The Forming Process in Nickel Positive Electrodes

Donald Tuomi

Roy C. Ingersoll Research Center, Borg-Warner Corporation, Des Plaines, Illinois

ABSTRACT

A detailed study has been made of the phases produced and their geometric distribution during formation of Edison-type tubular positive nickel electrodes. The initial charging in lithiated KOH electrolytes converts the $Ni(OH)_2$ to a beta phase having a solid solution range for di- and tetravalent nickel. The beta crystalline structure is related to $LiNiO_2$. This phase can be further oxidized to alpha phase, a tetravalent nickelate having appreciable trivalent nickel solid solubility. Alpha phase is most readily formed during $Ni(OH)_2$ oxidation in concentrated KOH or NaOH electrolytes, but does not form in LiOH electrolytes. The addition of LiOH to the battery electrolyte contributes to alpha phase discharge and limits alpha phase reformation. The contribution of alpha phase to electrochemical capacity is limited by a low effective exchange current as compared to the beta phase.

In the production of commercial storage batteries, electrode plates are generally given a particular electrolytic processing to bring the active materials into a suitable state of electrochemical activity. This process of improving the electrical capacity of a battery is described as "forming."

The forming process produces an active material composition and spatial distribution within the electrode which can be efficiently charged and discharged. Though this may be one of the simplest steps in the manufacturing operation, it is one of the most complex processes to describe from the viewpoint of physical and chemical theory. The contributing variables include the chemical constitution of the active phases, the electrolyte composition, the ionic and electronic equipotential surface distributions, and the detailed crystalline structures generated in the electrode, as well as the spatial distribution of the active material volume changes during the forming cycles.

Several facets of this art are illustrated by data accumulated during a microscopic and x-ray diffraction examination of experimental Edison tubular positive nickel electrodes at various stages of formation. The study provides insight into the complex mechanisms contributing to the electrode behavior.

The presentation is given in an evolutionary form. After first describing the basic experimental techniques, the discussion turns to the distinct chemical phases encountered during the electrochemical processing of the nickel hydroxide. This is followed by a description of the changes encountered during the oxidation-reduction cycles. The fundamental problems to be solved in developing an accurate physical model of the electrode are considered in the discussion.

Experimental Procedures

The electrode-forming process was investigated by using experimental Edison positive tubular electrodes (1a). The ¼ in. diameter, perforated-wall, nickel-plated steel tubes were packed with alternate layers of nickel hydroxide and nickel flake. The electrodes were mounted in individual nickel-plated steel frames and placed in individual plastic test cells containing nickel plate counterelectrodes. The test cells were filled with 180 cm^3 of mixed electrolyte: 4.3*N* KOH-1.0*N* LiOH. Neither the composition or quantity of electrolyte corresponds to those used in the Edison nickel-iron alkaline cell. The individual electrodes contained 9g of nickel hydroxide, $Ni(OH)_2$. During processing, the water level in the cells was maintained so that the experimental results were characteristic of the nominal electrolyte composition.

During the normal operations, the experimental cells were connected in series to a controlled current d-c power supply. A stepping-switch voltage-monitoring system[1] was used to indicate when the discharge voltage on a cell exceeded 1v *vs.* the sheet nickel electrode. At this stage the cell would be shunted out of the circuit. This discharge voltage limit is equivalent to discharging an electrode to the sharp potential decrease at the limiting ampere hour capacity, *i.e.*, the knee of the discharge curve.

When desirable, the electrode potential was recorded as a function of time, utilizing as a reference electrode a divalent-trivalent state, well-aged (1 year or longer), Edison tubular positive mounted in a tube attached to a Luggin capillary. This reference electrode had been processed and aged in the same electrolyte composition used in the experiment. Thus the recorded potentials directly measure the deviations in the potential distribution between the experimental electrode and the relevant reference electrode state. The reference potential corresponds to the electrode existing in an equilibrium state with respect to $Ni(OH)_2$-beta phase transformation.

After electrochemical processing the electrode was removed from the electrolyte into the laboratory atmosphere. No effort usually was made to wash the active materials with water; the small amount of electrolyte in the porous structure is quickly transformed to potassium carbonate as is shown by x-ray diffraction examination. There was no significant decomposition of trivalent nickel in this process. Because of the unique layer structure of the Edison electrode the active material could be readily separated from the nickel flake simply by passing the ground mixture through a magnetic field.

The active materials at various stages were characterized by microscopic examination and by x-ray powder diffractometer patterns. The x-ray data were obtained using a G.E. XRD3 spectrogoniometer with copper K_α radiation. The powder samples were prepared by mounting the tube in a lathe and drilling equal volume concentric samples. After flake removal, the samples were used to determine the tube x-ray diffraction patterns and chemical composition as a function of the radius.

The nickel valence state in the active material was determined by reaction with standard arsenious oxide solution followed by back titration of the excess reagent with standard $KMnO_4$. The nickel, subsequently was determined gravimetrically with dimethylglyoxime and the nickel valence state was calculated Samples were not washed free of alkali since this generally caused a slight decrease in the valence state, as well as decreasing the analyzed nickel content of the sample.

[1] Developed by S. S. Jaffe, T. A. Edison Research Laboratory McGraw-Edison Corp., W. Orange, N. J.

Nickel Oxide Phases

In the following sections the relevant observations are summarized regarding the di-, tri-, and tetravalent nickel phases encountered during the electrochemical oxidation and reduction of Edison tubular positive electrodes. This electrode is particularly suitable for this study since the physical state of the initial phase packed into the electrode can be controlled independently and the processed material can be subject to detailed examination independent of the electronic conductor matrix.

This phase of the investigation showed that three distinct nickel phases are encountered in KOH and mixed LiOH-KOH electrolytes. The discharged state is a nickel hydroxide $Ni(OH)_2$, and the charged phases include a trivalent nickelate-beta phase and a tetravalent nickelate-alpha phase.

Divalent nickel phase.—The divalent nickel hydroxide, $Ni(OH)_2$, is generally accepted as the discharged state for the nickel electrode. The phase, however, has a variable crystalline structure dependent on the preparative procedure. The phase can vary from a highly crystalline material to a turbostratic structure layer lattice, as in the thin films studied by Wynne-Jones, to a practically amorphous freshly precipitated hydrous material as illustrated in Fig. 1. Corresponding to variations in the nickel hydroxide crystallinity changes may occur in the chemical composition (1b).

For this study the starting material is a stoichiometric nickel hydroxide prepared by spraying $NiSO_4$ solution into tanks containing a hot NaOH solution. The precipitated nickel hydroxide is collected and dried. After the impurities of sodium hydroxide, carbonate, and sulfate are removed by leaching with hot water, the nickel hydroxide is dried again. The major constituent is a well crystallized $Ni(OH)_2$, as shown by the x-ray diffraction pattern in Fig. 2. The crystallite size is in the 1000Å range as shown by diffraction line half-breadth measurements at half-maximum intensity. There is no marked difference in the crystallite "a" or "c" direction dimensions. It is not an amorphous phase, and the diffraction lines are characteristic of the $Ni(OH)_2$ structure. The compound can be classed as an electrical insulator. To a very large extent the crystallite size of the discharged state $Ni(OH)_2$ was controlled

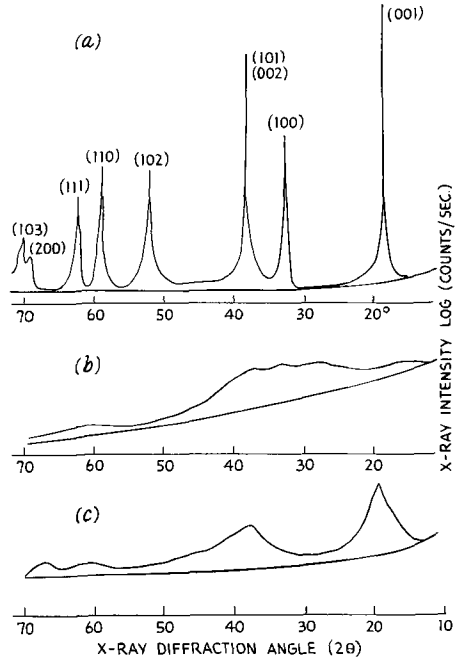

Fig. 1. $Ni(OH)_2$ crystalline structure variations: (a) stoichiometric crystalline nickel hydroxide, $(Ni(OH)_2$, (b) freshly precipitated nickel hydroxide, and (c) thin film $Ni(OH)_2$ discharge state. Copper K_α radiation, logarithmic intensity recording.

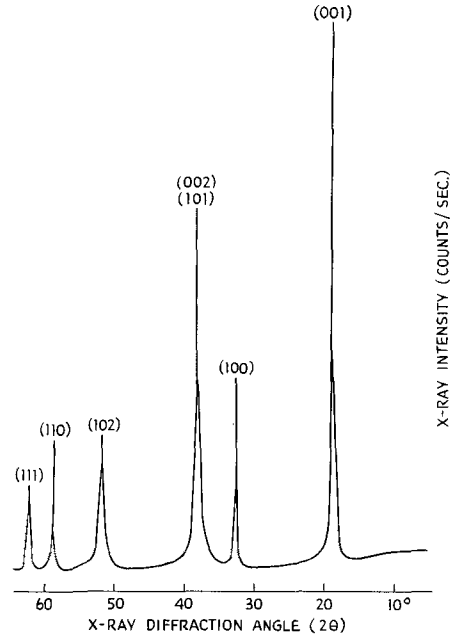

Fig. 2. X-ray diffraction pattern for well-crystallized stoichiometric, green, nickel hydroxide. CuK_α X-radiation.

by the initial crystallite size. The oxidation-reduction cycle conditions did not produce rapid reconstructive transformations of the $Ni(OH)_2$ lattice during beta-$Ni(OH)_2$ cycling. This does not imply, however, that the $Ni(OH)_2$ discharge state represents an ideal precisely stoichiometric material. Rather, the solid phase should represent some solid solution bound for the electrolytic system under examination.

Trivalent nickel phase.—The electrochemical oxidation of nickel hydroxide in an alkaline electrolyte based on KOH as the major component produces a trivalent nickel-containing phase which has a unique diffraction pattern. Glemser and Einerhand (2) introduced the designation β-NiOOH ($Ni_2O_3 \cdot H_2O$) for this oxidation product. Considering the structural and chemical properties outlined below, a more appropriate name for the trivalent nickel oxide is "beta" phase, without assigning a particular chemical formula.

If the well-crystallized nickel hydroxide is electrochemically oxidized to the trivalent state in 2M NaOH, or 2M KOH, or 5M LiOH at room temperature for 96 hr at 0.25 amp, the product obtained is characterized by the x-ray diffraction pattern shown in Fig. 3. The in-

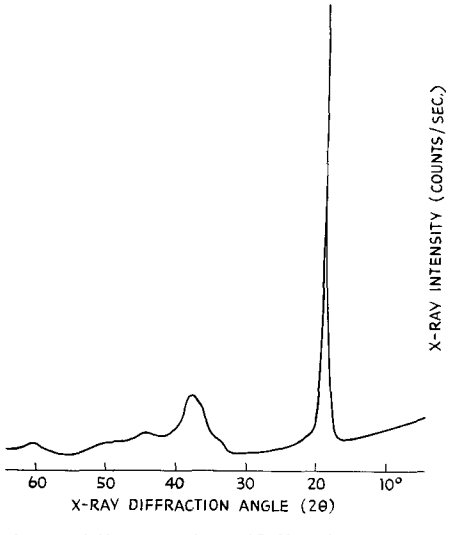

Fig. 3. X-ray diffraction data (CuK_α) for the first oxidation product obtained during crystalline $Ni(OH)_2$ electrochemical oxidation in 2M KOH or NaOH or 5M LiOH at room temperature.

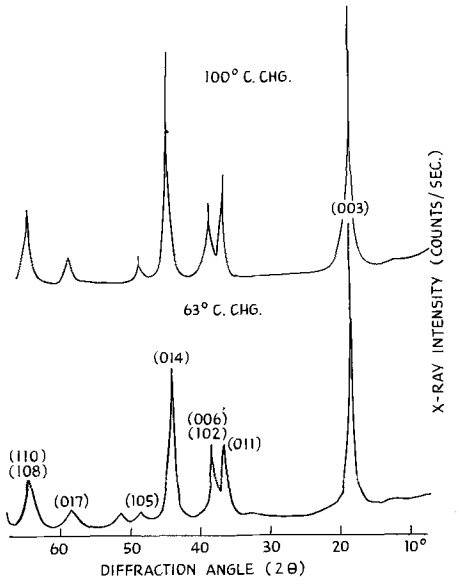

Fig. 4. X-ray diffraction data (CuK_α) for the oxidation product formed during the electrochemical oxidation of crystalline $Ni(OH)_2$ in 5M LiOH at 63° and 100°C.

tense diffraction line at 19° is practically coincident with the $Ni(OH)_2$ (001) plane reflection. This coincidence has led to the description of the $Ni(OH)_2$ oxidation as involving a simple removal of protons from the lattice corresponding to a continuous series of solid solutions from the di- to the trivalent states (3). The reaction within this framework would not be viewed as a conventional two-phase transformation process. It should be emphasized that the x-ray diffraction pattern of beta phase did not change significantly if the oxidation product was first examined wet as formed or after air drying without washing to remove the electrolyte. The nickel valence state in beta phase varied from 2.90 to 3.08.

Insight into a structural description of beta was provided through a study of the electrochemical oxidation of the $Ni(OH)_2$ in hot 5M Li(OH) electrolytes. At 63° and 100°C the oxidation product from crystalline $Ni(OH)_2$ is a well-crystallized trivalent nickel compound as shown in Fig. 4. This diffraction pattern can be related to the $LiNiO_2$ crystalline structure (4) as shown in Table I, rather than to $Ni(OH)_2$. The degree of ordering in the beta phase structure or the crystallite domain size is dependent on the electrochemical oxidation conditions, *i.e.*, electrolyte composition, temperature, and the cycling conditions including current density, cycle number, open-circuit times, and cycle depth.

Chemical analyses of the beta phase from the LiOH electrolyte showed a Li/Ni mole ratio of 0.40 for the low-temperature material unwashed compared to 0.72 for the more crystalline high-temperature material. The corresponding nickel valence states were 3.07 and 2.97. Thus, during the LiOH anodic oxidation of the nickel hydroxide significant amounts of electrolyte cation diffuse into the crystalline solid in apparent opposition to the applied electric field.

The chemical analyses of beta phase indicated that a unique chemical stoichiometry could not be assigned. Applying the electrical neutrality boundary condition on the chemical analyses for nickel, alkali, and carbonate ions indicated that virtually an anhydrous oxide phase was involved. Washing as-formed beta phase with water resulted in an extraction of alkali ions and a decided reduction in the total nickel content, *i.e.*, an increase in the water content. The phase has zeolitic exchange characteristics.

The x-ray diffraction peaks for beta phase can be assigned indices on the basis of the $LiNiO_2$ crystalline structure as shown in Fig. 5. Chemically beta phase is more appropriately described as a trivalent nickelate rather than as a trivalent nickel oxide. This beta phase is a low electrical resistivity, 1 ohm-cm or less, n-type semiconductor as indicated by thermoelectric power measurements, rather than the low electrical resistance p-type phase encountered in the lithium doped nickel oxides (5). Thermal decomposition results in the conversion of the n-type compound to a p-type phase. It should be recognized that the lithium-doped p-type NiO solid solutions have only a superficial electrochemical activity.

A rather direct comparison of the beta phase to the trivalent nickel products obtained by various oxidation procedures is given by the x-ray diffraction patterns summarized in Fig. 6. The logarithmic x-ray intensity data were obtained under conditions comparable to Fig. 1, whereas the linear x-ray intensity data are scaled to the same base used for the other patterns. The trivalent oxides prepared by chemical procedures are essentially amorphous. The Haissinsky thin film-anodic deposition oxide is identical to the material extensively studied by Wynne-Jones and associates (6). This oxide phase clearly is distinctly different from the beta phase oxide obtained during anodization of a well crystallized

Table I. X-ray diffraction data comparison

High-temperature $Ni(OH)_2$ electrochemical oxidation in 5M LiOH *vs.* Dyer *et al.* $LiNiO_2$ · CuK_α radiation

5M LiOH Product		Dyer *et al.* $LiNiO_2$		$Ni(OH)_2$	
2θ°	Intensity	2θ°	Intensity	2θ°	Intensity
18.7	100	17.3	100	18.9	100
—	—	—	—	32.6	60
36.67	35	36.6	66	—	—
—	—	37.8	16	—	—
38.31	21	38.03	23	38.2	60
44.37	182	43.87	161	—	—
48.55	26	48.60	25	—	—
—	—	—	—	51.4	22
58.53	34	58.67	28	58.5	23
—	—	—	—	62.2	16
64.21	77	64.43	42	—	—
64.75	93	64.77	41	—	—
68.15	25	68.07	21	68.9	4
—	—	—	—	70.0	6
—	—	—	—	72.1	7
—	—	76.77	9	—	—
77.42	24	77.60	15	—	—
—	—	81.37	7	—	—
82.28	30	81.87	17	82.0	4
84.02	15	84.6	12	—	—
—	—	—	—	87.8	1
93.10	10	93.00	12	—	—
98.00	5	98.13	12	—	—
115.5	23	—	—	—	—

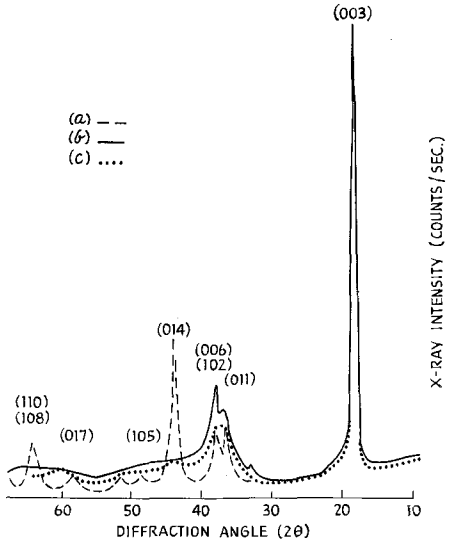

Fig. 5. Comparison of x-ray diffraction patterns for beta phase (a) high temperature $Ni(OH)_2$ oxidation in 5M LiOH, (b) room temperature 96 hr, —250 ma/tube 5M LiOH, (c) beta phase typical 2M KOH, NaOH, and 4.3*N* KOH plus 1.0*N* LiOH.

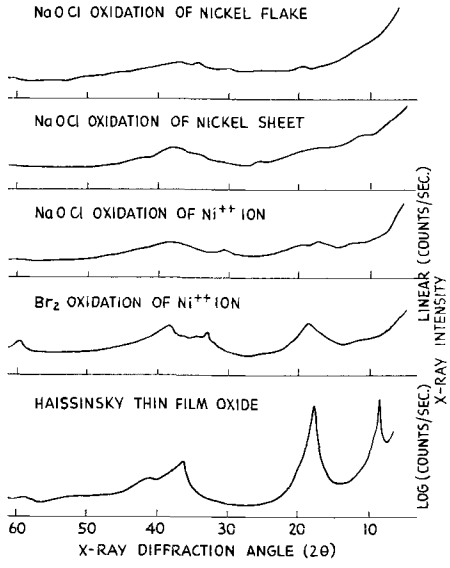

Fig. 6. X-ray diffraction patterns for various nickelic oxide products.

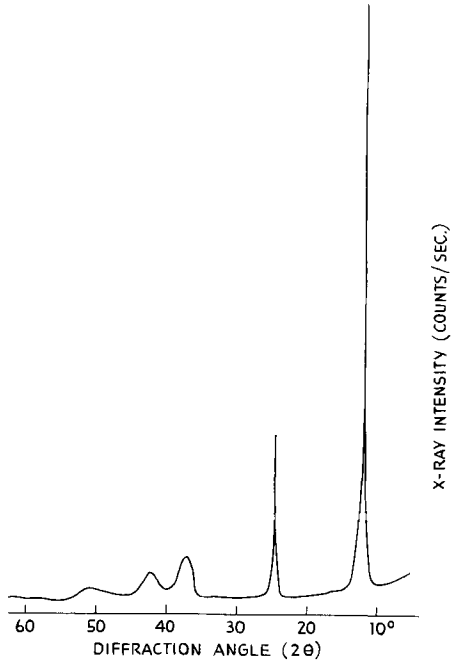

Fig. 7. X-ray diffraction pattern for typical alpha phase formed from well-crystallized $Ni(OH)_2$.

$Ni(OH)_2$. The general diffraction characteristics are consistent with the observations reported by Briggs and Wynne-Jones (7).

In summary the trivalent nickel crystalline structures depend markedly on the preparative techniques and on the starting material characteristics. For a given set of conditions reproducible products are obtained. For the electrochemical oxidation of crystalline $Ni(OH)_2$ a characteristic trivalent nickel material x-ray diffraction pattern is obtained. The material is best described as a trivalent nickelate conveniently designated as beta phase.

Tetravalent nickel.—At the T. A. Edison Research Laboratory in 1956, D. M. Meter and C. Y. Li discovered that prolonged oxidation of the trivalent beta phase in porous plaques resulted in the appearance of a new phase characterized by an intense x-ray powder diffraction line at 7.08Å (12.5° 2θ) replacing the intense beta phase line at 4.7Å. In previous survey studies on tubular, positive electrodes this 7.08Å line (the lowest diffraction angle line) had been designated as a measure of the concentration of an alpha phase. It now became obvious that the new phase, alpha, forming as an oxidation product from trivalent beta must involve tetravalent nickel. Further experimentation demonstrated that crystalline nickel hydroxide is readily oxidized at room temperature to alpha if very concentrated KOH or NaOH electrolytes are used.

The alpha phase is characterized by the x-ray diffraction pattern shown in Fig. 7. This pattern is characteristic of the products formed in greater than 4M KOH and NaOH. At lower alkali concentrations the overvoltage relationships with respect to oxygen evolution limit the extent of alpha formation.

Chemical analyses were performed on alpha phase prepared under various conditions. In the first study a set of tubes packed with crystalline $Ni(OH)_2$ was charged for 17 days at 125 ma [19 Faradays/mole $Ni(OH)_2$] in three different electrolytes. The products were washed free of nickel flake using the forming electrolyte, rinsed quickly with water, and dried in a desiccator. The observed valence states were as follows:

Electrolyte	Nickel valence
45% KOH	3.34
45% KOH saturated with LiOH	3.36
4.3*N* KOH plus 1.0*N* LiOH	3.22

The three products had practically identical x-ray diffraction patterns.

A second group of electrodes was charged for 160 hr at 125 ma in 45% KOH, 7.4 Faradays/mole $Ni(OH)_2$. The oxidized product had a very distinct gray metallic luster, a graphite appearance. This new phase had a much greater volume than the original $Ni(OH)_2$ or beta phase, thereby causing either electrode distortion or an ejection of the material through the tube perforations into the electrolyte. The valence state of the nickel varied with the material processing as follows: (*a*) the ejected gray metallic luster paste wet with 45% KOH, a 3.34 valence; (*b*) the tube product washed rapidly with water by decantation while magnetically separating the nickel from the liquor, followed by drying at room temperature, a 3.44 valence; (*c*) centrifugal separation of a dispersion of alpha in 45% KOH, followed by room temperature drying, a 3.48 valence. The initial alpha phase obtained immediately after removing the electrode from the circuit reacted very vigorously with alcohol; but the samples dried for analysis reacted comparatively slowly. Furthermore, the initial gray metallic luster had been replaced by a distinctly black appearance. Consequently, it appears certain that the valence of 3.48 is appreciably less than is possible for alpha at the end of electrolysis. On the other hand, the valence state of alpha could be reduced to practically 3.0 without producing significant changes in the x-ray diffraction pattern for alpha phase.

The chemical composition of alpha phase formed in a 45% KOH electrolyte was as follows: 50% Ni, 17% K, and 33% O, OH. Assuming all the nickel is present in the tetravalent form, the formula $K_{0.5}Ni_{1.0}O_{2.0}(OH)_{0.5}$ or $(KOH)_{0.5}NiO_2$ satisfies the electrical neutrality requirement corresponding to 16.5% K^+, 49.4% Ni^{+4}, 27% O^{-2}, and 7.1% OH^-.

For the 45% KOH electrolyte the K/Ni mole ratio for alpha phase was 0.412; but in the mixed electrolyte 4.3*N* KOH with 1.0*N* LiOH the K/Ni mole ratio was 0.237 and the Li/Ni ratio 0.0915. The quantities involved do not correspond to simple mole ratios.

The x-ray diffraction data for the alpha phase can be related to the results reported by Glemser and Einerhand (8) for γ-NiOOH as shown in Table II. The γ-NiOOH was obtained by reacting $NaNiO_2$ or $KNiO_2$ with water or by reacting their β-NiOOH with Na_2O_2. This γ-NiOOH phase could be readily oxidized to a +3.48 valence by hypobromite.

Table II. Electrochemical oxidation of $Ni(OH)_2$ in 45% KOH alpha phase x-ray diffraction data

Edison Alpha			Glemser-Einerhand γ-NiOOH			
$2\theta°$ Cu K_α	d/n, A	Intensity	$2\theta°$ Cu K_α	d/n, A	Intensity	hkil
12.5	7.08	100	12.8	6.25	VS	0003
25.2	3.53	24	25.9	3.44	S	0006
36.6	2.45	2	37.0	2.43	W	$10\bar{1}1$
37.5	2.40	4	37.9	2.37	S	$10\bar{1}2$
38.3	2.35	1				
42.4	2.13	4	41.0	2.20	VW	$10\bar{1}4$
44.4	2.04	3	43.1	2.10	S	$10\bar{1}5$
			48.4	1.88	W	$10\bar{1}7$
51.8	1.77	2.5	51.5	1.77	S	$10\bar{1}8$
61.0	1.605	1	58.7	1.67	W	$10\bar{1}10$
			62.9	1.48	S	$10\bar{1}11$
65.8	1.419	2	66.3	1.41	M	$11\bar{2}0$
67.0	1.40	1	68.0	1.38	M	$11\bar{2}3$
			71.0	1.33	W	$10\bar{1}13$
			72.5	1.30	W	$11\bar{2}6$
78.4	1.22	1	79	1.21	W	$20\bar{2}2$
82.0	1.175	1	82.5	1.17	W	$20\bar{2}5$

Alpha phase is readily formed only during prolonged anodization of $Ni(OH)_2$ in concentrated alkali containing K or Na cations, and only if the nickel has been oxidized through beta phase. The material is more appropriately described as a tetravalent nickelate within which trivalent nickel has appreciable solid solubility. An empirical formula describing this condition is

$$M_2 Ni^{+3}{}_{2(1-y)} Ni^{+4}{}_y O^{-2}{}_{4-y}$$

where M is a monovalent cation including H^+ or H_3O^+ along with the large atomic radius K^+ and Na^+ ions and y varies from 0.5 to an upper limit of 1.0. The phase designation "alpha" is preferable to the γ-NiOOH notation since it does not convey prejudices regarding the detailed chemical composition. This is analogous to the γ, δ, etc., notation applied to the MnO_2 electrochemically active materials. The alpha phase, as noted by Glemser and Einerhand, has a laminar structure.

Electrode Formation

Now consider the phenomena encountered during the formation of an Edison tubular positive electrode. This electrode can be visualized as a sandwiching of nickel flake and nickel hydroxide layers in a perforated tube. The nickel flake forms the electronic contact from the nickel hydroxide to the tube walls while the perforations in the tube walls provide ionic access between the porous bed-granular nickel hydroxide and the electrolyte.

First consider the direct observation of the initial charge process, then the effect of cycling on the microstructure and the x-ray diffraction effects, and finally, the electrochemical properties of the formed electrode.

Direct microscopic observation.—The initial study of the forming process involved the direct microscopic observation of the nickel hydroxide oxidation. The tube wall was carefully ground from a section of the tube exposing the edges of several layers. After mounting in a sample holder frame the electrode was immersed in the electrolyte. A binocular microscope was used to observe the changes produced during cycling.

The exposed surface of $Ni(OH)_2$ lamellae presented a distinct gray-green granular structure, having both a variable grain size and density distributed between nickel flake layers. The particles ranged from loose open-pore aggregations to dense green microporous grains, showing conchoidal fracture characteristics.

During electrode oxidation at the half normal rate, 125 ma/tube a series of changes was visible. The average behavior corresponded to the oxidation front (formation of black oxide) migrating from the metal contact surfaces into the hydroxide layer. The migration rate was fastest at the periphery near the nickel plated tube contact to the nickel flake and slowest in the center of the exposed layer.

During a 48 hr charge period in the lithiated electrolyte the green layer progressively changed to a distinctly black oxide beta phase which was gradually converted to a distinct gray metallic luster nickelate phase, alpha. Probing the oxidized surface with a needle showed that the brittle divalent nickel hydroxide phase had been transformed into a deformable, more or less plastic layer.

Several unusual phenomena were observed during the oxidation. The more dense, translucent green $Ni(OH)_2$ particles were the most difficult to oxidize. However, numerous isolated dense particles, even several located the maximum distance from the electronic current tap, were immediately oxidized to the black phase. Other grains showed a distinct transitional behavior, suggesting an initial rapid surface oxidation, followed by a slower bulk process.

The easily oxidized grains probably contained excess alkali incompletely removed during normal production processing. The excess alkali would decrease the local electrochemical potential required for the oxidation reaction. In the more slowly oxidized grains several parameters appeared to be rate-controlling. The very low porosity grain structures had a limited electrolyte accessibility. In the extremely porous, high-surface area structures secondary adsorption exchange processes within the porous bed or local reactions of alkali with adsorbed materials could slightly shift the electrochemical potential distribution. Finally, some grains did not appear to have good electronic contact with the substrate. This did not appear to be a major limiting variable, perhaps because the oxidized phases are good electronic conductors and only a small area contact is sufficient to provide adequate electronic conductivity.

Oxygen evolution during charging appeared to occur from the alpha phase surface. This gas evolution on a peripheral phase automatically serves to limit the extent of oxidation in the interior of the layer. During open-circuit stand, gas evolution was predominantly from interior void structure. The electrochemical couple contributing to oxygen evolution depended on internal local cell action. Within the close packed porous bed structure gas bubble formation was restricted by capillarity; the surface tension forces contributed to increased gas solubility as well as to controlling the gas bubble flow path out of the porous bed through the coarsest pore structure.

Metallographic and x-ray diffraction studies.—The extensive confounding of variables evident in the first observation of the formation led to a detailed metallographic and x-ray diffraction study of formation. The initial survey studies showed that the x-ray diffraction patterns of "air dried" active materials were not significantly different from freshly formed products.

For this second study a number of tubular electrodes were processed to various stages of formation under controlled charge and discharge conditions. Samples were periodically removed for detailed metallographic examination and for x-ray diffraction characterization.

The metallographic structures originally photographed in color by B. Bastian are illustrated by black and white prints in Fig. 8. The photographs span the central radial cross section from the tube center to the periphery (= ⅛ in.). The nickel flake is distributed in an approximate layer configuration.

Within the unformed tube, Fig. 8a, the nickel hydroxide shows the two extreme forms: (*a*) translucent green dense grains and (*b*) white or very pale green low-density grains. All gradations between these extremes can be found. More or less gray-black grains result from the crushing of dark blue-gray to black particles observed in the pure $Ni(OH)_2$. These grains apparently had a trace of surface thermal decomposition to NiO during drying.

After 4 hr charge at 125 ma, 1/12 the first cycle input or 0.2 Faraday/mole Ni, the structure appeared as

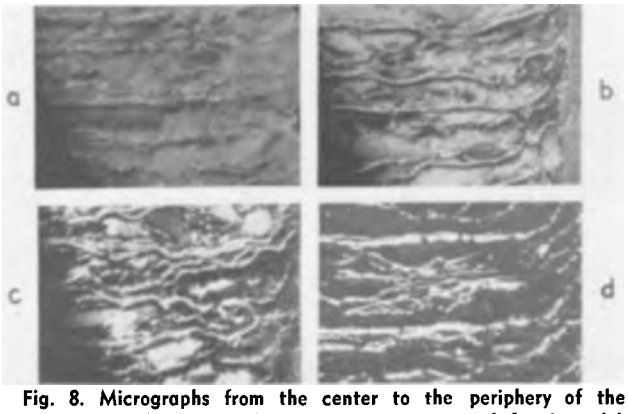

Fig. 8. Micrographs from the center to the periphery of the tubular electrode (right edge) at various stages of forming: (a) initial $Ni(OH)_2$ layer; (b) after 4 hr charge at 125 ma; (c) after 8 hr; and (d) after 48 hr.

shown in Fig. 8b. The black oxidized phase observed earlier formed at metal-electronic contact and migrated into the active material. The reaction is not restricted to the periphery of the tube only, but extends to the center of the electrode. As noted earlier, some interior grains quickly oxidized to the dark black form. In several regions the stereo-microscopic examination indicated that a thin superficial oxide penetrated into a porous grain, but that the electrochemical oxidation did not proceed rapidly into the crystallite interior. At this early stage the x-ray diffraction data indicated a progressive transformation of nickel hydroxide to beta phase from the periphery to the center of the electrode. This, obviously, was a statistical average behavior.

After 8 hr charge the uncharged $Ni(OH)_2$ distribution corresponded to Fig. 8c. Dense as well as porous green grains were present in both oxidized and unoxidized forms. The migration of the phase transformation front into the layers was apparent throughout the tube.

After 24 hr charge at 125 ma, 1.1 Faradays/mole Ni, the green $Ni(OH)_2$ had disappeared as shown in Fig. 8d. The granular characteristics of the layer were no longer evident, but probing with a needle revealed the presence of particulate structure in the layer. At this stage x-ray diffraction data as a function of tube radius showed that only slightly more than half the $Ni(OH)_2$ had been oxidized to beta phase. Thus, a surface oxidation had proceeded rapidly to a diffusion-length depth in the crystallites contacting the electrolyte. The absence of significant $Ni(OH)_2$ line broadening implied that below a certain size oxidation proceeded rapidly. As the reaction progressed the individual small crystallites were removed, a small fraction at a time, so no net broadening of x-ray diffraction lines was readily discernible.

The 24 hr charge was midway through the first charge cycle. At this time the peripheral region x-ray diffraction patterns showed that alpha phase was beginning to form from the beta phase though a considerable fraction of unoxidized $Ni(OH)_2$ was distributed throughout the tube.

Extending the charge to 48 hr at 125 ma, 2.2 Faradays/mole Ni, does not significantly alter the microscopic structure. The general shading of the black active material becomes more metallic. However, as shown by the x-ray diffraction data in Fig. 9, substantial conversion of beta to alpha phase was occurring in the peripheral half while appreciable $Ni(OH)_2$ was still present within this region of the electrode. The increase in active material volume during alpha phase formation should effectively reduce the local current density on the central volume of active material. Although a distinct grain structure still was present, the more highly charged material appeared to be more plastic during sample processing.

During the first discharge cycle the electrode delivered 0.6 Faraday/mole Ni. The active material changed to a

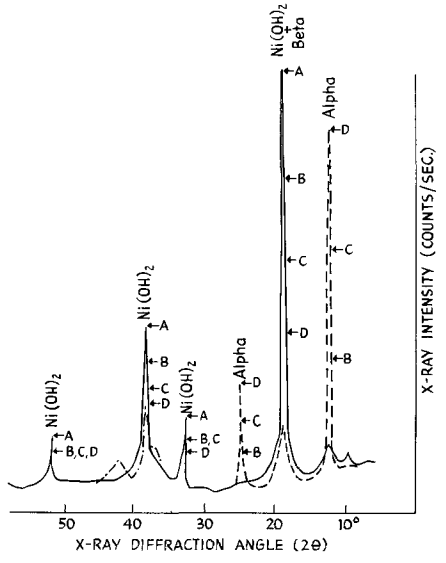

Fig. 9. X-ray diffraction data for concentric volumes of active material after first formation cycle 48 hr charge at 125 ma: (A) center quarter; (B) second quarter; (C) third quarter; and (D) peripheral quarter.

distinctly granular solid, losing its metallic luster. Both beta and $Ni(OH)_2$ appeared to be more or less hard crystalline solids. The x-ray diffraction data showed that at the normal rate only a portion of the alpha phase was discharged. The green nickel hydroxide was not recovered as a discharge product, rather the material was distinctly black in the discharged state. Re-oxidation again formed the more plastic lighter luster active material.

After several additional forming cycles in the lithiated electrolyte the nickel hydroxide was fully oxidized to beta phase. Simultaneously, the amount of peripheral alpha phase steadily decreased, both after charge and discharge. In the charged state the active material had a very high electronic conductivity in the range of 1 ohm-cm^{-1}. By contrast, the discharged phase was an electrical insulator, containing a large number of defect sites having strong optical absorption in the visible spectrum.

After the forming process was completed in the lithiated electrolyte the electrode no longer contained a significant alpha phase component. The charged phase was beta. The electrode similarly cycled in a 5M KOH electrolyte contained an appreciable amount of alpha which was cycled during charge and discharge, as well as remaining as a distinct phase not readily discharged at the operational current densities.

Electrochemical behavior. — The electrochemical processing of the electrode in lithiated electrolytes results in a series of structural changes in the active material which are not directly evident in the electrochemical ampere-hour capacity measurements.

The electrochemical capacity data on the electrodes are summarized in Table III. From the capacity measurements alone no indications are obtained of the complex changes occurring within the electrode during cycling. Generally, an exceptionally large initial cycle

Table III. Electrochemical capacity during electrode processing through a set of forming cycles in 4.3*N* KOH 1.0*N* LiOH electrolyte

Cycle No.	Cycle condition	Amp-hr capacity
1	48 hr 125 ma	1.70
2	8 hr 250 ma, 15 hr 125 ma	1.68
3	8 hr 250 ma, 15 hr 125 ma	1.69
4	15 hr 250 ma	1.63
5	7 hr 250 ma	1.33
6	7 hr 250 ma	1.33

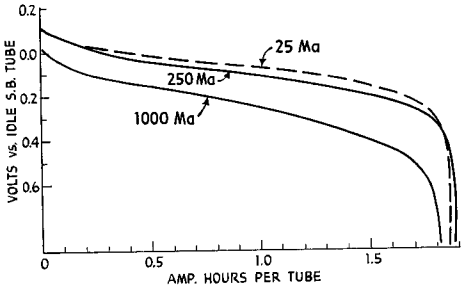

Fig. 10. Discharge potential vs. electrochemical capacity at 0.1, 1.0, and 4.0 normal discharge rates (25, 250, 1000 ma) after a 7 hr charge at 1½ normal rate (375 ma) for a tubular electrode fully formed in 4.3*N* KOH-1.0*N* LiOH electrolyte. Dotted curve obtained by subtracting initial polarization term from 100 ma curve.

capacity was associated with extensive alpha phase formation during charge along with a relatively efficient discharge.

An electrode formed in a pure KOH electrolyte did not show any drastic difference in capacity as compared to forming a lithiated electrolytes. However, on continued cycling the capacity tended to decrease as the amount of "floating" alpha phase increased. In a lithiated electrolyte the capacity remained stable or increased slightly as the efficiency of cycling beta phase improved and the last traces of alpha were eliminated. The electrode valence state during formation varied from slightly greater than 3.0 in the periphery to 2.5 to 2.7 in the center; but, after formation, the charged valence state was close to 3.0 throughout.

A fully formed electrode operating under equilibrated structure conditions in the 4.3*N* KOH-1.0*N* LiOH electrolyte shows a surprisingly small rate sensitivity of electrochemical capacity as illustrated by the potential-capacity curves in Fig. 10. This capacity at saturation charge corresponded to 0.71 Faraday/mole Ni output compared to normal rate condition delivering 0.5 Faraday/mole Ni. After correcting for the nickel valence state variation in the discharged electrode, this capacity corresponds closely to a 1.0 valence change in the active cycling material. Thus, the capacity of a cycling lithiated electrode after forming is complete corresponds to an oxidation reduction reaction between a trivalent and a divalent nickelate state. Extensive overcharge of the electrode formed in a lithiated electrolyte does not produce alpha phase. On the other hand, at the relatively low operational lithium concentrations the active material does not behave as a characteristic lithium nickelate in the charged state.

Discussion

The nickel hydroxide positive electrode is, inherently, a complex physical-chemical system. As yet, sufficient progress has not been made on the fundamental electrochemical theory to give a framework of logical simplicity within which to organize observations. On the other hand, only through attempts at data organization does there finally begin to evolve a description for the detailed structure presented within the functioning general electrochemical corrosion systems involving solid phases. The differences encountered between passive and active electrochemical systems are matters of degree, rather than differences involving fundamentally different conceptual frameworks.

With this in mind, now consider systematically various aspects of the functioning electrode. The over-all objective is to describe the three-dimensional system: electrolyte, phase I, phase II, and electronic contact. The discussion is conveniently divided into four areas: (*a*) the tetravalent oxide phase, (*b*) the nickel hydroxide phase transformation, (*c*) the gross electrochemical oxidation reduction process, and (*d*) the detailed kinetics problem.

Tetravalent nickel.—As noted by Falk (3) various formulas have been suggested for the charged materials in the nickel electrode. Generally speaking, excess electrochemical capacity beyond the trivalent state has been associated with a solid solution of tetravalent nickel in the trivalent oxide (9) although some have considered the excess capacity to be associated with adsorbed oxygen (10). General agreement that a distinct tetravalent nickel phase is not encountered in anodic oxidations has existed.

In this investigation a tetravalent nickel oxidation product, alpha phase, was obtained from a crystalline $Ni(OH)_2$ under particular experimental conditions. The alpha phase was readily formed during overcharge of the electrode in concentrated KOH or NaOH electrolytes. The degree of crystallinity of the alpha phase was determined by the crystallinity of the $Ni(OH)_2$. The ease of alpha phase formation increased with increasing alkali concentration and decreasing temperature. A further qualification was present, namely, that the system oxygen overvoltage had to be sufficiently high for an adequate driving voltage to be generated across the solid-electrolyte interface, space charge region to drive the oxidation reaction forward.

Although alpha phase has been undoubtedly encountered in many investigations, its existence as a distinct component was not readily recognized for several reasons. The phase is characterized by a significantly greater molar volume than the lower oxide phases; consequently, formation of the phase at the periphery of an electrode can restrict the oxidation of the interior phase. This can occur through a restriction of the ionic conduction into the interior as well as by the evolution of oxygen on the surface of alpha. A further complicating factor is the low effective exchange current for alpha phase. At the normal current densities it is not readily discharged to the divalent state. The presence of low oxygen overvoltage impurities in the systems can prevent alpha phase formation. Finally, the detailed crystalline form and prior processing of the active material may have provided a form which is not oxidizable to the tetravalent state.

The broad spectrum of solid-state structures encountered in the oxidation of nickel to the high valence states (ranging from amorphous to well-crystallized structure depending on the initial material) strongly implies that solution-precipitation processes are not significant factors in the reaction. The phase transformation cannot be viewed as simple proton migrations out of the $Ni(OH)_2$ lattice to form solid solutions, since the alkali cation is an essential component of the oxidized phase. The transport of large ionic radius cations into the crystal lattice during charge implies the presence of large ionic radius lattice imperfections comparable to K^+, OH^-, H_3O^+, and H_2O groups contributing to solid-state diffusional processes.

The metallic luster encountered in the most highly oxidized alpha phase implies a rather high density of conduction electrons in the n-type material. A detailed study of the electronic properties of the phase would be of intrinsic interest in the description of the electronic energy states of the nickel ion. A detailed charge and mass balance experiment involving the oxidation of green crystalline $Ni(OH)_2$ to the alpha phase form is needed to define clearly the chemical composition and nickel valence state limitations in the compound.

Trivalent nickel phase transformation.—Another area of confusion in the nickel electrode description is the form of the phase transformation in nickel hydroxide oxidation to the trivalent beta phase. Both Salkind (11) and Falk (3) consider the x-ray diffraction patterns in which some $Ni(OH)_2$ lines disappear and others appear as implying a solid solution phase transformation between $Ni(OH)_2$ and beta phase. On the other hand, Foerster (9) in 1907 considered the oxidation to proceed with the formation of a new phase, a solid solution of tetravalent nickel in a trivalent oxide. Briggs and Wynne-Jones (7) have shown that thin film nickel electrodes involve two distinct phases, a dis-

charged state, $Ni(OH)_2$, and a charged state designated NiOOH.

More recently, Conway and Gileadi (12) have found that a reversible potential is only obtained over a limited range of porous plaque oxidation in a KOH electrolyte, namely, 20-50% of the total charge capacity. They assumed that the potential was determined by a surface phase of constant composition superimposed on a bulk phase of varying degree of oxidation, but not potential determining. The possibility that the potential was characteristic of a two-phase system was considered unlikely because the transformation was viewed as a variation in the extent of solid solution oxidation. Furthermore, the kinetic data on electrode charging implied the existence of a surface phase intermediate in bulk phase charging.

The electrode potential dependence on the alkali and water activity can be used to determine a single electrode reaction equation (13). Unfortunately, such data have not been obtained for a broad range of experimental conditions. These data, however, have led to equations involving from 0.42 to 2.28 moles of water per mole of nickel oxidized. Generally, the alkali concentration dependence has been viewed as a KOH adsorption on the active material and not as an essential component of a crystalline solid.

Through the study of beta phase formation in different electrolytes at high temperature it was shown that in LiOH electrolytes a distinct crystalline phase could be obtained. This phase had the characteristic x-ray diffraction pattern of lithium nickelate. Thus, the observed coincidence of beta and nickel hydroxide x-ray diffraction patterns reflects a coincidence of $LiNiO_2$ and $Ni(OH)_2$ diffraction lines rather than showing a solid solution of trivalent nickel in the nickel hydroxide crystal lattice. The beta phase x-ray diffraction lines assigned by Glemser and Einerhand (8) as (001), (100), and (110) of β-NiOOH are, respectively, transformed to the (003), (006), (102) (011), and (110) (108) reflections in the $LiNiO_2$ structure.

The oxidation of nickel hydroxide produces a new phase, beta. The phase contains cations characteristic of the electrolyte, but not in stoichiometric quantities. Chemical analysis of beta phase produced under a variety of conditions showed a nickel valence range from 2.6 to 3.1. The phase was readily obtained as a single product during $Ni(OH)_2$ anodization in dilute KOH or LiOH electrolytes. The beta phase formed in NaOH electrolytes gave modified x-ray diffraction patterns suggestive of several distinct phases between the divalent and tetravalent states.

The observed variability of the beta valence state, as well as the limited range of charge state characterized by the reversible potential, can be partially explained by recourse to the observations made by Goodenough and associates (14). The chemical composition of lithium nickelate was shown to vary as

$$Li_x Ni^{+2}{}_{1-x} Ni^{+3}{}_x O$$

over a solid solution range $O < x \leq 0.3$ as cubic NiO, for $0.3 < x \leq 0.388$ as a hexagonal oxide, but for $0.388 < x \leq 0.5$ as rhombohedral $LiNiO_2$. Thus, the beta phase nickel valence state data can be made self-consistent if the compound involves a solid solution range for divalent nickel in a trivalent phase, as well as a tetravalent nickel in the trivalent nickelate.

This description of beta phase properties would explain partially the variability of the electrode potential characteristics during charge and discharge, as well as the anomalously large pseudocapacitance. When the active material exists in the solid solution state the electrode potential reflects the variation in the Ni^{+2} and Ni^{+4} ion activity in the Ni^{+3} lattice. The solid solution range will depend on the detailed conditions determining the solid solution free energy function, *i.e.*, the imperfections controlling the detailed trivalent phase crystalline structure.

For the electrochemical oxidation process a series of half-cell reactions can be written. The simplest case to consider is the oxidation of $Ni(OH)_2$ to a lithium nickelate solid solution saturated with divalent nickel, namely:

$$1.577\ Ni(OH)_2 + 1.0\ Li^+ + 2\ OH^- \rightarrow 2.577\ Li_{0.388}\ Ni^{+2}{}_{0.224}\ Ni^{+3}{}_{0.388}\ O + 2.577\ H_2O + 1.0\ e$$

or

$$1.577\ Ni(OH)_2 + 1.0\ Li^+ + 2\ OH^- \rightarrow LiNi^{+2}{}_{0.5773}\ Ni^{+3}{}_{1.00}\ O_{2.577} + 2.577\ H_2O + 1.0\ e$$

If a portion of the lithium sites are occupied by protons, then the oxidation reaction would correspond to an equation of the form

$$1.577\ Ni(OH)_2 + (1.0 - Y)Li^+ + (2 - Y)OH^- \rightarrow Li^+{}_{1-Y}\ H^+{}_Y\ Ni^{+2}{}_{0.577}\ Ni_{1.0}\ O_{2.5773} + (2.577 - Y)H_2O + 1.0\ e$$

Depending on the extent of H^+ substitution of Li^+, from 1.577 to 0.577 moles of H_2O may be formed per Faraday. The solid solution in equilibrium with the $Ni(OH)_2$ may be oxidized to a trivalent state as a single phase system according to the reaction

$$0.224\ Li^+ + 0.448\ OH^- + Li_{0.388}\ Ni^{+2}{}_{0.224}\ Ni^{+3}{}_{0.388}\ O \rightarrow 1.224\ Li_{0.5}\ Ni_{0.5}\ O + 0.224\ H_2O + 0.224\ e$$

For the lithium nickelate oxidation to an average valence of 3.1 the reaction could be written as

$$0.0984\ Li^+ + 0.1968\ OH^- + Li_{0.5}\ Ni_{0.5}\ O \rightarrow 1.098\ Li_{0.545}\ Ni^{+3}{}_{0.41}\ Ni^{+4}{}_{0.045}\ O + 0.0984\ H_2O + 0.0984\ e$$

As before, the substitution of protons for the lithium ion would diminish the net water evolved in the reaction.

The determination of the electrochemical reactions will require complex experimentation. The system mass balance should be determined as a function of the oxidation state. This requires an initial electrode impregnated or packed with a well-defined $Ni(OH)_2$ initial phase. The electrodes subsequently should be oxidized and reduced under controlled potential conditions in various composition alkaline electrolytes, using a combination of gas coulometry and electrolyte chemical analysis to establish the mass transport conditions.

The available data indicate that there are two distinct types of electrochemical oxidation-reduction reactions proceeding in the nickel positive electrode. One process is the transformation of phase A into phase B, the second, the oxidation-reduction of a component present in a solid solution single phase material.

Additive effects.—A long-standing puzzle has been the precise role of the lithium in the mixed KOH-LiOH electrolytes, which confers an increased capacity and a long life to the positive electrode (15). The increase in electrode potential observed with a lithiated electrolyte has been interpreted as an increase in the oxygen overvoltage permitting charge to higher nickel oxidation states (16). This hypothesis was substantiated by oxygen overvoltage measurements on nickel plates (17). From the electrode formation studies clearly a complex collection of phenomena accompany lithium addition to the electrolyte.

During formation in a mixed electrolyte both potassium and lithium ions move into the active material during charge and out during discharge. In a pure LiOH electrolyte the oxidation process only produces beta phase; no alpha phase is formed even under drastic overcharge conditions. In the mixed electrolyte alpha phase is initially formed, but during cycling it is discharged and disappears as a system component. On the other hand, in a pure KOH electrolyte the peripheral alpha phase contributes to the electrochemical capacity if the discharge rate local current density is sufficiently small. But if the current density is too

large, the alpha phase does not cycle and functions as an inert phase decreasing the effective amount of active material. Extensive overcharge of fully formed electrode in the lithiated KOH electrolyte does not result in alpha phase formation. Thus, the electrode capacity is increased by restricting the cycling to a beta phase with a negligible tetravalent phase contribution. The effective cycle life capacity is increased through the elimination of the floating alpha phase formation process.

The mixed electrolyte imposes further restrictions on the beta phase. With repeated sorption-desorption of K^+ and Li^+ during cycling, the beta phase is restricted to a unique degree of long range order (or disorder) typified by a unique x-ray diffraction pattern rather than gradually recrystallizing through a reconstructive phase transformation to the ordered lithium nickelate solid solution lattice. This minimizes the solid solubility range of divalent nickel with respect to the trivalent state. The nickel hydroxide is oxidized more or less directly to a trivalent state rather than to a lower level divalent nickel in solid solution in a trivalent $LiNiO_2$-type crystalline lattice.

The increased capacity attainable in the lithiated electrolyte can be attributed to the elimination of the rate-sensitive, low density alpha phase, which is not efficiently cycled at normal current densities. The elimination of alpha also permits ready oxidation of $Ni(OH)_2$ throughout the compacted layers. This is accompanied by an apparent increase in the oxygen overvoltage.

The effects are not to be directly attributed to growth of insulating barrier layers of one form or another, limiting electronic conduction processes as suggested by Tichenor (5). The increase in capacity through bismuth hydroxide addition to the $Ni(OH)_2$, as noted by Tichenor, is dependent on the formation during overcharge of an alpha phase which can be discharged efficiently at the operational current densities and is formed even in lithiated electrolytes. Thus, foreign ions can modify the phase transformation kinetics so that particular mass transport reactions are facilitated or inhibited.

In connection with the effect of additives, Tichenor noted that ferric hydroxide additions to the nickel hydroxide decreased the electrode capacity. This effect has been found to depend on a reduction of the effective oxidation potential distribution within the electrode. The oxygen overvoltage can be sufficiently reduced so that the interior nickel hydroxide is not oxidized. This type of phenomena is undoubtedly encountered in the porous plaque nickel electrodes which even on extensive overcharge are difficult to oxidize to the alpha phase state at the usual electrolyte concentrations.

This study does not provide a pat explanation for the role of lithium in the electrode processes. The data do emphasize the extreme care necessary in describing the influence of additives upon electrode processes. The effects may involve perturbations in electronic or mass transport processes in the solid phases, modifications in the Helmholtz electrical double-layer structure, space-charge field distributions in the solid or the electrolyte phases, or modifications in the local electrochemical exchange currents, not only for the phase transformation reactions, but also for the gas evolution processes.

Equipotential surface effects.—At the completion of electrode formation the electrochemical capacity had become relatively independent of the discharge rate. This contrasts with the observations of Kuchinski and Ershler (18) on the charge and discharge of a $Ni(OH)_2$ grain. They observed that the oxidation proceeds from the metal contact region into the grain starting at the three-phase contact area metal-electrolyte-nickel hydroxide. No rate-sensitivity effects were observed during charge. High rate discharge led to the isolation of active phase through the formation of an insulating layer near the metal contact. Placing a metal probe in contact with the surface opposite to the original contact area permitted discharge of the isolated phase. The implied conclusion is that the charged phase is a good electronic conductor, but the discharged phase is not.

In this forming study the oxidation progressed in a similar fashion proceeding into the porous matrix from the metal contact. The initial reaction is the formation of a surface-covering layer of a higher valence nickelate over the $Ni(OH)_2$ surface. This is followed by a migration of the reaction front into the nickel hydroxide to form beta phase. As anticipated, the initial gross reaction proceeds from the metal contact into the layer and from the periphery to the center of the tube. The oxidation state is highest at the periphery and lowest in the center.

After electrode formation the electrochemical capacity does not show the discharge rate sensitivity observed by Kuchinski and Ershler. The absence of rate sensitivity can be partially attributed to a change in the equipotential surface distribution for ionic conduction through the electrolyte in the porous bed and the electronic conduction through the active phase. The formed active material is in intimate electronic contact with the nickel flake layers which are oriented parallel to the ionic conduction paths. During formation the particulate structure of the original $Ni(OH)_2$ is formed into a fairly continuous porous bed. Thus, during discharge the electronic conduction path through beta phase moves from the periphery toward the center as the higher electrical resistivity discharge phase is formed from the periphery toward the center. This structure contrasts sharply with the point contact electrode present in Kuchinski and Ershler's experiments (18) or with the nickelate coating on a metallic substrate used in the thin film studies (19). An additional factor not to be neglected is the formation of an active material state which has a sufficiently large exchange current to maintain the required high local current densities.

Electrochemical kinetics.—Now turn to a discussion of the electrochemical process involved in active material oxidation reduction. Although solution-precipitation mechanisms can be postulated for the oxidation reduction of nickel oxides, the experimental evidence is that the phase transformations proceed primarily as a solid-state reaction, not depending on the solution of nickel ions. This is strongly supported by the observation that microcrystalline $Ni(OH)_2$ remains microcrystalline and macrocrystalline material remains macrocrystalline over long periods of cycling. Furthermore, in a cell very little material transport occurs between electrodes over a cycle life of many years.

Conway and Bourgault described the electrical behavior of the nickel electrode during open-circuit oxygen evolution as a large pseudocapacitance due to the discharge or desorption of oxygen containing radicals on its surface (20). The process is characterized as an electrochemical reaction rather than as a simple non-electrochemical decomposition or desorption of a surface phase from the nickelic oxide. During oxygen evolution on charging a large adsorption or pseudocapacitance was observed so that appreciable time was required for the potential to stabilize after a change in the applied current.

Conway and Gileadi (12), on the other hand, observed the presence of three distinct regions in the active material during charging, namely: (*a*) the initial charging of a surface phase, (*b*) the transition from a surface to a bulk-charging process, and (*c*) the bulk phase charging. This model is analogous to Foerster's (9) and Glemser-Einerhand's (2) model postulated to explain the difference between the anodic and cathodic potential curves. They assumed that oxidation produced primarily an NiO_2 phase with the trivalent oxide forming subsequently either through a decomposition process or by reaction with the divalent phase.

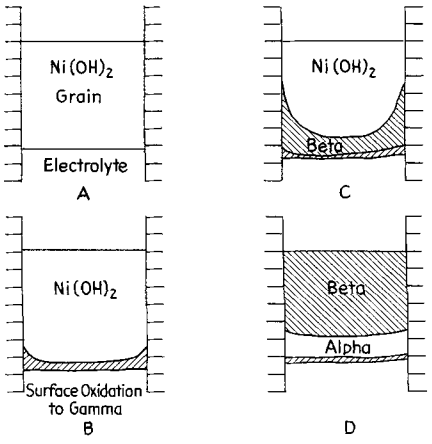

Fig. 11. Physical model for $Ni(OH)_2$ grain oxidation: (A) initial state; (B) surface layer charged to gamma phase; (C) beta phase formation; and (D) alpha phase formation.

This evidence implies an electrochemical process model based on a set of solid-state processes within the framework outlined by Croft and Tuomi (21) for reversible electrodes. Clearly a simple model will not adequately describe the complex data.

The gross features for the anodic conversion of a nickel hydroxide grain are illustrated in Fig. 11. The first stage involves the propagation of an electronic and ionic conductor high-nickel valence surface-oxide film from the three phase interface across the nickel hydroxide-electrolyte interface, *i.e.*, gamma phase. This is followed by a bulk phase process producing beta phase, also a mixed electronic and ionic conductor. Finally, the surface beta phase region is converted to alpha phase, and oxygen evolution occurs in the Helmholtz double layer surface region.

During the phase transformation process lattice imperfections must be introduced into the crystals so that the mass transport necessary for crystalline phase oxidation and reduction can proceed at a significant rate. The physical model must incorporate a driving force to convert the crystalline electronic insulator $Ni(OH)_2$ to an electronic-ionic conductor beta phase without dropping the electrical field across the insulating phase. Furthermore, a mechanism is needed for converting the semiconductor, beta, to a new semiconductor, alpha, without solution of the nickel ions.

For this discussion the discharge phase, $Ni(OH)_2$ is assumed to behave as a covalently bonded layer-lattice structure. The structure is formed from a divalent nickel layer octahedrally coordinated to two opposing oxygen layers. The layer configuration is maintained as electrically neutral by a hydrogen ion layer between two oxygen layers coordinated to separate nickel layers. The band structure corresponds to a large gap electrical insulator.

The oxidized phases in contact with the electrolyte are assumed to exist as low electronic resistance n-type semiconductors. Detailed Seebeck voltage measurements on the more crystalline beta phase from hot LiOH electrolytes showed that the charge phase was an n-type, low electronic resistance nickelate (22). Thus, lithium addition effects are not validly described by models based on the p-type lithium doped nickel oxide (5).

The beta phase, analogous to $LiNiO_2$ (4), is viewed as a $CsCl_2I$-type layer lattice structure. This is equivalent to a trivalent nickel layer octahedrally coordinated to a pair of oxygen layers. The electrical neutrality of layers is maintained by a set of cations (H^+, Li^+, K^+, Na^+) distributed on appropriate sites between the two layers of oxygen octahedrally coordinated to separate Ni layers.

In a general fashion the anodization of $Ni(OH)_2$ is considered to involve the oxidation of the divalent nickel layer to the tri- and tetravalent states without a reconstructive lattice transformation. The change in the Ni layer valence is equivalent in the octahedrally coordinated oxygen layer to a decrease in the required positive charge to maintain electrical neutrality from a $+2$ for $Ni(OH)_2$ to $+1$ for the trivalent state, to zero for the tetravalent Ni configuration. Thus, the mass transport process involved in the phase transformation proceeds in the H^+, OH^- layer region of $Ni(OH)_2$. The layer configurations are viewed as involving a combination of interlayer-interstitial compound structure along with tunnel and layer compound structures (23), depending on the state of oxidation. In other words, an ideal crystal lattice model would not give a valid representation. A reaction process, throughout which the nickel ion remains octahedrally coordinated to oxygen, is postulated. The nickel valence state is characteristic of the Ni-O bond, rather than corresponding to the classical viewpoint of an ionic lattice, *i.e.*, the Ni-O bonds are covalent.

The electrochemical processes involve the sequence: (i) an electrochemical exchange at the solid electrolyte interface involving a set of electronic-ionic lattice imperfections, (ii) electron transport through the oxidized phase region to the metallic contact, (iii) mass transport through the oxidized phase to the lower valence phase at the second interface, and (iv) electrochemical exchange at the second solid phase interface functioning as a source or sink for the ionic-electronic imperfections necessary to maintain the mass and charge balance.

Although a detailed model is difficult to describe, a hypothesis can be presented on several system characteristics which are necessary for self-consistency in the observed properties. The basic postulate is that a three-phase three-interface process is involved. An electrochemical exchange reaction at the solid electrolyte interface produces an internal space charge field, as well as being a source and sink for atomic and electronic imperfections. The electronic charge transport occurs through the higher valence state oxides contacting the metallic-electronic conductor. The driving force for the phase transformation depends on the source and sink characteristics of the two phase interface for both electronic and atomic imperfections. The space charge fields within the solid phases contribute to the required mass transport process.

The first oxidation stage is forming a covering layer of oxide or nickelate over the nickel hydroxide surface adjacent to the electrolyte. The nickel valence state in this surface film corresponds to a nonequilibrium distribution. The Helmholtz double layer is not visualized as a two or three atom layer region, but rather as a volume element extending into the solid as well as into the electrolyte. The surface region involves primarily adsorbed hydroxyl and alkali ions and water molecules. The electrochemical exchange process involves a complex set of phenomena. Through the injection of holes a surface space charge region of high valence state nickel atoms is formed. Accompanying this hole-trapping process, a proton depletion layer extending a diffusion length into the hydroxyl layer is produced, and lattice vacancies, alkali ions, and other imperfections are introduced. The mass transport processes are controlled by the lattice imperfection generating and consuming processes involved in the detailed balancing of the exchange reaction.

Using the notation summarized by Rees (24) and outlined by Croft and Tuomi (21) the following exchange reactions are contributing to the Helmholtz double layer exchange processes

$$OH_l^- + \square_s^- \rightleftharpoons OH^-/\square_s^-$$

$$\square_s^+ + H^+/\square_o^+ \rightleftharpoons \square_o^+ + H^+/\square_s^+$$

$$H^+/\square_s^+ + OH^-/\square_s^- \rightleftharpoons H_2O_l + \square_s^+ + \square_s^- + n$$

$$H^+/\square_s^+ + p + OH^-/\square_s^+ \rightleftharpoons H_2O_l + \square_s^+ + \square_s^-$$

$$K_l^+ + \square_s^+ \rightleftharpoons K^+/\square_s^+$$

$$Li_l^+ + \square_s^+ \rightleftharpoons Li^+/\square_s^+$$

where $\square_o$ is an interior site; $\square_s$, a surface site; the superscript + or — distinguishes cation or anion sites; and the subscript l the liquid phase. The p and n refer to the holes and/or electrons involved in the local site charge neutrality change due to the removal of local site anions near nickel ions. On interior sites the reactions may be described as

$$Ni^{+2}/\square_o^+ + p \rightleftharpoons Ni^{+3}/\square_o^+$$
$$Ni^{+2}/\square_o^+ \rightarrow Ni^{+3}/\square_o^+ + n$$

the charge carrier type depending on the semiconductor properties. Complementary reactions would include the mass transport processes

$$K^+/\square_s^+ + \square_o^+ \rightleftharpoons K^+/\square_o^+ + \square_s^+$$
$$Li^+/\square_s^+ + \square_o^+ \rightleftharpoons Li^+/\square_o^+ + \square_s^+$$
$$OH^-/\square_s^- + \square_o^- \rightleftharpoons OH^-/\square_o^- + \square_s^-$$
$$H^+/\square_o^+ + OH^-/\square_o^- \rightleftharpoons (H_2O/\square_o^+)\square_o^-$$

Within this framework the surface exchange processes produce an oxidized nickel layer without requiring solution or significant diffusion of the nickel ions. The distributed space-charge field does not correspond to a local field sufficiently large to result in oxygen evolution from electrolyte decomposition.

The electrochemical exchange reactions generate a surface region with a high electronic and atomic imperfection density. As a result, the nickel atoms in the region adjacent to the electrolyte will have an average valence state determined by a combination of factors. During anodization the local space-charge density of electrons will be decreased, corresponding to an increase in the nickel valence state. The actual space charge density will depend on the rate of atom movements tending to eliminate the space charge. Thus, during anodization a surface region p-n semiconductor junction is formed within a system containing mobile doping atoms.

During the initial oxidation stages rapid diffusional exchange proceeds between the interface and a diffusion length depth into the solid. As charging proceeds, the solid phase begins to show bulk semiconductor properties. An internal space charge region extending from the solid-electrolyte interface to the metal-semiconductor contact and to the beta-nickel hydroxide interface can be formed. Within beta the nickel valence state varies from an upper solid solution limit at the electrolyte interface to nearly the lower limit at the nickel hydroxide interface. The trapping of electrons from the divalent nickel in $Ni(OH)_2$ in the beta phase produces a local electric field at the beta-$Ni(OH)_2$ interface. This interface is a sink for holes generated at the electrolyte interface and a source and sink for the imperfections required for the mass transport process completing the electrochemical oxidation reaction.

A group of electrochemical exchange reactions at the beta-$Ni(OH)_2$ interface can be formulated as follows

$$Ni^{+2}/\square_{OH}^+ + p \rightleftharpoons Ni^{+3}/\square_{OH}^+$$
$$Ni^{+3}/\square_o^+ \rightleftharpoons Ni^{+2}/\square_o^+ + p$$
$$Ni^{+3}/\square_o^+ + Ni^{+2}/\square_{OH}^+ \rightleftharpoons Ni^{+2}/\square_{OH}^+ + Ni^{+2}/\square_o^+$$
$$OH^-/\square_{OH}^+ + \square_o^+ \rightleftharpoons OH^-/\square_o^+ + \square_{OH}^+$$
$$H^+/\square_{OH}^+ + \square_o^+ \rightleftharpoons H^+/\square_o^+ + \square_{OH}^+$$
$$Li^+/\square_o^+ + \square_{OH}^+ \rightleftharpoons Li^+/\square_{OH}^+ + \square_o^+$$
$$K^+/\square_o^+ + \square_{OH}^+ \rightleftharpoons K^+/\square_{OH}^+ + \square_o^+$$

where the first three reactions represent local valence changes in beta and $Ni(OH)_2$ and the remainder form the mass transport processes necessary to maintain local electrical neutrality.

During constant current charge a sequence of effects appears. The surface double layer region is first charged, producing a local interior space-charge field. With an extension of the semiconductor charge phase into the interior a distributed space charge field is formed. This field is characterized by a combination of the semiconductor band structure and the mobility of dopant imperfections. As the state of charge increases the magnitude of the space charge diminishes so that at the end of charge there is only an iR loss in the solid and the applied field is largely at the solid electrolyte interface. If charging is continued until steady-state oxygen evolution is reached, the distributed space charge will have vanished. The semiconductor is characterized by a flat band potential. If the electrode is placed on open circuit, the space charge field will gradually decay through atom movements in the solid phase, and a flat band potential condition will be approached.

In this model the anomalous relationships between the charge and discharge potentials are related to the space charge fields within the charged phases which contribute to mass and charge transport during cycling. Through their effects the nickel hydroxide could be oxidized to the high valence states without actually dropping the electric field across the nickel hydroxide. This distinguishes the Ni electrode oxidation reduction process from that in cadmium oxidation where a covering $Cd(OH)_2$ layer is formed over the cadmium.

When the electrode is placed on open circuit after charging, a local cell system is formed by a coupling of the oxygen evolution reaction on the semiconductor surface with a decay in the nickel valence state in the oxide. This decay process for isolated electrodes does not necessarily decrease the valence below 3.0 even on very long open-circuit stands. Though the oxygen evolution process is closely related to the "steady state" electrode potentials, the data do not give insight into the mechanism of nickel valence reduction. In certain isolated charged electrodes left on open circuit for several years, the nickel valence showed only a negligible decay although the normal rate capacity had decreased to a low value, *i.e.*, self-discharge had occurred. The electrodes, however, could be fully discharged at very low rates. An extended overcharge of the electrodes restored the original capacity. Considering the extent of overcharge required, it seemed unreasonable simply to postulate a surface-covering layer reduction. The results suggested that the imperfection density necessary for mass transport during discharge had diminished during open-circuit stand.

The experimental data suggest that the lattice imperfections involved in the mass transport are introduced into the solid phase during the charging process. Their characteristics depend on the forming conditions and electrolyte composition. The correlation of the oxygen evolution with the electrode potential may reflect mass transport limitations through the Helmholtz double layer into the solid at virtually flat band potential conditions. The experimental problem is to characterize the surface mass and charge transfer sites as a function of the solid phase structure. With a wide variety of structures experimentally accessible in the nickel electrode such detailed studies are practical.

Additives such as Li^+, K^+, Na^+, or Bi and other elements produce a number of subtle changes in the Helmholtz double layer structure and the electrochemical exchange reactions at the solid electrolyte interface. The ready transport of lithium into the electrode during charge implies that either a strong activity effect is involved or that only a small opposing electrical field is formed at the solid electrolyte interface on anodization.

For the transformation of beta to alpha phase the mass transport processes involve atom migration within good electronic conductors, 1 ohm-cm resistivities. The mass transport involves a separation of the oxygen-octahedrally coordinated nickel layers by the insertion of a K^+-H_2O layer between the opposing oxygen layers. Systematic studies of the structural relationships for the various electrolyte and impurity combinations should provide insight into the factors controlling the reaction kinetics. It is insufficient to describe the effects simply in terms of oxygen over-

voltage displacements and surface area variations or in terms of simple mixed potential functions.

The forming process study has shown that material which appears to be very disordered, and even amorphous, may have a variable electrochemical capacity. The existence of an amorphous structure does not assure the presence of many lattice imperfections capable of contributing to mass transport under the relatively low internal electric field conditions necessarily present in a practical active material for use in batteries. Definite local site symmetry boundary conditions exist, limiting the transition probabilities for atom jumps into neighboring vacant sites.

The research outlined in this report has emphasized the critical role played by electrochemical exchange reactions involving minor system components even in solid phases not having a high degree of lattice perfection. Studies over a large enough temperature range to define limiting conditions are of particular importance. There is no doubt that the electrolyte component can exert equally profound effects on the solid-state transformations encountered in many other corrosion systems.

Although a well-defined model cannot yet be formulated for the nickel electrode reactions, the experimental data clearly show that solid-state phase transformations are relevant. From a composite approach involving structural chemistry, solid-state physics, and electrochemistry, sufficiently extensive and varied data should become available to bring clarity and simplicity into the relevant physical mechanisms.

Summary

This study of forming processes in the nickel positive electrode has clarified several facets of the art. In summary, the main results obtained are as follows:

1. In LiOH and dilute KOH and NaOH electrolytes nickel hydroxide is readily oxidized to a trivalent state designated as beta phase nickelate.

2. In concentrated KOH or NaOH electrolytes the beta phase can be further oxidized to a tetravalent state designated as alpha phase nickelate.

3. The crystallinity of the oxidized phases depends on the crystallinity of the initial $Ni(OH)_2$ phase.

4. The effective electrochemical exchange current of alpha phase is smaller than for beta phase. Consequently, under normal conditions alpha is not efficiently cycled.

5. At elevated temperatures in LiOH electrolytes the $Ni(OH)_2$ is oxidized to a trivalent phase having the $LiNiO_2$ crystalline structure.

6. The effect of the lithium addition to KOH electrolytes is to eliminate alpha phase as a system component.

7. The variable potential characteristics during charge and discharge are related in part to solid solution ranges for di- and tetravalent nickel in the trivalent phase and, in part, to the distributed potential within the semiconductor phases constituting the active material.

8. Additive effects on the electrode properties may involve changes in the phases formed as well as changes in the oxygen overpotential for the electrode.

9. The spatial distribution of the charge and discharge phases within a cycling electrode depends on the equipotential surface distributions for ionic and electronic conduction within the electrolyte and solid, respectively.

10. A general model based on solid-state mass and charge transport processes has been used to interrelate the observed data.

Acknowledgments

An extensive study such as implied by the outlined results clearly depends on the cooperation of a number of people. The experimental work was largely performed by L. Middlecamp and Mrs. V. Tierney. The analytical services were kindly provided by R. Arzapalo, M. Maffia, and Miss J. Sareski under the supervision of B. D. Brummet. The research benefited from frequent discussions with Drs. G. T. Croft, J. B. Johnson, A. Fleischer, and P. F. Grieger at the T. A. Edison Research Laboratory.

The continued support of Dr. D. W. Collier was appreciated. Special acknowledgment is due to W. W. Smith and R. H. Weeks, Jr. at the Nickel Alkaline Battery Division of The Electric Storage Battery Company for their support and encouragement during the preparation of this paper for publication.

Manuscript received Dec. 19, 1963; revised manuscript received Sept 2, 1964. This paper was presented in part at the Houston Meeting, Oct. 9-13, 1960.

Any discussion of this paper will appear in a Discussion Section to be published in the December 1965 JOURNAL.

REFERENCES

1a. G. W. Vinal, "Storage Batteries," 4th ed., p. 86-7, John Wiley & Sons, Inc., New York (1955).
1b. T. Okada, T. Shiraishi, and K. Watanabe, *J. Chem. Soc. Jap. Ind. Chem. Soc.*, **51**, 129 (1948).
2. O. Glemser and J. Einerhand, *Z. Elektrochem.*, **54**, 302 (1950).
3. S. Uno Falk, *This Journal*, **107**, 661 (1960).
4. L. B. Dyer, B. S. Borie, Jr., and G. P. Smith, *J. Am. Chem. Soc.*, **5**, 107 (1958).
5. R. L. Tichenor, *Ind. Eng. Chem.*, **44**, 973 (1952).
6. G. W. D. Briggs, E. Jones, and W. F. K. Wynne-Jones, *Trans. Faraday Soc.*, **51**, 1433 (1955).
7. G. W. D. Briggs and W. F. K. Wynne-Jones, *ibid.*, **52**, 1272 (1956).
8. O. Glemser and J. Einerhand, *Z. Anorg. Chem.*, **261**, 46 (1950).
9. F. Foerster, *Z. Elektrochem.*, **13**, 414 (1907).
10. A. L. Pitman and G. W. Work, NRL Report 4845 (1956).
11. A. Salkind and P. F. Bruins, *This Journal*, **109**, 356 (1962).
12. B. E. Conway and E. Gileadi, *Can. J. Chem.*, **40**, 1933 (1962).
13. P. L. Bourgault and B. E. Conway, *ibid.*, **38**, 1557 (1960).
14. J. B. Goodenough, D. G. Wickham, and W. S. Croft, *J. Phys. Chem. Solids*, **5**, 107 (1958).
15. T. A. Edison, U. S. Pat. 876,447 (1907).
16. T. Okada, T. Shiraishi, and T. Yasuhara, *J. Chem. Soc. Jap., Ind. Eng. Chem. Sect.*, **53**, 578 (1950).
17. T. Okada, T. Shiraishi, and T. Yashuhara, *ibid.*, **54**, 16 (1951).
18. E. N. Kuchinski and P. V. Ershler, *J. Phys. Chem. U.S.S.R.*, **20**, 539 (1946).
19. E. Jones and W. F. K. Wynne-Jones, *Trans. Faraday Soc.*, **52**, 1270 (1956).
20. B. E. Conway and P. L. Bourgault, *Can. J. Chem.*, **40**, 1690 (1962).
21. G. T. Croft and D. Tuomi, *This Journal*, **108**, 915 (1961).
22. G. J. B. Crawford and D. Tuomi, In preparation.
23. A. D. Wadsley, *Rev. of Pure Appl. Chem.*, **5**, 165 (1955).
24. A. L. G. Rees, "Chemistry of the Defect Solid State," pp. 16-20, John Wiley & Sons, Inc., New York (1954).

Oxides on the Silver Electrode

II. X-Ray Diffraction Studies of the Working Silver Electrode

Charles P. Wales and Jeanne Burbank

United States Naval Research Laboratory, Washington, D. C.

ABSTRACT

Silver electrodes were examined in 20-50% KOH using a cell permitting simultaneous x-ray diffraction and electrochemical studies. Highly oriented smooth rolled sheet Ag developed randomly oriented Ag on its surface during early cycles. Charge-discharge capacity increased to a maximum as surface area increased. AgO crystal size and amount formed varied inversely with charging c. d. High charge rates gave tight coatings of small AgO crystals that limited further oxidation. Reactions took place initially at the outer surface of the electrode. Oxidation to Ag_2O and AgO and reduction to Ag_2O and Ag occurred by formation of distinct crystals rather than expansion or contraction of preexisting crystal lattices. Discharge capacity at the AgO/Ag_2O potential plateau depended more on surface area than on quantity of AgO. A slow discharge produced smoother Ag surfaces, lowering capacity of the next cycle. There was never evidence of a suboxide, oxidation state higher than AgO, solid solution, or alloy of oxygen and silver.

Investigation of the silver electrode in KOH solution is of interest since silver oxides comprise the positive active material of charged Ag-Zn and Ag-Cd storage batteries. It is therefore desirable to know the reactions and products occurring in alkaline solutions when oxidized silver electrodes are reduced cathodically, and when metallic Ag electrodes are oxidized anodically. In the persent work an electrolytic cell was used that permitted x-ray diffraction examinations to be made of the working electrode during charge and discharge, instead of interrupting electrolysis and removing the electrode for x-ray examination as was done previously (1).

There is general agreement that Ag_2O having the Cu_2O type of face-centered cubic structure is formed at the first potential plateau when a silver electrode is anodically oxidized (charged) using constant current in alkaline solution. Although there have been claims that a silver suboxide may form on a silver electrode, its presence was not detected, and indeed the existence of silver suboxide itself is quite dubious (1). When silver is anodized in KOH solutions, the potential rises to a peak after charging at the first plateau for sufficient time, and then monoclinic AgO forms at a second potential plateau. Finally, the potential rises again and oxygen evolution takes place. There have been unsubstantiated reports of higher oxides of silver, presumably containing trivalent silver, forming just before or during oxygen evolution. Some confusion has been caused by the report of Jones and Thirsk of what they believed was the x-ray diffraction pattern of AgO (2). Their pattern has since been shown to be that of the so-called silver peroxysulfate $Ag_7O_8SO_4$ and not AgO (1). The x-ray diffraction pattern for monoclinic AgO is well established now and has been given by Scatturin, Bellon, and Zannetti (3) and by Graff and Stadelmaier (4), among others. Standard reference patterns for Ag and Ag_2O appear in the ASTM Powder Diffraction File.

Three additional oxides of silver have been reported recently. Tetragonal AgO, which appears to be a peroxide containing mono- and divalent Ag, has a diffraction pattern closely resembling that of monoclinic AgO and was prepared by McKie and Clark through the action of ozonized oxygen on hot silver powder (5). Vol and Shishakov have reported that a silver peroxide having the NaCl type of cubic lattice forms when silver is heated in oxygen (6). A modification of Ag_2O having the CdI_2 structure has been obtained by Kabalkina *et al.* using high pressure and temperature (7). Only the face-centered cubic Ag_2O and the monoclinic AgO have been definitely established as being present on the silver electrode in alkali (1, 8-10).

Experimental Procedure

The test electrode was a half-submerged rotating Ag disk 57 mm in diameter, mounted vertically in a cell designed for use on a horizontal circle x-ray spectrogoniometer (11). The method of mounting the disk covered its edge and back, leaving only one side to contact the electrolyte. X-ray diffraction patterns, using CuK_α radiation, were made from this side of the disk as it rotated out of the electrolyte. Initially the disk was cut from 0.25 mm thick Ag of 99.99+% purity. This disk was not perfectly flat despite pressing, since it had been cut from a roll of sheet silver. Consequently the recording of the diffraction pattern from this disk showed some variations with sample rotation because the sample surface was not all in the same plane. Disks cut from 1.6 mm thick flat sheet Ag of similar purity removed this difficulty, and these were used for most of the work reported here. Satisfactory patterns have also been obtained from disks of sintered Ag cut from a storage battery electrode, but due to the porosity of this material the electrochemical reactions were not limited to one side, as was the case with sheet Ag.

A counterelectrode of sintered Ag, wrapped in cellulosic separator material, faced the submerged part of the continuously rotating specimen disk. The cell also contained a reference electrode of Ag/Ag_2O. Some work was done in 20% and 50% KOH, but the usual electrolyte was 35% KOH at 23°-26°C, and this was used except where otherwise specified. Charge and discharge were carried out with a wide range of constant currents. The Ag sample rotated at 60 rpm and, therefore, the diffraction pattern was registered 0.25 sec after the sample left the electrolyte, with the total time out of solution being 0.5 sec. Current did not need to be interrupted during the x-ray examinations because the test Ag electrode was always partially submerged. This experimental arrangement permitted x-ray diffraction patterns to be made during charge and discharge of a working electrode simultaneously with electrochemical measurements and visual observations. The use of this cell lowered the possibility of an unstable crystalline compound being present but undetected by x-ray diffraction.

Results

Before the initial anodic oxidation of the disks that were cut from smooth rolled sheet Ag, x-ray diffraction patterns showed strong preferred orientation: the (110) planes lying in the surface of the 0.25 mm sheet,

and the (110) and (100) planes lying in the surface of the 1.6 mm sheet. The initial charge produced first a thin layer of Ag_2O and then a thicker layer of AgO. A little randomly oriented Ag formed in the first discharge.

The highly oriented Ag substrate showed strongly through the randomly oriented oxide films in x-ray diffraction patterns made during early charge-discharge cycles. The amount of dendritic randomly oriented polycrystalline Ag present after discharge and the surface roughness of the Ag both increased gradually during the early cycles, and at the same time the amount of Ag visible by x-ray diffraction through the oxide film after charging to gas evolution gradually decreased. Capacity rose from its initial value of about 5-10 mah and reached a maximum of about 65-75 mah as the electrodes were cycled in 35% KOH, and a rough surface of dendritic polycrystalline Ag was produced. Although this Ag was in good electrical contact with the base Ag, it was easily broken from the surface. Randomly oriented Ag could also be obtained by abrading a smooth Ag disk with a fine polishing cloth before anodization, but this was not accompanied by any marked increase in discharge capacity, in contrast to the results when polycrystalline Ag was produced through repeated cycling.

There was never evidence of a suboxide, solid solution, or alloy of oxygen and silver during charge or discharge. Ag_2O lines gradually appeared in addition to the Ag lines of the x-ray diffraction patterns while dendritic randomly oriented Ag was charging at the Ag/Ag_2O potential plateau at a moderate current, for example the 12-24 hr rate. The diffraction lines for Ag did not broaden or shift as Ag_2O formed. The Ag_2O diffraction patterns were in close agreement with the standard Ag_2O pattern. The Ag_2O pattern had become moderately strong by the end of the Ag/Ag_2O potential plateau and was about the same intensity as the metallic Ag pattern, which had decreased from its initial strength. The potential was usually 25-50 mv above the Ag/Ag_2O equilibrium during most of this plateau. Sometimes there was a secondary plateau at about 70-100 mv, after the electrode had charged about 1/4 or 1/3 of the normal amount of the Ag/Ag_2O plateau in 20% KOH. This secondary plateau was not observed in 35% or 50% KOH.

The AgO diffraction pattern could be detected when only a very small amount of AgO had formed, for example when the charge at the Ag_2O/AgO plateau was 0.3-0.5% of the total capacity. The Ag_2O pattern did not broaden or shift as Ag_2O was oxidized to AgO. The AgO diffraction patterns closely resembled the standard AgO pattern. An AgO pattern made in 20% KOH using the experimental method described here was given as Fig. 4a of ref. (11).

The gas evolution potential plateau of the rotating electrode was about 0.1v lower than normal for O_2 evolution on AgO. This lower potential was an effect of rotating the electrode in and out of the electrolyte. Using a stationary electrode, the potential continued to rise for about 0.1v after the onset of O_2 evolution. Despite extensive gassing using various current densities, no pattern was ever observed that could be attributed to an oxidation state higher than AgO. The potential usually dropped rapidly to the Ag_2O/AgO plateau after a charge was terminated, but following very low rate charges the potential dropped more slowly than normal.

Low charging currents (1-10 day rates) resulted in a granular surface of light gray AgO. There was specular reflection from what appeared to be large crystal facets. The base Ag was greatly obscured or even undetected in diffraction patterns made after reaching oxygen evolution under these conditions. High charge currents (2-120 min rates) gave a thinner coating of dark gray AgO having what appeared visually to be a much smoother surface. Diffraction patterns of this

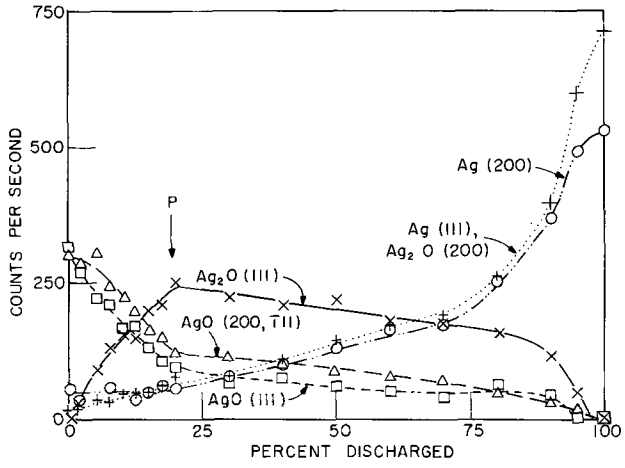

Fig. 1. Change in intensity of x-ray diffraction peaks during continuous discharge of AgO in 35% KOH. The Miller indices corresponding to the peaks are: AgO (111), □; AgO (200) and $(\bar{1}11)$, △; Ag_2O (111), X; Ag_2O (200) coincident with Ag (111), +; Ag (200), ○. The end of the first discharge plateau is indicated by the arrow at point P.

AgO were quite poor, and the randomly oriented Ag that had been produced through cycling was still detectable. Ag_2O was detectable after a moderate or high rate charge to gassing when using Ag that had developed the rough dendritic surface, but Ag_2O was not detected after low rate charges to gassing, or when using disks of smooth or sintered Ag. Oxides formed on a smooth Ag surface gave patterns of higher intensity than those obtained after the rough surface was developed. Strongest of all were the patterns from the sintered Ag disk.

Diffraction patterns were practically unchanged after an electrode was put on open circuit for 16 hr following a charge to 75% of capacity. After a fully charged electrode was on open circuit for 60 hr the AgO pattern was slightly weaker but Ag_2O was not definitely visible. The self-discharge rate was obviously quite low.

Ag_2O could be detected quite early in a discharge. It appeared to form first at areas that were the last to charge, where the AgO was thin. When using disks that had developed the rough dendritic surface, AgO was present in diffraction patterns until very near the end of discharge (Fig. 1). The first 2.5% of the discharge of Fig. 1 was done at the 40 hr rate following a charge at the 18 hr rate to oxygen evolution. X-ray diffraction patterns were made every ½% of discharge in this initial period, but for clarity only peaks when 0% and 2% discharged were included on Fig. 1. Current was increased to the 10 hr rate after the electrode was 2.5% discharged, and when 20% discharged, current was increased to the 2.5 hr rate. The Ag_2O/Ag potential plateau was reached after the discharge was 19.2% complete and is indicated by the arrow P. Total capacity of this discharge was 70.3 mah. Diffraction peaks for the (002) and $(\bar{2}02)$ reflections of AgO showed the same trend as the two AgO peaks plotted in Fig. 1, but with intensities about half as strong. The (220) reflection of Ag had peaks about 20 to 80 counts/sec stronger than the (200) peaks shown.

X-ray diffraction at the end of a discharge showed only metallic Ag, although at times small spots of Ag_2O could be seen visually. Rapid discharges (2 hr or faster rate) gave very good randomly oriented polycrystalline Ag patterns despite the speed of reduction. Slow discharges gave poorer Ag diffraction patterns having increased amounts of highly oriented Ag visible. The charge-discharge cycles following a slow discharge had less than normal capacity. Capacity could be restored by a low rate charge that required several days to reach gas evolution.

Charge-discharge efficiency was usually in the range 95-102% when using 35% KOH, but was only 70-80% in 20% KOH. This contrasted with results reported earlier in which only 0.5% loss was found in 20% KOH (12), and no loss in 35% KOH (13), when using Ag electrodes wrapped with semi-permeable separator material. Most of this loss was probably due to Ag going into solution during charge. Black particles that precipitated out of the 20% KOH were identified as metallic Ag.

Discussion

It was pointed out above that there were several changes in characteristics of the Ag electrode with cycling; charge-discharge capacity, surface roughness, and amount of randomly oriented Ag all increased, at least up to a degree. The capacity increase was caused by the increase in surface area and appeared to represent neither actual increase in oxidation depth nor an effect of oxidizing randomly oriented Ag instead of highly oriented Ag. A medium or slow rate discharge produced more highly oriented Ag and less capacity on the following cycle than did a rapid discharge, but this loss in capacity was due to a smoother surface resulting from a larger crystal size after using the lower discharge currents, rather than to an effect of Ag orientation.

The amount of oxides that was present after charging increased with cycling, as was indicated both by rising capacity and by Ag from the substrate gradually becoming weaker in x-ray patterns made during the initial cycling. Weaker diffraction patterns were obtained from the oxides after cycling, despite a 5-10 times increase in quantity, due to the great increase in surface roughness. The more porous surface absorbed and scattered the x-ray beam, resulting in less efficient diffraction. Surface roughness may be the cause of detecting Ag_2O at the end of some moderate or high rate charges after building up capacity, but not detecting Ag_2O in the thin films during the initial cycles of the smooth surface. Patterns of the rough surface, recorded from a porous mass of dendrites or spheroidal particles, may have viewed a greater effective cross section and thus given more intense Ag_2O patterns than a thin Ag_2O film on a smooth base could give. An alternative possibility was that roughness affected current density over the surface and deeper crevices were not charged as efficiently, with the result that Ag_2O remained on the electrode when charge current was high, but not when charge required at least ½ day for completion.

Ag_2O and AgO had random orientation regardless of whether they were formed on randomly or highly oriented Ag. Ag_2O formed as distinct crystals on the Ag surface and not through a gradual expansion of the Ag lattice as oxygen entered. A gradual expansion of the lattice was to be considered possible since both Ag and Ag_2O have a face-centered cubic lattice, but if this were the true mechanism of formation the diffraction lines for Ag should have broadened or shifted, with a progressive expansion of lattice parameters from metallic Ag to Ag_2O. Similar evidence showed that oxygen did not gradually distort or expand the Ag_2O crystal lattice in forming AgO, but AgO formed in its own definite crystal lattice. Finding AgO after charging 0.3-0.5% at the Ag_2O/AgO plateau indicated that initially AgO must be forming on the surface of the electrode next to the solution. The amount of AgO present at this point was less than that necessary for detecting one component of a mixture by x-ray diffraction, and this amount of AgO would not have been detected if it were distributed throughout the Ag_2O or were forming at the Ag-Ag_2O interface.

Assuming that AgO formed initially from Ag_2O and that no Ag was oxidizing simultaneously, the amounts of AgO and Ag_2O should be equal when the quantity of charge current exceeded that required to reach the beginning of the Ag_2O/AgO potential plateau by 50%. This was true, judging by the relative strengths of the Ag_2O and AgO diffraction patterns. This measurement was only sufficiently accurate to indicate that at least most current was oxidizing Ag_2O in this period, since a few per cent of the current could have oxidized Ag without it being detected. When the quantity of charge current was twice that required to reach the Ag_2O/AgO plateau, the Ag_2O pattern had become quite weak, but Ag_2O still being present indicated that additional Ag had oxidized by this point. It was calculated that 15-40% additional metallic Ag oxidized after reaching the Ag_2O/AgO plateau in typical low or medium rate charges.

The AgO coating obscured the base Ag much more at the end of a charge than did Ag_2O at the end of the Ag/Ag_2O plateau, even when the 15-40% additional oxide is considered. This may indicate a greatly increased thickness of AgO compared to Ag_2O. Yoshizawa and Takehara reported an oxide layer 1.5μ thick after oxidizing to the end of Ag_2O formation (electrode approximately 1/3 charged) and a layer 8μ thick after oxygen evolution (10). Since the base Ag was obscured to a large extent when heavy films of AgO were on the electrode, some Ag_2O may also be present at the Ag-AgO interface under these conditions, but masked by the AgO coating.

Charges at the 4-10 day rate were the most effective for oxidizing the Ag base and for building capacity up to the maximum reached by cycling. After dendritic randomly oriented Ag had been formed on the base Ag, low rate charges appeared to oxidize this polycrystalline Ag completely. The total amount of AgO and its crystal size both varied inversely with the charging current density. The best diffraction patterns were obtained after charging with medium currents, for example ½-1 day rates. This was probably the range of current densities giving the optimum particle size for x-ray diffraction. Oxygen evolution appeared to perfect crystallinity when using medium rates of charge, perhaps by perfecting the lattice or by changing the particle size.

The very poor diffraction patterns obtained after quite high charge rates were due to small AgO crystal size, and the AgO lattice may have been highly distorted. After charging the Ag electrode to oxygen evolution using a high current and then lowering the current, there was only a little further charge acceptance, AgO diffraction patterns remained poor, and the discharge capacity was less than if the low current had been used throughout the charge. The small AgO crystals made a more uniform coating and were more interlocking than the larger crystals obtained with slower charge rates. Thus OH^-, O^{--}, or Ag ions could not penetrate this tight AgO coating readily and further oxidation was limited. Nevertheless AgO of small particle size may be better in a primary or storage battery because the increased surface area may result in less polarization and improved electrical contact.

X-ray diffraction patterns indicated that during discharge Ag_2O formed as distinct crystals, and not by gradual shrinking of the AgO lattice. Ag_2O formed initially on the surface of the AgO, as was indicated by visual observations and by its early appearance in the patterns. A discharge reached the Ag_2O/Ag potential plateau after Ag_2O covered the electrode surface. Although only Ag_2O could be seen visually on the surface at this point, diffraction patterns often showed AgO also (Fig. 1). The amount of Ag_2O present decreased gradually from point P, as shown by the (111) reflection of Ag_2O. The apparent increase in Ag_2O (200) after point P was actually due to increase in the coincident Ag (111) reflection. The relative changes in the intensities of the diffraction peaks indicated that up to point P, while discharging at the upper plateau, the rate of growth of Ag_2O corresponded to the rate of discharge and covering over of the surface of AgO. The de-

crease in AgO counts per second by point P was largely due to Ag_2O covering the AgO, and represented only a 19% decrease in the total amount of AgO present. Beyond point P, the slopes for the Ag_2O (111) and the AgO (200, $\bar{1}11$ and 111) peaks indicated that both oxides were discharging simultaneously, with the layer of Ag_2O covering the AgO crystals remaining approximately the same thickness until near the end of the discharge. Ag did not trap any oxides during a discharge. When using the Ag electrode that had developed a rough surface, after Ag_2O had formed on the outer surface of the protrusions the discharge could then proceed from the inner surface outward, with relatively little Ag forming on the surface at first. Thus the diffraction patterns would continue to show Ag_2O and AgO until close to the end of discharge (Fig. 1). Smooth electrodes discharged more evenly.

It has been recognized that the discharge following a very slow charge exhibits an ususually short AgO/Ag_2O potential plateau, although the total discharge has a very large capacity. Explanations offered for this short plateau include assuming that the depth of oxidation was greater when charging with a low current due to AgO slowly reacting with base Ag. The resultant charged electrode then would have much Ag_2O in it, and Ag_2O could cover the surface after a relatively short discharge (12). As already mentioned above, however, no Ag_2O was detected after low rate charges. The slower fall in open-circuit potential to the AgO/Ag_2O plateau, following a low rate charge, could be another indication of little or no Ag_2O being present. Under these conditions Ag_2O must form before the AgO/Ag_2O potential was obtained. On the basis of the work reported here it is now believed that the unusually short higher potential plateau during discharge under these conditions resulted from having a coating of large AgO crystals on the electrode. Less Ag_2O needed to be formed to cover the AgO since the large crystals had a smaller surface area. Therefore the potential fell to the Ag_2O/Ag plateau during a discharge after relatively little AgO was reduced to Ag_2O, even though an unusually large amount of AgO was present. Another indication of a small surface area following a very slow charge was that the AgO plateau was entirely lacking during a rapid discharge; potential fell to a minimum at first and then rose to the Ag_2O/Ag plateau. Conditions differed when using a high rate charge, as then small AgO crystals formed having a large area, although a smaller total amount of AgO was present. It took longer to cover this surface with Ag_2O on discharge. The electrode contained considerably less AgO by the time the Ag_2O/Ag potential plateau was reached, and the lower plateau was relatively short.

Summary

The experimental method used permitted successful examination of a working electrode. It was found that reactions took place first on the surface of a silver electrode. Oxidation and reduction products formed as distinct crystals, rather than through expansion or contraction of existing crystal lattices. Surface area and crystal size, which depended on current density, were shown to be important in determining the charge-discharge characteristics of the silver electrode.

Manuscript received Aug. 5, 1964. This paper was prepared for delivery before the Washington Meeting, Oct. 11-15, 1964.

Any discussion of this paper will appear in a Discussion Section to be published in the December 1965 JOURNAL.

REFERENCES

1. C. P. Wales and J. Burbank, *This Journal*, **106**, 885 (1959).
2. P. Jones and H. R. Thirsk, *Trans. Faraday Soc.*, **50**, 732 (1954).
3. V. Scatturin, P. Bellon, and R. Zannetti, *Ric. Sci.*, **27**, 2163 (1957).
4. W. S. Graff and H. H. Stadelmaier, *This Journal*, **105**, 446 (1958).
5. A. S. McKie and D. Clark, "Batteries," (Proc. Third Int. Symp., Bournemouth, England) p. 285, Pergamon Press, New York (1963).
6. Yu. Ts. Vol and N. A. Shishakov, *Izv. Akad. Nauk SSSR, Otdel. Khim. Nauk*, **1962**, 586.
7. S. S. Kabalkina, S. V. Popova, N. R. Serebryanaya, and L. F. Vereshchagin, *Dokl. Akad. Nauk SSSR*, **152**, 853 (1963).
8. T. P. Dirkse, *This Journal*, **107**, 859 (1960).
9. G. W. D. Briggs, I. Dugdale, and W. F. K. Wynne-Jones, *Electrochim. Acta*, **4**, 55 (1961).
10. S. Yoshizawa and Z. Takehara, *J. Electrochem. Soc. Japan*, **31**, 91 (1963).
11. J. Burbank and C. P. Wales, *This Journal*, **111**, 1002 (1964).
12. C. P. Wales, *ibid.*, **109**, 1119 (1962).
13. C. P. Wales, *ibid.*, **108**, 395 (1961).

Catalytic Decomposition of Aqueous Formic Acid on Platinum Electrodes

D. R. Rhodes and E. F. Steigelmann

California Research Corporation, Richmond, California

ABSTRACT

Formic acid in 1*N* H_2SO_4 at 30°C dissociatively adsorbs onto a platinum electrode to form a species that acts electrochemically like adsorbed CO. This species inhibits the oxidation of other compounds and, therefore, can act as a poison on an anode. It can be removed by anodic oxidation at relatively positive potentials. These effects were studied using a potential-sweep technique.

Formic acid is an intermediate in the electrolytic oxidation of aqueous methanol solutions. At platinized porous carbon anodes (1), methanol oxidizes first to formaldehyde, then to formic acid, and finally to CO_2. In acid solution the oxidation of formic acid to CO_2 is relatively rapid and complete, but in base, when formic acid is present as formate ion, the rate of reaction is slow.

Thermodynamic calculations from free energy of formation data show that CO_2, H_2, CO, and H_2O can be formed from the decomposition of formic acid in water. The values are as follows (2)

$$\underset{-85.1}{HCOOH\ (aq)} \rightleftharpoons \underset{-92.3}{CO_2\ (aq)} + H_2\ (g); \quad \Delta F_f = -7.2 \text{ kcal/mole} \quad [1]$$

$$\underset{-85.1}{HCOOH\ (aq)} \rightleftharpoons \underset{-32.8}{CO\ (g)} + \underset{-56.7}{H_2O\ (l)}; \quad \Delta F_f = -4.4 \text{ kcal/mole} \quad [2]$$

Because the values for the free energy of formation of H_2 (aq) and CO (aq) are not available, those for the gaseous state were used. The values of CO_2 (aq) and HCOOH (aq) differ from the gaseous state values by only 2-3 kcal/mole, so those used for H_2 (aq) and

CO (aq) should be close approximations. The data show that the formation of CO_2 and H_2 is thermodynamically favored.

In concentrated sulfuric acid, formic acid decomposes to form carbon monoxide and water (3), but, at concentrations of less than 85% sulfuric acid in water, the rate of this reaction is very slow.

In more dilute acid solutions, formic acid can be photochemically decomposed to carbon monoxide, carbon dioxide, water, and hydrogen (4). The rate of this reaction reaches a maximum at 0.1M formic acid in 0.1N H_2SO_4.

Formic acid in aqueous acid solution is also catalytically decomposed on various metals. The rate of decomposition is greatest on palladium dispersed on $BaSO_4$ and much slower on platinum and rhodium. Other metals which were tested were inactive (5). During the decomposition on metals, the open-circuit potential of the system goes through a maximum, while the rate of hydrogen production on the metal decreases to a small constant value (6). The electrooxidation of aqueous formic acid on a number of different metal surfaces has also been studied (7). Platinum, rhodium, and palladium give the greatest rate of oxidation.

Griffith and Buck (8) studied the electrochemical oxidation of aqueous formic acid on platinized platinum over a large pH range using potential-sweep methods and chronopotentiometry. They found that the rate of oxidation goes through two maxima in going from acidic to basic solution. Also, their chronopotentiograms showed an inhibition toward formic acid oxidation after the electrode had been allowed to stand in solution. They did not study this phenomenon further. Munson (9) also reported chronopotentiometric studies of the oxidation of formic acid and formate ion as a function of pH. He interpreted his results as indicating the presence of a slow preelectrochemical reaction. In the pH range 1.4-6.0, two transition times were obtained, but, above 6.0, only one was obtained. The first transition wave was attributed to direct electrooxidation following a slow homogeneous reaction and the second to oxidation of adsorbed formate species. All his results were with a short wait-time between runs; the effect of wait-time between chronopotentiograms was not studied.

Slott (10) reported work on the oxidation of formic acid using chronopotentiometry. He also measured the double-layer capacitance of a platinum electrode in formic acid solution. He concluded that some reaction takes place which involves the slow adsorption of species from solution onto the electrode surface. Thus, the amount adsorbed seems to be a function of wait-time between chronopotentiograms.

The adsorption of formic acid, oxygen, and hydrogen onto platinum in perchloric acid solutions has been studied by Breiter (11). The effect of the catalytic decomposition reaction on the electrochemistry of formic acid was not observed. However, a detailed study of the reaction of formic acid on platinum during electrooxidation was made.

Gilman (12) studied electrochemical oxidations of CO on a platinum anode and concluded that CO adsorbs at a relatively rapid rate and covers 75% of the platinum surface at equilibrium.

The above articles clearly indicate that formic acid reacts catalytically on the surface of some metal electrodes. During our initial studies with formic acid electrooxidation on platinum, we realized that this catalytic reaction occurs at a fast enough rate to complicate seriously any electrochemical studies. This present investigation is concerned with this catalytic reaction and how it affects the electrochemistry of formic acid.

Experimental

The anodic oxidation of formic acid was studied in a conventional three-compartment-type electrolytic cell. A glass frit was used between the working and counter-electrode compartments to retard mixing of the solutions in the compartments. The reference electrode compartment was in electrolytic contact with the anode compartment by means of a salt bridge which was constructed from glass tubing. A closed stopcock in the salt bridge hindered the electrolyte in the working electrode compartment from mixing with the solution in the reference electrode compartment, but allowed electrolytic contact between the two solutions.

The working electrode was a rotating platinum disk electrode as previously described (13). (Geometric area is 0.15 cm^2.) This electrode was always cleaned in hot acid-dichromate cleaning solution and rinsed with boiling distilled water before being used. The surface roughness of the electrode was determined from the coulombs necessary to reduce a platinum electrode after a voltage sweep up to 1.4v *vs.* SCE (14) (0.5 x 10^{-3} coulombs/cm^2). A simple platinum foil counter-electrode and a Beckman sleeve-type saturated calomel reference electrode were used. All potentials are given with respect to the saturated calomel electrode at room temperature.

The solutions were made in the cell. Formic acid in 1*N* H_2SO_4 solution was prepared by adding 100 ml of 1*N* H_2SO_4 to the cell, deaerating with purified nitrogen, and adding the necessary amount of concentrated formic acid from a microsyringe to make the solution 0.085M in formic acid. (The acidity of the solution essentially does not change because of the low ionization constant of formic acid.)

All formic acid solutions were made with Baker's Analyzed Reagent Grade formic acid. The mixed solution of formic acid and CO was prepared by adding 100 ml of 1*N* H_2SO_4 to the cell, saturating with CO, and adding the formic acid as before. The CO-saturated solutions were prepared by bubbling gas through 1*N* H_2SO_4 in the cell. It was assumed that CO has about the same solubility in either 1*N* H_2SO_4 or 0.085M formic acid plus 1*N* H_2SO_4. However, this point is not important since the results were only qualitative. All experiments were carried out at 30.0° ± 0.01°C.

Potential-sweep voltammetry measurements were used in these studies. A triangular voltage-time wave, from a generator built by our Electronics Development Group, was coupled with a Wenking potentiostat to obtain the potential sweeps. The current-voltage (or time) curves were recorded on a Type 502 Tektronix oscilloscope or a Sargent MR recorder. A Tektronix Polaroid-Land camera back was used to record permanently the current-voltage traces from the oscilloscope.

The electrode was rotated at 600 rpm during all measurements except where noted. In all cases, three continuous potential sweeps of the electrode were made. The wait-time between each set of three continuous potential sweeps was carefully controlled; for the adsorption measurements, it was 5 min. (As shown later the accurate measurement of wait-time is not important so long as it is greater than 20 sec.) During the wait-time the electrode was held at 0.0v *vs.* SCE. The areas under the curves were determined with a planimeter. The cell, equipment, and techniques used to obtain the current-voltage curves for CO were similar to those used for formic acid. Here also the wait-time between sweeps was 5 min under similar conditions. Gilman (12) has shown that adsorption is essentially complete in 1 min.

Results

The oxidation of formic acid was studied by investigating five different aspects of formic acid electrochemistry. These are: (*a*) the general shape of the formic acid current-voltage curve; (*b*) the effect of wait-time between sweeps on the relative heights of the current peaks; (c) the current-voltage curves of a mixed formic acid-CO-1*N* H_2SO_4 solution; (*d*) the peak-current voltage for CO and formic acid oxidation

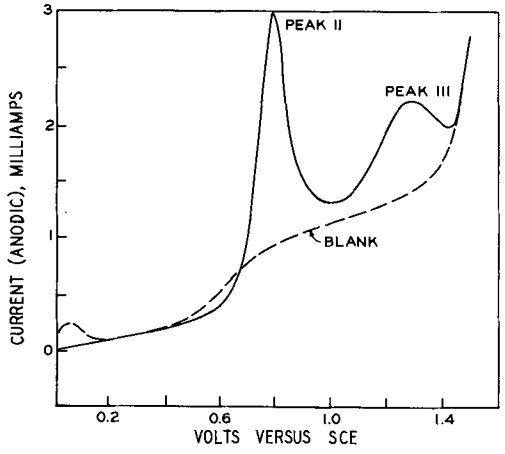

Fig. 1. First sweep of 0.085M HCO_2H in 1*N* H_2SO_4 at 30°C on a platinum disk electrode rotating at 600 rpm; 0.97 cm^2 real surface area; sweep rate of 1.2 v/sec.

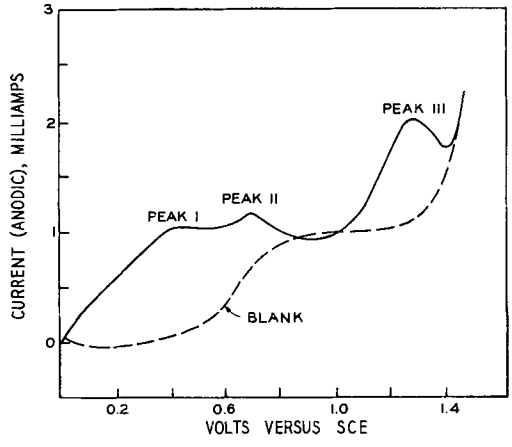

Fig. 2. Third consecutive sweep of 0.085M HCO_2H in 1*N* H_2SO_4 at 30°C on a platinum disk electrode rotating at 600 rpm; 0.97 cm^2 real surface area; sweep rate of 1.2 v/sec.

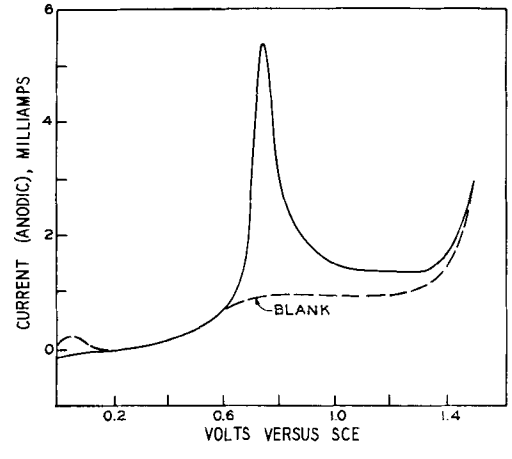

Fig. 3. First sweep of a saturated solution of CO in 1*N* H_2SO_4 at 30°C on a platinum disk electrode rotating at 600 rpm; 1.1 cm^2 real surface area; sweep rate of 1.2 v/sec.

as a function of sweep rate; (*e*) the coulombs necessary to oxidize adsorbed formic acid and CO.

In Fig. 1 to 4 are shown typical current-voltage curves for the oxidation of formic acid and CO in 1*N* H_2SO_4 at 30°C on platinum. The current-voltage curves for the platinum electrode in 1*N* H_2SO_4 (blank) are also shown for comparison. The blank curves for the first consecutive sweep (Fig. 1 and 3) are slightly different than those for the third consecutive sweep (Fig. 2 and 4). The small hydrogen wave at about +0.1v is absent during the sweep because hydrogen has no

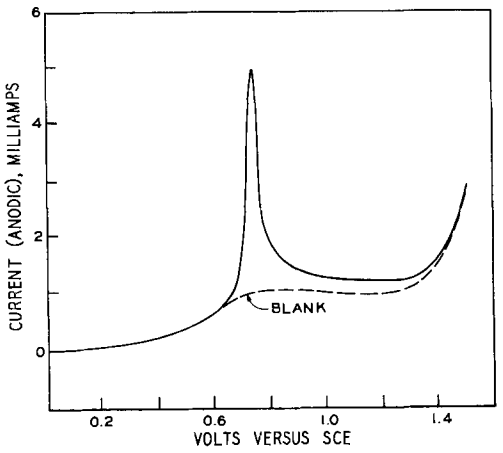

Fig. 4. Third consecutive sweep of a saturated solution of CO in 1*N* H_2SO_4 at 30°C on a platinum disk electrode rotating at 600 rpm; 1.1 cm^2 real surface area; sweep rate of 1.2 v/sec.

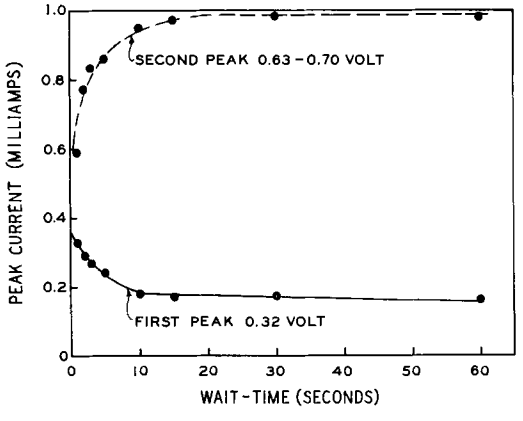

Fig. 5. Effect of wait-time between sets of sweeps on peak heights during first sweep; 0.085M HCO_2H-1*N* H_2SO_4; platinum disk electrode rotating at 600 rpm; 0.97 cm^2 real surface area; sweep rate of 0.26 v/sec.

opportunity to adsorb between sweeps. The blank curves in Fig. 1 and 3 or Fig. 2 and 4 are similar except for the difference in current levels. This was caused by a "real surface area" difference between the electrodes used in the formic acid and CO studies.

As shown in Fig. 2, three current peaks can be obtained for the oxidation of formic acid during the third consecutive sweep; peak I is at about 0.4v, peak II is at about 0.8v, and peak III is at about 1.3v. During the first consecutive sweep (Fig. 1), the peak at 0.4v is essentially gone. This and other effects led us to conclude that the relative heights of the three peaks are very sensitive to the recent history of the system.

Some of the variables which affect the current peak heights of formic acid oxidation on platinum in 1*N* H_2SO_4 at 30°C are:

1. *Sweep number.*—Three continuous sweeps were made. Peak I increased and peak II decreased from the first to the third sweep. Peak III remained relatively constant.

2. *Stirring.*—Peaks I and II decreased slightly when the solution was stirred by rotating the platinum disk electrode at 600 rpm; peak III increased significantly with stirring. Thus, the rate of oxidation of peak III is limited by diffusion. The decrease of current with stirring for peaks I and II might be caused by the forced diffusion of products from the nonelectrochemical adsorption reaction away from the electrode surface, *e.g.*, formic acid adsorbs to form CO and/or H_2 which are thrown away from the electrode surface by stirring before they can react.

3. *Wait-time between sweeps.*—The effect of wait-time between sweeps on the height of peaks I and II during the first sweep is shown in Fig. 5. The height

of peak I decreases, whereas, the height of peak II increases with increasing wait-time between sweeps. Evidently, an adsorbed layer is present which inhibits oxidation of peak I but is itself oxidized at peak II.

From previous literature and from these results we postulate that the following reactions take place. At open circuit or at about 0v (*vs.* SCE), formic acid in acid solution decomposes on a platinum electrode to form hydrogen atoms and/or other adsorbed species (3-10). At open circuit the adsorbed hydrogen atoms combine to form H_2 gas, whereas, when the electrode is held at 0.0v, the hydrogen atoms are ionized. Because hydrogen ionization is a relatively rapid process, the slow step must be the initial dissociative chemisorption of formic acid.

While this reaction is occurring, a competing but slower reaction takes place which results in the formation of a strongly adsorbed layer of material on the electrode surface. The adsorbed layer is oxidized during the second peak (0.8v); therefore, the longer the wait-time the more the material that dissociatively adsorbs and the larger the second peak. In contrast to this, the oxidation process giving the first peak (0.4v) cannot take place when the adsorbed layer is present. The height of the first peak decreases with increasing surface coverage by the adsorbed layer.

In Fig. 6 and 7 are shown potential sweeps of mixtures of formic acid and CO in H_2SO_4 at 30°C with and without stirring. These curves were at a potential sweep rate of 26 mv/sec. The peak at 0.7v for adsorbed formic acid and the peak for CO overlap. However, with stirring, a small postpeak shoulder is obtained on the peak at 0.7v for both sweeps. Gilman (12) indicated that the voltage of the CO peak for the adsorbed species is slightly more negative than the peak produced by CO diffusing to the surface and adsorbing during a peak. Also the decrease in height of peak I with stirring in Fig. 7 indicates that we have increased

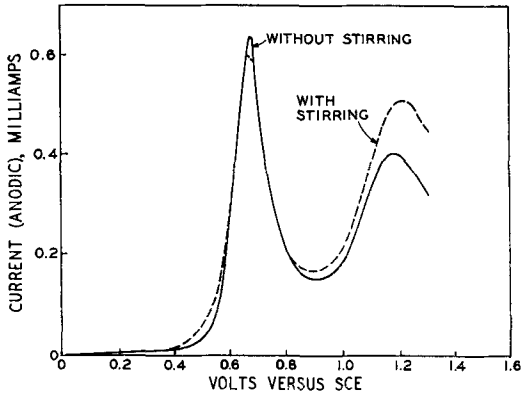

Fig. 6. First sweep of 0.085M HCO_2H in CO saturated 1*N* H_2SO_4 at 30°C on a platinum disk electrode rotating at 600 rpm; 0.97 cm^2 real surface area; sweep rate of 0.26 v/sec.

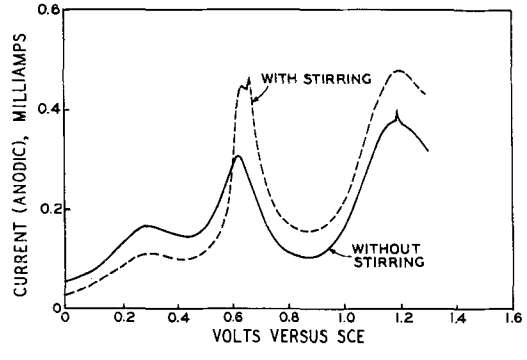

Fig. 7. Second consecutive sweep of 0.085M HCO_2H in CO saturated 1*N* H_2SO_4 at 30°C on a platinum disk electrode rotating at 600 rpm; 0.97 cm^2 real surface area; sweep rate of 0.26 v/sec.

Table I. Peak current voltage of CO and HCO_2H as function of sweep rate

Sweep rate, v/sec	CO, v *vs.* SCE	HCO_2H, v *vs.* SCE
0.13	0.69	0.68
0.26	0.70	0.68
0.64	0.73	0.70
1.2	0.76	0.73
2.4	0.79	0.76
5.8	0.85	0.80

the over-all rate of adsorption of the poisoning material by causing forced convection of the solution.

The peak voltages for the first sweep of CO and for peak II for the first sweep of formic acid are shown in Table I for various sweep rates. These results were obtained with stirring.

The coincidence of the current-voltage curves in Fig. 6 and 7 and the similar dependence on peak voltage as given in Table I suggest the possibility that the two peaks are caused by the oxidation of the same species. In Table I the formic acid peak is slightly more negative because of the influence of peak I and because CO is diffusing to the surface and adsorbing during a sweep. The potential of the current peak due to the oxidation of CO which has diffused to the surface is slightly more positive in potential than the current peak potential from the oxidation of CO already adsorbed on the surface. This was discussed earlier.

The adsorption of formic acid and that of CO were each studied as a function of sweep rate. The coulombs obtained during oxidation were measured by integrating the area under a selected portion of the current-voltage curve. For formic acid the area was determined up to a 0.26v increment beyond the peak at 0.7v. This was necessary to eliminate the third peak which is diffusion controlled and because the current peak shifts with sweep rate for a slow electrochemical process. The number of coulombs for the oxidation of CO was determined by integrating the area of the current-voltage (time) curves to the same ΔE increment beyond the peak.

Because these two peaks are not diffusion controlled, we can assume that

$$Q_{FA} = Q_{(FA+PtO)} - Q_{PtO} = Q_{ads} + Q_{film} \qquad [3]$$

where Q_{ads} is for the material which adsorbs during a sweep, Q_{film} is for the material which is adsorbed before the sweep begins, Q_{PtO} is the number of coulombs obtained during a blank sweep, and Q_{FA+PtO} is the number of coulombs obtained from the oxidation of formic acid and platinum. For this equation to be valid, we must assume that:

1. All the species which can be oxidized through the ΔE potential range are oxidized, regardless of sweep rate.
2. Because of efficient stirring with the rotating disk electrode, diffusion does not limit the reaction during either fast or slow sweeps.
3. The same number of coulombs is necssary to charge the double layer for the blank solution and the formic acid solutions or the blank solution and the CO solution. This is valid since even large double layer capacities gives small amounts compared to those obtained in these studies ($< 5\%$).
4. The formation of adsorbed oxygen on platinum is not hindered or changed in the presence of the compound being oxidized (11).

According to these assumptions, Q_{film} should be a constant for a given electrode and solution and independent of sweep rate. Q_{PtO} is determined for each condition and subtracted from $Q_{(FA+PtO)}$.

If it is assumed that at the bulk concentration of formic acid used in these experiments the adsorption rate is first order with respect to formic acid or CO concentration and free surface area, but independent of electrode potential, then in electrochemical units

$$i_{ads} = nFAk_fC_{FA}\,(1-\theta) \qquad [4]$$

where the electrochemical terms have their usual significance: C_{FA} is the concentration of formic acid at the electrode surface, θ is the fraction of surface covered with adsorbed formic acid, and k_f is a convenient rate constant which includes all effects due to potential, etc. The bulk concentration can be used instead of the surface concentration because they are essentially equal under these conditions of stirring. The reaction in the reverse direction is ignored.

The amount of material adsorbed during a sweep is given by

$$Q_{ads} = \int_{t=0}^{t=\tau} i_{ads}\,dt = \int_{t=0}^{t=\tau} nFAk_fC_{FA}\,(1-\theta)\,dt \qquad [5]$$

where τ is the time interval of a sweep. We assume that during a sweep the surface has constant coverage up to the peak at about 0.7v (11, 12). Beyond this point the coverage drops rapidly to a low value and becomes constant for the rest of the sweep. Because we integrate to a ΔE beyond the peak, we can consider the surface to have minimum coverage during about one fourth of the total sweep. It is reasonable to assume that an average surface coverage independent of sweep rate may be used. Then the amount adsorbed during a sweep may be expressed as follows

$$Q_{ads} = K\tau = K'/v \qquad [6]$$

where K and K' are constants and V is the sweep rate. (The total voltage interval is kept constant.) Equation [6] combined with [3] gives

$$Q_{FA} = Q_{(FA+PtO)} - Q_{PtO} = K'/v + Q_{film} \qquad [7]$$

A plot of Q_{FA} *vs.* $1/v$ should give a straight line with intercept at Q_{film} and with a slope equal to K'.

The same discussion holds for determining Q_{CO}.

In Fig. 8 are shown plots of Q_{FA} and Q_{CO} *vs.* the reciprocal of sweep rate. A straight line was drawn through these data points for each oxidation process. Extrapolation of these lines to infinite sweep rate ($1/v = 0$) gives Q_{film} which is an indication of the amount of adsorbed material on the electrode before the potential sweep was started. These lines intersect the Q axis at about the same point. Therefore, we conclude that the same number of coulombs is required to oxidize both adsorbed CO and the adsorbed intermediate from the catalytic decomposition of formic acid on platinum. Because the curves were not integrated over the entire potential sweep to oxygen evolution, Q_{film} does not give the total amount adsorbed on the surface.

This technique for determining surface coverage can be compared to that used by Breiter for formic acid (11) and Gilman for CO (12). A comparison of the results of the two authors shows that they also obtained about equal surface coverages of carbon monoxide and formic acid. If one assumes that oxygen adsorption on platinum gives 0.5 x 10^{-3} coulombs/cm^2, then Breiter obtains about 0.25 mc/cm^2 of real area for the oxidation of adsorbed formic acid. If a surface roughness of 1.8 is assumed, Gilman obtained about 0.28 x 10^{-3} coulombs/cm^2 of real surface area for the oxidation of adsorbed carbon monoxide. Our results give a value of 0.15-2.0 x 10^{-3} coulombs/cm^2. If one considers that we only integrated to a voltage increment beyond the peak and did not integrate to oxygen evaluation, the results of Breiter, Gilman, and this work compare quite well. The technique used in this study is better suited for comparing the two compounds since it eliminates the effect of the third peak of formic acid oxidation.

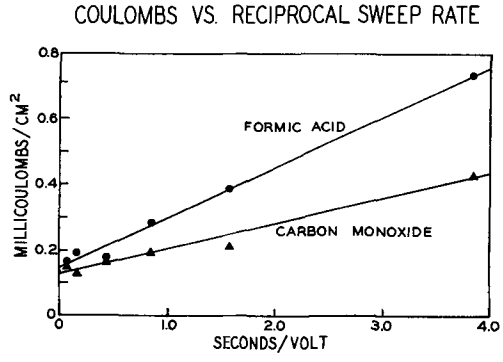

Fig. 8. Coulombs *vs.* reciprocal sweep rate for 0.085M HCO_2H in 1*N* H_2SO_4 or CO saturated solution in 1N H_2SO_4 at 30°C on a platinum disk electrode rotating at 600 rpm.

Conclusions

It is known from prior work that (5-7), on certain metal catalysts in aqueous solutions, formic acid decomposes to adsorbed hydrogen and an adsorbed carboxylate group. Hydrogen gas is given off from the surface until the surface is completely covered with the carboxylate groups. The open-circuit potential of such a metal goes through a maximum when the rate of hydrogen production decreases to a small constant value. Carbon monoxide is known to adsorb on platinum and to be oxidized electrochemically to carbon dioxide.

It is shown in this paper that formic acid reacts with the platinum electrode in aqueous solution to form an adsorbed species which behaves in a way similar to carbon monoxide. This adsorbed species blocks the surface of the electrode and prevents the adsorption of other species. This means that, if formic acid is present at an appreciable concentration, the surface of the electrode will become poisoned while the electrode is under no-load conditions. The electrode can be cleaned by allowing the voltage of the electrode to increase to about that for platinum oxide formation (about 0.7v) where the adsorbed species is oxidized. These conclusions are based on the following observations:

1. Some intermediate from the catalytic decomposition of formic acid adsorbs on the platinum surface and prevents the oxidation of formic acid at 0.4v.
2. Free energy calculations show that formic acid can decompose to H_2O and CO. However, this can happen at appreciable rates only on a catalyst.
3. The adsorbed intermediate can be oxidized at 0.8v. Its current-voltage curve is very similar to the CO curve; the peak voltages of the two curves are about the same over a large sweep-rate range.
4. The oxidation of adsorbed formic acid intermediate and of CO gives the same number of coulombs. During the adsorption of formic acid, adsorbed hydrogen is formed which can be oxidized to hydrogen ions when the electrode is held at 0v *vs.* SCE. The rate of this reaction is relatively slow because either there is a slow rate of adsorption of formic acid or there is a slow rate of dissociation of the adsorbed formic acid into species similar to carbon monoxide.

Acknowledgment

The authors gratefully acknowledge the support of the Army Materiel Command, Harry Diamond Laboratories, Washington, D. C., and the Advanced Research Projects Agency. They are indebted to Mr. Paul M. Abrahamson for a large part of the experimental work and wish to thank Doctors G. H. Denison, R. T. Macdonald, M. J. Schlatter, and L. R. Griffith for helpful discussions of this work.

Manuscript received Dec. 26, 1963; revised manuscript received July 1, 1964. This paper was presented at the Toronto Meeting, May 3-7, 1964.

Any discussion of this paper will appear in a Discussion Section to be published in the December 1965 JOURNAL.

REFERENCES

1. R. P. Buck *et al.*, "Mechanism and Kinetics of Reactive Groups in Organic Fuels," 15th Annual

Proceedings Power Sources Conference, May 9, 1961.
2. F. D. Rossini, "Selected Values of Chemical Thermodynamics Properties," *Natl. Bur. Standards, Circ.* 500, U. S. Dept. of Commerce, February 1952.
3. G. A. Ropp, *J. Am. Chem. Soc.*, **82**, 842 (1960); E. R. Schierz and H. T. Ward, *ibid.*, **50**, 3240 (1928).
4. G. E. Adams and E. J. Hart, *ibid.*, **84**, 3994 (1962).
5. E. Müller and K. Schwabe, *Z. Elektrochem.*, **34**, 170 (1928).
6. K. Schwabe, *ibid.*, **61**, 744 (1957).
7. E. Müller, *ibid.*, **33**, 561 (1927); E. Müller and S. Tanaka, *ibid.*, **34**, 256 (1928).
8. R. P. Buck and L. R. Griffith, *This Journal*, **109**, 1005 (1962).
9. R. A. Munson, Paper presented at the Pittsburgh Meeting of the Society (1963).
10. Robert Slott, Ph.D Thesis, Dept. of Chem. Eng., Mass. Inst. Tech. (1963).
11. M. W. Breiter, *Electrochim. Acta*, **8**, 447 (1963); *ibid.*, 457 (1963).
12. S. Gilman, *J. Phys. Chem.*, **66**, 2657 (1962).
13. L. R. Griffith and D. R. Rhodes, "On the Electrochemical Oxidation of Ethylene in Aqueous Sulfuric Acid," 50th National AIChE Meeting, Buffalo, N. Y., May 1963; *Chem. Eng. Prog.*, **59**, 54 (October 1963)
14. H. A. Laitinen and C. G. Enke, *This Journal*, **107**, 773 (1960).

The Effect of Ultraviolet Light on the Anodic Oxidation of Formic Acid

E. F. Steigelmann[1] and D. R. Rhodes

California Research Corporation, Richmond, California

ABSTRACT

The effect of 2537Å ultraviolet light on the anodic oxidation of formic acid was examined in 1*N* H_2SO_4 electrolyte on a platinum gauze anode. At potentials more negative than 0.5v *vs.* SCE when the uv light is turned on, the current increases for a short time before it decreases to a near-zero value. At potentials more positive than 0.5v, the current increases to a maximum value, the largest increase being at 0.65v *vs.* SCE. Most of the uv effects are due to the reaction of the photolysis products at the anode. At potentials more positive than 1.0v *vs.* SCE, electrode activation by uv light may be a factor.

Both the photolysis and the anodic oxidation of formic acid have been discussed extensively, but the effect of photolysis on the anodic oxidation of formic acid has not been discussed.

Of the many articles on the anodic oxidation of formic acid (1) some have reported that in acid electrolyte, formic acid is oxidized completely to carbon dioxide and water (2, 3). Recently Munson (4) studied the reaction of formic acid on a smooth platinum anode in acid electrolyte and found two different oxidation paths. The first was a direct electrooxidation without prior adsorption; the second was oxidation of an adsorbed formate species. Rhodes and Steigelmann (5) found a slow, preelectrochemical decomposition of formic acid on a platinum anode in acid electrolyte. One of the decomposition products reacts very much like carbon monoxide.

The photolysis of formic acid in aqueous H_2SO_4 electrolyte has also been extensively discussed (6, 7). The photolysis proceeds by radical intermediates which react further to yield carbon dioxide, carbon monoxide, formaldehyde, hydrogen, and water (6).

Dolin *et al.* (8) studied the effect of x-rays and ultraviolet light (wavelengths between 3000 and 4000Å) on the anodic oxidation of formic acid. When formic acid is oxidized anodically, it exhibits three peaks in the potential sweep-current curves; these peaks are centered near 0.4, 0.7, and 1.3v *vs.* SCE (5, 9). Dolin (8) showed that x-rays significantly increase the current at the first and third peaks in the potential sweep-current curves for formic acid. They attributed these effects to two different processes. The first process, which increased both peaks, was shown to be the reaction of the radiolysis products of water; the second (this one increases only the third peak) was shown to be electrode activation. In addition to using x-rays, Dolin also used uv light (wavelengths between 3000 and 4000Å). While light of these wavelengths does not decompose formic acid, Dolin did find a current increase at the third peak; this increase he ascribed to photoexcitation of the platinum oxides on the electrode surface.

While Dolin used two different energy regions to excite formic acid, *i.e.*, the very energetic x-rays and the near uv radiation, he did not use the far uv region (wavelengths between 2000 and 3000Å). This radiation can decompose formic acid and should have marked effects on its anodic oxidation. Therefore, in the experiments described here, the effects of 2537Å light on the anodic oxidation of formic acid were examined.

Experimental

Apparatus and materials.—The cell potential was controlled during the potential-sweep and potentiostatic experiments by a Wenking potentiostat which had a triangular-wave, potential-sweep generator connected to it. All measurements of the current-time curves were recorded on a Sargent MR recorder.

Before each experiment, the cell was thermally equilibrated in a constant temperature water bath (30.00° ± 0.05°C). The cell itself was the typical three-electrode cell of H design with anode and cathode compartments separated by a medium porosity glass frit. The cathode was a 1-cm^2 of platinum foil. The reference electrode was a Beckman sleeve-type, saturated calomel electrode and was connected to the anode compartment through a Luggin capillary. Flow of liquid between the reference and anode compartments was prevented by a Nalfilm-1 (National Aluminate Company) ion exchange membrane.

The essentially monochromatic (2537Å) source was a low-pressure, mercury-arc lamp. Around this was fitted a 52-mesh platinum gauze cylinder, 1 in. in length and ½ in. in diameter. This served as anode. The formic acid was Baker's AR grade, and the electrolyte was 1*N* H_2SO_4.

Experimental design.—Because of the many factors studied in the potential-sweep experiment, the principles of "experimental design" (10) were applied. Five factors were involved: the concentration of formic acid,

[1] Present address: The American Oil Company, Whiting, Indiana.

carbon monoxide, hydrogen, and oxygen, and the intensity of the uv light. The experiments consisted of all possible combinations of the five factors with formic acid being at zero and 6.6 millimolar, the gases at zero and one-fourth saturation at room temperature, and uv light off and on. (One volume of electrolyte saturated at atmospheric pressure with a given gas was mixed with three volumes of helium-saturated electrolyte to produce a one-fourth saturated solution. The saturated solutions were made by bubbling for 20 min the appropriate gas through the electrolyte.) The entire design was duplicated so that the number of trials (experiments) equaled 64.

Since the total number of trials is far greater than can be done on any one day, the daily electrode activity variation becomes important. This varaition is, at times, sufficiently large so as to mask some of the effects being sought. However, by "confounding" the design, this variation was eliminated. In each replicate, one 4-factor and two 3-factor interactions were sacrificed by confounding. More than likely these interactions are very small, if not zero; therefore, little, if any, information is lost by this process. The experiment was divided into eight blocks of eight trials each, and the order of the trials within each block was randomized. All the trials within each block were done on one day. Among the trials of a block, every effort was made to keep the electrode activity constant.

Experimental procedure.—Before any block of potential-sweep experiments was done, the cell and the two platinum electrodes were cleaned thoroughly in chromic acid cleaning solution and rinsed exhaustively with distilled water followed by 1*N* H_2SO_4 electrolyte. In order to minimize variation of the electrode activity between trials of a block, the glassware and electrodes were rinsed only with distilled water and 1*N* H_2SO_4; no cleaning solution was used. Since the order of the trials was random, any "history effect" introduced by not using the chromic acid does not prejudice the results.

Before each trial, the electrode was pretreated in the cell by twice cycling the electrode potential between 0 and 1.25v *vs.* SCE. Ten minutes were then allowed for the cell to come to equilibrium. Four successive potential sweeps between 0.1 and 1.25v were then made and the current-time curve was recorded. The sweep rate was constant at 0.92 v/min. The solution was not stirred.

In the potentiostatic experiments, the same cleaning procedure was used as above. Two electrode potentials were investigated, 0.40 and 0.65v *vs.* SCE; the formic acid concentration was 0.1M, but all other conditions were identical with those in the potential-sweep experiments. In a potentiostatic experiment, the current-time curve was recorded for 20 min before the uv light was turned on. This time interval allowed the cell to approach steady-state conditions. The light was then turned on for 10 min. After the light was turned off, the cell was allowed to run for an additional 20 min to again approach the off-light steady-state conditions.

Analysis of the Potential-Sweep Data

In the potential-sweep experiments, the anodic portion of the current-time curve was characterized by four measured variable quantities: the number of coulombs passed between 0.1 and 1.25v *vs.* SCE and the currents at the three formic acid potential peaks. Since the values for the above variable quantities are different for successive sweeps, the sweep number is an additional factor (at four levels, *i.e.*, the first four sweeps) which brings to 128 the total number of values for each variable (not including replication).

The data were analyzed in the usual manner with the fourth, fifth, and sixth order interactions comprising the variance. The results of these calculations and the 95% confidence limits for each value are given in Tables I through IV. Table I contains values of the variables describing the anodic oxidation of formic acid. Tables II, III, and IV cite the increases in each of these variables above its Table I value caused by hydrogen, carbon monoxide, and uv light, respectively.

Table I. Values for the variables describing the anodic oxidation of formic acid

	Sweep No. 1	2	3	4	95% Confidence limits
Coulombs × 10^3	70	107	98	91	±12
Current at 0.20v, ma	1.1	7.0	6.5	5.9	±1.2
Current at 0.65v, ma	8.0	4.1	3.7	3.1	±2
Current at 1.25v, ma	2.2	5.4	5.0	5.2	±0.6

Table II. Increase caused by hydrogen in the variables describing the anodic oxidation of formic acid

	Sweep No. 1	2	3	4	95% Confidence limits
Coulombs × 10^3	26	27	26	26	±18
Current at 0.20v, ma	0.1	0.1	0.1	0.0	±1.7
Current at 0.65v, ma	2.6	1.4	1.4	1.4	±2.8
Current at 1.25v, ma	0.8	0.8	0.8	0.8	±0.9

Table III. Increase caused by carbon monoxide in the variables describing the anodic oxidation of formic acid

	Sweep No. 1	2	3	4	95% Confidence limits
Coulombs × 10^3	7	8	8	7	±18
Current at 0.20v, ma	−0.4	−0.3	−0.4	−0.4	±1.7
Current at 0.65v, ma	4.6	2.1	1.3	1.7	±2.8
Current at 1.25v, ma	2.5	2.1	1.7	1.3	±0.9

Table IV. Increase caused by the ultraviolet light in the variables describing the anodic oxidation of formic acid

	Sweep No. 1	2	3	4	95% Confidence limits
Coulombs × 10^3	45	50	57	62	±18
Current at 0.20v, ma	0.5	1.3	2.1	2.9	±1.7
Current at 0.65v, ma	4.9	4.9	4.9	4.9	±2.8
Current at 1.25v, ma	2.0	1.9	1.9	1.8	±0.9

Discussion

The four following possible mechanisms for the current changes caused by uv light are considered in detail: (i) a thermal effect, if the lamp heats the electrode; (ii) oxidation of the radical intermediates from the photolysis of formic acid; (iii) uv activation of the electrode surface similar to that discussed by Dolin (8); and (iv) oxidation of some of the stable products of the formic acid photolysis, *i.e.*, carbon monoxide, hydrogen, and formaldehyde.

It will be shown that, at potentials less positive than 1.0v *vs.* SCE, the oxidation of the stable decomposition products (mechanism iv) accounts for all observed uv effects. At potentials more positive than 1.0v, both the oxidation of the photolysis products and electrode activation (mechanism iii and iv) contribute to the uv effect. But we have no way of separating these two mechanisms to assess their relative importances. Later we will show that mechanisms i and ii do not explain the observed current changes.

The oxidation of the stable photolysis products could cause the current changes in one of two ways: (*a*) diffusion gradients are set up next to the anode such that the total fuel concentration at the anode increases when the light is turned on, and (*b*) the photolysis products are more reactive than formic acid. It can be shown that when the lamp is turned on, the total con-

centration of reactants at the anode decreases. Therefore, only path (*b*) can account for the uv effect.

Of all the formic acid photolysis products, only hydrogen, formaldehyde, and carbon monoxide are oxidized anodically. Hydrogen is more reactive anodically than is formic acid. Buck and Griffith (3) have shown that formaldehyde is more reactive than formic acid in acid electrolyte. It can be shown that the carbon monoxide also is more reactive than formic acid at potentials greater than 0.6v *vs.* SCE (5, 9, 11). Thus, the uv effect can be explained simply on the basis that the reactivity of the anode fuel has been increased.

If the above mechanism is correct, results of experiments where the photolysis products were added one at a time should predict the effect of uv light. Conclusions drawn from the additive experiments are only qualitative since they do not duplicate the photolysis product concentration. In the additive experiments, the molar concentrations of CO and H_2 are calculated from their solubilities in water to be about 2.1×10^{-4} and 1.9×10^{-4}, respectively (12). It can be shown that the photochemical rates of production of CO and H_2 at the electrode are 2.1×10^{-4} and 1.5×10^{-4} moles liter^{-1} min^{-1}, respectively. [These values were calculated using the following information: (i) the lamp intensity is 4 μw cm^{-2} at 1 meter, (ii) the formic acid extinction coefficient assumed to equal its vapor phase extinction coefficient is 40 (13), and (iii) ϕ (H_2) and ϕ (CO) are 0.110 and 0.142, respectively (7).] In the photochemical experiment, the complex diffusion patterns of the different molecular species at the electrode do not lend to accurate calculation of H_2 and CO concentrations at the electrode. However, the photochemical rates for H_2 and CO are sufficient to make the concentrations of these species at the electrode as large as they are in the additive experiments.

In the experiment where hydrogen is added to the electrolyte (Table II), no significant increase in any of the formic acid peaks is evident, while an increase in the total number of coulombs is seen. In the carbon monoxide additive experiment (Table III), the only significant increases were seen at the 0.65 and 1.25v peaks, the largest one being at 0.65v, sweep No. 1. We did not perform an additive experiment for formaldehyde; but, from the work of Buck and Griffith (3), it appears that formaldehyde should be similar to carbon monoxide in its affect on the formic acid oxidation.

The results from the above additive experiments indicate that the uv light should cause the following changes in the anodic oxidation of formic acid:

1. The number of coulombs as evidenced by the area under the anodic portion of the potential-sweep curve should increase. Probably, this would be caused primarily by hydrogen oxidation.
2. Carbon monoxide and formaldehyde should affect the peak currents. The current at 0.65v should show the largest increase.

The results for the uv effect follow the trends predicted by the additive experiments, and the effect uv light has on the formic acid oxidation may be summarized from Table IV as follows:

1. The number of coulombs is increased by about 60%.
2. The current at 0.25v is increased but only during the third and fourth consecutive sweeps.
3. The current at 0.65v is increased greatly (greater than 100% during the second, third, and fourth sweeps).
4. The current at 1.20v is increased slightly.

Therefore, the predictions of the mechanism and the effect of uv light are consistent in the potential-sweep experiments.

Potentiostatic Experiments

In the potentiostatic experiments, the effect of uv light is different at 0.40v than at 0.65v. At 0.40v (Fig. 1) a transitory current surge is seen immediately after the light is turned on (point A). The current goes

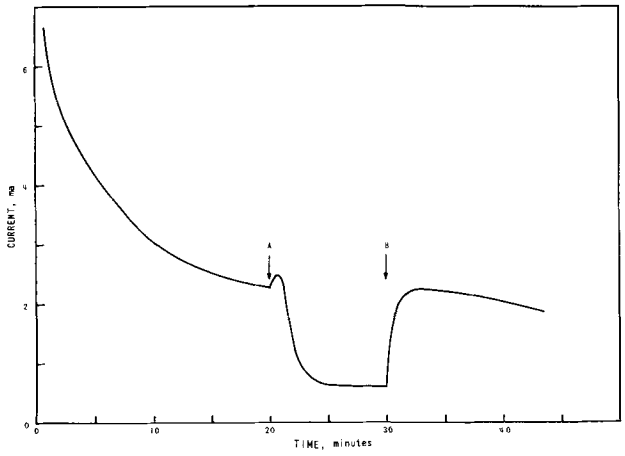

Fig. 1. Effect of uv light on the current during the oxidation of formic acid at 0.40v *vs.* SCE. A, Light on; B, light off.

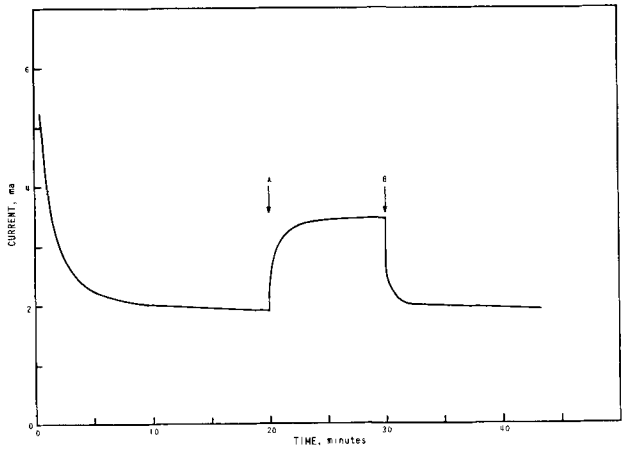

Fig. 2. Effect of uv light on current during the oxidation of formic acid at 0.65v *vs.* SCE. A, Light on; B, light off.

through a maximum and decays to 25% of the "off-light" value. At 0.65v (Fig. 2) after the light is turned on, the current increases to a steady-state value 80% greater than the "off-light" steady-state current. In both cases when the light is turned off, the current resumes its "off-light" value within a few minutes.

The mechanism at 0.40v would appear to be as follows. After the light is turned on, hydrogen, carbon monoxide, and formaldehyde are formed near the electrode. Of these, only hydrogen is oxidized appreciably, and its oxidation probably accounts for the current surge at this potential. Carbon monoxide, on the other hand, does not oxidize at any appreciable rate at 0.40v but does adsorb on the anode to block formic acid oxidation (5, 11). Probably, it is this adsorption and blocking (of the formic acid oxidation) which cause the current to decay.

At 0.65v (Fig. 2), the current increase caused by uv light may be explained in the following manner. All three photolysis products (including carbon monoxide) are oxidized at this potential, and the reactivity of the fuel mixture offsets not only any possible current decrease due to a decrease in the anode fuel concentration but causes the observed current increase. Thus, our mechanism for the uv effect can explain the potentiostatic results at 0.40v and 0.65v *vs.* SCE.

Other Mechanisms

The following mechanisms also were considered to explain the effect of uv radiation of the anodic oxidation of formic acid: (i) a thermal effect, if the lamp heats the electrode; (ii) uv activation of the electrode surface at potentials less than 1.0v; (iii) oxidation of

radical intermediates from the photolysis of formic acid.

None of these were able to account for the uv effect for the following reasons.

After the uv lamp was turned on, a 3.0°C temperature rise was measured at the electrode by a chromel-alumel thermocouple. The electrode will not experience greater localized heating than the thermocouple probe because of their relative sizes. Therefore, the lamp causes, at the most, a 3.0°C increase in electrode temperature. A 10°-20°C increase in electrode temperature would be required if electrode heating by the uv lamp caused the observed current increases.

Dolin *et al.* (9) suggested that both x-rays and uv light (between 3000 and 4000Å) activate a platinum electrode only at potentials greater than 1.0v. We used ethylene to check for electrode activation by 2537Å light at potentials more negative than 1.0v. No activation was found. From this, it seems likely that in the anodic oxidation of formic acid, electrode activation by 2537Å light is unimportant at potentials less positive than 1.0v *vs.* SCE.

The oxidation of the radical intermediates of formic acid photolysis could not account for the ultraviolet effect. In the potentiostatic experiments (Fig. 1 and 2), the current takes several minutes to regain the "off-light" value after the lamp is turned off. This slow recovery time does not suggest radical decay but, rather, diffusion of stable products away from the electrode.

Conclusion

We have seen that the anodic oxidation of formic acid is greatly altered by uv light. At potentials less than 1.0v, the effects of uv light are most likely caused by the anodic reaction of some of the formic acid photolysis products; these are carbon monoxide, formaldehyde, and hydrogen.

Acknowledgment

The authors gratefully acknowledge the support by the Harry Diamond Laboratories of the Army Materiel Command and by the Advanced Research Projects Agency. They are indebted to Professor Peter W. M. John, of the University of California at Davis, California, for designing the statistical experiment and to Mr. Louis J. Painter for the use of his computer program to do the statistical calculations. They also would like to thank Doctors G. H. Denison, R. T. Macdonald, and M. J. Schlatter for their many suggestions.

Manuscript received Feb. 11, 1964.

Any discussion of this paper will appear in a Discussion Section to be published in the December 1965 JOURNAL.

REFERENCES

1. E. Mueller, *Z. Elektrochem.*, **29**, 264 (1923); E. Mueller and S. Tanaka, *ibid.*, **34**, 256 (1928); K. Schwabe, *ibid.*, **61**, 744 (1957); H. Gerischer and J. Held, *ibid.*, **64**, 1111 (1960); U. B. Vasiliev and V. S. Bagotskii, *Dokl. Akad. Nauk. S.S.S.R.*, **148**, 132 (1963).
2. E. Mueller and G. Hindemith, *Z. Elektrochem.*, **33**, 562 (1927); C. E. Heath, B. L. Tarmy, E. L. Holt, D. G. Levine, A. W. Moerikofer, J. A. Shropshire, and C. H. Worsham (Esso Research and Engineering Co.), Contract DA-36-039-SC-89156, Report No. 1 (June 1962).
3. R. P. Buck and L. R. Griffith, *This Journal*, **109**, 1005 (1962).
4. R. A. Munson, *J. Electroanal. Chem.*, **5**, 292 (1963).
5. D. R. Rhodes and E. F. Steigelmann, To be published.
6. D. Smithies and E. J. Hart, *J. Am. Chem. Soc.*, **82**, 4775 (1960).
7. D. Berthelot and H. Gaudechon, *Compt. rend.*, **151**, 478 (1910); W. N. Herr and W. A. Noyes, Jr., *J. Am. Chem. Soc.*, **50**, 2345 (1928); G. E. Adams and E. J. Hart, *ibid.*, **84**, 3994 (1962).
8. P. I. Dolin, D. V. Kokoulina, S. A. Brusentseva, and S. A. Kabakchi, *Dokl. Akad. Nauk. S.S.S.R.*, **144**, 1081 (1962).
9. M. W. Breiter, *Electrochim. Acta*, **8**, 447, 457 (1963).
10. O. L. Davies, "The Design and Analysis of Industrial Experiments," Oliver and Boyd, London and Edinburgh, and Hafner Publishing Co., New York (1960).
11. S. Gilman, *J. Phys. Chem.*, 66, 2657 (1962).
12. "International Critical Table," Vol. 3, pp. 256 and 257.
13. E. E. Barnes, Thesis, 1961 (University of Washington).

The Specific Effects of Chloride and Sulfate Ions on Oxide Covered Aluminum

M. A. Heine, D. S. Keir, and M. J. Pryor

Metals Research Laboratories, Olin Mathieson Chemical Corporation, New Haven, Connecticut

ABSTRACT

The distribution of a-c resistance throughout the thickness of oxide film on aluminum specimens, conditioned by pre-exposure to 1.0*N* solutions of sodium chloride and sulfate, has been determined by an electrical method. This method involves measurement of series capacitance and dielectric loss of the oxide covered aluminum as the surface films thin slowly in a slightly alkaline, passivating, sodium chromate solution. Results show that chloride ions become included at certain selected locations in the oxide film, create additional current carriers, and lower the ionic resistance of the film. Sulfate ions do not appear to become included in aluminum oxide films under these conditions and do not lower the film resistance. Aluminum oxide films containing chloride ions dissolve more rapidly in the chromate solution than similar untreated films or films that have been treated in sodium sulfate solution. These observations are held to throw new light on the well defined tendency of oxide covered aluminum to pit severely in nearly neutral sodium chloride solutions.

One of the more widely investigated subjects in aqueous corrosion has been the specific effects exercised by various anions on the rate and form of metallic corrosion. Underlying many of these investigations is the desire to clarify the mechanism by which chloride ions, in particular, exercise such harmful specific effects on metals such as iron and aluminum.

In one of the earliest studies of specific anion effects on aluminum, Britton and Evans (1) measured the increase in current produced at an aluminum anode

maintained in an otherwise passivating chromate solution by the addition of standard amounts of normally corrosive salts. They were thus able to estimate from these experiments a "film penetrating power" of various added anions. In decreasing order, this was found to be Cl', Br', I', F', SO_4'', NO_3', and HPO_4''. Later one of the authors of this paper (2) determined the corrosion rate of super-purity aluminum after 2 and 4 weeks immersion in molar solutions of the sodium halides in the absence of chromate additions. Here it was found that the corrosion rate decreased in order of severity with the series F', Cl', Br', I' with the exception of the longer immersion time in sodium iodide where an enhanced rate of corrosion accompanied the formation of some elemental iodine in solution. The most heavily corroded specimens in the sodium fluoride solution also showed the deepest pitting which was even more severe than that in sodium chloride solution.

Probably the most definitive past study of the specific effect of chloride ions in pitting aluminum was that carried out by Edeleanu and Evans (3). This work confirmed a substantial *p*H drop at aluminum anodes during anodic polarization in potassium chloride solution. By calibration with an inert platinum anode, in similar solutions, it was found that a substantial proportion of soluble reaction product was formed at an aluminum anode in potassium chloride solution and that a much lesser quantity of the soluble product was formed under similar conditions in the less aggressive sodium sulfate solution. This work led to the formation of the "autocatalytic" mechanism for the pitting of aluminum in chloride solutions.

Despite the similarity in terms of acid strength of sulfuric and hydrochloric acids and despite the similarity in electrolytic conductivity of sodium sulfate and sodium chloride solutions of similar concentration, the former solution is substantially less corrosive to aluminum (4, 5) and has lesser tendency to promote aggressive pitting. This is consistent with the well-known ability to anodize aluminum in sulfate solutions, and with the observations of Petrocelli (6) on the stability of thin oxide films on aluminum immersed in sulfuric acid at potentials between −1.0 and +3.0v SCE scale.

The present work is primarily an investigation of the change in a-c resistance of oxide films on aluminum during immersion in sodium chloride and sodium sulfate solutions. Previously a-c capacitance bridge techniques over a wide range of frequency were applied to a study of the effect of immersing super-purity aluminum covered with various thicknesses of γ-Al_2O_3 film in sodium chloride solution at *p*H 6 (7, 8). The results showed that the a-c resistance of a γ-Al_2O_3 film on aluminum, measured at a frequency of 1000 cps, decreased with time to a constant value during contact with the sodium chloride solution; this resistance drop was obtained under conditions where gross corrosion did not occur and where the film thickness, crystal structure, and topography were not detectably changed. At the same time, similar immersion in chloride solution was without effect on the a-c film resistance measured at high frequency (100,000 cps and above). These results were interpreted as meaning that chloride ions entered the anion lattice of γ-Al_2O_3, thereby creating additional current carriers which appeared to lower the ionic resistance of the oxide film without changing the electronic resistance.

A further technique developed by two of the authors (9) has permitted determination of the distribution of a-c resistance throughout the thickness of γ-Al_2O_3 films on aluminum. This method involved measurement of capacitance and loss during the slow and reproducible thinning of γ-Al_2O_3 films by slightly alkaline, passivating, chromate solutions. It was established that contact with this solution did not introduce defects into the film that modified its resistance. The ultimate film thickness that can be achieved is the passive film thickness (around 25Å) which makes the method mainly applicable to the study of thicker compact alumina films. Accordingly, this technique has been employed in the present investigation to determine the magnitude and location of resistance changes in 240Å thick γ-Al_2O_3 films on super-purity aluminum following immersion in 1.0*N* solutions of sodium chloride and sulfate at *p*H 6 for times insufficient to cause detectable corrosion. Because of the earlier establishment of full frequency dispersion curves from 100-1,000,000 cps for these films the present work was confined to the two frequencies of 1000 and 100,000 cps which are particularly pertinent in the chloride substituted alumina system. Results are considered to throw new light on the specific effects of these anions on the corrosion rate of aluminum and serve to provide additional clarification of the cause of the strong tendency of chloride ions to promote pitting attack.

Experimental and Results

Materials.—The aluminum used in this investigation was 99.997% pure and contained 0.001% iron, 0.001% silicon, and 0.001% copper. Specimens used in electrical experiments conducted at a frequency of 1000 cps were in the form of annealed wire having a diameter of 2.5 mm. Specimens used in electrical experiments conducted at frequency of 100,000 cps were in the form of annealed sheet having a thickness of 0.37 mm. The 1.0*N* sodium chloride and sodium sulfate solutions were made up from CP chemicals and demineralized, distilled water and had their *p*H adjusted to 6.0 by the addition of the appropriate acid. The sodium chromate solution was made up from CP sodium chromate and demineralized, distilled water and had its *p*H adjusted to a value of 7.1 by the addition of sodium dichromate.

Sample preparation.—The wire specimens for the low-frequency capacitance and dielectric loss determination were degreased with benzene and etched with 1.0*N* sodium hydroxide for 10 min. They were then rinsed in demineralized distilled water, then in methanol, and finally masked with Tygon paint in order to leave a cylindrical surface area of 0.2 cm^2 exposed. The masked specimens were then stored for 24 hr over calcium sulfate before further treatment. Sheet specimens for electrical experiments at 100,000 cps were similarly etched and then anodized before being masked with the Minnesota Mining and Manufacturing Company's pressure sensitive Electroplaters Tape No. 470 from which a small hole of 0.02 cm^2 area had been punched.

The oxide films investigated in this study were composed of γ-Al_2O_3 and were formed anodically in an electrolyte consisting of 3% by weight of ammonium tartrate dissolved in demineralized distilled water. The *p*H of the solution was adjusted to 7.0 by the addition of a few drops of dilute ammonium hydroxide, so that anodizing conditions favored the formation of compact, uniform, anodic films. The anodizing method was identical to that used in previous studies (7-9). All films were formed at 20v and at 25° ± 0.05°C giving a thickness of approximately 240Å. The forming voltage was raised incrementally and at a fixed rate to the maximum value. The maximum permitted current surge and leakage current values were identical to those previously described (8, 9).

Experimental method.—Masked and anodized wire and sheet samples were first conditioned by immersion in either 1.0N sodium chloride or sodium sulfate solution, at *p*H 6, and at 25° ± 0.05°C for a period of 960 min; the *p*H values of these solutions remained at their original value to within an accuracy of ±0.5 *p*H units. During immersion, no detectable corrosion of the film covered aluminum occurred. Neither could any change in thickness, topography, or crystal structure of the outer surfaces of the 240Å thick films be detected by a combination of electron microscopy and reflection electron diffraction.

Following the above conditioning in either sodium chloride or sulfate solution the oxide covered speci-

mens were washed thoroughly and then immersed in 1.0M sodium chromate solution at pH 7.1 and at 25° ± 0.05°C together with unconditioned but otherwise similar control specimens. Measurement of the initial series capacitances and dielectric losses at different frequencies permitted determination of the total a-c resistance of the oxide films at the appropriate frequency. However, in this solution the films thinned uniformly and slowly, as described previously (9), to an ultimate film thickness of around 25Å, usually within a period of around 3000 min. Successive similar measurement of capacitance and dielectric loss at determined intervals of time during the slow film thinning permitted calculation of the resistance distribution throughout the various aluminum oxide films. The electrical properties of the various oxide films on aluminum were measured during thinning in separate, fresh, chromate solutions at the same pH and temperature (25° ± 0.05°C) in order to eliminate any possibility of interference from the small amounts of dissolved aluminum oxide (10).

A General Radio 716-C capacitance bridge assembly was used for the electrical determinations described in this paper. A constant, 50 mv p-p signal was applied to the oxide covered aluminum specimens in all measurements. A 3.2 cm diameter platinum gauze cylinder was used as a second conducting electrode, with the chromate solution acting as a solution electrode for the centrally located aluminum specimen. Electrical shielding of the measuring assembly was achieved by surrounding it with aluminum foil.[1] When experiments were conducted at a frequency of 1000 cps, the multiplying range of the 716-C bridge was used in order to obtain a suitably large capacitance range for specimens with an area of 0.2 cm². When experiments were conducted at 100,000 cps, where the multiplying range is not operative, a smaller specimen area of 0.02 cm² was employed together with a low loss external series capacitor (0.001 μF) to bring the capacitance of the series combination within the bridge range. In this case a 716-P4 guard circuit, which eliminated lead and other stray capacitances, was employed to develop maximum sensitivity. The current flow in the films due to the application of the AC signal was much less than 1% of the d-c anodic leakage current.

The low-frequency measurements at 1000 cps (50 mv p-p signal) provided direct values of the series capacitance (C_s) and the dielectric loss (D) of the cell containing the slowly thinning, oxide covered aluminum specimen. Previous work (9) showed that series resistance effects from the chromate solution and platinum electrode could be safely ignored at 1000 cps since they were less than 1% of the minimum resistance of the fully thinned oxide films. Accordingly, the average resistivity (ohm-cm) of the oxide film (ρ) could be calculated at any given thickness level from the relationship

$$\rho = \frac{4\pi}{K\omega D} \qquad [1]$$

where K is the dielectric constant of the oxide film,[2] D its dielectric loss at that thickness, and ω the angular frequency of the a-c signal. Using the analog of a capacitor with a parallel reistance, the average oxide film thickness at any given time, could be calculated from the parallel capacitance (C_p). C_p is related to the measured series capacitance (C_s) by

$$C_p = \frac{C_s}{1 + D^2} \qquad [2]$$

Since D never exceeded a value of 0.07 at 1000 cps (see for instance Fig. 1) the average film thickness at 1000 cps could be calculated directly from uncorrected values of C_s without incurring errors greater than 0.5%.

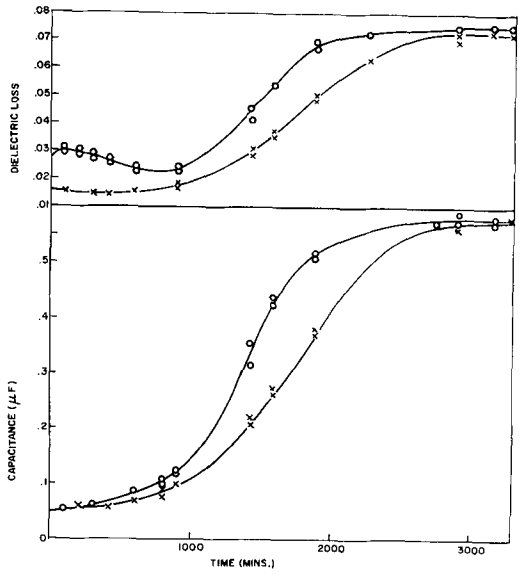

Fig. 1. Variation with time of the series capacitance and dielectric loss of chloride treated and untreated γ-Al_2O_3 films during their thinning in 1.0M sodium chromate solution at pH 7.1 at 25°C: X—X, original film; O—O, chloride treated film.

The foregoing method of calculating the average resistivity of a slowly thinning aluminum oxide film is not sufficiently accurate at higher frequencies of 100,000 cps (50 mv p-p signal). Here the measured C_s and D values include significant contributions not only from the oxide film itself, but also from the adsorbed double layers and chromate solution, together with the external low loss series capacitor. The effect of the external series capacitor can be measured and eliminated as described in a previous publication (9). The resulting corrected values of C_s and D for the oxide film plus chromate solution and associated double layers permit calculation of the parallel a-c resistance R_p ohms cm² of this combination from

$$R_p = \frac{1 + D^2}{D\omega C_s} \qquad [3]$$

The previous work (9) also developed values for the parallel a-c resistance of the chromate solution and associated double layers in the identical measuring cell and over a wide range of frequencies. This was achieved by substituting a smooth platinum specimen of the same area (0.02 cm²) in the same measuring cell for the oxide covered aluminum specimen. The parallel resistance of the solution component of R_p may be subtracted from the combination value in Eq. [3] thereby permitting calculation of the a-c resistance (ohm-cm²) of the oxide film alone at various thickness levels. Resistivity (ohm-cm) and parallel resistance (ohm-cm²) at any given thickness are, of course, directly related by the appropriate value of film thickness in centimeters.

Results.—The resistivity[3] of duplicate specimens of the original 20v γ-Al_2O_3 films was found to be around 1.5 x 10^{10} ohm-cm at 1000 cps and 1.5 x 10^7 ohm-cm at 100,000 cps. These values are quite similar to those determined at the same frequencies in earlier work (8). After immersion for 960 min in 1.0*N* NaCl solution at pH 6.0 and at 25° ± 0.05°C (during which no detectable corrosion or film thickening occurred) the average resistivity of duplicate specimens at 1000 cps decreased to a value of 7.7 x 10^9 ohm-cm whereas the average resistivity at 100,000 cps was unchanged. Simi-

[1] See Fig. 1 of ref. (8) for details.

[2] It has been shown previously (7, 8) that Cl' substitution in compact anodic films on aluminum does not significantly change the value of K.

[3] All resistance values are expressed as parallel resistances.

lar immersion of duplicate specimens in 1.0*N* sodium sulfate solution at the same *p*H and temperature and for the same time resulted in no significant decrease in resistivity either at 1000 or 100,000 cps.

Duplicate aluminum specimens carrying the original 20v films and similar specimens carrying originally similar films which had been immersed in sodium chloride and sulfate solutions as described above, were then immersed in 1.0M Na_2CrO_4 solution at *p*H 7.1 and at 25° ± 0.05°C in order to thin the films and thereby permit calculation of the resistance *vs.* thickness curves. Figure 1 shows the measured changes with time of the series capacitance and dielectric loss at 1000 cps of specimens carrying the original γ-Al_2O_3 films and of those specimens carrying similar films which had then been immersed in the sodium chloride solution. These experiments were conducted on masked wire specimens with an area of 0.2 cm^2 exposed to the various electrolytes. The curves for duplicate specimens carrying 20v films that had been immersed in sodium sulfate solution are not contained in Fig. 1 because the capacitance and dielectric loss *vs.* time curves are almost indistinguishable from those of the specimens carrying the original "as-formed" γ-Al_2O_3 films.

The results in Fig. 1 are depicted in Fig. 2 as curves relating film thickness to the average or cumulative resistivity (ohm-cm) of the three oxide films (calculated directly from Eq. [1]) at 1000 cps. Figure 3 depicts the relationship between film thickness and a-c resistance (ohm-cm^2) at 1000 cps; this curve is calculated from the "best fit" curves for the three conditions in Fig. 2 by multiplying the cumulative resistivity by the film thickness.

It may be immediately seen from Fig. 2 and 3 that immersion of the oxide covered aluminum specimens in sodium chloride solution, following film formation and prior to film thinning, results in a significant decrease in the a-c resistance of the oxide films at 1000 cps and that this resistance drop is confined to the outer 170Å of the 240Å thick film. However, similar immersion in sodium sulfate solution is without major effect on the resistance of the film, with the small changes in the outer 30Å of the film adjacent to the original oxide-solution interface being of doubtful experimental significance.

Immersion in either sodium chloride or sodium sulfate after film formation failed to reduce the a-c resistance at 100,000 cps of the original 20v oxide film. Accordingly, thinning experiments in 1.0M sodium chromate solution at *p*H 7.1 were performed only on duplicate specimens of the original 20v film and similar specimens that had been subsequently immersed in 1.0*N* NaCl solution at *p*H 6 for 960 min. Figure 4 shows the relationship between thickness and a-c resistance (ohm-cm^2) at 100,000 cps for both sets of films. The results were obtained using the smaller (0.02 cm^2) masked sheet specimens in combination with the low loss external capacitor. The results in Fig. 4 have been corrected for the external capacitor and for solution and double layer resistance as described earlier (9). As would be anticipated from the measurements on the initial unthinned films, immersion in sodium chloride (or sodium sulfate) solution has no effect on the dis-

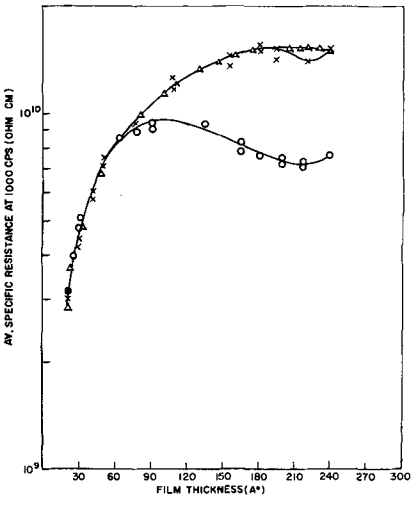

Fig. 2. Relationship between average specific resistance at 1000 cps and thickness of untreated γ-Al_2O_3 films 240Å thick and similar films which have been treated by 16 hr immersion in either 1.0*N* sodium chloride or sulfate solution at *p*H 6 and at 25°C: X—X, original film; O—O, chloride treated film; △—△, sulfate treated film.

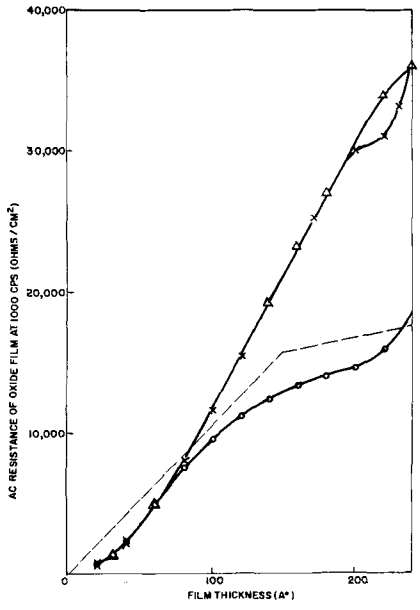

Fig. 3. Relationship between a-c resistance at 1000 cps and thickness of untreated γ-Al_2O_3 films 240Å thick and similar films which have been treated by 16 hr immersion in either 1.0*N* or sodium chloride or sulfate solution at *p*H 6 and at 25°C: X—X, original film; O—O, chloride treated film; △—△, sulfate treated film; — — —, from MacMullen and Pryor.

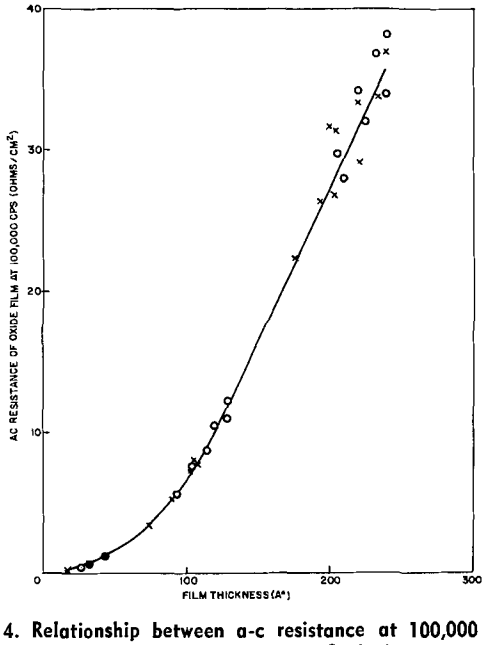

Fig. 4. Relationship between a-c resistance at 100,000 cps and thickness of untreated γ-Al_2O_3 films 240Å thick and similar films which have been treated by 16 hr immersion in 1.0*N* sodium chloride at *p*H 6 and at 25°C: X—X, original film; O—O, chloride treated film.

tribution of a-c resistance at 100,000 cps throughout the thickness of the film. Figure 5 shows the common relationship between average or cumulative resistivity (ohm-cm) at 100,000 cps and thickness for both the original and substituted aluminum oxide films. Figure 5 is calculated from the smoothed common curve in Fig. 4 and can be compared directly with the similar results at lower frequency in Fig. 2.

The results in Fig. 1-5 confirm earlier observations that immersion of oxide covered aluminum specimens in sodium chloride solution results in a decrease in a-c resistance of the oxide film only at bridge frequencies below 100,000 cps. This decrease in resistance occurs under the experimental conditions described (8) above without film thinning, contamination, and structural or topographical changes. However, Fig. 2 and 3 show that similar immersion in sodium sulfate solution produces no significant change in the distribution of a-c resistance at 1000 cps throughout the thickness of the film. Neither solution produces a significant change in the high (100,000 cps) frequency resistance distribution through the film thickness.

Figures 2 and 3 throw new light on the primary location of the low-frequency resistance change in oxide films exposed to sodium chloride. From these figures the resistance drop is clearly confined to the outer 170Å of the film adjacent to the original oxide-solution interface. The resistance decrease is considered to be due to the additional current carriers introduced by chloride ion substitution in the outer portion of the oxide film. Since the reciprocal resistivity, *i.e.*, conductivity, of a semiconductor is directly proportional to the number of current carriers, information on the distribution of additional current carriers introduced by Cl' substitution can be obtained by plotting the conductivity (cotangent to Fig. 3) of the original and chloride treated films as a function of film thickness. This plot is contained in Fig. 6 for the two oxide films. The difference in conductivity, *i.e.*, the dotted curve, represents the distribution of current carrier introduced by chloride ion substitution and therefore is directly proportional to the retained chloride ion concentration in the film.

It is also evident from Fig. 1 and also from similar results obtained at 100,000 cps, that the series capacitance of the chloride treated film increases more rapidly with time than that of the original film or the sulfate treated film. Since immersion in the sodium chloride does not significantly change the dielectric constant of the oxide film (8), the results in Fig. 1 indicate that the chloride treated films dissolve more rapidly in the chromate solution than either the untreated or the sulfate treated films. Figure 7 shows the relationship between the thickness of the two treated and the untreated aluminum oxide films and time of immersion in 1.0M Na_2CrO_4 solution at *p*H 7.1.

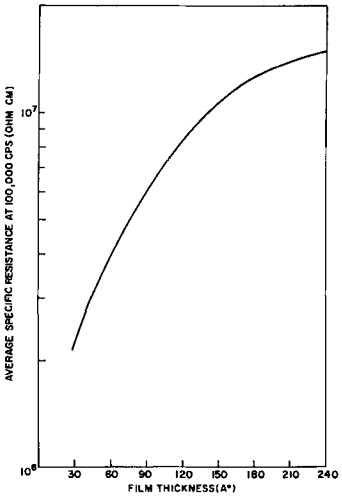

Fig. 5. Common curve relating average specific resistance at 100,000 cps to thickness of γ-Al_2O_3 films 240Å thick both with and without treatment in 1.0*N* sodium chloride solution for 16 hr at *p*H 6 and at 25°C.

Discussion

Initial electrical experiments on unthinned, 240Å thick γ-Al_2O_3 films before and after 16 hr immersion in sodium chloride solution, confirmed previous results (7, 8) that this chloride treatment decreases the average resistivity of the oxide films determined at 1000 cps. The magnitude of the decrease in resistivity in 1000 cps was also similar to that previously reported (7). These initial experiments showed that otherwise similar immersion in sodium sulfate solution had no significant effect on the average resistivity of the γ-Al_2O_3 films at 1000 cps. Neither did immersion in the chloride or sulfate solutions change the capacitance of the oxide covered aluminum specimens, and therefore, the oxide film thickness from the initial value.

Initial electrical experiments on similar unthinned films at 100,000 cps also gave resistance values identical to those determined in earlier work (8, 9) at this frequency, and confirmed that 16 hr immersion in sodium chloride and also sodium sulfate solution produced no change in the high-frequency resistance or capacitance of the oxide films.

Structure of the original oxide films.—The film thinning experiments give a great deal of more useful information on the variation of resistance throughout the thickness of these anodic γ-Al_2O_3 films formed by the rising voltage method and, in particular, how this nonuniform resistance distribution is modified by intervening treatment with sodium chloride or sulfate solutions. Figure 3 shows the relationship between a-c resistance (ohm-cm^2) at 1000 cps and thickness of the original 240Å thick γ-Al_2O_3 film formed at 20v in neutral ammonium tartrate solution. This resistance *vs.* thickness curve is similar to that established earlier (9) and consists of four distinct regions which have previously been described as follows:

1. A low resistivity[4] region some 60-80Å thick immediately adjacent to the oxide-metal interface where the resistivity increases from 5×10^9 ohm-cm at a distance of 25Å from the oxide metal interface to 2×10^{10} ohm-cm at 80Å from the oxide metal interface;
2. A characteristic overlying region around 100Å thick in which the resistivity at 1000 cps is constant at 2×10^{10} ohm-cm;
3. A 40Å thick region extending from 180 to 220Å from the oxide-metal interface in which the low-frequency resistivity decreases with increasing distance from the oxide-metal interface to as little as 5×10^9 ohm-cm; and
4. An outer region some 20Å thick, immediately adjacent to the oxide-solution interface, where the resistivity at 1000 cps is unusually high (5×10^{10} ohm-cm).

Figure 4 shows the much simpler relationship between a-c resistance of the original 240Å thick γ-Al_2O_3 films at 100,000 cps and thickness. This is also identical to the results of earlier work on similar films (9) and contains only two regions as follows: (i) a region around 80Å thick immediately adjacent to the oxide-metal interface in which the resistivity is as low as 3×10^6 ohm-cm and increases with increasing distance from the oxide metal interface, and (ii) a residual zone of constant resistivity (2.2×10^7 ohm-cm) extending from around 100Å from the oxide-metal interface out to the oxide-solution interface.

An explanation was offered earlier (9) for the presence of these zones of variable resistivity and for the strong effect of frequency. This explanation is briefly

[4] Obtained from the slope of the tangent to the a-c resistance (ohm-cm^2) *vs.* thickness (cm) curve at the appropriate film thickness value.

summarized below. Studies of dispersion peaks in dry γ-Al_2O_3 films at varying frequency and temperature (7) suggested that the relaxation time of defects introduced by impurity substitution of hydroxyl ions was somewhat less than 10^{-5} sec. It was later suggested (8, 9) that the measurement of C_s and D at frequencies of 100,000 cps and above would be mainly sensitive to electronic relaxation effects resulting from gross impurity substitution (including substantial departure from stoichiometry) and that similar measurements at lower frequencies than 100,000 cps would be sensitive to both ionic and electronic relaxation effects resulting from these causes.[5] Indirect evidence (8) was introduced to show that electronic and ionic relaxation effects, detected by these means, could be qualitatively related to the electronic and ionic resistances respectively of the aluminum oxide film. This view receives some support from the recent work of Strickler and Carlson (25).

Accordingly, the low resistivity region of the γ-Al_2O_3 film depicted in Fig. 4 at 100,000 cps was attributed primarily to electronic relaxation effects resulting from the anticipated presence of excess metal ions in the vicinity of the oxide-metal interface. Probably there exists an n-type defect structure in this region similar to the F′ defect structure proposed earlier by Grunberg and Wright (11). A similar low-resistivity region is seen in the vicinity of the oxide-metal interface at the lower frequency of 1000 cps (Fig. 3). It is believed that this lower frequency effect is also due primarily to electronic relaxation effects from the nonstoichiometric excess metal structure, although it is not possible to rule out some contribution from ionic relaxation effects. It was, however, suggested that these ionic effects are not predominant at 1000 cps in this region of the oxide film.

The zones of constant resistivity, which encompass the remainder of the oxide film at 100,000 cps (Fig. 4) and a 100Å thick zone at 1000 cps (Fig. 3) were previously defined as showing the characteristic resistivities of the γ-Al_2O_3 film at the two frequencies. The remaining two outer zones of varying resistivity at 1000 cps were attributed to ionic relaxation effects resulting from impurity substitution. The intermediate 40Å thick zone (3) of reduced specific resistance was believed to be due to field-aided entry of hydroxyl ions into the γ-Al_2O_3 structure during formation of the anodic film. This proposition finds good support in the recent elegant Xe^{125} marker studies of Davies *et al.* (12), who demonstrated clearly the existence of substantial inward migration of anions during the formation of similar anodic aluminum oxide films. One-for-one substitution of singly charged hydroxyl ions for doubly charged oxygen ions in the anion lattice should result in the creation of additional current carriers, a more strongly n-type defect structure, and an increase in ionic relaxation effects. The outer region (4) of very high specific resistance at 1000 cps (5×10^{10} ohm-cm) was attributed to the existence of a saturated anion lattice, due to the strongly oxidizing conditions during film formation; this outer area of the film was considered to exhibit a more strongly p-type character (9, 13). Again this structure modification resulted in a modification of ionic rather than electronic relaxation characteristics.

Changes in structure resulting from immersion in sodium chloride or sulfate solutions.—After this summary of the probable resistivity characteristics of the original oxide film, any changes resulting from immersion in sodium sulfate or chloride can now be considered in more detail. It should first be re-emphasized that the immersion times in these solutions were deliberately held to a sufficiently low value (16 hr at 25°C) that no detectable corrosion of the oxide covered aluminum occurred. Furthermore, no film thinning, contamination, or change in the surface topography was detected in the capacitance studies or in the electron microscopical studies reported previously (8, 9).

Immersion of aluminum covered with a 240Å thick aluminum oxide film having the foregoing structural characteristics in 1.0*N* Na_2SO_4 solution of *p*H 6 for 16 hr and at 25°C resulted in no change in thickness, in average resistivity, or in the a-c resistance distribution throughout the thickness of the oxide film at 100,000 cps. Therefore, treatment in the sulfate solution modifies neither the defect structure of the excess metal oxide adjacent to the oxide-metal interface, nor the characteristic high frequency resistivity of the remaining oxide. At the lower frequency of 1000 cps, the average resistivity of the unthinned oxide was again not changed by the 16 hr immersion in sodium sulfate. Thinning experiments on films pretreated with sodium sulfate solution again showed that there was no change in film thickness, in the characteristic zone of constant resistivity, or in the excess metal region of the oxide film adjacent to the oxide-metal interface (Fig. 2 and 3). Minor modifications in resistivity appear to have been made in the outer 40Å of the oxide film adjacent to the solution-oxide interface (Fig. 2). The experimental significance of these small changes is uncertain; however, they might be due to the entry of small concentrations of OH′ ions specifically adsorbed on the oxide surface (8), since the changes seem basically similar to those in zone 3 of the original film. Alternately, the slight modifications in the resistance *vs.* thickness curve which are seen in the outer 40Å of the film, may be due to partial annihilation of the mobile carriers in the two diverse defect structures in zones 3 and 4 of the original film (9, 13). Accordingly, the low-frequency results in Fig. 2 and 3 are held to imply either that sulfate ions themselves do not substitute in γ-Al_2O_3 structure to any significant degree, or else that any substitution in the γ-Al_2O_3 structure is unaccompanied by a significant change in a-c resistance, either at high or low frequency. The latter alternative is considered to be less likely.

When the a-c resistance *vs.* thickness curves are determined at 100,000 cps following similar treatment of oxide covered aluminum specimens with sodium chloride solution (where again no corrosion or detectable film thinning, etc., occurs), no change in the resistance distribution with thickness is again detected (Fig. 4). This observation is consistent with earlier work on unthinned films (8) and suggests that any chloride ion substitution obtained in these experiments has no added effect on the electronic relaxation characteristics of the γ-Al_2O_3 films. The situation is vastly different when the effect of treatment with sodium chloride solution on the a-c resistance *vs.* thickness curve at 1000 cps is determined (Fig. 3). Here the immersion in the sodium chloride solution results in a major decrease in resistance without film thinning and, of course, without corrosion. The change in the resistance distribution with thickness occasioned by the immersion in sodium chloride solution can be summarized as follows:

1. The low-resistivity zone adjacent to the oxide-metal interface is completely unaffected by chloride immersion. This is due only to the selection of a relatively thick initial film through which complete penetration of chloride ions was not anticipated.

2. The characteristic zone of constant low-frequency resistivity is completely eliminated.

3. The penultimate zone 3 of decreasing specific resistance with increasing film thickness, believed to be due to OH′ entry, is reinforced, magnified, and deepened to within 70Å of the oxide-metal interface.

[5] The experimental technique appears to be best adapted to investigation of the changes in resistance resulting from deliberately perturbing the original as-formed oxide. The major significance is, therefore, obtained by comparison of the resistance of the "perturbed" oxide with the original film which may be essentially regarded as a background. Electrical resonance effects that are easily detected are these with large relaxation times less than 10^{-5} sec.

4. The former outer zone of maximum specific resistance is largely suppressed, but is still detectable.

The actual a-c resistance distribution in chloride substituted γ-Al_2O_3 is therefore more complicated than the simple two zone (completely substituted and completely unsubstituted) model proposed earlier by MacMullen and Pryor (7) (dotted curve in Fig. 3) where the large variation in resistivity of the original film with thickness was not realized.

The results in Fig. 3 appear to be completely consistent with the already proposed entry of chloride ions into the aluminum oxide structure and their exchange with oxygen ions in the anion lattice (7, 8). The authors believe that this postulate is further supported by the evident reinforcement, by chloride treatment of the penultimate zone 3 in the original film, where original resistivity was believed to be lowered by hydroxyl entry during film formation. This zone from Fig. 3 becomes extended inward by around 110Å to within 70Å of the oxide-metal interface. Since these strong resistance effects of chloride substitution are seen only at frequencies below 100,000 cps (8), they should represent enhanced ionic relaxation effects from Cl′ substitution and should manifest themselves as a substantially decreased ionic resistance of the over-all oxide film. If a one to one chloride ion-oxygen ion exchange or substitution is visualized, the substituted oxide should exhibit a much stronger n-type defect structure. Support for the inclusion of chloride ions in aluminum oxide films during simple immersion in sodium chloride solution is also provided to some degree by the previous radiochemical studies of Verkerk (14).

The aqueous sodium chloride solution employed in this investigation, of course, contains hydroxyl ions as well as chloride ions. Both anions appear to be able to enter the γ-Al_2O_3 film structure, substitute for oxygen ions, and therefore produce the same number of additional current carriers for an equivalent number of substitutions. Since the relaxation times of the resulting defects could well be quite similar, the present experimental work does not permit quantitative assignment of the proportion of the total resistance drop in Fig. 3 to one or the other of these individual anions.

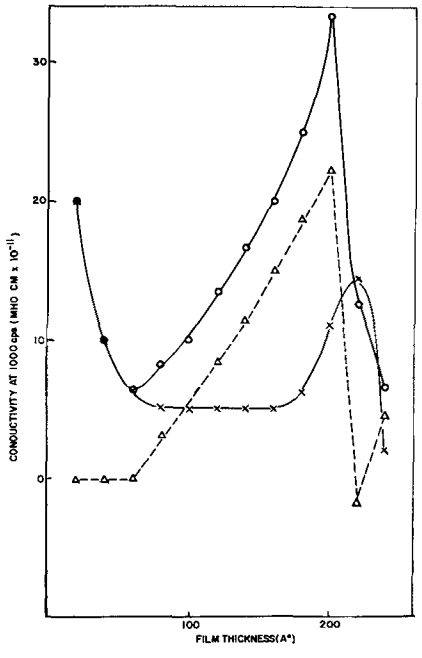

Fig. 6. Relationship between conductivity at 1000 cps and thickness of γ-Al_2O_3 films 240Å thick both with and without prior immersion in 1.0*N* sodium chloride solution for 16 hr at pH 6 and at 25°C: X—X, original film; O—O, chloride treated film; △—△, difference curve.

However, from the results in Fig. 3 on the effects of immersion in 1.0*N* Na_2SO_4 solution, which contained the same concentration of OH′ ions as the 1.0*N* NaCl solution, it appears that any effect of hydroxyl substitution during the immersion experiments is small compared with that resulting from Cl′ substitution.

The present work can now be applied to estimating the distribution of additional current carriers introduced into the aluminum oxide films by chloride treatment. In a semiconductor the number of current carriers is directly proportional to the reciprocal resistivity, *i.e.*, the conductivity or cotangent to Fig. 3. The conductivity distribution with film thickness at 1000 cps in the original untreated aluminum oxide film and in the otherwise similar chloride treated aluminum oxide film is shown in Fig. 6. The difference in conductivity at a given thickness should be directly proportional to the number of additional current carriers introduced by chloride treatment and therefore to the concentration of Cl′ (with possibly OH′) ions in the oxide film at that location; *i.e.*, the dotted difference curve in Fig. 6. It may be seen that the concentration of chloride ions in the outer 20Å of the oxide film is very low. The apparently "negative" concentration observed 20Å from the oxide-solution interface is probably due to the annihilation of the mobile carriers in the vicinity of the p-n junction. A low concentration of Cl′ in the p type layer is consistent with the view that this layer contains an essentially saturated anion lattice and that the early rapid entry of chloride ions primarily occurs at vacant sites in the anion lattice (7). The concentration of chloride ions increases sharply at the outer edge of the n-type zone in the aluminum oxide film and thereafter appears to decrease in an approximately linear fashion with increasing distance from the oxide-solution interface. The reasons for this approximately linear decrease in Cl′ ion concentration are at present not completely understood, and the present work does not permit a unique explanation of this phenomenon.

Effect of chloride ion substitution on the dissolution kinetics of aluminum oxide films.—Of particular significance from the standpoint of corrosion mechanisms is the higher dissolution rate exhibited by the γ-Al_2O_3 films pretreated in sodium chloride solution (Fig. 7). Probably the small difference in dissolution rate between the original films and those pretreated in sodium sulfate solution is not experimentally significant. However, in all experiments an enhanced dissolution rate of the films pretreated in sodium chloride solution was observed. From studies of the zeta potential of various oxides of aluminum (15, 16), it appears that the hydroxyl ions should be specifically adsorbed at *p*H 7.1 on aluminum oxide films in much greater numbers than hydrogen ions. Therefore, it is probable that the

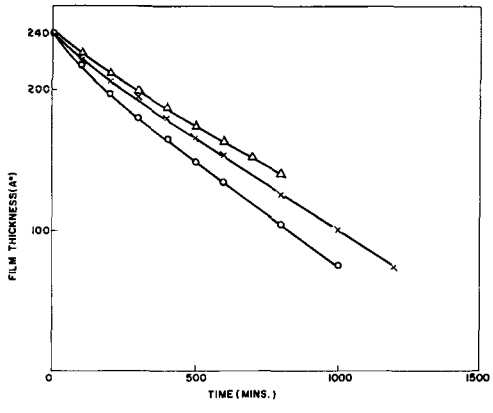

Fig. 7. Thickness of γ-Al_2O_3 films in the untreated condition and after treatment for 16 hr in either 1.0*N* sodium chloride or sodium sulfate solution as a function of time of immersion in 1.0*M* sodium chromate solution at *p*H 7.1 and at 25°C: X—X, original film; O—O, chloride treated film; △—△, sulfate treated film.

combination of specifically adsorbed hydroxyl ions with aluminum ions in the lattice of the aluminum oxide film and the removal of a combined species from the surface constitutes the rate-controlling step during dissolution of the oxide films in the thinning solution. Earlier studies on the mechanism of direct dissolution of α-Fe_2O_3 in noncomplexing acids (17) (where the rate-controlling step is the combination of adsorbed hydrogen ions with oxygen ions in the oxide lattice) showed that an increasing number of oxygen ion vacancies in the anion lattice favored more rapid dissolution of the oxide. This effect was attributed to a relaxation of the force-field around surface oxygen ions in the vicinity of oxygen ion vacancies thereby facilitating their removal from the crystal lattice. By analogy, substitution of the γ-Al_2O_3 films with chloride ions would be expected to create additional aluminum ion vacancies, thereby facilitating the removal of aluminum ions from the alumina lattice; under given dissolution conditions, this factor should speed the rate of dissolution. The results in Fig. 7 appear to be consistent with this suggestion.

Modifications of the aluminum oxide structure and its relation to pitting of aluminum in nearly neutral solutions.—The foregoing observations can be now applied to improving the understanding of why aluminum covered with its natural oxide film is much more susceptible to pitting corrosion in sodium chloride solution than in sodium sulfate solution. When film-covered aluminum is immersed in sodium chloride solution, the first reaction occurring in the induction period before gross corrosion begins should be the adsorption and entry of Cl′ ions into the oxide lattice. This should create additional current carriers and/or additional aluminum ion vacancies in the cation lattice and thereby reduce the ionic resistance of the oxide film. In turn, this will result in a reduction of anodic polarization and should permit more rapid outward diffusion of aluminum ions into the solution. Concurrently, the electronic resistance of the oxide film, which is important in controlling cathodic polarization (18), is probably not significantly changed as long as the over-all film thickness remains constant. In the natural oxide film, penetration of the chloride ions down to the oxide-metal interface must be anticipated from Fig. 2 and 3, and indeed earlier work (7) on thinner films shows this view to be justified. Furthermore, the chloride ions can hardly be distributed uniformly throughout the film, but instead should be concentrated at certain selected areas such as grain boundaries, dislocations, and other internal surfaces in the oxide film where rapid exchange and substitution has been anticipated (7, 8). At the local areas of highest Cl′ ion concentration in the film, not only will the resistance of the film (per unit of thickness) to the outward passage of aluminum ions be lowest, but also the film itself will be specially sensitive to enhanced dissolution. This will became even more pronounced as aluminum ions enter the solution, become precipitated as a hydrated aluminum oxide, thereby generating local concentrations of hydrogen ions around the anodic locations as shown by Edeleanu and Evans (3). Under these conditions, the microscopic areas of high chloride ion concentration could well be enlarged to macroscopic pits by the speeding action of the higher locally generated H^+ ion concentration but extreme localization of attack on a macroscopic scale must be anticipated since the oxide film at the local areas containing the highest concentrations of substituted Cl′ ions not only exhibit the lowest ionic resistivity, but also under steady-state conditions of film dissolution and repair, must exhibit a locally lower thickness than adjacent areas not containing as high a concentration of substituted chloride ions. In the truest sense, the pitting of aluminum in chloride solutions becomes "autocatalytic" due to these local, thin areas of maximum Cl′ concentration and lowest ionic resistivity in the film.

The state of affairs is entirely different when similar specimens are immersed in sodium sulfate solution at the same *p*H and temperature. The sulfate ions probably do not enter the lattice of the thin surface oxide films to a significant degree. Accordingly, prolonged contact of the oxide covered aluminum with sodium sulfate solution does not serve either to reduce the ionic resistivity of the surface film or to increase its dissolution rate. Therefore, although the specimen will corrode and the film may thin or thicken slowly with time, only local variations of *p*H and small metallurgical differences in the metal substrate, inherited in the oxide film, tend to localize the corrosion. The two primary oxide film factors of local reduction in ionic resistivity and superimposed local sensitivity to enhanced dissolution, so clearly produced by substituted chloride ions, are conspicuously absent during immersion in sodium sulfate solution. The major difference between the effects of Cl′ and SO_4'' ions on the oxide film may well also account for Edeleanu and Evans' (3) observation that anodic treatment of aluminum in sodium chloride solution produces more soluble anodic reaction products at between *p*H 5 and 6 than similar anodic treatment of aluminum in sodium sulfate solution.

It is tempting to apply the above reasoning to the pitting of aluminum in other aqueous solutions and to the pitting of other metals normally covered with thin oxide films. This extrapolation must be cautiously conducted in the absence of pertinent supporting data. Nearly neutral solutions of sodium fluoride pit aluminum even more readily than chloride (2). Doubtless, the explanation of this phenomenon also lies in the changes wrought by fluoride ions on the oxide film. Fluoride ions can be included in γ-Al_2O_3 films on aluminum to a substantially higher degree than chloride ions and, thereby, produce a greater decrease in low frequency resistivity (7, 8). It must also be anticipated that greater inclusion of substituted F′ ions will result in a further significant substantial increase in dissolution rate of the surface oxide film. These two factors, in combination, can be held to offer a satisfactory explanation of the more aggressive pitting action of sodium fluoride solutions upon aluminum.

Application of these concepts to the pitting of iron in chloride solutions raises many more uncertainties. Although the recent work of Engell and Stolica (19) on the effect of Cl′ ions on iron passivated anodically in sulfuric acid, is strikingly similar to the present work on the relative effects of Cl′ and SO_4'' ions on aluminum, there exists another powerful means of destroying the protective action of oxide film on iron, *i.e.*, reductive dissolution (20-22); this reaction must be carefully considered in relation to any film breakdown phenomena on iron. In solutions having *p*H values below 7.0 it may well be that the relationship between impurity substitution, including departure from stoichiometry, and the reductive dissolution characteristics of a substituted iron oxide film governs the choice between localized film breakdown and pitting, on one hand, and passivity on the other. Some preliminary consideration has been given to the problem (13, 23, 24), but insufficient data appear to exist at this time to permit real understanding of the complex atomic processes involved.

Acknowledgment

The authors wish to acknowledge the support given to this work by the Olin Mathieson Chemical Corporation and their permission to publish the results.

Manuscript received Nov. 22, 1963.

Any discussion of this paper will appear in a Discussion Section to be published in the December 1965 JOURNAL.

REFERENCES

1. S. C. Britton and U. R. Evans, *J. Chem. Soc.*, **1930**, 1773.

2. M. J. Pryor, *Z. Elektrochem.*, **62**, 782 (1958).
3. C. Edeleanu and U. R. Evans, *Trans. Faraday Soc.*, **47**, 1121 (1951).
4. J. E. Draley, International Conference on Aqueous Corrosion of Reactor Materials, Oct. 14-16 (1959).
5. J. E. Draley and W. E. Ruther, *Corrosion*, **12**, 31 (1956).
6. J. V. Petrocelli, *This Journal*, **106**, 566 (1959).
7. J. J. MacMullen and M. J. Pryor, "Proceedings of the 1st International Congress on Metallic Corrosion," p. 52 Butterworths (1961).
8. A. F. Beck, M. A. Heine, D. S. Keir, D. van Rooyen, and M. J. Pryor, *Corrosion Science*, **2**, 133 (1962).
9. M. A. Heine and M. J. Pryor, *This Journal*, **110**, 1205 (1963).
10. K. F. Lorking, *J. Appl. Chem.*, **10**, 449 (1962).
11. L. Grunberg and K. R. H. Wright, *Proc. Roy. Soc.*, **A232**, 403 (1955).
12. J. A. Davies, J. P. S. Pringle, R. L. Graham, and F. Brown, *This Journal*, **109**, 999 (1962).
13. M. J. Pryor, *ibid.*, **106**, 557 (1959).
14. B. Verkerk, UNESCO, International Conference on Radio Isotopes in Scientific Research UNESCO/NS/RIC44.
15. J. J. Modi and D. W. Fuerstenau, *J. Phys. Chem.*, **61**, 640, (1957).
16. D. J. O'Connor, P. G. Johansen, and A. S. Buchanan, *Trans. Faraday Soc.*, **52**, 229 (1956).
17. M. J. Pryor and U. R. Evans, *J. Chem. Soc.*, **1949**, 3330.
18. M. J. Pryor and D. S. Keir, *This Journal*, **102**, 605 (1955).
19. H. J. Engell and N. D. Stolica, *Z. Phys. Chem.*, **20**, 113 (1959).
20. U. R. Evans, *Proc. Roy. Soc.*, **A107**, 228 (1925).
21. U. R. Evans, *J. Chem. Soc.*, **1930**, 478.
22. M. J. Pryor and U. R. Evans, *ibid.*, **1950**, 1259, 1266.
23. M. Nagayama and M. Cohen, *This Journal*, **109**, 781 (1962).
24. M. Nagayama and M. Cohen, *ibid.*, **110**, 670 (1963).
25. D. W. Strickler and W. G. Carlson, *J. Am. Ceram. Soc.*, **47**, 122 (1964).

An Investigation of Porous Anodic Oxide Films on Aluminum by Comparative Adsorption, Gravimetric and Electronoptical Measurements

G. Paolini, M. Masoero, F. Sacchi, and M. Paganelli

Istituto Sperimentale dei Metalli Leggeri, Milano, Italy

ABSTRACT

Results of BET adsorption measurements on a-c and d-c sulfuric acid anodic films on aluminum have been compared with results of pore counts and with coating ratio figures. Both real surface and volume were measured. A roughness factor should be introduced in order to obtain an agreement between data from different sources.

Several means are available to investigate the porous structure of anodic films on aluminum, such as are industrially produced in dilute sulfuric acid. Direct examination by the electron microscope, gravimetric determinations of the oxide weight, density measurements, adsorption techniques (e.g., by the BET method), refraction properties, permeability, and electrical capacity measurements are some of the methods which have been employed for this purpose.

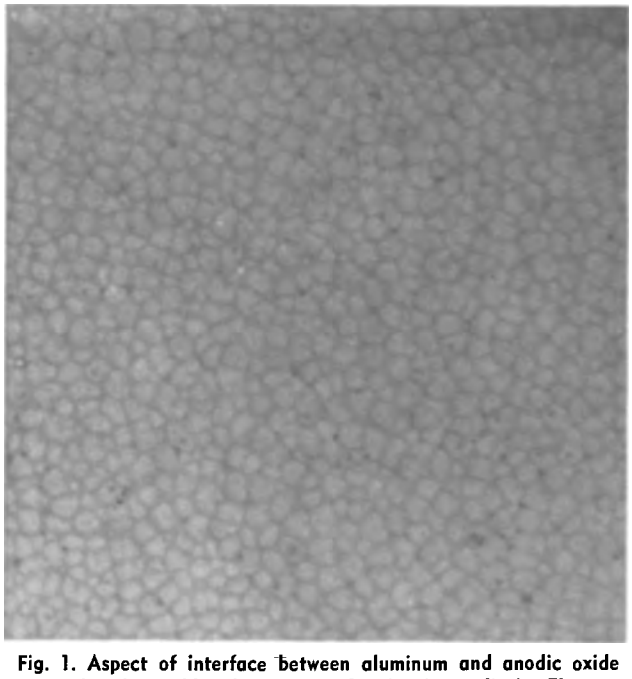

Fig. 1. Aspect of interface between aluminum and anodic oxide film produced at 30v d.c. in H_3PO_4 (oxide replica). Electron magnification 10,000X; total magnification 30,000X.

By comparing the results obtained with different methods, more information can be gained than by any single method taken by itself; unfortunately, in many cases the results obtained by one laboratory on one set of samples have to be compared with results obtained by other laboratories on different sets of samples.

The object of the present research was to apply gravimetric, electronoptical, and adsorption methods to a whole range of films that had been formed under strictly controlled conditions in order to delineate with closer accuracy the fine structure of the pore system.

Physical Methods

A first approximation to the pore structure could be easily obtained by simple physical methods:

Electron microscopy.—(1-3) By examining replicas of the cell structure engraved into the oxide-metal interface (Fig. 1), the number of cells, *i.e.* pores, can be counted; a confirmation can be had by direct transmission observation of thin porous films detached from the metal (Fig. 2, 3);

Gravimetric method.—The weight of oxide existing on the sample can be calculated by double weighing (before and after dissolving the oxide away in phosphochromic solution which does not dissolve the metal);

Geometric method.—The real oxide thickness can be measured directly on an Abbe micrometer, as the difference between the sample thickness before and after dissolving the oxide film.

Based on such measurements, a schematic pore structure can be drawn, provided the pore shape be considered as uniform and regular (cylindrical as a first approximation).

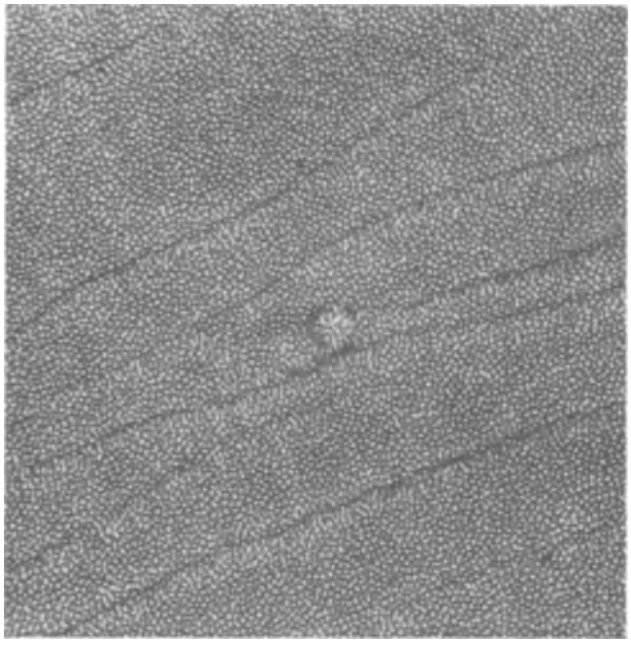

Fig. 2. Transmission electron micrograph of anodic film produced in H_2SO_4 d.c., 1 amp/dm^2. Pores were enlarged by attack in anodizing bath itself. Electron magnification 10,000X; total magnification 30,000X.

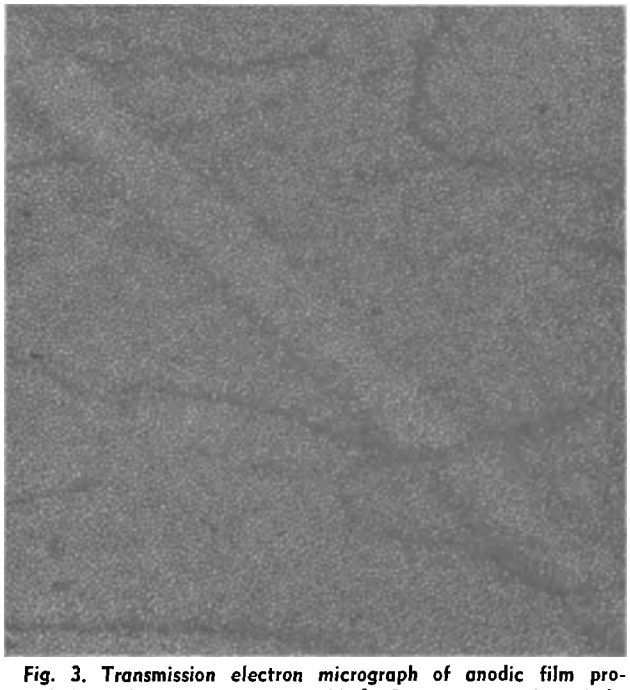

Fig. 3. Transmission electron micrograph of anodic film produced in H_2SO_4 a.c., 1.54 amp/dm^2. Pores were enlarged by attack in anodizing bath itself. Electron magnification 10,000X; total magnification 30,000X.

Let us call N the number of pores per cm^2 counted on the electron microscope, δ the density of the compact oxide forming the pore walls, h the film thickness measured on the Abbe micrometer, and P the oxide weight.

One can then calculate the over-all pore volume V_s and the average pore radius $\bar{R}$

$$V_s = \frac{\delta h - P}{\delta} \qquad [1]$$

$$\bar{R} = \sqrt{\frac{V_s}{\pi N h}} \qquad [2]$$

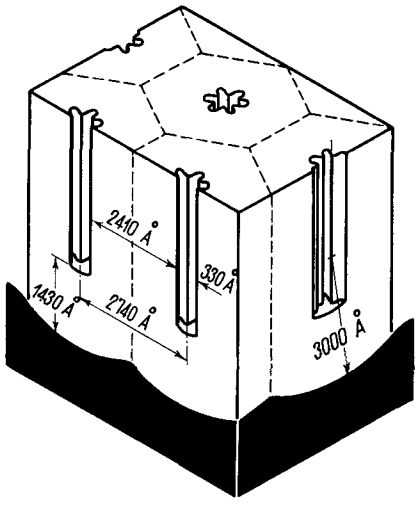

Fig. 4. Model of 120v H_3PO_4 film according to Keller

Fig. 5. Electron micrograph of aluminum oxide interface of 99.99% Al anodized in H_2SO_4. Oxide replica shadowed with Cr. Electron magnification 6000X; total magnification 18,000X.

Moreover, as the pore base radius has been calculated by Keller *et al.* (1), the taper of the pore can be deduced, as well as the real surface S_s

$$S_s = 2\pi\bar{R}Nh \qquad [3]$$

The accuracy of the data obtained by this way is somewhat limited by several difficulties.

The first difficulties arise when counting the pore numbers in the usual films formed in H_2SO_4; such films, as distinguished from H_3PO_4 films which form large cells (Fig. 4) have a very minute cellular structure which hardly allows for an exact direct counting of the cell number (Fig. 5, 6). Good direct counting on these films is only obtained by transmission observation of very thin oxide films detached from the metal and partially redissolved by a reaction which widens the pores (Fig. 2 and 3). This method, on the other hand, gives rise to several doubts: the pore count is somewhat uncertain because of the small pore size; some walls between the cells may be eaten up in the reaction, and some pores may be thus obliterated; such films which are examined by transmission must have a very reduced thickness and are produced by anodizing for a very short time (*e.g.*, 45 sec), which is of the same order of magnitude as the initial unstable stage of any anodizing process: the structure of such very thin films therefore might not be the same as for normal films formed under stable electrical conditions (Fig. 7).

Another source of error is the value of the density of the pore wall: according to Spooner (4) the value of 3.2 given by Russell for alumina should be assumed; however, hydrostatic measurements by Prati in 1953 (5) gave a figure in the neighborhood of 2.77. The large

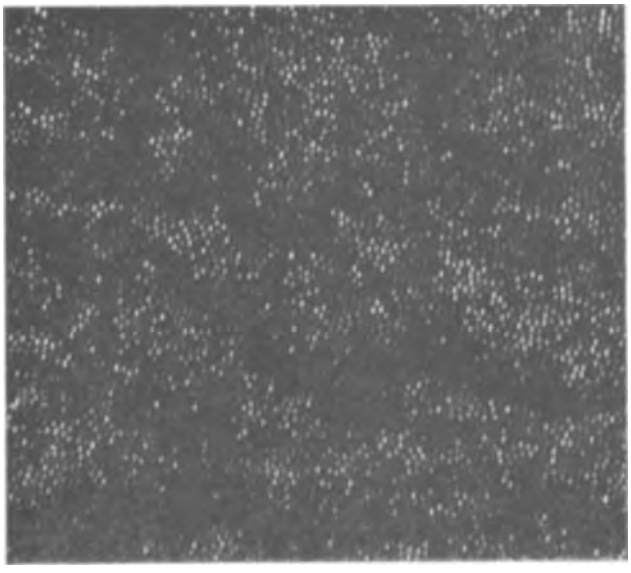

Fig. 6. Transmission electron micrograph of d-c H_2SO_4 film. The oxide films were not chemically attacked, and the pores cannot be counted clearly. Electron magnification 10,000X; total magnification 30,000X.

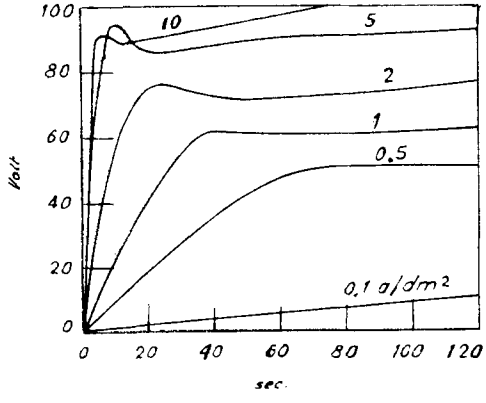

Fig. 7. Initial voltage-time relationships at constant current density for oxalic acid anodizing.

uncertainty in this value reflects on the geometrical considerations which can be deduced by the given formulas.

A further uncertainty is introduced by the hypothesis of cylindrical pores (which can be easily modified to account for gradual redissolution of the outer portion to a truncated conical shape). This hypothesis is assumed, but it has not been proven.

The adsorption method.—The above considerations show that in order to obtain a more precise definition of the pore structure, the over-all pore volumes and surfaces should be independently measured.

The most accurate method available in order to measure directly the pore volume and surface is the adsorption method.

The details of the Brunauer, Emmett, and Teller (BET) method for measuring the surface areas by means of low-temperature isotherms are well known.

Burwell *et al.* (7) report results of surface area obtained on an anodized aluminum sample by nitrogen and ethylene adsorption, and they also compare the three main methods of calculation: BET equation, "point B" and Harkins and Jura equation.

The value they accept as final is the one derived from BET equation and "point B" applied to nitrogen isotherms. On a single sample they also measure the pore volume at saturation and derive the pore diameter (107Å) from the ratio $2V/S$, as for perfect and smooth pores.

Some authors have calculated the pore diameter and the general film structure starting from the above adsorption measurements; however, more accurate conclusions can be obtained only if the pore volume is also known for a number of samples, and if the pore number is actually counted on the same samples that have been used for the adsorption test.

The present investigation is aimed at clarifying this point, in the meanwhile taking into account the influence of fundamental operating variables of the process itself, *i.e.*, current density, type of current (d.c. and a.c.), and film thickness.

Preparation of samples.—The samples used were 75 x 10 x 1 mm, 99.99% rolled Al with 70% cold-work.

Surface preparation was identical (etching in 10% NaOH at 50°C for 30 sec); concentration (20% by weight), and temperature (20°C) of the 200 liter sulfuric acid anodizing bath were also kept constant throughout the tests, and slight agitation by blown air was maintained.

Each anodizing condition was applied to 90 samples, suspended by means of 99.5 Al racks of known surface area.

The different treatments applied appear in the first four columns of Table I; as can be seen, an anodizing time of 30 min has been generally adopted, and the current density and type have been varied. However, current densities were not the same for a.c. as for d.c., as a previous reseach had shown the electrochemical efficiency of the a-c treatment to be markedly inferior. The current densities adopted therefore have been 1, 1.5, and 2.5 amp/dm² for d.c., and 1.54, 2.3, 3.8 amp/dm² for a.c. in order to obtain the same film thickness with the latter in the same time.

As a further precaution, any slight difference in film thickness has been compensated in the diagrams by plotting the properties against the "metal loss," *i.e.*, the amount of metal consumed in anodizing, which is faradaic, and is an accurate measure of the amount of electricity passed through the anode surface (10). In one case (d.c. at 1.5 amp/dm²) the time of treatment has been also extended to 60 min in order to observe the variations caused by doubling the film thickness, other conditions being kept constant.

For each set of conditions, some further samples were anodized separately in identical conditions, but the treatment was interrupted after 45 sec, whereby very thin films were produced, which could be detached and observed by transmission in the electron microscope.

Table I. Results of gravimetric and adsorption tests

Type of current	Current density, amp/dm²	Voltage eff.	Anodizing time, min	Abbe thickness, μ	Oxide weight, g/cm² · 10⁻⁴	Coating ratio, C_R	Experimental volume, V_s, cm³/cm² · 10⁻⁴	Experimental surface, S_s, cm²/cm²
d.c.	1	11.9	30	9.1	20.62	1.30	1.706	597
d.c.	1.5	14.1	30	14.6	33.04	1.342	2.590	880
d.c.	1.5	14.1	60	29.2	52.66	1.246	7.572	2093
d.c.	2.5	16.1	30	24.25	55.94	1.395	4.133	1230
a.c.	1.54	18*	30	9.35	19.83	1.263	—	716
a.c.	2.3	20*	30	14.8	31.96	1.310	—	1006
a.c.	3.8	23*	30	26.3	57.59	1.355	—	1473

* These voltages should be reduced to about half, as a-c anodizing is carried out between two aluminum electrodes and the oxide film is crossed twice by the current.

For each batch of 90 samples anodized under the same conditions, 10 samples were weighed before and after treatment, then their thickness was measured with the Abbe micrometer; subsequently, the samples were deoxidized in the phosphochromic solution and were weighed and measured again.

It was thus possible to calculate the average oxide weight and thickness formed on unit surface and the average metal loss which is a measure of electricity passed through the surface.

The main bulk of 80 samples for each batch was introduced in the container of the adsorption apparatus.

Results of Gravimetric and Micrometric Measurements

Results of gravimetric and micrometer measurements are shown in Table I, columns 5, 6, and 7.

It is apparent that films of practically identical thickness and weight have been obtained in equivalent processes with d.c. and a.c. by increasing the current density of the latter in the proportion found necessary to balance its lower oxide-forming efficiency.

The "coating ratio," *i.e.*, the ratio of oxide weight to the weight of metal consumed, has also been calculated (column 7): this figure has been widely used in the technical literature (9, 10) to give an idea of the efficiency of the anodizing process.

On the whole, the oxide thickness investigated ranges from 9 to 29μ, the oxide weight from 20 to 62 x 10^{-4} g/cm^2, and the coating ratio from 1.24 to 1.39: these values cover the range that is found with normal industrial processes.

Electron microscopy.—In order to count the pore number of the very thin films employed to this purpose, it was found to be necessary that the pores should be enlarged by dissolution in a chemical reagent.

This was accomplished by leaving the samples in the anodizing bath for 2 min after interrupting the anodizing current. The films slightly attacked by the sulfuric acid electrolyte were detached from the metal by the mercuric chloride method and were observed by transmission in the electron microscope.

Pore numbers were counted on micrographs of the type shown in Fig. 2-3, and are shown in Table III and Fig. 9, in comparison with numbers found by Keller *et al.* (1) on d-c films (no previous data were found for a-c films).

The pore numbers were quite reproducible on different areas of the same specimen (at least three samples from the same specimen were considered). As the metal was in the cold-worked state, it had a subgrain structure in the order of magnitude of 1μ, with no appreciable difference in pore numbers between the several subgrains appearing in the microscope field.

In this case, no "grain" effect was observed of the type described by Franklin and Stirland (11) for annealed material.

Cell size has been deduced from pore numbers, and has been plotted against anodizing voltage, in order to allow a comparison to be made with data similarly plotted by Keller *et al.* (Fig. 8). As can be seen in this figure, in the present case the pore numbers lie on a straight line, parallel to the line drawn by Keller *et al.*, and at a distance corresponding to a 15-20% increase in pore number or to a 2v increase in voltage.

Adsorption Measurements

These measurements were carried out by standard methods, employing a classical BET apparatus, provided with a cell large enough to contain the samples.

The isotherm given in Fig. 17 is typical of samples for which volume is reported, which required determining the whole isotherm.

Mathematical analysis of adsorption and desorption curves was not done, but the steepness of the isotherms at a relative pressure of 0.85 ÷ 0.90 indicates that the pore dimensions for such systems are quite monodisperse.

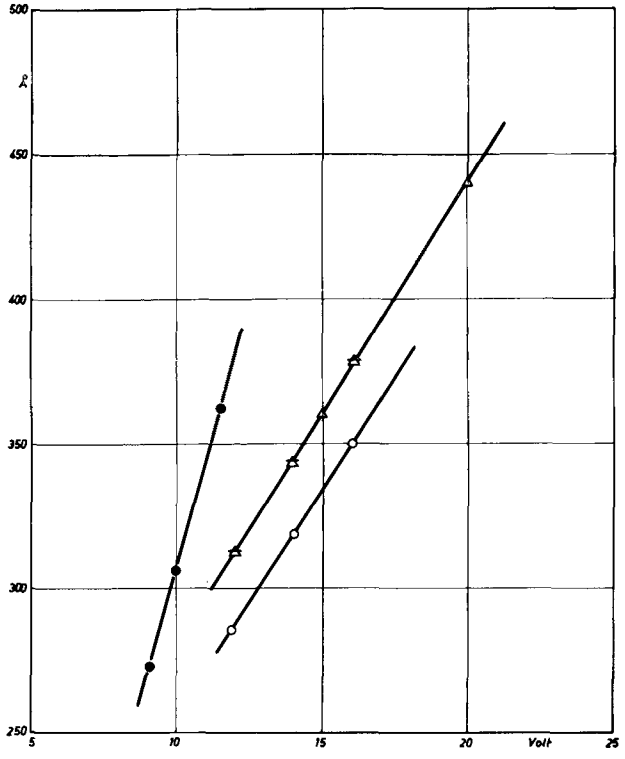

Fig. 8. Cell dimensions vs. anodizing voltage. ○, d.c. I.S.M.L.; ●, a.c. I.S.M.L.; △, d.c. Alcoa; triangle with line across, Alcoa values corresponding to I.S.M.L. voltages.

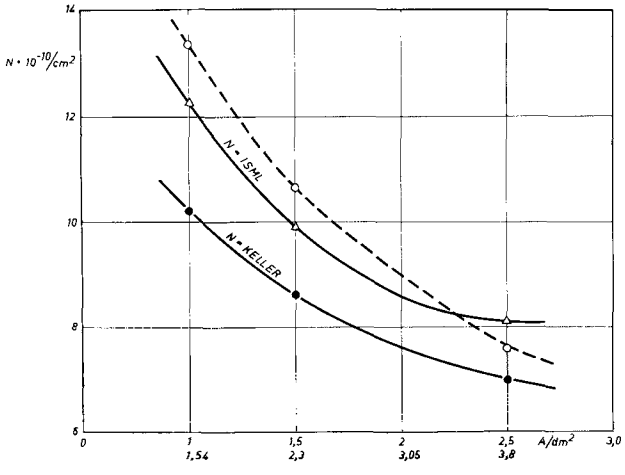

Fig. 9 Pore numbers vs. current density; — — —, a.c.; ———, d.c.

Results of volume and surface measurements are shown in Table I.

Results of volume measurements.—Volume measurements were carried out only on d-c films; the main purpose of these measurements was to obtain an independent confirmation of the density of the material forming the pore walls.

Results obtained are shown in Table I, column 8.

Volumes are comprised between extreme values of 1.7 and 7.5 x 10^{-4} cm^3/cm^2; of course, the pore volume is strongly dependent on film thickness: in order to allow comparison on an equal basis, unit volumes are given in column 4, Table II, *i.e.*, the volume of unit oxide thickness, which range between 0.17 and 0.26 10^{-4} cm^3/cm^2/μ.

The continuous lines in Fig. 10-11, showing total volume and unit volume variations for 30 min cc films, have good regularity, and repetition of the measurement for the highest current density confirmed the

Table II. Results of gravimetric, electronoptical, and adsorption tests

Type of current	Current density, amp/dm²	Anodizing time, min	Unit volume experimental, Vus, cm³/cm²/μ · 10⁻⁴	Unit volume calculated, Vuc, δ = 2,78, cm³/cm²/μ · 10⁻⁴	Unit surface experimental, S_{us}, cm²/cm²/μ	R_v, Å	Roughness factors, Fr: N I.S.M.L.	Roughness factors, Fr: N A.L.C.O.A.	Calculated density, δ-g/cm³
d.c.	1	30	0.1874	0.1849	65.6	69.8	1.221	1.338	2.788
d.c.	1.5	30	0.1773	0.1863	60.3	75.6	1.284	1.376	2.751
d.c.	1.5	60	0.2593	0.2294	71.7	91.4	1.263	1.354	2.897
d.c.	2.5	30	0.1705	0.1686	50.7	82.4	1.225	1.316	2.780
a.c.	1.54	30	—	0.2371	76.6	75.2*	1.214*	1.317**	—
a.c.	2.3	30	—	0.2236	68.0	81.8*	1.24*	1.345**	—
a.c.	3.8	30	—	0.2125	56.0	94.4*	1.245*	1.350**	—

* These values were calculated for δ = 2.78 and Vuc = Vus.
** These values were calculated for δ = 2.78 and Vuc = Vus and for N ISML reduced 15% (difference observed between ISML and ALCOA values in the case of d.c.)

straight line determined by single measurements for the two lower current densities.

In Fig. 10-11 the dotted lines for unit and total volumes of a-c films are not based on experimental values, but were calculated from geometrical considerations to be described in detail.

The good reproducibility of experimental values for 30 min films enables us to accept with confidence also the volume value obtained for the 60 min film, which does not appear in the figures.

Results of surface measurements.—A larger number of surface measurements were carried out, as these measurements are easier and quicker to make than volume measurements.

Results obtained for total and "unit" (per unit film thickness, μ) surface are shown in column 9, Table I, column 6, Table II, and Fig. 12-13.

The data obtained are more scattered than the volume data, because of the intrinsic nature of surface measurements discussed earlier.

However, the trends are clearly defined in Fig. 12-13, and average values entered in Tables I and II are reasonably acceptable.

Total surfaces vary between 600 and 2100 cm²/cm² as a function of film thickness and other properties;

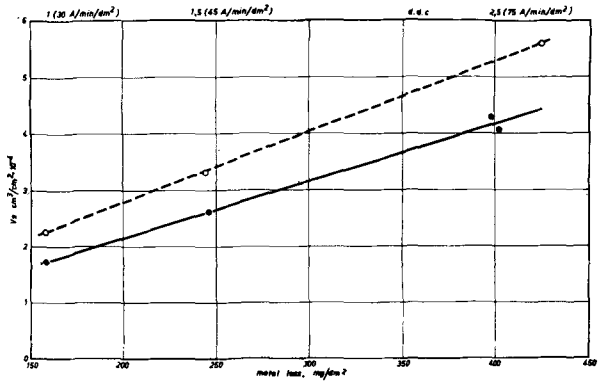

Fig. 10. Total pore volume vs. metal loss; — — —, a.c.; ———, d.c.

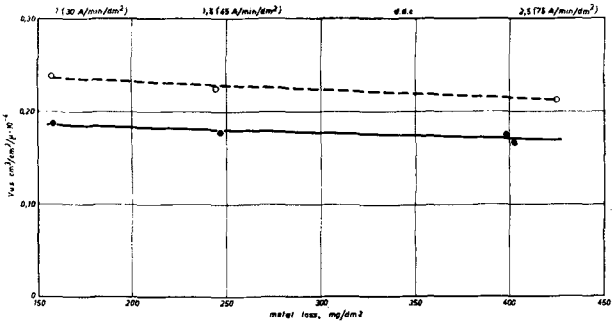

Fig. 11. Unit pore volume vs. metal loss; — — —, a.c.; ———, d.c.

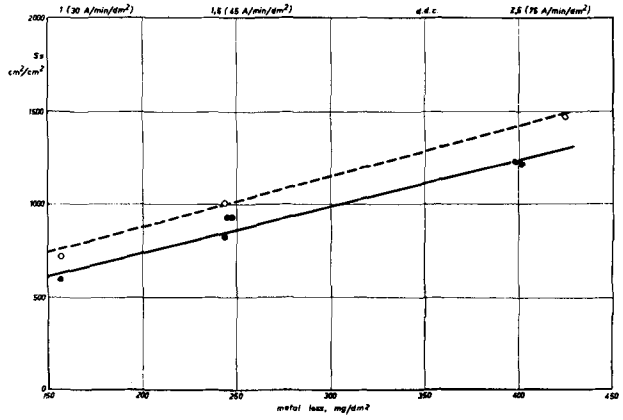

Fig. 12. Total pore surface vs. metal loss; — — —, a.c.; ———, d.c.

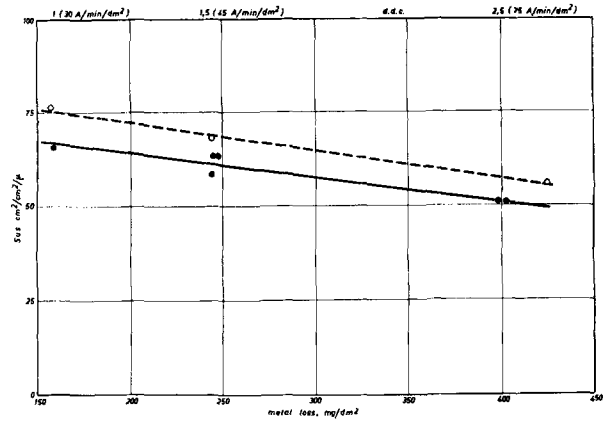

Fig. 13. Unit pore surface vs. metal loss; — — —, a.c.; ———, d.c.

unit surfaces vary between 50 and 77 cm²/cm²/μ of thickness.

A comparison may be made between films produced in cc at 1 and 1.5 amp/dm², and the Burwell-Smudsky-May films which were produced in similar conditions: our surfaces and volumes were about 20% higher, and the difference may be explained perhaps by the higher acid concentration employed in the present tests (20% instead of 15%).

Geometrical considerations.—The knowledge of real surfaces and volumes makes possible an independent calculation of the density of the material in the pore walls; the validity of the cylindrical pore model may also be controlled by applying the three equations [1], [2], [3] already mentioned.

If the pore could be assumed as cylindrical, then not only δ, but also $\overline{R}$ and N might be calculated from the above equations.

Calculation of δ.—δ values are immediately given by adsorption values through Eq. [1].

Table III. Comparison of pore numbers observed by electronoptical measurements (ISML and ALCOA) and pore numbers calculated by adsorption measurement supposing a cylindrical shape

Current type	Current density, amp/dm²	Voltage	Anodizing time, min	I.S.M.L. pore number, · 10¹⁰/cm²	Pore number from adsorption results, · 10¹⁰/cm²
d.c.	1	11.9	30	12.24	18.28
d.c.	1.5	14.1	30	9.88	17.2
d.c.	1.5	14.1	60	9.88	15.78
d.c.	2.5	16.1	30	8.12	11.77
a.c.	1.54	18.1*	30	13.36	—
a.c.	2.3	20*	30	10.64	—
a.c.	3.8	23*	30	7.58	—

* See footnote Table II.

Values of δ obtained in d-c tests are given in Table II, column 9. The values are between 2.75 and 2.89; the latter value, however, is the only one substantially different from average values, and it belongs to the 60 min film.

Apart from this case, a figure of 2.78 may be proposed for the oxide density (at least for 30 min films): this value is markedly lower than those given by several authors, but it is practically coincident with values reported by Prati in hydrostatic balance measurements (5).

If a value of 2.78 is chosen for δ, the pore volume can be calculated, by means of Eq. [1], also for a-c films: unit volumes so calculated are given in Table II, column 5. In the same table calculated values are also given for d-c films in order to show the good agreement between gravimetric and adsorption volumes that is obtained when a value of 2.78 is chosen for δ.

It can be seen that unit volumes of a-c films are in the range of $0.22 \pm 0.01 \times 10^{-4}$ cm³/cm²/μ and are about 20% greater than the volumes of corresponding d-c films. (An exception is the 60 min d-c film which has a larger unit volume, comparable to a-c films, because of attack on the pore walls caused by prolonged exposure to the anodizing solution.)

On the other hand, unit volumes were not appreciably influenced by the different current densities employed.

Pore distortion.—Values of real volumes and surfaces can be introduced in Eq. [2] and [3], and $\overline{R}$ and N values can be thus calculated (Table III), which are based on the assumption of a regular straight cylindrical pore.

Should these $\overline{R}$ and N values be inconsistent with values obtained by other methods, some modification of the pore shape would have to be introduced in order to account for the difference.

This is indeed the case when "adsorption" $\overline{R}$ and N values are compared with the values found by gravimetric and electronoptical values.

Adsorption values for N are definitely higher, and cell sizes do not follow a straight line in the Keller diagram; moreover, the two films produced in identical conditions for different times of 30 and 60 min should have different pore numbers, which would contrast with the accepted fact that identical voltages correspond to identical pore numbers.

A disagreement is also found in the case of $\overline{R}$, as "adsorption" $\overline{R}$ values are rather small, and in some case are smaller than Keller's base radius.

The hypothesis of cylindrical regular pores has therefore to be modified. The starting point is the volume measurements and the electronoptical pore numbers, which are considered to be the most reliable experimental data.

By introducing these values in Eq. [2], acceptable $\overline{R}$ values are obtained both when Alcoa and I.S.M.L. N values are used. However, when the $\overline{R}$ values so calculated are introduced in Eq. [3] along with electronoptical N values, surface values are obtained which are definitely smaller than the experimental ones.

This may be explained either by supposing that the shape of the pore section be distorted from the circular shape, or by slanting and distortion of the pore axis (11, 12). The latter is thought to have a minor influence, as the average angle should not be much different from 10° (11), which would cause a difference of only 1-2%.

Tentatively, a "roughness factor" might be introduced

$$F_r = \frac{S_s}{S_v} = \frac{SR_v}{2V}$$

where S_v is the theoretical surface calculated from adsorption volume measurements (*i.e.*, calculated from the average radius $\overline{R}$ obtained from volume measurements), and S_s is the real surface calculated by adsorption surface measurements.

The roughness factors shown in Table II, column 8, have been calculated both by assuming Alcoa and ISML values for the pore numbers; for a-c films, a 15% difference between the two numbers has been assumed, by analogy with d-c films, and calculated adsorption volumes have been assumed as in the preceding chapter.

The values of the roughness factors lie in the following regions:

1.345 ± 0.030 if calculated by Alcoa numbers

1.250 ± 0.035 if calculated by ISML numbers

Deviations from the mean value are quite small and in the order of magnitude of 3%, as if the pore "roughness" were independent from anodizing conditions.

Some examples of typical deviations from the circular shape, which would account for observed roughness factors in the worst case (Alcoa pore numbers) are shown in Fig. 14.

By introducing a roughness factor in Eq. [3], this becomes

$$\frac{S_s}{F_r} = S_v = 2\pi\overline{R}Nh \qquad [3a]$$

and the three equations [1], [2], and [3a] can be employed.

Pore "conicity".—The mean radii $\overline{R}_v$ calculated by the above reasoning are referred to cylindrical pores, and from now on they will be designated as $\overline{R}_{cyl}$.

Actually, the pores are not expected to be cylindrical because of progressive attack at the orifices; they are rather expected to be conical, so that their real mean radius $\overline{R}_{con}$ should be different from the mean radius calculated in the cylindrical hypothesis: the difference, however, is practically irrelevant.

Indeed, assuming a value of 60Å for the radius at the pore base (as calculated by Keller):

$$\overline{R}_{con} = 15 \cdot 10^{-8} + \frac{1}{2} \cdot \sqrt{3\,\overline{R}_{cyl}^2 - 2700 \cdot 10^{-16}}$$

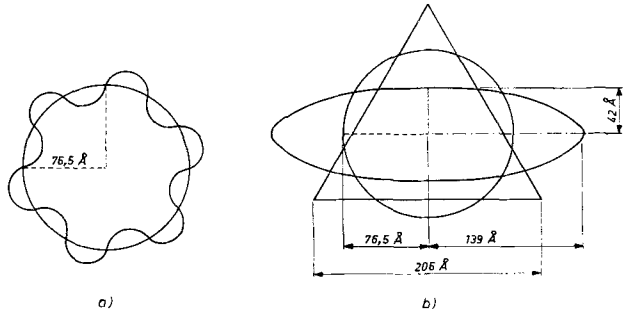

Fig. 14. Typical pore sections which give same volume as circular section, but increased area to satisfy relation $S_v = F_r S_s$.

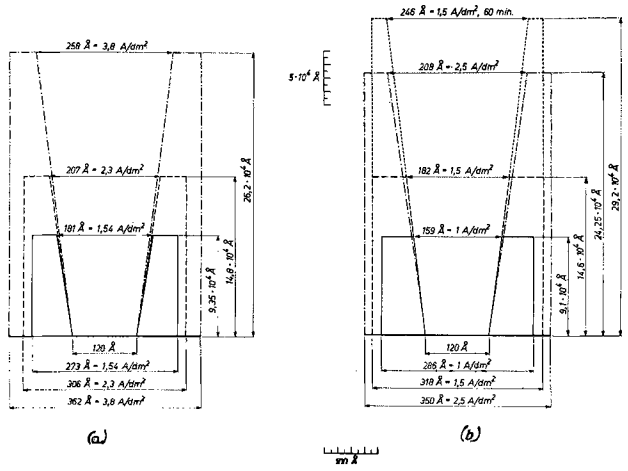

Fig. 15. Dimensional schemes for a-c films (a) and d-c films (b)

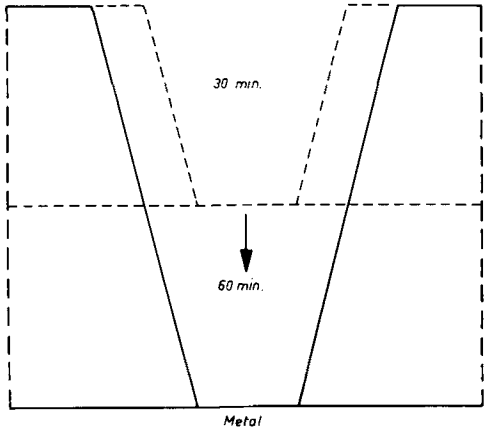

Fig. 16. Oxide growth into base metal by doubling anodizing time

By introducing in this formula the calculated values of $\overline{R}_{cil}$ (ranging from $70 \cdot 10^{-8}$ cm to $100 \cdot 10^{-8}$ cm), the maximum difference between R_{con} and R_{cyl} turns out to be about 2%. This can be disregarded, and in discussing the conical pore its mean radius can be assumed as equal to the calculated radius of the cylindrical pore.

Figure 15 shows the resulting dimensions for the different films. The slant of the pore walls is very slight in all cases (the vertical scale in Fig. 16 is 500 times reduced relative to the abscissas scale) and is practically the same for films produced at the same current density.

In general, pore walls are thicker for high current densities, for d-c films, and for the shorter anodizing time.

Nonhomogeneity of pore wall.—In an earlier paragraph it was shown that the pore wall density was nearly constant for all 30 min films, but increased for the 60 min film.

The 30 min film is expected to develop into the 60 min film as shown in Fig. 16: in this case, at the end of 60 min, the lower part of the pore will have taken up the same shape as the upper part had after the first 30 min, and the latter will have suffered surface dissolution causing enlargement of the outer radius.

The higher wall density of the thicker film may thus be explained by supposing that the pore wall be made up with material of increasing density from the pore surface to the interior; this might be connected with observations on barrier layers, which indicated

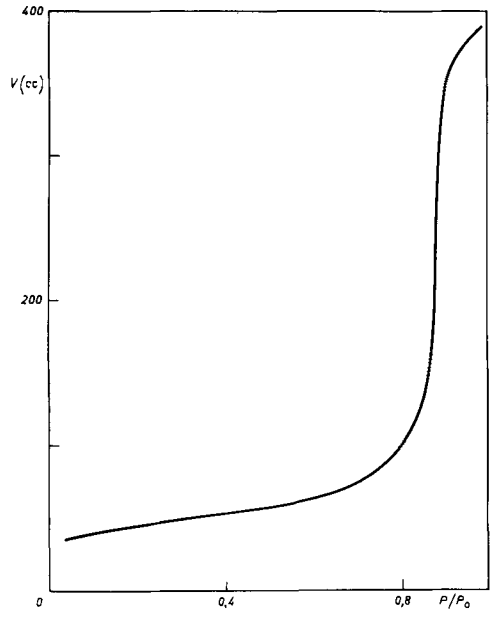

Fig. 17. Typical adsorption isotherm on sample 4 (N_2, -195°C)

that a more soluble material exists in the center of the cell (13).

Conclusions

An accurate description of the fine pore structure can be obtained by supplementing electronoptical and gravimetric measurements with adsorption techniques.

The real surface turns out to be 25-35% higher than that calculated from volume measurements; this discrepancy can be accounted for by deformation of the circular section.

The average density of the material in the pore walls is about 2.78 for 30 min films, higher for 60 min films.

All facts are in good agreement with the picture of the pores as truncated cones, with very slightly slanting walls. The wall slant does not vary considerably with the film thickness.

Acknowledgments

The authors are indebted to Professor C. Panseri, Director of the I.S.M.L., for encouragement, criticism, and permission to publish the results.

Manuscript received Feb. 13, 1964; revised manuscript received Sept. 8, 1964.

Any discussion of this paper will appear in a Discussion Section to be published in the December 1965 JOURNAL.

REFERENCES

1. F. Keller, M. S. Hunter, and D. L. Robinson, *This Journal*, **100**, 411 (1953).
2. M. Paganelli, *Alluminio*, **27**, 3 (1958).
3. I. S. M. L., *Rapporto*, **11**, 526/6207.095 (1962).
4. R. C. Spooner, *Proc.* 44th Annual Convention Am. Electroplaters' Soc., Montreal, June 17-20, 1957, cfr. pp. 132-142.
5. A. Prati, *Alluminio*, **22**, 148 (1953).
6. S. Brunauer, P. H. Emmett, and E. Teller, *J. Am. Chem. Soc.*, **60**, 309 (1938).
7. R. L. Burwell, P. A. Smudski, and T. P. May, *J. Am. Chem. Soc.*, **69**, 1525 (1947).
8. F. Sacchi, *Galvanotecnica*, **13**, 141 (lug. 1962).
9. R. B. Mason and P. E. Fowle, *This Journal*, **101**, 53 (1954).
10. A. Prati, F. Sacchi, and G. Paolini, *Alluminio-Nuova Metallurgia*, **30**, 467 (1961).
11. R. W. Franklin and D. J. Stirland, *This Journal*, **110**, 262 (1963).
12. A. Hone, *Metal Progr.*, **53**, 363 (1948).
13. R. W. Franklin, *Nature*, **180**, 1470 (1957).

Mechanism of the Oxidation of Zirconium in Oxygen and Liquid Sodium

Tennyson Smith

North American Aviation Science Center, Thousand Oaks, California

ABSTRACT

A rigorous analysis using Fick's second law diffusion equation (for film growth and diffusion into the metal) is given which explains the observed variation of apparent activation energy between about 28 and 50 kcal/mole for the oxidation process. This analysis also explains the observed differences between oxidation in oxygen and oxidation by oxygen in liquid sodium. An empirical equation is given that will accurately describe the experimental data of weight gain *vs.* time (for Zr, Ti, and Cu) as this relationship goes from approximately parabolic, to quasi-cubic, to parabolic again. The derivation of this equation stems from the hypothesis that the diffusion coefficient (for oxygen into the metal) decreases as the oxygen consumption increases.

From the many experimental studies (1-10) of the oxidation of zirconium and its alloys in oxygen and in liquid sodium, the following current problems have arisen as to the mechanism.

Oxide vs. metal diffusion control.—There has been some question as to whether the rate of oxidation of zirconium is controlled by the diffusion of oxygen through the oxide film or whether it is controlled by diffusion into the metal. Is oxidation controlled by one of these processes or can these concepts be expressed quantitatively so that the importance of each process (diffusion in the oxide layer and diffusion in the metal) can be evaluated at a given temperature and will this explain the wide variation of reported activation energies in the literature (18 to about 50 kcal/mole)?

Oxidation in liquid sodium.—It has been observed that zirconium oxidation in liquid sodium follows an approximate parabolic law and has an activation energy (10) of about 52 kcal/mole. What is the mechanism of oxidation in sodium and why is the rate constant about a factor of 100 larger (at 600°C) for oxidation in oxygen than for oxidation in liquid sodium?

Quasi-cubic rate law.—The oxidation process has been observed to follow approximately linear, parabolic, and cubic-rate laws. The word approximately is used because the exponent n in the equation

$$W^n = kt + C$$

has been found to vary from 1 to about 3.6 under various conditions, rather than to be the integers 1, 2, or 3. The various authors have been inclined to refer to the rate laws as linear, parabolic, or cubic if n was in the range 1, 2, 3, respectively. Is it necessary that n be an integer?

Although a theoretical basis has been proposed for parabolic oxidation of zirconium at the time this paper was written, no basis for the apparent cubic law was known to the author. However, it has been brought to the attention of the author that Kofstad and Hauffe (11) have proposed qualitatively a similar mechanism for the approximate cubic law as is expressed quantitatively in this paper.

Theoretical Analysis and Experimental Results

Metal or Oxide Diffusion Control

It is our purpose first to show under what conditions and at what temperatures oxidation shifts from primarily diffusion in the film to primarily diffusion in the metal. To do this we must calculate the parabolic rate constant in terms of the diffusion coefficient for oxygen in the oxide and in the metal. Since oxidation of zirconium has been shown to obey approximately linear and cubic rate laws, as well as parabolic, we wish to determine if the dissolution process in addition to film growth can account for this.

We assume that the mechanism of oxidation is the same for all oxide thicknesses, that is, that oxygen dissolves into the metal at all temperatures and that with an existing oxide film, this dissolution process creates anion vacancies which in turn allow oxygen diffusion across the film. For this mechanism, exposure of oxide-free zirconium to oxygen will cause dissolution of oxygen into what is essentially a semi-infinite medium as in Fig. 1a. In Fig. 1, $C_1(O)$ represents the oxygen concentration at the oxide-gas interface for stoichiometric oxide, $C_1(\delta)$ represents the oxygen concentration in the oxide at the oxide-metal interface, and $C_2(\delta)$ represents the oxygen concentration in the metal at the metal-oxide interface. Curves t_1, t_2, and t_3 in Fig. 1a represent the oxygen concentration profile in the metal at increasing time. When enough time has elapsed for the metal to become supersaturated with oxygen [concentration between $C_2(\delta)$ and $C_1(\delta)$] and for nucleation to occur, an oxide film will form as shown in Fig. 1b. The value of the oxygen concentration in the metal at the metal-oxide interface in Fig. 1b will be between $C_1(\delta)$ and $C_2(\delta)$, depending on the degree of supersaturation needed to form oxide (*e.g.*, if very little supersaturation is needed, curve 1 is appropriate at a particular time, for a large supersaturation curve 2 is appropriate).

Let us assume that attainment of equilibrium at the oxide-metal interface is rapid with respect to oxygen absorption by the oxide-metal system. Once an oxide film has been formed, the following consideration can be made. The oxygen dissolves into the metal and if the rate of transport through the film is faster than dissolution, supersaturation will occur at the oxide-metal interface and more film will be formed. If the dissolution is faster than transport through the film, then the oxygen concentration in the metal will fall below the equilibrium value, and the film will begin to dissolve.

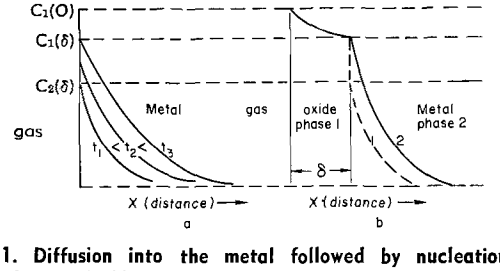

Fig. 1. Diffusion into the metal followed by nucleation and growth of an oxide film.

The process of diffusion through an oxide film and into the underlying metal, as illustrated in Fig. 1, is analyzed as a moving boundary problem in Appendix A. With the one assumption that D is independent of concentration, it is concluded in Appendix A that the parabolic rate equation can be expressed in terms of the two diffusion processes as follows

$$\frac{W^2}{t} = \frac{(M_1 + M_2)^2}{t} = k_p = [2\rho_1 f_{(O)} \alpha\sqrt{D_1} + B_2{}^1\sqrt{D_2}]^2 \quad [1]$$

where M_1 and M_2 are the weight (per square centimeter) of oxygen in the oxide film and metal, respectively, at time t, k_p is the parabolic rate constant, D_1 and D_2 are the diffusion coefficients for oxygen in the oxide film and the metal, respectively, $W = M_1 + M_2$, and the other symbols are constants defined in Appendix A. From Appendix A we have M_1, M_2, and k_p as a function of temperature

$$M_1 \approx 5.6 \times 10^3 \, e^{-\frac{14{,}600}{RT}} \quad [2]$$

$$M_2 \approx 1.6 \times 10^6 \, e^{-\frac{24{,}500}{RT}} \quad [3]$$

where M_1 and M_2 are expressed as mg/cm² at $t = 24$ hr, and

$$k_p \approx \left[19\, e^{-\frac{14{,}600}{RT}} + 5.5 \times 10^3 \, e^{-\frac{24{,}500}{RT}}\right]^2 (\text{mg/cm}^2)^2/\text{sec} \quad [4]$$

It is seen from Eq. [1] and [4] that at high temperatures $k_p \rightarrow M_2{}^2/t$ and the activation energy should approach 49 kcal/mole while at low temperatures $k_p \rightarrow M_1{}^2/t$ and the activation energy should approach 29 kcal/mole. At intermediate temperatures the apparent activation energy should increase from 29 to 49 kcal/mole.

Table I gives the experimental data of Debuigne and Lehr (12) for M_1, M_2, and W as a function of time and temperature. The calculation of W^2/t from the values of W at various times shows that the parabolic law is only approximated since the apparent k_p decreases slightly with increasing time. Values of M_1, M_2, and W^2/t from Table I are plotted in Fig. 2. The theoretical curves for M_1, M_2, and k_p (Eq. [2], [3], and [4]) are also plotted in Fig. 2. It is seen that if theoretical values of M_1, M_2, are multiplied by factors 1/2.5, 1/10, respectively, that the theoretical and experimental values correlate very well. It is not surprising to find that theoretical values differ in absolute value from experimental, considering the inaccuracy of the absolute values of D_1 and D_2. Also, it can be seen from Table I that the ratio M_1/M_2 is not constant with time as it should be if the parabolic law were strictly adhered to.

Table I. Quantity of oxygen in the oxide layer M_1, and the oxygen dissolved in the metal M_2 as a function of oxidation time and temperature [after Debuigne and Lehr (12)]

Temperature, °C	Time, hr	W, total wt gain, mg/cm²	M_1, oxygen in oxide, mg/cm²	M_2, oxygen in metal mg/cm²	M_1/M_2	W^2/t (mg/cm²)² hr
668	40.7	1.73 ± 0.02	1.49	0.24	6.2	0.073
668	92.6	2.63 ± 0.02	2.17	0.46	4.7	0.074
700	2.7	0.66 ± 0.07	0.67	0.06	11	0.16
700	16.4	1.50 ± 0.03	1.25	0.25	5	0.14
700	447	6.76 ± 0.16	3.42	3.34	1	0.10
750	7.5	1.87 ± 0.07	1.39	0.47	2.9	0.46
750	23	3.15 ± 0.02	1.97	1.18	1.7	0.43
800	6.4	2.35 ± 0.05	1.62	0.72	2.24	0.86
800	23	4.15 ± 0.15	2.53	1.62	1.56	0.75
800	78.7	7.05 ± 0.2	4.17	2.85	1.46	0.63
850	6	3.71 ± 0.1	2.24	1.46	1.53	2.3
	24	6.71 ± 0.2	2.98	3.73	0.8	1.9

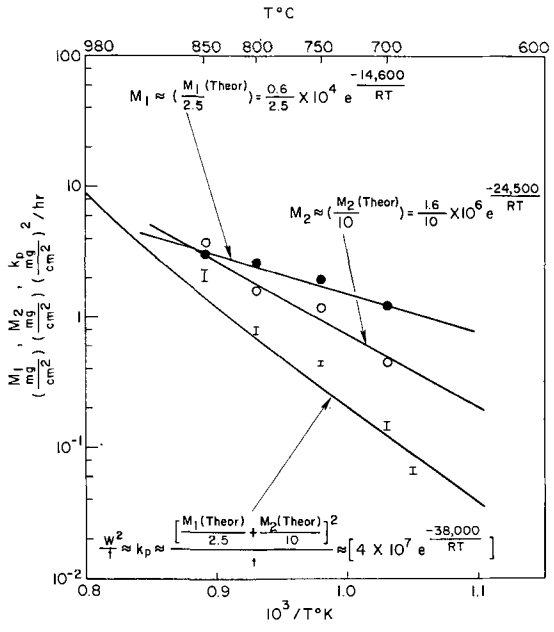

Fig. 2. Comparison of experimental data and theoretical equations for M_1, M_2, and k_p.

It is seen that M_1/M_2 becomes constant in less time as the temperature is increased. Since in the theoretical analysis the parabolic rate law was assumed over the entire time of the experiments, it is expected that some deviation would exist between the absolute values of the theoretical and experimental results. However, the fact that the experimental activation energies are predicted for M_1, M_2, and k_p as a function of temperature is considered to be confirmation of the theory.

From Eq. [2] and [3] at 24 hr

$$\frac{M_1}{M_2} \approx 3.5 \times 10^{-3} \, e^{\frac{9{,}900}{RT}} \quad [5]$$

and this ratio is plotted in Fig. 3 along with the experimental values from the data of various workers (9, 13, 14), and estimated from Table I at 24 hr. It is seen (Fig. 3) that an excellent correlation exists between the predicted curve and the experimental data. It is seen from Eq. [5] that $M_1/M_2 = 10$ at 450°C and $M_1/M_2 = 0.1$ at 1210°C, *i.e.*, 90% of the oxygen is going

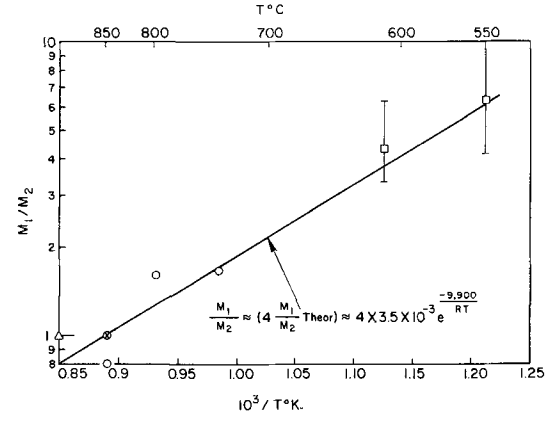

Fig. 3. Arrhenius plots of (M_1/M_2) vs. $1/T$ for the oxidation of zirconium (M_1 = wt of oxygen in the oxide film and M_2 = wt of oxygen in the metal) from the data of Debuigne and Lehr (12), Porte *et al.* (9), Pemsler (13), and Hussey and Smeltzer (14). The solid line is the predicted theoretical curve multiplied by a correction factor of 4. ○, Debuigne and Lehr (12), 24 hr; △, Porte *et al.* (9); circle with X, Pemsler (13); □, Hussey and Smeltzer (14).

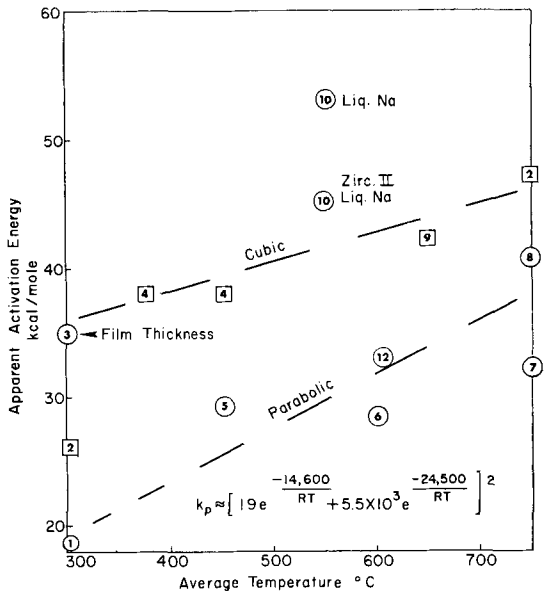

Fig. 4. Apparent activation energies for increasing temperature range from the literature. (Number identifies reference.) The circles indicate that an approximate parabolic rate law was followed; the squares indicate that an approximate cubic law was followed. The dashed lines indicate the trend of increased apparent activation energy for the parabolic and cubic data. The special case of oxidation in liquid sodium is given at the top of the figure.

into the oxide film at 450°C and 90% of the oxygen is going into the metal at 1210°C, if the mechanism holds for β zirconium above 862°C. Between these two temperatures both processes will be important. Since most of the experimental work has been done between 300° and 1000°C, it must be concluded that one cannot speak of diffusion control in the metal or diffusion control in the oxide but that each process plays a more or less important role, depending on the temperature. The quantitative contribution of each process is given by Eq. [4]. It is predicted that the effective activation energy will increase with temperature. For example, the curve W^2/t in Fig. 2 can be expressed as 10^7 exp $(-35{,}200/RT)$ in the low temperature region and 7×10^9 exp $(-40{,}600/RT)$ in the high temperature region. The curvature in the Arrhenius plot is within experimental error and would not have been detected from the experimental plot of W^2/t *vs.* $1/T$. In Fig. 4 values of apparent activation energy, reported by various authors, are plotted *vs.* the mean value of the temperature range of the oxidation study. It is seen that the apparent activation energy does increase as the temperature is increased, especially in the cases for which the parabolic law was approximately obeyed. We shall consider the effect of α in Eq. [1], on the oxidation of zirconium in liquid sodium next.

Oxidation in Liquid Sodium

An equation relating the rate constant for oxidation of zirconium in sodium, $k(\mathrm{Na})$, and temperature from Mackay's data (10) is

$$k(\mathrm{Na}) = 4.0 \times 10^{10}\, e^{-\frac{52{,}900}{RT}} \ (\mathrm{mg/cm^2})^2\ \mathrm{hr}^{-1} \qquad [6]$$

where $k(\mathrm{Na})$ is obtained from the equation

$$W^2 = k(\mathrm{Na})t \qquad [7]$$

and W is the weight gain (mg/cm²).

Equation [6] is within a factor of two of k_p from the theoretical Eq. [4] for the high temperature region ($M_2 >> M_1$) where diffusion into the metal is dominant.

The rate of film growth is proportional to α which is directly related to ΔC_1. For oxidation in oxygen this is just equal to the vacancy concentration in the oxide at the metal-oxide interface, $C(\square, \delta)$, since the vacancy concentration at the oxide-gas interface, $C(\square, o)$, is essentially zero. However, in liquid sodium, the reaction at the sodium-oxide interface is expressed by the equation

$$\mathrm{O(Na)} + 2e^- + \square(\mathrm{Na}) \overset{K(\mathrm{Na})}{\rightleftharpoons} \mathrm{O^=} \qquad [8]$$

where O(Na) represents the oxygen dissolved in sodium, e^- represents electrons in the oxide, $\square$(Na) represents oxygen vacancies in the oxide (in contact with Na), and $O^=$ represents lattice anions in the oxide. If we choose unit concentration as the standard state for $\square$(Na) and e^-, we can write

$$C(\square, \mathrm{Na}) = \left[\frac{a(\mathrm{O^=})}{4a(\mathrm{O, Na})\ K(\mathrm{Na})}\right]^{1/3} \qquad [9]$$

since $C(e^-) = 2C(\square, \mathrm{Na})$. A similar equation is obtained for the oxide-oxygen (gas) reaction except a (O,Na) is replaced by the activity (or partial pressure of oxygen) and K(Na) by the equilibrium constant $K(O_2, \mathrm{gas})$. It is because $[a(O_2, \mathrm{gas})\ K(O_2, \mathrm{gas})]$ is extremely large that $C(\square, o)$ approaches zero at the gas-oxide interface. Although $[a(\mathrm{O, Na})\ K(\mathrm{Na})]$ is not known, it is without doubt that

$$a(\mathrm{O, Na})\ K(\mathrm{Na}) << a(O_2, \mathrm{gas})\ K(O_2, \mathrm{gas}) \qquad [10]$$

and so

$$C(\square, \mathrm{Na}) >> C(\square, o) \qquad [11]$$

It is predicted that

$$\Delta C_1(\mathrm{Na}) \equiv |C(\square, \mathrm{Na}) - C(\square, \delta)| < C(\square, \delta) \qquad [12]$$

and the rate would be less than for oxidation in oxygen.

Since ΔC_1(Na) is predicted to be much smaller than ΔC_1 (oxygen), it follows that $\alpha(\mathrm{Na}) << \alpha(O_2)$. Consequently, W is shifted to predominantly M_2 with the resultant activation energy of 52 kcal/mole. In Mackay's experiments the rate law was between parabolic and cubic ($n \sim 2.3$ to 2.5). To verify this analysis, observe that from Mackay's work at 408°C and 500 hr, the film thickness proved to be 450 to 630Å (by comparison with a calibrated color step gauge) and had a total weight gain of 0.0158 mg/cm². With the equation, $M_1 = \rho_1 f_{(O)} \delta$ and an average value of $\delta \approx 540$Å, we calculate the weight of oxygen in the oxide film to be

$$M_1 \approx 5.83 \times 0.26 \times 5.4 \times 10^{-6} = 8.1 \times 10^{-6}\ \mathrm{g(O)/cm^2}$$

or 0.0081 mg/cm². It follows that the weight of oxygen in the metal was

$$M_2 \approx 0.0158 - 0.0081 = 0.0077\ \mathrm{mg/cm^2}$$

so that $M_1/M_2 \approx 1$. From Fig. 3 for oxidation in oxygen, it is predicted that the ratio of $M_1/M_2 \approx 20$. It is concluded that in liquid sodium, M_1 is much smaller than it would have been in oxygen at the same time and temperature, as predicted. Table II gives values for the

Table II. Comparison of the rate constants for the oxidation of zirconium in liquid sodium and in oxygen at approximately 600°C

	Oxidation of Zr in liquid Na at 630°C after Mackay (10)			Oxidation of Zr in O_2 gas at 600°C			
	$k(\mathrm{Na})$ $(\mathrm{mg/cm^2})^n/\mathrm{hr}$	n		Gas	$k(\mathrm{gas})$ $(\mathrm{mg/cm^2})^n/\mathrm{hr}$	n	Ref.
Pure Zr	3.2×10^{-4}	2.3	Zr	O_2	5.5×10^{-3}	2.9	9
			Zr	O_2	4×10^{-3}	2.0	3
Zircaloy II	3.2×10^{-4}	2.5	Zr(carbon melted)	O_2	1.4×10^{-1}	2.0	15
			Zr(carbon melted)	CO_2	4×10^{-3}	1.8	15

rate constants at about 600°C for oxidation of zirconium and its alloys in liquid sodium and for zirconium in oxygen. At 600°C, $W \approx M_1$ for oxidation in oxygen and $W \approx M_2$ in sodium so that $M_1/M_2 \approx [k(\text{oxygen})/k(\text{Na})]^{1/2} \approx 15$, from Table II. The predicted value of M_1/M_2 from Fig. 3 is ~4.

From Eq. [33A] for small α, $B_2' \approx C_2(\delta)$, and we calculate the diffusion coefficient for oxygen in the metal at 408°C and 500 hr to be

$$D_2 = \frac{M_2^2 \pi}{[C_2(\delta)]^2 4t} \approx \left(\frac{7.7 \times 10^{-3}}{1.14 \times 10^3}\right)^2 \cdot \frac{\pi}{4 \times 500 \times 3600} = 2 \times 10^{-17} \text{ cm}^2/\text{sec} \quad [13]$$

from Eq. [31A].

If we assume that the oxidation of zirconium in liquid sodium is due primarily to the diffusion of oxygen into the metal, then the diffusion coefficient, calculated from the sodium work should have the same relation to temperature as that found by Pemsler (16) for the diffusion of oxygen into zirconium metal, *i.e.*,

$$D_2 = 9.4e^{-\frac{51{,}780}{RT}} \text{ cm}^2/\text{sec} \quad [14]$$

It is seen from Mackay's results that the activation energy for oxidation in liquid sodium is approximately the same (52.9 kcal/mole) as for diffusion in the metal (51.78 kcal/mole). With Mackay's value of 52.9 kcal/mole and the value of D_2 at 408°C (Eq. [13]), we get

$$D_2 \approx 2e^{-\frac{52{,}900}{RT}} \text{ cm}^2/\text{sec} \quad [15]$$

for oxidation in liquid sodium, and this correlates very well with Eq. [14]. It is concluded that oxidation in liquid sodium is indeed due primarily to diffusion of oxygen in the metal for the temperature range of Mackay's work (about 400°-900°C). Table III gives a comparison of experimental values for the pre-exponential factor $D_{2,0}$, the diffusion activation energy Q_2, and D_2 at 386°C for pure zirconium and for Zircaloy 2 and Zircaloy 3. The fact that the activation energy for the oxidation of Zircaloy 2 in liquid sodium (~45 kcal/mole) compares well with independent measurements yielding a value of about 41 kcal/mole, is further evidence that oxidation in sodium is due to diffusion in the metal.

Quasi-cubic Rate Law

We wish to consider next a possible explanation for the fact that in a number of investigations (3, 9, 11, 20, 21) it has been found that the oxidation of zirconium, titanium, and copper, obey a rate law such as

$$W^n = k_c t \quad [16]$$

where n varies between 2 and about 3. It can be seen that according to Eq. [1] the parabolic law should be obeyed whether dissolution occurred or not. It is hoped that the following discussion (although speculative in nature) may point out important parameters for future investigation.

In the case of interstitial diffusion of oxygen in the metal, the diffusion coefficient should be proportional to the probability that an adjacent interstice is vacant. Consequently, the diffusion coefficient may be concentration dependent, as pointed out in Appendix A. A rigorous test to determine whether the quasi-cubic rate law can be attributed to this concentration dependency, must await an accurate investigation of the relation between D_2 and C_2. However, if $D_2(x)$ is proportional to the concentration of vacant sites at distance x in the metal, we may express an approximate local value as

$$D_2(x) \approx D_2^\circ (1 - C_2/C_2^1) \quad [17]$$

where D_2° is the diffusion coefficient at $M_2 = 0$ and C_2^1 is an effective value of C_2 for which $D_2(x) \to 0$. Placing the value for $D_2(x)$ (now a function of concentration) into Eq. [2A] yields a solution in numerical, rather than closed, form. Even though Eq. [17] has basis in theory, it is felt that the numerical analysis is unwarranted until the experimental relation between D_2 and C_2 has been determined. In the meantime, we can draw some conclusions concerning the quasi-cubic rate law as follows:

We know that C_2 is an increasing function of M_2 and as a working hypothesis we will make the assumption that $C_2/C_2^1 \equiv M_2/M_2^1$. Now, since M_1/M_2 is essentially constant at constant temperature, it follows that $C_2/C_2^1 \equiv W/W^1$, if the previous assumption is true. An approximate equation for an effective average value of D_2 is

$$\overline{D_2} \approx D_2^\circ (1 - W/W^1) \quad [18]$$

A more general equation than Eq. [1], which includes the property of concentration dependency (to a first approximation) can be written

$$W_c = W/[A + B(1 - W/W^1)] = t^{1/2} \quad [19]$$

where

$$A = 2\rho_1 f_{(O)} \alpha D_1^{1/2} \quad [20]$$

$$B = B_2^1 (D_2^\circ)^{1/2} \quad [21]$$

W^1 is the effective value of W at which $\overline{D_2} \to 0$, and W_c is defined as W divided by the term in brackets. Equation [19] has the property that at short time when

Table III. Experimental diffusion coefficients for oxygen in ZrO_2 and in Zr

$D = D_0 e^{-Q/RT}$

	Temp range, °C	C_1 (v) mole / cm³ × 10³	$D_{1,0}$ cm²/sec	Q_1 kcal/mole	At 386°C $D_1 \times 10^{13}$ cm²/sec	Ref.
Zr oxide	386	7	10^{-3}	28.7	3	This work
	499-900	—	10^{-3}	29.3	2.2	Debuigne & Lehr (12)
	700-1000	7.1	10^{-2}	28.1	55.0	Kingery *et al.* (17)
	700-1000	0.28	5×10^{-2}	33.4	5.5	Douglass (18)
			$D_{2,0}$	Q_2	$D_2 \times 10^{18}$	
Zr metal	400-585		9.4	51.8	80	Pemsler (16)
	408-635		2	52.9	8	Deduced from the data of Mackay (10)
	600-850		224	59.7	5	Debuigne & Lehr (12)
Zircaloy* 2 and 3	408-635		—	45.3	—	Deduced from the data of Mackay (10)
	1000-1500		0.2	41	6400	Mallett *et al.* (19)

* Zircaloy 2 contains in weight per cent, 1.5 Sn, 0.2 Fe, 0.05 Cr, 0.03 Ni.
Zircaloy 3 contains in weight per cent, 0.22 Sn, 0.34 Fe, 0.03 Cr, 0.005 Ni.

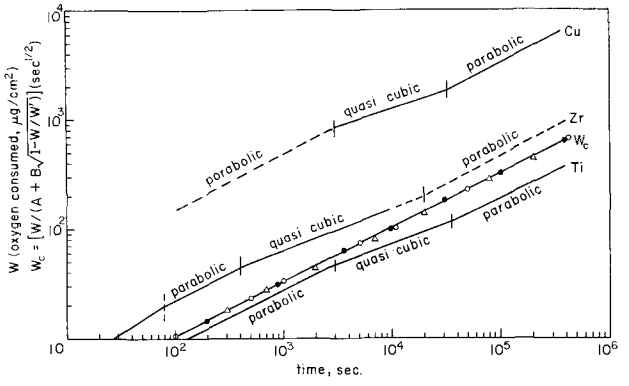

Fig. 5. Log log plot of W (weight oxygen consumed) vs. time (sec) for Zr, Ti, and Cu. The theoretical curve, $W_c = t^{1/2}$, is also plotted, where $W_c = W/[A + B\ (1 - W/W^1)]$. ○, Cu, 520°C, Tylecote; △, Zr, 500°C, Sense; •, Ti, 600°C, Kofstad and Hauffe.

$W << W^1$, $W_c = W/[A + B]$ and when $W \approx W^1$, $W_c = W/A$. Therefore at short and long time a log log plot of W *vs.* t should have a slope of 0.5 (parabolic), while at intermediate times as W/W^1 varies between approximately zero and unity the slope should be less than 0.5 (perhaps approximately 0.33 or quasi cubic). A log log plot of W_c *vs.* t should have a slope of 0.5 through the whole time period.

To illustrate that Eq. [19] has the correct form, we need values for A, B and W^1. Figure 5 shows a log log plot of W *vs.* t for the oxidation of Zr, Ti, and Cu, all of which dissolve oxygen to an appreciable extent. The solid lines labeled Zr, Ti, and Cu represent experimental data reported by Sense (20), Kofstad and Hauffe (11), and Tylecote (21), respectively. These curves have been divided into time periods for which approximate parabolic and cubic laws appeared to be obeyed. It is seen that the Ti curve follows the sequence parabolic, quasi-cubic, parabolic as predicted by Eq. [19]. The Zr curve is parabolic followed by quasi-cubic and the Cu curve is quasi-cubic followed by parabolic (the dashed lines represent presumed data, had it been reported in these time periods).

Let us first consider the zirconium experiment. From Eq. [20], [26A], and [27A] we obtain a value 1.45 $\mu g/cm^2\text{-}sec^{1/2}$ for A and from Eq. [21], [33A], and [28A] we obtain a value of approximately 0.8 for B, at 500°C. The experimental value of $A + B$ ($= W/t^{1/2}$, $t \sim 100$ to 400 sec) from Fig. 5 is about 2.2, which checks with the theoretical value. With these values for A and B and a value of 140 $\mu g/cm^2$ for the adjustable parameter W^1, values of W_c have been calculated and plotted (△) in Fig. 5. It is seen that the data falls close to the theoretical curve ($W_c = t^{1/2}$) in spite of the quasi-cubic period of the W *vs.* t curve.

It should be pointed out that D_2 in Eq. [28A] should be approximately equal to $D_2°$ in Eq. [21] because Pemsler (16) used pure crystal bar zirconium with anodized films. Calculation of M_2 for his experiments ($\sim 2 \times 10^{-5}$ cm oxide dissolved during an experiment) yields values of <30 $\mu g/cm^2$. As seen for the Zr curve in Fig. 5, this corresponds to the region where $W << W^1$. Consequently Pemsler's (16) experiments are not expected to show the concentration dependency. Kearns and Chirigos (22) also measured the diffusion coefficient of oxygen in zirconium and obtained results in accord with Pemsler. Although they state that they found no concentration dependency below 1.9 a/o (atomic per cent) oxygen, this would not invalidate Eq. [7]. For example, $C_2{}^1$ is probably of the order of 29 a/o (solubility of oxygen in zirconium) so that the change of $D_2(x)$ would be less than about 10% if C_2 varied between 0 and 2.9 a/o. This variation of $D_2(x)$ is probably less than experimental error in the Kearns and Chirigos experiments.

For the case of Ti oxidation, we have no theoretical values for A, B, and W^1, but we can obtain them from the experimental curves in Fig. 5. From a value of W during the short time (parabolic curve) we get $A + B \approx 0.87$, from the long time (parabolic curve) we get $A \approx 0.60$ so that $B \approx 0.27$. We know that the curve will change from quasi-cubic to parabolic as $W \to W^1$ and pick approximately 100 for W^1 from the Ti curve in Fig. 5. With these values for A, B, and W^1 values for W_c (solid points in Fig. 5) fall on the theoretical curve (W_c *vs.* t) over the whole experimental time period.

Simnad *et al.* (23) measured the rate of oxidation of both saturated (with oxygen) and unsaturated titanium as a function of temperature (800°-1200°C). They showed that the rate of oxidation was definitely a function of the oxygen content of the metal. From their data, we can obtain.

$$A\ (\mu g/cm^2\text{-}sec^{1/2}) = 1.2 \times 10^6\, e^{-\frac{25{,}000}{RT}}$$

for the saturated titanium. If we assume that in the high temperature range (800°-1200°C) that most of the oxygen enters the unsaturated metal we obtain

$$B \approx 2.3 \times 10^7\, e^{-\frac{32{,}000}{RT}}$$

At 600°C we calculate values for A and B of 0.7 and 0.25, respectively. These values are in excellent agreement with the values calculated above (0.6 and 0.27).

For the case of copper oxidation we can obtain values for A (~ 10 $\mu g/cm^2\text{-}sec^{1/2}$), W^1 ($\sim 1.8 \times 10^3$ $\mu g/cm^2$) but we cannot obtain B because the experimental data are not reported in the very short time period. However, if we assume that the parabolic curve would have been valid immediately proceeding the beginning of the reported data (~ 3000 sec) we obtain a value for $A + B$ of about 15 $\mu g/cm^2\text{-}sec^{1/2}$ so that B would be about 5. Calculated values of W_c for Cu (open circles in Fig. 5) also fall close to the theoretical curve.

Certainly an empirical equation having the form of Eq. [19], satisfactorily describes experimental data for which a quasi-cubic law seems to be obeyed. Equation [17] has theoretical basis and it is predicted from this analysis that an equation having the form of Eq. [18] will be valid for the diffusion of oxygen into Zr, Ti, and Cu, and perhaps other metals that dissolve oxygen. However, the substantiation of this prediction must await an experimental test.

It should be noted that it is predicted from Eq. [19] that when the quasi-cubic period is over ($W \to W^1$) that dissolution into the metal is essentially complete, the rest of the oxygen going into the film. If it is found experimentally that oxygen does continue to dissolve into the metal during the parabolic period (following the quasi-cubic period) the theory will remain essentially unchanged by multiplying $D_2°$ by a factor ($\gamma - W/W^1$) in Eq. [18] where γ is a constant greater than unity. In this case the constants A, B, and W^1 would be altered slightly.

It is seen then, that for metals that dissolve oxygen to an appreciable extent such as Zr, Ti, and Cu, a quasi-cubic rate law may be expected to be observed in some instances but not in others, depending on the values of A, B, and W^1, how long the experiment was allowed to continue, and the temperature range. The important parameters in A are α and D_1 and in B they are α, D_1/D_2 and $C_2(\delta)$. From Eq. [25A] and [33A] we see that low values of α will increase B but decrease A, so that α becomes a very important parameter with respect to which process will dominate at a given temperature. Equation [26A] reveals that α is directly related to ΔC, (the difference in defect concentration across the oxide film). According to Eq. [19] the quasi-

cubic law will not be observed unless the M_2 term is significant. However, regardless of the temperature range, if the M_2 term is significant, the apparent activation energy will tend to be closer to 49 kcal/mole (see Eq. [1] and [4]). This is seen to be the case in Fig. 4.

Conclusions

It is concluded that the mechanism of the oxidation of zirconium (and probably other metals such as titanium, hafnium, copper, tantalum, and perhaps niobium and vanadium, all of which dissolve oxygen to varying amounts) may be explained in detail by analysis of the diffusion of oxygen through an oxide film and diffusion of oxygen into the metal at all temperatures. Such an analysis reveals that both parabolic and higher order rate laws are to be expected during the oxidation of zirconium depending on experimental conditions. It is also concluded that apparent activation energies are expected to increase from about 30 kcal/mole at low temperatures to about 50 kcal/mole at high temperatures for experiments that obey the approximate parabolic law. For experiments that follow a higher order law (approximately cubic), it is expected that the activation energy would be closer to 50 kcal/mole at all temperatures.

Essentially all of the observed kinetic behavior can be explained from the unified theory presented, including oxidation in liquid sodium. However, the role of the concentration dependency of the diffusion coefficient must await experimental evidence before the explanation of the quasi-cubic nature is clearly established.

APPENDIX A

Solution of Fick's Second Law

Let us consider the moving boundary problem illustrated in Fig. 1 We let the oxide-gas interface be at $X = 0$ and the oxide-metal interface be at $X = \delta$. The oxygen concentration in the oxide (phase 1) is C_1 and in the metal (phase 2) is C_2. Since the density of the oxide is different from that of the metal saturated with oxygen, we will follow the method of Carlslaw and Jaeger (24). Consider the movement of the oxide-metal boundary in the X direction a distance $d\delta$. The mass of oxide $\rho_1 d\delta$ formed per unit area has been derived from a thickness $(\rho_1/\rho_2)\ d\delta$ of metal (saturated with oxygen). Thus the metal moves with a velocity v along the x-axis given by

$$v = -\left(\frac{\rho_1}{\rho_2} - 1\right)\frac{d\delta}{dt} \qquad [1A]$$

and Fick's second law can be written

$$D_2\left(\frac{\partial^2 C_2}{\partial X^2}\right) - \left(\frac{\rho_2 - \rho_1}{\rho_2}\right)\frac{d\delta}{dt}\cdot\frac{\partial C_2}{\partial X} = \frac{\partial C_2}{\partial t} \qquad [2A]$$

for diffusion in the metal. Since the diffusion coefficient for interstitial diffusion of oxygen would be concentration dependent, Eq. [2A] is only approximate.

Fick's second law for diffusion in the oxide can be expressed

$$D_1\left(\frac{\partial^2 C_1}{\partial X^2}\right) = \frac{\partial C_1}{\partial t} \qquad [3A]$$

The initial condition is

$$C_2 = C_2(\infty), X > 0, t = 0 \qquad [4A]$$

and the boundary conditions are

$$C_1 = C_1(O),\ X = 0, t > 0 \qquad [5A]$$

$$C_1 = C_1(\delta),\ X = \delta - 0,\ t > 0 \qquad [6A]$$

$$C_2 = C_2(\delta),\ X = \delta + 0,\ t > 0 \qquad [7A]$$

Conservation of mass gives

$$-D_1\frac{\partial C_1}{\partial X}\bigg|_{x=\delta-o} + D_2\frac{\partial C_2}{\partial X}\bigg|_{x=\delta+o} = C_1(\delta)\frac{d\delta}{dt} - C_2(\delta)\frac{d\delta}{dt} \qquad [8A]$$

The solution of Eq. [3A] satisfying the conditions [5A] and [6A] is

$$C_1 = C_1(O) - B_1\, erf\left(\frac{X}{2\sqrt{D_1 t}}\right) \qquad [9A]$$

which yields

$$C_1(\delta) = C_1(O) - B_1\, erf\left(\frac{\delta}{2\sqrt{D_1 t}}\right) \qquad [10A]$$

at $X = \delta$, and where B_1 is a constant with time. Since $C_1(\delta)$, $C_1(O)$, and B_1 are constant with time, then $\delta/\sqrt{t}$ must be constant. We let

$$\frac{\delta}{2\sqrt{D_1 t}} = \alpha \qquad [11A]$$

where α is a constant independent of time.

From Eq. [2A] and [11A]

$$D_2\left(\frac{\partial^2 C_2}{\partial \chi^2}\right) - \left(\frac{\rho_2 - \rho_1}{\rho_2}\right)\alpha\left(\frac{D_1}{t}\right)^{1/2}\frac{\partial C_2}{\partial X} = \frac{\partial C_2}{\partial t} \qquad [12A]$$

which has the solution

$$C_2 = C_2(\infty) + B_2\, erfc\left[\frac{X}{2\sqrt{D_2 t}} - \left(\frac{\rho_2 - \rho_1}{\rho_2}\right)\alpha\left(\frac{D_1}{D_2}\right)^{1/2}\right] \qquad [13A]$$

At $X = \delta$

$$C_2(\delta) = C_2(\infty) + B_2\, erfc\left[\alpha\phi^{1/2}\left(\frac{\rho_1}{\rho_2}\right)\right] \qquad [14A]$$

where $\phi = (D_1/D_2)$ and B_2 is a constant with time. According to Reddick and Miller (25), if

$$F(\alpha) = \int_{a(\alpha)}^{b(\alpha)} f(\chi, \alpha)\, d\chi \qquad [15A]$$

then

$$\frac{dF(\alpha)}{d\alpha} = \int_{a(\alpha)}^{b(\alpha)}\frac{\partial f(X,\alpha)}{\partial \alpha}\, dx - f(a,\alpha)\frac{da}{d\alpha} + f(b,\alpha)\frac{db}{d\alpha} \qquad [16A]$$

It follows from Eq. [16A] that

$$-D_1\frac{\partial C_1}{\partial \chi} = B_1\left(\frac{D_1}{\pi t}\right)^{1/2} e^{-\frac{X^2}{4D_1 t}} \qquad [17A]$$

and

$$-D_2\frac{\partial C_2}{\partial \chi} = B_2\left(\frac{D_2}{\pi t}\right)^{1/2} e^{-\left[\frac{X}{2\sqrt{D_2 t}} - \left(\frac{\rho_2 - \rho_1}{\rho_2}\right)\phi^{1/2}\alpha\right]^2} \qquad [18A]$$

so that

$$B_1\left(\frac{D_1}{\pi t}\right)^{1/2} e^{-\alpha^2} - B_2\left(\frac{D_2}{\pi t}\right)^{1/2} e^{-\alpha^2(\rho_1/\rho_2)^2\phi} = [C_1(\delta) - C_2(\delta)]\,\alpha\left(\frac{D_1}{t}\right)^{1/2}$$

or

$$B_1 e^{-\alpha^2} - \left(B_2 e^{-\alpha^2(\rho_1/\rho_2)^2\phi}\right)/\phi^{1/2} = [C_1(\delta) - C_2(\delta)]\,\alpha\sqrt{\pi} \qquad [19A]$$

Eliminating the constants B_1 and B_2 with Eq. [10A] and [14A], we get the transcendental equation for α

$$\frac{e^{-\alpha^2}}{erf\,\alpha} - \frac{[C_2(\delta) - C_2(\infty)]e^{-\alpha^2(\rho_1/\rho_2)^2\phi}}{[C_1(O) - C_1(\delta)]\phi^{1/2}\, erfc\,[\alpha\phi^{1/2}(\rho_1/\rho_2)]} = \left(\frac{C_1(\delta) - C_2(\delta)}{C_1(O) - C_1(\delta)}\right)\alpha\sqrt{\pi} \qquad [20A]$$

These equations are identical to those derived by Wagner (26) except for the factor ρ_1/ρ_2 since he did not consider the effect of change in density.

The parameters in Eq. [20A] have the following approximate values: $C_2(\delta) \approx 1.14$ g/cm^3, $C_2(\infty) = 0$, $C_1(O) \approx 1.46$ g/cm^3, $\rho_1 = 5.83$ g/cm^3, $\rho_2 = 6.72$ g/cm^3, and $\phi \approx$ (10-100).

From the thermodynamic data of Domagala and McPherson (27) and by choosing the appropriate standard states (*i.e.*, the concentration of the various species at 386°C), we get for the anion vacancy concentration at the oxide-metal interface

$$C(\square, \delta) \approx C(\square, \delta) \text{ (at 386°C) } K_v^{1/3} \approx 0.11\, e^{\frac{\Delta\bar{S}^\circ(v)}{3R}}\, e^{-\frac{\Delta\bar{H}^\circ(v)}{3RT}} \quad [21A]$$

Here $\Delta\bar{S}^\circ(v)$ and $\Delta\bar{H}^\circ(v)$ are the partial molar entropy and enthalpy of vacancy formation which prove to be 11 ± 0.3 e.u. and 7.1 ± 0.3 kcal/mole, respectively. In Eq. [21A], $C(\square, \delta)$ has been expressed in the units g/cm^3 rather than mole/cm^3.

It follows that

$$C(\square, \delta) = |C_1(O) - C_1(\delta)| \approx 0.7\, e^{-\frac{2{,}400}{RT}} \text{ g/cm}^3 \quad [22A]$$

and at 727°C, $|C_1(O) - C_1(\delta)| \approx 0.2$ and $C_1(\delta) \approx 1.26$ g/cm^3. An estimate of α from Eq. [20A] is about 0.2. Another way to obtain α is as follows: Let M_1 and M_2 be the quantity of oxygen in the oxide film and the metal per cm^2, respectively, at time t_1 ($W = M_1 + M_2$). If we assume diffusion through the film to obey Fick's first law, that the concentration gradient is essentially linear, and that D_1 is concentration independent, then at low temperatures when $M_2 << M_1$

$$\frac{dM_1}{dt} = \frac{\rho_1 f_{(o)} \Delta C_1 D_1}{M_1} \quad [23A]$$

where $f_{(o)}$ is the weight fraction of oxygen in zirconium dioxide. It follows that

$$M_1 = (2\rho_1 f_{(o)} \Delta C_1 D_1 t)^{1/2} \quad [24A]$$

From Eq. [11A]

$$M_1 = 2\rho_1 f_{(o)} \alpha (D_1 t)^{1/2} \quad [25A]$$

so that at 386°C

$$\alpha = \left(\frac{\Delta C_1}{2\rho_1 f_{(o)}}\right)^{1/2} = \left(\frac{0.11}{3.02}\right)^{1/2} \approx 0.2 \quad [26A]$$

which checks with the value obtained from Eq. [20A].

At 386°C the value for B_1 proves to be 0.05 and $B_2 \sim$ (3-70) depending on the absolute value of ϕ.

From Table III we choose the following as being the best approximate equations for D_1 and D_2

$$D_1 \approx 10^{-3}\, e^{-\frac{29{,}300}{RT}} \text{ cm}^2/\text{sec} \quad [27A]$$

$$D_2 \approx 10\, e^{-\frac{51{,}800}{RT}} \text{ cm}^2/\text{sec} \quad [28A]$$

Then

$$\phi = D_1/D_2 \approx 10^{-4}\, e^{\frac{22{,}500}{RT}} \quad [29A]$$

The values of $D_{1,o}$ and Q_1 in Eq. [27A] were chosen because they result from experiments for oxide films on zirconium; whereas, the work of Douglass was for sintered oxide powder and the work of Kingery *et al.* was for stabilized zirconia. The values of $D_{2,o}$ and Q_2 in Eq. [28A] were chosen because they result from direct measurement of oxygen into the metal.

Expressing M_1 as a function of temperature, at a time of 24 hr, yields

$$M_1 \approx 5.6 \times 10^3\, e^{-\frac{14{,}600}{RT}} \quad [30A]$$

where M_1 is in mg/cm^2.

The quantity of oxygen that has entered the zirconium metal at t is

$$M_2 = \int_o^t \left(-D_2 \frac{\partial C_2}{\partial X}\Big|_{x=\delta+o}\right) dt = 2B_2 \left(\frac{D_2 t}{\pi}\right)^{1/2} e^{-\alpha^2(\rho_1/\rho_2)^2\phi} \quad [31A]$$

At 24 hr

$$M_2 \approx 10^3\, B_2^1\, e^{-\frac{26{,}000}{RT}} \quad [32A]$$

where

$$B_2^1 = \frac{2}{\sqrt{\pi}} B_2\, e^{-\alpha^2(\rho_1/\rho_2)^2\phi} = \left[\frac{C_2(\delta)\, e^{-\alpha^2(\rho_1/\rho_2)^2\phi}}{erfc\,[\alpha\phi^{1/2}(\rho_1/\rho_2)]}\right] \frac{2}{\sqrt{\pi}} \quad [33A]$$

It is seen that at high temperatures when ϕ is small $B_2^1 \to C_2(\delta)$, while at low temperatures when ϕ is large, $B_2^1 \to C_2(\delta)\ \alpha\ (\rho_1/\rho_2)(\pi\phi)^{1/2}$, since for $y > 2$, $erfcy \approx e^{-y^2}/y\sqrt{\pi}$. In the temperature range 500° to 1000°C, B_2^1 can be expressed by the approximate equation

$$B_2^1 \approx 1.6\, e^{+\frac{1{,}500}{RT}} \quad [34A]$$

so that (changing to mg/cm^2)

$$M_2 \approx 1.6 \times 10^6\, e^{-\frac{24{,}500}{RT}} \text{ mg/cm}^2 \quad [35A]$$

in this temperature range.

From Eq. [25A] and [31A], we have

$$\frac{W^2}{t} = k_p = [2\rho_1 f_{(o)} \alpha \sqrt{D_1} + B_2^1 \sqrt{(D_2)}]^2 \quad [36A]$$

where k_p is the parabolic rate constant.

Acknowledgment

The author would like to acknowledge the help of Dr. J. H. Bick of the North American Aviation Science Center Mathematics Department for his help in solving Eq. [2A].

Manuscript received Feb. 10, 1964.

Any discussion of this paper will appear in a Discussion Section to be published in the December 1965 JOURNAL.

REFERENCES

1. E. A. Gulbransen and K. F. Andrew, *J. Metals*, **1**, 515 (1949).
2. J. Belle and M. W. Mallett, *This Journal*, **101**, 229 (1954).
3. E. A. Gulbransen and K. F. Andrew, *J. Metals*, **9**, 394 (1957).
4. D. Cubicciotti, *J. Am. Chem. Soc.*, **72**, 4138 (1950).
5. M. W. Fassell, NP-4246 (1952).
6. D. J. Garibotti, H. M. Green and W. M. Baldwin, Jr., AECU-3013 (1955).
7. P. Kofstad, *Acta Chem. Scand.*, **12**, 701 (1958).
8. R. G. Charles, S. Barnartt and E. A. Gulbransen, *Trans. Am. Inst. Mining Met. Engrs.*, **212**, 101 (1958).
9. H. A. Porte *et al.*, *This Journal*, **107**, 506 (1960).
10. T. L. Mackay, NAA-SR-6674 (1962), *This Journal*, **110**, 960 (1963).
11. P. Kofstad and K. Hauffe, *Werkstoff und korrosion*, **7**, 642 (1956).
12. J. Debuigne and P. Lehr, "Corrosion of Reactor Materials," p. 105, International Atomic Energy Agency, Vienna (1962).
13. J. P. Pemsler, *This Journal*, **111**, 381 (1964).
14. J. Hussey and W. W. Smeltzer, *ibid.*, **111**, 564 (1964).

15. A/conf. 15/P/1450, May 1958.
16. J. P. Pemsler, *This Journal*, **105**, 315 (1958).
17. W. D. Kingery *et al.*, *J. Amer. Cer. Soc.*, **42**, 393 (1959).
18. D. L. Douglass, "Corrosion of Reactor Materials," Vol. 2, 224, International Atomic Energy Agency, Vienna (1962).
19. M. W. Mallett *et al.*, *This Journal* **106** 181 (1959).
20. K. A. Sense, *ibid.*, **109**, 377 (1962).
21. R. F. Tylecote, *J. Inst. Metals*, **81**, 681 (1953).
22. J. J. Kearns and J. N. Chirigos, WAPD-TM-306, Feb. 1962.
23. M. Simnad, A. Spilners, and O. Katz, *J. Metals*, **7**, 645 (1955).
24. H. S. Carlslaw and J. C. Jaeger, "Conduction of Heat in Solids," p. 291, Oxford University Press (1960).
25. H. W. Reddick and F. H. Miller, "Advanced Mathematics for Engineers," p. 247, John Wiley and Sons, Inc., New York (1947).
26. W. Jost, "Diffusion in Solids, Liquids, and Gases," p. 71, Academic Press Inc., New York (1960).
27. R. F. Domagala and D. S. McPherson, *J. Metals*, **6**, 238 (1954).

Measurement of Overpotential Parameters on Passive Electrodes

J. L. Ord

Department of Physics, University of Waterloo, Waterloo, Ontario, Canada

ABSTRACT

Experimental measurements of overpotential parameters on passive electrodes often give results which depend on the technique used for the measurement. This dependence is illustrated for the widely studied system of a passive iron electrode in 1*N* H_2SO_4 at 25°C. Three different experimental techniques, all employing galvanostatic transients, are used for the measurements. The first method determines the overpotential parameters from the shape of the capacitive transient observed when the circuit is opened. In the second method the current is switched from one constant value to another, and the parameters are determined from the resulting potential shift. The third method determines the parameters from an analysis of the current dependence of the slopes of galvanostatic oxidation curves. The results obtained by the three methods differ significantly.

Studies of passivity commonly employ electrical measurements to study the state of the surface of the passive electrode. The properties of the electrode, such as layer thickness, are then deduced from the values of the electrical parameters measured. Many of the electrical measurements are concerned with the overpotential, measured from a Flade potential, and the dependence of current density on it, although some measurements, such as cathodic reduction, are concerned only with the removal of the passive layer. This investigation is designed to illustrate the results obtained when a number of techniques are used to study the overpotential on a passive electrode. The system studied is a passive iron electrode in 1*N* H_2SO_4 at 25°C. This system is used because a great deal of work has been done on it by a number of workers, and, although it is not suggested that the results obtained can be extrapolated to other systems, problems similar to those encountered in this system arise in most passive systems.

The three methods used in this investigation all employ galvanostatic transients. The first method determines the overpotential parameters from the shape of the capacitive transient observed when the circuit is opened. This method, referred to as the open-circuit method in this paper, is also known as the current-interrupter method (1, 2). In the second method, known as the rapid method (3), the current is switched from one constant value to another, and the parameters are determined from the resulting potential shift. The third method determines the parameters from a technique of analyzing galvanostatic oxidation transients which uses the current dependence of the slope of the oxidation curve, rather than the displacement between curves obtained at different charging currents. Galvanostatic oxidation transients have been used extensively in studies of passivity (4-6).

Experimental

Iron electrodes were prepared from high-purity vacuum-melted iron rods obtained from a number of sources. The only difference noted between electrodes prepared from different samples of iron was that only the highest purity iron could be heat treated to produce large uniform grains. Cylindrical electrodes with 0.2 cm^2 cross-sectional area were coated with epoxy, then mechanically and electrolytically polished to expose one end surface which was mounted vertically in the cell. The coating operation is critical with this geometry of electrode, and great care was taken to avoid leakage between the iron and the epoxy at the exposed surface. A jacketed five-neck flask with standard-taper joints was used as a cell. Electrodes, gas inlet tubes, and thermometers were all mounted on standard-taper adapters so that the cell could be sealed and yet be completely demountable. The cell was kept at 25° ± 0.1°C. The electrolyte used in the work reported here was hydrogen-saturated 1*N* H_2SO_4. Coiled platinum wire was used as a cathode, and a mercurous sulfate reference electrode was used in place of the more common calomel electrode in order to exclude chlorine ions from the electrolyte. All potentials were measured using the reference electrode then converted to the normal hydrogen electrode scale.

Potential is measured and recorded using a potentiometer, operated on voltage output, in series with a pair of electrometers connected in parallel. One of the electrometers is used as a VTVM with 8 mv maximum full-scale sensitivity, enabling potentials of greater than a volt to be read to fractions of a millivolt with high (10^4 ohm) input impedance. The other electrometer acts as the input coupler for the chopper-stabilized preamplifier of a fast (150 cps) recorder. The potentiometer can be used as a calibrated blocking voltage for the recorder. Currents are measured on an electrometer used as a micromicroammeter with a 3 mv full-scale voltage drop. The potentiostatic and galvanostatic supply circuits both use batteries and are connected in series. For potentiostatic measurements a relay shorts out the galvanostat. Galvanostatic transients are applied simply by opening this relay.

The results of electrical measurements in this system depend to a certain extent on the manner in which the electrode surface is prepared and also on the precise manner in which it is passivated. A description of this dependence is beyond the scope of this paper. The

results reported here were obtained using cathodic reduction as a final electrolytic pretreatment followed immediately by passivation using the potentiostatic circuitry. The electrode takes approximately 4 sec to reach the passive state. The electrolyte is then changed to remove reaction products. The electrical parameters, with the exception of the capacitance, reach their steady-state values quickly using this procedure. The large-grained electrode used for most of the measurements exhibited a steady-state current density of 5.5 $\pm$ 0.5 μa/cm^2 for passivating potentials between 0.9 and 1.4v, and 8.3 μa/cm^2 at a passivating potential of 0.71v. Other workers (7) report a current density of 7 μa/cm^2 for passivating potentials between 0.9 and 1.4v in this system.

Results

Experimental studies (4, 6, 8) on passive electrodes indicate that the current density, i, is exponentially related to the overpotential, V. This exponential dependence can be written most simply in the form

$$i = i_0 \exp(V/V_0) \quad [1]$$

where the parameters i_0 and V_0 have the same dimensions and units as the measured quantities i and V. Most other exponential expressions can be written in this simple form. For example (6), the expression

$$i = k \exp(\beta V - Q/B) \quad [2]$$

can be put into the form of Eq. [1] by setting $k \exp(-Q/B) = i_0$, and $\beta = 1/V_0$. The exponential dependence is experimentally found to be valid for transients in which V does not fall much below V_0. This result is consistent with the assumption that Eq. [1] describes an activation-controlled process at an overpotential which is high enough so that the reverse current can be ignored. Of the transients used in this work, only the open-circuit transient extends beyond the region of validity of Eq. [1], and its analysis is not carried beyond this region.

The open-circuit transient uses the fact that the overpotential appears across a capacitance. The differential equation of the transient is

$$C\,dV/dt + i_0 \exp(V/V_0) = 0 \quad [3]$$

and its solution is

$$V = V_0 \ln(CV_0/i_0) - V_0 \ln(t + CV_0/i_1) \quad [4]$$

where i_1 is the current density before the circuit is opened, in this case the steady-state current density, 5.5 μa/cm^2. In Fig. 1 an open-circuit transient is plotted on linear and logarithmic time scales. The time origin is adjusted on the logarithmic scale until the transient becomes linear. For the transient shown in Fig. 1 this time is 1.0 sec, and hence from Eq. [4] $CV_0/i_1 = 1.0$ sec. The slope of the logarithmic plot gives $V_0 = 0.186$v,

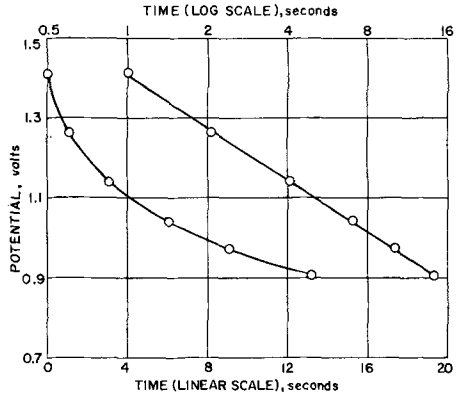

Fig. 1. Open-circuit transient from an initial passivating potential of 1.412v. The lower curve is plotted on a linear time scale; the upper curve, displaced 1 sec, is plotted on a logarithmic time scale.

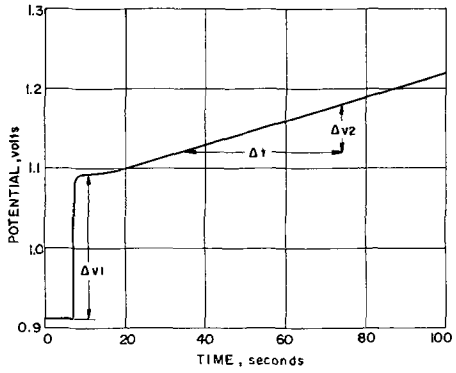

Fig. 2. Galvanostatic transient from a passivating potential of 0.912v at an anodic current density of 50 μa/cm^2. The rapid method determines V_0 from ΔV_1; the galvanostatic oxidation method studies the slope $\Delta V_2/\Delta t$ and its dependence on current density.

and therefore both C and V_0 can be determined. This transient cannot be fitted to a single exponential curve, and hence the electrode cannot be represented by a resistance in parallel with a capacitance. The transient can be fitted by a sum of exponentials to an accuracy dependent on the number of exponentials in the sum. This procedure gives an equivalent circuit which represents the electrode by a number of parallel R-C elements arranged in series. This approach is not taken here because other information, such as rapid-method measurements, indicates that current is exponentially related to overpotential through an equation of the form of Eq. [1].

Figure 2 shows a typical galvanostatic oxidation curve. The initial potential change, ΔV_1, enables V_0 to be determined. Since the value obtained does not agree with the value obtained from open-circuit transients, this value is designated V_0', and is obtained from

$$V_0' = \Delta V_1 / \ln(i_2/i_1) \quad [5]$$

where i_1 is the initial current, as in Eq. [4], and i_2 is the current of the oxidation transient. Equation [5] follows directly from Eq. [1]. In the rapid method complete oxidation transients generally are not recorded. The current is switched to another value as soon as the capacitive transient is complete, so that an average value for V_0' can be determined from a number of potential changes. The transient shown in Fig. 2 shows some initial overshoot. A complete oxidation curve can be analyzed either by taking ΔV_1 as shown in the figure or by extrapolating the linear portion of the curve back to intersect the initial rise to determine ΔV for use in Eq. [5]. In the rapid method the linear portion of the curve is not recorded, and hence ΔV_1 is used in Eq. [5] to determine V_0'. If the extrapolation technique is used, the difference between V_0' and the open-circuit V_0 is even greater than is indicated by the rapid method.

Complete galvanostatic oxidation curves are usually analyzed (4, 6) by plotting potential *vs.* the excess charge reaching the electrode, $(i_2 - i_1)t$, for a number of oxidation curves with different oxidation currents. The displacement between these curves for fixed values of the charge effectively gives V_0 through an equation of the form of Eq. [5]. This enables V_0 to be determined as a function of the excess charge reaching the electrode, rather than as a function of the steady-state passivating potential. This analysis assumes that the passive layer continues to dissolve at a rate equivalent to the steady-state current even when the electrode is not in a steady state. The passive layer is assumed to change its thickness in proportion to the excess charge reaching the electrode. The technique of analyzing the data outlined above is not used here because the displacement between curves is due, at least in part, to

the initial potential shift analyzed by the rapid method. Only the slopes of the galvanostatic oxidation curves are used in this work in order to obtain independent data from the rapid and oxidation methods.

The open-circuit and rapid methods are based on the assumption that the parameters i_0 and V_0 are unchanged over the course of the transient. The galvanostatic oxidation transient involves changes in i_0, V_0, or both. If V_0 changes and i_0 remains constant, Eq. [1] can be differentiated to give

$$dV/dq = dV_0/dq \ln(i_2/i_0) \quad [6]$$

If, on the other hand, i_0 changes and V_0 remains constant, differentiation of Eq. [1] yields

$$dV/dq = -V_0/i_0 \, di_0/dq \quad [7]$$

If analysis of the experimental data indicates that dV/dq is linearly dependent on $\ln(i_2)$, Eq. [6] is assumed valid, whereas if dV/dq is found to be independent of i, Eq. [7] is assumed valid. In systems where i_0 is large, such as the system under study in this paper, the factor $\ln(i_2/i_0)$ in Eq. [6] can be varied significantly by a suitable choice of oxidation currents. In systems where i_0 is small, such as in neutral electrolytes (6), the experiments must be performed with extreme care to enable the difference between Eq. [6] and [7] to be detected. This difference is important, since Eq. [6] and [7] lead to different models of a passive electrode. Integration of Eq. [7] casts Eq. [1] into the form of Eq. [2].

In Fig. 3 the values for V_0 obtained by the open-circuit and rapid methods are plotted *vs.* steady-state passivating potential. The two curves differ significantly, especially in their slopes. Fitting the data to straight lines using least squares gives

$$V_0 = 0.221 \ (V_p - 0.552) \text{ volts} \quad [8]$$

$$V_0' = 0.0664 \ (V_p + 0.408) \text{ volts} \quad [9]$$

where V_p is the steady-state passivating potential. If i_0 is assumed independent of passivating potential, it can be calculated directly from the steady-state current density and the slope of the V_0 *vs.* V_p curve. The measured values of i_1 are approximately independent of V_p, and if it is assumed that i_0 is also independent of V_p, Eq. [1] implies that the steady-state overpotential is equal to a constant times V_0. This constant is just the reciprocal of the slope of the V_0 *vs.* V_p curve plotted in Fig. 3. The assumption that i_0 is independent of V_p is equivalent to assuming that the zero of overpotential can be determined by extrapolating the V_0 *vs.* V_p curve in Fig. 3 to intersect the V_p axis. This assumption appears reasonable for the results of the open-circuit method, but not for the results of the rapid method. Using $i_1 = 5.5$ μa/cm^2 in Eq. [1], the open-circuit method gives $i_0 = 0.06$ μa/cm^2, and the rapid method gives $i_0 = 1.6 \times 10^{-6}$ μa/cm^2.

The open-circuit method enables the capacitance to be determined in addition to i_0 and V_0. The reciprocal

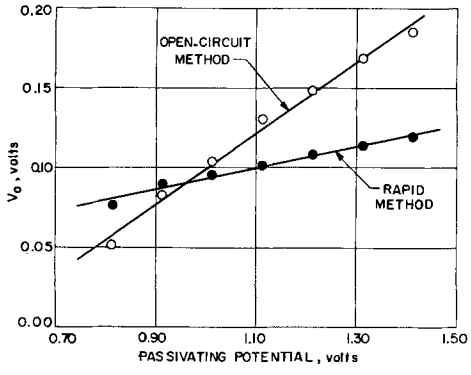

Fig. 3. Dependence of V_0 on passivating potential as determined by the open-circuit method and the rapid method.

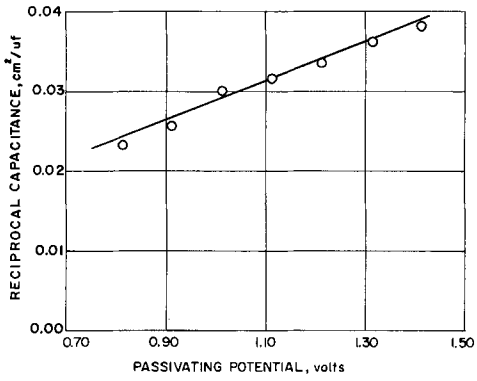

Fig. 4. Dependence of 1/C on passivating potential as determined by the open-circuit method.

capacitance is plotted *vs.* passivating potential in Fig. 4. A least squares fit of the data to a straight line gives

$$1/C = 0.0246 \ (V_p + 0.174) \text{ cm}^2/\mu\text{f} \quad [10]$$

The reciprocal capacitance changes by a factor of only 1.6 for a range of passivating potential over which V_0, measured by the same technique, changes by a factor of 3.6; hence both of these parameters cannot be proportional to the thickness of a layer on the electrode. The other methods do not enable capacitance to be determined, so no comparison is possible. It should be noted that capacitance is the parameter which is most sensitive to the history of the electrode, *i.e.*, the way in which the electrode is passivated, and the time spent at various passivating potentials. This behavior complicates the interpretation of capacitance measurements.

The results of the galvanostatic oxidation measurements are plotted in Fig. 5. In this figure and in calculations based on it, currents are expressed as multiples of the steady-state current, i_1. When currents are expressed in this manner, the data can be analyzed and compared with the results of the other methods without assuming a roughness factor. If Eq. [6] is multiplied through by i_1, one obtains

$$i_1/(i_2 - i_1) \, dV/dt = i_1 \, dV_0/dq [\ln(i_2/i_1) + \ln(i_1/i_0)] \quad [11]$$

In Fig. 5 the left hand side of Eq. [11] is plotted *vs.* $\ln(i_2/i_1)$. The linear dependence on $\ln(i_2/i_1)$ indicates that Eq. [6] rather than Eq. [7] describes galvanostatic oxidation transients. Fitting the data by least squares, one obtains

$$i_1/(i_2 - i_1) \, dV/dt = 0.0621 \ [\ln(i_2/i_1) + 0.843] \text{ mv/sec} \quad [12]$$

Using Eq. [11] and [12], one can compare this result with the results obtained by the other two methods by noting that $\ln(i_1/i_0)$ is just the reciprocal of the V_0 *vs.* V_p slope. The oxidation method gives this slope as

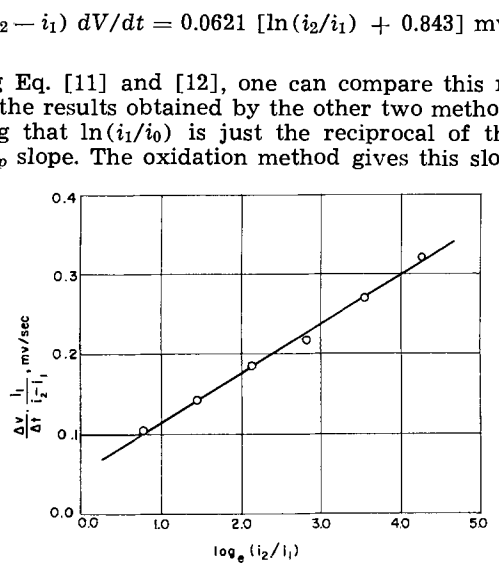

Fig. 5. Results of galvanostatic oxidation measurements from an initial passivating potential of 0.912v. i_1 is the initial steady-state current density, 5.5 μa/cm^2, and i_2 is the current density of the oxidation transient.

1.19, whereas the open-circuit method gave 0.221 and the rapid method gave 0.0664. These results differ significantly, and hence any conclusions concerning the variation in thickness of the passive layer with passivating potential must be drawn with great care. The difference between oxidation and rapid-method results can be obscured if the oxidation curves are analyzed by the more usual technique employing the displacement between curves, for this displacement has as one component the potential shift analyzed by the rapid method. The two techniques of analyzing oxidation curves will give consistent results only if the rapid method and oxidation method themselves give consistent results.

The results presented here cannot be extrapolated to other passive systems, but in most systems a similar study might be of value before an interpretation of the measured parameters is attempted. Ord and Bartlett (8), studying the passivity of iron in $2N$ H_2SO_4 at 20°C, attempt to interpret a wide range of measurements in terms of the state of the electrode and use a series of complex transients to study the reason for the difference between the values obtained by different methods.

Acknowledgment

This work was supported by the National Research Council of Canada under Grant No. A-1151. The author is indebted to Mr. W. J. Woitowetch for his assistance in preparing electrodes, and to Mr. A. B. Barabas for his assistance in performing the experiments.

Manuscript received May 25, 1964.

Any discussion of this paper will appear in a Discussion Section to be published in the December 1965 JOURNAL.

REFERENCES

1. D. C. Grahame, *J. Phys. Chem.*, **57**, 257 (1953).
2. P. E. Lake and E. J. Casey, *This Journal* **106**, 913 (1959).
3. G. Okamoto, H. Kobayshi, M. Nagayama, and N. Sato, *Z. Elektrochem.*, **62**, 775 (1958).
4. K. G. Weil, *ibid.*, **59**, 711 (1955).
5. K. J. Vetter, *ibid.*, **62**, 642 (1958).
6. N. Sato and M. Cohen, *This Journal*, **111**, 512 (1964).
7. U. F. Franck and K. G. Weil, *Z. Electrochem.*, **56**, 814 (1952).
8. J. L. Ord and J. H. Bartlett, *This Journal* (in press).

The Reaction of Hydrogen with Graphite at 1200° to 1650°C

Earl A. Gulbransen, Kenneth F. Andrew, and Fred A. Brassart

Physical Chemistry Department, Westinghouse Electric Corporation, Pittsburgh, Pennsylvania

ABSTRACT

The reaction was studied at 19 Torr pressure under static and flow conditions. Rates of reaction up to 6.0 x 10^{17} atoms of C per cm^2-sec were measured at 1650°C and 19 Torr. The rates of reaction were nearly independent of flow and pressure. The kinetic data could be fitted to an Arrhenius-type equation $dn'/dt = Ke^{-\Delta H/RT}$, where $\Delta H = 72 \pm 2$ kcal/mole. Mass spectrometer studies of the reacted gases in the flow experiments showed no evidence for methane and other carbon-hydrogen gases. This was interpreted as evidence for the decomposition of carbon-hydrogen compounds immediately after reaction. Since the reaction products cannot form a barrier layer, a chemical mechanism was proposed for the reaction for both flow and static conditions.

Graphite reacts with hydrogen at an appreciable rate at 1600°C although the reaction products methane and other hydrocarbons are unstable. The kinetics and mechanism of the graphite-hydrogen reaction at high temperatures is of scientific and technical interest since graphite has been proposed as a material in nuclear reactors operating in hydrogen atmospheres at high temperatures.

This paper will report a study of the kinetics of the graphite-hydrogen reaction using both static and flow conditions. Vacuum microbalance methods are used to study the kinetics of the reaction, and mass spectrometer methods are used to study the composition of the reaction products.

Clark, Woodley, and DeHalas (1) have given a review of the published work. Low-temperature carbon chars were used in the early kinetic studies (2). Carney and Thomas (3) and Blackwood (4-6) have studied the reaction of various carbons including graphite below 950°C. Blackwood (4-6) used a packed annular bed of carbon and hydrogen at pressures up to 40 atm. The rate of methane formation was found to be a linear function of pressure. For graphite, an energy of activation of 43 kcal/mole was found (4) for the temperature range 650°-950°C. A reaction mechanism was suggested (6) which involves the formation of $>CH_2$ groups on the carbon surface and subsequent reaction with H_2 to form methane.

Thermochemical Calculations

Table I shows three types of reactions which involve the specimen and reacting gas. The first group are reactions between hydrogen and carbon, the second group are vaporization reactions of carbon atoms and molecules, and the third reaction is the dissociation of hydrogen molecules. Heats of formation and equilibrium constants are tabulated for each of these reactions in Table II for temperature of 527°-1727°C (7). Except for the methane reaction all of the reactions show large positive heats of formation and negative values of the logarithms of the equilibrium constants. Molecular hydrogen is slightly dissociated at the higher temperatures.

Table III shows a second series of reactions. These are side reactions including the dissociation of the alumina furnace tube in vacua and the reactions of hydrogen and methane with alumina. These are undesirable reactions and their effects on the primary reactions must be carefully evaluated. Equilibrium constants are given for the reaction at 1627°C (1900°K).

The dissociation of Al_2O_3 to Al_2O and O_2 gases is the least unfavorable of the dissociation reactions. An oxygen pressure of 10^{-8} Torr is calculated at 1627°C.

Table I. Primary reactions

1.	Hydrogen reactions	
	$C(s) + 1/2H_2(g) \rightleftarrows CH(g)$	[1]
	$C(s) + H_2(g) \rightleftarrows CH_2(g)$	[2]
	$C(s) + 3/2H_2(g) \rightleftarrows CH_3(g)$	[3]
	$C(s) + 2H_2(g) \rightleftarrows CH_4(g)$	[4]
	$2C(s) + H_2(g) \rightleftarrows C_2H_2(g)$	[5]
	$2C(s) + 2H_2(g) \rightleftarrows C_2H_4(g)$	[6]
2.	Vaporization	
	$C(s) \rightleftarrows C_1(g)$	[7]
	$2C(s) \rightleftarrows C_2(g)$	[8]
3.	Dissociation	
	$H_2(g) \rightleftarrows 2H(g)$	[9]

Table II. Heats of formation‡ and equilibrium constants for carbon and hydrogen reactions

Temp, °C	[1]* CH(g) ΔH°_f	[1]* CH(g) log K_p	[2]* CH_2(g) ΔH°_f	[2]* CH_2(g) log K_p	[3]* CH_3(g) ΔH°_f	[3]* CH_3(g) log K_p	[4]* CH_4(g) ΔH°_f	[4]* CH_4(g) log K_p	[5]* C_2H_2(g) ΔH°_f	[5]* C_2H_2(g) log K_p
527	142.0	−32.91	66.0	−16.05	29.87	−9.58	−20.86	0.15	53.17	−11.78
727	141.8	−25.15	65.7	−12.45	29.28	−7.96	−21.48	−1.01	53.45	−8.86
927	141.5	−19.99	65.4	−10.06	28.86	−6.90	−21.85	−1.80	53.23	−6.91
1127	141.3	−16.31	65.2	−8.36	28.55	−6.16	−22.05	−2.37	53.04	−5.53
1327	141.0	−13.56	65.0	−7.09	28.30	−5.60	−22.14	−2.80	52.89	−4.50
1527	140.8	−11.42	64.8	−6.11	28.12	−5.17	−22.14	−3.14	52.77	−3.70
1727	140.5	−9.71	64.7	−5.37	27.96	−4.83	−22.10	−3.41	52.67	−3.06

Temp, °C	[6]* C_2H_4(g) ΔH°_f	[6]* C_2H_4(g) log K_p	[7]* C(g) ΔH°_f	[7]* C(g) log K_p	[8]* C_2(g) ΔH°_f	[8]* C_2(g) log K_p	[9]* H(g) ΔH°_f	[9]* H(g) log K_p
527	9.76	−6.69	171.6	−38.57	197.9	−43.75	52.84	−11.54
727	9.20	−6.17	171.6	−29.20	197.6	−32.95	53.12	−8.65
927	8.87	−5.84	171.5	−22.95	197.2	−25.76	53.38	−6.71
1127	8.70	−5.61	171.4	−18.49	196.7	−20.63	53.63	−5.32
1327	8.61	−5.45	171.2	−15.15	196.3	−16.80	53.85	−4.27
1527	8.59	−5.32	171.1	−12.55	195.8	−13.82	54.05	−3.45
1727	8.63	−5.21	170.9	−10.48	195.3	−11.45	54.23	−2.79

‡ ΔH°_f in kcal/mole.
* Refer to reactions in Table I.

Table III. Secondary reactions

Type	Equation		log K_p 1627°C (1900°K)
Thermal dissociation	$Al_2O_3(s) \rightleftarrows 2Al(g) + 3/2O_2(g)$	[10]	−28.81
	$Al_2O_3(s) \rightleftarrows Al_2O(g) + O_2(g)$	[11]	−21.72
	$Al_2O_3(s) \rightleftarrows Al_2O_2(g) + 1/2O_2(g)$	[12]	−18.46
Hydrogen reduction	$Al_2O_3(s) + 3H_2(g) \rightleftarrows 2Al(g) + 3H_2O(g)$	[13]	−17.15
	$Al_2O_3(s) + H_2(g) \rightleftarrows Al_2O_2(g) + H_2O(g)$	[14]	−15.03
	$Al_2O_3(s) + 2H_2(g) \rightleftarrows Al_2O(g) + 2H_2O(g)$	[15]	−13.94
Hydrogen atom reduction	$Al_2O_3(s) + 6H(g) \rightleftarrows 2Al(g) + 3H_2O(g)$	[16]	+1.46
	$Al_2O_3(s) + 2H(g) \rightleftarrows Al_2O_2(g) + H_2O(g)$	[17]	−8.82
	$Al_2O_3(s) + 4H(g) \rightleftarrows Al_2O(g) + 2H_2O(g)$	[18]	−1.53
Methane reaction	$Al_2O_3(s) + 3CH_4(g) \rightleftarrows 2Al(g) + 3CO(g) + 6H_2(g)$	[19]	+3.93
	$Al_2O_3(s) + CH_4(g) \rightleftarrows Al_2O_2(g) + CO(g) + 2H_2(g)$	[20]	−8.00
	$Al_2O_3(s) + 2CH_4(g) \rightleftarrows Al_2O(g) + 2CO(g) + 4H_2(g)$	[21]	+1.17
Carbon reduction	$Al_2O_3(s) + 3C(s) \rightleftarrows 2Al(g) + 3CO(g)$	[22]	−5.91

The reactions of molecular hydrogen with alumina are not feasible even at 1627°C. However, the reactions of atomic hydrogen with alumina are feasible. Due to the small concentration of atomic hydrogen in equilibrium with molecular hydrogen the reduction of alumina by hydrogen is not important at 1627°C.

The direct reaction of methane with alumina to form the metal or the suboxide Al_2O is favorable at 1627°C. This reaction is of special interest since methane is probably the major reaction product of the carbon-hydrogen reaction.

Experimental

The apparatus and method have been described (8-9). Spectroscopic grade of high-purity graphite (AGKSP) was used. The cylindrical shaped specimens weighed 0.05g and had surface areas of 0.55 cm^2. Ultra pure hydrogen containing 99.97% H_2 and 0.03% CO or N_2 was used in all of the experiments.

The furnace tube was a 2 cm I.D. high-density alumina tube. The specimens were supported centrally in the tube from one end of a Cahn microbalance by a tungsten wire. Temperature was measured at a point inside the furnace tube adjacent to the sample. The hydrogen gas was preheated in the furnace tube before coming into contact with the sample.

Results

Time and temperature.—Weight loss *vs.* time experiments were made at 19 Torr pressure and for temperatures between 1200° and 1650°C. Both static and flow environments were used. Flow rates of 0.84 to 2 x 10^{20} hydrogen molecules per second were used. These rates correspond to 256-610 cm/sec flow velocities at 1650°C.

Linear weight loss *vs.* time curves were found except at the highest temperatures where surface area changes occurred. Rates of reaction were evaluated from the initial part of the curve in units of grams of C/sec and in atoms of C/cm^2-sec. Geometrical surface areas were used in the calculations. Independent weight checks were made using an external microbalance.

Calculations could also be based on the real area of the graphite sample. Here the rates of reaction calculated on the geometrical area basis would be divided by the ratio of real surface area to the geometrical surface areas. This factor is of the order of 1000 for the size of specimens used and for the particular grade of graphite.

Table IV summarizes the kinetic results. For comparison flow rates are given in units of atoms of hydrogen per sec. Figure 1 shows a log rate *vs.* $1/T$ plot

Table IV. Rate of reaction, graphite and hydrogen 19 Torr, 0.050g sample, 0.545 cm^2

Flow

Reaction conditions		Rates of reaction	
Temp, °C	Flow, atoms H/sec	dw/dt, g/sec	dn'/dt, atoms C/cm^2-sec
1650	3.4×10^{20}	6.4×10^{-6}	5.9×10^{17}
1600	3.6×10^{20}	4.6×10^{-6}	4.2×10^{17}
1550	3.6×10^{20}	1.6×10^{-6}	1.5×10^{17}
1500	3.4×10^{20}	1.3×10^{-6}	1.2×10^{17}
1500	3.6×10^{20}	9.9×10^{-7}	9.0×10^{16}
1450	3.6×10^{20}	9.6×10^{-7}	8.8×10^{16}
1400	3.6×10^{20}	5.3×10^{-7}	4.9×10^{16}
1350	3.6×10^{20}	1.9×10^{-7}	1.7×10^{16}

Static

Reaction conditions		Rates of reaction	
Temp, °C	Flow, atoms H/sec	dw/dt, g/sec	dn'/dt, atoms C/cm^2-sec
1600	None	4.2×10^{-6}	3.8×10^{17}
1500	None	1.6×10^{-6}	1.4×10^{17}
1500	None	9.5×10^{-7}	8.9×10^{16}
1200	None	$<1.6 \times 10^{-8}$	$<1.5 \times 10^{15}$

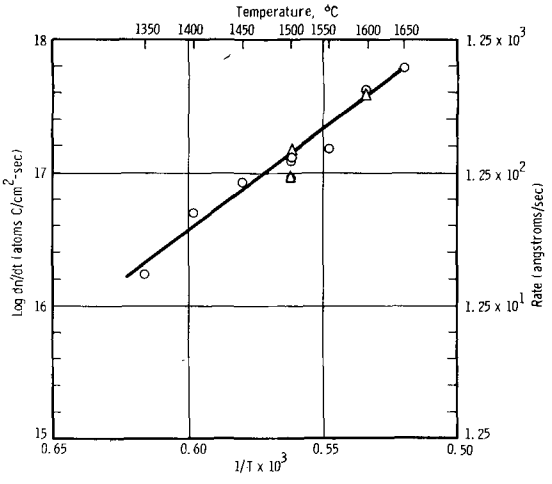

Fig. 1. Log *dn/dt* graphite + hydrogen, 19 Torr; ○, flow conditions; △, static conditions, samples 0.545 cm², ΔH = 72 ± 2 kcal/mole.

of the data. Rates are given in both atoms of C/cm²-sec and in angstroms of C/sec. At 1650°C and 19 Torr a reaction rate of 6.0 x 10^{17} atoms of C/cm²-sec or 10^3 Å/sec was measured. This rate is equivalent to an ablation rate of 0.86 cm of C/day.

Temperatures given are those of a thermocouple placed inside the furnace tube and adjacent to the sample. No temperature change was noted on adding hydrogen. This indicates that the hydrogen was adequately preheated and that the heat of reaction was not appreciably raising the surface temperature.

The results of both flow and static experiments fit the same straight line in Fig. 1. A heat of activation of 72 ± 2 kcal/mole was calculated.

Effect of pressure.—Table V shows a series of experiments made at 1500°C for pressures of 9.5 to 38 Torr for both static and flow conditions. The effect of pressure is small.

Mass spectrometer studies—Flow experiments.—Samples of the reacted gases were analyzed in both the flow and static experiments. Table VI shows the gas analyses for three flow experiments. From the rate of carbon reaction the expected methane concentrations should be 0.10, 0.03, and 0.01% for the 1500°, 1400°, and 1200°C experiments. No methane was found. The accuracy of the analyses was 0.01%. No evidence was found for either carbon monoxide or carbon dioxide.

Static experiments.—Table VII shows the results for the static experiments at 1500°C. Carbon monoxide was the major product of reaction. The cc-Torrs of carbon monoxide in the system could be related to the expected cc-Torrs from the amount of carbon reacted. No methane was found. The only source of oxygen in the reaction system was the alumina furnace tube. These experiments suggest that the carbon-hydrogen reaction products react with the alumina furnace tube wall at 1500°C to give carbon monoxide and hydrogen. This can only happen in a static experiment where sufficient time is available. In the flow experiments where velocities up to 615 cm/sec are used, the reacted gases are in the hot zone of the tube for less than 10^{-2} sec. This time is not sufficient for the reaction to form carbon monoxide. Since no methane or other carbon-hydrogen molecules are observed in the flow experiment, we propose that the carbon-hydrogen reaction products decompose to carbon and hydrogen immediately after formation. Carbon soot was observed in the exit line.

Table V. Effect of pressure on rates of hydrogen + carbon reaction, 9.5-38 Torr, 1500°C, 0.050g sample, 0.545 cm² area

P, Torr	Flow, H atoms/sec	*dw/dt*, g/sec	*dn'/dt*, atoms C/cm²-sec
9.5	3.6 x 10^{20}	8.9 x 10^{-7}	8.1 x 16^{16}
9.5	3.6 x 10^{20}	9.4 x 10^{-7}	8.6 x 10^{16}
19	3.6 x 10^{20}	9.9 x 10^{-7}	9.0 x 10^{16}
19	3.1 x 10^{20}	1.5 x 10^{-6}	1.4 x 10^{17}
38	4.0 x 10^{20}	1.4 x 10^{-6}	1.3 x 10^{17}
38	3.9 x 10^{20}	1.5 x 10^{-6}	1.4 x 10^{17}
19	None imposed	1.0 x 10^{-6}	9.0 x 10^{16}
19	None imposed	1.6 x 10^{-6}	1.4 x 10^{17}

Table VI. Mass spectrometer studies, carbon and hydrogen reaction, 19 Torr, flow rates = 3.4 x 10^{20} atoms of H/sec

Ultra pure hydrogen		Analysis in %*					
Temp, °C	Rate of reaction, atoms C/cm²-sec	H_2	N_2	O_2	CH_4	CO	CO_2
1200	1.2 x 10^{16}	99.80	0.14	0.04	<0.01	<0.01	0.01
1400	4.9 x 10^{16}	99.84	0.13	0.03	<0.01	<0.01	<0.01
1500	1.5 x 10^{17}	99.76	0.18	0.04	<0.01	<0.01	0.01

* Accuracy of analyses 0.01%.

Table VII. Mass spectrometer studies, carbon and hydrogen reaction, 1500°C 19 Torr, convection flow only, ultra pure hydrogen

Extent of reaction		Analyses in %*					
Total C, mg	Time, min	H_2	N_2	O_2	CH_4	CO	CO_2
1.42	10	96.86	0.05	0.01	<0.01	3.07	0.01
5.02	30	90.93	<0.01	0.02	<0.01	9.05	<0.01

* Accuracy of analyses 0.01%.

Alternative mechanisms.—Two alternative explanations may be given which must be considered. First, alumina dissociates giving oxygen and the gaseous suboxide Al_2O. The oxygen then reacts with the graphite sample giving carbon monoxide. Thermochemical data from Table III shows that the dissociation reactions do not occur at 1627°C to give a sufficient oxygen pressure to account for the rate of reaction. Leak rate studies on the reaction system also show that gas sources cannot account for more than 1% of the required oxygen. Second, hydrogen reacts with alumina to give the suboxide and water. The water then reacts with graphite to give carbon monoxide and hydrogen. Thermochemical data show that this reaction is not possible at 1627°C. To prove that this reaction is not contributing we exposed sheet specimens of pure alumina to hydrogen in a static system at 1500°C and 19 Torr pressure. No reaction occurred.

Alumina + methane reaction.—Thermochemical calculations given in Table III show that methane can react with alumina at 1627°C. To prove that this reaction is possible we added pure methane gas to the alumina furnace tube at 10 Torr and at 1600°C. A gas sample was taken after allowing the reaction to proceed for 30 min. The gas analyses showed 57.86% H_2, 18.12% CO, 0.03% CO_2, 23.83% methane, and 0.016% C_2H_2. 43% of the original methane was reacted. This experiment is not quantitative since only 40 cc of the 5000 cc volume was in the hot zone. In addition most of the gas source was connected to the furnace tube by 8 mm sections of stainless steel or nickel tubing. We conclude that methane can react with the alumina furnace tube at 1600°C.

Discussion

The kinetic data obtained in this study will be used in two ways. First, we will estimate the efficiency of the reaction and the fraction of kinetic theory collisions which result in reaction. Second, we will apply Blackwood's analyses (6) of the carbon + hydrogen reaction to our high temperature data.

Efficiency of reaction.—The efficiency E of a reaction is given by the equation

$$E = 4\frac{dn''/F}{dt} \qquad [23]$$

Here F is the flow rate in units of H atoms/sec, dn''/dt is the actual rate of reaction in the system and the factor 4 comes from the ratio of hydrogen to carbon atoms in methane. At 1650°C and 19 Torr, we calculate from Table IV an efficiency of 0.24%. Compared to the high efficiencies of 25-30% for the oxidation reaction only a small fraction of the hydrogen atoms passing over the sample react.

Kinetic theory.—Equation [24] gives the number of collisions n of hydrogen molecules with a 1 cm² surface

$$n = 3.5 \times 10^{22} \frac{P}{(MT)^{1/2}} \qquad [24]$$

Here P is the pressure in Torr, T is the absolute temperature in °K, and M is the molecular weight. At 1650°C and 19 Torr, a collision rate of 1.07×10^{22} molecules/cm²-sec is calculated. If the reaction product is methane, we calculate a maximum theoretical rate of reaction of 5.03×10^{21} carbon atoms per cm²-sec. The actual rate was 6×10^{17}. The fraction of the theoretical maximum was 0.0108.

Mechanism.—The kinetic study and the mass spectrometer analyses of the reaction products suggests a chemical mechanism is rate controlling in both static and flow environments. A barrier layer of gaseous reaction products is not formed since the methane is removed by dissociation or by reaction with the alumina furnace tube.

Blackwood (6) has proposed a three-step mechanism. The first step is the adsorption of two hydrogen atoms with one being attached to an active site and the other reacting anywhere on the surface including the original site.

$$C + H_2 \underset{j_1}{\overset{i_1}{\rightleftarrows}} (CH)H \qquad [25]$$

Here the activity of the surface is unaffected by the hydrogen atom. The second step is a rearrangement.

$$(CH)H \underset{j_2}{\overset{i_2}{\rightleftarrows}} (CH_2) \qquad [26]$$

The third step is the direct separation of methane from the surface by reaction with molecular hydrogen.

$$H_2 + (CH_2) + \underset{j_3}{\overset{i_3}{\rightleftarrows}} CH_4\uparrow \qquad [27]$$

The small letters refer to the velocities of the forward and reverse directions for the respective reactions.

Equations can be set up for the formation and decomposition of each intermediate and for methane in terms of the velocities of the several reactions and the fraction of surface occupied. These equations can be used to calculate the rate of formation of methane R. For low methane concentrations, we have

$$R = \frac{k_1 P_{H_2}^2}{1 + k_3 P_{H_2} + k_4 P_{H_2}^2} \qquad [28]$$

k_1, k_3, and k_4 are rate constants and are given by the following equations

$$k_1 = \frac{i_1 i_2 i_3}{j_1 j_2 + i_2 i_2} \qquad [29]$$

$$k_3 = \frac{i_1 i_2 + i_1 j_2 + i_3 j_1 + i_2 i_3}{j_1 j_2 + i_2 i_2} \qquad [30]$$

$$k_4 = \frac{i_1 i_3}{j_1 j_2 + i_2 i_2} \qquad [31]$$

Between 650° and 870°C, Blackwood found that R was a linear function of the pressure. Therefore, in Eq. [28], $k_3 P_{H_2} >> 1$ and $k_4 P_{H_2} << k_3 P_{H_2}$.

At 1600°C we find R to be nearly independent of pressure. In Eq. [28], $k_4 P_{H_2}^2 > 1 + k_3 P_{H_2}$. Equation [28] for these conditions is

$$R = \frac{k_1}{k_4} \simeq i_2 \qquad [32]$$

This suggests that the rate-limiting mechanism at high temperatures is a surface rearrangement of hydrogen atoms on the surface following reaction [26].

Summary

Equilibrium thermochemical calculations show that methane and other carbon-hydrogen compounds are not formed when graphite and hydrogen are reacted between 1200° and 1600°C. Reaction can occur if the products of reaction are removed from the furnace tube or by decomposition.

A kinetic study was made using ultra pure hydrogen and high-purity graphite. A sensitive microbalance was used to follow the weight loss-time curves as a function of temperature, pressure, and flow. A mass spectrometer study was made of the products of reaction.

Rates of reaction were studied both under flow and under static reaction conditions. Flow rates up to 2×10^{20} molecules of hydrogen were used at 19 Torr pressure. At 1650°C and 19 Torr a rate of reaction of 6×10^{17} atoms of C/cm²-sec was measured. This corresponds to an ablation rate of 1000 Å/sec. In terms of hydrogen flow the efficiency of reaction was 0.24%. In terms of kinetic theory collision calculations, 0.0108% of the maximum theoretical rate was measured.

Methane was not found in the products of reaction under flow conditions. Carbon monoxide was found in experiments carried out under static conditions. To explain these results we studied (i) the dissociation of alumina at 1600°C, (ii) the reaction of hydrogen with alumina, and (iii) the reaction of methane with the alumina furnace wall. Methane was found to react with alumina at 1600°C to give carbon monoxide. An analysis based on these studies showed that methane decomposes without reacting with alumina in flow environments. In static environments methane reacts with alumina to give carbon monoxide.

The graphite-hydrogen reaction showed an exponential temperature behavior with a heat of activation of 72 ± 2 kcal/mole. The rates of reaction were nearly independent of flow and of pressure.

Blackwood's kinetic interpretation of the graphite-hydrogen reaction was used to explain the data.

Manuscript received July 22, 1964.

Any discussion of this paper will appear in a Discussion Section to be published in the December 1965 JOURNAL.

REFERENCES

1. T. J. Clark, R. E. Woodley, and D. R. DeHalas, "Nuclear Graphite," Chap. 14, R. E. Nightingale, Editor, Academic Press, New York (1962).
2. C. W. Zielke and E. Gorin, *Ind. Eng. Chem.*, **47**, 820 (1955).
3. N. S. Corney and R. B. Thomas, British Rept. AERLE-C/R 2502, June 1958.
4. J. D. Blackwood, *Australian J. Appl. Sci.*, Sept. 1962, 199 (1962).
5. J. D Blackwood, *Australian J. Chem.*, **12**, 15 (1959).
6. J. D. Blackwood, *ibid.* **15**, 297 (1962).
7. JANAF Thermochemical Tables, The Dow Chemical Co., Midland, Mich. (1960).
8. E. A. Gulbransen, K. F. Andrew, and F. A. Brassart, *Carbon*, **1**, 413 (July 1964).
9. E. A. Gulbransen, K. F. Andrew, and F. A. Brassart, To be published.

The Role of Adsorbed CN Groups in the Hydrogen Embrittlement of Steel

W. Beck,[1] A. L. Glass, and E. Taylor

Aeronautical Materials Laboratory, Naval Air Engineering Center, Philadelphia, Pennsylvania

ABSTRACT

Specimens of ultra high strength steel were charged cathodically with hydrogen or immersed without charging in a NaOH solution of $NaC^{14}N$ and the adsorption of $C^{14}N$ groups determined by means of radioactivity measurements. In addition, the desorption of adsorbed $C^{14}N$ groups was also studied. Heats, designated heats of adsorption, energies of activation, and the surface coverage with $C^{14}N$ were calculated. Hydrogen embrittlement by measurement of bend ductility, negative overvoltage, and the relative hydrogen coverage were determined under similar conditions and with similar materials. It is concluded that $C^{14}N$ groups are strongly and preferentially adsorbed on highly active centers and the hydrogen recombination reaction retarded accordingly. The rapid increase in hydrogen embrittlement with increasing surface coverage by $C^{14}N$ is ascribed to a high surface concentration of the embrittling hydrogen atoms, followed by rapid migration into the steel.

It is most unfortunate that high strength steel parts, when plated from a cyanide bath, are badly embrittled, and in the presence of stress concentrations, their fatigue strengths and limits are reduced.

The transition from ductile to brittle is the result of presence of hydrogen atoms in the steel which have migrated into it during electroplating. Several mechanisms have been advanced which relate embrittlement induced by absorbed hydrogen atoms to changes in the submicroscopic metallographic structure (1).

It has been shown recently that there is a close relationship between hydrogen surface coverage and hydrogen embrittlement (2). Therefore, any embrittlement mechanism is not satisfactory in which the effect of the surface concentration of the embrittling hydrogen atoms on the inducement of hydrogen embrittlement is not integrated.

It has been reported that the CN group is adsorbed easily on metallic and nonmetallic solid surfaces, particularly iron, and effectively retards numerous decomposition and oxidation processes on them (3), as well as displacing less strongly adsorbed anions (4, 5).

The main objective of this study was the determination of whether CN groups were adsorbed on the steel surface, to obtain an idea about the strength of bonding of these groups to the metal, and to find out whether their presence increased the surface coverage of steel with atomic H.

The comparatively high surface concentration of hydrogen along with the marked embrittlement it induces in the steel in presence of CN groups was discussed in the light of an electrochemical mechanism.

Experimental Procedures

Materials.—The majority of measurements were conducted on a low alloy steel, AISI SAE 4340, which, heat treated to a strength level between 260 and 280 ksi UTS, becomes very sensitive to hydrogen embrittlement.

Some measurements were also made on AISI 1095 steel with a strength similar to that of the 4340 steel.

Hydrogen Embrittlement Production and Measurement

Standard test specimens (6) used for hydrogen embrittlement measurements in general were 2 in. diameter half rings having a width of 1 in. and a wall thickness of ⅛ in. Rings were embrittled by charging only the polished convex surface cathodically with hydrogen in a NaOH solution containing NaCN. Hydrogen embrittlement was evaluated by means of a compression bend test in a universal testing machine at a cross head speed of 0.01 in./min. The total cross head travel from the free height of the ring along the open diameter to the height at fracture is called deflection. This value, a measure of the ductility (embrittlement) of the specimen, was compared with the fracture deflection of an uncharged specimen and expressed in per cent reduction in deflection.

Measurement of Negative Overvoltage

Circular disks of 4340 steel were mounted in lucite, and metallographically polished to a high luster. Prior to immersion in the catholyte, the surface was degreased with benzene, rinsed with distilled water, and wiped with dry cotton.

The polarization cell assembly was composed of three Pyrex glass vessels which contained, respectively, a large platinum sheet anode, the steel disk cathode, and a Beckman calomel reference electrode. Electrolytic connection between the cathode and anode was by means of glass tubes, connected with Tygon tubing. The cathodic and anodic compartments were filled with 0.1M NaOH, and a 0.1M KCl agar bridge, kept a fixed distance of 1 mm from the steel surface, connected the cathodic compartment with the reference electrode.

A buret, inserted in the rubber stopper covering the container with the steel specimen, contained the NaCN solution.

Purified hydrogen was continuously bubbled into the agitated solution surrounding the steel electrode and over it. All containers were kept in a constant temperature bath at 30° ± 0.05°C.

A well-filtered rectifier supplied a constant current to the cell. The potential between cathode and reference electrode was recorded continuously by means of a sensitive potentiometer.

The experimental technique was similar to that used by Bockris and Conway (7) and also Amar and Awad (8). The direct method of measuring the overpotential was used, and new specimens with freshly prepared cyanide solutions were used for each run.

Immediately after immersion in the hydrogen presaturated NaOH solution, the specimen was polarized cathodically until attainment of a steady state, which was considered reached when the change of the potential did not exced 5 mv within a 15 min period. A small volume of the concentrated NaCN solution was then added from the buret to give the desired NaCN concentration and a new steady state polarization potential

[1] At temporary duty at the Office of Naval Research, Branch Office, London, England.

The opinions or assertions expressed in this paper are the private ones of the writers and are not to be construed as official or reflecting the views of the Department of the Navy or the Naval Service at large.

was then recorded. During addition of NaCN, the polarizing current was not interrupted but maintained constant by means of a variac on the power supply.

Relative Hydrogen Coverage

Devanathan, Stachurski, and Beck (2) have shown that if one side of a thin steel membrane is cathodically polarized, the current required for ionization of the hydrogen, which permeates the membrane and reaches the other anodically polarized side, is proportional to the hydrogen coverage of the cathode surface. With this apparatus, the hydrogen coverage of the cathode side of the membrane is maintained at a certain fixed level, whereas on the anode side, because of rapid H ionization, the H coverage is at about zero level. According to Faraday's law, the current in the anode circuit is a direct measure of the instantaneous rate of hydrogen permeation and hence of the rate controlling hydrogen coverage. The catholyte contained NaCN, the anolyte consisted of 0.1M NaOH solution.

The galvanostatically maintained cathode current density was 10 ma/cm^2. The membrane, 1 mm thick, consisted of ultra high strength AISI 4340 steel.

The relative hydrogen coverage Q_T is obtained from the following expression

$$Q_T = \frac{i_t}{i_{st}} \qquad [1]$$

where i_{st} signifies the permeation current, determined for conditions when the assumed coverage approaches unity and i_t is the measured steady permeation current.

Adsorption of $C^{14}N$ on Nonpolarized Surfaces

Since the adsorbed layers were found to be easily desorbed during rinsing, this phase of the investigation was conducted as follows: a Tracerlab Tg-C-4 Geiger tube was modified (9) by replacing its 1 in. diameter mica end window with a 0.5 mil thick Mylar sheet, covered with a thin iron layer.[2] This layer, produced by vacuum deposition of 4340 steel, had a bright and shiny appearance. The iron-coated Mylar sheets used were of a uniform thickness and their selection was based on the relative opacity which was determined photometrically.

The radioactivity of the sodium cyanide-C-14 solution was determined by moving the platform, containing the solution in the hot stage, up to the iron-Mylar window of the Geiger tube, and at fixed distances (3 in., 2 in., 1 in., etc.) between the Mylar window and the surface of the solution counts per minute were determined.

A curve was obtained by plotting these distances *vs.* the counts per minute at each distance. The curve was extrapolated to zero distance and the solution radioactivity determined as the intercept on the counts per minute axis. The solution temperature was regulated by means of a hot stage and when contact was finally made between the iron coating and the solution, the counter was simultaneously started. Counts per minute were obtained periodically until no increase was observed. Therefore, the radioactivity induced in the iron layer was the difference between the maximum counts per minute obtained on contact of layer with solution and the solution counts per minute. The specific activity of the $NaC^{14}N$ was 5.8 μc/mg or 1.28 x 10^7 dpm/mg. All measurements were conducted with hydrogen saturated solutions and a fresh specimen was used for every run.

Corrections for self adsorption and back scattering for these very low counts were deemed unnecessary. However, only those measurements were considered which satisfied the requirement for uniformity by the Chauvenet criterion.

[2] It is recognized that iron coatings vapor deposited on a Mylar film do not have the physical properties of the steel disks employed in the adsorption studies on polarized surfaces. However, electron diffraction patterns of the coatings and the surfaces of the polished steel disks showed no significant chemical differences.

Adsorption of $C^{14}N$ on Cathodically Polarized Surfaces

The experiments were conducted with 2 in. diameter 4340 steel disks, metallographically polished to a mirror finish. The polarization cell consisted of a 2¼ in. diameter petri dish with the electrodes arranged horizontally; the platinum anode was at the bottom of the dish and the steel cathode ⅛ to ¼ in. above the anode, was kept in position by a magnet. The constant current density was 10 ma/cm^2.

After completion of the polarization run the specimen was removed from the solution, rinsed, dried, and the radioactivity determined in a gas flow counter. The standard rinsing procedure consisted of a 5 min rinse in a slow stream of tap water, followed by two 2 min rinses in distilled water, and two short rinses in methyl alcohol.

All counts were corrected for background, backscattering and resolving time of the counter, and the averages, from three separately made measurements, were used in graphs and calculations. Counts/minute were converted to gCN/cm^2.

The specific activity of the solution was 25.4 mc/mM. Using radioactive sodium cyanide and the above radiochemical procedures, the surface concentration of CN was determined with respect to variations in solution concentrations (0.002 to 0.2M), temperature (20°-40°C) and immersion time (see graphs).

Desorption of CN from Pre-polarized and Non-polarized Surfaces

A part of this desorption study dealt with potential decay measurements on steel surfaces in order to determine the possible effect of desorption of CN on the surface concentration of hydrogen and hence the potential. However, the potential on a charged specimen is also affected by the hydrogen slowly diffusing out of the steel disk into the surrounding solution. As has been found, the quantity of hydrogen accumulating inside of the specimen depends on its thickness and is sharply decreased by reducing it. Since it was very difficult to obtain the necessary quantity of very thin high strength 4340 steel strips, those of AISI 1095 steel were used.

The specimens consisted of small strips of feeler gauge (AISI 1095 steel) with a bright and smooth surface finish. They were completely covered with an insulating plastic coating and immediately preceding a polarization run, a square window about 1/16 in. was cut out of the coating on each side of the strip.

The exposed metal area was solvent degreased, rinsed with distilled water, and finally with the solution to be used for the polarization run. After completion of polarization, the specimen was immediately removed from the solution, rinsed for 2 min in 0.1M NaOH and reimmersed either in a NaOH solution or a NaOH solution with NaCN. Potential measurements were started 2 min after reimmersion.

Desorption by means of radioactivity measurements was determined with an exposed area of 0.5 x 1 in. After polarization in the 0.1M NaOH solution of 0.02M $NaC^{14}N$, specimens were rinsed for 2 min in distilled H_2O and reimmersed into 5 ml 0.1M NaOH.

At predetermined time intervals, 0.1 ml samples were withdrawn and the radioactivity determined by means of liquid scintillation counting techniques at —14°C.

The total quantity of CN adsorbed on similar sheet specimens, after polarization and rinsing as described above, was determined in a gas flow counter. From this determination, and the counts obtained by liquid scintillation counting, the loss in surface concentration of CN due to desorption was determined at the various time intervals.

The desorption of $C^{14}N$ from nonpolarized iron films was determined by means of the technique described under "Adsorption of $C^{14}N$ on Nonpolarized Surfaces."

After attainment of maximum adsorption, the Geiger tube was immersed in 800 ml of NaOH solution and simultaneously, the recorder was turned on at a set

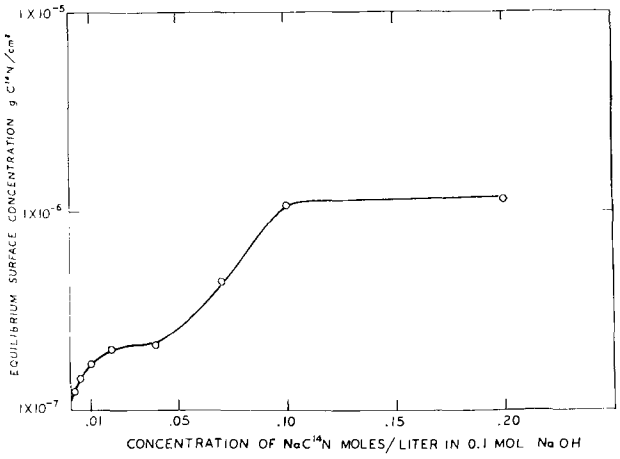

Fig. 1. Adsorption isotherm recorded at 20°C on specimens immersed in 0.1M NaOH solution containing $NaC^{14}N$ in various concentrations.

speed. The rapid decrease of counts with time was recorded until the background count was obtained.

Experimental Results

Effect of Concentration of Dissolved NaCN *and Temperature on the Surface Concentration of* $C^{14}N$ *Groups*

The "S" shaped curve in Fig. 1 indicates that in the range of low concentrations of NaCN (to about 0.04M), the adsorption may have the characteristics of a Freundlich or Tempkin isotherm. At concentrations exceeding this value, surface coverage increases rapidly and finally, beyond 0.1M, the adsorption on the nonpolarized surface approaches saturation conditions.

A log-log plot of the values of the surface concentration of $C^{14}N$ taken from the "S" shaped section of the curve in Fig. 1 (to a concentration of NaCN of about 0.04M) *vs.* the solution concentrations is almost linear. The deviations from the linearity appear to be more marked in a semilogarithmic plot, consisting of a plot of the log of the surface concentration of $C^{14}N$ or of the heat designated heat of adsorption *vs.* solution concentration of NaCN. This might indicate that the values fit more closely a Freundlich than a Tempkin adsorption isotherm.

The above analysis is quite preliminary in nature and was only presented because of the fact that the rapid drop in ductility is limited to a range of rather low concentrations of NaCN, actually appreciably below 0.04M.

With polarization (Fig. 2), the curve approaches linearity and begins to sweep upwards toward a saturation at a concentration of 0.2M NaCN, which is usually observed in an adsorption isotherm.

The curve illustrating the dependency of surface concentration of cyanide on adsorption temperature for a polarized surface (Fig. 3) increases linearly whereas the inverse is true with nonpolarized steel.

Heat, Designated Heat of Adsorption of $C^{14}N$

The heat of surface processes associated with the adsorption of systems containing the CN group (ΔH) was calculated for the polarized surface as a differential heat of adsorption (10).

Calculations by means of the Fisher, Hirschfelder, Taylor atom models have indicated high coverage of the polarized surface with CN, and ΔH actually may have been generated by several surface processes as will be discussed in another paper. The integrated form of the Clausius Clapeyron equation was used for these calculations

$$\Delta H = 4.574 \left(\frac{T_1 T_2}{T_2 - T_1} \right) \log c_2 - \log c_1 \qquad [2]$$

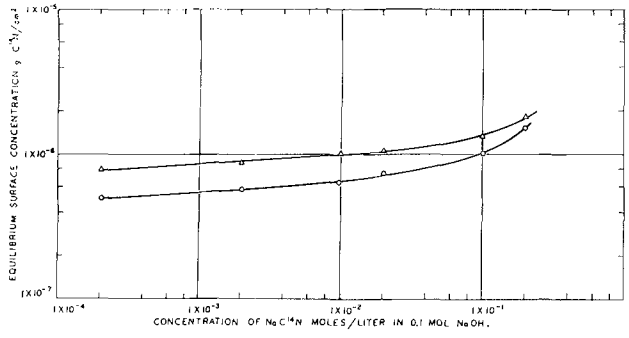

Fig. 2. Adsorption isotherms recorded at two different temperatures on specimens polarized cathodically at 10 ma/cm² for 30 min in 0.1M NaOH solution containing $NaC^{14}N$ in various concentrations. ○, Solution temperature 20°C; △, solution temperature 40°C.

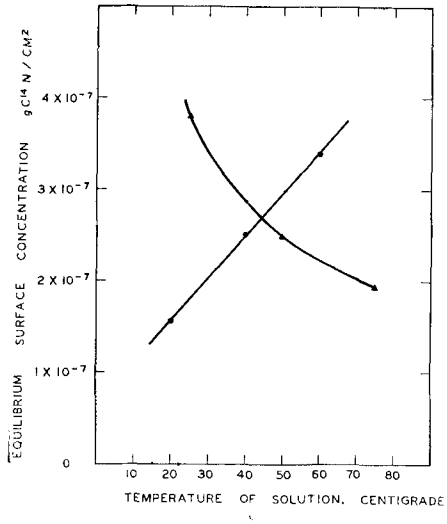

Fig. 3. Relationship between solution temperature and surface concentration of $C^{14}N$. ▲, Specimens immersed into a solution consisting of 0.02M NaCN + 0.1M NaOH until attainment of adsorption equilibrium; ●, specimens polarized cathodically in same solution at 10 ma/cm² for 30 min.

The two solution concentrations of NaCN, c_1 and c_2, necessary for production of the same surface concentration of CN at the absolute temperatures T_1 and T_2, respectively, are obtained graphically from the adsorption isotherms presented in Fig. 2. These values were substituted into the Clausius Clapeyron equation and the differential heat of adsorption (ΔH) was calculated. The above method is used extensively in gas adsorption.

The plot of ΔH *vs.* surface concentration of CN is depicted in Fig. 4. Its decrease with increasing surface concentration of CN is considered to be caused by the hetergeneous structure of the adsorbing steel surface. The first quantity of CN interacting with the most active sites reacts vigorously as indicated by the highly exothermic heat values. As the surface process progresses and the less active sites also become involved, the reaction diminishes and the heat values become less exothermic.

Additional information may be obtained from the ΔH curve in Fig. 4. The point corresponding to —10 kcal/mole represents an adsorption of 10.3×10^{-8} $gC^{14}N/cm^2$. When this value is subtracted from 14.7×10^{-8} $gC^{14}N/cm^2$, which is the total quantity of CN on the surface depicted by this curve, the remaining 4.4×10^{-8} $gC^{14}N/cm^2$ obviously represents a layer formed at heats less than —10 kcal/mole and is 22.4% of the total surface concentration. Therefore, since it may be expected that $C^{14}N$ is more easily desorbed from sites of comparatively low activity, and since

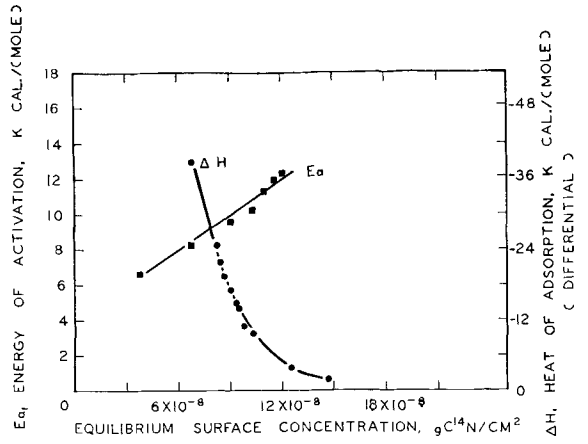

Fig. 4. Plot of ΔH and E_a vs. surface concentration of CN. As discussed in the paper, several surface processes are contributing to the generation of heat, designated in this figure as "Heat of Adsorption."

heats of adsorption less than —10 kcal/mole represent such sites, remarkable correlation is established between the fixation of CN on less active sites, as calculated above, and that actually found by radiochemical determination (25%) (comp. p. 57). The value of —10 kcal/mole is selected since many investigators equate heat of adsorption below this figure with comparatively weak adsorption that may occur on less active sites.

Energy of Activation for Adsorption of $C^{14}N$

In gas adsorption, the energy of activation E_a (11) is calculated from the Arrhenius equation. Tentative calculations of this energy were made from the integrated Arrhenius equation.

$$E_a = \ln\left(\frac{t_1}{t_2}\right)\left(\frac{R}{1/T_1 - 1/T_2}\right) \qquad [3]$$

Here t_1 and t_2 are the times required for adsorption of a given quantity of CN at the absolute temperatures T_1 and T_2, respectively. A plot of E_a *vs.* the surface concentration of CN is shown in Fig. 4. The E_a increases from 6.7 kcal/mole for the low level CN adsorption to about 13.0 kcal/mole for the higher concentrations of CN on the steel surface. This is considered strong evidence that with progressively increasing coverage, first the more active sites are covered in the adsorption process, since they require lower activation energies. Subsequently, those sites with less activity requiring comparatively higher activation energies are covered.

The Rate of Adsorption and Desorption of $C^{14}N$ *Groups*

The times and the surface concentrations of $C^{14}N$ plotted in Fig. 5 and 10 (to be shown below) were converted into rate values. Since bilogarithmic plots of these values gave straight lines, the adsorption or desorption can be represented mathematically by the following equation

$$y = at^n \qquad [4]$$

The constants a and n were obtained statistically by the least squares method. By differentiating the equations with respect to time, the rate of cyanide adsorbing on or desorbing from the steel surface can be computed at any given time.

As can be seen from Fig. 6, the rate of adsorption on polarized surfaces decreases rather rapidly with increasing time and increases moderately with temperature. The rapid decrease of the rate of adsorption again is considered a strong indication that with increasing time, the number of active areas decreases markedly. Selected rate values at various temperatures are listed in Table I.

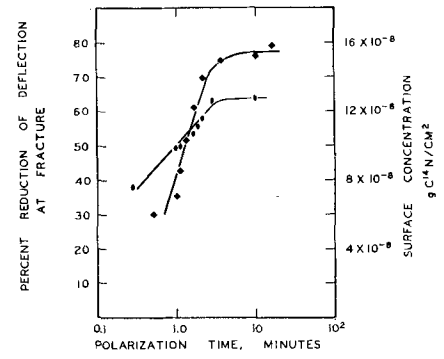

Fig. 5. Effect of polarization time on fracture deflection and surface concentration of $C^{14}N$. Specimens polarized cathodically at 10 ma/cm² in a solution consisting of 0.02M NaCN + 0.1M NaOH, 20°C. ●, Surface concentration; ◆, fracture deflection. Values recorded below 5 min are nonequilibrium surface concentrations, those above 5 min are equilibrium surface concentrations. Small half ring bend test specimen 2 x 7/16 x 1/8 in.

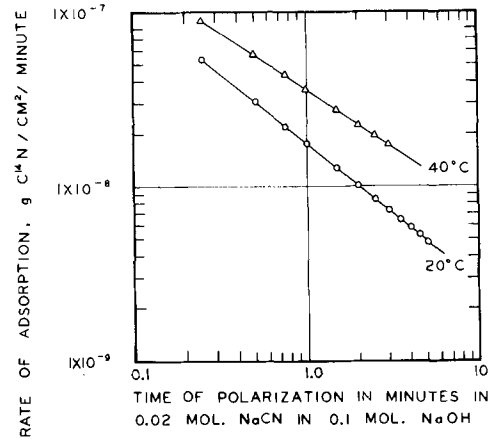

Fig. 6. Effects of time of cathodic polarization and solution temperature on adsorption rate.

Table I.

Steel surface not subjected to cathodic polarization		Steel surface polarized cathodically		
Temp. of solution, °C 0.02M NaCN + 0.1M NaOH	Time for attainment of adsorption equilibrium, sec	Adsorption Temp. of solution, °C 0.02M NaCN + 0.1M NaOH	Time for attainment of adsorption equilibrium, sec	Rate of adsorption g CN/min/cm² after seconds
25	18	20	300	120 sec—6.2 × 10^{-8} 300 sec—4.9 × 10^{-9}
50	4	40	180	120 sec— 1 × 10^{-7} 300 sec—6.2 × 10^{-8}
		Heat designated heat of adsorption (ΔH)		
	Approx. 2.0	$K_{cal/mole}$	39-1.5	
		Energy of activation (Ea)		
	Approx. 0-4	$K_{cal/mole}$	6.5-13	
	Time for complete desorption 19 sec	Desorption in 0.1M NaOH at 20°C	Time for maximum desorption 2400 sec 25% of total quantity of adsorbed CN was adsorbed reversibly	Rate of desorption g CN/min/cm² after seconds 120 sec—4 × 10^{-9} 2400 sec—1 × 10^{-10}

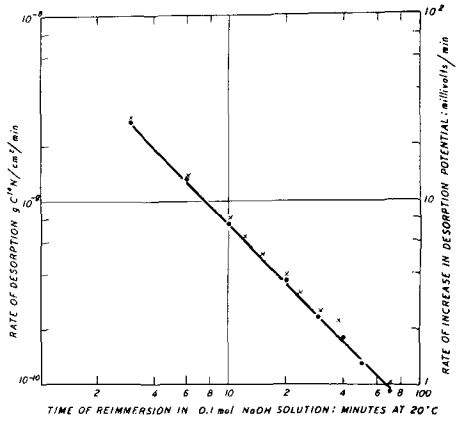

Fig. 7. Effect of time on rate of desorption of $C^{14}N$ and desorption potentials. X, Desorption of $C^{14}N$; •, desorption potential.

The rate of desorption from and respectively the rate of adsorption on nonpolarized surfaces was not calculated since the instrumentation employed did not yield sufficiently reproducible results for these fast reaction rates. However, we were able to determine that the reproducibility of the time necessary for maximum $C^{14}N$ coverage was satisfactory, and therefore, these values are incorporated in Table I.

The slope of the desorption curve in Fig. 7 is slightly higher than that for the adsorption curve in Fig. 6. This indicates the rate of desorption is decreasing faster than the rate of adsorption. In order to explain this phenomena, it may be speculated again that the $C^{14}N$ desorbed was largely physically adsorbed on less active sites and the CN which remains adsorbed is mainly held by strong bonds to the active areas.

Comparison of Significant Data

In Fig. 5, the effect of polarization time on reduction in deflection and surface concentration of CN can be compared. The trend of the two curves show the steep increase within an initial polarization period of about 5 min, and the final attainment of saturated conditions.

Figure 8 demonstrates the effect of temperature on reduction in deflection as well as surface concentration of CN. The trends of these curves are generally comparable between 20° and 60°C.

The plot in Fig. 9 is typical for the effect on NaCN concentration on the negative overvoltage of steel. Immediately upon addition of NaCN, the overvoltage rises rapidly and is higher for greater cyanide concentrations. In general, steady state in the pure NaOH

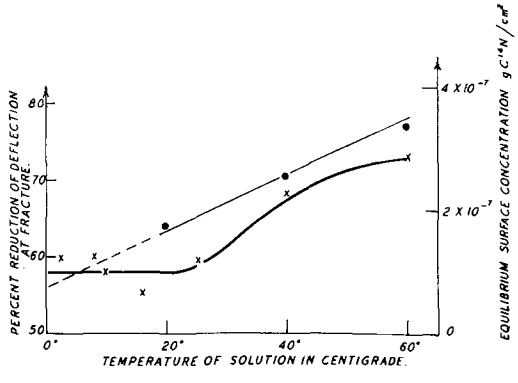

Fig. 8. Effect of solution temperature on equilibrium surface concentration of $C^{14}N$ and fracture deflection. Specimens polarized cathodically at 10 ma/cm² for 30 min in solution consisting of 0.02M $NaC^{14}N$ + 0.1M NaOH. •, Equilibrium surface concentration of $C^{14}N$; X, fracture deflection.

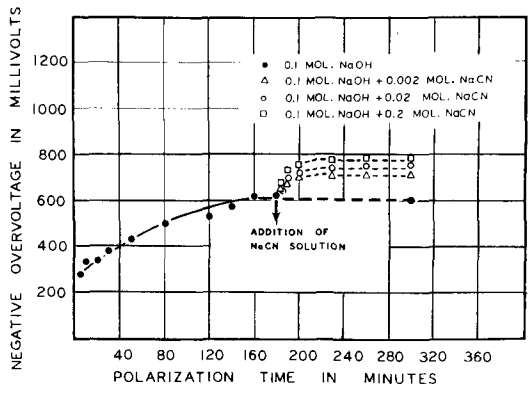

Fig. 9. Polarizing current density X-10 ma/cm², 30°C

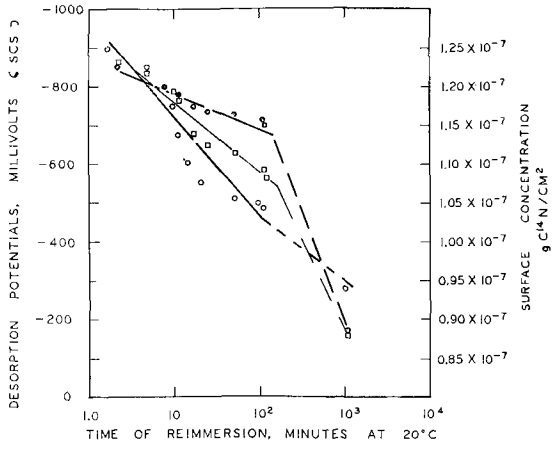

Fig. 10. Effect of immersion time on desorption potentials and surface concentrations of $C^{14}N$. Thin sheet specimens prepolarized cathodically for 5 hr at 10 ma/cm². Solution consisted of 0.02M NaCN + 0.1M NaOH. Potential at zero time between X-1250 and X-1300 mv (SCS). Equilibrium surface concentration at zero time is 1.30 x 10^{-7} g$C^{14}N$/cm². •, Specimens reimmersed in solution consisting of 0.02M NaCN + 0.1M NaOH; □, ○, specimens reimmersed in 0.1M NaOH sol; •, □, potential measurements; ○, radioactivity measurements.

solution is attained after 160 min. However, after addition of NaCN, about 70 min more are required.

The curves presented in Fig. 10 illustrate the effect of time on surface concentration and potential. After polarization, the specimens were reimmersed in a NaOH solution in the presence and absence of NaCN, respectively. The polarization time was selected to be 5 hr because shorter times resulted in a fast shift of the potential in the cathodic direction and poorly reproducible measurements.

As can be seen from Fig. 10, the slope of the line depicting the slow decay of the potential in 0.1M NaOH within a period of about 100 min is steeper than that for a NaOH solution of NaCN. The potential within this 100 min interval is more anodic in solutions containing NaCN than in those without this compound added and the lines depicting the fall of the potential or the decay of radioactivity have quite similar slopes. However, exceeding this 100 min period, dissimilarities in the trends of the curves occur.

Radioactivity measurements have indicated that the decrease in the surface concentration of $C^{14}N$ did not exceed 25% of the quantity of the totally adsorbed CN attained after an immersion period of 40 min. This value could not be exceeded, even when the specimen was immersed for a period as long as 20 hr at 20°C.

Adsorption and desorption studies on nonpolarized surfaces were conducted on a comparatively limited

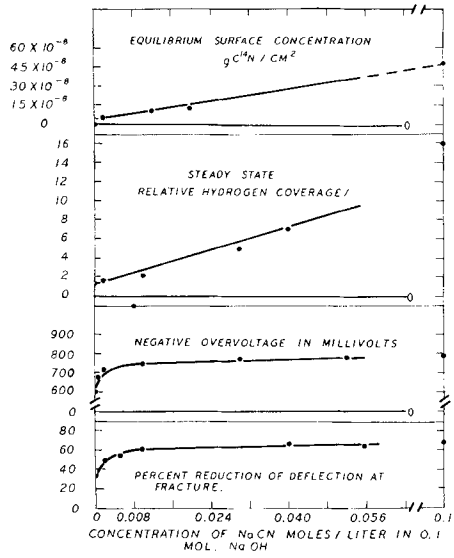

Fig. 11. Effect of solution concentration of $NaC^{14}N$ on a number of variables. Overvoltage measurements at 30°C; all other measurements at 20°C; polarizing current, 10 ma/cm².

basis and pertinent results will be presented in the Discussion Section.

As demonstrated in Table I, on cathodically polarized specimens, the times for attainment of adsorption equilibria are markedly longer than on nonpolarized surfaces, ΔH and E_a are strongly increased and desorption is very slow and incomplete.

These differences in the data presented herein are considered strong evidence that cathodic polarization when associated with $C^{14}N$ adsorption induces certain surface reactions which do not proceed on nonpolarized surfaces.

Finally, Fig. 11 demonstrates the effects of NaCN concentration on a number of variables. In all cases, an increase occurs as the NaCN concentration is increased to about 0.01M. Particularly, the similarity in the trend of the curves is noted with those depicting the concentration dependency of overvoltage and reduction in deflection and also those depicting the effect of CN solution concentration on cyanide surface concentration, and hydrogen coverage. Comparing the results obtained with 0.01M NaCN solution, at which reduction in deflection reached its maximum value, with those at zero concentration, the following may be seen:

The deflection is decreased from about 25 to 62%, the steady state relative hydrogen coverage has increased from 1 to 4, the negative overpotential changes from 600 to about 750 mv and surface concentration of CN goes from 0 to 7.5 x 10^{-8} g/cm².

Discussion

A mechanism is now discussed for the generation on and migration of the embrittling hydrogen atoms into the steel, based on the above presented discussion of the radiochemical data and those of electrochemical and ductility measurements.

Since a solution with an alkalinity as high as pH-13 has a negligibly low H ion concentration, it appears probable that the first step (a) in the formation of atomic H is a slow discharge of a solvated proton from a water molecule. Because of the comparatively low order of the negative overvoltage (12) determined in this study (<750 mv), it is further concluded that the desorption step (b) consists in a fast Tafel recombination.[3]

This reaction would proceed predominantly on places where the heat of H adsorption is high but the activation energy for H recombination relatively low. These highly active sites are designated Fe^B areas contrary to the Fe^A areas with relatively low surface activity.

Under idealized conditions, the total area of the steel surface Fe involved in the adsorption of H is

$$Fe = \Sigma Fe^A + \Sigma Fe^B \qquad [5]$$

The discharge reaction (a) and the catalytic cycle (b) on the highly active Fe^B sites may then be represented by the following equations (12)

$$\text{(a)}\quad 2H_2O + 2e_o^- \rightarrow 2\,OH^- + 2H$$

$$\text{(b)}\quad 2Fe^B + 2H \rightarrow 2Fe^B\text{——}H \rightarrow 2Fe^B + H_2 \qquad [6]$$

When k_R signifies the rate constant for the H recombination reaction in electrical units, C_{Hads} the surface concentration of the H adatoms, and i_c the constant density of the polarizing current, the following equation holds true, if the applicability of Tafel recombination is anticipated.

$$i_c = k_R\, C_{Hads}^2 \qquad [7]$$

However, in the presence of cyanide compounds, apparently due to their strong preferential adsorption, the number of active sites (as discussed above) still available for H adsorption is drastically reduced. Hence, the activation energy for H recombination is increased, and the rate of this reaction retarded accordingly. At constant density of the polarizing current i_c, the surface concentration of the H adatoms, C_{Hads}, must rise in order to compensate for the decrease in the rate constant k_R.

According to the diffusion laws (2, 14), the quantity of H absorbed in the steel specimen during unit time is proportional to C_{Hads}, and by increasing this concentration, the velocity of migration of the embrittling H atoms into the metal is also increased and embrittlement accelerated accordingly.

If the above discussed mechanism applies, it would be expected that a reactivation of the Tafel recombination can be brought about by preferential desorption of CN. As can be seen from Fig. 7 plotting the rate of increase of the potential and that of the CN desorption, *vs.* the time of immersion in a 0.1M NaOH solution, overlapping curves result. The intimate relationship between these two variables strongly indicates that the potential is determined by desorption of CN. In other words, the increase in potential is caused by CN progressively desorbing from the steel surface, and therefore this potential has to be considered a desorption potential. This process is also in agreement with the requirements of basic Eq. [6] and [7] because the increase in k_R is compensated for by the decrease in C_{Hads}. These facts indirectly confirm the above postulated mechanism of inhibition of hydrogen recombination.

Therefore, it is inferred that a desorption of CN, even as limited as 25%, is sufficient to reactivate (at least to a certain degree) the reaction necessary for recombination of H atoms.

Other investigators (2) have correlated hydrogen coverage of a cathodically polarized steel membrane surface with the hydrogen permeating through it. Fisher and Bärmann (15, 16) studied embrittlement by plating Cd from the cyanide bath or by cathodically charging high strength steel specimens in various sodium cyanide solutions. Even though the current density employed was tenfold greater than that reported herein and the embrittlement was evaluated by repeated flexure to fracture, their hydrogen embrittlement results in general are in agreement with those presented in this paper.

The reliability of their overvoltage measurements and, therefore, all pertinent conclusions seem to be doubtful, because they were conducted in presence of oxygen and it is open to question whether steady state

[3] Makrides (13) has advanced the concept that, with small fractional H coverage, the exchange rates for discharge and recombination in strongly alkaline solutions at equilibrium are about equal on Ni (and perhaps as well on Fe).

potentials ever had been attained. The assumption of a cathodic reduction of NaCN at higher concentrations, at the comparatively low potential at which hydrogen was charged into the steel is hardly conceivable. This assumption is not in agreement with the radiochemically determined increase in the surface concentration of cyanide with increased cyanide solution concentration.

The effect of adsorbed CN anions on the overvoltage may be explained by Frumkin's theory of the retarded hydrogen discharge (17, 18).

In the presence of specifically adsorbed anions, the ψ' potential, that is the potential of the external Helmholtz layer which represents the mean potential value at a distance of one ionic radius from the electrode surface, becomes more negative.

Replacing Eq. [7] by the following Eq. (1_b), one obtains for the polarizing current, i_c, when hydrogen atoms are generated by protonic discharge of water molecules, [Eq. (1_a)]

$$(1_a) \quad H_2O + e_0^- \rightarrow H_{ads} + OH^-$$
$$(1_b) \quad i_c = K_{a_{H_2O}} \exp(-\alpha F[\phi - \psi']/RT$$

One obtains further for the overvoltage

$$(2) \quad \eta = a_{CN^-} - \psi' - \frac{RT}{F} \ln OH^- + \frac{RT}{\alpha F} \ln i_c$$

and from this equation

$$(3) \quad \left(\frac{d\eta}{d \ln a_{CN^-}}\right)_{PH;\ i_c} = -\left(\frac{d\psi'}{d \ln a_{CN^-}}\right)_{PH;\ i_c}$$

The overvoltage, η, increase with increasing ψ' potential which is caused by increased adsorption of CN ions due to the increased solution activity of CN^-.

As can be clearly seen from Eq. (1_b), the rate of the hydrogen evolution reaction depends on the term $(\phi - \psi')$ on which again depends the activation energy. Since this energy increases linearly with the increase of $(\phi - \psi')$, it follows that the more negative ψ', the greater becomes the activation energy and the more marked the retardation of the reaction rate as indicated by the increase in the overvoltage η.

Acknowledgments

The authors are much indebted to Mr. N. Promisel, Head, Special Materials Branch, Bureau of Naval Weapons, for the great and continual interest taken in this study; to Mr. F. S. Williams, Superintendent, Metallurgical Division, Dr. G. K. Holmes, Superintendent, Chemical Engineering Division, and Mr. J. Smith, Head, Chemistry Branch, of the Aeronautical Materials Laboratory, Naval Air Engineering Center, for their helpful assistance. Gratefully acknowledged are the valuable discussions with Dr. H. Wroblowa and Z. Stachurski, both formerly with the Electrochemical Laboratory of the John Harrison Laboratory of Chemistry at the University of Pennsylvania. Thanks are also due to Mr. B. Baker for assistance with the experimental work during the initial phase of this investigation.

Manuscript received Dec. 13, 1963; revised manuscript received Aug. 31, 1964. This paper was presented at the Boston Meeting, Sept. 16-20, 1962.

Any discussion of this paper will appear in a Discussion Section to be published in the December 1965 JOURNAL.

REFERENCES

1. E. A. Steigerwald, F. W. Schaller, and A. R. Troiano, *Trans. Met. Soc.*, AIME, **218**, 835 (1960).
2. M. A. V. Devanathan, Z. Stachurski, and W. Beck, *This Journal*, **110**, 886 (1963).
3. H. Freundlich, "Kapillarchemie," Vol. 1, pp. 331-332 (1930).
4. K. Schwabe, K. Wagner, and Ch. Weissmantel, *Z., Physik. Chem.*, **206**, 309 (1957).
5. A. N. Balaschowa, *ibid.*, p. 347.
6. W. Beck and E. J. Jankowsky, *Proc. Am. Electroplaters Soc.*, **47**, 152 (1960).
7. J. O'M. Bockris and B. E. Conway, *J. Phys. Chem.*, **53**, 527 (1949).
8. I. A. Amar and S. A. Awad, *ibid.*, **60**, 871 (1956).
9. H. D. Cook, *Rev. Sci. Instruments*, **27**, 1081 (1956).
10. S. Brunauer and L. E. Copeland, "Surface Tension, Adsorption," in "Handbook of Physics," E. M. Condon and H. Odishaw, Editors, pp. 5-107, New York (1958).
11. *Ibid.*, pp. 5-112.
12. J. O'M. Bockris and M. A. V. Devanathan, Report of University of Pennsylvania, ONR No. 551 (22) NR 036-028, March 31, 1962.
13. A. C. Makrides, *This Journal*, **109**, 977 (1962).
14. Th. C. Franklin and F. Matsuda, Report Baylor University, Contract No. AF 19 (607)-8414, June 1962.
15. H. Fischer and H. Bärmann, *Korrosion u Metallschutz*, **16**, 405 (1940).
16. H. Fischer, *Z. Electrochem.*, **52**, 123 (1948).
17. A. Frumkin, *ibid.*, **59**, 816 (1955), *This Journal*, **107**, 469 (1960).
18. Tza Chyuan-Sin and Z. A. Zofa, *Proc.* Acad. of Sciences of USSR, Physical Chemistry, pp. 537-540 (1959).

June 1965 Discussion Section

A Discussion Section, covering papers published in the July-December 1964 JOURNALS, is scheduled for publication in the June 1965 issue. Any discussion which did not reach the Editor in time for the December 1964 Discussion Section will be included in the June 1965 issue.

Those who plan to contribute remarks for this Discussion Section should submit their comments or questions in triplicate to the Managing Editor of the JOURNAL, 30 East 42 St., New York, N. Y., 10017, *not later than March 1, 1965*. All discussion will be forwarded to the author(s) for reply before being printed in the JOURNAL.

Exchange of Silver Ions at Single Crystal/Solution Interfaces

Irvine I. Tingley

Mines Branch, Department of Mines and Technical Surveys, Ottawa, Ontario, Canada

ABSTRACT

The exchange of silver ions between the (111), (100), (110), and (311) surfaces of single-crystal silver and silver nitrate solutions has been studied, using Ag^{110} as tracer. The initial step is very rapid and is probably largely adsorption, since much of the radioactivity acquired during the first few seconds can be removed by soaking in distilled water. After about 15 min the rate-controlling process appears to be diffusion in the solid. In 0.01M $AgNO_3$ solution the radioactivity uptake continues steadily if the surfaces are frequently desorbed with distilled water, but if the adsorbed ions are allowed to remain, the rate of uptake is reduced. In 0.1M $AgNO_3$ solution the radioactivity on the surfaces reaches constant values after 4 days, whether or not desorption is carried out. The penetration profile and diffusion coefficient in the metal were obtained by "chemical sectioning." It was found that diffusion occurred by means of "dislocation pipes," and resembled grain boundary diffusion rather than lattice diffusion by a vacancy mechanism which occurs at high temperatures.

The exchange of silver ions between polycrystalline silver metal surfaces and aqueous solutions of silver salts has been investigated by a number of workers using radioactive silver isotopes as tracers (1-11). In general, all agree that a rapid exchange involving only a few atom layers takes place in the first few seconds, followed by a slower process which is affected by the concentration of the solution, the state of the surface, and the temperature. This slower uptake of ions from the solution is held to be controlled by diffusion in the solid. King and Levy (2) found that surfaces that were removed from the solution, and washed frequently, underwent more exchange than surfaces that were left undisturbed; they attributed this to the removal of adsorbed salt that slowed down the exchange. However, King and McKinney (3) concluded that the increased exchange was due, more likely, to increased diffusion caused by a rise in temperature due to the hot water used in the washing. They calculated a grain boundary diffusion coefficient of the order of 10^{-21} cm^2/sec. Sandor (8), who removed the radioactivity by electroetching, obtained a value of 1.37×10^{-20} cm^2/sec for the grain boundary diffusion coefficient.

The present work was undertaken to ascertain the behavior of specific single-crystal surfaces with respect to the exchange of silver ions with aqueous silver nitrate solutions, and to obtain a value for the room temperature volume diffusion coefficient.

Experimental Details

The single crystals of silver were grown in a horizontal furnace by the method of Chalmers (12), using 99.999% pure silver obtained from Johnson, Matthey and Mallory Limited, Toronto. The crystals were then sectioned and oriented along the desired direction, and the resulting surfaces were electroetched and/or chemically etched and polished, as described below. Most cuts were made using a spark cutter, but two specimens were cut by means of an "acid saw." The orientation of the surfaces was obtained by x-ray diffraction, and the cuts were made to within 5° of the plane desired. The disturbed material on the surfaces was removed by electroetching with the cyanide electropolishing solution of Gilbertson and Fortner (13), with a current of 4 ma/cm^2 and/or by chemical etching with 55% HNO_3 or with a solution of 15 ml of 30% H_2O_2 plus 25 ml of concentrated NH_4OH. The surfaces were then electropolished by the method of Gilbertson and Fortner (13), or chemically polished by the chromic acid-hydrochloric acid method of Levinstein and Robinson (14). Both of these methods produce very smooth surfaces with a minimum of microscopic imperfections. Square or rectangular specimens, with a small tab for handling, similar to those used by Sandor (8), were cut using an "Airbrasive" machine (S. S. White Dental Manufacturing Company, New York). These specimens had an area of 1 cm^2 on the surface exposed to the solution. The radioactive silver isotope was Ag^{110}; the radioactive metal was dissolved in nitric acid, evaporated to dryness, taken up in distilled water, evaporated to dryness again, redissolved in water, and made up to the required concentration with reagent grade silver nitrate. These solutions had a pH of 5.5.

The specimens were cemented onto a glass disk with paraffin, and their edges painted with paraffin to expose only the one surface. The surfaces were then wiped very carefully with absorbent cotton moistened with chloroform to remove any paraffin and grease immediately before being immersed in the radioactive solution. After removal from the solution, the disk, with the specimens on it, was rinsed with distilled water to remove any adhering solution. The specimens were then removed from the paraffin mounts, rinsed thoroughly with distilled water and then with chloroform before being counted. The chloroform rinse was made to remove any small pieces of paraffin which might adhere to the edges of the specimen and make a crevice where liquid might be entrained.

Counting was done with a well-type NaI(Tl) scintillation counter, the specimens being counted at the bottom of the well. Corrections for decay of the Ag^{110} and for day-to-day variation in the counter efficiency were made by comparing with counts taken on standards prepared by electroplating specimens in a radioactive silver nitrate solution at the beginning of these experiments. Corrections for absorption were not necessary because of the small distance penetrated and the energies of the γ-rays.

Experimental Results

The radioactivity taken up by polycrystalline silver surfaces during long periods of immersion in radioactive silver nitrate solution is shown in Fig. 1. Results for two electropolished polycrystalline surfaces that were immersed in 0.1M $AgNO_3$ solution that had a specific activity of 252,000 cpm/ml, are plotted for various periods totaling 46 days. The line was drawn by the method of least squares. The radioactivity uptake is seen to be proportional to the square root of the time, as it should be if a diffusion process is occurring.

During the first few minutes, however, the uptake of radioactivity follows a different pattern. Figure 2 shows this for (111), (100), and (110) surfaces immersed in a 0.01M solution of $AgNO_3$ having a specific activity of 984,000 cpm/ml. The rate of uptake of radioactivity is seen to be very rapid during the first few

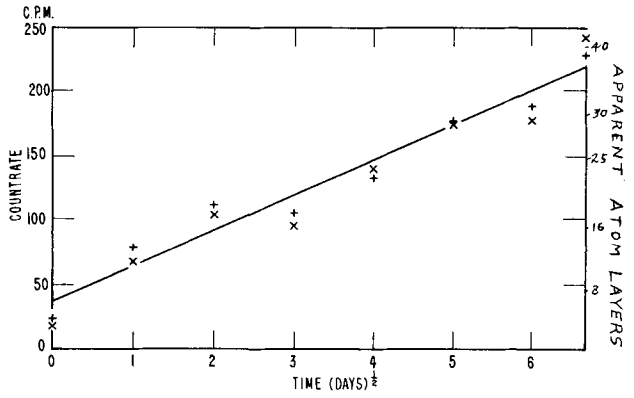

Fig. 1. Radioactivity uptake in polycrystalline silver, 0.1M $AgNO_3$ solution, 6 cpm = 1 apparent layer.

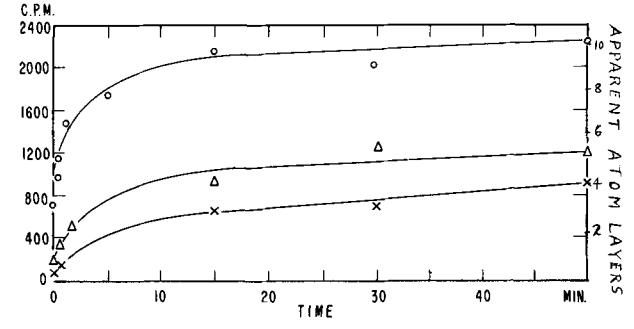

Fig. 2. Radioactivity uptake at beginning of exchange, 0.01M $AgNO_3$ solution, 226 cpm = 1 apparent layer: O, 111; △, 100; ×, 110.

seconds, then to decrease until after 15 min it becomes constant, and the curves become linear with the square root of the time. The curves for polycrystalline surfaces are very similar for the short times of immersion. The data for the single-crystal surfaces show that the initial uptake on the (111) surface is much greater than that on the (100) surface, and the uptake on the (110) and (311) surfaces follow in that order, the differences between the last three being much smaller than that between the (111) and (100) surfaces, however.

With longer periods of immersion in 0.01M $AgNO_3$ solution, the extent and manner of the radioactivity uptake depend on whether or not desorption of silver and nitrate ions is carried out. Figure 3 shows curves for (111), (100), and (110) surfaces, exposed for periods up to 9 days in 0.01M $AgNO_3$ solution, with desorption carried out after each immersion by soaking the specimens in distilled water for three 24-hr periods. Similar curves for an experiment with (111) and (100) surfaces show this linearity of uptake, when plotted against the square root of the time, for periods totaling 100 days. This indicates that diffusion of the radioactive silver atoms into the metal takes place after the surface exchange, and that these atoms are replaced by more radioactive silver ions from the solution, after desorption of inactive ions from the surface, thus causing the radioactivity of the specimen to increase.

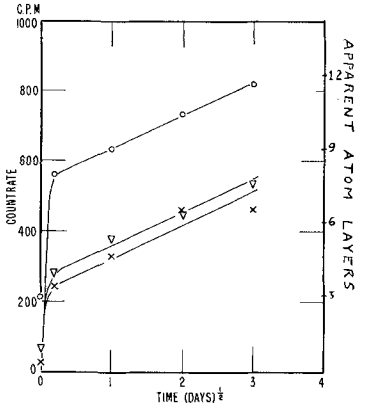

Fig. 3 Radioactivity uptake on single crystal surfaces with desorption at intervals, 0.01M $AgNO_3$ solution, 70 cpm = 1 apparent layer: O, 111; ▽, 100; ×, 110.

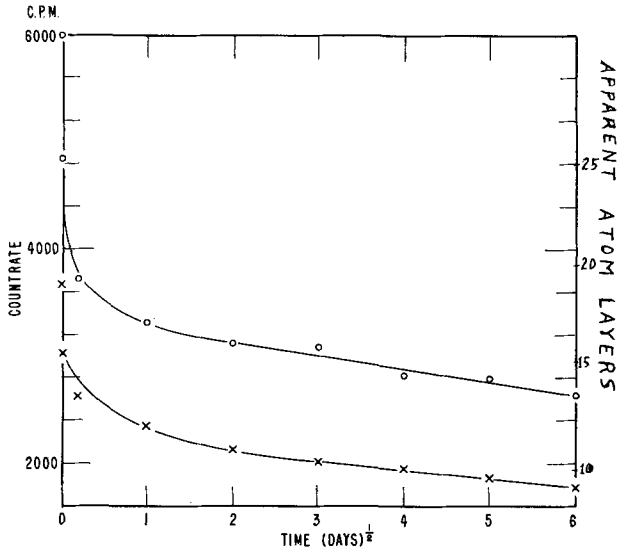

Fig. 4. Reverse exchange on single crystal surfaces, 0.01M $AgNO_3$ solution, 192 cpm = 1 apparent layer: O, 111; ×100.

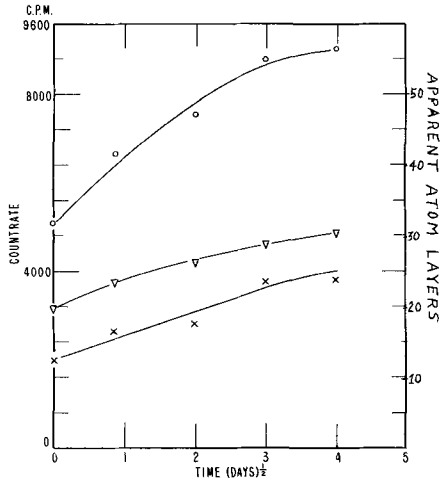

Fig. 5. Radioactivity uptake on single crystal surfaces without desorption, 0.01M $AgNO_3$ solution, 158 cpm = 1 apparent layer: O, 111; ▽, 100; ×, 110.

That the whole process is an exchange is shown by Fig. 4, in which surfaces that had become radioactive in radioactive solution are seen to lose their radioactivity in a similar manner when immersed in nonradioactive solution. If the surfaces are not desorbed after each immersion, however, the radioactivity uptake does not obey the same relation, but its rate decreases more rapidly, as shown in Fig. 5.

With 0.1M $AgNO_3$ solutions, however, an equilibrium point seems to be reached when the surfaces had been immersed for a total of 4 days. This is shown in Fig. 6, which contains the data for four differential planar surfaces. Again, desorption of these surfaces between immersions does not have the effect observed with surfaces exposed to 0.01M $AgNO_3$ solutions. The total uptake is reduced, but equilibrium is reached at about the same time. It would appear that, because of the higher concentration of ions in the solution, the adsorption of ions takes place much more rapidly than the

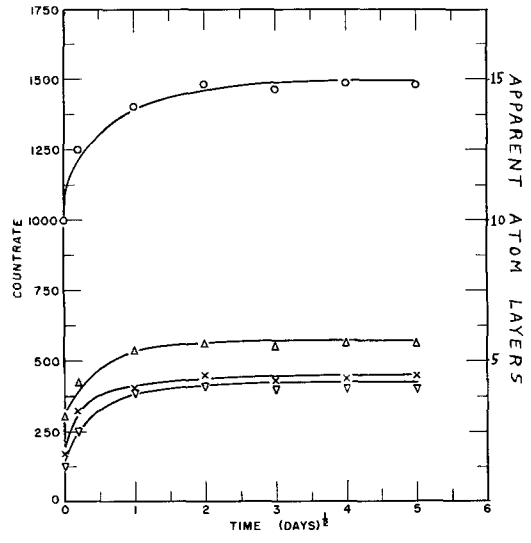

Fig. 6. Radioactivity uptake on single crystal surfaces, 0.1M $AgNO_3$ solution, 100 cpm = 1 atomic layer: ○, 111; △, 100; ×, 110; ▽, 311.

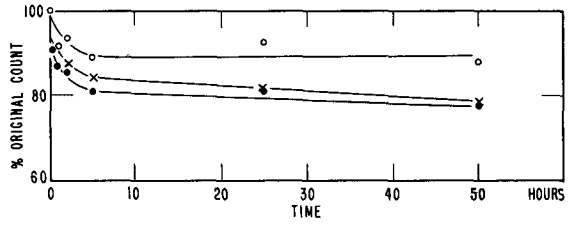

Fig. 7. Desorption of single crystal surfaces with distilled water: •, 100; ○, 111; ×, 110.

reverse process, even after restoration of the surface by massive desorption before immersion.

The extent of desorption by distilled water is shown in Fig. 7. One surface of each type was made radioactive by immersion for nine days, with desorptions between the immersion periods (*i.e.*, after 1, 4, and 9 days), and then a further immersion for 16 days without desorptions. The per cent removal of the radioactivity by desorptions with distilled water is shown. From surfaces immersed in radioactive solution for only very short periods, up to 30, 40, and 50% of the radioactivity can be desorbed by distilled water from the (111), (100), and (110) surfaces, respectively.

To obtain a diffusion profile, small "slices" of the specimens were removed by etching with a solution containing 20g of CrO_3 and 10g of H_2SO_4 in 2000g of distilled water. The technique of "chemical sectioning" has been described by Barr *et al.* (15). The solution that they used for copper, however, was found to pit silver surfaces, and so the chromic-sulfuric acid solution was substituted. It was found that a 5-sec dip in this solution, while it was boiling, followed by rinsing in distilled water, removed an amount of silver from a polished surface corresponding to a thickness of 0.2μ. The silver was removed very evenly, leaving the surface still polished, and the process was reproducible. The sides of the specimens were lightly ground to remove any silver that had diffused down along these surfaces, and the exposed surfaces were then etched in small beakers containing the solution. Both the solution and the specimen were counted and the results agreed within the experimental errors. Apart from the first slice, the logarithm of the removed activity was proportional to the thickness of metal removed, rather than to the square of the thickness as it would be if it followed the error function complement equation which holds for volume diffusion at temperatures above 600°C. The penetration curves obtained are shown in

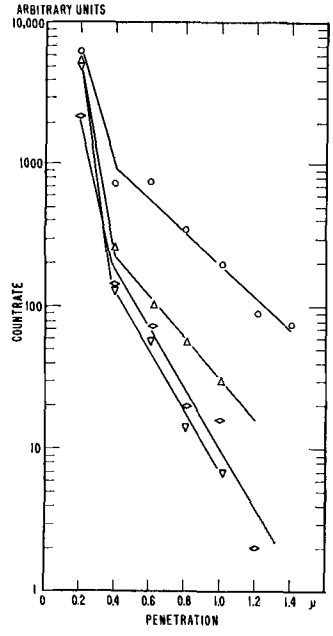

Fig. 8. Penetration profile of silver specimens with different plane surfaces: ○, (111); △, (100); ▽, (110); ◇, (311).

Fig. 8, in which the lines are drawn by the method of least squares.

Calculation of Diffusion Coefficient

The fact that the penetration of radioactive silver atoms into single-crystal specimens at room temperature follows a relation similar to that for grain-boundary diffusion rather than to that for volume diffusion at high temperatures suggests that silver diffuses at room temperature along dislocation "pipes," which behave like tiny grain boundaries. The equation derived by Fisher (16) for grain-boundary diffusion may then be used to calculate the diffusion coefficient. This equation is

$$D_d = 2D_v^{1/2}(\log e)^2 \Big/ \delta\left(\frac{d \log a_x}{dx}\right)^2 (\pi t)^{1/2}$$

where D_d will be the dislocation diffusion coefficient, D_v the volume diffusion coefficient, e the base of natural logarithms, δ the width of the dislocation pipe, a_x the radioactivity, x the distance penetrated normal to the surface, and t the time. Tomizuka and Sonder (17) obtained the equation

$$D = 0.4 \exp \frac{-44{,}100}{RT}$$

for the self-diffusion of silver in single crystals at high temperatures. Extrapolated to room temperature (25°C) this gives a value

$$D_v = 4.5 \times 10^{-33} \text{ cm}^2/\text{sec}$$

Using this value and 1.44×10^{-8} (the effective atomic radius of silver) for the width of a dislocation pipe the value for the dislocation diffusion coefficient at 25°C in silver is

$D_d = 2.1 \times 10^{-21}$ cm^2/sec for (111) surfaces

$= 1.5 \times 10^{-21}$ cm^2/sec for (100) surfaces

$= 6.1 \times 10^{-22}$ cm^2/sec for (110) and (311) surfaces

Discussion

The ease of removal, by soaking in distilled water, of a large proportion of the radioactivity acquired by these silver surfaces, suggests that the first step in the exchange process is adsorption of silver ions from the solution onto the top layers of atoms in the metal lattice. The number of atoms in 1 cm^2 of (111), (100), 110),

and (311) planes in silver is 1.4 x 10^{15}, 1.2 x 10^{15}, 8.5 x 10^{14}, and 7.2 x 10^{14}, respectively. The number of silver ions taken up by these surfaces is roughly proportional to the densities of atoms on the surfaces, *i.e.*, decreasing in magnitude from (111) through (100) and (110) to (311), but the fact that they are not exactly proportional shows that factors other than merely the number of adsorption sites, such as adsorption and exchange energies, are operating. This is also indicated by the ease of removal of freshly adsorbed ions by soaking in distilled water, which is inversely proportional to the quantities adsorbed, *i.e.*, decreasing in magnitude from (311) through (110) and (100) to (111).

That a certain time elapses before exchange is complete between the adsorbed ions and those in the metal lattice is shown by the fact that specimens immersed for longer periods (or even stored after exchange) are not desorbed to the same extent as those freshly activated by short periods of immersion. Referring to Fig. 2, it would seem that the initial very rapid uptake during the first few seconds is due to adsorption; the increase from the first few seconds until about 15 min is the result of exchange between adsorbed ions and atoms in the metal, followed by exchange between adsorbed inactive ions and radioactive ions in the solution, and then the slower increase of radioactivity after the first 15 min is due to diffusion of radioactive atoms along the surface and into the metal and their replacement on the surface by other radioactive atoms going through the processes of adsorption, exchange and diffusion into the metal.

The inhibition of the exchange by adsorbed ions, shown in Fig. 5 and 6, may be due to the formation of a double layer of silver and nitrate ions, the anion part of which tends to prevent the exchange of silver ions between the surface (or adsorbed layer) and the solution. Attempts to investigate the adsorption of nitrate ions on silver surfaces proved inconclusive. However, King and Schochet have shown that silver nitrate, as such, is adsorbed on silver surfaces (18).

Alternatively, if adsorption leads to a smaller effective surface, or the filling of "active sites" such as kinks, incomplete rows, steps *etc.*, this also might retard further adsorption. No sign of corrosion was observed on the surfaces used in the experiments reported in this paper. These surfaces were very smooth (14), were very carefully handled, and remained very smooth to microscopic observation and without a sign of tarnish throughout the duration of the experiments. Because of improper electropolishing, some surfaces were prepared which did tarnish slightly after several days. The pickup curves for these surfaces always showed an upward curvature, which is easily explained, because exchange between the solution and silver oxide and sulfide is more rapid than with the metal, and also because the corrosion roughened the surface and thus caused its area to gradually increase. The linearity of the pick-up curves in Fig. 3 and 6, and the lack of any visual corrosion, indicates that corrosion did not occur to such an extent that it affected the exchange.

As mentioned above, the self-diffusion of silver at high temperatures takes place by a vacancy mechanism, and may be represented by Fick's Second Law, for constant surface concentration, by the equation

$$C_{(x,\,t)} = C_0\, erfc \frac{x}{2\sqrt{Dt}}$$

where $C_{(x,\,t)}$ is the concentration of diffusant at thickness x and time t, C_0 is the constant concentration of the diffusant at the surface, and D is the diffusion coefficient (19). However, it was found that the diffusion at room temperature does not obey this equation, but instead follows the same law as grain-boundary diffusion. Extrapolation of the Arrhenius equation which obtains for silver at high temperatures would indicate that the atoms moved only 10^{-13} cm in the present experiment. This also indicates a different mechanism for the room temperature diffusion. On the other hand, the actual area of the surface is probably many times the measured area, due to vacancies, steps, *etc.*, and there is evidence that the dislocation density can vary extremely rapidly near the surface. Several papers during the last year or so have reported very low volume diffusion coefficients near the surface of a metal, indicating that the structure of the metal is markedly different in that region from what it is in the interior of the metal. For these reasons a calculation of the area of diffusion from the difference in radioactivity between the surface and planes in the interior seems impossible. If diffusion occurs along dislocation networks or pipes, the area through which diffusion is occurring is actually very much less than the geometrical area of the surface.

Hoffman and Turnbull studied grain-boundary self-diffusion in silver, and obtained curves similar to Fig. 8 (21). The high values in the first slice they explained as due to surface radioactivity which had not diffused. It now appears that the greater slope at the beginning of these diffusion profiles is due to the lower diffusion coefficient near the surface, mentioned above. They proposed a dislocation pipe theory to explain grain-boundary diffusion, and obtained an Arrhenius equation which covered the diffusion from 400° to 525°C. This equation is

$$D_b = 0.14 \exp \frac{-19{,}700}{RT}$$

Extrapolation of this equation to 25°C gives a value for D_b of 3.2 x 10^{-15} cm^2/sec, which is 5 to 6 orders of magnitude greater than those obtained by Sandor and by King *et al.* The experimental results fall between those obtained by this equation and those obtained by extrapolating the Arrhenius equation for volume diffusion at high temperatures.

Calculating from the amount of exchange, King obtained, for single crystal silver at room temperature, values of the self-diffusion coefficient from 1.3 to 1.5 (x10^{-21}) cm^2/sec, in good agreement with those obtained in the present work (22).

An alternative method for determining the actual area through which diffusion occurs is suggested in a paper by Foster *et al.* (23). Ag^{110} is not suitable for this purpose, because of its γ-emission, but Ag^{111} could be used, perhaps.

Acknowledgments

The author wishes to express his appreciation to Dr. G. G. Eichholz, former Head of the Physics and Radiotracer Subdivision, Mines Branch, for his direction of this research and help at all times, to Dr. J. D. Keys, of the Mines Branch, Dr. G. R. Piercey and Mr. G. V. Kidson, of the Research Metallurgy Branch, Atomic Energy of Canada, Ltd., Chalk River, Ont., and Mr. L. P. Trudeau, of International Nickel Company Ltd., stationed at Chalk River, Ont., for helpful discussions on diffusion mechanisms and techniques, to Mr. J. F. Rowland for the x-ray diffraction determinations, to Dr. Z. S. Basinski, of National Research Council, and Drs. D. M. Fegredo and K. G. Davis, of the Physical Metallurgy Division of the Mines Branch, for cutting crystals, and to other members of the Mineral Sciences Division of the Mines Branch for assistance in many ways.

Manuscript received April 20, 1964; revised manuscript received Aug. 13, 1964. This paper was presented at the Boston Meeting, Sept. 16-20, 1962.

Any discussion of this paper will appear in a Discussion Section to be published in the December 1965 JOURNAL.

REFERENCES

1. B. V. Rollin, *J. Am. Chem. Soc.*, **62**, 86 (1940).
2. C. V. King and Boris Levy, *J. Phys. Chem.*, **59**, 910 (1955).

3. C. V. King and N. E. McKinney, *Can. J. Chem.*, **37**, 205 (1959).
4. C. C. Coffin and I. I. Tingley, *J. Chem. Phys.*, **17**, 502 (1949).
5. I. I. Tingley and C. C. Coffin, *Proc. and Trans. Roy. Soc., Can.*, **43**, 214 (1949).
6. I. I. Tingley, I. H. S. Henderson, and C. C. Coffin, *Can. J. Chem.*, **34**, 14 (1956).
7. A. Baerg and C. A. Winkler, *ibid.* **31**, 319, 521 (1953).
8. J. E. Sandor, *ibid.*, **39**, 1869 (1961).
9. M. Do. Carma Anta and M. Cottin, *Compt. rend.*, **234**, 1686 (1952).
10. H. Gerischer and W. Vielstich, *Z. Elektrochem.*, **56**, 330 (1952).
11. H. Gerischer and R. P. Tischer, *ibid.*, **58**, 919 (1954).
12. B. Chalmers, *Proc. Roy. Soc.*, **A196**, 64 (1949).
13. L. I. Gilbertson and O. W. Fortner, *Trans. Electrochem. Soc.*, **81**, 199 (1942).
14. H. J. Levinstein and W. H. Robinson, *J. Appl. Phys.*, **33**, 3149 (1962).
15. L. W. Barr, D. A. Blackburn, and A. F. Brown, Radioisotopes in the Physical Sciences and Industry, Internationl Atomic Energy Agency, Vienna, 1962.
16. J. C. Fisher, *J. Appl. Phys.*, **22**, 74 (1951).
17. C. T. Tomizuka and E. Sonder, *Phys. Rev.*, **103**, 1182 (1956).
18. C. V. King and R. K. Schochet, *J. Phys. Chem.*, **57**, 895 (1953).
19. J. Crank, "Mathematics of Diffusion," Oxford University Press (1956).
20. P. B. Hirsch, *Progress in Metal Phys.*, **6**, 236 (1955).
21. R. E. Hoffman and D. Turnbull, *J. Appl. Phys.*, **22**, 634 (1951); *Acta Met.*, **2**, 419 (1954).
22. C. V. King, Todd Simmons, and Alice Berlin, *This Journal*, **110**, 1261 (1963).
23. L. M. Foster, A. S. Gillespie, Jr., T. H. Jack, and W. W. Hill, *Nucleonics*, **21**, 53 (April 1963).

Electrodeposited Nickel-Iron-Molybdenum Thin Magnetic Films

W. O. Freitag and J. S. Mathias

UNIVAC, Division of Sperry Rand Corporation, Research & Engineering Center, Blue Bell, Pennsylvania

ABSTRACT

Thin magnetic films of nickel-iron-molybdenum, 600-800Å thick, were electrodeposited from citrate complexed solutions containing sodium molybdate, nickel sulfate, and iron sulfate. The variation of magnetic properties of the films was determined as a function of the composition of the film, the *p*H of the plating solution, and the current density. All experiments were carried out at room temperature. Glass slides with vacuum evaporated chromium-gold layers were used as substrates. Magnetic films with H_k values of 1.0 oe have been obtained from these solutions.

The Ni-Fe-Mo alloy system was investigated as part of a program of continued development of thin magnetic films for computer memory use. The objective was to develop magnetic films having a low anisotropy field (H_k). The anisotropy field is the magnetic field required to saturate the film in a direction normal to the easy axis.

Most magnetic film memories now in use or being designed operate at drive currents of several hundred milliamperes (1). Techniques have been developed in our laboratories for the fabrication of memories which can operate at 20-30 ma (2) and which, therefore, will be compatible with molecular-type integrated circuits. One of the requirements for the design of such a low power memory was the availability of magnetic thin film material with anisotropy field on the order of 1 oe. This paper describes research directed toward this goal.

Engleman and Hardwick (3) have reported the preparation of thin films of permalloy having an H_k as low as 1.5 oe by a vacuum evaporation technique. Francombe and Noreika (4) have obtained magnetic films having an H_k of 2.5-4.0 oe by cathodic sputtering.

Wolf (5) has electrodeposited binary nickel-iron alloy films 1000Å in thickness which show an H_k of 3.5-4.0 oe. Electrodeposited Ni-Fe-P films having an H_k as low as 2 oe have been prepared in our laboratories and have been discussed previously (6). Exploratory work with electrodeposited Ni-Fe-Mo alloy films indicated that this alloy showed considerable promise with respect to producing films with H_k values to 1.0 oe.

Experimental

The plating apparatus was similar to that described previously (6) and consisted of a rectangular plastic vessel which was fitted with a suitable means of holding the cathode rigidly in a removable holder. Anodes were fabricated from high-purity nickel sheet. The bath was surrounded by a coil which generated a uniform vertical magnetic field of about 35 oe. The plating current was provided by a constant current regulated power supply. All experiments were carried out at room temperature without agitation.

The cathodes were Corning Microsheet approximately 8 mils in thickness measuring 43 mm x 50 mm and coated with evaporated layers of chromium and gold 1000-1200Å and 800-1000Å in thickness, respectively. Evaporations were carried out at about 1×10^{-5} Torr.

The electrolyte was a citrate complexed solution of nickel and iron sulfates containing sodium molybdate; bath compositions are shown in Table I.

Magnetic properties, coercive force, H_c and anisotropy field, H_k, were measured on a 60 cycle hysteresograph. A qualitative estimate of magnetostriction was made by flexing the film samples within the sense coil of the hysteresograph during H_k measurement. Since the hysteresograph was designed for samples of another size, only the sign of the H_k change was recorded, and no values for magnetostrictive coefficient are given in this work.

Deposits were analyzed by dissolving a known film area, diluting to volume, and applying standard colorimetric micromethods for Fe, Ni, and Mo. Thicknesses were estimated from the total amounts of metal found and are believed accurate to ±10%. Film compositions

Table I. Composition of electrolytes

Component, g/l	Solution Series 1	Series 2	62-27	62-51
$NiSO_4 \cdot 6H_2O$	60	80	60	80
$FeSO_4 \cdot 7H_2O$	1 to 8	2 to 5	3.5	4.0
$Na_2MoO_4 \cdot 2H_2O$	¼ to 2	1 to 2	1.5	1.5
Citric acid monohydrate	66	60	72	80
Saccharine	0.8	0.8	0.8	0.8
Na lauryl sulfate	0.4	0.2	0.4	0.2
NaCl	10	10	10	10
$NaOH/H_2SO_4$	As required to adjust to pH 5.2			

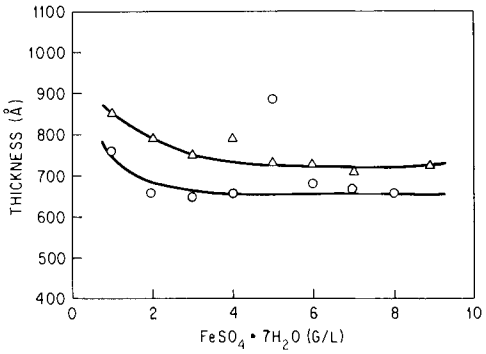

Fig. 1. Effect of ferrous sulfate concentration on film thickness at constant nickel sulfate concentration. Series I solutions, c.d. = 6 ma/cm^2; plating time 60 sec. △, 1.5 g/l $Na_2MoO_4 \cdot 2H_2O$; ○, 0.25 g/l $Na_2MoO_4 \cdot 2H_2O$.

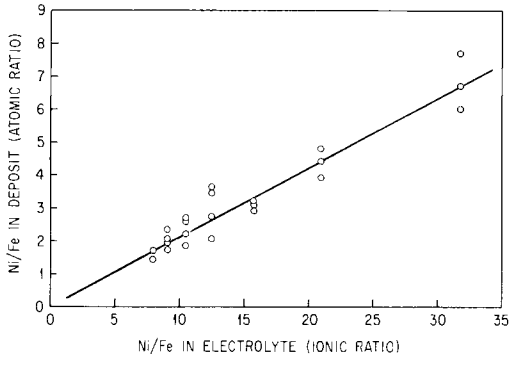

Fig. 2. Nickel-iron ratio in deposit *vs.* ionic ratio in electrolyte. Series I solution, c.d. = 6 ma/cm^2; plating time 60 sec.

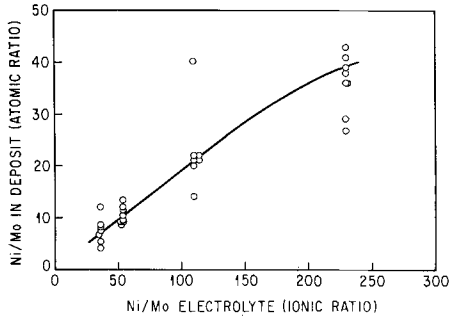

Fig. 3. Nickel-molybdenum ratio in deposit *vs.* ionic ratio in electrolyte. Series I solutions, c.d. = 6 ma/cm^2; plating time 60 sec.

up to about 30 wt. % Fe and 20 wt. % Mo were investigated.

Control of Film Composition

The composition of the deposit was controlled primarily by the composition of the plating bath. The data shown in Fig. 1 to 3 were obtained using solutions of Series I, Table I. The plating time was 60 sec at a current density of 6 ma/cm^2. Ferrous sulfate heptahydrate and sodium molybdate concentrations were varied giving a series of solutions having Ni^{++}/Fe^{++} ionic ratios of 63.3-7.9, and Ni^{++}/MoO_4^{--} ratios of 228 to 37.

Figure 1 shows a plot of film thickness obtained at a constant deposition time of 60 sec *vs.* iron content of the electrolyte, at two levels of molybdate concentration. No effort was made to determine cathode current efficiency quantitatively although a 60 sec plating cycle was calculated to yield a film about 1100-1200Å in thickness at 100% efficiency. We note from Fig. 1 that the efficiency is roughly independent of the iron content of the solution (except at very low iron) and is slightly better at higher molybdenum concentrations.

Figure 2 shows the relationship between the ionic ratio of nickel and iron in the electrolyte and the atomic ratio of nickel and iron in the deposit. A change in sodium molybdate concentration did not appear to affect the relative deposition rates of nickel or iron under our plating conditions. The vertical spread of the experimental points shows the range of Ni-Fe atomic ratios obtained at the four different levels of molybdenum concentration in the electrolyte. However, the four lines that result when one plots these data separately for each molybdenum concentration are very nearly the same line, and no systematic effect of molybdate concentration can be determined. Therefore, within the limits of accuracy of these data, the amount of molybdate ion present in the solution has no effect on the Ni/Fe ratio in the deposit, and the latter is a function only of the ratio of the nickel and iron ions in the electrolyte.

Figure 3 relates the nickel-molybdenum ratios for the same films. Again there is considerable experimental spread, but there was evidence that for solutions having low Ni/Mo ionic ratios, increasing amounts of iron sulfate gave decreasing Ni/Mo atomic ratios in the deposit. This effect was not sufficiently clear-cut to permit graphic presentation, however, and did not appear at all at the higher Ni/Mo ratios.

Variation of Deposit Composition with Plating Time

During the simultaneous discharge of more than one ionic species at a cathode, the relative deposition rates of the individual ions will vary at the start of the deposition cycle as their relative concentrations vary in the cathode double layer. The interplay of relative depletion rates in this double layer and diffusion rates into this layer eventually results in some equilibrium composition. During the deposition of these thin films, the total deposition time is not much longer than the time required to achieve this equilibrium. As a result composition gradients appear across the thickness of the films, and a film 500Å thick could have an average composition quite different from one 1000Å thick plated under exactly the same conditions. This effect has been discussed with respect to binary Ni-Fe films by several workers (7, 8). The ternary system Ni-Fe-P was studied by the present authors (6). During the deposition of Ni-Fe from uncomplexed sulfate solutions, the initial film layers are more iron-rich than layers deposited subsequently. The effect is ameliorated by the presence of sodium hypophosphite in the Ni-Fe-P system.

Figure 4 shows the average iron concentration as a function of plating time for Ni-Fe-Mo films. The initial layers of deposit are relatively more iron-rich than those deposited later as is the case in the nickel-iron deposition. Figure 5 shows the data for molybdenum content of these same films. The initial layers are Mo-rich, but an equilibrium composition is soon reached.

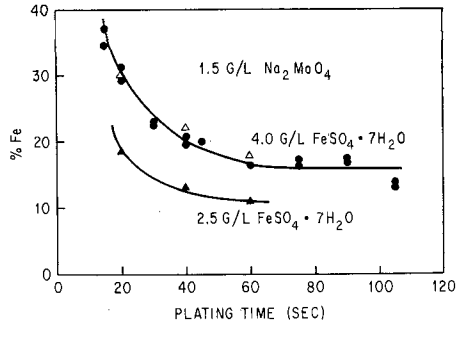

Fig. 4. Variation of average iron content of Ni-Fe-Mo films with plating time (film thickness) at a constant molybdate concentration. Two levels of ferrous sulfate concentration are shown. Current density was 6 ma/cm^2. Triangular points were from solutions of Series 2, round points from Solution 62-51 (Table I).

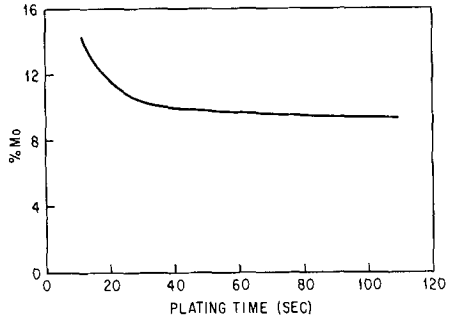

Fig. 5. Variation of average molybdenum content of Ni-Fe-Mo films with plating time (film thickness) for films deposited from solution 62-51, Table I: 1.5 g/l $Na_2MoO_4 \cdot 2H_2O$; 4.0 g/l $FeSO_4 \cdot 7H_2O$.

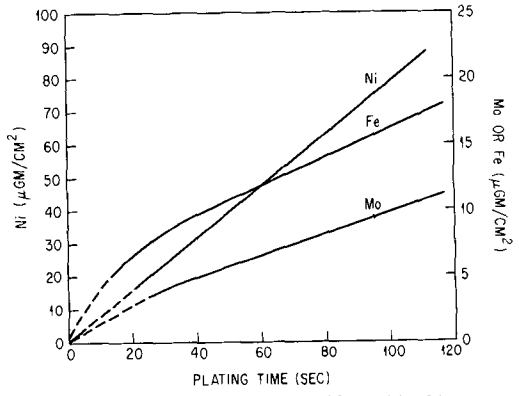

Fig. 6. Amount of each component in Ni-Fe-Mo films vs. plating time from solution 62-51. Current density was 6 ma/cm^2; 1.5 g/l $Na_2MoO_4 \cdot 2H_2O$; 4.0 g/l $FeSO_4 \cdot 7H_2O$.

These data are presented in a more significant manner in Fig. 6. The compositions are expressed in micrograms of each component per unit area of film and are plotted against plating time. When an equilibrium state is reached in the cathode double layer and some constant composition is being deposited, the rate of increase of the amount of each alloy component in the film should be a constant and the curve will be linear. This is seen to be the case for each metal species here. Iron approaches its straight line portion corresponding to a constant deposition rate in about 40-50 sec. Nickel, however, appears to deposit at a uniform rate from the beginning. This is not unexpected, since nickel is present in relatively larger amounts.

The slopes of the straight line portions of these curves yield the equilibrium deposition rates of the three components. These values are 0.085, 0.108, and 0.78 μg/cm^2/sec for Mo, Fe, and Ni, respectively. The equilibrium composition is therefore 9% Mo, 11% Fe, and 80% Ni for this solution. Assuming that the reduction of each Ni or Fe ion requires two electrons, and each molybdate ion requires six, one calculates that the current efficiency for this equilibrium deposit is about 57%.

Furthermore, since the slopes of the Fe and Mo lines in Fig. 6, that is, the deposition rates, are greater at a plating time less than that required for establishing the equilibrium deposit, the current efficiencies should be somewhat greater for thinner films. That this is indeed the case was shown by plotting total deposit thickness as a function of plating time; the slope of this curve, which should be a straight line, was greater in the region 15-40 sec than it was in the region greater than 40 sec.

It appears that after about 40 sec of plating, equilibrium concentration conditions are achieved in the cathode double layer, and after this a constant composition alloy is deposited.

Effect of Composition on Magnetic Properties

The variation of magnetic parameters with electrolyte and deposit composition is shown in Fig. 7 and 8. Figure 7 shows the effect of the ionic ratio of nickel to molybdate in the solution on the H_k of a 60 sec deposit. Several iron concentrations, expressed as ionic ratio of nickel to iron in the bath, are represented. For solutions high in iron, that is having a Ni/Fe ratio of 10 or lower, high H_k values are obtained at all molybdenum levels, although H_k decreases as the molybdate content is increased. Minimum H_k films were obtained at Ni/Fe ratios of 20 to 30 and at nickel to molybdate ratios of 35 to 50. At higher Ni/Fe ratio there is a sharp increase in H_k values.

The data shown in Fig. 7 are a composite of two sets of experiments, one based on Series 1 solutions (Table I), the other on Series 2 solutions. The two sets of data agreed well, showing that under the conditions used (which involved no agitation, a current density of 6 ma/cm^2, a plating time of 60 sec, and a pH of 5.2) the H_k of the film is dependent on the composition of the plating bath and hence on the composition of the deposit.

Figure 8 relates H_k to film composition directly. The low Fe, low Mo corner of the ternary Ni-Fe-Mo composition diagram is shown. The points represent the composition of films in the thickness range 600-800Å as determined by wet analysis. The points along the 0% Mo axis (binary Ni-Fe alloy) were taken from Wolf's data for 500Å films (5). These were included even though they do not fall within the thickness range of our data since Wolf showed no appreciable H_k change with thickness in this thickness range. The dashed lines roughly map out areas of points having the indicated H_k values.

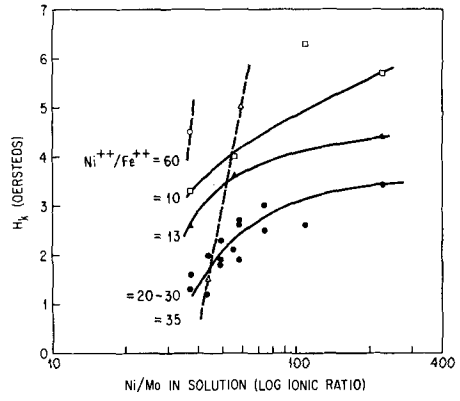

Fig. 7. Anisotropy fields of 60 sec deposits as a function of ionic ratio in electrolyte. Films plated from solutions of both Series I and II are represented; c.d. = 6 ma/cm^2; plating time 60 sec.

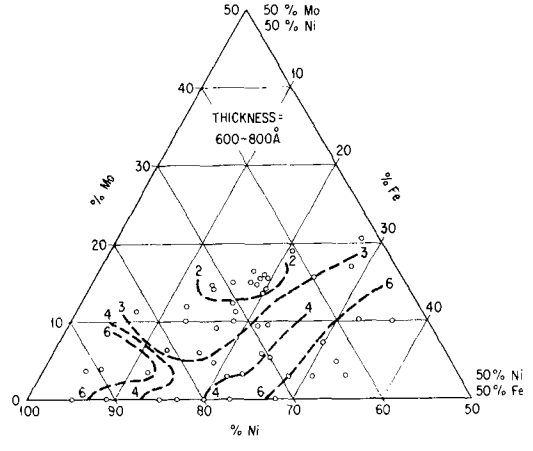

Fig. 8. Anisotropy field as a function of film composition. The dashed lines roughly map out areas of composition having the range of H_k values shown. A field of $H_k < 2$ oe appears at 15% Mo, 15-20% Fe.

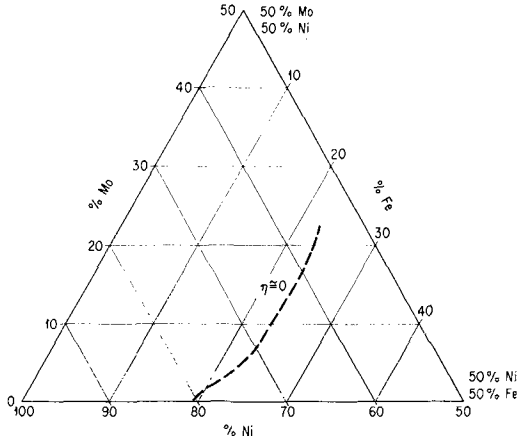

Fig. 9. Approximate locus of Ni-Fe-Mo film compositions having zero magnetostriction in the 600-800Å thickness range.

An area of minimum H_k (H_k — 1.0 to 2.0 oe) appears at approximately 15% Mo, 15 to 20% Fe, and 65 to 70% Ni.

Figure 9 shows the approximate locus of compositions with zero magnetostriction. Note that this line misses the area of minimum H_k; all films with suitably low H_k values were highly magnetostrictive.

Effect of Plating Conditions on Magnetic Properties

The magnetic properties of the electrodeposited Fe-Ni-Mo films are sensitive to the current density and pH during deposition. It is shown below that for a limited current density range the variation of H_k of the films with current density is traceable to variations in relative deposition rates of the three component metals. However, film quality as reflected by the squareness of BH loops deteriorated at higher current densities.

The effect of current density was studied with solution 62-27 (Table I). Current density was varied from 2 to 14 ma/cm^2 at a constant 360 ma-sec/cm^2. No deposit was obtained at 2, and incomplete coverage was found at 4 ma/cm^2. Films with "well-behaved" BH loops were found up to about 10 ma/cm^2; above this current density, distorted loops were obtained. The variation of H_k for these films is indicated in Fig. 10 which shows a slight increase in H_k as current density increases. Analysis of these films gave the results shown in Fig. 11. Both the iron and molybdenum contents of the deposits decrease as current density increases, and, as can be seen from Fig. 8, as the Fe concentration falls an increase in H_k is to be expected. Note also an increase in cathode current efficiency as current density is increased as expressed by the rising deposit thickness, even though a constant total charge was passed through the cell.

The effect of pH on the magnetic properties of the electroplate is striking and requires further study. Figure 12 illustrates the behavior observed for solution 62-27, and is typical of all solutions tested. Minimum H_k values are observed at pH of 5.2. Below pH 4, only films with distorted BH loops were obtained; no deposits were formed at pH 6 or above.

Summary

We have shown that the Ni-Fe-Mo alloy films can be deposited from mixed sulfate solutions complexed with citrate ion and containing sodium molybdate. The composition of the films may be controlled by controlling the plating time and the composition of the solutions. Magnetic films having anisotropy fields as low as 1.0 oe can be prepared, but these are highly magnetostrictive in the thickness range investigated.

Acknowledgments

The authors wish to express their appreciation to Guy DiGuilio, Charles Bell, and Victor Suchodoloski for fabrication of the films and the magnetic measurements, and to Edwin Schneider for the chemical analyses.

Manuscript received May 8, 1964; revised manuscript received Sept. 4, 1964. This paper was presented at the Pittsburgh Meeting, April 15-18, 1963.

Any discussion of this paper will appear in a Discussion Section to be published in the December 1965 JOURNAL.

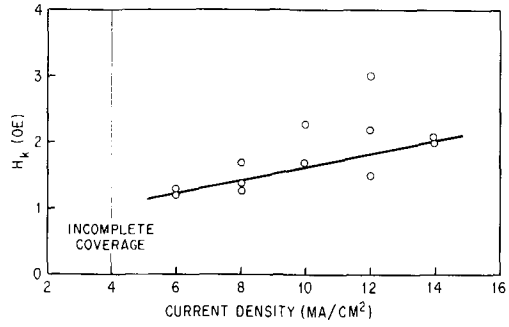

Fig. 10. Variation of H_k of Ni-Fe-Mo films with current density. The electrolyte (Solution 62-27) was a solution which yielded minimum H_k values at 6 ma/cm^2. A constant charge of 360 ma-sec/cm^2 was used.

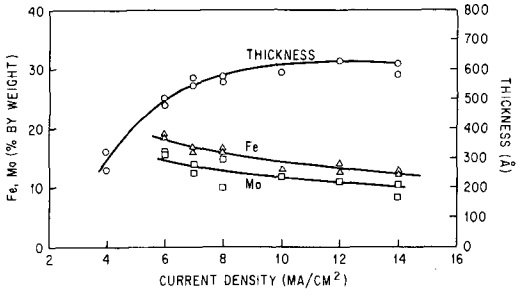

Fig. 11. Variation of deposit thickness and composition with current density (Solution 62-27).

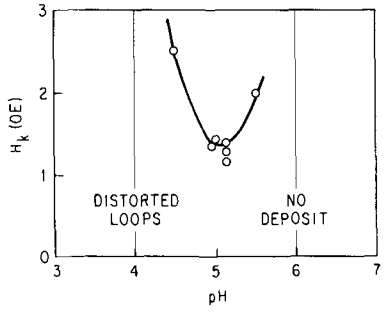

Fig. 12. Effect of pH on anisotropy field of 600-800Å Ni-Fe-Mo deposit (Solution 62-27).

REFERENCES

1. G. Fedde, *Proc. AFIPS Conference*, Washington, D. C., **22**, 213 (1962).
2. C. J. Kriessman, T. J. Matcovich, and W. E. Flannery, Intermag Conference, Washington, D. C., April 1963.
3. J. H. Engleman and A. J. Hardwick, Transactions, Ninth National Vacuum Symposium, The Macmillan Co., New York, 1962; A. J. Hardwich, *J. Appl. Phys.*, **34**, 818 (1963).
4. M. H. Francombe and A. J. Noreika, *ibid.*, **32S** (1961).
5. I. W. Wolf, *This Journal*, **108**, 959 (1961); *J. Appl. Phys.*, **33**, 1152S (1961).
6. W. O. Freitag, J. S. Mathias, and G. DiGuilio, *This Journal*, **111**, 35 (1964).
7. G. H. Cockett and E. S. Spencer-Tinns, *ibid.*, **108**, 906 (1961).
8. F. H. Edelman, *ibid.*, **109**, 440 (1962).

Extremely Intense Light Sources with Narrow-Band Spectral Emission

Jenny E. Rosenthal and Charles F. Eyer

Melpar, Inc., Falls Church, Virginia

ABSTRACT

The effect of a microwave field at 2.45 kMc on a sodium seeded oxyhydrogen flame is studied in some detail in the case when the microwave power is only about 1/8th of the thermal power of the flame. An average brightness enhancement by two orders of magnitude is observed raising the level to 2 million foot-lamberts. The enhanced emission is limited to the vicinity of the resonance lines which show quite extreme broadening with narrow reversal. Under pulsed operation, the light pulse is synchronized with the microwave pulse. Qualitative data are given for the enhancement at 10 kMc. Possible explanations of the observed effects are considered.

This is a report on work done toward the development of a lamp of high efficiency and high brightness level radiating over practically the entire range of 4π steradians. Operation can be either continuous or at any desired pulse rate up to a few kilocycles and possibly higher. Most of the emission is concentrated in a spectral band of the order of 50-300Å.

The operation can be illustrated by the following example: A sodium seeded flame is a light source activated by a cheap form of power. However, the efficiency, *i.e.*, the ratio of luminous power out to thermal power in, is less than 1%. If this light source is subjected to a microwave field whose power is only about ⅛th of the initial thermal power due to combustion, the result is more than a hundred fold increase in the brightness of the light source with an over-all operating efficiency approaching 50%. The enhancement is not limited to flames seeded with alkali metals, but appears to be a much more widespread phenomenon. A report on the more general aspects is deferred to a later date.

Experimental Arrangement and Results

The microwave field is produced inside a waveguide in the TE_{10} mode by a magnetron operating at 2.45 kMc with an average power output of nearly 1 kw. The waveguide has a cross section of 4.3 x 2.6 in., is open at the end, and has holes drilled to permit insertion of the flame with its axis perpendicular to the direction of the electric vector (see Fig. 1). A special tuning mechanism is provided to concentrate the microwave energy in the region of the flame. This arrangement is estimated to provide about 25% coupling between the flame and the microwave field, *i.e.*, some 250w are absorbed by the flame, the rest being reflected. According to calculations based on Stratton's book (1, 2), redesign of the microwave cavity and of the plasma envelope should bring the coupling up to 90%.

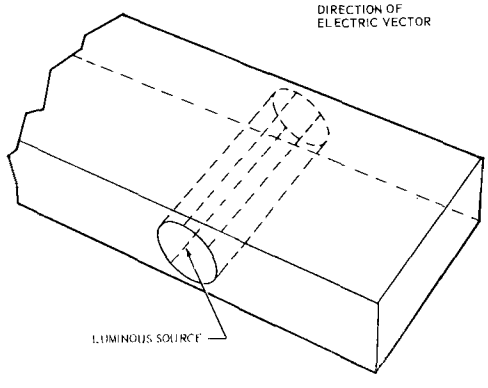

Fig. 1. Schematic of experimental set-up

The light source is formed by an oxyhydrogen torch confined laterally inside a quartz tube containing a charge of small NaCl crystals. This arrangement provides a simple way for impregnating the flame with sodium as the NaCl charge keeps being replenished.

The entire set-up is placed inside an exhaust cabinet which serves to exhaust the liberated chlorine and other gases that may be present and in addition provides shielding against microwaves. Viewing can be done either from the side or from the front through suitable openings in the walls of the exhaust cabinet, which are covered by a wire mesh for radiation shielding. A Spectra Spot Brightness Meter placed in front of the open end of the waveguide and focused on a small area of the quartz tube is used to measure the brightness of the lamp. It should be emphasized that the meter is sufficiently far away to keep any minor changes in its position from affecting the readings, given in ft-L.

When the torch is lit but the magnetron is not turned on, the brightness reading for a flame saturated with salt is of the order of 15,000 ft-L. When the magnetron is turned on, pulsed at 60 cycles, the brightness reading on the meter, which gives a time average, is increased by a factor of 130 to a value of 2 million ft-L. To study the behavior of the emitted light as a function of time, the light pulse is detected by a photodiode and displayed on an oscilloscope. Figures 2A and 2B show oscilloscope traces of the enhanced

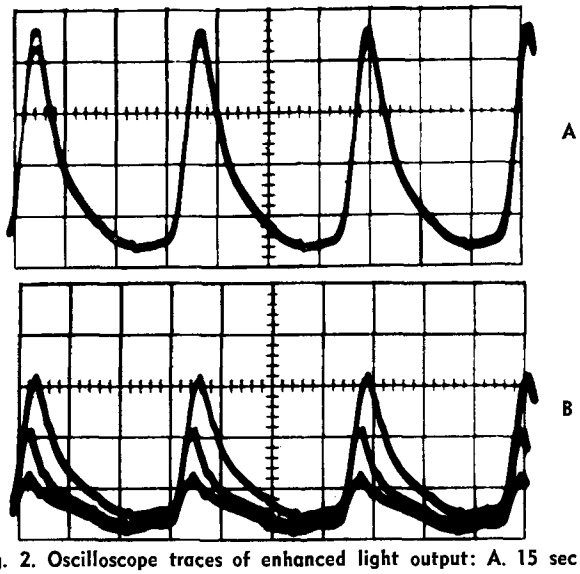

Fig. 2. Oscilloscope traces of enhanced light output: A. 15 sec after ignition; B. 3, 5, and 7 min after ignition.

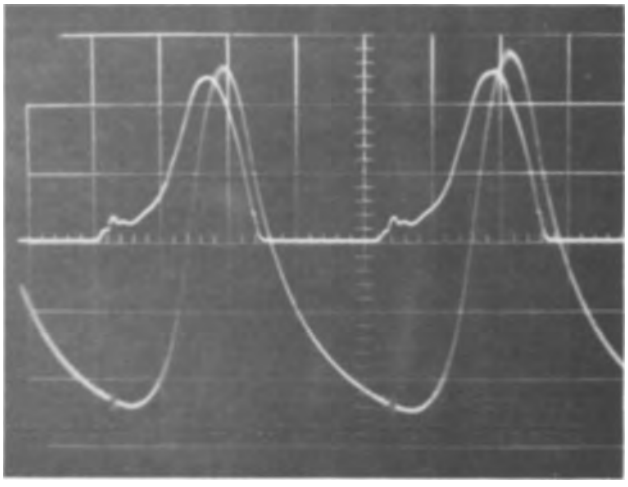

Fig. 3. Comparison of light pulse and magnetron pulse

light output at a 60 cycle pulsing rate. Each horizontal division represents 5 msec, the vertical (intensity) scale is arbitrary. Figure 2A represents conditions 15 sec after ignition and simultaneous turning on of the magnetron. With the arrangement used, the salt is slowly blown out through the open ends of the quartz tube. The three curves in Fig. 2B are oscilloscope traces of the light output at successive stages of salt depletion, 3, 5, and 7 min after ignition, respectively.

Since increased seeding raises the flame conductivity, the above data mean that enhancement increases with flame conductivity, *i.e.*, with plasma density. The higher the brightness of the flame before it is subjected to the microwave field, the greater the enhancement factor.

The following studies were carried out to obtain a better understanding of the observed basic phenomenon of enhancement.

The first set pertains to the time relationship between the emitted light pulse and the magnetron pulse. Figure 3 shows the degree of synchronization between the two. Different baselines were chosen to make the comparison more clear cut. Pulsing is at 120 cycles. The microwave pulse is referred to the upper line and the light pulse to the bottom one. Each horizontal division corresponds to 2 msec. We see that the enhanced light pulse does not start till the microwave pulse has reached a certain level, however, it continues to rise past the peak of the microwave pulse and proceeds to decay much more slowly. Pulsing rates as high as 2 kc have been used with 0.75 μsec pulse duration and a peak power of 1 kw. The emitted light was found to be pulsed at the same rate though the time-averaged enhancement was too low to be detected visually. This is to be expected in view of the very low duty cycle.

With regard to spectroscopic data, visual observation did not reveal OH bands under any operating conditions. In the absence of a microwave field, the observed spectrum is that of atomic sodium with such broadening characteristics as would be expected in a flame operating around 2500°C, the temperature listed (3) for a hydrogen-rich oxyhydrogen flame. These results are to be contrasted with the appearance of the spectrum in Fig. 4 produced by a flame subjected to the action of the microwave field. The spectrogram extends over the range from the sodium D-lines to the sodium green line, which would appear at the position indicated by the arrow. It is visible on the original plate but may be too faint to be seen in reproduction. Thus enhancement does not affect transitions other than the resonance lines. Reversal indicates the normal position of the D-lines. Broadening is obviously quite extreme.

Under certain conditions which are not yet fully understood, we also observed a faint continuum or

Fig. 4. Spectrogram of enhanced sodium flame

possibly a very dense band system extending for a few hundred angstroms on each side of the D-lines. This may be a secondary effect. In any case, the ratio of the intensity in the vicinity of the D-lines to that of the continuum is estimated to be at least of the order of 100. This is to be compared with conditions in the mercury high pressure lamp where the ratio of the intensity of the mercury green line to that of the surrounding continuum is less than 10.

Enhancement is also observed at 10 kMc. However, no quantitative comparison is possible with the 2.45 kMc case since the entire power output of the high frequency magnetron is only 250w.

No coupling has been observed between a d-c discharge and a microwave field even though the shape and orientation of the electrodes are chosen so as to prevent microwave reflection from them. The voltage and current values used were in the range required for an arc discharge. However, when the d-c discharge was combined with the microwave field, no enhancement could be noticed visually.

Discussion

The following salient facts appear from the experiments above:

1. The microwave energy acts as a trigger which permits efficient utilization of thermal energy in the production of visible radiation.
2. Enhancement appears to be restricted to the first excited state.
3. The broadening of the enhanced lines is quite extreme while the reversed portions at the center remain quite narrow.
4. No coupling is observed between a d-c discharge and a microwave field.

The following comments appear to be pertinent with regard to these facts:

a. Temperature rise has to be excluded as the cause of the enhancement since the temperature would rise only by about 1000°C even if the entire 250w of microwave energy were used for heating the gases in the flame. Calculations based on Planck's radiation function show that this increase in temperature would cause only a nine-fold increase in the radiation from a blackbody at the wavelength of the Na D-lines. Furthermore, at the higher temperature, the wavelength of a maximum emission from a blackbody would be shifted. If instead of a blackbody, we consider the actual case of an atom emitting discrete

lines, the temperature rise would increase the population of the more highly excited states and thus increase the intensity of transitions from these states relative to the intensity of the resonance radiation. As mentioned above, this is contrary to observations.

b. It is obvious that Doppler broadening at the existing temperatures is several orders of magnitude smaller than that shown in Fig. 4. Using conventional notation, the standard formula for collision broadening is (4)

$$\Delta\lambda/\lambda = N'd^2\lambda\sqrt{(3kT/4Mc^2)} \quad [1]$$

where $\Delta\lambda$ is the width of the line at half the intensity of the maximum, N' the number of atoms per unit volume, and d the effective diameter for a collision sufficiently close to affect the radiation process. To get this formula to agree with experiment, we must postulate a value for d some thirty times larger than its value obtained from kinetic theory. While results of this nature have been observed previously (5, 6), it should be emphasized that in our experiments the large increase in collision cross section occurs only under microwave action. The narrow width of the reversed lines indicates that whatever "perturbation" takes place, it affects solely the excited state.

Comparison with Other High Intensity Sources

In order to evaluate the usefulness of the microwave enhanced plasma source for practical applications, it is necessary to compare it with conventional high brightness sources, such as the Hanovia short arc xenon lamps. The performance of these conventional lamps is usually measured in terms of their luminous flux or their intensity. Since we measured the output of our enhanced sodium flame in terms of its brightness, it is necessary to correlate the two sets of parameters. For this purpose we use the expressions

$$B = 929L/4A,\ L/4\pi = C \quad [2]$$

where A is the source area in cm^2, B the brightness in ft-L, C the intensity in candles, and L the luminous flux in lumens. Strictly speaking, the relations in Eq. [2] are applicable only to sources radiating uniformly over a sphere. However, they should provide at least a good estimate of data for the sodium flame. The results of this comparison are listed in Table I. The value listed for the total power input into the enhanced flame is the sum of the thermal power input of 2.2 kw into the flame and the electrical power input of 2 kw into the magnetron. It is seen from the table that even for this total power input the efficiency of the enhanced sodium flame is far higher than that of either of the xenon lamps. Allowing for the fact that the coupling between the microwave field and the flame is only 25%, but with proper design can be made 90%, we can place the effective power input at only about 2.7 kw. The efficiency of the energy transformation is therefore as high as 220 lumens/w. Furthermore, since the enhanced sodium flame emits primarily in the region of the D-lines, it constitutes a source with the highest number of lumens per watt per angstrom. It has the additional attractive feature that it is capable of being pulsed to fit any desired pulse pattern.

Table I. Comparison of data for sodium flame

	Na flame	Xe arc, Lamp 1	Xe arc, Lamp 2
Power consumption (watts)	4,200	2,200	5,000
Luminous flux (lumens)	600,000	66,000	200,000
Intensity (candles)	50,000	5,300*	21,500
Efficiency (lumens/watt)	140	30	40

* Calculated from manufacturer's data using formula in Eq. [2].

Practical Considerations

No matter how efficient a lamp, it is not suitable for practical applications if it requires auxiliary gas tanks or a vacuum arrangement. We have therefore started work on simulating a flame by a completely self-contained system. The resonating cavity and the plasma enclosure are also in the process of being redesigned to provide more efficient coupling and to permit eliminating the tuning mechanisms.

Manuscript received July 8, 1964. This paper was presented at the Toronto Meeting, May 4-7, 1964.

Any discussion of this paper will appear in Discussion Section to be published in the December 1965 JOURNAL.

REFERENCES

1. J. A. Stratton, "Electromagnetic Theory," p. 490 ff, McGraw-Hill Book Co., New York (1941).
2. R. A. Kraushaar and A. Crivello, Private communication.
3. N. A. Lange, "Handbook of Chemistry," 10th Ed., p. 825, McGraw-Hill Book Co., New York (1961).
4. G. P. Harnwell and W. E. Stephens, "Atomic Physics," p. 110, McGraw-Hill Book Co., New York (1955).
5. H. E. White, "Introduction to Atomic Spectra," p. 430, McGraw-Hill Book Co., New York (1934).
6. R. W. Wood, "Physical Optics," 3rd Ed., p. 528, Macmillan Co., New York (1934).

On the Luminescent Properties of the Rare Earth Vanadates

L. H. Brixner and E. Abramson

Pigments Department and Central Research Department, respectively, E. I. du Pont de Nemours and Company, Inc., Wilmington, Delaware

ABSTRACT

X-ray examination of several Ln_2O_3/V_2O_5 systems indicated that compounds of the $LnVO_4$ type are the only ones formed by the rare earth sesquioxides and vanadium pentoxide. On the basis of this finding, we developed a flux-growing technique employing a V_2O_5 melt for the preparation of all rare earth vanadates in single crystalline form. With such monocrystals as well as with polycrystalline material we studied the fluorescent emission of the rare earth vanadates, and these data are reported and discussed.

The fact that YVO_4 crystallizes in the D_{4h}^{19}-I4/amd space group of zircon ($ZrSiO_4$) was first recognized by Broch (1), and since the ion radius of Y^{3+} is generally placed between Dy^{3+} and Ho^{3+} it was to be expected that at least some of the rare earth vanadates would crystallize in the same structure. Milligan, Watt, Rachford, and Vernon (2, 3) prepared all rare earth vanadates of the $LnVO_4$ type and found that with the exception of $LaVO_4$ they do indeed all crystallize in the $ZrSiO_4$ structure. Gambino and Guare (4) later con-

firmed these structures. Carron *et al.* (5) found that $LaVO_4$ has the monazite structure, which recently was confirmed by Schwarz (6) who conducted a comparative crystallographic study of all rare earth phosphates, arsenates, and vanadates.

The only information concerning the luminescent properties of the rare earth vanadates is given by Van Uitert (7) who investigated the $Y_{1-x}Eu_xVO_4$ system during a study on the role of f-orbital electron wave function mixing in the concentration quenching of Eu^{3+}. He used a $NaVO_3$ flux for the preparation of rare earth vanadates, but did not state anything about the size or quality of the obtained crystals. It still appeared desirable to look at the luminescent properties of all rare earth vanadates, particularly since the considerable thermal stability could make them excellent candidate materials for host lattices for optical maser materials if they can be grown in single crystal form by flame-fusion, Verneuil, or some other appropriate technique.

Experimental

All rare earth vanadates were prepared directly from high-purity V_2O_5 (obtained from the Vanadium Corporation of America), and the corresponding rare earth sesquioxides were obtained in 99.9% purity from the Lindsay Chemical Division of the American Potash and Chemical Corporation. Reaction was generally effected in two steps: first the stoichiometrically mixed powders of —200 mesh particle size were prereacted at 680°C (just below the melting point of V_2O_5) for some 10-14 hr. This reaction product was then ballmilled in a mechanical agate ballmill under acetone, dried, pressed into a 1-in. diameter pellet, and fired in a second step for some 10-14 hr at 1200°C. After this treatment, completely reacted, homogeneous materials were obtained, which failed to show any of the lines of the components upon x-ray examination. Weight losses for approximately 10g charges were generally below 0.1%. $CeVO_4$ and $PrVO_4$ were prepared under an inert atmosphere to avoid the possibility of oxidation of the trivalent rare earths to a higher valence state. Tb^{3+} in $TbVO_4$, which also forms higher oxides, did not show any tendency to oxidize and could be handled in air.

Small single crystals of all rare earth vanadates can be obtained from a V_2O_5 flux at 1000°C by simply charging a small quantity of any rare earth oxide (except Ce, Pr) into the V_2O_5 melt and letting it react for about 10-14 hr. Although crystals obtained in this fashion are rather small (up to 1 mm in cross section) they are of fair optical quality as an inspection under the microscope and in polarized light indicated. The major portion of the excess melt can be poured off while the remaining small quantity of V_2O_5 can be leached away with ammonia. Specifically for the systems Y_2O_3/V_2O_5 and Gd_2O_3/V_2O_5, we demonstrated that the $LnVO_4$ compound is the only existing phase by preparing eight different compositions of $Ln_2O_3:V_2O_5$ varying from 4:1 to 1:4. In each case, the $LnVO_4$ compound was the only new phase in addition to the excess component. Larger single crystals up to 1 cm long can be obtained by establishing a small temperature gradient in the flux and using a platinum wire seed, immersed about ¼ in. into the melt, as a "cold finger." Figures 1 and 2 show some single crystals of YVO_4 and $GdVO_4$, grown without seed in the above described way. Figure 3 gives a typical crystal cluster as obtained with the Pt seed.

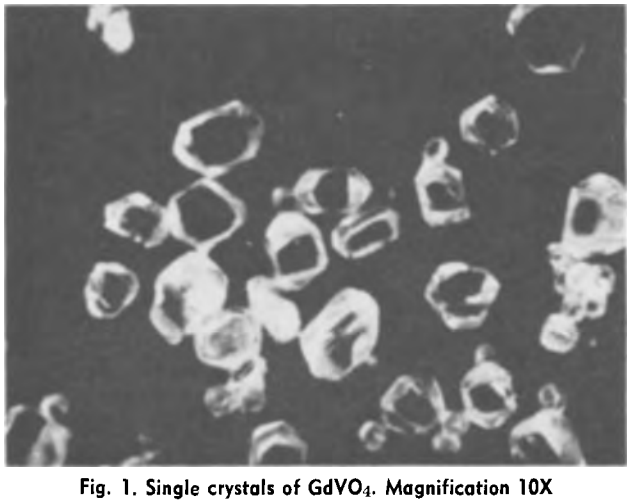

Fig. 1. Single crystals of $GdVO_4$. Magnification 10X

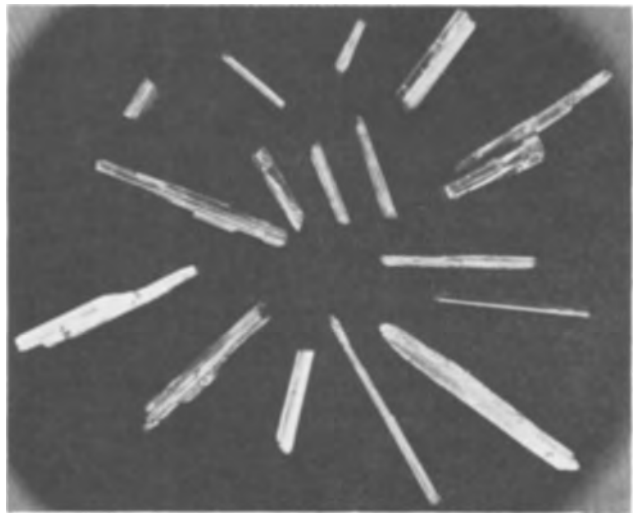

Fig. 2. Single crystals of YVO_4. Magnification approximately 7X

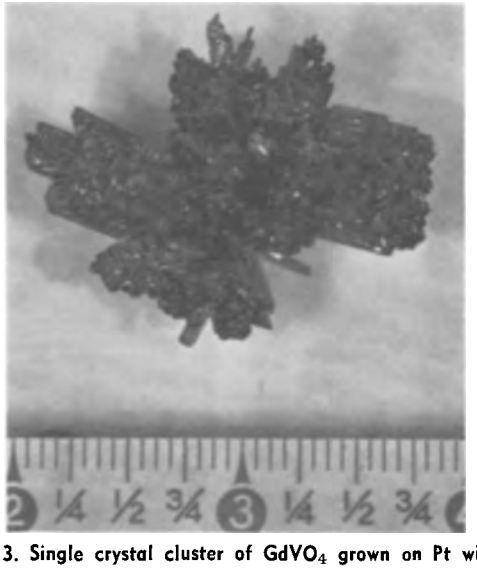

Fig. 3. Single crystal cluster of $GdVO_4$ grown on Pt wire

X-ray powder diffraction patterns were taken with a Philips 114.6 mm diameter camera at 25°C. The samples were sealed in 0.2 mm diameter Lindemann glass capillaries and were exposed to the K_α radiation of copper ($\lambda = 1.5418$Å) for 2-6 hr. Accurate parameters were obtained by extrapolation according to Nelson (8). Lattice dimensions and space groups of single crystals were determined by the rotating-crystal technique.

Crystallographic and Luminescent Properties

The measured lattice parameters are summarized in Table I, the asterisk denoting values obtained from single crystals. These parameters are in good agreement with those reported by Schwarz (*loc. cit.*)

Fluorescent emission in the visible region was first observed qualitatively under excitation by a 2537Å or

Table I. Luminescent and crystallographic data of the rare earth vanadates

Compound	Intrinsic color	Color of fluorescent emission 300°K 2537Å	300°K 3660Å	77°K 2537Å	77°K 3660Å	a_t, Å	c_t, Å
$ScVO_4$	Tan	S Orange	W Orange	S Green-yellow	S Yellow-green	6.78*	6.12
YVO_4	White	S Yellow	S Yellow	S Blue-white	M Yellow-white	7.12*	6.27
$LaVO_4$	White	M Purple	W Purple	S Orange-yellow	M Yellow	Not characterized	
$CeVO_4$	Green	—	—	—	—	7.412	6.488
$PrVO_4$	Green-yellow	—	—	—	—	7.364	6.461
$NdVO_4$	Light blue	—	—	—	—	7.333	6.432
$SmVO_4$	Yellow-white	—	—	—	—	7.265	6.388
$EuVO_4$	White	W Purple	W Purple	M Blue-white	M Red	7.229	6.374
$GdVO_4$	White	S Red	S Red	S White	M Creme	7.17*	6.32
$TbVO_4$	Yellow-white	—	—	—	—	7.143	6.320
$DyVO_4$	White	—	—	—	—	7.137	3.310
$HoVO_4$	Peach	—	—	—	—	7.119	6.288
$ErVO_4$	Pink	—	—	M Blue-white	M Yellow	7.093	6.277
$TmVO_4$	White	—	—	—	—	7.069	6.261
$YbVO_4$	White	—	—	—	—	7.051	6.239
$LuVO_4$	White	S Yellow-white	S Yellow-white	S Blue-white	M Yellow	7.02*	6.22

* The letters S, M, and W denote Strong, Medium, and Weak intensities.

3660Å u.v. mineral light. Coarse quantitative fluorescent scans were made with a Beckman DK2 recording spectrometer with a mercury and phosphor lamp F4T5/BL (General Electric Company designation) through a Schott UG-11 filter which cuts off above 4000Å. Thus, excitation was between 3000 and 4000Å. The detector used was a photomultiplier tube 1P28 (Radio Corporation of America). These observations are also summarized in Table I.

More refined spectra were taken with samples excited by a filtered AH-3 mercury discharge lamp (primarily 3660Å radiation) with a Leeds and Northrup 0.5 meter Ebert mount grating spectrometer using again a 1P28 photomultiplier detector. Representative spectra of YVO_4 and $GdVO_4$ are shown in Fig. 4 and 5, and the characteristic fluorescent wavelengths of all the compounds so examined are summarized in Table II. The numbers in parentheses on the spectra give the relative intensity of the lines after correction for the spectral response of the detector.

The excitation spectrum (fluorescence intensity as a function of exciting wavelength) of $GdVO_4$, shown in Fig. 6, indicates that the principal excitation of this material occurred in a strong band whose half-maximum points are at 2500 and 3250Å. Since Gd^{3+} does not have strong, broad absorption bands in this wavelength region, the excitation of fluorescence must involve the VO_4^{3-} complex. This same absorption band must exist in all of the rare earth vanadates and be responsible for the major portion of their excitation.

Reference to Fig. 4 and 5 and to Table II shows that a number of the observed fluorescence multiplets, namely those centered about 4800, 5250, 5550, and 5750Å, are common to many of the compounds which emitted visible light. These multiplets may be due to the presence of rare earth impurities. In particular, the emission at 4800 and 5750Å could be ascribed to Dy^{3+} and that at 5450Å to Tb^{3+}. Although the two remaining multiplets at 5250 and 5550Å do not closely match known fluorescent transitions in any of the trivalent rare earth ions, it is possible that they are due, respectively, to Pr^{3+} and Er^{3+} impurities. That the muliplets may be inherent to the vanadate compound cannot, however, be completely ruled out except by the investigation of compounds prepared with controlled dopings of trivalent rare earth ions. This has been done only in the case of Eu^{3+} as an impurity.

Although Tm^{3+} has energy levels at a separation corresponding to 4750Å, the 4f-4f transitions of trivalent rare earth ions are not known to occur in other than relatively sharp line multiplets. Hence, the broad band generally observed at 4750Å probably arises from

Table II. Emission wavelengths of visibly fluorescing rare earth vanadates at room temperature

Compound	Emission wavelengths (Å)							
$ScVO_4$ No. 1	4800	5250		5460	5570	5750		
$ScVO_4$ No. 2	4800	5250		5460	5570	5750	5950[c]	6180[c]
YVO_4	4800[a]	5250		5460	5540	5750		
$GdVO_4$	4800[a]	5250	5380[c]	5460	5540	5750	5950[c]	6175[c]
$LaVO_4$	4800[b]						5950[c]	6175[c]
$EuVO_4$	4750	(low resolution spectrum)					5950	6180

[a] Plus weak broad band centered at 4750Å.
[b] Plus strong broad band centered at 4750Å.
[c] These lines due to Eu^{3+} contamination.

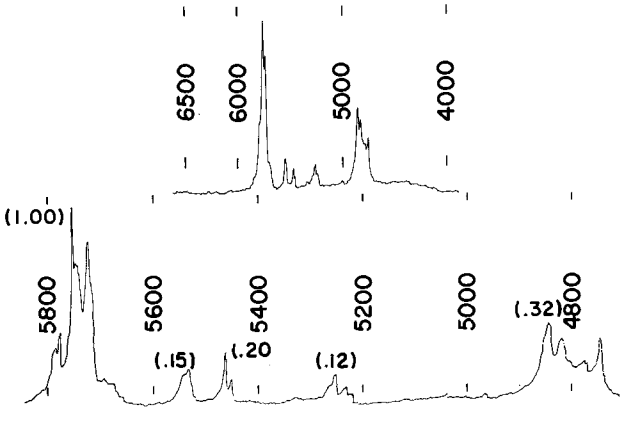

Fig. 4. Fluorescent emission spectrum of YVO_4 at 300°K. Excitation was by an AH3 Hg lamp. The wavelength markings are in Å and the numbers in parentheses are relative intensities corrected for the spectral sensitivity of the spectrometer system.

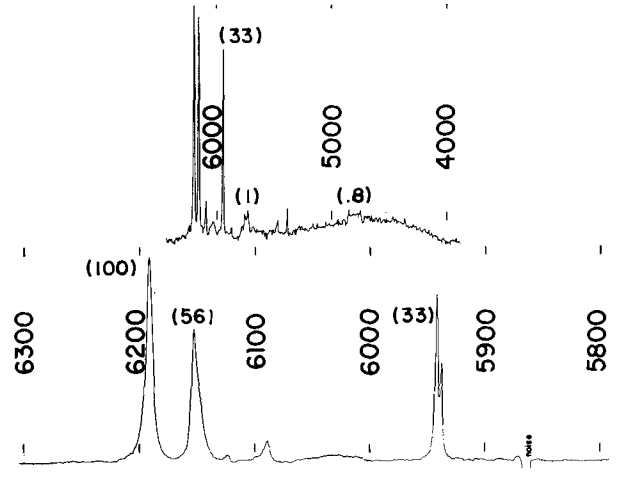

Fig. 5. Fluorescent emission spectrum of $GdVO_4$ at 300°K. Excitation was by an AH3 Hg lamp. The wavelength markings are in Å and the numbers in parentheses are relative intensities corrected for the spectral sensitivity of the spectrometer system.

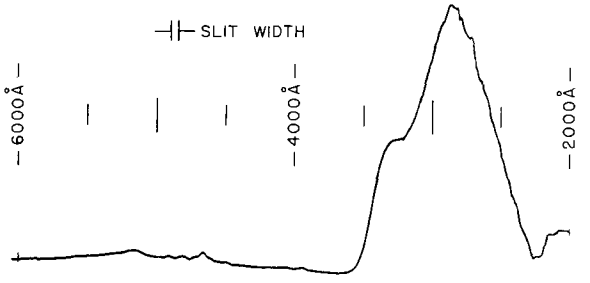

Fig. 6. Excitation spectrum of $GdVO_4$ at 300°K. This is the fluorescent intensity at ~6200Å per unit incident intensity as a function of the wavelength of incident light. The band pass of the monochrometer is indicated on the spectrum.

a "molecular" transition, and is further discussed later on. Some of the compounds also exhibit very bright, sharp line (a few angstroms wide) emission at 5950 and 6175Å. These lines are suspiciously close to the positions of the $^5D_0 \rightarrow {}^7F_1$ and $^5D_0 \rightarrow {}^7F_2$ transitions of Eu^{3+} in $Eu/LaCl_3$ (9), and hence we strongly suspected that in our case they are due to small amounts of Eu^{3+} contamination. This suspicion was further supported by the recently published fluorescent emission spectrum of $Eu_2(WO_4)_3$ (10), which is very similar to our $GdVO_4$ spectrum. The 5380Å line in our $GdVO_4$ spectrum is near the position of the $^5D_1 \rightarrow {}^7F_1$ transition of Eu^{3+}. Careful analysis by optical emission and x-ray spectroscopy confirmed the suspicion by establishing the presence of 0.06% Eu_2O_3 in Gd_2O_3. This analysis was in good agreement with the certified data later on supplied by the American Potash and Chemical Company, who gave 0.053% Eu_2O_3 in Gd_2O_3. The fact that Eu^{3+} did enter $GdVO_4$ via the flux growing technique indicated that the segregation coefficients of Eu_2O_3 and Gd_2O_3 are not different enough to effect purification during the growth of crystals. Eu^{3+} contamination of the other rare-earth sesquioxides was not investigated, but is presumably present to some extent.

In view of the observations regarding europium contamiantion, and because of the sharpness of these Eu^{3+} lines, we studied the system $Gd_xEu_{1-x}VO_4$ in more detail to establish the optimum fluorescent emission as a function of x. We prepared samples by the previously outlined technique with x varying from 0.002 to 0.2. A typical high resolution spectrum of $Eu/GdVO_4$ is reproduced in Fig. 7. Note that while the 5380, 5950, and 6175Å emission is still strong, the remainder of the lines have been quenched. The fluorescence emission intensity as a function of x is plotted in Fig. 8. This rather typical curve shows an increase of intensity with concentration at low concentrations followed by a maximum at $x = 0.08$, and then a gradual dropping off (concentration quenching) toward higher concentrations. While the characteristic shape of such

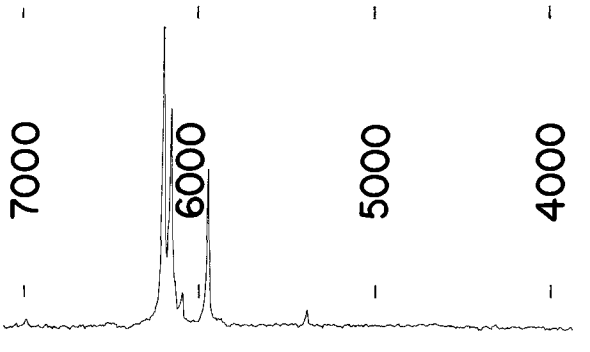

Fig. 7. Fluorescent emission spectrum of $Eu_{0.08}Gd_{0.92}VO_4$ at 300°K. Excitation was by an AH3 Hg lamp. The wavelength markings are in Å.

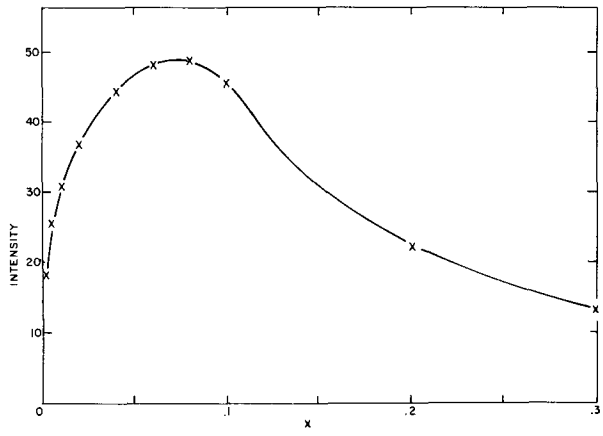

Fig. 8. Intensity of fluorescent emission as a function of x for the $Eu_xGd_{1-x}VO_4$ system.

curves is almost always identical even for such widely differing systems as $CaMoO_4$:Dy (11), $CaWO_4$:Tb (11), βAl_2O_3:Mn (12), $CaWO_4$:Eu (13), Mg-Li-tungstate:Mn (14), the optimum of the activator concentration varies over considerable ranges. In some of our own studies (15), we could show specifically for Eu^{3+} that the maximum emission can occur at as little as 0.5 mole % Eu^{3+} in $CaMoO_4$ for instance or at as high as 40 mole % in $GdPO_4$. Other examples for optimum Eu^{3+} activator concentrations are given by Borchardt (16) with 40 mole % in $Gd_2(WO_4)_3$ or 10 mole % in Y_2WO_6.

Discussion

Some of the rare earth vanadates described in this paper constitute interesting luminescing materials, which might find use in general fluorescent applications, such as fluorescent lamps or high-pressure mercury vapor lamps. Since the fluorescence did not quench up to 300°C, the latter applications, which require temperature stable phosphors, could be of especial interest. A most intriguing application would, of course, be as a solid state optical maser, particularly in the case of Eu^{3+} in $GdVO_4$. Preliminary melt experiments, however, indicated that if congruent melting occurs at all the melting point is above 1700°C. We could not obtain a melt in a 60% Pt-40% Rh crucible, which generally is quite suitable for the melting of $CaWO_4$ (mp 1630°C). Attempts to melt vanadates in iridium crucibles indicated that $GdVO_4$ can be homogeneously melted at approximately 1750°C at which temperature Ir metal evaporates at a rapid rate. This strongly suggests that some flame fusion process is necessary for the preparation of single-crystal $GdVO_4$ boules. Another problem which will have to be anticipated is the loss of oxygen from Eu_2O_3 which commonly occurs even in a $CaWO_4$ melt, turning crystals deep red, due to the presence of Eu^{2+}. Other parameters such as quantum efficiencies, fluorescent lifetime, excitation and absorption spectra, will also have to be determined before a complete evaluation of the $Eu_xGd_{1-x}VO_4$ system is possible as a laser material. The strong line at 6192Å would be the most likely one for laser emission.

In the case of YVO_4, the fluorescence is associated with either impurities or the VO_4^{3-} anion. The most intense fluorescence here is at 5750Å in a multiplet with a total width of 50Å. More interesting, however, is the wide multiplet near 4800Å. If these lines could be sufficiently pumped, there is the possibility that one might obtain laser action with a minimum transfer of heat energy to the lattice.

As a general speculation for the mechanism of fluorescence in the rare-earth vanadates, we postulate a mechanism similar to that invoked by Borchardt (17) for the rare-earth tungstates and 1:1 oxytungstates: ultraviolet energy is absorbed either by the VO_4^{3-}

anionic group of the material or by a "charge transfer" transition involving the rare earth ion and a neighboring oxygen. With the present data, no choice between these two possibilities can be made. Excitation is then transferred predominantly to the lowest energy fluorescent levels, from which emission occurs. If the fluorescent energy levels of the principal rare-earth ion lie lower than those of the vanadate ion, most of the excitation energy is transferred to the rare-earth ion, which then emits its characteristic spectrum provided that concentration quenching is not too severe. $EuVO_4$ is an example of this process. If rare-earth ions with levels lower than those of the principal rare earth ion are present as dilute impurities in a host of the YVO_4 type, only a portion of the energy will be transferred to the lowest energy level as exemplified by the $Eu_xGd_{1-x}VO_4$ series. The broad fluorescence band generally evident at 4750Å may be due to a Stokes-shifted transition from the absorbing level to the ground state. The relative intensity of such a band would depend on the ratio between its transition probability and the probability of energy transfer to rare earth ions.

Acknowledgment

The authors would like to thank Dr. G. Teufer of the Engineering Research Laboratory for obtaining single crystal data and Mr. A. T. Weinmann for his assistance in obtaining powder data. We are also grateful to Messrs. L. S. Brooks and J. S. Ariganello for running the fluorescent emission spectra and to Mr. F. Y. Tse for taking the excitation spectra.

Manuscript received July 8, 1964.

Any discussion of this paper will appear in a Discussion Section to be published in the December 1965 JOURNAL.

REFERENCES

1. E. Broch, *Z. Phys. Chem.*, **20**, 345 (1933).
2. W. O. Milligan and L. W. Vernon, *J. Phys. Chem.*, **56**, 145 (1952).
3. W. O. Milligan, L. M. Watt, and H. J. Rachford, *J. Phys. and Colloid Chem.*, **53**, 227 (1949).
4. J. R. Gambino and C. J. Guare, *Nature*, **198**, 1084 (1963).
5. M. K. Carron, M. E. Mrose, and K. J. Murata, *Am. Mineral.*, **43**, 985 (1958).
6. H. Schwarz, *Z. anorg. allgem. Chem.*, **323**, 44 (1963).
7. L. G. van Uitert, R. C. Linares, R. R. Soden, and A. A. Ballman, *J. Chem. Phys.*, **36**, 702 (1962).
8. J. B. Nelson and D. P. Riley, *Proc. Phys. Soc.*, **57**, 160 (1945).
9. L. G. DeShazer and G. H. Dieke, *J. Chem. Phys.*, **38**, 2190 (1963).
10. R. E. MacDonald, M. J. Vogee, and J. W. Brookmann, *IBM J. of Res. and Dev.*, **6**, 363 (1962).
11. L. H. Brixner, *This Journal*, **111**, 693 (1964).
12. F. A. Kröger, "Some Aspects of the Luminescence of Solids," p. 95, Elsevier Publishing Co., Inc. (1948).
13. L. G. van Uitert and R. R. Soden, *J. Chem. Phys.*, **32**, 1687 (1960).
14. H. Witzmann, K. Th. Wilke, J. Buhrow, and H. J. Bohm, *Z. Phys. Chem.*, **222**, 271 (1963).
15. L. H. Brixner, *This Journal*, To be published.
16. H. Borchardt, *J. Chem. Phys.*, To be published.
17. H. J. Borchardt, *ibid.*, **39**, 504 (1963).

Chemical and Optical Studies of Samarium Doped CaF_2 Type Single Crystals

P. F. Weller, J. D. Axe*, and G. D. Pettit

Thomas J. Watson Research Center, International Business Machines Corporation, Yorktown Heights, New York

ABSTRACT

Single crystals of CaF_2 and $Ca_{1-x}Sr_xF_2$ were grown by the Czochralski technique and doped with varying concentrations of samarium. Complete solid solution was found in the CaF_2-SrF_2 pseudobinary system with a minimum near 50% CaF_2 at 1330° ± 10°C. The concentration of Sm^{+2} depended on the melt concentrations of SmF_3 and Sm metal, and the samarium segregation coefficient did not change significantly with samarium concentration. The fluorescence efficiency of Sm^{+2} as a function of Sm^{+2} concentration appeared to go to a broad maximum at about 0.1% Sm^{+2}. The fluorescent emission in $Ca_{1-x}Sr_xF_2$: Sm^{+2} showed pronounced inhomogeneous line broadening.

The discovery of a CaF_2:Sm^{+2} laser (1) stimulated interest in the CaF_2-Sm system. In order to optimize laser efficiency, it seemed necessary to obtain more perfect crystals with better control of the doping levels, oxidation state ratios, and homogeneity. We have used the Czochralski technique to grow samarium doped CaF_2 and $Ca_{1-x}Sr_xF_2$ crystals (2). Crystal perfection has been indicated by the number of imperfections appearing as voids and growth "streamers," the number of dislocations, and the amount of light scattering that occurred in the crystals. Oxidation state variations were achieved by varying the amount of reducing agent, samarium metal, added to the sample charge. Doping homogeneity was improved considerably by a samarium segregation coefficient near unity which was essentially concentration independent over the range studied. However, crystal growth parameters such as the ratios of crystal diameter to crucible diameter and melt surface to melt volume did affect Sm^{+2} homogeneity considerably. Optimum Sm^{+2} doping levels for maximum fluorescence efficiency were indicated by studying the efficiency as a function of Sm^{+2} concentration. The strong effect of certain impurities on the Sm^{+2} fluorescence was shown by the severe line broadening in the $Ca_{1-x}Sr_xF_2$:Sm^{+2} fluorescence experiments.

* This research has been supported in part by the Army Research Office, Durham, North Carolina.

Crystal Growth

Starting materials.—CaF_2 was obtained from the Harshaw Chemical Company as random cut chips (highest quality). SrF_2 was prepared synthetically using a flux method (3).

$$SrCl_2 + 2KF \rightarrow SrF_2 + 2KCl \qquad [1]$$

The SrF_2 was then carefully fired in flowing HF gas at about 1300°C for several hours or crystallized using a Bridgman-Stockbarger technique with a PbF_2 oxygen "scavenger" added (4).

Samarium trifluoride and metal were obtained from the Lindsay Division of American Potash and Chemical Company. SmF_3 was HF fired at about 1200°C, and the samarium metal was H_2 fired at about 1000°C.

Growth procedure.—The crystals were grown in an apparatus described previously (5). Graphite, platinum, and molybdenum crucibles were used with molybdenum being most satisfactory. A graphite sus-

ceptor, inductively heated, held the crucibles. The dry, nitrogen atmosphere was either flowing at 1-2 liter/min or static at a pressure slightly greater than 1 atm.

Crystals were nucleated on single crystal seeds or on a platinum wire and pulled at speeds ranging between ½ and 4 in./hr with rotation speeds of around 60 rpm. Generally, the crystals were 1 to 4 in. long, ⅛ to ½ in. in diameter, and grew with random orientation around the [110] and [111] directions when not nucleated on an oriented seed. No cracking of any of the crystals was observed (6), regardless of size or of the Ca/Sr ratio, even though they were cooled to room temperature in 1 to 2 hr.

Crystal Perfection

CaF_2:Sm^{+2}.—*Light scattering.*—Experiments similar to those of Kaiser and Keck (7) showed that in the best CaF_2:Sm crystals less than 1% Tyndall scattering was observed; while in the worst, about 30% of the incident light was scattered by a crystal ½ cm long.

Imperfections.—Voids and gaseous inclusions were generally formed when the crystal diameter was changing rapidly and the growth speed was 2 in./hr or more.

Growth streamers, white, feather-like webbings that run along the growth direction angling out from the center, were present quite often, regardless of pull conditions. They were eliminated only when oxides were not present in the starting materials and H_2O was not present during growth.

Examination with a light microscope equipped with two nicol prisms detected no macroscopic strains in the grown crystals.

Dislocations were observed by etching the crystals with a warm, 20% HCl solution for 10 to 30 sec (8). Generally, between 10^5 and 10^6 triangular pits/cm^2 were observed. This same, randomly distributed, pit density was found for doped and undoped crystals and for Bridgman-grown crystals obtained from Harshaw, Optovac, and our own laboratory. No correlations could be made between growth conditions and pit counts.

Mixed crystals.—$Ca_{1-x}Sr_xF_2$ crystals were grown with x = 0.05, 0.1, 0.3, 0.5, 0.7, and 0.9. The crystals were 1 to 2 in. long and about ¼ in. in diameter. In all cases complete solid solution was found with no detectable segregation either radially or longitudinally along the crystal, as shown by x-ray diffraction powder patterns. These x-ray data, the sample compositions, and the melting points of the various mixtures determined during crystal growth yielded a tentative CaF_2-SrF_2 pseudobinary phase diagram with a minimum near 50% CaF_2 at 1330° ± 10°C, as shown in Fig. 1. Sm^{+2} fluorescence in this mixed system is discussed below.

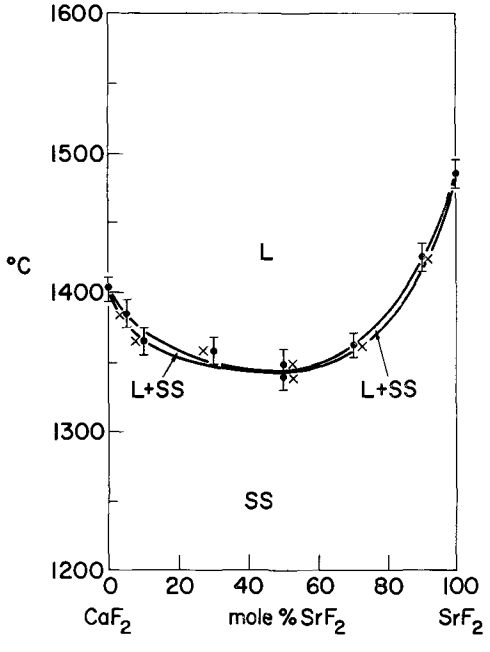

Fig. 1. Tentative phase diagram for CaF_2-SrF_2 solid solutions. •, Sample composition melting points; x, first solid to freeze.

Crystal Doping

Sm^{+2}/Sm^{+3} *ratios.*—Generally samarium was added to the sample charge as SmF_3 or SmF_3 and Sm in varying ratios. It was found that the concentration of Sm^{+2} obtained was a function of the amounts of SmF_3 and Sm present in the melt, as can be seen from Table I. The situation is complicated by the fact that Sm^{+2} is also produced when SmF_3 is present alone, as is shown in Table I. This indicates two methods for producing Sm^{+2}. The most obvious ones are

$$2SmF_3 + Sm \rightarrow 3SmF_2 \quad [2]$$

and

$$2SmF_3 \rightarrow 2SmF_2 + F_2 \quad [3]$$

The data in Table I, however, indicate a strong dependence of Sm^{+2} concentration on the amount of samarium metal added and a much weaker dependence on the amount of SmF_3. This is contrary to what the above equilibria predict, i.e., the concentration of Sm^{+2}, $[Sm^{+2}]$, should depend on $[SmF_3]^{2/3}$ and $[Sm]^{1/3}$ (assuming complete solution of the samarium metal). It seems, then, that either equilibrium has not been attained and Sm^{+2} production is kinetically controlled or that the equilibria involved are more complex and, for example, involve direct oxidation of the samarium metal by very small amounts of O_2 in the growth atmosphere. In any event, Eq. [2] and [3] above do not describe the situation satisfactorily.

Divalent samarium production can also, of course, be affected by impurities in the starting materials. As seen in Table I only about 0.002% Sm^{+2} is obtained when CaF_2 is doped with 0.1% SmF_3. This small amount of Sm^{+2} can be completely oxidized by impurities such as Eu^{+3} and Cd^{+2} according to the following equations

$$Sm^{+2} + Eu^{+3} \rightarrow Sm^{+3} + Eu^{+2} \quad [4]$$

and

$$2Sm^{+2} + Cd^{+2} \rightarrow 2Sm^{+3} + Cd \quad [5]$$

We have grown CaF_2 crystals containing no detectable Sm^{+2} by adding 0.01% EuF_3 or 0.01% CdF_2 to the sample charge along with 0.1% SmF_3. Eu^{+2} is easily observed so that the impurity can be noticed immediately in the case of europium contamination. With CdF_2, however, detection is difficult. Since many other chemical impurities can undergo similar reactions, the purity of the starting materials is quite critical in obtaining reproducible Sm^{+2} concentrations.

Doping homogeneity.—Variations of samarium concentration along the length of a crystal caused by

Table I. Sm^{+2} production as affected by varying Sm^{+3}/Sm ratios added to sample charge

Experiment	SmF_3/Sm molar ratio	Mole % Sm (total)	Mole % Sm^{+2}	% Conversion to Sm^{+2}
17	No Sm	0.10	0.00213	2.1
19	No Sm	0.10	0.00187	1.9
50	No Sm	0.13	0.0487	38
27	2/2	0.070	0.00842	12
23	2/2	0.12	0.0483	43
21	2/2	0.13	0.0482	37
26	2/2	0.25	0.115	46
34	2/2	1.2	0.668	56
20	2/1	0.10	0.00187	19
23	2/2	0.12	0.0483	43
21	2/2	0.13	0.0482	37
47	2/5	0.24	0.0671	28
37	2/10	0.44	0.305	69
20	2/1	0.10	0.0187	19
48	10/1	0.39	0.0779	20
49	20/1	0.86	0.126	15

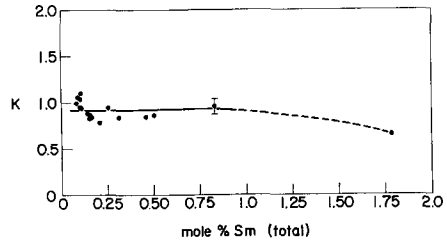

Fig. 2. Samarium segregation coefficient, $K = C_S/C_l$, as a function of total samarium concentration. The dotted portion of the curve is tentative. The approximate error is given only at the 0.83 mole % point for the sake of clarity.

segregation were not large since the segregation coefficient was about 0.90, and essentially independent of concentration as is shown in Fig. 2. The decrease in K between 1.0 and 1.8 mole % Sm is questionable since the x-ray fluorescence measurements are suspect in the high concentration region.

Divalent samarium concentrations, however, increased by as much as a factor of 3 from crystal top to bottom (2 to 3 in.) unless growth procedures were carefully controlled. The largest effects were caused by crystal diameter differences, with larger diameters giving more Sm^{+2}, and crystallization of a large portion of the melt. The latter effect can be seen for experiment No. 47 in Table I. In this experiment the crystal size was similar to that in No. 20, 21, 23, and 37, but the melt volume was about twice as great. The explanation for these observations is not obvious. The Sm^{+2} gradients are not caused by segregation ($K = 0.9$) nor does reoxidation to Sm^{+3} of the hot, growing boule seem appropriate since radial Sm^{+3} gradients were undetected except for the very outermost "skin" of the crystal. The most critical parameter appears to be the amount of samarium reaching the melt surface since increased crystal diameters increase stirring and a decrease in melt volume increases the melt surface to volume ratio. Variations of Sm^{+2} concentration can be kept to a minimum by using seeds to obtain relatively small and constant crystal diameters and by pulling small crystals from large melts.

Optical Properties

Absorption coefficients.—The absorption coefficients for Sm^{+2} and Sm^{+3} were obtained in the following way. A CaF_2:Sm single crystal was cut into three sections, the first 1 mm thick, the second 1 cm thick, the third 1 mm thick. Absorption spectra were run at 77°K on the thin slices for Sm^{+2} and for Sm^{+3} on the thick section (9), which was then carefully fired in flowing HF gas at 1200°C to oxidize all of the Sm^{+2}. The Sm^{+3} absorption spectrum was then rerun and the sample analyzed for total samarium content by x-ray fluorescence. Selected absorption coefficients for Sm^{+2} and Sm^{+3} are given in Table II. These values are smaller, by about a factor of five, than those reported by Kaiser, Garrett, and Wood (10) at 4°K. The greater portion of the discrepancy must be attributed to the determination of the Sm^{+2} concentration. We estimate that our error was ±10%.

Table II. Selected absorption coefficients for Sm^{+2} and Sm^{+3} at 77°K

Species	Wavelength (A)	$\alpha = \frac{1}{t}\log_{10}\frac{I_o}{I}$ (cm^{-1})	Concentration (mole %)
Sm^{+2}	6,905	9.0	0.12
	6,363	64	
	5,083	7.2	
	4,468	30	
	4,251	58	
Sm^{+3}	12,130	0.52	0.27
	12,260	0.37	
	12,373	0.37	

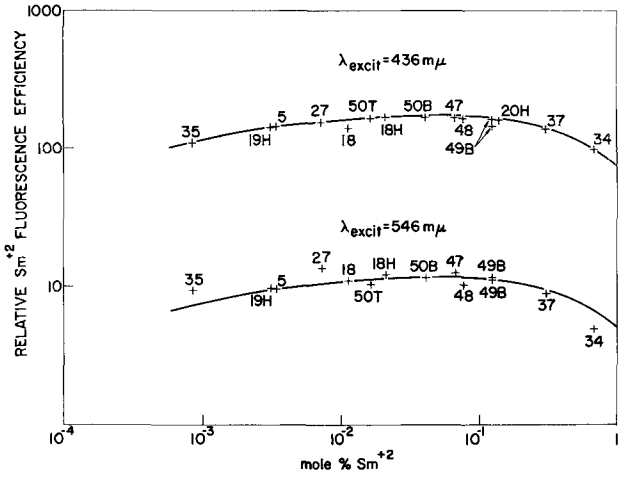

Fig. 3. Relative Sm^{+2} fluorescence efficiency vs. Sm^{+2} concentration at 77°K. The difference in fluorescence efficiency between the two excitation wavelengths is only approximate. The very similar concentration dependence of the two sets of points is shown by the identical curves drawn through them.

Fluorescence.—Some studies were made at 77°K of the relative fluorescence efficiency of Sm^{+2}, particularly as a function of Sm^{+2} concentration. For this purpose polished sections of crystals with previously determined absorption were excited by green (λ = 546 mμ) and blue (λ = 436 mμ) light from a high pressure Hg discharge which was rendered nearly monochromatic by a small grating monochromator. The resulting red emission was isolated by suitable filters and a fraction, g, detected with a photomultiplier. The relative emission intensity per absorbed photon, $g\ I(\text{incident})\left[\frac{I(\text{emitted})}{I(\text{absorbed})}\right]$, is shown in Fig. 3 for two incident wavelengths. The efficiencies at the two wavelengths have not been corrected for the wavelength dependence of I(incident). The decreasing efficiency at high concentration is a common characteristic of many fluorescence systems. The decreasing efficiency at the very low concentrations was an unexpected feature. One tentative explanation is that there are a small number of energetically favored Sm^{+2} sites in which the ions fluoresce either poorly or not at all, and that these sites become saturated at relatively low concentrations.

We have found no detectable influence of Sm^{+3} on the Sm^{+2} fluorescence efficiency although the Sm^{+2}/Sm^{+3} ratio in the samples investigated varied between 0.01 and 1.0. No attempt was made to determine an absolute quantum efficiency. Kaiser, Garrett, and Wood (10) indicate that under similar conditions the quantum efficiency is close to unity for Sm^{+2} doping of about 0.01 mole %.

Mixed crystals.—It is now well established (11) that the initial level of the Sm^{+2} fluorescence transition in CaF_2 is of the $4f^55d$ configuration whereas in SrF_2 the initial level is the $^5D_0$ state of the $4f^6$ configuration. Wood and Kaiser (11) have noted that the addition of small amounts of SrF_2 to CaF_2:Sm^{+2} has a strong influence on the Sm^{+2} emission. We thought it to be of some interest to investigate the Sm^{+2} fluorescence behavior over the entire range of compositions $Ca_{1-x}Sr_xF_2$. The emission characteristics of representative samples are shown in Fig. 4. For the purpose of this figure the integrated emission intensities of the various samples were approximately normalized. However, the fluorescence efficiency falls off noticeably with dilution at either extreme, the

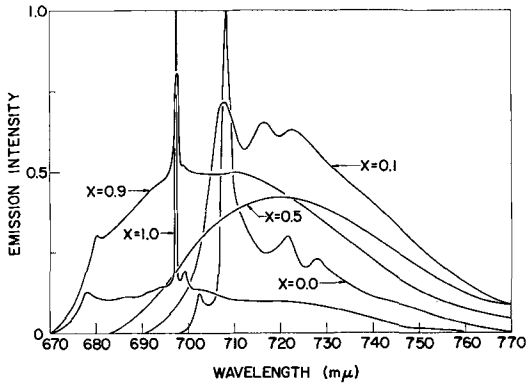

Fig. 4. Spectral emission characteristics of Sm^{+2} in $Ca_{1-x}Sr_xF_2$ at 77°K.

equimolar mixture being less efficient by more than one order of magnitude. The pronounced broadening of the emission bands must certainly be associated with the superposition of spectra of ions in nonequivalent environments. It appears, however, that no simple explanation based on a small number of possible near neighbor arrangements can account for the semicontinuous nature of the emission of the equimolar mixture. Obviously there seems to be little hope of "tuning" the frequency of the Sm^{+2} laser by continuous variation of the lattice composition.

Conclusions

1. CaF_2 type crystals of high optical quality can be grown easily and quickly using the Czochralski technique. Crystals with little or no light scattering can be obtained by eliminating O_2 and H_2O from the growth atmosphere and oxide impurities from the starting materials.

2. Divalent samarium concentrations are affected not only by oxygen containing impurities, but by other easily reduced impurities such as CdF_2 and EuF_3.

3. Varying Sm^{+2}/Sm^{+3} ratios can be obtained by using different amounts of SmF_3 and reducing agent, Sm. Sm^{+2} concentrations are more strongly dependent on the Sm metal than on the SmF_3 concentration. This seems to indicate that Sm^{+2} formation is more complicated than is shown in Eq. [2] and [3].

4. Although the samarium segregation coefficient in CaF_2 is 0.9, Sm^{+2} concentration variations can be caused by varying crystal diameters and melt volumes.

5. Absorption coefficients for Sm^{+2} and Sm^{+3} were determined at 77°K, and selected values are listed in Table II.

6. The fluorescence efficiency of Sm^{+2} as a function of Sm^{+2} concentration appears to go through a broad maximum at about 0.1% Sm^{+2}.

7. The fluorescent emission in $Ca_{1-x}Sr_xF_2:Sm^{+2}$ shows pronounced inhomogeneous line broadening.

8. The CaF_2-SrF_2 pseudobinary system showed solid solutions over the entire composition range. A tentative phase diagram was determined with a minimum near 50% CaF_2 at 1330° ± 10°C.

Manuscript received July 13, 1964, revised manuscript received Aug. 28, 1964.

Any discussion of this paper will appear in a Discussion Section to be published in the December 1965 JOURNAL.

REFERENCES

1. P. P. Sorokin and M. J. Stevenson, *IBM J. Res. Dev.*, **5**, 56 (1961).
2. H. Guggenheim, *J. Appl. Phys.*, **32**, 1337 (1961).
3. A. V. Shubnikov and N. N. Sheftal (Editors), "Growth of Crystals," Vol. 2, p. 86, Consultants Bureau, Inc., New York (1959).
4. D. C. Stockbarger, *J. Opt. Soc. Am.*, **39**, 731 (1949).
5. P. F. Weller and J. A. Kucza, *J. Appl. Phys.*, **35**, 1945 (1964).
6. K. Nassau, *J. Appl. Phys.*, **32**, 1820 (1961).
7. W. Kaiser and M. J. Keck, *J. Appl. Phys.*, **33**, 762 (1962).
8. B. Porter and E. A. Brown, *J. Am. Cer. Soc.*, **45**, 49 (1962).
9. J. R. O'Connor and H. A. Bostick, *J. Appl. Phys.*, **33**, 1868 (1962).
10. W. Kaiser, C. G. B. Garrett, and D. L. Wood, *Phys. Rev.*, **123**, 766 (1961).
11. D. L. Wood and W. Kaiser, *ibid.*, **126**, 2079 (1962).

The Preparation of High-Purity Rhenium Single Crystals

R. R. Soden, G. F. Brennert, and E. Buehler

Bell Telephone Laboratories, Inc., Murray Hill, New Jersey

ABSTRACT

Rhenium single crystals have been prepared by electron beam float zone melting with resistance ratios (R273°K/R4.2°K) exceeding 30,000. In one crystal a ratio in excess of 55,000 was obtained. It appears that purification occurs both by selective vaporization and zone refining.

Very high purity metal single crystals are necessary for the experimental determination of their intrinsic electronic properties. Zone refining techniques have made it possible to obtain a number of metals with the required purities and as a result, significant advances have been made in the understanding of their electronic structure. Electron beam floating zone refining is particularly useful for the purification and growth of refractory metal crystals. Crucible contamination is eliminated, the zone length is readily controlled, and the high vacuum, which is required for the electron beam, enhances the volatilization of impurities.

Ideally, one would like the impurities in a source material to have distribution coefficients favorable for zone refining or partial vapor pressures which will allow them to be removed by selective vaporization. Hence, the specific impurities present in the original material will specify the ease and rate of purification. Even if these ideal conditions exist, care must be taken before and during zone refining to keep contamination from outside sources to a minimum. This care includes the reduction of contamination by backstreaming oil vapor from the diffusion pump orifice in the vacuum station and contact by the molten zone or hot crystal to the electron gun mechanism. The technique used to preform a rod suitable for zone refining is also very important and has become quite evident in the present work on high purity rhenium.

Several investigators have prepared rhenium, single crystals by electron beam zone refining (1-5). The purest rhenium crystals grown previously, as determined by resistance ratio measurements (6), were by Hauser and Buehler (7) and by Sell (8) of Westinghouse Electric Corporation. Resistance ratios of 4000

and 6000 were obtained, respectively, by these workers. We have prepared Re single crystals by electron beam floating zone melting with resistance ratios exceeding 30,000 and in one crystal, a ratio in excess of 55,000 was obtained. A discussion of this work is presented in this paper.

Floating Zone Melting Apparatus

The vacuum floating zone melting apparatus was previously described (9). However, for this work, the rf coil was replaced by an electron gun which consists of a circular 0.0115-in. diameter thoriated tungsten filament and molybdenum focusing plates on the top and bottom. A mechanically driven variac control similar to that described by Schadler (10) was used to control the emission current.

The kinetics of purification by vaporization are often dependent on the ultimate vacuum attainable, especially in cases where solute partial pressures are significantly greater than the partial pressure of the solvent. Thus, a series of liquid nitrogen cooled traps was installed in the station to enhance the vacuum and to cut down back-diffusion of oil vapor from the diffusion pump orifice. These consisted of a baffle plate covering the diffusion pump orifice and a large coil extending up into the station. A vacuum of 2 to 8 x 10^{-6} mm of Hg was thus readily maintained during zone refining.

Material Preparation, Zone Melting, and Crystal Growth

High purity rhenium powder was obtained from the Johnson-Matthey Company. Spectroscopic analysis reveals this powder to contain less than one hundred parts per million total metallic impurities (Table I). The powder was received after the supplier's final purification step. No further manipulation was performed on the powder to produce, for example, a specific particle size.

A preformed rod of this powder was obtained by pressing it at approximately 30,000 psi in a ¼ by ¼ by 3-in. hardened split steel die. To the best of our knowledge, no contamination with Fe occurs during this operation. Since the compact is extremely fragile, it is carefully placed on a water cooled silver boat and sintered at approximately 1900°C by rf heating in a purified argon atmosphere (11). The temperature is increased during sintering in approximately 200°C steps every 10 min and held at 1900°C for 15 min. Multicolored deposits of mixed oxides of rhenium are formed on the quartz tube between 400° and 1500°C. The density of the sintered compact is ≅11 g/cc.

This technique for preforming the rod for floating zone melting has the following advantages:

1. Handling of the material is kept under laboratory control and hence no unnecessary contamination is introduced.
2. The preheat-treatment under argon reduces the problems associated with sputtering during zone melting due to adsorbed gases in the powder. The porous compact provides a large surface area for vaporization of oxide impurities.
3. High purity powder can be used as it comes from the final purification step of the supplier. Since the compact will be float zone melted into a single crystal, the only necessary prerequisite for the powder is that some form of rod can be prepared for suspension in the apparatus. Particular particle sizes are not required and a precise density is not necessary after the heat treatment.

Table I. Spectroscopic analyses of Johnson-Matthey Re No. 36083 (in ppm)

Al	<5
Ca	<5
Cu	<50
Fe	<5
Mg	<10
Si	<10

Not detected—Ag, Co, Cr, Mn, Ni, W and the noble metals.

Table II. Resistance ratio data for Re single crystals

Sample No.	Seed orientation	No. of zone melting passes	Lot No. of starting material or crystal source	Resistance ratios: Seed	Lead end	Tail end	Transition region*
51	R	3	29,862	—	5,000	—	—
52	R	10	29,862	—	13,300	—	—
53	[11$\bar{2}$0]	10	29,862	4,000	8,200	—	1,700
54	[11$\bar{2}$0]	10	29,862	8,200	13,300	—	—
55	R	10	36,083	17,700	17,700	—	4,000
56	[11$\bar{2}$0]	5	36,083	17,700	8,800	—	—
		10	36,083	17,700	17,300	—	—
		15	36,083	17,700	30,800	—	9,100
57	[11$\bar{2}$0]	15	36,083	17,000	20,000	—	—
58	[0001]	15	36,083	≅2,000	27,600	30,500	—
59	[10$\bar{1}$0]	15	36,083	≅12,000	19,500	15,100	—
60	[10$\bar{1}$0]	20	36,083	19,500	24,000	28,500	10,600
61	[0001]	1	59	30,000	23,400	—	—
63	[0001]	1	57	30,000	23,400	55,300	—

* The transition region is that portion of the zone melted rod between the "tail" end and unmelted portion.

The sintered compact is suspended in the vacuum station from a quartz hook by notching the rhenium bar and attaching a loop of five mil rhenium wire. The bottom of the compact is allowed to make contact to a rhenium rod (in most cases, a single crystal seed) held by an adjustable chuck. Focusing plates with large openings (~⅝-in. diameter) are used on the electron gun in order to accommodate the ¼-in. square bar. After an initial minimum 2-hr pump down, two fast passes, one up and one down, are made at temperatures of approximately 2000°C and just below the melting point of rhenium (3150°C) at 3000°C, to outgas the rod and to heat up the station and thus outgas the parts inside the bell jar. The tip of the bar is then melted into the seed. For the samples denoted as R (random seed orientation) in Table II, the gun was moved one-half inch up the sintered bar (after welding to the seed) before zone melting. The melting of the sintered bar is done progressively, since the molten metal which forms on the edges is drawn into the sintered compact by surface tension. This results in instability of the molten zone and, consequently, there is danger of losing the zone. Two or three passes are thus necessary to completely melt through the sintered rod. The emission current is controlled manually through these periods. New focusing plates (with openings of usually 1.4 times the rod diameter) are then placed on the gun and zone melting is started after evacuating the system. The molten zone travel rates employed are one, and one and one-half mils per second. No difference in the purification rate was noted for either travel speed. With the liquid nitrogen traps in operation, a vacuum of between 2 to 8 x 10^{-6} mm of Hg is maintained during zone melting and crystal growth. A typical sintered compact and a zone melted rhenium single crystal are shown in Fig. 1.

Resistance Ratio Measurements

We have used measurements of the residual resistance or resistance ratios ($R_{298°K}/R_{4.2°K}$) to determine

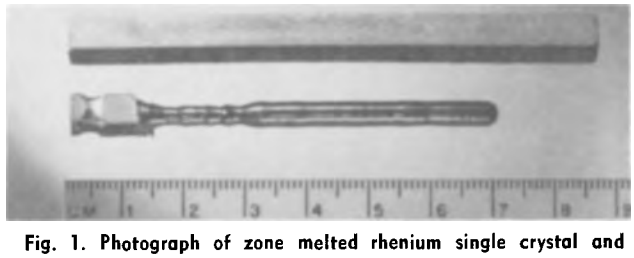

Fig. 1. Photograph of zone melted rhenium single crystal and sintered rhenium bar.

the extent of purification because standard analytical techniques are not adequate in determining the purity of very high purity metals. The resistance ratio technique and apparatus were described by Kunzler and Wernick (6). Each zone melted rod was prepared for measurement by ultrasonically soldering copper leads with an indium alloy solder at desired intervals along the sample axis. The specimens were then mounted on a phenolic holder assembly. Potentials were measured at room temperature and 4.2°K with a Beckman model 14 breaker amplifier, Leeds Northrup Wenner potentiometer and recorder. A constant d-c current source of 0.01 amp was employed for the room temperature meaurements, while 4.0 or 10.0 amp, depending on the size and purity of the sample, was used at 4.2°K. Our resistance ratio results are shown in Table II. Extrapolation of a plot of resistance ratio *vs.* the number of zone passes on sample 56 indicates the resistance ratio of the starting material (Table I) to be approximately 2000.

Discussion

Examination of the resistance ratio data in Table II, particularly the transition region, shows that some purification was accomplished by the movement of impurities, which have distribution coefficients less than one, to the tail end of the rod. Since the resistance ratio of the starting material is approximately 2000, it is apparent that purification by volatilization has also occurred.

The high melting point of rhenium is favorable for the selective vaporization of impurities. This is especially true when the ratio of the product of the partial pressure of the pure solute and its activity in the solvent rhenium to the partial pressure of pure rhenium is significantly greater than unity. Examination of the available vapor presure data for the impurities which were detected (Table I) shows that all except possibly iron and silicon, which are at the 5 to 10 ppm level, should be completely removed by vaporization at the melting point of rhenium if one assumes ideal solution behavior. The partial pressure of the i^{th} component over the solution, P_i, is K_iX_i (as $X_i \rightarrow 0$) where X_i is the mole fraction of the i^{th} component and K_i is the Henry's law constant at low values of X_i. This constant can equal p_i^*, the vapor pressure of pure i at the given temperature if the solvent and solute are similar in behavior; however, K_i usually deviates from p_i^*, although at these low levels of impurity content, the deviation should be very small. In the case of iron, and silicon, the only detected metallic impurities with vapor pressures close to rhenium, a plot of p_i *vs.* X_i at low concentrations as $K_i \rightarrow p_i^*$ shows that selective vaporization of these impurities may occur down to a minimum concentration of approximately 1 to 2 ppm. Even if the slope K_i deviates significantly from the assumed slope p_i^*, these impurities should be removed by selective vaporization to at least the 5 ppm level.

The resistance ratio increases nearly linearly with the number of passes as is evidenced by sample 56. There appears, however, to be an anisotropy effect on the rate of purification. Four samples were prepared of $[11\bar{2}0]$ orientation to work up to an 18,000 ratio seed before the 30,000 ratio on the fifteen-pass area of sample 56 was obtained. This was done because of the low ratio (~4000) of the initial $[11\bar{2}0]$ seed (sample 53). Sample 58 was prepared using an [0001] seed with approximately a 2000 ratio, and was made ostensibly to get a seed of suitably high ratio to grow a high purity crystal in the vicinity of 30,000; however, after fifteen passes, even with the relatively impure seed, 30,000 was obtained. Samples 59 and 60 were grown to prepare a third orientation ($[10\bar{1}0]$) of 30,000 resistance ratio. The rate of purification, however, is even slower than in the case of the $[11\bar{2}0]$ orientation. The ease of purification thus appears to increase with orientation of the crystal axis as $[10\bar{1}0] < [11\bar{2}0] < [0001]$. It is not known at this time whether this orientation effect on purification, as indicated by the resistance ratio data, is related to the anisotropy of the material (different temperature coefficients of resistivities) or is related to the mechanism of crystal growth. The data on sample 61, which was the lead end of sample 59 reoriented with one zone pass from $[11\bar{2}0]$ to [0001], would suggest that the effect is not due to different temperature coefficients of resistivity for the various crystal directions since the resistance ratio was virtually unchanged in this reoriented sample.

The data obtained during the course of this work suggests the need for a continued effort in ascertaining the specific purification parameters. The apparent effect of orientation on the purification needs further study and the role of zone refining also needs more definition since there are indications that impurities with segregation coefficients greater than unity are involved.

Summary

We have shown that extremely high purity rhenium crystals can be prepared consistently with resistence ratios above 30,000. Purification occurs both by selective vaporization and zone refining. The nature of the source material and the manner in which it is handled are important factors in determining the extent of purification.

Acknowledgment

The authors would like to thank J. H. Wernick and W. A. Reed for their guidance during the course of this work and for their helpful comments on this paper. The analytical work done by E. K. Jaycox and the assistance of E. Berry are gratefully acknowledged.

Manuscript received June 10, 1964.

Any discussion of this paper will appear in a Discussion Section to be published in the December 1965 JOURNAL.

REFERENCES

1. M. Davis and R. L. Lever, U.S. 2,809,905, October 15, 1957.
2. G. A. Geach, R. A. Jeffery, and E. Smith, *J. Less Common Metals*, **1**, 56 (1959).
3. A. Lawley, *Acta Met.*, **8**, 896 (1960).
4. E. M. Savitskii, *Issled. po. Zharaproch. Splavan Acad. Nauk. SSSR Inst. Met.*, **9**, 192 (1962).
5. E. Rexer, Proc. Symp. Electron Beam Technol. 4th, Boston, Massachusetts, 245 (1962).
6. J. E. Kunzler and J. H. Wernick, *AIME Trans.*, **212**, 856 (1958).
7. J. J. Hauser and E. Buehler, *Phys. Rev.*, **125**, 142 (1962).
8. H. Sell, Unpublished work.
9. E. Buehler, *AIME Trans.*, **212**, 694 (1958).
10. H. W. Schadler, "The Art and Science of Growing Crystals," J. J. Gilman, Editor (1963).
11. H. F. Sterling and R. W. Warren, *Metallurgica*, **67**, (August 1963).

Indium Antimonide of High Perfection

Sidney G. Parker, Oran W. Wilson, and Bill H. Barbee

Texas Instruments Incorporated, Dallas, Texas

ABSTRACT

InSb having mobilities at liquid nitrogen temperature of approximately 1 x 10^6 cm^2/v-sec with excess carrier concentrations in the $10^{13}/cm^3$ range was produced by extensive purification steps followed by controlled crystal growth. The number of dislocations was less than $500/cm^2$ as revealed by etch techniques.

Efforts have been made (1-4, 6-7, 13) to prepare indium antimonide (InSb) of high purity, but the effects of dislocations on electrical properties such as mobility of carriers have been neglected. Our goal was to prepare high perfection InSb by increasing the chemical purity and decreasing the number of crystalline imperfections. Extensive purification of In and Sb before compounding, followed by zone refining of the InSb, was planned. Further, the InSb was to be zone refined in single crystal form. Single crystals were to be grown by various techniques (2, 5) to study the effects of dislocations on electrical properties.

Source of materials.—Special Research Grade (SRG) In and Sb (99.9999% pure) and material of 99.999% purity were obtained from Consolidated Mining and Smelting Company. All acids and other reagents used for etching, degreasing, and rinsing were "Reagent Grade;" distilled water was used for preparing etch solutions and for rinsing. Pure H_2, the ambient during zone refining, was obtained by diffusion through hot Pd.

Quartz boats, sandblasted to provide a rough inside surface, were used during zone refining. These boats were thoroughly etched with a solution of $HF\text{-}HNO_3$, rinsed with distilled water, and air-dried in a dust free atmosphere. Quartz boats covered with a carbon coating formed by thermal decomposition of toluene or acetone, or graphite boats were used initially. The carbon coating was used to prevent wetting of the quartz; however, it was found that none of the materials (In, Sb, or InSb) would wet quartz if the system were dry. Since the carbon deposit contained traces of impurities, the uncoated quartz boats were preferable.

Compounding of InSb.—During the early phases of the program, InSb ingots were compounded singly from small ingots or pieces of In and Sb. These ingots varied in composition, which made it difficult to evaluate purification procedures, and an apparatus (8) was built to cast up to ten, 250g, InSb ingots from the same melt.

In this apparatus the In and Sb were melted and mixed together under an inert atmosphere, then transferred to quartz boats. The boats were held in a brass holder while being loaded. Chilled water circulating through the boat holder caused the melt to freeze instantly upon striking the chilled boats.

Ingots cast from this apparatus were homogeneous, and uniformity between ingots was achieved.

Purification of In *and* Sb.—An effort was made to improve the InSb by purifying In and Sb before compounding. These elements were distilled and zone refined, but the purities attained were no better than 99.9999%, the purity of the initial starting material in some experiments. Hence, the Special Research Grade materials were used without further purification.

Effects of Zone Refining InSb

Palladium-purified H_2 was used during zone refining because tank H_2 contained impurities that would yield highly compensated material. The H_2 atmosphere in the zone refining system reduced the loss of Sb by evaporation and provided a reducing ambient. Some impurities were probably volatilized from the molten zone, and the H_2 served as a carrier to sweep out these materials. The direction of H_2 flow, whether concurrent or countercurrent to the direction of zone refining, did not affect the purity. No differences were noted in InSb purity for H_2 flows over the range of 300 to 1500 cc/min, although one might expect increased losses of Sb and impurities at the greater flows.

Zone refining InSb at 1 in./hr gave more high purity, n-type material than did zone refining at greater speeds. Table I shows some of the variations in purity as reflected by resistivities, mobilities, and excess carrier concentrations for InSb ingots zone refined at various speeds. Ingots refined more slowly gave material with higher mobilities and less compensation. More efficient purification was also indicated in ingots zone refined slowly by the appearance of p-type regions on the last portion of freeze, because the impurities have more time to mix and establish true equilibrium conditions between the solid and the molten zone. Single crystal growth during zone refining is enhanced by slow zone travel speed. The zone width was about 1 in., and the melt-solid interface was planar.

The optimum zone refining speed for obtaining the highest purity InSb was not determined, and even slower speeds might give still better purification. Purity is a function of zone refining speed, the number of passes, and the crystalline state (polycrystalline *vs.* single crystal). The least number of zone passes at a specified refining speed needed to attain a certain purity could not be calculated because neither all the impurities nor their segregation coefficients were known. The optimum number of zone passes must be found by trial or by determining effective segregation coefficients at various zone refining speeds.

It had been reported (9) that material transfer over the edge of the boat by the last portion to freeze during zone refining aided purification; however, we did not find this true for InSb. With one exception, all ingots in which material was carried from the boat contained mixed regions of p-type and n-type material. Further, the n-type material from these ingots was highly compensated. Constant volume changes during material transfer probably caused the concentration of impurities to vary widely, hence the difficulty in maintaining the system at equilibrium.

Table I. Effects of zone refining speeds

Ingot No.	Zone travel speed, in./hr	Total No. of passes	Measurements on typical samples* Mobility, cm^2/v-sec	Resistivity, ohm-cm	No. excess carriers/cm^3
44B	1	55	636,000	0.06	1.7×10^{14}
42	2	52	87,000	4.82	2.96×10^{13}
47B	1	50	530,000	0.21	1.2×10^{14}
46	2	51	38,000	9.72	1.96×10^{13}
60	4	25	279,500	0.85	3.1×10^{13}
	2	31			
4	4	15			
	2	25	570,000	0.27	4.78×10^{13}
	1	12			

* All measurements were made at 80°K on single crystal samples cut from near the middle of the n-type region of the ingots.

Table II. Comparison of InSb ingots zone refined in single crystal state vs. polycrystalline state

Ingot No.	Total No. of zone passes	No. of single crystal passes	Single crystal orientation** on growth face	Measurements at 80°K: Mobility, cm²/v-sec	Resistivity, ohm-cm	n-type Carriers/cm³
69	40	35	<111> (grew naturally)	916,000	0.120	6.7×10^{13}
8	40	30	Unknown, (grew naturally)	735,000	0.104	9.6×10^{13}
37	60	0	Poly	442,494	0.107	1.62×10^{14}
38	60	10	<115>	425,196	0.04	4.3×10^{14}
63	42	25	<111>	670,000	0.127	8.6×10^{13}
33	44	0	Poly*	426,000	0.02	8.58×10^{13}
68	40	30	Unknown, (grew naturally)	919,000	0.11	6.9×10^{13}
91	42	0	Poly	424,000	0.19	8.7×10^{13}

* Single crystal regions were used for all measurements, even on polycrystalline material; all samples cut from near the center of the n-type region.
** Crystal orientation taken as normal to length of ingots.

The cropping (9) of a boat 1½ in. from each end of the ingot after 10 or 15 passes, followed by further zone refining, did reduce the total number of passes needed to attain a certain purity level and did improve the yield of high mobility n-type material. Cropping allowed greater purification because impurities which segregate to the ends were removed and did not back-diffuse into the ingot.

Zone refining in single crystal states greatly increased the mobility over that obtained by zone refining in the polycrystalline state, as illustrated in Table II. The material with highest mobility and lowest excess carrier concentration was found in ingots 68 and 69, which had the most passes in the single crystal state. It can readily be seen that greater mobility can be obtained with fewer passes for single crystal zone refining. Zone refining polycrystalline material is less effective for purification because impurities probably segregate at grain boundaries. Experiments with InSb ingots containing radioactive Zn showed that the segregation coefficient for Zn was 1.2 for polycrystalline zone refining but 1.9 for single crystal refining. It was difficult to obtain material with a mobility greater than 500,000 cm²/v-sec at 80°K by polycrystalline refining, even with 100 passes.

Uniformity of Zone Refined Ingots

The ingots produced by zone refining, even in single crystal form, vary in composition over the length of the ingot. The resistivity profile of such an ingot is shown in Fig. 1. This ingot, which was zone refined single crystalline for 30 passes, is rather uniform in resistivity over approximately 4 in. of its length.

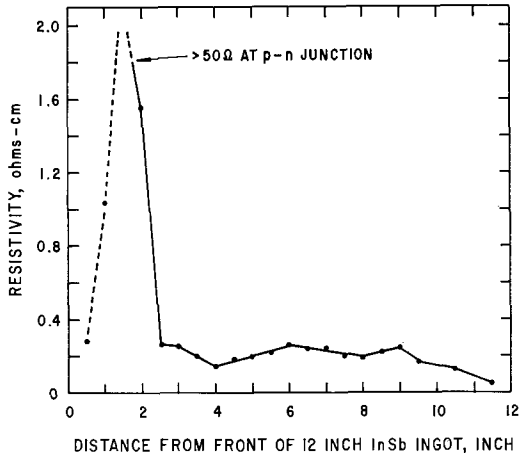

Fig. 1. Resistivity profile of zone refined InSb ingot. Measurements made by 4-point probe at 80°K; — — —, p-type; ———, n-type.

Table III. Profile of material properties in zone refined InSb Ingot

Position of sample from the ingot*	Type of material	Temperature, °K of measurement	Resistivity, ohm-cm	Hall mobility, cm²/v-sec	Number of excess carriers/cm³
4 in. from front	n	300	4.67×10^{-3}	78,000	2.01×10^{16}
	n	80	3.60	84,000	2.44×10^{13}
6½ in. from front	n	300	4.48×10^{-3}	82,000	2.02×10^{16}
	n	80	1.21×10^{-1}	917,000	6.70×10^{13}
10 in. from	n	300	4.46×10^{-3}	79,000	2.09×10^{16}
from	n	80	1.71×10^{-1}	423,000	1.01×10^{14}

* Total length of ingot was 12 in. Zone refined single crystal in <111> orientation for 30 passes. Measurements made at 80°K on n-type material.

Hall bars were cut from the ingots parallel to the growth face or normal to the length. Electrical measurements on samples taken from a refined ingot are shown in Table III. A wide variation in mobility is noted and indicates the degree of nonuniformity in the n-type material. However, there are regions of considerable uniformity, as shown by the resistivity profile. Samples were usually selected from these uniform resistivity regions.

An unsuccessful effort was made to form homogeneous ingots from high purity, n-type material by zone leveling. For material containing 10^{15}/cm³ excess carriers or more it was possible to obtain homogeneous ingots by zone leveling, but with n-type ingots containing fewer excess carriers, zone leveling produced very nonuniform ingots, as revealed by resistivity profiles. N-type InSb containing 10^{14}/cm³ excess carriers produced areas mixed with n-type material after zone leveling. Small variations in growth conditions and volume greatly influence the distribution of impurities during zone leveling. These subtle variations which arise in crystal growth with a moving molten zone are perhaps more noticeable at the lower carrier concentrations.

Effects of Dislocations on Mobility

The high purity InSb produced by zone refining in single crystal form exhibited rather high mobilities (600,000 to 919,000 cm²/v-sec), but the number of dislocations revealed by etch techniques was in the range of 10^4 to 10^5 per cm². Because it was known that dislocations usually cause decreased mobilities (13), it was thought that the mobilities could be increased still further by decreasing the number of dislocations. Horizontal growth of single crystal ingots in quartz boats gave a minimum of 10^4/cm² dislocations. Obviously, the growth conditions in a boat were not conducive to crystalline perfection.

By taking the n-type regions from the zone refined bars, loading into a vertical type puller, and using the Czochralski technique to grow a single crystal, we were able to reduce the dislocations to less than 500/cm² (Table IV) and in most cases to increase the mobility. With ingot 68 it was found that the mobility increased in the pulled crystal even though the num-

Table IV. Effect of dislocations on mobility

Ingot No.	Measurements at 80°K on crystal grown in zone refiner: No. of dislocations per cm²	No. of excess n-type carriers	Hall mobility, cm²/v-sec	Measurements at 80°K on crystal grown in crystal puller: No. of dislocations per cm²	No. of excess n-type carriers	Hall mobility, cm²/v-sec
68*	1×10^4	6.8×10^{13}	919,000	50	1.8×10^{14}	980,000
70**	2×10^5	2.62×10^{14}	550,000	150	5.37×10^{14}	720,000
8***	—	—	—	100	3×10^{13}	1,200,000

* Zone refined for 30 passes in single crystal form.
** Zone refined in polycrystalline form with single crystal sample taken for measurements.
*** Zone refined in single crystal form, but sample not cut out for analysis until after crystal grown by pulling.

ber of excess carriers increased. This increase in mobility has been attributed to the decrease in the number of dislocations. One pulled crystal gave a mobility of 1,200,000 cm^2/v-sec at 80°K on material which had previously been zone refined in single crystal form for about 40 passes. It appears that zone refining in single crystal form followed by crystal growth in a vertical puller to reduce dislocations produces InSb crystals of greatest perfection. The number of dislocations occurring even in crystals grown with a vertical puller was dependent on the number of dislocations present in the seed crystal. It was necessary to select InSb seed crystals containing a minimum of dislocations.

Discussion

It was not possible to obtain purities much greater than 99.9999% by vacuum distillation and zone refining of In and Sb. Whether continued zone refining or vacuum outgassing would produce In or Sb of greater purity is debatable, for the chance for pickup of impurities from the containers and ambient increases with time. The use of pure H_2 during zone refining was necessary to produce high purity, uncompensated material.

As anticipated, the zone refining conditions of the InSb ingots had a marked effect on chemical purity and electrical properties. The more slowly the zone refiner was run, the greater the purity. With a slow zone travel speed there is adequate time for establishment of equilibrium between the solid and liquid phase; there is also improved mixing. Zone refining in single crystalline rather than in polycrystalline form contributed greatly to improved purity and increased mobility. There also seemed to be preferred growth planes on the single crystal seeds used to initiate growth. Certain crystal faces were able to sustain single crystal growth, while the opposite faces fostered polycrystalline growth. The size of atomic and/or ionic radii of the incoming elements and the bonding energies involved determine the probability of incorporation of atoms into the lattice.

Nonuniformity of ingots over the length of the crystals may be attributed to differences in growth conditions, such as volume of the molten zone and nucleating centers on the boat wall. As one might expect, polycrystalline ingots, because of the tendency for impurities to segregate at grain boundaries, showed less uniformity than single crystal ingots. Crystal dislocations contributed to nonuniformity, since such defects often tend to behave as segregation centers.

Crystal dislocations affected the mobility of InSb, an effect that was also found with such materials as Ge (12). Dislocations may serve not only as scattering centers but also as traps for the carriers and might therefore influence the carrier mobility. Certain types of dislocations seemed to propagate during crystal growth, although the nature of these dislocations was not determined.

Manuscript received May 20, 1964.

Any discussion of this paper will appear in a Discussion Section to be published in the December 1965 JOURNAL.

REFERENCES

1. K. F. Hulme, *J. Electronics and Control*, **6**, 397 (1959).
2. L. I. Matkova and M. S. Mirgalovskaya, *Russian Journal of Inorganic Chemistry*, **5**, 750 (1960).
3. T. C. Harman, *This Journal*, **103**, 128 (1956).
4. K. F. Hulme and J. B. Mullin, *J. Electronics and Control*, **3**, 160 (1957).
5. K. F. Hulme and J. B. Mullin, *J. Phys. Chem. Solids*, **17**, 1 (1960).
6. A. L. Haughwout, Thesis, U.S. Air Force Institute of Technology, September 1959.
7. R. C. Bourke, S. E. Miller, and W. P. Allred, Jr., *This Journal*, **106**, 61*C* (1959).
8. S. G. Parker and O. W. Wilson, *Rev. Sci. Instruments*, **35**, 276 (1964).
9. W. G. Pfann, "Zone Refining," John Wiley and Sons, New York (1958).
10. C. Thurmond, "Semiconductors," N. B. Hannay, Editor, p. 157, Reinhold Publishing Corporation, New York (1959).
11. J. W. Faust and A. Sagar, *J. Appl. Phys.*, **31**, 331 (1960).
12. R. A. Logan, G. L. Pearson, and D. A. Kleinman, *Bull. Am. Phys. Soc.*, **3**, 261 (1958).
13. S. C. Liang, "Compound Semiconductors," Willardson and Goering, Editors, Vol. I, p. 227, Reinhold Publishing Corporation, New York (1962).

Some Properties of GeTe-PbTe Alloys

J. C. Woolley[1] and P. Nikolic[2]

Department of Physics, University of Nottingham, Nottingham, England

ABSTRACT

Solid solution between PbTe and GeTe of stoichiometric composition has been studied. It is found that for samples annealed at 600°C for periods of up to four weeks and then air quenched, single phase condition can be obtained at all alloy compositions, and the lattice shows a continuous transition from cubic to rhombohedral form. Room temperature values of lattice parameter a_0 and rhombohedral angle α, positive hole concentration p and mobility μ and optical energy gap E_g have been determined as a function of composition. The variation in percentage of vacant sites on the germanium sublattice, as determined from p, is correlated with the difference in cell volume for cubic and rhombohedral structures.

Although the properties of PbTe have been well studied in the past, it is only recently that any appreciable work has been carried out on GeTe and SnTe and on the pseudobinary alloy systems derived from the three compounds. The investigation of the properties of GeTe and SnTe has been complicated by the fact that each corresponds to a narrow single phase field in the corresponding metal-tellurium binary diagram; hence the electrical properties may vary considerably with the method of preparation.

In the case of GeTe, it has been shown (1) that the congruently melting alloy has a composition corresponding to $GeTe_{1.025}$. The material with a stoichiometric composition of GeTe is found (2) to have a positive hole concentration of 7.0×10^{20}/cc; if it is assumed that one lattice vacancy on the germanium sublattice produces two positive holes, this indicates the

[1] Present address: Department of Physics, University of Ottawa, Ottawa, Ontario, Canada.

[2] Present address: University of Belgrade, Belgrade, Yugoslavia.

presence of almost 2% vacancies on germanium sites with the corresponding amount of germanium present as a second phase. For PbTe, the range of solid solution of the individual elements in the compound is considerably less. The material of stoichiometric composition PbTe is usually found to be p-type at room temperature but with a considerably smaller carrier concentration of the order 10^{18}/cc (3).

When solid solution between the three compounds is considered, an important factor is that PbTe and SnTe have the cubic rock salt structure while GeTe shows this structure only above 430°C, below this temperature being rhombohedrally distorted. It has been shown that single phase solid solution across the whole range of composition is obtained for PbTe-SnTe (4-6) and for GeTe-SnTe alloys (5, 7, 8), but in the case of GeTe-PbTe alloys Mazelsky *et al.* (5) report only a very limited range of solid solubility of either compound in the other, the limits being temperature dependent.

Mazelsky and Lubell (2, 9) have also considered the solubility in GeTe, PbTe, and SnTe of the cross-substitutionally derived ternaries $TlSbTe_2$ and $TlBiTe_2$, finding a considerable range of solid solution in each case. They have investigated the effects of this solid solution on the carrier concentration and electrical properties of the binary compounds. Rosi *et al.* (10) have made similar investigations of the alloys of GeTe, PbTe, and SnTe with the derived ternary $AgSbTe_2$.

Experimental Procedure

Preparation of alloys.—The GeTe and PbTe were each synthesized separately from the elements which were 99.999% pure, and the alloys were then prepared by melting together appropriate amounts of the two compounds. The resulting ingots were annealed at 600°C until equilibrium at that temperature was obtained; they were then air quenched to room temperature. The necessary annealing time was determined by taking x-ray powder photographs of control samples after various times of annealing, the criterion for equilibrium being that no further change in the x-ray photograph could be observed with continued annealing. X-ray powder photographs of the test samples were then used to determine the variation of lattice parameters with composition.

Physical measurements.—Measurements were made at room temperature of the Hall coefficient and electrical conductivity for various alloy compositions, and also, where possible, infrared transmission measurements were made to determine the optical energy gap. The apparatus and methods used here were the same as described previously for other alloy systems (11).

Results and Discussion

Lattice parameter data.—The variation of lattice parameters with composition is shown in Fig. 1. In contrast to the results of Mazelsky *et al.* (5), single phase solid solution was obtained at all compositions when alloys were annealed at 600°C and then air quenched. However, while an annealing time of one week was sufficient to give good equilibrium conditions in the alloys near the ends of the composition range, alloys near the center of the range had to be annealed for at least four weeks and even then showed some blurring of the high angle x-ray lines. It is seen that there is a continuous transition from the cubic form of PbTe to the rhombohedral form of GeTe. The parameter a_0 varies almost linearly with composition, while the rhombohedral angle α has a value of 90° (*i.e.*, cubic) from 0 to 30 mole % GeTe and then varies continuously to the value of 88° 16′ for GeTe.

The difference from the data of Mazelsky *et al.* can probably be accounted for in terms of difference in treatment of the alloys. Mazelsky *et al.* showed for an alloy $Ge_{0.96}Pb_{0.04}Te$ that while this alloy was two phase at room temperature, at 275°C a single phase rhombohedral structure was observed which transformed to cubic at 390°C. In the present results, prolonged annealing produced a single phase condition in all alloys and this was quenched in at room temperature. Thus, our specimens most likely represent equilibrium conditions at 600°C. It is not clear therefore what is the room temperature equilibrium condition.

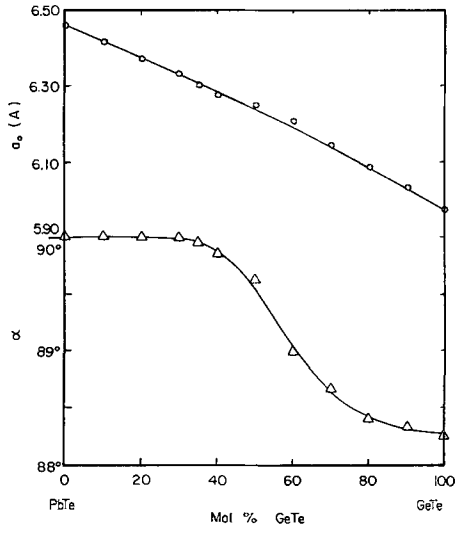

Fig. 1. Variation of room temperature values of rhombohedral lattice parameters a_0 and α as a function of composition.

Electrical data.—Measurements of Hall coefficient R_H showed that all alloys were p-type. The variation of positive hole concentration p $(= 1/eR_H)$ with composition is shown in Fig. 2, in addition to the value of Hall mobility $\mu (= \sigma R_H)$ as a function of composition. These electrical results show an interesting correlation with the crystallographic data in Fig. 1. Thus p remains at a value similar to that for the PbTe used here (*i.e.*, less than 10^{19}/cc) while the structure is cubic. Then it increases rapidly with GeTe content when the structure becomes rhombohedral, reaching a value of 6.5×10^{20}/cc for GeTe itself. This is in good agreement with the results of Mazelsky and Lubell for a material of stoichiometric composition GeTe. Similarly the mobility falls continuously from a value of 600 cm^2/v sec to 60 cm^2/v sec in the range of cubic structure, but then remains reasonably constant over the composition range where the structure is rhombohedral.

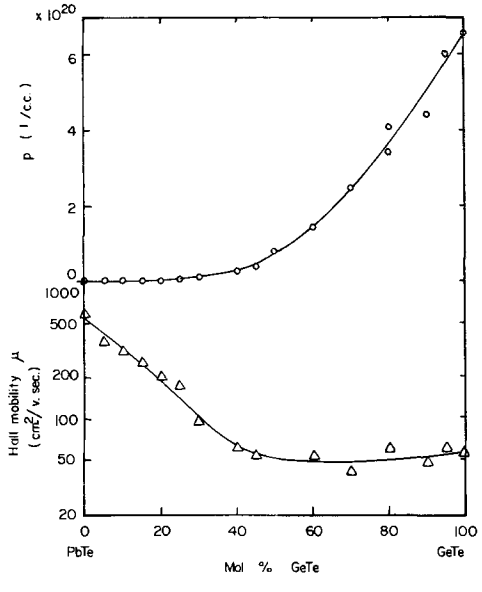

Fig. 2. Variation of room temperature values of positive hole concentration p and Hall mobility μ as a function of composition.

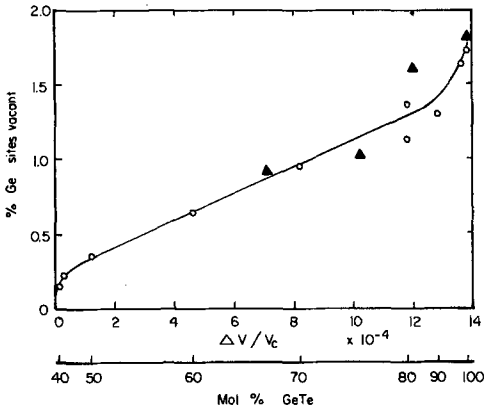

Fig. 3. Variation of percentage germanium sites vacant with $\Delta V/V_c$: ○, present data for GeTe-PbTe alloys; ▲, GeTe-Tl(Sb,Bi)Te_2 alloys (Mazelsky and Lubell).

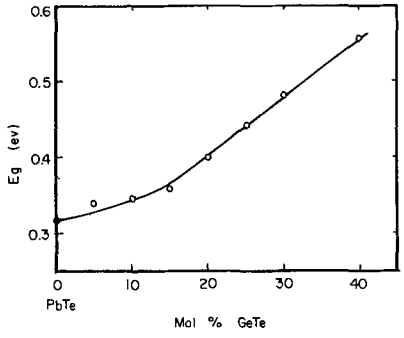

Fig. 4. Variation of room temperature values of optical energy gap E_g as a function of composition.

Consider first the carrier concentration data. It is clear that the increase in p is related to the onset of rhombohedral distortion in the lattice; assuming, as in the case of GeTe, that the positive holes are due to lattice vacancies on the (Pb, Ge) sublattice, this would indicate a correlation between lattice vacancy density and rhombohedral distortion. Since a_o varies almost linearly with GeTe content, the important factor appears to be the variation of the rhombohedral angle α or the corresponding variation in unit cell volume. To represent this volume variation, a parameter $\Delta V/V_c$ has been calculated, where ΔV is the difference between the volume of the rhombohedral cell and the volume V_c of the cubic cell with the same value of a_o. From the value of p, assuming two positive holes per lattice vacancy (2), the ratio of concentration of lattice vacancies to concentration of germanium atoms on the (Pb, Ge) sublattice has been calculated and expressed as percentage germanium sites vacant. The variation of this quantity with $\Delta V/V_c$ is shown in Fig. 3. This graph is linear over a large range of rhombohedral structure, showing deviations only at the onset of rhombohedral behavior and near to GeTe itself. This indicates that the number of lattice vacancies occurring is directly dependent on the volume defect $\Delta V/V_c$.

To check this suggestion, similar parameters can be calculated from the data of Mazelsky and Lubell (2) on the solid solution of Tl(Sb, Bi)Te_2 in GeTe. In this case, there is a range of solid solution of only 8 mole % $TlSbTe_2$ or $TlBiTe_2$ in GeTe, but this causes a rapid change in α toward the cubic condition. Since the positive hole concentration in the ternaries themselves is approximately 2 x 10^{19}/cc, which is small compared with the 7 x 10^{20}/cc for GeTe, again the variation in carrier concentration in the alloys can be attributed to changes in the vacancy concentration on the germanium lattice sites. Points corresponding to this data have been plotted in Fig. 3. Although it is not possible to obtain accurate figures from the published data, it is seen that the results for the Tl(Sb, Bi)Te_2 solid solution are in reasonable agreement with the data presented here.

Turning to the mobility data, this also can be correlated with the presence of lattice vacancies which must be considered effectively as ionized acceptors. Over the range from 0-40 mole % GeTe, the increase in p is small and hence the reduction in μ with increased GeTe content must be attributed to a considerable extent to alloy scattering, *i.e.*, to the introduction of increased disorder on the (Pb, Ge) sublattice. In the absence of any other major scattering effects, such alloy scattering might be expected to give a minimum mobility at approximately the equimolar composition. The mobility would rise again beyond this point as the degree of disorder decreases, *i.e.*, in this range the (Pb, Ge) sublattice is occupied predominantly by germanium atoms. However, although in the range 50-100 mole % GeTe the scattering due to the presence of lead atoms on the germanium sublattice decreases with increased GeTe content, this is compensated by an increase in ionized acceptor scattering. Thus the value of μ does not in fact increase, but remains roughly constant with alloy composition. A very approximate calculation from the values of p and lead content indicates that to obtain this result the scattering cross section of the vacancies must be of the order of 35 times that of lead atoms in the germanium sublattice.

Optical data.—Figure 4 shows the variation of room temperature optical energy gap E_g with alloy composition in the range 0-40 mole % GeTe. For alloys of higher GeTe content it was not possible to determine values of E_g as the absorption of the samples greatly increased with the rapid increase in carrier concentration. Over the range 15-40 mole % GeTe, the value of E_g varies approximately linearly with GeTe content; extrapolation of this line gives a value of 1.0 ev for GeTe itself in reasonable agreement with the expected value for GeTe.

Manuscript received June 22, 1964.

Any discussion of this paper will appear in a Discussion Section to be published in the December 1965 JOURNAL.

REFERENCES

1. J. R. McHugh and W. A. Tiller, *Trans. AIME*, **218**, 187 (1960).
2. R. Mazelsky and M. S. Lubell, *Adv. in Chem.*, **39**, 210 (1963).
3. W. W. Scanlon, "Solid State Physics," Vol. 9, p. 83, F. Seitz and D. Turnbull, Editors, Academic Press Inc., New York (1959).
4. T. Okada, *J. Phys. Chem. Solids*, **8**, 428 (1959).
5. R. Mazelsky, M. S. Lubell, and W. E. Kramer, *J. Chem. Phys.*, **37**, 45 (1962).
6. A. A. Machonis and I. B. Cadoff, *Trans. Met. Soc. AIME*, **230**, 333 (1964).
7. N. Kh. Abrikosov, A. M. Vasserman, and L. V. Poretskaya, *Dokl. Akad. Nauk. SSSR*, **123**, 279 (1958).
8. H. Krebs, K. Grün, and D. Kallen, *Z. anorg. Chem.*, **312**, 307 (1961).
9. R. Mazelsky and M. S. Lubell, *J. Phys. Chem.*, **66**, 1408 (1962).
10. F. D. Rosi, E. F. Hockings, and N. E. Lindenblad, *R.C.A. Rev.*, **22**, 82 (1961).
11. J. C. Woolley, C. M. Gillett, and J. A. Evans, *J. Phys. Chem. Solids*, **16**, 138 (1960).

Cadmium Selenide Thin Film Field Effect Transistors

Herbert L. Wilson and William A. Gutierrez

Melpar, Inc., Falls Church, Virginia

ABSTRACT

All thin film, insulated gate, field effect transistors (triodes) have been formed by standard vacuum deposition techniques. Comparison of the electrical parameters of devices formed with CdS, CdSe, or CdTe semiconductor layers indicated certain advantages, namely, higher mobility and better stability, of the CdSe units. Stability and life of CdSe devices was improved by use of aluminum rather than gold for the gate electrode. A preliminary investigation of the use of various materials for use as the dielectric layer indicates many compounds are suitable.

The transverse field effect phenomenon appears to be for amplifying thin film devices the most immediately utilizable of various suggested phenomena. The typical structure consists of two electrodes contacting a semiconductor with a third electrode being separated by a dielectric. Disclosures of field effect devices by Lilienfield (1) in 1930 and of completely thin film, nonjunction devices by Heil (2) in 1935 pointed out with amazing accuracy many device requirements. These early devices, however, never became popular despite the intensive effort to find solid-state amplifying devices in the ensuing years. The prime limitation of the thin film devices was the low sensitivity of the semiconductor to the applied transverse field. Shockley and Pearson's (3) efforts in 1948 to modulate the conductivity of germanium films, together with Bardeen's (4) theory of surface states, indicated that surface states may have a major influence on the field effect in materials. Nevertheless, despite the deleterious effects of surface states, Feldman (5) in 1961 reported thin film devices consisting of germanium semiconductor films and later Wilson, Layton, Gutierrez, and Feldman (6), in 1962 obtained germanium film devices that exhibited useful current and power gains.

The thin film cadmium sulfide devices of Weimer (7, 8) exhibited voltage gains in addition to current and power gains. Useful values of transconductance, voltage amplification, and other electrical characteristics indicated the practical applications of the devices to numerous circuits.

In the present investigation, cadmium selenide and cadmium telluride films have been employed in field effect devices and compared with cadmium sulfide devices. In addition, several metal and dielectric materials have been employed as gate and dielectric layers.

Experimental

The device formation was carried out in vacuum at pressures of 10^{-5} to 10^{-7} mm Hg. The semiconductor films were deposited from undoped semiconductor materials of 99.99+% purity (Harshaw, Light). A graphite crucible (heated by a close fitting tantalum heater) was utilized in the semiconductor evaporations. A quartz-wool filter was used to prevent spattering or loss of material. The insulator and electrode films were deposited from tantalum and tungsten boats, respectively. A relatively pure source material (> 99%) was used for these evaporations.

Drawn, amorphous glass, 25 mm square and approximately 0.5 mm thick, was used as substrates (Corning 0211). These were cleaned by standard ultrasonic procedures. The substrates were then outgassed in vacuum at 350°C for approximately 5 min before the initial deposition.

Standard heating, shuttering, and masking techniques were employed. The source to substrate distance used was about 20 cm.

Figure 1 shows a cross section of a basic thin-film, insulated-gate, field effect triode (transistor). Various film layers are identified and will be referred to in the text of this paper. The film thickness given for the electrodes are typical. The ranges of dielectric and semiconductor thickness are typical for the materials used. These thicknesses were varied to obtain the desired device characteristics. The results of alternate sequences, such as reversal of the layer order, structures involving gate electrodes above and below the semiconductor layer, etc., are not reported here. Five to one hundred such devices were deposited singularly or as "pairs" on a substrate. Figure 2 is a photograph of the top view of sixteen "pairs" of devices deposited with a common source electrode (CS) for each pair. A source-drain electrode spacing of 12μ was used ex-

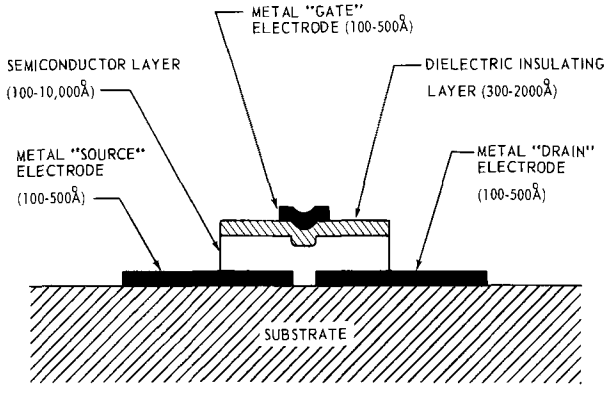

Fig. 1. Cross-sectional view of a thin film field effect triode

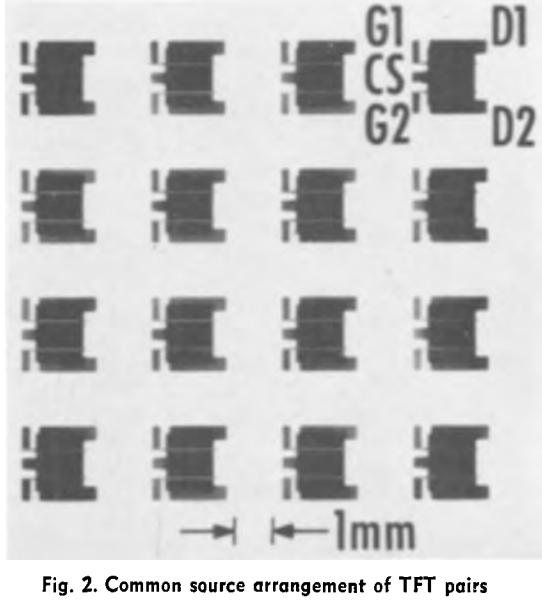

Fig. 2. Common source arrangement of TFT pairs

clusively. The width (gate electrode length) ranged from 1 to 5 mm.

The semiconductor films were deposited at a rate of approximately 10,000 Å/min. It appeared as though a rapid deposition of the semiconductor layer (all other parameters held constant) generally resulted in films of lower resistivity. This is believed due to either a more congruent evaporation of the elements or to a lesser reaction with oxygen during the formation of the film. Depending on the method used, a rapid deposition rate seemed preferable in obtaining field sensitive films. This may be due to the reasons mentioned above. The ability to make rapid depositions was achieved by the use of relatively large charges (up to 5g) dispersed in a shallow manner over the bottom of a large crucible. This appeared preferable to fast deposits by excessive heating in which considerable dissociation of smaller charges in smaller crucibles took place. A crucible temperature of about 900°C was used to evaporate the semiconductor material.

The semiconductor films were deposited over the previously deposited source-drain electrodes. Samples for Hall effect measurements and material analysis were generally of another configuration. No attempts were made to form single crystal layers. Dielectric film deposition ranged from 200 Å/min for Dy_2O_3 to 4000 Å/min for SiO. Rates were restricted somewhat by the relative ease of evaporation of the material used. The dielectric deposition was initiated at a substrate temperature of 25°C (room temperature). Due to source radiation it was noted that increases in substrate temperatures to 100°C occurred during the deposition of the higher temperature dielectrics. It appeared that a rapid deposition of oxide dielectrics was preferable in obtaining a decrease in the semiconductor film resistivity. This phenomena is discussed later in this paper. Metallic electrode depositions were made at rates of approximately 2000 Å/min.

Etched molybdenum or electroformed nickel masks were used to form the different film configurations. To achieve a high resolution fine gap between source and drain electrodes, tungsten wires (12μ in diameter) were spot welded to the basic masks. The device characteristics shown in this paper are photographs taken from a Tektronic, type 570, characteristic curve tracer. Values of μ, g_m, and r_D are readily calculated from these display curves.

The life and reliability tests on the devices were conducted by either observing their performance in an astable multivibrator circuit or by observing the change in their display characteristics with time on the curve tracer. These were continuous operation tests.

Results and Discussion

In the device fabrication, it was found that source-drain electrodes of gold were easily damaged in handling or mask movement. Therefore, several other materials, including platinum, indium, nichrome, chromium, nickel, copper, and aluminum, were investigated. Nichrome, chromium, and nickel formed hard films when deposited at a substrate temperature greater than 200°C and were not as subject to damage as were electrodes formed from the other materials. For various reasons not gone into here, nichrome was used extensively for source-drain electrodes. Any further heating of these nichrome electrodes such as the outgassing cycle shown in Fig. 6 required good vacuum of less than 10^{-5} mm Hg to prevent harmful surface oxidation.

In general SiO was used as the dielectric layer. Other dielectrics were investigated and compared with SiO. Thus far films formed from such oxides as SiO_2, La_2O_3, Yb_2O_3, Nd_2O_3, and Dy_2O_3 were found suitable for device use. Another oxide B_2O_3 was found very suitable for devices in that excellent high dielectric breakdown characteristics were obtained ($> 2 \times 10^6$ v/cm). This high breakdown strength was noted despite the fact that the evaporation was made from direct contact to a tantalum boat. Owing to the hydroscopic nature of B_2O_3 however, this film was utilized either sandwiched between or as a mixture with other dielectrics mentioned. The use of fluoride dielectrics such as AlF_3 and MgF_2 in addition to CaF_2 (9) were also successfully utilized. It appears that any material possessing reasonable dielectric properties in thin film form may be used unless, of course, it is destructively reactive in the atmosphere or with other contacting layers.

It was observed that different dielectric layers may influence the electrical properties of the semiconductor layer. The substrate temperature during deposition of the dielectric was also found to be a contributory factor. In addition, the manner in which the semiconductor layer was formed also determined the influence of the dielectric layer on its properties.

It was found that large drops of semiconductor resistivity ($> 100/1$) with the application of an overlying SiO dielectric layer (substrate held near room temperature and without previous air baking) assured that the semiconductor layer would exhibit high sensitivity to field effect. If no drop in resistivity was noted, the eventual device formed exhibited either poor sensitivity (transconductance) or required appreciable positive bias for good sensitivity. Other similarly formed semiconductor layers (*i.e.*, formed in the same run as those used with SiO dielectrics) exhibited similar response to the other oxide dielectrics listed. Fluoride dielectrics tested appeared less influential on the semiconductor layer resistivity. Use of either a sulfide (ZnS) or selenium as the dielectric layer usually resulted in an increase of the semiconductor resistivity. This latter experiment appears to coincide somewhat with the findings of Shallcross (10) in experiments involving use of selenium vapor on CdSe films. Devices utilizing ZnS or Se dielectric layers exhibited poor sensitivity characteristics.

At first, gold was used for the gate electrode. Life tests conducted on devices (to be discussed later) indicated, however, that use of another material would be preferable. Use of some materials, such as nichrome and nickel, created undesirable stresses in the underlying dielectric layer, and the resultant devices frequently exhibited gate area film peeling and/or a low dielectric-breakdown voltage. Devices with aluminum gate electrodes have thus far exhibited superior stability and reliability.

Of the three semiconductors studied, devices using CdTe were the most difficult to fabricate. The CdTe films generally exhibited resistivities which were too high for device applications. There was no apparent relation between film resistivity and film appearance. CdTe films were black and reflective, regardless of wide ranges of deposition rate and substrate temperature. In some cases crystal growth was observed.

Three techniques were used in forming lower resistivity CdTe films. The films were either heavily doped with cadmium or rapidly deposited on substrates cooled below room temperature, or baked in atmosphere. Doping with Cd was the most successful method although reproducibility was very difficult to achieve.

The CdTe films which exhibited field effect response were deposited at a substrate temperature of about 200°C. These films were doped by adding cadmium (about 1% by weight) to the high-purity CdTe source. After deposition, these films were annealed at 300°C in vacuum or at 500°C in air for approximately 5 min. At these anneal temperatures, crystal growth was observed, as shown in Fig. 3. These crystals often cause weak spots in the overlying dielectric layer. The films were usually deposited to a thickness of 5000Å. Figure 4 shows the I-V characteristics of a CdTe device. Saturation of drain current required voltages beyond the breakdown strength of the dielectric layer. The elec-

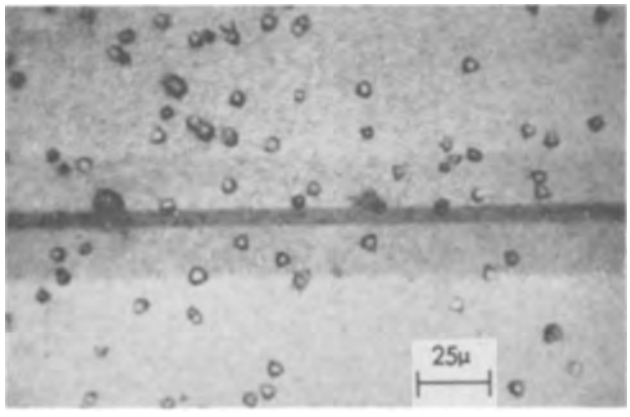

Fig. 3. CdTe crystal growth in the vicinity of the gap between source and drain electrodes.

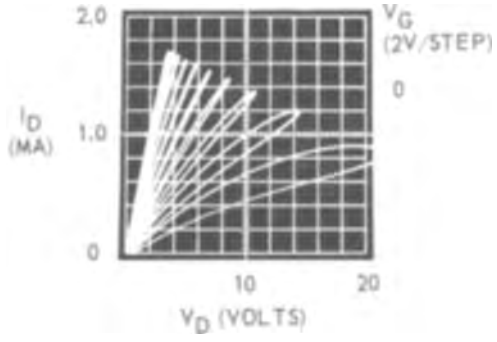

Fig. 4. Drain current *vs.* drain voltage characteristics of a CdTe device; $r_D \sim 16.7$ kohm; $g_m \sim 150$ μmhos; $\mu \sim 2.5$; $C_{in} \sim 100$ pf; $R_{in} > 50$ mohm; GB ~ 250 kc.

trical characteristics exhibited a rather unusual hysteresis effect. It was not uncommon to observe similar effects in CdS and CdSe devices. It appears that this hysteresis phenomena is associated principally with interelectrode RC time constants. Heating effects, surface states, and polarization are other possible causes.

CdTe devices generally exhibited low transconductances (g_m) of about 150 micro-mhos, amplification factors (μ) of about 5, and gain bandwidth products of about 200 kc. Most of the devices operated preferably in the enhancement mode (7).

The resistivity of a vacuum-deposited CdS film was generally related to its color. A dark brown or black film indicated a relatively low resistivity (<0.05 ohm-cm). Low resistivity films were formed by depositing at a substrate temperature of less than 50°C. Fast depositions also resulted in lower resistivity films. Such films were found to contain excess cadmium.

An orange-colored CdS film was usually of medium resistivity (0.5 to 500 ohm-cm). These films were formed by annealing dark films as described above by raising the temperature above 100°C for a time which is dependent on the anneal temperature. Another method was to deposit at a substrate temperature of about 70°-200°C.

The resistivity of yellow CdS films was usually high (> 5000 ohm-cm). These films were formed either by annealing the orange films for a longer time or by depositing at substrate temperatures above 200°C. Such films were found to contain excess sulfur.

The relation between color and resistivity for vacuum deposited CdS films was a general observation and no consideration has been given to the degree of crystallization or phase composition of the films.

The best CdS films for device use were obtained by depositing dark films (3000-6000Å thick) and annealing them in a vacuum at a temperature of about 200°C. The films were usually annealed until they appeared similar in color to the source material before evaporation. The Hall mobilities of these films were usually below 5 cm²/volt sec.

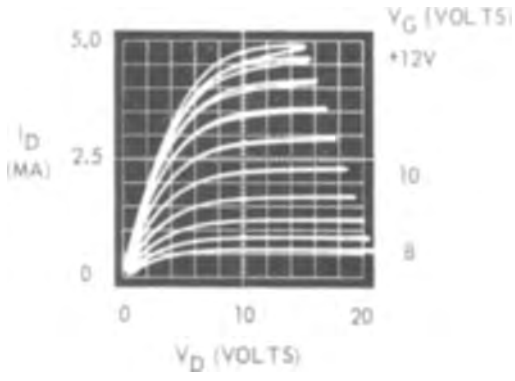

Fig. 5. Characteristics of a CdS field effect device operating in the enhancement mode; $r_D \sim 200$ kohms; $g_m \sim 1000$ μmhos; $\mu \sim 200$; $C_{in} \sim 100$ pf; $R_{in} > 100$ mohms; GB ~ 1.6 MC.

Figure 5 is a photograph of the I-V characteristics of a CdS device. The device parameters did not exhibit the quality of performance reported by Weimer (7). Perhaps this is due in part to the relative dielectric thickness utilized and the ability to form more sensitive CdS layers in atmospheric heat treatments (not utilized here). The device of Fig. 5 measured 2.5 mm width with 12μ spacing between source drain contacts. The CdS and SiO layers were approximately 5000 and 1500Å, respectively. Most of the CdS devices operated preferably in the enhancement mode. Transconductances (g_m) values up to 1500 micromhos, amplification factors (μ) greater than 200, and gain bandwidth products greater than 1 Mc were measured.

The color of a CdSe film did not strongly indicate its relative resistivity. The films were usually brown. In general, however, the lighter colored films were lower in resistivity, higher in mobility, and probably had a higher cadmium content than darker films of comparable thickness. The CdSe films had Hall mobilities ranging up to 50 cm²/volt sec. On the average, mobility values for CdSe were 5-10 times that of CdS films.

CdSe films were deposited to a thickness of up to 10,000Å at a substrate temperature of about 80°C. Postdeposition treatment consisted of three basic annealing procedures (the annealing procedure as used here includes the dielectric deposition). In the first procedure, the films were annealed in vacuum at a temperature of about 250°C for 2 to 3 min. After this part of the annealing, an increase in film resistivity (to a value above the pre-anneal value) was observed as the film cooled. This increase in resistivity is attributed to the absorption of oxygen (regardless of the vacuum utilized) as discussed by Bube (11) and by Somorjai (12). After allowing the film to cool in vacuum to about 50°C, the dielectric layer was then deposited. A significant drop in the resistivity of the CdSe film was noted upon the deposition of the SiO dielectric. Drops in resistivity of about a hundredfold were not uncommon. This phenomena as discussed later is not yet fully understood. Figure 8 shows the typical I-V characteristics of a CdSe device annealed in this manner.

The second type of annealing procedure was similar to that of the first except that a break in vacuum was made before the dielectric layer was deposited. An increase in resistivity was observed when the film was exposed to air. This was attributed to oxygen absorption. The film was then returned to the vacuum chamber and the dielectric deposited on it. Resistivity drops of a thousandfold were observed. This greater drop in resistivity was attributed to the relative exposure to atmospheric oxygen before the dielectric deposition. Figure 6 is a graph (second method) of substrate tem-

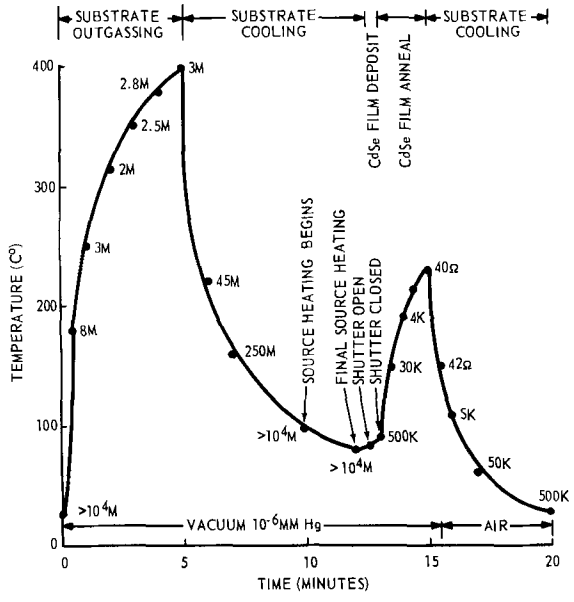

Fig. 6. Typical temperature and source-drain resistance values monitored in substrate outgassing and formation of a CdSe film.

perature *vs.* time during the substrate outgassing cycle, CdSe film deposition, CdSe film anneal, and withdrawal from vacuum. Values of resistance existing between source and drain electrodes (1/200 square) were monitored and are also shown on this graph.

At room temperature (25°C) the resistance between the source and drain electrodes is greater than 10,000 megohms. Upon heating via infrared quartz lamps the resistance decreased rapidly to 2 megohms at 315°C. This is explained by the thermal effect on the conductivity of the substrate (0.5 mm glass). A rise in resistance to 3 megohms was observed as the temperature further rose to 400°C. This appeared to be due to the desired removal of surface impurities, etc. With the outgas cycle completed the substrate is allowed to cool to the vicinity of 80°C (T = 12 min). At this temperature, the resistance between the source and drain electrodes is again greater than 10,000 megohms. At this point, the source containing the CdSe was elevated to 900°C. (Previously heated to 600°C from T = 10 min to T = 12 min). An additional time of 30 sec was allowed for the source to attain a temperature in the vicinity of 900°C. At this time (T = 12.5 min) the previously shuttered CdSe vapor is allowed to deposit on the substrate. After a 30-sec deposition, the substrate is again shuttered and the source heat turned off. The resistance of the deposited film was 500 kohms at this point. An anneal cycle was immediately initiated for 2 min (T = 15 min) during which the substrate attained a temperature of 230°C and the film resistance dropped to 40 ohms (at least half of this resistance is believed to be electrode resistance). Retention of the substrate in vacuum for 30 sec and cooling to 150°C resulted in only a very slight rise in film resistance (42 ohms). Removal of the substrate from vacuum and cooling to the vicinity of room temperature caused an increase in resistance of the film to 500 kohms.

Not shown on the graph, but of extreme importance, was the drop in resistance noted on the CdSe film upon deposition of the overlying dielectric layer. In this case the CdSe film resistance dropped to 3 kohms and remained at this value throughout device formation. The I-V characteristics of devices annealed in this manner are shown in Fig. 5, 7, 9, and 10.

With these first two methods of anneal, it was found that annealing at too high a temperature or for too long a time resulted in poor devices. It was also found that if the annealing was at too high a temperature or for too long a time, the resistivity of the semiconductor did not change appreciably when the dielectric was deposited. Such devices generally exhibited small values of transconductances or operated best in the enhancement mode ($V_G > +6v$). If the anneal was too low in temperature or for too short a time, the resultant device showed small values of amplification factor and large pinch-off voltages. These devices operated best in the depletion mode.

The third method of anneal was similar to the second method. However, it involved not only a break in vacuum, but also a further anneal in atmosphere before the deposition of the dielectric. The anneal in atmosphere was performed in an oven for 3 to 5 min at a temperature of 500°C. The heating in atmosphere reduced the resistivity of the film (100/1). The film was then placed in the vacuum chamber and the dielectric deposited on it. A decrease in resistivity of about tenfold was noted on application of the dielectric. The films annealed in this manner generally resulted in devices with unusually large hysteresis loops in their characteristic curves, short operational lifetimes, and comparably low dielectric breakdown voltages. In the formation of sensitive device structures it was noted that in each of the three methods of semiconductor formation discussed application of an overlying oxide dielectric caused a significant decrease in the semiconductor resistivity. This phenomena was noted for CdS and CdTe as well as for CdSe films. For devices operating in or near depletion mode it appears that this phenomena is a critical final activation phase of the semiconductor layer. Analysis of this phenomenon suggests either one or both of two physical changes in the semiconductor film structure is responsible.

It has been noted in previous reports by Bube (11) and Somorjai (12) and in the investigation of this paper that the increase in the resistivity of CdSe films on exposure to atmosphere is attributed to absorption of oxygen. It therefore appears reasonable that a drop in resistivity of the CdSe film on the dielectric deposition might be attributed in turn to the desorption of the oxygen either by bombardment of dielectric molecules or by chemical absorption of this oxygen by the dielectric layer. However, several questions are as yet not satisfied by this theory, *i.e.*, pertaining to the resistivity drop. The theory of oxygen desorption in the investigations carried out in this paper indicates chemical absorption of the oxygen atoms lying on the semiconductor surface by the dielectric layer. This is supported by the fact that thus far the greatest drops in resistivity of CdSe films have been noted when oxide dielectrics have been used. However, several reservations on this theory have continued to appear. One such reservation is the fact that CdSe films deposited to thicknesses of greater than 1μ and formed in the same manner as films of less thickness have more often shown little change in resistivity on dielectric deposition. This cannot be attributed to the film thickness due to the relative magnitudes of resistivity involved. In addition, thinner films formed with only slightly longer anneal cycles and with initial resistivities of less than one order of magnitude larger have also shown little influence by the dielectric film on their resistivity. These irregularities suggest that another theory might be justified. It is known that both the semiconductor layer and dielectric layer are under stress (revealed by occasional substrate breakage by the individual films involved). It is therefore possible that stress (known to influence semiconduction) produced in the semiconductor layer by the dielectric layer is possibly responsible for at least part of the resistivity drop. From many observations of electrical behavior change on the deposition of the dielectric layer this later theory of change of film stress appears reasonable. For instance it is somewhat more reasonable that some CdSe films do or do not change resistivity on dielectric application due to relative stress conditions within the films in-

volved rather than explanation of oxygen desorption. Conclusive evidence as to the exact phenomenon may be difficult to distinguish since stress itself may be the creation of oxygen exchange between layers.

Figure 7 shows the Id *vs.* Vd characteristics of a CdSe device utilizing a Dy_2O_3 dielectric. This device measured 1.5 mm in width with 12μ source-drain spacing. The CdSe and Dy_2O_3 layer thickness measured approximately 6000 and 700Å, respectively. These characteristics indicate as do those of Shallcross (13) that CdSe devices are comparable in performance to CdS units (7, 8, 14).

It has been reported that improvement in device pinch off characteristics could be obtained by use of a glow discharge cleaning of the substrate (15). This technique has not been utilized in the formation of devices reported in this paper. Initial experiments at this facility, however, tend to confirm the value of a proper glow discharge (16) cleaning in this respect.

Figure 8 illustrates the device characteristics of a CdSe unit utilizing very thin layers. This particular device had a semiconductor thickness of less than 400Å and an SiO_2 dielectric which was about 400Å. The over-all device thickness (4 layers) was less than 1000Å. This device illustrates the use of very thin layers and was almost completely photoinsensitive. The photosensitivity of the devices was highly dependent on the thickness of the semiconductor and on its annealing cycle. The thinner films which were annealed for a longer time in vacuum were found to be the more photoinsensitive. Preliminary tests have shown that the thinner, more photoinsensitive films were also more resistant to radiation effects. It is found, however, that better reproducibility of device parameters was achieved if a semiconductor thickness of about 8000Å was used.

Figure 9 shows a CdSe device which can be made to operate with high transconductance in either the depletion or the enhancement mode. This device measured 5 mm in width with 12μ spacing. It appeared that in forming CdS, CdSe, or CdTe devices by the methods used that it was easier to form CdSe units exhibiting the ability to operate either in the enhancement or depletion mode. Depletion mode CdSe units were fabricated by forming thicker CdSe films, reducing the CdSe anneal, and use of an oxide dielectric. In addition, use of thinner dielectrics (higher field intensity) reduced any bias requirement.

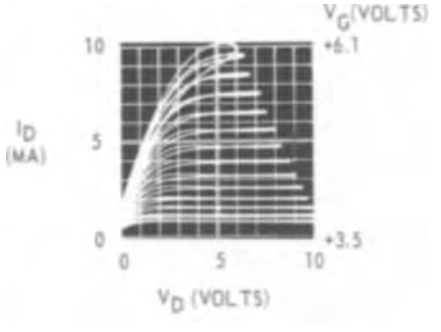

Fig. 7. Characteristic Id *vs.* Vd curves for a CdSe unit operating in the enhancement mode; $r_D \sim$ 100K; $g_m \sim$ 5000 μmhos; $\mu >$ 500; $C_{in} \sim$ 50 pf; $R_{in} >$ 500 mohms; GB $\sim$ 16 MC.

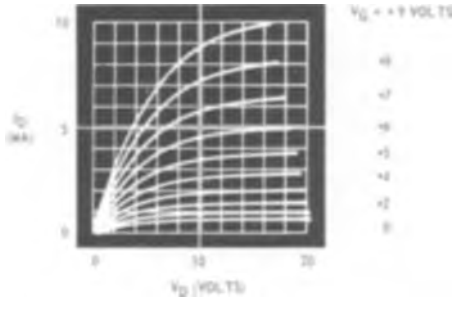

Fig. 8. Id *vs.* Vd characteristics of a very thin TFT structure; $r_D \sim$ 100 kohms; $g_m \sim$ 1000 μmhos; $\mu \sim$ 100; $C_{in} \sim$ 100 pf; $R_{in} >$ 100 mohms; GB $\sim$ 2 MC.

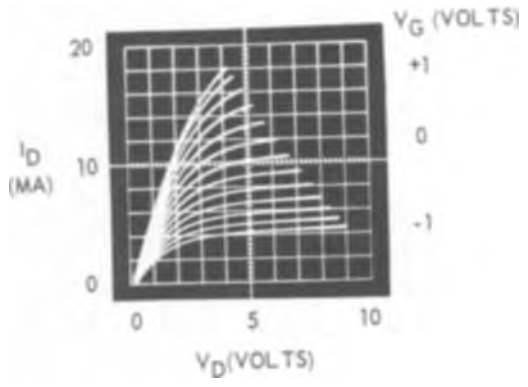

Fig. 9. Characteristics of a CdSe unit of relatively large transconductance operating in both enhancement and depletion mode; $r_D \sim$ 7 kohms; $g_m \sim$ 8000 μmhos; $\mu \sim$ 56; $C_{in} \sim$ 150 pf; $R_{in} >$ 100 mohms; GB $\sim$ 8.5 MC.

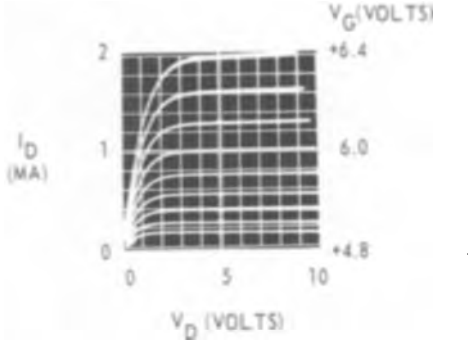

Fig. 10. Device characteristics of a CdSe unit utilizing a B_2O_3-SiO dielectric; $r_D =$ 250 Kohms; $g_m =$ 2000 μmhos; $\mu =$ 500; $C_{in} \sim$ 50 pf; $R_{in} >$ 100 megohms; GB $\sim$ 6.4 MC.

Special devices exhibiting large transconductance values in excess of 20,000 micromhos were formed utilizing a CdSe semiconductor layer. This was accomplished by either paralleling smaller devices, use of thinner dielectrics, decrease in source-drain spacing, harder driving of the device (increase drain and gate voltages), or combination of the above. As can be appreciated this improvement in transconductance was accompanied by various other degradations in device characteristics not gone into here.

The ability to fabricate devices of similar characteristics during the same deposition run was found to be primarily a problem of uneven heating of the substrates. It appeared that a slight variation of temperatures existing in areas of deposition caused variations in the semiconductor film properties.

Reproducibility from deposition to deposition was found dependent on the similarity of deposition parameters as expected. The most difficult parameter to control was that of the added influence of the graphite crucible in the semiconductor deposition. It appeared that oxidation or contamination of the graphite by one of the elements of the compound would affect the semiconductor films in differing amounts in succeeding

Figure 10 illustrates the more typical parameters obtained from 1.5 mm wide devices (12μ source-drain spacing). Although this device did not exhibit ultra-high transconductance, etc., it exhibited reasonably good characteristics coupled with good stability and life. This device utilizes a CdSe layer of approximately 5000Å thickness with a SiO and B_2O_3 dielectric of a total thickness of approximately 1000Å (approximately 500Å each).

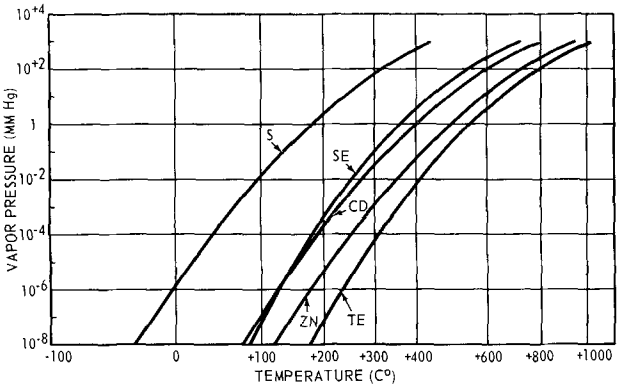

Fig. 11. Vapor pressure curves of elements of some II-VI compounds (after R. Honig).

evaporations. This was true regardless of whether the source charge (CdSe) was replaced with new material for each evaporation or if the same charge was used in succeeding depositions. Up to ten evaporations were made from each crucible before appreciable contamination (less sensitive CdSe layers). Good sensitivity of CdSe layers was obtained from the same charge for up to six depositions.

CdSe vs. CdS and CdTe Devices

By the techniques used CdSe semiconductor depositions appeared to result in a lesser contamination of the vacuum system interior. Devices utilizing the CdSe semiconductor layer were also more easily formed and reproduced. This later experience is attributed, in part to the relative closeness of the vapor pressure curves of Cd and Se as reported by Honig (17). Figure 11 shows these curves. The exact percentage of dissociation that occurs in a compound, in the vapor phase, is not known. Several investigators of CdSe (18, 19) have reported complete dissociation of the compound in the vapor phase. Investigators of CdS (20) have reported a dissociation of the compound which is dependent on the source temperature. Because of the dissociation that appears to occur, the more compatible vapor pressures of Cd and Se indicate a more congruent evaporation of the compound is possible. Experiments of Somarjai (21) have indicated this. It may therefore be possible to deposit CdSe films of closer stoichiometric ratio. X-ray diffraction studies have indicated that the deposited CdSe films were polycrystalline. It is not known whether a reformation of the compound had occurred on the substrate.

The bulk electron mobility of CdSe is reported greater than CdS (22). It might also be noted that photocells of CdSe are reported to have faster response times than CdS cells (23). Because of the lower resistivity of CdSe films, CdSe devices could conceivably be made smaller and thinner than CdS devices of comparable electrical characteristics. Preliminary tests at this facility have indicated the parameters of a thin device to be more resistant to radiation. The bulk electron mobility of CdTe is reported to be greater than that of either CdSe or CdS (22, 24). High mobility CdTe films however appear to be more difficult to form. Formation of CdTe films for use in TFT's seems at the present to be limited by reproducibilty of sensitive layers.

Life tests indicated CdSe devices to be more durable than CdS devices (gold gates). CdS units usually malfunctioned within a few hours under continuous operation. One such failure first appears as a rupturing of field plate. This is followed by an eventual decay in transconductance value, and finally a gate-drain breakdown occurs. Another type of failure noted was an increase with time of the source-drain resistance due probably to the growth of a barrier at one or both of these contacts. This phenomenon caused crowding of the Id *vs.* Vd characteristics or reduction of transconductance (9). Increase in positive bias was found to recover temporarily some of the loss, but often degradation continued. Although some CdSe devices exhibited the same type of failure as CdS devices it appears as though a method of formation is possible whereby a considerable life expectancy is realized. This is probably true for CdS devices as well. The CdSe devices which exhibited no substantial change in parameters after 24 hr of continuous operation appear able to have long life expectancies at room temperatures. Circuits employing CdSe devices have been operating continuously for over 5000 hr with only a 3000Å protective SiO layer over the device. Life tests were conducted in a room without humidity control. Other devices have been stored under nonoperating conditions for like periods of time and have not shown significant changes in characteristics. It was observed that CdSe devices with aluminum gate electrodes were more stable and had longer lifetimes than devices with gold gate electrodes.

The CdSe devices were used successfully in experimental thin-film integrated circuits, *i.e.*, multivibrators, oscillators, differential and operational amplifiers, logic elements, etc. These devices were also studied and used as current limiters (25).

Summary

Thin films, field effect triodes were formed with standard vacuum equipment. This was done to study the feasibility of using methods compatible with the formation of thin-film passive elements, for integrated thin-film circuits. In addition, materials other than those previously used by other investigators were studied. Devices were formed with CdTe, CdS, and CdSe as the semiconductor layer. CdTe devices were difficult to form principally because of the high resistivity encountered. Cadmium doping resulted in some operational devices, but reproducibility was inferior to CdS and CdSe devices.

Operational CdSe devices were the easiest to fabricate. These devices exhibited characteristics comparable to CdS devices. In general, the ability to use thinner and higher mobility CdSe layers indicate that higher frequencies of operation and improvements in microminiaturization and radiation resistance can be realized. The fabrication of operational CdSe devices was found to be compatible with standard vacuum techniques. This was attributed in part to the relative closeness of the vapor pressures of Cd and Se.

In the formation of devices it was found that under certain conditions a significant drop in semiconductor resistivity occurred when an oxide dielectric layer was deposited over it. Sensitive devices of long life generally exhibited this behavior during their processing.

The ability to reproduce devices of similar parameters was found to be strongly dependent on the use of identical deposition parameters.

Acknowledgments

The authors wish to express their appreciation to Dr. Charles Feldman and Wilbur T. Layton for their encouragement and suggestions, and to Kenneth Hoggarth, who formed some of the devices studied.

Manuscript received Dec. 13, 1963. This paper was presented at the Pittsburgh Meeting, April 15-18, 1963. This research was supported in part by the Bureau of Naval Weapons, United States Navy Department.

Any discussion of this paper will appear in a Discussion Section to be published in the December 1965 JOURNAL.

REFERENCES

1. J. Lilienfield, U. S. Pat. 1,745,175, Jan. 28, 1930; U. S. Pat. 1,900,018, Mar. 7, 1933.
2. O. Heil, U. K. Pat. 439,457, Mar. 4, 1935.
3. W. Shockley and G. L. Pearson, *Phys. Rev.*, **74**, 232 (1948).
4. J. Bardeen, *J. Phys. Rev.*, **71**, 717 (1947).

5. C. Feldman, Conference on Navy Laboratory Microelectronics Program, Applied Phys. Lab, The John Hopkins University, June 12-13, 1961, sponsored by the Office of Naval Research (OTS No. PB-181314) p. 53.
6. H. Wilson, W. Layton, W. Gutierrez, and C. Feldman, Paper presented at the Pittsburgh Meeting of the Society, April 14-18, 1963.
7. P. K. Weimer, "An Evaporated Thin Film Triode," IRE-AIEE Device Res. Conf., Stanford University, Stanford, Calif., June 26-28, 1961.
8. P. K. Weimer, *Proc. IRE*, **50**, 1462 (1962).
9. P. K. Weimer, F. V. Shallcross, and H. Borkan, *RCA Rev.*, **24**, 661 (1963).
10. F. V. Shallcross, *ibid.*, **24**, 676 (1963).
11. R. H. Bube, *J. Chem. Phys.*, **27**, 496 (1957).
12. G. A. Somorjai, *J. Phys. Chem. Solids*, **24**, 175 (1963).
13. F. V. Shallcross, *Proc. IRE*, **51**, 851 (1963).
14. H. Borkan and P. K. Weimer, *RCA Rev.*, **24**, 153 (1963).
15. First Quarterly Report on Field Effect & Space-Charge-Limited Thin Film Triodes, DA36-039-AMC-02374, US Army Electronics Materiel Agency, RCA (1963).
16. L. Holland, "Vacuum Deposition of Thin Films," p. 74, John Wiley & Sons, New York (1960).
17. R. Honig, *RCA Rev.*, **23**, 567 (1962).
18. D. DeNobel, Ph.D. Thesis, University of Leiden (1958).
19. P. Goldfinger, Tech. Rept., Univ. Libre Bruxelles, Jan. 1959.
20. E. Senkovits and R. Zuleeg, Paper presented at the Pittsburgh Meeting of the Society, April 18, 1963.
21. G. A. Somorjai, *J. Phys. Chem.*, **65**, 1059 (1961).
22. R. H. Bube, "Photoconductivity of Solids," p. 269, John Wiley & Sons, Inc., New York (1960).
23. H. Pollack, "Photoelectric Control," p. 100, John F. Rider Publishers Inc., New York (1962).
24. B. Segall *et al.*, *Phys. Rev.*, **129**, 2471 (1963).
25. W. A. Gutierrez and H. L. Wilson, *IEEE Trans. on Electron Devices*, **ED-11**, 466 (1964).

Electrical Resistivity and Diffusionless Phase Transformations of Zirconia at High Temperatures and Ultrahigh Pressures

E. Dow Whitney

Research and Development Division, The Carborundum Company, Niagara Falls, New York

ABSTRACT

The resistivity of chemically pure monoclinic zirconia has been investigated at pressures to 45,000 bars and temperatures to 1200°C. Measurements were made on thin, prepressed wafers of ZrO_2 situated between the opposed, cemented carbide Bridgman anvils of a uniaxial Griggs and Kennedy simple squeezer. Observation of discontinuous changes in electrical resistance at various temperatures under isobaric conditions have been used to define the phase diagram. The pressure dependence of the temperature of the reversible monoclinic $\rightleftharpoons$ tetragonal phase transition in zirconium dioxide agreed with the slope of the P-T equilibrium curve up to 15 kilobars as calculated from thermodynamics, *i.e.*, $dT/dP = -3.02 \times 10^{-2}$ degrees bar^{-1} (1). Activation energy for electrical conduction followed the Arrhenius equation and was found to be pressure dependent, decreasing from 3.56 ev at atmospheric pressure to an apparently constant value of 0.86 ev from 30 to 45 kilobars.

The existence of two structural modifications of zirconia was first reported by van Arkel (2) in 1924. Several years later Ruff and Ebert (3) definitely established the phenomenon of polymorphism in this material by measuring the lattice constants and densities of both the monoclinic (density = 5.68 g/cm^3), and tetragonal (d = 6.10 g/cm^3) forms. The existence of a modification of zirconia with hexagonal symmetry reported a decade later by Cohn (4) has never been confirmed, however. The reaction

$$\text{monoclinic } ZrO_2 \rightleftarrows \text{tetragonal } ZrO_2$$

at ~1200°C is reversible, and all attempts to stabilize the high-temperature tetragonal modification by rapid quenching have been unsuccessful to date (5, 6). Prior to 1962 it was generally assumed that a cubic modification of chemically pure zirconia could not exist (7-9). Very recent data have now indicated, however, that above 2200°C the reversible formation of a cubic form of ZrO_2 is indeed possible (10, 11).

The monoclinic $\rightleftharpoons$ tetragonal transition in zirconia occurs at a definite temperature and pressure and possesses a latent heat of transformation, involves a change of structural ordering, and therefore is a phase transition "of the first kind." Furthermore, as Wolten has pointed out (11), the ZrO_2 transformation is indeed both diffusionless, i.e., all atoms have the same neighbors in either phase, and is also of the martensitic-type."

In spite of the voluminous literature on zirconia, the influence of hydrostatic pressure, along with high temperatures on the course of the monoclinic-tetragonal transformation has received relatively little attention, although the fusion of ZrO_2 at 65,000 atm in a carbon tube has been reported (12). Vahldiek, Robinson, and Lynch have investigated the influence of pressure and temperature on the phase transformation of zirconia (13). They found that samples of chemically pure monoclinic zirconia after hot pressing at approximately 20,000 atm at temperatures of 1800°C and then rapidly quenched to room temperature, followed by decompression, subsequently exhibited a lower monoclinic-tetragonal phase transformation temperature on reheating. The new phase transition range was found to be 900°-1020°C compared with 1000°-1200°C before compression.

This author recently considered the thermodynamics of the monoclinic-tetragonal transition, and has presented a calculated P-T phase diagram of zirconia (1). The calculated pressure coefficient of the equilibrium transition temperature was found to be

$$dT/dP = -3.02 \times 10^{-2} \text{ deg/bar} \qquad [1]$$

Berezhnoi (14) has also calculated the slope of the monoclinic-tetragonal equilibrium curve from available thermodynamic data and has proposed a P-T diagram for pure ZrO_2. His value of $dT/dP = -3.58 \times 10^{-2}$ deg/bar^{-1} is in fair agreement with this author's, considering the assumptions involved in both calculations.

The purpose of this investigation was to experimentally verify the calculated P-T phase diagram for pure zirconia within the limits of the ultra-high pressure ap-

paratus described below. The monoclinic-tetragonal phase transition was detected by observing the discontinuous change in electrical resistivity associated with the crystallographic transformation (15-17).

Experimental

Monoclinic zirconium dioxide was prepared from recrystallized (from concentrated HCl solutions) low hafnium zirconyl chloride octahydrate ($ZrOCl_2 \cdot SH_2O$), obtained from the Carborundum Metals Division, The Carborundum Company, Akron, New York. The white crystalline solid was partially dehydrated by heating to constant weight in air under an infrared lamp, the temperature of the zirconyl salt being held at about 70°C. The product was a free-flowing white powder which analyzed to be $ZrOCl_2 \cdot 4H_2O$ in agreement with the studies of Komissarova *et al.* (18). The tetrahydrate was ignited in air in platinum dishes in a Harper electric furnace at 1200° for 3 to 4 hr. The resulting product was 100% monoclinic zirconia as determined by x-ray diffraction analysis. Emission spectrographic analysis of the material is given in Table I. Chemical analysis of the product gave: ZrO_2, 99.9%; water soluble chlorides, 0.1%.

The method of applying pressure was based on Bridgman's opposed anvil technique. Bridgman has shown that in such systems the stress developed in the compressed sample may be assumed to be hydrostatic if the thickness of the pressed sample disk is quite small. To a first approximation, then, the pressure on the sample can then be determined simply by the ratio of the load developed by the hydraulic rams and the working area of the tungsten carbide Bridgman anvils. The specific equipment employed in this study, referred to commonly as the "simple squeezer," has been described by Griggs and Kennedy (19) and is principally the Bridgman anvil unit modified to permit heating of the sample by means of an external furnace. Specimens were in the form of thin disks approximately 0.4 mm thick and 6.4 mm in diameter. These were prepared by prepressing monoclinic ZrO_2 to approximately 40,000 bars in the high-pressure apparatus. Working faces of the carbide pistons were faced with very thin disks (0.0004 in. thick x 0.250 in. in diameter) of platinum-10% rhodium foil to prevent possible contamination of the ZrO_2 samples. After pressing, the zirconia samples were found to be hard, lusterless white disks with a measured density of 97-100% of theoretical (x-ray) for monoclinic ZrO_2.

Myers, Dachille, and Roy have recently shown (20) that a "pressure multiplication effect" of as high as 2 to 2.5 times the nominal load pressure can occur when using Bridgman anvils, and that this "multiplication effect" is dependent on the diameter-to-thickness ratio of the sample undergoing compression. From their studies it was established that no pressure intensification occurred when the $d:t$ ratio was approximately 16:1, whereas a gain of over 2.5 times could be realized by reducing this ratio to 7:1, *i.e.*, the use of thicker samples. In the work reported here the $d:t$ ratio of the zirconia compacts was very close to 16:1.

The ZrO_2 disks, after being faced with platinum foil, were placed between the carbide anvils of the press, one anvil of the assembly being insulated from ground.

Table I. Spectrochemical analysis of ZrO_2

Element detected	Concentration in ppm	Element detected	Concentration in ppm
Ca	<10	Hf	not detected
Mg	<20	Co	<20
Ti	<20	Ni	<20
V	<20	Cu	<10
Cr	<20	B	20
Mn	<20	Al	<10
Fe	<100	Si + Pb	<20

The load developed by the hydraulic press was increased until the desired pressure was obtained on the sample. Pressures were calculated directly from press loads determined previously by calibration with a Type CXX SR-4 Baldwin-Lima-Hamilton Corporation precision load cell against a Heise, 0 to 10,000 lb/in.^{2} pressure gauge and areas of the high-pressure faces of the carbide anvils as determined with a precision cathetometer.

Temperature measurement and control were achieved by means of a L&N Speedomax® H recorder coupled with an L&N program control unit. Since the method employed for calibration of sample temperatures exactly followed the procedure given by Griggs and Kennedy, it need not be further described here. Resistance readings were taken at various temperatures with a General Radio Impedance Bridge, Model 650A using 1000 cps a.c. to avoid electrode polarization effects. A Ballatine Laboratories vacuum tube a-c voltmeter proved to be a sensitive external null detector. At the conclusion of a run the ZrO_2 disk was removed from the press, and the diameter and thickness of the compact measured with a micrometer. Resistivity values were calculated from the resistance readings and the final area/thickness ratios. It was not possible, however, to obtain resistivity values at the conclusion of every experiment. In several experiments severe deformation or destructive failure of the pistons occurred. When this happened the zirconia samples usually shattered, and final measurement of the samples was not possible. For this reason resistance data are given in terms of relative values only.

In some preliminary studies the monoclinic zirconia pellets were pressed within a retaining ring of unfired pyrophyllite, which is the usual procedure in conducting experiments with uniaxial-type high-pressure equipment. This, however, led to rather erratic results. The resistivity of pyrophyllite as a function of temperature at ambient and high pressures has been measured by Hall and Bundy (21) and is of the same order of magnitude as that of zirconia. Consequently, the problem of "parallel resistance" was avoided by eliminating the use of pyrophyllite rings in the experiments reported here.

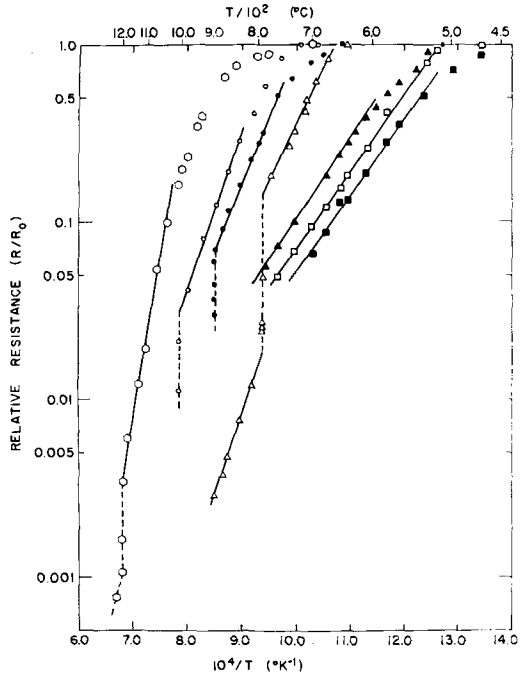

Fig. 1. Temperature dependence of resistance of ZrO_2 at various pressures: ○, 1 bar; ○, 5 kilobars; ●, 10 kilobars; △, 15 kilobars; ▲, 20 kilobars; □, 30 kilobars; ■, 45 kilobars.

Table II. Temperatures of discontinuous changes in resistance at various pressures

Pressure, kilobars	Temperature, °C	Theoretical $mZrO_2 \rightarrow tZrO_2$ transition temp. calc. from $dT/dP = -3.02 \times 10^{-2}$ deg/bar, °C
0.001	1200	1205
5.0	1000	1054
10.0	900	903
15.0	790	752
20.0	Not observed	601
30.0	Not observed	299
45.0	Not observed	—

Results and Discussion

Plots of relative resistance (R/R_o), *vs.* reciprocal temperature at various applied pressures ranging from atmospheric (1 bar) to 45 kilobars are shown in Fig. 1 where R_o represents the resistance of the samples at room temperature and constant pressure. Temperatures at which discontinuous breaks in the R/R_o *vs.* $1/T$ curves occurred are given in Table II. No discontinuous changes in the resistance of the zirconia samples with increasing temperature were observed at pressures higher than 15 kilobars. In experiments conducted at 20, 30, and 45 kilobars, sample temperatures were slowly increased up to the point of piston failure.

It will be noted in Fig. 1 that at each pressure deviations from the Arrhenius equation occurred at the lower temperatures. This curvature is indicative of two competing conduction mechanisms which in the case of unstabilized ZrO_2 is both ionic and electronic conduction. Both mechanisms will have different activation energies and will be influenced differently by temperature.

Figure 2 is a plot of the pressure dependence of the resistance of ZrO_2 at various temperatures. From this plot the initially rapid decrease of resistance with applied pressure is apparent, as are the discontinuities in the relative resistance curves up to 15 kilobars. Of particular interest is the leveling off of the resistance curves at the higher pressures indicating a rapidly decreasing pressure dependence of the resistance at pressures above ~30 kilobars.

The calculated phase diagram of zirconia showing regions of thermodynamic stability of the monoclinic-tetragonal crystallographic forms on the P-T plane is given in Fig. 3. Good agreement was found at 5, 10, and 15 kilobars between the points of observed discontinuities in resistance and the predicted monoclinic-tetragonal ZrO_2 equilibrium curve. It is reasonable to

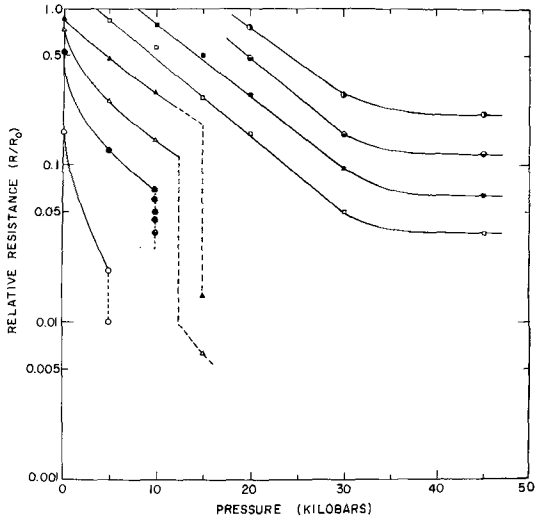

Fig. 2. Pressure dependence of resistance of ZrO_2 at various temperatures: in °C, half dark circle, right side, 600; half dark circle, bottom, 650; ■, 700; □, 750; ▲, 800; △, 850; •, 900; ○, 1000.

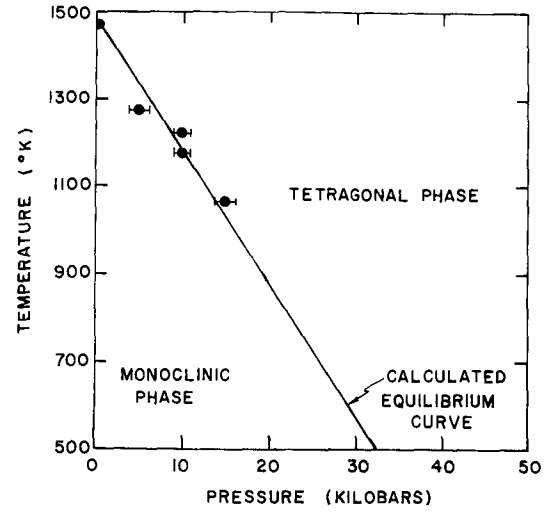

Fig. 3. Phase diagram for zirconia showing theoretical m ZrO_2-t ZrO_2 phase boundary calculated from $dt/dP = -3.02 \times 10^{-2}$ °/bar, and experimental transition temperatures.

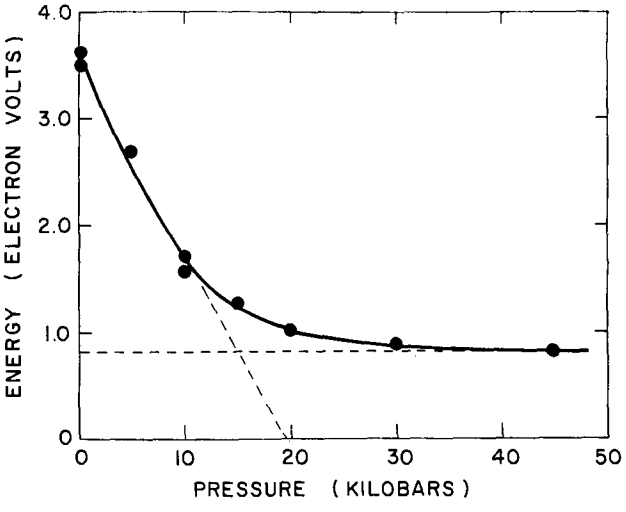

Fig. 4. Activation energy for electrical conduction in ZrO_2 vs. pressure.

assume, therefore, that such sudden changes in resistance are the result of crystallographic transformation of the zirconia lattice, and that in the pressure range 1-15,000 bars the theoretical monoclinic $ZrO_2 \rightleftarrows$ tetragonal ZrO_2 equilibrium curve has been verified. Indeed, the atmospheric pressure transition temperature of 1205° reported here is in excellent agreement with the sharp transition point temperature of 1200° reported by Kofstad and Ruzicka (16).

However, as has been mentioned previously, between 20 and 45 kilobars no breaks in the relative resistance curves were observed. This may be due in part to failure of the system to achieve equilibrium at these lower temperatures.

In Fig. 4 is shown the variation of activation energy for electrical conduction in zirconia as a function of applied pressure. Activation energies were calculated from linear portions of the curves shown in Fig. 1 via the Arrhenius equation which may be expressed as a function of pressure, *viz.*,

$$r(P) = r_o(P) \exp [E(P)/kT] \qquad [2]$$

Numerical values for the interesting pre-exponential term, $r_o(P)$, the electrical resistance of zirconia at infinite temperature as a function of pressure, could not be determined in many instances since, as mentioned previously, resistivity values were not always available.

At atmospheric pressure the activation energy in the monoclinic phase was found to be 3.56 ev in good agreement with a value of 3.8 ev for high-purity ZrO_2 found by Johansen and Cleary (22). With increasing pressure the activation energy decreased more or less exponentially reaching an apparently constant value of approximately 0.86 ev at 45,000 bars. Experiments were run in duplicate, and duplicate activation energies were found to agree within ±10%. The over-all activation energy *vs.* pressure curve in the monoclinic region may be decomposed into two linear relationships

$$\text{monoclinic } ZrO_2 \; dE/dP = -1.94 \times 10^{-4} \text{ ev/bar-mole} = -4.47 \text{ cal/bar-mole} \quad [3]$$

and

$$dE/dP = 0 \quad [4]$$

It is of interest to note that the former linear change of activation energy with applied pressure intersects the 0 activation energy level at approximately 20 kilobars. It would appear, therefore, that the particular conduction mechanism responsible for this slope is no longer operative at this pressure. Above 20 kilobars the second mechanism (apparently independent of pressure) is predominant.

Tien and Subbarao (23) determined the activation energy for conduction in ZrO_2-CaO cubic solid solutions over the concentration range 13-20 mole % CaO. Extrapolation of their data to zero CaO concentration yields an activation energy of 0.84 ev for conduction in chemically pure "cubic" ZrO_2. The decrease in E with pressure observed in this work may be due to a change in structure with the smaller molar volume cubic form of ZrO_2 being formed at high pressures.

Summary

1. By means of electrical resistance measurements the calculated P-T equilibrium curve for the reversible transformation monoclinic $ZrO_2 \rightleftharpoons$ tetragonal ZrO_2 has been experimentally verified up to 15 kilobars.

2. Activation energy for conduction in ZrO_2, obtained as a function of applied pressure, was found to decrease from 3.56 ev at atmospheric pressure to an apparently constant value of 0.86 ev in the range 30-45 kilobars.

Acknowledgments

The author acknowledges with thanks the assistance of several people during the course of this work. They are Professor Watt W. Webb for his valuable contributions and critical review of the manuscript, and H. Dean Batha for his keen interest and encouragement from the inception of this study to its conclusion. The very careful and thorough work of Dale D. Russell in conducting the electrical measurements and maintaining the high-pressure equipment in excellent working order is also gratefully acknowledged.

Manuscript received May 27, 1963. This paper was presented at the New York Meeting, Sept. 30-Oct. 3, 1963.

Any discussion of this paper will appear in a Discussion Section to be published in the December 1965 JOURNAL.

REFERENCES

1. E. D. Whitney, *J. Am. Ceram. Soc.*, **45**, 612 (1962).
2. A. E. van Arkel, *Physica*, **4**, 286 (1924).
3. O. Ruff and F. Ebert, *Z. anorg. u. allgem. Chem.*, **180**, 19 (1929).
4. W. M. Cohn, *This Journal*, **68**, 65 (1935).
5. R. F. Domagala and D. J. McPherson, *J. Metals*, **6**; Trans. AIME, **200**, 238 (1954).
6. C. T. Lynch, F. W. Vahldiek, and L. B. Robinson, *J. Am. Ceram. Soc.*, **44**, 147 (1961).
7. B. C. Weber and M. A. Schwartz, *Ber. deut. keram. Ges.*, **34**, 391 (1957).
8. F. A. Mumpton and R. Roy, *J. Am. Ceram. Soc.*, **43**, 234 (1960).
9. P. Duwez and F. Odell, *ibid.*, **33**, 274 (1950).
10. D. K. Smith and C. F. Cline, *ibid.*, **45**, 249 (1962).
11. G. M. Wolten, *ibid.*, **46**, 418 (1963).
12. R. H. Wentorf, Jr., *J. Phys. Chem.*, **63**, 1934 (1959).
13. F. W. Vahldiek, L. B. Robinson, and C. T. Lynch, *J. Chem. and Eng. Data*, **7**, 479 (1962).
14. A. S. Berezhnoi, *Dopovidi Akad. Nauk Ukr. SSR*, **1**, 65 (1962).
15. F. Trombe, M. Foëx,, and J. Wyart, *Compt. rend.*, **233**, 172 (1951).
16. P. Kofstad and D. J. Ruzicka, *This Journal*, **110**, 181 (1963).
17. R. W. Vest, "The Electrical Behavior of Refractory Oxides," ARL-63-116 Aerospace Research Laboratories, Wright-Patterson Air Force Base, Ohio, Contract AF 33(616)-7748, July, 1963.
18. L. N. Komissarova, V. E. Plyushchev, and I. N. Kremenskaya, *Russ. J. Inorg. Chem.*, **5**, 281 (1960).
19. D. T. Griggs and G. C. Kennedy, *Amer. J. Sci.*, **254**, 722 (1956).
20. M. B. Myers, F. Dachille, and Rustum Roy, *Rev. Sci. Instr.*, **34**, 401 (1963).
21. H. M. Strong, "High Temperature Methods at High Pressure," in "Modern Very High Pressure Techniques," p. 105, R. H. Wentorf, Jr. (Editor), Butterworth Inc., Washington, D. C. (1962).
22. H. A. Johansen and J. G. Cleary, *This Journal*, **111**, 100 (1964).
23. T. Y. Tien and E. C. Subbarao, *J. Chem. Phys.*, **39**, 1041 (1963).

Electrochemical Pseudo-Inductances

F. Gutmann[1]

The Electrochemistry Laboratory, The University of Pennsylvania, Philadelphia, Pennsylvania

ABSTRACT

The meaning of inductance is reviewed. Evidence is adduced that electrochemical systems may exhibit lagging currents, and it is proposed to explain this in terms of a pseudo-inductance, which is defined as the capability of a space to store electrical energy reversibly and kinetically. The kinetic process is ascribed to the visco-elastic behavior exhibited particularly at higher frequencies and/or in highly viscous systems as, *e.g.*, dry-cells. The relaxation time of ions may be calculated from the phase angle by means of visco-elastic theory. It is suggested that the pseudo-inductance may cancel out all or part of the capacitive time delay inherent in the transmission of nerve impulses across synaptic junctions and thus may play a significant part in such processes.

Impedance measurements are a well-known method for the study of electrochemical systems. A measurement at any one frequency yields, in effect, values for the components of an equivalent circuit consisting of a reactance, X, and a resistance, R, either in series or in parallel, depending on the method employed. Since the double layer represents a very large capacitance (1),

[1] On Leave from the Department of Physical Chemistry, The University of New South Wales, Sydney, Australia.

in the order of 16 $\mu F/cm^2$, it is assumed that X is purely capacitive.

Extension of the measurements over a range of frequencies shows that this simple model, while perfectly valid for any one frequency, fails to account for the observed change in the values of R and X with frequency, thus requiring the design of more complicated equivalent circuits.

These, however, are invariably thought to be made up of only linear resistive and capacitive elements, though it is well known that no such equivalent circuit can be devised which accurately represents the observed frequency dependence of X as well as of R (2). This matter will be further discussed in a later paper.

In measurements at higher frequencies, and/or on active electrochemical systems it is often found (3-7) that these behave as negative capacitances or exhibit a negative component of the imaginary part of the complex conductance. Both statements are tantamount to saying that the system behaves as an inductance, and indeed in some cases (6) equivalent circuits including an inductance have been devised.

In this paper we wish to adduce evidence for the general presence of inductive effects in electrochemical processes; we shall interpret these effects in terms of the visco-elastic properties of the system.

The Meaning of Inductance

Before discussing the—to electrochemists—perhaps less familiar concept of inductance, let us consider what is meant by a capacitance C; we can say that this is a property of an element of space dv which is capable of storing, reversibly, electrostatic energy, W

$$W = \int \frac{q^2}{C} dv \qquad [1]$$

where $q = f(v)$ is the local (space-) charge density. It should be emphasized that, of course, the seat of the stored energy is the dielectric and that thus the concept of capacitance has nothing to do with the presence, or absence, of electrodes. Even a measurement involving no electrodes whatever permits the evaluation of the capacitance of a region of space, which can be defined from Eq. [1].

Alternatively, we can define a capacitance in terms of the phase difference between an applied voltage and the current produced. Consider a sealed box with two terminals. The current through the box may be either in phase with the applied voltage, or be leading or lagging the same. If the current leads or lags the voltage by exactly 90°, one deals with pure capacitance or pure inductance, respectively. In all other cases, where the phase angle is less than ±90° the circuit element must contain a mechanism for the dissipation as well as for the storage of energy.

It should be emphasized that the concept of inductance has nothing to do with "coils of wire" or, more accurately, with the interaction of a conductor with an electromagnetic field. Exactly as two plates with an interposed dielectric are a sufficient, but not a necessary condition for exhibiting a capacitance, so is such an interaction a sufficient, but not a necessary condition for exhibiting an inductance.

We thus define inductance as the property of a region of space capable of reversibly storing electric energy kinetically.

We cannot conclude from a measurement at any one frequency only that the sealed box contains only one type of reactance, since all or part of a capacitive reactance may be cancelled by all or part of an inductive reactance which may also be present. Should both reactances cancel exactly, we speak of resonance.

This now permits us to illustrate our argument thus: consider a piezoelectric crystal, say quartz or thiourea. This crystal will exhibit a very sharp resonance if it is excited at its mechanical resonance frequency; such excitation need not necessarily involve even the application of electrodes to the crystal. At resonance, the crystal behaves as a pure resistance. Below resonance it behaves as a capacitance and above resonance as an inductance: in brief it behaves like a resonant circuit consisting of a capacitance and an inductance in series. There is kinetic storage of energy in the elastic deformation of the crystal, but there are no coils of wire and the interaction of the highly insulating crystal, considered as a conductor, with the current is quite negligible. In fact, this inductive behavior of piezoelectric crystals above resonance is being seriously considered to be used practically in integrated circuitry.

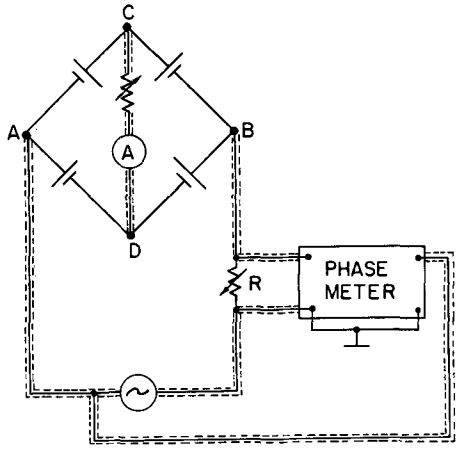

Fig. 1. Circuit for phase relation measurements on batteries

Experimental

We have carried out measurements on 1.5v Leclanchè type dry batteries (commercial Eveready dry cells) which were connected as shown in Fig. 1.

It is seen that there is no d-c voltage across the test terminals, A and B, and there is no a-c voltage between the current terminals, C and D, assuming the four cells to be identical. All leads were screened and tied to a single earthing point at the ground terminal of an Ad-Yu phase meter. This measures the time interval between the instants of intersection with the time axis, of the voltage wave and of the current wave. The read-out is directly in terms of the phase angle and is independent of waveform as long as the wave does not intersect the time axis more than twice every cycle. This property is important in view of the highly non-sinusoidal shape of the current wave.

The oscillator was a beat frequency signal generator with a range of up to 100 kc/sec and a rather constant output voltage of about 22v. The resistance, R, was adjusted to give a voltage drop of approximately 0.5v at the highest frequency employed in each run: thus about 98% of the total applied alternating voltage appeared across the system. The alternating voltage across each 1.5v dry cell thus at all times was considerably higher than the d-c voltage, being about 10v rms or more.

At low values of direct current, in the order of 1 ma, the phase angle remained substantially constant at 45°, as to be expected in a diffusion controlled electrochemical system (8). As the direct current drain was increased, the phase angle commenced to drop with increasing frequency, the onset of this effect shifting to lower frequency values as the current drain was raised. At a direct current of about 1.5 amp, the phase angle reached zero at a frequency of about 80 kc/sec and thence became inductive, increasing monotonically with increasing frequency.

These high values of current are rather excessive for the dry cells employed; it was difficult to maintain the current for any length of time, and the batteries were invariably discharged and rather unserviceable at the

Table I. Data from Powell and Rasmussen (3)

Frequency f = 300 kc/sec; temperature T = 24°C

Substance	Concentration, moles/liter	σ' in mhos/meter	σ'' in mhos/meter
CsCl	5	41.5	−0.4
$BaBr_2$	2.5	21.7	−0.2
CdI_2	1.25	2.92	−0.15
CdI_2	0.625	1.92	−0.09
$Pb(NO_3)_2$	1.25	7.72	−0.63
$Pb(NO_3)_2$	0.625	5.05	−0.19
Bi film	5.05×10^{-6} in. thick	4.33×10^{4}	-0.14×10^{4}
Sb film	3.3×10^{-6} in. thick	2.37×10^{5}	$+0.41 \times 10^{5}$

end of a run. The phase meter reading also tended to fluctuate by about 10% at high values of direct current, although the qualitative features of the experiment remained quite clear, *viz.*, that the impedance of the cells went through a true resonance at about 80 kc/sec and thence became inductive.

This rather surprising result prompted a search of literature in order to secure further corroborating evidence.

Further Experimental Evidence from Literature

Perhaps the most accurate quantitative data have been obtained by Powell and Rasmussen (3) at the National Bureau of Standards, Boulder, Colorado. They report that "measurements of strong electrolytic solutions have shown that the conductivity has a strong out-of-phase component which can be either leading or lagging, depending on the nature of the solution, and thus contributes either a positive or negative component to the permittivity." It should be pointed out that these authors employ a transformer bridge in which the unknown forms a single turn loop; the electrolyte is contained in a ring shaped container and no electrodes are required. There are no metal surfaces at all in contact with the electrolyte. The data in Table I were obtained at 300 kc/sec and 24°C. The table evaluates the electrolyte impedance in terms of a complex conductivity σ^* defined as

$$\sigma^* = \sigma' + j\sigma'' = jK_0\omega K^* \quad [2]$$

where

$$K^* = k' + jk'' \quad [3]$$

K^* being the complex permittivity, or dielectric constant, of the medium. A negative value of σ'' indicates a lagging current, *viz.*, the unknown behaves as an inductance.

It is seen that the impedance of the electrolyte becomes more inductive as the concentration rises and as the weight of the cation increases. It should be noted that also evaporated bismuth films exhibit a lagging current, while those of antimony, *e.g.*, do not.

A study of lead-acid storage battery impedances by Willihnganz and Rohner (6) showed that "the battery also possesses a measurable inductance" and "when large batteries are studied, the effect of inductance assumes a major importance." The battery was represented by an equivalent circuit as shown in Fig. 2, and the results are summarized in Fig. 3. It is seen that, for a 180 amp-hr battery, the two reactances become equal at about 80 c/sec; above that resonance, as would be expected in a series resonant circuit, the inductive reactance exceeds the capacitive reactance, resulting in a lagging current.

The resonance frequency is found to be independent of battery size, thus indicating that both reactances follow closely similar geometric relations.

Papers read at the recent 124th Meeting of the Electrochemical Society by Brodd (7) and by Lurie *et al.* (5) also report that the phase angle of primary and secondary cells becomes inductive at higher frequencies. They relate the changes in phase angle to the amount of charge stored in the device; Lurie *et al.* (5) report that the impedance of a Ni-Cd battery shows a

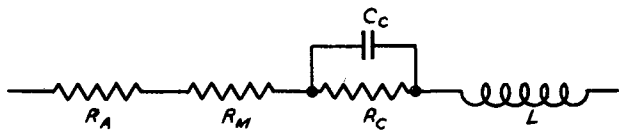

Fig. 2. Equivalent circuit of a lead-acid accumulator [after Willihnganz and Rohner, ref. (6)]. R_A here represents the resistance of the electrolyte, and R_M that of the metal plates of the battery. C_C and L represent the effective capacitance and inductance, respectively. The capacitance C_C shunted by a leakage resistance R_C.

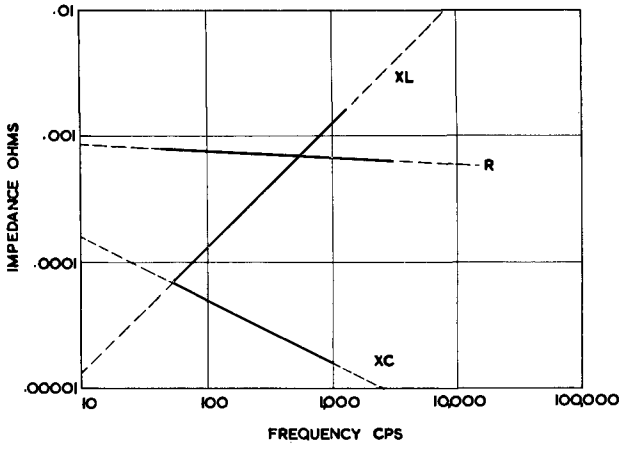

Fig. 3. Impedance components; 180 amp-hr lead-acid accumulator [after Willihnganz and Rohner, ref. (6)].

shallow minimum at about 1000 cps followed by a steep rise; this is equivalent to the presence of an inductance in the order of microhenries.

It is important to note that exactly the same effect occurs in nerve membranes (9): the parallel impedance of squid nerve membranes is strongly inductive at low frequencies, going through a resonance at about 100 cps and thence becomes capacitive. This behavior is illustrated in Fig. 4. It should be pointed out that these are parallel admittance components, referring to a parallel tuned circuit. Transposing these to a series equivalent circuit shows that well below resonance the equivalent series reactance approaches a limiting value of $-\omega Lp$, being capacitive, while above resonance the opposite holds, *i.e.*, a parallel L-C circuit behaves as a capacitance. Thus the behavior depicted in Fig. 4 for a

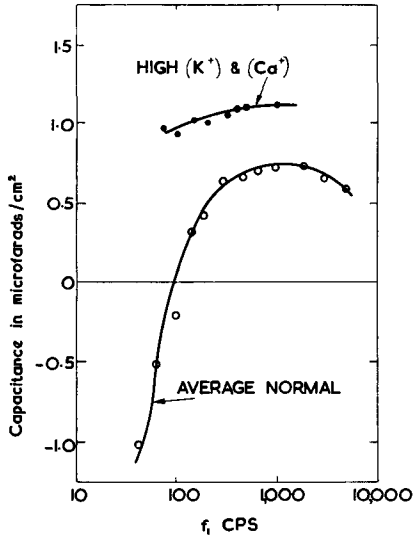

Fig. 4. Admittance components in squid nerve membranes [after Schmitt, ref. (9)]. The capacitance here refers to an equivalent circuit consisting of conductance and capacitance in parallel.

parallel L-C circuit is the mirror image of that valid for the series circuit thus far considered, with the sign of the ordinate reversed.

Electrochemical or Pseudo-Inductances

Exactly as a capacitance may arise from a variety of processes, so can an inductance be due to any one of many different mechanisms, the common factor being a reversible storage of electric kinetic energy. We shall apply the term pseudo-inductance to inductances arising in the course of electrochemical reactions in parallelism to the pseudocapacitance due to such reactions.

In the case of an active circuit element, a pseudo-inductance may arise from any energy yielding process containing a time delay. Carson (10) has pointed out that such a process would occur in a battery which is subjected to an alternating voltage of an amplitude substantially in excess of its direct terminal voltage: the battery is then alternately charged and discharged from the a-c source, and the lagging current is a consequence of the inherent time delay between a charge q being put into the battery and q being released again.

Another mechanism has been pointed out by Conway (11): In some adsorption experiments under quasi-equilibrium conditions the surface coverage θ may vary with the applied potential so that $d\theta/dV$ is negative, *i.e.*, an increase in potential shifts the equilibrium toward a desorption process. Since the charge q is proportional to θ this means that the dynamic capacitance dq/dV will also become negative and thus equivalent to a pseudo-inductance. The process can be readily interpreted along the lines suggested before. An increase in the applied potential causes a drop in adsorption because part of the energy supplied is being stored kinetically in desorbing some of the adsorbate, the process being reversible since reducing the potential causes re-adsorption, *i.e.*, release of the stored energy. This is in exact parallelism to kinetic electrode processes where a dynamic equilibrium between two equal and opposing exchange currents is attained at a certain potential.

The general differential equation for a diffusion-controlled electrochemical process is

$$\frac{\partial a}{\partial t} = D\frac{\partial^2 a}{\partial x^2} \qquad [4]$$

where a is the activity and D the diffusion coefficient of the reactant ion species. D is related to the viscosity η of the medium by the Einstein-Townsend relation

$$D = \frac{zkT}{6\pi\eta r_o} \qquad [5]$$

where z is the valency and r_o the mean radius of the ions, considered to be spherical.

The standard treatment (8) of electrode kinetics applies the following boundary conditions

$$a = a_{\text{Bulk}} \text{ for } x \to \infty$$
$$\frac{I \sin \omega t}{zF} = -D\left[\frac{\partial a}{\partial t}\right]_{x=0} \qquad [6]$$

The second condition implies that the current $i = I \sin \omega t$ at the electrode-solution interface is in phase with the diffusion wave. This treatment then yields the well known $\omega^{-1/2}$ dependence for the impedance of the system, which appears as an R/C combination at any one value of frequency.

However, this relation of the diffusion wave to the current need not necessarily hold and is inherently unlikely to hold at higher values of current, at higher frequencies, and in a visco-elastic medium.

The theory of visco-elasticity (12) treats the viscosity as a complex quantity, η^*. However, if one introduces

$$\eta^* = \eta_1 + j\eta_2 \qquad [7]$$

into Eq. [4] for the diffusion coefficient D, then the resulting differential equation

$$\frac{\partial a}{\partial t} = D^*\frac{\partial^2 a}{\partial x^2} \qquad [8]$$

no longer permits a solution in a closed form; also the boundary condition Eq. [6] no longer strictly applies because the viscosity now becomes a function of frequency. A computer solution, though, can, of course, be derived.

In Powell and Rasmussen's (3) careful conductivity measurements, no electrodes were in contact with the solution, and there is no question of any polarization effects. The system thus is truly diffusion or viscosity controlled, and the only forces limiting the motion of the ions are viscous forces.

It is thus reasonable to assume that the electrical impedance components are proportional to the components of the mechanical impedance as determined from conventional visco-elastic theory (12). Thus, the electric phase angle must equal the visco-elastic phase angle

$$\tan \phi = \sigma''/\sigma' = \eta_2/\eta_1 \qquad [9]$$

assuming a parallel circuit. The conductivity components, σ'' and σ', were defined in Eq. [1].

Powell and Rasmussen's data yield a value of 0.084 radians = 4°52′, for the lagging phase angle ϕ in a 1.25M lead nitrate solution. Transposing this into an equivalent series circuit, as in Fig. 2, yields for the pseudo-inductance L a value of 0.57 microhenries.

Representing the visco-elastic system by a Maxwell Model, it follows that

$$\tan \phi = \omega\tau \qquad [10]$$

where ω is the angular frequency, *i.e.*, $2\pi 3 \times 10^5$ cps and τ stands for the ionic relaxation time. For the present case, $\tau = 4.5 \times 10^{-8}$ seconds, which is certainly a reasonable value.

In general, the mechanical impedance Z_m is defined as

$$Z_m = \text{Force/Velocity} = b\eta^* \qquad [11]$$

where η^* is the complex viscosity and b a constant.

Let us consider a lamina vibrating in the x-direction in a liquid of density ρ and viscosity η. Let l denote the distance from the lamina at which the velocity has reached zero, *i.e.*, where the liquid may be considered stationary. Since viscosity necessarily involves the transfer of momentum in a direction perpendicular to the direction of motion, we can then say, following the treatment given by Correlli and Porreca (13), that a damped transverse viscosity wave spreads into the liquid in the y-direction, reaching zero amplitude for $y = l$, and having wave front surfaces parallel to the x—z plane of the lamina. The oscillation of the lamina then has been shown (11) to be determined by a mechanical impedance Z_m given by

$$Z_m = \eta\beta\frac{\sinh 2\beta l + \sin 2\beta l}{\cosh 2\beta l - \cos 2\beta l} + j\eta\beta\frac{\sinh 2\beta l - \sin 2\beta l}{\cosh 2\beta l - \cos 2\beta l}$$
$$j \equiv \sqrt{-1};\ \beta \equiv \left[\frac{\omega\rho}{2\eta}\right]^{1/2} \qquad [12]$$

If the viscosity η exceeds about 6 poises and the frequency remains below about 1 Mc/sec, then a series development yields

$$Z_m \cong \frac{\eta}{l} + j\omega\rho l/3 \qquad [13]$$

Thus, it is seen that the pseudo-inductance will be proportional to the frequency, the density of the ionized medium, and to the quantity l. The latter can be identified with the thickness of the diffusion layer, S, known from kinetic theory (14) to have a value in the order of 0.05 cm.

While the evaluation of a proportionality factor converting the mechanical into an electrical impedance, in terms of material constants, will be discussed in a later communication, it can be readily seen that Eq. [13] is in at least qualitative agreement with the experimental results: the pseudo-inductance increases with frequency and with the current passing.

For systems of low viscosity and measurements at higher frequencies (above 25 kc/sec for $\eta \cong 0.01$ poises) $\sinh \beta l \cong \cosh \beta l$ and the mechanical impedance can be approximated by

$$Z \cong \eta\beta + j\eta\beta \qquad [14]$$

so that the pseudo-inductance follows from $L = \dfrac{\eta\beta}{\omega}$ as

$$L = K\left[\frac{\eta\rho}{2\omega}\right]^{1/2} \qquad [15]$$

where K is a constant of proportionality depending on the physical dimensions of the system.

Since actually the reactance $X_L = \omega L$ is the measured quantity, it is again seen that the pseudo-inductive reactance increases with frequency and with the viscosity and density of the ionized medium. It should be pointed out that Eq. [15] also follows from conventional visco-elastic theory as a limiting case for a pure liquid; it is seen that then the phase angle will be 45° lagging at all frequencies. This refers to an ideal electrodeless and purely viscosity-controlled system: the counterpart to the ideal diffusion-controlled electrode reaction, which exhibits a phase angle of 45° leading current.

Matters are far more complicated in active systems which include physical electrodes, since the double layer capacitance as well as the pseudocapacitances arising at these interfaces will have to be compensated by the pseudo-inductance until, a resonance, and at frequencies above that, a lagging current can be observed.

Pseudo-Inductance and Synaptic Transmission

It has been pointed out by Schmitt (9) that "in a typical biological membrane the reactive element will for the most part include polarization phenomena, the physical capacitance of the membrane AND SOME OF THE ACTIVE PROCESSES (own capitals)." Now, the sharp leading edge of the action-potential spike represents a high-frequency component. If the signal transmission across the synaptic junction is indeed associated with the transport of acetylcholine across the junction which then triggers a signal, then it should be expected that the time delay due to the pseudo-inductance should be of importance. Its magnitude should affect the speed of the transmission process and *vice versa*. Any process, and any substance introduced into the snyaptic region, which interferes with the complex viscosity of that region thus should also affect the synaptic transmission by causing a time delay and altering the phase relation of the signal. The very fact that an impulse can be triggered by a signal transmitted across the synapsis in such a short time indicates that perhaps some sort of a physical resonance mechanism might be at work in which the capacitive time delay inherent in the junction is balanced by a pseudo-inductance caused by the out-of-phase component of the complex viscosity: energy is stored in a visco-elastic stress and suddenly released on arrival of the signal in order to make up for the capacitive time delay. In other words, we propose, in the synapsis, a visco-elastic energy storage mechanism governed by a storage modulus, which is in phase with the stress.

Acknowledgments

The writer wishes to thank Professor J. O'M Bockris and the Electrochemistry Laboratory of the University of Pennsylvania for their hospitality. This work forms part of a Research Program on the Electrical Properties of Psychotropic Substances carried out under Research Grant No. MH-06361 awarded by the National Institute of Mental Health, Bethesda, Maryland, which support is hereby gratefully acknowledged.

Manuscript received Jan. 15, 1964; revised manuscript received July 1, 1964.

Any discussion of this paper will appear in a Discussion Section to be published in the December 1965 JOURNAL.

REFERENCES

1. D. C. Grahame, *Chem. Rev.*, **41**, 441 (1947).
2. D. C. Grahame, *This Journal*, **99**, 378C (1952); H. Gerischer, *Z. Phys. Chem.*, **201**, 66 (1952).
3. R. C. Powell and A. L. Rasmussen, *IRE Trans. Inst.*, **I-9**, 179 (1960).
4. A. Bewick, M. Fleischmann, and M. Liler, *Electrochim. Acta*, **1**, 95 (1959).
5. M. Lurie, R. C. Shair, and H. N. Seiger, Paper presented at the New York Meeting of the Society, 1963.
6. E. Willihnganz and P. Rohner, *This Journal*, **106**, 259 (1959).
7. R. J. Brodd, Paper presented at the New York Meeting of the Society, 1963.
8. J. O'M. Bockris, Chapter 4 of "Modern Aspects of Electrochemistry," p. 194, Butterworths, London (1954).
9. O. H. Schmitt, in "Electrochemistry in Biology and Medicine," T. Shedlovsky, Editor, p. 91, John Wiley & Sons, New York (1955).
10. W. Carson, Private communication.
11. B. E. Conway, Private communication.
12. W. Phillipoff, "Viscositaet der Kolloide," Steinkopff, Leipzig (1942); B. Gross, "Mathematical Structure of the Theories of Viscoelasticity" Hermann, Paris (1953); M. Kornfeld, "Elastizitaet der Fluessigkeiten," Berlin (1952); J. D. Ferry, "Viscoelastic Properties of Polymers," J. Wiley & Sons, Inc., New York (1961); J. T. Bergen, "Viscoelasticity," Academic Press, New York (1960); W. Philipoff, Private communication.
13. A Carrelli and F. Porreca, *Nuovo Cimento*, **19**, 197 (1961).
14. S. Glasstone, "An Introduction to Electrochemistry," p. 451, P. van Nostrand, New York (1942). (6th Printing 1954).

The Effect of Composition and Structure on the Electrochemical Reactivity of Nickel

G. A. Di Bari and J. V. Petrocelli[1]

Paul D. Merica Research Laboratory, The International Nickel Company, Inc., Sterling Forest, Suffern, New York

ABSTRACT

The electrochemical reactivity of nickel is defined in terms of the parameters of the anodic polarization curve as determined potentiostatically. The effect of structure and the effect of the additives carbon, silicon, sulfur, selenium, tellurium, and phosphorus on the parameters of the polarization curve have been determined. It is concluded that small amounts of these elements affect the reactivity of nickel to a greater extent than large changes in structure. They increase the reactivity of nickel and inhibit passivity significantly.

Passivity is a general phenomenon of metals, accounting for some commercially useful properties of many of the primary metals and their alloys (1). The passive behavior of iron (2), nickel (3), and chromium (4), has been studied by many investigators. Great progress has been made in understanding the electrochemical behavior of iron and detailed information on the thickness, chemical composition, and structure of the passive film is available (5, 6). Similarly detailed information is not yet available for nickel.

In studying the passivity of nickel, Greene (7) indicated the complex polarization characteristics of nickel as compared to other metals. This complex behavior is probably partly responsible for the existing controversy over the significance and interpretation of the Flade potential of nickel. Vetter (3) has suggested that some of the apparent discrepancies in the reported behavior of nickel might be traced to the presence of impurities. Trumpler (8) has studied the effect of impurities on the electrochemical behavior of nickel. Hospadaruk and Petrocelli (9) in a determination of the relative reactivity of nickel electrodeposits, concluded that the reactivity and pitting tendency of nickel increase as the sulfur content increases. Wesley (10) described the effect of sulfur, and his discussion of the reactivity of nickel is especially pertinent to this study. In discussing the electrochemistry of dissolution processes, Petrocelli (11) noted that imperfections or zones of disarray might affect the rates of dissolution of metals. In this study, the electrochemical reactivity of nickel, as affected by structure and impurities, has been investigated.

Procedure and Nomenclature

Electrochemical reactivity.—The electrochemical reactivity of nickel may be defined in terms of the parameters of the anodic polarization curve as determined potentiostatically. A schematic semi-logarithmic curve of the anodic dissolution current as a function of potential is shown in Fig. 1. The indicated behavior is typical of metals that corrode actively on immersion in a given electrolyte and are readily passivated on anodic polarization. We will consider three regions:

1. *The Active Region, AB,* is characterized by the corrosion potential, E_{oc}, the corrosion current, i_{oc}, and the slope of the linear portion of the curve (the Tafel slope).

2. *The Active to Passive Transition Region, BC,* is defined by the parameters of the principal peak, E_{pp}-i_{pp}, which indicate the tendency to passivate. The slope of this descending curve is given significant meaning in Mueller's (12) treatment of the transition region, where the slope is related to the kinetics of film formation.

3. *The Passive Region begins at C* and is characterized by the passive potential, E_p, and the rate of dissolution in the passive region, i_p. The pertinent parameters in this region may be considered a measure of the extent of passivation.

In terms of the operational approach described, the object of this study was to determine how the parameters of the anodic polarization curve for nickel are affected by (i) structural changes, specifically changes in grain size, and (ii) the presence of electronegative elements in nickel.

Specimens.—Three kinds of pure nickel were included in this study: high-purity nickel prepared by Wesley (13), conventional electronickel deposited from a typical refinery-type electrolyte, and commercial wrought nickel (Nickel 200). To study the effects of structure, conventional electronickel was subjected to various degrees of cold-working and heat-treatments to obtain a variety of grain sizes. The nickel specimens containing sulfur, selenium, tellurium, and phosphorus were prepared by electrodeposition from nickel electrolytes containing suitable additives. Specimens containing silicon and carbon were prepared by casting *in vacuo* without the use of deoxidizers.

Test method.—The various nickel electrodes were mounted in Lucite and polished using standard metallographic techniques. Data obtained with silicon-bearing nickel in the presence and absence of Lucite were identical. The effect of Lucite was therefore judged to be negligible. The specimens were then etched in 1:1 nitric-acetic acid and photographed. The speci-

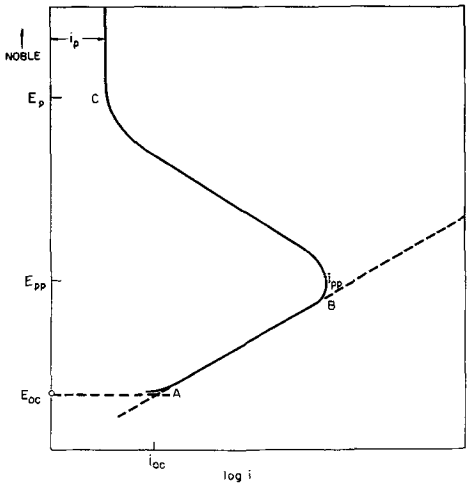

Fig. 1. Schematic anodic polarization curve

[1] Applied Research Office, Ford Motor Company, Dearborn, Michigan.

mens were repolished and etched prior to placing them in the polarization cell. The mounts were marked so that the same area could be examined and photographed after polarization.

Electrical contact to the specimen was made by means of a nickel rod that screwed into the Lucite mount. The specimen (exposed area of 1 cm^2, usually) was placed in a conventional two-compartment cell. Anodic polarization was begun after 30 min, or when the open-circuit potentials became steady.

The electrode potentials and polarization curves were determined by the direct method (14) using a Luggin capillary. The potentials were controlled within $\pm$ 1 mv by means of a Fairport potentiostat. The cell currents were automatically recorded (L&N Speedomax G). When the current reached a steady value, the potential was increased, usually by 10 mv. In the active region, a steady value of the current was obtained after about 2 min. In the transition and passive regions, the currents became steady slowly (greater than 1 hr). The reproducibility of the curves was excellent, except as will be noted later.

The test solution contained one mole per liter of nickel sulfate and the chloride concentration was maintained at less than 3 millimoles per liter. The temperature was controlled at 25° $\pm$ 0.1°C. The *p*H of the electrolyte was 2.0. The solutions were air-saturated. Oxygen may complicate the interpretation of polarization data. But at a *p*H value of 2.0, the effect of oxygen on the anodic polarization characteristics of nickel is negligible. All potentials were measured *vs.* a saturated calomel electrode and are so reported.

Results

High-purity vs. conventional electronickel.—A typical microstructure of conventional electronickel is given in Fig. 2. The as-deposited structure of the high-purity material was similar, although finer grained. The effect of annealing the electrodeposited nickel was to increase grain size and to destroy the dendritic structure characteristic of the as-deposited material. This can be seen in Fig. 3 which shows the structure of the high-purity material after annealing in hydrogen at 2000°F for 2 hr plus annealing *in vacuo* at 2000°F for 1 hr. The annealed high-purity nickel had an ASTM grain size of 4. The conventional electronickel which was heated in argon at 2200°F for 5 hr had an average grain size of 3 and the two materials were considered to have similar structures.

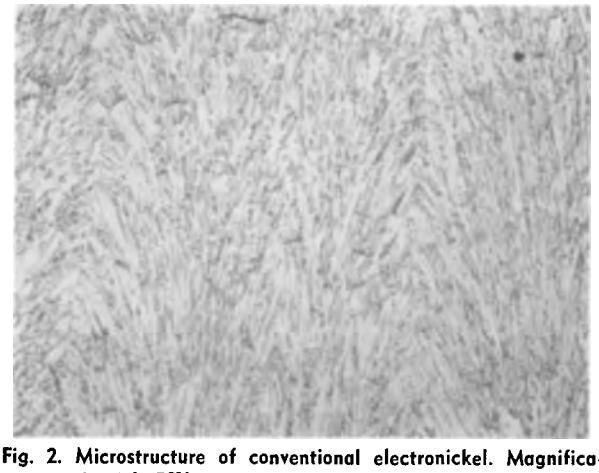

Fig. 2. Microstructure of conventional electronickel. Magnification approximately 50X.

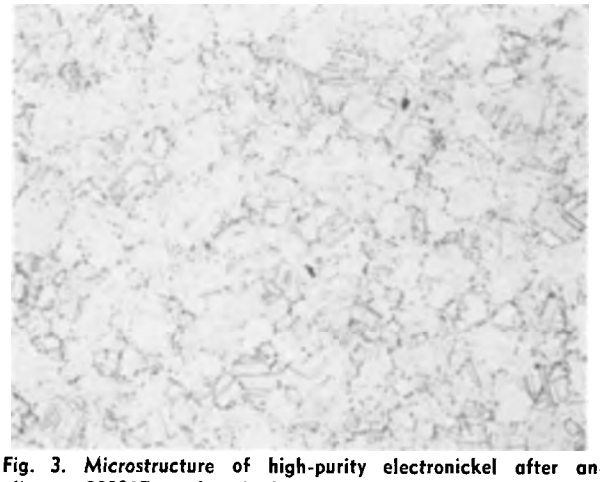

Fig. 3. Microstructure of high-purity electronickel after annealing at 2000°F, as-deposited. Magnification approximately 50X.

The anodic polarization curves of the as-deposited and annealed high-purity nickel, given in Figure 4, differed slightly. The value of the peak current, i_{pp} was somewhat higher for the annealed material, but the transition from the active to passive state was more abrupt. The values of E_{oc}, i_p and the Tafel slope were almost identical, however.

The corresponding data for the conventional electronickel before and after annealing, Fig. 5, indicated that it was more reactive than the high-purity nickel. The open-circuit potentials were shifted in the active direction and the values of i_{pp} and i_p were larger for the conventional material. The value of i_p was increased from 15 to 50 $\mu a/cm^2$ after annealing.

The results strongly indicate that the differences in reactivity were due to the differences in purity. The

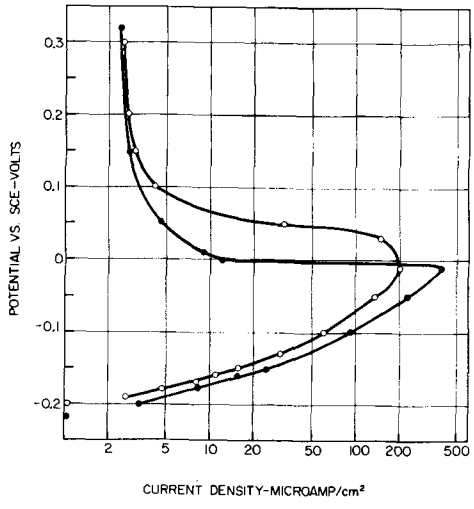

Fig. 4. Anodic polarization curves of high-purity electronickel, as-deposited (○) and annealed (●) in 1.0M $NiSO_4$, *p*H 2.0, 25°C.

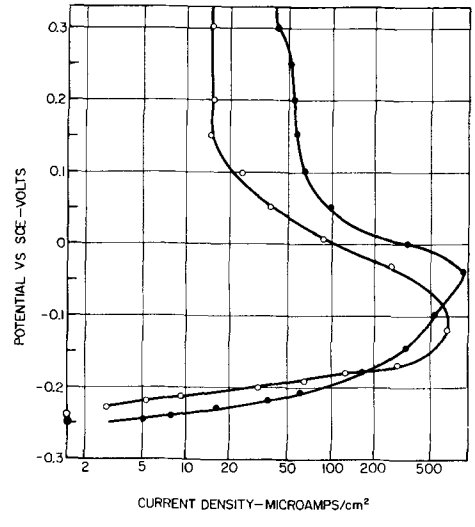

Fig. 5. Anodic polarization curves of conventional electronickel as-deposited (○) and annealed (●) in 1.0M $NiSO_4$, *p*H 2.0, 25°C.

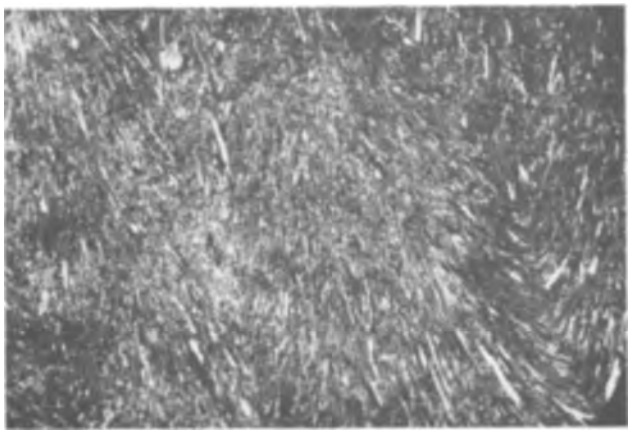

Fig. 6a. Microstructure of conventional electronickel, as-deposited, after polarization, in 1.0M $NiSO_4$, pH 2.0, 25°C. Magnification 50X.

Fig. 6b. Annealed at 2200°F. Magnification 50X

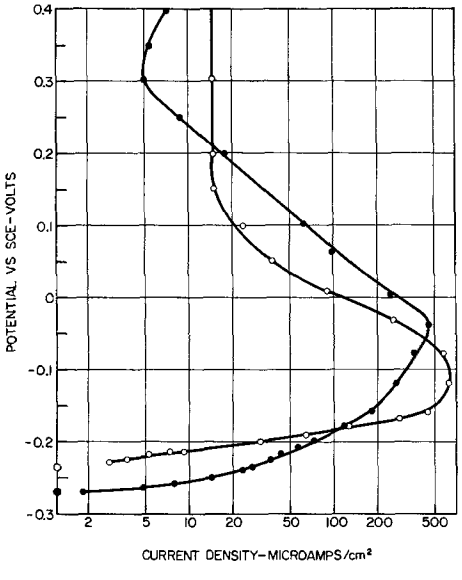

Fig. 7. Anodic polarization curves of conventional electronickel, as-deposited (○), and as-cast (●), in 1.0M $NiSO_4$, pH 2.0, 25°C.

differences in reactivity may have been due to localized activity. For example, after polarization, the as-deposited conventional electronickel showed a general etched surface, while the annealed material evidenced greater pitting-type corrosion (Fig. 6). The surface was covered with numerous tiny pits and several large circular ones. No pitting of the high-purity nickel was observed after polarization.

Effect of grain size.—To study the effects of structure further, the conventional electronickel was melted and cast *in vacuo*. The resultant material had a larger grain size (ASTM 1) than either of the annealed specimens described above.

The polarization data of the as-deposited and as-cast nickel are compared in Fig. 7. The cast material showed a change in the passive region. The value of E_p was shifted from 0.15v to 0.30v and i_p increased with potential.

Further variations in grain size were effected by combining cold-working and annealing treatments. Conventional electronickel was pre-annealed at 1200°F for 30 min and was then cold-worked to a 50% reduction in thickness. A portion of the material was stress-relieved at 350°F for 1 hr. Little change in the microstructure resulted. Some of the cold-worked material was also annealed at 800°F for 1 hr. The latter treatment resulted in very fine equiaxed grains having an ASTM grain size rating of 10.

The principal effect of cold-working and annealing on the polarization characteristics, as given in Fig. 8, was on the active to passive transition region. The

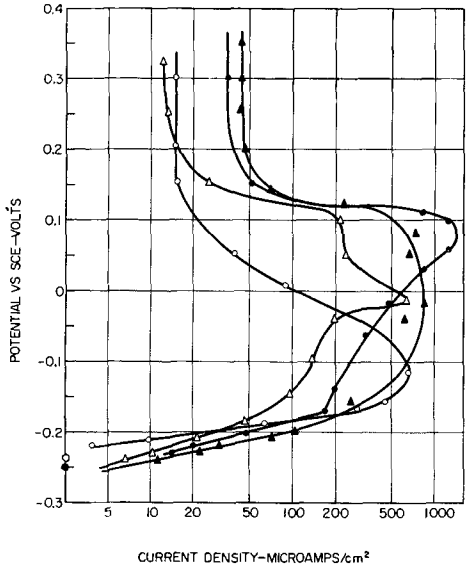

Fig. 8. Anodic polarization curves of conventional electronickel as affected by cold-working and annealing, in 1.0M $NiSO_4$, pH 2.0, 25°C. ○, As-deposited; △, 50% cold work; ▲, 50% cold work and stress relief, 350°F; ●, 50% cold work and annealed, 800°F.

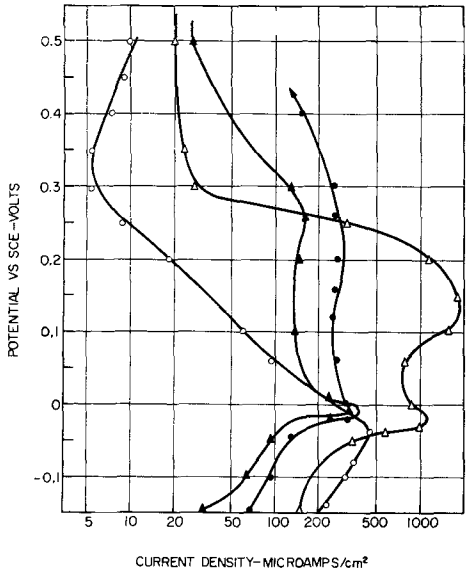

Fig. 9. Effect of silicon on the anodic polarization of cast nickel in 1.0M $NiSO_4$, pH 2.0, 25°C; per cent silicon: ○, 0.004; ▲, 0.3; ●, 0.6; △, 1.1.

dissolution rates (current densities) remained high over a broader potential range for the cold-worked material. The values of i_p were higher for the specimens which were stress-relieved or annealed. The reproducibility of the data presented in Fig. 8 was not determined. There was a tendency for the currents to increase with time in the active to passive transition region.

Commercial wrought nickel (Nickel 200).—The polarization characteristics of Nickel 200 were studied in the cold-rolled and annealed states (2200°F for 5 hr). The polarization curves were very similar to those for the cold-worked and annealed conventional electronickel given in Fig. 8. However, in the cold-rolled state extensive pitting occurred. The extent of pitting was markedly reduced by annealing.

Effect of electronegative elements.—The results with relatively pure nickel indicated that minor changes in the degree of purity affected the over-all reactivity of nickel. It was of interest to determine the effects of controlled amounts of added impurities. The impurities studied were silicon, carbon, sulfur, selenium, tellurium, and phosphorus.

Silicon.—The polarization curves of cast nickel containing various amounts of silicon are compared in Fig. 9. The effect of silicon on the polarization of nickel was to increase the current in the active to passive transition region and in the passive region. The result was that silicon tended to inhibit passivity. The silicon-containing material had an increased tendency for pit formation (Fig. 10).

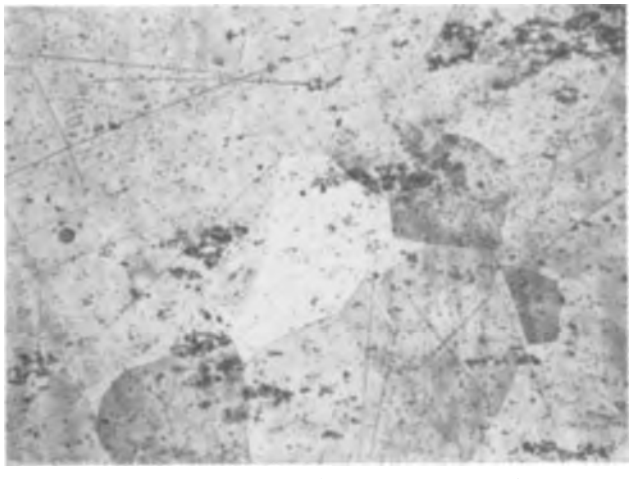

Fig. 10. Microstructure after polarization of cast nickel containing 1.1% Si. Magnification approximately 50X.

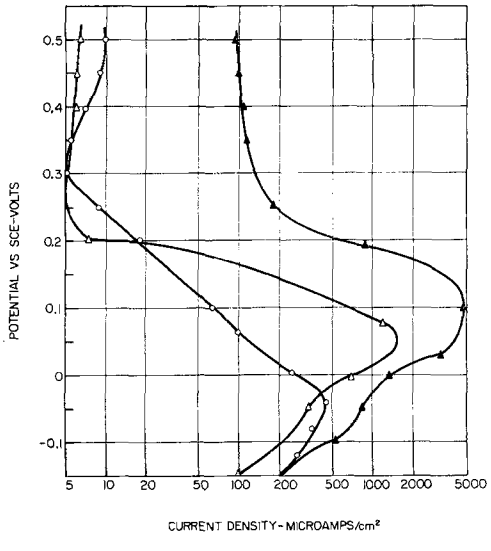

Fig. 11. Effect of carbon on the anodic polarization of cast nickel in 1.0M $NiSO_4$, pH 2.0, 25°C; per cent carbon: ○, 0.02; △, 0.15; ▲, 0.47.

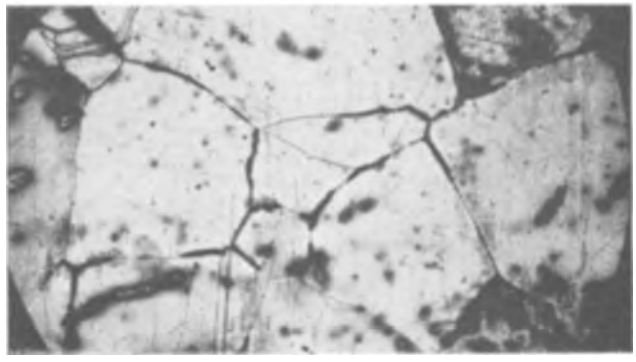

Fig. 12. Microstructure after polarization of cast nickel containing 0.47% carbon. Magnification approximately 50X.

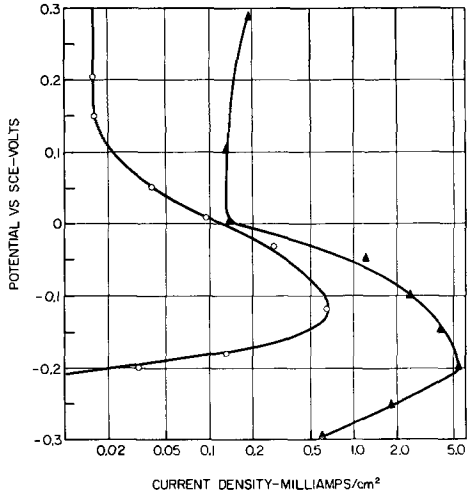

Fig. 13. Effect of phosphorus on the anodic polarization of electrodeposited nickel in 1.0M $NiSO_4$, pH 2.0, 25°C; ○, conventional electronickel; ▲, 0.05% phosphorus.

Carbon.—The effect of carbon on the polarization of cast nickel is shown in Fig. 11. The increased values of the primary passive current, i_{pp}, are indicative of the reduced tendency for carbon-bearing nickel to become passive. At the 0.47% level, carbon caused considerable increase in the passive current, i_p. The effect of carbon at the 0.47% level was to increase markedly the extent of intergranular dissolution (Fig. 12).

Phosphorus, selenium, tellurium, and sulfur.—The elements phosphorus, selenium, tellurium, and sulfur, unlike silicon and carbon, caused significant changes in reactivity in the active region. The open-circuit potentials were shifted in the active direction, as is evident in Fig. 13, 14, and 15.

The reduced tendency for passivation is indicated by the increased values of i_{pp}. Phosphorus increased the value of i_{pp} from about 0.6 to 5.0 ma/cm², selenium from about 0.6 to 5.0 ma/cm², tellurium from 0.6 to 1.0 ma/cm², and sulfur from 0.6 to 50 ma/cm².

The additives affected the rates of dissolution in the passive region as well. Small amounts of selenium and tellurium maintained the current in the passive region very close to the primary passive current, i_{pp}. While phosphorus-bearing nickel appeared to passivate, the value of i_p was higher than for conventional electronickel. Sulfur-bearing electronickel, however, did finally attain as low a value of i_p as did the conventional material, but at higher potentials.

The nickel containing phosphorus, selenium, tellurium, or sulfur had a somewhat increased tendency for pit formation.

Discussion

Effect of structure.—The increased reactivity of the conventional electronickel, as opposed to the high-

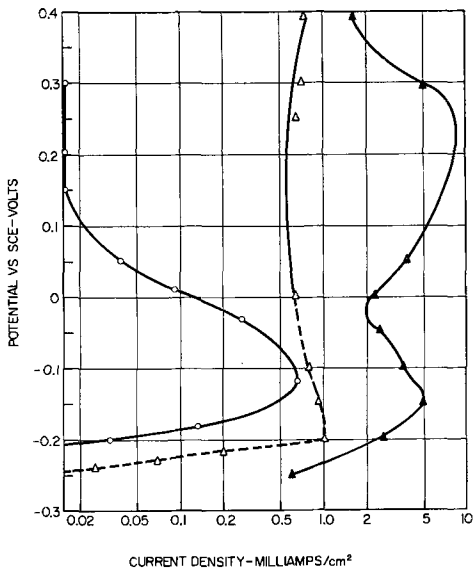

Fig. 14. Effect of selenium and tellurium on the anodic polarization of nickel in 1.0M $NiSO_4$, pH 2.0, 25°C; ○, conventional electronickel; ▲, 0.018% Se; △, 0.016% Te.

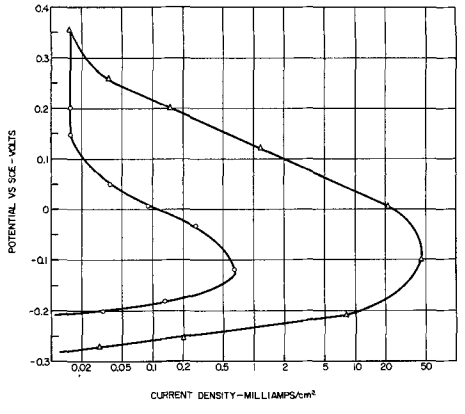

Fig. 15. Effect of sulfur on the anodic polarization of electrodeposited nickel in 1.0M $NiSO_4$, pH 2.0, 25°C; ○, conventional electronickel; △, 0.012% sulfur.

purity nickel, was probably due to the minor differences in purity, since the materials were of comparable microstructure. Although large changes in grain size resulted from annealing electronickel at 2200°F, minor effects on reactivity were observed. High-temperature annealing of the conventional electronickel increased the extent of localized corrosion, perhaps indicating an effect of distribution of impurities. The effect of impurities in increasing localized corrosion was particularly evident in the behavior of the wrought nickel.

The cold-working of electronickel interfered with its tendency to become passive. The effect of cold-work can be appreciated from a mechanism of conversion from active to passive states recently presented by Mueller (12). The model described is based on the relative rates of two opposing reactions, (i) the anodic dissolution of the metal in the active region as determined by the Tafel relation, and (ii) the rate of formation of a passivating film. The familiar S-shaped curve is then the resultant of these two opposing reactions. The data presented in Fig. 4 and 5 are in fair agreement with the proposed model. The effect of cold-work, in terms of Mueller's analysis, is to interfere with the ease of formation of the passivating film. Cold-work would be expected to increase the number of lattice imperfections. This is consistent with the retardation of film formation evident in the polarization data and agrees with the suggestions of Petrocelli (15) that lattice imperfections at or near the metal surface must be influential in determining the properties of the passivating film. Imperfections will influence the initiation and growth of the film.

Effect of Additives

With the exception of silicon, the additives studied have limited solid solubilities in nickel. Less than 0.03% carbon dissolves in nickel at room temperature, the excess segregating at grain boundaries as graphite when slowly cooled from annealing temperatures. The increased intergranular dissolution noted in nickel containing 0.47% carbon is indicative of this limited solubility. Sulfur, selenium, tellurium, and phosphorus dissolve to the extent of less than 0.001%, and the formation of intermetallic compounds is possible.

The effects of the additives on the anodic polarization characteristics, especially on the values of the primary passivating current, i_{pp}, make it possible to determine the relative effectiveness of the additives in increasing the electrochemical reactivity of nickel. Thus, it appears that at equal atomic concentrations the order of effectiveness is

$$S > Se > Te > P > C > Si$$

The effect of silicon is believed to be a specific one. The effect of silicon, at least up to 0.6%, appears to be confined solely to the passive region. The electrochemical dissolution of silicon and its subsequent precipitation as an amorphous silica gel has been observed while studying the anodic behavior of silicon-containing nickel. The reactions of silicon involved may be written

$$Si \rightarrow Si^{n+} + ne^-$$
$$Si^{n+} + n\,(OH^-) \rightarrow Si\,(OH)_n \downarrow$$

Thus the oxidation of silicon and its subsequent reaction would remove hydroxyl ions from the anode film. This specific effect of silicon would be consistent with the known pH dependence of the Flade potential. Further the effect of silicon indicates that the hydroxyl group is directly involved in the passivation of nickel.

The effect of impurities on the reactivity of nickel has been discussed by Wesley (10). He proposed that the observed electrochemical behavior of nickel might be usefully explained in terms of the electronic structure of the nickel atom. The fundamental cause of the passivation tendencies and the high anodic overvoltage for the dissolution of nickel lies in the existence of vacancies in the 3d orbitals. This view is consistent with Piontelli's classification (16) of metals. The "inert" metals, *e.g.*, nickel, cobalt, rhodium, palladium, platinum, chromium, all have incomplete electron subshells. Additional correlation between passivation tendencies and electronic structure may be found by considering the initiation of passivation as involving chemisorption of some species from solution. The usual order of decreasing heat of chemisorption values is

$$Ta > W > Cr > Fe > Ni > Rh > Cu > Au$$

Trapnell (17) has pointed out that this sequence correlates well with that of decreasing d-electron character of the metal bond. It should be pointed out that this sequence also correlates well with the known passivation tendencies of these metals.

As has been emphasized by Wesley, the outer electronic arrangement in the "free" nickel atom would be $(3d)^8\,(4s)^2$. However, in solid nickel the outer electronic arrangement on a statistical basis (18) would be $(3d)^{9.4}\,(4s)^{0.6}$. This then allows for the existence of atoms of nickel with configurations $(3d)^{10}\,(4s)^0$, $(3d)^9\,(4s)^1$ and $(3d)^8\,(4s)^2$. The first two configurations have been shown to predominate. In solution, the nickel-aquo complex has eight electrons in 3d orbitals. The high activation overvoltage of nickel is due to the rearrangement of the outer electronic structure [*e.g.*, $(3d)^{10}\,(4s)^0 \rightarrow (3d)^8\,(4s)^2$] necessary before the nickel atom goes into solution. The role of impurities then

was pictured as catalyzing the electron rearrangement and transfer. On this basis, Wesley concluded that the desirable impurity should be one which can accept an electron.

The ability of an atom to attract or accept electrons is the usual definition of electronegativity. A logical extension of the above ideas is that the effectiveness of an element in increasing reactivity should be related to its electronegativity. The electronegativities of some of the elements have been calculated using a new method (19) and the values are in good agreement with those calculated by Mulliken who defined electronegativity as the average of the sum of the first ionization potential and the electron affinity.

With respect to electronegativity, the relative effectiveness of the additives studied would be

$$S > P > C > Si$$

which is in agreement with the order deduced from the polarization studies. The electronegativities of selenium and tellurium would be expected to fall between those of sulfur and phosphorus.

A detailed mechanism for the activation effects cannot be offered on the basis of the evidence presented. The discussion in terms of electronic structure, however, does not preclude a mechanism involving specific adsorption of anions. Unpublished data indicate that adsorption of an anionic species containing one of the Group VI elements would account for the effects of the additives on the reactivity of nickel.

Conclusions

Small amounts of impurities have considerably greater effect on the reactivity of nickel than large changes in structure. Cold-working of nickel interferes with its tendency to passivate on anodic polarization.

The elements sulfur, selenium, tellurium, and phosphorus increase the reactivity of nickel and inhibit passivity significantly. The relative effectiveness of the additives is related to their electronegativities.

Acknowledgments

The authors acknowledge with appreciation the permission of The International Nickel Company, Inc., to publish the data in this paper. They would also like to dedicate this paper to Dr. W. A. Wesley on the occasion of his retirement from the Research Laboratory.

Manuscript received April 30, 1964; revised manuscript received Sept. 25, 1964.

Any discussion of this paper will appear in a Discussion Section to be published in the December 1965 JOURNAL.

REFERENCES

1. H. Gerischer, *Angew. Chem.*, **70**, 285 (1958).
2. For detailed bibliography see: K. J. Vetter, *Z. Physik. Chem.*, **202**, 1 (1953); *Z. Elektrochem.*, **64**, 244 (1960).
3. K. Arnold and K. J. Vetter, *Z. Elektrochem.*, **64**, 407 (1960); G. Okamato and N. Sato, *J. Japan Inst. Metals*, **23**, 662 (1959); **24**, 130 (1960); L. F. Trueb, G. Trumpler, and N. Ibl, *Helv. Chim. Acta*, **44**, 960 (1961).
4. Y. M. Kolotyrkin, *Zhur. Fiz. Khim.*, **36**, 1232 (1962); *Z. Elektrochem.*, **62**, 50 (1958); **62**, 664 (1958).
5. K. J. Vetter, *Z. Elektrochem.*, **62**, 642 (1958).
6. M. Nagayama and M. Cohen, *This Journal*, **109**, 781 (1962).
7. N. D. Greene, First International Congress on Metallic Corrosion, p. 113, Butterworths, London (1962).
8. G. Trumpler, *Helv. Chem. Acta*, **35**, 1304 (1952); **36**, 1630 (1953).
9. V. Hospadaruk and J. V. Petrocelli, *Plating*, **48**, 479 (1961).
10. W. A. Wesley, Hothersall Memorial Lecture, *Trans. Inst. Metal Finishing*, **33**, 1 (1956).
11. J. V. Petrocelli, "The Surface Chemistry of Metals and Semi-conductors," p. 345, John Wiley & Sons, Inc., New York (1960).
12. W. A. Mueller, *This Journal*, **107**, 157 (1960).
13. W. A. Wesley, *ibid.*, **103**, 296 (1956).
14. G. Kortum and J. O'M. Bockris, "Electrochemistry," Vol. II, p. 398, Elsevier Publishing Co., New York (1951).
15. J. V. Petrocelli, *op. cit.*, p. 348.
16. R. Piontelli, *J. Chim, Phys.*, **45**, 115 (1958); *Z. Elektrochem.*, **55**, 128 (1951).
17. B. M. W. Trapnell, "Chemisorption," Academic Press, Inc. New York (1955). Discussed in A. W. Adamson, "Physical Chemistry of Surfaces," p. 540, Interscience Publishers, Inc., New York (1960).
18. W. Hume-Rothery, "Atomic Theory for Students of Metallurgy," p. 57, The Institute of Metals, London (1948).
19. R. P. Iczkowski and J. L. Margrave, *J. Am. Chem. Soc.*, **83**, 3547 (1961).

Nonaqueous $AgNO_3$ Solutions: Electrical Conductance and Viscosity in CH_3CN and C_6H_5CN

George J. Janz, A. E. Marcinkowsky, and Iqbal Ahmad

Department of Chemistry, Rensselaer Polytechnic Institute, Troy, New York

ABSTRACT

The electrical conductance, viscosity, and density of silver nitrate solutions in anhydrous acetonitrile and benzonitrile in the concentration range up to 6M at 25°C are reported. The Bjerrum and Fuoss- Kraus criteria for ionic aggregates clearly confirm the formation of ion pairs as the concentration increases from the dilute range, with evidence for higher aggregates (triple ions) with further concentration increase. The partial molar volume data support the view that CH_3CN has a more open solvent structure than either C_6H_5CN or H_2O. The solvation interactions, and the equivalent conductances are examined from current semi-empirical viewpoints and discussed relative to aqueous solutions of comparable $AgNO_3$ concentrations.

In nonaqueous media the inorganic solutes are, all too frequently, sparingly soluble. Selection of electrolytes for the investigation of concentrated solution in organic media is more limited than in aqueous media. Silver nitrate is one of the few inorganic solutes having a high solubility in polar organic solvents, such as acetonitrile (12 moles liter^{-1}) and benzonitrile (> than 4 mole liter^{-1}). The present communication reports the results of conductance and viscosity measurements for $AgNO_3$ in these two solvents up to 6M concentrations. In the very dilute range Walden and Birr (1), and Griffith and Lawrence (2) have reported

data for $AgNO_3$ in CH_3CN and C_6H_5CN; results for the concentrated range are almost nonexistent. Concentrated aqueous solutions of $AgNO_3$ have been thoroughly investigated, especially by Campbell and Kartzmark (3). The present results are examined in light of current viewpoints for ionic interactions and solvation in concentrated electrolytes.

Experimental

The procedures for the purification of CH_3CN and C_6H_5CN have already been described (4, 5). The physical constants of the solvents used were as follows: CH_3CN; bp 81.7°C; $d^{25/4}$, 0.7768; κ, 5.9×10^{-8} ohm^{-1} cm^{-1}; η, 0.359 cp; C_6H_5CN; bp 190.7°C; $d^{25/4}$, 1.0088; κ, 7.6×10^{-8}; η, 1.024.

Silver nitrate (analytical grade) was vacuum dried at moderately high temperatures (120°C) and stored over $Mg(ClO_4)_2$ until required.

The conductance measurements were made with a Jones bridge (L&N) with accessories. The cell constants of the cells were 32.177, 1.258, and 0.054 cm^{-1}. Correction for polarization effects at the bright platinum electrodes was by extrapolation to infinite frequency, and all measurements were also corrected for the conductance of the solvent. Values of equivalent conductance of the two series of the solutions are in Table I. The phoreograms[1] are in Fig. 1 and 2.

Densities were determined to an accuracy of ±0.004% (25°±0.02°C) using a 25 ml pycnometer (Fisher Scientific Company, Weld Type). Viscosity measurements (25°±0.02°C) for the $AgNO_3$ solutions (CH_3CN and C_6H_5CN) were with Ostwald viscometers (Cannon Fenske design, Fisher Scientific Company). Calibrations were with conductivity water and benzene (Fisher Reagent Grade) as standards. Exits to room atmosphere were vented through $Mg(ClO_4)_2$ guard tubes. The viscosities were corrected for the kinetic energy term by calculation (6). Tables II and III summarize the results.

Strict precautions were observed to maintain anhydrous conditions during all solvent and solution transfers.

Discussion

An estimate of the solute-solvent interactions can be gained from a knowledge of the molar volumes of the solvated electrolyte. Using the extension of Einstein's theory of viscosity (7) for solutions by Vand (8), it follows that the expression

$$\log \eta_{rel} = \frac{AC}{1 + Q'C} \quad [1]$$

may be used to gain $\overline{V}$, the effective molar volume of the solvated electrolyte. Here η_{rel} is the relative viscosity of the solutions, A and Q' are 2.5 $\overline{V}$/2.303 and $Q\overline{V}$, respectively.[2] Using the data in Tables II and III, values for $\overline{V}$ for $AgNO_3$ in CH_3CN and C_6H_5CN are, respectively, 0.230 and 0.293 liter mole^{-1}. Correcting for the molar volume of $AgNO_3$ (0.039) and dividing by the molar volume of the solvent, the solvation number in the two solvents are found to be 3.7 and 2.5, respectively. These solvation numbers appear valid for increasing concentrations up to 5M for CH_3CN and 4M for C_6H_5CN. Above 5M in CH_3CN, the molecular ratio ($CH_3CN/AgNO_3$) is less than 3 (*e.g.*, at 6.2M, this ratio is 2.6). At still higher concentrations the solvent may well be present almost entirely as "bound" solvent, *i.e.*, the ions are dispersed in a solvent medium present almost entirely as primary solvation sheath solvent. Discussion of the properties of $AgNO_3$ in this concentration range awaits completion of vibrational and magnetic resonance spectroscopic studies in progress in this laboratory.

The question of solvation interactions for $AgNO_3$ has been investigated by Strehlow and Kopp (9) using CH_3CN solutions in Hittorf-type electrolyses. It is recognized (10) that such measurements give an estimate of the total solvation number as distinct from the number bound in the primary solvation sheath. Values of 9 and 4 were thus reported for the Ag^+ ion and NO_3^- ion, respectively, in CH_3CN solutions. This very marked solvation undoubtedly contributes directly to the high solubility of this solute in CH_3CN. Comparable measurements have not been reported for $AgNO_3$ solutions in C_6H_5CN.

From the densities of the solutions given in Table III, the apparent molal volumes of the solution were calculated from the expression (11)

[1] Refer "Nomenclature For Conductance," *J. Chem. Ed.*, **32**, 527 (1955). A phoreogram is defined as the curve in which the equivalent conductance is plotted against the square root of the concentration.

[2] Q is an interaction parameter dealing with mutual interference between the particles and with their Brownian motion; various authors agree only that it does not differ greatly from unity.

Table I. Electrical conductance, 25°C

(A) $AgNO_3$-CH_3CN c, mole liter^{-1}	$\sqrt{c}$	Specific cond, ohm^{-1} cm^{-1} × 10^3	Λ, ohm^{-1} cm^{-1}
0.000	—	—	188.80
0.0099_2	0.0996	1.2330	124.27
0.0421_9	0.2054	3.5716	84.65
0.1576	0.3970	8.5269	54.10
0.2863	0.5351	12.337	43.09
0.7329	0.8561	21.352	29.13
1.807	1.345	33.424	18.50
2.695	1.642	38.215	14.18
3.427	1.851	38.791	11.32
4.313	2.077	37.371	8.665
6.162	2.483	27.710	4.497
(B) $AgNO_3$-C_6H_5CN			
0.00544	0.0731	0.0717	13.184
0.01156	0.1073	0.1215	10.510
0.02504	0.1595	0.1660	6.606
0.04400	0.210	0.240	5.560
0.14370	0.378	0.592	4.120
0.3119	0.559	1.1251	3.607
0.3730	0.611	1.310	3.500
0.3995	0.631	1.360	3.420
0.5176	0.719	1.573	3.079
0.5830	0.764	1.650	2.830
0.9070	0.951	2.700	2.980
1.2731	1.138	2.997	2.354
1.891	1.375	3.960	1.950
3.140	1.722	3.773	1.074_3
3.513	1.874	3.246	0.9240

Table II. Viscosity of $AgNO_3$ solutions, 25°C

(A) $AgNO_3$-CH_3CN c, mole l^{-1}	η, cp	η/η_0
0.00000	0.359	1.000
0.00992	0.365	1.016
0.0412	0.372	1.037
0.1576	0.394	1.098
0.2863	0.423	1.178
0.7329	0.534	1.486
1.807	0.956	2.660
2.695	1.561	4.341
3.427	2.37	6.589
4.313	3.71	10.312
6.162	11.44	31.831
(B) $AgNO_3$-C_6H_5CN		
0.0856	1.3330	1.075
0.1993_2	1.4006	1.130
0.4987	1.8529	1.495
1.1343	2.8810	2.325
2.4720	8.4568	6.810
2.8962	12.452	10.003

Table III. Densities and apparent molar volumes (calculated) of $AgNO_3$ solutions, 25°C

c, mole l^{-1}	CH_3CN ρ, g ml^{-1}	CH_3CN φV, ml mole^{-1}	C_6H_5CN ρ, g ml^{-1}	C_6H_5CN φV, ml mole^{-1}
0.0	0.7748		1.0088	
0.9			1.0722	27.23
1.0	0.9340	16.33	1.1432	27.55
1.5	1.0120	17.05		
2.0	1.0880	18.67	1.2850	27.81
2.5	1.163	19.81		
3.0	1.239	20.37	1.4260	28.16
4.0	1.390	21.35		

$$\Phi_V = \frac{1000}{cd_o}(d_o - d) + \frac{M_2}{d_o} \qquad [2]$$

where Φ_V is apparent molal volume, c is concentration in mole liter^{-1}, d_o and d are the densities of the solvent and the solution, respectively, and M_2 is the molecular weight of the solute. The Φ_V values thus calculated are given in Table III. Inspection shows that Φ_V in CH_3CN varies from 16.3-21.4 ml mole^{-1} in the conc. range 1-4 mole liter^{-1}, while in C_6H_5CN it varies from 27.2 to 28.2 from 0.5-3 mole liter^{-1}; this is to be compared with aqueous solutions where it increases from 31.6-34.4 cc mole^{-1} in the conc. range 1-6 mole liter^{-1}. The theoretical significance of the partial molal volumes relative to the solute and solvent have been reviewed by Stern and Amis (10). Two points may be noted in the present results. The value for Φ_V for comparable concentrations is considerably smaller in CH_3CN than in C_6H_5CN and aqueous solutions, and less than the molar volume for $AgNO_3$ in the solid state (39.0). The concentration dependence for Φ_V is much larger in CH_3CN solutions. It follows from the relatively small values of Φ_V in the dilute concentration range in CH_3CN that this solvent has a more open or "loose" structure than either C_6H_5CN or H_2O.

Comparison of the electrical conductivities for $AgNO_3$ in CH_3CN and C_6H_5CN with the corresponding aqueous concentration range in light of the solvent viscosities is of interest. The high value for Λ_o, 188.8$_0$, in CH_3CN undoubtedly reflects directly the relatively low values for viscosity, 0.36 cp and dielectric constant, 35. (cg. H_2O. η, 0.897 c.p., ϵ, 78.5 Λ_o, 133.3$_6$). Comparison of the Λ_o values for $AgNO_3$ in CH_3CN and C_6H_5CN (ϵ, 25; η, 1.024) shows more clearly the viscosity effect since the latter has a dielectric constant more nearly that of CH_3CN and viscosity closely comparable to H_2O. The values for Λ_o in CH_3CN and C_6H_5CN are, respectively, 188.8$_0$ and 52.4. Similarly the marked decrease of Λ with increasing concentrations (6M: 4.5 and 40 for $AgNO_3$ in CH_3CN and H_2O, respectively) also correlates with the viscosity changes (6M: 10.4 and 1.7 cp for $AgNO_3$ in CH_3CN and H_2O, respectively). Any attempt at a complete description of the properties of electrical conductance for $AgNO_3$ in these nonaqueous media must take due cognizance of these factors. An evaluation of the semi-empirical Wishaw-Stokes conductance equation (12)

$$\Lambda = \left(\Lambda_o - \frac{\beta\sqrt{c}}{1 + Ba\sqrt{c}}\right)\left(1 - \frac{\delta\sqrt{c}F}{1 + Ba\sqrt{c}}\right)\frac{\eta_o}{\eta} \qquad [3]$$

is nevertheless of interest in view of its moderate success for concentrated aqueous solutions. As with aqueous $AgNO_3$ solutions (3), calculations show that the experimental data are approached if moderately small values for a (2.3Å) are used in Eq. [3] for the dilute region; at concentrations greater than about 2 mole l^{-1}, an ion size parameter of 4.35Å must be used to approximate the experimental values. Larger values for a (*e.g.*, 6-8Å) give poorer agreement in this concentration range. Values for a for comparable $AgNO_3$ aqueous concentrations found by Campbell and Kartzmark (3) were, respectively 2.3 and 4.35Å. The calculations serve to emphasize the empirical nature for the values of a in this conductance equation. Inspection of the phoreograms for the CH_3CN, C_6H_5CN, and H_2O solutions, Fig. 1(i), 2(i), and 3 (i), respectively, shows that the former two are quite characteristic of highly associated electrolyte solutions. The criteria for ion-pair and triple-ion aggregates based on the Bjerrum and Fuoss-Kraus ionic interaction schemes (13-15) are illustrated by the log Λ-log c graphs, and the effect of taking cognizance of the viscosity differences, *i.e.*, log $\Lambda\eta/\eta_o$, is also shown, Fig. 1(ii), 2(ii), and 3(ii), for these three solvent systems.

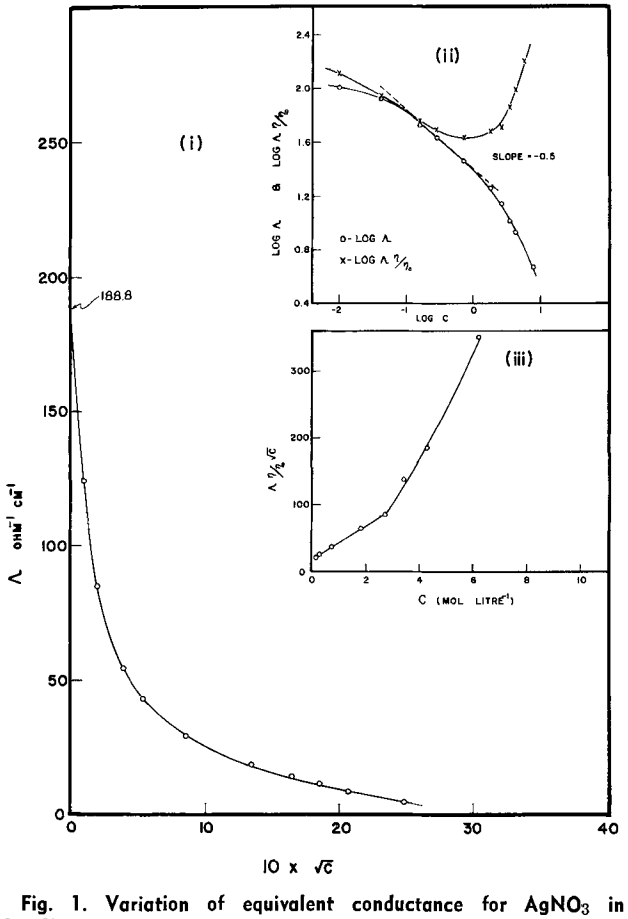

Fig. 1. Variation of equivalent conductance for $AgNO_3$ in CH_3CN, 25°C.

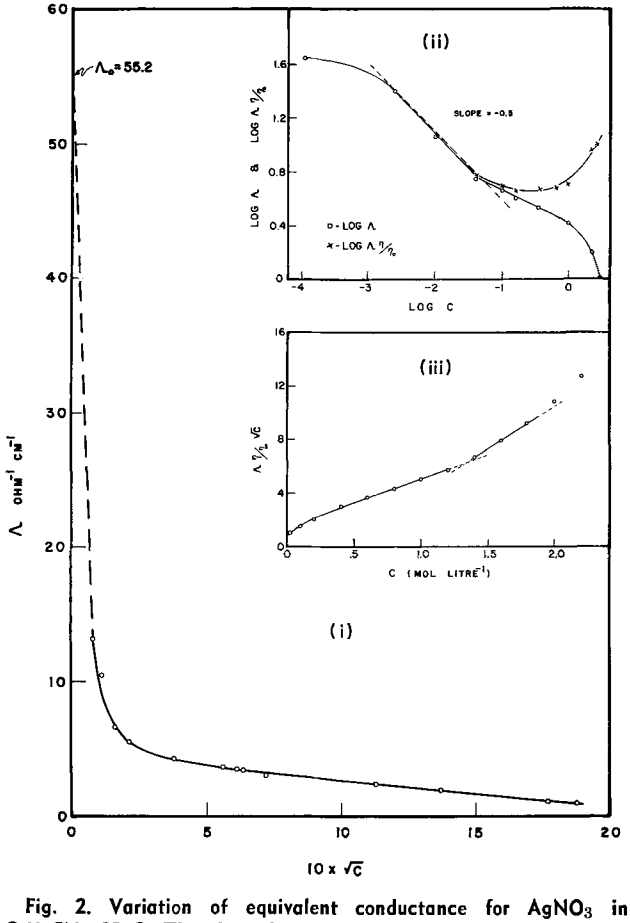

Fig. 2. Variation of equivalent conductance for $AgNO_3$ in C_6H_5CN, 25°C. The dashed extrapolation to infinite dilution is the data of Griffiths, Lawrence, and Pearce (2).

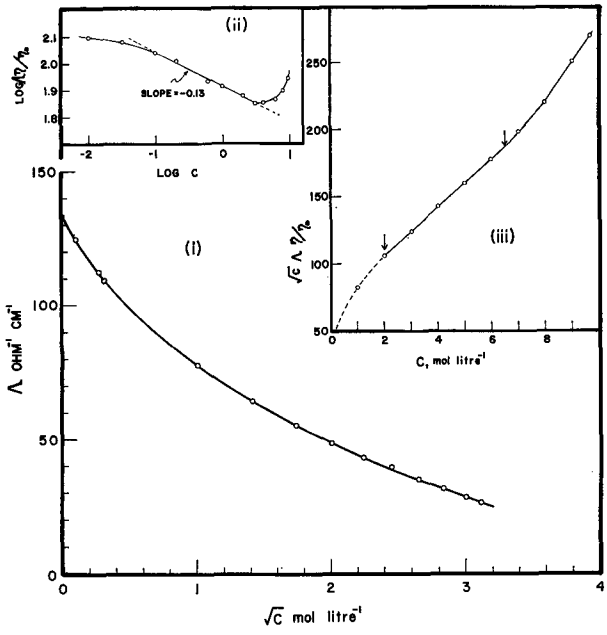

Fig. 3. Variation of equivalent conductance for $AgNO_3$ in water, 25°C, based on the data of Campbell and Kartzmark (3). The arrows (3.1A) indicate the limits proposed for triple-ion formation.

It is seen that in both the nonaqueous systems the value of the slope predicted for ion-pair formation, namely, $-\frac{1}{2}$, holds for a short range as the concentration is increased from the very dilute range. With increasing concentrations the log $(\Lambda\eta/\eta_0)$, curves show the minimum characteristic of triple-ion aggregate formation (8, 9). For the corresponding aqueous solutions, Fig. 3(ii), the log Λ and log $(\Lambda\eta/\eta_0)$ graphs are quite similar, but the value for the slope of the linear region prior to the minimum is markedly less than $-\frac{1}{2}$.

The minima in the log $(\Lambda\eta/\eta_0)$ curves, Fig. 1-3(ii), shift to higher concentrations as the dielectric constant of the solvent increases; this is in accord with the prediction for ionic interactions based on the solvent dielectric properties.

A possible additional empirical criterion for ion aggregate formation in electrolytes is the $(\Lambda\eta/\eta_0)\sqrt{c}$-c graphical analysis illustrated as (iii) in Fig. 1-3, respectively. The linear regions correlate well with the regions for ionic association (c.f. Fig. 1-3, ii), pairwise and higher aggregates; the inflexion point corresponds approximately with the transition from the region of predominant ion-pair aggregates to triple-ion aggregates in these solutions.

Acknowledgments

The authors thank Mrs. M. P. Klotzkin for measurements of the densities and viscosities of $AgNO_3$ in benzonitrile. Financial assistance of U.S. Atomic Energy Commission, Division of Research, Washington, D.C., is gratefully acknowledged.

Manuscript received May 13, 1964; revised manuscript received July 22, 1964.

Any discussion of this paper will appear in a Discussion Section to be published in the December 1965 JOURNAL

REFERENCES

1. P. Walden and E. J. Birr, *Z. Physik. Chem.*, **144A**, 269 (1929).
2. V. S. Griffiths, K. S. Lawrence and M. L. Pearce, *J. Chem. Soc.*, **1958**, 3998.
3. A. N. Campbell and E. M. Kartzmark, *Can. J. Chem.*, **33**, 887 (1955).
4. G. J. Janz and S. S. Danyluk, *J. Am. Chem. Soc.*, **81**, 3846 (1959).
5. G. J. Janz, I. Ahmad and H. V. Venkatasetty, *J. Phys. Chem.*, in press.
6. G. Barr, "A Monograph of Viscometry," Humphry Milford, New York (1931).
7. A. Einstein, *Ann. Phys.*, **19**, 389 (1906).
8. V. Vand, *Phys. Chem.*, **52**, 277 (1948).
9. H. Strehlow and H. Kopp, *Z. Elektrochem.*, **62**, 373 (1957).
10. K. H. Stern and E. S. Amis, *Chem. Rev.*, **59**, 1 (1959).
11. H. J. Harned and B. B. Owen, "The Physical Chemistry of Electrolytic Solution," Reinhold Publishing, Inc., New York (1958).
12. B. F. Wishaw and R. H. Stokes, *J. Am. Chem. Soc.*, **76**, 2065 (1954).
13. D. A. MacInnes, "The Principles of Electrochemistry," p. 373, Dover Publication, Inc., New York (1961).
14. N. Bjerrum, *Det. Kegl. Danske visden*, **9**, 12 (1926).
15. R. M. Fuoss and C. A. Kraus, *J. Am. Chem. Soc.*, **57**, 1 (1935).

Technical Notes

Intergranular Corrosion Penetration in an Age-Hardenable Aluminum Alloy

H. Nichols and W. Rostoker

Metals and Ceramics Division, IIT Research Institute, Chicago, Illinois

It is common knowledge that the commercial aluminum alloy 2024 (nominally 4.5% Cu, 1.5% Mg, 0.6% Mn) is susceptible to stress corrosion cracking in saline solutions. Even in the absence of stress, the loss of tensile strength from protracted immersion in these solutions is appreciable (1). This latter effect results from a form of intergranular attack which is generally termed intergranular corrosion. As may be seen in Fig. 1, whereas the stress corrosion cracks follow a fairly sharply directed intergranular path, the intergranular corrosion zone moves in from the surface as a plane front behind which the individual grains have been separated from their neighbors. It is to be noted also that the depth of the zone of intergranular separations is often not much less deep than the maximum penetration of the stress corrosion cracks.

This paper describes the unusual temperature dependence of the penetration of this intergranular penetration zone in the absence of externally applied stress. Small coupons were cut from commercial sheet of 0.125 in. thickness. The edges were carefully machined and the coupons were re-heat-treated after machining to size so that the metallurgical condition at the edges was restored to that of the bulk of the material and residual macrostresses from the manufacturing history were eliminated. The oxide film from heat-treatment was dissolved off by a brief immersion in dilute caustic solution. The washed and dried specimens were totally immersed for 70 min in a solution containing 53 g/l of NaCl, 50 g/l of Na_2CrO_4 and HCl in amount sufficient to adjust the *p*H to about 2. Upon removal, washing, and drying, the specimens were sectioned and the depth of penetration of the intergranular attack measured with a metallurgical microscope. Because of the friability of the surface, the depth of penetration was calculated from the center section between the two approaching zones of intergranular penetration. The temperature of the solution was varied between 0° and 80°C. Results are summarized in Fig. 2 (a, b, c) for three states of aging.

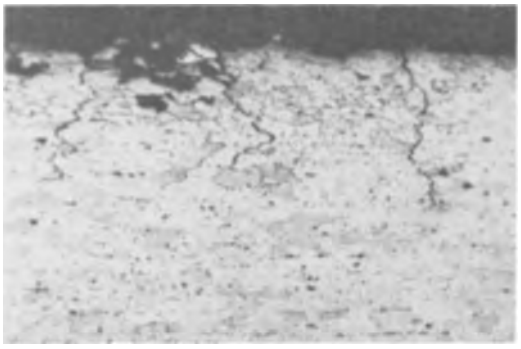

Fig. 1. Illustration of intergranular penetration of stress corrosion cracks in a tensile specimen of age-hardened Al 2024 alloy which had been immersed under stress in a $NaCl\text{-}Na_2CrO_4\text{-}HCl$ solution. Magnification 75X.

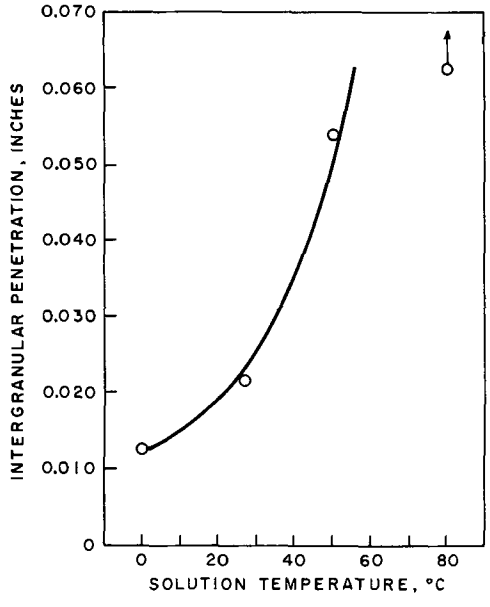

Fig. 2a. Intergranular penetration of Al 2024 alloy in three heat-treated states; solution $NaCl\text{-}Na_2CrO_4\text{-}HCl$; immersion time, 70 min; alloy annealed (furnace cool).

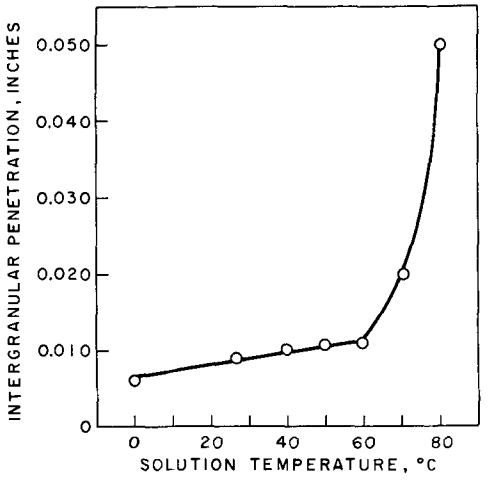

Fig. 2b. Alloy aged 210°C, 30 min

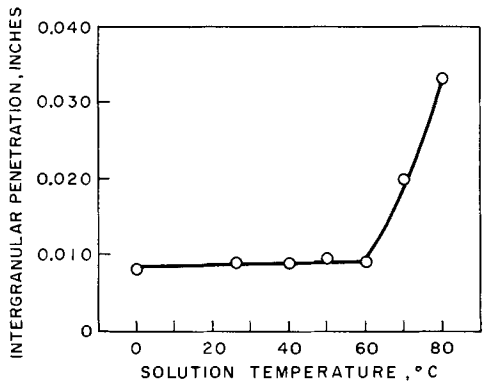

Fig. 2c. Alloy aged 100°C, 30 min

The trends have some unusual aspects. For the 100°C aged condition, intergranular penetration is finite but independent of temperature from 0° to 60°C. Above 60°C, the rate of penetration increases abruptly. For the 210°C aged condition, there is a slight temperature dependence between 0° and 60°C and, again, above 60°C an abrupt increase. For the annealed condition, a strong temperature dependence exists over the whole range of temperatures. The data point with the arrow at 80°C in Fig. 2(a) indicates that intergranular attack in 70 min had penetrated to the center of the specimen which, in fact, had disintegrated. From these observations we may deduce that two processes are operative, one of which is limited to the lower range of temperatures and is peculiar to the age-hardened state.

In that a strong temperature dependence is operative over the whole range of temperatures, the behavior of the annealed state conforms to the expectation of a corrosion process. The independence (or near independence) of the age-hardened states in the temperature range of 0°-60°C is clearly not the expected behavior of a corrosion process.

The temperature independence of the intergranular penetration rate is, however, closely similar to the corresponding behavior of cracking under externally applied stress (2). In this previous publication it was shown that stress corrosion cracking rates for this alloy in the same state of heat-treatment are constant in the same temperature range. It seems reasonable, therefore, to consider the role of internally existing stresses. We postulate that in the age-hardened state, significant stresses exist transverse to grain boundaries and that at the lower temperatures, intergranular penetration is a process of stress corrosion cracking on a microscale. For this material, microscale, stress corrosion cracking is more rapid in the range 0°-60°C but not being appreciably temperature dependent is supplanted at some higher temperature by a process of selective corrosion along intergranular paths which is strongly temperature dependent.

It is inescapable that a question should be raised as to the compatibility between a demonstrated, temperature-independent process of intergranular penetration and the theory of stress corrosion cracking which is based on an intergranular corrosion mechanism (3). It is the purpose of this paper to do just this.

Acknowledgment

This work was supported by a contract from the Pitman-Dunn Laboratories of Frankford Arsenal and permission to publish is gratefully acknowledged.

Manuscript received July 29, 1964; revised manuscript received Oct. 1, 1964.

Any discussion of this paper will appear in a Discussion Section to be published in the December 1965 JOURNAL.

REFERENCES

1. D. O. Sprowls and R. H. Brown, *Metals Progress*, p. 79-85, April, 1962.
2. H. Nichols and W. Rostoker, *Trans. ASM*, **56**, 494 (1963).
3. R. B. Mears, R. H. Brown, and E. H. Dix, ASTM-AIME Symposium on Stress-Corrosion Cracking of Metals, 1944, p. 323.

Shaped Electrode Design

F. H. Edelman and R. W. Klopfenstein

RCA Laboratories, Radio Corporation of America, Princeton, New Jersey

In the deposition of a magnetic alloy film on to a metallized glass capillary, it was found that there were large compositional and thickness gradients along the length of the tube which could be attributed to the substrate resistance. The cell used is shown in Fig. 1. The cathode is rotated during the electrodeposition and is surrounded by the stationary concentric cylindrical anode. The cell is essentially one of concentric cylindrical electrodes whose ends are insulating planes at right angles to their common axis. This configuration

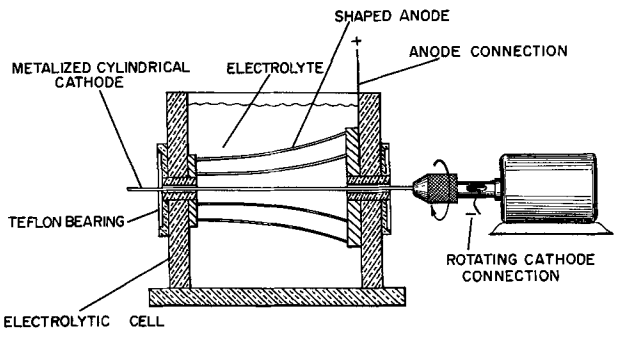

Fig. 1. Shaped anode cell

using electrodes of negligible resistance results in a uniform primary current distribution.

Methods for calculating the effect of an appreciable electrode resistance on current density distribution in an electrolytic cell, for substrates of various geometries, have been proposed (1-3). Waber, assuming that the overvoltage was a linear function of the current density, added a polarization term (4) and showed that for concentric cylinders the change of current along the length of the electrode takes the form of

$$\frac{d^2 I}{dx^2} - \frac{\rho_m}{2\pi a t\left[\frac{\rho_e}{2\pi}\ln\left(\frac{b}{a}\right) + \frac{1}{p}\right]} I = 0 \quad [1]$$

It is seen from Eq. [1] that a knowledge of the polarization is required in order to calculate the current distribution.

One method for compensating for the high cathode resistance is to shape the electrode in such a manner that the annular space between the electrodes is made to vary with the distance from the plating contact in a predetermined manner which will be derived.

In the following development, the assumption is made that the electrolytic current flows entirely in a radial direction. There will, in fact, always be a small

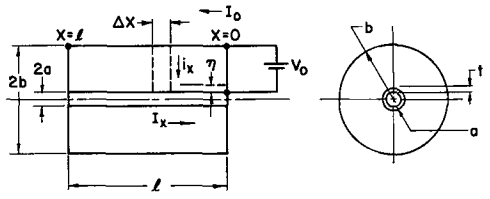

Fig. 2. Electrolytic circuit

component of current flow in the axial direction near the shaped electrode. The effect of this axial component will be quite small, however, when the change of conductor shape is reasonably gradual. The same type of approximation is often introduced in other similar design problems as in the design of tapered transmission lines (5).

Referring to Fig. 2, the voltage drop per unit length along the thin layer conductor

$$\frac{dV}{dx} = -\frac{I\rho_m}{2\pi at} \qquad [2]$$

and $\rho_m/2\pi at$ is the resistance of the metallized conductor. The electrolytic current is equal to the decrease in current per unit length

$$i = -\frac{dI}{dx} \qquad [3]$$

The voltage drop in the electrolytic system at a point x is

$$V = \eta + \left[\frac{\rho_e}{2\pi}\ln\left(\frac{b}{a}\right)\right] i \qquad [4]$$

where polarization is a function of the electrolytic current density

$$\eta = f(i) \qquad [5]$$

and $\rho_e/2\pi \ln b/a$ is the resistance per unit length of the electrolyte between concentric cylindrical electrodes of radius a and b.

Differentiating [4] with respect to distance

$$\frac{dV}{dx} = \frac{d\eta}{di}\frac{di}{dx} + \frac{\rho_e}{2\pi}\ln\left(\frac{b}{a}\right)\frac{di}{dx} + \frac{1}{b}\frac{\rho_e}{2\pi} i \frac{db}{dx} = -\frac{\rho_m}{2\pi at} I \qquad [6]$$

where the outer radius b is a function of x but the inner radius a is constant. For uniform current density

$$\frac{dI}{dx} = K = -\frac{I_o}{l} \qquad [7]$$

It follows from [7] that

$$I = I_o\left(1 - \frac{x}{l}\right) \qquad [8]$$

and substituting [3] in [6]

$$\frac{d\eta}{di}\frac{d^2I}{dx^2} + \frac{\rho_e}{2\pi}\ln\left(\frac{b}{a}\right)\frac{d^2I}{dx^2} + \frac{\rho_e}{2\pi b}\left(\frac{db}{dx}\right)\left(\frac{dI}{dx}\right) = \frac{\rho_m}{2\pi at} I \qquad [9]$$

Substituting [7] and [8] into [9] and rearranging

$$\int_{b_o}^{b}\frac{db}{b} = \int_{o}^{x} -\frac{\rho_m(l-x)}{at\,\rho_e}dx \qquad [10]$$

Integrating

$$\ln\frac{b}{b_o} = -\frac{\rho_m x\left(l - \frac{x}{2}\right)}{at\,\rho_e} \qquad [11]$$

and letting

$$A = \frac{\rho_m}{at\,\rho_e} \qquad [12]$$

$$b = b_o \exp\left[-Ax\left(l - \frac{x}{2}\right)\right] \qquad [13]$$

It is interesting to note that there is no polarization term in Eq. [13], which describes the change in radius of the anode along its length in order to achieve a uniform current density. Under the condition of uniform current density, the effect of polarization is to introduce a constant voltage drop along the line (no assumption concerning the linearity of the relationship between polarization and current density need be made). Polarization, therefore, has no influence on the shape of the electrode required to produce uniform current. When the ratio of the specific resistivity of the electrode to that of the electrolyte is very small (as is the case for bulk conductors), the value of A in Eq. [13] approaches zero. This results in b being almost identical with b_o, and no shaping of the electrode is required for uniform current density.

Manuscript received May 20, 1964; revised manuscript received Sept. 9, 1964. The research reported in this paper was sponsored by the United States Army Electronic Research and Development Laboratory, Fort Monmouth, N. J., under Contract No. DA 36-039-AMC-03248(E).

Any discussion of this paper will appear in a Discussion Section to be published in the December 1965 JOURNAL.

REFERENCES

1. C. Kasper, *Trans. Electrochem. Soc.*, **77**, 359 (1940).
2. W. W. Harvey, *This Journal*, **109**, 638 (1962).
3. C. W. Tobias and R. Wijsman, *ibid.*, **100**, 459 (1953).
4. J. T. Waber, *Trans. Electrochem. Soc.*, **90**, 243 (1946).
5. R. W. Klopfenstein, *Proc. IRE*, **44**, 31 (1956).

SYMBOLS

i	electrolytic current per unit length
I_o	initial current
l	length of sample
x	distance along length of electrode
ρ_m	specific resistiviy of the conducting film
ρ_e	specific resistivity of the electrolyte
b	radius of outer electrode
a	radius of inner electrode
$1/p$	polarization constant
t	thickness of electrodeposited film
η	polarization voltage
V	voltage between electrodes

Fluorescent Properties of Red-Emitting Europium-Activated Phosphors with Cathode Ray Excitation

A. Bril, W. L. Wanmaker, and C. D. J. C. de Laat

N. V. Philips'Gloeilampenfabrieken, Eindhoven, Netherlands

Some years ago data were reported on the efficiencies of phosphors for color television tubes and, moreover, the lumen contributions of the blue, green, and red phosphors required for obtaining a white fluorescence were calculated (1, 2). These calculations were made for various sets of primary phosphors for color television.

The factors which together determine the lumen contributions for each primary phosphor are: (*a*) the radiant efficiency; (*b*) the lumen equivalent (*i.e.*, the lumen efficiency for 100% radiant efficiency); (c) the "weight" of a lumen, which is proportional to $1/y$ (where y is the C.I.E. chromaticity coordinate of the light emitted by the phosphor). For red phosphors used at present, *viz.*, $Zn_3(PO_4)_2$-Mn and (0.2 Zn, 0.8 Cd) S-Ag, the second factor was rather unfavorable due to the broad emission band of these phosphors and the third because of the relatively high y-value of the phosphors.

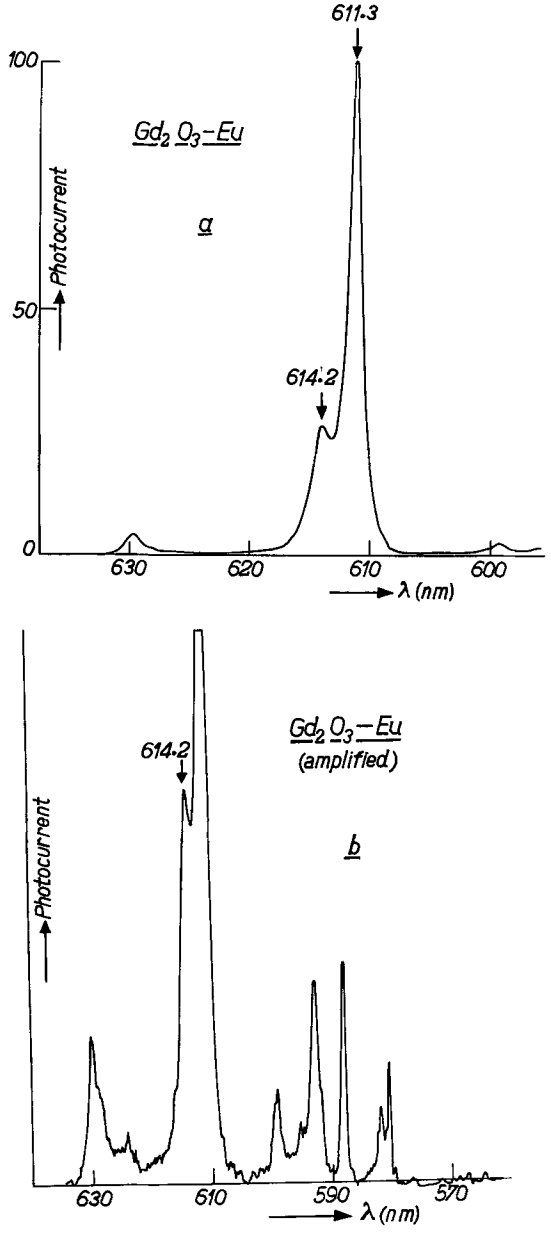

Fig. 1a and b. Spectral energy distribution curve of the emission of Gd_2O_3-Eu. Cathode-ray excitation. Many weak lines in green and blue are also present.

From the much higher lumen efficiency of the sulphide phosphor, we concluded that this phosphor was more suitable as a red component than the $Zn_3(PO_4)_2$-Mn phosphor [See ref. (1) and (2)].

We stated in ref. (1) that, when searching for better red phosphors, one should keep in mind that, apart from having a good efficiency, the phosphor should have a narrow band emission peaking at about 610 nm, because the color coordinates corresponding to this wavelength are about the same as those chosen for the red primary, being about $x = 0.66$, $y = 0.34$. However, at that time such phosphors were not known.

Later on we found though, that phosphors activated with europium have emission lines quite near 610 nm, corresponding to transitions from the $^5D_0$ to the $^7F_2$ energy level. For more details we refer to ref. (3). Many other lines also occur due to the fact that the ground level of the Eu^{3+} ion is split sevenfold, while further splitting of the levels occurs owing to the crystal field (Stark splitting). In many Eu-activated phosphors, then, orange lines in the region 580-590 nm are as strong as or even stronger than the lines near 610 nm.

We found that europium-activated gadolinium-oxide and yttrium-oxide are very favorable for the purpose described above, the red lines at 611.3 and 614.2 nm being very much stronger than the other lines. The photoluminescence of these phosphors, which was first described by Urbain (4), has also been studied by Wickersheim and Lefever (5), by Ropp (6), and by Chang (7). Y_2O_3-Eu, like the Gd_2O_3-Eu, shows a very strong 611.3 nm emission peak, being about 10 times more intense than the 580-590 nm emission lines. In europium-activated Gd-borates, $GdPO_4$, La-borates and $EuPO_4$ studied by us (3), the orange lines are much stronger than in Gd_2O_3-Eu. In Fig. 1 the spectral energy distribution of Gd_2O_3-0.06 Eu for 20 kv cathode ray excitation is given. The spectral energy distribution of Y_2O_3-Eu is quite similar to that of Gd_2O_3-Eu. The location of the emission peaks in various host lattices is about the same; apparently the transition probabilities are much more sensitive to the effects of the surroundings of the Eu-ions than the position of the energy levels. The width of the lines is about 1.0 nm at room temperature.

In the preparation of the Eu phosphors we started with EuF_3 (99.9%), La_2O_3 (99.99%), and Y_2O_3 (99.9%) as obtained from the Lindsay Chemical Division of American Potash and Chemical Corporation; Gd_2O_3 (99.9%) and Eu_2O_3 (99.9%) were obtained from Michigan Chemical Corporation. In general, the thoroughly mixed starting materials were fired once or twice for 2 hr at a temperature of 1200°C. Better results were obtained when a fluorine compound was added to the firing mixture. The fluorine was added as ammonium-fluoride and europium-fluoride. In Fig. 2 data are given for some phosphors made with various amounts of

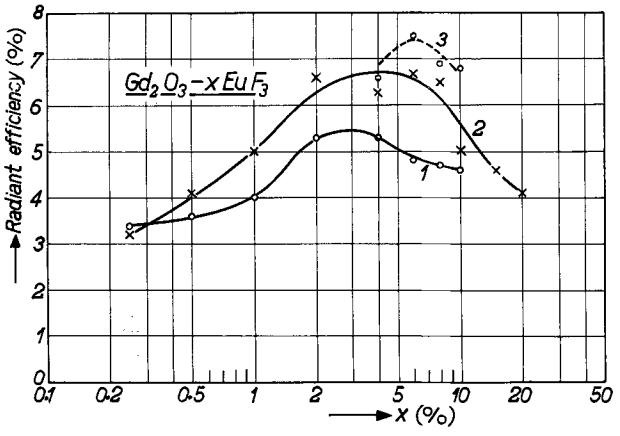

Fig. 2. Effect of Eu- content added on the radiant efficiency (cathode ray excitation) of Gd_2O_3-Eu phosphors: curve 1, firing once; curve 2, firing twice; curve 3, firing three times; all for 2 hr at 1200°C.

europium-fluoride added; moreover, before firing 0.10 mole of ammonium-fluoride per mole of Gd_2O_3 was added to each sample.

In Table I, a comparison is given of the efficiency of Eu-activated Gd_2O_3, Y_2O_3, and La_2O_3. Furthermore, some figures are given for Gd_2O_3-Eu prepared with Eu_2O_3, Eu_2O_3 + NH_4F, and EuF_3, respectively. With a low Eu-content, *viz.*, lower than about 0.04-0.06 gram atom Eu per mole rare earth oxide, the intensity of the 580-590 nm emission lines becomes more intense. The preparation conditions also have an influence on this effect.

Table II presents the efficiency of Gd_2O_3-Eu together with the efficiencies of the red fluorescent phosphors, which are used to-day as a red primary in color television tubes.

The radiant efficiency of Gd_2O_3-Eu is as high as or even higher than efficient manganese-activated phosphors, like willemite and zinc phosphate. It can be seen further from Table II that Gd_2O_3-Eu, due to its high lumen equivalent, has a much higher lumen efficiency than the (0.2 Zn, 0.8 Cd) S-Ag phosphor, in spite of its lower radiant efficiency compared with the latter phosphor. This means, too, that the lumen efficiency of a white color obtained with the blue, green, and red primaries (for equal signal ratio) increases to the same extent when Gd_2O_3-Eu is used (*i.e.*, the light output is about 100% higher than with the use of zinc cadmium sulfide).

The red zinc cadmium sulfide phosphor, activated with silver, has not only a higher light output, but also a much shorter decay time (about 0.04 msec) than $Zn_3(PO_4)_2$-Mn (about 12 msec). This is of advantage

Table I. Radiant efficiency (cathode ray excitation) of europium activated rare earth oxides

Cathode rays at 20,000v and 1 μa/cm². RE_2O_3 = Rare Earth Oxide. Phosphors fired twice for 2 hr at 1200°C.

Phosphor	Moles added/mole RE_2O_3 Eu_2O_3	EuF_3	NH_4F	Radiant efficiency, %
Gd_2O_3-Eu	0.04	—	—	5.1
	0.04	—	0.24	5.9
	—	0.08	—	5.9
Y_2O_3-Eu	—	0.06	0.10	5.8
La_2O_3-Eu	—	0.06	—	2.2

Table II. Characteristics of red-emitting cathode ray phosphors

Cathode rays at 20,000v and 1 μa/cm²

Phosphor	Radiant efficiency η, %	Lumen equivalent L, lm/w	Lumen efficiency l, lm/w	Decay time τ, msec
$Zn_3(PO_4)_2$-Mn	5.5	140	7.7	12-30
(0.2 Zn, 0.8 Cd) S-Ag	17	75	13	0.04
Gd_2O_3-0.06 Eu	8	330	26	0.9

in the case of slowly moving objects in television pictures. When the decay time becomes too long (of the order of the time in which one image is described) trailing of pictures occurs.

The Eu-activated phosphors have an exponential decay with $1/e$ value of 0.9 msec. This is not so short as the decay time of sulfides but, as far as we can see, short enough to give no troubles with moving objects.

Acknowledgments

The authors wish to express their thanks to Mr. J. G. Verlijsdonk and Mr. A. A. L. Sleutjes for preparing the phosphors and to Mr. J. A. A. Bertens for the assistance in the measurement of the spectral distribution.

Manuscript received Aug. 20, 1964.

Any discussion of this paper will appear in a Discussion Section to be published in the December 1965 JOURNAL.

REFERENCES

1. A. Bril and H. A. Klasens, *Philips Research Repts.*, **10**, 305 (1955).
2. H. A. Klasens and A. Bril, *Acta Electronica*, **2**, 143 (1957).
3. A. Bril and W. L. Wanmaker, *This Journal*, **111**, 1363 (1964).
4. G. Urbain, *Ann. Chim, Phys.*, **18**, 293 (1909).
5. K. A. Wickersheim and R. A. Lefever, *This Journal*, **111**, 47 (1964).
6. R. C. Ropp, *ibid.*, **111**, 311 (1964); Proc. Third Rare Earth Conference, Clearwater, 1963.
7. N. C. Chang, *J. Appl. Phys.*, **34**, 3500 (1963).

Solid Solubility in the System GaSb-GaAs

M. E. Straumanis and C. D. Kim

Department of Metallurgical Engineering, School of Mines and Metallurgy, University of Missouri at Rolla, Rolla, Missouri

No data have been published until recently (1, 2) on the mutual solubility in the system GaSb-GaAs. However, in one article (1) only one point in the solid solubility region is mentioned.

Ivanov-Omskii and Kolomiets (3) reported that the zone equilibration method is an effective one to achieve an equilibrium condition for GaSb and InSb solid solutions. Since zone equilibration causes a change of composition in the heat-treatment ingot (GaAs may decompose), this method could not be used where the same stoichiometric composition had to be retained throughout the sample. Therefore, the method of long time annealing was used for all samples.

GaSb and GaAs were prepared from the elements of 99.99-99.999% purity and mixed to provide the compositions shown in Fig. 1. Small quartz vials were nearly filled with the finely ground powders, evacuated, and sealed. The small size was necessary in order to heat the vials uniformly from all sides to prevent segregation (4).

Each of the mixtures was initially heated at constant temperatures between 670° and 720°C for periods of

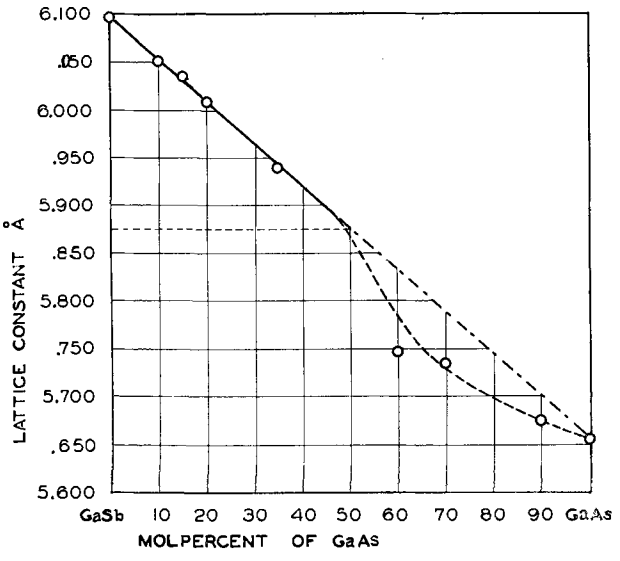

Fig. 1. Change of lattice constant a within the system GaSb-GaAs

5-10 days, and then quenched in ice water. On detection of lines of the starting products on x-ray powder photographs, the grinding and heating procedure was repeated until a uniform end product was achieved. The heating temperature was raised slightly from cycle to cycle. However, temperatures higher than 760°C cannot be applied because of decomposition.

The lattice parameters were determined at constant temperature of the sample (± 0.05°C) by placing the powder camera (64 mm in diameter) into a thermostated jacket. Asymmetric patterns, requiring no knowledge of the camera diameter for Bragg angle measurements, were obtained using Cr $K\alpha_1$, radiation ($\lambda = 2.28965$Å). As the powder mounts were very thin and nearly transparent for x-rays (about 0.2 mm in diameter) no absorption correction was made. The exposure time was about 50 min. The lattice parameter determination procedure has been described previously (5, 6).

The lattice constant of each cubic sample was computed from the last single line, which was $422\alpha_1$ (Bragg angle ~ 82°) for GaAs and $333\alpha_1$, (Bragg angle ~ 78°) for GaSb. The solid solutions yielded the same back reflection lines. Although these lines were fairly broad, the lattice parameter was determined with sufficient precision (± 0.0004Å). Figure 1 shows the changes in lattice parameters *vs.* composition of the solid solutions.

The lattice constants of the starting substances with the refraction correction included were:

GaSb $a = 6.09592 \pm 0.00004$Å at 25°C

GaAs $a = 5.65321 \pm 0.00003$ at 25°C

These lattice constants agree with those calculated from the tetrahedral atomic radii of Ga, As, and Sb for homopolar compounds (7). The lattice constants of all the solid solutions were in between these two values.

Due to the decomposition of the solid solutions above 760°C (the melting points of GaAs and of GaSb are 1237° and 712°C, respectively), their formation arises through solid-state diffusion reactions. Thus long periods of reaction are necessary. The same was observed for the system InAs-InSb (8).

It was interesting to note that the GaAs reacted much faster with the GaSb than the latter with the former to form the solid solutions; thus, the uptake of GaSb by pure GaAs was very slow. It took 20 days to dissolve 65 mole % GaSb in 35 of GaAs at temperatures up to 720°C. Nevertheless, weak lines of the pure GaAs were still present on the patterns. Assuming that the amount of unreacted GaAs was about 3 mole %, the lattice parameter of this composition is about 0.013Å too high. On the other hand, for the 50-50 point a value of 5.87 ± 0.02Å was obtained by Müller and Richards (1), which is nearly on the Vegard line. Therefore, a straight line was drawn through the first 5 points (there were no GaAs lines on the patterns for samples containing more than 65% GaSb), extending nearly to the 50-50 composition (Fig. 1). Beyond this point there is still solid solubility, but homogeneity could not be reached. There is a deviation from Vegard's law. It would be interesting to find whether equilibrium solid solutions with high GaAs content could be prepared by the flash evaporation method (2).

The difficult solid solubility is in agreement with the large difference of more than 15% in the atomic radii of Sb (1.36Å) and of As (1.18Å). Evidently upon contact of the GaSb and GaAs grains, the compounds diffuse into each other only very slowly because of the large size of their molecules. The initial diffusion is molecular because otherwise free Ga would remain, but none was observed in the x-ray patterns. Furthermore, it has been shown that Ga does not dissolve in GaSb and only in very small amounts in GaAs (9). After the formation of an extremely thin solid solution surface layer, the As atoms diffuse at a considerably more rapid rate than Sb into the grains causing a lattice contraction. This process is also faster than molecular diffusion. Thereby the replacement of the larger Sb atoms of the ternary system by the smaller As atoms (with resulting shrinkage of the lattice) is easier. The reverse process (Sb into GaAs) must be much slower, which explains the difficulty of formation of ternary solid solutions rich in As.

Acknowledgment

The authors are grateful to Dr. W. J. James, Professor of Chemistry of the Department of Chemistry, for assistance with the manuscript.

Manuscript received June 18, 1964; revised manuscript received Sept. 21, 1964.

Any discussion of this paper will appear in a Discussion Section to be published in the December 1965 JOURNAL.

REFERENCES

1. E. K. Müller and J. L. Richards, *J. Appl. Phys.*, **35**, 1233 (1964).
2. E. K. Müller, B. J. Nicholson, and G. L'E. Turner, *This Journal*, **110**, *969* (1963).
3. V. I. Ivanov-Omskii and B. T. Kolomiets, *Soviet Physics, Solid State*, **1**, 834 (1959).
4. V. J. Lyons and V. J. Silvestri, *J. Phys. Chem.*, **65**, 1275 (1961).
5. M. E. Straumanis, *J. Appl. Phys.*, **20**, 726 (1949).
6. M. E. Straumanis in G. L. Clark's "Encyclopedia of X-rays and Gamma Rays," p. 700, Reinhold Publishing Co., New York (1963).
7. L. Pauling and M. L. Huggins, *Z. Kristallogr.*, **87**, 205 (1934).
8. J. C. Wooley and B. A. Smith, *Proc. Phys. Soc.*, **72**, 214 (1958).
9. M. E. Straumanis and C. D. Kim, In preparation for publication.

The Effect of Ionic Species on the Etching of Germanium

J. W. Faust, Jr.

Research Laboratories, Westinghouse Electric Corporation, Pittsburgh, Pennsylvania

The basic ingredient of most etchants is an oxidizing agent (1). In some cases, particularly semiconductors, a complexing agent is necessary to take the oxidized species into solution. Other ingredients, for example heavy metal ions, are sometimes added to vary the surface appearance. If cupric nitrate is added to a mixture of HF and HNO_3 (in the ratio of HF:HNO_3:5% $Cu(NO_3)_2$; 4:2:4), a chemical polish is obtained (2); the same mixture without the cupric nitrate yields a surface completely covered with terraced pyramidal pits. On the other hand, if silver nitrate is added, a preferential etch results whose pits are faceted by {111} planes (3). In studies directed toward deducing the etching mechanism of such etchants, the question arose as to what species was actually responsible for the preferential nature of the silver etch; one would naturally suspect the silver ion. In an effort to clarify this question, the following study was undertaken. Since the HF in this solution is a complexing agent and thus plays only a passive role in the dissolution mechanism, it was decided to investigate the other ions, *i.e.*, the hydrogen, nitrate, and heavy metal ions.

It has already been shown that certain of the heavy metal ions plate out on germanium (4); removal of the plated material yields a deeply pitted and nondescript surface. It was found, however, that the use of ultrasonic vibration during etching prevented the heavy metal from building up a deposit on the germanium thus leaving a fresh surface for further attack. It was thus possible to obtain etching of germanium by heavy metal ions (acting as the oxidizing agent) by the use of water as a complexing agent. For these experiments, two ultrasonic generators were used (*a*) a 400-watt unit operating at 20 kc, and (*b*) a 65-watt unit operating at 40 kc. Both units gave similar results. For actual operation, the beaker containing the etching solution was placed in the water bath of the ultrasonic generator and the power adjusted until cavitation resulted. Water solutions of the ions investigated are given in Table I along with their etch rates on {111} surfaces and a description of the surface.

As can be seen from Table I, the basic nitrate and the Cu ions give a nondescript etch pattern as shown by Fig. 1. The acid nitrate, however, gives excellent {111} planes parallel to the surface as shown in Fig. 2. All other etchants gave reasonably well-defined {111} etch patterns as shown in Fig. 3. The etch rate data is included only for comparison purposes, since the ultrasonic agitation generally increased the temperature of the etchant approximately 25° during the etching time. It is interesting to note, however, that the effectiveness of the ions in removing germanium (*i.e.*, the etch rates) is roughly in the order one would expect from free energy calculations based on such a reaction (*i.e.*, galvanic). The theoretical sequence is

$$Au > Pd > Ag > Hg > Cu >> Na$$

Table I shows only Pd out of place. It should also be

Table I. Experimental conditions and results obtained on {111} surfaces of germanium with ultrasonic agitation

Etchant	Etch rate, mg/cm²/min	Microscopic appearance of surface
5% $AgNO_3$	0.63	Mottled triangles
1% $AgC_2H_3O_2$	White ppt	When ppt wiped off, well-developed triangles were visible
Sat'd. AgF	0.22	Well-developed triangles
46% HNO_3	0.23	Roughly circular patterns with flat bottoms
1% $NaNO_3$	0.002	Nondescript pattern
10% NaOH	0.000	No attack
5% $Cu(NO_3)_2$	0.04	Nondescript pattern
5% $Hg(NO_3)_2$	0.15	Reasonably well-defined triangles
1%$PdCl_2$	0.05	Well-defined triangles
1% $AuCl_3$	0.29	Well-defined triangles

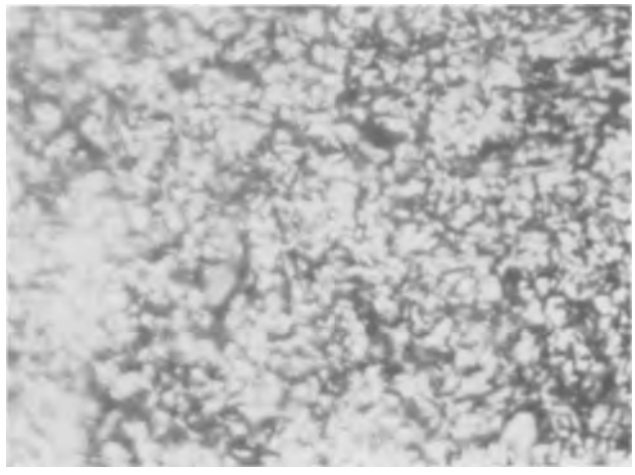

Fig. 1. Nondescript surface resulting from copper ion. Magnification 500X.

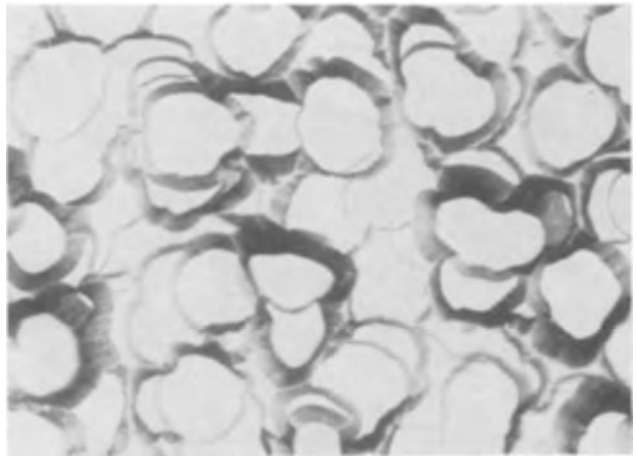

Fig. 2. Pits produced by nitric acid. Magnification 500X

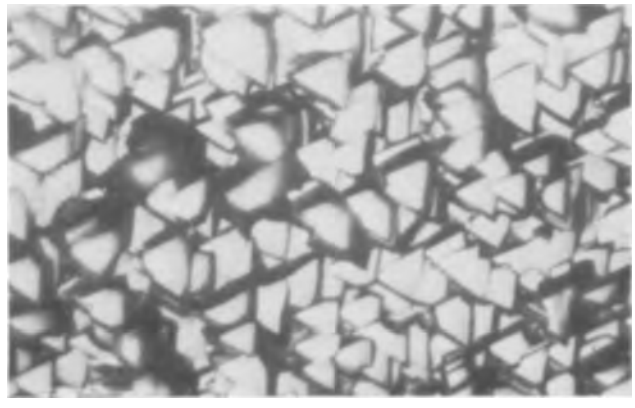

Fig. 3. Triangular pits produced by palladium ions. Magnification 500X.

pointed out that these etch rates are very much higher than those obtained by Harvey and Gatos (5) for dissolved oxygen in water showing that this is a negligible factor compared to the galvanic attack.

The results indicate that neither the hydrogen, nitrate, hydroxyl, nor copper ions are responsible for the preferential attack on the {111} planes. Several heavy metal ions, in addition to silver, were found to give preferential attack on these planes. Furthermore, the results indicate that the use of ultrasonics in etching may be a very important parameter.

Manuscript received May 27, 1964.

Any discussion of this paper will appear in a Discussion Section to be published in the December 1965 JOURNAL.

REFERENCES

1. J. W. Faust, Jr., "Methods of Experimental Physics," Vol. 6A, K. Lark-Horovitz and V. Johnson, Editors, p. 165, Academic Press, New York (1959).
2. K. Lark-Horovitz, U. S. Pat. 2,514,879, July 1950.
3. R. H. Wynne and C. Goldberg, *Trans. AIME*, **197**, 436 (1953).
4. J. W. Faust, Jr., IRE-AIEE Devices Conference, State College, Pa., June 1953.
5. W. W. Harvey and H. C. Gatos, *This Journal*, **105**, 654 (1958).

Manuscripts and Abstracts for Fall 1965 Meeting

Papers are being solicited for the Fall Meeting of the Society, to be held at the Statler-Hilton Hotel in Buffalo, N. Y., October 10, 11, 12, 13, and 14, 1965. Technical sessions probably will be scheduled on: Batteries (including symposia on Charging Characteristics of Batteries and Characteristics of Electrodes during Charging, Corrosion, Electrodeposition (including Symposium on Thin Film Technology), Electronics—Semiconductors, Electrothermics & Metallurgy (including a Symposium on Zirconium and Its Alloys).

To be considered for this meeting, **triplicate copies of the usual 75-word abstract, as well as of an extended abstract of 500-1000 words** (see notice on page 274C of the December 1964 issue), must be received at The Electrochemical Society, 30 East 42 St., New York, N. Y., 10017, *not later than May 14, 1965.* (Papers solely sponsored by the Corrosion Division **do not** require an extended abstract.) *Please indicate on 75-word abstract for which Division's symposium the paper is to be scheduled, and underline the name of the author who will present the paper.* No paper will be placed on the program unless one of the authors, or a qualified person designated by the authors, has agreed to present it in person. Clearance for presentation of a paper at the meeting should be obtained before the abstract is submitted. An author who wishes his paper considered for publication in the JOURNAL or ELECTROCHEMICAL TECHNOLOGY should send triplicate copies of the manuscript to the Managing Editor of the appropriate publication 30 East 42 St., New York, N. Y., 10017. Concerning papers to be published in the JOURNAL, see notice on per page charge on page 14C of this issue.

Presentation of a paper at a technical meeting of the Society does not guarantee publication in the JOURNAL or ELECTROCHEMICAL TECHNOLOGY. However, all papers so presented become the property of The Electrochemical Society, and may not be published elsewhere, either in whole or in part, unless permission for release is requested of and granted by the Editor. Papers already published elsewhere, or submitted for publication elsewhere, are not acceptable for oral presentation except on invitation by a Divisional program Chairman.

A New High-Performance Fuel Cell Employing Conducting-Porous-Teflon Electrodes and Liquid Electrolytes

L. W. Niedrach and H. R. Alford

Research Laboratory, General Electric Company, Schenectady, New York

ABSTRACT

A low-temperature, aqueous electrolyte fuel cell employing new, "conducting-porous-Teflon electrodes" is described. The new electrodes show excellent performance characteristics with a variety of fuels (including hydrocarbons) and with both oxygen and air as the oxidant. Preparation methods are discussed, and performance data obtained with ambient temperature, hydrogen-oxygen and hydrogen-air cells are presented to illustrate their properties.

In earlier publications the use of "Conducting-Porous-Teflon Electrodes" in regenerative, matrix-type cells has been described (1, 2). While these cells are of some interest, particularly for applications in gravity-free space, they have not been given serious consideration for operation on a continuous feed basis. Under the latter conditions the matrix is responsible for some operational disadvantages; *e.g.*, at high current densities concentration polarization can occur at the electrodes, maintenance of the proper water balance in the electrolyte introduces design problems, and the internal resistances of the cells are higher than desired. In order to overcome these difficulties, work was directed at modifying and improving the original electrode structure so that the matrix could be eliminated. This has resulted in a new, high-performance fuel cell which operates with an aqueous electrolyte.

In seeking this objective two important restrictions concerning operation were deliberately imposed as being desirable: (i) The fuel (oxidant) gas-electrolyte interface was to be established within the electrode structure by "controlled wetting," and (ii) the electrodes were to be capable of operation at ambient atmospheric pressure. In addition emphasis was placed on retaining a relatively thin structure.

The new electrodes which are 5-10 mils thick, consist of a Teflon-catalyst mix that is pressed and sintered onto a suitable supporting screen which also serves as an excellent electronic conductor to carry current to the terminals of the cell. A porous Teflon film on the gas side of the electrode provides for proper control of wetting so that both the electrolyte and reacting gas have satisfactory access to the catalyst incorporated into the electrode. While alternative means of preparing electrodes were considered, *e.g.*, use of high Teflon-to-catalyst ratios and laminar structures with two different Teflon-to-catalyst ratios, the results obtained with the film covered electrodes were by far the most encouraging. These electrodes were found to be exceedingly reliable and readily manufactured in the laboratory. It was therefore elected to concentrate on electrodes of this type. The present paper is devoted to a discussion of their preparation and properties as exemplified by their performance in ambient temperature, hydrogen-oxygen and hydrogen-air cells. Platinum black was used almost exclusively as the electrocatalyst in the work to be reviewed and 6*N* KOH and 5*N* H_2SO_4 were the principal electrolytes.

The electrodes are exceedingly versatile, and some performance data obtained with other fuels and electrolytes have already been published. Thus, excellent performances have been reported for a variety of hydrocarbons, with a sulfuric acid electrolyte up to 89°C (3) and with a phosphoric acid electrolyte up to 200°C (3-5). In addition they have also been used effectively with methanol and a cesium carbonate electrolyte at temperatures up to 185°C (6).

Structure of the New Electrodes

Examples of the new electrodes are shown in Fig. 1. These were prepared by bonding platinum black-Teflon mixtures to the central areas of nickel screens. One quarter-inch-wide rings of 5-mil-thick Teflon sheet (du Pont's FEP Fluorocarbon Film) were used as seals around the peripheries. In mounting the electrodes in cell housings these seals are buried under the gaskets that are used. In another version the outer ring has been eliminated and the catalyst-Teflon mix has been spread uniformly over the entire circular area of the screen. Such electrodes perform equally well electrically and retain the electrolyte more reliably.

The important differences in the two surfaces of the electrodes are shown clearly in Fig. 1. The surface of the electrode on the left is coated with the porous Teflon film and is obviously exceedingly hydrophobic. In operation this side faces one of the gases. The untreated, electrolyte side of the electrode on the right has been wetted by drops of water placed upon it.

The photomicrograph in Fig. 2 brings out additional details of the electrode structure. It shows the surface film clearly at the top. As shown by the wire at the left, the screen is entirely imbedded in the catalyst-Teflon mix. It is pertinent to note that the starting catalyst consists of agglomerates of particles about 0.01μ in size. The ultimate size of the Teflon particles is about 0.2-0.5μ.

Experimental

Preparation of electrodes.—Most of the electrodes used in this work were prepared by a standard procedure. A Teflon suspension (du Pont's Teflon-30, which contained 59.6% solids by weight) was the

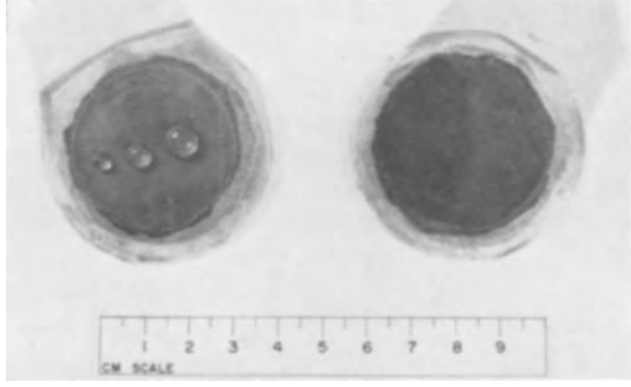

Fig. 1. Typical electrodes showing wetting characteristics

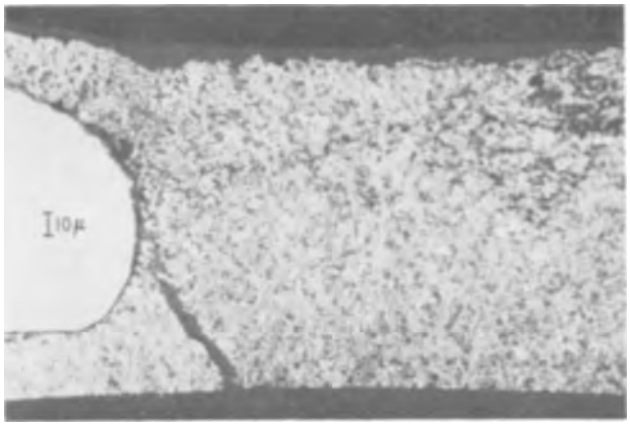

Fig. 2. Photomicrograph of a sectioned electrode showing the surface film on one side. Electrode No. 375. Body: 34 mg Pt black, 3.1 mg Teflon/cm^2; film: 2.4 mg Teflon/cm^2; nickel screen, 40 mesh; 4.5 mil wire. Magnification approximately 330X.

source of the binding material. Platinum black from Engelhard Industries, Inc., was used as the catalyst in most cases, but a few other catalysts were also used. Screen materials that were employed are listed in Table I. The nickel and silver were satisfactory in alkaline cells while the platinum screens could be used with the acidic cells as well.

While electrodes can be made with finer mesh screens of smaller wire size, it has been found that their resistances are high enough to be unattractive. In most of the work, therefore, 40- to 45-mesh screen made of 5- to 8-mil wire was used. In order to minimize the thickness of the electrodes, such screens were regularly rolled to a thickness corresponding to that of the individual wires. It was found necessary to leave wide tabs on the screens in order to reduce ohmic losses during operation of cells at high current densities.

Before making the electrodes themselves, a supply of Teflon films was prepared for use as surface coatings. This was done by spraying a Teflon-30 suspension diluted with seven volumes of water onto an aluminum foil using an air brush (Paasche, Type V). Films corresponding to 0.79, 1.6, 2.4, and 3.9 mg Teflon per cm^2 were used. In preparing these films a 5- by 5-in.^{2} area was marked on the aluminum foil, and an appropriate amount of the diluted Teflon suspension was used to coat this area to the desired thickness. Before spraying, a pattern of four circles having the diameter of the ultimately desired electrodes was scribed within the square to facilitate later steps in the preparation.

A fine spray was used so that several retracings of the pattern could be made in order to obtain a uniform thickness. During application, the aluminum foil was mounted on the bed of a hot plate which was maintained at 120°-150°C to facilitate evaporation of the water from the spray. The rate of application was such that wet areas did not develop and run on the foil.

Following the spraying, the foil was placed on the bed of the press (6-in. bed Carver press with individually heated platens) at 350°C and the jaws were closed to a gap of about ⅛ in. for about a minute. During this treatment the nonionic wetting agent in the Teflon suspension was rejected, and sintering of the Teflon particles occurred to form the desired film (7).

Spreads of platinum black (or other catalyst) with the Teflon-30 suspension were then prepared on circular areas on two aluminum foils, one of which had previously been coated with Teflon as described above. In preparing a typical spread to cover the entire circular area of the screen (17.7 cm^2), a 0.03 cc aliquot of the Teflon-30 suspension was first placed on the foil along with a suitable volume of dilution water, about 0.6 cc. After mixing, 0.3g of platinum black (previously sifted through a 325-mesh screen) was added and a thin, cream-like slurry was made by mixing with a small spatula. This was then dispersed as uniformly as possible over the area and slowly dried on a hot plate. It was necessary to raise the temperature very slowly during the initial phases to obtain a satisfactory deposit. Ultimately, however, the bed of the hot plate was raised to 250°-350°C to dispel the wetting agent as white fumes from the Teflon suspension.

The screen having a tab was then centered over one of the spreads, and a strip of Teflon sheet was placed across the tab as a seal. The second spread was then placed on top of the screen with the catalyst mix again facing the screen. This assembly, with the two aluminum foils facing outward, was sandwiched between two ferrotype plates and placed on the bed of the press. Sintering was performed at 350°C for 2 min at the desired pressure, usually 1800-3000 lb/in^2 of electrode surface.

Following the heat treatment, the aluminum foil was dissolved from the electrode with warm 20% NaOH. A water rinse and an air drying then resulted in a finished electrode. In most of the work, electrodes, either with or without the peripheral Teflon rings, were prepared as outlined above. The occasional variations that were introduced will be described as they arise.

Test cell.—The completed electrodes were housed as shown in the exploded view of a cell in Fig. 3. The two electrodes were separated by a ⅛-in. thick spacer which formed a 1½-in. diameter pocket for the free electrolyte. Appropriate gaskets and face plates formed chambers for the fuel and oxidant gases. All plastic parts were of Lucite, and gaskets were of silicone rubber or poly(ethylene-butene) copolymer. Gasketing was such that the effective working areas of the electrodes were 1½-in. diameter circles. Platinum and Teflon tubing were used for the connections that encountered electrolyte. Gases were flowed through polyethylene tubing. For operation on air one of the faceplates contained a 1½-in. diameter hole. This gave free access of air to the electrode.

Electrolytic hydrogen and purified oxygen were employed during operation. At low current densities static gases could be used, but at high current densities (>250 ma/cm^2) it was generally found desirable to maintain slow flows of the gases through a cell. This was particularly true of the oxygen which contained enough nitrogen and argon as impurities to accumulate rapidly in the cell chambers and cause "smothering."

Table I. Reinforcing screens used in electrode fabrication

Metal	Mesh, wires/in.	Wire size, diameter, mils
Platinum	80	3
	45	7.8
Nickel	40	4.5
Silver	40	7.5

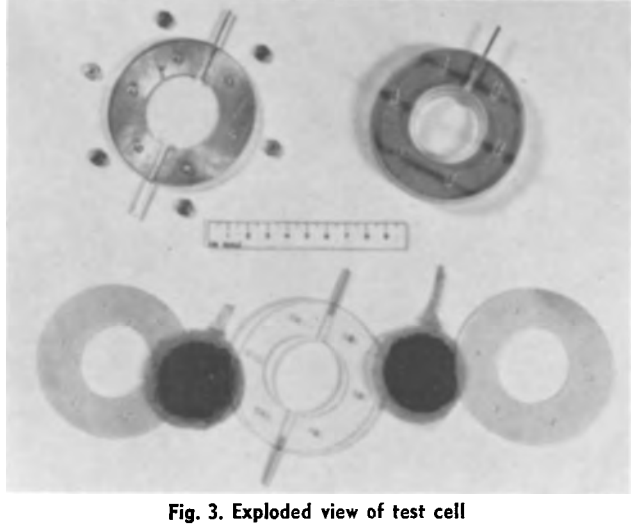

Fig. 3. Exploded view of test cell

In order to prevent the water produced in the cell reaction from diluting the electrolyte excessively, the electrolyte was circulated between the cell and a relatively large reservoir. In initial experiments, forced circulation was achieved by means of gravity flow from a reservoir above the cell level. Electrolyte which drained from the cell was then returned to the reservoir with the aid of a Teflon bellows pump.

It was soon found that the circulation provided by means of a thermal loop was adequate to maintain the cell performance. This simpler arrangement was therefore used for most of the work. A polyethylene bottle connected to the cell with Teflon tubing served as the reservoir.

A reference electrode was prepared by mounting one of the new-type electrodes in a separate housing and exposing one side to hydrogen. Electrolyte in the other chamber of the reference cell then made contact with the working system, *via* a bridge of Teflon tubing filled with the common electrolyte. Individual electrode performances in the cell under test were then obtained *vs.* the reference from measurements with a Kordesch-Marko bridge (8). Use of the bridge also permitted the measurement of IR-free voltages.

Although most of the measurements were made with the aid of the Kordesch-Marko bridge, over-all polarization curves were frequently obtained during direct discharge of cells through resistive loads. These invariably agreed well with the over-all curves obtained with the pulsating current derived from the bridge.

Results and Discussion

Before examining the effects of a number of individual parameters, it is of interest to consider the general performance characteristics of the new cells with alkaline and acidic electrolytes. For this purpose polarization curves for cells employing 6*M* KOH and 5*N* H_2SO_4 electrolytes are shown in Fig. 4 and 5, respectively. It is significant to note that current densities as high as 1000 ma/cm² have been delivered by the alkaline cells operating on hydrogen and oxygen. At such high current densities, of course, considerable internal heating occurs, and operation is therefore not isothermal. For example, electrolyte and electrode temperatures of about 70°C have been measured on both acidic and alkaline, hydrogen-oxygen cells at current densities of about 500 ma/cm². While the voltage (and hence efficiency) is low at these high current densities, the polarization curve gives assurance that the new electrodes will be able to handle surge currents well above the 100-200 ma/cm² that might be considered as the normal operating range. The performance of hydrogen-oxygen cells with acidic electrolytes is similar to that observed with the alkaline electrolyte.

Even when air is used as the oxidant, relatively high current densities can be obtained with the new cell before evidence of mass transfer polarization appears in the form of a sharp decline in the voltage with increasing load. Somewhat lower voltages are observed when air is substituted for oxygen, *e.g.*, at 200 ma/cm² 0.70v *vs.* 0.76v for the alkaline cell and 0.60v *vs.* 0.69v for the acidic cell. While partially resulting from the concentration effect involved in the Nernst equation, the lower voltages obtained with air probably also reflect the fact that better cooling is accomplished during air operation. As a result, internal resistances are higher and electrode reactions are more sluggish than when oxygen is used and higher temperatures are reached in the cell.

The new electrodes also do an excellent job of retaining the aqueous electrolytes. A small amount of seepage has, however, been observed with all the electrodes tested to date. In practice then, it may be necessary to provide some means of recycling the seepage.

Effect of the thickness of the surface film.—The first series of experiments was devoted to an examination of the effect of the thickness of the Teflon surface film on cell performance. All electrodes used in this series were prepared with rolled 40-mesh nickel screens having wire diameters of 4.5 mils. Two identical electrodes with peripheral Teflon rings were used in each of the test cells. Surface films of 0.79, 1.6, 2.4, and 3.9 mg Teflon/cm² were tested. All of the experiments were performed with alkaline electrolytes, 6*M* KOH. Most of the polarization data shown in Fig. 6 and 7 were obtained with the Kordesch-Marko bridge and show the potentials of the fuel and oxidant electrodes against the hydrogen reference. Also shown are the over-all performance curves (IR drop included) for the cells

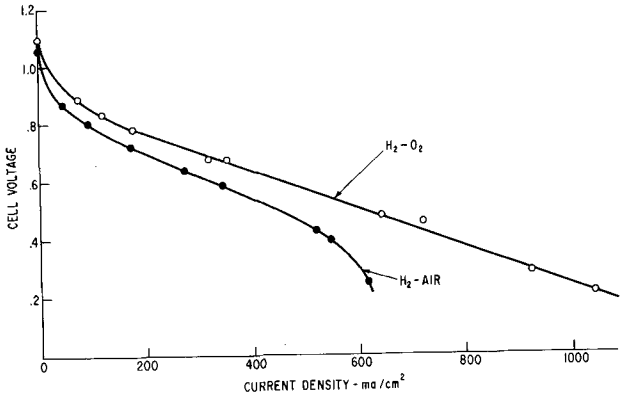

Fig. 4. Performance with alkaline electrolyte. Cell LFC-267. Electrolyte, 6M KOH; electrodes: body (35 mg Pt, 3.2 mg Teflon)/cm²; film, 1.6 mg Teflon/cm².

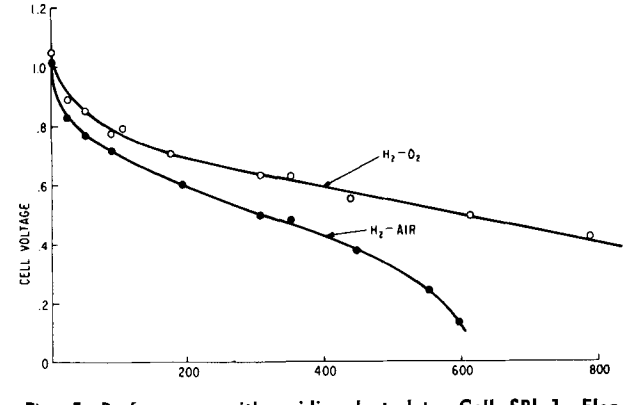

Fig. 5. Performance with acidic electrolyte. Cell SPL-1. Electrolyte, 5N H_2SO_4; electrodes: body (35 mg Pt, 3.2 mg Teflon)/cm²; film, 1.6 mg Teflon/cm².

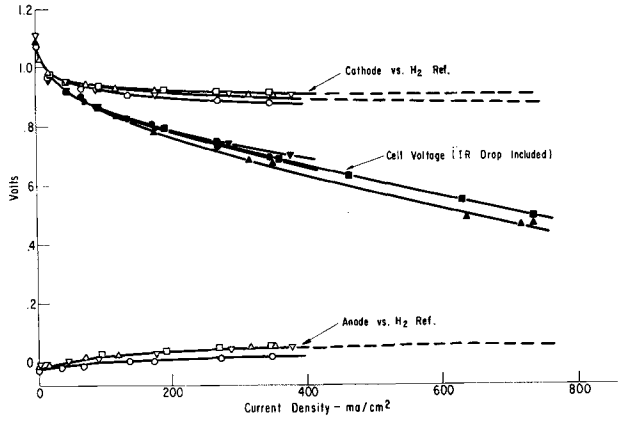

Fig. 6. Effect of film thickness on performance with H_2 and O_2. Electrolyte, 6M KOH; electrodes, body (35 mg Pt, 3.2 mg Teflon)/cm²; film: ○, ●, 0.79 mg Teflon/cm² LFC-270; △, ▲, 1.6 mg Teflon/cm² LFC-267 (9); ▽, ▼, 2.4 mg Teflon/cm² LFC-271; □, ■, 3.9 mg Teflon/cm² LFC-275.

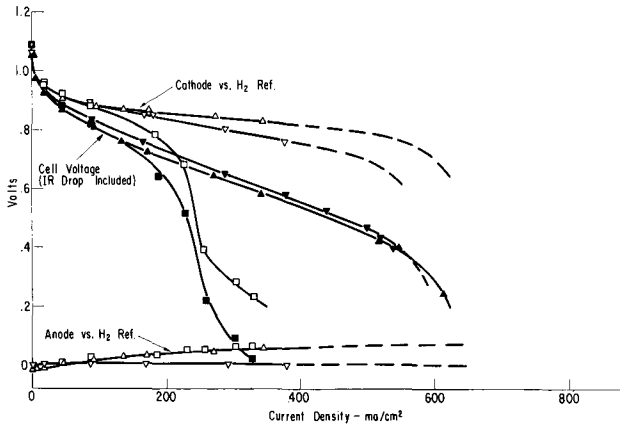

Fig. 7. Effect of film thickness on performance with H_2 and air. Electrolyte, 6M KOH; electrodes, body (35 mg Pt, 3.2 mg Teflon)/cm²; film: △, ▲, 1.6 mg Teflon/cm² LFC-267 (9); ▽, ▼, 2.4 mg Teflon/cm² LFC-271; □, ■, 3.9 mg Teflon/cm² LFC-275.

operating on oxygen and on air. At the time that these tests were made the bridge could handle a maximum current of about 4.5 amp. The data obtained at higher current densities were therefore obtained by direct discharge of the cells through resistive loads. The agreement between both types of data attest to the satisfactory functioning of the system.

It is seen that the effect of the film thickness on the performance of oxygen and hydrogen electrodes is not very pronounced. With air as the oxidant, however, it is evident from the data in Fig. 7 that the thinner films result in better performances. This is reasonable in view of the lower permeability that would be anticipated for the heavier films, and hence the greater tendency toward blockage with nitrogen.

Since an important purpose served by the film is the prevention of electrode drowning, as well as gross leakage of the electrolyte through larger pores, a word is in order about these aspects of performance. Electrode drowning manifests itself by severe polarization over a narrow range of current density. It is therefore evident from the data for the hydrogen and oxygen electrodes in Fig. 6 and 7 that drowning is not a problem.

Some electrolyte leakage occurred with all of the electrodes used in this series of tests, but it was found to be concentrated in the boundary region between the active area and the peripheral Teflon rings. It was therefore impossible to obtain meaningful quantitative data. Qualitatively, however, it was observed that the active electrode areas were freer from seepage droplets, the thicker the film.

It would therefore appear that practical electrodes, particularly air electrodes, will require an optimization between rate of seepage and gas accessibility. From the above, as well as repeated experiments with similar electrodes, it is our opinion that at the present state of development, film thicknesses between 0.79 and 2.4 mg Teflon/cm² are the most attractive with regard to over-all performance.

Effect of Other Electrode Parameters and Processing Variables

With the platinum black catalyst several other electrode parameters and processing variables were examined briefly. These included: (*a*) effect of screen wire size, mesh, and material; (*b*) effect of pressure used in final sintering; (*c*) effect of ratio of catalyst to Teflon; (*d*) effect of amount of platinum and Teflon; and (*e*) effect of using a commercially available Teflon film for the surface layer.

Screen characteristics.—Changes in the supporting screens manifested themselves by affecting the cell resistance and the associated IR drop. Even in the small laboratory cells, electrodes constructed with 80-mesh, 3-mil platinum wire screens showed excessively high ohmic drops, particularly when electrodes with narrow tabs were used. At the other extreme were electrodes employing low-resistance silver screens with 7.5-mil wires and wide tabs. The 40- to 45-mesh platinum and nickel screens that were used in most of the work were intermediate in performance.

Sintering pressure.—Variation in the pressure used in preparing electrodes was not examined in detail nor over a wide range. Those prepared at the lowest pressure tested, 180 lb/in.² were lacking in strength, although their electrical performance was excellent. With these electrodes, however, the gaskets from the cell were capable of inducing appreciable flow of the catalyst-Teflon mix and failures occurred around the edges. In general, pressures of the order of 1800 to 3000 lb/in.² were considered most satisfactory for the preparation of electrodes.

Ratio of catalyst to binder.—Electrodes of satisfactory strength and performance can be obtained within the range of platinum-to-Teflon weight ratios from 1:0.05 to 1:0.5. Most of the work was done with the ratio 1:0.09 (*i.e.*, 1g platinum black to 0.10 cc Teflon-30 solution).

Amount of platinum and Teflon.—Experiments were run with alkaline cells using electrodes containing from 17 to 45 mg platinum/cm² (a constant weight ratio of platinum-to-Teflon binder of 1:0.09 was used and the film thickness was maintained at 2.4 mg Teflon/cm²). Pronounced effects were not observed although the thinnest electrodes leaked excessively. Electrodes containing in the range 30-40 mg platinum/cm² appeared to be quite satisfactory and were adopted for most of the remaining work.

Commercial films as surface coatings.—While the major portion of the effort employed sprayed films of Teflon, a few electrodes were made with commercially available Teflon films that had a nominal thickness of ⅛ mil (obtained from Dielectrix, Inc.). These electrodes were prepared in the standard fashion except that the film was added in an extra pressing operation at the end of the regular procedures. At 200 ma/cm² hydrogen-oxygen cell potentials of greater than 0.70v can be realized with such electrodes. Current densities of 500 to 600 ma/cm² can be supported on hydrogen and oxygen but at greatly reduced potentials.

In this connection it is of interest to note that the permeation rates shown in Table II were obtained for the film with the mass spectrometer.[1] Because all spectrometer peaks were established rapidly on placing the gases on the high-pressure side of the film, it was concluded that pores were present. Assuming linear relationships, the tabulated data correspond to permeation rates of 0.073 and 0.063 cc (STP)/min/cm² of the ⅛-mil film for hydrogen and oxygen, respectively, at a pressure differential of 1 atm. The observed currents

[1] The authors are indebted to Dr. F. J. Norton for these measurements.

Table II. Permeation rates for Dielectrix, Inc., ⅛-mil Teflon film

permeation rate, p, in $\frac{\text{cm}^3\text{(STP)}}{\text{sec}} \cdot \frac{\text{mm thickness}}{\text{cm}^2\text{ area} \cdot \text{cm Hg pres.}}$

Temp, °C	H_2	He	O_2	N_2	Ar	SF_6
28	5.1×10^{-8}	2.7×10^{-8}	4.4×10^{-8}	6.8×10^{-8}	2.45×10^{-8}	—
53	2.4×10^{-7}	1.6×10^{-7}	1.45×10^{-7}	1.3×10^{-7}	1.2×10^{-7}	2.55×10^{-8}

of about 500 ma/cm² call for gas consumption rates of about 3.4 and 1.75 cc/min for the hydrogen and oxygen. This would indicate that the film ruptured sufficiently during processing to permit the passage of the additional gas to the catalyst.

While the electrical properties of these electrodes were comparable with the others, seepage of electrolyte through the pores was also comparable.

Effect of Operating Conditions on Cell Performance

Several important operating parameters were varied during the course of the work. In particular, the effects of the liquid and gas pressure heads were considered, as was the effect of the electrolyte concentration. In addition, tests were made to determine the need for an external circulation loop and reservoir.

Effect of electrolyte head.—Polarization data were obtained for several alkaline cells as the electrolyte heads were varied over the range 3-24 in. above the tops of the electrodes. During these tests the circulating loop to the reservoir was not closed. Instead, a "standpipe" arrangement was used with a thin tube filled with electrolyte serving to provide the hydrostatic pressure. Hydrogen and oxygen gas pressures of about 2-3 in. of water were used. The range of pressures covered should easily include the highest excess electrolyte pressures which will be encountered in practical size cells having electrodes up to 20 in. on a side.

Increasing the liquid head results in little change in the electrical performance of the cell or in that of the individual electrodes. A slightly poorer over-all polarization curve obtained with the largest liquid head does, however, appear to be real and may reflect some penetration of the electrolyte into the pores of the electrodes. Reduction of the pressure reversed this effect.

In the small laboratory cells the pressure gradient varies by only 1½ in. from the top of the electrode to the bottom. In a practical device, with its larger electrodes, the gradient will vary considerably more. These experiments indicate, however, that the electrical performance at the different levels will not differ significantly.

Effect of gas pressure.—In looking at the effect of gas pressure on cell performance, a range from 1 to 22 in. of water was covered. The cells were arranged with the electrolyte in a closed loop with a head of 2 or 6 in. above the tops of the electrodes. In these tests a ⅜ in. thick spacer was used between the electrodes to minimize the danger of bridging the gap should gases bubble into the electrolyte. The cells therefore had a somewhat higher internal resistance than normal. As a result the over-all polarization curves obtained with these cells were slightly inferior to others in this paper. It was found that the cells could be operated with gas pressures exceeding the hydraulic head of the electrolyte by as much as 20 in. of water without bubbling into the electrolyte occurring. No pronounced effects that can be attributed directly to changes in the gas pressures were encountered. Indeed, the data were exceptionally reproducible even at the higher current densities.

At the higher current densities the temperatures in the cells were also high. For example, with a cell containing 6*M* KOH as electrolyte at a current density of 580 ma/cm², an electrolyte temperature of 83°C was measured. Under these conditions the anode and cathode temperatures were 82° and 88°C, respectively, and the reservoir measured 38°C. Similar temperatures were obtained with acidic electrolytes. At such temperatures the partial pressure of water is fairly high, particularly at the water-producing electrode where the electrolyte is diluted. For this reason, as well as the fact that cell performance at high current densities is sensitive to gas flow rate, it appears highly likely that steam blanketing of the electrodes may occur.

Effect of the electrolyte concentration.—As noted in the previous section, some cells operating on hydrogen and oxygen and employing 6*M* KOH or 5*N* H_2SO_4 as the electrolytes have shown evidence of some steam blanketing at the electrodes. In an effort to reduce this effect, a number of cells were run with more concentrated electrolytes over which the vapor pressure of water was considerably less.

When 12*M* KOH was used there was, indeed, a slight improvement in performance at high current densities. Unfortunately, however, because of its higher resistivity, this electrolyte tended to heat more than 6*M KOH* at corresponding current densities. In addition, its higher viscosity resulted in less circulation through the external loop and this also contributed to a higher temperature in the cell, *e.g.*, 96° *vs.* 83°C at a current density of 580 ma/cm². This attempt to reduce the vapor pressure of the water was therefore largely self-defeating. In general, however, 12*M* KOH appeared to be an attractive electrolyte. In particular, its higher viscosity resulted in lower seepage rates through the electrodes than were seen with 6*M* KOH.

Attempts to examine the effect of increasing the electrolyte concentration with the acid were unsatisfactory. Sulfuric acid is less effective than potassium hydroxide in reducing the vapor pressure of water, and a 23*N* solution is required to accomplish the reduction equivalent to 12*M* KOH. This concentration of acid proved unsatisfactory. When it heated to a temperature of 60°-70°C, direct reaction with the hydrogen occurred, and hydrogen sulfide formed and poisoned the fuel electrode. A similar behavior was observed with 17*N* H_2SO_4, but in this case when the temperature reached 80°-90°C.

Effect of electrolyte circulation.—Because an external circulation loop such as that used in much of the present work may prove cumbersome in the designing of practical cells, it was of interest to determine whether this is required for satisfactory operation. For this purpose an air-breathing, acid cell was placed in operation without any external circulation. Instead, a small funnel was attached to the top inlet tube on the electrolyte chamber, and water (to compensate for evaporation losses) was added directly to the cell chamber.

That adequate mixing of the electrolyte can be achieved in this way was clearly attested to by steady operation at 0.68 ± 0.02v when the current was held constant at 88 ma/cm². The steady potential was maintained for 25-hr periods both during operation of the cell in this fashion and during operation with a thermal loop when the makeup water was added to the reservoir. Even with larger cells, thermal mixing within the electrolyte chamber should be more than adequate to prevent stratification of the electrolyte when the water is introduced at the top. If stratification were to occur and a water layer formed at the top, the resistance across that layer would be much greater than in the lower acidic region. The current would therefore be concentrated at the bottom of the cell and more power would be dissipated there than at the top. The heat so generated would therefore be distributed in a way to promote convective mixing and thereby destroy concentration gradients within the electrolyte.

If desired, however, makeup water could be introduced at the bottom of the cell chamber. In this case density differences between the makeup water and the electrolyte already in the cell would contribute to the mixing.

Alternative Electrocatalysts

A few exploratory experiments were performed with alternative electrocatalysts. These included silver and activated carbons. Electrodes of both types performed reasonably well with oxygen. This is shown by the data in Fig. 8. The silver electrode used in cell LFC-264 contained approximately 70 mg Silflake-131 (Handy and Harmon) and 7 mg Teflon binder/cm². It was coated with a surface film containing 2.4 mg Teflon/cm². The platinized carbon electrode of cell LFC-282 contained 17 mg amorphous carbon containing 10%

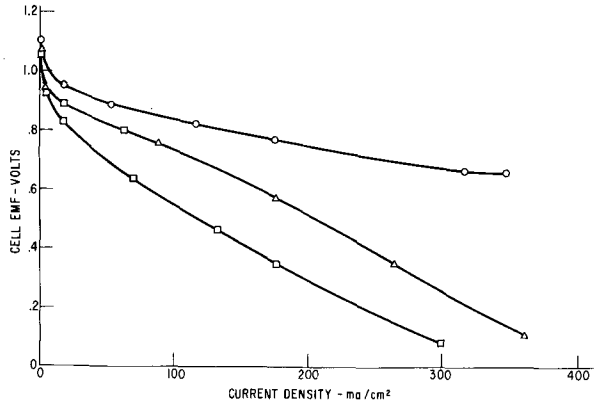

Fig. 8. Performance of cells with various oxygen electrode catalysts. Electrolyte, 6M KOH; anodes, Pt black; cathodes: ○, Pt black LFC-269; △, 10% Pt on amorphous carbon LFC-282; □, Silflake LFC-264; IR drop included.

platinum and 3 mg Teflon binder/cm². It too was coated with a surface film containing 2.4 mg Teflon/cm². The anodes in both of these cells were made with platinum black.

These data are included merely to indicate the promise of some of these less expensive materials as practical electrocatalysts. Actually, the carbon-base material has shown even better performance with both oxygen and hydrogen in the earlier matrix type cells (9). This implies strongly that the carbon electrode of the present example does not represent the optimum in wetting control.

Alternative Electrolytes

In most applications it is desirable to be able to operate a fuel cell on air. With an acidic electrolyte this is no problem since carbon dioxide from the air is not absorbed. However, such electrolytes are more corrosive than caustic electrolytes, and the latter therefore have some advantages in practical cells. These electrolytes, however, are converted to carbonates by the carbon dioxide in the air.

While the resistances of carbonate electrolytes are higher than those of caustics or acids, the difference is not enough to preclude their consideration for use in fuel cells (6,10, 11). It was therefore of interest to examine the performances of a number of them covering the range of compositions that might be encountered as equilibrium electrolytes in air-breathing cells. Room temperature polarization curves for a family of electrolytes from KOH to K_2CO_3 are shown in Fig. 9. The ohmic drop has been eliminated from all of these

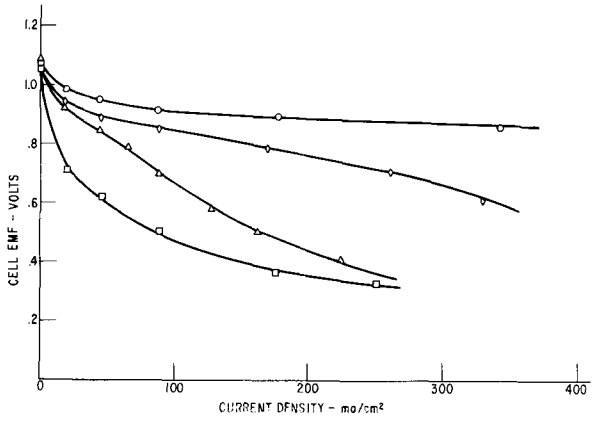

Fig. 9. Effect of carbonate on H_2-O_2 cell performance. Cell LFC-273. Electrodes: body, 35 mg Pt, 3.2 mg Teflon/cm²; film, 2.4 mg Teflon/cm². ○, 6M KOH; ◇, 3M KOH, 1.5M K_2CO_3; △, 1.5M KOH, 2.25M K_2CO_3; □, 3M K_2CO_3; IR drop eliminated.

Table IV. Phosphate solutions tested as fuel cell electrolytes

Solution No.	Electrolyte and concentration	pH
1	5*M* H_3PO_4	<0.0
2	2.5*M* H_3PO_4-2.5*M* NaH_2PO_4	0.8
3	5*M* NaH_2PO_4	3.4
4	2.5*M* NaH_2PO_4-2.5*M* K_2HPO_4	7
5	1.25*M* NaH_2PO_4-1.25*M* K_2HPO_4	7
6	5*M* K_2HPO_4	9

curves, but in no case was the total cell resistance greater than 0.08 ohm.

It is evident that the carbonate has a pronounced effect on performance, largely in the form of adverse effects on electrode polarization. From work with carbonate and bicarbonate electrolytes in the older, low-temperature, matrix-type cells, it was found that the hydrogen electrode is the one that is strongly affected; this appears to be the result of direct reaction between hydrogen and carbonate to form CO or a related species on the electrode surface which then inhibits the electrooxidation of hydrogen (9).

Because of the volatility of CO_2 the composition of the equilibrium electrolyte in an operating cell will be affected by such parameters as temperature, current density, concentration and volume of electrolyte, and other variables. From the data presently available, it is therefore impossible to predict the magnitude of inhibition that will be experienced with such an electrolyte under practical conditions. It is possible, however, that an appreciable penalty will be paid.

In view of the adverse effect of carbonate on cell performance, some attention was given to the possibility of using phosphate solutions as CO_2 rejecting electrolytes. Some of the solutions tested had moderate buffer capacity in the intermediate *p*H region where corrosion problems would be less severe than with strong acids. The electrolytes in Table IV were examined.

It is to be noted that the sodium and potassium salts were chosen for solutions 3 and 6, respectively, on the basis of solubility considerations. The mixture used for solution 4 was also chosen in an effort to avoid precipitation. This was not entirely successful, and some precipitate formed slowly. The less concentrated solution 5 was therefore prepared for additional tests at essentially the same *p*H.

At ambient temperature all of these phosphate electrolytes were inferior to sulfuric acid. In part this was a result of their higher resistances, but there were also pronounced effects on electrode behavior. The oxygen electrode was affected more strongly than the hydrogen electrode, and the effect became more pronounced as the *p*H increased. It is possible that these effects were caused by adsorbed phosphate ions (especially $HPO^{-}{}_4$-), but a straight *p*H effect cannot be precluded. In either case, phosphate solutions, with the exception of those containing phosphoric acid, do not appear attractive as electrolytes.

Performance during Continuous Operation

Seven cells were placed on continuous operation at current densities of 88, 176, or 263 ma/cm² for periods of from 5 days to over 5 months. The first cell was operated with forced circulation of the electrolyte. All of the remaining units were operated with thermal loops.

The hydrogen supply was sufficiently pure to permit operation on static heads of gas with an occasional short purge (a few seconds) to sweep out impurities that slowly accumulated in the fuel electrode's gas chamber. Because the impurity level of the oxygen was higher, it was necessary to continuously vent a slow stream of oxygen from the cells; a rate of less than 1 cc/min was maintained.

Graduated traps in the vent lines permitted the collection of liquid that accumulated in the gas chambers. This included seepage as well as water which distilled from the electrodes to the faceplates of the cells. All

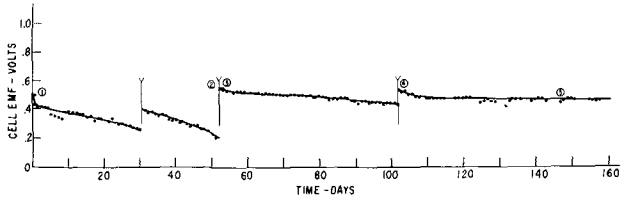

Fig. 10. Performance of acidic H_2-air cell with platinum black electrodes on continuous load. Cell LFC 260. Electrodes, platinum black; electrolyte, 5*N* H_2SO_4; load, 2 amp (176 ma/cm^2). Circled numbers refer to polarization curves; Y refers to replacement of electrolyte.

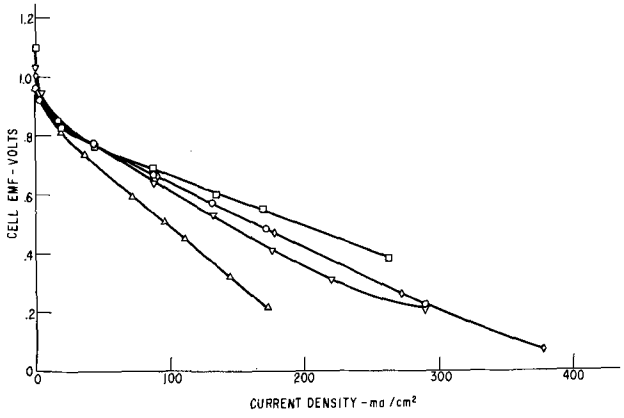

Fig. 11. Polarization curves obtained during tests on continuous load. Cell LFC-260, air cell. Electrodes, platinum black; electrolyte, 5*N* H_2SO_4; ○, initial operation; △, after 52 days' operation; □, after 52 days' operation and cleaning of electrodes; ▽, after 102 days' operation; ◇, after 147 days' operation; IR drop included.

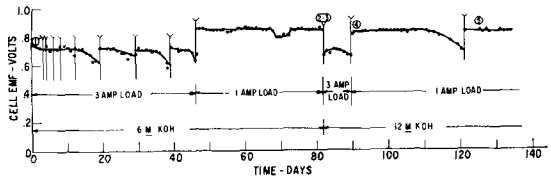

Fig. 12. Performance of alkaline H_2-O_2 cell with platinum black electrodes on continuous load. Cell LFC 269. Electrodes, platinum black; electrolyte, 6 and 12*M* KOH; load, 1 amp (88 ma/cm^2) and 3 amp (263 ma/cm^2). Circled numbers refer to polarization curves; Y refers to replacement of electrolyte.

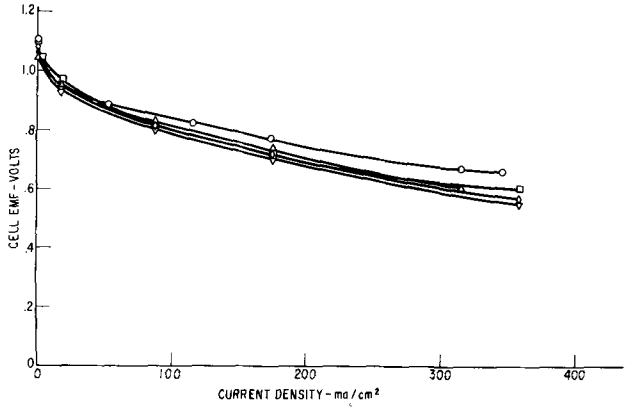

Fig. 13. Polarization curves obtained during tests on continuous load. Cell LFC 269. Electrodes, platinum black; electrolyte, 6 and 12*M* KOH; ○, 6*M* KOH initial operation; △, 6*M* KOH after 82 days' operation; □, 12*M* KOH after 82 days' operation on 6*M* KOH; ▽, 12*M* KOH after 90 days' operation; ◇, 12*M* KOH after 126 days' operation; IR drop included.

was recycled back to the reservoirs. To minimize seepage, electrolyte heads were held to about 1 in. above the tops of the electrodes.

During air operation with a fully exposed electrode, more water was evaporated than was produced in the cell reaction. In such cases makeup water was added periodically to the reservoir.

During operation on oxygen the water formed in the cell reaction gradually diluted the electrolyte so that periodic replacement was required. The need for replacement was generally indicated by a decline in cell performance; the response of the cell to fresh electrolyte was immediate. During early tests about 80 cc of electrolyte were used in charging a system. Later this was increased to about 250 cc in order to extend the periods between replacements.

Some representative performance data are summarized in Fig. 10 through 13. Shown are cell voltages on load as well as polarization curves obtained after various periods of operation. No cell failures occurred during these tests apart from leaks which developed in cell housings.

Cell LFC-260 was one of the first cells to be assembled. Its electrodes are reinforced with 80-mesh, 3-mil wire, platinum screens having narrow tabs. As a result its internal resistance was high, 0.12 ohm, and a drop of about 0.15v occurred in the tabs themselves at the operating current of 2 amp (176 ma/cm^2). Nevertheless, this acid cell gave excellent performance on hydrogen and air for over 160 days as attested to by the data in Fig. 10 and 11.

A word is in order about the performance of this cell during the first 52 days. During this period silicone rubber gaskets were used on the cell. Gradual attack from the acid produced silica which accumulated in the pores of the electrodes. On the 52nd day the cell was disassembled and the electrodes were leached with warm sodium hydroxide. After reassembly with poly(ethylene-butene) copolymer gaskets, the cell performed excellently for over 110 additional days.

Cell LFC-269 contained the same electrodes as provided the data in Fig. 4. They were reinforced with 40-mesh, 4.5-mil wire, rolled nickel screens having wide tabs. This alkaline cell had a considerably lower resistance than LFC-260, *i.e.*, 0.06 ohm. It was operated on hydrogen and oxygen for over 140 days at the current densities indicated in Fig. 12. During the first 19 days a small reservoir charged with 80 ml of electrolyte was used. This was subsequently changed to a larger reservoir with charges of about 250 ml of fresh electrolyte, although the amount was reduced again upon switching to 12*M* KOH. In general, the performance of this cell was excellent, and as shown by the polarization data in Fig. 13 there was no decline in its ability to handle overloads.

Summary and Conclusions

The structure of conducting-porous-Teflon electrodes has been improved with regard to strength, conductivity, and wetting characteristics. In their new form these very thin electrodes (5-10 mils thick) may be employed with aqueous electrolytes without the need for the matrix-type support previously used. The result is a fuel cell having excellent performance characteristics. These include an ability to operate on air at practical current densities of 100-200 ma/cm^2. In other work the new electrodes have also been shown to have excellent performance characteristics with hydrocarbon fuels and with methanol.

The new cells may be operated with the electrolyte circulated through an external loop by thermal pumping, or the electrolyte may be used without such circulation.

A number of cells have been operated continuously for periods of months with encouraging results. One of our first hydrogen-oxygen cells was operated with an acid electrolyte and air as oxidant at a current density

of 176 ma/cm² for over 5 months. A similar alkaline cell was operated on hydrogen and oxygen at current densities of 263 and 88 ma/cm² for a similar period.

Acknowledgments

The authors are indebted to H. A. Liebhafsky, E. J. Cairns, and W. T. Grubb for helpful discussions during the course of this investigation. They also appreciate the assistance of F. J. Norton who measured the permeability of one of the Teflon films, and that of E. F. Koch and R. R. Russell who obtained the photomicrographs of electrodes.

Manuscript received July 1, 1964. This paper was presented at the Washington Meeting, Oct. 11-15, 1964.

Any discussion of this paper will appear in a Discussion Section to be published in the December 1965 JOURNAL.

REFERENCES

1. J. S. Bone, S. Gilman, L. W. Niedrach, and M. D. Read, Proceedings 15th Annual Power Sources Conference, Atlantic City, N. J., p. 47 (1961).
2. L. W. Niedrach, Belgian Pat. No. 617,375 (1962).
3. W. T. Grubb and L. W. Niedrach, Proceedings 17th Annual Power Sources Conference, Atlantic City, N. J., p. 69 (1963).
4. W. T. Grubb and L. W. Niedrach, *This Journal*, **110**, 1086 (1963).
5. W. T. Grubb and C. J. Michalske, *This Journal*, **111**, 1015 (1964).
6. E. J. Cairns and D. C. Bartosik, *This Journal*, **111**, 1205 (1964).
7. Information Bulletin No. -X-50d, E. I. du Pont de Nemours & Co.
8. K. Kordesch and A. Marko, *This Journal*, **107**, 480 (1960).
9. L. W. Niedrach, Unpublished results.
10. E. J. Cairns and D. I. Macdonald, *Electrochem. Technol.*, **2**, 65 (1964).
11. E. Justi, "High Drain Hydrogen-Diffusion Electrode Operating at Ambient Temperature and Low Pressure," 1959. Trans. by T. E. Burton, Res. Inf. Service, Div. Pergamon International Corp., 40 East 23rd St., New York 10, N. Y.

The Active Iron Electrode

I. Iron Dissolution and Hydrogen Evolution Reactions in Acidic Sulfate Solutions[1]

Eugene J. Kelly

The Chemistry Division, Oak Ridge National Laboratory, Oak Ridge, Tennessee

ABSTRACT

The *p*H and potential dependencies of the steady-state iron dissolution and hydrogen evolution reactions were determined for zone-refined iron in H_2-saturated acidic sulfate solutions. The mechanistic significance of the data is examined in detail. The results of this investigation serve to resolve the conflict concerning the mechanism of iron dissolution in noninhibiting media and to provide an experimental and mechanistic base for the interpretation of the electrochemical behavior of the active iron electrode in inhibiting media.

A comparative study has been made of the electrochemical behavior of the active iron electrode in typical inhibiting and noninhibiting media. The purpose of the investigation was to determine the changes produced in the kinetics and mechanistics of a noninhibited system as a result of specific adsorption of an inhibitor. Such information is not only essential to the understanding of corrosion inhibition, but is also relevant to the interpretation of kinetic data for other electrode processes involving adsorption.

The many recent investigations of the active iron electrode in noninhibiting media such as deoxygenated acidic sulfate, perchlorate, and chloride solutions have led to a variety of conflicting results. According to Bonhoeffer (1, 2) and Heusler (1-3), the mechanism of the iron dissolution reaction in sulfate and perchlorate solutions is given by Eq. [1]-[3],

$$Fe + OH^- \rightleftharpoons (FeOH)_{ads} + e^- \quad [1]$$

$$Fe + OH^- + (FeOH)_{ads} \rightarrow (FeOH)_{ads} + (FeOH)^+ + 2e^- \quad [2]$$

$$(FeOH)^+ + H^+ = Fe^{++} + H_2O \quad [3]$$

in which the surface species, $(FeOH)_{ads}$, serves simply as a catalyst for reaction [2]. This system of reactions may be described by Eq. [4] and [5]

$$i_a/\mathbf{F} = \bar{k}_1 a_{(OH^-)}(1-\theta) - \bar{k}_{-1}\beta\theta + 2\bar{k}_2 a_{(OH^-)}\beta\theta \quad [4]$$

$$\beta d\theta/dt = \bar{k}_1 a_{(OH^-)}(1-\theta) - \bar{k}_{-1}\beta\theta \quad [5]$$

where i_a is the net anodic current density corresponding to the iron dissolution reaction, and $\bar{k}_j$ are electrochemical rate constants which, assuming transfer coefficients of ½, are equal to $k_j \exp(\pm\lambda_j \mathbf{F}E/2RT)$, where λ_j is the number of electrons transferred per occurrence of the j^{th} reaction, and the plus and minus signs refer to anodic and cathodic processes, respectively. The definitions of β and θ follow from $(FeOH)_{ads} = \beta\theta$, where $(FeOH)_{ads}$ is the concentration of the catalyst expressed in moles/cm², θ is the fraction of the surface occupied by the catalyst, and β is a proportionality constant. The other symbols have their customary meanings. If $2\bar{k}_2 a_{(OH^-)}\beta\theta >> \bar{k}_1 a_{(OH^-)}(1-\theta) - \bar{k}_{-1}\beta\theta$, *i.e.*, if the contribution of reaction [1] to the net anodic current density is negligible compared to that of reaction [2], then Eq. [4] reduces to Eq. [6]

$$i_a/\mathbf{F} = 2\bar{k}_a a_{(OH^-)}\beta\theta \quad [6]$$

With $d\theta/dt$ equal to zero and $(1-\theta) \approx 1$, Eq. [5] and [6] lead to the steady-state solution

$$\frac{i_{a,\infty}}{\mathbf{F}} = 2k_2\left(\frac{k_1}{k_{-1}}\right) a^2_{(OH^-)} \exp(2\mathbf{F}E/RT) \quad [7]$$

i.e., the steady-state system should be characterized by an anodic Tafel slope of 30 mv/decade, 2.303 $RT/2\mathbf{F}$, and a second order dependency on the hydroxyl ion activity. Using fast polarization techniques, these authors were also able to observe a transient anodic Tafel line having a slope of 60 mv/decade, 2.303 $RT/\mathbf{F}$. This result was accounted for assuming that during the short time interval required to fix the transient anodic Tafel

[1] Research sponsored by U.S. Atomic Energy Commission under contract with the Union Carbide Corporation.

line, θ remains constant at θ_o. Then Eq. [6] becomes Eq. [8]

$$i_{a,o}/\mathbf{F} = 2k_2 a_{(OH^-)}\beta\theta_o \exp(\mathbf{F}E/RT) \quad [8]$$

which shows the first order dependency of reaction [2] on the hydroxyl ion activity, as well as the observed effect of potential on this reaction.

According to Bockris *et al.* (4-6), in sulfate solution the steady-state anodic dissolution reaction is characterized by an anodic Tafel slope of 40 mv/decade, (2/3)(2.303 $RT/\mathbf{F}$), and a first order dependency on the hydroxyl ion activity. To account for their results, they suggested the mechanism

$$Fe + H_2O \rightleftharpoons (FeOH)_{ads} + H^+ + e^- \quad [9]$$

$$(FeOH)_{ads} \rightarrow (FeOH)^+ + e^- \text{ (rate-determining)} \quad [10]$$

$$(FeOH)^+ + H^+ = Fe^{++} + H_2O \quad [11]$$

in which the surface species, $(FeOH)_{ads}$, acts as a reaction intermediate rather than a catalyst. This reaction mechanism is described by Eq. [12] and [13]

$$i_a/\mathbf{F} = \bar{k}_1(1-\theta) - \bar{k}_{-1}a_{(H^+)}\beta\theta + \bar{k}_2\beta\theta \quad [12]$$

$$\beta d\theta/dt = \bar{k}_1(1-\theta) - \bar{k}_{-1}a_{(H^+)}\beta\theta - \bar{k}_2\beta\theta \quad [13]$$

where $a_{(H^+)}$ is the proton activity, and the other symbols retain their previous definitions. For the steady-state case, $d\theta/dt$ is equal to zero. Then, if $\bar{k}_{-1}a_{(H^+)}\beta\theta >> \bar{k}_2\beta\theta$ and $(1-\theta) \approx 1$, Eq. [12] reduces to Eq. [14]

$$\frac{i_{a,\infty}}{\mathbf{F}} = 2\frac{k_1k_2}{k_{-1}a_{(H^+)}}\exp(3\mathbf{F}E/2RT) \quad [14]$$

which is consistent with the observed 40 mv/decade Tafel slope and the first order dependency on the hydroxyl ion activity. These authors also reported a transient anodic Tafel line having a slope of approximately 2.303 $RT/\mathbf{F}$. This was interpreted by assuming that in the process of anodic charging, reaction [9] rapidly attains a state of pseudo-equilibrium, during the attainment of which, the diffusion of protons from the double layer to the bulk of the solution is negligible. Consequently, Eq. [14] gives the current density corresponding to the pseudo-equilibrium state, but with $a_{(H^+)}$ now referring to the pseudo-equilibrium activity of protons, $a_{(H^+),o}$, in the double layer. If the change in potential is sufficiently large to justify the approximation, $a_{(H^+),o} = \beta\theta_o$, then Eq. [14] may be written as Eq. [15]

$$i_{a,0} = i_{a,1}\left(\frac{a_{(H^+)}}{\beta\theta}\right)_1^{1/2}\exp\left[\frac{\mathbf{F}}{RT}(E-E_1)\right] \quad [15]$$

where the subscript one refers to the initial steady state from which the transient measurements originate.

In partial confirmation of the Heusler mechanism, Heusler and Cartledge (7) reported steady-state and transient anodic Tafel slopes of 30 mv/decade and 60 mv/decade, respectively, in 0.5f H_2SO_4, and used the mechanism of reactions [1]-[3] as a basis for the interpretation of the inhibition of iron dissolution by iodide ion and carbon monoxide. Lorenz, Yamaoka, and Fischer (8) reported a steady-state anodic Tafel slope of 30 mv/decade in HCl and (HCl + KCl) solutions, subject to the condition that pH > 1.5 and pH > 2 for the two types of solutions, respectively. These authors criticized the mechanism of Bockris and co-workers, who had earlier criticized the Heusler mechanism. In sulfate and chloride solutions, Hoar (9) and Hurlen (9, 10) found a 30 mv/decade steady-state anodic Tafel line, but a first rather than second order dependency of the anodic reaction on the hydroxyl ion activity. Steady-state anodic Tafel slopes of 30-40 and 50-60 mv/decade in sulfate solution have been reported by Makrides (11), 30 mv/decade in perchlorate solution by Kaesche (12), approximately 100 mv/decade in sulfate solution by Okamoto *et al.* (13), 54 mv/decade in chloride solution by Makrides *et al.* (15), and 68 mv/decade in chloride solution by Stern and Roth (14). Neither order determinations nor detailed mechanisms were included in this latter group of studies.

There is general agreement that the cathodic Tafel line corresponding to the hydrogen evolution reaction in these media has a slope of —120 mv/decade, —2(2.303 $RT/\mathbf{F}$). That the reaction is first order in proton activity would also appear to be reasonably well-established (4, 10). The steady-state current density, $i_{c,\infty}$, is therefore given by Eq. [16]

$$|i_{c,\infty}|/\mathbf{F} = k_c a_{(H^+)}\exp(-\mathbf{F}E/2RT) \quad [16]$$

The mechanistic significance of this equation will be considered in the discussion section.

Relations between the corrosion potential and pH and the corrosion current density and pH may be determined by equating the expressions for the steady-state anodic and cathodic current densities, for example, Eq. [7] and [16] or Eq. [14] and [16]. Bockris and co-workers reported values of —60 mv/pH or —2.303 $RT/\mathbf{F}$ and —½ for (dE_{corr}/dpH) and (d log i_{corr}/dpH), respectively, values which are consistent with Eq. [14] and [16]. Hurlen gave corresponding values of —48 mv/pH or —(4/5)(2.303 $RT/\mathbf{F}$) and —3/5, values which are consistent with Eq. [16] and his expression for the steady-state anodic current density

$$i_{a,\infty}/\mathbf{F} = k_a a_{(OH^-)}\exp(2\mathbf{F}E/RT) \quad [17]$$

On the other hand, Bonhoeffer and Heusler found the corrosion rate to be independent of pH, in agreement with Stern (16), and reported a value of —45 mv/pH for (dE_{corr}/dpH). An inspection of Eq. [7] and [16] shows these observations to be internally inconsistent with the mechanism proposed by these authors, a fact noted by Bockris *et al.* (4). A few of the many other values reported for (dE_{corr}/dpH) are —60 mv/pH by D'Ans and Breckheimer (17), —56 mv/pH by Stern (16) who emphasized the fact that the result was less than —2.303 $RT/\mathbf{F}$, —52 mv/pH by Kaesche (12), and —47 mv/pH by Makrides *et al.* (15) who also reported a logarithmic relation between the corrosion rate and pH.

The preceding review clearly suggests that, prior to attempting to resolve the more complicated inhibited systems, the electrochemical behavior of active iron in noninhibiting media should be re-examined. This paper reports on the results obtained in acidic sulfate solution.

Experimental

In order to circumvent contamination problems associated with the use of rubber, lubricants, etc., the entire cell assembly was made of Pyrex glass and Teflon. The apparatus was so designed that essential operations, such as rapid addition of pre-electrolyzed solutions and the removal of used solutions, could be accomplished without opening the apparatus to the atmosphere. The test electrode compartment, a flat-bottomed cylinder, was fashioned from the male component of a 55/50 TS ground glass joint. The ground surface was carefully removed by fire-polishing, and the rest of the cylinder was provided with a glass jacket by means of which, in conjunction with a circulating water bath, a constant solution temperature of 25.00° ± 0.03°C was maintained. The cap was machined from Teflon, and had a total of nine ports, four standard-taper ports for electrode holders and the remainder for variable position hydrogen inlet and outlet tubes, solution inlet tubes, and a Haber-Luggin capillary probe. These tubes were connected *via* flexible Teflon "spaghetti" tubing (1/16 or 1/8 in. ID) to a hydrogen manifold, reservoirs containing pre-electrolyzed, hydrogen-saturated solutions, and an external reference electrode compartment, respectively. The

reference electrode compartment, holding a saturated calomel electrode, was also jacketed and maintained at 25.00° ± 0.03°C. A tube passed from the bottom of the test electrode compartment, through the wall of the jacket, to a Teflon "T-bore" stopcock. The second arm of the stopcock led to an external counterelectrode compartment, while the third arm served to drain both compartments. A Teflon coated bar-magnet provided stirring in the test electrode compartment.

Iron electrodes studied in this investigation were machined from a small ingot of high-purity, zone-refined electrolytic iron.[2] The analysis of the ingot (Bar 27, Specimen D, Lot 7) in parts per million was as follows: C(10), N(2), H(0.1), S(5), Al(15), Cr(5), Co(1), Cu(2), Mn(0.5), Ni(12), Si(10), and (Sb, As, Ca, Cd, Pb, Mo, Sn, Ti, W, Va, Zn, Zr) not detected.[3] The electrodes were cylindrical, ½ in. long, and either ⅛ (small) or ¼ (large) in. in diameter. The electrodes were mounted on conventional Teflon electrode holders (19).

Sulfuric acid and sodium sulfate solutions were prepared from reagent grade materials and triply distilled water. All solutions were pre-electrolyzed, using an iron cathode, and saturated with hydrogen. Electrolytic hydrogen was purified at 450°C over copper and palladium, and presaturated with water vapor at 25°C.

In a typical experiment, the cell and auxiliary apparatus were cleaned in hot acid solution (equal parts of concentrated H_2SO_4, concentrated HNO_3, and distilled water), rinsed in distilled water, assembled, and leached with test solution. Test electrodes were initially etched in the same acid solution, rinsed in distilled water, and transferred to the cell. Test electrodes remained in test solution from one to several days prior to recording any data, during which period the test solution was replaced frequently by fresh solution from a reservoir. A well-behaved system exhibited no polarization hysteresis phenomena, and this fact was used as the basic criterion by which the suitability of the system for investigation was determined.

Potentials were measured with a high impedance (10^{11} ohms) L&N Model 7664 *p*H and EMF meter, and recorded with a 10 mv Brown recorder. In this investigation, concerned only with the steady-state behavior of iron, a galvanostat was employed in the determination of polarization curves. Steady-states were established within the response time of the recorder, *i.e.*, approximately 3 sec full-scale. For current densities in excess of roughly 1 ma/cm², it was necessary to employ an internal iron counterelectrode in place of the external counterelectrode. A stream of hydrogen through the test solution was maintained at all times, enabling the solution *p*H to be measured with a platinum-hydrogen electrode. The platinum was immersed in the solution only momentarily and then retracted to a position above the solution in order to prevent contamination. Ferrous ion concentration was held to a negligible level by frequent change of the test solution.

Results

A Tafel diagram of typical data obtained in 0.5M H_2SO_4 is shown in Fig. 1, in which the absolute value of the net current density, $|i_n|$, is represented by the solid line passing through the encircled experimental points. The partial cathodic current density, $|i_c|$, corresponding to the hydrogen evolution reaction, exhibits Tafel behavior with the cathodic Tafel line (dashed) having a slope of $-2(2.303\ RT/\mathbf{F})$. Concentration polarization accounts for the deviation from Tafel behavior at high cathodic current densities. The partial anodic current density, i_a, corresponding to the iron dissolution reaction, shows a Tafel region over which the slope is 40 mv/decade, *i.e.*, $(2/3)(2.303\ RT/\mathbf{F})$. No concentration polarization is observed on the anodic side, but at current densities above those shown in Fig. 1, deviation from Tafel behavior as a result of IR-drop becomes significant. The extrapolated anodic and cathodic Tafel lines (dashed) intersect at the observed open-circuit potential, E_{corr}, and fix the magnitude of the corrosion current density, i_{corr}. The partial and net current densities satisfy the relation, $i_n = i_a + i_c$.

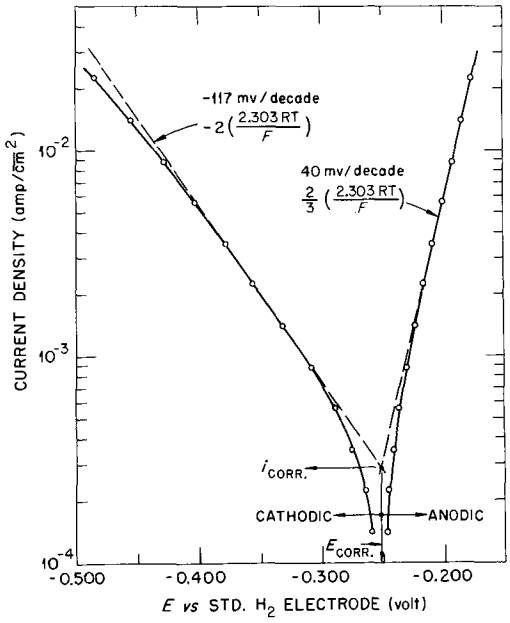

Fig. 1. Polarization of iron in H_2-saturated 0.50M H_2SO_4; T = 30°C.

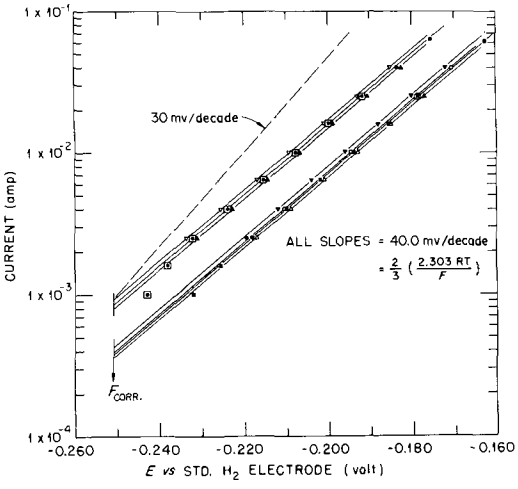

Fig. 2. Anodic polarization of iron in H_2-saturated 0.50M H_2SO_4 (T = 30°C). Data shown for 4 large and 4 small electrodes, each in freshly prepared solution; initial apparent area ratio = 2.86 cm²/1.35 cm² = 2.12.

The purpose of the experiment summarized in Fig. 2 was to resolve the conflict concerning the magnitude of the steady-state anodic Tafel slope. To this end, the anodic polarization characteristics of numerous iron electrodes, each in freshly prepared 0.5M H_2SO_4, were determined. The results clearly show that the steady-state anodic Tafel slope is 40 mv/decade, *i.e.*, $(2/3)(2.303\ RT/\mathbf{F})$, and not 30 mv/decade, as frequently reported, or some other value of less diagnostic significance. For comparative purposes, a line having a slope of 30 mv/decade has been included in Fig. 2. The results also show that a rather high degree of accuracy may be expected when comparing polarization data for different electrodes on the basis of apparent surface areas. At a given potential, the ratio of the average current for the four large electrodes to

[2] Prepared, analyzed, and distributed by Battelle Memorial Institute on behalf of the American Iron and Steel Institute.

[3] See Table I of ref. (18) for limits of detection.

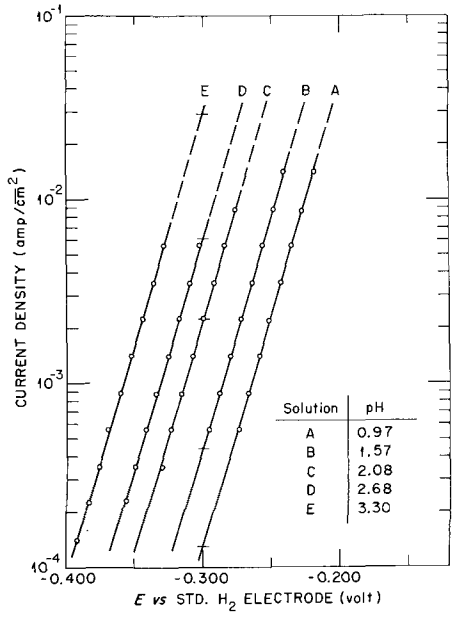

Fig. 3. Anodic polarization of iron in H_2-saturated 0.50M (H_2SO_4 + Na_2SO_4) at various pH values; T = 30°C.

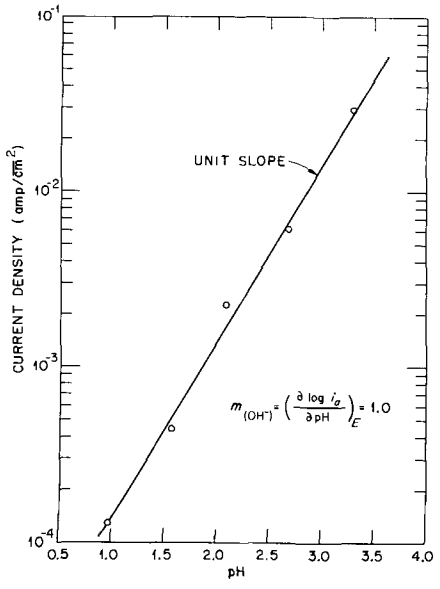

Fig. 4. Anodic current density of iron electrode as function of pH at constant potential (E = —0.300v vs. std. H_2 electrode) in H_2-saturated 0.50M (H_2SO_4 + Na_2SO_4); T = 30°C.

that for the four small electrodes is 2.19, while the apparent area ratio of the large and small electrodes is 2.12. Contamination of the electrode surface by solution impurities, as evidenced by the presence of slow polarization hysteresis phenomena, was occasionally encountered in studies at higher pH values, *i.e.*, in solutions prepared from Na_2SO_4. In such cases, the electrode was found to be less polarizable than normal, and no true Tafel behavior was observed. Normal behavior was restored by replacing the solution and re-etching the test electrode.

On the basis of the results just described, the partial anodic and cathodic current densities may be expressed by Eq. [18] and [19], respectively

$$i_a = k_a a_{(OH^-)}^m \exp(3\mathbf{F}E/2RT) \quad [18]$$

$$|i_c| = k_c a_{(H^+)}^n \exp(-\mathbf{F}E/2RT) \quad [19]$$

in which the reaction orders, m and n, remain to be determined. A direct evaluation of the order of the anodic reaction with respect to the hydroxyl ion activity was made. A single test electrode was placed in solution having a pH of 3.30, and the anodic Tafel line was determined. The pH was then lowered by running H_2-saturated, pre-electrolyzed dilute sulfuric acid directly from a storage reservoir into the cell *via* Teflon tubing and stopcocks connecting the two compartments. In this fashion, the system was maintained in a completely closed state. At each pH, the anodic Tafel line was determined. The results of this experiment are summarized in Fig. 3 which shows the displacement of the anodic Tafel line accompanying changes in solution pH. According to Eq. [18], the reaction order is given by Eq. [20]

$$m = (\partial \log i_a/\partial \mathrm{pH})_E \quad [20]$$

Using the current densities observed at E = —0.300v (marked in Fig. 3 by a horizontal bar), the order plot shown in Fig. 4 was constructed. As the figure shows, a straight line drawn with a unit slope fits the data very closely. Consequently, the anodic reaction is first order in hydroxyl ion activity, and not second order.

According to Eq. [21], which follows directly from Eq. [18]

$$(\partial E/\partial \mathrm{pH})_{i_a} = -(2m/3)(2.303\ RT/\mathbf{F}) \quad [21]$$

the electrode potential at a constant anodic current density should be a linear function of pH and, if m = 1, the proportionality constant should be equal to —40 mv/pH. Using this approach, the results of anodic order determinations performed on several different electrodes are conveniently summarized in Fig. 5. The straight line drawn with a slope of —40 mv/pH fits the data, further confirming the fact that m = 1.

A satisfactory direct evaluation of n, the order of the hydrogen evolution reaction with respect to proton activity, is precluded by concentration polarization. However, at open-circuit, $i_a = |i_c| = i_{corr}$, and $E = E_{corr}$. Consequently, it follows from Eq. [18] and [19] that

$$(dE_{corr}/d\mathrm{pH}) = -(m + n)(2.303\ RT/2\mathbf{F}) \quad [22]$$

i.e., a plot of E_{corr} *vs.* pH should yield a straight line having a slope of $-(m + n)(2.303\ RT/2\mathbf{F})$. Since it has already been established that m = 1, this approach allows an indirect evaluation of n to be made. The results of experiments performed on several different electrodes are shown in Fig. 6. In some instances the data were obtained in a matter of minutes by following the procedure used to determine m, *i.e.*, by starting at the highest pH and then reducing the pH in steps by running H_2SO_4 into the cell from a reservoir. In other cases, the electrodes remained several days at each pH, during which time they were subjected to various polarization experiments. The results confirm the linear

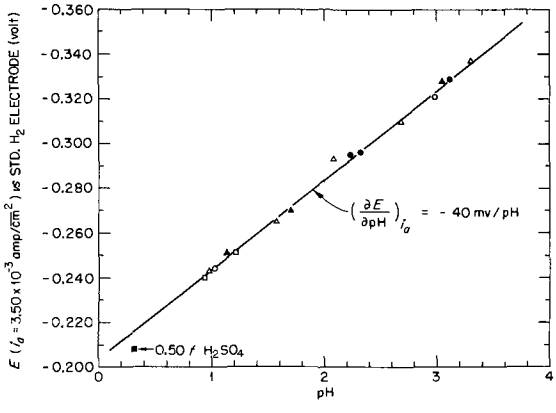

Fig. 5. Variation of the potential corresponding to a partial anodic current density of 3.50 x 10^{-3} amp/cm² with pH for several iron electrodes in H_2-saturated 0.50M (H_2SO_4 + Na_2SO_4); T = 30°C.

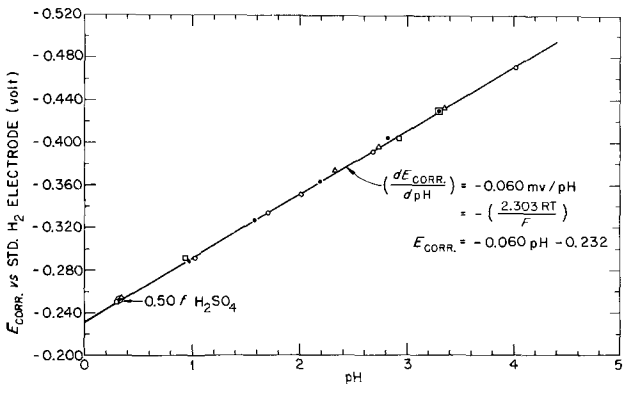

Fig. 6. Variation of the corrosion potential of iron with pH in H_2-saturated 0.50M (H_2SO_4 + Na_2SO_4); T = 30°C. Different electrodes are represented by different symbols (○ and • by fast technique).

relation between E_{corr} and pH and, according to Eq. [22], the observed slope of precisely —60 mv/pH, —2.303 $RT/\mathbf{F}$, means that the hydrogen evolution reaction is first order in proton activity.

Discussion

The experimental results of this investigation are summarized in the following set of self-consistent equations

$$i_{a,\infty} = k_a a_{(OH^-)} \exp(3\mathbf{F}E/2RT) \quad [23]$$

$$|i_{c,\infty}| = k_c a_{(H^+)} \exp(-\mathbf{F}E/2RT) \quad [24]$$

$$E_{corr} = -0.232 - (2.303\,RT/\mathbf{F})\,pH \quad [25]$$

$$\log i_{corr} = -3.15 - (1/2)\,pH \quad [26]$$

in which current densities are expressed in units of amp/cm², and the electrode potential, in volts, is referred to the standard hydrogen electrode. The value of the constant appearing in Eq. [26], —3.15, is based on data obtained in Na_2SO_4 solutions, Fig. 3-5. For 0.5M H_2SO_4, Fig. 1, 2, the constant has a slightly more negative value of —3.38. Equations [25] and [26] show that (dE_{corr}/pH) and (d log i_{corr}/pH) are equal to —60 mv/pH and —½, respectively, and these values may be compared with those cited in the introduction. As a matter of convenience, the hydrogen evolution and iron dissolution reactions are discussed separately.

Hydrogen evolution reaction.—The general reaction scheme for the hydrogen evolution reaction is given by Eq. [27]-[29]

$$H^+ + e^- \rightleftharpoons H_{ads} \quad [27]$$

$$H_{ads} + H^+ + e^- \rightarrow H_2 \quad [28]$$

$$2H_{ads} \rightarrow H_2 \quad [29]$$

in which for the prevailing experimental conditions, dissociation of H_2 can be neglected. If reaction [27] is coupled with reaction [28], the appropriate kinetic equations are Eq. [30] and [31]

$$-i_c/\mathbf{F} = \bar{k}_1 a_{(H^+)}(1-\theta_H) - \bar{k}_{-1}\beta_H\theta_H + \bar{k}_2 a_{(H^+)}\beta_H\theta_H \quad [30]$$

$$\beta_H d\theta_H/dt = \bar{k}_1 a_{(H^+)}(1-\theta_H) - \bar{k}_{-1}\beta_H\theta_H - \bar{k}_2 a_{(H^+)}\beta_H\theta_H \quad [31]$$

in which $\bar{k}_j$ are electrochemical rate constants. The definitions of β_H and θ_H derive from the relation, $[H_{ads}] = \beta_H\theta_H$, where $[H_{ads}]$ is the concentration of adsorbed hydrogen atoms expressed in mole/cm², θ_H is the fraction of the surface occupied by the hydrogen atoms, and β_H is a proportionality constant. In order to achieve agreement with Eq. [24], it is necessary that $(\bar{k}_1 a_{(H^+)} + \bar{k}_2 a_{(H^+)}\beta_H) >> \bar{k}_{-1}\beta_H$, in which case, with $d\theta_H/dt = 0$, Eq. [30] and [31] lead to the steady-state solution represented by Eq. [32] and [33]

$$\theta_{H,\infty} = k_1/(k_1 + k_2\beta_H) \quad [32]$$

$$-i_{c,\infty}/\mathbf{F} = 2\bar{k}_2 a_{(H^+)}\beta_H\theta_{H,\infty} = 2k_2 a_{(H^+)}\beta_H \left(\frac{k_1}{k_1 + k_2\beta_H}\right) \exp(-\mathbf{F}E/2RT) \quad [33]$$

If reaction [27] is coupled with reaction [29], the kinetics are described by Eq. [34] and [35]

$$-i_c/\mathbf{F} = \bar{k}_1 a_{(H^+)}(1-\theta_H) - \bar{k}_{-1}\beta_H\theta_H \quad [34]$$

$$\beta_H d\theta_H/dt = \bar{k}_1 a_{(H^+)}(1-\theta_H) - \bar{k}_{-1}\beta_H\theta_H - 2k_3\beta_H^2\theta_H^2 \quad [35]$$

In this case, agreement with Eq. [24] requires that $2k_3\beta_H^2\theta_H^2 >> \bar{k}_{-1}\beta_H\theta_H$ and $(1-\theta_H) \approx 1$. With these restrictions, the steady-state solution derived from Eq. [34] and [35] is given by Eq. [36] and [37]

$$\theta_{H,\infty} = (k_1 a_{(H^+)}/2k_3\beta_H^2)^{1/2} \exp(-\mathbf{F}E/4RT) \quad [36]$$

$$-i_{c,\infty}/\mathbf{F} = 2k_3\beta_H^2\theta_{H,\infty}^2 = k_1 a_{(H^+)} \exp(-\mathbf{F}E/2RT) \quad [37]$$

The preceding analysis shows that the observed results are consistent with three well-known mechanisms (20),

(*A*) slow discharge-fast electrochemical desorption; Eq. [32], [33], $k_2\beta_H >> k_1$, $(1-\theta_H) \approx 1$

(*B*) fast discharge-slow electrochemical desorption; Eq. [32], [33], $k_1 >> k_2\beta_H$, $\theta_H \approx 1$

(*C*) slow discharge-fast catalytic desorption; Eq. [36], [37], $(1-\theta_H) \approx 1$.

The inability to distinguish among these mechanisms merely on the basis of the dependence of the current density on pH and potential, the inaccessibility of a stoichiometric number for actively corroding iron, and the conflicting opinions generated by various theoretical attempts to establish the rate-determining step (21,22), have resulted in a dilemma which has only recently been resolved with any degree of certainty.

Under certain conditions (23), the steady-state flux of hydrogen atoms diffusing through an iron membrane electrode which divides a cell into two otherwise isolated compartments is given by Eq. [38]

$$f_\infty = \frac{Dk_i\theta_{H,\infty}/k_o l}{1 + (2D/k_o l)} \quad [38]$$

where D is the diffusion coefficient of hydrogen in iron, l is the thickness of the membrane, and k_i and k_o are rate constants associated with the transfer of adsorbed hydrogen atoms from the surface to the interior of the membrane and *vice versa*, respectively. The flux results in a net transfer of hydrogen atoms from the "polarization" side of the membrane, where the surface coverage by adsorbed hydrogen atoms is $\theta_{H,\infty}$, to the "diffusion" side of the membrane. According to Eq. [32], which applies to mechanisms (*A*) and (*B*), $\theta_{H,\infty}$ and, consequently, f_∞ are independent of the potential of the polarization side of the membrane. For mechanism (*C*), Eq. [36] applies and, therefore, $\partial \ln f_\infty/\partial E$ is equal to $-\mathbf{F}/4RT$. This latter result was observed by Devanathan (24), who employed an Armco iron membrane in acidic sulfate solution. At very large cathodic overvoltages, electrochemical desorption predominated, *i.e.*, mechanism (*C*) was replaced by mechanism (*A*). Again, according to Eq. [33], [37], and [38], the steady-state flux should be proportional to $|i_{c,\infty}|$ for mechanisms (*A*) and (*B*), and to $(|i_{c,\infty}|)^{1/2}$ for mechanism (*C*). The latter observation has been reported many times for Armco and comparable irons (23).

In experiments of the type just described, the kinetics of the hydrogen evolution reaction occurring on the polarization side of the membrane are examined. An alternative approach is to study the effects produced by diffusing atomic hydrogen on the kinetics of

the hydrogen evolution reaction occurring on the diffusion side of the membrane (25). Differentiation of Eq. 34 leads to Eq. [39]

$$\left(\frac{dE}{d\theta_H}\right)_{ic} = \frac{(-2RT/F)(\bar{k}_1 a_{(H^+)} + \bar{k}_{-1}\beta_H)}{\bar{k}_1 a_{(H^+)}(1-\theta_H) + \bar{k}_{-1}\beta_H\theta_H} \quad [39]$$

from which it is apparent that $(dE/d\theta_H)_{ic}$ is negative, *i.e.*, for mechanism (*C*) an increase in θ_H resulting from diffusion of hydrogen from the polarization side of the membrane to the diffusion side causes the potential of the latter surface, under cathodic polarization at a constant current density, to become less noble. Similarly, differentiation of Eq. [30] gives Eq. [40]

$$\left(\frac{dE}{d\theta_H}\right)_{ic} = \frac{(-2RT/F)(\bar{k}_1 a_{(H^+)} + \bar{k}_{-1}\beta_H - \bar{k}_2 a_{(H^+)}\beta_H)}{\bar{k}_1 a_{(H^+)}(1-\theta_H) + \bar{k}_{-1}\beta_H\theta_H + \bar{k}_2 a_{(H^+)}\beta_H\theta_H} \quad [40]$$

and if $\bar{k}_1 a_{(H^+)} > \bar{k}_2 a_{(H^+)}\beta_H$, as in mechanism (*B*), then $(dE/d\theta_H)_{ic}$ is again negative. On the other hand, if $\bar{k}_2 a_{(H^+)}\beta_H > \bar{k}_1 a_{(H^+)}$, then $(dE/d\theta_H)_{ic}$ is positive except for the unlikely case where $\bar{k}_2 a_{(H^+)}\beta_H - \bar{k}_1 a_{(H^+)} < \bar{k}_{-1}\beta_H$, a condition which when coupled with the restriction leading to Eq. [32], [33], $\bar{k}_1 a_{(H^+)} + \bar{k}_2 a_{(H^+)}\beta_H >> \bar{k}_{-1}\beta_H$, would require $k_1 \approx k_2\beta_H$. With $\bar{k}_2 a_{(H^+)}\beta_H >> \bar{k}_1 a_{(H^+)}$, as in mechanism (*A*), $(dE/d\theta_H)_{ic}$ is positive. Kovba and Bagotskaya (26) found that for zone-refined iron in 0.5M H_2SO_4, $(dE/d\theta_H)_{ic}$ is positive, *i.e.*, mechanism (*A*) prevails. For Armco iron in the same medium, the results were less definitive, but were interpreted as being indicative of mechanism (*C*), in agreement with Devanathan's findings.

Bockris and Koch (27) examined the relative rates of hydrogen and deuterium evolution on spectroscopically pure iron and found the results to be consistent only with a slow discharge mechanism. The absence of any significant pseudocapacity associated with changes in θ_H, together with the fact that $(1-\theta_H) \approx 1$, also establishes slow discharge as the rate-determining reaction, both on zone-refined (6) and Armco (24) iron.

Contrary to previous reports favoring slow electrochemical desorption as the rate-determining step, [28], [29], all of the results just described confirm slow proton discharge, $H^+ + e^- \rightarrow H_{ads}$, as the rate-determining reaction for hydrogen evolution on iron. For zone-refined iron, the preceding discussion indicates that the experimental results of the present investigation, Eq. [24], may be attributed to mechanism (*A*), slow discharge-fast electrochemical desorption.

Iron dissolution reaction.—As is shown by Eq. [23], the steady-state anodic Tafel slope, $(\partial E/\partial \log i_{a,\infty})_{pH}$, is equal to 40 mv/decade, *i.e.*, (2/3) (2.303 *RT*/**F**), and the reaction is first order in hydroxyl ion activity. These results are in agreement only with those of Bockris *et al.* (4-6), as may be seen by comparing Eq. [23] and [14]. Equation [23] may be interpreted in terms of the following mechanism

$$Fe + H_2O \rightleftharpoons Fe(H_2O)_{ads} \quad [41]$$

$$Fe(H_2O)_{ads} \rightleftharpoons Fe(OH^-)_{ads} + H^+ \quad [42]$$

$$Fe(OH^-)_{ads} \rightleftharpoons (FeOH)_{ads} + e^- \quad [43]$$

$$(FeOH)_{ads} \rightarrow (FeOH)^+ + e^- \text{ (rate-determining)} \quad [44]$$

$$(FeOH)^+ + H^+ = Fe^{++} + H_2O \quad [45]$$

which takes formal account of the simultaneous coverage of the electrode surface by adsorbed water molecules, hydroxyl ions, and the surface intermediate, $(FeOH)_{ads}$. A kinetic description of this mechanism is given by Eq. [46]-[49]

$$i_a/\mathbf{F} = \bar{k}_3\beta\theta_2 - \bar{k}_{-3}\beta\theta_3 + \bar{k}_4\beta\theta_3 \quad [46]$$

$$\beta d\theta_1/dt = \bar{k}_1(1-\theta_T) - \bar{k}_{-1}\beta\theta_1 - \bar{k}_2\beta\theta_1 + \bar{k}_{-2}a_{(H^+)}\beta\theta_2 \quad [47]$$

$$\beta d\theta_2/dt = \bar{k}_2\beta\theta_1 - \bar{k}_{-2}a_{(H^+)}\beta\theta_2 - \bar{k}_3\beta\theta_2 + \bar{k}_{-3}\beta\theta_3 \quad [48]$$

$$\beta d\theta_3/dt = \bar{k}_3\beta\theta_2 - \bar{k}_{-3}\beta\theta_3 - \bar{k}_4\beta\theta_3 \quad [49]$$

in which $\bar{k}_j$ are electrochemical rate constants, and θ_1, θ_2, and θ_3 represent the fractions of the electrode surface occupied by $Fe(H_2O)_{ads}$, $Fe(OH^-)_{ads}$, and $(FeOH)_{ads}$, respectively, *i.e.*,

$$Fe(H_2O)_{ads} = \beta\theta_1, \quad Fe(OH^-)_{ads} = \beta\theta_2, \quad (FeOH)_{ads} = \beta\theta_3$$

where the surface concentrations are expressed in mole/cm^2, and β is a proportionality constant. The total fraction of the surface occupied, θ_T, is equal to $(\theta_1 + \theta_2 + \theta_3)$. Equations [46]-[49] reduce to the steady-state solution

$$i_{a,\infty}/\mathbf{F} = 2k_4\beta\frac{k_3k_2}{k_{-3}k_{-2}a_{(H^+)}}\left(\frac{k_1}{k_1 + k_{-1}\beta}\right)\exp(3\mathbf{F}E/2RT) \quad [50]$$

which agrees with the observed results, Eq. [23]. The conditions leading to Eq. [50] are $\bar{k}_{-3} >> \bar{k}_4$ and $1 >> (\theta_2 + \theta_3)$. With $\theta_T \approx 1$, the latter condition means that $\theta_1 \approx 1$, *i.e.*, $k_1/(k_1 + k_{-1}\beta) \approx 1$. An alternative approach is to assume that for an instantaneous value of θ_3, the remainder of the occupied surface is divided between θ_1 and θ_2 in accordance with reaction [42] in equilibrium, *i.e.*, $\theta_1/\theta_2 = \bar{k}_{-2}a_{(H^+)}/\bar{k}_2$. Then, with $\theta_1/\theta_2 >> 1$ and $\theta_T \approx 1$, Eq. [46] and [49] reduce to Eq. [51] and [52].

$$i_a/\mathbf{F} = \bar{k}_3\beta(\bar{k}_2/\bar{k}_{-2}a_{(H^+)})(1-\theta_3) - \bar{k}_{-3}\beta\theta_3 + \bar{k}_4\beta\theta_3 \quad [51]$$

$$\beta d\theta_3/dt = \bar{k}_3\beta(\bar{k}_2/\bar{k}_{-2}a_{(H^+)})(1-\theta_3) - \bar{k}_{-3}\beta\theta_3 - \bar{k}_4\beta\theta_3 \quad [52]$$

If $\bar{k}_{-3} >> \bar{k}_4$ and $(1 - \theta_3) \approx 1$, then in the steady-state, $d\theta_3/dt = 0$, the current density is again given by Eq. [50].

A comparison of Eq. [51], [52], and [50] with Eq. [12], [13], and [14], respectively, reveals that the mechanism presented here, Eq. [41]-[45], is basically equivalent to that proposed by Bockris *et al.* (4-6), Eq. [9]-[11], in which the adsorption of water and hydroxyl ions was ignored. The necessity for taking into account the adsorption of these species becomes evident when specific adsorption of an anion inhibitor is considered, as in the second paper of this series. In advocating a modified form of the Heusler mechanism, Lorenz, Yamaoka, and Fischer (8) criticized the Bockris mechanism on several counts. Their objections may be dealt with more effectively if, first, the original and modified forms of the Heusler mechanism are examined. The modified version is shown by Eq. [53]-[56]

$$Fe + OH^- \rightleftharpoons (FeOH)_{ads} + e^- \quad \text{fast} \quad [53]$$

$$(FeOH)_{ads} + Fe \rightleftharpoons Fe(OHFe)_{ads} \equiv K \quad \text{slow} \quad [54]$$

$$Fe(OHFe)_{ads} + OH^- \rightleftharpoons FeOH^+ + (FeOH)_{ads} + 2e^- \quad \text{r.d.s.} \quad [55]$$

$$FeOH^+ + x\cdot H_2O \rightleftharpoons Fe^{++}\cdot aq + OH^- \quad \text{fast} \quad [56]$$

In both the original and modified versions, the steady-state and transient anodic current densities are given by Eq. [7] and [8], respectively, although in the modified version, $k_2\beta\theta_o$ is replaced by k_3K_o in Eq. [8] and k_2 is replaced by k_3k_2/k_{-2} in Eq. [7]. Equating $i_{a,\infty}$ and $|i_{c,\infty}|$, the latter being given by Eq. [19], one finds that $(dE_{corr}/dp\text{H})$ and $(d \log i_{corr}/dp\text{H})$ are equal to $-(2/5)(n+2)(2.303\ RT/\mathbf{F})$ and $-(4n-2)/5$, respectively. The order of the hydrogen evolution reaction with respect to proton activity was not determined by Heusler, but with the reported value of zero for $(d \log i_{corr}/dp\text{H})$, n would necessarily be equal to ½,

and (dE_{corr}/dpH) would then be $-2.303\ RT/\mathbf{F}$, *i.e.*, -60 mv/pH. Not only does $n = \frac{1}{2}$ have no theoretical basis, but it is now established that $n = 1$. With $n = 1$, (dE_{corr}/dpH) and $d \log i_{corr}/dpH)$ would be equal to $-(6/5)(2.303\ RT/\mathbf{F})$, *i.e.*, -70 mv/pH, and $-2/5$, respectively. The reported values of -45 mv/pH and 0 constitute an internal inconsistency in both versions of the mechanism. According to Eq. [7] and [8], the steady-state and transient current densities are second and first order in hydroxyl ion activity, respectively. In view of the discrepancies just cited, it is of interest to examine the method employed in determining these reaction orders. Equations [7] and [8] are of the form

$$i_a = k_a a_{(OH^-)}^m \exp(\alpha \mathbf{F}E/RT)$$

from which it follows that m is given by Eq. [57]

$$m = \left(\frac{\partial \log i_a}{\partial pH}\right)_E = -\left(\frac{\partial E}{\partial pH}\right)_{i_a} \Big/ \left(\frac{\partial E}{\partial \log i_a}\right)_{pH} \quad [57]$$

However, $(\partial E/\partial pH)_{i_a}$ was identified with (dE_{corr}/dpH), which is possible only if $(d \log i_{corr}/dpH)$ is zero. With (dE_{corr}/dpH) equal to -45 mv/pH and $(\partial E/\partial \log i_a)$ equal to 60 mv/decade and 30 mv/decade for the transient and steady-state, respectively, the corresponding reaction orders were 3/4 and 3/2. Conceding that (dE_{corr}/dpH) should probably be -60 mv/pH, the orders were promoted from 3/4 and 3/2 to 1 and 2. One can only conclude that either $n = \frac{1}{2}$, an experimentally and theoretically unacceptable value, or Eq. [7] and [8] are incorrect. A further discrepancy in the original Heusler mechanism is revealed by a consideration of anodic transients under potentiostatic conditions. Heusler found that at constant potential log $(i_{a,\infty} - i_{a,t})$ was a linear function of time. Data were presented for two values of the electrode potential, and a 40 mv increase in the potential was accompanied by a decrease in the time constant, $-dt/d\ln(i_{a,\infty} - i_{a,t})$, from 0.28 sec to 0.25 sec. At constant potential, Eq. [5] may be solved for θ as a function of time, and if the result is substituted into Eq. [4], the anodic current density is given by Eq. [58]

$$(i_{a,\infty} - i_{a,t}) = (i_{a,\infty} - i_{a,o}) \exp(-\bar{k}_{-1}t) \quad [58]$$

which shows that the time constant is actually $1/\bar{k}_{-1}$ and, consequently, potential-dependent. In contrast to the observed effect, an increase of 40 mv in the potential should have caused the time constant to increase by a factor of 4.64. In the modified version of the mechanism, this discrepancy, the existence of which was not noted, has been inadvertently overcome since in this formulation the time constant would be equal to $1/k_{-2}$ and, therefore, potential independent. An additional difficulty in either version arises from the fact that the hydroxyl ion concentration is far too low in acid solution to support the current densities observed. This problem is not circumvented by the suggestion (3) that the hydroxyl ion concentration at the electrode surface can be much greater than in the interior of the solution if hydroxyl ions are more strongly adsorbed than water dipoles for, from a kinetic viewpoint, it would still be necessary to replace Eq. [1] and [53] by Eq. [41]-[43], and OH^- by $Fe(OH^-)_{ads}$ in Eq. [2] and [55]. However, this would raise a question concerning the potential dependency of reactions [2] and [55], since the pre-electrode plane could no longer be identified with the outer Helmholtz plane. Finally, the use of two electron transfer reactions such as reactions [2] and [55] has been appropriately criticized by Bockris *et al.* (4). In reply to the criticism, it has been suggested (8) that two electron transfer reactions may be regarded as the sum of two parallel one electron transfer reactions, but this would result in the reaction having a potential dependency characteristic of a one electron transfer reaction, *i.e.*, $\mathbf{F}E/2RT$ and not $\mathbf{F}E/RT$.

In contrast to the serious defects present in the original and modified forms of the Heusler mechanism, the criticisms leveled by Lorenz, Yamaoka, and Fischer (8) against the Bockris mechanism and, by equability, the mechanism of Eq. [41]-[45], may be shown to be without substance. The following criticisms were leveled against the Bockris mechanism:

1. The steady-state relation derived from the transient current density-potential relation calls for a Tafel slope of 40 mv/decade instead of the reproducible experimental value of 30 mv/decade.
2. The steady-state relation also calls for an electrochemical reaction order with respect to hydroxyl ion activity of 1 instead of 2.
3. The transient current density-potential relation offers no precise statement concerning the electrochemical reaction order.
4. The initial polarization value in the potential-time curve does not disappear when an iron rotating-disk electrode ($\omega = 4800$ rpm) is used.

The first two points require no comment beyond pointing out that the steady-state results, Eq. [23], derive only from direct steady-state measurements and not from transient measurements. Interpretations of transient data which lead to a conflict with Eq. [23] must necessarily be incorrect. The present investigation, being limited to steady-state measurements, offers no direct experimental confirmation of the interpretation suggested by Bockris *et al.* (5, 6) for the transient anodic Tafel line. However, the feasibility of their interpretation, an interpretation which is not in conflict with steady-state results, is not lessened by the third and fourth criticisms listed above. The third point can only be regarded as a matter of semantics for, as was shown in the introduction, the relation between the anodic current density and proton activity is precisely defined, *i.e.*, the anodic current density is inversely proportional to the existing proton activity in the double layer, both in the transient and steady states. With regard to the fourth point, the interpretation of the transient Tafel line observed during anodic charging is based on the assumption that during the time required for reaction [9] to attain a pseudo-equilibrium state, $\bar{k}_{-1}\beta\theta_H a_{(H^+,D.L.)} >> f_{diff}$ (here f_{diff} represents the net diffusion flux of protons from the double layer, where the proton activity is $a_{(H^+,D.L.)}$, to the bulk of the solution). Rotation of the electrode does not necessarily invalidate this inequality and, consequently, although it would affect the rate of decay of the transient, it may have no effect whatsoever on the transient Tafel line, *i.e.*, the observation that the initial polarization value does not disappear (or diminish) can not be regarded as evidence against the interpretation proposed by Bockris *et al.* (5, 6) for the transient Tafel line.

The diversity in the results obtained by other investigators may be attributed to contamination of the electrode surface, as evidenced by the presence of slow polarization hysteresis phenomena. In such contaminated systems, illusory steady-state Tafel behavior is observed if the time lapse in the determination of log *i vs. E* curves is small compared to the time required to significantly alter the state of the electrode surface (30).

Summary

The electrochemical behavior of the active iron electrode in the absence of an inhibitor has been determined, and the results may serve as an experimental and mechanistic base for the interpretation of the electrochemical behavior of iron in inhibited systems. In addition, the results of this investigation suggest that the electrochemical behavior of cobalt in noninhibiting media be carefully re-examined since, in acidic sulfate solution, the system has been interpreted (31-32) in terms of the Heusler mechanism for iron, although there is earlier evidence (33) which indicates that the mechanism presented here may be more appropriate.

Acknowledgment

The author is especially indebted to Dr. G. H. Cartledge for his continued encouragement and resolute support. He also wishes to acknowledge the kind support of Dr. P. H. Emmett.

Manuscript received July 20, 1964.

Any discussion of this paper will appear in a Discussion Section to be published in the December 1965 JOURNAL.

REFERENCES

1. K. F. Bonhoeffer and K. E. Heusler, *Z. physik. Chem., N.F.*, **8**, 390 (1956).
2. K. F. Bonhoeffer and K. E. Heusler, *Z. Elektrochem.*, **61**, 122 (1957).
3. K. E. Heusler, *ibid.*, **62**, 582 (1958).
4. J. O'M. Bockris, D. Drazic, and A. R. Despic, *Electrochim. Acta*, **4**, 325 (1961).
5. J. O'M. Bockris and H. Kita, *This Journal*, **108**, 676 (1961).
6. J. O'M. Bockris and D. Drazic, *Electrochim. Acta*, **7**, 293 (1962).
7. K. E. Heusler and G. H. Cartledge, *This Journal*, **108**, 732 (1961).
8. W. Lorenz, H. Yamaoka, and H. Fischer, *Ber. Bunsenges. Physik. Chem.*, **67**, 932 (1963).
9. T. P. Hoar and T. Hurlen, Proc. 8th Meeting CITCE, Madrid, 1956, p. 445, Butterworths, London (1958).
10. T. Hurlen, *Acta Chem. Scand.*, **14**, 1533, 1555, 1564 (1960).
11. A. C. Makrides, *This Journal*, **107**, 869 (1960).
12. H. Kaesche, *Z. Elektrochem.*, **63**, 492 (1959).
13. G. Okamoto, M. Nagayama, and N. Sato, Proc. 8th Meeting CITCE, Madrid, 1956, p. 72, Butterworths, London (1958).
14. M. Stern and R. M. Roth, *This Journal*, **104**, 390 (1957).
15. A. C. Makrides, N. W. Komodromos, and N. Hackerman, *ibid.*, **102**, 363 (1955).
16. M. Stern, *ibid.*, **102**, 609 (1955).
17. J. D'Ans and W. Breckheimer, *Z. Elektrochem.*, **56**, 585 (1952).
18. R. E. Heffelfinger, D. L. Chase, G. W. Regnstorff, and W. Henry, *Anal. Chem.*, **30**, 112 (1958).
19. R. E. Meyer, *This Journal*, **106**, 930 (1959).
20. J. O'M. Bockris and H. Mauser, *Can. J. Chem.*, **37**, 475 (1959).
21. B. E. Conway and J. O'M. Bockris, *J. Chem. Phys.*, **26**, 532 (1957).
22. L. I. Krishtalik, *Zh. Fiz. Khim.*, **34**, 117 (1960).
23. L. I. Freiman and V. A. Titov, *ibid.*, **34**, 23 (1960).
24. M. A. V. Devanathan and Z. Stachurski, *This Journal*, **111**, 619 (1964).
25. A. N. Frumkin, *Zh. Fiz. Khim.*, **31**, 1875 (1957).
26. L. D. Kovba and I. A. Bagotskaya, *ibid.*, **38**, 217 (1964).
27. J. O'M. Bockris and D. F. A. Koch, *J. Phys. Chem.*, **65**, 1941 (1961).
28. N. Pentland, J. O'M. Bockris, and E. Sheldon, *This Journal*, **104**, 182 (1957).
29. J. O'M. Bockris, Proc. 4th Conf. Electrochem., Moscow, 1956, pp. 56, 101, Academy of Science, Moscow (1959).
30. E. J. Kelly, Chem. Div. Ann. Prog. Rept. June 20, 1963, ORNL-3488, p. 93.
31 K. E. Heusler, *Z. Elektrochem.*, **66**, 177 (1962).
32. Z. A. Iofa and Bao-Min Bei, *Zh. Fiz. Khim.*, **36**, 2558 (1962).
33. V. I. Kravtsov and O. G. Lokshtanova, *ibid.*, **36**, 2362 (1962).

On the Initiation and Growth of Stress Corrosion Cracks in Tarnished Brass

A. J. McEvily, Jr., and A. P. Bond

Scientific Laboratory, Ford Motor Company, Dearborn, Michigan

ABSTRACT

Stress corrosion cracking of α-brass was studied in nearly neutral ammoniacal copper sulfate. Under the test conditions, this solution produced a thin, adherent oxide film on the brass. Microstructural studies of the fracture surfaces suggest that alternate formation and rupture of this film leads to initiation and propagation of stress corrosion cracks. Crack propagation rates were measured in sheet specimens with a central notch and found to be proportional to $\sigma_g^2 l$, where σ_g is the applied stress and l is the semicrack length.

Among the various mechanisms proposed for stress corrosion cracking are those based on film rupture (1), on structure sensitive sites together with dislocation interactions, on stacking faults, on short range order (2-7), on strain assisted anodic dissolution (8, 9), on stress-sorption (10), and on solid solution effects (11). Such a variety of proposals is an indication that no general mechanism exists, but that one or another is applicable under certain circumstances. However, the lack of a comprehensive study of the role of stress on the initiation and growth of stress corrosion cracks contributes to the uncertainty in deciding which of the many proposed mechanisms is applicable to a case at hand. In the present investigation the role of stress in crack initiation and growth was determined for the stress corrosion of α-brass in an ammoniacal solution. Since it has been suggested (12, 13) that the tarnish which forms on α-brass plays an important role in stress corrosion cracking, it appeared desirable to examine the characteristics of this tarnish in some detail.

Experimental

Materials.—α-brass (70 w/o Cu-30 w/o Zn) (w/o is weight per cent) in both the annealed as well as a cold-worked condition, was chosen for this study because information is available on its susceptibility to stress corrosion cracking under various environmental conditions (13, 14). Annealed specimens, obtained from sheet material, were 0.031 in. thick, and were heat-treated for 2 hr at 500°C in an argon atmosphere. The cold-worked specimens (75% reduction) were 0.015 in. thick. The tensile properties of the materials used were as follows:

	Proportional limit, psi	Yield strength, psi	Tensile strength, psi
Cold Rolled	60,000	95,000	98,000
Annealed	15,000	18,000	52,000

Specimens.—An electropolished tensile strip, ½ in. wide, was used primarily to study the characteristics of the tarnish. A second type of specimen, shown in Fig. 1, was used to study crack growth. A centrally located stress-raising slit localized the region of crack initiation and was made by drilling a hole and then slitting further in the width direction to the desired slit length. Slitting was accomplished by the reciprocating action of a thread impregnated with diamond paste, and provided a reproducible stress-raiser essentially free of

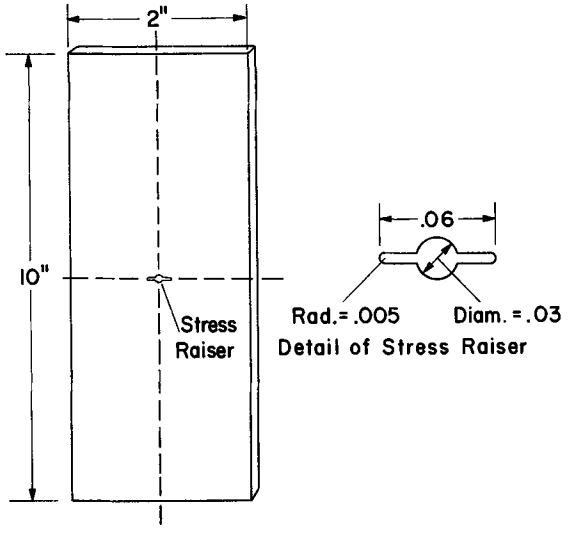

Fig. 1. Specimen used in the determination of rate of crack propagation.

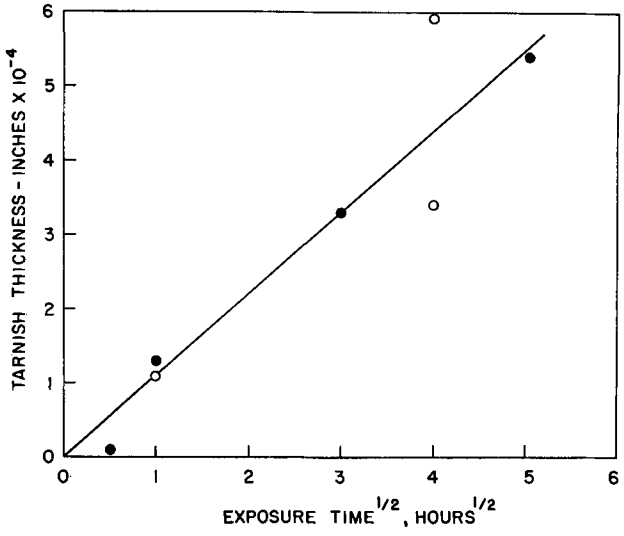

Fig. 2. Tarnishing of brass in 0.05M $CuSO_4$ + 0.48M $(NH_4)_2SO_4$ of pH = 7.25; ○, annealed; ●, cold rolled.

the residual stresses which are characteristic of machined slits or notches. The surfaces of these specimens were lightly polished using metallographic techniques to facilitate the observation of crack growth.

Solution.—The solution shown by Mattson (13) to lead to rapid stress corrosion cracking of α-brass was used. It was 0.05M in $CuSO_4$ and 0.48M in $(NH_4)_2SO_4$ with the *p*H adjusted to 7.25 ± 0.05 with NH_4OH. As Mattson noted (13), the reproducibility is somewhat improved by aging the solution about 24 hr. A small amount of precipitate is formed during this period, but little if any further precipitation was observed subsequently, even during long-time stress corrosion runs.

Tests.—Specimens were tested in a dead-weight, lever-type creep machine, load being transmitted to the specimen through a universal joint to eliminate bending stresses. A plexiglass container, sealed to the specimen below the notch by means of a rubber gasket, was filled with solution after loading. To minimize changes in solution composition, fresh solution was continuously introduced into the cell at a rate of about 80 ml/hr. Initial experiments revealed that attack was rapid at the solution-air interface. To avoid this effect, specimens were coated with Glyptal in the vicinity of the interface.

Crack growth was observed with a low-power microscope (30X) equipped with a micrometer eyepiece. A light source was used to illuminate the specimen surface, and cracks were easily visible through the solution. The lengths of the cracks developed from each end of the slit on both faces were recorded as a function of time. A timer equipped with a cut-off switch automatically recorded the total time to rupture. The applied load was fixed during most of the tests, but in a few instances was altered during a test in order to study the influence of prior load history on the rate of growth of the cracks.

Results

The tarnish.—Forty and Humble (12) concluded that tarnish consists of Cu_2O platelets in a dezincified matrix, with the volume of tarnish about the same as that of the brass replaced. Pickering and Swann (4) have also observed Cu_2O particles in the surface of α-brass exposed to an ammoniacal atmosphere. The tarnish is not the only corrosion product since our tarnished specimens exhibited a weight loss rather than a weight gain. Thus an appreciable fraction of the corrosion products is soluble.

The rate of formation of tarnish, measured by taper-sectioning unstressed specimens which had been immersed in the tarnishing solution for various periods of time, is shown in Fig. 2. Some difficulty was experienced in preparing these taper sections as a consequence of the weak and friable nature of the tarnish. The thickness of the tarnish, x, can be approximated by the equation

$$x = c\sqrt{t} \qquad [1]$$

where c is a constant equal to 1.1 x 10^{-4} in./$hr^{1/2}$, and t is the immersion time in hours. This relation indicates that the rate of tarnish formation is governed by a diffusion process. Figure 2 shows that the average rate of tarnish formation was about the same for annealed and cold-worked specimens, and this is consistent with Pickering and Swann's observation that static dislocations are not sites of preferential chemical attack. It has been reported that in annealed brass the rate of tarnish formation at grain boundaries is greater than within the grains (12).

A micrograph of a taper section through the tarnish layer is shown in Fig. 3. Electron micrographs of replicas stripped from the tarnished surfaces showed that the surface roughened with increasing exposure time.

In order to determine the effect of stress applied during tarnishing, tensile strips of cold-worked brass were loaded to various levels below the proportional limit, and the change in length was noted as a function of time. In the absence of the solution, no extension occurred. Results for tarnished specimens are shown in Fig. 4. Although the specimens were tested within the supposed elastic range, in each case the rate of extension of the specimens increased with time until rupture occurred. Examination of the specimens revealed distribution of cracks in the tarnish, so that the observed extension is a result of the growth of these cracks prior to

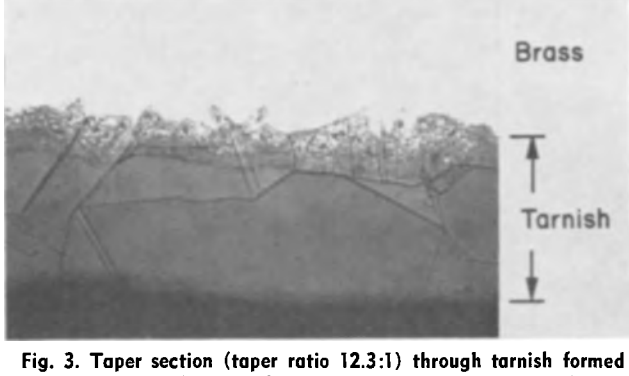

Fig. 3. Taper section (taper ratio 12.3:1) through tarnish formed on annealed brass by a 16 hr exposure to the tarnishing solution. Magnification approximately 300X.

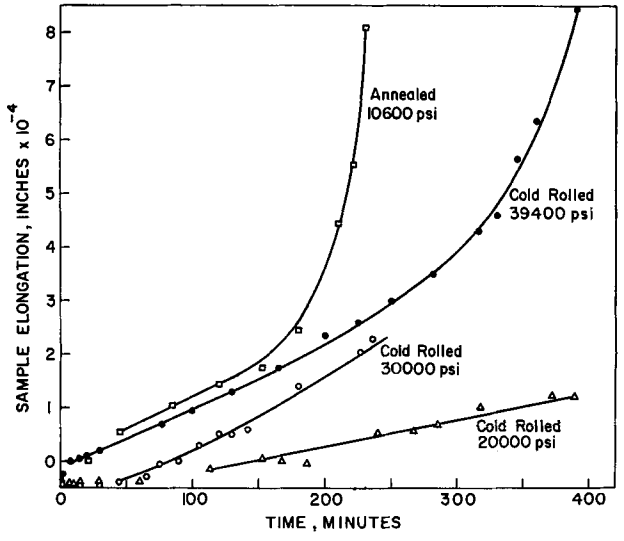

Fig. 4. Elongation of tensile specimens of brass exposed to the tarnishing solution at the indicated stress levels.

final rupture. This result was somewhat unexpected since the work of Forty and Humble, with annealed specimens, appears to indicate that plastic deformation involving slipbands in the brass substrate would be required to initiate cracking of the tarnish. To check on this further, an annealed specimen with a proportional limit of 15,000 psi was tested at 10,000 psi, and behavior similar to that for the cold-worked brass was observed, as shown in Fig. 4. Failure of annealed α-brass below the yield strength in an ammoniacal environment has been previously noted (3, 15). It appears therefore that, although the exact mode of failure is uncertain and may indeed involve dislocation motion on a microscale within the tarnish or at the tarnish-metal interface, massive plastic deformation associated with slip bands is not necessary. Massive plastic deformation can, of course, rupture a surface film, but this would be true for any surface film, such as aluminum oxide, whether or not the material is susceptible to stress-corrosion cracking.

As observed by Forty and Humble (12), the cracking appeared to be confined to the tarnish layer, with cracks being blunted and arrested at the interface between the brittle tarnish and the ductile substrate as shown in Fig. 5 for a cold-worked specimen.[1] It has been suggested (16) that pore formation due to dezincification of the brass might serve to advance the crack in a brittle manner beyond the tarnish layer. In order to obtain some indication of the effect of porosity on ductility, a brass specimen was dezincified by annealing for 30 hr in a vacuum at 850°C, which resulted in a void volume of 17%. Nevertheless, the material was quite ductile, thereby indicating that only the tarnish is brittle in the present case.

Short range order has also been considered to influence the process of stress corrosion cracking by providing a preferred path for corrosive attack due to the destruction of short range order by dislocation motion (4). To check on this point for brass, the time to rupture for tensile specimens of disordered material was compared with that for material possessing a degree of short range order. Disordered material was obtained by water quenching from an annealing temperature of 450°C (the bulk of the tests described in this paper involved disordered material); short range ordered material was obtained by heating quenched material to 190°C and maintaining that temperature for 24 hr (17). The times to failure at three stress levels of the disordered and short-range-ordered α-brass specimens in the tarnishing solution were as follows:

Condition	Applied stress, psi	Time to failure, hr
Short-range-ordered	16,000	4.2, 11.32
Disordered	16,000	2.5, 6.76
Short-range-ordered	18,600	2.77, 4.01
Disordered	18,600	3.0, 4.55
Short-range-ordered	22,700	2.0, 3.08
Disordered	22,700	1.75, 2.65

These results show no obvious correlation between degree of short range order and time to failure. The above results indicate that stress corrosion cracking occurs because of the weak nature of the protective tarnish film and that the strength of the tarnish does not depend on the condition of the underlying brass.

Crack growth.—The experimental approach employed in determining the rate of growth of cracks was similar to that used for fatigue cracks (18). In the latter case, a centrally located slit serves as a stress raiser at which cracks are initiated. The growth of the cracks is observed with a low power microscope and related to the number of load cycles applied; from these data the rate of growth is determined. It has been shown that the rate can be expressed as a single valued function of the parameter $\sigma_g\sqrt{l}$, where σ_g is the maximum applied gross-section stress in the loading cycle, and l is the semilength of the fatigue crack (19). This correlation is not unexpected, since $\sigma_g\sqrt{l}$ is related to the stress intensity at the tip of a growing crack (20) if the crack length is less than half the sheet width.

In the present study the rate is, of course, expressed as a function of time rather than of the number of load cycles.

General Observations

For annealed specimens, the level of stress required to initiate cracks in a short time also caused extensive plastic deformation in the vicinity of the central slit. As a consequence, many cracks appeared in time (Fig. 6). The main crack advanced by a linking up of the smaller cracks, a circumstance which made the determination of a crack front uncertain; therefore, quantitative information with annealed specimens could not be obtained. The cracks in these specimens were usually intergranular. As the cracks deepened, they became much more blunt (Fig. 7).

Crack growth along the surface of cold-worked brass

[1] These cracks are "transgranular," but it is noted that they do not penetrate the α-brass grains themselves.

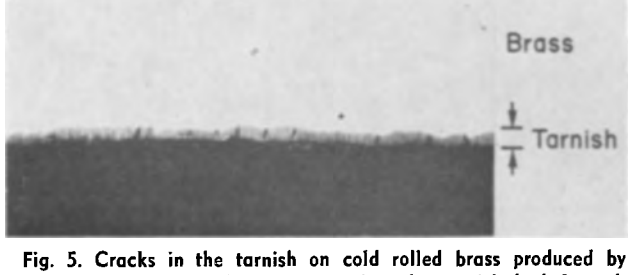

Fig. 5. Cracks in the tarnish on cold rolled brass produced by stressing the base metal in tension after the tarnish had formed. Note that cracks do not penetrate the untarnished metal. Magnification approximately 800X.

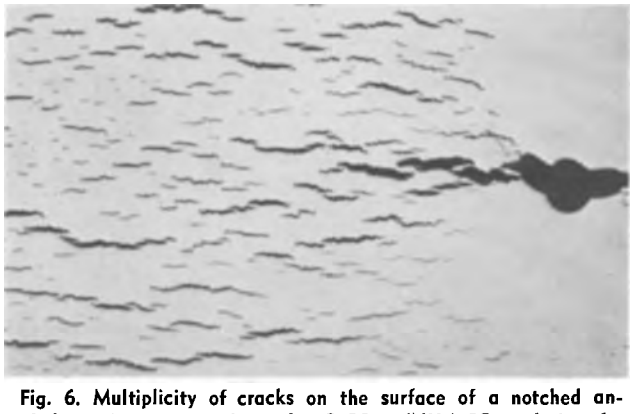

Fig. 6. Multiplicity of cracks on the surface of a notched annealed specimen exposed to the $CuSO_4$—$(NH_4)_2SO_4$ solution for 21 hr at a stress of 13,000 psi. Magnification approximately 7X.

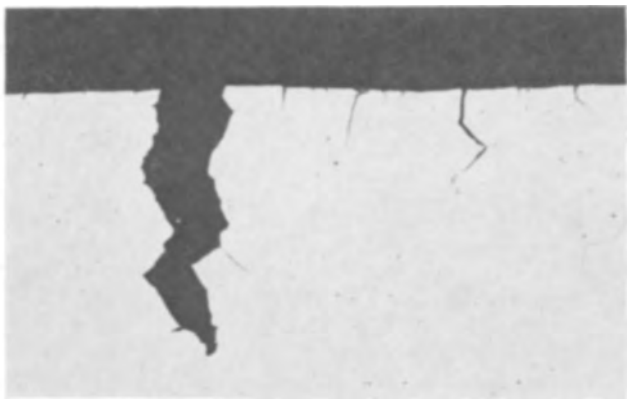

Fig. 7. Cross section of stress corrosion cracks in annealed brass. Magnification approximately 170X.

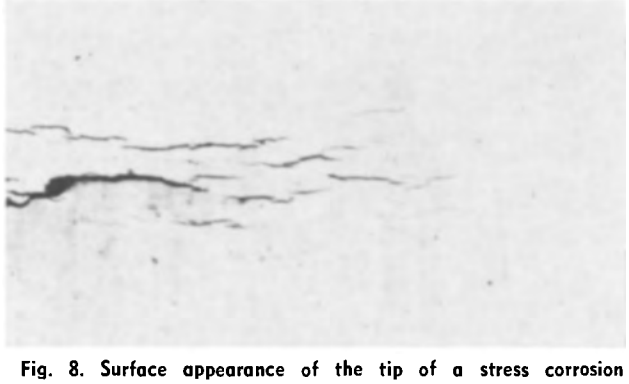

Fig. 8. Surface appearance of the tip of a stress corrosion crack growing in a notched, cold rolled brass specimen exposed 5 hr at 57,000 psi. Magnification approximately 170X.

was much easier to follow. A well-defined main crack advanced along the surface by linking up with microcracks formed in the small plastic zone at the tip of the crack. Microcracks were not visible through the low power microscope, and therefore only the advance of the main crack was recorded. An example of this microcracking is shown in Fig. 8.

In both the annealed and cold-worked specimens the plane of initial crack growth was perpendicular to the specimen surfaces. As the cracks increased in length, the average plane gradually shifted toward 45° to the specimen surfaces, the distance to the transition region being an inverse function of the applied stress. It is noted that the greater proportion of total crack life was spent in the first of these two modes. A shift in crack plane orientation is also observed in fatigue crack growth and can be explained (21) in terms of the size of the plastic zone at the tip of the crack. When the zone size is small with respect to the thickness of the sheet, plane strain conditions prevail at the tip and the fracture plane is normal to the surface. As the crack increases in length, the size of the plastic zone increases also, and when it approaches the sheet thickness a condition of plane stress exists in the plastic zone at the crack tip with the result that the fracture plane shifts to a 45° inclination with respect to the surface.

The shape of the crack front itself depended on the applied stress level. At low stresses, the cracks were well advanced along the surface with respect to the interior. As the stress level increased, the disparity between the two was considerably reduced. An extreme example of the crack leading at the surface was found in the case of a crack formed at 17,000 psi. This crack apparently stopped growing after developing along the surface to a length of 0.094 in. As shown in Fig. 9, its length in the interior was only 0.023 in.

As viewed through the microscope, the growth of cracks in both annealed and cold-worked specimens appeared to be continuous in time; that is, no pauses

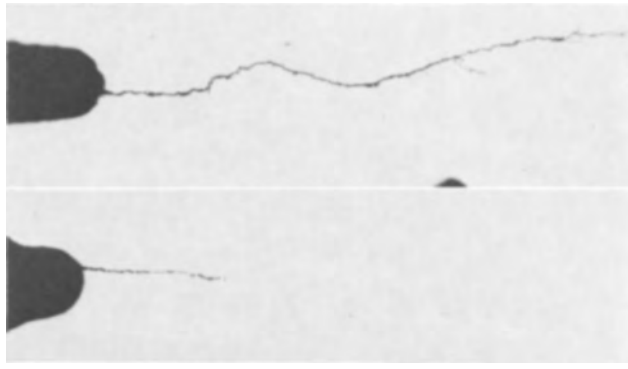

Fig. 9. Crack lengths in a notched, cold rolled brass specimen after 53 hr exposure to the cracking solution at a stress of 17,000 psi; (top), near surface; (bottom) near center of the specimen. Magnification approximately 30X.

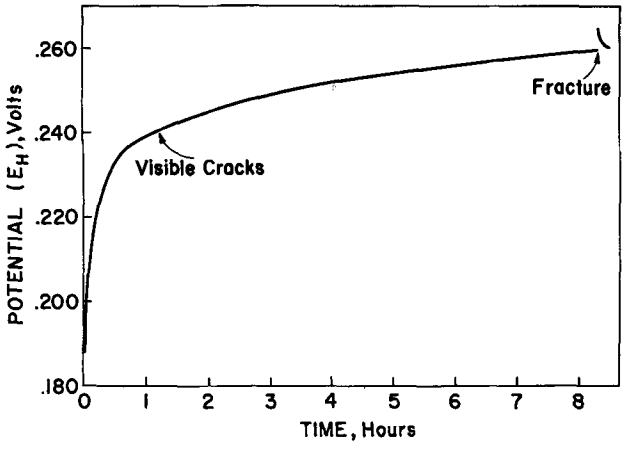

Fig. 10. Potential of a cold rolled, notched stress corrosion specimen as a function of time exposed in 0.05M $CuSO_4$ + 0.48M $(NH_4)_2SO_4$, pH = 7.25 at 50,000 psi.

and subsequent bursts of crack growth were noted. Electrode potential measurements, which have been reported to be sensitive to bursts of crack growth in other systems (22), did not show bursts of growth in the present instance. After an initial fairly rapid drift in the noble direction, the rate of potential change slowed considerably (Fig. 10). Except at fracture, no pronounced discontinuities were observed, and no detectable change in potential occurred at the onset of visible cracking, even though the Luggin capillary employed in these measurements was placed near the crack tip. These results suggest that any active metal surface exposed by the cracking process was too small a fraction of the total surface to have an appreciable effect on the electrode potential. Similar results were obtained for both annealed and cold-worked specimens. In all cases, the potential is in the region corresponding to Cu_2O as the reaction product according to Mattson's calculated potential-pH diagram for this system.

Replicas of the fracture surfaces examined in an electron microscope indicated that discontinuities in growth occurred on a very fine scale. An example of a fracture surface of an annealed specimen is shown in Fig. 11a. Figures 11b and 11c show the appearance of the fracture surfaces of cold-worked brass at two different stress levels. Scanning of the replicas showed that the fracture markings remained parallel over distances much larger than the grain diameter. These markings are similar to those observed on the fracture surfaces of fatigue specimens as a consequence of the advance and blunting of the fatigue crack during each loading cycle.

Rate of Crack Growth

The log of the rate of crack growth for cold-worked brass is a single valued function of the crack stress tip

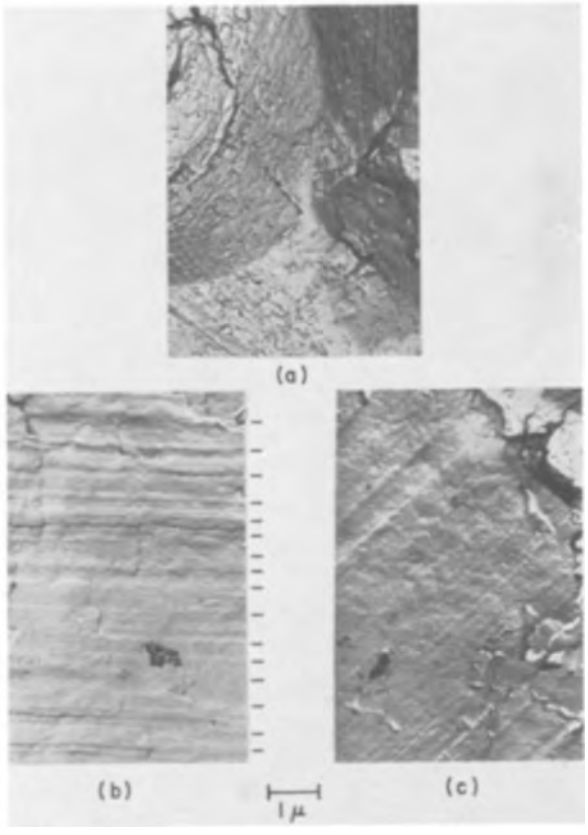

Fig. 11. Electron micrographs of replicas of stress corrosion fracture surfaces. (a) annealed brass at 14,600 psi; (b) cold rolled brass at 30,900 psi (main rupture markings indicated in margin); (c) cold rolled brass at 67,000 psi. Magnification approximately 7000X.

intensity parameter, $\sigma_g\sqrt{l}$, over a wide range of values (Fig. 12). The data can be approximated by a line whose equation is

$$\log dl/dt = \log A + 2 \log \sigma_g\sqrt{l} \qquad [2]$$

or

$$dl/dt = A\sigma_g{}^2 l \qquad [3]$$

where A is a material constant.

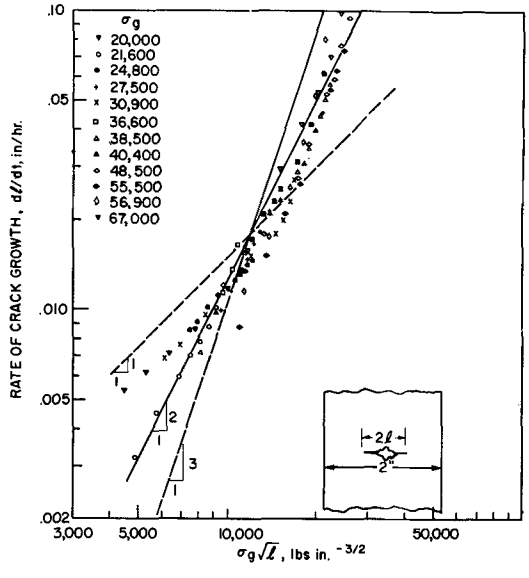

Fig. 12. Rate of stress corrosion crack propagation in cold rolled brass exposed to 0.05M $CuSO_4$ + 0.48M $(NH_4)_2SO_4$, pH = 7.25.

This equation holds for values of $\sigma_g\sqrt{l} > 4000$ lb-in.$^{-3/2}$. Below this value cracks propagate at a much slower rate than given by Eq. [3].

Equation [3] may be integrated to give

$$\ln l_R/l_o = A\sigma_g{}^2 t_R \qquad [4]$$

where t_R is the time to rupture, if crack initiation occurs instantaneously, l_o is the initial crack length, and l_R is the crack length at rupture. Since most of the time is spent in growing the crack at lengths much below l_R, variations in l_R, a number which would actually decrease with increasing applied stress, can be neglected with only small error. If this is done, then

$$t_R \propto \frac{1}{\sigma_g{}^2} \qquad [5]$$

A logarithmic plot of the data *vs.* time to rupture is given in Fig. 13; the observed slope of −2 shows that the time to rupture does indeed depend inversely on the square of the applied stress level. If the numerical value of A determined from the rate plot (Fig. 12) is used, then the quantitative prediction is with 20% of the measured value, indicating that the assumptions used above are reasonable.

Specimens which were prestressed in compression to introduce a state of residual tensile stress at the notch tip and an increase in notch sharpness, cracked at stress levels below the minimum for specimens not prestressed. Specimens prestressed in tension, required much longer times for development of cracking than in the absence of the preload.

When the amplitude of tensile loading was varied during the test the results also reflected the influence of prior load history. Denoting the time spent at the nth stress level as t_n and t_{Rn} as the time to rupture at the nth level, then changing from high loads to low increased the total life as given by

$$n = \sum_{1,2}^{n} \frac{t_n}{t_{Rn}} \qquad [6]$$

whereas going from a low load to a high had little effect on the rate of growth at the higher load level. It appears then that the above summation will yield a

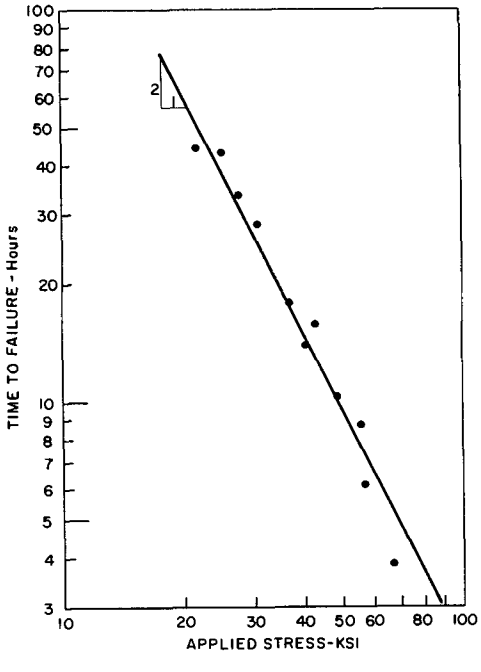

Fig. 13. Time to rupture as a function of applied stress for notched, cold rolled brass specimens exposed to the cracking solution.

value equal to or greater than unity for tensile loading. Therefore a simple prediction based on the time spent at each load level would lead to a conservative prediction of total lifetime. However, if a compressive load were applied, it would accelerate cracking in the next stage of tensile loading due to its effect on residual stresses and shape of the crack tip. In this event the above summation would be reduced. These effects of prior load history on the growth of stress corrosion cracks are similar to those observed in the case of fatigue crack growth.

Discussion

Of the various suggested mechanisms for stress corrosion cracking, our results are in best accord with the film rupture mechanism proposed by Logan (1). Exposure of brass to ammoniacal cupric sulfate solution rapidly produces a protective film, consisting mainly of cuprous oxide, which reduces the over-all corrosion rate to a fairly low level. Cracking of this film exposes a small area of bare metal which is anodic to the film. Rapid anodic attack on the exposed brass leads to reformation of the protective film. After the protective tarnish is again established its rate of thickening is expected to be controlled by diffusion processes within the film.

Stress corrosion cracking was found experimentally to consist of three steps: (*a*) crack initiation, followed by (*b*) crack advance along the surface into regions already tarnished, and simultaneously, (*c*) crack penetration from the surface into the interior of the specimen.

Crack initiation.—Cracks appeared in the notched specimens within the plastic zone at the tip of the stress raiser as the tarnish layer formed. It seems unlikely that the formation of an extremely thin film could have caused a motion of the static array of dislocations initially present in the substrate and thereby rupture the film. It seems more likely that rupture involved a decrease in resistance to fracture of the film with increasing thickness. That such a strength-thickness relationship exists is inferred from the work on thin films of silver and gold which has demonstrated that the fracture stress decreases sharply with increasing thickness up to about 1000Å (23, 24). In addition, epitaxial stresses in the tarnish, which would be expected to increase with thickness, may also lower the fracture resistance. Such an interpretation is consistent with the behavior of unnotched specimens which extended and failed, even in the nominally elastic range, at rates which increased with the stress level.

Crack growth along the surface.—This mode of crack advance in the plastic zone ahead of the main crack (Fig. 8) is associated with the advance of the crack into a region which has already been tarnished. Plastic deformation of the underlying brass results in the opening up of microcracks already present in the tarnish and the further cracking of the tarnish. The mechanism is probably similar to that described by Forty and Humble: planar glide, induced by a low stacking fault energy, introduces a severe stress concentration when blocked by the surface layer.

Crack growth in interior.—The cracking of the subsurface section of the specimens controls the over-all rate at which cracks propagate. Because of the accelerated cracking in the unconstrained plastic zones at the surface, the crack front takes on a curved shape which is more pronounced at low stress levels. Since cracks penetrate only to the tarnish-metal interface, the important step in crack propagation is the repeated formation and rupture of the tarnish layer along the crack front; therefore, the process of crack growth has much in common with crack initiation. This view is supported by the regular nature of the markings found on the fracture surface (Fig. 11). Such markings are not expected if a simple dissolution process or some random blocking of the crack tip occurred. These markings are thought to be due to the plastic deformation which occurs each time the tarnished film ruptures and the crack advances to the interface where it is arrested by plastic blunting, as shown in Fig. 14. The figure also indicates how secondary markings due to slip bands may be present on the fracture surface and between main markings.

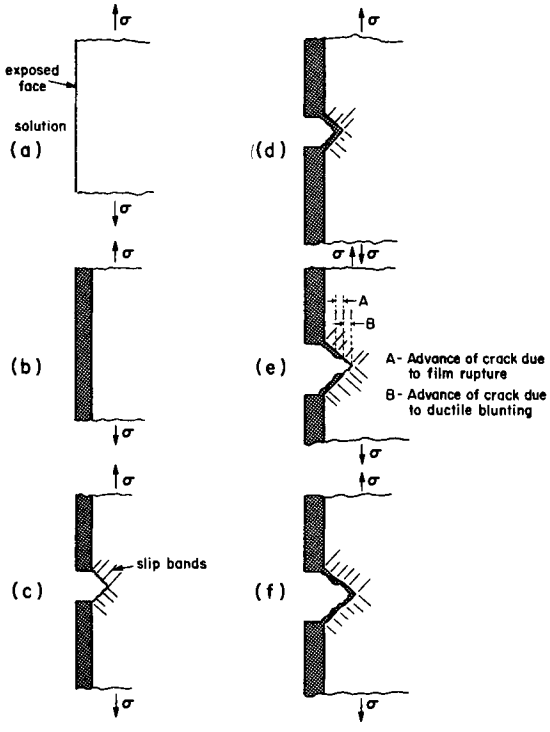

Fig. 14. Schematic representation of initiation and growth of stress corrosion cracks by the process of tarnish rupture.

The rate of formation of cracked area by such a mechanism is given by

$$r = B\frac{\Delta l}{\Delta t_R} = B\frac{\Delta l_T + \Delta l_B}{\Delta t_R} \qquad [7]$$

where B is a numerical factor that relates the shape of the crack front to the dimensions and shape of the specimen. This factor is considered in the present example to be independent of stress, but in fact does depend somewhat on the applied stress, particularly at low stress levels. Δl is the increment of crack growth due to tarnish rupture and plastic blunting (A + B, Fig. 14) and is the sum of the incremental advance due to tarnish rupture, Δl_T, plus that due to plastic blunting, Δl_B; and Δt_R is the time for the formation of the film measured from the end of one increment of crack advance until the tarnish ruptures again.

If we neglect the contribution of plastic blunting to the advance of the crack and assume the rate of thickening of the film at the tip is a diffusion controlled process, we can write

$$\Delta l = \Delta l_T = c\sqrt{\Delta t_R} \qquad [8]$$

With respect to this assumption, it is of course likely that when the film is very thin the rate of reaction is controlled by the activation polarization characteristics of the brass. It has been shown that copper can dissolve at very high anodic rates (25), and it is reasonable to expect that brass does also. In this case, the film soon thickens to the point that diffusion processes within the film become rate controlling so that during most of the period of film growth, the rate-determining step is diffusion within the film. However, another possibility to be considered is that diffusion within the crack of reactants to the tip or products to the bulk solution is rate controlling. Hines has shown that this concentration polarization is unlikely to be of im-

portance in the cracking of austenite stainless steels (9). In the present case the principal anodic reaction is $2Cu+H_2O \rightarrow Cu_2O+2H^+$. Thus the only reactant supplied by diffusion is water which is present in great excess and the only product removed by diffusion is the hydrogen ion which has the highest diffusivity of all ions. Also the buffer capacity of the electrolyte should minimize effects of changes in hydrogen ion concentration. This system is therefore less likely to be subject to considerable concentration polarization within the crack than would the stainless steel system considered by Hines so that concentration polarization does not seem to be rate controlling in the present case. It therefore appears reasonable that diffusion within the tarnish controls the rate at which the tarnish forms.

Upon substituting for Δt_R in Eq. [8] we obtain

$$r = \frac{Bc^2}{\Delta l_T} \qquad [9]$$

From the data on the rate of formation of the film, c^2 is equal to 1.2×10^{-8} in.^{2}/hr, assuming that a bulk measurement can be extended to the thin tarnish layer at a crack tip.[2] For a value of B close to unity, the rate of advance of the crack is given by

$$r = \frac{1.2 \times 10^{-8}}{\Delta l_T} \text{ in./hr} \qquad [10]$$

If the distance between the main markings in Fig. 11 is taken as the thickness of the tarnish film at the time it ruptures a calculation of the rate of crack advance can be made using Eq. [10]. This leads to rates of cracking of 0.0025 in./hr at a gross stress of 67,000 psi and 0.0006 in./hr at a gross stress of 30,900 psi. These replicas were taken close to the crack origin where the corresponding experimentally determined rates are about 0.017 and 0.004 in./hr, respectively. The observed and calculated rates could be brought into closer agreement if approximately one-half of the distance between markings were attributed to the advance due to plastic blunting. Because of uncertainties in the tarnishing process at the tip of a crack and in making measurements from the replicas it does not seem possible to make a more rigorous calculation of these rates at present.

From the experimental findings it has been shown that the rate of growth is proportional to $\sigma_g^2 l$. This indicates that the advance of the crack front is related to Eq. [7], and can be expressed as

$$\sigma_g^2 l \propto \frac{1}{\Delta l_T}\left(1 + \frac{\Delta l_B}{\Delta l_T}\right) \qquad [11]$$

If the advance due to blunting is linearly related to the advance due to tarnish rupture, then the above proportionality can be reduced to

$$\sigma_g^2 l \propto \frac{1}{\Delta l_T} \qquad [12]$$

A rationalization of this empirical relationship is not straightforward in that the factors responsible for the rupture of the film at the tip of a crack are quite complex. It is known, however, that the radius of a crack tip is directly related to the quantity $\sigma_g^2 l$ (26). The smaller the size of the radius the more the stress state will approach one of plane strain, a condition which would tend to cause a rapid decrease in shear stress immediately ahead of the curved crack front. Since tensile fracture usually is the result of shear deformation, fracture of the tarnish and the advance of the crack front may also depend on the magnitude of the shear stresses encountered as the film thickens and its fracture resistance decreases. The lower the value of $\sigma_g^2 l$, the greater will be the thickness attained before rupture because of the lower magnitude of shear stresses involved.

[2] Since the grain boundaries in annealed brass are replicated in the oxide (Fig. 4), enhanced diffusion along these oxide grain boundaries may be associated with the intergranular cracking mode in annealed brass. Heavy cold work would tend to reduce the structural difference between matrix and boundaries.

Concluding Remarks

1. It is concluded that both the initiation and propagation of stress corrosion cracking in tarnished α-brass involves the formation and rupture of a weak, protective film, and that cracking occurs because rupture of the film localizes the effects of stress and environment. This localized cracking process is avoided if the film is not sufficiently protective to restrict general corrosion. For example, we have observed this to be the case for copper in the ammoniacal copper sulfate solution. It can also be avoided if the film is strong enough to sustain the applied stress without rupturing.

2. The process of film rupture does not require massive plastic deformation of the substrate. This finding does not preclude the possibility that dislocation motion within the tarnish or on a microscale at the tarnish-brass interface occurs and is involved in the rupture process.

3. The rate of growth of stress corrosion cracks for a wide range of crack growth rates is a single valued function of the parameter $\sigma_g^2\sqrt{l}$, and the rate is proportional to $\sigma_g^2 l$. From this relationship it follows that the time to rupture varies inversely as the square of the applied stress level. σ_g.

Acknowledgment

The authors express their appreciation to Drs. T. L. Johnston, A. S. Tetelman, and G. F. Bolling for helpful discussions during the course of this investigation. The capable assistance of Mrs. P. McAlpine, Mr. R. Benoit, and Mr. J. Ingall is also acknowledged.

Manuscript received Aug. 10, 1964.

Any discussion of this paper will appear in a Discussion Section to be published in the December 1965 JOURNAL.

REFERENCES

1. H. L. Logan, *J. Research Natl. Bureau Standards*, **48**, 99 (1952).
2. R. Bakish and W. D. Robertson, *Acta Met.*, **4**, 342 (1956).
3. W. D. Robertson and A. S. Tetelman, "Strengthening Mechanisms in Solids," ASM, Metals Park, Ohio (1962).
4. H. W. Pickering and P. R. Swann, *Corrosion*, **19**, 373t (1963)
5. D. Tromans and J. Nutting, "Fracture of Solids," p. 637, Gilman and Drucker, Editors, Interscience Publishers, New York (1963).
6. A. J. Forty, "Physical Metallurgy of Stress Corrosion Fracture," T. N. Rhodin, Editor, Interscience Publishers, New York (1959).
7. D. L. Douglass, G. Thomas, and W. R. Roser, *Corrosion*, **20**, 15t (1964).
8. T. P. Hoar, *ibid.*, **19**, 331t (1963).
9. J. G. Hines, *Corrosion Sci.*, **1**, 21 (1961).
10. H. H. Uhlig, "Physical Metallurgy of Stress Corrosion Fracture," T. N. Rhodin, Editor, Interscience Publishers, New York (1959).
11. L. Graf, "Stress Corrosion Cracking and Embrittlement," W. D. Robertson, Editor, John Wiley & Sons, Inc., New York (1956).
12. A. J. Forty and P. Humble, *Phil. Mag.*, **8**, 247 (1963).
13. E. Mattson, *Electrochim. Acta*, **3**, 279 (1961).
14. A. R. Bailey, *Met. Rev.*, **6**, 101 (1961).
15. G. Edmunds, Symposium on Stress Corrosion Cracking of Metals, ASTM-AIME (1944).
16. A. J. Forty, "Recent Advances in Stress Corrosion," A. Bresle, Editor, Bulletin 25, Corrosion Committee, Royal Swedish Academy of Engineering Sciences, 22 (1961).
17. R. Feder, A. S. Nowick, and D. B. Rosenblatt, *J. Appl. Phys.*, **29**, 984 (1958).
18. A. J. McEvily, Jr. and W. Illg, U. S. National Advisory Committee for Aeronutronics, T. N. 4394 (1958).
19. P. C. Paris, M. P. Gomez, and W. E. Anderson, *Trend in Engineering*, **13**, 9 (1961).

20. H. F. Hardrath and A. J. McEvily, Jr., Proceedings of the Crack Propagation Symposium, Cranfield, College of Aeronutronics, **1**, 231 (1963).
21. H. W. Liu, Private communication.
22. H. J. Engell and A. Bäumel, "Physical Metallurgy of Stress Corrosion Fracture," T. N. Rhodin, Editor, Interscience Publishers, New York (1959).
23. J. W. Menter and D. W. Pashley, "Structure and Properties of Thin Films," Neugebauer, Newkirk, and Vermilyea, Editors, John Wiley & Sons, New York, p. 111 (1959).
24. J. W. Beams, *ibid.*, p. 183.
25. B. E. Conway and J. O'M Bockris, *Plating*, **46**, 321 (1959)
26. B. A. Bilby, A. H. Cottrell, and K. H. Swinden, *Proc. Roy. Soc.*, **A272**, 304 (1963).

Adsorption of Monomeric and Polymeric Amino Corrosion Inhibitors on Steel

R. R. Annand[1] **and R. M. Hurd**[2]
TRACOR, Inc., Austin, Texas
and Norman Hackerman
Department of Chemistry, The University of Texas, Austin, Texas

ABSTRACT

The adsorption of 4-ethylpyridine, 4-ethylpiperidine, and very low molecular weight poly(4-vinylpyridines) was studied in cyclohexane solutions containing hydrogen reduced steel powder. Isotherms were obtained for the monomers at 30°C. They show that an amount equivalent to monolayer formation is adsorbed at equilibrium concentrations in the range 2.5 to 5.0 x 10^{-3}M. The polymer was adsorbed to a much greater extent. Using a specially designed chromatographic method, the heat of adsorption of the piperidine derivative from cyclohexane was determined. Simultaneous measurements of the adsorption of the polymer and the corrosion of the steel in aqueous hydrochloric acid have shown that the corrosion rate decreases by 80% as the polymer adsorbs to form a very incomplete layer. From these results, it is concluded that these compounds chemisorb to the steel surface and that the 4-ethylpiperidine is bonded at the nitrogen atom but that the 4-ethylpyridine is adsorbed in a position with the plane of the ring parallel to the steel surface. Attachment of polymer is at multiple sites in the molecule, but appreciable portions of the chains are left in the solution phase. The area which is deactivated toward corrosion by adsorption of poly(4-vinylpyridine) from HCl is considerably greater in extent than that which is physically covered by the adsorbed molecules, *i.e.*, a large neighboring area of steel surface is ennobled by the adsorbed polymer molecules.

In corrosion inhibitor research, it has long been recognized that preferential adsorption of organic inhibitors interferes with the reaction between the corrodant species and the metal surface. At first, this interference was believed to result from electrostatic attraction between cations and cathodic areas, or between anions and anodic areas. This concept alone has since been shown to be untenable (1), and other types of adsorption have had to be considered. In 1954 Hackerman and Makrides proposed a chemisorption mechanism of inhibitor action (2), and Finley and Hackerman showed that a persistent, inhibiting adsorption of amines could be obtained in benzene (3). Other investigators have discussed various other types of adsorption or combinations of types to account for the observed results (4, 5). Recently radiochemical and spectrophotometric measurements of the adsorption of thiourea derivatives have been reported (6, 7). However, solution adsorption measurements on steel surfaces for inhibitor amines with similar molecular character but dissimilar inhibitor action have been lacking.

The work reported here was undertaken in conjunction with an inhibition study (8) to examine the adsorption behavior of amine inhibitors and to elaborate the relationship between adsorption and inhibition. A dual approach was chosen: (i) a study of two simple compounds, 4-ethylpiperidine and 4-ethylpyridine, which are similar in size, base strength, solubility, and chemical nature, but which are not so similar as might be expected in their inhibitor effectiveness; and (ii) a study of the relative adsorbabilities of a monomer amine, 4-ethylpyridine, and a polymer, poly(4-vinylpyridine), which had very short chains and whose repeating units had the same structure as the monomer. To keep the reactions at the steel surface simple and therefore to focus attention on the adsorption, the adsorption experiments were carried out in cyclohexane on steel powder which was carefully freed of oxide by reduction in a hydrogen atmosphere.

[1] Present address: Petrolite Corporation, St. Louis, Missouri.

[2] Present address: Continental Oil Company, Ponca City, Oklahoma.

Experimental Procedures

Static adsorption measurements.—These experiments were designed to study adsorption from cyclohexane solutions onto reduced steel powder in the absence of oxygen. The steel powder was reduced in hydrogen, weighed, and then introduced to the thermostated adsorption cell under the surface of the cyclohexane without exposure to air. In some cases, the adsorbable amine was present in the solution before the steel powder was added; in others, the amine was added later. There was no observable difference in the equilibrium amount adsorbed due to the different procedures. The adsorption cell was provided with a paddle stirrer and was maintained under a positive nitrogen pressure of 3 or 4 lb by means of a mercury columun on the exit line. Tank nitrogen was bubbled through a zinc-vanadyl sulfate tower to remove oxygen, then through a sulfuric acid scrubber to remove any water spray, and finally a Drierite tower to remove any acid spray. The nitrogen was then passed through a cyclohexane bubbler which was kept in the thermostated water bath with the adsorption cell. All of the connections between the bubbler and the adsorption cell were made of glass. Teflon sleeves were used to seal

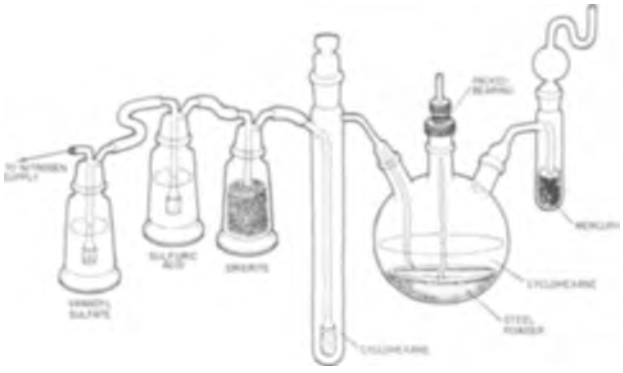

Fig. 1. Adsorption cell and gas train

the ground-glass joints. The arrangement of this equipment is shown in Fig. 1.

The adsorption cell was assembled from a one-liter, three-neck Morton flask with a Trubore packed stirrer bearing assembly[3] combined with a shop modified lubricant trap. When connected to a Waco stirrer motor to complete the apparatus, it could be kept sealed and operating continuously for at least as long as 30 days without a net loss of cyclohexane and without contamination of the solvent with lubricant or chemicals from the gas train.

The bubbler and the adsorption cell were immersed in a stirred water bath maintained at 30° ± 0.005°C by a Sargent Thermonitor, with water level in the bath maintained by a simple float valve arrangement. In the usual case, samples of the solution for analysis were taken systematically over a period of about 10 days and were used to determine the course of the adsorption process. Samples from a portion of the thermally equilibrated initial solution, taken before introduction of the steel, were used as standards for this comparison.

The steel powder used for these experiments was obtained from the Vanadium-Alloys Steel Corporation, Latrobe, Pennsylvania. Chemical analysis supplied by the manufacturer was in the typical range for the SAE 1020 composition. Sieve analysis produced 85.0% of the particles in the range 140-200 mesh or 74-105μ. BET determination showed 0.0571 m^2/g for the specific surface of the reduced powder. This indicates a surface roughness factor of 5.8.

The powder, contained in a Vycor tube, was prepared for the adsorption experiments by reducing it with hydrogen at 650°C maintained in a controlled temperature furnace, Completeness of reduction was determined by absorbing the water formed in a Drierite tower and weighing. Hydrogen, predried with Drierite, was used for the reduction. This procedure was adopted after several trials to determine the best compromise between absence of sintering and rapid reduction. Following reduction, the hydrogen flow was replaced with oxygen-free, dry argon, and the steel was maintained at temperature for several hours to allow any absorbed hydrogen to escape. Any oxidation was detected by the change in color of the powder.

Oxygen was removed from the argon by passage through a purification train similar to that used for the nitrogen in the adsorption system. For added insurance, before introduction to the powder samples, it was also passed through a steel powder bed held at temperature. The steel powder was transferred to the adsorption cell by means of a purified nitrogen stream which blew it out of the reduction tube and through a glass tube inserted into the adsorption cell under the surface of the cyclohexane. The weight of powder transferred was determined by weighing the reduction tube before and after transfer.

Spectrophotometric analysis was the method chosen for concentration determination. By appropriate adjustment of sample size and light-path length, a wide range of concentrations could be covered accurately. In some cases in which only a small relative concentration change occurred, the differential technique was applied. In general, the adsorption cell was filled with 200 ml of solution and a pipetted 4 ml sample was taken each time. This was split into triplicate 1 ml samples which were carried through the analysis scheme. Before contact with the steel, a portion of the amine solution was reserved to furnish the triplicate standards which were run concurrently with the samples.

For the experiments with 4-ethylpyridine and poly(vinylpyridine), spectrophotometric measurements were made on the diluted samples using the pyridine absorbance peak at 225 mμ and a prepared standard calibration curve.

For the experiments with 4-ethylpiperidine, it was necessary to introduce a chromophore into the molecules before the spectrophotometric measurements could be made. For this purpose, 2,4-dinitrofluorobenzene was used as a reagent to introduce a dinitrobenzene moiety at the nitrogen site (9). Contrary to the usual procedure, the reaction was carried out in cyclohexane held in a water bath at 60°C.

After the appropriate time for maximum color development and cooling to room temperature, spectrophotometric measurements were made at 352 mμ on the reacted solution without further treatment except to dilute to a known volume. The absorptivity of the unreacted 2,4-dinitrofluorobenzene is small enough at 352 mμ, and the reaction is sufficiently complete that, by using an excess of reagent, the background absorbance could be reliably blanked out using the same amount of reagent in the blank as in the sample. The concentration of piperidine in the measured volume was determined from a standard calibration curve.

From the analytical concentration, the sample volume, and the volume contained in the adsorption cell combined with the weight of steel contained in the cell, the amount adsorbed was calculated in terms of micromoles of amine per gram of steel. For the polymer, these calculations were in terms of micromoles of r-mer per gram of steel, since the analytical method produced this result. The number of micromoles of polymer per gram of steel were obtained from the molecular weight.

Measurement of adsorption from HCl.—Use of the spectrophotometric procedure for poly(vinylpyridine) in acid solutions is complicated by the general absorbance of the iron at the wavelengths of interest. Since corrosion of the steel continuously increased the iron concentration over the time period in which the polymer was adsorbing, a problem developed. However, by using the criteria cited by Mellon (10) for choosing the best wavelengths for measurement, a simultaneous method was developed for determining both iron and poly(vinylpyridine) concentrations by measuring at two wavelengths, 255 and 239 mμ. It was necessary to combine the spectrophotometric cell and adsorption cell because of the rapidity of the adsorption and corrosion phenomena. Also, because of the interrelationships between such factors as HCl concentration, rate of corrosion, solubility of poly(vinylpyridine) hydrochloride, and inhibitor effectiveness, it was found that an acid concentration of 0.01*N* gave the best compromise between time available for data taking and optimum range of concentrations measured.

The procedure was to start with a known volume of the uninhibited acid and a known weight of steel powder in a regular spectrophotometric cell and to take enough data to determine the corrosion rate. Then a known volume of a concentrated solution of the poly(vinylpyridine) hydrochloride in 0.01*N* HCl was added and the solution thoroughly agitated before spectrophotometric measurements (now including the simultaneous determination of the inhibitor) were resumed. These measurements were continued at short intervals over about an hour and were only terminated

[3] Obtained from Ace Glass Company, Vineland, New Jersey.

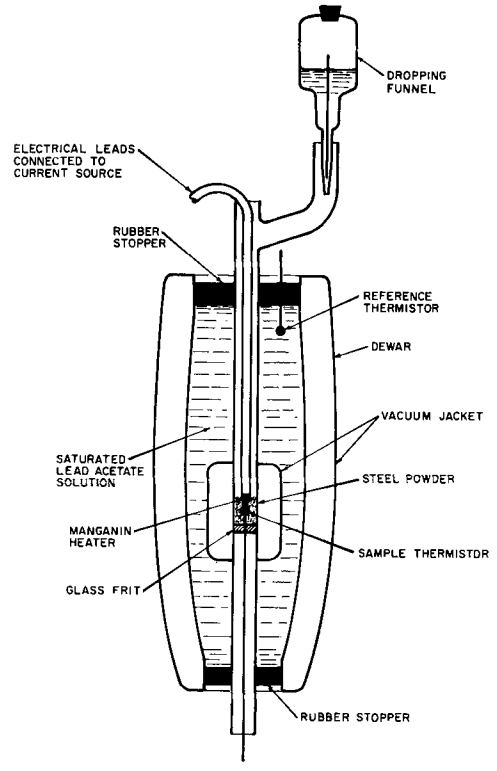

Fig. 2. Apparatus for dynamic adsorption measurements

when the absorbance increase due to iron dissolution pushed the total absorbance out of the range of the spectrophotometer. The concentrations of iron and of pyridine r-mers were determined by substituting the absorbance data into a set of simultaneous equations and solving in the usual way (11). The equations were derived and checked with standard solutions and mixtures.

Heat of adsorption measurements.—These experiments, based on a modification of the procedure of Groszek (12), were carried out in the flow calorimeter schematically outlined in Fig. 2. A known weight of steel powder rests on a glass frit with a glass-jacketed thermistor[4] inserted through a small hole drilled in its center. The steel was placed in the center of a double-walled bulb which was about halfway down a glass column. The thermistor was placed in the center of the mass of steel powder. A small coil of manganin heater wire was put in the steel on the same axis as the thermistor and slightly above. The heater was connected to a constant-current source. The column passed down the axis of a double-walled outer container, and the bulb was centered in this volume. The space between the walls of both the double-walled structures was evacuated. The large vessel was filled with a concentrated lead acetate solution to increase its heat capacity, and a second matching thermistor was located in this solution close to the outside wall of the column.

The thermistors were made part of a Wheatstone bridge circuit in combination with a set of mercury cells and with a Helipot which formed the third and fourth legs. The balance condition of the bridge was detected by a 5 mv stripchart recorder. A specially designed dropping funnel (which completes the apparatus) was used to obtain the slow flow rates required. In use, pure solvent was allowed to flow down the walls and adjusted to a rate of about 0.25 ml/min. The bridge, which was balanced initially, registered a large unbalance in the hot direction as the solvent reached the steel powder. Flow was continued until the balance condition was again obtained indicating that the heat released by solvent wetting had been removed from the inner bulb by the flowing solvent. At this time, the solvent funnel was quickly exchanged for a similar funnel containing a solution of the adsorbate in the same solvent and flowing at the same rate.

When this solution, temperature equilibrated by its contact with the thermostated column walls, reached the steel powder, a positive temperature excursion due to the heat of adsorption was registered by the recorder. It was followed by a somewhat slower fall in temperature as the continuing flow carried this heat out of the steel sample bulb. For calibration, a known constant-current pulse was then sent through the heater for a predetermined time, and a similar curve was traced by the recorder. Empirical adjustment of the geometrical arrangement of the heater wires and of the pulse time and magnitude were required to obtain a curve comparable to that produced by the amine solution so that the areas under the curves could be compared. This procedure gives a value which is the difference between the heat of adsorption of adsorbate and the heat of desorption of solvent.

Synthesis and characterization of the compounds used.—The 4-ethylpyridine was obtained from Reilly Tar and Chemical Company and was distilled immediately before use through a vacuum-jacketed, highly efficient column under a nitrogen atmosphere.

The poly(4-vinylpyridine) was prepared from freshly distilled 4-vinylpyridine (obtained from the same source) by polymerization in ethanol under nitrogen. A specially designed, high-dilution method was used in which the initiator, 2,2′-azoisobutyronitrile, and methanol solution were each added slowly to a large volume of an ethanol solution of the monomer held under nitrogen just below the reflux temperature. The resulting solution was then allowed to stand at temperature and under nitrogen for several days. Using this method, only slightly disperse samples of polymer were obtained. By properly adjusting the ratio of initiator to monomer and the over-all concentration of each, the molecular weights obtained could be controlled to give samples ranging from five r-mer units up to about one hundred. Molecular weights were determined with a Mechrolab Vapor Osmometer. Because the isolation procedures produced a partially hydrated polymer, it was necessary to use a dehydration procedure to obtain cyclohexane solutions. This procedure involved refluxing a solution of the polymer in methanol over calcium hydride followed by addition of cyclohexane and elimination of the methanol by repeated exhaustive distillation. The resulting cyclohexane solution was separated from the insoluble dehydration products (from hydrolysis of the hydride) by decantation.

Cyclohexane obtained from Phillips Petroleum Company (99 mole % minimum) was used for all of the experiments. It was distilled under nitrogen before use. A similar grade of n-heptane was used in some of the experiments.

The 4-ethylpiperidine used in the experiments was obtained by catalytic hydrogenation of purified 4-ethylpyridine in a Parr apparatus over palladium charcoal. It was purified by distillation in the vacuum-jacketed still, and the absence of the pyridine was verified by ultraviolet spectrophotometric analysis.

Results

Static adsorption experiments.—Adsorption-time curves illustrating the results of the adsorption experiments conducted in cyclohexane are presented in Fig. 3 for samples of poly(4-vinylpyridine) and for 4-ethylpyridine. The curves for 4-ethylpiperidine were similar. In the adsorption-time runs for the 4-ethylpyridine and 4-ethylpiperidine, the initial concentration of adsorbate was varied over a range sufficient to produce a change in the final, equilibrium concentration covering the range 5-50 x 10^{-4}M. These limits were estab-

[4] Obtained from Victory Engineering Corporation, Springfield, New Jersey.

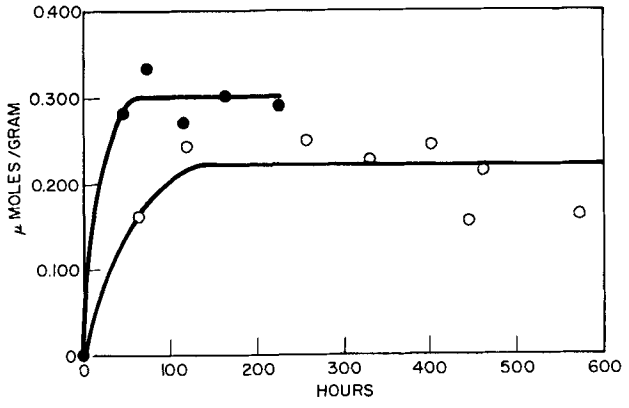

Fig. 3. Adsorption-time curves: ●, poly(vinylpyridine), MW = 3200; ○, 4-ethylpyridine.

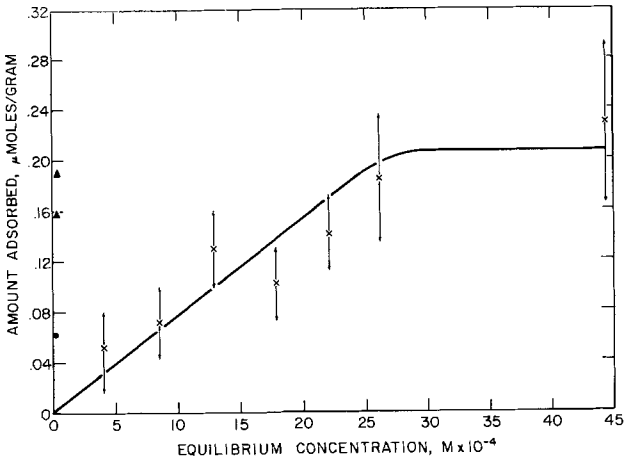

Fig. 4. Composite adsorption isotherm for 4-ethylpyridine solutions in cyclohexane: △, polymer 512 MW; ●, polymer 1200 MW; X, monomer.

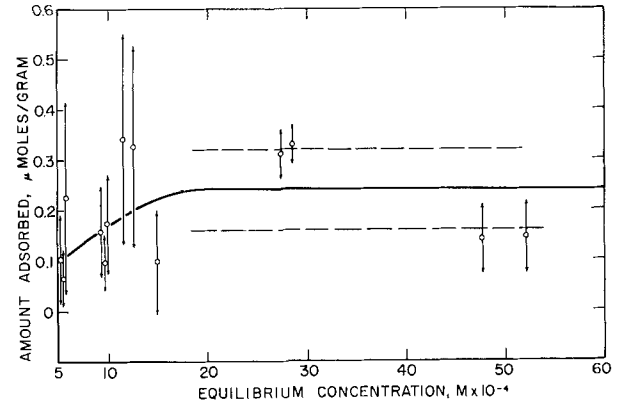

Fig. 5. Adsorption isotherm for 4-ethylpiperidine

lished by the limitations of the spectrophotometric analysis. In the case of the polymer solutions, it was not possible to cover so wide a range because of added limitations posed by the low solubility and high adsorbability of the polymers. Each point on the curves is the average of the differences between triplicate samples and triplicate standards. The standards were obtained from that portion of the original solution which was removed prior to introduction of the steel powder. No difference in the adsorption was observed between hydrogen-saturated steel and steel which had been outgassed in argon.

The adsorption levels indicated by the plateaus in the individual adsorption-time curves were used to define the isotherms for 30°C shown in Fig. 4 and 5. The average value for all of the points on the plateaus of the adsorption-time curves were used for the points on the isotherms. The points plotted in Fig. 4 are derived from at least two determinations of the adsorption-time curve, and the arrows reflect the composite standard derivation of the averages. The individual points from each of three polymer runs are included in Fig. 4 to show greater extent of adsorption at low concentrations.

Using the BET area of the steel powder and the amount adsorbed on the plateaus of the isotherms, the surface area available to each adsorbed molecule was calculated. These data are contained in Table I, along with a summary tabulation of the amount adsorbed, the projected area covered by each molecule, and the resulting number of layers of adsorbate.

The area/molecule figures in the table were obtained by arranging scale models of the molecules in the appropriate adsorption position using a flat surface to represent the steel surface. Several photographs of each molecule were then taken from a vertical position directly centered over the model. The total area covered by the molecule was computed by using the picture to outline the molecule on a grid and then counting the squares inside the outline. The scale dimensions of the squares (in terms of Å) were determined from the diameter of the hydrogen atoms.

For the polymer molecules, the area per ring was derived by dividing the total area by the number of rings. Multiple determinations on various photographs and models varied by 2%. Both possible arrangements

Table I. Summary of adsorption data

Compound	Amount adsorbed, μmoles/g	Area/molecule, Å²		No. of layers
		Experimental[a]	Model[b]	
4-Ethylpiperidine	0.24 ± 0.08	39 ± 13	33	0.84 ± 0.28
4-Ethylpyridine	0.21 ± 0.07	46 ± 15	49	1.1 ± 0.4
			21[c]	0.46 ± 0.15[c]

Poly(4-vinylpyridine)	Calculated in terms of Rings	Molecules	Rings	Molecules	Rings	Molecules	
MW 512 (4 units)	0.19 ± 0.02	0.048 ± 0.006	54 ± 6	216 ± 24	45	180	0.83 ± 0.09
MW 1160 (10 units)	0.42 ± 0.03	0.042 ± 0.003	31 ± 3	310 ± 31	45	450	1.45 ± 0.14
MW 3200 (30 units)	1.05 ± 0.06	0.035 ± 0.002	9.5 ± 0.6	284 ± 18	45	1395	4.74 ± 0.30

[a] Calculated using the number of amine rings removed from solution and the BET area of the steel powder.
[b] Projected area calculated from scale models: Assuming flat orientation for the pyridine rings in both monomer and polymer; assuming chain form for the piperidine rings.
[c] Calculated assuming perpendicular orientation of the pyridine ring.
NOTE: The values under the columns headed "Rings" are calculated on the basis of the pyridine ring concentrations; the values in the columns headed "Molecules" are calculated on the basis of polymer molecule concentrations. These values were not obtained from isotherms, but instead for individual adsorption-time runs.

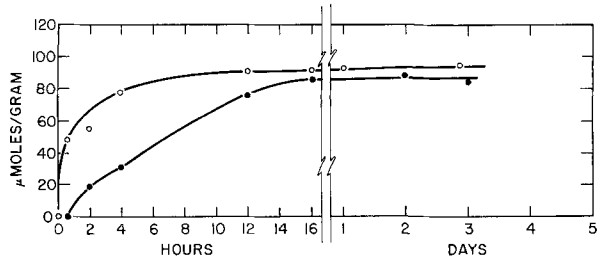

Fig. 6. Adsorption-time curves for 4-ethylpyridine on completely reduced (○) and lightly oxidized (●) steel powders.

for the pyridine, *i.e.*, with the plane of the ring perpendicular to the surface and parallel to the surface, are quoted in the table. For 4-ethylpiperidine, the chair form was assumed in the table, although all of the possible arrangements in either configuration covered essentially the same area within experimental error.

As an incidental observation, the adsorption behavior of 4-ethylpyridine was observed on a sample of steel powder which had been slightly oxidized by a brief exposure to a small amount of air while the steel was still hot, which resulted in a slight discoloration. The adsorption-time curve shown for this material is compared in Fig. 6 to the usual adsorption-time curve obtained on carefully protected (unoxidized) steel powder. It may be seen that the total amount of adsorption has not been affected (within experimental error), but that the rate of adsorption on the oxidized surface was appreciably slower.

Both of the analytical procedures for these experiments produced triplicate analyses (on the same sample) which were within the precision range of good analytical practice. In addition, the analyses of the standard solutions were consistent throughout the course of an experiment and conformed to Beer's law in experiments with different concentrations. The pooled standard deviations (representing the dispersion of the triplicates) over the course of a run in all these cases were in the range of 0.5-1.5% of the average. Triplicate analyses which were run on duplicate samples taken from the cell at the same time were also comparable to the over-all precision. In view of the good precision of the measurements of the individual points, the scatter exhibited in the adsorption-time curves is greater than expected, and it is concluded that the scatter must originate from the adsorption process itself. The deviations among multiple runs at

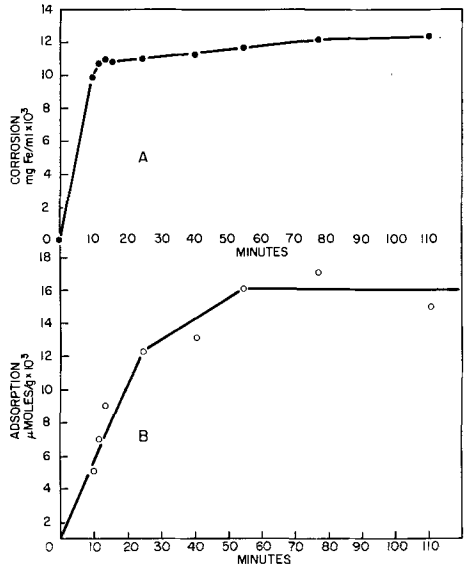

Fig. 7. Comparison of adsorption and corrosion in polypyridine inhibited 0.01*N* HCl.

Table II. Adsorption of poly(vinylpyridine) (MW 1160) from aqueous 0.01*N* HCl

Grams steel	Adsorption, μmoles/g	% Inhibition
2.0	0.014	n.d.
4.0	0.017	80
4.0	0.016	80
8.0	0.020	80

low concentration as shown in Fig. 5 also reflect this cause.

Adsorption of poly(vinylpyridine) from HCl.—Typical curves obtained in these experiments are presented in Fig. 7, and the results of four experiments are summarized in Table II. Curve A in Fig. 7 has been normalized by subtracting the amount of iron present at the time the polymer solution was added. Zero time, therefore, corresponds to the time at which the polymer solution was added. The data points in curve B were derived from the absorbance measurements by the procedure previously described for the cyclohexane solutions. The level portion of the adsorption curve (B) corresponds to 0.016 μmoles of polymer adsorbed per gram of steel. This amount is less than one-tenth monolayer (calculating as for Table I and assuming no appreciable area change).

The results from all of the experiments are summarized in Table II. The figures quoted in Table II in the column headed % Inhibition were derived from the equation

$$\% \text{ Inhibition} = \left(1 - \frac{\text{Rate inhibited}}{\text{Rate-uninhibited}}\right) \times 100$$

The corrosion rates used in this equation were derived from the slopes of the iron curves, in inhibited and uninhibited solution. In all cases, the initial polymer concentration was 3.9×10^{-5}M in terms of pyridine rings or 3.9×10^{-6}M in polymer molecules. Because the uninhibited rate falls off after a long time compared to the experimental interval, it is concluded that diffusion eventually limits both reactions.

Heat of adsorption experiments.—These experiments are briefly included here primarily to demonstrate further evidence for the chemisorption of 4-ethylpiperidine. Typical curves for the amine in cyclohexane and for a calibration experiment are reproduced in Fig. 8. In successive experiments using in-

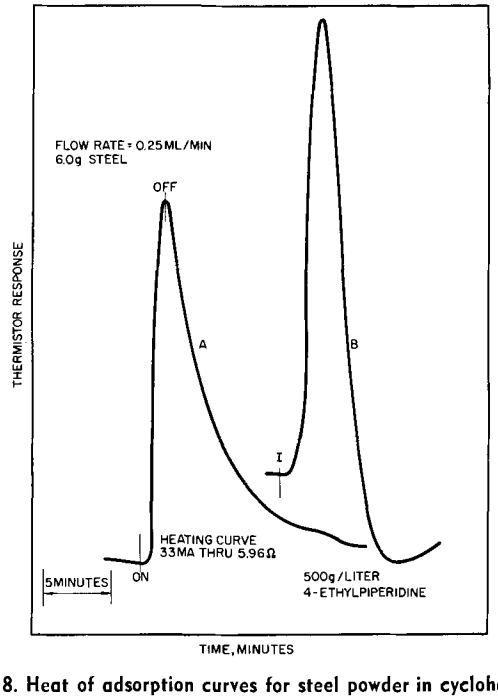

Fig. 8. Heat of adsorption curves for steel powder in cyclohexane

creasing concentrations of amine, the curves observed gradually became narrower and peaked at higher and higher temperatures until at 400 g/l, and thereafter their shape and height stabilized at that shown in Fig. 8. Above 400 g/l concentration, saturation is achieved and the coverage is assumed to be that obtained in the static experiments (Table I).

The calibration curve shown was developed empirically by adjusting the geometrical relationship between the heater and thermistor and by adjusting the magnitude and interval of current flow. The same amount of steel and the same rate of solvent flow were used as in the experiment with 4-ethylpiperidine. The current used to produce the calibration curve corresponds to 16.8 millicalories. Using this figure and assuming saturation of the steel at 0.24 μmoles of 4-ethylpiperidine adsorbed per gram of steel, the heat of differential adsorption is calculated to be 13 kcal per mole. This value was shown to be substantially free of heat-of-solution effects in an experiment using solvent only in the sample chamber. In this experiment 300 μl of the amine in one slug were injected into the solvent stream flowing into a 3.0 ml volume of the same solvent surrounding the thermistor. A small negative heat of solution was observed. However, this amount of heat is insignificant because the total quantity of amine available for adsorption is 3000 times the amount adsorbed at equilibrium.

In other experiments, a small positive heat of adsorption was observed for cyclohexane adsorbed onto steel from n-heptane (99 mole% minimum), and both benzene and 4-ethylpyridine were found to adsorb exothermically onto steel from cyclohexane. When n-heptane was used as solute in cyclohexane, its adsorption on steel is endothermic.

Discussion

From the data collected in Table I, it is concluded that both 4-ethylpiperidine and 4-ethylpyridine are adsorbed to the extent of an essentially complete monolayer.

It is concluded that the pyridine rings are adsorbed with the plane of the rings parallel to the local plane of the metal surface, primarily because the isotherm for 4-ethylpyridine shows monolayer formation when this position is assumed. The alternative vertical position would require participation of solvent molecules in the adsorbed layer which, in turn, would seem to require a close solvent-solute association, a conclusion which belies the closer association expected between the structurally similar cyclohexane and 4-ethylpiperidine molecules. Finally, both benzene and 4-ethylpyridine adsorb exothermically from cyclohexane, indicating that participation of the π-electron system does occur in adsorption bond formation.

The possibility that the apparent adsorption was really due to hydrogenation of the pyridine chromophore by hydrogen absorbed in the steel was investigated by treating samples from one run with the piperidine reagent (which will react with any primary or secondary nitrogen). There was no detectable reaction. Furthermore, there was no difference between adsorption runs with hydrogen-saturated steel and those with argon-degassed steel. Finally, it was observed during the synthesis work that pyridine ring reductions are difficult even with platinum metal catalysts and much higher temperatures and hydrogen pressures. For these reasons, it is concluded that the decrease in solution concentration during an adsorption run is truly the result of accumulation of pyridine molecules at the iron surface.

In the case of 4-ethylpiperidine adsorption the difference in projected areas covered by different orientations and different steric arrangements of the molecule are much smaller than experimental error due to the ball-like shape of the molecule. From the heat of adsorption data, it is concluded that the nitrogen atom participates strongly in the formation of the adsorption bond, and therefore the molecules at the surface are arranged with the nitrogen in close proximity to the surface and not with the ethyl tail down. This conclusion is supported by the recent observation by other investigators of a charge-transfer type spectrum for a long-chain amine adsorbed on chromium (13). Dehydrogenation reactions are ruled out in this case also because of the dual experiments with hydrogen-saturated and argon-degassed steel.

Even short poly(vinylpyridine) chains (4 units) are much more strongly adsorbed than the monomer. This is shown by the individual points included in Fig. 4 and by the data in Table I. There is a definite tendency for the adsorption to increase with time on the plateau portion of the adsorption-time curves. In addition, increasing the length of the chains greatly increases the adsorption tendency. Apparently, the polymer molecules all adsorb to about the same extent, as shown by the consistent values for amount adsorbed calculated in Table I in terms of molecules. This means that the number of rings removed from the solution by adsorption increases with chain length. It also means that all of the rings on a chain are not adsorbed, but some of them remain partly in the solution phase. However, adsorption of the polymers at more than one point in the molecule makes them very difficult to displace and accounts for the greatly increased inhibition by these molecules.

The aqueous solution measurements show that a considerable portion of the metal surface in excess of the amount covered is deactivated toward corrosion because adsorption of less than one-tenth monolayer produced 80% inhibition. This is probably the result of overlapping of domains of ennoblement when more than one ring is absorbed from a molecule in which they are close together.

Conclusions

1. Molecules of 4-ethylpiperidine are strongly chemisorbed on a steel surface to form a monolayer of molecules adsorbed in the chair configuration and bonded at nitrogen.
2. Molecules of 4-ethylpyridine are chemisorbed on steel in a monolayer and in a position with the plane of the ring parallel to the metal surface.
3. Adsorption of poly(vinylpyridine) molecules is by attachment at several of the adsorbable chain members so that strong adsorption is rapid and desorption is difficult even from solution in aqueous hydrochloric acid.
4. Adsorption of the polymers from acid solutions produces ennoblement of a much greater area of the steel surface than that which is physically covered.

Acknowledgment

The authors gratefully acknowledge the able assistance of Dr. J. S. Payne, Jr., and Mr. R. N. Foote, who carried out the syntheses and of Messrs. J. W. Dooley and D. H. McLendon and Mrs. Peggy Glass, who made many of the measurements. In addition, they thank Drs. P. D. Gardner and R. M. Roberts for their advice and constructive criticisms of the organic portions of the work. The work was done under Contract No. DA-23-072-ORD-1590 for the Army Research Office, Department of the Army. One of the authors (NH) expresses his appreciation of the support by the Robert A. Welch Foundation of Houston, Texas, and of the Office of Naval Research of the work in his laboratory which led in part to this research.

Manuscript received Sept. 3, 1964.

Any discussion of this paper will appear in a Discussion Section to be published in the December 1965 JOURNAL.

REFERENCES

1. M. Stern and A. L. Geary, *This Journal*, **104**, 56 (1957).
2. N. Hackerman and A. C. Makrides, *Ind. and Eng. Chem.*, **46**, 523 (1954).
3. H. F. Finley and N. Hackerman, *This Journal*, **107**, 259 (1960).

4. H. Fischer, Symposium Europeen sur Les Inhibiteurs De Corrosion, Xeme Manifestation de la Federation Europeeme de la Corrosion, Ferrara (italie) 1960, (Universita Degli) Studi Di Ferrara, 1961, p. 1-71.
5. L. I. Antropov, "Kinetics of Electrode Processes and Null Points of Metals," Ranchi, India, Catholic Press (1960).
6. T. K. Ross and D. H. Jones, Symposium Europeen sur Les Inhibiteurs De Corrosion, Xeme Manifestation de la Federation Europeeme de la Corrosion, Ferrara, (italie) 1960, (Universita Degli) Studi Di Ferrara, 1961, pp. 163-182.
7. L. Cavallaro, L. Felloni, and G. Trabanelli, Symposium Europeen sur Les Inhibiteurs De Corrosion, Xeme Manifestation de la Federation Europeeme de la Corrosion, Ferrara (italie) 1960, (Universita Degli) Studi Di Ferrara, 1961, pp. 111-135.
8. R. R. Annand, R. M. Hurd, and N. Hackerman, *This Journal*, **112**, 144 (1965).
9. F. C. McIntire, L. M. Clements, and M. Sproull, *Anal. Chem.*, **25**, 1757 (1953).
10. M. G. Mellon, "Analytical Absorption Spectroscopy," pp. 369-373, John Wiley & Sons, Inc., New York (1950).
11. M. G. Mellon, "Analytical Absorption Spectroscopy," pp. 374-376, John Wiley & Sons, Inc., New York (1950).
12. A. Groszek, *J. Chromatog.*, **3**, 454 (1960).
13. D. Churchill and L. S. Bartell, *J. Phys. Chem.*, **67**, 2518 (1963).

Inhibition of Acid Corrosion by Soluble Monomer and Polymer Amines Containing Identical Functional Groups

R. R. Annand,[1] and R. M. Hurd,[2]
TRACOR, Inc., Austin, Texas
and Norman Hackerman
Department of Chemistry, The University of Texas, Austin, Texas

ABSTRACT

Samples of three kinds of very low polymer amines were examined in aqueous HCl solutions to determine their inhibitor effectiveness. The results show that soluble molecules containing multiple repeating units which are identical in functionality are more efficient corrosion inhibitors than the corresponding monomers, presumably because of multiple adsorption bonding. The compounds used in these experiments are (i) poly(4-vinylpyridine), (ii) poly(4-vinylpiperidine), and (iii) polyethyleneamines. Chains four units in length and longer produce inhibition equivalent to monomer at concentrations which are nearly four orders of magnitude lower than those required for the monomer. This effect is due to the increased stability of the adsorption bonding and also to some overlapping of ennobled micro areas. In the high ranges, the inhibition is not linearly related to coverage. The differences in inhibitor effectiveness among the three monomers are retained in parallel by the polymers.

The experiments reported here are part of a study of the influence of molecular structure on inhibitor effectiveness. Previous work (1) has shown that in a series of saturated cyclic amines which have a progression in the orbital character of the secondary nitrogen atom, both the adsorption bonding and inhibitor effectiveness progressed in parallel. The present work sought to test the hypothesis that soluble molecules containing multiple repeating units with identical functionality would be more efficient corrosion inhibitors than the corresponding monomers because of multiple adsorption bonding. Accordingly, three series of compounds were examined for inhibitor effectiveness in hydrochloric acid: (i) 4-vinylpyridine polymers with 4-ethylpyridine as monomer, (ii) 4-vinylpiperidine polymers with 4-ethylpiperidine as monomer, and (iii) polyethyleneamines with ethylenediamine as monomer.

The experimental procedures were designed to give the best reproducibility of the data and to spread the results from the individual compounds so that reliable comparisons of their individual behavior could be made. They were so chosen that the comparisons among compounds would be valid, *i.e.*, so that identical conditions of solubility, H^+ concentration, etc., were obtained. In general, this required working in strong mineral acid solutions. A wide range of inhibitor concentration was investigated, and the three different polymer systems were tested to check the general applicability of the individual results.

[1] Present address: Petrolite Corporation, St. Louis, Missouri.

[2] Present address: Continental Oil Company, Ponca City, Oklahoma.

Experimental Procedure

Weight-loss experiments.—Both belt polished SAE 1010 steel coupons with an area of about 15 cm^2 and hand polished low carbon shim steel coupons with much larger areas were corroded in 3*N* HCl for periods of time long enough to give an easily determined weight change even in highly inhibited solutions. The usual length of time was 2-4 hr for the small coupons and 1-2 hr for the large ones. Inhibition results were the same for both types of coupons. All coupons were run twelve at a time with at least triplicates of each concentration of inhibitor. Triplicate blanks always took up three out of the twelve coupons. In this manner, a large body of blank runs was collected during the course of the experiments, and any significant deviation of the blanks in a set of twelve coupons [determined statistically by the t-test (2)] was taken as cause for a rerun of that set of experiments.

Reproducibility was aided by running the experiments with the coupons and solutions contained in individual test tubes which were immersed in a controlled temperature bath. Gasometric checks of both the inhibited and uninhibited solution were performed by connecting the tube to a gas buret and measuring the volume of hydrogen evolved as a function of time over the course of the experiment. These plots were all linear and passed through the origin. The volume of gas evolved corresponded to the weight of metal lost according to stoichiometry.

Experiments were run in which the concentration of inhibitor[3] was changed from the order of 1*N* to

[3] Concentrations throughout this paper are expressed in terms of nitrogen atoms, *e.g.*, the equivalent weight of a molecule containing four nitrogen atoms = MW/4.

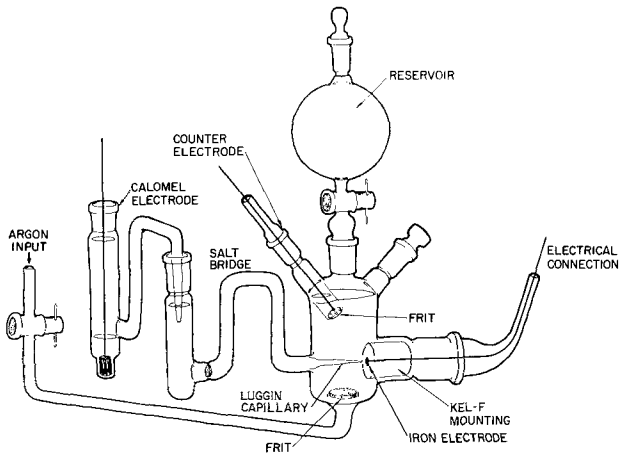

Fig. 1. Polarization cell

about $10^{-6}N$, or until acceleration of the corrosion reaction was observed. In the experiments with significant amounts of basic inhibitor present, the acid concentration was adjusted to maintain it at 3.0*N* in the inhibited solutions. All of the inhibitors were completely soluble under the conditions of the experiments.

Polarization experiments.—Polarization experiments were performed using the cell design shown in Fig. 1. The steel samples used were obtained by punching circular disks out of some of the small SAE 1020 coupons. A length of iron wire was spot welded to one face of each disk. A premolded Kel-F cylinder drilled axially to accept the wire was used to mount the iron disk electrode. The disk was mounted in the Kel-F and bonded to it by reheating and pressing in the original mold. Finally the wire end of the cylinder was turned on a lathe to a standard taper and the electrode face was polished uniformly with emery paper. The whole Kel-F electrode assembly was mounted in the cell by firmly seating it in the female portion of a demountable female-male double TS joint section.

Polarization curves were taken in the usual way using a platinum counterelectrode in a separate compartment and a calomel reference electrode connected through a salt bridge to a Luggin capillary. Placement of the bridge capillary was not extremely critical because the solutions were highly conducting. However, by adjustment of the over-all length of the Kel-F mounting, a distance of a few millimeters was maintained. Electric current was supplied by a parallel pair of 90v radio batteries operated through a variable high resistance to make them a constant-current source. Electrode potentials were measured with a potentiometer, and currents were measured by the IR drop through a standard resistance.

The usual procedure was to insert the polished electrode into the empty cell, fill it with degassed 1.0*N* HCl, and then wait to allow the open-circuit potential to stabilize while the solution was further degassed and stirred with argon. Polarization data were first taken in the cathodic (hydrogen evolution) direction, and then after rechecking the open-circuit potential, in the anodic (iron dissolution) direction. In most experiments with inhibitor, a weighed amount of inhibitor was added after the open-circuit potential had stabilized with a fresh electrode and then the polarization curves were taken. In some cases, uninhibited polarization curves were taken first and then the inhibitor added and the inhibited polarization curves taken. Repetitive experiments agreed well when a freshly polished electrode and a fresh solution bath were used each time a set of experiments was run. Changes in ferrous ion concentration throughout a run were not large enough to affect the potentials. After periods of continuous or consecutive exposure to the acid of several days' duration, the electrodes showed evidence of preferential corrosion around the edge of the metal. This corrosion proceeded from the flat side of the edge and not from the curved side which was effectively bonded to the Kel-F. The presence of these areas was indicated by distortions in the polarization curves.

Synthesis and purification of compounds used.—The polyethyleneamines were obtained from Distillation Products Industries and were distilled before use. The 4-ethylpyridine was obtained from Reilly Tar and Chemical Corporation, and before use it was distilled in a nitrogen atmosphere through a highly efficient, vacuum-jacketed still. It was also stored under nitrogen. The poly(4-vinylpyridine), poly(4-vinylpiperidine), and 4-ethylpiperidine were synthesized in the laboratory. The monopiperidine was obtained by catalytic hydrogenation in a Parr apparatus using a palladium-charcoal catalyst. After distillation in a nitrogen atmosphere, the product was checked spectrophotometrically for absence of the pyridine. This product was also stored under nitrogen.

After many trials, a procedure was designed for obtaining very low molecular weight poly(vinylpyridines) by polymerizing 4-vinylpyridine (obtained from Reilly Tar and Chemical Corporation and freshly distilled before use) using 2,2'-azoisobutyronitrile as initiator. The procedure finally adopted consisted in polymerizing in a very dilute ethanol solution which was kept under nitrogen almost at the reflux temperature. By properly adjusting the extent of dilution in the polymerization media and the ratio of monomer to initiator, polymer samples could be obtained which ranged in chain length from four to about one hundred units. Number average molecular weights were determined using a Mechrolab Vapor Osmometer. The number of initiator fragments per chain was determined by infrared spectral analysis. This indicated two fragments per chain.

The 4-vinylpiperidine polymers were obtained from the corresponding polypyridine by catalytic reduction in a high-pressure stainless steel autoclave. During the course of a great many trial reductions using different catalysts and at various operating temperatures and pressures, it was found that the necessary catalytic function was the ability to cause reduction at the lowest possible temperature so that degradation was a minimum. Using ruthenium on carbon and the highest hydrogen pressure safely obtainable in the autoclave at 250°C, a satisfactory reduction was obtained with only slight degradation. Only a very small percentage of unreduced pyridine units remained, but a

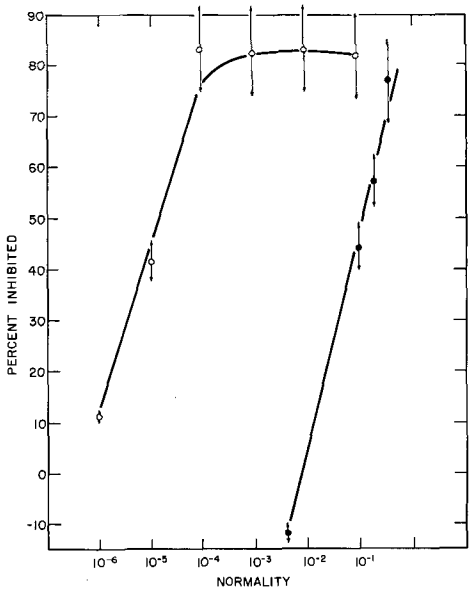

Fig. 2. Per cent inhibition *vs.* log concentration for mild steel at 40°C in 3.0*N* HCl; ○, poly(vinylpyridine) (MW 160); ●, 4-ethylpyridine.

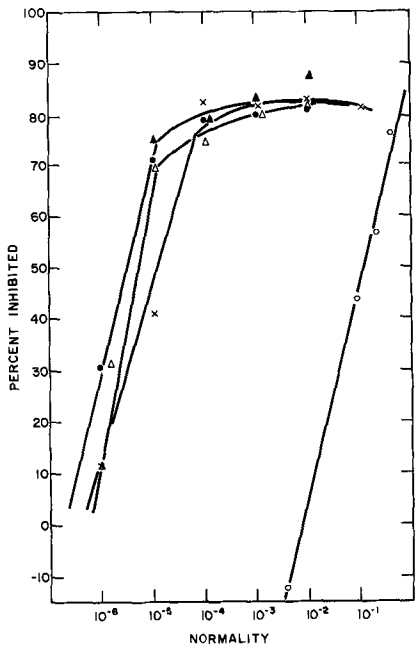

Fig. 3. Effect of polymer chain length on inhibitor effectiveness for mild steel polypyridines in 3.0*N* HCl at 40°C. Chain length: ○, 1 unit; ●, 4 units; X, 10 units; ▲, 14 units; △, 67 units.

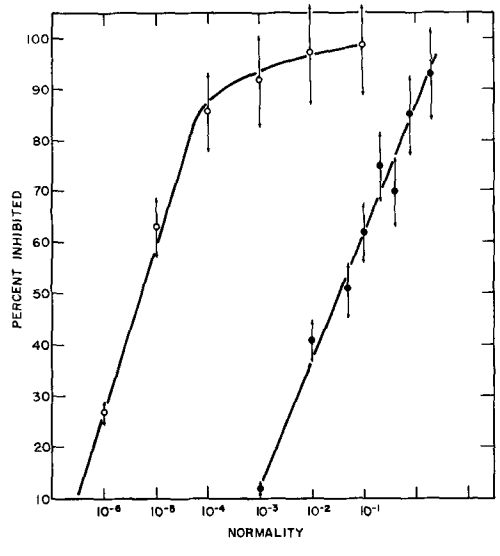

Fig. 4. Per cent inhibition *vs.* log concentration for mild steel at 40°C in 3.0*N* HCl; ●, 4-ethylpiperidine; ○, poly(vinylpiperidine) (MW 400).

ruthenium-polymer complex was formed in the autoclave reaction. It was necessary to wash out the ruthenium by extraction into n-butanol from an acidic aqueous solution. Dicyclohexylthiourea was added to the butanol to force the extraction by competitive complexation of the ruthenium. The complex thus formed had a distinctive blue color and therefore could be used as its own indicator to signal complete removal of the ruthenium. The purified polymer was then recovered by making the solution basic, filtering, washing and vacuum drying.

Discussion of the Results

The curves obtained from the weight loss experiments for the three series of compounds are shown in Fig. 2, 3, 4, and 5. From these, it is readily seen that the hypothesis which was tested is indeed valid. Polymer chains above 3 to 4 units in length produce the same inhibition as the monomer at concentrations up to four

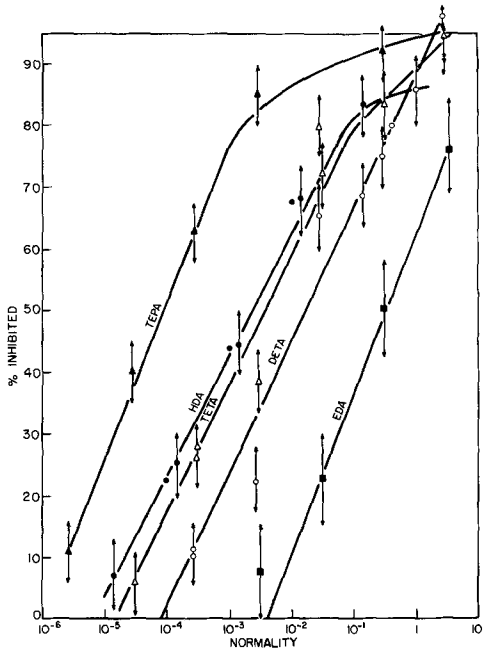

Fig. 5. Per cent inhibition *vs.* log concentration for mild steel at 40°C in 3.0*N* HCl; ●, hexamethylenediamine; ○, diethylenetriamine; ■, ethylenediamine; △, triethylenetetramine; ▲, tetraethylenepentamine.

powers of ten lower in magnitude. In all of the experiments, the inhibitor was completely soluble; no emulsions were used.

Because two and three unit polypyridines and polypiperidines were not available, one of the reasons for the work with the polyethyleneamine series was to determine whether the increase in inhibitor effectiveness of polymers is progressive from one up to four or five units. The data of Fig. 5 show that it is progressive up to four units, but the data of Fig. 3 show that this progression ceases above four units. These data show that the stability of the adsorption bonding to the metal determines the inhibitor effectiveness. That is, a soluble species which adsorbs readily and which is not easily removed when once adsorbed will be most effective. It is interesting to note that among the three types of compounds, the same trends in inhibitor effectiveness (in terms of the position of the curves on the log axis) exhibited by the monomers on the rising portion of the curve are retained by the polymers. This suggests that adsorption of polymers provides a multiplying effect to the relationships between the kind of individual adsorption bonds and the inhibitor effectiveness of that bond.

A possible alternative mechanism for the effectiveness of the polymers is the precipitation of a metal polymer complex in the immediate vicinity of the metal surface. This is rejected on the following grounds: (i) Complexes of hexamethylenediamine would be expected to be much less soluble (and therefore more effective) than those of either diethylenetriamine or triethylenetetramine, yet they all have nearly the same inhibition effect; (ii) in no case has a complex containing precipitate been observed in the presence of excess iron(II) or iron(III); (iii) a continuous tendency to precipitate and therefore to inhibit would be expected as the chain length is increased, particularly for very long chains and when several iron atoms are complexed by one chain; no such tendency was observed with the polypyridines or polypiperidines above the level of four units (Fig. 3); and (iv) no visible film was formed on the coupons under any inhibited conditions.

An unexpected feature of the results is the existence of the log-linear portion which extends over about two decades on the log concentration axis. This feature has

been found to be a general one for a wide variety of compounds tested in this laboratory. As shown in the 4-ethylpyridine curve (Fig. 2), even points which represent an increase in corrosion rate lie on the line when plotted in terms of negative inhibition. The negative numbers are derived on the same basis as the others, *i.e.*, from the equation

$$\% \text{ Inhibited} = \left(1 - \frac{\text{Rate inhibited}}{\text{Rate uninhibited}}\right) \times 100$$

where the rate terms are in the same units, *e.g.*, mg lost/hr/cm^2.

The fact that the curves for per cent inhibition as a function of log concentration are linear over an appreciable range for the polyethyleneamines, the polypiperidines, polypyridines, and other compounds indictate a linear relation between adsorption from acid solution and log concentration. Such a relationship is found in the Temkin isotherm (3, 4),

$$\theta = -\frac{RT}{\beta \Delta H_o} \ln AC$$

In this expression, β is a constant; A is a complex function of ΔH_o and other parameters; and ΔH_o is the heat of adsorption for very low coverage, (θ). For adsorption from dilute aqueous solution, ΔH_o will be influenced by contributions from the heats of desorption of solvent and of neutralization of the inhibitor conjugate acid.

The ionization constants for all of the polyethyleneamines have been published (5-8). Using these values, the normalities of amine, and the concentration of HCl, it can be shown that at the highest concentration plotted for tetraethylenepentamine, only 0.74% of the molecules are not fully protonated. The free amine (completely unprotonated) is present at a concentration of the order of $10^{-36}N$ at an analytical concentration (*i.e.*, amount of amine added per unit volume of solution) corresponding to good inhibition. Furthermore, under the experimental conditions of high, constant H^+ ion concentration, the concentration of any of the possible species, *i.e.*, from completely unprotonated to completely protonated, is a linear function of the analytical concentration. The base strengths in the polyethyleneamine series range upward from tetraethylenepentamine. The polypyridines and piperidines are expected to be quite similar for comparable chain-length. On this basis, if it can be assumed that per cent inhibition is proportional to per cent coverage (θ), then

$$\%I = K\theta = -\frac{KRT}{\beta \Delta H_o} \ln A - \frac{KRT}{\beta \Delta H_o} \ln C$$
$$= m \log C + \text{Constant}$$

where K is the proportionality constant. That is, the slope of the line, $\%I = F(\log C)$, is proportional to the reciprocal of the net heat of adsorption. Furthermore, since β is an independent constant, if the ΔH_o's, the K's, and the β's are similar, the slopes of the lines, $\%I = F(\log C)$, should be the same.

The data in Table I were obtained by a statistical treatment of the data shown graphically in Fig. 5 to get average values of the slopes of the rising portion of the individual curves. It can be seen that the slopes are very nearly uniform for all of the polyethyleneamines. This must mean that only small differences occur in the ΔH_o's and β's due to the different ratios

Table I. Slopes of the curves of Fig. 5

Compound	Slope, %I per log cycle
EDA	17.9
HDA	17.2
DETA	18.5
TETA	17.5
TEPA	18.9
Average	18.0

Table II. Slopes of the curves of Fig. 2, 3, and 4

Compound	Slope, %I per log cycle
Ethylpyridine	42.0
Polypyridine (MW 514)	40.0
Polypyridine (MW 1160)	32.0
Polypyridine (MW 1549)	44.2
Polypyridine (MW 6954)	58.8
Ethylpiperidine	25.5
Polypiperidine (MW 400)	32.5

of the number of primary to secondary amino nitrogens. However, it may represent large contributions by the heats of neutralization and desorption of solvent which are the same for all the compounds. These may be masking the relatively smaller differences in the heat of formation of the chemisorption bond among the different compounds.

For comparison, the slopes of the curves from Fig. 2, 3, and 4 are included in Table II for polymer and monomer pyridines and piperidines. The higher slopes of these curves are consistent with either a large solvent contribution to the heats of reaction or with a difference of a factor of about two in either β or K, because the inhibitor effectiveness at saturation is not appreciably different for the two kinds of polymers. There is, however, a greater spread in the data of Table II, indicating a greater difference between monomer and polymer.

The factor, K, in the above discussion is used because adsorption experiments from acid solutions (9) have shown that in 0.01N HCl polypyridines are capable of producing 80% inhibition under conditions where less than one-tenth monolayer coverage is obtained. Furthermore, polarization curves taken with and without both monomer and polymer show that the metal is ennobled by 20 mv or more due to the adsorption of these inhibitors (10). An example of this is presented in Fig. 6. These observations strongly suggest that in the plateau portion of the polymer curves where θ ceases to be proportional to the per cent inhibition efficiency, the proportionality breaks down because the ennobled areas of the surface begin to overlap as θ increases, and thus K is no longer constant.

Conclusions

1. Very short chains of adsorbable groups improve inhibitor effectiveness by orders of magnitude compared to monomeric species.

2. This effect is interpreted in terms of a greatly increased stability of the net total adsorption bonding

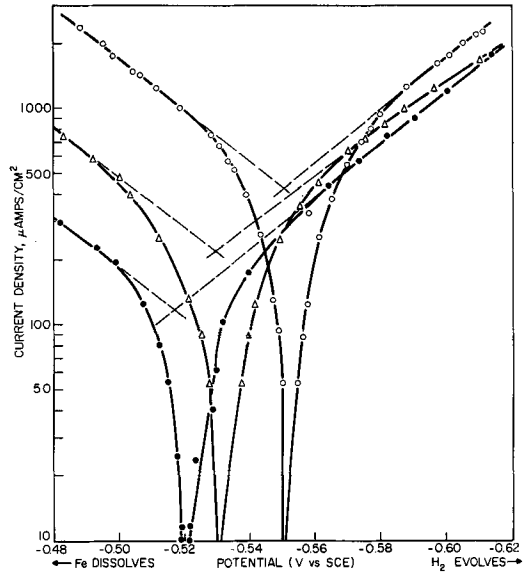

Fig. 6. Polarization curves for uninhibited monomer and polymer solutions; △—△, 0.1M 4-ethylpyridine in 1N HCl; ○—○, 1N HCl uninhibited; ●—●, 0.031M poly(vinylpyridine) 512 MW in 1N HCl.

in the polymer species, *i.e.*, a high tendency to adsorb, to stay adsorbed, and to form strong metal/inhibitor bonds which contribute an enhanced ennobling effect.

3. In the case of adsorption which ennobles the metal surface, the inhibition is not linearly related to coverage in the high inhibition ranges.

4. In agreement with 3, the variations in effectiveness of the individual adsorbable groups (exemplified by the monomers) are retained in the polymer.

Acknowledgment

The authors gratefully acknowledge the assistance of Dr. J. S. Payne, Jr., and Mr. R. N. Foote, who carried out the organic syntheses and of Dr. I. Y. Chang, who took the polarization data. This work was carried out under Contract No. DA-23-072-ORD-1590 for the Army Research Office, Department of the Army. One of the authors (NH) also expresses his appreciation to the Robert A. Welch Foundation of Houston, Texas, and to the Office of Naval Research for support of research in his laboratory over the years which in part led to this work.

Manuscript received Sept. 3, 1964. This paper was presented in part at the 20th Annual NACE Conference, March 1964, Chicago, Illinois.

Any discussion of this paper will appear in a Discussion Section to be published in the December 1965 JOURNAL.

REFERENCES

1. N. Hackerman, R. M. Hurd, and R. R. Annand, *Corrosion*, **18**, 37t (1962).
2. W. J. Youden, "Statistical Methods for Chemists," pp. 24-28, John Wiley & Son, New York (1959).
3. S. Brunauer, K. S. Lore, and R. G. Keenan, *J. Am. Chem. Soc.*, **64**, 751 (1942).
4. A. Frumkin and A. Slygin, *Acta Physicochim. URSS*, **3**, 791 (1935).
5. Alexander Gevo, *J. Am. Chem. Soc.*, **76**, 5159 (1954).
6. H. B. Jonassen, F. W. Frey, and A. Schaefsma, *J. Phys. Chem.*, **61**, 504 (1957).
7. H. B. Jonassen, R. B. LeBlanc, A. W. Meibohm, and R. M. Rogan, *J. Am. Chem. Soc.*, **72**, 2430 (1950).
8. R. Rometsch, A. Marxer, and K. Miescher, *Helv. Chim. Acta*, **34**, 1611 (1951).
9. R. R. Annand, R. M. Hurd, and N. Hackerman, *This Journal*, **112**, 138 (1965).
10. R. R. Annand and N. Hackerman, "Corrosion Inhibition," in "Encyclopedia of Electrochemistry," C. A. Hampel, Editor, Reinhold Publishing Co., New York (1964).

The Influence of Crystal Orientation on the Oxidation of Tungsten

R. W. Bartlett and J. W. McCamont

Philco Research Laboratories, Newport Beach, California

ABSTRACT

The oxidation of tungsten above 1800°C is described in terms of deviations from gas collision theory (Hertz-Knudsen equation). The probability that a colliding oxygen molecule will react with tungsten is strongly dependent on crystal orientation. Of the crystal faces examined, (100) surfaces oxidize most rapidly with a reaction probability of 0.4. (111) and (110) surfaces oxidize at approximately the same rate as polycrystalline tungsten. The morphology of oxidized (100) surfaces is smooth with the exception of occasional stepped octahedral pyramids each bound by {111} faces. The morphology of (111) surfaces is smooth except for numerous stepped tetrahedral pyramids each bound by {100} faces. Initiation of these shapes is not associated with dislocations or detectable impurities. However, dislocations subsequently cluster at mature octahedral pyramids. The morphology of oxidized (110) tungsten surfaces consists of extremely irregular surfaces and macroscopic ledges, but shapes clearly related to crystal geometry were not identified.

Oxidation of tungsten at temperatures above 1300°C involves collision, chemisorption of oxygen on the tungsten surface, chemical reaction, and evaporation of tungsten oxides. Oxidation rates are linear and have been determined from pressure measurements (1-4) and by measurements of sample dimension changes (5-7) taken during oxidation. Below approximately 1800°C the oxidation rate increases with temperature in an exponential manner characteristic of activated chemical processes. Above 1800°C the rate is independent of temperature except at very low pressures and high temperatures. There is evidence that oxygen atoms chemisorb in two distinct monolayers with different binding energies (2, 8). Oxide polymers, particularly $(WO_3)_3$ and $(WO_2)_3$, have been shown to be the predominant vapor species in equilibrium with tungsten oxides (9). However, a recent mass spectrometric study (10) indicates that monomers are the species evaporated from oxidizing tungsten surfaces. Polymerization evidently occurs later as a result of collisions in the gas phase. Above 2000°C the WO_2 monomer is produced in greater abundance than WO_3 (10).

The nonactivated oxidation rate behavior of tungsten has been explained in terms of deviations from the rate at which oxygen molecules collide with the tungsten surface, since this is the maximum possible rate. Using gas kinetic theory (Hertz-Knudsen equation)

$$J = \epsilon P_{O_2}/(2\pi mkT)^{1/2} \qquad [1]$$

Where J is the number of oxygen molecules which react each second and ϵ is the probability that each O_2 molecule striking the surface will react; $\epsilon \leq 1$. Since the rate is not limited by a prior or subsequent activated step or endothermic step, the reaction probability is equivalent to the sticking probability (condensation coefficient) of oxygen. In a previous study (7), with polycrystalline tungsten, rate data at oxygen pressures from 10^{-6} atm to 1 atm were described with a constant value of the reaction probability, $\epsilon = 0.06$. This correlation included an independent correction for the lowered oxygen pressure at the surface caused by the tungsten oxide gas boundary layer which is present at high pressures. This correction was based on free convection theory.

A study of the effect of metal crystal orientation on oxidation rates at temperatures where condensed oxides form has been made for tungsten (11) and several other metals (12). Similar studies at high temperatures where the oxide products vaporize are rare in general and have not been made for tungsten. The purpose of this study was to determine the reaction probabilities and observe variations in tungsten morphology during oxidation of low index faces.

Experimental

One half inch diameter single crystals of known [hkl] orientation were wafered to produce short cylindrical samples each bound by parallel (hkl) faces. Using a 2% NaOH electrolyte, these surfaces were electropolished, and some were electroetched to develop etch marks and to outline subgrain boundaries. The oxidation procedure is described below. Samples were set on a thin tungsten pedestal located in a vacuum chamber. A stable mounting was accomplished using an insertion hole drilled in the side of the sample. The chamber was evacuated and backfilled with dry oxygen to 1 x 10^{-6} atm. Pressure was maintained by controlling the flow of oxygen through the system. This oxygen pressure was chosen and used exclusively because of several advantages. First, this pressure was high enough to permit removal of considerable tungsten. This allows full development of morphological changes and insures accurate rate measurements. Second, although this pressure is higher than typical condensation-evaporation experiments in metal systems, it is lower than required to form a gas boundary film sufficient to affect the rate of oxidation. Third, at this pressure, there is comparative rate data for polycrystalline tungsten from two sources (4, 7). All samples were oxidized at 2050° ± 50°C using an R.F. induction coil. Temperature was measured with a calibrated disappearing filament pyrometer using corrections for the spectral emissivity of tungsten and calibrated window absorptivity. The oxidation rate was determined by measuring the decrease in distance between opposite (hkl) faces with micrometer calipers accurate to ±0.0001 in. These measurements were made on samples which had been oxidized 420 min, and the decrease in interface distance varied between 0.0195 and 0.045 in.

The tungsten crystals used as samples were grown by the Linde Company using a plasma arc Verneuil technique, Table I. In all cases misorientation of crystal faces with the surface was less than 5°.

Since the orientation and appearance of etch marks generated in aqueous solutions were used to correlate the morphological results of high-temperature oxidation, a brief introductory discussion of wet etch marks on tungsten is necessary. Etch pits in tungsten have been studied extensively by Schadler (13) using a $CuSO_4 \cdot NH_4OH$ solution and by Berlec (14) using both a $CuSO_4 \cdot NH_4OH$ solution and a 2% NaOH solution. The results using either etchant are identical. Square etch pits are developed on (100) surfaces, and elongated triangular pits develop on (112) surfaces of tungsten. In both cases, the defining sides of the etch pits are {110} planes. Plastic deformation experiments and matched etch pit patterns in cleaved surfaces indicate that the etch pits coincide with dislocations intersecting the surface. Berlec (14) has observed small oriented etch hillocks with a triangular outline on heavily etched (111) surfaces of tungsten. Neither etch pits nor hillocks occur on (110) surfaces of tungsten. All of these results were confirmed during the present study. We have also found that the wet etch pyramids on (111) surfaces cluster at subgrain boundaries, suggesting an association with dislocations.

Table I. Nominal composition tungsten crystals

C	6 ppm	Fe	0.01%
O	5 ppm	Mg	0.001
Al	0.01%	Mn	0.01
Co	0.003	Mo	0.1
Cu	0.001	Ni	0.01
Cr	0.01	Si	0.01

Table II. Measured reaction probabilities based on an oxidation period of 420 min at 2050°C and: $W + O_2 \rightleftharpoons WO_2(g)$

$$P_{O_2} = 1 \times 10^{-6} \text{ atm}, \; T = 300°K;$$

$$\epsilon = (\text{rate}) \left(\frac{\rho_W N_O}{M_W P_{O_2}} \right) (2\pi mkT)^{1/2}, \; \epsilon = 9.84 \times 10^8 \; (\text{rate})$$

Sample	Face	Avg. face recession	Recession rate, in./min	ϵ
W-12	(100)	0.0176	4.2×10^{-5}	0.41
W-13	(100)	0.0172	4.1×10^{-5}	0.40
W-20	(100)	0.0186	4.3×10^{-5}	0.42
W-4	(110)	0.0032	7.7×10^{-6}	0.076
W-7	(110)	0.0032	7.6×10^{-6}	0.075
W-8	(110)	0.00295	7.0×10^{-6}	0.069
W-31	(111)	0.0040	9.5×10^{-6}	0.093
W-32	(111)	0.0040	9.5×10^{-6}	0.093
W-33	(111)	0.00395	9.4×10^{-6}	0.092

Vicinal surfaces composing the faces of structural anomalies, hillocks and pits, formed on tungsten were identified from (*a*) the height or depth of the structure measured by oil emersion microscopy, (*b*) the projected geometry of the structure, and (c) the orientation of the crystal with respect to the orientation of the hillock or pit. Crystal orientation was determined by x-ray diffraction.

Results

The measured values for reaction probabilities on (100), (110), and (111) faces are shown in Table II. These data are also shown in graphical form and compared with polycrystalline data at the same pressures in Fig. 1. The values for (110) and (111) faces are similar to the polycrystalline values, but the reaction probability on the (100) face was much faster, approaching half of the total collision rate.

The differences in morphology of the tungsten surface were more striking, but the results were equally reproducible. Polished (100) and (111) surfaces tended to remain smooth while (110) surfaces were jagged. Grooving of subgrain boundaries occurs on (100) and (111) surfaces. Etch pits or other indications of accelerated oxidation at dislocations were not observed on any of the crystal faces as a result of oxidation. Wet etch pits introduced before oxidation lost definition as a result of oxidation but did not change otherwise.

(100) Surface.—Examination of the 90-min oxidation micrographs reveals occasional marks similar to the wet etch pits. These hillocks are the initial appearance of growth anomalies on (100) surfaces which remain for extended periods of oxidation and eventually become octahedral pyramids. These growth forms also appear as small rounded craters in their early stages.

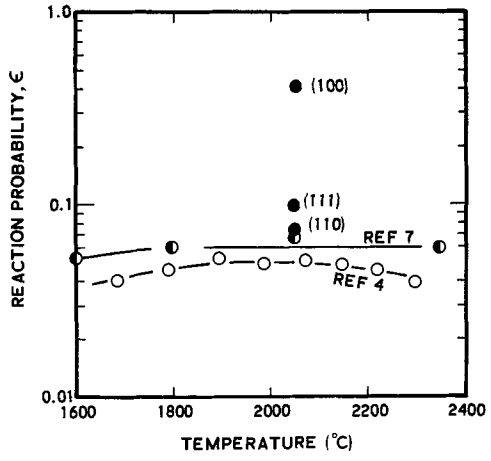

Fig. 1. Reaction probability for polycrystalline tungsten wire (4) and rod (7) and single crystal low index faces at 1 x 10^{-6} atmospheres oxygen pressure.

Fig. 2. Carbon replica of stepped pyramid on (100) tungsten surface. Magnification 1500X.

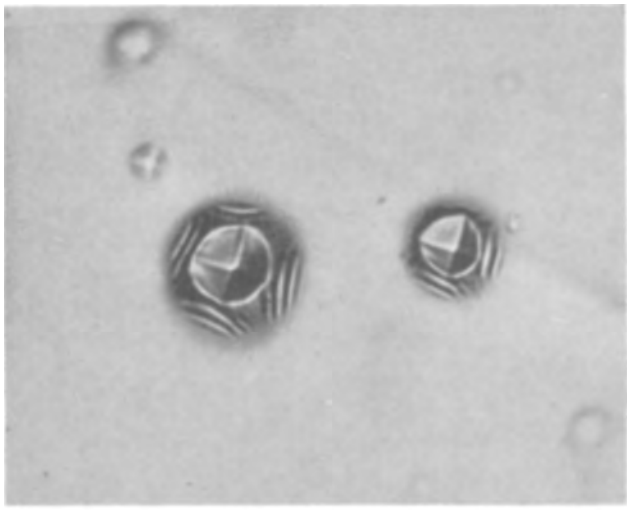

Fig. 3. Octahedral pyramids on (100) surface with cores having the shape of shallow polyps. Small craters slightly out of focus can be seen in the background; oxidation 7 hr at 2070°C. Magnification approximately 500X.

Sometimes they appear as shallow polyp structures containing fourfold symmetry. An electron micrograph replica of a mature octahedral pyramid is shown in Fig. 2. It is considerably larger than a wet etch pit. Its sides are {111} faces rather than the {110} faces observed for wet etch pits. The octahedral faces are stepped to provide for a flatter total pyramid shape without sacrificing the exposure of low index faces at the surface. However, the edges of each pyramid, where the {111} planes intersect, are not stepped. This shape leads to the appearance of fourfold inverted rings in optical micrographs. The center of these pyramids may simply be a continuation of the pyramid structure or contain the shallow polyps. Two examples of the latter are shown in Fig. 3.

The mature stepped pyramid structures are slow to develop. Those shown in Fig. 2 and 3 were formed by an oxidation period of 7 hr. There were comparatively few of these structures on the (100) surface, but they were observed on all samples oxidized more than 3 hr. They have been seen at subgrain boundaries, but there was no preference for this location and little tendency to cluster at any location. Their orientation is fixed by their {111} faces and the orientation of the crystal, Fig. 4. Small misorientations between adjacent subgrains were indicated by small changes in orientation of the stepped pyramids contained within them. As with wet etch pits, slight misorientation of the surface with respect to the (100) plane caused distortions of the symmetrical shape of the pyramids.

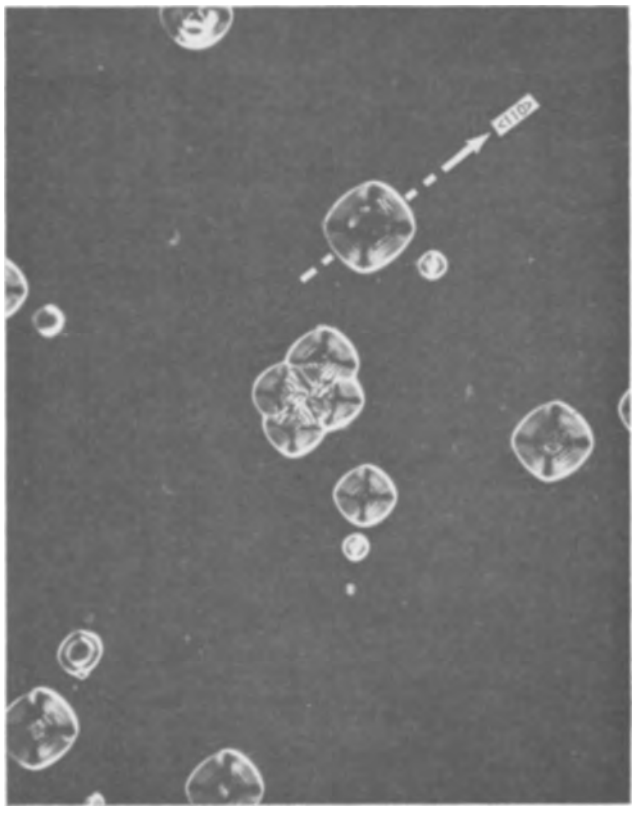

Fig. 4. Orientation of stepped octahedral pyramids on (100) tungsten surface; darkfield illumination. Magnification approximately 130X.

Extensive oxidation after dislocation etching has shown that octahedral pyramids are not initiated at dislocations. However, mature pyramids subsequently act as traps for dislocations. A polished (100) surface was oxidized 7 hr and later marked with a referencing hardness indentation near two octahedral pyramids. The sample was then etched in 2% NaOH to develop wet etch pits. This is shown in the second micrograph of Fig. 5. Dislocations clustered within the strain hardened area around the indentation mark as expected. However, equally dense dislocation clustering has occurred within the octahedral pyramid. Because the wet etch pits are bound by {110} faces their outline is rotated 45° with respect to the square outline of the octahedral pyramids.

Electron microprobe analysis of the tungsten surface at the stepped pyramids was undertaken to determine if impurities were influencing this behavior. Elements other than tungsten were not present in detectable amounts. Furthermore, the tungsten x-ray emission intensity was not diminished at octahedral pyramids relative to the rest of the sample. If tungsten oxides, borides, carbides, or nitrides were present in appreciable quantities, a measurable reduction in tungsten x-ray intensity would have been detected.

(111) Surface.—The morphology development on (111) surfaces was similar to the (100) surfaces. The surface remained smooth; but gradually stepped tetrahedral pyramids matured, Fig. 6. They were more numerous than the octahedral pyramids observed on the (100) surface. Electron micrographs show the steps more clearly than light micrographs. In many instances the hillocks are rounded and only approximate tetrahedral shape. These oxidation pyramids are oriented differently than the wet etch pyramids. This is shown

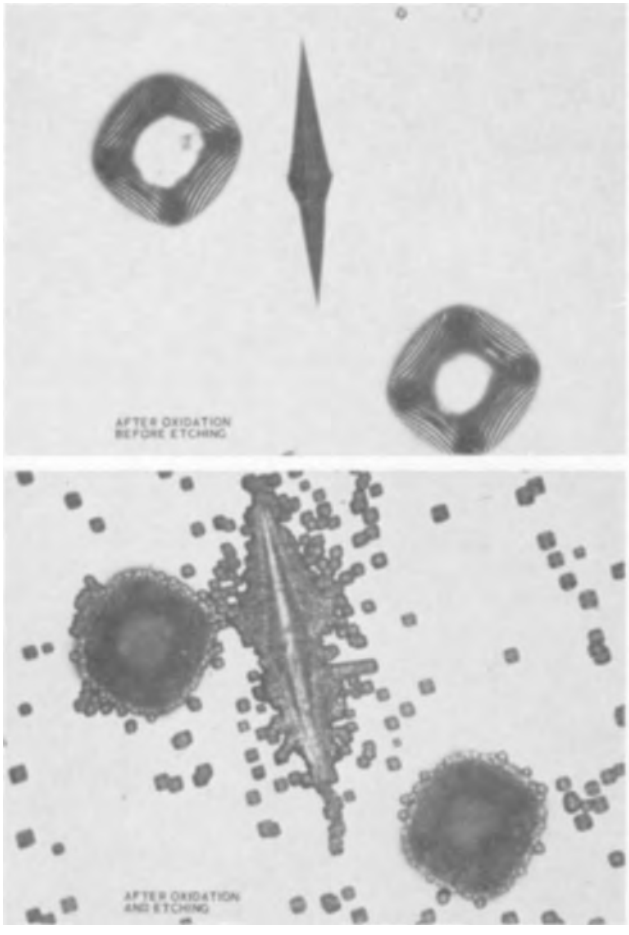

Fig. 5. Post oxidation wet etching treatment shows accumulation of dislocations at stepped pyramids on (100) tungsten surface. Magnification approximately 260X.

in Fig. 7. Both micrographs were taken in the same area and identified by hardness indentations, not shown. The sample was wet etched prior to oxidation, left micrograph. The triangles formed by the intersection of the wet etch pyramids with the (111) surface are pointing down and to the left. The results of a 1-hr oxidation treatment are shown in the right micrograph. A stepped pyramid has formed at the top of the photographed surface, but its triangular outline on the surface is pointing upward and to the right. Oxidation has rounded the wet etch pyramids and is tending to reorient them as triangles pointing in the opposite direction of their original orientation. From a comparison of crystal orientation, as determined from x-ray diffraction studies, with pyramid orientation on the (111) surface we determined that the wet etch pyramids are bound by {110} faces while the stepped oxidation pyramids are bound by {100} faces. The apparent change in orientation of the wet etch pyramids during high temperature oxidation is caused by the preference for {100} faces rather than {110} faces under these conditions. Consequently, the {100} faces advance and the {110} faces recede as defining surfaces for the hillocks.

(110) Surface.—Pyramids or other definite crystallographic shapes do not form on the (110) surface. Grooving of subgrain boundaries also does not occur although these boundaries usually can be detected and followed in a microscope field because of slight differences in shading which occur at the boundaries. The mature morphology developed after a 7-hr oxidation treatment consists of: (*a*) long serrated ridges; (*b*) triangular shapes with saw-tooth edges pointing toward shallow depressed areas and all oriented in a common direction; and (*c*) numerous parallel striations. These are shown in Fig. 8. Rare examples of isolated dodecahedral (110) faces occurred as small

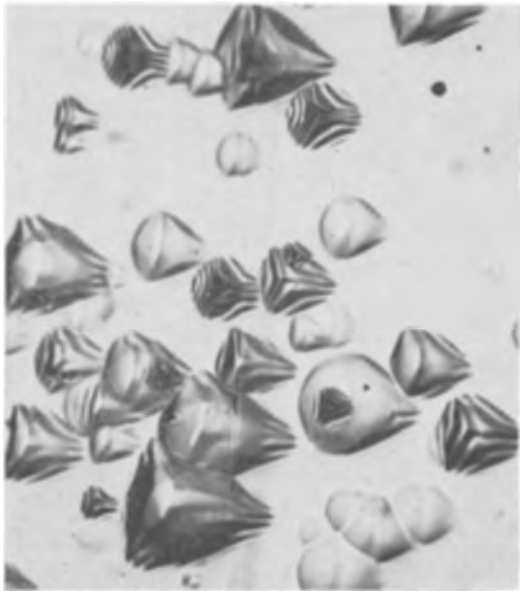

Fig. 6. Mature tetrahedral pyramids on the (111) surface of tungsten oxidized 7 hr at 2050°C. The photograph is bisected by a subgrain boundary.

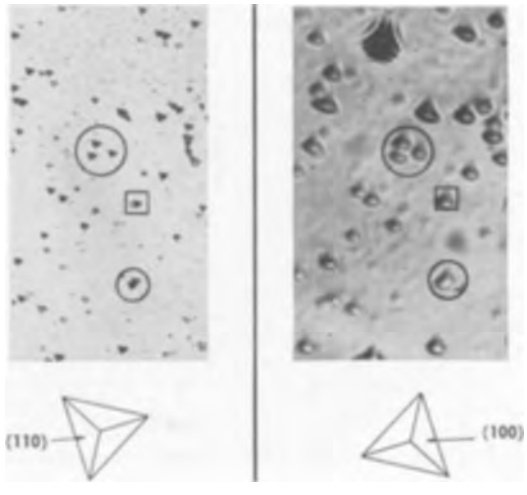

Fig. 7. Orientation of wet etch pyramids on (111) before oxidation, left; reverse orientation of oxidation triangular pyramid developed during a 1-hr oxidation period at 2050°C in the same area, right. Photographs were matched with indentation marks. Magnification approximately 375X.

sections of the tungsten crystal projecting outward from the surface.

Discussion

The results of this study are not easily explained by other published data or models for evaporation and condensation. The order of oxidation rates measured in this study, (100) > (111) > (110>, is different from the rates of formation of thin oxide films on tungsten measured by Metrofanov (11) at 400°-450°C. The order of the latter study was (111) > (100) > (110), and rate increases were correlated with reductions in electronic work functions. The oxidation mechanisms are different, and agreement is not necessarily expected.

Batterman (5) studied faceted hillocks and pits formed during the etching of germanium in a H_2O_2-HF solution. He reasoned that a stable hillock required that the recession rate of the hillock face be less than the product of the recession rate of the base plane and cosine of their angle of intersection. Batterman's results were generally consistent with this rule, but not consistent in all cases. The prevalent formation of

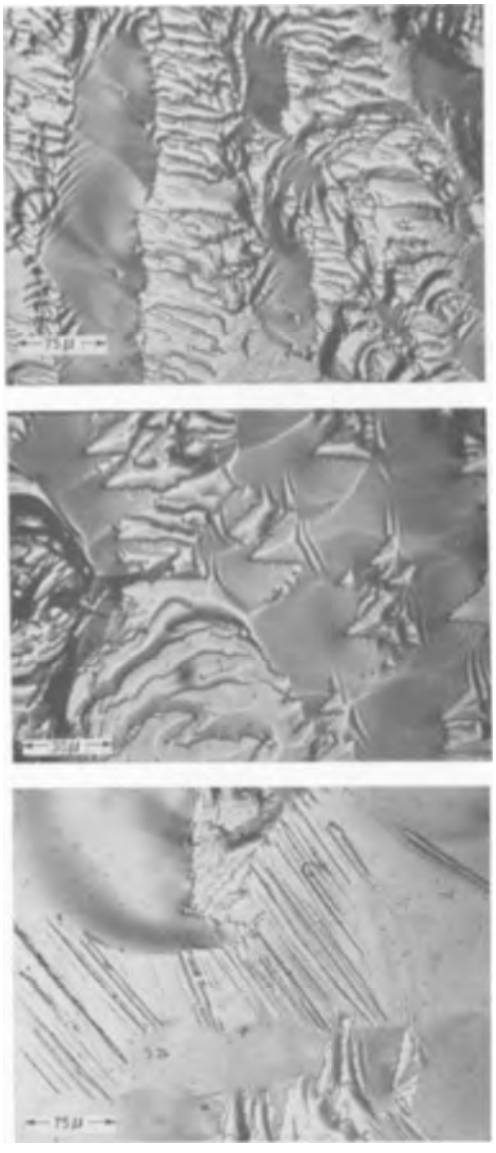

Fig. 8. Characteristic patterns on the (110) tungsten surface resulting from oxidation.

tetrahedral pyramids with {100} faces on a (111) base plane of tungsten does not conform with Batterman's rule.

Sticking coefficients of diatomic molecules have been attributed to entropy decreases involved in transforming from the gas phase to the chemisorbed state. In particular, hindered rotation of the molecule in the chemisorbed state appears to be a plausible cause of a sticking coefficient less than unity (16). On this basis, the sticking coefficient is the ratio of the partition functions for the chemisorbed state and gas state. Since vibration frequencies cannot be evaluated, the approximation that vibrational partition functions have values of unity is taken, and the sticking coefficient is reduced to the reciprocal of the rotational partition function for oxygen

$$\epsilon = \frac{\sigma h^2}{8\pi^2 IkT} \qquad [2]$$

The calculated value for ϵ at 300°K is 0.014. This does not conform with the experimental results, and the model fails to account for the observed rate anisotropy.

When entropy effects are absent, evaporation coefficients are expected to be high and macroscopic ledges absent unless impurities are present (17). Impurities may be contributing to the observed morphologies, but without positive evidence no conclusions can be drawn.

Acknowledgments

The authors are grateful to Mr. R. W. Walker and Mr. J. P. Pope for experimental assistance and to Dr. W. M. Fassell for his helpful discussions. This study was sponsored by Aeronautical Systems Division, U. S. Air Force under Contract AF 33(657)-8654.

Manuscript received June 15, 1964; revised manuscript received Aug. 24, 1964. This paper was presented at the Washington Meeting, Oct. 11-15, 1964.

Any discussion of this paper will appear in a Discussion Section to be published in the December 1965 JOURNAL.

REFERENCES

1. I. Langmuir, *J. Am. Chem. Soc.*, **105**, 35 (1913); *ibid.*, **37**, 1139 (1915).
2. J. Eisinger, *J. Chem. Phys.*, **30**, 412 (1959).
3. J. A. Becker, E. J. Becker, and R. G. Brandes, *J. Appl. Phys.*, **32**, 411 (1961).
4. H. U. Anderson, "Kinetic Studies of the Reactions Occurring Between Tungsten and Gases at Low Pressures and High Temperatures," (Ph.D. Thesis, University of California 1962); UCRL 10135, April 1962.
5. R. A. Perkins and D. D. Crooks, *J. Metals*, **13**, 490 (1961).
6. R. A. Perkins, W. L. Price, and D. D. Crooks, "Oxidation of Tungsten at Ultra-High Temperatures," Lockheed Report 6-90-62-98, November 1962, Sunnyvale, Calif.
7. R. W. Bartlett, *Trans. AIME*, **230**, 1097 (1964).
8. J. A. Becker in "Solid State Physics," Vol. 7, p. 379-424, F. Seitz and D. Turnbull, Editors, Academic Press, New York (1958).
9. J. Berkowitz, W. A. Chupka, and M. G. Inghram, *J. Chem. Phys.*, **27**, 85 (1957).
10. Joan Berkowitz-Mattuck, A. Buchler, J. L. Engelke, and S. N. Goldstein, *J. Chem. Phys.*, **39**, 2722 (1963).
11. O. V. Mitrofanov, "Soviet Physics-Crystallography," **8**, No 2, 229-231 (Trans) (1963).
12. A. T. Gwathmey and K. R. Lawless, "The Influence of Crystal Orientation on the Oxidation of Metals," in "The Surface Chemistry of Metals and Semiconductors," pp. 483-521, H. C. Gatos, Editor, John Wiley & Sons, New York (1960).
13. H. W. Schadler, "Correlation of Etch Pits and Dislocations in Tungsten," in "Direct Observations of Imperfections in Crystals," pp. 593-608, J. B. Newkirk and J. H. Wernick, Editors, Interscience Publishers, New York (1962).
14. I. Berlec, *J. Appl. Phys.*, **33**, 197 (1962).
15. B. W. Batterman, *J. Appl. Phys.*, **28**, 1236 (1957).
16. F. M. Wanlass and H. Eyring, "Sticking Coefficients," in "Advances in Chemistry Series No. 33," p. 140, American Chemical Society (1961).
17. J. P. Hirth and G. M. Pound, "Condensation and Evaporation Progress in Materials Science," Vol. XI. Chap. D., The MacMillan Co., New York (1963).

Low-Pressure Oxidation of Niobium at 1200°-1700°C

Per Kofstad and Svein Espevik

Central Institute for Industrial Research, Blindern, Oslo, Norway

ABSTRACT

The oxidation behavior of niobium has been studied at 1200°-1700°C at oxygen pressures ranging from 2×10^{-4} to 0.5 Torr. The oxidation involves dissolution of oxygen in the metal, formation of NbO, NbO_2, and Nb_2O_5. The oxidation may be divided into 3 main stages: (*a*) an initial linear oxidation which is followed by (b) a parabolic oxidation which, in turn, transforms into (c) a final linear oxidation. The initial linear oxidation involves dissolution of oxygen in the metal and the oxidation is governed by the rate of chemisorption on the metal surface. The parabolic oxidation is due to formation of protective NbO_2, which is further oxidized to porous nonprotective Nb_2O_5 at a linear rate. The oxidation is affected by the presence of liquid Nb_2O_5 at and above 1500°C, and at higher temperatures evaporation of Nb_2O_5 becomes an increasingly important part-process.

A major shortcoming of refractory metals is their poor high-temperature oxidation resistance. When considering applications of these metals or their alloys at elevated temperatures, even under "vacuum" conditions, a knowledge of their oxidation behavior is required. Also for applications of these metals in coated condition, such knowledge is desirable as it provides the margin of safety in case of coating failure.

Inouye (1) studied the oxidation of niobium at 850°, 1000°, and 1200°C at oxygen pressures ranging from 3×10^{-5} to 5×10^{-3} Torr. The initial oxidation was found to proceed principally by dissolution of oxygen in the metal, and this was followed subsequently by formation of NbO, NbO_2, and Nb_2O_5. NbO_2 was shown to form a protective scale, which was further oxidized to a nonprotective layer of Nb_2O_5. Other investigators have studied the oxidation behavior of niobium at higher oxygen pressures at temperatures up to 1200°C (2-6). Close to 1 atm O_2 the oxidation has been found to involve primarily the dissolution of oxygen in the metal and the formation of Nb_2O_5. However, on the basis of Inouye's work (1) it seems safe to conclude that NbO and NbO_2 are formed as intermediate reaction products also at higher oxygen pressures, although they may only be present in small amounts.

No detailed studies of oxidation of niobium at temperatures in excess of 1200°C appear to have been reported previously in the literature.

Experimental Methods

Materials.—The niobium metal sheet was obtained from Murex Ltd., England. Estimates of metallic impurities were as follows: Fe and Al, each 0.05%; Si, 0.02%; Cr, Pb, and Hg, each 0.01%, and C_T 0.1%. The hardness of the as-received sheet was VHN 75 (10 kg load).

Prior to oxidation the specimens were polished with alumina, rinsed in distilled water and acetone. The metal was recrystallized in high vacuum ($<10^{-5}$ Torr) in the oxidation apparatus prior to the start of the oxidation run. Commercial tank oxygen dried over phosphorus pentoxide was used.

Methods.—Rates of oxidation were measured thermogravimetrically with a Cahn automatic recording balance. The specimens were suspended in a Pt-13% Rh wire ($d = 0.2$ mm). Above 1600°C the Pt/Rh-wire became alloyed with niobium, probably through the formation of liquid alloy phase, and under these conditions a thin niobium wire was used to suspend the specimen in the hotter part of the furnace. The surface area of the niobium wire was small compared to that of the specimen.

The furnace is shown schematically in Fig. 1. An alumina tube (Morgan recrystallized alumina) served as reaction chamber, and it was mounted directly on the baffle valve of an Edwards F203 oil diffusion pump which has an unbaffled pumping speed of 70-80 liters/sec and a speed through the baffle valve of 50-55 l/sec. The alumina tube had an inner diameter of 33 mm and a length of 50 cm. A small alumina bucket was placed in the lower end of the tube to catch any specimens which might fall down due to breaking of the suspending wire. The reaction temperature was measured with Pt-5% Rh/Pt-20% Rh or Ir/Ir-60% Rh thermocouples located inside the reaction chamber next to the specimen.

The complete furnace system consisted of two separate high-vacuum systems serving, respectively, the reaction chamber and the heating element chamber. The latter contained the molybdenum heating element (wire with a diameter of 1 mm wound directly on the alumina tube and embedded in alundum cement) and three molybdenum and tantalum heat shields. The outer wall of the reaction chamber consisted of a Pyrex tube which was cooled by a tight-fitting, water-cooled copper shell. High vacuum was always maintained in the heating element chamber.

The specimens were introduced at room temperature and the system was evacuated to $<10^{-5}$ Torr. The temperature was subsequently raised and equilibrated. Due to outgassing of the furnace during the heating period, the temperature was slowly increased to the desired level, and 3-4 hr was used to raise the temperature to 1500°C. The outgassing and small unavailable leaks in a furnace system of this type unquestionably cause some contamination in addition to the original impurities in the niobium specimens. On the other

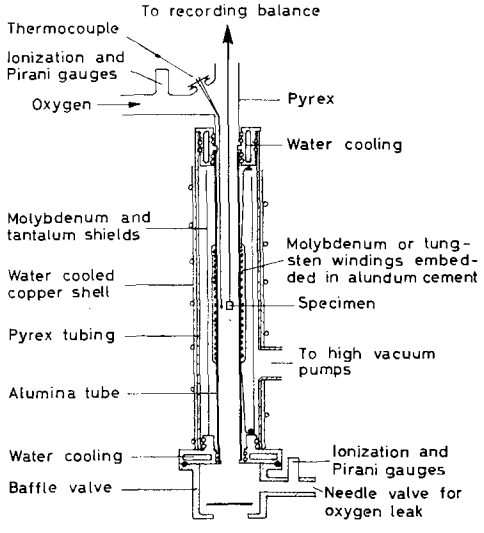

Fig. 1. Schematic illustration of the furnace system

hand oxygen impurities at temperatures above 1600°-1700°C may to some extent be removed through oxide evaporation. In a later improvement of the system a vacuum lock has been incorporated which permits an introduction of the specimens into the furnace after outgassing and temperature equilibration of the system.

The oxidation run was started by introducing oxygen in the system, and up to 1 min was necessary before establishing the correct oxygen pressure. During oxidation at the lower pressures the baffle valve was kept open, and oxygen was continuously pumped through the reaction chamber. The oxygen pressure was monitored at both ends of the reaction chamber by means of calibrated Pirani (LKB) and ionization (Leybold) gauges. Below approximately 0.01 Torr a pressure drop developed along the reaction chamber. Under these conditions the desired pressure was first established at the top of the chamber, and a small oxygen leak was subsequently introduced in the baffle valve to equalize the pressures. During oxidation the same oxygen pressure was maintained at both ends of the reaction chamber.

When the reaction rate measurements were completed, the specimens were cooled slowly in high vacuum in the oxidation apparatus. As this procedure could cause changes in the appearance of the reacted specimens, specimens for metallographic examinations were also oxidized in another furnace system and quenched from the reaction temperature by dropping them onto niobium metal ships in quartz tube beneath the furnace. The quartz tube, which was also part of the high vacuum system, was precooled in liquid nitrogen.

The x-ray diffraction studies were made with a GE-XRD-3 recording x-ray diffractometer. The metallographic studies were performed with a Reichert universal camera microscope (Model MeF).

Experimental Results

Reaction rate measurements.—Rates of oxidation of niobium were measured at temperatures from 1000° to 1700°C at oxygen pressures ranging from 2 x 10^{-4} to 0.5 Torr O_2. The initial studies were made on specimens measuring approximately 11 x 11 x 1.9 mm (total surface area of about 3.3 cm^2), but as will be discussed below, it was also later necessary to study oxidation rates as a function of sample size.

Results of the thermogravimetric studies on 3.3 cm^2 specimens are presented in Fig. 2-5, in which the weight change (in mg/cm^2) is plotted as a function of time (in minutes). The weight change was evaluated using the original geometrical dimensions of the specimens. No attempts were made to study reaction rates at oxygen pressures lower than 2 x 10^{-4} Torr O_2 due to possible effects of degassing of walls, etc., on the oxidation. No measurable weight changes were observed during heating of the specimens provided the pressure in the system was $<10^{-5}$ Torr. If the pressure rose to 10^{-4} Torr during the heating period, small weight gains could result prior to the run, but such contamination (<0.02 mg) were not found to affect the subsequent oxidation within the reproducibility, which could be estimated to be within 15%.

Figures 2 and 3 show the effect of oxygen pressure on the rate of oxidation at 1400° and 1600°C, respectively. In Fig. 4 and 5 is shown the effect of tempera-

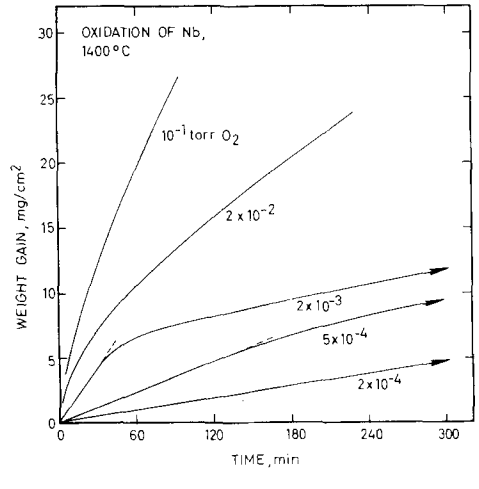

Fig. 2. Effect of oxygen pressure on oxidation of niobium at 1400°C

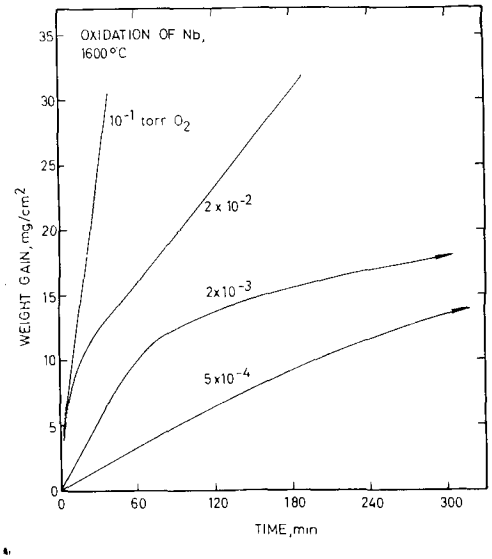

Fig. 3. Effect of oxygen pressure on oxidation of niobium at 1600°C

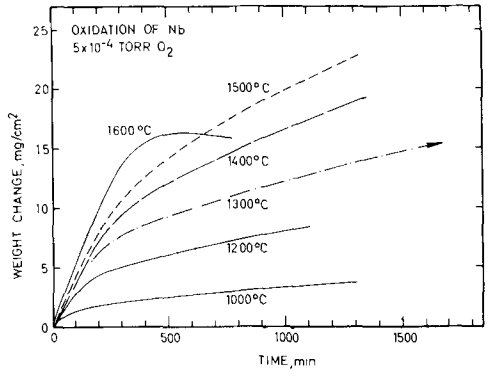

Fig. 4. Effect of temperature on oxidation of niobium at an oxygen pressure of 5 x 10^{-4} Torr.

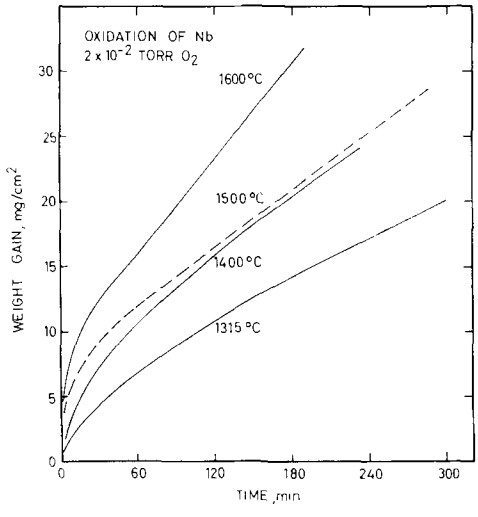

Fig. 5. Effect of temperature on oxidation of niobium at an oxygen pressure of 2 x 10^{-2} Torr.

ture on the rate of oxidation at oxygen pressures of 5×10^{-4} and 2×10^{-2} Torr.

The reaction rate measurements show that the oxidation may be divided into three main stages: (i) an initial linear rate of oxidation which is followed by (ii) a parabolic stage (<1500°C), which in turn after longer periods of oxidation transforms into (iii) a final linear rate of oxidation. The rate of oxidation during all three stages exhibits a large oxygen pressure dependence. The duration of the two first stages is a function of oxygen pressure and becomes shorter the higher the oxygen pressure. At 2×10^{-2} Torr O_2 the duration of the initial linear stage is a few minutes at most.

Between 1400° and 1500°C a change in the temperature dependence of the oxidation during the final linear oxidation is observed (Fig. 5). This change is concluded to be associated with the transition from solid to liquid Nb_2O_5. The melting point of Nb_2O_5 is about 1490°C (7, 8).

Above 1500°C oxide evaporation also becomes an important part-process as evidenced by the weight loss observed during later stages of oxidation at and above 1600°C (Fig. 4). Rates of oxide evaporation into vacuum ($\sim 2 \times 10^{-5}$ Torr) from oxidized specimens were measured at 1550°, 1600°, and 1650°C.

Studies on oxidized specimens.—When oxidation was stopped during the initial linear stage, no visible changes of the specimen could be observed, and no oxide phase could be identified either by x-ray diffraction or metallographic studies. However, x-ray diffraction studies showed that the lattice parameter of the niobium metal had increased during oxidation. From this it is concluded that oxygen dissolves in the metal during the linear stage (9, 13).

X-ray diffraction studies on the surface of specimens oxidized into the parabolic stage only gave reflections due to NbO_2. At 1700°C an additional, unidentified reflection with $d = 2.21$Å was observed. The color of the surface oxide was black, and the oxide adhered extremely well to the substrate. Metallographic cross sections closely resembled those previously published by Inouye (1). The scales were often broken up, but this is concluded to be a result of the cooling of the specimens and the resultant stresses which are built up due to the difference in thermal expansion of the oxide and the substrate. It was also difficult to preserve the scales during polishing.

NbO was present beneath the NbO_2 scales, and the metallographic cross section shows that it is preferentially formed at grain boundaries and that it grows as irregularly shaped crystals in the niobium metal. Examples of cross sections of niobium specimens oxidized at 1500° and 1600°C are shown in Fig. 6a and b. The amount of the NbO phase present in a specimen appeared to be larger the higher the temperature.

The final linear stage of the oxidation was found to be associated with formation of Nb_2O_5 on the NbO_2 scale. After cooling to room temperature, the pentoxide was identified as the high-temperature modification, α-Nb_2O_5. The oxide was in the form of a porous and voluminous scale which easily detached at room temperature. The color was gray.

When liquid Nb_2O_5 was formed, sudden weight losses were observed during the thermogravimetric measurements, and this was probably due to a dripping off of the liquid oxide. After oxidation most of the pentoxide was also found, in one case in the form of a drop, at the lower end of the specimen.

Discussion

The oxidation behavior of niobium at 1200°-1700°C exhibits the same general features as described by Inouye (1) for the temperature range 850°-1200°C. The oxidation involves three main stages: (i) an initial linear oxidation, (ii) a subsequent parabolic stage, and (iii) a final linear oxidation. Above the melting point of Nb_2O_5 the oxidation is affected by the presence of the liquid oxide phase, and above 1500°C evaporation of

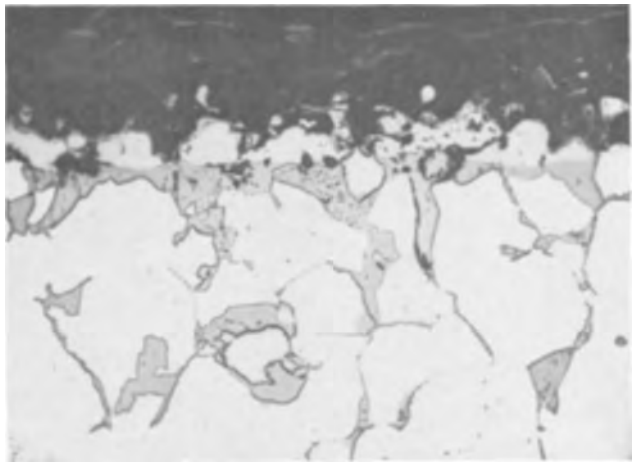

Fig. 6. Metallographic cross section of specimen oxidized for 4100 min at 1500°C and 2×10^{-4} Torr O_2. The gray oxide is NbO. Magnification 80X.

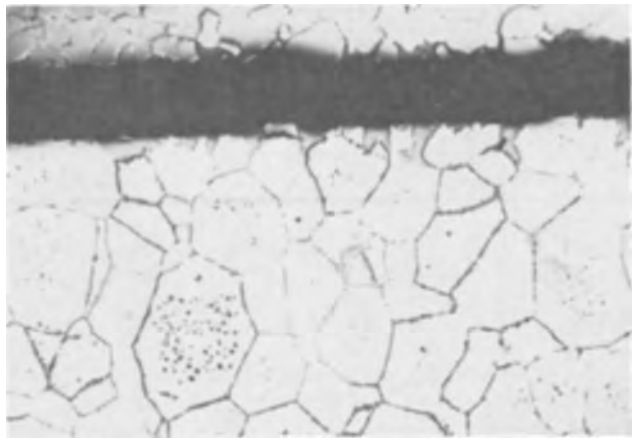

Fig. 6b. Metallographic cross section of specimen oxidized for 60 min at 1600°C and 5×10^{-3} Torr O_2. Magnification 80X.

Nb_2O_5 also becomes important during the later stages of the reaction. In the following the various stages and the associated mechanisms and rate-determining processes will be discussed.

The Initial Linear Oxidation

Oxygen dissolution.—During the initial linear oxidation oxygen dissolves in the metal. During later stages and during the transition to the subsequent parabolic oxidation it is concluded that oxidation also comprises formation of NbO at the metal surface.

The initial linear oxidation shows a large oxygen pressure dependence, and the shorter duration of this stage with increasing oxygen pressure partly reflects that the niobium becomes more rapidly saturated with oxygen. However, at higher oxygen pressures a competing oxide formation on the surface also tends to shorten the linear stage, and above about 10^{-2} Torr O_2 the initial linear oxidation becomes too short to be evaluated accurately from the thermogravimetric studies. Under these conditions a simultaneous oxygen dissolution and oxide formation take place.

At sufficiently low oxygen pressures the duration of the initial linear stage will be determined by the solubility of oxygen in niobium, and thus on the size and thickness of the specimens. In this respect a knowledge of the solubility of oxygen in niobium is important.

The solubility of oxygen in niobium in equilibrium with NbO has been studied by Seybolt (9), Elliot (10), Pemsler (11), Bryant (12), and Gebhardt and Rothenbacher (13). A summary of their results is shown in Fig. 7. Both the heat of solution and the solubilities at 1000° and 1100°C reported by Seybolt may be too high, as an extrapolation leads to unreasonably high solu-

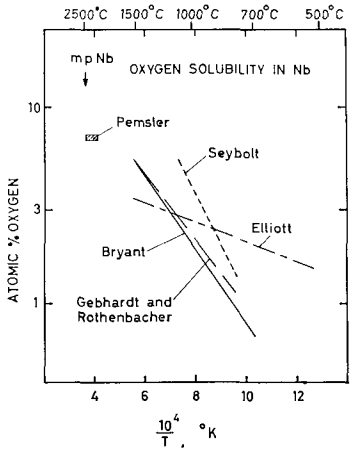

Fig. 7. Solid solubility of oxygen in niobium in equilibrium with NbO as a function of the reciprocal absolute temperature.

bilities at temperatures close to the melting point of niobium. At low temperatures one may fail to reach equilibrium between NbO and the niobium-oxygen solid solution due to slow kinetics. Below 700°C the formation of suboxides of niobium (18-20), which are probably metastable, may also yield too high apparent solubilities. Pemsler reports a solubility of about 7 at. % in the temperature range 2170°-2470°C. There is good agreement between the results of Bryant and of Gebhardt and Rothenbacher, and it is believed that these results represent the better values for the oxygen solubility in niobium.

Using Bryant's values the maximum weight gain due to oxygen dissolution for specimens measuring 11 x 11 x 1.9 mm amounts to about 3.8 mg/cm² at 1300°C, 5.15 mg/cm² at 1500°C, and 6.45 at 1700°C. At the lower oxygen pressures employed in this work (2×10^{-4} and 5×10^{-4} Torr O_2), the initial linear rate persists until the specimens become close to saturated before appreciable oxide formation begins to take place.

Temperature and oxygen pressure dependence.—Figure 8 shows the initial linear rate of oxidation as a function of oxygen pressure. Both the results of this work and those of Inouye are included. The results suggest that the initial linear rate is proportional to the oxygen pressure at low oxygen pressures and that a transition to a gradually smaller pressure dependence occurs with decreasing pressure.

In considering the initial oxidation it is found, as described below, that a large fraction of the impinging oxygen molecules reacts with the metal. Under such conditions the danger exists that the measured rate of reaction may be partially or completely governed by the rate of transport of oxygen through the reaction tube to the specimen. This will be a function of the dimensions of the tube, the reaction rate, and the total

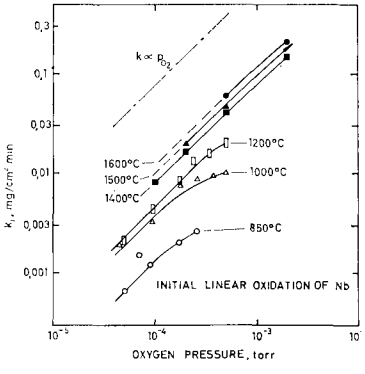

Fig. 8. The rate constant for the observed initial linear oxidation, k_i, as a function of oxygen pressure. The open points show Inouye's results (1) while the filled points represent this work.

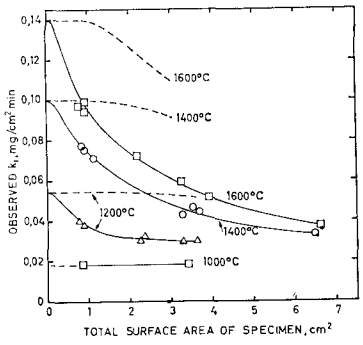

Fig. 9. Observed initial linear rate of oxidation as a function of total surface area of specimen.

surface area of the specimens. In order to test and thus possibly correct for such an effect, the rate of oxidation was measured as a function of specimen size. The results of such measurements are illustrated in Fig. 9, which shows the initial linear rate as a function of the total surface area of the specimen. As seen the observed reaction rate above 1200°C was found to increase markedly with decreasing surface area, thus indicating that the oxidation was in fact partially governed by transport of oxygen in the reaction chamber.

At sufficiently small rates of total oxygen consumption of the specimens the rate should be independent of specimen surface area, and thus an extrapolation of the curves in Fig. 9 to zero surface area should give the rate of reaction of the metal. From the results in Fig. 9 it is seen that an exact extrapolation is difficult to make at the higher temperatures. In the present case the reaction rates at zero surface area was estimated by comparing with rates measured in another apparatus for which a rate-limiting transport of oxygen was not equally critical. The latter values are indicated by the broken lines. Below 1200°C, at which transport limiting effects are not important, both apparatus gave the same rates of oxidation. It may also be noted that during subsequent parabolic oxidation below 1500°C and during the final linear oxidation the reaction rates become slow enough that transport-limiting factors are of no importance.

Although the observed reaction rates above 1200°C are partly limited by transport of oxygen in the reaction chamber, it may still be concluded that the reaction is proportional to the oxygen pressure as the results in Fig. 8 represent relative values at the same surface area. The same pressure dependence is also suggested by Inouye's results below about 2×10^{-4} Torr O_2. This pressure dependence suggests that adsorption of oxygen on the surface is an important rate-limiting factor.

In considering adsorption on metals we shall follow Ehrlich's (14) treatment and assume that oxygen molecules first become physically adsorbed on the surface and that subsequent chemisorption occurs on specific surface sites from the reservoir of physically adsorbed molecules. Accordingly the adsorption is written as

$$O_{2(g)} \underset{k_{-1}}{\overset{k_1}{\rightleftharpoons}} O_2 \text{ phys. ads.} \qquad \text{phys. ads.} \quad [1]$$

$$2 \text{ sites} + O_2 \text{ phys} \xrightarrow{k_2} O_{\text{chem}} + O_{\text{chem}} \quad \text{chemisorption} \quad [2]$$

If adsorption of oxygen limits the rate of oxidation, the subsequent steps in the reaction, which may involve incorporation of the chemisorbed oxygen atoms and subsequent diffusion into the metal, are relatively rapid processes, and the oxidation mechanism is described by Eq. [1] and [2].

$k_1 p_{O_2}$ denotes the rate of adsorption of physically adsorbed molecules. When assuming a condensation coefficient of unity (15), $k_1 p_{O_2}$ is equal to the rate of

impingement of oxygen molecules, which from the kinetic gas theory is given by

$$k_1 p_{O_2} = \frac{p_{O_2}}{(2\pi mkT)^{1/2}} \qquad [3]$$

k_{-1} and k_2 represent the rate constant for desorption and chemisorption of physically adsorbed molecules. The temperature dependence of k_{-1} and k_2 may be given the general formula

$$k_n = \alpha_n \exp(-E_n/RT) \qquad [4]$$

where E_n is the activation energy and α_n accounts for the frequency and probability factors associated with the process.

The above model neglects effects due to interactions of physically adsorbed molecules and desorption of chemisorbed oxygen molecules.

During linear oxidation one may further assume that the concentration of the intermediate species, *i.e*, the physically adsorbed molecules, does not change with time and that the condition of stationary states may be applied. This leads to the following expression for the initial linear rate of oxidation, k_i

$$k_i = k_1 p_{O_2} \frac{k_2(1-\theta)^2}{k_{-1} + k_2(1-\theta)^2} \qquad [5]$$

where θ represents the fraction of chemisorption sites occupied by chemisorbed oxygen.

From Eq. [5] it is seen that $k_i \propto p_{O_2}$ at sufficiently low oxygen pressures, *i.e.*, when $1-\theta \cong 1$, while a transition to a gradually smaller oxygen pressure dependence will be observed with increasing oxygen pressure, *i.e.*, when θ can no longer be neglected. As seen in Fig. 8 this is in agreement with Inouye's results. It should furthermore be noted that the deviation from $k_i \propto p_{O_2}$ probably occurs at lower oxygen pressures the lower the temperature.

When $k_i \propto p_{O_2}$ the temperature dependence is given by

$$k_i = \frac{p_{O_2}}{(2\pi mkT)^{1/2}} \cdot \frac{\alpha_2 \exp(-E_2/RT)}{\alpha_2 \exp(-E_2/RT) + \alpha_{-1}\exp(-E_{-1}/RT)} \qquad [6]$$

and accordingly an Arrhenius plot of k_i should not give a straight line relationship. This is also suggested by the experimental results as shown in Fig. 10, where the logarithm of k_i has been plotted as a function of the reciprocal absolute temperature under conditions where $k_i \propto p_{O_2}$, *e.g.*, at 10^{-4} Torr O_2. The values of k_i represent extrapolated values at zero surface area

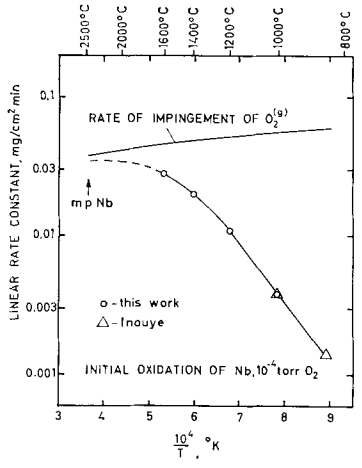

Fig. 10. Logarithm of k_i (extrapolated values at zero surface area of specimen) as a function of the reciprocal absolute temperature.

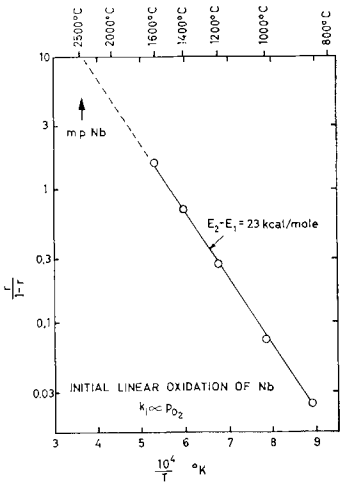

Fig. 11. Logarithm of the quantity $r/1-r$ as a function of the reciprocal absolute temperature; r is the reaction coefficient.

(Fig. 9), and the values have furthermore been extrapolated from 5 x 10^{-4} to 10^{-4} Torr O_2 in order to allow a comparison with Inouye's results under conditions where $k_i \propto p_{O_2}$. Equation [6] does, of course, also apply at other oxygen pressures as long as $k_i \propto p_{O_2}$. The calculated weight gain if all oxygen molecules which impinge at 10^{-4} Torr O_2 were to react with the metal is also shown in Fig. 10.

In order to confirm the above mechanism (Eq. [1] and [2]) one may introduce the term reaction coefficient, $r = k_i/k_1 p_{O_2}$, which denotes the fraction of the impinging molecules that react with the metal. The term $r/1-r$ is given by

$$\frac{r}{1-r} = \frac{k_2}{k_{-1}} = \frac{\alpha_2}{\alpha_{-1}} \exp\{-(E_2 - E_{-1})/RT\} \qquad [7]$$

and a plot of log $r/1-r$ as a function of $1/T$ should thus give a straight line relationship where the slope is determined by the difference in activation energies between that of chemisorption and that of desorption of physically adsorbed molecules. Figure 11 shows that the initial linear oxidation of niobium obeys Eq. [7] under conditions when $k_i \propto p_{O_2}$ and that $E_2 - E_{-1} = 23$ kcal/mole.

It may be noted that the value of r increases from 0.024 to 0.61 from 850° to 1600°C, and at the latter temperature about 60% of the impinging oxygen molecules react with the metal. Tantalum exhibits a closely similar oxidation behavior under corresponding conditions (15), but for this metal the reaction coefficient r is about half of that for niobium. Both metals have therefore excellent gettering properties at high temperatures.

In Fig. 11 the value of $r/1-r$ has been extrapolated to the melting point of niobium. Corresponding values of k_i have been evaluated and these are indicated by the broken part of the curve in Fig. 10, and these thus represent estimated values if the mechanism is valid up to the melting point. It may be possible, however, that a direct desorption of chemisorbed oxygen to the gas phase becomes significant at temperatures near the melting point of niobium, and this could cause a larger decrease in the "apparent" activation energy k_i with increasing temperature than indicated by the extrapolated values in Fig. 10. Depending on the associated activation energies an appreciable desorption of molecules could even cause a reversal in temperature dependence. Niobium metal may also be deoxidized by high-vacuum treatment at very high temperatures, probably through the evaporation of niobium oxides, and such effects would further be expected to influence the oxidation behavior of niobium. At low partial pressures of oxygen near the melting point of niobium the oxygen solubility will also be a function of the

oxygen pressure (11) and the duration of linear stage will be correspondingly limited.

Parabolic Oxidation

During the transition from the initial linear to the parabolic oxidation, it is concluded that the oxidation mainly results in formation of NbO. This does not occur as a plane-parallel film or scale on the metal, but as a growth of NbO crystals into the metal from the surface. The NbO crystals are irregularly shaped and often show large variations in size. It is reasonable to conclude that the growth of NbO depends on the orientation of the individual grains in the metal. The growth and penetration of NbO into the metal is also favored at grain boundaries. Qualitatively it appears that NbO formation is governed by the crystal growth in the solid phase, but from this work it is not possible to evaluate specific details of this process or its temperature dependence. Qualitatively it may, however, be concluded that the amount of NbO becomes relatively larger the higher the temperature.

The parabolic oxidation itself is concluded to be associated with NbO_2 formation. Metallographic examinations after cooling to room temperature show in places a broken-up scale, but this is probably a result of cooling as in the places where the NbO_2 scale is intact, it exhibits excellent adherence to the substrate. NbO_2 probably forms a compact, protective scale during the oxidation, as is also previously found by Inouye (1), and the parabolic rate is concluded to reflect a Wagner-type mechanism with a rate-determining diffusion through NbO_2.

For a further evaluation of the diffusion process associated with the parabolic oxidation the oxygen-pressure dependence of the parabolic rate constant, k_p, has been evaluated, and the results are shown in Fig. 12. In estimating the rate constant it was assumed that the amount of NbO in the metal beneath the scale remained unchanged during the oxidation. Below 1500°C $k_p \propto p^{1/2}{}_{O_2}$, while at 1500°C the results indicate a smaller and also a varying oxygen pressure dependence. At 1600° and 1700°C the reaction rate measurements did not permit an evaluation of the parabolic rate constant. This may possibly be due to an increased importance of NbO formation, to the presence of liquid Nb_2O_5, or to effects of oxide evaporation (see below).

Judging from the growth of the oxide scale on niobium, a rate-determining transport of oxygen in NbO_2 appears probable. If the Wagner mechanism applies, an oxygen pressure dependence of $k_p \propto p^{1/2}{}_{O_2}$ is unusually large. It also rules out a defect structure involving oxygen vacancies. However, a possible explanation could be that the defects in NbO_2 involve interstitial oxygen according to the relationship

$$1/2\ O_2(g) \rightleftharpoons O_i^{z-} + ze^+ \qquad [8]$$

and that diffusion of oxygen takes place through an interstitially mechanism. A pressure dependence of $p^{1/2}{}_{O_2}$ could in principle be obtained either if the electron holes, e^+, are associated with the interstitial oxygen ion or if intrinsic ionization of electrons from the conduction to the valence band ($\text{nil} \overset{K_e}{\rightleftharpoons} e^+ + e^-$) yields an electron hole concentration which is very much larger than that produced from Eq. [8], *i.e.*, if $\{e^+\} = K_e{}^{1/2} >> O_i{}^{z-}$.

According to Eq. [8] NbO_2 is proposed to contain excess oxygen relative to the stoichiometric oxide. NbO_2 has possibly a small homogeneity range (17), but otherwise little is known about its defect structure. The above considerations (Eq. [8]) are therefore at this stage purely speculative and are put forth solely to explain the oxygen pressure dependence of the parabolic oxidation.

In the temperature range 1200°-1400°C the parabolic oxidation has an activation energy of $E = 44$ kcal/mole. In view of the lack of knowledge of the defect structure of NbO_2 a detailed interpretation of this value is not possible.

NbO_2 is further oxidized to Nb_2O_5, and the growth of the latter oxide is, at least during the later stages of the reaction, linear with time. During the parabolic growth of NbO_2 traces of Nb_2O_5 may be present on the surface although it is not detected in the x-ray diffraction studies. The fact that the parabolic oxidation does exhibit an oxygen pressure dependence shows that Nb_2O_5 has no protective properties. This is also suggested by the appearance and by the metallographic cross sections of oxidized specimens which show porous scales of Nb_2O_5. The growth of NbO_2 + solid Nb_2O_5 thus probably involves a Loriers-type mechanism **(17)**.

Final Linear Oxidation

Growth of solid Nb_2O_5.—As mentioned above the solid Nb_2O_5 has no protective properties and forms a voluminous and porous scale. When this stage is reached during the oxidation, the thickness of the NbO_2 scale will, according to a Loriers-type mechanism, approach a limiting thickness, and the final linear rate essentially represent formation of Nb_2O_5.

The rate of formation of Nb_2O_5, k_f, also shows a large oxygen pressure dependence. This is shown in Fig. 13 where log k_f is plotted as a function of log p_{O_2}. Results from ref. (4) are also included, and these are represented by the open points. At 1000°C k_f is proportional to $p^{1/2}{}_{O_2}$ over the whole oxygen pressure range studied. The same applies to the higher oxygen pressure at 1200° and 1300°C.

An oxygen pressure dependence of $k_f \propto p^{1/2}{}_{O_2}$ suggests that a dissociative adsorption equilibrium is established on the surface (14, 15). Following Eq. [1] and [2] the reaction may in this case be written

$$O_2 \overset{K_1}{\leftrightharpoons} O_2 \text{ phys. ads.}$$
$$2 \text{ sites} + O_2 \text{ phys. ads.} \overset{K_2}{\rightleftharpoons} O_{chem} + O_{chem} \qquad [9]$$

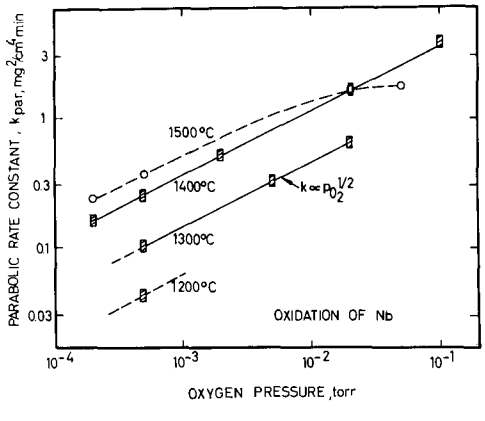

Fig. 12. Parabolic rate constant for formation of NbO_2 as a function of oxygen pressure.

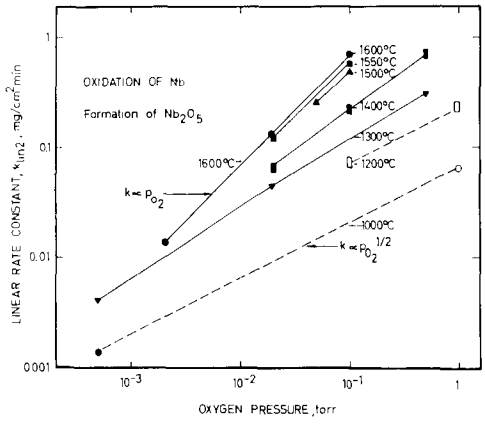

Fig. 13. Rate constant for the final linear oxidation, k_f, as a function of oxygen pressure.

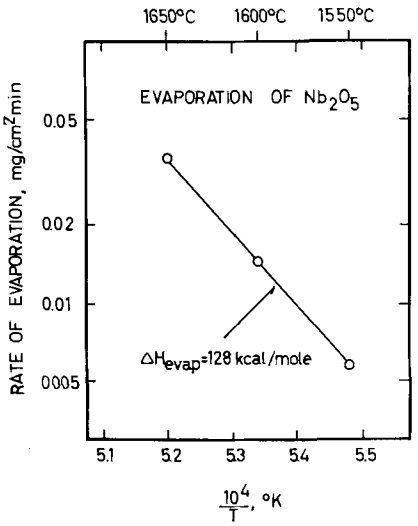

Fig. 14. Logarithm of the rate of evaporation from liquid Nb_2O_5 on oxidized Nb specimens as a function of the reciprocal absolute temperature.

$$O_{chem} \xrightarrow{k_3} \text{products} \qquad [10]$$

where $K_1 = \frac{k_1}{k_1}$ and K_2 represent the equilibrium constants. The rate of oxidation is accordingly given by

$$k_f = k_3 [O_{chem}] = k_3 K^{1/2}_{12} (1-\theta) p^{1/2}_{O_2} \qquad [11]$$

where $K_{12} = K_1 K_2$. At low coverage, *i.e.*, when $1-\theta \cong 1$, the rate of oxidation will be proportional to $p^{1/2}_{O_2}$ as observed for k_f. It should also be noted that at sufficiently high oxygen pressures, the rate of oxidation will as a limit become independent of oxygen pressure.

At very low oxygen pressures the assumption of chemisorption equilibrium will no longer be valid, and at sufficiently low oxygen pressures the rate of adsorption will become rate-determining. As a limit the rate of oxidation will become proportional to p_{O_2} as described above for the initial oxidation. The change to a somewhat larger oxygen pressure dependence at the lower pressures at 1300° and at 1400°C is believed to reflect such a transition in the rate-determining process.

When $k_f \propto p^{1/2}_{O_2}$ the activation energy amounts to about 24 kcal/mole. In this connection it should be noted that the value of k_3 increases while that of K_{12} decreases with increasing temperature, and the activation energy associated with k_f (when proportional to $p^{1/2}_{O_2}$) represents the difference between the activation energy associated with k_3 and the "enthalpy of chemisorption" associated with K_{12} (Eq. [11]).

Formation of liquid Nb_2O_5.—The rate of formation liquid Nb_2O_5 shows a different dependence on oxygen pressure and temperature than that of the growth of solid Nb_2O_5. As seen in Fig. 13 $k_f \propto p_{O_2}$ for the formation of $Nb_2O_{5\,liq}$. At low oxygen pressures this difference in pressure dependence leads to a smaller rate of formation of Nb_2O_5 when it is in liquid form (*e.g.*, 1600°C) than when it is solid (*e.g.*, 1300°C).

From the relationship $k_f \propto p_{O_2}$ it is concluded that the rate of chemisorption is the rate-determining process. When liquid Nb_2O_5 is formed, the whole specimen surface is probably always covered by a continuous layer of liquid oxide. When relatively large amounts are formed the oxide also drips off the specimen. The rate-determining chemisorption takes place on the liquid oxide surface, and the oxygen rapidly diffuses through the liquid phase to the solid oxide phase where it reacts to form Nb_2O_5.

The apparent activation energy for the formation of $Nb_2O_{5\,liq}$ as determined from the results at 1500°, 1550°, 1600°C amounts to 16 kcal/mole. Following the treatment for the initial linear oxidation this value approximately corresponds to the difference in activation for the chemisorption and the desorption of the molecules physically adsorbed on liquid Nb_2O_5.

Oxide evaporation.—Above 1550°C an appreciable evaporation of Nb_2O_5 takes place, and at 1600°C, for instance, a resultant weight loss of the specimen occurs during later stages of the oxidation at the lower oxygen pressure (Fig. 4).

The rates of evaporation in vacuum ($\sim 2 \times 10^{-5}$ Torr) was measured at 1550°, 1600°, and 1650°C and the results are presented in Fig. 14. The evaporation rates per unit surface area were evaluated using the original geometrical dimensions of the unoxidized specimens. Corrections due to the increase in surface area resulting from oxide formation would be small.

The enthalpy of evaporation is 128 kcal/mole. As this value is much larger than the activation energy for the formation of liquid Nb_2O_5 (~ 16 kcal/mole), the oxide evaporation will become increasingly important the higher the temperature. The rate of oxide evaporation may be considered to be approximately independent of oxygen pressure at oxygen pressures employed in this work, while the rate of formation is proportional to p_{O_2}. The amount of liquid Nb_2O_5 on the surface or whether it evaporates as soon as it is formed, will consequently at a specific temperature be determined by the oxygen pressure.

The rate of evaporation from a free surface into a vacuum is related to the pressure of the evaporation species by the Hertz-Langmuir equation

$$z_i = \alpha_i p_i / (2\pi m_i kT)^{1/2} \qquad [12]$$

z_i is the number of molecules evaporating per unit time per unit area, m_i is the molecular weight of the gas molecule, p_i is the equilibrium pressure, and α_i is the evaporation coefficient. When the molecule in the condensed phase is the same as the vapor species, the value of α_i has been found to be close to unity. In this work the liquid Nb_2O_5 may be expected to be deficient in oxygen relative to stoichiometric composition, but the exact composition is not known.

No mass-spectrometric analysis has been made of the evaporating species, but, assuming an evaporation coefficient equal to unity and that the molecules are Nb_2O_5, the observed evaporation rates give (Eq. [12]) the following values for the equilibrium pressure of Nb_2O_5: 4.3×10^{-6} Torr at 1550°C, 9.5×10^{-6} Torr at 1600°C, and 2.8×10^{-5} Torr at 1650°C.

Acknowledgment

This work has in part been sponsored by the Air Force Materials Laboratory, Research and Technology Division, AFSC, through the European Office of Aerospace Research, United States Air Force.

The authors are indebted to the members of the staff at the Central Institute for Industrial Research who have participated in the experimental work.

Manuscript received Feb. 14, 1964; revised manuscript received Sept. 8, 1964.

Any discussion of this paper will appear in a Discussion Section to be published in the December 1965 JOURNAL.

REFERENCES

1. H. Inouye, "The Oxidation of Columbium at Low Oxygen Pressures," in "Columbium Metallurgy," AIME Metallurgical Society Conferences, Vol. 10, D. L. Douglass and F. W. Kunz, Editors, Interscience Publishers, New York (1961).
2. H. Inouye, "Scaling of Columbium in Air," Reactive Metals Proceedings, (MD) Special Report Series No. 5, Met. Soc., AIME (1956).
3. W. D. Klopp, C. T. Sims, and R. I. Jaffee, Battelle Memorial Institute, BMI-1170, 1957.

4. P. Kofstad and H. Kjøllesdal, *Trans. AIME.*, **221**, 285 (1961).
5. V. I. Arkhorov, A. F. Gerasimov, and T. V. Ushkova, *Fiz. metal. metalloved.*, **12**, 761 (1961).
6. T. Kolski, *Trans. Quart.*, **55**, 119 (1962).
7. A. J. Pollard, *J. Am. Ceram. Soc.*, **44**, 630 (1961).
8. J. J. Diamond and S. J. Scheider, *ibid.*, **43**, 1 (1960).
9. A. U. Seybolt, *J. Metals*, **6**, 774 (1954).
10. R. P. Elliott, *Trans. AIME.*, **200**, 990 (1954).
11. J. P. Pemsler, *This Journal*, **108**, 744 (1961).
12. R. T. Bryant, *J. Less-Common Metals*, **4**, 62 (1962).
13. E. Gebhardt and R. Rothenbocher, *Z. Metallkunde*, **54**, 623 (1963).
14. G. Ehrlich, *J. Phys. Chem.*, **59**, 473 (1955).
15. P. Kofstad, *J. Less-Common Metals*, **7**, 241 (1964).
16. G. Brauer, *Z. anorg. u allgem. Chem.*, **248** (1941); *Naturwiss.*, **28**, 30 (1940).
17. J. Loriers, *Compt. rend.*, **229**, 547 (1949).
18. N. Norman, *J. Less-Common Metals*, **4**, 52 (1962).
19. N. Norman, P. Kofstad, and O. J. Krudtaa, *ibid.*, **4**, 124 (1962).
20. G. Brauer, H. Müller, and G. Kühner, *ibid.*, **4**, 533 (1962).

Electrical Behavior of Passive Iron

J. L. Ord[1] and J. H. Bartlett

Department of Physics, University of Illinois, Urbana, Illinois

ABSTRACT

From a study of the steady-state and of galvanostatic transients, it is concluded, in agreement with Vetter and Weil, (i) that there exists a layer on iron when it is passive, (ii) that an electric field drives ions through this layer, and (iii) that the resistance to the flow of these ions is nonohmic. In the steady state, the thickness of this layer varies linearly with passivating potential from about 8Å to about 68Å. Transition from the steady passive state to the active state can occur slowly (probably by uniform thinning) for anodic current constant and less than the steady-state value, or rapidly (probably without thinning) for cathodic currents. The results indicate that, when the system is in a nonsteady state, there is a nonzero charge distribution within the layer. Even if the steady-state current be restored, it may take a long time for this charge distribution to relax back to the neutral steady state.

The nature of passivity, as exemplified by the electrical behavior of a passive iron electrode, has been the subject of much debate. Interest has centered around such questions as: (i) Is there a thin monolayer or a layer of appreciable thickness on the surface? (ii) What are the mechanisms for formation and removal of such layers? (iii) What is responsible for the large (600 mv) overpotential necessary to maintain iron in the passive state?

Previous studies of the electrical properties of passive iron have not been very extensive. Some work has been done in alkaline solutions, but the most information has been obtained with acid solutions. Some early investigations were made using nitric acid (1) but this is a rather complicated system, and later studies (2-4), including those reported here, are all with sulfuric acid. Franck and Weil (2) demonstrated the existence of a nonzero steady current, which is called the corrosion current and which is just sufficient to form new layer at a rate which balances the loss rate due to dissolution by the acid. Vetter (4) recorded galvanostatic transients from the steady state, measuring the rise of potential as a function of net charge added. He suggested the existence of an electrical field across a passive layer of appreciable thickness. His potentiostatic measurements also indicated that current through the layer is an exponential function of this field. Weil (3) repeated these measurements with more refined techniques, and concluded that "it is correct to assume that particle transport through the passive layer occurs by ions moving in an electric field." Vetter later (5) speculated that the layer is a composite oxide, the part nearest the metal being Fe_3O_4 and the outer part being Fe_2O_3.

The present work, using entirely different methods of analysis, confirms the essential ideas of Vetter and of Weil that there is an electric field driving ions through the layer and that the resistance offered to their flow is nonohmic in nature. In addition, it indicates that there is a nonzero charge density within the layer during the course of a galvanostatic charging process. The system is not then in a steady state, and it takes a considerable time, even when the steady-state current has been restored, for the system to relax back to normal. Reliable estimates of the thickness can as yet be made only for the steady state, where the thickness varies linearly with passivating potential from about 8Å to around 68Å.

Activation comes about in two different ways. For large cathodic current, the process is independent of layer thickness, so that activation corresponds to a rapid breakdown of protection at the metal-layer interface. On the other hand, when an anodic current of less than steady-state value flows, activation does depend on the initial thickness, which is taken to mean that the acid must eat away the layer until finally there is a breakthrough with consequent disruption.

Experimental

Transients were recorded by photographing an oscilloscope trace. This technique enables very fast transients to be recorded and is convenient also for transients of several minutes duration. Slow transients were recorded by setting the sweep rate at 5 sec/cm and adjusting the sweep length to 10 cm. The dead time between sweeps is negligible at this setting. An example of a slow transient recorded in this manner is given in Fig. 5.

The circuitry used is shown schematically in Fig. 1. The potentiostat consists of a 10-turn Helipot placed across a bank of 2v batteries. The galvanostat consists of a variable resistor in series with a 180v battery bank. These simple arrangements offer a number of advantages over more sophisticated electronic circuitry. (*A*) The galvanostat and potentiostat can be placed in series, and switching from one to the other can be accomplished by shorting or opening the galvanostat output. (*B*) Complex transients can be applied using a relay bank with calibrated time intervals between the closing of the relays. For example, one can switch in succession from constant potential to one constant current to open circuit to another constant current, with all switching controlled by the relay bank. (*C*) Auxiliary electrodes are not needed in the cell. The galvano-

[1] Present address: Department of Physics, University of Waterloo, Waterloo, Ontario, Canada.

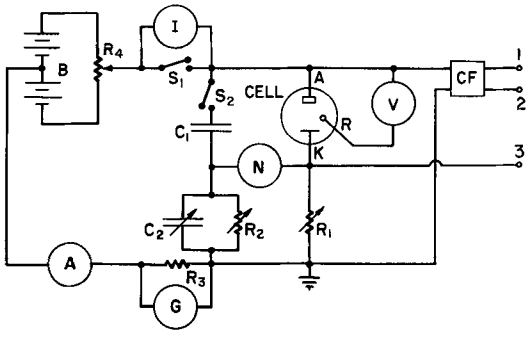

Fig. 1. Circuit diagram: A, anode; K, cathode, R, reference electrode; V, VTVM; CF, cathode follower; N, null detector; G, signal generator; I, constant current source; B, battery bank; A, microammeter.

stat kept the current constant to within 0.5% for all potential transients of interest. When the Helipot was replaced by fixed resistors for potentiostatic transients, the potential stayed constant to within 1 mv for current changes of 100 μa.

The Schering impedance bridge, consisting of R_1, R_2, C_1, and C_2 along with the cell, is shown in Fig. 1 (it does not affect the potentiostatic circuitry). The a-c signal was introduced by connecting a 5-ohm resistor in series with the potentiostat, and connecting a low-frequency oscillator across it. A high-gain null detector allowed the bridge to be operated with 10 mv a-c across the cell.

The measuring and recording circuitry is more critical than the cell supply circuitry. A VTVM with 100 megohm input impedance and a 20 μa panel meter can be used for most simple measurements. For more critical measurements a Keithley d.c. VTVM Model 200B (input impedance greater than 10^{14} ohms) was used to measure potential, and a Keithley Micro-microammeter Model 414 to measure current. A low-noise cathode follower with bandwidth greater than 100 kc is needed to operate the oscilloscope, especially for open-circuit transients. Either a conventional triode (6F5, grid current 6×10^{-9} amp) or a triode-connected electrometer tube (CK 5886, grid current less than 10^{-14} amp) can be used in a battery-operated cathode-follower circuit to achieve this performance.

The electrolyte used for all experiments except those studying the effect of pH was 2*N* H_2SO_4. The behavior of a passive iron electrode in this electrolyte does not appear sensitive to dissolved gases; oxygen-saturated, nitrogen-saturated, and hydrogen-saturated electrolytes yield identical results. Since a platinized-platinum electrode was made the cathode, hydrogen-saturated electrolyte was usually used to stabilize the potential of the cathode. Measurements were normally made at room temperature (22°C). A mercurous sulfate (0.1*N* $K_2SO_4/Hg_2SO_4/Hg$) electrode was used as reference. All potentials are given with respect to this reference. At room temperature in 2*N* H_2SO_4 this electrode has a potential of approximately 0.725v with respect to a reversible hydrogen electrode.

The anodes were prepared from a polycrystalline iron rod of 99.99% purity. An anode consisted of a ½ in. segment of this rod machined to a cross-sectional area of 0.2 cm^2 and mounted on a copper rod covered by glass tubing. The iron was first coated with a compound such as WD-4 shellac or Cenco Sealstix. After the coating had been removed from the end, the rod was mechanically polished. The anode surface was mounted so as to be vertical in the cell. It is usually desirable to work with a mildly etched surface whose roughness factor does not change rapidly. With the anode geometry described above (even after deep etching) a nominally plane surface of 0.2 cm^2 area can be restored by mechanical polishing. To enable data obtained using anodes of different roughness factors to be compared, the assumption has been made here that at

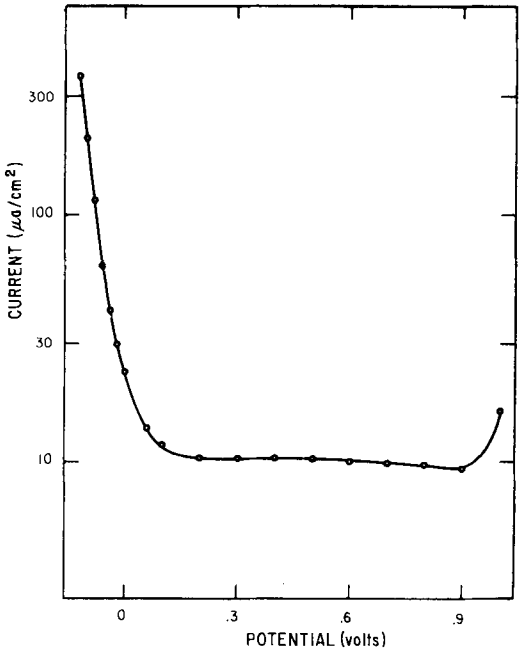

Fig. 2. Steady-state current *vs.* potential

room temperature (22°C) in 2*N* H_2SO_4 the current density at potentials in the middle of the passive region is 10 μa/cm^2. An electrode which exhibits this current density probably has a roughness factor near 1.5. (No measurement of the roughness factor was made.)

Results

Potentiostatic measurements.—If an iron electrode is placed in solution and a constant potential is applied, the current is found to reach a steady state after a certain interval, and the dependence of steady-state current on potential is represented by a so-called current *vs.* potential curve. The shape of this curve in the active region was given by Bartlett and Stephenson (6), and in the passive region by Franck and Weil (2). In the present measurements, where the electrode was passivated at constant potential, the current reached the steady state within 30 min and then stayed constant for at least 10 hr. Figure 2 shows the steady-state current density as a function of potential for the passive region. (The active-state corrosion potential is located at −1.03v on the potential scale, *vs.* mercurous sulfate, used in Fig. 2.) Franck and Weil (2) have reported longer times to reach the steady state, but they passivated at constant current and reached oxygen evolution, where there is presumably a fairly thick oxide layer, before switching to constant potential. (The longer times would be expected because of the fact that the oxide layer must become thinner to correspond to a steady state of a lower potential, and both thinning and readjustment take place slowly.)

As is seen from Fig. 2, the current density is approximately constant in the passive region between about 0.2v and 0.9v. Above 0.9v, it rises steeply with increasing potential due to oxygen evolution, and below 0.2v it also rises rapidly with decreasing potential, which represents an increase in rate of dissolution of the electrode.

The steady-state current density depends strongly on temperature and pH. The temperature dependence[2] is consistent with an activation-controlled process with energy of about 17 kcal/mole, as reported by Vetter (4). The pH range from 0 to 3 was studied using mixtures of H_2SO_4 and K_2SO_4, and it was found that the logarithm of the current density decreases linearly with increasing pH over this range. The current density changes by a factor of 10 for a pH change of 3.

[2] This measurement has been made for the range of 5°-70°C, at a potential of 0.4v, by D. DeSmet (private communication).

Only a limited amount of information about the electrode can be obtained from potentiostatic transients. When the potential is switched from one constant value to a higher one, the current density has an initial (infinite) discontinuous rise, because of the relation $i = C\ dV/dt$, which is followed by a slower decline to its initial value (7). If one measures the value of the current density just subsequent to the above capacitive transient, the indications are that it depends exponentially, not linearly, on the potential. For a quantitative study of this dependence, it is more convenient to use galvanostatic transients.

Measurements of a-c impedance were made in conjunction with the steady-state potentiostatic measurements. The a-c impedance, corrected for electrolyte resistance, may be expressed in terms of an equivalent parallel resistance, R_p, and capacitance, C_p. Both resistance and capacitance decrease with increasing frequency. The capacitance changes by a factor of 2 and the resistance by a factor of 10^3 over the frequency range from 1 to 10^4 cps. The resistance and capacitance are plotted against steady-state potential in Fig. 3 and Fig. 4 for a frequency of 100 cps.

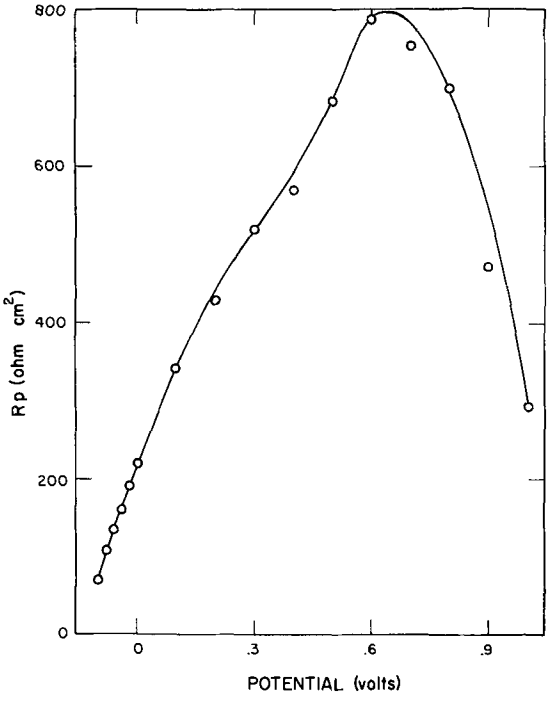

Fig. 3. Parallel resistance vs. potential; frequency, 100 cps

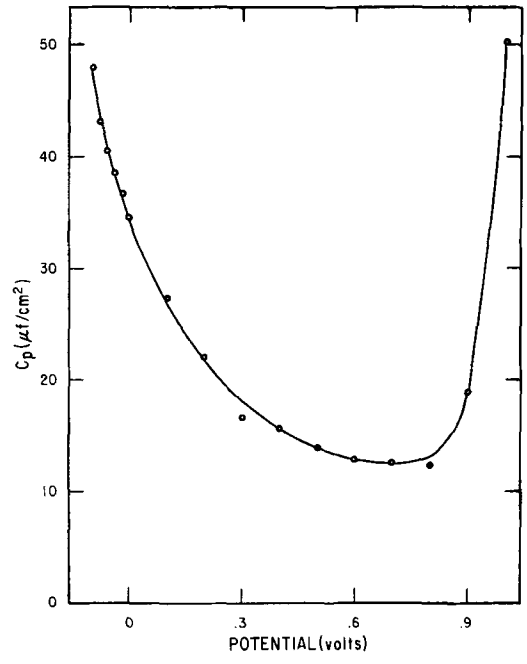

Fig. 4. Parallel capacitance vs. potential; frequency, 100 cps

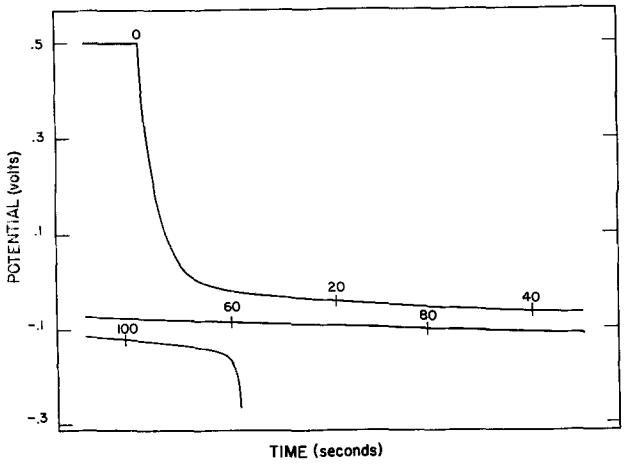

Fig. 5. Open-circuit potential transient. The corrosion potential (—1.03v) is not shown.

Galvanostatic measurements.—Figure 5 shows the potential transient observed when a steady state is interrupted by opening the circuit. This galvanostatic transient can be divided roughly into three parts: an initial capacitive transient, a sloping plateau,[3] and a sharp transition to the corrosion potential (not shown in the figure). Transients starting from different steady-state potentials differ mainly in the height of the capacitive transient.

An examination of the variation with current of the initial slope of a galvanostatic transient shows that the electrode does have a definite capacitance C which is given by the equation

$$i = C\ dV/dt + i_{ss} \qquad [1]$$

where i_{ss} is the steady-state current. The dependence of the reciprocal capacitance on the initial steady-state potential is shown in Fig. 7. Also shown is the reciprocal a-c equivalent capacitance at 100 cps.

In experiments such as the above, the times are so short that the potential V cannot change appreciably. To describe the behavior for longer times, let us assume that the potential is given by

$$i = C\ dv/dt + f(v) \qquad [2]$$

where v is the overpotential measured from a zero to be defined below. Since the observed transient is not a linear function of the time, the quantity $f(v)$ cannot be a constant. Furthermore, although the transient appears roughly exponential, the fit to a single exponential curve is not close, and so we cannot assume $f(v) = v/R$ (equivalent circuit as a resistance in parallel with a capacitance). However, if the parallel leakage current $f(v)$ be assumed to depend exponentially on v (as might be expected if activation processes control), then the transient can be fitted reasonably well. Accordingly, let us assume that

$$f(v) = i_o \exp\ (v/v_o) \qquad [3]$$

where i_o and v_o are constants.

When $i = 0$ (open circuit), the differential equation of the capacitive transient is, from [2] and [3],

$$C\ dv/dt + i_o \exp\ (v/v_o) = 0 \qquad [4]$$

and the solution is

[3] Attempts to define precisely a "Flade potential" at the end of this plateau meet the difficulty that the plateau itself curves downward well before the sudden transition to the active state.

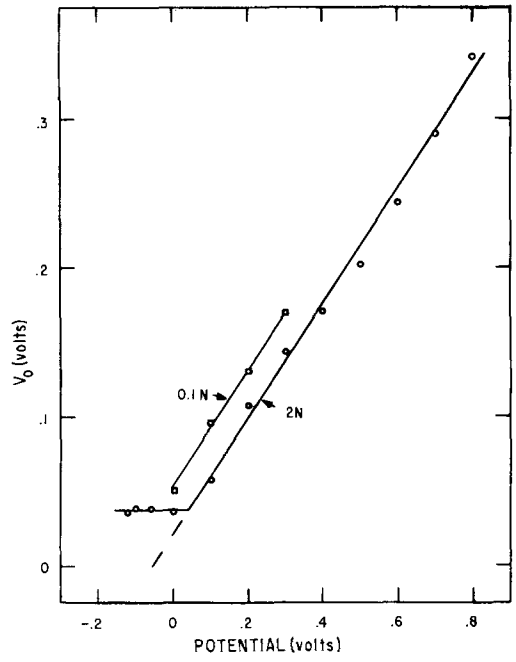

Fig. 6. v_0 vs. potential

$$v = v_o \ln(Cv_o/i_o) - v_o \ln(t + Cv_o/i_I) \quad [5]$$

where i_I is the current prior to opening the circuit. An equation of this form has been derived by Grahame (8), and applied to a study of the anodic oxidation of cadmium (8a). By choosing θ suitably, one can fit the initial two-thirds of the capacitive transient by a straight line

$$v = \text{const} - v_o \ln(t + \theta) \quad [6]$$

The slope of this straight line is v_o, and it is a well-defined experimental parameter.

Figure 6 shows the values of v_o which are obtained when the circuit is opened from a definite steady-state potential, as a function of that potential. This function is linear in the region where the current density is constant, and is constant (and equal to 37 mv) at lower potentials (below about 0.05v for $2N$ H_2SO_4).

In order to calculate the parameter i_o, it is necessary to determine the zero of overpotential. Since the overpotential under consideration is associated with the capacitive transient, it will be zero when that transient has died out. However, there is another much slower process occurring which causes the plateau to slope. Accordingly, it is natural to suppose that the above overpotential is zero on the plateau extrapolated backwards. When this is done, it turns out that i_o is approximately constant over the potential region where the steady-state current i_{ss} is constant. Because the plateau is not exactly linear, this extrapolation is difficult. However, one can obtain a well-defined zero of overpotential by assuming i_o is constant when i_{ss} is, and extrapolating as in Fig. 6. The zero is located at -0.055v, and $i_o = 0.75$ μa/cm^2 when $i_{ss} = 10$ μa/cm^2, and the acid is $2N$ H_2SO_4.

Since the exponential nature of $f(v)$ has been established, and since the steady-state current density has a temperature dependence indicating the existence of an activation energy, it is now in order to discuss the theoretical equation relating current density to overpotential across an activation barrier. This, according to various authors (9), is of the form

$$i/i_o = \exp(\alpha\lambda\eta/kT) - \exp(-(1-\alpha)\lambda\eta/kT) \quad [7]$$

where η is the overpotential measured from the reversible potential, α is the fraction of the overpotential which aids the forward current, λ is the valence of the charge carriers, and i_o is the exchange current at zero overpotential. If η is large, the last term may be neglected and this equation has the same form as Eq. [3]. If η is small, however, Eq. [3] and its consequence Eq. [5] are no longer valid, and this may account in part for the fact that the bottom third of the capacitive transient deviates from the curve of Eq. [6].

Assuming temporarily that η is large, let us try to correlate it with the measured overpotential v. If we should equate v to η, then it folows that $v_o = kT/\alpha\lambda$, a constant independent of v. This result is not consistent with Fig. 6, where v_o depends linearly on v, and hence the entire overpotential cannot appear across the activation barrier.

It seems more reasonable to assume (10) that a layer of thickness D is present at the interface and that only a fraction of the overpotential appears across the activation barrier. In this event, we can relate $\alpha\eta$ to the field E by the equation $\alpha\eta = aE$, where a defines a "jump distance" for forward motion of particles across the activation barrier. Then, from Eq. [7] and [3], we have

$$E = (kT/a\lambda)(v/v_o) \quad [8]$$

for the field across the barrier. If there were no charge within the layer, then (by Gauss' theorem) the field would be constant across the layer, $v = ED$, and the thickness

$$D = (a\lambda/kT)v_o \quad [9]$$

If we assume that in the steady state the layer is neutral, then its thickness will be proportional to v_o, which can be determined experimentally. Figure 6 then indicates that (i) the layer has a limiting thickness below which it does not decrease and (ii) that the thickness increases linearly with steady-state potential up to about ten times this minimum thickness.

As mentioned above, the steady-state current density depends strongly on pH. Comparison of the two curves in Fig. 6, representing $0.1N$ H_2SO_4 and $2N$ H_2SO_4, respectively, shows that v_o depends only on v and not on pH.

In reaching the steady state, for a given overpotential, the system parameter i_o somehow adjusts itself so that the final value is in accordance with Eq. [3], where the current density i is itself equivalent to the rate at which the acid removes the layer, this rate depending on pH and temperature.

A comparison of Fig. 6 with Fig. 7 shows that the reciprocal capacitance is a linear function of v_o in the steady state. Apparently the capacity is related to the

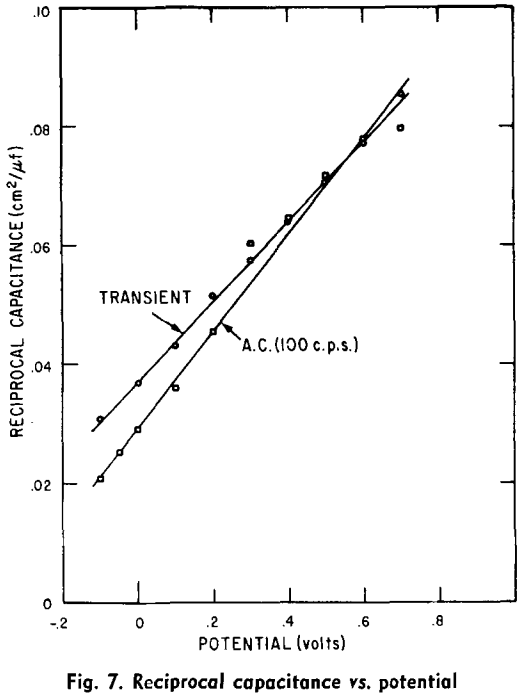

Fig. 7. Reciprocal capacitance vs. potential

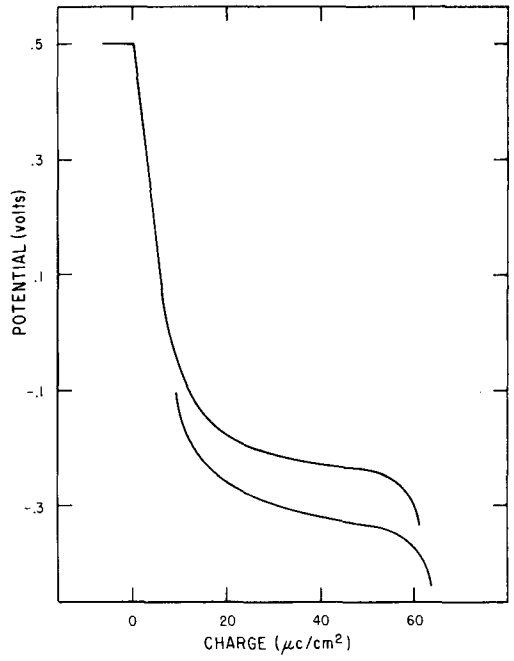

Fig. 8. Cathodic potential transients. Cathodic current: upper curve, 0.256 ma/cm²; lower curve, 2.56 ma/cm².

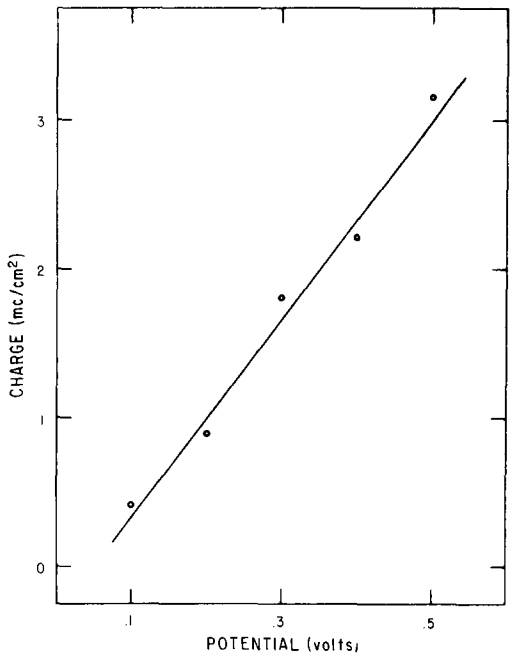

Fig. 9. Charge to activate vs. potential. Anodic current 3μa/cm²

thickness of the layer. The discussion section below shows that this is to be expected if one adopts a rather general model for the layer.

Transition to the Active State

If the electrode is initially passive and in a steady state with anodic current i_{ss}, a transition to the active state may be effected if one applies a constant current $i < i_{ss}$. This current can be anodic or cathodic.

The case where the current is cathodic and large with respect to the corrosion current is illustrated by Fig. 8, where potential has been plotted *vs. it*, with t the time the current i has flowed. The two curves are for two different values of the current, and it is seen that the length of the plateau[4] depends only on the charge and not on the current density. (Strictly speaking, activation might be expected to depend on $(i_{ss} - i)t$, but $|i_{ss}| < i$ and hence one may use it for the charge involved, without causing appreciable error.) The amount of charge required, before the transition to the active state occurs, is equivalent to a fraction of a monolayer. Other authors (3) have observed this, and have suggested that a "hole" is created in the layer. But then the charge to make a hole should depend on the layer thickness (as measured by the initial potential) and this is not found. An alternative explanation is that large cathodic currents cause disruption of a monolayer, followed by a general breakdown and a transition to the active state.

Activation with anodic current $i < i_{ss}$ is different from that with large cathodic current, because the initial thickness is important in the former case. In Fig. 9, for an anodic current density of 3 μa/cm², the activation charge is shown as a function of initial steady-state potential. This charge is greater than that for cathodic activation, and it increases linearly with the thickness of the surface layer. During anodic activation, the erosion of the layer by the acid may be assumed to continue at the rate i_{ss}, while formation occurs at the rate i. As long as there is an anodic current, this will tend to flow where the layer is thinnest and thus automatically keep the thickness of the layer uniform. However, continued erosion will eventually make the layer so thin that disruption must occur. With this picture, the anodic activation charge corresponds to a layer at least several atoms thick, and so will be greater than the cathodic activation charge, which seems to involve less than a monolayer.

If the current is zero or cathodic and small, the transition to the active state is intermediate in behavior between the above types of activation. Presumably the erosion culminates in the formation of a hole through the layer, there being nothing to prevent it. For zero applied current (open circuit) the time to activate is not entirely reproducible, which apparently is due to the thinning being nonuniform, or in other words to the existence of "local action currents."

Layer Growth

To study the increase in thickness of a passive layer, we have recorded galvanostatic transients with anodic currents greater than the steady-state current, and a typical one is shown in Fig. 10. Starting from the steady state, there is at first a capacitive rise in potential, which may be regarded as a rapid adjustment to the increased current. The potential goes through a maximum, decreases slightly to a plateau and then rises linearly with time. (The experiments of Weil (3) were such that the maximum and plateau were not recorded.) At higher passivating potentials, the length of

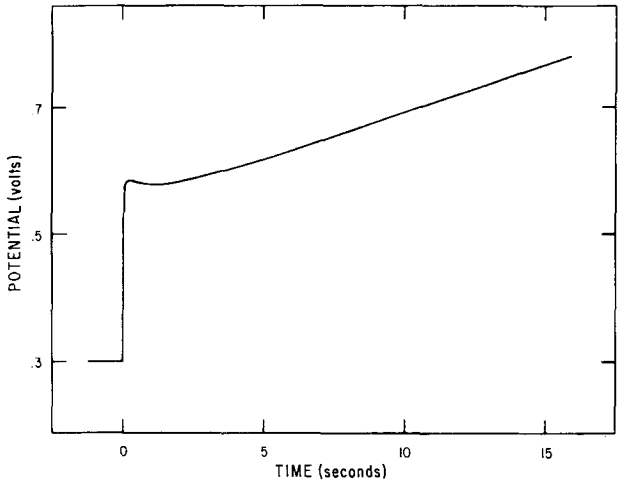

Fig. 10. Galvanostatic potential transient. Anodic current, 183 μa/cm².

[4] The plateau itself shifts to more negative potentials as the cathodic current is increased, according to $\Delta V = 0.04 \ln i$, which relation is practically independent of thickness.

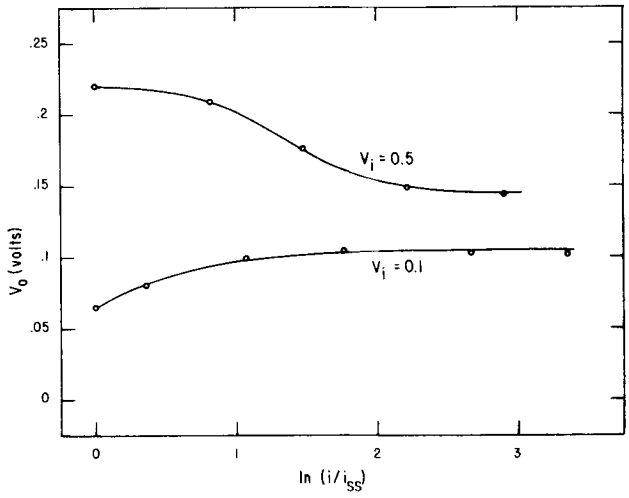

Fig. 11. Dependence of v_o on current. Initial steady-state potential: upper curve, 0.5v; lower curve, 0.1v.

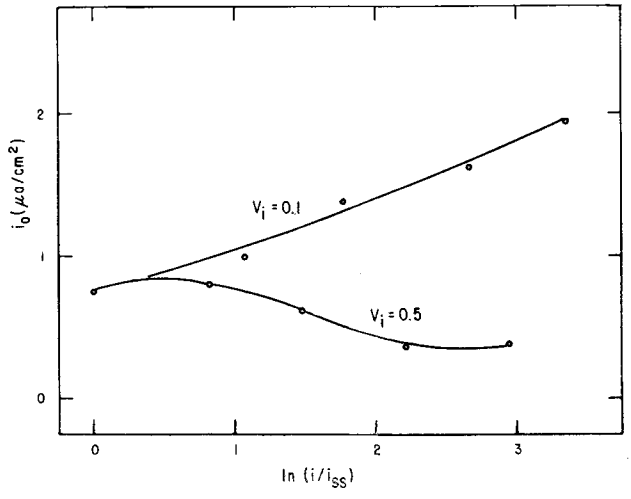

Fig. 12. Dependence of i_o on current. Initial steady-state potential: upper curve, 0.1v; lower curve, 0.5v.

the plateau shows little potential dependence, but does vary approximately inversely with excess current, indicating that a constant amount of charge is required to reach the end of the plateau. The slope of the linear potential rise is approximately proportional to $i - i_{ss}$, as would be expected if the layer is thickening.

Closer investigation reveals that a point on the above linear rise does not correspond to a steady state, for the field is not constant across the layer. If the circuit be opened when an excess charge of 0.05 mc/cm^2 (enough to complete the capacitive transient and arrive on the plateau, without appreciably changing the layer thickness) has passed, then it is found that the field across the activation barrier has changed from its steady-state value. [The open-circuit transient can be fitted by a $\ln(t + \theta)$ function over a wide range of potential, and so one can obtain good parameters v_o and i_o. These are shown in Fig. 11 and 12, for 2 different values of the initial steady-state potential v_i, as a function of the applied current i.] Now with a given potential v and a thickness D, the average field is v/D, which will be the actual field in the steady state. If the field across the activation barrier is different from this average, so must the field in the remainder of the layer be different, and the field cannot be constant. By Gauss' theorem, $\partial E/\partial x = 4\pi\rho$, so the interior of the layer has a nonzero charge density at the end of the plateau (and on the linear rise as well).

Relaxation from the charged condition to the neutral steady state can be followed by switching down to the

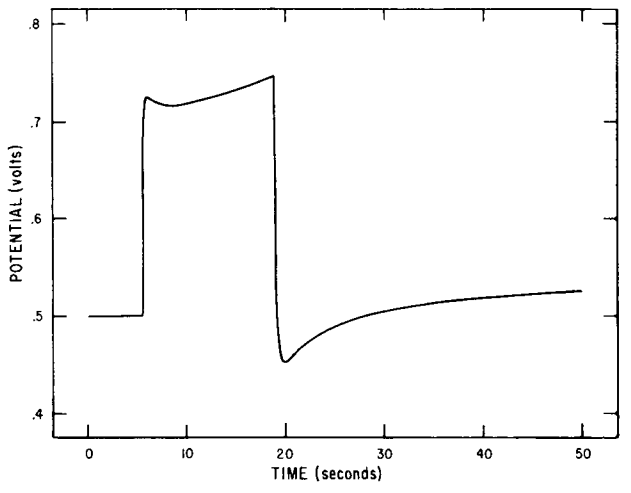

Fig. 13. Galvanostatic potential transient. Current switched from 10 to 73 μa/cm^2, then back to 10 μa/cm^2.

corrosion current, at any point of the linear rise. Figure 13 shows the resulting behavior. The rapid drop of potential (capacitive transient) is followed by a slow rise. After about a half a minute, i_o and v_o return to their steady-state values, which are consistent with the final potential. But an open-circuit transient from the linear rise drops very rapidly, so that i_o and v_o can be expected to be nearly constant during the drop, which is in fact found.

In general, then, i_o and v_o can change rapidly if a large change of current is made, but quite slowly if redistribution of charge over the whole layer is involved. If, for instance, the solution be changed from 0.1N H_2SO_4 to 2N H_2SO_4, keeping the potential constant, the quantity v_o takes about 2.5 min, and i_o as long as 10 min, to reach new steady values (unpublished experiments by D. DeSmet). Apparently i_o and v_o serve to describe local conditions at an activation barrier, which conditions adjust rapidly to electron flow, but only slowly to motion of ions.

The thickness of the layer can be estimated by indirect methods in a manner similar to that used by Vetter and Weil (1), and our results are roughly the same. If excess charge ΔQ is given to the layer, and relaxation at $i = i_{ss}$ is allowed to proceed to completion, then the increase of potential ΔV is related to ΔQ in a linear fashion, as shown in Fig. 14. If this charge ΔQ all goes to build layer, the increase in thickness ΔD is given by the equation $\Delta D = M(\Delta Q/\sigma A)/s\lambda F$, where M is the molecular weight, σ the roughness factor, A area, s specific gravity, and λ the valence of ion. Thus we can relate ΔD to ΔV if we make assumptions about M, σ, s, and λ. But since Fig. 6 shows a linear connection between v_o and V, ΔD will be proportional to Δv_o. This is in agreement with Eq. [9], the factor of proportionality being $a\lambda/kT$. Assuming that the layer is composed of Fe_2O_3, that $\sigma = 1.5$ and $\lambda = 3$, and that $D = (a\lambda/kT)v_o$ from Eq. [9], the minimum thickness is calculated to be 8Å. the thickness at $v = 800$ mv is 68Å, and the jump distance a is 1.9Å. [A somewhat similar dependence of thickness on potential was found in the anodic oxidation of platinum (11, 12)].

Discussion

Now that the evidence indicates the existence of a nonzero charge within the layer, it becomes natural to inquire how this charge builds up, relaxes, and causes the layer to change in thickness. One can obtain at least partial answers by considering the behavior of a layer with an arbitrary distribution of charge.

If the charge density is ρ and the dielectric constant is ϵ, then Gauss' theorem states that

$$\epsilon E = 4\pi \int \rho dx \qquad [10]$$

The drop in potential across the layer is

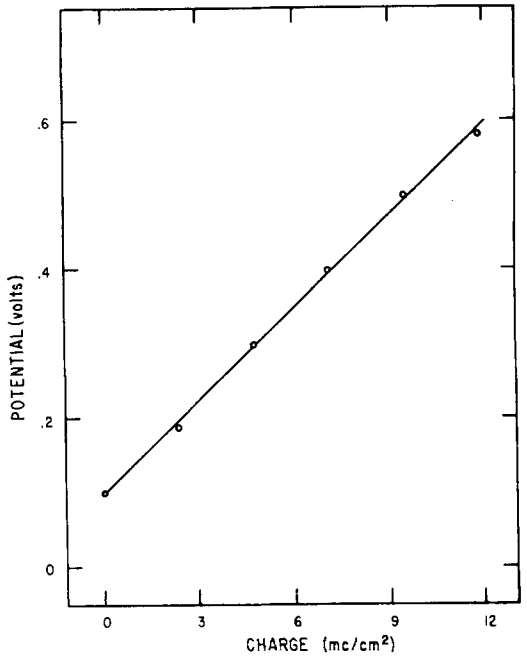

Fig. 14. Steady-state potential *vs.* charge. Potential measured 100 sec after switching down to steady-state current. Charge = $(i - i_{ss})t$.

$$v = -\int_0^D E dx \qquad [11]$$

This may change because the charge density changes, or because the layer increases in thickness. The total amount will be

$$\Delta v = \int_0^D \Delta E\, dx + E\Delta D \qquad [12]$$

Furthermore, by continuity, the time rate of change of charge density is given by

$$\frac{\partial \rho}{\partial t} = -\frac{\partial i}{\partial x} \qquad [13]$$

where i is the current density.

Now let us discuss a galvanostatic charging process, using the above equations. When the current is increased at $t = 0$, electrons flow without delay, leaving ionized iron atoms behind, ready to migrate in the opposite direction under the influence of the field E. Suppose that these ions are contained in a small length Δx. Then, from [13]

$$\Delta\rho\, \Delta x = \Delta i\, \Delta t$$

By [10], $\epsilon\Delta E = 4\pi\, \Delta\rho\, \Delta x = 4\pi\, \Delta i\, \Delta t$.

If the region Δx is at the metal interface and $\Delta x << D$,

$$\Delta v = -D\Delta E = \frac{4\pi}{\epsilon} \Delta i\, \Delta t\, D \qquad [14]$$

Since capacity is defined in general by the equation $C = -i/(dV/dt)$, we see that our system behaves as if there were a capacitative element (in parallel with the normal resistance) through which the current Δi flows. Its capacity is, from [14],

$$C = \epsilon/4\pi D \qquad [15]$$

This equation is consistent with our experimental observations that the reciprocal capacity in the steady state varies linearly with the potential (and thus with the thickness). Since there is nothing in the above derivation which restricts the system to be in the steady state, we should be able to find the thickness by measuring the capacity and applying Eq. [15].

To proceed further, let us attempt to describe the thickening process, making what seem to be natural assumptions. Vetter (4) has suggested that at the layer-electrolyte interface negative oxygen ions are produced and that these can migrate through the layer toward the metal. Exactly where they combine with positive ions to produce added layer has been left open, so let us suppose that this occurs somewhere in the middle of the layer, the position being determined by the relative mobilities of the various types of ion. If, except where the ions are combining, the charge density is steady, then $\Delta E = 0$ and Eq. [12] results in $\Delta v/\Delta t = E_c(\Delta D/\Delta t)$, E_c being the field at the site of combination. If the thickening (thinning) occurs at a constant rate, then the potential will rise (fall) linearly with time. For a galvanostatic transient with $i > i_{ss}$, we do observe a linear rise, and for $i > i_{ss}$ a linear fall, during the latter part of the transient.

More quantitative statements about changes in thickness and about the factors governing the exchange current and electric field seem to demand further experimentation, especially in connection with the relaxation process. Qualitatively, however, the above model does tie together phenomena which are otherwise inexplicable, and thus furnishes guidelines toward further progress in understanding the structure of a passive layer.

Acknowledgment

This work was supported by the U.S. Army Research Office (Durham) under contracts DA-11-022-ORD-2525 and DA-11-022-ORD-3442, and by the University of Illinois Research Board.

Mr. W. P. Perkins rendered invaluable assistance both in performing the experiments and in analyzing the data. Mr. L. D. Ferguson assisted with studies of capacitance and of concentration dependence. Mr. J. E. Orme helped with the a.c. measurements, and Mr. P. O. Schemmel and Mr. W. H. Trester with the data analysis.

For all this support and assistance, we are deeply appreciative.

Manuscript received May 7, 1962; revised manuscript received Oct. 14, 1964. This paper was presented at the 2nd International Passivity Conference, Toronto, September 1962.

Any discussion of this paper will appear in a Discussion Section to be published in the December 1965 JOURNAL.

REFERENCES

1. K. J. Vetter, *Z. Elektrochem.*, **55**, 274 (1951).
2. U. F. Franck and K. G. Weil, *ibid.*, **56**, 814 (1952).
3. K. G Weil, *ibid.*, **59**, 711 (1955).
4. K. J. Vetter, *ibid.*, **58**, 230 (1954).
5. K. J. Vetter, *ibid.*, **62**, 642 (1958).
6. J. H. Bartlett and L. Stephenson, *This Journal*, **99**, 504 (1952).
7. Ya. M. Kolotyrkin, *Z. Elektrochem.*, **62**, 664 (1958).
8. D. C. Grahame, *J. Phys. Chem.*, **57**, 257 (1953).
8a. P. E. Lake and E. J. Casey, *ibid.*, **106**, 913 (1959).
9. J. O'M. Bockris and E. C. Potter, *This Journal*, **99**, 169 (1952).
10. N. Cabrera and N. F. Mott, *Repts. Progr. Phys.*, **12**, 163 (1948-49).
11. J. Giner, *Z. Elektrochem.*, **63**, 386 (1959).
12. H. A. Laitinen and C. G. Enke, *This Journal*, **107**, 773 (1960).

The Structure of Electrodeposited Copper Examined by X-Ray Diffraction Techniques

E. M. Hofer[1] and H. E. Hintermann

Laboratoire Suisse de Recherches Horlogères, Neuchâtel, Switzerland

ABSTRACT

X-ray diffraction line profiles of copper, electrodeposited from an acid plating bath in the presence of thiourea, have been analyzed by Fourier techniques. From the coefficients data on microstrains, crystallite size, twin fault, and stacking fault densities were obtained. The stored energy and the dislocation density have been derived from the value of the rms strains. The sums of the determination of the Fourier coefficients of the various diffraction peaks were calculated with a computer. The particle size as determined by the Fourier analysis varies between 1350 and 180Å. The smallest particle size is obtained in a plating bath with a thiourea concentration of 20 mg/l. The deposits contain no stacking faults; the microtwin density is high. The microstrains are strong, indicating high values for the stored energy, ≈0.25 cal/g, and the dislocation density, ≈2 x 10^{11}/cm^2. A relationship was established between hardness and strain. X-ray results were compared with those obtained from electron microscopical observations on the same specimens.

The mechanical properties of electrodeposits have been the subject of many studies (1). The properties are due to definite microstructural features comparable to those produced by cold-work, such as small grain size and strong internal tensions. Fischer (2) explained that strong inhibition can entirely block a crystal's active growth sites during deposition and thus cause a notable decrease in the grain size with increasing amounts of the additive. Vermilyea and co-workers proved quantitatively that the rate of electrodeposition of metal whiskers is controlled by this mechanism (3), and that the formation of polycrystalline electrodeposits can be explained by the same mechanism (4).

Strains in galvanic deposits are similar to those produced by cold-work. Their presence has been known for almost a century (5, 6). They are the result of distortions in the mosaic structure influenced by the deposition parameters (7, 8). Strain can result from the transformation of atomic hydrogen enclosed in the crystalline body of the metallic deposit into molecular hydrogen (9-11), the retaining and releasing of atomic hydrogen during electrodeposition (10, 11), and the presence of dislocations created by growth accidents (9, 12). Steinemann and Hintermann (13) measured dislocation densities in copper deposits of 10^8 to 10^{11} dislocations/cm^2. Another reason for the presence of strains is the inclusion of the additive or a reaction product thereof in the deposit (13). By electron microscopical techniques an occlusion density of 10^{17}/cm^3 was determined (13). Jan (14) measured the occlusion density by x-ray small angle scattering and obtained similar results. The pinning of dislocations between inclusions, as observed in copper sheets electroplated in the presence of gelatine, is still another cause for the improved mechanical properties of electrodeposited metals (13, 15).

An accurate and extended knowledge of the microstructure of electrodeposits was necessary if a relation between certain deposition parameters and the resulting mechanical properties of the electrodeposits were to be found. One possible and promising method of investigation was a Fourier analysis of the x-ray diffraction peaks obtained from electrodeposits (16, 17). This method renders a better statistical value for the crystallite size than does the electron microscope, since the examined surface of the specimen is much larger. Moreover, from the analysis of the diffraction peaks by Fourier techniques, additional data on the magnitude of microstrains and the density of growth faults can be obtained. This technique has the further advantage of being nondestructive. Its results combined with hardness measurements contribute to a better understanding of the structural defects and their influence on the mechanical properties of electrodeposited metals.

[1] Present address: Central Research Laboratory, American-Standard, New Brunswick, New Jersey.

Experimental

Sample preparation.—Copper deposits of 30μ thickness were produced on laminated and annealed copper sheets of 50μ thickness. The electrolytic cell was of cylindrical shape with a rotating cathode and a stable concentric anode of the following dimensions: cathode, diameter 40 mm, height 100 mm, effective height[2] 82 mm; anode, diameter 80 mm, height 100 mm. This cell was constructed for good reproductibility of the following parameters: (*a*) current density *i*, (*b*) temperature *T*, (*c*) geometry *G*, (*d*) agitation *A*. These parameters were kept constant for all depositions.

Seven deposits were made. Analytical grade thiourea[3] was used as an additive. The initial composition of the plating bath was 1*N* $CuSO_4$, 1*N* H_2SO_4, prepared as described by Fischer and co-workers (18, 19). A fresh solution was used for each plating. The thiourea was added in quantities of 5, 10, 15, 20, 25, 40, and 100 mg/l solution immediately before the electrodeposition. The other deposition parameters were: $i = 28$ ma/cm^2 and $T = 22° \pm 1°$C. The samples were chosen from an area exhibiting the least of preferred crystallite orientation, usually from the central region of the cathode. In order to prevent recovery at room temperature, the specimens were held under liquid nitrogen until investigated by x-ray diffraction.

Heat treatments were made for 1 hr at temperatures of 100°, 175°, 250°, 350°, 450°, and 550°C, respectively.

X-ray methods.—The x-ray diffraction patterns were recorded with a Philips proportional counter diffractometer. Filtered Co Kα radiation (voltage 30 kv, current 10 ma, Fe filter) was used, thus eliminating the copper fluorescent radiation from the sample. The width of the divergence slit was 1°, that of the receiving slit 0.2 mm. The scanning speed was ¼ degree 2θ/min, the chart speed 800 mm/hr.

The electrodeposits were mounted in a stainless steel specimen holder in order to provide reproducible experimental conditions during the recording of the various diffraction patterns. The heat-treatment was performed while the specimen was kept in the holder. The background was determined from a sample annealed at 550°C and substracted from each diffraction pattern of the samples to be analyzed.

[2] Height of the sheet on which the copper actually was deposited.

[3] Merck p.a.

If a fcc metal is considered to be composed of a stacking of (111) layers whose normal sequence would be ABCABCABC . . ., a stacking fault is a break in this sequence ABC↓BCABC . . ., whereas a reversal in the sequence ABCACBA represents a twin fault. The probability α of finding a stacking fault between two (111) layers can be determined from the relative positions of the 111 and 200 reflections of the sample as deposited and the annealed standard (20, 21), *i.e.*

$$(2\theta_{200} - 2\theta_{111})_{\text{untreated}} - (2\theta_{200} - 2\theta_{111})_{\text{annealed}} = -\left(\tan\theta_{200} + \frac{1}{2}\tan\theta_{111}\right)\frac{45\sqrt{3}\,\alpha}{\pi^2} \quad [1]$$

The Fourier analysis of the recorded diffraction peaks was carried out with an electronic computer, IBM 1620. The program was established in such a way that, after the function to be analyzed had been introduced in form of discrete values P'_ν spaced in regular intervals θ_ν, the Fourier coefficients and the position of the center of gravity with regard to the peak maximum, ΔCG, of each peak were obtained (17). For the calculation of the Fourier transform and ΔCG, intervals equal to 2 sin θ/λ were used. The ordinates were previously divided by $f^2(1 + \cos^2 2\theta)/\sin^2\theta$, f being the atomic scattering factor. Once the ΔCG value was known, the probability β of finding a twin fault between two (111) layers could be determined by the method of Cohen and Wagner (22)

$$\Delta CG(^\circ 2\theta)_{111} - \Delta CG(^\circ 2\theta)_{200} = \beta\,(11\tan\theta_{111} + 14.6\tan\theta_{200}) \quad [2]$$

The cosine Fourier coefficient A_L, for which the line broadening due to instrumental effects (23) is corrected by the method of Stokes (24), can be considered as the product of two coefficients A_L^S and A_L^D. L is the real distance in the crystal normal to the diffracting planes, equal to na_3; n is the harmonic number, and a_3 is the unit cell dimension in the direction perpendicular to the diffracting planes. A_L^S is due to the particle size, A_L^D to the rms strain averaged over the distance L : $\langle\epsilon_L^2\rangle^{1/2}$

$$\ln A_L = \ln A_L^S - 2\pi^2(L/a_o)^2 h_o^2 \langle\epsilon_L^2\rangle \quad [3]$$

where $h_o^2 = (h^2 + k^2 + l^2)$ is the order of the reflection and a_o is the true lattice parameter. Only the term due to the strain is a function of h_o^2. Thus, if A_L is plotted as a function of different orders of reflection $(h_1^2 + k_1^2 + l_1^2)$ a straight line is obtained, whose intersection with the ordinate furnishes the value of A_L^S. This value, a function of L, renders $\langle D\rangle_{\text{eff }hkl}$, the size of the coherently diffracting domains. This effective dimension of the particles includes the effects of grain boundaries, small angle boundaries, stacking faults, and twin faults

$$\frac{1}{\langle D\rangle_{\text{eff }hkl}} = -\left[\frac{dA_L^S}{dL}\right]_{L\to o} = \frac{1}{\langle D\rangle} + \frac{1.5\alpha + \beta}{a_o} c_{hkl} \quad [4]$$

c_{hkl} is a coefficient which depends on the reflection under study. In this work the orders 111 and 222 have been used for which c_{hkl} is equal to $\sqrt{3}/4$. The expression $[(1.5\alpha + \beta)/a_o]\ 3/4 = \langle D\rangle^{-1}_{F\,111}$. The term $\langle D\rangle_{F\,111}$ is the calculated particle size due to the presence of faults only.

The diffraction peaks of all seven samples with and without heat treatment at different temperatures were analyzed by Fourier techniques. To apply the correction of Stokes for the instrumental line broadening, a sample annealed at 550°C was used as a standard. Moreover, to check if there was any annealing effect on freshly deposited coatings at ambient temperature, these samples were stored after deposition under liquid nitrogen and their x-ray diffraction patterns recorded at a sample temperature of —160°C. For this purpose a low-temperature goniometer head analogous to the one described by Wagner (25) was used. It was experimentally verified that neither the width nor the form of the diffraction peaks were influenced by the use of this goniometer attachment.

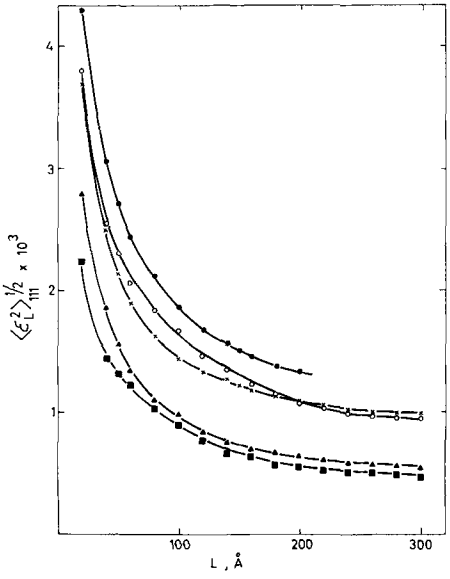

Fig. 1. rms strain $\langle\epsilon^2_L\rangle^{1/2}$ *vs.* the averaging distance normal to the diffracting planes L, for copper deposited from 1*N* H_2SO_4, 1*N* $CuSO_4$ with 40 mg/l thiourea and for different annealing temperatures: •, —160°C; ○, 25°C; X, 100°C; ▲, 175°C; ■, 250°C; 40 mg/l.

Results

Strains.—The rms strains of the seven specimens were calculated as a function of L (example in Fig. 1). If it is assumed that the distribution of the strains within the crystal is random, it is possible to calculate the stored energy due to the elastic distortions in the lattice with the formula of Faulkner (26)

$$V = \frac{15\,E}{2(3 - 4\nu + 8\nu^2)}\langle\epsilon^2\rangle$$

where E is Young's modulus in the direction $[hkl]$ of the deformation and ν is Poisson's ratio.

The rms strain $\langle\epsilon_L^2\rangle^{1/2}$ is a component normal to the reflecting planes, averaged over a column length L, then squared and averaged over all sample regions. According to McKeehan and Warren (27), the true value of the strain is only obtained at small values of L. Therefore V has been chosen to be calculated for $L = 20$Å, a value which seemed sufficiently small to satisfy this condition, yet sufficiently great that $\langle\epsilon_L^2\rangle^{1/2}$ could be determined precisely. Values of V were calculated for each annealing temperature T_a at various thiourea concentrations (Fig. 2 a-g). Also listed in Fig. 2 are the size of coherently diffracting domains, rms strain, and Vickers DPH values. The curves were drawn taking into account for the maximum deviation from V, as indicated in the appendix. The point at —160°C indicates that the sample was actually kept at this temperature during the recording of the diffraction pattern. From the plotted curves it is evident that the release of the stored energy with increasing temperature does not proceed in a parallel manner for the seven specimens. Hence the recovery mechanism depends on the concentration of the additive which itself influences the structure, the number of occluded impurities, and the number of faults in the plate. Several authors (28-30) have studied the recovery of pure copper after irradiation or cold-work and have distinguished five recovery stages. Although the numerous publications on this subject agree on the activation energy of the different stages and also on the

temperature ranges within which the transitions are supposed to occur, they disagree somewhat on the interpretation of the kinetics of these phenomenons.

The first recovery stage, between —240° and —225°C, is attributed to close-pair annihilation by the motion of interstitials immediately adjacent to a vacancy (28-30), or to a local rearrangement process occurring in displacement spikes (29). The second stage, between —160° and —60°C, is associated with di-interstitial (30) or interstitial (28) migration or with the migration of divacancies or "wide" pair recombination (29). The third stage, between —60° and +40°C, is characterized by divacancy migration (28), diffusion of interstitials, and their recombination with vacancies (29), vacancy migration, or the breaking up of interstitial clusters (30). All the authors attribute the fourth stage, from

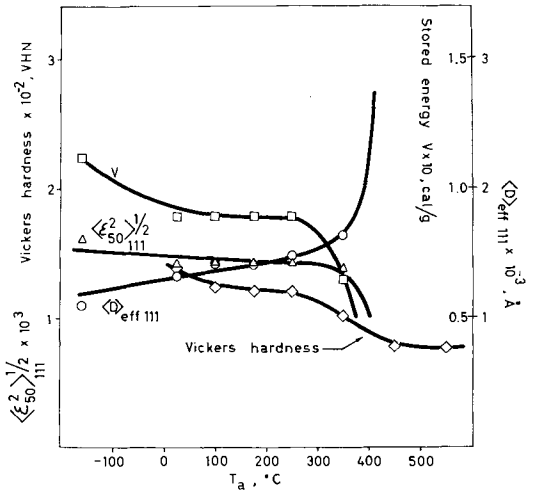

Fig. 2. Size of the coherently diffracting domains $\langle D \rangle_{eff\ 111}$, rms strain $\langle \epsilon^2_{50} \rangle^{1/2}_{111}$, stored energy V and Vickers hardness number VHN for 20g load as function of the annealing temperature T_a. (a) 5 mg/l thiourea.

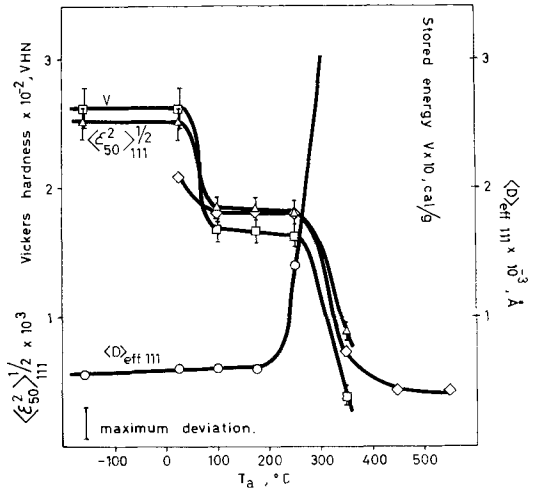

Fig. 2b. 10 mg/l thiourea

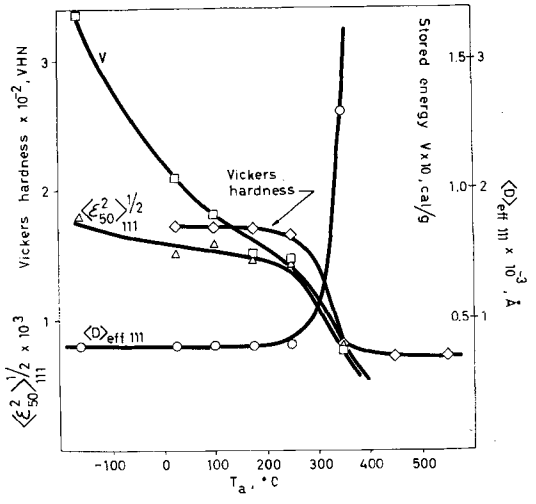

Fig. 2c. 15 mg/l thiourea

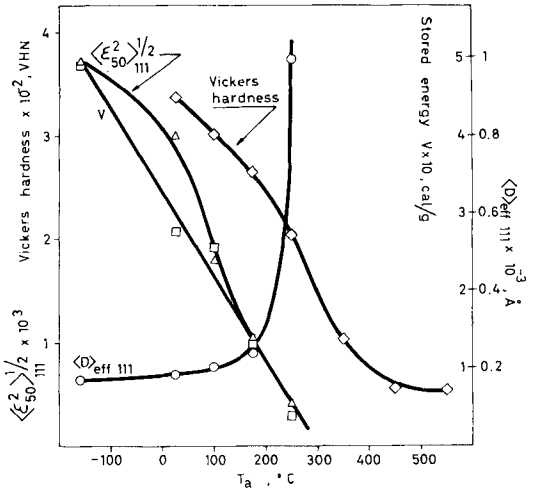

Fig. 2d. 20 mg/l thiourea

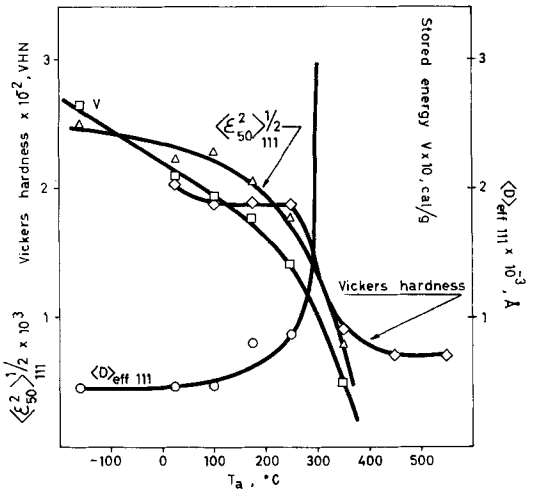

Fig. 2e. 25 mg/l thiourea

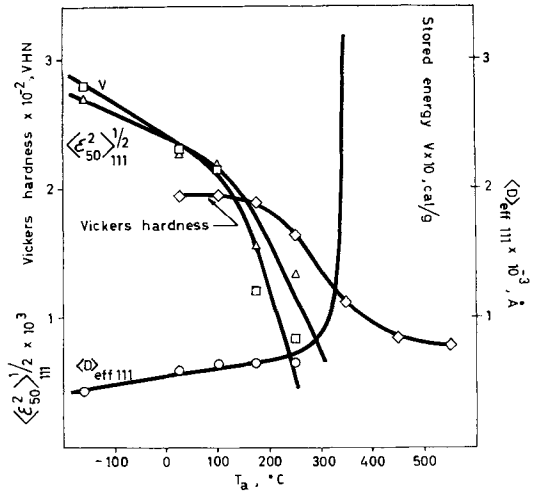

Fig. 2f. 40 mg/l thiourea

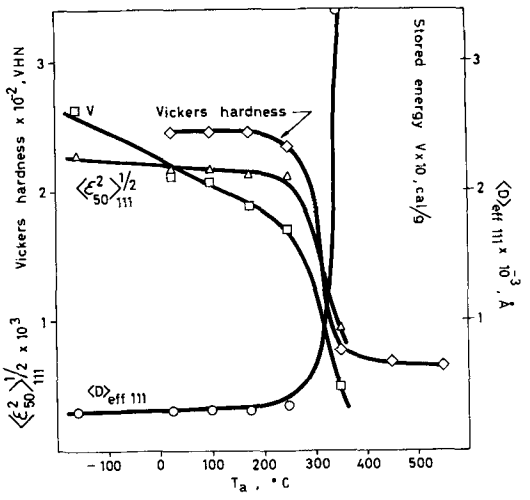

Fig. 2g. 100 mg/l thiourea

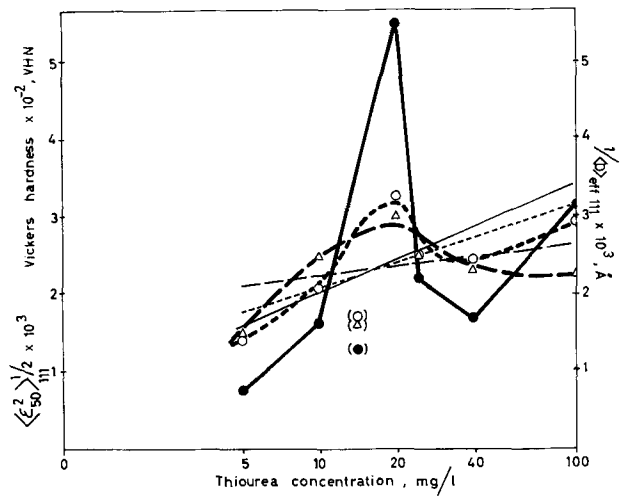

Fig. 3. rms strain $\langle\epsilon^2_{50}\rangle^{1/2}_{111}$, inverse of the size of the coherently diffracting domains $1/\langle D\rangle_{\text{eff }111}$ and Vickers hardness number VHN vs. thiourea concentration in the bath: —— •, $1/\langle D\rangle_{\text{eff }111}$; — — △, $\langle\epsilon^2_{50}\rangle^{1/2}_{111}$; - - - - ○, Vicker's hardness.

100° to 200°C, to the migration of isolated vacancies and to their disappearance at grain boundaries or dislocations. The fifth stage, at about 240°C, is unanimously considered as the stage of reorganization of the crystal by self-diffusion and migration of dislocations occurring before the recrystallization or simultaneously with it.

This information is summarized in Table I. An attempt was made to compare the recovery behavior of the copper electrodeposits of this study to samples of pure copper processed in a different manner as described in the literature.

In the case of the electrodeposits only the stages III, IV, and V could be observed, because the bath temperature at the time of the deposition was 22°C. The only purpose of the diffraction under liquid nitrogen was to prevent a recovery of the deposit at ambient temperature. From Fig. 2 it is evident that the three later recovery stages could generally be observed on all deposits. The different stages have been separated by taking into account (i) the limiting temperature as stated in Table I, (ii) the course of the curves as indicated by the measured points, and (iii) for stage V also the onset of the rapid grain growth. The percentages of recovery were calculated from the curves representing V as a function of T_a (Fig. 2), assuming that 50% of the entire stored energy is represented by the latter three recovery stages, as is actually the case for irradiated and cold-worked metals. However, two remarks must be made: (*A*) The presence of a rather high number of impurities occluded in the crystalline structure of the deposits retards the different recovery steps so that the processes succeeding one another become less pronounced and tend to overlap. (*B*) It is more the secondary effects of the recovery stages III and IV which can be observed by x-ray diffraction methods, namely the vacancy migrations. Their occurrence makes a rearrangement of the dislocation network within the crystal lattice possible and thus diminishes the microstrains. Results are reported in Table I. Those obtained from the deposits produced at low and medium thiourea concentrations compare reasonably well with the values given by the literature, those deposits produced at high thiourea concentrations do not. But rather than to look for a good agreement between literature and experimental results this comparison reveals the complexity of the structure and the recovery behavior of these electrodeposits.

Crystallite size and recrystallization.—The crystallite size varies as a function of the additive's concentration in the plating solution. The inverse of the crystallite size, $1/\langle D\rangle_{\text{eff }111}$, was plotted as a function of the initial thiourea concentration in the bath (Fig. 3). As a maximum had previously been found for the strains at 20-25 mg/l thiourea, a minimum of the grain size was observed in the same concentration range.

The average diameter $\overline{D}$ as obtained from an electron microscopical study of these electrodeposits was determined by the method of Braun (31) which relates the average volume $\overline{v}$ of the grains to its average linear dimension $\overline{\mathcal{L}}$ measured on the micrographs,

Table I. Release of stored energy in copper electrodeposits compared to the release of stored energy in cold-worked and irradiated copper

		Stage I	Stage II	Stage III	Stage IV	Stage V
Activation energy	(29)	0.1 ev	0.2-0.5 ev	0.72 ev	1.19 ev	2.1 ev
Temperature interval	(28)	−245° to −230°C	−180° to −70°C	−60° to 50°C	130°C	230°C
Values admitted for this work		−240° to −225°C	−160° to −60°C	−60° to 40°C	100°-200°C	240°C
Model	(28) (29)	close-pair annihilation id. + rearrangement in spikes	interstitial migration migration of vacancy clusters	di-vacancy migration interstitial migration	vacancy migration id.	self-diffusion id.
Release of stored energy after cold-work	(28)	0%	40%	30%	10%	10%
Release of stored energy after irradiation	(28)	25%	25%	30%	10%	10%
Release of stored energy in the electrodeposits	additive: mg/l					
	5			25%	25%	
	10			20%	30%	
	15			30%	10%	10%
	20			25%	15%	10%
	25			15%	15%	20%
	40			15%	20%	15%
	100			12%	10%	28%

Table II. Copper-thiourea, principal results of the structural analysis

Thiourea concentration, mg/l	$\overline{D}$ Electron microscope, Å	$<D>_{eff\ 111}$, Å	$<D>_{F\ 111}$, Å	Stored energy, v, cal/g	Twin fault density, β	ρ_{WS}, cm^{-2}	ρ_c, cm^{-2}	$<\epsilon_{50}^2>_{111}^{1/2}$, %	Hardness, VHN
5	1500	1350	1640	0.09	0.005	0.50×10^{11}	0.50×10^{11}	0.15	139
10	620	620	780	0.26	0.011	1.55×10^{11}	1.65×10^{11}	0.25	206
15	990	780	1640	0.11	0.005	0.65×10^{11}	0.75×10^{11}	0.16	170
20	250	180	400	0.28	0.021	2.20×10^{11}	2.30×10^{11}	0.30	335
25	470	450	1050	0.21	0.008	1.55×10^{11}	2.30×10^{11}	0.25	205
40	615	600	870	0.23	0.009	1.30×10^{11}	1.50×10^{11}	0.23	197
100	350	310	700	0.21	0.012	1.20×10^{11}	3.00×10^{11}	0.22	245

i.e., $\overline{v} = 2.57\ (\overline{\mathcal{L}})^3$. The values in Table II indicate an excellent concordance between $<D>_{eff\ 111}$ and $\overline{D}$.

The results from the electron microscopical study on the various electrodeposits are summarized in Table III.

A minimum grain size is observed at an original thiourea content of 20-25 mg/l solution.

The growth of the coherently diffracting domains with the annealing time and temperature is different for each specimen (Fig. 2). By observing the curves relating the crystallite growth to the annealing temperature at constant annealing time, a slow increase of the grain size is noticed, previous to the fast raise which gives evidence of the actual recrystallization. This slow grain growth is perhaps induced by the diffusion of vacancies from sites of high local strain toward grain boundaries and dislocations. The absorption of vacancies by dislocations leads to a complete rearrangement of the dislocation network within the lattice, thus causing an increase in crystallite size $<D>_{eff\ 111}$ as measured by Fourier techniques. These mechanisms have been described and discussed by van Bueren and Hornstra (32).

Twin faults.—No shifts of the 111 and 200 reflections were found on the x-ray diffraction patterns of the electrodeposits. This indicates a low stability or a very small number of stacking faults in the plates. The same findings were obtained from the electron microscopical study of these deposits. On the other hand the microtwin faults are numerous and easily detectable. Different interpretations exist concerning their formation in a metal electrodeposited in the presence of an additive. Most theories explain them as caused by a blocking of one of the crystal's growth directions by the additive (9). Hinton, Schwartz, and Cohen (16) explain the formation of the twin faults on the basis of a particular stacking mechanism of the (111) layers. The arrival of an additive molecule or a molecule of a reaction product thereof can have either of two effects on the structure of the crystallite: (*A*) An adsorbed foreign molecule, if similar in size to the metal atom to be deposited, may let pass an advancing growth step and permit the crystal layers to pile up continuously in a correct stacking sequence. The region around the molecule may be strained, causing dislocations, but no faults will be produced. (*B*) If the adsorbed foreign molecule is considerably larger than the metal atoms of the deposit, an advancing growth step is forced by this obstacle to change its growth direction, and the growth layers continue to pile up in a stacking sequence in reverse to the former until the molecule is covered. Thus a fault is created. In most cases the plating solution does not contain the additive dissolved in a simple molecular form but rather in

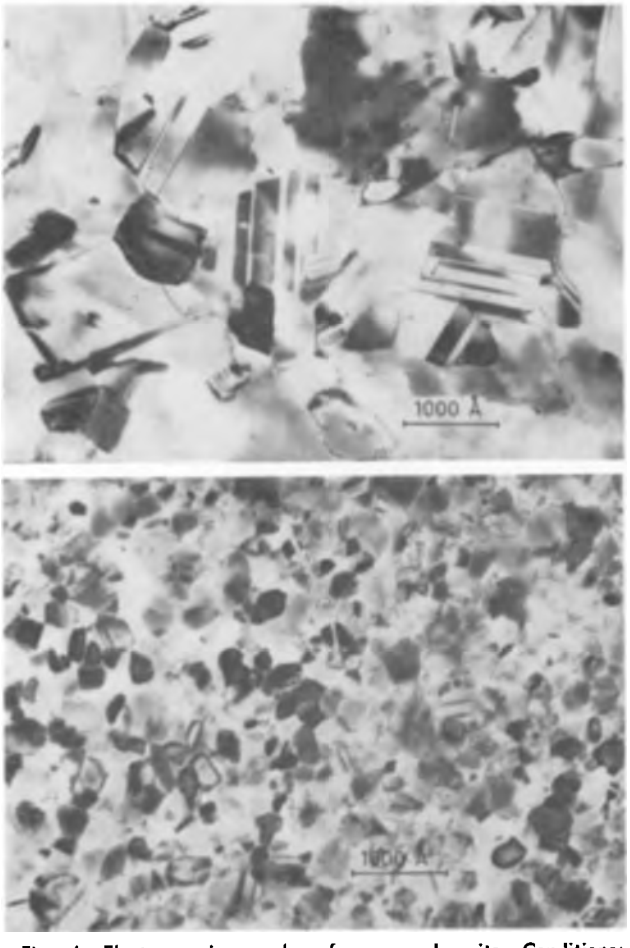

Fig. 4. Electron micrographs of copper deposits. Conditions: 1*N* H_2SO_4, 1*N* $CuSO_4$, 28 ma/cm^2, room temperature. (a) (top) solution containing 10 mg/l thiourea; (b) (bottom) solution containing 20 mg/l thiourea.

Table III. Evaluation of the electron micrographs

Additive conc, mg/l	Average grain size $\overline{D}$, Å	Appearance
5	1500	Large grains, broken up in subgrains by small angle boundaries and microtwins. Occlusions preferentially arranged in chains.
10	620	Grains of rounded shapes; occlusions more numerous and more randomly distributed than in the former deposit (Fig. 4a).
15	990	Structure different from the structure of the other deposits. Elongated grains in preferential directions. Chains of occlusions arranged in the direction of the longer axis of the crystallites. Microtwins not uniformly distributed over the plate.
20	250	Very small grains of rounded shapes and homogeneous in size (Fig. 4b).
25	470	Similar to the preceding deposit but with larger grains.
40	615	Similar to the plating deposited in the presence of 10 mg/l thiourea, but less uniform.
100	350	Needle-like structure. Small grain size. Boundaries faded and difficult to estimate.

Table IV. Reproductibility of the Fourier analysis

	$<D>_{eff\ 111}$ %	$<\epsilon_{20}^2>_{111}^{1/2}$ %	$<\epsilon_{50}^2>_{111}^{1/2}$ %	$<\epsilon_{100}^2>_{111}^{1/2}$ %	$<D>_{F\ 111}$ %
Maximum deviation	±5	±3	±5	±6	±5
Standard deviation	±2.5	±1.3	±1.7	±2.4	±2.6

complex compounds with the metal ions, the formation parameters and exact stoichiometric composition of which are not yet well understood. It is very possible that these complex compounds present themselves, according to the experimental conditions, in a form more or less favorable for the formation of microtwin faults. However, since these phenomena occur either as chemical or electrochemical reactions in the bulk of the plating solution or in the diffusion and double layer immediately adjacent to the electrode surface during electrodeposition, they do not come within the scope of this paper.

The probability of finding a twin or growth fault, *i.e.*, of finding two or more layers in an incorrect sequence, was calculated by the method of Cohen and Wagner. The influence of the instrumental line broadening and the $K\alpha_1\alpha_2$ doublet was minimized by an appropriate choice of the slits in the pathway of the incident and diffracted beams, respectively. Furthermore, a recent study by Witt and Schoening (33) makes it evident that the $K\alpha_1\alpha_2$ doublet introduces a negligible error in the determination of β, if the asymmetry of the peak is measured over the entire line profile, as is actually done in this study by means of an IBM 1620 electronic computer.

Table II reports the calculated β values of the seven plates as deposited. β varies between 0.005 and 0.021. With these probability values it is possible to calculate $<D>_{F\ 111}$, *i.e.*, the crystallite size due only to the presence of faults. The absolute value for the twin fault density as such is perhaps of little significance. What seems to be more important is the comparison between $<D>_{\text{eff }111}$ and $<D>_{F\ 111}$. There are in fact samples with high β-values for which $<D>_{F\ 111}$ is much larger than $<D>_{\text{eff }111}$ (20 mg/l and 25 mg/l thiourea). This indicates that the relative twin fault density in the deposit is low. Yet, for other samples (5, 10, and 40 mg/l thiourea) this difference between $<D>_{F\ 111}$ and $<D>_{\text{eff }111}$ is small. Hence the grains of the deposit are divided by a great number of twin faults, which is also confirmed by the electron microscopical study. Thus, the investigated samples may be classified in two groups: (*a*) deposits with predominant influence of the twin faults, $<D>_F/<D>_{\text{eff}} < 2$ (5, 10, and 40 mg/l thiourea), and (*b*) deposits for which the smallness of the coherently diffracting domains is due to other causes, $<D>_F/<D>_{\text{eff}} > 2$ (20 and 25 mg/l thiourea).

Dislocations.—Considering the fact that local strains caused by occlusions of impurities fall off with $1/r^3$, and the strains due to dislocations with only $1/r$, it can be concluded that $<\epsilon_{50}^2>^{1/2}$ is mainly due to dislocations. Furthermore, knowing the values for the rms strains and postulating a maximal separation and a minimal interaction of the dislocations as a working hypothesis, it is possible to calculate the dislocation density in the sample with the formula of Williamson and Smallman (34)

$$\rho_{WS} = \frac{16 <\epsilon_{50}^2>}{b^2}$$

where b is the Burgers vector of the dislocation ($a_o/2$ [110]). Admitting moreover the hypothesis that the recovery stages are due only to mechanisms anticipated by the literature, and also assuming that the entire energy remaining in the metal lattice in recovery stage V is the sum of the energies of individual dislocations only, and finally knowing the energy of a simple dislocation, it is possible to calculate the dislocation density. According to Cottrell (35) the energy of a single dislocation is 1.5×10^{-4} erg/cm. The dislocation densities were calculated according to both methods, the results of which are reported and compared in Table II. A good agreement between the results of the two methods was observed, the value ρ_c generally being slightly higher than ρ_{WS}. The accuracy of this method depends on the estimation of the onset of recovery stage V, which is rather hazardous at certain instances. The differences between the two methods are small indeed. In the former, it is postulated that only in the recovery stage V the energy due to dislocations alone is released. Thus it is possible to separate the strains caused by dislocations from those due to other causes. In the latter, the strains due to dislocations are separated from those of other origins, considering that they fall off with $1/r$. In both methods the hypothesis of the maximal separation and the minimal interaction between the dislocations is made. No consideration is given, however, to annexed effects as, *e.g.*, the pinning of dislocations by occlusions.

Hardness.—Microhardness measurements were made on the deposits using a Zeiss D 30 Hardness Tester, type Hanemann. All hardness values reported here, expressed in Vickers hardness number (VHN), were determined using a load of 20g. Test samples were chosen from the same area of the cathode as those used for the x-ray investigation.

Three factors seem to influence the hardness: (i) the fineness of the grain, (ii) the dislocation density, and (iii) the pinning of the dislocations by impurities. The fineness of the grain and a high dislocation density restrict the mobility of the dislocations. For this reason, the Vickers hardness number (VHN) was reported as a function of the annealing temperature T_a, together with the rms strains $<\epsilon_{50}^2>^{1/2}_{111}$ and the crystallite size as determined by the Fourier analysis of the diffraction peaks, $<D>_{\text{eff }111}$. All are variables of the same function (Fig. 2). An excellent agreement is noticed in the behavior of these quantities with the temperature, which proves that the hardness depends on $<D>_{\text{eff }111}$ and $<\epsilon_{50}^2>^{1/2}_{111}$. Furthermore it may be noted (Fig. 3) that the deposits presenting the smallest grain size and the highest strains are also those with the highest hardness number. Thus again one observes a concurrent behavior of the hardness, the inverse of the crystallite size, and the rms strains of the deposits.

Conclusions

Figure 3 could serve as a summary of the structural study carried out on the copper-thiourea system. Based on a least square calculation straight lines have been drawn between the points of measurement of the inverse of the grain size, the microstrains, and the Vickers hardness. These lines show the trend of these parameters to increase with the logarithm of the concentration of thiourea, indicating a direct action of the quantity of the additive on the structure and mechanical properties of the deposit.

The same points[4] have been connected also by curves, all of which indicate a maximum in the region of 20 mg/l thiourea. This may be interpreted as follows:

1. The region between 5 and 10 mg/l thiourea. This could be designated as the "region of normal interaction," meaning that the additive produces the expected effects on the electrodeposits, such as small grain size, strong preferred orientation,[5] and numerous twin faults. These are all effects which can be explained by relatively simple mechanisms, for example the blocking of certain growth layers by the additive.

2. The region between 15 and 30 mg/l thiourea. It could be called the "region of strong interaction." The high number of additive molecules can block all growth directions of the crystallite, thus causing large strains and producing structures of small grain sizes. For the same reason the relative twin fault density decreases and the preferred orientation of the crystallites disappears. The deposit is very homogeneous, the mechanical properties are optimal. It is the region of the additive's highest power.

3. The region between 30 and 100 mg/l thiourea. This region could be designated as the "region of complex interaction" because the effects are diverse. They seem to have a recurrent tendency, the grain size and the

[4] Except those for 15 mg/l thiourea, for which the authors feel that the measurements are not reliable enough to influence the trend of the curve.

[5] This preferred orientation was measured using a Schultz goniometer (36).

relative twin fault density increase, the preferred orientation of the crystallites reappears and the hardness number decreases. The molecules of the additive are too numerous; hence they either disturb one another in their action of blocking the growth centers, or they form less inhibitive complex compounds with the copper ions. These deposits contain within themselves areas which strongly resemble deposits of the first type of this classification (large number of twin faults, preferred crystallite orientation) and areas which resemble deposits of the second type (small grains of homogeneous size and shape).

A more detailed study of the copper-thiourea system is imperative. It should explain which one of the two interpretations: linear increase of the parameters with the logarithm of the thiourea concentration or maximum at a certain well-defined value of the additive's concentration is correct. However, our mastery of certain electrochemical problems is incomplete, and our knowledge of the reciprocal actions between electrolyte and additive in the bulk of the solution and at the electrode-electrolyte interface is fragmentary. A better understanding of these reactions is necessary before the present study can be refined and extended.

Acknowledgments

The authors are grateful to Professors P. Dinichert and J. Rossel for helpful discussions. They thank Ph. Javet for the preparation of the deposits, J. Béguin for taking the electronmicrographs, Dr. A. Braun for the hardness measurements, and E. Saurer for assistance in the numerical computations.

Manuscript received April 30, 1964; revised manuscript received Oct. 8, 1964.

Any discussion of this paper will appear in a Discussion Section to be published in the December 1965 JOURNAL.

APPENDIX

The limits of reproductibility of the Fourier analytical treatment of the profiles of x-ray diffraction lines have been determined on a coper electrodeposit by performing the following operations five succeeding times: (*a*) mounting the specimen in the specimen holder, performing the diffraction; (*b*) measuring the ordinates P'_ν according to equal intervals with a pantograph; (*c*) calculating the Fourier transforms and applying the correction of Stokes, on an electronic computer IBM 1620; (*d*) separating graphically the grain size effect from the effect of the microstrains; (*e*) calculating the quantities $<D>_{\text{eff }111}$ (size of the coherently diffracting domains), $<\epsilon_L^2>^{1/2}{}_{111}$ (rms strains) and $<D>_{F\,111}$ (crystallite size due only to the presence of faults).

The maximum deviation and the standard deviation have been calculated for these different quantities and are reported in Table IV.

From the maximum deviation on $<\epsilon_{20}^2>^{1/2}{}_{111}$ of $\pm 3\%$ the maximum deviation on V was calculated to be $\pm 6\%$.

In one case it was shown that the results obtained from two different deposits, produced under identical electrochemical conditions, strayed less than 10%. However, further investigations of this sort are needed to assert this value.

REFERENCES

1. S. Steinemann, J. P. Renaud, H. E. Hintermann, and A. Braun, *Bull. Soc. Suisse Chronométrie*, **4**, 230 (1958).
2. H. Fischer, *C.I.T.C.E.* CR. 4 Réunion Cambridge, London (1952).
3. P. B. Price, D. A. Vermilyea, and M. B. Webb, *Acta Met.*, **6**, 524 (1958).
4. D. A. Vermilyea, *This Journal*, **106**, 66 (1959).
5. B. Mills, *Proc. Roy. Soc. (London)*, **26**, 504 (1877).
6. Bouty, *Compt. rend.*, **88**, 714 (1879).
7. L. G. Palatnik, E. L. Gebstein, and J. S. Lukoz, *J. Tech. Phys. (USSR)*, **10**, 1756 (1940).
8. H. Fischer, P. Huhse, and F. Pawlek, *Z. Metallkunde*, **47**, 43 (1956).
9. H. Fischer, "Elektrolytische Abscheidung und Elektrokristallisation von Metallen," Springer-Verlag, Berlin (1954).
10. M. R. J. Wyllie, *J. Cem. Phys.*, **16**, 52 (1948).
11. R. M. Bozorth, *Phys. Rev.*, **26**, 390 (1925).
12. N. Cabrera and D. A. Vermilyea, "Growth and Perfection of Crystals," John Wiley & Sons, Inc., New York (1958).
13. S. Steinemann and H. E. Hintermann, *Schweiz. Arch. angew. Wiss. Techn.*, **26**, 202 (1960).
14. J. P. Jan, *Z. angew. Math. Phys.*, **14**, 1 (1963).
15. E. M. Hofer and P. Javet, *Bull. Soc. Suisse Chronométrie*, **4**, 779 (1962).
16. R. W. Hinton, L. H. Schwartz, and J. B. Cohen, *This Journal*, **110**, 103 (1963).
17. E. M. Hofer and P. Javet, *Helv. Phys. Acta*, **35**, 369 (1962).
18. H. Binder and H. Fischer, *Z. Metallkunde*, **53**, 161 (1962).
19. H. Seiter and H. Fischer, *Z. Elektrochem.*, **63**, 249 (1959).
20. M. S. Paterson, *J. Appl. Phys.*, **23**, 805 (1952).
21. B. E. Warren, "Progress in Metal Physics," Vol. 8, p. 147, Pergamon Press, New York (1959).
22. J. B. Cohen and C. N. J. Wagner, *J. Appl. Phys.*, **33**, 2073 (1962).
23. L. Alexander, *ibid.*, **21**, 126 (1950); **25**, 155 (1954).
24. A. R. Stokes, *Proc. Phys. Soc.*, **361**, 382 (1948).
25. C. N. J. Wagner, Thesis, Saarbrücken University (1957).
26. E. A. Faulkner, *Phil. Mag.*, **5**, 519 (1960).
27. M. McKeehan and B. E. Warren, *J. Appl. Phys.*, **24**, 52 (1953).
28. H. G. van Bueren, "Imperfections in Crystals," North-Holland Publishing Company, Amsterdam (1960).
29. A. Seeger, in "Handbuch der Physik," Vol. 7/1, S. Flügge, Editor, Springer-Verlag, Berlin (1955).
30. J. M. Corbett and R. M. Walker, *Phys. Rev.*, **110**, 767 (1958).
31. A. Braun, *Rev. mét.*, **52**, 676 (1955).
32. H. G. van Bueren and J. Hornstra, "Proc. 4th Symp. Reactivity of Solids," Elsevier, Amsterdam (1960).
33. F. Witt and F. R. L. Schoening, *J. Appl. Phys.*, **33**, 2464 (1962).
34. G. K. Williamson and R. E. Smallman, *Phil. Mag.*, **1**, 34 (1956).
35. A. H. Cottrell, "Dislocations and Plastic Flow in Crystals," p. 38, The Clarendon Press, Oxford (1963).
36. L. G. Schultz, *J. Appl. Phys.*, **20**, 1030 (1949).

Preparation and Properties of Electrodeposited Cylindrical Magnetic Films

M. W. Sagal

Bell Telephone Laboratories, Incorporated, Murray Hill, New Jersey

ABSTRACT

A process is described for the electrodeposition of cylindrical permalloy films with near zero magnetostriction. The design of a plating cell intended to achieve good uniformity of electrolyte agitation over the plating region is given. The steps used in the preparation of the wire substrate are discussed. Results showing the dependence of average alloy composition on electrolyte flow rate and pH are given, along with typical magnetic characteristics of the plated wire.

Most of the work described in the literature on the preparation and characteristics of magnetic thin films for memory applications has been concerned with films evaporated or electrodeposited on flat insulating or metallic substrates (1, 2). An alternative configuration, an anisotropic film deposited on the surface of a small diameter wire, offers a number of advantages from the device point of view (3). A process for the fabrication of this material by a continuous electrodeposition process using high agitation conditions for achieving high current densities and compositional uniformity has been described previously (4, 5). In this earlier work the importance of proper substrate preparation, including the use of a copper preplate, was pointed out. This paper describes an advanced design of a continuous plating system in some detail, including a sequence of substrate cleaning and preplate steps which has been found to give a satisfactory surface for the subsequent plating of a nickel-iron film with desirable magnetic properties. Further, the degree of composition control that can be routinely achieved by proper regulation of the plating parameters is discussed, along with typical data showing the dependence of average film composition on electrolyte flow rate and pH. Finally, values of magnetic parameters closely related to the ultimate performance of the material as a memory device are given.

The process is shown schematically in Fig. 1. The substrate is a 0.005 in. diameter hardened Be-Cu wire which is carefully drawn in order to minimize scratches caused by dirt particles collecting on the dies. It is pulled through the apparatus at 6 in./min. The wire is protected from the laboratory atmosphere by a nitrogen blanket between each process step. An electrolytic alkaline cleaner removes organic soil and loose dirt, and an acid dip removes surface oxide. The wire surface at this state, although superior to that of ordinary commercially drawn wire, still shows (Fig. 2a) a large number of pits and small scratches under high magnification. In general, 1μ magnetic films plated onto this surface with no further preparation do not have satisfactory properties. The wire is then plated with 1μ of copper from a commercial plating bath.[1] Figure 2b shows the appearance of the wire surface after copper plating. This copper plate may serve to

[1] Unichrome copper plating process of M and T Chemicals, Inc.

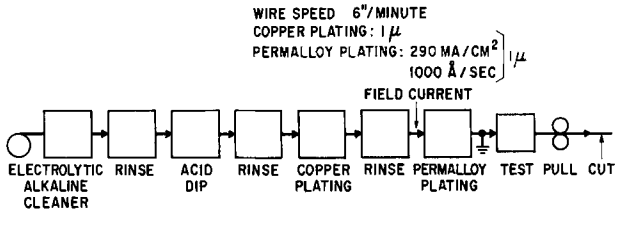

Fig. 1. Schematic view of plating process

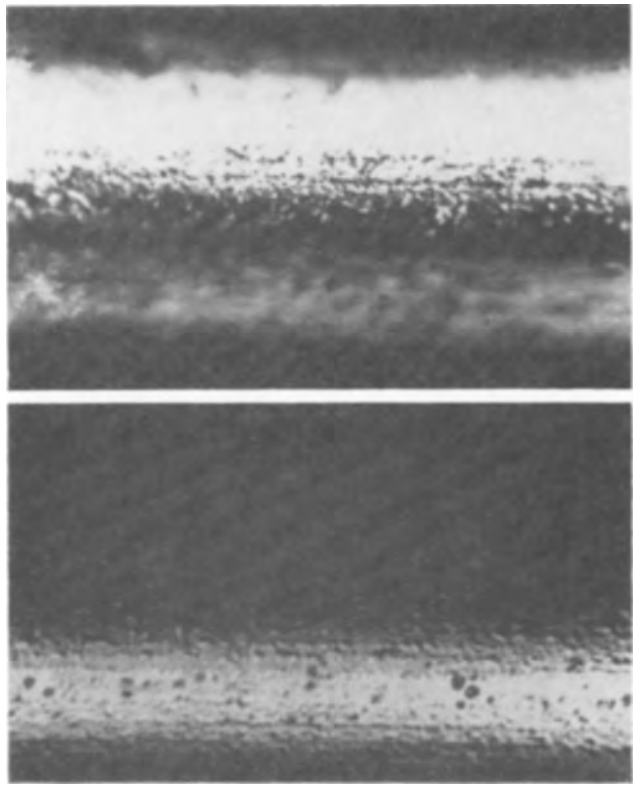

Fig. 2. Photomicrographs of Be-Cu wire surface with Nomarski type interference microscope (560X): (a) (top) after cleaning and acid dip; (b) (bottom) after copper plating.

smooth the surface although it clearly does not eliminate the surface imperfections completely. The omission of the copper plating step in the process has the effect of raising the values of dispersion and minimum bit writing current (see discussion of magnetic properties for definitions) by a factor of from 2 to 4, depending on the local surface roughness of the substrate. The wire is rinsed in ultrasonically agitated deionized water between each of these preparatory steps.

Electrical contact is made to the wire by means of a gold plated brass wheel following the last rinse tank to permit the introduction of direct current into the wire while the permalloy film is being deposited. The circumferential magnetic field from this current results in a circumferential easy axis in the film where the application requires it. Alternatively, if an easy axis along the wire length is desired, a field is applied by means of Helmholtz coils mounted outside the permalloy plating chamber.

In the high current density-high agitation permalloy plating process used here, the composition of the plated

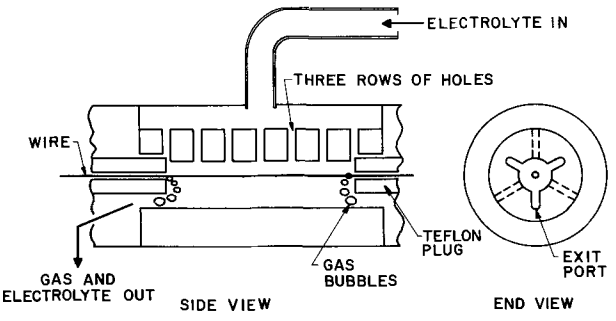

Fig. 3. Plating cell

alloy is a sensitive function of the electrolyte agitation at the wire surface. The permalloy plating chamber is designed to give uniformly high agitation along the entire length of wire being plated in order to reduce the possibility of composition gradients in the film. A centrifugal pump forces the electrolyte through the cell. Provision is made for regulating the electrolyte temperature, pH, and flow rate. The heart of the plating chamber is a Lucite tube with three staggered rows of holes drilled through the wall (shown schematically in Fig. 3). The electrolyte is forced through these holes and impinges on the surface of the moving wire at high velocity. It is removed through low impedance exit ports at both ends of the chamber. The wire passes in and out of this Lucite tube through Teflon plugs which extend into the region of high electrolyte agitation. Nitrogen gas is bubbled through the Teflon plugs to establish a plating region whose length is determined by the maximum penetration of gas bubbles into the Lucite tube. The bubbles penetrate past the Teflon tips by about one bubble diameter, which is approximately equal to the hole diameter of the Teflon plugs. The gas is swept out through the low impedance exit ports at each end by the high velocity electrolyte. This bubble seals serves two purposes. It prevents leakage of the electrolyte from the plating chamber into the rest of the apparatus, and it insures that the electrolyte agitation at the entrance and exit points of the wire is very nearly the same as the agitation in the central portion of the plating cell.

The nitrogen gas swept out from the plating region leaves the system through a tube in the outer part of the plating chamber. Since the electrolyte is not sealed off from air, a gradual drop of Fe^{2+} concentration is observed. This oxidation problem has not been serious since a change in electrolyte composition can be compensated by an adjustment in another process variable.

The importance of a near-zero magnetostriction composition in uniaxial magnetic films has been generally recognized (1). The stresses in evaporated or electrodeposited films cause severe degradation in uniaxial properties if the film is very far from the zero magnetostriction composition. For the plated wire, the composition requirements are even more severe because of the bending and twisting of the small diameter wire substrate which occurs during handling. It has been found that the average composition of the film should be held to within about $\pm$ 0.2% of the zero magnetostriction composition to avoid difficulties from strain-induced skew during memory assembly. In contrast, a detectable increase in dispersion of the film in an unstressed wire (resulting from internal stresses in the film) occurs when the film composition deviates from the zero magnetostriction composition by more than about $\pm$ 1%.

The required control of composition can be obtained by proper control of plating parameters. The composition of the plated alloy depends on bulk bath composition, temperature, pH, agitation, and plating current density. Electrolyte agitation affects the composition of the plated film through its effects on depletion layer

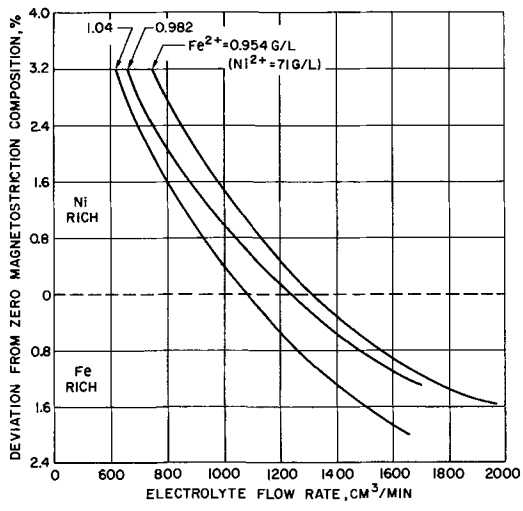

Fig. 4. Dependence of film composition on electrolyte flow rate (sulfamate bath). The zero on the ordinate corresponds to about 20% Fe. A composition "0.8% Fe rich" is therefore 20.8% Fe.

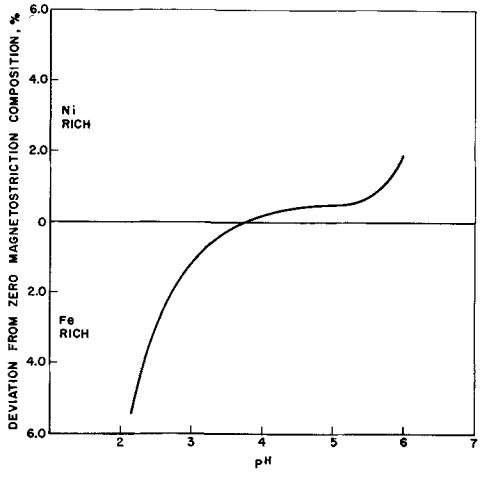

Fig. 5. Dependence of film composition on electrolyte pH (sulfate-chloride bath).

thickness and the composition of the electrolyte next to the substrate (which is in general different from the bulk composition). For a fixed plating cell geometry, agitation is dependent on the electrolyte flow rate. Figure 4 shows how the composition of the film, determined by x-ray fluorescence, depends on electrolyte flow rate with other parameters held constant. The probable effect of a change in plating cell geometry will be to move the curves of Fig. 4 along the flow rate axis. The increase in Fe content of the film with increasing flow rate (*i.e.*, increasing agitation) is in accord with the expected effect of decreased depletion layer thickness on the deposition rate of the more readily deposited metal (6) (Fe in this case).

Figure 5 illustrates the dependence of film composition on bath pH with other parameters held constant. The increase in Fe content below pH = 4 may be associated with a slight drop in cathode efficiency at low pH. This would increase the proportion of the more readily deposited metal in the alloy in a way similar to a decrease in current density (6).

In routine operation, the composition is measured indirectly by a magnetostriction measurement. One end of a plated wire is clamped and the other end twisted through a known angle. The resultant helical stress in the film introduces an easy axis skew, which is measured by the method of Belson (7). The sense and magnitude of the induced skew is a measure of

Table I. Magnetic characteristics

	$I_{b_{MIN}}$, ma	$I_{b_{MAX}}$, ma (with $H_\perp = 0$)
$H_{\perp_{WRITE}} = 9$ oe:	4	35
6 oe:	8	38
4 oe:	14	48
3 oe:	23	57
Belson α_{90}	$= 1.2°$	
Belson skew	$= 0.3°$	
H_K (loop tracer)	$= 3$ oe	

the deviation of the average film composition from the zero magnetostriction alloy.[2]

The plating conditions are then adjusted until the magnetostriction is as close to zero as possible (corresponding to a composition of about 20% Fe, balance Ni). For example, the electrolyte flow rate or pH can be changed to modify the alloy composition, as indicated in Figs. 4 and 5. The average film composition can be controlled to ± 0.1%.

X-ray fluorescence composition measurements are based on an average over 3 feet of plated wire. The magnetostriction test provides a measurement of average composition over 1 in. lengths of wire. Measurements of magnetostriction over a series of adjacent 1 in. segments give the same result which shows that any composition variations along the wire length must be on a scale $<<$ 1 in. Further, the absence of bad bits resulting from magnetostriction effects when the wire is incorporated into experimental memory planes with approximately 0.05 in. bit centers (3) indicates that significant compositional variations along the wire are absent. Although the type of plating cell described here is designed to minimize agitation inhomogeneities along the plating length, experiments have not yet been carried out to measure composition gradients through the film thickness. In principle, one source of composition gradient often found in plated films because of the build-up of a depletion layer (8) should be absent here, since wire entering the plating cell encounters a steady state depletion layer.

Both sulfate-chloride (2) and sulfamate (4) baths have been used successfully.

Magnetic Properties

The most significant magnetic characteristics of the plated wire, as determined by an on-line pulse test, are given in Table I. The on-line test permits continuous monitoring of memory characteristics as the wire is produced. Only properties of films with the easy axis around the wire circumference are described here, since this type of film has been most thoroughly studied. Some of the characteristics of these films have been previously given (3).

A ½ in. long coil which supplies a hard direction field is mounted at the end of the plating apparatus. This coil defines the length of wire under test, and is long enough to effectively eliminate the geometry-dependent demagnetizing field in the hard direction. The pulse program is shown in Fig. 6. The parameters of primary interest are:

1. $I_{b_{min}}$, the bit writing current (*i.e.*, the current producing the easy direction field) needed to switch 90% of the available flux at a particular value of hard direction writing field $H_\perp$; and
2. $I_{b_{max}}$, the bit disturb current (with $H_\perp = 0$) which reduces the 90% written-in bit to 81% of full flux on the application of 100 disturbs. (For a 0.005 in. diameter wire, 1 ma ≡ 0.032 oe.)

[2] This technique is due to T. R. Long (to be published).

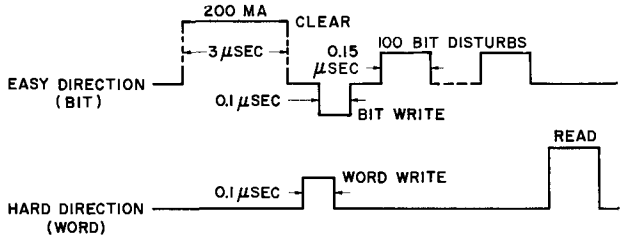

Fig. 6. Pulse program for on-line test of wire with circumferential easy axis.

Values of $I_{b_{min}}$ and $I_{b_{max}}$ for a typical film are given in Table I. Since variations of about ±20% in bit current amplitude and pulse width should be anticipated in actual memory operation, a good criterion for acceptable film quality is $I_{b_{max}} \geqq 1.5\ I_{b_{min}}$. In addition, in order to be conservative, the measurements are made using a disturb pulse width 1.5 times the bit write pulse width since the disturb effect increases with pulse width (3).

The increase of $I_{b_{max}}$ with an increase in $I_{b_{min}}$ is a general phenomenon in these films. This result implies that the specification of an undisturbed read signal equal to 90% of available flux is not a complete description of the state of the film before the application of disturb pulses. The particular combination of $H_{\perp_{WRITE}}$ and bit writing current which is chosen to switch 90% of available flux affects the resistance to domain wall motion when easy axis disturb pulses are subsequently applied.

The effects of a larger number of disturb pulses and the simultaneous application of easy and hard direction disturb pulses are measured off-line, and have been discussed elsewhere (3).

Table I also contains values of α_{90} (dispersion) and skew as measured by the Belson technique (7), as well as the anisotropy field H_K measured by a loop tracer method. These measurements are of some use in qualitatively evaluating film samples, but are a poor means of quantitatively predicting performance under pulse switching conditions.

Acknowledgments

It is a pleasure to acknowledge the contributions of J. T. Chang, I. Danylchuk, U. F. Gianola, C. E. Johnson, T. R. Long, and A. J. Perneski. The author would also like to thank K. M. Olsen and R. F. Jack for samples of Be-Cu wire and Miss S. M. Vincent and J. E. Kessler for x-ray fluorescence analysis of the films.

Manuscript received June 30, 1964; revised manuscript received October 1, 1964.

Any discussion of this paper will appear in a Discussion Section to be published in the December 1965 JOURNAL.

REFERENCES

1. E. W. Pugh, "Magnetic Films of Nickel-Iron," in "Physics of Thin Films," Vol. 1, George Hass, Editor; Academic Press, New York (1963).
2. I. W. Wolf, *J. Appl. Phys.*, **33**, 1152 (1962).
3. I. Danylchuk, A. J. Perneski, and M. W. Sagal, Proc. of the 1964 Conference on Nonlinear Magnetics, Washington, D. C.
4. T. R. Long, *J. Appl. Phys.*, **31**, 123S (1960).
5. T. R. Long, Paper presented at the Detroit Meeting of the Society, Oct. 1-5, 1961.
6. "Electrodeposition of Alloys," Vol. I, Chap. 6 and 11, Abner Brenner, Academic Press, New York (1963).
7. H. Belson, Proc. of the 1963 Conference on Nonlinear Magnetics, Washington, D. C.
8. G. H. Cockett and E. S. Spenser-Timms, *This Journal*, **108**, 906 (1961).

Fluorescent Emission Spectra in II-VI Compounds

R. E. Halsted, M. Aven, and H. D. Coghill

Research Laboratory, General Electric Company, Schenectady, New York

ABSTRACT

Fluorescent emission spectra in "pure" and variously doped single crystals of CdTe, ZnTe, and to a lesser extent CdSe and ZnSe, have been recorded at temperatures of 25°K or below. These data have been tabulated and graphically presented along with prior low-temperature data on these materials, CdS, and ZnS. The pattern of results provides evidence for the existence of analogous defects throughout the II-VI family of compounds.

The fluorescent emission properties of the large band-gap II-VI compounds, particularly ZnS and CdS, have been investigated extensively in the past. Preparative procedures for maximizing specific emission bands in these materials in powder form have been established. Much attention has been given to models which at least provided a conceptual basis for organizing the results (1). Currently considerable attention is being given to the development of improved techniques for the preparation and purification of single crystals of II-VI compounds (2-4). Much progress has been made. One can therefore anticipate increasing application in the near future of diverse optical and electrical measurements to the determination of the position and nature of defect levels in these materials.

This work should be significantly expedited by making maximum use of evidence that analogous defect levels may exist in the various members of a given class of compounds. Similarities in preparative procedures, experimental behavior, and interpretation of results can thus be exploited. Prior studies of the ZnCdS phosphor system have provided a nice illustration of the utility of fluorescent emission data for establishing such analogs. With improved preparative control, it was established that the emission bands attributable to a given impurity exhibit a systematic shift in wavelength with host lattice variation from ZnS to CdS (5-7). Comparatively limited attention has been given to an extension of this evidence for analogous emission bands from the sulfides into the selenides and tellurides of zinc and cadmium (8-10).

In the course of investigations of II-VI compounds at this Laboratory, we have recorded emission spectra in "pure" and doped single crystals of these materials, generally at ~25°K. Data on the compounds CdTe and ZnTe provide a substantial addition to prior work. Emission due both to near-band-edge radiative recombination processes and deep impurity levels has been observed. Because of the survey nature of this work, these results will eventually be extended and perhaps some cases of inaccurate identification established.

We have noted, however, that the results do indeed provide a rather convincing extension of the evidence for analogous emission processes found in the ZnCdS system. A compilation of these data with prior work has been found to have current value in suggesting probable analogs between the transitions in different compounds. For example, it has provided a basis for appraising the relevance of electrical transport and optical measurements in p-type ZnTe and CdTe to a general understanding of acceptor defects in this class of materials. For this reason we have prepared the following tabulation of our data and selected prior published data on the positions of fluorescent emission bands for impurities from columns I, III, and VII of the periodic table in the sulfides, selenides, and tellurides of zinc and cadmium. Column V and other impurities were not included because of the limited amount of data now available for more than one II-VI compound. The information is also presented graphically. In addition to cataloging the new results, this form of presentation dramatizes the evidence suggested by the order in the data for probable analogs in the fluorescent emission processes in these materials. Some questions arising from these correlations are noted. However, no attempt is made to provide a critical examination of the evidence for the nature of the various recombination processes involved.

Experimental Procedure

Our method for taking fluorescent emission data has been conventional in nature. For data at liquid hydrogen temperature, samples were mounted with an adhesive varnish (G.E. 7031) on a coolable copper substrate in an evacuated housing. They were masked, except for an observation slit, with indium foil. A thermocouple, cemented in pressure contact with the edge of the crystal but shielded from exposure to the excitation radiation by the foil, was generally used to monitor the temperature of the sample. Samples were immersed in liquid helium for 4°K data. A 1000-w filtered high-pressure mercury arc (G.E. AH-6) was used as an excitation source. Both LiF prism and grating spectrometers were employed as dictated by resolution and wavelength range requirements. Spectrometer output was measured with either cooled PbS, infrared sensitive photomultiplier (RCA 7102), or 1P21 photomultiplier detectors. Spectrometer and detector combinations were calibrated in wavelength and response with standard sources.

Our results have been obtained primarily on single crystal material prepared at this Laboratory. Single crystals of all materials except CdTe have been grown from the vapor (11). CdTe crystals were grown from the melt (3). Samples of commercially available vapor-grown CdS and CdSe were also employed (12, 13). Data on material doped both before crystal growth and by diffusion after crystal growth have been recorded. Cleaved surfaces were preferably employed for observations of fluorescence. In order to obtain comparable results on chemically etched surfaces, some experimentation with etching procedures for each material was generally required.

Compilation Procedure

Tables I through VI present a compilation of our emission data and prior published data for the compounds ZnS, CdS, ZnSe, CdSe, ZnTe, and CdTe, respectively. For convenient reference we have also cited the low temperature band gap, E_g; the energy for exciton formation, E_{ex}; and the longitudinal optical phonon energy, $E_p(\mathrm{LO})$. E_g is established by adding to E_{ex} the exciton binding energy determined by observation of both ground and first excited states. Our somewhat arbitrary selection of prior data was prompted by considerations such as the following.

Data taken at 80°K or below have been cited wherever possible for several reasons. The position of low-temperature emission peaks can be related to well-defined band-gap energies for estimates of the binding energy of the defect levels involved. The emis-

sion peaks are also narrower and their maxima better defined. In some cases LO phonon structure can be resolved providing a measure of the transition energy unobscured by LO phonon emission. Between 0° and 80°K the band gap decreases in energy only ~0.01 ev. References were also favored which were concerned with tracing a given emission band through a variation in host lattice composition. Some recent references are cited to supply an entry into the literature concerned with providing a detailed description of specific recombination mechanisms. In some cases our data have been tabulated and prior references also listed. In most such cases we are assuming responsibility for some difference in detail, *e.g.*, temperature, but the results are regarded as being in agreement.

The peak positions given for emission bands with unresolved LO phonon structure are the energy equivalent of the wavelength of maximum emission on an energy per unit wavelength ($E/\Delta\lambda$) *vs.* wavelength plot. Most published data on these compounds are so plotted. The use of the physically more significant photons per unit photon energy ($P/\Delta E_p$) *vs.* photon energy plot would shift the position of broad peaks to somewhat lower energies since $(P/\Delta E_p) \propto \lambda^3(E/\Delta\lambda)$. Widths at half-height of these broad emission peaks are tabulated in parentheses after the peak position to provide an approximate description of the emission band. Evidence for small variations in the position of these spectra with crystal structure and identity of compensating defects have been omitted even though well established (5). However, some cases of extreme variation are noted.

Fluorescent emission of near-band-gap energy in II-VI compounds at low temperatures occurs as resolved sets of equally spaced emission lines formed by the simultaneous emission of photons and 0,1,2,--LO phonons (14). The relative intensities of lines within a set have been described by a relation of the form $I_n = I_o N^n/n'$ (15). I_n is the relative intensity of the $(n+1)$th line involving the emission of a photon plus n LO phonons. N is the mean number of emitted phonons. Although the accuracy of this description appears to be poor when applied to experimental results with sufficiently small N, we have used it as a basis for characterizing spectra with resolved LO phonon structure. We have tabulated the position of

Table I. Data on fluorescent emission spectra in ZnS

E_g(14°K) = 3.84 ev (cubic), 3.91 ev (hexagonal).
E_{ex}(14°K) = 3.800 ev (cubic), 3.873 ev (hexagonal) (18).
E_p(LO) = 0.044 ev (14).

Dopant	Peak position [N] or (W/2)	Temp, °K	References
U, Cl	3.782* ev	10	(19)
U, Cl	3.76*	10	(19)
U, Cl	3.64* [1.0]	10	(19, 16)
U, Cl	3.00 (~0.25)	80	(19, 5)
U, D	2.63-2.75 (0.30)	80	(19, 20)
Ag > D	3.20 (0.25)	80	(5)
Ag ≈ D	2.86 (0.25)	80	(5)
Ag, Ag-D	2.0 (0.6)	80	(5, 21, 22)
Cu > D	2.85 (0.25)	80	(20)
Cu ≈ D	2.38 (0.28)	80	(20)
Cu	1.83 (0.50)	80	(21)
Cu-In	1.55 (0.50)	80	(23, 5)
Cu	0.84 (structured)	80	(24, 25)
Au-D	2.64 (0.28)	80	(6, 26)
Au-D	2.34 (0.26)	80	(6)
Au-In, Au-Ga	1.5 (0.5)	80	(5)

Table II. Data on fluorescent emission spectra in CdS

E_g(4.2°K) = 2.583 ev.
E_{ex}(4.2°K) = 2.554 ev (27).
E_p(LO) = 0.038 ev (14).

Dopant	Peak position [N] or (W/2)	Temp, °K	References
U	2.554* ev	1.6	(27, 42)
U	2.547* [3 × 10⁻⁴]	1.6	(27, 42)
U	2.536* [8 × 10⁻³]	1.6	(27, 42)
U	2.39*-2.42* [0.8]	25	(16)
U, D	1.70 (0.25)	80	(23, 28)
U, D	1.40 (0.36)	80	(23)
Ag	2.00 (0.20)	80	(5)
Ag	1.68 (0.25)	80	(5)
Au	1.94 (0.22)	80	(6, 29)
Au	1.55 (0.4)	300	(6)
Au	1.05 (0.28)	80	(6, 29)
Cu	1.57 (0.23)	80	(29)
Cu	1.18 (0.24)	80	(29)
Cu	0.75 (structured)	80	(24, 25)

Table III. Data on fluorescent emission spectra in ZnSe

E_g(4°K) = 2.820 ev (cubic).
E_{ex}(4°K) = 2.800 ev (cubic) (30).
E_p(LO) = 0.031 ev (14).

Dopant	Peak position [N] or (W/2)	Temp, °K	References
U, Cl	2.802*	4	(23)
U, Cl	2.797* [1 × 10⁻²]	4	(23)
U	2.793* [5 × 10⁻²]	4	(23, 32)
U	2.783* [0.3]	4	(23, 32)
U	2.69*-2.75* [0.6]	25	(23, 32, 16)
U	2.53 (0.15)	25	(23, 32)
U, D	2.07 (0.25)	25	(23, 32, 33)
Ag	2.61 (0.16)	25	(23)
Ag	2.22 (0.22)	25	(23)
Cu	2.34 (0.18)	25	(23, 8)
Cu	1.95 (0.18)	25	(23, 8, 33, 34)
Cu	1.25 (0.21)	25	(23, 35)
Au	1.78 (0.36)	170	(34)
U	1.45 (0.20)	25	(23)
U	0.78 (0.2)	25	(23, 35)
U	0.63 (0.2)	25	(23, 35)
U	0.56 (0.2)	25	(23, 35)

Table IV. Data on fluorescent emission spectra in CdSe

E_g(1.8°K) = 1.840 ev.
E_{ex}(1.8°K) = 1.824 ev (36).
E_p(LO) = 0.027 ev (14)

Dopant	Peak position [N] or (W/2)	Temp, °K	References
U	1.82*	25	(23)
U	1.81*	25	(23)
U	1.74*	25	(23, 16)
U	1.53 (0.15)	25	(23)
U	1.44 (0.15)	25	(23)
Ag-D	1.35 (0.20)	80	(29)
Cu-D	1.03 (0.20)	80	(29, 23)
Au-D	0.85 (0.20)	80	(29)

Table V. Data on fluorescent emission spectra in ZnTe

E_g(4°K) = 2.39 ev.
E_{ex}(4°K) = 2.382 ev (37).
E_p(LO) = 0.026 ev (14).

Dopant	Peak position [N] or (W/2)	Temp, °K	References
U	2.381*	25	(23)
U	2.375* [1 × 10⁻²]	25	(23)
U	2.31*-2.35* [0.23]	25	(23, 16)
U, Cu	2.24*, 2.21 (0.07)	25	(23)
Ga, In	2.11 (0.12)	25	(23)
U	1.88 (1.986*)	25	(38, 23)
U, Ga	1.65, 1.56 (0.25)	25	(23)
U	1.05 (0.12)	25	(23)
U	0.98 (0.12)	25	(23)
Ag	2.28*	25	(23)
Ag	1.92 (0.19)	25	(23)
Cu	1.97 (0.13)	25	(23)
Cu	1.47 (0.18)	25	(23)
Au	1.33 (0.2)	25	(23)
Ga	0.67 (0.16)	25	(23)

Table VI. Data on fluorescent emission spectra in CdTe

E_g(2.1°K) = 1.605 ev.
E_{ex}(2.1°K) = 1.595 ev (39, 40).
E_p(LO) = 0.021 ev (14).

Dopant	Peak position [N] or (W/2)	Temp, °K	References
U	1.595*	25	(14)
U	1.593* [1 × 10⁻²]	25	(14)
U	1.589* [4 × 10⁻²]	25	(14)
U	1.52*-1.56* [0.3]	25	(16)
U	1.45*	25	(14)
D	1.40-1.44 (0.08)	25	(14)
U	1.10-1.15 (0.11)	25	(23)
D	1.05-1.11 (0.11)	25	(23)
Ag	1.49*	25	(14)
Ag	1.19 (0.15)	25	(23)
Cu	1.23 (0.14)	25	(23)
Cu	0.88 (0.18)	25	(23)
Cu	≤0.55 (0.08)	25	(23)
Au	1.27 (0.11)	80	(41)
Au	0.72 (0.10)	25	(23)

the highest energy peak of the series and identified such energies with an asterisk. $N(\equiv I_1/I_0)$ is given in square brackets for a number of cases where the peaks were reasonably well resolved. We have attempted to select those band-edge spectra which appear to be dominant *in pure materials*. Some variability has been observed in the position of the exciton absorption line, and hence in the band gap in nominally pure materials (30). We have therefore tabulated band-edge emission data from one source for each compound, although citing other references. This procedure should permit a more significant determination of the energy differences between the various transitions listed.

Emission bands are identified with the addition of specific dopants. Generally speaking, there remains uncertainty in II-VI compounds as to the specific nature of the defect at which an emission process originates. Compensating native defects, isolated or associated, may be involved as well as the dopant. The specified impurity addition is therefore indicative of preparative procedure, but cannot be regarded as identifying the origin of the emission in any precise way. In presenting the data some abbreviations were introduced. The symbols for specific elements are generally employed with the exceptions of U and D denoting "undoped" (but not necessarily pure) and "donor" impurity, respectively. The use of D indicates that essentially the same result has been obtained with several impurities from columns III or VII of the periodic table. If D is linked to another element by other than a comma, *e.g.*, Ag > D, Ag ≈ D, Ag — D, the presence of both impurities is believed to be required. In some compounds the results have been shown to be dependent on the relative proportion of impurities; hence, *e.g.*, Ag > D.

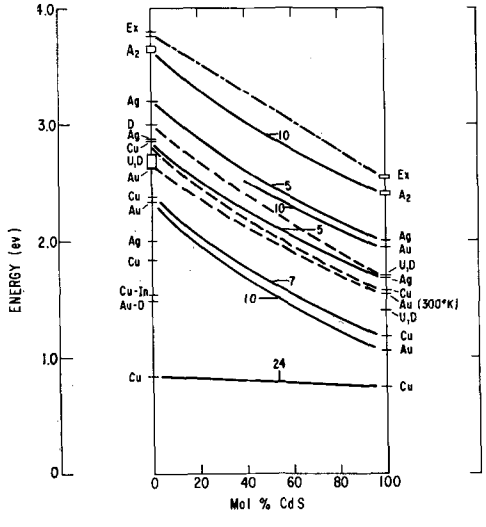

Fig. 1. Fluorescent emission energies in ZnCdS system

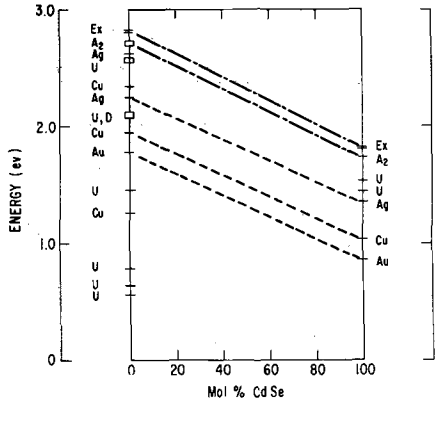

Fig. 2. Fluorescent emission energies in ZnCdSe system

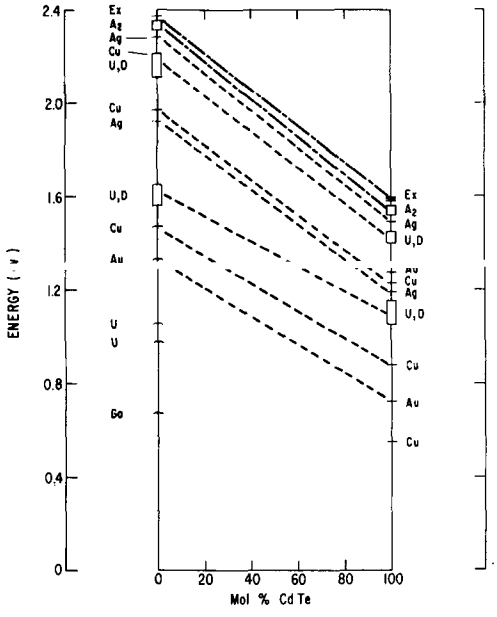

Fig. 3. Fluorescent emission energies in ZnCdTe system

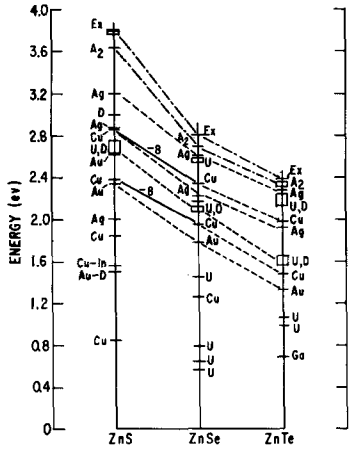

Fig. 4. Fluorescent emission energies in ZnSSeTe system

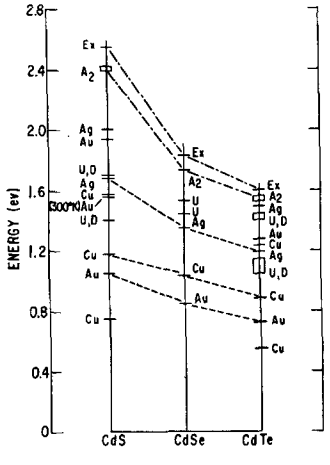

Fig. 5. Fluorescent emission energies in CdSSeTe system

This information is presented graphically in Fig. 1 to 5. The pattern of analogous emission processes suggested by the data is indicated by the connecting lines. Solid lines are employed where correlations have been previously established by a study of the relevant ternary compounds through a range of compositions. A reference is cited for each case of this type. Broken lines are used in two cases where the validity of the correlation appears assured even though their position

in compounds of intermediate composition has not been ascertained. Emission attributed to bound or free excitons is termed "exciton" emission and identified by its proximity in energy with exciton absorption or reflectance data. The energy scale of Fig. 1 to 5 does not permit an indication of the detail observable with high resolution in this region. Analogs of the "green edge emission" or "A_2" emission of CdS are identified by the unique characteristics of their spectra (16). Dashed lines are employed where the correlations are suggested by the pattern of results but have not otherwise been confirmed. If the correlations prove generally valid, one might expect the connecting lines to approximate the positions of emission bands in intermediate compounds. The curvature of these lines can, however, be substantial. It may perhaps be extreme in the case of ZnSeTe compounds where the band gap has been reported to go through a minimum at a composition $ZnSe_{0.35}Te_{0.65}$ (17).

Discussion

The data presented in Fig. 1 through 5 demonstrate that there exists a general regularity in the way the positions of the levels belonging to the different luminescence centers vary from compound to compound. Examination of the data for the more detailed features of such correlative relationships, however, generates many questions which at present have no simple or unambiguous answers. Some examples are illustrative.

Emission attributed to the recombination of excitons bound to various defects gives rise to quite complex spectra at liquid helium temperatures. Some prominent examples are included in Tables I and VI, although not resolved in Fig. 1 to 5. In the case of CdS, Zeeman effect studies of these emission and associated absorption spectra have identified three types of transitions present as: (*a*) exciton bound to a neutral donor defect, (*b*) exciton bound to an ionized donor, and (*c*) exciton bound to a neutral acceptor (27, 42). Free exciton recombination is also observed and identified by its coincidence in energy with exciton absorption. It becomes relatively more prominent at higher temperatures where the binding energy of an exciton to the above defects is small compared to kT. Analogous recombination processes occur in other compounds (43-45). Tentative identification of bound exciton processes in II-VI compounds other than CdS may be feasible by assuming that the energy by which the exciton is bound to a defect, E_{ex}-E_{exd}, is approximately a constant fraction, F, of the defect binding energy, E_d, for a given type of shallow defect. Here E_{exd} is the formation or recombination energy for an exciton bound to the defect. If the nature of a transition becomes known from magneto-optical studies, a knowledge of F should conversely permit an estimate of the position of the defect level involved. In silicon $F \approx 0.1$ for excitons bound to either donors or acceptors with defect binding energies up to 0.15 ev (43). The applicability of this relationship to the II-VI class of compounds requires the approximate validity of the effective mass approximation and a relatively constant ratio of hole-to-electron masses. For an exciton bound to a neutral donor in CdS a value for F of $0.0066/0.033 = 0.20$ was found (27). Comparable ratios for the dominant emission in the exciton region for n-type CdTe and ZnSe are indicated. The magnitude of F for the exciton bound to a neutral acceptor is uncertain in CdS since the depth of the active acceptor level is not known. Since the effective mass of electrons is smaller than the effective mass of holes in II-VI compounds, F may be smaller for acceptor defects than for donor defects (46).

Analogs of the green edge emission in CdS have been identified by their unique doublet structure. Currently two types of defect levels observed in electrical transport measurements could provide recombination transitions of appropriate energy. A correlation has recently been made between these spectra and the presence of double-acceptor levels near the conduction band in II-VI compounds (47). An explanation of the emission energy and structure, the temperature dependent characteristics, and the variability of the spectra with crystal doping appears possible on this basis (16). However, electrical measurements have also shown the presence of acceptor levels approximately 0.05 ev from the valence band in CdTe and ZnTe (48-50). Analogs of these levels in the selenides and sulfides would permit donor-acceptor-pair emission (51) in the energy ranges of interest. It remains to be determined whether one or both of these mechanisms are operative.

Figures 1 to 5 suggest that the pattern of "high" and "low" energy emission bands identified in the literatube for Cu, Ag, Au, and "self-activated" ZnCdS phosphors exists for the entire II-VI family of compounds. Thus the extensive effort which has been devoted to the identification of such emission processes as those occurring at 2.85 and 2.38 ev for ZnS:Cu, 2.7 ev for self-activated ZnS and 2.00 ev for CdS:Ag has immediate relevance in other compounds if the correlations are valid (52). Discrepancies remain to be resolved. For example, the "high energy Ag" band occurring at 2.00 ev in CdS:Ag has been attributed to a transition between a level near the conduction band and the valence band (53). The suggested analog in ZnTe, however, appears to involve a transition between the conduction band and a relatively shallow acceptor level which can be seen electrically (50).

In ZnS and CdS a structured emission band can be observed at ~0.8 ev. The structure is attributed to internal Cu transitions that are relatively uninfluenced by host lattice composition. Other transitions occur in the red and near infrared in ZnS which appear to depend strongly on the identity of both donor and acceptor impurity. ZnSe and ZnTe samples generally are found to exhibit infrared emission at photon energies below those discussed above. Further investigation may establish analogs among these.

Acknowledgments

The authors gratefully acknowledge contributions by their colleagues at the Research Laboratory, both by way of informative discussions and material for spectral analysis. L. H. Esmann provided skillful assistance with much of the experimental work.

This investigation has been supported in part by the U.S. Army Engineer Research and Development Laboratories, Fort Belvoir, Virginia, and in part by the Aerospace Research Laboratory, Office of Aerospace Research, U.S. Air Force.

Manuscript received Sept. 11, 1964. This paper was presented at the Toronto Meeting, May 3-7, 1964.

Any discussion of this paper will appear in a Discussion Section to be published in the December 1965 JOURNAL.

REFERENCES

1. See, *e.g.*, H. W. Leverenz, "Luminescence of Solids," John Wiley & Sons, Inc., New York (1950), or the more recent work D. Curie, "Luminescence in Crystals," John Wiley & Sons, Inc., New York (1963).
2. M. Aven and H. H. Woodbury, *Appl. Phys. Letters*, **1**, 53 (1962).
3. M. R. Lorenz and R. E. Halsted, *This Journal*, **110**, 343 (1963).
4. L. R. Shiozawa, J. L. Barrett, G. P. Chotkevys, S. S. Devlin, and J. M. Jost, Aeronautical Research Laboratory Contract No. AF33(616)-6865, Final Report, Period January 1960-December 1961 (unpublished).
5. W. van Gool, *Philips Research Repts.*, **13**, 157 (1958); Philips Research Repts. Suppl. No. 3 (1961).
6. M. Avinor, *This Journal*, **107**, 608 (1960).
7. H. Ortmann and H. Treptow, *Z. Naturforsch*, **16a**, 910 (1961).
8. F. F. Morehead, *J. Phys. Chem. Solids*, **24**, 37 (1963).

9. A. A. Bundel, Z. I. Guratskaya, and M. N. Noskova, *Optics and Spectroscopy*, **11**, 352 (1961).
10. M. Avinor and G. Meijer, *J. Chem. Phys.*, **32**, 1456 (1960).
11. W. W. Piper and S. J. Polich, *J. Appl. Phys.*, **32**, 1278 (1961).
12. Eagle-Picher Company, 1948 American Building, Cincinnati, Ohio.
13. Harshaw Chemical Company, 10064 Chester Ave., Cleveland, Ohio.
14. R. E. Halsted, M. R. Lorenz, and B. Segall, *J. Phys. Chem. Solids*, **22**, 109 (1961).
15. J. J. Hopfield, *ibid.*, **10**, 110 (1959).
16. R. E. Halsted and B. Segall *Phys. Rev. Letters* **10** 392 (1963).
17. S. Larach, R. E. Shrader, and C. F. Stocker, *Phys. Rev.*, **108**, 587 (1957).
18. J. L. Birman, H. Samelson, and A. Lempicki, *General Telephone and Electronics Research and Development Journal*, **1**, 2 (1961). Exciton binding energy of 0.04 ev estimated.
19. H. Samelson and A. Lempicki, *Phys. Rev.*, **125**, 901 (1962) reports data on cubic ZnS. Other data are on hexagonal ZnS.
20. W. van Gool and A. P. Cleiren, *Philips Research Repts.*, **15**, 238 (1960).
21. M. H. Aven and R. M. Potter, *This Journal*, **105**, 134 (1958). Data converted to energy/$\Delta\lambda$ *vs.* λ plot to give tabulated λ_{max}(ev).
22. E. F. Apple and F. E. Wiliams, *ibid.*, **106**, 224 (1959).
23. Our data.
24. P. F. Browne, *J. Electronics*, **2**, 1 (1956). Position given for highest energy peak of structured emission band.
25. I. Broser, R. Broser-Warminsky, H. J. Schulz, Proc. Internat'l Conf. on Semiconductor Physics, Prague, 1960, p. 771.
26. S. T. Henderson, P. W. Ramby, and M. B. Halstead, *This Journal*, **106**, 27 (1959).
27. D. G. Thomas and J. J. Hopfield, *Phys. Rev.*, **128**, 2135 (1962); *ibid.*, **122**, 35 (1961).
28. B. A. Kulp, *ibid.*, **125**, 1865 (1962); B. A. Kulp and R. H. Kelley, *J. Appl. Phys.*, **31**, 1057 (1960).
29. See ref. (10). Absence of high energy Ag, Cu, or Au bands with excess activator is noted in CdSe.
30. M. Aven, D. T. F. Marple, and B. Segall, *J. Appl. Phys.*, **32S**, 2261 (1961). This reference notes a variability between samples which is believed due to variable content of sulfur impurity in General Electric ZnSe. Band edge data cited are from cubic crystals grown from high purity Eagle Picher ZnSe powder. (See M. Aven and P. R. Kennicott, Scientific Report No. 8, Contract No. AF19(628)-329, August 1964). Data on hexagonal ZnSe have also been reported (31).
31. E. F. Gross and L. G. Suslina, *Soviet Phys.-Solid State*, **4**, 2689 (1963).
32. D. C. Reynolds, L. S. Pedrotti, and O. W. Larson, *J. Appl. Phys.*, **32S**, 2250 (1961) enumerates additional emission bands in this energy region.
33. S. Larach, *J. Chem. Phys.*, **21**, 756 (1953).
34. L. Ya. Markovskii and R. I. Smirnova, *Optics and Spectroscopy*, **10**, 98 (1961).
35. B. A. Kulp and R. M. Detweiler, *Phys. Rev.*, **129**, 2422 (1963).
36. J. O. Dimmock and R. G. Wheeler, *J. Appl. Phys.*, **32S**, 2271 (1961).
37. A. C. Aten, C. Z. van Doorn, and A. T. Vink, Proc. Internat'l Conf. on Semiconductor Physics, Exeter, 1962, p. 696.
38. R. E. Dietz, D. G. Thomas, and J. J. Hopfield, *Phys. Rev. Letters*, **8**, 391 (1962).
39. D. T. F. Marple and B. Segall, To be published.
40. D. G. Thomas, *J. Appl. Phys.*, **32S**, 2298 (1961).
41. D. de Nobel, *Philips Research Repts.*, **14**, 361 (1959).
42. D. C. Reynolds and C. W. Litton, *Phys. Rev.*, **132**, 1023 (1963).
43. J. R. Haynes, *Phys. Rev. Letters*, **4**, 361 (1960).
44. D. G. Thomas, M. Gershenzon, and J. J. Hopfield, *Phys. Rev.*, **131**, 2397 (1963).
45. D. R. Hamilton, W. J. Choyke, and Lyle Patrick, *ibid.*, **131**, 127 (1963).
46. W. Kohn, footnote ref. (43).
47. M. R. Lorenz, B. Segall, and H. H. Woodbury, *Phys. Rev.*, **134**, A751 (1964).
48. M. R. Lorenz and B. Segall, *Phys. Rev. Letters*, **7**, 18 (1963).
49. D. G. Thomas and E. A. Sadowski, *J. Phys. Chem. Solids*, **25**, 395 (1964).
50. M. Aven and B. Segall, *Phys. Rev.*, **130**, 81 (1963).
51. D. G. Thomas, M. Gershenzon, and F. A. Trumbore, *ibid.*, **133**, A269 (1964).
52. See, *e.g.*, S. Shionoya, T. Koda, K. Eraand, and H. Fijiwara, *J. Phys. Soc. Japan*, **19**, 1157 (1964).
53. C. C. Klick, *Phys. Rev. Letters*, **2**, 418 (1959).

Luminescence of Europium in the Ternary System: La_2O_3-Gd_2O_3-Y_2O_3

R. C. Ropp[1]

Sylvania Electric Products Inc., Towanda, Pennsylvania

ABSTRACT

A detailed study of a rare-earth oxide ternary system activated by Eu^{+3} has shown that these phosphors are host-sensitized. There are matrix excitation bands present as well as a band attributed to perturbation of excited states of Eu^{+3}. An exciton mechanism is believed responsible for the matrix band and the field perturbation of the excited Eu^{+3} state.

The broad field of phosphors comprising rare-earth oxides activated by rare earths has been neglected in the past, primarily because of availability and purity of rare-earth materials. Recently, however, there has been a renaissance of interest in the fluorescence of rare earths, chiefly because of their applicability to the field of lasers. The earliest work by Urbain (1) stressed the cathodoluminescent properties of Gd_2O_3 and Y_2O_3 activated by small amounts of Eu, Er, Sm, or Tb. Subsequent investigations included description of the ultraviolet properties of La_2O_3:Pr (2), as well as Lu_2O_3, Sc_2O_3, or Y_2O_3, all activated by Sm (3). Later studies concentrated on Y_2O_3. Rosenberger (4) studied Y_2O_3:Er and La_2O_3:Er, and the spectroscopic transitions associated with Er^{+3} luminescence. Chang (5) studied conditions necessary for laser action of Eu^{+3} in Y_2O_3. Wickersheim and Lefever (6) gave general properties of luminescence of phosphors based on Y_2O_3 and La_2O_3, while in the most recent work, Axe and Weller (7) studied the effect of other rare-earth impurities on the luminescence of Eu^{+3} in Y_2O_3.

In an earlier work by the author (8), it was established that only three rare-earth oxides were effective as matrices in promoting rare-earth fluorescence: La_2O_3, Gd_2O_3, and Y_2O_3.[2] Of the rare-earth ions, only Sm^{+3}, Eu^{+3}, Tb^{+3}, and Dy^{+3} gave appreciable room-temperature luminescence. A study of the ternary system was conducted to define some of the mechanisms which produce luminescence in rare-earth oxide phos-

[1] Present address: Westinghouse Electric Corporation, Bloomfield, N. J.

[2] Here we designate Y_2O_3 and La_2O_3 as rare-earth compounds, although they contain no 4f electrons as does Gd_2O_3 [$4f^7$]. They do have similar chemical behavior.

phors, and to determine the energy processes which occur during the luminescent transitions. Compound formation in the ternary system is limited to the monoclinic $LaYO_3$ and to the hexagonal compound La_3YO_6 (9). Presumably, similar gadolinium compounds form.

Experimental Methods

The nitrates (or the oxides dissolved in concentrated nitric acid) of the requisite rare earths were dissolved to form 0.40M solutions. Mixtures of the ions in solution were made so that the required volumes totaled one liter before precipitation. The activator content was maintained at 2.5 mole % of the total cation content. Oxalic acid as a 10% solution was used as the precipitant, knowing the reaction to be quantitative in the presence of 5 mole % excess acid (10).

$$2M^{+3} + 3(C_2O_4) = \rightarrow M_2(C_2O_4)_2 \cdot xH_2O$$

where x = 2 to 6 when the precipitation is carried out at 80°C. The precipitate was dried overnight at 110°C and fired in air at temperatures ranging between 500° and 1100°C to form the phosphor, using open silica crucibles.

La_2O_3 is unstable in air, spontaneously forming the hydroxide $La(OH)_3$ which is nonluminescent. Appropriate precautions to prevent hydrolysis are required prior to measurement of spectral properties.

The optical spectra were obtained with the aid of a commercial instrument (11) having two monochromators. The excitation monochromator provided a constant energy excitation beam over the range of 46,000 to 20,000 cm^{-1}. Either monochromator may be programmed separately to provide excitation or fluorescence spectra. The spectra are automatically compensated for wavelength energy but not for relative intensity. Resolution in the instrument varies from a few angstroms in the ultraviolet to about 10Å in the red region of the spectrum.

Experimental Results

Single-oxide systems.—All three single oxides are activated by Eu^{+3}, as shown in Fig. 1. The excitation properties differ, while the emission occurs in the same spectral region, the strongest line being a red emission line close to 6100Å.

La_2O_3 has the hexagonal A-type structure, while Y_2O_3 and Gd_2O_3 form the cubic C-type structure, both typical of the rare-earth oxides, depending on the atomic number and firing temperature (12). Table I lists published data found for these oxides as well as cell constants determined in this work.

The most intense emission line for Eu^{+3} in La_2O_3 is positioned at 16,100 cm^{-1}, while those for Gd_2O_3 and

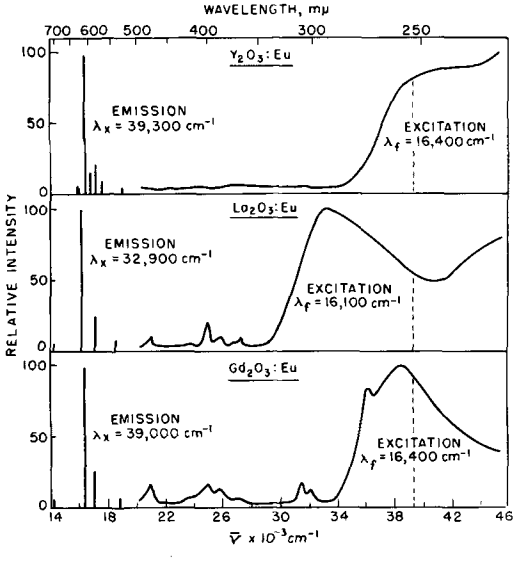

Fig. 1. Excitation-emission of Eu^{+3} in rare-earth oxide matrices

Table I.

Oxide	Firing temp, °C	Structure	a_o	c_o	Cation site symmetry	Number of oxide neighbors
La_2O_3	1000	Hexagonal	3.937Å	6.130Å	Distorted octahedral	7
Y_2O_3	1000	Cubic	10.604	—	Distorted cubic	6
Gd_2O_3	1000	Cubic	10.8	—	Distorted cubic	6
Gd_2O_3	1400	Monoclinic	Not determined		Distorted trigonal	7

Y_2O_3 are positioned at 16,400 cm^{-1}. These differences are attributed to symmetry changes at the cationic site where Eu^{+3} in Gd_2O_3 or Y_2O_3 can substitute in either of two sites having C_{2v} or S_6 symmetry. The site in La_2O_3 involves a peculiar sevenfold coordination having C_3 symmetry (13).

There are three distinct features in the excitation spectra. The low-intensity narrow bands are probably 4f → 4f transitions between levels of the activator atoms. There are two broad, intense excitation bands, one of which always appears at the same wavelength, regardless of activator (8). These are probably matrix excitation bands. The position and intensity of the other broad excitation band (thought to be an activator excitation band) are dependent on both the matrix and the incorporated activator (8).

The matrix excitation band of Y_2O_3:Eu occurs at about 2000Å. Those phosphors based on La_2O_3 all show the same broad matrix excitation band at 2200Å. The rather narrow excitation band in Gd_2O_3:Eu found at 36,000 cm^{-1} (2780Å) is caused by an excitation transition in the Gd^{+3} ion ($^8S_{7/2} \rightarrow {}^6I_J$). There is a broad excitation band peaking at about 47,600 cm^{-1} for Gd_2O_3:Eu because of matrix excitation.

The nature of the activator excitation band is more obscure. The bands might be attributed to 4f → 5d transitions or to a perturbed 4f → 4f transition in the Eu^{+3} activator center. Previous authors have favored the former, primarily because it is difficult to visualize or justify a mechanism involving perturbation of the "shielded" 4f electronic states.

The effect of structure on excitation.—The three matrices, La_2O_3, Y_2O_3, and Gd_2O_3, offer an ideal group for studies of matrix-activator interactions and the effect of site symmetry of fluorescent properties. Referring to Table I, it may be seen that all structures involve sites in which a departure from a regular symmetry is prevalent.

In a phosphor where host sensitization plays a primary role, long-range energy transport mechanisms would be expected to occur only in those matrices having a high degree of lattice-ordering. In noncrystalline materials, host sensitization (matrix excitation) does not generally occur.

Thus, the differences in excitation band position observed for the three systems would lead to the expectation that the matrix bands should be dependent on structure. The fact that Gd_2O_3 is dimorphic offers a method for determining the effect of structure on excitation bands. It would be expected that the intensity of the matrix excitation band would be highly dependent on the crystallinity of the matrix, and its position perhaps dependent on structure. Substantiating experimental data are presented in Fig. 2. Note that the monoclinic form has a broad peak apparent at 42,000 cm^{-1} (as well as the band due to Eu^{+3}). The cubic form, identified by x-ray analysis, also has two peaks whose relative intensities depend on firing temperature. The material fired at 600°C has one main peak at 39,400 cm^{-1}; another band appears at 44,000 cm^{-1}. The difference in intensity of this latter band is due to differences in crystallinity of the materials. Thus, according to x-ray diffraction analysis, the 600°C-fired material is much less crystalline and the matrix excitation band is much less intense than the

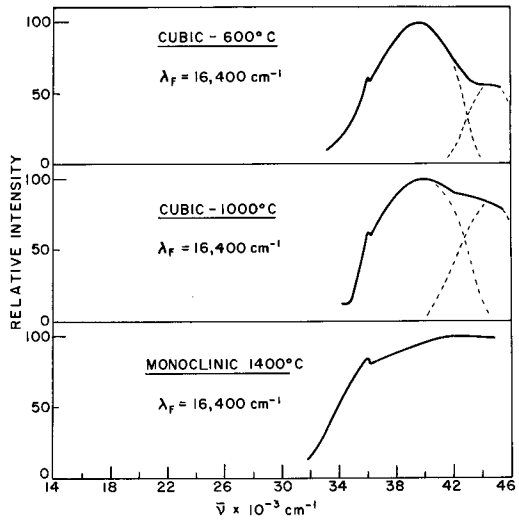

Fig. 2. Effect of structure on Gd_2O_3 : Eu excitation spectra

material fired at 1000°C. A previous paper (14) has shown that decomposition of the oxalates begins at 400°C and is complete at 600°C if given enough time for reaction. The materials were identified, by x-ray analysis, as cubic Gd_2O_3. The chief difference was in crystallite size (*i.e.*, crystallinity). Thus, the matrix excitation band intensity is a function of the degree of lattice-ordering.

There is one energy transfer process which occurs in the Gd_2O_3 phosphor, but not in Y_2O_3 or La_2O_3. This is the excitation transfer process corresponding to absorption within the Gd^{+3} ion (2780Å) by a transition within the 4f shell, with subsequent excitation of Eu^{+3}. This process is a separate excitation mechanism from the activator or matrix excitation processes.

The ternary system.—The ternary system forms only four compounds: $LaYO_3$ is monoclinic (9), and presumably $LaGdO_3$ has the same structure; La_3YO_6 is hexagonal, and likewise its conjugate, La_3GdO_6. No other compounds are known. Figure 3 shows a phase diagram found for the ternary system fired at 1000°C. Three separate single-phase regions were found: cubic, monoclinic, and hexagonal. Two-phase regions connect each with the other. The phase diagram must be regarded as approximate, since no specific effort was made to determine composition after firing. The data represent the initial cation ratios of ions in solution before oxalate precipitation and subsequent firing. Since these steps are essentially quantitative, no serious error is believed to have resulted (7). At 1400°C, the phase diagram changes so that the area of the cubic phase is reduced and the monoclinic region expands to include monoclinic Gd_2O_3.

It was found that the ultraviolet plaque response (2537Å irradiation) was a function of structure and not of composition (see Fig. 4). Thus, the hexagonal and monoclinic regions can produce 65% of standard manganese-activated cadmium-borate phosphor brightness. In the mixture having the cubic structure,

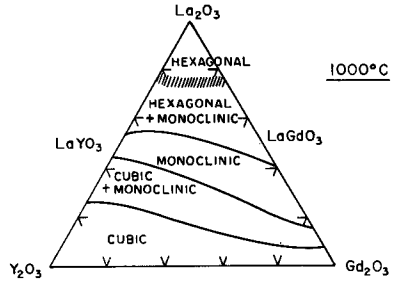

Fig. 3. Phase diagram of the ternary system La_2O_3-Gd_2O_3-Y_2O_3

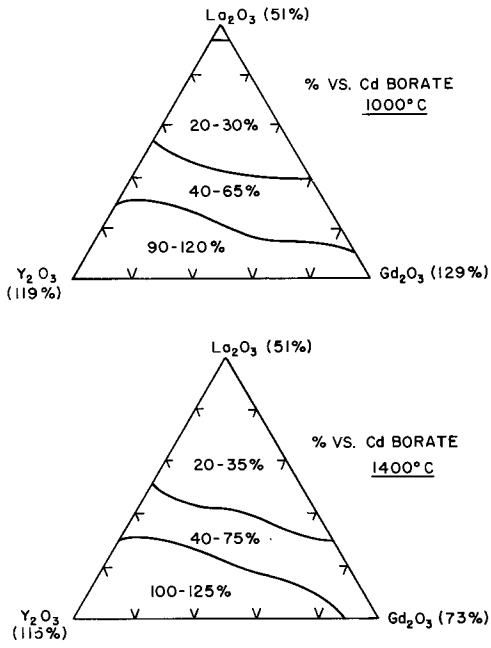

Fig. 4. Plaque brightness as a function of composition

those compositions containing no La have the highest brightness. Of these, the ultraviolet response seems to increase with Gd_2O_3 content, which would be predicted since the excitation-band maximum of Gd_2O_3:Eu is closer to 2537Å than that of Y_2O_3:Eu. The experimental data, accordingly, indicate simple solid-solution formation between Y_2O_3 and Gd_2O_3. However, the systems fired at 1400°C show decreased ultraviolet response as the transition from cubic to monoclinic symmetry occurs. Consequently, high ultraviolet response is found only in compositions having cubic symmetry.

In the ternary system, the differences in the excitation bands attributed to Eu^{+3} were determined as a function of composition. Since these excitation bands appear at widely separated points in the spectra, it is possible to classify the bands as to type. These data are given in Table II. Note that these are the excitation bands attributed to perturbation of excited states of the Eu^{+3} cation incorporated within the matrix.

It is readily seen that the excitation peak observed is not a function of structure but is due to the presence or absence of La. When La is present, the excitation is typical of the La_2O_3 spectrum, regardless of structure.

Discussion of Results

It has been demonstrated that there are two broad, intense excitation bands present in Eu^{+3}-activated rare-earth oxide phosphors. Of these, the band peaking at the higher energies has been shown, by correlation of x-ray and excitation data, to be associated with

Table II. Excitation as a function of composition

Composition La	Y	Gd	Structure	Excitation peak, cm^{-1}	Type of Eu^{+3} band
1.0	—	—	Hexagonal	33,600	La
—	1.0	—	Cubic	40,200	Y
—	—	1.0	Cubic	38,600	Gd
0.8	0.2	—	Hexagonal	34,600	La
0.7	—	0.3	Monoclinic + hexagonal	34,000	La
0.6	—	0.4	Monoclinic + hexagonal	33,700	La
0.5	0.4	0.1	Monoclinic	34,200	La
0.4	0.4	0.2	Cubic + monoclinic	34,500	La
0.4	0.6	—	Cubic + monoclinic	34,200	La
0.4	0.2	0.4	Cubic + monoclinic	34,100	La
0.2	—	0.8	Cubic + monoclinic	34,900	La
0.2	0.8	—	Cubic	34,700	La
0.1	0.1	0.8	Cubic + monoclinic	35,500	La + Gd
0.1	0.8	0.1	Cubic	37,500	Gd + Y
—	0.4	0.6	Cubic	38,000	Gd + Y
—	0.6	0.4	Cubic	38,200	Y + Gd
—	0.2	0.8	Cubic	37,700	Gd
—	0.8	0.2	Cubic	38,500	Y + Gd

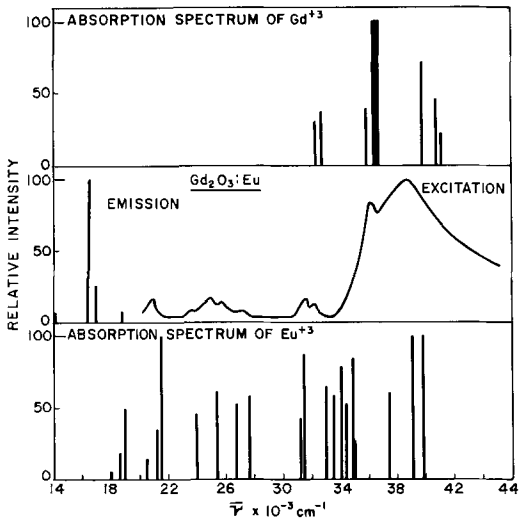

Fig. 5. Comparison of absorption spectra of Eu^{+3} and Gd^{+3}

matrix excitation, at least in Gd_2O_3:Eu. Because the matrix band intensity is dependent on lattice-ordering, one is led to the conclusion that this band is the result of exciton processes (excited states of the lattice). There are at least two possibilities of exciton formation. In one process, the exciton formation involves an oxygen p^6 electron in analogy to the alkali halides (15). In the other, cation exciton states in the lattice are involved. Such behavior has been observed also in the alkali halides, particularly KCl (16). Of the two mechanisms, the latter is preferred because of the behavior of the excitation bands in the ternary system. In the ternary system, the matrix excitation may occur by formation of "bound-states" in which a cation p^6 electron is excited to a p^5d or p^5s state, and the wave is propagated throughout the lattice (17). Such a mechanism gives rise to host sensitization and requires high lattice perfection. Experimental evidence supports these conclusions because of the fact that there are "typical" matrix excitation bands for all three compounds. Such bands are a function of the cation, not of the structure.

As mentioned previously, the nature of the activator excitation band is not at all clear. The broad, intense excitation bands found at lower energies might be attributed to one of three causes: (i) the matrix, (ii) the isolated activator center, or (iii) the interaction of matrix with activator center. Case (i) can be shown to be improbable by consideration of the energy levels of Gd^{+3} and Eu^{+3}, as shown in Fig. 5. The energy levels were determined by absorption measurements (18) of Gd^{+3} and Eu^{+3} in solution. Although the triplet absorption of Gd^{+3} appears shifted in Gd_2O_3:Eu, the main excitation band cannot be attributed to Gd^{+3}, but must be due to Eu^{+3} energy levels perturbed by the crystal field or some other factor.

Case (ii) must be eliminated because only narrow bands would be expected for $f^n \rightarrow f^{n-1}f^*$ transitions (and perturbation of the $f^n \rightarrow f^{n-1}d^*$ excited state would involve the crystal field interaction).

Case (iii) can be subdivided into two possibilities: (a) where the interaction arises between cation pairs M^{+3}-Eu^{+3}, and (b) where the perturbation is due to the interaction of a field on the activator center, *i.e.*, the perturbation of the excited state is dependent on crystal structure. In the ternary system, if (a) proved to be true, we would expect La_2O_3:Eu, which has poor response to 2537Å, to improve in brightness when small amounts of Gd, Y, or both, were present. Experimental results, given previously, eliminate this possibility.

Thus, one is left with the conclusion that the broad excitation band is due to perturbed excited states of the activator, Eu^{+3}. A possible explanation is that perturbation is caused by the exciton field. The exact nature of the perturbation mechanism, whether field-interaction or vibronic coupling, is unknown. However, the experimental evidence shows that the La_2O_3 matrix possesses the lowest energy exciton states, so that even a cubic structure containing but 20% La still possesses an excitation spectrum typical of La_2O_3 containing Eu^{+3}. With this mechanism, one would expect the position of the band (*i.e.*, the minimum energy required for excitation) to be a function of composition, not of structure, as observed.

Correlation (19) of the published values of the energy levels of Eu^{+3} (20) to the emission spectra shows that in La_2O_3 emission occurs from the $^5D_1$ level, whereas in the other cubic oxides, emission occurs from the $^5D_0$ state. This difference is attributed to the local site symmetry of the Eu^{+3} activator in the oxide structures.

It has been observed that a mechanism, in which $4f \rightarrow 4f$ transitions can possess high oscillator strengths with strong transition probabilities, can exist (21) and that such a transition would involve an enforced dipole type of transition at the C_{2v} site in the cubic crystal because of the lack of a center of inversion. Polarization of emission along the $\bar{1}1\bar{1}$ plane would then be expected. It remains for more direct measurements to demonstrate the accuracy of the proposed mechanism.

Acknowledgment

The author is indebted to Dr. C. W. W. Hoffman for the x-ray powder diffraction measurements, to H. D. Layman for preparation of the samples, and to Dr. R. W. Mooney, M. A. Aia, and Dr. H. J. Borchardt for helpful discussions.

Manuscript received April 1, 1964.

Any discussion of this paper will appear in a Discussion Section to be published in the December 1965 JOURNAL.

REFERENCES

1. G. Urbain, *Ann. Chim. Phys.*, **18**, 293 (1909).
2. H. Gobrecht and R. Tomaschek, *Ann. Phys.*, **29**, 324 (1937).
3. F. A. Kröger, "Some Aspects of The Luminescence of Solids," Elsevier Publishing Co., New York (1948).
4. F. Rosenberger, *Z. Phys.*, **167**, 349, 360 (1962).
5. N. C. Chang, *J. Appl. Phys.*, **34**, 3500 (1963).
6. K. A. Wickersheim and R. A. Lefever, *This Journal*, **111**, 47 (1964).
7. J. D. Axe and P. F. Weller, *J. Chem Phys.*, **40**, 3066 (1964).
8. R. C. Ropp, *This Journal*, **111**, 311 (1964).
9. J. Cassedanne and H. Forestier, *Compt. rend.*, **253**, 2953 (1961).
10. K. G. Broadhead and H. H. Heady, *Anal. Chem.*, **32**, 1603 (1960).
11. W. Slavin, R. W. Mooney, and D. T. Palumbo, *J. Amer. Opt. Soc.*, **51**, 93 (1961).
12. I. Warshaw and R. Roy, *J. Phys. Chem.*, **65**, 2048 (1961).
13. L. Pauling, *Z. Krist.*, **69**, 415 (1928).
14. R. C. Ropp and E. E. Gritz, "Proceedings of the Fourth Rare Earth Conference," Gordon and Breach, New York, To be published (1964).
15. R. S. Knox and N. Inchaupe, *Phys. Rev.*, **116**, 1093 (1959).
16. F. Fischer, *Z. Phys.*, **160**, 194 (1960); see also: E. Ilmas, R. Kink, G. Liidja, and Ch. B. Lushchik, *Tr. Inst. Fiz. i Astron. Akad. Nauk. Est*, **23**, 221 (1963); V. L. Broude, A. F. Prikhot'ko, and E. I. Rashba, *Uspekhi fiz. Nauk (USSR)*, **67**, 99 (1959).
17. M. Trlifaz, *Czech. J. Phys.*, **13**, 631 (1963).
18. R. Prandtl and W. Scheiner, *Z. anorg. allgem. Chem.*, **220**, 107 (1934).
19. R. C. Ropp, Unpublished data.
20. G. S. Ofelt, *J. Chem. Phys.*, **38**, 2171 (1963).
21. B. R. Judd, *Phys. Rev.*, **127**, 750 (1962).

Diffusion-Induced Imperfections in Silicon

M. L. Joshi and F. Wilhelm

Components Division, International Business Machines Corporation, Poughkeepsie, New York

ABSTRACT

Diffusion-induced dislocations and precipitates have been studied through electron microscopy as a function of the diffusion depth. High concentrations of phosphorus and arsenic were diffused in (111) Si wafers to a shallow depth under the condition of constant solute surface concentration. Extensive dislocation networks were observed in phosphorus diffused wafers, whereas only a few single dislocations were detected in arsenic-diffused wafers. The results are shown to be in general agreement with Prussin's model of dislocation generation by relief of the stress due to solute lattice contraction of P and As.

The generation of dislocations in crystals by solute concentration gradients is well known (1-3). Such gradients can, for instance, be set up by fluctuations of the freezing rate during solidification. The solute concentration gradients imposed by shallow diffusion of large dopant concentration have been shown to cause the generation of dislocations in silicon (4-6). Queisser (4) found regular arrays of line patterns following crystal symmetry on silicon diffused with a high concentration of boron into a shallow surface layer and etched subsequently. These patterns were interpreted as slip lines due to the stress introduced into silicon lattice by the nonuniformly distributed, undersized, substitutional boron impurity. Prussin (5) produced etch pits marking dislocation sites on cleavage planes normal to the plane of diffusion in (111) silicon wafers symmetrically diffused with boron and phosphorus. It was shown that the stresses introduced by the solute lattice contraction were sufficient to produce dislocations. X-ray microscopy (6) and electron probe analysis (7) using essentially the reverse current of an irradiated diode as a read-out have given support to these findings. Jaccodine (8) reported the observation of individual dislocations forming networks in a phosphorous-diffused (111) silicon slice by transmission electron microscopy.

In this article, we present a study of diffusion induced dislocations as a function of the impurity diffusion depth in a (111) silicon wafer by the technique of transmission electron microscopy. Transmission electron micrographs were also obtained at the surface and near the junction in an arsenic-diffused wafer with surface concentration $\approx 5 \times 10^{20}$ cm^{-3}. This was done to explore the influence of the atomic size factor in the generation of defects by diffusion. On the basis of Pauling's tetrahedral covalent radii, P is undersized in Si, whereas As is almost the same size.

There is a considerable interest in regard to the diffusion-induced imperfections, other than dislocations. The detailed analysis of thin phosphorus-diffused layers in p-type silicon by Tannenbaum (9) has shown that at high concentrations of phosphorus ($>10^{20}$/cm^3) there is a significant difference between the profiles determined by sheet resistivity (corrected for ionization) and by radio tracer measurements. Tannenbaum interpreted this difference by postulating that part of the phosphorus is present not in the substitutional sites, but in the interstices or as precipitates. The detection of phosphorus precipitation by transmission electron microscopy in the diffused profile should be very informative in the light of the above consideration.

Experimental

Diffusion.—Three slices 10-mil thick and ~1 in. in diameter were cut parallel to (111) from a Czochralski-grown boron-doped ($\sim 10^{15}$ cm^{-3}) silicon crystal. The dislocation density of the crystal section from which the slices were cut was found by the etch pit technique to be less than 500/cm^2. The silicon wafers were lapped and chemically polished to remove any surface damage. Two of the wafers were symmetrically diffused on both sides with phosphorus in an open tube configuration at a temperature of 1150°C from a P_2O_5 source that was held at 300°C. The wafers were removed from the diffusion furnace and allowed to cool in room air on the quartz platform.

The third nondiffused wafer annealed at 1150°C served as a control to detect any possible defects introduced during specimen preparation. Both the etch pit technique and the electron microscopy revealed no such defects.

One of the diffused wafers was used for the determination of the solute profile, and the other for the study of the diffusion-induced imperfections. The surface impurity concentration was greater than 10^{21}/cm^3, as determined from the sheet resistance measurements and Irvin's curves (10). The p-n junction depth was about 2μ. The phosphorus-diffusion profile as obtained by the anodization-sectioning technique (9) in conjunction with the sheet resistivity measurements is shown in Fig. 1. This profile represents the ionized phosphorus distribution. The diffusion-induced imperfections were examined at the surface and at the depths 1/4, 1/3, 1/2, 1 and 1 1/2μ in the solute profile, as indicated in Fig. 1.

Specimen preparation.—The diffused wafer was cut by diamond-scribing into strips ⅛ in. wide. These strips were subjected to anodic oxidation, on the side to be studied. By successive removal of the oxide layers with HF, the appropriate depth in the solute profile was reached. The thickness of the removed silicon

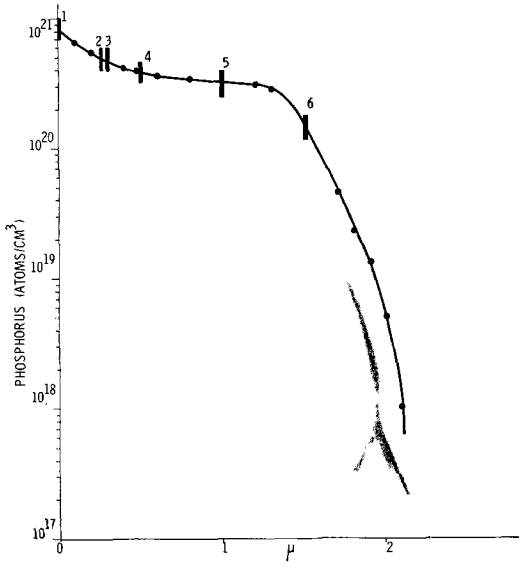

Fig. 1. Diffusion profile indicating levels of depth in the specimen where imperfections were studied; electron micrographs at point 1 to 6; four-point probe profile; diffusion: silicon 1150°C, P_2O_5 300°C.

layer per sectioning strip was determined from a comparison of the silicon oxide color to a standard film thickness gauge. The accuracy of this measurement is about ±50Å in 1000Å. Each strip was cut into ⅛ x ⅛ in. samples.

In order to obtain transparency to the electron beam in the microscope, the specimen had to be thinned to a few thousand angstroms. The samples were chemically polished down from the other side of the diffused surface under study by chemical polishing, using the solution: 300 cc of HNO_3 (70%), 200 cc of CH_3COOH (glacial), 100 cc of HF (47%), and 3g of iodine crystals. The surface to be studied was well protected from the chemical attack. Occasionally, samples were thinned by the electrolytic jet etch technique using a mixture of isopropyl alcohol and HF.

Electron Microscopic Observations

A Philips electron microscope (100B) was used for diffraction electron microscopy of the specimens. Individual dislocations are found in all investigated layers of the P-diffused wafer, down to a depth of 1½μ in the diffusion profile. At the surface (0μ depth) and at the depth of ¼μ (Fig. 2 and 3), rather complete networks were seen. Many threefold nodes are observed, joined by sections of almost straight dislocations. The network cells are of dimensions ½ to 1μ across. Dislocation densities up to 10^9 cm/cm^3 were measured. At the depth of 1/3μ into the diffused layer (Fig. 4), the dislocation networks appeared to be broken into smaller patches, sparingly connected with each other. At still greater depths (½ to 1½μ), the networks have practically disappeared (Fig. 5 and 6) and individual dislocations, some straight and some branched with one or two threefold nodes, are present.

The spreading of the network and the length of the component dislocations indicate that the dislocations lie in the plane of observation, *i.e.*, in the (111) plane. In many cases, where dislocations leave the (111) plane to terminate at the specimen surface, an abrupt change of direction takes place, revealed by the wavy appearance of the dislocations. The waviness [explained by the dynamical theory of diffraction contrast (11)] is due to inclination of the dislocation line with respect to the foil.

No stringent regularity exists in the network studied. Whenever small range regularity is detected, network cells tend to be hexagonal (Fig. 3), with dislocations joining in nodes under angles of 120°. Straight disloca-

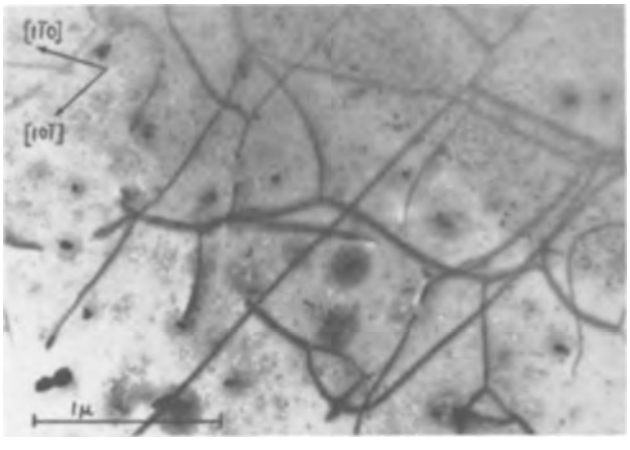

Fig. 2. Dislocation structure near the surface (depth 0μ)

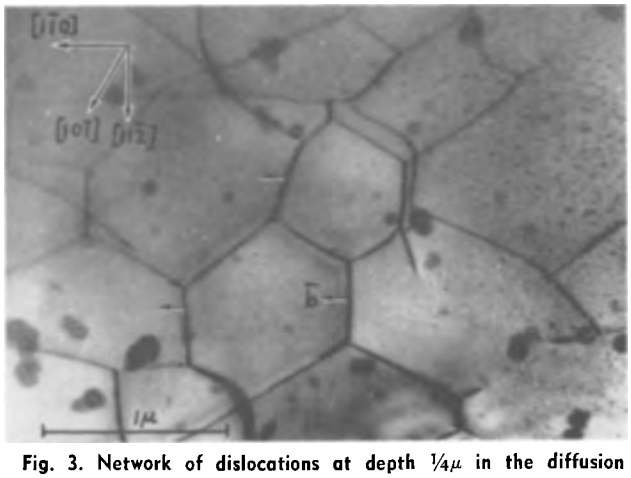

Fig. 3. Network of dislocations at depth ¼μ in the diffusion profile; arrows indicate Burgers vector.

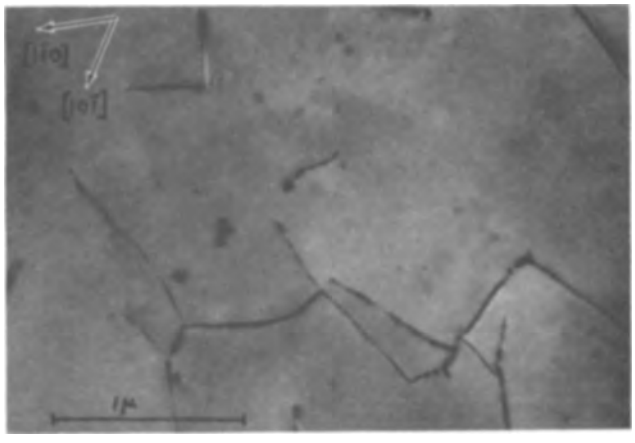

Fig. 4. Breaking-up of dislocation network at depth 1/3μ

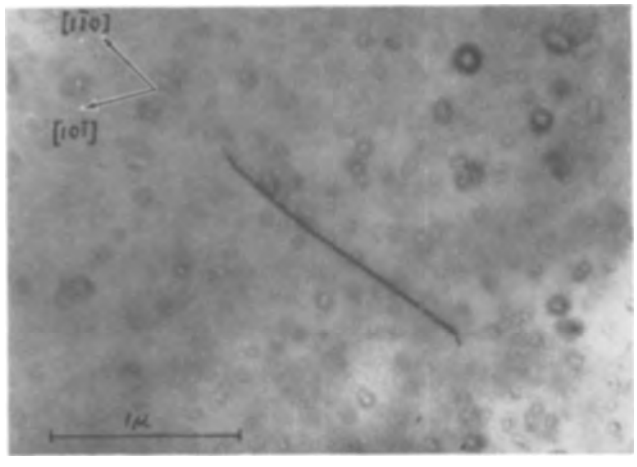

Fig. 5. Single dislocation at depth ½μ; only a few dislocations are found at this and at deeper levels.

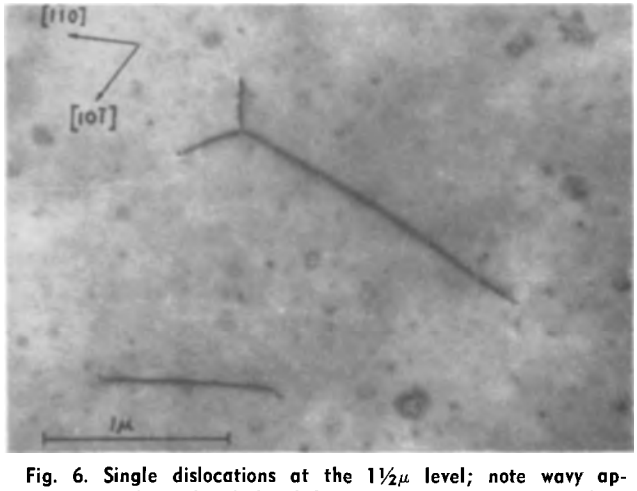

Fig. 6. Single dislocations at the 1½μ level; note wavy appearance at the ends of the dislocations, indicating tilt of these dislocation parts out of the plane of observation.

tions often lie in <112> directions. Isolated nodes, however, are occasionally found with their dislocations lying in a <110> direction.

The Burgers vector was determined on some of the dislocations (Fig. 3) by darkfield observation under illumination from a selected diffracted beam, indicating the edge character of the dislocations. They are of $a/2$ <110> type, in agreement with the findings of other researchers (6, 8).

Tilt of the specimen in the electron microscope revealed no other dislocations other than those shown in Fig. 3. The threefold nodes of the dislocation networks observed were contracted; no indication of extension is present. Figure 7 represents several groups of almost-straight parallel dislocations at $1/3\mu$ depth at the magnification of 12,000X. They seem to form a triangular pattern, with dislocations lying in <110> directions—interpreted as lying on {111} planes other than the plane of the specimen.

Dislocations in the specimen studied are rather immobile. No dislocation motion under the stress of the electron beam was observed in the electron microscope. Occasionally microcracks are observed in the material, created during the specimen preparation.

A (111) silicon wafer from a pulled silicon crystal doped with P ($>5 \times 10^{20}/cm^3$) was investigated for comparison with the diffusion-induced defects. Only very few dislocations inclined to the plane of observation were found in these specimens (Fig. 8). No other defects than dislocations were found.

On the magnification scale employed (30,000X), the dislocation distribution is considerably inhomogeneous.

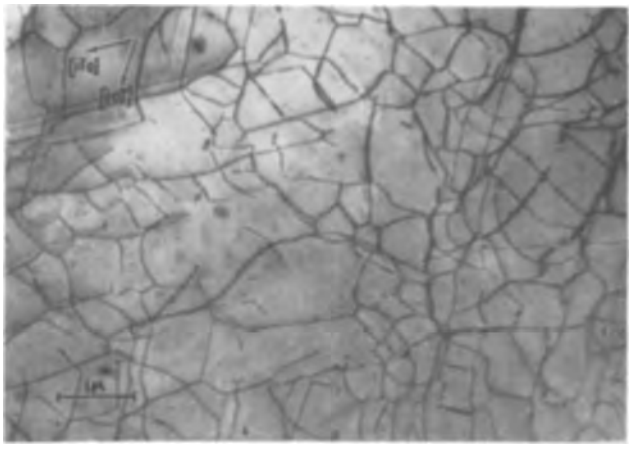

Fig. 7. Low-magnification micrograph reveals traces of dislocations lying in the three {111} planes, projected upon the plane of observation. In this micrograph (taken at a depth of $1/3\mu$), an unusually high dislocation density (for this depth) is found, not characteristic for this level when compared to many other observations.

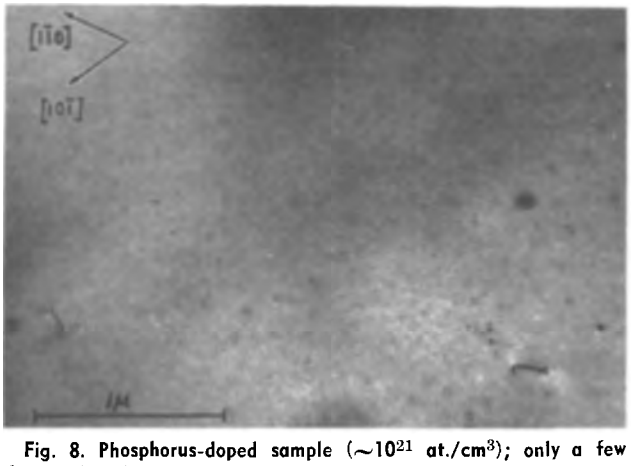

Fig. 8. Phosphorus-doped sample ($\sim 10^{21}$ at./cm^3); only a few short dislocations are present.

Frequently, particles of crystalline shapes (Fig. 9) are found in the diffused specimen throughout the diffusion profile studied herein. Their distribution also varies considerably in the different areas investigated. There are square, hexagonal and elongated particles of various apearances, with sizes ranging from 500Å to about 1μ. It is strongly suspected that these particles are phosphorus precipitates. Dark-field imaging did not give any indication of coherence of these particles with the parent lattice. The particles retain their shapes even in very fine detail when the specimen is washed in concentrated HNO_3 and subsequently in concentrated HF. They appear, however, to be lightened in contrast after the acid treatment.[1]

Arsenic diffused (surface concentration, $5 \times 10^{20}/cm^3$) boron-doped ($\sim 1.5 \times 10^{16}/cm^3$) silicon samples were examined at the surface and near the junction. Only a few single dislocations were observed; they often seem to lie almost perpendicular to the plane of observation (Fig. 10). Needle-type precipitates were observed at some places near the surface. No precipitation was detected near the junction.

Discussion

The electron microscope investigation gives evidence of the presence of dislocations and precipitates in silicon specimens, with a diffusion gradient of a high concentration of phosphorus. The absence of any significant amount of dislocations in the uniformly doped phosphorus ($> 5 \times 10^{20}/cm^3$) specimen should indicate that it is not necessarily the high solute concentration that induces dislocations. The small distribution coefficient ($k_0 = 0.35$) in phosphorus doping of single crystals could cause local concentration fluctuations, giving rise to the few dislocations seen in Fig. 9. The extensive dislocation networks seen in the diffused-phosphorus specimens are the result of relief of the stress gradient introduced by the solute lattice contraction of phosphorus diffused in silicon. Incidentally, the origin of the diffuse regions of extra x-ray scattering power observed on the glide plane traces in the case of silicon grown by floating-zone process has been suggested by other researchers to be these dislocation networks (12, 8). In addition, the regular arrays of the line markings (4) revealed by etching seem to be slip lines caused by glide on {111} planes, which our observations on dislocation networks corroborate.

The determination of the Burgers vectors in some experiments (Fig. 2), indicates that these particular dislocations seem to possess almost-pure edge character. These dislocations are oriented very closely in a <112> direction. The pure-edge dislocation on the (111) plane with a/2 <110> Burgers vector in the case of a diamond lattice is a composite dislocation which

[1] In a similar investigation, Schmidt and Stickler (14) have recently reported the identification of a silicon phosphide phase by transmission electron microscopy.

Fig. 9. Photo shows particles found in many areas throughout the diffused profile.

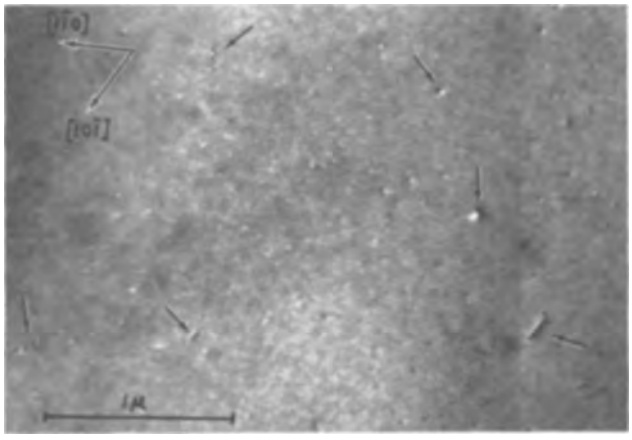

Fig. 10. Small dislocations in an As-diffused specimen; some are pointed out by arrows; micrograph taken near the surface.

occurs when the axis of a simple 60° Read's dislocation (with 1.4 broken bonds per lattice constant) changes alternately from one <110> orientation to another (13). Under the conditions of diffusion and solute lattice contraction such a dislocation (which requires 1.63 broken bonds per lattice constant) could be energetically possible.

The dislocation networks in the (111) plane of observation give credence to Prussin's concept of the stress relief by diffusion-induced dislocations. Since the dislocations must lie in the diffusion plane for the stress relief, only the six {111} slip systems with Burgers vectors a/2 <110> lying in {111} planes other than the plane of diffusion can be activated (according to Prussin). Only the edge components of these Burgers vectors contribute to the strain relief in the diffusion plane. The generation of the dislocations with predominant edge character is also consistent with this model. In the case of diffusion from a constant solute surface concentration (*i.e.*, for a strictly erfc distribution), Prussin derived a Gaussian dislocation distribution from the surface to a point in the diffused layer where the dislocation density drops to zero. The etch-pit density distribution on the cleaved plane extended half way into the diffusion profile in Prussin's own experiment (of deep diffusion of phosphorus in silicon). The significant feature of our study is that a dislocation density of 10^9 cm/cm^3 extends from the surface to about $1/3\mu$ depth and then begins to drop very rapidly and is negligible beyond a quarter of the way into the profile.

The surface dislocation density (according to Prussin's model on the basis of the solute lattice contraction coefficient $\beta \approx 10^{-24}$ cm^3/atom) is $\approx 3 \times 10^8$ cm, which is within one order of magnitude of our experimental observation. However, the dislocation penetration into the interior in our experiment seems shallower than expected. Considering the inhomogeneity of dislocation distribution on the scale of observation, it is not possible to compare the distribution actually obtained by electron microscopy to the expected one. The total number of dislocations created at the beginning of the diffusion process is dispersed into the interior of the sample during transport of the solute. This dispersion is likely to be restricted because of the nodes tending to anchor the dislocation networks.

It is also invariably observed that solute profiles are not erfc-type when high amounts of impurities are diffused into very shallow depths. Both of these considerations (anchoring and solute profiles) may be responsible for the deviations of the dislocation distributions-based strictly on the erfc distribution of the solute. The likely effect of dense dislocation networks in the diffused surface affecting the sheet resistivity measurements should not be neglected in estimating impurity concentration from Irvin's curves.

The absence of dislocation networks in the case of a large amount of arsenic diffusion indicates the importance of the degree of atomic misfit. The misfit ratio r/r_o (where r and r_o are Pauling's tetrahedral covalent radii of the solute and silicon) for P and As is 0.932 and 1.0, respectively. The incorporation of As in Si, consequently, would involve very little strain. The high surface concentration of P ($> 10^{20}$/cm^3) in comparison with that of B ($\approx 3 \times 10^{19}$/cm^3) needed for observation of slip patterns (4) is another example of the solute lattice contraction effect ($r/r_o = 0.746$ for B).

The observation of particles believed to be phosphorus precipitates indicates that the strains introduced into the diffused samples are locally inhomogeneous. The origin of the precipitates lies in the diffusion process, and well-defined shapes imply crystallinity (14). The incorporation of such particles may contribute to the deviation of the diffusion profile from the expected one. It should not be surprising if these precipitates, which extend almost to the p-n junction, affect the electrical behavior of the devices containing large amount of P diffusant.

Acknowledgments

The authors wish to express their gratitude to E. S. Wajda for suggesting the problem and helpful discussions. They also wish to thank F. W. Schneider, J. N. Ramsey, J. G. Christ, and G. A. Silvey for their valuable help and encouragement. They are grateful to S. Mader for his helpful comments.

Manuscript received June 5, 1964.

Any discussion of this paper will appear in a Discussion Section to be published in the December 1965 JOURNAL.

REFERENCES

1. A. J. Goss, K. E. Benson, and W. G. Pfann, *Acta. Met.*, **4**, 332 (1956).
2. F. C. Frank, *Advances in Phys.*, **1**, 91 (1952).
3. W. A. Tiller, *J. Appl. Phys.*, **29**, 611, (1958).
4. H. J. Queisser, *ibid.*, **32**, 1176 (1961).
5. S. Prussin, *ibid.*, **32**, 1876 (1961).
6. G. H. Schwuttke and H. J. Queisser, *ibid.*, **33**, 1540 (1962).
7. J. J. Lander, H. Schreiber, Jr., T. M. Buck, and J. R. Mathews, *Appl. Phys. Letters*, **3**, 206 (1963).
8. R. J. Jaccodine, *ibid.*, **4**, 114 (1964).
9. E. Tannenbaum. *Solid State Elect.*, **2**, 123 (1961).
10. J. C. Irvin, *Bell System Tech. J.*, **41**, 387 (1962).
11. A. Howie and M. J. Whelan, *Proc. Roy. Soc.*, **A267**, 206 (1962).
12. A. E. Jenkinson and A. R. Lang, "Direct Observations of Imperfections in Crystals," p. 471, Interscience Publishers, New York (1962).
13. J. Hornstra, *J. Phys. Chem. Solids*, **5**, 129 (1958).
14. P. F. Schmidt and R. Stickler, Recent News Paper presented at the Toronto Meeting of the Society, May 3-7, 1964.

TriPyramid Growth of Epitaxial Silicon

Morio Inoue

Research Laboratory, Matsushita Electronics Corporation, Takatsuki, Osaka, Japan

ABSTRACT

The tripyramids in vapor grown epitaxial silicon on substrates of (111) orientation were examined by chemical etching and x-ray diffraction techniques. The growth patterns of the tripyramids were brought out clearly by etching the epitaxial layer with the Sailer etch and the iodine etch successively. The tripyramids consist of twinned crystallites of [511] orientations. They originate at the interface between the substrate and the epitaxial layer. The cause of twinning was proved to be the formation of silicon carbide on the surface of the substrate. A crystallographic model was derived from the experimental results.

Epitaxial silicon films grown on single crystal substrates by the vapor decomposition method often contain stacking faults and tripyramids. The stacking faults have been investigated by many authors using chemical etching (1) and electron transmission techniques (2). It has been shown that the number of the stacking faults depends on both the physical perfection and amount of surface contamination of the substrate (3).

In addition to the stacking faults, growth hillocks, called tripyramids (4), have been observed on {111} substrates (5, 6). Batsford *et al.* reported that the residual water and organic solvents during chemical polishing induce the stacking faults and the tripyramids (3). Those were produced during the film growth, and they have been often found to be associated with the stacking faults. The tripyramids seen on epitaxial silicon layers obtained by reduction of silicon halide have also been observed on some germanium layers deposited by cathodic sputtering (7). Miller *et al.* (5) proposed a crystallographic model and a formation mechanism for the pyramids. However their model does not seem satisfactory to explain our geometrical observation by chemical etching and x-ray diffraction. A new model is proposed and the geometry and origin of the tripyramid growth are discussed in this paper.[1]

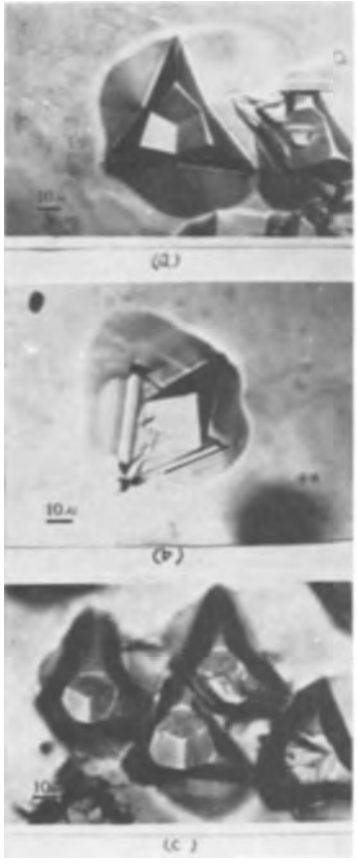

Fig. 1. Microphotographs of tripyramid growth on Si (111): (a) a typical tripyramid, (b) a monopyramid, (c) modified tripyramids.

Experiments

Epitaxial growth.—The epitaxial layers were prepared by silicon tetrachloride vapor decomposition at 1250°C in a hydrogen atmosphere (8). Chemically etched silicon wafers of (111) orientations were used as substrates. A substrate was placed on a graphite susceptor and heated by induction. The final removal of oxide was carried out in a hydrogen stream for 15 min at a temperature of 1260°C. The growth rate was approximately 1μ min^{-1}. The grown layers were usually $10 \sim 1000\mu$ in thickness.

Figure 1 shows a starlike hillock on the epitaxial layer called a tripyramid. The size and height of the tripyramid hillocks vary proportionally to the deposition thickness of the layer. They originate at the interface between the substrate and the epitaxial layer. Usually they exhibit figures similar to the one shown in Fig. 1a, but in a particular case monopyramids (Fig. 1b) and modified tripyramids (Fig. 1c) were observed. The geometry of the tripyramids were clarified by measuring the height and length under the optical microscope (Fig. 7).

Chemical etching study.—The internal crystallographic structure of the growth pyramids has been investigated by chemical etching techniques. The Sailer

[1] After this work was completed, a paper on the tripyramid imperfections was published by T. L. Chu and J. R. Gavaler, *Phil. Mag.*, 9, 993 (1964). They had studied the structure of tripyramids by chemical etching and optical microscope techniques. Their crystallographic analysis is similar to that of this work. However, their work does not contain the nucleation mechanism of the tripyramid.

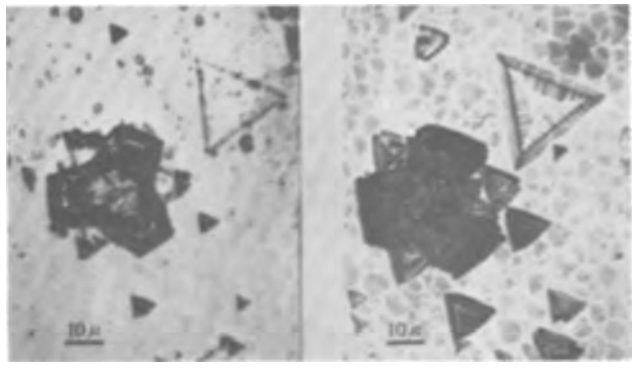

Fig. 2. Etch figure of tripyramid etched with Sailer etch: (a) (left) 2 hr, (b) (right) 3 hr. Dislocation etch pits and triangular etch figures of the stacking faults are revealed simultaneously.

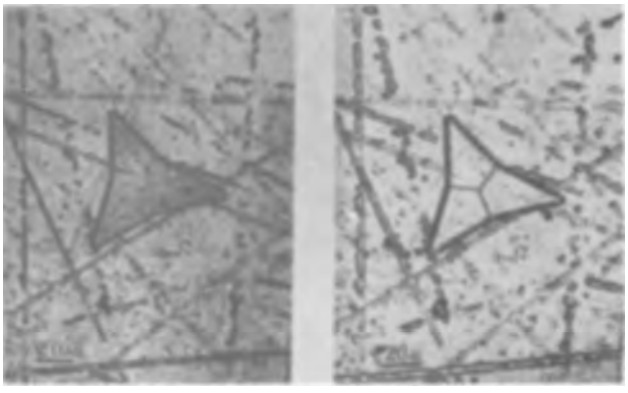

Fig. 3. Etch figure of tripyramids: (a) (left) etched with Sailer etch for 1 hr after partial removing of the hillock; (b) (right) the same samples were etched successively with iodine etch for 10 sec.

etch[2] and the iodine etch[3] were used in this work to bring out clearly the growth pattern of the pyramids. Figure 2 shows an etch figure of a tripyramid etch with the Sailer etch for 2 ~ 3 hr at room temperature. The copper deposited on the surface during Sailer etching was removed with nitric acid. Triangular defect boundaries associated with the tripyramids and isolated stacking faults were definitely revealed. As the Sailer etch shows clearly the area of a tripyramid, but does not reveal its inner structure, a modified etching was tried.

The samples were subjected to the Sailer etch for 1 hr and to the iodine etch for about 10 sec after hillocks were removed by lapping the surface with alundum powder and diamond paste. Whereas etching with the Sailer etch for 1 hr only reveals outlined boundaries (Fig. 3a), a following short period of iodine etching definitely etches the Y-shaped inner boundary between three incoherent crystallites (Fig. 3b). The angle at the tip of the starlike figure is 43°. Surrounding defect boundaries exhibit faster etch rates than inner Y-shaped boundaries. Besides these outer and inner boundaries, stacking faults and twin boundaries are also etched definitely by this technique as shown in Fig. 4. Figure 4 shows the etch figure after the double etching described above. Growth pyramids often associate with stacking faults (Fig. 2a and Fig. 4). It is noted that the stacking faults and the tripyramids are concentric in their configuration and are rotated 60° to each other.

In Fig. 4 the length of an equilateral triangle due to a stacking fault is equal to the distance between two adjacent tips of a starlike tripyramid configuration. This shows that the tripyramids originate at the substrate-epitaxial layer interface and grow in a similar way to the stacking faults. Moreover, it was proved by etching the cross section, that in the presence of stacking faults, the tripyramids originate at the same point as the stacking faults.

[2] 3000 ml NHO_3 + 600 ml HF + 2 ml Br_2 + 23g Cu $(NO_3)_2$ dilute 10:1 with deionized water before use.

[3] 110 ml glacial CH_3COOH + 100 ml HNO_3 + 50 ml HF + 0.3g I_2.

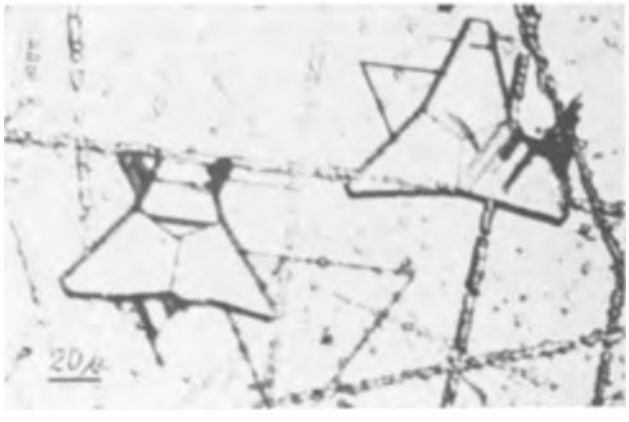

Fig. 4. Etch figure of tripyramids and stacking faults. Etched with Sailer etch for 1 hr and iodine etch for 10 sec.

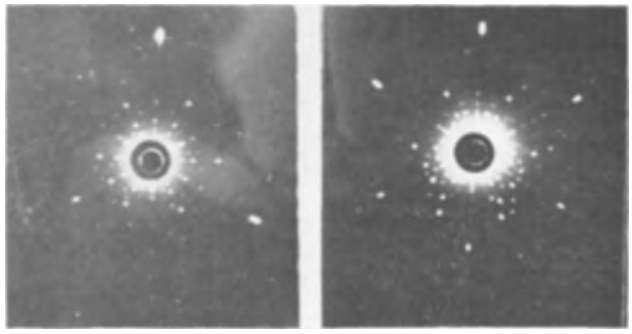

Fig. 5. X-ray back Laue reflection photograph: (a) (left) substrate silicon of [111] orientation; (b) (right) tripyramid hillock region of an epitaxial layer.

However, a tripyramid as shown in Fig. 3b, not associated with the triangular defects of a stacking fault, is often observed. This figure suggests that stacking faults are not essential to the growth of tripyramids.

X-ray back reflection.—The orientation of the crystallite can be shown up by x-ray back reflection. Laue photographs were taken on epitaxial layers with a 80μ growth thickness. A grown layer whose density of tripyramids was more than 5 x 10^4 cm^{-2} showed the following mixed Laue spot pattern (Fig. 5b). (On the sample, whose tripyramid density was less than 1 x 10^3 cm^{-2}, the spot pattern due to only the [111] orientation was observed.)

(I)	[111] substrate
(II)	[111] 180° rotated twin
(III)	[511] due to the rotation about $[\bar{1}11]$ as twin axis.
(IV)	[151] due to the rotation about $[1\bar{1}1]$ as twin axis.
(V)	[115] due to the rotation about $[11\bar{1}]$ as twin axis.

(I) is the substrate orientation and the epitaxial area free from the tripyramids which has substantially a [111] orientation (Fig. 5a). (II) is 180° rotated twins about the [111] substrate orientation. (III), (IV), and (V) are also twin orientations to the substrate crystal, although their axes are not parallel to the substrate [111] direction. Above five axes gave nearly the same intensities, but sometimes one of the intensities of (III), (IV), and (V) became predominantly when one of the three crystallites of the tripyramid grew exclusively as shown in Fig. 1b.

The crystallite orientations of the tripyramids were clarified by the correspondence between the boundary figure of etching and the results of x-ray diffraction (described in detail in the discussion).

Electron diffraction study.—In order to know the origin of four kinds of twins, substrate surfaces were examined by electron diffraction. It was proposed that the overgrowth of SiC on silicon originate twinning of the crystal (5). A silicon wafer of (111) orientation on which carbon of a few angstrom in thickness was deposited in vacuum, was heated at a temperature of 1175°C for 15 min in a hydrogen stream. Electron diffraction showed that the carbon coated silicon surface reacted with the carbon to form silicon carbide (α-SiC). When carbon-coated silicon wafers were used as substrates, the epitaxial layer inevitably produced many tripyramids. Figure 6 shows the effect of carbon deposition on tripyramid nucleation. On the left half

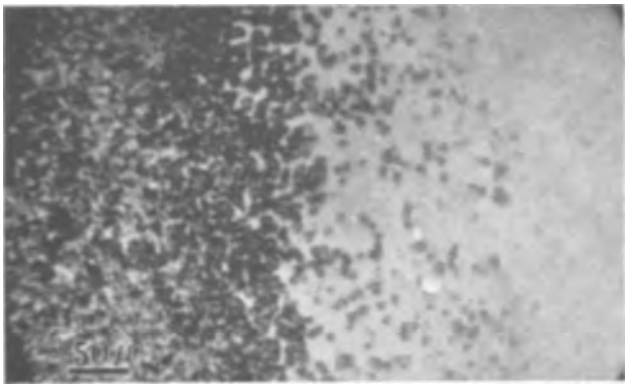

Fig. 6. Effect of carbon deposition on tripyramid nucleation. A carbon film was deposited on the left half region before epitaxial growth.

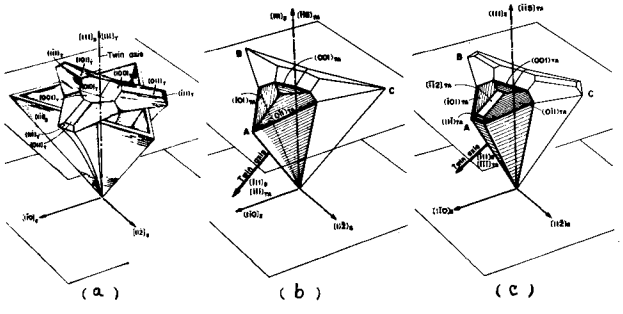

Fig. 7. Three-dimensional diagram illustrating the geometry of the tripyramid: (a) Miller's model, (b) and (c) author's model.

region, a carbon film was deposited before epitaxial growth. In the growth system, a graphite pedestal used as RF heater is the active source of carbon contamination. However in an all silicon-quartz system where no carbon is present, the tripyramid growth was very rare or not observed.

Discussion

Miller *et al.* proposed a crystallographic model and a formation mechanism for the pyramids (5). After their model the tripyramid associates with the twin lamella as shown in Fig. 7a. Tripyramids are 60° twinned to the substrate resulting from overgrowth of the silicon carbide.

From the experimental results of the etching and the x-ray reflection the author derived a model different from that by Miller (5). The schematic diagrams are shown in Fig. 7b and 7c. In the following paragraphs the crystallographic models are discussed in comparison to the Miller model (Fig. 7a).

The orientations of the crystallites in a tripyramid were [511], [151], and [115]. Three crystallites A, B, and C in Fig. 7c are incoherent to each other and were connected through the Y-shaped boundary as shown in Fig. 3b. Since the tripyramids have [511] orientations, they exhibit faster etch rates with the Sailer etch than the surrounding (111) region in Fig. 2. It was shown by partial removing and etching that the tip of the starlike tripyramid grows rectilinearly as shown in Fig. 7b.

The crystallographic indices of the exposed planes of the tripyramid were (110) and (100) (Fig. 7b). The modified form of Fig. 1c exposed (211) and (111) planes too (Fig. 7c). These indices were determined by measuring the height and length under the optical microscope on the basis of the criteria of the [511] and [111] orientations which were established by x-ray diffraction. The results do not agree with the model in Fig. 7a. The interfaces in the layer marked by oblique lines in Fig. 7b were determined in the same way and they appear to be (221) planes to the twinned crystallite.

The tripyramid and the substrate silicon are combined by multiple and complicated twinnings. In a diamond structure 60° twinning axes <111> exist in four ways, [111], [$\bar{1}$11], [1$\bar{1}$1], and [11$\bar{1}$]. All of the twinnings were detected by x-ray diffraction. Twinnings [$\bar{1}$11], [1$\bar{1}$1] and [11$\bar{1}$] correspond to the crystallites A, B, and C, respectively, in Fig. 7b (cf. Fig. 2c).

Although a crystallite A combines with a surrounding (111) layer by twinning about the [$\bar{1}$11] axis, the interfaces between them are not ($\bar{1}$11) plane but have a more complicated boundary. The striped bands in Fig. 4 correspond to the [111] 180° rotation twins. In fact these twins are always present in x-ray diffraction patterns. Because tripyramids without stacking faults are observed (Fig. 3), stacking faults are not essential to growth mechanism.

The cause of twinning was proved to be the formation of silicon carbide by Miller *et al* (5). After their results, the formation of α-SiC (hexagonal) layers on the silicon surface brings forth the twinning by the packing effect. SiC (0001) is parallel to the Si (111). The twin in the diamond lattice is produced when two extra SiC (0001) planes are inserted into a crystal. SiC nucleates at sites along the steps bounded by the (111) planes (5). These steps are produced by the thermal etching or by a reaction of $SiCl_4$ and H_2. Twinning about each of three ($\bar{1}$11) planes of the steps or etch pits on the (111) substrate surface introduces the crystallite of [511] orientation as shown in Fig. 7b. The effect of carbon or silicon carbide on tripyramid nucleation was experimentally proved (Fig. 6). In practical growth conditions, there are some origins which appear to be capable of depositing silicon carbide on the substrate surface beside the carbon pedestal. They are the small quantities of organic solvents such as methane, carbon tetrachloride, etc. (3, 9, 10). Vapor transport reactions of the carbon and silicon have been proposed (5).

It has been concluded that the tripyramid is introduced into the vapor-grown silicon layer through a few atomic layers of silicon carbide formed at the substrate interface. The graphite pedestal and the organic solvents are the active source of carbon contamination. To produce highly perfect epitaxial layers free from the tripyramids, it is necessary to clean the substrate and to remove carbon from the reaction system.

Acknowledgments

The author wishes to thank Dr. S. Takayanagi and Dr. I. Teramoto for their helpful discussions.

Manuscript received July 31, 1964.

Any discussion of this paper will appear in a Discussion Section to be published in the December 1965 JOURNAL.

REFERENCES

1. T. L. Chu and J. R. Gavaler, *This Journal*, **110**, 388 (1963).
2. G. R. Booker and R. Stickler, *J. Appl. Phys.*, **33**, 3281 (1963).
3. K. O. Batsford and D. J. D. Thomas, *Elec. Commun.*, **38**, 354 (1963).
4. T. B. Light, "Metallurgy of Semiconductor Materials," Metallurgical Soc. Conf., Vol. 15, p. 137, Interscience Publishers, New York (1962).
5. D. P. Miller, S. B. Watelski, and C. R. Moore, *J. Appl. Phys.*, **34**, 2813 (1963).
6. T. L. Chu and J. R. Gavaler, "Metallurgy of Advanced Electronic Materials," Metallurgical Soc. Conf., Vol. 19, p. 209, Interscience Publishers, New York (1963).
7. E. Reizman and H. Basseches, "Metallurgy of

Semiconductor Materials," Metallurgical Soc. Conf., Vol. 15, p. 169, Interscience Publishers, New York (1962).
8. H. C. Theuerer, *This Journal*, **108**, 649 (1961).
9. K. Sato, *Oyo Buturi*, **32**, 777 (1963).
10. R. C. Newman and J. Wakefield, "Solid State Physics in Electronics Telecommunications, Proceedings of an International Conference, Brussels," Vol. 1, pt. 1, p. 318, Academic Press Inc., New York (1960).

Vapor Phase Transport and Epitaxial Growth of $GaAs_{1-x}P_x$ Using Water Vapor

G. E. Gottlieb

RCA Laboratories, Princeton, New Jersey

ABSTRACT

It was found that $GaAs_{1-x}P_x$:Te doped layers can be homogenously transported by a vapor phase technique using water vapor. Epitaxial layers of the same As-P ratio as the melt-grown source wafers were grown onto [$\bar{1}\bar{1}\bar{1}$] and [100] GaAs substrates. The reaction proceeds via the following equation

$$2GaAs_{1-x}P_x + H_2O \rightleftarrows Ga_2O + (1-x)\ As_2 + (x)\ P_2 + H_2$$

Ga_2O is the actual transporting species. At a water vapor pressure of 0.286 mm (ice at −30°C) an activation energy of 85 kcal/mole was calculated. The amount of material transported was found to be a function of (*a*) $\sqrt{P_{H_2O}}$ entering the system, (*b*) the temperature difference between source and substrate, (*c*) the composition of the source material, and of course (*d*) the absolute source temperature. The transport of GaAs with water vapor was found to have an activation energy that is nonconcentration dependent within the range of water vapor pressures studied. Certain aspects of Te doping were studied; the oxygen content of the epitaxial layers was studied via mass spectrographic techniques.

The useful and interesting electrical characteristics of GaAs and GaP are well known. A logical extension of the work on these compounds is a study of the properties of the alloys $GaAs_{1-x}P_x$. As in the case with the pure compounds (especially GaP) the alloys are difficult to prepare by normal melt growth techniques. The usual problems encountered in the melt-growth of high melting point materials are concerned with purity and crystallinity. The alloys present the additional problem of homogeneity, *i.e.*, a constant ratio of As to P throughout the matrix.

This paper will discuss the growth of $GaAs_{1-x}P_x$:Te doped layers by a vapor phase technique. This work was instituted in order to obtain a compound having a band gap of 1.72 ev, so that by injection luminescence it emits at 7200Å and thereby stimulates a $CaF_2:Dy^{+2}$ laser. This experiment was performed (1), and it was found that the light emitted by the $GaAs_{1-x}P_x$ diodes was sufficient to stimulate the above-mentioned laser. The difficulties inherent in the melt-growth technique, just mentioned, suggested that vapor phase growth should be used as a preparative technique. Schäfer (2) discussed various aspects of vapor phase transport, the preparation of high melting point materials via volatile intermediates. Antell and Effer (3) applied the technique to III-V compounds, using iodine and chlorine as the transporting agent. Pizzarello (4) synthesized large polycrystalline boules of $GaAs_xP_{1-x}$, using GaAs and P or GaAs and GaP as starting materials and iodine as the transporting agent. Holonyak (5) reported the epitaxial growth of GaAs and GaP, using various chlorides as transporting agent. In the present work oxygen transport was utilized, in contrast to the above worker's use of halide transport. Gershenzon and Mikulyak (6) have also reported the growth of GaP, via a Ga_2O transport mechanism. Previous experience (7) with the transport of GaAs via Ga_2O, in a close-spaced system, indicated that Ga compounds can be transported successfully in this manner. Therefore, the close-spaced system with water vapor as the source of oxygen seemed the logical choice of method.

Frosch (8) has reported the growth of GaP and $GaAs_{1-x}P_x$ utilizing a Ga_2O vapor transport mechanism in an open tube apparatus, with the bulk of the paper devoted to GaP. In contrast to the above, the present paper is largely concerned with the growth of $GaAs_{1-x}P_x$ in the close-spaced system, via Ga_2O. Some of the topics discussed in the above paper are common to those reported in the present work, for example, growth rates, doping, crystal morphology, and usable growth parameters. However, the work reported here is devoted solely to $GaAs_{1-x}P_x$, presenting quantitative data on (a) the effects of temperature, (b) the $\sqrt{P_{H_2O}}$ relationship, (c) the homogeneity of the grown layers, and (d) incorporation of the transport agent into the grown layer.

Experimental

The close-spaced system of Nicoll (9) was used. The source and substrate wafer temperatures were each controlled by separate heaters. To insure an equal temperature over the entire wafer heavy molybdenum disks were placed between the wafers and their respective heaters. Temperature measurement and control were achieved by thermocouples placed in small holes in the molybdenum disks. A spacing of 10 mils was used between the source and substrate. Palladium diffused hydrogen, at a flow rate of 6 cc/min, was passed over ice at −20° to −30°C; the ice temperature was maintained by a salt-ice bath, or by an ethylene glycol-water bath. This technique controlled the amount of water vapor admitted to the system. The various growth parameters were studied by observing the weight loss of the source wafer as a function of the parameter of interest. A detailed description of the apparatus and of the experimental procedure has been given previously (7).

The $GaAs_{1-x}P_x$:Te source wafers were cut from melt-grown ingots. These source wafers were polycrystalline, with a varying As-P ratio. Mechanically polished (111) and (100) GaAs wafers, etched in 1:1:10 $H_2O:H_2O_2:H_2SO_4$ prior to growth were used as substrates.

Results and Discussion

The actual transport is assumed to proceed as follows

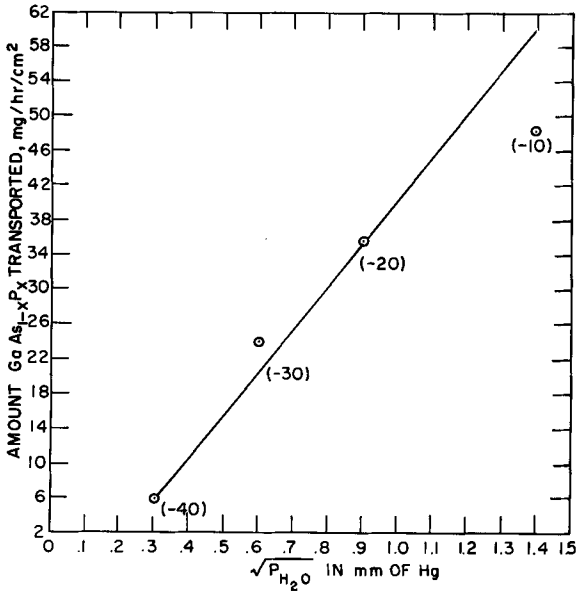

Fig. 1. Amount of $GaAs_{1-x}P_x$ transported as a function of water-vapor pressure. Figures in the parenthesis are the temperatures corresponding to the indicated vapor pressures. T_H, 935°C; T_C, 920°C.

$$2GaAs_{1-x}P_x + H_2O \rightleftarrows Ga_2O + (1-x)\,As_2 + (x)\,P_2 + H_2 \qquad [1]$$

Ga_2O is the transporting species, as demonstrated by several authors (10, 11). It was previously found (7) that the transport of GaAs by H_2O is proportional to $\sqrt{P_{H_2O}}$; this study shows that the amount of $GaAs_{1-x}P_x$ transported (Fig. 1) is also dependent on $\sqrt{P_{H_2O}}$, with some deviation at higher H_2O concentrations. This deviation from the expected relationship could be due to the formation of Ga_2O_3, which was observed in this work at higher water vapor concentrations; (P_{H_2O} above 9 mm). Previous work (12) on the Ga_2O-Ga_2O_3 system is in agreement with the above.

Figure 2 shows a plot of the reciprocal temperature *vs.* the log of the amount of $GaAs_{1-x}P_x$ transported. The activation energy for the reaction, calculated from this graph is 85 kcal/mole, at a water vapor pressure of 0.286 mm (ice at —30°C). Comparative activation energies are 74 kcal/mole, for GaP, at a water vapor pressure of 0.286 mm, and 49 kcal/mole, for GaAs at a water vapor pressure of 4.58 mm (ice at 0°C) (7). The closeness of the activation energies indicates that essentially the reaction is "Ga transport," via Ga_2O.

It was found that the GaAs-H_2O transport reaction has a non-concentration dependent activation energy, within the range of water vapor pressures studied. At 4.58 mm H_2O pressure, the activation energy is 49 kcal/mole and at 0.77 mm the activation energy is 47.4 kcal/mole. This indicates that within the above mentioned limits there are no competing source reactions, ruling out the formation of Ga_2O_3 as represented by the following equation

$$2GaAs + 3H_2O \rightarrow Ga_2O_3 + H_2 + As_2$$

The formation of Ga_2O_3 would also lower the efficiency of the reaction by 1/3 putting an upper limit of 67% on the deposition efficiency. In the present study 80-90% of the weight loss of the source was gained on the substrate.

This lack of dependence of the activation energy on the H_2O concentration is in direct contrast to the GaAs-HCl (13) situation, in which the activation energy is very dependent on the HCl concentration (pressure).

The layers of $GaAs_{1-x}P_x$ obtained in this study were

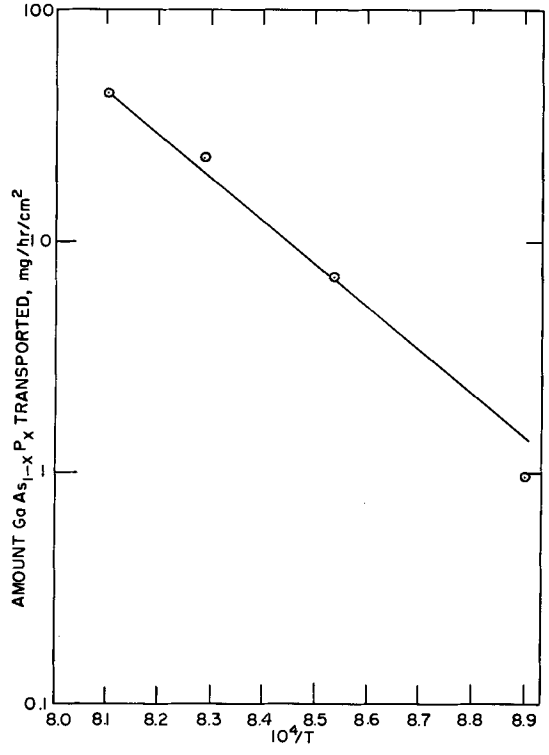

Fig. 2. Temperature dependence of the transport rate plotted as the amount of $GaAs_{1-x}P_x$ transported *vs.* $10^4/T$.

single-phase, single-crystal solid solutions of the above material. A completely mirror-like layer was usually obtained, at a growth rate of one-four mils/hour. Among the factors influencing growth rate are source composition, temperature of source and substrate, temperature difference, and wafer geometry. A good growth rate is not in itself sufficient to produce useful layers. Other factors of importance to be discussed, are substrate perfection, doping and impurities in the films.

It was found that the growth rate varied significantly with the source composition. As shown in Fig. 3, growth rate increased as the percentage of GaP increased. A possible reason for these results is the effect of the reverse reaction. GaAs can be transported at much lower temperatures than GaP. Therefore, at higher temperatures the reverse reaction becomes appreciable, and tends to limit the amount of material transported with a small temperature difference. These results are at temperatures of 935°-920°C (935° hot zone, or source, 920° cold zone, or substrate).

Small changes in the temperature difference have striking effects on the appearance of the grown layers. A $GaAs_{1-x}P_x$ layer grown at 950°-900°C, (900°-cold zone, or substrate), is usually very rough, 940-900 improves the appearance somewhat, but a startling change occurs when 940-920 is used. Under these con-

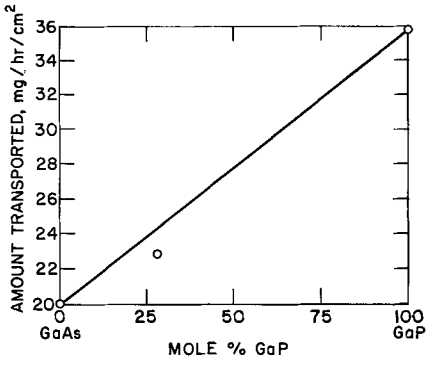

Fig. 3. Dependence of the amount of material transported on source composition. T_H, 935°C; H_2O, at 30°C; flow rate, 6 cc/min.

ditions the layer is mirror-like, with only occasional growth defects. This strong temperature dependence is in direct contrast to the GaAs situation, in which a variation of 50°C in the temperature difference between source and substrate produced hardly discernible changes in the grown layers.

The above facts are partially explained by Fig. 4. This shows that as the temperature difference between source and substrate is decreased, the amount transported also decreases. Although the concentration of Ga_2O in the gas phase is determined by the source temperature, the rate of removal of Ga_2O is determined by the substrate temperature. The same amount of material is therefore arriving at the substrate, but the "sticking probability" is lowered, due to the higher substrate temperature. For this reason, less material is deposited per unit area per unit time. Furthermore, the higher substrate temperature produces an increased surface mobility; this along with the lower deposition rate explains the improved crystallinity observed with small temperature differences. The effect of the temperature difference on the amount of material transported is demonstrated by two experiments performed at a source temperature of 980°C. In the first experiment the substrate temperature was 965°C, and 33 mg/cm²/hr were transported. In the second experiment, all the conditions were the same except that the substrate temperature was decreased to 930°C. In this case 110 mg/cm²/hr were transported.

The dependence of the amount of $GaAs_{1-x}P_x$ transported on the substrate temperature is due to the close-spacing, and the resultant interaction between source and substrate parameters. The close-spaced system approaches the behavior of a sealed system, in which the substrate temperature, by affecting the concentration of Ga_2O in the gas phase, has a profound effect on the amount of $GaAs_{1-x}P_x$ transported, as shown in Fig. 4.

Most of the source wafers were Te doped in the 1-5 x 10^{18} atoms/cm³ range; however, 10^{17} Te/cm³ doping was also studied. Both mass spectroscopic and electrical measurements indicated that in the range 10-100 ppm (2 x 10^{17}-2 x 10^{18}), the Te concentration in the epitaxial layer is the same as that in the source wafer. However, source wafers with up to 300 ppm of Te produced epitaxial layers containing only 100 ppm. This data is shown in Table I. Since the vapor pressure of elemental Te is large, it is not clear whether the Te transports as Te or as TeO_2.

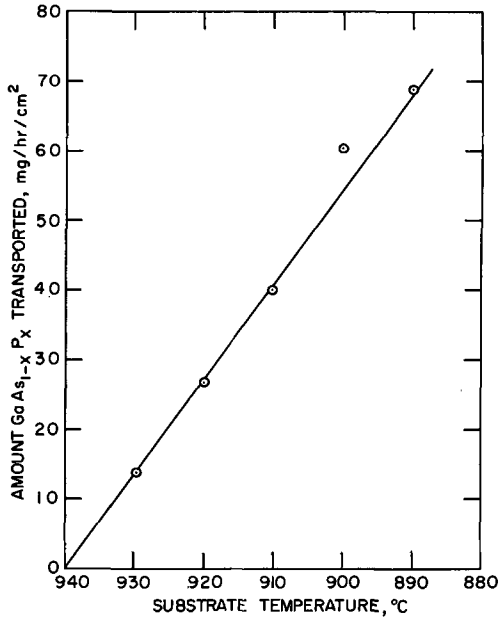

Fig. 4. Amount of $GaAs_{1-x}P_x$ transported as a function of the substrate temperature, at a constant source temperature. T_H, 940°C; H_2O, at 30°C.

Table I.

Number	Oxygen content of source, at. ppm†	Oxygen content of grown layer, at. ppm	Tellurium content of source, at. ppm	Tellurium content of growth layer, at. ppm	Growth rate, mg/hr/cm²
32	—	330	100	100	100
84	3	135	10	10	38.4
97	3	1350	10	10	16.9
116	—	1300	100	100	23.3
122	—	—	7.5 x 10^{17}*	2 x 10^{18}*	24.8
124	—	135	—	10	29.7
126	10	400	—	29	—
143	30	—	300	100	20.4
150	30	330	300	100	20.4

* Determined by Hall measurements.
† At. ppm = atomic parts per million.

The uniformity of the grown layers was studied by ultrasonically cutting small disks (0.040 in. diameter) from an epitaxial layer and corresponding source wafer, and then analyzing the composition of these disks via lattice constant measurements. The results of one such analysis are shown in Fig. 5. The grown layer had a maximum over-all variation in composition of 2%; the diffraction lines were sharp, indicating a variation within each disk of less than ±0.5%. Both the internal variation, and the over-all variation are much less in the grown layer than in the source. The As-P variation in the source is usually about 15%.

The layer shown in Fig. 5 was grown at a rate of ~12 mils/hr. A similar analysis (not shown) was performed on a layer grown at ~1.6 mils/hr. It was found that the maximum over-all compositional variation was also ~2% in this layer. However, the point to point variation was much less in the layer grown slowly, than in that grown more rapidly. Most of the slowly grown layer was one composition, with a single point deviating from this composition by ~2%. This indicates that the compositional variation within the grown layer is dependent on the growth rate. As would be expected, regrowth of a wafer further reduces compositional variation.

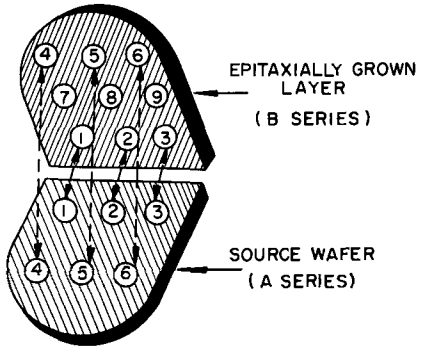

Fig. 5. The relationship between the source composition (A series) and the epitaxial layer composition (B series) is shown. Identical numbers from each series indicate areas adjacent to each other during growth. The substrate in this case was [100] GaAs wafer, grown at 920°C (substrate temperature).

Sample	Lattice Constant Å	Mole % GaAs	Mole % GaP
B_1	5.592	69.9	30.1
B_2	5.596	71.7	28.3
B_4	5.596	71.7	28.3
B_5	5.591	69.3	30.7
B_6	5.596	71.8	28.2
B_7	5.593	70.5	29.5
B_8	5.595	71.0	29.0
A_1	5.586-5.607	67.0-77.2	33.0-22.8
A_2	5.580-5.598	64.0-72.6	36.0-27.3
A_5	5.584-5.609	66.0-78.0	34.0-22.0
A_6	5.581-5.603	64.4-75.2	35.6-24.8

A very few layers had areas of smeared Laue patterns, indicating some type of crystalline imperfection. In order to determine whether these irregularities are already present in the substrate wafers, or whether they are originating in the epitaxial layers, GaAs substrate wafers were etched in 1:1:10 $H_2O:H_2O_2:H_2SO_4$. Of a large number of substrate wafers etched in this manner, only a few showed any type of defect; the majority of the wafers polished in the above etch. The defective wafers were used as substrates, and the layers grown on these wafers had areas of smeared Laue patterns. Correlating these areas with the corresponding substrate areas showed that the substrate irregularity has propagated into the grown layers, manifesting itself as a "smeared" Laue pattern. Microphotographs of this effect are shown in Fig. 6.

Three separate areas on an individual $[\bar{1}\bar{1}\bar{1}]$ GaAs substrate were photographed. Each area is shown prior to growth and after growth of the epitaxial layer; the Laue pattern of the layer in each area is also shown. The substrate and layer photos are magnified 150X. The layer was grown at a substrate temperature of 920°C and a growth rate of 4.6 mg/hr/cm² (0.37 mils or 9 μ/hr). Figure 6(a) shows a severely distorted area. The irregularities are already evident in the substrate and are manifested as a dark area on the deposit photo. The Laue pattern shows broken dots, and the start of ring formation. In Fig. 6(b) the disturbances are less severe. The dots in the Laue pattern are somewhat distorted and broken. Figure 6(c) shows a nondistorted area, with nonbroken dots, essentially defect free single crystal material. Layers grown on the (100) plane were found by visual and microscopic examination to have fewer crystalline defects than (111) growth.

Typical wafer surfaces are shown in Fig. 7. Figure 7(a) exhibits an epitaxial layer grown on a [100] GaAs substrate. The layer was grown at 920°C at a growth rate of 5.4 mg/hr/cm², or 0.43 mil/hr. The mirror-bright surface is manifested by the reflection of the graph paper from the surface. Figure 7(b) depicts a typical epitaxial layer grown on a $[\bar{1}\bar{1}\bar{1}]$ GaAs substrate. The layer was grown at 920°C, at a growth rate of 47 mg/hr/cm², or 3.7 mils/hr.

In a transport reaction the amount of transporting agent incorporated into the grown layer is of interest. For this purpose, mass spectrographic studies were utilized. Table I shows that the source wafers were

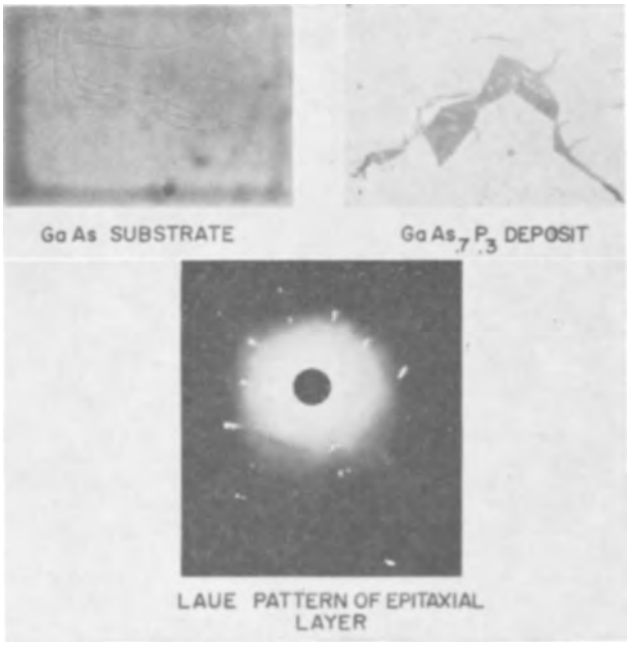

Fig. 6. Three areas on a GaAs substrate prior to growth, the resulting layers, and their Laue patterns are shown: (a) defective area.

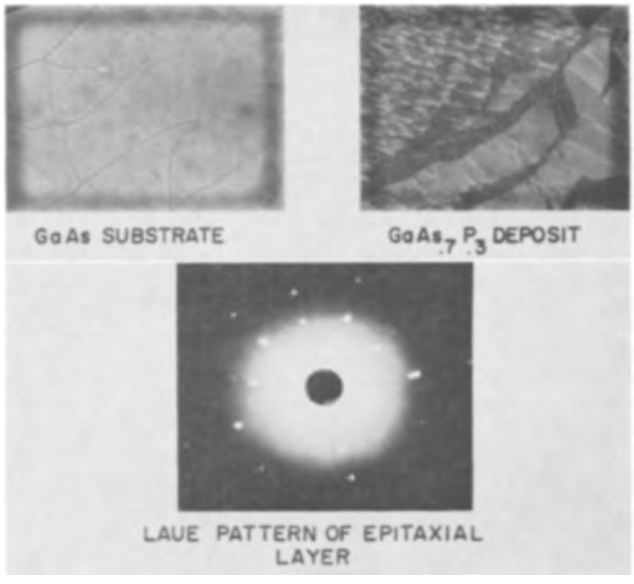

Fig. 6(b). Intermediate area.

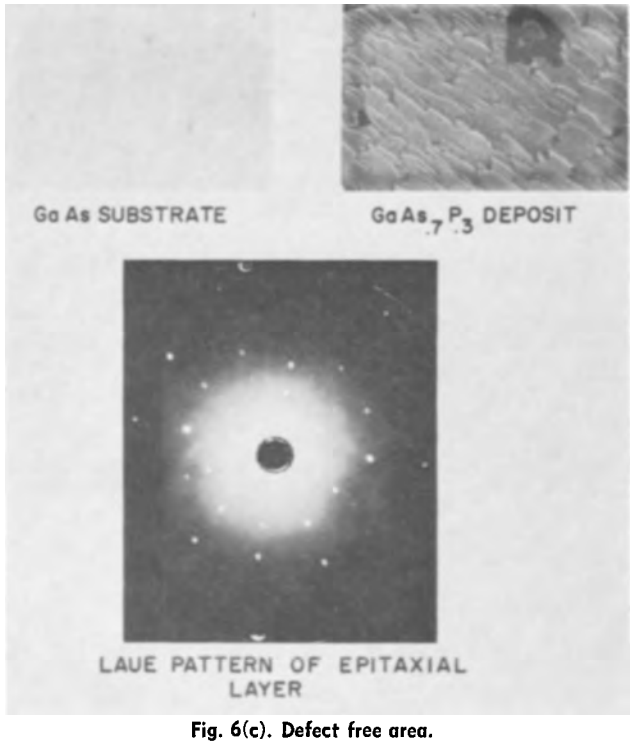

Fig. 6(c). Defect free area.

reasonably low in oxygen concentration. The oxygen content of the grown layers was found to be 100-1000 ppm, or 0.01-0.1 atomic per cent. This is the same range that previous workers (13, 14) found for the incorporation of halide transporting agents in halide vapor grown III-V compounds. A recent report (15) indicates that molybdenum is attacked by oxygen at 550°C; mass spectrographic analysis did not show the presence of any molybdenum in the epitaxial layers. This indicates that the reaction of water vapor with $GaAs_{1-x}P_x$ is favored over the molybdenum reaction.

Single-crystal, single-phase layers of $GaAs_{1-x}P_x$:Te were also grown using powdered sources. Both powdered $GaAs_{1-x}P_x$, and GaAs plus GaP were used. Preliminary investigations on the uniformity of these layers indicate that they are at least as homogenous as the layers grown from melt-grown source wafers.

Summary and Conclusions

It was found that $GaAs_{1-x}P_x$:Te can be homogenously transported in the close-spaced system. A con-

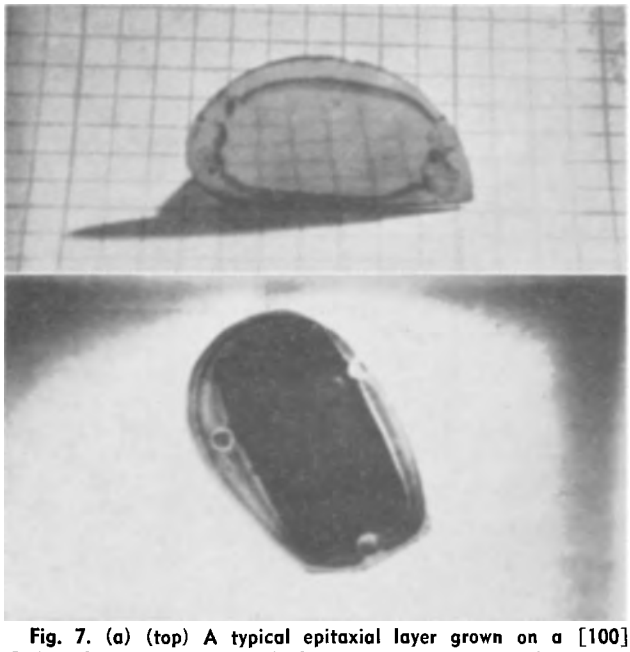

Fig. 7. (a) (top) A typical epitaxial layer grown on a [100] GaAs substrate is shown. (b) (bottom) Depicts a typical epitaxial layer grown on a [$\bar{1}\bar{1}\bar{1}$] GaAs substrate.

trolled amount of water vapor added to the hydrogen stream is the transporting agent. The rate of transport is dependent on $\sqrt{P_{H2O}}$. In the range 2 x 10^{17} — s x 10^{18} Te/cc, the grown layer concentration corresponds to the source concentration in a 1:1 ratio. It was found that the amount of $GaAs_{1-x}P_x$ transported is dependent not only on the source temperature, but also on the temperature difference between source and substrate.

Acknowledgments

It is a pleasure to acknowledge the experimental acumen of J. F. Corboy, Jr. The author is indebted to P. G. Herkart for advice, encouragement, and useful discussions. Thanks are due to R. J. Paff for performing the lattice constant measurements, and to H. H. Whitaker for the mass spectrographic analysis. The author is indebted to P. Robinson for useful discussions and to D. Richman for a critical reading of the manuscript.

Manuscript received April 9, 1964; revised manuscript received Oct. 9, 1964.

Any discussion of this paper will appear in a Discussion Section to be published in the December 1965 JOURNAL.

REFERENCES

1. S. A. Ochs and J. I. Pankove, *Proc. IEEE.*, **52**, 713 (1964).
2. H. Schafer, H. Jacob, and K. Etzel, *Z. anorg. und allgem. Chem.*, **286**, 27 (1956); *ibid.*, 42; H. Schäfer and B. Morcher, *ibid.*, **290**, 279 (1957).
3. G. R. Antell and D. Effer, *This Journal*, **106**, 509 (1959).
4. F. A. Pizzarello, *ibid.*, **109**, 226 (1962).
5. N. Holonyak, "Metallurgy of Semiconducting Materials," p. 49, Interscience Publishers, Inc., New York (1962).
6. M. Gershenzom and R. M. Mikulyak, *This Journal*, **108**, 548 (1961).
7. G. E. Gottlieb and J. F. Corboy, Jr., *RCA Review*, **24**, 585 (Dec. 1963).
8. C. J. Frosch, *This Journal*, **111**, 180 (1964).
9. F. H. Nicoll, *ibid.*, **110**, 1165 (1963).
10. S. Antkiv and V. H. Dibeler, *J. Chem. Phys.*, **31**, 1890 (1953).
11. C. J. Frosch and C. D. Thurmond, *J. Phys. Chem.*, **66**, 877 (1962).
12. C. J. Frosch and C. D. Thurmond, *This Journal*, **111**, 184 (1964).
13. R. Moest, *ibid.*, **109**, 1061 (1962).
14. W. J. McAleer, H. R. Barkemyer, and P. I. Pollak, *ibid.*, **108**, 168 (1961); G. R. Antell, *J. Appl. Phys.*, **31**, 1686 (1960).
15. E. A. Gulbransen, K. F. Andrew, and F. A. Brossart, *This Journal*, **110**, 952 (1963).

Measuring Mobility and Density of Charge Carriers Near a P-N Junction

D. Pomerantz

Laboratory for Physical Science, P. R. Mallory, Burlington, Massachusetts

ABSTRACT

Two types of probe measurement are described which allow the determination of the conductivity mobility and the density of majority carriers in the neighborhood of p-n junctions. The first of these measures the change in sheet conductivity of a layer as a function of the reverse bias applied to a junction bounding the layer. The second measures the capacitance of the junction *vs.* the reverse bias. The techniques are applied to silicon p-n junctions of both the epitaxial and diffused variety. A significant difference is observed in the mobility variation near these two types of junction.

As an aid in the analysis of junction semiconductor devices it is valuable to measure directly the physical properties of the semiconductor in the neighborhood of the junctions. The main properties of interest are the concentration, mobility, and lifetime of charge carriers. This work will describe a method of measuring the first two of these parameters and its application to two widely used silicon junction types; (i) junctions between a lightly doped epitaxial layer grown on a lightly doped substrate of opposite conductivity type and (ii) junctions produced by a heavily doped diffused layer in a lightly doped substrate of opposite conductivity type.

Experimental

Figure 1 illustrates a technique for measuring the differential sheet conductivity of a layer bounded by a junction. The experimental arrangement is similar to a conventional four point resistivity probe (1) except that two additional probes have been added, making contact with the substrate. The current probes, I_1 and I_2, supply a constant current, I, which flows in the n-layer of the sample illustrated, the junction acting as a barrier to current flow in the p-region. The voltage probes, V_1 and V_2, are connected to a high impedance voltmeter so that they do not draw any current and therefore measure the transverse potential drop in the

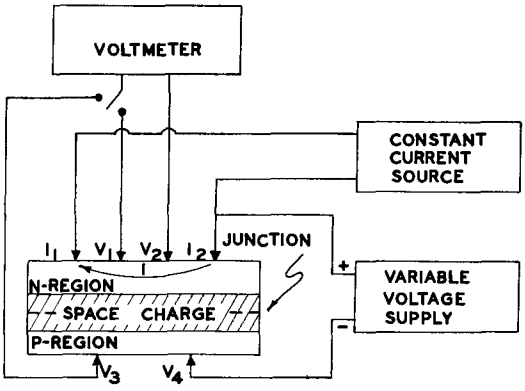

Fig. 1. Experimental arrangement for measurement of differential sheet conductance.

n-layer due to the current I. From this the sheet conductivity may be deduced. The voltage probe, V_4, applies a variable potential to the substrate with respect to the current probe I_2. The sign of this potential is such as to reverse bias the junction. Since the leakage current of the junction flows through probe V_4, it is not suitable for measuring the potential of the p-region. Another probe, V_3, is provided for this purpose which may be connected to the voltmeter through the switch. The voltage applied to the junction is then measured between probes V_2 and V_3. By increasing this applied reverse bias, the junction space charge region is caused to sweep mobile carriers out of the n-layer, decreasing its sheet conductivity. The measurement consists in determining the voltage difference between V_1 and V_2 as a function of the voltage applied to the junction, measured between V_2 and V_3.

The difference between two conductivity measurements at slightly different voltages is a measure of the conductivity of the particular lamina swept out by the space charge when the increment of voltage is applied. The principle of operation is similar to modulation of the channel resistance of a field effect transistor, except that care is taken to operate at sufficiently low currents so that the transverse voltage drop in the layer is small compared to the voltage applied to the junctions, *i.e.*, remote from pinchoff. The measurement may be made with either sign of current flow in the n-region, but more accurate results are obtained if the direction of the current I is such as to forward bias the point contact diode, I_2, through which voltage is applied to the n-layer. When this diode is reverse biased, variations in its reverse characteristic due to noise or surface effects produce variations in the potential of the n-layer. Excess junction leakage current flowing transversely in the n-region will produce an error in the voltage measured between V_1 and V_2. For the polarity of the current, I, shown in Fig. 1, this will increase the measured voltage. The amount of increase may be measured with the current source disconnected. This error voltage is then subtracted from the original reading to obtain the effect of the current I alone. The correction is unmeasurably small for junctions of good quality. The current I is adjusted to be sufficiently large to produce an accurately measurable voltage, but small enough so that injection of minority carriers into the base by the forward biased current probe is negligible. The latter effect is observable as a rapid increase in the current flowing in V_4, as I is increased. This is avoided as it signifies the presence of nonequilibrium carrier concentrations which produce modulation of the n-layer conductivity. Typical values of current lie between 0.2 and 0.5 ma. The measurement of differential sheet conductivity may be made on a whole slice if the junction is sufficiently free of defects. In this way different areas may be measured nondestructively. In practice this situation is rare, and it is convenient to etch onto the slice, through the junction, a pattern of rectangular mesas with dimensions of aproximately 1 by 4 probe spacings. For measuring the properties of both the n- and p-regions, rectangular dice of these dimensions are used.

In addition to the differential sheet conductivity, the carrier density as a function of position must be known in order to determine how the mobility varies in the n-layer. This is determined from capacitance *vs.* voltage measurements as shown in Fig. 2. Here a variable voltage is supplied to the two probes, C_1 and C_2, through a capacitance bridge. Two separate probes, V_2 and V_3, determine the voltage applied to the junction. To avoid errors due to the capacitance of the probes, C_1 and C_2, which are in series with the junction, two additional current supplies are used to forward bias these point contact diodes. The effect is to provide a low resistance in parallel with the capacitance of the contacts. Without this current flowing, the point contacts will be at almost zero bias and can easily have a capacitance which is comparable to the junction. This leads to an erroneously small result. The currents I_1 and I_2 are adjusted so that further increase produces no reduction in capacitance. In practice this leads to values of 20-50 μa.

Theory of Measurement

Figure 3 illustrates the distribution of space charge density near a reverse biased p-n junction. The dotted lines give the net amount of ionized fixed charge. To the right of the origin is plotted the charge density due to ionized donors net of ionized acceptors (N_d) as a function of distance into the n-region which has a thickness, t. To the left is plotted the charge density of ionized acceptors net of ionized donors (N_a) as a function of distance into the p-region.

The solid lines show the total space charge density, $\rho(v,x)$, which is produced when the fixed charge is stripped of its neutralizing mobile carriers by the built-in plus the applied voltage. For the purpose of calculating mobilities, it is not necessary to assume that the charge drops abruptly to zero at the edge of the space charge region. Figure 3 illustrates the more

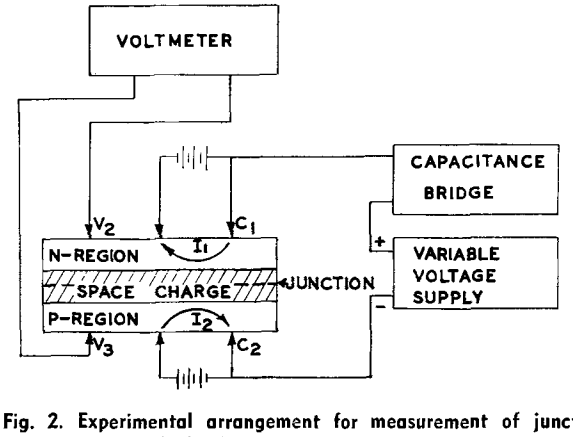

Fig. 2. Experimental arrangement for measurement of junction capacitance *vs.* applied voltage.

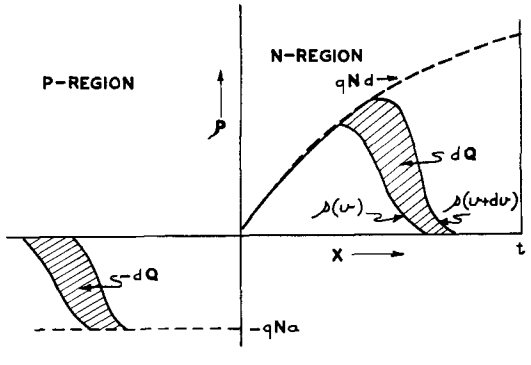

Fig. 3. The net fixed charge density (dashed) and the space charge density (solid) near a p-n junction.

gradual reduction characteristic of small applied voltages. An increase in applied voltage, dv, produces an increase, dQ, in the space charge on the n-side of the junction as shown in the figure. Over-all neutrality requires a space charge, $-dQ$, be produced on the p-side. The small signal capacitance per unit area at this particular voltage is just the ratio of the induced charge per unit area, dQ, to the inducing voltage, dv

$$c(v) = \frac{dQ}{dv} \quad [1]$$

where

$$Q(v) = \int_0^t \rho(v,x)\, dx \quad [2]$$

We now consider the change in sheet conductivity due to the same change, dv, in voltage. It will be seen that to a very good approximation this is attributable to the mobile charge of magnitude $-dQ$ which is removed from the fixed charge dQ in Eq. [1]. The total sheet conductivity of the n-layer is

$$\sigma_s = \int_0^t (nq\mu_n + pq\mu_p)\, dx \quad [3]$$

where n, p, μ_n, μ_p, the electron and hole concentrations and their mobilities are functions of x, the distance from the junction; and q is the electronic charge. The charge density is given by

$$\rho(x) = qp(x) - qn(x) + qN_d(x) \quad [4]$$

Substituting $n(x)$ from Eq. [4] into Eq. [3] gives

$$\sigma_s = -\int_0^t \rho(v,x)\mu_n\, dx + \int_0^t pq(\mu_p + \mu_n)\, dx + \int_0^t N_d(x)\, q\mu_n\, dx \quad [5]$$

In Eq. [5] the second integral is the contribution due to minority carriers plus an equal number of neutralizing majority carriers. This is entirely negligible except for near intrinsic silicon (*i.e.* > 1000 ohm-cm). Since the third integral is not a function of v we have

$$\frac{d\sigma_s}{dv} = -\mu_n \frac{dQ}{dv} \quad [6]$$

The quantity dQ, which is the differential of Eq. [2], is illustrated in Fig. 3. It is equal in magnitude (and opposite in sign) to the area density of mobile charge swept out of the region shown cross hatched in Fig. 3. The average mobility of these charge carriers is μ_n. The expression for the mobility is obtained by eliminating dQ/dv between Eq. [1] and Eq. [6]

$$\mu_n = -\frac{1}{c}\frac{d\sigma_s}{dv} \quad [7]$$

It is to be noted that μ_n is the true conductivity mobility for majority carriers, a quantity normally derived on theoretical considerations from the Hall or drift mobilities. Here it may be determined directly from measurable quantities. The mobility will normally be a function of the applied voltage v, reflecting the variation in crystal properties or impurity concentration at the edge of the space charge region. This voltage will in turn be related to distance from the junction through the capacitance measurement described below. In this way the edge of the space charge, probing into different laminae, determines the variation of mobility within the p- or n-region.

For an infinite sheet, thin compared to the probe spacing, the quantity σ_s in Eq. [7] is given by $\sigma_s = I(\ln 2)/\pi V$ (2) where V is the voltage measured between probes V_1 and V_2, Fig. 1. If the sample area is limited, other correction factors are required. These have been calculated by Smits (2). In the case of a rectangular sample comparable in width or narrower than the probe spacing, some precision is added to the mobility determination by the fact that the width of the sample drops out of Eq. [7]. In this case σ_s is given by (2).

$$\sigma_s = Is/VC'd \quad [8]$$

where s is the probe spacing, d the rectangle width, and C' a numerical factor tabulated in (2) and closely approximating unity for a narrow rectangle. This approximation corresponds to parallel current flow past the voltage probes. If the measurement is made at constant current, the following expression is obtained by differentiation of Eq. [8]

$$\frac{d\sigma_s}{dv} = -\frac{I}{V^2}\frac{dV}{dv}\frac{s}{C'd} \quad [9]$$

The capacitance per unit area c, is determined from the measured capacitance C, by $c = C/da$, where a is the rectangle length. Substituting this expression along with Eq. [9] in Eq. [7] gives

$$\mu_n = \frac{I}{V^2}\frac{dV}{dv}\frac{sa}{C'C} \quad [10]$$

from which d, the sample width, drops out. This expression has been used for obtaining the results described below. The accuracy of the determination is limited mainly by the measurement of the small voltage increment dV. In the measurements described below, dV is of the order of 10 mv and is determined to an accuracy of better than 1% using a precise high impedance differential voltmeter. Such accuracy is necessary to determine the relatively small variation of mobility with doping.

The equations for determining impurity concentration and distance from the junction from the measured values of $c(v)$ are

$$\frac{d}{dv}\left(\frac{1}{c^2}\right) = \frac{2}{qe}\left(\frac{1}{N_d} + \frac{1}{N_a}\right) \quad [11]$$

$$c = \frac{\epsilon}{s_a + s_d} \quad [12]$$

$$N_d\, ds_d = N_a\, ds_a \quad [13]$$

where ϵ is the dielectric constant and s_a, s_d, are the widths of the space charge layer in the p- and n-regions, respectively. Equations [11] and [12] are a generalization of those originally derived by Schottky (3) for the case where either N_d or N_a is large compared to the other. Equation [11] is proved by substituting Eq. [12] and then Eq. [13] into it, remembering that $qN_d\, ds_d = dQ = cdv$.[1] Equation [13] expresses the condition of over-all charge neutrality where ds_d and ds_a are the incremental increases in space charge penetration into n- and p-regions, respectively. In the derivation of these equations it is necessary to assume a sharp edged space charge region, a good assumption for applied voltages large compared to the built-in voltage. For small applied voltages the position coordinates s_a and s_d derived from the above relations must be considered to have an uncertainty of the order of the distance over which the space charge drops from qN_d or qN_a to zero. The mobility and impurity concentration which are determined as a function of s_a and s_d must therefore be considered as averages over this range.

In addition to Eq. [11]-[13] one other relationship is needed to determine the four quantities $N_a(s_a)$ and $N_d(s_d)$, when N_a and N_d are of comparable size. For the case of an epitaxial layer it is reasonable to assume a constant substrate doping, which is then measurable. As will be seen, this assumption may be verified from the results. For the case of a diffused junction there will be a narrow region on both sides of the junction which will be linearly graded, *i.e.*, $N_a = N_d$. As the space charge penetrates into the heavily diffused side of the junction this impurity concentration increases to a large value, eliminating its term from the right side of Eq. [11]. Using each of these assumptions in turn, N_d and N_a, determined from Eq. [11], are plotted as a function of $s_a + s_d$, the total space charge

[1] The author is indebted to E. Pittelli for this result.

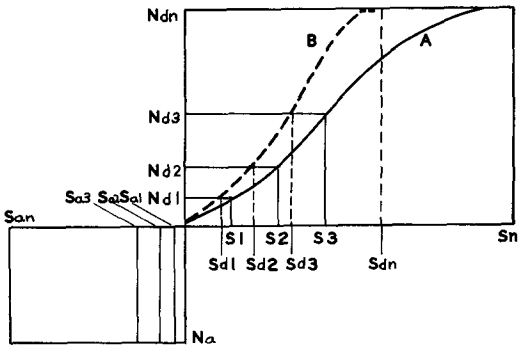

Fig. 4. Method of determining the relative penetration of space charge into the p and n-regions.

width, determined from Eq. [12]. The actual variation of $N_d(s_d)$ is then found by interpolating a curve which approaches the first situation asymptotically for a narrow space charge region and the second situation for a wide space charge region. While this process is not entirely free of ambiguity, a typical example, illustrated in Fig. 6, shows that the error incurred cannot be large.

It is now possible to relate the mobility directly to the net impurity concentration since both have been determined as a function of the total space charge width, $s_a + s_d$, through its dependence, Eq. [12], on the measured value of c. Examples of this result are illustrated by the curves of Fig. 5 and 6. If the differential sheet conductivity measurement is made on both sides of the junction, this relationship can be separately established in the p-and n-regions.

It only remains to separate the space charge into its two components, s_a and s_d. This is especially significant in epitaxial layers on lightly doped substrates since, in this case, a large part of the space charge region may penetrate into the substrate. If, as assumed previously, this region contains a uniform impurity concentration, N_a, the relative penetration of the space charge may be obtained by graphical integration of Eq. [13]. The process is illustrated in Fig. 4, where $s_1, s_2, \ldots s_n$, are successive values of space charge width, increasing incrementally; $N_{d1}, N_{d2}, \ldots N_{dn}$, are the corresponding values of net donor density on the n-edge of the space charge region; $s_{d1}, s_{d2}, \ldots s_{dn}$, are the corresponding penetrations of the space charge into the n-region and $s_{a1}, s_{a2}, \ldots s_n$, the penetrations of space charge into the p-region. The difference equations arising from Eq. [13] are

$$s_{d1} N_{d1} = 2 s_{a1} N_a, \quad s_{d1} + s_{a1} = s_1 \qquad [14]$$

$$(s_{d2} - s_{d1})\ (N_{d2} + N_{d1}) = 2 (s_{a2} - s_{a1}) N_a,$$

$$s_{d2} + s_{a2} = s_2 \qquad [15]$$

etc.

These equations are solved by choosing closely spaced values of s_1, etc., and determining the values of N_{d1}, etc., from the curve derived from Eq. [11], [12], *e.g.*, curve A of Fig. 4. The values of s_1 and N_{d1}, along with the measured N_a, are substituted into Eq. [14] which are solved for the two unknowns: s_{a1}, s_{d1}. These are substituted along with s_2 and N_{d2} into Eq. [15] which are then solved for s_{a2}, s_{d2}. The process continues as far as measurements have been made. The values of s_{d1}, etc., *vs.* N_{d1}, etc., give the actual variation of net donor concentration with distance from the junction, *e.g.*, curve B of Fig. 4. Using this result the position coordinates s_a, s_d, may now be related individually to C and hence to v since $C(v)$ is a measured function. In this way the mobility, previously determined as a function of N_d, is directly related to distance from the junction. For diffused junctions, such as Fig. 6, the penetration on the diffused side is normally quite small and may generally be neglected. When this is not the case it is again possible to use Eq. [13] and through a process of graphical integration determine the quantities s_a, s_d.

It is of interest to determine the range over which the above measurements may be carried out. To do this, we observe from Gauss' electrostatic theorem that the maximum field, which occurs at the junction, $E_{max} = Q/\epsilon \approx 300$ kv/cm. From this we obtain the maximum net area density of donors or acceptors which can be included in the space charge region before breakdown, *i.e.*, $Q/q \approx 3 \times 10^{12}/\text{cm}^2$. Thus, for example, impurities at an average density of $10^{15}/\text{cm}^3$ can be measured out to a distance of 30μ from the junction, a value which is not affected by the distribution of impurities on the other side of the junction. On the other hand, E_{max} may be calculated by integrating the charge due to the measured distribution of net donors or acceptors out to the point of breakdown. This technique is useful for detecting premature breakdown of junctions due to surface effects or field concentrators in the space charge region.

Results

The results of measurements of n-type epitaxial layers on p-substrates and n-type wafers with diffused p-type surface layers are shown in Fig. 5 and 6. For the epitaxial layer of Fig. 5, the solid lines give the net donor concentration, calculated from Eq. [11], and the mobility, calculated from Eq. [10], as a function of total space charge width, calculated from Eq. [12]. The value of N_a used in Eq. [11] was measured as $3.0 \times 10^{15}/\text{cm}^3$. The dashed curves are the result of the graphical integration of the solid curves using Eq.

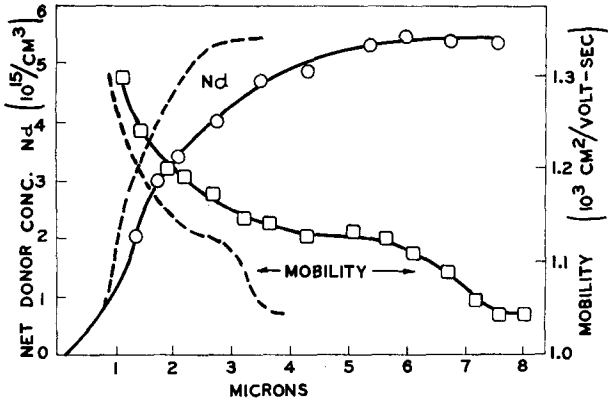

Fig. 5. Variation of mobility and impurity concentration in an n-type epitaxial layer on a p-type substrate. For the solid curves the abscissa is total space charge width. For the dotted curves abscissa is distance into the n-region measured from the junction.

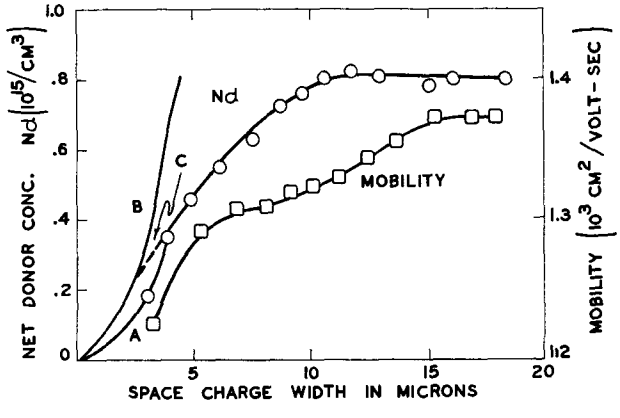

Fig. 6. Variation of mobility and impurity concentration in an n-type substrate with a p-type diffused layer. Curve A is for infinite impurity concentration on p-side of junction. Curve B is for a symmetrical junction. Curve C (dashed) is interpolated between A and B.

[13] as described above. In this case the abscissa is distance from the junction. In the net donor concentration we observe a slow increase in impurity concentration, approaching an asymptote about 3μ from the junction. This increase has been explained (4) as due to etch back of the relatively pure substrate material which dilutes the n-type impurity in the gas phase, so that the first deposited layer is less heavily doped. An alternative explanation is that during the initial growth stage the ratio of n-type impurity to Si deposited is lower than its ratio in the gas phase owing to selective decomposition of $SiCl_4$. This results in a boundary layer next to the growth interface which is enriched in impurities, the process continuing until a steady state is reached. In either case, a reduction in mobility is expected owing to the build-up of impurities in the layer as distance from the junction increases. This is observed as plotted in the two lower curves. The mobility appears to approach an asymptote at about the same position as the impurity concentration asymptote but then suffers another reduction as the surface of the layer is approached. The latter effect is not explained at the present time. As a simultaneous check on this determination of the impurity and mobility profiles it is observed that by integrating the product of these quantities and the electronic charge over the layer, the total sheet conductivity of the layer is obtained, a quantity which can be directly measured by the four probe technique. The limit of integration is determined by a bevel and stain measurement of the layer thickness. The result is expressed by

$$\sigma_s = \int_0^t q\mu_d(s_d)\, N_d(s_d)\, ds_d \qquad [16]$$

Since it is usually necessary to extrapolate μ_d and N_d some distance to the surface of the layer, Eq. [16] is only a rough check. For the specimen of Fig. 5 the difference between the calculated and measured values of σ_s is less than 5%.

In the case of the diffused junction, the mobility variation in the substrate as shown in Fig. 6 is opposite to its variation in the epitaxial layer. The sample is a deep (40μ) gallium diffused p-type region on a 5 ohm-cm n-type substrate. In this case the measured variation in μ_d is due to compensation of the substrate impurities by the tail of the gallium diffusion, so that the total impurity concentration increases as the junction is approached from the n-side, causing a reduction in mobility.

Summary

It has been shown that the conductivity mobility and carrier density may be directly measured in the vicinity of blocking junctions. The probe method of measurement does not require the application of permanent contacts and is therefore useful for characterization of materials to be fabricated into semiconductor devices. In epitaxial layers the mobility is found to increase as the junction is approached. In diffused junctions the mobility is found to decrease as the junction is approached from the substrate side. The difference is attributable to the fact that the diffused junction is produced by compensation, which results in a greater density of scattering centers at the junction than in the substrate, whereas the nature of epitaxial growth is such as to produce a smaller density of scattering centers at the junction than in the layer.

Manuscript received July 27, 1964.

Any discussion of this paper will appear in a Discussion Section to be published in the December 1965 JOURNAL.

SYMBOLS

I	total current in amperes flowing in probe I_1, Fig. 1.
N_a	atoms/cm^3 consisting of the excess of ionized acceptors over ionized donors.
N_d	atoms/cm^3 consisting of the excess of ionized donors over ionized acceptors.
t	thickness in cm of layer being measured.
ρ	space charge density in coulombs/cm^3.
v	voltage applied to junction, v.
x	distance in cm from junction.
Q	total space charge per unit area on the n-side of junction in coulombs/cm^2.
c	small signal capacitance per unit area of junction, farad/cm^2.
σ_s	sheet conductivity, mho/square.
n	number of mobile electrons per cm^3.
p	number of mobile holes per cm^3.
μ_n	conductivity mobility of electrons in cm^2/volt sec.
μ_p	conductivity mobility of holes in cm^2/volt sec.
q	electronic charge, 1.6×10^{-19} coulombs.
V	voltage measured between inner probes, V_1, V_2, Fig. 1.
s	probe spacing in cm.
d	width of sample or mesa in cm.
C'	dimensionless correction factor for sheet conductivity.
a	length of sample or mesa in cm.
C	capacitance of junction in farads.
ϵ	dielectric constant of semiconductor in farad/cm.
s_a	distance in cm between the junction and the edge of the space charge region in the p-region.
s_d	distance in cm between the junction and the edge of the space charge region in the n-region.
E_{max}	maximum value of electric field within the space charge, volts/cm.

REFERENCES

1. L. Valdes, *Proc. IRE*, **42**, 420 (1954).
2. F. M. Smits, *Bell Syst. Tech. J.*, **37**, 711 (1953).
3. W. Schottky, *Z. Physik*, **118**, 539 (1942).
4. D. Kahng, C. O. Thomas, and R. C. Manz, *This Journal*, **110**, 394 (1963).

Diffusion of Gold into Silicon Crystals

G. J. Sprokel and J. M. Fairfield

International Business Machines Corporation, Endicott and Poughkeepsie, New York, respectively

ABSTRACT

Profiles are obtained for gold diffusing into silicon wafers of finite thickness. The profiles do not obey Fick's law. The effects of shallow diffusions of phosphorous and boron on the gold concentration are described; gold concentration is higher in areas of high phosphorous concentration.

Gold is used quite extensively to control the charge storage time of high speed diodes and transistors. Therefore, the diffusion of gold into silicon wafers of finite thickness is important in the design and fabrication of these devices. The diffusion of gold into silicon has been discussed by Struthers (1), Boltaks (2), Dash (3), and more recently by Wilcox and LaChapelle (4). It has become apparent from these publications that gold diffuses quite fast (1, 2), probably occupying interstitial positions of the silicon lattice, and that at least part of these interstitial atoms may convert to substitutionals (3).

In the above diffusion studies experimental conditions were such that the diffusing gold never pene-

trated through the whole specimen. If, however, gold is allowed to reach the opposite surface, as it is in practical applications, unexpected effects are observed. The concentration near the opposite surface is higher than expected and is affected by the state of that surface. It is the purpose of this paper to discuss these effects in some detail.

Experimental Procedures

Briefly, the experimental procedure is as follows. Gold labeled with Au 199 is plated on and diffused into silicon wafers in an argon atmosphere. Thin slices are etched off sequentially, starting at the side opposite the plated surface. The amounts of gold and silicon in each etchant sample are determined, and concentration profiles are constructed from these data.

Wafers are cut from pulled silicon crystals, and the surfaces are lapped and etched. The concentration of electrically active impurities is about 10^{13} at./cm^3. The wafers are approximately 25 mil thick.

Some of these wafers were diffused with phosphorus or boron to study the effects of these diffusions on the gold concentration. Planar structures were used, having been prepared in the conventional way. Silicon oxide was grown thermally; windows were etched in using photolithography; phosphorus or boron was diffused in the window areas to a depth of approximately 1μ. Then gold was plated on the opposite side and diffused in.

Detail.—Carrier-free Au 199 obtained as gold chloride[1] is dissolved in HNO_3/HCl and freeze-dried. The residue is taken up in 1 ml of a plating bath containing $KAu(CN)_2$ 0.01*N*; KCN 0.2*N*; Na_2HPO_4 0.03*N* (5). Immediately before plating the surface is "roughed" using 600 grit SiC paper and cleaned ultrasonically. Adhering plates were obtained on all wafers. The plate contains 1.5 x 10^{18} at. of Au, sufficient for an average concentration of 4 x 10^{19} at./cm^3 in the wafer. The ratio of Au 199 to Au 197 is adjusted to about 10^{-4}, sufficient for a detection sensitivity of 5 x 10^9 at. Au/cpm.

The gold is diffused in an argon atmosphere to prevent oxidation of the wafer surface. The argon gas was monitored for Au 199. Evaporation of gold is negligible.

In preparation for the etching sequence, the wafer is cemented to a Teflon[2] rod with the plated side toward the Teflon. The rod is inserted into a polypropylene test tube, containing 5 ml etching solution cooled to about 0°C in melting ice, and rotated to provide gentle agitation. The etching solution used in most of this work is a mixture of 3 parts HNO_3 s.d. 1.4; 2 parts glacial acetic acid; and 1 part HF 48%. Etching times are adjusted to remove the amount desired, then the etching solution is replaced and the process repeated until the wafer is dissolved.

Immediately after etching all samples are assayed for gold by counting the Au 199 gamma peak at 0.158 Mev in a single channel gamma spectrometer. By comparing the count rates of the etchant samples with the count rate of known aliquots of the plating bath, the amount of gold in the etchant is calculated. The amount of silicon in the etchant is determined by neutron activation analysis. The etchant solution, transferred into a suitable polypropylene container, is irradiated with fast neutrons produced by the reaction T(d, n) He 4.[3] The assay of silicon is based on the reaction Si 28 (n, p) Al 28. The only interfering reaction is O 16 (n, p) N 16. Compton scattering from the O 16 gammas causes considerable background at the silicon peak. Therefore the etchant samples are cooled for 2.5 min before they are counted. The O 16 activity has now decayed to 10^{-6} of the original amount, while Al 28 activity has decreased only to 0.46. The neutron flux is not constant enough for quantitative work, therefore each etchant sample is irradiated together with a silicon standard. From this one can calculate the total flux for the particular irradiation period, but since the fast neutron flux is moderated by the etchant solution (essentially water) a correction is necessary. The correction can be obtained by irradiating a silicon standard together with a solution made by dissolving a known amount of silicon in etching solution. The sensitivity of the method for pure silicon, under the experimental conditions of this study, is about 5 μg/cpm at a background of about 4 cpm, and for the etchant solution about 10 μg/cpm at a background of about 10 cpm. This background depends on the chemicals used; in particular HNO_3 contains measurable amounts of silicon. The samples of etchant solution contain 5-20 mg of silicon. Therefore the sensitivity is quite adequate. Since chemical operations are not involved the method of assay is quite fast, about 10 min/sample.

The amount of silicon in the etchant solution determines the thickness of the slice removed from the wafer. The amount of gold in the etchant solution and the volume of the slice determine the local concentration of gold. The sum of the thickness of the slices should add up to the thickness of the wafer. The difference is usually less than 0.001 in., the average for all wafers checks within 0.0002 in. However, the standard deviation for one sample is about 25% of the average. Since this would cause a similar spread in the data for the gold concentration, determination of the actual amount removed greatly improves the accuracy of the data.

Results

Concentration profiles.—Figures 1 and 2 show concentration profiles after diffusion at 1000° and 1100°C, respectively. All profiles are characterized by a nearly horizontal central region. Near the gold side the concentration drops 2 or 3 orders of ten in a distance of 1 or 2 mils. Near the opposite side the concentration tends to increase. The concentration in the central

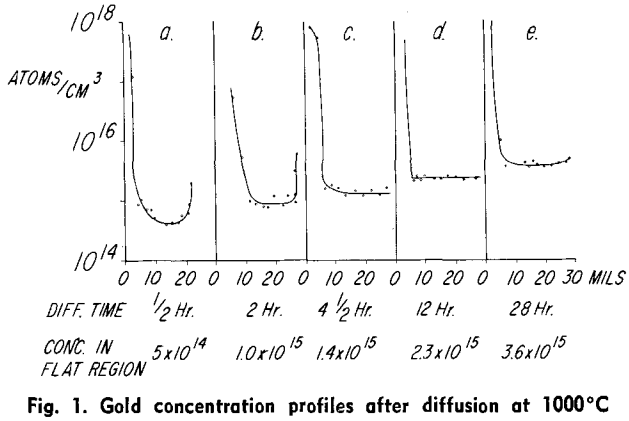

Fig. 1. Gold concentration profiles after diffusion at 1000°C

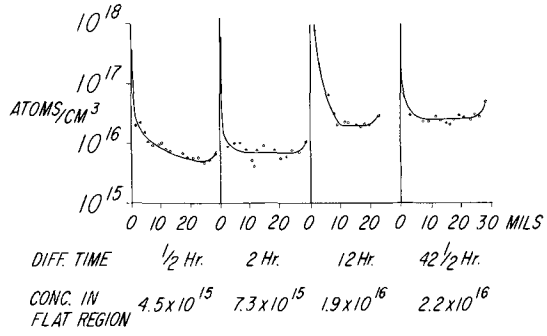

Fig. 2. Gold concentration profiles after diffusion at 1100°C

[1] Western New York Nuclear Research Center, Buffalo, New York.

[2] Registered Trade Mark, E. I. du Pont de Nemours Company, Wilmington, Delaware.

[3] The neutron generator is built by Texas Nuclear Corporation, Austin, Texas.

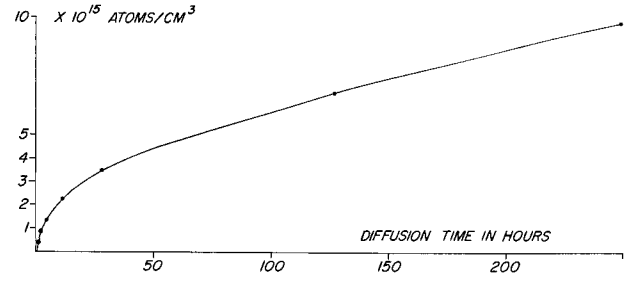

Fig. 3. Gold concentration in central region plotted vs. time, temperature 1000°C. Data are those given in Fig. 1 except the points at 128 and 256 hr. These were obtained by neutron activation analysis.

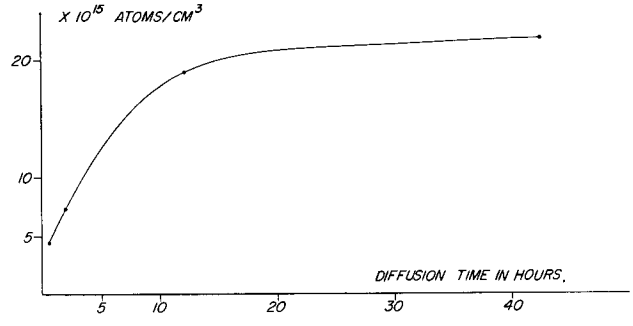

Fig. 4. Gold concentration in central region plotted vs. time, temperature 1100°C. Data from Fig. 2.

region increases with diffusion time as indicated in Fig. 3 and 4, but the location of the steep gradient near the gold side is independent of time. Therefore the steep gradient must be considered an artifact of the experiment. At the plated surface gold-silicon eutectic is formed. The eutectic melt does not wet the surface but may well extend, in localized spots, to a depth of a few milli-inches.

Radial homogeneity.—Data in the previous section refer to the average gold concentration in a slice. Autoradiograms of etched wafer surfaces indicate substantial homogeneity across the surface. However, nearly all autoradiograms made in the course of this study show spots of much higher gold concentration. The number of such spots is small except near the original wafer surface. Spots tend to conglomerate at the original surface, but a shallow etch removes most of this activity. The size of single spots on the film is of the order of 10μ. The activity in one spot cannot be measured directly from the optical density because the x-ray film is overexposed at that spot. To make an appreciable contribution to the total, the activity in one spot would have to be 10^6 times larger than the average, which is unreasonable. Therefore, wherever the number of spots is small, the contribution of this localized gold can be neglected.

Often the same configuration of spots appears in autoradiograms from several sequential etches. In such cases gold has clearly accumulated along lines extending into the crystal, probably dislocations. These lines may extend 5 mils or more. Since their number is small, typically less than 1/mm^2 they cannot contribute to a fast transfer of gold through the wafer.

If a wafer which has been shown to contain this type of gold accumulation is heated for a long time (20 hr or more), no appreciable change in the number of spots is found. Under these conditions there is no external supply of gold, and since the lattice is far from saturated one would expect the accumulations to disappear completely if they contributed to the transfer.

Surface effects.—The amount of gold collecting near a wafer surface depends on the surface preparation. It is smaller for etched surfaces than for etched and oxidized surfaces. If a gold diffused wafer is etched and heated again, gold collects near the surface mostly in localized spots which can be removed by a shallow etch in agreement with an earlier observation (7). The increase in the gold concentration under an oxide layer can be used to prepare autoradiograms of oxide-masked wafers. The window areas appear lighter.

Shallow phosphorous diffusions also affect the gold concentration. At high phosphorous concentrations (8 x 10^{20} at. P/cm^3 at the surface) the window areas are darker and have therefore collected more gold (Fig. 5a). However, at low concentrations (2 x 10^{20} at. P/cm^3 or less) the masked areas are darker. Therefore the mask dominates at low concentration (Fig. 5c).

The electrical junctions are about 1-2μ from the surface. If substantially more than this is etched-off, a pattern as in Fig. 5a reverses; the window areas are now lighter. A pattern as in Fig. 5c remains unchanged. Therefore, the effect of the masking still persists 10 or 20μ from the SiO_2/Si interface (Fig. 5b and 5d). The window areas in Fig. 5b and 5d are no longer sharply delineated but appear diffuse. Examining autoradiograms of gold in a phosphorous diffused area under a microscope shows that the gold is not uniformly distributed over the area but tends to build up near the edges (Fig. 6). Boron diffusion does not produce comparable effects but the highest concentration used was only 1 x 10^{20} at. B/cm^3.

Discussion

From Fig. 1-4 it is seen that the concentration of gold in bulk silicon, introduced from an infinitely large source at the surface, increases smoothly with time, rapidly for short diffusion times but only slowly for longer diffusion times. At 1100°C the gold concentration is 2.2 x 10^{16} at./cm^3 after 42 hr diffusion time. At 1000°C the concentration is 9.8 x 10^{15} at./cm^3 after 250 hr. Collins, Carlson, and Gallagher (7) have reported data on the solubility of gold in silicon. Details are not given, but by interpolating the graph in Fig. 1 of their paper, the solubility may be shown to be approximately 3 x 10^{16} at./cm^3 at 1100°C and 9 x 10^{15}

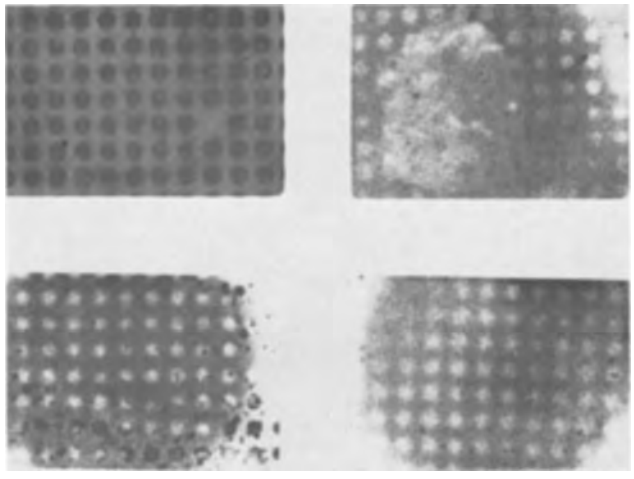

Fig. 5. Au 199 autoradiograms of P diffused wafers. Circular windows (diameter 400μ) etched in oxide mask. P diffused from PH_3. Junction depth 1-2μ. Au 199 diffused from a plate on the opposite surface. Excess removed prior to exposure. (a) (top left) 8 x 10^{20} P/cm^3. After Au diffusion oxide mask removed in HF. Window areas contain more gold than masked areas; (b) (top right) same as 5a but etched to a depth of 10μ. Window areas are now lighter. The area in the center indicates the spot where the oxide mask was removed prior to gold plating (to assure good contact); (c) (bottom left) 2 x 10^{20} P/cm^3. Window areas contain less gold than masked areas. Autoradiogram shows the original surface, before cleaning in HF. Notice spots of high Au concentration in 5c, absent in 5a; (d) (bottom right) Same as c but etched to a depth of 25μ. The pattern remains unchanged.

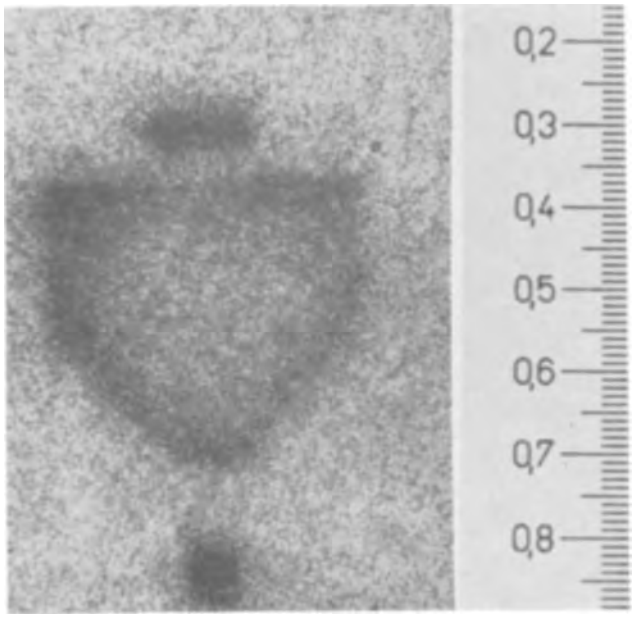

Fig. 6. Accumulation of gold in a phosphorous diffused area, starting at the circumference and proceeding inward. It appears that the intersection of mask and window has a larger effect on the gold concentration than the diffused phosphorous itself. (Scale 10μ/div.).

at./cm^3 at 1000°C. Numerically these data agree well; however from the slope of the curve in Fig. 3 it is doubtful whether solubility has been reached. The true solubility is probably slightly higher. The data in Fig. 3 and 4 will be used in a forthcoming paper (8).

The buildup of gold occurs much faster around areas of lattice imperfections or discontinuities (*e.g.*, surfaces, dislocations, phosphorous diffusion, etc.). This phenomenon can be explained by an interstitial-substitutional model, as discussed by Frank and Turnbull (9) for copper in germanium and used by LaChapelle and Wilcox (4). Gold diffuses rapidly as an interstitial but converts to a relatively immobile substitutional by combining with a lattice vacancy. This conversion occurs more rapidly near sources of vacancies.

Surfaces are sources of vacancies; thus the total concentration builds up near the surface as evidenced by the graphs in Fig. 1 and 2. Thermally oxidized surfaces can produce more vacancies than unoxidized surfaces. Mechanical damage of the surface can produce more vacancies still.

The observed accumulation of gold along lines extending into the crystal may well represent dislocations. A mechanism discussed by Dash (3) in which the collecting gold induces dislocations to climb could well be operative. The stability of these accumulations emphasizes the relative immobility of gold atoms in the substitutional state.

Finally, damage or dislocations from high surface concentrations of phosphorus act as sources of vacancies and thereby collect gold relatively rapidly. This fact is particularly important when high surface concentration phosphorous diffusions are used to make high speed diodes and transistors. In such devices, the amount of gold is intimately related to the charge storage times.

Conclusion

There is qualitative evidence for the interstitial-substitutional mechanism; a gold atom diffuses as an interstitial but is converted to a nearly immobile substitutional. The conversion occurs everywhere but is particularly prominent near sources of vacancies. Gold collects especially fast in areas prediffused with a large concentration of phosphorus.

Gold can be used to study damage done to a lattice by phosphorous diffusion or oxidation.

Manuscript received July 22, 1964; revised manuscript received Sept. 14, 1964. This paper was presented at the Toronto Meeting, May 3-7, 1964.

Any discussion of this paper will appear in a Discussion Section to be published in the December 1965 JOURNAL.

REFERENCES

1. J. D. Struthers, *J. Appl. Phys.*, **27**, 1560 (1956); **28**, 516 (1957).
2. B. I. Boltaks, G. S. Unlikov, and R. S. Malkovich, (English) *Sov. Phys. Solid State*, **2**, 2134 (1961). Also, B. I. Boltaks, "Diffusion in Semiconductors," Academic Press, New York (1963).
3. W. C. Dash, *J. Appl. Phys.*, **31**, 2275 (1960).
4. W. R. Wilcox and T. J. LaChapelle, *ibid.*, **35**, 240 (1964)
5. W. Blum and G. B. Hogaboom, "Principles of Electroplating," 3rd ed., McGraw-Hill Publishing Co., New York (1949).
6. G. Bemski and J. D. Struthers, *This Journal*, **105**, 588 (1958).
7. C. B. Collins, R. O. Carlson, and C. J. Gallagher, *Phys. Rev.*, **105**, 1168 (1957).
8. G. J. Sprokel, To be published.
9. F. C. Frank and D. Turnbull, *Phys. Rev.*, **104**, 617 (1956).

A Study of the Dissolution of Zinc in Buffered Acetic Acid Solutions

Robert S. Alwitt[1] and Robert S. Kapner

Department of Chemical Engineering, Rensselaer Polytechnic Institute, Troy, New York

ABSTRACT

The kinetics of zinc dissolution in buffered acetic acid solutions are described. The dissolution process occurred along the walls of zinc tubes with acid solutions passing through the tubes in laminar flow. Only a moderate degree of diffusional resistance in transporting reactants to the reaction surface was observed. The data indicate that molecular acetic acid as well as hydrogen ions participate in the cathodic reaction. Possible dissolution mechanisms are proposed based on simultaneous reactions involving hydrogen ion and molecular acid discharge at the metal surface. Only at high acid concentrations does the molecular acetic acid discharge reaction become important.

The purpose of this investigation was to obtain information on the kinetics of the dissolution of zinc by acetic acid. Using buffered acid solutions, in which the *p*H and molecular acid concentration could be varied independently, information was obtained on the role of the weak acid molecule in the dissolution process. There is little information in the literature on this point.

Kilpatrick and Rushton studied the dissolution of rotating zinc and magnesium cylinders in deaerated solutions of HCl, acetic acid (HAc), and other weak acids (1). They found the reaction rate to be dependent on rotational speed and viscosity, both indicative of a significant degree of diffusion control. However, for both HCl and HAc, the activation energy was about 10 kcal/mole, far greater than the 3-4 kcal/mole to be expected for a reaction under complete diffusion control. The reaction rate was first order with respect to total acid concentration, but not to the hydrogen ion concentration alone. They concluded that the surface reaction was due to both ionic and molecular acids, but the results were not clear-cut. Levich (2) reported a study of the dissolution of rotating magnesium disks in 0.1*N* HCl, 0.15*N* HAc, and 0.15*N* HCOOH. The data indicated that in all cases the reaction rate was determined by the diffusion of acid to the surface. Allbutt and Tolley (3) determined the dissolution rate of zinc in dioxan-water solutions of HCl. At sufficiently high dioxan concentrations an appreciable fraction of the HCl was present in molecular form. In these solutions the data indicated the possibility of direct reaction between zinc and covalent HCl.

The dissolution of a metal by an acid can be considered as consisting of simultaneous anodic and cathodic electrochemical processes. According to the Wagner-Traud theory of mixed potentials (4), which has been substantiated for simple systems, each process can be analyzed independently of the other. In this paper only the cathodic processes occurring on the zinc surface are discussed. In a strong acid, the usual cathodic reaction is reduction of hydrogen ions to atomic hydrogen and thence molecular hydrogen. With a weak acid, another possible cathodic reaction is reduction of the molecular acid species.

It was anticipated that dissolution would be under significant diffusion control, which would result in the reactant wall concentration being less than the bulk concentration. In such a situation it is imperative that the experimental reactor be of a design that will permit calculation of wall concentrations from experimentally measurable quantities. The two designs most frequently used for this purpose are the rotating disk and the tubular reactor. The latter was used in this study.

The "quasi-stationary" technique of Frank-Kamenetskii (5) was used to calculate wall concentrations. This method assumes that the conditions of diffusional transport can be considered independent of the course of the surface reaction. The fact that the diffusion and reaction processes are coupled by a surface boundary condition is neglected. This results in consideration only of transport in the direction normal to the surface, neglecting reactant that arrives due to longitudinal convective transport. Any error inherent in this method can be substantially reduced provided longitudinal concentration differences are kept very small. This can be easily accomplished in a differential reactor, one in which reactant conversion is minimized.

With these assumptions, the amount of reactant supplied at steady state to an element of reactor surface is

$$q = \beta (C - C_W) \qquad [1]$$

At steady state, q must equal the surface reaction rate. The definition of β, the diffusion velocity constant (or mass transfer coefficient) is $\beta = N_{Nu}D/d$. Since diffusion is considered to be independent of the surface reaction process, β can be determined from analogous heat transfer data or theory. With q and C determined experimentally it is a simple matter to calculate C_W.

Experimental

The dissolution of zinc by buffered and unbuffered solutions of acetic acid was studied in a tubular reactor. The ranges of the independent variables were: C_{HAc}, 10^{-3} to 10^{-2}M; *p*H, up to 6.0; N_{Re}, 50-1000. Sodium acetate was used as the buffering salt. Except for runs to determine the heat of activation, the temperature of the test section was maintained at 30° ± 1°C. Prepurified nitrogen was bubbled through the acid solution for 4 to 12 hr prior to the start of a run to remove dissolved oxygen. Reagent grade chemicals and distilled water were used throughout. The reactor section was made of 99.999% zinc. As-received zinc billets were pickled, recast in Pyrex tubes, machined to the dimensions of schedule 80 ¼ in. pipe, and chemically polished. These zinc tubes were annealed in an argon atmosphere for 24 hr at 350°C and then repolished. Metallographic examination at 400X showed no evidence of cold-work on the inner surface of a sample.

The test apparatus is pictured in Fig. 1. The test section consisted of three lengths of zinc tube connected by flange and O-ring assemblies to give a total length of 33.3 cm. The dissolution rate was low enough so that the inside diameter of the tubes did not change significantly during these runs. Entrance and exit

[1] Present address: Engineering Laboratories, Sprague Electric Company, North Adams, Massachusetts.

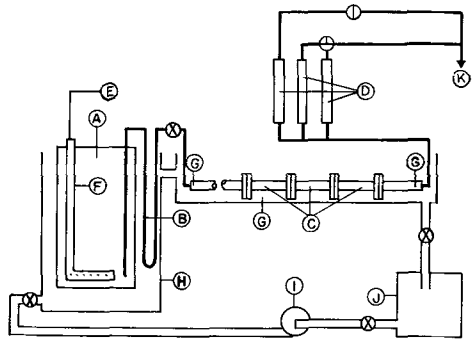

Fig. 1. Experimental apparatus: A, acid reservoir; B, glass heat exchanger; C, zinc tubes; D, Rotameters; E, N_2 supply; F, N_2 header; G, thermocouples; H, water drum; I, water pump; J, water surge tank; K, effluent.

sections were schedule 80 ¼ in. PVC pipe of sufficient length to insure well-developed laminar flow in the test section. Acid solution was fed through the reactor by maintaining a constant positive head at the outlet of the acid reservoir with a pressure-regulated source of nitrogen. Flow rate was regulated with the stopcocks after the rotameters. Reaction conditions were such that the hydrogen concentration never exceeded the solubility of hydrogen. The test section and polyethylene acid reservoir were held at constant temperature by a temperature controlled circulating water bath heated by immersion heaters not illustrated in Fig. 1.

Procedure.—When not in use, the test section was filled with distilled water. At the start of a run, 2 x $10^{-3}N$ HAc was run through for 40 min to remove any oxide build-up on the tube surface during storage in water. Acid made up to the desired composition in the reservoir was passed through the reactor at several flow rates. At the slowest flow rate it was found that after running for 20 min steady-state conditions were assured. At all flow rates, 20 min were allowed before collecting effluent samples. The concentration of zinc in the effluent was determined for each flow rate using a modification of the spectrophotometric method of Rush and Yoe (6, 7). At each acid composition 3-6 flow rates were run in random order. Corresponding to each effluent sample the potential of the zinc was determined with reference to a saturated calomel electrode (SCE) kept at 30°C in the same water bath. Potential readings were made with a Beckmann Model G *p*H meter. Further details of the experimental apparatus and procedure can be found elsewhere (8).

Results

From the data of replicate runs it was found that reaction rates were reproducible within ± 15.8% and corrosion potentials were reproducible within ± 6 mv, both at the 95% confidence level.

For each acid composition the least squares line for log C_{Zn} *vs.* log N_{Re} was determined. Some typical results are shown in Fig. 2. The average slope of all runs was —0.930 ± 10.3%. The slope was not a function of HAc concentration or *p*H. In the absence of diffusional effects the slope would be —1 and for complete diffusion control it would be —2/3. There is no theoretical reason for a linear relationship in the region of intermediate control. In the present case the justification is that the residual variance of the least squares lines was not significantly greater than the variance of replicate points.

Since there were some diffusional effects, the concentration of reactants at the wall were less than the bulk concentrations. The wall concentration of HAc was calculated using the approximate method of Frank-Kamenetskii (5) described above. For each acid composition the calculation was made at N_{Re} = 150, using the C_{Zn} from the least squares line to determine the average reaction rate over the reactor. The average Nusselt number for a tube of length L is $1.61(N_{Pe}d/L)^{1/3}$ (9). Over the range of bulk concentration used, the diffusivity of acetic acid varies less than 1% and was calculated to be 1.34 x 10^{-5} cm²/sec at 30°C (10). Using these values and the dimensions of the reactor, the value of β in Eq. [1] was 3.78 x 10^{-4} cm/sec. An experimental determination of β agreed within 5% with the calculated value. The fraction of acid reacted was always less than 3%, so the reactor was considered a differential reactor with bulk acid concentration equal to the inlet value.

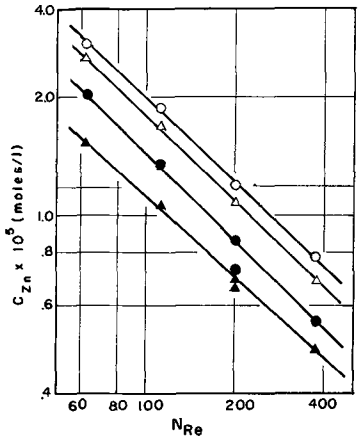

Fig. 2. Typical experimental results. ${}_BC_{HAc} \times 10^3$: ▲, 2.00; •, 3.92; △, 7.76; ○, 10.04.

The average value of the ratio ${}_WC_{HAc}/{}_BC_{HAc}$ calculated from Eq. [1] was 0.895. Ninety-five per cent of the values were greater than 0.75. Assuming no concentration gradient in acetate ion, the gradient in C_{H^+} was proportional to that in C_{HAc}. Figure 3 shows the relationship between C_{Zn} at N_{Re} = 150 (proportional to reaction rate) and wall concentration of HAc at various bulk *p*H values.

The electrode potential of the zinc was independent of flow rate. It was a function of acid concentration

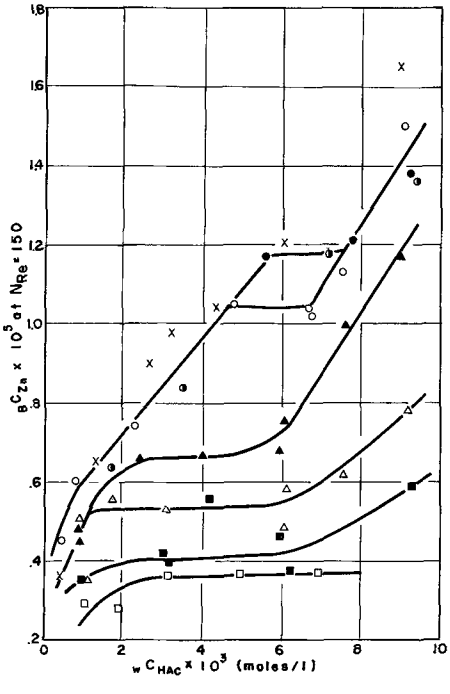

Fig. 3. Reaction rate vs. wall concentration of acetic acid. N_{Re} = 150; *p*H: X, no buffer; •, 3.50; half dark circle, 3.80; ○, 4.10; ▲, 4.50; △, 5.00; ■, 5.50; □, 6.00.

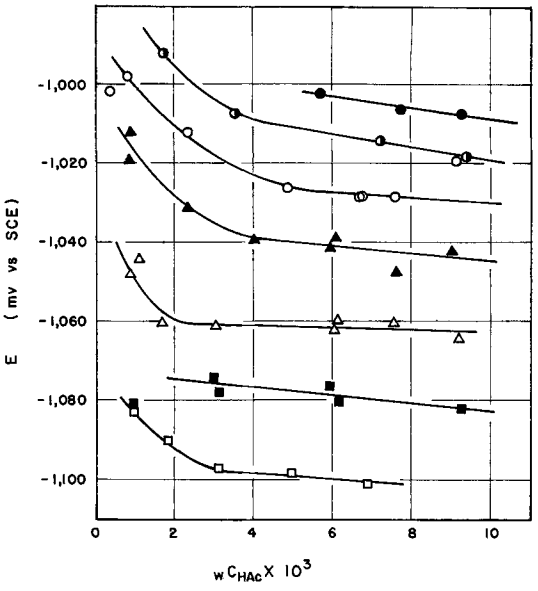

Fig. 4. Zinc potential vs. wall concentration of acetic acid. N_{Re} = 150; pH: ●, 3.50; half dark circle, 3.80; ○, 4.10; ▲, 4.50; △, 5.00; ■, 5.50; □, 6.00.

and pH, as shown in Fig. 4. Values of potential with unbuffered acid are not given since it was very difficult to obtain steady or reproducible results with these solutions. At a concentration of 5 x 10^{-3}M, acetic acid has a conductivity of only 100 μmhos. With this acid the impedance of the solution path between the zinc and the reference electrode was about one megohm. This is high enough to account for the observed erratic potential readings.

The change of reaction rate with temperature was determined for three solution compositions. The apparent energy of activation was determined from the slope of the log rate *vs.* $1/T$ plots shown in Fig. 5. The results were corrected for diffusional effects using a graphical relationship developed by Rosner (11). The results with each solution were as follows:

Solution $C_{HAc} \times 10^3$	pH	Activation energy (kcal/mole) Exptl.	Corr.
1.37	4.08	4.55	5.83
5.23	5.98	4.62	4.87
9.70	4.10	4.90	5.50

An average value of 5.4 kcal/mole would apparently be accurate within ± 10% over the range of experimental conditions.

Discussion

The transport of reactants to the zinc surface played a much smaller role in the over-all reaction rate than had been expected. The use of ultrahigh purity zinc (99.999%) and a reaction surface free of cold work apparently reduced the surface reaction rate sufficiently so that diffusion was not the predominant slow step.

The calculated wall concentrations are those that would exist at the zinc-solution interface in the absence of all other effects except convective forces and concentration gradients. However, at a metal-electrolyte interface there will exist an electric double layer (edl) with its associated electric field. The thickness of the edl varies, but is usually considerably less than 1000Å. Thus, within any reasonable experimental accuracy, the calculated wall concentration can be taken as that existing at the solution boundary of the edl. Uncharged species will be little affected by the edl, so the calculated wall concentration of HAc molecules are representative of the true interfacial concentration. However, ionic concentration in the edl is a function of potential and ionic strength as well as bulk

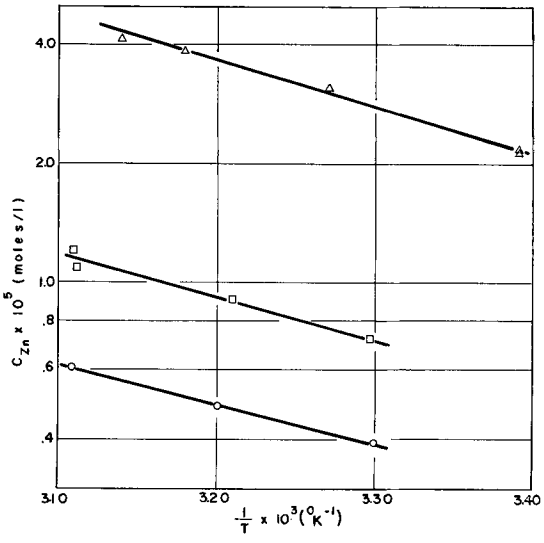

Fig. 5. Arrhenius plot for determination of over-all activation energy:

Symbol	$_BC_{HAc}$	pH	N_{Re}
□	1.37×10^{-3}	4.08	125
○	5.23×10^{-3}	5.98	200
△	9.70×10^{-3}	4.10	100

(wall) concentration.[2] At high ionic strength (> 1M), it can usually be assumed that ionic concentrations within the edl are the same as those outside the edl. In this study ionic strength was determined primarily by the sodium acetate added to adjust pH, and was always less than 1M. Thus, it was not possible to analyze the rate data quantitatively to evaluate possible reaction mechanisms without introducing several assumptions about the properties of the edl. However, qualitative analysis of the data yields some interesting information.

Examination of Fig. 3 shows that at each pH there is a range of C_{HAc} over which rate is independent of C_{HAc}. At lower and higher C_{HAc} the rate depends on C_{HAc}. In Fig. 4 it is seen that at each pH the electrode potential changes rapidly at low C_{HAc} and then changes little with further increase in C_{HAc}. The increasing reaction rate at low C_{HAc} and constant pH could be due to the changing potential rather than to a dependency on C_{HAc}. Since the potential is relatively stable at each pH at high C_{HAc}, the increase in reaction rate in this region appears to be a function of C_{HAc}. It is interesting that the data at high C_{HAc} can be extrapolated linearly to the origin with a slope dependent on pH and/or E. This is indicative of a reaction that is first order with respect to HAc.

The experimental data may be explained by a reaction scheme in which at low C_{HAc} the rate-controlling step of the cathodic reaction is a function of pH and E. At high C_{HAc} the rate-controlling step is a function of pH, E, and C_{HAc}. The simplest way for this to occur would be by means of parallel reaction paths, one path involving a proton and the other an HAc molecule. As the HAc concentration increased, the second reaction would be favored.

It is generally accepted that reduction of H^+ on a metal proceeds in the following sequence

$$H^+ + e \rightarrow H \qquad [2a]$$

followed by either

$$H + H \rightarrow H_2 \qquad [2b]$$

or

$$H + H^+ + e \rightarrow H_2 \qquad [2c]$$

[2] Breiter *et al.* (12) give a brief description of the effect of the edl on surface reactions. More detailed information is in chapters by Parsons and Frumkin in ref. (13).

It is possible that reactions analogous to [2a] and [2c] can occur involving HAc molecules, *e.g.*,

$$HAc + e \rightarrow H + Ac^- \quad [3a]$$

$$H + HAc + e \rightarrow H_2 + Ac^- \quad [3b]$$

At low C_{HAc} the rate-controlling step might be [2a], followed by [3a] at high C_{HAc}. Or, at low C_{HAc} the rate-controlling step might be [2b] or [2c] followed by [3b] at high C_{HAc}. The standard electrode potential is —0.280v for the reaction, $HAc + e = \frac{1}{2} H_2 + Ac^-$. When compared with the standard electrode potential of —0.763v for the reaction, $Zn = Zn^{+2} + 2e$, it is seen that the reduction of molecular acid is quite feasible in this system.

Other reactions first order with respect to C_{HAc} are also possible. For example, reduction to acetaldehyde

$$CH_3COOH + 2H^+ + 2e = CH_3CHO + H_2O \qquad E_o = -0.118v$$

Yakhontov (14) found small amounts of acetaldehyde present after reacting zinc with 40% and 60% acetic acid at 100°C. However, considering the conditions of the present experiment, it is doubtful that this reaction contributed significantly to the observed rate.

For a discharge reaction such as [2a] or [3a] the energy of activation is generally greater than 10 kcal/mole. The observed energy of activation was significantly less than this. If surface coverage with atomic hydrogen was high, a reaction between adsorbed H atoms or between adsorbed H atoms and a species in solution might proceed with a much lower activation energy. Among others, Bockris and Potter (15) reported a study that showed that on tungsten and nickel surfaces the heat of adsorption of H atoms falls considerably at coverages above about 70% until at about 90% coverage the heat of adsorption is about 5 kcal. Thus, the observed heats of activation may be indicative of significant surface coverage. Such coverage could explain the relative constancy of the heat of activation even when measured at conditions at which different reactions might be rate-controlling.

On this basis it does not seem likely that discharge of H^+ or HAc were rate-controlling steps. The data do not permit distinguishing whether reaction [2b] or reaction [2c] was rate-controlling at low C_{HAc}. Whichever one of these was controlling at low C_{HAc}, it appears that a reaction such as [3b] became dominant at high C_{HAc}.

Additional work to confirm these suggested reactions is in progress. Experimental studies are being made using sufficient supporting electrolyte which will permit estimates of wall concentrations of ionic species. With these data a quantitative treatment of the dissolution mechanism can be undertaken. The effect of soluble inhibitors on the kinetics of this dissolution process is also being studied.

Conclusions

1. The dissolution of zinc in acetic acid can proceed under only slight diffusion control.
2. Molecular acetic acid can take part in the cathodic reaction on zinc in acid solution.
3. The dissolution reaction appears to occur through parallel reaction paths, one path involving a proton and the other an HAc molecule. As the HAc concentration increases, the second reaction is favored.

Acknowledgment

The material presented here is part of a research program made possible by National Science Foundation grant G23484. One of the authors (RSA) was the recipient of a National Science Foundation Cooperative Fellowship during part of this program.

Manuscript received April 29, 1964; revised manuscript received Sept. 16, 1964.

Any discussion of this paper will appear in a Discussion Section to be published in the December 1965 JOURNAL.

REFERENCES

1. M. Kilpatrick and J. H. Rushton, *J. Phys. Chem.*, **34**, 2181 (1930); **38**, 269 (1934).
2. V. G. Levich, "Physicochemical Hydrodynamics," Prentice-Hall, Englewood Cliffs, N. J. (1962).
3. M. Allbutt and G. Tolley, *J. Appl. Chem.*, **11**, 52 (1961).
4. C. Wagner and W. Traud, Z. Elektrochem., **44**, 391 (1938).
5. D. A. Frank-Kamenetskii, "Diffusion & Heat Exchange in Chemical Kinetics," translated by N. Thon, Chapt. II, Princeton University Press, Princeton (1955).
6. J. T. McCall, G. K. Davis, and T. W. Stearns, *Anal. Chem.*, **30**, 1345 (1958).
7. R. M. Rush and J. H. Yoe, *ibid.*, **26**, 1345 (1954).
8. R. S. Alwitt, PhD thesis, Rensselaer Polytechnic Institute, Troy, New York (1963).
9. W. H. Linton and T. K. Sherwood, *Chem. Eng. Progr.*, **46**, 258 (1950).
10. V. Vitagliano and P. A. Lyons, *J. Am. Chem. Soc.*, **78**, 4538 (1956).
11. D. E. Rosner, AIChE Preprint No. 135, 54th Annual Meeting Dec. 1961.
12. M. Breiter, M. Kleinerman, and P. Delahay, *J. Am. Chem. Soc.*, **80**, 5111 (1958).
13. P. Delahay, Editor, "Advances in Electrochemistry & Electrochemical Engineering," Vol. 1, Interscience, New York (1961).
14. V. D. Yakhontov, *J. Gen. Chem.* (*USSR*), **17**, 2054 (1947).
15. J. O'M. Bockris and E. C. Potter, *J. Chem. Phys.*, **20**, 614 (1952).

SYMBOLS

β	diffusion coefficient.
C	concentration, moles/liter.
D	diffusivity, cm^2/sec.
d	tube diameter.
E	electrode potential *vs.* reference electrode.
edl	electric double layer.
L	tube length.
mv	millivolts.
N_{Nu}	Nusselt number.
N_{Re}	Reynolds number.
q	flux.
SCE	saturated calomel electrode.
T	absolute temperature.

Subscripts: B, bulk solution; H^+, hydrogen ion; HAc, acetic acid; W, wall; Zn, Zinc ion.

Conductance of Glass Immersed in Molten Salts

Kurt H. Stern

National Bureau of Standards, Washington, D. C.

ABSTRACT

The electrical conductance of high SiO_2 glass was measured when immersed in a number of molten salts and salt mixtures between 800° and 900°C. Sodium and lithium ions diffuse into the glass, both from their own chlorides and from low concentrations in KCl. The glass comes to equilibrium with each melt composition, the time of equilibration depending on the particular ions in the melt. The activation energy of sodium and lithium ion conduction in glass is 75-84 kJ (18-20 kcal), with potassium it is variable between 105 kJ (25 kcal) and 167 kJ (40 kcal). The conductance method is not sufficiently precise to detect silver and cuprous ion diffusion into glass.

In spite of several studies of the behavior of glass in molten salt media the detailed processes involved in the interaction between various glasses and salts are not yet well understood. The present state of knowledge may be summarized as follows: (*A*) Electrical conduction in silica glasses is ionic (1, 2), the magnitude of the current depending on the kinds of ions, their concentration, and the temperature. (*B*) Silica glasses containing alkali metal oxides are cationic conductors, the oxide anions remaining fixed in the glass structure (2). (*C*) Activation energies for conduction are similar to those for diffusion, typically 84-168 kJ (20-40 kcal) (3). (*D*) When a glass initially containing ions is placed into a molten salt, ion exchange may take place, ions from the glass diffusing out and ions from the melt diffusing in (4, 5). Factors determining this exchange are not well known. (*E*) When a high-purity (low ion content) glass, such as fused silica, is placed in a molten salt, ions from the salt diffuse into the glass (7). There is some evidence that the smaller of two ions in a salt mixture will diffuse preferentially into the glass (7), but specific ion-glass interactions may also be significant (6). (*F*) The surface composition of an ion-containing glass may differ from that in the bulk, both in the presence and absence of salt. The equilibrium composition is that giving the minimum surface free energy (8). (*G*) Some glasses, *e.g.*, Vycor, contain bound water as OH groups in the silica structure. In a water vapor environment these OH groups move, leading to net diffusion of H_2O through the glass (9, 10). Nothing is known of the effect of this bound water on the transport of ions through the glass. (*H*) If a glass initially containing no ions, *e.g.*, pure silica, is exposed to a molten salt whose cations diffuse into the glass, electrical neutrality requires that an equivalent amount of anions migrate into the glass also. Information on this point is largely lacking, although there is some evidence that anions migrate through glass under an applied field (11).

The present paper reports a study of the electrical conductance of high-silica glass, mainly Vycor, immersed in various molten salts. Two effects were studied: (i) changes of conductance with time, caused by the immersion of the glass in a salt or salt mixture, (ii) changes of conductance caused by changes in the melt composition and temperature, which are independent of time.

Experimental

The conductance cells consisted of 13 mm O.D. Vycor glass U-tubes ~ 25 cm high, with a 1 mm thick glass partition in the center of each cell separating the legs. The bright platinum electrodes, 1 cm^2 in area, were suspended by sealed-on platinum wires from glass caps which fitted over the ends of the cell. Thus the electrodes could be removed easily for addition of salt to the cell and repositioned. Since the resistance of the salt had been found (in a similar tube without partition) to be negligible compared to that of the partition, the precise position of the electrodes did not affect the measurement.

In each measurement the salt composition in both compartments was the same. 15g of the salt or salt mixture under study was placed in the preheated cell, already positioned in the center of the furnace, melted, the electrodes were introduced, and measurements begun.

Using a Marshall control panel and packing the cell in vermiculite kept the temperature constant to within ± 1°. The temperature was measured by a chromel-alumel thermocouple whose hot junction was positioned just outside the center of the cell. Resistance was measured with a Jones and Josephs-type bridge with Wagner ground at 1 kc. Between 1 and 10 kc resistance was independent of frequency. High resistances were measured in parallel with a high-precision 10^4 ohm resistor. In a typical measurement the cell was filled with one salt and allowed to equilibrate; the resistance was measured as a function of temperature. The desired amount of a second salt was then added and the procedure repeated. Further additions were made until the cell was full. Each new experiment was started with a new cell. In some experiments the conductance was measured as a function of time until equilibrium was reached.

Since it proved impossible to reproduce precisely the cross section and thickness of the glass partitions in the various cells, the actual values of $1/R$ have little significance when comparing measurements made in different cells. Changes occurring with time and melt composition in the same cell and the temperature coefficient of conductance both in the same and different cells are significant, however.

Reagent grade NaCl, KCl, and KBr were dried under vacuum at 500°C; LiCl was vacuum dried above its melting point. Anhydrous CuCl was prepared by reduction of $CuCl_2$ by sulfurous acid (12). Reagent grade AgCl was used without further purification.

Results and Discussion

In many of the experiments the salt initially put in the cell was KCl because it was known that potassium ions diffuse into glass only to a slight extent (7). Thus the addition of a salt whose ions diffuse into glass to a greater extent can be detected by an increase in conductance. Since, in addition to diffusion of ions into the glass, ions may also diffuse out, only relatively large changes in conductance can be considered significant. Thus, although a noticeable change in conductance on addition of salt is evidence for some glass-salt interactions, the absence of such a change does not necessarily imply absence of interaction.

Since most experiments were carried out with Vycor the subsequent results refer to that glass unless otherwise indicated.

General observations.—In the initial experiments, carried out with KCl, the cell was heated to 800°C

and the salt added. Fluctuations in conductance occurred for several hours, both with Vycor and fused silica, the conductance decreasing during this period by as much as a factor of four. If the empty cell was kept at 800°C for several days before introducing the salt, fluctuations were much reduced. A slow decrease in conductance still occurred for several days subsequent to the addition of salt, probably because the diffusion of sodium ions out of the glass is the predominant effect. The removal of fluctuations on heating the empty cell suggests that structural changes or loss of bound water are taking place.

In all experiments the conductance eventually reached a steady value, although this usually required several days. After the first few hours, changes were quite slow. When a steady value had been reached the temperature dependence of the conductance was measured between 800° and 900°C. In virtually all cases the conductance ($1/R$) was a linear function of $1/T$ so that the activation energy (E_a) is independent of temperature in this range. The addition of a second salt to the KCl already in the cell may or may not produce a change in conductance. If the former, the process described above generally repeats, *i.e.*, the conductance changes again, in some cases over a period of several days until another equilibrium value is reached.

Experiments with specific systems are described below.

KCl-NaCl

The addition of either KCl or NaCl to a cell which has only been heated to bring it to the temperature of the experiment (800°-900°C) leads to a fairly rapid decrease of conductance for several hours. Since the effect occurs even with NaCl it cannot be attributed to the diffusion of Na^+ ions out of the glass, (as it can for KCl) but is probably due to structural rearrangements of the glass, *e.g.*, loss of bound water. It appears likely also that Na^+ ions do not diffuse immediately into such a glass.

If the glass has been heated for several days prior to salt addition only a slow decrease of $1/R$ takes place with KCl, as expected for the diffusion of Na^+ out of the glass.

To study the effect of NaCl addition on the equilibrium conductance value the empty cell was first heated at 650°C for three days. After KCl had been added, $1/R$ decreased slowly for three days at 830°C from 1.04×10^{-5} to 0.245×10^{-5} reciprocal ohms after which $1/R$ remained constant. The temperature was then varied randomly for several hours between 800° and 900°. All points fell on the same linear $1/R$ *vs.* $1/T$ plot. A weighed quantity of NaCl was then added. The conductance became steady in a few hours and the temperature coefficient was again determined. The procedure was repeated several times until the cell was full. Results are shown in Fig. 1. The mole fraction of NaCl (X_{NaCl}) is shown to the right of each curve. The conductance increases with increasing X_{NaCl} and the temperature coefficient decreases. Both effects are linear in X_{NaCl} as shown in Fig. 2, where the Arrhenius activation energy has been calculated from the conductances at 814° and 890°C.

If KCl is added to glass originally equilibrated with NaCl the effect is much smaller and in the opposite direction, *i.e.*, the conductance decreases slightly. For example, with NaCl alone $1/R = 10.1 \times 10^{-5}$ reciprocal ohms, with $X_{KCl} = 0.34$, $1/R = 6.4 \times 10^{-5}$ reciprocal ohms. The Arrhenius activation energy E_a remains virtually constant at 77.4 kJ (18.5 kcal). These results indicate that potassium ions replace sodium ions only slightly in the glass, but that because of their larger size they block some of the available conductance paths in the glass structure. The much higher activation energy observed for KCl alone and its decrease with added NaCl are consistent with this view and with recent observations of membrane potential measurements on this system (7).

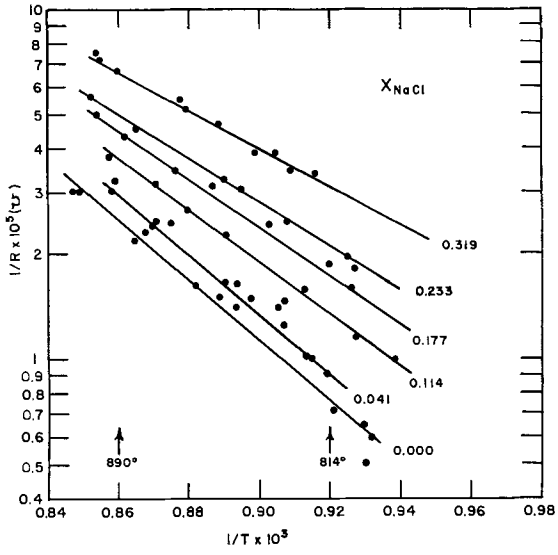

Fig. 1. Equilibrium conductance values of Vycor in various KCl-NaCl mixtures as a function of $1/T$.

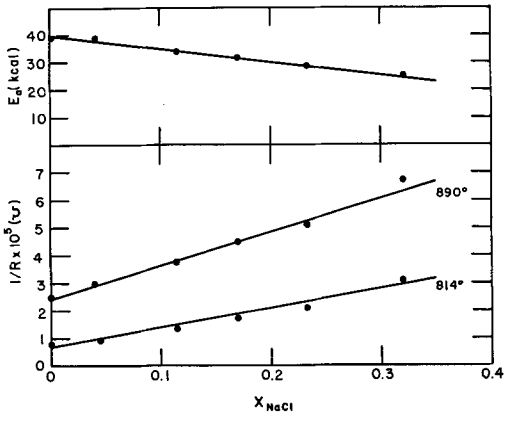

Fig. 2. Change in conductance and activation energy on the addition of NaCl to KCl, data of Fig. 1.

Similar, but less extensive, experiments were also carried out with fused silica (Vitreosil). The results were the same qualitatively, but much longer periods of time were required before constant conductance values were reached, possibly because this glass has less open pores than does Vycor.

KCl-LiCl

When LiCl is added to glass equilibrated with KCl, as described above, the conductance increases linearly with time, showing that lithium ions are diffusing into the glass. Figure 3 shows a typical plot for $X_{LiCl} = 0.055$. Even at this very low concentration lithium ions

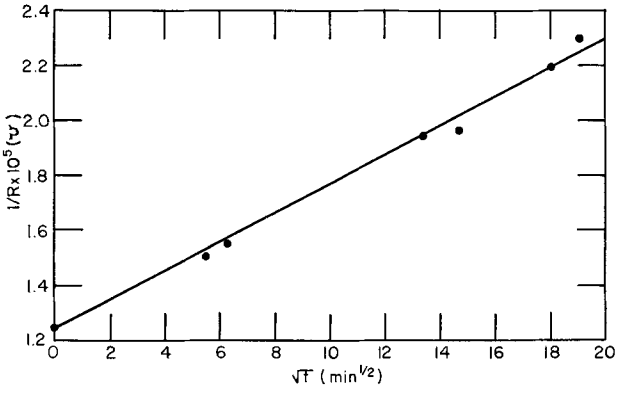

Fig. 3. Change in conductance of Vycor equilibrated with KCl on the addition of 5.5 mole % LiCl, 830°C.

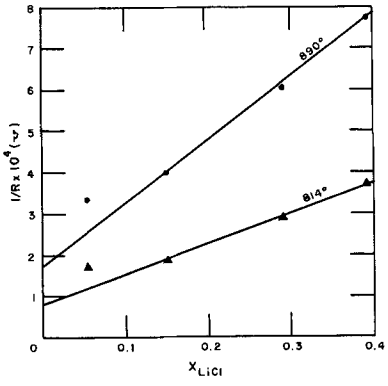

Fig. 4. Change in conductance of Vycor on the addition of LiCl to KCl.

are either displacing the slower potassium ions already in the glass or moving through unoccupied channels in the glass.

As with NaCl, new equilibrium conductance values are reached with successive additions of LiCl. Similarly, the conductance is linear in X_{LiCl} (Fig. 4). The activation energy remains constant as LiCl is added.

KCl-CuCl, KCl-AgCl

The addition of CuCl and AgCl to KCl produces no significant change in glass conductance up to 10 mole % added salt, the highest concentration used. This result does not imply that cuprous and silver ions do not diffuse into glass. That they in fact do so from their own pure molten salts is well known (6). However, when the glass has already been equilibrated with a salt whose ions penetrate the glass preferentially, diffusion of Cu^+ and Ag^+ is greatly reduced. For example, glass membrane potential experiments in the AgCl-NaCl (13) and CuCl-NaCl (14) systems indicate that nearly all of the cationic current is carried through the glass by sodium ions.

NaCl-LiCl

When the glass is initially equilibrated with NaCl instead of KCl the conductance is approximately ten times as great. This large increase indicates that both concentration and mobility of sodium ions in the glass are greater than those of potassium ions since the ionic mobilities probably do not differ by that much. The same conclusion was reached previously from experiments with NaCl additions to KCl.

When even small amounts of LiCl are added to NaCl the conductance rises still further. In contrast to the KCl-LiCl system, however, the increase in conductance occurs so rapidly, within a few minutes, that it cannot be followed accurately. A comparison of the two systems implies that the prior equilibration with NaCl has had a different effect on the glass structure than that with KCl (*cf.* Fig. 3), making it more permeable to Li^+ ions. Successive additions of LiCl cause corresponding increases in the conductance, the equilibrium values being linear functions of X_{LiCl}. Both this dependence and that on temperature are shown in Fig. 5 and 6. It thus appears that sodium ions do not occupy all of the possible conductance paths in the glass, possibly because some of them are too small for Na^+, although they can accommodate Li^+.

The effect of high NaCl concentration on glass can also be seen by comparing the increase in conductance produced by a given amount of salt. The addition of 10 mole % of NaCl and LiCl added to KCl increases the conductance by 8×10^{-7} and 12×10^{-7} reciprocal ohms, respectively; the addition of 10 mole % LiCl added to NaCl gives a change of 475×10^{-6}. This conductance increase is, however, almost entirely due to the very much larger initial conductance with NaCl as compared to KCl. Thus, the conductance increases by 22% when 10% LiCl is added to NaCl and by 15%

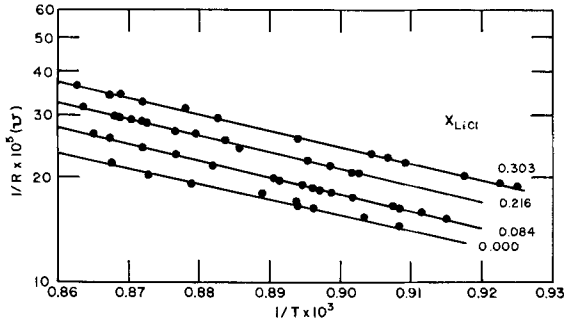

Fig. 5. Equilibrium conductance values of Vycor in various NaCl-LiCl mixtures as a function of $1/T$.

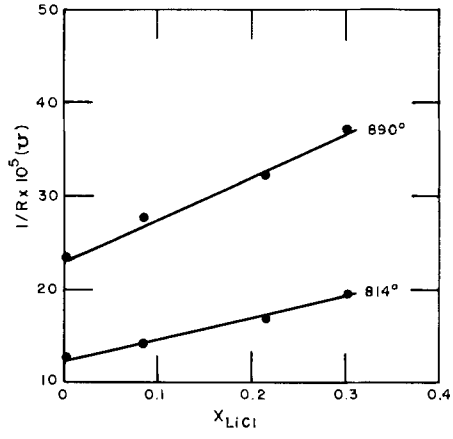

Fig. 6. Change in conductance of Vycor on addition of LiCl to NaCl

when it is added to KCl. These data suggest that the interaction of Na^+ ions with glass differs from that of the other alkali metal cations, but it is not known how.

The activation energy remains virtually constant at 75-84 kJ (18-20 kcal), as LiCl is added to NaCl, but this is not surprising since most of the current is still being carried by sodium.

KBr-KCl-NaBr

To see if a change in anion had any effect on the conductance a cell was initially filled with KBr. The conductance was low, as with KCl, and similarly decreased with time. Over a three-day period $1/R$ decreased from 4.9 to 3.1 x 10^{-6} reciprocal ohms while E_a increased from 26 to 29 kcal. The addition of KCl up to 20 mole % produced no significant change, the

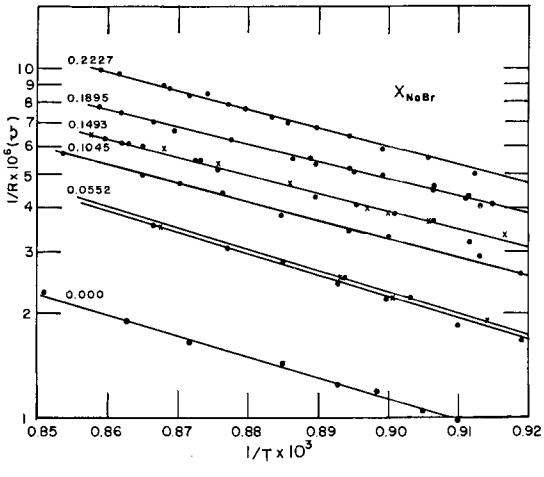

Fig. 7. Equilibrium conductance values of Vycor in NaBr-(76 mole % KBr-24 mole % KCl) as a function of $1/T$.

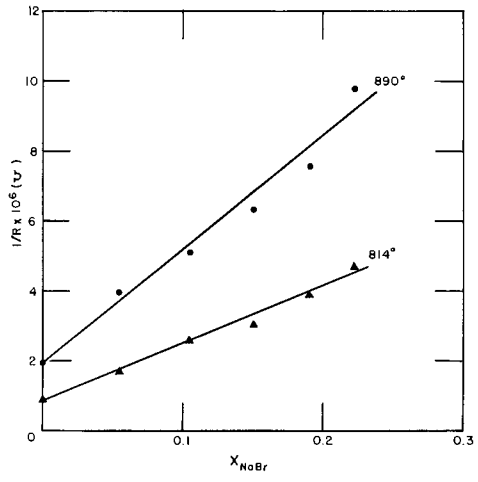

Fig. 8. Change of conductance of Vycor on addition of NaBr to a KBr-KCl melt, data of Fig. 7.

conductance decreasing slowly over a period of weeks. Evidently the effect of adding the smaller Cl^- ion is insignificant compared to the conductance decrease produced by Na^+ diffusion out of the glass.

After two weeks of equilibration with the above KBr-KCl mixture, 24 mole % KCl, NaBr was added. The conductance increased rapidly, the increase being linear in time, as expected. Subsequent additions of NaBr gave the data shown in Fig. 7. The two curves for $X_{NaBr} = 0.0552$ show the change in $1/R$ after one day, the increase with time being clearly much less than that due to a concentration change. As shown in Fig. 8 the increase in conductance is linear in X_{NaBr}, E_a decreasing from 11.2 to 96 kJ (27 to 23 kcal) over the concentration range shown.

Conclusions

The results of the present study are in general agreement with previous work bearing on the behavior of high-purity silica glass in molten salts.

1. The diffusion of potassium ion into glass is very small even when it is the only cation in the melt. In that case the predominant effect appears to be the diffusion of Na^+ out of the glass.

2. From KCl-NaCl and KCl-LiCl melts sodium and lithium ions, respectively diffuse into the glass. The glass comes to equilibrium with a given melt composition fairly rapidly, showing that a uniform ionic composition in the bulk of a $\sim$ 1 mm thick glass is established in a few hours.

3. When LiCl is added to NaCl in equilibrium with glass, Li^+ diffuses rapidly into the glass, showing that not all interstices are filled with Na^+, perhaps because some of them will only accommodate the smaller Li^+.

4. Although Cu^+ and Ag^+ are known to diffuse into glass from their own salts and probably also, although to a much lesser extent, from mixtures with alkali halides, the conductance method is not sufficiently sensitive to detect such diffusion.

5. The present work allows no definite conclusion to be drawn about anion diffusion into glass. Addition of Cl^- to Br^- produces no detectable change in conductivity. However, if the glass is to preserve its electrical neutrality as cations diffuse into it, anions must follow. It is conceivable, however, that partial charge separation in the glass occurs, with anions occupying only the surface layer (adsorption).

6. In general, the activation energy increases with decrease in permeability to a given ion, similar to the behavior with gases (15). The lowest values of E_a, 75 kJ (18 kcal), was observed for NaCl. With KCl E_a fluctuated considerably, probably depending on the residual sodium content of the glass. The highest value obtained was 163 kJ (39 kcal), but an occasional E_a as low as 105 kJ (25 kcal) was obtained with the salt. The addition of NaCl to KCl always lowered E_a.

Manuscript received Sept. 4, 1964. This paper was presented at the Toronto Meeting, May 3-7, 1964.

Any discussion of this paper will appear in a Discussion Section to be published in the December 1965 JOURNAL.

REFERENCES

1. G. W. Morey, "The Properties of Glass," Chap. XVII, Reinhold Publishing Co., New York (1938).
2. J. E. Stanworth, "Physical Properties of Glass," Chap. VI, Clarendon Press, Oxford (1950).
3. J. Halberstedt, *Z. anorg. u allgem. Chem.*, **211**, 185 (1933).
4. B. Lengyel, *Z. phys. Chem.*, **164**, 295 (1933).
5. B. Lengyel and A. Sammt, *ibid.*, **181**, 55 (1937).
6. J. A. Pask and C. W. Parmelee, *J. Am. Ceram. Soc.*, **26**, 265 (1943).
7. K. H. Stern and J. A. Stiff, *This Journal*, **111**, 893 (1964).
8. Ref. (2), Chap. VII.
9. A. J. Moulson and J. P. Roberts, *Trans. Faraday Soc.*, **57**, 1208 (1961).
10. T. Drury, G. J. Roberts, and J. P. Roberts, *Adv. Glass Techn.*, 249 (1962).
11. A. Berlin, Private communication.
12. "Inorganic Syntheses," Vol. II, p. 1, McGraw-Hill Book Co., New York (1946).
13. K. H. Stern, *J. Phys. Chem.*, **67**, 893 (1963).
14. K. H. Stern and S. E. Meador, To be published.
15. cf. Ref. (2), Chap. V.

June 1965 Discussion Section

A Discussion Section, covering papers published in the July-December 1964 JOURNALS, is scheduled for publication in the June 1965 issue. Any discussion which did not reach the Editor in time for the December 1964 Discussion Section will be included in the June 1965 issue.

Those who plan to contribute remarks for this Discussion Section should submit their comments or questions in triplicate to the Managing Editor of the JOURNAL, 30 East 42 St., New York, N. Y., 10017, *not later than March 1, 1965.* All discussion will be forwarded to the author(s) for reply before being printed in the JOURNAL.

Investigations of the Kinetics of Hydrogen and Oxygen Reactions on a Platinum Electrode in Acid Solution Using Pulse and Decay Techniques

Sigmund Schuldiner and Theodore B. Warner[1]

U. S. Naval Research Laboratory, Washington, D. C.

ABSTRACT

The influence of hydrogen partial pressure, current density, and temperature on the anodic oxidation of sorbed H and the anodic generation of sorbed O were determined. Electrode processes were evaluated and separated to give the following quantities: (*a*) the amount of H associated with a Pt surface and its immediate vicinity, (*b*) the extent of reaction of H atoms, absorbed in the metal interior, that migrate to the surface of the metal and are either ionized or react with O atoms, (*c*) the extent of reaction of H_2 from the solution phase, (*d*) the amount of O adsorbed on the Pt surface, and (*e*) the amount of O absorbed in the Pt surface layers (skin).

The kinetics of the open-circuit reaction of galvanostatically determined amounts of sorbed O with H_2 were determined. This investigation showed that absorbed O in Pt significantly affects coulometric measurements at pulse lengths longer than about 1000 μsec. The presence of absorbed O in the Pt can also materially affect the reaction rate of chemisorbed O with H_2. Under the experimental conditions, transport of reactants on the solution side was fast enough so that diffusion did not limit processes in either the H ionization or O sorption regions. The data indicated that migration of adsorbed species on the Pt surface to active sites was rate controlling in the O sorption region, except in the case of reaction of adsorbed O with H_2 when significant amounts of O were absorbed in the skin of the Pt. In this case the chemical reaction rate between adsorbed O and H_2 was retarded so that this chemical step appeared to be rate determining. Reaction rates of the adsorbed O and H_2 reaction under open-circuit conditions were determined at varying temperatures, adsorbed and absorbed O concentrations, and H_2 partial pressures.

This investigation was carried out to determine the influence of hydrogen partial pressure, current density, and temperature on (*a*) the anodic oxidation of adsorbed hydrogen

$$Pt - H \rightarrow H^+ + Pt + e^- \qquad [1]$$

where Pt— indicates a chemisorbed species, and (*b*) the anodic generation of atomic oxygen

$$H_2O + Pt \rightarrow Pt - O + 2H^+ + 2e^- \qquad [2]$$

on a platinum electrode. By use of relatively fast (*i.e.*, high current density) constant current anodic pulses, only that hydrogen already sorbed on the Pt electrode is ionized, and a given number of O atoms are generated and adsorbed on the electrode surface without a significant number of these O atoms absorbing into the outermost layers (skin) of Pt (1—3), or combining to O_2 and diffusing away into solution. By use of longer charging times (*i.e.*, low current densities), some H_2 in solution is ionized in addition to the originally sorbed hydrogen, and a large part of the deposited O atoms may be absorbed into the surface layers of Pt during the time of the applied pulse and more than a monolayer is deposited. Previous work at this Laboratory (1, 3), as well as the work of others, has indicated that O atoms formed during anodic polarization in the O sorption region primarily will either be chemisorbed on the Pt electrode surface or be absorbed in the surface layers of the Pt electrode. In addition, if H atoms are dissolved in the Pt bulk, they may migrate to the surface and either be ionized or react with O atoms.

It has been shown (1, 4) that the rate of reaction of molecular hydrogen in solution with chemisorbed O atoms at potentials above 0.9v (*vs.* NHE) is relatively slow, hence low-current-density-charging pulses were used to determine the combined amount of adsorbed and absorbed O and the reaction of adsorbed O with H_2. The amount of reaction involving H_2 can be determined by comparing such curves with charging curves obtained in hydrogen-free solution. The amount of H_i which migrates to the surface where it is oxidized can be determined in H_2-free solutions by subtracting the number of coulombs required to charge a Pt electrode, free of H_i, to the O_2 evolution potential from the number of coulombs required to charge the same Pt electrodes containing H_i over the same potential range. Thus, the amount of fast-reacting sorbed hydrogen, H_s, the additional hydrogen reacting from solution, H_2, and from the metal interior, H_i, the amount of O atoms adsorbed on the Pt surface, O_{ad}, the amount of O atoms absorbed into the skin of the Pt, O_{ab}, and the amount of reaction of H_2 with adsorbed O atoms can all be determined using the operational definitions of these quantities.

Experiments were conducted to determine the kinetics of the reaction of O_{ad} with H_2 under open-circuit conditions. Here the electrode was coulometrically charged (see Fig. 1b) with a known amount of O_{ad} or O_{ad} plus O_{ab} and the pulse terminated. The potential decay with time was then photographically recorded from an oscilloscope trace (see Fig. 1b) from which the time for reaction of O_{ad} with H_2 in solution plus H_i which migrates to the surface could be measured.

Breiter (5) also used a kinetic technique involving the reduction of chemisorbed oxygen with H_2. However, the method used in this paper varies in several important respects from that of Breiter. In our work we can distinguish between O chemisorbed on the electrode surface and that absorbed into the skin of the metal. Breiter's potentiostatic method (5) undoubtedly included both O_{ad} and O_{ab}. In this paper we shall show that the presence of O_{ab} can materially affect the rate of the reduction of O_{ad} with H_2. Breiter (5) determined the amount of sorbed O at a given anodic potential by using a cathodic sweep which did

[1] National Academy of Sciences Postdoctoral Resident Research Associate.

not clearly separate the oxygen region from the double layer region. In our work we form a given amount of O with an anodic charging pulse where we can separate the amount of O_{ad} present from the amount of O_{ab} dissolved in the Pt electrode. We can also correct for the double layer charge (1). The significance of Breiter's determination of reaction rates at given decay potentials is difficult to assess since his electrode probably contained both O_{ad} and O_{ab}. His reaction rates for different polarization potentials decreased with increased polarization potential, and since potentiostatic charging for 60 sec is adequate time for considerable absorption of O, his decrease in reaction rate can be explained by increased amounts of O_{ab} at higher polarizing potentials.

Our method does suffer in that it does not determine reaction rate as a function of decay potential, but yields the integrated reaction rate over the entire decay potential range. We can, however, limit the potential to which the electrode is anodically charged and thereby successively decrease the amount of O formed. This permits us to show the effects of reduced surface coverage of O on its reaction rate with H_2.

Experimental

The electrochemical system, gas purification trains, and general procedures have been described elsewhere (1-3). True areas (about 0.3 cm^2) of the working Pt bead electrode were defined using the method previously reported (1, 6), and cleanliness of the working electrode and solution was verified by the configuration of the anodic charging curve in the O sorption region (6). The electrolyte was 1M H_2SO_4 solution and was maintained at a constant temperature (±0.5°C) with a water bath. Water bubblers used to saturate the helium or hydrogen going into the cell were kept in the same constant temperature bath to maintain the same partial pressure of water vapor and thereby to keep the electrolyte concentration in the cell constant.

After pre-electrolysis of the solution, the temperature of the water bath was set at a given value and an appropriate mixture of hydrogen and helium (or one of these pure gases) was bubbled through the cell at given rates (0-1300 ml/min) as determined with one or two flowmeters. Zero stirring rate measurements were taken shortly after stopping the flow of a given gas or gas mixture into the cell. The electrometer, pulse generator, and oscilloscope used were the same as previously reported (3), as were the reference (Pt wire and miniature glass) and counter (Pd tube) electrodes. In order to polarize the Pt bead electrode up to the O_2 region with low current density pulses (< 5 ma/cm^2), long duration pulses (> 0.5 sec) were required. These pulses were generated with an Electronic Measurements Solid State (Model C612) Constant Current power supply, using a telegraph key to switch the current on and off. The resulting charging curves were photographed from the oscilloscope screen.

Single-shot, constant-current pulses were used to determine the anodic charging curves. After a current pulse, the electrode was permitted to recover to its normal open-circuit potential before the next pulse was applied. Pulse current densities, known to ±3%, were varied from 780 $\mu a/cm^2$ to about 3 amp/cm^2. The $\mu coul/cm^2$ of hydrogen ionized and oxygen formed were corrected for double layer charging by using a previously determined relationship between double layer capacitance and potential (1).

After anodic charging curves were taken under a variety of conditions, a series of photographs were made showing the polarization decay in H_2-saturated solution (varying H_2 partial pressures and temperatures) at the Pt bead electrode, which was previously charged with a known number of coulombs to a given potential in the O sorption region or somewhat beyond in the O_2 formation region. (Figure 1a delineates the various regions for the charging and decay traces.) In these experiments a charging pulse was set for a given duration and an oscillogram taken (see top charge curve in Fig. 1b). The oscilloscope sweep rate was then considerably slowed and the voltage amplification increased so that the pulse itself was largely off the screen and lasted only a very small fraction of the total time displayed. Then the decay curve (see decay curves in Fig. 1b) following pulse cut off ran for the length of the horizontal sweep until the potential and shape of the decay curve showed complete removal of sorbed oxygen. Thus, with this technique a known number of O atoms could be formed on the surface and the time required for their subsequent open-circuit reaction with molecular hydrogen in solution determined.

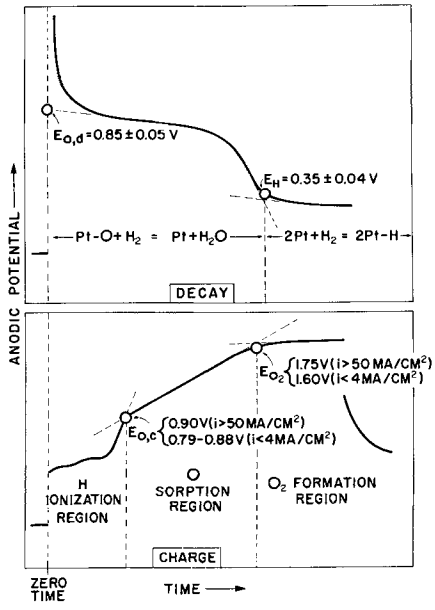

Fig. 1a. Oscilloscope traces: delineation and definition of the major reaction regions and potentials in charge and decay traces.

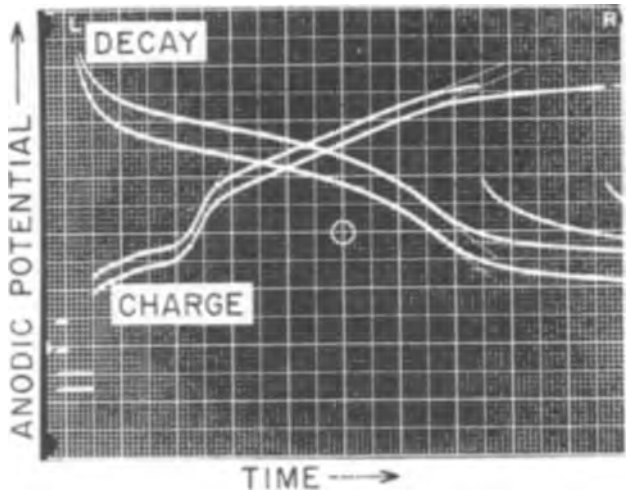

Fig. 1b. Typical anodic charging curves (50 μsec per horizontal division, 0.5v per vertical division, i = 2.61 A/cm^2) and decay curves (2000 μsec per horizontal division, 0.2v per vertical division) at 50°C and p_{H_2} = 0.88 atm.

Anodic Charging Reactions

From the photographed anodic charging traces (Fig. 1b), the number of $\mu coul/cm^2$ of both ionized H and O formed on the Pt bead electrode was determined. These values were corrected for double layer charge. For high-current-density anodic pulses (1-3 amp/cm^2) only O_{ad} is formed and the number of coulombs

used to charge the O sorption region at room temperature was used to define the surface area (1) of the Pt bead. Under these conditions the O sorption region was assumed to require 420 μcoul/cm^2 to charge (equivalent to one monolayer, one-to-one correspondence with surface Pt atoms); the H ionization region was found to require 230 μcoul/cm^2 to charge. The 230 μcoul/cm^2 of H oxidized represents the amount of H (H_s) associated with the Pt surface under open-circuit conditions (p_{H_2} = 1 atm). Experimental evidence (1, 7) indicates that part of this hydrogen is chemisorbed on the Pt surface as atoms and part is absorbed primarily in the outermost layers of the Pt. The experimental data at 23°C showed that within experimental error, this quantity of H, for the higher current density pulses, was virtually independent of the hydrogen partial pressure in the cell (0.02 to 1 atm). This indicated that the amount of chemisorbed hydrogen in rapid equilibrium with H_2 gas above the solution is very small at room temperature and verified previous work from this Laboratory (1, 8).

At lower current densities the amounts of charge consumed in both the H and the O regions exceeded 230 and 420 μcoul/cm^2, respectively. These excesses of charge, q_{ex}, represented: (*a*) the amount of hydrogen in the H ionization region, $q_{H,ex}$, oxidized beyond the amount of hydrogen, H_s, originally associated with the surface before imposition of the anodic pulse, and (*b*) the excess charge in the O sorption region, $q_{O,ex}$, which was due primarily to the oxygen, O_{ab}, formed beyond that needed to form a single monolayer of O atoms, O_{ad}, plus any H_2 and H_i oxidized.

Figure 2 shows both the current density and the hydrogen partial pressure effects on $q_{H,ex}$ and $q_{O,ex}$. The $q_{H,ex}$ can come from two sources, the molecular hydrogen, H_2, bubbled into the cell and the hydrogen dissolved in the interior, H_i, of the Pt bead diffusing out to the surface. Estimations of the amount of H_i which diffused to the surface and then was oxidized were made in pure helium-saturated solutions (the electrode was first saturated with H_2, p_{H_2} = 1 atm, then the H_2 was replaced with He and charging curves were obtained). These experiments showed that with current density pulses of higher than 0.203 amp/cm^2, virtually no hydrogen diffused from the interior of the Pt bead to the surface during the charging pulse. At lower current densities, some hydrogen coming from this source was detected and the p_{H_2} = 0 points in Fig. 2a roughly indicate their values. Interestingly, the amount of H_i (about 300 μcoul/cm^2) diffusing to the surface at current densities of 3.53 ma/cm^2 and lower was essentially independent of current density.

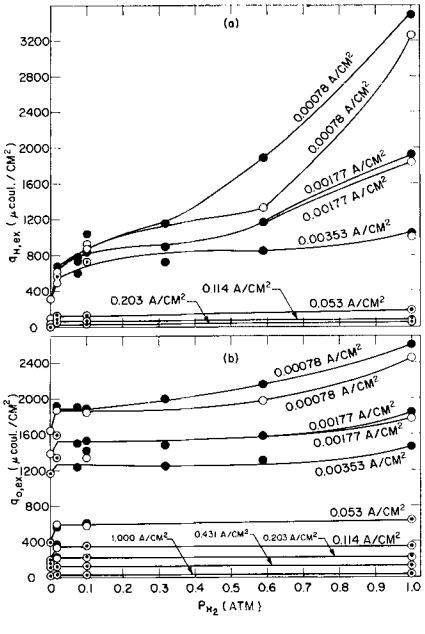

Fig. 2. Data from anodic charging curves at 23°C. Effects of current density, stirring, and hydrogen partial pressure on excess of charge in (a) the H ionization region, $q_{H,ex}$, and (b) the O sorption region, $q_{O,ex}$; ○, quiescent solution; ●, vigorously stirred solution.

The $q_{O,ex}$ appears to represent primarily the amount of O_{ab} in the skin of the Pt bead plus the possible reaction of H_2 and the H_i which diffused to the surface during anodic charging. Lack of stirring effects at current densities above 0.053 amp/cm^2 made it unlikely that a significant amount of oxygen was lost from the surface in the form of O_2 in the O sorption region. Reaction of O_{ad} with H_2 at potentials in the O sorption region has been shown to be slow (1, 4); however, the data in Fig. 2b show that at current densities of 3.5 ma/cm^2 and lower, a significant amount of reaction of O_{ad} with H_2 must occur. Here both stirring and increased hydrogen partial pressure cause an increase in the amount of charge consumed in the O sorption region. However, as the hydrogen partial pressure is decreased, eventually the number of coulombs of charge transferred does not vary even with stirring. But even at these low hydrogen partial pressures there evidently is some reaction of O_{ad} with H_2, because when the hydrogen partial pressure is reduced to zero, the amount of charge expended decreases. In fact, even at current densities as high as 0.203 amp/cm^2 there appears to be a significant amount of reaction of O with H_2. The fact that there are conditions under which hydrogen partial pressure and/or increased stirring does not affect the apparent amount of hydrogen reaction with O_{ad} means that under these conditions the transport of H_2 to the electrode surface by convection and diffusion is faster than the reaction of H_2 with O_{ad}.

At the lowest current density pulse applied (0.78 ma/cm^2), increased stirring rates above those used in the Fig. 2a data considerably lengthened the hydrogen ionization region on the oscilloscope trace. With a small decrease in current it was impossible to polarize the electrode beyond the hydrogen region. This showed that the exchange current density, i_o, for the hydrogen reaction is close to 0.78 ma/cm^2 and that extremely fast stirring is necessary to minimize diffusion polarization. This value checks previous steady-state measurements (9) from this Laboratory when the previous values are adjusted to correspond to the definition of true surface area used here. On the other hand, the length of the O_{ad} region was virtually independent of further increases in the hydrogen stirring rate, beyond the corresponding values shown in Fig. 2b, at 0.78 ma/cm^2. This demonstrated that i_o, for the reaction of H_2 with O_{ad}, is considerably less than 0.78 ma/cm^2, and it also follows that diffusion polarization of H_2 in the vigorously stirred solution was insignificant.

The data shown in Fig. 2b for the helium-stirred solution (p_{H_2} = 0, Pt electrode containing H_i) primarily gives the sum of H_i atoms which diffuse to the surface and are ionized and of O_{ab} generated during the anodic pulse. At the lowest current density this amounts to the equivalent of about four atomic layers of O.

Experiments conducted in helium-saturated solution in which H_i in the Pt bead was completely removed (potential *vs.* NHE was 0.47-0.59v) showed that the amount of O_{ab} in the skin of the metal was 910, 1020, and 1260 μcoul/cm^2 at current densities of 3.53, 1.77, and 0.78 ma/cm^2, respectively. The p_{H_2} = 0 values shown in Fig. 2b, for the same series of current densities, include oxidized H_i and O_{ab} and are 1170, 1400, and 1630 μcoul/cm^2, respectively. The amount of H_i which diffuses to the surface and is oxidized appears to level off at about 400 μcoul/cm^2 at the two lowest current densities, but at all these low current densities the H_i contribution is significant.

The $p_{H_2} = 0$ values shown in Fig. 2b therefore account for both oxidized H_i and O_{ab} and the difference between $q_{O,ex}$ values at $p_{H_2} > 0$ and $p_{H_2} = 0$ represents the amount of H_2 from solution which is ionized. The high $q_{O,ex}$ values for the low current density data indicate that the top layers of Pt atoms in the metal skin may be fairly well saturated with oxygen. As will be shown later this can have a marked effect on the catalytic behavior of Pt.

The data in Fig. 2 show large differences in $q_{H,ex}$ and $q_{O,ex}$ for given current density pulses. Using these curves the amount of H_2 ionized in the H ionization region and H_2 reacting in the O sorption region were separated from the total q_{ex} values and compared. This comparison showed that at current densities of 3.53 ma/cm^2 and lower, the number of equivalents of H_2 reacting in the O sorption region is considerably less than the number of equivalents of H_2 being ionized in the hydrogen region, even though the duration of the O sorption region is about twice as long. At current densities of 0.053 amp/cm^2 and higher the reverse occurs; here considerably more H_2 reacts per unit time in the O sorption region than in the H ionization region. These experimental facts show (*a*) that hydrogen diffusion cannot be rate controlling in both the H ionization and O sorption regions, otherwise the number of coulombs of H_2 per unit time reacting in both regions would be identical, (*b*) at low current densities, H_2 is ionized much faster in the H ionization region than H_2 reacts with O_{ad} in the O sorption region, therefore, H_2 diffusion cannot be rate controlling in the O sorption region, and (*c*) at the higher current densities, H_2 reacts with O_{ad} faster in the O sorption region than these molecules are ionized in the H ionization region; here one concludes that H_2 diffusion cannot be rate controlling in the H ionization region.

The exchange current densities of both the charge transfer and molecular dissociation steps of the hydrogen reaction have been shown (1, 8, 9) to be independent of the charging rate. Hence, the differences in the reaction rates of H_2 at the anodized Pt bead at low and high current densities must be in the O sorption region. We believe that the rate of reaction of H_2 with O_{ad} is faster with high current density pulses because less O is absorbed into the skin of the Pt under these conditions. The work which will be reported in the last section of this paper will further verify that the rate of the reaction between H_2 and O_{ad} is strongly dependent on the amount of O_{ab} in the skin of the Pt electrode.

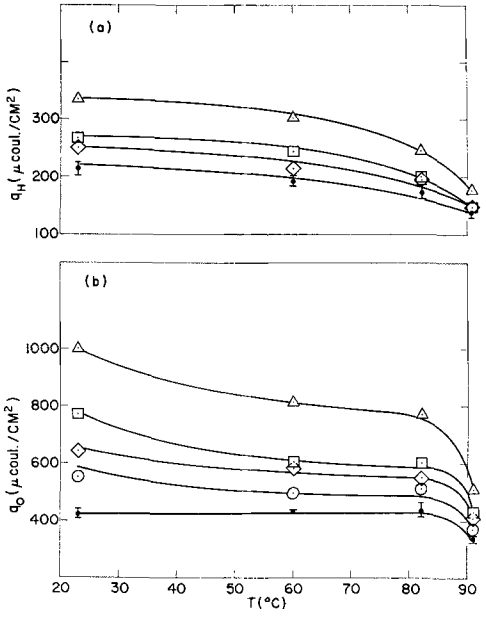

Fig. 3. Temperature effects on anodic charging curves: (a) q_H in hydrogen ionization region [Solid circle with I thru it, 0.43, 1.00, 1.69, 2.52 amp/cm^2; other symbols same as (b)]; (b) q_O in oxygen sorption region; △, 0.053 amp/cm^2; □, 0.114 amp/cm^2; ◇, 0.203 amp/cm^2; ○, 0.43 amp/cm^2; solid circle with I thru it, 1.00, 1.69, 2.52 amp/cm^2.

Temperature effects.—The effects of temperature on both the H ionization and O sorption regions are shown in Fig. 3. Data scatter is indicated for the high current pulses and was approximately the same for the other pulses. The curves in Fig. 3a for the H ionization region indicate that the effect of temperature is essentially the same for all current densities, the lower current density pulses showing additional discharge due to reaction of H_2 that comes from the solution. The fact that there is an inverse temperature effect seems to indicate that the lower H_2 partial pressure at higher temperatures would be an important factor. Nevertheless, the data in Fig. 2a clearly show that at the current densities involved the effect of H_2 partial pressure is essentially negligible at 23°C.

One important factor brought out by these curves (Fig. 3a) is that the amount of H_s decreases as the temperature increases. This can be seen especially for the high current density curve where the ionization of extra H_2 from solution would be unimportant. This decrease in the amount of H_s could be due essentially to the lower H_2 partial pressure at higher temperatures. Thus, even though the 23°C case apparently shows independence of the amount of H_s with p_{H_2}, this may be due to the fact that at this temperature the equilibrium between H_s and H_2 may take a relatively long time to be established. It could also well be that the loss of the bulk of the hydrogen from Pt is not through equilibration with H_2 dissolved in the solution, but is due to reaction with trace amounts of oxygen which leak into the system. Higher temperatures could both increase the amount of the oxygen leak and the rate of reaction of O_2 with H_s.

Because the curves in Fig. 3a are essentially parallel, the effect of temperature on $q_{H,ex}$ can be considered to be constant. Unfortunately, it is not possible with this data to separate H_2 partial pressure effects from temperature effects. Measurements were taken in both quiescent and stirred solution (zero and 1300 ml/min gas flow, respectively). Under both conditions, the numbers of coulombs measured for the data (except at the lowest current densities) shown in Fig. 2a were essentially the same. Where there is no stirring effect, we are led to believe that diffusion of H_2 from the solution was not the controlling factor. Hence, we conclude that the rate-controlling step for the ionization of the molecular hydrogen which comes from solution is the dissociation of H_2 to H.

Temperature effects (Fig. 3) in the O sorption region are quite different from those in the H ionization region. Figure 3b shows that at high current densities, where only surface adsorption of O occurs, q_O is independent of temperature with the exception of the 91°C value. The temperature invariance indicates that a transport or charge transfer step may be rate controlling. Here also diffusion in solution can be ruled out by the lack of stirring effects. The transport here would most likely involve either the migration of a water molecule to a site where it can be oxidized or the migration of an O atom to a suitable site on the electrode surface. The sudden drop in q_O at 91°C is difficult to explain. There are several possibilities: (*a*) the effects of electrode poisons would most likely increase at higher temperatures, and the reproducibility of the data being poorest at this temperature would tend to support this, and (*b*) the bonding of O_{ad} at 91°C may be such that a linear bond with surface Pt atoms no longer predominates and therefore full coverage would be less than 420 μcoul/cm^2. Our cleanliness tests at 91°C and after immediate lowering of temperature did not indicate impurity adsorption; however, we cannot be sure that some self-poisoning process did not occur at this temperature.

The lower current density (0.053-0.43 amp/cm^2) data in Fig. 3b show a definite temperature effect of $q_{O,ex}$ throughout the entire temperature range. The curves are roughly parallel, and here again diffusion control in solution is unlikely due to the absence of stirring effects. The fact that there is an inverse temperature effect may be due to a decrease in the solubility of O in the metal skin as the temperature increases and thereby the rate of absorption which gives $q_{O,ex}$ decreases. Decreased hydrogen partial pressure is probably also a factor.

These temperature effects indicate that important changes are taking place, not only on the surface but in the surface layers of the Pt electrode. More work is contemplated on the absorption of O into the skin and the effects of these absorbed atoms on the surface reaction kinetics.

Chemical Reaction of Molecular Hydrogen with Chemisorbed Oxygen Atoms

The unique feature of the technique used to study the reaction of H_2 with O_{ad} is that electrochemical measurements were used not only to determine the kinetics of a chemical reaction occurring on a metal surface under open-circuit conditions, but the effects of the various sorbed species could be isolated. Accurate control of the amount of O_{ad} was possible by coulometric means. Also, the effects of O_{ab} on the rate of the surface reaction between O_{ad} and H_2 could be determined.

The data in Fig. 4 give the reaction rate

$$i_r = \frac{\text{number of } \mu\text{coul/cm}^2 \text{ of O generated during the anodic phase}}{\mu\text{sec required to reduce O with } H_2 \text{ which migrates to the surface}}$$

where i_r is expressed in amp/cm^2. The chemical reaction involved is

$$Pt - O + H_2 \rightarrow H_2O + Pt \qquad [4]$$

With the high current densities (1.66-3.36 amp/cm^2) used to collect the data shown in Fig. 4, absorption of O during anodic charging was found to be negligible. The data for $q_O > 420$ μcoul/cm^2, $E_{O_2} \approx 1.8$v, also indicate that an excess of adsorbed O can be formed in the O_2 formation region. These excess O atoms are evidently not lost by diffusion into solution as O_2 in the fast pulse times used. This may indicate that initially at E_{O_2} at least as much as about another monolayer of O atoms can be held on the electrode surface. These extra O atoms may easily go into the interstitial holes in the Pt lattice (especially in the 110 plane). The potential may simply be a function of the coverage of surface atoms with O_{ad}. After these surface atoms are saturated, the holes in the lattice are filled without apparently affecting the potential and, as the data in Fig. 4 show, the reaction rate, i_r, of Eq. [4] is independent of the surface coverage from one monolayer up to about two monolayers. It is also possible that the extra oxygen is in the molecular form and is held in position firmly enough so that losses are negligible during both the formation of oxygen and reaction with H_2. A third possibility is that PtO_2 is formed at E_{O_2} before the generation of O_2. Molecular hydrogen then reacts with both PtO_2 and Pt-O at essentially the same rate.

Blank runs were made at 23°C to estimate the effects due to a terminating resistance used to maintain pulse shape. The electrode was first exposed in 1 atm H_2 saturated solution and then the H_2 was replaced with pure He. After sweeping out the solution with He for about 20 minutes, the potential became more anodic by about 60 mv. Decay traces in this solution (p_{H_2} calculated <0.01 atm) gave i_r values equal to a little over one-half of the i_r values found in the H_2 swept solutions. This means that i_r values shown in Figs. 4 and 5 should be reduced by about ½ to give true i_r values for the reaction of O_{ad} with H_2. Check runs were made also with the terminating resistance removed from the pulse output. These runs gave essentially a zero blank showing that the contribution of H_i to i_r was negligible, and the results checked those found using the terminating resistance corrected for its blank.

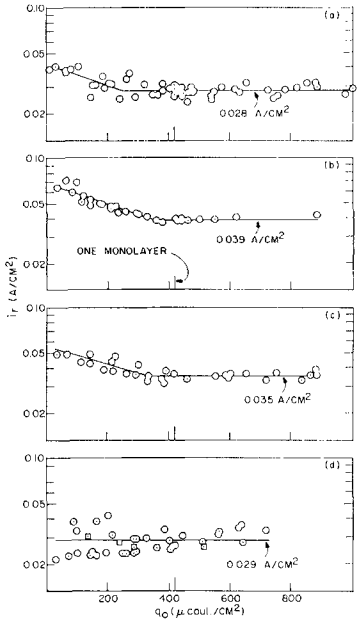

Fig. 4. Rates of reaction, i_r, of O_{ad} with H_2 obtained from decay curves following high current density anodic pulses terminated at various points in the O sorption or O_2 formation regions (no O_{ab} generated). (a) 23°C, 1.0-0.1 atm H_2; (b) 50°C, 0.88 atm H_2; (c) 70°C, 0.69 atm H_2; (d) 90°C, ⊙, 0.31 atm H_2; □, 0.09 atm H_2.

The values of i_r in the plateau regions of Fig. 4 can be considered to be essentially independent of both temperature and hydrogen partial pressure. (The data in Fig. 4a showed a random scatter of points at 0.1, 0.5, and 1 atm H_2 partial pressures.) The values shown in Fig. 4 were taken also at stirring rates beyond which i_r did not increase with increasing stirring. The lack of stirring rate and H_2 partial pressure effects eliminates the diffusion of H_2 from solution as the rate-controlling mechanism. The lack of H_2 partial pressure and temperature effects also eliminates the direct chemical reaction of H_2 with O_{ad} as a possible rate-determining step. A third possible controlling step is one which involves a dissociation of H_2 into atoms and its migration across the surface to active sites bearing O atoms where the reaction in Eq. [4] can occur. It is also possible that the rate-controlling step may be the migration of O_{ad} to the active sites where it can react with either atomic or molecular hydrogen.

The fact that i_r at $p_{H_2} = 1$ atm after subtracting the i_r at $p_{H_2} < 0.01$ atm gives values somewhat higher than 0.01 amp/cm^2, which is about one order of magnitude higher than i_o for the molecular hydrogen ionization reaction (0.00078 amp/cm^2 or 0.0015 amp/cm^2 on an apparent area basis), demonstrates that (*a*) diffusion of H_2 cannot be rate-controlling in the H ionization region because the reaction with H_2 shown in Eq. [4] occurs faster under equal stirring rates, and (*b*) that H_2 does not dissociate into atoms before reacting with O_{ad}, because here again the reaction of

O_{ad} with H_2 is faster than the ionization of H_2 which requires dissociation into atoms. Taking all of these facts into consideration, the most likely rate-controlling step for the reaction between H_2 and O_{ad} is the migration of O_{ad} atoms to active sites where they can directly react with H_2. Hence a reasonable rate-determining step can be postulated, even though the detailed reaction steps which comprise the over-all mechanism are not known.

At lower surface coverages, θ ($\theta < 1$), the data in Fig. 4 show that i_r increased as the surface coverage decreased. This suggested, since the most active sites would be covered with O_{ad} first, that the decrease in the number of inactive sites covered with O_{ad} reduced the amount of necessary migration to active sites and thereby i_r tended to increase. This argument also supports the O_{ad} migration step as the rate-controlling one.

When charging pulses from 0.053 to 1.0 amp/cm^2 were used to form the O sorption region, the rate of charging was slow enough so that some of the O atoms formed absorbed into the skin of the Pt bead and, possibly, some H_i atoms migrated to the surface (as shown in the previous section). Under these conditions, at the end of the charging pulse part of the O atoms formed were adsorbed on the Pt surface and part absorbed in the skin of the electrode. Loss due to reaction with H_i and with H_2 from solution during charging was significant mainly at current densities below 0.2 amp/cm^2, even at the lower current densities used only a fraction of the O_{ad} reacted with H_i or H_2 (see Fig. 2b).

The data in Fig. 5 were obtained with pulses which were terminated just at the end of the O sorption region (see, for instance, upper charge curve in Fig. 1b), but which were of such low current density that additional amounts of oxygen could dissolve in the Pt. This is in contrast to the data in Fig. 4, which were obtained with high current density pulses. Some of these latter pulses were long enough to charge well into the O_2 formation region, some were terminated just at the end of the O sorption region, and some were terminated at various points within the O sorption region.

Figure 5 shows that O_{ab} has a marked effect on i_r. The reaction current density, i_r, of Eq. [4] is sharply diminished as the amount of O_{ab} increases (correction of i_r for any reduction of O_{ad} due to migration of residual H_i to the surface during charging would tend to decrease i_r further). Figure 5a shows that i_r is a direct function of p_{H_2}. Figure 5b shows that although increased temperature tends to increase i_r (see i_r values in Fig. 5a at comparable partial pressures), the lowering of H_2 partial pressure with increasing temperature (owing to increased partial pressure of water vapor) exerts a stronger effect than temperature.

The data in Fig. 5 were also taken under vigorous stirring conditions where increased stirring rates did not change i_r; therefore diffusion control of H_2 was minimized. The results shown in Fig. 5 indicate that the reaction mechanism for Eq. [4] must be quite different than for the case where O_{ab} is insignificant. The dependence on H_2 partial pressure indicates that the reaction is controlled by the chemical reaction of H_2 with O_{ad}. The tendency of a positive temperature dependence also indicates such a reaction control. The increase in i_r as $q_{O,ex}$ decreases shows that the reaction rate increases as the amount of sorbed O decreases, and the change to the higher slope at low $q_{O,ex}$ values indicates that the reaction step is becoming so fast that the over-all rate i_r, approaches the comparable values shown in Fig. 4 where O_{ad} migration is the indicated rate-controlling step. Hence, in the region of the steeper slope (Fig. 5) there appears to be a mixed control of the reaction. This is also verified by the coming together of the curves in Fig. 5 at the lowest $q_{O,ex}$ values. This indicates that H_2 partial pressure and temperature effects become less important as in the data shown in Fig. 4.

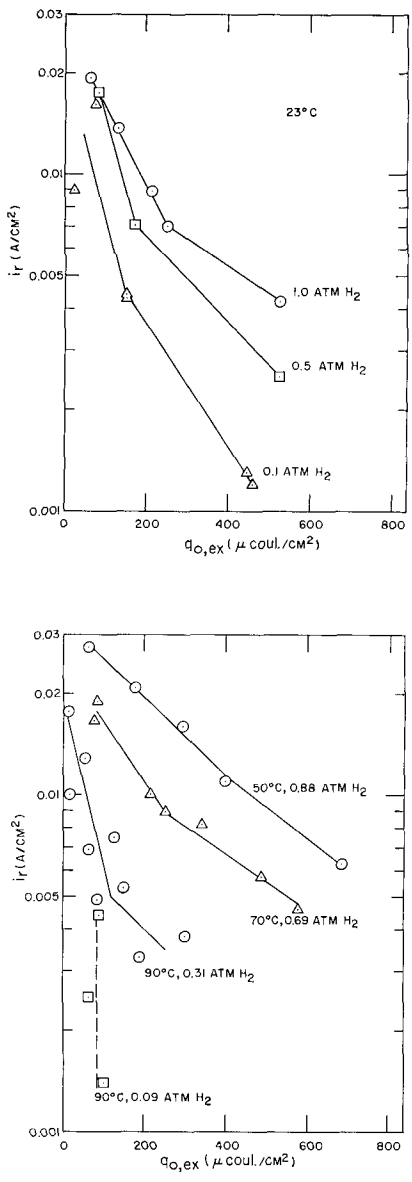

Fig. 5. Rates of reaction, i_r, of O_{ad} with H_2 obtained from decay curves following low current density anodic pulses terminated at end of O sorption region (O_{ab} present).

It is felt that the presence of O_{ab} in the Pt bead markedly lowers the heat of adsorption of O_{ad}. This in turn evidently slows the rate of the chemical combination of O_{ad} and H_2.

One of the most important results of this investigation is considered to be the application of the described technique for separating differently sorbed species associated with a surface and determining their effects on the rates of chemical reactions.

Conclusions

Use of the techniques described here has led us to conclude:

1. That platinum electrodes in sulfuric acid solution can absorb considerable quantities of oxygen and hydrogen in excess of the quantity present on the surface. In this work the oxygen was generated on the electrode surface electrolytically; the hydrogen was present in the solution.

2. That this absorption is fast. Measurable quantities of absorbed oxygen are found after anodic polarizations of 1000 μsec or longer.

3. That multiple monolayers can be absorbed if sufficient time of contact is allowed.

4. That desorption is slow. An effort is necessary to obtain an electrode free of these dissolved species. Coulometric studies involving oxidation or reduction of substances adsorbed on the surface of a platinum electrode can be seriously affected by the presence of these dissolved species as an unrecognized reactant (10).

5. That catalytic behavior of a platinum electrode is drastically affected by such absorbed species.

These conclusions, in turn, lead to the conclusion that the use of anodic pulses to clean an electrode prior to use may create more problems than it solves, and if used, extreme care must be taken to insure that the above processes do not influence the measurements.

Acknowledgments

The authors gratefully acknowledge the help of Professor P. H. Emmett of Johns Hopkins University, especially his suggestion that the surface migration of adsorbed species to active centers may be applicable for the reaction of O_{ad} with H_2.

Manuscript received June 8, 1964; revised manuscript received Sept. 23, 1964. This paper is to be presented at the San Francisco Meeting, May 9-13, 1965.

Any discussion of this paper will appear in a Discussion Section to be published in the December 1965 JOURNAL.

SYMBOLS

(Figure 1a delineates and defines the major reaction regions and potentials in the charge and decay traces. Wherever a quantity of material was determined coulometrically, double layer capacitance charging was corrected for.)

H_s hydrogen atoms associated with Pt atoms on the surface and immediately below the surface. Operationally, H_s is the time-independent amount of H atoms coulometrically measured with an anodic pulse that polarizes the electrode through the H ionization region in less than 1000 μsec. At a Pt electrode under 1 atm H_2 at 25°C, H_s = 230 μcoul/cm^2.

H_i hydrogen atoms located in the interior of a Pt electrode. Operationally, these H atoms do not migrate to the surface and react under the conditions referred to under H_s. H_i atoms only add to the measured number of coulombs at polarization times longer than 1000 μsec.

H_2 molecular hydrogen in the solution phase.

i_r number of μcoul/cm^2 of O generated during an anodic pulse divided by the time, in μsec, required to reduce this O with H_2 plus H_i which migrates to the surface.

O_{ad} oxygen atoms chemisorbed on the Pt electrode surface. By the definition of area used, these atoms are in a one-to-one correspondence with surface Pt atoms. Operationally, O_{ad} is the time-independent amount of O atoms coulometrically measured with an anodic pulse that polarizes the electrode through the O sorption region in less than 1000 μsec. At 25°C, O_{ad} = 420 μcoul/cm^2.

O_{ab} oxygen atoms absorbed in the skin of the Pt electrode. Operationally, these atoms only add to the measured number of coulombs at polarization times longer than 1000 μsec.

q_H the number of μcoul/cm^2 of reaction in the H ionization region.

q_O the number of μcoul/cm^2 of reaction in the O sorption region.

$q_{H,ex}$ the number of μcoul/cm^2 of hydrogen oxidized in the H ionization region in excess of the amount of hydrogen atoms (H_s) originally associated with the electrode surface before imposition of the anodic pulse. $q_{H,ex}$ is due to oxidation of H_i and H_2.

$q_{O,ex}$ the number of μcoul/cm^2 of charge expended in the O sorption region in excess of the amount required to generate the O atoms (O_{ad}) chemisorbed on the Pt surface. $q_{O,ex}$ is due to the formation of O_{ab} and of the oxidation of H_i and H_2.

fraction of available sites on the surface covered.

REFERENCES

1. S. Schuldiner and R. M. Roe, *This Journal*, **110**, 332 (1963).
2. S. Schuldiner and R. M. Roe, *ibid.*, **110**, 1142 (1963).
3. T. B. Warner and S. Schuldiner, *ibid.*, **111**, 992 (1964).
4. W. Nernst and E. Merriam, *Z. Phys. Chem.*, **53**, 235 (1905); O. Sackur, *ibid.*, **54**, 641 (1906); M. W. Breiter, *Electrochim. Acta*, **7**, 601 (1962).
5. M. W. Breiter, *This Journal*, **109**, 425 (1962).
6. S. Schuldiner and T. B. Warner, *J. Phys. Chem.*, **68**, 1223 (1964).
7. T. C. Franklin and S. L. Cooke, *This Journal*, **107**, 556 (1960).
8. C. H. Presbrey, Jr. and S. Schuldiner, *ibid.*, **108**, 985 (1961).
9. S. Schuldiner, *ibid.*, **106**, 891 (1959).
10. S. Schuldiner and T. B. Warner, *Anal. Chem.*, **36**, 2510 (1964).

Polarography of Lead Complexes in Glycolic Acid and Malonic Acid as Competing Chelating Agents

Tsai-Teh Lai and Ching-Chiang Hsieh

Department of Chemical Engineering, Cheng Kung University, Tainan, Taiwan, China

ABSTRACT

The polarography of lead complexes in glycolic acid, malonic acid, and in a mixture of glycolic acid and malonic acid has been studied in detail. With glycolic acid, $Pb(G)^+$ and $Pb(G)_2$ were identified. With malonic acid, evidence for the existence of $Pb(HA)^+$, $Pb(HA)_2$, and $Pb(A_2)^{-2}$ was obtained. In a mixture of glycolic acid and malonic acid as competing ligands to the lead ion, the complex species of $Pb(G)^+$, $Pb(G)(HA)$, and $[Pb(G)(A)]^-$ were formed. The electrode reactions and concentration dissociation constants of the complexes were given. The coordination ability between the lead ion with the following groups decreased in the order: $-COO^- > -OH > -COOH$.

The polarographic behavior of the complexes of uranium (VI) with glycolic (1) and malonic acid (2) has been investigated. The malonate complexes of iron (3) and chromium (III) (4) have been studied polarographically.

Although the polarography of lead complexes with tartaric acid has ben reported by Iwase (5), it was found that little has been done with other carboxylic or hydroxylic acids. In an attempt to determine what complexes of lead existed in the competing chelating

agents of glycolic acid and malonic acid, and to estimate their concentration dissociation constants, a detailed investigation by polarography was undertaken.

Experimental

Apparatus.—The apparatus and procedure used in this work were described previously (1).

The characteristics of the capillary were 1.10 $mg^{2/3}$ $t^{-1/2}$ at a mercury column height of 61 cm and an applied potential of —0.500v *vs.* SCE.

All polarographic solutions were allowed to stand at least 30 min before measurements were made to assure equilibrium. No maxima were encountered, and no suppressors were added to the solutions.

All experiments were carried out at 30° ± 0.1°C.

Chemicals.—The stock solution of 0.01M lead nitrate was standardized complexometrically with standard EDTA solution (6). A 2M stock solution of malonic acid and 1M stock solution of glycolic acid were prepared, and their exact concentrations were determined with carbonate-free sodium hydroxide solution which was standardized with potassium biphthalate of the National Bureau of Standards.

Results and Discussion

The half-wave potential for the lead complex PbA_x^{2-nx} at the dropping mercury electrode may be represented by

$$(E_{1/2})_c = (E_{1/2})_s + \frac{0.060}{2}\log K_c - \frac{0.060}{2}x \log [A^{-n}] \text{ (at 30°C)} \quad [1]$$

Here K_c is the concentration dissociation constant of the lead complex and $[A^{-n}]$ is the concentration of ligand.

If A^{-n} and B^{-m} represent chelating agents that compete for the electron pair donor groups to the lead ion, the half-wave potential of the resulting complex $PbA_xB_y^{(2-nx-my)}$ is expressible as

$$(E_{1/2})_c = (E_{1/2})_s + \frac{0.060}{2}\log K_c - \frac{0.060}{2}x \log [A^{-n}] - \frac{0.060}{2}y \log [B^{-m}] \quad [2]$$

When the ligand number x of A^{-n} is identical to the ligand number y of B^{-m}, Eq. [2] can be simplified to

$$(E_{1/2})_c = (E_{1/2})_s + \frac{0.060}{2}\log K_c - \frac{0.060}{2}x \log [A^{-n}][B^{-m}] \quad [3]$$

We then obtain

$$\frac{\Delta(E_{1/2})_c}{\Delta \log [A^{-n}][B^{-m}]} = -0.030\,x \quad [4]$$

This equation shows that if the value of the slope of $E_{1/2}$ *vs.* log $[A^{-n}][B^{-m}]$ is an integral multiple of 0.030, the ligand number of A^{-n} and B^{-m} are the same. That is, the ligand A^{-n} and B^{-m} will have identical coordination ability to the lead ion when the solution has the same concentration of A^{-n} and B^{-m}.

Reversible and diffusion controlled reduction.—Figure 1 shows the typical polarograms and the plots of log $i/(i_d - i)$ *vs.* $E_{d.e.}$ for lead ion solutions (curve I), containing glycolic acid (curve II), malonic acid (curve III), and glycolic acid and malonic acid (curve IV). It is obvious from Fig. 1 that the half-wave potential of simple lead ion in 0.1M KNO_3 solution at pH 3.50 is —0.397v *vs.* SCE and the half-wave potentials are all shifted to negative side by chelation with glycolic acid, malonic acid, and a mixture of glycolic acid and malonic acid.

The slopes of the conventional log plots for the polarograms of lead-glycolate, lead-malonate, and lead-glycolate-malonate system at various pH values were rounded up in Table I. The temperature coefficients of

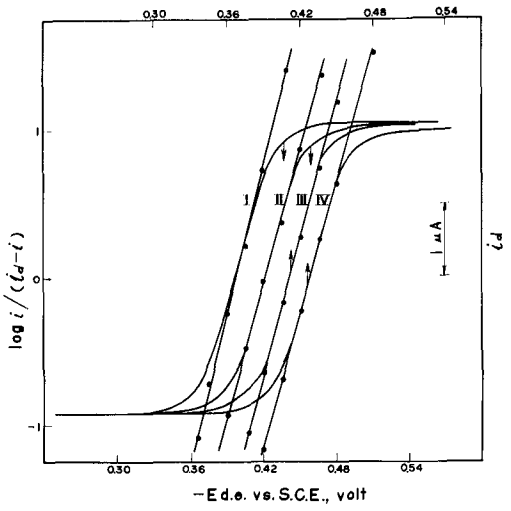

Fig. 1. Typical polarograms and log $i/(i_d-i)$ *vs.* $E_{d.e.}$ Polarograms of solutions containing 1.116 mM $Pb(NO_3)_2$, 0.1M KNO_3, at pH 3.50 with various chelating agents: (I) no chelating agent; (II) 0.1027M glycolic acid; (III) 0.0976M malonic acid; (IV) 0.1027M glycolic acid and 0.0976M malonic acid.

half-wave potential and diffusion current were also determined with the data listed in Table II. From Tables I and II, it is obvious that the three systems are all 2-electron reversible and diffusion-controlled reduction.

Lead-glycolic acid system.—Curve I in Fig. 2 represents the effect of pH on the half-wave potential of a lead-glycolic acid system. At pH < 2.35, the half-wave potentials are independent of pH and remain constant at $(E_{1/2})_s$ value, indicating that no chelation occurred. In the pH range 2.35-4.15, the slope of $E_{1/2}$ *vs.* pH is —0.028 showing that one hydrogen ion was required in releasing the coordinated glycolate anion from one mole of lead-glycolate complex to form glycolic acid. At pH > 4.15, the half-wave potentials became independent of pH value again, showing that no hydrogen ion was involved in the reduction of the complexes.

To determine the ligand number of the lead-glycolate complexes, the variation of half-wave potential with the concentration of glycolate ion was measured (Fig. 3). The concentration of glycolate anion was calculated from the nominal concentration of glycolic acid, the pH of the solution, and the pKa (3.82) (7), for glycolic acid.

In curve I of Fig. 3, the half-wave potentials are essentially independent of glycolic acid concentration

Table I. Slopes of $E_{d.e.}$ *vs.* log $i/(i_d-i)$

Systems	pH range	No. of polarograms	$E_{d.e.}$ *vs.* $-\log i/(i_d - i)$ low val.	high val.	avg.
Pb-Gly.	1.5-7.5	52	0.028	0.031	0.030
Pb-Mal.	1.5-7.5	54	0.028	0.032	0.030
Pb(Mal.)(Gly.)	1.5-7.5	65	0.028	0.031	0.030

Table II. Temperature coefficients of half-wave potential and diffusion current

Systems	pH	Temp range, °C	Temp coefficient of $E_{1/2}$ (mv/°C)	i_d (%/°C)
Pb-Gly.	5.3	13-25	−0.44	+1.7
		25-47	+0.27	
Pb-Mal.	5.3	13-47	−0.13	+1.4
Pb(Gly.)(Mal.)	5.3	13-47	−0.13	+1.6

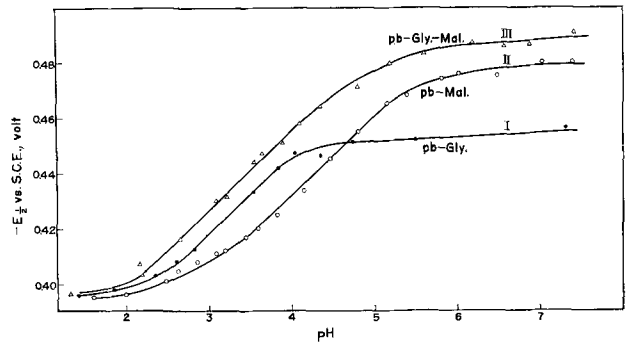

Fig. 2. Effect of pH on half-wave potential. Polarographic solutions containing 1.116 mM $Pb(NO_3)_2$, 0.1M KNO_3, and various chelating agents: (I) 0.205M glycolic acid; (II) 0.218M malonic acid; (III) 0.205M glycolic acid and 0.218M malonic acid.

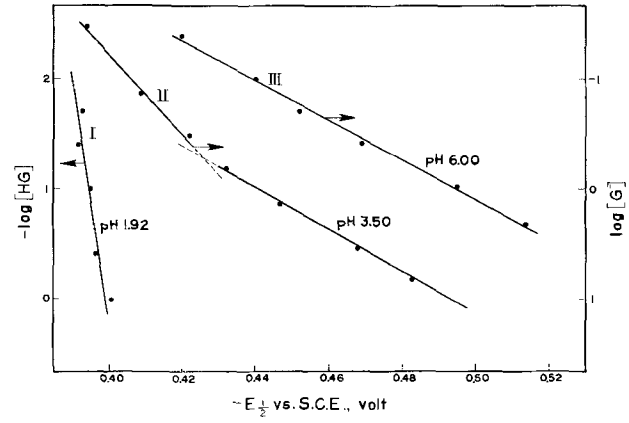

Fig. 3. Variation of half-wave potential of lead-glycolic acid system with ligand concentration: 1.116 mM $Pb(NO_3)_2$, 0.1M KNO_3.

at pH 1.92. This is in good agreement with the fact that no chelation occurred in the low pH region as mentioned above. Curve II in Fig. 3 consists of two straight lines which intersect at glycolate concentration 0.055M. The slopes of the lines are 0.028 and 0.055, corresponding to the ligand number of 0.92 and 1.83, respectively. Thus, the chelate species and electrode reactions in the pH range 2.35-4.15 can be written

$$[G^-] < 0.055M,$$
$$PbG^+ + H^+ + 2e + Hg = Pb(Hg) + HG \qquad (a)$$

$$[G^-] > 0.055M,$$
$$Pb(G)_2 + H^+ + 2e + Hg = Pb(Hg) + HG + G^- \quad (b)$$

The slopes of curve III in Fig. 3 is 0.055, corresponding to the ligand number of 1.83. Thus, the chelate species and electrode reaction at pH > 4.15 may be expressed as

$$Pb(G)_2 + 2e + Hg = Pb(Hg) + 2G^-$$

Lead-malonic acid system.—It is obvious from curve II in Fig. 2, the half-wave potentials are independent of pH at pH < 2.25 and pH > 5.40. However, in the pH range 2.25-5.40, the half-wave potentials are dependent on pH, and the $\Delta E_{1/2}/\Delta pH$ is —0.028, indicating that one hydrogen ion was consumed in the electrode reduction.

As shown in Fig. 4, the diffusion current constants remain constant at 3.12 at pH lower than 5.25 and at 2.88 at pH greater than 5.25, revealing that two kinds of chelate species transform at pH 5.25. This result and the pK_2 value 5.36 (8) of malonic acid, evidenced that the ligand species is hydrogenmalonate ion at pH lower than 5.25, and is malonate ion at pH greater than 5.25.

The ligand number of the chelates were estimated from Fig. 5, in which the concentration of the hydrogenmalonate ion and malonate ion were calculated

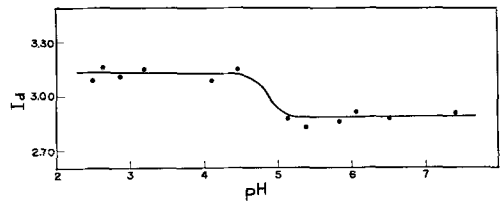

Fig. 4. Effect of pH on diffusion current constant of lead-malonate complexes.

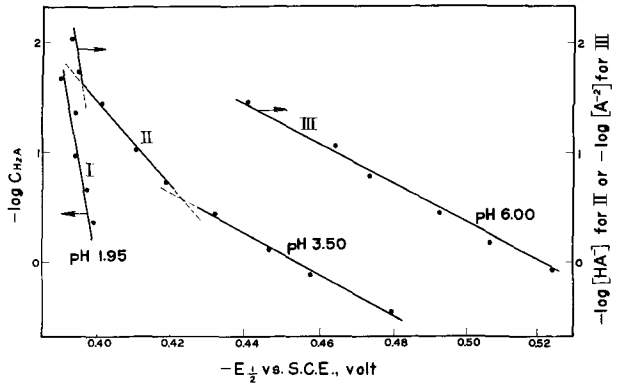

Fig. 5. Variation of half-wave potential of lead-malonic acid system with ligand concentration: 1.116 mM $Pb(NO_3)_2$, 0.1M KNO_3.

from the added concentration of malonic acid, the pH of the solution and using $pK_1 = 2.75$ and $pK_2 = 5.36$ (8).

Curve I in Fig. 5 shows that the ligand number is nearly equal to zero, *i.e.*, essentially no chelation occurred at pH lower than 2.25, which is in good agreement with the result of curve II in Fig. 2.

Curve II in Fig. 5 shows two breaking points at the hydrogenmalonate ion concentration of 0.025 and 0.27M. The first breaking point at 0.025M shows the starting point for chelation, namely, a concentration of hydrogenmalonate ion greater than 0.025M is required to assure the chelation with 1.116 mM lead ion. The ligand number of the lead-hydrogenmalonate chelates were found to be 0.87, and 1.80, as evidenced by the slopes of 0.026, and 0.055, respectively (curve II, Fig. 5).

Based on the forgoing discussion, the chelate species and electrode reactions in the pH range 2.25-5.25 can be expressed as

$$0.025M < [HA^-] < 0.27M,$$
$$Pb(HA)^+ + H^+ + 2e + Hg = Pb(Hg) + H_2A \qquad (a)$$

$$[HA^-] > 0.27M,$$
$$Pb(HA)_2 + H^+ + 2e + Hg = Pb(Hg) + HA^- + H_2A \qquad (b)$$

Above pH 5.40, the malonate ligand took the place of the hydrogenmalonate ligand, as predicted by the sudden drop of the diffusion current constant from 3.12 to 2.88 (Fig. 4). The slope of curve III in Fig. 5 is 0.057 from which the malonate ligand number is 1.90. Thus, above pH 5.40, the formula is $Pb(A)_2^{-2}$ and the electrode reaction will be

$$Pb(A)_2^{-2} + 2e + Hg = Pb(Hg) + 2A^{-2}$$

Lead-glycolic acid-malonic acid system.—Two kinds of chelating agents, glycolic acid and malonic acid, were used in competing for the electron pair donor groups to the lead ion, at the condition of nearly identical concentrations.

The $E_{1/2}$ *vs.* pH plot for this system appears as curve III of Fig. 2. The chelation starts at pH 2.1. The line obtained by varying the pH from 2.1 to 5.3 has a slope of —0.029, indicating that one hydrogen ion was involved in the reduction.

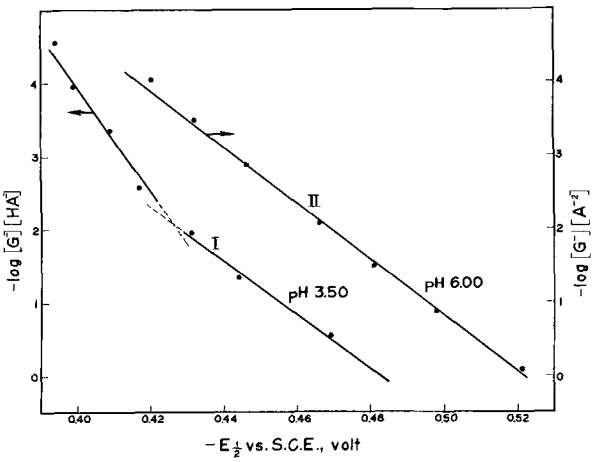

Fig. 6. Variation of half-wave potential of lead-glycolic acid-malonic acid system with ligand concentration: 1.116 mM $Pb(NO_3)_2$, 0.1M KNO_3.

In an attempt to apply Eq. [4], the plots of $E_{1/2}$ *vs.* log $[G^-]$ $[HA^-]$ for *p*H 3.50 and $E_{1/2}$ *vs.* log $[G^-]$ $[A^{-2}]$ for *p*H 6.00 are shown as curves I and II of Fig. 6, in which G^- and A^{-2} denote, respectively, glycolate ion and malonate ion.

In curve I of Fig. 6, the break occurs at $[G^-][HA^-] = 7.9 \times 10^{-3}$ M; the slope is 0.015 for the upper line and is 0.027 for the lower line. Let x and y be the ligand number of G^- and HA^- or A^{-2}. Applying the value of slope, 0.015, in Eq. [4], we get $x \neq y$ when $[G^-]$ $[HA^-] < 7.9 \times 10^{-3}$ M. It was already shown that the glycolate ion can complex with the lead ion only in a 1:1 ratio at lower ligand concentration. The same is true of the hydrogenmalonate ion. Hence $x = 1$ and $y = 0$ or $x = 0$ and $y = 1$ for the case $x \neq y$. This relation indicates that the chelate formed in the competing agents, may be either $Pb(G)^+$ or $Pb(HA)^+$ when $[G^-]$ $[HA^-] < 7.9 \times 10^{-3}$M. However, because of the greater stability of the $Pb(G)^+$ complex (as will be shown in the next section) the $Pb(G)^+$ rather than $Pb(HA)^+$ was considered as the most probable species. On the other hand the slope of the lower line, 0.027, is sufficiently close to 0.030, to yield a value of $x = y = 1$. This shows that the chelate species is Pb(G) (HA) when $[G^-]$ $[HA^-] > 7.9 \times 10^{-3}$M. Thus, the electrode reactions in the *p*H range 2.1-5.3 can be formulated as

$[G^-]$ $[HA^-] < 7.9 \times 10^{-3}$M,

$$Pb(G)^+ + H^+ + 2e + Hg = Pb(Hg) + HG \quad (a)$$

$[G^-]$ $[HA^-] > 7.9 \times 10^{-3}$M,

$$Pb(G)(HA) + H^+ + 2e + Hg = Pb(Hg) + HA^- + HG \quad (b)$$

Similarly, the slope of curve II in Fig. 6 at *p*H 6.0 is 0.026, giving $x \cong y$ and a chelate species of $[Pb(G)(A)]^-$. Thus, the electrode reaction at *p*H greater than 5.3 is

$$[Pb(G)(A)]^- + 2e + Hg = Pb(Hg) + G^- + A^{-2}$$

Concentration dissociation constants of chelates.— The over-all concentration dissociation constants of the chelates were determined by application of Eq. [1] and [2] in which $(E_{1/2})_s$ is —0.397v *vs.* SCE (curve I, Fig. 1). The *p*K values obtained for the chelates are summarized in Table III.

Table III. Concentration dissociation constants of lead complexes

Chelating agents	Ligand number	Chelate species	*p*K
Glycolic acid	0.92	$Pb(G)^+$	2.13 ± 0.03
	1.83	$Pb(G)_2$	3.24 ± 0.05
Malonic acid	0.87	$Pb(HA)^+$	1.37 ± 0.01
	1.80	$Ph(HA)_2$	1.88 ± 0.06
	1.90	$Pb(HA)_2^{-2}$	4.19 ± 0.07
Mix. of glycolic acid and malonic acid	0.90	Pb(G)(HA)	2.89 ± 0.07
	0.87	$[Pb(G)(A)]^-$	4.13 ± 0.06

The $Pb(G)^+$ chelate has the five-membered ring structure

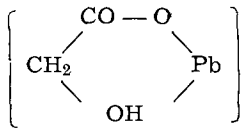

and the $Pb(HA)^+$ has the six-membered ring structure

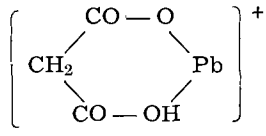

Pfeiffer (9) has shown that, in general, a five-membered ring is more stable than a six-membered ring when the ring is entirely saturated. This was proved by the *p*K values of 2.13 for $Pb(G)^+$ and 1.37 for $Pb(HA)^+$ as shown in Table III. These facts show that the coordination ability of the lead ion with —OH is stronger than that of the lead ion with —COOH.

As listed in Table III, the *p*K value of $Pb(A_2)^{-2}$ is 4.19 and that of $Pb(G)_2$ is 3.24, indicating that the coordination ability between the lead ion and $—COO^-$ is stronger than that between the lead ion and —OH. Thus, it was concluded that the coordination ability between the lead ion with the following groups decreases in the order $—COO^- > —OH > —COOH$. This order is in excellent agreement with the order of *p*K values (Table III): $Pb(A_2)^{-2}$ (4.19) > $[Pb(A)(G)]^-$ (4.13) > $Pb(G)_2$ (3.24) > Pb(G)(HA) (2.89) > $Pb(HA)_2$ (1.88)

Acknowledgment

The authors thank the National Council on Science Development, which supported the work described.

Manuscript received Aug. 27, 1964.

Any discussion of this paper will appear in a Discussion Section to be published in the December 1965 JOURNAL.

REFERENCES

1. T. T. Lai, S. N. Chen, B. C. Wang, and C. C. Hsieh, *Anal. Chem.*, **35**, 1531 (1963).
2. T. T. Lai and C. C. Hsieh, *J. Inorg. Nucl. Chem.*, **26**, 1215 (1964).
3. W. B. Schaap, H. A. Laitinen, and J. C. Bailar, Jr., *J. Am. Chem. Soc.*, **76**, 5868 (1954).
4. R. E. Hamm and R. H. Perkins, *ibid.*, **77**, 2083 (1955).
5. A. Iwase, *J. Chem. Soc. Japan*, **78**, 1411 (1957).
6. H. Flaschka and F. Huditz, *Z. Anal. Chem.*, **137**, 172 (1952).
7. R. T. Morrison and R. N. Boyd, "Organic Chemistry," p. 715, Allyn & Bacon, College Division, Rockleigh, N. J. (1959).
8. A. E. Matell and M. Calvin, "Chemistry of Metal Chelate Compounds," p. 514, Prentice-Hall Inc., Englewood Cliffs, N. J., (1956).
9. P. Pfeiffer, *Angew. Chem.*, **53**, 93 (1940).

Conductivity through Hydrogen Bonded Organic Compounds and Their Homogeneous Solutions

I. Conductivity of Aliphatic Alcohols and Their Benzene Homogeneous Solutions

M. F. Mayahi and A. E. Habboush

Department of Chemistry, College of Science, University of Baghdad, Iraq

ABSTRACT

The conductivity of methanol, ethanol, n-butanol, n-pentanol, and n-hexanol was measured at 30°C. The effect of an increase of one (—CH_2—) group in the carbon chain was determined by plotting molar conductivities *vs.* molar volumes (ml) of each pure alcohol; the slope of the straight line obtained was —55 units. The conductivity of these alcohols in benzene solution at 30°C was found to show a characteristic rise with concentration; the conductivity rises sharply at about 6M concentration of each alcohol. Such points are referred to as inflection points. The plot of molar conductivities of solutions *vs.* the volume of the solution containing one mole of each alcohol at the inflection point gives a straight line, the slope of which is —38 units.

The effect of the hydrogen bond on the conductivity of alcohols (1), solid organic (2) acids, and acidic solutions of water and alcohols (3) has been investigated previously. Mecke *et al.* (1) studied the conductivities of pure methanol, isopropanol, tertiary butyl alcohol, and benzyl alcohol, and the conductivities of their solutions in CCl_4, chlorobenzene and benzene. They found that conductivity decreased as branching in the carbon chain increases. Ubbelohde *et al.* (2) studied the conductivity of solid organic acids and found that the conductivity of the interhydrogen-bonded acids was a hundred times greater than those with intrahydrogen-bonded acids.

Conway *et al.* (3) worked on proton conductance in water and alcohols and observed the lower mobility of the proton as the alcohol hydrocarbon chain length increases. Our work is concerned with the conductivity of hydrogen-bonded compounds and in this paper we report the conductivities of pure methanol, ethanol, n-butanol, n-pentanol, n-hexanol, and also the conductivities of their solutions in benzene at 30°C.

Experimental

Materials.—Methyl alcohol was supplied by Fisher Scientific Company (certified reagent) containing 0.01 % water and was used without further treatment. Ethyl alcohol and benzene were of Analar grade of the British Drug Houses Company and used without further treatment. Butyl alcohol and hexanol were supplied by B.D.H. and were treated with $MgSO_4$ and distilled. Amyl alcohol was Analar grade of Merck & Company and was treated with $MgSO_4$ and distilled.

Apparatus.—A Wayne Kerr Universal bridge B221 was used with a special cell designed for low conductivity measurement, the distance between the platinized platinum electrodes being 0.35 cm.

Method.—Conductivity measurements were made at 30° ± 0.1°C. 5 ml of benzene or alcohol was transferred to the cell using syringe-type graduated 5-ml pipet. After reaching thermal equilibrium, the alcohol or benzene was added from an automatic 1-ml closed buret, graduated to 0.005 ml, to benzene. The cell was sealed immediately with strong adhesive tape to prevent further contact with air. The cell was stirred and readings were taken immediately until a constant value was obtained, experimentally found to be about 2 min. Separate experiments showed that the readings stay constant for 20 min except for solutions containing very high percentages of methyl or ethyl alcohols. For methanol and ethanol the value changed quickly with time, and the value after 2 min was taken. For further additions of alcohol or benzene the adhesive tape was removed from the buret inlet in the cover of the cell, and the buret tip was inserted in the inlet for quick delivery, and the cell was immediately resealed. Each titration curve was done completely in less than 2 hr.

The buret stopcock was treated with vacuum silicone grease which was soaked for two days in alcohol, boiled, the supernatant alcohol decanted, and the grease dried at 100°C before use.

Results and Discussion

The large increase in the initial values of pure methanol and ethanol are due to absorption of water from the air. The results show decrease in conductivity of the pure alcohols as shown in Fig. 1 and 2, as the carbon chain increases in line with observations made by Conway *et al.* (3) for proton mobility in alcohols. This decrease in conductivity is directly related to the per cent hydrogen bonding in these alcohols, such hydrogen bonding decrease with increasing carbon chain, as reflected from their boiling points, heat of vaporization, and thermal conductivities (4).

The effect of an increase of —CH_2— groups on conductivity can be estimated by plotting molar conduc-

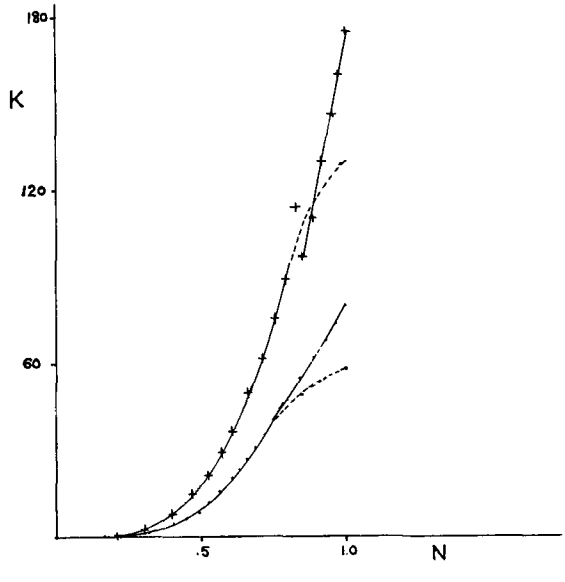

Fig. 1. Specific conductivity (K) x 10^8 ohm^{-1} cm^{1-} *vs.* mole fraction (N) for methyl alcohol (+) and ethyl alcohol (•) in benzene at 30°C. The straight line in each curve shows the effect of water in each system. The dotted parts are the extrapolation to the lowest reading of each alcohol.

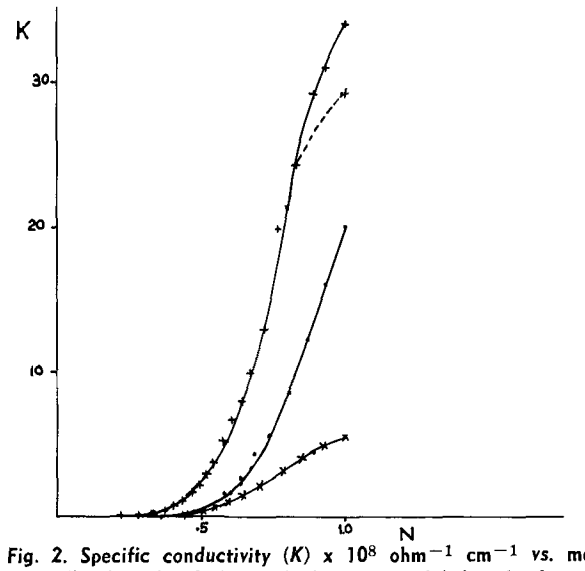

Fig. 2. Specific conductivity (K) x 10^8 ohm^{-1} cm^{-1} vs. mole fraction (N) for n-butyl alcohol (+), n-pentonol (•) and n-hexanol (X) in benzene. The dotted part is the extrapolation to the lowest reading for n-butanol at 30°C.

tivity *vs.* molar volume, Fig. 1. The slope of the straight line is —55 units.

The addition of an inert solvent to these alcohols should affect conductivities in the same manner as increasing the carbon chain in each alcohol. Such an effect is observed in the conductivities of alcohols when diluted with benzene. Plots of specific conductivity against mole fraction are shown in Fig. 1 and 2: for each alcohol there is a particular concentration at which the conductivity rises sharply with increasing concentration. These concentrations will be referred to as inflection points. This inflection indicates that the per cent hydrogen bonding of the alcohol has reached critical value, the meaning of which will be explained later. The inflection points were obtained from each curve by the usual method used to find end points in conductimetric titration; that is by drawing tangents to both ends of the curve, the point on the actual curve which corresponds to the intersection point of the tangents. The conductivity of the solution at that concentration corresponding to the inflection points was read directly from the curve. The inflection points are listed in Table I.

At the inflection points the hydrogen bond formation reaches a critical value, and the conductivity through such hydrogen-bonded chains rises sharply because the effective collisions between these chains is much greater than that between smaller chains present in solutions of lower concentrations. The increase in hydrogen bond formation when the concentration of alcohol is increased is amply verified in the literature by spectral work (4, 5). The inflection point of each alcohol occurs where the same number of moles of the different alcohols are present per unit of solution (*ca.* 6 moles/liter, Fig. 1 and 2, Table I). Table I shows that the conductivity of methanol at its inflection point is higher than that of hexanol at its inflection point, although there is the same number of

Table I. Inflection points taken from Figs. 1 and 2

Alcohol	Mole fraction of alcohol	Specific conductivity ohm^{-1} cm^{-1}, at inflection points	% v/v of alcohol	No. of moles/liter
Methanol	0.43	11.0 × 10^{-8}	26	6.35
Ethanol	0.50	8.0	36	6.18
Butanol	0.61	6.8	58	6.15
Pentanol	0.67	3.6	63	6.52
Hexanol	0.70	2.0	65	6.16

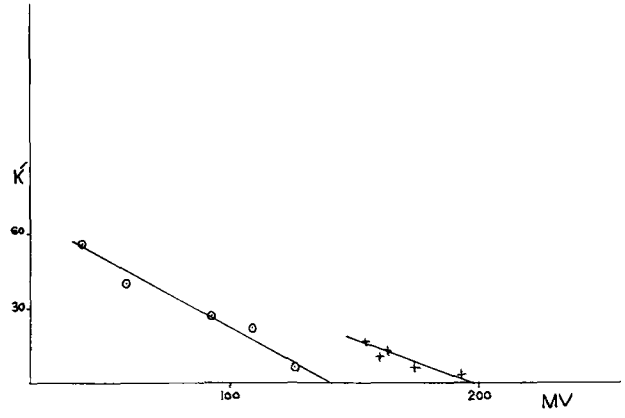

Fig. 3. Molar conductivity (K') x 10^6 ohm^{-1} cm^{-1} vs. molar volume (MV) for pure alcohols (⊙), and for alcohols in benzene at their inflection points (+) at 30°C.

moles/liter involved in each case. This is due to the fact that conductivity can proceed only through hydrogen bonds produced by effective collisions. The increased carbon chain length in the higher alcohols reduces these effective collisions by shielding the (OH) group in the alcohol molecule. This shielding is reduced to some extent in benzene solution but not entirely. The reduced shielding effect of the longer carbon chain is indicated by comparing the slopes obtained by plotting molar conductivities *vs.* molar volumes for the pure alcohols (—55 units) and for the solutions at the inflection points (—38 units) (Fig. 3).

The meaning of the slopes, as indicated earlier, is the decrease in molar conductivity brought about by an increase of one —CH_2— group in the carbon chain of the alcohol. The lower slope obtained for the inflection points in benzene solution indicates a reduction of the steric effect of the longer carbon chain and polymer chains also; the benzene straightens up these chains, thus reducing the shielding of the (OH) group and therefore increasing the effective collisions, which in turn causes the conductivity of the higher alcohols to increase relative to that of methanol. The large increase in conductivity caused by the small amount of absorbed water can be explained by the same reasoning: that is, the small water molecule, when hydrogen bonded between alcohol molecules, reduces the steric effect of the longer carbon chain, thus increasing the extent of hydrogen bonding in the whole system.

Our work, and that of Mecke (1), indicates the necessity of the hydrogen bonds for the conductivity of pure alcohols and their solutions. The solvents used in such systems were benzene, CCl_4, and chlorobenzene. The conductivity of these solvents, although small, is not negligible, especially at higher temperature (1).

It is difficult to explain the conductivity of such inert solvents as CCl_4 by the mechanism proposed by Mecke for the alcohol system, $HROH^+$----------O^-R $\rightleftarrows$HOR--------HOR. A different mechanism involving tunneling of electrons through solvent molecules might explain the conductivity of the inert solvents as that of CCl_4 (6, 7). This mechanism might also be involved in the conductivity of alcohols. The tunneling of electrons is easier through the hydrogen bonds (3) making the conductivity of alcohols higher than those of the inert solvents; accordingly the conductivity of alcohols should decrease with dilution.

Manuscript received Jan. 17, 1964; revised manuscript received July 14, 1964.

Any discussion of this paper will appear in a Discussion Section to be published in the December 1965 JOURNAL.

REFERENCES
1. R. Mecke and H. Zeininger, *Z. Elektrokem.*, **52**, 49 (1948); H. Zeininger and R. Mecke, *ibid.*, **54**, 174 (1950).
2. J. Mc. Pollock and A. R. Ubbelohde, *Trans. Faraday Soc.*, **52**, 1112 (1956).
3. B. E. Conway, J. O'M. Bockris, and H. Linton, *J. Chem. Phys.*, **24**, 834 (1956).
4. G. C. Pimentel and A. L. McClellan, "The Hydrogen Bond," Freeman (1960).
5. C. M. Huggin and G. C. Pimentel, *J. Phys. Chem.*, **60**, 1615 (1956).
6. D. D. Eley, *Research*, **12**, 293, (1959).
7. D. D. Eley and M. R. Willis, *J. Chem. Soc.*, **1963**, 1534.

Conductivity through Hydrogen Bonded Organic Compounds and Their Homogeneous Solutions

II. Conductivity of Phenol, o- and p-nitrophenol in Benzene and Ether

M. F. Mayahi and A. E. Habboush

College of Science, Baghdad University, Baghdad, Iraq

ABSTRACT

The conductivity of p-nitrophenol is more than that of o-nitrophenol in ether at 21°C. The solvent effect on conductivity is shown by measuring the conductivity of phenol in benzene and in ether at 21°C. The participation of the hydrogen-bonded complex C_6H_5OH-----$O(C_2H_5)_2$ in the conductivity of the system is postulated. Such complexing lowers the rate of increase in conductivity with concentration of phenol in ether compared to that in benzene.

The important influence of the hydrogen bond on conductivity was shown in Part I (1) for methanol, ethanol, butanol, n-pentanol, and n-hexanol. In this part we report the conductivities of phenol and benzoic acid in benzene and in ether, also o- and p-nitrophenol, and o- and p-nitrobenzoic acid in ether, all at 21°C.

Ubbelohde *et al.* (2) had shown that the conductivities of interhydrogen bonded solid organic acids are some hundred times greater than those of intrahydrogen bonded acids. Mecke *et al.* (3) studied the conductivities of o- and p-chlorophenol in CCl_4 at 20°C and found that the conductivities of the p-isomer is some hundred times greater than that of the o-isomer at 0.066 mole fraction.

Our work on the o- and p-nitrophenol and on o- and p-nitrobenzoic acid in ether shows differences similar to those reported by Ubbelhode (2) and Mecke (3).

Experimental

Materials.—o- and p-nitrophenol were commercial products and were twice recrystallized from alcohol before use. Benzoic acid and its o- and p-nitro compounds, phenol, benzene, and ether were of analytical grade and were used without further treatment

The method and apparatus for conductometric titrations were as described in Part I.

Results and Discussion

Figures 1 and 2 are plots of specific conductivity *vs.* molarity for phenol in benzene and in ether at 21°C. As in the case of alcohols (1) the conductivity is lowered as concentration is decreased. This decrease of conductivity is brought about by the decrease in per cent hydrogen bonding with dilution. Spectral evidence shows that phenol is interhydrogen bonded, and such bonds are broken on dilution with inert solvents (4). Thus interhydrogen bonding is important in the conductivity of phenol. Any other process which breaks the hydrogen bonding of phenol should bring about a decrease in conductivity. On this premise, the o-substituted phenol should have much lower conductivity than their p-isomer owing to the formation of the intrahydrogen bonding as indicated by spectral work (5). Such low conductivity was observed in our study of the conductivity of p- and o-nitrophenol in ether at 21°C. Figures 3 and 4 show the plot of specific conductivity *vs.* molarity for each isomer. The highest molarity used in each case was about the saturation point of each isomer. It is evident that the conductivity of p-nitrophenol is about six times more than that of o-nitrophenol in ether, even when the concentration of the latter compound is much higher. This ratio in conductivity would be still higher in noncomplexing solvents. This result is in good agreement with that found by Ubbelohde (2).

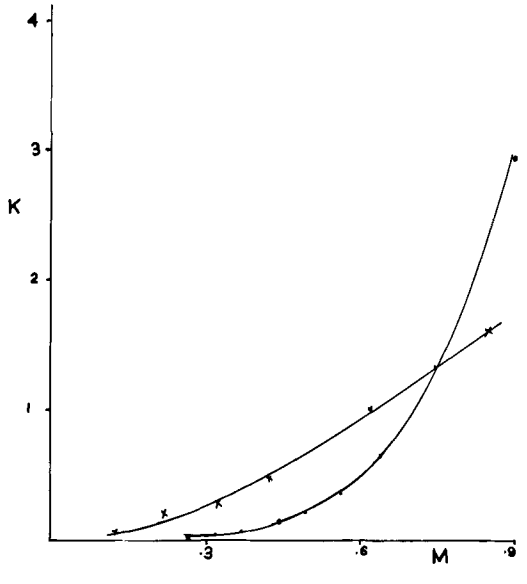

Fig. 1. Specific conductivity (K) x 10^{-8} ohm^{-1} cm^{-1} *vs.* molarity (M) for phenol in benzene (•) and in ether (X) at 21°C.

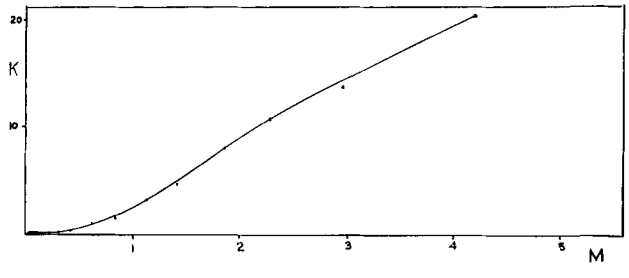

Fig. 2. Specific conductivity (K) x 10^{-8} ohm^{-1} cm^{-1} *vs.* molarity (M) for phenol in ether at 21°C.

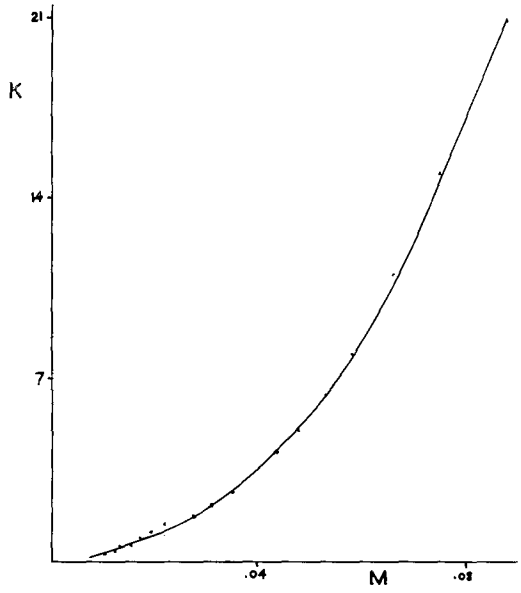

Fig. 3. Specific conductivity (K) x 10^{-8} ohm^{-1} cm^{-1} vs. molarity (M) for p-nitrophenol in ether at 21°C.

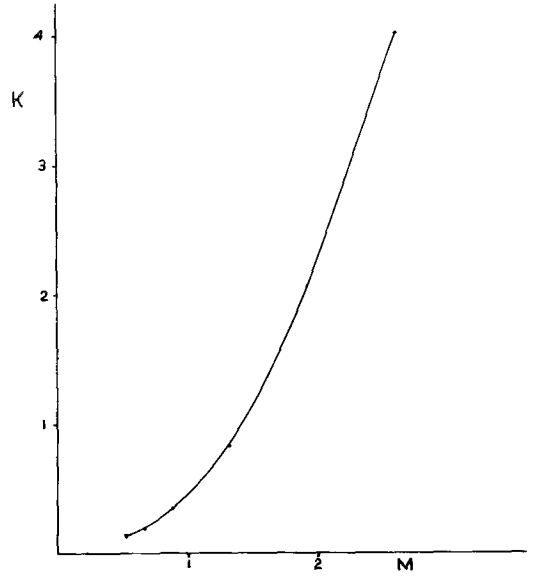

Fig. 4. Specific conductivity (K) x 10^{-8} ohm^{-1} cm^{-1} vs. molarity (M) for o-nitrophenol in ether at 21°C.

Inspection of Fig. 1, 2, and 4 shows that the conductivity of phenol is higher than those of o-nitrophenol in ether, indicating again the effect of intermolecular hydrogen bonding on conductivity. Also, the conductivities of benzoic acid which forms dimers and its o-NO_2 and p-NO_2 derivatives gave very small conductivities compared with that of phenol in ether (1.6M benzoic acid has a conductivity of 0.060 x 10^{-8} ohm^{-1} cm^{-1}).

The effect of solvent on conductivity is shown by comparing the conductivity of phenol in benzene and in ether (see Fig. 1 and 2). The rate of increase of conductivity of phenol is benzene is more than that of phenol in ether, as concentration is increased. This is due to the fact that the interhydrogen bonding of phenol is broken by the ether molecule, since the hydrogen bonding ether and phenol is stronger than between phenol molecules, as indicated by infrared study (6). However, Fig. 1 shows that the conductivity of phenol in ether is higher than that of phenol in benzene at the lower concentrations. Since the conductivity of an organic compound is increased when hydrogen bonding is involved, and (as indicated above) such hydrogen bonding is interrupted by ether molecules, then the higher conductivity of phenol in ether at the lower concentration must indicate that the hydrogen bonded complex between phenol and ether, *i.e.*, C_6H_5OH----$O(C_2H_5)_2$, is participating in the conductivity of the whole system. This involves an equilibrium between the phenol polymers and the indicated complex. After the intersection point of the two lines in Fig. 1 the conductivity of phenol in benzene is higher than that of phenol in ether, where the same concentrations are involved. This can be explained by assuming that there is greater increase in the formation of polymerized phenol in benzene than in ether.

A further example on the effect of solvent on conductivity is that of the difference in conductivity of benzoic acid in benzene (0.8M conductivity 0.0032 x 10^{-8} ohm^{-1} cm^{-1}) and in ether (0.8M conductivity 0.050 x 10^{-8} ohm^{-1} cm^{-1}). This difference is expected because benzoic acid is known to form closed dimers in benzene; these dimers are largely opened by the ether molecules (7).

Manuscript received Jan. 17, 1964; revised manuscript received July 14, 1964.

Any discussion of this paper will appear in a Discussion Section to be published in the December 1965 JOURNAL.

REFERENCES

1. M. F. Mayahi and A. E. Habboush, *This Journal*, **112**. 222 (1965).
2. J. M. Pollock and A. R. Ubbelohde, *Trans. Faraday Soc.*, **52**, 1112 (1956).
3. H. Zeininger and R. Mecke, *Z. Elektrochem.*, **54**, 174 (1950).
4. C. M. Huggin and G. C. Pemental, *J. Phys. Chem.*, **60**, 1615 (1956).
5. W. Luttke and R. Mecke, *Z. Phys. Chem.*, **196**, 56 (1950).
6. W. Luttke and R. Mecke, *Z. Electrochem.*, **53**, 241 (1949).
7 H. Hosoya, J. Tanaka, and S. Nagakura, *J. Molec. Spect.*, **8**, 257 (1962).

Hydrogen Evolution at a Solid Indium Electrode

James N. Butler and Manfred Dienst

Tyco Laboratories, Inc., Waltham, Massachusetts

ABSTRACT

Measurements of hydrogen overvoltage on solid indium electrodes were made in 0.1M $HClO_4$ at temperatures from 21° to 59.5°C. The slow step in the hydrogen evolution reaction is probably discharge of a hydrogen ion, as indicated by the exchange current (10^{-11} amp/cm^2), transfer coefficient (0.5), effect of added iodide ion, and effect of acid concentration. The enthalpy of activation is 14.1 ± 0.5 kcal/mole at the reversible hydrogen potential and 10.0 ± 0.2 kcal/mole at the zero-charge point. From these values, an estimate of 50 ± 10 kcal/g atom is obtained for the heat of adsorption of hydrogen atoms on indium. The reaction is very sensitive to traces of oxygen, and the formation and removal of oxide films are discussed.

Indium offers an unusual opportunity for a detailed study of the hydrogen evolution reaction. In dilute acid, hydrogen evolution is the principal reaction over a potential range of more than 0.8v. The variation in reaction rate due to the influence of the double layer is greatest near the zero-charge point, which is known for indium and lies within the accessible range of hydrogen overpotential measurements. Thus indium is a good electrode on which to study how the hydrogen evolution reaction is influenced by the double layer. Indium also provides an interesting comparison with mercury, which has a similar hydrogen overpotential, but quite a different zero-charge point.

Although considerable work has been done on the dissolution of indium and indium amalgams and on the deposition of indium from solutions containing In^{+3} ions, no adequate measurements have been made of hydrogen overpotential on pure indium.

Bockris (1) made a brief survey of hydrogen overvoltage on eight metals in 1*N* HCl in the current density range from 10^{-3} to 10^{-1} amp/cm^2, and among these was indium. The results of this study are included in Fig. 1. Because no attempt was made to exclude oxygen rigorously from the electrolyte or to remove all traces of superficial oxide films from the electrode, the results of this study must be regarded as preliminary.

Hydrogen evolution has been noted by several workers (2-4) when the rate of indium deposition in acid solution becomes limited by diffusion of In^{+3} to the electrode surface. Kangro and Weingärtner (2) made a study of the deposition of indium from acid solutions containing $In_2(SO_4)_3$ and H_2SO_4, on an indium-coated platinum electrode. They noted that at sufficiently high current densities hydrogen evolution, rather than indium deposition, was the primary process. Their current-potential curve obtained in a solution of pH = 0.86, containing 1% of $In_2(SO_4)_3$ is also shown in Fig. 1. Although the results agree roughly with those of Bockris, a large discrepancy exists in the slope of the Tafel line.

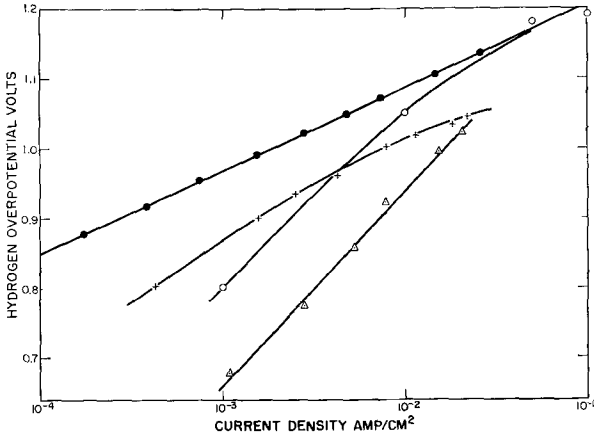

Fig. 1. Comparison of measurements of hydrogen overpotential by various workers: •, this work; ○, Bockris (1); +, Kangro and Weingärtner (2); △, Kochegarov *et al.* (3).

Kochegarov, Zaburdaeva, and Zyablova (3) performed a similar experiment, depositing indium from $In_2(SO_4)_3$-H_2SO_4 solutions onto a copper electrode. Their results, obtained at pH = 2.5 in a solution containing 0.1M $In_2(SO_4)_3$ (Fig. 1), agree with the results of Kangro and Weingärtner (2) at the highest current density, but the overvoltage values are generally much lower and the slope is closer to that of Bockris (1). In neither of these experiments was oxygen excluded from the solution, so that the current observed probably resulted not only from hydrogen evolution, but also from indium deposition and oxygen reduction. It is apparent from the above discussion that no systematic study has been made of In electrodes under conditions where hydrogen evolution is the only process taking place (34).

The necessity for rigorously removing oxygen from the solution when making measurements of hydrogen overvoltage has often been emphasized (5, 6), and the presence of differing amounts of oxygen in the electrolyte and on the electrode surface could account for the disagreement among the results of the three studies mentioned above. Furthermore, the slope of the Tafel lines in Fig. 1 varies between 120 and 280 mv. Although 120 mv is consistent with a slow-discharge mechanism for hydrogen evolution, a higher Tafel slope indicates that an additional process, such as indium deposition or oxygen reduction, is taking place (7, 8).

We have made accurate measurements of the hydrogen overpotential on indium in perchloric acid at several temperatures. These results are reported in this paper and discussed in terms of the transition state theory of reaction rates and the structure of the electrical double layer at the indium-electrolyte interface.

Experimental

A conventional three-compartment cell was used, with platinized platinum counter and reference electrodes. A Luggin capillary was positioned within 4 mm of the working electrode, and under the conditions of measurement, the resistance between the tip of the capillary and the electrode surface was 3-8 ohms. Measurements were made potentiostatically, using a Wenking electronic potentiostat (Brinkmann Instruments) together with a microammeter (Griebach, 0.5% accuracy).

The electrolyte was prepared from triple-distilled conductivity water and reagent grade perchloric acid (Baker). Except where noted, the concentration of perchloric acid was 0.100M. The solution was purified

by pre-electrolysis for 16 hr at a current of 10 ma, using a platinized platinum electrode as cathode. This cathode was removed from the solution before measurements were made. The solution was saturated with purified hydrogen throughout pre-electrolysis and all measurements. An oil-bath thermostat maintained the temperature constant within ±0.2°C from 20° to 60°C.

The cylindrical working electrode was made from 99.999% indium (American Smelting and Refining Company) and had a surface area of approximately 0.5 cm². It was electropolished in a 2:1 mixture of methanol and nitric acid, at an anodic current density of 0.3 amp/cm². After electropolishing, the electrode was thoroughly washed with conductivity water and introduced to the cell. The most reproducible measurements were obtained after the electrode had been polarized overnight in the cell at −1.0v. This effect was related to the removal of an oxide film and will be discussed in detail later.

The capacity of the electrode was measured by suddenly changing the current and observing on an oscilloscope the corresponding change in the potential of the electrode. For this measurement, the electrode was polarized galvanostatically.

From the initial linear increase of potential, the capacity was calculated using the relation

$$C = \Delta i(dt/dV)$$

where Δi is the current increment. If the current was increased by about 1 ma, the electrode potential increased linearly by about 4 mv in 16 μsec, corresponding to a capacity of about 4 μf (8 μf/cm²).

Results

In order to achieve reproducible values for the current-potential curve at low current-densities, it was necessary to prepolarize the indium electrode cathodically (usually at −1.0v with respect to a reversible hydrogen electrode) for an extensive period of time. Apparently the electropolished electrode was covered with a thin film of indium oxide, even though it appeared brightly metallic. At a temperature of 30°C, prepolarization for 16 hr at −1.0v was sufficient to remove the oxide film completely, as indicated by the fact that further prepolarization did not change the current-potential curve. During a typical prepolarization period, approximately 0.3-0.4 coul/cm² were passed in addition to the hydrogen evolution current observed on a clean electrode. If this were due entirely to removal of oxide film, the film on the electrode would have been approximately 0.1-0.2μ in thickness. Such a thick oxide film should have resulted in the appearance of interference colors, which were not observed. More likely, a large part of the additional current passed during prepolarization resulted from reduction of traces of dissolved oxygen in the electrolyte.

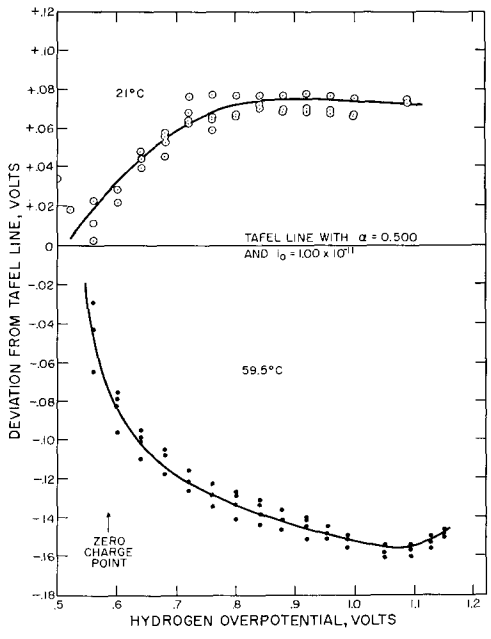

Fig. 2. Deviation of experimental current-potential curve from an arbitrary Tafel line with $\alpha = 0.500$ and $i_0 = 1.00 \times 10^{-11}$.

The measured potential values were corrected for the iR drop to obtain overpotential values, which are listed in Table I. Each set of values is the average of two to four current-potential curves, taken with the potential increasing and with the potential decreasing.

In Fig. 2 are shown two sets of current-potential measurements at 21° and 59.5°C. To show the small differences between the measurements clearly, we have plotted the deviation of the experimental values from a Tafel line

$$\eta = \frac{RT}{\alpha \mathbf{F}} \ln(i/i_0) \qquad [1]$$

with arbitrarily chosen values of exchange current $i_0 = 1.00 \times 10^{-11}$ amp/cm² and cathodic transfer coefficient $\alpha = 0.500$. Although there is a systematic deviation from the arbitrary Tafel line, the average difference between two points taken at a given potential at the same temperature is only about 4 mv. As can

Table I. Hydrogen overpotential on solid indium

Temperature dependence											
21.0°C		25.0°C		30.0°C		41.0°C		50.5°C		59.5°C	
η	i	η	i	η	i	η	i	η	i	η	i
η in volts, corrected for iR drop. i in μa/cm²											
0.500	0.10	0.480	0.078								
0.520	0.20	0.560	0.42	0.560	0.54						
0.560	0.52	0.600	0.78	0.600	1.24	0.600	0.80				
0.600	0.82	0.640	1.60	0.640	2.80	0.640	2.06	0.600	1.40		
0.640	1.30	0.680	3.55	0.680	6.39	0.680	5.25	0.640	3.45	0.600	2.20
0.720	4.05	0.720	7.85	0.720	14.5	0.720	12.5	0.680	8.95	0.640	5.03
0.760	9.15	0.760	17.1	0.760	31.9	0.760	29.3	0.720	21.9	0.680	11.6
0.800	18.9	0.800	37.8	0.800	74.3	0.800	64.5	0.760	50.3	0.720	28.3
0.840	39.3	0.839	82.0	0.839	167.	0.840	134.	0.800	110.	0.760	64.8
0.880	87.5	0.879	175.	0.878	377.	0.879	297.	0.839	231.	0.800	144.
0.920	191.	0.918	370.	0.917	833.	0.918	623.	0.879	490.	0.839	312.
0.959	427.	0.955	753.	0.953	1750.	0.955	1318.	0.917	1033.	0.878	665.
i in μa/cm²											
0.998	0.960	0.990	1.53	0.985	3.50	0.991	2.72	0.954	2.10	0.916	1.38
1.092	5.48	1.022	2.80	1.050	12.4	1.062	11.4	0.988	4.10	0.952	2.53
		1.071	7.10	1.093	26.4	1.111	27.0	1.055	15.1	0.985	5.26
		1.091	10.65	1.118	44.5	1.142	47.5	1.102	33.0	1.050	18.0
		1.107	14.35	1.141	63.5			1.135	55.8	1.093	38.0
		1.135	25.3	1.153	85.0					1.126	61.8
										1.150	88.8

be seen in Fig. 2, at 21°C, the deviations from the Tafel line became more positive at higher overpotentials, and at 59.5°C, the deviations became more negative at higher overpotentials. The data obtained at intermediate temperatures showed current-potential curves which were intermediate in shape bewteen the two extremes shown in Fig. 2.

As we shall explain in the discussion section, it seems likely that the slow step in the hydrogen evolution reaction on indium is the discharge of a hydrogen ion. For a reaction in which discharge of an ion is the rate-determining step, the measured overpotential includes not only the potential drop across the compact (Helmholtz) double layer, which drives the reaction, but also a potential drop across the diffuse (Gouy-Chapman) double layer, which does not influence the reaction rate (9-12). We have therefore used the relations derived by Frumkin (9, 13, 14) to obtain parameters which describe the experimental data. Unlike mercury, indium has a zero-charge point which falls at the lower end of the accessible range of overvoltage measurements: at —0.580v with respect to a reversible hydrogen electrode in 0.1M $HClO_4$ (15). This means that the contribution of the diffuse double layer to the total potential drop will vary appreciably over the range of potentials where we have measured the current-potential curves.

In order to apply Frumkin's equation to correct for the potential drop across the diffuse double layer, it is necessary to obtain ϕ_2, the potential of the outer Helmholtz plane, which is identified with the transition state for the hydrogen discharge reaction in the absence of specific adsorption. This potential is given by the equation (9, 16)

$$K\phi_0 = \left[\frac{2RT\,D\,D_0}{\pi}C_+\right]^{1/2}\sinh\left(\frac{\phi_2\mathbf{F}}{2RT}\right) \quad [2]$$

where R is the gas constant, T is the absolute temperature, D is the dielectric constant of water, $D_0 = 1.128 \times 10^{-12}$ coul volt^{-1} cm^{-1}, C_+ is the concentration of univalent electrolyte, $\mathbf{F}$ is the Faraday constant, K° is the integral capacity of the Helmholtz layer, and ϕ_0 is the rational potential of the electrode [potential with respect to the zero-charge point (16)].

The measured values of capacity are shown in Fig. 3, together with the interpolated curve which was used in the calculations, corresponding to the empirical equation

$$K = 8.9 + 2.75\ \phi_0 + 1.25\,\phi_0^2 \quad [3]$$

The measured capacity was somewhat lower than the 15 to 20 μf/cm^2 obtained with mercury (16), gallium (17), and lead (18), which may result from a thin residual oxide film.

For comparison, an alternative capacity function was obtained by extrapolating results obtained on a series of indium amalgams (19). This function presumably

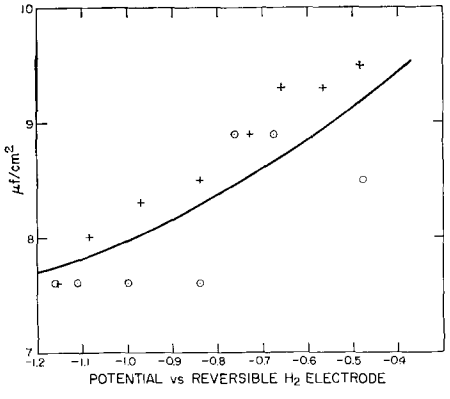

Fig. 3. Experimentally measured capacity values and interpolated curve used for calculations (Eq. [3]). ○, Clean electrode; +, oxidized electrode; ——, interpolated curve Eq. [3].

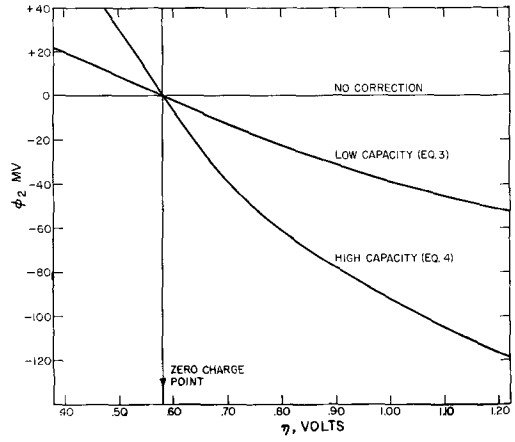

Fig. 4. Calculated values of the potential of the outer Helmholtz plane, ϕ_2, at 32°C.

is a good approximation to the capacity of pure supercooled liquid indium, and was

$$K = 42.0 + 46.6\,\phi_0 + 54.0\,\phi_0^2 \quad [4]$$

Equation [4] gave values in the range from 30 to 40 μf/cm^2.

In Fig. 4 are plotted two typical curves giving ϕ_2, the potential of the outer Helmholtz plane with respect to the bulk of the solution, as a function of the hydrogen overpotential. These were calculated using Eq. [3] and [4] to approximate K° in [2]. Note that when the high-capacity function given by Eq. [4] is used, the values of ϕ_2 obtained are nearly twice as large as when the low-capacity function given by Eq. [3] is used.

The overpotential for a reaction, where discharge of a hydrogen ion is the slow step, is given by the equation (9, 13, 14)

$$\eta = \frac{1-\alpha}{\alpha}\left(\phi_2 - \frac{RT}{\mathbf{F}}\ln[H^+]\right) + \frac{RT}{\alpha\mathbf{F}}\ln i - g_H + \text{const.} \quad [5]$$

where α is the cathodic transfer coefficient, i the current density, g_H the free energy of desorption of a hydrogen atom for the surface of the electrode, and $[H^+]$ the bulk concentration of hydrogen ions. Since we are holding the composition of the electrode and the concentration of hydrogen ion in the electrolyte constant, we can lump the constant terms into a corrected exchange current i_o'

$$\eta = \frac{1-\alpha}{\alpha}\phi_2 + \frac{RT}{\alpha\mathbf{F}}\ln(i/i_o') \quad [6]$$

where

$$\ln i_o' = (1-\alpha)\ln[H^+] + \frac{\alpha\mathbf{F}}{RT}g_H + \text{const.}$$

The corrected exchange current i_o' is different from the exchange current obtained from the simple Tafel Eq. [1] because of the term in ϕ_2, which corrects for the potential drop across the diffuse double layer. If $\phi_2 = 0$, Eq. [6] reduces to the simple Tafel equation.

Equation [5] can be cast into the form of a straight line

$$y = \alpha x + B \quad [7]$$

where

$$y = \frac{RT}{\mathbf{F}}\ln i + \phi_2$$

$$x = \eta + \phi_2 \quad [8]$$

The slope of this line is α and its intercept is

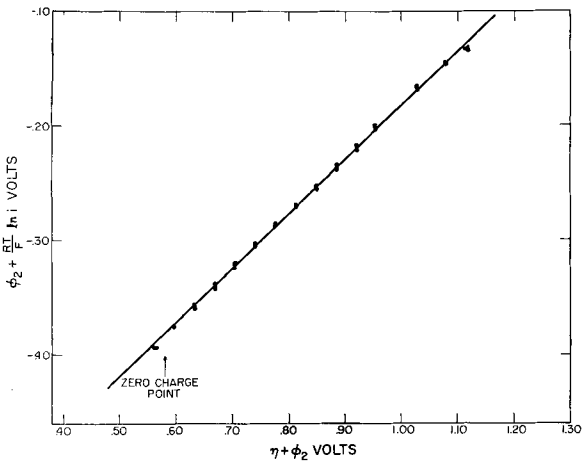

Fig. 5. Fit of experimental data to Eq. [5]. The temperature was 32°C, and the low-capacity function (Eq. [3]) was used to calculate ϕ_2. The correlation coefficient for the least-squares straight line is 0.9995. The best values for the parameters are $\alpha = 0.472 \pm 0.003$ and $-\log i_o' = 10.82 \pm 0.05$.

$$B = \frac{RT}{\mathbf{F}} \ln i_o' \qquad [9]$$

To obtain the parameters for each of the experiments conducted, ϕ_2 was calculated from Eq. [2] using the capacity function defined by either [3] or [4], and for each data point the quantities x and y, given by Eq. [8], were calculated. A least-squares straight line (Fig. 5) was fitted to the function $y(x)$, and from its slope and intercept were obtained the best values for α and $-\log i_o'$. The 95% confidence limits provide an estimate of the probable error in the measurements. These calculations were performed on an IBM 7094 computer.

The values so obtained are listed in Tables II and III, along with the values of α and $-\log i_o$ obtained when no correction is made for the potential drop across the diffuse double layer. From Table II, we can see that the larger the capacity, the smaller is α and the larger is i_o'.

Comparing the confidence limits on the parameters calculated with the high-capacity function, the low-capacity function, and with no correction, we can see that the best over-all fit is obtained with the low-capacity function. The high-capacity function gives a slightly better fit at the high temperatures, and no correction at all gives a slightly better fit at the low temperatures. The results obtained using the low-capacity function are probably the most realistic and will be used in the subsequent discussion.

Discussion

Mechanism.—In our calculations and in the following discussion of the results, we assume that discharge of a hydrogen ion is the rate-determining step in the hydrogen evolution reaction on solid indium. This mechanism is suggested by a number of observations, which we shall discuss here.

Table III. Effect of electrode preparation

Temperature 30°-32°C

History of electrode	Parameters of current-potential curve[a] α	$-\log i_o'$	No. points
1. Electropolished, reduced at −1.0v for 40 hr as 30°C	0.489 ± 0.004	10.83 ± 0.06	35
2. Electropolished, reduced at −1.0v for 16 hr at 25°C	0.472 ± 0.003	10.82 ± 0.04	59
3. Treatment 2, followed by redn. at −1.0v for 16 hr at 60°C	0.482 ± 0.002	10.80 ± 0.04	30
4. Clean electrode, oxidized for 5 min in air at 25°C (only points with $i > 10^{-4}$ amp/cm²)	0.459 ± 0.009	10.36 ± 0.14	16
5. Treatment 4, followed by redn. at −1.0v for 16 hr at 30°C	0.486 ± 0.004	10.84 ± 0.06	23
6. Clean electrode, left on open circuit (−0.4v) for 15 min	0.485 ± 0.006	10.84 ± 0.08	20

[a] Calculated using experimental capacity values given by Eq. [3].

The exchange current on indium is approximately 10^{-11} amp/cm² at 30°C, of the same order of magnitude as the exchange current on lead and mercury, metals for which considerable evidence indicates a slow discharge mechanism (8, 9, 20). As shown in Fig. 5, the data fit Eq. [5] over a wide range of potentials, including the zero-charge point of indium, where the largest deviation from Eq. [5] would be expected if discharge were not the slow step. The observed effect of the diffuse double layer is thus the same as is expected for a slow discharge mechanism. The observed transfer coefficient is very close to 0.50, indicating a symmetrical activation energy barrier. This also implies that discharge is the slow step (21).

One important effect of the slow-discharge mechanism is the extreme sensitivity of the hydrogen overvoltage to adsorbed species on the electrode (9, 20). A specifically adsorbed anionic species on the electrode lowers the overvoltage at small current densities. In a few experiments, we added potassium iodide to the electrolyte and observed that, at current densities below 10^{-4} amp/cm², the overvoltage was approximately 0.1v lower than in the absence of potassium iodide. This agrees qualitatively with the results observed on mercury, lead, and gallium (9, 17, 20). However, the effect observed could have been at least partially due to small amounts of oxygen or free iodine in the electrolyte, since the results were very irreproducible.

A further consequence of the slow-discharge mechanism is that the dependence of overvoltage on pH should be given by Eq. [5]. An experiment with 0.01M $HClO_4$ as electrolyte gave the results summarized in Table IV. According to Eq. [6], the quantity

$$-\log i_o' + (1 - \alpha) \log [H^+]$$

should be independent of the electrolyte composition. In Table IV we see that it is the same within experimental error for both 0.1 and 0.01M $HClO_4$.

In view of the foregoing observations, it seems reasonable to assume that discharge of a hydrogen ion is the slow step of the hydrogen evolution reaction on indium.

Table II. Parameters of the current-potential curve

(errors are 95% confidence limits)

Temp, °C	Low-capacity[a] α	Low-capacity[a] $-\log i_o'$	High-capacity[b] α	High-capacity[b] $-\log i_o'$	Uncorrected[c] α	Uncorrected[c] $-\log i_o$	No. points
21.0	0.389 ± 0.011	10.19 ± 0.14	0.290 ± 0.020	9.27 ± 0.25	0.445 ± 0.009	10.74 ± 0.12	52
25.0	0.449 ± 0.003	10.86 ± 0.04	0.372 ± 0.011	9.98 ± 0.15	0.498 ± 0.002	11.15 ± 0.03	37
30.0	0.489 ± 0.004	10.83 ± 0.06	0.441 ± 0.004	10.55 ± 0.06	0.530 ± 0.004	11.19 ± 0.07	35
41.0	0.495 ± 0.005	10.77 ± 0.07	0.441 ± 0.005	10.41 ± 0.07	0.538 ± 0.005	11.14 ± 0.07	51
50.5	0.502 ± 0.006	10.44 ± 0.08	0.445 ± 0.005	10.05 ± 0.07	0.546 ± 0.006	10.81 ± 0.09	53
59.5	0.510 ± 0.006	10.22 ± 0.07	0.454 ± 0.004	9.87 ± 0.06	0.552 ± 0.006	10.57 ± 0.08	56

[a] Integral capacity obtained using Eq. [3].
[b] Integral capacity obtained using Eq. [4].
[c] No correction for potential drop across diffuse double layer.

Table IV. Effect of electrolyte concentration[a]

Conc. of $HClO_4$, moles/liter	0.100	0.010
Low-capacity[b]		
α	0.489 ± 0.004	0.40 ± 0.02
$-\log i_o'$	10.83 ± 0.06	10.3 ± 0.3
$-\log i_o' + (1 - \alpha)$ Log $[H^+]$	11.34 ± 0.06	11.5 ± 0.3
Uncorrected[c]		
α	0.530 ± 0.004	0.48 ± 0.02
$-\log i_o$	11.19 ± 0.07	10.8 ± 0.3

(a) Temperature 30°C.
(b) Integral capacity obtained using Eq. (3).
(c) No correction for diffuse double layer.

Enthalpy of activation.—According to the transition state theory (8, 21, 23), the enthalpy of activation for the discharge reaction is given by

$$\Delta H^{\ddagger} = RT^2 \left(\frac{\partial \ln i}{\partial T} \right)_{\eta} \qquad [10]$$

and depends on the potential at which the temperature coefficient is measured.

The temperature dependence of the corrected exchange current is shown in Fig. 6. These values were obtained using the capacity function given by Eq. [3]; however, the uncorrected values of exchange current, and the values obtained using the capacity function given by Eq. [4] differ only by an additive constant. The best straight line through the points obtained at the three highest temperatures gives $\Delta H^{\ddagger} = 14.1 \pm 0.5$ kcal/mole for the enthalpy of activation at the reversible hydrogen potential. The values obtained at the lower temperatures have been omitted because the effect of adsorbed oxygen or a thin oxide film makes Eq. [10] inapplicable.

Although it is conventional to calculate the enthalpy of activation at the reversible hydrogen potential, it is also significant to look at the enthalpy of activation at the zero charge point of the electrode. In Fig. 7 is plotted the current at the zero charge point [$\eta = 0.58$v (15)] as a function of the reciprocal temperature. The slope of the best line defined by the high temperature points is 10.0 ± 0.2 kcal/mole. In principle, the current at the zero charge point should be independent of the capacity function used to calculate the diffuse double layer correction. The effect of the capacity function on i_z, apparent in Fig. 7, reflects the effect of scatter in the current-potential values on the interpolation at the zero charge point.

In order to compare the enthalpy of activation for indium with that for mercury, it is desirable to refer

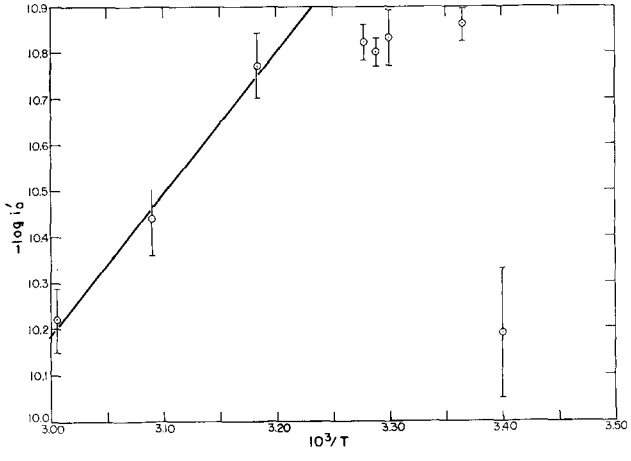

Fig. 6. Temperature dependence of the corrected exchange current. The straight line corresponds to an enthalpy of activation of 14.1 ± 0.5 kcal. The low-capacity function was used in calculating i_o'.

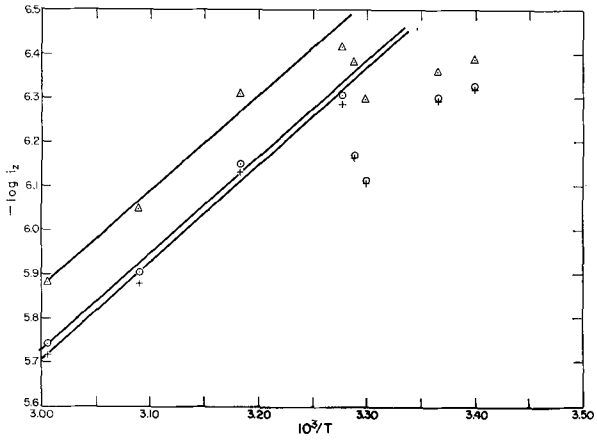

Fig. 7. Temperature dependence of the current at the zero charge point. All three straight lines have a slope corresponding to an enthalpy of activation of 10.0 ± 0.2 kcal. ○, Low capacity; △, high capacity; +, uncorrected.

both to the same potential relative to the zero-charge point. The reversible hydrogen potential in 0.1M $HClO_4$ is 0.165v positive with respect to the zero-charge point of mercury, but is 0.58v positive with respect to the zero-charge point of indium (15). Consequently, a comparison of $\Delta H^{\ddagger}$ at the reversible hydrogen potential will contain contributions from the temperature dependence of the double layer structure.

At the reversible hydrogen potential, $\Delta H^{\ddagger}$ for the hydrogen evolution reaction on mercury was determined by Post and Hiskey (23) to be 21.7 ± 0.2 kcal, and by Iofa and Mikulin (24) to be 21.1 ± 0.5 kcal. The potential dependence of the enthalpy of activation is given approximately by (23)

$$\Delta H^{\ddagger} = \Delta H^{\ddagger}_{rev} - \alpha \mathbf{F} \eta \qquad [11]$$

where $\Delta H^{\ddagger}_{rev}$ is the enthalpy of activation at the reversible hydrogen potential, and η, the cathodic overvoltage, is positive.

Equation [11] does not hold as well for indium as it does for mercury. This can be seen by calculating the difference in the enthalpy of activation on indium between the reversible hydrogen potential and the zero charge point. Using Eq. [11], this difference is calculated to be 6.7 kcal; the experimentally observed difference is only 4.1 kcal. For this reason, we feel it is more accurate to extrapolate the results for mercury than the results for indium.

Thus, at the zero charge point, $\Delta H^{\ddagger}$ for the hydrogen evolution reaction on mercury is 19.8 kcal, which may be compared with 10.0 kcal which we have observed for $\Delta H^{\ddagger}$ at the zero charge point on indium.

Similarly, but with less accuracy, we may compare the enthalpy of activation on mercury at the reversible hydrogen potential (+0.165v with respect to the zero-charge point) with that for indium at a potential of +0.165v with respect to the zero-charge point, an overpotential of 0.415v. For mercury, $\Delta H^{\ddagger}$ is 21.7 kcal; for indium, $\Delta H^{\ddagger}$ is 11.9 kcal.

Parsons and Bockris (22) have estimated, for mercury and nickel, the theoretical dependence of enthalpy of activation on the heat of adsorption of hydrogen atoms. Using a similar method, Rüetschi and Delahay (26) have calculated heats of adsorption for hydrogen atoms and correlated them with experimental values of overvoltage at constant current density.

Because of the similarity in hydrogen overvoltage between mercury and indium, it seems likely that the values of all parameters involved in the dependence of $\Delta H^{\ddagger}$ on heat of adsorption are approximately the same for mercury and indium (15). The curve of this dependence, calculated for mercury by Parsons and Bockris (22), is shown in Fig. 8. To show the uncertainty in such a calculation, two extreme estimates are

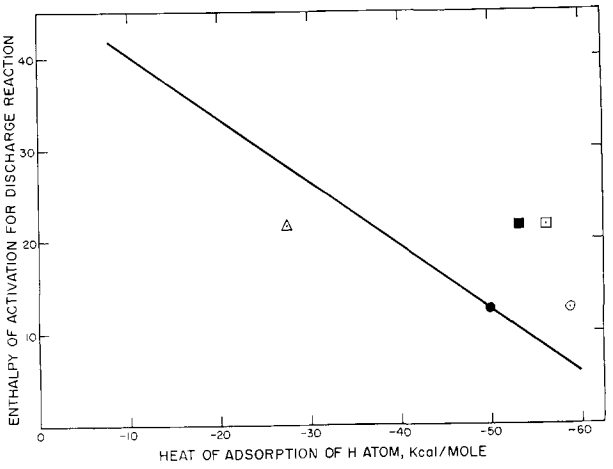

Fig. 8. Relation between enthalpy of activation and heat of adsorption of hydrogen atoms, with estimated values for mercury and indium. ——, Theoretical curve (22); •, indium, this work; △, mercury (24, 25); □, mercury (27); ■, mercury (26); ○, indium (26).

shown for the heat of adsorption of hydrogen atoms on mercury: Frumkin, Iofa, and Bagozky (25) estimated this quantity to be approximately 28 kcal, whereas Conway and Bockris (27) estimated it to be approximately 57 kcal. The theoretical curve calculated by Parsons and Bockris (22) falls between these two extremes. Our value of 11.9 kcal for the enthalpy of activation for the hydrogen evolution reaction on indium (at a potential of +0.165v with respect to the zero-charge point) allows us to estimate that the heat of adsorption of hydrogen atoms on indium is 50 ± 10 kcal. This value is consistent with the value (56.6 kcal) estimated by Rüetschi and Delahay (26).

Effect of oxide film.—We have mentioned that, before reproducible measurements of overpotential could be obtained, it was necessary to remove the oxide film on the electrode by prolonged cathodic polarization. At temperatures below 30°C, this oxide film was not removed even after polarization for 16 hr at — 1.0v.

The oxide film we have observed is probably similar to the film formed on passivation of indium. Popova and Simonova (32) showed that anodic polarization of indium in both acid and alkaline solutions produce a passive oxide layer which corresponded approximately to a monolayer of oxygen. In 0.1M $HClO_4$, this passive oxide layer was apparently stable, even though In_2O_3 is thermodynamically unstable in acid solutions (33). A similar type of oxide film has been observed on solid gallium (18, 28). Indium antimonide is known to form a stable, coherent film of In_2O_3 both on thermal oxidation (29, 30) and on anodic oxidation (31). This film is difficult to reduce, even in acid solution (29).

Our observations on the oxide film formed on indium are in accord with these results. In our experiments, polarization of the indium electrode at — 0.6v for 16 hr failed to remove the oxide film; complete removal required an elevated temperature, as well as prolonged cathodic polarization at — 1.0v (See Table III).

The fact that indium forms such a stable oxide film causes a hysteresis effect in the current-potential curve when traces of oxygen are present. In Fig. 9, we see the current-potential curve observed when a freshly prepared electrode is introduced into the cell. As the cathodic overpotential is increased, the lower curve is obtained; the wave resulting from both the reduction of the oxide film and the diffusion-limited reduction of oxygen in the solution. If the electrode is held for several hours at 1.0v cathodic polarization, the current decreases. If the overpotential is then decreased, the upper curve is obtained. The wave for oxygen reduction is shifted to lower current densities, both because the concentration of oxygen in the solution is smaller and because part of the oxide film has been removed from the electrode.

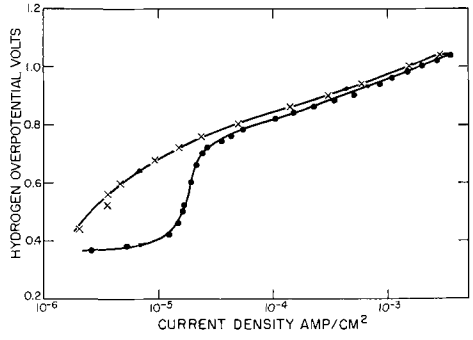

Fig. 9. Current-potential curve taken using a freshly prepared electrode. The lower curve was taken with overpotential increasing; the electrode was held at an overpotential of 1.04v for 2 hr and then the upper curve was taken, with overpotential decreasing.

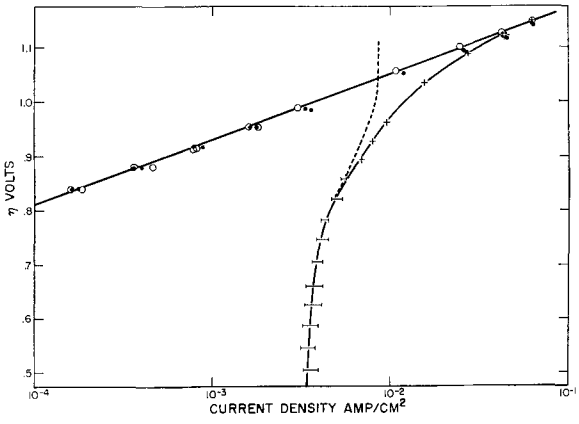

Fig. 10. Current-potential curve taken on a clean and oxidized electrode in the absence of oxygen and on an electrode in a solution saturated with oxygen. The oxygen reduction current was obtained by subtracting the current given by the upper curve from that given by the lower curve. Without oxygen: •, clean; ○, oxidized. With oxygen: ———, total current; — — —, O_2 reduction current.

This wave definitely results from oxygen reduction, and not from In^{+3} reduction. If the electrode is prepolarized until the current-potential curve shows no hysteresis and obeys Eq. [5] over the accessible range of overpotentials, we may assume that the oxide film has been completely removed. If such an electrode is left on open circuit for 15 min, no effect is observed on the current-potential curve (Table III), indicating that no appreciable amount of In^{+3} exists in the solution due to chemical dissolution of the electrode. In contrast, if the electrode is removed from the cell and exposed to the air for only 1½ min, the subsequent polarization curve shows hysteresis and has the shape shown in Fig. 9. In order to restore the electrode to its former condition, it is necessary to polarize it cathodically for 16 hr. During this time, approximately 0.5 coulombs of charge pass through the cell in addition to that required to evolve hydrogen. This additional current is probably due both to reduction of oxide on the electrode and to the reduction of oxygen in the solution. These results are summarized in Table III.

The effect of bubbling oxygen over the electrode is shown in Fig. 10. The oxygen reduction current (dotted line) has been obtained by subtracting, from the total current, the current for hydrogen evolution at the same potential. Note that although the oxygen reduction current appears to be diffusion limited in the range of potentials shown, the limiting current in fact increases by about a factor of two at approximately

0.8v. This effect probably results from stirring by evolved hydrogen. At lower potentials, the limiting current for oxygen reduction is controlled by diffusion of oxygen through a boundary layer at the electrode surface. When the rate of hydrogen evolution becomes large enough, hydrogen bubble formation at the electrode surface disturbs this boundary layer and increases the maximum rate at which oxygen can diffuse to the electrode.

Another possible explanation of this phenomenon can be made in terms of the kinetics of reduction of the oxide film. If the rate of reduction of oxygen on the oxide film is slower than the rate of reduction of oxygen on a clean electrode, then, at potentials between 0.4 and 0.8v, a steady state is set up. The oxide film is reduced, but is regenerated by oxygen diffusing from the solution. However, at potentials above 0.8v, reduction of the oxide film itself is sufficiently fast that the electrode becomes free of oxide and oxygen reduction takes place directly on the surface of the metal. Because this reaction is faster, a higher limiting current controlled by diffusion of oxygen is reached.

An alternative kinetic explanation for the increase in oxygen reduction current at high potentials is that the oxide film catalyzes the hydrogen evolution reaction. This explanation is not correct. In Fig. 10 the data are given for an oxidized electrode and an oxide-free electrode under the same conditions. In the region covered by Fig. 10, the current-potential curves for hydrogen evolution, in the absence of oxygen, are identical on clean and oxidized electrodes. The oxide does not catalyze the hydrogen evolution reaction.

Acknowledgments

This work was supported by the Office of Naval Research, Materials Sciences Division, Contract No. NOnr-3765(00), ARPA Order No. 302-62. The authors thank Dr. A. C. Makrides for the penetrating criticism and helpful suggestions which he gave during the course of this work. Miss Evelyn Barron assisted with the calculations.

Manuscript received June 17, 1964; revised manuscript received Oct. 16, 1964. This paper was presented at the Washington Meeting, Oct. 11-15, 1964.

Any discussion of this paper will appear in a Discussion Section to be published in the December 1965 JOURNAL.

REFERENCES

1. J. O'M. Bockris, *Trans. Faraday Soc.*, **43**, 417 (1947).
2. W. Kangro and F. Weingärtner, *Z. Elektrochem.*, **58**, 505 (1954).
3. V. M. Kochegarov, F. I. Zaburdaeva, and E. A. Zyablova, *Zh. Priklad. Khim.*, **35**, 1376 (1962).
4. G. Serravalle and B. Mazza, *Electrochim. Acta*, **8**, 313 (1963). (Previous work by the Italian school is cited in this paper).
5. J. O'M. Bockris and R. Parsons, *Trans. Faraday Soc.*, **45**, 916 (1949).
6. A. Azzam, J. O'M. Bockris, B. E. Conway, and H. Rosenberg, *ibid.*, **46**, 918 (1950).
7. J. O'M. Bockris and E. C. Potter, *This Journal*, **99**, 169 (1952).
8. J. O'M. Bockris, "Modern Aspects of Electrochemistry," Vol. **I**, p. 209, Butterworths, London (1954).
9. A. N. Frumkin, "Hydrogen Overvoltage and Adsorption Phenomena. Part I. Mercury," in Vol. I. of "Advances in Electrochemistry and Electrochemical Engineering," p. 65, P. Delahay, Editor, Interscience, New York (1961).
10. R. Parsons, "Structure and Influence of the Double Layer," *ibid.*, p. 1.
11. M. Breiter, M. Kleinerman, and P. Delahay, *J. Am. Chem. Soc.*, **80**, 5111 (1958).
12. P. Delahay and M. Kleinerman, *ibid.*, **82**, 4509 (1960).
13. A. N. Frumkin, *Z. Physik. Chem.*, **A164**, 121 (1933).
14. A. N. Frumkin, *Discussions Faraday Soc.*, **1**, 57 (1947).
15. J. N. Butler and A. C. Makrides, *Trans. Faraday Soc.*, **60**, 1664 (1964).
16. D. C. Grahame, *Chem. Rev.*, **41**, 441 (1947).
17. K. Sabo and I. A. Bagotskaya, *Dokl. Akad. Nauk SSSR*, **149**, 139; **150**, 128 (1963).
18. U. V. Pal'm and V. E. Past, *ibid.*, **146**, 1374 (1962).
19. J. N. Butler, M. L. Meehan, and A. C. Makrides, *J. Electroanal. Chem.*, In Press (1965).
20. A. N. Frumkin, "Hydrogen Overvoltage and Adsorption Phenomena, Part II," in Vol. III of "Advances in Electrochemistry and Electrochemical Engineering," p. 287, P. Delahay, Editor, Interscience, New York (1963).
21. R. Parsons, *Trans. Faraday Soc.*, **47**, 1332 (1951).
22. R. Parsons and J. O'M. Bockris, *ibid.*, **47**, 914, (1951).
23. B. Post and C. F. Hiskey, *J. Am. Chem. Soc.*, **72**, 4203 (1950).
24. Z. A. Iofa and K. P. Mikulin, *Zhur. Fiz. Khim.*, **18**, 137 (1944).
25. A. Frumkin, Z. A. Iofa, and V. S. Bagozky, *ibid.*, **25**, 1117 (1951); **26**, 1854 (1952).
26. P. Rüetschi and P. Delahay, *J. Chem. Phys.*, **23**, 195 (1955).
27. B. E. Conway and J. O'M. Bockris, *J. Chem. Phys.*, **26**, 532 (1957).
28. G. Wolf, *Z. Physik. Chem. (Leipzig)*, **223**, 249 (1963).
29. A. J. Rosenberg and M. C. Lavine, *J. Phys. Chem.*, **64**, 1135 (1960).
30. A. J. Rosenberg, *ibid.*, **64**, 1143 (1960).
31. J. F. Dewald, *This Journal*, **104**, 244 (1957).
32. T. I. Popova and N. A. Simonova, *Isv. Akad. Nauk, SSSR, Ser. Khim.*, 1187 (1963).
33. M. Pourbaix, "Atlas d'Equilibres Electrochimiques," p. 439, Gauthier-Villars, Paris, 1963).
34. Note added in proof: Murtazaev and Nikol'skaya [*Dokl. Akad. Nauk Uz. SSR*, **21**, 31 (1964), *Chem. Abstr.*, **61**, 15661 (1964)] have studied hydrogen evolution on indium in KOH, HCl, and H_2SO_4. At 10^{-3} amp/cm^2 in acid, $\eta \cong 0.85$ volts compared to our value of 1.00 volts. This low overvoltage, together with the high Tafel slope (200-250 mv) indicates considerable oxygen in the electrolyte. Hence their current-potential curves do not correspond to hydrogen evolution alone.

Improved Porous Electrode for Studying Electrocatalytic Reactions of Gases and Vapors

G. Bianchi

Laboratory of Electrochemistry and Metallurgy, University of Milan, Milan, Italy

ABSTRACT

An improved porous electrode is described which is a convenient basis for a comparative study of electrocatalytic activity of noble metals and/or for investigations of electrocatalytic processes on gases. The suggested technique makes use of porous graphite disks having a part of their surface covered with a thin layer of catalyst kept in position by means of a thin network of sintered Teflon drops. Such an electrode is to be disposed horizontally with its upper catalyst side kept in the atmosphere of the concerned gas, the remaining part being immerged in the solution. Solution by capillarity moves upward to moisten catalyst. Teflon prevents solution from reaching a too high level which would submerge the catalyst. This way the triple contact electrode-solution-gas is complete and efficient, and both solution level and graphite porosity are not critical factors. Polarization curves and charge-discharge curves have been determined in order to evaluate performances of that porous electrode in various electrochemical systems and processes.

Investigation of electrochemical processes of gas sparingly soluble in aqueous solutions has its chief obstacle in the set up to be deviced to realize the contact electrode-solution-gas. Such a contact may be obtained by means of a porous electrode wet-proofed so that the contact between the gas and the solution is in the pores of the electrode itself. A similar artifice is applied in the fuel cells where porous electrodes with controlled porosity are used. However this method does not give satisfactory results when applied to draw polarization curves or charge-discharge curves or to make analogous determinations.

The structure of the electrode gives origin to concentration polarization in the gas phase and in the solution inside the pores of the electrode itself. Furthermore it is unavoidable to have incorrect determinations of polarization by ohmic losses taking place inside the porous electrode. On top of that must be put the hindrance offered to the construction of electrodes with reproducible properties, when electrodes activated in different ways are to be used, by the fact that the activation must be realized by deposition of the catalyst inside the pores of the electrode.

A different problem is the perfection of an experimental set up valid for studying and evaluating catalysts as Pt-Pd-Rh, etc., blacks involving electrochemical methods. This problem has been recently considered by Grubb and Michalske (1) who proposed a metal screen as a support for the pasted catalyst. The necessity for a method to evaluate the electrocatalytic activity of noble metals has been outlined recently in the case of ethylene anodic oxidation in acid solutions (2). Such a method can be perfected easily and rapidly as the evaluation of the catalysts may be done only by measuring the current at controlled potential for selected reactions of the electrode.

Suggested Technique

The newly suggested technique makes use of the properties of a porous graphite electrode suggested by Elmore and Tanner (3) having a part of its surface covered with a thin layer of an appropriate catalyst kept in position with Teflon. The electrode is disposed horizontally with the part covered with the catalyst kept in an atmosphere of gas and the remaining part immersed in the aqueous solution. The solution moves upward by capillarity through the pores of the electrode and moistens the catalyst layer. The Teflon wetproof layer also helps to prevent solution from reaching a too high level which would completely submerge the catalyst. On the other hand, this porous Teflon layer is very thin (about 0.2 mm) so that the concentration polarization on the gas side is negligible as long as very high current densities are not reached. This way the contact electrode-solution-gas is complete and satisfactory, and solution level is not a critical factor.

The detailed electrode previously described is shown in Fig. 1 together with the polarization cell used and the correct disposition of the Luggin-Haber's capillary to prevent ohmic losses in the polarization measurements (4).

The electrode is prepared in conformity with the following specifications: a disk of porous graphite 4 mm thick and 25 mm in diameter, pierced in the center to settle a Luggin-Haber's capillary, is covered over by a thick paste of the catalyst finely ground in distilled water, a slight depression being applied

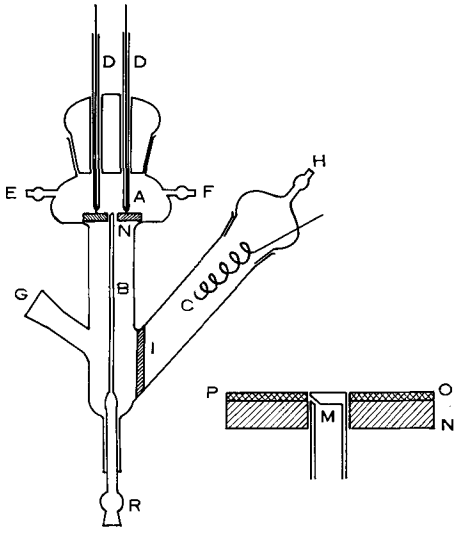

Fig. 1. Complete view of the cell using the porous electrode with capillary imbibition for measures of polarization with detail of the electrode and disposition of the Luggin-Haber's capillary: A, gas chamber; B, solution; C, counterelectrode; D, wires for connection with polarizing circuit and potentiometric circuit; E, inlet of the gas or vapor; F, outlet of the gas or vapor; G, connection with reservoir of solution; H, outlets of gas evolved at counterelectrode; I, sintered glass diaphragm; M, Luggin-Haber capillary with lateral opening positioned in the hole at the center of the electrode; N, porous graphite electrode; P, O, layer of catalyst; R, to reference electrode.

underneath the disk during the process. Both in the case of Pt black and of graphite powder activated with platinum the deposited catalyst amounts to about 5 mg/cm^2. The disk dried in a muffle furnace at 120°C is sprayed with an aqueous suspension of Teflon (du Pont 30) and afterwards heated *in vacuo* at 300°C for 3 hr to sinter the Teflon. The spraying of Teflon suspension should be done so that the Teflon cover results in a net involving 3 or 4 layers of drops, whose mean diameter is about 50μ. This can be achieved by spraying the Teflon, drying with hot air, spraying the Teflon again, drying, and so on. This wetproof Teflon cover protects the catalyst from mechanical damage and prevents the formation, during operation, of a veil of solution over the activated surface of the electrode without screening the catalyst itself.

If the studied catalyst can be damaged during the heating at 300°C necessary to sinter Teflon, the electrode could be used without the Teflon layer, too. In this case, however, the solution level is critical, and the current which the electrode can now supply is reduced to about 25%.

Such an electrode may be used as a research tool for studying electrochemical processes involving gases and vapors. In the latter case the vapors are flushed round the electrode by a stream of inert gas as disturbing phenomena of concentration polarization in the gas phase are unimportant as in the case of porous wet-proofed electrode.

Results

The performances obtained with this electrode are explained in some of the accompanying figures. Figure 2 shows potentiostatic curves of polarization related to the anodic ionization of hydrogen.

Curves A and B are obtained with two electrodes prepared by using graphite at different porosity but according to the same technique. The results are equivalent and prove that the properties of the porous graphite are not critical for the behavior of the electrode. Curves C and D are obtained with a catalyst different from that used for curves A and B and show the anodic ionization of pure hydrogen (curve C) or of a mixture 50% H_2 and 50% N_2 by volume.

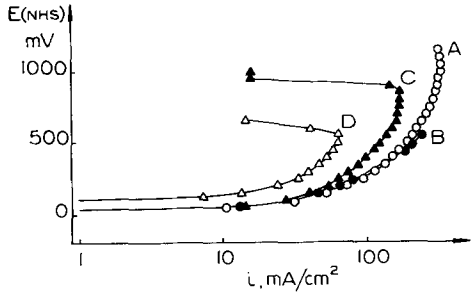

Fig. 2. Potentiostatic polarization curves for the hydrogen anodic ionization in acid solution 0.5M H_2SO_4 at 25°C. A, B, C, pure hydrogen; D, mixture of 50% H_2 and 50% N_2 by volume. For curves A and B the same catalyst is used but the supporting electrode is different: in one case (A) being graphite National S 2368, grade 45, porosity 48%; in the second one (B) being graphite Stackpole Carbon Co. PC 57 H, porosity 68%. For curves C and D the same electrode and the same catalyst is used. The catalyst is different from that used for curves A and B.

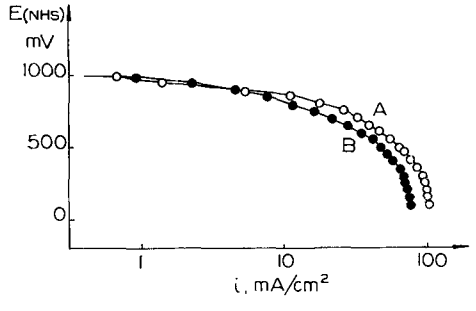

Fig. 3. Cathodic polarization curves for the reduction of O_2 in acid solutions at 50°C: A, electrode cathodically activated at + 200 mv, NHS; B, electrode after functioning for long time at + 700 mv, NHS.

The O_2 cathodic reduction on Pt black in 2.5M H_2SO_4 at 50°C is shown in Fig. 3. Polarization curve A is obtained with an electrode activated by cathodic polarization at + 200 mv (NHS); curve B with an electrode that worked for long time at + 700 mv. The variation of current is immediate when air is substituted for oxygen and *vice-versa* (Fig. 4). This fact, more than the ratio 5:1 between the current verified in the two cases, shows that the concentration polarization on the gas side is so low that no appreciable effect is produced.

Figure 5 illustrates the anodic oxidation of methanol in acid solution at 25°C. Methanol vapors are carried by a nitrogen stream.

Performances of various catalysts (platinum, iridium, rhodium, and ruthenium blacks) in the anodic

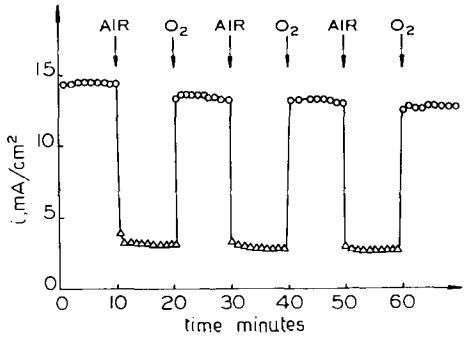

Fig. 4. Current response during cathodic reduction of oxygen at 700 mv, NHS, in acid solutions at 50°C, on alternated substitutions of oxygen for air and *vice versa*.

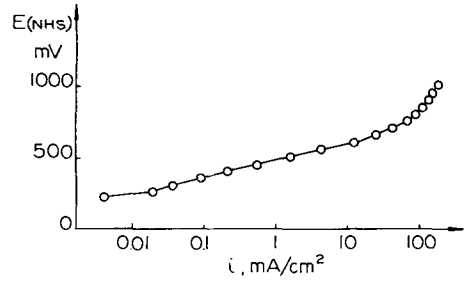

Fig. 5. Polarization curve for the anodic oxidation of methanol vapors carried by a stream of nitrogen in acid solution (0.5M H_2SO_4) at 25°C.

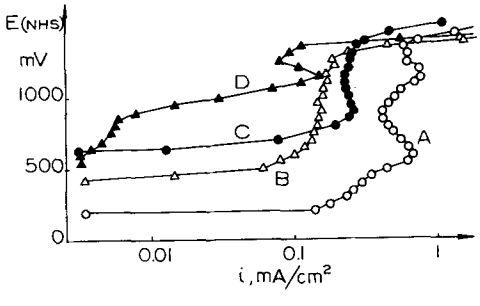

Fig. 6. Polarization curves for the anodic oxidation of propane in acid solution (0.5M H_2SO_4) in the presence of various catalysts at 25°C: A, platinum black (Engelhard); B, iridium black (Johnson and Matthey); C, rhodium black (Engelhard); D, rutenium black (Johnson and Matthey).

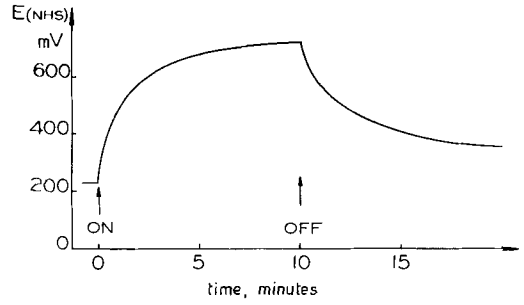

Fig. 7. Anodic charging curves at constant current (i = 0.5 ma/cm^2) and decay curve after anodic polarization for propylene in acid solution (0.5M H_2SO_4) at 25°C; platinum black as catalyst.

oxidation of propane in acid solution at 25°C are compared through the potentiostatic curves in Fig. 6, which confirm that platinum is the best catalyst for propane anodic oxidation (5).

The anodic charging curves related to propylene in acid solution in presence of platinum black are in Fig 7. The electrodes were activated by anodic formation of platinum oxides followed by cathodic reduction at 200 mv (NHS). It is evident that during the anodic oxidation of propylene, the catalyst undergoes a process of slow poisoning.

Discussion

The results quoted in this paper put into evidence that the capillary imbibition porous electrode can be advantageously used as a research tool for studying the electrochemical processes of gases and vapors. It can furthermore be employed as a support for a hydrogen reference electrode, reliable and simple, with exchange currents as high as 10 ma/cm^2. It is also possible to foresee the utilization of such an electrode in fuel cells and industrial plants.

Acknowledgment

This research was sponsored by Consiglio Nazionale delle Ricerche, Roma.

Manuscript received Feb. 24, 1964.

Any discussion of this paper will appear in a Discussion Section to be published in the December 1965 JOURNAL.

REFERENCES

1. W. T. Grubb and C. J. Michalske, *This Journal*, **111**, 477 (1964).
2. H. Dahms and J. O'M. Bockris, *ibid.*, **111**, 728 (1964).
3. G. V. Elmore and H. A. Tanner, *ibid.*, **108**, 669 (1961).
4. R. Piontelli, G. Bianchi, *et al.*, *Z. Electrochem.*, **56**, 86 (1952); **58**, 54 (1954); **58**, 86 (1954).
5. W. T. Grubb, 16th Annual Power Sources Conf., p. 31 (1962).

Technical Notes

Oxidation by Transport through Blocking Pores

P. L. Harrison

Central Electricity Research Laboratories, Leatherhead, England

Under certain conditions the oxidation of mild steel in aqueous solutions in the temperature range 250°-400°C produces a double layer magnetite film, the inner layer of which is protective (1). In dilute alkaline solutions, the growth of this inner layer becomes extremely slow at a thickness of a few tens of microns, and there is some indication of a limiting thickness of about 50 μm. Under weakly acidic or strongly alkaline conditions (2, 3) the magnetite does not form as a protective layer and corrosion continues at a rapid rate. The mechanism of the corrosion process and the conditions leading to a nonprotective oxide have been the subject of many recent studies (4-6).

Some of this work (4, 5) has shown that the magnetite layer formed is porous. Measurements of the density of laboratory-grown magnetite (4) indicated a porosity of about 10% volume/volume, and electron microscopy of magnetite films 1000-2000Å thick (5) indicated that pores of 100-500Å are present between the particles of magnetite. Porosimetry studies (7) of an exceptionally thick magnetite deposit from part of a power-station boiler were in agreement with these measurements. Such porosity can be reconciled with a protective oxide layer by assuming that the pores gradually become blocked during the course of oxidation. It is known (1) that during oxidation metal ions pass out through the oxide as oxidant passes in. There is a possibility, therefore, of reaction taking place within the pores.

The growth of a porous oxide under conditions such that the pores become blocked during oxidation has been treated by Evans (8). He considers two cases. One case represents self-blocking in which the pores through which the reactants diffuse become blocked by the reaction taking place within them. If w represents the weight of metal oxidized and n represents the number of pores per unit area, then we have $\frac{dw}{dt} = k_1 n$ and $-dn = k_2 dw$ which give the asymptotic equation

$$w = \frac{n_o}{k_2}(1 - e^{-k_1 k_2 t}) \qquad [1]$$

where n_o is the value of n at $t = 0$.

The other case, termed mutual pore blocking by Evans, is one in which the oxide formed within a pore causes a compressive strain in the surrounding oxide, which closes up neighboring pores. The number of pores so blocked is proportional to the density of pores, so that the equations become

$$\frac{dw}{dt} = k_1 n \text{ and } -dn = k_3 n dw$$

These give the direct logarithmic equation

$$w = \frac{1}{k_3}\log_e (k_1 k_3 n_o t + 1) \qquad [2]$$

It is to be noted that, in the case of self-blocking, the weight of metal oxidized cannot exceed an amount represented by $w = n_o/k_2$. No such limit applies in the case of mutual blocking, so that at large values of t the extent and rate of oxidation is greater for the

mutual blocking case than for the self-blocking case. This arises because implicit in the equation $-dn = k_3\, ndw$ is the assumption that the pores responsible for causing blocking of neighboring pores do not themselves become blocked. Evans (9) suggests that the oxide growing within the pore becomes wedged across the pore in such a way that it fills part only of the cross section. As this oxide continues to grow, compressive strains are set up at the points of contact between it and the pore surface. The transmission of these strains through the bulk oxide causes neighboring pores to become blocked even though the intrapore oxide does not completely block the pore in which it is growing. Evans suggests that the effective resistance of this pore to the passage of reactants is unaltered, because, although the cross section is reduced at the site of the intrapore oxide, the strains this oxide imposes cause the cross section of neighboring lengths of the pore to be increased. He suggests that the two effects can be assumed to cancel each other out.

A further case of pore-blocking which is of interest is one in which the intrapore oxide responsible for the blocking of neighboring pores also causes blocking of the pore in which it is forming. This is a combination of the two cases considered by Evans. The relevant equations are

$$\frac{dw}{dt} = k_1 n \text{ and } -dn = k_2\, dw + k_3\, n\, d\, w$$

which give for the relation between extent of oxidation and time, the equation

$$w = \frac{1}{k_3} \log_e \left[1 + \frac{k_3 n_o}{k_2} (1 - e^{-k_1 k_2 t}) \right] \qquad [3]$$

The curves for this case and for the case of self-blocking pores only are given in Fig. 1. In order to aid comparison, the nondimensional quantities

$$W = \frac{w k_2}{n_o},\ T = k_1 k_2 t \text{ and } G = \frac{k_3 n_o}{k_2}$$

have been used.

Equations [1] and [3] then become

$$W = 1 - e^{-T} \qquad [4]$$

and

$$W = \frac{1}{G} \log_e [1 + G\,(1 - e^{-T})] \qquad [5]$$

respectively.

Curves for $G = 0.0$, 0.1, 1.0, and 10.0 are given in Fig. 1. Putting $G = 0$ reduces Eq. [5] to [4] the equation for self-blocking pores.

At small values of T Eq. [5] approximates

$$W = \frac{1}{G} \log_e (1 + G\,T) \qquad [6]$$

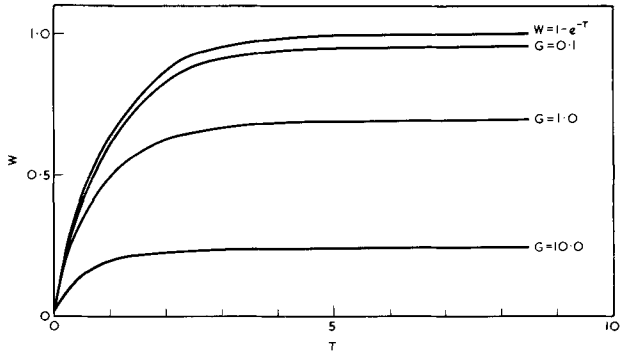

Fig. 1. Oxidation curves for pore blocking mechanism giving protective oxide: ord, W, dimensionless weight gain; abs, T, dimensionless time.

At large values of T, Eq. [5] approximates

$$W = \frac{1}{G} \log_e (1 + G) - \frac{1}{1 + G} e^{-T} \qquad [7]$$

From Eq. [6] and [7] it is seen that Eq. [5] represents a transition from a direct logarithmic growth law to an asymptotic growth law. In the early stages of oxidation when the pore density is relatively high, mutual blocking of pores will have the greatest influence on the growth law giving a direct logarithmic growth law. Measurements on the corrosion of mild steel to magnetite in alkaline solutions have suggested a logarithmic growth law at least in the early stages (4, 10). In the late stages of oxidation, when the pore density is relatively low, mutual blocking of pores will be relatively unimportant and self-blocking will have the greatest influence giving an asymptotic growth law. Such a transition would be consistent with the high degree of protection that magnetite formed during aqueous corrosion is capable of giving.

Under more strongly alkaline or weakly acidic conditions the magnetite formed does not afford protection, and a near linear oxidation rate is observed. There is no reason to assume that pore blocking does not occur under these conditions even though the oxide is nonprotective. However, with the rapid in-filling of pores that can be expected in the more corrosive conditions, the stresses built up within the oxide may become too large to be completely relieved by the blocking of neighboring pores. This excess stress could be relieved by shear strains which would create additional pores or cracks in the neighborhood of the blocked pore. Such a mechanism would introduce a term $-k_4\, dw$ into the expression for $-dn$ so that we have $-dn = (k_2 - k_4)\, dw + k_3 n\, d\, w$. The effect of the production of pores in this way is to reduce the importance of self-blocking of pores in the growth law, that is, to reduce the effective value of k_2. In the particular case of $k_4 = k_2$, the oxide grows wholly according to the direct logarithmic law. If $k_4 > k_2$, then effectively, $k_2 < 0$, and $-W$, $-G$ and $-T > 0$. Equation [5] then becomes

$$(-W) = \frac{1}{(-G)} \log_e [1 + (-G)\,(e^{(-T)} - 1)] \qquad [8]$$

For large $(-T)$ this approximates to the form

$$W = A + BT \qquad [9]$$

representing a linear growth law. This occurs at a time when the pore density approaches a value sufficient to give a balance between the rate of pore blocking and the rate of pore production. Curves of Eq.

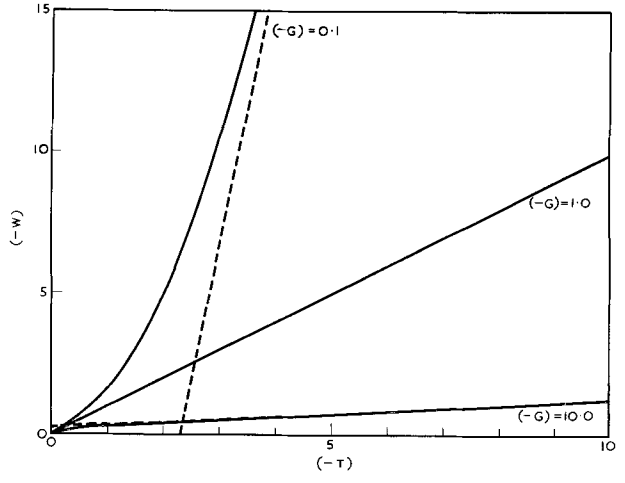

Fig. 2. Oxidation curves for pore blocking mechanism giving nonprotective oxide: ord, $(-W)$ dimensionless weight gain; abs, $(-T)$, dimensionless time.

[8] for values of (—G) of 0.1, 1.0, and 10.0 are given in Fig. 2.

It is seen that a nonprotective oxide is not inconsistent with a pore blocking mechanism. The situation that is most likely to occur is that the stresses produced in the oxide do not become fully relieved in the early stages of oxidation, but slowly increase as the oxide thickens. This would have the effect of slowly increasing the value of k_4, perhaps to a limiting value, as the oxidation proceeded. If this limiting value of k_4 is greater than the value of k_2, the effective value of k_2, positive at the beginning of the oxidation, would eventually become negative. This would give the sequence, with increasing time of logarithmic, asymptotic, accelerating to linear for the oxide growth law, representing a transition from a protective to a nonprotective oxide layer.

Both protective and nonprotective magnetite layers have been produced on mild steel oxidized in aqueous solutions at high temperature. A simple extension of the theory of pore blocking by Evans can explain the appearance of these two oxide forms, and suggests that their appearance may depend on the same basic mechanism.

Acknowledgment

The work described in this note was carried out at the Central Electricity Research Laboratories, Leatherhead, and is published by permission of the Central Electricity Generating Board.

Manuscript received Oct. 2, 1964.

Any discussion of this paper will appear in a Discussion Section to be published in the December 1965 JOURNAL.

REFERENCES

1. E. C. Potter and G. W. W. Mann, "Proc. 1st Int. Congr. Metallic Corrosion," 49, Butterworths, London (1961).
2. E. C. Potter and G. W. W. Mann, *Chem. and Ind.*, 1768 (1963).
3. W. A. Fraser and M. C. Bloom, *Corrosion*, **18**, 163t (1962).
4. A. M. Adams, E. M. Field, D. R. Holmes, and R. C. Stanley, 2nd Int. Congr. Metallic Corrosion, New York, 1963.
5. E. M. Field, Corrosion Science Society Meeting, Cambridge, 1963.
6. M. C. Bloom, M. Krulfeld, and W. A. Fraser, *Corrosion*, **19**, 327t (1963).
7. British Coal Utilisation Research Association, Private communication.
8. U. R. Evans, "The Corrosion and Oxidation of Metals," Edward Arnold, London (1960).
9. U. R. Evans, Private communication.
10. A. J. Panson, Paper presented at the Houston Meeting of the Society, Oct. 9-13, 1960.

Synthesis of GaAs by Vapor Transport Reaction

H. R. Leonhardt

IBM Watson Research Center, Yorktown Heights, New York

Within the last few years vapor growth processes have become a common method to prepare single crystalline GaAs (1-6). In most cases the following reaction is used

$$3\,GaX + \frac{1}{2}\,As_4 \rightarrow 2\,GaAs + GaX_3 \qquad [1]$$

where X = Cl or I. The iodide disproportionation reaction is usually employed in closed tubes because iodine is a solid which makes the loading procedure of the ampoules fairly simple. For most purposes, however, flow systems are more attractive. Therefore, an iodide process suitable for such an open tube apparatus has been developed.

Elemental gallium and arsenic were used as the source materials, H_2-HI being the transporting agent. The hydrogen iodide was prepared *in situ* from hydrogen and iodine to insure sufficiently high purity of the carrier gas (7). There were mainly two reasons for combining synthesis and epitaxial growth of GaAs: (i) Since gallium and arsenic are available in high purity, one can expect that such a system has the potential to produce high-purity GaAs, especially since the low-temperature iodide process is utilized. (ii) Separate sources for the two components permit a wide variation in the composition of the reactive gas.

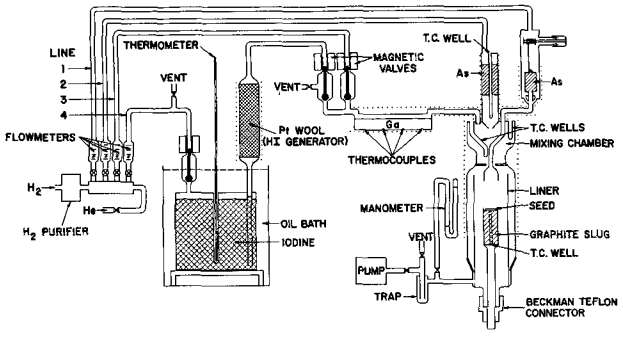

Fig. 1. Flow chart of GaAs vapor growth system

Figure 1 shows the basic features of the apparatus. Purified hydrogen can be fed into the system through four input lines. During the initial heat up period, the GaAs substrate is placed in a bell shaped shelter into which line 1 terminates, and hydrogen containing some arsenic is passed over it. The purpose of the arsenic is to prevent decomposition of the seed. Therefore, its pressure which is controlled by the temperature of the arsenic source in line 1 has to be kept above the dissociation pressure of the seed crystal. Assuming solid-vapor equilibrium for the arsenic, thermodynamic calculations show that the arsenic temperature has to be $\geq$ 190°C for a substrate preheating temperature of 750°C which was generally used. Data for the calculations were taken from the literature (8-10). For the actual decomposition process, lines No. 2 and 4 are used. The arsenic in line 2 is transported in elemental form. In 4, iodine is evaporated and converted to hydrogen iodide which reacts subsequently with gallium to form gallium iodides. The arsenic and gallium source are heated by multizone furnaces which provide a constant temperature over the entire length of the two zones. The gas streams from lines 2 and 4 are mixed in a chamber which is kept sufficiently hot so that no GaAs can form in it, the appropriate temperature being determined by calculations which will be described in the next section. In the deposition chamber the gases are cooled down so that GaAs precipitates.

Such a two-line system brings some complications with it since the conditions in the different zones have to be adjusted to each other. The best theoretical approach to this problem possible at the present time is a thermodynamic analysis which has been made with the following assumptions: (A) Thermodynamic

equilibrium is achieved in each part of the system. (B) All important vapor phase species are known. (C) The partial pressures of the various species follow the ideal gas law. (D) The total pressure p_t equals 1 atm throughout the entire system. (E) All solids and liquids are pure phases. (F) The conditions are chosen so that the gas streams from line 2 and 4 in Fig. 1 yield a mixture in the mixing chamber which is in equilibrium with solid GaAs.

The first assumption has been checked for the three most critical zones: the iodine, the gallium, and the arsenic source. Studies on the evaporation rate of iodine by Reisman, Berkenblit, and Alyanakyan (11), and on the rate for the Hi-Ga reaction by Silvestri (12) have been used to demonstrate the validity of the assumption for the iodine and the gallium source. For the arsenic source kinetic calculations were made based on data given by Brewer and Kane (13). Under all conditions the relaxation time of the solid-vapor equilibrium for the arsenic was found to be orders of magnitude shorter than the residence time of the transporting hydrogen gas in the source chamber, which means that also at the arsenic source equilibrium obtained. In order to check the assumption on the total pressure, p_t has been measured at the input side of the system. It was found to be only a few Torr above atmospheric pressure, *i.e.*, $p_t = 1$ atm is a good approximation.

Table I. Vapor phase species in the system

Abbreviations: A, arsenic source; G, gallium source; D, deposition chamber; M, mixing chamber; I, iodine source; p_t, total pressure; f_n, flow rate in line n, c, $\left(\frac{\text{gallium content}}{\text{arsenic content}}\right)_M$

Zone	Vapor phase species
A	As_2, As_4, H_2
I	I_2, H_2
G	GaI, GaI_3, HI, I_2, I, H_2
M, D	GaI, GaI_3, HI, I_2, I, H_2, As_2, As_4

It can be readily demonstrated that the system is defined thermodynamically by specifying the following experimental parameters: 1, the ratio of the flow rates; 2, the temperature T_A of the arsenic source; 3, the temperature T_M and the ratio c between the gallium and arsenic content of the vapor phase of the mixing chamber; and 4, the temperature T_D in the deposition chamber. These specifications and a series of independent equilibria provide a sufficient number of equations, shown in Table II, to calculate the partial pressures of the various vapor phase species (Table I) and the appropriate temperatures at the iodine and the gallium source.

From the partial pressures in the mixing and deposition chamber one can determine the gallium to

Table II.

Zone	Equation or equilibrium[a, b]		Reference
A	$4As(s) \rightleftarrows As_4$	$\log K_1 = -\frac{6{,}777}{T} + 7.678$	(9)
A, M, D	$As_4 \rightleftarrows 2As_2$	$\log K_2 = -\frac{13{,}029}{T} + 7.981$	(10)
M, D, G	$GaI_3 \rightleftarrows GaI + I_2$	$\log K_3 = -\frac{10{,}250}{T} + 6.71 \log T - 14.2$	(8, 14, 15)
M, D	$GaI_3 + 2GaAs(s) \rightleftarrows 3GaI + \frac{1}{2}As_4$	$\log K_4 = -\frac{23{,}650}{T} + 19.4$	(8)
M, D, G	$2HI \rightleftarrows H_2 + I_2$	$\log K_5 = -\frac{622.4}{T} - 0.834$	(16)
M, D, G	$I_2 \rightleftarrows 2I$	$\log K_6 = -\frac{7{,}991}{T} + 5.481$	(17)
I	$I_2(s) \rightleftarrows I_2$	$\log K_7 = -\frac{3{,}513}{T} - 2.013 \log T + 13.374$	(18)
G	$2Ga(l) + GaI_3 \rightleftarrows 3GaI$	$\log K_8 = -\frac{11{,}000}{T} + 12.4$	(8)
A, M, D, G, I	Total pressure condition: $\Sigma p_i = p_t = 1$ atm all species	(p_i = partial pressure of species i)	
M	Conservation of arsenic and hydrogen: $\left(\frac{4p_{As_4} + 2p_{As_2}}{2p_{H_2}}\right)_A = \left(\frac{4p_{As_4} + 2p_{As_2}}{2p_{H_2} + p_{HI}}\right)_M \frac{f_2 + f_4}{f_2}$		
M	Specification of gallium to arsenic ratio in M: $c = \frac{p_{GaI} + p_{GaI_3}}{4p_{As_4} + p_{As_2}}$		
I	Conservation of hydrogen and iodine: $\left(\frac{p_{GaI} + 3p_{GaI_3} + 2p_{I_2} + p_I + p_{HI}}{2p_{H_2} + p_{HI}}\right)_M = \left(\frac{p_{I_2}}{p_{II_2}}\right)_I \frac{f_4}{f_2 + f_4}$		
G	$= \left(\frac{p_{GaI} + 3p_{GaI_3} + 2p_{I_2} + p_I + p_{HI}}{2p_{H_2} + p_{HI}}\right)_G \frac{f_4}{f_2 + f_4}$		
D	$= \left(\frac{p_{GaI} + 3p_{GaI_3} + 2p_{I_2} + p_I + p_{HI}}{2p_{H_2} + p_{HI}}\right)_D \frac{f_1 + f_2 + f_4}{f_2 + f_4}$		
G	Conservation of gallium and iodine: $\left(\frac{p_{GaI} + p_{GaI_3}}{p_{GaI} + 3p_{GaI_3} + 2p_{I_2} + p_I + p_{HI}}\right)_M = \left(\frac{p_{GaI} + p_{GaI_3}}{p_{GaI} + 3p_{GaI_3} + 2p_{I_2} + p_I + p_{HI}}\right)_G$		
D	Stoichiometry of gallium arsenide: $\left(\frac{(p_{GaI} + p_{GaI_3}) - (4p_{As_4} + 2p_{As_2})}{2p_{H_2} + p_{HI}}\right)_M = \left(\frac{(p_{GaI} + p_{GaI_3}) - (4p_{As_4} + 2p_{As_2})}{2p_{H_2} + p_{HI}}\right)_D$		

[a] Pressure unit: 1 atm
[b] (s) = solid
(l) = liquid
unindicated = vapor species

iodine ratio y_M and y_D in the two zones. The difference Δy between these quantities is the amount of gallium which should precipitate as GaAs according to thermodynamics in the deposition chamber per equivalent of iodine:

$$\Delta y = y_M - y_D$$

$$= \left(\frac{p_{GaI} + p_{GaI_3}}{p_{GaI} + 3p_{GaI_3} + 2p_{I_2} + p_I + p_{HI}} \right)_M - \left(\frac{p_{GaI} + p_{GaI_3}}{p_{GaI} + 3p_{GaI_3} + 2p_{I_2} + p_I + p_{HI}} \right)_D$$

Δy represents the maximum value for the experimental growth rate which one can expect in the system for a given set of conditions.

A large number of cases with different values for the parameters was calculated on an IBM 7090 computer. For practical use, a few were selected on the basis of high Δy values and reasonable temperatures for the gallium and iodine source.

Epitaxial GaAs has been grown successfully in this open tube iodide system using gallium[1] of 99.9999% and arsenic[2] of 99.999% purity. The substrate surfaces were prepared by means of a chemical polishing technique which has been developed recently by Reisman *et al.* (19).

Some of the results are shown in Table III and Fig. 2. Under the conditions indicated in Table III the effective deposition rates (*i.e.*, only the growth on the seed crystal is taken into account) were appreciably smaller than the calculated values. This is at least partly due to the fact that GaAs precipitated not only on the substrate but also on the walls of the reaction tube and on the seed holder.

Figure 2 shows the effect of deposition temperature on the surface perfection. Deposits grown at 620°C on substrates oriented in the <111> A direction (which is the gallium terminated side) developed many pyramids within a short time (Fig. 2a), and as the growth continued a few big pyramids took over (Fig. 2b). Better results in terms of surface smoothness were obtained at higher deposition temperatures (Fig. 2c). Above 650°C, however, the deposition rate started to decrease appreciably. The rates between 620° and 650°C were in the order of 20 μ/hr. Runs were also made with substrates oriented in the <111> B and the <100> direction. In agreement with results reported for the closed tube iodine process (1) only polycrystalline growth could be obtained on <111> B substrates. Deposits grown in the <100> direction were epitaxial, but the surfaces showed a very dense pattern of pyramids.

The electrical properties of the vapor grown material summarized in Table III were determined from

Fig. 2. Deposits grown for different lengths of time t and at different deposition temperatures T: (left) t_a = 45 min, T_a = 620°C; (center) t_b = 4 hr 30 min, T_b = 620°C; (right) t_c = 45 min, T_c = 650°C.

Hall and resistivity measurements. All deposits were n-type. The results were obtained from samples which had been grown thick enough so that the original substrate could be removed. Two series of experiments were made under different conditions. Between the first and the second one the arsenic source had to be replenished. Aside from that the various source materials were not changed between runs. In Table III the runs are listed in chronological order. The increase in mobility and the decrease of the carrier concentration in the course of the first series shows that the system became cleaner from run to run. The abrupt deterioration of the vapor grown material after the arsenic source had been reloaded indicates that a substantial fraction of the impurities came either from the arsenic or was introduced during the loading procedure (*e.g.*, the system might have become contaminated with silicon when the arsenic container was sealed).

In the two series of runs the deposits were grown under different arsenic pressures. Theoretically one would expect that with increasing arsenic pressure the concentration of free electrons in the grown GaAs would decrease and the hole concentration increase due to a decrease in arsenic and an increase in gallium vacancies.[3] However, this effect was apparently much smaller than the effect of contaminants on the electrical properties so that it could not be observed.

In Table III the best values for the mobilities are appreciably higher than what has been found normally in vapor grown GaAs (22). Together with their strong temperature dependence this might be an indication that the material was not severely compensated.

Acknowledgments

The author would like to thank Mr. J. V. Lyons for participating in the initial part of this work, Dr. A. Reisman for helpful discussions, and Mr. E. Baran for his assistance in the experimental work. He also wants to acknowledge the support which he received from Miss A. Kuhlke and Dr. R. Kelisky by making the computer calculations, from Dr. S. E. Blum by supplying the GaAs substrates, and from Dr. J. F. Woods and Mr. S. Baliozian by making the electrical measurements.

[1] Alcoa Chemicals.

[2] Cominco Products, Inc.

[3] This has been observed in a number of II-VI compounds (20, 21).

Table III. Deposition rates and electrical properties of vapor grown GaAs

Growth conditions	Calculated growth rate, mg/hr	Experimental growth rate, mg/hr	Exp. growth rate / Calc. growth rate %	Carrier conc. [10^{16} cm^{-3}] Room temp.	Carrier conc. [10^{16} cm^{-3}] 77°K	Mobility [cm^2/v sec] Room temp.	Mobility [cm^2/v sec] 77°K
T_{As} = 407°C T_I = 76°C T_{Ga} = 434°C T_{mix} = 800°C T_{dep} = 620°C $f_{As} = f_{Ga}$ = 50 cm^3/min Substrate orientation: <111>A Growth time: 11 hr	232 232 232 232 232	10 15.7 13.8 13.1 14.0	4.3 6.8 6.0 5.6 6.0	2.6 2.9 2.3 1.5 1.4	1.9 1.6 1.6 1.1 1.0	5,370 5,680 5,800 6,150 6,530	9,680 12,670 11,870 14,600 16,170
T_{As} = 487°C T_I = 82°C T_{Ga} = 410°C T_{mix} = 800°C T_{dep} = 620°C $f_{As} = f_{Ga}$ = 50 cm^3/min Substrate orientation: <111>A Growth time: 10 hr	276 276	17.3 18.0	6.3 6.5	2.1 0.7	1.5 0.5	5,710 5,850	8,050 9,870

Manuscript received Aug. 18, 1964. This paper was presented at the Toronto Meeting, May 3-7, 1964.

Any discussion of this paper will appear in a Discussion Section to be published in the December 1965 JOURNAL.

REFERENCES

1. V. J. Lyons and V. J. Silvestri, *This Journal*, **108**, 177C (1961).
2. A. Hagenlocher, *ibid.*, **108**, 213C (1961).
3. R. L. Newman and N. Goldsmith, *ibid.*, **108**, 213C (1961).
4. F. V. Williams and R. A. Ruehrwein, *ibid.*, **108**, 177C (1961).
5. R. R. Moest and B. R. Shupp, *ibid.*, **109**, 1061 (1962).
6. C. J. Frosch and C. D. Thurmond, *ibid.*, **109**, 301C (1962).
7. A. Reisman and M. Berkenblit, *ibid.*, **111**, 60C (1964).
8. V. J. Silvestri and V. J. Lyons, *ibid.*, **109**, 963 (1962).
9. Landolt-Börnstein, "Zahlenwerte und Funktionen," Vol. II, 2a, Springer Verlag, Berlin (1960).
10. D. R. Stull and G. C. Sinke, "Thermodynamic Properties of the Elements," Advances in Chemistry Series, No. 8 (1956).
11. A. Reisman, M. Berkenblit, and A. Alyanakyan, *This Journal*, **110**, 186C (1963).
12. V. Silvestri, Paper presented at the Washington Meeting of the Society, Oct. 11-15, 1964.
13. L. Brewer and J. S. Kane, *J. Phys. Chem.*, **59**, 105 (1955).
14. L. L. Quill, "The Chemistry and Metallurgy of Miscellaneous Materials, Thermodynamics," University Microfilms Inc., Ann Arbor, Mich.
15. W. Fischer and O. Jubermann, *Z. anorg. u Allgem. Chem.*, **227**, 227 (1936).
16. G. M. Murphy, *J. Chem. Phys.*, **4**, 344 (1936).
17. "Selected Values of Chem. Thermodyn. Prop.," Circ 500 Ser. III, Nat. Bureau of Standards (1961).
18. L. J. Gillespie and L. H. D. Fraser, *J. Am. Chem. Soc.*, **58**, 2260 (1963).
19. A. Reisman and R. L. Rohr, *This Journal*, **111**, 1425 (1964).
20. R. F. Brebrick, *J. Phys. Chem. Solids*, **24**, 27 (1963).
21. J. Bloem, *Philips Research Repts.*, **11**, 273 (1956).
22. F. V. Williams, *This Journal*, **111**, 886 (1964).

A Chemical Polish for Lead Telluride

M. R. Lorenz

IBM Watson Research Center, Yorktown Heights, New York

The preparation of PbTe surfaces free of damage has been investigated by several workers using various techniques. The results of these studies have recently been tested and summarized (1). Briefly there exists a satisfactory electrochemical polish (2). A chemical polish (3) which can produce film (1) and damage free flat surfaces (3) is also known. Although the reported chemical polish may be ideal for flat surface preparation, it has the disadvantage of requiring a mounted sample. The purpose of this communication is to describe a new and simple chemical polish for PbTe which does not have any limitation with regard to geometry. The polished surfaces are indistinguishable from those obtained by use of the electrochemical polish (2).

Test samples consisted of both single and polycrystalline wafers as well as irregular shaped PbTe crystals. The polishing solution was composed of saturated aqueous $K_2Cr_2O_7$ and concentrated nitric acid. The volume ratio of the two components is fairly limited and is between 4.2 and 5.0 with the optimum at about 4.5. A typical polishing solution would consist of 40 cc saturated $K_2Cr_2O_7$ solution and 9 cc concentrated HNO_3. For large crystal charges or dissolution of thick layers the solution volume would of course require a corresponding increase to avoid rapid dilution of the polish strength. The PbTe samples were placed in a Pyrex basket which was fused to a Pyrex rod. By rotating the basket while suspending it in the solution, at room temperature, the test samples were subjected to a good polishing action. Similarly good action was achieved by placing samples directly into a solution beaker and stirring the solution vigorously with a magnetic stirrer. When surfaces appeared satisfactory the samples were well rinsed in H_2O and dried. The rate of material removed for the above conditions was measured on a number of samples for various periods of time. The results show a dissolution rate which varied between 20 and 40 μ/min. Temperature control during polishing appears not extremely critical. However, tests at 45°C indicate a dissolution rate nearly double that at 25°C without any appreciable change in the surface finish.

Sometimes a smooth polished crystal may have a barely perceptible golden colored film on the surface. The occasional appearance of the film is not understood but is no cause for concern since it can be readily removed. Film covered samples were placed in 50% NaOH solution. The solution was heated to 100°-120°C and then left to cool back to room temperature. The samples were rinsed in dilute HCl solution and then thoroughly rinsed in distilled water and dried. The above treatment removed any visible surface film but does not lead to cracking of samples due to thermal shock as had been noted earlier (3, 1).

The procedure described here is simple and quick. It suffers no restriction with regard to geometry. However, as any chemical polish it requires slight variations on the part of the experimentalist to achieve the desired results.

The application of the PbTe polishing solution to GeTe, SnTe, and SnSe was attempted with little success. Variations of the $K_2Cr_2O_7$ to HNO_3 ratio did not lead to any improvement. A mixture of 20 parts of saturated $K_2Cr_2O_7$, 11 parts of HCl, and 1 part of HNO_3 gave visibly smooth shiny surfaces on SnTe. After a few minutes, the shiny surfaces showed slight discoloration which was easily removable by dipping into 20% NaOH solution. Microscopic investigation, however, indicated that the SnTe surfaces were in general ripply and pitted. Similar surfaces could be obtained on GeTe when a mixture of 20 parts of saturated $K_2Cr_2O_7$ and 1 part of HNO_3 was used.

Acknowledgment

The author wishes to thank Mr. L. Buszko for his diligent assistance in this work.

Manuscript received Sept. 3, 1964.

Any discussion of this paper will appear in a Discussion Section to be published in the December 1965 JOURNAL.

REFERENCES

1. M. K. Norr, "Polishes and Etches for Tin Telluride, Lead Sulfide, Lead Selenide and Lead Telluride," NOLTR 63-156, U.S. Naval Ordnance Laboratory, White Oak, Maryland (1963).
2. M. K. Norr, *This Journal*, **109**, 433 (1962).
3. P. H. Schmidt, *ibid.*, **109**, 879 (1962).

Transpiration Studies of the Ge-I_2-Inert Gas System

A. Reisman, M. Berkenblit, and S. A. Alyanakyan

IBM Watson Research Center, Yorktown Heights, New York

Recently, the results of thermodynamic analyses of the Ge-I_2 solid-vapor system in the presence of inert and/or reactive gases at constant total pressure were presented (1, 2). The data derived from these analyses were intended as guides in designing and operating an open tube disproportionation system for growing Ge single crystals epitaxially via reaction [1]

$$GeI_4 + Ge \rightleftarrows 2GeI_2 \qquad [1]$$

Use of the data in an experimental system, however, depends on the degree of equilibrium that is achieved in equilibrating a carrier gas with solid phases at certain critical points in the open tube flow train. In the Ge-He-I_2 system these points are; the halogen source, the germanium source, and the deposition region.

The present report describes studies of transpiration phenomena in the above system. In essence these studies involved determining the flow conditions at different temperatures which were necessary for a He stream to equilibrate physically with an iodine source, and for an I_2-He mixture to equilibrate chemically and physically with a Ge bed. Because of the results obtained, it will be seen that there are interesting aspects in the flow rate ranges in which the I_2-He gas is not in equilibrium with the Ge. Studies of the deposition region have not been conducted pending the construction of a complete vapor transport train.

Experimental Procedure

Figure 1 is a schematic representation of the iodine bed employed. The design of this bed enables passing of the incoming gas stream through either the iodine source or a bypass. Both the source and bypass chambers contain glass beads to increase the heat capacity of the bed to offset cooling effects due to gas flow and evaporation. Figure 2 is a schematic representation of the train used in the experimental evaluation of the iodine bed efficiency. The He carrier gas was purified in a John Mickel Associates purifier, which in turn is followed by a flow meter, the iodine source, thiosulfate absorption traps, and a wet test meter. Without prepurification of the carrier gas, the thiosulfate solutions, maintained at a starting pH of 7, invariably decomposed with the liberation of sulfur due to the presence of CO_2 as an impurity in the He.

All experiments were conducted on as-received semiconductor grade iodine. Before using this material, the packed bed was flushed for several hours with the carrier gas.

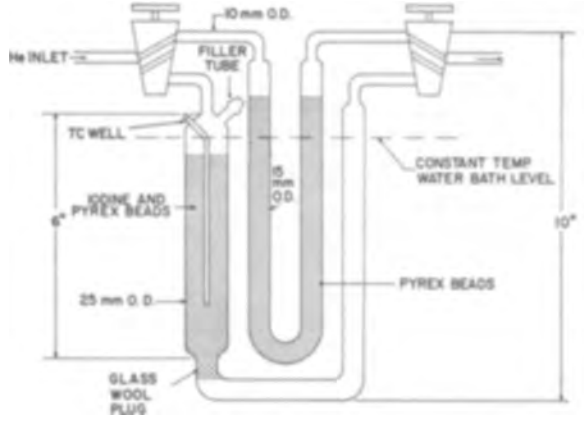

Fig. 1. Iodine source bed design

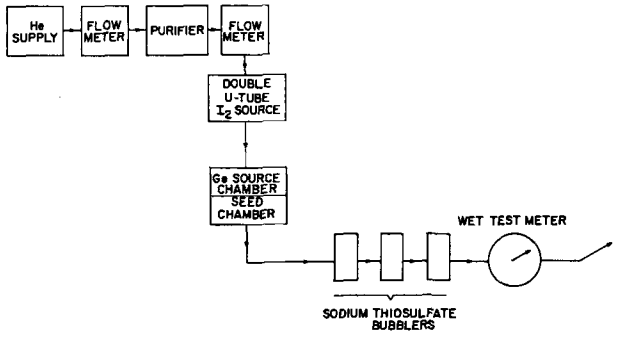

Fig. 2. Schematic representation of I_2 transpiration train

Since no convenient method analogous to that employed for the iodine analysis suggested itself for the Ge system, it was decided to determine the Ge quantity removed from the source bed by a weight loss method. Figure 3 shows the experimental arrangement used to obtain data at 400°, 450°, and 620°C. The design employed facilitates disassembly of the reaction train to enable weighing the Ge bed.

Results and Discussion

Iodine transpiration studies.—Although the equilibrium flow rate range can be evaluated by plotting iodine gas phase concentration *vs.* flow rate for each of the iodine source temperatures investigated, values of the halogen source vapor pressure were also computed. Comparison of these values with those in the literature insure against the possibility of a systematic error in our method of evaluating iodine gas phase concentration leading to incorrect absolute values. These values are important in comparing the Ge-I_2 reaction data with the thermodynamic results mentioned previously. Two series of transpiration experiments were conducted, one with an iodine source at 50.5°C, the other with the iodine source at 61.8°C. At all flow rates up to approximately 0.9 l/min, the systems appeared to be in equilibrium.[1] The calculated vapor pressures for the two temperatures were 2.14 ± 0.06 mm and 4.79 ± 0.07 mm, respectively. Comparison of these approximate values with those of Baxter and Grosse (3) who used a more sophisticated transpiration technique indicates that no major systematic errors

[1] Vapor pressures were calculated with the aid of the equation below. Assuming ideal gas behavior and a constant value of atmospheric pressure (1 atm), the partial pressure of iodine in atm is given by

$$p_{I_2} = n_{I_2}/[n_{I_2} + \frac{V}{RT_M}(1 - p_{H_2O})]$$

where n_{I_2} is the number of moles of iodine, determined by titration of the thiosulfate solutions, that are carried in the volume V measured at a wet test meter whose temperature is T_M and where p_{H_2O} is the vapor pressure of water at T_M.

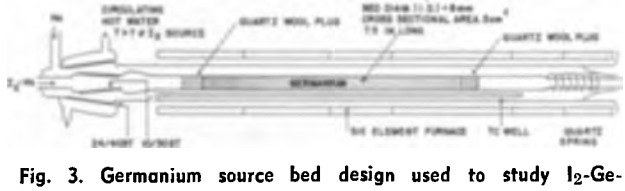

Fig. 3. Germanium source bed design used to study I_2-Ge-He system.

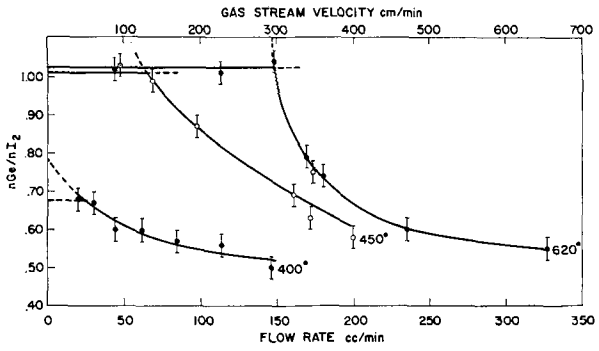

Fig. 4. Transpiration data for the Ge-I_2-He system

were involved in the iodine analysis. The values obtained by them were 2.24 and 4.83 mm, respectively.

Ge-I_2 *transpiration studies.*—On the basis of the thermodynamic analyses (1, 2) in the temperature interval 350°-650°C, the value of the vapor phase component mole ratio Ge/I_2 as a function of temperature is limited at the lower temperature by a value of 0.5 coinciding with the semiconductor-halogen species stoichiometry GeI_4. At the higher temperature, the limiting value of this ratio is 1.0 coinciding with the semiconductor-halogen species stoichiometry GeI_2. Consequently, it was expected that for the three temperatures studied, 400°, 450°, and 620°C, the flow rates at which solid-gas phase equilibrium are attained would lead to values of the Ge/I_2 ratio within the limits defined by the thermodynamic analyses. Again, as with the studies involving iodine equilibrium, the equilibrium flow rate region for Ge can be evaluated by plotting Ge vapor phase concentration *vs.* flow rate. As a check to insure against some systematic error leading to incorrect absolute Ge transport values, the I_2 and Ge transpiration data were used to calculate Ge/I_2 component mole ratios in both the equilibrium and nonequilibrium flow rate regions.

In measurements of the type under consideration linear gas stream velocities are more significant than gas flow rates since the latter are independent of equipment geometry. As no simple means of establishing the linear gas stream velocities in the packed Ge bed could be evolved, a reference velocity scale based on the hypothetical velocities that would have obtained in an unpacked bed of the dimensions shown in Fig. 3 was calculated for the flow rates employed. This velocity scale is meant only to provide some feeling for the gas residency time in the Ge bed. The arbitrary Ge particle size distribution used in this investigation was 52.2% retained on No. 8 U.S. Standard Sieve Series, 18.2% retained on No. 12, 16.3% retained on No. 20, 8.6% retained on No. 40, 2.7% retained on No. 60, and 2.0% passing hrough No. 60. Repeated bed packing of newly crushed, sieved, and "white etched" Ge provided reasonably reproducible data. It is to be noted that the use of any other arbitrary particle size distribution would merely have shifted the flow rate at which the gas effluent from the Ge bed became saturated, but would not have altered the equilibrium Ge/I_2 ratio obtained at a given temperature.

Figure 4 presents the Ge/I_2 mole ratios derived from both the iodine and Ge measurements as a function of flow rate (also in terms of the hypothetical linear gas stream velocity mentioned above).

The significant features of this figure may be summarized as follows:

1. At 400°C, it could not be established whether equilibrium was achieved at the lowest measurable flow rate. The smooth curve can be extrapolated to zero flow in two ways, one assuming that equilibrium has been achieved at finite flows, the other assuming equilibrium is achieved only at zero flow. In the latter instance, the zero flow intersection provides an equilibrium Ge/I_2 ratio in reasonable agreement with that predicted thermodynamically, *i.e.*, 0.78 and 0.83, respectively.
2. At higher temperatures, equilibrium appears to have been achieved within the limits of experimental uncertainty, the equilibrium flow rate range increasing with increasing temperature. Thus at 450°C, a theoretical value of 0.95 is predicted and 1.01 ± 0.04 is obtained experimentally. At 620°C, a theoretical value of 0.99 is predicted and 1.03 ± 0.03 is obtained experimentally.
3. Most significant, however, are the implications concerning the reaction mechanism between Ge and I_2 that may be drawn from the data in the nonequilibrium regions of the three curves. In each instance it is observed that with increasing flow rate the curves tend toward a limiting value of 0.5. This implies that the reaction of Ge with iodine proceeds via the two step mechanism

$$Ge_{(s)} + 2I_{2(v)} \rightleftarrows GeI_{4(v)} \quad [2]$$

$$GeI_{4(v)} + Ge_{(s)} \rightleftarrows 2GeI_{2(v)} \quad [3]$$

The first of these reactions appears to be rapid since even at the fast flow rates we have never observed free iodine passing through the Ge source bed (the asymptotic approach of the curves to a value of 0.5 supports this visual observation). The second reaction is markedly slower than the first. As the latter is the desired one in this vapor transport reaction, it represents a serious experimental limitation in the design of an efficient, reproducible germanium-iodine disproportionation open tube scheme. Thus, if one operates within the nonequilibrium linear gas stream velocity range, the tendency to form GeI_4 increases with increasing flow rate, resulting ultimately in a readily achievable worst case of zero transport efficiency (4).

Manuscript received April 9, 1964; revised manuscript received Nov. 2, 1964. This work was supported in part by AFCRL Contract No. AF 19(628)-2648. The paper was presented in part at the New York Meeting of the Society, Sept. 29-Oct. 3, 1963.

Any discussion of this paper will appear in a Discussion Section to be published in the December 1965 JOURNAL.

REFERENCES

1. A. Reisman and S. A. Alyanakyan, Paper presented at the New York Meeting of the Society, Sept. 29-Oct. 3, 1963.
2. A. Reisman and S. A. Alyanakyan, *This Journal*, **111**, 1154 (1964).
3. G. P. Baxter and M. R. Grosse, *J. Am. Chem. Soc.*, **37**, 1061 (1915).
4. Recently, P. Balk of this laboratory in studies of the Ge-Cl_2, Ge-I_2, and Ge-Br_2 interactions by other techniques has concluded that a two-step mechanism is involved in the Ge-Br_2 case and very probably also involved in the other two systems. See Proc. of the Int. Conf. of the Phys. and Chem. of Solid Surfaces, June 21-26, 1964, Brown University.

Brief Communications

An A-C Conductive Adhesive for Testing Electroluminescent Devices

Alexander Baczewski

General Telephone & Electronics Laboratories, Inc., Bayside, New York

This communication deals with the compounding of an inexpensive material which allows temporary adhesion of the conductor to an electroluminescent device.

Many electroluminescent devices consist of a conductive transparent material, an electroluminescent layer and an aluminum back electrode prepared by high-vacuum evaporation. It is very difficult to repair pinholes and small blemishes in the electroluminescent layer once the aluminum back electrode has been applied. A temporary electrode that would make it possible to find such defects before the aluminizing step would allow the preparation of defect-free devices. Such an electrode must provide good electrical contact to the sometimes very rough electroluminescent layer, and it should be easy to apply and remove. Although water dispersions of graphite can be used for this purpose, the water is deleterious for most devices and may magnify or even cause defects. In addition, the black color of the conductor will detract from the brightness of a device. Alloys of mercury, indium, and thallium can be used for this purpose since they have very low melting points and wet almost any surface; these alloys, however, are extremely toxic and quite expensive (1).

It is well known that the reaction products of boric acid and aliphatic polyhydroxy compounds and their ammonium salts are good conductors of electricity (2). Some of these compounds dissolve in ethylene glycol; such solutions are also good conductors and are colorless, water-free liquids. They have been used formerly in the manufacture of capacitors (3). A solid polyhydric alcohol increases the viscosity without decreasing the conductivity; hence, it is possible to mix ethylene glycol, mannitol, boric acid, and ammonia in such a way that a very viscous, clear mass results which may be used as an adhesive; the amounts are not critical. Table I gives a few examples.

Table I. Polyol-ammonia-boric acid combinations

Constituent	% by weight			
Ethylene glycol	44	44	44	23
Mannitol	7	7	28	28
Boric acid	35	28	21	42
Ammonia	14	21	7	7

The solutions were prepared in the following manner. Various amounts of ethylene glycol, mannitol, and boric acid were mixed and aqueous ammonia was added while the temperature was slowly raised to 125°C with vigorous stirring. The temperature was maintained at 125°C for 5 min and then at 100°C for 2 hr without stirring. The resulting adhesive was kept in a desiccator.

One of these compounds was spread on paperbacked aluminum foil and the coated foil pressed onto a non-aluminized electroluminescent lamp. When the lamp voltage was increased slowly, thin spots lit up, and pinholes could be found before shorting occurred. The foil was removed and the adhesive was washed off with methanol. After elimination of the defects, and subsequent application of the evaporated electrode, the lamp brightness was equivalent to that of defect-free lamps that had not undergone this treatment.

Acknowledgment

Most of the experimental work was performed by V. Quistorff.

REFERENCES

1. V. J. King, *Rev. Sci. Instr.*, **32**, 1407 (1961).
2. T. Moeller, "Inorganic Chemistry," p. 763, John Wiley & Sons, New York (1957).
3. Standard Handbook for Electrical Engineers, p. 5-27, McGraw Hill Book Co., Inc., New York (1949).

The Formation of $FeSn_2$ during the Electrodeposition of Tin on Iron

W. Roger Buck, III, and Henry Leidheiser, Jr.

Virginia Institute for Scientific Research, Richmond, Virginia

The resistance to corrosion of commercial tinplate in some environments appears to be related to the characteristics of the iron-tin alloy $FeSn_2$ which is formed at the interface between the two metals during heat-treatment following the electrodeposition step (1). The purpose of this communication is to point out that fine-grained $FeSn_2$ is formed during electrolysis of iron in an alkaline bath but is not formed during electrolysis in an acid bath. This experimental result may have important consequences in focusing attention on a variable which appears to be subject to control.

Tin was electroplated on ⅜ in. iron cylinders (both Ferrovac-E and type-L steel) with a hemispherical end from the following two baths: acid bath: $SnSO_4$ 100 g/l, H_2SO_4 30 g/l, tartaric acid 30 g/l; alkaline bath: $Na_2SnO_3 \cdot 3H_2O$ 90 g/l, NaOH 7.5 g/l, NaOAc 15 g/l, 30% H_2O_2 0.5 ml/l. Both baths were operated

at 70°. The majority of the experiments were carried out at a current density of 3 amp/dm^2 and a plating time of 30 sec. These conditions are equivalent to an average deposit thickness of approximately 6000Å in the acid bath assuming 100% current efficiency, and to an average deposit thickness of approximately 2300Å in the alkaline bath assuming deposition from the Sn(IV) state and a current efficiency of 75%. The iron samples were polished in a commercial chemical polishing reagent, MirroFe, and were abraded with levigated alumina immediately before plating. The grain size of the deposit from the acid bath was of the order of 10^{-2} mm in diameter and of the order of 10^{-4} mm in diameter in the alkaline bath as indicated by x-ray diffraction analysis. Grain-size modifiers were not added to the acid bath as is the commercial practice.

The deposits were examined by x-ray diffraction using unfiltered iron radiation and grazing incidence on the hemispherical surface. This technique is remarkably sensitive to small amounts of crystalline material when the strong diffraction line occurs at planar spacings above 2.5Å. The diffraction line of iron at 2.03Å and the diffraction lines of tin at 2.92 and 2.79Å were clearly visible in all experiments. The strongest diffraction line of $FeSn_2$ at 2.56Å was used to determine its presence.

A faint line due to $FeSn_2$ was occasionally visible when the sample was x-rayed immediately after deposition of tin from the alkaline bath: it was always visible when the sample was annealed at 100° in boiling water for 10 min or more after deposition. $FeSn_2$ was not detected when deposition was carried out from the acid bath. Annealing the sample for as long as 60 hr at 100° in boiling water did not result in the formation of $FeSn_2$ identifiable by x-ray diffraction techniques.

The alkaline bath differs from the acid bath in many respects but particularly in the fact that hydrogen is codeposited with tin in the alkaline bath. The importance of hydrogen was examined by several methods: (*A*) the sample was electrolytically precharged with hydrogen immediately before electrodeposition of tin from the acid bath; (*B*) the tin concentration in the acid bath was lowered to 0.001 of its ordinary value (0.1 g/l $SnSO_4$) and deposition was carried out at 8 amp/dm^2 and low current efficiency; (*C*) tin was electrodeposited from solutions containing 0.002-0.010 g/l of dissolved tin at 100°. $FeSn_2$ was occasionally detected in (*A*), it was detected in (*B*) after annealing at 100° for 10 hr, and it was always detected in (*C*). These experiments suggest that the codeposition of hydrogen favors the formation of $FeSn_2$.

The $FeSn_2$ diffraction line was very clear on samples in which iron was subjected to electrolysis at 1 amp/dm^2 for 6 hr in boiling 0.1M Na_2CO_3 solutions containing 0.002 g/l dissolved tin. Based on prior studies with radioactive tin (2) the rate constant for the pickup of tin by metallographically polished iron at 100° is 2×10^{-8} g/cm^2-sec$^{1/2}$. If the tin forms $FeSn_2$ as a continuous film, this rate constant indicates that a film 30Å thick should be formed in 6 hr. The clear diffraction line suggests that appreciably more $FeSn_2$ is present at the interface than is expected on the basis of thermal diffusion only. These experiments agree with experiments in the indium-antimony system (3) in which it was found that electrolysis increased the rate of formation of InSb.

Manuscript received Sept. 22, 1964.

Any discussion of this paper will appear in a Discussion Section to be published in the December 1965 JOURNAL.

REFERENCES

1. G. G. Kamm and A. R. Willey, "1st Int. Congress on Metallic Corrosion," p. 495, Butterworth's Press, London (1961).
2. W. Roger Buck, III, A. N. J. Heyn, and Henry Leidheiser, Jr., *This Journal*, **111**, 386 (1964).
3. Melvin C. Hobson and Henry Leidheiser, Jr., To be published.

The Platinum-on-Carbon Catalyst System for Hydrogen Anodes

I. Characterization of the Catalyst and Support

L. J. Hillenbrand and J. W. Lacksonen

Battelle Memorial Institute, Columbus, Ohio

ABSTRACT

A high degree of hydrogen electrode activity in alkaline media can be achieved with less than 1 mg Pt/cm^2 of electrode, if a properly chosen carbon support is used. For a complete description of the platinum-on-carbon catalyst systems, the physical and chemical states of both platinum and carbon must be considered. In this paper the measurements of total electrode area, metal area and dispersion, pore size distribution, and the location of the Pt within the carbon structure are considered, and the importance of the choice of carbon is illustrated. The control of the chemical interactions between the platinum and the carbon is essential if high activity per unit weight of platinum is to be obtained.

Despite the large amount of work that has been done on platinized carbon electrodes for fuel cells, little information has been published on the choice of materials and methods for construction of a hydrogen anode. This situation is due to the extremely complicated surface chemistry of carbon and the many important variations that are possible in its production.

In the present work on catalytic electrodes for fuel cells, means were sought to characterize the catalyst and its support. Out of this work arose the realization that the possible chemical variations of the carbon surface had large effects on the activity of the platinum catalyst. This and the following paper, Part II, describe the observations that were made of the platinum-on-carbon catalyst system.

Platinized platinum electrodes are commonly recognized to have much better activity for hydrogen than those made from bright platinum. Similarly, a dispersion of platinum on carbon can show a much better performance as a hydrogen anode than that obtainable from an equivalent area of bright platinum, and with the use of substantially less platinum than required for either bright or platinized electrode structures. The complications that arise in the interpretation of such results stem from the fact that the different activities may result either from difference in surface area or from altered chemical states of the surfaces, or both. For the platinized carbon electrodes, the situation is especially complicated since there is the question of the role of the carbon. In the present work, a study was made of the changes in activity produced by the platinum-carbon interactions, and an attempt was made to differentiate these from the changes resulting from physical differences. The platinum-carbon interactions have proved to be of primary importance to the activity of the platinum catalyst.

One of the most important needs was a means to measure the metal area of the electrode. This need extends even to electrodes made from bright foil or wire because they have true areas considerably greater than the geometric area. Measurements (1) of the surface roughness, that is the ratio of true to geometric area, for commercial platinum foil or wire give values somewhat greater than 2, and the redox or etching treatments usually required to activate such electrodes can be expected to increase the roughness. At the other extreme, platinized platinum was found by Bowden and Rideal (1) to have a surface roughness in excess of 1800. Almost certainly this variation in surface roughness is accompanied by changes in surface chemical heterogeneity. The variations in the chemical state of the surface that can accompany these physical changes might be expected to lead to marked changes in electrode activity. A number of theories have been suggested for platinum catalysts as hydrogen electrodes in which the surface heterogeneity is the controlling feature: see for example Hill and Ives (2) and Davtyan (3).

The variations in surface roughness and surface heterogeneity that are possible for the platinum-on-carbon system are much more complicated because of the influences of the carbon surface. For this case, the total surface area can be measured by BET physical gas adsorption, and active metal areas can be differentiated from the remainder of the surface by hydrogen chemisorption. The information gained by these methods is described in the following sections.

The description of a platinized-carbon electrode includes three types of information: (i) the amount of carbon surface and the distribution of the pore diameters present; (ii) the amount and distribution of platinum surface; and (iii) the chemical conditions of the platinum and carbon surfaces and their interactions.

The first of these can be obtained by conventional BET gas-adsorption methods and by mercury-intrusion measurements. The third item is discussed in a separate paper (4). The second can be obtained by hydrogen-chemisorption measurements on appropriate portions of the electrode. However, some improvements in available hydrogen-chemisorption techniques have been necessary.

Measurement of the Surface Area of Platinum on Carbon

In recent years, hydrogen-chemisorption methods have been developed for measurement of platinum-metal areas of platinum-on-alumina catalysts. In these techniques, the samples are reduced in hydrogen and evacuated at 300°-500°C for prolonged periods to provide the required clean metal surface prior to the chemisorption measurement. Unfortunately, this heat treatment is unsuitable for unsupported platinum or for platinum on carbon. The thermal instability of platinum black has been reported by a number of workers, Benton (5) for example. Some of the recent data that show this thermal instability are summarized in Table I, where methods using nitrogen and krypton are based on physical adsorption and for hydrogen on chemisorption.

The data of Table I for the several samples of platinum black clearly show the sintering of unsupported platinum at 500°C. Battelle data shown for Baker Black were assembled from a variety of measurements made at different times and on two different lots of platinum black from the same supplier. There is little doubt that, in the absence of air, sintering of platinum black above 200°C caused noticeable reduction of the

Table I. Surface area of platinum black by gas adsorption (Values assembled from several sources)

Platinum source	Surface area, m^2/g Hydrogen	Nitrogen	Krypton
Fisher Black	—	—	36 (150°C)[a]
Bishop Black	2.2 (250°C)[b]	2.4 (250°C)[b]	19 (150°C)[a]
Baker Black	0.55 (500°C)[c]	0.54 (500°C)[c]	32 (150°C)[a]
Baker Black (Battelle)[d]			
26°C, He	—	21	—
150°C, vacuum	—	23	—
60° to 200°C, He	—	18-19	—
300°C, H_2 + vacuum	1.5-2.0	3-3.5	—
500°C, H_2 + vacuum	—	<1.0	—

[a] General Electric Company, "Research on Low Temperature Fuel Cell Systems," Progress Report No. 14, to U.S. Army Engineer Research and Development Laboratories, Ft. Belvoir (December 15, 1960). Contract DA-44-009-ENG-3771.
[b] H. Gruber, *J. Phys. Chem.*, **66**, 48 (1962).
[c] L. Spenadel and M. Boudart, *J. Phys. Chem.*, **64**, 204 (1960).
[d] Baker Platinum Division, Englehard Industries. The data shown are from determinations made at Battelle after treatment as shown in the table.

surface area. Recently, Fisher (6) showed that this sintering occurred more readily with clean platinum black than it did with platinum covered by a monolayer of oxygen. Because of the sintering, hydrogen-chemisorption measurements could not be used for any platinum-catalyst preparation in which the platinum might be suspected to show thermal sensitivity similar to that shown for unsupported platinum.

In the case of platinum black, the distinction between the total area by nitrogen adsorption and the metal area by hydrogen chemisorption has not been of major concern for properly cleaned samples, although it may be important if partial poisoning of the platinum surface is suspected. On the other hand, supported platinum such as platinized carbon cannot be properly investigated unless a distinction can be made between the active platinum-metal area and the remainder of the surface. To develop a method for hydrogen chemisorption that was suitable for platinum-on-carbon catalysts, a suitable treatment of the platinum at temperatures no higher than about 200°-250°C was needed. Experiments made to examine the effects of heat treatments on the chemisorption of hydrogen by platinum on carbon are illustrated in Table II.

Table II shows that conventional high temperature (300°-500°C) treatments of experimental samples yield platinum-metal areas of 20 to 30 m^2/g of platinum. The platinum was applied by preparing a slurry of carbon in the appropriate amount of chloroplatinic acid, dried, and heated to 165°C in an air oven over night. This platinum is located on the carbon support originally having a surface area of over 400 m^2/g. If the platinum that was used had been dispersed as a molecular layer, it should have had an area of about 276 m^2/g of platinum. Hence, the values in Table II amount to about 10% of that which could be obtained with a good dispersion. The crystallite sizes shown are calculated values based on this surface-area measurement, assuming that the platinum is dispersed as a regular shape such as a cube. They are not experimental measurements of actual platinum particle sizes.

Table II. Dispersion of platinum on carbon measured by hydrogen adsorption

Treatment	Number of samples	H_2/g, cc	Platinum area[a], m^2/g	Calculated crystallite size[b], Å
300°, H_2, 1/500°, vacuum, 17 hr[c]	6	4.6-6.2	20-30	105-78
300°, H_2, 1/400°, vacuum, 17 hr	1	4.2	20	115
300°, H_2, 1/300°, vacuum, 17 hr	2	4.8-5.4	23-26	101-90
As above, Baker 5% platinum on carbon	1	20.6	99	24
250°, H_2, 1/26°, He, vacuum, 48 hr[d]	1	11.0	53	44
As above, Baker 5% platinum on carbon	1	19.4	93	25
As above, platinum on Barnebey-Cheney Carbon K2046	1	40.0	192	12
As above, platinum on mineral carbon	1	32.2	155	15

[a] Platinum area calculated assuming 0.208 cc H_2 (STP) adsorbed per square meter of metal area. See for example L. Spenadel and M. Budart, *J. Phys. Chem.*, 64, 204 (1960).
[b] Calculated assuming the platinum area is distributed as the surface area of cubic crystallites of uniform size.
[c] This shorthand notation should be read: heat at 300°C in flowing H_2 for 1 hr, then at 500°C in vacuum for 17 hr.
[d] This shorthand notation should be read: heat at 250°C in flowing H_2 for 1 hr, then evacuate and purge with He occasionally at 26°C for 48 hr.

When a sample of platinum on carbon with this 300°-500°C treatment was examined for electrode activity, it was found that the heat treatment had destroyed most of the activity that was originally present.[1] Similar samples examined by x-ray line broadening revealed that the crystallites had grown appreciably during the treatment as compared with the crystallite sizes in the original preparations.

Subsequently, it was found that, since degassing could be accomplished in a flowing stream, the sample for chemisorption could be prepared by heat treating to temperatures not above about 200°-250°C for only 1 hr. The table shows that twice as much platinum area was found in this way as compared with that obtained by the old technique. Furthermore, there appeared to be no change when the treatment was repeated on the same samples. Material treated by this technique showed good electrode activity. Some of the differences in platinum dispersion that could be noted by such measurements are suggested by the values given in the remaining entries of the table. As shown in the final two entries, well-dispersed platinum was measurable by this technique. Since the Baker catalysts shown in Table II gave the same surface area by both methods and the treatment could be repeated on Battelle samples without change in area, the procedure appeared to be valid for the measurement of the dispersion of platinum. This conclusion was further supported by the observation that samples treated in this way remained active as hydrogen electrodes.

Amount and Distribution of Platinum

The platinized carbon was used to prepare dual-porosity carbon structures in which the platinum was located only in the outer layer. The general construction of these electrodes is shown in Fig. 1. The inner layer was made from a macroporous carbon which served as a support for the outer or catalytic layer and which also distributed the gas to the outer layer. The outer layer was microporous and contained the catalyst. When the electrode had become thoroughly wetted by the electrolyte, the gas pressure used was sufficient to hold the liquid interface out of the inner layer but permitted the electrolye to penetrate the

[1] Compare, for example, samples K, U, V, T with samples S, R, B of Table I in accompanying paper, Part II.

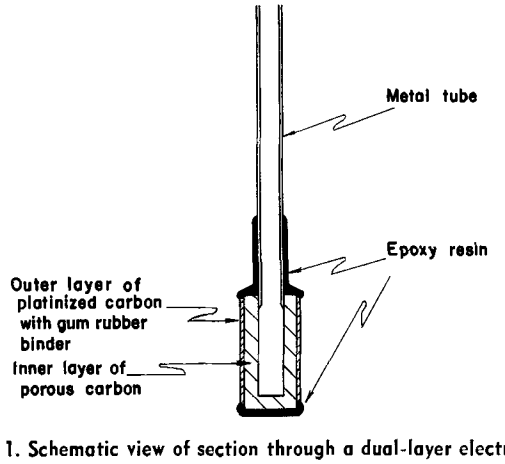

Fig. 1. Schematic view of section through a dual-layer electrode

Table III. Effect of variations in the amount and distribution of platinum in dual-layer electrodes

Samples	Weight of outer layer[a], g/cm²	Amount of platinum[b], %	Anodic limiting current density[c], ma/cm² Initial	Final	Special conditions of sample preparation[a]
			Variation of platinum content		
18736-24A	0.124	0	0	0	—
D	0.136	0.1	<1	<1	—
C	0.127	1	30	40	—
F	0.127	3	12.5	175 (110)[d]	—
B	0.119	5	15	95	—
G	0.121	5	15	105	—
H	0.130	7	25	115	—
			Variation of platinum distribution		
P	0.127	5	0.5	20	Outer layer is physical mixture of Darco S-51 and Baker's platinum black.
O	0.133	100	215	235	Outer layer is all Baker's platinum black. Poor continuity of outer layer.
W	0.135	6	95	90	Platinum black painted on outside of prefabricated, noncatalyzed dual-layer electrode.
Z	0.139	16	155	170	Platinum black painted on outside of prefabricated, noncatalyzed dual-layer electrode.
X	0.127	5.3	<1	<1	Platinum black painted on NC-60 support, followed by noncatalyzed outer layer of Darco S-51 carbon.
I	0.114	8.5	30	140	0.06g platinum painted on NC-60 support, then 5% platinized carbon outer layer applied.
Y	0.132	10	95	105	Platinum black painted on outside of 5% platinized outer layer of electrode.
18978-87	0.017	5	—	106	About 1 mg of platinum/cm² geometric area.

[a] With the exception of samples O and P, all samples were dual-layer electrodes and were activated by heating in air at 165°C. The support is NC-60 carbon and the outer layer is made of Darco S-51 carbon, except as noted. The binder used was gum rubber.
[b] Listed as weight per cent of the outer layer, except as noted.
[c] The electrodes were loaded as hydrogen anodes initially, then cycled cathodically and anodically two times. The polarizations are not corrected for IR drop from ohmic resistance in the cell. The limiting current represents polarization down to zero volts *vs.* SCE.
[d] The value of 110 ma/cm² was obtained at the end of the normal cycling. However, an increase in electrode back pressure occurred suddenly, and the subsequent performance was improved as shown.

micropores of the outer layer. The three-phase contact between solid electrode, liquid electrolyte, and gaseous fuel occurred in this layer. The two layers were bound together by a minor amount of gum rubber binder incorporated into the powdered carbon used to form the outer layer. The outer layer could be applied by painting or spraying techniques. Because of the low degree of wettability of the carbon itself and because of the binder used to form the dual-layer structure, even the outer layer was not completely wetted by the aqueous electrolyte. This means that, although the electrolyte generally penetrates the outer layer of the electrode, it probably does not enter any of the finer pore areas of that layer.

With this electrode construction a series of experiments was made to determine the requirements for the amount and distribution of platinum catalyst needed for hydrogen anode service.

For the electrodes described in this paper, the inner layer was generally National Carbon NC-60 carbon cut from a cylinder about 0.5 x 1.0 in. The outer layer was powdered carbon chosen from one of several sources but frequently was Darco S-51. Unless otherwise noted, the platinum was applied to the powdered carbon of the outer layer as chloroplatinic acid and then, after drying, the platinum compound was decomposed by heating the carbon to 165°C overnight in air. A comparison of several conditions for pretreatment is shown in Table III. For each of these electrodes the active geometric area of the electrode was about 15 cm². The electrodes were tested as hydrogen anodes in 30 w/o (weight per cent) KOH electrolyte using a half-cell apparatus. All performances are listed with correction for IR drop in the electrolyte.

The half-cell apparatus consisted of a saturated calomel reference electrode, a platinum foil counter-electrode and the test electrode. A constant and known current was impressed between the test and counter-electrodes with a 6-v battery. The current was adjusted with a potentiometer, and the voltage of the test electrode was compared with the calomel reference electrode. In this work the reference electrode was located in the same position with regard to the other electrodes in all experiments. The IR drop in this arrangement was not measured, but in cells of comparable geometry an IR drop of 300 mv was estimated at 100 ma/cm² for a 20 cm² electrode.

Table III shows effects of variation in the amount and distribution of platinum in this dual-layer electrode structure. The activities listed were obtained from the current needed to polarize the electrode to 0v *vs.* a saturated calomel electrode. This was not a diffusion-limited current, but rather an arbitrary stopping point for these electrode structures. The data are not corrected for IR drop in the electrolyte.

In each case the electrode was activated by cycling the electrode between anodic and cathodic polarizations. In Table III, the results of the first and the third, or final anodic polarization are shown. It is clear that the electrode activity is markedly improved by this cycling and in most cases, at least for electrodes of good activity, the slope of the curve became nearly constant throughout the complete anodic and cathodic cycle so that the electrode system is approximately reversible.

In Table III, it appears that the maximum final activity was approached by platinum concentrations in the outer layer of about 3%; an increase of platinum content up to 7% had only a small additional effect on the final activity. However, improvement in current-voltage characteristics was more pronounced with cycling when the electrodes contained less platinum.

For Electrode 18978-87, the weight of the outer layer was decreased to 0.25g of platinized carbon so that the platinum amounted to about 1 mg/cm² of geometric area. Tests of this and similar electrodes indicated that this amount of platinum was sufficient for good activity.

The role played by the carbon used in the outer layer is illustrated in Table III by electrodes P and O, in which the electrodes had an outer layer of platinum black rather than chemically deposited platinum on carbon. The physical mixture of platinum black and Darco S-51, electrode P, is obviously a poor electrode structure. Electrode O, made using all platinum for the outer layer, had good activity, but the amount of platinum used was about 20 times that for the platinum-on-carbon preparations.

Large differences in activity were observed with changes in the location of the platinum. Electrodes W, Z, X, and I show that platinum located between the two layers of the dual-layer electrode was quite ineffective, whereas platinum located on the outside of the dual-layer structure had quite good activity. Elec-

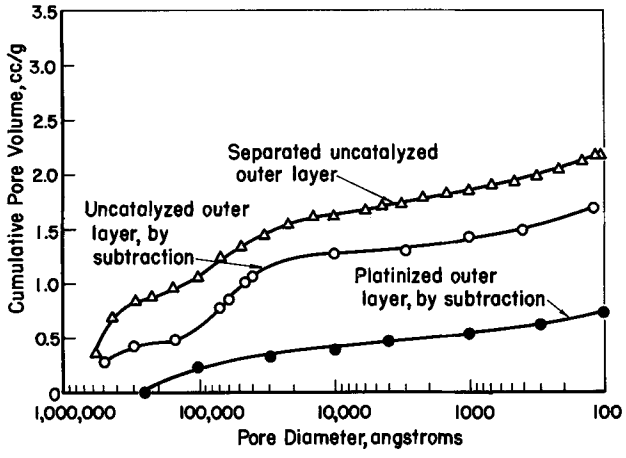

Fig. 2. Mercury-porosimeter measurements of pore distribution for microporous activated Darco S-51 carbon plus gum-rubber binding.

trode Y indicated that platinum black painted on the outside of the dual-layer structure did nothing to further the activity of previously catalyzed dual-layer structure.

Thus, the highest activity for platinum on a weight basis was obtained by chemical deposition of the platinum on a suitable carbon used as the outer layer of the electrode. The platinum had little effectiveness when located btween the electrode layers, but was quite active if located in or near the outer surfaces of the outer layer.

The importance of the choice of carbon is illustrated by the last two entries in Table II. Although the highest dispersions of platinum were obtained with these two carbons, the electrode made using the mineral carbon was almost totally inactive, whereas that made using the Barnebey-Cheney K2046 carbon showed good activity. Thus, it appears that the achievement of a good dispersion of platinum does not insure good activity. The importance of the chemical state of the carbon surfaces is discussed in a second paper (4).

Pore Structure of the Catalyzed Outer Layer

Further information on the location of the platinum in the catalyzed dual-layer structure, and also on the exact nature of the porosity of the completely fabricated electrode, was obtained by examining the pore-size distribution and surface areas for a variety of samples. In each of these structures, gum rubber was the binder.

The results of examining one dual-layer electrode for distribution of macropores by mercury-porosimetry measurements are shown in Fig. 2. To get the proper pore distribution for the outer layer, a method had to be devised to measure the porosities of the two layers separately. In one experiment, the porosity of the NC-60 substructure was measured and subtracted from the porosity shown for an uncatalyzed dual layer structure. The middle curve shown in Fig. 2 gives the pore-size distribution for the uncatalyzed outer layer obtained in this way. A similar curve is shown for the outer layer measured after it had been physically removed from the NC-60 substructure. Some cracking and pulverizing of the outer layer occurred during this separation, and the increase in large pores shown by the top curve of Fig. 2 is a reflection of this crumbling. Otherwise, the two curves referred to in Fig. 2 are quite similar. When the carbon was platinized and then applied to the NC-60 substructure in the normal way, the large reduction in macropores occurred as shown by the lowest curve in Fig. 2. This indicated that the platinum had plugged some of the pores of the carbon.

The micropore distribution below 100Å pore diameter was not obtained for platinum on carbon, but was measured for silver-catalyzed samples. The silver catalyst did not markedly enter the micropores of the carbon. Since the carbon was not readily wetted by water, entry of the aqueous impregnating solution into the micropores of the carbon was not expected, so the conclusions appeared reasonable.

Additional information about the effects of catalyst impregnation and application of the binder on the final pore structure of the outer layer of the electrode was obtained by measuring the total surface area of samples in various stages of preparation. The surface areas were measured by N_2 adsorption in a flow method using the Brenauer-Emmett-Teller technique and were degassed in a stream of helium at 25°C to avoid changes in the gum rubber binder present in one of the samples. The surface area of the Darco S-51 was 463 m^2/g. After deposition of 5 w/o Pt by impregnation with chloroplatinic acid and heat treatment at 165°C, the surface area dropped to 290 m^2/g. This reduction of the total surface area could be explained only by a removal of a large part of the microporosity below 100Å pore diameter, perhaps as a result of plugging by the deposits in the larger pores.

After the gum rubber solution was added, the slurry was used to form a dual-layer electrode. The outer layer then was removed and its surface area was found to be 107 m^2/g. The additional plugging produced by the gum rubber raised the question of the compatibility of the platinum and the gum-rubber binder and of the possible coverage of platinum surface by the binder. Hydrogen chemisorption measurements made on one gum-rubber-treated sample indicated that the platinum area was still totally available after the application of the rubber binder. It appears probable that the binder can be pictured as a porous network which, although it adheres to and bonds the carbon particles together, does not interact strongly with the platinum catalyst and remains porous to hydrogen.

Viton A, a copolymer of vinylidene fluoride and perfluoropropylene, has been used in recent electrodes to replace the gum rubber used as a binder in earlier work. Electrodes prepared with Viton A, cured at 200°C for 24 hr, have good activity and are physically much stronger than those made by using gum rubber.

Conclusions

Based on the observations presented, a few of the details of the structure of the active electrodes can be described. Thus, for the electrodes used in this work, platinum dispersions of about 50 m^2/g on carbon were effective as hydrogen electrodes. This platinum was most effective if located in or near the outer surfaces of the outer layers. The degree of dispersion indicated corresponded to crystallites on the order of 40-50Å size, and these seemed to be located in the macropore portion of the outer layer. Indeed, since the carbons used were all poorly wet by aqueous solutions, it is doubtful if the micropore portion of the carbon ever became wetted by either the platinum solution or the alkaline electrolyte. It is conceivable that these micropores served as gas passages for supply to the active centers of the electrode. In this connection it was of interest to note that the physical mixtures of Pt and C used for one electrode had extremely poor activity.

With proper choice of carbon and control of the electrode preparation, as little as 3 w/o platinum on carbon was sufficient to generate an electrode of high activity. Good hydrogen anodes were made with 1 mg Pt per cm^2 (geometric) or electrode area. There was no evidence that this was the lower limit of the useful range of platinum contents.

Although these measurements served to describe in some detail the microstructure for an active electrode, the achievement of a good dispersion of platinum catalyst did not assure good activity. To complete the picture, a knowledge was required of the chemical

limitations posed by the carbon surfaces present. Thus, although the highest dispersions of platinum were achieved with the last two carbons listed in Table II, the platinum on K2046 carbon showed good activity and the sample made using the mineral carbon was almost totally inactive. The chemical requirements for the carbon surfaces used is the subject of another paper (4).

As a result of these observations, it became apparent that the most efficient use of platinum catalyst for hydrogen anode service could be obtained only if many factors, both physical and chemical, were taken into account. One of the most important of these factors is the chemical interaction between platinum and carbon which must be controlled if high activity per unit weight of platinum is to be obtained.

Acknowledgment

The authors wish to thank the members of the Fuel Cell Research Group for their permission to publish this work. They also wish to acknowledge the assistance and advice of the other personnel assigned to this project, especially C. L. Faust, D. M. Johnson, E. J. Kahler, B. A. Petro, and W. T. Reid.

Manuscript received Aug. 20, 1964. This paper was presented at the Boston Meeting, Sept. 16-20, 1962.

Any discussion of this paper will appear in a Discussion Section to be published in the December 1965 JOURNAL.

REFERENCES

1. F. P. Bowden and E. K. Rideal, *Proc. Roy. Soc. (London)*, **A120**, 59 (1928).
2. G. J. Hills and D. J. G. Ives, "The Hydrogen Electrode," Chapt. 2, *Reference Electrodes*, by Ives and Janz, Academic Press, New York (1961).
3. O. K. Davtyan and co-workers, "Mechanism of Oxidation, Hydrogenation and Electrochemical Combustion on Solid Catalysts." A series of papers in *Russian J. Phys. Chem.*, with various co-authors, especially: Part V., **35** (11), 1276 (1961); Part VI., **35** (12), 1346 (1961); Part VII., **36** (4), 353 (1961). All Consultants Bureau Editions.
4. L. J. Hillenbrand and J. W. Lacksonen, *This Journal*, **112**, 249 (1965).
5. A. F. Benton, *J. Am. Chem. Soc.*, **48**, 1850 (1926).
6. R. A. Fisher, "Adsorption Properties of Hydrogen and Oxygen on Platinum Black and Carbon Supported Platinum From 20 to 300 K," Ph.D. Thesis, Pennsylvania State University (1961).

The Platinum-on-Carbon Catalyst System for Hydrogen Anodes

II. Chemical Requirements of the Carbon Surface

L. J. Hillenbrand and J. W. Lacksonen

Battelle Memorial Institute, Columbus, Ohio

ABSTRACT

The large differences in the activity of platinum-on-carbon anodes that could be produced by the choice of carbon indicated that an important chemical interaction existed between the platinum and the carbon surface. A chemical interaction was also indicated by electron-spin-resonance measurements on plain and platinized carbon. Subsequently it was found that the activity of the platinum anode was reduced to negligible values if the carbon surface was cleaned in N_2 at 1000°C before application of the platinum. If the carbon was reoxidized using CO_2 at 1000°C before application of the platinum, full activity of the platinum deposit was obtained. The effect of N_2 and CO_2 was reversible. Graphitic carbons were unsuitable for this work and did not respond greatly to these treatments. These effects do not seem to be explainable by the surface area changes that are produced. The effect appears to be explainable by adapting the catalyst poisoning theory of Maxted.

In the earlier paper, Part I (1), a dual-layer hydrogen anode was described which used less than 1 mg of platinum per square centimeter on a suitable carbon. The choice of the carbon was found to be important. The highest temperature to which the electrode was exposed was the 165°C heat treatment in air used to decompose the chloroplatinic acid and to activate the electrode. In this heat treatment, the carbon support apparently participated as a reducing agent for the deposition of platinum. Since it was not known whether this reduction provided a clean catalyst of maximum activity, other heat treatments were checked, especially in the presence of hydrogen. This work was part of an investigation of the optimum conditions for activation of the platinum catalyst and led to the experiments that showed the importance of the chemical state of the carbon surface.

Heat Treatments of the Platinized Carbon

The results of the various heat treatments in vacuum, air, and hydrogen presented in Table I show that the treatments at 300°C or above usually were detrimental to the platinum on carbon catalyst. On the other hand, completely fabricated dual-layer electrodes that had been heated in hydrogen at 200°C for several hours had good activity. Also, the hydrogen chemisorption measurements previously reported (1) were made on samples activated at 250°C and were known to remain active as hydrogen anodes following this treatment. On occasion, electrodes of moderate activity appeared to be somewhat improved by the 200°C treatment in hydrogen, so it was concluded that some residual contamination of the platinum surface was removed in this way.

The detrimental effects of heat treatments above 300°C were at least partially explained by the sintering of the platinum catalyst. The x-ray line-broadening examinations (1) showed that the platinum crystallites grew considerably when samples were heat treated at 500°C. However, the large differences in activity related to the type of carbon (1) also suggested that an important chemical interaction existed between the platinum and the carbon surface. Therefore, that part of the effects of heat treatment conceivably was produced by chemical changes that occurred at the platinum-carbon interface.

Investigation of the Carbon Support

The suspicion that platinum-carbon interactions were influencing the activity of the final electrode was strongly supported by the failure of some carbons to yield an active electrode preparation regardless of how the platinum was deposited. Thus, Table II shows that poor activity might be obtained even though the dis-

Table I. The effect of H_2 pretreatment and temperature on the activity of dual-layer electrodes, with 5% platinum on carbon[b]

	Weight of outer layer[a], g/cm²	Anodic limiting current density[c], ma/cm² Initial	Final	Special conditions of sample preparation[a]
18736-24K	0.120	15	35	Evacuated, then exposed to hydrogen at 300°C and evacuated at 500°C for 16 hr
U	0.128	10	12	Evacuated, then exposed to hydrogen at 300°C and evacuated at 500°C for 16 hr
V	0.140	17.5	40	Evacuated, then exposed to hydrogen at 300°C and evacuated at 400°C for 16 hr
T	0.125	12.5	50	Evacuated, then exposed to hydrogen at 300°C and evacuated at 300°C for 16 hr
Q	~0.10	93.5	133	Outer layer is Baker's 5% platinum on charcoal, evacuated, then exposed to hydrogen at 300°C for 16 hr
S	0.131	15	97.5	Evacuated at 300°C for 2 hr
M	0.133	20	60	Heated at 300°C in air for 1.5 hr
N	0.120	5	15	Heated at 500°C in air for 1.5 hr
R	0.127	55	148	Decomposition temperature for H_2PtCl_6 on carbon lowered to 50°C; no further heat treatment
B	0.119	15	95	Decomposition temperature was the normal 165°C; no further heat treatment
G	0.121	15	105	Decomposition temperature was the normal 165°C; no further heat treatment

[a] All samples were prepared as dual-layer electrodes (1), and were activated by heat treatment in air at 165°C, except as noted. The support is NC-60 and the outer layer is Darco S-51 carbon, except as noted.
[b] Listed as weight per cent of the outer layer.
[c] The electrodes were loaded as hydrogen anodes initially; then they were cycled cathodically and anodically two times. The polarizations are not corrected for the IR drop due to ohmic resistance in the cell; the limiting current represents polarization down to 0v *vs.* SCE.

Table II. The effect of choice of carbon on electrode activity

Carbon	ESR, 10^{16} unpaired electrons per gram Carbon alone	Carbon with 5% Pt	Platinum area for 5% deposit, m²/g	Hydrogen electrode activity, ma/cm² at 0 v *vs.* SCE
Barnebey-Cheney K2046	100	0	192	150
Darco S-51	20	1.4	50	140
Mineral carbon[a]	0	No resonance[b]	155	<1
Saran carbon[a]	0	—	—	<10
NC-60 (pulverized)	<1	—	—	60

[a] Prepared for research purposes by Union Carbide Consumer Products Corporation.
[b] Sample could not be run because its electrical conductivity was too high.

persion of the platinum, as measured by hydrogen chemisorption, appeared good. The data for the mineral carbon are a good example of this. Further evidence for a platinum-carbon interaction that controls catalytic activity was obtained from chemical treatment of the carbon surface and by the use of electron-spin resonance (ESR) for samples of plain and platinized carbon.

Electron-spin-resonance measurements.—Essentially, ESR is a means for estimating the number of unpaired electrons in a structure. The unpaired electrons represent single electrons that are not involved in chemical-bond formation and are considered to be a measure of the number of free-radical structures trapped in the material. At least two types of interaction can be observed by changes in ESR. One is a physical and the other a chemical interaction. If two electrons interacted magnetically without actually becoming paired, this physical interaction would result in a broadening of the ESR signal and an apparent decrease in the observed intensity. If the unpaired electrons of the free-radical structures are brought together to form a chemical bond, the resulting electron pair formation also results in a decrease in the ESR signal. Where the interaction is chemical, the unpaired electrons involved in the bond formed are totally removed from the resonance, and the signal received is not broadened in spectral width. The interesting differences that appear in ESR among many carbons have been discussed by a number of workers; for example, Kraus and Collins (2), and Collins, Bell, and Kraus (3). The formation and removal of unpaired electrons by direct oxidation of the carbon surface have been discussed by Antonowicz (4), who also indicated the participation of these unpaired electrons in the conduction band for carbon. The relationship of ESR to charge carriers in carbon was discussed by Singer and Wagoner (5).

A relationship between ESR for platinum on carbon and its catalytic activity was the subject of papers by Nicolau and co-workers (6). Nicolau believed that a laminar sandwich-type complex formed between the metal and the graphite crystallites in which a partial sharing of the electrons occurred between these two phases. This appeared to be his explanation for the relationship which he found between the ESR for the material and its catalytic activity in organic hydrogenation reactions. Unfortunately, Nicolau worked with only one particular carbon, and the generality of this relationship is not indicated by his work. In the current studies, it was decided to determine whether the ESR for platinum on carbon could be used as an indicator of electrode catalytic activity.

Because of the relatively high electrical conductivity of carbon, ESR could be obtained for this material only if it was finely divided. Following Collins (3), pulverized carbon samples were contained in melting-point tubes and sealed in ampoules for the control of the sample environment. In each case, the carbon was pulverized to obtain a mixture that was 1/3 (−100 + 325) sieve size and 2/3 (−325). This amount of grinding is considered insufficient to affect markedly the resonance obtained. The samples were usually evacuated at room temperature for several hours and then heated and evacuated at 100°C. Helium was used as a purge gas to sweep the vapors out of the sample tube at various stages during this evacuation. Table II shows some comparative data for the ESR of several carbons before and after application of platinum.

Table III shows that preliminary heat treatments of several carbons in air up to 165°C had no appreciable effect on the resonance for Darco S-51 or Barnebey-Cheney carbons. The mineral carbon appeared to give some signal as received, but after the heat treatment at 165°C, it showed no resonance whatsoever. Pretreatment of the carbon at 165°C was adopted as standard treatment prior to its use in electrode preparations for the ESR studies.

Figure 1 and Table IV show the effects of heat treatment of the carbon at temperatures up to 500°C in air and the effects of the application of platinum to these

Table III. Electron-spin resonance of carbon samples with various pretreatments

Preliminary treatment	Unpaired electrons per gram × 10^{16} Barnebey-Cheney K-2046 carbon	Darco S-51 carbon	Mineral carbon
As received	85	14-25	49-88
Add H_2O, dry 100°C, 24 hr	100	16	—

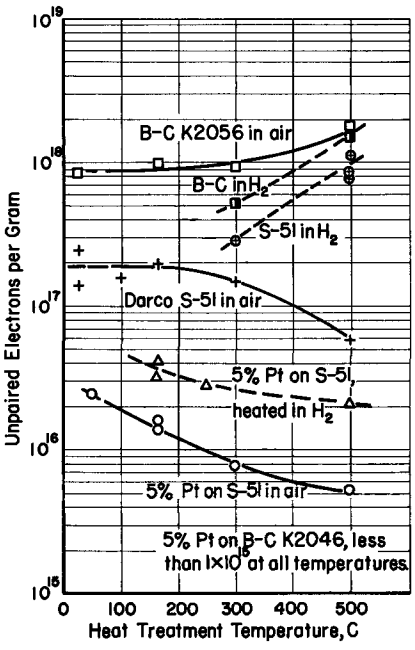

Fig. 1. Electron spin resonance for carbon and platinized carbon. B-C is Barnebey-Cheney.

carbons. The number of unpaired electrons was obtained from the ESR measurements. There also appeared to be a large decrease in the number of unpaired electrons after the application of platinum to the carbon. These decreases in ESR occurred without line broadening, which was strongly suggestive of a chemical interaction of the platinum with the substrate carbon. Barnebey-Cheney carbon K2046 showed a large decrease in resonance after application of the platinum. These formulations had good electrode activity so that the decrease in resonance in this case did not appear to indicate any appreciable deactivation. Since chemical interactions between the two phases were indicated, it may be assumed that these interactions led to the various degrees of electrode catalytic activity that were observed for these carbons. If some of these interactions were particularly detrimental to the catalytic activity while others were not, the chemical distinction between these two types of interactions would help to define the required properties of the platinum-on-carbon catalyst system. The chemical interactions discussed in the next section were investigated for this purpose.

Chemical alteration of the carbon surface.—The chemical changes induced by heating in air and in hydrogen, as shown in Table IV and Fig. 1, led to a study of the activity changes that could be produced by heating the carbon in various oxidizing and reducing environments. Darco S-51 samples shown in Fig. 1 that had been heated in hydrogen showed poor electrode activity, and a sample of the Barnebey-Cheney carbon which was ground while immersed in

Table IV. Effect of pretreatment of Darco S-51 on the activity of the platinum deposit

Carbon temperature	ESR, 10^{16} unpaired electrons per gram: Carbon alone	ESR, 10^{16} unpaired electrons per gram: Carbon with 5% Pt	Hydrogen-anode activity, ma/cm² at 0v *vs.* SCE
As received	20 ± 5	1.4	140
165°C in air	17 to 20	1.9	133
300°C in air	15	—	—
400°C in air	12	2.0	70
500°C in air	6	—	—
500°C in H_2/N_2	112	8	10
1038°C in N_2	<<1	<<1	8
1038°C in N_2, then SO_2 at 25°C	<<1	<<1	96

Table V. Chlorine analysis of carbon samples

Sample identification	Chlorine, %	Mole ratio, Cl/Pt
19115-1-1, Darco S-51	0.19	—
-3, mineral carbon	1.4	—
-4, Barnebey-Cheney K2046	0.15	—
-5, NC-60	0.10	—
-6, Saran carbon	0.09	—
18736-21, Pt/S-51/decomposed 50°C	3.2-4.1	3.5-4.5
18736-64-1, Pt/S-51/decomposed 165°C	0.5-1.8	0.6-2.0
19115-9-1, Pt/S-51/decomposed 165°/H_2 reduced	0.18	0.2
19115-9-2, Pt/S-51/decomposed 165°/hot H_2O washed	0.2	0.2
18736-64-3, Pt black	<0.05	<0.1
18353-27-1, Baker 5% Pt/charcoal	<0.05	<0.1

Table VI. Approximate composition of ash for carbon samples, arc spectrographic analysis

Sample	Ash, %	Constituent[a]: Major	Constituent[a]: Minor
Darco S-51	17.5	Si	Fe, Al, Ti
Mineral carbon	0.78	Si	Fe, Al
Barnebey-Cheney K2046	4.8	Si	Fe, Mg, Al, Na, Cu, Ca
NC-60	0.36	Si	Fe, Mg, Al, Na, Ni, Cu, Ca, Zn
Saran carbon	0.82	Fe	Si, Al, Na, Ni, Cu, Zn

[a] Trace-element analysis deleted. Minor constituents arbitrarily defined as at least 1% of ash; since only approximate analysis was obtained, the distinction between minor and trace is uncertain. Traces were found for many elements.

chloroplatinic acid was equally poor. In both cases, the suggestion seems to be that the stronger interactions which were possible with clean or fresh carbon surfaces deactivated the platinum catalyst.

It was realized that the carbon surfaces could contain considerable oxygen. Also, chlorine remained from the decomposition of the chloroplatinic acid. There were also ash constituents in these carbons that could have responded to the oxidizing and reducing environments used to treat the carbon. For this reason, the carbons of interest were analyzed for chlorine and ash. The results are shown in Tables V and VI. From these data it appears that the active samples prepared in this work had relatively high ash content and high chlorine content. The importance of these two variations was not investigated further at this time because large and reproducible activity differences resulted from variations which seemed to be dependent only on changes in the oxygen content of the surface, see for example Table VII.

To vary the surface state of the carbon, samples were treated in hydrogen, nitrogen, air, CO_2, and SO_2. The results obtained from these treatments are illustrated in Tables IV and VII. In each case, the treatment was applied to the carbon alone, and then the platinum was deposited by impregnation with chloroplatinic acid followed by heat treatment overnight at 165°C. The data of Table IV illustrate the loss in ESR with high-temperature treatment either in air or in nitrogen. In Table IV, the large reduction in ESR that accompanied application of the platinum, and the regular decrease in hydrogen-anode activity with increasing carbon treatment temperature, indicated a chemical reaction between the carbon and the platinum. Heating in nitrogen at 1038°C produced a very large reduction in activity, which suggested that the carbon surface treated in this way had a detrimental effect on activity. The SO_2 treatments seem to have had a beneficial effect on carbons that had been partially deactivated by heating.

Cleaning and reoxidation of the surface produced by these treatments led to the experiments summarized in Table VII, which clearly illustrates the large changes in activity produced by cleaning the carbon surface and then reoxidizing the surface using carbon dioxide. The data in Table VIII show that the deactivation produced by nitrogen treatment cannot be

Table VII. Effects of heating carbon at 1000°C in nitrogen and carbon dioxide

Carbon used[b]	Hydrogen-anode activity, ma/cm² at 0v vs. SCE		
		Carbon treatment[c]	
	165°C, air	1000°C, N_2[a]	1000°C, N_2, then 1000°C, CO_2
Darco S-51	140	10	180
Barnebey-Cheney K2047	118	32	110

[a] All carbons were dried at 165°C overnight before use.
[b] The S-51 is a Darco carbon; K2047 is an experimental carbon from Barnebey-Cheney.
[c] The carbon treatments at 1000°C were for 1 to 2 hours.

Table VIII. Total surface area[a] for typical materials used to form outer layer of electrode

Material	Surface area, m²/g, for indicated carbon treatment		
	165°C, air	1000°C, N_2[b]	1000°C, N_2, then 1000°C, CO_2
Darco S-51	463	649[d]	1061
Darco S-51 + 5% Pt	290	378[d]	853-925[d]
5% Pt/S-51 + gum rubber[c]	107	94-144	422

[a] To avoid change in gum-rubber distribution, samples were degassed in dry helium at 25°C.
[b] All carbons were heated at 165°C overnight before use.
[c] These samples were formed as dual-layer electrodes. The outer layer was then removed and used for these tests.
[d] Samples other than those for which values are given were degassed at 150°C for comparison. No significant differences in the area were noted.

explained by changes in surface area. Similarly, the activation produced by CO_2 is not believed to be related to the change in surface area.

Conclusions

The experimental data presented in this paper show that the activity of the catalytic-platinum anode is strongly influenced by the surface state of the platinum catalyst. Further, the effects produced by chemical alteration of the carbon surface indicate that the platinum catalyst is deactivated by a reaction between platinum and a cleaned carbon surface. Oxidation of the surface of the carbon support appears to protect the platinum from this deactivation and perhaps contributes further to the activity of the platinum by effecting changes in the heterogeneity of the surface.

The platinum-carbon interactions described in this research are thought to be altering the catalytic activity of the platinum through the electronic interactions that occur between the two components. The ESR data show some evidence for this interaction. The oxidation of the carbon surface, with the formation of carbon-oxygen structures, presumably leads to an entirely different electronic interaction between the small platinum crystallites and the carbon substrate than occurs with cleaned carbon surfaces. The evidence indicates that the interactions that occur on the oxidized surface are much more desirable for catalysis of the hydrogen anode.

The beneficial effect of the oxidation of the carbon surface seems to be in accord with the theory of catalyst poisoning discussed by Maxted (7). In the present work, the toxic carbon atom is assumed to provide a strong dative bond to the platinum atoms in the Pt-C interface, thereby poisoning the entire crystallite when it is small. Hypothetically, oxidation of the carbon surface shields the platinum from this reaction and provides a readily reducible surface interaction with the platinum crystallite.

In the present study, the catalytic electrodes were intended to use a minimum amount of platinum dispersed as small crystallites on a large amount of carbon surface. For these preparations, the platinum-carbon interactions may be expected to have the maximum influence on activity. Alternatively, in preparations where the platinum crystallites are agglomerated as a platinum black deposit on a small amount of carbon surface, the influence of the Pt-C interface may not be observable.

Manuscript received Aug. 20, 1964.

Any discussion of this paper will appear in a Discussion Section to be published in the December 1965 JOURNAL.

REFERENCES

1. L. J. Hillenbrand and J. W. Lacksonen, *This Journal*, **112**, 245 (1965).
2. G. Kraus and R. L. Collins, *Rubber World*, 219, (November, 1958).
3. R. L. Collins, M. D. Bell, and G. Kraus, *J. Appl. Phys.*, **30**, 56 (1959).
4. K. Antonowicz, *J. Chem. Phys.*, **36**, No. 8, 2046 (1962).
5. L. S. Singer and G. Wagoner, *J. Chem. Phys.*, **37**, No. 8, 1812 (1962).
6. C. S. Nicolau and H. G. Thom, *Z. anorg. allgem. chem.*, **303**, 133 (1960).
7. E. B. Maxted, *Advances in Catalysis*, Vol. III, 129-177 (1951).

Design of Primary and Secondary Cells

I. Effect of Polarization and Resistance on Cell Characteristics

Clarence M. Shepherd

U. S. Naval Research Laboratory, Washington, D. C.

ABSTRACT

The current density distribution in a battery is a function of electrode height, electrode resistance, electrolyte resistance, and polarization. Mathematical solutions have been obtained for those cases where the polarization curves are either linear, logarithmic, or cubic. A numerical method is indicated for finding a general solution. In the case of linear polarization, the results are presented in graphs which show the current density distribution and other cell characteristics over a wide range of operating conditions. The determination of these cell characteristics can be of considerable importance in cell design. For practical applications, the complex mathematical calculations involved in the cases of logarithmic and cubic polarization can be eliminated by the use of transformations which convert them to the linear case.

This is the first of a projected series of papers whose main purpose is to determine and describe a theoretical approach to the problem of designing batteries having optimum characteristics such as maximum output. Particular emphasis will be placed on the minimization of battery weight or volume. The effect of polarization and internal resistance on the current density distribution and other battery characteristics will be discussed in this paper.

In most commercial batteries the I-R drop down the grid or electrode is negligible. The term "I-R drop" refers here to the potential drop that occurs when a

current flows through a resistance and is not related to the separate terms I and R as defined later. Thin grids are often used in low weight batteries and in batteries that are to be discharged at high rates. Thus the I-R drop down the electrode may be appreciable. In such a case, consider the paths of two hypothetical units of current, one of which travels a short distance down the anode before it crosses over to the cathode, and the other which travels much farther down the anode before crossing over. In both paths the total potential drop inside the cell, due to I-R drops and polarization, must be the same. In the first path, the I-R drop down the grid is much smaller than it is in the second path, and as a result, the potential drop due to polarization and I-R drop in the electrolyte must be much higher. Consequently, the current density in the upper part of the battery must be greater than it is in the lower part. This variation in current density over the face of the electrode can be quite large and may cause serious overheating at the top of the cell. In any case, the discharge potential and the efficiency will be lower, the capacity at a given discharge rate will be lower, and the maximum discharge rate will be less. Such conditions are undesirable, particularly in a cell that is being designed for optimum characteristics such as minimization of weight. These factors place a limit on how thin a battery grid may be. Consequently, in optimum cell design, it is necessary to determine quantitatively the effects of internal resistance and polarization on the current density distribution.

Tobias and Wijsman (1) have solved the theoretical case for linear polarization. The results are mathematically complex and difficult to evaluate numerically. Moreover, they are limited to the case where the polarization is linear. It can be shown from their work that it is safe to assume in conventional types of batteries that the current flow in the electrolyte is perpendicular to the electrodes whenever the distance between the electrodes is less than approximately one-tenth of their height. This assumption greatly simplifies the mathematical analysis and makes it possible to include the cases where the polarization is logarithmic, cubic, and inverse cubic. The latter case will not be discussed here since it has no practical value.

Mathematical Discussion

The mathematical derivations that follow are obtained by using a model based on the following assumptions:

1. The electrodes are flat, parallel, rectangular, and of uniform width and the spacing between electrodes is less than one-tenth of the electrode height.
2. The path of the current is perpendicular to the electrodes.
3. The grids are uniformly thin sheets of negligible thickness.
4. The current enters and leaves the system uniformly along the tops of the electrodes.
5. The electrode assembly fits snugly in the cell case on both sides and the bottom and the electrolyte level coincides with the top of the electrodes. This assembly eliminates boundary effects and makes the problem two-dimensional.
6. The electrodes and electrolyte are homogeneous and isotropic conductors at uniform temperature.
7. The discharge current is constant.

In actual battery construction, variations from the first five assumptions are generally small and their effect will be negligible. In almost all batteries, assumption six will be true at the beginning of the discharge. In the case of a large current density variation, the electrolyte will be heated unevenly. Also, the active material at the top of the cell will be consumed more rapidly than at the bottom, thus causing an uneven distribution of unused active material which results in the current density distribution changing appreciably throughout discharge. In this case, the mathematical equations that follow will hold true only at the beginning of the discharge. In a cell having optimum characteristics, the current density distribution will be fairly even and consequently the results that follow will be approximately true throughout a major portion of the discharge.

There are other factors that may affect these results during the course of a discharge, the most important of which is change in composition of electrolyte due to its reaction with the active materials. This causes the cell potential and the electrolyte resistance to vary and often results in stratification of the electrolyte. However, it seems highly probable that most batteries designed for minimum weight or volume will use a system in which the electrolyte composition does not change appreciably during discharge.

A base cell is shown in Fig. 1. N of these base cells can be assembled together, anode to anode and cathode to cathode to give a multiplate cell having $N + 1$ electrodes and N electrolyte compartments. It is important to note that each electrode separating a compartment in this multiplate cell is twice the thickness of the electrode in the base cell and will carry twice the current.

In the discussion that follows, lower case letters usually denote variables and capital letters usually indicate factors that are constant for a particular battery:

h, the height of a particular point above the bottom of the electrode, cm. It is the major independent variable.

H, total electrode height, cm.

i, the current density and is the amount of current flowing between the electrodes per unit area of apparent electrode surface at a point that is height h above the bottom of the electrode, amp cm^{-2}.

i_H and i_o are the values of i at the top and the bottom of the electrode, respectively, amp cm^{-2}.

I, the discharge current per unit width of the base cell, amp cm^{-1}. The total discharge current equals $N\,I$ times the width of the electrode.

x, the current per unit width of base cell, flowing vertically past a point on the electrode that is a height, h, above the bottom of the electrode, amp cm^{-1}.

e, the sum of the potential drop in the anode and cathode measured from the top of the electrode to a point that is height, h, above the bottom of the electrodes, volts.

R, the sum of the resistances, measured vertically, of the anode and cathode unit electrodes in the base cell, ohms. Each unit electrode is one unit wide, one unit deep, and one-half the thickness of the actual electrode that is separating compartments in a multiplate cell. In most cases, the resistance of the active material is comparatively high and consequently, the resistance of the pasted electrode is approximately equal to the grid resistance.

L, the actual resistance of a parallelogram one square unit in cross section extending from grid to grid and

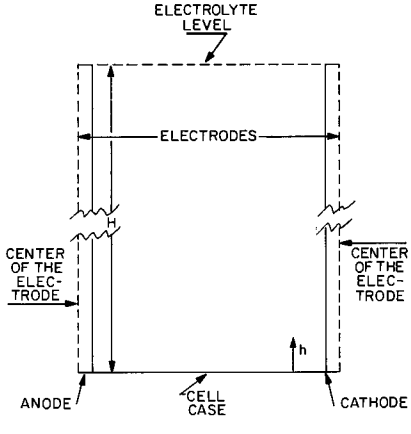

Fig. 1. Base cell

including any spacers or separators, ohm-cm^2. If no spacers or separators are present, L equals the electrolyte resistivity times the distance between the plates.

E_d, a potential drop in the cell that is equal to the difference between the open circuit potential and the discharge potential when the cell is being discharged at a current density equal to i, volts.

$F(i)$, the voltage drop due to polarization, volts. It is defined for the purposes of this paper as follows: E_d equals the sum of the I-R drop in the electrodes, the I-R drop in the electrolyte and the polarization, $F(i)$. In the case of linear polarization, $F(i)$ is defined as being equal to $Ki + K_1$.

K, a constant, the slope of the linear term in the polarization curve, ohm-cm^2.

K_1, the value of the constant term in the polarization curve, volts.

$E^\circ = E_d - K_1$, volts. Since K_1 is usually small in value, E° is generally a good approximation of E_d. If an error were made in determining the value of the open-circuit potential, the same error would be present by definition in E_d and K_1. Such an error would not affect the value of E° nor would it affect any of the derivations and results that follow in this paper. Consequently the open-circuit potential could be redefined or replaced by a new potential such that K_1 would equal zero, $F(i)$ would equal Ki, and E° would equal E_d without affecting any subsequent results.

$$S = L + K, \text{ ohm-cm}^2$$

$$V = (R/S)^{1/2}, \text{ cm}^{-1}$$

$$\Psi = VH = (R/S)^{1/2} H, \text{ dimensionless} \quad [1]$$

If a mathematical equation is to be determined for $F(i)$, it needs to apply only in the range of current densities, i, in which the battery is operating. Since our ultimate goal is an optimum battery in which the range of current densities is usually narrow, it should be fairly easy to find simple equations that will describe the polarization curve adequately.

From the definitions of e, h, R, x, i, and E_d, it can be seen that

$$\frac{de}{dh} = -Rx \quad [2]$$

$$\frac{dx}{dh} = i \quad [3]$$

$$\frac{di}{dh} = \frac{dx}{dh} \cdot \frac{di}{dx} = i\frac{di}{dx} \quad [4]$$

$$E_d = e + Li + F(i) \quad [5]$$

Differentiating Eq. [5] and substituting Eq. [2] and [4] give

$$Rx = Li\frac{di}{dx} + iF'(i)\frac{di}{dx} \quad [6]$$

On integrating

$$Rx^2 = B + Li^2 + 2\int iF'(i)\,di \quad [7]$$

If $iF'(i)$ can be integrated, an equation involving i, x, and the integration constant, B, is obtained, which can be solved for i as a function of x.

$$i = \frac{dx}{dh} = f(x,B) \quad [8]$$

Solving for dh and integrating gives

$$h = f_1(x,B) + C \quad [9]$$

B and C are determined from the boundary conditions, and Eq. [9] is solved for x to give

$$x = f_2(h) \quad [10]$$

which is differentiated to obtain the current density distribution

$$i = f_2'(h) \quad [11]$$

There are a very limited number of mathematical equations for $F(i)$ which will allow a mathematical completion of the analyses in Eq. [5] to [11]. If the steps cannot be completed or if $F(i)$ is available only as a graph, the solution can be achieved by graphical, numerical, or computer methods. In most cases, the simplest practical solution for the general case described by Eq. [5] utilizes a transformation which enables the results to be described as if the polarization were linear.

Linear polarization.—In the case of linear polarization, $F(i)$ is represented by the equation

$$F(i) = Ki + K_1 \quad [12]$$

Substituting Eq. [12] in Eq. [5] gives

$$E_d = e + Si + K_1 \quad [13]$$

Differentiating, substituting Eq. [2] and [4], and integrating gives

$$\frac{S}{2} i^2 = \frac{R}{2} x^2 + C_1 \quad [14]$$

Solving for the current density

$$i = \frac{dx}{dh} = \left(V^2x^2 + 2\frac{C_1}{S}\right)^{1/2} \quad [15]$$

which gives on integration

$$h = \frac{1}{V}\sinh^{-1}\frac{R^{1/2}x}{(2C_1)^{1/2}} + C_2 \quad [16]$$

The integration constants, C_1 and C_2, are determined from the boundary conditions ($h = 0$, $x = 0$), ($h = H$, $x = I$), and substituted in Eq. [16] to give

$$Vh = \sinh^{-1}[(x/I)\sinh(VH)] \quad [17]$$

The following four equations are easily derived from Eq. [17], [2], [3], and [13].

$$\frac{x}{I} = \frac{\sinh[(VH)(h/H)]}{\sinh VH} = \frac{\sinh[\Psi(h/H)]}{\sinh\Psi} \quad [18]$$

$$\frac{iH}{I} = (VH)\frac{\cosh[(VH)(h/H)]}{\sinh VH} = \Psi\frac{\cosh[\Psi(h/H)]}{\sinh\Psi} \quad [19]$$

$$\frac{e}{HIR} = \frac{\coth(VH)}{(VH)} - \frac{\cosh[(VH)(h/H)]}{(VH)\sinh(VH)} = \frac{\coth\Psi}{\Psi} - \frac{\cosh[\Psi(h/H)]}{\Psi\sinh\Psi} \quad [20]$$

$$\frac{E^\circ}{HIR} = \frac{\coth(VH)}{(VH)} = \frac{\coth\Psi}{\Psi} \quad [21]$$

The quantities (x/I), (Ψ), (h/H), (iH/I), (e/HIR), and (E°/HIR) are dimensionless. If K_1 is small compared to E_d, E° will be the approximate potential drop in the cell. Equations [18] to [21] are plotted in Fig. 2 through 5. These equations have also been confirmed experimentally.

The ratio of the current density, i, to the average current density has been plotted as a function of the fractional electrode height, h/H, in Fig. 3. The ideal distribution, obtained at $\Psi = 0$, is a horizontal line. At Ψ equals 5, the ratio of the current density at the top of the battery, i_H, to the current density at the bottom of the battery, i_o, is theoretically more than seventy. It is unlikely that the polarization curve would be linear over this wide a range of current densities. In addition, there are other factors present which will cause the ratio of i_H to i_o to vary from the theoretical value when it is high. At lower values of Ψ, where the batteries are more efficient, the theoretical value of

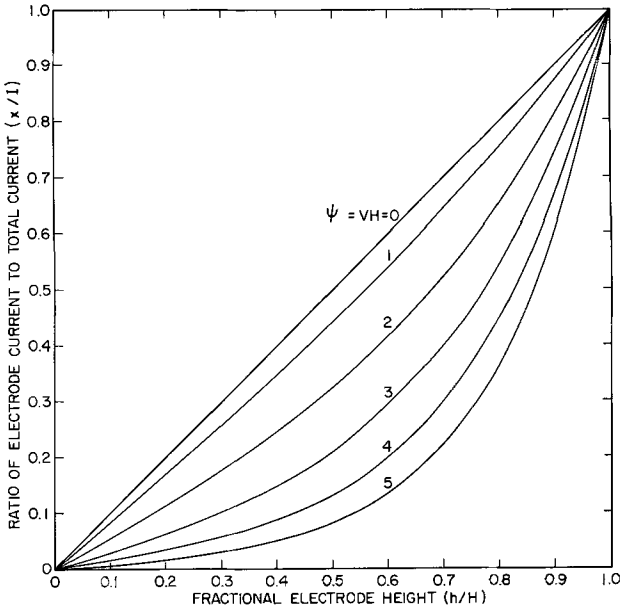

Fig. 2. Variation of current flowing in electrode with electrode height and Ψ for linear polarization.

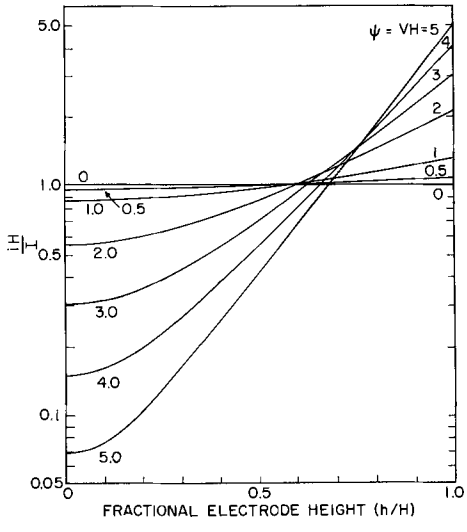

Fig. 3. Effect of electrode height and Ψ on current density distribution for linear polarization.

i_H/i_o will be more accurate. At Ψ equal to one, i_H/i_o equals 1.54. This is fairly close to the level at which an optimum cell will operate. Fortunately, most commercial cells have low values of Ψ.

There are a large number of other equations that can be derived for the linear polarization case. For example

$$i/i_o = \cosh Vh, = \cosh [\Psi(h/H)] \qquad [22]$$

$$i_H H/I = \Psi \coth \Psi \qquad [23]$$

and

$$\frac{eH}{SI} = \frac{H}{I}(i_H - i) = \frac{E^\circ H}{SI} - \frac{iH}{I} \qquad [24]$$

Cubic polarization.—With cubic polarization, $F(i) = K_2 i^3 + Ki + K_1$, and Eq. [5] becomes

$$E_d = e + Si + K_2 i^3 + K_1 \qquad [25]$$

where K_2 is positive in value.

Differentiate Eq. [25], substitute Eq. [2] and [4], and integrate.

$$\frac{R}{2}x^2 = \frac{S}{2}i^2 + \frac{3}{4}K_2 i^4 - C_1 \qquad [26]$$

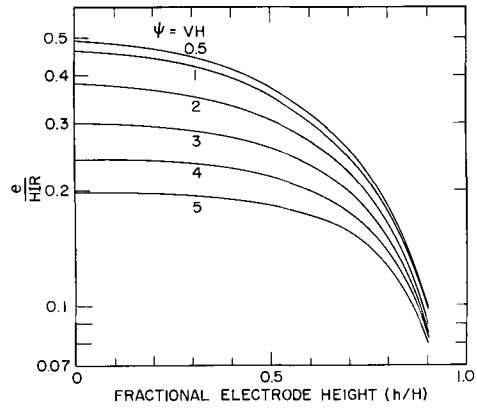

Fig. 4. Effect of electrode height and Ψ on potential drop in electrode for linear polarization.

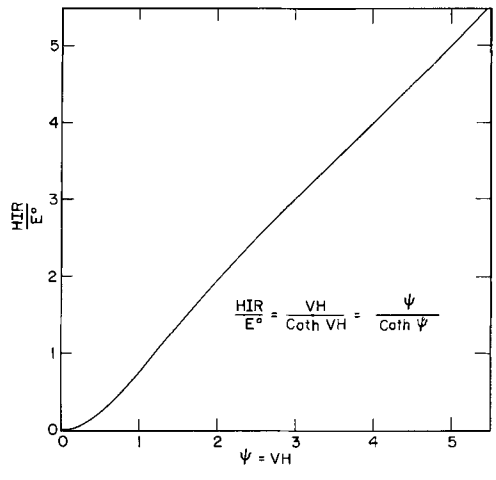

Fig. 5. Effect of Ψ on the approximate potential drop in cell for linear polarization.

$$i = \frac{dx}{dh} = \left[(B + Dx^2)^{1/2} - \frac{1}{2}F \right]^{1/2} \qquad [27]$$

where $F = \frac{2S}{3K_2}$, $B = \frac{S^2 + 12K_2C_1}{9K_2^2}$, and $D = \frac{2R}{3K_2}$.

Equation [27] is not readily integrable. It can be expanded in a Maclaurins series to give

$$h = i_o^{-1}x - \frac{1}{12}i_o^{-3}DB^{-1/2}x^3 + \frac{3}{160}i_o^{-5}(DB^{-1/2})^2x^5 - \frac{5}{896}i_o^{-7}(DB^{-1/2})^3x^7 + \ldots.$$

$$+ \frac{1}{80}i_o^{-3}B^{-1/2}(DB^{-1/2})^2x^5 - \frac{3}{448}i_o^{-5}B^{-1/2}(DB^{-1/2})^3x^7$$

$$- \frac{13}{3360}i_o^{-3}B^{-1}(DB^{-1/2})^3x^7 + \ldots \qquad [28]$$

where $i_o = \left(B^{1/2} - \frac{1}{2}F \right)^{1/2}$.

By the use of dimensional analysis, it can be shown that the coefficient of x^n in any term in Eq. [28] is equal to a constant times the quantity,

$$V_1^{n-1} i_o^{-n} (i_o^2 B^{-1/2})^\Phi \qquad [29]$$

where Φ is some positive integer, including zero, and

$$V_1^2 = \frac{1}{2} DB^{-1/2} = R(S^2 + 12K_2C_1)^{-1/2} \quad [30]$$

When Eq. [29] and [30] are substituted in Eq. [28], it becomes

$$V_1 h = \left[\Psi_1 \frac{x}{Hi_o} - \frac{1}{6}\Psi_1^3 \left(\frac{x}{Hi_o}\right)^3 + \frac{3}{40}\Psi_1^5 \left(\frac{x}{Hi_o}\right)^5 - \frac{5}{112}\Psi_1^7 \left(\frac{x}{Hi_o}\right)^7 + \dots \right] + g \quad [31]$$

where

$$g = \frac{1}{20} i_o^2 B^{-1/2} \Psi_1^5 \left(\frac{x}{Hi_o}\right)^5 - \frac{3}{56}(i_o^2 B^{-1/2})\Psi_1^7 \left(\frac{x}{Hi_o}\right)^7 - \frac{13}{420}(i_o^2 B^{-1/2})^2 \Psi_1^7 \left(\frac{x}{Hi_o}\right)^7 + \dots \quad [32]$$

and $\Psi_1 = V_1 H$.

By definition

$$i_o^2 B^{-1/2} = \left(B^{1/2} - \frac{1}{2}F\right) B^{-1/2} = 1 - \frac{S}{(S^2 + 12K_2C_1)^{1/2}} \quad [33]$$

Since i must have a positive value at the boundary condition, $(h = 0,\ x = 0)$, it can be seen from Eq. [26] that the integration constant C_1 must be positive in value. Consequently, Eq. [33] shows that $i_o^2 B^{-1/2}$ varies in value between one and zero. Therefore, g will become small in value whenever $\Psi_1(x/Hi_o)$ is less than one. Under these conditions, Eq. [31] can be seen by inspection to be approximately

$$V_1 h = \sinh^{-1}[\Psi_1(x/Hi_o)] \quad [34]$$

When $h = H$, $x = I$ and Eq. [34] becomes

$$V_1 H = \Psi_1 = \sinh^{-1}[\Psi_1(I/Hi_o)] \quad [35]$$

When Ψ_1 is less than 0.88, $\Psi_1(I/Hi_o)$ is less than one, g is small in value, and Eq. [34] and [35] are approximate solutions. If Eq. [34] is divided by Eq. [35], the following equation is obtained.

$$\frac{x}{I} = \frac{\sinh[\Psi_1(h/H)]}{\sinh \Psi_1} \quad [36]$$

Equation [36] can also be obtained by substituting Ψ_1 for Ψ in Eq. [18]. An accurate description of the cell characteristics can be obtained by substituting Ψ_1 for Ψ in Eq. [18], [19], and [20]. Cell characteristics can be predicted over a much wider range of conditions by the use of an empirical method which can also be applied to other types of polarization. If there were no polarization during a constant current discharge, Eq. [5] would be

$$E_d = e + Li \quad [37]$$

L would equal S, and the cell characteristics would be described perfectly by the equations for linear polarization. The potential drop due to polarization, $F(i)$, would be in all cases a monotonic increasing function of i containing no sharp breaks, as long as the value of $VH = \Psi$ was under 2 or 3 and the current density variation over the face of the electrode was not large, a condition that would be true in a well-designed battery. Under these conditions, the introduction of the polarization term, $F(i)$, would convert Eq. [37] to Eq. [5] and would cause the existing current density distribution curve to be flattened while retaining much the same shape. If $F(i)$ is linear, the new current density distribution curve is described by Eq. [19]. Since the current density variation is small for low values of VH and since the summation of the current density over the face of the electrode equals I, the new current density distribution curve that results by the introduction of a nonlinear polarization term, $F(i)$, into Eq. [37], should be described approximately by Eq. [19] if Ψ in this equation is replaced by $\Psi_k = V_k H$ where Ψ_k is a suitable function of Ψ and $F(i)$. Ψ_k can be calculated from the numerical value of a single point such as i_H on the true current density distribution curve through the use of Eq. [23]. The approximation curve and the true current density curve both pass through the same point i_H, both have the same integral and have much the same shape. Consequently any difference between the two curves would be expected to be small for low values of Ψ.

Assume a theoretical case where there is no polarization and Eq. 37 applies. Let the value of L be such that $\Psi = 3$. Then the current density distribution over the face of the electrode is completely described by the curve for $\Psi = 3$ in Fig. 3. The introduction of any polarization would flatten this curve toward the limit where $\Psi = 0$ and the current density distribution is uniform. If a linear polarization term as described in Eq. [12] is introduced such that $K = 1.25L$ then Ψ would be reduced in value from 3 to 2 and the current density distribution over the face of the electrode would be completely described by the curve for $\Psi = 2$ in Fig. 3. If a nonlinear polarization term of a suitable size had been introduced instead of the linear term, a flattening of the $\Psi = 3$ curve could be obtained which would be fairly well approximated by the $\Psi = 2$ curve and it could be assigned a value of $\Psi_k = 2$. Under normal conditions such approximation should be accurate enough for use in Eq. [18], [19], and [20] but definitely not in [21].

$\Psi_k = \Psi_2$ has been determined for the case of cubic polarization and its applicable range is shown in Fig. 6 where it is plotted as a function of Ψ and the dimensionless factor F_1.

$$F_1 = \left(\frac{2S}{3K_2}\right)\left(\frac{H}{I}\right)^2 = \frac{FH^2}{I_2}$$

Accurate values of the current flowing in the electrodes, the current density distribution and the potential drop in the electrodes can be obtained by substituting Ψ_2 for Ψ in Eq. [18], [19], and [20], respectively, or in Fig. 2, 3, and 4, respectively. Satisfactory values of $E°/HIR$ cannot be obtained by substituting Ψ_2 in Eq. [21]. Accurate values of $E°/HIR$ can be determined from Fig. 7.

Logarithmic polarization.—In the case of logarithmic polarization, $F(i) = K_3 \ln i + Ki + K_1$ and Eq. [5] becomes

$$E = e + Si + K_3 \ln i + K_1 \quad [38]$$

Differentiate Eq. [38], substitute Eq. [2] and [4] and integrate

$$\frac{R}{2}x^2 + C_1 = \frac{S}{2}i^2 + K_3 i$$

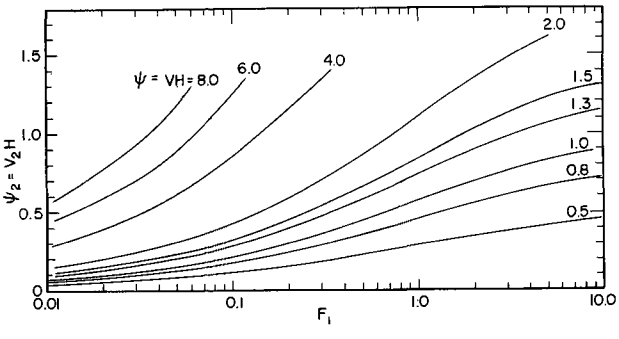

Figure 6. Plot showing Ψ_2 as a function of Ψ and F_1

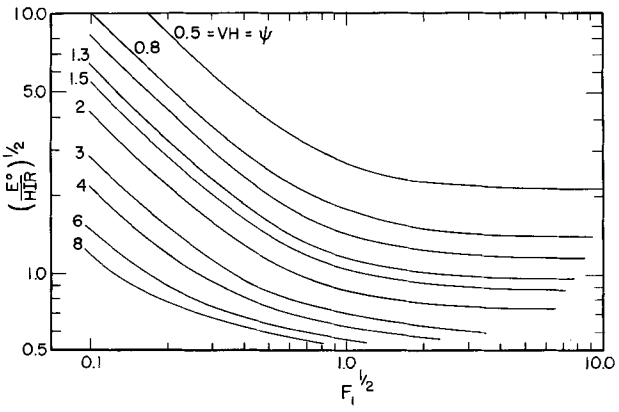

Fig. 7. Approximate potential drop in cell for cubic polarization

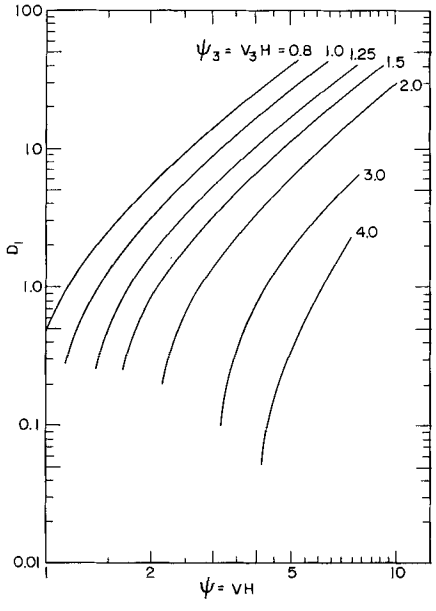

Fig. 8. Plot showing Ψ_3 as a function of Ψ and D_1

Solving for i and x gives

$$i = (V^2x^2 + A)^{1/2} - D \quad [39]$$

and

$$x = \frac{1}{V}(i^2 + 2iD + D^2 - A)^{1/2} \quad [40]$$

where $A = \frac{2C_1}{S} + \frac{K_3^2}{S^2}$ and $D = \frac{K_3}{S}$

$$dx = i\,dh = \frac{(i + D)\,di}{V(i^2 + 2iD + D^2 - A)^{1/2}} \quad [41]$$

which gives on integration

$$h = \frac{1}{V}\ln\left[2(i^2 + 2iD + D^2 - A)^{1/2} + 2i + 2D\right] + \frac{D}{V}\frac{1}{(A - D^2)^{1/2}}\sin^{-1}\left[\frac{2Di + 2D^2 - 2A}{2iA^{1/2}}\right] + C_7 \quad [42]$$

Substituting Eq. [39] and [40] in Eq. [42] gives

$$h = \frac{1}{V}\ln\left[2Vx + 2(V^2x^2 + A)^{1/2}\right] + \frac{1}{V}\frac{D}{(A - D^2)^{1/2}}\sin^{-1}\left[\frac{D(V^2x^2 + A)^{1/2} - A}{A^{1/2}\{(V^2x^2 + A)^{1/2} - D\}}\right] + C_7 \quad [43]$$

When $h = 0$, $x = 0$, and

$$C_7 = -\frac{1}{V}\ln 2A^{1/2} - \frac{1}{V}\frac{D}{(A - D^2)^{1/2}}\sin^{-1}(-1) \quad [44]$$

Equation [44] is substituted in Eq. [42] and [43] to give

$$Vh = \Psi\left(\frac{h}{H}\right) = \cosh^{-1}\left[\frac{(iH/I) + D_1}{A_1^{1/2}}\right] + \frac{D_1}{(A_1 - D_1^2)^{1/2}}\sin^{-1}\left[1 - \frac{\{D_1(iH/I) + D_1^2 - A_1\}^2}{A_1(iH/I)^2}\right]^{1/2} \quad [45]$$

and

$$\Psi\left(\frac{h}{H}\right) = \sinh^{-1}\left[\frac{\Psi(x/I)}{A_1^{1/2}}\right] + \frac{D_1}{(A_1 - D_1^2)^{1/2}}\sin^{-1}\left[\frac{\Psi(x/I)\,(A_1 - D_1^2)^{1/2}}{A_1^{1/2}\{\Psi^2(x/I)^2 + A_1\}^{1/2} - A_1^{1/2}D_1}\right] \quad [46]$$

where $A_1 = AH^2I^{-2}$ and $D_1 = DHI^{-1}$. A_1, D_1, Ψ, (x/I), (h/H), and (iH/I) are dimensionless. When D_1 is negative in value and D_1^2 is larger than A_1, Eq. [45] and [46] become

$$\Psi\left(\frac{h}{H}\right) = \cosh^{-1}\left[\frac{(iH/I) + D_1}{A_1^{1/2}}\right] + \frac{D_1}{(D_1^2 - A_1)^{1/2}}\sinh^{-1}\left[\frac{\{D_1(iH/I) + D_1^2 - A_1\}^2}{A_1(iH/I)^2} - 1\right]^{1/2} \quad [47]$$

and

$$\Psi\left(\frac{h}{H}\right) = \sinh^{-1}\left[\frac{\Psi(x/I)}{A_1^{1/2}}\right] + \frac{D_1}{(D_1^2 - A_1)^{1/2}}\sinh^{-1}\left[\frac{\Psi(x/I)\,(D_1^2 - A_1)^{1/2}}{A_1^{1/2}\{\Psi^2(x/I)^2 + A_1\}^{1/2} - A_1^{1/2}D_1}\right] \quad [48]$$

The function, $\sin^{-1}$, is multivalued. The $\sin^{-1}$ in Eq. [46] is a monotonic function starting at zero for $h/H = 0$ and continuously increasing in value up to h/H = one.

When h/H equals 1, $x/I = 1$, and Eq. [46] and [48] each becomes an equation which gives A_1 as a function of the two known variables D_1 and Ψ and can be solved for A_1 numerically. When these numerical values of A_1 are substituted in Eq. [45], [46], [47], and [48], numerical values are obtained of x/I and iH/I as functions of h/H, D_1, and Ψ. These calculations are quite lengthy. It was found that the numerical work could be greatly reduced by transforming to the linear case through the use of Ψ_k as previously described. The empirical term $\Psi_k = \Psi_3 = V_3H$ has been plotted in Fig. 8 as a function of D_1 and Ψ.

The solutions for the current and potential distributions for logarithmic polarization can be calculated with a high degree of accuracy from the linear polarization equations by substituting Ψ_3 wherever Ψ occurs, in Eq. [18], [19], and [20], or in Fig. 2, 3, and 4. Ψ_3 may not be substituted in Eq. [21]. Ψ_3 can be calculated over the range covered in Fig. 8 from the equation

$$\log(\Psi/\Psi_3) = 0.1520 + 0.2452\log D_1 + 0.12226(\log D_1)^2 - 0.01676(\log D_1)^3 \quad [49]$$

Conclusion

It seems highly likely that the current density distribution and other cell characteristics discussed here can be described fairly accurately for low values of Ψ in any ordinary battery where the polarization is nonlinear, by substituting properly calculated values of Ψ_k for Ψ in Eq. [18], [19], and [20], or in Fig. 2, 3, and 4, thus eliminating most of the mathematics and greatly simplifying the calculation of the cell characteristics. However, values of E° cannot be determined in this manner by substituting Ψ_k for Ψ in any of the linear polarization equations involving E° such as Eq. [21]. In such cases, E_d, the potential drop in the cell, can be calculated by the use of Eq. [5].

Manuscript received June 10, 1964; revised manuscript received Nov. 20, 1964.

Any discussion of this paper will appear in a Discussion Section to be published in the December 1965 JOURNAL.

REFERENCE

1. C. W. Tobias and R. Wijsman, *This Journal*, **100**, 459 (1953).

A Bacterial Methane Fuel Cell

Willem van Hees

Baltimore Gas and Electric Company, Baltimore, Maryland

ABSTRACT

Fuel cells with a *Pseudomonas methanica* suspension at the anode and sterile medium at the cathode developed 0.5-0.6v on open circuit, methane and air being used. Maximum power density was 2.8 $\mu w/cm^2$ (2.6 mw/ft^2) at 0.35v. Hydroxyl ions are the source of oxygen at the anode. The immediate fuel is hydrogen, probably supplied by a flavoprotein. The free energy efficiency of the fuel cell is 14.2% at very low drain and 8.2% at the maximum power point. Its improvement depends on finding energetically more advantageous ways of interfering electrochemically in the natural respiratory sequence. Current density can be improved, possibly by one order of magnitude.

The problem of cheaply and simply catalyzing the electrochemical oxidation of methane under ambient conditions has been approached but not solved (1). Certain micro-organisms are capable of producing and maintaining a system of organic catalysis and energy transfer by which methane can be oxidized at a rate of about 4×10^{-12} ml/hr/organism at 30°C. Part of the ingested carbon is yielded as carbon dioxide; the remainder is used for bacterial substance. It was not known at which point in the metabolic sequence electrochemistry could take over from nature or whether a soluble intermediate useful in a fuel cell is excreted. Similarly, although on general biochemical grounds the free energy conversion efficiency was expected to be low, no estimations involving electrochemistry had been attempted (2). If 100 ml of a vigorous culture with an organism count of 0.5×10^9/ml use methane at the quoted rate, and if one half of the chemical energy of the methane were convertible in a biofuel cell, a current of 1.0 ma could be expected. These, and other considerations motivated an investigation of some of the properties of a methane bio-anode using a strain of *Pseudomonas methanica* (Söhngen).[1] This organism obligately depends on methane (or methanol) for growth (3).

Apparatus and Experimental Procedures

Electrode potentials were determined at 30°C with a saturated calomel electrode as reference. They are given below in terms of the potential of the normal hydrogen electrode.[2] A Hildebrand type gas electrode was used in 50 ml fluid, while carbon dioxide free gas was bubbled through at a rate of 5 l/hr such that stirring was vigorous. When anode potentials were measured, special care was taken to prevent diffusion of air to this electrode. Bridges were made with the fluid used at the electrode with 2% agar and saturated with potassium chloride.

For fuel cell studies a bio-anode was coupled with an air (oxygen) cathode in a three-compartment device made of a transparent polymer material.

It is similar to a cell described by Davis and Yarbrough (4). Figure 1 shows a schematic longitudinal cross section of three compartments formed by three cylindrical pieces and two membranes. The cylinder wall thickness is 9 mm. The ends of the middle cylinder were machined to mate with the open ends of the two other cylinders. When aligned, and after placing the membranes, the three parts could be tightly pressed together with auxiliary equipment (not shown). Thus, three compartments would be formed. The membranes, made of a regenerated cellulose[3] were then clamped between the cylinder edges. The cellulosic material was permeable to inorganic ions and to dyes but not to protein molecules or bacteria.

The end compartments had electrodes placed close to the membranes and made of helically wound platinized platinum wire with a nominal surface of 12.6 cm^2 each. This material had been selected for the anode because it was expected that hydrogen would be the anode reactant. Furthermore, it was used for the cathode because it had a more negative potential than smooth platinum and several forms of silver,[4] gold or nickel in the medium employed (see below). The bacterial medium was used as electrolyte.

The electrode compartments each had a wide opening facing upward, into which a short access tube was fitted. This permitted the existence of a meniscus of 45 mm diameter, and it prevented the loss of bacteria through froth flotation. The gases were introduced at points directly under the electrodes through polyethylene tubes. Gas inlet and outlet tubes passed through rubber stoppers closing off the short wide access tubes.

The compartment that was supplied with methane (left-hand side, Fig. 1) contained the bacterial suspension and the anode. The other two compartments were filled with sterile medium. Oxygen was bubbled through the cathode half-cell in the form of air. When the fuel cell was in operation, electrons could pass through the external circuit from anode to cathode.

The purpose of the two-membrane arrangement, in preference to a one-membrane two-compartment cell, was to restrict severely the diffusion of dissolved oxygen from cathode to anode. The central compartment had inlet and outlet tubes for purging the fluid in it with oxygen-free nitrogen.

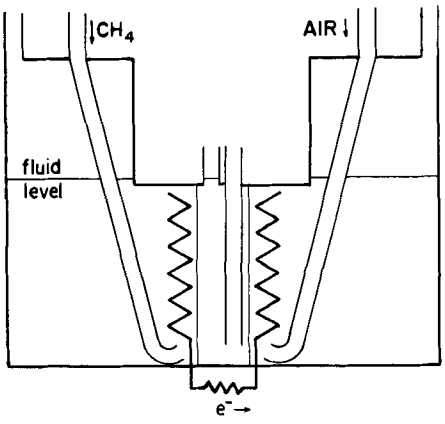

Fig. 1. Schematic diagram of the fuel cell

[1] Received from J. W. Foster, University of Texas, Austin, Texas.

[2] The American convention regarding the sign of electrode potentials is followed. The oxygen electrode potential is negative.

[3] Supplied by A. H. Thomas Co. The average pore diameter is 4.8 $m\mu$, the wall thickness is 0.04 mm. The dialysis bag later referred to is of the same material, but with a wall thickness of 0.02 mm.

[4] Contrary to expectation, *P. meth.* was found to grow well in the presence of pure metallic silver.

The membranes had an area of 25.5 cm^2 each; the electrode compartments had volumes of 153 ml. the middle compartment volume was 41 ml. The inner diameter of the compartments was 57 mm, the over-all inside length after assembly about 136 mm, the distance between the membranes 16 mm.

Carefully purified methane or nitrogen was used in the anode half-cell. These gases were prepared from technical grades by passing them through a purification train to remove thoroughly any electrochemically active impurities, such as hydrogen, oxygen, nitrogen oxides, or unsaturated hydrocarbons, if present. The methane initially was of 95-96% purity, the remainder consisting of saturated hydrocarbons, mainly ethane. These hydrocarbons constitute an insignificant admixture. This is because *P. meth.* is an obligate methane oxidizer, as stated. Furthermore, the nonbacteriological electrochemical reactivities of methane and its C_2 to C_4 homologs are fully expected to be extremely small and virtually the same under the given conditions.[5]

When carbon dioxide was used, a concentration of 8.0% (beverage grade, purified as described above) was maintained in both anode and cathode gases. All gases or gas mixtures were saturated with water vapor at 30°C prior to their entry into the fuel cell, which was operated at that temperature in all experiments. Gas flow to each half-cell was at the rate of 5.0 l/hr.

Emf measurements were made with a sensitive potentiometer preset before circuit closure to a value taken from the chart of a recording potentiometer with a very high off balance input impedance. Thus emf "seeking" and concomitant current drains were avoided. Fuel cell load current was calculated from the voltage drop across known resistances, measured with a recording millivolt meter (0-10 mv scale).

Equilibrium was assumed to exist if a recorded value was maintained without significant fluctuation for at least 30 min. Polarization curves, involving six to eight data points taken over as many or more hours, were obtained after open-circuit equilibrium had been reached overnight.

Pseudomonas methanica was propagated in a completely inorganic medium with methane as the sole source of carbon. The gas over the fluid had the following initial composition by volume: methane 50%, carbon dioxide[6] 10%, oxygen 40%. These culture conditions are highly selective, minimizing the danger of contamination. Frequent tests for invading species always gave negative results. In bulk, the mature culture has a pink color. Unless stated otherwise, an organism count of 0.5 x 10^9/ml obtained at the start of each experiment.

The composition of the medium was: $MgSO_47H_2O$ 0.40g; $CaCl_2$ 0.02g; K_2HPO_4 0.67g; KNO_3 1.00g; NaCl 0.50g; H_2O 1000g.

Results and Discussion

When an electrode is immersed in a suspension of *P. meth.* newly taken from a culture flask, an emf of about —0.6v, mainly due to dissolved oxygen and carbon dioxide, may be observed. The obligately aerobic *P. meth.* will gradually remove the oxygen, a process that may be hastened by scrubbing the fluid with methane or nitrogen. Without scrubbing carbon dioxide will not be fully removed. Equilibrium was found at various emf values between —0.10v and 0v and occasionally above 0v, with a culture that initially had a *p*H of 6.5. A value of about —0.05v represents a majority of cases. In these, the final *p*H was below 8. In the cases that were excluded, bacterial decay had caused a *p*H value above 8 and sometimes above 9. Maintaining bacterial vigor is not compatible with establishing a bacterial electrode potential equilibrium, which requires zero current. When neither gaseous nor dissolved oxygen can reach the bacteria, they depend on ions capable of releasing oxygen upon their discharge at the electrode. At zero current there is no net discharge. Eventually the bacteria will perish. Reaching a potential plateau generally took over one day.

The carbon dioxide free air (oxygen) electrode potential in the medium at *p*H 7.0 usually was quite close to —0.58v. An open-circuit fuel cell emf of approximately 0.53v was thus to be expected. An actual value of about 0.50v was found with the three compartment cell at *p*H 6.0-6.5 (initial). This illustrates that diffusion of dissolved oxygen from cathode half-cell to anode half-cell was indeed very slight.[7]

In order to give the bacteria as natural a set of conditions as possible under the circumstances, carbon dioxide was always used in both halves of the fuel cell. Oxygen, except for apparently negligible diffusion, could only reach the bacteria after discharge of oxygen carrying ions at the anode. Thus the withdrawal of electric power is the only (relatively) substantial means of providing the bacteria with oxygen. This must be true for any obligate aerobe functioning in an anode half-cell. (Facultative anaerobes seem more suited for such a role. When no current is being taken, they can continue producing an electrochemically usable material.)

Methane is not an electrochemically active species at the anode. This may be shown by replacing it by nitrogen, which causes little change in emf as long as the bacteria remain vigorous. In the prolonged absence of methane the organism count dwindles. The cell emf also decreases.

The maximum current in the cell described was of the order of 1μa/cm^2 of electrode area.[8] However, the use of a hydrogen transfer (redox) intermediate enhanced the current density. 1-naphthol 2-sulfonate indo 2, 6-dichlorophenol was found to be suitable under the anode half-cell conditions. At *p*H 7 and 30°C this indicator has a redox potential of —0.119v (5). Its blue (oxidized) form became decolorized when the bacteria had raised the (negative) emf sufficiently through oxygen scavenging and subsequent addition of hydrogen to the dye molecules, and the light pink bacterial color than would prevail. The dye concentration was 0.0028M. The polarization curve obtained with this dye present is shown in Fig. 2 (curve D). The open-circuit fuel cell emf was the same whether the dye was present or not. This suggests that the dye functions as a transfer agent rather than as an electrochemical species.

The dye is decolorized by hydrogen addition, not by oxygen removal. This occurs in the anode half-cell, as well as in an oxygen starved culture, indicating that a naturally occurring dehydrogenation of some substrate molecule also occurs in the fuel cell.

Organisms from a culture with a count of 0.9 x 10^9/ml were centrifuged and washed, then resuspended in a small volume of medium and sonically destroyed at a temperature between 0° and 5°C. The insoluble debris was removed by centrifuging and the pink supernatant solution diluted with medium to the original culture volume. The fluid thus obtained was used in an anode half-cell potential determination with methane as the scrubbing gas. A potential of —0.120v

[5] It would be very difficult to obtain relative reactivity data at ordinary temperatures using a dilute neutral electrolyte. For comparative data obtained under conditions much more conducive to electrochemical oxidation of saturated hydrocarbons, see "Fuel Cells," W. Mitchell, Editor, pp. 285-6, 373-4, New York (1963).

[6] Growth in a newly inoculated medium is extremely slow if this gas is absent. Although methane is the original carbon source, carbon dioxide apparently is both made and used by this species, its presence ensuring rapid growth. This has been observed by others. See C. E. Zobell, *Bacteriol. Revs.*, **10**, 1 (1959), and *Advances in Enzymol.*, **10**, 443 (1950).

[7] Without bacteria, but under otherwise similar conditions, an open-circuit emf of about 0.3v was extremely slowly approached.

[8] Replacement of methane by hydrogen gas under otherwise unchanged conditions, causes a current increase of more than two orders of magnitude, showing that the bacterial anode process severely limits the over-all process rate. The cell geometry, furthermore, was not optimal for power production.

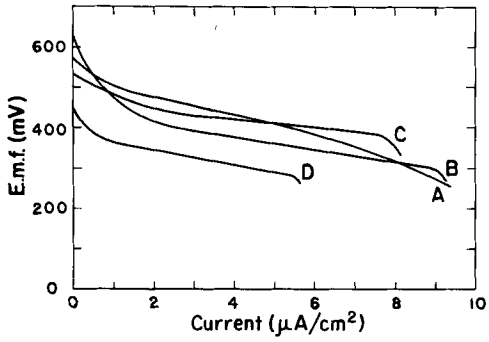

Fig. 2. Polarization curves obtained under different conditions

established itself slowly. This is somewhat below but fairly close to the values usually obtained with live material of "equivalent strength." This shows that the contents of the bacteria play a role in the events taking place in the fuel cell, and that the open-circuit fuel cell emf can be established substantially without involving substances excreted by the bacteria. In order to ascertain whether such substances, if present, have an electrochemical function, physical contact between the bacteria and the anode was prevented in another experiment. This was effected by enclosing this electrode in a slender dialysis bag[3] filled with medium. Under these circumstances, open-circuit emf was established extremely slowly even though the indophenol dye was present; the current at any emf was insignificant. This shows that physical contact between electrode and the bacteria is necessary for charge transfer. The hydrogen used for the anodic formation of water is thus not available from a water-soluble substance excreted by the bacteria, nor from the reduced form of the dye. The latter conclusion further implies that this dye is not a true electrode reactant in this cell. Although *P. meth.* can grow in very dilute methyl alcohol, which probably is an intermediary in the methane oxidation sequence, it is not the immediate fuel. Prior to its removal hydrogen is attached to a substance inside (or on) the bacteria.

The dye, in either form, is easily taken up by or removed from the bacteria, as was shown by dialysis and other experiments. Bacterial contact with the anode is necessary nonetheless. This is due to the fixed ratio maintained between the concentrations of oxidized and reduced dye molecules at any given anode potential and *p*H of the electrolyte. Reduction of dye molecules in (or on) a bacterium required simultaneous oxidation of as many leuco molecules, with the aid of ubiquitous hydroxyl ions and removal of an even number of electrons from the bacterium. The bacteria briefly function as macro-ions on impact with the anode.

By adjusting the fluid *p*H to 7.5 with potassium carbonate prior to start-up of a newly assembled fuel cell, higher open-circuit emf and higher current densities may be obtained. The former varies according to

$$E = 0.753 - 0.03 \log ([HO_2^-]/[OH^-])$$

This relation (6) represents the cell's emf as a function of cathodic peroxide concentration. Higher current densities stem from a lower cathode emf, from the higher redox potential of the dye at higher *p*H (at *p*H 6.5, redox potential $E_o' = -158$ mv; at *p*H 7.5, $E_o' = -80$ mv) and to a minor degree from the added potassium carbonate.[9] Under otherwise equal conditions a higher concentration of the oxidized form of the dye will be available at higher *p*H, which permits an increased rate of reaction with the hydrogen donor substance of the bacteria. Curves obtained after an initial *p*H adjustment to 7.5 are shown in Fig. 2. Curve A represents results after *p*H adjustment only. Curve B was obtained with a strain of *P. meth.* grown in the same medium, but with potassium nitrate replaced by ammonium sulphate on a weight for weight basis. In the case of curve C, the strain was grown in a medium with four times the usual amount of potassium nitrate. *p*H adjustments were also made in these two cases.

Adustment of *p*H has a greater effect than the changes in medium (electrolyte) composition. From the fact that cell performance in the presence of nitrate is not poorer than in its absence, it may be concluded that nitrate is not involved in supplying oxygen to the bacteria at the anode (a nitrate-nitrite mechanism would not involve charge transfer across the cell). This is not surprising; *P. meth.* is a true aerobe incapable of utilizing nitrate oxygen.[10]

Hydroxyl ions are the only ions present that are, under the existing conditions, capable of supplying oxygen at an anode. Whether these ions originate from water molecules at the anode or whether they are formed at the cathode cannot now be stated. For the first case, a mechanism can be written involving a net positive ion (hydrogen ion) transport from anode to cathode, where these ions then are bound. In the second possible mechanism, a net negative ion (hydroxyl ion) transport occurs in the opposite direction. Which mechanism prevails is expected to depend on *p*H and on ion transport rates.

In order to decide approximately where the respiratory chain is interrupted and provided with an electrochemical termination, the anode potential should be compared with known redox potential (E_o') values of the oxidative enzymes.

It is current understanding that bacterial substrate (in this case methane or its derivatives) yields hydrogen which is transferred via a sequence of complex substances, eventually to reach a terminal acceptor (7). This sequence consists of two parts. In each dehydrogenation event, in the first part, two atoms are enzymatically removed from the substrate and bound to an intermediate transfer substance which, in turn, passes two electrons and two protons to the next species in the sequence. At the end of the first part of the sequence hydrogen ions enter into the surrounding fluid and electrons pass on to the next transfer substance. The second or terminal part of the sequence of transfer agents consists of cytochromes. These only transfer electrons, one at a time, until at the last cytochrome step oxygen is reduced and free hydrogen ions from the surroundings are also bound. In each transfer event some energy is used, representing a fraction of the original bonding energy of the hydrogen.

In general, the steps in the dehydrogenation sequence may be formulated as (8)

$$AH_2 + B \rightleftarrows BH_2 + A$$

In the case of aerobic bacteria, the over-all process then becomes

$$AH_2 + \frac{1}{2} O_2 \rightarrow A + H_2O$$

Redox potentials of five intermediates (or types of intermediates) have been determined (9).

The anode potential, measured with a "bridge cell" is 0.05v as stated. The uncertainty in this value is very likely to be within ±0.05v. This potential may be represented by

$$E = E_o' - RT/2f \ln ([AH_2]/[A])$$
$$= E_o' - 0.03 \log 10c = E_o' - 0.03c$$

in which E_o' is the redox potential of the electrochemically active hydrogen transfer substance involved and E the measured culture (anode) potential. E varies very little whether the indophenol dye is used or not. Under the existing conditions the dye is de-

[9] The use of oxygen instead of air results in an approximate doubling of the current density in the middle part of the emf range, other experimental conditions being the same.

[10] Cultures of *P. meth.* die if no O_2 is present, even if extra nitrate used (medium C). Nitrate cannot act here as oxygen donor.

colorized (visually observed). The reduced (hydrogenated) form is present in a relatively high concentration at the anode. This means that the dehydrogenated form (A) of the transfer substance may well be present in a relatively high concentration, so that exponent c will have a fairly small (positive) value. E and E_o' will not be greatly different, and electrochemical interference with the natural metabolic sequence may then be said to occur at the flavoprotein or at the cytochrome b level. These substances have redox potentials of 0.08v and —0.08v, respectively. It appears to be less likely that transfer agents immediately prior to or following those mentioned, are involved. These would be a pyridine nucleotide (E_o' = 0.32v) and a cytochrome c (E_o' = —0.27v) (9).

The fuel then is constituted by hydrogen ions and electrons, produced in equal numbers. Either both are removed from a flavoprotein, or the hydrogen ions come from a flavoprotein and the electrons from a cytochrome b.

It is of interest to note that in an ordinary culture of *P. meth.* "almost certainly the oxygenation step(s) takes place at the stage prior to the conversion of methane to methanol" (10). In the fuel cell this does not hold true if the foregoing considerations are valid.

The cell emf may be used to estimate the efficiency of the conversion of free energy into electrical energy. Free energy conversion efficiency equals the product of current efficiency (observed current/current equivalent of gas consumed) and voltage efficiency (observed voltage/theoretical voltage). If there is no interelectrode diffusion and no internal electrical leakage, the free energy conversion efficiency will be approximately equal to the voltage efficiency (11).

In the present case hydrogen is oxidized electrochemically, but this hydrogen stems from the methane used by the bacteria. To calculate a realistic free energy conversion efficiency, the voltage efficiency value must be multiplied by $\Delta F(H_2)/\Delta F(CH_4)$.

$$\text{Eff.} = E_{\text{obs.}}/E_{\text{theor.}} \times \Delta F(H_2)/\Delta F(CH_4)$$

$\Delta F(H_2)$ represents the free energy change accompanying the oxidation of a mole of hydrogen; $\Delta F(CH_4)$ indicates the same for methane. As was seen (Fig. 2) under certain conditions an open circuit of about 0.6v was reached.

$$\text{Eff.} = 0.60/1.23 \times (-56.7)/(-195.5) \times 100 = 14.2\%$$

This efficiency value, which is quite low for a fuel cell, may be looked on as the maximum so far attainable.[11] Based on current draw at 0.35v (the maximum power point on curve C in Fig. 2) a more realistic value of 8.2% may be found. The current density at this maximum power point is 2.8 μw/cm^2 (2.6 mw/ft^2). Until a means can be devised to interfere electrochemically at an earlier stage in the oxidative chain, efficiencies substantially in excess of some 14% cannot be expected. It is assumed that each pair of hydrogen atoms originates from one methane molecule or its equivalent derivative. The use of inorganics by the bacteria is ignored in this calculation.

The experimental device used was not designed to yield maximal power. However, even with a design perfect for this purpose, power density has to be low because it is geared to bacterial metabolism. It has not been investigated what fraction of the available energy may be removed from the fuel cell over a longer period of time without harming the culture. As was seen, too long a period of lack of oxygen (no power being taken) causes a decrease in bacterial count. But also, it was often noticed when determining polarization curves, that the cell emf should not be taken below a certain value other than briefly. Doing this would result in extremely slow recuperation of the emf on load decrease and frequent inability to regain or even to approach the original open-circuit value.

The persistence of this polarization cannot be satisfactorily explained by assuming the presence of chemisorbed oxygen on the anode. Such an oxide layer could impede the oxidation of fuel at the anode, but only temporarily. The bacteria normally are capable of yielding hydrogen ions (and electrons), and no reason is apparent why this hydrogen would not after load decrease or removal, sooner or later react with the chemisorbed oxygen. The bacterial inability to overcome this polarization, once a relatively substantial amount of energy has been removed to the external circuit in a short time, must be sought in the bacterial physiology.

The bacteria will grow very slowly if carbon dioxide is absent, and only methane and oxygen are available.[6] If only carbon dioxide and oxygen are present but not methane, growth will not be observed. If all three gases are present, growth is rapid, under comparable conditions. It is then concluded that methane is the original carbon source, and it is surmized that carbon dioxide is needed for the synthesis of bacterial substance via a partial reduction. The energy needed for this reduction is less than that obtained from the complete oxidation of methane. An actively multiplying culture of *P. meth.* keeps on producing carbon dioxide (3), however. This means that more energy is liberated in oxidizing methane than is used in reducing carbon dioxide. The difference, it is further assumed, is available for electrochemical conversion. If these considerations have merit, it may then be said that if energy removal from the bacterial system takes place at a rate substantially higher than the rate at which the energy difference referred to is generated, the bacterial metabolism cannot function normally. If this condition is maintained too long, damage occurs, and the organisms lose the ability to recuperate fully and to re-establish the usual open circuit emf. A "physiological polarization" has set in. Although this phenomenon has not been systematically investigated, there is no doubt that determining the high current density end of the polarization curve is detrimental to the bacterial culture. A bacteriological fuel cell with *P. meth.* in the anode half-cell can neither sustain prolonged periods at open circuit, nor under high current drain. It is expected that this will be true for other obligate aerobes.

Under moderate current drain (3μa/cm^2) no deterioration was observed during a period of over 24 hr.

On the basis of a normal methane consumption rate in an active culture (outside of the fuel cell), an estimate of the order of magnitude of the attainable may be formed.

About 15 ml of methane may be used in 24 hr by 153 ml of suspension, under ordinary culture conditions.[12] If it could be arranged that 14% of the chemical energy of this volume of methane were converted electrochemically in the fuel cell described in 24 hr, a current of 0.75 ma should be expected. In actuality, a current of slightly more than 0.1 ma was recorded (Fig. 2).

There is little doubt that improved cell geometry and the use of coarsely porous electrodes would lead to higher current values. Forced bacterial suspension circulation may again improve these, but the net effect might well be smaller due to auxiliary power consumption. A current density, higher than reported by more than one order of magnitude cannot be expected unless a more advantageous access to the metabolic pathways and thus a higher efficiency becomes available. It may serve a purpose to try to adapt strains of *P. meth.* or other methane oxidizing organisms, to a medium with higher conductivity and higher *p*H than used in this work.

[11] The free energy change and the enthalpy change accompanying the oxidation of methane are virtually equal. All stated free energy efficiency values are therefore also thermal efficiency values.

[12] The volume of the anode half-cell; 1.0 × 10^9 organisms/ml. Meniscus area 25 cm^2; culture was briefly shaken twice a day.

Conclusions

1. The potential measured on a platinum electrode immersed in a de-aerated culture of *Pseudomonas methanica* is near —0.05v. (*P. meth.* uses only methane as its source of carbon).

2. A methane and air fuel cell utilizing *P. meth.* in the anode half-cell has an open-circuit emf of 0.5-0.6v near neutrality.

3. Physical contact between bacteria and anode is necessary for the removal of electrons into the external circuit. The electrochemistry takes place in or on the bacteria, not via an excreted (direct) fuel.

4. If methane is replaced by nitrogen the anode potential is not changed at first. However, the bacteria begin to die out. The ability of a fuel cell, of the type described, to produce electrical energy decreases slowly but continuously after methane is replaced by nitrogen. Methane is the original source of the electrochemically active species.

5. The actual fuel species is hydrogen removed from a flavoprotein, and possibly involving a cytochrome b. Hydroxyl ions are the immediate source of oxygen at the anode.

6. Prolonged periods of open-circuit condition and also a very high current drain should be avoided. Both are detrimental to the bacteria. An obligate aerobe, such as *P. meth.* is best suited to functioning under moderate current drain.

7. The free energy conversion efficiency is maximally 14% if methane is considered to be the indirect fuel. At 0.35v, the maximum power point, this efficiency is 8.2%. These values were calculated after the assumption was made that each pair of hydrogen (fuel) atoms oxidized stems from one molecule of bacterial substrate (methane).

8. Current density, in the presence of an indophenol redox intermediate is of the order of milliamperes per square foot in the simple device used. The normal metabolic rate of *P. meth.* in a culture contains no promise that improved cell geometry will result in a current density improvement greater than about one order of magnitude.

Manuscript received Aug. 20, 1964; revised manuscript received Oct. 17, 1964.

Any discussion of this paper will appear in a Discussion Section to be published in the December 1965 JOURNAL.

REFERENCES

1. W. T. Grubb and C. J. Michalske, Paper presented at the 18th Annual Power Sources Conf., May 19, 1964, Atlantic City.
2. A free energy conversion efficiency of about 30% was calculated by L. G. M. Baas-Becking and G. S. Parks, *Physiol. Revs.*, **7**, 85 (1927). They used analytical data obtained from conventional cultures of *P. meth.* by the discoverer of this organism, N. L. Söhngen, *Rec. Trav. Chim. Pays Bas*, **29**, 238 (1910).
3. M. Dworkin and J. W. Foster, *J. Bacteriol.*, **72**, 646 (1956).
4. J. B. Davis and H. F. Yarbrough, *Science*, **137**, 615 (1962).
5. "Manual of Microbiological Methods," H. J. Conn., Editor, p. 95, New York (1957).
6. K. V. Kordesch, in "Fuel Cells," W. Mitchell, Editor, p. 338, New York (1963).
7. "The Life of Bacteria," K. V. Thimann, 2nd ed., Chap. 5, New York (1963).
8. A. J. Kluijver, "The Chemical Actions of Micro-organisms," London (1931).
9. E. Ball (1944), J. Colpa-Boonstra and F. A. Holton (1959), K. Burton and T. H. Wilson (1953), quoted by K. V. Thimann, "The Life of Bacteria," 2nd ed. p. 235, New York, (1963).
10. J. W. Foster in "Oxygenases," O. Hayaishi, Editor, pp. 244-6, New York (1963).
11. H. H. Chambers and A. D. S. Tantram, in "Fuel Cells," G. H. Young, Editor, pp. 103-4. New York (1960).

Electrochemical Behavior of TiO_x Solid Solutions in Aqueous HF and HF-HCl Mixtures

M. E. Straumanis, K. C. Chuang,[1] J. L. Ratliff,[2] and W. J. James

Departments of Metallurgical Engineering and of Chemistry, University of Missouri at Rolla, Missouri

ABSTRACT

TiO_x electrodes coupled to platinum exhibited very low hydrogen evolution rates, V_2, during anodic polarization in aqueous hydrofluoric acid as compared with V_1, the open circuit rates. The difference, V_1-V_2, was independent of the HF concentration and of the composition of the TiO_x electrodes within the compositional range 0-5% b.w. oxygen. Therefore, these TiO_x alloys are polarizable to the same extent (polarizability about 81%) by equivalent current densities in hydrofluoric acid. A more pronounced effect (polarizability 82 to 138%) was observed for TiO_x dissolving in HF-HCl mixtures. The difference, V_1-V_2, increased with both the oxygen content of the solid solution electrodes and the HCl concentration.

In the search for the reasons of such a pronounced decrease in hydrogen evolution rates of the electrodes during passage of an anodic current, it was found that the dissolution potential, ϵ', of TiO_x electrodes in HF became more noble with time, with the increase of oxygen content of the alloys, and with the increasing concentration of HCl in the HF-HCl mixtures as electrolytes. The ϵ' became more active with increasing concentration of HF. In all cases, increasing anodic current density shifted ϵ' strongly toward positive values. Interpretations of the various ϵ'-changes are given in terms of protective layer formation. These layers formed during anodic dissolution as well as the potential changes (polarization) cause the pronounced decrease in hydrogen evolution at the anodes. Ti-O solid solutions exhibit, because of thermodynamical reasons, a more noble potential than the pure metal.

The kinetics of dissolution of TiO_x alloys in HF was explored previously (1). Simultaneously it was found that these alloys, containing about 5-10% oxygen by weight, when coupled to platinum, were so strongly polarized that the hydrogen evolution or open circuit rate, V_1, was reduced by 9.5 $mm^3\ cm^{-2}\ min^{-1}\ ma^{-1}$ (2, 3). This indicated TiO_x electrodes to be more strongly polarizable than pure titanium dissolving in HF, for which a reduction of 5.7 $mm^3\ cm^{-2}\ min^{-1}\ ma^{-1}$

[1] Present address: Department of Metallurgy, Massachusetts Institute of Technology, Boston, Massachusetts.

[2] Present address: Battelle Memorial Institute, Columbus, Ohio.

Table I. *K*-values, Eq. [2], in HF for various TiO_x alloys at 25°C

% b.w.	Formula	K values in mm/ma min. HF 0.25*N*	0.50*N*	0.75*N*	Average
0.785	$TiO_{0.024}$	5.38	5.56	5.19	5.38
1.22	$TiO_{0.037}$	5.82	5.71	5.72	5.75
2.62	$TiO_{0.081}$	6.59	6.11	5.97	6.23
3.30	$TiO_{0.102}$	5.77	5.59	5.48	5.61
4.11	$TiO_{0.128}$	5.17	5.29	5.50	5.32
4.63	$TiO_{0.145}$	5.42	5.78	6.51	5.90
5.01	$TiO_{0.158}$	5.12	5.50	5.20	5.28
			Average		5.64 ± 0.30

Table II. Summary of *K* values obtained for TiO_x solid solutions in HF-HCl mixtures at 25°C

Oxygen content in % b.w.	Formula	HF, *N*	HCl, *N*	*K*, $mm^3/ma\ min\ cm^2$
About 0	Ti	0.1-2.0	0	5.7
3.30	$TiO_{0.102}$	0.5	0	5.56
3.30	$TiO_{0.102}$	0.5	0.1	5.56
3.30	$TiO_{0.102}$	0.5	1.0	7.47
3.30	$TiO_{0.102}$	0.5	2.0	8.98
4.11	$TiO_{0.128}$	0.25	1.0	6.35
4.63	$TiO_{0.145}$	0.25	1.0	6.51
4.97	$TiO_{0.157}$	0.1-0.75	1.0	9.70
5.01	$TiO_{0.158}$	0.50	0	5.50
5.01	$TiO_{0.158}$	0.50	0.50	7.63
5.01	$TiO_{0.158}$	0.50	1.0	8.28
7.02	$TiO_{0.226}$	0.1-0.75	1.0	9.6
10.84	$TiO_{0.305}$	0.1-0.75	1.0	9.3

was found (4). Thus it was decided to study the effect of alloy composition on the rate of anodic dissolution and to try and explain the results by appropriate potential measurement.

Experimental

The TiO_x *samples.*—Ten specimens of the alpha solid solution of oxygen in titanium were prepared ranging in composition from 0.785 to 10.84% b.w. oxygen (see Tables I and II). Calculated amounts of Ti and TiO_2 powders, excepting the samples of smallest oxygen content where titanium hydride was also added to reduce the oxygen content, were mixed and compacted at 50 tsi. Each compact was placed in an alumina crucible and presintered for 1 hr *in vacuo* at 500°C. Titanium hydride in the sample of lowest oxygen content decomposed at this temperature. The samples were then heated at 1350°C for 4 hr. Following furnace cooling, the surface layer of each sample was removed and the specimen finished for accurate measurement of surface area. Trimmings were retained for chemical analysis. Samples were examined optically and by x-rays to determine porosity and homogeneity. Each sample was then mounted in Lucite so as to expose a known surface area to the acid.

Chemical analysis of each sample was made using the hydrogen evolution method (5).

Apparatus and procedure.—The apparatus and procedure used have been thoroughly described previously (4). The dissolution flask of recent construction is shown in Fig. 1.

The cell, TiO_x-Pt, was immersed (external circuit switch open) into the acid (300 ml at 25° ± 0.1°C) the stirring mechanism turned on, and the constant hydrogen evolution rate, V_1, recorded. Then the circuit was closed, the current I in ma registered, and the total rate, V_t, with hydrogen evolving from both electrodes was determined.

The difference Δ in the open and closed circuit rates, $V_1 - V_2$, was calculated from the equation

$$\Delta = V_1 - V_2 = V_1 - V_t + 6.97I \qquad [1]$$

As all the H_2 evolution rates are in $mm^3\ cm^{-2}\ min^{-1}$ at STP, V_2, the closed circuit rate at the TiO_x electrode could be calculated from $V_2 = V_t - 6.97\ I$, where $6.97\ I$ is the faradaic rate equivalent of H_2 evolution in $mm^3\ ma^{-1}\ min^{-1}$ at the Pt cathode (assuming this reaction to be the entire cathodic process there). Thus

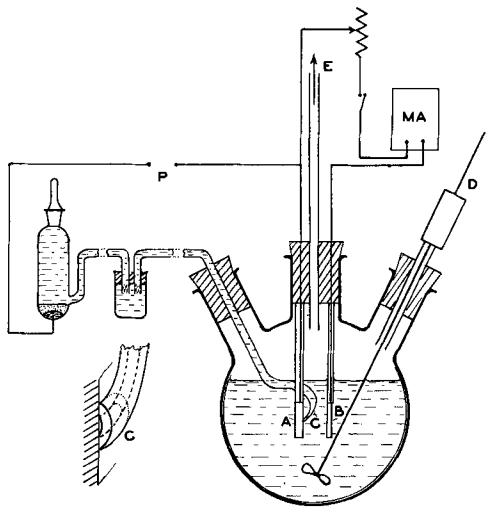

Fig. 1. Apparatus for measurement of anodic potentials during determinations. A, TiO_x electrode mounted in Lucite; B, Pt electrode; C, capillary tube to the salt bridge and calomel electrode; D, stirrer with Hg seal; E, tube to gas buret; P, potentiometer; M.A., milliameter.

Δ (in $mm^3\ cm^{-2}\ min^{-1}$) is the reduction in the rate of hydrogen liberation at titanium caused by the current due to coupling with platinum. In all experiments, a stirring speed of close to 300 rpm was maintained. A simple model illustrating the significance of Δ has been published previously (6).

Dissolution potentials.—The dissolution potentials of four specimens in the absence of an anodic current were determined, measuring the emf of the cell

$$TiO_x/HF, \text{ or } HF + HCl, KCl\ (1N), Hg_2Cl_2/Hg$$

The potential of the anode was reduced to the hydrogen scale. The electrolyte was agitated by a magnetic stirrer at approximately 300 rpm. Potential readings were taken as soon as possible after the electrodes were immersed and then at 5-min intervals.

As Δ is proportional to the anodic current density, the effect of the latter on the potential of the TiO_x electrode was found by coupling it to a platinized Pt cathode at a distance of 10 mm to accommodate the capillary tube, the tip of which was in the TiO_x-acid interface. ϵ' determinations were also carried out during the measurement of the anodic hydrogen evolution rates.

Starting with the highest current density delivered by the cell (no external current was used), each measurement was made 5 min after the change in current density. Three readings were recorded for each current density at 1-min intervals. Two potential readings were taken at each time interval, and the current was adjusted to every other potential reading. A schematic diagram of the apparatus is shown in Fig. 1.

Results

Changes in anodic dissolution rates.—The Δ values (Eq. [1]) were plotted *vs.* current density I. There is a straight line relationship (Eq. [1] and Fig. 2)

$$\Delta = KI \qquad [2]$$

The slope constant K has the units $mm^3ma^{-1}min^{-1}$, meaning that the hydrogen evolution rate of 1 cm^2 of anode surface is reduced by the value of K. Similar straight lines were obtained with the other alloys of Table I, revealing the independence of Δ with regard to both composition and acid concentration.

However, it was found that K did not remain constant when mixtures of HF and HCl were used as solvents. Although the addition of HCl does not alter the diffusion controlled mechanism of dissolution, it

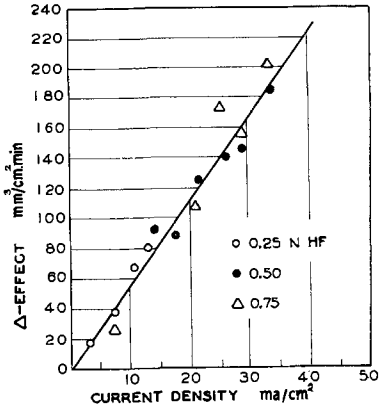

Fig. 2. Effect of current density on Δ for $TiO_{0.102}$ dissolving in HF at 25°C; slope $K = 5.61$.

undoubtedly influences the nature of the metal surface and the composition of the interfacial layers thus altering the K values. Because of this, measurements in HF-HCl mixtures were made, and the results are summarized in Table II.

Although the values obtained with HCl added to the HF, fluctuate to some extent, the increase of K with the increase in HCl concentration and also with the oxygen content can be easily seen. To show the latter increase more clearly, the K values are plotted *vs.* the O/Ti ratio in Fig. 3. At compositions above the dashed line, the total rate of H_2-evolution decreases if an anodic current is applied to the TiO_x electrode. In terms of polarizability, P, (2) for pure Ti, $P = 81.8\%$, and for $TiO_{0.36}$, $P = 138\%$. At the composition of $TiO_{0.07}$, the decrease in H_2-evolution rate at the anode due to the anodic current is exactly balanced by that of the increase at the cathode.

The following phenomena were also observed during these experiments: (*a*) the lower the circuit resistance, the greater were the current fluctuations; severe fluctuations occurred (± 15 ma) at zero ohm box resistance; (*b*) current readings at 0 resistance were less than those at 1 ohm, and sometimes less than 2 ohms box resistance; (c) highest K values were found in most cases from the measurement at 0 ohm box resistance.

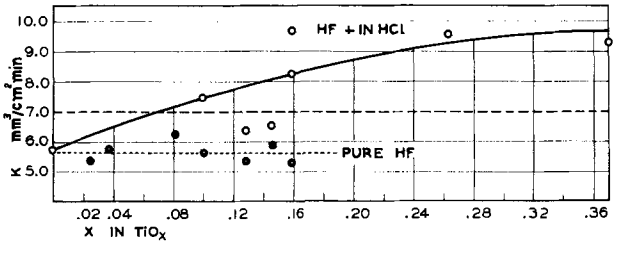

Fig. 3. K values, Eq. [1], obtained in pure HF and in mixtures of HF + HCl (1N) *vs.* x of TiO_x; dashed line: $K = 6.97$ mm³/min at the cathode.

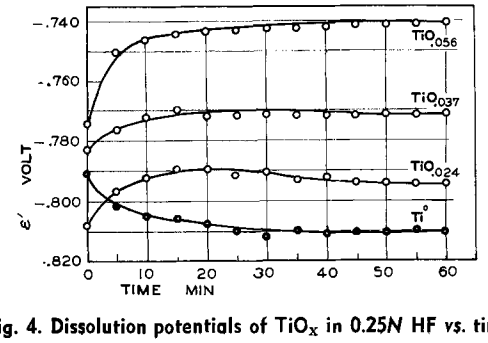

Fig. 4. Dissolution potentials of TiO_x in 0.25N HF *vs.* time

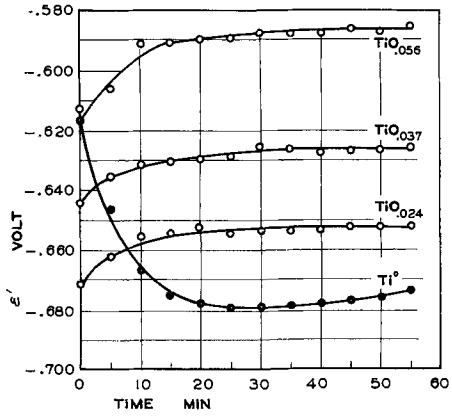

Fig. 5. Dissolution potentials of TiO_x in 0.105N HF-1.0N HCl *vs.* time.

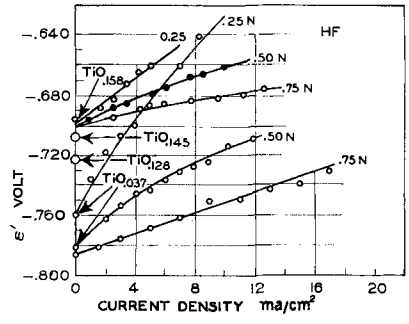

Fig. 6. Effect of current density on the dissolution potential of $TiO_{0.037}$ and $TiO_{0.158}$; ϵ' of $TiO_{0.128}$ and $TiO_{0.145}$ is in between (curves omitted).

Dissolution potentials.—Figure 4 represents the time-potential plots for TiO_x in 0.25N HF and Fig. 5 the same for TiO_x in 0.105N HF-1.0N HCl mixture (hydrogen scale).

From the graphs we note that (*a*) the higher the oxygen content, the more noble is ϵ' for the same acid concentration, (*b*) for the same alloy, ϵ' is more noble in the lower acid concentration, (c) for a given HF concentration, the addition of HCl shifts ϵ' to more noble values, and (*d*) pure Ti becomes less noble with time (except after 30 min in mixed acid).

The effect of current density on ϵ' was studied for $TiO_{0.037}$, $TiO_{0.128}$, $TiO_{0.145}$, and $TiO_{0.158}$ dissolving in 0.25, 0.50, and 0.75N HF. The ϵ' of pure Ti was determined in 0.1, 0.25, 0.50, and 1.0N HF. Plots of ϵ' *vs.* current density are shown in Fig. 6.

It can be seen that an increase in current density is associated with a shift of ϵ' to more noble values. The increase in ϵ' is greater, the lower the acid concentration, and the larger the O-content of the alloy.

Similar data were obtained using a closed cell during the anodic rate measurements (Fig. 1). Apparently, dissolved oxygen in solution had little if any effect on the results.

Discussion and Conclusions

Explanations have to be found (*a*) for the ϵ'-time curves of TiO_x; (*b*) for the ϵ'-current density curves; and (*c*) for the large Δ value in both pure HF and in mixtures of HF and HCl.

It is already known that the potential of pure Ti in aqueous HF becomes more negative with increasing concentration of the acid, approaching a limiting value at about 0.3-0.4N (7). However, in HCl no similar active potential could be observed (8). The most negative value in 10N HCl was —0.37v. Accordingly, it was assumed that HCl, unlike HF, is incapable of dissolving the protective oxide layer on the surface of Ti, which shifts the dissolution potential ϵ' toward

noble values. This hypothesis could now be confirmed using oxygen-containing alloys for potential measurements.

The ϵ'-time curves.—The alpha solid solution has the h.c.p. structure of titanium with interstitial oxygen bonded to a limited number of titanium atoms. Dissolution experiments reveal two Ti associated with three O. Accordingly, the alpha phase may be viewed as a solution of Ti_2O_3 in Ti (5).

The stoichiometry of the dissolution reactions is, for the parts of the alloy containing an excess of Ti, as follows

$$Ti + 3HF = TiF_3 + 1.5H_2 \quad [3]$$

The oxygen present in the metal accumulates on the surface possibly as Ti_2O_3, and since the latter is soluble in HF, it dissolves (chemical reaction)

$$Ti_2O_3 + 6HF = 2TiF_3 + 3H_2O \quad [4]$$

A third equation of verified stoichiometry (5) expressing the dissolution of TiO_x is obtained from [3] and [4]

$$TiO_x + 3HF = TiF_3 + xH_2O + 0.5(3 - 2x)H_2 \quad [5]$$

The electrochemical reaction due to the action of local elements as applied to the Ti in the solid solution is

$$Ti + 3H^+ = Ti^{+3} + 1.5H_2 \quad [6]$$

In the above cases, the Ti ion is, of course, complexed with fluoride ions.

The interpretation of the ϵ'-time curves is as follows: as HF attacks the oxide on the Ti surface, the acid comes in direct contact with the metal, and a very negative potential is measured; since dissolution requires time, the drop in potential occurs along a curve shown in Fig. 4 and 5 for pure Ti. The more concentrated the HF, the faster the drop. As HCl does not dissolve the surface oxide, the ϵ' of Ti remains comparatively noble.

If the metal contains oxygen in solid solution, its dissolution potential will be more noble, the higher the oxygen content (Fig. 4 and 5). This can be explained in terms of the decrease of the free energy of the alloy (9). The further change of the dissolution potential will depend on the solubility of the oxide in the acid. Since in HF the domains rich in Ti° dissolve rapidly according to Eq. [3], the oxide of the alloy slowly accumulates to a certain degree and the excess spalls from the surface and dissolves, Eq. [4]. Thus a nearly constant thickness of film is maintained. Formation of more dense oxide layers, although not perceptible, will cause more noble potentials. Dilution of HF shifts the potentials to more noble values (decrease of oxide layer solubility in HF), as do additions of HCl to the HF. ZrO_x alloys behave similarly (10). Be metal behaves slightly differently (9).

The ϵ'-current density curves.—It is now possible to interpret these curves. When an anodic current is flowing through a TiO_x electrode, at first, the metallic Ti atoms will go into solution according to Eq. [6] and an oxide (probably Ti_2O_3) will accumulate on the surface, causing a rise in anodic potential (Fig. 6). Of course, the potential will also increase as a function of anodic current density.

Since at high concentrations of HF (0.75*N*) the oxide dissolves more rapidly in the acid, the *K* values (Tables I and II) and the inclination of the curves will be lowest. The inclination as well as the starting points of the curves will increase with decreasing HF concentration and increasing concentration of oxygen in the TiO_x electrodes (Fig. 6).

The large Δ values.—A possible explanation is that during self-dissolution reactions [3], [4], and [5] contribute. When anodic current is applied, the rate increase of reaction [6] increases the accumulation of Ti_2O_3 on the electrode surface as Ti° passes into solution. Since reaction rate [4] is slow, the oxide layer reduces the rate of reaction between molecular HF and the domains rich in Ti by increasing the diffusion barrier and probably by covering a portion of the local elements. Thus, as is seen in Fig. 2, the decrease in rate of H_2 evolution at the anode during closed circuit is manifested by the more noble potential of the coupled titanium resulting in a large positive Δ. The constancy of *K* (Fig. 3) in pure HF can then be explained on the basis that variation in oxygen content is insufficient to change the dissolution rate of the oxide layer. In fact, it has been reported that the rate of H_2 evolution from TiO_x alloys is nearly independent of the oxygen content (1).

On the other hand (Table II), the *K* values are much higher in HF-HCl mixtures and dependent upon the HCl concentration and the content of O in Ti. The increase in electrical conductivity as well as the increase in molecular HF concentration speeds up reactions [3] and [6] as shown by the higher dissolution rates (1). Therefore, on application of anodic current, the oxide layer grows more rapidly than in HF alone but the dissolution rate of Ti_2O_3 is affected only slightly. Therefore, at high current densities, the rate of oxide accumulation approaches its dissolution rate. Only a few spots of Ti° remain on the anode and hence, the H_2 development drastically decreases. When the oxide layer exceeds an optimum thickness, breakdown begins and results in current fluctuations. The fact that the current measured at 0 ohm box resistance is less than the current at 1 ohm lends support to the presence of a thick protective film on the electrode surface. The possibility also exists that the oxide film contains less metal than corresponds to the formula thus making it more resistant to acid attack as is the case for NiO (11).

The increase in *K* with increasing HCl concentration is more difficult to explain. In some way, this acid must affect the thickness, porosity, solubility, or adherability of the oxide layer. This is confirmed to some degree by the strong increase in ϵ' with increasing current density (Fig. 6). Therefore, not only the emf of the local circuits causing the self-dissolution of the anode (12) decreases (during the passage of the anodic current), but also the thickness of the oxide layer increases by accumulation (low solubility in HF in presence of HCl), even faster than in pure HF. The consequence is that the drop in rate of anodic hydrogen evolution cannot be compensated any further by the H_2 evolution on the cathode by the current. The *K* constant in such cases becomes larger than 6.97, suggestive of passivation phenomena.

All these experiments show in a direct manner that the presence of oxide layers or even of dissolved oxygen in a metal causes an increase in potential towards noble values with increasing oxygen content.

Acknowledgment

The authors thank the U.S. Atomic Energy Commission (Contract No. AT 11-1-73, project 5) and the Office of Naval Research for financial assistance.

Manuscript received July 24, 1964; revised manuscript received Oct. 30, 1964.

Any discussion of this paper will appear in a Discussion Section to be published in the December 1965 JOURNAL.

REFERENCES

1. M. E. Straumanis, W. J. James, and J. L. Ratliff, *J. Less-Common Metals*, **3**, 327 (1961).
2. M. E. Straumanis and Y. N. Wang, *This Journal*, **102**, 304 (1955).
3. M. E. Straumanis, W. J. James, and W. C. Custead, *ibid.*, **107**, 502 (1960).
4. M. E. Straumanis and P. C. Chen, *ibid.*, **98**, 351 (1951).
5. M. E. Straumanis, C. H. Cheng, and A. W. Schlechten, *ibid.*, **103**, 439 (1956).
6. M. E. Straumanis, *ibid.*, **108**, 1087 (1961).

7. M. E. Straumanis and P. C. Chen, *Metall*, **7**, 85 (1953).
8. M. E. Straumanis and P. C. Chen, *Corrosion*, **7**, 229 (1951).
9. M. E. Straumanis and D. S. Gnanamuthu, *Corros. Sci.*, **4**, 377 (1964).
10. W. J. James, W. G. Custead, and M. E. Straumanis, *ibid.*, **2**, 237 (1962).
11. U. R. Evans, "Corrosion and Oxidation of Metals," pp. 32, 222, Edward Arnold Ltd. (1960).
12. M. E. Straumanis, *Korros. u. Metallsch.* **14**, 71 (1938).

Electrodeposition of Coherent Deposits of Refractory Metals

I. Niobium

G. W. Mellors and S. Senderoff

Development Department, Parma Research Laboratory, Union Carbide Corporation, Parma, Ohio

ABSTRACT

A general method has been found for the electrodeposition of coherent, dense deposits of refractory metals by electrolysis of molten salts. By dissolving the refractory metal fluoride in mixtures of alkali metal fluorides, one may deposit coherent thick coatings of chromium, hafnium, molybdenum, niobium, tantalum, tungsten, vanadium, and zirconium. Not only do the deposits in all cases have the theoretical density, but in most cases are extremely pure and equal to or better in mechanical properties than electron beam melted material available commercially. While differences exist from metal to metal in the details of the compositions of the electrolyte and the valence state of the refractory metal, the general process can be described in terms of one of the first metals studied, niobium. Niobium metal is electrodeposited from a solution about 10 w/o NbF_5 in a mixture of alkali fluorides at a temperature of about 775°C and a current density of about 50 ma/cm^2 with commercially pure niobium as anode material. Anode and cathode efficiencies are close to 100% and deposits with hardness of 85-100 DPH are obtained regularly. Deposits with densities of 99.8% of theoretical and higher are obtained and the throwing power of the bath is better than that usually associated with commercial nickel plating. There is no major restriction on substrates, since steel, stainless steel, graphite, copper, Hastelloy alloys, and others have been used. Thicknesses up to ¼ in. have been electrodeposited with a surprisingly smooth surface. The microstructures of the deposits are the typical columnar grain structure usually observed in electrodeposits without addition agents and their soundness has been confirmed by mechanical testing. Also, successful electrorefining has been accomplished.

The metals of Group IV-B, V-B, and VI-B have long been a challenge to electrochemists because their compounds cannot be reduced electrolytically to metal in either aqueous or organic media (except for Cr). Alloys of some of them in which the major ingredient is Fe, Ni, or Co have been electrodeposited from aqueous media (1), but all attempts to increase the refractory metal content to that of a useful high temperature alloy have failed. It has been known for many years that compounds of most, if not all, of these metals can be reduced to metal in molten salts but only in the form of powder or dendrites (2, 3, 4). With the exception of Balke's (5) tantalum process, these have not proved to be commercially acceptable because the working up of the mixture of metal crystals and salts which constitutes the cathode product is expensive and results in a comparatively impure product in most cases.

The exceptional cases in which coherent deposits were obtained on a laboratory scale involved highly specific electrolytes. The all-chloride (2) electrolyte from which coherent molybdenum may be deposited is unsuitable for titanium (6). Borate or phosphate melts used successfully with tungsten (3), are completely unsuitable for coherent Ti or Mo deposition. In this series of papers we shall describe a general method for the electrodeposition of coherent deposits of eight of the nine metals of Groups IV-B, V-B, and VI-B (the inapplicability to titanium will be discussed below), their alloys and compounds with each other, and with other elements. In this first paper the electrodeposition of coherent deposits of niobium will be considered.

Despite the considerable body of literature on the electrodeposition of niobium, this metal has not been electrodeposited previously in coherent sheets and its electrodeposition even as powder has been unsuccessful commercially. Niobium as powders or dendrites can be electrodeposited from oxide-fluoride melts (7, 8) but only as a brittle rather impure material (9). Only NbP can be obtained from oxide-phosphate melts (10). Comparatively pure powders have been obtained from mixed chloride-fluoride systems (9, 11) but when they contained oxyfluoride as in one process (12) the powder obtained was impure (9). A process described in two patents (13) claiming the "Method of cladding a base metal with a corrosion resistant metal of the group Ti, Zr, Hf, V, Ta, Nb, Cr, Mo, and W . . . . ." actually produces diffusion alloys of some of these refractory metals with the substrate, and build-up stops when the outer layer of the coating becomes too highly concentrated with respect to the refractory metal. At this point deposition of dendrites of the refractory metal begins.

The solution from which coherent deposits of niobium are electrodeposited in a mixture of the fluorides of niobium and alkali metals, the detailed formulation of which is described below.

Operating Procedures

The mixture of alkali fluorides[1] was melted in a graphite crucible in air in order to expel most of the moisture in the salts and allowed to cool. The slug so obtained was transferred to a nickel crucible, K_2NbF_7[2] was added and the crucible placed in the bottom of the Hastelloy X[3] can be shown in Fig. 1. The Hastelloy can was 4½ in. in diameter and 15 in. from the bottom to the flange. A sheet of niobium for use as anode had

[1] ACS specification from Harshaw Chemical Company.

[2] Kawecki Chemical Company.

[3] Stellite Division of Union Carbide Corporation.

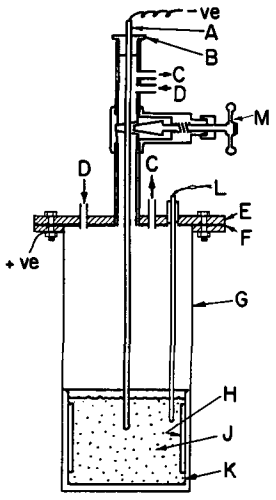

Fig. 1. Apparatus for electrodeposition of niobium. A, stainless steel cathode; B, "Teflon" stopper; C, Argon outlets; D, Argon inlets; E, steel lid; F, "Teflon" or Sauereisen gasket; G, "Hastelloy X" can; H, niobium anode; J, fluoride melt; K, nickel crucible; L, thermocouple and well; and M, gate valve (1 in.).

Fig. 2. Niobium electroplates and electroforms. Upper, 5 mils niobium plate on copper; lower, electroformed niobium crucible and nozzle. All in as-deposited state except crucible, which was ground.

been bent into a cylinder and previously inserted into the crucible in contact with its wall.

An inert atmosphere was maintained within the Hastelloy can by flowing Linde cylinder argon through the system. The bronze gate valve was used as a gas lock during insertion and removal of cathode.

The Hastelloy can containing the crucible with the plating solution was placed in a Hoskins furnace (Type FD104) which was controlled by a chromel-alumel thermocouple and Wheelco controller.

A new electrolyte was electrolyzed for a short while to eliminate residual impurities and to establish the correct valence state for satisfactory deposition.

Plating Range and Effects of Operating Variables

A typical formula for a niobium plating solution is shown in Table I. This corresponds to 10 w/o (weight per cent) NbF_5 dissolved in the ternary eutectic of LiF, NaF, KF. The eutectic composition melts at 454°C. Coherent niobium plates and electroforms of the type shown in Fig. 2 are produced between 700° and 825°C at current densities from 5 to 125 ma/cm². The cell voltage is between 0.1 and 0.25v.

Electrolyte composition.—The composition of the electrolyte is, in general, not critical. Lower concentrations of NbF_5 reduce the limiting current density so that at about 5 w/o the limiting current density is below 20 ma/cm². High concentrations raise the liquidus temperature so that at about 30 w/o CbF_5, the necessary operating temperature (approximately 825°C) approaches a level at which the coherence of the plate begins to deteriorate. The composition of the solvent may be varied widely. The eutectic compositions of KF-LiF and KF-NaF have been used instead of the ternary eutectic with equally good results. A higher operating temperature (minimum 775°C) is required when KF-NaF is used as solvent because of the higher liquidus in this system, but in general the composition of the solvents is largely determined by its effect on the melting point of the solution.

Valence state.—The mean valence[4] of the niobium in the electrolyte must be close to four, the steady state valence in baths operated over long periods of time usually is between 4.1 and 4.2 and under these conditions the cathode and anode current efficiencies are essentially 100% based on the reaction $Nb^{4+} + 4e \rightleftharpoons Nb^0$. This high efficiency is maintained until the mean valency of the bath exceeds about 4.5 when the cathode current efficiency falls rapidly. Although the efficiencies are very irreproducible when the valence of the niobium increases, the values given in Table II, observed in isolated runs, give an indication of the sensitivity of the cathode current efficiency to valence state.

Simple immersion of niobium metal in the solution of KF-LiF-NaF and NbF_5 results in the reaction

$$Nb + 4NbF_5 \xrightarrow[810°C]{KF\text{-}LiF\text{-}NaF} 5NbF_4$$

which proceeds until a mean valence of about 4.5 has been reached. It is for this reason that the anode current efficiency exceeds 100% when the valence of the electrolyte exceeds 4.5. Experiments performed when the bath was stirred either mechanically or by bubbling argon showed that it was possible to reduce the mean valence to about 4.1 (90% as Nb^{IV}) by reaction with Nb metal, but that on standing this reverted to about 4.5. The most desirable lower valency state, that below about 4.3, can only be maintained by electrolysis and the reaction responsible for reduced efficiency of metal deposition at higher valencies is $Nb^{5+} + e^- \rightarrow Nb^{4+}$.

Since not only is the efficiency reduced but impurities in the plate are increased when the valence rises, it is necessary to avoid oxidizing conditions of all types. The valence is increased by oxygen and moisture contamination, and by insufficient anode area. In the latter case, however, anode current densities in excess of 100 ma/cm² did not appreciably oxidize the solution even after long periods of electrolysis. In the case of oxygen or dry air contamination or electrolytic oxidation at the anode, the process may be reversed by correcting the condition and electrolyzing. Hydrolytic

[4] The mean valence is determined by dissolving the frozen electrolyte in the presence of excess $FeCl_3$ and titrating with $K_2Cr_2O_7$ to determine the reducing power. This result is then compared with the value for total Nb obtained by the usual gravimetric procedure.

Table I. Typical formula for niobium plating solution

	w/o	Mole %
LiF	26.2	47.6
NaF	10.5	11.8
KF	47.0	38.2
K_2NBF_7	16.2	2.50

Table II. Sensitivity of cathode current efficiency to valence state

Valence	Cathode current efficiency, %
4.1	100
4.2	98
4.3	85
4.5	35
4.6	~0

oxidation, however, is irreversible. Material balance studies have shown that a solution which has been hydrolytically oxidized has a permanent increase in its valence state. Addition of fresh, pure K_2NbF_7 results in complete reduction of the added Nb^{5+} to Nb^{4+}. The resultant steady state mean valence of the solution is what one would expect on adding the same amount of Nb^{4+} to a bath with Nb content and valence state of the solution prior to the addition.

Temperature.—The lower limit of operation is determined by the liquidus of the plating bath. It has been found that poorer deposits are obtained as one approaches to within 25° or 35° of the liquidus. This may be the result of the increased viscosity and decreased diffusion coefficients combining to reduce the limiting current density to a very small value. The upper limit is established by the gradual loss of coherence of the deposit, proceeding with increasing temperature through a pseudo-plate state to the deposition of powder and dendrites. This probably results from the dissociation of the complex ionic species that is normally reduced at the cathode. This will be discussed below.

Current density.—The lower limit is controlled by the concentration of noble impurities such as iron whose deposition becomes appreciable compared to that of niobium at low current densities. Extremely pure baths have no lower limit to the current density. The upper limit increases with temperature and concentration of Nb^{4+} to the value of the diffusion limited current. Above this current alkali metal is deposited with disastrous effects on the deposits, producing first powders and dendrites, and finally slimes.

Impurities.—The harmful effects of moisture, oxygen, and more noble metal ions have already been indicated. Anions such as oxide, hydroxide, chloride, bromide, and iodide have been found undesirable in varying degrees. The presence of oxide and hydroxide results in hard and brittle metal deposits while the halogen ions reduce the operating range within which coherent deposits are obtainable. Replacement of KF-LiF-NaF with KCl-NaCl as the solvent for NbF_5 results in deposits of dendrites and powders under all conditions. However, as is frequently the case in electrodeposition, trace quantities of some of these impurities have shown addition agent action; for example, by reduction of the grain size of the deposited metal.

In this connection the deposits obtained at 775°C and a cathode current density of 30 ma/cm² of Fig. 3 are of interest. The melt from which these deposits were made was contaminated with moisture or oxygen and it proved impossible to obtain dense coherent deposits from this system, although all efforts were made to "work-in" and electrolytically purify the electrolyte. The five deposits (a to e), run in the indi-

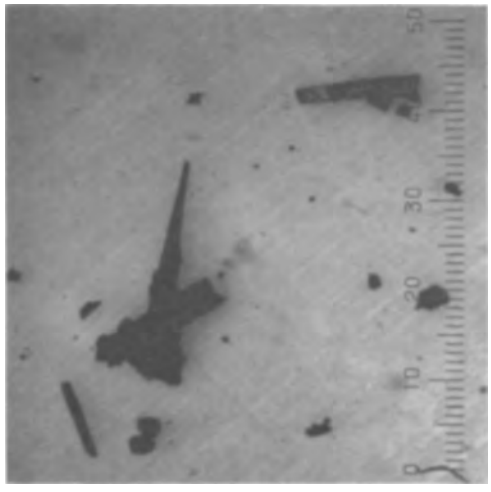

Fig. 4a. Photomicrograph of dendrites from surface of deposit shown in Fig. 3a. Magnification approximately 28X.

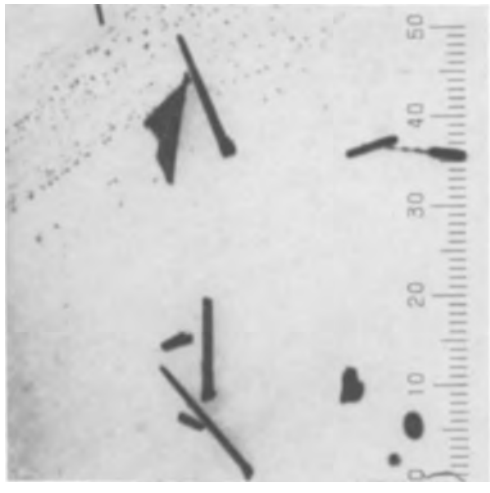

Fig. 4b. Photomicrograph of dendrites from surface of deposit shown in Fig. 3b. Magnification approximately 28X.

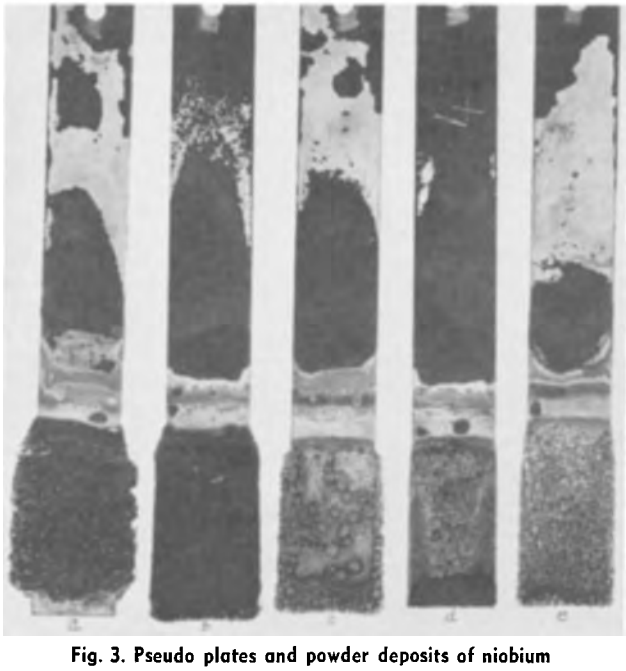

Fig. 3. Pseudo plates and powder deposits of niobium

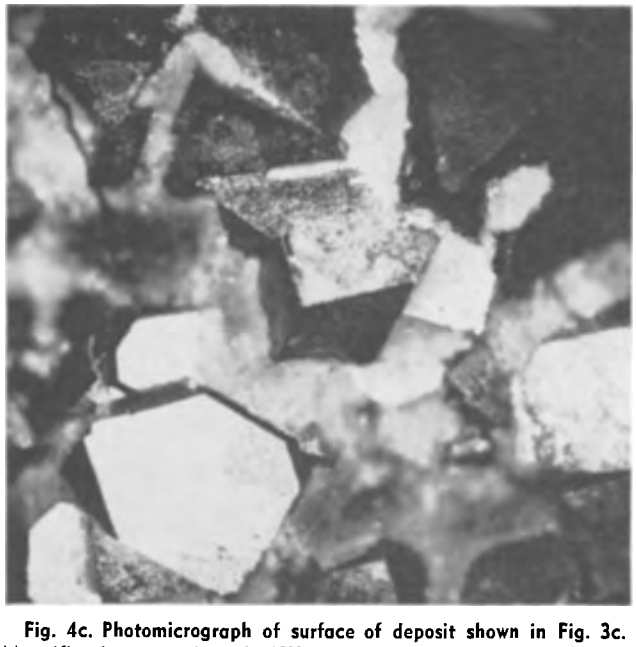

Fig. 4c. Photomicrograph of surface of deposit shown in Fig. 3c. Magnification approximately 60X.

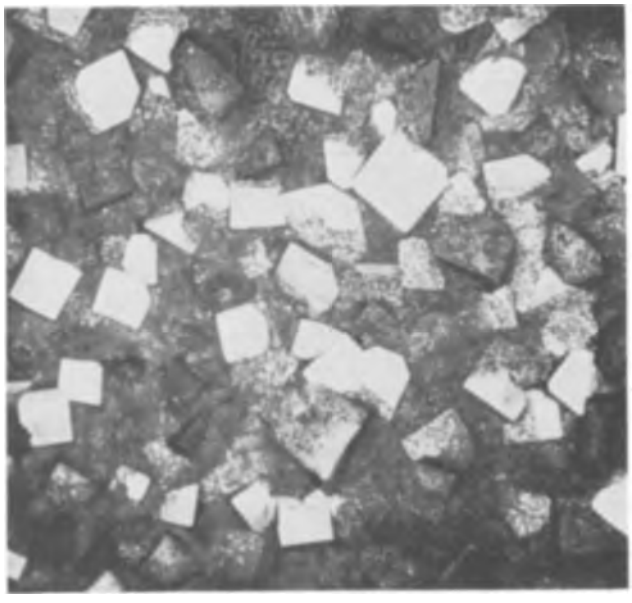

Fig. 4d. Photomicrograph of surface of deposit shown in Fig. 3d. Magnification approximately 60X.

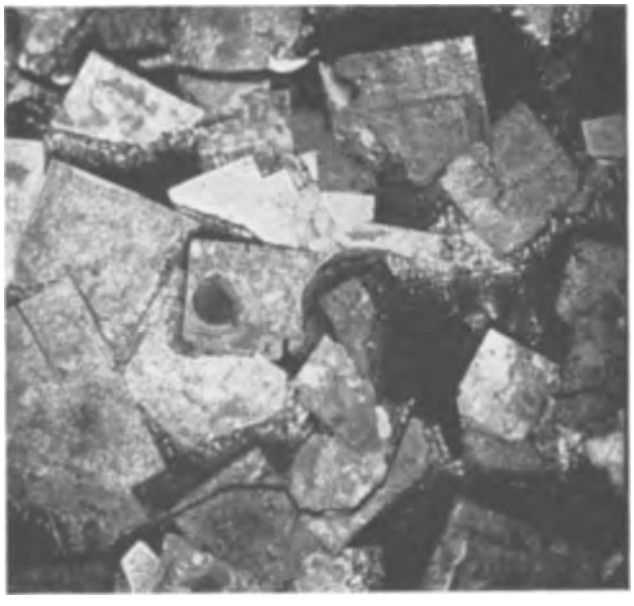

Fig. 4e. Photomicrograph of surface of deposit shown in Fig. 3e. Magnification approximately 60X.

cated order, represent a total electrolysis time of over 100 hr. In Fig. 4a and b are seen the dendrites deposited on the surface of the first two cathodes of Fig. 3. The disappearance of the dendrites and conversion of the deposit to a "pseudo-plate" consisting of coarse-grained niobium powders compacted by some finer grain material is seen in the photomicrographs (Fig. 4c, d, e) of the surfaces of the deposits shown in Fig. 3. In Fig. 4c there still remains some of the salts which fill the large number of voids of the typical compacted powder deposit. The uselessness of this deposit is recognized when one realizes that to obtain metal of even moderate purity it is necessary to pulverize the deposit finely and leach the impurities out of it. Nevertheless, "pseudo-plates" such as this have been the basis of innumerable patents. In Fig. 5d and e, cross sections of the deposits of Fig. 3d and e show that even the initial "plate" is particulate and, in fact, already a powder, though not as easily discernible if the plating is terminated when the deposit is very thin. It is interesting to note that some of the dendrites taken from the Fig. 3a and b cathodes may be single crystals of niobium.

Fig. 5d. Photomicrograph of cross section of deposit shown in Fig. 3d. Magnification approximately 60X.

Fig. 5e. Photomicrograph of cross section of deposit shown in Fig. 3e. Magnification approximately 60X.

Characteristics of Deposits

Purity.—In Fig. 6 is shown a typical niobium deposit 20 mils thick, on a copper substrate produced from the standard composition electrolyte described above. The usual columnar structure of electrodeposits without addition agents is observed. The good bond to the base metal, the absence of inclusions and grain boundary precipitates is evident. The hardness of the plate is 93 ± 3 DPH and its impurity content is as follows: Fe 0.029%, Cr <0.01, Cu <0.01, Ni 0.022, Ta <0.01, N 0.001, H 0.003, and O 0.039.

Another deposit from an electrolyte using the same concentration of NbF_5 in the NaF-KF eutectic solvent had a DPH hardness value of 70 and an interstitial content as follows: O 0.021%, H 0.0005, N <0.0005, and C ~0.0001. It is not yet established that the indicated change in electrolyte is directly responsible for the difference in purity of the deposit.

Comparatively high oxygen contents have been consistently noted in spite of very low hardness values. It is possible that the most critical contribution to hardness from interstitials comes from the nitrogen and hydrogen content which tend to be very low in the electrodeposited niobium. Plates have been produced with oxygen content as low as 0.007%, but work is still in progress on the reduction of oxygen content to values consistently below 0.01%.

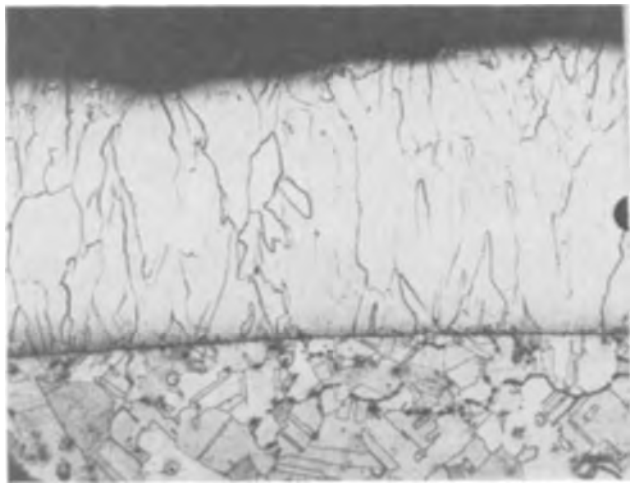

Fig. 6. Cross section of niobium plate on copper (copper at bottom). Magnification approximately 100X.

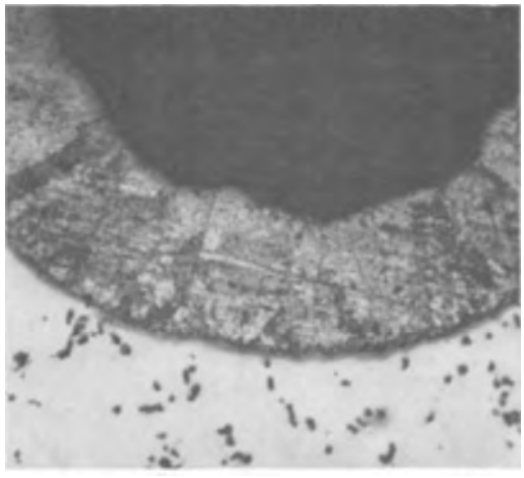

Fig. 7. Cross section of niobium deposit in a recess of a mat of a turbine blade. Magnification approximately 150X.

It is noteworthy that the oxygen content of the cathode in all cases is less than that of the anode. With niobium roundels containing 0.12% oxygen as anode material[5] the plate stabilized at 0.04% oxygen; with roundels containing 0.018% oxygen; 0.006% oxygen was found in the plate, but air contamination of the electrolyte increased the oxygen content of the plate to 0.045% in the next two-day run. Carbon in niobium roundel anodes is also refined out; with 0.037% C in the anodes, the plates stabilized at about 0.0006% C. Nitrogen likewise is reduced from 0.035% in the anodes to 0.0009% in the cathodes in steady state. Iron and nickel impurities in the anodes are concentrated in the cathode and chromium is transferred with only slight refining. With 2% tantalum in the anodes, cathodes are obtained in which tantalum is not detected by emission spectroscopy. The ultimate steady state impurity content of the cathodes must be equal to or less than that of the anode. It is lower in the cases of carbon and oxygen because these elements are apparently lost by precipitation from the melt.

Properties.—The deposits are produced at 100% of the theoretical density of niobium and behave in all matters as arc-melted or electron beam-melted niobium. The columnar structure causes the tensile strength normal to the columns to be a little lower than that of annealed niobium, *i.e.*, 42 to 47 ksi compared to 56 to 57 for electron beam-melted material. The ductility of the plated material is excellent showing an elongation of 25-30% compared to 26-28% for EBM material. The electrodeposited niobium may be directly rolled, a 39 mil plate having been rolled to 9 mils with no intervening annealing.

The resistance ratio[6] has been measured for a representative sample and found to be 30 ± 10. Undoubtedly reduction of the oxygen from the value of 290 ppm in this sample will improve this value.

The properties of electrodeposited niobium as a capacitor were determined by anodizing a plated coating and determining the leakage current at the forming voltage (100v) and at 50v. This was found to be 138 μa and 4.6 μa compared to values for tantalum of the same size and shape of 190 and 50 μa.

Coating properties.—Niobium deposits with exceptional throwing power. While none of the standard boxes or cells were used to measure this property, deposits inside of tubes and in recessed areas of irregular objects showed greater uniformity than is normally encountered with Watts nickel plating. In Fig. 7 is shown a niobium deposit in the recess between the teeth in the root of a turbine blade, where 5.8 mils was deposited in the recess.

Pore-free deposits on reasonably smooth surfaces can be made with certainty in moderate thicknesses. Three to five mil plates on silver are routinely tested by immersion overnight in 1:1 HNO_3. Where the substrate is extremely smooth, as in the case of an optically flat surface of copper, a 1 μin. plate of niobium prevented attack during overnight immersion in nitric acid.

Excellent adhesion is obtained on iron, stainless steel, nickel, copper, and graphite. Uranium and other active metals must be protected before plating with a strike coat, and certain alloys such as Hastelloy C and cupronickel alloys form brittle diffusion layers which impair adhesion. When substrates are cleaned and prepared for plating according to the appropriate ASTM recommended practices with little or no modification, satisfactory adherence is usually obtained.

Discussion

Perhaps the most surprising feature of the study was the importance of essentially pure fluoride melts. While chloride and mixed chloride-fluoride systems have been studied for years and found to produce only dendrites, powders, or sometimes diffusion alloy layers covered with powder, the fluoride melt in the absence of chlorides consistently produces coherent deposits. In the case of zirconium and zirconium diboride the tolerance for chlorides in the electrolyte is very low. Niobium and tantalum have somewhat greater tolerance for chlorides; but even in the latter case, a chloride content in excess of about 10 w/o causes serious deterioration of the coherence of the deposit.

The specific effect of anions can be understood at least qualitatively if one assumes that deposition of coherent deposits from molten salts requires that a complex anion of the correct thermodynamic stability be available in the electrolyte for reduction at the cathode. One must postulate that if the complex anion is insufficiently stable (*i.e.*, has too large a dissociation constant), dendrites and powders will deposit by reduction of the free metal cation available in high concentration from the dissociation of the complex. If on the other hand the complex is too stable (too small a dissociation constant), its reduction potential will reach that of the alkali metals and the codeposition of liquid or gaseous alkali metals with the refractory metal can lead only to particulate cathode deposits or even cathode slimes. In the range of complex compound stability between these two extremes it is probably the direct reduction of the complex anion which produces coherent metal deposits. In the absence of

[5] When niobium roundels were used as anode material they were contained in a nickel screen basket. The nickel was unattacked so long as niobium remained in contact with it.

[6] The ratio of the electrical resistance at 300°K to that at 4.2°K with a sufficiently large magnetic field applied to keep the sample in the normal conducting state.

more quantitative information at present we can only say that the importance of fluoride ion in these systems arises from its effect on the strength of the anionic complexes formed by the transition metals in these molten systems.

There is no doubt that anionic fluoro complexes are more tightly bound than anionic chloro complexes so that since chloro complex systems produce powder deposits with no evidence of alkali metal production, the use of fluoride melts should tend to improve coherence according to the above reasoning.

It was shown in previous publications (15, 16) that the stability of a chloro complex was strongly affected by differing solvent cations. For example, changing from potassium chloride to sodium chloride as solvent for cerium chloride increases the activity of cerium ion by a factor of about 20 (15) and changing sodium to calcium chloride increases the cerium ion activity by an additional factor of about 100. It was also noted (16, 17) that a correlation existed between the quantity Z/r^3 (Z = valence, r = crystal ionic radius) for the solvent cation and strength of the chloro-cerium complex in the system. It appeared that the smaller the "charge density" (Z/r^3) of the solvent cation the stronger was the bonding of the chloro cerium complex. Semiquantitative relationships of this type involving the charge and radius of the ion have been found by many others (18, 19). That this exists in fluoride systems has been shown by surface tension measurements (20, 21) from which it is clear that fluorozirconate complexes are considerably stronger in a KF-LiF solvent than in a NaF-LiF solvent, which again demonstrates that substitution of potassium ion for sodium ion, in this case in a ternary melt, increased the stability of the anionic transition metal complex.

While it is clear that the predominant effect on the strength of the anionic complex is that of the anion, within a given anion series an effect of the solvent cation on the stability of the anion complex can be discerned.

In order to extend this concept to ternary and multicomponent systems it is convenient to define a "molar dissociation coefficient" M, for the solvent such that $M = \sum n_i \frac{Z_i}{r_i^3}$ (where n_i = mole fraction of cation i in the solvent), for the solvent and correlating this with the Z/r^3 for the solute transition metal ion in the valence state from which it is reduced to metal at the cathode. As M for the mixed solvent increases, or Z/r^3 for the transition metal ion decreases, the dissociation of the fluoride complexes of the transition metal ion would increase. Several examples involving Zr, Nb, Ti, and Ta will be used to demonstrate this concept of the solvent effect on coherence of deposits.

Flinak	LiF	NaF	KF	
Mole fraction	0.465	0.115	0.42	
Pauling cation radius	0.60	0.95	1.33	
Z/r^3	4.63	1.17	0.426	$M = \sum n_i \frac{Z_i}{r_i^3} = 2.47$
$n_i \frac{Z_i}{r_i^3}$	2.15	0.135	0.179	

The value of M for the KF (0.50)-LiF (0.50) eutectic is 2.53, that for the NaF-LiF eutectic is 3.246, while for the KF (0.60)-NaF (0.40) eutectic it is 0.724. Thus, the "molar dissociation coefficients" for the lithium-containing solvents have about the same values while that for NaF-KF is much smaller. However, the specific steric effects of Li^+ cannot be ignored. It has been shown (22), for instance, that in the molten alkali nitrates, the Li^+ effectively restricts the rotation of the nitrate ion, while the other alkali ions do not. Therefore, it is likely that the desirable value of the molar dissociation coefficient would be different for Li^+-containing solvents than for others.

It is possible to calculate $\left[\frac{Z}{r^3}\right]$ values for the refractory metal ions, again using the radii of Pauling. No value for Ta^0, Ta^{1+} or Ta^{5+} is given by Pauling, but since $r_{Ta0} \approx r_{Nb0}$ it would be reasonable to assume that the pentavalent ions are approximately the same size. One may further assume that there is little difference, at the most 0.03Å, between the radius of Nb^{4+} and that of Nb^{5+}. No value is given for the radius of Ti^{2+}, but Ti^{4+} is 0.68. Ti^{3+} has been reported as 0.68 ~ 0.69Å, not very different from Ti^{4+}, so it may be reasonable, as a first approximation, to say that Ti^{2+} is of the same order, *i.e.*, 0.67Å. The values of Z/r^3 in Table III are calculated in which Z is the valence state of the ion in the species which is reduced at the cathode.

Table III. Values of Z/r^3

	Valence	Radius	Z/r^3
Ti	2	0.67	6.65
Zr	4	0.80	7.81
Nb	4	0.73	10.3
Ta	5	0.70	14.7

Table IV. Arithmetic product, $M\frac{Z}{r^3}$

	NaF-KF-LiF eutectic	KF-LiF eutectic
Ti	16.4	16.8
Zr	19.3	19.7
Nb	25.4	26.0
Ta	35.9	36.8

Consider now the arithmetic product, $M\frac{Z}{r^3}$, for the four metals and the two-lithium-containing solvents, Table IV.

It is significant that in these two solvents (and also in the NaF-KF solvent) the deposition of coherent zirconium is difficult, though successful, and that of titanium unsuccessful. In the case of zirconium slight departures from the desired composition resulted in the production of potassium vapor probably from a reaction of the type

$$Zr + 4KF \rightarrow ZrF_4 + 4K$$

and in the case of titanium large amounts of potassium vapor were liberated. Since it previously had been established that titanium cannot be deposited coherently at all in the absence of KF, an attempt was made to formulate a ternary solvent for titanium deposition such that $M\frac{Z}{r^3} > 19.3$, that is one with an M of about 2.90. Such a solvent, given that it must contain KF, might be the composition 0.36NaF, 0.54LiF and 0.10KF $\left(\sum n_i \frac{Z_i}{r_i^3} = 2.96\right)$ and experiments carried out in this laboratory indicate that Ti plates of limited thickness may be obtained from this solution provided the KF/TiF_4 ratio is approximately four. The thickness limitation and other difficulties probably caused by the incomplete suppression of potassium deposition, have thus far prevented the application of this general process to titanium deposition as successfully as in the case of the other refractory metals, but the usefulness of this concept of the solvent effect is definitely indicated.

Summary

The electrodeposition of coherent deposits of the refractory metals, Cr, Mo, W, V, Nb, Ta, Zr, Hf and some of their alloys and compounds can be accomplished by electrolysis of molten fluoride systems. In this paper the deposition of niobium from a solution consisting of KF 26.2 w/o, LiF 10.5, NaF 47.0, and K_2NbF_7 16.2 at 775°C, and a current density of 50 ma/cm² has been described. The major variables have proved to be tem-

perature, valence state, and impurity level. The composition is not critical but the presence of a substantially pure fluoride system is required and a tentative explanation based on the maintenance in the solution of a complex anion of appropriate stability for reduction at the cathode to form coherent deposits is advanced. The properties of the deposited niobium are identical in most respects to metallurgically produced metal of equivalent purity and structure. While there are differences among the refractory metals in detail which require specific accommodations in the plating system, niobium may be considered, in general, an example of the group. Additional papers on the other metals are in preparation. These processes are the subjects of patent applications in the United States and foreign countries (23).

Acknowledgments

The authors wish to express their thanks to their colleagues in Union Carbide Corporation for assistance, including B. H. Eckstein, R. B. Puyear, and R. F. Ashton, who performed many of the electrorefining experiments; W. D. Forgeng and J. D. Ruggiero for metallography, W. E. Chambers and I. H. S. Fraser for analyses and R. W. Meyerhoff and F. E. Cariou for the determination of the electrical properties of the deposits. They would also like to acknowledge the interest and encouragement of Dr. R. G. Breckenridge throughout the course of the work.

Manuscript received Aug. 2, 1964; revised manuscript received Nov. 19, 1964. This paper was delivered at the New York Meeting, Sept. 29-Oct. 3, 1963.

Any discussion of this paper will appear in a Discussion Section to be published in the December 1965 JOURNAL.

REFERENCES

1. A. Brenner, "Electrodeposition of Alloys," Vol. II, Academic Press, New York (1963).
2. S. Senderoff and A. Brenner, *This Journal*, **101**, 16 (1954).
3. (a) G. L. Davis and C. H. R. Gentry, *Metallurgia*, **53**, 3 (1956); (b) F. X. McCawley, C. B. Kenahan, and D. Schlain, *This Journal*, **110**, 180C (1963), Abstract only.
4. A. R. Stetson, *Materials in Design Engineering*, **57**, 81 (March 1963); U.S. Pat. 3,024,174 (March 1962).
5. C. W. Balke, U.S. Pat. 1,799,403 (1931).
6. (a) A. Brenner and S. Senderoff, *This Journal*, **99**, 223C (1952); (b) G. D. P. Cordner and H. W. Worner, *Anal. J. Appl. Sci.*, **2**, 358 (1951).
7. F. H. Driggs, U.S. Pat. 1,815,054 (1931); 1,874,090 (1932).
8. C. W. Balke, *Trans. Electrochem. Soc.*, **85**, 89 (1944).
9. A. J. Kolk, M. E. Sibert, and M. A. Steinberg, "Technology of Columbium," E. B. Gonser and E. M. Sherwood, Editors, John Wiley & Sons, Inc., New York (1958).
10. H. Hartman and W. Massing, *Z. anorg. allgem. chem.*, **266**, 98 (1951).
11. P. Drossbach, *Z. Electrochem.*, **58**, 691 (1954).
12. C. C. Ma, *Ind. Eng. Chem.*, **44**, 352 (1952).
13. B. C. Raynes, U.S. Pat. 2,782,156 (1957); 2,786,809 (1957).
14. Y. B. Kim, C. F. Hempstead, and A. K. Strnad, *Phys. Rev. Letters*, **9**, 306 (1962); *Phys. Ref.* 129, 528 (1963); *J. Appl. Phys.*, **34**, 3226 (1963).
15. S. Senderoff, G. W. Mellors, and R. I. Bretz, *Ann. N. Y. Acad. Sci.*, **79**, 878 (1960).
16. S. Senderoff, G. W. Mellors, and R. I. Bretz, *This Journal*, **108**, 93 (1961).
17. G. W. Mellors, "Proc. 1st Austr. Conf. on Electrochem.," A. Friend and F. Gutman, Editors, p. 521, Pergamon Press Inc., New York (1964).
18. M. F. Lantratov and A. F. Alabyshev, *J. Appl. Chem. U.R.S.S.*, **26**, 235, 321 (1953); **27**, 685 (1954).
19. D. M. Gruen and R. L. McBeth, *J. Phys. Chem.*, **63**, 393 (1959).
20. G. W. Mellors and S. Senderoff, "Proc. 1st Austr. Conf. on Electrochem.," A. Friend and F. Gutman, Editors, p. 578, Pergamon Press Inc., New York (1964).
21. G. W. Mellors and S. Senderoff, *This Journal*, at press.
22. J. K. Wilmshurst and S. Senderoff, *J. Chem. Phys.*, **35**, 1078 (1961).
23. G. W. Mellors and S. Senderoff, Canadian Pat. 688,546 (1964).

Electrolytic Capacitor Anodes Derived from Tantalum-Titanium and Niobium-Titanium Alloys

Thaddeus L. Kolski

Pigments Department, Experimental Station, E. I. du Pont de Nemours & Company, Inc., Wilmington, Delaware

ABSTRACT

Porous sheets of tantalum or niobium can be prepared by volatilization of titanium from sheets of tantalum-titanium or niobium-titanium alloys at high temperatures in vacuum. Removal of titanium from the initial alloy results in significantly increased surface area, nearly all of which is available for anodic film formation. Conventional anodization of material prepared in this manner produces anode-dielectric systems of excellent quality. Pore dimensions within the porous anodes are large with respect to anodic film thickness, and formation to 600v can be achieved with only minor loss of effective anode area.

The fundamental relationship determining the capacitance of a parallel plate capacitor is

$$C = 8.85 \times 10^{-14} \epsilon A/d$$

where C is capacitance, f; ϵ, dielectric constant of medium separating plates; A, plate area, cm^2; d, plate separation, cm. In an electrolytic capacitor, the dielectric separating the "plates" is the oxide layer formed on the anode by electrolytic oxidation; therefore d refers to the thickness of this layer and ϵ to its dielectric constant. For a given anode material and set of formation conditions, which determine the nature and thickness of the anodic layer, and assuming perfect contiguity with the counterelectrode, the remaining variable which can influence capacitance is the available surface area of the anodized substrate. In the case of a foil anode, available surface area may be increased by any process which increases the ratio of true area to apparent geometric area, that is, increases the surface enhancement factor. A widely used method of achieving this effect is electrochemical etching. In order to maximize the benefits accruing from increased surface area, however, it is important that the dimensional magnitude of the irregularities be large with respect to thickness of the anodic oxide film to be formed thereon in order that effective area of

the counterelectrode-oxide layer interface conform closely with that of the anode-oxide layer interface.

In addition to high capacitance, good anodic oxide quality is imperative in electrolytic capacitors to be used in applications requiring reliability. By the term "anodic oxide quality," reference is directed toward desirable characteristics such as good barrier properties, resistance to nucleation and crystallization under conditions of elevated temperature or field stress, resistance to damage during counterelectrode application (as in solid electrolyte devices) or other fabrication steps, and resistance to any change over long time periods under conditions of both use and disuse. Obviously, anodic oxide quality cannot be fully assessed without fabrication of statistically significant quantities of finished capacitors and subjecting these to appropriate tests. However, "wet-cell tests" involving metal substrates covered by anodic oxide layers are helpful in providing information which may be used to estimate the potential value of anode materials.

It is the purpose of this paper to describe the properties of two new electrolytic capacitor anode materials which are characterized by high surface enhancement factors and, on the basis of initial evaluation, excellent electrical quality of surface oxide layers which are formed by the process of anodization. These materials are superficially tantalum and niobium; therefore the high dielectric constants and low thicknesses of anodically formed layers of the corresponding oxides are utilized in application of the materials as capacitor anodes.

Preparation and Composition

The preparation of the new materials involves the high-temperature vacuum heating of tantalum-titanium and niobium-titanium binary alloys. Under these conditions, prolific pore formation occurs in the metal bodies as a result of titanium volatilization, with the extensive creation of new surface. Figures 1 and 2 are photomicrographs showing polished sections of typical products prepared in this manner. The total area generated is dependent on several parameters involving the initial alloy body and conditions of vacuum heating; this will be discussed in subsequent publications. The present paper is concerned only with properties of the porous valve metal resulting from this process. It should be kept in mind, however, that although excellent reproducibility of product characteristics is obtained under constant preparation conditions, the nature of the resultant porous body may be varied as a result of changing preparation parameters.

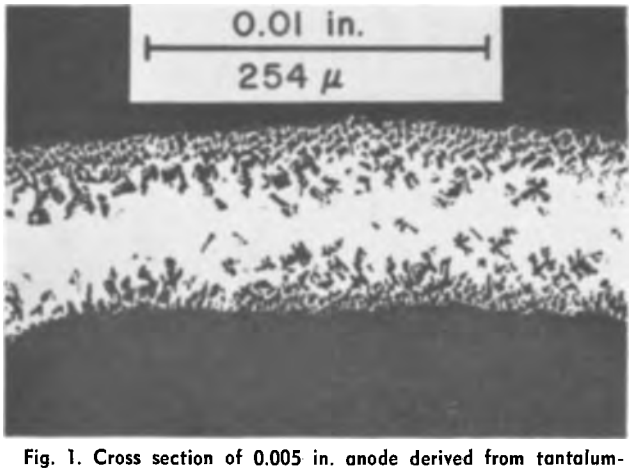

Fig. 1. Cross section of 0.005 in. anode derived from tantalum-titanium alloy sheet. Surface enhancement ratio 14.2.

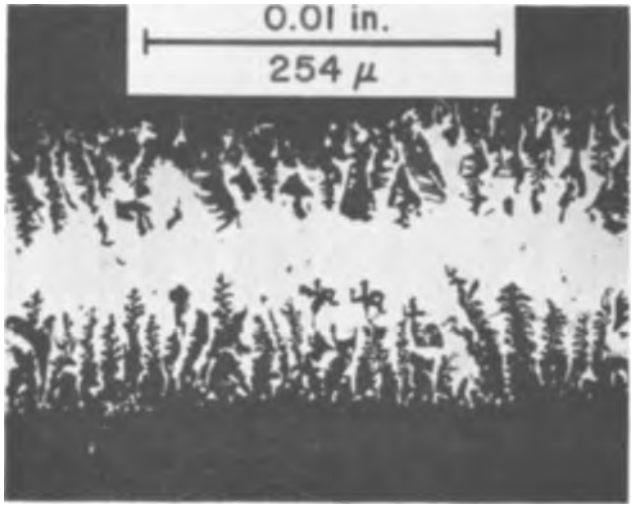

Fig. 2. Cross section of 0.009 in. anode derived from niobium-titanium alloy sheet. Surface enhancement ratio 17.6.

Most of the original titanium content is removed from the alloy as a result of the volatilization process. It would be expected that significant amounts of residual titanium are to be found only deep within the nonporous portion of the anode, *i.e.*, that the anode surface after the vacuum heating step may be considered, to a first approximation, essentially tantalum or niobium. This was confirmed by comparison of x-ray fluorescence from the surfaces of a sheet specimen of niobium-titanium alloy and the product obtained by heating the same material in vacuum. An x-ray probe of sufficient energy to penetrate to an effective depth of about 5μ produced radiation completely devoid of titanium peaks from the vacuum heated specimen; the unheated specimen was characterized by very strong titanium peaks. The limit of titanium detection in this case was below 0.1%.

To characterize further the surface of anodes prepared by vacuum heating tantalum-titanium sheet, the anodic oxide layers formed to different voltages on this substrate were isolated and analyzed by emission spectrography. General aspects of anodization, which in this case was carried out in aqueous 0.01% propionic acid, have been described previously (1). Anodic film isolation was effected by leaching away metal from the anodized specimens with a solution of 10% (by volume) bromine in anhydrous methanol. As shown in column 6 of Table IV, titanium values in the isolated anodic films are independent of film thickness for anodized layers formed from 50 to 500v at room temperature. These analyses confirm that titanium concentration in the superficial regions of alloy-derived tantalum anodes prepared in this manner is no greater than about 0.07% (by weight) to a depth of at least 0.36μ, which is the approximate tantalum thickness required to generate a 500v anodic layer (2).

Surface Enhancement

The highly developed surface of the alloy-derived anodes, as evident from optical microscopy, is manifest in high capacitance values after formation and testing in suitable electrolyte systems. For example, these materials may be anodized conveniently in aqueous 0.01% H_3PO_4 at 25°C and tested in aqueous 10% H_3PO_4 at 25°C using the methods described earlier (1). Formation to 200v with a 1-hr current decay period results in wet-cell test capacitance values such as those shown in Tables I and II. The capacitance per area values are based on apparent, or geometric, area. Upon comparison with the capacitance values obtained using 0.0005 in. foil specimens of tantalum and niobium anodized under identical conditions, it is evident that the true area of the alloy-derived anodes which is effectively available for anodic oxide film formation to 200v is much greater than the geometric area. Other things being equal, the surface enhancement ratio increases with increasing thickness of the anode, because of increasing pore depth.

The high capacitance level of the alloy-derived anodes is entirely accounted for by available surface area, as demonstrated by comparison of surface area values deduced from capacitance measurements after anodization, with those from determination of absolute

Table I. Comparison of tantalum-titanium alloy sheet derivatives with plain tantalum foil and sintered compacts of tantalum powder

	Ta-Ti derivatives				Ta foil[a]	Ta sintered powder compacts[b]
Thickness, in.	0.0013	0.003	0.005	0.010	0.0005	3/16 diam
Surface enhancement ratio	4.1	8.2	14.2	27.3	1.00	—
Capacitance,[c] μf/in.^{2}	1.79	3.62	6.24	12.01	0.44	—
Capacitance,[c] μf/g	14.9	16.7	16.9	17.2	6.6	12.5
Capacitance,[c] μf/cm^3	168	164	184	148	110	125
D-C leakage at 160v, μa/μfv	0.007	0.007	0.005	0.009	0.0020	0.0006[d]
Dissipation factor, %	1.00	1.44	1.70	2.08	0.90	12.7

[a] Heated in vacuum at 2100°C for 1 hr.
[b] Made from a typical commercial "hi cap" powder; sintered at 2150°C for ½ hr; current decay period 2 hr.
[c] 200v formation.
[d] Test voltage 140v.

Table II. Comparison of niobium-titanium alloy sheet derivatives with plain niobium foil and sintered compacts of niobium powder

	Nb-Ti derivatives				Nb foil[a]	Nb sintered powder compacts[b]
Thickness, in.	0.0013	0.003	0.006	0.009	0.0005	3/16 diam
Surface enhancement ratio	4.1	6.6	13.5	17.6	1.00	—
Capacitance,[c] μf/in.^{2}	2.07	3.31	6.77	8.79	0.50	—
Capacitance,[c] μf/g	32.4	29.3	25.3	30.2	14.3	11.4
Capacitance,[c] μf/cm^3	194	161	135	129	123	67
D-C leakage at 160v, μa/μfv	0.013	0.010	0.010	0.016	0.0060	0.004[d]
Dissipation factor, %	1.16	1.64	2.14	2.64	0.80	9.0

[a] Heated in vacuum at 2100°C for 1 hr.
[b] Made from a typical −200 mesh powder; sintered at 2100°C for 2 hr; current decay period 2 hr.
[c] 200v formation.
[d] Test voltage 140v.

surface area by means of BET krypton sorption. To illustrate, six specimens were prepared from niobium-titanium alloy sheet by vacuum heating. The value for charge per unit apparent area for two specimens, after formation to 100 and 200v in aqueous 0.01% H_3PO_4, was 1220 μfv/in.^{2}; this value corresponds to a surface enhancement ratio of 12.2 as compared to 100 μfv/in.^{2} obtained with plain niobium foil vacuum heated and formed under identical conditions. Measurement of absolute surface area of the four unanodized samples of the same alloy-derived material resulted in the data summarized in Table III, from which it is clear that the true area of these specimens is an average of 14.2 times the geometric area. A somewhat higher value is to be expected from gas adsorption measurements than from capacitance determinations, since a portion of the surface reached by krypton atoms is inaccessible to anodizing electrolyte. That some 85% of the anode surface area is reproduced by a 200-v anodic layer, which is about 0.44μ thick (3, 4, 1), attests to the high degree of smoothness in the pore walls and absence of very small pores in these anodes. Further discussion of pore sizes is found below.

Much of the over-all volume of the alloy-derived anodes is essentially a network of pores, resulting in excellent anode material utilization values. It is evident from Tables I and II that gravimetric capacitance efficiencies of the alloy-derived anodes are from 2 to 2½ times those of 0.0005 in. foil specimens of pure tantalum or niobium. The alloy-derived anodes are more efficient on a weight basis than sintered compacts made of tantalum and niobium powders, as well. The advantage is more striking in the case of niobium than tantalum; this is related to the lower melting point of niobium and the excessive surface loss which occurs on sintering niobium powder compacts at temperatures sufficiently high to produce pellets which display low leakage current on anodization (1). Volumetric capacitance efficiencies of alloy-derived anodes also are higher than those of anodes prepared from plain 0.0005 in. foil or sintered powder compacts of pure tantalum or niobium, as based on physical dimensions of anode specimens. However, the volumetric capacitance efficiencies can be misleading unless interpretation in terms of anode configuration for insertion into a specific case size is possible.

Table III. Surface area of 0.0055 in. specimens derived from niobium-titanium sheet

	1	2	3	4
Geometric area after vacuum heating, cm^2	20.5	25.8	32.9	58.7
Absolute (BET) surface area, cm^2	299	356	479	821
Surface enhancement ratio*	14.6	13.8	14.6	14.0

* Compare with 12.2 from capacitance measurements.

Capacitance data listed in Tables I and II are close to the optimum values which have been achieved for anodes of the respective thicknesses. These data were determined early in this research, using small specimens (approx. 1 x ½ in.) which were vacuum heated only a few at one time. Later during the investigation it was found that the simultaneous vacuum heating of many and/or larger specimens in a single batch resulted in anodes which displayed considerably lower d-c leakage levels after formation than the values shown in Tables I and II. With large furnace loads, d-c leakage values as low or lower than those obtained with plain foil vacuum annealed at 2100°C are readily attained. This fact indicates that an important role might be played by titanium vapor which evolves from the alloy sheet under heat-treatment. There seems good reason to speculate that presence of titanium vapor in the furnace hot zone serves to getter the residual atmosphere, and thus decrease or prevent the absorption and accumulation of interstitial impurities in the titanium-containing alloy undergoing vacuum heating.

Conservation of Effective Anode Area to High Formation Voltages

Visual examination of sectioned specimens of the alloy-derived anodes indicates that the pores are smooth-walled and predominantly greater than 5μ in diameter. Since this dimension is large as compared to the thickness of anodic layers, reported to be about 15 Å/v for tantalum (2, 5) and 22 Å/v for niobium (3, 4, 1) in the case of films formed at room temper-

Table IV. Characterization of 0.0045 in. anodes derived from tantalum-titanium sheet

Formation,[a] v	Capacitance[b], μf/in.²	D-C leakage,[c] μa/μfv	Dissipation factor,[d] %	Charge value (CV product), μfv/in.²	Ti conc. in anodic oxide, %
50	23.0	0.0015	4.00	1148	0.068
100	11.67	0.0009	2.10	1167	0.065
200	5.32	0.0007	1.40	1064	0.042
300	3.72	0.0006	1.00	1116	0.052
400	2.48	0.0013	0.80	992	0.056
500	2.04	0.0030	0.96	1020	0.074

[a] Formed in aqueous 0.01% propionic acid at 25°C, using current density of 1 ma/in.² based on absolute surface area of anode; final voltage maintained for 1 hr.
[b] Based on geometric anode area.
[c] Measured at 70% of forming voltage in aqueous 0.01% propionic acid.
[d] Measured at 120 cps in aqueous 10% H_3PO_4.

ature, little effective anode surface loss should occur as a result of anodic film growth. This is verified experimentally and is evident from the nearly constant charge values shown in Table IV for anodes derived from tantalum-titanium sheet which were formed to voltages from 50 to 500v.

A plot of reciprocal capacitance *vs.* formation voltage is linear if effective anode surface is constant. Such a plot for anodes derived from niobium-titanium sheet is shown in Fig. 3. Formation in this case was carried out at 25°C in aqueous 0.01% H_3PO_4. The fact that essentially no deviation from linearity is evident up to 500v formation constitutes a demonstration that effective anode surface is not detectably dependent on anodic oxide thickness up to this level, assuming that dielectric constant and field strength within the anodic layer also are independent of thickness.

A definite limit on the thickness of anodic layers which may be formed in dilute aqueous acid electrolytes is imposed by scintillation phenomena which occur at potentials near 500v at room temperature. The use of certain essentially nonaqueous electrolytes allows formation to potentials well in excess of 500v. An electrolyte which has proven particularly suitable for anodization of alloy-derived tantalum is made by dissolving 125g boric acid in a solvent consisting of 250g ethylene glycol and 250g diethylene glycol, and adding concentrated ammonium hydroxide dropwise to a resistivity of 2000 ohm-cm at 125°C. In the following discussion, this electrolyte is referred to as EDBA-2000. Formation may be carried out conveniently at temperatures considerably above room temperature in this electrolyte, thus serving to form thicker oxide layers as a result of the increased temperature as well as higher potentials.

Alloy-derived tantalum anodes surface-enhanced 30.5-fold were used to study the effect of forming to high voltages in the EDBA-2000 electrolyte. These anodes contain more internal surface than those which

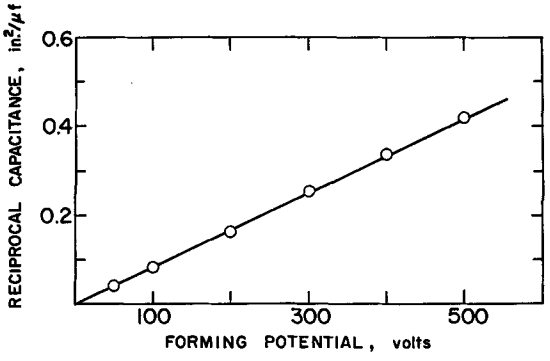

Fig. 3. Reciprocal capacitance vs. formation voltage for 0.0055 in. anodes derived from niobium-titanium alloy sheet. Surface enhancement ratio 12.2.

Fig. 4. Cross section of 0.014 in. anode derived from tantalum-titanium alloy sheet. Surface enhancement ratio 30.5.

are characterized by Table IV and Fig. 3 because of greater anode thickness, 0.014 in., and consequently deeper pores. The specimen shown in Fig. 4 has been formed to 600v at 125°C in EDBA-2000, and the anodic oxide layer, estimated to be 1.2μ in thickness, is visible in the photomicrograph. It appears that some of the smaller pores may be filled with oxide, but the photomicrograph is deceptive because any significant offsetting of the plane of section from the center of a pore gives the illusion of a filled or partially filled pore. Further, the apparent thickening of oxide layer in certain regions is due to large deviations from normality in the angle between the plane of section and the surface of a pore wall.

To measure quantitatively the extent of surface loss at high formation voltages in EDBA-2000 at 125°C, and to compare the capacitance of anodes formed in EDBA-2000 at 125°C and in aqueous 0.01% propionic acid at 25°C, specimens of the 0.014 in. thick, 30.5-fold surface-enhanced alloy-derived tantalum were formed to various voltages in both electrolytes. A summary of capacitance and dissipation factor values for these specimens, measured at 25°C in 10% H_3PO_4, is tabulated in Table V. The decrease in CV product with increasing formation voltage reflects the loss in effective anode area at high formation voltages. The

Table V. Capacitance-formation voltage relationship for 0.014 in. anodes derived from tantalum-titanium sheet

Formation,[a] v	Capacitance,[b] μf/in.²	Dissipation[c] factor, %	CV product, μfv/in.²	CVT product 10^3 μfv°K/in.²
Formation in aqueous 0.01% propionic acid at 25°C				
50	53.7	6.60	2680	800
100	27.2	4.34	2720	810
150	17.86	2.60	2680	798
200	13.28	2.06	2660	791
250	10.53	1.60	2630	784
300	8.67	1.50	2600	775
350	7.01	2.10	2450	731
400	6.14	1.30	2460	735
450	5.28	1.10	2380	708
500	4.56	1.10	2280	680
Formation in EDBA-2000 at 125°C				
50	38.9	4.60	1940	774
100	20.0	3.34	2000	796
150	13.30	1.90	2000	794
200	9.87	1.76	1970	786
250	7.73	1.32	1930	770
300	6.07	1.30	1820	725
350	5.12	1.20	1790	713
400	4.29	1.10	1740	691
450	3.62	1.04	1630	648
500	3.14	1.04	1570	625
550	2.93	1.00	1610	642
600	2.56	1.00	1540	611

[a] Current density 1 ma/in.², based on absolute surface area of anode; final voltage maintained for 1 hr.
[b] Based on geometric anode area.
[c] Measured at 120 cps in aqueous 10% H_3PO_4.

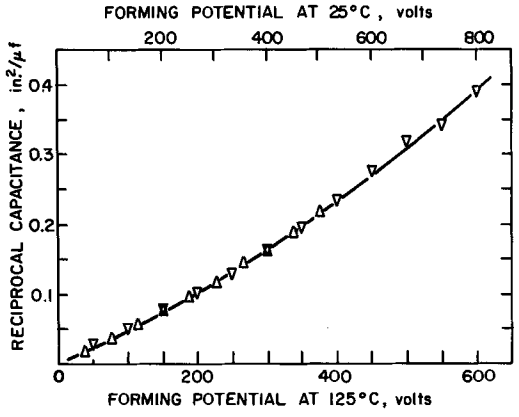

Fig. 5. Reciprocal capacitance vs. formation voltage for 0.014 in. anodes derived from tantalum-titanium alloy sheet. Surface enhancement ratio 30.5. △, 25°C; ▽, 125°C.

loss is moderate. Formation to 500v in aqueous 0.01% propionic acid at 25°C results in an effective loss of about 15% of the anode area available at formation up to 200v. Similarly, formation to 600v in EDBA-2000 at 125°C results in an effective anode area about 22% lower than that obtained as a result of formation up to 200v.

Constancy of the product of capacitance, formation voltage, and formation temperature (CVT product) has been demonstrated by Torrisi in the case of plain tantalum foil (6). Comparison of the CVT products shown in Table V for the 30.5-fold surface-enhanced alloy-derived tantalum specimens formed under the two different conditions shows that at low formation voltages, corresponding to negligible area loss due to oxide film growth, both formation conditions yield values near 800,000 μfv°K/in.^{2}. Thus the CVT product appears to be a constant, within experimental error, for the alloy-derived tantalum anodes as well. Plots of reciprocal capacitance as a function of formation voltage are exactly superimposable, as shown in Fig. 5, if formation voltages under the two temperature conditions are reduced to equivalent film thicknesses by the use of the CVT relation. Constancy of the CVT product strongly indicates that the dielectric constant of the anodic layer formed at 125°C in EDBA-2000 is the same as that formed at 25°C in aqueous 0.01% propionic acid.

The slight concavity of the plot in Fig. 5 is due, of course, to filling in of minor pores with anodic oxide, and the 22% area loss as a result of formation to 600v at 125°C may be considered slight indeed in view of the fact that the resultant film thickness is equivalent to that of an hypothetical room temperature film formed to 802v. Even this moderate loss would be lowered in the case of thinner alloy-derived tantalum anodes or those prepared under conditions such that the lower pore size limit in the final product be larger.

The conservation of anode area to high forming voltages shown by the alloy-derived materials is in marked contrast to the case of electrochemically etched foils. The latter materials are characterized by a surface enhancement factor, commonly referred to as the etch ratio, which decreases rapidly with increasing formation voltage. For this reason, as well as the excellent quality of the anodic film, the alloy derivatives are of particular interest for application in high voltage devices.

The large pore size characteristic of these anodes is a major factor contributing to the low dissipation factors shown upon formation and testing in a suitable electrolyte. Typical values are listed in Tables I and II. Access to all anodized internal surfaces through low resistance paths results in a low equivalent series resistance component of the total electrical loss.

High Electrical Quality of Anodic Oxide Layer

Choice of a criterion by which anodic oxide quality may be assessed is not obvious. For example, measurement of d-c leakage at a given voltage level is open to question because the voltage level is in itself arbitrary, and also because the leakage value obtained may be influenced by anodization kinetics during initial film formation if an electrolyte of high resistivity is used. To avoid scintillation at relatively low voltages, it is not unusual to employ electrolytes of high resistivity for investigations at high voltages. Also, spuriously high d-c leakage values may result from capillary rise of test electrolyte past the limit of anodized area on the test specimen. Similarly, mere formation to high voltages is not a definitive test because many substances can be formed to levels well beyond those at which irreparable damage to the anodic layer is done in the form of field-induced crystallization.

Because of these objections, an attempt has been made to design an evaluation procedure which yields information concerning the barrier oxide film quality at several voltages up to the ultimate formation voltage. The technique used involves slow formation at constant current density with intermittent pauses at various voltage levels to note current decay at derated voltages. In effect this corresponds to the measurement of leakage current at many voltages over a wide range, although without holding time at formation voltage. The advantage of this technique lies in permitting definition of a formation level above which an increased rate of change of terminal current during the decay period with formation voltage is observed. Such an increase is interpreted as corresponding to a degradative change in the nature of the barrier oxide film, or what is often called "incipient crystallization." Using an abrupt change in the decay current-formation voltage relationship, rather than the absolute magnitude of the decay current, as the significant response of the quality test reduces objections centered on capillary rise of electrolyte past the anodized area of the specimen as well as slow anodization rate. Interference from the latter factor is further decreased by employing low current densities in the test.

The quality tests were conducted using a current density of 1 ma/in.^{2}, anode area being taken as the total area exposed to anodizing electrolyte. Area was deduced from capacitance measurements on similarly prepared samples, after 200-v formation. Except in the case of the 0.014 in. anodes, no lead wires were attached to the specimens used in these experiments; connection to the power supply circuit was made directly through a narrow tab of the anode which intersected the electrolyte level. Current decay readings were taken at 50-v or shorter intervals. On reaching

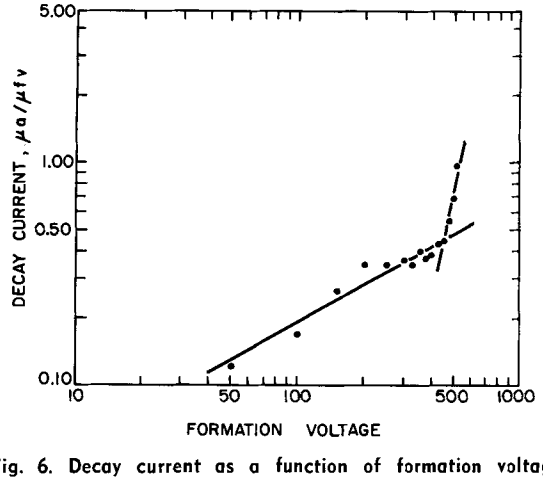

Fig. 6. Decay current as a function of formation voltage in aqueous 0.01% H_3PO_4 at 25°C for 0.006 in. anodes derived from niobium-titanium alloy sheet. Surface enhancement ratio 13.5. Scintillation at 510v.

the formation voltage at which a value for decay current was desired, the potential was dropped back to 70% of forming voltage over a period of 1 min and current allowed to decay at this potential for 3 min. The value used as the decay current was that after 3 min at 70% of forming voltage, or after a total of 4 min under derated voltage. Voltage was then increased back to formation voltage over the period of 1 min, and formation at 1 ma/in.^{2} was resumed. Testing was extended to the highest voltage attainable before anodization rate became seriously slowed or severe scintillation limited higher formation. The values for observed scintillation voltages which are reported in the subsequent discussion are those at which visible sparking is first seen in a darkened room. Scintillation voltages defined in this way were reproducible within a range of 5-10v.

A logarithmic plot of decay current as a function of formation voltage in aqueous 0.01% H_3PO_4 (2950 ohm-cm) at 25°C is shown in Fig. 6, for anodes derived from niobium-titanium alloy sheet. The break in the curve indicates that anodic oxide film degradation sets in at about 450v under these formation conditions. Visible scintillation is observed slightly above 500v.

A similar test in aqueous 0.01% propionic acid (approximately 19,000 ohm-cm) at 25°C for anodes derived from tantalum-titanium alloy sheet is summarized in Fig. 7. Remarkably, at no voltage level does the plot show an upward trend; decay current decreases with increasing voltage past 500v, at which point visible scintillation is first noticeable, to 565v, a level at which scintillation is so extensive that further potential increase across the anodization cell is not possible without increasing current density. The high decay current values at low voltages shown in Fig. 7 are a result of the high electrolyte resistivity. A significant voltage drop across the electrolyte results in a lag in anodic film growth and continued film growth occurs at derated voltages. The relative effect is much greater at low voltages than high voltages, in agreement with the downward trend of the plot. With electrolytes of higher conductivity, delay of anodic film growth is greatly lessened. For example, using aqueous 1% propionic acid electrolyte (1950 ohm-cm) at 25°C, decay current is independent of formation voltage up to the scintillation potential (500v), as shown in Fig. 8. The higher conductivity of this electrolyte, however, allows greater current flow in the event of a triggering mechanism at the oxide-electrolyte interface, and degenerative changes in the anodic film occur shortly beyond the scintillation voltage.

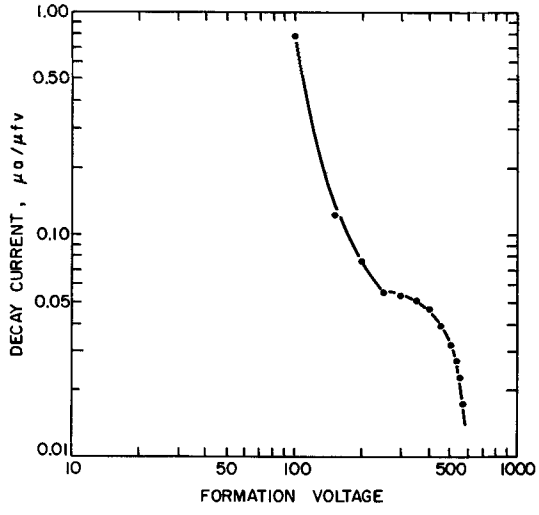

Fig. 7. Decay current as a function of formation voltage in aqueous 0.01% propionic acid at 25°C for 0.005 in. anodes derived from tantalum-titanium alloy sheet. Surface enhancement ratio 14.2. Scintillation at 500v.

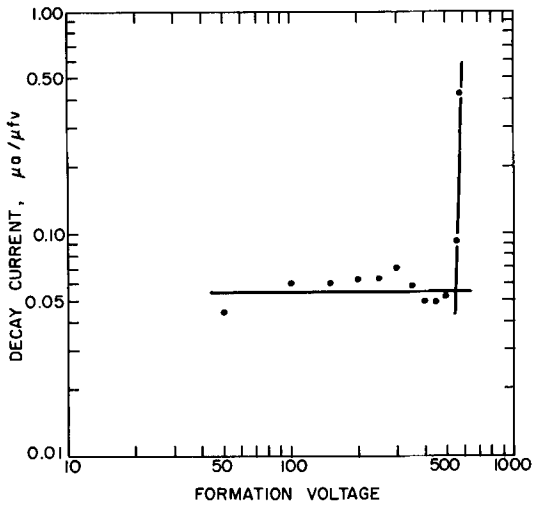

Fig. 8. Decay current as a function of formation voltage in aqueous 1% propionic acid at 25°C for 0.005 in. anodes derived from tantalum-titanium alloy sheet. Surface enhancement ratio 14.2. Scintillation at 500v.

Because the theoretical implications of the anodic oxide quality test, as described above, are subject to further clarification, it is important to use the same test with anodes of well-characterized properties; when used on a comparative basis, the quality test is shown to be significant as a purely operational tool. For comparison, a logarithmic plot of decay current at derated voltage *vs.* formation voltage in aqueous 0.01% propionic acid at 25°C for 0.0005 in. commercial tantalum foil ("high reliability" capacitor grade) is shown in Fig. 9. Formation of foil which is cleaned only by washing and degreasing can be carried to 440v at which level scintillation occurs, but evidence for incipient crystallization as defined above, appears at about 250v. A vacuum purification-anneal heat treatment of such foil at 2100°C for 2 hr, however, results in markedly improved anodization behavior. After such treatment, formation can be continued to 480v without evidence of incipient crystallization.

The excellent quality of the anodic layer formed on an alloy-derived porous tantalum body in EDBA-2000 at 125°C, using as a criterion the change in decay current at 70% of forming voltage as a function of forming voltage, is demonstrated by the logarithmic current-voltage relationship shown in Fig. 10. These data were observed during formation of a 0.014 in. thick, 30.5-fold surface-enhanced anode. Visible scintillation occurs at 640v and evidence of anodic film

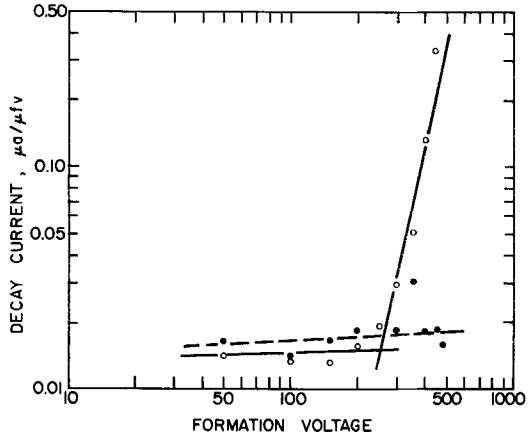

Fig. 9. Decay current as a function of formation voltage in aqueous 0.01% propionic acid at 25°C for 0.0005 in. plain tantalum foil. • - - - •, 2100°C for 2 hr, scintillation at 480v; ○—○, washed only, scintillation at 440v.

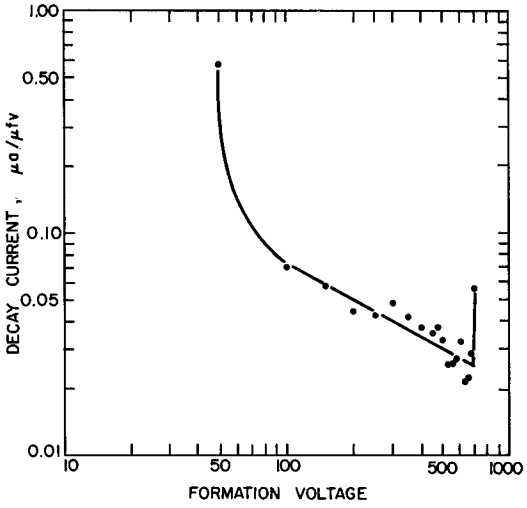

Fig. 10. Decay current as a function of formation voltage in EDBA-2000 at 125°C for 0.014 in. anodes derived from tantalum-titanium alloy sheet. Surface enhancement ratio 30.5; scintillation at 640v.

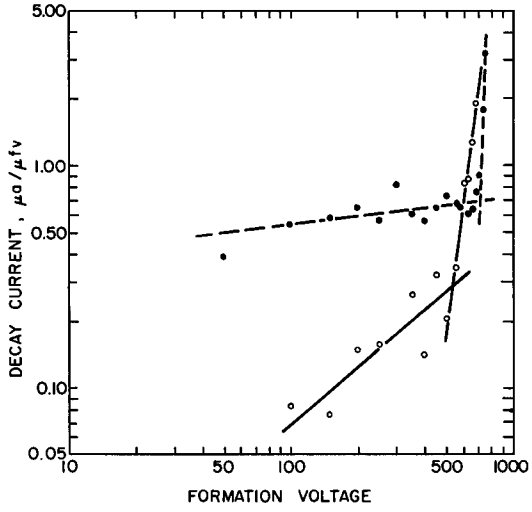

Fig. 11. Decay current as a function of formation voltage in EDBA-2000 at 125°C for 0.0005 in. plain tantalum foil. ● - - - ●, 2100°C for 2 hr, scintillation at 650v; ○ — ○, washed only, scintillation at 625v.

degradation at about 680v is indicated by the sharp increase in decay current. The decreasing tendency of decay current with increasing formation voltage is similar to that observed in Fig. 7 for anodization in aqueous 0.01% propionic acid. From the similarity in electrolyte resistivities, it might be expected that formation in EDBA-2000 would yield a decay current-voltage relationship more like that observed with aqueous 1% propionic acid, as shown in Fig. 8. However, the deeper pores in the 0.014 in. thick specimen contribute significantly to a lag in anodic film growth, the effect of which is pronounced at low formation voltages. In this respect, anodes derived from thick alloy sheet resemble conventional porous pellets made from pure metal powder compacts.

For comparison, the evaluation of 0.0005 in. commercial tantalum foil in EDBA-2000 at 125°C is summarized by the logarithmic plots of decay current *vs.* formation voltage for vacuum heated and unheated foil, shown in Fig. 11. Quality degradation begins near 500v for the unheated foil and near 680v for the foil heated in vacuum at 2100°C for 2 hr. The high decay current levels observed on vacuum heated tantalum foil prior to reaching voltage levels at which oxide degradation occurs are caused by enhanced wetting of the specimen tab by the electrolyte, with the result that oxidation is not limited at a sharp boundary just above the electrolyte-air interface during the test. For an unknown reason, the unheated specimen does not exhibit the same wetting characteristics, as indicated by the generally lower decay current levels below the breakdown voltage.

Another method of comparing the anodic characteristics of the alloy-derived tantalum with those of commercial tantalum foil is to measure current decay as a function of time at some arbitrary voltage level. Current decay curves at 600v in EDBA-2000 at 125°C after slow formation to this voltage at 1 ma/in.^{2} (based on absolute anode area) are shown in Fig. 12. The alloy-derived anode in this case is the same high surface enhancement material as that used in the quality test summarized in Fig. 10. In spite of the higher surface area of the alloy-derived anode, its anodic layer heals more rapidly at 600v in EDBA-2000 at 125°C, as compared to commercial tantalum foil. Both the alloy-derived tantalum material and vacuum heated commercial tantalum foil exhibit decay currents which still diminish after 6 hr, whereas the commercial tantalum foil not heated in vacuum shows a reversal after about 2½ hr.

Resistivity of EDBA-2000 electrolyte increases from 2000 to 2350 ohm-cm over a 6-hr period at 125°C,

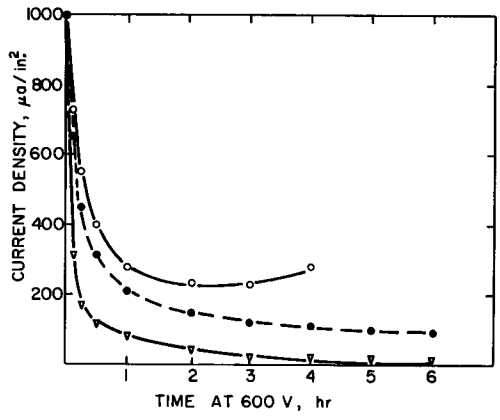

Fig. 12. Current decay at 600v in EDBA-2000 at 125°C for 0.0005 in. plain tantalum foil and for 0.014 in. anodes derived from tantalum-titanium alloy sheet, surface enhancement ratio 30.5. ○ — ○, Ta foil, washed only; ● — ●, Ta foil, 2100°C for 2 hr; ▽ — ▽, alloy-derived Ta anode.

primarily as a result of ammonia evaporation. Although this has the effect of depressing decay current slightly during anodic evaluation in this electrolyte, intercomparison of alloy-derived tantalum and commercial tantalum foil is justified because the test was carried out in the same manner for each sample.

Among the factors leading to the good anodic quality apparent in the alloy-derived anodes, several would appear to be of primary importance. The possible effect of gettering the furnace hot zone with evolved titanium already has been mentioned. Certainly the fact that essentially all of the anode surface is newly created during the vacuum heating step, and in no way mechanically handled prior to anodization, represents a degree of surface cleanliness unmatched in conventional foil or sintered powder compacts. During the vacuum heating step, which is carried out at temperatures near the melting point of the initial alloy, diffusion of impurities is more rapid than in pure tantalum or niobium; this can be expected to result in a more efficient operation of the various physical and chemical processes which serve to produce and remove volatile impurities. Removal of the volatile impurities is further facilitated by the *in situ* development of pores in the metal body. Not to be disregarded is the surface smoothness inside the pores formed during titanium volatilization. The smooth contours presented by the inner pore walls are conducive to the formation of

anodic layers of uniform thickness and freedom from defects induced by sharp field gradients.

Conclusions

The new forms of porous tantalum and niobium, which result from high-temperature vacuum removal of titanium from binary alloys of tantalum and niobium with titanium, appear highly suitable for use as electrolytic capacitor anode materials. Two outstanding advantages inherent in these materials are high surface enhancement ratios which are diminished only slightly by formation to voltages up to 600v and excellent anodic oxide quality. These characteristics indicate that anodes made from the alloy-derived materials will be especially useful for application in high voltage capacitors.

Publications to follow describe capacitors (7) made using anodes such as those described above.

Acknowledgment

The author wishes to express grateful appreciation to Mr. Charles E. Perry, who performed much of the experimental work, to Mr. Karl Moeglich for valuable discussion of anodic oxide quality which led to the quality evaluation test employed in this investigation, and to Dr. Kurt F. J. Heinrich for the surface x-ray fluorescence examination.

Manuscript received May 21, 1964. This paper was presented at the Toronto Meeting, May 3-7, 1964.

Any discussion of this paper will appear in a Discussion Section to be published in the December 1965 JOURNAL.

REFERENCES

1. R. B. Hand, H. W. Ling, and T. L. Kolski, *This Journal*, **108**, 1023 (1961).
2. L. Young, *Proc. Royal Soc. (London)*, **A244**, 41 (1958).
3. L. Young, *Trans. Faraday Soc.*, **52**, 502 (1956).
4. L. Young, *Can. J. Chem.*, **38**, 1141 (1960).
5. D. A. Vermilyea, *This Journal* **102**, 655 (1955).
6. A. F. Torrisi, *ibid.*, **102**, 176 (1955).
7. T. L. Kolski and H. W. Ling, *Electrochem. Tech.*, In print.

Dielectric Films in Titanium Electrolytic Capacitors

Akio Yamashita and Hiroshi Hagiwara

Research Laboratory, Industrial Apparatus Division,
Matsushita Electric Industrial Company, Ltd., Toyonaka, Osaka, Japan

ABSTRACT

The effects of pretreatment and various formation parameters on the properties of anodic films produced on titanium were investigated. It was found that the anodic film on titanium could be improved by a pretreatment of the titanium in nitric acid. Titanium oxide films were formed anodically in a molten salt electrolyte at constant potential, and the leakage current at room temperature showed a v-type curve for the forming time. Physical and electrical properties of the anodic films to obtain minimum leakage current are discussed. The thickness of anodic film was determined and a dielectric constant of about 107 was obtained.

Aluminum and tantalum are commonly used as the base metals for electrolytic capacitors (1, 2). In the case of titanium, relatively little conclusive information is available, and it is still difficult to form a suitable dielectric film for electrolytic capacitors.

It was the purpose of this investigation to study the effects of pretreatment of the anode and various formation parameters on the character of the anodic films produced. The formation parameters include the molten salt electrolyte composition, forming time, potential, and temperature.

In the study of anodic films on metals, factors of significance in evaluation of films include thickness, porosity, density, and electrical properties. Films prepared in this study were evaluated through measurements of thickness, dielectric constant, and electrical properties.

Many studies on the anodic formation of certain metals have been reported. These include common metals such as tantalum. Titanium, about which little is known with respect to its anodizing characteristics, might be expected to have a high capacitance per unit area, if the oxide film formed is the rutile modification, with a bulk dielectric constant on the order of 100. In most cases, however, the oxide films formed have been neither a pure rutile structure nor insulating in nature. Most researchers (3-5) employed various acids or aqueous solutions of common salts as formation electrolytes. Sibert (3) employed various acid electrolytes. Of the basic electrolytes he tried, the phosphate-based materials gave by far the best results. Huber and Bloxson (4) employed a mixed aqueous solution of weak organic acid and alcohol. McLean *et al.* (5) utilized hydrochloric-nitric-sulfuric acid baths for polishing the surface followed by anodizing in a buffered borate solution. They could not obtain, however, satisfactorily low leakage currents for titanium oxide dielectrics anodically formed in these electrolytes.

The leakage current of an electrolytic capacitor presumably depends on the presence of impurities in titanium (1, 6, 7). Major impurities in commercial titanium are iron and oxygen. It is known that the presence of iron generally causes an increase in the leakage current. Oxygen will be in the form of titanium oxide.

Experimental

Preparation of specimens.—Specimens of 99.7% purity titanium foil were employed as strips 0.5 x 5 cm in a thickness of 0.05 mm. The specimens were cleaned by washing in reagent grade toluene and by polishing the metal surfaces in hydrofluoric and nitric acid to remove surface impurities. The acids and reaction products were removed by pure water rinses lasting several hours. Moreover, specimens were immersed in an appropriate pretreatment solution before anodic formation.

Anodization.—Specimens were centered in cylindrical titanium cathodes 80 mm in diameter. Molten salt electrolytes containing different mixtures of sodium nitrate and calcium nitrate were employed, and films were anodized by the instantaneous application of constant voltage utilizing a battery source. Effects of such parameters as type of electrolyte, forming time, and forming voltage on the properties of the dielectric are shown in the following section.

After removal from the cell, specimens were rinsed in pure water and allowed to dry in air. In most cases, electrical testing was done in 10% nitric acid at room

temperatures with a titanium cathode. Leakage current was noted 5 min after a test potential of 10v was applied across the cell. The capacitance and dissipation factor were determined at 120 or 1000-cps using a bias of 3v d.c. and a signal voltage of 1.5v a.c.

Results

Pretreatment.—It was found that the anodic film could be improved by immersing the anode material in various concentrations of nitric acid which nominally is noncorrosive to titanium. The specimens subjected to the immersion treatment were anodically formed at constant formation voltage of 40v in a mixed molten salt electrolyte of 300°C. Table I illustrates the effects of the immersion time on the electrical properties of anodic films of titanium. The leakage current decreases with the increase in immersion time in every concentration of nitric acid over the range studied. Values of the leakage current after 400-hr immersion are about 1/10 as large as the values obtained with no immersion.

Dissipation factor also decreases with the increase in immersion time. Capacitance remains virtually unchanged (Table I, p. 283).

We think that the effect of pretreatment is as follows: an oxide film of the anatase type was formed on the titanium surface by immersion in nitric acid (8) and was left intact prior to anodic oxidation. That is, we presumed from our investigation that this oxide film greatly influenced the later anodic oxidation. Since titanium is very active, it is easily oxidized in comparison with iron. As a result, after all of the titanium surface is oxidized in a dilute acid, iron will be gradually dissolved away from the surface, and the leakage current will be reduced as the immersion time is extended.

Anodization.—Electrolyte.—The effect of forming conditions on the electrical properties of capacitors is illustrated in Table II, p. 283.

Since a molten salt electrolyte consisting of 25 w/o (weight per cent) sodium nitrate and 75 w/o calcium nitrate has a higher melting point than other combinations, the forming temperature is higher. The composition of the molten salt electrolyte, in which the following data for Fig. 1, 2, 3, 4, 5, and 6 were obtained, consists of 75% w/o sodium nitrate and 25 w/o calcium nitrate.

Forming time.—In the case of titanium the leakage current is largely affected by the forming time.

Figure 1 illustrates the relationship between the forming current and the forming time in a molten salt electrolyte of 320°C. The formation was carried out at constant potential. The forming current decreases with the increase of forming time. It is commonly considered that the forming current decreases with an increase of insulation properties of anodic films. However, the leakage current in $\mu a/(\mu f\text{-}v)$ of an electrolytic capacitor at room temperature does not decrease with the increase of forming time. The relationship between the leakage current in $\mu a/(\mu f\text{-}v)$ at a test potential of 10v and the forming time in minutes for various forming potentials in volts are illustrated in Fig. 2. The leakage current shows a v-type curve for the forming time: that is, a time shorter than that necessary to diminish substantially the forming current gives the smallest leakage current. It is presumed that the decrease in current with forming time does occur in a molten salt electrolyte indicating an increase in insulation character. In an aqueous electrolyte at room temperature a new electrochemical mechanism appears which gives higher leakage for longer formation times.

Figure 3 illustrates the relationship between capacitance, dissipation factor and the forming time. Except in the case where specimens were anodically formed at 10v, capacitance decreased slightly with the increase

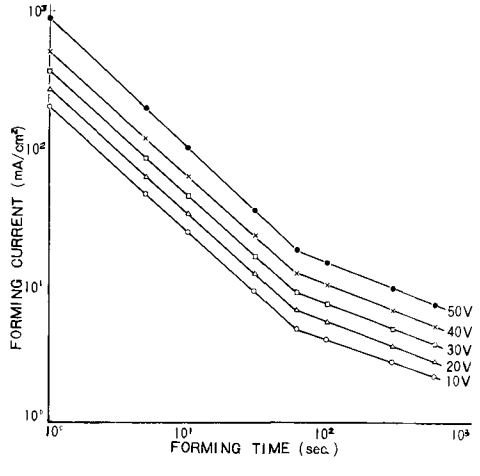

Fig. 1. Relationship between forming current and forming time for various forming potentials.

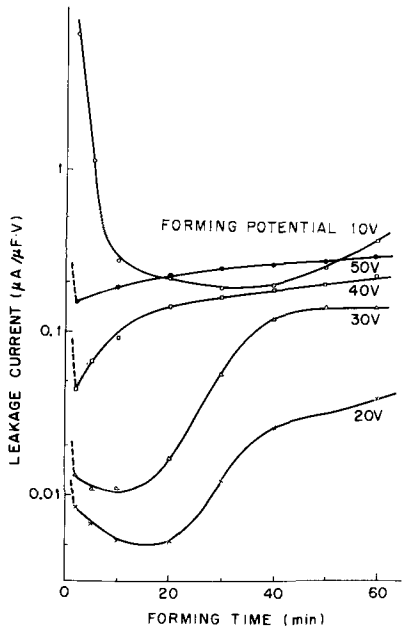

Fig. 2. Relationship between leakage current and forming time for various forming potentials.

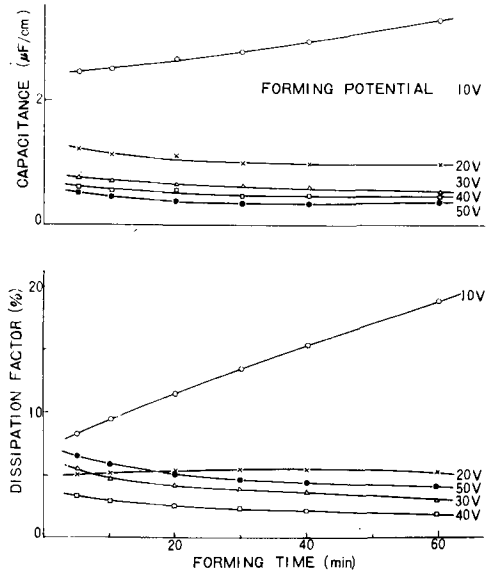

Fig. 3. Dependence of the capacitance and dissipation factor at 1 kc/s on the forming time for various forming potentials.

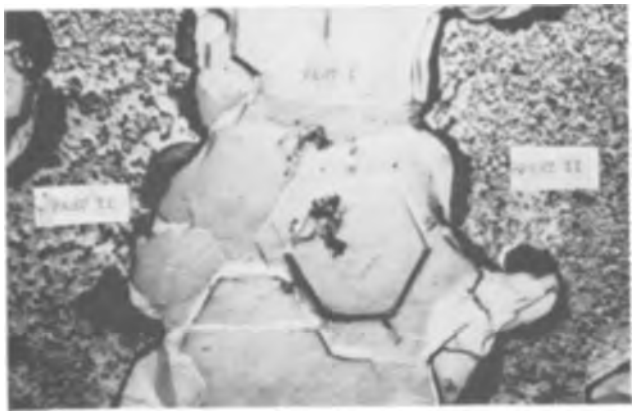

Fig. 4. Electron micrograph of the etched surface formed for a time shorter than that necessary to obtain the minimum leakage current. Magnification 10,000X.

Fig. 5. Electron micrograph of the etched surface formed for a time longer than that necessary to obtain the minimum leakage current. Magnification 10,000X.

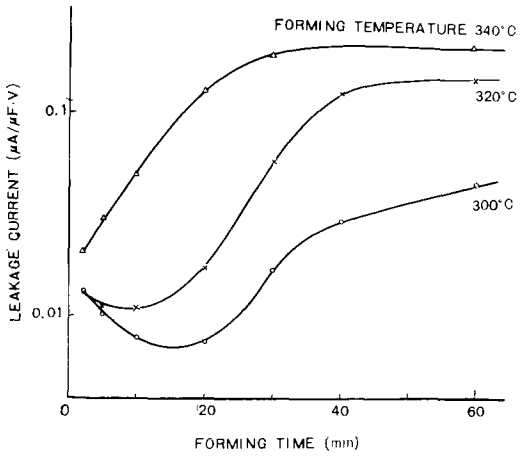

Fig. 6. Relationship between leakage current and forming time for various forming temperatures at the forming potential of 30v.

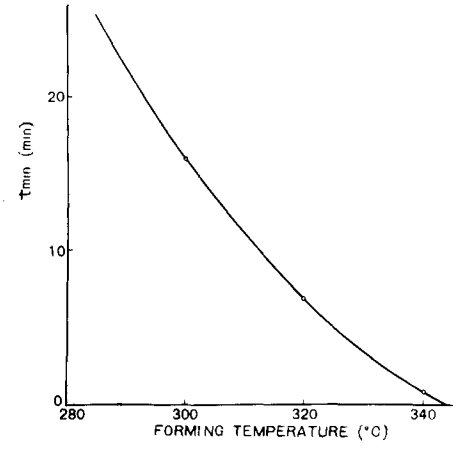

Fig. 7. Relationship between forming time to obtain minimum leakage current and forming temperature.

of the forming time. The capacitance decrease is caused by an increase in the thickness of the anodic oxide film, and very little additional film is formed after 5 min. The dissipation factor decreased with the time except for specimens anodically formed at 10v. It was found that the etching solution CP-4 easily removed the anodic film formed at 10v, and so this film was presumed to be very porous or have a different structure.

Figure 4 is the electron micrograph replica of the surface formed for 10 min at the formation voltage of 10v, which is shorter than the time required to reach the minimum leakage current, and subsequently etched in CP-4. Figure 5 is the electron micrograph of a similar surface but originally formed for 120 min at 30v which is longer than the time required to reach the minimum leakage current. Part I of these photographs shows the titanium surface from which the anodic oxide film has been removed by the etchant, and Part II shows the surface of the anodic film. Since the lattice structure of the titanium molecule is that of a densely packed hexagon, the hexagonal crystal structure is observed in the central part of Fig. 4. The surface of the 10v anodic film (Fig. 4) is rather rough compared with the 30v film (Fig. 5), indicating that the anodic film of the former is etched easier than the latter. The reason is presumably due to insufficient crystallization of the anodic film of the former.

Forming potential.—As shown in Fig. 2, the length of the forming time which gives the smallest leakage current value changes according to various forming potentials. The forming time necessary to obtain the smallest leakage current is less at a high potential (40v) than at a low potential (10v). The minimum in leakage current at 50v is presumed to occur at such a short formation time that it cannot be experimentally detected. Generally the forming time necessary to obtain the minimum leakage current decreases with increasing forming potential. This relationship may be empirically fitted to the data in Fig. 2, using one point at 10v, by the following equation:

$$t_{\min} = 314/v_f - 0.14\,v_f \qquad [1]$$

where $t_{\min}$ is the forming time to obtain minimum leakage current at a 10v test potential, and v_f is the forming potential. This equation indicates that when a lower forming potential is used, a longer forming time will be necessary to obtain the smallest leakage current value. Moreover, it predicts that a minimum leakage current does not exist if specimens are formed at potentials higher than 47.5v. In the capacitor formed at 50v, the leakage current increases as the forming time increases. We think that this increase results from crystallization of the anodic film. Since it is known that the rate of crystallization increases with formation voltage in the case of tantalum (9), it is assumed that the minima of the other formation voltages are also caused by the onset of crystallization.

Forming temperature.—Figure 6 illustrates the relationship between the leakage current and the forming time obtained for various forming temperatures at a forming potential of 30v. The forming time to obtain the minimum leakage current decreases with an increase in the forming temperature. The relationship between the forming time to reach minimum leakage current and the forming temperature is shown in Fig. 7. The curve crosses the x-axis at 343°C. At higher forming temperatures, the leakage current increases with the increase of forming time.

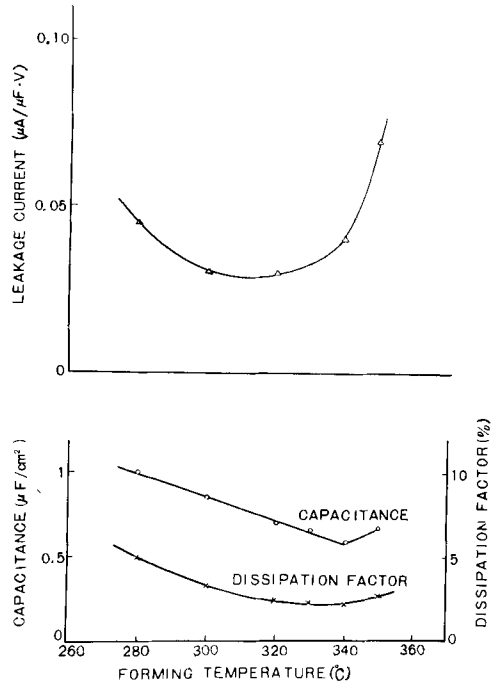

Fig. 8. Variation of capacitance, dissipation factor, and leakage current with forming temperature.

Furthermore the relationship between the electrical characteristics of the film and the forming temperature is shown in Fig. 8. Capacitance decreases linearly with an increase in forming temperature up to about 340°C. At 350°C the capacitance increases somewhat: leakage current increases rapidly between 340°C and 350°C, and the dissipation factor increases slightly at 350°C.

We will attempt to explain the critical temperature in the growth of film due to the theory of Cabrera and Mott (10). When the growth of one layer of atoms takes 10^5-sec[10], it is assumed that the growth of the film is infinitely slow. The thickness of film at that time is X_L

$$X_L = (va'q)/(w - 39kT) \qquad [2]$$

where v is the potential difference across the oxide, a' is the distance from the minimum to maximum potential energy during a jump into oxide, q is the charge on the metal ion entering the oxide, w is the activation energy to enter the oxide in the absence of a field, k is the Boltzmann constant, and T is the absolute temperature. Thus, for temperatures below the critical temperature, $T_c = w/39k$, a stable film is formed: for temperatures above this, the growth continues indefinitely. For titanium at 310°C, the activation energy, w, is 2.09v (11), so the critical temperature T_c should be 348°C. Above 348°C no limiting film will be formed, and the growth will proceed according to the parabolic law. As mentioned above, electrical characteristics show considerable variation between 340° and 350°C, presumably due to the critical temperature of 348°C.

Film Characteristics.—The v-type curve was obtained in the relationship between the leakage current and forming time. The determination of the dielectric constant of the anodic film formed to a minimum leakage current is described in the following sections. The specimens were formed at 40v for 10 min in a molten salt electrolyte whose temperature was 285°C.

Film Thickness.—The thickness of film was ascertained by three methods: measurement of the total amount of charge passed across film during formation, measurement of the interference color, and measurement with an electron microscope. An equation for the total amount of charge passed across the film is $i = A \exp$

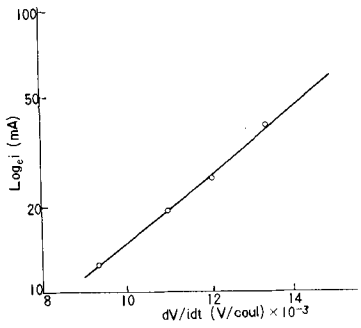

Fig. 9. Relationship between $\log_e i$ and $dv/(idt)$

(BE) according to Cabrera and Mott (10) (A, B = constant). This equation is rewritten as follows

$$\log_e i = \log_e \{SA/\eta\} + 0.4343B \{(S\rho F/M\eta)\, dv/(idt)\} \qquad [3]$$

where i is the circuit current, S the anode surface area, η the current efficiency, ρ the density of oxide film, F the Faraday constant, M the molecular weight of oxide film. The relationship between $\log_e i$ and dv/idt is shown in Fig. 9. The formation was carried out at constant current density at a potential increasing up to 40v. Comparing B (11) obtained directly from the relationship between $\log_e i$ and field F with B obtained from the slope of the line in Fig. 9, the current efficiency should be 0.0208.

By using this current efficiency, the thickness of film is obtained by Faraday's law as follows

$$d_1 = 1830 \text{ (Å)} \qquad [4]$$

This thickness of film was formed with a constant current density at a potential increasing up to 40v, but it is distinct in Eq. [2] that the thickness of film is determined by formation potential. Accordingly the thickness of film formed with constant potential of 40v is approximately equal to the former.

Measurement of the film thickness formed at 40v can also be obtained from the interference color (12, 13). By dividing the thickness of air film giving the same color in transmitted light by the refractive index of bulk rutile (2.62), the thickness of the oxide film is obtained as follows

$$d_2 = 1900 \text{ (Å)} \qquad [5]$$

Furthermore the film thickness is obtained by measurement with an electron microscope. After casting specimens in epoxy resin containing titanium dioxide powder, the oxide film is cut perpendicularly. Figure 10 shows an electron micrograph replica of the cross section of the oxide film. The black line in the center of the graph is the cross section of the oxide film, Part I is titanium, and Part II is the epoxy casting resin. Measuring the film thickness from this photograph results in an average value as follows

$$d_3 \simeq 2000 \text{ (Å)} \qquad [6]$$

The value of film thickness shown in Fig. 11 has been obtained by these methods.

Dielectric constant.—Using the mean value of film thickness formed at 40v, the dielectric constant is obtained as follows

$$\epsilon = (3.6 \times 10^6 \pi C d)/S = 107 \qquad [7]$$

where C is the capacitance, S the anode surface area, $C/S = 0.50 \mu f/cm^2$, d the film thickness of 1900Å. Considering the dielectric constant of the film, the crystal structure is presumed to be a rutile type of titanium dioxide.

Conclusions

It was found that the anodic film could be improved by immersing the anode material in various concen-

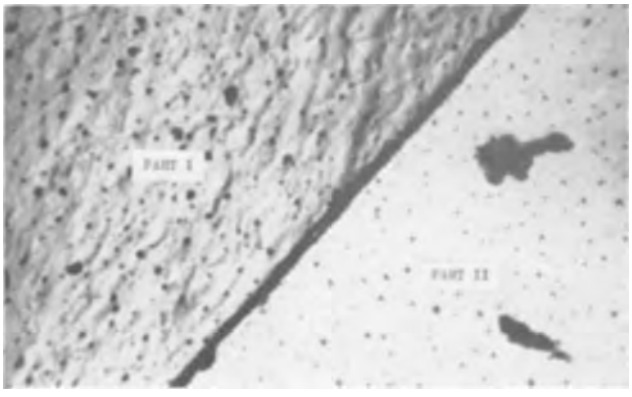

Fig. 10. Micrograph of cross section of oxide film

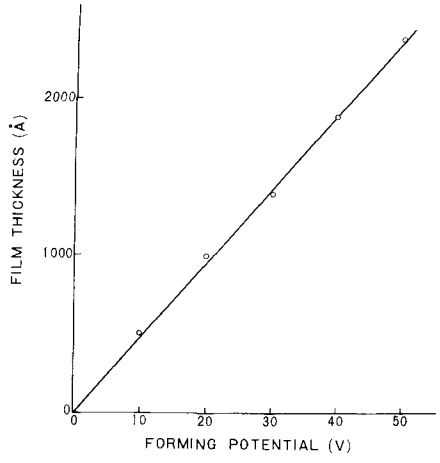

Fig. 11. Relationship between film thickness and forming potential

trations of acid. The leakage current decreases with the increase in immersion time in every concentration of nitric acid.

The leakage current of titanium electrolytic capacitors shows a v-type curve for the forming time, that is, a time shorter than that necessary to substantially diminish the forming current gives the smallest leakage current. The effects of molten salt electrolytes, formation potential, and forming temperature were investigated by a measurement of electrical and chemical properties of anodic oxide films. A critical temperature of 348°C for titanium anodization was obtained and compared with a change of electrical properties.

The measurement of anodic oxide film thickness was obtained by three methods: measurement of the total amount of charge passed across the film, measurement of the interference color, and measurement with an electron microscope. A dielectric constant of 107 was obtained for film formed at 40v. Considering the dielectric constant of the film, the crystal structure is presumed to be rutile type of titanium dioxide.

Acknowledgment

The authors would like to express their hearty thanks to Dr. Miyabe, Professor of Waseda University, who advised them concerning the writing of this paper, Mr. Shimada, manager of the Business Department, Dr. Tsukamoto, chief of the Laboratory, Dr. Yamauchi, deputy chief of the Ist Research Department who encouraged them in their development, and the members of the Central Laboratory who co-operated with them in analyzing the films.

Manuscript received July 1, 1963; revised manuscript received March 5, 1964.

Any discussion of this paper will appear in a Discussion Section to be published in the December 1965 JOURNAL.

REFERENCES

1. J. Burnham, *IRE Trans. Component Parts,* pp. 73-82, Sept., (1957).
2. R. L. Taylor and H. E. Haring, *This Journal,* **103**, 611 (1956).
3. M. E. Sibert, *ibid.,* **110**, 65 (1956).
4. F. Huber and J. Bloxson, *IRE Trans. on Component Parts,* June, 1961.
5. D. A. McLean, N. Schwartz, J. K. Werner, and M. Gresh, Bell Tel. Labs., U.S. Army Signal R&D Laboratories Report, ASTIA AD-232-690, Jan. 15, 1960, pp. 14-15.
6. G. Muriset, *This Journal,* **99**, 285 (1952).
7. D. A. Vermilyea, *Acta Met.,* **2**, 476 (1954).
8. J. Chiba, Research Report for Practical Use, **10**, 1653 (1961), published by Institute of Physical and Chemical Research in Japan.
9. D. A. Vermilyea, *This Journal,* **102**, 207 (1955).
10. N. Cabrera and N. F. Mott, *Repts. Progr. Physics,* **12**, 163 (1949).
11. Nagasaki and Ishida, *Keikinzoku in Japan,* 25 (1957).
12. L. Young, *Trans. Faraday Soc.,* **50**, 153 (1954).
13. D. A. Vermilyea, *Acta Met.,* **1**, 282 (1953).

Table I. Effect of pretreatment in nitric acid on the electrical properties of anodic films of titanium

Immersion time, hr	0			0.1			1			20			400		
	i[1]	C[2]	$D.F.$[3]	i	C	$D.F.$	i	C	$D.F.$	i	C	$D.F.$	i	C	$D.F.$
Concentration, volume, %	μa/cm²	μf/cm²		μa/cm²	μf/cm²		μa/cm²	μf/cm²		μa/cm²	μf/cm²		μa/cm²	μf/cm²	
1	0.19	0.49	0.041	0.14	0.51	0.032	0.11	0.56	0.030	0.10	0.57	0.025	0.02	0.55	0.027
10	0.18	0.47	0.039	0.12	0.50	0.038	0.11	0.52	0.029	0.09	0.52	0.025	0.03	0.51	0.020
30	0.19	0.51	0.043	0.08	0.53	0.027	0.08	0.57	0.023	0.07	0.52	0.023	0.03	0.51	0.022
60	0.21	0.46	0.045	0.08	0.52	0.026	0.07	0.54	0.025	0.06	0.51	0.023	0.04	0.50	0.018

[1] i, leakage current at 10v dc.
[2] C, capacitance at 120 cps.
[3] $D.F.$, dissipation factor at 120 cps.

Table II. Effect of forming conditions on the electrical properties of capacitors

Mixture weight per cent $NaNO_3$: $Ca(NO_3)_2$		Melting point, °C	Formation temp., °C	Formation voltage, v	Formation time, min	Cap., μf/cm²	D.F.	Leakage current, μa/μf-v
%	%							
75 :	25	245	320	30	10	0.48	0.031	0.0054
55 :	45	236	320	30	10	0.47	0.030	0.011
25 :	75	368	370	30	10	0.57	0.053	0.070

Glow Discharge Formation of Silicon Oxide and The Deposition of Silicon Oxide Thin Film Capacitors by Glow Discharge Techniques

S. W. Ing, Jr.,[1] and W. Davern

Electronics Laboratory, General Electric Company, Syracuse, New York

ABSTRACT

A process is described for the formation of silicon oxide thin films by the low-temperature decomposition of tetraethoxysilane in an a-c glow discharge. The effects of various process parameters on the film deposition rate and the resultant film characteristics have been studied and are described. It has been shown that thin silicon oxide films prepared by glow discharge techniques can be used effectively as the dielectric in thin film capacitors. The resultant capacitors have low dielectric losses and are very stable under various life test conditions.

A number of techniques have been developed for forming thin amorphous films (less than 1μ) of SiO_2 on various substrates. The most commonly used methods include: (*a*) oxidation (thermal or electrolytic) of silicon (1); (*b*) sputtering of silicon in oxygen (2, 3); (c) evaporation of silicon suboxide in oxygen (4); (*d*) pyrolytic decomposition of organic silicate compounds (5).

The oxidation process is not versatile enough; only silicon substrates can be used. Some success has been achieved with sputtering and evaporation techniques; these can be used in conjunction with a variety of substrate materials. However, the sputtered films that have thicknesses of the order of 1000Å or less usually contain a certain amount of pinholes (2), and show occlusion of large grains with sizes up to 500Å in diameter (3). The evaporated SiO_2 films have ben reported to be hygroscopic (4). The pyrolysis of organic-silicate compounds yields high quality SiO_2 films but only at temperatures greater than 700°C (5); this high-temperature requirement restricts the method to the use of substrate materials that are inert under the conditions of deposition.

A new method based upon a glow discharge has recently been developed (6). Tetraethoxysilane is used, but instead of pyrolyzing at high temperatures, an a-c induced glow discharge is employed to supply the necessary energy for decomposing the tetraethoxysilane and producing silicon oxide. The exact chemical composition of the oxide has not been determined. However, the oxide is amorphous and shows an infrared absorption peak at around 9.4μ, which is characteristic of Si-O bond. Its chemical inertness and its stability at high temperatures are not unlike fused silica.

Previous work in related areas include the electron bombardment formation of thin organic and metallic films (7), the d-c glow discharge deposition of thin films (8), and the d-c gaseous anodization of aluminum (9).

The substrate during the glow discharge deposition of silicon oxide is at near room temperature; thus the technique offers the possibility of depositing films on a wide variety of substrate materials. Furthermore, the oxide films formed by the glow discharge method are quite pin-hole free (6). Consequently, these films have enjoyed a wide range of application. For example, the films have been used effectively as masks against certain impurity diffusions in silicon (6) and GaAs (10) at elevated temperatures.

This paper describes in more detail the glow discharge process that has been developed for depositing thin silicon oxide films. In addition, the paper describes the effects of various process parameters on the film deposition rate and the characteristics of the resultant films. The utilization of glow discharge deposited silicon oxide films as dielectrics in thin film capacitors has been explored and is also reported.

Apparatus and Procedure

The main purpose of the glow discharge apparatus is to expose the substrate to a controlled atmosphere in a partial vacuum. In the present case, the controlled atmosphere consists of a background gas, usually oxygen, and the organic-silicate vapor. A plasma is then formed in the gas which surrounds the substrate where the chemical reactions take place. A flow system is used to feed continuously the background gas (such as argon or oxygen) and the tetraethoxysilane vapor to the reaction chamber; the reaction products are then pumped out. The flow system is shown in Fig. 1. Oxygen is introduced through a leak valve and its flow rate is measured with a rotameter. Tetraethoxysilane is introduced into the chamber through a capillary tube under its own vapor pressure; the vapor pressure is regulated by controlling the source temperature. It has been found that it is necessary to cool the source. In our work this has been accomplished by employing a thermoelectric cooler. The pressure inside the chamber is monitored continuously by a McCleod gauge and controlled by regulating the pumping speed. An adjustable valve is placed in the line leading from the cold trap to the vacuum pump for performing this function.

A schematic of the reaction chamber is shown in Fig. 2. Oxygen is fed into the reaction chamber through the narrow section where the plasma is generated. The

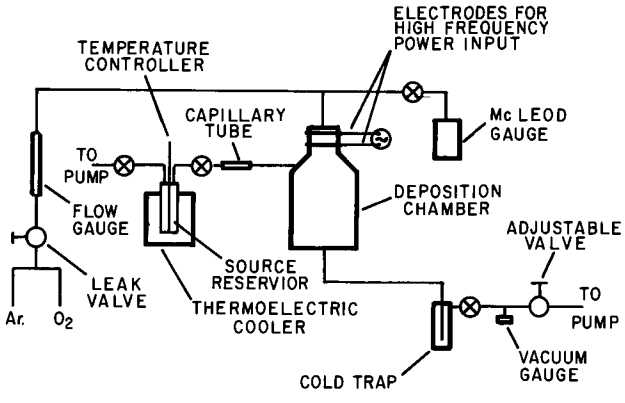

Fig. 1. Flow system used for glow discharge deposition

[1] Present address: Fundamental Research Laboratory, Xerox Corporation, Webster, New York.

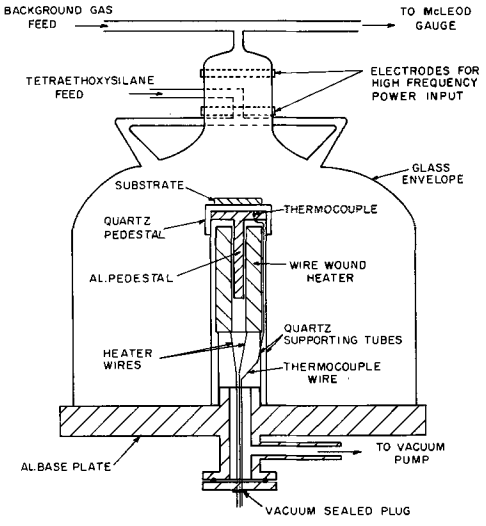

Fig. 2. Glow discharge reaction chamber

Table I. Glow discharge deposition of silicon oxide thin film capacitors

P_{O_2}, mm Hg	T, source, °C	Deposition time, hr	Measured oxide thickness, Å	Capacitance, μμf	Dielectric constant as calculated	Loss tangent
0.09	15.56	½	2850	1580	5.3 ± 0.3	0.015
0.09	15.56	1	3700	1240	5.4 ± 0.2	0.012
0.09	15.56	2	9400	480	5.3 ± 0.1	0.016
0.09	15.56	½	2000	2260	5.3 ± 0.4	0.011
0.18	15.56	1	1800	2800	5.9 ± 0.5	0.006
0.250	15.56	1	1930	3090	6.9 ± 0.5	0.0095
0.18*	15.56	1	1890	2060	4.9 ± 0.5	0.0009
0.09*	15.56	1	1620	2800	5.4 ± 0.5	0.0012
0.09	12.78	2	3540	1090	4.5 ± 0.2	0.0135
0.09	12.78	1	1930	2500	5.4 ± 0.4	0.0045
0.09	12.78	½	750	6390	5.5 ± 1.0	0.006
0.09	12.78	3	5400			
0.18	12.78	1	1200	3380	4.8 ± 0.6	0.002
0.09*	12.78	1	1500	2840	5.0 ± 0.5	0.001
0.09	10.0	2	1860	2030	4.3 ± 0.4	0.0025
0.09	10.0	2	1650	2430	4.7 ± 0.5	0.002
0.09	10.0	3	1800	2330	4.7 ± 0.5	0.001
0.09	10.0	1	770	5540	5.0 ± 1.0	0.0026
0.09*	10.0	2	1350	3350	5.3 ± 0.6	0.002
0.09	7.22	3	660	6340	4.9 ± 1.0	0.0024
0.09	7.22	2	400	11640	5.4 ± 1.8	0.003

* Substrate was heated to 200°C.

ionized and the disassociated species have a long enough lifetime, so that glow follows the gas stream and extends itself into the region where the substrate is located. Tetraethoxysilane vapor is introduced into the plasma downstream of the narrow section. This step accomplishes the important function of confining the reaction (as much as possible) to the vicinity of the substrate. Using this arrangement, the plasma color intensity is uniform in the region of the substrate.

High-frequency power is applied to the gas through two copper electrodes strapped to the outside wall of the narrow section of the chamber. A half-megacycle, 1-kw induction generator is used as the power source. Electrical coupling between the electrodes and the gas is good in the gas pressure range of several hundredth to several tenths of mm of Hg.

The substrate is placed on a quartz pedestal and floats electrically when surrounded by the plasma. A heater is available for use with an aluminum pedestal when substrate heating is required. The substrate would be in direct contact with the aluminum. A thermocouple, imbedded in the aluminum pedestal, monitors its temperature.

At the start of a run, the source reservoir is cooled to the desired temperature, and the oxygen flow rate and the reaction chamber pressure are adjusted to the desired conditions. The oxygen flow rate, once set, is not affected significantly by the pressure inside the chamber because of a high-pressure drop across the oxygen leak valve. Next, the power is turned on, and a plasma is generated to outgas the chamber and clean the substrate. After a few minutes, the valve leading from the source reservoir to the chamber is opened and the silicon oxide deposition is started. Due to the large volume of reaction products, the pressure inside the reaction chamber begins to increase and a steady state is soon reached. This steady-state pressure has been found to be reproducible from one run to the next.

The vapor pressure of the tetraethoxysilane, (manufacturer specification, 99.9% pure), as a function of temperature was extrapolated based on the original data of Stull (11). The source temperatures employed ranged from 7.22° to 15.55°C, corresponding to a vapor pressure range of 0.52 to 0.92 mm Hg, and were controlled to ±0.5°C.

Fabrication and measurement techniques.—Thin film silicon oxide capacitors were deposited on 1 x ½ in. glass slides. An aluminum electrode was first evaporated lengthwise on one surface of the slide. The silicon oxide film was then deposited over the aluminum strip. A second evaporation of aluminum was then carried out to form the counterelectrode strips, oriented perpendicular to the first aluminum strip. The thickness of the aluminum electrodes is approximately 2000Å. Six capacitors are formed on a single slide, each having an area of 0.097 cm^2.

A piece of polished silicon located adjacent to the substrate was used to determine the thickness of the silicon oxide layer and its refractive index. The measurement was made by first masking half of the silicon surface and then etching the oxide away from the unmasked half with hydrofluoric acid, thus forming a step. A portion of this step was covered with a film of evaporated aluminum to form a reflecting surface. The wafer surface was then examined with an interference microscope using light of a known wavelength. The fringe shifts at the step, with and without the evaporated aluminum, were photographed and measured. The oxide thickness was then calculated from the number of fringe shifts which appeared on the reflecting side of the step. The uncertainties in the thickness measurements are estimated to be ±150Å. Next, the refractive index of the oxide film was calculated from the ratio of the fringe shifts between the aluminum coated and uncoated regions of the step.

Capacitance and loss tangent measurements at 1 k-c were made on each of the capacitors using a bridge circuit. Some of the capacitors were measured at frequencies from 0.1 kc to 3 Mc.

A number of the thin-film silicon oxide capacitors were also subjected to a variety of life test conditions. Their capacitances and loss tangents were measured as a function of the time duration of the tests. Other tests, such as the dielectric strength and the ability to withstand thermal stresses, were also carried out.

Results and Discussion

Deposition of silicon oxide thin films.—The conditions of deposition and the results are presented in Table I. The oxygen pressure shown in the first column refers to the initial pressure within the reaction chamber prior to the introduction of the organic vapor. Parameters that have been investigated include initial oxygen pressure, source temperature, time length of deposition, and substrate temperature. The power input, the chamber and the electrode geometry, and the pumping speed were fixed.

The substrate temperature rise due to the plasma bombardment has been estimated by exposing the aluminum pedestal, which is well insulated from heat sinks, to the plasma under the deposition conditions, using an O_2 pressure of 0.09 mm Hg and a source temperature of 12.78°C. The steady-state temperature of the aluminum was measured to be 75°C. This temperature should be reasonably close to the steady-state bulk substrate temperature during deposition since the plasma is quite uniform in the aluminum pedestal region.

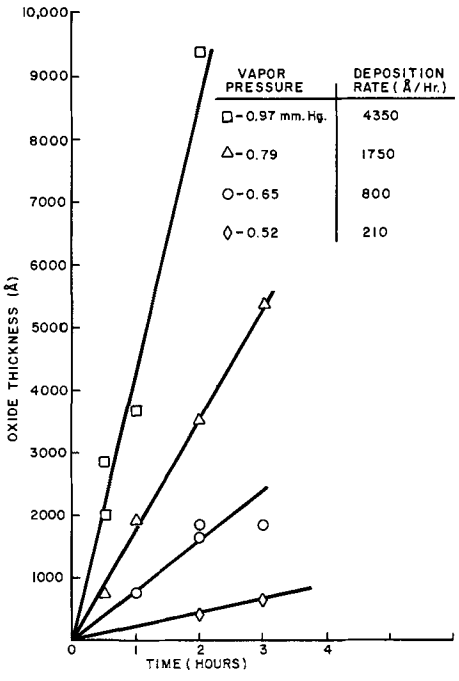

Fig. 3. Deposited oxide thickness *vs.* deposition time

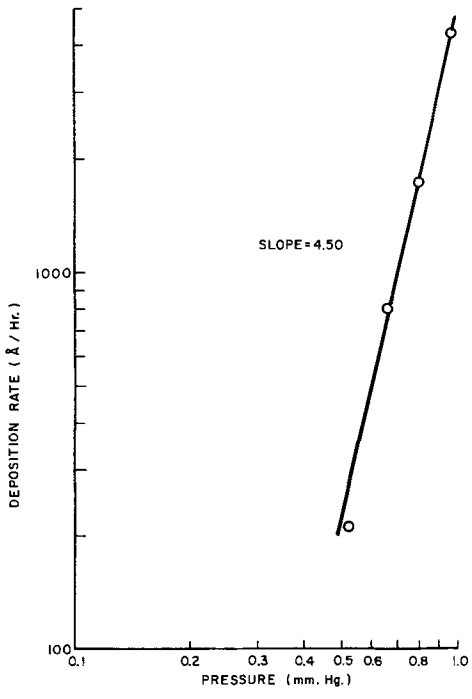

Fig. 4. Oxide deposition rate *vs.* vapor pressure of tetraethoxysilane in reservoir.

In Fig. 3, the oxide thickness is shown as a function of the deposition time for a constant oxygen feed rate, at various partial pressures of tetraethoxysilane in the reservoir. A family of straight lines was obtained, indicating a constant growth rate of the oxide. No initiation periods were observed.

The effect of the source temperature, which is a direct function of the concentration of the source in the reaction chamber, is extremely pronounced. The flow rate of the tetraethoxysilane vapor into the reaction chamber is controlled primarily by the capillary tube (1 mm ID, 2 cm long), as shown in Fig. 1. The capillary tube assures that the source flow rate will not be a function of the geometry of the reservoir. At the capillary inlet the partial pressure of the tetraethoxysilane can be assumed to be in equilibrium with the liquid source. However, the organic flow rate itself is difficult to estimate because the diffusivity of the tetraethoxysilane through the stagnant gas layer in the capillary is not known. In addition, any calculation based on the source depletion rate would be inaccurate, since for each run, the amount of the source consumed is small.

The deposition rate, when plotted as a function of the partial pressure of tetraethoxysilane at the source, yields the straight line shown in Fig. 4. From this line it can be established that R is proportional to p raised to the 4.5 power, where R is the deposition rate and p is the vapor pressure of the source. This relationship is not a universal one and is only applicable under the present set of conditions. However, it does indicate the extent of the deposition rate dependence on the source feed rate.

When the initial oxygen pressure was increased to 0.18 mm Hg (see Table I), a substantial decrease in the deposition rate was observed. The source flow rate into the chamber should not be significantly affected by the increase in the total pressure since the rate of flow across the capillary is governed mainly by the concentration gradient of the source material, assuming that there is no appreciable change in the diffusivity. The explanation may lie in the fact that there is a thick layer of plasma separating the source inlet into the chamber from the substrate. An appreciable portion of the tetraethoxysilane must have decomposed and deposited on the chamber wall before it could reach the substrate. Under higher oxygen partial pressures, a larger portion of the source material can be expected to react in the vicinity of the source inlet; hence, there is a larger amount of material deposited on the wall and a smaller amount on the substrate.

When the substrate is heated to 200°C at an oxygen pressure of 0.09 mm Hg, the deposition rate again decreases. This may be due to a slight upward convection current around the substrate caused by the temperature gradient between the substrate heater and the air-cooled chamber wall. Such a current would tend to lower the concentration of the reactants in the substrate region.

In Fig. 3 the deviations of the data points from straight lines can be attributed to variations in the source temperature (±0.5°C). The deposition rate can more precisely be reproduced when the source temperature is more carefully maintained at a constant value.

The variation in the thickness of the oxide film across a 1-in. diameter substrate can generally be held to ±5% of the total film thickness. The uniformity of the film seems to be a function of the ratio of the substrate area to the cross-sectional area of the reaction chamber. The lower this ratio is, the more uniform is the film thickness.

The product gas has been analyzed using a mass spectrometer. The detectability of the short chain hydrocarbons, alcohols, and other organic species is of the order of 1% minimum concentration in the gas sample. Water vapor could not be analyzed due to the interfering background water content of the apparatus. The species detected were CO, CO_2, O_2, and N_2 indicating that the oxidation of the organic silicate was quite complete within the reaction chamber.

Effect of deposition rate on silicon oxide film characteristics.—The influence of the deposition rate on the characteristics of the thin film silicon oxide capacitors is shown in Table I. The loss tangents of the capacitors made at the higher source temperatures and lower oxygen concentrations (where the oxide growth rates are faster), are generally higher than those made with a lower source temperature and a higher oxygen concentration (where the oxide growth rates are slower).

A few of the capacitors, grown at different rates, were measured for their capacitances and loss tangents as a function of frequency, from 0.1 kc to 3 Mc. Two sets of data were plotted and are shown in Fig. 5 and 6.

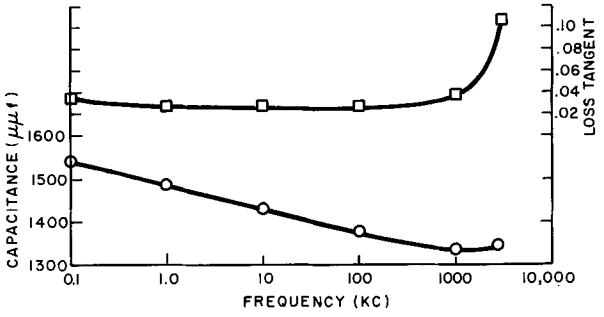

Fig. 5. Capacitance (lower curve) and loss tangent (upper curve) vs. applied frequency; oxide film deposited at a rate of 3700 Å/hr, oxide film thickness, 2800Å.

The curves of Fig. 5 are for films which were grown at rates of 3500-5000 Å/hr; the curves in Fig. 6 are for films grown at rates below 2000 Å/hr. The capacitors formed at the faster growth rates show a consistent decrease of capacitance as the applied frequency increases; the capacitors formed at the lower growth rates remain unchanged in their capacitances as the applied frequency is increased. The slight upturn in capacitance at frequencies greater than 1 Mc is most likely due to series resistances and inductances. The loss tangents of both types of capacitors remain essentially constant up to 100 kc and then begin to increase. Most of the increased losses can be attributed to series resistances in the thin film electrodes. The effect of growth rate can again be observed when the films are etched in hydrofluoric acid. Films that were grown at rates above 3500 Å/hr always yield a brownish residue when rinsed in HF; the films grown at slower rates dissolved completely. The brownish residue is probably organic material that has been occluded in the oxide structure during the deposition process, indicating an incomplete decomposition of the organic-silicate when the growth rate is too high. These entrapped organic functional groups could give rise to a dipolar contribution to the capacitance of the film. The decrease of capacitance with increasing frequency occurring at relatively low frequencies in these high-growth-rate deposited films indicate that these polar molecular segments have long dielectric relaxation times.

Properties of silicon oxide films prepared by glow discharge techniques.—The dielectric constant values of the films lie mostly in the range of 4.5-5.5 as shown in Table I. It is not possible to ascertain the effect of the deposition rate on the film dielectric constant since the variations in the dielectric constants between the films are within the uncertainty limits of the measurements. The refractive index obtained from the interferometer measurements, using 5460Å light, is 1.5 ± 0.1. No density measurements have yet been made. Electron diffraction measurements show that the films are amorphous.

Capacitor Testing

Capacitor life test results are shown in Fig. 7 to 9. The high humidity (with and without applied bias)

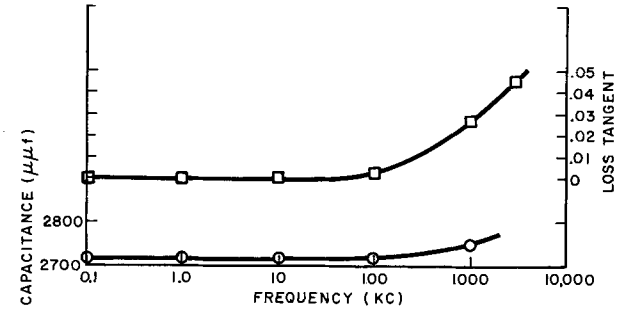

Fig. 6. Capacitance (lower curve) and loss tangent (upper curve) vs. applied frequency; oxide film deposited at a rate of 825 Å/hr; oxide film thickness, 1500Å.

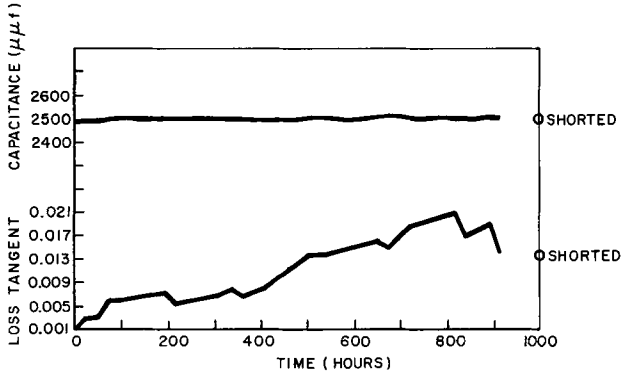

Fig. 7. Capacitance and loss tangent measured at 1 kc vs. test time; test condition: 100% relative humidity at 23°C; deposition rate of the oxide film, 1900 Å/hr; oxide film thickness, 1700Å.

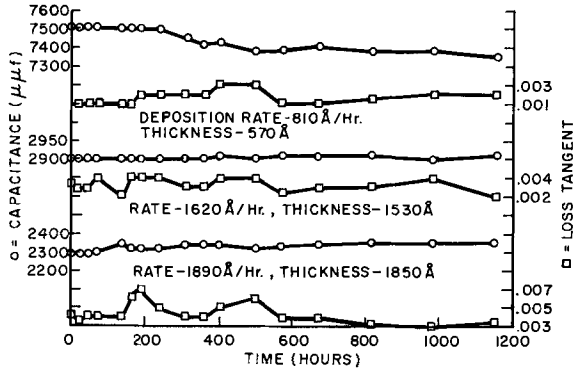

Fig. 8. Capacitance and loss tangent measured at 1 kc vs. test time; test condition: 70% relative humidity at 23°C with 10½v bias.

tests were conducted on capacitors that were formed at slow deposition rates (less than 2000 Å/hr) and without substrate heating. Figure 7 shows the test results of a capacitor exposed to a 100% relative humidity ambience at 23°C with no applied bias. The capacitance and the loss tangent were measured at approximately 50-hr intervals. The capacitance remained essentially constant, but the loss tangent tended to increase with time. A short did develop after 900 hr of testing. Figure 8 shows plots of capacitance and loss tangent *vs.* time of three capacitors that were tested in a 70% relative humidity ambience at 23°C with 10.5v bias applied across the capacitor. Both the capacitance and the loss tangent of these samples remained quite constant over a period of 1150 hr.

Thin film capacitors formed without substrate heating were tested at 100°C and 10.5v applied bias at room ambience. Results are shown in Fig. 9. The initial capacitances and loss tangents were measured at 23°C. The capacitor formed at a slower rate exhibits a very slight decrease in capacitance in the first 50 hr of test with no significant change in loss tangent. However, the capacitor grown at a higher rate exhibits an appreciable decrease in capacitance with time at the start of the test; it then levels off and the capacitance remains constant. The loss tangent seems to maintain its value with time. These changes in capacitances due to heating are irreversible. However, once stabilized, these capacitors show very low thermal coefficient of capacitance; generally less than 20 ppm/°C in the temperature range 23°-100°C.

The dielectric strengths of these films, calculated on the basis of the bulk breakdown voltages, are in the range 5 x 10^6 to 10^7 v/cm. These values compare closely to the dielectric strength of fused quartz, which is reported to be around 10^7 v/cm.

The capacitors were also tested for their ability to withstand thermal stresses. The sandwich assembly was cooled very rapidly from room temperature by

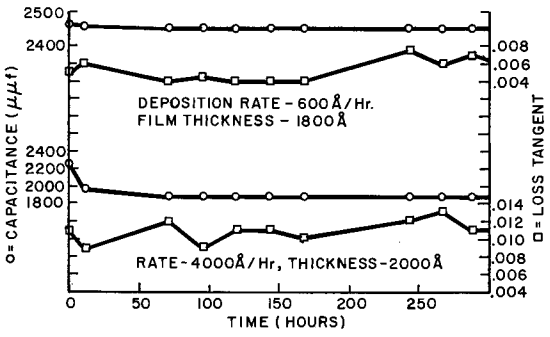

Fig. 9. Capacitance and loss tangent measured at 1 kc vs. test time; test condition: 100° in room ambient with 10½v bias.

immersing it quickly into liquid nitrogen, where it remained for 10 to 15 min. The assembly was then quickly withdrawn and warmed in the room ambient. The cycle was repeated three times. Two capacitors, of film thicknesses 1800 and 2000Å, respectively, were used for the test. The capacitances and the loss tangents were measured before and after the test and no significant changes were observed. Microscopic examinations of these capacitors revealed no cracking or peeling.

Effect of Background Gas

The effect of the background gas on the deposited film was briefly investigated. Both argon and hydrogen plasmas were used. A much slower deposition rate (less than 1000 Å/hr) was required to ensure that the deposited films yield no organic residue when etched with HF. It can therefore be surmised that, although the source itself has a high oxygen content, an oxidizing plasma is still needed to assist in the completion of the decomposition reaction and to provide an ample supply of oxygen for the formation of the silicon-oxygen network.

Proposed Mechanism for Glow Discharge Deposition

A reaction mechanism has been postulated. The mechanism is based on a high energy particle bombardment decomposition of the organic-silicate source in the gas phase, followed by a polymerization of the free radicals into silicon oxide clusters. The clusters are then deposited onto the substrate surface and bonded to the surface atoms. Any attached organic functional groups could also be dissociated from the deposited layer by a subsequent bombardment step.

During deposition the mobility of the clusters on the solid surface must be quite high, since the films as deposited are coherent even when they are very thin (on the order of a few hundred Angstroms). The film adherence to the glass substrate surface is good. For example, the oxide film could not be lifted off by using a "Scotch" tape indicating that strong bonds have been formed between the substrate surface and the first layer of the deposited oxide film.

Conclusions

The glow discharge formation of silicon oxide in an oxygen plasma, using tetraethoxysilane as a source material, has been studied. The resultant silicon oxide films are amorphous, coherent, and exhibit good adherence characteristics. The parameters investigated included oxygen pressure, source material feed rate, and substrate temperature. The oxide film deposition rate has been shown to be a strong function of the source feed rate. The deposition rate is slowed as the oxygen pressure or the substrate temperature is increased, probably due to a lower mass transport rate of the source to the substrate.

The quality of the deposited oxide films, as indicated by their electrical stability and low dielectric loss, is dependent on the deposition rate. At rates below 2000 Å/hr, the films are generally of high quality. The films formed at rates above 3000 Å/hr seem to have a substantial amount of organic material occluded in their structure and are less stable electrically. They also have higher dielectric losses. The dielectric constant of the films are in the range of 4.5-5.5.

The thickness of the film has been controlled so that variations of less than ±5%, across a 1-in. square substrate area, has been achieved. In addition, the deposition rate has been controlled to within ±10%.

Capacitors have been made from the glow discharge deposited films that have specific capacitances in the range of 4,800-110,000 $\mu\mu f/cm^2$. These capacitors have shown good stability in high humidity tests and in room ambient 100°C tests with or without applied bias. The capacitors have low temperature coefficients of capacitance and are able to withstand extreme thermal shocks. The bulk breakdown strengths of the films lie in the range 5 x 10^6 to 10^7 v/cm.

Manuscript received March 6, 1964; revised manuscript received Nov. 6, 1964. This paper was presented in part at the New York Meeting, Sept. 29-Oct. 3, 1963.

Any discussion of this paper will appear in a Discussion Section to be published in the December 1965 JOURNAL.

REFERENCES

1. M. M. Atalla, E. Tannenbaum, and E. J. Scheibner, *Bell Syst. Tech. J.*, **38**, 749 (1959).
2. W. R. Sinclair and F. G. Peters, *J. Am. Ceram. Soc.*, **46**, 20 (1963).
3. E. E. Smith and D. R. Kennedy, *Proc. Inst. Elec. Eng. (Lon.)*, **109** (Part B Suppl. 22), 504 (1962).
4. F. S. Maddocks and R. E. Thun, *This Journal*, **109**, 99 (1962).
5. E. L. Jordan, *ibid.*, **108**, 478 (1961).
6. L. L. Alt, S. W. Ing, Jr., and K. W. Laendle, *ibid.*, **110**, 465 (1963).
7. R. W. Christy, *J. Appl. Phys.*, **33**, 1884 (1962); *ibid.*, **31**, 1680 (1960); A. G. Baker and W. C. Morris, *Rev. Sci. Instr.*, **32**, 458 (1961).
8. V. A. Russell and D. L. Stockman, General Electric Company, Internal Report, Jan. (1962).
9. J. L. Miles and P. H. Smith, *This Journal*, **110**, 1240 (1963).
10. S. W. Ing, Jr., and W. Davern, *ibid.*, **111**, 120 (1964).
11. D. Stull, *Ind. Eng. Chem.*, **39**, 517 (1947).

The Infrared Spectra of the Adsorbed Phase on Tantalum Oxide Films

F. Vratny

Bell Telephone Laboratories, Incorporated, Murray Hill, New Jersey

ABSTRACT

An investigation of the adsorbed phase on anodic and thermally grown tantalum oxide on sputtered tantalum has been carried out using infrared reflectance and transmission spectral techniques. After exposure to air (50% RH), it was possible to identify water, carbon dioxide, and hydrocarbon residues. Both the water and carbon dioxide were removed on evacuation and heating while the hydrocarbon residues were retained by the sample. It is proposed that the hydrocarbon residues occur as a result of gettering processes in the residual gases during sputtering of the original tantalum film, or by incorporation of the organic electrolyte used for anodizing.

The infrared spectrum of a solid can be a very helpful tool in characterizing the nature and existence of adsorbed phases on solids (1). Under appropriate conditions it has been used to determine adsorption isotherms (1-4), and to establish the nature of an adsorbent (5, 6) and the type of interaction between adsorbent-adsorbate (3, 4). Further, it is known that the presence of an adsorbed phase on a solid can have a pronounced effect on the electrical properties of both the bulk and the surface of a solid (7-14). As a particular example, it is known that the presence of an adsorbed layer of water can have a decided effect on the dielectric properties of many oxides (15, 16) as anodic aluminum oxide (17) and anodic tantalum oxide (18). Further, based on charge storage data for tantalum oxide it may be possible that the presence of a second adsorbate may be necessary to explain the pronounced effect at present attributed only to water (18). In order to characterize the various species on tantalum oxide the infrared spectrum of the adsorbate phase was obtained.

It was possible to obtain the spectrum of the adsorbed phase in the 2.5-13μ range without undue complications due to the fact that tantalum oxide presents no interfering band in this region of the spectrum (19). Although techniques are directly available for observing the spectrum of an adsorbed phase on a solid, the particular case of tantalum oxide offers a number of singular peculiarities which required an evaluation of preparative and observational techniques. These factors were evaluated by preparing tantalum oxide by both thermal oxidation and anodization on several different kinds of substrates. Further, spectra were observed by more than one method, including specular reflectance, multiple reflectance, and direct transmission. In this way it was possible to rule out spurious results and to make definite assignments to adsorbate materials. Of the techniques employed it is felt that the method of direct transmission proved the more useful and flexible.

Experimental

Tantalum oxide films were used to evaluate the reflectance method. These samples were prepared by deposition of tantalum on 1 x 3 in. quartz microscope slides. The slides were first cleaned in detergent and rinsed in distilled water and isopropyl alcohol. Tantalum was then deposited by cathodic sputtering at 4 kv and 3 ma/cm^2 from an arc melted tantalum plate. The metallic film had a total thickness of $\sim$ 5000Å and a specific resistivity of $\sim$ 100 μohm-cm. The film was anodized to an appropriate voltage in an electrolyte of 1:2:3 water, oxalic acid, ethylene glycol at 105°C to obtain the desired thickness of oxide.

The samples used for the transmission experiments were deposited as above; however, the substrate was either sapphire or barium fluoride. Anodization was carried out in an identical fashion. The metallic base was removed by anodic etching in a lithium chloride-alcohol electrolyte. This technique made it possible to obtain metal-free areas of at least 2 mm^2 which were suitable for direct transmission experiments (18).

It was not possible to oxidize tantalum thermally at 400°-600°C on potassium chloride or barium fluoride without affecting the substrate. The potassium chloride substrates became opaque while the barium fluoride substrates showed definite carbonate bands. The infrared spectra of samples produced in this way indicated the presence of large amounts of oxide and carbonates from the substrate as well as metallic fluorides arising from the firing process. Consequently, the thermal oxidation was performed only on sapphire substrates at 800°C, where these interferences were controlled by the greater stability of the sapphire. It was possible, however, to obtain a slight trace of an oxide band due to the presence of a metal-metal oxide (M-O-M') stretching frequency arising as a result of the possible interfacial diffusion between tantalum oxide and sapphire.

The specular reflectance spectrum was obtained by means of a Perkin Elmer specular reflectance attachment. In this method light is reflected specularly from the sample surface, collected by a spherical mirror, and focused onto the slit of the spectrometer. In all cases a gold or tantalum surface of high specular reflectance was used in the reference beam.

It was found that if the spectrometer was used at a scale expansion of (1X) the specular reflectance of tantalum oxide was nearly constant and structureless in the 4.5-12μ region of the spectrum. At a scale expansion of (10X) it was possible to identify the presence of adsorbed water ($\sim$ 3600 cm^{-1}) and carbon dioxide ($\sim$ 2350 cm^{-1}). An indication of adsorbed aliphatics or carboxalate OH ($\sim$ 2700 cm^{-1}) was also noted. Possible metal-oxide bands occurred at $\sim$ 1925 and 925 cm^{-1}.

For a further discussion of assignment of absorption bands, see the Discussion.

Multiple Reflectance Spectra (Oblique Incidence)

Although it was possible to obtain a significant picture of the adsorption species on tantalum oxide by the specular reflectance methods, the intensities were marginal due to a single reflection from the sample surface. By the use of a method of multiple reflection from the surface it was possible to intensify the characteristics found by the single reflectance method. Thus, the above samples were investigated by the method of multiple reflectance.

The multiple reflectance spectrum was obtained by means of a special reflectance attachment. The optical system (Fig. 1 and 1b) relies upon polychromatic

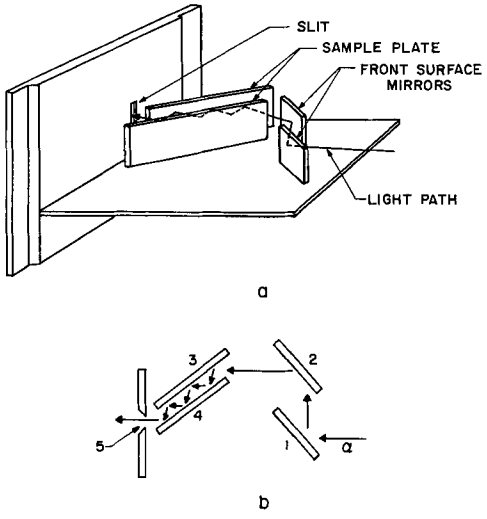

Fig. 1. Optical system for multiple reflection spectroscopy. A, Pictorial view; B, Schematic view, 1,2, front surface mirror, 3,4 sample, 5, slit, α, angle of incidence.

infrared radiation which is reflected from mirrors 1 and 2 onto the sample plates 3 and 4 where multiple reflection occurs between the two parallel sample surfaces. This configuration permits the absorption spectra of an adsorbed specie on a surface to be obtained without interference from the body of the sample. It is quite flexible in that it may be used in oblique or grazing incidence to obtain respectively simple multiple reflection from the sample surfaces or internal reflection in the oxide. This difference results from reflected radiation at angles greater than Brewster's angle ($\tan \theta = \mu$) and internal reflection to a greater extent as this angle is approached, *i.e.*, internal reflection occurs at an angle θ greater than θ' where $1/\sin \theta = n$ (20). At less than the Brewster angle the radiation is totally internally reflected. This is a technique perfected by Harrick (21) and Francis and Ellison (22).

Due to loss of intensity from reducing the effective size of the beam and due to energy losses through scattering and unusual optical densities it was found necessary to compensate the reference beam. A comb attenuator was designed for this purpose. This device has the particular utility of being easily and precisely adjusted to any desired optical density.

Employing the first technique of oblique reflection (surface reflection), with a sample separation of 0.070 in. and an angle of 30° incidence to the light source, it was possible to identify infrared absorption bands (Fig. 2) for carbon dioxide at D (about 2350 to 2500 cm^{-1}), hydrocarbon C-H or carboxalate OH vibrations at C (2600 to about 2800 cm^{-1}), physically adsorbed water evident by the band at B from about 3200 to about 3400 cm^{-1}, and finally chemisorbed water at A at 3580 cm^{-1} and 3630 cm^{-1}. These bands do not have the same appearance as they would have in transmission due to the fact that for a given band the transmission of the samples register changes proportional to k, the absorption coefficient, while in reflection they register changes which are proportional to both n and k, the index of refraction and the absorption coefficient, respectively. Thus, bands will be found to move from their established position to a different frequency (23-26), dependent on the change of n with frequency.

From an estimate of absorption coefficients it is estimated that the band due to chemisorbed water corresponds to about four to eight molecular layers while the physically adsorbed water corresponds to about two monolayers. Correspondingly the CH residues and CO_2 occur at about two to four molecular layers. These estimates represent upper limits to the concentration and are probably too large by an order of magnitude

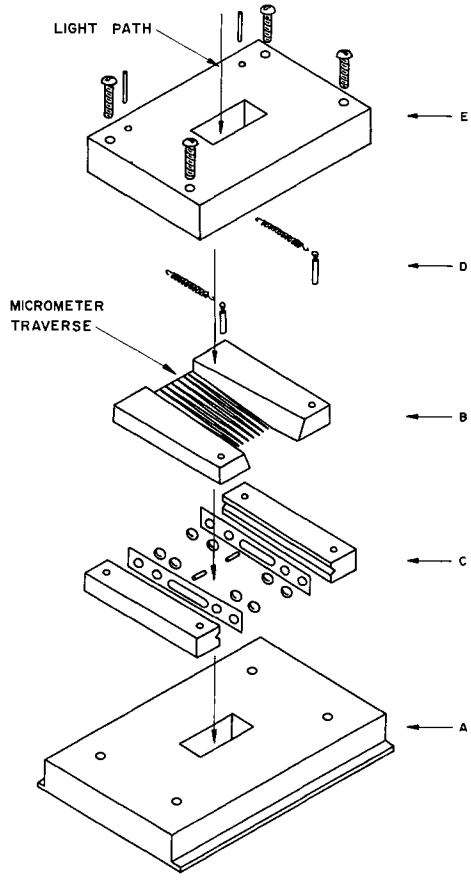

Fig. 1a. Light attenuator, exploded view

in light of comparisons to known surface coverages, see general reference (27).

Multiple Reflectance (Grazing Incidence)

Using the technique of grazing incidence multiple reflectance it was possible to delineate and expand on the features obtained by the oblique incidence method. The same procedure was followed as in the preceding section with the exception that the angle of incidence between the light beam and the sample was ~ 10° and the data were recorded at a scale expansion of (20X). A large number of absorption bands were noted in the 5-7μ region of the spectrum. These are due to atmospheric water vapor (28).

In addition, it was possible to establish the presence of many adsorbed species. In Fig. 3 and 4 the spectrum obtained from an anodic tantalum oxide sample which had been dried for 24 hr at 110°C is compared with the spectrum from a sample which had been held at 100% humidity for 4 hr. In this set of figures as well as following figures, the breaks in the spectra represent experimental translations along the re-

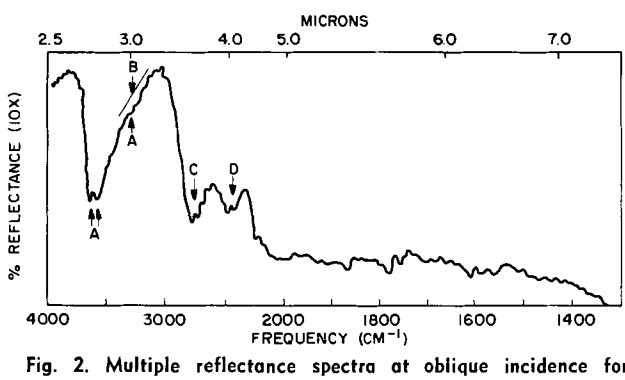

Fig. 2. Multiple reflectance spectra at oblique incidence for anodic tantalum oxide. A, Chemisorbed water; B, physisorbed water; C, CH-residues, D-CO_2. The ordinate is zero to 10% reflectance.

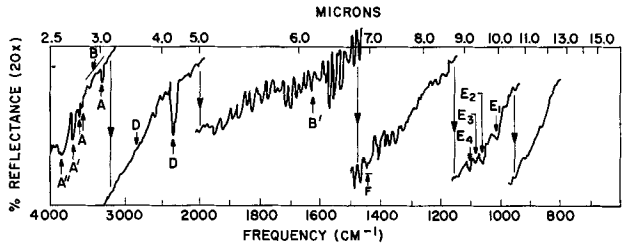

Fig. 3. Multiple reflectance spectra at grazing incidence for dry anodic tantalum oxide. A, Chemisorbed water (OH^-); A', chemisorbed water or CO_2; A", chemisorbed water; B, physisorbed water; C, CH-residue; D, CO_2. The ordinate is zero to 5% reflectance with roughly a 5% increase in base line at each discontinuity.

flectance axis. This was caused by the lack of adequate compensation in the reference beam and the rapidly changing intensity level which occurs with decreasing frequency. Since the spectra were taken with overlapping regions it may be seen that in general this adjustment corresponds to an axis translation of at most a change of 5% reflectance.

The major difference is the large background slope in the 3μ region found in the wet sample. This is quite characteristic of extreme surface coverage by water. This characteristic also masks many of the bands found in this region which are seen in the dry sample. There is also a pronounced water band in the 6.1μ region in the wet sample which is greatly reduced in intensity in the dry sample. In addition, there are indications of CH residues (C), C' is carboxalate OH, CO_2 (D), metallic oxide bands (E), and carbonate or chemisorbed CO_2 (F). Fairly predominant CH Bands are observed, which are comparable to aliphatic CH_{2n+2} and aromatic phthalate configurations. Bands were also observed in the 4-7.0μ region which are due to the carboxylate group.

From an estimate of intensities the chemisorbed water bands may be due to 1-3 monolayers of water while the physisorbed water bands cannot be suitably resolved. The CO_2 band represents about four molecular layers. This is in distinct contrast to the results obtained from oblique reflectance and represents the distinction between internal and oblique reflection.

Transmission Spectra of Thermally Produced Tantalum Oxide

The transmission spectrum of thermally oxidized tantalum on sapphire was obtained by direct transmission at (5X) scale expansion.

The spectrum (Fig. 5) indicated a large amount of carbon dioxide (D) and possibly carbonate ion or chemisorbed CO_2 (F) ($\sim$ 1430 and 2350 cm^{-1}) as well as substantial amounts of adsorbed water (band at $\sim$ 3300 cm^{-1}) (B). Quite distinct to this sample were the intense bands at 1180, 1120, and 1090 cm^{-1} which are suggestive of metal-oxide bands (E). The physisorbed water band corresponds to about 50-150 molecular layers of water while the CO_2 band is due to about

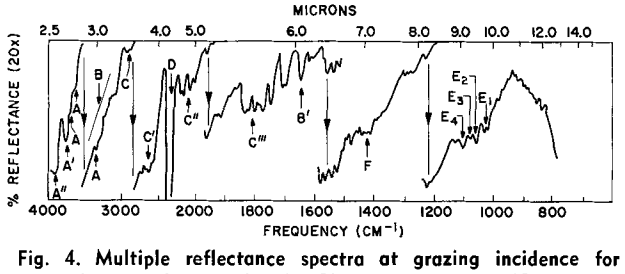

Fig. 4. Multiple reflectance spectra at grazing incidence for wet anodic tantalum oxide. A, Chemisorbed water (OH^-); A', chemisorbed water or CO_2; A", chemisorbed water; B, physisorbed water, note large slope; C, CH-residues; D, CO_2; E, metal oxide; F, $CO_3^=$. The ordinate is zero to 5% reflectance with roughly a 5% increase in base line at each discontinuity.

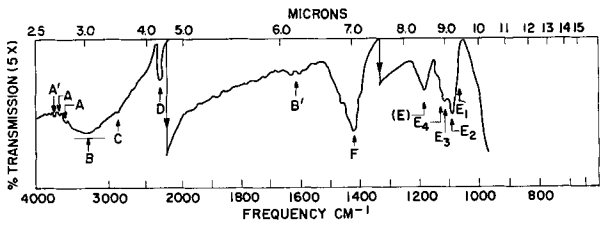

Fig. 5. Transmission spectra of thermally produced tantalum oxide on sapphire. A, Chemisorbed water (OH^-); A', chemisorbed water or CO_2; B, physisorbed water; C, CH-residues; D, CO_2; E, metal oxide; F, $CO_3^=$. The ordinate is zero to 20% with roughly a 10% increase in base line at each discontinuity.

10-50 molecular layers. The unusually large amount of water and CO_2 is probably due to the thermal nature of the sample which is highly porous.

Transmission Spectra of Anodically Produced Tantalum Oxide

The transmission spectrum was obtained for anodic tantalum oxide on barium fluoride. It was found that the transmission was relatively constant out to the cutoff of the barium fluoride windows. At a scale expansion of 10X (Fig. 6) it was possible to identify both CO_2 (D) and H_2O (A, B). Physically adsorbed water may be identified at $\sim$ 3300 cm^{-1} while chemisorbed water is indicated by the bands at $\sim$ 3700 cm^{-1}. On heating the anodic oxide sample, the 3300 cm^{-1} band diminished in intensity while the 3700 cm^{-1} band increased in intensity due to a reduction in the background as a result of the decrease in hydrogen bonded surface water (29, 30). The presence of physically adsorbed CO_2 (D) is established by the band at $\sim$ 2350 cm^{-1} which corresponds to the ν_3 vibration of CO_2. Chemisorbed CO_2 (F) or carbonate is also suggested by the bands at $\sim$ 1500 cm^{-1} and 1410 cm^{-1}; however, it is recognized that fluorite windows are prone to this type of interference. A further adsorbed specie is indicated by the band at $\sim$ 2950 cm^{-1}. This is due to a CH vibrational mode from adsorbed hydrocarbons (C). The concentration of chemisorbed water has only slightly altered from the thermally produced sample while the physisorbed water has decreased by at least a decade, *i.e.*, 5-15 monolayers of water.

As an extension of the above investigation, an anodic tantalum oxide film on barium fluoride was mounted in a special infrared cell (31), and spectra were obtained as a function of cell pressure and temperature. The results are classified according to active functional groups. Attention is directed to two regions of the spectrum from 4000 to 2700 cm^{-1} (Fig. 7) and 2700 to 1950 cm^{-1} (Fig. 8). In both cases a number of spectra are superimposed at a common origin in order that the results of the pressure-temperature treatment may be seen readily. The sample was first equilibrated at normal atmospheric conditions (O) *i.e.*, 25°C and $\sim$ 50% RH. On reducing the pressure over the sample to 10^{-3} Torr, (O'), a substantial amount of physically adsorbed water ($\sim$ 3250 cm^{-1} corresponding to OH with hydrogen bonding) was lost. The

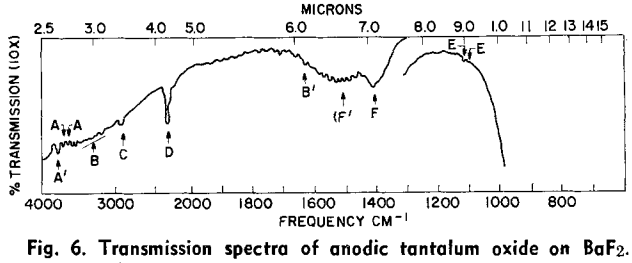

Fig. 6. Transmission spectra of anodic tantalum oxide on BaF_2. A, Chemisorbed water (OH^-); A', chemisorbed water or CO_2; B, physisorbed water; C, CH-residues; D, CO_2; E, metal oxide; F, $CO_3^=$.

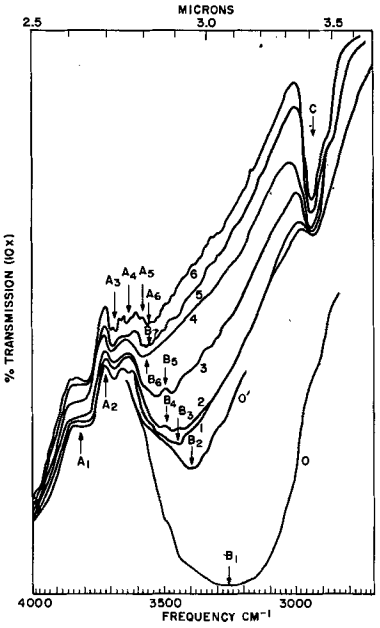

Fig. 7. Transmission spectra of anodic tantalum oxide (O) on evacuation (O'), on heating to 200°C in vacuum (1-6). A, Chemisorbed water; A_1, ω_0 for $VO(OH)_2$; A_2, ω_0 for $SiO_2 \cdot xH_2O$; A_3, ω_0 for $Mg(OH)_2$, $Co(OH)_2$; A_4, γ for Mica (OH), γ for $VO(OH)_2$; A_5, γ for $VO(OH)_2$, B-physisorbed; B, physisorbed water; B_1, $\theta \simeq 1.0$ (150 monolayers); B_2, $\theta \simeq 0.6$ (60 monolayers); B_4, $\theta \simeq 0.3$ (30 monolayers); B_7, $\theta \simeq 0.1$ surface coverage, (1-5 monolayers), C, CH-residues.

sample was then heated in a sequential fashion to ~200°C. The progression 1 to 6 is representative of this temperature cycle, *i.e.*, about 30°C intervals (coverage approximated from ref. (12), molecular layer coverage estimated from intensities). It may be noted that two bands due to chemisorbed water persist at ~ 3520, 3680, and 3800 cm^{-1} due to free hydroxyl while greater and greater amounts of physically adsorbed water are lost. The band at ~2950 cm^{-1} seems to grow in intensity due to a decrease in the magnitude of the water band. This band is due to organic C-H vibrational states. Due to its persistence the associated CH is equally or more strongly held (bonded) than the chemisorbed water. The source of this hydrocarbon contaminant is hydrocarbon cracking during the deposition of the film or incorporation of the organic electrolyte during anodization. Liquid nitrogen trapping of the pumping system during observation of the spectra mitigate the possibility of contamination from this source. The band at ~ 2300 cm^{-1} is assigned to the ν_3 band of CO_2. It appears as a reversal in intensity due to the lack of compensation in the reference beam. With this in mind it may be seen that on heating there is an apparent increase in the amount of CO_2, up to ~ 100°C, followed by a very rapid loss of CO_2 as a temperature of 200°C is approached. This increase occurs as a result of the rapid change in background due to the rapid loss of water from the sample. Although the loss of CO_2 in the region of 200°C is real the loss in the 100°C region can only be inferred.

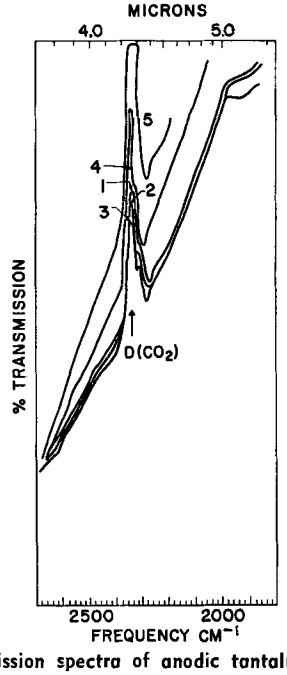

Fig. 8. Transmission spectra of anodic tantalum oxide on heating to 200°C in vacuum (1-5).

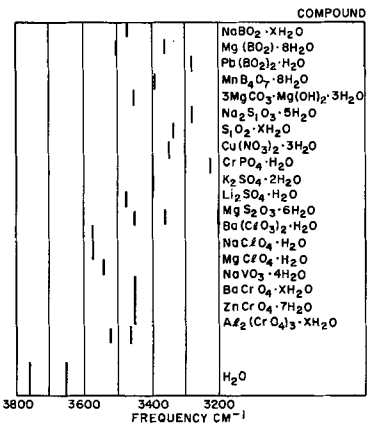

Fig. 9. Correlation diagram for crystalline hydrates [Ref. (40), (42)].

Discussion

The assignment of infrared bands to adsorbed water or associated hydroxyl groups is primarily a process of correlation with information obtained from assignments made upon bulk materials. In this regard it may be seen from Fig. 9 that water of crystallization ordinarily leads to bands in the 3400 cm^{-1} region. As the degree of association becomes greater, as in the highly complexed water in the chlorates and perchlorates, the bands move to higher energies to ~ 3500 cm^{-1}. Finally, in the case of free hydroxyl groups, as in hydroxides (see Fig. 10) the bands move to ~ 3600 cm^{-1} and even 4000 cm^{-1}. In gas absorption studies, it has been noted that the band associated with water adsorbed on synthetic Zeolite (6) tends to assume a shape dependent upon the degree of surface coverage, Fig. 11. The 3μ band of water is associated with the stretching frequency of the O-H band in water. In

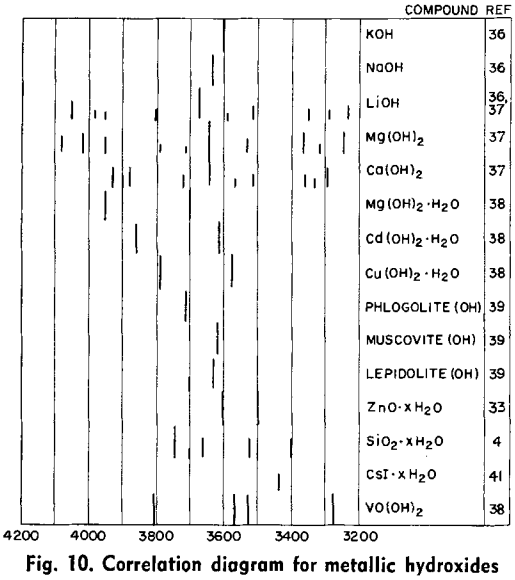

Fig. 10. Correlation diagram for metallic hydroxides

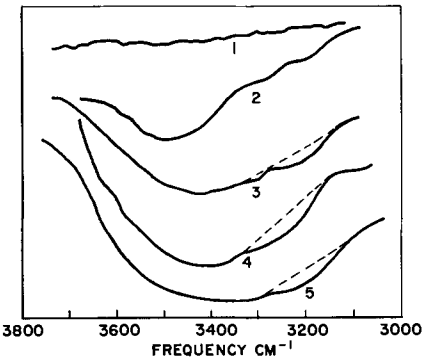

Fig. 11. Spectra of water absorbed on Zeolite. 1, Dehydrated on zeolite; 2, $\theta \simeq 0.34$ surface coverage; 3, $\theta \simeq 0.69$, 4 — $\theta \simeq 1.0$, 5 — liquid water, (6).

this regard it was observed that on increasing surface coverage the band broadened and moved from ~ 3486 to 3377 cm^{-1} with structure at 3200 cm^{-1}. This has been interpreted in terms of the polarity of the water molecule which will tend to orient its hydrogen atoms toward oxygen in the substrate. Since the observed value of the O-H stretching frequency was always found to be less than that for the vapor, its association is probably due to "hydrogen bonding." The broadening is assumed to be due to clustering, mutual interaction between water molecules, rather than further substrate association. This has been substantiated further by Cross, Burnham, and Leighton (43) who predicted that a di-coordinated water molecule, bonded through its hydrogen atoms, should have a stretching frequency of ~ 3500 cm^{-1}. Thus, the highly ionic materials, as potassium hydroxide, sodium hydroxide, etc., have a fundamental closer to that of the free water vapor than can be expected from materials having a high degree of hydrogen bonding.

A second means of assignment is by correlation based on similarity of structure. It may be noted that there is a pronounced mass effect in the alkali metal hydroxides which produce a shift in the fundamental stretching mode. Thus, one may expect a correlation between tantalum oxide and say vanadium oxide. The spectrum for this material has been obtained (38) and contains a fundamental frequency at 3804 cm^{-1} and bands at 3529 and 3566 cm^{-1} which are due to the independent or "free" OH stretching frequency. Further, the 3276 cm^{-1} band is due to an associated or hydrogen bonded mode. In this manner, it is seen that the simple picture of $VO(OH)_2$ is inadequate in that it does not encompass the complexities of this material which is more likely pictured as an interhydrogen bonded hydroxide. Passing on now to the case of tantalum oxide, a certain degree of similarity to vanadium oxide may be assumed, dependent on mass and bonding effects. The degree of similarity is pointed out in Fig. 7.

Finally, a third mode or approach is considered in assignment of water bands associated as an adsorbed phase. It has been proven in numerous structures that the degree of association of water to a substrate is a direct indication of the bonding strength. Thus, on heating the substrate, it is possible to distinguish the bands that leave or diminish in intensity, indicating a physically adsorbed phase in contrast to bands that remain, indicating a chemisorbed or tightly bonded phase. This may be seen in Fig. 7 by direct comparison to Fig. 11. At total surface coverage ($\theta = 1$) there is a large band centered at 3200 cm^{-1}. As the physically adsorbed layer is decreased (approximated at $\theta = 0.6$, 0.3, 0.1) the band decreases in intensity and moves to a higher frequency, indicating a greater degree of surface association (30).

Moving now to the case of the adsorption of carbon dioxide, it is fully documented that CO_2 will give bands at 2.688, 2.765, and 4.225μ (42). However, its effect in the adsorbed state is less understood. In work carried out on zinc oxide, it was found that the prime process was physical adsorption as indicated by the 4.225μ band. It should be pointed out that this is immediately in accord with the present observations, indicating also a prime process of physical adsorption of CO_2, followed by desorption on evacuation and heating.

Finally the identification of hydrocarbon residues must be considered. The fact that hydrocarbons, in general, give bands in the 3.5μ region is fully documented in ref. (41). It has also been shown that hydrocarbons produce essentially the same bands in the normal process of adsorption. This may be seen in the work of Eischens and Pliskins (1, 34) and many others (23, 44-47).

From the present study of the vibrational spectra of the adsorbed phase on tantalum oxide, it is evident that this oxide is prone to adsorption of substantial amounts of water and carbon dioxide. Further, a substantial portion of these adsorbed gases are removed under modest vacuum conditions (10^{-2}-10^{-3} Torr), while a further quantity of gas is removed only on heating. Carbon dioxide is removed at these pressures at ~ 100°C, while removal of strongly adsorbed water requires temperatures as high as 200°C. Two distinct types of adsorbed water were observed; physically adsorbed, and chemisorbed (3, 4, 5, 33, 34). A similar assignment can be made for carbon dioxide (1). In this regard it was noted in the thermal study of these samples that temperature cycling tended to accentuate the formation of chemisorbed water. It would be of interest to determine whether this will have a long term effect on the structure of the oxide as well as an effect on the dielectric properties.

An additional point was raised in this phase of the investigation with regard to the origin of the CH vibrational modes. Their position and band shape is strongly suggestive of chemisorbed CH residues (1, 34, 35). The fact that the residues were not removed on heating suggests a strongly bonded-heavy residue, yet does not preclude the possibility of actual structural incorporation. A possible source of such strongly adsorbed residues is the plasma used to prepare these films. Tantalum is deposited in an argon sputtering plasma at about 20μ pressure. However, it is known that the hydrocarbon background pressure can rise at least as high as 10^{-7} Torr. This will result in incorporation in the deposited film as cracked fractions. A further source of hydrocarbons occurs during the anodization of the tantalum film. Ethylene glycol and organic acids are employed as electrolytes. These will be adsorbed during the anodization and may account for the existence of carboxalate lines found in Fig. 3 and 4.

Without further information on the electrical properties of tantalum oxide during the adsorption, it is impossible to arrive at a definite statement regarding the electronic effects suggested by this information. However, it is known that adsorption of gases on a material having a measurable band gap will result in a process of charge compensation between the adsorbate and adsorbent. There is some physical evidence to indicate that these compensation processes are quite complex (48, 49). On the other hand, Sasaki (50) and others (51-56) have postulated the existence of a p-type layer on n-type or intrinsic Ta_2O_5. A possible source of this is the production of a high density of charged sites. Due to the localized nature of the compensation process in an insulator it seems evident that significant deviations from the average net charge may occur at selected regions of probable charge transfer. This will cause a material which may have been slightly extrinsic to become highly conductive through an accumulation layer or an inversion layer. Such layers may have characteristically large charge storage and transient decay as well as the unusually large rectification characteristics.

Manuscript received May 18, 1964; revised manuscript received Nov. 11, 1964. This paper was presented at the Pittsburgh Meeting, April 15-18, 1963.

Any discussion of this paper will appear in a Discussion Section to be published in the December 1965 JOURNAL.

REFERENCES

1. R. P. Eischens and W. A. Pliskin, *Advances in Catalysis and Related Subjects*, **IX**, 1 (1958).
2. M. J. Low, *Chem. Rev.*, **60**, 267 (1960).
3. M. Folman and D. J. C. Yates, *J. Phys. Chem.*, **63**, 183 (1959).
4. R. S. McDonald, *ibid.*, **62**, 1168 (1958).
5. J. T. Brunhultz, G. E. Hall, F. G. Mann, and N. Sheppard, *J. Chem. Soc.*, **1959** 868.
6. G. J. C. Frohnsdorff and G. L. Kingston, *Proc. Roy. Soc.*, **247A**, 469 (1958).
7. N. B. Hannay, "Semiconductors," Chap. 16, Reinhold Publishing Co., New York (1959).
8. P. Kislick, *Bell System Tech. J.*, **37**, 925 (1958).
9. J. H. Forster and L. E. Miller, *ibid.*, **35**, 766 (1956).
10. I. A. Myasnikov and S. Ya. Pshevzetski, *Doklady Akad. Nauk. SSSR*, **99**. 125 (1954).
11. M. H. Bortner and G. Parravano, *Advances in Catalysis and Related Subjects*, **IX** (1957).
12. G. W. Gobeli and F. G. Allen, *J. Phys. Chem. Solids*, **14**, 23 (1960).
13. P. Zwertering, H. L. T. Koks, and C. Van Heerden, *ibid.*, **11**, 18 (1959).
14. H. J. Krusemeyer and D. G. Thomas, *ibid.*, **4**, 1/2, 78 (1958).
15. G. Dorz, *Czech. J. Phys.*, **11**, 406 (1961).
16. B. J. Goldsmith and J. Muir, *Trans. Faraday Soc.*, **56**, 1656 (1960).
17. A. C. Jason and J. L. Wood, *Proc. Phys. Soc. (London)*, **B68**, 1105 (1960).
18. N. Schwartz and M. Gresh, *This Journal*, **112**, 295 (1965).
19. F. Vratny, M. Dilling, F. Gugliotta, and C. N. R. Rao, *J. Sci. and Ind. Res.*, **20B**, 590 (1961).
20. G. Joos, "Theoretical Physics," 2nd ed., pp. 351-2, Hafner Publishing Co.
21. N. J. Harrick, *Phys. Rev. Letters*, **4**, 224 (1960); *J. Phys. Chem.*, **64**, 1110 (1960).
22. S. A. Frances and A. H. Ellison, *J. Opt. Soc. Amer.*, **49**, 121 (1959).
23. F. Vratny and N. Micale, *Trans. Faraday Soc.*, **59**, 2739 (1963).
24. F. Vratny and J. J. Kokalas, *App. Spect.*, **16-6**, 176 (1962).
25. F. Vratny, *J. Chem. Phys.*, **34**, 1377 (1961).
26. F. Vratny, *J. Inorg. Nucl. Chem.*, **16**, 263 (1961).
27. (*a*) W. E. Garner, "Chemisorption," Butterworth, London (1957); (*b*) L. E. Copeland, "Solid Surfaces," Amer. Chem. Soc. Adv. or Chem. Series #33, Washington, 1961. (*c*) F. R. Eirich, *Ann. N.Y. Acad. Sci.*, **141**, #3 (1963).
28. A. R. Downie, M. C. Magoon, T. Purcell, and B. Crawford, Jr., *J. Opt. Soc. Amer.*, **43**, 941 (1953).
29. A. Chevet, *J. Phys. Radium*, **14**, 493 (1953).
30. R. S. McDonald, *J. A. C. S.*, **79**, 850 (1957).
31. F. Vratny and B. Graves, *Rev. Sci. Instr.*, **31**, 65 (1960).
32. S. Matsushita, *J. Chem. Phys.*, **32**, 982 (1960).
33. J. H. Taylor and C. H. Amberg, *J. Chem.* **39**, 535 (1961).
34. W. A. Pliskin and R. P. Eischens, *J. Chem. Phys.*, **24**, 482 (1956).
35. D. J. C. Yates and P. J. Lucchesi, *ibid.*, **35**, 243 (1961).
36. J. K. Wilmshurst, *ibid.*, **34**, 941 (1961).
37. R. W. Hexter, *ibid.*, **34**, 941 (1961).
38. C. Cabannes-Ott, *Compt. rend.*, **242**, 2825, 355 (1956).
39. J. M. Serratosa and W. F. Bradley, *Nature*, **181**, 111 (1958).
40. F. A. Miller and C. H. Wilkins, *Anal. Chem.*, **24**, 1253 (1952).
41. W. C. Price, W. F. Sherman, and G. R. Wilkinson, *Proc. Roy. Soc.*, **A247**, 467 (1958).
42. H. M. Randall, R. G. Fowler, N. Fusan, and J. R. Dangl, "Infrared Determination of Organic Structures," D. Van Nostrand, New York (1949).
43. P. C. Cross, J. Burnham, and P. A. Leighton, *J. Am. Chem. Soc.*, **59**, 1134 (1937).
44. R. P. Eischens, *Z. Elektrochem.*, **60**, 782 (1956).
45. D. J. Yates and N. Sheppard, Proc. Second International Congress of Surface Activity (1957).
46. L. H. Little, N. Sheppard, and D. J. C. Yates, *Proc. Roy. Soc.*, **A259**, 242 (1960).
47. R. P. Eischens, 1959—Fifth World Petroleum Congress, V#3, Ap. (1959).
48. G. H. Wannier, Internal Publication, Bell Telephone Labs., April 20, 1949.
49. N. F. Mott and R. W. Gurney, "Electronic Processes in Ionic Crystals," p. 107, Oxford Press, (1953).
50. Y. Sasaki, *J. Phys. Chem. Solids*, **13**, 177 (1960).
51. Y. Ishikawa, Y. Sasaki, Y. Seki, and S. Inowaki, *J. Appl. Phys.*, to be published.
52. D. A. Vermilyea, *Acta. Met.*, **5**, 113 (1957).
53. J. D. Memory, Internal Publication, Bell Telephone Labs., 1957.
54. M. Kobayashi, Ext. Abstr. IRE Convention, Philadelphia, May 1959.
55. W. A. Van Geel, *Physica*, **17**, 761 (1951).
56. R. L. Taylor and H. E. Haring, *This Journal*, **103**, 611 (1956).

Effect of Ambients and Contact Area on the Asymmetric Conduction of Anodic Tantalum Oxide Films

N. Schwartz and M. Gresh

Bell Telephone Laboratories, Incorporated, Murray Hill, New Jersey

ABSTRACT

The effect of moisture and metallic contact area has been investigated on the asymmetry properties of anodic tantalum oxide films, approximately 2400Å thick. Moisture has been reversibly desorbed and adsorbed by vacuum baking followed by exposure at 50-85% RH. The cathodic currents are not affected significantly by this cycle, while the anodic leakage and charging current can be changed by factors of 10^6 and 10^2, respectively. The contact area experiment confirm previous results that the asymmetry is due to local inhomogeneities in the oxide film, since nonpolar characteristics, in the absence or presence of moisture, can be obtained with a contact area less than 0.01 mm^2. This result indicates that the moisture effect is associated with defects in the oxide film. The oxide film can thus be considered as a normal dielectric with high symmetrical anodic and cathodic breakdown voltages. Distributed on the average 0.1 mm apart throughout the film are heterogeneities of an unknown nature which cause a symmetrical but lower breakdown than the rest of the oxide. The asymmetry results from an increase in the anodic breakdown at these distinct sites due to the presence of water.

Many investigations have been make on the current transport properties of anodic oxide films. These films when measured in an aqueous electrolyte are capable of passing large currents when the parent metal is cathodic compared to the blocking features when it is anodic. The mechanisms that have been proposed for this effect (1,2) may be arbitrarily classified as heterogeneous or homogeneous phenomena. The first of these depends on local inhomogeneities in the oxide film which are responsible for the asymmetric current flow, with the rest of the oxide film having normal insulating dielectric properties. Evidence for this mechanism is based on the varying resistivity of an anodic tantalum oxide film determined by probe measurements (3), on deductions based on measurements with anodized tantalum rods (4), and on experiments with electrodes evaporated at different angles (5). The homogeneous mechanisms depend on detailed proposals concerning the electronic band structure of the oxide (6) on interactions with the aqueous electrolyte contact (1), and on transport of protons through the film (7).

Studies have been made on the differences between aqueous and nonaqueous electrolytes, the effect of salts in nonaqueous solvents, and the comparison between solvent or metallic contacts in attempts to evaluate the contribution of the counterelectrode to the asymmetry (1). In all of this work, however, there has been no definitive investigation of the effect of water on the conduction properties. The results in liquid sulfur dioxide indicate that the cathodic currents are considerably lower than those in aqueous solution (1), but it is difficult to determine to what extent moisture was excluded. In the normal aqueous electrolyte measurement, of course, the concentration of water cannot be readily varied. The printed tantalum oxide capacitor (8) is an excellent example of the characteristics obtained with uniform anodic oxide films with evaporated metallic contacts. With this capacitor the measurement of asymmetry does not depend on an electrolyte contact, and moisture can be reversibly desorbed or adsorbed. The present work is a preliminary one to phenomenologically define the effects of water on the conduction properties of anodic tantalum oxide films, using the printed capacitor as the vehicle. Moreover, since the counterelectrode contact area can be easily varied with this capacitor, it should be possible to distinguish between the heterogeneous and homogeneous mechanisms without confusion with respect to the variable pressure of a metallic probe (1).

The conduction properties of the printed capacitor do not exactly correlate with those of conventional capacitors, since the cathodic breakdown voltages are much larger than observed for either wet or solid electrolytic types. A strong similarity does exist, however, since there are asymmetric cathodic and anodic breakdown voltages (8). Moreover, anodic tantalum oxide formed on sputtered tantalum films demonstrates a cathodic current characteristic similar to the normal types when measured in aqueous electrolytes (1).[1] These features indicate that information gained by this study will be applicable to anodic oxide films in general.

Experimental Methods

Tantalum films were sputtered from high-purity tantalum cathodes through masks on cleaned soft glass microscope slides to a thickness of about 4500Å. The films were anodized to 100v at 105°C in an oxalic acid-ethylene glycol-water bath resulting in oxide films about 2400Å thick (8). In all cases, the anodization was interrupted to etch electrochemically the tantalum films in lithium chloride in methanol which has been proven beneficial in reducing anodic leakage or shorts (9), but by repeated experiments has been shown not to affect the asymmetry characteristics. The last step in the fabrication was the evaporation of a gold counterelectrode by tungsten filament evaporation techniques at pressures of 1×10^{-4} to 1×10^{-6} Torr.

Two forms of finished capacitor structures are shown in Fig. 1. By limiting the depth of immersion of the tantalum coated slide in the anodization electrolyte the upper contact area (marked Ta in Fig. 1) is not oxidized. Type 1C was used primarily in these studies with capacitors of about 0.035 μF. Type 1A permitted an anode area variation of about 3×10^{-2} to 10 mm^2 with corresponding capacitance values from 50 to 10,000 picofarads for 100v anodization at 105°C. The results reported in general represent the average of four or more capacitors.

Measurements of current-voltage characteristics were performed in two ways: (*a*) a normal current measurement after 1 min at a given voltage; and (*b*) an almost transient value. For this latter measurement,

[1] More detailed measurements with aqueous electrolytes indicate a higher complexity than originally reported (1) and these will be discussed in a later communication.

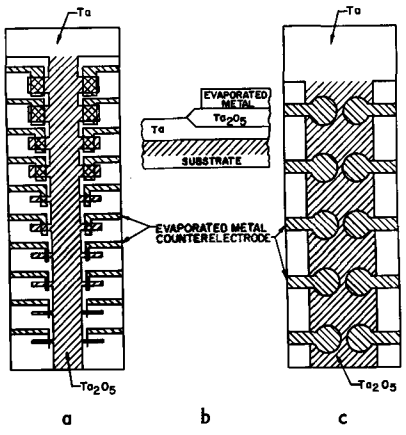

Fig. 1. Structures for the evaluation of printed tantalum oxide capacitors: (a) tantalum anode area variation; (b) schematic capacitor structure; (c) normal capacitor sample.

a motor driven potentiometer generated a single triangular wave at about ±1 v/sec or about 0.002 cps. The micromicroammeter is a direct current amplifier, and the output of the amplifier and the voltage from the potentiometer are displayed on an X-Y recorder. The voltage drop across the micromicroammeter is small compared to that of the test capacitor. A schematic diagram for the output of the measurement is shown in Fig. 2. The voltages are shown as anodic or cathodic with respect to the tantalum electrode of the capacitor. I_C, the ideal charging current generated by the constant increase or decrease in voltage, is given by Eq. [1]

$$I_C = C\frac{dV}{dt} \qquad [1]$$

and is directly proportional to the capacitance in farads and the rate of voltage rise in volts per second. $I_L{}^V$ is the usual leakage current, and $I_P{}^V$ is a polarization current, both of which are voltage dependent. This measurement does not separate the leakage current from the polarization current. No attempts have been made to fit the current-voltage curves analytically, and therefore arbitrary anodic, $V_A{}^B$, and cathodic, $V_C{}^B$, breakdown voltages have been defined as the voltages at which the currents (*i.e.*, ~ 0.1 μa) are three times the charging currents. This dynamic technique allows a rapid evaluation of the d-c properties of many capacitors and their "breakdown" voltages.

The effect of moisture on the properties of the capacitors was determined by baking at pressures from 1 x 10^{-5} to 1 x 10^{-6} Torr at 85° to 125°C for periods of 3 to 4 hr. The capacitors were then cooled to room temperature, and their a-c or d-c properties measured while they were still in the vacuum system through a multiheaded wire seal. Subsequently, moisture or air was admitted to the system and the properties of the films measured.

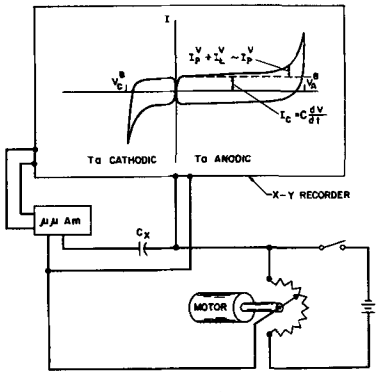

Fig. 2. Schematic output of the dynamic method for determining I-V characteristics.

The structural investigation of the anodic oxide films was performed in a Siemens Elmiskop electron microscope. The oxide films were anodized to 10-20v, since greater thicknesses do not allow sufficient electron transmission. The oxide films were stripped from the metal film by an electrochemical tantalum etching technique. A V-shaped pattern with about 0.25 in. legs and a 30° angle was scratched through the oxide being careful not to penetrate the glass. The tantalum film was etched anodically in a solution of 0.01 w/o (weight per cent) lithium chloride in methanol at room temperature at a potential of 10-20v. For a 3000-4000Å tantalum film, 0.5 cm^2/hr of tantalum was removed. The slide was washed and stored in methanol. When desired, the excess methanol was removed by a nitrogen gas stream, and a 0.25 mm layer of collodion was applied to the exposed tantalum oxide film. After drying overnight, the collodion was cut into convenient sections, and the sections were manually transferred to a screen and the collodion dissolved in butyl acetate.

Results

Effect of Moisture

Effect of moisture on the current-voltage characteristics.—A typical curve for a change in current characteristic after baking in vacuum at 125°C for 3 hr is shown in the upper part of Fig. 3. The anodic breakdown voltage has decreased by approximately 60v, while there has been little change in the cathodic breakdown voltage. In all cases studied, the vacuum baking cycle effected the cathodic current only negligibly, but increased the anodic current profoundly. Moreover, the decrease in anodic breakdown voltage is completely irreversible if the desiccated sample is exposed to dry air, but completely reversible when exposed to moist air. The rate of return to a high anodic breakdown voltage at 50% relative humidity in

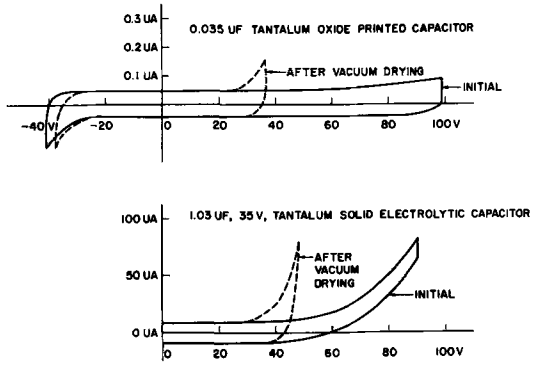

Fig. 3. Comparison of I-V characteristics determined by the dynamic method before and after vacuum baking; upper curve, printed tantalum oxide capacitor; lower curve, tantalum solid electrolyte capacitor.

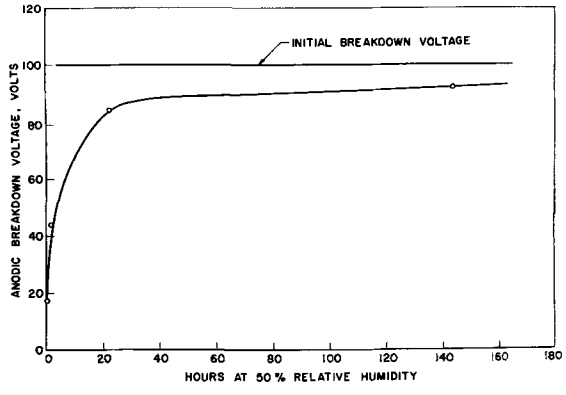

Fig. 4. Anodic breakdown voltage of a printed tantalum oxide capacitor at 50% relative humidity in air as a function of time after vacuum baking.

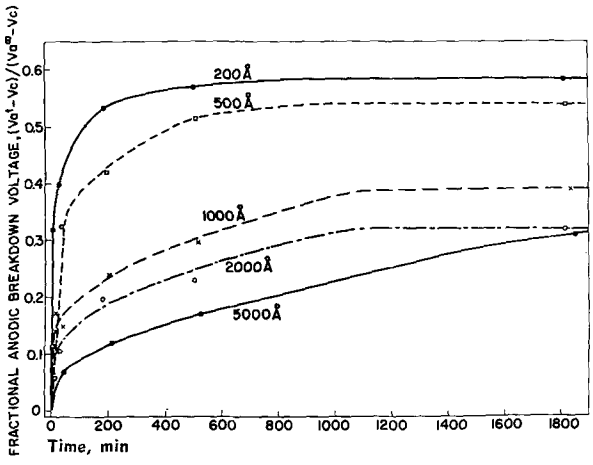

Fig. 5. Fractional anodic breakdown voltage at 45% relative humidity as a function of time after vacuum baking for capacitors with varying thickness of the gold counterelectrode. ($V_a{}^t$ is the anodic breakdown voltage at time t, $V_a{}^\infty$ is the maximum anodic breakdown voltage at infinite time at 85% RH, and V_c is the cathodic breakdown voltage).

air is demonstrated in Fig. 4 for a sample originally desiccated in vacuum at 125°C.

Figure 5 indicates the dependence of the rate of return on the thickness of the gold counterelectrode layer. Since the rate of return depends on the gold thickness it implies that the moisture must be diffusing through the metal electrode. Transmission electron micrographs of stripped gold films indicate that there are many cracks between islands for the thinnest films, which gradually decrease in number for the thicker films. This figure also demonstrates that the anodic breakdown voltage depends on the relative humidity, since for 85% RH the fractional anodic breakdown voltage is 1, rather than 0.3-0.6 illustrated for 45% RH.

When the moisture is removed from the dielectric by vacuum baking, there is only a 3% loss in capacitance over the entire frequency range of 0.1-5 kc, while the dielectric loss decreases by approximately 40%. Depending on the specific model assumed, this loss in capacitance may be associated with a 2-50Å layer in the surface, or a 0.1 μg/cm^2 of bulk water in the oxide film. Both of these values are approximate since a 1.5% loss in capacitance occurs where there is no large change in the d-c characteristics. This background change in capacitance may result from the annealing of the oxide film (6).

The influence of moisture is not specific to tantalum oxide films made from sputtered or evaporated tantalum metal anodes. A similar drying treatment has

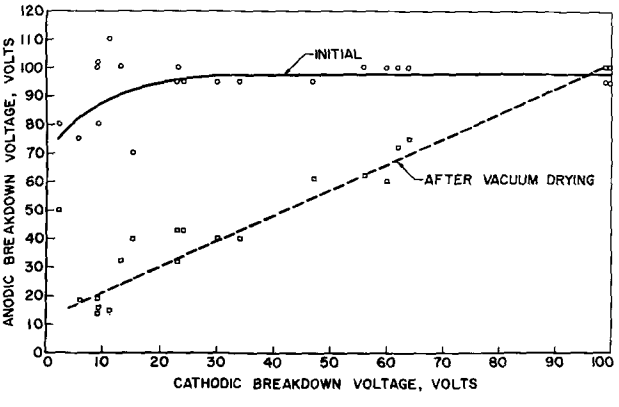

Fig. 6. Dependence of the anodic breakdown voltage of printed tantalum oxide capacitors on the initial cathodic breakdown voltage.

been applied to tantalum solid electrolyte capacitors where the anode is a sintered pellet of tantalum powder and the cathode is a porous layer of manganese dioxide (10). Baking a 1.0 μf capacitor at 125°C for 4 hr at 10^{-6} Torr, caused the anodic breakdown voltage[2] (Fig. 3) to decrease from 67 to 39v. As observed with the printed capacitor the presence or absence of moisture in the oxide has negligible effects on the cathodic characteristic. When this sample was exposed to 50% relative humidity, the anodic voltage characteristic was identical to the value before bake out within 30 min. This fast recovery for such a large area confirms that the slow rate of return for the printed capacitor may be limited by the penetration of the moisture through the gold counterelectrode. In the solid electrolytic capacitor, the manganese dioxide layer is porous enough to allow moisture to be adsorbed rapidly on the tantalum oxide layer.

During the course of this work, many capacitors have been investigated where the cathodic breakdown voltage had a range from 7 to 100v. The top curve in Fig. 6 indicates the anodic breakdown voltages before vacuum baking, and it is apparent that the initial values have no strong dependence on the original cathodic voltage. The lower curve illustrates the anodic breakdown voltages after the vacuum baking. A linear relationship exists between the final anodic breakdown voltage after baking and the original cathodic breakdown voltage. When the cathodic breakdown is in the range of 80-100v there is little change during the baking procedure.

Comparison of dynamic and static leakage measurements.—The data have been presented only when determined by the dynamic method described in the experimental section. For anodic oxide films a long polarization process occurs during current measurements. The dynamic method may tend to emphasize the polarization effect since the transit time is only of the order of 1 sec/v. Many different kinds of comparisons were made between the "static" and dynamic methods, which indicated that, although the latter did measure a high fraction of the polarization current, qualitatively it was a direct measure of the change in anodic characteristics due to the removal of moisture.

This conclusion was best illus rated by experiments on the effect of moisture on the charging rate and terminal leakage current, evaluated by current measurements as a function of time after the instantaneous ap-

[2] The breakdown voltage in this case is defined as for the printed capacitor type in the section on experimental methods.

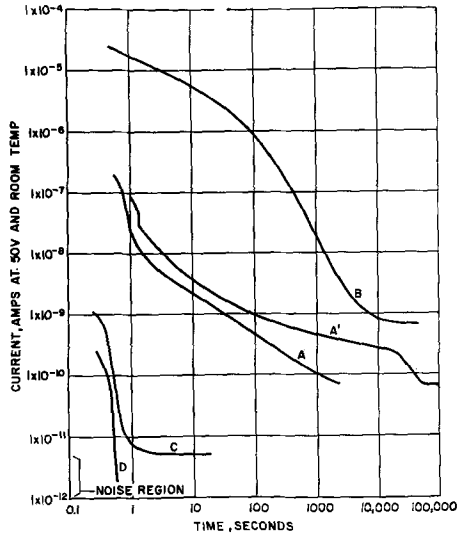

Fig. 7. 50V charging current measured at 25°C as a function of drying. a. In room ambient. b. In vacuum after bake out. c. In 17 Torr of water. a'. After return to room ambient. d. Polystyrene capacitor.

plication of 50v. The capacitors chosen for this study had a cathodic breakdown voltage of 10v in order to obtain a maximum sensitivity of electrical properties to moisture. Curve A (Fig. 7) is the result in a normal room ambient (*i.e.*, ~ 50% RH) and consists of a fast initial charging process followed by a slow step which approaches an analytical form given by Eq. [2].

$$I = At^{-n} \qquad [2]$$

The terminal leakage value appears to be about 5 x 10^{-11} amp for a time approaching 10,000 sec. This two-stage process is quite similar to the results reported for tantalum oxide films in aqueous electrolytes (11), where the first stage was attributed to a RC charging process, but with calculated R values considerably higher than that anticipated from the external circuit resistance. The second stage had the same analytical form of Eq. [2], and this process was presumed to be determined by trapping levels in the dielectric. These charging curves correspond to times beyond the normal expected dielectric charge and represent residual polarization of relatively large relaxation time.

Curve B (Fig. 7) is the result of measurement in vacuum after baking at 125°C at a pressure of 1 x 10^{-3} Torr for 3 hr. The fast initial charging process has disappeared, and the terminal leakage value is 7 x 10^{-10} amp. Curve C is the result of subsequently introducing into the vacuum system water vapor to a pressure of 17 Torr at room temperature (~ 70% humidity). The initial process has reappeared, and is now many times faster than that of curve A. The terminal leakage value is less than 5 x 10^{-12} amp, and could not be determined precisely because of background noise in the measuring circuit. This entire series of steps is essentially reversible, because the successive step of equilibrating the sample in a room ambient resulted in curve A'. Curve D is for a polystyrene capacitor of equivalent capacitance, and indicates the expected result for a low residual charge dielectric film.

Superficially these results confirm the interpretation that the presence of water in or on the oxide film determines both the charging rate and terminal leakage current. Depending on the moisture level, the initial charging rate varies by a factor of 10^6, while the terminal leakage value varies by a factor of 10^2.

There is a serious objection to concluding that the removal of moisture affects the initial charging rate by altering the parameter of a single mechanism. For the condition illustrated by curve B, the vacuum dried condition, the total charge passed in the first 100 sec is approximately 250 times larger than expected on the basis of the initial capacitance and charging voltage. This excess charge can arise in two possible ways: (*A*) The high initial current is truly a value associated with a dielectric breakdown process, but the dielectric can be "reformed" with continued application of a potential. This "reforming" designation does not imply only ionic transfer and may be related to the slow build up of an electronic barrier in some portion of the oxide. (*B*) An improbable large voltage dependent capacitance may arise from the removal of moisture, and its charging process may be exceptionally slow.

This latter possibility could be eliminated by capacitance measurements as a function of bias, and preliminary measurements indicate no large changes in capacitance with bias. For the purposes of this paper, therefore, it will be assumed that the dynamic technique gives a true measure of the breakdown voltage on drying the sample.

Cathodic Breakdown Voltage and Area Dependence

Vermilyea (3) has demonstrated by probe measurements on tantalum oxide prepared on bulk anodes that an area effect exists with respect to the cathodic currents. Despite the large cathodic currents that can be passed through these films in aqueous electrolytes, very small metallic probe measurements indicated that different areas were either highly insulating or conducting. This would imply that the rectification phenomenon observed in electrolytic solutions is related to discrete points in the oxide films rather than being a homogeneous effect associated with the entire film. These experiments have been criticized in several ways, but perhaps the most valid one is that it is difficult to use metal probes and to know conclusively whether the probe is puncturing the oxide films due to point pressures in some cases, and not making contact in other cases. It has been confirmed in this study that it is quite easy to puncture the oxide films even when lightly touching it with a metallic probe. For the tantalum oxide printed capacitor, however, small area evaporated counterelectrodes are easily attained, and this type of contact avoids the ambiguity associated with variable pressure of probes. Moreover, the area of the contact is easily determined by capacitance measurements. The structure used for these experiments is illustrated in Fig. 1a. These slides were prepared by the usual procedure utilizing gold counterelectrodes, and the important variable for study was the cathodic breakdown voltage. These results are plotted in Fig. 8 for two different sputtering runs.

The results demonstrate that down to about 300 picofarads (or 0.3 mm^2) the cathodic breakdown voltage is fairly constant. The voltage rises sharply as the capacitance decreases to the order of 50 picofarads. The shape of the curve depends to some extent on the sputtering run. An interpretation of these curves is that the cathodic breakdown voltage depends on discrete inhomogeneities in the oxide films. The probability of making contact to such a local defect becomes much smaller as the area of the capacitor is decreased. In some of these curves, at about 50 picofarads the full expected cathodic breakdown voltage of tantalum oxide is realized. These data, therefore, entirely confirm Vermilyea's experiments with respect to local defects determining the cathodic characteristics of anodic oxide films.

There is a surprising feature about these data. For each capacitance value, four individual capacitors were tested, and at each capacitance value there is very little spread for the breakdown voltage. If a local inhomogeneity mechanism was of importance, a much broader distribution at high cathodic breakdown voltages would be expected. This feature has not been entirely resolved, but similar measurements have been obtained for a large number of capacitors with values of the order of 50-100 picofarads. For these data (Fig. 9), slides from three different runs were used. One of these slides had capacitors with very low breakdown voltage, and high breakdown voltages could not be obtained at all. For the other two slides, there is a distribution of cathodic breakdown voltages as would

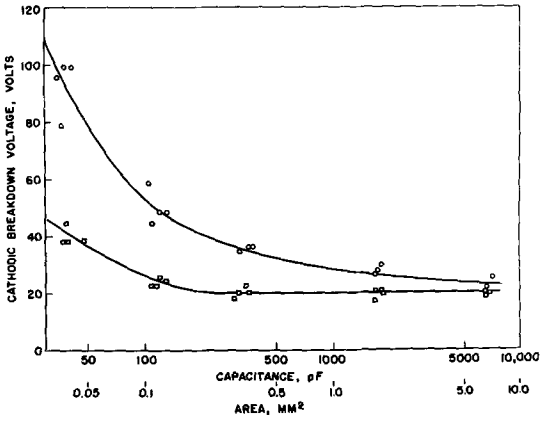

Fig. 8. Cathodic breakdown voltage as a function of the capacitance of printed tantalum oxide capacitors. All formations at 100v at 110°C.

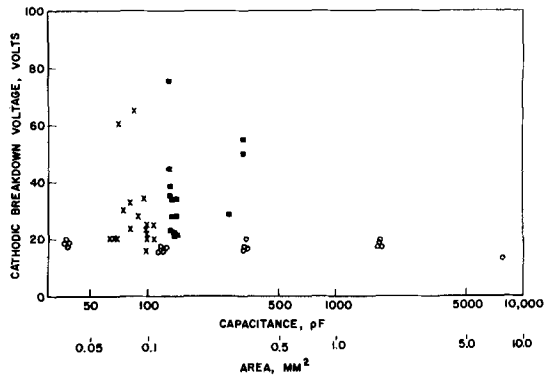

Fig. 9. Distribution of cathodic breakdown voltages for small area capacitors. Each symbol represents an individual sputtering run.

be expected from a local defect mechanism. The tight distribution of the initial data of Fig. 8 may only be due to the small sample size. In attempting to quantitatively fit these data to a model based on localized defects (12) some anomalies have appeared with respect to the exact shape of the curve, and further work is required on this problem. However, in general, it may be concluded that a localized defect mechanism is responsible for the change in breakdown voltage with the variation of area.

As has been indicated previously, the moisture effect for the anodic characteristics depends on the cathodic breakdown voltage. As the cathodic breakdown value approaches 70- 80v the humidity dependence essentially disappears. In fact, the data presented in Fig. 6 is a representation of capacitors of different areas.

Electron Microscope Investigations

Since the previous experiments indicate that local defects exist in the oxide films, some initial electron microscope investigations have been made in an effort to confirm their presence. When the stripped oxide films were investigated by electron transmission, a variety of defect types could be found. They consisted of small crystallized areas, pores which did not completely penetrate the films, and long cracks. Generally, the major fraction of the oxide film was homogeneous and consisted of amorphous tantalum oxide. The defects when they were observed were generally localized in an area of 100 μ^2, but at least one defect was always observed on every specimen screen which has an area of 1 mm^2. At present, it is not clear whether these defects were present originally or were introduced during the stripping of the film. More extensive work is required with respect to the stripping process, the type of defects, their incidence, and their relation to electrical properties and variation of process techniques.

Discussion

The results presented in the previous sections can be summarized in the following conclusions with respect to the conduction properties of anodic tantalum oxide:

(*A*) The anodic currents are decreased by a specific interaction with water, but not with oxygen or nitrogen. However, a possible interaction with a mixture of water and oxygen has not been completely excluded.

(*B*) The interaction with water involves the mechanism of the anodic leakage and capacitive decay currents, but not the cathodic currents.

(*C*) The cathodic currents are related to a local defect, or heterogeneous mechanism, in the oxide film.

(*D*) Since the interaction with moisture described in (*B*) disappears when high cathodic breakdown voltages are obtained by area variation, the moisture effect as well must depend on a local defect mechanism.

The implication of these results is that at defect sites there is a nonpolar oxide film with an anodic breakdown strength roughly equivalent to the cathodic breakdown value. At these sites, however, there is an anodic barrier to current flow caused by the presence of moisture, resulting in high anodic breakdown voltages. Over the remaining area of the oxide, the moisture effect is not important, and the film is nonpolar with cathodic and anodic breakdown strengths approximating the original anodization voltage. Unfortunately, most of these conclusions depend on an interaction with local defects, and no specific mechanism can be proposed until more information is gained about their nature, incidence, and origin. The initial electron microscope studies have revealed physical defects in the oxide film, but they have not been reported in detail since it is not completely certain that they were present in the unstripped oxide films. Compositional defects caused by deviations of stoichiometry or impurities are other possible suspects.

This conclusion of the importance of water in determining the anodic characteristics is sharply different than other interpretations of the asymmetry which emphasize an abnormal cathodic current relative to the expected properties of a normal dielectric. The present interpretation indicates that the cathodic currents are normal, while the anodic breakdown is unusually high due to the presence of moisture.[3]

The two unusual features of these results are the sensitivity to moisture of the anodic leakage and charging currents. In an effort to establish a single mechanism to explain these results, it is tempting to resort to a local defect mechanism proposed by Young (4). The local defect is specifically a microfissure (*i.e.*, a crack or hole) in the oxide. When the tantalum is the cathode in an aqueous solution, large currents can flow because hydrogen is liberated, which because of size and tantalum embrittlement considerations, would not be trapped in the microfissure. When the tantalum is anodic, oxygen would be liberated which would be trapped as bubbles and thus maintain the full dielectric strength of the oxide. To adapt this proposal to the present results, it is conceivable that the vacuum bake out would remove both moisture and oxygen from the microfissures. This would imply that the cathodic characteristics would greatly improve, while the anodic characteristics would not change essentially. It is difficult to rationalize the increase in anodic leakage, unless due to the vacuum treatment the oxide essentially collapsed around the fissure resulting in more intimate contact of the gold to a thinner portion of the oxide film. Of greater consequence, however, is the difficulty in relating the charges in the capacitor current decay process to a microfissure mechanism. Recent studies (11) have indicated that this process is determined by electron traps in the oxide film, which if true, indicates that water is intimately involved in the dissociation and recombination of traps and electrons. In general, the microfissure mechanism, though having interesting features, fails to correlate the general conclusions in detail.

Further studies are required in order to obtain a more detailed understanding of this problem, with an investigation of the defect type perhaps being the most important. One of the interesting questions is whether the presence of moisture affects the oxide as a whole as well as being important in local areas. This is of importance in understanding the influence of moisture on the capacitor charging mechanism. Studies on the charging and discharging process with ultraviolet illumination and varying amounts of moisture as variables might be quite fruitful. An associated study (13) on the infrared spectra of the surface adsorbed species has already indicated the presence of water, carbon dioxide, and hydrocarbons, whose concentration change with temperature and pressure. Experiments with tritiated water have also indicated the

[3] This conclusion holds only within the evaporated electrode configuration. As has been indicated earlier, an aqueous electrolyte contact does cause a change in the cathodic breakdown voltage.

presence of water in or on the oxide film (14). Further studies are required to relate these changes in concentration with electrical properties of the tantalum oxide film.

Acknowledgments

The authors wish to express their appreciation to M. Urban for designing the switching circuits for the dynamic method for determining I-V characteristics, and to C. J. Calbick for his electron microscope studies of thin tantalum oxide films.

Manuscript received Aug. 11, 1964; revised manuscript received Nov. 5, 1964. This paper was presented in part at the Indianapolis Meeting, April 30-May 3, 1961.

Any discussion of this paper will appear in a Discussion Section to be published in the December 1965 JOURNAL.

REFERENCES

1. P. F. Schmidt, F. Huber, and R. F. Schwarz, *J. Phys. Chem. Solids*, **15**, 270 (1960).
2. L. Young, "Anodic Oxide Films," Academic Press, New York (1961).
3. D. A. Vermilyea, *J. Appl. Phys.*, **27**, 963 (1956).
4. L. Young, *Trans. Faraday Soc.*, **55**, 842 (1959).
5. M. Kleefstra, *Ann. Radioelectricité*, **57**, 223 (1962).
6. Y. Sasaki, *J. Phys. Chem. Solids*, **13**, 177 (1960).
7. A. Middlehoek, *This Journal*, **111**, 379 (1964).
8. R. W. Berry and D. Sloan, *Proc. I.R.E.*, **47**, 1070 (1959).
9. R. W. Berry and N. Schwartz, *Proc. 4th National Convention of Military Electronics*, **4**, 214 (1960).
10. D. A. McLean and F. S. Power, *Proc. I.R.E.*, **44**, 872 (1956).
11. K. Lehovec and R. Dreiner, Abstract Electrochemical Society Meeting, Indianapolis, Ind., May 1961.
12. B. Epstein, *J. Appl. Phys.*, **19**, 544 (1948).
13. F. Vratny, *This Journal*, **112**, 289 (1965).
14. G. M. Krembs, *ibid.*, **110**, 938 (1963).

The Preparation and Properties of GaAs-InAs Mixed Crystals

Henry T. Minden

Sperry Rand Research Center, Sudbury, Massachusetts

ABSTRACT

Mixed crystals of $Ga_xIn_{1-x}As$ have been prepared by a halogen vapor transport method. The entire composition range was covered and electroluminescent diodes were made. The dependence of emission energy at 77°K on composition was determined. Conditions were determined for the epitaxial deposition of GaAs-InAs mixed crystal layers on pure GaAs needs. A halogen-flow system was used, and liquid Ga-In solutions were used in the source. It was discovered that considerable fractionation occurred in the deposition reaction.

Both GaAs and InAs are direct band-gap semiconductors. P-N junctions in single crystals show strong injection electroluminescence, especially at low temperatures. Stimulated emission has been observed in GaAs and InAs junction diodes which were made in the form of optically resonant cavities (1, 2). At 77°K the emission peak in GaAs is at .8400μ, while for InAs the emission is at 3.5μ. Electroluminescence and stimulated emission have also been observed in diodes which were made from quasi-binary mixed crystals of GaAs and InAs (3). The optical emission fell at wavelengths between the extremes represented by the two pure materials. It remains to determine the dependence of emission wavelength on composition, much as has been done with GaAs-GaP mixed crystals (4).

The electroluminescent emission in direct III-V compounds occurs at energies which are about 0.02 ev lower than the band gap, and the emission energy varies with temperature much as does the gap. The variation with composition of the energy gap at room temperature has been determined for the GaAs-InAs system by optical absorption measurements (5). The mixed crystals were prepared from the melt, however, and there was considerable uncertainty in the measurement of both the composition and the band gap.

It has been found, however, that homogeneous mixed crystals of controllable composition can be grown by halogen vapor transport techniques (6, 7). This technique was used to prepare mixed crystals of GaAs-InAs throughout the whole composition range. Electroluminescent diodes were prepared and the peak emission wavelength was determined as a function of composition. Mixed crystal epitaxial layers were also prepared by deposition on pure GaAs in a halogen-flow system.

Material Preparation

Closed-tube transport.—To prepare bulk crystals of InAs-GaAs we used a slight modification of the so-called closed-tube technique (7). Weighed amounts of powdered GaAs and InAs were sealed in a small, evacuated quartz tube along with some Cl_2 gas. The Cl_2 reacted with the arsenides at room temperature, and all of the material was at one end of the tube. The tube was put in a furnace which had a large temperature gradient. The reactants were at the hot end of the tube (at about 700°C). Complete transport occurred in about ½ hr, and the deposit was generally in the form of small flakes. The tube was then placed in a close-fitting Inconel bomb which had thermocouples placed at either end. The bomb was centered in a cylindrical furnace in such a way that the temperature difference across the quartz tube was roughly 10°C. As before, the source was at the hot end. A mean temperature of 850° was used for low GaAs concentrations, while for GaAs concentrations of greater than about 50% temperatures up to 950° were needed for large crystal growth. The runs were generally made overnight, although longer times were used. Usually the transport was incomplete. As might be expected, the larger the temperature gradient, the faster the transport, and the smaller the crystallite size.

Typical crystals are shown in Fig. 1. They generally had a lamellar structure with well-developed tetrahedral sides. The sides were {111} facets, as determined by x-ray diffraction and by the way the crystallites cleaved. The polarity of the facets was not determined.

Open-tube deposition.—The flow system which was used to deposit epitaxial layers on seed crystals has been described elsewhere (8). A mixture of H_2 and HCl was passed over arsenic metal at 500° and then over a boat filled with a Ga-In solution which was at 850°-900°. Downstream there was a seed crystal of GaAs which was held at temperatures ranging from 650°-750°. Both the H_2 and HCl flow rates were 2-4 x 10^{-3} mole/min, and the indications were that the transport and deposition were almost quantitative in the amount of HCl. Of course, most of the actual deposi-

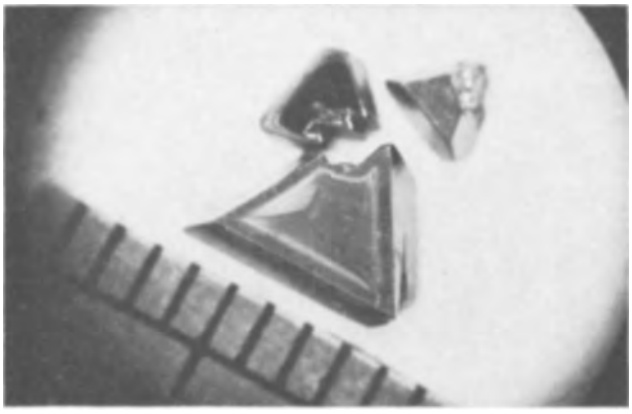

Fig. 1. InAs-GaAs crystallites obtained by the closed-tube halogen vapor transport process. The scale is in millimeters.

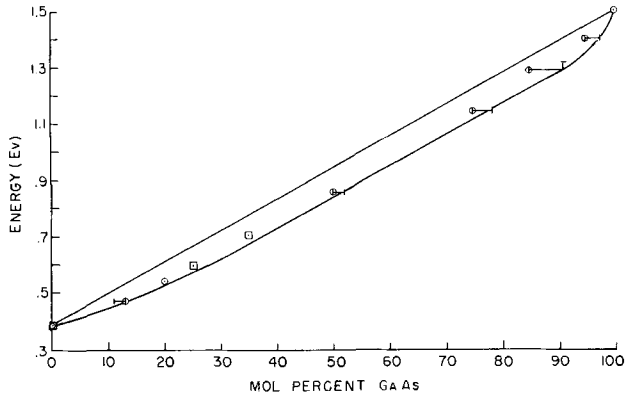

Fig. 2. Dependence of electroluminescence energy on composition for InAs-GaAs mixed crystal diodes. The peak emission wavelength was measured at 77°K. Squares are data of Strauss *et al.* (3) taken at 2°K.

tion occurred on the walls of the tubes and on the seed holder. The deposition rates on the seed were about 15-40 μ/hr; layer thicknesses of 20-50μ were used.

Diode Fabrication

All the material we prepared for this study was unintentionally doped n-type. The crystallites which were obtained from the closed-tube transport were lapped flat on one side. The other side was a naturally formed specular facet. Several such crystallites were sealed in an evacuated tube along with a few mg each of Zn and As. The diffusion runs lasted 2 hr, and temperatures from 650° to 700° were used, depending on the GaAs concentration. The junctions so formed were about 30μ deep.

The crystallites were cleaved or ultrasonically cut into pellets, and the lapped side was alloyed to a conventional transistor header which was In-Au plated. The contact to the specular p-side was made by alloying an In sphere. Occasionally, the n-side of the pellet was alloyed across a hole in the header in order that the radiation could be viewed from the broad area of the junction rather than edge-on.

The epitaxial material was treated in a similar fashion, except that the diffusion times were shorter to prevent the diffusion from penetrating to the GaAs substrate.

Measurements

The closed-tube technique gave compositions which were definitive and reproducible. The initial measurement was the proportion of InAs and GaAs which was weighed out at the start of the preparation. The lattice constant of the synthesized crystals was then measured for several samples by means of x-ray powder patterns.[1] The diffraction lines were sharp and well-defined, and they corresponded to known reflections. From the lattice constants and Vegard's law (9) the composition was determined.

The electroluminescent spectra of diodes made from these crystals were measured at 77°K. The I-V characteristics were measured as a matter of course. Quite naturally, there was a good correlation between the energy of the emission peak and the voltage at which the forward-current break occurred. For a given composition, the maximum variation of the emission peak was about $\pm$ 2%.

The composition which was obtained in the flow system was not so well-defined as for the closed-tube technique. In particular, the composition of the deposit was not simply related to the composition of the source. Therefore, in order to determine the relationship between the source and deposit compositions, several techniques were used to determine the nature of the epitaxial layer. Lattice constants were measured with an x-ray diffractometer. For some samples the optical absorption edge was measured at room temperature.

[1] These measurements were done by W. Croft and R. Carter.

As with the lattice constant, a linear interpolation was made on an energy scale to determine the composition. Although this is not strictly justified, it is sufficiently accurate considering the scatter of our results in these experiments. Finally, on some samples diodes were made and the electroluminescent emission peak was determined at 77°K. Again, a linear interpolation to determine the composition was deemed sufficient for our purpose.

Results

Figure 2 shows the variation of electroluminescence energy with composition. Where a composition range is indicated, the left-hand end of the line represents the composition as determined by the starting proportions, while the right-hand end gives the x-ray composition. There was obviously a slight fractionation which favored GaAs in the deposit. We believe that this can be minimized by repeated grinding and retransport of the deposit. Table I shows the starting compositions which were used and the actual lattice constants which were measured for the transported material. (Note that at around 10% GaAs the deposit was richer in In than the source.)

The peak of the emission spectrum was measured at 77°K. The lines were about 0.02 ev wide, and there was no detectable shift of the peak or line narrowing with increasing diode current. No attempts were made to observe stimulated emission. The emission energy was consistently below the value calculated for a given composition by a linear interpolation between the terminal energies. This is in agreement with work done on the variation of band gap with composition (5) except that our deviations from linearity were not so great.

As mentioned above, the composition of the epitaxial layers which were deposited in the flow system could not be predicted from the proportions of Ga and In in the source. Figure 3 shows the relationship between the source composition and the composition of the deposit. GaAs definitely tended to deposit more readily than InAs. Moreover, between source compositions of 5% and 10% Ga the concentration of GaAs in the deposit varied between 15% and 60%. This made it diffi-

Table I. Starting compositions

Starting proportion, mole % GaAs	Lattice constant, A	Peak diode emission wavelength at 77°K, μ
13	6.012	2.65
20	5.984	2.38
20	5.977	2.33
50	5.845	1.47
75	5.738	1.095
85	5.688	0.95-0.98
95	5.663	0.895

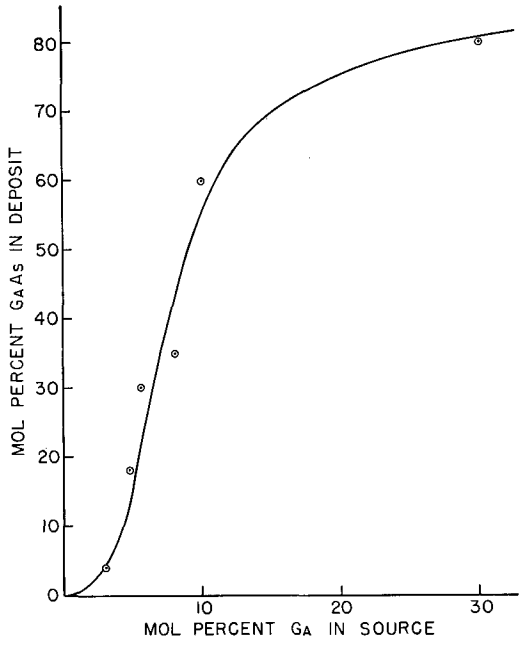

Fig. 3. Fractionation in the epitaxial deposition of InAs-GaAs by an open-tube flow system. The source was a In-Ga liquid metal solution; GaAs seed crystals were used.

cult, but not impossible, to control the deposit concentration in this range. On the other hand, above deposit concentrations of 80% GaAs the composition of the source had little effect on the deposit. Other factors, such as the seed temperatures and the flow rates, were relatively more important. For instance, we observed that higher seed temperatures favored the deposition of GaAs. We have not investigated this region of compositions in detail, but there were indications that when there was as much as 10% In in the source, the amount of In which appeared in the deposit was negligible. In any case, deposit concentrations having less than 10% InAs would be quite difficult to control in the flow system.

The deposition temperatures for InAs and its alloys with GaAs were substantially below those required for GaAs. At these temperatures no observable etching of the GaAs seed occurred. Deposits on polished seeds were sectioned and the interfaces were flat and also abrupt compared to the layer thickness. When pure In was used as the source, x-ray diffraction analysis showed that even thin layers were indeed composed of pure InAs. These results seem to preclude the possibility that the excess GaAs content in the layers came from an etching and redeposition of the seed as has been observed for Si and GaAs-GaP.

As a given boatful of source material was used up during the course of a series of runs, the composition of the deposited layers remained essentially constant. The halogen take-up reactions appeared to follow a Raoult's law type of behavior, while the fractionation took place on deposition. Although the source composition was the principal factor which affected the deposit composition, the deposition temperature played a role. Higher temperatures favored the deposition of GaAs. In fact, efficient deposition of pure InAs took place only at temperatures below about 700°, whereas GaAs deposition was readily possible up to about 780°. This result is to be contrasted with the observation that GaAs and GaP deposit at the same temperature (8). Quite obviously, the deposition reaction is dependent on the group III halide rather than the group V element. No inference can be drawn from our experiments, however, as to whether there was any interaction between the indium and gallium chlorides during the deposition process.

Conclusion

The closed-tube halide transport process is a very good method for obtaining homogeneous mixed crystals of III-V compounds. This has now been shown in the cases of GaAs-GaP and InAs-GaAs, but there is no reason why it should not work for such systems as InAs-InP (10) and possibly GaAs-AlAs (11). The closed-tube method for InAs-GaAs is superior to the flow system for composition control. On the other hand, if epitaxial layers are desired, the advantages of the closed-tube technique are not so clear. Unless extreme care is taken, etching of the GaAs seed takes place, and the deposited composition will be markedly and uncontrollably different from that determined by the proportion of the reactants which are initially used. Similar effects have been noted for GaAs-GaP layers which were deposited in a closed tube.

There is one final disadvantage to layers which were deposited in the flow system. The electroluminescent emission from junctions made in our epitaxial material was relatively weak. Also, the reverse leakage in the diode I-V characteristics was large even at 77°K. We concluded that our layers had a high electron concentration in spite of the fact that they were not intentionally doped. From past experience we suspect that the contaminant was Si. The Si could have readily been picked up from the quartz boat in which the In-Ga liquid source was contained. This contamination might be overcome by using other boat materials, such as high purity graphite or boron nitride. Also, the finely divided, meltgrown mixed crystal could be used as a source.

Acknowledgment

The author wishes to thank Dr. R. Sirrine for communicating the results of his closed-tube experiments which were done at the MIT Lincoln Laboratory. Mr. A. Sears did most of the material preparation and made most of the diodes. Mr. J. Donahue assisted in the measurements.

Manuscript received Sept. 30, 1964. This work was supported by the U.S. Air Force Avionics Laboratory, Wright-Patterson AFB, under Contract No. AF33 (615)-1120.

Any discussion of this paper will appear in a Discussion Section to be published in the December 1965 JOURNAL.

REFERENCES

1. For good reviews of the early work which was done on GaAs *see* R. N. Hall, *Solid State Electronics*, **6**, 405 (1963); and M. I. Nathan, *ibid.*, **6**, 425 (1963).
2. I. Melngailis, *Appl. Phys. Letters*, **2**, 176 (1963).
3. I. Melngailis, A. J. Strauss, and R. H. Rediker, *Proc. IEEE*, **51**, 1154 (1963).
4. S. M. Ku and J. F. Black, *Solid State Electronics*, **6**, 505 (1963).
5. M. S. Abrahams, R. Braunstein, and F. O. Rosi, *J. Phys. Chem. Solids*, **10**, 204 (1959).
6. F. A. Pizzarello, *This Journal*, **109**, 226 (1962).
7. R. Sirrine, *ibid.*, **111**, 750 (1964).
8. S. W. Ing and H. T. Minden, *ibid.*, **109**, 995 (1962).
9. J. C. Wooley in "Preparation of III-V Compounds," pp. 3-20, R. K. Willardson and H. L. Goering, Editors, Reinhold, New York (1962).
10. F. B. Alexander *et al.*, *Appl. Phys. Letters*, **4**, 13 (1964).
11. S. M. Ku and J. F. Black, Late News Paper, Electrochemical Soc. Meeting, Toronto, May 1964.

Calcium Orthovanadate $Ca_3(VO_4)_2$–A New Laser Host Crystal

L. H. Brixner and P. A. Flournoy

Pigments Department and Engineering Physics Laboratory, respectively,

Experimental Station, E. I. du Pont de Nemours & Co., Inc., Wilmington, Delaware

ABSTRACT

The fluorescent emission of Nd^{+3}, Sm^{+3}, Eu^{+3}, Tb^{+3}, and Dy^{+3} in a $Ca_3(VO_4)_2$ host were determined as functions of rare earth concentrations, and the optimum rare earth concentration for maximum fluorescence was established for each case. Single crystals containing these elements as active ions were grown by the Czochralski technique, and fluorescent lifetime and linewidth were determined for some. Excitation spectra for $Eu_{0.3}Na_{0.3}Ca_{2.4}(VO_4)_2$ indicate energy exchange between VO_4^{-3} and Eu^{+3}. A comparison of absorption spectra for $Ca_3(VO_4)_2$:Nd and $CaMoO_4$:Nd shows the considerably stronger absorption of the vanadate host especially in the 5800Å region. A single crystal of the specific composition $Nd_{0.08}Ca_{2.88}\phi_{0.04}(VO_4)_2$ was machined into a Fabry-Perot resonator and stimulated emission was observed at 300°K with a threshold of 3000 joules.

Many hosts for rare earth ions comprising ternary calcium-oxo-metallates have been studied, with $CaWO_4$ (1) receiving the most intensive investigation. Recently calcium niobate [$Ca(NbO_3)_2$] (2) was added, and now we can also include $Ca_3(VO_4)_2$ in this group. In a previous note (3), the growing of single crystal $Ca_3(VO_4)_2$, as well as its structure and some other properties, were described. This paper deals with fluorescent emission studies of various rare earths substituted in the $Ca_3(VO_4)_2$ lattice as a host. Since a trivalent rare earth ion is introduced into the cation site of divalent calcium, some valence compensating scheme has to be applied to restore electroneutrality. In the absence of any other ions, the simplest balancing occurs according to the vacancy mechanism given in Eq. [1]

$$(1-x)\ Ca_3^{+2}(VO_4)_2 + 2x\ Ln^{+3}VO_4 \rightarrow Ca_{3-3x}^{+2}Ln_{2x}^{+3}\phi_x(VO_4)_2 \quad [1]$$

One can see that for each three calcium ions, only two rare earth ions are substituted and the third site is left vacant, as indicated by the symbol ϕ. In the case of $Ca_3(VO_4)_2$, this deficiency apparently does not create any particular stress or strain in the lattice, since crystals of these compositions can be grown quite readily. A second mechanism involves univalent sodium and compensation occurs in the cation sites according to Eq. [2]

$$(3-2x)\ Ca_3^{+2}(VO_4)_2 + 2x\ Na_{1.5}^{+1}Ln_{1.5}^{+3}(VO_4)_2 \rightarrow 3Ca_{3-2x}^{+2}Na_x^{+1}Ln_x^{+3}(VO_4)_2 \quad [2]$$

Obviously each Na^{+1}/Ln^{+3} pair replaces two divalent calcium ions in this case and, due to the rather good match of ionic radii, solid solubility of $Na_{1.5}Ln_{1.5}(VO_4)_2$ in the $Ca_3(VO_4)_2$ is rather high (up to about $x = 0.6$). The $Na_{1.5}Ln_{1.5}(VO_4)_2$ structure, at least for the case where Ln is Nd, however, is different from that of $Ca_3(VO_4)_2$; it is tetragonal with $a_t = 7.338$Å, $c_t = 5.456$Å.

A third valence compensation mechanism involves compensation in the anion site and is represented by Eq. [3].

$$(1-x)Ca_3^{+2}(V^{+5}O_4)_2 + xCa^{+2}Ln_2^{+3}(Ti^{+4}O_4)_2 \rightarrow Ca_{3-2x}^{+2}Ln_{2x}^{+3}(V_{1-x}^{+5}Ti_x^{+4}O_4)_2 \quad [3]$$

Electroneutrality in this scheme is restored by replacing a pentavalent vanadium ion by tetravalent titanium for each neodymium introduced in the calcium site. Here again the structure of $CaNd(TiO_4)_2$ is different from that of $Ca_3(VO_4)_2$ but has not yet been determined. Similar compensation techniques for other hosts have been used by Nassau (4) and Ballman (2).

Fluorescent emission studies were carried out on samples prepared according to all three schemes. Laser action was observed on a Nd-doped crystal compensated according to scheme [1]. In growing single crystals this mechanism gave the best quality. Scheme [2] was next best, and scheme [3] posed the greatest problem. Ti^{+4} compensated single crystals invariably turned deep brown and opaque on growing, and even subsequent annealing under oxygen failed to yield optically clear crystals.

Fluorescence Studies

All samples for these studies were in polycrystalline form, prepared from the best commercially available chemicals. The rare earth oxides were from the Lindsay Chemical Division, V_2O_5 from the Vanadium Corporation of America, and $CaCO_3$ as well as Na_2CO_3 were standard Baker and Adamson analytical grade chemicals. The preparation was done in two steps: first the constituent components, weighed to the nearest 1/10 mg, were carefully mixed and heated in platinum containers to 650°C (just under the melting point of V_2O_5) for 10 to 14 hr. Homogenization was then achieved by ballmilling under acetone in a mechanical agate ballmill. The dried powders were subsequently compacted into 1 in. diameter pellets and refired at 1200°C for another 10 to 14 hr. Coarse fluorescent scans of the samples emitting in the visible were obtained with a Beckman DK2 recording spectrometer with a mercury lamp F4T5/BL (GE designation) through a Schott UG-11 filter which cuts off above 4000Å. The detector used was a photomultiplier tube 1P28 (RCA). More refined spectra were taken from samples excited by a filtered AH-3 mercury discharge lamp (primarily 3660Å radiation) and a L&N 0.5 meter Ebert mount grating spec-

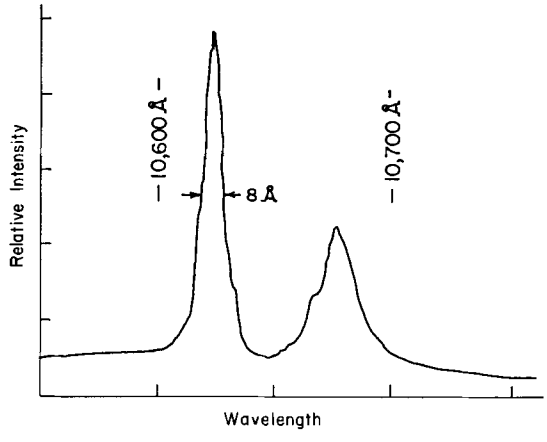

Fig. 1. Fluorescent emission spectrum of $Nd_{0.08}Na_{0.08}Ca_{2.84}(VO_4)_2$ at 77°K.

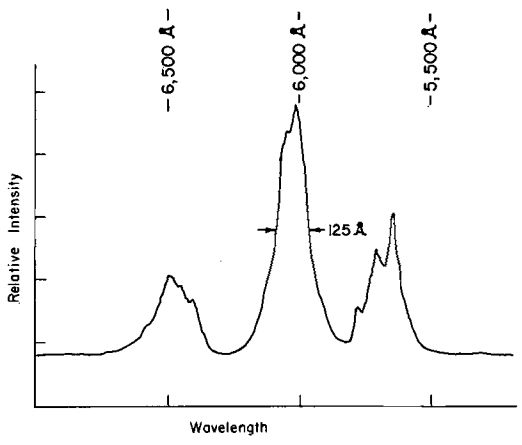

Fig. 2. Fluorescent emission spectrum of $Sm_{0.08}Na_{0.08}Ca_{2.84}(VO_4)_2$ at 300°K.

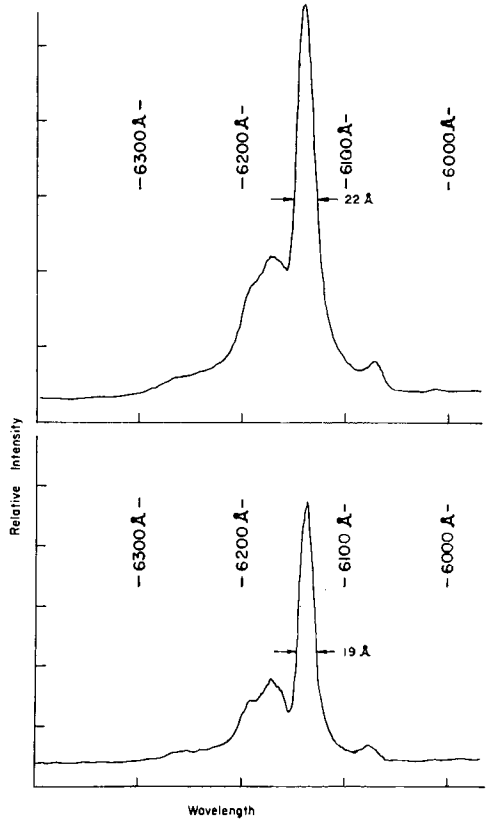

Fig. 3. Fluorescent emission spectrum of $Eu_{0.30}Na_{0.30}Ca_{2.40}(VO_4)_2$ at 300°K (top) and 77°K (bottom).

trometer using again a 1P28 photomultiplier detector. For the infrared spectra a Bausch and Lomb 2-meter grating spectrograph was used in conjunction with Kodak 1-Z infrared sensitive spectroscopic plates. Typical spectra for some characteristic compositions are given in Fig. 1-4. Figure 1 shows emission from a sodium compensated Nd sample where the main fluorescence peak at 1.063μ clearly dominates the other weak emission lines at 77°K. The linewidth is 8 cm^{-1} at 77°K and 40 cm^{-1} at 300°K. In Fig. 10 we will show the fluorescent emission of Nd from a vacancy compensated single crystal, where the lines are considerably broader with width of 180Å at 300°K and 90Å at 77°K. Figure 2 represents the room temperature spectrum of the most intensely fluorescing Sm-composition, and one can see that it consists of essentially three very broad lines centered around 5635, 6010, and 6490Å. The halfwidth of the predominant center line is about 120Å. Surprisingly, this line narrowed only slightly

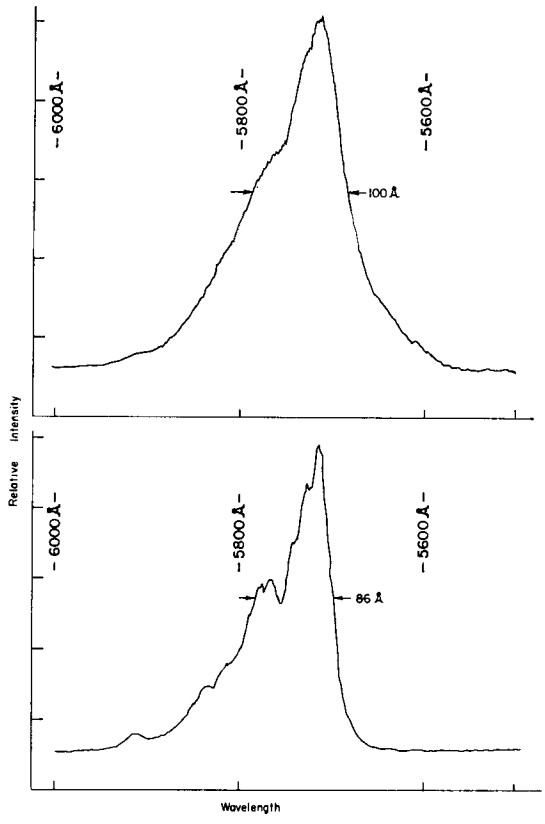

Fig. 4. Fluorescent emission spectrum of $Dy_{0.10}Na_{0.10}Ca_{2.80}(VO_4)_2$ at 300°K (top) and 77°K (bottom).

in going to liquid nitrogen temperature. This indicates that the broadening might be due to crystal imperfections and strain, since the first spectra in the visible were run with very fine powders exhibiting relatively large surface to volume ratios. However subsequent fluorescent emission studies of a single crystal of the composition $Sm_{0.08}\phi_{0.04}Ca_{2.88}(VO_4)_2$ again showed only rather insignificant line narrowing in going from 300° to 77°K. This small spectral difference between room temperature and liquid nitrogen temperature was also observed for the europium case and is best demonstrated in Fig. 3 by giving the spectra for both temperatures. One can see that the spectra are essentially identical with the most intense line at 6137Å. Another series of four weak lines is centered around 5935Å, and there is a weak line at 6075Å. Here again a single crystal of the composition $Eu_{0.3}\phi_{0.15}Ca_{2.55}(VO_4)_2$ gave an essentially identical spectrum with a halfwidth of 19.2Å at 77°K and 16.8Å at 300°K, indicating that the nonnarrowing of lines is not associated only with the powders.

The emission spectrum for the terbium doped sample is extremely weak and almost completely quenched due to the fact that the host absorbs in this region. The spectrum consists essentially of one very broad line centered around 5380Å with a halfwidth of some 125Å. Finally in Fig. 4 the room temperature as well as the liquid nitrogen spectrum of Na-compensated Dy-doped $Ca_3(VO_4)_2$ is given. Here again only insignificant line narrowing occurs, for the powder as well as a single crystal of the composition $Dy_{0.03}\phi_{0.015}Ca_{2.955}(VO_4)_2$. The predominant emission is centered around 5715Å. This band of lines of about 100Å halfwidth narrows to some 80Å at liquid nitrogen and begins to get resolved into a number of individual lines. However, even at 77°K line splitting is not very sharp. Another weaker emission band not represented in Fig. 4 is centered around 4800Å and a somewhat sharper line occurs at 4915Å.

The optimum doping concentration yielding maximum intensity of fluorescence for Nd^{+3} in Nd_xNa_x-

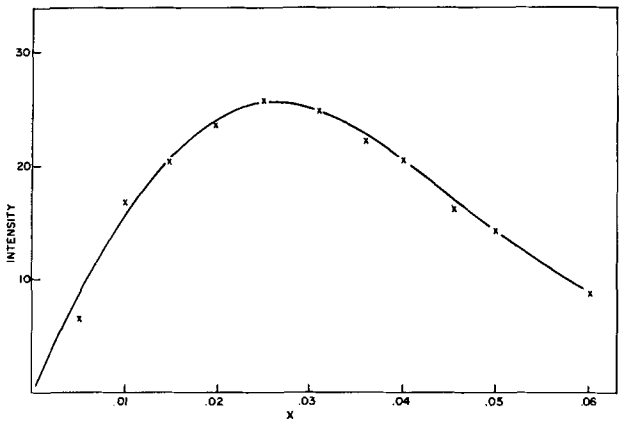

Fig. 5. Fluorescent emission as a function of X for the $Nd_{2x}\phi_xCa_{3-3x}(VO_4)_2$ system.

$Ca_{3-2x}(VO_4)_2$ was found to be at $x = 0.1$. In the case of the Nd compositions, the Ti^{+4} as well as the vacancy compensating mechanism was also applied, and it was of interest to see that the location of this optimum shifted to the considerably lower Nd^{+3} concentrations of $x = 0.02$ for the Ti^{+4} compensation. The optimum x for Nd^{+3} in $Nd_{2x}\phi_xCa_{3-3x}(VO_4)_2$ was found to be 0.025, and the rather typical plot for intensity of fluorescent emission as a function of the Nd concentration is given in Fig. 5. Starting from $x = 0$, one can see the rather steep increase to the optimum and then gradual intensity decrease until eventually complete concentration quenching occurs. The shape of the curve for fluorescence *vs.* concentration for the other rare earths studied was very similar, and for the purpose of a comparison the peak intensities of the strongest line are summarized in Table I for those rare earths emitting in the visible. Fluorescent lifetime for a number of vacancy compensated $Ca_3(VO_4)$:Nd crystals is given in Fig. 6 as a function of Nd concentration.

The predominant excitation wavelength was 3660Å, and since this comparison is not corrected for monochromator dispersion and photomultiplier sensitivity differences, we can only state qualitatively that in this particular host europium is the best emitter in the visible. A direct comparison with the Nd intensities was not possible, since they were not measured under identical conditions.

The outstanding intensity of the europium emission makes one suspect that some form of energy exchange between the host and the Eu^{+3} ion occurs, particularly in view of the fact that such an exchange had been demonstrated for the similar YVO_4:Eu (5) and $Eu_xGd_{1-x}(VO_4)$ (6) systems. We therefore ran an excitation spectrum for $Ca_3(VO_4)_2$:Eu and compared it to Eu^{+3} in $CaWO_4$ in Fig. 7. The data were obtained with monochromatic excitation which was accomplished by using a 1000-watt xenon source and a ½ meter Jarrell-Ash monochromator with a 16Å band pass. A fraction of the excitation energy was monitored with a Perkin-Elmer model 12 spectrometer stripped of all active elements except the thermocouple. Emission at 6150Å at room temperature was detected with an S-11 type photomultiplier through a multilayer dielectric filter optimized for 6150Å. The photomultiplier and thermocouple signal were monitored on a two-channel ratio recording strip-chart recorder presenting a normalized excitation spectrum. A comparison of the two spectra shows evidence for energy transfer from vanadate to europium ions since the excitation of the vanadate host is at least twice as efficient and the wavelength dependence is radically different in the region of vanadate absorption. In a separately run spectrum for the 3000-4000Å region with ½ the gain setting for vanadate, its emission was still considerably more intense than that from the tungstate sample so that the high intensity observed with excitation below 3700Å for the vanadate can only be explained by assuming energy exchange between the VO_4^{-3} and Eu^{+3} ion. Another interesting comparison is made in Fig. 8, where the absorption spectra are compared for Nd^{+3} in a scheelite host, such as $CaMoO_4$ and in $Ca_3(VO_4)_2$. These data were obtained with the Cary spectrophotometer set for approximately 2Å resolution. The

Table I. Comparison of fluorescent emission intensity for various $Ln_xNa_xCa_{3-2x}(VO_4)_2$ systems

System, Ln	Optimum x	Peak emission at Å	Relative intensity at identical slit width (0.2)
Sm	0.08	6010	25
Eu	0.30	6137	516
Tb	0.08	5380	10
Dy	0.10	5715	81

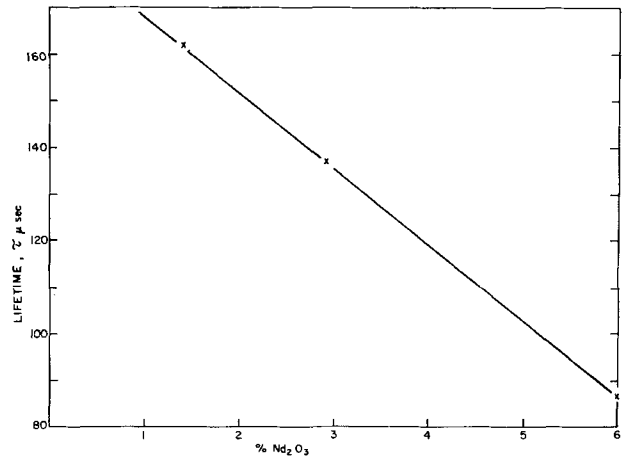

Fig. 6. Fluorescent lifetime as a function of Nd^{+3} concentration for $Nd_{2x}\phi_xCa_{3-3x}(VO_4)_2$ single crystals.

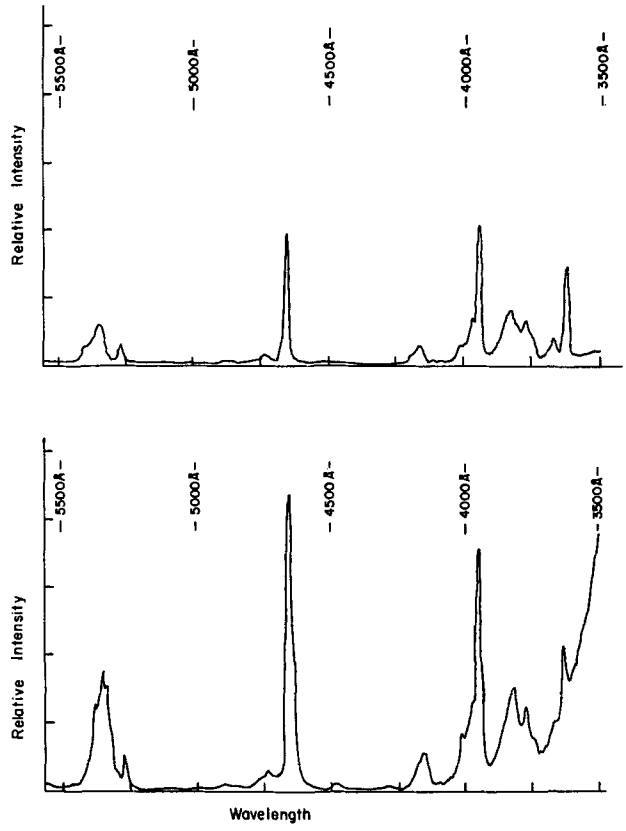

Fig. 7. Comparison of excitation spectra for $CaWO_4:Eu^{+3}$ (top) and $Ca_3(VO_4)_2:Eu^{+3}$ (bottom) at 300°K.

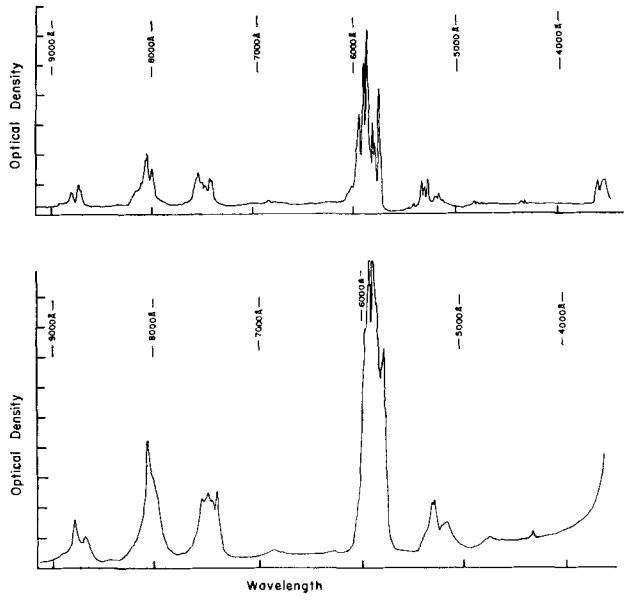

Fig. 8. Comparison of absorption spectra for $CaMoO_4:Nd^{+3}$ (top) and $Ca_3(VO_4)_2:Nd^{+3}$ (bottom) at 300°K.

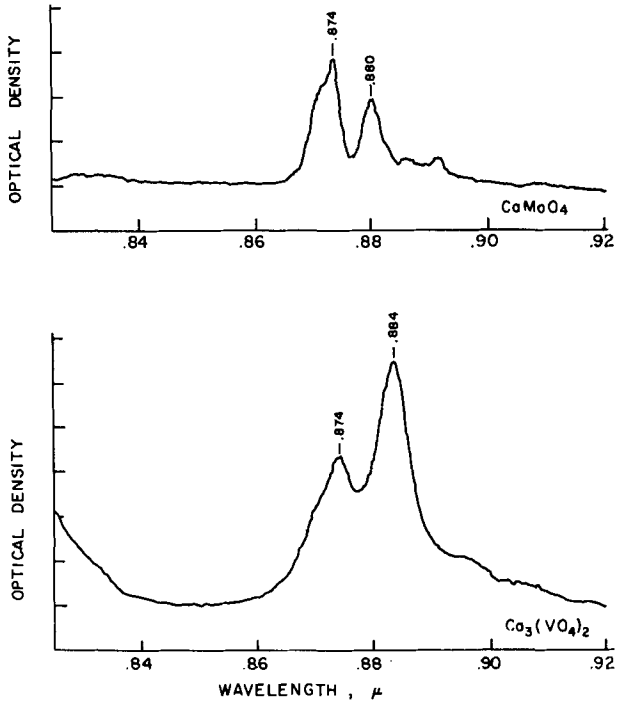

Fig. 9. Relative location of the $4F_{3/2}$ level for Nd^{+3} in $CaMoO_4$ (top) and $Ca_3(VO_4)_2$ (bottom) at 300°K.

wavelength was scanned from 3000 to 10,000Å. The infrared and visible regions were scanned separately using a PbS and an S-11 type photomultiplier, respectively, and the charts were then joined at 6300Å before reproduction. Comparison of the spectra shows that the vanadate absorption is an order of magnitude stronger than that of $CaMoO_4$:Nd. There are several qualitative differences in the spectra in addition to the obvious intensity changes. Particularly interesting is the difference in the 8800Å region where injection laser pumping is used. This region is reproduced in Fig. 9. Unfortunately in addition to the intensity reversal the shift for the vanadate is toward the higher rather than the desired (8400Å) shorter wavelength region. Generally the absorption bands for the vanadate are broader and consequently exhibit less detail. The vanadate host should be particularly good for pumping with a tungsten source in continuous wave experiments since the absorption is so strong in the near infrared region.

Crystal Growing

The predominant feed starting material was $Ca_3(VO_4)_2$. It was prepared in two steps: by first precipitating $Ca_2V_2O_7$ from purified solutions of $Ca(NO_3)_2 \cdot 4H_2O$ and NH_4VO_3. $Ca_2V_2O_7$ was obtained as a microcrystalline lemon-yellow powder with the typical analysis: CaO, 37.77%; V_2O_5, 61.53%; calc. CaO, 38.14%; V_2O_5, 61.86%. In a second step, $Ca_3(VO_4)_2$ was prepared by interacting $Ca_2V_2O_7$ with the stoichiometric amount of reagent grade $CaCO_3$. Polycrystalline $Ca_3(VO_4)_2$ is practically white; large single crystals, however, do have a distinct light yellow-to-orange color, due to absorption in the blue region of the visible spectrum. The rare earth oxides as well as the other constituents were added to the $Ca_3(VO_4)_2$ powder and melted in Ir crucibles from which crystals were grown. As a rf power source a 25 kw/450 kc/sec Westinghouse generator was used in conjunction with an automatic voltage regulator keeping the current steady to within 2½%. Crystals were grown in air at speeds between ½-¾ in./hr. The crystal cross section was invariably circular with three distinct growth lines along the sides indicating that the principle growth axis has threefold symmetry. Optically this axis corresponds to the a-axis of a scheelite-type oxide, such as $CaMoO_4$, and thus exhibits the expected optical birefringence. Crystals up to 6 in. in length can be grown readily. In comparison with Nd in $CaMoO_4$ (7), they are deeper in color due to the intrinsically colored host. Since considerable difficulty was encountered in growing clear crystals of the titanium compensated compositions, all crystals were grown from either sodium or vacancy-compensated compositions. It was particularly interesting that contrary to experience with the sodium-compensated tungstate case (1), excess sodium was quite detrimental to the quality of the crystals and segregation coefficients even at the 1:1 Na:Nd level were exceptionally close to 1. The calculation of segregation coefficients ($K = c_s/c_l$ where c_s is the concentration in solid, c_l the concentration in liquid) was done by Pfann's (8) method, based on analytical information obtained by x-ray fluorescence analysis of the top and bottom of a crystal. Table II summarizes some typical results for Na as well as vacancy-compensated crystals. Segregation coefficients for the corresponding rare earth vanadates were also determined for single crystals of $Eu_{0.20}\phi_{0.10}Ca_{2.7}(VO_4)_2$, $Sm_{0.08}\phi_{0.04}Ca_{2.88}(VO_4)_2$, and $Dy_{0.03}\phi_{0.015}Ca_{2.955}(VO_4)_2$. They were found to be 0.98, 0.98, and 0.99, respectively.

Since the Na content of the compounds listed in Table II could not be determined by the x-ray fluorescence techniques, we had to estimate it by difference; indications were that hardly any sodium entered the single crystals. It was this result which prompted us to synthesize and study the properties of the vacancy-compensated systems.

Table II. Some typical analyses of doped and undoped calcium vanadates

Nominal composition	CaO%	V_2O_5%	Nd_2O_3%	Total %	Segregation coefficient K for Nd_2O_3	CaO: V_2O_5 ratio
$Ca_2V_2O_7$	37.8	61.5	—	99.3	—	1:0.50
$Ca_3(VO_4)_2$	47.8	51.6	—	99.4	—	1:0.33
$(NaNd)_{0.04}Ca_{2.92}(VO_4)_2$	45.7	51.5	2.4	99.6	1.1	—
$(NaNd)_{0.10}Ca_{2.80}(VO_4)_2$	42.8	51.0	6.1	99.9	1.2	—
$Nd_{0.025}\phi_{0.0125}Ca_{2.9625}(VO_4)_2$	46.9	51.5	1.5	99.9	1.1	—
$Nd_{0.08}\phi_{0.04}Ca_{2.88}(VO_4)_2$	44.5	50.9	4.8	100.2	1.1	—
$Nd_{0.10}\phi_{0.05}Ca_{2.85}(VO_4)_2$	43.4	50.9	6.0	100.3	1.0	—

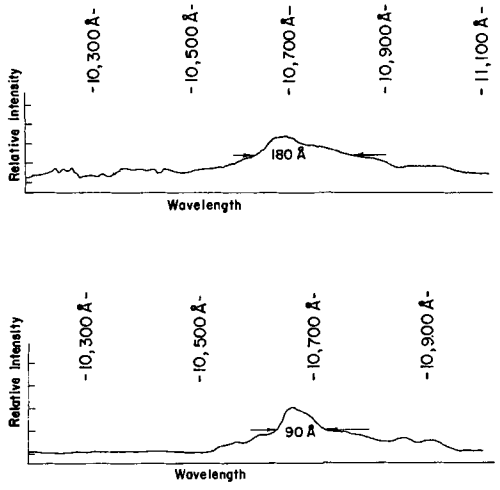

Fig. 10. Fluorescent emission spectrum of single crystalline $Nd_{0.05}\phi_{0.025}Ca_{2.925}(VO_4)_2$ at 300°K (top) and 77°K (bottom).

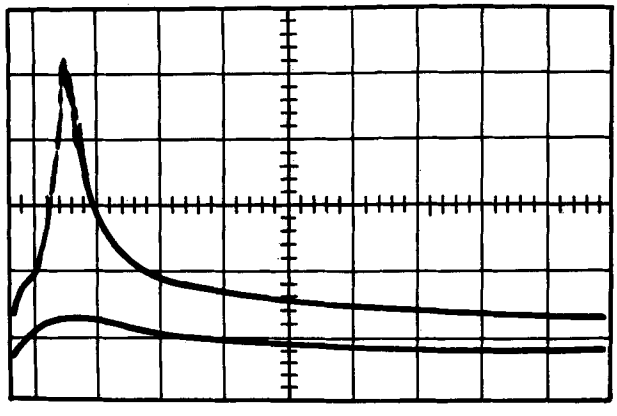

Fig. 11. Stimulated emission of $Nd_{0.08}\phi_{0.04}Ca_{2.88}(VO_4)_2$ at 300°F (lower trace below, upper trace above threshold).

The fact that even without Na compensation we obtained such favorable segregation coefficients is very interesting and particularly useful in single crystals where the Nd^{+3} distribution is nearly homogeneous from top to bottom.

Laser Experiments

Single crystal boules were cut and ground into cylindrical rods 6.3 mm, 4.8 mm, and 3.2 mm diameter and 2 in. long. The cylindrical surfaces were left rough and the ends polished to form a Fabry-Perot resonator. Silver was evaporated onto the end surfaces; one end was 5% transmissive and the other completely opaque. Laser characteristics at 300°K were measured under pulsed illumination in a Lear-Siegler LS-3 laser head with a Kemlite FT100B helical xenon flash lamp. The stimulated emission was detected with a Dumont K1485 photomultiplier through a 3 mm silicon filter. Figure 11 shows typical laser emission just above threshold. Thresholds are typically 3000 joules under these conditions. The spectral output above threshold was determined by focusing the emitted radiation on the entrance slit of a Bausch and Lomb 2-meter grating spectrograph and recording the output on hypersensitized Kodak 1-Z spectroscopic plates. Stimulated emission was observed at 1.067μ with the line width narrowing to 20Å from the normal spontaneous emission linewidth of 180Å at room temperature, as seen in Fig. 10.

Table III. Comparison of Eu^{+3} emission in different hosts

Compound or system	Optimum mole % Eu^{+3}	Strongest line mμ	Intensity
$(EuTaO_4)_x(CaWO_4)_{1-x}$	10	610	17
$(EuTaO_4)_x(CaMoO_4)_{1-x}$	0.5	610	64
$(EuNbO_4)_x(CaMoO_4)_{1-x}$	0.5	610	132
$(EuVO_4)_x(CaMoO_4)_{1-x}$	30	610	210
$Eu_xGd_{1-x}PO_4$	40	585	81
$Eu_xGd_{1-x}NbO_4$	40	610	87
$(EuNa)_xCa_{3-2x}(VO_4)_2$	30	610	516
$(EuNbO_4)_x(CaWO_4)_{1-x}$	10	610	110
$Eu_xGd_{1-x}NaSiO_4$	30	585	120
$Eu_xGd_{1-x}VO_4$	8	610	288
$Eu_xNa_xZn_{1-2x}B_2O_4$	30	580	69
$Eu_xNa_xCd_{1-2x}B_2O_4$	30	580	150
$Eu_xGd_{2-x}ZnO_4$	30	610	120

Discussion and Miscellaneous Data

Since $Ca_3(VO_4)_2$ constitutes another laser host, it appeared desirable at this point to measure as many pertinent parameters as possible and also to compare the influence of the host on the fluorescent emission of the active ion in it.

In Table III, a summary of the fluorescent emission output of Eu^{+3} under comparable conditions is given for a number of different hosts. It is quite obvious that not only the intensity, the optimum doping level but even the spectral characteristics themselves change significantly as a function of the host.

Eu^{+3} shows relatively narrow line emission in a $Ca_3(VO_4)_2$ host, and the excitation spectrum clearly indicates that some energy exchange occurs between VO_4^{3-} and Eu^{+3}. Therefore this system shows potential as a good laser material, particularly in view of a recent publication by Chang (9) who reported stimulated emission from trivalent europium in yttrium oxide. Furthermore, as can be seen from Table II at least among the cited examples for 3660Å excitation, Eu^{+3} shows the strongest emission in the $Ca_3(VO_4)_2$ host with quantum efficiencies approaching 100% for several lines. It is also interesting to note that the three strongest emitters all contain the VO_4^{-3} ion.

In Table IV we summarize some of the other parameters. In order to put these data in perspective with another laser host we compare them to $CaMoO_4$. In view of this comparison, one would say that $Ca_3(VO_4)_2$ has little to offer as a laser host and merely adds another member to the ever increasing list of established laser hosts. The fact that it is the first intrinsically colored and piezoelectric laser host plus the energy exchange still makes it an interesting candidate, and

Table IV. Comparison of some properties of two laser hosts

	$Ca_3(VO_4)_2$	$CaMoO_4$
Optimum laser composition	$Ca_{2.925}Nd_{0.05}\phi_{0.025}(VO_4)_2$	$(CaMo)_{0.99}(NdNb)_{0.01}O_4$
Molecular weight	354.3475	201.0415
Weight % Nd^{+3}	2.036	0.717
Structure	Monoclinic C2	Tetragonal $I4_1/a$
Lattice parameters	a = 8.35Å, b = 10.77Å c = 7.00Å, β = 95°	a = 5.213Å c = 11.395Å
Expansion coefficients	in a = 5.5 × 10^{-5} in c = 3.5 × 10^{-5}	in a = 1.9 × 10^{-5} in c = 2.5 × 10^{-5}
Thermal conductivity	14.5 mwatts/cm-deg (300°K)	39.5 mwatts/cm-deg (300°K)
Hardness, mohs	4.3	4.3
Refractive index	1.89	1.98
Dielectric constant	13.3 (at 1KC)	12.5 (at 1KC)
Melting point	1430°C	1480°C
Typical threshold	3000 joules	1 joule
Lifetime at optimum	108 μ-sec	160 μ-sec
Linewidth	90Å	5Å

certainly more detailed studies of the laser characteristics, particularly power measurements, have to be carried out before final judgement can be made as to the qualification of $Ca_3(VO_4)_2$ as not only a novel but also a useful laser host.

Manuscript received Sept. 8, 1964.

Any discussion of this paper will appear in a Discussion Section to be published in the December 1965 JOURNAL.

REFERENCES

1. K. Nassau and A. M. Broyer, *J. Appl. Phys.*, **33**, 3064 (1962).
2. A. A. Ballman, S. P. S. Porto, and A. Yariv, *ibid.*, **34**, 3155 (1963).
3. L. H. Brixner, P. A. Flournoy, and Keith Babcock, *This Journal*, **111**, 873 (1964).
4. K. Nassau and G. M. Loicano, *Phys. Chem. of Solids*, **24**, 1503 (1963).
5. L. G. Van Uitert, R. R. Soden, and R. C. Linares, *J. Chem. Phys.*, **36**, 1793 (1962).
6. L. H. Brixner and E. Abramson, *This Journal*, **112**, 70 (1965).
7. L. H. Brixner, *ibid.*, **111**, 690 (1964).
8. W. G. Pfann, "Zone Melting," p. 11, John Wiley & Sons, Inc., New York (1958).
9. N. C. Chang, *J. Appl. Phys.*, **34**, 3500 (1963).

Observation of Impurity Redistribution During Thermal Oxidation of Silicon Using the MOS Structure

B. E. Deal, A. S. Grove, E. H. Snow, and C. T. Sah

Fairchild Semiconductor, Division of Fairchild Camera & Instrument Corporation, Palo Alto, California

ABSTRACT

The redistribution of impurities during thermal oxidation of silicon has been investigated using the metal-oxide-semiconductor (MOS) system. It has been demonstrated that the MOS technique permits a semiquantitative observation of both n- and p-type impurity profiles in the silicon surface region. Results are presented for redistribution of aluminum, boron, gallium, indium, antimony, arsenic, and phosphorus. In addition, the effects of oxidation variables (oxidation time, temperature, rate, and ambient) on redistribution, predicted by previous work in these laboratories, have been studied in detail for boron-doped silicon.

The formation of a silicon dioxide layer is an important step in the fabrication of "planar" silicon transistors and other devices. Such oxide layers are used to mask portions of the silicon surface from impurity diffusion as well as for passivation of the surface (1A). In addition, surface-controlled silicon devices, which employ the oxide layer as the dielectric of a capacitor, have become increasingly important in recent years (1B).

Because of these important practical applications considerable effort has been directed to the study of the properties of the silicon dioxide-silicon system. One particularly useful tool that emerged in such investigations is the metal-oxide-semiconductor (MOS) capacitor structure (2, 3) which has been employed in extensive studies of the electrical properties of the oxide-silicon interface (4-8).

It has been shown (9, 10) that thermal oxidation of silicon brings about a redistribution of the doping impurity near the silicon surface. It is clear that those characteristics of semiconductor devices which are dependent on the impurity concentration near the surface will be affected by this redistribution process. Accordingly, the MOS capacitance method might be expected to yield a means of observing the impurity redistribution phenomenon through the influence of this phenomenon on the capacitance-voltage characteristics of MOS structures.

The present work presents the results of such an investigation. We shall begin by describing the principles on which the method is based. Next we shall consider the factors which affect the impurity redistribution profile as well as the relationship between the impurity redistribution in the semiconductor and the electrical characteristics. Experimental results obtained with seven different acceptor- and donor-type impurities are presented and discussed in light of the theory of the redistribution process and of the MOS structure. Finally, the redistribution of boron is studied in detail under a variety of conditions.

Basic Considerations

Principles of the MOS method.—The MOS structure is illustrated schematically in Fig. 1. In essence, it consists of an evaporated aluminum field plate (referred to as the "gate"), the oxide dielectric, and the silicon substrate. Contact to the silicon is through an evaporated aluminum back contact.

The theory of the MOS structure has been developed in detail elsewhere [see for instance ref. (7), (8)], and therefore only a brief qualitative description is given here for the case of a p-type semiconductor. If the voltage applied to the field plate, V_G, is negative, holes are attracted to the vicinity of the interface so that the semiconductor is much like a metal and the capacitance of the MOS structure is approximately the same as the capacitance of the oxide layer alone. On the other hand, if the applied voltage is made positive, holes are repelled from the vicinity of the interface, leaving behind a region from which the majority carriers are depleted so that their concentration in this region is much smaller than the ionized acceptor ion concentration. We shall refer to this as the electrical depletion region. Because the depletion region in effect adds to the thickness of the dielectric, the capacitance decreases. Upon further increase in the applied voltage, electrons are attracted to the vicinity of the interface and form an extremely narrow inversion region. Additional charge induced in the semiconductor

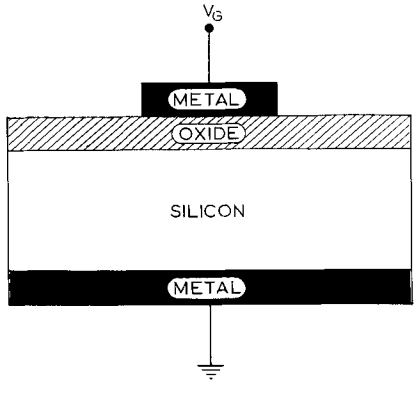

Fig. 1. Metal-oxide semiconductor (MOS) structure

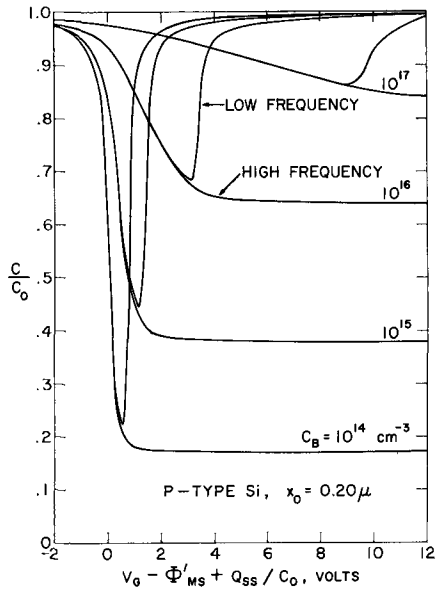

Fig. 2. Theoretical MOS capacitance-voltage characteristics

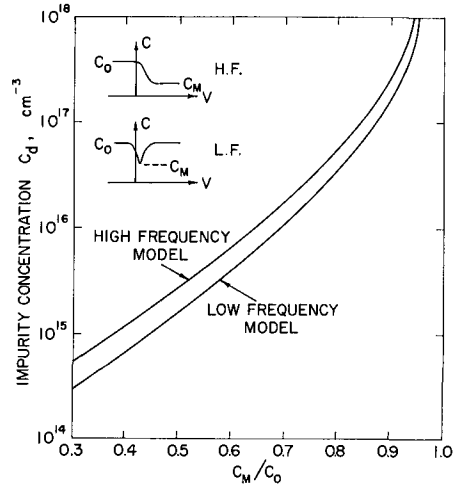

Fig. 3. Relationship between impurity concentration and minimum capacitance for the two MOS models ($x_o = 0.20\mu$).

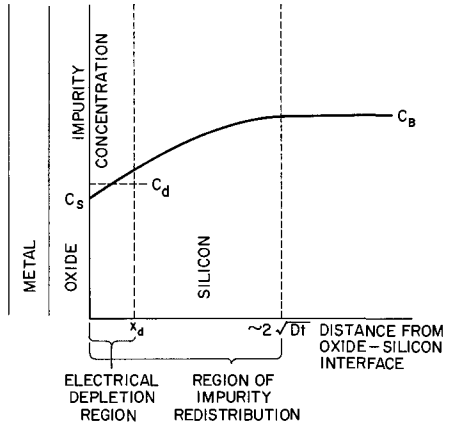

Fig. 4. Relationship of effective surface concentration C_d to impurity redistribution profile.

by further increase in the applied voltage will almost entirely appear in the inversion region and therefore the depletion region stops increasing in size. Correspondingly, the capacitance reaches a minimum value. In the case when the measurement frequency is low enough in comparison with the generation rate of minority carriers, the electrons in the inversion region will be able to follow the variation of the a-c measurement signal, and the capacitance will rise again to the value of the oxide capacitance. The maximum width of the depletion region, however, is independent of frequency (7).

Figure 2 shows the capacitance-voltage characteristics of a MOS structure calculated on the basis of both the high- and the low-frequency theories (8) as a function of the impurity concentration within the semiconductor. Here C and C_o denote the capacitance per unit area of the MOS structure and of the oxide layer, respectively; ϕ'_{MS} is the metal-semiconductor work function difference, and Q_{SS} is the surface state charge density. It is evident that the value of the minimum capacitance, in both theories, is a sensitive function of the impurity concentration. This is further illustrated in Fig. 3 where the ratio of the minimum capacitance to the capacitance of the oxide layer is plotted as a function of the impurity concentration in the semiconductor for the case of 0.2μ oxide thickness.[1]

The analysis on which the theoretical curves shown in Fig. 2 and 3 are based assumes a uniform impurity distribution in the silicon. If the impurity concentration at the surface is different from that in the bulk, this effect might be observed through the minimum value of the MOS capacitance. Impurities are, in fact, known to redistribute near the silicon surface during thermal oxidation (9, 10) so that the situation corresponding to an inverted MOS device might be as depicted in Fig. 4 for the case of impurity depletion from the silicon. It is reasonable to expect that the concentration which affects the MOS characteristics will be some effective concentration, C_d, across the electrical depletion region x_d.

Thus, the experimentally determined minimum MOS capacitance should provide a measure of the effective impurity concentration in the vicinity of the surface. Admittedly, the method is at best an approximate one since it applies a theory which is based on the assumption of a uniform impurity concentration in the semiconductor to the determination of a deviation from this condition. More exact, and much more complicated, approaches are possible through calculating the MOS characteristics based on a nonuniform impurity distribution (11). However, the present method is simple, easy to use and interpret, and, as detailed comparison of the results with those obtained in an earlier more accurate investigation (10) shows, it gives consistently very good results.

Impurity redistribution.—The theory of the impurity redistribution process which takes place upon thermal oxidation of silicon has been presented elsewhere (10). A general equation is derived there which gives the surface or interfacial concentration in the silicon resulting after oxidation as a function of the parameters of the system. This equation is

$$\frac{C_S}{C_B} = \frac{1 + (C_o/C_B)\lambda}{1 + (1/m - \alpha)\sqrt{\pi}\exp(\alpha^2A^2/4D_2)\operatorname{erfc}(\alpha A/2\sqrt{D_2})\,A/2\sqrt{D_2} + \lambda/m} \quad [1]$$

where C_S is the impurity concentration in the silicon, near the oxide-silicon interface; C_B the impurity concentration in silicon bulk; C_o the impurity concentration at outer surface of the oxide during oxidation; $\lambda \equiv r \exp[(\alpha^2r^2-1)A^2/4D_2r^2]\operatorname{erfc}(\alpha A/2\sqrt{D_2})/\operatorname{erf}(A/2\sqrt{D_1})$; $r \equiv \sqrt{D_1/D_2}$; D_1 is the diffusion coefficient

[1] Approximate formulas for the minimum capacitance ratio are given in the Appendix. However, minimum capacitance ratios for other oxide thicknesses can also be readily obtained from Fig. 3 using the series capacitance formula, Eq. [4A].

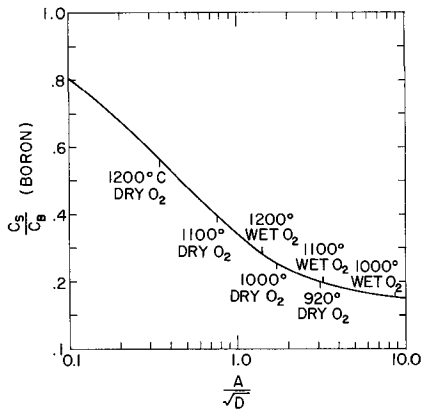

Fig. 5. Redistribution of boron at the silicon surface due to thermal oxidation as a function of the ratio of oxidation rate, A, to square root of diffusivity, $\sqrt{D}$.

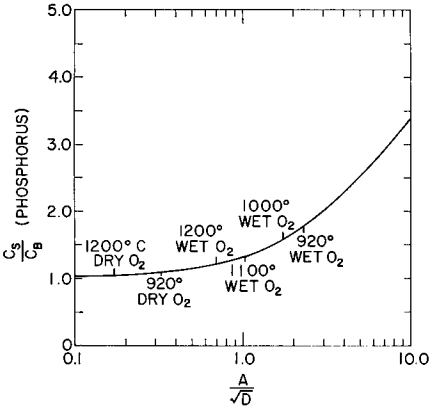

Fig. 6. Redistribution of phosphorus at the silicon surface due to thermal oxidation as a function of the ratio of oxidation rate, A, to square root of diffusivity, $\sqrt{D}$.

of impurity in the oxide; D_2 the diffusion coefficient of impurity in the silicon;

$$\alpha = \frac{\text{Thickness of silicon oxidized}}{\text{Thickness of silicon dioxide produced}} = 0.44;$$

m = (segregation coefficient at Si-SiO_2 interface)

$$\equiv \frac{\text{Equilibrium impurity concentration in silicon}}{\text{Equilibrium impurity concentration in oxide}};$$

A is the oxidation parabolic rate constant, $x_o/\sqrt{t}$; and x_o the oxide thickness.

For boron and phosphorus, we can consider the diffusion in the oxide to be negligible, since r is small (12, 13). As a result, the term λ drops out of Eq. [1]. The values of the segregation coefficient m for boron and phosphorus are taken to be 0.3 and 10, respectively (10). Plots of C_S/C_B *vs.* $A/\sqrt{D}$ are presented in Fig. 5 and 6 for thermal oxidation of boron- and phosphorus-doped silicon based on the above values and Eq. [1]. As mentioned above, A is the parabolic rate constant for thermal oxidation and D (= D_2) is the diffusivity of the impurity in silicon, so that the dimensionless quantity $A/\sqrt{D}$ represents the relative rates of oxidation and diffusion in the silicon. Indicated on the two curves are various oxidation conditions corresponding to oxidation rates and diffusivities at various temperatures in wet and dry oxygen. Diffusivity values for boron are taken from Kurtz and Yee (14) while those used for phosphorus are from Fuller and Ditzenberger (15). The oxidation rate constants used were based on previous work by one of the authors (16). [Wet O_2 indicates oxygen bubbled through water at 95°C. This is referred to as "steam" oxidation in (10).] It should be noted that thermal oxidation of silicon below 1000°C is no longer controlled by diffusion but rather by a surface reaction. Hence the oxidation rate will not be strictly parabolic at 920°C. Nevertheless, data for this temperature, based on an effective parabolic rate constant, are still included in Fig. 5 and 6 as approximations.

Figures 5 and 6 indicate that boron depletes from the silicon surface region during thermal oxidation while phosphorus piles up. It is apparent that the value of $A/\sqrt{D}$ increases with decreasing temperature owing to the fact that diffusivity values decrease more rapidly with temperature than oxidation rate constants. Also, at any particular temperature, the value of $A/\sqrt{D}$ is higher for oxidation in a wet atmosphere than in a dry atmosphere due to the higher oxidation rate of the former (16).

As the $A/\sqrt{D}$ ratio decreases in Fig. 5 and 6, C_S/C_B approaches unity corresponding to no redistribution. On the other hand C_S/C_B decreases for large values of $A/\sqrt{D}$ in the case of boron and increases in the case of phosphorus. This, of course, can be expected on intuitive grounds. Thus it is apparent from these curves that minimum redistribution of both phosphorus and boron occurs at high oxidation temperatures (1200°C) and at a low rate of oxidation (dry O_2).

The actual impurity distribution after oxidation is error-function type (10), so that the extent of the region of redistribution may be approximated by $2\sqrt{Dt}$ where D is the impurity diffusion coefficient in silicon and t is the oxidation time. For a 0.2μ dry oxide $2\sqrt{Dt}$ will vary from 0.12μ at 920° to 1.2μ at 1200°C for boron-doped silicon, and from 1.1μ at 920° to 2.4μ at 1200° for phosphorus doped silicon.

Relationship between the electrical depletion region and the extent of the region of impurity redistribution. —The relative size of the electrical depletion region compared to the region of impurity redistribution is a very important consideration in the MOS method. It has been mentioned above that the impurity concentration which affects the MOS device characteristics is an effective concentration C_d over the width of the electrical depletion region. This width, designated by x_d, is in turn a function of the impurity concentration and the bias voltage. In this work we are interested only in the minimum MOS capacitance which occurs at a sufficiently high bias voltage that x_d has reached its maximum size. A plot of maximum x_d *vs.* impurity concentration,[2] based on the calculations in ref. (8), is shown in Fig. 7. This graph is based on the results of calculations given in ref. (8) which assumed a uniform impurity concentration within the silicon. It is evident from Fig. 7 that, as the impurity concentration increases, the maximum electrical depletion region width decreases.

In the case of impurity redistribution it is necessary to know both x_d and $2\sqrt{Dt}$ in order to determine what portion of the redistribution profile is influencing the MOS characteristics. For instance, let us assume that an impurity depletes at the silicon surface with a redistribution length, $2\sqrt{Dt}$, of 1.0μ and that the interfacial concentration C_S is equal to 0.5 C_B. This example is shown in Fig. 8. In Fig. 8A, an electrical depletion width, x_d, of 0.1μ is shown. Since the minimum MOS capacitance will be determined by the impurity concentration over the region x_d, the resulting value of the effective concentration, C_d, will be fairly close to the concentration at the surface, *i.e.*, C_d will equal say, 0.55 C_B. Figure 8B shows a second possibility where conditions result in an electrical depletion width of 1.0μ. Now the minimum MOS capacitance will correspond to some average concentration over the region between the silicon surface and 1.0μ from the surface,

[2] The maximum of x_d will be referred to simply as x_d in the rest of this work.

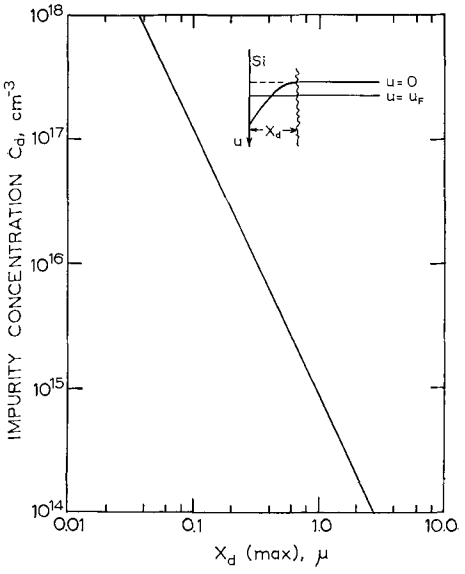

Fig. 7. Relationship between maximum electrical depletion region width and impurity concentration for MOS structure.

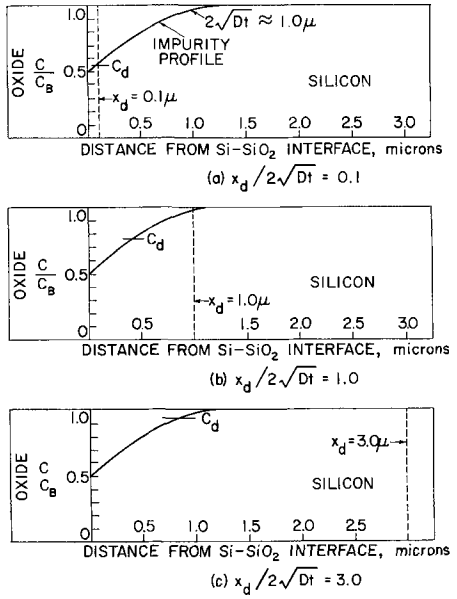

Fig. 8. Variation of effective surface concentration, C_d, for different ratios of electrical depletion region width, x_d, to impurity redistribution length, $2\sqrt{Dt}$.

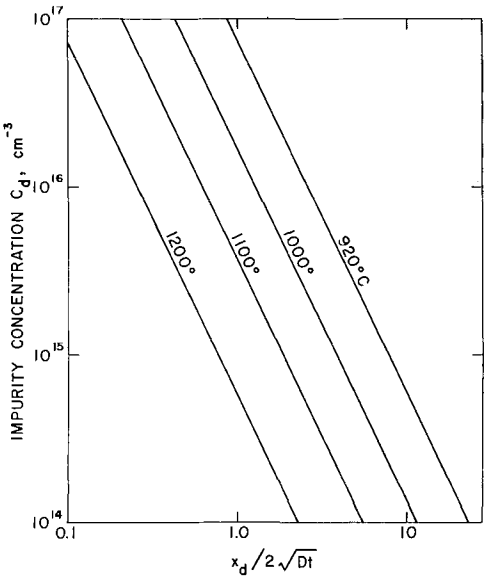

Fig. 9. Dependence of effective surface concentration, C_d, on the ratio $x_d/2\sqrt{Dt}$ for different oxidation temperatures (dry oxygen, $x_o = 0.20\mu$).

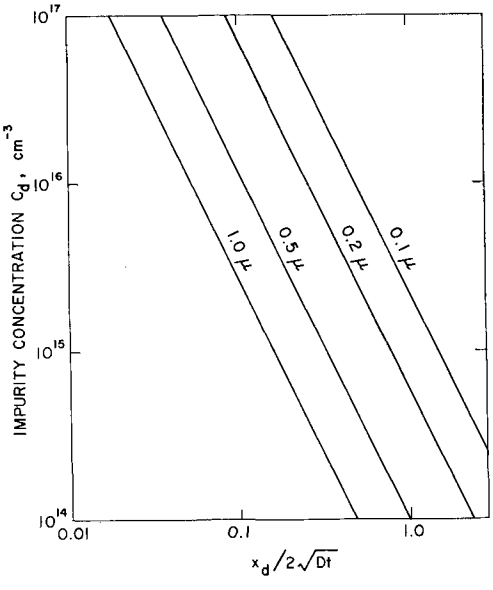

Fig. 10. Dependence of effective surface concentration, C_d, on the ratio $x_d/2\sqrt{Dt}$ for different oxide thicknesses (dry oxygen, 1200°C).

and the value of C_d will be about 0.8 C_B. Finally, in Fig. 8C, an electrical depletion region of 3.0μ is depicted, with a corresponding effective concentration of about 0.95 C_B. It can therefore be noted that while the impurity redistribution remains the same, the C_d value changes considerably depending on the ratio of x_d to $2\sqrt{Dt}$.

The ratio, $x_d/2\sqrt{Dt}$, is thus a significant quantity in the analysis of impurity redistribution. As discussed above, the value of x_d depends only on the impurity concentration over the electrical depletion region, while the quantity $2\sqrt{Dt}$ will be dependent on impurity type, oxidation temperature, and time. Plots of $x_d/2\sqrt{Dt}$ *vs.* impurity concentration are presented in Fig. 9 and 10 for various oxidation temperatures and oxide thicknesses. Both figures represent dry oxygen ambient. If it is desired to know the silicon impurity concentration very near the oxide-silicon interface, a low value of $x_d/2\sqrt{Dt}$ is required. From Fig. 9, for instance, it can be observed that a highly doped substrate oxidized at 1200°C will give the lowest $x_d/2\sqrt{Dt}$ ratio. Similarly, a low ratio is obtained for a 1.0μ oxide on a highly doped substrate as seen in Fig. 10. Other conditions can be selected using these relationships to determine the redistribution profile from the surface into the bulk.

On the other hand, if conditions are fixed, then the ratio $x_d/2\sqrt{Dt}$ will determine what portion of the impurity profile will have a part in determining C_d. In presenting the results for cases where $x_d \gtrless 2\sqrt{Dt}$, C_d will be taken to correspond to the impurity concentration at a point halfway between the silicon surface and x_d, *i.e.*, at distance $x_d/2$.

Experimental

Silicon used in this investigation was single crystal Czochralski type, (111) surface oriented with an initial dislocation count of less than 100 cm^{-2}. After slicing and lapping to 250μ thickness, the bulk impurity concentration was determined using a four-point probe

and a precision micrometer. The slices were cleaned and chemically polished to 150μ thickness in a 4 HF: 10 HNO_3 solution immediately prior to oxidation. Oxidizing ambients included both dry and wet oxygen (oxygen bubbled through water at 95°C). A description of the oxidation apparatus and procedure is given in ref. (16). P-type and n-type silicon slices were oxidized in separate furnaces. Oxide was removed from the back, and aluminum deposited on the top oxide and the back silicon by conventional evaporation techniques (1A). Dots, 250μ in diameter, were prepared from the aluminum over the oxide using photoresist techniques. The sample was then alloyed at 550°C to insure good ohmic contact to the back side. Good ohmic contact to both the field plate metal and the silicon during MOS measurements is important since any oxide in series affects capacitance values and causes erroneous measurements. Oxide thicknesses were determined for each oxidation using multiple-beam interferometry techniques on a mechanically polished test slice.

MOS capacitance-voltage characteristics were determined for several devices on each slice using an automatic recording system. The resulting curve for each unit was analyzed by comparison to the corresponding high frequency or low-frequency MOS theory (8). In most cases the curves followed the high-frequency theory at a 100 kc test frequency. Such samples were selected for more precise measurements on a Boonton capacitance bridge. The ratio of minimum capacitance to oxide capacitance was obtained for each device. Oxide capacitance values used were those measured at large negative bias in the case of p-type silicon and at large positive bias for n-type silicon. (Comparison of measured oxide capacitances with oxide thickness gave the value of the dielectric constant, $K_o = 3.9$). Using a curve of the type shown in Fig. 3, the value of the effective impurity concentration near the silicon surface, C_d, was determined. A specific example is illustrated in Fig. 11.

Results

General survey.—A survey involving several different dopants, both acceptors and donors, was conducted to determine redistribution characteristics caused by thermal oxidation. All oxidations were carried out at 1200°C in dry oxygen. Oxide thickness was 0.20μ in all cases. MOS devices were prepared, C-V plots obtained, and effective surface concentrations determined from capacitance minima. A value of x_d was determined from the effective surface concentration using Fig. 7. Values of $2\sqrt{Dt}$ were calculated based on the conditions of oxidation. The results consisting of the ratio of the effective impurity concentration across the electrical depletion region to the bulk doping, C_d/C_B, are tabulated in Table I. Also shown are values of the ratio $(x_d/2)/2\sqrt{Dt}$ which indicate the position along the impurity profile to which C_d is assigned. The corresponding redistribution values reported in ref. (10) are given for comparison. Following is a short summary of the results.

Antimony and Arsenic.—In ref. (10), these two donor impurities are reported to pile-up slightly under the above oxidation conditions. The present results indicate a small pile-up, of the same order as obtained in the previous study.

Phosphorus.—Figure 6 predicts that phosphorus will pile-up to the extent of $C_S/C_B = 1.1$ at all dry oxidation temperatures. This has been found to be the case for a number of MOS devices, with the exact value varying from 1.1 to 1.2.

Aluminum and indium.—Indium was found in ref. (10) to deplete to a very low value at the oxide-silicon interface. This was found to be the case also in the present experiments. Aluminum behaves in a similar manner. The results indicate that the concentrations of these two impurities right at the silicon surface are much smaller than in the bulk, *i.e.*, $C_S/C_B \ll 1$.

Gallium.—This p-type impurity was the subject of a detailed study described in ref. (10). It was shown that even though its segregation coefficient favors pile-up, the rapid diffusion of gallium through the oxide (17) results in considerable depletion. Results of three separate gallium concentrations are given in Table I. The results indicate, as with aluminum and indium, that the gallium concentration at the surface is near zero.

Boron.—Boron is predicted from Fig. 5 to deplete to $C_S/C_B = 0.6$ under the above oxidation conditions. For $(x_d/2)/2\sqrt{Dt}$ values of 0.1 to 0.2, the observed values of C_d/C_B range from 0.7 to 0.8. A more detailed investigation of boron redistribution is discussed in the next section

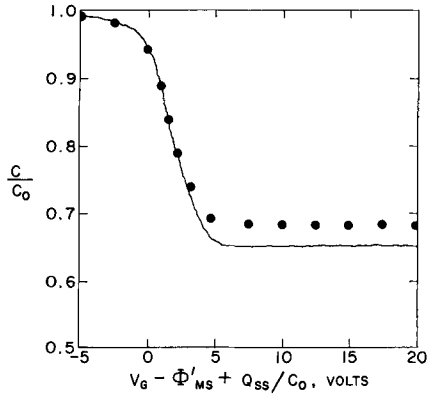

Fig. 11. An example showing comparison between theoretical (solid circles) and experimental (solid line) MOS C-V characteristics. Calculations correspond to the bulk doping, $C_B = 1.45 \times 10^{16}$ cm^{-3} and $x_o = 0.20\mu$. Minimum capacitance ratio of experimental curve, $C_M/C_o = 0.65$, corresponds to an effective surface concentration $C_d = 1.10 \times 10^{16}$ cm^{-3} from Fig. 3. Oxidation was in dry O_2 at 1200°C for 60 min. Value of $x_d/2\sqrt{Dt}$ is 0.24.

Table I. Redistribution of various impurities

Dry O_2 oxidation, 1200°C, 60 min, $x_o = 0.20\mu$

Dopant	C_B, cm^{-3}	$\sqrt{D}$, $\mu/\sqrt{\text{hr}}$	$\frac{x_d/2}{2\sqrt{Dt}}$	C_d/C_B	C_d/C_B*
Antimony	1.0×10^{16}	0.35	0.22	1.2-1.5	1.2
Arsenic	2.5×10^{15}	0.35	0.40	1.1-1.3	1.2
Phosphorus	4.0×10^{15}	1.13	0.10	1.1-1.2	1.1
Aluminum	5.5×10^{15}	2.35	0.10	0.2	—
Boron	1.4×10^{16}	0.60	0.12	0.7-0.8	0.66
Gallium	5.0×10^{16}	0.78	0.14	0.1	0.17
Gallium	1.5×10^{16}	0.78	0.18	0.2	0.21
Gallium	8.0×10^{14}	0.78	0.35	0.8	0.40
Indium	1.8×10^{17}	0.57	0.11	0.1	0.15

* Corresponding data from Grove, Leistiko, and Sah (10).

Table II. Redistribution of boron as a function of oxide thickness and oxidation type

$C_B = 1.4 \times 10^{16}$ cm^{-3}

Oxide type	Oxidation temp, °C	Oxidation time, min	Oxide thickness, μ	$\frac{x_d/2}{2\sqrt{Dt}}$	C_d/C_B
Dry oxygen	1200	1440	1.0	0.03	0.52
Dry oxygen	1200	360	0.5	0.05	0.77
Dry oxygen	1200	60	0.2	0.12	0.83
Dry oxygen	1200	15	0.09	0.25	0.83
Dry oxygen	1200	6	0.05	0.33	0.78
Wet oxygen*	1200	85	1.0	0.12	0.50
Wet oxygen	1200	22	0.5	0.24	0.65
Wet oxygen	1200	4	0.2	0.47	0.72
Pyrolytic	750	5	0.2	250	1.0
Anodic	25	35	0.2	∞	1.0

* Oxygen bubbled through 95°C H_2O.

Table III. Redistribution of boron as a function of oxidation temperature and bulk concentration

Dry O_2 oxidation, $x_o = 0.20\mu$

Temp, °C	Oxidation Time, min	C_B, cm^{-3}	$\sqrt{D}$, $\mu/\sqrt{hr}$	$\frac{x_d/2}{2\sqrt{Dt}}$	C_d/C_B
1200	60	5.5×10^{16}	0.6	0.06	0.69
1200	60	1.4×10^{16}	0.6	0.12	0.72
1200	60	3.2×10^{15}	0.6	0.26	0.72
1200	60	1.4×10^{15}	0.6	0.37	0.75
1200	60	2.3×10^{14}	0.6	0.90	0.9
1200	60	1.1×10^{14}	0.6	1.15	1.0
1100	138	6.5×10^{16}	0.2	0.17	0.52
1100	138	1.4×10^{16}	0.2	0.30	0.72
1100	138	2.9×10^{15}	0.2	0.70	0.82
1100	138	1.4×10^{15}	0.2	0.90	1.0
1000	360	6.0×10^{16}	0.055	0.27	0.40
1000	360	1.4×10^{16}	0.055	0.55	0.57
1000	360	2.8×10^{15}	0.055	1.15	1.0
920	960	6.8×10^{16}	(0.015)	(0.90)	(0.34)
920	960	1.4×10^{16}	(0.015)	(1.40)	(0.61)
920	960	3.1×10^{15}	(0.015)	(2.25)	(1.0)

Boron redistribution.—Redistribution of boron in silicon due to thermal oxidation was investigated over the temperature range 920°-1200°C. Two main effects were considered in this investigation: (*a*) factors influencing the relationship of x_d, (the width of the electrical depletion region), to $2\sqrt{Dt}$, (the length of the redistribution region); (*b*) factors influencing the impurity redistribution itself.

Results are reported in terms of oxidation type and oxide thickness (Table II); and oxidation temperature and boron concentration, (Table III). The quantity, $(x_d/2)/2\sqrt{Dt}$ to which the effective concentration, C_d, corresponds, is given in both tables.

Oxidation type and oxide thickness.—MOS devices were prepared using four different types of oxidation. Bulk concentration of the boron in the silicon slice was the same in all cases: 1.4×10^{16} cm^{-3}. The value of x_d (the maximum width of the electrical depletion region) corresponding to the bulk impurity concentration was 0.28μ.

From Table II, the differences in boron redistribution caused by various types of oxidations can be noted. For instance, when $(x_d/2)/2\sqrt{Dt} = 0.25$, wet oxygen results in a C_d/C_B value of 0.65 compared to 0.83 for dry oxygen. This trend agrees with predictions based on Fig. 5. In the case of pyrolytic and anodic oxides, where the low oxidation temperatures (hence very low diffusivities) result in very high $(x_d/2)/2\sqrt{Dt}$ ratios, no redistribution can be observed.

It can be noted in the case of both dry and wet oxidation that, as the oxidation time increases and hence the $(x_d/2)/2\sqrt{Dt}$ ratio decreases, the C_d values obtained represent concentrations nearer to the surface.

Oxidation temperature and boron concentration.—Let us first consider the effect of oxidation temperature on boron redistribution. Table III includes results of dry oxygen oxidation of boron-doped silicon at four different temperatures. All oxides are 0.20μ thick. The predicted effect of temperature on the boron surface concentration was presented in Fig. 5. Thus, while at 1200° the boron concentration at the silicon surface was predicted to be 0.6 C_B, at 920° it should be only about 0.2 C_B. If the lowest concentration at each temperature listed in Table III is considered, a uniform decrease in C_d/C_B can be noted going from 1200° down to 920°C. Furthermore the values agree quite closely with predictions based on Fig. 5. Values at 920°C are in parenthesis since oxidation no longer is parabolic at this temperature and the redistribution theory (10) can only be applied as an approximation. The value of $(x_d/2)/2\sqrt{Dt}$ at 920° seems to be too high, perhaps reflecting an uncertainty in $\sqrt{D}$.

At any particular temperature, the variation of boron bulk concentration should affect only the maximum width of the electrical depletion region x_d. As an increasing x_d value causes the $(x_d/2)/2\sqrt{Dt}$ ratio to approach unity, C_d should approach C_B. This is indeed the case at 1000°, 1100° and 1200°. As mentioned above, the $\sqrt{D}$ value of 920° is in question and should apparently be about twice the value listed, i.e., $\sqrt{D}$ at 920° should be 0.03 $\mu/\sqrt{hr}$ according to these results.

The results of Table III are more clearly understood if redistribution profiles based on the theory given in ref. (10) and a segregation coefficient $m = 0.3$ are plotted in Fig. 12. It can be noted that, as the oxidation temperature is lowered, the interfacial concentration of boron and the redistribution length (approximated by $2\sqrt{Dt}$) both decrease. Also included on the graph are x_d distances for several impurity concentrations. It is evident that the higher the boron concentration, the closer C_d will be to the actual interfacial concentration, C_s. At low boron concentrations, the MOS device will merely "observe" the bulk concentration, even for oxides grown at 1200°C.

All dry oxygen boron data from Tables II and III are also shown in Fig. 13 where C_d/C_B is plotted *vs.* $(x_d/2)/2\sqrt{Dt}$. This results in an approximate impurity distribution profile. The predicted distributions are shown by the solid lines. Reasonable agreement is obtained between experimental results and the theoretical profiles, especially in the light of the fact that the MOS method described here is only semiquantitative. The 920°C data are not shown due to the considerations discussed above.

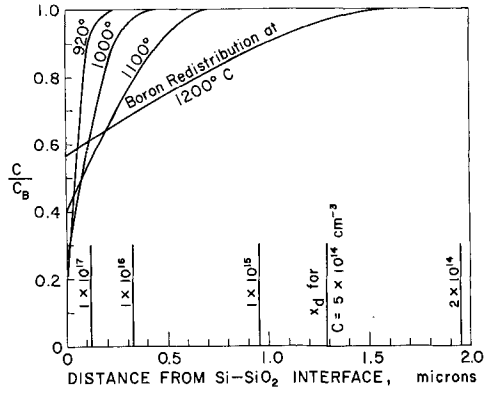

Fig. 12. Predicted redistribution profiles for boron in silicon due to dry oxygen oxidation at various temperatures. The electrical depletion region width, x_d, is also shown for various impurity concentrations.

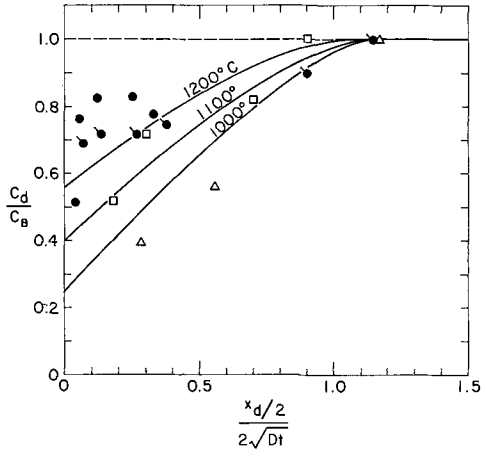

Fig. 13. Experimental results of boron redistribution due to oxidation in dry oxygen. Predicted profiles are also shown. Solid circle 1200°, $C_B = 1.4 \times 10^{16}$ cm^{-3}, varying t ($\rightarrow x_o$); solid circle with line to the left 1200°, open square 1100°, open triangle 1000°, $x_o = 0.2\mu$ varying C_B ($\rightarrow x_d$).

Conclusions

The MOS field-effect capacitance method has proven satisfactory as a semiquantitative method for observing the impurity redistribution in silicon due to thermal oxidation. Concentration values obtained by this method represent effective average values across the electrical depletion region. By a careful choice of conditions this method can even yield the actual impurity redistribution profile.

The results obtained in this study for seven different acceptor and donor-type impurities were found to be in complete agreement with the results of the earlier investigation (10). In addition the effects of oxidation temperature and ambient, not covered experimentally in ref. (10), were investigated in detail for boron. The MOS results agree with the theoretical predictions of ref. (10).

In conclusion, it should be pointed out that the MOS method is relatively nondestructive and can be used with regular device processing by placing MOS field plates over an oxide either at the edge of a wafer or in between conventional devices.

Acknowledgment

The authors wish to thank Mrs. D. S. Sklar for her assistance in the experimental portion of this program.

Manuscript received Aug. 17, 1964. This paper was presented at the Washington Meeting, Oct. 11-15, 1964.

Any discussion of this paper will appear in a Discussion Section to be published in the December 1965 JOURNAL.

REFERENCES

1A G. E. Moore, "Microelectronics," E. Keonjian, Editor, Chap. 5, McGraw-Hill Book Company, New York (1963).
1B C. T. Sah, *IEEE Trans. Electron Devices*, **ED-11**, 324 (1964).
2. J. L. Moll, IRE Wescon Convention Record Part 3, p. 32 (1959).
3. W. G. Pfann and C. G. B. Garrett, *Proc. IRE*, **47**, 2011 (1959).
4. L. M. Terman, *Solid State Electronics*, **5**, 285 (1962).
5. R. Lindner, *Bell System Tech. J.*, **41**, 803 (1962).
6. K. Lehovec, A. Slobodskoy, and J. L. Sprague, *Phys. Stat. Sol.*, **3**, 447 (1963).
7. A. S. Grove, E. H. Snow, B. E. Deal, and C. T. Sah, *J. Appl. Phys.*, **35**, 2458 (1964).
8. A. S. Grove, B. E. Deal, E. H. Snow, and C. T. Sah, Paper presented at IEEE Solid State Research Conf., Boulder, Colo., July 1964; abstracted in *IEEE Trans. Electron Devices*, **ED-11**, 531 (1964); to be published in *Solid State Electronics*.
9. M. M. Atalla and E. Tannenbaum, *Bell System Tech. J.*, **39**, 933 (1960).
10. A. S. Grove, O. Leistiko, Jr., and C. T. Sah, *J. Appl. Phys.*, **35**, 2695 (1964).
11. J. Lindmayer, *Solid-State Electronics*, **6**, 137 (1963).
12. C. T. Sah, H. Sello, and D. A. Tremere, *J. Phys. Chem. Solids*, **11**, 288 (1959).
13. S. Horiuchi and J. Yamaguchi, *Jap. J. Appl. Phys.*, **1**, 314 (1962).
14. A. D. Kurtz and R. Yee, *J. Appl. Phys.*, **31**, 303 (1960).
15. C. S. Fuller and J. A. Ditzenberger, *ibid.*, **27**, 544 (1956).
16. B. E. Deal, *This Journal*, **110**, 527 (1963).
17. A. S. Grove, O. Leistiko, Jr., and C. T. Sah, *J. Phys. Chem. Solids*, **25**, 985 (1964).
18. K. Lehovec and A. Slobodskoy, *Solid-State Electronics*, **7**, 59 (1964).
19. D. R. Frankl, *ibid.*, **2**, 71 (1961).

APPENDIX

Approximate Formulas for the Calculation of the Minimum Capacitance Ratio

In the present work, values of the minimum capacitance of the MOS structure as a function of the impurity concentration were based on exact calculations. However, approximate expressions have also been derived which enable their rapid estimation.

The maximum width of the electrical depletion region can be estimated on the basis of the simple model presented in ref. (7).[3] If, in the case of a p-type semiconductor, the maximum depletion region width, $x_{d\max}$, is assumed to be reached when the electron surface concentration in the inversion region equals the concentration of holes in the bulk of the semiconductor, *i.e.*, $n_s = N_A$, this width will be given by

$$2\phi_F = \frac{q\,N_A\,x_{d\,\max}^2}{2K_s\,\epsilon_o} \qquad [1A]$$

where the notation is the same as in ref. (7) and (8). This formula yields values in good agreement with Fig. 7.

The minimum high-frequency space charge capacitance per unit area of the semiconductor will then be given approximately by

$$C_{s\,\min} = \frac{K_s\,\epsilon_o}{x_{d\,\max}} = \frac{K_s\,\epsilon_o}{L_D}\sqrt{\frac{N_A}{2n_i}}\,[4\ln(N_A/n_i)]^{-1/2} \qquad [2A]$$

where

$$L_D \equiv \left[\frac{kT}{q}\,\frac{K_s\,\epsilon_o}{2\,q\,n_i}\right]^{1/2}$$

The minimum low-frequency space charge capacitance can be obtained by setting $dC/dV_G = 0$ since in the low-frequency case the characteristics exhibit a true minimum. This was done by Frankl (19) whose calculations lead to the approximate result

$$C_{s\,\min} = \frac{K_s\,\epsilon_o}{L_D}\sqrt{\frac{N_A}{2n_i}}\,[1 + 0.542u_F - 0.0115u_F^2 + 1.25\times10^{-4}\,u_F^3]^{-1} \qquad [3A]$$

where $u_F = \ln(N_A/n_i)$.

The minimum capacitance ratio of the MOS structure is then given for either case by

$$\frac{C_M}{C_o} = \left[1 + \frac{C_o}{C_{s\,\min}}\right]^{-1} \qquad [4A]$$

where $C_o = K_o\,\epsilon_0/x_o$ is the capacitance per unit area of the oxide layer.

[3] Similar considerations have been advanced by Lehovec and Slobodsky (18).

Substrate Orientation Effects and Germanium Epitaxy in an Open Tube HI Transport System

A. Reisman and M. Berkenblit

Thomas J. Watson Research Center, International Business Machines Corporation, Yorktown Heights, New York

ABSTRACT

The results of the thermodynamic analysis of the system Ge-I_2-H_2-He was used as a guide in designing a germanium epitaxial reactor. The equipment incorporates an instantaneous demand HI generator and is free of lubricated joints and valves. Cleaning of the apparatus is effected by the use of liner tubes and the system operates semiautomatically. Vapor growth studies were conducted to determine the effects on the surface morphology of grown layers caused by substrate parameters such as crystal orientation, resistivity, and conductivity type. It was found that the latter two parameters did not affect surface morphology, but that small crystal misorientations off of <111> surfaces had pronounced effects. Growth rates in the system were of the order of 0.7 μ/hr under the conditions used, and values of N_D-N_A of 10^{15} electrons/cm^3 were obtained routinely using undoped sources. Mobilities for the deposits were in the 14,000 cm^2/v sec range at liquid nitrogen temperature.

The low temperatures associated with Ge epitaxial growth in an iodine process offer some distinct advantages when diffusion processes must be minimized. On the other hand, surface morphology obtainable with this growth procedure is generally inferior to that obtained in a high temperature reduction process. An additional disadvantage in such a disproportionation growth scheme is the low growth rate obtained, necessitating extended time periods during which experimental parameters must be controlled. The recent thermodynamic analysis of the system Ge-I_2-H_2-He (1) indicated that regions of temperature insensitivity for source and seed sites could be used to advantage in achieving long term stability of an open tube Ge-HI disproportionation train in which Ge transport occurs via reactions [1] and [2]. This provided the impetus for designing

$$Ge_{(s)} + 2HI_{(v)} \rightleftarrows GeI_{2(v)} + H_{2(v)} \quad \text{(at source)} \quad [1]$$

$$2GeI_{2(v)} \rightleftarrows Ge_{(s)} + GeI_{4(v)} \quad \text{(at seed)} \quad [2]$$

an apparatus to study possible parameters effecting surface morphology at the temperatures in which Ge epitaxy occurs in an HI transport system.

Experimental Procedure

HI *transport system.*—Examination of the curves of Fig. 1 (1) indicate that for F values [$H_2/(H_2 + He)$ mole fraction] of 0.1, and 0.2, the mole ratio nGe/nI_2 at potential source and seed sites is relatively temperature insensitive. Thus, a plateau is generated at 600°C which is a useful source temperature, and a minimum occurs at around 350°C which represents a useful seed temperature. Using this information as a guide, an apparatus was designed for effecting Ge epitaxy. As a matter of convenience, and in order to assure more rapid attainment of equilibrium, the iodine emanating from the source bed was converted to HI since preliminary experiments had revealed that the conversion $I_2 + H_2$ to HI in the Ge source does not go to completion.

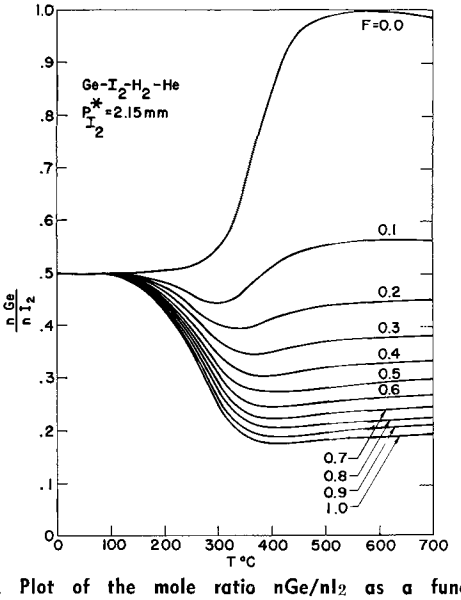

Fig. 1. Plot of the mole ratio nGe/nI_2 as a function of temperature.

HI *generator.*—A problem that existed in the use of HI as a transporting agent was the unavailability of a high purity commercial source. The available HI was found to be contaminated with phosphorus, due probably to the use of phosphoric acid lubricated joints in the synthesis of the reagent. In addition, the available regulators corroded badly in operation making flow control difficult to achieve. It was decided to explore the possibility of developing an *in situ* controlled source of HI free of corrodible or lubricated valves. The apparatus shown in Fig. 2 was evolved and is based on the work of Caley and Burford (2). In place of the catalyst suggested by the authors, platinum wool was used (1 mil crumpled Pt wire). Instead of the "red heat" used by them a temperature of 350°-450°C

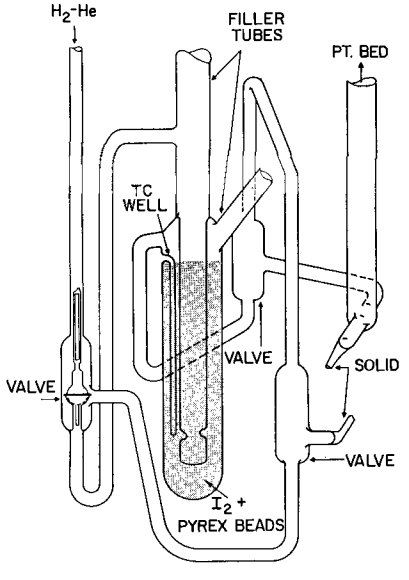

Fig. 2. HI generator

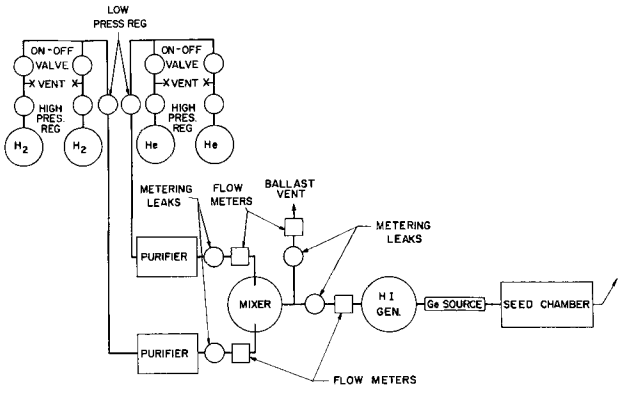

Fig. 3. Schematic representation of deposition reaction train

Fig. 4. Detail of gas entry nozzles into deposition chamber

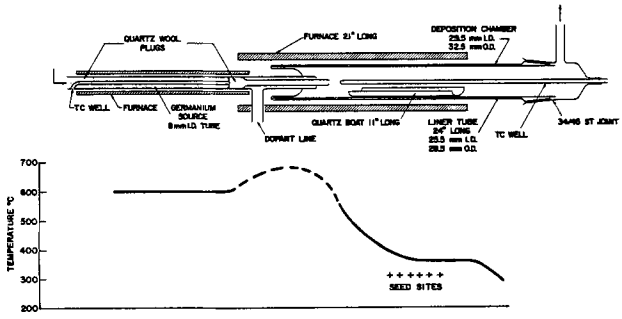

Fig. 5. Germanium source bed and deposition chamber

was found to be adequate. The need for joints and stopcocks was eliminated by using magnetically operated ball joints and a by-pass arrangement as shown in Fig. 2. To obtain more positive valve seating, each magnet assembly is comprised of two coils so that both opening and closing are effected magnetically. The iodine path lengths necessary for equilibrium to obtain between the carrier gas and the bed have been discussed in a paper dealing with transpiration studies in the system Ge-I_2-He (3). For a Pt bed 10 in. long and 20 mm ID heated to 420°C, complete reaction is achieved with linear gas velocities to 1000 cm/min (input flow rate of 1400 cm^3/min) at iodine pressures to 35 mm. If greater flow rates and/or higher iodine pressures are necessary, longer or greater diameter Pt columns and/or higher temperatures may be required. In operation, the efficiency of the synthesis is readily discernible by observing the disappearance of the iodine color at some point in the Pt wool packing. At flows of 75-150 cm^3/min, the iodine color disappears almost immediately within the Pt bed. The glass assembly, up to the Pt bed, is kept in a constant temperature oil bath. Condensation of the effluent HI from the generator and analysis of the condensate failed to reveal any traces of platinum.

The reaction train.—Figure 3 schematically depicts the entire reaction train. H_2 (Matheson, Ultra Pure Hydrogen, 10 ppm impurities) and He (Matheson Helium, 100 ppm impurities) are mixed and purified in a molecular sieve type purifier (J. Mickel Associates). The purifier has a rated capacity of 3 liters/min and provides an output in the 10 ppB impurity range. Flows for the entire system are controlled by Granville-Phillips metering leaks and are monitored by flow meters (Predictability Flowmeters from the Manostat Corp.).

The remaining portions of the system were designed in accord with results obtained in a study of Ge-I_2 transpiration phenomena previously reported (3). Thus, the Ge source was contained in a quartz tube 8 mm ID and 12 in. long heated by a 6 element furnace. The deposition chamber was 24 in. long with an ID of 35 mm again heated by a 6 element furnace.

Since the entire glass portion of the system is constructed free of joints, it was necessary to incorporate a simple clean up procedure which did not require disassembly of the glassware after each deposition. This was achieved by the use of a removable liner in the deposition chamber. Figure 4 shows the construction of the gas entry nozzles into the deposition chamber[1] and the recess surrounding these nozzles into which the liner tube fits, and Fig. 5 shows the design of the Ge source bed and deposition chamber. In order to minimize diffusion between the liner tube and wall of the reactor, the liners were chosen so as to provide a close fit with the wall of the deposition chamber. The use of removable liners has enabled operation without shutdown for cleaning for months at a time.

Temperature and flow conditions.—All of the epitaxial growth experiments were conducted in a carrier gas containing a $H_2/(H_2 + He)$ ratio of 0.2 and an input iodine partial pressure of 2.5 mm. The Ge source was maintained at 600° ± 10°C and the seeds at 365°-405°C. From Fig. 1 it is seen that the equilibrium Ge/I_2 ratio decreases from 0.443 to 0.394 in the temperature interval 600°-365°C. This corresponds to a theoretical dropout of 0.049 moles Ge/mole input iodine.

Figure 5 also shows the temperature profile of the HI reaction train. Following the Ge bed, the temperature was raised to >600°C to prevent premature deposition of Ge, and to increase the temperature gradient past the nozzle. The gradient terminates in a 4 in. long flat deposition region at 360°-365°C. Flow rates were 75 cc/min. At this flow rate the theoretical dropout of Ge in the deposition chamber is 1.8 mg/hr.

Substrate preparation.—Substrate wafers were saw cut from preoriented single crystals. Both Czochralski pulled and zone leveled germanium crystals were used as noted below, although most depositions were conducted on pulled material. The wafers were lapped to uniform thickness with a succession of Al_2O_3 grit sizes of 9.5, 5, and 3μ and then mechanically polished with 0.3μ Al_2O_3 (Linde A) followed by a 0.05μ (Linde B) final polish. These finished substrates exhibit a high polish but are surface damaged.

After mechanical polishing, the wafers were ultrasonically cleaned in deionized water. Then in order to remove surface damage they were etched in a 5:1 HNO_3/HF solution for 30 sec, rinsed in deionized water, ethyl alcohol, and dried in a stream of warm N_2 immediately prior to use. They were then placed in the

[1] The apparatus contains two gas lines into the deposition region, one for Ge and the other potentially for a dopant. The latter was not used in these studies and the gas flowing through the second leg served as a diluent in the deposition chamber. The effect of dilution on growth rate will be described in a later report.

apparatus and given a 15 min HI cleaning etch at 365°C in order to remove surface oxides. This etching did not result in a measurable weight loss (±0.1 mg) nor in a change in surface appearance, but etch products were observed at the outlet portion of the reactor.

Results

Characteristics of deposits and growth rates.—Under the conditions of the experiment as outlined above, growth rates have been of the order of 0.7 μ/hr at 365°C, and approximately half this rate for a seed temperature of approximately 400°C, with depositions conducted for periods up to 96 hr. Most of the deposits have been x-ray analyzed, and generally exhibit crystal perfections which may be termed perfect within the limits of conventional x-ray detectability (4).

Thermoelectric probing showed all deposits to be n-type although the Ge source was 40 ohm cm p-type material. Van der Pauw samples were prepared and net carrier concentrations, N_D-N_A, were determined to be in the range 1-4 x 10^{15} electrons/cm^3. Hall mobilities at liquid N_2 temperature ranged around 14,000 cm^2/v sec. Attempts were made to determine the nature of the impurities present in the system, *i.e.*, such impurities might arise from leaching of the quartz ware, gaseous impurities not trapped by the gas purification system, or impurities in the I_2 source. None of these, however, at the present time can be traced as the source of impurities.

Substrate orientation effects.—Initial deposits were obtained on substrates cut from a p-type, 30 ohm-cm pulled crystal, nominally oriented perpendicular to the <111> direction. The surfaces of these deposits did not show the gross pyramidal overgrowths normally associated with low temperature disproportionation growth (5). Instead, a relatively smooth, matte finish was obtained. Subsequently layers grown on substrates cut from at 1.2 ohm-cm, p-type zone leveled crystal, yielded the more characteristic <111> pyramidal growths. Figure 6 shows both types of surfaces as they were obtained in a single growth experiment using wafers from the two crystals as substrates. This experiment demonstrated that the observed surface morphology differences were not due to system variations, but in some way were related to differences between the substrates.

The differences that were considered included the following: (*a*) The substrate source in one case was a pulled crystal and in the other a zone leveled crystal. Imperfections might have been significantly different in both due to the method of single crystal preparation, and their number and type might influence growth morphology. (*b*) The doping levels of the two crystals were different and might influence surface morphology. (*c*) Though the wafers were all nominally oriented perpendicular to the <111>, the slices from the pulled crystal were found to be approximately 4° off the <111> orientation.

In order to test (*a*) and (*b*) it was felt that the orientation parameter would have to be evaluated first. Consequently, a series of wafers was prepared from a new p-type 30 ohm-cm pulled crsytal. These wafers were cut in three different orientations, all nominally perpendicular to the <111>. The directions of misorientation intentionally introduced are best seen with reference to Fig. 7 which is a simplified stereographic projection perpendicular to the <111>. Because of the three-fold symmetry present, two major misorientations are possible, toward the closest <211>, and toward the closest <110>. It should be noted that in addition to the misorientations described, there are intermediate misorientations possible; namely, those in which the misorientation vector lies in between the two possible major misorientation directions. This gives rise to a misorientation involving two coordinate specifications, a ρ value indicative of the angular misorientation from the <111>, and a ϕ value which locates the intersection of a perpendicular from the surface studied to the stereographic plane within the directions bounded by the <111>-<211> and <111>-<110> vectors. The three types of wafers studied are denoted by <111>, <111> → <211> and <111> → <110>, where the angle off the <111> toward either the <211> or <110> was 3°-5°. After polishing, each wafer was x-ray analyzed to determine its precise orientation.

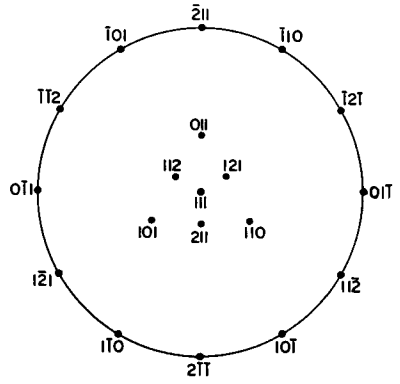

Fig. 7. Simplified stereographic projection perpendicular to the <111>. Angles: ∢ 111-211 = 19°28′; ∢ 111-110 = 35°16′.

The three types of wafers were included in each experiment, their positions in the reactor being randomly changed from run to run. On the basis of a series of such experiments, the following results were obtained reproducibly. Wafers oriented with $\rho \leq 1°$ and ϕ varying from 0 to 60° always developed pyramidal overgrowths. The density of pyramids was dependent on the seed position in the furnace. Thus, <111> wafers first encountering the gas stream developed

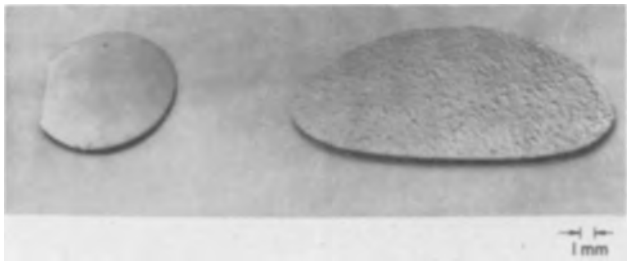

Fig. 6. Simultaneous growth on pulled and zone leveled wafers

Fig. 8. Deposit on substrate with orientation <111>.

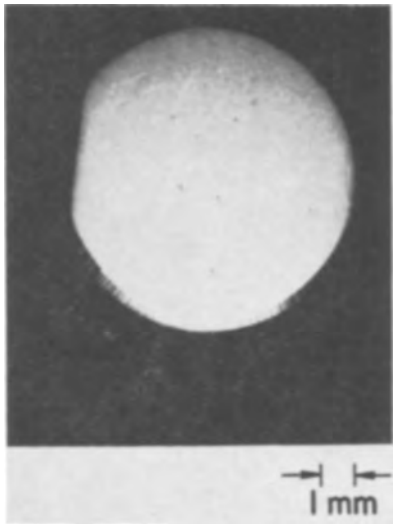

Fig. 9. Deposit on substrate with orientation <111> → <110>.

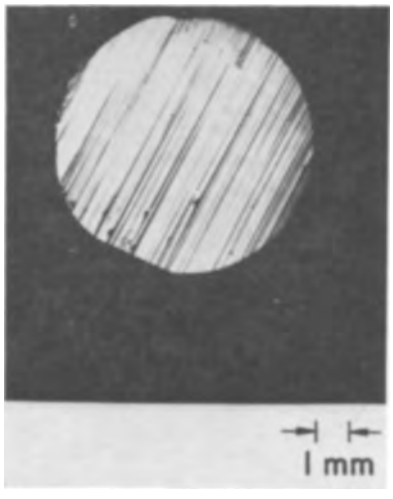

Fig. 10. Deposit on substrate with orientation <111> → <211>.

numerous pyramidal overgrowths, but did not show the greatest weight gain. The <111> wafers further down stream developed fewer, but larger pyramids. Figure 8 shows a typical deposit obtained on a <111> wafer. Wafers misoriented toward the <110> with $\rho = 3°\text{-}5°$ and a ϕ angle of 0-15° from the <111>-<110> vector were free of pyramidal overgrowths, exhibiting the structure shown in Fig. 9. Wafers misoriented 3°-5° toward the <211> with a low ϕ angle yielded shiny deposits which were, however, striated. These are shown in Fig. 10.

While the effects of ρ angle with small ϕ angle in either of the major misorientation directions was predictable, the effects of variation in ϕ angle with $\rho = 3°\text{-}5°$ were not as definable. Thus, when the major misorientation direction was toward the nearest <110> a measurable ϕ angle was always attended by the formation of a bevel around a portion of the wafer edge. This bevel was striated. No definitive, simple way of determining the directions of the striae could be found, although they appeared to be <110> directions. The edge of the wafer on which the bevel formed did not relate to the direction of the gas stream relative to the wafer in the deposition chamber. At higher ϕ angles, 20°-30°, hybrid surfaces developed which did not resemble too closely the surfaces obtained with $\rho = 3°\text{-}5°$ toward either of the two major misorientations. Thus, the surfaces were partially striated and shiny like those obtained on the <111> → <211> and partially matte finish similar to that obtained on the <111> → <110>. Because measurement of the ϕ angle is subject to more error than measurement of the ρ angle, the exact ϕ values at which these hybrids were observed cannot be stated precisely. Less extensive studies with zone leveled wafers gave similar results to those described above.

Studies of substrates with resistivities between 1 and 40 ohm-cm both n and p type from either pulled or zone leveled crystals, showed no further effects on the growth characteristics other than those derived by appropriate misorientation of the wafers. Thus, it may be concluded that the variation in growth characteristics observed is attributable to orientation effects. It is of further interest to note that aside from the furnace position effect observed in <111> oriented wafers, neither position nor temperature effects were observed on the growth habit of the misoriented substrates.

Although detailed studies of other orientations have not been conducted, preliminary studies of growth on <211> and <110> surfaces qualitatively show similar misorientation effects. <211> surfaces were found to be free of striae, <110> surfaces grew nonuniformly and both appeared extremely sensitive to surface condition.

Acknowledgment

We wish to thank C. Fisher for designing and fabricating the magnetic valve system, R. Rohr for assisting in the design of the reactor, N. Stemple and E. Maschler for the x-ray analyses of substrates, C. Lent for the preparation of single crystal germanium, and C. Duncombe for cutting the wafers.

Manuscript received Sept. 24, 1964; revised manuscript received Nov. 19, 1964. This paper was presented in part at the Toronto Meeting, May 3-7, 1964. This work was supported in part by AFCRL Contract No. AF19(628)-2468.

Any discussion of this paper will appear in a Discussion Section to be published in the December 1965 JOURNAL.

REFERENCES

1. A. Reisman and S. A. Alyanakyan, *This Journal*, **111**, 1154 (1964).
2. E. R. Caley and M. G. Burford, "Morganic Synthesis," Vol. 1, H. S. Booth, Editor, pp. 159-162, McGraw-Hill Book Co., New York.
3. Presented at the New York Meeting, Sept. 29-Oct. 3, 1963, Abstract 142.
4. H. Cole and N. R. Stemple, *J. Appl. Phys.*, **33**, 227 (1962).
5. J. C. Marinace, *IBM Journal of Res. & Dev.*, **4**, 248 (1960).

Kinetics of the Silicon-Silicontetrachloride Reaction in a Flow System

Ole Alstrup and Carl O. Thomas[1]

Physics Department, Section III, Technical University of Denmark, Lyngby, Denmark

ABSTRACT

The kinetics of the heterogeneous reaction

$$Si + SiCl_4 = 2SiCl_2$$

have been studied in a flow system with helium as the carrier gas. For this reaction the postulated rate expression

$$\frac{d\,Si}{dt} = -1.0 \times 10^6 \exp\left(-\frac{67000}{RT}\right) P_4^{1/2} + 9 \exp\left(-\frac{29000}{RT}\right) P_2$$

$$g\ Si\ cm^{-2}\ sec^{-1}$$

was shown to describe the experimental results. The flow system data has been analyzed in terms of quantitatively measurable system parameters. Consequently true rather than apparent constants are found.

The reduction of silicon and germanium tetrahalides in a hydrogen atmosphere is widely used as a method for preparing epitaxial films of these materials. The type reaction is written usually as

$$MX_4 + 2H_2 = M + 4HX \qquad [1]$$

where M is the group-IV element and X is the halogen. This form is not even an accurate indication of the material balance. For example, a variety of other products occurs in the silicon-chlorine process including $SiHCl_3$ and miscellaneous polymeric forms. In spite of the large amount of experimental work in this field, a high level of uncertainty remains as to the mechanism by which hydrogen is involved in the over-all process. However, there is a general consensus in the literature [silicon (1-5) and germanium (6-7)] that the type disproportionation

$$M + MX_4 = 2MX_2 \qquad [2]$$

is one of the reactions in the over-all process. The equilibrium for the Si-$SiCl_4$ reaction following Eq. [2] has been studied quantitatively by Schäfer and Nickl (8-9). They concluded that no other molecular species were present to any significant degree. Bylander (2) and Monchamp, McAleer, and Pollack (5) have studied the disproportionation reaction in a flow system, but no quantitative kinetic data were obtained in either case. Monchamp *et al.* then used a low-pressure closed system, somewhat similar to that used by Heinecke and Ing (10) in germanium studies, for the investigation of the kinetics of the disproportionation reaction. They found that

$$\frac{dN_o}{dt} = -8.23 \times 10^{24} \exp\left(-\frac{49100}{RT}\right) P_4^{1/2}$$

$$atoms\ Si\ cm^{-2}\ sec^{-1} \qquad [3]$$

where N_o is the number of atoms in the silicon sample divided by its surface area, and P_4 the $SiCl_4$ pressure. A rate expression of this form indicates that the reaction must go to completion, and that the equilibrium constant must be either zero or infinite. The equilibrium constant is known to have a finite value (8), and consequently the rate expression of Monchamp *et al.* cannot be strictly valid. We postulate, subject to subsequent experimental verification, that the complete rate expression is of the following form

$$\frac{dN_o}{dt} = -k'_1 P_4^n + k'_2 P_2^{2n} \qquad [4]$$

where P_2 is the $SiCl_2$ pressure (P_{SiCl_2}) in the reaction zone, and k'_1 and k'_2 are rate constants. In Eq. [4] the factor-of-two relationship between the exponents is a requirement imposed by the form of the equilibrium constant, since this is found to be equal to P_2^2/P_4. At high flow rates, *i.e.*, not near equilibrium, $|k'_2 P_2^{2n}| << |k'_1 P_4^n|$ and Eq. [3] and [4] become similar in form. As one approaches equilibrium at low flow rates, the right-hand term becomes increasingly significant. We have determined the numerical values of k'_1 and k'_2 and n. The data, when extrapolated to zero flow rate, yield an equilibrium constant in reasonable agreement with that reported earlier by Schäfer and Nickl (8).

Experimental

The reaction chamber is shown in Fig. 1. The normal flow direction was in through the larger tube and out through the smaller central tube. The lower linear velocity through the external tube provided better temperature equilibration for the incoming gases. The influence of the flow direction was only detectable for flow rates above about 1 cc sec^{-1}. The close annular fit between the two concentric pieces and the capillary tip on the inner piece was intended to minimize back-streaming of gases. The volume of the reaction zone could be changed by changing the distance which the central piece was inserted into the larger tube.

At the highest flow rates used, the input pressure was less than 10 mm (Hg) above atmospheric pressure. Since the pressure terms enter to the one-half power and to the first power, the error in neglecting this pressure increment was considered to be negligible.

The flow rate was measured by means of a soap-film flow meter (11). A cold trap and a short capillary were placed between the exit of the reaction chamber and the flow meter to prevent halide products from getting into the flow meter. The flow rate data were

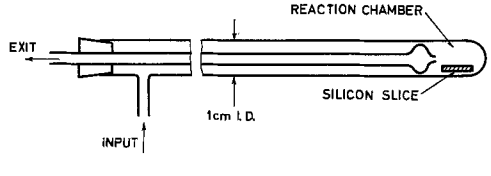

Fig. 1. Quartz reaction chamber

[1] Present address: Department of Physics, University of Tennessee, Knoxville, Tennessee.

corrected to standard conditions (cc sec^{-1} at 25°C and 760 mm Hg).

In the range of about 0.2 cc sec^{-1} to several cc sec^{-1} the flow control and reproducibility were better than ±5%. At flow rates below about 0.2 cc sec^{-1} the reproducibility degenerated rapidly. Therefore, at very low flow rates a motor-driven oil piston pump was used. In this way, a known volume of helium was pumped through the reaction chamber in a given time. The flow rate reproducibility was about ±10%.

A platinum-wound Heraeus furnace was used for heating. The furnace profile was flat to ±2°C for more than the length of the reaction zone. The temperature was stable to about ±2°C for the duration of the runs, usually about ½ hr. The control thermocouple was mounted adjacent to the furnace windings, and the measurement thermocouple was in contact with the end of the reaction chamber. A rather high activation energy was found for the reaction. Consequently the rate will be quite sensitive to the temperature variations, and this may be one of the sources of the scatter in the data.

The silicon slices were cut to a (111) orientation (±0.5°). They were then mechanically polished on both sides to a final thickness of about 0.5 mm. The final polish was with 1μ aluminum oxide. The slices were then waxed down and sawed to specified dimensions. The area figures used in subsequent calculations include both faces and the total edge area of these slices.

The etch rate of the reaction was determined by weight loss measurements on a microbalance. Blank weight loss runs were made with helium alone. The blank weight losses were consistently lower than 3% of the smallest weight losses produced by the reaction, so this correction was disregarded.

The downstream deposit in the cooler portion of the system was silicon, with no evidence of polymeric formation.

Mathematical Analysis

We assume complete mixing in the reactor volume. For this condition, where mixing is very rapid compared to the rate, the composition will be uniform throughout the reaction volume and equal to the output composition. This is of course a limiting condition, but it is apparently fulfilled in the reaction chamber used here as is later shown in the discussion of the results. For this condition the depletion rate of $SiCl_4$ in the reaction chamber is

$$-\frac{dm_4}{dt} = v_o\,(\rho_4^o - \alpha\rho_4) \qquad [5]$$

where m_4 is the weight of the incoming $SiCl_4$ vapor, ρ_4^o the density of $SiCl_4$ in the incoming gas, ρ_4 the density of $SiCl_4$ in the reaction chamber, and v_o the flow-rate of the unreacted gas mixture. α is a correction for gas expansion produced by the chemical reaction and is equal to $(1 + P_4^o)/(1 + P_4)$, where P_4^o is the $SiCl_4$ pressure in the incoming gas and P_4 the $SiCl_4$ pressure in the reaction chamber. Equation [5] may be rewritten as

$$-\frac{dm_o}{dt} = -\frac{M_0}{M_4}\frac{dm_4}{dt} = \frac{M_0}{M_4}v_o\,(\rho_4^o - \alpha\rho_4) \qquad [6]$$

where m_o is the weight of the silicon sample, M_0 the atomic weight of Si, and M_4 the molecular weight of $SiCl_4$. Combined with the postulated rate expression which may be written

$$\frac{1}{A}\frac{dm_o}{dt} = -k_1P_4^n + k_2P_2^{2n} \qquad [7]$$

where A is the total surface area of the sample we get

$$\frac{1}{A}\frac{M_0}{M_4}v_o\,(\rho_4^o - \alpha\rho_4) = k_1P_4^n - k_2P_2^{2n} \qquad [8]$$

For $P_4^o = 0.1$ atm and P_4 equal to the equilibrium value at 1170°C α is equal to 1.023. This is larger than any value applicable to our experimental conditions and consequently we drop the α term at this point. At larger values of P_4, the α term can of course become significant. For $\alpha = 1$ we have

$$P_2 = 2(P_4^o - P_4) = 2\,\Delta P_4$$

Inserting this in Eq. [8] and converting the ρ_4 term to P_4 dimensions by multiplication with M_4/RT we get

$$\frac{v_o}{A}\frac{M_0}{M_4}\frac{M_4}{RT}\Delta P_4 = k_1P_4^n - k_2(2\,\Delta P_4)^{2n}$$

or

$$\frac{v_o}{A}\frac{M_0}{RTk_1} + \left(\frac{4}{K}\right)^n(\Delta P_4)^{2n-1} = \frac{P_4^n}{\Delta P_4} \qquad [9]$$

where K is the equilibrium constant $= P_2^2/P_4 = (k_1/k_2)^{1/n}$. It is significant that for conditions where complete mixing obtains the reactor volume is not one of the system variable or constants.

The derivation ignores the "back-streaming" effect which often can introduce an error at low flow rates. The form of this correction was derived by Merten (12) and used by Thurmond and Frosch (13). We have checked the weight loss from the reaction in our system at zero flow and found it to be about the same magnitude as the blank weight loss. This was done by first blowing $SiCl_4$ through the system for 3 min to insure that a steady-state condition was established. Then the system was closed and allowed to stand at the reaction temperature for 1 hr. The system was then quickly purged with helium and the weight loss measured. After subtracting the calculated weight loss for the first 3 min (obtained from data in other runs) the difference is then due to back-streaming.

Results and Discussion

Evaluation of n.—P_4, the ambient $SiCl_4$ pressure in the reaction chamber, can be determined from the flow rate, the initial $SiCl_4$ pressure P_4^o, and the silicon weight loss by using the equation for the material balance

$$\Delta P_4 = -\frac{1}{v_o}\frac{dm_o}{dt}\frac{RT}{M_0} \qquad [10]$$

where $-dm_o/dt$ is set equal to the weight loss of the sample divided by the time for the experiment. We use these values to construct Fig. 2, which is a log-log plot of etch rate *vs.* P_4. This neglects the second right hand term of Eq. [7]. A straight line can be drawn through the high flow rate points, with a slope of $n = 0.49 \pm 0.01$ in agreement with Monchamp *et al.* Figure 2 is based on nine runs made at a reaction temperature of 1170°C and $v_o/A \geq 3$ cm/sec. The straight

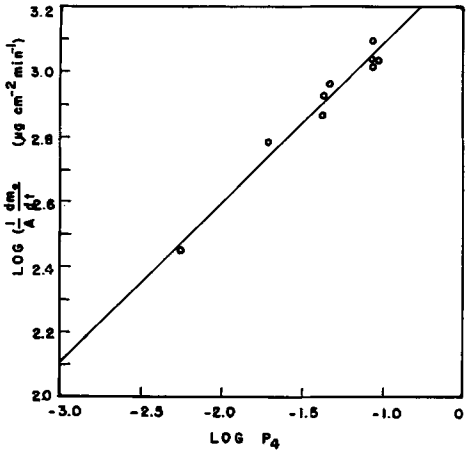

Fig. 2. Etch rate in g Si per cm^2 per min *vs.* the $SiCl_4$ pressure. In log-log plot the slope is equal to the exponent *n*.

line shows that one can neglect the second term in Eq. [7] for the high flow rate experiments. The low flow rate data points can lie far from the line. The validity of the above procedure is further supported by Fig. 5 which will be discussed later.

Evaluation of k_1.—For the special case on $n = 0.5$ Eq. [9] simplifies

$$\frac{v_o}{A}\frac{M_0}{RT}\frac{1}{k_1} + \left(\frac{4}{K}\right)^{1/2} = \frac{P_4^{1/2}}{\Delta P_4} \qquad [11]$$

In Fig. 3 we have plotted $P_4^{1/2}/\Delta P_4$ *vs.* v_o/A for the 1170°C data. The slope of the line is M_0/RTk_1 and the intercept at $v_o/A = 0$ is $2K^{-1/2}$, so that we can determine both the rate constant k_1 and the equilibrium constant K. (k_1 can also be determined from Fig. 2 and checks within 3%). The lower curve is a least-squares fit to 39 runs. The reaction chamber volume was from 1.5 to 4 cc for this group. The upper curve is for three additional runs at 6 cc volume. For these runs the volume was large enough to invalidate the complete mixing assumption, and to produce an apparently lower rate constant. For the remainder of the runs at other temperatures the reactor volume was kept small enough to be in the complete mixing range and no dependency on the volume was observed.

Schäfer and Nickl (8) give 0.050 (in atm) for the 1170°C equilibrium constant. From Fig. 3 we find a value of 0.035 ± 0.015 which is in tolerably good agreement with Schäfer and Nickl's result.

The slope of the lower curve in Fig. 3 yields a value of $k_1 = 79 \times 10^{-6}$ g Si cm^{-2} sec^{-1} $atm^{-1/2}$ which is about five times as large as the k_1 value calculated at 1170°C from Monchamp's rate expression.

Runs similar to those previously described were made at reaction temperatures of 1000° and 1080°C. For each reaction temperature a least squares plot as shown in Fig. 3 was made. Since the slope is M_0/RTk_1, the rate constant k_1 at each temperature can be determined. The intercept in each case was again $2K^{-1/2}$. For these temperatures, K was in closer agreement with Schäfer and Nickl's result.

The three values of k_1 are plotted *vs.* reciprocal temperatures in Fig. 4. The activation energy is found to be 67 ± 7 kcal $mole^{-1}$, which gives

$$k_1 = 1.0 \times 10^6 \exp\left(-\frac{67000}{RT}\right) \text{ g Si } cm^{-2}\ sec^{-1}\ atm^{-1/2} \qquad [12]$$

This activation energy is even higher than that reported by Monchamp *et al.* Both Monchamp and Heinecke have indicated that for flow system measurements they found a very low apparent activation energy, about 5 kcal in the case of silicon (5). We are unable to account for the great difference between their flow system data and ours. We would expect the apparent activation energy to be lower in the closed system where the mass transport is limited in part by diffusion and convection currents in the gas phase. This could account in part for the difference between 49 kcal reported for a closed system by Monchamp and the 67 kcal found in the present work for an open flow system.

Calculation of k_2.—One cannot, of course, derive the rate expression from the equilibrium constant directly. However, if the rate expression is correctly formulated in Eq. [4], we can calculate k_2 and its activation energy from the data available at this point. At equilibrium

$$k_1 P_4^{1/2} = k_2 P_2 \qquad [13]$$

and $k_2 = k_1 K^{-1/2}$. We have found both k_1 and K as functions of temperature, but since our value of the equilibrium constant is in agreement with Schäfer and Nickl's and the latter is determined with more accuracy we have used their value for calculating k_2, *i.e.*, we use

$$K = 1.21 \times 10^{10} \exp\left(-\frac{75000}{RT}\right) \text{ atm}$$

Therefore by use of Eq. [12] we can go directly to

$$k_2 = 9.0 \exp\left(-\frac{29000}{RT}\right) \text{ g Si } cm^{-2}\ sec^{-1}\ atm^{-1} \qquad [14]$$

and the complete rate expression

$$\frac{1}{A}\frac{dm_o}{dt} = -1.0 \times 10^6 \exp\left(-\frac{67000}{RT}\right) P_4^{1/2} + 9 \exp\left(-\frac{29000}{RT}\right) P_2 \text{ g Si } cm^{-2}\ sec^{-1} \qquad [15]$$

The two activation energies are consistent with the H value for the reaction as calculated from the heats of formation of the dichloride and of the tetrachloride.

Flow rate dependency.—Rearrangement of Eq. [11] gives

$$\Delta P_4 = \frac{k_1 P_4^{1/2}}{2k_2 + v_o M_0/ART} \qquad [6]$$

Figure 5 illustrates the etch rate, stated as weight loss per cc of gas, as a function of the v_o/A parameter. The solid line is calculated from Eq. [16] (Recall that $1/v_o \times dm_o/dt$ is proportional to ΔP_4, Eq. [10]) for a reaction temperature of 1170°C and P_4^o equal to 0.045 atm. The broken line is calculated using only the $k_1 P_4^{1/2}$ term from Eq. [7]. For low flow rates the curve is too high and approaches complete reaction rather than the equilibrium value. For $v_o/A \geq 3$ cm/sec one is allowed to disregard the second term in Eq. [15].

By inserting Eq. [10] in Eq. [16] we get

$$-\frac{dm_o}{dt} = \frac{k_1 P_4^{1/2}}{\frac{1}{A} + 2k_2\frac{RT}{M_0}\frac{1}{v_o}} \qquad [17]$$

or

$$-\frac{1}{A}\frac{dm_o}{dt} = \frac{k_1 P_4^{1/2}}{1 + 2k_2\frac{RT}{M_0}\frac{A}{v_o}} \qquad [18]$$

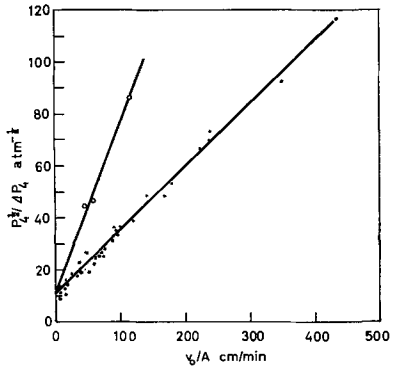

Fig. 3. Data plot based on Eq. [11] for determination of k_1

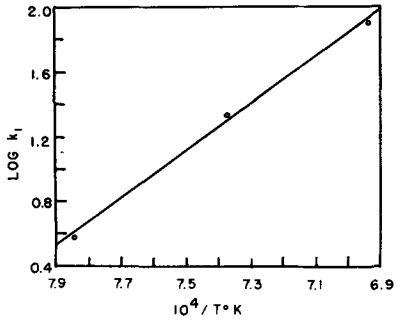

Fig. 4. Temperature dependence of k_1

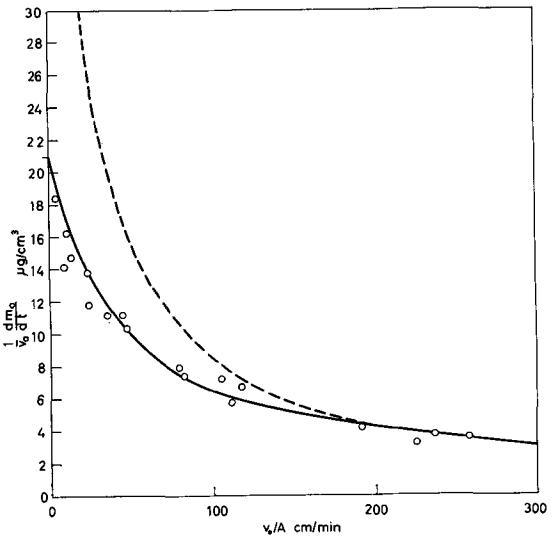

Fig. 5. Etch rate in g Si per cc of the gas *vs.* the flow rate divided by the sample area.

At sufficiently low flow rates Eq. [18] gives

$$-\frac{1}{A}\frac{dm_o}{dt} \cong \frac{M_0}{RT}\frac{k_1}{2k_2}\frac{v_o}{A}P_4^{1/2} = \frac{M_0}{RT}\left(\frac{K}{4}\right)^{1/2}\frac{v_o}{A}P_4^{1/2} \quad [19]$$

At high flow rates

$$-\frac{1}{A}\frac{dm_o}{dt} \cong k_1P_4^{1/2} \cong k_1P_4^{o1/2} \quad [20]$$

By plotting $1/A$ x dm_o/dt *vs.* v_o/A as with Eq. [19] and [20] one gets a curve with asymptotes in 'both ends.' From the asymptotes one can calculate k_1 and K. However the low flow rate region often is so small that the asymptote is determined with a high uncertainty.

Equation [17] and Eq. [18] are consistent as to asymptotes. However if one uses samples of different area, it is seen from Eq. [17] that one cannot get a curve in the intermediate region by plotting dm_o/dt *vs.* v_o. We see that the flow dependency is expressed by the ratio v_o/A rather than by v_o.

The dimensions of v_o/A are cm/sec, a linear velocity, but should not be construed as being the actual linear velocity of the gas in the system, since the area is that of the sample and not the cross section of the reactor. Mathematical normalization to unit area, introduced in Eq. [7] leads to the v_o/A form.

General comments.—The temperature measurement of the reaction chamber is done with a thermocouple placed outside the reaction chamber. Because of the possibility of a temperature difference between the outside and inside of the reaction chamber there may be a systematic error in the temperature measurement. There are different sources of error. The incoming gas may not be sufficiently warm. As mentioned previously this was the case when the gas was let in through the narrow inner tube. When we use the outer tube the temperature profile in the furnace is so flat that the gas obtained the right temperature at all flow rates. This can be seen by the following argument. If the gas temperature is lower than the stated reaction temperature, the temperature difference will increase with increasing flow rate as the time of heat transfer per cc of gas from the wall will decrease. Consequently for two "identical" experiments, where v_o/A is the same but v_o is different, we should get a lower etch rate for the experiment at higher flow rate. This is not observed within the experimental uncertainty. Another source of error could be the heat of the reaction. Also, an error may appear since there may be a temperature difference between the gas and the furnace walls. In fact some later experiments carried out in a quite different system gave etch rates that all were 10% higher than those given here. It may be explained by the two last sources of error. Including these experiments in the calculations would change k_1 about 15% and K about 40%, whereas n would be unchanged. These figures may indicate the uncertainty of the experiments.

Comparing our results with those of Monchamp *et al.* we see that the n-value is the same whereas we get different values for the activation energy of k_1. The difference is so large that it cannot be explained by an error in our temperature measurement. We believe it more likely that Monchamp's etching is partly diffusion limited. This is the case for our experiments with the large reaction chamber as shown in Fig. 3 (upper line). The value of k_1 is lower but the value of n is still 0.5.

Another difference between Monchamp's and our results is that we in the rate expression use the actual pressures of $SiCl_4$ and $SiCl_2$ in the reaction chamber, whereas Monchamp apparently uses the initial pressure P_4^o or an over-all pressure $P_4 + P_2$. However this cannot explain the difference in our k_1 values.

The high activation energy for the etching reaction and the fractional order of the reaction imply that the rate limiting step is surface adsorption or desorption as suggested by Monchamp *et al.* In this case we would expect to see a relationship to the surface roughness factor. However no difference in etch rate was observed on chemically polished and on lapped samples. In most of the runs, the total thickness reduction was about 250μ. Consequently the initial roughness produced by different surface treatments would be smoothed out early in the runs, and the roughness variation could be hidden, along with other experimental variables, in the standard deviation. There was no detectable rate difference between the (111), (110), and (100) planes. Also, there was no noticeable preferential development of crystal faces near the edges or corners of the samples. On the other hand if the rate-limiting step is surface adsorption or desorption, one would expect n to vary with pressure, which is not found in the pressure region used.

Acknowledgments

The authors wish to thank Mrs. I. Lund and Mr. S. Mathiesen for preparing the samples and assisting with the runs; C. D. Thurmond and N. I. Meyer for helpful discussion: the Bell Telephone Laboratories and Haldor Topsøe for contributing the materials used in the work.

Manuscript received July 27, 1964; revised manuscript received Oct. 28, 1964. This paper was abstracted in part from one submitted in partial fulfillment of the requirements for the Lic. Techn. degree by one of the authors (O.A.) and the work was supported in part by grants from the United States Educational Foundation in Denmark and from the American Scandinavian Foundation in New York.

Any discussion of this paper will appear in a Discussion Section to be published in the December 1965 JOURNAL.

REFERENCES

1. W. Steinmaier, *Philips Research Repts.*, **18**, 75 (1963).
2. E. G. Bylander, *This Journal*, **109**, 1171 (1962).
3. R. C. Newman and J. Wakefield, *ibid.*, **110**, 1068 (1963).
4. H. Basseches, R. C. Manz, C. O. Thomas, and S. K. Tung, in "Proceedings of the AIME Technical Conference on the Metallurgy of Semiconductor Materials," Interscience Publishers, New York (1962).
5. R. R. Monchamp, W. J. McAleer, and P. I. Pollack, *This Journal*, **111**, 877 (1964).
6. J. J. Grossman, *ibid.*, **110**, 1065 (1963).

7. N. Kyle and J. J. Grossman, Paper presented at New York Meeting of the Society, Oct., 1963.
8. H. Schäfer and J. Nickl, *Z. anorg. u. allgem. Chem.*, **274**, 250 (1953).
9. H. Schäfer, *ibid.*, p. 265.
10. W. J. Heinecke and S. Ing, *J. Appl. Phys.*, **32**, 1498 (1961).
11. A. I. M. Keulemans, "Gas Chromatography," pp. 56-57, Reinhold Publishing Co., New York (1957).
12. U. Merten, *J. Phys. Chem.*, **63**, 443 (1959).
13. C. D. Thurmond and C. J. Frosch, *This Journal*, **111**, 184 (1964).

LIST OF SYMBOLS

A surface area of the sample.
α correction factor to account for the volume expansion in the reaction chamber.
K equilibrium constant $= P_2^2/P_4$.
k_1,k_2 rate constants, associated with P_4 and P_2, respectively.
M_0 atomic weight of Si.
M_4 molecular weight of $SiCl_4$.
m_o weight of Si sample.
N_o number of Si atoms in the sample per unit surface area.
P_4^o $= P^o_{SiCl4} = SiCl_4$ pressure in the incoming gas.
P_4 $= P_{SiCl4} = SiCl_4$ pressure in the reaction zone.
P_2 $= P_{SiCl2} = SiCl_2$ pressure in the reaction zone.
ΔP_4 $= P_4^o - P_4$.
R gas constant.
ρ_4^o density of the incoming $SiCl_4$.
ρ_4 density of $SiCl_4$ in the reaction chamber.
T absolute temperature.
t time (sec).
v_o flowrate of the incoming gas mixture (cc/sec) corrected to 298°K and 1 atm.

Localized Enhanced Diffusion in NPN Silicon Structures

R. Gereth, P. G. G. van Loon, and V. Williams

ITT Semiconductor, Shockley Laboratory, Palo Alto, California

ABSTRACT

Extensive studies of the Emitter Dip Effect (EDE) in npn silicon structures are reported. Typically, 1 ohm-cm n-type silicon starting material was used. Boron diffusion into this material resulted in a 0.7μ base depth and surface concentrations of 1.8 x 10^{20} cm^{-3}. The emitter regions had surface concentrations of 3 x 10^{20} cm^{-3} and 0.4μ junction depths. The dip was typically 0.3μ, *i.e.*, the base penetrated 0.3μ deeper under the emitter than elsewhere. Important experimental findings are: (*A*) Crucible grown, zone refined, and epitaxial silicon give the same results. (*B*) The EDE occurs only if phosphorus doping is sufficient to overcompensate the base doping. (*C*) Multiple emitter diffusion causes multiple dips. (*D*) Slow cooling from diffusion temperature enhances the dip. (*E*) An enhanced boron diffusion constant in the base layer apparently causes the dip rather than the rejection of boron by the region of high phosphorus concentration. (*F*) The dip is not present for lightly doped (10^{17} cm^{-3}) base layers.

Localized enhanced diffusion of the base collector junction underneath the emitter regions has been observed in double diffused high-frequency transistors (1-3). This phenomenon is often referred to as Emitter Dip Effect (EDE). Not very much attention has been given to the EDE in the relevant literature during recent years. This was mainly due to lack of reproducibility complicating the study of the EDE and its theoretical explanation. The EDE was first reported by Miller (1), who described the phenomenon and suggested the possibility that the effect was caused by impurity interactions such as published by Reiss *et al.* (4) for lithium in germanium. Later, the EDE was discussed by Baruch and co-workers (2). Based on a vacancy enhanced diffusion mechanism they developed an hypothesis which partially explained the EDE observed in a npn structure made with gallium base diffusion.

The earliest work which was done in the course of the investigation reported here was concerned with the reproducibility of the effect. Previously, the EDE had been observed only sporadically and was found to be connected in some way with the time and temperature of predeposit of both the base and the emitter dopants, subsequent diffusion and oxidation steps, and operator technique, as well as general cleanliness of the furnaces. After a schedule had been found which gave reproducible results from run to run, intensive studies were made to establish the experimental conditions for the creation of the EDE. Most emphasis was put on a shallow diffused silicon npn transistor. The experiments were extended later to pnp structures.

Experimental Results

Starting material and standard diffusion schedule.— The starting material used in the majority of the experiments was n^-n^+ epitaxial material obtained from Merck, Monsanto, Allegheny, and Texas Instruments. The vapor grown n^- silicon film was about 10μ thick and had a resistivity of 1 ohm-cm, corresponding to a carrier concentration of 5 x 10^{15} cm^{-3}. The resistivity of the n^+ substrate ranged from 0.002 to 0.04 ohm-cm. The same results were obtained when experiments were carried out using crucible grown silicon material of equivalent doping level. The schedule which was followed in most of the work is described below and illustrated in Fig. 1.

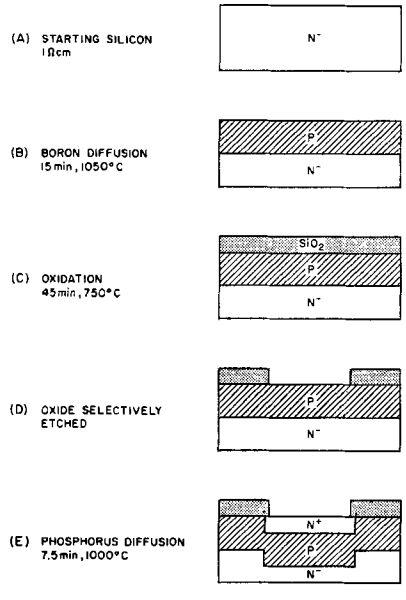

Fig. 1. Processing steps for fabrication of shallow diffused npn silicon structures.

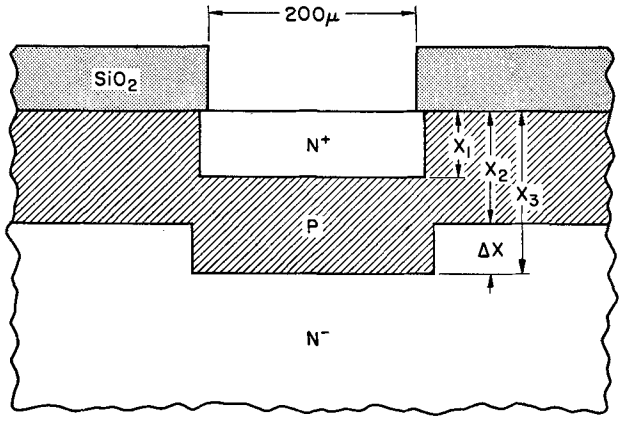

Fig. 2. Schematic drawing of a beveled cross section through npn structure exhibiting the EDE (note the different scale in horizontal and vertical direction). Standard npn structure: $X_1 = 0.4\mu$; $X_2 = 0.7\mu$; $X_3 = 1.0\mu$; $\Delta X = 0.3\mu$.

After standard cleaning steps, the base was diffused in at 1050°C for 15 min using 1% diborane in hydrogen as the dopant source and dry nitrogen as the carrier. This procedure gave a junction depth of 0.7μ and a surface concentration of 1.8×10^{20} cm^{-3}. Following the base diffusion a surface layer of silicon dioxide was grown by means of the thermal decomposition of ethyl silicate (5) in vacuum at 750°C for 45 min. Emitter windows were then opened in this oxide layer. The emitter regions were produced by diffusion of phosphorus at 1000°C for 7.5 min. The diffusion source was P_2O_5 at a temperature of 240°C; the ambient was dry nitrogen.

Beveling and staining the slice following the emitter diffusion revealed the "standard" EDE. An enlarged illustration of the EDE is shown in Fig. 2. For the purpose of this paper, certain distances have been defined as noted in Fig. 2. The emitter base junction depth is defined as X_1, the base collector junction under the oxide as X_2, and the base collector junction under the emitter as X_3. It can be seen that the magnitude of the dip is equal to $X_3 - X_2 = \Delta X$. The distances X_3, X_2, and ΔX are independently measurable and since $X_3 - X_2 = \Delta X$, a check is provided for the value of ΔX. Another advantage of the schedule is that comparatively low temperatures are involved. At temperatures in the range of 1000-1050°C, complicating factors such as thermal diffusion, outdiffusion through the open windows, and diffusion into the oxide mask during the time involved are minimized.

Influence of emitter diffusion on EDE.—Having established a schedule which reliably produced the EDE,

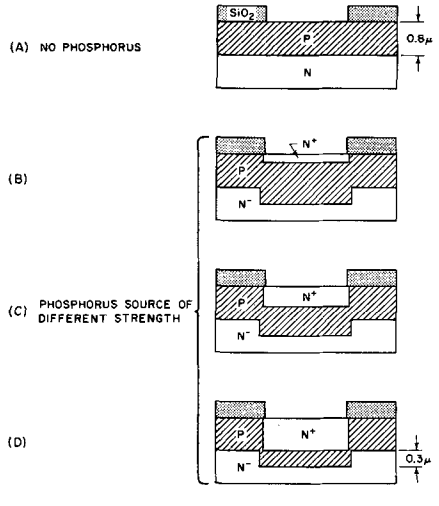

Fig. 3. Emitter dip as a function of emitter junction depth; heat treatment, 15 min, 1000°C.

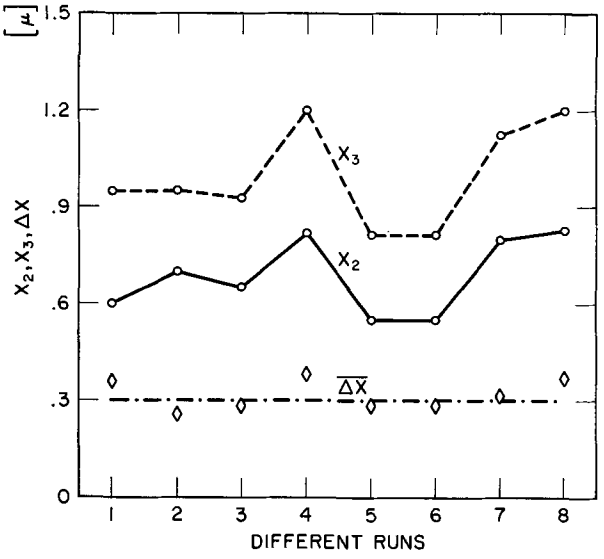

Fig. 4. Observed scatter of X_2, X_3, and ΔX over eight repeated experiments. Emitter diffusion time was 7.5 min. ◇, $\Delta X = X_3 - X_2$.

the influence of the emitter diffusion on the EDE was investigated. It was shown that the presence of a phosphorus doped emitter was necessary to produce the EDE. A dip was never observed unless staining revealed n-type doping in the emitter window. The magnitude of the EDE, however, was independent of the phosphorus concentration above that necessary to produce an emitter. If windows were opened in the oxide over the base layer and the slice diffused for periods of time up to 15 min at 1000°C in a clean tube, no dip was observed. In contrast to this observation, it was found that appreciable outdiffusion of boron occurred if material with opened windows was diffused at 1100°C for 20 min in a clean tube. This outdiffusion resulted in a reverse dip. The experiment also showed that diffusion of boron into the oxide which could result in the EDE did not play an appreciable role at 1000°C.

Deliberate variation in the emitter concentration was obtained by aging a P_2O_5 source for 15 min and then removing it. Doping of the silicon material was then a result of residual P_2O_5 in the tube. In all cases the extent of the dip was 0.3μ, within the limits of experimental error. This observation is in contradiction to earlier findings (1). Figure 3 illustrates our observations. In all cases, the base was the result of the standard diffusion, and the heat treatment thereafter

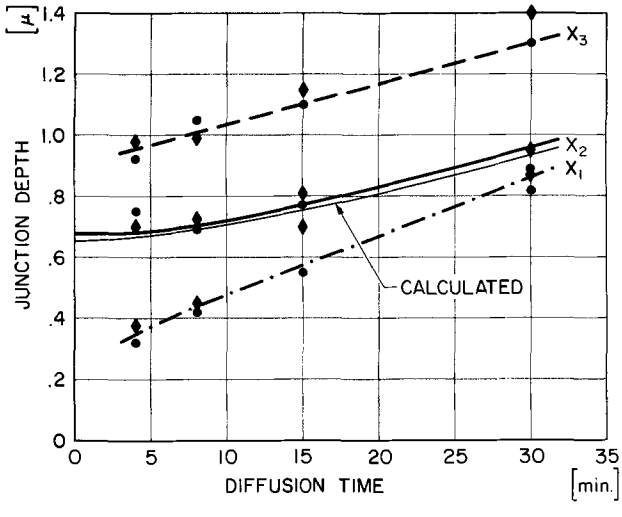

Fig. 5. Junction depths X_j ($j = 1, 2, 3$) as a function of emitter diffusion time. X_j's are defined in Fig. 2; ●, operator A; ◆, operator B.

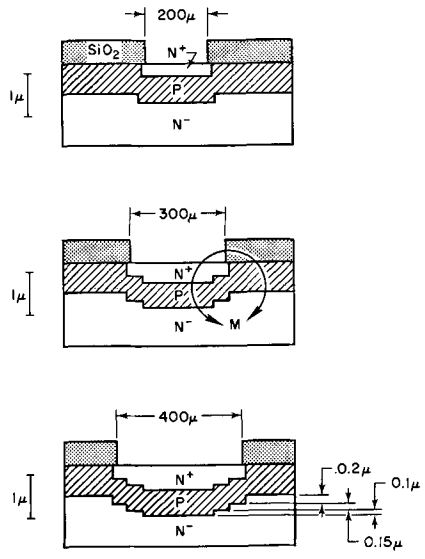

Fig. 6. Multiple EDE caused by multiple emitter predeposition steps.

was for 15 min at 1000°C in a nitrogen ambient. The magnitude of the EDE is seen to remain constant although the emitter junction depth increases with source strength.

Additional studies of the effect of the phosphorus emitter doping level on the EDE are plotted in Fig. 4 and 5. The scatter of X_2, X_3, and ΔX observed over eight repeated experiments are presented in Fig. 4. The emitter diffusion time was 7.5 min, all other parameters were maintained constant. Although the magnitude of X_2 varies, ΔX stays nearly constant with an average value of 0.3μ. Figure 5 shows the junction depths as a function of phosphorus emitter diffusion time. The data represent average values obtained by operators A and B. The average value of ΔX is again 0.3μ. The diffusion of the base collector junction under the oxide X_2 is in good agreement with the calculated values using the boron diffusion constant as published by Fuller and Ditzenberger (6). Of interest is the finding that the dip seems to be produced almost instantaneously. Only in phosphorus diffusion times of less than 2 min was the dip found to decrease in magnitude. This decrease can be attributed, however, to insufficient time for the slice to reach the temperature of the furnace. Further evidence for the observation that the dip is formed in time intervals which are short compared to the over-all diffusion times at 1000°C was provided by an experiment illustrated in Fig. 6. A 200μ wide window was opened in the oxide coating of a slice which contained the standard base. An emitter was then predeposited for 4 min at 1000°C. Following this treatment, the window was widened. The slice was returned to the diffusion furnace for another 4 min. The window was again widened, and the slice was predeposited for a final 4 min. Beveling and staining the material revealed a dip after each diffusion. The initial dip was 0.2μ in this particular slice, and each successive predeposit produced a dip although it became smaller. It should be pointed out that the total EDE produced by the triple phosphorus predeposition steps of 4 min each is 50% larger than that found as a result of a single 12 min emitter diffusion. The base under the oxide remained constant at 0.7μ throughout the experiment. Figure 7 is a microphotograph revealing the "true structure" of a small section labeled "M" in Fig. 6.

Variation of base layer.—Most of the work discussed above was done on material containing a 0.6-0.7μ deep base layer. The surface concentration of acceptors in this material as determined by four-point probe measurements was 1.8×10^{20} cm^{-3}.

An obvious experiment was the determination of the effect of a thicker base layer. The standard silicon epitaxial material was diffused in diborane at 1050°C for 2, 16, and 64 hr. The base collector junction in this material was 2.5, 3.9, and 6μ, respectively. After oxide growth and 7.5 min of phosphorus diffusion at 1000°C an EDE of approximately 0.3μ was visible in the material containing the 2.5μ base. A slight rounding was visible under the emitter of the material containing the 3.9μ base. No EDE was visible in the 6.0μ base layer. The dip in the 3.9μ base material was not reproducible.

Figure 8 is an illustration of another experiment done to determine what influence the base concentration has on the EDE. As described above, a pyrolytic oxide (5) was grown on material which had been diffused in diborane at 1050°C for 2 hr. After opening emitter windows, part of the base layer was etched away in the emitter windows. Subsequently, the slice was predeposited in the P_2O_5 furnace at 1000°C for 4 and 8 min, respectively. No dip was visible. Details of this experiment are illustrated in Fig. 8. From this experiment it was concluded that the EDE occurred only when phosphorus was predeposited in material containing relatively high acceptor concentration levels. The concentration of the boron acceptors in the "tail end of the diffusion" is apparently too low to produce a dip.

Using a series of epitaxially deposited base layers (7) of different doping concentrations, the influence of the base doping level on the EDE was investigated. The substrate was 1 ohm-cm n-type silicon in all cases. The results are summarized in Table I. Only the heavily doped epitaxial layers show the EDE. Run 1 was re-

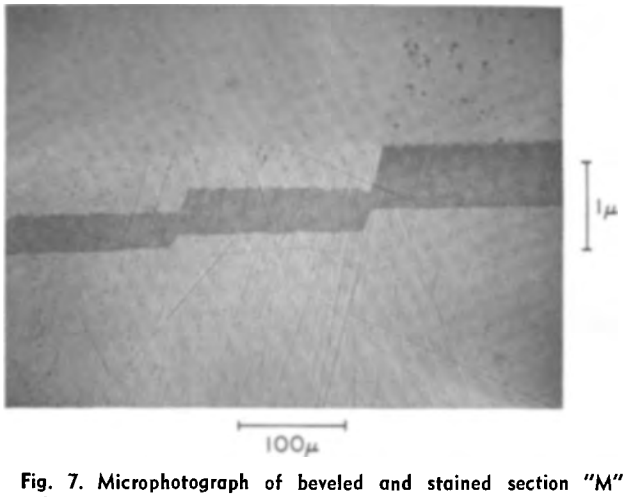

Fig. 7. Microphotograph of beveled and stained section "M" as schematically illustrated in Fig. 6.

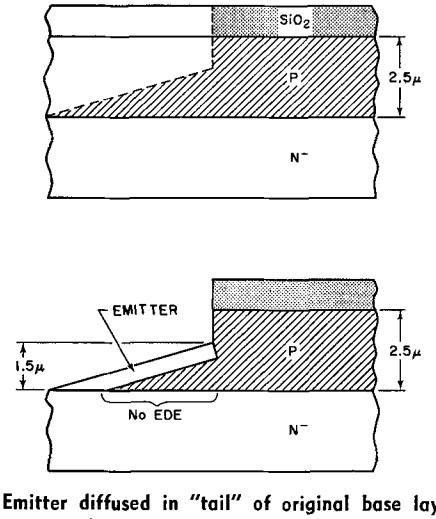

Fig. 8. Emitter diffused in "tail" of original base layer. Dotted line in the upper drawing indicates how the structure was etched prior to emitter diffusion.

Table I. EDE experiments performed with epitaxial base layers. The phosphorus emitter diffusion was carried out at 1000°C for 7.5 min. X_2 and ΔX are defined as shown in Fig. 2

Run	Boron concentration, cm^{-3}	X_2, μ	ΔX, μ
1	1.3×10^{17}	0.6	0
2	1.0×10^{18}	0.9	0
3	3.0×10^{18}	0.9	0.1
4	1.2×10^{19}	0.9	0.15

peated with a silicon slice which had the identical starting epitaxial base layer. Prior to the emitter diffusion, however, a shallow p^+ layer (approximately 0.3-0.4μ deep) was formed in the regions of the emitter windows by exposing the slice at 1050°C for 4 min to a diborane nitrogen gas stream as described earlier. No EDE was found in this slice after the subsequent emitter diffusion (7.5 min at 1000°C). This last experiment clearly demonstrates that it is the magnitude of the base concentration in the region of the base collector junction as opposed to the surface concentration which is important for the formation of the EDE. The influence of the base surface concentration is only indirect since it obviously determines the impurity profile in the diffused base layer and thus the concentration in the vicinity of the base collector junction.

Cooling rate and EDE.—Baruch (2) observed a drastic influence of the cooling rate on the EDE. He reported an increase of the magnitude of the dip by a factor of 2 in a silicon slice containing a gallium doped base and phosphorus doped emitter when the slice was cooled at the rate of 5°C/min and not quenched. With this idea in mind, the following experiment was carried out. Two slices containing the standard base were diffused at 1000° in a phosphorus predeposit furnace. After 7.5 min, one slice and the P_2O_5 source were removed from the furnace. The other slice remained in the furnace. On removal of the phosphorus source, the furnace temperature was allowed to drop at an average rate of 3°C/min from 1000 to 680°C; the slice was then taken out of the furnace and quenched to room temperature. It was found that the EDE in the material which served as the reference slice was the standard one ($\Delta X = 0.3\mu$). On the other hand, the EDE in the slowly cooled material was 0.5μ. The depth of the base under the oxide was exactly the same in both slices. The experiment was done several times and close agreement between runs was found. Part I of Fig. 9 illustrates the effect.

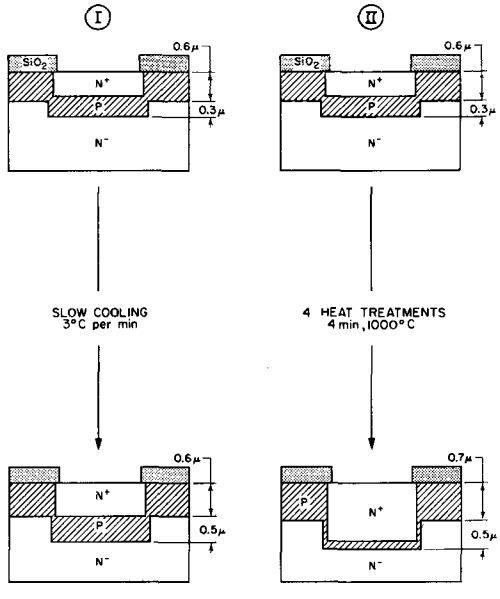

Fig. 9. Influence of heat treatments on standard EDE

Another interesting result was obtained when a slice exhibiting the standard EDE ($\Delta X = 0.3\mu$) was given 4 heat treatments at 1000°C. Each heat treatment was of 4 min duration and was done in a clean furnace without phosphorus source present. After each heating step the slice was rapidly taken out of the diffusion furnace and quenched to room temperature. The time required for removal and cooling was 10-11 sec. Part II of Fig. 9 shows the influence of the heat treatments on the EDE. The total heating time of 16 min during which the slice had been in the hot zone of the furnace, caused a slight movement of the base collector junction underneath the oxide (X_2 changed from 0.6 to 0.7μ) and a strong inward diffusion of the phosphorus atoms forming the emitter region. The dip in the base collector junction was also increased. However, after the four heat treatments it approached the same value of 0.5μ as was found in the "slow cooling" process described above. This observation shows for the first time that the EDE can be influenced by a simple heat treatment without an external phosphorus source.

In the subsequent experiment the function of the emitter in producing the EDE was explored. The EDE was produced following the standard procedure. One half of the slice was treated for 45 sec in an etch which removed the emitter region while leaving the oxide and base layer intact. Both halves were then cooled from 1000 to 700°C over a period of 2 hr in a clean tube without source. It was found that the dip had increased from about 0.2 to 0.4μ in the slice containing the emitter whereas the EDE remained constant at about 0.2μ in the slice from which the emitter region had been removed.

After it was found that the rate of cooling was important in the formation of the EDE, an attempt was made to determine the effect of rapid cooling. The average time required to remove a slice from the phosphorus diffusion furnace was 11 sec. A modification in procedure resulted in decreasing this time to about 1 sec. Phosphorus diffusion for 4 min at 1050°C into silicon containing the standard base followed by this rapid cooling resulted in a 27% decrease in the dip as compared to a slice cooled at the ordinary rate.

Determination of concentration profiles[1].—All results on the EDE described thus far were obtained from cross section evaluation of diffused npn structures. In

[1] This Section was partly supported by Contract No. AF 33(657)-11403.

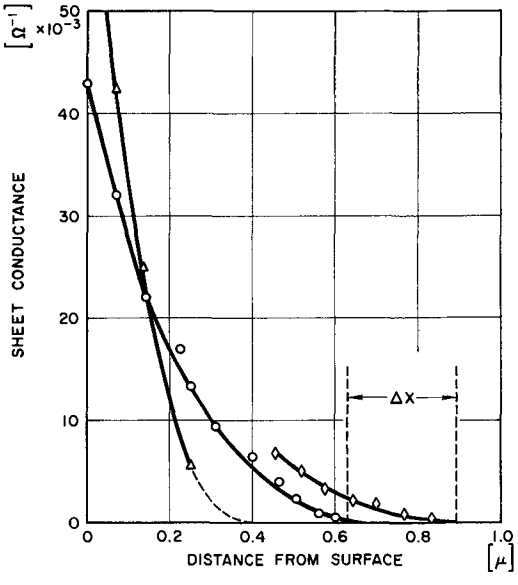

Fig. 10. Sheet conductance measurements as a function of distance from surface, ○, Base only; ◇, base under emitter; △, emitter.

order to gain more information on the EDE, the concentration profile in the standard test structure was determined using the technique of anodic sectioning (8). Two epitaxial silicon slices (n-type, 1 ohm-cm resistivity) were prepared. The first slice referred to as the "base only slice" contained the standard diffused base layer formed at 1050°C for 15 min as described in Fig. 1. The second slice referred to as the "base under emitter slice" contained the standard base plus a shallow phosphorus layer over the entire slice which was produced by a 4 min phosphorus diffusion step at 1000°C. This additional 4 min heat treatment at 1000°C was also applied to the first slice after the actual base diffusion; however, in this case no phosphorus source was present.

Each slice was anodically sectioned separately. The silicon was removed in increments of 0.05-0.06μ as determined by microbalance weighings. Sheet conductance calculations were made using the results of four point probe measurements (9). For further details of the method see paper by Tannenbaum (8). Figure 10 reproduces the experimental results. The sheet conductance is plotted as a function of distance from the surface. The "circles" correspond to the data obtained from the slice which contained only the base layer. In the second slice, the sheet conductance of the base (denoted by "diamonds" in Fig. 10) could be measured only after the emitter was removed. Since the emitter junction depth was 0.4μ, the first reliable sheet conductance measurement of the base underneath the emitter could be performed at a depth of 0.46μ. The emitter dip effect is clearly visible in Fig. 10 as the difference between the extrapolated base collector junction depths of the two slices. The junction depths as revealed by the sectioning procedure were in good agreement with those determined by staining.

The concentration profiles of the diffused boron base layers are plotted in the upper part of Fig. 11. These curves were prepared from Fig. 10 by determining the conductivity from the derivative of sheet resistance in respect to sectioning depth. The concentration of the boron atoms was then found by referring to Irvin's paper (10). The notation of Fig. 11 is the same as that of Fig. 10. The boron concentration as a function of distance from surface was calculated in steps of 0.05μ. At the surface, the boron impurities reach a concentration of 1.8×10^{20} cm^{-3}.

In addition to the measured profiles of the diffused boron layers in the two slices, the profile observed in a

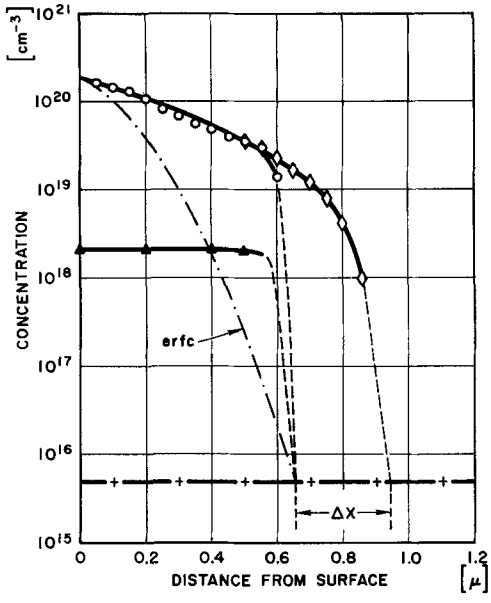

Fig. 11. Concentration profiles of diffused and epitaxial base layers: ○, base only; ◇, base under emitter; ▲, epitaxial base; +, collector (1 ohm-cm, n-type).

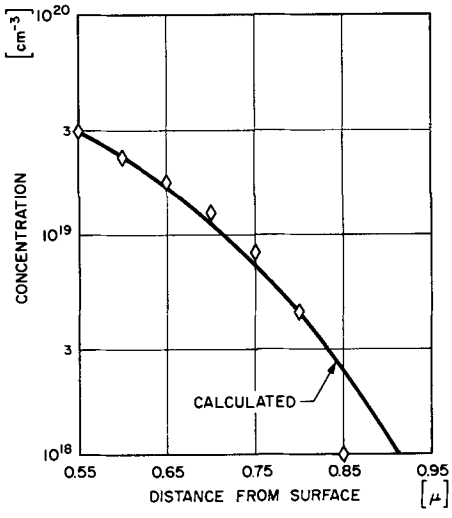

Fig. 12. Concentration profile in base layer of three layer npn structure. The emitter junction depth was 0.4μ deep. The calculated curve corresponds to an erfc distribution. ◇, Base under emitter.

control test specimen in an epitaxially grown base layer is shown; this indicates the precision of the technique. A theoretical erfc distribution for a diffused layer with a surface concentration of 1.8×10^{20} cm^{-3} and a junction depth of 0.65μ is shown for comparison with the two diffused slices.

The results of the concentration profile measurements illustrated in Fig. 11 suggest that (*a*) there is no pile up of boron impurities in the "base under emitter" slice directly in front of the phosphorus emitter (no "snowplow effect") and (*b*) the EDE is not caused by a normal thermal diffusion process. The fact that the snow plow effect is not operative is indicated by the identical curvature which both base layer sheet conductance curves (Fig. 10) exhibit at distances between 0.45 and 0.55μ.

At a depth of 0.6μ the concentration of the base in the "base only" slice drops off rapidly (see Fig. 11) while the profile of the "base under emitter" shows a more gradual decrease. This section of Fig. 11 is redrawn in Fig. 12. The experimentally obtained points are shown together with a calculated curve representing an ideal erfc distribution. This distribution is based on a model which is equivalent to the assumption that the flat concentration profile below 0.55μ in Fig. 11 acts as a constant concentration source leading to an erfc distribution as a function of depth beyond 0.55μ. This curve is shown in Fig. 11 with a "surface concentration" of 3×10^{19} cm^{-3} and $\sqrt{Dt} = (0.12 \pm 0.01) \times 10^{-4}$ cm, where D is the effective diffusion constant and t the time interval for the diffusion. The data of Fig. 12 allow the estimation of a minimum value for the effective D necessary to produce the EDE of Fig. 10. Earlier it was reported that the EDE is created during emitter predeposition steps as short as 3 min. Therefore from this maximum possible time a minimum value for D is given by

$$D_{\min} = \frac{1.44 \times 10^{-10}}{1.8 \times 10^{2}} = 8 \times 10^{-13}\ \text{cm}^2\ \text{sec}^{-1} \quad [1]$$

This value is 30 times larger than that published for normal boron diffusion at 1000°C by Fuller and Ditzenberger (6). The actual effective D may be much greater: The "slow cooling studies" reported earlier actually indicate that the EDE is formed while the slice is taken out of the diffusion furnace. This step normally requires from 10 to 11 sec. For this time which is about 18 times less than 3 min, the apparent diffusion constant which would govern the dip formation must then be at least 500 times larger than normal (6). These estimates clearly show that the EDE can-

not be explained by a normal thermal diffusion process.

Another interesting feature of the data plotted in Fig. 11 is the fact that the profiles of the two diffused base layers coincide at a distance of 0.5μ from the surface. This observation, together with results of spreading resistance measurements (3) underneath the emitter, seems to indicate that the EDE is caused by an enhanced diffusion only of the boron impurities present in the vicinity of the base collector junction prior to the emitter predeposition step. Since the concentration profile of the three layer npn structure could not be measured at distances smaller than 0.5μ from the surface, one might question the conclusion that both profiles coincide. This statement is based only on two measured values (at $x = 0.5\mu$ and $x = 0.55\mu$) and the over-all shape of the concentration curves. However, the following calculation shows that an enhanced movement of the boron atoms occurring throughout the entire base layer would have resulted in a profile differing so drastically from that observed, that it would not have been masked by lack of accuracy in the sheet conductance measurements.

The concentration $C(x)$ of the diffused base profiles of Fig. 11 can be represented in the range between $x_1 = 0.15\mu$ and $x_2 = 0.55\mu$ (x is distance from surface) by the following relation

$$C(x,t) = C(x_1) \exp \{-\alpha(x - x_1) + \beta t\} \quad [2]$$

α is the decay constant and is obtained from Fig. 10 as

$$1/\alpha = 0.28\mu \quad [3]$$

Since Eq. [2] is a solution of Fick's law, one finds that

$$\beta = \alpha^2 D \quad [4]$$

where D is the diffusion constant. During a time interval Δt the exponential concentration profile would move by a distance $\Delta x = x - x_1$ which is given by

$$\Delta x = \alpha D \, \Delta t \quad [5]$$

Assuming the value of $\sqrt{Dt}$ to be $(0.12 \pm 0.01) \times 10^{-4}$ cm, as found for the enhanced diffusion of the boron atoms in the region $x > 0.55\mu$, one can calculate a value of Δx as

$$\Delta x = 0.05\mu \quad [6]$$

A shift of the concentration profile of 0.05μ was not observed for $x < 0.55\mu$ thus suggesting that the enhanced diffusion of the boron atoms forming the EDE takes place only in regions underneath the emitter layer.

EDE in pnp structures.—To our knowledge, the EDE in pnp structures has never been reported. Attempts were therefore made to produce an EDE in this type of structure. It was felt that concentrations and junction depths should be as nearly the same as in the npn structure as possible.

A slice of boron doped silicon ($C_B = 1.5 \times 10^{15}$ cm^{-3}) was diffused for 15 min at 800°C with a P_2O_5 source followed by diffusion in a clean tube for 15 min at 950°C. This treatment resulted in a junction depth of 0.6μ and a surface concentration of about 2×10^{20} cm^{-3} which is in agreement with the junction depth and surface concentration of the base in the npn structure. After pyrolytic oxide growth (5), boron was diffused into the opened windows using a platinum box and B_2O_3 as the source for 5 min at 1100°C. Beveling and staining did not reveal a dip in the pnp structure.

Summary and Discussion

Experimental evidence for the EDE has been collected. The main results of the investigations described in preceding sections can be summarized as follows:

1. The EDE has been observed only in npn structures.

2. The EDE is not caused simply by the presence of phosphorus in the emitter oxide windows. EDE occurs only if the phosphorus doping is so high that it compensates the base doping.

3. The EDE is only observable in npn transistors with sufficiently high phosphorus surface concentration N_D so that at the diffusion temperature $N_D > n_i$, n_i being the intrinsic carrier concentration at this temperature ($n_i = 7 \times 10^{18}$ cm^{-3} for $T = 1000$°C).

4. The EDE does not depend on the diffusion time used to form the emitter. Therefore, multiple emitter predepositions cause multiple dip formation.

5. The dip can be enhanced by slow cooling and reduced by quenching. This suggests that the dip is created during the time the slice is being removed from the diffusion furnace.

6. The EDE is not the result of rejection of boron by the region of high phosphorus concentration, but is rather the result of an increased diffusion constant for boron near the collector junction.

7. The EDE is not caused by the oxide mask since no dip is observed if a slice having open windows in its oxide mask is heat-treated in the absence of phosphorus in a nonoxidizing atmosphere.

8. The base concentration but not the concentration gradient in the vicinity of the collector junction prior to the emitter diffusion determines the magnitude of the EDE.

At this time no hypothesis can be presented which can consistently explain the results of the EDE studies. All features listed above are in qualitative agreement with Baruch's model.

Baruch *et al.* (2) observed the EDE while studying vacancy enhanced diffusion in silicon under high-energy proton bombardment. They found that in the irradiated regions the depth of a diffused layer increased. Such effects had been predicted by Shockley (11-13) who suggested that thin irradiated layers close to the crystal surface may act as a source of vacancies which can diffuse in part toward the interior of the crystal causing an enhanced diffusion of substitutional impurities. Strack (14-15) bombarded silicon samples with low-energy ions in a d-c glow discharge and simultaneously doped the samples with phosphorus and boron. The results are consistent with Shockley's vacancy model. A direct connection between vacancy enhanced diffusion and EDE became obvious when Amadei (16) observed the EDE in an npn transistor which had phosphorus emitters produced by selectively ion bombarding (17) a silicon slice containing a boron diffused base layer. In this case, the EDE could be explained by excess vacancies created while forming the n-type emitter which diffused toward the base collector junction. There they enhanced the diffusion constant of the boron atoms which were already present and produced the EDE.

From the foregoing it becomes apparent that an explanation for the EDE in regular double diffused structures assuming vacancy enhanced diffusion must first of all explain the mechanism which can cause the emitter to act as a source of vacancies. Baruch (2) employed the following model: the introduction of donors to form the emitter increases the local concentration of charged vacancies. His approach is based on the fact that heavy donor doping increased the vacancy concentration (18-22) assuming that vacancies act like acceptors. The emitter could thus be a reservoir for a large number of vacancies which might produce the EDE. Baruch proposed that a fraction of these excess vacancies diffuse toward the base collector junction while the slice cools after being taken out of the diffusion furnace. However, Shockley (23) pointed out that this process is unlikely because the potential barrier for escape of negative charges from emitter to base becomes larger with decreasing slice temperature. The excess amount of negatively charged vacancies will therefore prefer to diffuse toward the surface of the

silicon slice. On the other hand, the results of heat treatments described earlier strongly support the idea that whatever mechanism governs the EDE, the driving force can be "frozen in" by quenching the slice or can come to full development if enough time is allowed in a slow cooling process. The observation that the EDE present in a quenched sample can be influenced by simple heat treatments without the presence of phosphorus is also interesting. This is a completely new aspect which will be pursued in more detail in future experiments. It is hoped that the experimental data reported in this paper may stimulate further investigations.

Acknowledgment

The authors are very grateful to Dr. W. Shockley for his interest in this work, for many stimulating discussions, and for his critical revision of the manuscript.

Manuscript received Aug. 10, 1964; revised manuscript received Oct. 23, 1964. This work was supported by U.S. Army Research Office, Durham, N. C., Contract No. DA-04-200 ORD-1166(X).

Any discussion of this paper will appear in a Discussion Section to be published in the December 1965 JOURNAL.

REFERENCES

1. L. E. Miller, "Properties of Elemental and Compound Semiconductors," p. 321, by H. Gatos, Editor, Interscience, New York (1960).
2. P. Baruch, C. Constantin, J. C. Pfister, and R. Saintespring, *Discussion Faraday Soc.*, **31**, 76 (1961).
3. G. E. Moore, "Microelectronics," p. 262, E. Keonjian, Editor, McGraw-Hill Book Co., New York-Toronto-London (1963).
4. H. Reiss, C. S. Fuller, and A. J. Pietruszkiewicz, *J. Chem. Phys.*, **25**, 650 (1956).
5. J. E. Sandor, Paper presented at the Los Angeles Meeting of the Society, May 6-10, 1962.
6. C. S. Fuller and J. A. Ditzenberger, *J. Appl. Phys.*, **27**, 544 (1956).
7. H. C. Theuerer, *This Journal*, **108**, 649 (1961).
8. E. Tannenbaum, *Solid State Electronics*, **2**, 123 (1961).
9. L. B. Valdes, *Proc. IRE*, **42**, 420 (1954).
10. J. C. Irvin, *Bell Syst. Tech. J.*, **41**, 387 (1962).
11. W. Shockley and R. N. Noyce, *Bull. Am. Phys. Soc.*, **II/1**, 380 (1956).
12. W. Shockley, "Dislocations and Mechanical Properties of Crystals," p. 581, J. Fisher, W. G. Johnston, R. Thomson, and T. Vreeland, Jr., Editors, John Wiley & Sons, Inc., New York (1957).
13. W. Shockley, Private communication.
14. H. Strack, *Bull. Am. Phys. Soc.*, **1**, 543 (1962).
15. H. Strack, *J. Appl. Phys.*, **34**, 2405 (1963).
16. L. Amadei, Private communication.
17. L. Amadei and A. Goetzberger, *Solid State Electronics*, **7**, 487 (1964).
18. H. Reiss and C. S. Fuller, "Semiconductors," N. B. Hannay, Editor, pp. 222-268, Reinhold, New York (1956).
19. R. L. Longini and R. F. Greene, *Phys. Rev.*, **102**, 992 (1956).
20. M. W. Valenta and C. Ramasastry, *ibid.*, **106**, 73 (1957).
21. M. F. Millea, *Bull. Am. Phys. Soc.*, **II/3**, 102 (1958).
22. W. Shockley and J. L. Moll, *Phys. Rev.*, **119**, 1480 (1960).
23. W. Shockley, Private communication.

Vapor Deposition of Germanium on Molybdenum

I. L. Kalnin and J. Rosenstock

American-Standard Research Division, New Brunswick, New Jersey

ABSTRACT

The vapor deposition of germanium on single and polycrystalline molybdenum substrates by hydrogen reduction of $GeCl_4$ vapor has been studied as a function of deposition temperature (600°-950°C), $GeCl_4$ concentration (0.2-4 mole %) and total gas flow (200-600 Std. cc/min). The activation energy of this process was 12 kcal/mole. A multiphase intermediate region containing several molybdenum germanides was found between the Mo and the polycrystalline Ge deposit. The molybdenum germanide phases were identified by x-ray diffraction and delineated by sectioning and selective etching. Their microhardness, electrical resistivity, and adherence were investigated.

The metal-semiconductor system Mo-Ge has received little attention in comparison to other neighboring systems, such as the Mo-Si, for example. Even the phase diagram has not been available (1) until recently (2).[1] Searcy and Peavler *et al.* have reported the preparation of some molybdenum germanides and their x-ray diffraction patterns (3,4). Since the Mo in a nonoxidizing ambient is an excellent material for high-temperature electrical and thermal contacts, it was of interest to examine the extent of interaction between the Ge and the Mo at elevated temperatures as well as the composition and structure of their interface. Preliminary experiments using diffusion couples indicated that the Ge diffusion into Mo was noticeable at 700°C. Satisfactory bonding of the Ge to the Mo was prevented, however, by the α-$MoGe_2$ which was invariably present next to the Ge. The vapor deposition of Ge on the Mo was then resorted to as a possible means of providing a stronger bonding, either because of a cleaner, oxide-free Mo substrate or a molybdenum germanide, other than $MoGe_2$, more adherent to the substrate. Since the effects of epitaxy might be important, the deposition was done on both single-crystal and polycrystalline Mo slices.

[1] The Mo-Ge phase diagram, ref. (2), was published after most of our experimental work was completed.

Experimental

The Mo was obtained commercially either as circular single-crystal slices, 0.5-1.0 mm thick, deposited area 1 cm^2, oriented 2° off the [100] direction or as polycrystalline rod, > 99.95% pure, which was cut into slices of similar size. These slices were mechanically polished with alumina powder of successively smaller grit to a bright finish of approximately 0.2μ peak-to-peak roughness, then etched for 2 min prior to deposition with a boiling concentrated formic acid-hydrogen peroxide mixture, 7:3 vol ratio, to remove about 4μ from the surface. After etching, the single-crystal Mo slices often showed clusters of large pores, probably gas inclusions, up to 0.1 mm in diameter, distributed irregularly over the otherwise smooth surface. These pores were filled with Ge during the deposition and became additional reactive diffusion sources creating pipes of Mo_xGe_y which were sometimes visible in the sectioned substrate (cf. Fig. 8). The $GeCl_4$ was made at our Research Laboratories and was quite pure, since the spectrographic analysis of Ge prepared from it

showed less than 25 ppm of any of the customary impurities, including Si, in it. The cylinder H_2 (> 99.5% pure) was further purified by passage through a commercial deoxydizer-dehydrator assembly.

The deposition apparatus was a conventional flow system made up of a set of gas sources, H_2 and N_2, a set of flow meters, a saturator trap filled with liquid $GeCl_4$ and a vertical, R. F. heated quartz reaction tube, 45 mm OD and 30 cm long. The tube was capped on both ends by brass couplings using neoprene O-ring compression seals and brass flanges. The top flange contained a quartz sighting window, the bottom one a sheathed chromel-alumel thermocouple which also supported a cylindrical graphite susceptor. A cold trap at the outlet end was used to collect the condensable waste products.

Briefly, the deposition was as follows: The Mo slice was introduced onto a quartz slide on top of the susceptor. The apparatus was evacuated and any leakage was eliminated. After the Mo had been preheated in H_2 for 15 to 30 min at 1000°C, the deposition temperature was set and the $GeCl_4$ vapor was introduced by bubbling the H_2 through the saturator trap. The $GeCl_4$ concentration was calculated from the measured weight loss of the trap. It was adjusted by means of a constant temperature cold bath around the trap. After the deposition the specimen was cooled to room temperature at a rate of about 100°C/min.

The specimen evaluation generally involved the following steps: determination of the weight gain and calculation of the average deposit thickness assuming bulk density and geometrical surface area; visual and microscopic inspection of the surface; measurement of the electrical resistance across the interface; identification of the surface phases by means of Laue backreflection photographs; low angle (5°) bevel lapping with alumina abrasives to expand the interface region by a factor of approximately 11; examination of the microstructure of the sectioned region by means of selective etching techniques, microhardness indentations, photomicrography, etc.; and selective removal of portions of the deposit by scratching or grinding for x-ray studies or chemical analysis.

Results and Discussions

Kinetics of the deposition.—The weight gain of the Mo was reasonably linear with time up to our longest deposition time, 90 min. The deposition rate was determined as a function of temperature (600°-950°C), $GeCl_4$ concentration in the H_2 (0.2- 4.0 mole %) and the total gas flow (200-600 Std. cc/min). Figure 1 shows the deposition rate *vs.* reciprocal temperature at the flow rate, F = 550 cc/min and the $GeCl_4$ vapor concentration, C = 0.2 and 1.0 mole %, respectively.

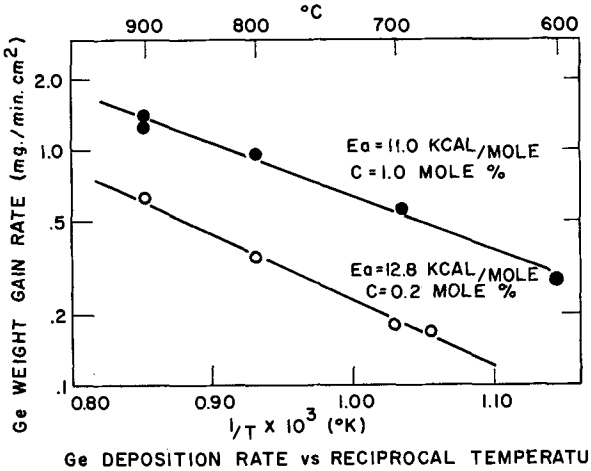

Fig. 1. Ge deposition rate *vs.* reciprocal temperature (F = 550 cc/min).

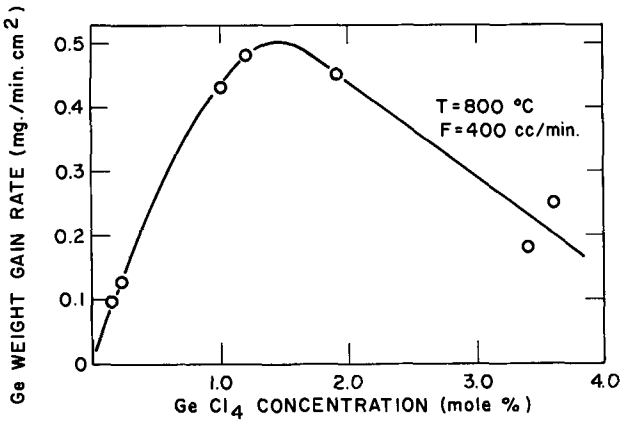

Fig. 2. Ge deposition rate *vs.* $GeCl_4$ concentration (F = 400 cc/min, T = 800°C).

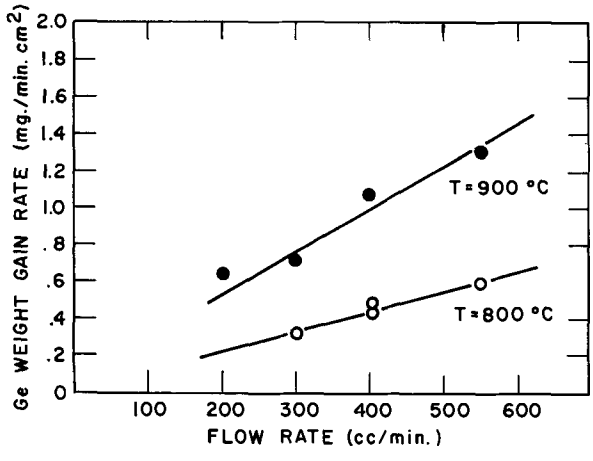

Fig. 3. Ge deposition rate vs. flow velocity (C = 1.0 mole %)

The calculated activation energies for the two concentrations are fairly close, 11.0 and 12.8 kcal/mole, confirming the linearity of the deposition process. The finally estimated activation energy was 12 ± 2 kcal/mole. To convert the weight gain rate to thickness gain rate for Ge (μ/min) one would multiply the ordinate by 1.9. Since the Ge, however, has partially reacted to form molybdenum germanides, Mo_xGe_y, the true thickness would certainly differ from the calculated one. Figure 2 gives the deposition rate as a function of the $GeCl_4$ concentration at 800°C and F = 400 cc/min. A maximum at about 1.5 mole % is observed. Similar maxima, but at different concentrations have been reported for the epitaxial vapor depositions Ge on Ge (5) and Si on Si (6). The dependence of the deposition rate on the total gas flow is seen in Fig. 3. The increase is linear up to our largest flow, 600 cc/min, corresponding to a linear flow of 1 cm/sec. The published data for Ge on Ge and Si on Si indicate a leveling-off at still higher flow rates, at or above 1.5 liters/min. The kinetic data of the Ge vapor deposition thus are similar to those reported for the epitaxial Ge/Ge and Si/Si depositions. The reaction mechanism at the hot Mo surface, therefore, should also be similar, consisting mainly of two simultaneous two-electron redox reactions

$$GeCl_4 + H_2 = GeCl_2 + 2HCl$$

$$GeCl_2 + H_2 = Ge_{(g)} + 2HCl$$

which lead to the steady state between the gaseous germanium-containing species

$$GeCl_4 + Ge_{(g)} = 2\,GeCl_2$$

An analysis of the analogous reaction mechanism for Si was made by Steinmaier (7) and was shown to be in good qualitative agreement with the experimental evidence.

Composition and structure of the Ge-Mo *interface region.*—Above 600°C the reactive diffusion of Ge into Mo became noticeable and a multiphase intermediate region consisting of several molybdenum germanides, Mo_xGe_y, was formed. Unless the deposition was done at high $GeCl_4$ concentrations (> 3 mole %) at which the deposition rate was lower and the deposit surface smoother, elemental Ge was present on the Mo substrate indicating that the vapor deposition rate ordinarily was higher than the Ge disappearance rate through the Mo_xGe_y formation. Near the melting point of Ge, the diffusion rate became comparable to the deposition rate (approximately 4 μ/min), and free Ge was sometimes absent. Figure 4 shows a fairly typical surface appearance of Mo slices deposited for 20 min at (a) 700°, (b) 800° and (c) 900°C, respectively, using 0.2 mole % $GeCl_4$. With increase in the deposition temperature, the Ge layer becomes more uniform and coherent. The slice (d) which has a thin, smooth coating has been deposited at 700°C and 3.4 mole % Ge for the same time. The Ge deposit usually was finely polycrystalline, and no preferential orientation was observed, either in the polycrystalline or single-crystal slices, from the Laue backreflection photographs. Above 900°C, however, the Ge sometimes contained large grains some of which were etched more rapidly than others by aqueous H_2O_2-HF and appeared to be of different orientation, Fig. 5. Also, another phase had segregated along the Ge grain boundaries. Figure 6 shows the needle like pattern of this phase at 1000X magnification. It is assumed that this phase is α-$MoGe_2$,

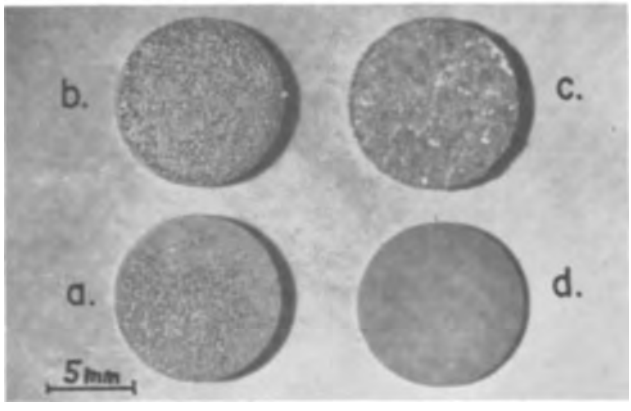

Fig. 4. Ge deposited on Mo substrate at: (a) 700°, (b) 800°, (c) 900°C using 0.2 mole % $GeCl_4$, and (d) 700°C and 3.4 mole % $GeCl_4$.

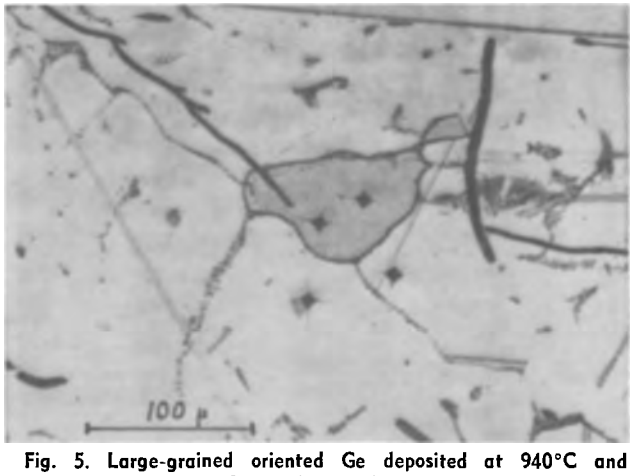

Fig. 5. Large-grained oriented Ge deposited at 940°C and etched with aqueous H_2O_2-HF (3:1:1). Note the segregated phase, the indentation cracks and the thermal stress cracks.

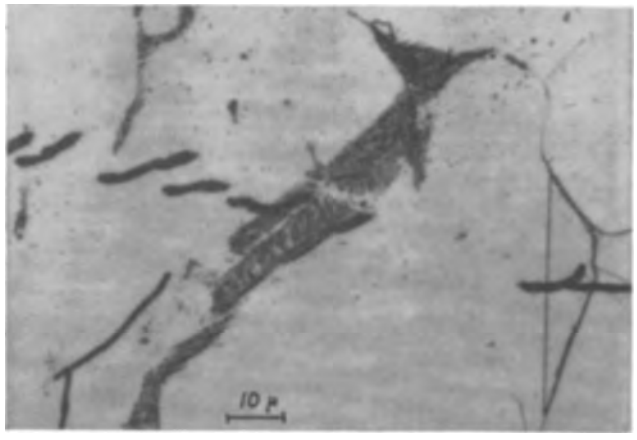

Fig. 6. Appearance of the segregated phase in the Ge, probably $MoGe_2$.

since x-ray diffraction data indicated its presence in the surface layer. The layer closest to the Ge formed by the reactive diffusion was always $MoGe_2$. The interface between the Ge and the $MoGe_2$ was very rough, although the initial Mo surface had been smooth. This indicates either solubility of the Mo in the Ge, or more likely, the reaction of the $GeCl_4$ with the Mo substrate, the thermodynamically most favorable reaction being

$$GeCl_4 + Mo = GeCl_2 + MoCl_2;$$
$$\Delta F\ 1000°K = +\ 9\ \text{kcal/mole}$$

Assuming typical values: F = 500 cc/min, $GeCl_4$ conc. = 1 mole % a deposition efficiency of 5%, and the above reaction in the steady state, the Mo removal rate was calculated as approximately 1 μ/min. Removal of Mo for the first few minutes of deposition would thus suffice to alter the original surface to the observed roughness of a few microns. The bulk of the $MoCl_2$ is probably reduced immediately to Mo which then reacts further to form Mo_xGe_y. Traces of Mo were identified in the waste products deposited on the chamber wall by means of potassium thiocyanate and stannous chloride spot tests (8). A mixture of several molybdenum germanides, usually Mo_3Ge, Mo_5Ge_3 and Mo_2Ge_3 up to 4μ thick, was found in the surface layer deposited at 600° at which the Ge diffusion is yet negligible. Since the thickness of this layer varied rather irregularly with the experimental conditions, the determination of growth rates of the various Mo_xGe_y phases was not possible. As the Ge diffusion proceeded during the deposition at higher temperatures, the mixed surface layer was converted completely into $MoGe_2$ and Mo_2Ge_3.

The Mo_xGe_y compounds reported by Searcy and Peavler (4) were $MoGe_2$, Mo_2Ge_3, Mo_5Ge_3,[2] and Mo_3Ge. All of these phases have been identified in the intermediate layer at one time or another. Ordinarily, the phases were present in separate layers which could be delineated by selective etching. The single-phase character of the thicker layers, $MoGe_2$ and Mo_2Ge_3, could be established by x-ray diffraction analysis of successive thin layers removed from the deposited surface by means of a diamond-point tool. The thinner layers near the Mo could not be analyzed separately, and it was assumed that the other two delineated layers were the phases Mo_5Ge_3 and Mo_3Ge. These phases were delineated best by successive application of two etchants, one acidic, the other alkaline. The acid etchant was a mixture of conc. H_2O_2 (30%), conc. HF (50%), H_2O in vol. ratio 1:1:3. Since it etched Ge at a rate of approximately 5 μ/min at room temperature, it could be used to remove the Ge deposit if desired. The Mo_xGe_y etched much more slowly, 0.1-0.3 μ/min and the Mo least (< 0.05 μ/min). The alka-

[2] Originally called Mo_3Ge_2, but identified later as Mo_5Ge_3 (9).

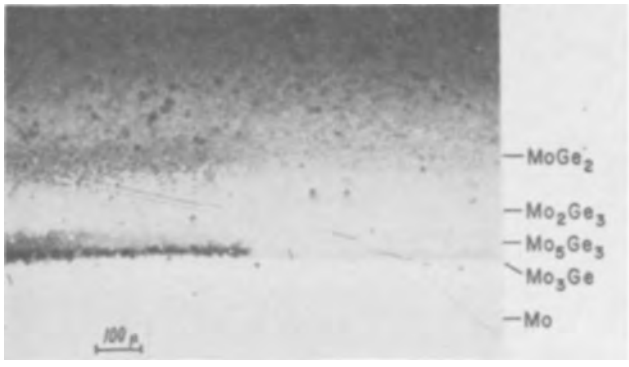

Fig. 7. Beveled section of the Ge-Mo interface at 800°C having four Mo_xGe_y phases present. Ge has been removed.

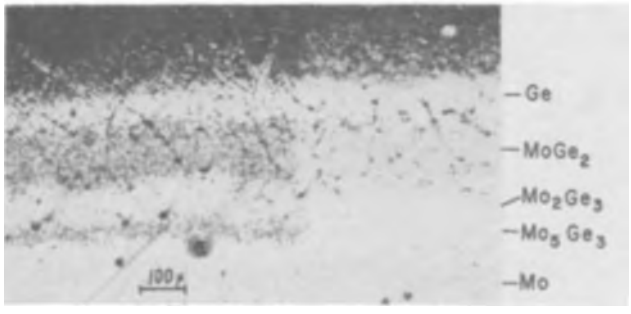

Fig. 8. Beveled section of the Ge-Mo interface at 900°C. Ge has not been removed.

line ferricyanide etchant was an aqueous solution of 10 w/o (weight per cent) KOH and 10 w/o $K_3Fe(CN)_6$. This reagent etched some of the molybdenum germanides selectively whereas Mo and Ge were essentially unetched. The application time was 10-30 sec for the alkaline and 1 min or longer for the acidic etchant. The acidic etchant outlined the boundaries: $Ge/MoGe_2$ and $MoGe_2$ Mo_2Ge_3/Mo_5Ge_3, Mo_3Ge and Mo_3Ge/Mo. Application of the alkaline etch outlined the boundaries $MoGe_2/Mo_2Ge_3$ and Mo_5Ge_3/Mo_3Ge of the sectioned specimen. Figure 7 shows a typical beveled section (5°) of the intermediate Mo_xGe_y layers present in a specimen deposited at 800°C for 60 min. The Ge on the top has been etched off with aqueous H_2O_2-HF. The area on the right has been etched with H_2O_2-HF only, whereas that on the left was further treated with the the ferricyanide etchant. The application of the latter provides a much better contrast between the phases, all four of which are seen. The contrast seems to be caused by selective etching and not by the formation of stained surface films. In Figure 8 the intermediate layer formed at 900° is seen. The light top layer is elemental Ge. The dark bottom layer (Mo_3Ge) near the Ge has disappeared. The Mo rich phases, in general, were present either at the surface at 700° or below or in the diffused layer at temperatures below 900°C. Above 900°C, the amount of $MoGe_2$ and Mo_2Ge_3 increased, while that of Mo_3Ge decreased. It has been observed that $MoGe_2$ decomposes into Mo_2Ge_3 + liquid above 1095°C (4).

The $MoGe_2$ and Mo_2Ge_3 layers displayed a network of broad grain boundaries which terminated at the Mo_5Ge_3 layer (Fig. 9). The disturbed appearance of these layers, which are nearly as hard and brittle as the Ge, may be ascribed to the thermal stresses created by the post-deposition cooling. The Mo rich phases, Mo_5Ge_3 and Mo_3Ge, were undisturbed and, therefore, would appear more suitable for thermal stress resistant contacts than the Ge rich ones.

Adherence.—Attempts to remove the surface layer from the substrate by means of adhesive tape sometimes resulted in the separation of Ge from the underlying $MoGe_2$. The strength of adhesion was qualitatively estimated to be much better than in the case of

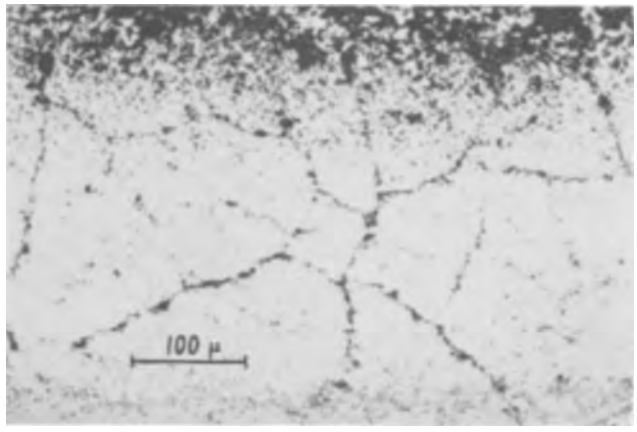

Fig. 9. Appearance of wide grain boundaries in the $MoGe_2$, Mo_2Ge_3 layer.

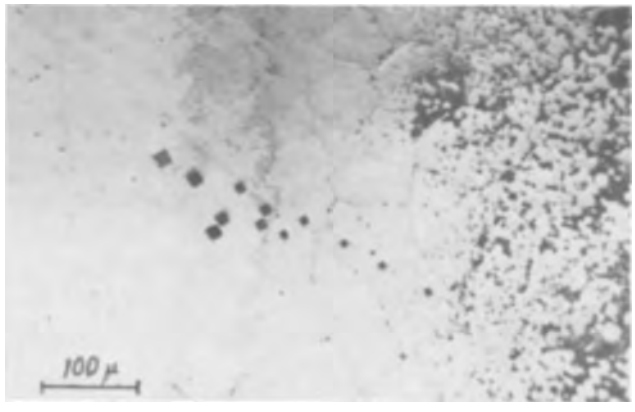

Fig. 10. A series of indentations showing the microhardness discontinuities across the interface.

diffusion-bonded elements. Since Ge was in contact with $MoGe_2$ in either case, the improvement was probably due to stronger mechanical bonding provided by the roughened, $GeCl_4$-etched Mo surface. Separation between the Mo_xGe_y phases or between the Mo_3Ge and the Mo substrate did not occur.

Hardness.—Microhardness measurements with Vickers diamond pyramid tester at 50g load indicated that the hardness of the Ge deposit depends on its grain size. The apparent hardness of small Ge crystallites imbedded in the polycrystalline matrix was 1340 ± 80; on large polycrystalline grains, it was 1140 ± 70; and on small polycrystalline aggregates it decreased to 930 ± 70 kg/mm². The $MoGe_2$-Mo_2Ge_3 phase hardness was 900 ± 30 kg/mm². There is a rapid decrease in microhardness and rather wide fluctuation from 600 to 350 kg/mm² in the Mo_5Ge_3-Mo_3Ge region. Another sharp hardness drop occurs at the Mo substrate, for which the hardness value agrees well with that of pure Mo, 210 ± 30 kg/mm². Figure 10 illustrates a series of microhardness measurements showing the two discontinuities across the beveled section of the Ge-Mo interface. The Ge has been etched off.

Electrical resistivity.—The resistance of the intermediate layer was measured by clamping the deposited specimen between two brass holders. The contact resistance was decreased to a negligible value by means of (*a*) brass foil which was inserted between the holder and the specimen and was wetted on both sides with In-Ga alloy and (*b*) four-point measuring technique using a Keithley 503 milliohmeter. The series resistance of Mo was sufficiently low to be disregarded. The resistance values obtained ranged from 0.5 to 0.05 milliohms, depending on the amount of Ge present. The lowest values were measured on specimens containing no free Ge. Attempts to remove the Ge by etching were not very successful because some

series resistance would arise, presumably from a thin oxide-containing surface film. Using specimens containing the least amounts of free Ge, the resistivities of the intermediate layer were between 6 and 20 milliohm cm, which in our opinion, should correspond to the upper resistivity limit.

Acknowledgments

The authors thank G. P. K. Chu for the encouragement of this work, and R. Oliva of the Analytical Section for conscientious identification of the various molybdenum germanides.

Manuscript received Aug. 18, 1964. This paper was delivered before the Toronto Meeting, May 3-7, 1964.

Any discussion of this paper will appear in a Discussion Section to be published in the December 1965 JOURNAL.

REFERENCES

1. M. Hansen and K. Anderko, "Constitution of Binary Alloys," 2nd ed., p. 767, McGraw-Hill Book Co., New York (1958).
2. P. Stecher, F. Benesovsky, and H. Nowotny, *Monatsh. Chem.*, **94** [6], 1154 (1963).
3. A. W. Searcy, R. J. Peavler, and H. J. Yearian, *J. Am. Chem. Soc.*, **74**, 566 (1952).
4. A. W. Searcy and R. J. Peavler, *ibid.*, **75**, 5657 (1953).
5. E. I. Givargizov, *Soviet Physics-Solid State* (Engl. Transl.) **5**, 840 (1963).
6. H. C. Theuerer, *This Journal*, **108**, 649 (1960).
7. W. Steinmaier, *Philips Research Repts.*, **18**, 75 (1963).
8. F. Feigl, "Spot Tests in Inorganic Analysis," p. 115, Elsevier Publishing Co., New York (1958).
9. C. H. Dauben, P. H. Templeton, and C. E. Myers, *J. Phys. Chem.*, **60**, 443 (1956).

Anodic Oxidation of Methanol at Palladium Electrode in Alkaline Solution

Tsutomu Takamura and Ken'ichi Minamiyama

Central Research Laboratory, Tokyo Shibaura Electric Company, Ltd., Kawasaki, Japan

ABSTRACT

Carbonate formation from methanol at active palladium electrodes was confirmed in alkaline solution by measuring current-voltage curves for methanol and other related compounds and by determining the oxidation products formed at the test electrode. The current efficiency in the anodic oxidation was observed to be over 80% in the current density range from 20 to 400 mamp/cm^2. A probable mechanism was proposed for the oxidation reaction by determining the electrochemical reaction order (z). The z values obtained for methanol and hydroxide ion were 1/3 and 2/3, respectively. The activation process of the transfer reaction was considered to be the oxidation of methoxy radical by hydroxide ion.

Methanol is an attractive fuel for fuel cells because of its electrochemical reactivity, availability, and low cost. Several studies have been reported on the mechanism of the anodic oxidation of methanol at platinum electrode both in acidic and alkaline media (1-3). In acidic media, methanol could be oxidized at platinum electrode to carbon dioxide and water (1, 2), while in alkaline media, the main oxidation product was reported to be formate ion (3).

In view of the energy utilization, complete oxidation to carbonate ions is desirable, which was supposed by the present authors to be partially accomplished by the use of palladium electrode because palladium has a particular affinity for hydrogen (4). Preliminary experiments on the anodic oxidation of methanol at an active palladium electrode in alkaline solution showed that the fuel could be converted into carbonate ion.

In this paper quantitative studies on the anodic oxidation of methanol are described and a probable mechanism concerning the transfer reaction is proposed.

Experiment

Test electrode.—Pure palladium black (99.997%) was deposited electrolytically on the cleaned palladium plate from 0.2M solution of palladium chloride. The palladized palladium plate was washed thoroughly, then heated to expel occluded hydrogen at 200°C in nitrogen stream. The obtained disk had 1.2 cm diameter.

Electrolytic solution.—Commercial reagent of KOH was dissolved in distilled water, to which known amounts of K_2CO_3 and a test material (fuel) such as methanol, ethanol, etc., were added. Although pre-electrolysis of the solution is said to be necessary before adding test material in order to obtain a reversible potential, an identical stable potential was obtained for the test material in the present solutions regardless of pre-electrolysis. Accordingly, the measurements were carried out without pre-electrolysis.

The electrode, however, gave no stable potential in the solution whose concentrations of KOH and test material were less than 0.1 and 0.02M, respectively. Then all the measurements were done in the solution containing these reagents more than 0.2M.

Potential measurements.—Potentials were measured at 25°C by the direct method with a Luggin-capillary, a mercuric oxide half cell (2M NaOH) being used as a reference electrode. The change in the liquid junction potential due to the concentration variation in the test electrode compartment was corrected with the Lewis-Sargent equation.

Determination of current efficiency.—An H-type cell whose two parts were connected through a porous glass was used as an electrolysis cell, a smooth platinum plate being used as a counterelectrode. The concentration of the electrolytic solution was kept at 5.5M and 5.0M for KOH and methanol, respectively. Carbonate ion in the solution was previously removed by adding appropriate quantities of $Ba(OH)_2$. By polarizing the test electrode anodically, constant current electrolysis was carried out for several 10-min periods in the nitrogen stream. Carbonate ions formed at the test electrode were determined gravimetrically in the form of $BaCO_3$. On the other hand, the total numbers of electron used during the electrolysis were calculated from the current intensity and the electrolysis time.

Results

Current-voltage curves.—Examples of current-voltage curves of methanol at varied concentrations are

given in Fig. 1, which shows that methanol is very reactive at the test electrode. Each curve falls on a Tafel line with $\alpha = 0.50$ in the current density range below 30 mamp/cm^2. At larger current densities the current-voltage relation deviates from Tafel line, indicating that a diffusion process contributes in the region.

If the rate of methanol oxidation to carbonate at the test electrode (Eq. [1]) is sufficiently fast, only a small polarization is expected even at high anodic current density for solutions of formalin or formate, both of which are considered to be stable intermediates in the course of the methanol oxidation. If, for example, the final product were formate ions, very large polarization would be observed for formate even at very low anodic current densities.

$$CH_3OH + 8\,OH^- \rightarrow CO_3^{2-} + 6H_2O + 6e \qquad [1]$$

Current-voltage curves obtained for these two oxidizable substances are given in Fig. 2, which shows that even formate is very reactive at the test electrode. Unlike the case with platinum electrode, formate gives high current densities at small polarizations. These results suggest that methanol can be oxidized into carbonate at the test electrode.

Determination of current efficiency.—Existence of the oxidation reaction to form carbonate was expected in the measurement of current-voltage curve, but as the method is indirect, the formation of carbonate was determined in order to confirm that the carbonate formation is the main reaction. Carbonate ions formed at the test electrode were determined as $BaCO_3$.

The current efficiency was also determined coulometrically. In the oxidation reaction [1], one mole of carbonate ions should be formed from an equivalent mole of methanol, whereby six moles of electron are released at the test electrode. The efficiency is then defined as the mole ratio of the amount of carbonate determined analytically to that calculated from the observed electrical quantities. The efficiency was found to be always over 80% throughout the current densities studied. This shows that the activation process of the oxidation is independent of the current density. That the oxidation reaction to form carbonate was a main reaction was thus confirmed by the direct determination of oxidation product.

Reactivity of palladium for several substances.—Bearing in mind that palladium has a particular affinity to hydrogen and that the carbonium band occurs in the infrared spectrum for the gaseous adsorption of methanol on nickel (5), we can expect that methanol is likewise adsorbed on palladium with the hydrogen atom on the methyl group.

However, hydrogen atoms belonging to any alkyl group are not necessarily considered to combine with palladium. In order to check what kind of hydrogen atom is liable to undergo the oxidation, reactivity at the test electrode was measured for the following species: ethanol, isopropanol, glycerine, ethylether, acetone and acetic acid. Current-voltage curves for these compounds are shown in Fig. 3. Substances not shown in the figure are ether and acetic acid, which gave no stable potential even at very small current density. Contrary, alcohols, formalin, and formic acid were proved to be suitable as fuels. All these suitable substances have one or more hydrogen atoms attached to the carbon atom adjacent to the terminal oxygen atom, while unsuitable ones have not such hydrogen atoms. The hydrogen atom is considered to be liable to adsorb on palladium, bringing C-H bond scission.

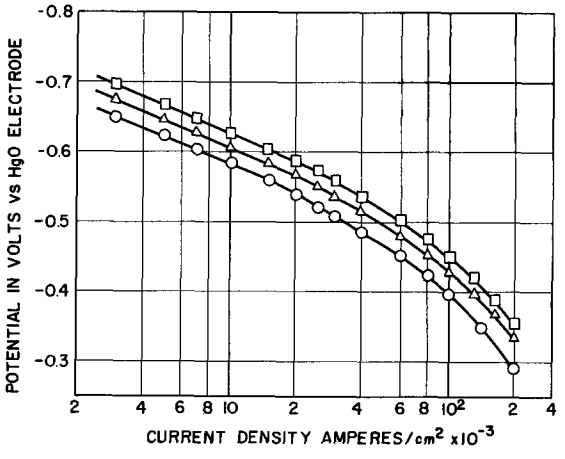

Fig. 1. Current-voltage curves of methanol at palladium electrode in KOH solution. [KOH] = 4M, [K_2CO_3] = 1M, 25°C. □, 4.97 methanol; △, 2.48 methanol; ○, 0.75M methanol.

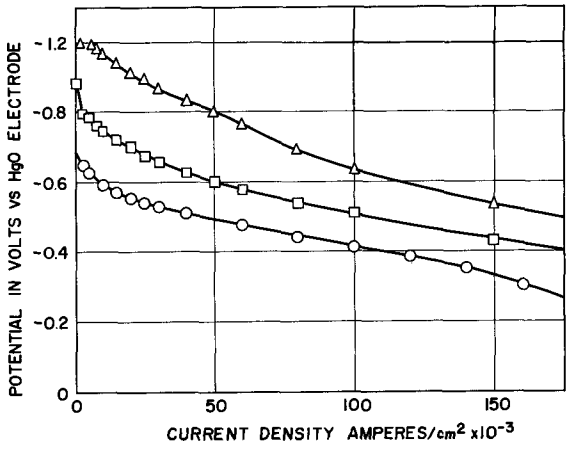

Fig. 2. Current-voltage curves of methanol, formalin, and potassium formate at palladium electrode in KOH solution. Fuel concentration = 1M, [KOH] = 4.5M, [K_2CO_3] = 0.1M, 25°C. ○, 1M methanol; △, 1M formalin; □, 1M formate.

Discussion

Vetter introduced the electrochemical reaction order, z_{rj} (or z_{oj}), into the analysis of electrode reaction (6). The probable mechanism of the oxidation of methanol will be considered here with the Vetter's method. Observed current i flowing across the test electrode at an appropriate anodic polarization is expressed by Eq. [2]

$$i = k_+ K_r C_{CH_3OH}^{zr'} \cdot C_{OH^-}^{zr2} \cdot \exp\left[\frac{n\alpha FE}{RT}\right] \qquad [2]$$

where notations are the same as those expressed in Vetter's text (6). With the condition that the poten-

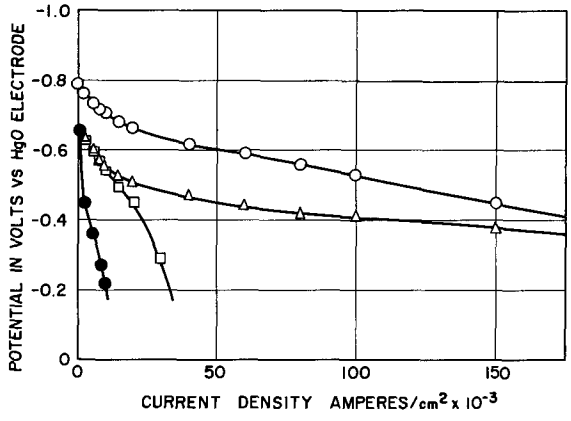

Fig. 3. Current-voltage curves of alcohols and acetone at palladium electrode in KOH solution. Fuel concentration = 1M, [KOH] = 4.5M, [K_2CO_3] = 0.1M, 25°C. ○, 1M ethanol; △, 1M, glycerin; □, 1M 2-propanol; •, 1M acetone.

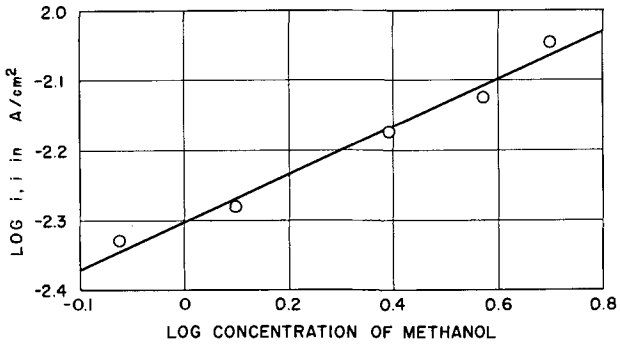

Fig. 4. Plots of log i vs. log c of methanol at $E = -0.625$v *vs.* HgO electrode. The potential variation due to the change in methanol concentration was corrected by assuming that the activity coefficient of methoxide is constant. [KOH] = 4M, [K_2CO_3] = 1M, 25°C.

tial difference between the Helmholtz double layer and the bulk of the solution is negligible, we obtain [3] at fixed C_{OH^-} and E.

$$\left(\frac{\partial \log i}{\partial \log C_{CH_3OH}}\right)_{C_{OH^-},E} = z_{r1} \qquad [3]$$

z_{r1} can thus be obtained from the plotting of log i measured at fixed E against log C_{CH_3OH}.

Current-voltage curves were measured at fixed concentrations of KOH(4M) and K_2CO_3(1M) by varying the methanol concentration. The curves were observed to be independent on the stirring rate of the solution. Since the presence of excess electrolyte is considered to maintain the condition supporting [3], z_{r1} can be obtained from the current-voltage curves measured at varied concentrations. The plottings of log i at 0.625v *vs.* HgO electrode against the logarithm of methanol concentration are shown in Fig. 4, which gives a straight line to give $z_{r1} = 1/3$.

Similarly z_{r2} was obtained by varying the hydroxide concentration at fixed concentrations of other species. The effect of the variation of the activity coefficient on E was evaluated from the mean activity coefficient of KOH (7) and the ion size parameter (8) in the ionic strength range between 2.5 and 7.5. Variation of the activity term in E in this range was estimated to be within a few millivolts, which is not an adequate quantity to allow a different conclusion. Plots of log i *vs.* log C_{OH^-} showed that z_{r2} was 2/3. This indicates that hydroxide ions participate in the activation process by a factor of 2/3.

A part of methanol in alkaline solution dissociates into methoxide ion, (9)

$$CH_3OH + OH^- \rightleftharpoons CH_3O^- + H_2O \qquad [4]$$

This could also be ascertained by the decrease of the infrared band at 1110 cm^{-1} with the increase of hydroxide concentration. Thus formed CH_3O^- would be adsorbed on palladium electrodes and easily release one electron to form methoxy radical, $CH_3O\cdot$ (10)

$$CH_3O^- \rightleftharpoons (CH_3O^-)_{ad} \qquad [5]$$

$$(CH_3O^-)_{ad} \rightarrow (CH_3O\cdot)_{ad} + e \qquad [6]$$

where $(\ )_{ad}$ denotes adsorbed species. $CH_3O\cdot$ has three identical hydrogen atoms which can be adsorbed on palladium.

The value of z introduced by Vetter is considered to correspond to b' given by Parsons (11), and b' is the mole number of species B', for example methanol, to form one mole of activated complex in the transfer reaction. z obtained for methanol at the test electrode was 1/3, showing that three moles of activated complexes are formed from one mole of methanol, while OH^- was shown to participate in the complex formation by a factor of 2/3. With reactions [4], [5], and [6] we can reasonably suppose that the activated complex ($A^{\ddagger}$) is formed through the activation reaction [7].

$$(CH_3O\cdot)_{ad} + 2\,OH^- \rightarrow (CO_2^-)_{ad} + 3A^{\ddagger} + H_2O + e$$

with

$$A^{\ddagger} \rightarrow (H)_{ad} \qquad [7]$$

In this reaction $(H^A)_{ad}$ would easily be combined with OH^- through

$$(H)_{ad} + OH^- \rightarrow H_2O + e \qquad [8]$$

and at the same time $(CO_2)_{ad}$ would be oxidized to carbonate ion through the rapid reaction [9].

$$(CO_2)_{ad} + 2\,OH^- \rightarrow CO_3^{2-} + H_2O \qquad [9]$$

This mechanism may be probable because $(CO_2^-)_{ad}$ is the adsorbed form of formate whose hydrogen atom attached to the carbon atom is released and because the reaction [8] was observed to be more rapid as compared to the methanol oxidation reaction.

Summarizing reactions [4] to [9], we obtain the over-all oxidation reaction [1]. The mechanism proposed here will be examined further by other methods.

Acknowledgments

The authors wish to express their deep thanks to Dr. Y. Miura, manager of this laboratory and to Dr. H. Shiratori a senior researcher of this laboratory for their helpful discussions and encouragement.

Manuscript received July 20, 1964; revised manuscript received Nov. 22, 1964.

Any discussion of this paper will appear in a Discussion Section to be published in the December 1965 JOURNAL.

REFERENCES

1. B. L. Tarmy, *Proc. 16th Ann. Power Source Conf.*, 29 (1962).
2. M. W. Breiter, *This Journal*, **111**, 449 (1963); S. Gilman, *J. Phys. Chem.*, **68**, 70 (1964).
3. R. P. Buck, L. R. Griffith, R. T. MacDonald, and M. J. Schlatter, *Proc. 15th Ann. Power Source Conf.*, 16 (1961).
4. M. von Stackelberg and W. Jahns, *Z. Elektrochem.*, **62**, 349 (1958).
5. G. Blyholder and L. D. Neff, *J. Cat.*, **2**, 138 (1963).
6. K. J. Vetter, "Elektrochemische Kinetik," p. 114 Springer-Verlag, Berlin, (1961).
7. B. E. Conway, "Electrochemical Data," p. 77, Elsevier Publishing Co., Amsterdam, (1952).
8. J. Kieland, *J. Am. Chem. Soc.*, **59**, 1675 (1937).
9. J. Koskikallio, *Suomen Kemistilehti*, **30B**, 111 (1957).
10. S. Nagaura and K. Sasaki, Presented at the 17th Meetings of the Chem. Soc. Japan in Tokyo (1964).
11. R. Parsons, *Trans. Faraday Soc.*, **47**, 1332 (1951).

Electromotive Force Studies of Cadmium Chloride in Water, Water-Methanol, and Methanol Solutions

Jack D. Hefley[1] and Edward S. Amis

Chemistry Department, University of Arkansas, Fayetteville, Arkansas

ABSTRACT

The emf of cadmium chloride was determined in water, water-methanol, and methanol solvents over a concentration range of 0.0050 to about 0.1000*M*. Measurements were made using a L&N Type K-3 potentiometer and an amalgam cell without transference. In order to determine the standard potential of cadmium chloride in the various solvents it was necessary to extrapolate the molality to zero by a suitable linear function of the observed emf. Satisfactory values of the standard potential were determined over the entire solvent, temperature, and concentration ranges by assuming only one method of ionization and simultaneously varying the equilibrium constant as the solvent composition was varied. The justification for decreasing the dissociation constant as the dielectric constant was decreased was based on Bjerrum's theory of ionic association in media other than water. The laborious calculations involved in the determination of the standard potentials were accomplished by using an I.B.M. 7040 computer. The standard potentials which were determined were used to calculate the mean ionic activity coefficients of cadmium chloride in the various solvents. The calculations were made by using the form of the Nernst equation which is applicable to a 2-1 electrolyte. The activity coefficients of cadmium chloride in the various solvent systems are similar to those determined by other investigators for electrolytes in mixed and nonaqueous solvents. The general behavior is that deviations from the Debye-Hückel theory occur at lower concentrations as the dielectric constant of the solvent is decreased.

This is the second paper (1) on the emf studies of cadmium chloride in pure and mixed solvents.

Measurements of the emf of the cell

$$Cd\text{-}Cd_xHg(11\%) \mid CdCl_2(m) \mid AgCl\text{-}Ag$$

have been made at 25°, 30°, and 35°C throughout a cadmium chloride concentration range of 0.0005 to about 0.1000*M* and over the complete solvent range for the water-methanol system. From the results, the standard potentials of the cells, E_o, and the activity coefficients of cadmium chloride in the various solvent systems have been computed.

Experimental Procedure

The silver-silver chloride electrodes of the kind designated by Harned (2) as type 2 were used. The cadmium amalgam was prepared from distilled mercury and high-purity cadmium metal supplied at special request from the E. H. Sargent Company. The amalgam electrodes containing 11% of the total cadmium were made individually in each cell vessel according to the method of Harned and Fitzgerald (3).

A standard concentrated stock solution was made from Baker Analytical Reagent cadmium chloride and conductivity water. Its strength was found by gravimetric determination of its chloride content. More dilute solutions were prepared by adding weighed amounts of the standard solution to known weights of water. This same procedure was used in mixed solvents.

In order to prepare solutions in pure nonaqueous solvents, a known weight of the standard concentrated aqueous stock solution mentioned above was evaporated and dried at 150°C for 24 hr and the solute dissolved in the methanol which had been purified according to the procedure of Foster and Amis (4). More dilute solutions in the nonaqueous solvent were then prepared in a manner similar to that for aqueous and mixed solvents.

Oxygen was removed from each cell by purging it with argon saturated with vapor whose composition and temperature were the same as the solvent in the individual cell. The cells came to equilibrium in 1-2 hr after preparation. The temperature control was within ± 0.01°.

The emf of each cell was measured seven times with a L&N Type K-3 Universal Potentiometer, and each observed emf value which is recorded in this work is the average of these seven measurements.

[1] Present address: Union Carbide Chemicals Company, South Charleston, West Virginia.

Table I. EMF measurements in international volts of cadmium chloride in water solutions at 25°C

Sample No.	m	$E \pm 0.02$ mv
1	0.00086	0.83447
2	0.00288	0.79710
3	0.00653	0.77074
4	0.01030	0.75690
5	0.01620	0.74657

Experimental Results

When the emf was measured on the cell containing cadmium chloride in water solutions at different values of the molality, the values in Table I were obtained. A graphical presentation of this raw data is shown in Fig. 1 where the observed electromotive force is

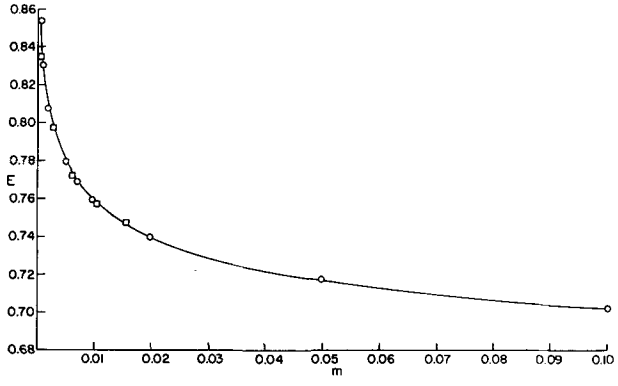

Fig. 1. EMF of the Cd-Cd$_x$Hg (11%) |CdCl$_2$(m)| AgCl-Ag cell in water at 25°C plotted against the cadmium chloride molality. ○, Data of Harned and Fitzgerald (3); □, data of this work.

Table II. EMF measurements in international volts of cadmium chloride in methanol-water mixtures

Sample No.	m	EMF ± 0.03 mv, 25°	EMF ± 0.03 mv, 30°	EMF ± 0.03 mv, 35°
		30% MeOH		
6	0.000465	0.81846	0.82513	0.82845
7	0.00121	0.78948	0.79273	0.79451
8	0.00224	0.77078	0.77672	0.77718
9	0.00450	0.75205	0.75454	0.75665
10	0.00543	0.74721	—	—
11	0.00796	0.73736	0.73964	0.74048
12	0.01270	0.72587	0.72838	0.72953
13	0.0206	0.71474	0.71621	0.71704
14	0.0525	0.69299	0.69396	0.69512
15	0.0969	0.68176	0.68284	0.68355
		60% MeOH		
16	0.000536	0.77967	0.78144	0.78252
17	0.00114	0.75816	0.76944	0.76071
18	0.00220	0.74202	0.74265	0.74351
19	0.00439	0.72482	0.72544	0.72614
20	0.00765	0.71193	0.71203	0.71249
21	0.0129	0.70077	0.70102	0.70160
22	0.0201	0.69175	0.69206	0.69236
23	0.0402	0.67805	0.67896	0.67970
24	0.0916	0.66431	0.66506	0.66569
		90% MeOH		
25	0.000563	0.73178	0.73397	0.73597
26	0.00124	0.71277	0.71406	0.71521
27	0.00213	0.70495	0.70637	0.70750
28	0.00530	0.68873	0.68978	0.69066
29	0.00875	0.67901	0.67968	0.68024
30	0.0123	0.67283	0.67370	0.67432
31	0.0205	0.66617	0.66686	0.66753
32	0.0375	0.66249	0.66300	0.66371
33	0.0876	0.65504	0.65599	0.65655
		100% MeOH		
34	0.000614	0.71652	0.71851	0.72007
35	0.00132	0.70792	0.70921	0.71032
36	0.00257	0.69610	0.69752	0.69865
37	0.00553	0.68296	0.68401	0.68481
38	0.00821	0.67602	0.67670	0.67721
39	0.0129	0.66789	0.66877	0.66930
40	0.0198	0.66079	0.66187	0.66354
41	0.0279	0.65831	0.65883	0.65945
42	0.0578	0.65421	0.65483	0.65537

plotted against the molality. It can be seen from Fig. 1 that the data of this work, which is indicated by squares, is in very good agreement with the data of Harned and Fitzgerald (3), which is represented by circles.

The emf measurements of cell containing cadmium chloride in water-methanol and methanol solutions are shown in Table II and Fig. 2. Because of the small temperature coefficients, only those data for 25°C are shown graphically. It can be seen from Fig. 2 that the emf data in the various methanol solutions are a smooth function of the molality.

The experimental precision in aqueous solutions was in general of the order of 0.02 mv. In the alcoholic solutions the precision was somewhat less, about 0.03 mv. Due to the nature of the calculations, the accuracy of the values of the standard potentials discussed below is believed to be at least ± 2.0 mv.

Evaluation of the Standard Potentials

The determination of the standard potentials of cadmium chloride in the different solvent systems was based on the method used by Harned and Fitzgerald (3) to determine the standard potential of cadmium in an aqueous solution. In their work they assumed that cadmium chloride is an incompletely dissociated electrolyte and then corrected for the degree of dissociation, α, from the equilibrium constant, K, and the activity coefficient of barium chloride by using the Law of Mass Action and the Debye and Hückel theory.

In this work it was necessary to modify the method of Harned and Fitzgerald (3) in two ways. These two modifications will be discussed below.

Representing the electromotive force of the cell by the equation

$$E = E_o - k \log 4m^3\gamma_\pm^3 \qquad [1]$$

and replacing $\log \gamma_\pm$ by $(-S_{(f)}\sqrt{m} + B'm)$ one obtains the equation

$$E + k \log 4m^3 - 3kS_{(f)}\sqrt{m} = E_o - 3k'Bm = E_H \qquad [2]$$

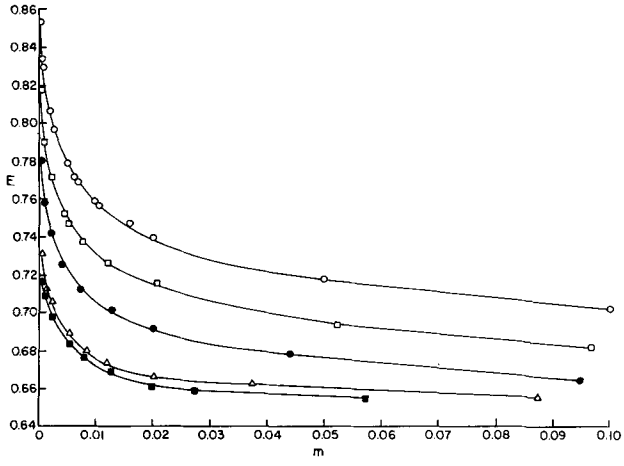

Fig. 2. EMF of the Cd-Cd$_x$Hg (11%) $|CdCl_2(m)|$ AgCl-Ag cell in water, water-methanol, and methanol at 25°C. ○, H_2O; □, 30% MeOH; ●, 60% MeOH; △, 90% MeOH; ■, 100% MeOH.

In the above equations E_o is the standard cell potential, m is the molality, $\gamma_\pm$ is the mean ionic activity coefficient, k is $2.303RT/2F$, and $S_{(f)}$ is the limiting slope of the Debye-Hückel theory. E_H is a function that should be linear with m in dilute solutions when the Debye-Hückel theory holds and provided the electrolyte were completely dissociated. $S_{(f)}$ is later used as the limiting slope of a 1-1 electrolyte.

If cadmium chloride were a completely dissociated electrolyte, according to Eq. [2] a plot of E_H and therefore of $E + k \log 4m^3 - 3kS_{(f)}\sqrt{m}$ should, in dilute solutions, be linear with m. However, cadmium chloride is not completely dissociated as indicated by conductance data, and hence the plot is not linear.

Equations [3] and [4] below give the dissociation data most in harmony with the data in this report.

$$CdCl_2 \rightarrow CdCl^+ + Cl^- \qquad [3]$$

$$CdCl^+ \rightleftarrows Cd^{++} + Cl^- \qquad [4]$$

The first step in the dissociation is represented as complete, while the $CdCl^+$ ion is only partially dissociated. Cadmium chloride itself is probably only partially ionized; however, the incompleteness of this dissociation is neglected in the assumed mechanism of dissociation for dilute solutions represented by Eq. [3] and [4].

If one assumes that $\gamma' = \gamma'_{Cl^-} = \gamma'_{CdCl^+}$; where γ' is the activity coefficient; if $\gamma'_{Cd^{++}} = \gamma'' = (\gamma')^4$; and if the concentrations of the $CdCl^+$, Cd^{++}, and Cl^- ions are, respectively, $m(1-\alpha)$, $m\alpha$, and $m(1+\alpha)$, then the equilibrium constant for step two from Eq. [4] becomes

$$K = \frac{(\alpha m\gamma'')(1+\alpha)\gamma' m}{m(1-\alpha)\gamma'} = \frac{m\gamma''\alpha(1+\alpha)}{1-\alpha} \qquad [5]$$

where α is the degree of dissociation of the $CdCl^+$ ion. Solving for α yields

$$\alpha = \frac{1}{2}\left[-\left(1 + \frac{K}{m\gamma''}\right) + \sqrt{\left(1 + \frac{K}{m\gamma''}\right)^2 + \frac{4K}{m\gamma''}}\right] \qquad [6]$$

Noyes and Falk (5) estimated K to be between 0.007 and 0.002 from the conductance data of Wershoven (6) taken at 20°C in aqueous solutions. Reghellato and Davies (7) found K to be 0.010 at 25°C by applying Onsager's theory to the same data and assuming a reasonable value for the mobility of the $CdCl^+$ ion.

Harned and Fitzgerald (3) treated the cadmium chloride data by first calculating α employing Eq. [6] and assuming the values of K to be between 0.005 and 0.015. They then computed γ''-values from the Debye-Hückel equation

$$\log \gamma'' = -\frac{4S_{(f)}\sqrt{\mu'}}{1 + A\sqrt{\mu'}} \quad [7]$$

In this equation γ'' and $S_{(f)}$ have their usual significance, and A is the Debye-Hückel constant and is given by the equation

$$A = \frac{\sqrt{2}\,(35.57)\,\overset{\circ}{a} \times 10^8}{(DT)^{1/2}} \quad [8]$$

where $\overset{\circ}{a}$ is the mean diameter of the ions, that is the distance between their centers in the position of closest approach of the ions. In the above equations, a quantity is sometimes primed and sometimes unprimed. The primed quantities are real the unprimed ones are stoichiometric. Thus

$$\mu' = \frac{1}{2}\sum m_i' z_i^2 \quad [9]$$

where m_i' represents the actual ionic concentrations.

The calculations were made by assuming a value of α, say 0.80, for the values of K and of m being used. The value of μ' for the assumed value of α and the selected value of m was calculated using the equation

$$\mu' = (2\alpha + 1)m \quad [10]$$

and γ'' was obtained from Eq. [7]. This value of γ'' was used in Eq. [6] to recalculate α, from which, using Eq. [10], a better value of μ' was calculated. This better value of μ' substituted in Eq. [7] yielded a better value of γ''. This process was repeated until the same value of α, to within a few thousandths of a unit, was obtained twice. These calculations were carried out for each concentration in each solvent, at each temperature to obtain values of α and of K under these conditions.

Equation [1] in terms of the stoichiometric activity coefficient may be written in terms of the real activity coefficient $\gamma'_{\pm}$ and the actual ionic concentration as follows

$$E = E^o - k \log \alpha(1 + \alpha)^2 m^3 \gamma^3_{\pm} \quad [11]$$

and by subtracting E^o from both sides of Eq. [2] one can write

$$E_H - E^o = E - E^o + k \log 4m^3 - 3kS_{(f)}\sqrt{2\mu} \quad [12]$$

Substituting the value of $E - E^o$ from Eq. [11] into Eq. [12] there results

$$E_H - E_o = k \log 4 - k \log \alpha(1 + \alpha)^2 - 3k \log \gamma'_{\pm} - 3kS_{(f)}\sqrt{2\mu} \quad [13]$$

Harned and Fitzgerald (2) computed the right-hand side of Eq. [13] for various values of K using the activity coefficients of barium chloride obtained by Tippetts and Newman (8) for the real activity coefficients of cadmium chloride. These computed values were plotted *vs.* $\sqrt{m}$ and compared with E_H calculated from Eq. [2] and plotted against $\sqrt{m}$. The values of K which caused the curve of Eq. [13] to be most nearly symmetrical with the curve of Eq. [2] was taken as the dissociation constant. Values of the right hand member of Eq. [13] were read from the proper curve and subtracted from the original unsmoothed E_H function. According to Eq. [12] and [13] this gives

$$E^o = E + k \log \alpha(1 + \alpha)^2 m^3 \gamma^3_{\pm} \quad [14]$$

Harned and Fitzgerald averaged the values of E^o obtained in the above described manner by drawing a straight line of zero slope through the points resulting by plotting the values of E^o against $\sqrt{m}$. They obtained a value of 0.57300v for E^o.

In this work, data on cadmium chloride in aqueous solutions were taken initially to check the experimental procedure for reproducibility. Since this data compared favorably with the data of Harned and Fitzgerald (3), the two sets of data were listed together and treated according to the above theory with the aid of an IBM 7074 computer. The value of E^o obtained from the mixed data was 0.57340v.

The next step in the treatment of the data was to replace the activity coefficients of barium chloride by the value of γ'' for cadmium chloride from which the best value of α was computed in the reiterations by the use of Eq. [6], [7], and [10]. The complete procedure described above was then applied. The value of E^o determined in this case was 0.57162v. Since this treatment of the data gave a value within 1.5 mv of the value determined by Harned and Fitzgerald (3), it was decided to write a program for the IBM 7074 computer which was similar to the above treatment except for the two changes listed below.

The first change naturally was that γ'' cadmium chloride was used instead of γ barium chloride.

The second change was that the curves corresponding to Eq. [2] and [13] were not considered separately, but rather their difference was computed since this difference is E^o. The obtaining of the final form of the equation is shown below.

At 25°C Eq. [2] becomes

$$E_H = E + 0.08875 \log m - 0.1557\sqrt{m} + 0.01781 \quad [15]$$

Equation [13], at 25°C, reduces to

$$E_H - E^o = 0.01781 - 0.02958 \log \alpha(1 + \alpha)^2 - 0.08875 \log \gamma_\alpha - 0.08987\sqrt{\mu} \quad [16]$$

where γ_α is the value of γ'' calculated from the proper modification of Eq. [7] using the best value of α determined in the reiterations described above. $\gamma_\alpha = [\gamma'']^{1/2}$.

When one substitutes the value of E_H from Eq. [15] into Eq. [16], the following equation is obtained

$$E^o = E + 0.08875 \log m\gamma_\alpha - 0.1557\sqrt{m} + 0.08987\sqrt{\mu} + 0.02958 \log \alpha(1 + \alpha)^2 \quad [17]$$

This is the final form which was used to evaluate E^o for each observed value of E at a given molality. The values of E^o computed from this equation for each value of E and m were averaged. The IBM 7074 computer program was stated so that different values of K and a selected value of $\overset{\circ}{a}$ were tried until the correct combination gave an average E^o value with an average deviation of 1.5 mv. This amounts to the difference between the curves from Eq. [2] and [13] being a straight line with a slope of zero within 1.5 mv. In the higher alcohol solutions the average minimum deviation of E^o was somewhat higher. The points on the Harned and Fitzgerald plot showed comparable deviations to those in Table III.

In Table III the E^o values which were determined are listed. In addition the values of the equilibrium constants and the mean distance of approach of the ions which were necessary for E^o to reach a suitable minimum deviation are listed. Other derived quantities and the dielectric constants of the media are presented in this table.

In order for E^o to reach this minimum deviation it was not necessary to change the value of $\overset{\circ}{a}$ as the solvent was varied from water to 100% methanol. Oiwa (9) found a trend for $\overset{\circ}{a}$ when HCl was studied in the water-methanol solutions, although the range of variation for $\overset{\circ}{a}$ for HCl was not great in this study. He indicated that this was due to a preferential solvation effect of the ions. It has been found that the value for $\overset{\circ}{a}$ for cadmium chloride in water-ethanol solvents did not change (1).

Table III. Tabulated values of derived quantities in different solvents and at different temperatures

Solvent	T°K	D	K	$\overset{\circ}{a}$ (A)	E° international volts	Deviation in E°	$-\Delta F^\circ$ calories per mole ± 200 cal	$-\Delta H^\circ$ calories per mole ± 200 cal	$-\Delta S^\circ$ e.u. ± 0.6 e.u.
H_2O	298.16	78.5	0.07	5	0.57162	0.00130	26,400		
								33,800	25
H_2O	303.16	76.8	0.07	5	0.56890		26,200		
								32,400	20
H_2O	308.16	75.0	0.07	5	0.56670		26,100		
30% MeOH	298.16	64.6	0.05	5	0.53611	0.00137	24,700		
								27,300	8.7
30% MeOH	303.16	62.7	0.05	5	0.53502	0.00097	24,700		
								31,400	22
30% MeOH	308.16	61.3	0.05	5	0.53262	0.00074	24,600		
60% MeOH	298.16	50.1	0.02	5	0.49510	0.00152	22,800		
								27,000	22
60% MeOH	303.16	48.6	0.02	5	0.49362	0.00157	22,800		
								36,600	46
60% MeOH	308.16	47.1	0.02	5	0.48864	0.00114	22,500		
90% MeOH	298.16	35.8	0.01	5	0.44253	0.00184	20,400		
								26,900	22
90% MeOH	303.16	34.6	0.01	5	0.44019*	0.00192	20,300		
								37,700	57
90% MeOH	308.16	33.7	0.01	5	0.43396	0.00162	20,000		
100% MeOH	298.16	31.6	0.001	5	0.41033	0.00183	18,900		
								30,900	40
100% MeOH	303.16	30.7	0.001	5	0.40598	0.00176	18,700		
								34,100	51
100% MeOH	308.16	29.9	0.001	5	0.40050	0.00183	18,500		

* Smoothed values.

In Fig. 3 the E° values listed in Table III are plotted against the reciprocal of the dielectric constant of the medium in which each E° value was determined. The resulting lines are almost straight in agreement with the data taken by Hefley and Amis in the ethanol-water system (1). Corsaro (10) studied zinc chloride in water-methanol solutions. He found that the E° of that solution varied linearly with the reciprocal of the dielectric constant of the medium in which the E° was determined, when methanol and methanol-water solutions were used. These data have been discussed theoretically by Harned and Owen (11) and by Amis (12).

Variations in the values of the dissociation constant K were discussed in the case of ethanol water solvents, and the same discussion would apply here. In brief the dissociation and hence the dissociation constant decreased as the dielectric constant of the media decreased due to the addition of increasing quantities of methanol. This is in agreement with Bjerrum's (13) theory of ionic association in liquid media. The decrease in the dielectric constant of the ethanol-water solvents by a factor of about 2.5 caused K to decrease by a factor of about 10^{-2} as was found in the methanol-water media. Fuoss and Kraus (14) found a decrease of 10^{-3} fold in the K values for tetraisoamylammonia nitrate when the dielectric constant of the dioxane-water media decreased by threefold.

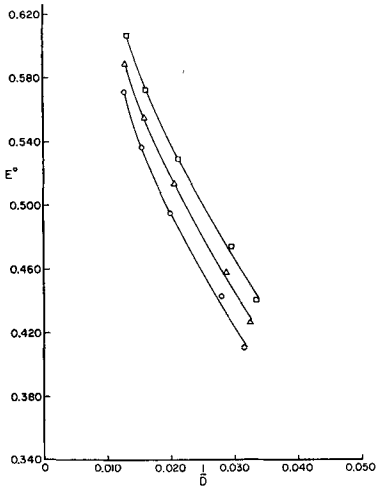

Fig. 3. Standard potentials of the Cd-Cl_xHg (11%) $|CdCl_2(m)|$ AgCl-Ag cell plotted against $1/D$ using methanol solutions. ○, MeOH solutions at 25°C; △, MeOH solutions at 30°C + 0.02000v; □, MeOH solutions at 35°C + 0.04000v.

The value of 5Å found for the distance of closest approach of the ions of cadmium chloride is not unreasonable since the divalent cadmium ion has a radius of about 0.95Å and the monovalent chloride ion a radius of about 1.90Å. The solvent would no doubt play a part in the determination of the value of $\overset{\circ}{a}$, making this value greater than the sum (0.95Å + 1.95Å) or 2.85Å. Therefore $\overset{\circ}{a} = 5$Å is reasonable.

Values of ΔF°, ΔH°, and ΔS° recorded in Table III were calculated using standard equations for these quantities. The chemical reaction to which these calculations apply is the cell reaction. Thus

$$Cd(s) \rightarrow Cd^{++}(m) + 2\epsilon \text{ (anode reaction)} \quad [18]$$

$$2Ag^+(s) + 2\epsilon \rightarrow 2Ag(s) \text{ (cathode reaction)} \quad [19]$$

$$Cd(s) + 2Ag^+(s) \rightarrow Cd^{++}(m) + 2Ag(s) \text{ (cell reaction)} \quad [20]$$

In the methanol-water as in the ethanol-water system, the change in standard free energy increases (becomes less negative continually) as the per cent of nonaqueous component in the solvent increases. This means that the process becomes less spontaneous with increasing amounts of methanol in the solvent. As discussed in the ethanol paper, this decrease in spontaneity might result from one or several causes. Difference in nature and extent of solvation, change in the structure of the solvent, and increased association of the ions at the lower dielectric constants might be among the pertinent factors. However, here again the latter factor is perhaps the predominant one. That this is true is supported by the observation that the standard free energy change toward a more positive value is less in going from water to 100% methanol than in going from water to 100% ethanol, and the change in dielectric constant is also less in the water-methanol case.

As in the case of ethanol water. the ΔH°-values have been rounded off to three significant figures because the quantities depend on differences in ΔF°-values and hence are no doubt not so reliable as the ΔF°-values themselves. Nevertheless, the quantities are presented here so as to be available for comparison with future data. The reaction is exothermic throughout and shows

a negative entropy increment in all instances. In ethanol-water the process was exothermic throughout and showed a negative entropy increment in all instances. The ΔS^o-values were rounded off to two significant figures since the differences in ΔF^o and ΔH^o contained only two, or at most, three significant figures. The precision of these values were calculated from the precisions of the ΔF^o- and ΔH^o-values.

The negative entropy increments for the process probably indicate an ordering process as discussed in the ethanol-water paper. In this paper the ordering process is apparently greater at the higher temperature interval and is probably related to the lower viscosity and reduced dielectric constant at the higher temperature permitting a more ready orientation of the molecules.

Activity Coefficients

After the E^o values were determined for each solvent composition, the activity coefficients were calculated from Eq. [1].

The logarithm of the activity coefficients which were determined in this manner are listed in Tables IV and V. A graphical representation of this data in which

Table IV. Activity coefficients of cadmium chloride in water at 25°C

m	m	$-\log \gamma_\pm$
0.000500	0.0224	0.080
0.000861	0.0293	0.097
0.00100	0.0316	0.11_2
0.00200	0.0447	0.15_4
0.00288	0.0537	0.20_1
0.00500	0.0707	0.23_1
0.00653	0.0808	0.26_0
0.00700	0.0837	0.26_6
0.0100	0.100	0.30_6
0.0103	0.101	0.30_1
0.0162	0.127	0.38_7
0.0200	0.141	0.40_0
0.0500	0.224	0.54
0.100	0.316	0.67

Table V. Activity coefficients of cadmium chloride in methanol-water solvents

m	$\sqrt{m}$	$-\log \gamma_\pm$, 25°C	$-\log \gamma_\pm$, 30°C	$-\log \gamma_\pm$, 35°C
		30% Methanol		
0.000465	0.02156	0.0499	0.0830	0.094
0.00121	0.03478	0.139	0.139	0.13_9
0.00224	0.04733	0.195	0.229	0.21_7
0.00450	0.06708	0.287	0.287	0.25_7
0.00543	0.07369	0.314	—	—
0.00796	0.08922	0.369	0.369	0.36_8
0.0127	0.11269	0.443	0.447	0.45_1
0.0206	0.14352	0.528	0.522	0.52_5
0.0525	0.22912	0.689	0.682	0.69
0.0969	0.31129	0.828	0.825	0.83
		60% Methanol		
0.000536	0.02315	0.137	0.119	0.13_4
0.00114	0.03376	0.222	0.202*	0.22_4
0.00220	0.04690	0.326	0.303	0.32_2
0.00439	0.06626	0.432	0.412	0.43_8
0.00765	0.08746	0.528	0.505	0.52_5
0.0129	0.11357	0.629	0.610	0.63
0.0201	0.14177	0.720	0.703	0.73
0.0402	0.20049	0.867	0.859	0.89
0.0916	0.30265	1.069	1.062	1.0_9
		90% Methanol		
0.000563	0.02373	0.211	0.231	0.24_4
0.00124	0.03521	0.339	0.353	0.36_1
0.00213	0.04615	0.486	0.503	0.51_1
0.00530	0.07280	0.699	0.715	0.72
0.00875	0.09355	0.808	0.821	0.83
0.0123	0.11091	0.886	0.902	0.91
0.0205	0.14318	1.033	1.048	1.0_6
0.0375	0.19365	1.253	1.268	1.2_8
0.0876	0.29597	1.538	1.559	1.5_7
		100% Methanol		
0.000614	0.02418	0.439	0.452	0.47_3
0.00132	0.03633	0.675	0.682	0.70
0.00257	0.05070	0.831	0.841	0.86
0.00553	0.07436	1.016	1.024	1.0_4
0.00821	0.09061	1.109	1.115	1.1_3
0.0129	0.11357	1.214	1.223	1.2_4
0.0198	0.14071	1.320	1.333	1.3_7
0.0279	0.16073	1.441	1.448	1.4_7
0.0578	0.24041	1.711	1.720	1.7_4

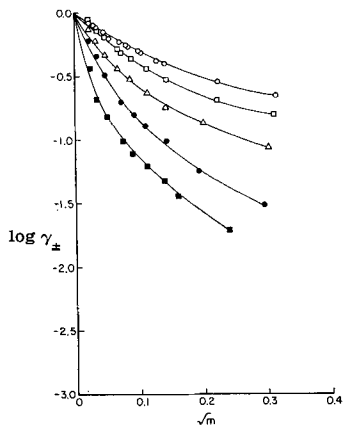

Fig. 4. Activity coefficients of the Cd-Cd$_x$Hg (11%) $|CdCl_2(m)|$ AgCl-Ag cell in the water-methanol system at 25°C. ○, H_2O; □, 30% MeOH; △, 60% MeOH; ●, 90% MeOH; ■, 100% MeOH.

log $\gamma_\pm$ is plotted against $\sqrt{m}$ is shown in Fig. 4. Only those data for 25°C are shown graphically due to the small temperature coefficient.

The variation of the activity coefficients of cadmium chloride with the dielectric constant (or solvent composition), as shown in the figures, follows the same general trends which Harned and Morrison (15, 16) observed for hydrochloric acid in water-dioxane solvents. This trend is a deviation from the straight line limiting slope of the Debye and Hückel theory at a lower value of the molality as the dielectric constant is decreased.

Acknowledgment

The authors wish to thank the United States Atomic Energy Commission which supported this work financially under contract AT-(40-1)-2069. Thanks is also due Union Carbide Chemicals Company for use of its IBM 7074 computer in calculating the values of E^o.

Manuscript received Aug. 21, 1964. This paper is based on a Dissertation presented to the Graduate School, University of Arkansas, in partial fulfillment of the requirements for the Ph.D. degree by one of the authors (J. D. H.).

Any discussion of this paper will appear in a Discussion Section to be published in the December 1965 JOURNAL.

REFERENCES

1. J. D. Hefley and E. S. Amis, *J. Phys. Chem.* In press.
2. H. S. Harned, *J. Am. Chem. Soc.*, **51**, 416 (1929).
3. H. S. Harned and M. E. Fitzgerald, *ibid.*, **58**, 2624 (1936).
4. N. G. Foster and E. S. Amis, *Z. physik Chem. N. F.*, **3**, 365 (1955).
5. A. A. Noyes and Falk, *J. Am. Chem. Soc.*, **34**, 475 (1912).
6. F. J. Wershoven, *Z. physik. Chem.*, **5**, 481 (1890).
7. E. C. Reghellato and C. W. Davies, *Trans. Faraday Soc.*, **26**, 592 (1930).
8. E. A. Tippetts and R. E. Newman, *J. Am. Chem. Soc.*, **56**, 1675 (1934).
9. I. T. Oiwa, *J. Phys. Chem.*, **60**, 754 (1956).
10. G. Corsaro and H. L. Stephens, *This Journal*, **104**, 512 (1957).
11. H. S. Harned and B. B. Owen, "The Physical Chemistry of Electrolyte Solutions," pp. 336-340, Reinhold Publishing Corp., New York (1950).
12. E. S. Amis, *J. Electroanal. Chem.*, in press.
13. N. Bjerrum, *Kgl. Danske Vidensk Selskob*, **7** [9], 1 (1926).
14. R. M. Fuoss and C. A. Kraus, *J. Am. Chem. Soc.*, **55**, 1019 (1933).
15. H. S. Harned and J. O. Morrison, *Am. J. Sci.*, **33**, 161 (1937).
16. H. S. Harned and J. O. Morrison, *J. Am. Chem. Soc.*, **58**, 1908 (1936).

Significance of Nonsteady-State A-C and D-C Measurements in Electrochemical Adsorption Kinetics

Applications to Galvanostatic and Voltage Sweep Methods

B. E. Conway, E. Gileadi,[1] and H. Angerstein-Kozlowska[2]

Department of Chemistry, University of Ottawa, Ottawa, Canada

ABSTRACT

Information obtainable from nonsteady-state electrochemical studies is examined with particular reference to the determination and significance of capacitance associated with adsorbed intermediates in consecutive reactions. The frequency dependence of the capacity in a-c measurements is related to the rise-time dependence in d-c charging transients and the concept of an equivalent frequency in d-c measurements is proposed. The nonsteady-state kinetics for a galvanostatic charging process is examined for a reaction sequence involving adsorbed intermediates, and it is shown how the capacitance behavior depends on the charging current density. Applications to the triangular voltage sweep method are made, and it is shown that for this case where neither steady-current nor steady-state kinetics apply, care must be exercised in interpretation of results derived from this method. The nonsteady-state kinetics for this case are derived and the dependence of the capacity on sweep-rate is deduced. The differential galvanostatic method leads to results which can be much more explicitly analyzed in a rigorous kinetic manner, for irreversible charging processes. Applications to experimental results which support the treatment given are discussed.

The adsorption pseudocapacitance (1) arising in certain electrochemical reactions, where an initial discharge step is at quasi-equilibrium when followed by a rate-determining step, may be defined as

$$C = k\,(d\theta/dV) \qquad [1]$$

where θ is the fractional surface coverage by intermediates formed by the discharge of an ionic species, V is the metal-solution potential difference, and k is a proportionality constant, representing the Faradaic charge which has to cross the metal-solution interface for a complete monolayer of discharged species (*e.g.*, adsorbed radicals, metal adions) to be formed on unit real surface area of the electrode.

Experimental methods for determining the adsorption pseudocapacitance have been reviewed recently (2-4) and the form of the $C - V$ relationship has been derived, assuming that the electrode system obeys an ideal Langmuir isotherm (5, 6) and for the more general and experimentally applicable case when the variation of the heat of adsorption with coverage (Temkin type of isotherm) is also taken into account (1, 7). Cases for which the assumption of quasi-equilibrium in the initial ion discharge step cannot be made have also been considered (7, 8).

The capacitance at the metal-solution interface can be obtained from a-c impedance determinations by a compensating bridge method or from phase angle measurements. The electrode is first polarized to a steady-state by applying a constant current or potential, and its impedance with respect to a small a-c signal is measured and resolved into its capacitative and resistive components. The amplitude of the a-c signal is maintained very low so that the steady current condition at the electrode is not significantly disturbed. The capacitance measured by the method is usually found to depend on the frequency and at any frequency it is the sum of the ionic double-layer capacitance $C_{d.l.}$ and the adsorption pseudocapacitance C. Dolin and Ershler (9) have shown that the total capacitance C_p measured in a parallel circuit arrangement depends on frequency according to the equation

$$C_p = \frac{C}{1 + \omega^2 r^2 C^2} + C_{d.l.} \qquad [2]$$

where C is the value of the adsorption pseudocapacitance at zero frequency (referred to by the above authors as the "equilibrium value"), and r is the reaction resistance in the initial ion discharge step, obtainable by extrapolation of the observed resistance R_p in the same parallel arrangement to infinite frequency. From Eq. [2], it is clear that $C_{d.l.}$ and r can be obtained by measuring C_p and R_p at high frequencies and extrapolating the results to infinite frequency. With these quantities known, the adsorption pseudocapacitance can be obtained from a single measurement of the total capacity C_p at an accurately known frequency. Equation [2] was derived assuming a completely homogeneous electrode or would correspond to a heterogeneous one with completely unhindered lateral motion of the adsorbed species on the surface. That this model is not quite realistic, was already realized by Dolin and Ershler (9) who found that the value of C calculated from Eq. [2] at various frequencies was still strongly frequency dependent. The capacity C could in principle, be obtained by extrapolating the measured value C_p to $\omega = 0$ and subtracting from it $C_{d.l.}$, but the measurement becomes experimentally difficult at very low frequencies ($\nu <$ 10 cycles sec^{-1}), and the experimental error is much larger. Thus, while the a-c bridge method can usually yield the most accurate experimental results, the interpretation of the values obtained is by no means straightforward.

An alternative group of methods, widely used to determine the total capacity at the metal solution interphase, depends on the relation

$$i = C\,(dV/dt) \qquad [3]$$

in which i is the direct current used to charge the capacitance C. Constant current charging curves (taken over an interval of potential where the part of the current used for the relevant over-all Faradaic process is negligible) have been used by Frumkin *et al.* (10)

[1] Present address: John Harrison Laboratory of Chemistry, University of Pennsylvania, Philadelphia, Pennsylvania.

[2] On leave of absence from the Technical University, Warsaw, Poland.

and by Butler (11), and the method has since become a generally used technique. Initial rates of decay of overpotential on open-circuit have also been used (12, 13) to determine C. This method is based on the assumption that the electrode reaction continues on open-circuit by a self-discharge process which momentarily, at the commencement of the open-circuit transient, has the same rate as that corresponding to the steady-state polarizing current density. The latter method has been extended (12, 14-16) to enable the calculation to be made of the adsorption pseudocapacity effective at any potential along the whole open-circuit decay curve, provided that the steady current-potential relation is known in an independent experiment. The assumption made in this case is that the rate-determining Faradaic reaction continues on open-circuit and acts as a potential dependent resistance shorting the terminals of the "pseudocapacitor." The value of the current to be used in Eq. [3] to evaluate C at any potential is equal to the current observed during steady-state polarization at the same potential. For current-potential relations which show hysteresis between the ascending and descending direction of change of potential, the results obtained potentiostatically for descending currents and potentials are to be used for the calculation of C.

When d-c techniques are applied, it is implicitly assumed that the pseudocapacity measured is the "equilibrium" value, namely, that which would be obtained by extrapolating the measured a-c values to infinitely low frequencies. This assumption is usually made irrespective of the magnitude of the constant current used for charging or discharging the electrode and, in fact, in the study of adsorption of atomic hydrogen, use of high current densities is required (1, 3, 17-19) to minimize readsorption of hydrogen.

The question whether the capacity measured during a constant current charging process is, in principle, the "equilibrium capacity" in the sense defined above (*i.e.*, the value corresponding to extrapolation to zero a-c frequency), or if a change in charging current and/or a change in dV/dt during charging at a given total constant current, can be looked on as a change in "equivalent frequency" (see below) is of great importance in the study and quantitative interpretation of the shape of transients for electrochemical reactions. Thus, if the effective capacity does depend on i and/or dV/dt during a galvanostatic transient (as indeed it does in certain cases to be discussed below), it is evident that this dependence should be considered when an attempt is made to evaluate kinetic and coverage parameters from transient behavior (5, 7, 8, 20).

It is the purpose of the following discussion to provide a physical picture and mathematical treatment for the variation of adsorption pseudocapacity with frequency and rise-time or charging current, and to predict the effect of variation of applied current on the shape of galvanostatic transients and on the values of the pseudocapacitance calculated from them. Experimental tests of these predictions will also be presented, which qualitatively support the theory given.

Physical Origin of Frequency Variation of Pseudocapacitance

Amplitude.—It is convenient to consider a general anodic reaction

$$M + A^- \underset{k_{-1}}{\overset{k_1}{\leftrightarrows}} MA + e \qquad \text{(I)}$$

$$2MA \xrightarrow{k_2} 2M + A_2 \qquad \text{(II)}$$

and it will be assumed that the rate constants k_1, k_{-1} for reaction (I) are relatively large compared with that for step (II), so that (I) is at quasi-equilibrium with step (II) rate-determining throughout the potential range studied. The concentration of intermediates will hence be determined solely by the equilibrium in step (I)[3] and will not be significantly affected by the kinetics of step II. If an a-c signal of small amplitude and very small frequency were now superimposed on the d-c current or potential used to polarize the system to a steady-state, the value of the coverage at any time would be that corresponding to the electrochemical steady-state at the momentarily prevailing net potential. Under these conditions, the true "equilibrium" pseudocapacity would be measured. If, on the other hand, the frequency of the a-c signal were sufficiently high, it is clear that the equilibrium in step (I) would not be disturbed at all, and the impedance at the metal-solution interface would be only that associated with the ionic double layer. Between these two extreme conditions, there can exist a frequency interval in which the rate of change of coverage can be comparable with the rate of change of potential and a dispersion of the measured capacity is observed.[4] In this range of frequencies, the coverage cannot change fast enough with the change in potential, and the smaller change in coverage then corresponds to a smaller observed pseudocapacity. It can therefore be concluded that as long as $dV/dt >> d\theta/dt$ the tendency would be for little or no pseudocapacity to be observed. When $dV/dt << d\theta/dt$, the equilibrium pseudocapacity is observed and when $dV/dt \doteq d\theta/dt$, a variable pseudocapacity can be observed which depends on dV/dt and hence on frequency. If the applied a-c signal has a sinusoidal form, the time-dependent value of the potential may be written as

$$V = V_o + A \sin(\omega t) \qquad [4]$$

where A is the amplitude of the a-c signal and V_o is the steady-state (d-c) value of the potential. Differentiating Eq. [4] with respect to time gives

$$dV/dt = A\,\omega \cos(\omega t) \qquad [5]$$

hence

$$|dV/dt|_{\text{max.}} = A\,\omega = 2\pi A\nu \qquad [6]$$

$$|dV/dt|_{\text{ave.}} = \frac{2A\omega}{\pi} = 4A\nu \qquad [7]$$

The *max*imum and *ave*rage absolute values of the rate of change of potential with time are hence proportional to the product of frequency multiplied by the signal amplitude.

The results in Eq. [6], [7] would seem somewhat unexpected since it is known experimentally, and has been shown theoretically (22), that the observed pseudocapacity is independent of the amplitude of the a-c signal (so long as it is kept small enough so that the steady-state polarization is not significantly disturbed). This apparent disagreement can be explained as follows: since it has been assumed that step I remains at quasi-equilibrium during steady-state polarization, we may regard the a-c signal as a small overpotential of variable magnitude applied to a step which is otherwise at equilibrium. The net rate of a reaction close to equilibrium is proportional to the so-called "affinity" in terms of Prigogine's terminology (23, 24), and in the case of an electrochemical reaction is proportional to the overpotential (25). Also since only step I is considered, the net reaction rate is proportional to $d\theta/dt$ and we may write

$$\frac{|dV/dt|_{\text{max.}}}{|d\theta/dt|_{\text{max.}}} = \frac{2\pi\nu A}{i_o FA/kRT} = \frac{(2\pi kRT)}{i_o F}\nu \qquad [8]$$

[3] See, however, ref. (7), (8) for a discussion of the limitations of this statement when a large dependence of apparent standard free energy of adsorption of the intermediate upon surface coverage is involved (Temkin-type conditions).

[4] It is important to realize that the above explanation (which also applies to the model leading to Eq. [2]) only predicts a variation of capacity over a relatively narrow range of frequency, *i.e.*, *ca.* two orders of magnitude in ν. The fact that, experimentally, C is found to be a function of ν over a much wider frequency range (5, 21), coupled with the apparent frequency dependence of C calculated from Eq. [2] [cf. ref. (9)], can be regarded as evidence for the existence of surface heterogeneities at which step (I) proceeds with a distribution of rate constants.

where k is the charge associated with formation of a monolayer of adsorbed intermediates (cf. Eq. [1]) and i_o is the exchange current density for the initial ion discharge step I. Equation [8] may be rewritten as

$$\frac{|dV/dt|_{max.}}{|d\theta/dt|_{max.}} = (2\pi kr)\nu \qquad [8a]$$

in which r is the reaction resistance for step I (cf. Eq. [2]), given by $r = RT/i_oF$ at low overpotentials. Thus, both quantities on the l.h.s. of Eq. [8a] are proportional to the amplitude A of the a-c signal, and their ratio is independent of it.

Phase shift.—The approach outlined above can lead to a phenomenological understanding of the origin of the phase shift arising from adsorption pseudocapacitance. Thus if the frequency of the signal is low enough, it may be assumed that equilibrium in the initial ion-discharge step is maintained at all times, and the coverage θ_t at any time t is equal to the coverage which could be observed in the steady-state condition (no a-c signal) when the electrode is polarized to a potential V_t. In order to maintain this condition, the coverage must change at a rate $d\theta_t/dt$ proportional to the rate of change of potential (dV_t/dt). Since for the system defined here, the a-c component of the current is proportional to $d\theta/dt$ (it is assumed that the d-c rate of production of A_2 is virtually unchanged) it follows that $i = k(dV_t/dt) = K' \cos \omega t$ while the a-c contribution V_t to the potential is $V_t = A \sin(\omega t)$, *i.e.*, a phase shift of $\pi/2$ arises limitingly between current and potential.

It can also be seen immediately that if the frequency is higher, so that θ_t cannot change fast enough with V_t, the current will lag behind compared with the situation at very low frequency (apart from it being on the average smaller) and thus the phase difference between i and V will be smaller than $\pi/2$. This is electrically equivalent to adding a resistance in series with the capacitor in an electric circuit, and corresponds physically to the finite reaction resistance $r = (RT/i_oF)$ and to a deviation from complete equilibrium conditions in the initial ion-discharge step.

Rapid Galvanostatic Charging

Equivalent frequency.—The situation during a charging or discharging process conducted at constant current density will now be considered. It will be assumed that in the interval of potential studied, practically all the current is used to deposit or ionize the adsorbed layer of intermediates (*i.e.*, the current due to the steady-state over-all Faradaic process is negligible). The rate of the net discharge reaction, proportional to the rate of change of coverage with time, is thus kept constant under the above conditions (but see below) during a galvanostatic pulse, but may be changed between experiments.

For the case of a-c impedance measurement, Eq. [8a] can be written as

$$\alpha = K\nu \qquad [8b]$$

where

$$\alpha = \frac{|dV/dt|_{max}}{|d\theta/dt|_{max}} = \frac{|dV/dt|_{ave}}{|d\theta/dt|_{ave}} \qquad [8c]$$

and

$$K = 2\pi kr$$

Correspondingly, on a constant current charging curve we have

$$\alpha' = \frac{|dV/dt|}{|d\theta/dt|} = \frac{|dV/dt|}{i/k} \qquad [9]$$

where α' is now an experimentally determined quantity and the equation

$$\alpha' = K\nu \qquad [9a]$$

will then define an equivalent frequency ν' corresponding to the same degree of departure from equilibrium in the initial ion discharge step as occurs during an a-c measurement taken at a frequency ν. For a given constant current charging curve, i = const. and hence α' and consequently ν' are proportional to dV/dt and change with V and t during the charging process. It is also apparent that the equivalent frequency ν' is not only a function of dV/dt but also of i for charging curves taken at different rates, *i.e.*, at different i values since for a given capacity, dV/dt will be larger for larger charging currents.

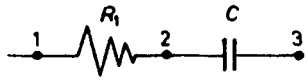

Fig. 1. Equivalent circuit for charging the pseudocapacitance in the nonsteady-state.

The frequency dependence of adsorption pseudocapacitance may be viewed in terms of an electrical model. The fact that a deviation from the equilibrium value of θ and C is observed during an a-c cycle is due to a small change of polarization of the discharge step giving rise to a current which is proportional to potential. Hence the reaction resistance acts as a simple ohmic resistance and a series "R.C." type of circuit (Fig. 1) applies. The same considerations could be applied to d-c charging at constant current. In this case the measured potential is given by

$$V = ir + V_c$$

where R is the reaction resistance and V_c the potential on the plates of the equivalent capacitor. Hence

$$\frac{dV}{dt} = \frac{dV_c}{dt}$$

so that the correct capacities will be observed but at potentials displaced to an extent iR from the reversible value.

However, during galvanostatic charging, i is usually large, and therefore the reaction resistance is potential dependent to an appreciable extent (Tafel behavior). Thus, $\Delta V = ir$ would be a function of V and the C values would depend on i and V in addition to a simple parallel displacement with respect to C (Fig. 2).

The latter explanation provides a basis for correlation of the physical model with the formal calculation.

The fact that the initial ion-discharge step (reaction I) is displaced from its equilibrium condition during galvanostatic charging or discharging, resulting in a distortion of the C-V relationship obtained, was realized already by Dolin and Ershler (9). In later literature (2, 17-19) the surface concentration of adsorbed hydrogen was studied by the "fast charging method," *i.e.*, by applying a constant, high anodic current pulse to the electrode; the effect of current density on the resulting pseudocapacity was not, however, discussed, except

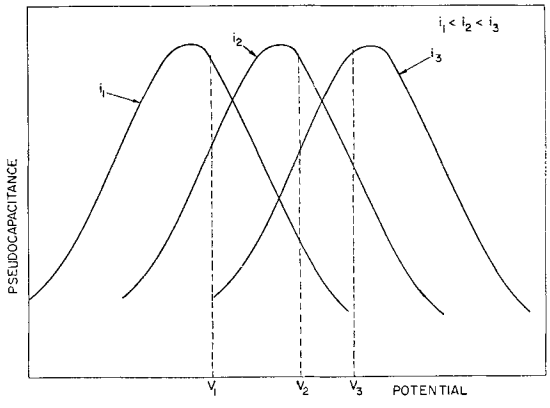

Fig. 2. Effect of irreversibility in the charging reaction on the capacity-potential profiles (schematic); effects shown for low overpotential in the charging step.

with regard to the problem of readsorption of hydrogen (1, 17).

Irreversibility in the discharge step.—We shall consider here, for simplicity, the h.e.r. and assume that a constant anodic current i is applied to the system which is initially on open-circuit at its equilibrium potential. Under these conditions, the only electrochemical reactions which can take place are the formation or ionization of adsorbed hydrogen atoms represented by step I above. It is clear that if i is less than or comparable with the exchange current for step I, the equilibrium in step I will be practially undisturbed during the anodic transient, and the coverage and adsorption pseudocapacitance calculated from the rate of change of potential with time, dV/dt, at each potential V are the true "equilibrium" values. Normally, however, high current densities must be used to ionize the adsorbed hydrogen on the surface [in order to avoid readsorption of hydrogen and other vitiating effects (2, 4)] so that i may become of the same order of magnitude or even larger than i_o.

When i is of the order of magnitude of i_o or smaller, the current is linearly related to the overpotential, *i.e.*, a constant reaction resistance r is involved and given by

$$r = \frac{RT}{i_o F} \qquad [10]$$

The quantity r represents physically the degree of reversibility of the reaction considered and the potential drop across this reaction resistance when a current i is passed is simply the overpotential η

$$ir = \frac{i}{i_o}\left(\frac{RT}{F}\right) = \eta \qquad [11]$$

Under the conditions specified above, the electrode acts as a series combination of a capacitor (equal in value to the sum of the d.l. capacitance [assumed relatively negligible] and the adsorption pseudocapacitance) and a resistor, as shown schematically below (Fig. 1)

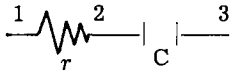

In theoretical discussions of the potential dependence of adsorption pseudocapacitance, the relevant potential is V_c across the capacitance C as would be measured between the points 2 and 3 above, since it is assumed that equilibrium is not disturbed. Experimentally, however, the potential V_{13} is measured between the points 1 and 3 in Fig. 1a, *i.e.*

$$V_{13} = ir + V_c \qquad [12]$$

Then differentiation with respect to time gives

$$\frac{dV_{13}}{dt} = \frac{dV_c}{dt} \qquad [13]$$

since both i and r are assumed to be constant during the transient. The capacity at the metal-solution interface is obtained from the equation

$$\frac{1}{C} = \frac{1}{i}\left(\frac{dV_{13}}{dt}\right) = \frac{1}{i}\left(\frac{dV_c}{dt}\right) \qquad [14]$$

and would therefore seem to be unaffected by the finite irreversibility of the reaction. From Eq. [12], however, it is clear that the potential V_{13} will differ from that (V_c) which is theoretically significant (1, 5, 6) in determining the potential at which a given value of C is attained, by an amount $\Delta V = ir$ depending on the kinetics of the reaction (its r value) and on the current i. Changing the current density i used in a galvanostatic transient would thus have the effect of shifting the C-V curve without change in shape (but see below) along the potential axis. This is shown schematically in Fig. 2. It is important to realize that while the shape of the C-V relationship is not in the above sense affected by the irreversibility of the reaction, the measured value of C at a particular potential, will depend on the applied current density i. Moreover, for a given V, the value of C may increase or decrease with i depending on the relative positions of the C-V curves for the various i values. Thus, referring to Fig. 2 where three curves are shown corresponding to increasing values of i_1, the value of C measured at a potential V_1 would decrease with increasing i ($i_1 < i_2 < i_3$) while at V_3 it would increase with increasing i. At some intermediate potential V_2 it may first increase and then decrease as i is increased.

It is of interest to consider the case when $i >> i_o$ so that the adsorption equilibrium is highly disturbed. In this case, the reaction resistance may be expressed as

$$r = \frac{RT}{\beta F}\frac{i}{i_o}\exp\left[\frac{\beta\eta F}{RT}\right] \qquad [15]$$

for an anodic process. The reaction resistance is clearly a function of η in the discharge step, but it must be remembered that during the galvanostatic transient, η (with respect to step I) remains practically constant while the change in potential is due mainly to a change in the quasi-reversible potential of the system (step I), associated with the change of coverage (1).[5] Thus the equivalent circuit represented in Fig. 1 is still valid and Eq. [13] and [14] can be applied. The shift of the C-V curve by $V = ir$ will in this case not be proportional to i since r itself is a function of i. When r has the nonlinear form given in [15], the analysis below will apply.

Nonsteady state kinetic theory of charging.—A galvanostatic charging curve corresponds to a steady-current condition but not to a chemical steady-state condition, since a total "charging" current i is made up of components i_C, the capacitative true charging current, and any Faradaic current i_F. The situation also depends on the nature of the consecutive reaction mechanism, *i.e.*, whether or not the desorption step (as in hydrogen evolution) proceeds by a chemical atom recombination step or by an electrochemical atom-ion discharge step. In the former case, all the current passes through the reaction resistance of the discharge step since the desorption is nonelectrochemical; in the latter case, part of the current is involved in electrochemical removal of the intermediate, *e.g.*, adsorbed H, and part in formation of H. The equivalent circuits are hence somewhat different (Fig. 3a, 3b) and a special symbol is required (see Fig. 3b) for the reaction resistance for the electrochemical atom-ion desorption step; electrons and H^+ ions arising from the metal and solution, respectively, are discharged from the ionic double-layer capacitance while charge corresponding

[5] This is only an approximation. As the potential is changed during the galvanostatic charging process, the exchange current density is changed due to (*a*) a change in coverage (19); (*b*) a change in the metal-solution potential difference at the changing reversible potential. Thus, even though i is kept constant, r will change due to the variation in i_o and, hence, η will also change. This would have the effect of changing the shape of the C-V relationship slightly in addition to the lateral shift in the curves. A numerical analysis, however, shows that in most practical cases this effect will be quite small.

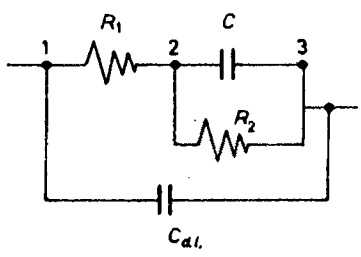

Fig. 3a. Complete equivalent circuit for step I followed by a nonelectrochemical desorption (charging process nonohmic).

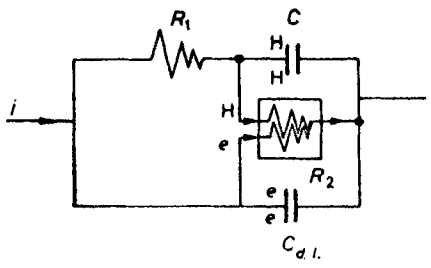

Fig. 3b. Complete equivalent circuit for step I followed by an electrochemical (e.g., atom + ion) desorption step.

to H atoms is withdrawn from the adsorption pseudocapacitance. No representation alternative to the dual channel symbol shown in Fig. 3b is possible for the electrochemical desorption type of process without "short-circuits" being involved.

The general electrochemical reaction sequence[6]

$$M + A^- \rightleftarrows MA + e \qquad (I)$$

$$MA + A^- \rightarrow M + A_2 + e \qquad (III)$$

may be considered. The steady-current condition (see Fig. 3b) is

$$i = i_1 + i_3 \qquad [16]$$

and

$$i_1 = \vec{i}_1 - \overleftarrow{i}_1 = i_C + i_3 \qquad [17]$$

where i_C is the net charging current for the pseudocapacitor.

In the steady state, $i = 2i_3$ ($i_C \rightarrow 0$); i_3 is the leakage current from the pseudocapacity associated with desorption of adsorbed A by step III and is also the electron + ion leakage current across the ionic double-layer capacity $C_{d.l.}$ associated with step III, (in regard to the charge transfer involved).

If θ is the coverage by A at a metal-solution potential difference V, the steady-current condition under Langmuir conditions (cf. 1) gives, in abbreviated form[7]

$$i = k_1 (1-\theta) e^{V/b} - k_{-1}\theta e^{-V/b} + k_3\theta e^{V/b} + C_{d.l.}\left(\frac{dV}{dt}\right) \qquad [18]$$

which gives θ as

$$\theta = \frac{k_1 e^{V/b} - i}{k_1 e^{V/b} + k_{-1} e^{-V/b} - k_3 e^{V/b}} \qquad [19]$$

neglecting the $C_{d.l.}$ term.

In Eq. [18] and [19], the k terms are the indicated "rate constants" which include for brevity of representation also the ion concentration terms allowing for double-layer ion distribution effects. For the purpose of the present calculations, it will not be necessary to specify the k terms nor the potential quantity V in more detail.

Calculating the pseudocapacity (Eq. [1]), we obtain

$$C = kd\theta/dV = \frac{2kk_1k_{-1}/b}{[k_1e^{V/b} + k_{-1}e^{-V/b} - k_3e^{V/b}]^2} - \frac{ki[k_{-1}e^{-V/b} - k_1e^{V/b} + k_3e^{V/b}]/b}{[k_1e^{V/b} + k_{-1}e^{-V/b} - k_3e^{V/b}]^2} \qquad [20]$$

The term in rate constants and V is separated from that involving current i since it is seen [cf. (1), (7), (8)] that the first term becomes the equilibrium pseudocapacitance for A as a function of V when k_1, $k_{-1} >> k_3$ (quasi-equilibrium conditions). For the latter condition then, C differs from its equilibrium value[8] by a kinetic term involving the measured rate i of the galvanostatic pulse (note: this is limiting only the rate of surface charging when the potential range corresponds to negligible net over-all reaction for the mechanism I, II).

[6] An anodic reaction is chosen purely for convenience of representation of the kinetic equations.

[7] Here the symmetry factor for step I and its reverse, and III are, for convenience, assumed equal to 0.5 so that all the b terms are the same. Also, the ionic double-layer charging current $C_{d.l.}(dV/dt)$ has been included in Eq. [18]. This part of i will, however, generally be negligible in potential regions where the adsorption pseudocapacitance is appreciable, which is the condition considered here.

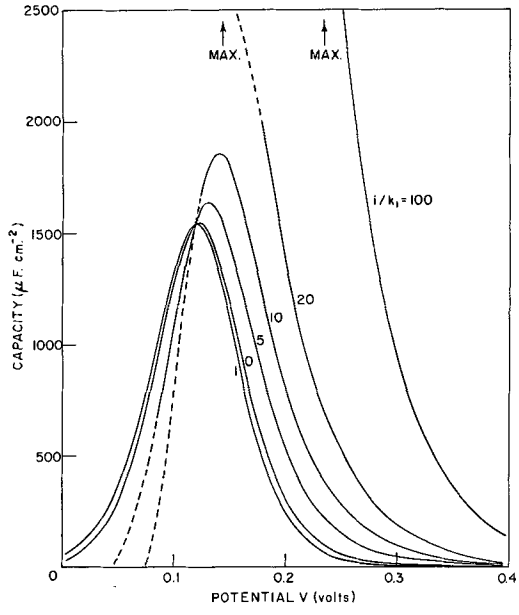

Fig. 4. Capacity-potential profile for galvanostatic charging at various currents expressed as the ratio i/k_1 where k_1 is the kinetic constant in Eq. [20] for the forward direction of step I. (Dotted regions are not experimentally realizable). K_1 the quasi-equilibrium constant in step I is taken as 0.01 [cf ref. (1) and (7)].

The behavior of C with respect to V for a range of i values (expressed as i/k_1) has been computed from Eq. [20] for the "quasi-equilibrium" condition k_1, $k_{-1} >> k_3$ with a value of K_1, the equilibrium constant for step I, equal to 10^{-2} ($= k_1/k_{-1}$) as in previous calculations of C as a $f(V)$ (1, 7, 8). Choice of other values of K_1 simply shifts the scale of potentials over which the variation of C with V occurs (1). The results for C as $f(V)$ are shown in Fig. 4a and 4b, and for θ as $f(V)$ in Fig. 5.

[8] The calculations here differ from those we have given previously (7, 8) which concerned the dependence of C on extent of disturbance of I from equilibrium in the steady current and chemical steady state. Here the analysis applies only to the steady-current condition in transients.

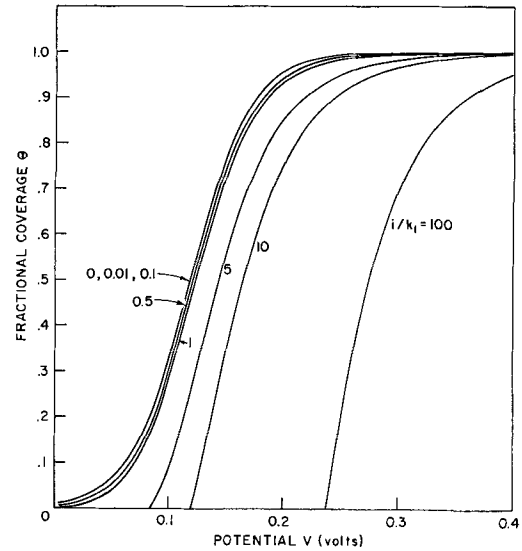

Fig. 5. Coverage θ-potential (V) profiles corresponding to Fig. 4 for various values of the charging rate parameter $1/k_1$.

The calculations indicate that C may either decrease or increase, depending on the potential, with increasing current in the galvanostatic pulse as was concluded qualitatively above and in Fig. 2. The decrease of C occurs over those potentials less than that for which $C = C_{max.}$ in the equilibrium case (k_1, $k_{-1} >> k_3$ and $i \rightarrow 0$) while the increase of C with increasing i occurs at potentials corresponding to $C > C_{max.}$. The change of capacity is linear with i/k_1 as required by Eq. [20], but negative values of θ would appear to be indicated for $i > k_1 e^{-V/b}$. This is, however, a physically impossible condition since the pseudocapacitance can only be charged by the discharge step I which cannot proceed at a rate greater than that defined by its rate constant and respective V and b values, *i.e.*, at the rate $k_1 e^{-V/b}$ when $\theta \rightarrow 0$). The maximum over-all rate in the steady state for the mechanism I, III is $2k_3 e^{V/b}$ which will be less than $k_1 e^{V/b}$ if III is rate-controlling. It is clear therefore that while $k_1 e^{V/b}$ or $k_{-1} e^{-V/b}$ may be greater than i, i cannot be greater than $k_1 e^{V/b}$. Hence the limit for i/k_1 is $i/k_1 = e^{V/b}$ for a potential V.

If the desorption step occurs by a recombination type of process II, the same type of analysis as above will hold provided that the condition k_1, $k_{-1} >> k_2$ is maintained. However, the equivalent circuit will not involve the special element shown in Fig. 3b since no charge transfer is involved in the desorption step. The pseudocapacitance is hence in parallel simply with the leakage resistance corresponding to k_2 and this whole combination provides a parallel leakage admittance across $C_{d.l.}$.

Linear Potential Sweep Method

Here the potential of the system is controlled potentiostatically and is made to change at a predetermined (usually constant) rate. The situation here is thus, in principle, similar to that during galvanostatic charging. Here for α (Eq. [8c]) we would have

$$\alpha = \left| \frac{dv/dt}{d\theta/dt} \right| = f\left(\frac{dV}{dt}, i\right) \qquad [21]$$

where dV/dt rather than i is now the quantity fixed by a device, *e.g.*, a potentiostat controlled by a ramp or triangular wave function, in the external circuit and the observed current is a function of potential and time. A point along the $i - t$ curve obtained experimentally can again be related to an equivalent frequency through Eq. [9a] and the pseudocapacity value, determined by the time-dependent charging current $i_v (= C_v\, dV/dt)$ at potential V, may become a function of the rate of change of potential with time, and of the degree of reversibility of the initial ion discharge step (*e.g.*, step I). Under such conditions $i_V/(dV/dt)$ would not be constant but a function of (dV/dt). This is observed in some cases (27).

The theory of the triangular wave potential sweep method was originally given by Sevcik (28), and the method was examined by Delahay and Perkins (29), for diffusion-controlled reactions; however, the analysis of Sevcik is inapplicable to most of the recent applications to anodic oxidation and electrocatalytic reactions where adsorbed intermediates are involved (4) and the currents are pseudo-Faradaic charging currents or kinetic currents modified by potential-dependent adsorption of intermediates (4). In most of the recent applications, this method has been used somewhat uncritically to obtain qualitative information on possible steps in anodic oxidation reactions. Since neither a steady-state nor a steady-current condition obtains, rigorous kinetic analyses have not previously been made. However, the essential nonsteady-state kinetic theory can be developed as we show below.[9]

We assume that a current i_t is passing at time t in the sweep when the potential is V. For a given sweep $dV/dt = m$, a constant. The current for a charge transfer step involving the production or ionization of an intermediate, *e.g.*, as in reaction I, will be

$$i_t = k_1 (1 - \theta_t)\, e^{V/b} - k_{-1} \theta_t e^{-V/b} \qquad [22]$$

in ranges of V where the rate of the desorption step II is negligible; θ_t is the coverage of the intermediate produced in the discharge step I and prevailing at time t when the potential is V. In the sweep method, this coverage θ_t will not be the same as that in the galvanostatic method at the same potential, since in the latter case the potential adjusts to the coverage with a microscopic extent of charge transfer while here the potential is momentarily set at V, but the coverage must take some time to reach the value it would have in the galvanostatic method at this potential. Generally we shall expect for an ascending (anodic) sweep that $\theta_G > \theta_P$ where G and P represent the galvanostatic and potentiodynamic coverages attained at potential V. The change of coverage during a sweep from potential V_1 to V_2 is obviously

$$\Delta\theta = k \int_{t_1}^{t_2} i_t\, dt \qquad [23]$$

where k is as defined earlier and t_1 and t_2 are times proportional to V_1 and V_2. By analogy with the operations used to obtain Eq. [19], we obtain

$$\theta_t = \frac{k_1 e^{V/b} - i_t}{k_1 e^{V/b} + k_{-1} e^{-V/b}} \qquad [24]$$

where i_t is now dependent on t,V, instead of being constant as in the case of the relation [19]. Separating the term in i_t gives

$$\theta_t = \frac{k_1 e^{V/b}}{f(V)} - \frac{i_t}{f(V)} \qquad [25]$$

where $k_1 e^{V/b} + k_{-1} e^{-V/b}$ has been represented by $f(V)$. Differentiation of [25] enables the capacitance C_V to be expressed in terms of an equilibrium capacitance $C_{V,E}$ [cf. (1, 7, 8)] corresponding to zero net charging rate and a term dependent on dV/dt. Thus

$$\frac{C_V}{k} = \frac{d\theta_t}{dV} = \frac{2k_1 k_{-1}/b}{[f(V)]} + \frac{[f(V)]\left[\frac{i_t}{b} - \frac{di_t}{dV}\right] - \frac{2k_{-1} i_t e^{-V/b}}{b}}{[f(V)]^2} \qquad [26]$$

The first term is recognized (7, 8) as $C_{V,E}$ and i_t can be expressed as

$$i_t = C_V\, dV/dt; \text{ also } \frac{di_t}{dV} = C_V (d^2V/dt^2) + \frac{dV}{dt} \cdot \frac{dC_V}{dV} = \frac{dV}{dt} \cdot \frac{dC_V}{dV}$$

since dV/dt = constant. Hence Eq. [26] gives

$$\frac{C_V}{k} = \frac{C_{E,V}}{k} + \left(\frac{dV}{dt}\right) \frac{\left\{ f(V)\left[\frac{C_V}{b} - \frac{dC_V}{dV}\right] - \frac{2k_{-1} e^{-V/b} C_V}{b} \right\}}{[f(V)]^2} \qquad [27]$$

This has the expected form since $C_V \rightarrow C_{E,V}$ when $dV/dt \rightarrow 0$. C_V is not, however, linear in dV/dt as follows by expressing C_V explicitly as a function of dV/dt. The most explicit form is

$$\frac{C_V}{k} = \frac{\frac{C_{E,V}}{k}[f(V)]^2 - \left(\frac{dV}{dt}\right) f(V) \left(\frac{dC_V}{dV}\right)}{[f(V)]^2 - \frac{k}{b}\left(\frac{dV}{dt}\right)(f(V) - 2k_{-1} e^{-V/b})} \qquad [28]$$

For a given sweep, dV/dt is constant and dC_V/dV could be obtained experimentally [or calculated (1, 7, 8)] by

[9] A brief communication on this matter has been published elsewhere (*J. Electroanal. Chem.*, in press).

means of a differentiating amplifier using a dual beam oscilloscope (cf. 30). The rate constants in $f(V)$ might then be estimated by measurements of dC_V/dV at two or more sweep rates if the processes involved were purely of an adsorption-desorption type. However, this is rarely the case except perhaps for H and O adsorption reactions occurring below their respective reversible potentials.

It is seen that a differential galvanostatic method, *e.g.*, that of Kozlowska and Conway (30), leads to a much simpler and direct analysis of nonequilibrium electrochemical adsorption behavior than is the case for the sweep method which gives a simple result only under equilibrium conditions, *i.e.*, for relatively "reversible" processes.

A rather simpler but only approximate solution which may apply at low sweep rates may be derived by assuming that the capacity C_V differs from $C_{E,V}$ simply by the effect of the finite current i_V given by the galvanostatic current relation [18], *i.e.*, assuming $\theta_t \doteq \theta$ which is equivalent to the condition that θ_t can follow V with a degree of irreversibility which is small. Then

$$C_V = C_{E,V} - k_V i_V \qquad [29]$$

where $C_{E,V}$ is the equilibrium capacity contribution and the second term, proportional to i, has been written as k_V where k_V is a function of V and is defined by comparison of [29] with [20]; it may take a positive or negative sign depending on the partial rate terms in Eq. [20]. The current i_V in Eq. [29] is simply the charging current $C_V dV/dt$ determined by C_V and the potential sweep rate. Then

$$C_{E,V} = C_V + k_V i_V = C_V(1 + k_V\, dV/dt) \qquad [30]$$

At very slow sweep rates it is hence clear that $C_V \rightarrow C_{E,V}$, the experimentally significant equilibrium value, since the charging currents are then limitingly small and the equilibrium in the step of type I is least disturbed.

At somewhat higher sweep rates

$$i_V = (C_{E,V} - k_V i_V)\, dV/dt \qquad [31]$$

or

$$i_V/(dV/dt) = \frac{C_{E,V}}{1 + k_V\left(\frac{dV}{dt}\right)} \qquad [32]$$

The left-hand-side of Eq. [32] is the measured capacity at the given dV/dt, *i.e.*, C_V so that approximately

$$C_V = \frac{C_{E,V}}{1 + k_V\left(\frac{dV}{dt}\right)} \qquad [33]$$

The result will also depend on electrode potential through the potential-dependent terms in k_V (see Eq. [20] and [29]).

From the foregoing discussion, it may be suggested that data derived from the potential sweep method should always be obtained as a function of the sweep rate (cf. 35) and extrapolated to zero frequency. This would apply to calculated capacities, charge corresponding to the area $\int i dt$ under the peak, and the position of the peak currents on the potential axis.

It has been supposed in previous work [*e.g.*, (27)] that a current peak, in the potential-sweep method, which gives an $\int it$ independent of dV/dt is one that is associated with an electrochemical adsorption process. This is a reasonable assumption, but the converse is not necessarily true, *viz.*, that a peak which gives an it product dependent on dV/dt must be associated with steady kinetic or diffusion-controlled process rather than an adsorption. Thus, the charge passed is a pseudo-Faradaic process in which deposition or ionization of an intermediate is involved will depend on the sweep rate. If the sweep is fast enough, in a repetitive sweep experiment, there will be negligible charging of the adsorption pseudocapacitance; the capacity will tend to the double-layer capacity and the charge to that associated with the change of charge held in double layer between the extremes of the signal potential. In a single sweep (ramp signal) experiment, this limitation will, however, not apply since the potential will be steady at the top or bottom of the ramp. It must also be pointed out that the rate of a kinetic process exhibiting an inhibition or passivation, *e.g.*, by coadsorbed oxide intermediates (37), will give a potentiostatic current-voltage relation in the sweep method which can be dependent on the sweep rate since the extent of coverage by the inhibiting species at a given (momentary) potential will be dependent on dV/dt as discussed above in the general case (Eq. [23]).

Applications to Experimental Results

Charging curves.—Charging curves have recently been obtained for the formate oxidation reaction at Pt (cf. 32) by Kozlowska and Conway (31) by the direct and differential galvanostatic method (30) at various cathodic current densities. The results may be used to examine the applicability of Eq. [20]. The capacities associated with the coverage by the electrode of formate radical species (14, 32) are shown in Fig. 6 as a function of the charging current density. It is seen that the capacities increase with increasing cathodic charging current density as indicated by Eq. [20] at high anodic overpotentials when $k_{-1}e^{-V/b} << k_1 e^{V/b}$. The experimental conditions in this work are as indicated in the caption to Fig. 6. Anhydrous formic acid was used as the solvent (cf. 32) in order to minimize complications by reactions involving anodically formed surface oxides of Pt.

Similar conclusions may be obtained from the data of Conway and Vijh (33, cf. 34) for direct and differential galvanostatic charging in the Kolbe reaction at Au in anhydrous trifluoroacetic acid from which residual traces of water were removed by treatment with a

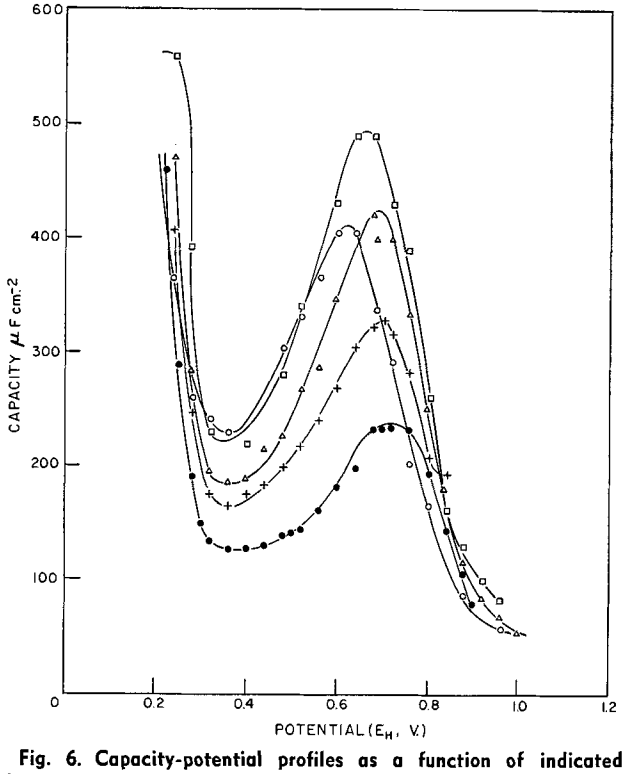

Fig. 6. Capacity-potential profiles as a function of indicated charging current density for the adsorbed species in the formate oxidation; 1M HCOOK in anhydrous HCOOH, 5°C; smooth Pt electrodes fired in hydrogen; previous anodic polarization for 5 min at 10^{-3} amp/cm^{-2}. Cathodic c.d. (in amp/cm^{-2}): •, 2.1 x 10^{-4}; +, 4.6 x 10^{-4}; △, 8.0 x 10^{-4}; ○, 1.8 x 10^{-3}; □, 3.9 x 10^{-3}.

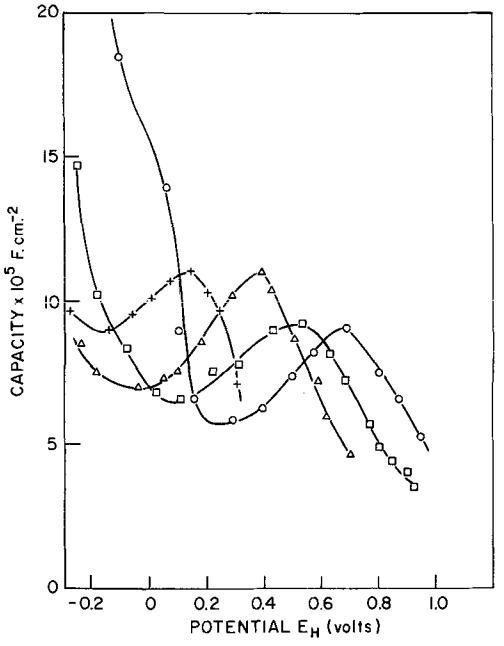

Fig. 7a. Capacity-potential profiles as a function of charging current density for the adsorbed species in the Kolbe oxidation; 1M K.TFA in anhydrous trifluoracetic acid. Cathodic c.d. (in amp/cm^{-2}): ○, 5.02 x 10^{-3}; □, 10.03 x 10^{-3}; △, 21.0 x 10^{-3}; +, 32.8 x 10^{-3}.

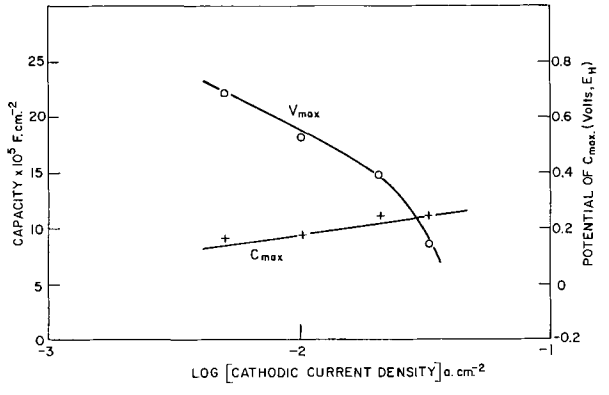

Fig. 7b. Dependence of maximum capacity and potential at which it occurs on cathodic current density (conditions as for Fig. 7a).

small quantity, (<1%) of trifluoroacetic anhydride. Here the adsorbed intermediate responsible for the pseudocapacity is believed (34) to be the CF_3COO radical. The capacity-potential relationships are shown in Fig. 7, for various cathodic discharging rates; again the capacities are dependent on the discharging current density as required theoretically.

Few experimental results exist from which suitable data for a simple irreversible system can be obtained to test the dependence of capacities on sweep rate in the potential sweep method. Will and Knorr (35) have studied the hydrogen ionization reaction in some detail by the sweep method and have experimentally examined the dependence of the potential of the current maximum and of the current itself on dV/dt. This reaction is, however, a relatively reversible one. Gilman and Breiter (35, 36) have studied the anodic oxidation of methanol at various sweep rates. Apart from better resolution of charging detail at the lower sweep rates, the position of the peak current is found to depend on sweep rate and approaches a constant value of potential at the smaller sweep rates. The data derived from their curves are plotted out in Fig. 8 and indicate a variation of the maximum with changing dV/dt, and hence transient current, in the expected manner. However, in these more complex reactions, it is not always pos-

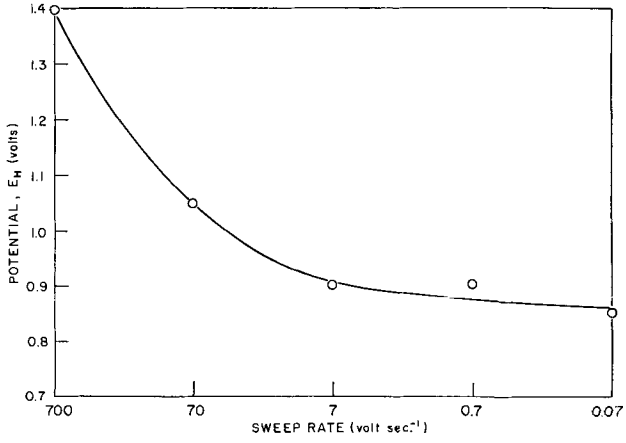

Fig. 8. Potentials of the current maximum in triangular potential sweep curves for methanol oxidation at Pt, as a function of sweep rate [ref. (35)].

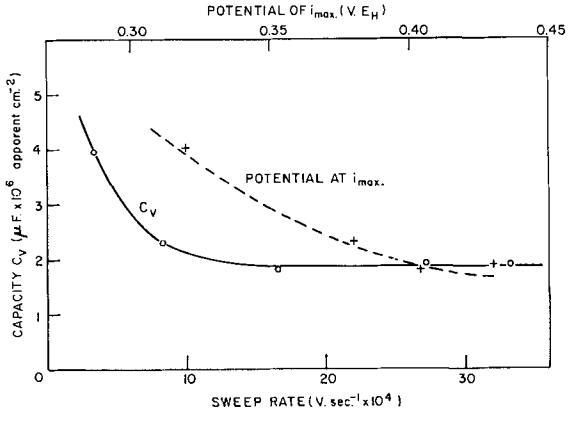

Fig. 9. Maximum capacitance as a function of sweep rate for the adsorption peak in methanol oxidation (27) at platinized platinum. Potentials of current maxima (cf. Fig. 8) also shown.

sible to distinguish between kinetic Faradaic currents and pseudo-Faradaic currents involved in the build up or removal of adsorbed intermediates. In complex reactions, *e.g.*, the oxidation of methanol and of formate in aqueous media both kinetic and pseudo-Faradaic currents, *e.g.*, for surface oxide films function, may pass in the same potential range and influence each other (37). The analysis made above for the capacitance behavior will then not be applicable. In most of the previous work using the potential-sweep method, it is believed that insufficient attention has been paid to these complications.

In another case, the oxidation of methanol at platinized platinum (27), the peak was observed between 0.25 and 0.6v. E_H has been characterized as an adsorption peak on account of the independence of the *it* product (but see above) under the peak on anodic sweep rate. This therefore provides a case of interest in relation to the present discussion. The capacity maxima may be calculated as a function of dV/dt and are shown in Fig. 9 together with the potentials of the capacity maxima. The variation of both quantities with sweep rate is as expected on the foregoing theory. The capacity maxima decrease in this case with increasing charging current (dV/dt) and are displaced to higher anodic potentials (overpotential effect). The actual values of C_V are very large but the electrodes used were platinized so the actual capacities per real cm^2 of electrode area are probably of the order of at least 2000 μF cm^{-2}, a result which could arise under Langmuir conditions (1, 4, 6). However, the above figure for C_V per real cm^2 is on the high side and this apparent large value may in fact indicate some participation of kinetic currents

in the sweep currents observed, a problem we have emphasized above.

Open-Circuit Decay Measurements

Various experimental methods have been proposed (2, 3, 12-16) by which the adsorption pseudocapacitance can be evaluated by studying the rate of decay of potential on open-circuit following steady-state polarization. The situation here is quite different from that in the two cases considered above since the potential of the system is allowed to change by a self-discharge process, without external control of potential or current. Thus the rate of decay of overpotential will be a function of time, but will always be determined by the intrinsic electrochemical time constant RC of the reaction comprised of an equivalent capacitor and a resistor in parallel.[10] The current density flowing internally in the system at any potential will be equal to the steady-state current density measured at the same potential (14). If our initial assumption that the electrode reaction is studied in the potential range where the ion discharge step can effectively be regarded as being at quasi-equilibrium, holds, then the pseudocapacity obtained by any method based on open-circuit decay will represent the true equilibrium value as would be measured at an infinitely low frequency. This is the capacitance quantity required in kinetic interpretations and for relation to isotherms (1, 6-8). The interpretation of results obtained by this method (12) is hence more straightforward than in the other two methods discussed.

Conclusions

It is shown that measurements of the adsorption pseudocapacitance by any method where the current or the potential is controlled by the external circuit may be a function of the externally controlled quantity. While the frequency dependence of the adsorption pseudocapacitance, as measured by an a-c impedance bridge is well known, little regard seems to have been given hitherto to a similar effect which will prevail during galvanostatic or polarographic potential-sweep studies.

The concept of an "equivalent frequency" in d-c transients is introduced and the significance of its variation with time (potential) during a constant d-c charging transient is emphasized, in relation to the theoretical interpretation of the shape of the transient.

The experimentally observed dependence of the adsorption pseudocapacity on the frequency of the applied a-c signal (when measured by the a-c bridge method) over a wide range directly indicates the existence of intrinsic heterogeneities on the electrode surface, coupled with significant hindrance to lateral motion of the adsorbed species on the surface.

Any method depending on the study of the rate of decay of potential on open circuit will yield the "equilibrium" pseudocapacitance value and is therefore to be preferred.

A quantitative kinetic treatment of the dependence of the observed pseudocapacity on the applied current in a galvanostatic charging transient is given and the result is applied to the calculation of analogous effects which arise in the potentiostatic potential-sweep method.

A kinetic treatment is given for the voltage sweep method with regard to the behavior of the pseudocapacitance in adsorption processes. It is concluded that the differential galvanostatic method is preferable.

Applications to experimental results are given.

[10] The capacitor is actually a parallel combination of the ionic double-layer capacity and the adsorption pseudocapacity, but we shall assume here that the former is negligible with respect to the latter. The resistor is the nonohmic differential reaction resistance, defined as $(di/dV)^{-1}$ which is normally a function of exp. [V], or of V at low overpotentials.

Manuscript received Aug. 26, 1964.

Any discussion of this paper will appear in a Discussion Section to be published in the December 1965 JOURNAL.

REFERENCES

1. B. E. Conway and E. Gileadi, *Trans. Faraday Soc.*, **58**, 2493 (1962).
2. J. O'M. Bockris and M.A.V. Devanathan, Office of Naval Research Report No. CNR 551, (22) (1957).
3. E. Gileadi, Ph.D. Thesis, Ottawa (1962).
4. E. Gileadi and B. E. Conway in "Modern Aspects of Electrochemistry," J. O'M. Bockris and B. E. Conway, Editors, Vol. III, Butterworths Sci. Publ. London (1964). See also B. E. Conway, "Theory and Principles of Electrode Processes," Ronald Press, New York, in press.
5. A. Eucken and B. Weblus, *Z. Electrochem.*, **55**, 114 (1951).
6. J. O'M. Bockris and H. Kita, *This Journal*, **108**, 676 (1961).
7. B. E. Conway and E. Gileadi, *Can. J. Chem.*, **42**, 90 (1964).
8. E. Gileadi and B. E. Conway, *J. Chem. Phys.*, **39**, 3420 (1963).
9. P. Dolin and B. Ershler, *Acta Physicochim. U.R.S.S.*, **13**, 747 (1940); see also A. R. Despic and D. R. Jovanovic, *Doc. Chem. Yugoslav*, **25-26**, 427 (1961).
10. A. Slygin and A. N. Frumkin, *Acta Physicochim. U.R.S.S.*, 3, 719 (1935); *ibid.*, **4**, 991 (1936); *ibid.*, **5**, 819 (1936).
11. G. Armstrong and J. A. V. Butler, *Trans. Faraday Soc.*, **29**, 1261 (1933).
12. B. E. Conway and P. L. Bourgault, *ibid.*, **58**, 593 (1962); see also V. E. Past and E. A. Iofa, *Zh. Fiz. Khim. S.S.S.R.*, **33**, 1230 (1959).
13. H. B. Morley and F. E. W. Wetmore, *Can. J. Chem.*, **34**, 359 (1956).
14. B. E. Conway, E. Gileadi, and M. Dzieciuch, *Electrochim. Acta*, **8**, 143 (1963).
15. V. V. Sobol and Z. A. Iofa, *Doklady Akad. Nauk S.S.S.R.*, **138**, 1151 (1961).
16. U. Palm and V. E. Past, *ibid.*, **146**, 1374 (1962).
17. M. Breiter, C. A. Knorr, and W. Volkl, *Z. Elektrochem*, **59**, 881 (1955).
18. M. A. V. Devanathan, J. O'M. Bockris, and W. Mehl, *J. Electroanal. Chem.*, **1**, 143 (1959/60).
19. M. A. V. Devanathan and M. Selvaratnam, *Trans. Faraday Soc.*, **56**, 1820 (1960).
20. H. Kita, M. Enyo, and J. O'M. Bockris, *Can. J. Chem.*, **39**, 1870 (1961).
21. M. Breiter in "Transactions of the Symposium on Electrode Processes," John Wiley & Son, Inc., New York (1961).
22. D. C. Grahame, *This Journal*, **99**, 370C (1952).
23. J. Prigogine, "Thermodynamics of Irreversible Processes," C. C. Thomas Publishers, Springfield, Ill. (1955).
24. J. Prigogine, P. Outer, and C. Herbo, *J. Phys. Chem.*, **52**, 321 (1948).
25. A. C. Makrides, *This Journal*, **104**, 677 (1957).
26. A. Damjanovic, Private communication.
27. J. Giner, *Electrochim. Acta*, **9**, 63 (1964).
28. A. Sevcik, *Coll. Czech. Chem. Comm.*, **13**, 349 (1948).
29. P. Delahay and G. Perkins, *J. Phys., Coll. Chem.*, **55**, 586, 1146 (1951).
30. H. A. Kozlowska and B. E. Conway, *J. Electroanal. Chem.*, **7**, 109 (1964).
31. H. A. Kozlowska and B. E. Conway, To be published.
32. B. E. Conway and M. Dzieciuch, *Can. J. Chem.*, **41**, 21, 55 (1963).
33. B. E. Conway and A. Vijh, To be published.
34. B. E. Conway and N. Dzieciuch, *Can. J. Chem.*, **41**, 38 (1963).
35. F. Will and C. A. Knorr, *Z. Elektrochem.*, **64**, 258 (1960); cf. F. Will, Abstracts Electrochem. Soc. Meeting, Toronto, May (1964).
36. J. Gilman and M. Breiter, *This Journal*, **109**, 1099 (1962).
37. D. J. Gilroy and B. E. Conway, *J. Phys. Chem.*, In press.

The Effect of Pressure on *p*H and Dissociation Constants from Measurements with Buffered and Unbuffered Glass Electrode Cells

Acetic, Formic, Phosphoric, Carbonic Acids Adenosinetriphosphate and Phosphorylcreatine

A. Distèche and S. Distèche

Laboratory of General Biology, Zoology Institute, University of Liege, Liege, Belgium

ABSTRACT

The cell Ag-Ag Cl $\left|\begin{matrix}\text{HCl } (m_1)\\ \text{KCl } (m_2)\end{matrix}\right|$ glass $\left|\begin{matrix}\text{HR or HR + MR}\\ (m_1 + m_2)\ \text{KCl}\end{matrix}\right|$ AgCl-Ag

is used to measure the effect of pressure on the ionization constant K of weak acids (HR) in the presence or not of the corresponding Na or K salt (MR). Double extrapolation, to zero weak electrolyte concentration and zero KCl concentration, yields log K_p/K_1 values at $p = 1000$ kg cm^{-2} and the molal volume change on ionization for the reaction HR $\rightleftharpoons$ R$^-$ + H$^+$ is computed at 1 atm for acetic acid, formic acid, carbonic acid (buffered and unbuffered solutions), phosphoric acid (2^d step), adenosinetriphosphate and phosphorylcreatine.

It has been shown in previous papers (1-3) that the cell

$$\text{Ag-AgCl}\left|\begin{matrix}(m_1)\text{HCl}\\ (m_2)\text{KCl}\end{matrix}\right|\begin{matrix}\text{glass}\\ (\text{Corning}\\ 015)\end{matrix}\left|\begin{matrix}\text{HR or HR + MR}\\ (m_1 + m_2)\text{KCl}\end{matrix}\right|\text{Ag-AgCl}$$

can be used to measure the effect of pressure on the ionization of a weak acid HR in the presence or absence of its Na or K salt (MR). Dissociation constants K can be computed from the emf measurements by extrapolation to zero ionic strength and zero weak electrolyte concentration, and the volume change (ΔV_p^o) induced by pressure p can be calculated at any pressure from the well-known equation

$$\left(\frac{\partial \ln K}{\partial p}\right)_{m,T} = \frac{-\Delta V^o}{RT} \qquad [1]$$

More recently, Hamann (4) used the cell Ag-AgCl | (m_1) HCl | Li — glass | (m_2) KCl + (m_3) KOH | AgCl-Ag to derive ΔV_1^o for water.

In the present paper, we shall investigate in more detail the pressure dependence of the ionization constants of acetic, formic, phosphoric (2nd step), and carbonic acids, either in buffer solutions or in pure acid solutions. Data for organophosphorus compounds such as adenosinetriphosphate and phosphorylcreatine are also described.

Experimental

The equipment described in 1962 (2) is used. It was found that slight hysteresis effects, which sometimes appear when new Ag-AgCl or glass electrodes are tried, are minimized by applying several pressure cycles before making the final experiment.

Methods.—The methods used to derive ionization constants from emf measurements are classic and can be used, in principle, to calculate K and ΔV^o at any pressure with the aid of Eq. [1].

In practice, the choice of a particular method is limited by the fact that the glass electrode cell under pressure exhibits two types of asymmetry potentials: one, normal, which can be taken into account by measuring the emf of the cell with the reference solution on both sides of the glass membrane, and another which arises (2) when the KCl concentration is different in the two compartments. To eliminate this last cause of error, it was found convenient to use the following three cells

1. Ag-AgCl	HCl (0.01M) KCl (0.09M)	HR or HR + MR KCl (0.1M)	Ag-AgCl
2. Ag-AgCl	HCl (0.001M) KCl (0.009M)	HR or HR + MR KCl (0.01M)	Ag-AgCl
3. Ag-AgCl	HCl (0.001M)	HR or HR + MR KCl (0.001M)	Ag-AgCl

The asymmetry due to KCl in cell 3 can be neglected.

The emf (E) of the cells at 1 atm or at pressure p is expressed by the relation

$$E_{1,p}\mathbf{F}/2.3RT = \log (m_H)_{1,p}^{ref.} - \log (m_H)_{1,p}^{x} + 2\log \frac{(\gamma_{HCl})_{1,p}^{ref.}}{(\gamma_{HCl})_{1,p}^{x}} \qquad [2]$$

where m_H is the hydrogen ion concentration (molal scale), γ_{HCl} the mean activity coefficient for HCl, and where *ref.* and x, respectively, refer to the reference half-cell and the cell compartment containing the weak acid HR or its buffer HR + MR (M = Na or K) at concentrations m_{HR} and m_{MR}.

The dissociation constant K of the weak acid is given by the relations

$$\log K = \log \frac{m_H^2}{m_{HR} - m_H} + 2\log \gamma_A = \log k - (A\sqrt{\mu} \pm B\mu) \qquad [3]$$

in the unbuffered half-cell, and

$$\log K = \log \frac{m_H(m_{MR} + m_H)}{m_{MR} - m_H} + 2\log \gamma_A = \log k - (A\sqrt{\mu} \pm B\mu) \qquad [4]$$

in the buffered half-cell

Here $2\log \gamma_A = \log \gamma_H\gamma_R/\gamma_{HR}$ and $(A\sqrt{\mu} \pm B\mu)$ is the usual function of the ionic strength μ used to estimate $2\log \gamma_A$.

The combination of [2], [3], and [4] leads to the expressions

$$2(E_1 - E_p)\mathbf{F}/2.3RT = \log \frac{K_p}{K_1} + \log \frac{(m_{HR} - m_H)_p}{(m_{HR} - m_H)_1} + 2\log \frac{(\gamma_A)_1}{(\gamma_A)_p} + 4\log \frac{(\gamma_{HCl})_1^{ref.}}{(\gamma_{HCl})_p^{ref.}} - 4\log \frac{(\gamma_{HCl})_1^{x}}{(\gamma_{HCl})_p^{x}} \qquad [5]$$

and

$$(E_1 - E_p)\mathbf{F}/2.3RT = \log \frac{K_p}{K_1} + \log \frac{(m_{HR} - m_H)_p}{(m_{HR} - m_H)_1} \cdot \frac{(m_{MR} + m_H)_1}{(m_{MR} + m_H)_p} + 2\log \frac{(\gamma_A)_1}{(\gamma_A)_p}$$

$$+ 2 \log \frac{(\gamma_{HCl})_1^{ref.}}{(\gamma_{HCl})_p^{ref.}} - 2 \log \frac{(\gamma_{HCl})_1^{x}}{(\gamma_{HCl})_p^{x}} \quad [6]$$

for the unbuffered and buffered half-cells, respectively.

When m_H is negligible compared to m_{HR} and m_{MR}, the ionic strength remains constant in the x compartment. The effect of pressure on γ_{HCl} is small

$$\left[\log \frac{(\gamma_{HCl})_{1000}}{(\gamma_{HCl})_1} = 0.003 \text{ in HCl } 0.1\text{M } (5) \right]$$

and as a first approximation one can neglect the terms containing γ_{HCl} which cancel each other at infinite dilution of the weak electrolyte because of the symmetry of the cells.

Equations [5] and [6] then simplify to

$$2(E_1 - E_p)\mathbf{F}/2.3RT = \log \frac{K_p}{K_1} + 2 \log \frac{(\gamma_A)_1}{(\gamma_A)_p} = \log \frac{k_p'}{k_1'} \quad [7]$$

and

$$(E_1 - E_p)\mathbf{F}/2.3RT = \log \frac{K_p}{K_1} + 2 \log \frac{(\gamma_A)_1}{(\gamma_A)_p} = \log \frac{k_p'}{k_1'} \quad [8]$$

for the unbuffered and buffered half-cells, respectively.

The primes indicate that log k' is only known with approximation. The choice of the best suited concentration scales to eliminate log $(\gamma_{A1}/\gamma_{Ap})$ by extrapolation to zero concentration of both weak electrolyte and KCl, is based on the following considerations.

Activity coefficients and pressure are related by the well-known equation

$$\left(\frac{\partial \ln \gamma}{\partial p} \right)_{m,T} = \frac{\overline{V}_2 - \overline{V}_2^\circ}{RT} \quad [9]$$

where $\overline{V}_2$ and $\overline{V}_2^\circ$ are the partial molal volumes of the solute (subscript 2), respectively, at any concentration m, and in the standard state (unit activity, or at infinite dilution in the pure solvent). Integration of [9] yields the simplified relation (5)

$$\log \gamma_p = \log \gamma_1 + C(p-1)\sqrt{m d_o} \quad [10]$$

in which C is a constant and d_o the density of water.

Infinite dilution in 0.1M KCl (cell 1), 0.01M KCl (cell 2), and 0.001M KCl (cell 3) can be used to define three other reference states and for each medium the partial molal volumes in the standard state will be shifted in first approximation, according to Eq. [11] (6).

$$^{KCl}\overline{V}_2^\circ = \overline{V}_2^\circ + A_V \sqrt{2d_o}\sqrt{\mu} \quad [11]$$

where A_V is a constant.

It follows that extrapolation of $E_1 - E_p$ (Eq. [7] and [8]) on the $\sqrt{m}$ scale will yield values of log K_p/K_1 corresponding to each auxiliary reference state. Equations [1], [9], and [11] show that subsequent extrapolation on the $\sqrt{\mu}$ scale to zero KCl concentration will give log K_p/K_1 in pure water. Further, it is to be expected, if p is not too great, that the two extrapolations will be linear.

When m_H is not negligible, it is practical to calculate m_H' from Eq. [2] using γ_{HCl} values corresponding to the ionic strength at pressure 1 and p. The prime indicates the approximation introduced by the fact that the effect of pressure on the activity coefficient is neglected and that it is assumed that γ_{HCl} in KCl or NaCl is not affected by the weak electrolyte. The values used for γ_{HCl} are taken from Harned and Owen (7). $(m_H')_{1,p}$ is used to calculate $(\log k' - A\sqrt{\mu'})_{1,p}$ from Eq. [3] and [4], again neglecting the effect of pressure on the constant A, which is close to unity.

$(-\log k' + \sqrt{\mu'})_p - (-\log k' + \sqrt{\mu'})_1 = \Delta pK'$, or log k_1'/k_p' is then calculated and can be used for the double extrapolation on the $\sqrt{m}$ and $\sqrt{\mu}$ scales as above.

An alternative consists in twice extrapolating, either $(-\log k' + \sqrt{\mu'})$ or $-\log k' + A\sqrt{\mu'} \pm B\mu'$ or simply, log k', at pressures 1 and p, on the best suited concentrations scale ($\sqrt{\mu}$ or μ) depending on the nature of the electrolyte.

Since the effect of pressure on the activity coefficients is neglected in the calculations, it can be deduced from the difference between the slopes of the extrapolated functions. If needed, the corrected activity coefficients can be used to calculate the ionization functions k (Eq. [3] and [4]) with more accuracy, which in turn will lead to a more precise knowledge of K after a second double extrapolation.

The volumes change on ionization at infinite dilution, (ΔV_1°), is calculated from the slope of a graph of log K_p/K_1 *vs.* pressure at 1 atm (Eq. [1]).

When simplified Eq. [7] and [8] are valid, ΔV_1 values can be read from the slope of $E_1 - E_p = f(p)$ at 1 atm and yield ΔV_1° by double extrapolation.

It is easy to show (2) that $\Delta V_1 = 1.016 \times (E_1 - {}^*E_{1000})$ if V is expressed in cm^3 mole^{-1}, E in millivolts, p in kg cm^{-2}.

*E_{1000} is measured on the tangent of $(E_1 - E_p) = f(p)$ drawn through $p = 1$. In most cases $(E_1 - E_p)$ is a linear function of p up to 1000 kg cm^{-2} and therefore the values for log $K'_{1000}/K_1' = \Delta pK'$ or simply the direct experimental emf shift $(E_1 - E_{1000})$ can be used to extrapolate. In practice, for the media investigated, it was found that whenever $(E_1 - E_p) = f(p)$ graphs displayed some slight curvature, the tangent through $p = 1$ safely could be drawn through E_p at $p = 500$ kg cm^{-2}, with $\Delta V_1 = 2 \times 2.1016 \times (E_1 - E_{500})$ if the effect of dissociation of the weak electrolyte can be neglected.

Corning 015 glass membranes give the correct hydrogen electrode constant, 2.3 $RT/\mathbf{F} \pm 1$ mv or 2%, independently of pressure, the uncertainty being within the limits of the experimental errors.

Results

Acetic acid and acetate buffer.—Figure 1 gives $2\mathbf{F}/2.3RT\ (E_1 - E_p) = \Delta pk' = \log k_p'/k_1'$ $(p = 500$ kg cm$^{-2})$

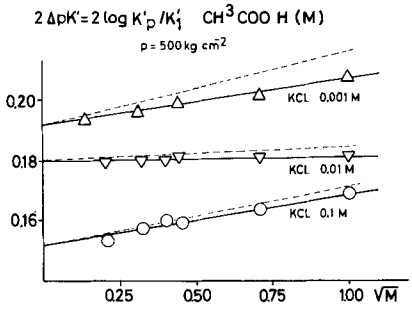

Fig. 1. Acetic acid in KCl 0.1, 0.01 and 0.001M KCl. Extrapolation of log k_p'/k_1' and log K_p'/K_1' to zero acetic acid concentration. Solid lines, log k_p'/k_1' (eq. [7]); dotted lines, $-\log k_p' + \sqrt{\mu_p'} + \log k_1' - \sqrt{\mu_1'} = \Delta pK'$ (eq. [2] and [3]).

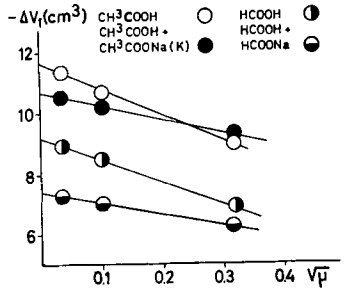

Fig. 2. Extrapolation of $-\Delta V_1$ (cm^3 mole^{-1}) to zero KCl concentration for acetic acid, acetate buffer, formic acid, and formate buffer.

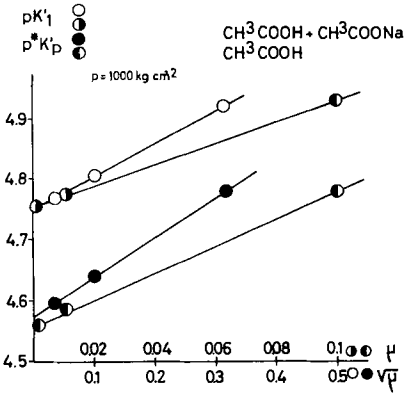

Fig. 3. Extrapolation of pK_1' and pK_p' values obtained at zero acetic acid and acetate buffer concentration, to zero KCl concentration; μ scale, acetic acid; $\sqrt{\mu}$ scale, acetate buffer. p^*K_p' at 1000 kg cm^{-2} is calculated from the slope of $(E_1 - E_p) = f(p)$ at 1 atm for acetic acid; $p^*K_p' = pK'_{1000}$ for acetate buffer where $(E_1 - E_p) = f(p)$ is linear.

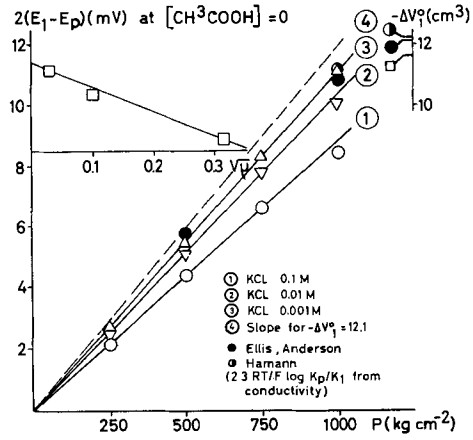

Fig. 4. 2 $(E_1 - E_p) = 2.3\ RT/F \log k_p'/k_1' = f(p)$ at zero acetic acid concentration, in 0.1, 0.01, and 0.001M KCl. Inserts: extrapolation of 2 $(E_1 - E_p)$ to zero KCl concentration and corresponding $-\Delta V_1°$ value (11.6 cm^3 mole^{-1}). 2.3 $RT/F \log K_p/K_1$ and $\Delta V_1°$ from conductivity data [Ellis and Anderson (8); Hamann (9, 10)] are indicated together with the limiting slope of 2 $(E_1 - E_p) = f(p)$ for $-\Delta V_1° = 12.1$.

for acetic acid solutions as a function of $\sqrt{m}$ (Eq. [7]; $2 \times \Delta pK'$ is taken as ordinate to facilitate comparison with Fig. 5 for acetate buffer and for simplicity the symbol K' is used instead of k'). Corresponding values of ΔV_1 at $[CH_3COOH] = 0$ are extrapolated to $[KCl] = 0$ in Fig. 2, which gives $-\Delta V_1° = 11.6$ cm^3.

The slope of the extrapolated function depends both on the ionic strength and the undissociated acid concentration. This explains the difference between the slope for 0.01M KCl and that observed for 0.1M and 0.001M KCl.

A more elaborate treatment (Eq. [2] and [3]) where $pK' = -\log k' + \sqrt{\mu'}$ is first extrapolated on the μ scale to $\mu = 0.1$, 0.01, and 0.001, and then (Fig. 3) to $[KCl] = 0$ on the $\sqrt{\mu}$ scale, yields $-\Delta V_1° = 11.5$ cm^3 mole^{-1}. The * sign of p^*K_p in Fig. 3 denotes that the dissociation constant at $p = 1000$ kg cm^{-2} is calculated from $2 \times 2\ (E_1 - E_{500})$ values (see page 351). The dotted lines in Fig. 1 represent $-\log k_p' + \sqrt{\mu_p'} + \log k_1' - \sqrt{\mu_1'} = \Delta pK'$ derived from these more complicated calculations which give the same result as the simple treatment used to draw the solid lines.

Figure 4 shows $2(E_1 - E_p) = f(p)$ (Eq. [7]) at $[CH_3COOH] = 0$ in KCl 0.1M, 0.01M, and 0.001M, where the $(E_1 - E_p)$ values were obtained from extrapolations of the emf readings on the $\sqrt{m}$ scale at $p = 250$, 500, 750, and 1000 kg cm^{-2}.

The curvature in $2(E_1 - E_p) = f(p)$ is apparent at $p = 1000$ kg cm^{-2} but only in 0.1 and 0.01M KCl. The extrapolation at $[KCl] = 0$ is also given on Fig. 4 and the corresponding $-\Delta V_1°$ value is 11.6 cm^3 mole^{-1}.

This figure is in agreement with our previous preliminary determinations (2) and in reasonable agreement with density and conductivity data (Table I).

The $-\Delta V_1°$ values, published by Ellis and Anderson (8) for $p = 1$, $p = 500$, $p = 1000$ kg cm^{-2} and by Hamann and Strauss (9) for $p = 1$ and $p = 1000$ kg cm^{-2} are indicated on Fig. 4 either in cm^3 mole^{-1} or converted into emf values, together with the limiting slope corresponding to $-\Delta V_1° = 12.1$ cm^3 mole^{-1} (8).

It is clearly seen that the main difference between the conductivity data and our determinations lies in the estimation of the curvature of $2(E_1 - E_p) = f(p) = 2.3RT/\mathbf{F} \log k_p'/k_1'$.

In a buffer containing equal molalities of acetic acid and sodium acetate, $E_1 - E_p$ is a linear function of p up to 1000 kg cm^{-2} at all the KCl concentrations investigated. $(E_1 - E_{1000})$ together with $\Delta pK' = \log K_{1000}'/K_1'$ is given in Fig. 5 as a function of the square root of the total salt and acid concentrations.

The drop of $(E_1 - E_{1000})$ at high dilutions shows that Eq. [7] is no longer valid, and that it is necessary to take the dissociation of acetic acid into account (Eq. [4]) to get the correct values for $\Delta pK' = -\log k_1' + \sqrt{\mu_1'} + \log k_p' - \sqrt{\mu_p'}$.

Extrapolation on the $\sqrt{\mu}$ scale is given in Fig. 2 and shows that $-\Delta V_1° = 10.7$ cm^3 mole^{-1} which agrees with our previous determinations (2) but is 0.9 cm^3 smaller than $-\Delta V_1°$ in acetic acid solutions.

Extrapolation of $-\log k' + \sqrt{\mu'}$ at $p = 1$ and $p = 1000$ kg cm^{-2} first on the μ scale to zero buffer concentration and then to $[KCl] = 0$ on the $\sqrt{\mu}$ scale (Fig. 3), gives identical results. No difference was found with potassium acetate or when the buffer ratio MR/HR is reduced to 1/8.

The value of pK_1 in the unbuffered cell is 4.76, and 4.75 when the buffer is used, in agreement with the results obtained by Hamann (9, 10) (4.77), and by Ellis and Anderson (8) (4.75) from their conductivity determinations. (The extrapolation line for acetate buffer in Fig. 3 has been shifted 0.01 pK unit to coincide with the data for acetic acid, to better show the difference of the effect of pressure).

Formic acid and formate.—Formic acid has been extensively studied in a previous paper (2) from which

Table I. Volume change for ionization of some weak acids at 1 atm, 22°C

	Glass electrode $-\Delta V_1°$	Density $-\Delta V_1°$	Conductivity $-\Delta V_1°$
Acids and buffers	cm^3 mole^{-1}	cm^3 mole^{-1}	cm^3 mole^{-1}
Acetic acid	11.6	12.5 (10) 9.2 (6) 11.5 (14)	12.2 (9) 12.1 (8)
Acetate buffer	10.7		
Formic acid	9.2[1] (2)	8.0 (10)	8.8 (10)
Formate buffer	7.4		
Carbonic acid $K_{(1)}$	26.6	29.0 (6)	26.5 (13)
Bicarbonate buffer	25.5		
Phosphoric acid $K_{(1)}$	17.7[1] (2)		15.5 (8)
Phosphate buffer $K_{(1)}$	15.7[1] (2)		
Phosphate buffer $K_{(2)}$	24.0	28.1[2] (15)	
Adenosine triphosphate (pH 7.0)	24.0		
Phosphorylcreatine (pH 7.0)	21.2		
Volume change for ionization of water at 1 atm, 25°C, Hamann (4).			
	20.4 (4)	20.55 (16) 23.4 (6)	

[1] Average values taken from Distèche (2) multiplied by the factor 1.016 (see page 35) which was neglected in the 1962 paper.
[2] $\Delta V_1 = -24.1$ cm^3 mole^{-1} is reported from dilatometric experiments by Linderstrom-Lang and Jacobsen (11).

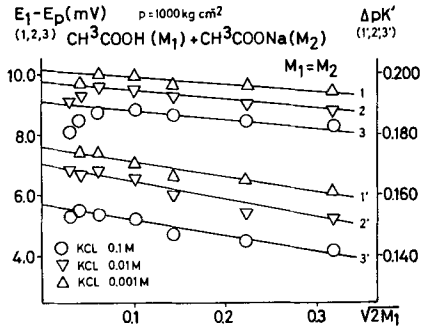

Fig. 5. Acetate buffer in 0.1, 0.01, and 0.001M KCl. 1, 2, 3: $(E_1 - E_p) = 2.3\ RT/F \log k_p'/k_1'$ as a function of the total acetate and acetic acid concentration. 1', 2', 3': extrapolation of $\Delta_pK' = -\log k_1' + \sqrt{\mu_1'} \log k_p' - \sqrt{\mu_p'}$ (Eq. [2] and [4]) to zero buffer concentration.

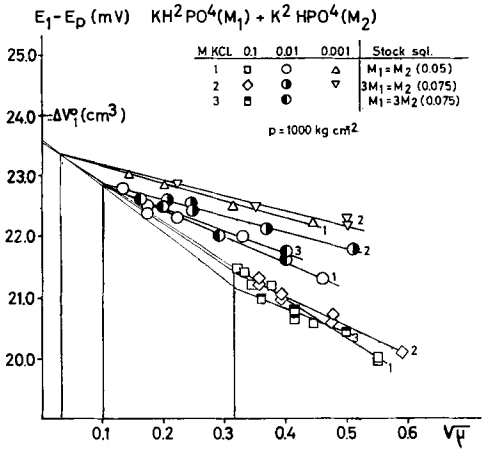

Fig. 6. Phosphate buffer $K_{(2)}$ in 0.1, 0.01, and 0.001M KCl. Extrapolation of $(E_1 - E_p) = 2.3\ RT/F \log k_p'/k_1'$ to zero KCl and buffer concentration at three different buffer ratios; $-\Delta V_1^\circ = 24.0$ cm^3 mole^{-1}.

we take the necessary data to extrapolate $-\Delta V_1$ to [KCl] = 0 on the $\sqrt{\mu}$ scale as shown in Fig. 2. $-\Delta V_1^\circ = 9.2$ cm^3 mole^{-1} in fairly good agreement with the conductivity determinations (Table I) [8.8 cm^3 mole^{-1}, Hamann (10)]. Data for formate buffer, treated in the same way as the acetate buffer, yield $-\Delta V_1 = 7.4$ cm^3 mole^{-1} (Fig. 2).

It is seen on this same figure that the curves for acetic acid and formic acid, for acetate buffer and for formate buffer, run nearly parallel with each other.

Phosphate buffer (2nd step).—In Fig. 6, the results obtained for three different buffer ratios are plotted on the $\sqrt{\mu}$ scale and the double extrapolation leads without any difficulty to $-\Delta V_1^\circ = 24.0$ cm^3 mole^{-1}, which is to be preferred to a preliminary estimate, 23.4 cm^3 mole^{-1}, published in 1962.

Density measurements predict $-\Delta V_1^\circ = 28.1$ cm^3 mole^{-1} (14) but dilatometric experiments by Linderstrom-Lang and Jacobsen [see ref. (11)] give 24.1 cm^3 mole^{-1}.

Adenosine triphosphate and phosphorylcreatine.—Figure 7 indicates that $-\Delta V_1^\circ$ (24.0 cm^3 mole^{-1}) is the same in phosphate buffer and in ATP solutions at pH = 7.0, the double extrapolation being done on the $\sqrt{m}$ and $\sqrt{\mu}$ scales. A slightly smaller value is obtained if both extrapolations are made on the $\sqrt{\mu}$ scale (dotted line).

Figure 8 shows the corresponding results for phosphorylcreatine. $-\Delta V_1^\circ = 21.2$ cm^3 mole^{-1} and is considerably smaller than the volume change observed for phosphate buffer ($K_{(2)}$) and ATP.

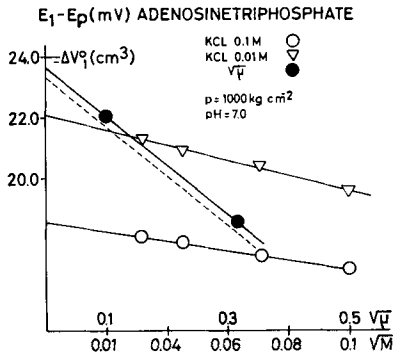

Fig. 7. Adenosinetriphosphate in 0.1 and 0.01M KCl. Extrapolation of $(E_1 - E_p) = 2.3\ RT/F \log k_p'/k_1'$ to zero ATP concentration ($\sqrt{m}$ scale) and to zero KCl concentration ($\sqrt{\mu}$ scale); $-\Delta V_1^\circ = 24.0$ cm^3 mole^{-1}. Dotted lines, both extrapolations are made on the $\sqrt{\mu}$ scale.

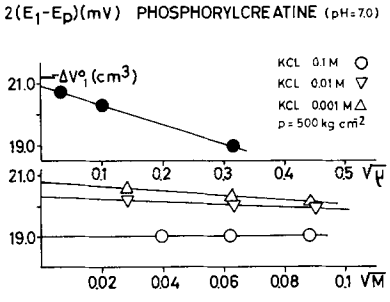

Fig. 8. Phosphorylcreatine in 0.1, 0.01, and 0.001M KCl. Extrapolation of 2 $(E_1 - E_p) = 2 \times 2.3\ RT/F \log k_p'/k_1'$ to zero phosphorylcreatine concentration (lower curves) and to zero KCl concentration (upper curve); $-\Delta V_1^\circ = 21.2$ cm^3 mole^{-1}.

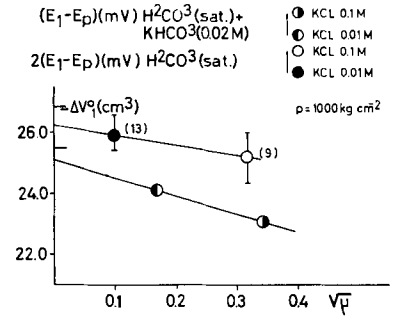

Fig. 9. Extrapolation of 2 $(E_1 - E_p) = 2.3\ RT/F = \log k_p'/k_1'$ for carbonic acid (saturated solution) and $(E_1 - E_p) = 2.3\ RT/F \log k_p'/k_1'$ for bicarbonate buffer (H_2CO_3 sat. + 0.02M $KHCO_3$) to zero ionic strength; $-\Delta V_1^\circ = 26.6$ cm^3 mole^{-1} and 25.5 cm^3 mole^{-1}. The circles on the upper curve represent average values derived from 13 and 9 determinations in 0.01M KCl and 0.1M KCl respectively; the horizontal lines indicate the highest and lowest values.

The ΔV values are calculated from readings at 500 kg cm^{-2} because of the rather marked curvature of the $(E_1 - E_p) = f(p)$ curve.

Control analysis before and after a pressure run failed to indicate any hydrolysis.

It is well known (12) that the $pK_{(2)}$ of phosphoric acid in phosphorylcreatine is strongly affected by the methylguanidinium group, its value being 4.6 instead of 7.2. The difference observed for ΔV_1° is related to this phenomenon insofar as it is related to the ionic solvation energy difference between H_3PO_4 and its ester.

Carbonic acid and bicarbonate buffer.—Our previous determinations of ΔV_1 for carbonic acid in 0.1M KCl (1) gave values as high as 31.0 and 32.3 cm^3 mole^{-1}, but only 22.8-23.9 cm^3 mole^{-1} for the bicarbonate buf-

fer (values corrected for the asymmetry due to KCl when 0.1M HCl is used as reference half-cell). Density data (6) predict 29.0 cm^3 $mole^{-1}$ and conductivity data give 26.5 cm^3 $mole^{-1}$ (13).

Experimental difficulties were encountered especially with carbonic acid solutions, the pH of which shows long-term instability under pressure. The curves giving $(E_1 - E_p) = f(p)$ were constructed from readings taken immediately after quick pressure steps separated by long intervals.

The same problems were met with at the start of the new determinations. Later, however, it was found that stable readings can be obtained provided the silicone oil used in the glass electrode cell is saturated with CO_2 as well as the aqueous solutions and the cell filled from pipettes where the gas phase is pure CO_2. These precautions limit the possibility of CO_2 exchanges between both liquid phases and the escape of CO_2 in the pressure bomb or elsewhere.

The circles on the upper curve of Fig. 9 correspond to the average value of, respectively, 9 and 13 determinations in 0.1M KCl and 0.01M KCl saturated with CO_2.

Extrapolation at $\sqrt{\mu} = 0$ gives $-\Delta V_1^\circ = 26.6$ cm^3 cm^{-3} in agreement with the conductivity experiments.

Bicarbonate buffer containing 0.02M $KHCO_3$ was tested in the same way. The results show very much less dispersion, are in reasonable agreement with our previous determinations, and yield on extrapolation $-\Delta V_1^\circ = 25.5$ cm^3 $mole^{-1}$.

Extrapolation at zero buffer concentration was not tried in this case because of the difficulty of maintaining the buffer ratio constant. The effect of H_2CO_3 on log K_p'/K_1', however, is small (5) compared to the effect of the ionic strength, so that it seems safe to extrapolate.

Discussion

Table I summarizes the ΔV_1° determinations made with a glass electrode cell compared with the data from density and conductivity measurements.

The agreement with conductivity data is fairly good for acetic, formic, and carbonic acid, but the value found for H_3PO_4 from emf measurements is about 2 cm^3 higher. It should be noticed that H_3PO_4 is highly dissociated in diluted solutions which means relatively small pH shifts for large $\Delta pK'$ changes when pressure is applied. This makes ΔV calculations much more sensitive to experimental errors. The ΔV found for phosphate buffer $K_{(1)}$ is in close agreement with the conductivity determinations, but this might be fortuitous since we notice that systematically ΔV values for buffers, from pH measurements, are smaller than the values obtained for pure acid solutions.

The difference is much larger than possible experimental errors: 0.9, 1.8, 2.0, 1.1 cm^3 for acetate, formate, phosphate $K_{(1)}$, and bicarbonate buffer, respectively.

The difference is identical with Na or K salts. This practically eliminates the possibility of an error due to asymmetry in cation composition between the cell compartments since the reference half-cell always contains KCl except for the experiments in 0.001M KCl where the effect of KCl is negligible. However, the cell cannot be made symmetrical with respect to anions. Though it seems rather unlikely, these could be adsorbed on the glass membrane and cause errors in the buffer measurements.

pK values are difficult to determine with precision when dissociation is appreciable and it is known that, for example, the data for phosphoric acid $K_{(1)}$ buffer at different buffer ratios extrapolate to different values of log K depending on the choice of the function to estimate the activity coefficients (17). It can however be shown that a change of the activity coefficients used to calculate m_H shifts both K_p and K_1 and has but little effect on log K_p/K_1 for phosphoric acid, phosphate buffer $K_{(1)}$, and formic acid. For acetic acid, acetate buffer and formate buffer m_H is small except at very high dilutions and can be completely neglected for carbonic acid and bicarbonate buffer.

The fact that the observed differences exist even at infinite dilution eliminates as explanation all the effects which affect the activity coefficients: ionic associations, uncomplete dissociations, salting in and out effects, etc., unless one admits that some of these effects only disappear at extreme dilutions where emf measurements become impossible.

More experiments on, for example, acetate buffer, covering a very wide range of buffer ratios, perhaps will throw more light on this unsolved problem.

Acknowledgment

The authors wish to express their gratitude to Dr. S. D. Hamann, Dr. R. G. Bates, and Professor B. B. Owen, for helpful criticism of the manuscript.

Manuscript received July 27, 1964; revised manuscript received Oct. 27, 1964.

Any discussion of this paper will appear in a Discussion Section to be published in the December 1965 JOURNAL.

REFERENCES

1. A. Distèche, *Rev. Sci. Instruments*, **30**, 474 (1959).
2. A. Distèche, *This Journal*, **109**, 1084 (1962).
3. A. Distèche and M. Dubuisson, *Bull. Inst. Océanographique Monaco*, **1174**, 1 (1960).
4. S. D. Hamann, *J. Phys. Chem.*, **67**, 2233 (1963).
5. H. S. Harned and B. B. Owen, "The Physical Chemistry of Electrolytic Solutions," 2d ed., Reinhold Publishing Corp., New York (1958).
6. B. B. Owen and S. R. Brinkley, *Chem. Rev.*, **29**, 461 (1941).
7. H. S. Harned and B. B. Owen, *J. Am. Chem. Soc.*, **52**, 5079 (1930).
8. A. J. Ellis and D. W. Anderson, *J. Chem. Soc.*, **342**, 1765 (1961).
9. S. D. Hamann and W. Strauss, *Trans. Faraday Soc.*, **51**, 1684 (1955).
10. S. D. Hamann, "Physico-chemical Effects of Pressure," Butterworths Scientific Publications (1957).
11. F. K. Johnson, H. Eyring, and M. J. Polissar, "The Kinetic Basis of Molecular Biology," John Wiley & Sons, New York (1954).
12. W. D. Kumler and J. J. Eiler, *J. Am. Chem. Soc.*, **65**, 2355 (1943).
13. A. J. Ellis, *J. Chem. Soc.*, **750**, 3689 (1959).
14. O. Redlich and J. Bigeleisen, *Chem. Rev.*, **30**, 171 (1942); see ref. (5).
15. J. S. Smith, Dissertation Yale Univ. (1943); see ref. (5).
16. A. Bodanszky and W. Kauzmann, *J. Phys. Chem.*, **66**, 177 (1962).
17. R. Bates, *J. Res. Nat. Bureau Standards*, **47**, 127 (1951).

Electrochemical Oxidation of Certain Hydrocarbons and Carbon Monoxide in Dilute Sulfuric Acid

H. Binder, A. Köhling, H. Krupp, K. Richter, and G. Sandstede

Battelle-Institut e.V., Frankfurt(Main), Germany

ABSTRACT

For the hydrocarbons methane through heptane, ethylene, and carbon monoxide anodic potential/current density curves were measured in a galvanostatic half-cell arrangement. Raney platinum proved to be an active catalyst for the conversion of the hydrocarbons. In $3N$ H_2SO_4 at 100°C a stationary current density of 200 ma/cm² was measured for ethane, propane, butane, ethylene, and carbon monoxide, and 100 ma/cm² for methane and pentane. By coulometric analyses the conversion of methane, ethane, and propane to CO_2 was found to be 100%. Complete conversion of butane, pentane, hexane, and heptane apparently requires conditions different from those employed here. In $5N$ H_2SO_4 potential oscillations with time were observed, which were caused by partial poisoning of the electrode on reduction of H_2SO_4 to H_2S and the subsequent self-regeneration of the electrode.

Experiments made at several laboratories (1-8) during the last few years have shown that a variety of hydrocarbons are anodically oxidized in acids and alkalies at temperatures below 100°C and potentials far below the oxygen potential. However, the current densities achieved were very small compared with those obtained on use of hydrogen. For this reason experiments were carried out at working temperatures of up to 200°C (9-12), and a current density of about 200 ma/cm² was obtained in phosphoric acid (11). It is, of course, advantageous to use an electrolyte which does not dissolve the carbon dioxide produced during the reaction. Such an electrolyte is preferably an acid one. At atmospheric pressure and temperatures above 100°C the concentration of, in particular, sulfuric acid is so large that it cannot be used as electrolyte, since it is reduced at such temperatures.

We used Raney platinum metals as fuel cell catalysts (13, 14) at first in the electrochemical combustion of methanol. It was found in further experiments (15, 16) that, in the presence of a Raney platinum catalyst, the derivatives of the saturated hydrocarbons with one to three carbon atoms per molecule, alcohols, aldehydes, and carboxylic acids, are completely converted to CO_2 in $5N$ H_2SO_4 at 80°C. Subsequent investigations were concerned with the conditions at which both hydrocarbons and carbon monoxide can be electrochemically oxidized in sulfuric acid and, for comparison, also in phosphoric acid. In the experiments with the fuels discussed here the anodic potential/current density curves were measured in a galvanostatic half-cell arrangement. Furthermore, coulometric analyses were carried out.

Half-Cell Arrangement

Figure 1 shows the measuring setup for the galvanostatic measurements. The gaseous fuel flows through the porous electrode. Thus the electrodes were tested as bubble electrodes, and only a distinct proportion of the passing fuel was oxidized. The electrodes operated at a gas pressure of about 1.5 atm. The disk-shaped porous test electrode is fixed in a holder of polypropylene providing the gas supply. It is supported at its edge by a Viton gasket, to which it is pressed by means of a cap nut. The electric contact is made by means of two springy insulated wires of platinum-iridium; one of them is designed as a current lead, the other for potential measurements.

The potential of the test electrode was measured by means of a Luggin capillary against a hydrogen electrode kept in the same solution at the same temperature. This reference electrode is an autogenous hydrogen electrode. It consists of a Raney platinum electrode, suspended by a platinum wire, at which hydrogen is evolved electrolytically at a cathodic current density of about 1 ma/cm², another platinum wire forming the anode. At this current density the overvoltage for hydrogen evolution is negligibly small, so that the potential equals the reversible hydrogen potential. For every solution and temperature employed this potential is assumed to be zero.

The counterelectrode, a platinum wire, is contained in a separate vessel joined by a liquid junction. Thus, cathodic reaction products are prevented from reaching the anode.

The anode vessel is closed by means of a ground cover with attached reflux condenser.

The test electrode was subjected to a constant current load, and the potential was recorded. The first reading for every set of conditions was taken after 24 hr of operation; subsequent readings were taken at intervals of about 2 hr each.

Electrodes and Reactants

The electrodes were prepared in the form of porous disks by compacting a mixture of gold powder, forming the electrode skeleton, and powdered Raney platinum aluminum alloy at a pressure of 10^9 dyne/cm². Subsequently, the aluminum of the Raney alloy was dissolved by treating the disk first with dilute KOH solution and then with $7N$ KOH, finally at a temperature of 90°C. These test electrodes were 13 mm in diameter and about 1 mm in thickness. They contained about 180 mg of Raney platinum per square centimeter of geometric surface area.

The Raney platinum alloy was $PtAl_4$. It was prepared by heating an intimate mixture of platinum and aluminum powder in the form of a compacted disk.

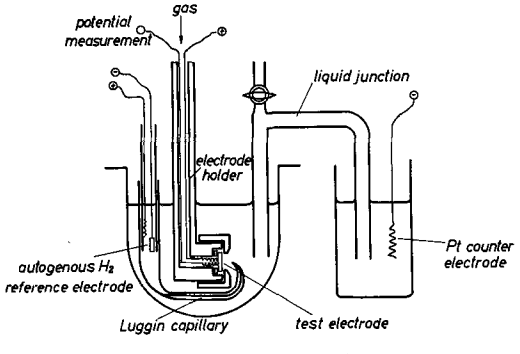

Fig. 1. Half-cell arrangement for galvanostatic measurement with a gas electrode.

The resulting regulus of the alloy was powdered and the 10-25μ size fraction was used for the test electrode in an amount of 60% by volume together with the <60μ size fraction of gold powder which amounted to 40% by volume.

The purity of the gases involved was 99.5 mole %. Technical grade propane was used for reference. The liquid hydrocarbons pentane, hexane, heptane were kept in an evaporator, which was placed on top of the electrode support by means of a short connection tube. The evaporator was heated by a jacket which permitted adjustment of temperatures at which the vapor pressure of the liquid hydrocarbon reached the operating pressure of the electrode (approximately 1.5 atm). In this way the pure hydrocarbon vapor was passed through the electrode.

Experiments in 5N H_2SO_4

The galvanostatic anodic oxidation of propane at the Raney platinum electrode in 5N H_2SO_4 at 100°C failed to yield stationary potentials. At a current density of 50 ma/cm² a potential of 350 mv was measured after a few hours. In the course of several days the potential rose to about 900 mv and then increased more rapidly until the evolution of O_2 started. The electrode could, however, be regenerated by the evolution of O_2 and subsequent cathodic reduction of the oxygen surface layer.

If the current density is reduced to 30 ma/cm², the electrode is capable of self-regeneration. As illustrated in Fig. 2, oscillations of the potential with time are observed. The potential increases within 10-15 hr to about 550 mv, and in the next 30 min rises by some further 150 mv, then remains constant for about 2 hr, and finally drops to about 400 mv within a few minutes. This process recurs periodically. The probable source of these oscillations is seen in a blocking of the electrode surface by a sulfur layer rather than by the oxidation products of propane. In the anodic oxidation of a hydrocarbon water is consumed according to the equation

$$C_nH_{2n+2} + 2n\ H_2O = n\ CO_2 + (6n + 2)\ H^+ + (6n + 2)\ e^-$$

Hence, the sulfuric acid is concentrating in the pores of the electrode and is then reduced by the hydrocarbons. Following the increase in the potential, the sulfur is oxidized and, consequently, the surface of the catalyst is decontaminated.

On use of hydrogen and carbon monoxide in 5N H_2SO_4, gaseous H_2S is formed on the Raney platinum catalyst at 100°C. These reducing agents are so powerful that even 5N H_2SO_4 is reduced. The catalyst is poisoned at open circuit, and the rest potential increases.

Potential Current Density Plots in 3N H_2SO_4

The evolution of H_2S observed in 5N H_2SO_4 at 100°C is avoided if the concentration of the sulfuric acid is reduced. In 3N H_2SO_4 at 100°C H_2S is no longer formed even with carbon monoxide fuel except by selecting a very large flow rate of the gas. The potentials remain constant. At this concentration oscillation of the potentials during the oxidation of the hydrocarbons is no longer encountered.

Table I. Reversible potentials at 100°C and rest potentials of a Raney platinum electrode in 3N H_2SO_4 at 100°C

Fuel	Rev. pot., mv	Rest pot., mv
H_2	0	0
CO	−132	0
C_2H_4	33	210
CH_4	130	140
C_2H_6	96	120
C_3H_8	85	130
C_4H_{10}	83	150
C_5H_{12}	80	150
C_6H_{14}	80	150
C_7H_{16}	78	150

Table II. Degree of conversion of some alkanes to CO_2 in 3N H_2SO_4 at 90°C

Reactant	Potential, mv	ψ_{CO_2}, %
CH_4	380	100.2
	620	100.1
C_2H_6	450	99.8
	550	100.5
C_3H_8	320	100.5
	450	99.5
C_4H_{10}	460	101.3
	550	100.8

Table I depicts the rest potentials measured in 3N H_2SO_4 at 100°C, along with the reversible potentials at 100°C calculated from the thermodynamic data. The reversible oxygen potential at 100°C amounts to 1166 mv.

The rest potential of carbon monoxide is larger than the reversible potential. The fact that carbon monoxide yields the hydrogen potential suggests that this compound reacts with water to give carbon dioxide and hydrogen.

The rest potential of ethylene is much larger than the reversible potential, in contrast to saturated hydrocarbons where the variation of the rest potential from the reversible potential is relatively small.

In the case of methane the rest potential closely approximates the reversible potential, but it is unlikely that we should be dealing with a "reversible methane electrode" rather than with a mixed potential.

The stationary potential/current density curves measured with the Raney platinum electrode in 3N H_2SO_4 at 100°C are depicted in Fig. 3 and 4. Carbon monoxide yields a linear characteristic. Its slope is somewhat larger than in the case of hydrogen. Hydrocarbons, too, furnish linear characteristics, except at small current densities where the slope increases towards zero current.

On use of methane the potential is still steady with time at as large a current density as 150 ma/cm². At larger current densities the potential increases with time, since a chemisorbed layer of oxygen starts forming on the platinum surface at potentials above, say, 800 mv. Polarization in the case of methane slightly

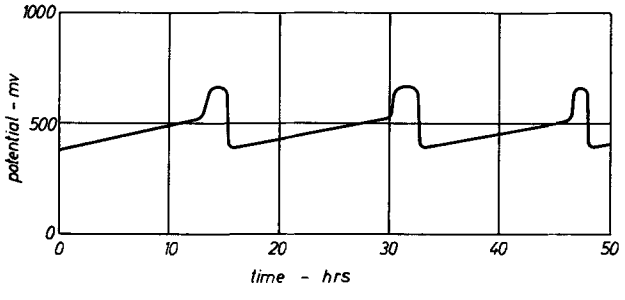

Fig. 2. Potential-time plot of a Raney platinum electrode with propane in 5N H_2SO_4 at 100°C.

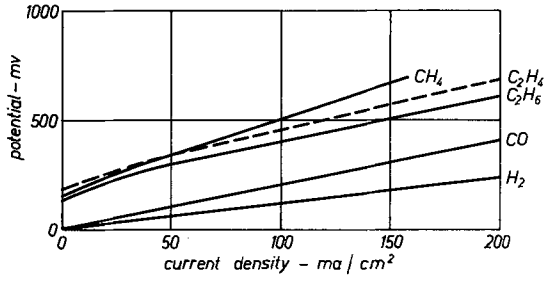

Fig. 3. Potential/current density plots of a Raney platinum electrode with methane, ethane, ethylene, carbon monoxide, and hydrogen in 3N H_2SO_4 at 100°C.

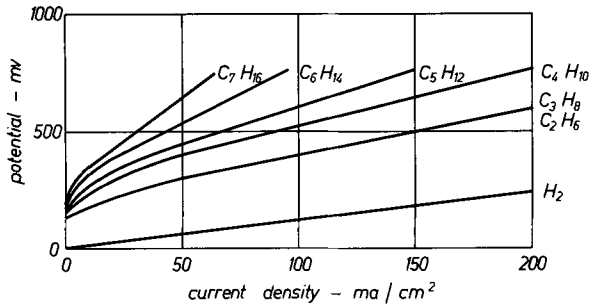

Fig. 4. Potential/current density plots of a Raney platinum electrode with saturated hydrocarbons (and hydrogen for reference) in 3*N* H_2SO_4 at 100°C.

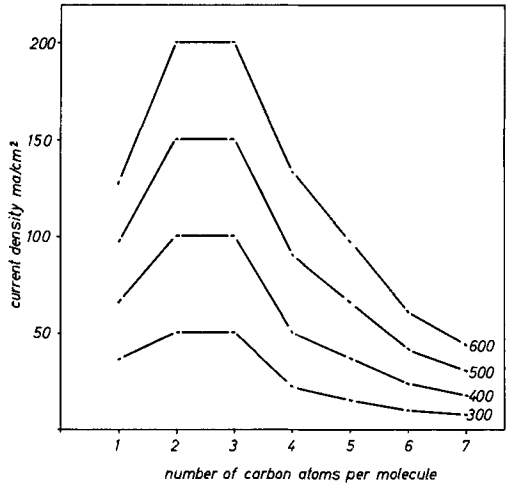

Fig. 5. Current density of a Raney platinum electrode with alkanes in 3*N* H_2SO_4 at 100°C vs. the number of carbon atoms per molecule with the potential as a parameter.

exceeds that with ethane; this is plausible on account of the high thermodynamic stability of the methane molecule. Ethylene likewise leads to a larger polarization than ethane, which, on the basis of the available evidence, may be attributed to rather stable sorbate/catalyst bonds. With ethylene the limiting current density is larger than 300 ma/cm² and the limiting potential larger than 1000 mv.

As is evident from Fig. 4, a stationary current density of at least 200 ma/cm² is obtained with ethane, propane, and butane in the presence of Raney platinum catalyst. If we want to compare the anodic polarization of hydrocarbons with that of hydrogen it should be noted that the reversible potential (cf. Table I) has to be subtracted from the hydrocarbon values, *e.g.*, 85 mv in the case of propane. With increasing chain length of the saturated hydrocarbons the slope ($\Delta\psi/\Delta i$) of the potential/current density

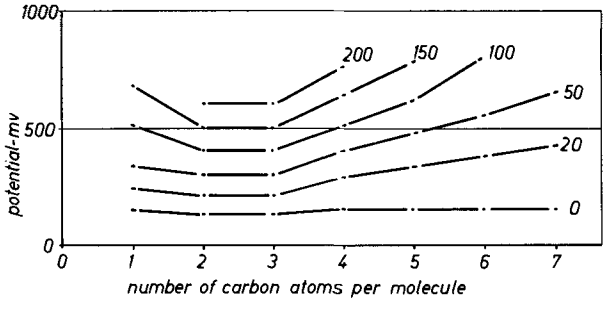

Fig. 6. Potential of a Raney platinum electrode with alkanes in 3*N* H_2SO_4 at 100°C vs. the number of carbon atoms per molecule with the current density (ma/cm²) as a parameter.

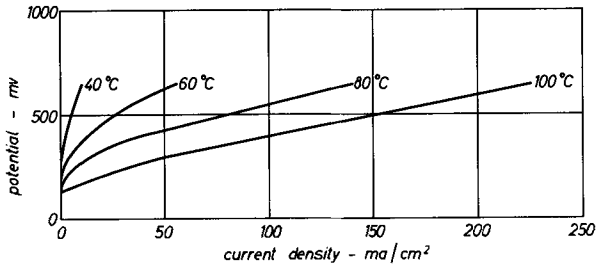

Fig. 7. Potential/current density plots of a Raney platinum electrode with propane in 3*N* H_2SO_4 with the temperature as a parameter.

curve at a given current density increases too. The limiting current density decreases correspondingly. Methane is an exception; with methane the slope is somewhat larger than that with ethane (*cf.* Fig. 3).

The effect of the chain length and hence of the number of carbon atoms per molecule on the oxidation rate is depicted in Fig. 5 and 6. When changing from methane to ethane, the current density increases at a given potential, then remains constant if an additional carbon atom is added and finally drops as the chain length grows.

In Fig. 6 the current density is used as a parameter. It is noted that the potential shows a minimum in the case of ethane and propane. The same applies to the rest potential. The limiting potential is found at about 800 mv. Above this potential a chemisorbed oxygen layer is formed on platinum in sulfuric acid if other substances are absent.

Temperature Dependence of Propane Oxidation

Figure 7 shows potential/current density plots of a Raney platinum electrode with propane in 3*N* H_2SO_4 at various temperatures. There is a marked increase in polarization with falling temperature. At 60°C the potential is 450 mv at a current density of 20 ma/cm², whereas its value drops to 200 mv at 100°C.

A plot of the current density *vs.* the temperature is depicted in Fig. 8, the potential being 500 mv. At 40°C the current density is as small as 5 ma/cm², but strongly rises with increasing temperature to a total of 140 ma/cm² at 100°C.

Replacement of pure propane by technical grade propane at 100°C likewise yields stationary potentials which are only slightly above those of pure propane. Hence, the electrode is not poisoned by possible common contaminations.

Coulometric Analysis

In order to determine the degree of conversion of the hydrocarbons in the anodic oxidation, the carbon dioxide evolved by the reaction was collected and weighed. The quantity of electricity involved was

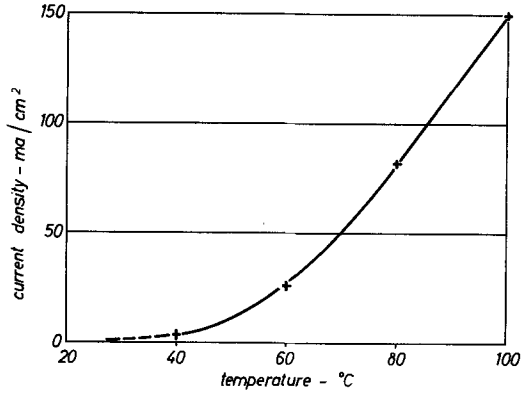

Fig. 8. Current density of a Raney platinum electrode with propane in 3*N* H_2SO_4 vs. the temperature at a potential of 500 mv.

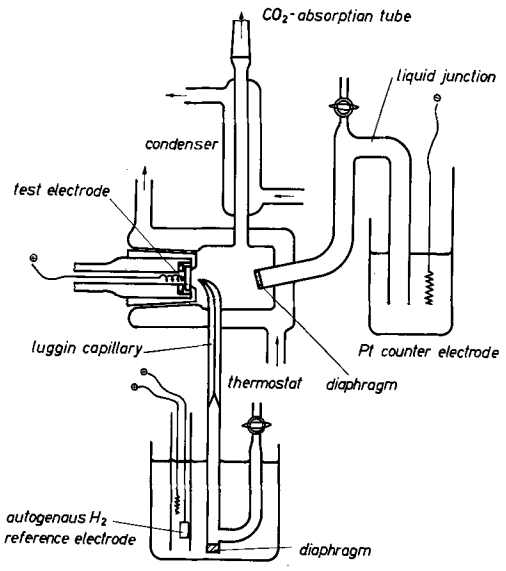

Fig. 9. Apparatus for coulometric analysis with a gas electrode

measured simultaneously. The glass apparatus used in these experiments, again a half-cell arrangement, is shown in Fig. 9. The electrolyte volume in this case is kept as small as possible in order to minimize both the dissolved quantity of gas and the stay period of the gas while passed through the apparatus. This allows the effect of minor variations of flow rate and temperature on the measuring result to be neglected.

The holder for the Raney platinum electrode consists of polypropylene and is provided with a ground section for connecting it to the glass vessel. The vessel is provided with a jacket through which the thermostat liquid flows. The counterelectrode is located in a second vessel which is separated from the anode compartment by a diaphragm in order to avoid undesired reactions. The reference electrode, again an autogenous hydrogen electrode, is contained in a separate tube which is connected to the reaction vessel via a capillary tube.

The escaping gas flows through a small condenser into a tube filled with phosphorus pentoxide and finally reaches a tube packed with NaOH-asbestos for absorption of the carbon dioxide. The flow rate was adjusted such that about 10% of the gas was converted.

The experiments were performed at constant potential. Methane, ethane, propane, butane in $3N$ H_2SO_4 were used at 90°C. The degree of conversion ψ_{CO_2} is derived from the measured quantity m_{exp} of CO_2 and the quantity m_{calc} of CO_2 calculated from the reaction equation and the quantity of electricity involved, as follows

$$\psi_{CO_2} = \frac{m_{exp}}{m_{calc}} 100\%$$

The results are summarized in Table II.

As Table II indicates, the degree of conversion of methane, ethane, and propane is 100%, within the limit of error. Hence, no by-products are formed in the electrochemical oxidation of these hydrocarbons under the conditions applied. This result was obtained at potentials involved in fuel cells.

The complete conversion to CO_2 suggests that all intermediates remain chemisorbed at the catalyst surface. Thus, the hydrocarbon is adsorbed on the electrode surface where it reacts with H_2O molecules that may likewise be adsorbed, and emits electrons to the electrode and protons to the electrolyte until only CO_2 is left on the surface which then is desorbed.

For butane conversion values above 100% were found which are outside the limit of error. This result suggests that the oxidation of butane, at the condition of large flow rates, does not proceed up to the carbon dioxide stage and that partially oxidized products are desorbed. These products are absorbed in the tube packed with NaOH-asbestos so that a larger degree of conversion is erroneously indicated.

At 100°C instead of 90°C, the conversion of propane is no longer complete. As a consequence of the increase in temperature, desorption of partially oxidized hydrocarbons takes place and the desorption products are carried away by the streaming gas.

Since all intermediates can be converted quantitatively (16) to carbon dioxide and water, we believe that propane and butane can also be completely oxidized to carbon dioxide at certain conditions,[1] in particular at flow rates that are compatible with the current intensity, a requirement fulfilled in practical fuel cells anyhow.

Conclusions

The hydrocarbons are oxidized on Raney platinum in dilute sulfuric acid at large current densities; the reaction rate decreases with growing chain length. It is expected from the experimental results that a propane fuel cell can be operated at 100°C which, at a voltage of 0.5v, yields a current density of 100 ma/cm^2. While the exclusive products of the anodic oxidation of methane, ethane, and propane are carbon dioxide and water, complete conversion of butane, pentane, hexane, and heptane apparently requires conditions different from those employed here.

Acknowledgment

This work was conducted under a contract and in cooperation with the Robert Bosch GmbH, Stuttgart, Germany. Their permission to publish these results is gratefully acknowledged. The authors greatly appreciate the interest and the valuable suggestions of Drs. Ilge, Neumann, Herrmann, and Jahnke, members of the sponsoring company.

Manuscript received April 22, 1964. This paper was presented at the Toronto Meeting, May 3-7, 1964.

Any discussion of this paper will appear in a Discussion Section to be published in the December 1965 JOURNAL.

REFERENCES

1. J. C. Balaceanu, *Compt. rend. 4e Congr. Natl. Pétrole*, **1**, 37 (1960).
2. M. J. Schlatter, Preprints Am. Chem. Soc. Meeting, Chicago, 1961, **6**, [4-B] 149; "Fuel Cells," G. J. Young, Editor, Vol. 2, p. 190, Reinhold Publishing Corp., New York (1963); Preprints Am. Chem. Soc. Meeting, New York, 1963, **7** [4], 234.
3. W. T. Grubb, *Proc. 16th Ann. Power Sources Conf.*, 34 (1962).
4. W. T. Grubb and L. W. Niedrach, *Proc. 17th Ann Power Sources Conf.*, 69 (1963).
5. G. T. Young and R. B. Rozelle, "Fuel Cells," G. J. Young, Editor, Vol. 2, p. 216, Reinhold Publishing Corp., New York (1963).
6. H. Wroblowa, B. J. Piersma, and J. O'M. Bockris, *J. Electroanal. Chem.*, **6**, 401 (1963).
7. L. W. Niedrach, Paper presented at the New York Meeting of the Society, 1963.
8. V. R. José and V. D. Long, *J. Appl. Chem.*, **14**, 64 (1964).
9. C. E. Heath and C. H. Worsham, Paper presented at Chicago Meeting of the Am. Chem. Soc., 1961; "Fuel Cells," G. J. Young, Editor, Vol. 2, p. 182, Reinhold Publishing Corp., New York (1963).
10. W. T. Grubb and L. W. Niedrach, *This Journal*, **110**, 1086 (1963).
11. W. T. Grubb, *Nature*, **201**, 151 (1964).
12. W. T. Grubb and C. J. Michalske, *ibid.*, **201**, 287 (1964).

[1] Further experimental results on the oxidation of hydrocarbons were reported at the Washington Meeting of the Society, Oct. 11-15, 1964.

13. H. Krupp, H. Rabenhorst, G. Sandstede, G. Walter, and R. McJones, *This Journal*, **109**, 553 (1962).
14. G. Sandstede, Dechema-Monographien. **49**, 303 (1964).
15. H. Binder, A. Köhling, H. Krupp, K. Richter, and G. Sandstede, Paper presented at New York Meeting, Am. Chem. Soc., **7** [4], 232 (1963); "Advances in Chemistry Series," in print.
16. H. Binder, A. Köhling, and G. Sandstede, *ibid.*

Technical Notes

The Distribution of Defects in Aluminum Oxide Films near the Metal-to-Oxide Interface

M. A. Heine and P. R. Sperry

Metals Research Laboratories, Olin Mathieson Chemical Corporation, New Haven, Connecticut

Thin oxide films which form on metal surfaces by thermal or anodic oxidation are known to depart from the bulk stoichiometric composition and to contain impurities and lattice defects. Defects in the oxide structure may contribute to ionic or electronic conduction, depending on their nature and concentration. Hence, they influence the kinetics of formation and the subsequent reactions of the surface films with the environment to which they are exposed. Despite the broad background of experimental data available on bulk semiconductors, little or nothing has been determined about the actual defect structure of that important class of metal oxide films in the order of a few hundred Ångstroms or less in thickness. The great difficulty of obtaining direct experimental data on distribution of defects in such films limits the interpretation of their dry or wet corrosion behavior to some assumed model of homogeneous or inhomogeneous distribution of the defects.

There is indirect evidence that thin, room temperature oxide films on aluminum depart from stoichiometry and contain excess metal and/or oxygen vacancies in the vicinity of the oxide metal interface. Grunberg and Wright (1) have demonstrated this particularly well for aluminum, and also for magnesium and zinc which are similarly believed to form thin excess metal oxides. They were able to show a spectrum of electron emission photosensitized within the visible light range on freshly abraded or vacuum deposited aluminum. They gave particular attention to a prominent sharp peak found at a wavelength of 4700Å and concluded that the most likely lattice imperfection contributing to this effect would be a missing oxygen site trapping two electrons and giving rise to an F'-center. The electron emission was attributed to trapped electrons at shallow surface sites. Decay of the emission occurred on further oxidation, with the rate of decay being a function of oxygen partial pressure. Thus, their investigative method could not be extended to stable thicker films.

Work in progress at the authors' laboratory has been aimed toward a more direct study of the nature and distribution of defects in γ-Al_2O_3 films formed on 99.997% pure aluminum. Capacitance and dielectric loss measurements over a wide range of a-c frequency have been used and have been supplemented by electron-optical and other methods, as described in previous publications (2, 3). The experimental method briefly consists of constructing a parallel plate capacitor in which the aluminum substrate forms one electrode, the oxide film is the dielectric, and the other electrode is formed by an aqueous chromate solution connected through a platinum screen. It has been clearly shown in the previous work that contact with this electrolyte introduces no changes into the structure of the film. Corrections for the resistance and capacitance of the solution can be made readily when necessary. From the measured and corrected capacitance and dielectric loss values and from the electrical analog to the film of a capacitance and resistance in parallel, a frequency dependent value of a-c parallel resistance, R_p, can be calculated. Differences of this value between films of equal thickness have been attributed to differences in the ionic or electronic relaxation effects due to gross impurity substitution or departure from stoichiometry (2). At frequencies somewhat greater than 10 kc, it is believed that only the electronic relaxation effects from impurity substitution can be seen, whereas at lower frequencies combined ionic and electronic relaxations contribute to R_p (2).

The a-c resistance determined as above is a total value for the entire film thickness, and it does not give any indication of defect distribution. A valuable extension of the technique was the development of a means of chemically dissolving or thinning the films (3) in a uniform fashion by immersion in a slightly alkaline, passivating chromate solution; the solution again did not affect the structure and composition of the remaining film. Thus, the distribution of the a-c resistance at different frequencies could be determined throughout the thickness of the films, down to a limiting passive film thickness of 20-25Å. All measurements were made at 25°C. Details of the method and some results appear elsewhere (3).

It is of particular interest to examine the high-frequency resistance values (100 kc) in the immediate vicinity of the oxide-metal interface. These high-frequency resistance values have been considered to reflect primarily electronic relaxation effects resulting from departure from stoichiometry or from relatively gross impurity substitution. Previous work (2, 3) was conducted on barrier layer-type films formed anodically in neutral ammonium tartrate solution. Two dissimilar regions of high-frequency a-c resistance were found in these films. First was an inner region, extending to about 90Å from the metal-oxide interface in which the R_p *vs.* total thickness was not linear and in which high-frequency resistivity increased with increasing distance from the oxide-metal interface. Second was a region from 90Å out to the outer oxide surface in which R_p was a linear function of thickness; therefore, this was a region of constant high-frequency resistivity. The latter was attributed to the uniform characteristic γ-Al_2O_3 formed under anodic conditions. It was concluded that the lower resistivity, inner

region was associated with the excess metal defect nature of the film adjacent to the oxide-metal interface.

In the new work reported herein, a similar analysis has been applied to thermal films formed by oxidation of annealed 99.997% pure aluminum sheet, 0.016 in. thick, in dry oxygen and at temperatures from 350° to 500°C. The surface pretreatment, consisting of a 15-min etch in 0.5*N* NaOH followed by a dip in 50% HNO_3, has been found to give a fairly smooth surface free from contamination which would affect subsequent oxidation. The resulting oxide films were composed of γ-Al_2O_3 and had thicknesses ranging between 40 and 85Å. One of the films, formed at 500°C, contained well-developed crystals (Fig. 1a) which gave sharp γ-Al_2O_3 electron diffraction patterns. Those films formed at 450°C and below appeared structureless to the electron microscope (Fig. 1b) and showed rather diffuse rings upon transmission electron diffraction, a characteristic of so-called "amorphous" γ-Al_2O_3. The change from amorphous to mixed crystalline and amorphous film in the range of 450° to 500°C is in agreement with Dignam (4) and others. In spite of these differences in structure, it was found that the R_p *vs.* thickness curves for all of the thermal films coincided almost exactly with that obtained from the inner region of the anodic film; *i.e.*, the entire thermal film within this thickness limit was an excess metal film with varying resistivity. This finding is qualified to the extent that measurements made at 25°C can be considered characteristic of the films as they existed at the elevated temperatures only insofar as these characteristics could be retained during rapid cooling after oxidation.

The curve, R_p *vs.* thickness, for both the anodic and the thermal films in the excess metal region proved to be parabolic, as shown by Fig. 2 in which R_p is plotted against the square of the thickness, giving excellent fit to a straight line. The thickness was calculated from the capacitance measured at 1 kc which is in the frequency range which Lorking (5) considered most suitable for this purpose. The failure of this line to extrapolate to zero resistance at zero thickness may be due to minor residual inaccuracies of obtaining an absolute measure of film thickness and/or to small errors introduced in the high-frequency solution corrections (3). Assuming that the real intercept would be negligibly small in value, the data can be simply described by

$$R_p = kX^2$$

where X is the total thickness at which R_p was measured. Since the incremental resistivity, *i.e.*, the resistivity of any extremely thin element parallel to the metal surface, is directly proportional to the thickness, it follows that the high-frequency conductivity, σ, for a given element of film is inversely proportional to the distance of that element from the metal-oxide interface. An expression for the number of defects, N, contributing to the electronic relaxation is obtained from the general expression for conductivity

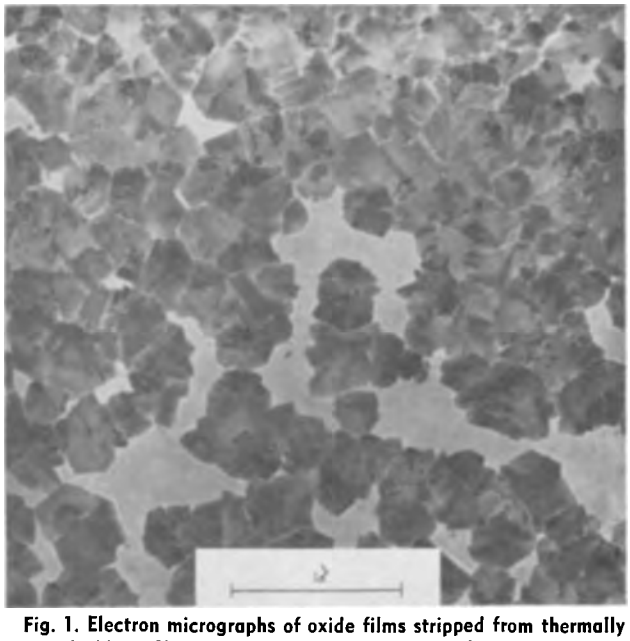

Fig. 1. Electron micrographs of oxide films stripped from thermally oxidized 99.997% pure aluminum: (a) oxidized at 500°C for 20 hr. Magnification approximately 26,500X.

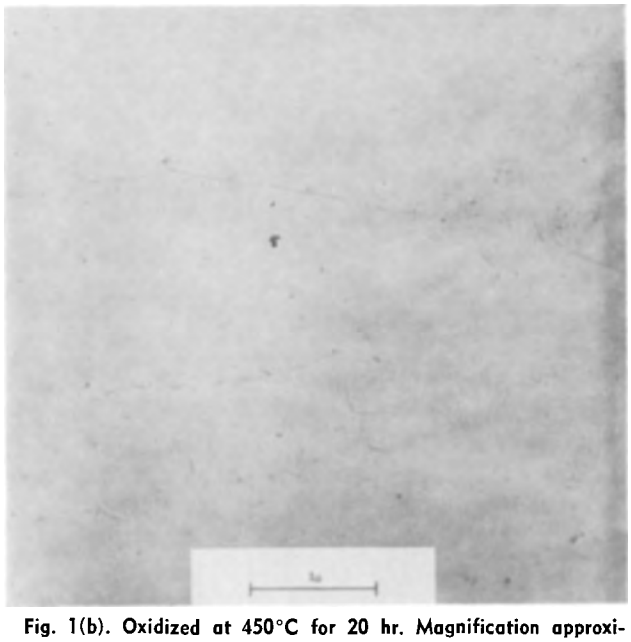

Fig. 1(b). Oxidized at 450°C for 20 hr. Magnification approximately 19,500X.

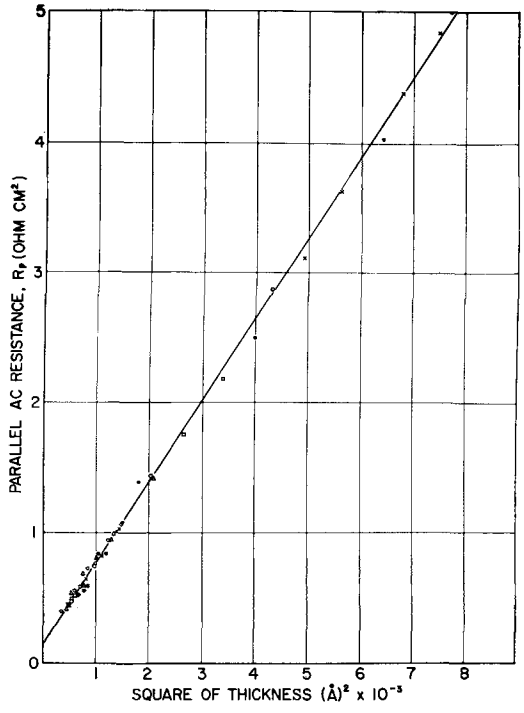

Fig. 2. High-frequency (100 kc) a-c resistance of a variety of γ-Al_2O_3 films plotted against the square of the thickness. The separate points for each individual film are individual measurements made during uniform thinning of the film: X, 500°C; □, 450°C; ○, 400°C; △, 350°C; •, anodic.

where r is the rate in moles sec^{-1} cm^{-2}, c is the concentration of KNO_3 in moles $liter^{-1}$, and P_o and E are constants.

The activation energy, E, is 17.1 kcal $mole^{-1}$ and P_o, which can be regarded as a frequency factor, was found to be 9.2×10^6 cm sec^{-1}.

Discussion

Capacitance studies (1) have revealed that freshly prepared anodic zirconium oxide films are permeable to electrolyte solutions, but microscopic evidence indicates that the surface of the oxide is virtually featureless (3). Several suggestions have been made to account for this permeability, the most reasonable being the existence of invisible cracks perpendicular to the film surface (4). Our experimental observations lead to some tentative conclusions about the nature of the oxide film and the permeation process.

The permeation rate is fairly reproducible. The small deviations in results can be attributed to variations in the ratio of actual film area to apparent film area. This indicates that a reproducible network of interstices, rather than random gross flaws, serve as paths for permeation. Furthermore, the activation energy for the free diffusion of KCl in water is 4.4 kcal $mole^{-1}$ (5) which is nearly four times smaller than the observed activation energy for permeation through the oxide. This also supports the contention that the process is not merely a simple bulk diffusion through large flaws.

The relative concentration independence of the constant, P, is difficult to account for if a pore-free barrier layer similar to that found in porous anodic aluminum oxide (6) exists at the oxide-dilute solution interface. The termination of an interstice by a relatively perfect layer would probably lead to a bottleneck. It is probable, however, that this barrier layer which would most likely be found at the oxide-metal interface during anodization, is removed during the film stripping process. Permeation runs carried out with the oxide surfaces reversed with respect to the KNO_3 solution indicate that the permeation is the same in both directions.

It is likely then, that in the case of these isolated zirconium oxide films we are dealing with a permeation through a network of small interstices where the activation process may be adsorption and desorption of ions upon interstice walls.

Acknowledgment

This work was supported by the Pitman-Dunn Institute for Research, Frankford Arsenal, Philadelphia, Pennsylvania.

Manuscript received Oct. 28, 1964.

Any discussion of this paper will appear in a Discussion Section to be published in the December 1965 JOURNAL.

REFERENCES

1. R. D. Misch, "Characteristics of Anodic and Corrosion Films on Zirconium," Report No. ANL-6149, Argonne National Lab., May, 1960.
2. R. E. Salomon, W. M. Graven, and G. B. Adams, Jr., *J. Chem. Phys.*, **32**, 310 (1960).
3. R. W. Franklin, *Nature*, **180**, 1470 (1957).
4. D. L. Douglass, *Corrosion*, **17**, 589t (1961).
5. W. V. Malik and Fasih A. Siddiqi, *J. Colloid Sci.*, **18**, 161 (1963).
6. R. L. Burwell and T. P. May, *This Journal*, **94**, 195 (1948).

Growth and Characterization of Uranium-Doped Germanium Single Crystals

H. R. Killias,[1] S. N. Dermatis, and H. C. Gatos

Department of Metallurgy and Center for Materials Science and Engineering, Massachusetts Institute of Technology, Cambridge, Massachusetts

In the course of a study of fission fragment damage in bulk germanium (1), several germanium single crystals doped with uranium were grown successfully. Since such doping experiments have not been reported previously, growth procedure, distribution coefficient, and preliminary results of electrical measurements are presented here.

The crystals were grown from the melt by the Czochralski method using a graphite crucible and prepurified nitrogen as furnace atmosphere. Because of the relatively large atomic size or uranium, a high seed rotation (60 rpm) and a very low pulling rate (0.28 in./hr) were found necessary for successful growth. In a typical charge, a previously prepared master alloy was added containing 0.1 weight per cent (w/o) enriched uranium.[2] The presence of oxygen impurities in the furnace atmosphere was found to be critical because of the rapidly formed uranium oxide particles in the melt which tend to agglomerate at the solid-liquid interface and interfere with the crystal growth leading to the formation of irregularly sized twin bands.

Because the distribution coefficient of uranium in germanium was expected to be low, exceptionally pure uranium had to be used as doping material in order to prevent the preferred incorporation of impurities which have a relatively high solubility in germanium. The following impurity concentrations have been given for the enriched uranium: Al 7 ppm, P < 10 ppm, Zn 3 ppm on an atom basis. These concentrations are small enough not to affect the present results significantly.

An analytical determination of the uranium concentration in the grown single crystals was made by a method recently reported by Price and Walker (2). It is based on the fact that fission fragment tracks in mica crystals can be revealed by etching. Accordingly, a freshly cleaved mica crystal is placed next to the polished surface of the crystal to be analyzed. After an exposure to a thermal neutron flux ϕ the number of fission fragments per unit area (ρ) which have crossed over into the mica is

$$\rho = (1/2) R_o N \eta \sigma \phi \qquad [1]$$

where η is the isotopic abundance of U^{235}, σ the fission cross section of U^{235}, and R_o the effective fission fragment range in germanium. If R_o is taken as 7×10^{-4} cm and the fission track density determined with a microscope, the uranium concentration N can be obtained from Eq. [1]. Such determinations were made on both sides of samples which were later used for electrical measurements. The fission track densities of both sides always agreed within 2% and led to uranium concentrations between 1.5×10^{14} and 2.5×10^{14} at./cm^3 for different samples. Using these values and the uranium concentrations in the melt, the distribution coefficient of uranium in germanium was calculated as $k_o = 4.5 \times 10^{-5}$ with an estimated accuracy of

[1] Present address: General Electric Research Laboratory, Schenectady, New York.

[2] 99.7% U^{235}, obtained from Oak Ridge National Laboratory, Oak Ridge, Tennessee.

Fig. 1. Anomalous x-ray transmission topograph of uranium-doped germanium crystal, $(\bar{2}20)$ reflection, CuK_α radiation; note twin bands and segregated particles. Magnification approximately 7X.

25%. A semiquantitative discussion of this value in terms of a tetrahedral radius or heat of sublimation, as it has been done for other impurities in germanium (3), is not applicable for uranium. As far as the order of magnitude is concerned, however, the present value of k_o seems to be reasonable.

The mica detector method has also been used to study the distribution of uranium in the grown crystals. It was found that the fission track distribution was uniform over the whole sample except for a few small but very dense track clusters which indicated the presence of uranium-containing, segregated particles. This indication was confirmed by anomalous x-ray transmission microscopy (4) (Fig. 1). Embedded in a network of dislocations with Burgers vectors [101] and [011], small circular spots of about 30μ diameter are being observed. Confirmation that these spots are not due to damaged surface areas, such as etch pits, was obtained by the following experiment. A series of topographs was taken of a specimen whose thickness was reduced after each exposure. Individual spots could be followed through the crystal until they disappeared at a certain thickness. No spots were found at any reduced thickness which were not present in the first topograph. By comparing topographs of different (hkl) reflections, it could further be concluded that the observed spots represent particles of spherical shape.

The density of segregated particles varied from 300-400 cm^{-3}. The particle size is probably very close to the observed spot size of 30μ because the strain field of an inclusion falls off very rapidly with distance. Thus, the number of uranium atoms concentrated in these particles is of the order of 10^{17} at./cm^3. The nature of the segregated material could not be determined directly, but it is felt that the particles consist of metallic uranium rather than of uranium oxide or of an intermetallic uranium-germanium compound.

Electrical resistivity and Hall effect for some of the uranium-doped crystals were measured between 80° and 400°K. All crystals investigated are n-type with carrier concentrations between 1×10^{14} and 2×10^{14} cm^{-3}. A comparison of carrier concentration and concentration of dissolved uranium gives an apparent net contribution of 0.80 ± 0.10 electrons per uranium impurity. However, in these preliminary measurements, there were no indications of any donor or acceptor levels over the investigated temperature range. This is somewhat surprising since uranium might be expected to introduce deep multiple impurity levels corresponding to different ionization stages. A close investigation will have to include counter-doping with elements of groups III and V in order to sweep the Fermi level through the energy gap and the extension of electrical measurements to lower temperatures.

Acknowledgment

It is a pleasure to thank C. Herman for his skillful assistance in growing the crystals and Dr. T. B. Reed for helpful discussions. This work was supported by the Advanced Research Project Agency under Contract SD-90 and the Office of Naval Research under Contract Nonr-1841(84).

Manuscript received Oct. 22, 1964.

Any discussion of this paper will appear in a Discussion Section to be published in the December 1965 JOURNAL.

REFERENCES

1. H. R. Killias, Ph.D. Thesis, Massachusetts Institute of Technology, May 1964.
2. P. B. Price and R. M. Walker, *Appl. Physics Letters*, **2**, 23 (1963).
3. F. A. Trumbore, *Bell Syst. Tech. J.*, **39**, 205 (1960).
4. See for instance, G. H. Schwuttke, *J. Appl. Phys.*, **33**, 2760 (1962).

Brief Communications

Phase Diagram for the Pseudo-binary System Germanium and Gallium Arsenide

Y. Takeda, T. Hirai, and M. Hirao

Central Research Laboratory, Hitachi Ltd., Kokubunji, Tokyo, Japan

It has been reported by Jenny and Braunstein (1) that the Ge-GaAs alloy system was not a solid solution-type, but its phase diagram has not been established previously. In this communication, we report the phase diagram for the pseudobinary system Ge-GaAs determined by means of thermal analysis, microscopic observation, and x-ray microanalysis. The thermal analysis was made by melting appropriate amounts of Ge and GaAs mixtures in a sealed, evacuated silica ampule with a thermocouple hole at the bottom, holding it above the melting point of GaAs for about an hour and then cooling the melt at 1°C/min.

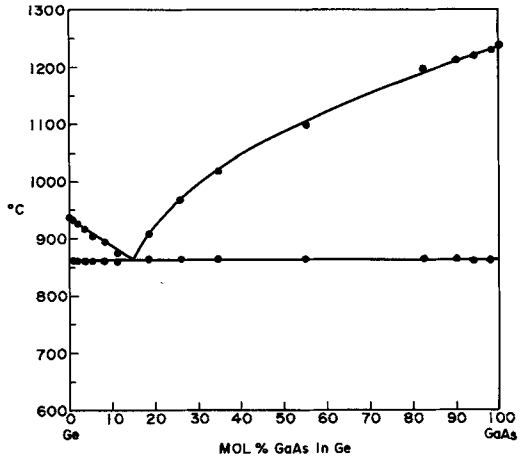

Fig. 1. Phase diagram for the GaAs-Ge system. Estimated solubility of Ge into GaAs and GaAs in Ge is less than 0.5 mole % Ge and 0.25 mole % GaAs, respectively.

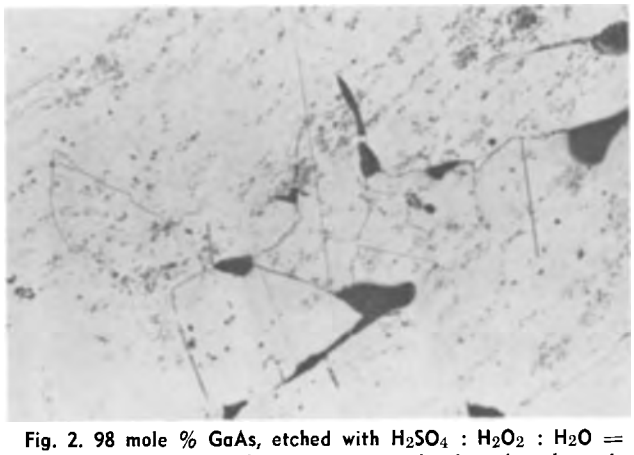

Fig. 2. 98 mole % GaAs, etched with H_2SO_4 : H_2O_2 : H_2O = 1:1:1 solution. The black areas are cracks brought about in solidification. Magnification approximately 145X.

The resultant phase diagram is shown in Fig. 1. This alloy system has a simple eutectic type phase diagram and no intermediate compound was found. The eutectic point lies at 15 mole % GaAs and its temperature is 865°±2°C.

The microstructure of the alloy with the composition of 98 mole % GaAs etched with H_2SO_4:H_2O_2:H_2O = 1:1:1 solution is shown in Fig. 2. This composition showed no sign of the existence of eutectic phase by thermal analysis, but a small amount of a second phase was observed at the grain boundaries of GaAs and this phase was confirmed to be the eutectic composition by x-ray microanalysis.

Figure 3 shows the microstructure of the alloy containing 2 mole % GaAs. The eutectic phase is clearly observed in this alloy, and almost the same pattern is observed for the 0.25 mole % GaAs alloy.

So the estimated solubilities of Ge in GaAs and GaAs in Ge from thermal analysis data are lower than 2 mole % Ge and 0.25 mole % GaAs, respectively.

Kolm *et al.* (2) have reported the solubility of Ge in GaAs to be lower than 0.5 mole % Ge by lattice parameter measurements of Ge-GaAs alloys. We could

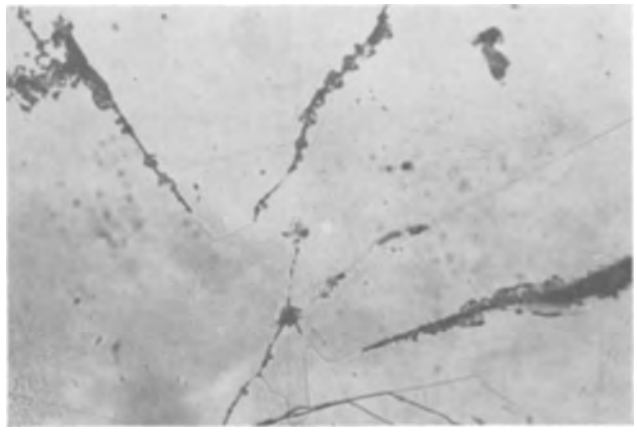

Fig. 3. 98 mole % Ge, etched with H_2SO_4 : H_2O_2 : H_2O = 1:1:1 solution. Magnification approximately 145X.

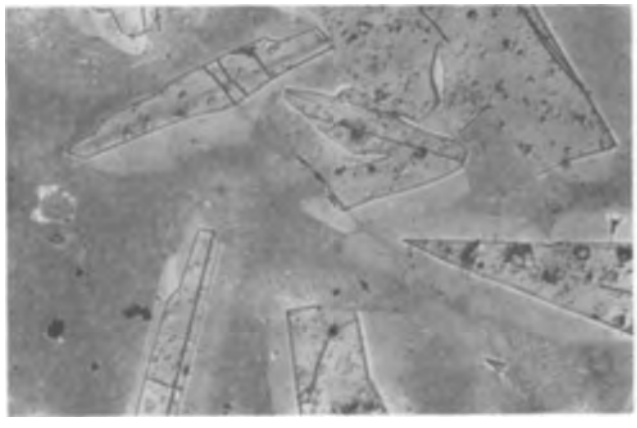

Fig. 4. 50 mole % GaAs, etched with H_2SO_4 : H_2O_2 : H_2O = 1:1:1 solution. Magnification approximately 145X.

not determine the precise solubility limits of Ge in GaAs and GaAs in Ge, but these results indicate that both solubilities are very low, although they do not show true equilibrium solubility limits because of the fast cooling rate.

Figure 4 shows the microstructure of the alloy containing about 50 mole % of GaAs. This appears to show three different phases, GaAs primary crystals, eutectic phase, and the third phase surrounding the GaAs primary crystals. This third phase looks different from the eutectic phase, but it was confirmed to be almost the same eutectic composition by x-ray microanalysis. The reason why the same eutectic phase shows two different patterns is not clear, but this probably results from slight deviation from the eutectic composition due to a difference in diffusion rate of Ga between As, or from a difference in etching condition, near the GaAs primary crystals.

Manuscript received Sept. 29, 1964.

Any discussion of this paper will appear in a Discussion Section to be published in the December 1965 JOURNAL.

REFERENCES

1. D. A. Jenny and R. Braunstein, *J. Appl. Phys.*, **29**, 596 (1958).
2. C. Kolm, S. A. Kulin, and B. L. Averbach, *Phys. Rev.*, **108**, 965 (1957).

Equilibria of the Mn_2O_3-Mn_3O_4-O_2 Systems

N. G. Schmahl and B. Stemmler

Institut für physikalische Chemie of the University of Saarland, Saarbrücken, West Germany

In the paper of Otto (1) the report of Schmahl and Shenouda (2) could hardly have been referred to. It may be stated that the selected temperatures (2) for Mn_2O_3-Mn_3O_4 to give 1 atm and 0.209 atm (= 1 atm air) are in rather good agreement with the work of Otto.

Since the publication (2) further investigations have been made by us and the results will be published (3). We were able to obtain practically univariance of the Mn_2O_3-Mn_3O_4 system. This could be achieved by treating the samples with oxygen-pressures a little over the univariance pressure within times up to a month. By this procedure lattice defects were removed. We found the temperature dependence of the oxides on the oxygen pressure is different from that usually observed. The values obtained by approaching equilibrium from the higher oxygen pressure side are in agreement with those obtained by approaching from the lower side. (Time required was up to 48 hr.)

It is to be stated, furthermore, that not one but two temperature dependent systems exist. The corresponding straight lines obtained for log pO_2 as a function of $1/T$ meet at 937°C. The line involving the higher pressures is attributed to the α system and that involving the lower to the β system. At temperatures above 937°C only pressures of the α system have been observed. Below 937°C spontaneous transition from β to α occurred several times. The case of a system with higher pressure being stable as compared with a system with lower pressure being metastable was discussed by Schmahl and Shenouda (2).

In light of the above mentioned observations we are compelled to postulate the existence of a third, a metastable modification of Mn_3O_4 in addition to the well-known tetragonal Hausmannite and the well-known spinel, stable above 1172°C. There is a probability that Hausmannite participates in the α system.

Similar results had been reported in a thesis by Eckert (1950) and the results incorporated in ref. (2). (The log pO_2 *vs.* $1/T$ lines meet at 952° instead of 937°C.) These results had been rejected because the possibility of a change in modification in only the Mn_2O_3 had been considered and this does not explain the situation. Data on the β system seem to have been obtained also by Tatievskaya, Chufarov, and Antonov (4). In x-ray investigations of Mn_3O_4 quenched by withdrawing specimens of the α or β system from the furnace the same pattern resulted.

Data for the reaction $6Mn_2O_3 = 4Mn_3O_4 + O_2$

α system: $-4.5758 \log pO_2(\text{atm}) = 45{,}345/T - 35.785$

Values determined at 830°-960°C

β system: $-4.5758 \log pO_2(\text{atm}) = 51{,}526/T - 40.891$

Values determined at 830°-937°C

	α system	β system
pO_2 760 Torr	994°C	(994°C / 898°C)
pO_2 159 Torr	892°C	
$\Delta H_T°$, per mole O_2	45.3 ± 0.7 kcal	51.5 ± 1.3 kcal
$\Delta S_T°$, per mole O_2	35.8 ± 0.6 cal/deg	40.9 ± 1.1 cal/deg

Transformation $1Mn_3O_4$ (metastable) to $1Mn_3O_4$(stable)

$\Delta H_T = -1.55$ kcal $\quad \Delta S_T = -1.28$ cal/deg

Since the Cp value of Mn_3O_4 is known only for Hausmannite and since it has not been established that this material participates in the α system, standard values have not been calculated for the α system or for the β system.

Manuscript received Nov. 2, 1964.

Any discussion of this paper will appear in a Discussion Section to be published in the December 1965 JOURNAL.

REFERENCES

1. E. M. Otto, *This Journal*, **111**, 88 (1964).
2. N. G. Schmahl and F. Shenouda, *Arch. Eisenhüttenw.*, **34**, 511 (1963).
3. B. Stemmler, Thesis, Saarbrücken University; to be published.
4. E. P. Tatievskaya, G. J. Chufarov, and V. K. Antonov, *Chem. Abstracts*, **42**, 6624 (1948).

Equilibrium Pressures of Oxygen over MnO_2-Mn_2O_3 at Various Temperatures

Earl M. Otto

National Bureau of Standards, Washington, D. C.

ABSTRACT

Oxygen pressures of the pyrolusite form of MnO_2 have been determined in a temperature range of 441°-642°C. The dissociation reaction $4MnO_2(c) \rightleftarrows 2Mn_2O_3(c) + O_2(g)$ has been found to reach a steady state in the forward direction; reaction in the reverse direction was exceedingly slow and did not reach a steady state. $\Delta H°$ and $\Delta S°$ for the reaction at 813°K are 37.87 kcal[1] and 51.28 cal/deg, respectively. With little error these values can be used in the equation

$$-4.5756 \log pO_2(\text{atm}) = 37{,}870/T - 51.28$$

to calculate the pressure for any temperature in the above mentioned range. Conversion to 298.15°K resulted in $\Delta H°_{298} = 38.8$ kcal and $\Delta S°_{298} = 52.8$ cal/deg for the dissociation. The limits of uncertainties are not given here because equilibria were not attained by recombination.

Although many investigations of original experimentation, theoretical calculations and collation of data reported in the chemical literature give information which relate temperature of MnO_2 and oxygen pressure, there is such a lack or omission of critical detail and there is so much disagreement that it was felt desirable to attempt to clear up the discrepancies. There is a lack of measuring and/or reporting precise temperatures and pressures. Frequently there is evidence that no equilibrium was reached. For example, in many instances the temperature of the MnO_2 was raised a few degrees per minute. Preparation of the sample is not always specified, nor is there assurance the sample was dry or desiccant included in the system. Among the investigators there is disagreement not only in the pressure-temperature relationship, but also regarding composition, crystal structure, and nomenclature of the sample and regarding the existence of reversibility of the MnO_2 dissociation. Table I gives in very concise form, pertinent observations made by the various investigations (1-24). When sufficient data were available, pressure-temperature graphs were made and some of these are shown in Fig. 5.

Values for thermodynamic constants of oxides of manganese have been determined experimentally in recent years by Millar (25), Siemonsen (26), Southard (27), Shomate (28), Moore (29), Kelley and Moore (30), Orr (31), and King (32). These values have been collated, adjusted to correlate with newly accepted reference values, and are tabulated by Kelley (33), Rossini (34), Brewer (35), Coughlin (36), Glassner (37), Mah (38), and Dushman (39). Brewer has stated (40) that "further work at higher temperatures and with long heating times is necessary to clarify the equilibrium limits of the solid-solution ranges."

It became evident, therefore, that precise determinations of oxygen pressure-MnO_2 temperature relationships at equilibrium were needed. Furthermore, the question of reversibility needed to be studied.

[1] One thermochemical calorie = 4.1840 joules. $R \ln pO_2 = 2.302585 \times 8.31433$ joules ÷ 4.1840 joules/cal = 4.57563 cal log pO_2.

Experimental

For the lowest two temperatures (441° and 491°C) the apparatus was identical with that previously described by this author (41). A diagrammatic sketch of the apparatus is shown in Fig. 1. For 555°C the sample was contained in a Vycor cup set in a nickel bomb. A nickel delivery tube led outside the furnace to ⅜-in. stainless steel tubing attached by Swagelok fittings to a heavy wall glass manometer containing mercury. Steel capillary tubing then lead to a 250 psi gauge and a high-pressure valve. From mercury to pressure gauge and almost to the valve the system was filled with

Table I. Observations of various investigators

Literature reference	Brief summary of pertinent observations
Moissan (1)	H_2 over heated MnO_2. Reaction began at 230°.
Wright and Luff (2)	H_2 over heated MnO_2. Reaction began at 390°.
Gorgeu (3)	Several varieties MnO_2 heated in air. O_2 evolved at about 400°.
Meyer and Rötgers (4)	MnO_2 prepared from $Mn(NO_3)_2$. Decomposed at 530° in air and at 565° in O_2; 86 hr required; no reversibility.
Askenasy and Klonowski (5)	MnO_2 heated in closed system; 0.26 atm in <5 hr at 478° and >1.37 atm in <5 hr at 536°; reversibility claimed.
Kendall and Fuchs (6)	MnO_2 heated in closed system; 1 atm as 419°; reversibility claimed.
Drucker and Hüttner (7)	MnO_2 heated. Pressure equilibria not constant; reversible below 480°.
Simon and Feher (8)	MnO_2 heated; 0.9 atm at 525°.
Bahr and Sackur (9)	MnO_2 heated in closed system: 1.07 atm at 572° in 68 hr; irreversible.
Von Krüll (10)	MnO_2 heated. Concluded no definite decomposition temperature obtainable.
Blumenthal (11)	Pyrolusite, crystalline, amorphous. See Fig. 5 for pyrolusite.
LeBlanc (12)	X-ray diffraction studies. No solid solutions exist.
Dubois (13)	Various types MnO_2 heated. Decomposed at 300°-600°. Proposes $MnO_{1.90}$.
Herman and Slonim (14)	Several natural MnO_2 ores. No >0.4 atm at no >583°. X-ray diffractions showed no solid solutions.
Kapustinskii and Bayushkina (15)	Heated MnO_2 prepared from $Mn(NO_3)_2$. See Fig. 5.
Sakai, Hukuyama and Okuno (16)	Several kinds MnO_2 heated in air. Decomposed at 500°-580°.
Matsuno (17)	Pyrolusite heated. Decomposed about 650°; temperature depends on crystal size.
Tatievskaya (18)	Decomposition temperature of 627° at 1.24 atm calculated by thermodynamics.
Kulp and Perfetti (19)	In DTA (12.5° rise/hr) break in curve at 580°-670°.
Brenet and Grund (20)	Thermogravimetric analysis. Weight loss at 500°.
McMurdie and Golvato (21)	DTA of pyrolusite. Endothermic break at 670°.
Pascal (22)	More than 150 oxides of manganese exist.
Grasselly and Klivenyi (23)	Product analysis after heating for 3 hr in air. Weight loss at 460°.
Földvari-Vogl and Koblencz (24)	DTA of pyrolusite. Endothermic break at 640°.

All temperatures are in °C. DTA = Differential Thermal Analysis.

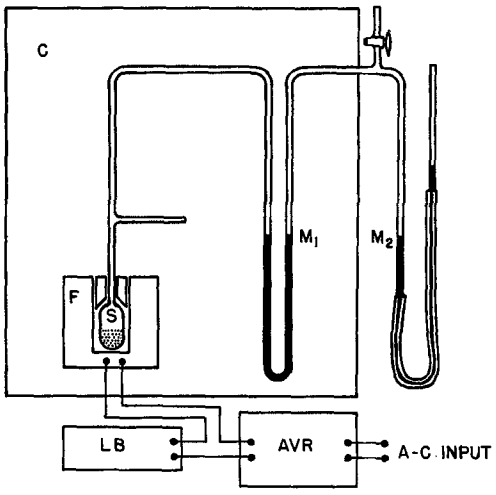

Fig. 1. Diagrammatic sketch of apparatus: C, temperature controlled cabinet; S, Vycor tube containing sample, M_1 and M_2, manometers, M_2 serves as leveling device; AVR, automatic voltage regulator; LB, lamp bank; F, furnace.

trichlorethylene on which the pressure could readily be increased by passing cylinder nitrogen through the high-pressure valve. For 642° the sample was again in a Vycor cup. Now the nickel bomb was very thick walled and was attached to nickel tubing and then stainless steel capillary tubing. A 2500 psi gauge and an oxygen servicing high-pressure valve completed the system. For all temperatures except 642°, pressure readings were taken at constant volume.

In all cases the furnace was located in the thermostatted cabinet (c). Regulated constant current was continuously supplied by means of an automatic voltage regulator connected in series with a lamp bank and the furnace.

The manganese dioxide used was reagent grade pyrolusite assaying 99.5% MnO_2. In a sieve test 9% remained on the 100 mesh sieve, 88% on the 200 mesh, and 3% through the 200 mesh. Further grinding was done sometimes. The sample was dried at 120°C overnight and then weighed into the Vycor capsule. Further drying was done by operating the furnace at 350°C while the system was being evacuated for several hours. The furnace temperature was increased and then held constant for hundreds or several thousand hours while the pressure was approaching an equilibrium or steady value. At each temperature, data on pressure-time relationships were obtained and plotted. Figures 2 and 3 are typical.

By lowering the temperature or by increasing the oxygen pressure attempts were made to reverse the dissociation reaction. The resulting reduction in pressure was so slow in contrast to Mn_2O_3 dissociations (41) that at first it was considered that there was no reduction and the dissociation is irreversible. Figures 2 and 4 show that there is recombination, but that equilibrium was never re-established.

The first sample used in this investigation was mortar ground so fine that it all readily passed through a 100 mesh sieve. After drying the sample at 300°C the system was evacuated to several mm pressure and sealed. The temperature was raised to 513° for a few hours during which time the pressure rose to 1200 mm. The system was cooled to 441°, again evacuated and resealed. It was concluded after 1199 hr that the equilibrium pressure had been reached. That the supply of oxygen was not exhausted was proven by again evacuating and heating to a higher temperature during which time the pressure reached 7.3 atm. The second sample reported was likewise heated to about 500° and the system evacuated before being stabilized at 491° for a total of 524 hr, 336 hr being required to reach a steady pressure. The third sample was preheated to about 580° and the evolved oxygen (18 atm) removed. Then, after 477 hr at 555° by which time the pO_2 was 14 atm and after a partially successful reversal, a second build-up of pressure was allowed to take place, this one reaching 15 atm in 1400 hr and maintaining that pressure for

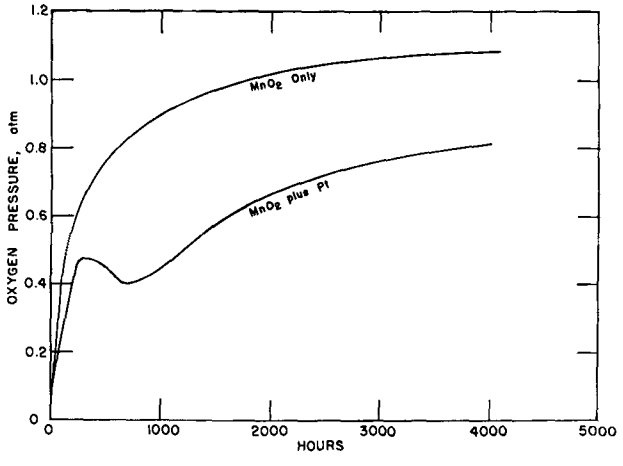

Fig. 3. Dissociation of pyrolusite. Effect of time on attainment of equilibrium at 474°C; also the effect of the presence of platinum black at 474°C.

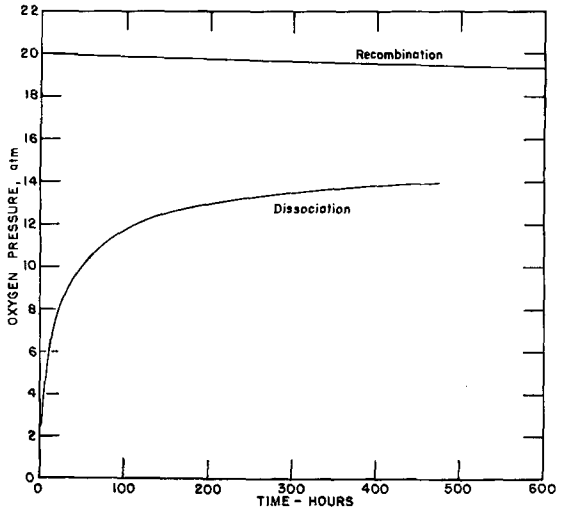

Fig. 2. Dissociation of pyrolusite. Effect of time on attainment of equilibrium at 555°C; also evidence of partial recombination at 555°C.

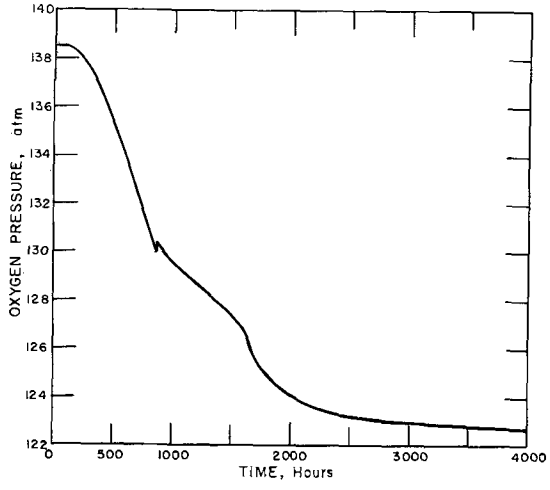

Fig. 4. Reoxidation at 475°C of pyrolusite dissociated at 642°C. Equilibrium pressure is 1.4 atm.

Table II. Equilibrium data for four temperatures

Temperature, °K	pO_2, atm	Compressibility factor	Fugacity, atm	$-R\ln$ fugacity	"Correction" C	$\Delta Y°/T$, cal/deg
714.15	0.410	1.0001	0.4100	+1.7716	−0.0222	+1.7494
764.15	2.45	1.0007	2.4517	−1.7822	−0.0066	−1.7887
828.15	15.0	1.0046	15.069	−5.3907	−0.0028	−5.3934
915.15	142.7	1.045	149.12	−9.9457	−0.0145	−9.9602
[813]						[−4.6884*]

Compressibility factors were obtained by interpolation and extrapolation of data taken from "Tables of Thermal Properties of Gases" Circular 564 National Bureau of Standards. Fugacity equals the compressibility factor times the pressure.

* This is the predicted value of $\Delta Y°/T$ at 813° as given in the section on Treatment of Data.

1600 additional hr. A noteworthy observation is that 800 hr were needed to reach 14 atm in the second build-up compared to 477 hr in the first. The sample studied at 642° was evacuated at 350° and slowly heated to 642° until the pO_2 was 125 atm. Some oxygen was released; the pressure fell to 110 atm. From 1500 to 1800 hr at 642° the pressure was constant at 142.7 atm. Following this experiment the temperature was raised, and it was noted that, after thermal equilibrium was obtained, the pO_2 again rose indicating some MnO_2 was dissociating. An unsuccessful attempt was made to reach the equilibrium pressure by lowering the temperature from 642° to 475°. Figure 4 shows that the Mn_2O_3 did not undergo recombination in the first 200 hr. Recombinations then became relatively rapid until a total of 870 hr had passed, at which time there was a temporary rise in oxygen pressure and then a decrease, but at a lower rate than the initial. If the recombination taking place between 3000 and 4000 hr were to continue at the same rate, the remaining pressure drop of 115 atm to the equilibrium pressure of 1 atm at 475° would have required a number of years. After the partially successful reversal attempt sufficient MnO_2 remained to obtain essentially the equilibrium pressure at 530° in 3700 hr. The equilibrium data obtained for the four temperatures are given in Table II and Fig. 5. For comparison purposes experimental data from the literature are included in Fig. 5. It is to be noted that the oxygen pressures observed in the present investigation are much greater than any heretofore observed for corresponding temperatures.

Platinum black was blended with pyrolusite in an attempt to catalyze the dissociation of MnO_2 or the reverse action. Figure 3 shows that the platinum actually consumed much of the oxygen and was of no benefit to the study.

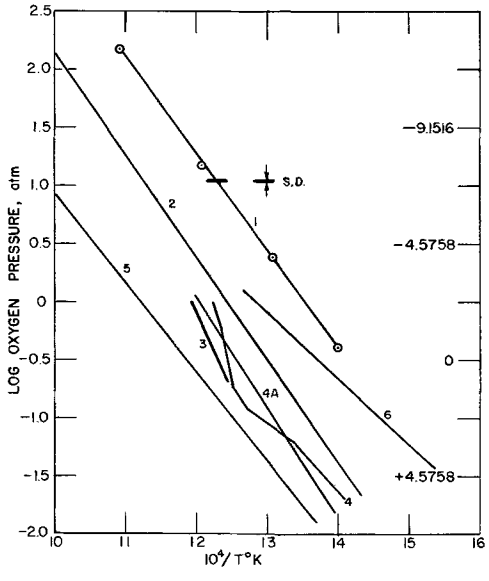

Fig. 5. Oxygen pressure-manganese dioxide temperature. Curve 1, present work on pyrolusite; line thickness aside curve 1 shows the uncertainty of the fit of the equation at 813°K; curve 2, Mah; curve 3, Meyer and Rötgers; curve 4, Blumenthal (experimental) curve 4A, Blumenthal (calc.); curve 5, Ulich and Siemonsen.

Treatment of Data

In spite of the inability to attain complete reversibility, it is assumed that equilibrium was reached in the forward direction. Since the range in oxygen pressure exceeded 100 atm, it is necessary to use fugacity (fO_2) in calculating values for thermodynamic constants (heat and entropy) of the reaction to give precise correlation of pressure and temperature. In other respects the treatment of the data is similar to that used in the previous paper (41). The method of Prosen (42) was again used to convert the data to yield a theoretical straight line plot of $\Delta Y°/T$ against $1/T$, where this line is the tangent to the $\Delta F°/T$ curve at a selected temperature of 813°K, an approximate midpoint temperature in this study. The pertinent equations involved are

$$\Delta Y°/T = \Delta H°_{813}/T - \Delta S°_{813}$$

and

$$\Delta Y°/T = -4.5756 \log fO_2 + C$$

where C is the correction given by

$$C = -\Delta(H°_t - H°_{813})/T + \Delta(S°_t - S°_{813})$$
$$= -1/T\,\Delta C°_p\,dT + (\Delta C°_p/T)\,dT$$

The $\Delta C°_p$ value for the reaction, obtained from data given by Kelley (33), is

$$\Delta C°_p = -9.78 + 8.00 \times 10^{-3} T + 8.66 \times 10^5/T^2$$

For the 813°K region the correction is

$$C = 3.9311 + 0.004T - 6{,}374.45/T$$
$$+ 4.33 \times 10^5/T^2 - 22.5233 \log T/813$$

Table II gives in successive columns for each equilibrium the temperature, the observed pressures, the compressibility, the fugacity, R ln of fugacity, the Prosen correction, and $\Delta Y°/T$. Also Fig. 5 indicates there is no noticeable difference on this scale between the plot of pO_2 against $1/T$ and the theoretical tangent at 813°K. The constants of this tangent

$$\Delta Y°/T = \Delta H°_{813}/T - \Delta S°_{813}$$

were determined to be

$$\Delta H°_{813} = 37.87 \pm 0.56 \text{ kcal}$$

$$\Delta S°_{813} = 51.28 \pm 0.70 \text{ cal/deg}$$

and the predicted value at 813 was

$$\Delta Y°/813 = -4.688 \pm 0.065 \text{ cal/deg}$$

The indicated uncertainties are the standard deviations of the associated quantities as determined from the least squares fit to the four points of Table II. The uncertainty in the log pO_2 value at 813°K is indicated by the standard deviation shown by the thickness of the line aside curve 1 of Fig. 5. This is evidence that the difference from the other curves cannot be accounted for by errors in measurement. Systematic error due to not actually reaching equilibria could only mean

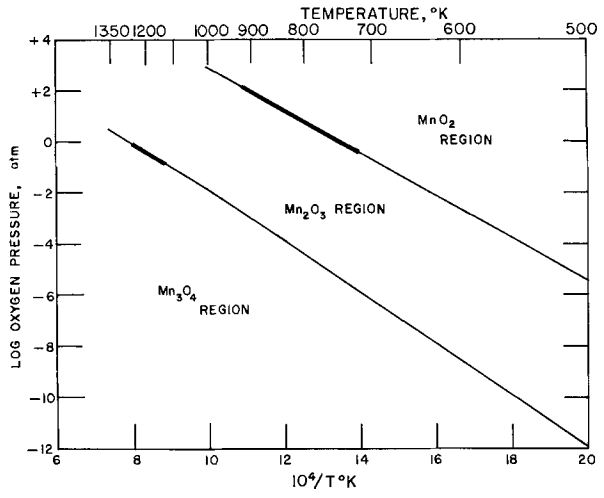

Fig. 6. Regions of stable existence of oxides of manganese

that pressures would have been even higher than those shown here.

If one subtracts from the above constants —0.88 kcal, $(H_{813} - H_{298})$, and —1.50 cal/deg, $(S_{813} - S_{298})$, calculated from the tabulated heat content and entropy data given by Kelley for the substances involved, the resultant constants for the reaction at 298.15°K become

$$\Delta H^\circ_{298.15} = 38.76 \pm 0.6 \text{ kcal}$$

$$\Delta S^\circ_{298.15} = 52.78 \pm 0.7 \text{ cal/deg}$$

Then

$$\Delta F^\circ_{298.15} = 23.0 \text{ kcal}$$

These values may be compared with those given in the literature. Rossini *et al.* (34) selected —124.5 kcal for the ΔHf°_{298} of MnO_2 and —232.1 kcal for that of Mn_2O_3. These yield +33.8 kcal for ΔH°_{298} for the reaction. Mah (38) selected —124.4 kcal for ΔHf°_{298} of MnO_2 and —228.4 kcal for that of Mn_2O_3 giving +40.8 kcal for the reaction. Brewer (35) chose —124.2 kcal and —229.2 kcal for these respective constants which result in 38.4 kcal for the reaction. Using the newly determined value of —228.7 kcal derived by Otto (41) for the ΔHf°_{298} of Mn_2O_3 one obtains for the ΔHf°_{298} of MnO_2 a value of —124.0 kcal. This is in good agreement with those cited above.

The value of ΔS°_{298} may also be compared with that obtained from entropy values given in the literature. Glassner (37) selected entropies at 298°K for MnO_2, Mn_2O_3, and O_2 as 12.7, 26.4, and 49.0 cal/deg, respectively. These yield 51.0 cal/deg for the dissociation of MnO_2 while the value obtained as a result of this investigation is 52.8 cal/deg.

It may be of interest to compare, in tabular form, the present results with those given by Mah.

Temp, °K	298	700	800	900	1000
Present work, atm	4.3×10^{-17}	0.242	7.23	101.5	849
Mah's table, atm	1.71×10^{-19}	0.0238	0.855	14.1	132

Now that equilibrium studies of MnO_2-Mn_2O_3 and Mn_2O_3-Mn_3O_4 have been completed, it is possible to delineate the mutual boundaries of these oxides. By use of tables (38) of entropy and heat-content changes the boundaries (Fig. 6) have been extended above and below the range of temperatures and pressures of the experimentation. At an oxygen pressure of 1.000 atm the equilibrium temperature is 468°C (741°K), while in air at 1.000 atm it is 424°C (697°K).

Acknowledgment

The author wishes to express his gratitude to Dr. W. J. Hamer under whose direction the work was conducted and who maintained keen interest in the study despite the thousands of hours required to obtain equilibria.

Manuscript received Aug. 6, 1964. This paper was presented at the Boston Meeting, Sept. 16-20, 1962.

Any discussion of this paper will appear in a Discussion Section to be published in the December 1965 JOURNAL.

REFERENCES

1. H. Moissan, *Ann. Chim. Phys.*, [5] **21**, 231 (1880).
2. C. R. A. Wright and A. P. Luff, *J. Chem. Soc.*, **33**, 522 (1878).
3. A. Gorgeu, *Compt. rend.*, **110**, 1134 (1890).
4. R. J. Meyer and K. Rötgers, *Z. anorg. Chem.*, **57**, 104 (1908).
5. P. Askenasy and S. Klonowski, *Z. Elektrochem.*, **16**, 104 (1910).
6. J. Kendall and F. Fuchs, *J. Am. Chem. Soc.*, **43**, 2017 (1921).
7. C. Drucker and R. Hüttner, *Z. Phys. Chem.*, **131**, 237 (1928).
8. A. Simon and F. Feher, *Z. Elektrochem.*, **38**, 137 (1932).
9. F. Bahr and O. Sackur, *Z. anorg. chem.*, **73**, 101 (1912).
10. V. F. Von Krüll, *Z. anorg. u. allgem. chem.*, **208**, 134 (1932).
11. M. Blumenthal, *Bull. soc. chim. (France)*, **53**, 1418 (1933).
12. M. LeBlanc and G. Wehner, *Z. phys. chem.*, **168**, 59 (1934).
13. M. P. Dubois, *Ann. chim.*, [11] **5**, 432 (1936).
14. Z. Herman and Ch. Slonim, *Monatshefte*, **70**, 84 (1937).
15. A. F. Kapustinskii and K. C. Bayuskhina, *Zhur. fiz. khim. (USSR)*, **11**, 77 (1938).
16. W. Sakai, H. Hukuyama, and T. Okuno, *J. Soc. Chem. Ind. Japan*, **45**, 25 (1942).
17. S. Matsuno, *ibid.*, **46**, 605 (1943).
18. E. P. Tatievskaya, G. I. Chufarov, and V. K. Antonov, *Izvest. Akad. Nauk. SSSR*, 371 (1948).
19. L. Kulp and J. Perfetti, *Mineralog. Mag.*, **29**, 239 (1952).
20. J. Brenet and A. Grund, *Compt. rend.*, **240**, 1210 (1955).
21. H. F. McMurdie and Golvato, *U. S. Natl. Bur. Standards J. Research*, **41**, 589 (1948).
22. P. Pascal, "Nouveau Traité de Chimie Minerale," Vol. XVI, p. 748, Masson et Cie, Paris (1960).
23. G. Grasselly and E. Klivenyi, *Acta Univ, Szegediensis Acta Mineral. Petrog.*, **9**, 15 (1956).
24. M. Foldvari-Vogl and V. Koblencz., *ibid.*, **9**, 7 (1956).
25. R. W. Millar, *J. Am. Chem. Soc.*, **50**, 1875 (1928).
26. H. Siemonsen, *Z. Elektrochem.*, **45**, 637 (1939).
27. J. C. Southard, *J. Am. Chem. Soc.*, **63**, 3142 (1941).
28. C. H. Shomate, *ibid.*, **66**, 928 (1944).
29. G. E. Moore, *ibid.*, **65**, 1398 (1943).
30. K. K. Kelley and G. E. Moore, *ibid.*, **65**, 782 (1943).
31. R. L. Orr, *ibid.*, **76**, 857 (1954).
32. E. G. King, *ibid.*, **76**, 3289 (1954).
33. K. K. Kelley, *U. S. Bur. Mines Bull. 584* (1960).
34. F. D. Rossini, *U. S. Natl. Bur. Standards Circ. 500* (1952).
35. L. Brewer, *Chem. Rev.*, **52**, 1 (1953).
36. J. P. Coughlin, *U. S. Bur. Mines Bull. 542* (1954).
37. A. Glassner, *U. S. Argonne Nat. Lab. ANL 5750* (1957).
38. A. D. Mah, *U. S. Bur. Mines Repts. Invest. 5600* (1960).
39. S. Dushman, "Scientific Foundations of Vacuum Techniques," p. 742, 2nd Ed., John Wiley & Sons, New York (1962).
40. L. Brewer, Private communication.
41. E. M. Otto, *This Journal*, **111**, 88 (1964).
42. E. J. Prosen, To be published.

Effects of Foreign Ions on Nickel Hydroxide and Cadmium Electrodes

E. J. Casey, A. R. Dubois, P. E. Lake,* and W. J. Moroz

Defence Chemical Biological and Radiation Laboratories, Ottawa, Ontario, Canada

ABSTRACT

The behavior of individual positive and negative electrodes of the sintered-plate nickel-cadmium battery system in the presence of foreign ions in KOH solutions has been examined. Carbonate choke: The variation of electrochemical capacity as a function of carbonate contamination of the electrolyte, temperature, and current density was measured for both positive and negative electrodes. The effect of carbonate on the negative cadmium electrode is much greater than on the positive. The general mechanism and the role of intermediate complexes are discussed. Nitrate shuttle: Self-discharge occurs in cells containing nitrate, as a result of reduction of NO_3^- to NO_2^- at the cadmium electrode with subsequent reoxidation to NO_3^- at the nickel hydroxide electrode. Cations on the positive: Addition of Li^+, Ag^+ Sb^{+3}, Al^{+3}, and As^{+3} to the electrolyte had effects on capacity and on charge-retention of well-formed nickel hydroxide positive electrodes. Lithium promoted the highest average oxidation, particularly at high temperatures (55°C). Arsenic was the best inhibitor of loss of charge. Possible mechanisms are discussed.

Carbonate.—Previous investigations have had as their objective the understanding of the effects on nickel-cadmium batteries of the carbonate which is formed by the reaction of the alkali electrolyte with carbon dioxide absorbed from the air (1). The interest of this Laboratory in these phenomena was awakened several years ago when it was observed that sintered-plate cells with more than 5% carbonate by weight sometimes behaved very peculiarly (2) and always delivered less capacity (3, 4) at low temperatures. However, the unpredictability of when and where it would occur made the verification of a true carbonate effect difficult.

On cadmium metal surfaces the mechanism of the carbonate effect has been studied (4-7) at a more fundamental level, in the absence of the porous sintered nickel matrix. It was concluded (6) that $CO_3^=$ competes with OH^- for adsorption sites on the underlayer which forms as the primary product of the oxidation reaction; and, further, that this competition varies with variation in current, electrolyte composition, and temperature. The important role of an inner double layer, in the underlayer, was stressed.

Another way of looking at this effect might be through the model of Croft and Tuomi (8-9). In their model the polarizations of the electrode are related to the number and kind of structural defects principally at the electrolyte-oxide interface and in the covering layer itself. The number and kinds of defects are determined by their rate of formation by the anodic current, their rate of combination with each other and with existing defects, and their rate of reaction with the components of the electrolyte.

The fibrous nature and the probable role of the hydroxycarbonate anodic reaction products on cadmium were discussed by Huber (10). Although their chemical composition was reported as early as 1936 (11), and that of the related bicarbonates since 1957 (12), there is still no reliable means of identifying small quantities formed on an anode. To complicate matters, these compounds are unstable. The problem of identification will be discussed in a subsequent report.

The nickel hydroxycarbonates are better known. Gagnon *et al.* (11, 13) showed chemically that nickel hydroxycarbonates can be formed if precipitating conditions are carefully controlled. However, like the cadmium compounds, sufficiently rapid identification of small quantities formed at electrodes is still not possible. There have been some very good recent studies made of the chemical precipitation and properties of nickel hydroxycarbonates (14) which may be used as a starting point in the attempt to understand at least qualitatively the electrochemical behavior. Thus compounds of the general formula $yNiCO_3 \cdot Ni(OH)_2 \cdot H_2O$, where $y = 1$, 3, or 4 have been identified chemically, and they give unique x-ray diffraction patterns (14). They are unstable in strong caustic. Longuet-Escard and Méring (15) have tackled the critical problem of the distortion of the nickel hydroxide lattice by incorporated carbonate ions; and Vasserman and Fomina (16) have followed changes in composition and in x-ray diffraction pattern during ageing, the compound becoming more basic at high *p*H (~12) and less basic at low *p*H (~7). Feitknecht (17) has given a broad and informative perspective of this problem.

Nitrate.—The loss of charge of a nickel-cadmium cell via the "nitrate shuttle" (18) was not recognized until cells with little or no free electrolyte were manufactured. Observations of odd effects of nitrate on voltage have been noticed [*e.g.*, (19)]. It seems to be a unique redox system: both the oxidized (NO_3^-) and reduced (NO_2^-) species are soluble in the electrolyte, are uncomplexed with either the electrolyte or the electrodes, and diffuse at a rate which increases with concentration gradient and temperature. Because nitrate is readily reduced by cadmium metal, and nitrite readily oxidized by charged nickel hydroxide, a mechanism for loss of charge exists by means of electron exchange within the cell.

Positive ions.—Following up a rather ingenious prediction from the solid-state structure of cadmium and its hydroxide, Fleischer (20) was able to demonstrate that the addition of indium metal to the cadmium negative electrode made a sharp decrease in the loss of capacity which usually occurs during cycling. With the above exception, most of the published work within the past few years on cationic additions, including that undertaken by this Laboratory, has dealt with their effect on the behavior of the nickel hydroxide electrode. The addition of lithia to the electrolyte has been standard practice in the pocket-plate battery industry for years. Its effect has been described in the trade as keeping the nickel hydroxide active material "loosened up," with the result that the electrochemical storage capacity does not decrease with prolonged use of the battery. Normally lithia does not need to be added to the sintered-plate battery; this is presumed to be so because the positive active material is spread so thinly over the surface of the sintered matrix that it is substantially all available for electrochemical action at normal temperature. However, to facilitate the formation of plates made by the thermal impregnation

* Present address: 448 Briar Avenue, Ottawa, Ontario, Canada.

process (21) used now by at least two manufacturers, it is sometimes necessary to add lithia to the electrolyte during the forming process. That lithium ions are also beneficial in the sintered plate positive at high temperatures will be demonstrated later.

Although cobalt hydroxide has often been incorporated in pocket-plate batteries since the time of Edison, the introduction of cobalt into the positives of sintered-plate batteries was first made by a European manufacturer during the early 1950's, and most other manufacturers have since followed suit. An additional stimulus for the commercial introduction of cobalt was Winkler's paper (22) in 1955 in which he reported "brilliant improvement" in performance. In general terms, cobalt raises the voltage of the electrode during discharge (*i.e.*, either it raises the reversible emf or it lowers the overvoltage). Further, cobalt has been reported (19) to improve greatly the charge-retention of the positive, and data published recently (23) support this view. After Winkler's paper, the first published systematic study on the effects of cobalt was that of Doran in 1958 (24). With lightly impregnated plates he demonstrated that, in contrast with plates containing pure nickel hydroxides, whose electrochemical storage capacity slowly decreases toward a final steady value (about 60% of the original) during repetitive cycling, the "electrodes containing moderate proportions of cobalt maintain indefinitely a capacity at least as high as that of the pure nickel hydroxide electrode at its transient best." He also found that whereas other ions (Zn^{++}, Mn^{++}, and Cd^{++}) made only minor modifications to the charge (oxidation) and discharge (reduction) curves, Mg^{++} had the very important practical effect of raising the discharge voltage (*i.e.*, lowering the cathodic overvoltage of the positive) by about 50 mv. However, Mg^{++} ions were found to increase the rate of loss of charge from the oxidized nickel hydroxide mass during an idle period.

Further, Doran found (25) that replacement of 5% of the nickel ions by cobalt and 5% by magnesium ions combined the best characteristics of both additions; thus, a stabilized high capacity, as well as discharge at a higher voltage resulted. In his paper, Doran cautioned that one could not extrapolate from his results, obtained with lightly impregnated plates, to battery performance. Subsequent evaluations of complete cells have been inconclusive (26).

In later work (27) it was demonstrated that scandium alone has the combined beneficial effects of the $Mg^{++} - Co^{++}$ addition, and that the discharge voltage is even higher with scandium than with magnesium. Further, "compared with the pure nickel electrode, in addition to the much higher discharge potential, the separation of anodic and cathodic potential is less, and the oxygen overpotential (top-of-charge potential) is higher." Of course, all of these effects are desirable in battery applications.

A basic difficulty arises in a study such as the present one, because the crystal structure of the active nickel hydroxide mass may be different from one experiment to the next on the same material, or from one preparation to another [see ref. (28), *e.g.*]; and, further, the crystal structure may change with "age" and even during "rest" when it is not being oxidized and reduced (8, 29, 30). One preparation (loose, open structure) may be expected to show marginal effects of positive ion additions, while another preparation (more perfectly formed crystallites) may show marked effects. These and other published claims [ref. (31-58)] about electrochemical effects of positive ions have been collected and are recorded in Table I, for comparison later with results of the present work.

Consider what might be the effects of foreign cations on the electrical conductivity of the active nickel hydroxide mass. Two concepts provide the background: (*a*) the mass consists of lamellar hexagonal arrays of positive ions, negative ions and water molecules whose positions are known from x-ray diffraction studies [colorfully described and illustrated by Doran (24), *e.g.*]; and (*b*) the idea (59), that the oxygen atoms of the water and hydroxide ions of the mass remain relatively fixed in the lattice while protons from the electrolyte and electrons from the metallic grid move into the mass during discharge (reduction) and out of the mass during charge (oxidation). Divalent foreign cations should distort the lattice, being of different size, and introduce anion (OH^-) vacancies as the mass becomes oxidized. Into these vacancies water molecules may fit, and facilitate protonic conduction. Doran's results on Mg^{++} and Sc^{++} especially tend to support

Table I. Reported effects of added cations on properties of nickel hydroxide electrodes

	Ionic radius, A	Coulombic capacity, C	Capacity-stabilization with cycling	Voltages			Charge retention (open circuit)	Potential decay (open circuit)			Electrical conductivity of oxides	Rate of recrystallization of hydroxides	References
				disch	chge	o'chge		b_A	b_B	b_C			
Li^+	0.68	++	+	0	0	++	+	0	+	+	++	(−)	(35), (29), (55), (45), (39), *, (83), (86)
Na^+	0 97	0	0	0	0	0	0	0	0	0		0	**, (33), (83)
K^+	1.33	+				(−)	(+)	0	0	0		(−)	(48), (50), (52), (83)
Rb^+	1.48	(+, −)		(−)	(+)								(41), (58), (86)
Cs^+	1.69	(+, −)		(−)	(+)								(41), (58), (86)
Ag^+	1.26	+		+	0	0	0	0	d	d		(−)	*
Mg^{+2}	0.65	+	+	+	(0)	0	−						(25)
Cu^{+2}	0.69			(−)	(+)								(25)
Ni^{+2}	0.69											+	(40), (42)
Zn^{+2}	0.74	0, =	=	0, −	0	0	0						(25), (55), (56), (87)
Cd^{+2}	0.97	0		0	0	0	0						(24), (57)
Hg^{+2}	1.10	++	+										(43)
Ba^{+2}	1.34	+, −	+, −				−						(85), (29), (2), (55), (44), (76)
B^{+3}	0.35	(−)											(36)
Al^{+3}	0.51	0		−	+	+	0	0	d	0			*
Fe^{+3}	0.53	+, −	+										(35), (49)
Ce^{+3}	0.63	+, 0	+	+	+	−	+	+	++	+	+	(−)	(20), (25), (54), (31), (47), (51), (55), (22), (38), (23)
Sc^{+3}	0.81	+		+	+	0	+						(25), (27)
Mn^{+4}	<0.80 (+2)	0, −		0	0								(25), (46)
Sn^{+4}	0.75	+											(64)
Sb^{+5}	0.62	+		0	+	0	+	0	d	0			*
As^{+5}	0.56	+		0	+	+	++	0	d	0			*
Bi^{+5}	<1.16 (+3)											+	(35)
Mo^{+6}	<0.68 (+4)					−							(47)
Cr^{+6}	<0.55 (+3)					−							(47)
W^{+6}	0.64					−		0					(87)

0, no change; +, increased; − decreased; $b = \partial E/\partial \log t$, where t is time and E is potential; A, B, and C, 1st, 2nd, and 3rd sections of open-circuit voltage decay; d, disappeared; *, this work; **, taken as standard or reference behavior.

this idea. Monovalent cations should do the same, even to the discharged mass [as $Ni(OH)_2$]. Trivalent cations may introduce cation vacancies and so facilitate electronic conduction; or trivalents may be more heavily hydrated, because of smaller size, and facilitate protonic conduction. If electronic conduction through the mass can be made lower relative to protonic conduction, the mass can be anodically oxidized to a higher free energy state at the mass-electrolyte interface before oxygen evolution sets in. An attempt has been made to study these possibilities experimentally.

The rate of self-discharge during an idle period following charging may also be affected by foreign cations. The present work has been designed around the simple premise that the charge, or the oxidation capability of the charged mass, is composed of two parts: (*a*) the "normal capacity," associated with the transformation $Ni(OH)_2 \rightarrow NiOOH$;[1] and (*b*) the "over-capacity"—extra oxygen forced into the NiOOH during charging and trapped there. Thus the charged mass may be represented as

$$\beta\text{-NiOOH[O]}$$

where the extra O is in, as well as on, the crystallites. [See ref. (65) for discussion of $(\beta\text{-NiOOH})_2(O)_{ads.}$] Both the overcapacity and the normal capacity are lost during an idle period, the former faster than the latter. In the present work an attempt has been made to separate the two and then to assess the effects of monovalent and trivalent foreign ions on each decay.

Experimental Methods

The experimental cells consisted of the test electrode suspended between two counter electrodes in a lucite or nylon container. A reference electrode (Hg/HgO), with Luggin capillary tip which was proximal to the test electrode, was added. The stock electrolyte was 30% KOH in distilled water, and protected from rapid CO_2 absorption by a ½-in. layer of mineral oil. The electrolyte was replaced when necessary.

Experiments were of two kinds: (*a*) Charge-discharge cycles were done on a program (Table II) which has been shown [see ref. (3), for example] to reflect quantitatively and reliably the operational electrochemical properties of the electrode. The capacity (charge delivered), 5-sec and mid-point discharge voltages, the shape of the charging curve, and the top-of-charge voltage were recorded at several current densities. (*b*) Charge-retention studies were also carried out: potential decay and capacity loss as a function of time were carefully measured. The decay of open-circuit potential (test electrode to Hg/HgO reference

continuous recording on a potentiometer which was fed only a fraction of the potential of the cell via a high resistance (200,000 ohms) voltage divider; (ii) intermittent measurements of cell potential at appropriate intervals with a L&N slide-wire potentiometer; and (iii) continuous recording of potential by a Type 1230-A General Radio electrometer-amplifier (input impedance minimum 10^9 ohms) coupled with an Esterline Angus recording ammeter. The precision of the measurements was: for the recording potentiometer ±2 mv; L&N ±0.1 mv; 1230-A electrometer ±2 mv.

The cycling and charge-retention programs [(*a*) and (*b*) above] were carried out on duplicate cells to which Li^+, Ag^+, $Sb^{+3} \cdot As^{+3}$ or Al^{+3} had been added. No study of charge retention was done on carbonate-

[1] Note that although the composition NiOOH is manifested in three fairly well-defined physical structures (see X-ray diffraction patterns and cell constants, Fig. 1 and Table I of ref. (60), for example), there is still no unequivocal evidence that the nickel in the compound is trivalent. On the contrary, the x-ray K-edge absorption results of Hanson and Milligan (61) offer no evidence at all for valences other than two in the "higher oxides." Tsutsumi (62) later found similar results with higher oxides, but introduced an uncertainty which has not yet been clarified (63). Perhaps $Ni(OH)_2$ is simply a good container for O and OH, with certain compositions [4 $Ni(OH)_2 \cdot NiOOH$, $Ni_3O_2 \cdot Ni_3O_2(OH)_4$, NiOOH] more stable than others. However, it is believed that trivalent and tetravalent nickel can be stabilized in complexes with certain foreign elements such as phosphorus and arsenic (64).

Table II. Cycling routine and program used to study output vs. current density

Cycling routine* Discharge at the following rates:		Test program for each added cation	
1.	3 hr	I	At 27°C, with no additive; then
2.	20 hr		
3.	3 hr	II	At 27°C, with additive; then
4.	1 hr	III	At 55°C, with additive, then
5.	6 min		charge-retention studies at 55°C; then
6.	3 hr		
7.	3 hr	IV	At 55°C, with additive; then
8.	3 min	V	At 27°C, with additive
9.	3 hr		
10.	2 min		
11.	3 hr		
12.	3 hr		
13.	20 hr		
14.	3 hr		

* All charging done at the 1-hr rate for 2 hr.

contaminated electrodes. Duplicate controls, containing no additive, were run simultaneously. All cells containing positive ion additives were thermostated at 55° ± 1°C during most of experiments, with cycling at 27°C done both before and after the high-temperature studies. The electrodes used in the positive ion studies were prepared from commercial (Clevite) sintered nickel plaques made from carbonyl nickel. Impregnation was carried out by the thermal method (21). The plates were then formed, and given 14 electrical cycles on the routine outlined in Table II. This procedure established the "normal" behavior of the electrode. After the characteristics had stabilized, the impurities were introduced into the electrolyte: the Ag^+ first as nitrate, later as oxide, the Li^+ as hydroxide, the As^{+3} as oxide, the Sb^{+3} as oxide and the Al^{+3} as oxide.

For the carbonate studies, electrodes from two commercial sources [prepared by the electrolytic method (66, 67)] as battery plates (by North American and European manufacturers) were used. After electrochemical cycling in 30% KOH (7.2*N* KOH) to constant "normal" capacity, the electrodes were cycled in electrolyte made up of mixtures of various proportions of 7.2*N* KOH and 7.2*N* K_2CO_3 so that the concentration of K^+ remained constant at 7.2*N*. These mixtures correspond roughly to the practical situation after 30% electrolyte has absorbed CO_2 from the air. Experimental data were collected at temperatures of 27°, −18°, −40°, and −54°C. Electrodes were charged at the 1-hr rate for 2 hr, put on open circuit stand for approximately a half-hour, and subsequently discharged at current densities of 3.9, 15.6, or 39 ma/cm² of electrode. Electrolyte compositions[2] of 0, 5, 10, 25, 50, 75 and

only nominal, the actual $CO_3^=$ concentration being closer to a value of 1-1.5%). As a check on reproducibility, at least two electrodes of the same type were used for each experiment. The cycle was repeated from two to five times with each electrode and the results for each particular condition were averaged. In addition, some cadmium electrodes were examined to determine whether the capacity loss during aging is temporary or permanent. The early experiments (3, 4) have been carefully repeated by further experiments on plates from different sources. Selected results which establish the main features of the processes are reported in this paper.

After introduction of the impurity, cycling was continued (Table II) until new stable characteristics had been obtained. In the carbonate studies it was found advantageous to re-cycle in 30% KOH at room temperature before changing the electrolyte composition; but in the positive ion studies this was done only at the very end of the experiment. During the cycling of cells containing added positive ions the experiments were interrupted at convenient times so that measure-

[2] $100\left[\frac{\text{equiv. of } CO_3^=}{\text{equiv. of } CO_3^= + \text{equiv. of } OH^-}\right]$, called "equiv. % $CO_3^=$"

ments of both the decay of voltage and the loss of charge during open circuit stand could be taken. For charge-retention studies the charge was measured as the coulombic output during reduction at the 2-hr rate. The minimum stand time was 30 min, and the longest was six weeks.

Some x-ray diffraction spectra were taken in support of this work by the Physics Section of this Laboratory. In addition, standard qualitative chemical analytical techniques were employed for the identification of impurity ions found at the end of the experiment in both the electrolyte and the electrodes. Corroborative analytical work was done by the Analytical Section. Mines Branch, Ottawa. Basicity and carbonate were determined by double titration, with phenolphthalein and methyl purple indicators. The nickel in the electrodes which was soluble in hot NH_4Cl-NH_4OH was determined quantitatively by the dimethylglyoxime method (68).

Changes in nitrite concentration in the electrolyte were followed by the sensitive sulfanilic acid-alpha naphthylamine hydrochloride color development for NO_2^-, as described by Snell and Snell (69).

Results and Discussion

The Carbonate Choke

The aim of this series of experiments, which was to establish the effects of contamination by carbonate ion on nickel hydroxide and cadmium electrodes and to be able to predict carbonate effects on nickel-cadmium batteries, has not been fully achieved. The results on single electrodes were reproducible to within only about ±10%, even when a fixed parallel geometrical arrangement was used and when the most obvious variables, temperature, concentration and charge and discharge rate, were carefully controlled. The work has pointed up the importance of further variables, some of which cannot be controlled in experiments in which the active material is held within the pores of a sintered plaque. For instance, until more is known of the physical properties of anodically formed hydroxides and hydroxycarbonates of cadmium and nickel, the full explanation of the effects of carbonate contamination, and under what conditions these effects will occur, cannot be predicted. However, the results obtained in the present work permit certain general conclusions to be made and point out suitable directions for further study. The results are discussed in the following two sections.

On cadmium electrodes.—The general trends and measurements on a particular plate for a particular set of conditions were reproducible, but the detailed behavior varied from plate to plate, and also was found to be dependent on the age and electrical history of the plate. In this report the results are summarized in terms of a qualitative model which, in our opinion, includes the principal dependent variables. The general behavior is illustrated with examples selected from experimental results on plates. Essentially the model [summarized in ref. (28)] is as follows: Cd metal oxidizes anodically to a "CdO" underlayer, the primary product,[3] and in all but the very initial stages either metal ions or oxygen-containing species must penetrate the film of CdO if reaction is to continue. Therefore the thickness of CdO is important. It is removed at the CdO-electrolyte interface by a "conversion reaction," in which CdO is complexed into the adjacent electrolyte as $Cd(OH)_4^{-2}$ or $Cd(CO_3)_3^{-4}$ (7), at a rate depending on the composition of the electrolyte at the interface, and settles out on the surface of the CdO layer as $Cd(OH)_2$, $CdCO_3$, or as a hydroxycarbonate. The reaction can continue as long as ions can penetrate the CdO more easily than water can be oxidized to oxygen and the electrons so liberated penetrate the CdO in the opposite direction. Therefore the rate of the conversion reaction is of prime importance: if it is slow, the available capacity will be low. This rate increases with temperature and exposed area. The reaction can go by two routes, via the hydroxy-complex (at rate v_{OH^-}) and via the carbonate-complex ($v_{CO_3^=}$). These complexes are not very soluble and probably also precipitate on the CdO surface. Hence the complicated problem of physical interference by reaction product logically arises, and it cannot be avoided. This introduces the second variable.

The second variable thought to be important is the specific volume of final precipitate. In addition to the complexes $Cd(OH)_4^{-2}$ and $Cd(CO_3)_3^{-4}$, solid, basic cadmium carbonates, $xCdCO_3 \cdot Cd(OH)_2$, can also be formed. Huber stated (10) that these are formed as fibrous (gelatinous) precipitates at the reaction interface where Cd^{++} from the metal meets OH^-, $CO_3^=$, and H_2O from the electrolyte. Several years ago Gagnon *et al.* (11), using a controlled precipitation of weak $Cd(NO_3)_2$ and K_2CO_3 solutions, formed two such compounds, which were chemically distinguishable, corresponding to $x = 10$ and $x = 5$. We have repeated, confirmed, and extended this work and, chemically, have been able to distinguish a third compound corresponding to $x = 4$ (Fig. 1). By the time they were dried and mounted, all gave x-ray spectra basically of $CdCO_3$, but sometimes with additional weak lines due to $Cd(OH)_2$, splitting in two of the three strongest lines and with intensity differences at short spacings. All three are quite unstable, and change composition, to $Cd(OH)_2$ or $CdCO_3$, if washed for a long time or digested in the mother liquor depending on the *p*H. Details of this work will be published elsewhere.

The precipitates found after $Cd(NO_3)_2$ solutions are mixed with 7.2*N* ($KOH + K_2CO_3$) solutions in which the concentration is varied from 0 to 100 equivalent % K_2CO_3 show some striking physical difference (see Fig. 2). In the central, 20-70 equivalent % region, the precipitates are voluminous and gelatinous and when analyzed are found to be composed of $Cd(OH)_2$, K_2CO_3, and $CdCO_3$ with slight variations in x-ray spectra. Those in the end regions of concentration (<20%, >70%) are nearly pure hydroxide or carbonate and

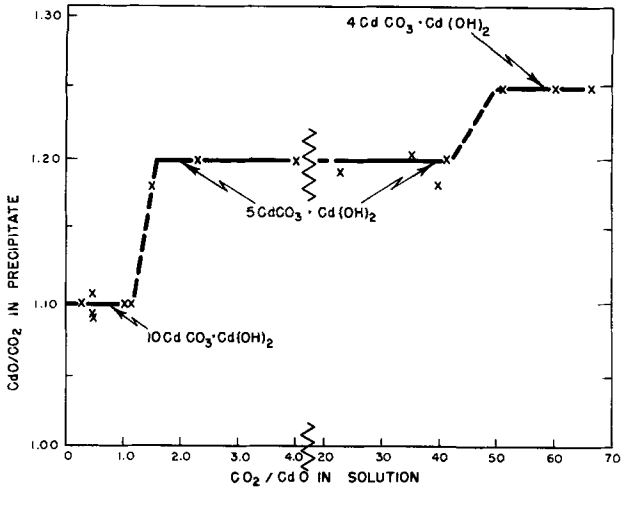

Fig. 1. Analytical results on precipitates and their mother liquors made by controlled mixing of $Cd(NO_3)_2$ with K_2CO_3 of different concentrations.

[3] There has been discussion on this point in the recent literature. We called it "CdO" for reasons discussed in ref. (6) on the basis of interference colors, existence of the conversion reaction, carbonate effects, exponential decay of overpotential, and consideration of likely primary processes. CdO was earlier (70) reported found by electron diffraction techniques, and was found again more recently (71), but others have tried to find it without success (8, 65). This divergence of experience can be rationalized as follows: The rate of the conversion reaction is high, and the underlayer very thin. Thus, during oxidation of cadmium planar electrodes at 0.33 ma cm^{-2} at 27°C in 7.2*N* KOH, the rate of conversion was found (5) to have a value equivalent to 0.26 ma cm^{-2} when the conversion layer was thin, and smaller values as the conversion layer built up. As conversion slows down the thickness of the underlayer increases. Its maximum thickness, at passivation, was estimated (28) to be a few hundred angstroms during current flow. It is rapidly converted to $Cd(OH)_2$ or $CdCO_3$ once the circuit is broken.

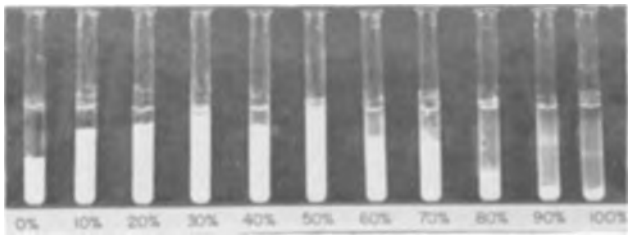

Fig. 2. Precipitates formed by mixing one part of 0.5N $Cd(NO_3)_2$ with one part of 7*N* K^+ in which the K^+ is present from 0 to 100 equiv. % carbonate in hydroxide.

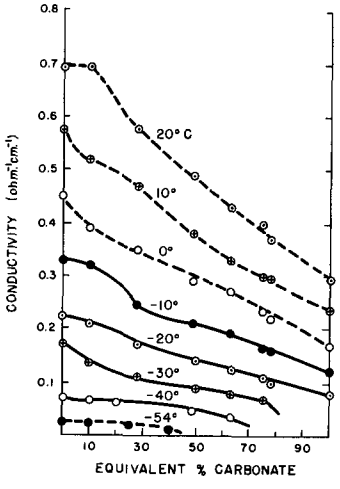

Fig. 3. Conductivity of mixed KOH-K_2CO_3 electrolytes at different temperatures. Total alkalinity: 7.2*N* K^+.

are flaky and/or granular. The specific volume of the final reaction product could be quite important in a porous electrode. For example, a small weight of precipitate could conceivably have a volume large enough to block the "neck" of a pore or displace the electrolyte and cut off all ionic contact between active material and the bulk of the electrolyte. This would make the active material within the pore unavailable for further electrochemical oxidation or reduction.

The third variable is the group of transport properties of the bulk electrolyte: conductance, diffusion, and fluidity. Electrical conductance, for example, falls off nearly linearly with increasing equivalent % carbonate, as is shown in Fig. 3, drawn from our earlier work (4). Presumably, as is usually the case, the corresponding specific rates of diffusion and fluid flow fall off similarly. At high rates and at low temperatures, soon after reduction starts, the ohmic voltage drop almost immediately reduces the cell voltage below the acceptable, useable, cut-off or end value. Decreased diffusion of KOH and K_2CO_3 in the solutions with higher equivalent % carbonate would also be expected to have the same effect, because the concentration gradients set up in the pores of the plate can disperse only slowly. Convective effects within pores and "extrusion" or forced flow of electrolyte into or out of pore due to changes in volume or physical structure of active material are not well understood but, such a transfer of fluid could dramatically affect the electrical output of heavily impregnated plates.

Figure 4a is a schematic illustration of speed of the processes on which the electrical output is thought to depend. A trend downward in the function plotted means there will be a trend downward in the coulombic output obtained. Since the processes are consecutive, the slowest one limits the output. Each of these curves represents a family of similar curves, there being a member for each set of experimental conditions. For example, the curves of Fig. 4b are the results of linear combinations of members of the four families introduced in Fig. 4a. Thus capacity *vs.* composition

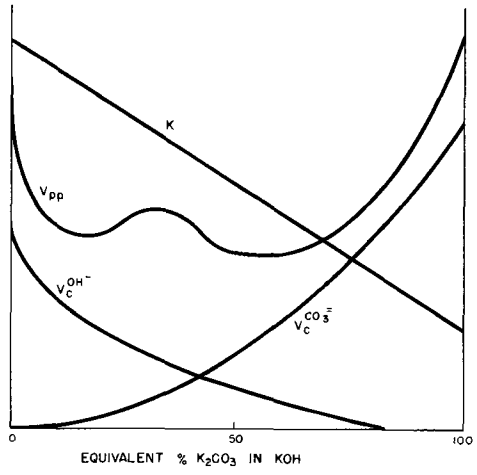

Fig. 4a. Schematic curves depicting how the rates of four critical processes probably vary with increasing carbonate in 7.2*N* K^+ electrolyte during anodic oxidation of cadmium.

$v_c^{OH^-}$ — rate of conversion reaction via $Cd(OH)_4^{-2}$

$v_c^{CO_3^=}$ — rate of conversion reaction via $Cd(CO_3)_3^{-4}$

K — specific conductance

v_{pp} — rate of penetration of reactants and products through precipitate (i.e. $v_{pp} \propto$ 1/ volume)

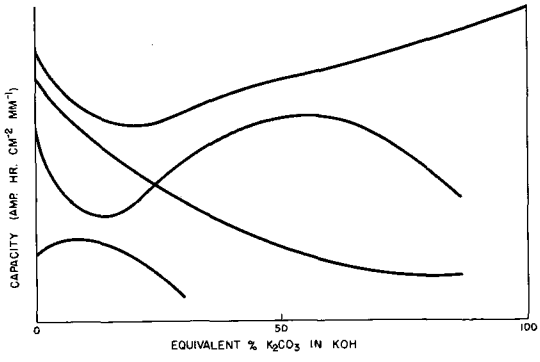

Fig. 4b. Effects of electrolyte composition on charge delivered by negative electrodes under various conditions (schematic).

(*C*/c) curves may take many shapes. Figures 5 to 7 are examples of results chosen from both the earlier report (4) and our more recent confirmatory work.

In addition to the transient effects on the three variables just considered, the results show that plates used in carbonated electrolyte can "age" or develop a permanent decrease in capacity. Although no cadmium has left the plate, some of it becomes passivated in the sense that it cannot be oxidized or reduced. This may be due to a permanent sealing of pores, to a redistribution of the active materials, or to the formation of a nonconducting (salt? oxide?) mass. The three sets of curves in Fig. 5 (25°C) were taken on plates which had a substantial history (at least 100 cycles) in batteries before these tests were done. Not only is the transient carbonate concentration effect very pronounced, but also in two cases, the capacity permanently "lost" was very large. Figure 6 (data at —18°C) illustrates this point even better: the output of a plate (No. 12) early in the tests is contrasted against the output of the same plate near the end of the tests, about 100 cycles later: the capacity *vs.* composition characteristic has changed markedly. Apparently the internal physical character of the plate has changed (*i.e.*, the plate has "aged") so that the capacity *vs.* composition curve has moved to the left and down, as if some solid carbonate had become permanently sealed into the plate, accounting for part of the loss (the permanent loss), while the carbonate in the electrolyte had caused

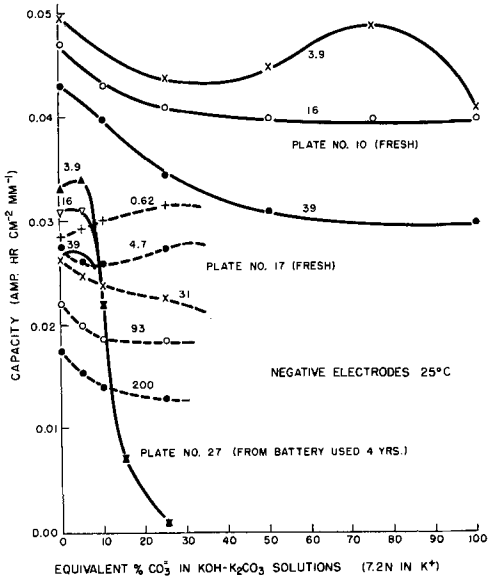

Fig. 5. Electrochemical capacity delivered, at c.d. shown (ma cm^{-2}), by good fair and poor cadmium negative plates at 25°C.

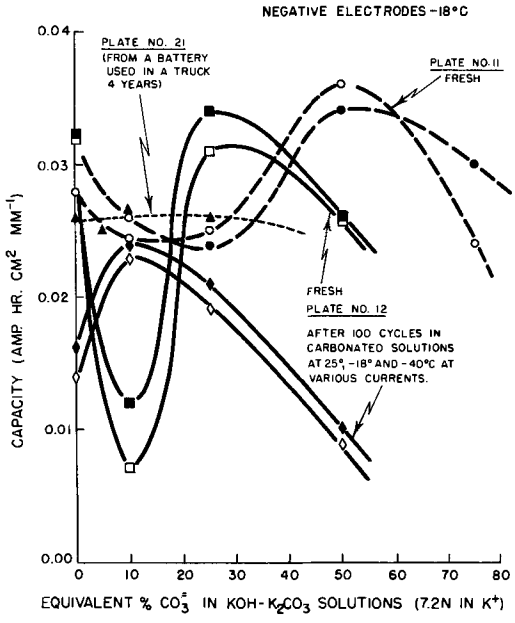

Fig. 6. Electrochemical capacity delivered, at c.d. of 160 ma cm^{-2}, by three different cadmium negative plates at —18°C, in KOH-K_2CO_3 mixtures. Solid symbols, charged at 25°C; open symbols, charged at —18°C.

the rest (the transient loss). The initial characteristics of another plate from the same group (No. 11) and with the same history, are also plotted in Fig. 6. Note the similarity of trend but difference in detailed behavior between supposedly duplicate specimens, plates 11 and 12.

Although somewhat tedious to obtain, these characteristic capacity *vs.* composition (*C*/c) curves clearly display the important, though subtle, differences between supposedly identical porous plates. They are much more sensitive than the Peukert curves (log *C* *vs.* log cd), which have been used to good advantage in assessing the early stages of development of the sintered plate technique [See ref (3) and (21), for example].

Figure 7 shows that differences in detail can be very pronounced at —40°: remarkably good output can be obtained from some plates, very much less from others. These differences are more pronounced the higher the discharge current density. The figure also illustrates the fact that better capacities can usually be obtained at low temperatures (—40°) if charging is also done at low temperatures. Generally at low temperatures the differences are less reproducible than at room temperature. Charge acceptance may be better at low temperature, but it seems to be more likely that the extra charge is due to hydrogen trapped in the pores and in grain boundaries of the nickel sinter, and as nickel hydride.

In summary, there now exists an accumulation of evidence that two kinds of detrimental effects due to carbonate occur on the negative plate: permanent effects related to the history of the plate and due to carbonate locked in the pores, and transient effects related to pore dimensions and the composition of the electrolyte. These effects have been observed on planar cadmium electrodes (5), and now, amplified greatly, on sintered negative plates. Three dependent variables seem to be important: the rate of the conversion reaction, the volume of reaction product (discharge), and the transport properties of the bulk electrolyte. These variables are dependent on electrolyte composition, temperature, and apparent current density, and probably also on pore size, pore size distribution, and interconnections of pores (*i.e.* electrolyte channels) within the plate.

On nickel hydroxide electrodes.—No appreciable effect of carbonate was found on the coulombic capacity of the nickel hydroxide electrode at 25°C. Tran-

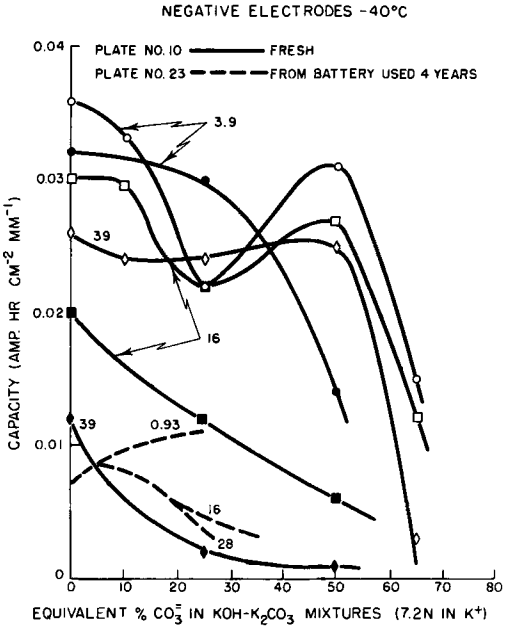

Fig. 7. Electrochemical capacity delivered, at c.d. shown (ma cm^{-2}), by two cadmium negative plates at —40° in KOH-K_2CO_3 mixtures. Solid symbols, charged at 25°C; open symbols, charged at —40°C.

sient effects, but no permanent effects, were found at low temperatures, during studies on 12 plates with upwards of 100 cycles per plate. Since the mechanism of discharge of the positive is still poorly understood, the presentation here is limited substantially to the effects of carbonate found experimentally.

At —18° and —40°C, the loss in capacity due to carbonate was found to be larger for plates which contained a greater amount of active material. In the more heavily loaded plates the capacity was a multivalued function of composition, a behavior similar to that of the negative. Figure 8 shows output at —18°C (following charge at —18°C) for two different plates, one twice as heavily loaded as the other. The general downward trend of the capacity as the electrolyte became more

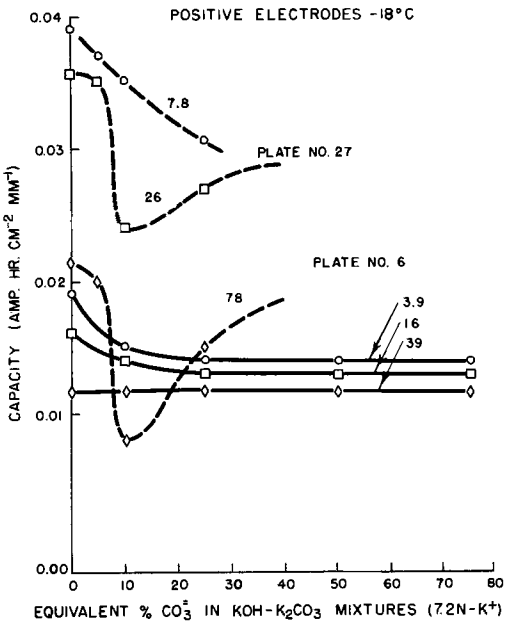

Fig. 8. Electrochemical capacity delivered at —18°C, at c.d. (ma cm^{-2}) shown, by two positive plates, which differ by a factor of two in the amount of nickel hydroxides per unit volume, in KOH-K_2CO_3 mixtures.

heavily carbonated is a behavior similar to that of the negative and is probably related to the decreasing rate of mass transport. The minimum at 10% may be the influence of the formation of bulky nickel hydroxycarbonates as intermediates in the process of electrochemical reduction, for it is evident that the effect was manifested only in the more heavily loaded plates. Unfortunately with nickel, as with cadmium, very little is known about the formation of its hydroxycarbonates as intermediates in the electrode process. Alternatively, possibly the carbonate acts by its ability to penetrate the layer lattice of the nickel hydroxide and distort it (15).

Figure 9 shows capacities delivered at —40°C. It is rather striking that the effect is actually fairly small until the carbonate content becomes so high that the electrolyte becomes glassy (at about 60 equiv. % carbonate), when the rate of transport of water, needed for the discharge reaction

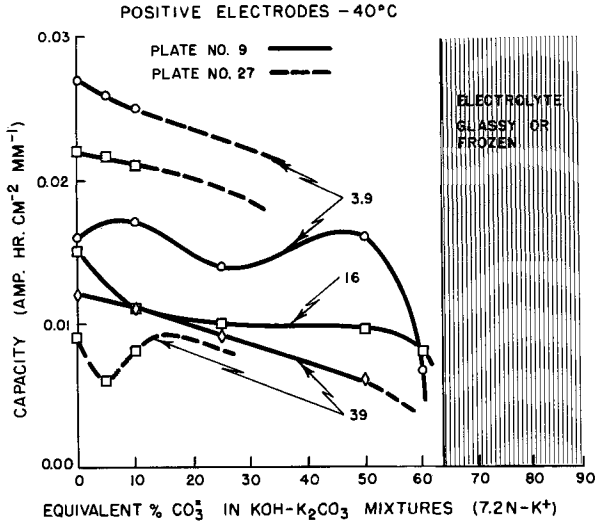

Fig. 9. Electrochemical capacity delivered at —40°C, at c.d. shown (ma cm^{-2}), by two nickel hydroxide plates in KOH-K_2CO_3 mixtures. All charging done at —40°C. (Charging at 25°C gave about the same outputs).

$$H_2O + e^- + NiOOH = Ni(OH)_2 + OH^-$$

falls practically to zero. Perhaps the readily available carbonate ions are literally frozen out of the layer lattice at —40°.

The Nitrate Shuttle

During preliminary work in this study, some positive ions were added to the electrolyte as nitrates. The most notable effect of the additions was the rather impressive loss of capacity during charged stand. Although the loss of charge was first attributed to the cation, a systematic elimination of possibilities by adding oxides instead of nitrates, and finally by adding KNO_3 itself, revealed that the anion was responsible for the effect. The results of experiments with the active materials added directly to the KOH electrolyte showed that Cd metal reduces nitrate rapidly to nitrite and that the oxidized positive plate material (nominally NiOOH) oxidizes nitrite to nitrate. Tests on a three-plate cell confirmed the suspicion that the $NO_3^- — NO_2^-$ couple can conduct a shuttle for electrons from the negative to the positive plate, and thus discharge the cell. Results are shown in Fig. 10. Since negative capacity was well in excess of positive in the test cells, the additive always ended up as nitrite, after the positive had become fully discharged. Subsequently it was shown that charged positive active material can stand alone in nitrate-containing KOH without accelerated self-discharge.

From these results the general mechanism of the nitrate shuttle is clear. Nitrate ion diffuses to the negative and is reduced to nitrite; the nitrite diffuses to the positive and is oxidized to nitrate. The result reported, for the cell containing 7 x 10^{-3} moles/1 KNO_3, in Fig. 10 was the approximate electrical equivalent at 55°C of a 100-ohm resistor connected directly across the terminals. The shuttle probably operates at a rate which is transport-controlled, since the reactions with the solids seemed to be relatively very fast at both the positive and negative electrodes. Since the transport rate (and hence the value of the equivalent resistance) is a function of cell geometry, concentration of nitrate, and temperature, as well as of the permeability constant of the separator, no detailed examination of transport for the experimental cells was worthwhile, and such work was not undertaken.

As a check on current industrial practice, sealed cells (4 AH) from the production line of two manufacturers were opened, and the contents refluxed in a Soxhlet extractor with distilled water for 3 hr. The leachant was then made neutral, and tested for nitrate. Tests for nitrate in both were positive. One had enough nitrate to make the electrolyte of the cell 0.005*N* in nitrate! The nitrate effect and its implications were reported briefly in an earlier paper (18). Reduction of NO_3^-

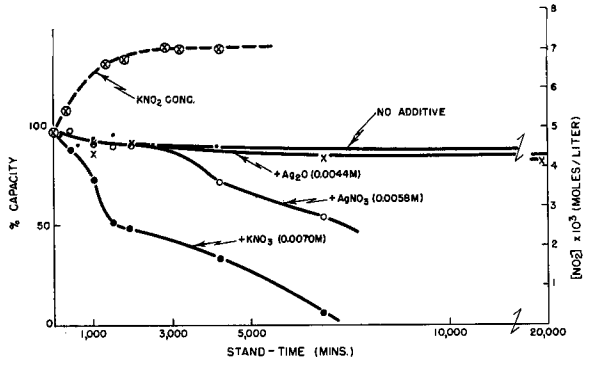

Fig. 10. Effect of nitrate ion on charge retention of positive plates in a 3-plate test cell; 7.2*N* KOH; 55°C; total nitrate added: 7x10^{-3}M. % capacity = 100 $C_t/C_{30\ min}$, where C_t is capacity after charged stand of *t* min, and $C_{30\ min}$ is capacity after charged stand of 30 min.

ultimately to NH_3 and N_2 in sealed cells at high temperatures during prolonged charged stands has been recently reported (72).

A search was made for other possible shuttles, but none was found. The requirements are actually quite stringent: good solubility of both the oxidized and reduced form; rapid oxidation of the reduced form by the charged positive; rapid reduction of the oxidized form by the charged negative; (redox potential E between $Cd/Cd(OH)_2$ and $NiOOH/Ni(OH)_2$ in 7*N* KOH). This search consisted of examination of the redox tables, and then experimentation with likely candidates (*e.g.*, I^-/IO_3^-, Tl^{+1}/Tl^{+3}, quinhydrone, etc.). All these couples lack at least one of the pertinent qualifications. The nitrate shuttle seems to be unique in the alkaline Ni-Cd system. [The iron (Fe^{+2}/Fe^{+3}) shuttle is well known in the $Pb/H_2SO_4/PbO_2$ system.]

There was some indication in this work that the nitrate-nitrite system depressed the voltage of the test cells during overcharge, but more work is required to establish this point.

Foreign Cations in the Nickel Hydroxide Electrode

General observations.—The effect of positive ion additions on (*a*) electrochemical capacity and (*b*) charge-retention and voltage-decay during charged stand were measured and analyzed. The experiments were intended to test the lamellar hydroxide-proton transfer model of nickel hydroxide electrodes.

Duplicate test cells were made up with added Li^+, Ag^+, Al^{+3}, and As^{+3}. These positive ions were added to the electrolyte of the test cells as $Al(OH)_3$, Sb_2O_3, As_2O_3, LiOH, and silver ion as Ag_2O. They were put through a cycling program and a charged-stand program at 55°C, at which temperature the aging effects should be accelerated. Although the information was gained under conditions (full impregnation, high temperature) in which the plate is often found in practice, it may be that introduction of the rapid aging effects has precluded the possibility of isolation of any but the gross effects of the ions added, *i.e.*, all the subtle effects may have been masked by the changes in crystalline form which occur during aging (8, 29, 30). Hence our discussion is limited to those effects which were observed under the specific conditions of this study.

The end-of-charge voltage did not vary appreciably from cycle to cycle. All charging (oxidation) was done for 2 hr at the 1-hr rate based on the theoretical capacity. The shapes of the charging curves varied (slightly), both from cycle to cycle and with different additives, but in no systematic fashion, and are not discussed here. [Lightly impregnated plates show some systematic variations (25).] High end-of-charge voltages with correspondingly high "overcapacities" were obtained with the Li^+-containing cells. This fact will be discussed later.

Other than one isolated inhibition caused by aluminum, no inhibition of the electrochemical oxidation or reduction which could be ascribed to the mono- or trivalent foreign ions was observed on the positive. A fast, sensitive amplifier-oscillograph apparatus was used for several high-rate (5-min) discharges at normal temperatures and at low temperatures (down to —30°C), but no large effects on overpotential were observed which could be ascribed unambiguously to foreign cations. This result may be a significant blow to the proton transfer theory of charge transfer within the active mass, because trivalent cations were expected to trap out anion vacancies into which protons could jump. However, there may be other explanations.

The cations are not as easily lost cathodically from the electrolyte as one might imagine. No silver was found plated out on cadmium; nor was any of the alloy AgCd detected by x-ray diffraction. Aluminum and lithium cannot be plated out in KOH_{aq}. Although AsH_3 and SbH_3 are evolved rapidly, along with H_2, from a cathode in acid solution, the processes are somewhat

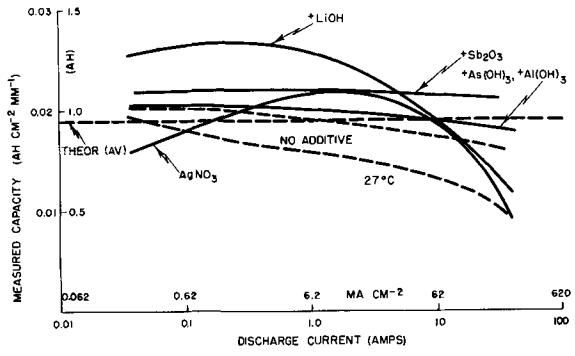

Fig. 11. Charge delivered at 27°C as a function of discharge current density for nickel hydroxide electrodes whose charge retention had been studied for nearly 2 years at 55°C.

different in basic solution. Thus, the silver nitrate-paper test for arsine revealed that when arsenic is added as As_2O_3 to KOH solution it does escape at the cathode as AsH_3, whereas if added as As_2O_5 it does not escape. The As_2O_3 added to a cell behaves as if it were quickly converted to As_2O_5 at the positive and then stayed there. No stibine could be detected either, but the case of antimony is not certain because analysis is difficult.

Charge delivered during reduction.—A progressive increase in the measured capacity with prolonged use was observed for all positive plates. The greatest increase was obtained with those containing foreign cations. This was reflected at all discharge rates, from the 20-hr to the 2-min rate. Better use is made of the active material within the plate when cycled at 55° than at 27°C. Once the "active mass" has become fully active at 55°C, however, the output at 27° approaches that at 55°C, behavior that perhaps could have been predicted from earlier work (73) on the role of water and alkali in the active mass. Figure 11 shows the charge delivered at 27°C by seven plates following protracted studies of charge retention at 55°C, conducted over a two-year period.

The source of increased capacity with life was determined by chemical analysis of the plates. The question posed was: Is the same amount of nickel hydroxide oxidized to a higher average level of oxidation (*i.e.*, to contain more oxygen), or is some of the sintered metal plaque oxidized slowly to give an extra amount of chargeable hydroxides? At the end of the tests the plates were washed in distilled water until neutral; the hydroxides were leached out in warm $NH_4OH = NH_4Cl$, and the leachant analyzed for soluble nickel using the dimethylglyoxime method (68, 69). A substantial increase in soluble nickel occurred during the tests [Table III: row (4) minus row (1)]. The fact that some of the original sinter was converted into active material was confirmed by the loss in weight of the sintered plaques, *i.e.*, 10-15% of their original weight per unit volume. The oxidation probably occurred during the prolonged (weeks) charge-retention tests at 55°C, not during the relatively insignificant charging time (2 hr). The rate of this corrosion reaction is doubtless a function of purity of the nickel powder from which the sinters were made.

The definite effects which could be ascribed unambiguously to the presence of the foreign cations were: (*a*) In all cells containing foreign cations, the sintered nickel matrix oxidized more during the tests than did the control electrodes with no foreign cations. (*b*) One positive in a cell containing $Al(OH)_3$ at one stage (cycle 55) was fully charged, yet could not be electrolytically reduced (discharged). This "passivation" was finally broken by an anodic pulse of high current density. Perhaps it was the physical breakdown of a skin of gamma alumina (an electronic conductor at high field strengths) formed on the exposed active sites of the active mass. This condition was observed only once.

Table III. Theoretical and measured electrochemical capacity of nickel hydroxide electrodes

Condition	100 × capacities, amp-hr cm^{-2} mm^{-1}				
	Normal	+ LiOH	+ $As(OH)_3$	Sb_2O_3	+ $Al(OH_3)$
1. Theoretical, based on weight gain (before tests)	1.80	1.85	1.80	2.05	1.97
2. Last measured (3-hr rate) 27°C	1.6	1.8	1.5	1.4	1.6
3. Last measured (3-hr rate) 55°C	2.3	2.8	2.4	2.1	2.2
4. Theoretical, based on soluble nickel (after tests)	3.0	3.6	2.6	3.0	2.8

Notes on each condition: 1, All weight gained during impregnation was assumed to be due to $Ni(OH)_2$; 2, cycle 56; 3, cycle 80; 4, Leached in a mixture of 1*N* NH_4OH + 1*N* NH_4Cl at 60°C for at least 24 hr.

Although values given for theoretical capacities are averages of 4 determinations, the errors are such that the numbers are reliable to only ±5%. In addition, numbers in row 1 might be systematically low because of excess drying; numbers in row 4 might be systematically low because of incomplete leaching. Reproducibility of measurements of electrochemical capacity during test program (Table II), as determined from the 3-hr rate discharge was ±4%.

(c) Positives in Li^+-containing cells consistently showed high "overcapacities," to be discussed next.

Charge retention.—Figures 12 and 13 show the charge (normalized: $C_r \equiv C/C_{Theor}$) delivered at the 2-hr rate by 12 plates after they had been stored for various lengths of time in the electrolyte at 55°C. This converging decay is linear in log time (t) for upwards of 2 months at 55°C, and can be expressed as

$$C_r \propto \log (t + \theta)$$

where θ is very small, of the order of minutes. [The same relationship was found by others, for example Conway and Bourgault (74), who measured the oxygen evolved from the charged active material at 25°C]. Beyond about 40 days the relationship breaks down. Thus a linear plot C_r *vs.* t, from 10^3 to 10^5 min, discloses that the decay rate, $-\partial C_r/\partial t$, at long times is more or less constant [similar observations have been reported before (75)]. If C_r^o is defined as C_r at the first marked deviation from the linearity of the C_r *vs.* log $(t + \theta)$ curve, and if it is assumed that to a first approximation all C_r above this value is excess capacity over that due to $NiOOH/Ni(OH)_2$, that is, "overcapacity," one can analyze the decay of this overcapacity, $Q(\equiv C_r - C_r^o)$, by standard kinetic techniques. Figure 14 shows a linear plot of Q *vs.* stand-time. Tangential slopes ($-dQ/dt$) express the rate of decay, v, at various values of the excess capacity. If the order of the reaction with respect to concentration of overcapacity is n, then

$$v \propto Q^n$$

from which

$$\partial \log v/\partial \log Q = n$$

From plots of log v *vs.* log Q for all the results, n was found to be about 5 (consider the insensitivity of the log-log plot). Integration and introduction of the boundary condition that Q must have some well-defined value, Q_o, at the end of charge (*i.e.*, at a stand-time of zero) gives

$$Q = Q_o(1 + 4k\,Q_o^4\,t)^{-0.25}$$

where k is the specific rate constant for the decay. In Fig. 15 the charge retained after different times of charged stand is plotted up for four electrodes in a manner which displays the inverse quarter-power dependence upon time.

In the system under study here, an order of reaction of about five can be interpreted in at least two ways, neither of which directly results from the chemistry of the system:

1. An unknown concentration-dependent force may be operative when excess higher oxide material begins to accumulate. This could be a physical repulsion of oxygen (as O_2?; as OH?; as O?) trapped under high internal pressure (dU/dV) in distorted (stretched ?) crystallites; or possibly an electrostatic repulsion of trapped OH^- ions, since high orders of reaction are observed when strong repulsive forces can become operative.

2. An erosion reaction, very rapid at first, but slowing down quickly, may be operative, perhaps a recrystallization, or a "digestion," as suggested by

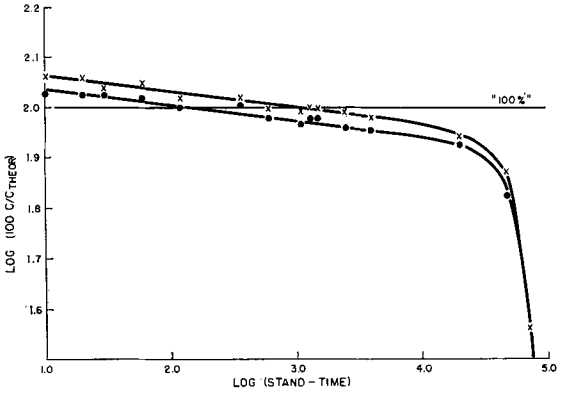

Fig. 12. Charge retention of thermally impregnated nickel hydroxide electrodes at 55°C, with no foreign ions added to the electrolyte, stand-time in minutes.

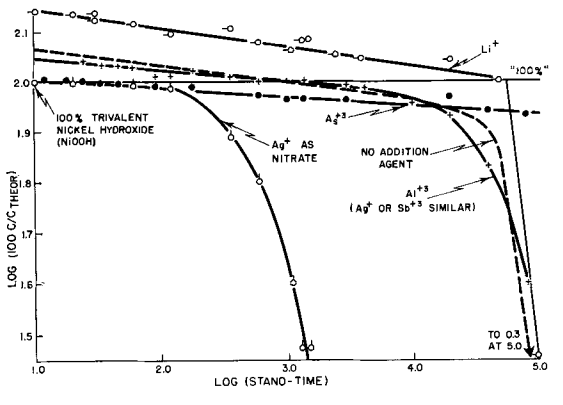

Fig. 13. Charge retention at 55°C, of thermally impregnated nickel hydroxide electrodes with foreign cations added to the electrolyte, stand-time in minutes.

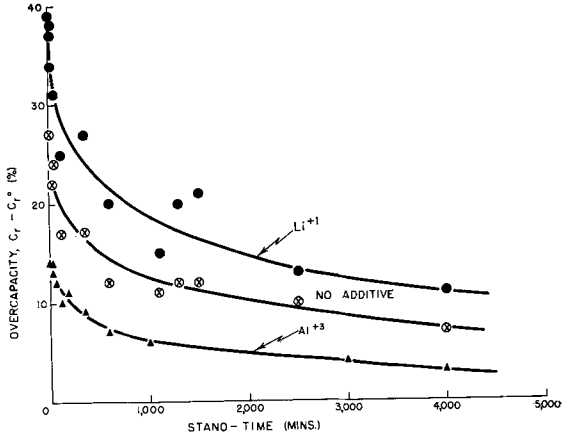

Fig. 14. Decay of overcapacity (C_r—C_r^o) of fully impregnated sintered plate nickel hydroxide electrodes at 55°C.

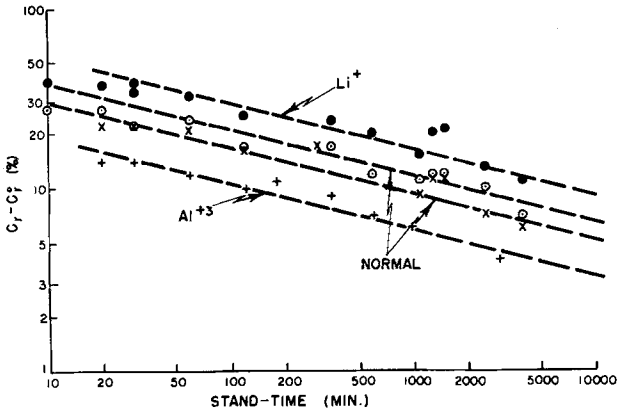

Fig. 15. Decays plotted as log ($C_r - C_r°$) vs. log (stand-time), with broken lines drawn in at slopes consistent with 5th order decay.

Seiger *et al.* (76). In this case the rate of decay of the overcapacity would simply follow the rate of the physical erosion of the mass, because it would be the erosion reaction which presents the overcapacity to the electrolyte.

On the assumptions that crystallites of charged active material have some particular (normal ?) size distribution, that little ones lose their extra oxygen faster (higher area/volume), and that Li^+ acts either by making the crystallites uniformly large or by helping to trap the extra oxygen in the crystallites, a study of the kinetics of loss of charge from very thin films, of the order of a few molecular layers in average thickness, has been started. Results on nickel wire, and then on nickel foil (Fig. 16) have shown, first, that the loss of charge is very much more rapid from open surfaces than from porous ones, and, second, that early in the decay from open surfaces the order of reaction with respect to overcapacity is only 2 not 5. We infer that the loss of charge from porous electrodes immediately after anodic oxidation is not controlled by an erosion reaction, but rather by the movement of trapped oxygen-containing species from the inside of the crystallites to the surface. The effect of the foreign cations, then, and of lithium in particular, can be ascribed to their modifying the elastic restoring forces, within the crystallites. This view is consistent with known modifications of lattice dimensions observed by Briggs (30) in 1957 in doped crystallites of nickel hydroxides.

Overpotential decay.—During studies of charge-retention of impregnated, sintered plate nickel hydroxide electrodes, the cell was allowed to stand on open circuit, and the open-circuit potential was traced as a function of time. The values so obtained were plotted in the manner introduced by Armstrong and

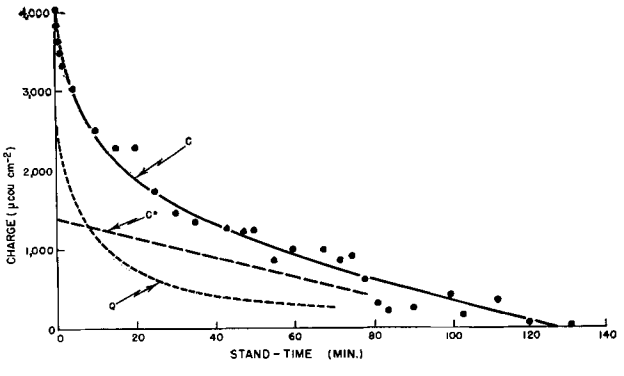

Fig. 16. Charge, C, delivered at 12 $\mu a/cm^2$ by oxidized nickel foil electrodes after various lengths of charged stand; $T = 30°C$; Q, overcapacity; C°, normal capacity.

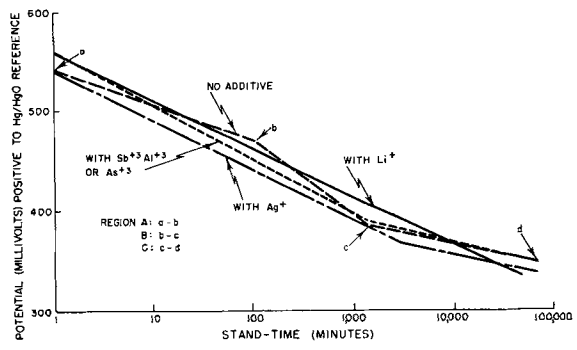

Fig. 17. Open-circuit decay of overpotential of nickel hydroxide electrodes, with and without foreign cations added.

Butler (77), *i.e.*, as E *vs.* log $(t + \theta)$. The slope, related [see ref (78), *e.g.*] to Tafel's "b" ($\partial E/\partial \log i$) could be evaluated. Figure 17 shows a typical plot. Three distinct regions A, B, and C are evident from inspection of the potential decay curves. Two of these regions, A and C, have been discussed rather fully by Conway and Bourgault (74); B is a transition region between A and C which has been examined by Seiger *et al.* (76). Average values of $\partial E/\partial \log t$ for the three regions are given in Table IV.

The three regions were not always observed in an electrode. For instance, plates containing Li^+ did not make the transition from A to B, and the C region was never observed. By contrast, plates with no additive spent most of their stand life in the C region. More or less complete loss of capacity did not further affect the open-circuit potential of the cells which had no additives: they remained in the C region.

As Conway and Bourgault, and earlier, Bockris, pointed out, if certain assumptions are made, the slopes, or b-values, may be interpreted in terms of specific rate determining steps in the self-discharge process. For instance, one can compare the value of 26 ± 2 mv for region C with the value of 25 (*i.e.*, 2.3 $2RT/5F$ at 55°C), which by Bockris' analysis is consistent with a rate-determining step in which HO_2 is being formed on the surface as follows

$$O_{ads} + OH^- \rightleftharpoons HO_2 + e^- \qquad [1]$$

However, the reaction

$$O_{ads} + OH_{ads} \rightleftharpoons HO_{2\ ads} \qquad [1a]$$

should give (78) a slope 2.3 $RT/3F$, or 22; which, although it is slightly less than our assignment of precision would allow (Table IV), would agree explicitly with the reaction assigned by Conway and Bourgault (74) to their values.[4]

Table IV. "b"-Values for different regions of self-discharge of nickel hydroxide electrode

		$b = -\partial E/\partial \log t$ (mv/decade of time)		
Decay	Region	No additive	Monovalent additive	Trivalent additive
Overcapacity	A	45 ± 8 (42 ± 0.2)*	50 ± 12	50 ± 12
	B	70 ± 5	None	None
	C	26 ± 2 (22 ± 0.3)*	None	22 ± 3
Normal capacity		Same as C	Same as C	Same as C

* Values given in parentheses are from reference (74) Table I, recalculated for 55°C. In our work individual decay plots did not give b-values (slopes) with high precision. However, repeated runs with the same electrode did not reproduce the value so exactly, and the accuracy reflects the variation observed.

[4] An undetected constant error is not impossible here although calibrations were done periodically to reduce the probability. The presence of Cd negatives may have made our decay slopes high. Further, the theoretical deductions of the numerical value of "b" invariably, and apparently quite arbitrarily for oxide electrodes, assume a "symmetry factor" of 0.5, which has not yet been unequivocally proven. With these reservations in mind, such an explicit statement of the reacting species gives the clue that it is O (and OH ?) which accounts for the overcapacity described earlier; and that self-destruction of NiOOH is slow.

Within the reproducibility in measurements, more than one deduced slope (said to be a characteristic of a certain step of the decay) can sometimes be made to fit the facts. The slope $-\partial E/\partial \log t$ of the reaction

$$OH_{ads} + OH^- \rightleftharpoons O_{ads} + H_2O + e^- \quad [2]$$

is said (78, 79) to be 2.3 $2RT/5F$, or 42 mv/decade of time at 55°C. This value falls within the range of values observed in the A region, and could be taken as an indication that this is the rate-controlling step early in the decay. Although such a reaction may exist under conditions of high overvoltage, the result on plates with Li^+ added show that this region of decay can continue to either the B or the C regions, and well below the overvoltage at which transition usually occurs. In this interpretation, Li^+ either promotes reaction [1] or inhibits reaction [2].

The B region has been given no assignment to date. It is short (a few hours) in solutions with no additives; it is absent altogether in weak caustic, and in solutions with additives (Fig. 17, Table III).

Milner's treatment [see ref (80)], and more recently Hale's (81), would involve diffusion processes, not necessarily activation processes alone, to explain the facts. Especially interesting is the fact that antimony and to a greater extent arsenic inhibit the loss of overcapacity. Perhaps arsenate is adsorbed on and poisons sites which would otherwise be involved in oxygen evolution.

Present status of the problem.—Many reported effects of cations on the measurable properties of the nickel hydroxide electrode are poorly founded in fact. Table I contains a summary of the claims and inferences drawn by various workers who have studied the question. Controlled experiments have been done in only a few cases, and the reported effects of others have to be considered more as lore than as scientific fact. This is understandable if the premise is accepted that the effect of a cation on the parameter being investigated is closely related to the physical condition of the nickel hydroxide (*viz.*, crystallite size distribution, defect structure, water content of the layer lattice, etc.) during the measurement. Reproducibility is bound to be poor. Of the reports on effects of 24 ions, reports on 7 draw particular attention: Li^+, Mg^{+2}, Zn^{+2}, Hg^{+2}, Co^{+3}, Sc^{+3}, and As^{+5}. The suppression of charge available from the electrode in the presence of Zn^{+2} and the increased charge available in the presence of both Hg^{+2} and Mg^{+2} ions require confirmation, for if the effects of divalent cations on coulombic capacity are as claimed (Table I), at least two interesting possibilities exist to account for the effects: (i) polarization of water of hydration might exist due to the strong electric field about the small Mg^{+2} ion (Doran's suggestion), and (ii) the layer-lattice crystallites might retain less water of hydration at the important defects occupied by large ions such as Hg^{+2} and Ba^{+2}.

Information on the transition metal cations is sparse and conflicting, with the exception of that on cobalt. Cobalt must exist as Co^{+3} even in the discharged nickel hydroxide material. There seems to be some agreement that Co^{+3} improves charge retention, stabilizes capacity during repetitive cycling, raises the charge and discharge voltages and increases the b-values, all indications that it promotes higher overcapacities. In this respect its effects resemble those of the Li^+ ion. The scandium ion seems to belong to this group also. However, its trivalent cousins (Fe^{+3}, Al^{+3}, B^{+3}), which have a strong tendency to form insulating oxides, clearly do not.

Arsenic and antimony, which must be present as pentavalent ions at the potential of the nickel hydroxide electrode, suppress the B region of potential decay and promote better charge retention; perhaps they adsorb, as AsO_4^{-3} or SbO_4^{-3}, on the oxygen evolution sites and inhibit the process. The fact that the arsenic ion can stabilize higher valence states of nickel (82), and increases the overpotential during charge and overcharge is supporting evidence.

Nickel hydroxide remains an enigma. As a semiconductor NiO will change conductivity by many orders of magnitude if it is doped with Li^+. The proton-transfer theory of ionic conduction seems well entrenched in the literature. Indeed the recent experiments on proton-penetrable Ni foil electrodes even permit the evaluation of the proton-transfer current during anodic oxygen evolution (83). (This current is highest in KOH, less in NaOH, and lowest in LiOH.) The present work emphasizes a possible movement of oxygen-containing species in the active mass, akin to mass transfer processes suggested for MnO_2, V_2O_5, and PbO_2 (84). Crystal deformation of the layer lattice can be effected by several cations (30), by carbonate (15) and probably by other anions such as nitrate. At the present time we may usefully consider nickel hydroxide to be a remarkable matrix through which electrons (or positive holes) and protons and oxygen-containing species can be forced, at relative rates which depend intimately on a time-dependent molecular structure, as well as on the nature of the applied force, or potential gradient. In this sense, nickel hydroxide may indeed be the most versatile, and *ipso facto* the most exasperating, member of the electrochemically active (hydr)oxide family.

General Summary

1. Electrodes were studied in which the electrochemically active material was supported within the pores of sintered nickel plaques. Detrimental effects of carbonate ion have been demonstrated on both the nickel hydroxide positive and cadmium negative electrodes.

2. On negative electrodes both permanent and transient effects occur, both of which lower the coulombic or ampere-hour output. The transient effects are a complicated function of the amount of carbonate in the electrolytes, and are dependent also on current density and temperature. Processes which seem to be involved are rate of conversion of primary reaction product into hydroxide or carbonate, specific volume of precipitate, and transport properties of electrolyte through the porous mass. Aging effects were demonstrated via the capacity *vs.* composition data.

3. On positive plates only transient carbonate effects were observed, quite complicated if the plate is heavily loaded.

4. Interpretations of these effects have been offered. Quantitative prediction of when they will occur is not yet possible. The possible roles of the hydroxycarbonates of cadmium and nickel as reaction intermediates are discussed.

5. The mechanism of the "nitrate shuttle" has been demonstrated. The nitrate-nitrite redox system within the cell seems to be unique in that it can be oxidized and reduced by the positive and negative, respectively. Since both species are soluble, it acts as an electronic short-circuit. A search for other systems which would do this was unsuccessful.

6. Prolonged (1-2 years) operation of pure nickel hydroxide electrodes at high temperature (55°C) resulted in a marked increase in the electrochemical capacity of the electrode. Analyses for soluble nickel showed that most of the increase could be attributed to oxidation of the sintered nickel matrix. However, there is evidence that the electrode gradually becomes able to be charged to a higher average oxidation state, especially in the presence of Li^+.

7. Practical conclusions from parts 1 to 6 include: (*A*) Nitrate from the processing of plates must be removed from cells, otherwise self-discharge may be rapid. (*B*) Special precautions must be taken to keep CO_2 from the air and carbonate from other sources (oxidation of separator ?) from processed plates and from assembled cells, otherwise the capacity may not be reproducible and the plates may show aging effects

and unpredictable outputs, especially at low temperatures. (*C*) Only extra high purity nickel powder should be used for the sintered matrix for nickel hydroxide electrodes, if corrosion of the matrix at high temperatures is to be avoided.

8. Loss of charge by charged nickel hydroxide seems to occur by two main processes: a rapid but convergent decay of the overcapacity, and a slower, linear decay of the normal capacity. The former may take days in a sintered plate, minutes on a nickel foil. The latter takes weeks in the sintered plate, hours on a foil.

9. Decay of the overcapacity consists of two, and perhaps three, consecutive steps, separable by analysis of the concurrent potential decay, and rather markedly affected by foreign cations. Possible controlling reactions are discussed. Kinetic analysis of the decay of charge, and analysis of the concurrent overpotential decay, suggest that the controlling reactions involve adsorbed oxygen atoms which are continuously supplied from within the crystallites.

10. Reported effects of foreign cations on the behavior of the nickel hydroxide electrode were collected and reviewed. The roles of certain uni- and trivalent positive ions on the nickel hydroxide electrode were investigated at length. None had any reproducible measurable effect on the ability of well-formed, charged nickel hydroxide to deliver its charge, even up to very high (20-min) rates, from 25° to −30°C. All promoted the oxidation of the sintered nickel matrix to active material at 55°C.

11. At 55°C Li^+ increased the overcapacity, and it also lowered the rate of loss of overcapacity. It blocked the onset of the second and third (B and C) stages in the potential decay which runs concurrent with the decay of overcapacity.

In an isolated, but interesting, instance, Al^{+3} blocked the reduction of a fully oxidized electrode, an effect that was finally broken by a strong anodic pulse of current. Arsenic, probably as As^{+5}, adsorbed on cathodic sites, affected the potential decays during loss of overcapacity, and then seemed to inhibit the protracted decay of the normal capacity which followed.

12. Inferences are drawn about the mechanisms of the various processes studied, and the present status of each is given.

Acknowledgments

Mr. D. G. Scraba, a summer student from the University of Alberta, did the nitrite analyses, and along with Mr. J. L. Lackner contributed technical assistance. Dr. J. R. Coleman, and Drs. I. H. S. Henderson and T. E. King who read the manuscript, offered many very helpful suggestions.

A special word of thanks is offered to the many friends in other laboratories who have encouraged the preparation of this paper.

Manuscript received Dec. 11, 1961; revised manuscript received Dec. 15, 1964. The manuscript is issued as DCBRL Report No. ———.

Any discussion of this paper will appear in a Discussion Section to be published in the December 1965 JOURNAL.

SYMBOLS

equivalent % of carbonate:

$$\frac{\text{Equiv. of } CO_3^=}{\text{Equiv. of } OH^- + \text{Equiv. of } CO_3^=} \times 100$$

x = No. of moles of $CdCO_3$ contained in solid basic cadmium carbonate of general formula x $CdCO_3$ $Cd(OH)_2$.

C = measured electrochemical capacity, or charge, in ampere-hours per unit volume (cm^2 area x mm thickness of electrode)

C_{Theor} = theoretical capacity based on weight gain during impregnation of sintered plaque, it being assumed that all weight gain is due to $Cd(OH)_2$ (negative) or $Ni(OH)_2$ (positive)

C_r = reduced, or normalized, capacity = $100\ C/C_{Theor}$ (%)

c.d. = current density

C_r° = value of C_r at which the linear C_r *vs.* log $(t + \theta)$ relationship breaks down, denoting last of the overcapacity

$Q = C_r - C_r^\circ$ = overcapacity (normalized)

Q_o = overcapacity immediately at the end of charging

v = $-d(C_r - C_r^\circ)dt$, rate of decay of overcapacity

n = order of reaction (decay of overcapacity) with respect to overcapacity

k = specific rate constant for decay of charge

U = internal energy; V, specific volume; $\partial U/\partial V$, internal pressure

E = potential (mv) positive to Hg/HgO reference

b = $-\partial E/\partial \log t$ during open-circuit stand

REFERENCES

1. A. P. Hauel, *Trans. Electrochem. Soc.*, **76**, 435 (1939); U. B. Thomas, Private communication, 1953; E. J. Casey, *Proc. 4th DRB Symposium*, p. 51-61, 1952.
2. E. J. Casey and B. Ogden, "Some Factors Affecting the Low Temperature Operation of Sintered Plate Nickel Cadmium Batteries," DRCL Report No. 117, October, 1952.
3. P. E. George and E. J. Casey, "The Electrical Output of Sintered Plates of Nickel Cadmium Batteries. I," DRCL Report No. 156, March, 1954.
4. P. E. Lake and E. J. Casey, "Sintered Plates of Nickel Cadmium Batteries. II. Extent of Effects of Carbonate Contamination on Electrical Output," DRCL Report No. 186, April, 1955.
5. P. E. Lake and E. J. Casey, *This Journal*, **105**, 52 (1958); **106**, 913 (1959).
6. P. E. Lake and E. J. Casey, *ibid.*, **106**, 532 (1960).
7. P. E. Lake and J. M. Goodings, *Can. J. Chem.*, **36**, 1089 (1958).
8. D. Tuomi, Private communication, 1963.
9. G. T. Croft and D. Tuomi, *This Journal*, **108**, 915 (1961).
10. K. Huber, *Z. Elektrochem.*, **62**, 675 (1958).
11. L. Cloutier, P. E. Pelletier, and P. E. Gagnon, *Trans. Roy. Soc. Can.*, **33**, III, 149 (1936).
12. K. C. Grover and L. M. R. Noyar, *Agra Univ. J. Res.*, **6**, Part 2, 67 (1957).
13. P. E. Gagnon, L. Cloutier, and R. Martineau, *Can. J. Res. B.*, **19**, 179 (1941).
14. J. T. Carriel and W. J. Singley, *J. Am. Chem. Soc.*, **76**, 3839 (1954); O. Bagno, *Compt. rend.*, **236**, 1275 (1953); J. Francois-Rossetti and B. Imélik, *J. Chim. Phys.*, **51**, 451 (1954); and *Bull. soc. chim. France*, p. 1115 (1957).
15. J. Longuet-Escard and J. Méring, *Compt. rend.*, **246**, 1231 (1958).
16. I. M. Vasserman and E. A. Fomina, *Zhur. Priklad. Khim.*, **34**, 90 (1961).
17. W. Feitknecht, *Kolloid Z.*, **136**, 52 (1954). See also *Kolloid Z.*, **93**, 66 (1940).
18. T. E. King, E. J. Casey, and I. H. S. Henderson, *Proc. 16th Annual Power Sources Conf.*, USASERDL, May, 1962.
19. R. Hérold, Private communications, 1960-1962.
20. A. Fleischer, "Vented Ni-Cd Batteries," *Proc. 11th Ann. Battery Research and Development Conference*, p. 83, U.S. Army Signal Engineering Lab., 1957.
21. P. L. Bourgault, P. E. Lake, E. J. Casey, and A. R. Dubois, *Can. J. Tech.*, **34**, 495 (1957); U.S. Pat. No. 2,831,044, Dec. 13, 1956; E. J. Casey, *Proc. 10th Annual Battery Conference*, USASCEL, Fort Monmouth, N. J., May, 1956.
22. H. Winkler, *Elektrotechnik*, **8**, 300 (1955).
23. J. P. Harivel and J. F. Laurent, *Electrochim. Acta*, **9**, 703 (1964).
24. R. J. Doran, "Impurity Effects in Metal Hydroxide Electrodes", Paper Y, *Proc. 1st Internat. Symposium on Batteries*, Signal Research and Development Laboratories, Christchurch, England, October, 1958.
25. R. J. Doran, "Further Studies of Aging and Impurity Effects in the Nickel Hydroxide Electrode", Paper 26, *Proc. 2nd Internat. Symp. on Batteries*, Signal Research and Development Establishment, Christchurch, England, October 1960; Brit. Pat. No. 848,922 (1960).
26. R. J. Doran, Private communication, 1962.
27. R. J. Doran, "The Nickel-Scandium Hydroxide Electrode", *Proc. 3rd Internat. Symp. on Bat-*

teries, Admiralty Engineering Labs., West Drayton, England, 1962; Brit. Pat. Appl. No. 34429/60.
28. E. J. Casey, *Chem. in Canada*, **12**, 49 (1960).
29. T. A. Edison, U.S. Pat. No. 678,722, July 16, 1901, and many others since.
30. G. W. D. Briggs *et al.*, *Trans. Faraday Soc.*, **51**, 1433 (1955); *ibid.*, **52**, 1272 (1956); *J. Chem. Soc.*, **1957**, 1846; *Electrochim. Acta*, **7**, 241 (1962); *ibid.*, **7**, 249 (1962).
31. T. A. Edison, U.S. Pat. No. 1,083,356, Jan. 6, 1914.
32. Edison's notebooks, which contain his work over many years, are available to the public at the Edison Library and Museum, Orange, N. J. They have never been edited with respect to his work on addition of foreign ions to alkaline cells.
33. V. I. Kosul'nikov and V. A. Tikhov, Russian Pat. No. 51, 380, July 31, 1937.
34. F. M. Bowers, Prog. Rept. by Thos. A. Edison Co. to U.S. Army Signal Corps on Contr. W36-039-sc-32137, Sept. 2, 1947.
35. R. L. Tichenor, *Ind. Eng. Chem.*, **44**, 973 (1952); see also E. J. W. Verwey, in "Semiconducting Materials," p. 151, Pergamon Press, Amsterdam (1951).
36. S. Z. Roginskii and N. I. Element, *Isvest. Akad. Nauk SSSR, Otdel. Khim. Nauk*, **1951**, 350.
37. J. M. Moulton, U.S. Pat. No. 2,634,303, April 7, 1953.
38. K. Sakata, T. Sakata, and K. Kigoshi, *Rept. Inst. Sci. and Technol.*, Univ. Tokyo, **8**, 39 (1954).
39. F. J. Morin, *Phys. Rev.*, **93**, 1195 (1954).
40. M. C. Rastogi, *Z. anorg. u. allgem. Chem.*, **276**, 316 (1954).
41. R. S. Coolidge, U.S. Pat. No. 2,683,102, July 6, 1954.
42. O. Bagno and J. Longuet-Escard, *J. Chim. Phys.*, **51**, 434 and 438 (1954); *Mem. serv. chim. etat* (Paris), **40**, 215 (1955).
43. I. P. Samokhvalov, D. B. Zlotnikova, and A. A. Maklyarskaya, USSR Pat. No. 108,324, Oct., 1957.
44. N. A. Marasonov, and B. V. Ershler, USSR Pat. No. 108,327, Oct. 25, 1957.
45. I. Sanghi and W. F. K. Wynne-Jones, *J. Sci. Ind. Research* (India), **16B**, 376 (1957).
46. I. I. Koval and V. N. Vorob'eva, *Vestnik Elektroprom.*, **29**, 46 (1958).
47. G. P. Loschinina and A. M. Murtazaev, *Dokl. Akad. Nauk. (SSSR)*, **11**, 37 (1958).
48. B. C. Bradshaw, "Adsorption Measurements on Nickel Oxide Electrodes," *Proc. 12th Ann. Battery R. and D. Conf.*, USASRDL, Fort Monmouth, N. J., 1958.
49. V. Herold, U.S. Pat. No. 2,646,454.
50. H. Winkler, *Proc. CITCE Mtg.*, **1958**, 383.
51. H. Winkler, German (East) Pat. No. 14,368, Feb. 17, 1958.
52. Ya. I. Tur'yan and I. A. Gershkovich, *Zhur. Fiz. Khim.*, **35**, 1879 (1961), by analogy with effects of Li^+, Na^+, and K^+ on cobalt.
53. J. M. Moulton, U.S. Pat. No. 2,870,234, Jan. 20, 1959.
54. S. Januskiewicz, "Addition of Cobalt to Ni-Cd Batteries." *Proc. 13th Ann. Power Sources Conf.*, USASDRL, 1959.
55. V. N. Flerov, *Zhur. Priklad. Khim.*, **32**, 1306 (1959).
56. V. N. Flerov, *Trudy Gor'kovsk Politekh, Inst.*, **15**, 41 (1959).
57. Y. A. Gindelis, USSR Pat. 125,589, Jan. 15, 1960.
58. Inference only, by analogy with behavior of silver oxide electrodes: C. M. Shepherd and H. C. Langelan, U.S. Naval Research Lab. Report No. 5635, July, 1961.
59. W. Feitknecht, *Bull. Soc. Chim. France*, **1949**, 15. The germ of this idea goes back at least to 1933 (*Helv. Chim. Acta*, **16**, 427), when in a paper on the layer structure of basic salts Feitknecht states "Attack takes place along the layers, not perpendicular to them."
60. J. Labat, *J. Chim. Phys.*, **60**, 1253 (1963); H. Bode, *Angewandte Chem.*, **73**, 553 (1961).
61. H. P. Hanson and W. O. Milligan, *J. Phys. Chem.*, **60**, 1144 (1956).
62. K. Tsusmi, *J. Phys. Soc. Japan.* **13**, 586 (1958).
63. R. A. Van Nordstrand, *Adv. in Catalysis*, **12**, 149 (1960).
64. J. D. Moulton, Unpublished result, 1948.
65. S. U. Falk, *This Journal*, **107**, 661 (1960).
66. A. Fleischer, *J. (and Trans.) Electrochem. Soc.*, **94**, 289 (1948).
67. H. W. Koren and G. Baumstark, U.S. Pats. No. 2,708,211 and 2,708,212, May, 1955.
68. I. Kolthoff and E. B. Sandell, "Textbook of Quantitative Inorganic Analysis," 3d ed., Macmillan New York (1952).
69. F. D. Snell and C. T. Snell, "Colorimetric Methods of Analysis," Vol. II, p. 334 for nickel, p. 803 for nitrite. D. Van Nostrand Co., Inc., New York (1949).
70. K. Huber, *This Journal*, **100**, 376 (1953).
71. S. Yoshisawa and Z. Takehara, *Electrochim. Acta*, **5**, 240 (1961).
72. S. F. Pensabene and A. J. Catotti, *Extended Abstracts*, Battery Div., Electrochemical Soc., Oct., 1964.
73. See, *e.g.*, F. Kornfeil, Proc. 12th Ann. Battery Research and Development Conference, USASRDL, Fort Monmouth, N. J., 1958, p. 18.
74. B. E. Conway and P. L. Bourgault, *Can. J. Chem.*, **37**, 292 (1959).
75. U. B. Thomas and R. J. Baker, Private communication, 1955.
76. H. N. Seiger, R. C. Shair, *et al.*, Gulton Industries, Inc., Final Report (Report No. 8) on U. S. Army Contract No. DA 36-039-SC-85390. June, 1962.
77. G. T. Armstrong and J. A. V. Butler, *Trans. Faraday Soc.*, **29**, 1261 (1933).
78. J. O. Bockris, *J. Chem. Phys.*, **24**, 817 (1956), Eq. 4.144.
79. B. E. Conway and P. L. Bourgault, *Trans. Faraday Soc.*, **58**, 593 (1962); B. E. Conway and E. Gilsadi, *ibid.*, **58**, 2493 (1962).
80. P. C. Milner and U. B. Thomas, "The Nickel Cadmium Cell," in "Advances in Electrochem. Eng.," in press.
81. J. M. Hale, "Kinetics in the Nickel Hydroxide Electrode," *Proc. 4th Internat. Symp. on Batteries*, Brighton, England, Sept., 1964.
82. R. S. Nyholm, *Chem. Rev.*, **53**, 263 (1964).
83. G. Ya. Slaidin and P. D. Lukovtsev, *Dokl. Akad. Nauk SSSR*, **142**, 1130 (1962).
84. See, *e.g.*, J. J. Coleman, *Trans. Electrochem. Soc.*, **90**, 545 (1946); F. Kornfeil, *This Journal*, **109**, 349 (1962); N. V. Watson and A. B. Scott, *Extended Abstracts*, Battery Division, Electrochem. Soc., Oct., 1964; B. N. Kabanov, E. S. Weisberg, I. L. Romanova, and E. V. Krivolapova, *Elektrochim. Acta*, **9**, 1197 (1964).
85. M. Seiger and R. Shair, "Studies on Sealed Ni-Cd Batteries," *Proc. 15th Ann. Power Sources Conf.*, U. S. Army Signal R&D Lab., Ft. Monmouth, N. J., 1961.
86. F. Alliegro, W. E. Ryan, G. Baumstark, and A. B. Mundel, "Design and Manufacture of Sealed Ni-Cd Cells of Cylindrical Design," Final Report by Sonotone Corp. to U. S. Army Electronics R&D Lab., March 31, 1963.
87. P. D. Lukovtsev and G. Ya. Slaidin, *J. Phys. Chem. USSR*, **36**, 1227 (1962).

Studies of the Oxidation of Nickel in the Temperature Range of 900° to 1400°C

Kazuo Fueki[1] and J. Bruce Wagner, Jr.

Materials Research Center and Department of Materials Science, Northwestern University, Evanston, Illinois

ABSTRACT

The parabolic oxidation of nickel has been studied between 900° and 1400°C at pressures from the dissociation pressure of nickel oxide to 1 atm of oxygen. The activation energies in various atmospheres were found to range from 36.3 to 43.6 kcal/mole. The usual equation for parabolic oxidation, $k_p = c[p_{O_2}{}^{1/n} - p_{O_2}{}^{1/n}$ (eq.)] did not hold over the entire pressure range because the value of $1/n$ varied with temperature. A marker study showed that the markers were located close to the metal-oxide interface. A method for obtaining the self-diffusion coefficient of the more mobile ionic species in the oxide is proposed.

The dependence of the parabolic constant of metal oxidation on the oxygen partial pressure can provide valuable information about ionic transport in the oxide and the mechanism of oxidation. In the early work of Wagner and Grünewald (1) on the oxidation of nickel, the parabolic constants were found to be proportional to $p_{O_2}{}^{1/5}$. The electrical conductivity of nickel oxide was found by von Baumbach and Wagner (2) to be dependent on $p_{O_2}{}^{1/4}$. On the basis of these results it was concluded that nickel oxide is a metal deficit p-type semiconductor and that the nickel oxide layer on nickel grows by the simultaneous diffusion of nickel ions via cation vacancies and of electron holes. Baur and his collaborators (3) carried out a study of the pressure dependence of nickel oxidation between 1000° and 1200°C at oxygen pressures from 6.5 x 10^{-3} to 20.4 atm. They found that the measured rates above 1 atm are insensitive to oxygen pressure and that the rates below 1 atm closely followed $p_{O_2}{}^{1/4}$. The pressure dependence was explained on the basis of Langmuir's adsorption isotherm and of vacancy creation by adsorbed oxygen. Since both oxidation studies and the measurements of diffusion (4, 5) and electrical conductivity (2, 6, 7) of nickel oxide have been confined to pressures above about 10^{-4} atm of oxygen, it has not been confirmed that the aforementioned mechanism still holds in lower oxygen pressures.

Marker studies are useful for identification of the predominant ionic species diffusion through oxides during metal oxidation. Sartell and Li (8) observed in their marker study that the nickel oxide formed on nickel consists of a black outer layer and a green inner one and that the markers were always located at the boundary between the two layers. They proposed a mechanism whereby the outer layer grows by the outward diffusion of nickel ions and that the inner layer grows by the inward diffusion of oxygen ions.

The results of von Baumbach and Wagner and of Baur and his collaborators are not consistent with that of Sartell and Li. To clarify further the ionic transport in nickel oxide, the present authors have studied the oxidation rate of nickel over a wide pressure range between the dissociation pressure of nickel oxide and 1 atm of oxygen. Marker studies have also been carried out. It is the purpose of this paper to report the results of these measurements and also to propose a method by which the self-diffusion coefficient is obtained as a function of oxygen partial pressure from oxidation data.

Table I. Analysis of nickel sheet*

	%
Silver	0.001
Aluminum	0.01
Cobalt	0.004
Chromium	0.001
Copper	0.002
Iron	0.02
Manganese	0.002
Molybdenum	0.001
Lead	0.04
Silicon	0.01
Tin	0.001
Titanium	0.001

* The above analysis was furnished by the Charles C. Kawin Company of Chicago, Illinois.

[1] Present address: Department of Industrial Chemistry, University of Tokyo, Tokyo, Japan.

Experimental and Results

Oxidation rate measurement.—Nickel sheet, 6 mil thick, containing impurities listed in Table I was used in these studies. Specimens, 1 cm wide by 2 cm long, were cut from the sheet, polished using 1/0, 2/0, 4/0 metallographic papers and using Linde "A" fine abrasive on a polishing wheel, washed with soap and water and with acetone, and then dried. The polished specimens were annealed in hydrogen at 550°C overnight to remove strain and to reduce any surface oxide.

The gravimetric measurements below 1190°C were carried out using an Ainsworth automatic-recording balance and its accessories described by Pettit and Wagner (9). Measurements above 1300°C were made using the weighing apparatus described by Pettit, Yinger, and Wagner (10) with modifications to the furnace and reaction tube. An ATT-type Globar tubular heating element, 1⅛-in. ID and 22-in. long, was used for the furnace. Through the hollow of the heating element an alumina reaction tube, 9/16-in. in ID and 36-in. long, was placed. There was a 3-in. section in the center over which the temperature was constant within ±3°C at 1400°C. The temperature was controlled at a given point within ±2°C by means of a platinum-10% rhodium thermocouple and a L&N Speedomax G.

The oxidizing atmospheres were oxygen of 1, 10^{-1}, 10^{-2}, 5 x 10^{-4}, and 1.35 x 10^{-4} atm, CO_2, and CO-CO_2 mixtures containing 0.25 and 0.50% CO at a total pressure of 1 atm. When a pressure of oxygen less than 1 atm was required, purified argon was used as the diluent gas. Flow rates of 0.9 and 2.7 cm/sec were employed below 1190° and above 1300°C, respectively.

Figures 1 and 2 show the parabolic plots of oxidation in various atmospheres at 1190°C. The slope changes with time during the initial oxidation period and eventually reaches a constant value. As seen from the comparison of two runs for 10^{-2} atm of oxygen, the rate for the later period is more reproducible than that for the initial period. Therefore, in this paper the parabolic constants were determined from the slope for the later period.

The Arrhenius plots of parabolic constants in various atmospheres are given in Fig. 3. The plots for oxidation in high oxygen pressures and in CO_2 are straight over the entire temperature range, but those

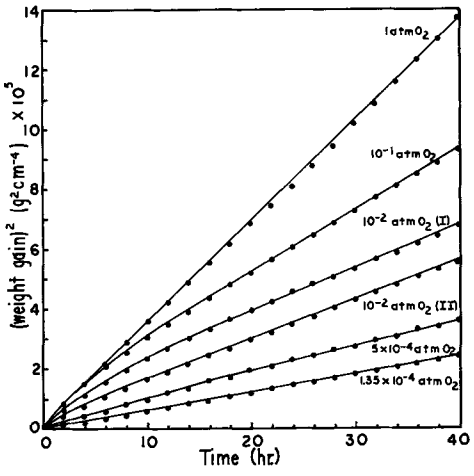

Fig. 1. Parabolic plot of oxidation at 1190°C

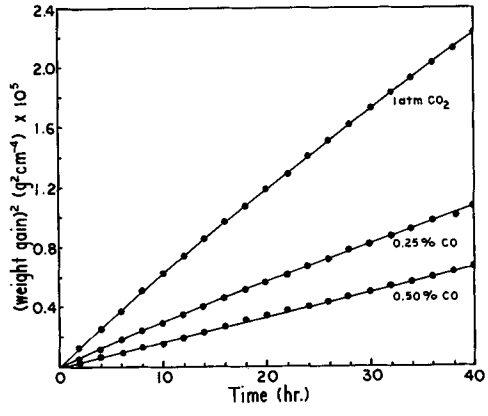

Fig. 2. Parabolic plot of oxidation at 1190°C

for low oxygen pressures and for CO-CO_2 mixtures are curved. The activation energies determined from the slopes of the straight-line portions are listed in Table II. For comparison, results obtained by previous investigators are summarized in Table III.

When an oxide with metal deficit and predominant electronic conduction is formed, the pressure dependence of parabolic constant is usually analyzed by the equation (16, 17)

$$k_p = c[p_{O_2}{}^{1/n} - p_{O_2}{}^{1/n}(\text{eq.})] \qquad [1]$$

where p_{O_2} and p_{O_2} (eq.) represent the oxygen partial pressures at the gas-oxide interface and at the oxide-metal interface respectively, c is a constant, and $1/n$ is a constant characterized by the mechanism of creation of a vacancy and electron hole(s), in this case, trivalent nickel. Figure 4 shows the plots of log k_p *vs.* log $[p_{O_2}{}^{1/n} - p_{O_2}{}^{1/n}(\text{eq.})]$ at constant temperatures. The oxygen pressures for CO-CO_2 mixtures were calculated assuming that the equilibrium of the reaction $2CO + O_2 \rightleftarrows 2CO_2$ was attained at the surface of nickel oxide. The value of n was chosen so that as many data points as possible could be located on a straight line with a slope of unity. As seen in Fig. 4 the data for low oxygen partial pressures deviate from the straight line except for the reactions at 1300° and 1400°C. A similar deviation has been reported by Pettit and Wagner for the oxidation of cobalt (9).

The data for oxidation in CO_2 were also plotted in Fig. 4. The oxygen partial pressures were calculated assuming that the equilibrium of self-dissociation $2CO_2 \rightleftarrows 2CO + O_2$ was attained on the surface of nickel oxide. These data, denoted by the symbol, *X*, are located close to the straight lines.

Marker study.—Platinum paste was put on a polished nickel specimen and heated at 900°C for 30 min

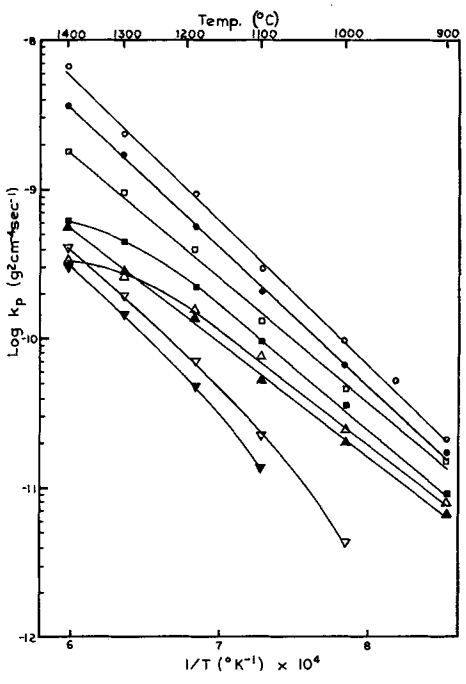

Fig. 3. Temperature dependence of parabolic constants in various atmospheres: ○, 1 atm O_2; ●, 10^{-1} atm O_2; □, 10^{-2} atm O_2; ■, 5×10^{-4} atm O_2; △, 1.35×10^{-4} atm O_2; ▲, 1 atm CO_2; ▽, 0.25% CO—CO_2; ▼, 0.50% CO—CO_2.

in a 1:1 mixture of CO-CO_2 to convert it into a thin and porous metallic film of about 1-2μ thickness. The specimen coated with the thin platinum layer was oxidized in oxygen of 1 atm or in carbon dioxide of 1 atm and cross-sectioned to examine the location of the platinum marker. Figure 5 shows the cross section of a specimen oxidized for 42 hr in 1 atm of oxygen at 1190°C. The oxide consists of a single layer and platinum markers are located close to the metal-oxide interface. When fine alumina powder was employed, markers were found to be located at the metal-oxide interface. The results of the present work clearly differ from those of Sartell and Li and show that nickel ions migrate much faster than oxygen ions.

Discussion

According to Wagner's theory of metal oxidation the rate constant for the formation of an oxide with predominant electronic conduction is given by the equation (16, 17)

Table II. Activation energies for the oxidation of nickel in various atmospheres in the present study

Atmosphere	Temperature range, °C	Activation energy, kcal/mole
1 atm O_2	900-1400	43.6
1×10^{-1} atm O_2	900-1400	42.5
1×10^{-2} atm O_2	900-1400	39.0
5×10^{-4} atm O_2	900-1190	37.7
1.35×10^{-4} atm O_2	900-1190	36.7
1 atm CO_2	900-1400	36.3

Table III. Comparison of activation energies

Investigators	Temperature range, °C	Activation energy, kcal/mole
Sartell and Li (8)	950-1200	67.0
Gulbransen and Andrew (11)	900-1050	68.3
Berry and Paĭdassi (12)	1000-1400	49.0
Frederick and Cornet (13)	800-1400	51.0
Baur, Bartlett, Ong, Jr., and Fassel (3)	1000-1200	50.0
Zima (14)	980-1260	45.1
Phillips (15)	700-1300	38.0

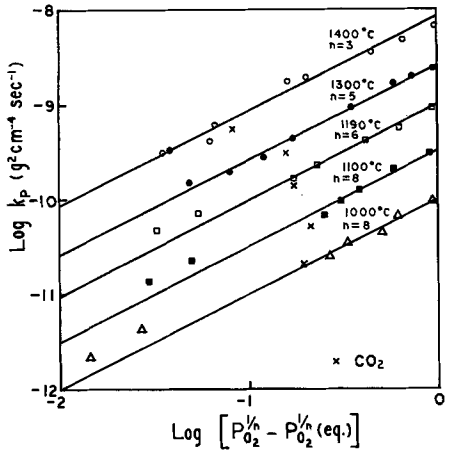

Fig. 4. Plots of log k_p vs. log $[p_{O_2}{}^{1/n} - p_{O_2}{}^{1/n}$ (eq.)]

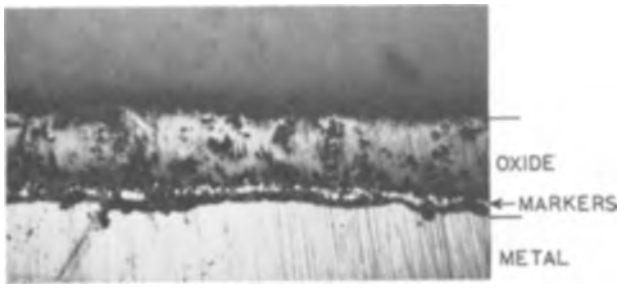

Fig. 5. Cross section of an oxide film with platinum markers. (1190°C, 1 atm O_2, 40 hr). Magnification 135X.

$$k_r = c_{eq} \int_{a_{x'}}^{a_{x''}} \left(\frac{Z_1}{|Z_2|} D_1{}^* + D_2{}^* \right) d \ln a_x \qquad [2]$$

where k_r is "rational rate constant" in equivalents per centimeter per second, $D_1{}^*$ and $D_2{}^*$ are the self-diffusion coefficients of cations and anions, respectively, Z_1 and Z_2 are units of charge on the cations and anions, respectively, a_x is the activity of nonmetallic element,[2] and c_{eq} is the concentration of ions in equivalents per cubic centimeter. Equation [1] is derived from Eq. [2] under the following assumptions: (*a*) oxidation is governed by the diffusion of cations via cation vacancies; (*b*) cation vacancies are created by a mechanism whereby n is independent of oxygen partial pressure, and (*c*) $D_1{}^*$ is proportional to the vacancy concentration. As shown above, Eq. [1] does not hold for the parabolic oxidation of nickel. Moreover, it is difficult to interpret a value of $n = 8$ for oxidation at 1000° and 1100°C. Therefore, a new method for the analysis of the pressure dependence of parabolic oxidation is proposed. As seen in Eq. [2], k_r consists of two kinds of terms, one of which is a function of a_x'' and the other a function of a_x'. a_x' is not a variable but a constant at a constant temperature. Therefore, k_r is differentiated by $\ln a_x''$ as follows,

$$\frac{Z_1}{|Z_2|} D_1{}^* + D_2{}^* = \frac{1}{c_{eq}} \cdot \frac{d k_r}{d \ln a_x''} \qquad [3]$$

In the case of the oxidation of nickel $Z_1/|Z_2|$ is unity and $D_2{}^*$ is eliminated because the marker study showed that cations migrate much faster than anions. Moreover, $d \ln a_x''$ is replaced by $\frac{1}{2} d \ln p_{O_2}$. Accordingly

$$D_1{}^* = D_{Ni}{}^* = \frac{2}{c_{eq}} \frac{d k_r}{d \ln p_{O_2}} \qquad [4]$$

c_{eq} is represented by the molecular weight M_{NiO} and the density ρ_{NiO} of nickel oxide (7.44 g/cc) as follows

$$c_{eq} = \frac{2 \rho_{NiO}}{M_{NiO}} \qquad [5]$$

[2] In the present case the single prime refers to the activity at the oxide-metal interface and the double prime that at the oxide-gas interface.

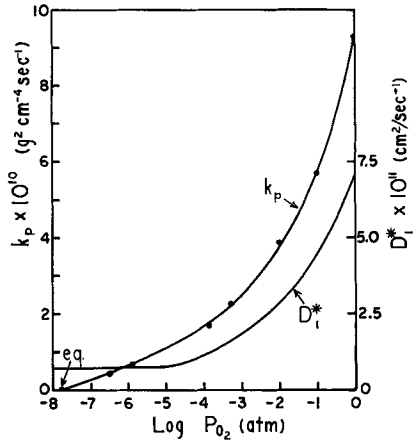

Fig. 6. Plots of k_p and D^*_1 as functions of p_{O_2} (1190°C)

For the present studies, the rational rate constant, k_r in units of eq/cm-sec, is related to the rate constant, k_p in units of $g^2 \cdot cm^{-4} \cdot sec^{-1}$, by an equation

$$k_r = \frac{M_{NiO}}{M_o{}^2 \rho_{NiO}} \cdot k_p \qquad [6]$$

where M_o is atomic weight of oxygen. Insertion of Eq. [5] and [6] into Eq. [4] yields

$$D_1{}^* = D_{Ni}{}^* = \left(\frac{M_{NiO}}{M_o \rho_{NiO}} \right)^2 \frac{d k_p}{d \ln p_{O_2}} = 0.1704 \cdot \frac{d k_p}{d \log p_{O_2}} \qquad [7]$$

Equation [7] shows that the self-diffusion coefficient of nickel ions is obtained as a function of log p_{O_2} by differentiating k_p with respect to log p_{O_2}. Figure 6 shows the plots of k_p *vs.* log p_{O_2} and of $D_1{}^*$ *vs.* log p_{O_2}. $D_1{}^*$ was obtained by differentiating the curve of k_p graphically and multiplying a factor of 0.1704. The plots of log $D_1{}^*$ *vs.* log p_{O_2} at different temperatures are given in Fig. 7. The value of log $D_1{}^*$ is independent of log p_{O_2} in the low-pressure range below about 10^{-6} atm and increases linearly with log p_{O_2} in the intermediate pressure range. The slopes determined in this range are given in Fig. 7. In the high-pressure range the slope appears to decrease gradually. In the intermediate

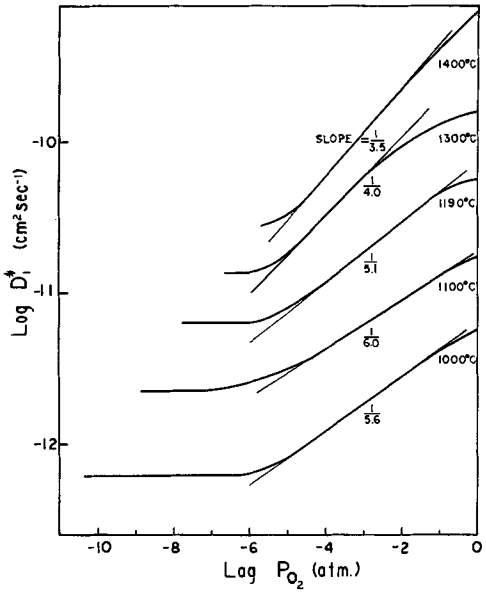

Fig. 7. Pressure dependence of self-diffusion coefficient D^*_1 calculated by the proposed method.

pressure range, the cation vacancies would be created by the following mechanisms

$$\frac{1}{2}O_2 \rightleftarrows [Ni_{\square''} \cdot \oplus] + \oplus + NiO \qquad (I)$$

or

$$\frac{1}{2}O_2 \rightleftarrows Ni_{\square''} + 2\oplus + NiO \qquad (II)$$

where $Ni_{\square''}$ is a cation vacancy and $\oplus$ is an electron hole. At 1300° and 1400°C the slope of the plot of log D_1^* *vs.* log p_{O_2} is about ¼. Mechanism (I) is inferred to predominate at these temperatures. Mechanism (II) would be predominant at 1000° and 1100°C. It is difficult to reconcile values of n in the pressure dependence of the parabolic rate constant (Fig. 4) and of the self-diffusion coefficient (Fig. 7) which decrease with increasing temperature. Such behavior would not be predicted on the basis of the ideal mass action law whereby the activities of each of the species are equated to their respective concentrations and whereby any trapping or association of electron holes onto vacancies would be expected to be more prevalent at the lower temperatures than at the higher temperatures.We do not have an explanation for this behavior. Additional data on the thermodynamics (activity coefficients of the respective species) are needed. The layers of NiO found in the present study were always adherent and free from pores under microscopic examination. While some oxygen transport in the NiO layers may aid in explaining the foregoing, the agreement of the present diffusion data with tracer diffusion studies (see below) suggests that the present analysis is correct.

There are no data available for the oxygen pressure dependence of the self-diffusion coefficient of nickel. One possible explanation for the apparent independence of D_{Ni}^* on oxygen pressure in the low-pressure range is as follows: In the low pressure range, the concentration of cation defects created by the excess oxygen would be small. Near the stoichiometric composition the defects would be created by a Frenkel mechanism,

$$\text{null} \rightleftarrows Ni_{\square''} + Ni_{O..} \qquad (III)$$

or by a Schottky mechanism

$$\text{null} \rightleftarrows Ni_{\square''} + O_{\square..} \qquad (IV)$$

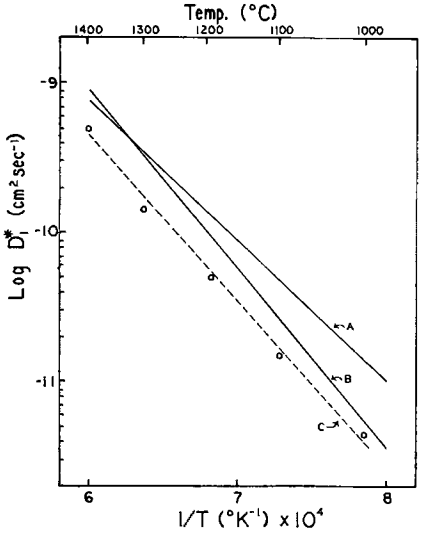

Fig. 8. Comparison of diffusion data: A, Shim and Moore, $D = 3.9 \times 10^{-4}$ exp (—44.2/RT) cm^2 sec^{-1}; B, Lindner and Åkerström, $D = 1.7 \times 10^{-2}$ exp (—56.0/RT) cm^2 sec^{-1}; C, This work, $D = 1.1 \times 10^{-3}$ exp (—50.3/RT) cm^2 sec^{-1}.

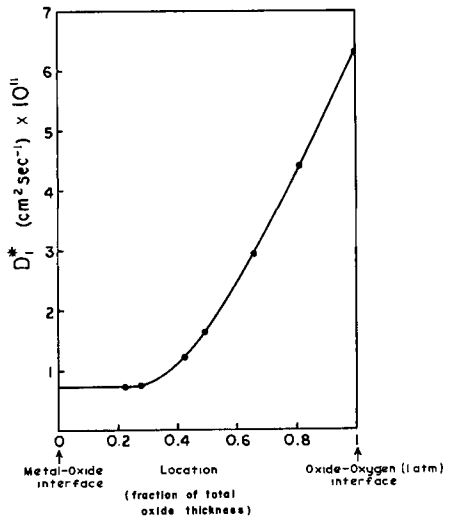

Fig. 9. Self-diffusion coefficient as a function of location in the oxide layer growing in 1 atm of oxygen at 1190°C.

where $Ni_{\square''}$ is a cation vacancy, $Ni_{O..}$ is an interstitial ion, and $O_{\square..}$ is an anion vacancy. If the concentration of defects created by mechanism (III) or (IV) greatly exceeds that created by the excess oxygen at low oxygen pressures, the mass action law yields

$$[Ni_{\square''}] \cdot [Ni_{O..}] = K_{III}(T) \qquad [8]$$

and

$$[Ni_{\square''}] \cdot [O_{\square..}] = K_{IV}(T) \qquad [9]$$

Since $[Ni_{\square''}]$ is equal to $[Ni_{O..}]$ or to $[O_{\square..}]$ as the case may be, the constant concentrations of cation vacancies and interstitial cations result in the self-diffusion coefficient being independent of oxygen pressure.

Baur and his collaborators found that the parabolic constant is insensitive to oxygen above 1 atm. In the present studies, the gradual decrease in the slope of k_p in the high-pressure range might be due to the transition to the pressure insensitive region. The Arrhenius plot of calculated D_1^* values at 0.2 atm is given in Fig. 8. The diffusion data of Shim and Moore (4), and of Lindner and Åkerström (5) are also plotted for comparison. The values of the self-diffusion coefficient of the nickel oxidation data agree well with those obtained independently using tracer techniques. This shows the self-consistency of the foregoing analysis.

The equilibrium oxygen pressure in a growing oxide decreases gradually from p_{O_2}, the oxygen partial pressure of ambient gas, to p_{O_2} (eq,), the dissociation pressure of the oxide. The location in the growing oxide where the equilibrium oxygen pressure is p_{O_2}' (p_{O_2} (eq.) $\leqq p_{O_2}' \leqq p_{O_2}$) is given by $(k_p'/k_p)^{1/2}$, where k_p' and k_p are the parabolic rate constants when the oxygen partial pressures are p_{O_2}' and p_{O_2}, respectively. Since the self-diffusion coefficient of nickel as a function of oxygen pressure is given in Fig. 7, one can obtain a relationship between the value of the self-diffusion coefficient and the location in terms of fraction of the total oxide thickness in the growing nickel oxide. Figure 9 shows the self-diffusion coefficient as a function of location in nickel oxide growing in 1 atm of oxygen at 1190°C. The linear gradient of D_1^* is seen in the outer portion of oxide and the independence of D_1^* on location is seen in the inner portion.

Summary

From the results of parabolic oxidation and of marker studies, the self-diffusion coefficient of nickel ions in nickel oxide is obtained as a function of oxygen partial pressure. The calculated self-diffusion coefficient is independent of oxygen pressure in the low

oxygen pressure range and is proportional to $p_{O_2}^{1/6}$ to $p_{O_2}^{1/3.5}$ in the intermediate pressure range. The dependence on $p_{O_2}^{1/4}$ is explained by the ionization of one electron hole from the cation vacancy while a $p_{O_2}^{1/6}$ dependence results if 2 electron holes are ionized. The calculated self-diffusion data at 0.2 atm of oxygen agree well with published tracer-diffusion values.

Manuscript received July 20, 1964. This work was supported by a grant from the Advanced Research Projects Agency through Northwestern University's Materials Research Center.

Any discussion of this paper will appear in a Discussion Section to be published in the December 1965 JOURNAL.

REFERENCES

1. C. Wagner and K. Grünewald, *Z. physik. Chem.*, **B24**, 455 (1938).
2. H. H. von Baumbach and C. Wagner, *ibid.*, **B24**, 59 (1934).
3. J. P. Baur, R. W. Bartlett, J. N. Ong, Jr.. and W. M. Fassell, Jr., *This Journal*, **110**, 185 (1963).
4. M. T. Shim and W. J. Moore, *J. Chem. Phys.*, **26**, 802 (1957).
5. R. Lindner, and Å. Åkerström, *Discussion Faraday Soc.*, **23**, 133 (1957).
6. S. P. Mitoff, *J. Chem. Phys.*, **35**, 882 (1961).
7. N. G. Eror and J. B. Wagner, Jr., *Amer. Ceram. Soc.* 65th Annual Meeting, April 27-May 2, 1963; Abstract No. 33-B-63. *Am. Ceram. Soc. Bull.*, **42**, No. 4, 199 (1963); to be published.
8. J. A. Sartell and C. H. Li, *J. Inst. Metals*, **90**, 92 (1961-62).
9. F. S. Pettit and J. B. Wagner, Jr., *Acta Met.*, **12**, 41 (1964).
10. F. S. Pettit, R. Yinger, and J. B. Wagner, Jr., *ibid.*, **8**, 617 (1950).
11. E. A. Gulbransen and K. F. Andrew, *This Journal*, **104**, 451 (1957).
12. L. Berry and J. Paidassi, *Compt. rend.*, **255**, 2253 (1962).
13. S. F. Frederick and I. Cornet, *This Journal*, **102**, 285 (1955).
14. G. E. Zima, *Trans. A.S.M.*, **49**, 924 (1957).
15. W. L. Phillips, Jr.. *This Journal*, **110**, 1014 (1963).
16. C. Wagner, *Z. physik. Chem.*, **B32**, 447 (1936).
17. C. Wagner, "Diffusion and High Temperature Oxidation of Metals," "Atom Movements", Am. Soc. for Metals, Cleveland, p. 153 (1951).

Determination of the Refractive Index and Thickness of Oxide Films on Anodized Zirconium from Transmission Interference Measurements

J. C. Banter

Oak Ridge National Laboratory, Oak Ridge, Tennessee

ABSTRACT

A method is described for the determination of the refractive index of thin oxide films stripped from anodized zirconium by dissolution of the metal. This new technique involves measurement of the interference patterns produced in the light transmitted through the films at various angles of incidence. The film thickness is also calculated from the data, and results show the refractive index does not vary with film thickness for films approximately 3000 to 5500Å thick. These films exhibit normal dispersion behavior over the ultraviolet, visible, and near infrared regions of the spectrum, with the refractive index varying from 2.07 to 2.50 at wavelengths of 1μ and 250 mμ, respectively.

In recent years, many experiments in the field of metallic corrosion have concerned the measurement of the optical properties and thickness of the thin oxide films formed in the early stages of corrosion. Frequently, reflection interference methods were used to make these measurements (1-4), but transmission measurements would serve just as well. This paper describes a transmission interference method applied to the determination of the refractive index and thickness of thin oxide films formed on zirconium. The technique was developed using anodically formed films with the hope of extending the measurements to films formed in other corrosive environments such as high-temperature water, air, and steam.

Theory

As the wavelength of light incident on a thin film is varied, the intensity of the transmitted beam exhibits alternate maxima and minima due to interference effects in the film. The wavelengths at which these extremes occur depend on the optical properties and thickness of the film as well as on the angle of incidence of the light. Vasícek (5) gives the equation describing the intensity, I_t, of light transmitted by a thin homogeneous film as

$$I_t = \frac{(1 - r'^2)(1 - r''^2)}{1 + r'^2 r''^2 + 2r'r'' \cos X} \qquad [1]$$

where r' and r'' are the Fresnel amplitude reflection coefficients for light incident from the same direction on the first and second surfaces of the film, respectively, and

$$X = 4\pi\eta_1 d_1 \cos\phi_1/\lambda \qquad [2]$$

η_1 and d_1 are the refractive index and thickness of the film, respectively, ϕ_1 is the angle of refraction of the light into the oxide, and λ is the wavelength of the incident light. Since $r'' = -r'$, the maxima occur at those wavelengths where $X = 2m\pi$; and the minima at those wavelengths where $X = (2m + 1)\pi$ with m, the order of interference, being an integer.

As the angle of incidence increases, the positions of the extremes for any given order of interference shift to shorter wavelengths in the spectrum. If the angle of incidence is increased sufficiently, the position of a given maximum or minimum can be shifted to the same wavelength as the minimum or maximum which was immediately adjacent to it at a lower wavelength at normal incidence. With known order numbers (which are easily determined) values for X as given by Eq. [2] can be calculated for both the extremes at normal incidence and those at the higher angle of incidence. Since $\cos\phi_1 = 1$ at normal incidence, the ratio of these two values of X yields $\cos\phi_1$ for the higher angle of incidence. The refractive index at this wavelength can then be calculated from Snell's law of refraction

$$\eta_0 \sin \phi_0 = \eta_1 \sin \phi_1 \quad [3]$$

where η_0 is the refractive index of the medium from which the light is incident on the film, and ϕ_0 is the angle of incidence of the light. The film thickness is determined by then substituting this value of η_1 into Eq. [2].

Experimental Procedure

Specimens ¾ in. x 1¾ in. were cut from 0.020-in.-thick zirconium foil and the surfaces chemically polished in a solution consisting of 50 ml lactic acid, 50 ml nitric acid, 20 ml water, and 10 ml hydrofluoric acid. Specimens were washed with copious amounts of water, dried, then anodized at constant voltages in a solution consisting of 40 ml glycerin, 20 ml lactic acid, 70 ml water, 120 ml ethyl alcohol, 10 ml phosphoric acid, and 4g citric acid. Specimens were anodized in such a manner that oxide film was formed on all surfaces. The film was then abraded from the center of one side of the specimen over an area approximately ⅜ x ⅝ in., and the metal in this area was dissolved by immersing the specimen in a 20% solution of bromine in ethyl acetate. This left a clear window of the oxide film supported by a surrounding frame of the undisturbed metal. The film and frame were then carefully washed in ethyl alcohol to remove all traces of bromine and dried in a stream of warm air.

The variation with wavelength of the intensity of light transmitted through these windows was measured in a Perkin-Elmer Model 4000 A spectrophotometer. For this purpose, two special specimen mounts were designed which allowed the rotation of the specimen about a vertical axis passing through the center of the spectrophotometer light beam. Figure 1 shows these two specimen mounts, one of which was used to make the measurements in air and has a specimen mounted in place. The second mount allows the measurements to be made with the specimen immersed in a liquid with refractive index higher than that of air. This mount was used with water as the immersion liquid in those instances where coincidence of the extremes could not be achieved at reasonable angles of incidence in air. The water immersion reduces the angle of incidence required to obtain coincidence of the extremes by increasing η_0.

Transmitted intensity measurements were first made on each specimen at normal incidence in the visible and/or ultraviolet regions of the spectrum, and then the angle of incidence at the appropriate wavelengths was gradually increased to obtain the angles required to produce coincidence of the extremes. Equation [2] was then applied to obtain η_1 and d_1 at each wavelength.

Results

Figure 2 shows typical interference patterns developed in the visible regions of the spectrum for one of the anodic oxide films and illustrates the shift to shorter wavelength of a given extreme as the angle of incidence is increased. At $\phi_0 = 60°$, maximum A has not shifted quite enough to come into coincidence with the position of minimum B at normal incidence,

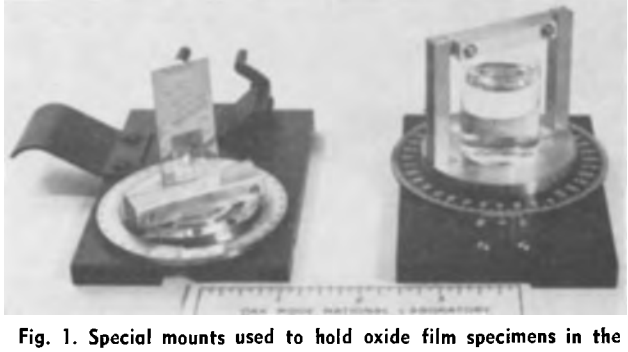

Fig. 1. Special mounts used to hold oxide film specimens in the spectrophotometer.

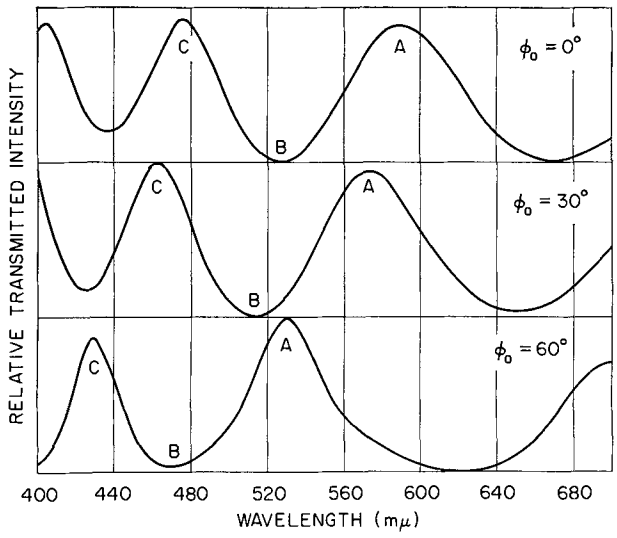

Fig. 2. Interference patterns developed in the visible regions of the spectrum at various angles of incidence by a film formed at 400v. A, 4th order maximum; B, 4th order minimum; C, 5th order maximum.

while minimum B has shifted beyond coincidence to a wavelength lower than that corresponding to the position of maximum C at normal incidence. Data for the calculation of η_1 and d_1 for this specimen in the visible region of the spectrum and the results of the calculation are listed in Table I. The average value for d_1 taken from this calculation was used in Eq. [2] to calculate values for η_1 at other wavelengths where extremes occurred outside the visible region. The calculated variation of the refractive index with wavelength of films formed at 200, 300, and 400v is shown in Fig. 3. The thicknesses of these films were calculated as 3159, 4318, and 5493Å, respectively.

Unfortunately, strong adsorption of light in the visible and ultraviolet regions of the spectrum obliterated the interference patterns of oxide films which were formed in high-temperature water and air to such an extent that this method could not be applied to them.

Discussion

Calculated values for both the refractive index and film thickness of the anodic zirconium oxide films are believed to be accurate to 1% or better, and within this limit the refractive index does not appear to change with film thickness. The refractive index of these films exhibits normal dispersion behavior with no appreciable absorption throughout the ultraviolet, visible, and near infrared regions of the spectrum, and varies from 2.07 at a wavelength of 1μ to 2.50 at a wavelength of 250 mμ. It should be noted, however, that the refractive index measured by this technique is not necessarily the same as that of the oxide film

Table I. Data for the calculation of the refractive index and thickness of an oxide film formed on zirconium anodized at 400v. Measurements were made with the specimen immersed in water.

Wavelength, λ, Å	Angles of incidence for coincidence of extremes	Order of interference of extremes $\phi_0 = 0°$	Order of interference of extremes $\phi_0 > 0°$	Index of refraction	Film thickness
6575	54° 12′	3	3	2.096	5490
5797	49° 48′	4	3	2.104	5510
5132	46° 24′	4	4	2.112	5460
4682	43° 48′	5	4	2.125	5508
4293	41° 48′	5	5	2.145	5504
3973	40° 12′	6	5	2.170	5493
3700	38° 48′	6	6	2.193	5483
Average					5493 ±33

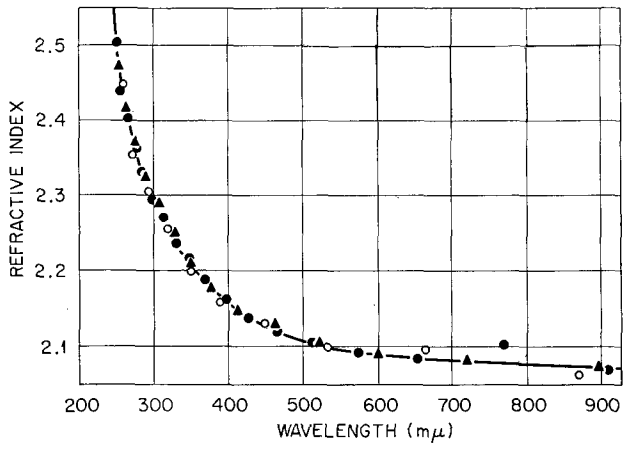

Fig. 3. Dispersion curve for three anodic zirconium oxide films. Anodized at: ●, 400v; ▲, 300v; ○, 200v.

in situ on the metal since the removal of the metal from the films tends to relieve certain strains existing in the film. These strains would be expected to affect the optical properties of the oxide. However, the calculated film thicknesses should not be appreciably different from those of the films in place.

The transmission interference method described here cannot, of course, be used with films such as the thermally formed films mentioned above which are strongly absorbing in both the visible and ultraviolet regions of the spectrum. The method is further limited by a lower limit on the thickness of the film for which coincidence of the interference extremes can be obtained at angles of incidence which are practically and accurately measurable. Proper choice of the liquid for use in the immersion mount can lower this limit considerably.

This method has one distinct advantage over the reflection interference methods often used for refractive index and thickness measurements. It completely eliminates the phase change occurring on reflection at the oxide-metal interface from the interference equations. This factor is often improperly treated. For example, Charlesby and Polling (6) developed interference equations for measurements similar to those reported using reflection techniques. Although these equations contained the phase change, its variation with angle of incidence was neglected completely in their use.

Furthermore, this method can undoubtedly be applied to other oxide films, both anodic and thermal, which can be separated from the substrate metal and which do not absorb strongly enough to obliterate the interference patterns normally developed.

Acknowledgment

The author wishes to express gratitude to Dr. M. L. Picklesimer for his many discussions of this project and his criticism of the manuscript.

Manuscript received Oct. 14, 1964. This paper was presented at the Washington Meeting, Oct. 11-15, 1964. The research was sponsored by the United States Atomic Energy Commission under contract with the Union Carbide Corporation.

Any discussion of this paper will appear in a Discussion Section to be published in the December 1965 JOURNAL.

REFERENCES

1. F. Abeles. *J. Phys. Radium*, **11**, 310 (1950).
2. N. J. M. Wilkins, *Corr. Sci.*, **4**, 17 (1964).
3. W. P. Ellis, *J. Opt. Soc. Am.*, **53**, 613 (1963).
4. O. S. Heavens, "Optical Properties of Thin Solid Films," Butterworths, London (1955).
5. Antonin Vasícek, "Optics of Thin Films," North-Holland, Amsterdam (1960).
6. A. Charlesby and J. J. Polling, *Proc. Roy. Soc. (London)*, **227A**, 434 (1954).

The Role of Copper During the Oxidation of Transformer Oils

John J. Melchiore and Ivor W. Mills

Research Laboratories, Sun Oil Company, Marcus Hook, Pennsylvania

ABSTRACT

Air oxidation of two transformer oils, differing mainly in the fact that one contained metal deactivator, was studied at 95°C in the presence and absence of metallic copper. Power factor, hydroperoxide and carbonyl oxidation intermediates, and copper contents were measured as a function of time. In the absence of metallic copper, oxidation of the two oils is quite similar. Curves of power factor and oxidation intermediates show no striking differences. There appears to be a relation between power factor and carbonyl content in these cases. In the presence of metallic copper, the oil containing metal deactivator is capable of resisting the catalytic effects of copper. The oil without deactivator is grossly degraded by <0.2 ppm soluble copper which the oil rapidly dissolves. The relation between copper content, hydroperoxide content, and power factor is discussed in terms of a proposed mechanism.

It is well known that oxidative degradation of electrical oils results in the loss of electrical insulating properties of the oil. This has led to a search for electrical oils with superior oxidation resistance, especially in the presence of copper. A number of comparative accelerated laboratory tests have been devised, hopefully to predict what will actually happen to a transformer oil in service over a period of years. A particularly convenient and useful comparative test involves periodic measurement of the power factor of an oil at 95°C exposed to air and copper over a period of several days. Although the correlation of this test with actual oil performance in use has yet to be demonstrated, the mechanism of oil degradation should be the same, since in both cases the oil at elevated temperature is exposed to air and metallic copper. This test, described in detail in the Experimental Section, was used throughout the present study.

The mechanism of oil degradation in the presence of copper is not clear. Proposals for both heterogeneous and homogeneous copper catalysis have been made (1), but more convincing evidence has been reported supporting the homogeneous theory (2). Although transformer oils in service are reported to dissolve about 0.2-0.6 ppm copper, the ability of an oil to retain soluble copper apparently depends on many diverse factors (3). However, detailed quantitative data on copper solubility during the early hours of oxidation are lacking as well as the mechanisms responsible for copper solubilization. Similarly, the role of metal deactivators is another related aspect of the over-all problem. The work presently reported, there-

Table I. Properties of transformer oils A and B

Physical	ASTM method	Transformer oil A	Transformer oil B
Specific gravity, 60°F	D1250	0.904	0.904
Flash, OC, °F	D92	295	295
Fire, °F	D92	325	325
Viscosity, SUS/100°F	D446	60	58.6
Pour point, °F	D97	−50	−50
IFT, dynes/cm	D971	40	41
Dielectric strength, kv	D877	32	35
Differential infrared and UV spectra		No Detectable Differences	
Refractive index/20°C		1.4951	1.4963
Chemical			
Neutralization No., mg KOH/g	D974	0.00	0.00
Inorganic chlorides & sulfates	D878	0	0
Free sulfur	D989	0	0
Total sulfur, weight per cent (w/o)		0.12	0.12
Average molecular weight, osmometric		271 ± 5	260 ± 5
Total aromatics, w/o		35	34.5
Monocyclic, w/o		27.4	25.7
Dicyclic		6.3	7.9
Tricyclic		1.3	0.9

fore, was undertaken to help answer these questions, with particular emphasis on the processes occurring during the early hours of oxidation.

In this investigation, air oxidations of two transformer oils, A and B, were studied at 95°C in the presence and absence of metallic copper. Power factors of the oxidizing oils were recorded automatically each hour. From small aliquots withdrawn periodically, hydroperoxide and carbonyl contents were measured polarographically. The soluble copper content was determined by neutron activation analysis. Thus, data are available for plotting continuous curves of power factor, copper content, and oxidation intermediates.

Physical and chemical properties of oils A and B are summarized in Table I, with infrared and ultraviolet spectra given in Fig. 1 and 2. The most important difference between these oils is the fact that oil B contains a metal deactivator, that is, a material capable of significantly decreasing the catalytic activity of copper. This metal deactivator was derived

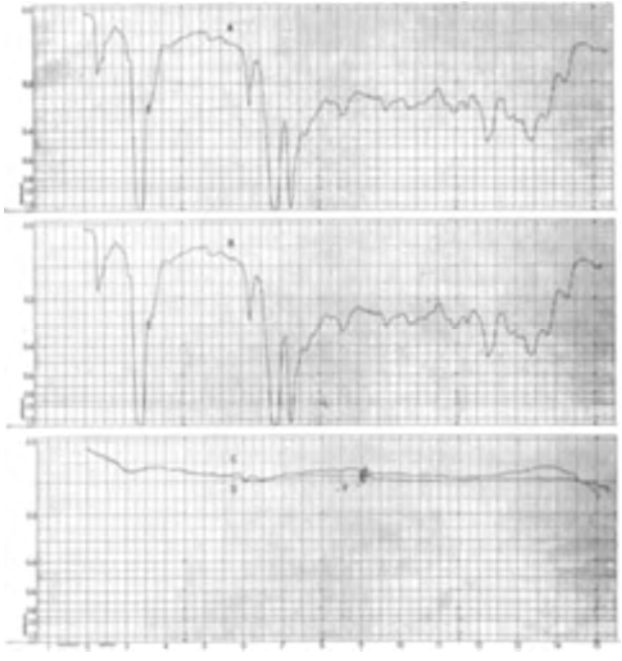

Fig. 1. Infrared spectra. Curve A is conventional transformer oil (A), liquid phase, 0.1 mm thickness. Curve B is oil containing metal deactivator (B), 0.1 mm thickness. Curve C is the differential spectrum of oil A vs. oil B, 1.008 mm thickness. Curve D is the differential spectrum of oil A vs. oil A, 1.008 mm thickness. Absorbance vs. wavelength.

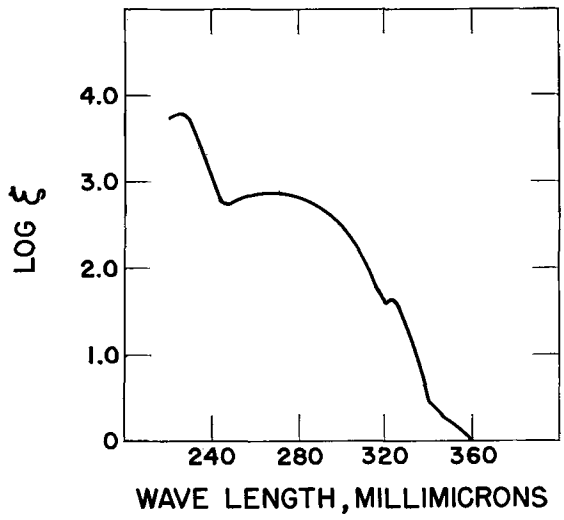

Fig. 2. Ultraviolet spectrum of conventional transformer oil (A) in isooctane, with cell thickness of 1 cm. Spectrum of oil containing metal deactivator (B) is identical. Log molar extinction coefficient (ε) vs. wavelength.

from naturally occurring sulfur compounds contained in oil A by the method detailed in the Experimental Section. The concentration of deactivator present in oil B is estimated to be about 100 ppm. Due to difficulties imposed by its low concentration, the exact chemical structure of this deactivator has not yet been determined. The effectiveness of deactivator is indicated in Fig. 3, which shows that deliberately introducing soluble copper does not markedly catalyze the oxidation of oil B, whereas the same quantity of copper grossly degrades oil A. Further evidence for the effectiveness of this deactivator is presented in Fig. 4, showing that a minor amount of oil B will protect oil A from the catalytic effect of soluble copper. These charts are presented simply to show the effectiveness of the deactivator when soluble copper is deliberately added to the oil to accelerate oxidation. In actual use, transformer oil is exposed to metallic copper and, in many cases, to air as well. Therefore, the studies described here were aimed at a better understanding of interactions between oil and metallic copper in the presence of oxygen.

Experimental

Generation of deactivator in situ.—Transformer oil A is obtained from a naphthenic distillate stock by treating the stock conventionally with sulfuric acid and

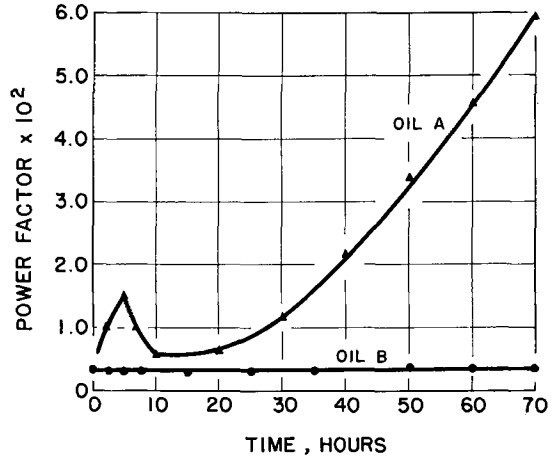

Fig. 3. Effect of 0.5 ppm Cu^{+2} and air on the power factor of conventional transformer oil (A) and oil containing metal deactivator (B) at 95°C.

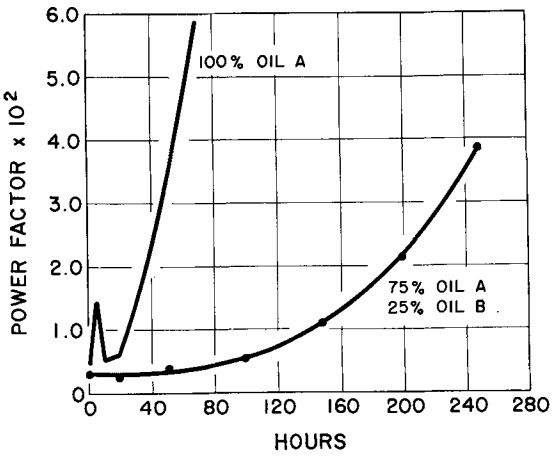

Fig. 4. Effect of 0.5 ppm Cu^{+2} and air on the power factor of blended transformer oils at 95°C.

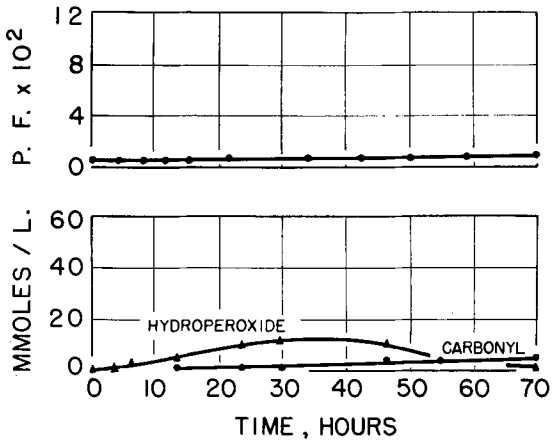

Fig. 5. Air oxidation of conventional transformer oil (A) at 95°C in the absence of copper. Power factor values and oxidation intermediates concentrations vs. time.

adsorptive clay according to procedures widely used in the petroleum industry. When oil A is reacted with sodium isopropoxide, species capable of deactivating copper are generated in very low concentrations (~100 ppm). Specifically, the deactivated oil, oil B, is typically obtained by the following laboratory procedure.

A 1-liter Morton flask, equipped with thermometer, high-speed stirrer, reflux condenser, and gas inlet tube, containing 500 mls oil A and 2.3g sodium, is heated to 110°C under nitrogen with vigorous agitation in order to disperse the sodium. The contents are cooled to room temperature and 7g anhydrous isopropanol are added. The oil and sodium isopropoxide are reacted at 110°-140°C for 30 min, continuing good agitation. When cooled below 90°C, the contents are added carefully, with agitation, to 1 liter of cold distilled water. The oil phase is separated and thoroughly washed five times with equal volumes of water. After drying at 105°C under vacuum, 14g adsorptive clay are added and slurried with the oil for 20 min at 105°C. The oil is then filtered through paper and finally vacuum filtered through a 0.45μ millipore filter.

Oxidation procedure.—Before oxidation, each oil is refiltered through a 0.45μ millipore filter, and 250 ml of filtered oil is then preheated in an oven to 95°C. The oil is placed in a thoroughly cleaned test tube 11 x 2½ in. A stainless steel cell, containing two concentric electrodes, is immersed in the oil. This cell has an air capacitance of 47 x 10^{-12} farads or a measured capacitance of 105 x 10^{-12} farads using material of dielectric constant of 2.2. A coil containing 100 in. of 0.06 in. diameter copper wire is placed within the cell. An air delivery tube extends to the bottom of the oil, through the copper coil. The test tube containing the oil, electrodes, copper coil, and air delivery tube is immersed in a constant temperature oil bath maintained at 95° ± 1°C. Air is supplied to the oil according to the specifications of ASTM D1904. Once each hour, the d-c conductivity of the oxidizing oil is measured, amplified using a L&N #98360A amplifier and recorded using a Varian G-10 recorder. Current is allowed to flow only 5-6 sec each hour. Using an applied voltage of 2.7v from standard mercury cells and the measured current, the resistance of the oil is calculated from Ohm's law. The power factor is related to the resistivity through the equation

$$\text{Power factor} = \frac{1}{\sqrt{(2\pi fCR)^2 + 1}}$$

where f equals 60 cycles and C is capacitance (assumed constant).

Periodically during the oxidation, 3 ml aliquots are withdrawn. Using the Sargent XXI polarograph according to the method of Loveland (4), the hydroperoxide content is determined on a 1 ml aliquot from the half-wave potential in the —0.9v region and the carbonyl content measured from the half wave at —1.6v (*vs.* saturated calomel electrode). The copper content of the sample is determined from the remaining 2 ml aliquot, using neutron activation analysis (5).

Results and Discussion

Oxidation in the absence of copper.—Data on the oxidation of oils A and B with air at 95°C in the absence of copper are summarized in Fig. 5 and 6. The figures show that the power factors of the oils during the first 70 hr of oxidation remain low and essentially unchanged, indicative of little oxidative degradation during this period.

Also plotted on the same time scale are the relative concentrations of hydroperoxides and carbonyl compounds, namely, aldehydes and ketones. The rate of appearance of these oxidation intermediates is essentially the same for both oils. Within a few hours hydroperoxide is detected, rising to a maximum concentration of about 10 mmoles per liter and gradually falling to a steady state of about 4 mmoles per liter. Carbonyl compounds show a slow steady rise during this oxidation period.

Results are consistent with a generally accepted free radical autoxidation mechanism, with hydroperoxide as the first isolatable oxidation intermediate. Decomposition of hydroperoxide and subsequent rearrangement and oxidation of its fragments would result in the appearance of aldehydes and ketones, fol-

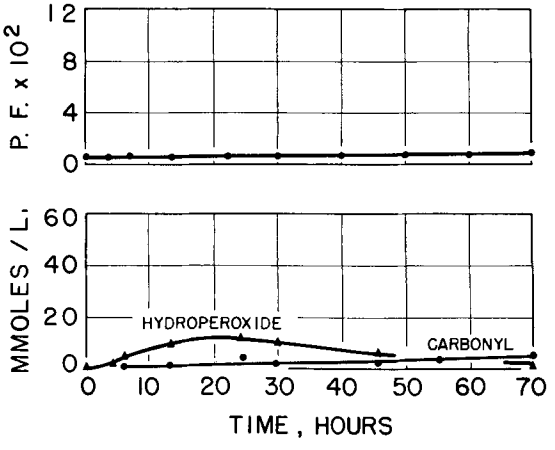

Fig. 6. Air oxidation of oil containing metal deactivator (B) at 95°C in the absence of copper. Power factor values and oxidation intermediates concentrations vs. time.

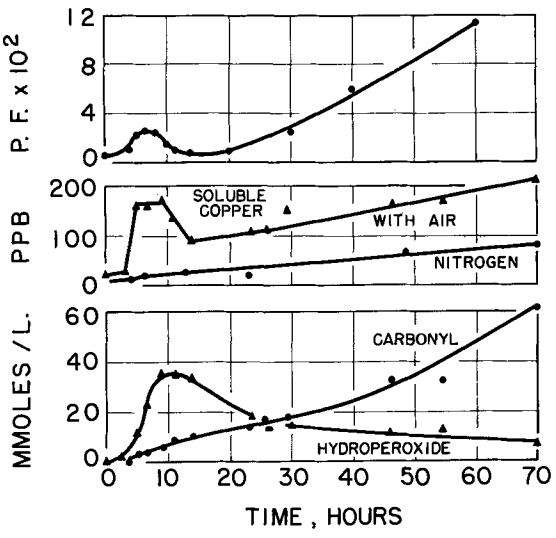

Fig. 7. Air oxidation of conventional transformer oil (A) at 95°C in the presence of metallic copper. Power factor values, parts per billion soluble copper, and oxidation intermediates concentrations vs. time.

lowed finally by the appearance of carboxylic acids. We can also reasonably conclude from the data that both oils, in the absence of copper, oxidize in a similar manner.

Figures 5 and 6 stop at 70 hr; however, if oxidation is continued longer, the power factor curves rise slowly. Although carboxylic acids and alcohols are known to make only small contributions to power factor (6), the parallel rise of power factor and carbonyl content suggests that they are related. Such a relation has not been previously reported, and we have not yet examined it in detail, but it is scheduled for further experimental studies.

Oxidation in the presence of metallic copper.—Power factor, oxidation intermediates, and copper solubility data for the air oxidation of oils A and B in the presence of metallic copper at 95°C are summarized in Fig. 7 and 8. It is immediately obvious that the oxidation of oil A is dramatically catalyzed by copper, whereas oil B is able to resist this copper catalysis.

Oxidation of oil A.—From a detailed examination of Fig. 7 the following observations are made:

1. Oxidative degradation of oil A is rapidly catalyzed by copper although the soluble copper content is less than 200 parts per billion (ppb) for most of the test period.

2. The power factor curve of the oxidizing oil exhibits a peak at 7 hr after which it falls nearly to its initial value before beginning a steady rise.

3. The copper content also rises to a peak between 5 and 10 hr, then drops before starting a gradual rise. The similarity between the power factor and soluble copper curves suggests that conductive copper in solution may affect power factor, particularly in the peak area. This copper solubility data is in sharp contrast to the copper solubility observed when the oil is maintained under nitrogen (Fig. 7). In this case, copper dissolves very slowly over a long period of time, never reaching the level of solubility obtained under oxidizing conditions. The power factor under nitrogen (not shown in Fig. 7) is low and flat over the entire test period.

4. The maximum hydroperoxide content of oil A during copper-catalyzed oxidation is about 3½ times greater than during the noncatalyzed oxidation (Fig. 5). It is interesting to note that maximum hydroperoxide content is achieved after the maximum amount of copper has entered solution, strongly supporting the hypothesis that soluble copper acts catalytically to accelerate hydroperoxide formation. From a comparison of the power factor and hydroperoxide curves, it is evident that hydroperoxides themselves make only a small contribution to the observed power factor.

5. The carbonyl content of the catalyzed oxidation becomes appreciable early in the oxidation and rises rapidly, greatly exceeding the carbonyl content of the uncatalyzed oxidation (Fig. 5) throughout the entire oxidation period, again indicating gross degradation of the oil.

The data are again consistent with a typical free radical chain autoxidation mechanism, catalyzed by soluble copper. The hydroperoxide and carbonyl curves are those that would be expected from such a mechanism. The copper solubility results summarized in Fig. 7 were somewhat unexpected and their interpretation warrants further discussion.

It is interesting to speculate on the nature of the processes occurring during the copper catalyzed oxidation of oil A at 95°C. This oil carried in it, before oxidation, 10-20 ppb soluble copper. Although processes initiating oxidation have received little attention and are not well understood, the initially contained soluble copper may be capable of initiating free radical chains according to previously proposed schemes (7). Once started, the first isolatable product of the oxidation will be hydroperoxides. It has been proposed that reaction of peroxides with metallic copper results in the solubilization of copper (8). It is generally accepted that copper forms an oxide film when exposed to oxygen (9, 10). It has recently been shown that at temperatures in the vicinity of 100°C, copper will form an oxide film having the unusual stoichiometry of $CuO_{0.67}$ (11). This film presumably is a gross defect structure of cuprous oxide. We propose, therefore, that solubilization of copper results from the reaction of hydroperoxide with this oxide film, which for simplicity we will simply consider as cuprous oxide as depicted in Eq. [1]. Possible disproportionation to the cupric salt is depicted in Eq. [2]

$$2ROOH + Cu_2O \rightarrow 2Cu^+(O_2R)^- + H_2O \quad [1]$$

$$2Cu^+(O_2R)^- \rightleftharpoons Cu + Cu^{+2}(O_2R)_2 \quad [2]$$

Metal salts of hydroperoxides, as proposed in reaction [1], are prepared by reaction of an appropriate metal oxide with hydroperoxide (12). The limited solubility of these salts in hydrocarbon media would depend on the nature of R, the ionic character of the salt, and any further organic material associated or complexed with it. From the coincidence of the power factor and copper solubility peaks of Fig. 7, it seems reasonable to conclude that the power factor peak observed at 7 hr is due largely to the conductivity of soluble copper.

For simplicity we have designated the first isolatable oxidation intermediate simply as hydroperoxide, ROOH. We do not imply that this is simply a hydroperoxide derived from a strictly hydrocarbon precursor. On the contrary, independent evidence indicates that sulfur and/or nitrogen containing organic compounds in the oil are the first to hydroperoxidize and it is these materials which we suspect tend to solubilize copper through reaction [1].

With the soluble copper present in solution, the typical catalytic reactions of metal ions with hydroperoxide would be expected according to Eq. [3] and [4], resulting in the formation of new chains and the appearance of carbonyl compounds from well-known reaction sequences (13).

$$ROOH + Cu^{+2} \rightarrow Cu^{+1} + H^+ + RO_2\cdot \quad [3]$$

$$ROOH + Cu^{+1} \rightarrow Cu^{+2} + OH^- + RO\cdot \quad [4]$$

In addition, the postulated copper salts would be expected to be unstable (14) and may decompose by Eq. [5] or [6].

$$Cu^+(O_2R)^- \rightarrow CuO + RO\cdot \quad [5]$$

$$Cu^{+2}(O_2R)^-_2 \rightarrow CuO + RO\cdot + RO_2\cdot \quad [6]$$

Consequences resulting from Eq. [5] and [6] would be initiation of new chains with subsequent appearance of hydroperoxides, alcohols, and carbonyl compounds, and a mechanism for removal of soluble copper from solution.

Alternate explanations for the observed net decrease in copper content (Fig. 7) are found in known reactions of hydroperoxides and their salts (15). Thus, hydroperoxide is known to react with its salt to produce an alcohol. Using the cuprous salt as an example, the reaction is summarized in Eq. [7].

$$Cu(O_2R) + ROOH \rightarrow ROH + O_2 + CuOR \quad [7]$$

Alternatively, primary and secondary alcohols are known to react with hydroperoxide salts according to Eq. [8].

$$Cu(O_2R) + RCH_2OH \rightarrow CuOH + ROH + R\text{-}CHO \quad [8]$$

The copper hydroxide produced would not be soluble in hydrocarbon media. The polar alcohol and carbonyl compounds produced via Eq. [7] and [8] or from the free radical chain autoxidation would be adsorbable on the copper oxide surface film, thus decreasing the rate of copper solubilization by reaction [1]. Eventually copper removal by Eq. [5], [6], or [8] predominates, resulting in a net decrease of soluble copper.

Although the experimental data clearly indicate a decrease in soluble copper content, visually we do not see any dispersed insoluble material, no doubt due to the extremely low concentration of soluble copper. The oxidizing oil and the aliquots withdrawn from it are perfectly clear. We do, however, observe the formation of varnish colored deposits on the copper coil and on the electrodes, after prolonged oxidation. The nature of these deposits was not investigated due to the minute quantities involved.

After passing through a minimum at about 14 hr, the copper content starts to rise again, probably due to the known solubilizing tendencies of carbonyl compounds and carboxylic acids (16).

Oxidation of oil B.—Oxidation data for oil B in the presence of copper, summarized in Fig. 8, is markedly different from oil A, since oil B contains material capable of reducing, but not completely eliminating, catalysis by copper. The oxidation is characterized by the following:

1. The power factor curve exhibits no peak early in the oxidation and rises only slightly over the entire oxidation period.

2. Oil B dissolves less copper than oil A. At equilibrium, oil B dissolves approximately 50 ppb soluble copper. Significantly, the copper concentration curve does not peak early in the oxidation, in good agreement with the lack of peak noted for the power factor curve.

3. The hydroperoxide curve approximates that found for oil B in the absence of copper. The carbonyl content is several times greater than that observed without copper, but still substantially less than that observed in oil A.

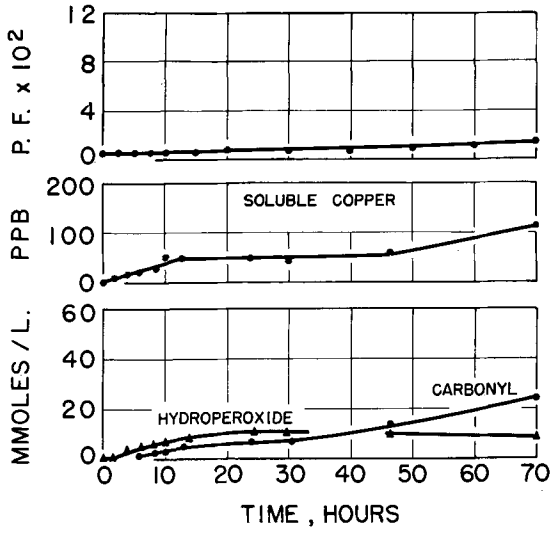

Fig. 8. Air oxidation of oil containing metal deactivator (B) at 95°C in the presence of metallic copper. Power factor values, parts per billion soluble copper, and oxidation intermediates concentrations vs. time.

The results clearly demonstrate that the catalytic effects of copper have been sharply reduced, but not completely eliminated. A striking difference is noted in the abilities of oils A and B to solubilize copper under oxidizing conditions. Oil B dissolves substantially less copper than oil A, although oil B oxidizes to produce appreciable hydroperoxide early in the oxidation. In fact, oil B after 4 hr of oxidation contains enough hydroperoxide to dissolve at least 70 ppm copper. Why then, if our postulated solubilization mechanism between hydroperoxide and copper oxide film is correct, does not more copper dissolve? A reasonable explanation is simply that the polar metal deactivator is adsorbed on the copper oxide surface, thus decreasing the solubilization of copper by Eq. [1]. Copper contained in solution, although at low concentrations, is capable of exerting some catalytic activity as evidenced by the increased carbonyl content over oxidation conducted in the absence of copper.

Therefore, based on this study, the function of metal deactivator appears to be twofold: (*a*) to coat the copper oxide surface and thus decrease the quantity of copper solubilized, and (*b*) to decrease the catalytic activity of solubilized copper, presumably by chelation.

Summary and Conclusions

This study of the processes occurring during the early hours of transformer oil oxidations has indicated that the oxidation rate of similar oils is slow and almost identical in the absence of copper, even though one contains metal deactivator. Dielectric loss, as measured by power factor, seems to be related to the carbonyl content of the oil in these cases.

The situation in the presence of copper is quite different. The oil without deactivator is rapidly degraded in the presence of metallic copper. The solubiltiy of copper rises quickly during the early hours of oxidation to a peak concentration of 170 ppb. The coincidence of this soluble copper peak and the observed power factor peak strongly suggests that copper enters solution in a conductive form contributing to power factor losses in the early stages of the oxidation. A mechanism of copper solubilization has been proposed, involving reaction of hydroperoxide derived from nitrogen and/or sulfur containing impurities in the oil, and a copper oxide surface film. The catalytic effect of the soluble copper is clearly demonstrated from the rate of appearance and concentration levels of hydroperoxide and carbonyl compounds.

In the presence of copper, a metal deactivator is very effective in preserving the oil. The quantity of copper dissolved is less, the rate of appearance and concentration of oxidation intermediates is also less. A twofold effect for the metal deactivator is apparent; namely, a coating effect on the metal which decreases copper solubilization and a decrease of catalytic activity of the soluble copper due to chelation.

Continuous power factor measurements have interesting but largely unexploited potential for following the oxidation of organic substances. Further fundamental work on factors contributing to observed power factor is needed to extend its usefulness. Particularly, quantitative correlations of power factor with oxidation intermediates and with valence and nature of soluble metal species are needed.

Finally, the present study emphasizes the effect of truly trace quantities of copper. The quantitative aspects of this effect could not have been appreciated were it not for the advent of neutron activation anal-

ysis, a superb tool for this and other trace element studies. It is hoped that this and later studies will contribute not only to a better understanding of oil oxidation as catalyzed by copper but to eventual significant improvement in the useful life of electrical oils.

Acknowledgments

The authors wish to acknowledge Mr. G. R. Dimeler and Mr. I. H. Johnson for their helpful assistance in polarographic analyses and power factor determinations, respectively.

Manuscript received Aug. 20, 1964. This paper was presented at the Toronto Meeting, May 3-7, 1964.

Any discussion of this paper will appear in a Discussion Section to be published in the December 1965 JOURNAL.

REFERENCES

1. F. Morton and R. T. T. Bell, *J. Inst. Petrol.*, **44**, 268 (1958).
2. C. N. Thompson, *ibid.*, **44**, 295 (1958).
3. J. C. Wood-Mallock, H. Steiner, and L. G. Wood, *ibid.*, **44**, 320 (1958).
4. J. W. Loveland, G. R. Dimeler, L. G. Bostwick, and L. J. Cali, *Proc. A.P.I., Div. of Refining*, **40**, 410 (1960).
5. R. W. King, C. C. Cerrato, and J. J. Melchiore, *29th Meeting of A.P.I., Div. of Refining*, May 12, 1964, Preprint No. 25-64.
6. A. R. Von Hippell, "Dielectric Materials and Applications," Chapter on Liquid Dielectrics, p. 16, John Wiley & Sons, New York (1954).
7. W. O. Lundberg, "Autoxidation and Antioxidants," Vol. 1, chapter by N. Uri, "Physico-Chemical Aspects of Autoxidation," pp. 95-99, John Wiley & Sons, New York (1961).
8. E. D. Eich, G. Fieck, and W. F. Olds, Paper presented at the Philadelphia Meeting of this Society, May 3-7 (1959).
9. U. R. Evans, "Corrosion and Oxidation of Metals," p. 32, Edward Arnold Publishers, London (1960).
10. L. Young, "Anodic Oxide Films," p. 308, Academic Press, London (1961).
11. H. Wieder and A. W. Czanderna, *J. Phys. Chem.*, **66**, 816 (1962).
12. A. G. Davies, "Organic Peroxides," Butterworth & Co., London (1961).
13. C. Walling, "Free Radicals in Solution," p. 445, John Wiley & Sons, New York (1957).
14. E. G. E. Hawkins, "Organic Peroxides," p. 11, F. F. Spon Ltd., London (1961).
15. A. G. Davies, *loc. cit.*, p. 187.
16. J. C. Bailar, "Chemistry of the Coordination Compounds," pp. 41-45, Reinhold Publishing Co., New York (1956).

Growth Mechanism of Thin Anodic Oxide Films on Tantalum

I. Self-Anodization Using an External Load Resistor

R. Dreiner, K. Lehovec, and J. Schimmel

Research Laboratories, Sprague Electric Company, North Adams, Massachusetts

ABSTRACT

The growth of an anodic oxide film on tantalum metal immersed in diluted sulfuric acid has been investigated using potential and capacitance measurements. The tantalum metal was connected through an external resistance to a platinum electrode in the electrolyte. An analysis of voltage *vs.* time confirms the exponential field dependence of the ionic current for the later phases of oxide growth. Analysis of current (I) *vs.* time (t) measurements provides BF_o and λF_o where B is the field coefficient,[1] F_o is the initial field in the oxide, and λ is the growth rate per unit current, provided that the emf of the reaction, E, is known. E can be determined by matching the B-values derived from I *vs.* t to those derived from capacitance measurements. For sufficiently thin oxide films the growth rate exceeds the value expected from Faraday's law based on the external current which indicates the presence of internal electron currents for which the empirical expression

$$I_E = I_E^o \, e^{-d/l}$$

with $I_E^o \sim 3 \times 10^{-4}$ amp/cm^2 and $l \sim 3.0$Å, was obtained. There are indications that either the inverse Tafel slope, B, or the emf, E, varies with film thickness in the range where the internal electron current is appreciable.

It has been found (1) that the ionic current promoting the growth of anodic oxide layers depends exponentially on the field across the oxide. Determination of the constants involved in this relation usually requires the measurement of the oxide thickness by such techniques as capacitance-, optical-, or weight-measurement.

We have explored the applicability of the exponential field law for very thin anodic oxide films on tantalum. Since the determination of the oxide thickness becomes increasingly difficult the thinner the oxide film, a method was used which does not involve thickness measurements, namely, the analysis of the time dependence of the external current through a resistor connecting Ta and Pt electrodes in an electrolyte. This current arises from the electromotive force of the reaction of Ta with water and decreases with time as the oxide grows on the tantalum.

This general procedure of analysis could be applied also to cases where an external power source is placed in series with the external resistor. However, in order to investigate the growth of thin oxide films we must limit the external current to fairly small values to obtain a slow growth rate. Initially the oxide resistance is very low so that the current is limited by the external resistor. In this range the current *vs.* time relation is not sensitive to the oxide resistance. In order to investigate the properties of thin oxide films we must reduce the external resistor as much as possible which is incompatible with the former condition of a fairly small current if a large external voltage were employed. For this reason we have not applied an external voltage and have studied in detail the growth of thin anodic films by means of the emf associated with the formation of Ta_2O_5 (so-called self-anodization).

We have compared the experimental time dependence of the external current with a theoretical equation based on well-known relations valid for thick oxide films, but not necessarily applicable to the thin oxide films here investigated. By this comparison the numerical values of certain parameters for thin oxide films were determined and the following anomalies were discovered:

[1] Sometimes referred to as "inverse Tafel slope."

1. The presence of electron currents through the oxide which govern the growth of sufficiently thin oxide films, and
2. Some time or thickness dependence of the "emf" or of the "inverse Tafel slope" for the ionic current.

These anomalies have then been investigated in more detail using capacitance measurements.

Experimental Procedure

Tantalum foil of 99.9% purity supplied by Fansteel was degreased, chemically polished, leached in boiling deionized water for 10 min, "vacuum" annealed at pressures less than 10^{-4} Torr at 2100°C for 30 min, etched in hydrofluoric acid, briefly rinsed in deionized water, and immediately inserted in 0.1% (by weight) aqueous sulfuric acid at room temperature. The sample had a narrow neck extending out of the H_2SO_4 solution to provide an electric contact. The macroscopic contact area with the electrolyte was 18.8 cm^2. The tantalum was connected through a load resistor, R_L, to a platinum electrode immersed into the electrolyte, and the current through the load resistor was measured as a function of time. Resistors of 10^3 ohms were used to investigate the current decay over many orders of magnitudes within a reasonable time, *i.e.*, about one day. Resistors of 10^5 ohms were used when emphasis was placed on the capacitance measurements during the initial phase of oxide growth. The external resistors were large with respect to the electrolyte resistance so that the potential drop across the electrolyte could be neglected.

The voltage between the platinum electrode and the electrolyte (during a run) was monitored by using a saturated calomel electrode in the electrolyte. Except during the initial few seconds, no significant variation in polarization was observed. The voltage was about 0.6v with the platinum (Pt) positive with respect to calomel.

The initial voltage across the resistor was about 1v (tantalum negative) for freshly etched foils.

The equivalent series capacitance of the cell was measured at 1000 cps with a General Radio impedance comparator and a recorder. This permitted the continuous recording of the capacitance with time. The equivalent series resistance observed was approximately 50 ohms which agreed reasonably well with the specific resistivity of the electrolyte and the geometry of the electrolyte cell. From this capacitance an "oxide thickness," d^*, was derived by

$$d^* = S\epsilon\epsilon_0/C \qquad [1]$$

where S is the area, and ϵ is the dielectric constant of tantalum oxide. This procedure ignores capacitances of space charge layers in the electrolyte adjacent to the platinum and adjacent to the tantalum oxide. By investigating the equivalent series capacitances of gold *vs.* gold and gold *vs.* platinum in the electrolyte, we have found that the capacitance for the platinum electrode could indeed be ignored. The solution double layer capacitance adjacent to the tantalum oxide should remain fairly constant during the oxide growth, so that the true oxide thickness would be smaller than the oxide thickness, d^*, by a constant amount, Λ. The equivalent series capacitance of the arrangement Au-electrolyte-Au was found to be $C_S = 2.4\ \mu F/cm^2$.[2] If the solution double layer capacitance adjacent to the tantalum oxide were the same as that adjacent to gold, we would have $\Lambda = S\cdot\epsilon\cdot\epsilon_0/2C_S = 5.1$Å.

Since the capacitance depends somewhat on frequency, the significance of an "oxide thickness" as derived by Eq. [1] for capacitance measurements at the frequency of 1000 cps may be questioned. It has been observed on niobium oxide (3) that the frequency dependence between 60 cps and 8 kcps is the same for various oxide films of thicknesses ranging from a few tens of angstroms to several 1000 angstroms. If this is the case in our films, the correction factor for converting the apparent thickness (*i.e.*, that of Eq. [1], as calculated from C at 1000 cps) to the true thickness should be the same for all values of d, and the frequency dependence of the capacitance may be taken into account by a corresponding frequency dependence of the dielectric constant. When using the capacitance value at 1000 cps in Eq. [1], we must then use the dielectric constant at 1000 cps which was determined by Young (4) to be $\epsilon = 27.6$ based on the density $\rho = 7.93$.

[2] The equivalent series resistance per double layer Au/electrolyte was 20 ohms/1 cm^2 area.

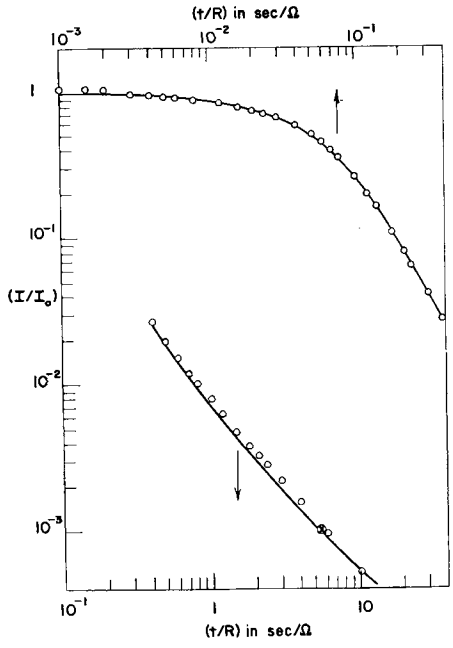

Fig. 1. Current decay during self-anodization of tantalum of area $S = 18.8\ cm^2$ in 0.1% aqueous H_2SO_4. Tantalum connected to a platinum electrode through a resistor $R = 1000$ ohms. Experimental points; Theoretical curve by Eq. [2] matched to the experimental points by using the following parameters: $I_o = 1.1$ ma, $E = 1.83$v, $BF_o = 35.6$, $\lambda F_o = 13.75$ v/coul.

Analysis of Current Density during Oxide Growth

Figure 1 shows the dependence of the current, I, in the external circuit on time. The ordinate is the ratio of the observed current to an extrapolated initial current, I_o, which was obtained by a procedure to be described later. The theoretical curve drawn represents the equation

$$\lambda F_o t/R = \left(1-\frac{1}{BF_o}\right)\ln\frac{I_o}{I} + \frac{E}{RI_o}\,\frac{BF_o}{[BF_o-\ln(I_o/I)]^2}\left(\frac{I_o}{I}-1\right) \qquad [2]$$

which follows from the accepted field dependence of the ionic current density

$$I_I = A\,e^{BF} \qquad [3]$$

with

$$F = (E-RI)/d \qquad [4]$$

and from Faraday's law

$$\frac{\partial d}{\partial t} = \lambda\cdot I_I \qquad [5]$$

with the ionic current I_I equal to the current, I, in the external resistor

$$I_I = I \qquad [6]$$

Equation [2] was derived as follows: Substitute d of Eq. [4] into [5], and replace $\frac{\partial F}{\partial t}$ by $\frac{1}{BI}\frac{\partial I}{\partial t}$ using [3] and [6] to obtain

$$\lambda I = \left[-\frac{R}{F}\left(1-\frac{1}{BF}\right) - \frac{E}{BF^2 I} \right] \frac{\partial I}{\partial t} \qquad [7]$$

Since F changes quite slowly (logarithmically) with I according to [3], we may treat F in Eq. [7] as a constant when integrating to obtain

$$\lambda t/R = \frac{1}{\bar{F}}\left(1-\frac{1}{B\bar{F}}\right)\ln\frac{I_o}{I} + \frac{E}{RI_o}\frac{1}{B\bar{F}^2}\left(\frac{I_o}{I}-1\right) \qquad [8]$$

where $\bar{F}$ is a suitable average value of F over the integration interval $0 \leq \tau \leq t$. Equation [2] was obtained by using the terminal value

$$F_{\tau=t} = F_o\left(1+\frac{1}{BF_o}\right)\ln\frac{I_{\tau=t}}{I_o} \qquad [9]$$

for $\bar{F}$ in the second term on the right of Eq. [8], since the largest contribution in the integration of Eq. [7] comes from the values near the boundary $\tau \approx t$. In the first term on the right of Eq. [8] $\bar{F}$ can be replaced simply by F_o since this term is important only in the range where $I_\tau \sim I_o$. The error committed by using [9] for $\bar{F}$ is estimated in Appendix I.

For $(I_o/I) - 1 << 1$ one may approximate $\ln (I_o/I) \approx (I_o/I) - 1$, showing that initially the ratio of the second term on the right of Eq. [2] to the first term is $\dfrac{E}{RI_o(BF_o - 1)}$. Since E/RI_o is of the order of unity, but BF_o is about 30, the first term dominates initially. It is interesting to note that the first term arises essentially without the aid of Eq. [3]. If we consider the field F in Eq. [4] as a constant, then it follows from Eq. [5] and [4] that $\lambda Ft/R = \ln I_o/I$ which is very approximately the first term of Eq. [2] since $BF_o >> 1$. Thus good agreement between Eq. [2] and the experimental data in the range $(I_o/I) - 1 << 1$ does not necessarily indicate that Eq. [3] is satisfied.

The second term on the right side of Eq. [2] results from the approximate variation of the field with thickness $F \approx E/d$, which is approached once $RI << E$, in conjunction with the exponential field dependence of the ionic current, Eq. [3], and Faraday's law, Eq. [5]. The second term on the right side of Eq. [2] is also pertinent to the decay of current with time when a constant voltage, V_A, is applied. The emf, E, is then to be replaced by $E + V_A$, and one obtains

$$I = \frac{B(E+V_A)}{[BF_o - \ln(I_o/I)]^2 \lambda t} \qquad [10]$$

Similar forms of the $1/t$-law of current decay during constant voltage formation have been previously derived (5, 6). However, Eq. [10] should be valid only if electron leakage currents through the sample are absent, if Faraday's law (5) and the field dependence (3) of the ionic current are fulfilled, and if there is no field distortion by space charges in the oxide.

Figure 2 shows a plot of $I(t)$ on a semilogarithmic scale. The straight line fits the experimental data well in the range $0.6 \lesssim RI \lesssim 1.05$v, *i.e.*, 400 sec $< t <$ 4500 sec. Such a straight line relationship is expected from Eq. [2]. Deviations of the experimental points from

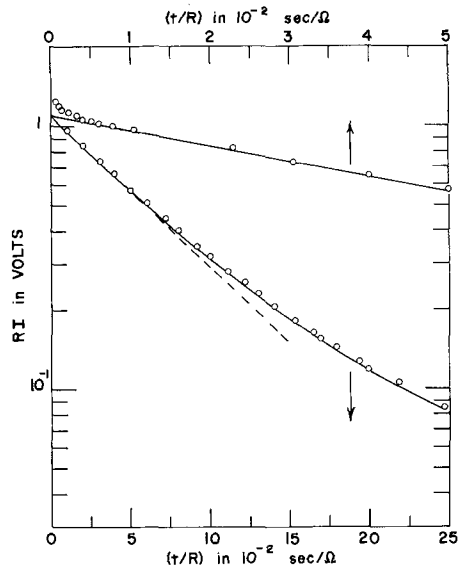

Fig. 2. Current decay during self-anodization of tantalum of area 18.8 cm² in aqueous 0.1% H_2SO_4 with $R = 10^5$ ohm connecting the tantalum to a Pt electrode. The straight line approximation provides $I_o = 1.1 \times 10^{-5}$ amps and $(\lambda F_o)^o = 13.2$ v/coul. Experimental points; —— theoretical curve Eq. [2] with $I_o = 1.1 \times 10^{-5}$ amp, $E = 1.83$v, $BF_o = 30.75$, $\lambda F_o = 13.48$ v/coul.

the straight line for $t \gtrsim 4500$ sec are expected due to the second term on the right side of Eq. [2]. The deviations of the experimental data from the straight line for $t \lesssim 30$ sec indicate that one or several of the Eq. [4]-[6] are not satisfied in this range. This will be discussed in more detail in conjunction with the capacitance measurements. Extrapolation of the straight line to $t = 0$ yields I_o, while its slope, according to Eq. [2] is

$$\left(\frac{\partial \ln (I_o/I)}{\partial\, t/R}\right)_{t\to 0} = \frac{\lambda F_o}{1+\dfrac{(E/RI_o)-1}{BF_o}} \equiv (\lambda F_o)^o \qquad [11]$$

As seen from Fig. 1, Eq. [2] fits well the entire range of experimental data $I(t)$ except for the initial range, as already mentioned. The constants BF_o and λF_o required to calculate the theoretical curve in Fig. 1 have been determined by matching the theoretical curve to the experimental data using the procedure described in Appendix 2.

Numerical values for BF_o and λF_o for four samples are listed in Table I, based on the value $E = 1.83$v. The value $E = 1.83$v was selected by comparing data of BF_o and λF_o derived from $I(t)$ with those derived from the capacitance measurements to be discussed in the next section. The values of λF_o differ very little among the four samples. The variation in BF_o is somewhat larger, which suggests that either B differs among various samples or that E might vary. The latter is not impossible considering that E in Eq. [4] is not only the emf but may include some contact potential.

Table I. Evaluation of the current vs. time relationship for self-anodization of tantalum oxide, assuming $E = 1.83$v

Sample	R, ohms	RI_o, v	BF_o	λF_o, v/coul	B/λ, farads	B^*, 10^{-6} cm/v	A^{**}, amp
1/21/63	10^6	1.1	35.6	13.75	2.59	8.03	3.8×10^{-19}
II	10^5	1.1	30.75	13.48†	2.28	7.07	4.9×10^{-19}
I	10^5	0.87	23.9	14.23	1.68	5.21	3.6×10^{-16}
1/16/63‡	10^4	0.45	27.1	14.02	1.93	5.98	7.6×10^{-17}

* Using $\lambda = 3.1 \times 10^{-6}$ cm/coul.
** $A = I_o e^{-BF_o}$.
‡ Sample remained unetched following the vacuum anneal.
† $\lambda F_o = 13.2$ using Eq. [11] and taking the denominator to equal 1.

Table II. Dependence of BF_o and λF_o on the choice of E for sample II

E, v	BF_o	λF_o, v/coul
1.7	20.08	13.45
1.83	30.75	13.48
1.9	31.61	13.50

To indicate the influence of the choice of E on the values of BF_o and λF_o of Table I, we have listed in Table II values of BF_o and λF_o for sample II, which would result from three different values of E.

Inserting the values of I_o and of BF_o into Eq. [3], the pre-exponential factor A has been calculated. These values scatter considerably. However, an error in BF_o by 10% would account for the large deviations of A from the mean value of about 10^{-17} amp.

Time Dependence of Capacitance

The time dependence of capacitance during oxide film growth was measured for the samples I and II listed in Table I. Self-anodization of these samples was carried out with the comparatively large resistance $R = 10^5$ ohm in order to slow down the initial oxidation rate so that fairly accurate capacitance measurements could be made.

As discussed in the previous section, the time dependence of the current is not strongly affected by relation [3] during the initial stages of oxide growth. However, the dependence of current on oxide thickness, obtained from Eq. [3], [4], and [6] is strongly dependent on the field dependence of the ionic current. Using the "apparent film thickness," d^*, derived from capacitance measurements by means of Eq. [1], and the external current, we have derived the field intensity as a function of current by means of Eq. [4] with $d = d^*$. These values are quite sensitive to the choice of the emf, E. In Fig. 3 these curves are plotted pertaining to the values $E = 1.9$, 1.83, and 1.7v, on a greatly expanded ordinate scale. The sample is the same as used for Fig. 2.

In spite of the scatter of the experimental points, three ranges of $F(I)$ are clearly apparent. The boundaries between these ranges correspond to the "apparent thicknesses" of 30 and 42Å, respectively. The middle range (b) becomes less pronounced for increasing E.

Range (a): For $d \gtrsim 42$Å, the field decreases linearly with the logarithm of current as expected from Eq. [3] with [6]. The straight lines fitting the experimental data of Fig. 3 in this range have slopes from which the values of B[3] (the first line of Table III) have been obtained. Extrapolation to $I = I_o$ of Table I provides F_o, and extrapolation to $F = 0$ provides the pre-exponential factor, A, of Eq. [3]. These values are listed in the second and last lines of Table III.

Comparison of BF_o values of Table III with the values derived from the analysis of $I(t)$ (Table II) shows that fairly good agreement exists for $E = 1.83$v. This value will be adopted, therefore, in the subsequent discussion of sample II. The value $E = 1.83$ has been used also for evaluating the $I(t)$ data of the other samples listed in Table I.

[3] B is defined as $\partial \ln I/\partial F$.

Table III. Evaluation of the straight lines in the region (a) marked in Fig. 3

	E = 1.7v	E = 1.83v	E = 1.9v
B (10^{-6} cm/v)	9.2	7.7	6.8
F_o (10^6 v/cm)*	3.61	3.94	4.13
BF_o	33.2	30.34	27.85
λF_o (v/coul)**	11.2	12.2	12.8
A (amp)	4.2×10^{-20}	5.1×10^{-19}	1.1×10^{-18}

* F_o is F extrapolated to $I_o = 1.1 \times 10^{-5}$Å.
** Using $\lambda = 3.1 \times 10^{-6}$ cm/coul.

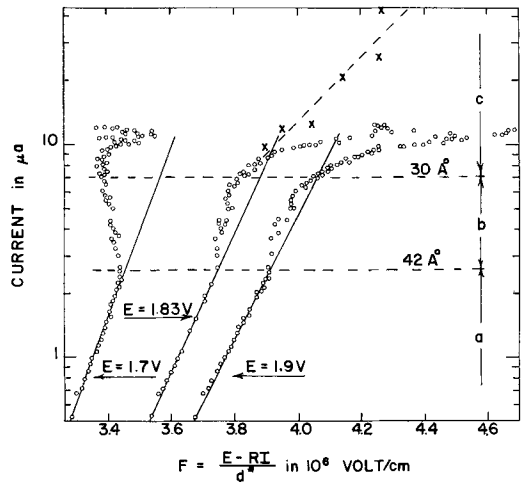

Fig. 3. Field intensity as a function of current, derived by Eq. [4] from current and capacitance measurements during self-anodization assuming three values of E. Values of Table III were derived from the straight line approximations in range (a).

Range (b): In the range corresponding to thickness between 30 and 42Å, the field derived by Eq. [4] changes much more slowly with current (*i.e.*, with time and thickness) than in the range (a).

Range (c): In the range $d \lesssim 30$Å, the field rises quite steeply with the external current.

It is obvious that for $d \lesssim 42$Å, at least one of the Eq. [3] to [6] ceases to be valid or, respectively, the parameters A, B, E, or λ in these equations are not constants but depend on t or d. For instance, the "emf" in this range might be a function of thickness or current density. Or else, the parameters A and B in Eq. [4] might not be constant; *e.g.*, B in the region (b) might be about twice the value in region (a). The region (c) could be explained by an ionic current which is much larger than the external electronic current due to internal flow of electrons so that Eq. [6] becomes invalid. Evidence for this interpretation of the region (c) will be discussed shortly. Lack of validity of Eq. [3] for $d \lesssim 42$Å should not significantly affect Eq. [2] since in the corresponding current range ($I \gtrsim 2 \cdot 10^{-6}$ amp), the condition $I > I_o/BF_o \approx 4 \times 10^{-7}$ amp prevails.

Using the external current, I, and the thickness, d^*, derived from capacitance by means of Eq. [1], we have calculated the "apparent growth efficiency"; *i.e.*, the growth efficiency based on the external current

$$\lambda^* = \frac{1}{I} \cdot \frac{\partial d^*}{\partial t} \qquad [12]$$

These values are plotted in Fig. 4 *vs.* oxide thickness. For thicknesses between 32.5 and 50Å, the average apparent growth efficiency was $\lambda^* = 3.2 \times 10^{-6}$ cm/coul. For smaller thicknesses, the apparent growth efficiency increases with decreasing current. Qualitatively, this accounts for the discrepancies between Eq. [2] and the experimental data in the range $t/R \lesssim 5 \times 10^{-3}$ sec/ohm of Fig. 2. For a given I and t, I_o of Eq. [2] would increase with an increase in λ.

The value $\lambda^*_\infty = 3.2 \times 10^{-6}$ cm/coul, approached by the apparent growth efficiency, λ^*, for $d^* \gtrsim 32.5$Å, is in reasonable agreement with the theoretical value $\lambda = \dfrac{M}{F \cdot \rho \cdot S \cdot 2z} = 3.1 \times 10^{-6}$ cm/coul, where the molecular weight of Ta_2O_5 $M = 442$, the Faraday constant $F = 96{,}500$ coul/g·equivalent, the density $\rho = 7.93$ g/cm^3, and the area $S = 18.8$ cm^2 have been used.

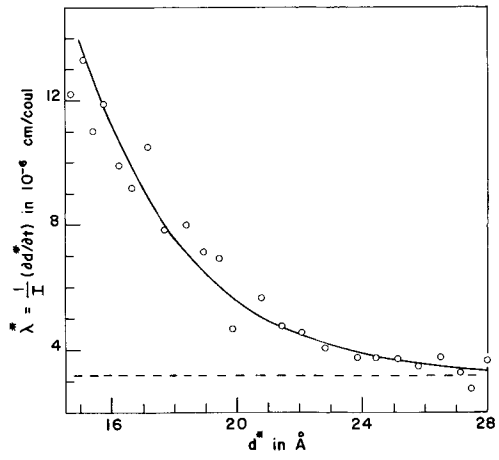

Fig. 4. Apparent current efficiency, λ^*; *i.e.*, current efficiency based on the external current, for oxide growth during self-anodization. Experimental points and theoretical curve from Eq. [13] with [14], assuming $I_E^o = 6.0 \times 10^{-3}$ amp, $l = 3.0$Å and $\lambda_\infty = 3.2 \times 10^{-6}$ cm/coul.

The fact that the apparent growth efficiency for $d^* \lesssim 32$Å exceeds significantly the value $\lambda = 3.1 \times 10^{-6}$ cm/coul can be explained by assuming that electrons flow through the oxide film together with the five-valent tantalum ions. This transfer may take place as an ionic current of tantalum ions of valency less than five (*i.e.*, one or several electrons attached to a five-valent ion), or else by electrons flowing through the oxide film unattached to tantalum ions.

Flow of a significant internal electron current, rather than transport by lower-valency tantalum ion, is indicated by the fact that the oxide also grows under open circuit conditions.[4] Considering the range of film thickness with which we are dealing, electron transfer is likely to occur by tunneling. Thus we shall refer to the electron current through the oxide tentatively as the tunnel current, I_E. The tunnel current has been obtained from

$$I_E = I \cdot \left(\frac{\lambda^*}{\lambda^*_\infty} - 1 \right) \qquad [13]$$

The full line drawn in Fig. 4 was calculated from [13] assuming an exponential dependence of tunnel current on thickness

$$I_E = I_E^o \, e^{-d/l} \qquad [14]$$

with $I_E^o = 6.0 \times 10^{-3}$ amp, $l = 3.0$Å and $\lambda = 3.2 \times 10^{-6}$ cm/coul. The data of Fig. 4 have been used to calculate the total ionic current, $I + I_E$ by means of Eq. [13]. If this total current would have been used as abscissa in Fig. 3 instead of the external current I, the points in the region (c) of the curve would have shifted to the left as indicated by the crosses for the case $E = 1.83$v. Thus correcting for the tunnel current removes much of the steep rise of the curves shown in Fig. 3 in the region (c).

However, the B-value derived by Eq. [3] for the range (c) in Fig. 3, after correction for the tunnel current, still remains significantly lower ($B \approx 3.3 \times 10^{-6}$ cm/v) than that in the region (*a*) ($B \approx 7.7 \times 10^{-6}$ cm/v).

Instead of the interpretation in terms of a constant E and a variable B, one might postulate a constant B [equal to that in region (*a*)] and a variable E, in the regions (*b*) and (c) which would be determined by the intersect of curves $E =$ const. with the extrapolated curve from the region (*a*). Assuming that $E = 1.83$v in the region (*a*), the E values would be higher in region (*b*) but lower in region (c). The changes in E required would be less than 0.1v.

[4] This will be the subject of the next paper in this series.

Discussion

The following discussion concerns mainly the validity of some of the basic equations used and the interpretation of certain parameters occurring in them.

Equation [4] expresses the electric field in the oxide in terms of the emf of the chemical reaction, E, the external voltage drop, RI, and the oxide thickness, d. Equation [4] implies that the electrical field is space independent throughout the oxide, *i.e.*, space charges are neglected. Actually, E is not only the emf of the reaction

$$2Ta + 5H_2O = Ta_2O_5 + 5H_2 \qquad [15]$$

but may include also electrostatic potentials which might exist between the metal and the electrolyte interface in analogy to the contact potential between two solids. This contact potential should be a function of surface states at the oxide-electrolyte interface as might arise from adsorbed ions. Thus E in Eq. [4] is not necessarily the true emf of chemical reaction [15], and its magnitude might change with current density and time during growth, contrary to the assumption of a constant E used in deriving Eq. [2] and the data of Fig. 3. Furthermore E might differ for different samples. The agreement between the value $E \sim 1.83$v derived from the experimental data with the theoretical emf 1.79v [Ta *vs.* Pt equal to Ta *vs.* $H_2 = 0.81$ (2) plus H_2 *vs.* Pt $= 0.98$] is therefore surprising.

Equation [3] contains also the tacit assumption that there is no overpotential during film growth across the space charge layer in the electrolyte adjacent to the oxide. In general, a fraction of the external potential RI might be required to modify the potential across this space charge layer when current flows, and only the remaining portion of RI would modify the field across the oxide.

We have already discussed the difficulties arising from the possible capacitance of the electrolyte space charge layer adjacent to the oxide for the determination of the true oxide thickness. Because of this difficulty the apparent oxide thickness d^* determined by Eq. [1] from capacitance measurements contains an unknown additive constant, Λ, the true oxide thickness being $d = d^* - \Lambda$. This constant, Λ, has been ignored in Fig. 3. The constant Λ has no effect on the effective growth efficiency λ^* of Fig. 4, and on the tunnel curcent, Eq. [14], derived from λ^*.

The determination of E by matching BF_o as obtained from $I(t)$ to BF_0 derived from capacitance measurements as shown in Fig. 3 is questionable for the following reasons: (*a*) if the apparent oxide thickness d^* is corrected by Λ to obtain the true oxide thickness, one has

$$\frac{1}{B_\Lambda F_\Lambda} = \frac{1}{BF} \cdot \frac{F_\Lambda}{F} + \frac{RI_\Lambda}{F\,d^{*2}} \cdot \frac{F_\Lambda}{F} \qquad [16]$$

where B_Λ, F_Λ are the values obtained from the corrected thickness, and B, F are those obtained from the uncorrected thickness ($\Lambda = 0$). The corrected product, $B_\Lambda F_\Lambda$, is smaller than the uncorrected one, since $F\Lambda/F > 1$. Thus the corrected values $B_\Lambda F_\Lambda$ would be less than those of Table III and by matching these corrected values to those of Table II a smaller value of the emf, E, would have been derived. Correcting d^* of Eq. [1] by Λ increases the field F by an amount which is larger for smaller d^*, so that the region (*b*) of Fig. 3 might be removed, and the region (*a*) would be enhanced.

For $E = 1.83$ and $\Lambda = 6$Å, region (*b*) in Fig. 3 would just about vanish. However, in order to match F_o and B from Fig. 3 (modified by $\Lambda = 6$Å) to the values obtained from $I(t)$, the value for the emf would have to be decreased to about 1.60v. Since region (*b*) becomes more pronounced by decreasing the value of E, the increase in Λ and the decrease in E would partially compensate and the region (*b*) would reappear. The sensitivity of various parameters to the choice of Λ is illustrated in Table IV. The values of BF_0 and λF_o

Table IV. Effect of the correction Λ for the oxide-electrolyte capacitance

Λ, Å	E, v	from $I(t)$				from $C(I)$			
		BF_o	λF_o, v/coul	B, 10^{-6} cm/v	F_o, 10^6 v/cm	BF_o	λF_o, v/coul	B, 10^{-6} cm/v	F_o, 10^6 v/cm
0	1.83	30.75	13.48	7.07	4.35	30.34	12.2	7.7	3.94
4	1.83	30.75	13.48	7.07	4.35	23.2	13.7	5.25	4.42
0	1.69	28.8	13.1	6.8	4.23	33.2	11.2	9.2	3.61
4	1.69	28.8	13.1	6.8	4.23	27.2	12.5	6.75	4.03

as determined from the analysis of $I(t)$ and $C(I)$ agree reasonably well for $\Lambda = 0$, $E = 1.83$ and also for $\Lambda = 4$, $E = 1.69$. However there is a large disagreement in BF_o obtained by the two methods for $\Lambda = 4$, $E = 1.83$ and for $\Lambda = 0$, $E = 1.69$.

The value λF_o of Table II is pertinent to the initial range of the $I(t)$ curve, while the value F_o of Table III is derived by extrapolation of F from the later ranges of current flow to the initial range using relation [3]. If this relation is not valid, as suggested by Fig. 3, the values of λF_o from Tables II and III cannot be expected to coincide.

The value of F_o derived from Table II with $\lambda = 3.1 \times 10^{-6}$ cm/coul should coincide with the F-value of Fig. 3 pertinent to the "initial current range," *i.e.*, the current range where the straight line approximation to the semilogarithmic plot of Fig. 2 is valid.

In view of all these difficulties, the B-values derived from Fig. 3 can be accepted only with great caution.

The B-values for region (a) as given in Table I are in reasonable agreement with those of the literature ($B \sim 5 \times 10^{-6}$ cm v^{-1}) (Young, p. 93).

Conclusions

1. The time dependence of the external current during self-anodization of tantalum in an electrolyte can be used to evaluate the combinations BF_o and λF_o of the "Tafel" slope, $1/B$, the growth efficiency, λ, and the initial field strength, F_o, provided that the emf, E, is known.

2. Combining the current *vs.* time measurements with those of capacitance *vs.* time, the emf, E, and the initial field can be derived. However, this evaluation involves some questionable assumptions.

3. For films of thickness $d > 40$Å the values of B and λ agree with those observed for the transport of five-valent tantalum ions.

4. At smaller film thicknesses, the following anomalies occur: (a) An electron current flows through the oxide film of magnitude $I_E^o \exp^{-d/l}$ with $I_E^o \sim 3 \times 10^{-4}$ amp/cm^2 and $l \approx 3.0$Å. (b) This simulates an effective growth efficiency, *i.e.*, a growth efficiency based on the external current which exceeds the value of Faraday's law for five-valent ions. (c) There is some indication that either the inverse Tafel slope of the ionic current varies in this range or else the emf, E, varies with film thickness.

Manuscript received July 16, 1964. This paper was presented at the Toronto Meeting, May 3-7, 1964.

Any discussion of this paper will appear in a Discussion Section to be published in the December 1965 JOURNAL.

REFERENCES

1. For a summary, see L. Young, "Anodic Oxide Films," Academic Press, London and New York (1961).
2. D. A. Vermilyea, *This Journal*, **101**, 389 (1954).
3. L. Young, *Faraday Soc.*, **51**, 1250 (1955).
4. L. Young, *Proc. Roy. Soc.*, **A244**, 41 (1958).
5. W. Ch. van Geel and H. Emmens, *Z. Phys.*, **87**, 220 (1933).
6. A. Charlesby, *Proc. Phys. Soc.*, **66**, 317 (1953).

APPENDIX 1

Estimate of Error in Eq. [2]

The error committed by using [9] for $\bar{F}$ can be estimated as follows. Since

$$F_{\tau=t} < \bar{F} < F_o \qquad [1.1]$$

we expect the relative error of the true t pertaining to the current I to be smaller than $(t_\tau - t_o)/t_o$ where t_τ is calculated from Eq. [8] using $\bar{F} = F_{\tau=t}$ and t_o is calculated from [8] using $F = F_o$. The error increases with decreasing I, and we shall be concerned, therefore, mainly with the range where the $\ln(I_o/I)$ term in Eq. [2] can be neglected *vs.* the I_o/I-term. Then

$$(t_\tau - t_o)/t_o \approx \frac{2}{BT_{\tau=t}} \cdot [\ln(I_o/I)] \cdot \left[1 + \frac{\ln(I_o/I)}{2BF_{\tau=t}}\right] \qquad [1.2]$$

Since the main contributions at the integration of Eq. [7] come from the I-values near the boundary $I_{\tau=t}$, we expect $F_{\tau=t}$ to be a better approximation to $\bar{F}$ than F_o. Thus the error by inserting [9] for $\bar{F}$ should be somewhat less than

$$(t - t_o)/2t_o \approx \ln(I_o/I)/BF_{\tau=t}) \qquad [1.3]$$

For $I_o/I \approx 10^3$ and $BF_{\tau=t} \approx 25$, the error in t by Eq. [2] should thus be somewhat less than 28%. The error can be bracketed closer by the relation

$$F_{\tau=t} < F < F_{\tau=t} + \frac{I - I_{\tau=t}}{BI_{\tau=t}} \qquad [1.4]$$

instead of [1.1] where the right side comes from the development of F as a function of I in the vicinity of $I_{\tau=t}$, $F_{\tau=t}$. For $E/RI_o = 1$, $BF_o = 30$ and $I_o/I = 10^3$, the following values are obtained: $\lambda t_o/BR = 1.33$ from Eq. [8] with $\bar{F} = F_o$; $\lambda t/BR = 2.09$ from Eq. [2]; and $\lambda t/BR = 1.69$ by integrating Eq. [7] with $\bar{F}$ replaced by the value on the right side of the inequality [1.4] prior to the integration. The exact value lies between 1.69 and 2.09.

APPENDIX 2

Determination of BF_o and λF_o by Matching Eq. [2] to Experimental Data $I(t)$

From a semilogarithmic plot as shown in Fig. 2, I_o and $(\lambda F_o)^o$ are obtained. Rearranging Eq. [2]

$$BF_o = 2\ln(I_o/I) - \frac{[\ln(I_o/I)]^2}{BF_o} + \frac{\frac{E}{RI_o}\left(\frac{I_o}{I} - 1\right)}{\frac{(\lambda F_o)^o}{R} t\left[1 + \left(\frac{E}{RI_o} - 1\right)/BF_o\right] - \left(1 - \frac{1}{BF_o}\right)\ln(I_o/I)} \qquad [2.1]$$

with $(\lambda F_o)^o$ defined by Eq. [11]. This form is convenient for calculating BF_o from a single experimental point of $I(t)$ in the range where the second term on the right side of Eq. [2] is dominant and assuming a suitable value of E. Equation [2.1] then becomes a good approximation

$$(BF_o)^{(o)} = 2\ln(I_o/I) + \frac{\frac{E}{RI_o}\left(\frac{I_o}{I} - 1\right)}{\frac{(\lambda F_o)^o}{R} t - \ln(I_o/I)} \qquad [2.2]$$

since the terms containing BF_o on the right side of Eq. [2.1] are only small corrections. By inserting $(BF_o)^{(o)}$ calculated from Eq. [2.2] on the right side of Eq. [2.1] and using an experimental point of $I(t)$,

one obtains the first order approximation $(BF_o)^{(1)}$; inserting $(BF_o)^{(1)}$ into the right side of Eq. [2.1], one obtains the second order approximation $(BF_o)^{(2)}$, etc.[5]

The series $(BF_o)^{(o)}$, $(BF_o)^{(1)}$, etc. converges so rapidly that we have found it rarely necessary to proceed beyond $(BF_o)^{(2)}$.

Using BF_o and $(\lambda F_o)^{(o)}$, one may calculate λF_o by Eq. [11].

SYMBOLS

I_I	ionic current
$I,(I_o)$	current (initial current) in the external resistor
A	preexponential factor in the ionic current-field relation
$F,(F_o),(\bar{F})$	field, (initial field), (time average of the field) across the oxide layer
B	field coefficient or "inverse Tafel slope"
λ	growth rate per unit current
λ^*	apparent growth rate as calculated from the external current
λ^*_∞	apparent growth rate for film thicknesses larger than 32Å
E	emf of reaction
I_E	internal electron current
$I_E{}^o$	preexponential factor in the electronic current-thickness relation
l	attenuation length of the internal electron current
d	true film thickness
d^*	film thickness as calculated from capacitances
Λ	(d^*-d)
C	capacitance
ϵ_o	permittivity of free space
S	area
R	external resistor
t	time
B_Λ,F_Λ	values of B and F after correcting for Λ

[5] Since BF_o is about 30, the first step in this procedure can be saved by inserting 30 for $(BF)^{(o)}$, instead of the value given by Eq. [2.2].

The Structure and Mechanical Properties of Electroless Nickel

Arthur H. Graham,[1] Robert W. Lindsay, and Harold J. Read

Department of Metallurgy, College of Mineral Industries,
The Pennsylvania State University, University Park, Pennsylvania

ABSTRACT

Effects of variations in phosphorus content of electroless nickel from 4.6 to 9.4 w/o on structure, strength, ductility, and hardness were studied. Electron diffraction proved the crystallinity of many as-plated alloys, and x-ray data established a conventional precipitation hardening mechanism during heat treatment. Changes in properties after heat treatment at 200°-750°C have been correlated with structural changes shown by x-ray diffraction and with those revealed in optical and electron back scatter micrographs. Abrupt changes in the structure, strength, and ductility of as-plated alloys and of alloys heat treated at 750°C occurred at phosphorus contents of about 7%.

Although electroless nickel plating has achieved considerable popularity in the somewhat more than a decade and a half since attention was drawn to its possibilities by the work of Brenner (1) and his colleagues, most of the literature on the subject concerns the process rather than the product. Some notice has been given to structure, but aside from hardness measurements, little has been done in the evaluation of mechanical properties.

Goldenstein, Rostoker, Schossberger, and Gutzeit (2) in their study of deposits containing 7-10 w/o (weight per cent) phosphorus concluded on the basis of x-ray diffraction and some other considerations that as-plated electroless nickel is amorphous. Other investigators reached similar conclusions. It is not impossible, however, to account for the typical diffraction patterns through a consideration of the combined effects of extremely small grain size, internal stress, and nonhomogeneous solid solution. Some hint of possible crystallinity in as-plated deposits appears in a paper by Zusmanovich (3), but he made no actual claim in this direction. The relationship between structure and phosphorus content of the deposits has not been studied, although the work of Brenner, Couch, and Williams (4) on electrodeposited nickel-phosphorus alloys contains evidence that phosphorus concentration is an important variable in determining structure.

More attention has been given to optical microstructure than to fine structure, but only a portion of the work has taken into account the phosphorus variable. The changes that take place on heat treatment have been extensively studied and most investigators have claimed that the final microstructure is a dispersion of Ni_3P in a nickel matrix (1, 2, 5, 6). Ziehlke, Dritt, and Mahoney (7) maintain, however, that heat treated, high-phosphorus alloys are dispersions of nickel in a matrix of Ni_3P. Because the mechanical properties would be markedly affected by the nature of the matrix, the effect of phosphorus on this variable needs further study.

The increase in hardness of electroless nickel as a result of heat treatment is a notable effect and has received much attention (2, 3, 5, 7). In general, agreement is good among investigators as to the effects of time and temperature on hardness, and the data resemble those for known precipitation-hardenable alloys. It has been generally assumed, therefore, that precipitation hardening is the mechanism that prevails in spite of the fact that the accepted theory of precipitation hardening, which requires a crystalline lattice, is not compatible with the amorphous structure that is also generally accepted. Only Goldenstein (2) and Ziehlke (7) and their colleagues recognized this point and postulated vague expedients to resolve it.

Almost nothing has been done on the determination of the strength of electroless nickel and most of the work on ductility has involved rather qualitative bend tests on composite samples of deposit and basis metal. Phosphorus content has not been regarded as an important variable, but Lee (5) as well as Ziehlke, Dritt, and Mahoney (7) published some observations that intimate that phosphorus content should not be ignored in work on mechanical properties.

The investigation described here had as its objectives (*a*) the study of the effects of phosphorus content on structure and mechanical properties, (*b*) correlation of changes in mechanical properties after heat treatment with structural changes, and (*c*) elucidation of the mechanism of hardening. Strength and ductility, as measured by the hydraulic bulge test, and microhardness were used to evaluate mechanical pro-

[1] Present address: Engineering Materials Laboratory, Experimental Station, E. I. du Pont de Nemours & Co., Inc., Wilmington, Delaware.

Table I. Details of electroless nickel processes

Designation	Bath composition, g/l			Plating conditions	
		First modification	Second modification		
Alkaline-chloride process	$NiCl_2 \cdot 6H_2O$	45	45	pH	8.2-8.4
	Sodium citrate dihydrate	82	82	Temperature	90°C
Modification of process developed by MacLean and Karten (10)	NH_4Cl	50	50	Rate of deposition	0.4-0.6 mil/hr
	$NaH_2PO_2 \cdot H_2O$ (rate of replenishment)	16 (2.1 g/l/hr)	24 (2.7 g/l/hr)	Ratio of area plated to bath volume	5 sq in./l
	NH_4OH	added to maintain pH		Agitation	stirrer
Acid-sulfate process	$NiSO_4 \cdot 6H_2O$	75		pH	4.2-5.7
	Sodium acetate	7.5		Temperature	93°C
After Girard (11)	H_3BO_3	8		Rate of deposition	0.6-1.0 mil/hr
	NH_4Cl	6		Ratio of area plated to bath volume	12 sq in./l
	$NaH_2PO_2 \cdot H_2O$	24		Agitation	stirrer

perties. Some preliminary findings on the crystallinity of electroless nickel have been reported previously (8).

Experimental Procedure

Specimen Preparation

Because of the large number of different electroless nickel plating processes that have been developed, it was not possible to select what might be considered a typical one. The selection of plating processes for this study was based principally on their ability to produce deposits that were free from internal stress and that did not contain macrovariations in phosphorus content across a thickness of 1 mil.[2] The microvariations in composition reported by Gutzeit (9) which occure over increments of approximately 0.02 mil in thickness could be tolerated. But, macrovariations in the average phosphorus content across the deposit would severely curtail, if not render impossible, the investigation of the effect of phosphorus on structure and mechanical properties. Internal stresses would also be detrimental to the objectives of this study because they would affect properties and influence the position and breadth of lines in diffraction patterns. The two processes selected for the preparation of specimens are specified in Table I.

Most of the specimens were prepared by alkaline-chloride processes that differ only slightly from the process developed by MacLean and Karten (10). Careful control of the periodic additions to the plating baths resulted in the formation of electroless nickel deposits that were free from internal stress, that is, they were not warped or distorted. Control of the periodic additions of sodium hypophosphite was based on the assumption that the amount required to maintain a constant rate of deposition would be sufficient to replace the amount consumed. The periodic additions of nickel chloride were determined by a calculation of the amount of nickel being deposited based on prior knowledge of the rate of deposition and the surface area of the basis metal.

As a result of the unavoidable changes in bath composition during 500 hr of plating from a particular alkaline-chloride bath, the average phosphorus content of the specimens deposited gradually increased from 4.6 to 9.4 w/o. Fortunately, the bath composition changed so slowly that the average phosphorus content, as indicated by electron-probe microanalysis, was constant across the thickness of deposits from a particular plating run.

The deposits from the acid-sulfate bath developed by Girard (11) were slightly stressed and had a phosphorus gradient that ranged from 5 w/o at the surface adjacent to the basis metal to 10 w/o at the outer surface. The increase in the phosphorus content during plating appeared to be related to the rapid decrease in the pH of the bath. A similar relationship between phosphorus content and the pH of acid electroless nickel baths has been observed by Gutzeit (9).

[2] All specimens were plated to approximately the same average thickness to avoid possible effects of variations in thickness on mechanical properties.

The electronprobe microanalysis traverses in Fig. 1 contrast the uniform distribution of phosphorus across a deposit from an alkaline-chloride bath with the steep phosphorus gradient across a deposit from the acid-sulfate bath. A limited number of specimens was prepared from the acid-sulfate bath to determine whether a significant difference in plating bath composition would affect the structure and the properties of the deposits.

The basis metal for bulge-test specimens was annealed copper sheet attached to a glass plate to give sufficient rigidity for handling. The surface of the copper sheet adjacent to the glass plate was coated with a stop-off lacquer. At the completion of a plating run, the stop-off lacquer was removed with acetone, and the copper substrate was stripped from the deposits in a solution of chromic acid (500 g/l) and sulfuric acid (50 g/l). Extensive experience with this stripping solution has shown that there is neither chemical attack nor mechanical disturbance of nickel or nickel-phosphorus deposits.

Strips of low-carbon steel served as the basis metal for hardness specimens.

Heat treatments were conducted at 200°, 400° 600°, and 750°C in a purified argon atmosphere. At the completion of a heat treatment, the specimens were cooled to below 100°C under the argon atmosphere before they were exposed to air.

X-ray Diffraction Studies

X-ray pinhole transmission patterns were taken of as-plated and heat-treated deposits to reveal the presence of any preferred orientation. Plated coatings with a preferred orientation usually have a fiber texture in which a certain crystallographic direction [hkl] of most of the grains is parallel, or nearly parallel, to an axis normal to the surface of the coating. To reveal the presence of any fiber texture in the electroless nickel deposits, it was necessary to tilt the specimen so that

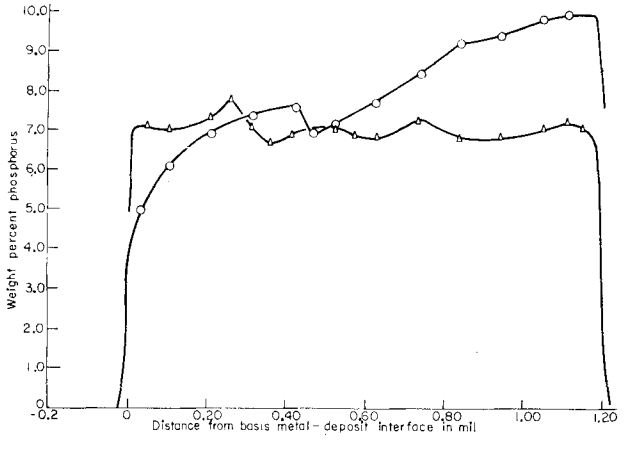

Fig. 1. Typical electron-probe microanalysis traverses of as-plated electroless nickel deposits. △—△, deposit from alkaline-chloride bath; ○—○, deposit from acid-sulfate bath.

the [hkl] fiber axis was not parallel to the x-ray beam. If the fiber axis is parallel to the beam, continuous Debye rings of uniform intensity will appear on the transmission patterns even though a strong preferred orientation exists (12). Preferred orientation will greatly diminish the intensity of many of the Debye rings on the pattern and might eliminate some of them.

An x-ray diffractometer study was conducted on the effect of phosphorus content on the position and breadth of the strong x-ray reflection from as-plated alloys. To compensate for instrumental errors in the diffractometer, the (220) reflection from a powdered-silicon standard was used as a reference for the calibration of the position of the electroless nickel reflection. The breadth of the reflection was measured at half maximum intensity.

The apparent grain size of as-plated electroless nickel alloys was estimated with the Scherrer formula which is based on diffraction broadening, as expressed in the following equation

$$t = \frac{0.9\,\lambda}{B \cos \theta_{hkl}}$$

where t is the apparent thickness of the grain in Å, λ is the wavelength of the radiation in Å, and B is the broadening of the reflection at half its maximum intensity in radians. The estimates of the grain size given by the Scherrer formula were compared with actual grain size measurements made on electron transmission micrographs.

Electron Diffraction Study

The deposits of electroless nickel for the electron diffraction investigation were thinned by electropolishing until they would transmit an electron beam accelerated by a potential of 75 kv. All the diffraction patterns were made with the electron beam perpendicular to the surface of the thin film.

Because excessive heating could cause the crystallization of an initially amorphous film, a finely focused beam and the smallest possible filament saturation current were used to minimize the heating due to electron bombardment. According to Thomas (13), such precautions can decrease the temperature rise of metallic specimens to approximately 20 centigrade degrees. As an additional precaution to insure that the structure of the specimens was not affected by electron bombardment, the beam was focused for diffraction before the specimen was moved into its path in the center of the microscope column. From the instant that the beam touched the specimens up to times as long as 1 hr, no change was observed in the diffraction patterns.

Because of the extremely small wavelength of the electrons (0.04Å), the radius of the Debye ring on a diffraction pattern is directly proportional to the magnitude of the reciprocal lattice vector for the reflection (d^*_{hkl}). A thin layer of polycrystalline nickel oxide or single crystals of nickel sulfate hexahydrate served as internal standards for the determination of the proportionality constant between the radius and d^*_{hkl}. The nickel sulfate hexahydrate crystals became attached to the electroless nickel films during the electropolishing of deposits in a sulfuric acid electrolyte with a high concentration of nickel ions. The thin layer of nickel oxide was intentionally formed on the films by electropolishing at low current densities.

Measurement of Mechanical Properties

The microhardness of the electroless nickel deposits was measured with a Tukon tester equipped with a Knoop indenter. Measurements were made on both the surface and the cross section of an adequate sample of as-plated deposits and heat-treated deposits. A 100-g indenting load was used on most of the specimens. For some specimens that had been heat treated above 400°C, the indenting load was decreased to 50g to avoid the anvil effect and to keep the indents well within the cross section of the deposit. Every hardness number reported is the average of measurements from at least 5 indents that were free from cracks and distortion.

A detailed description of the hydraulic bulge tester used to measure the strength and ductility of the electroless nickel deposits appears in an article by Read and Whalen (14). The theoretical and mathematical interpretation of the test results is presented in an article by Prater and Read (15). Strength is expressed as significant stress at fracture ($\bar{\sigma}$) and ductility is expressed as significant strain at fracture ($\bar{\delta}$). The only experimental data needed for the determination of $\bar{\sigma}$ and $\bar{\delta}$ are the oil pressure measured by appropriate gauges, and the bulge height determined by measurement of the travel of a microscope focused on the center of the bulge.

The significant strain was read directly from a master curve of $\bar{\delta}$ vs. bulge height experimentally determined by Prater.

The significant stress was calculated from the equation

$$\bar{\sigma} = \frac{PR}{2t_i}$$

where P is the pressure, R the radius of curvature of the bulge, and t_i is the instantaneous thickness of the specimen. Values for the instantaneous thickness were calculated by multiplying the original average thickness (t_o) by the ratio of t_i/t_o obtained from a curve determined by Prater.

Results and Discussion

Diffraction Patterns of As-plated Alloys

Although as-plated electroless nickel alloys have been considered to be amorphous by previous investigators, the electron transmission diffraction patterns in Fig. 2 and 3 provide definite evidence that the alloys are crystalline. There can be no doubt as to the crystallinity of the alloys with less than 7 w/o phosphorus because of the appearance of eight to eleven reflections in their diffraction patterns. Difficulties were encountered in the determination of lattice type and in indexing the patterns, but all the reflections could be attributed to nickel regardless of the lattice type assumed. Therefore, the as-plated alloys are supersaturated solid solutions of phosphorus dissolved in crystalline nickel.

Perhaps it should be made clear that as little as 2 v/o (volume per cent) of Ni_3P would produce lines in the diffraction patterns. A deposit with 7 w/o phosphorus would contain 50 v/o of Ni_3P if the phosphorus

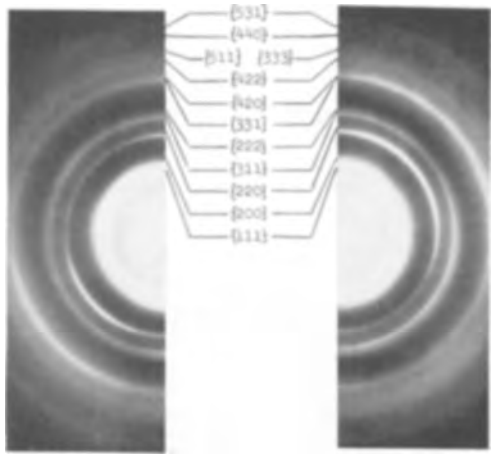

Fig. 2. Electron transmission diffraction pattern of as-plated electroless nickel from the alkaline-chloride bath, phosphorus content 5.0 w/o, indexed according to a fcc structure.

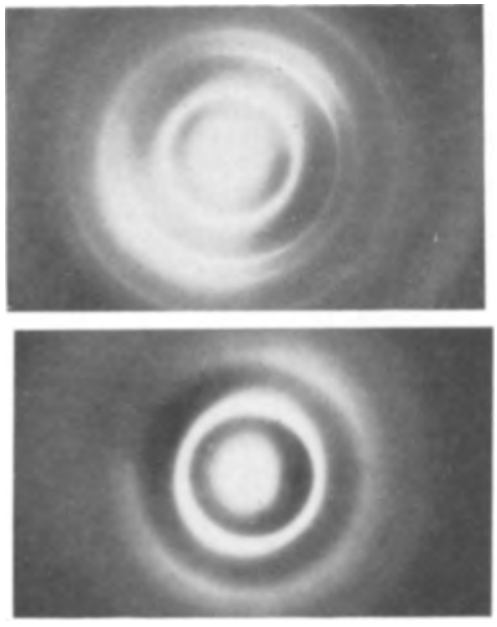

Fig. 3. Electron transmission diffraction patterns of as-plated electroless nickel alloys from the alkaline-chloride bath. (a) phosphorus content 6.6 w/o, (b) phosphorus content 8.6 w/o.

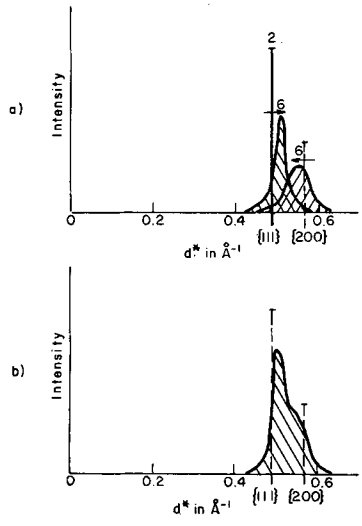

Fig. 4. Schematic sketch of the predicted effect of stacking faults on the {111} and {200} reflections from fcc nickel. (a) Effect on individual components of reflections, heavy vertical line represents unaffected components, shaded areas represent components that are broadened and shifted (after Paterson (16)). (b) Effect on over-all intensity profile.

were all combined with the nickel in the form of the compound. There is no indication that any compound other than Ni_3P is involved. Inasmuch as no compound lines were observed in the patterns, a supersaturated solid solution is indicated.

The patterns from the low-phosphorus alloys with less than 7 w/o phosphorus can be reasonably indexed according to either a hexagonal-close-packed (hcp) or a face-centered-cubic (fcc) structure (hcp nickel has often been reported). The most important factor in attempting to distinguish between the two possible structures is the {200} reflection for the fcc structure. The presence of a strong {200} reflection would be indicative of a fcc structure, whereas its absence would indicate a hcp structure. In all the electron transmission diffraction patterns, the {200} reflection was either absent or extremely weak. The difficulties in indexing can be attributed to stacking faults in the structure of fcc nickel.

The effect of stacking faults on the {111} and {200} reflections from a fcc structure as shown by Paterson (16) is illustrated schematically in Fig. 4a. The presence of stacking faults not only shifts all six components of the {200} reflection to a lower d^* value, but also diminishes their intensity by increasing their breadth. Although the (111) and $(\bar{1}\bar{1}\bar{1})$ components are not affected, the other six components of the {111} reflection are broadened and shifted to a higher d^* value. The predicted over-all intensity profile in the vicinity of the {111} and {200} reflections shown in Fig. 4 closely resembles the observed intensity profile on electron diffraction patterns of as-plated electroless nickel alloys. The d^*_{hkl} for the other reflections indexed in Fig. 2 is compatible with the assumption that the as-plated alloys consist of a single phase having the fcc structure of nickel with a high density of stacking faults. Evidence which might account for the presence of stacking faults in the as-plated alloys is presented in the section on the hardening mechanism.

As the phosphorus content of electroless nickel alloys increases from 7 to 9 w/o, all the reflections in the electron transmission diffraction patterns are severely broadened and many are destroyed. Only three or four reflections are discernible in patterns from alloys with more than 8 w/o phosphorus. However, these alloys still appear to be crystalline if their electron diffraction patterns are compared with patterns from glasses. Electron diffraction patterns of the amorphous structure of glasses have only one diffuse reflection that cannot be accurately located. On the negative of the diffraction pattern in Fig. 3b, which is typical of patterns from electroless nickel alloys with high phosphorus contents, four diffuse rings corresponding to the {111}, {220}, {311}, and {331} reflections are discernible.

Contradiction between Electron and X-ray Diffraction Results

The same specimens of as-plated electroless nickel that yield electron diffraction patterns indicative of a crystalline structure because of the appearance of eight to eleven reflections give x-ray diffractometer and x-ray pinhole transmission patterns that appear to be indicative of an amorphous structure because of the appearance of only one or two reflections. A strong {111} reflection and a weak {222} reflection were observed in diffractometer patterns from the alloys with less than 7 w/o phosphorus. As the phosphorus content increases from 7 to 9 w/o, the {111} reflection becomes less intense and the {222} reflection disappears.

Only the {111} Debye ring appears in x-ray pinhole transmission patterns produced with copper radiation. If an electroless nickel deposit is mounted so that the x-ray beam is perpendicular to its surface, the continuous {111} ring has a uniform intensity as shown in Fig. 5a. When a deposit with less than 7 w/o phosphorus is tilted so that the angle (β) between a normal to its surface and the x-ray beam is approximately 70°, a nonuniform intensity distribution indicative of a weak [111] fiber texture with an axis perpendicular to the surface of the deposit is revealed as shown in Fig. 5b. X-ray pinhole transmission patterns of the copper sheets that served as a basis metal reveal a random orientation; therefore, the preferred orientation in the electroless nickel deposits has no epitaxial relationship to the substrate. The electron transmission diffraction patterns in Fig. 2 and 3a also reveal the presence of the preferred orientation. In both the electron and the x-ray transmission patterns, the preferred orientation becomes weaker and eventually disappears as the phosphorus content increases above 7 w/o.

The detection of a [111] fiber texture in x-ray pinhole transmission patterns tends to support the electron diffraction evidence of crystallinity even though only one or two x-ray reflections are observed. A preferred orientation not only presupposes the existence of order, but also can cause the diminution of the in-

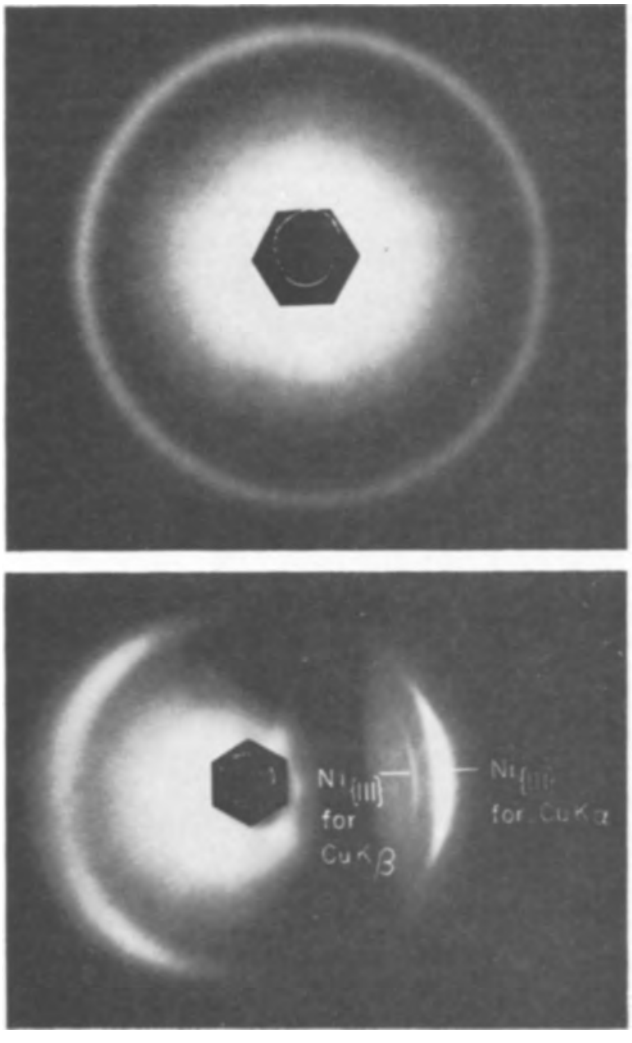

Fig. 5. X-ray pinhole transmission patterns of as-plated electroless nickel from the alkaline-chloride bath, phosphorus content 6 w/o, unfiltered copper radiation. (a) $\beta = 0°$, (b) $\beta = 70°$.

tensities of many x-ray reflections in diffractometer and pinhole transmission patterns. As a result of the basic design of conventional x-ray diffractometers, the crystallographic planes that are responsible for the appearance of a diffraction peak must be parallel to the surface of the specimen. An extremely strong [111] fiber texture perpendicular to the surface of a fcc metallic coating could cause the destruction of all x-ray reflections except those from the {111} planes and similar higher order planes because these would be the only planes parallel to the surface of the specimen. Although the weak [111] fiber texture in the low-phosphorus electroless nickel alloys would diminish the intensities of all the missing reflections in the diffractometer patterns, the preferred orientation is not strong enough to account for the absence of these reflections. The intensities of many reflections in the x-ray and electron transmission diffraction patterns would also be diminished by the weak [111] fiber texture if the beam of radiation were approximately parallel to the fiber axis.

The apparent contradiction between the x-ray diffraction results which led previous investigators to conclude that the structure of as-plated electroless nickel was amorphous, and the electron diffraction results which are indicative of crystallinity can be explained by a consideration of the effects of fine grain size and other factors that diminish the intensities of x-ray reflections. Reflections in x-ray patterns are broadened and become less intense as the grain size decreases to diameters less than 10,000Å. In electroless nickel, the

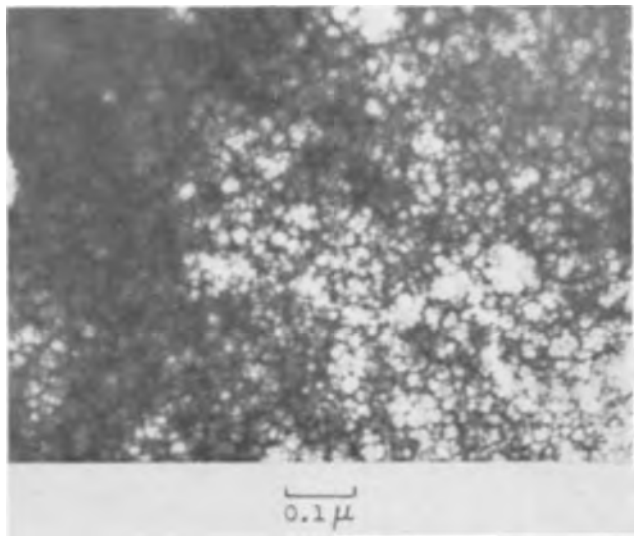

Fig. 6. Electron transmission micrograph of as-plated electroless nickel from the alkaline-chloride bath, phosphorus content 6.1 w/o, X 124,000.

apparent grain size, as indicated by electron transmission micrographs similar to that in Fig. 6, is of the order of 100Å; therefore, only the most intense x-ray reflections should appear. Although the x-ray diffraction pattern of a crystalline material with a particle size of 100Å should probably contain more than one or two reflections, the added effects of internal stress, solid solution, stacking faults, and preferred orientation on the diminution of the intensities of the reflections can reasonably account for the destruction of all but the strong {111} x-ray reflection from as-plated electroless nickel. In the x-ray diffractometer patterns of low-phosphorus alloys, the detection of a weak {222} reflection, which has not been observed by previous investigators, might be due to the absence of internal stress in the deposits prepared for this investigation.

Solution of the Scherrer formula (see section on experimental procedure) for the amount of broadening caused by fine grain size gives the equation

$$B = \frac{0.9\lambda}{t \cos \theta_{hkl}}$$

which indicates that the tendency of a fine-grained material to broaden reflections is greatly diminished as the wavelength of the radiation is decreased. The broadening is diminished not only because the numerator of the equation depends directly on the wavelength, but also because the cos θ_{hkl} term in the denominator increases as the wavelength decreases. The fine grain size of the electroless nickel does not preclude the production of electron-diffraction lines because the wavelength of electrons accelerated through a potential of 75 kv is almost two orders of magnitude smaller than the wavelength of x-rays used in diffraction work.

The existence of an abrupt change in the effect of phosphorus content at 7 w/o on the position and breadth of lines in diffraction patterns of as-plated electroless nickel alloys is clearly revealed by the graphs in Fig. 7 for the {111} x-ray reflection. The d_{111} and the peak breadth plotted for alloys deposited from the alkaline-chloride bath are averages of measurements made on the surface of the deposits adjacent to the basis metal and of measurements made on the outer surface. For alloys deposited from the acid-sulfate bath, the measurements from the two surfaces were plotted individually at phosphorus contents determined from electron-probe microanalysis traverses.

Variations in phosphorus content appear to have no significant effect on the position and breadth of the {111} reflection from alloys containing from 4.6 to

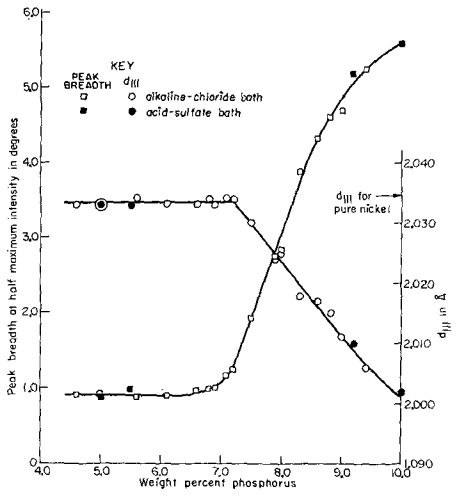

Fig. 7. Peak breadth of the {111} x-ray reflection and d_{111} for as-plated electroless nickel vs. weight per cent phosphorus.

7 w/o. As the phosphorus content increases from 7 to 10 w/o, d_{111} decreases and the reflection is broadened considerably. Both the shifting and the broadening of the reflection are associated with the development of an asymmetrical tail on the high-angle side of the {111} diffraction peak.

At present, the exact cause for the effects of an increase in phosphorus content above 7 w/o on diffraction patterns of as-plated electroless nickel alloys can only be the subject of speculation. Even though a decrease in grain size could contribute to the broadening of the {111} reflection, it would not result in asymmetry. Therefore, the observed increase in peak breadth with increasing phosphorus content must be caused by some phenomenon which can result in asymmetrical broadening, such as an increase in the density of stacking faults.

Goldenstein, Rostoker, Schossberger, and Gutzeit (2), in support of their contention that electroless nickel is amorphous, state that the apparent grain size obtained by measuring the breadth of the {111} x-ray peak and applying the Scherrer formula is only a few atomic diameters. The new data reported in Table II show that estimates given by the Scherrer formula are not valid indications of the actual grain size of alloys with more than 7 w/o phosphorus. In Table II, the Scherrer formula estimates, calculated from measured peak breadths that have been corrected for instrumental broadening, are compared with actual grain size measurements made on several electron transmission micrographs similar to that in Fig. 6. For the alloy containing 8.8 w/o phosphorus, the measured grain size is approximately five times greater than the estimate given by the Scherrer formula, which attributes all the broadening to fine grain size. The fact that the estimated grain size for alloys with 5.0 and 6.1 w/o phosphorus is fairly close to the measured value indicates that fine grain size makes a significant contribution to the total breadth of the x-ray reflections from the low-phosphorus alloys.

Table II. Comparison of estimated grain size given by the Scherrer formula with average grain size determined from electron transmission micrographs of as-plated electroless nickel

Weight per cent phosphorus	B radians	Grain size in Å: Estimate from Scherrer formula	Grain size in Å: Average of measurements on micrographs
5.0	0.0154	98	150
6.1	0.0153	98	150
7.5	0.0335	46	—
8.8	0.0803	19	100
9.4	0.0917	16	—

Effect of Heat Treatment on Preferred Orientation

An observed increase in the strength of the preferred orientation of the nickel phase of all electroless nickel alloys after heat treatments at temperatures ranging from 200° to 750°C is indicative of recrystallization and grain growth. Even the high-phosphorus alloys with more than 7 w/o phosphorus that seemed to have a random orientation in the as-plated condition develop a weak [111] fiber texture at temperatures as low as 200°C. After heat treatments at 200°C, the weak preferred orientation of the as-plated, low-phosphorus alloys is slightly stronger and a very weak {200} reflection appears on the x-ray pinhole transmission patterns. No evidence for the formation of a Ni_3P phase appears in electron or x-ray transmission diffraction patterns of alloys heat treated at 200°C for times as long as 240 min.

The initial particles of Ni_3P that form in alloys heat treated at 400° and 600°C also have a distinct preferred orientation. There seems to be no reason for this behavior unless the deposits are crystalline before heat treatment. This is one more bit of evidence for crystallinity of the as-plated deposits. In the low-phosphorus alloys, the preferred orientation of the Ni_3P phase is still strong after a heat treatment at 400°C for 120 min as shown by the {321} reflection in Fig. 8. An analysis of the preferred orientation in the Ni_3P phase and its implications concerning the hardening mechanism in electroless nickel will be presented in a subsequent section.

The strength of the [111] fiber texture in the nickel phase of all the electroless nickel alloys increases as the temperature of heat treatment increases from 200° to 600°C. At 750°C, the preferred orientation developed in the nickel phase of the high-phosphorus alloys is just as strong, if not stronger, than that developed in the same interval of time at 600°C. In the low-phosphorus alloys heat treated at 750°C for 120 min, the preferred orientation of the nickel phase is considerably weaker than that developed at 600°C, as shown by a comparison of Fig. 9 and 10a. Furthermore, the reflections from the nickel phase of the low-phosphorus alloys heat treated at 750°C are extremely spotty in character compared to the continuous reflections from the high-phosphorus alloys after a similar heat treatment. After heat treatments at 750°C, the differences in the character of the reflections and in the strength of the preferred orientation shown in Fig. 10 are indicative of recrystallization with excessive grain growth in the low-phosphorus alloys and recrystallization with restricted grain growth in the high-phosphorus alloys. Recrystallization is possible only if the as-plated deposits were crystalline.

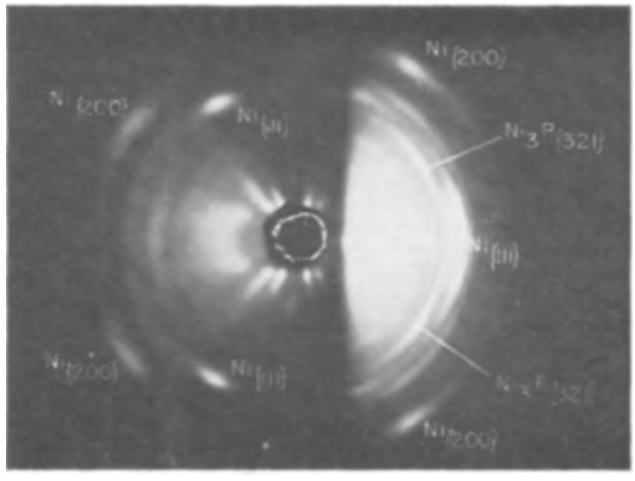

Fig. 8. X-ray pinhole transmission pattern of electroless nickel deposited from the alkaline-chloride bath and heat treated at 400°C for 120 min, phosphorus content 6.1 w/o, unfiltered copper radiation, $\beta = 70°$.

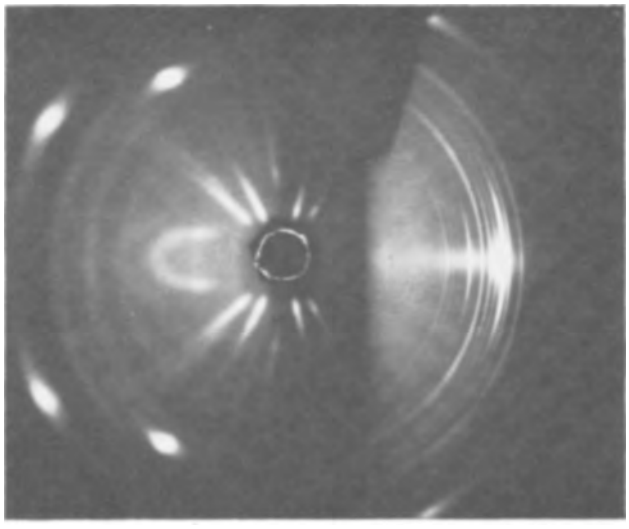

Fig. 9. X-ray pinhole transmission pattern of electroless nickel deposited from the alkaline-chloride bath and heat treated at 600°C for 120 min, phosphorus content 6.1 w/o, unfiltered copper radiation, $\beta = 70°$.

The results of the preferred-orientation study of electroless nickel alloys after heat treatments at temperatures ranging from 400° to 750°C are summarized in Table III. The qualitative estimates of the strength of the preferred orientation that appear in Table III were made on x-ray pinhole transmission patterns similar to those in Fig. 8, 9, and 10. The importance of inclining the specimen at various angles to the x-ray beam cannot be overemphasized, otherwise the variations in [111] fiber texture may not be detected.

Microstructure

The micrographs of as-plated electroless nickel in Fig. 11 and 12 show the lamellar structure observed by previous investigators and also reveal a significant difference in the thickness of the lamellae of deposits from the two plating baths. In the microstructure of the as-plated deposit from the alkaline-chloride bath shown in Fig. 11, the lamellar thickness is approximately 0.2 mil. The lamellae in the microstructure of the acid-sulfate deposit shown in Fig. 12, which closely resembles the appearance of micrographs published in the literature, are only about 0.02 mil thick.

After heat treatments at temperatures as high as 400°C, the microstructures of the electroless nickel alloys have the same lamellar appearance of as-plated alloys even though the supersaturated solid solution has transformed to the equilibrium phases of nickel and Ni_3P.

Heat treatments at 600°C for 120 min result in the disappearance of the lamellar structure, as shown by the micrograph in Fig. 13. The two equilibrium phases

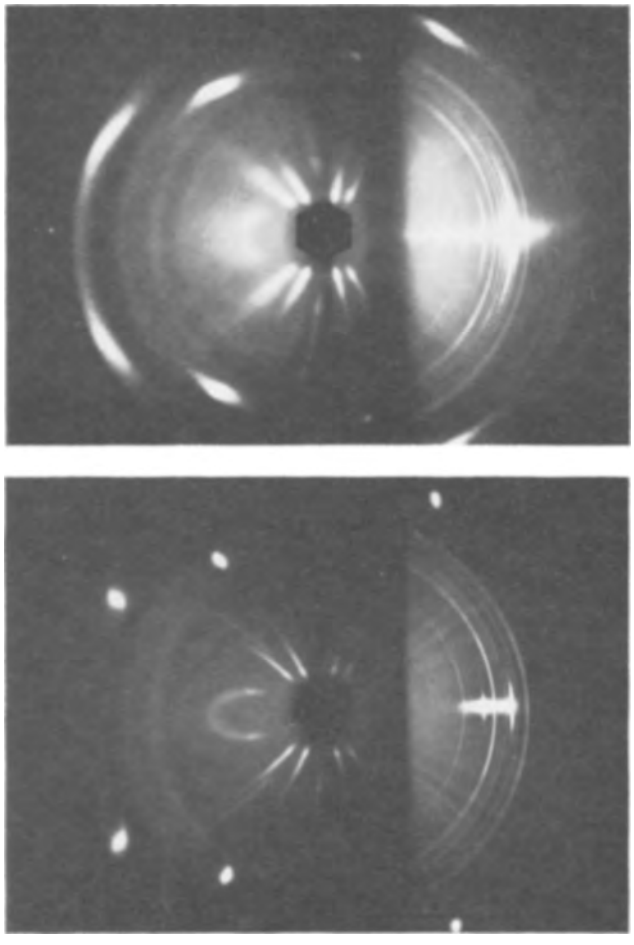

Fig. 10. X-ray pinhole transmission patterns of electroless nickel alloys deposited from the alkaline-chloride bath and heat treated at 750°C for 120 min, $\beta = 70°$, unfiltered copper radiation: (a) phosphorus content 5.0 w/o, (b) phosphorus content 8.8 w/o.

are evident in the micrograph, but the structure is too fine to be clearly resolved.

Optical micrographs of the electroless nickel alloys heat treated at 750°C for 120 min show clearly resolved particles dispersed in a matrix. The electron backscatter micrographs in Fig. 14 definitely establish that there is a change in the phase forming the matrix as the phosphorus content increases from 5.0 to 9.0 w/o. The intensity of electron backscattering diminishes with a decrease in mass density or with a decrease in the atomic number of the elements present. On the electron backscatter micrographs of electroless nickel, the Ni_3P phase should appear as a dark region not only because its mass density is less than nickel, but also because it contains 25 a/o (atomic per cent) of

Table III. Qualitative summary of preferred-orientation study of electroless nickel after heat treatments at temperatures ranging from 400° to 750°C

Phase	Plating bath	Weight per cent phosphorus	Strength of preferred orientation after heat treatment				
			at 400°C		at 600°C		at 750°C
			10-30 min	120 min	14-30 min	120 min	120 min
Ni	Alkaline-chloride	6	W-S	S	S	VS	W-S
		9	W	W-S	S	VS	VS
	Acid-sulfate	5*	W-S	S	S	VS	
		10**	VW	W	S	VS	
Ni_3P	Alkaline-chloride	6	S	S	W-S	VW-R	VW-R
		9	VW	VW-R	VW-R	R	R
	Acid-sulfate	5*	S	S	W-S	VW-R	
		10**	VW-R	R	VW-R	R	

Key: R random orientation, W weak, VS very strong, VW very weak, and S strong.
* Surface adjacent to basis metal.
** Outer surface.

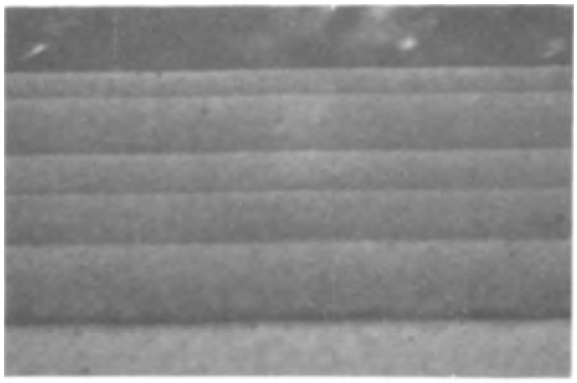

Fig. 11. Microstructure of as-plated electroless nickel from the alkaline-chloride bath, phosphorus content 7.1 w/o, NaCN-$(NH_4)_2S_2O_8$ etch, X 1000.

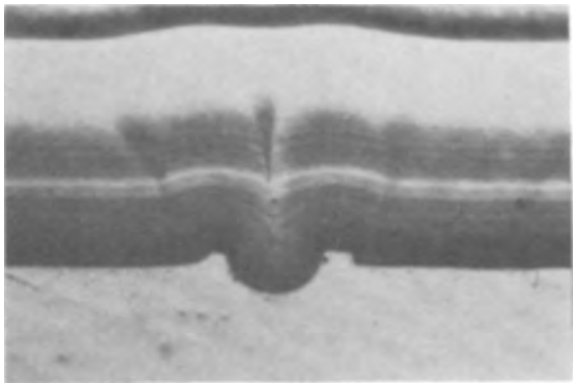

Fig. 12. Microstructure of as-plated electroless nickel from the acid-sulfate bath, phosphorus content varies from 5 w/o at surface adjacent to basis metal to 10 w/o at outer surface, NaCN-$(NH_4)_2S_2O_8$ etch, X 1000.

phosphorus, whose atomic number is considerably below that of nickel. Even though the particles of the dispersed phase are not clearly resolved, the electron backscatter micrographs indicate that the light nickel phase is the matrix in the alloys containing 5.0 w/o phosphorus and the dark Ni_3P phase is the matrix in the alloys containing 9.0 w/o phosphorus.

The evidence from x-ray pinhole transmission patterns for restricted grain growth of the nickel phase of high-phosphorus alloys heat treated at 750°C in contrast to the excessive grain growth in the low-phosphorus alloys can be attributed to the change in the phase forming the matrix as the phosphorus content increases. The continuous Ni_3P phase would act as a natural barrier to the growth of a dispersed nickel phase in the high-phosphorus alloys.

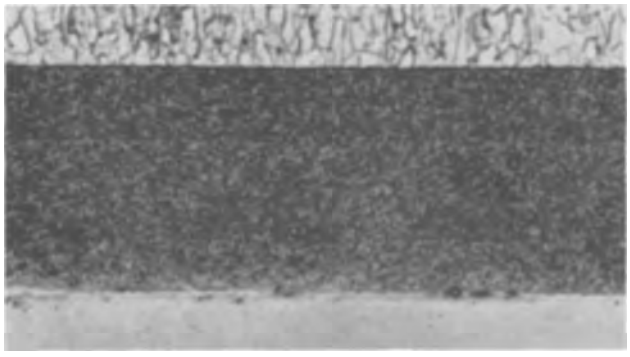

Fig. 13. Microstructure of electroless nickel deposited from the alkaline-chloride bath and heat treated at 600°C for 120 min, phosphorus content 9.0 w/o, NaCN-$(NH_4)_2S_2O_8$ etch, X 1000.

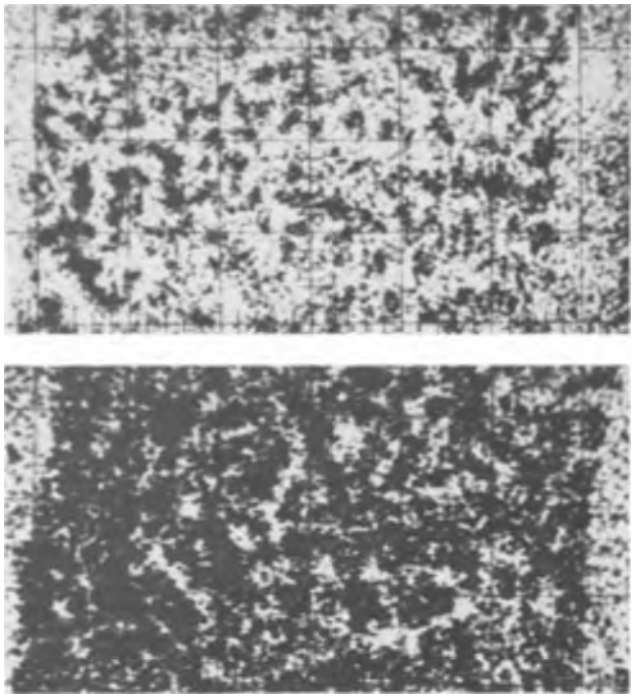

Fig. 14. Electron backscatter micrographs of electroless nickel alloys deposited from the alkaline-chloride bath and heat treated at 750°C for 120 min, unetched, X 2500. (a) phosphorus content 5.0 w/o, (b) phosphorus content 9.0 w/o.

The fact that the change in the phase forming the matrix occurs in the vicinity of 7 w/o phosphorus, which according to the equilibrium phase diagram corresponds to 50 v/o Ni_3P, can be ascertained from the series of micrographs in Fig. 15. The continuous nickel phase appears as light regions on the optical micrograph of the alloy with 5.0 w/o phosphorus in contrast to the gray regions representing the continuous Ni_3P phase in the micrograph of the alloy with 9.0 w/o phosphorus. In the microstructure of the alloy containing 7.1 w/o phosphorus shown in Fig. 15b, neither phase is continuous across the entire thickness of the deposit. The Ni_3P phase appears to be the matrix at the basis metal-deposit interface, whereas nickel seems to be the matrix near the outer surface. All optical micrographs in this section are oriented so that the basis metal is at the bottom.

Mechanical Properties

The bulge-test specimens deposited from the alkaline-chloride bath were grouped according to phosphorus content. As-plated specimens or specimens for a specific heat treatment were randomly selected from a group representative of a particular phosphorus content in order to eliminate any effect that plating conditions during a particular run might have on the properties of the deposits. The strengths and ductilities plotted on the graphs in this section are sample means or averages for measurements on several specimens. The limits of the averages indicated by dashed lines on some of the graphs are 90% confidence intervals for the true mean calculated from Student's "*t*" distribution.

For an adequate sample of as-plated specimens and heat-treated specimens, there was no significant difference between the hardness measurement on the surface of a deposit and the hardness measurement on its cross section. Therefore, it was not necessary to make two measurements on all specimens. If measurements were made on both the surface and the cross section, the Knoop hardness number (KHN) reported was the average of the two measurements. The maximum deviation of two measurements from their mean was less than 5%.

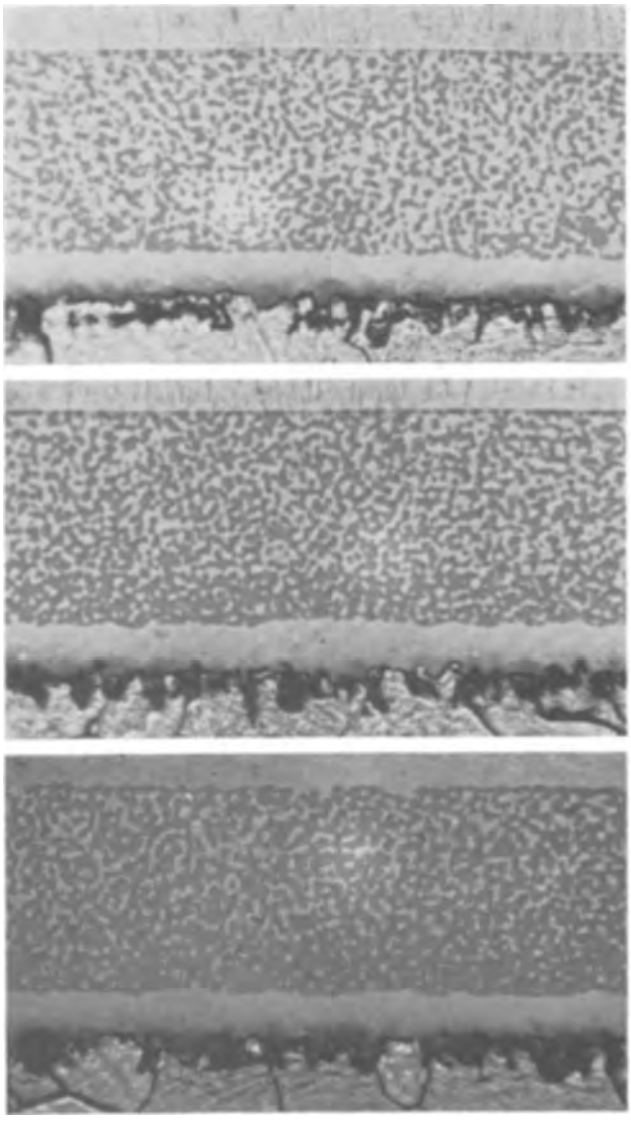

Fig. 15. Microstructure of electroless nickel alloys deposited from the alkaline-chloride bath and heat treated at 750°C for 120 min, NaCN-$(NH_4)_2S_2O_8$ etch, water rinse, 2% nital etch, X 1000. (a) phosphorus content 5.0 w/o, (b) phosphorus content 7.1 w/o, (c) phosphorus content 9.0 w/o.

The graphs in Fig. 16 indicate that both the strength and the ductility of as-plated electroless nickel alloys increase with a rise in phosphorus content. These results contradict qualitative observations of Brenner, Couch, and Williams (4) who reported a decrease in the strength and ductility of similar electrodeposited alloys with increasing phosphorus content. In the vicinity of 7 w/o, both the strength and the ductility of electroless nickel alloys rise abruptly and the strength appears to reach a maximum. The changes in strength and ductility are not reflected in the hardness, which remains practically constant as the phosphorus content increases.

The increase in the strength of the as-plated alloys can reasonably be attributed to either solid solution hardening or to the effects of localized coherency stresses in regions where phosphorus atoms are collecting and attempting to form a nucleus of the phosphide phase. At present, no reasonable hypothesis can be offered to explain the unusual direct relationship between strength and ductility with increasing phosphorus content of as-plated electroless nickel. A similar direct relationship was described by Read in his discussion of the effects of addition agents on the mechanical properties of copper and nickel electrodeposits (17).

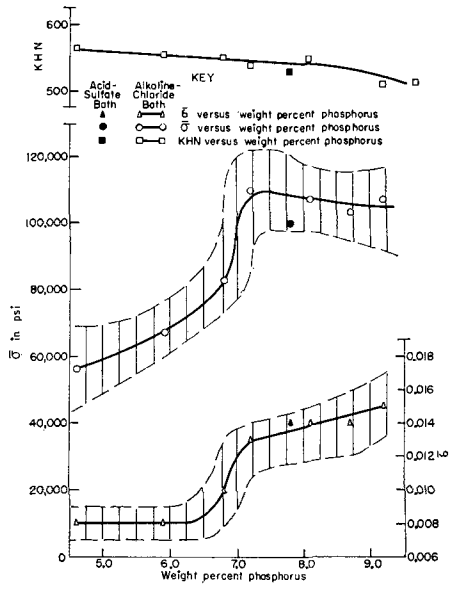

Fig. 16. Effect of phosphorus content on the mechanical properties of as-plated electroless nickel alloys.

The strength and ductilities reported in Fig. 16 for as-plated alloys containing 7 to 10 w/o phosphorus are in good agreement with those obtained by Jovanovic and Smith (18) for similar alloys. These investigators, whose method for analyzing bulge test results differs from that used in this investigation, report strengths at fracture ranging from 109,000 to 120,000 psi and strains at fracture ranging from 0.0069 to 0.0080. If the bulge test results of this study for alloys containing 7 to 10 w/o phosphorus were treated according to the method employed by Jovanovic and Smith, the average strength at fracture would be 106,000 psi and the average strain at fracture would be 0.0095.

Although heat treatments at 750°C for 60 and 120 min significantly improve both the strength and the ductility of the low-phosphorus alloys, they greatly decrease the strength and the ductility of the high-phosphorus alloys as shown by a comparison of the data in Fig. 16 and 17. The fact that alloys with greater

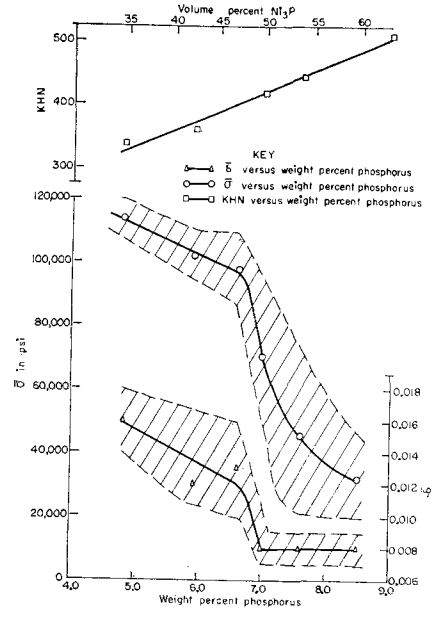

Fig. 17. Effect of phosphorus content on mechanical properties of electroless nickel alloys deposited from the alkaline-chloride bath and heat-treated at 750°C for 120 min.

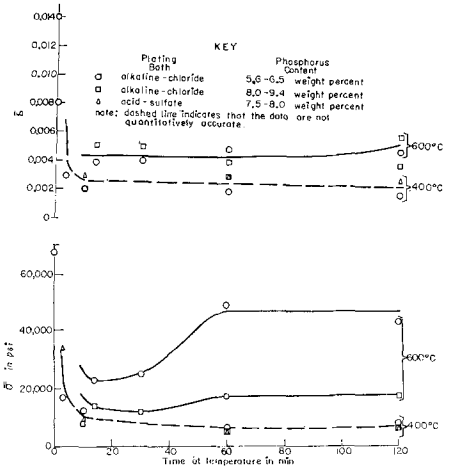

Fig. 18. Effect of heat treatments at 400° and 600°C on the strength and ductility of electroless nickel alloys.

than 7 w/o phosphorus are more brittle after heat treatments at 750°C than as-plated alloys of comparable phosphorus content confirms the qualitative observations of Brenner *et al.* for similar electrodeposited alloys and contradicts claims in the literature that prolonged heat treatments above 600°C improve the ductility of all electroless nickel alloys.

The graphs in Fig. 17 show that the strength and ductility of alloys heat treated at 750°C for 120 min decrease abruptly with increasing phosphorus content in the vicinity of 7 w/o. The abrupt loss in strength and ductility is indicative of the fact that a ductile nickel phase is the matrix in the low-phosphorus alloy and a brittle phosphide phase is the matrix in the high-phosphorus alloy. Once again, hardness measurements give no indication of the potent effect of phosphorus content in the vicinity of 7 w/o on strength and on ductility. The data plotted in Fig. 17 indicate that hardness is not only directly proportional to the weight per cent phosphorus in the alloys, but is also directly proportional to the volume per cent Ni_3P, as suggested by Ziehlke, Dritt, and Mahoney (7).

Heat treatments at 400° and 600°C result in a drastic decrease in the strength and ductility of all electroless nickel alloys as shown by the graphs in Fig. 18. After 10 min at 400°C, the alloys were so brittle that their strength and ductility could not be measured accurately even by the bulge test, which is particularly suitable for the determination of the properties of many brittle metallic coatings. The ductilities reported in Fig. 18 for the specimens tested are not quantitatively accurate because the bulge heights at fracture were far below the lower limit of the calibration graph for the bulge tester. At the lower limit, the curvature of the calibration graph changes rapidly so that precise extrapolation is not possible. Valid measurements of the strength were not obtained because the specimens fractured so early in testing that the oil pressure could not be accurately determined. For alloys heat treated at 400°C, phosphorus content seems to have no effect on the apparent strengths or the apparent ductilities which, at best, are only qualitative indications of these properties.

Even though the quantitative accuracy of the ductilities reported for alloys heat treated at 600°C is also questionable, the strength measurements are considered to be valid because all the specimens fractured at a measurable pressure. Heat treatments of the low-phosphorus alloys for more than 30 min result in the recovery of a significant portion of the original loss in strength. The high-phosphorus alloys are still extremely weak even after 120 min at 600°C.

There are probably many plausible explanations for the severe embrittlement indicated by the drastic decrease in the strength and ductility of electroless nickel after heat treatments at 400° and 600°C. One hypothesis could be based on the assumption that the Ni_3P phase initially precipitates as very thin platelets with edges that act as severe stress raisers. If this assumption were true, the recovery of the strength of the low-phosphorus alloys after prolonged heat treatments at 600°C could be attributed to the elimination of the stress raisers due to the natural tendency of the platelets to form spheroids and thereby decrease their surface energy.

A second hypothesis could be based on the assumption that many of the phosphorus atoms in as-plated electroless nickel alloys are segregated at grain boundaries. If this assumption were valid, the initial phosphorus-rich phase precipitated during heat treatments would form a continuous grain boundary network that could reasonably account for the embrittlement of the alloys. In the low-phosphorus alloys, a phosphide grain-boundary network would also tend to spheroidize during heat treatments at high temperatures. In the high-phosphorus alloys, the grain-boundary network would be stabilized due to the high volume percentage of the phosphide present.

There is some evidence on the x-ray pinhole transmission patterns of alloys heat treated at 400° and 600°C and on the micrographs of alloys heat treated at 750°C which would support both hypotheses suggested to account for the severe embrittlement. The observed preferred orientation of the phosphide phase in the x-ray pinhole transmission patterns suggests that some of the initial Ni_3P particles may precipitate as platelets with a particular crystallographic plane parallel to a habit plane in the parent nickel structure. The preferred orientation of the phosphide phase becomes stronger as the phosphorus content of the alloys decreases. However, even in the low-phosphorus alloys, the preferred orientation is not strong enough to preclude the existence of a randomly oriented precipitate at grain boundaries. The micrographs in Fig. 15a and 15b show irregularly shaped phosphide particles that appear to be the remnants of a grain-boundary network and also reveal small isolated phosphide spheroids which could have originally been platelets.

The data in Fig. 19 indicate that the embrittlement of electroless nickel after heat treatments at 400°C is accompanied by the substantial increase in hardness observed by previous investigators (2, 3, 5, 7). After 3 min at 400°C, the hardness of an alloy containing 6.1 w/o phosphorus is greater than that of an alloy containing 9.0 w/o. However, the hardness of alloys after heat treatments at 400°C for 10 min or longer is not significantly affected by phosphorus content. In Fig. 19, the stability of the maximum hardness developed at 400°C is compared with the rapid decrease in hardness during heat treatments at 600°C. The hardness

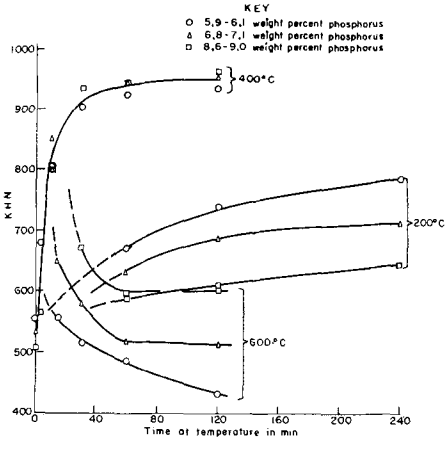

Fig. 19. Effect of heat treatment on the hardness of electroless nickel alloys deposited from the alkaline-chloride bath.

of alloys after identical heat treatments at 600°C appears to be directly proportional to the volume per cent of Ni_3P present.

After heat treatments at 200°C, an increase in the hardness was observed for all the electroless nickel alloys. In the low-phosphorus alloys, the rate of hardening was significantly greater than that in the high-phosphorus alloys as shown in Fig. 19. The observed dependence of the rate of hardening on phosphorus content partially accounts for the contradictory results of previous investigators concerning the tendency of electroless nickel to harden at 200°C. Goldenstein *et al.* (2), who reported no increase in hardness at 200°C, were studying high-phosphorus alloys. Zusmanovich (3) and Lee (5), who observed hardening, probably were studying low-phosphorus alloys.

In the high-phosphorus alloys, the relatively slow rate of hardening at 200°C seems to be indicative of the presence of an activation energy barrier, dependent on the phosphorus content, that retards the initial stages of the transformation and the hardening of the supersaturated solid solution. After a heat treatment at 400°C for 3 min, the low hardness of the alloy containing 9.0 w/o phosphorus compared to that of the alloy with 6.1 w/o phosphorus is further evidence for the existence of an activation energy barrier. If an activation energy barrier were not present, the high-phosphorus alloys should transform and harden faster than the low-phosphorus alloys because the instability of the solid solution and the free energy available for transformation should increase as the phosphorus content increases. Although in a few instances rate of precipitation may decrease with increasing solute concentration, we know of no reason to suspect that such a phenomenon should prevail here.

The strength and the ductility of the alloys heat treated at 200°C increase with a rise in phosphorus content as shown in Fig. 20. The measurements of strength of the alloys heat treated at 200°C for 120 min give a much more positive indication than hardness measurements that the low-phosphorus alloys start to transform before the high-phosphorus alloys. A comparison of the data in Fig. 16 and 20 indicates that a heat treatment at 200°C for 120 min decreases the strength of the low-phosphorus alloys by a factor of two but does not significantly affect the strength of the high-phosphorus alloys. The loss in strength in the low-phosphorus alloys resembles the embrittlement

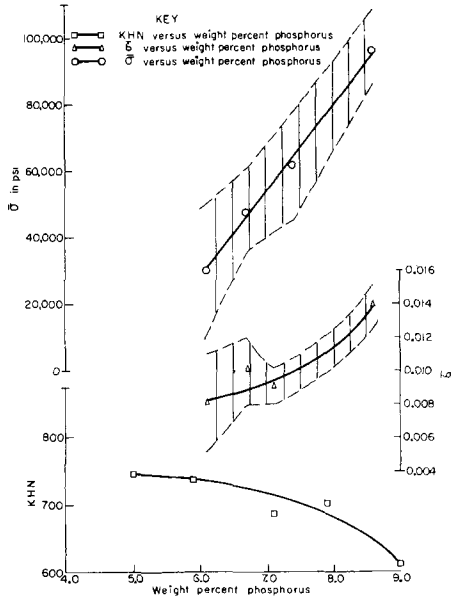

Fig. 20. Effect of phosphorus content on the mechanical properties of electroless nickel alloys deposited from alkaline-chloride bath and heat treated at 200°C for 120 min.

that accompanies the transformation of alloys during heat treatments at 400°C.

The decrease in ductility after heat treatments at 400°C is not observed after heat treatments at 200°C. Although the average values reported for the ductility of as-plated alloys and those reported for alloys heat treated at 200°C are almost identical, it is probably important to note that the scatter in the data for the low-phosphorus alloys heat treated at 200°C is much greater than that for as-plated alloys of comparable phosphorus content. Furthermore, changes in the mechanical properties of brittle materials are almost always indicated by variations in strength rather than in ductility because tests employed to measure strain are not sensitive enough. Even though the hydraulic bulge test is one of the most sensitive tests for detecting slight differences in the strain at fracture for brittle materials, its sensitivity is not very great at the strains at which electroless nickel deposits fracture.

Hardening Mechanism

The structural observations from x-ray pinhole transmission patterns and many of the characteristics of the increase in hardness after the heat treatment of electroless nickel tend to indicate the occurrence of conventional precipitation hardening. In the initial stages of precipitation hardening of a supersaturated solid solution, the atoms of the solute diffuse to a specific crystallographic plane with an atomic arrangement that resembles the array of atoms on a plane in the structure of the precipitate. As the atoms attempting to precipitate collect, they are forced to conform to the structure of the solvent. The forced coherency between atoms of the solvent and atoms attempting to form the structure of the precipitate causes severe, localized, elastic stresses that are responsible for the increase in hardness. When a sufficient number of solute atoms have collected, the structure of the precipitate is formed and the localized elastic stresses are relieved because the forced coherency no longer exists. After the formation of a significant number of precipitate particles at various locations throughout the specimen, the rate of hardening decreases and the hardness approaches a maximum.

The fact that there is no x-ray evidence for the presence of a phosphide precipitate in the low-phosphorus alloys that have been hardened by heat treatments at 200°C or by a heat treatment at 400°C for 3 min is in agreement with the established mechanism for precipitation hardening. After heat treatments at 400°C for more than 10 min, reflections from Ni_3P appear in x-ray diffraction patterns and the hardness approaches a maximum.

The strongest evidence obtained for the occurrence of conventional precipitation hardening in electroless nickel is based on the analysis of the relationship between the [111] fiber texture of the nickel phase and the preferred orientation of the Ni_3P phase, as revealed in the x-ray pinhole transmission pattern in Fig. 8. The presence of a preferred orientation in both the Ni_3P precipitate and the parent nickel phase implies the existence of a plane of coherency between the two crystal structures.

The habit plane on which a precipitate forms in the solvent is usually a plane of low indices. In the pattern in Fig. 8 and similar patterns, an analysis of the locations of the intense arcs on the {321} reflection of Ni_3P indicates that the {111} planes of fcc nickel are parallel to the {110} planes of Ni_3P, which has a body-centered-tetragonal structure with 32 atoms per unit cell. The arrangement of atoms associated with the $(\bar{1}10)$ Ni_3P plane shown in Fig. 21 bears a striking resemblance to the hexagonal array of atoms on the {111} planes of nickel. Furthermore, the average interatomic distance of 2.6Å on the {110} planes of Ni_3P is very close to the interatomic distance of 2.5Å in pure nickel. Therefore, the {111} planes of nickel

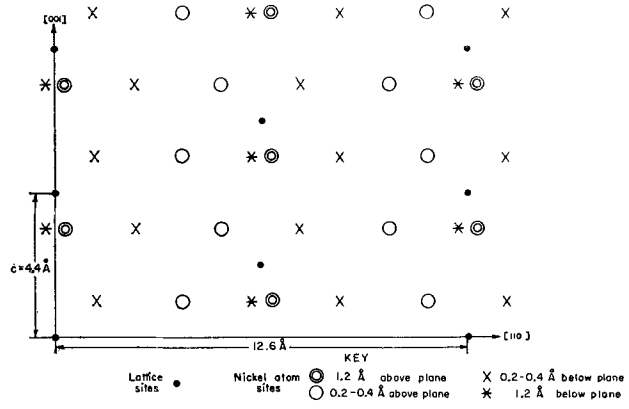

Fig. 21. Schematic sketch of the arrangement of atoms associated with the (110) plane of Ni_3P.

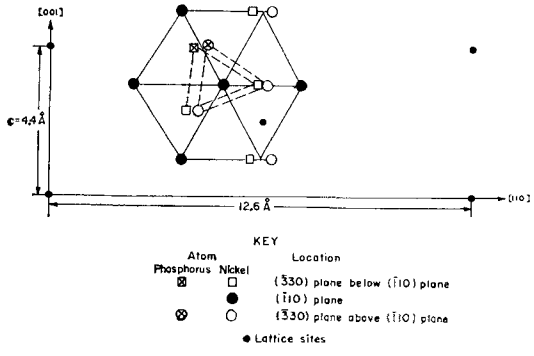

Fig. 22. Schematic sketch showing the pseudo hcp stacking sequence in the vicinity of a nickel atom on the (110) plane of Ni_3P.

satisfy all the requirements of a habit plane for the precipitation of Ni_3P.

The evidence that the {110} planes of the initial Ni_3P particles formed are parallel to the {111} planes of the nickel phase also tends to account for the existence of stacking faults in the as-plated deposits. In the Ni_3P structure, all of the phosphorus atoms may be considered to be located on a set of {330} planes which are immediately adjacent to the {110} planes. If one considers certain nickel atoms on {110} planes of Ni_3P and their nearest neighbors on adjacent {330} planes, a pseudo hcp stacking sequence is apparent, as shown in Fig. 22. This stacking sequence would correspond to a stacking fault in the fcc structure of the supersaturated solid solution in as-plated electroless nickel. If some of the phosphorus atoms in the as-plated alloy were segregated on {111} planes in the structure of the nickel solvent, they would tend to stabilize stacking faults because of the resemblance between the faults and a coherent structure of Ni_3P.

One important characteristic of the hardening of electroless nickel that is markedly different from conventional precipitation hardening is the inverse relationship between hardness and strength. In conventional precipitation hardening, an increase in hardness is accompanied by an increase in strength. The hypotheses that were proposed to account for the loss in strength during heat treatment of electroless nickel at 400°C do not explain why an increase in strength is not observed in the initial stages of hardening. In speculating on a plausible explanation for the unusual inverse relationship between strength and hardness in the initial stages of hardening, it is probably important to note that the established mechanisms and characteristics of conventional precipitation hardening are based on alloys with a grain size two to five orders of magnitude greater than that of as-plated electroless nickel. Very little is known concerning the relationships between strengthening mechanisms and the mechanical properties of extremely fine-grained alloys such as electroless nickel. Some of the characteristics of the hardening in fine-grained alloys might be different from those observed in alloys with a much coarser grain size.

Comparison of Alkaline-Chloride Deposits and Acid-Sulfate Deposits

No significant differences were observed between the x-ray diffraction patterns of alloys deposited from the alkaline-chloride bath and the patterns of deposits from the acid-sulfate bath. In the study of the effect of phosphorus content on the position and breadth of the {111} reflection from as-plated alloys, the data for the acid-sulfate deposits shown in Fig. 7 are extremely close to the curves established for the alkaline-chloride deposits. The data in Table III indicate that heat treatments have similar effects on the preferred orientation of the phases in alloys of comparable phosphorus content from the two baths.

In the microstructure of the as-plated deposits, the difference of one order of magnitude in the thickness of lamellae did not affect the mechanical properties shown on the graph in Fig. 16. However, it is possible that the steep phosphorus gradient across the acid-sulfate deposits obscures the effects on mechanical properties of differences in microstructure and plating bath composition. After heat treatments at 400°C, the mechanical properties of alloys deposited from the two plating baths were also similar, as shown by the data in Fig. 18.

Summary

An analysis of electron and x-ray diffraction patterns indicates that as-plated electroless nickel alloys are supersaturated solid solutions of phosphorus dissolved in crystalline nickel. An increase in phosphorus content above 7 w/o not only broadens and shifts electron and x-ray reflections, but also decreases the strength of a [111] fiber texture in the nickel-rich solid solution. Both the strength and the ductility of the as-plated alloys increase with a rise in phosphorus content whereas the hardness remains constant.

During heat treatments at temperatures ranging from 200° to 750°C, the development of a strong [111] fiber texture in the nickel phase is indicative of recrystallization and grain growth.

Differences in the mechanical properties of alloys after identical heat treatments at 200°C indicate that the phosphorus content affects the kinetics of the initial stages of transformation and hardening prior to the formation of a Ni_3P precipitate. The absence of a Ni_3P phase during the initial stages of hardening at 200° and 400°C is in agreement with the established mechanism for precipitation hardening. Additional definite evidence for the occurrence of precipitation hardening is the existence of a logical habit plane for the coherent precipitation of the Ni_3P phase.

Heat treatments at 400° and 600°C greatly decrease the strength and ductility of all the alloys. Low-phosphorus alloys heat treated for more than 30 min at 600°C recover a significant portion of the original loss in strength, but high-phosphorus alloys are still weak after 120 min at 600°C.

Heat treatments at 750°C that significantly improve the strength and ductility of low-phosphorus alloys greatly decrease the strength and ductility of high-phosphorus alloys. Hardness measurements give no indication of the abrupt changes in strength and ductility with increasing phosphorus content. The loss of strength and ductility in the vicinity of 7 w/o phosphorus indicates that a ductile nickel phase is the matrix in the low-phosphorus alloys, and a brittle Ni_3P phase is the matrix in the high-phosphorus alloys. Evidence in micrographs, x-ray diffraction patterns, and electron-probe microanalysis traverses confirms the change in the phase forming the matrix.

The x-ray diffraction patterns of alloys deposited from the acid-sulfate bath were similar to the patterns of alloys with comparable phosphorus contents deposited from the alkaline-chloride bath. The difference of one order of magnitude in the thickness of lamellae in the microstructure of as-plated alloys from the two plating baths has no apparent effects on mechanical properties.

Acknowledgment

One of the authors (AHG) was supported by a fellowship from the General Electric Educational Foundation during most of this investigation.

Manuscript received April 10, 1964; revised manuscript received Nov. 27, 1964. This paper was presented at the New York Meeting, Sept. 29-Oct. 3, 1964.

Any discussion of this paper will appear in a Discussion Section to be published in the December 1964 JOURNAL.

REFERENCES

1. A. Brenner, "Symposium on Electroless Nickel Plating," Spec. Tech. Publ. No. 265, A.S.T.M., Philadelphia, 1 (1959).
2. A. W. Goldenstein, W. Rostoker, F. Schossberger, and G. Gutzeit, *This Journal*, **104**, 104 (1957).
3. G. G. Zusmanovich, Metal Science and Heat Treatment (Russian), No. 4, 48 (1960).
4. A. Brenner, D. F. Couch, and E. K. Williams, *J. Research Nat'l. Bur. Standards*, **44**, 109 (1950).
5. W. G. Lee, *Plating*, **47**, 288 (1960).
6. W. H. Metzger, Jr., "Symposium on Electroless Nickel Plating," Spec. Tech. Publ. No. 265, A.S.T.M., Philadelphia, 13 (1959).
7. K. T. Ziehlke, W. S. Dritt, and C. H. Mahoney, *Metal Progress*, **77**, 84 (February 1960).
8. A. H. Graham, R. W. Lindsay, and H. J. Read, *This Journal*, **109**, 1200 (1962).
9. G. Gutzeit, *Plating*, **46**, 1158 (1959).
10. J. D. MacLean and S. M. Karten, *ibid.*, **41**, 1284 (1954).
11. A. Kreig, "Symposium on Electroless Nickel Plating," Spec. Tech. Publ. No. 265, A.S.T.M., Philadelphia, 21 (1959).
12. B. D. Cullity, "Elements of X-Ray Diffraction," p. 280, Addison-Wesley, Reading, Mass. (1956).
13. G. Thomas, "Transmission Electron Microscopy of Metals," p. 188, John Wiley & Sons, New York (1962).
14. H. J. Read and T. J. Whalen, *Proc. Am. Electroplaters' Soc.*, **46**, 318 (1959).
15. T. A. Prater and H. J. Read, *Plating*, **36**, 1221 (1949).
16. M. S. Paterson, *J. Appl. Phys.*, **23**, 805 (1952).
17. H. J. Read, *Plating*, **49**, 602 (1962).
18. S. Jovanovic and C. S. Smith, *J. Appl. Phys.*, **32**, 121 (1961).

Relationship between Deposit Thickness and Current Density during the Early Stages of Electrodeposition

Joseph B. Kushner[1]

Engineering School, Evansville College, Evansville, Indiana

ABSTRACT

Some experiments have been performed to determine how long it takes at a given current density to put a continuous copper deposit on a simple planar platinum cathode and what the average thickness of the copper deposit is at that time. The results indicate a hyperbolic power type of relationship between the current density and the time of full coverage and the current density and the deposit thickness at full coverage. A simple theory is proposed to explain the results obtained.

This is a preliminary report in connection with some experiments performed dealing with the origins of stress in electrodeposited metals. In a previous paper (1) the present author proposed that the stress in electrodeposited metals reaches a maximum value at the time the deposit becomes essentially continuous on the cathode. It is of interest therefore to determine for a given current density how thick the deposit is at the time continuity is achieved and how long it takes to arrive at this thickness.

At first glance this appears to be a rather elementary problem, but it is not as simple as it looks. If a deposit grows uniformly over the cathode surface, atom layer by atom layer, then at the time the cathode surface is continuously covered, the thickness of the deposit should be exactly one atom layer. But deposit growth does not occur like this. There is a certain amount of growth normal to the plane of the cathode as well as parallel to it. Furthermore it is well known that electrocrystallization on a cathode begins in many instances only after starting nuclei have formed. Evans and Shome (2) clearly demonstrated that in the case of a simple nickel plating bath growth starts from nuclei formed at the very beginning of the plating process and little or no additional nucleation occurs after that.

Electrocrystallization is very much similar to other kinds of crystallization, and thermodynamic reasoning leads one to the conclusion that the size of these starting nuclei should become smaller as the current density is increased. And since fewer atoms are required to form a nucleus there should be more of them at the start of plating at a higher current density than there would be at a lower current density. Furthermore, as current density is increased the rate of deposition is increased, and each of these starting nuclei grow at a faster rate. In accordance with this, therefore, it can be expected that at high current densities the cathode will be very quickly covered and the deposit thickness at that time will be very small whereas at low current densities, since less nuclei are formed, it will take longer to cover and the deposit will be thicker when full coverage is achieved. The purpose of the experiments described below was to determine what relationship, if any, existed between the current density used and the average thickness of the deposit at the time full coverage of a simple cathode surface occurred.

Experimental Equipment

The electrolyte used for the experiments was a 0.5M copper sulfate, 0.5M sulfuric acid solution. It was chosen because of its simplicity and because over a fairly wide range of current densities it is capable of producing microscopically resolvable deposits. Two liters of solution were made from analytical grade chemicals and distilled water. The solution was filtered through acid washed activated carbon and was preelectrolyzed using a strip of high-purity copper (99.-

[1] Also Director, Joseph B. Kushner Electroplating School, Evansville, Indiana.

999) as anode, as an additional purification. The solution was used in a specifically designed cell made of Lucite which held 16.4 ml of solution. The cell was drained after each test and filled with fresh solution for each succeeding test.

It is well known that exceedingly small amounts of impurities can have important effects in electrodeposition from acid copper sulfate baths, and no doubt the purification given the electrolyte was less than desirable, but it was felt that since each experimental bath would on the average contain the same kind and amount of impurities their effect on the deposit would be the same in all the experiments performed. The platinum strip was handled with considerable care to prevent bending and scratching of the surface beyond that already present in the as-received condition.

The cathode used was a thin strip of C.P. platinum (99.99+). Its dimensions were 0.01 in. thick, 0.25 in. wide and 4.00 in. long. The actual plating because of the cell design, occurred only on one side over a length of 1.00 in. so that the active cathode surface had an area of 0.25 in.^{2} (1.61 cm^2). Platinum was selected because it is known to give a reproducible surface (3, 6).

It has been shown quite convincingly that nucleation takes place at dislocation arrays such as polygonization boundaries, in the presence of impurities which at sometime during the previous history of the cathode have diffused to the dislocations (4, 5). For almost any other metal than platinum, surface cleaning would be sure to affect nucleation centers, leading to irreproducibility. In addition, the platinum surface gave a strong contrast to the pink colored copper deposit, a marked advantage in determining coverage.

The next question was how would continuity of the deposit be established? The criterion was the human eye, both unaided and with a microscopic amplification of 800 diameters. The plated cathode area was deemed fully covered when to the eye the deposit was uniformly spread over the surface and examination of random and selected areas at a magnification of 800 x showed no bare regions greater in area than 1/1000 of the total area of the field of view. Figure 1 shows a result in which the deposit was considered continuous. Figure 2 shows what was considered a discontinuous deposit. The human eye is amazingly sensitive to color, and some preliminary experiments indicated that the eye could detect films of copper only a few hundred angstoms thick.

The temperature of the plating bath was room temperature, 27°C + 1°. The cleaning procedure was as follows: The platinum strip, handled by tweezers at the nonplating end was heated in concentrated nitric acid for 2 to 3 min or long enough to remove the previous copper deposit. It was rinsed thoroughly in running distilled water and then anodically electrolyzed in a 10% solution of C.P. sulfuric acid using another platinum strip as cathode, at a potential of 6v so that there was copious oxygen evolution at the anode. This was followed by a distilled water rinse and then plating was started after permitting the strip to sit in the bath for 2 min without current.

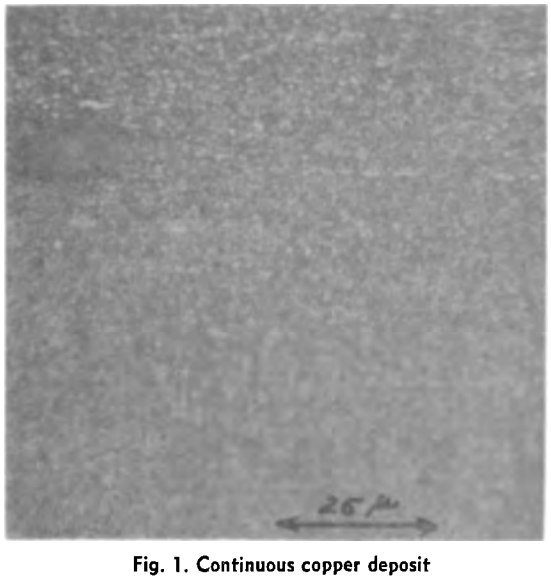

Fig. 1. Continuous copper deposit

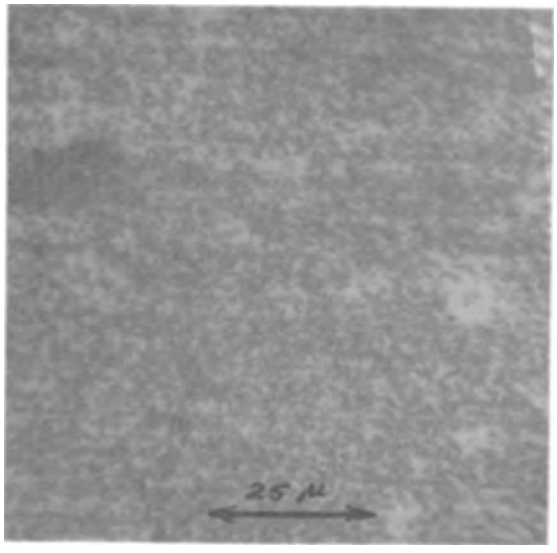

Fig. 2. Discontinuous copper deposit

It has been found by Becker (6) in the case of silver electrodeposition on platinum from a silver nitrate solution that random nucleation is produced whenever the platinum is given a cleaning treatment involving oxidation, such as dipping in nitric or sulfuric-chromate solution or flaming or anodic treatment in acid. He hypothesizes that oxygen is adsorbed on the cathode surface by these treatments, increasing the work of nucleation, and leading more or less to random nucleation. On the other hand he finds that cathodic treatment in nitric acid removes such an adsorbed oxygen layer, if formed, and leads to reproducible nucleation at easy nucleation sites with many many more nucleation sites available.

Use of a cathodic treatment in sulfuric acid was tried at first, but it was found that the hydrogen treatment led to nonuniformity of the copper deposit. Almost invariably for the same number of coulombs of electricity passed at several different current densities, the anodic treatment produced uniform coverage of the surface whereas the cathodic treatment resulted in bare areas. At this time no explanation is offered for this rather strange behavior. Possibly adsorbed hydrogen may be the cause of it. At any rate, on the basis of these tests, the anodic treatment was selected to help insure more random nucleation if this is what was occurring.

In order to determine the time of coverage as closely as possible, a pulse generator[2] producing an essentially square wave was used as the source of current. With this generator it was possible to produce either a single pulse or a series of pulses of known pulse width, spacing, and amplitude. The reasoning behind the use of a pulse generator was that the time element in the plating could be kept under closer control at the higher current densities when the time of plating was short. Thus, at higher current ranges full coverage might be obtained in a second or two with continuous current. With a pulse generator by using pulses of relatively small width compared to the pulse spacing the time factor could be magnified. For example, with a pulse spacing of 100,000 μsec and a pulse width of 10,000 μsec, the time of plating is magnified by a factor of 10.

Before using the pulse generator this way certain points had to be checked out. Basically these were:

[2] Servo Corporation of America, Model 3450D.

(*A*) Would the average thickness of the pulsed deposit be the same as for a continuous d-c deposit at the same number of coulombs? (*B*) Would pulse plating produce the same type of deposit, with reference to grain size, as continuous plating?

Regarding point *A*, it was found at once that some dissolution of the deposit took place during the off time particularly at low current densities. Thus at a current density below 4 ma/cm^2 the on-off ratio had to be 1 to 1 or better for an efficiency value as good as that for direct current. This was verified a number of times by plating the weighed platinum cathode with d.c. equivalent to the pulsed d.c. in terms of current density and coulombs passed. Efficiencies measured with the d.c. checked out very well with efficiencies at the same current density as measured by Turner (7) on an acid copper solution of similar composition. The efficiency with the pulsed current was likewise determined by weighing the platinum strip after a definite number of pulses producing the same current density and total number of coulombs was passed. These results came to within 2% or less of the d.c. results when the pulse width was at least one-half of the pulse spacing in the lower current density ranges. At higher current densities it was found possible to get results identical to the d.c. results with a wider pulse spacing; that is, a ratio of 1:10 could be used, thus magnifying the time by a factor of 10.

The attack on the copper deposit (and nickel in some other experiments) is no doubt due to the corrosive couple set up between the platinum and the copper. It appears that at relatively high plating current densities the interfacial film is depleted of ions or ion combination (most probably sulfate ions) that are capable of oxidizing the copper. The diffusion back to the interface of these attacking ions takes time and the next pulse puts on another layer of copper and retards the return of these ions. At lower current densities the attacking ions move only a short distance away from the cathode interface or are thinned out less extensively and, if the next pulse does not come quickly enough, some of the copper put on by the previous pulse is dissolved back into the solution, and the overall efficiency of the process becomes less than that of the d-c process. From the few pilot experiments tried, it appears that a considerable amount of information on diffusion and related subjects may be obtained by means of pulsing techniques.

With regard to the nature of the deposits, under the microscope the deposits produced by pulsed d.c. showed the same crystal size and general structure as those put down with the same number of coulombs of d.c. at the same current density. It may be that there are more subtle structure changes but these were not apparent to the eye.

It is also interesting to note that the copper deposits seemed almost invariably to nucleate along rolling lines, scratches, and other defects on the platinum strip. In most of the pictures taken a surface defect which can be seen in Fig. 1 and 2, was used as a landmark for positioning the surface so the same area could be photographed each time when desired. The circuit and apparatus layout is shown schematically in Fig. 3.

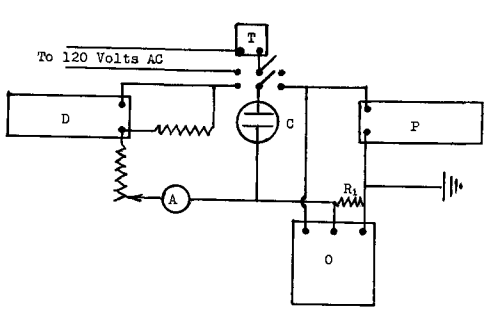

Fig. 3. Schematic of circuit used: T, electric timer; C, plating cell; P, pulse generator; A, ammeter; O, oscilloscope; D, constant current supply d.c.; R_1, precision resistor.

Table I. Time and deposit thickness at full coverage of platinum cathode

Actual plating time, sec, *t*	Coulombs passed, *Q*	Current density, ma/cm^2, *I*	Average thickness of deposit, Å, *T*
6.00	0.144	14.8*	329
17.5	0.280	9.88	638
30.0	0.360	7.41	822
80.0	0.640	4.94	1460
175.0	1.05	3.70	2400
400.0	1.60	2.47	3640
750.0	2.40	2.06	5470
1330	3.19	1.48	7280

* Measurements above this current density were not made due to difficulty in resolving crystal size.

The instantaneous current in the plating cell during pulses was determined from the measured instantaneous voltage drop across a precision resistor in series with the cell, as determined by means of a calibrated oscilloscope. Continuous direct current when used was produced by a constant current power source[3] and was measured by a precision Weston ammeter. During pulsed plating, the number of coulombs passed was determined by multiplying the number of pulses per second by the pulse width by the instantaneous current through the plating cell. The number of pulses (total) multiplied by the pulse width gave the actual plating time in seconds.

Data were obtained in the following way: At a given total current a known number of pulses were passed. The platinum strip was removed, rinsed in distilled water followed by a pure acetone spray, air dried and examined first with naked eye and then under the microscope at 800X. If the deposit showed bare areas, the strip was cleaned in hot nitric acid as previously described, given an anodic treatment in the 10% sulfuric, and plated again for a longer number of pulses and re-examined until finally the strip appeared to be fully covered (99.9%). The number of coulombs required for full coverage was determined by approaching full coverage from both the low coulomb side and the high coulomb side. The reproducibility of the method was good. It is estimated the maximum error is no greater than 10%. Each coulomb value (or time value) given in Table I is the result of at least two such determinations. The average thickness of each deposit was computed from the known number of

[3] Universal Electronics, Model 1020-2A.

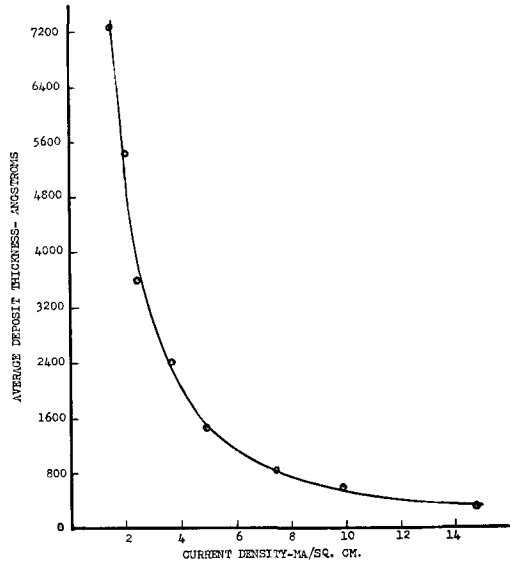

Fig. 4. Relationship between current density and average deposit thickness at time full cathode coverage is reached.

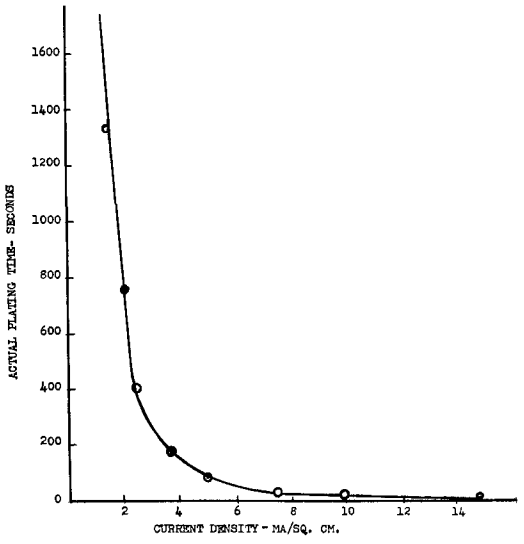

Fig. 5. Relationship between current density and time to reach full cathode coverage.

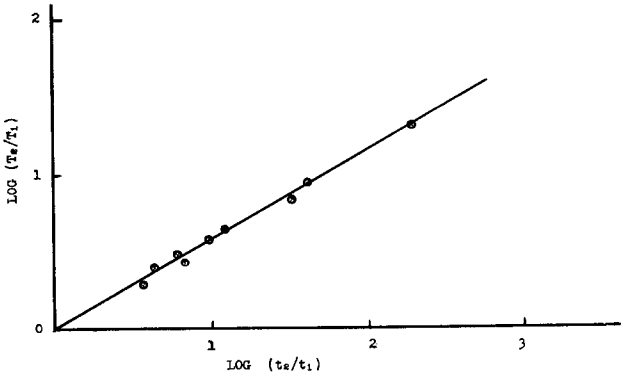

Fig. 6. Relationship between (T_2/T_1) and (t_2/t_1) at time full cathode coverage is reached.

coulombs passed, the nominal plated area, the electrochemical equivalent, and the bulk density of copper. Results for the copper solution described and the platinum strip used are given in Table I.

Three graphs have been plotted from the data. Figure 4 is a plot of the average deposit thickness *vs.* the current density used, at the time full coverage is reached. Figure 5 is a plot of the time to reach full coverage *vs.* the current density used and Fig. 6 is a plot of the log of (T_2/T_1) *vs.* the log of (t_2/t_1) where t_1 is the time in seconds to produce a deposit of average thickness T_1 angstroms, etc. Figures 4 and 5 show a hyperbolic type of relationship betweeen the thickness, time, and a power of the current density. Figure 6 gives what appears to be a straight line, with a slope of 0.57. The reason for this last plot will appear in the theory and discussion which follows.

Theory and Discussion

According to Evans and Shome (2) the area covered by a deposit on a flat cathode of area A_o in time t, is given by

$$A = A_o(1 - e^{-\pi v 2 t 2 N}) \qquad [1]$$

where v is the velocity of lateral spreading of the deposit (assumed constant for a given current density) and N is the number of nuclei originally formed. At the time of full coverage, assuming 99.9% to be full coverage, for different nucleation numbers, velocities, and times (different current densities) it can be said

$$\ln(1000) = \text{constant} = \pi v_1^2 t_1^2 N_1 = \pi v_2^2 t_2^2 N_2 = \pi v_3^2 t_3^2 N_3 \ldots \qquad [2]$$

What this series of equations is saying is that when coverage is complete, the lateral area of each grain deposited, multiplied by the number of grains (number of nuclei) is equal to the total area of the cathode surface A_o, or

$$A_1 N_1 = A_2 N_2 = A_3 N_3 = \ldots\ldots = A_o \qquad [3]$$

and

$$A_1/A_2 = N_2/N_1 \qquad [4]$$

Assuming all directions of lateral growth equally possible, the lateral growth that occurs from a given nucleus in time t must be equal to $a\sqrt{A}$, where a is a geometric constant. As a first approximation, the normal growth or thickness, T, can be assumed to be a simple linear function of the lateral growth. That is, $T = k\sqrt{A}$ where k is some proportionality constant. Solving for A gives $A = (T/k)^2$. Substitution of this value for A in [3] gives

$$(T_1/T_2)^2 = N_2/N_1 \qquad [5]$$

Electrocrystallization is very similar to other forms of crystallization, and by thermodynamic reasoning (8) it can be shown that the minimum radius of a crystal nucleus that will continue to grow is given by $R = Cs/G$ where C is a constant having to do with shape and interfacial relations, s is the surface energy (interfacial energy), and G is the free energy of the newly formed phase, all in consistent units.

In the case of electrocrystallization at a fixed temperature the interfacial energy is constant, and the free energy of the newly arriving metal ions will be measured by the difference between the energy they had as ions in solution and the energy they possess on sitting down on the substrate. This is given by the overpotential for deposition, e, the difference between the equilibrium potential and the actual potential required to produce deposition. Accordingly it can be said that

$$R = K/e \qquad [6]$$

where K is a new constant involving previous factors and the faraday.

If we consider the nucleus to be two dimensional at the start which is probably the case, and r is the radius of each individual atom of metal, then

$$\pi(K/e)^2 = bnr^2\pi$$

where n is the number of atoms in the nucleus and b is a constant having to do with the geometry of the arrangement. As a simple approximation in the case of copper, since the overpotential is relatively small, we can assume that the overpotential is directly proportional to the current density, I. This being so, the number of atoms forming a nucleus at a given current density, is proportional to one over the square of the current density, or

$$n \propto 1/I^2$$

Let m be the number of atoms deposited per unit of time per unit area which according to Faraday's law is proportional to I. Assuming the nuclei are formed in the first instant of time, the average number of nuclei formed at the start will be given by $m/n = N$. Thus N is proportional to $I/(1/I^2)$ or I^3. This line of reasoning, therefore, leads to the result that the number of nuclei formed at the start is proportional to the cube of the current density and as a result,

$$N_2/N_1 = (I_2/I_1)^3 \qquad [7]$$

Substitution of this value for N_2/N_1 in [5], gives

$$T_1/T_2 = (I_2/I_1)^{3/2}$$

or

$$T(I)^{3/2} = T_2(I_2)^{3/2} = T_1(I_1)^{3/2} = \text{a constant} \qquad [8]$$

But the average thickness of an electrodeposit varies directly with the number of coulombs $I\,t$, and accordingly,

$$T_1/T_2 = I_1 t_1 / I_2 t_2$$

If alternate substitutions are made for T and I in [8], using this last relationship, there results

$$t(I)^{5/2} = t_1(I_1)^{5/2} = t_2(I_2)^{5/2} = \text{a constant} \quad [9]$$

and

$$T_1/T_2 = (t_1/t_2)^{3/5} \quad [10]$$

If this theory is correct, we would expect that the relationship between current density and time and current density and thickness to take the forms shown in Eq. [8] and [9]. Likewise if a plot is made of the log of T_1/T_2 against the log of (t_1/t_2) the slope of the straight line, if it is a straight line, should be equal to 0.60 (3/5). The slope of the actual experimental line is 0.57 which is in excellent agreement with the theoretical value. A plot of Eq. [8] and [9] fits the experimental data fairly well but if $T(I)^{1.33}$ = a constant is plotted rather than $T(I)^{1.50}$ = a constant the smooth line through the experimental points shown in Fig. 4 is obtained and if $t(I)^{2.33}$ = a constant is plotted the smooth curve through the points of Fig. 5 results.

By assuming that the growth normal to the cathode is proportional to a power of the lateral growth, *i.e.*, $T = k(A)^{P/2}$ where p is an unknown power, and using the same type of procedure given above, we end up with the following relationships to replace [8], [9], and [10]:

$$T_1(T_1)^{3p/2} = T_2(I_2)^{3p/2} = \text{constant} \quad [8a]$$

$$t_1(I_1)\frac{3p+2}{2} = \text{a constant} \quad [9a]$$

$$T_1/T_2 = (t_1/t_2)\frac{3p}{3p+2} \quad [10a]$$

If $3p/3p + 2$ is set equal to 0.57, this gives $p = 0.883$ and substitution into [8a] and [9a] of this value gives $TI^{1.33}$ = constant and $tI^{2.33}$ = constant, with a better fit, as can be seen from the figures. It appears therefore on the basis of this evidence that the rate of growth normal to the cathode surface is almost but not quite a linear function of the rate of lateral growth. Because of possible errors in measurement and the appearance of exponential relationships, it may be that the first hypotheses is the correct one. Additional experiments will have to be performed in order to verify this. The hyperbolic power relationship shown here for copper is probably applicable to other deposits from simple solutions, at relatively low activation overpotentials. In the case of nickel which deposits at high activation overpotentials the number of nuclei formed will be very great (very fine crystals), and the technique used here for copper would be difficult to apply. Additional experiments are in progress in connection with the maximum stress in copper deposits in relation to these findings, which will be reported on in future papers.

Acknowledgment

The author would like to thank Mr. Wilfred Hung for assisting with the laboratory work, Mr. Russell Schoene for advice and assistance in connection with the electronic equipment, and Mr. Ed Reine for construction of the cell and other essential equipment.

This work was supported in full by National Science Foundation Research Grant GP-1678.

Manuscript received Sept. 22, 1964; revised manuscript received Dec. 18, 1964.

Any discussion of this paper will appear in a Discussion Section to be published in the December 1965 JOURNAL.

REFERENCES

1. J. B. Kushner, *Proc. Amer. Electroplaters' Soc.*, **45**, 28 (1958).
2. U. R. Evans and S. Shome, *J. Electrodepositers' Tech. Soc.*, **27**, 45 (1950-51).
3. J. K. Prall and L. L. Schreir, *Trans. Inst. Metal Finishing*, **38**, 9 (1961).
4. S. Weissman, *et al.*, Air Force Cambridge Labs., Project, 4608, Report No. 1, July, 1962.
5. T. B. Vaughn and H. J. Pick, *Electrochima Acta*, **2**, 179 (1960).
6. J. J. Becker, *This Journal*, **111**, 480 (1964).
7. D. R. Turner and G. R. Johnson, *ibid.*, **109**, 798 (1962).
8. G. M. Pound, "Liquid Metals and Solidification," p. 90, American Society for Metals, Cleveland (1958).

Growth of Single Crystal Cuprous Oxide from the Melt and Luminescence of Cuprous Oxide

Richard S. Zucker

Astrionics Division, Aerojet-General Corporation, Azusa, California

ABSTRACT

A number of crucible materials were evaluated for melting Cu_2O. Only MgO appears to be sufficiently nonreactive for use in crystal growing. A melt of cuprous oxide contained in a magnesia crucible when cooled at a rate of 2.5°C per hour produced large single crystals. Attempts to accelerate growth by cooling at a rate of 13.5°C per hour produced only small polycrystals. A (100) seed cut from the single crystal along natural cleavage lines was used to pull a crystal from the melt by the Czochralski method. A tendency to grow off-axis resulted in beautiful subsurface facets of transparent ruby-red material. Two new forms of luminescence were observed during rapid cooling of solid cuprous oxide. From 1175° to 1145°C continuous light emission was observed in the yellow-green region. From 1125° to 975°C flashing points of light were observed in the same spectral region.

Polycrystalline cuprous oxide rectifiers have been in use since 1929 as instrument and power rectifiers because of their excellent frequency response, resistance to pulse damage, and exceptionally high reliability and long life. These have been prepared by partial oxidation of copper sheets of the desired shape. Recently large area single crystals have been formed by annealing of polycrystalline cuprous oxide (1). No reports of crystal growth from the melt have been observed in the literature. One observer in 1933 reported failure to obtain crystal growth by the Bridgman or hydrothermal techniques (2). This paper describes the growth of ingots of single crystal cuprous oxide by the Czochralski method and some interesting phenomena observed during these experiments.

Experimental

A graphite resistance heated crystal furnace with sapphire Radiamatic control and linear down-drive (motor-driven downward adjustment of the tempera-

Table I. Evaluation of crucible materials for melting cuprous oxide

Run No.	Crucible material	Results at 1230°C in presence of Cu_2O
1	Alumina[6]	Highly reactive, not satisfactory.
2	Tantalum	Highly reactive, not satisfactory.
3	Graphite	Highly reactive, Cu_2O reduced to Cu.
4	Molybdenum	Reactive, alloys with metallic copper.
5	Magnesia (sintered)[6]	Best of all materials tried, only slightly reactive with melt over long periods of time.
6	Crystolon 63[1] (silicon carbide, oxynitride bonded)	Wetting, partial reduction to Cu, scum on surface.
7	Cerac 4[2] (aluminum nitride 95% silicon carbide 5%)	Violet wetting occurs, N.G.
8	Cerac 6[2] (aluminum nitride 55% silicon carbide 45%)	Violet wetting occurs, N.G.
9	Magnesia (single crystal)[6]	Melting without wetting occurs for 5 minutes. May be OK.
10	Lecotherm ceramic[3]	Soaked right through crucible on melting.
11	Zirconium silicate[4]	Soaked right through crucible on melting.
12	Cerac 2[2] (boron disilicide)	Strongly reductive, glass binder in crucible reactive with melt.
13	Boron nitride[5]	Most violent reaction of all, evolution of gas and ejection of contents from crucible.
14	Thoria[3]	Entire contents reduced to copper, which permeated walls of crucible.
15	Calcium zirconate[3]	Entire contents reduced to copper, which permeated walls of crucible.
16	Quartz[7]	Violently reactive to form copper silicate.
17	Zirconia[6]	Wetting of crucible, but no violent reaction. Scum formation limits time available.

Notes: [1] Carborundum Corp.; [2] Allis-Chalmers Corp.; [3] Leco Corp.; [4] Saxonburg Ceramic; [5] National Carbon Co.; [6] Norton Corp.; [7] Englehard Industries.

ture-set-point of the furnace controller) was used throughout this work. Baker Cu_2O powder was washed with benzene to remove the antioxidant (pine oil), dried, and weighed into the crucible. Argon (99.998%) or helium at 10 CFH was used for the furnace atmosphere. Subsequent experiments proved that the same results were obtained by weighing the unwashed Cu_2O directly into the crucible and removing the antioxidant by a vacuum heat treatment prior to melting. The crucible materials used are shown in Table I. About one-third reduction in volume of the powder is observed prior to melting, and a gradual change in color of the powder from ruby red to violet to black was noted. Norton RM-5480 Magnesia crucibles were used when pulling crystals using (100) seeds 5 x 5 x 25 mm cut from slow cooled runs. The seeds showed an approximate 70°32′ cleavage angle characteristic of (111) $\wedge$ (111) cuprite octahedrons. A natural crystal of cuprite may also be used as a seed. Slow cooling at a linear rate of 2.5°C per hour was easily obtained by automatic reduction of the power input to the furnace. Cooling at a rate of 13.5°C per hour produces polycrystalline material. At the melting point of cuprous oxide (1230°C) a change in apparent emissivity is evident, the melt appearing much brighter than the solid. The optimum pulling rate was found to be 1.75 cm/hr. The crucible was rotated at a speed of 10 rpm throughout all 28 runs in order to minimize uneven heating of the crucible. In addition, during some runs it became necessary to rotate the seed in an opposite direction at the same rate (10 rpm), making a total rotation rate of 20 rpm. The thermal fluctuations observed on the recorder during a typical run at equilibrium at the melting point of Cu_2O amounted to a maximum of 1.7°C, but the actual stepless controls of the furnace provide probably 0.2°C responsivity or better, if properly adjusted. A number of small crystals approximately 1 cm in diameter were easily grown using seeds. However, only one large irregular shaped crystal was grown which is shown in Fig. 4. The maximum diameter of this crystal was about 3 cm. The gross impurity in this crystal consisted of microscopic tree-like growths of metallic copper as determined by viewing a section of the crystal through a strong light. These apparently did not affect the single crystal of Cu_2O. In addition, some areas of this crystal were covered with a thin black surface layer of cupric oxide, CuO, which was easily removed in dilute hydrochloric acid before examination. No spectrographic or other methods were used to determine trace impurities, although from examination of the crucible attack after the run, it is strongly suspected that magnesium was picked up by the melt during a period up to several hours' contact with the molten cuprous oxide. The crystal, when viewed from the top during pulling, will show characteristic fourfold symmetry with light reflected off the (100) facets. These may not be present in all cases, as they seemed to predominate only when the crystal tended to grow off axis. Also, the crystal may tend to be lopsided due to freezing out of crucible reaction products on the crucible walls. Considerably more difficulty in growing cuprous oxide may be expected compared with silicon crystals due to the reactivity of the melt with magnesia. The single crystal character of the pulled crystal was confirmed by x-ray diffraction techniques (forward and back reflection Laue photographs).

After pulling is completed and during rapid cooling (approximately 100°C per min) of the remainder of the solid in the crucible, one or two luminescence phenomena may be observed, depending on the crucible material used. From 1175° to 1145°C the solid will instantaneously emit a burst of yellow-green light, L_1, which will diminish in intensity as the melt cools further, extinguishing at approximately 1145°C. No attempts were made to study the spectral characteristics of this high-temperature luminescence phenomenon, L_1. Over a much wider range of temperature (1125°-975°C) intermittent flashes of yellow-green light of 0.2-2 sec duration, L_2, will be observed. Cinespectrograph film measurements of the radiation of cuprous oxide over the temperature range 1125°-975°C show an absorption band in the yellow region of 0.56-0.60μ, and no emission lines or bands in this region are evident. The cinespectrograph used in this experiment consisted of a conventional slit, collimator, grating, lens, and film system. The film handling mechanism was a 35 mm cine camera permitting a sequence of spectra to be made at a rate of 10/sec. A lens in front of the slit serves as a light-gathering device for use with distant sources. It was not possible to focus this lens on the nearby source used in this experiment. Under these circumstances, therefore, emission lines from a blinking low-intensity point source on top of a 1200°-1300°K black body might easily have remained undetected. The emission wavelength is unknown at the present time. A more elaborate system would be required to determine the wavelength of emission of this radiation. These flashing lights appear at random throughout the solid and are especially intense wherever the Cu_2O has wetted (reacted with) the crucible walls. They remain of constant intensity throughout the above temperature range and then suddenly disappear at approximately 975°C. The high-temperature (continuous) light phenomena will be referred to as L_1, since it is the first to be observed on the cooling curve, and the lower temperature (flashing) light phenomena will be referred to as L_2 throughout the discussion. Both L_1 and L_2 can be repeated at will without any loss of intensity by reheating the contents of the crucible and cooling at the same rapid rate. Neither can be observed by cooling at a slow rate (10°C per min or less) or on the normal heating cycle.

Discussion

The best crucible materials are those which were compacted to the greatest degree during manufacture. To that extent the best results might be obtained from the use of single crystals of the respective materials, if available, by hollowing them out to form crucibles. On the basis of observed order of chemical reactivities with the melt, it might be predicted that crucibles made of beryllia would be less reactive than magnesia

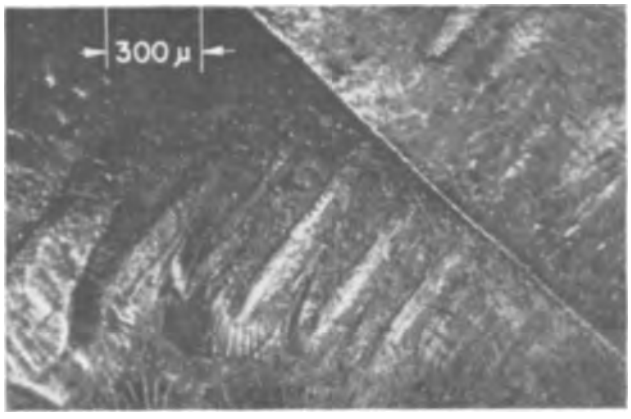

Fig. 1. Single crystal of cuprous oxide showing ridge along (100) sub-surface facet.

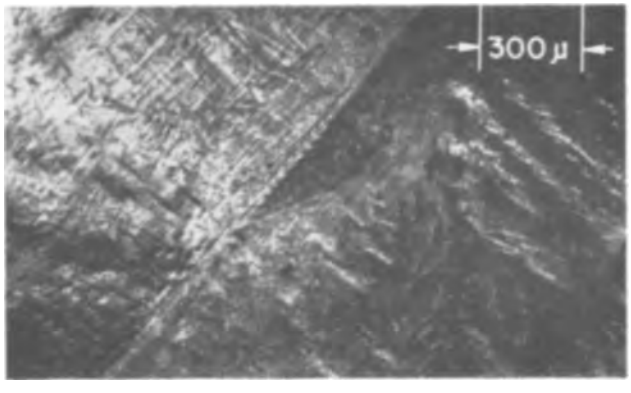

Fig. 2. Single crystal of cuprous oxide showing ridge along (100) sub-surface facet and light reflected off facet (left).

which is less reactive than alumina. Due to toxicity BeO crucibles were not tried, however. Crucibles made by pressing MgO slurries in a laboratory press were unsatisfactory due to porosity. However, use of a Pt crucible coated with MgO has been reported (3).

A microscopic view of the grown surface of a single crystal of cuprous oxide is shown in Fig. 1 and 2. The ridge along the edge of the facet is clearly shown here. The plane angle of the facet measured 90° ± ½°, characteristic of a (100) face (see Fig. 3). However, the vertex of this angle is inclined approximately 45° toward the seed axis indicating a shortening of the third cubic axis to form a rhombohedral pseudo-symmetry (4), although not clearly shown in Fig. 3 or 4. Cuprite (natural cuprous oxide mineral) belongs to the plagiohedral or gyroidal class of the isometric system because the faces of the general form (hkl) are arranged in spiral order. This class is rare among minerals and is represented, almost uniquely, by cuprite. It is interesting to note that because of this character, cuprous oxide may be expected to show circular polarization of light.

All material grown was p-type except one run made in a Ta crucible, which was strongly n-type and highly impure due to reaction of the melt with the tantalum crucible. It is suspected that almost degenerate doping with Ta resulted in this anomaly. Attempts to repeat this with 1% TaC (tantalum carbide) added to Cu_2O in a magnesia crucible resulted only in p-type material. Measurements made on typical crystals using silver paste to provide ohmic contacts are shown in Table II. These results show a hole mobility somewhat higher (about one order of magnitude) than that shown in the literature (5, 6).

A simple etch for revealing grain boundaries was 28% ammonium hydroxide for 5-30 min. For removing CuO deposits 3*N* HCl was found to be suitable.

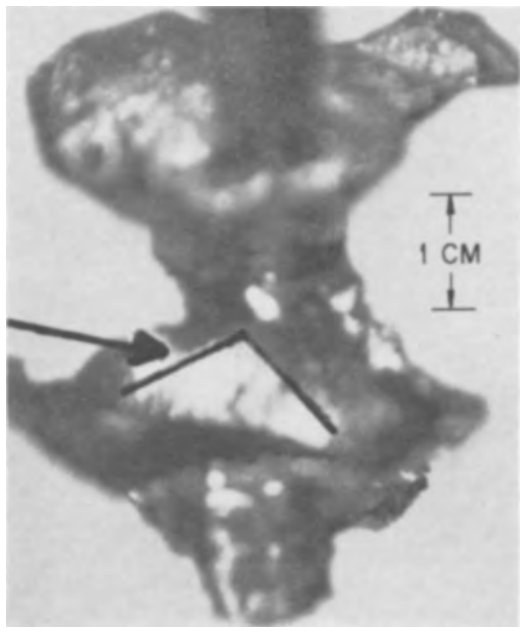

Fig. 3. Side view of pulled crystal of cuprous oxide showing light reflected off sub-surface (100) facet (arrow) and 90° plane angle (lines). Crystal was pulled out of melt rapidly to freeze the growth pattern, hence difference in diameter. The plane angle measured 90 ± ½°. Apparent distortion is due to perspective of the camera.

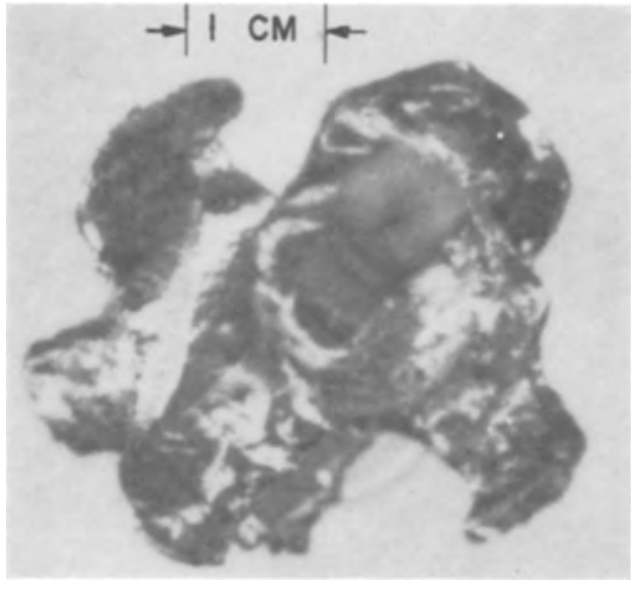

Fig. 4. Top view of Cu_2O crystal showing (100) seed

Luminescence

It is obvious from the limited data presented in this paper that a mechanism for the observed light emission cannot be put forth, particularly in view of the lack of data on the wavelength of emission. The two luminescence phenomena may not even be related in their mechanisms. Furthermore, both phenomena correspond to an "inverse thermoluminescence" since the emission is observed only on the cooling curve and not

Table II. Typical properties of single crystal cuprous oxide

Conductivity type	p
Resistivity, ohm-cm	4×10^3-16×10^3
Hall constant, cc/coulomb	2.1×10^6-2.2×10^7
Mobility, cm²/volt-sec	480-1300
Carrier concentration, carriers/cm³	3×10^{11}-3×10^{12}

on the heating curve. This is exceedingly difficult to explain. One is therefore forced to look for less obvious reasons such as possible phase changes in the system or the excitation of an impurity in the material. A brief review of the literature given below may be of interest at this point.

1. An anomalous vapor pressure curve has been reported for cuprous oxide (7, 8), because of the formation of a eutectic with cupric oxide. The vapor pressure of oxygen in equilibrium with liquid Cu_2O at 1230°C (mp of Cu_2O) is 0.6 Torr. This vapor pressure increases to 402 Torr in cooling to 1080°C (CuO-Cu_2O eutectic). Since the observed emission of L_2 is in the range of 1125°-975°C, this emission may in some cases be related to the CuO-Cu_2O eutectic at 1080°C, since it is known that CuO is present at least on the surface of the melt.

2. A rapid cooling rate of over 100°C per min is certainly a nonequilibrium condition, which may under these circumstances allow electronic transitions to occur which might otherwise be forbidden (9, 10).

3. Differential thermal analysis is indicated to explore the region 400°-1300°C to correlate light emission with perhaps extremely minute changes in the localized rate of cooling. No high-temperature phase changes have been reported for Cu_2O. However, crystallographic changes between 25° and 400°C have been reported (11) for cuprous oxide and similar changes for cuprous chloride (12).

4. The photoconductivity of Cu_2O is very complex (13), a maximum occurring at 0.57μ but complicated by "steps" in the absorption edge due to multiple level transitions, particularly in the yellow and green series of exciton absorption spectra (14) at 77.3°K. It is not known how this might affect the results observed.

In conclusion, it may be said that more precise measurements of the radiation observed will be required to resolve the exact nature of this luminescence. This may be rather difficult, in view of the transient as well as high-temperature nature of the phenomena.

Acknowledgments

The author is pleased to acknowledge the technical discussions of Dr. P. N. Russell and Dr. R. H. McFee. Interpretations of the cinespectrograms by Mr. Carleton W. Clench are greatly appreciated.

Manuscript received Oct. 13, 1964.

Any discussion of this paper will appear in a Discussion Section to be published in the December 1965 JOURNAL.

REFERENCES

1. R. S. Toth, R. Kilkson, and D. Trivitch, *J. Appl. Phys.*, **31**, 1117 (1960).
2. E. Englehard, *Ann. Phys.*, **17**, 501 (1933).
3. F. H. Smyth and H. S. Roberts, *J. Am. Chem. Soc.*, **42**, 2582 (1920).
4. W. E. Ford, "Dana's Textbook of Mineralogy," 4th ed., John Wiley & Sons, New York (1958).
5. J. S. Anderson and N. N. Greenwood, *Proc. Roy. Soc. (London)*, **A215**, 353 (1952).
6. J. Bloem, *Philips Research Repts.*, **13**, 167 (1958).
7. M. Randall, R. F. Nielsen, and G. H. West, *Ind. Eng. Chem.*, **23**, 391 (1931).
8. H. S. Roberts and F. H. Smyth, *J. Am. Chem. Soc.*, **43**, 1061 (1921).
9. J. H. deBoer and J. W. Verway, *Proc. Phys. Soc. (London)*, **49**, 59 (1937).
10. W. Schottky and F. Waibel, *Phys. Z.*, **36**, 912 (1935).
11. T. Ikada, *J. Phys. Soc. Japan*, **4**, 140 (1949).
12. M. R. Lorenz and J. S. Prener, *Acta Cryst.*, **9**, 538 (1956).
13. E. F. Gross, *Uspekhi Fiz. Nauk.*, 575 (1957).
14. F. L. Weichman, Ph.D. Thesis, Northwestern University (1958).

Poisoning and Gettering Effects in Silicon Junctions

E. J. Mets

Rectifier Components Department, General Electric Company, Auburn, New York

ABSTRACT

A study was made to obtain an understanding of the factors involved in the "poisoning" phenomena which are responsible for high reverse currents in silicon junctions. A tentative model has been proposed which describes the conditions by which fast diffusing metal impurities can precipitate within junction regions under certain high-temperature ambients and yet not under others. Oxygen appears to be a significant factor which can control the degree and location of such metal precipitation. The role of oxygen was investigated in its relation to impurities and defects in silicon. Its importance was demonstrated by copper-oxygen reactions, oxygen tie up complexing to form SiO_4^+ donor states, and by the effect of induced dislocations.

Considerable effort has been applied to the study of soft reverse characteristics of p-n junctions as indicated by excess reverse current below their normal avalanche breakdown voltage. The origin of this high leakage current is believed to be localized high electric fields caused by precipitated metal particles within the junction region. Goetzberger and Shockley (1, 2) have shown that metals with temperature dependent solubilities in silicon, such as Cu and Fe, can form precipitates through which current flows by Zener tunneling as a result of the high fields. However, certain diffusion processes do yield devices which have good electrical characteristics whereas other high-temperature processes cause degradation of junctions. Prior to this work no explanation as to why and how these precipitates occur in the bulk and junction regions of Si has been offered. As these undesired impurities are introduced into silicon to some degree by all such processes, there must be some controlling factors which reduce or prevent these impurities from collecting in junction regions in some cases but not in others. It is the purpose of this study to investigate those conditions which lead to the poisoning phenomenon and to establish a tentative model by which such precipitates locate in bulk silicon.

Previous observations.—It has been observed that diffused p-n-p structures as formed by Ga sealed-tube techniques yield "hard" breakdown (*i.e.*, devices which show negligible poisoning effects but exhibit avalanche breakdown characteristics). Subsequent oxidation procedures cause these reverse characteristics to become "soft" or poisoned. Typical characteristics are shown in Fig. 1.[1] Later phosphorus diffusion generally causes a poisoned unit to return to its original characteristics. The following discussion of the effects of each of these

[1] All devices were surface contoured to confine the avalanche regions to the body rather than the surface of the device. Further information concerning this technique can be found in a paper by R. L. Davies and F. E. Gentry entitled, "Control of Electric Fields at the Surface of p-n Junctions," *IEEE Transactions on Electron Devices*, July, 1964.

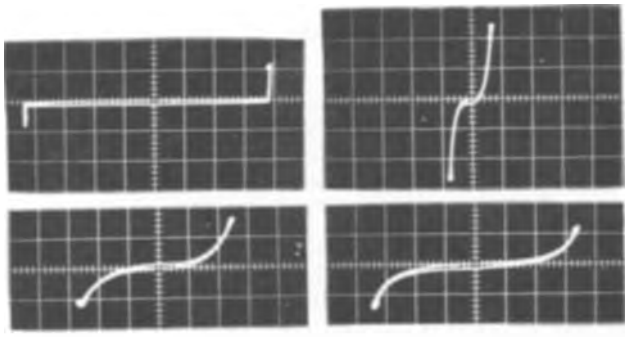

Fig. 1. Typical reverse characteristics of Ga diffused p-n-p junctions showing relative effect of cooling rate exposure to oxygen ambient at 1200°C: Vertical axis 5 ma/div; Horizontal axis 200 v/div. (a) (top left) as diffused; (b) (top right) furnace cool, 250°C/hr; (c) (bottom left) slow cool, 15°C/hr; (d) (bottom right) quenched.

three high-temperature operations results in a model which describes mechanisms that affect precipitation of these impurities in junction regions.

The formation of p-n-p structures by the normal sealed tube technique employs a Ga source along with silicon wafers which are sealed in a quartz capsule and back filled with argon through a liquid nitrogen trap. Avalanche-type electrical characteristics are ascribed to three possible effects. (*A*) The system is clean, free of poisoning impurities; (*B*) simple, glassy phase gettering occurs on the silicon surface; (*C*) fast diffusing impurities are removed by surface reactions which occur due to a lower partial pressure of oxygen in the sealed tube. In practice the first two are not probable. Deliberately poisoned Ga p-n-p structures, sealed in argon and heat-treated without a Ga source, are brought back to their original sharp characteristics with a significant increase in minority carrier lifetime. As no liquid phase is present, some other mechanism than glassy phase gettering must take place. This is probably the same means by which good p-n-p structures are originally formed. At the diffusion temperature (1250°C), metallic impurities are considered to be present from the source, quartz, gas ambient and on or in the silicon. The solid solubility of these impurities in silicon will be in equilibrium with phases present (such as oxides or gas) and dependent on temperature. On cooling, precipitation of these metallic impurities can occur because of decreasing solubility. A driving force to the surface is necessary to prevent precipitation in the vicinity of the junction. Such surface reactions can take place under a low partial pressure of oxygen by forming stable compounds of an oxygen complex. It has been shown by Schwuttke (3) that impurities such as copper will locate preferentially at regions of high oxygen concentration. This migration of residual oxygen in the silicon toward the surface would be a sufficient driving force for the removal of these fast diffusing impurities.

Under conditions of open-tube oxidation, silicon is exposed to temperatures 1100°-1250°C under wet or dry oxygen ambient to form an oxide phase on the silicon surface. Simultaneously, oxygen diffuses into the silicon along with undesired impurities. On cooling, precipitation of these impurities will occur at structural defects in the bulk with the size and location of the precipitates governed to some degree by the cooling rate. Sites of high oxygen concentrations can be formed in the bulk, thus preventing the mechanism of transport of fast diffusing impurities to the surface.

In fabricating p-n-p-n devices, phosphorus diffusion of the n-type emitter junctions often will restore p-n-p units which have been previously poisoned by the oxidation-mask step. In this two-step phosphorus diffusion process, first a phosphorus-silicate glass is formed under nitrogen or oxygen. Here an apparent liquid phase gettering effect (1) takes place. Normally, after this first predeposition step, the glass formed is removed prior to a higher temperature diffusion anneal under oxygen. It can be assumed that under these conditions liquid phase gettering is not present but rather some other mechanism is responsible for the prevention of downgrading. This might be explained by high surface doping concentrations which strain the lattice and thereby form dislocations at the surface. Prussin (4) and Quiesser (5) have shown that the stress introduced by solute contraction of phosphorus and boron in silicon is sufficient to generate dislocations. With these dislocations present, a "sink" can be formed, trapping fast diffusing impurities as "atmospheres" of the dislocations or by complexing with oxygen in these regions.

A poisoning model.—The model suggests that a controlling relationship exists between the gas ambient (particularly oxygen) and the type of diffused donor or acceptor impurity in silicon. It appears that the degree and location of such precipitation of fast diffusing metal impurities is influenced by the oxygen movement in the silicon. Clustering or precipitation of these impurities will occur at sites of high oxygen concentration, forming oxygen complexes and thus reducing the metal impurity level in other regions of the silicon. Oxygen will form atmospheres around diffusion induced dislocations thus depleting adjacent areas of oxygen and metallic impurities. Considerable evidence has been obtained to support this concept. These experiments have been based on copper-oxygen reactions, oxygen complexing to form SiO_4^+ donor states and surface induced dislocations.

Experimental

In an effort to determine the source of contamination, various parameters of the open tube systems were evaluated. Ga-diffused p-n-p wafers were chosen for this initial study. These structures offered good initial reverse avalanche-type characteristics which are sensitive to the poisoning phenomena.

Gallium diffused p-n-p structures, which were formed in chemically polished 20-22 ohm-cm n-type Si, generally had a junction depth of 3 mils and a base region of 3 mils so that avalanche voltages of 700-900v were obtained. Wafers were pelletized to a diameter of 0.640 in. and subsequently edge beveled to a 6° angle to eliminate surface effects. In all tests only avalanche type p-n-p wafers were selected for evaluation. Cleaning prior to heat-treatments were kept the same for all tests, except when specifically altered to study the effect of different cleaning cycles. This standard cleaning consisted of hot solvents, hot alkaline cleaning; HF:HNO_3 etch modified with iodine, and HNO_3 boil. Each step was followed by a large number of deionized water rinses.

From these initial experiments it was established that poisoning of the reverse characteristics of Ga p-n-p's could be accomplished at temperatures greater than 700°C under an oxygen ambient. With increasing temperatures, up 1250°C, there appears to be no significant correlation between temperature and the degree of electrical characteristic softening. This effect is observed regardless of prior pellet cleaning treatments and special care observed to prevent contamination by the furnace and the quartz tube, the latter being coated with a sodium-silicate glass to form a gettering sink on the surface. The use of an ultra-pure ambient oxygen did indicate some improvement in reverse currents.

Under a given set of experimental conditions, cooling rate of the p-n-p structures from 1250°C in oxygen did show pronounced effects in the degree of softening observed. Typically, a quenching rate such as 500°C/min in an oxygen ambient causes the least degree of poisoning whereas a furnace cool of 250°C/hr from 1250° to 900°C resulted in the highest degree of poisoning. By approaching equilibrium conditions with a cooling rate of 3-7°C/hr from 1250° to 900°C, harder avalanche breakdowns resulted than the furnace cool.

These typical reverse characteristics are shown in Fig. 1. Interrupted cooling was carried out by furnace cooling from 1250° to 1000°C and holding for 15 hr, then moderately quenched to room temperature by pulling the pellets out of the furnace slowly. The purpose of this experiment was to form SiO_2 precipitates as described by Kaiser (6); these precipitates should serve as complexing sites for metallic impurities. This process did result in considerable improvement over the normal furnace cool with reverse characteristics similar to that obtained by rapid quenching.

The most significant parameter was that effect observed by different gas ambients. No downgrading resulted at any temperature up to 1200°C when exposed to an argon ambient and allowed to furnace cool. On quenching some small degree of softening occurred. From these results it was felt that downgraded units could be "gettered" back under these conditions. Such p-n-p units obtained from various conditions of heat-treatment were sealed in a quartz ampoule under argon, heated at 1200°C for 1 hr, and allowed to furnace cool. In every case avalanche type characteristics were obtained with voltage 10-20% less than the original values. Lifetime values were increased by a factor of two to four above the initial values immediately following diffusion (hereafter defined as "as diffused"). Poisoning was also prevented by exposure of the p-n-p's in a hydrogen ambient at 1000-1100°C. However, electrical characteristics previously softened by oxidation treatments were severely poisoned on exposure to hydrogen. Under nitrogen at temperatures above 800°C, significant softening occurred.

Effect of Oxygen with Impurities and Defects in Silicon

The results from preliminary experiments indicated the oxide phase and/or oxygen ambient have some influence in the transport mechanism of impurities in Si. Motivated by these results, further investigations were made to determine the role of oxygen and its relation to impurities and defects in Si. In these experiments the behavior of oxygen was evaluated by converting the dissolved oxygen into SiO_4^+ donor states. The effects of diffused Cu and surface induced dislocations during oxygen diffusion and the subsequent effect on this oxygen-formed donor level was the basis of evaluation.

Oxygen complex (SiO_4^+).—Oxygen when diffused into Si can form donor states under suitable time and temperature conditions (7). These donor states, SiO_4^+, appear to form by association of groups of four oxygen atoms with one Si atom at a temperature of 450°C and reach a maximum level in about seventy hours. The degree to which the donor level will form is dependent on the dissolved oxygen. Logan and Peters (8) report the maximum solubility of oxygen in Si at 1250°C to be 3×10^{17} at./cm^3, which offers a maximum donor level of 1×10^{15}/cm^3 (8).

Experimentally, oxygen was diffused into polished p-type Si slices of 30-100 ohm-cm resistivity (net impurity concentration less than 3×10^{14} at./cm^3). One half of this lot was sealed in a quartz ampoule under argon, and the other half was used as a control lot. In the sealed tube, a portion of the slices had the oxide removed, and the other half the oxide was left intact. These were heat treated at 1250°C for the same periods of time as they were originally oxygen diffused, *i.e.*, 30 min to 3 hr. After this heat-treatment they were annealed at 450°C for 72 hr along with control slices which were not heat treated previously in argon.

From microscopic examination of stained cross sections, n-type layers were observed on the control slices to depths up to 1.5 mils depending on resistivity of the starting material. Those slices which were argon heat-treated with the oxide removed did not show any conversion. Silicon with the oxide left on converted, but to a lesser degree.

This effect was also observed when cooling rates that approached equilibrium conditions were used following open tube oxidation. In an earlier investigation, we had found that cooling rates of 3-15°C/hr, from 1250° to 900°C, prevented the formation of SiO_4^+ complexes. From these results it was postulated that this cooling rate would permit oxygen to form stable precipitates (SiO_2) or possibly diffuse to the surface of the slice. Under these conditions, therefore, the oxygen is tied up or reduced to level below which the conversion to donors is detectable.

Role of copper and oxygen.—The relationship between oxygen and the poisoning impurity should be determined. It appears that some residual oxygen is required to form favorable sites for nucleation and precipitation of such impurities away from the junction region but near or at the surface. The presence of an oxide phase on Si (always prevalent under an oxidizing ambient) would allow such precipitation to occur internally within the Si at many possible structural defect sites. The size of such precipitates would be governed by the precipitation kinetics of the species involved.

Some idea of these kinetics may be gleaned by examining the effects of Cu and oxygen such as offered by the investigations of Schwuttke (3). Results from that study show Cu to precipitate at regions of high oxygen concentrations with the possible formation of copper-oxygen complexes. It was also shown that dissolved oxygen will form atmospheres around dislocations thereby depleting adjacent areas of oxygen. Therefore, the presence of high concentrations of diffused oxygen should be a favorable location for the precipitation of impurities such as Cu during cooling.

As the normal impurity level of a species such as Cu is too low to be resolved by infrared examination, Cu was diffused into Si to decorate dislocation (9) sites with and without diffused oxygen. By observing the degree of decoration, as to size and shape, and to the level at which it occurs, a correlation with diffused oxygen appeared possible.

Chemically polished 20 ohm-cm n-type Si was oxygen diffused at 1250°C with a maximum surface concentration of 3×10^{17} at./cm^3. The time of diffusion was adjusted so that complementary error function gradient of probable oxygen would result in a level $\sim 1 \times 10^{14}$ at./cm^3 at a distance of three mils from the surface. A shallower diffusion was also made to the same level one mil from the surface. Along with controls containing only residual oxygen, Cu was diffused at 900°C for 10 min and rapidly quenched to room temperature.

By polishing in 0.2 mil increments from the surface and examining the slices with infrared, Cu was found to be precipitated in the high oxygen concentration regions near the surface. Unlike the control slices which showed fine dispersion of decorated dislocation tails, the samples containing oxygen were decorated by copper in the form of star-like clusters. This is similar to that observed by Schwuttke.

Effect of dislocation traps.—Realizing the effect of dislocations as trapping sites for oxygen and impurities such as copper, it was felt that such a site, if it can be introduced at the surface during diffusion, would offer a sink for fast diffusing impurities. The effect of cold working, introducing a stress, and subsequent heat-treatment to elevated temperatures would result in the formation of dislocations. Such line defects must be terminated, either by a surface, a grain boundary, or they may form closed loops. We could expect that in single crystals they would either propagate through the crystal, or form a loop with one surface. If such terminated loops could be produced at the surface, trapping at elevated temperatures of these impurities with an affinity for forming "atmospheres" with dislocations would appear possible.

It is known that a certain amount of damage is introduced into the surface of Si by impact loading, resulting in a stressed surface condition. On heating to some specific temperature, this stress will be re-

lieved with some resultant plastic deformation and subsequent formation of dislocations. Beveled Ga-diffused p-n-p pellets were stressed in this manner by sandblasting the surfaces lightly with a fine grit of 10μ size. Alternate surfaces and both surfaces of beveled pellets were sandblasted to evaluate directional effects of gettering. These units, along with control pellets were exposed to the standard oxidizing conditions of 1200°C for 30 min and furnace cooled. Etching the pellets first in HF to remove the oxide followed by 20 sec in CP-6 modified with iodine was sufficient to obtain the original avalanche characteristics on all the sandblasted units, regardless of the side on which the dislocations were introduced. Control pellets were badly downgraded.

Further experiments were made under longer oxidizing conditions up to 5 hr at 1250°C, always resulting in unpoisoned units. If the sandblasted pellets were quenched very rapidly from any of the oxidizing conditions, downgraded characteristics were obtained. However, reheating at 1200°C in oxygen for 30 min and furnace cooling restored the original electrical characteristics.

To evaluate trapping ability of the introduced dislocation "sponge" at the surface, Ga diffused p-n-p wafers were Cu diffused at temperatures of 900°-1200°C under oxygen and furnace cooled. No poisoning occurred with those pellets having surfaces in a lapped or sandblasted condition. By infrared examination, Cu precipitation effects could not be observed whereas the control slices always showed a large degree of either finely dispersed or gross precipitates in the crystal. Quenching of Cu diffused p-n-p wafers from 900°-1200°C under oxygen always resulted in severely poisoned units. Fine dispersed decorated dislocations were always present in the crystal and subsequent removal of this precipitation was accomplished to a large degree by reheat-treating at 1200°C followed by a furnace cool.

The rapid mobility of copper was first demonstrated by the following experiment: One side of a p-n-p wafer was chemically polished and the other side was finely sandblasted. Then drops of $CuNO_3$ solution were placed on the polished side with care being exercised to keep the sandblasted side free of copper. Next the slice was heat treated in oxygen at 1000°C for 30 min and quenched at a rate of 500°C/min. No downgrading of the reverse characteristics resulted. Moreover, after chemically polishing the sandblasted side, no copper precipitation was observable by infrared examination. However, p-n-p slices that were chemically polished on both sides and subjected to the same process had electrical characteristics which were badly softened and also showed heavy copper precipitation throughout the slices.

Surface induced dislocations on copper and oxygen.— It has been shown in this study that surface induced dislocations have a definite effect in preventing the downgrading phenomena, both in the formation and oxidation of p-n-p units. Copper decoration and infrared examination showed that impurities such as Cu are removed to a very significant degree by dislocation effects. However, it is possible that oxygen also contributes to this mechanism by forming atmospheres around these dislocations sites at the surface.

Oxygen was diffused into p-type Si having chemically polished, sandblasted and lapped surfaces with resistivities of 30, 54, 63, and 100 ohm-cm for 3 hr at 1250°C under wet O_2. One lot was allowed to furnace cool (250°C/hr) and the second lot was quenched to room temperature. After removing the oxide, both lots were annealed at 450°C for 84 hr. These were cross sectioned and stained to reveal any n-type conversion caused by oxygen-silicon interaction to form SiO_4^+. These results are illustrated in Fig. 2. Typically, n-layers were formed in the polished wafers, in some cases with a thin p-layer at the surface. In the lapped and sandblasted wafers, a thin 0.1-0.2 mil but nonuniform n-layer formed at the surface. This thin surface n-region was delineated by a p-type layer and another deeper n-region. Only a p-region more highly doped than the base was observed under the shallow n-surface layer in the sandblasted samples. In the resistivity range tested, no significant difference was observed between the type of structure formed by quenching or furnace cooling. By re-annealing at 575°C for 20 hr, the deep n-type conversion layers formed in the polished and lapped slices were removed. Under these conditions, the SiO_4^+ complex is disassociated. The thin n-surface layer on the lapped and sandblasted slices could not be annealed out at this temperature.

Fig. 2. Typical effect of various surface treatments on the formation of the SiO_4^+ complex from oxygen diffused into 54 ohm-cm p-type Si at 1250°C for 3 hr, 250°C/hr cooling rate; after 72 hr anneal at 450°C; beveled X-section depth magnified 10X. Microscope 60X.(a) Chemically polished surface.

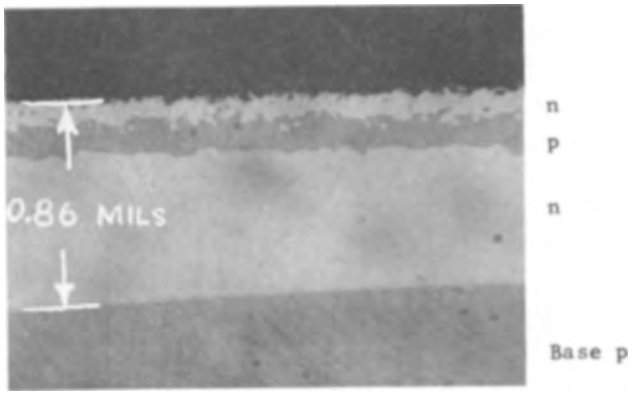

Fig. 2b. Lapped surface

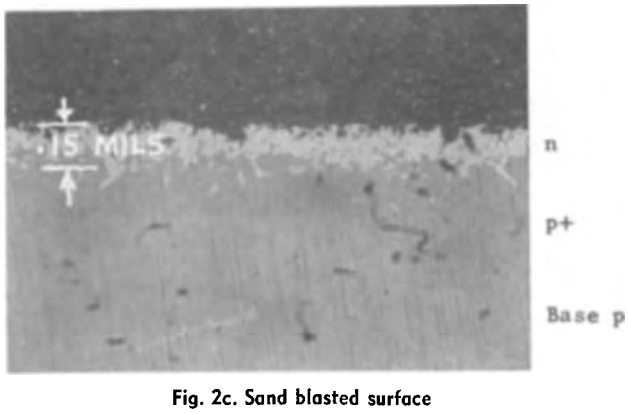

Fig. 2c. Sand blasted surface

The previous experiments were repeated except that Cu was diffused into the oxidized Si prior to annealing at 450°C. The diffusion of Cu was carried out under two temperature conditions; one at 900°C for 15 min and another at 1200°C for 20 min, to obtain different copper solute levels in the Si. A sig-

Fig. 3. Effect of Cu diffusion on the formation of the SiO_4^+ donor level in 54 ohm-cm p-type Si; beveled X-section depth magnified 10X; microscope 60X. (a) Typical n-layer formed by diffused oxygen.

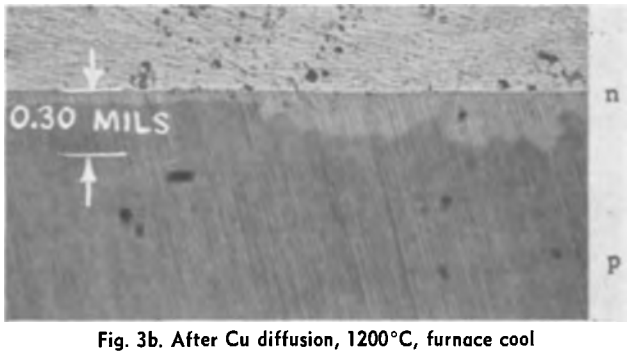

Fig. 3b. After Cu diffusion, 1200°C, furnace cool

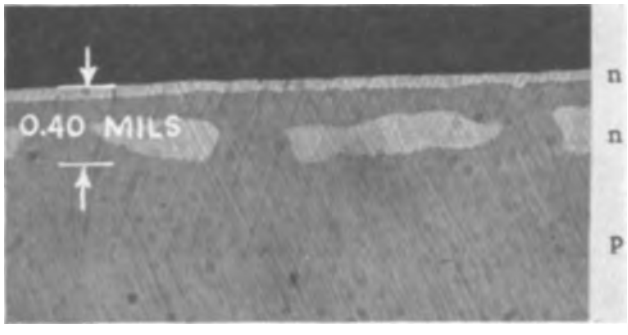

Fig. 3c. After Cu diffusion, 1200°C, quenched

nificant effect of Cu was observed in the donor formation after annealing at 450°C.

Typical results are shown in photomicrographs of Fig. 3. Directly after Cu diffusion from 1200°C, both quenched and furnace cooled polished slices showed an n-layer ~ 0.1 mil deep not observed on slices diffused with Cu at 900°C. After annealing at 450°C, n-layers formed on polished control slices (no Cu) and were partially eliminated on those which were Cu diffused. The effect was more pronounced when the Cu was quenched from diffusion temperatures. No significant effect of Cu on the oxygen formed donor level was found between sandblasted and lapped wafers as compared to polished control slices.

Oxygen-transport concept.—The concept of fast diffusing impurities locating at the silicon surface during nonoxidizing heat-treatments was further tested qualitatively. Wafers of 20 ohm-cm n-type silicon were prepared in three lots having chemically polished, lapped, and sandblasted surface finishes. These were oxidized in wet O_2, forming 12,000Å of oxide on their surfaces. The oxide was removed from one half of each lot and, along with control wafers which were not previously oxidized, they were Ga diffused in the standard sealed tube process. Typically, p-n-p junctions formed through the oxide on the polished slices showed downgraded reverse characteristics. Those formed without an oxide present had hard breakdowns, but the breakdown voltages were slightly less than the standard control slices. Sandblasted and lapped wafers with the oxide left on showed the same hard avalanche voltage breakdown as the control slices; whereas, those units with sandblasted surfaces from which the oxide had been removed, showed slightly higher voltages.

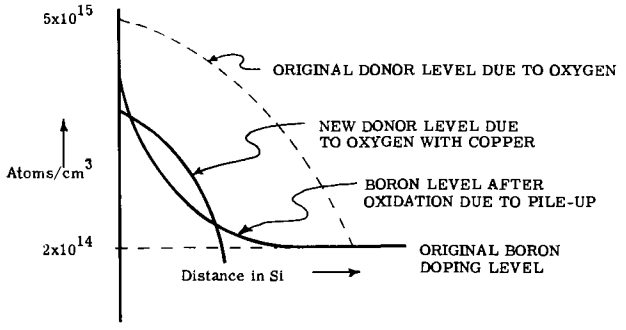

Fig. 4. Concentration profile diagram showing probable effect of Cu on the donor level (formed by oxygen).

Discussion

The purpose of this investigation was to show that a relationship exists between oxygen, the oxide phase, and fast diffusing metal impurities in terms of both the degree and location of metallic precipitation in silicon. The effects of Cu used as an example in these experiments does not necessarily indicate that other fast diffusing metal impurities behave in the same manner. Dash (10) has shown that Au does not offer any observable precipitation. The precipitation kinetics of other metals such as Fe and Ni can be different than that of Cu. However, results have been obtained here which show that such precipitation in the bulk can be effectively prevented without glassy-phase surface gettering. The experiments with Cu and its effects in repressing the SiO_4^+ donor complex indicates ion-pairing as a possible mechanism. The SiO_4^+ donors formed as a result of diffused oxygen can be used as a sensitive measure of the oxygen level and can indicate effectively changes that take place within the silicon.

The effect of Cu on oxygen donor formation on chemically polished slices may be explained as follows. From photomicrographs of Fig. 2a and 3a, we can see the typical donor layer which is formed by oxygen conversion with no added Cu present. In some cases a p-layer has formed on the surface. This can be depicted by the concentration profile diagram of Fig. 4.

From the appearance of the layers formed, the p-type surface layer is assumed to be the result of boron pile-up during oxidation. If this pile-up at the surface exceeds the concentration of donors formed, a p-layer will predominate.

With Cu subsequently diffused into the Si, depending on its solubility level, and whether it was quenched or furnace cooled, the original donor level would be reduced by the tie-up of diffused oxygen and Cu. The p-layer which forms in the lapped wafers can be attributed to boron pile-up. The formation of the shallow n-type surface layer on both the lapped and sandblasted surfaces is probably due to the reaction of oxygen and dislocations. Thus an indication of the depth of damage and of the magnitude of dislocation formation was provided. Sheet resistance measurements indicate this level to be ~ 5 x 10^{15}/cm^3. The absence of oxygen-formed donors in sandblasted specimens might be the result of greater boron pile-up to a level high enough to exceed the donor formation.

To examine more closely the effect of damage to the surface of Si, 2000 ohm-cm, p-type polished wafers were scribed with a diamond pencil leaving a number of scratches on the surface. These were oxidized and annealed at 450°C. As shown in Fig. 5, the depth of

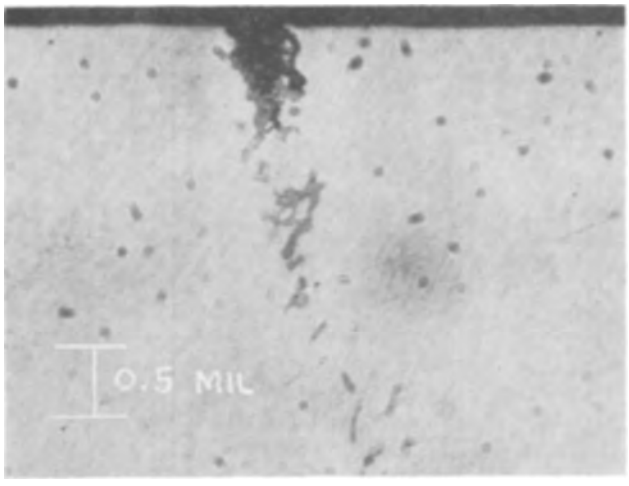

Fig. 5. Photomicrograph showing effect of damage due to scribe mark on polished 2000 ohm-cm p-type Si; after 1 hr oxidation at 1250°C and 450°C anneal for 72 hr; beveled X-section depth magnified 10X. a. Dark p-type regions within oxygen diffused and converted n-region. 75X.

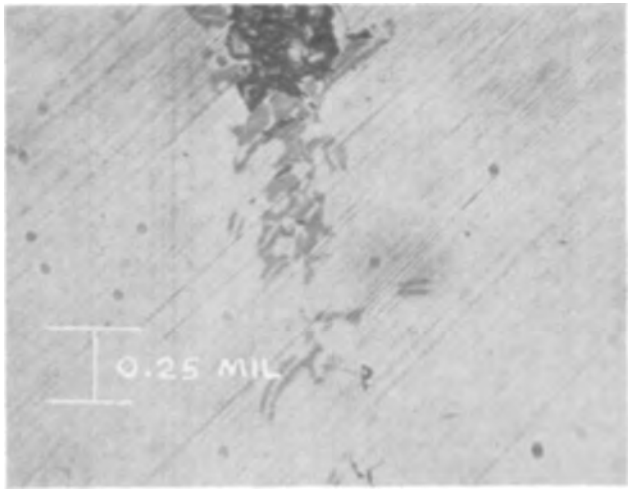

Fig. 5b. Enlarged view showing probable dislocation loops of high oxygen content within depleted dark stained regions. 150X.

the scribe mark was approximately 0.5 mil, but damage and subsequent dislocation formation extended to 2.5 mils. In this region of damage, darkly stained p-regions are present in the background of the n-type region where the latter is obtained because of oxygen conversion. These p-regions are assumed to be areas depleted of oxygen and are adjacent to dislocation loops containing atmospheres of oxygen removed from the depleted regions. From this observation, it is possible that the p-layer, assumed to be due to pile up, is also formed by the depletion of oxygen by reaction with surface induced dislocations.

The evidence indicates that oxygen can react with dislocations thereby forming shallow nonuniform n-type layers on the sandblasted and lapped surfaces. Further, there seems to be a reaction of Cu with oxygen as shown by their effects on the SiO_4^+ complex in polished wafers.

With the effect of a dislocation "sponge" at the surface, reheat-treating under oxygen of previously quenched wafers is of considerable interest. First it indicates that the introduced dislocations are not annealed out even with repetitive temperature cycles up to 1250°C. In addition the recovery of quenched and poisoned p-n-p units shows that fast diffusing impurities are responsible for the downgrading phenomena. A period of time, slower than rapid quenching, is needed to permit the diffusion of these impurities to the dislocation "sponge." As oxygen cannot out-diffuse in the time of cooling evaluated and because the SiO_2 phase is always present on the Si surface, the introduced dislocations must be the major influence in the prevention and recovery of poisoned p-n-p structures.

It was also shown that a metal impurity such as copper can be transported from bulk Si, probably to some surface layer by heat-treatment under argon ambients. Such an ambient also resulted in depletion of the diffused oxygen level from the body of the silicon. The recovery of the reverse characteristics of Cu poisoned p-n-p junctions by this argon treatment would indicate that oxygen-copper complexing or tie-up occurs at or near the surface. Infrared examination of these structures support this view.

An explanation may be offered concerning the effect of cooling rate in an oxygen ambient. In quenching, impurities can precipitate at sites throughout the wafer in a more dispersed form. Under a moderate cooling rate such as a furnace cool, metal impurities can coalesce because of their rapid mobility; however, oxygen levels would not be significantly affected by precipitation or agglomeration. A cooling rate approaching equilibrium conditions affects the oxygen level either by outdiffusion or by precipitation as indicated by the absence of oxygen formed donors. Although the metal impurity level in the bulk Si can be assumed to be the same in all these cases, the resulting reverse leakage currents are not. The lower leakage observed with quenched samples indicates that the over-all effect of more finely dispersed precipitates is less than that of larger coalesced precipitates. If equilibrium cooling resulted in a depletion of oxygen levels by outdiffusion (because of precipitation as SiO_2 at the surface), a significant reduction in reverse currents should be achieved. Therefore, it appears that coalescence of oxygen occurs within the bulk during such a slow cool thus permitting oxygen-metal impurity complexing. Similar reverse currents are obtained to those of slow cooling by holding the slices at 1000°C for long periods of time. Precipitation of oxygen as SiO_2 here causes a reduction in oxygen level within the body of the silicon.

Under nitrogen ambients, downgrading is probably due to a nitride formation. No explanation is offered for the serious poisoning effect of hydrogen on p-n-p slices which have been exposed to oxygen.

Acknowledgments

The author wishes to acknowledge the effort of R. I. Jurgensen, who helped plan and carry out the many experiments in this study and to F. E. Gentry for many helpful discussions and for reviewing this work.

Manuscript received Oct. 22, 1964. This paper was presented at the Washington Meeting, Oct. 11-15, 1964.

Any discussion of this paper will appear in a Discussion Section to be published in the December 1965 JOURNAL.

REFERENCES

1. A. Goetzberger and W. Shockley, *J. Appl. Phys.*, **24**, 1821 (1960).
2. W. Shockley, *Solid State Electronics*, **2**, [1], 35 (1961).
3. G. H. Schwuttke, *This Journal*, **108**, 163 (1961).
4. S. Prussin, *J. Appl. Phys.*, **32**, 1876 (1961).
5. H. J. Quiesser, *ibid.*, **32**, 1776 (1961).
6. W. Kaiser, *Phys. Rev.*, **105**, 1751 (1957).
7. C. S. Fuller and R. A. Logan, *J. Appl. Phys.*, **28**, 1427 (1957).
8. R. A. Logan and A. J. Peters, *ibid.*, **30**, 1627 (1959).
9. W. C. Dash, *ibid.*, **27**, 1193 (1956).
10. W. C. Dash, *ibid.*, **31**, 2275 (1960).

The Preparation of Homogeneous and Reproducible Solid Solutions of GaP-GaAs

M. Rubenstein

Research Laboratories, Westinghouse Electric Corporation, Pittsburgh, Pennsylvania

ABSTRACT

Solid solutions of GaP-GaAs were prepared using the sealed tube iodine transport method. The initial charge was iodine, powdered GaP, and powdered GaAs. These powders were ground and treated with aqueous hydrochloric acid to remove the damaged layers. The resulting GaP-GaAs solid solutions were more homogeneous than other such series of solid solutions which are described in the literature. Polycrystalline sound masses as well as single crystals with reproducible and predictable compositions can be produced using these treated powders.

Solid solutions of two or more compounds or elements can offer a method of changing many characteristics of either of the original constituents. It has been shown that silicon and germanium exhibit continuous solid solution and continuous variation of energy gap over the entire range of compositions (1-4). This type of semiconductor investigation was extended to the III-V compounds (5-10). Investigations on the system GaP-GaAs began in 1955 with Folberth's work (5) and were continued by other workers (11-15).

This paper demonstrates that solid solutions having formula $GaP_{(1-x)}As_x$ (the system GaP-GaAs) can be prepared more homogeneously than previous papers have indicated (13, 14), and the primary reason for this homogeneity is due to the use of powders as the initial charge. The solid solutions prepared in this work involved the sealed tube iodine transport technique (11-17).

Preparation of $GaP_{(1-x)}As_x$

First, the preparation of the solid solutions with formula $GaP_{(1-x)}As_x$ will be sketched quickly since this method has been described in detail (13, 14). Then a detailed description of the preparation of the charge (the powdered GaP and GaAs) will be presented.

The initial charge consists of iodine, GaP, and GaAs. The amount of iodine is such that a maximum pressure of 3 atm would be reached in the ampule if the average temperature were 1000°C, if all the iodine were converted to iodine atoms, if the iodine atoms underwent no reactions, and if no iodine were lost during the evacuation of the ampule. The GaAs and GaP powders (a total of 2g) and I_2 were placed in the ampule (having a volume of about 70 cc) as indicated in Fig. 1. The ampule with the charge was evacuated using a mechanical pump. The ampule was cooled using an ice-water bath to prevent excessive loss of I_2 during evacuation. A liquid nitrogen trap was placed between the pump and ampule to prevent hydrocarbons from getting into the ampule. The pressure in the ampule was about 4×10^{-2} Torr.

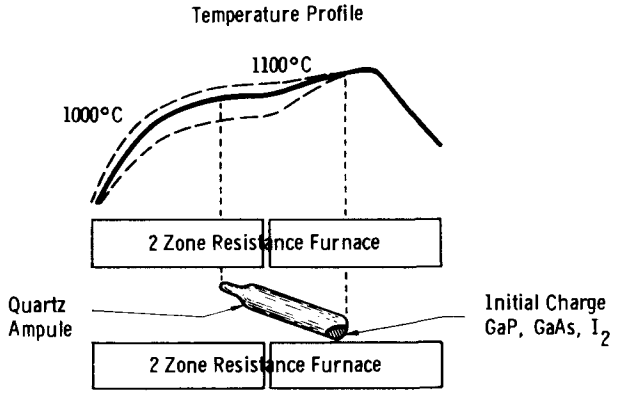

Fig. 1. Diagrammatic representation of ampule in furnace with temperature profiles.

The ampule was sealed off and placed in a temperature gradient such that the maximum temperature was 1100°C and the minimum temperature was between 1090° and 900°C. The time for transport varied between 15 min to four days. No attempt was made to seed the transported material.

Preparation of the Powdered GaP *and* GaAs

The GaP used in the charge for the iodine transport of $GaP_{(1-x)}As_x$ was material grown from a stoichiometric or nearly stoichiometric melt (this GaP was horizontally zone refined at about 1500°C at phosphorus pressures between 10 and 20 atm). The GaP was then crushed in a Plattner's diamond mortar and pestle, ground in a porcelain mortar and pestle, sieved, and then treated with aqueous hydrochloric acid (HCl) to remove contaminants introduced in crushing and sieving and to remove the damaged layer.

Since phosphine is produced when one grinds GaP (this compound is easily identified by its odor), the gallium (or the GaP) must undergo some change. Either Ga_2O_3, Ga_2O, or $GaPO_4$ is formed. Of course, any combination of these three could be produced. Some of the possible reactions which can be written are as follows

$$2GaP + 3H_2O \rightarrow 2PH_3 + Ga_2O_3 \quad [1]$$

$$2GaP + 3H_2O \rightarrow 2PH_3 + Ga_2O + O_2 \quad [2]$$

$$GaP + 4H_2O \rightarrow GaPO_4 + 4H_2 \quad [3]$$

$$GaP + 2\,O_2 \rightarrow GaPO_4 \quad [4]$$

Although GaP is usually considered a rather inert solid, one or more of these reactions could proceed at a damaged layer especially since grinding can produce large local thermal spikes in a material. It is also possible that GaP seems to be rather inert because the oxidized surface film protects the layers under this film.

It is difficult to prove which of these reactions most accurately describes this system since the grinding of GaP does not produce much product. It is fortuitous that a change in body color of the GaP on grinding is quite noticeable to the eyes, and it is also fortuitous that the olfactory nerves are quite sensitive to PH_3. The limit of perceptibility to PH_3 is 1.5-3 ppm, the limit for "serious effects after several hours" is 7 ppm, and the threshold limit is 0.05 ppm (19).

The treatment of the GaP with concentrated hydrochloric acid is an interesting reaction chemically. GaP is attacked very slowly by concentrated hydrochloric acid. GaP which has been ground is attacked at a much faster rate; there is an evolution of bubbles and a change in body color of the GaP. The color change is from brown to red-orange or yellow-orange (de-

Table I. Particle distribution

U.S. sieve No.	Diameter of particles, mm	Designation in this paper
80-100	0.177-0.149	1
100-120	0.149-0.125	2
120-140	0.125-0.105	3
140-170	0.105-0.088	4
170-200	0.088-0.074	5
Smaller than 200	Smaller than 0.074	6
Ground, treated with hydrochloric acid		I
Ground, treated with hydrochloric acid, slurried, decanted, sieved		II
Ground, sieved		III
Ground, slurried, decanted, sieved		IV

pending on the particle size of the GaP).

Table I shows some information about the particle distribution used as well as the treatment used in preparing the GaP powders. In Fig. 2 the diffuse reflectance is presented for all four treatments (as indicated in Table I) for the finest distribution of particles. Figure 3 shows the diffuse reflectance for all four treatments for the coarsest distribution of particles.

The difference between treatments III and IV (Fig. 2) is a slurrying operation. This operation consists of mixing the powder with water and decanting the water. The very fine particles are removed by this operation. The difference between treatments I and II is the same as between III and IV. The difference between treatments I and III is the hydrochloric acid treatment. The same may be said concerning treatments II and IV. This HCl operation increases the diffuse reflectance over the entire range of wavelengths. The change from yellow-orange to brown on grinding GaP can be seen in Fig. 2 and 3 by noting that the diffuse reflectance for the brown material falls off at wavelengths from 0.65 to 0.57μ. At these same wavelengths, GaP which has been treated with hydrochloric acid has a much higher diffuse reflectance.

There is one other observation which was made on GaP which did not have the slurrying and decanting operation. Not only did the coarser particle distributions (after sieving) contain some of the very fine particles, but these larger particles were coated with these very fine particles. Perhaps an electrostatic attraction holds these very fine particles to the coarser particles even during the entire sieving operation. The sieving operation may even be the cause of the electrostatic build-up of charge. The slurrying and decanting operation allows one to obtain samples having particle distributions without the very fine particles.

When one grinds a crystal using a mechanical force, a damaged layer is produced. This damaged layer is composed of a variety of disorders such as a deformed layer, sharp edges, cracks, an increase in the dislocation and vacancy densities, and a reactive surface. Such grinding also produces thermal spikes. These thermal spikes together with a reactive surface could produce a reaction with the surrounding atmosphere. Some of the reactions of GaP with H_2O and/or O_2 mentioned earlier might take place. Grinding GaP produces such a damaged layer which can be observed visually and nasally. There is another technique which can be used to observe a difference between this damaged layer and GaP without this damaged layer, the rate of dissolution. The rate of dissolution of this damaged layer is much larger than the rate of dissolution of GaP without this damaged layer. Any analysis of this rate would include all types of disorders, but since there obviously is a chemical reaction associated with the formation of this damaged layer, it will be assumed that a new compound is, at least, partially covering the surface of the ground GaP.

GaP was ground, slurried, decanted, and sieved. The particle distribution was 0.149-0.125 mm in diameter. Several samples were treated in the following manner. A weighed amount (about 2g) of GaP was placed in aqueous concentrated HCl (about 250 ml) and the mixture was slowly stirred. After 3 hr the GaP was washed with water, dried, and weighed. This weighed sample was returned to the HCl for three more hours, washed, dried, and weighed. This operation was repeated again and again. The curve in Fig. 4 labeled "3 hour runs" is typical of such an experiment. Note that the rate of dissolution of the ground GaP is still falling after a total of eighteen hours of HCl treatment. The curve in Fig. 4 labeled "24 hour runs" was treated in the same way as described above for the "3 hour runs" except the

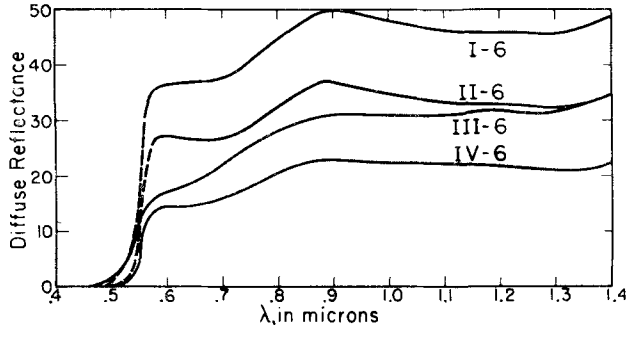

Fig. 2. Per cent diffuse reflectance vs. wavelength for GaP having undergone 4 different treatments (see Table I): the particle distribution is the finest.

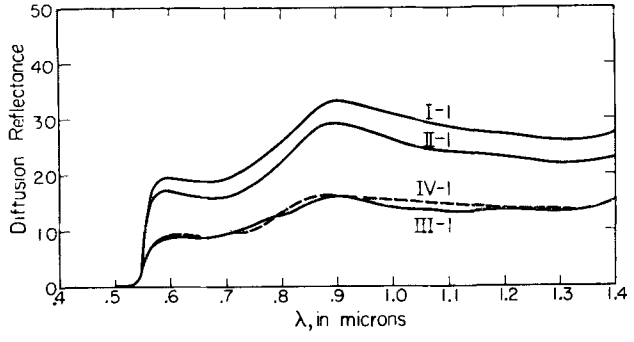

Fig. 3. Per cent diffuse reflectance vs. wavelength for GaP having undergone 4 different treatments (see Table I): the particle distribution is the coarsest.

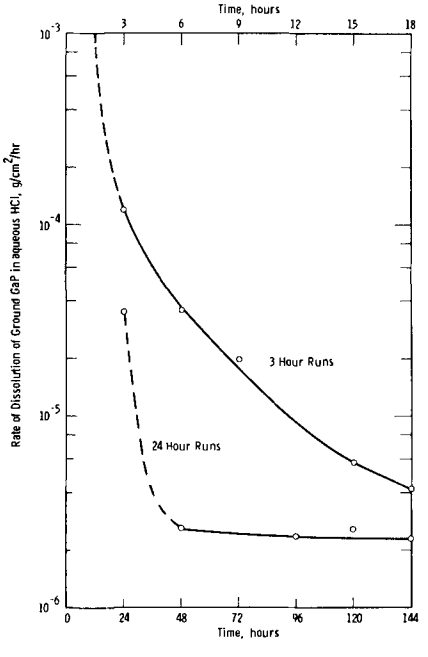

Fig. 4. Rates of dissolution of ground GaP vs. time

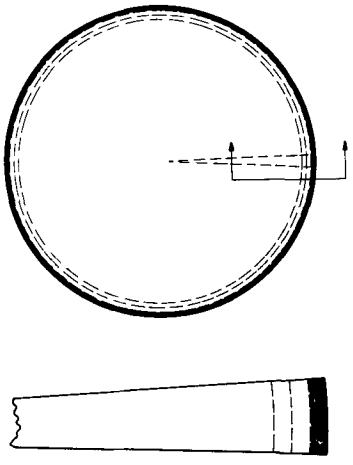

Fig. 5. Diagrammatic cross section of a particle of GaP with a damaged layer (top); (below) portion of sector of cross section of particle with damaged layer.

samples were treated for 24-hr periods instead of 3-hr periods. After 48 hr (two 24-hr HCl treatments) the rate of dissolution of the ground GaP does not fall appreciably. Figure 5 shows diagrammatically what the above experiments show. A particle has a damaged layer but this damaged layer is not a uniform one. It is most damaged on the outer periphery, and as one leaves the surface toward the interior of the particle this damaged layer shows less and less damage. The GaP in Fig. 4 shows a high rate of dissolution initially and a smaller rate of dissolution as more and more of the damaged layer or layers are removed. In the case of the curve labeled "3 hour runs" at the end of 18 hr, all of the damaged layers are not yet removed. In the case of the curve labeled "24 hour runs" at the end of the first 24-hr period the rate is greater than 18 total hr of 3-hr periods because this rate is a combination of higher rates and some lower rates of dissolution. Therefore, the room temperature dissolution rate of GaP with a damaged layer (caused by grinding) is greater than 1×10^{-4} g/cm^2/hr. The room temperature dissolution rate of GaP (without a damaged layer) in aqueous concentrated HCl is 2.3×10^{-6} g/cm^2/hr. The thickness of the damaged layer for several samples were calculated from the weight loss and rate of dissolution experiments to be about 2μ on a radius of about 70μ. After about 20 hr in HCl, GaP is removed at the rate of about 0.01 μ/hr. Initial rates of removal of GaP which has a damaged layer are about two orders of magnitude greater. This discussion may be concluded by saying that the rate of dissolution is not a constant since the degree of damage along a radius of a particle is not constant. It should also be pointed out that the calculation for the area of the particles assumes that these particles are spheres. Since these particles are not spheres, the real surface area is larger than calculated. This would mean that the true dissolution rates are smaller than those presented in this paper.

One other observation may be made correlating damaged layers with visual observation. As one treats ground GaP with HCl, there is a decided color change which one may easily observe from brown to red-orange or to yellow-orange. When the color change is noted, the most damaged material has been removed, and the rate of dissolution has fallen appreciably. The less damaged layers do not have diffuse reflectance much different from GaP without damaged layers and the dissolution rate in HCl of these layers is not much different from GaP without damaged layers. A good discussion on damaged layers and their chemical reactivity may be pursued in ref. (18).

GaAs in many respects is similar to GaP. Although their chemical reactivity is similar, GaAs is somewhat more reactive than GaP with respect to halogens, hydrogen halides, aqueous hydrogen halides, aqua regia, and nitric acid. GaAs powders were prepared in exactly the same way as the GaP powders. The discussion on damaged layers would equally apply to GaAs.

Table II. Lattice constants for 48 samples

State of sample after transport experiment*	Sample designation	Composition $GaP_{1-x}As_x$, x	Per cent transported**	Lattice constant, a_o
Single	20 N-2	0	80	5.4508
Not transported†	20 N-2	0	80	5.4505
	SID	0		5.4506
	S 20 P-2	0.1		5.4706
Single crystal	S 20 P-2	0.1		5.4700
	S 20 P-1	0.1		5.4709
	S 20 P-1	0.1		5.4707
	SIE	0.1		5.4704
	SIF	0.2		5.4894
Single crystal	20 R-2	0.2	40	5.4894
Single crystal	20 R-2	0.2	40	5.4883
Not transported†	20 R-2	0.2	40	5.4883
Transported	20 R-1	0.2	94	5.4893
Not transported†	20 R-1	0.2	94	5.4899
Single crystal	20 R-1	0.2	94	5.4899
Single crystal	20 S	0.3	59	5.5094
Transported	20 S	0.3	59	5.5093
	SIG	0.3		5.5100
Not transported†	S 20 T	0.4	28	5.5317
	SIH	0.4		5.5296
	SIK	0.5		5.5482
	S9E	0.5		5.5486
Single crystal	S9E	0.5		5.5483
Transported	S9D	0.6	65	5.5679
Not transported	S9D	0.6	65	5.5676
Single	S9D	0.6		5.5676
	S 49 W-1	0.6		5.5662
	S 49 W-1	0.6		5.5662
	S 49 W-2	0.6		5.5692
	S 49 W-2	0.6		5.5689
Single crystal	SIL	0.7		5.5895
Not transported	SIL-1	0.7	86	5.5891
Single crystal	SIL-1	0.7	86	5.5889
Single crystal	SIL-1	0.7	86	5.5893
Single crystal	SIL-1	0.7	86	5.5895
Single crystal	S9C	0.7		5.5888
Single crystal	S9C	0.7		5.5890
	SIL-2	0.7		5.5888
Single crystal	SIOH	0.8		5.6103
Single crystal	SIOH	0.8		6.6095
Single crystal	S2E	0.8		5.6104
Single crystal	S2E	0.8		5.6103
	S2M	0.8		5.6107
	S9B	0.9		5.6301
	S 2N-2	0.9		5.6305
Not transported†	S2F	1.0	81	5.6532
	S2F	1.0	81	5.6531
	S2P	1.0		5.6532

* If nothing is indicated concerning the "State of the Sample," the sample was polycrystalline.
** If no per cent transport is indicated, the samples were totally transported.
† Not transported samples were polycrystalline.

Results

$GaP_{(1-x)}As_x$ samples were prepared where $x = 0.1, 0.2, 0.3, \ldots, 1.0$. Table II contains lattice constants for 48 samples prepared in 28 independent preparations in this solid solution system GaP-GaAs. The samples were taken from single crystals and polycrystalline deposits. The samples were taken from preparations in which all of the GaP-GaAs was transported and in which as little as 28% of this material was transported. The time of transport varied from four days to 15 min. The difference in temperature between source and deposit varied from 10° to 200°C. The lattice constants in Table II are plotted in A of Fig. 6.[1] Whether the particle size of the source material had diameters between 0.177-0.149 mm or less than 0.074 mm no differences could be noticed in the material transported or material which did not transport. The length of time of the transport experiments (whether 4 days or 15 min) does not in any way affect the transported or non-transported material, other than the amount which transported. These lattice measurements were made using the Debye-Scherrer technique, a 57.32 mm radius of Straumanis-type camera with nickel filtered copper radiation. A trigonometric extrapolation was used to obtain the precision lattice constants (21).

[1] The lattice constants for GaP and GaAs at 18°C are 5.4505 ± 0.0001Å and 5.6534 ± 0.0002Å respectively (20).

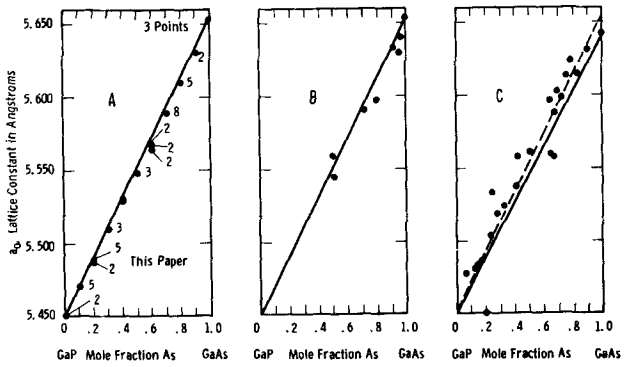

Fig. 6. Lattice constants of $GaP_{(1-x)}As_x$ *vs.* composition. "A" curve is from data obtained in this paper: "B" curve and "C" curve are from ref. (14) and (13), respectively.

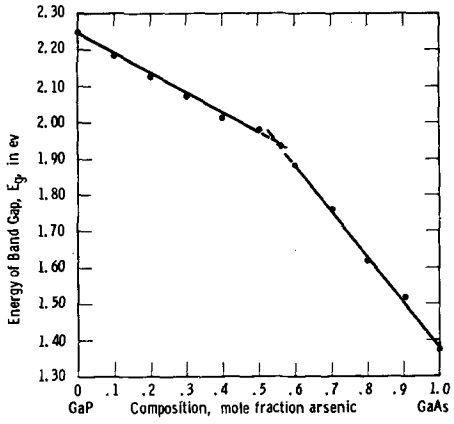

Fig. 7. Energy band gap *vs.* composition for the system $GaP_{(1-x)}As_x$

These points in Fig. 6, Curve A, lie quite close to the line connecting the lattice constants of pure GaP and GaAs; Vegard's law is followed quite well. Also plotted in Fig. 6 are two other curves from the literature (13, 14). The scatter of the points from data in this paper is much less than the scatter observed in data taken from the other two papers. One can observe in Table II that the so-called nontransported material has lattice constants which are either identical with or very close to the lattice constants of the transported material. This was observed not only in these samples listed in Table II, but in a number of other samples. One may conclude that the nontransported powders in these experiments did not remain as GaP and GaAs powders, but rather quickly formed the solid solution under the influence of iodine at a temperature of 1100°C.

Also included in this paper is a plot of band gap energy *vs.* composition, Fig. 7. The data was obtained from room temperature optical transmission measurements on samples which were about 0.4 mm thick. There are enough points plotted in this figure to merit the drawing of 2 straight lines with different slopes rather than a curved line as others have drawn for similar data (5, 13).

Conclusions

GaP and GaAs form a complete range of solid solutions obeying Vegard's law quite well. All of the points in A of Fig. 6 are below the line drawn (assuming Vegard's law is obeyed) indicating slight negative departures from Vegard's law.

One can obtain samples of $GaP_{1-x}As_x$ which are relatively homogeneous and reproducible as indicated in A of Fig. 7 by using crushed GaP and GaAs as the source of an iodine transport experiment.

When one crushes GaP and GaAs a damaged layer is produced. This layer may be removed by treatment with HCl. This treatment not only removes the damaged layer, but also any contaminants introduced on crushing and sieving.

Other workers were not able to obtain, in a reproducible manner, homogeneous solid solutions primarily because they did not know the composition of their solid solutions (their points show a scatter off the Vegard's law line). If they used large pieces of GaP and/or GaAs as their initial charge, the rates of GaP and GaAs leaving the sources and entering the gas phase were determined by the surface area of the source materials. If they crushed the source materials and did not remove the damaged layer, the source materials had already lost phosphorus and/or arsenic, formed oxides and/or phosphates (or arsenates), and were contaminated by impurities on crushing.

The author of this paper has noted (from the lattice constants of nontransported material) that before any solid solution is transported, the solid solution is formed at the source position when powdered GaP and GaAs are used as source material. This is experimental confirmation of a postulate previously set fourth (13). It is easier to understand the homogeneity and reproducibility of the solid solution presented in this paper, if the source material before transport were the solid solution already.

Acknowledgment

The author would like to thank Mr. Donald Sestrich for his help in the experimental efforts in this paper.

Manuscript received Sept. 16, 1964; revised manuscript received Nov. 27, 1964.

Any discussion of this paper will appear in a Discussion Section to be published in the December 1965 JOURNAL.

REFERENCES

1. H. Stohr and W. Klemm, *Z. anorg. Chem.*, **241**, 305 (1939).
2. A. Levitas, C. C. Wang, and B. H. Alexander, *Phys. Rev.*, **95**, 846 (1954).
3. M. Glicksman, *ibid*, **102**, 1496 (1956).
4. F. Herman, M. Glicksman, and R. H. Parmenter, "Progress in Semiconductors" (1957).
5. O. G. Folberth, *Z. Naturforsch.*, **10a**, 502 (1955).
6. F. Seitz and D. Turnbull, "Solid State Physics," Vol. 3, Academic Press, New York (1956).
7. W. Koster and B. Thoma, *Z. Metallkunde*, **46**, 293 (1955).
8. J. C. Wooley, B. A. Smith, and D. G. Lee, *Proc. Phys. Soc.*, **B69**, 1339 (1956).
9. J. C. Wooley and C. M. Gillett, *J. Phys. Chem. Solids*, **17**, 34 (1960).
10. F. A. Trumbore, P. E. Freeland, and A. D. Wells, *This Journal*, **109**, 645 (1962).
11. G. R. Antell and D. Effer, *ibid.*, **106**, 509 (1959).
12. N. Holonyak, Jr., D. C. Jillson, and S. F. Bevacqua, "Metallurgy of Semiconductor Materials," J. B. Schroeder, Interscience Publishers, Aug. 30-Sept. 1, 1961.
13. F. A. Pizzarella, *This Journal*, **109**, 226 (1962).
14. San-Mei Ku, *ibid.*, **110**, 991 (1963).
15. E. M. Hull, Paper presented at the New York Meeting of the Society, Electronics Division Abstracts, **12**, 43 (1963).
16. I. C. Marimace, *I.B.M. J. of R & D*, **4**, 248 (1960).
17. E. S. Wajdo, B. W. Keppenhan, and W. H. White, *ibid.*, **4**, 288 (1960).
18. H. C. Gatos, "The Surface Chemistry of Metals and Semiconductors," John Wiley & Sons, Inc., New York (1960).
19. F. A. Patty, "Industrial Hygiene and Toxicology," Vol. II, Interscience Publishers, New York (1962).
20. Von G. Giesecke and H. Pfister, *Acta Cryst.*, **11**, 369 (1958).
21. A. Taylor and H. Sinclair, *Proc. Phys. Soc.*, **57**, 126 (1945).

Thermal Oxidation of Heavily Doped Silicon

B. E. Deal and M. Sklar

Research & Development Laboratory, Fairchild Semiconductor, Palo Alto, California

ABSTRACT

Oxidation characteristics of heavily doped silicon were investigated in dry and wet (95°C H_2O) oxygen ambients over the temperature range 920°-1200°C for oxide thicknesses of 0.10-1.0μ. Silicon uniformly doped with boron (1×10^{16} to 2.5×10^{20} cm^{-3}) or phosphorus (4×10^{15} to 1.5×10^{20} cm^{-3}) was studied, as well as silicon surfaces predeposited with these two elements. Boron concentrations greater than 1×10^{20} cm^{-3} cause an increase in oxidation rates at all temperatures, the greatest effect occurring in dry oxygen. Above 1000°, no such rate increase occurs for phosphorus doped silicon. At 920°C, however, phosphorus concentrations of 1×10^{19} cm^{-3} or more result in a significant increase of oxidation rates. The latter effect is most pronounced in wet oxygen. The results can be explained satisfactorily by considerations which take into account redistribution of impurities during thermal oxidation of silicon. These considerations also enable a tentative prediction of the effect of heavy doping concentrations of other impurities on the oxidation rate.

Silicon reacts in various oxidizing atmospheres at elevated temperatures to form silicon dioxide (SiO_2). The kinetics of this thermal oxidation of single crystal silicon has been the subject of several recent papers (1-5). The authors of these papers reported no dependence of oxidation rate on bulk impurity concentration over the concentration ranges investigated. These concentrations extended from very low values (intrinsic silicon) to as high as approximately 1×10^{20} cm^{-3} acceptor and donor impurities. It has also been noted, however, that when silicon having surface impurity concentrations greater than 10^{20} cm^{-3} is oxidized, deviations from the standard values of oxidation rate constants are encountered (6, 7). For the most part these deviations have been found with samples subjected to diffusion processes used in device fabrication.

Recently, silicon oxides have assumed an increasingly important role in the development of surface controlled devices and integrated circuits, and the close control of oxide thickness has become of vital interest (8, 9). A study was undertaken therefore to determine the effect of impurity doping, if any, on thermal oxidation rates. This study included both p-type (boron doped) and n-type (phosphorus doped) silicon oxidized in dry and wet oxygen (95°C H_2O) in the temperature range 920°-1200°C. Samples of both uniformly doped crystals and diffused surfaces were examined.

Experimental

Silicon used in this program was obtained from the Kollstan Semiconductor Elements Company, Westbury, New York. It was in the form of circular slices, cut from Czochralski crystals, and lapped to 250μ thickness. In all cases, surface orientation was (111). Material used for subsequent diffusion processing was 1.3-1.5 ohm-cm, either p-type (boron doped) or n-type (phosphorus doped) silicon. Dislocation count was specified to be less than 100 cm^{-2}. For the heavily doped p-type silicon, material with boron concentration of 1×10^{20} and 2.5×10^{20} cm^{-3} was used. Similarly, the heavily doped n-type silicon contained 3.7×10^{19} and 1.5×10^{20} cm^{-3} phosphorus. For both types, the higher values represent the maximum concentration available for boron and phosphorus. In examining these materials some segregation of impurities was noted, especially at the edges of the slices. However it was possible to obtain a sufficient number of slices with large areas of uniform impurity concentration which could be used in this investigation.

Apparatus

The oxidation system was similar to the one described in ref. (3). Both dry oxygen and wet oxygen ambients were used. The latter consisted of oxygen bubbled through deionized water at 95°C. The resulting partial pressure of water vapor in the ambient was assumed to be 634 mm Hg, the vapor pressure of water at 95°C. For the dry oxygen, the gas was dried and purified using a molecular sieve trap. Furnace temperature was controlled to ±1.0°C in the range 920°-1200°C. Silicon slices were placed flat on a thin quartz boat during oxidation. Separate quartz tubes were used for n-type and p-type silicon.

Procedure

The silicon slices were mechanically polished on one side to assure optimum conditions for oxide thickness measurements. Previous experiments had demonstrated no difference in oxidation kinetics between chemically and mechanically polished surfaces for the thickness range studied in this program (3). The slices were cleaned, and resistivity measurements were made on the lapped side. Immediately prior to oxidation, they were carefully cleaned again. The cleaning procedures involved prolonged rinses in organic and inorganic solvents using ultrasonic agitation.

Each particular run, representing a certain oxidation condition, included a standard silicon slice, *i.e.*, $C_B = 1 \times 10^{16}$ cm^{-3}, and two slices of higher impurity concentration. Thickness measurements of the oxides produced were obtained using multiple-beam interferometric techniques. Accuracy and reproducibility of this method is estimated to be ±40Å. Results of the standard sample were compared with corresponding oxides prepared in a separate furnace. The run was repeated if any deviation was noted, although agreement among standard oxides produced in the same furnace with heavily doped crystals and those prepared separately was generally very good.

Dry oxidation characteristics of predeposited[1] silicon were also examined in this program. In these experiments the surfaces were first prepared in regular predeposition furnace systems (9). For boron doped surfaces, methyl borate [$(CH_3)_3BO_3$] and boron tribromide [BBr_3] sources were used. In the case of phosphorus the sources were phosphorus pentoxide [P_2O_5] and phosphorus oxychloride [$POCl_3$]. Surface concentrations of these predeposited surfaces were estimated by measuring junction depths and sheet resistance, and using calculated relationships of the kind presented in ref. (10). A complementary error function-type impurity distribution was assumed. Surface concentration values calculated by this method ranged from $5\text{-}8 \times 10^{20}$ cm^{-3}. The samples were then oxidized at 1200°C. On

[1] "Predeposition," according to common usage, denotes a relatively short diffusion step (the impurity being present in the ambient) usually resulting in a high surface concentration of the impurity (9).

some samples the oxide glass formed during the predeposition step was removed by HF treatment before oxidation; on others it was left on. A standard slice was included in each oxidation, and thicknesses of oxides produced were measured as described above. Again, thicknesses of these standard oxides agreed quite closely with those of corresponding oxides prepared alone in a clean system. Thicknesses of the oxide glasses produced during the predeposition step were also determined.

Results

The oxidation results of silicon uniformly doped with boron or phosphorus are presented graphically in Fig. 1-4. These graphs are log-log plots of oxide thickness *vs.* oxidation time for dry and wet oxygen. Four different oxidation temperatures are included, with data obtained with three different impurity concentrations for each temperature. The lower line for each temperature represents oxidation characteristics of the standard, and these values agree quite closely with previous data (3). The deviation from the standard oxidation rates for more heavily doped boron or phosphorus under certain conditions is readily noted. The significance of these differences is discussed in the following section. In general, experimental values were reproducible to within 100Å, close to the accuracy of the oxide thickness measurement technique.

Oxidation rates obtained using predeposited samples (with the glass removed) were compared with the results in Fig. 1-4. With the exception of the methyl borate samples, the rates fell on the line corresponding to heaviest doping in both the boron and phosphorus cases, *i.e.*, C_B(boron) = 2.5 x 10^{20} cm^{-3}, C_B(phosphorus) = 1.5 x 10^{20} cm^{-3}. The oxides produced on the methyl borate predeposited surfaces were nonuniform in thickness, indicating nonuniform surface concentrations.

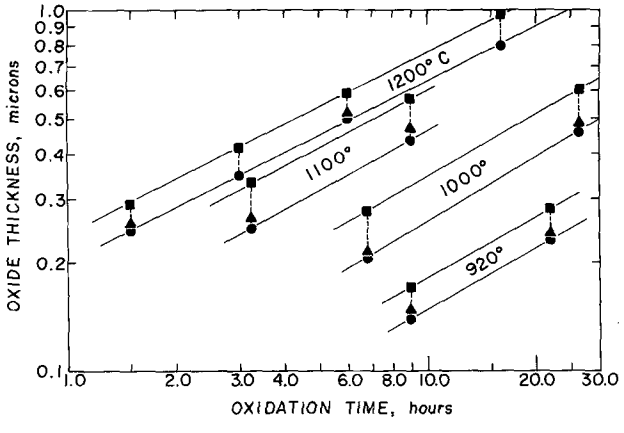

Fig. 1. Oxidation of boron-doped silicon in dry O_2 for three different boron concentrations at four oxidation temperatures: ■, C_B = 2.5 x 10^{20} cm^{-3}; ▲, C_B = 1.0 x 10^{20} cm^{-3}; ●, C_B = 1.0 x 10^{16} cm^{-3}.

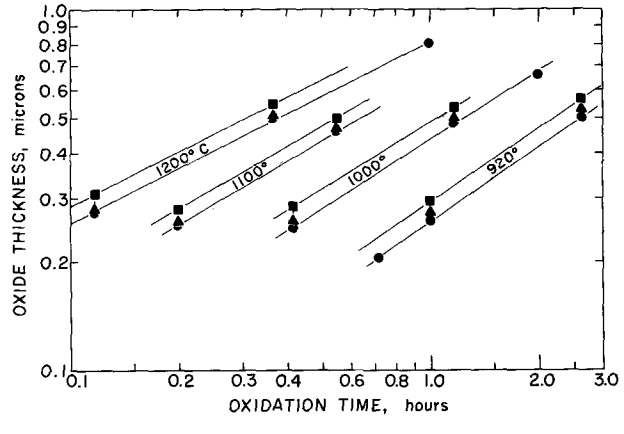

Fig. 2. Oxidation of boron-doped silicon in wet O_2 (95°C H_2O) for three different boron concentrations at four oxidation temperatures: ■, C_B = 2.5 x 10^{20} cm^{-3}; ▲, C_B = 1.0 x 10^{20} cm^{-3}; ●, C_B = 1.0 x 10^{16} cm^{-3}.

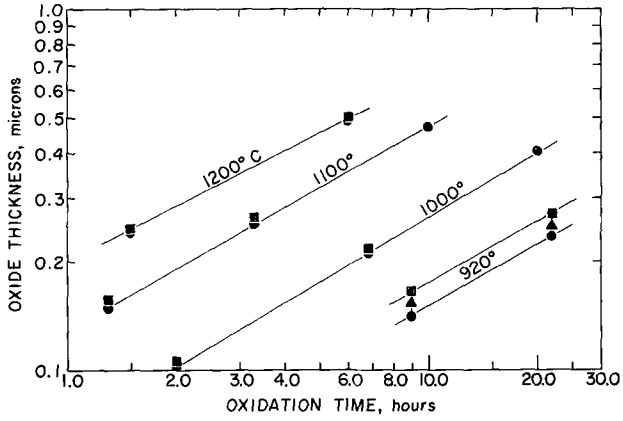

Fig. 3. Oxidation of phosphorus-doped silicon in dry O_2 for three different phosphorus concentrations at four oxidation temperatures: ■, C_B = 1.5 x 10^{20} cm^{-3}; ▲, C_B = 3.7 x 10^{19} cm^{-3}; ●, C_B = 4.0 x 10^{15} cm^{-3}.

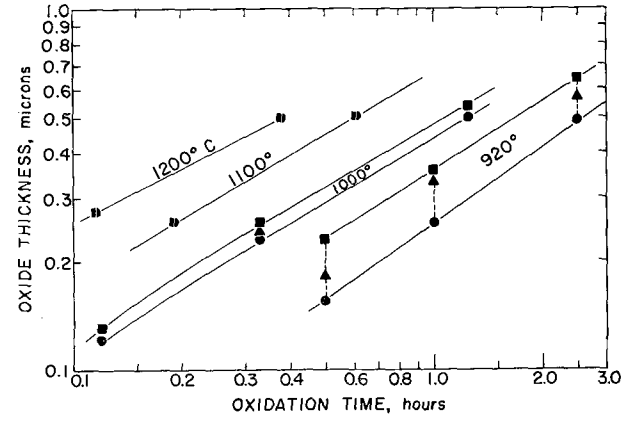

Fig. 4. Oxidation of phosphorus-doped silicon in wet O_2 (95°C H_2O) for three different phosphorus concentrations at four oxidation temperatures: ■, C_B = 1.5 x 10^{20} cm^{-3}; ▲, C_B = 3.7 x 10^{19} cm^{-3}; ●, C_B = 4.0 x 10^{15} cm^{-3}.

Discussion

Boron doped silicon.—In order to interpret the results of Fig. 1 and 2, we must first consider the nature of silicon oxidation. It has been demonstrated (1, 2, 11) that oxidation proceeds by diffusion of some oxidizing species through the oxide already formed to react at the silicon surface. At temperatures above 1000°, the oxidation rate is limited by this diffusion process resulting in the parabolic relationship

$$w = Kt^{1/2}$$

where w is oxide weight or thickness, t, oxidation time, and K is the rate constant, It follows that a change in the oxide structure may affect the oxidation characteristics. By purposely changing the structure, one may observe this effect. The experiments described above concerned with oxidation of predeposited surfaces with boron glass left on the silicon provided an indication of what effect the presence of boron in SiO_2 could provide on further oxidation.

Let us assume a boron glass of thickness 0.2μ is already present on a silicon surface. Then let the sample be exposed to a dry oxygen ambient for 6 hr at 1200°C. Several possibilities arise as to the resulting oxide formation, some of which are shown in Fig. 5. First, if there was no glass present originally, the resulting thickness-time plot would be represented by curve (A) with a final oxide thickness of 0.5μ. Second, if the

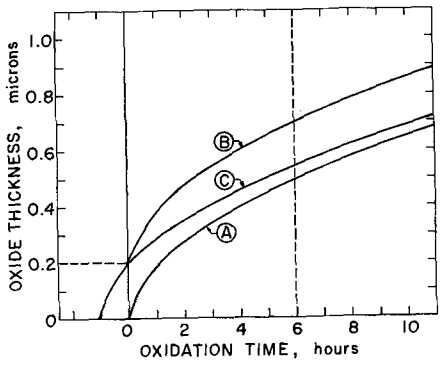

Fig. 5. Possible variations in subsequent oxidation characteristics due to 0.2μ glass formed on silicon surface during predeposition.

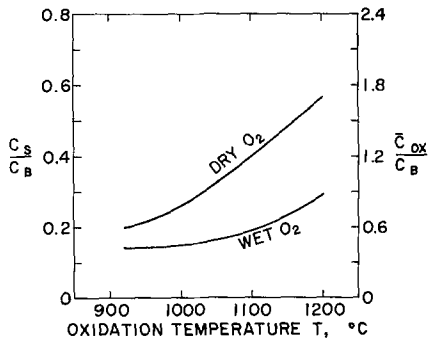

Fig. 6. Predicted boron concentration at the silicon surface (C_S) and in the oxide ($\bar{C}_{ox}$) due to impurity redistribution during thermal oxidation in two ambients at various temperatures.

diffusion of any oxygen species through the glass was much faster than through SiO_2, curve (A) would merely be displaced 0.2μ up along the thickness axis and curve (B) would result. Here the final oxide thickness would be the sum of two thicknesses, *i.e.*, 0.7μ.

The other simple case would exist if both the original glass and the final oxides produced had identical structures, *i.e.*, the diffusion coefficients of oxygen would be the same in both. This case is represented by curve (C), where the additional oxidation starts at the 0.2μ point of the original curve. In other words the original curve is shifted along the time axis so that 0.2μ coincides with 0 min. It can be observed that the final oxide thickness of this case will be 0.55μ. Of course other intermediate possibilities exist where the oxygen diffusivity through the original glass may be greater or less than through the final oxide.

Experiments involving subsequent oxidation of boron predeposited surfaces were performed in several variations. In a typical case the oxidation was conducted in dry oxygen for 90 min at 1200°C. Prior to this oxidation a borate glass was produced by BBr_3 predeposition in an oxygen-nitrogen atmosphere.

The results are: thickness of borate glass, 0.082μ; thickness of oxide on predeposited surface, borate glass removed, 0.294μ; thickness of oxide on predeposited surface, borate glass not removed, 0.372μ; thickness of standard SiO_2, 0.248μ.

It can be noted that the sum of the oxide thickness for the predeposited surface and the borate glass thickness (0.294μ + 0.082μ) is essentially equal to the total oxide thickness where the glass was not removed (0.372μ). Thus the latter result corresponds to case (B) of Fig. 5, and it follows that the borate glass presents very little resistance to the diffusion of oxygen. This effect has been noted previously by Thurston (12) and is in agreement with other comparisons of oxygen diffusion coefficients in glasses (13). The boron probably produces defects in the SiO_2 lattice, resulting in a structure which provides an increase of oxygen diffusion rate.

We are now in a position to discuss the increase of oxidation rates shown in Fig. 1 and 2 for uniformly doped silicon containing high concentrations of boron. These increases can be explained on the basis of the above results if boron is incorporated into the oxide during thermal oxidation. Results of experiments involving redistribution of impurities due to thermal oxidation indicates that this indeed does occur (14, 15). Figure 6 based on considerations of ref. (14, 15) shows the ratio of the boron concentration in the silicon, near the oxide-silicon interface, to the bulk concentration (C_S/C_B) for dry and wet oxygen oxidations as a function of temperature. Since a depletion of boron from the silicon takes place, this ratio is less than one. If a segregation coefficient[2] of 0.33 for the system is also assumed from ref. (14), the average boron concentration in the oxide can also be plotted in Fig. 6 as $\bar{C}_{ox}/C_B$ (see Appendix). At the higher temperatures, there is a considerable amount of boron in the oxide, especially in the dry oxygen case. This boron could cause a weaker bond structure and permit a more rapid oxidation, (assuming that diffusion through the oxide is the rate-determining step at the oxidation temperature). The boron concentration in wet oxides is less according to Fig. 6, and the increase in oxidation rate for heavily doped silicon accordingly should be less pronounced. This is indeed true as shown by comparing Fig. 1 and 2.

Figure 6 also indicates that as oxidation temperature decreases the average boron concentration in the oxide decreases. Thus, the effect of heavy doping should be less pronounced at lower temperatures. This is not observed from Fig. 1 and 2 perhaps because of the change in oxidation mechanism in the vicinity of 1000°C (see ref. 3).

Calculations indicate a dry oxide produced at 1200°C on silicon having a boron concentration of 2.5 x 10^{20} cm^{-3} should contain approximately 1% boron. Gravimetric analysis of such an oxide did show greater boron content than for a standard silicon oxide (C_B(std) = 1 x 10^{16} cm^{-3}), but the method was not sufficiently accurate for quantitative results. Much more significant results were obtained using an infrared examination. Samples were prepared by oxidizing to a thickness of 1.0μ. Using the photoresist and chlorine etch technique (1), a hole was etched through the silicon from the back side. A window of oxide, supported by a frame of silicon, remained on top for infrared transmission examination. Figure 7 shows spectra in the range 6.5-13.5μ wavelength for four different samples. (Total range examined was 2-15μ with no structure indicated beyond the limits included in the figure.) The spectrum for the standard oxide (either wet or dry oxygen) prepared from silicon whose bulk concentration is 1 x 10^{16} cm^{-3} is shown by curve (1). The characteristic absorption peak for fused silica (16) is shown at 9.2-9.3μ. A second peak attributed to an SiO bond, also exists at 12.5μ. Curve (4) represents a wet oxide also on 1 x 10^{16} cm^{-3} material, but covered with a borate layer produced in a methyl borate predeposition system. Additional peaks are now observed at 7.5 and 11.1μ. According to Jellyman and Proctor (17), these peaks are representative of a B_2O_3 glass.[3] Finally, curves (2) and (3) of Fig. 7 are for wet and dry oxygen oxides on 2.5 x 10^{20} cm^{-3} boron doped silicon. The peaks at 7.5μ have shifted slightly to the left (7.2μ) which is more typical of a mixed SiO_2-B_2O_3 system (17). Also present are the boron peaks at 11.1μ. The most significant fact about the two peaks at 7.2μ is the ratio of dry oxygen boron absorption to the wet oxygen value (about 2:1). This same ratio of boron concentration in the oxide is

[2] Segregation coefficient = m = $\frac{\text{equilibrium concentration of impurity in silicon}}{\text{equilibrium concentration of impurity in oxide}}$

[3] The data of ref. (17) are based on reflection spectra, but we as well as other investigators have found reasonable agreement between absorption and reflection data.

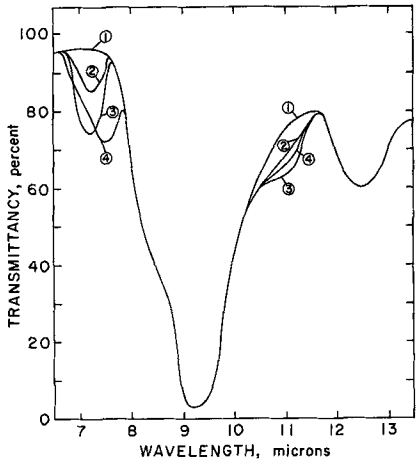

Fig. 7. Infrared absorption spectra of various silicon oxides: 1, standard dry and wet oxide, $C_B = 1 \times 10^{16}$ cm^{-3}; 2, wet oxide, $C_B = 2.5 \times 10^{20}$ cm^{-3}; 3, dry oxide, $C_B = 2.5 \times 10^{20}$ cm^{-3}; 4, wet oxide plus borate glass, $C_B = 1 \times 10^{16}$ cm^{-3}.

predicted from Fig. 6 (at 1200°C, $\bar{C}_{ox}/C_B$ for dry $O_2 = 1.7$, $\bar{C}_{ox}/C_B$ for wet $O_2 = 0.85$). Thus the presence of boron in the oxide is clearly verified by independent means.

Phosphorus doped silicon.—The phosphorus data of Fig. 3 and 4 may be analyzed in a manner similar to the heavily doped boron results. First, experiments involving oxidation of silicon covered with a phosphate glass indicated an increased diffusion rate of oxygen through the glass, although not to the same extent as with the borate glass system. The diffusion coefficient through the glass was estimated to be about 5 times that of pure SiO_2. This finding agrees with the results of Thurston who also noted that phosphorus in fused silica causes an increased rate of oxygen diffusion through the structure, but in a different manner than boron (12). If the phosphate glass data are applied to Fig. 5, the resulting curve would be somewhere in between curves (B) and (C).

Examination of Fig. 3 and 4 reveals that between 1000° and 1200°, a high bulk concentration of phosphorus causes little change in oxidation rates. This is consistent with results of ref. (14, 15): Phosphorus "piles-up" slightly at the silicon surface, and its concentration in the oxide is low. This effect is shown in Fig. 8. Even at 920°, the concentration of phosphorus in a wet oxide (the maximum case) is less than 0.2 that of the bulk. As a result the oxide produced will be essentially SiO_2 and subsequent oxygen diffusion through it will not be significantly affected. However, Fig. 3 and 4 show a marked increase of oxidation rate at 920°C, especially in wet oxygen. This apparent contradiction can be readily explained, however, if the mechanism of silicon oxidation is considered. It has been proposed that below 1000°C, thermal oxidation is no longer completely diffusion controlled, but depends considerably on the reaction at the silicon surface (3). The "pile-up" of phosphorus, especially in wet oxygen, could cause a change in the surface reaction rate and thereby affect the oxidation rate. From Fig. 8 this effect should be more pronounced in wet oxygen, and Fig. 3 and 4 indicate that this is indeed the case.

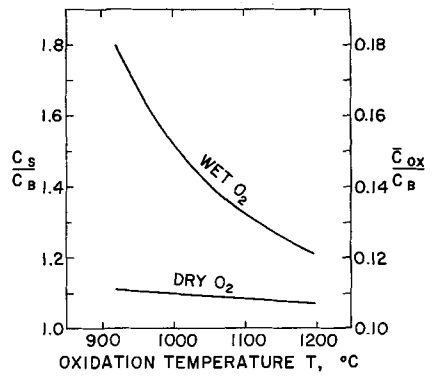

Fig. 8. Predicted phosphorus concentration at the silicon surface (C_S) and in the oxide ($\bar{C}_{ox}$) due to impurity redistribution during thermal oxidation in two ambients at various temperatures.

Table I. Relationship of parabolic oxidation rate constants for heavily doped silicon to standard values

Oxide ambient	Oxidation temp, °C	Rate constant K_{std}, $\mu/\sqrt{hr}$	Boron-doped silicon* K_B/K_{std}	Phosphorus-doped silicon† K_P/K_{std}
Dry O_2	1200	0.206	1.21	1.02
Dry O_2	1100	0.155	1.29	1.03
Dry O_2	1000	0.093	1.31	1.03
Dry O_2	920	(0.050)	1.20	1.18
Wet O_2 (95° H_2O)	1200	0.840	1.11	1.00
Wet O_2	1100	0.675	1.10	1.00
Wet O_2	1000	0.480	1.11	1.09
Wet O_2	920	(0.325)	1.13	1.30

* K_B is the rate constant for $C_B = 2.5 \times 10^{20}$ boron at./cm^3; K_{std} is the rate constant for $C_B = 1 \times 10^{16}$ boron at./cm^3.
† K_P is the rate constant for $C_B = 1.5 \times 10^{20}$ phosphorus at./cm^3; K_{std} is the rate constant for $C_B = 4 \times 10^{15}$ phosphorus at./cm^3.

Thus far, it has not been possible to establish the presence, or perhaps in this case, absence of phosphorus in the oxide by infrared examination. The only P_2O_5 absorption peak (over the wavelength range investigated) falls at 9.2-9.3μ, that of SiO_2. The latter completely masks any effect due to phosphorus.

Correlation of all data.—A general comparison of both boron and phosphorus results may now be made. Table I contains a partial summary of the data plotted in Fig. 1-4. Oxidation rate constants for the silicon with the heavier concentrations of boron and phosphorus ($C_B = 2.5 \times 10^{20}$ and 1.5×10^{20} cm^{-3}) expressed as K_B and K_P, are compared with the standard values, K_{STD}. It should be kept in mind that oxidation at the lower temperatures and for thiner oxides is not truly parabolic. However rate constants are still listed in terms of $\mu/\sqrt{hr}$ for the thicker oxides at each temperature for purposes of comparison. Table I shows a reasonable correlation with Fig. 6 and 8, in that at higher temperatures the concentration of boron in the oxide (Fig. 6) determines the amount of increase in oxidation rate. At 920°C, where the reaction has been proposed to be more surface controlled, wet oxygen oxidation of phosphorus-doped silicon results in the highest surface concentration and also the highest oxidation rate.

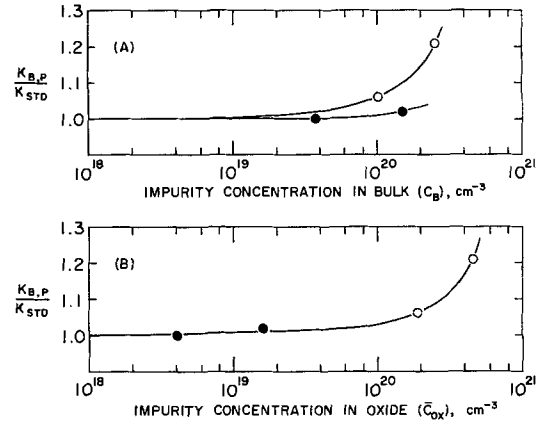

Fig. 9. Dependence of oxidation rate constants for heavily doped silicon on: (A) impurity concentration in the bulk; (B) impurity concentration in the oxide. Data are based on oxidation in dry oxygen at 1200°C; ○, boron; ●, phosphorus.

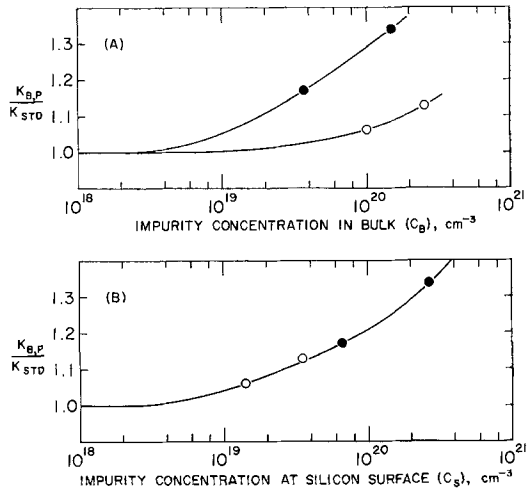

Fig. 10. Dependence of oxidation rate constants for heavily doped silicon on: (A) impurity concentration in the bulk; (B) impurity concentration at the silicon surface. Data are based on oxidation in wet oxygen (95°C H_2O) at 920°C; ○, boron; ●, phosphorus.

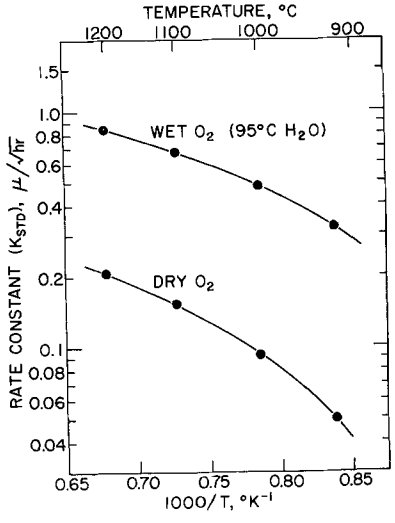

Fig. 11. Log of rate constant, $K_{STD} \equiv w/\sqrt{t}$, plotted against reciprocal of absolute temperature for dry and wet O_2 oxidation of silicon (C_B = 1 x 10^{16} at./cm^3).

In Fig. 9A, the K_B/K_{STD} and K_P/K_{STD} ratios for dry oxygen oxidation at 1200°C are plotted against bulk impurity concentration C_B. Two separate curves result. However, if the ratios are plotted against average impurity concentration in the oxide, $\bar{C}_{ox}$, one curve is obtained in Fig. 9B. Similarly, 920°C wet oxygen data are plotted in Fig. 10. In this case, whereas ratios of K_B/K_{STD} and K_P/K_{STD} plotted against C_B again result in two curves (see Fig. 10A), a plot of the ratios against surface concentration C_S gives one continuous curve. In this case if the results were plotted against $\bar{C}_{ox}$, the resulting curves would be even more divergent than Fig. 10A.

The above two cases (dry oxygen at 1200° and wet oxygen at 920°C) were selected as examples since they represent the two extremes in the effects of heavy doping on oxidation characteristics. It should be noted that wet oxygen data at 1200°C could be included in Fig. 9 (and dry oxygen data at 920°C in Fig. 10) with reasonable agreement with the existing curves. These results further indicate that the oxidation rate of heavily doped silicon is chiefly dependent on the impurity concentration either in the oxide (above 1000°C) or at the surface (below 1000°C).

A plot of the logarithm of parabolic rate constant versus the reciprocal of absolute temperature is shown in Fig. 11 for dry and wet oxygen silicon oxidation. The points represent the data from Table I for standard rate constants (K_{STD}). The curves help to illustrate the change in oxidation mechanism from one primarily diffusion controlled ($w = K_1 t^{1/2}$) to that where a reaction at the silicon oxide-silicon interface at least partially controls the oxidation rate ($w = K_2 t$). Above 1000°C the curves (based on parabolic rate constants) are more linear while below this temperature a more rapid change in slope is noted. The best fit of a straight line through the points in the 1000° to 1200° region in Fig. 11 will give activation energies of 14.75 and 10.25 kcal/mole for dry and wet O_2, respectively (where $K_{STD} \equiv w/\sqrt{t}$). These values correspond to 29.5 and 20.5 kcal/mole (for $k \equiv w^2/t$) which are in close agreement with previous results (3).

The fact that the curves in Fig. 11 are not strictly linear but have continuously changing slopes indicates that there is no sudden change in oxidation mechanism at any particular temperature. If we consider some concepts of oxidation mechanisms proposed by Evans (18), the nature of these results can be better understood. In the case of silicon, oxidation will depend on two main processes: the diffusion of the oxidizing species through the oxide and the reaction of this species with the silicon at the oxide-silicon interface. The slower of the two processes will be the actual rate-determining step. Temperature will be an important factor in determining the comparative rates and thus the relative importance of these two processes. This is indicated by the changing slopes in Fig. 11. The results described in this investigation involving oxidation rates of heavily doped silicon are also in agreement with this concept.

Mention should be made of the relationship of these results to the few data that have already been presented concerning oxidation of heavily doped silicon. Yeh (6) indicated that the oxidation rate of silicon with an estimated diffused phosphorus surface concentration of 2 x 10^{21} cm^{-3} increased if the oxidation occurred at 970°C in steam. The only data presented in support of this was a plot of oxide thickness *vs.* square root of time. The slopes and thus the oxidation rate constants, of the two plots (C_S = 2 x 10^{21} and 2 x 10^{16} cm^{-3}) were identical, while the intercepts were different. This indicated an initial porous oxide might have been present on the diffused surface, causing a shift of the type shown in Fig. 5 from curve A to curve B. According to the results of the present investigation, Yeh should have obtained a significant increase of oxidation rate in steam at 970° for the surface concentration indicated. Yeh did present data for a boron diffused surface (estimated C_s = 5 x 10^{18} cm^{-3}) which if plotted in a manner similar to the phosphorus data indicates a rate constant increase of about 10%. This increase would be of a magnitude similar to the boron results given in this paper, but such increases were found only when the boron surface concentration was at least 5 x 10^{19} cm^{-3}. The difficulty of accurately determining diffused surface concentrations might account for Yeh's results.

The other finding that heavily doped surfaces provide an increased oxidation rate was reported by Ligenza (7). Silicon with a phosphorus surface concentration of 10^{21} cm^{-3} was oxidized at 650°C for 1 hr in 120 atm steam. An oxidation rate five times that of high resistivity silicon was obtained. For this type of oxidation, the oxide thickness-time relationship is entirely linear which means the oxidation is controlled completely by a reaction at the silicon-silicon oxide interface. Such an increase in oxidation rate would therefore be expected from the results and considerations of the present investigation.

Conclusions

It has been shown that the thermal oxidation rate of heavily doped silicon (C_B of boron and phosphorus $\geq$10^{20} cm^{-3}) at temperatures above 1000°C depends on

the amount of impurity in the oxide. This finding is consistent with the diffusion-controlled mechanism of thermal oxidation in this temperature range. The amount of impurity in the oxide in turn is a function of the redistribution characteristics of the impurity and the oxidation ambient. Little effect is noted unless the impurity concentration in the oxide is greater than 10^{20} cm^{-3}.

At 920°C, where thermal oxidation is partially controlled by a surface reaction the rate of oxidation is a function of the impurity concentration at the silicon surface. This concentration, determined by redistribution phenomena, must be at least 10^{19} cm^{-3} before an appreciable change in rate occurs.

The effect of other impurities (for $C_B \geqq 10^{20}$ cm^{-3}) on oxidation rates may also be predicted, provided their redistribution characteristics are known. These predictions can be based on the four cases of the redistribution process as presented in ref. (14). Where the oxide rejects impurities and diffusion of these impurities in the oxide is slow (case 2A, ref. 14) such as phosphorus, antimony, and arsenic, no increase in oxidation rate should occur above 1000°C. However the rates should increase below 1000°C. If the oxide takes up an impurity, and again the impurity diffuses slowly in the oxide (case 1A), an increase of oxidation rate should occur at least at temperatures above 1000°C, and possibly below, as with boron. Gallium, aluminum, and indium, which deplete at the silicon surface and also probably diffuse rapidly through the oxide (either case 1B or 2B) should not cause an increase in oxidation rates at any temperature even at high bulk concentrations.

Acknowledgments

The authors are indebted to A. S. Grove, E. H. Snow, and C. T. Sah for helpful discussions regarding various aspects of this program. The calculations in the Appendix were performed by A. S. Grove. R. Tanner assisted in the preparation and evaluation of the oxides.

Manuscript received Sept. 22, 1964; revised manuscript received Nov. 23, 1964.

Any discussion of this paper will appear in a Discussion Section to be published in the December 1965 JOURNAL.

REFERENCES

1. M. M. Atalla, "Properties of Elemental and Compound Semiconductors," Vol. 5, H. Gatos, Editor, pp. 163-181, Interscience Publishing Co., New York (1960).
2. J. R. Ligenza and W. G. Spitzer, *J. Phys. Chem. Solids*, **14**, 131 (1960).
3. B. E. Deal, *This Journal*, **110**, 527 (1963); *ibid.*, **110**, 1292 (1963).
4. H. C. Evitts, H. W. Cooper, and S. S. Flaschen, *ibid.*, **111**, 688 (1964).
5. C. R. Fuller and F. J. Strieter, Paper presented at the Toronto Meeting of the Society, May 3-7, 1964, Abstract No. 74.
6. T. H. Yeh, *J. Appl. Phys.*, **33**, 2849 (1962).
7. J. R. Ligenza, *This Journal*, **109**, 73 (1962).
8. C. T. Sah, *IEEE Trans. Electron Devices*, **ED-11**, 324 (1964).
9. G. E. Moore, Chap. 5 in "Microelectronics," E. Keonjian, Editor, McGraw-Hill Book Co., New York (1963).
10. J. C. Irvin, *Bell System Tech. J.*, **41**, 387 (1962).
11. P. J. Jorgensen, *J. Chem. Phys.*, **37**, 874 (1962).
12. M. O. Thurston and K. D. Kang, "The Mechanisms of Oxidation and Diffusion Into the Oxide," Seventh Quarterly Technical Report No. RF 1233-7Q, U. S. Army Signal Supply Agency Contract No. DA-36-039-SC-87426, October (1962).
13. R. H. Doremus, Chap. 1 in "Modern Aspects of the Vitreous State," Vol. 2, J. D. MacKenzie, Editor, Butterworth and Co., Washington, D. C. (1962).
14. A. S. Grove, O. Leistiko, Jr., and C. T. Sah, *J. Appl. Phys.*, **35**, 2695 (1964).
15. B. E. Deal, A. S. Grove, E. H. Snow, and C. T. Sah, *This Journal*, **112**, 308 (1965).
16. I. Simon, Chap. 6 in "Modern Aspects of the Vitreous State," Vol. I, J. D. MacKenzie, Editor, Butterworth and Co., Washington, D. C., (1962).
17. P. E. Jellyman and J. P. Proctor, *Trans. Soc. Glass Tech.*, **39**, 173T (1955).
18. U. R. Evans, "The Corrosion and Oxidation of Metals," pp. 819-859, Edward Arnold Ltd., London (1960).
19. H. S. Carslaw and J. C. Jaeger, "Conduction of Heat in Solids," Appendix II, Oxford University Press, London (1959).

APPENDIX

The Average Impurity Concentration in the Oxide Layer

Because of the redistribution process taking place during thermal oxidation, some of the impurities which were originally in the silicon substrate will end up within the silicon dioxide film. The resulting average concentration of impurities within the oxide can be readily calculated on the basis of the redistribution theory (14), as follows.

The total amount of impurity (per cm^2) contained within the oxide layer is given by

$$Q_{ox} = \int_o^{z_o} C_1(z,t)\,dz \qquad [A\text{-}1]$$

where z_o denotes the oxide thickness, and $C_1(z,t)$ denotes the concentration of the impurity within the oxide film. [The notation follows that of ref. (14).] Incorporating Eq. [15] of ref. (14) into equation [A-1], and performing the integration yields the average concentration of the impurity in the oxide film

$$\bar{C}_{ox} \equiv \frac{Q_o}{z_o} = C_o + \left(\frac{C_s}{m} - C_o\right)\left[1 + \frac{\text{ierfc}(K/2\sqrt{D_1}) - 1/\sqrt{\pi}}{K/2\sqrt{D_1}}\right] \qquad [A\text{-}2]$$

where ierfc indicates the integral of the complementary error function and is tabulated in ref. (19). C_o denotes the concentration of the impurity at the outside surface of the oxide layer (this concentration is very small if the impurity has a tendency to leave the solid); C_s denotes the concentration of the impurity in the silicon near the oxide-silicon interface; and m is the segregation coefficient. The bracketed term has been evaluated and is shown in Fig. 12 as a function of $K/2\sqrt{D_1}$, the ratio of the parabolic oxidation rate constant to the square root of diffusivity of the impurity in the oxide layer. It can be noted that the limits of very small and very large diffusivities, Eq. [A-2] reduces to

$$\bar{C}_{ox} = C_s/m, \quad K/2\sqrt{D_1} \to \infty \qquad [A\text{-}3]$$

$$\bar{C}_{ox} = C_o, \quad K/2\sqrt{D_1} \to 0 \qquad [A\text{-}4]$$

The first of these equations corresponds to the case of boron and phosphorus; the second to gallium. These are the approximations used in the text of the present work.

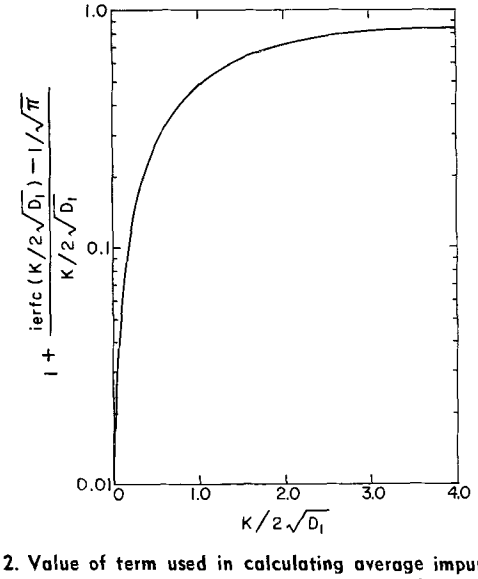

Fig. 12. Value of term used in calculating average impurity concentration in oxide as a function of the ratio $K/2\sqrt{D_1}$.

The Effects of Substrate Orientation on Epitaxial Growth

S. K. Tung

Bell Telephone Laboratories, Incorporated, Allentown, Pennsylvania

ABSTRACT

The effect of substrate orientation on the quality of silicon epitaxial layers was studied in terms of deposition rate and surface topography. The layer was deposited by the hydrogen reduction of silicon tetrachloride. Deposition rate was determined from the time of deposition and from the layer thickness obtained by angle lapping and staining. Deposition rate was lowest on accurately oriented <111> substrates and increased as the degree of misorientation from the <111> direction increased. The frequently observed surface pyramid defect was found to be a function of (*a*) deposition rate and (*b*) substrate orientation. These pyramidal defects were not observed for low deposition rates, and when the substrate was misoriented from the <111> direction. These observations are consistent with the proposal that the deposition rate used in practice is determined by two fundamental rate processes, namely, (*a*) reaction rate and (*b*) growth rate.

During the development of epitaxial deposited silicon layers, there has been interest in the effect of the orientation of the silicon substrate and in the change of orientation after surface processing and layer deposition. This paper reports a study of these effects on the quality of the silicon epitaxial layer in terms of deposition rate and surface topography.

Experimental Procedure and Results

Orientation change during silicon substrate processing.—A silicon substrate surface was lapped and chemically polished before epitaxial deposition. The surface orientation was measured by x-ray goniometry after each processing step, *i.e.*, lapping, chemical polishing, and epitaxial layer deposition. The precision of the employed technique was estimated to be within ± 10 min of arc. The data of this study are summarized in Table I. It is concluded that there was no substantial orientation change of the silicon surface through the orientation range investigated, either after chemical polishing or after layer deposition. The small orientation difference seen in Table I is believed to be experimental error.

Substrate orientation related to deposition rate.—To study the effects of substrate orientation on deposition rate a silicon layer was deposited on a polycrystalline silicon substrate whose surface was mechanically polished. This substrate contained two or three large grains. The orientations of these large grains were determined by the Laue back-reflection technique. An epitaxial silicon layer was deposited by the hydrogen reduction of silicon tetrachloride using a vertical type machine similar to that reported previously (1, 2). This deposition was normally done at a slice temperature of 1200°C and a 0.2 vol % concentration of silicon tetrachloride. After the layer deposition, the grain boundaries were delineated by the differences in thickness of silicon deposited on each grain. Figure 1 shows such a silicon wafer surface after epitaxial layer deposition. The grain boundaries can be seen clearly in this picture, but they could not be located before deposition because the wafer surface had been mechanically polished. The difference in layer thickness is further illustrated in Fig. 2 by an angle-lapped section. In this case the two large grains had <111> and<115> orientations. The layer thickness on the <111> grain was 11.2μ, and on the <115> grain it was 13.0μ. Because the two adjacent grains were deposited in the same run, other deposition parameters such as temperature, silicon tetrachloride vapor concentration, and flow rates were the same. The difference in layer thickness on different grains was thus due to the variation in orientation.

Figure 3 is a plot of deposition rate at 1200°C as a function of substrate orientation. Deposition rate was determined from the time of deposition and from layer thickness obtained by angle lapping and staining. The data of this plot were obtained from depositions on individual single crystal silicon substrates with different orientations. It is of interest to note that the deposition rate increased as misorientation from the <111> direction increased. Also, the curve shows that the <111> orientation had the lowest deposition rate of all low index orientations, while the <110> orientation had the highest deposition rate. These results were similar to those reported by Mendelson (3).

Table I. Surface orientation change after processing

Slice No.	Substrate resistivity, ohm-cm	Orientation, angle from <111> After lapping	After chemical polishing	After deposition
3619-78	0.014	3° 5′	3° 16′	2° 57′
3619-79	0.017	3° 11′	3° 24′	3° 11′
3642-2	0.006	2° 43′	—	2° 55′
3642-3	0.006	2° 46′	—	2° 38′
3642-4	0.006	2° 33′	—	2° 34′
3642-7	0.006	2° 24′	—	2° 29′
3642-8	0.006	2° 27′	—	2° 26′
3642-27	0.006	2° 38′	2° 36′	—
3642-30	0.006	2° 32′	2° 33′	—
3642-31	0.006	2° 26′	2° 29′	—
3642-32	0.006	2° 51′	2° 34′	—
3642-34	0.006	2° 26′	2° 39′	—

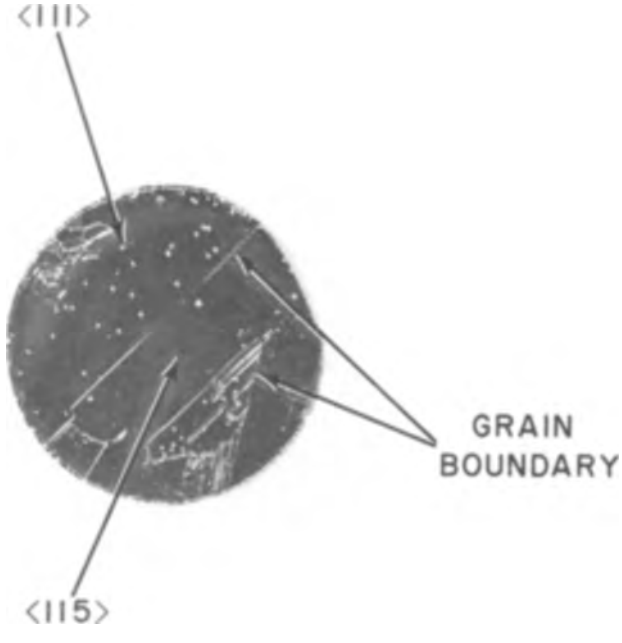

Fig. 1. Surface of silicon layer on polycrystal silicon substrate

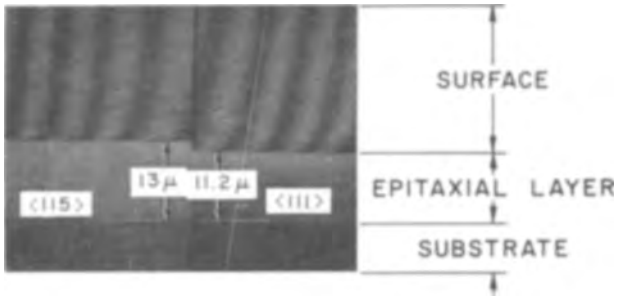

Fig. 2. An angle-lapped picture showing different layer thickness

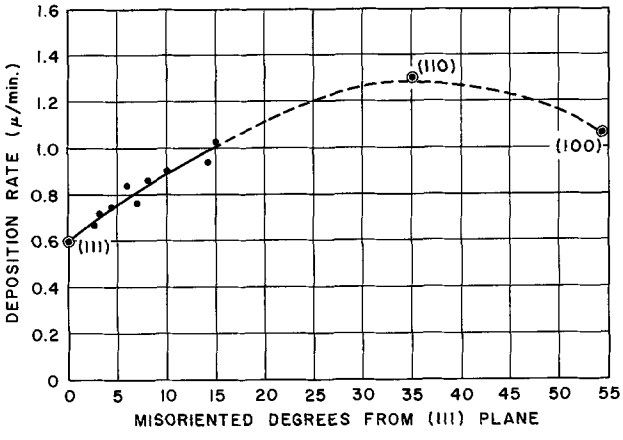

Fig. 3. Deposition rate vs. substrate misorientation

He observed a minimum growth rate and a high stacking fault density on <111> substrates.

Because the deposition rate depends strongly on other processing parameters (2), the orientation effect discussed here can be differentiated only when other process parameters are held substantially constant.

Substrate orientation and surface layer topography.— A surface defect of "pyramidal" shape was found in depositions upon <111> oriented substrates when the deposition rate exceeded a critical value (4). This type of surface defect is shown in Fig. 4. In general, this defect is a prominence on the surface and has a ridgelike tail associated with it. The size of the pyramids varied as the growing conditions changed. Normally, they are easily seen with the unaided eye.

A tetrahedral growth defect has been observed by Miller *et al.* (5) who attributed such a defect to the presence of silicon carbide. It should be emphasized that the type of surface defect observed here developed only when the deposition rate exceeded a critical value for that particular substrate orientation. That is the surface defect is a combination effect of both the substrate orientation and the deposition rate. Impurities play a less determining factor. For example, pyramids grew on a substrate with <111> orientation but no pyramids grew on a substrate with <115> orientation when both the substrates were deposited simultaneously at 1200°C with a deposition rate of 1.4 μ/min. In another experiment pyramids did not grow on either <111> or <115> oriented substrates because a lower deposition rate of 0.4 μ/min was used at the same deposition temperature. The deposition rate was adjusted by varying silicon tetrachloride concentrations. In general one can conclude that the pyramids were grown at a certain deposition rate for a particular substrate orientation. In this paper this deposition rate is called the "critical deposition rate" for that orientation.

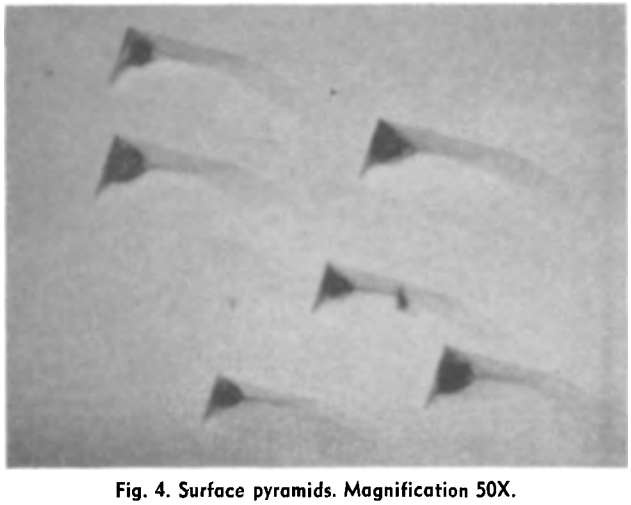

Fig. 4. Surface pyramids. Magnification 50X.

Table II. Summary of data

Substrate orientation	Critical deposition rate
<111>	1.0μ/min ±25%
½° from <111>	1.5μ/min ±25%
2° from <111>	3.5μ/min ±25%

Because the deposition rate is a function of the substrate orientation, it was expected that the critical deposition rate for pyramids grown depended on the substrate orientation. Experimental results showed that on a silicon substrate which had been misoriented from the <111> direction, a high deposition rate could be utilized without pyramids growing on the surface. Also, when a silicon substrate surface was closely oriented to the <111> direction, pyramids might develop on the surface unless a deposition rate less than the critical deposition rate was used.

The critical deposition rates for various misorientations from the <111> direction were found experimentally. Table II shows the critical deposition rate at 1200°C to be about 1 μ/min for a substrate oriented on the <111> direction, about 1.5 μ/min for a substrate with a ½ degree misorientation from the <111> direction, and about 3.5 μ/min for a substrate with a 2 degrees misorientation from the <111> direction. It should be pointed out that the critical deposition rate is also dependent on the depositing system and the data discussed was derived from the system described in a previous publication (2).

Discussion

One may ask "What is the critical deposition rate?" In answering this question it will be convenient to discuss the results in terms of heterogeneous rate reaction theory (6). In general the over-all deposition process can be separated into two main steps: (*a*) the reaction or series of reactions which take place on or near the substrate surface; this rate will be called the reaction rate; (*b*) the addition of atoms to proper sites of the substrate surface; this will be called the growth rate. These two rate processes complement each other during deposition. The slower process will control the over-all deposition process. Thus the observed deposition rate is either controlled by the reaction rate or by the growth rate. The controlling rate depends on how the deposition process is carried out and how the process parameters are arranged.

Figure 5 shows a schematic drawing of the observed deposition rate *vs.* silicon tetrachloride concentration. One may visualize that the growth rate or the rate at which atoms are added to the substrate surface is dependent on the substrate surface plane. Consequently the growth rate is a strong function of substrate orientation. On the other hand, the reaction rate should not depend too much on substrate orientation. Thus the critical deposition rate on a perfect substrate surface plane can be assumed to be the growth rate. Also, the deposition rate, whether controlled by the reaction rate or by the growth rate, depends on other process parameters in the deposition.

The theoretical treatment of surface structures in crystal growth from the vapor was given by Cabrera

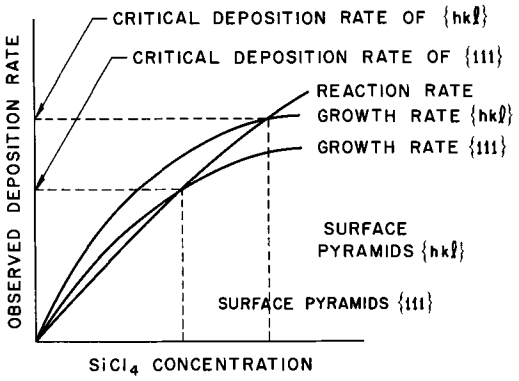

Fig. 5. Schematic drawing of the observed deposition rate vs. silicon tetrachloride concentration.

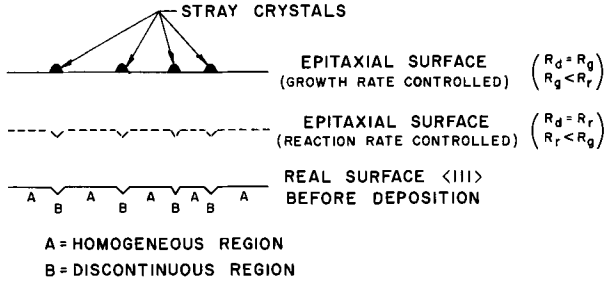

Fig. 6. Schematic drawing of a <111> surface after deposition

Fig. 7. Schematic drawing of a misoriented <111> surface

and Coleman (7). Assume a real surface to be almost homogeneous everywhere but with some inhomogeneities or discontinuities at several locations. These inhomogeneities will also have local orientation changes. It is predicted (7) that the growth rate at such discontinuities will be greater than the growth rate on the homogeneous region because nucleation will occur more readily at the discontinuities than at the homogeneous region. Figure 6 shows a schematic drawing of the epitaxial layer growth on a real surface having <111> orientation. If the deposition process is reaction rate controlled, then the over-all process is not orientation dependent. Consequently there are no differences in the growth features on the homogeneous regions and the inhomogeneous regions. The resultant epitaxial layer surface is merely an image of the substrate surface on which the layer was deposited. This result normally can be accomplished by depositing at a low silicon tetrachloride concentration. However, if the deposition process is growth rate controlled, then the over-all process is strongly orientation dependent and the reaction rate is greater than the growth rate. The difference between the reaction rate and the growth rate is shown by forming a stray crystal at an inhomogeneity at which the growth rate is greater than at other homogeneous regions on the surface. As shown in Fig. 3 the <111> oriented surface had the lowest growth rate when compared to other orientations. Consequently a "pyramid" on the surface is formed. In general, this result can be observed by depositing at a high silicon tetrachloride concentration.

The same general arguments can be applied for the case of a substrate surface which has an orientation other than the <111> orientation. Thus it is proposed that the atomic configuration of a misoriented {111} plane can be resolved into many steps which are parallel to the original {111} plane surface. This is shown schematically in Fig. 7. Such a misoriented {111} plane surface can have a greater growth rate than the {111} plane surface since it is expected that nucleation will occur more readily at the step corners formed by the {111} plane surfaces. Consequently the difference between the reaction rate and the growth rate on a misoriented {111} plane surface is less than the difference between the reaction rate and the growth rate on a {111} plane surface if the reaction rate is considered unchanged. Thus a substrate surface misoriented from the <111> direction can tolerate a higher deposition rate without developing pyramids on the surface.

Conclusions

The deposition rate was found to vary with substrate orientation. The deposition rate increased to a limit as the substrate was misoriented from <111> orientation. The <111> oriented substrate had the lowest deposition rate when compared to other major orientations, *i.e.*, <110> and <100>.

A pyramidal surface defect was found to be a function of both the deposition rate and the substrate orientation. The pyramidal defects were not observed when the deposition rate was slow, and/or when the substrate was misoriented from the <111> direction. These observations were explained by a proposed mechanism in which the deposition rate used in practice is considered to be composed of two fundamental rate processes reaction rate and growth rate which complement each other during the actual deposition.

Acknowledgment

The author wishes to thank Mrs. M. H. Read, Bell Telephone Laboratories, Murray Hill, for her x-ray work in determining the crystal orientations. Also, he is indebted to Dr. R. E. Caffrey for his valuable discussions.

Manuscript received Sept. 23, 1964.

Any discussion of this paper will appear in a Discussion Section to be published in the December 1965 JOURNAL.

REFERENCES

1. H. C. Theuerer, *This Journal*, **108**, 649 (1961).
2. S. K. Tung, *Metallurgy of Semiconductor Materials*, **15**, 87 (1962).
3. S. Mendelson, *J. Appl. Phys.*, **35**, 1570 (1964).
4. Private communication: G. H. Edmunds and W. C. Gibson at Bell Telephone Laboratories, Laureldale, Pennsylvania also reached the same results through their investigations.
5. D. P. Miller, S. B. Watelski, and C. R. Moore, *J. Appl. Phys.*, **34**, 2813 (1963).
6. A. Van Hook. "Crystallization: Theory and Practice," 22 (1961).
7. N. Cabrera and R. V. Coleman, "The Art and Science of Growing Crystals," 3 (1963).

Mechanism of Hydrocarbon Formation in the Electrolytic Reduction of Acetone in Aqueous Sulfuric Acid

Taro Sekine, Akira Yamura, and Kiichiro Sugino

Department of Applied Electrochemistry, Tokyo Institute of Technology, Tokyo, Japan

ABSTRACT

A tentative mechanism or hydrocarbon formation is proposed which, by combining the usual mechanism of pinacol and isopropanol formation, will contribute to one clarification of the over-all electrode process of acetone reduction.

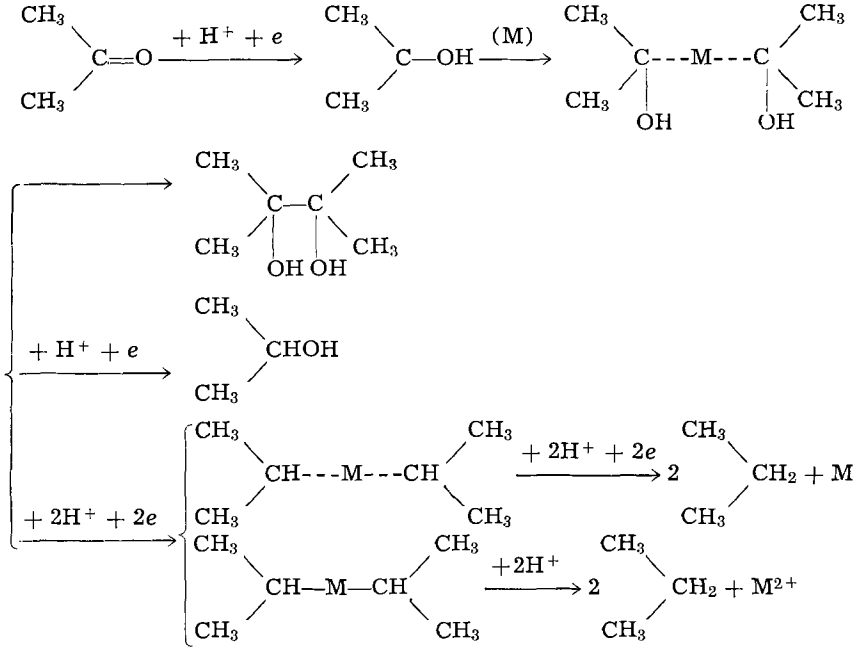

The main point lies in the fact that the radical $(CH_3)_2\dot{C}OH$ is further reduced with dehydration of propane through the isopropyl radical which is combined with the cathode metal. In certain cases (mercury and lead, etc.) the reaction products with metal (organometallic compound) can be isolated in a relatively stable form. Generally speaking, cathode material having a negative standard electrode potential tends to follow this hydrocarbon formation process.

In the electrolytic reduction of aliphatic ketones in acidic medium it is known that pinacol, secondary alcohol, and hydrocarbon are obtained as the main products. In the case of acetone, the reduction products were pinacol, isopropanol, and propane (1). Depending on the kind of cathode used, the amounts of the products obtained will differ considerably; at cadmium (1) and amalgamated zinc (2), the hydrocarbon was mainly obtained.

It is still not clear, however, why the use of different kinds of cathodes produces different types of products. It is impossible at this time to establish a complete mechanism of the electrolytic reduction of aliphatic ketones, although attempts have been made.[1]

The authors have undertaken this study in order to clarify the over-all electrode process of acetone reduction by trying to solve the problem of why the different kinds of cathodes cause the formation of different types of products, and in particular why the hydrocarbon is obtained.

Experimental

Assembly of the apparatus.—Arrangement of the electrolysis equipment and cell design are shown in Fig. 1. Two different types of cell, cylindrical and H type cell, were utilized for the convenience of preparative study and accurate gas analysis.

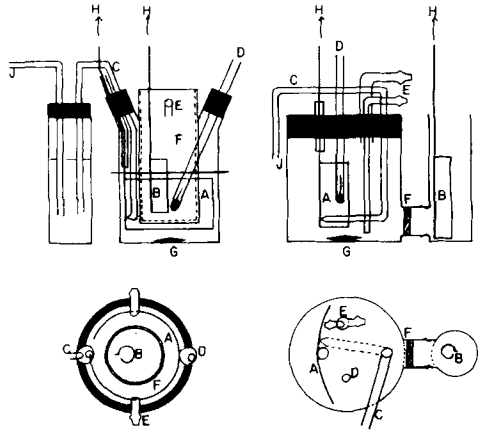

Fig. 1. Cell design: A, cathode; B, anode; C, salt bridge; D, thermometer; E, gas outlet to buret; F, diaphragm; G, stirrer (magnetic drive); H, to controlled potential electrolyzer; J, to saturated calomel electrode.

[1] Recently, S. Swann, Jr. reviewed the electrolytic reduction of keto groups to methylene groups in aliphatic compounds and he showed a tentative mechanism in which the metal of the cathode takes part in the reaction (3). This was originally put forth by Schall *et al.* (9).

Table I. Conditions of gas chromatographic analysis

Product stationary phase, 2m	Pinacol P.E.G.*	Isopropanol P.E.G.	H_2 M.S.†	C_2H_6 S.G.‡	C_3H_8 S.G.	C_3H_6 S.G.
Carrier gas	H_2	H_2	Ar	H_2	H_2	H_2
Flow rate, cc/min	40	40	40	40	40	40
Temperature, °C	200	100	20	100	100	100
Retention time, min	9.3	7.2	1.8	2.6	7.0	12.0

* P.E.G., polyethyleneglycol 1500.
† M.S., molecular sieve 5A.
‡ S.G., silica gel.

Preparation of electrolyte.—Acetone was purified by distillation after standing for several days with potassium permanganate. HCl-KCl buffer solution (*p*H 1.55) and 0.2*N* sulfuric acid solution were used for the background solution of polarographic measurement.

Pretreatment of electrodes.—With the exception of mercury, which was carefully distilled before use, lead, cadmium, zinc, aluminum, nickel, tin, and copper cathodes were washed successively with dilute hydrochloric acid and water. The fresh electrodes were used immediately in the following experiments.

Analysis of the products.—A gas chromatographic technique (4) was utilized to determine the products which were formed during the electrolysis and those formed by the decomposition of organo-metallic intermediate.

The conditions of gas chromatographic analysis used are condensed in Table I.

At the same time, pinacol was separated from the electrolyte and determined by the following procedure.

The catholyte was neutralized with anhydrous potassium carbonate, filtered, and the resulting solution was distilled at reduced pressure to remove acetone and 2-propanol. The residue was extracted with ether and after drying, the ether solution was evaporated. Colorless needles were obtained having a melting point of 38°C.

With the exception of mercury, the ions of metals such as lead, cadmium, zinc, aluminum, nickel, tin, and copper in the electrolyte or in the decomposition product or organo-lead intermediate were determined polarographically at 20° ± 1°C after 5-30 min of deoxygenation by nitrogen. Mercury was determined by E.D.T.A. titration (5).

To confirm the structure of organo-metallic intermediate, the I.R. spectroscopic method was tried by using "Shimadzu I.R. spectrophotometer Type IR-27" at 35°C.

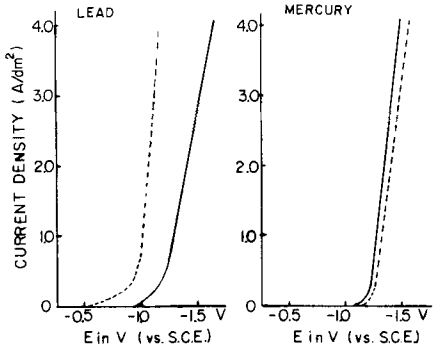

Fig. 2a. I-E curves in acetone sulfuric acid mixture at lead and mercury cathode: ——115g acetone and 28 cc 20% sulfuric acid; - - - - - 130 cc 10% sulfuric acid (reference).

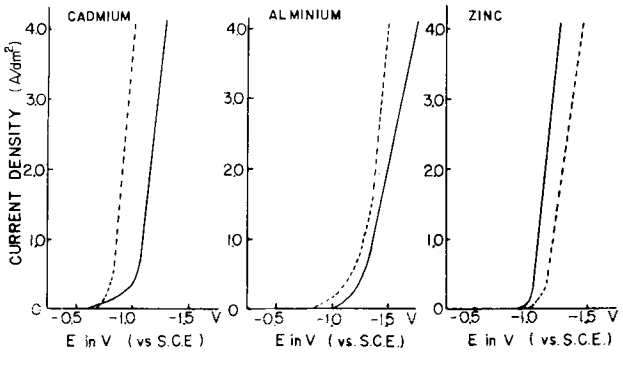

Fig. 2b. I-E curves in acetone sulfuric acid mixture at cadmium, aluminum, and zinc cathode: ——115g acetone and 28 cc 20% sulfuric acid; - - - - 130 cc 10% sulfuric acid (reference).

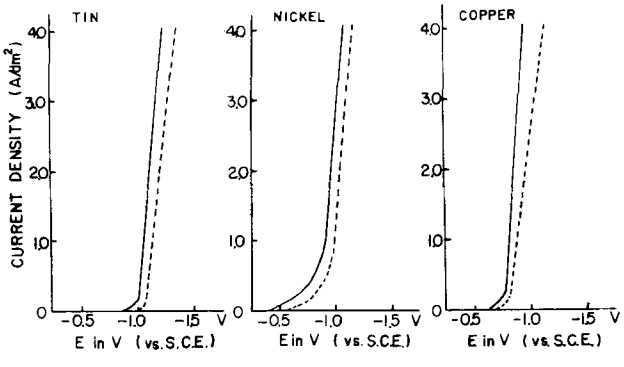

Fig. 2c. I-E curves in acetone sulfuric acid mixture at tin, nickel, and copper cathode: ——115g acetone and 28 cc 20% sulfuric acid; - - - - 130 cc 10% sulfuric acid (reference).

Results and Discussion

Current density-cathode potential curve.—A plot of current density *vs.* cathode potential was made in the catholyte described below by using controlled potential electrolyzer (Yanagimoto EV-3). Figure 2 shows the current density *vs.* cathode potential curves which were measured in a cylindrical cell at mercury, lead, cadmium, zinc, aluminum, nickel, tin, and copper cathodes, respectively. All measurements were carried out at 20° ± 1°C.

Polarographic measurement[2] was also carried out for the catholyte containing 1-10 x 10^{-3} mole/liter acetone in 0.2*N* H_2SO_4 or a HCl-KCl buffer. Polarograms of acetone are shown in Fig. 3. Current increases at mercury in Fig. 2 and 3 were seen at about —1.20v and are considered to be the reduction potential of acetone in sulfuric acid.

Although no noticeable reduction wave (showing half-wave potential) was observed on the polarogram of acetone reduction,[3] the interesting results were observed when the "controlled potential electrolyzer" was used on current-potential curve measurement. That is, at lead, cadmium and aluminum, a negative shift of current-potential curves was induced when

[2] Yanagimoto's High Sensitive Polarograph PA-201 was used.

[3] Nearly the same result was reported by Shikata and Tachi (6) and Zuman (7) for the same conditions.

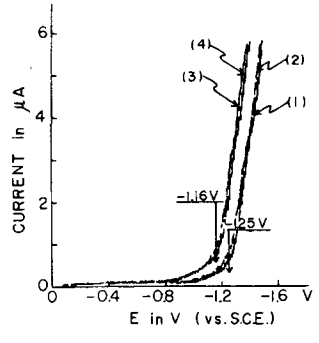

Fig. 3. Polarograms of acetone. 1, 5-500 x 10^{-3} mole acetone in HCl-KCl buffer; 2, HCl-KCl buffer (pH = 1.55); 3, 1-50 x 10^{-3} mole acetone in 0.2*N* H_2SO_4; 4, 0.2*N* H_2SO_4. Sensitivity 0.04 μa/mm.

Table II. Controlled potential electrolysis at various cathodes

Cathode	Hg	Pb	Cd	Zn	Al	Ni	Sn	Cu
Catholyte acetone, g	47	58	110	110	110	145	145	110
20% H_2SO_4 cc	10	13	21	21	21	36	36	21
Cathode potential, v (*vs.* S.C.E.)	−1.375	−1.375	−1.375	−1.375	−1.375	−1.300	−1.200	−1.000
Average current density, amp/dm²	3.0	1.5	3.2	4.3	1.6	5.6	4.0	1.0
Current consumed, amp-hr	12.5	12.3	14.1	12.8	4.6	12.4	5.5	3.6
Current efficiency, %	73	86	90	86	45	1	0	3
Products obtained								
Pinacol, g	0.18	0.74	0	0	0	0	0	0
%*	2.9	7.1	0	0	0	0	—	0
Isopropanol, g	7.9	6.5	0	0.2	0	0	0	0
%*	94.9	67.7	0	3.0	0	0	—	0
Propane, cc	74	930	2596	2157	434	138	0	120
%*	2.2	25.2	100	97.0	100	100	—	100
Hydrogen, cc	1400	730	496	117	1031	5127	2400	1500

* Per cent of total product.

acetone was added to the electrolyte, and at mercury, zinc, nickel, tin, and copper, a positive shift resulted.

Controlled potential electrolysis at various cathodes.—A controlled potential reduction of acetone in sulfuric acid was carried out at a reference potential of −1.375v, at various cathodes (mercury, lead, cadmium, zinc, aluminum, nickel, tin, copper) and was followed by the accurate determination of the products. The condition of electrolysis and its results are shown in Table II.

It was found that even when the reduction potential was the same, the types of products as well as the amounts differed substantially with the cathode used. For example, at mercury, 95% isopropanol, 3% pinacol, and 2% propane were obtained with a current efficiency of 73%. At lead, reduction occurred with a current efficiency of 86%, but the amount of isopropanol decreased to 68% while pinacol and propane increased to 7 and 25%, respectively. In these cases, aside from these reduction products, a small amount of organo-metallic compound which is considered to be reaction product of an intermediate and the cathode, was obtained. On the other hand, at cadmium, zinc, and aluminum cathodes, propane was the only product of electrolysis. At cadmium, reduction, for example, occurred with a current efficiency of 90% and formed 100% yield of propane. The current efficiency for propane formation *vs.* cathode potential is shown more clearly in Fig. 4.

Propane is formed at a potential more negative than −1.10v at a rapid rate and is accompanied by a slow evolution of hydrogen.

At nickel, tin, and copper, current efficiency was very much lower because of the low hydrogen overvoltage and film formation.

To obtain more insight into the mechanism of hydrocarbon formation, the electrolytic reduction of pinacol and 2-propanol was carried out at various cathodes under similar conditions and found to yield no propane.

Isolation of organo-metallic compounds and their decomposition.—The above results give no clue to the mechanism of the hydrocarbon formation and only indicate that a more negative electrode is necessary for the formation of hydrocarbon.

The observation that hydrocarbon formation was accompanied by pitting of the cathode suggested that the electrode had been attacked by a free radical.

This type of reaction was substantiated further by an interesting discovery during our experiments using mercury and lead cathodes. When the catholyte was allowed to stand after the electrolysis, there was a gradual formation of gas which turned out to be propane. Meanwhile, as previously reported (8), the above electrolyses produced also a small amount of oily substances which were considered to be organo-metallic compounds. Therefore, it seems to us that this propane might be formed as a result of the decomposition of the above-mentioned organo-metallic compounds.

To confirm this further, the catholyte containing the oily substance was taken out from the cell after the electrolysis and added to a saturated sodium chloride solution. The rate of decomposition and the composition of gas produced were then determined by gas buret and gas chromatography. The results are plotted in Fig. 5 and are listed in Table III.

As evident from the table, the oily substances seem to be the intermediate for propane formation.[4] Therefore, an attempt was made to isolate organo-metallic compounds and to clarify their properties. Although difficult, we succeeded in obtaining almost pure organo-mercury and organo-lead compound by careful procedure.

[4] An organo-metallic compound was postulated as an intermediate for the first time, by Schall and Kirst (9), in the electrolytic reduction of menthone to menthane.

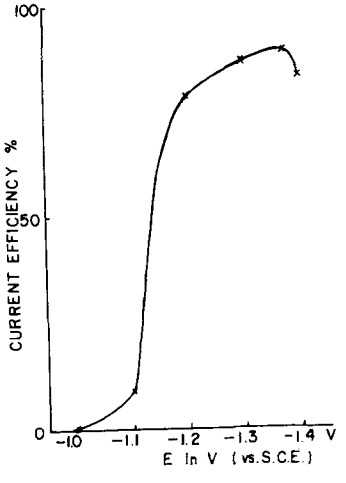

Fig. 4. Influence of cathode potential on current efficiency of propane formation at cadmium cathode.

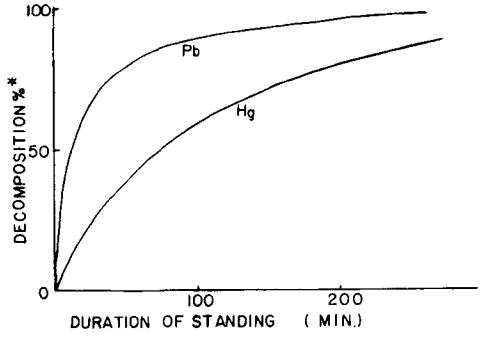

Fig. 5. Decomposition of organo-mercury and organo-lead compounds

* Decomposition % = (volume of gas evolved up to t min / total volume of gas evolved (final state)) x 100.

Table III. Decomposition of the oily substances in aqueous acidic medium

Proportion of gas produced, %	Hg cathode	Pb cathode
C_3H_8	91.5	93.5
C_3H_6	8.5	6.0
H_2	0.1	1.0

Isolation of organo-metallic compounds.—The separation and purification of the oily substances were carried out in the glass apparatus shown in Fig. 6. The crude oily substance collected on filter paper by filtration of the catholyte was dissolved in ether and the solution was quickly introduced to "reservoir A" with anhydrous potassium carbonate. The atmosphere in the system was then completely replaced by nitrogen. After standing for about 10 min in the dark, the solution was transferred into "container B" through a glass filter attached at the bottom of the glass pipe inserted in "A." Evaporation of ether in "B" was then carried out by bubbling nitrogen gas in the dark and gave a pure organo-metallic compound. The decomposition of this compound was also carried out in the same vessel "B."

The mercury compound thus obtained had properties (b.p. 118°C, 125mm Hg, $d_4^{20} = 2.125$, $n_D^{20} = 1.526$) which were identical with those of diisopropyl mercury (10). The infrared absorption spectrum of this compound pointed to the presence of only methyl and methane groups and excluded the presence of any oxygen groupings. These data confirmed the structure of the compound as diisopropyl mercury. This structure was further verified by the identification of its decomposition products. For the lead compound, the measurement of physical contents was difficult due to its instability in air. Its composition as diisopropyllead was clearly indicated from the results of the decomposition study.

Decomposition of organo-metallic compounds.—The decomposition of the mercury compound under the exposure of mercury lamp was carried out in a nitrogen atmosphere. The results are shown in Table IV.

The rate of decomposition of the lead compound seemed to be more rapid than that of the mercury compound. The results are shown in Table V. The products confirmed the structure as diisopropyl lead.

The results indicate that the organometallic compounds are the source of the propane in the electrolysis. Decomposition in the presence of 20% sulfuric acid is accelerated by light and gives practically a quantitative yield of propane and metallic ions.

The formation of propane and propylene under other conditions points to the formation of an isopropyl radical which undergoes disproportionation. This reaction apparently occurs to a slight extent in acidic medium.

The sensitivity of the organometallic compounds to light is in agreement with the work done on lead tetramethyl and mercury dimethyl by Leighton and Mortensen.

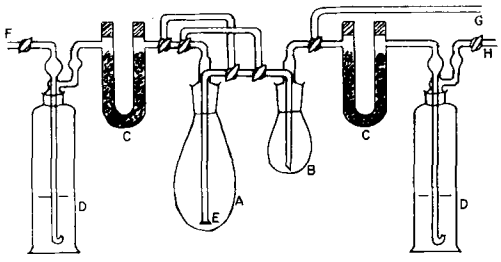

Fig. 6. Assemble glass work for purification and decomposition of organo-metallic compound: A, reservoir for crude sample; B, container of purified organo-metallic compound; C, calcium chloride for dehydration of nitrogen; D, pyrogallol alkali solution for deoxygenation of nitrogen; E, glass filter; F, gas inlet; G, to gas buret; H, gas outlet during evaporation of ether.

of hydrogen from the ether by an isopropyl radical with the formation of ethyl radicals.

Attempts to isolate an organocadmium compound in the electrolysis at a cadmium electrode, which produces a quantitative yield of propane, was not successful in agreement with the sensitivity of the compounds to acid.

In the absence of light this electrolysis gave large amounts of hydrogen and a current efficiency for propane formation of 37%. The results are shown in Table VI.

Table IV. Decomposition of organo-mercury compound in nitrogen atmosphere

Products	Organo-mercury compound	1.16 g	4.0 m mole*
	Propane	80.6 cc	3.6 m mole
	Propylene	73.3 cc	3.3 m mole
	Mercury	0.74 g	3.7 m mole

* As diisopropyl mercury.

Table V. Decomposition of organo-lead compound by light

			In N_2	In O_2	In C_6H_6	In 20% H_2SO_4	In ethyl ether
Organo-lead compound		mg	609	741	524	650	508
		m mole*	2.1	2.5	1.8	2.2	1.7
Gas produced	C_3H_8	cc	48.5	55.2	39.4	94.4	17.7
		m mole	2.2	2.5	1.8	4.2	0.8
	C_3H_6	cc	49.8	57.2	40.5	0	12.8
		m mole	2.2	2.6	1.8	0	0.6
	H_2	cc	4.5	11.2	9.0	0	0
		m mole	0.02	0.05	0.04	0	0
	C_2H_6	cc	0	0	0	0	29.8
		m mole	0	0	0	0	1.3
Residue	Total	mg	421	589	402	656	442
	Pb	mg	412	557	351	468	335
		m mole	2.0	2.7	1.7	2.3	1.6
		%**	97.7	94.6	87.3	71.3	75.6

* As diisopropyl lead.
** Pb % in residue.

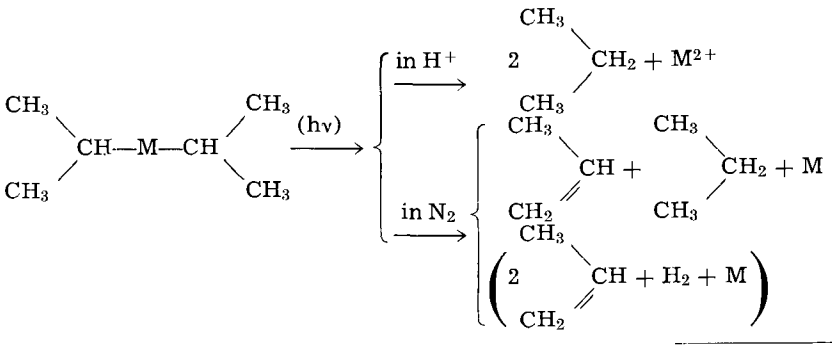

The formation of ethane in the decomposition of diisopropyl lead in ethyl ether points to the abstraction

Light had an appreciable effect also on the electrolysis at a mercury cathode. In the dark the current ef-

Table VI. Electrolysis at cadmium cathode. Effect of light

	Dark	Light
Catholyte acetone, g	82	82
20% H_2SO_4, cc	19	19
Cathode potential, v (vs. SCE)	−1.375	−1.375
Average current density, amp/dm²	1.9	6.1
Current consumed, amp-hr	3.3	3.4
Current efficiency, %	37	89
Products obtained		
Propane, cc	256	633
Hydrogen, cc	876	150

ficiency for the total reduction fell off to 55% or three quarters of that observed in the presence of light.

This is probably due to the slower decomposition in the dark of the intermediate organo-metallic compound.

Manuscript received Jan. 30, 1964; revised manuscript received Dec. 14, 1964. This paper was presented at the New York Meeting, Sept. 29-Oct. 3, 1963.

Any discussion of this paper will appear in a Discussion Section to be published in the December 1965 JOURNAL.

REFERENCES

1. J. Tafel and W. Schepps, *Z. Elektrochem.*, **17**, 972 (1911).
2. E. Muller, *ibid.*, **33**, 253 (1927).
3. S. Swann, Jr., *Bull.* Central Electrochem. Research Institute (India), **2**, 6 (1955).
4. K. Sugino, T. Sekine, and N. Sato, *Electrochem. Technology*, **1**, 112 (1963).
5. G. Schwarzenbach, "Die Komplexometrische Titration," Ferdinand Enke Publisher, Stuttgart (1956).
6. M. Shikata and I. Tachi, *Bull. Agr. Chem. Soc. Japan*, **4**, 91 (1928).
7. P. Zuman, *Nature*, **165**, 485 (1950).
8. J. Tafel, *Ber.*, **44**, 323 (1911).
9. C. Schall and W. Kirst, *Z. Elektrochem.*, **29**, 537 (1923).
10. M. Goret, *Bull. Sci. Pharmacol.*, **29**, 297 (1922); W. J. Jones, D. P. Evans, T. Gulwell, and D. C. Griffiths, *J. Chem. Soc.*, 45 (1935).
11. P. A. Leighton and R. A. Mortensen, *J. Am. Chem. Soc.*, **58**, 448 (1936).

Transpiration in an Open Tube GaAs/HI/H_2 System

G. Hellbardt

IBM Laboratories, Boeblingen, Germany

ABSTRACT

Etching rates and deposition rates have been measured in an open tube GaAs/HI/H_2 system for various iodine concentrations, flow rates, and temperatures between 500° and 850°C. Etching as well as deposition reactions are close to equilibrium at the surface of the solid GaAs. However, the amount of material of the vapor phase coming into contact with the solid is different in the two cases. At low flow rates the total flux through the tube takes part in the etching reaction whereas a certain fraction only takes part in the deposition reaction. It is suggested that different diffusion processes in the vapor phase cause this difference.

It has already been shown (1, 2) that etching rate measurements in open tube systems may yield results concerning the reaction mechanism.

Now the method of etching as well as deposition rate measurements has been applied to the system GaAs/HI/H_2. Whereas the thermodynamic data for the systems GaAs/H_2O/H_2 and GaAs/HCl/H_2 investigated in (2) had not been sufficiently and reliably known, in the system GaAs/HI/H_2 all the species in the gas phase and their mutual reactions are well known from thermodynamical equilibrium studies by Silvestri and Lyons (3) as well as by spectroscopic measurements by Richman (4). Furthermore, Leonhardt (5) calculated from these equilibrium data the partial pressures of all species in the vapor for a wide range of temperature. Thus we were able to compare immediately the results of our measurements with the equilibrium data. The question to be answered was how close to equilibrium the chemical reactions occur under the conditions of actual open tube vapor growth experiments.

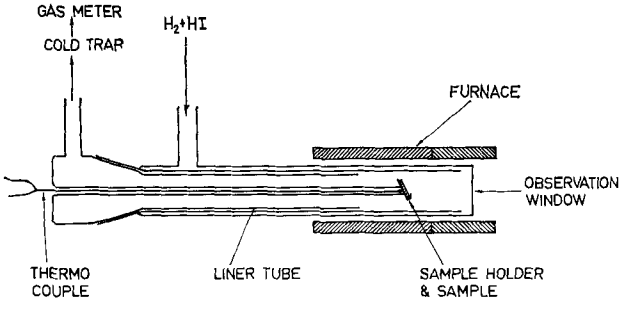

Fig. 1. Vapor etching apparatus

Experimental

Etching rate measurements.—The apparatus used in these experiments is shown in Fig. 1. Highly purified hydrogen is loaded with iodine in a U-tube filled with iodine and quartz granules and heated by a water bath to a temperature of $T_I = 50.3° \pm 0.1°C$. Additional experiments ascertained that the hydrogen/iodine mixture leaving the U-tube is saturated with iodine for all flow rates between 10 cm³/min and 500 cm³/min. The partial pressure of iodine which we found at the above mentioned temperature was $p_{I2} = 2.01$ mm Hg. The H_2/I_2 mixture is then passed through a reaction chamber containing platinized quartz wool at 450°C approximately after which the vapor consists of H_2 + HI only. This mixture is led into the double walled apparatus in which it is heated before it reacts with the GaAs sample. The reaction products leave the apparatus through a linear tube which is exchanged after each run and which prevents severe contamination of the reaction chamber.

All reaction products plus the unreacted HI are condensed in a liquid nitrogen cooled cold trap. The total volume of the pure H_2 leaving the cold trap is measured in a precision gas meter.

The face of the GaAs sample exposed to the vapor is the chemically polished (111) oriented Ga side.

Deposition rate measurements.—These experiments have been done in a simple connected tube apparatus (Fig. 2). In the first (lower) tube the seed is heated under the protection of pure H_2. In the meanwhile H_2 + HI stream over the source basket containing polycrystalline GaAs as source material. As soon as

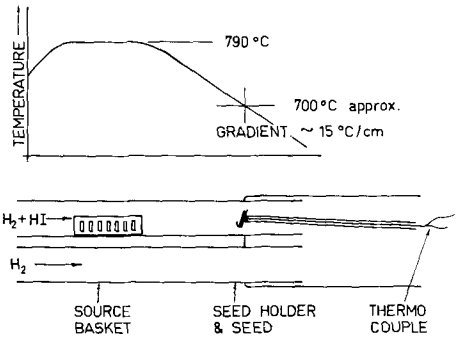

Fig. 2. Schematic sketch of the vapor deposition apparatus

the seed reaches the proper temperature it is pulled out of the lower tube and pushed into the upper one. The apparatus permits this operation to be done without opening a tube. Growth begins immediately.

The temperature profile which is the same in both tubes is such that the temperature in the source basket region is uniform within ±2°C, and the temperature gradient is constant in the vicinity of the seed. It is about 15°C/cm. Source temperature T_s and the temperature of the wafer T_w are measured by thermocouples during the run. Here, too, the exposed face of the sample is (111) oriented, Ga side.

Results

Etching rates.—Figure 3 contains all results of our etching rate experiments. The ratio of the total flux of gallium atoms in the vapor phase to the total flux of iodine atoms

$$y = \frac{n_{Ga}}{n_I} \qquad [A]$$

is plotted *vs.* the temperature of the wafer T_w. Since n_I is constant for a constant flow rate and n_{Ga} is proportional to the etching rate (cf. Eq. [1]) y itself is proportional to the weight loss per unit of time w/t in etching rate experiments. The full lines represent the theoretical values of y calculated by Leonhardt (5). The parameter is

$$\frac{P_I}{P_{tot}} = \frac{2 \times \text{partial pressure of iodine}}{\text{total pressure}} \qquad [B]$$

as measured in the iodine generator. P_{tot} used in that calculation is $P_{tot} = 1$ atm $= 735$ mm Hg, whereas we have a total (atmospheric) pressure of 720 mm Hg. We neglected this difference of 2% and calculated

$$\frac{P_I}{P_{tot}} = \frac{2 \times 2.01}{720} = 0.0056$$

This is between the values of $P_I/P_{tot} = 0.0025$ and 0.0125 available from the data of Leonhardt.

Most of the points are below the two curves. Apparently this is due to an effect of flow rate. Figure 4 shows this effect for two temperatures $T_w = 650$°C and $T_w = 800$°C; y decreases with increasing flow rate.

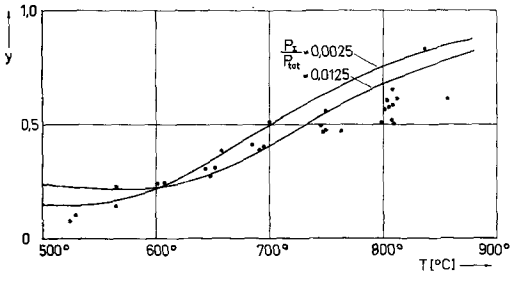

Fig. 3. Ratio of the total amount of gallium in the vapor phase to the total amount of iodine in etching experiments.

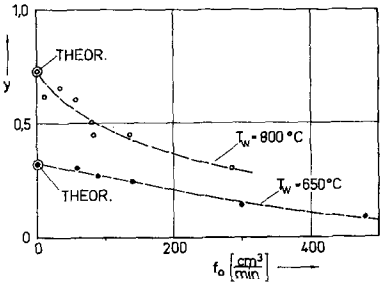

Fig. 4. Dependence of the etching rate on flow rate

The flow rate on the abscissa is in standard cm³/min. The linear velocity at $f_o = 100$ cm³/min and $T_w = 800$°C is $v = 138$ cm/min.

The theoretical values plotted at zero flow rates have been found by interpolation from the two theoretical curves in Fig. 3. Two lines can be drawn from these values through the experimental points of $T_w = 800$°C and 650°C, respectively. It appears that there is a dependence of the etching rate on the flow rate, but that for low flow rates the etching rates approach the equilibrium values.

Deposition rates.—For two different iodine concentrations corresponding to two different iodine generator temperatures T_I deposition experiments have been made. The iodine vapor pressures as determined in separate experiments were

$$T_I = 50.3, \quad P_{I_2} = 2.01 \text{ mm Hg}$$

$$T_I = 60.3, \quad P_{I_2} = 3.94 \text{ mm Hg}$$

The experimental deposition rates have been calculated from

$$g_{exp} = \frac{\Delta w}{M \cdot t \cdot A_w} \qquad [C]$$

where Δw, gain in weight of the wafer; M, molecular weight of GaAs; t, duration of the run; and A_w, area of the wafer.

The drawn curves (Fig. 5) represent values calculated according to

$$g_{calc.} = n_I[y_{T_s} - y_{T_w}]/A_T \qquad [D]$$

where n_I is the number of moles of iodine flowing through every cross section of the apparatus per unit of time, T_s the source temperature, T_w the wafer (seed)

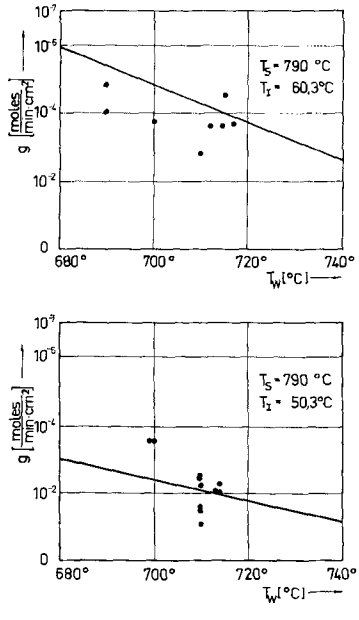

Fig. 5. Deposition rates for two different iodine concentrations

temperature, and A_T the area of the reaction tube. n_I can be calculated from the partial pressure of iodine in the iodine source and the flow rate.

For $T_I = 50.3°C$ with $P_I/P_{tot} = 0.0056$ $y_{theor.}$ has been taken from the curve of $P_I/P_{tot} = 0.0025$, while for $T_I = 60.3°C$ and $P_I/P_{tot} = 0.011$ the values have been taken from the curve of $P_I/P_{tot} = 0.0125$. In view of the scatter of the experimental points no serious error should be introduced by this approximation. The experimental points are scattered around the theoretical curves.

Discussion

Two diffusion effects have to be considered in etching rate experiments.

The first one has already been discussed in principle by Wagner and Stein (6) and others. If there is a concentration gradient along the axis of transportation, transport of the considered species will take place not only by linear flow but by diffusion also.

To calculate the magnitude of this effect in our etching rate experiments we assume the reaction

$$GaAs_s + HI_g \rightleftarrows GaI_g + \frac{1}{2}H_{2g} + \frac{1}{4}As_{4g} \qquad [1]$$

to take place.

Neglecting the partial pressure of GaI_3 is at least justified at 800°C. The mass action equation is

$$K = \frac{P_{GaI} \cdot P^{1/2}_{H2} \cdot P^{1/4}_{As4}}{P_{HI}} \qquad [2]$$

Furthermore, we write down an equation expressing the conservation of iodine during this reaction. HI enters the system at a partial pressure P^1_{HI}. Behind the GaAs the partial pressure of HI is constant and equal to P^o_{HI}. Consequently, no diffusion effects enhancing the transport of HI take place behind the GaAs. The amount of HI used up in the formation of GaI is given by

$$F = \frac{w \cdot q}{RT}(P^1_{HI} - P^o_{HI}) \qquad [3]$$

The flow F' of GaI from the GaAs is

$$F' = \frac{q}{RT}\left[-D\frac{dP_{GaI}}{dx} + wP_{GaI}\right] \qquad [4]$$

with D the diffusion constant of GaI in H_2, q the cross section area of the tube, x the coordinate parallel to the axis of the tube, and w the linear velocity of flow.

Under the conditions of steady state $F = \text{const}$ and $P_{GaI} = P^o_{GaI}$ at $x = 0$, *i.e.*, at the site of the GaAs, and $P_{GaI} = 0$ at a distance L behind the GaAs, Eq. [4] yields an expression for P_{GaI} as has been shown by Wagner and Stein (6).

$$P_{GaI} = \frac{P^o_{GaI}}{1 - \exp -\frac{w}{D}L}\left(1 - \exp -\frac{w}{D}(L - x)\right) \qquad [5]$$

$F = F'$ means the conservation of iodine and yields

$$P^1_{HI} - P^o_{HI} = P^o_{GaI}\frac{1}{1 - \exp -\frac{w}{D}L} = P^o_{GaI} \cdot \alpha \qquad [6]$$

With $P_{H_2} \approx \text{const} \approx 1$ atm and

$$P_{GaI} = 4P_{As4}$$

we get from [2] at $x = 0$

$$\frac{P^{o\,5/4}_{GaI}}{P^o_{HI}} = \frac{K}{0.707} = K' \qquad [7]$$

From [6] and [7] we arrive at

$$P^{o\,5/4}_{GaI} + K' \alpha P^o_{GaI} - K' P^1_{HI} = 0 \qquad [8]$$

The value of α is 1 with no diffusion going on. If α is varied by $d\alpha$ P^o_{GaI} is varied by dP.

We then get

$$\frac{F + dF}{F} = \left(1 + \frac{dP}{P^o_{GaI}}\right)\left(1 + \frac{d\alpha}{\alpha}\right) \qquad [9]$$

From [8] we obtain

$$\frac{dP}{P^o_{GaI}} = -\frac{1}{1 + 5P^{o\,1/4}_{GaI}/4K'}d\alpha \qquad [10]$$

With $T = 800°C$, $D = 1$ cm²/sec,[1] $f_o = 20$ cc/min, $q = 3$ cm², $L = 10$ cm, $d\alpha$ becomes $d\alpha = 0.01$. Since it is $P^o_{GaI} = 0.0019$ atm and $K = 0.45$ at 800°C (5) we get

$$\frac{dP}{P^o_{GaI}} = -0.007$$

The change in transport rate is

$$\frac{dF}{F} = 0.003$$

At lower temperatures w/D becomes larger, since it is $w \sim T$ and $D \sim T^{3/2}$, so that diffusion effects become still less important. Consequently, the partial pressures of GaI and GaI_3 are still less changed by diffusion drain from the GaAs source.

The second diffusion effect concerns the transport of reactants from the gas stream to the surface of the GaAs. The etched or grown surfaces on the wafer very often show striations not necessarily crystal oriented which can be explained as sort of flow patterns. These could not exist if the flow in the neighborhood of the wafer were turbulent. If, however, the flow is laminar, we must assume that a diffusion process is responsible for the mass transport from the vapor to the surface of the solid GaAs. Due to this effect the etching rate should decrease as the quantity w/D increases.

A quantitative model should be able to explain Fig. 4. It should also give different magnitudes of this diffusion effect at the source and at the seed because of the different numbers and types of species diffusing to and from the surface of the GaAs. However, we have not pursued this idea to a point where we can give quantitative answers.

Since the first diffusion effect has been shown to be negligible at least at flow rates above 20 cc/min, Fig. 4 means that the concentrations approach the equilibrium values in the vicinity of the solid GaAs with decreasing flow rates. In other words, almost all of the material passing the solid GaAs in our system reacts with the GaAs to equilibrium at 20 cc/min. We therefore assume that at higher flow rates there is also equilibrium at the surface of the solid. However, not all of the material in the gas phase can get to that surface in time before it passes by. This causes a decrease in the etching rate.

A similar thing happens at the seed. Since the same reactions take place at the source and at the seed, and the temperature region is about the same, we have no reason to assume that there is no equilibrium at the surface of the solid GaAs seed. However, the diffusion of material to and from the seed can be different as explained above. Therefore, the ratio of the amount of material reacting with the GaAs to the amount of material passing by unreacted is different.

Comparison of Eq. [C] and [D] shows that in calculating the experimental g values we referred to the wafer area whereas we calculated the theoretical values referring to the cross-sectional area of the tube.

[1] This diffusion constant has been assumed to be valid at 800°C for this estimate of the diffusion effect. Assuming the $T^{3/2}$ dependence on temperature this corresponds to a value of 0.13 cm²/sec at 0°C, which is about right if one compares it with the diffusion constant of metals in H_2 (7). One has to take into account that the molecule of GaI is larger than the metal atoms, *e.g.*, Hg.

Since we used a relatively large amount of polycrystalline GaAs as source we are sure from our etching rate experiments that we are in equilibrium there. Then the coincidence of the theoretical and experimental values (Fig. 5) actually means that the ratio as quoted above is equal to the ratio $A_w:A_T$ and that very little diffusion transport takes place.

Conclusions

Etching rate as well as deposition rate measurements in the GaAs/HI/H_2 open tube system showed that chemical reactions in vapor growth experiments go on close to equilibrium at the surface of the solid GaAs in the source region as well as in the seed region. However, the amount of material from the vapor which comes into contact with the solid depends on linear flow velocities. It is much higher in the source region than at the seed.

With the results of these experiments it is possible to predict deposition rates and efficiencies of vapor growth experiments in the open tube GaAs/HI/H_2 system. However, for a better understanding of the different kinetics at the source and the seed it is highly desirable to know more about the diffusion processes taking part in open tube experiments.

Acknowledgments

The author wishes to express his appreciation of the stimulating discussion with W. Kappallo and M. Michelitsch as well as his thanks to H. Leonhardt for furnishing the tabulated results of his calculations and for permission to publish these. The help of Miss G. Fritsche and Mr. M. Schlack in the experiments is gratefully acknowledged.

Manuscript received Mar. 2, 1964; revised manuscript received Nov. 27, 1964.

Any discussion of this paper will appear in a Discussion Section to be published in the December 1965 JOURNAL.

REFERENCES

1. R. R. Fergusson and T. Gabor, *This Journal*, **111**, 585 (1964).
2. M. Michelitsch, W. Kappallo, and G. Hellbardt, *ibid.*, **111**, 1248 (1964).
3. V. J. Silvestri and V. J. Lyons, *ibid.*, **109**, 963 (1962).
4. D. Richman, *RCA Rev.*, **24**, 596 (1963).
5. H. Leonhardt, IBM Research Report, RC-997, June 1963.
6. C. Wagner and V. Stein, *Z. Phys. Chem.*, **192**, 129 (1943).
7. W. Jost, "Diffusion," p. 413, Academic Press, New York (1960).

The Thermodynamic Properties of Dilute Solutions of Oxygen in the Liquid Binary Cu-Ni Alloys

E. S. Tankins, J. F. Erthal, and M. K. Thomas, Jr.

Naval Air Engineering Center, Aeronautical Materials Laboratory, Philadelphia, Pennsylvania

ABSTRACT

Thermodynamic properties of dilute solutions of oxygen in the Cu-Ni systems have been studied by means of the hydrogen-water vapor equilibrium The following reaction

$$H_2\ (g) + [O]_{soln} = H_2O\ (g)$$

was studied for which an equilibrium ratio can be written

$$K = \frac{P_{H_2O}}{P_{H_2}[a/o\ O]} \qquad [1]$$

where P_{H_2O} and P_{H_2} are the partial pressures of water vapor and hydrogen and [a/o O] is the amount of dissolved oxygen in atomic per cent. The equilibrium reaction [1] has been investigated over a wide temperature range and also for various composition ranges. Equations are presented which show the variation of the equilibrium constant [1] as a function of composition and temperature. Equations are also presented which show the variation of the standard free energy of solution of oxygen as a function of temperature for various compositions. Evidence is presented which shows Henry's law is obeyed by oxygen within experimental error over a substantial composition range.

The copper nickel system forms a series of very important commercial alloys. Pure nickel and pure copper are resistant to oxidation. The Cu-Ni equilibrium diagram (1) shows only one solid solution and the only solid-state change is the magnetic change in the high nickel end of the diagram.

Data on the reaction between liquid metal and gases are of great practical importance to the process metallurgist as well as to the theoretical metallurgist who is trying to develop a dilute solution theory to make predictions of properties of the various multicomponent systems.

Alcock and Richardson (2, 3) have discussed the dilute solutions of molten liquids and alloys. They applied the quasi-chemical model with some success to the Cu-Ni-S system. Recently, Oriani and Alcock (4) reviewed some simple models of solution.

The object of this investigation was to determine equilibria in the following reaction from 1400° to 1600°C at the high nickel end

$$H_2\ (g) + [O]_{soln} = H_2O\ (g)$$

$$K = \frac{P_{H_2O}}{P_{H_2}[a/o\ O]} \qquad [1]$$

where P_{H_2O} and P_{H_2} are the partial pressures of water vapor and hydrogen and [a/o O] is the amount of dissolved oxygen in atomic per cent.

Experimental Procedures

Materials.—The metals used in the investigation in the equilibrium apparatus were high-purity Mond Nickel Pellets and Spectrographic Purity Copper. There was no detectable nitrogen and the initial oxygen contents were less than 0.0050 weight per cent (w/o).

Two high-purity argon-hydrogen mixtures were used with hydrogen contents of 1.02 and 0.20 in volume per cent (v/o). Further purification of the gas mixtures was effected by passing them through magnesium chips held at 630°C in a stainless steel tube furnace.

Equilibrium apparatus.—The purified hydrogen-argon mixture was led via a capillary type flow meter through a water presaturator to a condenser system submerged in a thermostatically controlled water bath. The resulting gas mixture was led through heated glass tubing to a vertical resistance heated, equilibrium furnace. Within the equilibrium furnace, the gas mixture was led through a ⅛ in. bore alumina inlet tube to the surface of the melt which was held in a pure alumina crucible, ¾ in. in diameter and 2 in. high. The pedestal which supported the crucible allowed the surface of the melt to touch the alumina inlet tube. A detailed description of the apparatus and associated electrical system has been published elsewhere (5, 6).

The temperature in the uniform temperature zone of the furnace was measured principally by a L&N Optical Pyrometer sighted through an optical flat onto the crucible pedestal. A Pt-Pt-10% Rh thermocouple was inserted from time to time into the alumina tube which supported the crucible pedestal; this served as a means of calibrating the optical pyrometer and as a double check on the temperature.

The water bath temperature was controlled by means of a mercury thermostat to better than ±0.1°C, the temperature being measured on a calibrated mercury thermometer which could be read to 0.1°C.

Analysis.—The samples were prepared for oxygen analysis by splitting the entire solidified ingot, usually vertically, with a hack-saw and then grinding at least 1/32 in. off the outside. If there were any blow holes in the sample, they were carefully ground out to ensure that any oxide which might have been formed during the quenching operation was removed and to make certain that no abrasive materials were trapped. Only the high copper alloys exhibited such blow holes. The samples were numbered, degreased, weighed, and kept in a dessicator until analyzed. Care was taken to avoid manual contact with the samples once they had been cleaned.

The oxygen analysis was by an improved vacuum fusion method which has recently been described (7). The major alloying elements were not determined since previous analysis of other alloy systems indicate that the desired composition was very close to the actual.

Procedure.—The apparatus was prepared for an experiment by replacing the alumina inlet tube, cleaning the sight window, adjusting the thermostat temperature, setting the furnace in the desired temperature range, and starting the gas flow in order to purge the system. The presaturator was adjusted until excess water precipitated in the condenser at the rate of a few cubic centimeters per hour. A pure alumina crucible was charged with a 10g heat and placed on the crucible pedestal in the bottom of the furnace tube. The pedestal was then slowly raised until the crucible was in the constant temperature zone of the furnace. When the charge had melted, the pedestal was further raised until the inlet tube was just touching the surface of the melt and a back pressure of 1-4 cm was indicated on a small water manometer placed in the gas train. The pedestal support tube was then clamped in position.

The in-flow pressure of water corresponding to the temperature of the saturator was taken from the published tables (8), and the P_{H_2O}/P_{H_2} ratio derived in the usual manner from the composition of the in-going hydrogen-argon gas mixture, with the necessary corrections for barometric pressure and the small back pressure within the apparatus. No fugacity corrections were made, as it was considered that these were too small to be significant within the experimental error.

Results and Discussion

The reactions investigated in this work may be represented by

$$H_2\ (g) + O\ [\text{in Ni-Cu}] = H_2O\ (g)$$

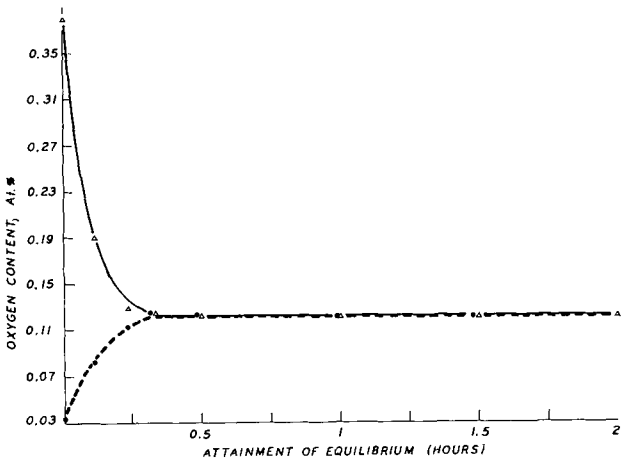

Fig. 1. Attainment of equilibrium for a 50Cu-50Ni alloy with a fixed gas composition, 1550°C: △ ——, initial oxygen 0.3800 a/o; ● - - - -, initial oxygen 0.0305 a/o.

$$K = \frac{P_{H_2O}}{P_{H_2}[\text{a/o O}]} \qquad [2]$$

where K is the equilibrium constant. The experimental results and their discussion are presented in the ensuing sections.

Attainment of equilibrium.—The attainment of equilibrium for a 50Cu-50Ni alloy with a fixed gas composition is shown in Fig. 1. The results show that in all cases except in the top line corresponding to a high oxygen content, equilibrium was reached in less than 30 min. The higher oxygen contents reached equilibrium in 30 min. The initial points on the curve probably are not as accurate because the control of temperature at the beginning is not as close as later on during each experiment. The results are also tabulated in Table I.

The melts were held at temperature with a gas flow rate of approximately 120 cc/min for at least 40 min. Earlier work on the pure metals (6) had shown equilibrium was attained in 20 min for this particular arrangement. It was assumed that copper behaved similarly to nickel, but as a further check, several duplicate runs were carried out for longer times for an alloy at the higher copper end. There was no significant change in oxygen content.

Equilibrium results for 1550°C.—In order for the derived value of K to be meaningful, either the dissolved oxygen must obey Henry's law, or a suitable extrapolation to the infinitely dilute solution must be made. It has been shown in earlier work (6) that oxygen obeys Henry's law over a substantial composi-

Table I. Experimental results obtained for a series of 50Cu-50Ni alloy at 1550°C from the attainment of equilibrium studies

Heat No.	Time	P_{H_2O}/P_{H_2}	Oxygen, a/o
	From high end Initial oxygen 0.3800 a/o		
E-1a	7 min	4.26085	0.1906
E-2a	14 min	4.26202	0.1296
E-3a	20 min	4.25417	0.1258
E-4a	30 min	4.25853	0.1220
E-5a	45 min	4.25620	0.1222
E-6a	1 hr	4.26202	0.1220
E-7a	1½ hr	4.25301	0.1216
E-8a	2 hr	4.25417	0.1220
	From low end Initial oxygen 0.0305 a/o		
E-1b	7 min	4.26085	0.084
E-2b	14 min	4.26202	0.1144
E-3b	20 min	4.25504	0.1216
E-4b	30 min	4.25853	0.1220
E-5b	45 min	4.25736	0.1220
E-6b	1 hr	4.26202	0.1224
E-7b	1½ hr	4.25301	0.1224
E-8b	2 hr	4.27311	0.1220

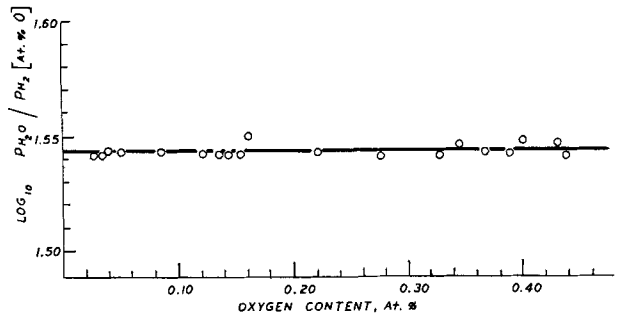

Fig. 2. Variation of the equilibrium constant $K = P_{H_2O}/P_{H_2}$ [a/o O] with oxygen content for a 50Cu-50Ni alloy at 1550°C.

tion range for pure Fe, Co, and Ni at 1550°C. Table II and Fig. 2 show the experimental results over a wide range of oxygen contents in the 50Cu-50Ni binary alloy at 1550°C. The independence of the equilibrium constant relative to the oxygen content is shown in Fig. 2. All the additional experimental runs were carried out at the lower oxygen content to insure compatability with Henry's law. A comprehensive discussion of possible discrepancies in Henry's law has been made (6).

Equilibrium results for various temperatures.—The results for various compositions of the nickel-copper alloy system are shown in Table III. The results can be represented in the usual form $\log_{10}K$ *vs.* $1/T$.

Experimental results were obtained with a computator for the least mean square calculation. Probable errors in the slopes and intercepts of the derived straight lines were calculated by the methods of Birge (9). The resulting equation for $\log_{10}K$ with probable error, are listed in Table IV.

The standard energy change for the reaction

$$H_2\ (g) + \tfrac{1}{2}\ O_2\ (g) = H_2O\ (g) \qquad [3]$$

was taken as

$$F^\circ = -59{,}905 + 13.78T \qquad [4]$$

The straight line equations for $\log_{10}K$ were converted to standard free energy equations for reaction [2] by application of the relationship

$$F^\circ = -RT \log K \qquad [5]$$

The derived equations were subtracted from Eq. [4] to yield a series of equations representing the standard free energy change, $F^\circ\%-F^\circ$ for the reaction

$$\tfrac{1}{2}\ O_2\ (\text{gas}) = [O]\ \text{soln} \qquad [6]$$

Table IV lists the derived equations; no account was taken of possible error in Eq. [4] in the listed probable errors.

The free energy of solution for the three are very close to 22 kcal at 1550°C. This means that the maximum solubility of oxygen is probably about the same in this range of alloys. The activity coefficient of oxygen due to the presence of copper in the nickel matrix is relatively constant over the 20-60% range.

Table II. Experimental results obtained for the 50Cu-50Ni alloy at 1550°C over a range of oxygen contents

Heat No.	P_{H_2O}/P_{H_2}	Oxygen, a/o	K
H-1	0.98193	0.0282	34.820
H-2	1.20632	0.0347	34.764
H-3	1.38020	0.0395	34.942
H-4	1.79659	0.0514	34.953
H-5	2.98374	0.0853	34.979
H-6	4.82476	0.1384	34.861
H-7	4.25853	0.1220	34.905
H-8	5.07400	0.1453	34.921
H-9	5.42943	0.1552	34.983
H-10	5.68682	0.1600	35.542
H-11	7.69338	0.2203	34.922
H-12	9.66969	0.2780	34.783
H-13	11.61103	0.3336	34.805
H-14	12.12911	0.3439	35.269
H-15	12.83537	0.3668	34.993
H-16	13.58081	0.3889	34.921
H-17	14.37024	0.4004	35.889
H-18	15.19531	0.4373	34.748
H-19	15.2053	0.4308	35.295

Table III. Experimental results obtained for binary alloys over a temperature range

Heat No.	Temp, °C	P_{H_2O}/P_{H_2}	Oxygen a/o	K
		80 Ni-20 Cu		
1-1	1410	6.46758	0.0570	113.466
1-2	1415	6.46758	0.0599	107.993
1-3	1420	7.07798	0.0666	106.276
1-4	1425	6.46939	0.0644	100.456
1-5	1435	6.63425	0.0714	92.917
1-6	1440	5.68843	0.0643	88.467
1-7	1450	7.07798	0.0864	81.921
1-8	1450	5.06305	0.0640	79.110
1-9	1475	5.68682	0.0851	66.825
1-10	1485	6.63044	0.1065	62.258
1-11	1490	4.26660	0.0718	59.423
1-12	1500	5.06445	0.0912	55.531
1-13	1500	4.66678	0.0830	56.226
1-14	1510	5.68361	0.1113	51.066
1-15	1525	6.61144	0.1440	45.913
1-16	1535	6.60955	0.1549	42.670
1-17	1545	4.05973	0.1020	39.801
1-18	1550	5.68361	0.1512	37.590
1-19	1550	3.31161	0.0872	37.977
1-20	1550	5.07117	0.1337	37.930
1-21	1550	4.26718	0.1119	38.117
1-22	1555	3.30873	0.0908	36.440
1-23	1575	3.30873	0.1061	31.185
1-24	1590	2.34268	0.0819	28.604
1-25	1600	2.34331	0.0875	26.781
1-26	1610	2.34208	0.0938	24.969
1-27	1620	2.34108	0.1001	23.387
		60 Ni-40 Cu		
2-1	1380	6.64285	0.0510	130.252
2-2	1390	6.47030	0.0522	123.952
2-3	1400	6.46939	0.0564	114.704
2-4	1410	6.46934	0.0620	104.345
2-5	1420	7.07798	0.0749	94.499
2-6	1435	6.63998	0.0796	83.225
2-7	1450	3.79099	0.0507	74.773
2-8	1460	3.79487	0.0549	69.123
2-9	1475	5.68682	0.0927	61.346
2-10	1485	6.62473	0.1178	56.237
2-11	1490	6.07420	0.1112	54.624
2-12	1490	5.05786	0.0927	54.561
2-13	1495	4.64765	0.0889	52.279
2-14	1500	3.80195	0.0753	50.491
2-15	1505	5.06445	0.1071	47.287
2-16	1510	5.68763	0.1226	46.392
2-17	1510	5.68763	0.1226	46.392
2-18	1515	4.05754	0.0908	44.687
2-19	1535	6.62093	0.1690	39.177
2-20	1550	5.68521	0.1632	34.836
2-21	1550	4.26718	0.1222	34.919
2-22	1550	3.83149	0.1100	34.832
2-23	1550	4.82210	0.1381	34.917
2-24	1575	3.82622	0.1309	29.230
2-25	1590	2.34108	0.0889	26.334
2-26	1600	2.34108	0.0953	24.565
2-27	1610	2.34012	0.1021	22.920
2-28	1620	2.33821	0.1090	21.451
		40 Ni-60 Cu		
3-16	1500	3.80716	0.0731	52.082
3-17	1500	6.07420	0.1165	52.134
3-18	1500	5.05849	0.0961	52.638
3-24	1550	4.82210	0.1342	35.932
3-25	1550	5.68843	0.1589	35.799
3-26	1550	6.07420	0.1692	35.899
3-27	1550	4.26718	0.1188	35.919

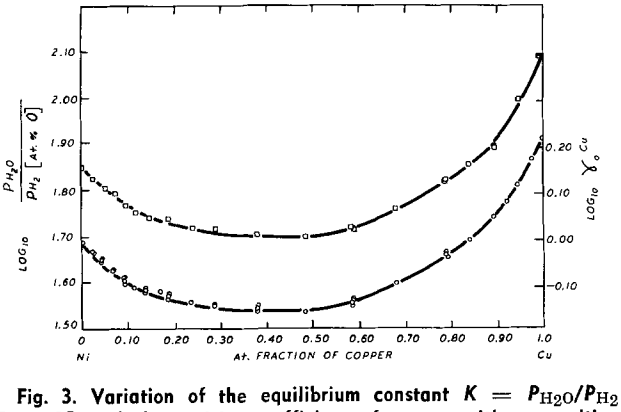

Fig. 3. Variation of the equilibrium constant $K = P_{H_2O}/P_{H_2}$ [a/o O] and the activity coefficient of oxygen with composition in the Ni-Cu alloys at 1550° (□—□—□—) and 1500°C (○—○—○—).

Table IV. Equations representing equilibrium constant and standard free energy of solution as a function of temperature

Copper w/o	$\log_{10} k$	F° $\frac{1}{2}O_2$ (g) = O soln.
20	$\frac{10{,}439\ (\pm 29)}{T} - 4.146\ (\pm 0.0165)$	$-12{,}136\ (\pm 133) - 5.192\ (\pm 0.076)T$
40	$\frac{10{,}355\ (\pm 25)}{T} - 4.138\ (\pm 0.0142)$	$-12{,}521\ (\pm 116) - 5.155\ (\pm 0.065)T$

From the consideration of the maximum uncertainties in the temperature, water ratio and oxygen analysis, one of the authors earlier suggested (6) a maximum probable error of about ±5% on the derived value of K; in general, the experimental scatter reported in this paper is consistent with this view. Analyses of many alloys in previous work for various binary alloys chosen at random showed no significant deviation in metal content (0.3%) from the stated compositions; this was ignored in considering the probable errors. The probable errors listed in Table IV suggest that the maximum probable error in the standard enthalpies of solution is of the order of 1 kcal.

Equilibrium results for binary alloys at 1550° and 1500°C.—Additional equilibrium runs are tabulated in Table V and are shown plotted in Fig. 3 for 1500° and 1550°C. There are additional runs above 60 w/o (weight per cent) Cu in order to see how the curve goes; however, the emphasis is being placed on the high nickel end of the system.

The copper-nickel system is a unique series. These alloys form a face-centered cubic lattice. The copper atom contains one more electron than the nickel atom, and to a first approximation, if a nickel atom is replaced by a copper atom in the alloy, the lattice is unaltered except that an electron is added which will raise the surface of the Fermi distribution and the lattice parameters show only slight changes.

Table V. Summary of additional data obtained for binary alloy at 1500° and 1550°C

Heat No.	Cu w/o	P_{H_2O}/P_{H_2}	Oxygen a/o	K
		Ni-Cu alloy at 1500°C		
4-1	2.50	6.07429	0.08955	67.831
4-2	5.00	6.07261	0.0940	64.602
4-3	7.50	6.06923	0.0983	61.742
4-4	10.0	6.06586	0.1034	58.664
4-5	12.0	6.06502	0.1078	56.262
4-6	13.0	6.06249	0.1091	55.568
4-7	15.0	6.12776	0.1115	54.957
4-8	25.0	6.06670	0.1169	51.896
4-9	30.0	6.12776	0.1195	51.278
4-10	50.0	6.12690	0.1222	50.138
4-11	50.0	7.06467	0.1410	50.104
4-12	70.0	6.12776	0.1064	57.592
4-13	80.0	6.07336	0.0918	66.159
4-14	80.0	3.81623	0.0578	66.025
4-15	85.0	6.06502	0.0857	70.770
4-16	90.0	6.12776	0.0780	78.561
4-17	90.0	4.64895	0.0591	78.662
4-18	95.0	6.12690	0.0688	89.054
4-19	95.0	5.06169	0.0566	89.429
4-20	100	6.07029	0.0505	120.204
		Ni-Cu alloys at 1550°C		
5-1	2.50	5.67478	0.1227	46.249
5-2	2.50	4.27815	0.09127	46.873
5-3	5.00	5.6738	0.1241	45.719
5-4	5.00	5.06536	0.1178	42.999
5-5	5.00	4.27698	0.0960	44.552
5-6	7.50	5.67798	0.1354	41.935
5-7	7.50	4.27229	0.1004	42.553
5-8	10.0	5.67959	0.1419	40.025
5-9	10.0	5.06978	0.1235	41.051
5-10	10.0	4.07144	0.0991	41.084
5-11	10.0	4.27464	0.1064	40.175
5-12	12.0	4.24863	0.1095	38.803
5-13	13.0	4.27054	0.1113	38.369
5-14	15.0	4.26704	0.1115	38.269
5-15	15.0	5.68843	0.1484	38.332
5-16	15.0	5.07119	0.1332	38.072
5-17	18.0	4.26470	0.1119	38.111
5-18	25.0	5.07259	0.1383	36.678
5-19	30.0	5.68361	0.1575	36.086
5-20	30.0	5.07259	0.1408	36.027
5-21	70.0	5.68412	0.1434	39.638
5-22	80.0	4.25612	0.0935	45.520
5-23	80.0	5.39536	0.1183	45.607
5-24	80.0	6.07958	0.1334	45.574
5-25	80.0	4.82210	0.1058	45.577
5-26	85.0	3.28285	0.0674	48.707
5-27	85.0	5.07330	0.1030	49.255
5-28	90.0	5.69005	0.1035	54.976
5-29	92.50	5.68412	0.0949	59.896
5-30	95.50	3.28728	0.0506	64.966
5-31	97.50	3.28728	0.0448	73.377
5-32	100	6.07113	0.0740	82.042

Since the phase diagrams of the Cu-Ni system show an almost ideal solid solution alloy, one would suspect that Raoult's law for the liquid state would be obeyed and that the activity coefficient would be unity or close to unity. The conclusion to be drawn is that the free energy of solution would be a linear function of alloying addition for the dissolved oxygen. Figure 3 shows that this is not the case. The excess free energy of solution of dissolved oxygen is a function of the equilibrium constant. The value of $\log_{10}K$ decreases with the addition of Cu to the nickel matrix, and after reaching a minimum value remains almost constant over a wide range of composition. At the high copper end, there is a rapid increase in $\log_{10}K$ which has been observed in other binary systems. At the present time, there is no theoretical explanation for this behavior.

The equilibrium constant for the pure nickel is from an earlier publication (6). Two runs were made with pure copper to see how the results compare with Girardi and Siebert (10) and Sano and Sakao (11). The results are somewhat lower than those of Siebert or Sakao's; however, they are sufficient to show the trend of the curve. There is no explanation at present for the discrepancy, and an intensive investigation on pure copper is forthcoming in the near future.

Figure 3 shows the change in the activity coefficient of oxygen at the high nickel end, and then a constant range and at 0.6 copper the activity coefficient of oxygen changes. This behavior is very similar to what Alcock and Richardson (2) noted for the Cu-Ni-S system. It is interesting to note that at the corresponding composition in the solid state the alloy changes in magnetic properties.

Alcock and Richardson (2) discuss the work of Himmler (12) on the electronic effects and applied their results on the dissolved sulfur in various alloys to the model. Himmler assumed that the chemical potential of the free electrons increased as the ratio of the free electrons to atom ratio in the alloy increased. There was an excellent correlation for the chemical potential of hydrogen; however, Alcock and Richardson's work with sulfur in the several alloy systems showed that the behavior of sulfur could not be explained solely in terms of the electron to atom ratio. The electronic effect may have some effect on the dissolved oxygen and may be important, but at present there is insufficient data to make any correlation and to separate the electronic effects from other effects. The quasi-chemical model as described in great detail by Alcock and Richardson (3) was applied to the present work. The model gives the proper sign and shape to the curve for the activity coefficient of oxygen. To apply the equations that Alcock and Richardson derived (3), accurate data are needed for the activities of copper and nickel in the Cu-Ni alloy system. If one assumes Raoult's law to hold over the entire composition range for the Cu-Ni system, then the calculated values for the activity coefficient of oxygen is greater than the experimental results plotted in Fig. 3. It is interesting to note that, if one considers that the copper-nickel system exhibits positive deviation from Raoult's law, then the calculated results for the activity coefficient for oxygen will be in closer agreement with the experimental results.

Activity and interaction parameter studies.—It is convenient to use a reference state which can be defined for the infinitely dilute solution of oxygen in nickel, where $a_o = 1$. The oxygen activities in the Cu-Ni alloys, therefore, are based on an activity relative to that in pure nickel.

The equilibrium for the reaction studied may be rewritten in the form

$$K_1 = \frac{P_{H_2O}}{P_{H_2}} \cdot \frac{1}{N_o{}^a \gamma_o{}^a} \qquad [7]$$

where $N_o{}^a$ is the mole fraction of oxygen in the alloy and $\gamma_o{}^a$ is the activity coefficient of oxygen in the alloy. By taking logarithms of Eq. [7] and rearranging the following expression is obtained

$$\log \gamma_o{}^a + \log K_1 = \log \frac{P_{H_2O}}{P_{H_2}} - \log N_o{}^a \qquad [8]$$

The expression on the right hand side is the experimentally determined quantity, but K_1 cannot be determined directly because of the lack of information on oxygen activity. A new equilibrium constant K_2 is defined as

$$K_2 = \frac{P_{H_2O}}{P_{H_2}} \cdot \frac{1}{N_o{}^a} \qquad [9]$$

$$\log K_2 = \log P_{H_2O}/P_{H_2} - \log N_o{}^a \qquad [10]$$

or

$$\log N_o{}^a = \log P_{H_2O}/P_{H_2} - \log K_2$$

Comparing Eq. [8] with Eq. [10], the following expression is obtained

$$\log \gamma_o{}^a = \log K_2 - \log K_1 \qquad [11]$$

Since K_2 is constant with composition, the activity coefficient is constant and, therefore, $\log K_1 = \log K_{Ni}$. Log $\gamma_o{}^a$ can be computed from the following equation

$$\log \gamma_o{}^a = \log K_2 - \log K_{Ni} \qquad [12]$$

Values for log K_2 were the experimental values determined in this study, and log K_{Ni} is obtained from earlier work (6). A plot of log K as composition, Fig. 3, will give log $\gamma_o{}^a$ which is parallel to the curve for log K with its zero at the pure Ni end of the curve.

Figure 4 shows an expanded view at the high nickel end of the diagram. Results are tabulated in Table V.

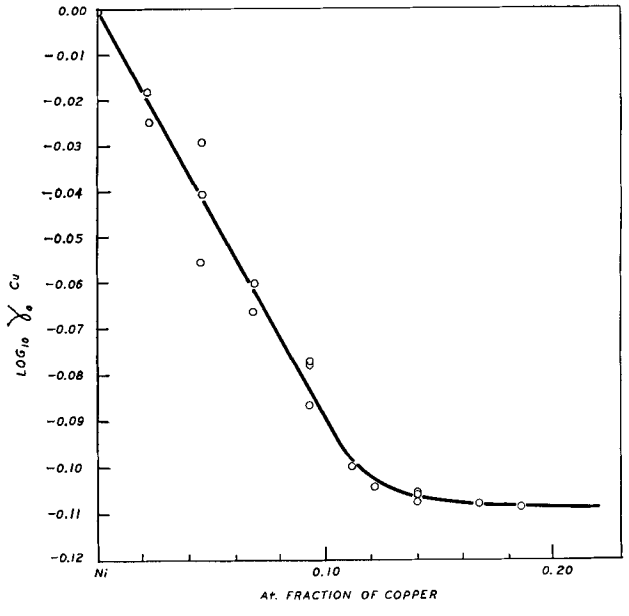

Fig. 4. Expanded view of the activity coefficient of oxygen at the nickel end of the Ni-Cu alloys at 1550°C to show the effect of Cu on the activity coefficient of oxygen in Ni.

A useful quantity can be derived from a measure of the terminal effects. The interaction parameter due to Wagner (13) can be obtained by differentiating the natural log of the activity coefficient of oxygen with respect to the mole fraction.

$$\epsilon = \left(\frac{\partial \ln \gamma_o{}^a}{\partial \text{Ni}} \right)_{\text{as Ni} \to 0} \qquad [13]$$

where ϵ is the interaction parameter, $\gamma_o{}^a$ the activity coefficient of oxygen in the alloy, and N the mole fraction of copper. From Fig. 4, one obtains a value of

$$\epsilon = -2.07$$

This value is valid up to 10% copper in nickel. The interaction parameter will allow one to calculate the excess free energy of solution.

Summary

A number of related thermodynamic equations, *e.g.*, $\Delta F°$, for the transfer of oxygen in the liquid Cu-Ni alloys have been investigated in great detail. The experimental results are represented as linear functions of $1/T$, and the related standard free energy changes are expressed as linear functions of temperature. It has been established that the dissolved oxygen in these metals follows Henry's law well within experimental errors.

The equilibrium relationships for dissolved oxygen have been investigated over a wide range of compositions for the copper-nickel alloys at two temperatures.

The interaction parameter has been determined at the high nickel end of the Ni-Cu alloy system.

Acknowledgments

Financial support for the work was from Foundational Research Project No. 9. The authors would like to thank Mr. J. Thompkins from AML for his assistance and Mr. J. Ryan for the computer work. The authors also would like to acknowledge the technical assistance of Mr. J. Hirl from AML.

The opinions expressed are the private ones of the authors and are not to be construed as official or reflecting the view of the Department of the Navy or the Naval Service at large.

Manuscript received May 11, 1964; revised manuscript received Jan. 4, 1965. This paper was presented at the Toronto Meeting, May 3-7, 1964.

Any discussion of this paper will appear in a Discussion Section to be published in the December 1965 JOURNAL.

REFERENCES

1. M. Hansan and K. Anderko, "Constitution of Biary Alloys," McGraw Hill Book Co., New York (1958).
2. C. B. Alcock and F. D. Richardson, *Acta Met.*, **6**, 385 (1958).
3. C. B. Alcock and F. D. Richardson, *ibid.*, **8**, 882 (1960).
4. R. A. Oriani and C. B. Alcock, *Trans. AIME*, **224**, 1104 (1962).
5. N. A. Gokcen, *ibid.*, **206**, 1558 (1956).
6. E. S. Tankins, N. A. Gokcen, and G. R. Belton, *ibid.*, **230**, 820 (1964).
7. N. A. Gokcen, *ibid.*, **212**, 93 (1958). N. A. Gokcen and E. S. Tankins, *J. Metals*, **14**, 584 (1962).
8. "Selected Values of Chemical Thermodynamics Properties," National Bureau of Standards, Series 111, 1956.
9. R. T. Birge, *Rev. Mod. Phys.*, **13**, 13 (1941).
10. D. J. Girardi and C. A. Siebert, *Trans. AIME*, **188**, 1168 (1950).
11. Kokich, Sano, and Sakao, *Nippon Kinzoku Gakkaishi*, **19**, 431 (1955).
12. W. Himmler, *Z. Phys. Chem.*, **195**, 244 (1950).
13. C. Wagner, "Thermodynamics of Alloys," Addison-Wesley Press, Cambridge, Mass., 1952. See also M. Ohtani and N. A. Gokcen, *Trans. AIME*, **218**, 533 (1960).

Hydrogen Adsorption on Platinum Single Crystal Electrodes

I. Isotherms and Heats of Adsorption

Fritz G. Will

Research Laboratory, General Electric Company, Schenectady, New York

ABSTRACT

The adsorption of hydrogen on the three main faces (100), (111), and (110) of platinum single crystal electrodes has been studied in 8*N* H_2SO_4 at different temperatures with the voltage sweep method. As on polycrystalline platinum electrodes, hydrogen adsorbs on each of the faces in two distinctly different binding states which present themselves as two pronounced maxima in the current-voltage sweep curves. There are indications for a third binding state giving rise to a third, less pronounced maximum. The potentials at which the maxima occur are essentially the same for polycrystalline and for each of the three single crystal electrodes. However, the relative heights of the maxima are different in each case. The adsorption isotherms and the heats of adsorption are also notably different on the three faces. Under the usual assumption of one hydrogen atom adsorbed per platinum surface atom, initial roughness factors of 1.0-1.9 result which increase to 1.9-2.4 during the experiments. The results suggest that, in fact, each of the crystal faces exposes more than one crystal plane. The left pronounced maximum is assigned to a (110) plane, the right pronounced maximum to a (100) plane, and the third small maximum to a (111) plane. Different proportions of these planes determine the different shape of the curves obtained on the different nominal faces and on polycrystalline electrodes.

The adsorption of hydrogen on polycrystalline platinum electrodes has been studied extensively in the past. Three different methods are available for these studies, (*a*) charging curves (1), (*b*) polarization with an alternating current (2), and (*c*) polarization with a triangular voltage sweep (3) also referred to as cyclic voltammetry or surface coulometry. All these methods are based on the fact that a change of the electrode potential in a certain range causes a change of the coverage of the electrode surface with hydrogen atoms. The adsorption-desorption process occurs through the charge transfer reaction

$$M\text{—}H \leftrightarrows M + H^+ + e^- \qquad [1a]$$

$$M\text{—}H + OH^- \leftrightarrows M + H_2O + e^- \qquad [1b]$$

in acid and alkaline solutions, respectively. For polarizations larger than about 50 mv, the charge transfer reaction [1] is much faster (4) than the dissociation-recombination reaction

$$H_2 + 2M \leftrightarrows 2M\text{—}H \qquad [2]$$

Hence, for a given polarization, a certain coverage of the surface with hydrogen atoms is established and maintained by fast discharge of hydrogen ions or hydroxyl ions according to the discharge reaction[1].

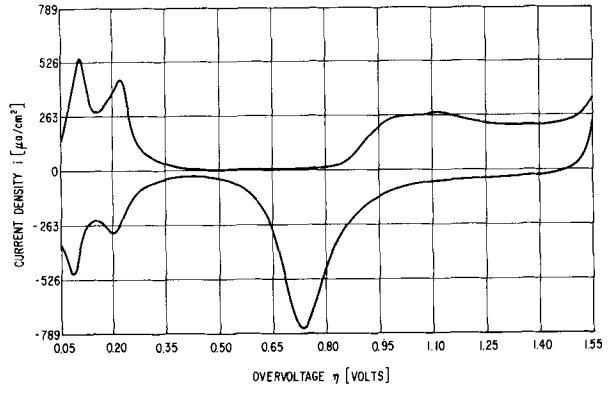

Fig. 1. Current-voltage sweep curve on polycrystalline platinum, obtained earlier (3). Sweep range 50-1550 mv, sweep rate 0.1 v/sec; surface area of electrode 0.19 cm².

The partial pressure of molecular hydrogen near the electrode surface which corresponds to that given polarization, on the other hand, is established much slower due to the slower rate of the dissociation reaction [2]. For any given polarization, the partial pressure of molecular hydrogen can be calculated from Nernst's law. At 0 volt (1 atm hydrogen pressure), the platinum surface is nearly saturated with hydrogen; at 0.4v ($\approx 10^{-14}$ atm), the surface is essentially free of hydrogen. It can thus be seen that a change of the electrode potential has the same effect on the hydrogen coverage of the surface as a change of the partial pressure of molecular hydrogen. In contrast to the latter method, however, the first method does not depend on the slow dissociation equilibrium [2].

In general, adsorption isotherms obtained on "active" polycrystalline platinum electrodes with either of the three methods exhibit three inflection points. These manifest themselves in two waves in the charging curves (5-7), and in two distinct maxima and one minimum in the differential capacity curves (8,9) and in the current-voltage sweep curves (3,10). Figure 1 shows a typical curve obtained on polycrystalline platinum with the sweep method. Apparently, hydrogen adsorbs on platinum preferentially at two distinct voltages or hydrogen pressures, *i.e.*, hydrogen exists in a strongly and a weakly bound state. Increasing voltage corresponds to decreasing hydrogen pressure, and hence the left maximum corresponds to weakly bound hydrogen and the right maximum to strongly bound hydrogen. Little conclusive information is available about the nature of the two states of adsorption.

Slygin and Frumkin (6,11) measured the amounts of anions and cations which are adsorbed on platinum as a function of the potential. They found that these amounts are influenced notably by the adsorption of hydrogen and interpret (12) their results as the adsorption of negatively polarized hydrogen at larger potentials (small coverages) followed by the adsorption of positively polarized hydrogen at smaller potentials (large coverages). Wicke and Weblus (8) found that the right maximum is influenced by the nature of the anions in the electrolyte while the left maximum does not show such a dependence. From this Eucken and Weblus (8) believe that the two maxima are not due to adsorption on two different crystallographic planes of the platinum but are due to adsorption on bare platinum (right maximum) and on oxygen atoms (left

maximum). Böld and Breiter (13) found values for the heat of adsorption of hydrogen on platinum in excess of 10 kcal/mole H_2 for coverages smaller than 0.5. This indicates that the strongly bound hydrogen is adsorbed as atoms. Kinetic considerations lead Breiter (14) to believe that the weakly bound hydrogen is also adsorbed as atoms.

Studies of hydrogen adsorption on platinum in the gas phase have also revealed the existence of strongly and weakly bonded hydrogen. Disagreement exists concerning the polarity of the two types of hydrogen and whether the weakly bound hydrogen is adsorbed as atoms or as molecules. Mignolet (15) measured the changes in the work function of a clean platinum film, which occur as a function of time, when hydrogen is being adsorbed at —190°C. Using both the condenser and the thermionic method, he found that the first 40% of the hydrogen which adsorbs increases the work function by 0.11v while the remaining 60% decreases the work function of the clean metal by 0.23v. At 20°C, under vacuum, only the initial 40% hydrogen which increases the work function remains adsorbed. These findings suggest that the initially adsorbed hydrogen is strongly bonded and negatively polarized and the subsequent 60% hydrogen weakly adsorbed and positively polarized. Mignolet also found that a volume of carbon monoxide almost equal to that of the weakly bonded hydrogen could be adsorbed in addition to the strongly bonded hydrogen. From this he believes that the weakly bonded hydrogen is adsorbed as molecules. It has been shown (16), however, that carbon monoxide displaces the weakly and strongly bonded hydrogen from the surface. Hence, the foregoing contention does not seem to be valid. Rootsaert *et al.* (17) adsorbed and desorbed hydrogen on a platinum tip in a field emission microscope by changing the temperature at a constant hydrogen pressure of 10^{-7} mm Hg. They found in agreement with Mignolet that on adsorbing hydrogen the work function first increases, passes through a maximum at a coverage of about 0.4, and then decreases with further increasing coverage. Pliskin and Eischens (18) obtained two absorption bands in infrared spectra of hydrogen adsorbed on alumina-supported platinum. When working with hydrogen and deuterium mixtures, they could not find any band corresponding to H — D^+ bonds. From this they deduce that the weakly bonded "positive" hydrogen is not adsorbed as molecules. Toya (19) showed that the two absorption bands correspond to a difference in heats of adsorption of only 0.8 kcal/mole H_2. This small difference makes it unlikely that the strongly and weakly bonded hydrogen discussed earlier is identical with the two types causing the two absorption bands. For the former, differences in heat of adsorption are found (10,20) which are of the order of 8 kcal/mole H_2.

The following study was undertaken to find out more about the nature of the two states of hydrogen adsorption. In particular, this study is concerned with the question whether the two states are due to adsorption on two different crystallographic planes preferentially exposed by the polycrystalline platinum. In order to test this possibility, the adsorption of hydrogen on the three main faces (100), (111), and (110) of platinum single crystals was studied. The voltage sweep method was applied because it affords a convenient and accurate way to determine the quantities of adsorbed hydrogen (3).

Experimental

The platinum single crystal was obtained by zone melting a platinum rod of 99.999% original purity in an electron beam. After orientation the crystal was cut with a diamond cutting wheel to give single crystals presenting the main faces (100), (111), and (110). These faces were then polished to optical flatness using for the final finish a 0.1μ alumina powder. The three single crystals were subsequently annealed in vacuum at 680°C for 24 hr and finally sealed into lime glass so that only the three faces of interest remained uncovered. The geometric surface areas were 0.181 cm^2 for (100), 0.328 cm^2 for (111), and 0.225 cm^2 for (110). The three crystals were symmetrically arranged in one cell compartment opposite the counter electrode. A hydrogen reference electrode was located in a second cell compartment which communicated with the main compartment via a capillary. All potentials are referred to this hydrogen electrode. The 8*N* H_2SO_4 used in the experiments was prepared with ultrapure water (21) and pre-electrolyzed for 15 hr. Although the measurements were carried out without gas-bubbling, the electrolyte was periodically flushed with prepurified argon to remove traces of hydrogen and oxygen.

Despite the cleaning procedures, reproducible results could be obtained only by applying a periodic sweep of such an amplitude that an oxide layer was formed and reduced during each sweep (compare Fig. 1) prior to the adsorption and desorption of the hydrogen layer. A sweep range of 50-1550 mv was chosen to achieve this and at the same time, hold the formation of molecular hydrogen and oxygen to a minimum. The applied sweep rate was 0.1 v/sec and, hence, the duration of one sweep was 30 sec. A modified (22) Hewlett Packard Function Generator 202A in conjunction with a potentiostat was used to apply the voltage sweeps. The resulting current-voltage (or time) curves were displayed on a Tektronix 502 x-y oscilloscope. For each face and each given temperature, photographs were taken of the first four sweeps and every 5 min thereafter for 20 min. A 35 mm "ROBOT" automatic transport and rewind camera was used for this purpose. The integration of the enlarged curves was performed graphically with an "Ott" planimeter No. 144 to a precision of 2%. Measurements on the three crystal faces were made at 0°, 10°, 25°, 40°, 60°, and 80°C. A specially designed circulating air thermostat allowed the temperature to be controlled within ±0.1°C.

While one particular face was being studied, the other two faces were kept in the solution on open circuit. When proceeding to the next face, a potential of 50 mv was always applied for 3 min before starting the periodic sweep from this potential. During the experiments which are reported here, each face was subjected to some 240 sweeps. In preceding preliminary experiments, about 160 sweeps had already been applied to each individual face.

Results

Current-voltage sweep curves.—As mentioned before, hydrogen desorbs from polycrystalline platinum electrodes preferentially at two different potentials corresponding to two distinct maxima in the current-voltage sweep curve. Figure 1 shows one such curve which was previously (3) obtained on polycrystalline platinum wires under conditions similar to those in the present study. The ratio of the currents of the "first" (less anodic) and "second" maximum I_1/I_2 is 1.2. Figure 2 shows curves which were obtained on the (100), (111), and (110) faces of platinum single crystals at 25°C. The curves correspond to sweep 260 and were photographed 10 min after starting the periodic sweep. The two striking features of the curves for (100) and (111) are: (*a*) as on a polycrystalline electrode there are still two distinct desorption maxima, and (*b*) while for the (100) face the first maximum is smaller than the second, the opposite is true for the (111) face; in fact the ratio I_1/I_2 is 0.8 for (100) and 1.5 for (111). The curve for the (111) face exhibits a small third maximum which degenerates to a shoulder in the curve for the (100) face. The curve obtained on the (110) face looks strikingly similar to the curve for (111), and the ratio I_1/I_2 is essentially the same for the two faces. However, the current densities i_1 and i_2 corresponding to the two maxima of the (110) curve are some 30% smaller than i_1 and i_2 for (111).

The effect of temperature on the curves is such that with increasing temperature the height of the maxima increases and their position is shifted toward less anodic

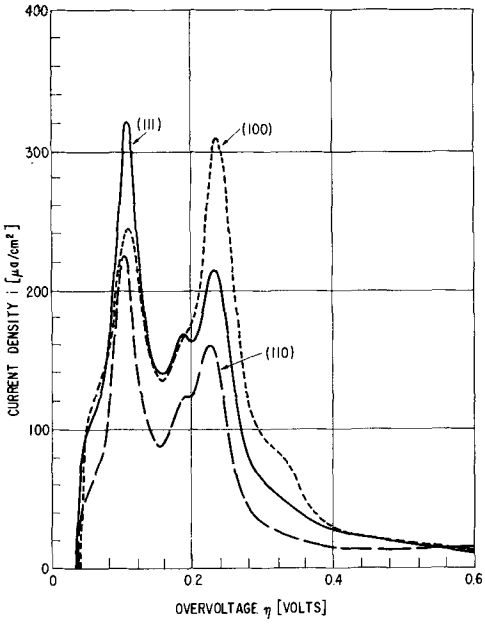

Fig. 2. Current-voltage sweep curves on platinum single crystal faces (100), (111), and (110) at 25°C. Sweep range 50-1550 mv, sweep rate 0.1 v/sec.

potentials. Both effects are larger for the first maximum.

During the 20-min duration of one experiment, the shape of the curves from the fourth sweep on remained essentially unaltered. The first curve and, to much lesser extent, the second and third curve always looked quite different from the succeeding curves.

The effect of the number of sweeps on the shape of the curves was quite pronounced, however, during the first 20 or 30 sweeps that were applied to the virgin crystal faces. Figure 3 shows this effect for the (110) face, where it is most pronounced. Curve I resulted when the 10th sweep was applied to the virgin surface. Curve II is identical to the (110) curve in Fig. 2 and was obtained after about 250 sweeps had been applied to the (110) face. While maximum 1 did not change too much, maximum 2 increased considerably with increasing number of sweeps. In fact, maximum 2 is smaller than maximum 3. After 10 sweeps, the ratio of the maxima currents I_1/I_2 is 2.9, and after 260 sweeps this ratio is 1.45. The corresponding figures for the (111) face are 2.1 (10 sweeps) and 1.5 (260 sweeps) and for the (100) face 0.79 and 0.80.

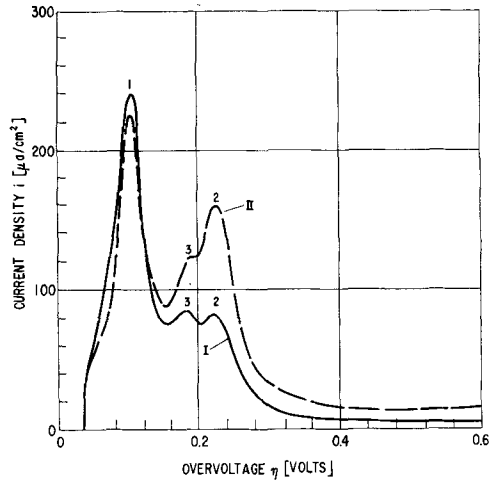

Fig. 3. Current-voltage sweep curves on the (110) face at 25°C after 10 sweeps (curve I) and after 260 sweeps (curve II).

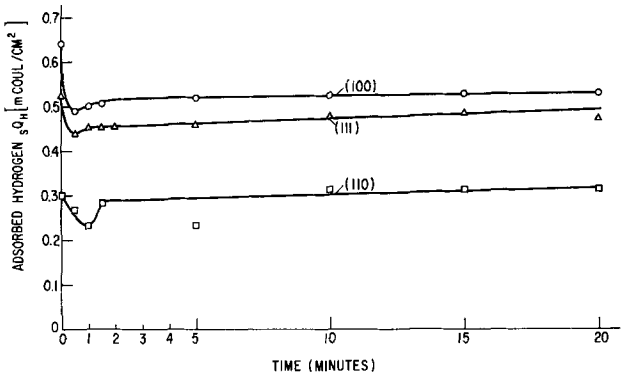

Fig. 4. Saturation amounts of hydrogen adsorbed on the three faces at 25°C.

Saturation concentration of adsorbed hydrogen.—Since a voltage is applied which changes linearly with time, the current-voltage curves in Fig. 1 and 2 also represent current-time curves. Hence, an integration of these curves yields the charge corresponding to the amount of adsorbed hydrogen plus the charge of the double layer capacity. The double layer capacity is almost constant between 50 and 400 mv (11). Its charge is only about 2% of the charge of adsorbed hydrogen and shall be neglected. The small current above potentials of about 400 mv is mostly due to the charge of the double layer (3). Below 50 mv the current decreases steeply. Therefore, the saturation concentration of hydrogen $_sQ_H$ adsorbed on the surface can be determined by integrating the curves from 50 to 400 mv. This was done for different times in the temperature range of 0° to 80°C. The result at 25°C for sweeps 240 to 280 is plotted in Fig. 4. During the first two or three sweeps of each experiment, erratic values are found for $_sQ_H$. From then on, $_sQ_H$ changes but slightly with time. This finding agrees with the finding concerning the changes in the shape of the curves with time.

For the first 10 sweeps that were applied to the virgin faces, considerably smaller amounts of hydrogen were found. The $_sQ_H$ values for 10 sweeps are 0.39 m-coul/cm² for (100), 0.23 for (111) and 0.24 for (110).[1] The corresponding values after 260 sweeps are 0.51 m-coul/cm² for (100), 0.46 for (111), and 0.30 for (110).

For the first sweep of each experiment, the total anodic charge, *i.e.*, adsorbed hydrogen plus oxygen, is always between 14% and 34% larger than the total cathodic charge. However, for the succeeding sweeps, the total anodic charge is consistently smaller than the cathodic charge, namely, by 1 to 12%.

Except for the (110) face, temperature has no systematic effect on the $_sQ_H$ values. For the (110) face, $_sQ_H$ stays roughly constant between 0° and 40°C and then decreases by about 20% from 40° to 80°C.

Adsorption isotherms.—The sweep curves obtained after 10 min for different temperatures were integrated in intervals of 50 mv between 50 and 400 mv. The degree of coverage $\theta = Q_H/{}_sQ_H$ at, *e.g.*, 300 mv, is the ratio of the charges resulting from an integration between 400 mv and, *e.g.*, 300 mv, and between 400 mv and 50 mv. The resulting adsorption isotherms for the (100) face are presented in Fig. 5. Applying Nernst's law and correcting for the vapor pressure of the sulfuric acid, the overvoltages are converted into partial pressures of molecular hydrogen. As one would expect for an exothermic process, the degree of coverage decreases with decreasing hydrogen pressure and increasing temperature. The curves display three inflection points in accordance with the three extrema

[1] Note added during revision of manuscript: According to a private communication on October 12, 1964, Dr. J. E. Oxley, Leesona Moos Laboratory, in similar experiments on Pt single crystals obtained $_sQ_H$ values of 0.30 mcoul/cm² for (100), 0.29 for (100), and 0.21 for (110). The results were obtained at a sweep rate of 18 v/sec.

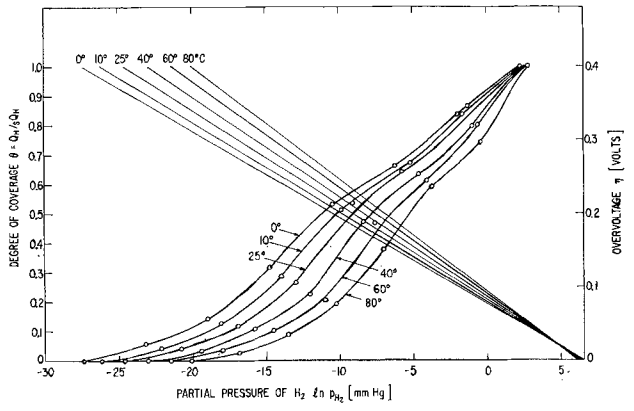

Fig. 5. Adsorption isotherms on (100) face. Straight lines relate voltage on right ordinate to partial pressure of hydrogen.

of the current-voltage sweep curves. Figure 6 shows the adsorption isotherms for the three crystal faces at 0° and 80°C. For constant hydrogen pressure, the degree of coverage decreases distinctly in the whole temperature range in the order (100)>(111)>(110). The effect is more pronounced at lower temperatures.

Heats of adsorption.—The Clausius-Clapeyron equation

$$dp/dT = \Delta H/T\Delta V \quad [3]$$

(ΔH, ΔV enthalpy and volume change on transferring 1 mole of hydrogen from the gas phase into the adsorbed phase) may be written as

$$d \ln p_{H_2}/dT = W/RT^2 \quad [4]$$

if one assumes ideal conditions in the gas phase and neglects the volume of the hydrogen in the adsorbed phase. The heat of adsorption $W \equiv \Delta H$ is negative for an exothermic process. If the heat of adsorption is temperature independent the integration of equation [4] gives

$$\ln p_{H_2} = -W/RT + \text{const.} \quad [5]$$

In a plot ln p_{H_2} against $1/T$ straight lines should result whose slope is proportional to the heat of adsorption (10, 13). While this is indeed the case for the (100) and (111) faces, the heat of adsorption increases noticeably with increasing temperature for the (110) face at temperatures above 40°C.

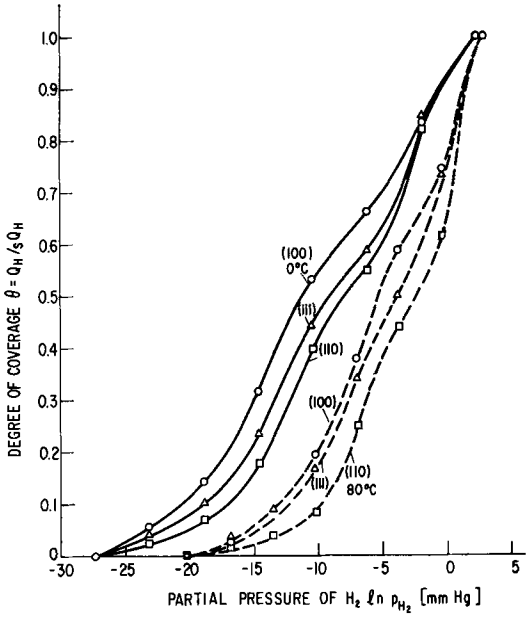

Fig. 6. Adsorption isotherms on (100), (111), and (110) at 0° and 80°C.

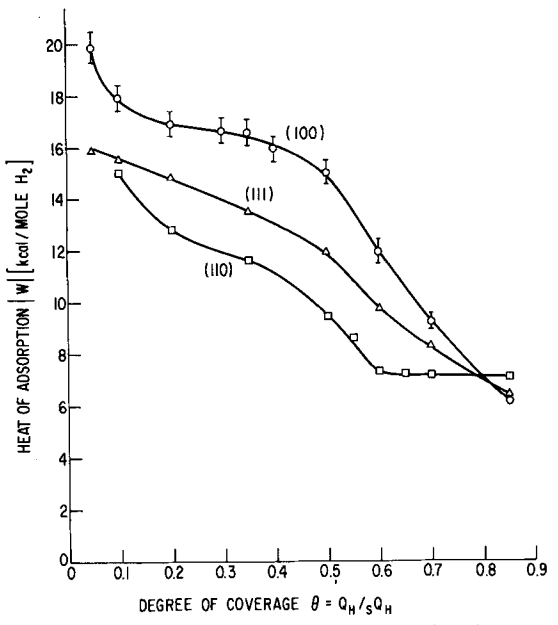

Fig. 7. Heats of adsorption of hydrogen on the three crystal faces as a function of coverage.

The heats of adsorption for the three crystal faces are plotted in Fig. 7 as a function of the degree of coverage. For the (110) face the temperature-independent values of W between 0° and 40°C are shown. For all three crystal faces, the heat of adsorption decreases substantially with increasing coverage. This agrees with results obtained on polycrystalline platinum in electrolytes (10, 13) and in the gas phase (20). Especially in the curve for the (110) face one can clearly distinguish between strongly and weakly bonded hydrogen; the latter prevails at $\theta > 0.6$ and has a heat of adsorption of about 7 kcal/mole. An increase of θ from 0.1 to 0.85 causes a decrease in the heat of adsorption of 66% for (100), 59% for (111), and 53% for (110). The other noteworthy finding is the comparatively large difference in the heats of adsorption for the different faces. Except for coverages larger than 0.8 the heats of adsorption decrease in the order (100)>(111)>(110). At coverages larger than 0.8, near saturation, this order is reversed. For coverages smaller than 0.6 the difference in W between the three faces averages between 2 and 3 kcal. For $\theta = 0.5$ the heats of adsorption are 15 kcal/mole H_2 for (100), 11.9 for (111), and 9.4 for (110).

Discussion

Roughness of the surface.—The number of platinum atoms in the surface planes of the three crystal faces are $1.5 \cdot 10^{15}$ atoms/cm^2 for (111), $1.3 \cdot 10^{15}$ for (100), and $0.92 \cdot 10^{15}$ for (110). If one makes the usual assumption that one hydrogen atom is adsorbed per platinum surface atom, the corresponding charges are 0.24 mcoul/cm^2 for (111), 0.208 for (100), and 0.147 for (110). The amounts of hydrogen that are found are considerably larger, particularly after the faces have been subjected to a large number of sweeps. This may be interpreted as a large initial roughness of the virgin faces which further increases with the number of sweeps applied. For the (100) face, for example, the roughness factor would be 1.87 after 10 sweeps and 2.45 after 260 sweeps. With such a large surface roughness, it is probable that the surface exposes more than one crystal face. The fact that the current maxima on all three faces occur to within ±5 mv at the same potentials (compare Fig. 2) could indicate that each of the faces is, in truth, a mixture of essentially two faces with a small fraction of a third face, particularly in the case of the nominal (111) and (110) face.

Effect of sweep on curve shape.—The effect of the number of sweeps on the shape of the curves (com-

pare Fig. 3) might be explained as follows. Initially (curve I), the nominal (110) face exposes a large fraction of (110) (maximum 1) and small fractions of (111) (maximum 3) and of (100) (maximum 2). After 260 sweeps have been applied (curve II), the amount of (110) has decreased slightly, the fraction of (111) stayed almost constant, but the fraction of (100) increased sharply. The periodic voltage sweep might cause the formation of etch pits with the exposure of preferred crystal faces. In this connection, it is interesting to note that the development of low-index planes by chemical etching is a standard technique in the determination of the orientation of various metal crystals (23).

The curve obtained on the (111) face (compare Fig. 2) looks always quite similar to that on the (110) face. This implies that the nominal (111) face exposes, in fact, always a large fraction of (110) (maximum 1), a considerable fraction of (100) and only a small fraction of (111). In order to rationalize this conclusion one has to assume that a thin surface layer exhibits a polishing and recrystallization texture which exposes the preferred orientations that are found. Indeed, a preferred orientation has been found on cold rolled and of polished copper and gold, with (110) planes lying parallel to the surface (24). The recrystallization texture on annealing may or may not resemble the polishing texture, depending on the severity of the surface damage and the particular annealing conditions (23). As mentioned before, the platinum crystals were annealed at 680°C for 24 hr. On platinum single crystals that had been annealed at 1100°C for 48 hr, Tucker (25) did not find evidence for faceting. However, the detection of crystal facets smaller than about 100Å in diameter is beyond the sensitivity of the slow electron diffraction apparatus.

Adsorption isotherms and heats of adsorption.—In the preceding discussion, maximum 1 has been assigned to a (110) plane, maximum 2 to a (100) plane, and maximum 3 to a (111) plane. This assignment is based on the relative heights of the current maxima for the different nominal faces in Fig. 2. It implies that the hydrogen bond is weakest on the (110) plane and strongest on the (100) plane. This agrees with the heats of adsorption for the three faces shown in Fig. 7, which increase in the order (110)<(111)<(100) for coverages smaller than 0.8. Based on considerations involving the number of nearest neighbors and their degrees of unsaturation, one would argue, however, that the bond should be weakest on the (111) plane and strongest on the (110) plane. More experiments are needed to solve this apparent contradiction.

Qualitatively, the different adsorption isotherms for the different faces can be understood with the proposed assignment of the current maxima. Since, for example, the nominal (110) face exposes a much smaller surface fraction of (100) than the nominal (100) face, it is evident that at smaller partial pressures of hydrogen, where (100) adsorbs preferentially, the surface coverage is smaller for the nominal (110) face than for the nominal (100) face. On a similar basis, the difference in heats of adsorption can be understood.

Current-voltage curves on polycrystalline wires.—The two pronounced maxima of current voltage curves obtained on polycrystalline platinum wires (compare Fig. 1) occur at essentially the same potentials as those obtained on the single crystal faces. The texture of cold-drawn wires of face-centered cubic metals, like platinum, is usually a double fiber texture with a [111] and a [100] direction parallel to the wire axis (23). With the possibility of so many different crystal planes exposed it seems surprising that only two maxima are observed. This difficulty can be reconciled by postulating that the wire surface becomes etched in the usual pretreatments of the electrodes prior to the experiments. In this etching process, the low-energy main faces are expected to develop at the expense of the large number of high-index planes.

Conclusions

The finding that the maxima have different heights for the different faces, but occur at almost the same potentials, suggests that each of the nominal faces exposes, in fact, several crystal planes in different proportions. Such an interpretation is consistent with the assumption that the large measured amounts of adsorbed hydrogen are due to a considerable surface roughness. The left pronounced maximum has been tentatively assigned to a (110) plane, the right pronounced maximum to a (100) plane and the third small maximum to a (111) plane. This implies that the bond strength of hydrogen and, hence, its heat of adsorption is smallest on (110) and largest on (100). This has been actually found. The two adsorption states of hydrogen that exist on polycrystalline platinum electrodes are also likely to be due to adsorption of hydrogen on two different crystallographic planes. The two current maxima occur within ±5 mv at the same potentials as the two pronounced maxima on the single crystals. Hence, it is concluded that cold-worked, polycrystalline platinum electrodes expose mainly crystallites with {110} and {100} planes. This conclusion is in agreement with the fact that the texture of all cold-rolled face-centered cubic metals is one in which {110} planes are parallel to the rolling plane (23). To reconcile the occurrence of only two or three current maxima on cold-drawn platinum wires with their texture of [111] and [100] parallel to the axis, one has to assume etching of the surface during the process of "activating" the electrodes. Studies with better defined crystal planes and under extreme clean conditions are needed to confirm these tentative conclusions.

Acknowledgments

The author gratefully acknowledges the loan of the platinum single crystals by C. W. Tucker which were prepared by J. W. Rutter and V. J. DeCarlo.

Manuscript received July 20, 1964. This paper was presented at the Toronto Meeting, May 3 to 7, 1964.

Any discussion of this paper will appear in a Discussion Section to be published in the December 1965 JOURNAL.

REFERENCES

1. F. P. Bowden, *Proc. Roy. Soc.*, **A125**, 446 (1929).
2. P. Dolin and B. Ershler, *Acta physicochim. URSS*, **13**, 747 (1940).
3. F. G. Will and C. A. Knorr, Internat. Polarograph. Kolloqu., Bonn 1958; *Z. Analyt. Chem.*, **173**, 87 (1960); *Z. Elektrochem.*, **63**, 1008 (1959); *ibid.*, **64**, 258 (1960).
4. J. Giner, *Z. Elektrochem.*, **63**, 386 (1959).
5. J. A. V. Butler and G. Armstrong, *Proc. Roy. Soc.*, **A137**, 604 (1932).
6. A. Slygin and A. Frumkin, *Acta physicochim. URSS*, **3**, 791 (1935).
7. M. Breiter, C. A. Knorr, and W. Völkl, *Z. Elektrochem.*, **59**, 681 (1955).
8. A. Eucken and B. Weblus, *ibid.*, **55**, 114 (1951); E. Wicke and B. Weblus, *ibid.*, **56**, 169 (1952).
9. M. Breiter, H. Kammermaier, and C. A. Knorr, *ibid.*, **60**, 37 (1956).
10. M. Breiter and B. Kennel, *ibid.*, **64**, 1180 (1960).
11. A. Slygin, A. Frumkin, and W. Medvedovsky, *Acta physicochim. URSS*, **4**, 911 (1936).
12. A. Frumkin and A. Slygin, *ibid.*, **6**, 819 (1936).
13. W. Böld and M. Breiter, *Z. Elektrochem.*, **64**, 897 (1960).
14. M. Breiter, *Electrochim. Acta*, **7**, 25 (1962).
15. J. C. P. Mignolet, *J. Chim. Phys.*, **54**, 19 (1957).
16. S. Gilman, *J. Phys. Chem.*, **67**, 78 (1963).
17. W. J. M. Rootsaert, L. L. Van Reijen, and W. M. H. Sachtler, *J. Catalysis*, **1**, 416 (1962).
18. W. A. Pliskin and R. P. Eischens, *Z. phys. Chem. N. F.*, **24**, 11 (1960).
19. T. Toya, *J. Res. Inst. Catalysis* (Hokkaido University), **10**, 236 (1962).
20. J. G. Aston, *J. Phys. Chem.*, **67**, 2042 (1963).
21. R. W. Powers, *Electrochem. Technol.*, **2**, 274 (1964).
22. F. G. Will, To be published.
23. C. S. Barrett, "Structure of Metals," McGraw-Hill Book Co., New York (1952).
24. C. S. Lees, *Trans. Faraday Soc.*, **31**, 1102 (1935).
25. C. W. Tucker, *J. Appl. Phys.*, **35**, 1897 (1964).

Technical Notes

The Preparation and Luminescence of Molybdenyl Phosphate

V. Chiola and C. D. Vanderpool

Chemical and Metallurgical Division, Sylvania Electric Products Inc., Towanda, Pennsylvania

In 1955, Schulz (1) reported the preparation and x-ray identification of molybdenyl phosphate, $MoO_2(PO_3)_2$, as one of several crystalline compounds isolated from the binary system, $MoO_3 \cdot P_2O_5$. Kierkegaard (2) investigated and proposed a crystal structure for $MoO_2(PO_3)_2$ and a number of other molybdenum phosphate compounds having low Mo:P ratios (3). In this laboratory, recent investigations of molybdenum trioxide-phosphoric acid systems led to the isolation of a crystalline product identified as molybdenyl phosphate, $MoO_2(PO_3)_2$. In the course of examining this material, it was discovered that molybdenyl phosphate, $MoO_2(PO_3)_2$, is a phosphor responding to irradiation by 3650 and 2537Å. It was found also that the same phosphor possesses electroluminescent properties. The purpose of this note is to report the preparation and properties of molybdenyl phosphate as a luminescent and electroluminescent material.

Schulz (1) prepared $MoO_2(PO_3)_2$ by heating a five-fold excess of P_2O_5 with MoO_3 to about 500°C in a steel bomb. The reaction was complete in 3-4 hr. A light-blue to light-green crystalline product was recovered after leaching the glassy reaction mixture with water to remove excess P_2O_5. Kierkegaard (2) prepared $MoO_2(PO_3)_2$ by autoclaving a mixture of 1.5 g MoO_3 and 6.6g P_2O_5 in a platinum crucible at 500°C for one week. The reaction mixture was washed and filtered to recover crystals.

Molybdenyl phosphate was prepared in this laboratory by heating one mole of MoO_3 with six moles of phosphoric acid in a silica crucible to 450°C while agitating the mixture. Crystalline $MoO_2(PO_3)_2$ began precipitating at 325°C, but a glassy mixture was formed on cooling. A bluish-white product was recovered by aqueous leaching to remove excess phosphoric acid, filtering and drying at 110°C.

An alternate procedure involved heating one mole of MoO_3 with two moles of phosphoric acid to 600°C for 1 hr to form a solid, white crystalline mass. After cooling, soluble matter was removed by leaching, and the molybdenyl phosphate product was recovered by filtration, washing with water, washing with 7% ammonium hydroxide solution, and drying at 110°C.

The typical impurity content of the molybdenyl phosphate prepared by the above procedures was determined by spectrographic qualitative analysis as follows: Al, 1-10 ppm; Ca, 1-10 ppm; Cu, 1-10 ppm; Fe, 1-10 ppm; Mg, 1-10 ppm; Mn, <10 ppm; and Si, 100-1000 ppm.

X-ray diffraction films were taken on a Philips Norelco unit having a camera diameter of 114.6 mm and using Ni-filtered CuKα radiation of 1.542Å wavelength.

Observed $1/d^2$ values agreed very well with $1/d^2$ values calculated from cell parameters furnished by Kierkegaard (2) for the compound, $MoO_2(PO_3)_2$. The observed 2θ values agree with those given by Schultz (1) for the compound having the stoichiometric composition $MoO_3 \cdot P_2O_5$.

The emission spectra were obtained with a Perkin-Elmer spectrofluorimeter (4). The spectral response of molybdenyl phosphate under 3650Å radiation is a broad-band emission which peaks at 6100Å (Fig. 1). Under 2537Å excitation a similar broad-band emission between 6100 and 6300Å is observed. Response is significantly greater at 3650 than at 2537Å radiation.

The fluorescent intensity of molybdenyl phosphate under 3650Å excitation is 79% greater than that measured on a standard calcium silicate phosphor, JEDEC No. P-25, (Sylvania No. 156). Under 2537Å radiation, the intensity is only 33% of that measured on the standard.

Electroluminescent brightness measurements were obtained using cells having dimensions of 1 x 1 x 0.006 in. and a castor oil dielectric. The electrode materials were brass and transparent conductive glass. A Photovolt Model 520 Photometer was used in conjunction with a photomultiplier detector. Figure 2 shows a semi-logarithmic plot of brightness *vs.* the reciprocal of the square root of the voltage. Although the level of brightness was low, it varied linearly with $v^{-1/2}$ from about 400 to 900v. At 400v, brightness was about 0.2% of that measured for a conventional ZnS:Cu,Cl phosphor.

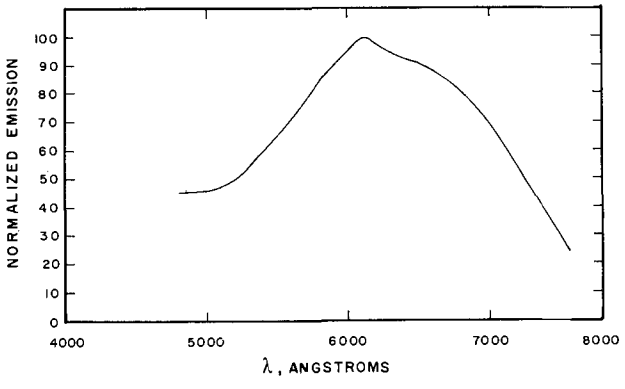

Fig. 1. Spectral response of $MoO_2(PO_3)_2$ to 3650Å excitation

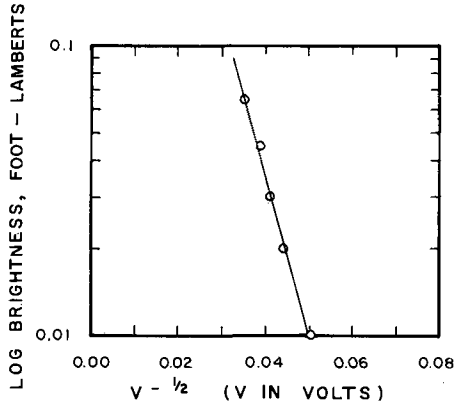

Fig. 2. Log brightness *vs.* (voltage)$^{-1/2}$

Molybdenyl phosphate electroluminesces blue-green at 60 cycles and blue at 6 kc. The results show that $MoO_2(PO_3)_2$ can be prepared from molybdenum trioxide-phosphoric acid reaction mixtures and that $MoO_2(PO_3)_2$ possesses luminescent and electroluminescent properties.

Acknowledgments

The authors wish to thank S. Faria for performing the spectral emission and electroluminescent brightness measurements and for helpful discussions concerning luminescent materials and their properties. They are also indebted to Dr. C. W. W. Hoffman and E. A. Wesley for x-ray diffraction measurements and to Dr. R. W. Mooney for advice and encouragement.

Manuscript received Aug. 18, 1964.

Any discussion of this paper will appear in a Discussion Section to be published in the December 1965 JOURNAL.

REFERENCES

1. I. Schulz, *Z. Anorg. u. allgem. Chem.*, **281**, 99 (1955).
2. P. Kierkegaard, *Arkiv Kemi*, **18**, 521 (1962).
3. P. Kierkegaard, *ibid.*, **19**, 51 (1962).
4. W. Slavin, R. W. Mooney, and D. T. Palumbo, *J. Opt. Soc. Amer.*, **51**, 93 (1961).

The Correlation between Water Contact Angle and KPR Adherence on SiO_2 Surfaces

A. A. Bergh

Bell Telephone Laboratories, Incorporated, Allentown, Pennsylvania

Kodak Photo Resist (KPR) is used in the processing of silicon planar transistors to protect selected areas of oxidized silicon surfaces from etching. KPR is an organic solvent solution of an ultraviolet-sensitive plastic. When applied to the oxide surface a thin coating is formed, and the areas where the oxide is to be protected are exposed to ultraviolet light. The nonexposed areas developed in organic solvents leaving a resist pattern that offers chemical resistance to oxide removal etchants. The oxide is usually 0.5-1.2μ thick, and the width of unprotected areas varies from a few microns to several mils. The resolution of the oxide edges depends on the adherence of the KPR to the oxide during etching. "Adherence" cannot be measured quantitatively, and it is best defined by the current of undercutting during etching as shown in Fig. 1. The sharp lines show good resolution, and the interference fringes indicate undercutting. The photoresist is not attacked by the etchant; it is only lifted at the edges. The instructions to apply KPR (1) recommend a high degree of cleanliness for both the silica surface and the photo resist solution and low relative humidity ambient to achieve good adherence. These conditions yield good results only on oxides heated to temperatures exceeding 850°C during or after oxidation. Undercutting was observed on oxides partially removed with an etchant containing fluoride ions, on oxides grown at lower temperatures, and on some deposited oxides. All the above oxides are wetted by water to a greater extent than those yielding good KPR resolution after etching.

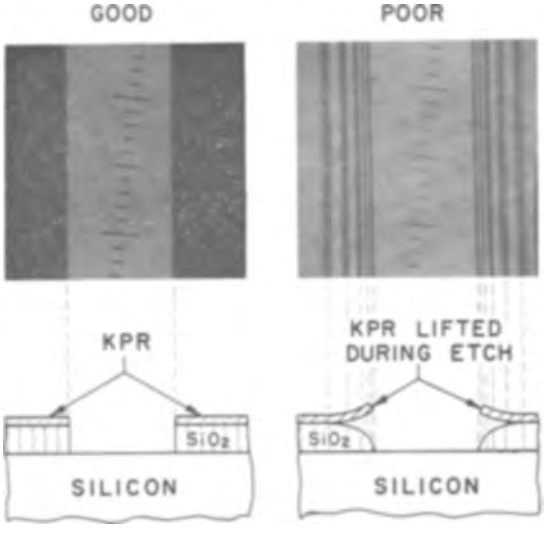

Fig. 1. Effect of KPR adherence on resolution (KPR has been removed before taking the photographs). Scale, 10 microns/division.

Experimental

One inch diameter, 5-6 mils thick, and 0.01 to 2 ohm-cm n-type silicon slices were used throughout the experiment. Oxides in the range of 0.6-1.0μ were produced under the following conditions: (*a*) 1 atm steam at 1050°C (1050°C-oxide); (*b*) 1 atm oxygen bubbled through 95°C water at 1050°C;(c) 120 atm steam at 650°C (650°C-oxide); (d) CO_2-oxide, deposited from a gas phase reaction at 1200°C (CO_2-oxide) (2); (*e*) reactive plasma sputtering at ~450°C (RPS-oxide) (3).

Water contact angles were measured with a reflection goniometer (4) using 4 x 10^{-3} ml size drops of high-purity water from a glass-Teflon micrometer syringe. KPR was applied over various patterns and unprotected areas of the oxide were removed with buffered HF solutions containing 15 ml of HF (49%) per 100 ml of a stock solution of 17M NH_4F. The etching rate of pure, amorphous SiO_2 is approximately 0.1 μ/min. The rate rapidly increases with increasing contamination of the oxide.

A minimum of six slices were taken from each group and contact angles were measured within 30 min after oxidation. Following this measurement slices were kept in hot concentrated HNO_3 for 10 min, rinsed in deionized water, and dried in a dust-free ambient at temperatures lower than 100°C. This treatment was used to remove any surface contamination and to evaluate the effect of water rinsing on the contact angle. (Boiling for 20 min in D.I. water produces the same change in θ.) Contact angles were measured on dry slices, KPR was applied, and the unprotected areas were etched away. The results of both readings and KPR adherence are listed in Table I. Oxides produced in atmospheric steam and wet oxygen at 1050°C showed identical values of θ and they are listed at "1050°C-oxide." Among the rinsed slices only the first group, average θ = 24°, gave good resolution.

Table I. Contact angles after oxidation and after rinsing

Type of oxide	θ After oxidation		θ After rinse		After rinse
	Average	Range	Average	Range	KPR adherence
1050°C-oxide	32	26-36	24	18-32	Good
650°C-oxide	3	0-8	3	0-8	Poor
CO_2-oxide	21	11-38	4	3-12	Poor
RPS-oxide	32	19-38	7	5-12	Poor

Table II. Change in θ after sequential treatments

Type of oxide	Treatment before heat	θ before heat	θ after heat*	θ after rinse**
1050°C-oxide	Buffered HF	4	36	24
650°C-oxide	None	<3	36	19
CO_2-oxide	HNO_3, H_2O	4	36	9
RPS-oxide	HNO_3, H_2O	13	35	9
Quartz plate	H_2O_2, H_2O	7	37	14

* 90 Min exposure to dry O_2 at 1200°C.
** 20 Min rinse in boiling DI water.

Correlation between low contact angles and poor KPR adherence was substantiated by another series of experiments. Different types of freshly oxidized slices were exposed to a buffered HF for 30 sec (etch rate~ 0.1 μ/min), rinsed in D.I. water and dried. All contact angles were lower than 6°, and poor adherence was observed on all slices with KPR.

A method to produce a low contact angle on any oxide has thus been established; different ways were tried to achieve the opposite effect. Heat-treatment in dry oxygen proved to be effective as shown in Table II. Similar results were obtained in vacuum and N_2, but O_2 is preferred because it prevents organic (usually hydrophilic) contamination. A limiting contact angle of $\theta = 40 \pm 5°$ was observed on all oxides after high-temperature baking.

Discussion

The significance of water contact angle on the structure and chemistry of SiO_2 surfaces will be discussed in detail in a forthcoming paper (5). The conclusions necessary to understand the adherence of KPR are listed below:

1. Low contact angles ($\theta < 3°$) indicate a strong adherence of water to SiO_2. Minimum contact angles are observed on completely hydroxylated surfaces.

2. The limiting value of $\theta = 40° \pm 5°$ observed on all oxides after exposure to high temperatures indicate a relatively weak bond between water and the SiO_2 surface. Heating removes water from the surface converting the silanol groups (Si — OH) into siloxane bridges (Si-O-Si). Siloxane is more hydrophobic ($\theta = \sim 40°$) than silanol ($\theta < 3°$).

3. The following can be said concerning the reaction

$$2Si{-}OH \leftrightarrows Si{-}O{-}Si + H_2O$$

(*a*) It can be completely shifted to the right at temperatures in excess of 850°C; (*b*) It can be shifted to the left only partially by boiling in water (or HNO_3). Deposited oxides hydrate easier than grown oxides (Table II, last column). (c) Complete hydration can be achieved (reaction shifted to the left) by breaking the siloxane bridges with HF, and hydrating the fluorinated silicon atoms, *i.e.*,

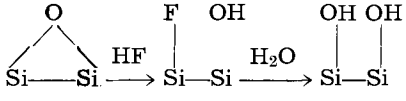

This accounts for the low contact angles after exposure to buffered HF and rinsing in water.

Table III. Effect of etch rate on the adherence of KPR

Etch rate, A/min	Etching time, min	Hydrophobic oxide	Hydrophilic oxide
4000	2.5	Not undercut	Slight undercut
1000	10	Not undercut	Undercut
330	32	Not undercut	Heavy undercut
140	70	Undercut	All oxide removed

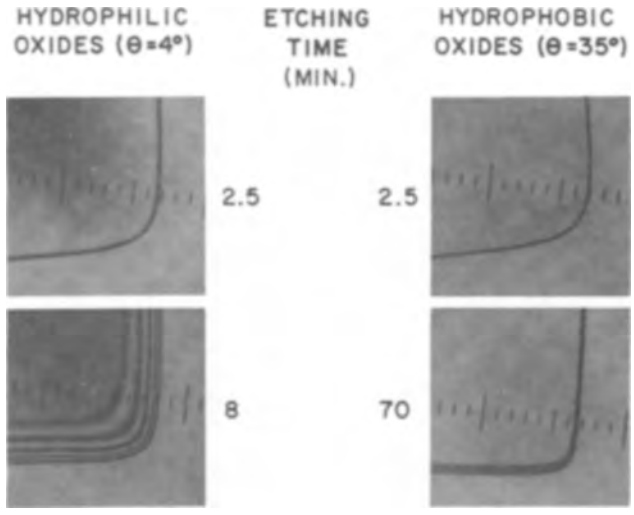

Fig. 2. Effect of etching time on undercutting. Scale, 10 microns/division.

A mechanism to explain that KPR is lifted during etching on hydrophilic surfaces can be obtained by considering the relative bond strengths at the KPR-oxide and water-oxide interfaces. Low contact angles indicate stronger, and high contact angles indicate weaker water-oxide bonds.

The contact angle of KPR, on the other hand, is nearly identical ($\theta \sim 20°$) on both hydrophilic and hydrophobic surfaces. In other words, the relative bond strengths between water-SiO_2 and KPR-SiO_2 is shifted in favor of the water on hydrophilic surfaces. Consequently, water has a greater tendency to penetrate the KPR-oxide interface on hydrophilic oxides. In view of this theory, two conditions enhance undercutting: (*a*) strong bonds at the water-oxide interface and (*b*) long exposure to aqueous solutions, *i.e.*, slow etching rates and excessive rinsing. A series of experiments were carried out, therefore, employing low and high contact angle oxides and different exposure times by changing the *p*H and thus the etch rate of the oxide removal etch. Results are shown in Table III, and some of the resolutions are illustrated in Fig. 2. Good agreement with theory can be observed. It is also evident that *p*H has an effect on the water penetration. The lifting of KPR increases with decreasing *p*H's faster than would be expected from the exposure time.

It can be concluded that the important effect of hydrophobic oxides is not in a better coupling between resist and silicon oxide, but in the decrease in the tendency of water to penetrate the resist-oxide interface.

Manuscript received Oct. 13, 1964; revised manuscript received Dec. 30, 1964. This paper was presented at the Washington Meeting, Oct. 11-15, 1964.

Any discussion of this paper will appear in a Discussion Section to be published in the December 1965 JOURNAL.

REFERENCES

1. Kodak, Photosensitive Resists for Industry, Industrial Data Book P-7, Eastman Kodak Co. (1962).
2. W. Steinmaier and J. Bloem, *This Journal*, **111**, 206 (1964).
3. J. R. Ligenza and E. I. Povilonis, Paper presented at the Washington Meeting of the Society, October 1964; W. C. Erdman and A. Androshuk, Paper presented at the Washington Meeting of the Society, October 1964.
4. T. Fort, Jr., and H. T. Patterson, *J. Colloid Sci.*, **18**, 217 (1963).
5. A. A. Bergh and M. L. White, To be published.

Strain Patterns in $GaAs_{(1-x)}P_{(x)}$ Alloy Overgrowths

R. Rosenberg

State University of New York, Stony Brook, New York

and M. Kozlowski, W. J. McAleer, and P. I. Pollak

Merck, Sharp and Dohme Research Laboratories,
Division of Merck & Company, Incorporated, Rahway, New Jersey

The objective of this note is to illustrate the occurrence of a particular type of strain pattern characteristic of $GaAs_{(1-x)}P_{(x)}$ alloy overgrowths on GaAs single crystal wafer substrates. The ultimate importance of such a strain field lies in its effect on the light emission characteristics of the heterojunction region because of disruption of crystal regularity and distortion of energy bands. Overgrowths were produced by vapor transport from GaAs and GaP charge chips to the substrate surface in an iodine ambient. The growth direction was <111>, the growth rate about 400Å/sec, and the growth surface gallium in all cases. Preparation of the wafers for observation in the <111> direction after growth consisted of removing the GaAs substrate base by lapping with a fine grit abrasive and then polishing opposite faces of the overgrowth with 0.25μ diamond paste. The strain patterns were observed by the birefringence technique and in the case of compositions transparent only to infrared lighting polaroid HR IR filters were used as polarizer and analyzer and observations made with an IR image converter tube.

Representative birefringence strain patterns are illustrated in Fig. 1 for a $GaAs_{0.8}P_{0.2}$ overgrowth. No strain was observed in pure GaAs overgrowths when viewed either parallel or transverse to the growth direction; that is, the fields were uniformly black under polarized light. The strain pattern produced in the alloy overgrowth when viewed in the <111> direction, as shown in Fig. 1a, consists of a regular block-type array of discontinuous lines which extends uniformly over the entire cross section. Figure 1b shows the strained region to extend from the original growth interface to the surface (the GaAs substrate is shown to be strain free.)

The strain was observed as a function of deposition temperature, overgrowth thickness, and overgrowth composition. Growth at 660°C (normal temperatures exceeded 800°C) did not eliminate the strain pattern, but increased the average block size suggesting a decrease in strain magnitude. Changes in overgrowth thickness did not appear to affect the strain pattern within limits of reproducibility between tests. Chem-

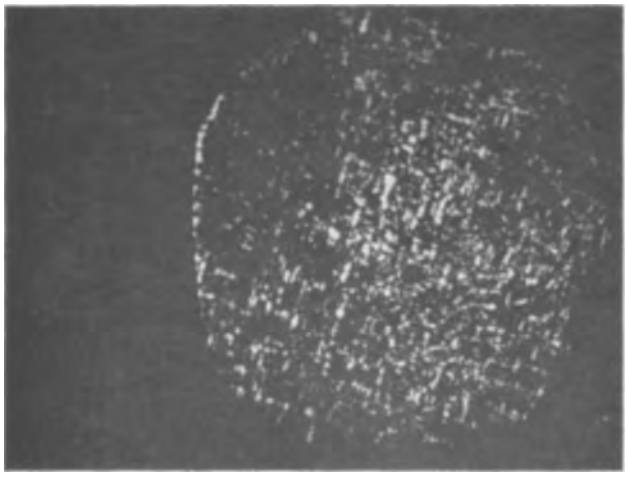

Fig. 1a. Strain pattern in $GaAs_{0.80}P_{0.2}$ alloy overgrowth produced by birefringence using polarized infrared light. Observation in <111> direction (growth direction).

Fig. 1b. Cross-section transverse to <111> direction

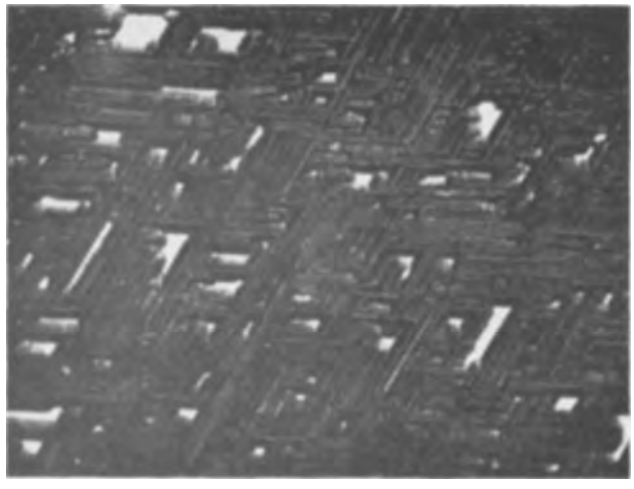

Fig. 2a. Etch-pit structure at the surface of alloy overgrowths. Slip line configuration in sample > 1 mm in thickness. Magnification approximately 100X.

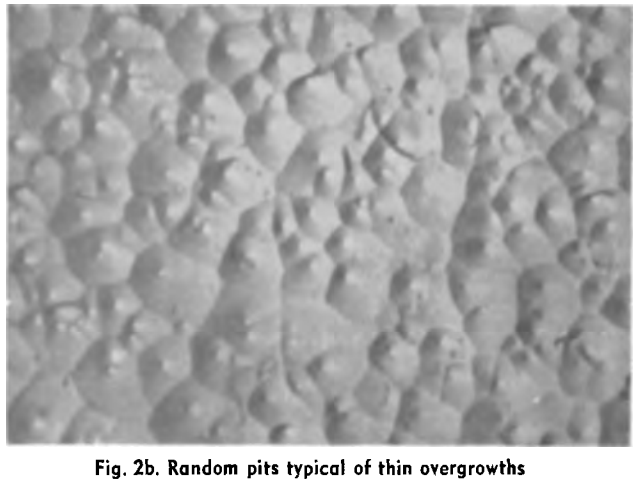

Fig. 2b. Random pits typical of thin overgrowths

ical etching of overgrowth surfaces revealed slip line configurations such as those of Fig. 2a in samples with overgrowths greater than 1mm thick, but random etch pit patterns in thinner samples, Fig. 2b. There did not seem to be a connection between the occurrence of slip and the birefringence pattern. Midrange overgrowth compositions, $0.40 < x < 0.60$, showed a tendency to fracture on cooling, with slight reduction in the observed residual strain. This was especially prevalent at low growth temperatures where release of elastic energy by deformation cannot readily take place. The strain pattern was already clearly defined in a 10% GaP alloy.

Relative rotation of the polarizer and analyzer with respect to the samples caused individual birefringence lines to be intermittently light and dark. This suggests a homogeneously distributed strain over the entire area rather than just within the observed pattern lines; the lines reflect the anisotropy produced in the crystal structure by the strain field.

Discussion

Three possible explanations can be suggested for formation of the strain pattern: lattice mismatch, thermal stresses and slip, and segregation. The lattice mismatch at the substrate overgrowth interface does not appear to be the most significant factor on several counts. First, the difference in lattice parameter between pure GaAs and pure GaP is about 4%; therefore the 10% GaP alloy has about a 0.4% mismatch (Vegard's law applies). Since the observed transition region in composition between substrate and overgrowth was found by x-ray analysis to be sufficiently broad to spread the mismatch over tens of micron distances, the resulting strain should be negligible. Second, the substrate was removed prior to observation so that the interface region was not present when observing strain patterns such as those depicted in Fig. 1a. Third, the transverse observation of Fig. 1b shows the field to extend over macroscopic distances, several orders of magnitude greater than expected on the basis of interface mismatch.

Stresses arise from thermal gradients during the cool-down period as the surface contracts more rapidly than the interior. The resulting tensile stresses, if sufficiently large, can produce slip structures such as those in Fig. 2a, or fracture in cases where slip is difficult. A recent observation by Gershenzon and Mikulyak (1) on a "pure" GaP overgrowth on GaAs showed a strain pattern similar to Fig. 1a. They attributed the pattern to the slip lines produced by the thermal stresses on cooling, relating the pattern to the familiar birefringence striations characteristic of bent crystals; also, it was argued that the strain lines were of the same orientation as slip plane traces. Several observations appear to indicate that cooling stresses were not the major cause of the strain patterns in the present work.

1. Strain patterns produced by cooling stresses usually take on a gross appearance, much like the fourfold symmetry birefringence as shown by Lederhandler (2) in silicon. The patterns in the sample of Fig. 1a and the rectangular-shaped specimen of Gerhenzon and Mikulyak were homogeneous over the entire cross section, including corners which should be most susceptible to stress concentration.
2. In the present work in which the growth direction was <111>, the strain pattern did not correspond to slip plane orientations.
3. The maximum effect of cooling should be at the outer surface of the overgrowth where the stresses are maximized. From Fig. 1b, however, it is apparent that the strain is uniform over the entire thickness of overgrowth.
4. Under exactly the same conditions of growth and cooling, pure GaAs overgrowths showed no strain patterns whereas alloy overgrowths did.
5. The GaAs substrate was found to be strain free even though the overgrowth was highly strained (see Fig. 1b). Both surfaces of the wafer were subject to approximately the same cooling rate.

The major cause of the observed strain as deduced from the findings seems to be a segregation effect. The presence of segregated impurities in silicon crystals was shown by Lederhandler (2) and Dash (3) to produce a fine striated birefringence pattern which was homogeneous with respect to the specimen cross section, much like the pattern found in the present work. As indicated by the strain-free GaAs overgrowths, the segregation effect was not produced by an impurity in the ambient or in the charge material; thus, it appears that it is the segregation of the alloy species As and P which occurs during growth (Ga segregation is probably not influential, again relying on the strain-free GaAs overgrowth). The segregation taking place must necessarily be of a local nature to give rise to the fine uniform strain pattern, and of small dimension as indicated by the homogeneous strain field suggested in a prior discussion concerning the effects of rotating the polarizer and analyzer. Segregation at sub-boundary walls is improbable on the basis that none were observed in the etch pit patterns of either the substrate or overgrowth. Also, it is difficult to conceive of segregation at individual dislocation sites causing the massive strain observed under polarization of IR or visible radiation. Two further possibilities are segregation of the species on specific habit planes, and short range ordering in the form of coherent islands, each island being consistent in composition and distribution within itself but differing from its neighbor such that a coherency strain would exist at the interfaces between islands; the sum of the local strains then appear as a long range strain. No direct evidence is available on which to base a mechanism at this time although it would seem that the driving force for segregation on habit planes should be low in this completely miscible system. Local ordering can be a result of the nucleation problem on the <111> growth surface. If it can be assumed that As, P, and Ga arrive at the surface at the same rate, then easy nucleation would give rise to a random distribution. In this case, however, the 4-atom, 2-layer triangular nucleus needed results in a nucleation problem. [Over-all growth of the nucleus occurs readily in a lateral <112> direction in the form of <110> zigzag chain units, as per Sangster (4)]. The number of stable nuclei will control the rate of growth of the surface layer. If the most stable nucleus is one which contains three atoms of P or As (the growth surface is Ga) rather than a composite, then the growth face will contain islands of GaAs and GaP nuclei. Lateral growth would then produce regions either high in As or P, with high stresses resulting in the planes of intersection between islands from lattice mismatch and differences in elastic thermal contractions on cooling. The stressed areas would be randomly oriented with respect to the growth surface and found throughout the thickness of the overgrowth, which seems to be the case. Since deposition is controlled by a chemical reaction of the growth surface, growth at low temperatures is characterized by fewer stable nuclei, slower growth, and larger and more uniform islands, resulting in a reduced strain field. Also, at the lower temperature the temperature gradients on cooling are less, decreasing contraction strains. Although experimental evidence directly confirming the above mechanisms is not available, the dependence of the strain pattern on segregation appears to be a reasonable explanation of the observations presented.

Manuscript received Oct. 19, 1964; revised manuscript received Dec. 29, 1964.

Any discussion of this paper will appear in a Discussion Section to be published in the December 1965 JOURNAL.

REFERENCES

1. M. Gershenzon and R. M. Mikulyak, *J. Appl. Phys.*, **35**, 2132 (1964).

2. S. R. Lederhandler, *ibid.*, **30,** 1631 (1959).
3. W. C. Dash, in "Growth and Perfection of Crystals," p. 383, J. Wiley & Sons, Inc., New York (1958).
4. R. C. Sangster, in "Compound Semiconductors, Vol. 1, Preparation of III-V Compounds," p. 241, Reinhold Publishing Co., New York (1962).

Thermal Expansion of GaSb at High Temperatures

J. C. Woolley

Department of Physics, University of Ottawa, Ottawa, Canada

Most of the available data on the thermal expansion of GaSb is for temperatures close to room temperature or below. Welker and Weiss (1) give a temperature coefficient α of 6.9 x 10^{-6}/°C without indicating the relevant temperature range; Sirota and Golobov (2) quote a mean expansion coefficient of 5.7 x 10^{-6}/°C over the range —100° to +20°C, whlie in a more detailed study Novikova and Abrikosov (3) have determined α as a function of temperature in the range 20-340°K and have shown a change in α from a negative value below 52°K to an almost constant value of about 6.5 x 10^{-6}/°C at 250°K and above. At temperatures above room, Bernstein and Beals (4) using an interferometric method with samples a few millimeters dimensions, give a value of α of 6.0 x 10^{-6}/°C up to 300°C. However they report that α increases rapidly above 300°C and they were unable to determine the expansion at 436°C.

It has been found (5) in electrical measurements on GaSb that the standard plot of log np/T^3 *vs.* $1/T$ shows a change in slope at approximately 450°C indicating different values of energy gap E_0 above and below this temperature. It was thought therefore that a change in α at this temperature could indicate some phase change in GaSb, which would cause the change in E_0. Although x-ray powder photographs of GaSb taken at 560°C still showed a zinc blende type of line distribution (5), this did not rule out the possibility of some transition such as that from a zinc blende structure to a defect antifluorite structure, since both structures would give the same pattern of lines in a powder photograph and would differ only in the relative intensities of the lines (6).

In order to check the results of Bernstein and Beals and to extend them to higher temperatures, x-ray powder photographs have been obtained for GaSb samples in the temperature range 25°-600°C, a Unicam 19 cm high-temperature camera being used with CuKα radiation. From these photographs the change in lattice parameter of GaSb relative to its value at 25°C has been determined. Figure 1 shows the variation of δ as a function of temperature where $\delta = a_T - a_{25}/a_{25}$, a_T being the lattice parameter at temperature T and a_{25} the parameter at 25°C. It is seen that within the limits of experimental error the graph is linear, showing a constant expansion coefficient of $+(6.7 \pm 0.1)$ x 10^{-6}/°C in the temperature range 25°-600°C. There is no indication of any anomalous behavior in the range 300°-450°C and no evidence of any structure change.

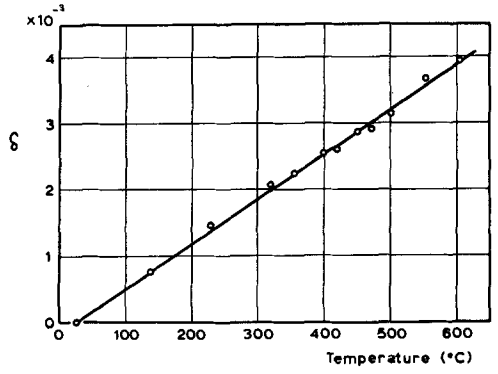

Fig. 1. Variation of δ as a function of temperature where $\delta = \frac{a_T - a_{25}}{a_{25}}$, a_T being the lattice parameter at temperature T and a_{25} the parameter at 25°C.

Acknowledgment

The author is grateful to Dr. W. B. Pearson of National Research Council, Ottawa, for the use of the high-temperature x-ray camera.

Manuscript received Oct. 28, 1964.

Any discussion of this paper will appear in a Discussion Section to be published in the December 1965 JOURNAL.

REFERENCES

1. H. Welker and H. Weiss, "Solid State Physics," Vol. 3, p. 51, F. Seitz and D. Turnbull, Editors, Academic Press, Inc., New York (1956).
2. N. N. Sirota and E. M. Golobov, *Doklady Akad. Nauk. SSSR,* **144,** 398 (1962).
3. S. I. Norikova and N. Kh. Abrikosov, *Sov. Phys. Solid State,* **5,** 1558 (1964).
4. L. Bernstein and R. J. Beals, *J. Appl. Phys.,* **32,** 122 (1961).
5. J. C. Woolley and C. M. Gillett, *J. Phys. Chem. Solids,* **17,** 34 (1960).
6. B. R. Pamplin, Thesis, Nottingham University, (1960).

The Heats of Fusion of InSb, InAs, GaAs, and InP

D. Richman and E. F. Hockings

RCA Laboratories, Princeton, New Jersey

During a study of the thermochemical properties of III-V compounds (1), information about their heats of fusion was needed. Only two compounds InSb (2, 3) and GaSb (2) have been measured by standard calorimetric methods. A rapid semiquantitative method has been used here to obtain the heats of fusion of InAs, GaAs, and InP. The application of standard techniques to these compounds is complicated by the high vapor pressures existing over the melts. This high pressure also necessitates making the measurements during the heating cycle, since quenching does not produce homogeneous, single phase materials.

The heats of fusion for the III-V compounds InSb, InAs, GaAs, and InP have been measured by a differential thermal analysis technique using apparatus of the type described by Gasson (4). Temperatures and temperature differentials were measured with Pt-Pt 13% Rh thermocouples whose outputs were displayed on an x-y recorder. Differential signals were amplified to provide a chart sensitivity of 20 μv/in. Heats of fusion were obtained from the areas of the DTA peaks after calibration with materials having known heats of fusion.

Table I. Properties of III-V compounds

Compound	Melting point, °C	Heat of fusion, kcal/mole This work	Other
InSb	525 ± 3	9 ± 3	12.2 ± 0.5 (2) 11.2 ± 0.4 (3)
InAs	942 ± 3	26 ± 3	
GaAs	1245 ± 5	21 ± 5	
InP	1058 ± 3	12 ± 3	15.2 (5)

The III-V compounds examined were in the form of crushed samples of single crystal, high-purity materials which had been prepared from stoichiometric melts. Heats of fusion and the melting points of these compounds are shown in Table I.

The heats of fusion for InAs and GaAs are higher than those for the other III-V compounds by an amount which exceeds the experimental error and the entropies of fusion for the arsenides are also high with respect to the other compounds. At their melting points the solids all have the zinc blende crystal structure. The liquids above the melting points can be considered as mixtures of group III atoms with monatomic and polyatomic group V species. The higher values for the entropies of fusion of the arsenides arise from differences in degree of association between arsenic and the other group V elements in these melts. Thus the observed heat of fusion of a III-V compound can be considered as composed of a heat of melting and a heat of association of the group V element.

Manuscript received March 26, 1964; revised manuscript received Jan. 8, 1965. This research was sponsored in part by the Electronics Research Directorate, Air Force Cambridge Research Center, Air Force Systems Command, under Contract AF19(604)-6152.

Any discussion of this paper will appear in a Discussion Section to be published in the December 1965 JOURNAL.

REFERENCES

1. D. Richman, *J. Phys. Chem. Solids*, **24**, 1131 (1963).
2. W. F. Schottky and M. B. Bever, *Acta Met.*, **6**, 320 (1958).
3. N. H. Nachtrieb and N. Clement, *J. Phys. Chem.*, **62**, 876 (1958).
4. D. B. Gasson, *J. Sci. Instruments*, **39**, 78 (1962).
5. M. Shafer and K. Weiser, *J. Phys. Chem.*, **61**, 1424 (1957).

Brief Communication

A Simplified Calculation of Tafel Slopes for Successive Electrochemical Reactions

G. H. Fraser[1] and R. G. Barradas

Lash Miller Chemical Laboratories, Department of Chemistry, University of Toronto, Toronto, Ontario, Canada

An electrochemical reaction may be a sequence of several elementary reactions involving one or more intermediates. To calculate the Tafel slope, if a particular step in the sequence were rate determining, the commonly employed method is to assume "quasi-equilibrium" for all preceding steps and thus to obtain the concentration of the intermediates as a function of overpotential (1, 2).

In an alternative treatment, Parsons (3) considered the passage of the representative point of a system over a series of free energy barriers. He derived the following expressions for the Tafel slopes of cathodic and anodic reactions, respectively

$$b_c = (\partial\eta/\partial \ln i)_{T,a_i} = -(\nu RT/\beta nF) - [(1-\beta)\nu/\beta nF](\partial p/\partial \ln i)_{T,a_i} - (\nu/nF)(\partial q/\partial \ln i)_{T,a_i} \quad [1]$$

$$b_a = (\partial\eta/\partial \ln i)_{T,a_i} = (\nu RT/(1-\beta)nF + (\nu/nF)(\partial p/\partial \ln i)_{T,a_i} + [\beta\nu/(1-\beta)nF](\partial q/\partial \ln i)_{T,a_i} \quad [2]$$

where a_i is the product of the activities of the reagents of the over-all reaction, n is the number of electrons involved in the over-all reaction, the stoichiometric number ν is the number of times the rate-determining step occurs when the over-all reaction occurs once, p and q are electrical work terms and η, i, β, R, T, and F have their usual significance.

In calculating Tafel slopes, most workers have preferred to use the quasi-equilibrium analysis rather than Parsons' treatment (*loc. cit.*), possibly because of uncertainty in handling the terms p and q. We shall show that these terms are really quite simple and that the method of Parsons is just as easy to use as the quasi-equilibrium treatment.

[1] Present address: Johnson, Matthey and Mallory Ltd., Toronto, Ontario, Canada.

Calculations of Tafel Slopes

For the general electrochemical reaction

$$xX + gG^{+z} + ne = wW + cC^{+(gz-n)/c} \quad [3]$$

to occur, the electrochemical systems must pass over a series of free energy barriers (3, 4). Four states must be considered: namely, the initial state I, the final state F, the state P immediately before the highest free energy barrier and the state Q immediately after. The standard electrochemical free energies of these states are given by

$$\overline{G}_I^\circ = (x/\nu)\mu_x^\circ + (g/\nu)\mu_G^\circ + (gz/\nu)\phi_s F + (n/\nu)\mu_e^\circ - (n/\nu)\phi_M F \quad [4]$$

$$\overline{G}_F^\circ = (w/\nu)\mu_W^\circ + (c/\nu)\mu_c^\circ + [(gz-n)/\nu]\phi_s F \quad [5]$$

$$\overline{G}_P^\circ = \mu_P^\circ + (gz/\nu)\phi_s F - (n/\nu)\phi_M F + p \quad [6]$$

$$\overline{G}_Q^\circ = \mu_Q^\circ + [(gz-n)/\nu]\phi_s F + q \quad [7]$$

where ϕ_M is the inner potential of the electrode and ϕ_s that of the solution. p and q are the electrical parts of the standard free energies required to transfer the system from the state I to the state P and from the state F to the state Q, respectively. From these equations Parsons derived [1] and [2].

There are two sources of work in the terms p and q; namely, work done in the physical adsorption of an ion into the Helmholtz double layer, where it can be discharged, and work done in discharging an ion. The former is proportional to ψ, the potential of the Gouy-

Helmholtz boundary of the double layer and the latter to $\Delta\phi$, where

$$\Delta\phi = \phi_M - \phi_s \quad [8]$$

Generalizing the analysis of Parsons, one derives

$$p = k^1\psi F + kF\Delta\phi; \qquad q = l^1\psi F + lF\Delta\phi \quad [9]$$

where k is the number of electrons which must be taken from the electrode to permit the rate-determining step to occur once and $(-l)$ is the number which must be removed to permit the products formed by the occurrence of one rate-determining step to be transferred to the final state F. k^1 and l^1 are defined in an analogous manner for the physical adsorption of ions. When

$$\eta = 0, \quad \Delta\phi = \Delta\phi_R$$

$$\eta = \Delta\phi - \Delta\phi_R \quad [10]$$

Therefore

$$(\partial p/\partial \ln i)_{T,a_i} = kF(\partial\eta/\partial \ln i)_{T,a_i} = kFb$$

and

$$(\partial q/\partial \ln i)_{T,a_i} = lFb \quad [11]$$

For a process occurring on a cathode [3], the Tafel slope associated with any step proceeding in the forward direction is

$$b_c = -(RT/F)[k + \beta(l - k + n/\nu)]^{-1} \quad [12]$$

from [11] and [1]. Similarly, from [11] and [2], the Tafel slope associated with any step in a cathodic reaction proceeding in the reverse direction is

$$b_a = (RT/F)[(1-\beta)(l - k + n/\nu) - l]^{-1} \quad [13]$$

For processes occurring on anodes, the direction of the forward reaction is the opposite to that of cathodic processes, *i.e.*, anodic reactions proceed from the state formerly designated as F to the state I. We must now define l as the number of electrons which must be removed from the electrode to permit the rate-determining step to occur once, *i.e.*, to move the system from state F to state Q. Accordingly, $(-k)$ is the number of electrons which must be removed to permit the products of one occurrence of the rate-determining step to be transferred to the final state, namely to move the system from the state P to state I.

Using these new definitions of k and l, the Tafel slopes associated with any elementary reaction in an anodic process proceeding in the forward and reverse direction can be again given by [13] and [12], respectively. However, it is conventional to use the symbol β for the symmetry factor of the forward reaction (1). Therefore, for processes occurring on anodes, [13] is rewritten as

$$b_a = (RT/F)[\beta(l - k + n/\nu) - l]^{-1} \quad [14]$$

and by analogy, [12] as

$$b_c = -(RT/F)[k + (1-\beta)(l - k + n/\nu)]^{-1} \quad [15]$$

k and l are not necessarily integers. Consider the reaction scheme proposed by Conway and Bourgault (5) for the evolution of oxygen

$$M + OH^- = MOH + e \quad [16]$$

$$MOH + OH^- = MO + H_2O + e \quad [17]$$

$$MO + MOH = MHO_2 + M \quad [18]$$

$$MHO_2 + MOH = 2M + H_2O + O_2 \quad [19]$$

The [MOH] formed in [16] is converted to the final products in three ways: by [17] followed by [18] and [19], by [18] followed by [19], and by [19] alone. The first path involves an electron; the next two require no charge transfer. The average number of electrons required is 1/3, *i.e.*, $k = 1/3$. The analysis of this reaction scheme is shown in Table I as an example of the application of this method. The results agree with those of the quasi-equilibrium analysis performed by Conway and Bourgault (5).

Table I. Kinetic parameters

Rate-determining step	n	ν	l	k	b_a
[16]	4	3	0	1/3	$RT/\beta F$
[17]	4	1	−1	2	$RT/(1+\beta)F$
[18]	4	1	−3	1	$RT/3F$
[19]	4	1	−4	0	$RT/4F$

Thus the Tafel slope for an electrochemical reaction can be calculated by noting the number of electrons appearing before and after the rate-determining step.

The above treatment has, of course, the same limitations as Parsons' original treatment. It is applicable only when low-coverage Langmuir kinetic equations can be used, and when the current does not depend on ψ.

General Equivalence of the "Electron Count" Analysis to the Quasi-Equilibrium Analysis

$(n/\nu) - (k - l)$ is the number of electrons involved in the rate determining step. Let this quantity be m (m may be zero). For a rate-determining step in a cathodic reaction

$$i = A([I_1]^{x1}[I_2]^{x11}[I_3]^{x111}\ldots)\exp(-m\beta\eta F/RT) \quad [20]$$

where A is a constant made up of the rate constant and the activities of the reagents, the I's represent intermediates formed by the discharge of reacting ions, and the x's represent the numbers of the corresponding intermediates appearing in the rate-determining step. The terms involving the intermediates may be symbolized by $[I]^X$. Therefore

$$i = A[I]^X \exp(-m\beta\eta F/RT) \quad [21]$$

In the quasi-equilibrium analysis, one obtains $[I]^X$ as a function of overpotential. The assumption of quasi-equilibrium implies that $\bar{G}_I = \bar{G}_P$, where these electrochemical free energies are no longer defined for the standard state. $\bar{G}_P$ can be obtained by adding a term $x(RT)\ln[I]$ to Eq. [6].

$$\bar{G}_P = \mu_P^\circ + x(RT)\ln[I] + (gz/\nu)\phi_s F - (n/\nu)\phi_M F + p \quad [22]$$

The activities of the reagents are considered to be constant. Therefore $\bar{G}_I$ differs from [4] only by constants. Thus

$$p = \text{constants} - x(RT)\ln[I] \quad [23]$$

From [23], [9] and [10]

$$[I]^X = (\text{constant})\exp(-\eta kF/RT) \quad [24]$$

Therefore

$$b_c = -(RT/F)(k + \beta m)^{-1} \quad [25]$$

which is identical to [12].

Similarly for anodic reactions

$$i = A[I]^X \exp(\beta\eta mF/RT) \quad [26]$$

$$q = \text{constants} - x(RT)\ln[I] \quad [27]$$

$$[I]^X = (\text{constant})\exp(-l\eta F/RT) \quad [28]$$

and therefore

$$b_a = (RT/F)(\beta m - l)^{-1} \quad [29]$$

which is identical to [14]. Thus the method of analysis developed in the previous section leads to the same Tafel slopes as in the quasi-equilibrium analysis.

Summary

The kinetic analysis of electrochemical reactions consisting of several steps, which was derived by Parsons, has not been widely used. By an extension of his treatment we have derived expressions by which

it is possible to calculate Tafel slopes merely by counting the number of electrons which are involved in various parts of the reaction, *i.e.*, those that appear before and those that appear after the rate-determining step, as well as the total number of electrons involved in the reaction. The stoichiometric number of each step must also be known. The general equations for the Tafel slopes of cathodic and anodic reactions, which we have derived, make Parsons' treatment just as convenient as the better known quasi-equilibrium analysis. It is shown that both treatments predict the same Tafel slopes.

Acknowledgments

The authors are indebted to the National Research Council of Canada and to the University of Toronto for financial assistance. One of them (G.H.F.) wishes to record his gratitude to the Province of Ontario Government for the award of a Postgraduate Fellowship.

Manuscript received Aug. 11, 1964; revised manuscript received Nov. 20, 1964.

Any discussion of this paper will appear in a Discussion Section to be published in the December 1965 JOURNAL.

REFERENCES

1. J. O'M. Bockris, *J. Chem. Phys.*, **24**, 817 (1956).
2. B. E. Conway, *Trans. Royal Soc. Canada*, **54**, (III), 19 (1960).
3. R. Parsons, *Trans. Faraday Soc.*, **47**, 1332 (1951).
4. J. O'M. Bockris, "Modern Aspects of Electrochemistry," pp. 180 *et seq.*, No. 1, Butterworth's, London (1954).
5. B. E. Conway and P. L. Bourgault, *Can. J. Chem.*, **37**, 292 (1959).

Manuscripts and Abstracts for Fall 1965 Meeting

Papers are being solicited for the Fall Meeting of the Society, to be held at the Statler-Hilton Hotel in Buffalo, N. Y., October 10, 11, 12, 13, and 14, 1965. Technical sessions probably will be scheduled on: Batteries (including Symposia on Charging Characteristics of Batteries and Characteristics of Electrodes during Charging), Corrosion, Electrodeposition (including Symposium on Thin Film Technology), Electronics-Semiconductors, Electrothermics and Metallurgy (including a Symposium on Zirconium and Its Alloys).

To be considered for this meeting, **triplicate copies of the usual 75-word abstract, as well as of an extended abstract of 500-1000 words** (see notice on page 112C of this issue), must be received at The Electrochemical Society, 30 East 42 St., New York, N. Y., 10017, *not later than May 17, 1965.* (Papers solely sponsored by the Corrosion Division **do not** require an extended abstract.) *Please indicate on 75-word abstract for which Division's symposium the paper is to be scheduled, and underline the name of the author who will present the paper.* No paper will be placed on the program unless one of the authors, or a qualified person designated by the authors, has agreed to present it in person. Clearance for presentation of a paper at the meeting should be obtained before the abstract is submitted. An author who wishes his paper considered for publication in the JOURNAL or ELECTROCHEMICAL TECHNOLOGY should send triplicate copies of the manuscript to the Managing Editor of the appropriate publication 30 East 42 St., New York, N. Y., 10017. Concerning papers to be published in the JOURNAL, see notice on per page charge on page 105C of this issue.

Presentation of a paper at a technical meeting of the Society does not guarantee publication in the JOURNAL or ELECTROCHEMICAL TECHNOLOGY. However, all papers so presented become the property of The Electrochemical Society, and may not be published elsewhere, either in whole or in part, unless permission for release is requested of and granted by the Editor. Papers already published elsewhere, or submitted for publication elsewhere, are not acceptable for oral presentation except on invitation by a Divisional program Chairman.

The Catalysis of the Electrochemical Oxidation of Formaldehyde and Methanol by Molybdates

J. A. Shropshire

Process Research Division, Esso Research and Engineering Company, Linden, New Jersey

ABSTRACT

The electrooxidation of formaldehyde and methanol on platinum has been shown to be catalyzed in sulfuric acid solution by the presence of molybdates. Decreased polarization has been shown to result from a cycle involving chemical reaction of the fuels with an oxidized molybdate species with subsequent electrooxidation of the reduced molybdate. The process requires the adsorption of molybdate at the electrode surface throughout the entire cycle.

The existence of catalytic currents during the electrochemical reaction of a variety of substances is well known (1). Catalytic currents in general arise when the product of an electrochemical reaction reacts with another species in solution in a subsequent chemical step, thus to regenerate the original form. The net observed result is an increase in the effective concentration of the electroactive species near the electrode and a corresponding increase in the observed current due to its reaction. In many cases this unique feature has been found useful in improving the polarographic determination of trace constituents in solution (1, 2).

An interesting variation of this principle has been investigated in the course of a recent study of the electrochemical oxidation of low molecular weight alcohol and aldehyde fuels for fuel cell use. This variation involves the catalytic reaction of HCHO or CH_3OH with a molybdate species at a platinum black electrode in H_2SO_4. In this case the molybdate species apparently is adsorbed and remains adsorbed at the electrode surface during both the electrochemical and chemical reaction steps.

This "surface redox" reaction, as it will be referred to hereafter, has been of particular interest in fuel cell studies on HCHO and CH_3OH. Through its use the electrochemical oxidation of these fuels to CO_2 may be carried out at a considerable decrease in polarization over that normally found on platinum based electrodes. A series of studies has been carried out to define the advantages and limitations of this system and to determine if in fact a catalytic mechanism is responsible for the observed improvements.

Experimental Techniques and Equipment

All electrochemical measurements in these systems were carried out in conventional glass "H" cells with anode and cathode compartments separated by glass frits. Voltage measurements were made against commercial saturated calomel reference electrodes through Luggin capillaries containing H_2SO_4 of concentration equal to that in the cell proper. All measurements were made using Keithley 610 A or 610 electrometers. Acid solutions were prepared from reagent grade 96% H_2SO_4 and deionized water of conductivity $< 10^{-6}$ mho/cm. Due to the practical necessity of high conductivity for fuel cell electrolytes, studies were carried out in 3.7M H_2SO_4, a solution exhibiting near-optimum conductivity. Absolute methanol and sodium molybdate were reagent grade chemicals. Formaldehyde was obtained as USP Formaldehyde solution (37% in water with a small amount of CH_3OH added for stabilization). Due to the higher reducing activity of HCHO no effect of the added CH_3OH was ever observed.

Electrodes used in this study were of two types. For performance studies (polarization-log current) of CH_3OH and HCHO in molybdate-containing electrolytes, the electrodes were prepared by pressing powdered platinum black into platinum screens. The platinum, prepared by the reduction of H_2PtCl_6 by $NaBH_4$ in aqueous solution, was found to have high surface area and to provide high activity for this purpose. In the chronopotentiometric studies on this system, small platinized platinum electrodes of about 0.25 cm^2 apparent area were used.

In one phase of this study oscilloscopic chronopotentiograms were obtained on the 0.25 cm^2 platinized electrode. Constant current for these transients was obtained from a 30v regulated d-c supply through a high series resistance. Transients were displayed on a Tektronix 545 A oscilloscope with type-D plug-in preamplifier and photographed with the aid of a Dumont type-453 A Polaroid attachment. Potentiostatic studies, where indicated, were carried out using the Duffers Model 600 potentiostat. Other pertinent experimental details will be found in the text where necessary. All polarizations in this study are referred to a hydrogen electrode in the same acid solution (NHE) or to the saturated calomel electrode (SCE), measured difference in these reference voltages being 0.194v at 25°C in the systems involved.

Oxidation of CH_3OH and HCHO on Pt in the Presence of Molybdate

The electrochemical oxidation of CH_3OH or HCHO on platinum black in strong acid media is a highly irreversible process. Passage of practical currents with either fuel is accompanied by polarizations up to 0.6v from the thermodynamically calculated potentials. Both fuels react at about the same potential level on platinum despite a computed difference of about 0.14v in theoretical potential ($E°_{25}CH_3OH = +0.03$v, $E°_{25}$HCHO (g) $= -0.11$v *vs.* NHE). This behavior has led to widespread belief that oxidation of both fuels involves a common slow step. The product of the oxidation of either fuel in acid has been shown by several investigators to result in essentially 100% production of CO_2 at steady state (3-5). Typical measured performances of 1M CH_3OH and 1M HCHO on $NaBH_4$-reduced platinum black in 3.7M H_2SO_4 at 82°C are shown in Fig. 1. Tafel slopes of about 0.06 v/decade are commonly found for oxidation of these fuels on platinum catalysts.

The addition of Na_2MoO_4 to the electrolyte before fuel addition results in a significant alteration of the performance curves (Fig. 1). The polarization at low current densities decreases by as much as 0.3v from that observed with platinum alone. Furthermore, the similarity of HCHO and CH_3OH performance largely disappears with HCHO in this system capable of sustaining currents 100 times as great as CH_3OH at the improved voltage. Also, neither fuel shows evidence of a well-defined Tafel behavior. Instead, the low polarization region exhibits a limiting current, beyond

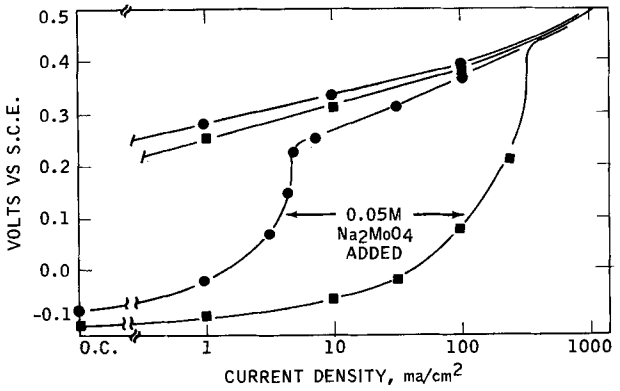

Fig. 1. Effect of Na_2MoO_4 on oxidation of CH_3OH and HCHO on Pt black ($NaBH_4$ reduced); 3.7M H_2SO_4, 82°C; •, 1M CH_3OH; ■, 1M HCHO.

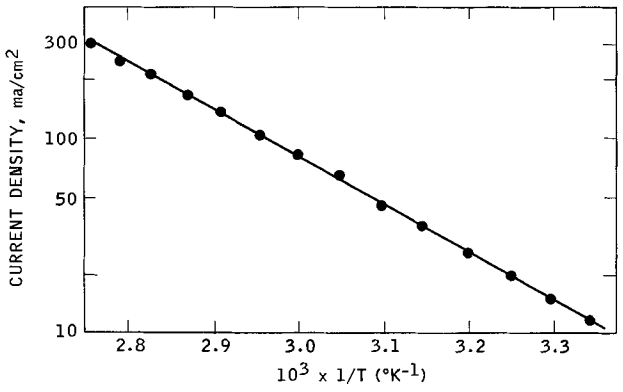

Fig. 2. Effect of temperature on reaction of HCHO on Pt black in presence of Na_2MoO_4. 1M HCHO; 0.05M Na_2MoO_4; 3.7M H_2SO_4; E = 0.1v vs. SCE; ΔE^* = 11.4 kcal/mole.

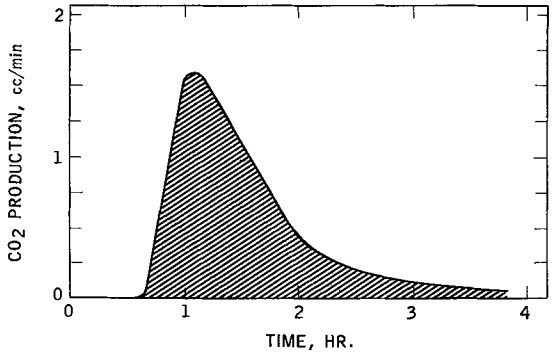

Fig. 3. Chemical reaction of CH_3OH with Na_2MoO_4 in presence of Pt black. 1M CH_3OH, 82°C; initial Na_2MoO_4 = 0.025 mole; 0.42g Pt black catalyst; total CO_2 = 0.0045 mole.

which polarization increases in both cases approximately to the level of the original platinum system. It was found that, if current was decreased following severe polarization of the system, the voltage followed the behavior found on platinum black in the absence of molybdate. This hysteresis was not evident until the limiting current of the initial plateau was exceeded. Thereafter, anodization of the electrode in fresh electrolyte without fuel was necessary to restore activity. It is significant to note that decreased polarization requires that the molybdate be added before the fuel is present. This point will be discussed in a later section.

An activation energy was obtained for the electrode reaction using 0.05M molybdate and 1M HCHO fuel at +0.10v *vs.* SCE using potentiostatic control. This voltage level lies in the region of the curve near the initial reaction limit, but not yet in a region where the normal reaction of HCHO on platinum black would be expected (see Fig. 1). Currents were measured at constant voltage in the temperature range 25°-90°C. The activation energy (Fig. 2) was about 11.4 kcal/mole, much too high to be indicative of a mass transport limitation.

Chemical Reaction of Molybdate with CH_3OH and HCHO

With these early indications of catalytic currents, it was discovered with some surprise that the chemical reaction between molybdate and these hydrocarbon fuels required a catalyst. It was found that with no catalyst present no significant reaction occurred between molybdate and CH_3OH or HCHO in 3.7M H_2SO_4. In the presence of platinum, however, reaction appeared to occur readily with the formation of a product which colored the strong acid solution red-brown. The molybdate equivalent in the reaction with CH_3OH was determined by monitoring the CO_2 production during the complete reaction of 0.025 moles of Na_2MoO_4 with CH_3OH in the presence of 0.42g of Pt black powder (82°C, 3.7M H_2SO_4). The CO_2 produced from the reaction was carried by a fixed flow of nitrogen to the absorption cell of a Liston-Becker Model 15A IR analyzer calibrated at a fixed wavelength for CO_2 analysis. The continuous record of CO_2 production versus reaction time is reproduced in Fig. 3. The peak CO_2 production corresponds roughly to a current of 14 ma/cm² on the type of electrode discussed previously. Although this value is undoubtedly subject to some error caused by lag in the nitrogen carryover system, it indicates a rough rate to be expected from the initial system. Integration of the entire CO_2 production *vs.* time curve was used to establish the moles of molybdate required to produce 1 mole of CO_2. This value was found to be about six, indicating a valence change of one for the reacting molybdate, in view of the six electron oxidation of CH_3OH to CO_2.

Although a similar complete curve was not recorded and analyzed for the reaction of molybdate with HCHO, the peak CO_2 production at the start of that reaction corresponded to about one half the value found for CH_3OH. In view of the greater reducing power of HCHO, this observation would seem inconsistent. An explanation of this result will be reserved to a later section.

Coulometry

As mentioned earlier, the product of the molybdate chemical reaction with fuel in 3.7M H_2SO_4 forms a red-brown solution. It was found that solutions identical in appearance were formed by electroreduction of an acid solution containing Na_2MoO_4 at a platinum electrode at 0.0 *vs.* SCE. (This voltage is about 0.2v negative to $E_{1/2}$ recorded in Fig. 4.) Since the chemical equivalent of molybdate to CH_3OH determined in the previous section would be wrong if CO_2 were not the sole product in the chemical reaction, an independent test of the valence change was made. Two coulometric determinations were carried out for reduction of the molybdate in 3.7M H_2SO_4 to equilibrium on a platinum basket held at 0.0v *vs.* SCE. This voltage level was fixed by means of a potentiostat and current *vs.* time recorded from the voltage drop across a fixed precision resistor in the auxiliary electrode lead. Auxiliary electrode was segregated using an agar plug to minimize bulk mixing of the electrolyte compartments. The data obtained leaves no doubt that a one electron reduction of the molybdate takes place.

Run	Coulombs calc. for 1 electron	Coulombs observed
1	571	573
2	398	390

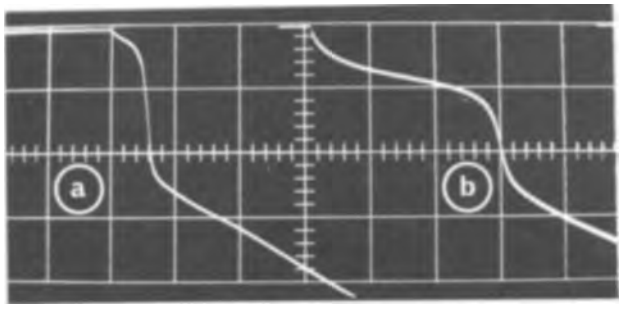

Fig. 4. Chronopotentiograms on platinized Pt in (a) 3.7M H_2SO_4; (b) 3.7M H_2SO_4-0.05M Na_2MoO_4. Top line, 0.0v *vs.* SCE, 300 mv/div (positive downward), 1 sec/div (left to right), 40 ma/cm^2, 25°C.

An attempt was made to confirm the equivalence value in run No. 1 by complete reoxidation of the reduced molybdate at potentials up to +0.8v vs. SCE. Such attempts were completely unsuccessful, however, resulting in very low current production over long periods of time. It appears that the pentavalent species is combined in solution in some relatively inert form, and reoxidation currents are limited by a slow release of the electroactive species.

Chronopotentiometry on Platinized Platinum

A typical anodic chronopotentiogram for a platinized platinum micro-electrode (0.25 cm^2 apparent area) in 3.7M H_2SO_4-0.05M Na_2MoO_4 at 25°C is shown in Fig. 4b. The electrode was polarized to 0.0v *vs.* SCE immediately prior to recording the voltage transient produced by impressing a constant current of 40 ma/cm^2 on the electrode. Under the conditions observed here, a well-defined wave is formed, with $E_{1/2} \simeq$ 0.2v *vs.* SCE (one-quarter wave). Formation of platinum oxide is evident when the voltage reaches +0.7v *vs.* SCE.

Since it was apparent that the over-all reaction of CH_3OH and molybdate involved other than a free molybdate species in solution, an attempt was made to use this well-defined transient to study the factors involved in molybdate adsorption on platinized platinum. Information on both molybdate and formaldehyde adsorption was obtained at 25°C by the anodic stripping technique originally used by Pavela (6). In this method, the preconditioned electrode was placed in the solution of adsorbate for a desired interval, removed rapidly to a 3.7M H_2SO_4 rinse solution to remove excess bulk solution, then placed in a cell containing 3.7M H_2SO_4 and the (anodic) stripping transient recorded. While this technique suffers the drawback of permitting determination of only the material strongly adsorbed, it nonetheless allows the separation of the independent factors in molybdate and fuel adsorption.

The 0.25 cm^2 platinized electrode used for this study was preconditioned by evolving H_2 and O_2 successively a few times (in H_2SO_4 solution) with final equilibration at 0.0v *vs.* SCE before removal to adsorbate solutions. Adsorbate solutions referred to in the following paragraphs are 1M HCHO in 3.7M H_2SO_4 and 0.05M Na_2MoO_4 in 3.7M H_2SO_4 in all cases not otherwise noted. Anodic transients, with the exception of Fig. 9, were recorded in pure 3.7M H_2SO_4.

It was found that a second immersion of this platinized electrode in 3.7M H_2SO_4-0.05M Na_2MoO_4 with no fuel present was sufficient to produce a tenaciously held layer of molybdate, yielding about 40 millicoulombs/cm^2 in the subsequent anodic stripping, Fig. 5b. The blank transient, also shown in Fig. 5a, clearly shows the initial regions of pseudocapacitance from oxidation of chemisorbed hydrogen atoms, the steep so-called double layer region, followed by platinum oxide formation at more positive voltages. By comparison, the electrode with adsorbed molybdate retained much of the initial pseudocapacitance of oxidation of adsorbed hydrogen, indicating that the adsorbed molybdate is not seriously blocking hydrogen sites. This single chemisorbed layer of molybdate was found to be sufficient to produce steady-state performance in a subsequent test with HCHO fuel, in 3.7M H_2SO_4, provided excessive polarization was avoided.

Immersion of the platinized electrode in 3.7M H_2SO_4-1M HCHO with no molybdate results in the rapid formation of a layer of tightly bound HCHO with an oxidation transient as shown in Fig. 6. Oxidation of this strongly held HCHO appears to occur only at or near voltages at which platinum oxidation occurs. Note the marked decrease in double layer capacity in the presence of this adsorbed HCHO, as evidenced by the very steep rise of voltage between 0.0 and +0.3v *vs.* SCE compared to the blank in Fig. 6. Absence of hydrogen pseudo-capacitance is taken as an indication that formaldehyde occupies the majority of the surface, including sites normally held by adsorbed hydrogen atoms. While HCHO was used as the fuel in this and subsequent studies of transients on platinum, the observations made apply in a general way to CH_3OH as well. Due to a stronger adsorption of HCHO, however, effects with that fuel are somewhat more pronounced and therefore have been used to illustrate the behavior.

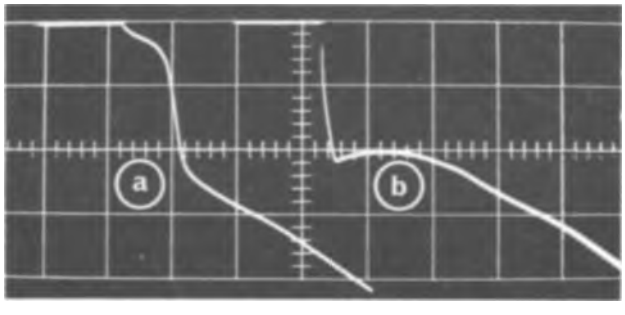

Fig. 6. Chronopotentiograms on platinized platinum in 3.7M H_2SO_4 (a) blank; (b) after 2-min dip in 1M HCHO-3.7M H_2SO_4 and rinse. Coordinates and conditions as in Fig. 4.

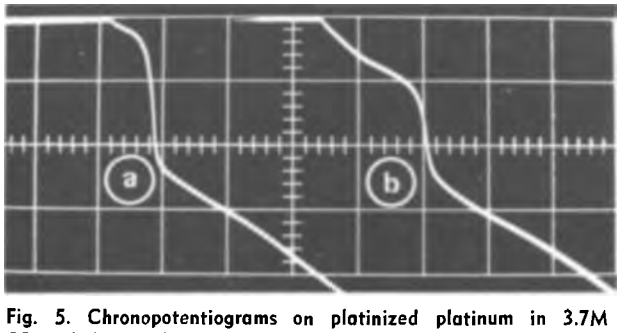

Fig. 5. Chronopotentiograms on platinized platinum in 3.7M H_2SO_4 (a) blank; (b) following 2-min dip in 0.05 Na_2MoO_4-3.7M H_2SO_4 and subsequent rinse in 3.7M H_2SO_4. Coordinates and conditions as in Fig. 4.

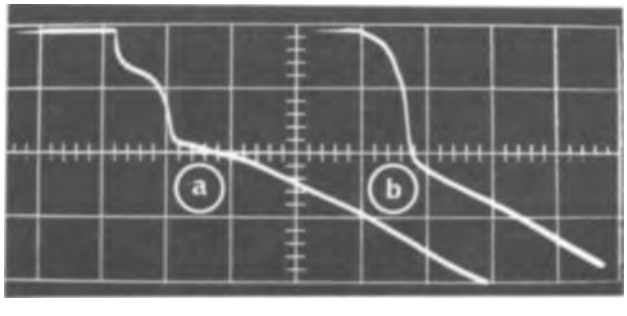

Fig. 7. Chronopotentiograms on platinized platinum in 3.7M H_2SO_4 (a) after 2-min dip in acid-molybdate solution, rinse, 2-min dip in acid-formaldehyde solution and rinse; (b) first subsequent transient on same electrode.

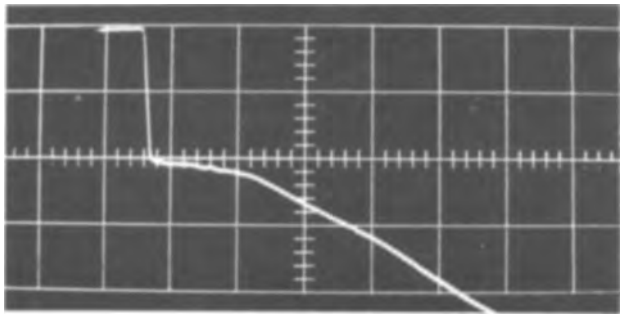

Fig. 8. Chronopotentiogram on platinized platinum in 3.7M H_2SO_4 following 2-min dip in acid-formaldehyde solution, rinse, 2-min dip in acid-molybdate solution, rinse. Coordinates and conditions as in Fig. 4.

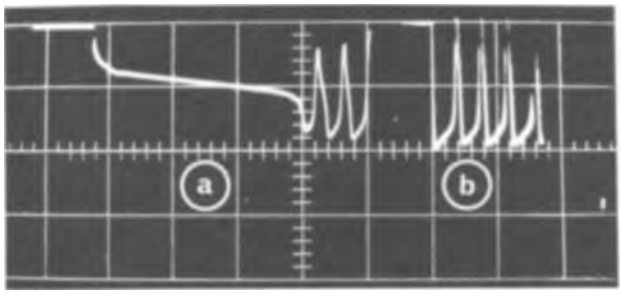

Fig. 9. Chronopotentiograms on platinized platinum in 1M HCHO-3.7M H_2SO_4 (a) after 2-min dip in acid-molybdate and rinse (3.7M H_2SO_4); (b) first subsequent transient on same electrode. Coordinates as in Fig. 4 except 2 sec/div (left to right).

If the electrode is immersed in molybdate solution, rinsed, and then immersed in formaldehyde, both components occupy the surface simultaneously as evidenced by the presence of both characteristic waves in the transient of Fig. 7a. The quantity of molybdate adsorbed appears to be only slightly less than that adsorbed in the previous case of Fig. 5, and absence of adsorbed hydrogen pseudocapacitance makes it seem probable that the strongly adsorbed formaldehyde is present on the hydrogen-type sites not occupied by molybdate.

It is important to recognize in this sequence that the molybdate oxidation wave is not catalytically enhanced through interaction with the HCHO that is strongly adsorbed on the surface. This is evidenced by the fact that the adsorbed HCHO remains on the surface until electrooxidized (Fig. 7a). As shown in Fig. 7b, however, a single anodic transient here serves to eliminate essentially all molybdate as well as formaldehyde.

If the electrode is treated in the reverse order (*i.e.*, contacted with HCHO first) no chemisorbed molybdate is found on the electrode (Fig. 8). The preadsorbed HCHO layer is apparently completely impervious to replacement by molybdate. (This is not completely true in the case of CH_3OH.) Thus, once the formaldehyde layer is formed at the platinum surface in a formaldehyde-containing solution, the electrode must be removed to a plain acid solution and adsorbed HCHO anodized off before the electrode once more is active for molybdate adsorption.

In contrast, anodic stripping of the preadsorbed molybdate layer in the presence of the 1M HCHO-H_2SO_4 solution at 25°C results in a sevenfold increase in transition time before voltage increases to the oscillatory level characteristic of constant current oxidation of HCHO on platinum in these solutions at 25°C (4, 7). This catalytic enhancement of the molybdate oxidation wave is shown in the transient of Fig. 9a. The second transient, Fig. 9b, shows no trace of remaining molybdate, only the oscillating trace of HCHO electrooxidation.

Proposed Mechanism

Based on the foregoing observations, the Pt-molybdate-HCHO (CH_3OH) interaction in H_2SO_4 would seem best summarized as follows:

Chemical reaction:

$$n[Mo^{+6}]_{(ads)} + \left\{\begin{matrix}HCHO\\CH_3OH\end{matrix}\right\} \rightarrow n[Mo^{+5}]_{(ads)} + CO_2 + (n-1)H_2O \text{ (slow)}$$

Electrochemical reaction:

$$n([Mo^{+5}]_{(ads)} + (H_2O) \rightleftarrows [Mo^{+6}]_{(ads)} + H^+ + e^-) \quad \text{(potential determining)}$$

Irreversible failure (to normal Pt levels)

$$[Mo^{+6}]_{(ads)} \rightarrow [Mo^{+6}]_{(soln)} \text{ (near PtO Levels)}$$

$$\left\{\begin{matrix}HCHO\\CH_3OH\end{matrix}\right\}_{(soln)} \rightarrow \left\{\begin{matrix}HCHO\\CH_3OH\end{matrix}\right\}_{(ads\ strongly)}$$

Thus, this reaction differs from a normal catalytic current-producing reaction in that the active intermediate must be fixed at the surface in order to be effective. This characteristic has given rise to the designation "surface redox" or "immobilized redox."

In this scheme no pretense of knowledge is made as to the exact nature of the adsorbed molybdate species. Based on the decrease in transition times for coadsorbed HCHO, however, it appears that strongly held molybdate occupies less than half the electrode surface, primarily those sites not involved in the (most anodic) hydrogen atom adsorption. Fuel on the other hand, especially HCHO, is capable of occupying the entire surface, blocking molybdate adsorption.

Based on the lack of Tafel behavior and dissimilarity of CH_3OH and HCHO performance, the slow step in this catalytic mechanism would seem to arise in some phase of the chemical reaction. Recalling that strongly adsorbed HCHO does not appear to react with adsorbed molybdate, it would seem that the observed rates are determined by the chemical reaction of adsorbed molybdate and nonadsorbed fuel. The high (limiting) activation energy is in accord with this reasoning. In this connection, adsorbed fuel refers to that fuel strongly chemisorbed and does not eliminate the possibility that a weaker, perhaps physical, state of adsorption exists for reactive fuel molecules. Mass transport considerations are eliminated by the fact that the molybdate can be fixed at the electrode, and HCHO (CH_3OH) diffusion is capable of supporting much higher currents (as shown by the subsequent reaction on Pt alone). The difference in performance, then, of HCHO and CH_3OH reflects the true difference in reducing power toward molybdate in the chemical step. If the Nernst equation can be assumed to apply to the surface species involved here, it would appear that Mo^{+5} concentration on the surface is very high during this reaction. Thus, for example, in order to operate at 0.0v *vs.* SCE with $E_{1/2}$ = 0.2v, a Nernst ratio for Mo^{+5}/Mo^{+6} of over 1000 would be required.

It would seem possible, since all molybdate is removed during anodization in the presence of fuel solutions, that the irreversible failure step might involve complexing surface molybdate with a product formed during the direct electrooxidation of HCHO (CH_3OH). Alternatively the absorbed molybdate layer may be forced off by formation of platinum oxides as the potential moves in a positive direction. In any event, once molybdate is lost from the surface, rapid and essentially irreversible replacement by the organic molecule occurs. Thus, as pointed out in a previous section, the sequence of contacting the electrode with molybdate and fuel becomes all important.

The proposed mechanism makes it apparent that the chemical reaction rate observed between fuel and molybdate need have no relation to the electrochemical rates which may be achieved in the "surface redox" process. Thus, the observed chemical reaction requires the desorption of reduced (pentavalent) molybdate in order to perpetuate the reaction, while

the electrochemical cycle does not. If this desorption process is slow, or readsorption of fuel in preference to molybdate occurs, the rates may differ widely. Thus, as pointed out previously, the low apparent chemical rate for reaction of HCHO with molybdate is not inconsistent with the mechanism, but indicates high coverage of the surface with formaldehyde and the inability of molybdate to replace it at a reasonable rate. In the case of CH_3OH this displacement does occur more readily and higher apparent rates are observed.

Summary

The use of molybdates as cocatalysts in the complete oxidation of HCHO and CH_3OH on platinum in acid electrolyte can result in a higher efficiency of this reaction. This improvement has been shown to arise from the catalytic chemical reaction of the fuel with an adsorbed (oxidized) molybdate species with subsequent electrooxidation of its reduced form. To remain operative the molybdate species must remain adsorbed at the electrode surface. Molybdate is lost from the surface under conditions of excessive polarization where HCHO is directly electrooxidized and performance subsequently is characteristic of the levels found with platinum alone. Strong adsorption of fuel under these operating conditions makes the failure irreversible.

The molybdate-fuel-platinum interaction outlined here is probably of little interest for a practical fuel cell system since HCHO is not at present a practical fuel and current densities for CH_3OH reaction are too low to be of interest. The surface redox concept, however, may have broad implications in the search for new fuel cell catalysts. Thus, other compounds may exist which would undergo this same type of redox reaction with fuel and whose adsorption at the electrode interface is not irreversible in the sense described above.

Acknowledgments

The work reported in this paper was made possible by the support of the Advanced Research Projects Agency under Order No. 247 through the U.S. Army Electronics Laboratories (Contract No. DA 36-039 SC-89156). Permission to publish is gratefully acknowledged. The author wishes to thank H. E. Frew for carrying out much of the experimental work.

Manuscript received Oct. 30, 1964. This paper was presented at the Washington Meeting, Oct. 11-15, 1964.

Any discussion of this paper will appear in a Discussion Section to be published in the December 1965 JOURNAL.

REFERENCES

1. P. Delahay, "New Instrumental Methods in Electrochemistry," p. 100, Interscience Publishers, New York (1954).
2. I. M. Kolthoff and J. J. Lingane, "Polarography," 2nd. ed., Vol. I, Chap. XV, Interscience Publishers, New York (1952).
3. H. Krupp, H. Rabenhorst, G. Sandstede, and G. Walter, *This Journal*, **109**, 553 (1962).
4. B. L. Tarmy, *et al.*, Report No. 1, Contract DA 36-039 SC-89156, Esso Research and Engineering Co., 1 Jan. 1962-30 June 1962.
5. M. J. Schlatter, Preprint of the Div. of Petroleum Chemistry, ACS 6 B-149 (1961).
6. T. O. Pavela, *Ann. Acad. Sci. Fennicae, Ser. A*, 2, 59 (1954).
7. R. P. Buck and L. R. Griffith, *This Journal*, **109**, 1005 (1962).

The Solubility and Diffusivity of Oxygen in Electrolytic Solutions

Keith E. Gubbins and Robert D. Walker, Jr.

Department of Chemical Engineering, University of Florida, Gainesville, Florida

ABSTRACT

Measurements of the solubility of oxygen in sulfuric acid, phosphoric acid, and potassium hydroxide are reported, together with values of the diffusivity of oxygen in potassium hydroxide solutions at 25°C. It is shown that for the electrolyte concentrations commonly employed in fuel cells the solubility and diffusivity of oxygen may each be reduced to as little as 2% of their corresponding values for pure water.

It seems probable that in some cases the current obtainable from fuel cells is limited by diffusion of the reacting gas through the liquid (electrolyte) phase to active sites on the surface of the electrode. Under these conditions it follows from Fick's law that the limiting current that may be drawn from a given electrode will depend on the concentration of the gas in the bulk electrolyte and on its diffusivity. In order to enable calculations concerning the performance of such electrodes to be made experimental measurements of solubilities and diffusivities of oxygen in fuel cell electrolytes have been carried out.

Experimental

Solubility.—Gas chromatography was used to determine the solubilities; a diagram of the apparatus is shown in Fig. 1. A sample of electrolyte was equilibrated with oxygen in a constant temperature bath controlled to ±0.1°C. A sample of known volume was withdrawn by means of a syringe and injected into a glass gas stripping cell. This cell contained a medium porosity glass frit and had a volume of about 7 ml; it was also equipped with an injection point consisting of a rubber serum cap. The sample size used was 5 ml. Helium carrier gas passed through the reference side of the thermal conductivity detector and into the sample cell; dissolved gases were rapidly and completely removed from solution by the dispersed carrier gas, and the gas mixture passed through drying tubes before entering the molecular sieve column. Since there was only one component to be analyzed the separating column was not really necessary; however it was included as an experimental convenience in providing a

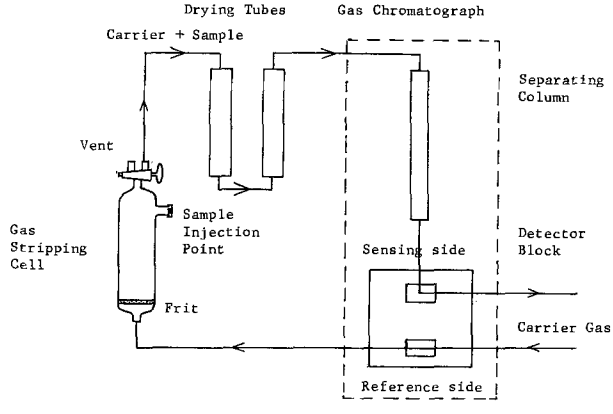

Fig. 1. Apparatus for measurement of solubility

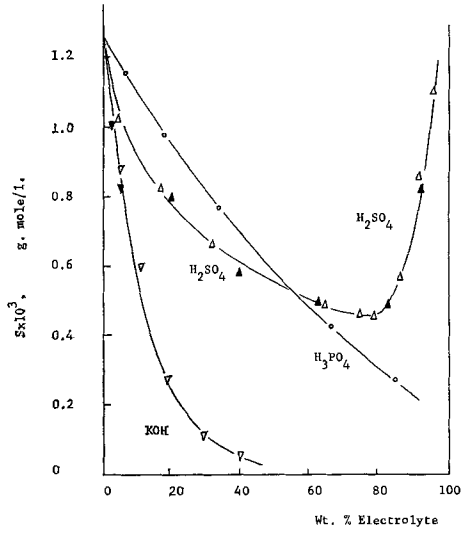

Fig. 2. Solubility of O_2 at 25°C: ○, experimental results for H_3PO_4; △, experimental results for H_2SO_4; ▽, experimental results for KOH; ▲, results of Bohr for H_2SO_4 (corrected to 1 atm assuming Henry's law); ▼, results of Geffcken for KOH.

suitable time interval between sample injection and the arrival of the peak. The peaks obtained by this method were somewhat broader than normal, but there was no excessive "tailing." The gas chromatograph was calibrated for oxygen by injecting a sample of pure water saturated with oxygen at 25°C. The solubility in this case has been accurately determined by chemical methods.

Diffusivity.—The diffusivity of oxygen in potassium hydroxide solutions was obtained by a polarographic method involving measurement of the limiting current during the reduction of the oxygen to hydrogen peroxide at the dropping mercury electrode. The apparatus was similar to that used by Lingane and Laitinen (7). A well-defined limiting current region was observed over the voltage range —0.2 to —1.0v *vs.* a saturated calomel electrode; this wave corresponds to reduction of oxygen to hydrogen peroxide. The second oxygen wave, corresponding to the reduction of hydrogen peroxide to hydroxyl ion, was less well-defined; in addition the mass flow rate and drop-time vary fairly rapidly with change in voltage in this region. The diffusivity (D) was therefore calculated from measurements made on the first wave, using the modified Ilkovic equation (8, 11)

$$i_d = 607\, n\, D^{1/2}\, C\, m^{2/3}\, t^{1/6} \left(1 + \frac{A\, D^{1/2}\, t^{1/6}}{m^{1/3}} \right)$$

where A is a constant; n the number of electrons involved in reaction = 2; i_d the limiting diffusion current, μa; C the concentration of oxygen, millimoles/liter; m the mass flow rate of mercury electrode, mg/sec; t the drop time of mercury electrode, sec.

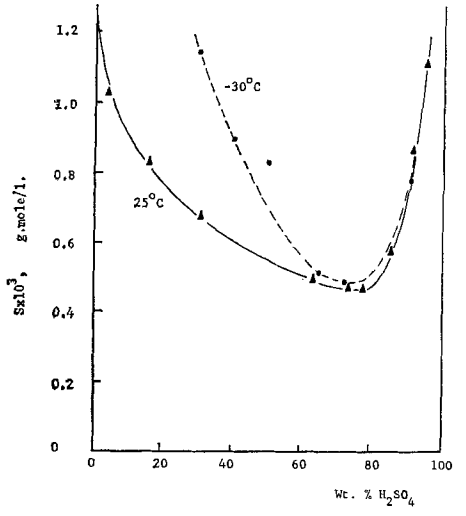

Fig. 3. Solubility of O_2 in H_2SO_4 at 25° and —30°C

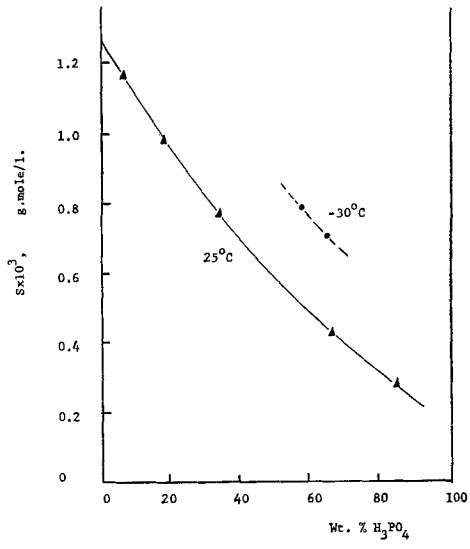

Fig. 4. Solubility of O_2 in H_3PO_4 at 25° and —30°C

The limiting current depends on both the solubility and the diffusivity. However, since the solubility was known from independent measurements, the diffusivity could be calculated from measurements of the limiting current. Different workers have given somewhat different values for the constant A. Strehlow and von Stackelberg (11) predicted the value 17 theoretically and claimed that this value was supported experimentally; Lingane and Loveridge (8) predicted a value of 39 from theory and found values of 31.7 and 33.5 by experiment. Meites and Meites (9) give the value of 31.5. Since experimental evidence supports the higher values for A (5) the value 31.5 given by Meites and Meites was used. Under normal experimental conditions the value obtained for D is not highly sensitive to changes in the value of A; thus changing the value of A from 31.5 to 39 produces a change in the value of D obtained of only about 4%. Jordan (4) has used polarography to determine the diffusivity of oxygen in glycerol-water mixtures and aqueous sucrose solutions

Results

Solubility.—The solubility of oxygen in sulfuric acid, phosphoric acid, and potassium hydroxide solutions has been determined. The results for 25°C are shown in Fig. 2. The solubility values plotted are gram moles of oxygen per liter for a solution equilibrated with oxygen gas at 1 atm pressure (*i.e.*, excluding water vapor pressure). The reproducibility of these results was of the order ±2%.

Figure 2 shows that the solubility of oxygen falls off rapidly and continuously with increasing concentration of potassium hydroxide or phosphoric acid. The solubility in sulfuric acid solutions shows a pronounced minimum at about 75 w/o (weight per cent) H_2SO_4, however. Bohr (1) has reported data for the solubility of air in sulfuric acid at 21°C; these data also show a minimum solubility in the range 70-80% H_2SO_4, and the values are in good general agreement with those shown in Fig. 2. Geffcken (2) has presented data on the solubility of oxygen in dilute solutions of potassium hydroxide (up to 2N); these results are in quite good agreement with those shown in Fig. 2.

Figure 3 compares solubilities in sulfuric acid at —30° with values at 25°C; at concentrations less than about 35% or greater than 90%, solid freezes out of solution at —30°C. Figure 4 shows the solubility in phosphoric acid at —30° compared with values at 25°C. Some additional experimental difficulties occurred at low temperatures owing to the high viscosity of the

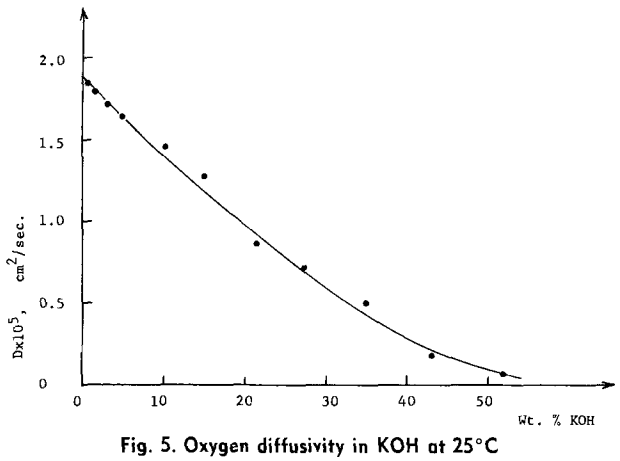

Fig. 5. Oxygen diffusivity in KOH at 25°C

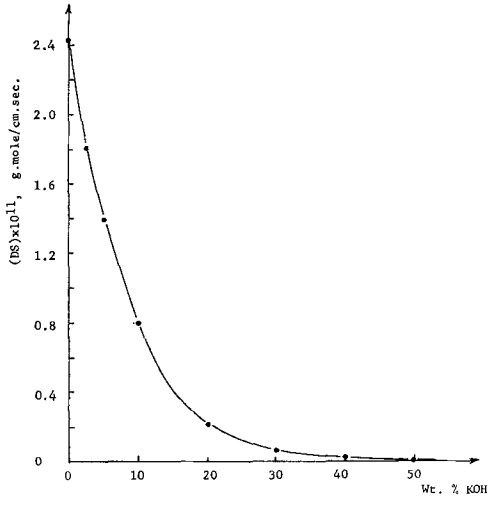

Fig. 6. Rate of diffusion, KOH at 25°C

solutions; this caused difficulty in saturating the solution with the gas and in transferring solution by means of a syringe.

Diffusivity.—Figure 5 presents diffusivity values for oxygen in potassium hydroxide at 25°C. Extrapolation of the curve back to zero concentration gives a value of 1.90 x 10^{-5} cm^2/sec for the diffusivity of oxygen in water at 25°C. This is in good agreement with values determined by other workers (3); thus Kreuzer (6) gives 1.90 x 10^{-5}, Semerano (10) gives 1.87 x 10^{-5}, and Jordan (4) gives 2.12 x 10^{-5}. Taking into consideration the uncertainty in the value of constant *A*, and experimental errors in the measurement of the variables in the Ilkovic equation, it is estimated that the maximum error of the diffusivity values reported is about ±6%.

Discussion

Figures 2 and 5 indicate that both the solubility and diffusivity of oxygen in potassium hydroxide decrease rapidly with increase in concentration. The rate of mass transport of dissolved oxygen to an electrode is proportional to the product of the diffusivity and the solubility. Figure 6 shows this product for potassium hydroxide at 25°C. From this figure it is seen that for a 35% KOH electrolyte the oxygen mass transport rate is less than 2% of that obtainable in pure water. Calculations of the current expected from a mass transport-limited fuel cell in which data for pure water are assumed will therefore give current values that are much too high.

Acknowledgments

The authors wish to express their appreciation to the Harry Diamond Laboratories, U. S. Army Materiel Command, for sponsoring the work reported here. The encouragement and suggestions of Mr. Nathan Kaplan of the Harry Diamond Laboratories, and the assistance of co-workers in this laboratory are also gratefully acknowledged.

Manuscript received Nov. 9, 1964; revised manuscript received Jan. 16, 1965. This paper was presented at the Washington Meeting, Oct. 11-15, 1964.

Any discussion of this paper will appear in a Discussion Section to be published in the December 1965 JOURNAL.

REFERENCES

1. C. Bohr, *Z. Physik. Chem.*, **71**, 47 (1910).
2. G. Geffcken, *ibid.*, **49**, 17 (1904).
3. D. M. Himmelblau, "Diffusion of Gases in Aqueous Solutions," Final Report, March 1, 1963, University of Texas, Austin, Texas.
4. J. Jordan, E. Ackerman, and R. L. Berger, *J. Am. Chem. Soc.*, **78**, 2979 (1956).
5. I. M. Kolthoff and J. J. Lingane, "Polarography," Vol. 1, 75, Interscience Publishers, Inc., New York (1952).
6. F. Kreuzer, *Helv. Physiol. et Phamacol. Acta*, **8**, 505 (1950).
7. J. J. Lingane and H. A. Laitinen, *Ind. Eng. Chem., Anal. Ed.*, **11**, 504 (1939).
8. J. J. Lingane and B. A. Loveridge, *J. Am. Chem. Soc.*, **72**, 438 (1950).
9. L. Meites and T. Meites, *ibid.*, **73**, 395 (1951).
10. G. Semerano, L. Riccoboni, and A. Foffani, *Gazz. Chim. Ital.*, **79**, 395 (1949).
11. H. Strehlow and M. von Stackelberg, *Z. Elektrochem.*, **54**, 51 (1950).

Scaling of Fe-26Cr Alloys at 870°-1200°C

D. Caplan and M. Cohen

Division of Applied Chemistry, National Research Council, Ottawa, Ontario, Canada

ABSTRACT

The oxide layers formed on Fe-26Cr alloy are wrinkled, porous, and blistered, and the metal/oxide interface markedly roughened. This is interpreted as evidence that compressive stresses are generated continuously in the growing oxide, hence that anion diffusion participates in the growth process. Smooth oxidation curves are observed if the wrinkled scale is adherent, even though non-uniform. However, when blistering and cracking occurs, as with electropolished specimens, the weight-gain/time curves are irregular. Similar irregularities occur wih Fe-26Cr-0.5 Si, Fe-26Cr-1Mn, type 446 and pure Cr. Manganese decreases oxidation resistance.

An earlier publication (1) described the oxidation of Cr at 980°, 1090°, and 1200°C. In this paper the oxidation of an Fe-26Cr alloy is examined under the same experimental conditions in a continuing program to investigate the physical nature and mechanism of growth of protective oxide scales. Also included are some experiments with Fe-26Cr containing additions of Mn or Si and with a 26% Cr commercial alloy.

The literature on the oxidation of Fe-Cr alloys has been reviewed recently by Seybolt (2, 3), Kubaschewski and Hopkins (4), Lai *et al.* (5), and most extensively by Wood (6). It is evident that a large effort has gone into investigating this system, but the accumulated information is in many cases contradictory and poorly reproducible. A wide range of scaling rates and a variety of oxide phases is observed. The reviewers

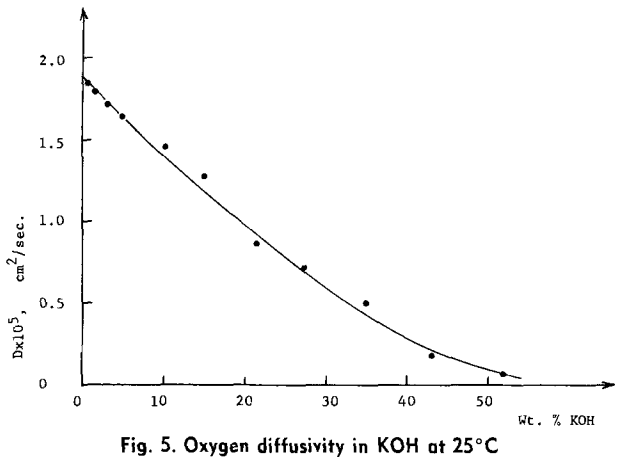

Fig. 5. Oxygen diffusivity in KOH at 25°C

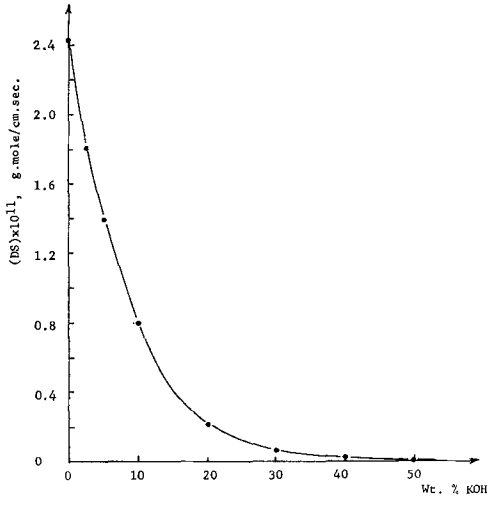

Fig. 6. Rate of diffusion, KOH at 25°C

solutions; this caused difficulty in saturating the solution with the gas and in transferring solution by means of a syringe.

Diffusivity.—Figure 5 presents diffusivity values for oxygen in potassium hydroxide at 25°C. Extrapolation of the curve back to zero concentration gives a value of 1.90 x 10^{-5} cm^2/sec for the diffusivity of oxygen in water at 25°C. This is in good agreement with values determined by other workers (3); thus Kreuzer (6) gives 1.90 x 10^{-5}, Semerano (10) gives 1.87 x 10^{-5}, and Jordan (4) gives 2.12 x 10^{-5}. Taking into consideration the uncertainty in the value of constant *A*, and experimental errors in the measurement of the variables in the Ilkovic equation, it is estimated that the maximum error of the diffusivity values reported is about ±6%.

Discussion

Figures 2 and 5 indicate that both the solubility and diffusivity of oxygen in potassium hydroxide decrease rapidly with increase in concentration. The rate of mass transport of dissolved oxygen to an electrode is proportional to the product of the diffusivity and the solubility. Figure 6 shows this product for potassium hydroxide at 25°C. From this figure it is seen that for a 35% KOH electrolyte the oxygen mass transport rate is less than 2% of that obtainable in pure water. Calculations of the current expected from a mass transport-limited fuel cell in which data for pure water are assumed will therefore give current values that are much too high.

Acknowledgments

The authors wish to express their appreciation to the Harry Diamond Laboratories, U. S. Army Materiel Command, for sponsoring the work reported here. The encouragement and suggestions of Mr. Nathan Kaplan of the Harry Diamond Laboratories, and the assistance of co-workers in this laboratory are also gratefully acknowledged.

Manuscript received Nov. 9, 1964; revised manuscript received Jan. 16, 1965. This paper was presented at the Washington Meeting, Oct. 11-15, 1964.

Any discussion of this paper will appear in a Discussion Section to be published in the December 1965 JOURNAL.

REFERENCES

1. C. Bohr, *Z. Physik. Chem.*, **71**, 47 (1910).
2. G. Geffcken, *ibid.*, **49**, 17 (1904).
3. D. M. Himmelblau, "Diffusion of Gases in Aqueous Solutions," Final Report, March 1, 1963, University of Texas, Austin, Texas.
4. J. Jordan, E. Ackerman, and R. L. Berger, *J. Am. Chem. Soc.*, **78**, 2979 (1956).
5. I. M. Kolthoff and J. J. Lingane, "Polarography," Vol. 1, 75, Interscience Publishers, Inc., New York (1952).
6. F. Kreuzer, *Helv. Physiol. et Phamacol. Acta*, **8**, 505 (1950).
7. J. J. Lingane and H. A. Laitinen, *Ind. Eng. Chem., Anal. Ed.*, **11**, 504 (1939).
8. J. J. Lingane and B. A. Loveridge, *J. Am. Chem. Soc.*, **72**, 438 (1950).
9. L. Meites and T. Meites, *ibid.*, **73**, 395 (1951).
10. G. Semerano, L. Riccoboni, and A. Foffani, *Gazz. Chim. Ital.*, **79**, 395 (1949).
11. H. Strehlow and M. von Stackelberg, *Z. Elektrochem.*, **54**, 51 (1950).

Scaling of Fe-26Cr Alloys at 870°-1200°C

D. Caplan and M. Cohen

Division of Applied Chemistry, National Research Council, Ottawa, Ontario, Canada

ABSTRACT

The oxide layers formed on Fe-26Cr alloy are wrinkled, porous, and blistered, and the metal/oxide interface markedly roughened. This is interpreted as evidence that compressive stresses are generated continuously in the growing oxide, hence that anion diffusion participates in the growth process. Smooth oxidation curves are observed if the wrinkled scale is adherent, even though non-uniform. However, when blistering and cracking occurs, as with electropolished specimens, the weight-gain/time curves are irregular. Similar irregularities occur wih Fe-26Cr-0.5 Si, Fe-26Cr-1Mn, type 446 and pure Cr. Manganese decreases oxidation resistance.

An earlier publication (1) described the oxidation of Cr at 980°, 1090°, and 1200°C. In this paper the oxidation of an Fe-26Cr alloy is examined under the same experimental conditions in a continuing program to investigate the physical nature and mechanism of growth of protective oxide scales. Also included are some experiments with Fe-26Cr containing additions of Mn or Si and with a 26% Cr commercial alloy.

The literature on the oxidation of Fe-Cr alloys has been reviewed recently by Seybolt (2, 3), Kubaschewski and Hopkins (4), Lai *et al.* (5), and most extensively by Wood (6). It is evident that a large effort has gone into investigating this system, but the accumulated information is in many cases contradictory and poorly reproducible. A wide range of scaling rates and a variety of oxide phases is observed. The reviewers

Table I. Composition of specimen materials (weight per cent, w/o)

	Fe-Cr	Fe-Cr-Si	Fe-Cr-Mn	Type 446
C	0.022	0.022	0.012	0.18
Mn	0.003	0.004	1.00	0.75
Si	0.02	0.55	0.01	0.86
Ni	0.02	0.02	0.02	0.32
Cr	26.2	26.2	25.7	25.9

see two main causes. One is the complexity created by experimental variations including alloy composition, impurities, specimen shape, specimen preparation, atmosphere, and procedure in carrying out the oxidation runs. The other is mechanical and structural: pores, blisters, cracks and plastic flow due to stress, local attack and non-uniform scales, phase changes caused by selective oxidation and loss of adhesion are superimposed on the scaling process and obscure the effect of the variables being investigated.

The particular object of the present work was to compare the results to the scaling of unalloyed Cr already carried out and thus disentangle the effects of composition variations in metal and oxide. Further, it was hoped to reduce confusion by using a high-purity Fe-26Cr alloy, oxidizing in purified oxygen, and giving considerable attention to surface preparation and experimental procedure. Since the only oxide formed on Fe-26Cr is Cr_2O_3 containing a small amount of Fe_2O_3 in solution, oxidation behavior similar to that of Cr metal is to be expected; spinel does not form unless surface metal were to become depleted below 13% Cr (2).

As will be seen, clarification was achieved only in part. The structural-mechanical factors are an intrinsic part of Cr alloy scaling and cannot be eliminated. Metallographic cross sections demonstrated their nature and permitted an interpretation of their origins.

Experimental

A high-purity, vacuum-melted Fe-26Cr alloy was used for most of the work. In addition, two similar alloys containing 0.5% Si or 1% Mn and a 26% Cr type 446 commercial steel were oxidized at 1090° only. Table I shows the composition of the four specimen materials. Rectangular specimens 1.1 x 0.5 x 4 cm were machined from 1.3 cm diam rolled rods. A few runs were made with cylindrical specimens 0.6 cm diam x 4 cm long and sheet specimens 1.1 x 0.035 x 5 cm, machined or rolled from the same rods.

The specimens were smoothed by abrading through 600 grit SiC paper and a 10μ layer of metal electropolished off in glacial acetic-70% perchloric acid (20 to 1) to remove surface contamination. They were then annealed for structural stability at 1100°C in purified argon at 20 Torr and electropolished to remove a further 10μ layer of metal. The second polish removed the Cr-depleted surface layer caused by preferential evaporation of Cr and any contaminant that formed during annealing; a precipitate of Cr carbide that apparently nucleated at the surface during cooling also was removed. Some specimens were not annealed, in which case the second electropolish was omitted. After electropolishing, the specimens were either rinsed in water and methanol and blotted dry or immediately etched for 15 sec in 1.38*N* HF (7), or in deoxygenated 4*N* HCl for 45 sec with the specimen polarized cathodically at 10 $\mu a/cm^2$ (1).

The oxidation runs were carried out at 870°, 980°, 1090°, and 1200°C in a vertical tube furnace in flowing oxygen from which CO_2 and moisture had been removed (1). Details of the experiments are included in Table II. For experiments in wet oxygen the gas was saturated with moisture at 25°C corresponding to a P_{H_2O} of 24 Torr. Weight increase was recorded continuously on an automatic balance. The open-insertion method was used in which the cold prepared specimen is lowered quickly into the hot reaction tube with oxygen flowing. Specimens required 0.5-3 min to reach temperature depending on cross section, and weight recording began at about 0.5 min. It is of prime importance to make an accurate estimate of the specimen weight at zero time. This differs from its weight in still air at room temperature by a factor involving convection, buoyant force, a piston effect, and a magnetic correction. It cannot be predicted and may take as long as 5 min to reach a steady state. The weight recording is most uncertain at the very beginning when, unfortunately, the weight is changing most rapidly. Satisfactory correction factors, accurate to 0.01 mg/cm^2, could be obtained from facsimile experiments with nonoxidizing specimens and by other means (1). Different correction factors were obtained if the specimen hung inside a Cr_2O_3 baffle crucible which was sometimes used at the higher temperatures to minimize volatilization of Cr oxide (1, 8).

After removal from the furnace the specimens were observed microscopically as they cooled under argon

Table II. Summary of oxidation runs

Run	Alloy	Temp, °C	Surface prep.	Time, hr	Oxidation curves: Fig. No.	Oxidation curves: Plotting symbol	Early waves in curves: Time of breaks, hr	Early waves in curves: Wt gain at breaks, mg/cm^2
1	Fe-26Cr	870	Etch	97	1a	———		
2	Fe-26Cr	980	Etch	29	1a	◑		
3	Fe-26Cr	980	Etch	50	1a	○		
4	Fe-26Cr	980	Etch	93	1a	●		
5	Fe-26Cr	980	Etch	94	1a	———		
6	Fe-26Cr	1090	Etch	0.4	1a			
7	Fe-26Cr	1090	Etch	23	1a	■		
8	Fe-26Cr	1090	Etch	100	1a	◨		
9	Fe-26Cr	1090	Etch	100	1a, 9a	———		
10	Fe-26Cr	1090	Etch	136	1a	□		
11	Fe-26Cr	1200	Etch	70	1a	———		
12	Fe-26Cr	980	E.P.	0.8	1b			
13	Fe-26Cr	980	E.P.	4	1b	———	0.8, 2.0	0.2, 0.4
14	Fe-26Cr	980	E.P.	23	1b	———	1.2, 1.7	0.3, 0.4
15	Fe-26Cr	980	E.P.	24	1b	———	1.7, 3.1	0.3, 0.7
16	Fe-26Cr	1090	E.P.	0.4	1b		0.2	0.4
17	Fe-26Cr	1090	E.P.	20	1b	———	0.2, 0.6	0.3, 0.7
18	Fe-26Cr	1090	E.P.	64	1b	———	0.3, 0.6	0.4, 0.7
19	Fe-26Cr	1090	E.P.	100	1b, 9b	———	0.2, 0.6	0.4, 0.8
20	Fe-26Cr	1200	E.P.	0.6	1b	———	0.2, 0.4	0.9, 1.6
	Cr	980	Etch	99	1a	— — —		
	Cr	1090	Etch	100	1a, 9a	— — —		
	Cr	1200	Etch	42	1a	— — —		
	Cr	980	E.P.	96	1b	— — —		
	Cr	1090	E.P.	21	1b, 9b	— — —		
	Cr	1200	E.P.	1.2	1b	— — —		
21	Fe-26Cr-0.5Si	1090	Etch	363	9a	———		
22	Fe-26Cr-1Mn	1090	Etch	20	9a	———		
23	446	1090	Etch	166	9a	———		
24	Fe-26Cr-0.5Si	1090	E.P.	92	9b	———		
25	Fe-26Cr-1Mn	1090	E.P.	20	9b	———		
26	446	1090	E.P.	191	9b	———		
Runs in wet oxygen								
27	Fe-26Cr	980	Etch	43				
28	Fe-26Cr	980	E.P.	24			1.2, 3.7	0.3, 0.6
29	Fe-26Cr	1090	Etch	140				

and then examined by x-ray diffraction, chemical analysis, and metallographically in cross section.

Results

Figure 1(a) summarizes the oxidation data for 11 etched Fe-26Cr specimens in 1 atm dry oxygen at 870°, 980°, 1090°, and 1200°C, and Fig. 1(b) the data for 9 electropolished specimens at 980°, 1090°, and 1200°C. The dashed lines are the oxidation curves for pure Cr metal at 980°, 1090°, and 1200°, etched or electropolished, repeated from an earlier publication (1).

Comparison of Fig. 1(a) and 1(b) shows that electropolished Fe-26Cr oxidized more rapidly than the etched alloy. [Cr had shown the same E.P. effect to an even greater degree (1). The etched alloy oxidizes as fast or faster than Cr; after electropolishing, Cr oxidizes faster than the alloy.] The etched specimens yield smooth oxidation curves but those of electropolished specimens all show irregularities near the beginning of the runs as evident in the sub-plot inset in Fig. 1(b). Usually, two such early waves occur between 0.2 and 2 hr. In general, the weight gain before the breaks increases and the time at which they occur decreases with increasing temperature (last two columns of Table II).

Scale structure on etched Fe-26Cr.—Figures 2 to 5 show the structure of the scale formed on the etched Fe-26Cr alloy. The outer surface is wrinkled and the metal surface very roughened, sometimes scalloped in high-crested waves; *e.g.*, compare Fig. 3(c) or 4(d) with the smooth metal as prepared for oxidation [Fig. 2(b)]. The oxide layer is blistered and porous and contains islands of metal [Fig. 3(b), 3(c), and 5(b)] that give the appearance of having been dragged from the metal surface. [The thin scale formed at 870° (Fig. 2) has developed only some of these characteristics and that at 1200° (Fig. 5) is incomplete, much of it having spalled during cooling after the run.] The rugged metal/oxide interface cannot be the result of local or intergranular attack since the oxide is too thin in the metal troughs in relation to the trough depth; it is often thicker over the metal projections instead of where least metal remains. A related phenomenon is shown in Fig. 5: at temperatures and run durations great enough to develop thick scale, the edges of

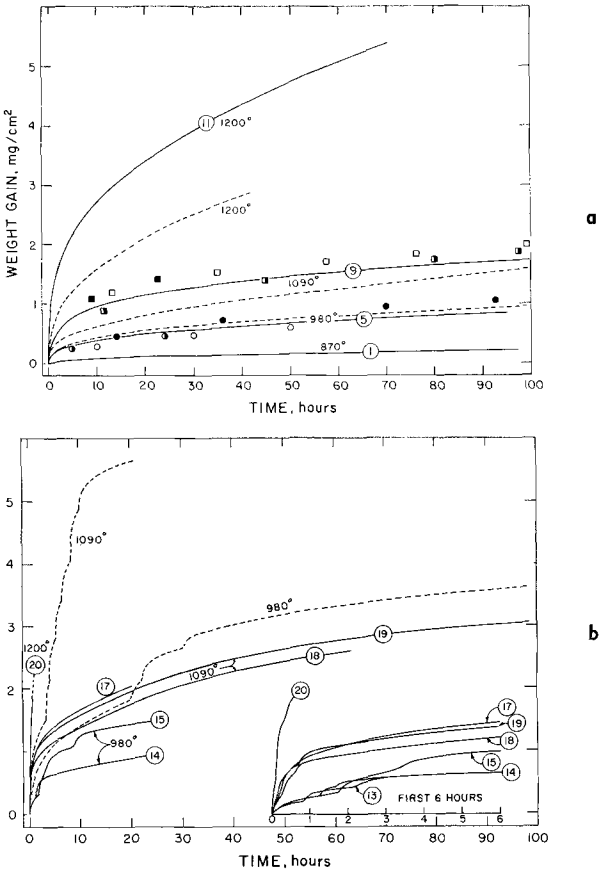

Fig. 1. Oxidation of Fe-26Cr alloy in 1 atm dry oxygen. Fig. 1a. Etched. Curves, 1, 5, 9, and 11 are at 870°, 980°, 1090°, and 1200°C, respectively; symbols half dark circle, open circle, and dark circle represent duplicate runs 2, 3, and 4 at 980°; symbols dark box, half dark box and, open box represent duplicate runs 7, 8, and 10 at 1090°. Fig. 1b. Electropolished. Runs 13, 14, and 15 at 980°; 17, 18, and 19 at 1090°; run 20 at 1200°. In the subplot of the first 6 hr the time scale is expanded to illustrate the early waves. Dashed lines in (a) and (b) show Cr oxidized at 980°, 1090°, and 1200°, repeated from Fig. 2 and 3 of ref. (1).

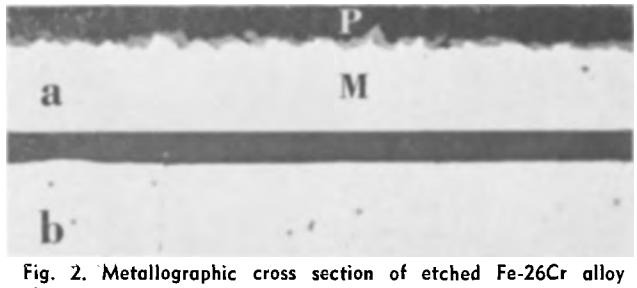

Fig. 2. Metallographic cross section of etched Fe-26Cr alloy oxidized for 97 hr at 870° (curve 1). P is mounting plastic; M is metal. Photograph (b) is a cross section of the etched alloy as prepared for scaling to show the contrast in roughness of the metal surface before and after scaling. Magnification 800X.

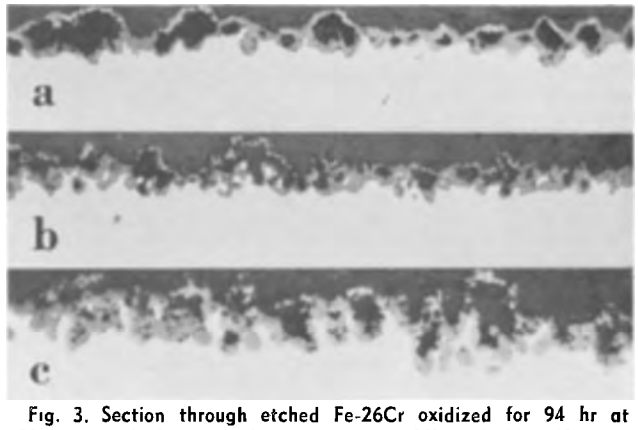

Fig. 3. Section through etched Fe-26Cr oxidized for 94 hr at 980° (curve 5). (a) and (b) magnification 400X; (c), Magnification 800X.

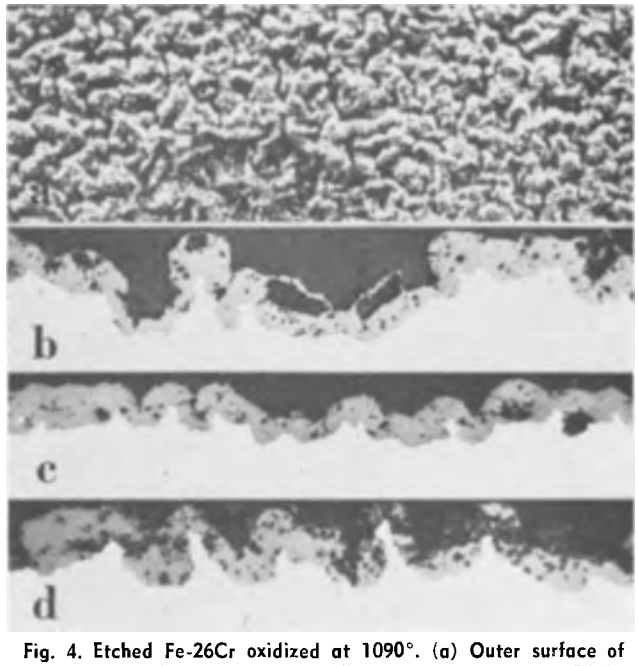

Fig. 4. Etched Fe-26Cr oxidized at 1090°. (a) Outer surface of oxide after 100 hr run (curve 9); (b) cross section after 136 hr (run 10); (c) and (d) cross section after 100 hr (run 8). Fragmentation and some porosity in (d) is artifact. Magnification: (a), 80X; (b) and (c), 400X; (d), 600X.

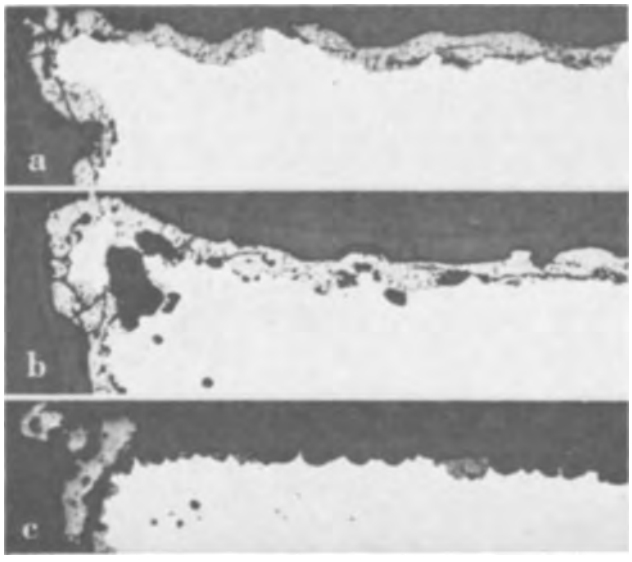

Fig. 5. Section through etched Fe-26Cr oxidized 70 hr at 1200° (curve 11). Scale layer not complete; approximately 50% lost by spalling during cooling at end of run. Magnification 120X.

the rectangular specimens showed a sharply peaked ridge of oxide. In cross section, the metal of the corners also may show a peak [Fig. 5(a)], whereas before oxidation the corners had been smoothly rounded by electropolishing. Measurements of the diagonal distance of the metal core after scaling showed an increase over the original dimension rather than the decrease expected due to metal having been consumed; *e.g.*, in run 11, the diagonals increased by 75μ while, on the average, 32μ of metal were oxidized. It follows from these observations that oxide and metal have been subjected to considerable lateral plastic flow, probably as a result of compressive stresses generated in the oxide layer by the growth process.

Scale structure on electropolished Fe-26Cr.—The scales formed on electropolished Fe-26Cr at 980°, 1090°, and 1200° are illustrated in Fig. 6 to 8. All show an outer separated layer and a more solid inner layer. The early waves in the weight-gain/time curves appear to be related to the outer blistered layer. Usually only one blistered layer is observed even though the oxidation curves show two waves; presumably the two sides of the specimen fail at different times. Figure 6(a) is a plan view of the oxide formed in 0.8 hr at 980°; the layer is poorly adherent and wrinkled or blistered but has not yet failed since no irregularity has occurred in the oxidation curve. Figure 6(b) and (c) are sections through the scale formed in 24 hr under the same conditions; the second layer of adherent, nonblistered scale formed when gaseous oxygen

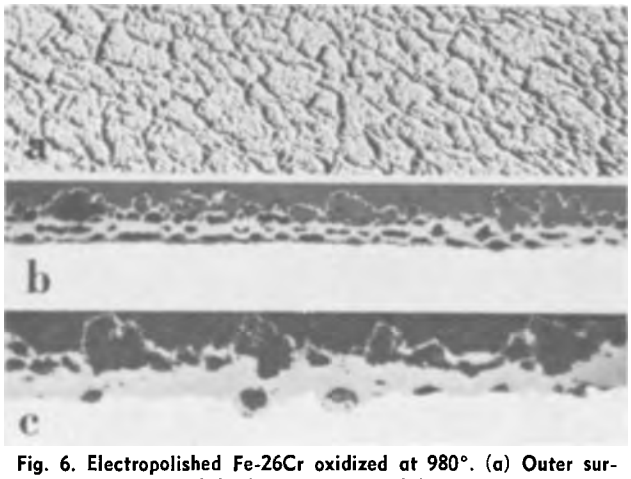

Fig. 6. Electropolished Fe-26Cr oxidized at 980°. (a) Outer surface of oxide after 0.8 hr (run 12); (b) and (c) cross section after 24 hr (curve 15). Some pores next to metal may be artifact. Magnification (a), 80X; (b), 400X; (c), 800X.

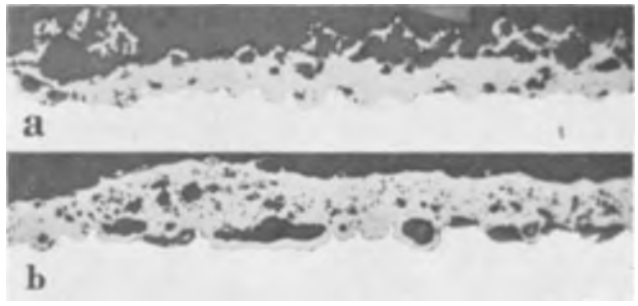

Fig. 7. Section through electropolished Fe-26Cr oxidized at 1090°. (a) Curve 17, 20 hr; (b) curve 19, 100 hr. Pores probably enlarged by polishing. Magnification 400X.

Fig. 8. Section through electropolished Fe-26Cr oxidized 0.6 hr at 1200° (curve 20). Magnification 400X.

was admitted to the bare metal by failure of the outer, wrinkled, first-formed layer at 1.7 (or 3.1) hr. At 1090° the outer blistered layer is less evident, especially after 100 hr [Fig. 7(b)], even though the weight gain before the break was no less than at 980° (last column of Table II); this might be accounted for by the increased sintering and evaporation of oxide (8) that would occur at the higher temperature and longer time. In the 0.6 hr run at 1200° (Fig. 8) the outer ballooned layer is much in evidence, consistent with the greater weight gain before the break and too short a time for significant sintering and evaporation to have occurred.

X-ray diffraction of Fe-26Cr.—The only oxide detected by x-ray diffraction was $(Cr,Fe)_2O_3$. Thermodynamically, a spinel is possible if the surface metal were to become depleted in Cr below 13% (2). Attempts to induce spinel by scaling for short times at high temperatures, under which conditions the reaction rate and hence Cr depletion would be greatest, were unsuccessful; no spinel was detected. The lattice parameter of the oxide corresponded to pure Cr_2O_3 which signifies an Fe_2O_3 content of less than 3% [based on the 0.01% accuracy of the x-ray method used and the known lattice parameter of the Fe_2O_3-Cr_2O_3 solid solution (9)].

Chemical analysis of Fe-26Cr.—The Fe_2O_3 content found by chemical analysis ranged from 0.4 to 2.5%, consistent with the x-ray result. There was a tendency for oxide formed at more rapid rates (electropolished, high temperatures, and short times) to contain more iron, but this could not be confirmed because of the difficulty of sampling thin oxide layers without contamination by the substrate metal.

Moisture.—Three runs were carried out in wet oxygen as duplicates to dry oxygen runs, etched and electropolished at 980° and etched at 1100° (see Table II). The oxidation curves were little different from the dry oxygen runs except at the higher temperature after the first several hours. The presence of moisture increases the rate of evaporation of Cr oxide (8) which decreases the weight gain but increases the consumption of metal. As the rate of weight gain slows due to increasing oxide thickness, the loss in weight caused by evaporation of Cr_2O_3 becomes relatively important especially if not suppressed by use of the Cr_2O_3 baffle crucible. Hence, the curve of the last 80 hr of run 29 was essentially flat and the final weight gain only half that of run 10 in dry oxygen.

Other alloys.—Figure 9 compares the 1090° oxidation curves of the Fe-26Cr alloy, etched and electropolished, with the three other Fe-26Cr alloys, the compositions of which are shown in Table I. The 1090° curves for Cr are included for reference.

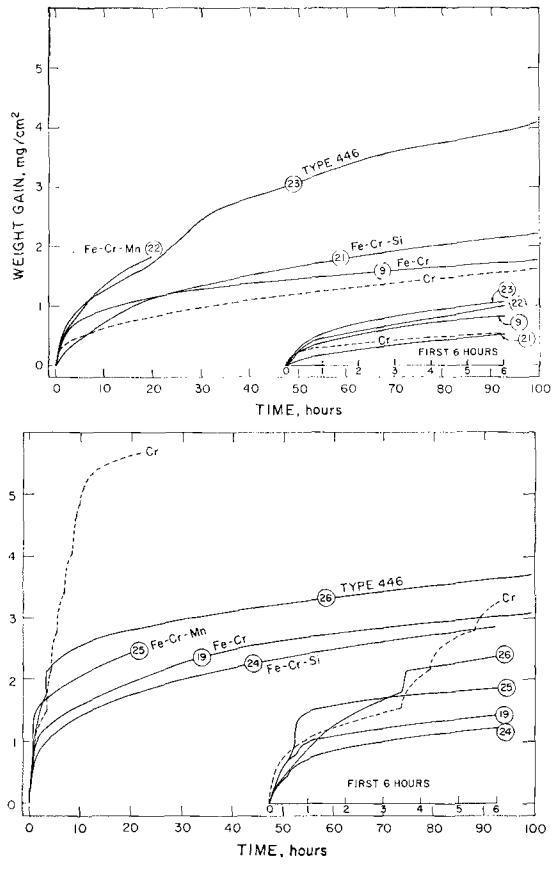

Fig. 9. Oxidation of Fe-26Cr, Fe-26Cr-0.5Si, Fe-26Cr-1Mn, type 446, and pure Cr at 1090° in 1 atm dry oxygen; (a) etched; (b) electropolished.

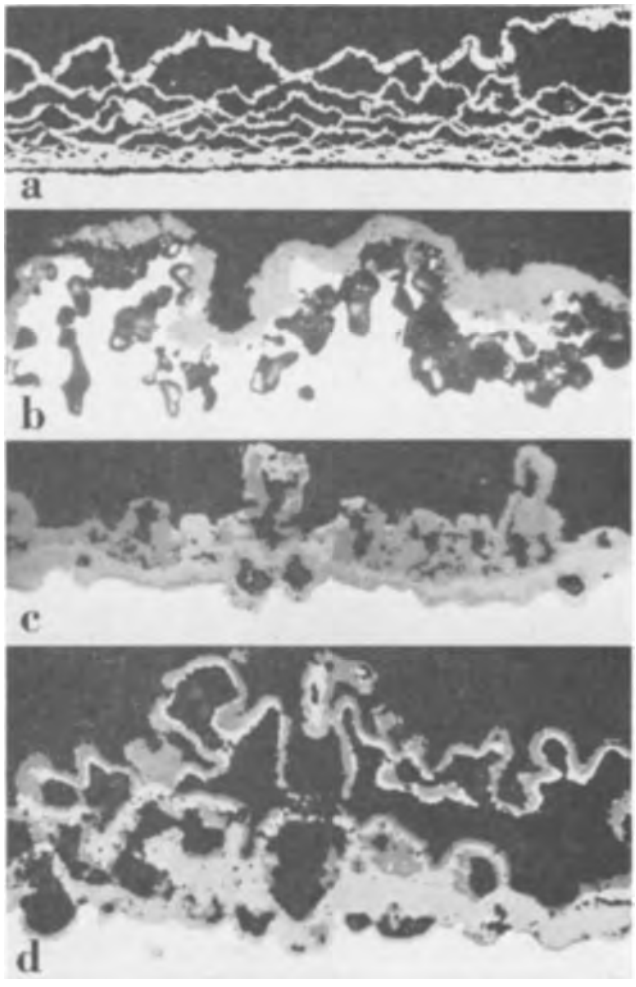

Fig. 10. Sections through Cr, Fe-26Cr-0.5Si and Fe-26Cr-1Mn oxidized at 1090°, illustrating irregular scale structures. (a) electropolished Cr, 21 hr. (Black gap between metal and scale is artifact.) Magnification 200X. (b) etched Fe-26Cr-0.5Si, 117 hr; islands of internal oxide in metal are mainly silica. Magnification 800X. (c) etched Fe-26Cr-1Mn, 20 hr (curve 22). Darker oxide is spinel; lighter oxide is M_2O_3. Magnification 800X. (d) electropolished Fe-26Cr-1Mn, 20 hr (curve 25). Darker oxide is spinel; lighter oxide is M_2O_3. Magnification 800X.

The increase in rate of oxidation due to electropolishing, which was observed with Cr and Fe-26Cr binary alloy, also occurs with Fe-26Cr-0.5Si, Fe-26Cr-1Mn, and type 446. For all five materials the initial reaction rate is faster after electropolishing than after etching, and all five show early breaks or waves after electropolishing [Fig. 9(b) inset] but not after etching [Fig. 9(a) inset]. The two alloys containing Mn oxidize faster than the others.

Scale structures are shown in Fig. 10. Highly irregular layers are formed. The multiple layers of Cr_2O_3 in Fig. 10(a) correspond directly to the segments of the Cr oxidation curve of Fig. 9(b). In the Fe-26Cr-0.5Si alloy, Si oxidized preferentially to form silica islands or subscale [Fig. 10(b)] below the outer layer of $(Cr,Fe)_2O_3$. Mn also oxidizes preferentially but forms a $MnO{\cdot}Cr_2O_3$ spinel (10) [Fig. 10(c), 10(d)] at the expense of some of the $(Cr,Fe)_2O_3$.

Discussion

The general oxidation behavior of the Fe-26Cr alloy is similar to that of Cr in regard to scaling rate and general topography of the scale.[1] Both of these are markedly affected by stress formation in the oxide and the prior chemical preparation of the surface, particularly electropolishing. All five specimen materials show a faster initial oxidation rate after electropolishing. [Pure Fe, on the contrary, oxidizes at the same rate whether electropolished or etched (11).] The compressive stress generated in the oxide leads to wrinkling and separation of the scale and to distortion and roughening of the surface metal.

[1] It is not unreasonable that Cr and Fe-26Cr should exhibit similar oxidation behavior since the 74% Fe content changes the system surprisingly little. The alloy is a substitutional solid solution, b.c.c. like Cr, and of nearly identical lattice parameter. The only oxide phase formed is the solid solution of rhombohedral $(Fe,Cr)_2O_3$ containing less than 3% Fe_2O_3 and indistinguishable in lattice parameter from the rhombohedral Cr_2O_3 on Cr. A spinel phase would develop between metal and $(Fe,Cr)_2O_3$ if preferential oxidation were to deplete the surface metal below 13% Cr (2) but no spinel was detected by x-ray diffraction. Attempts to produce spinel in short runs at high temperature, where depletion might be a maximum, were unsuccessful. In one instance spinel did form after a very long, hot run (500 hr at 1200°) when no baffle crucible was used to suppress volatilization of Cr oxide: boils of spinel as large as 3 mm were found at the bottom (upstream) corners where Cr depletion would be greatest.

Scaling Mechanism

The scaling mechanism proposed for Fe-26Cr is closely allied to that deduced for the oxidation of Cr. To account for the observed compressive flow it appears necessary to infer, as with Cr, that oxygen diffusion participates in film growth causing oxide to form below the oxide/gas boundary. Since evidence exists that Cr diffuses in the rhombohedral oxide on Fe-Cr alloys (2), it is assumed that both cations and anions participate in the diffusion process. Thus the zone of oxide formation is within the body of the growing oxide, reasonably accounting for the observed compressive stress.

Plastic flow of the oxide layer on the etched specimens induces extensive deformation in the adherent surface metal. The consequent rugged oxide/metal interface is observed at temperatures as low as 870° (Fig. 2) and at 1200° the effect is sufficient to cause gross deformation of the specimen (Fig. 5). With pure Cr, adhesion between oxide and metal appeared to be weaker since less flow of the metal surface was observed. The explanation for this is not known but some speculations are possible. The hot strength of

metal and oxide will be decreased by the presence of Fe. This will not only make the metal more readily deformable but will facilitate subsidence of the oxide on to the retreating metal to lessen loss of adhesion. Adhesion would be improved further by collapse of pores via plastic flow of the oxide and annihilation of cation vacancies at suitable sinks, *e.g.*, by dislocation climb. The effect of Fe on the defect structure of the oxide is unknown. If anion diffusion becomes relatively favored, as in α-Fe_2O_3, the zone of stress generation would shift toward the oxide/metal interface. Greater metal creep would then be expected. Whatever the reason, the result observed is a very rugged metal surface and peaked edges.

With the alloy, enhancement of diffusivity due to stress and continuing plastic strain is not directly apparent as was the case with Cr where nodule formation was explained in this way. Nevertheless, it is reasonable to assume its existence because the oxides are similar and stress so apparent. The effect of enhanced diffusivity on reaction kinetics should be a maximum initially and decrease progressively as the reaction rate slows.

The early waves in the E.P. oxidation curves can also be explained by the development of compressive stress. The fastest oxidation rate, hence the highest rate of stress generation, is with an electropolished specimen at the start of a run. Stress relief by creep normal to the surface will then be least effective and the stress can come to exceed the force of adhesion between oxide and metal. As a result, the oxide layer blisters away from the metal. A contributing or perhaps alternative cause of loss of adhesion is the higher rate of arrival at high oxidation rate of cation vacancies at the metal/oxide interface which may decrease adhesion by condensing into pores. The scaling process can continue in spite of separation between oxide and metal by transfer of Cr at points of contact and as vapor through the vacuum of the gap (1). Whereas with Cr the blistered layer could persist unbroken for 100 hr or more, with Fe-26Cr it fails in 2 hr or less, creating the early waves. The earlier failure might be because the oxide has lower hot strength than pure Cr_2O_3 or because the vapor pressure of Cr for the alloys is too low, especially after the metal surface becomes depleted in Cr. When the blistered layer perforates at some point, oxygen at 1 atm rushes into the vacuum gap and a second layer of oxide begins on the bare metal; the second layer does not blister because the surface on which it forms is no longer electropolished. The cause of the E.P. effect is believed to be related to the prior oxide produced during electropolishing having a higher concentration of lattice defects or of leakage paths for easy diffusion. This same speculation was proposed for pure Cr.

Oxidation Kinetics

The electropolished specimens are not considered because of the mechanical failure of the blistered first layer. The photomicrographs have shown that the oxide formed on the etched specimens is highly irregular with a rough outer surface, nonuniform thickness, rugged oxide/metal interface and containing blisters, pores and islands of metal. The effective area differs from the geometric area, not all the oxide participates in the protective process, and these factors change nonsystematically with time. As a result, meaningful analysis of the oxidation kinetics is not possible. It is surprising that the oxidation curves, at least of the etched specimens, are so smoothly well-behaved and the reproducibility as good as it is; apparently, despite so many processes operating simultaneously, local events are on a fine enough scale not to perturb the weight-gain/time record perceptibly.

Plotted on parabolic coordinates, $(\text{weight})^2$ *vs.* time, the oxidation curves generally are concave downwards. Possible reasons for this type of deviation from normal parabolic behavior are some oxide being nonparticipating, increasing cavity formation, loss of Cr oxide by volatilization, and improvement of the barrier by sintering; if, as postulated previously, plastic deformation resulting from compressive stress enhances diffusion, the effect would decrease as the reaction slows with time.

Double log plots of the oxidation data (log W *vs.* log t) yield good straight lines, in some cases over the entire time period of 0.1 to 100 hr, with slopes indicating values of n (in the relation $W^n = kt$) usually less than 3 and as low as 2.3 ($n - 2$ for parabolic). Nevertheless, this treatment has even less significance than the parabolic plot. The markedly nonideal character of the barrier layer precludes a systematic treatment and renders derivation of rate constants and consequent activation energies pointless. With Cr it was possible to estimate a local rate constant from areas on the metallographic cross sections where short lengths of ideal barrier layer could be found (1); no such areas of smooth, single-layer, nonporous oxide appeared on the alloy.

Moisture

The companion runs in wet oxygen demonstrate as with Cr that moisture does not significantly change the protectiveness of the M_2O_3 scale. This is in contrast to earlier observations on commercial stainless steels where gross increases and decreases were found depending on alloy type (12, 13). Much of the differences were due to mechanical factors: the huge breaks were obviously the result of separation and cracking of the barrier layer. Certainly moisture can be expected to change the sinterability of the oxide and hence affect plastic deformation and cracking. But increased plasticity cannot explain all the results. The moisture effect still is unexplained.

Other Alloys

In the ternary alloys, Si and Mn both oxidize preferentially and form second oxide phases. The silica formed under the $(Cr,Fe)_2O_3$ scale on the Fe-26Cr-0.5Si alloy does not develop into a continuous layer and for this reason has no appreciable effect on oxidation resistance. The protectiveness of the $(Cr,Fe)_2O_3$ layer is not affected. If the Si content were higher or the experimental conditions different, a continuous layer could form and isolate the Cr oxide from the substrate (12). The oxidation resistance would be increased temporarily until mechanical failure of the isolated layer occurred and rapid oxidation resumed.

The Fe-26Cr-1Mn ternary and the 446 stainless alloy, also containing Mn and 26% Cr, scale more rapidly than Cr, Fe-26Cr and Fe-26Cr-0.5Si. The $MnO \cdot Cr_2O_3$ spinel forms as a continuous layer, in part replacing the $(Cr,Fe)_2O_3$. The reaction rate is higher because diffusion is faster in the spinel (10) and also because Mn promotes excessive blistering, hence nonparticipating oxide.

Summary

The wrinkled and blistered oxide layers, peaked corners and roughened metal surface indicate that compressive stresses develop continually in the growing oxide. This points to anion diffusion as one of the processes contributing to film growth, resulting in a zone of formation of new oxide within the oxide layer. The consequent compressive stress causes the oxide and metal to deform plastically, creating highly irregular structures and mechanical failure of the barrier layer.

The nonuniformity of the scale structure interferes with the analysis of the reaction kinetics even when smooth oxidation curves are obtained. No rate constants or activation energies were deduced. The several complicating factors, including porosity, nonparticipating oxide, unknown effective area and varying oxide thickness, themselves change nonsystematically with time. If diffusion is enhanced by the continuing plastic flow, as is believed, diffusion coefficients in the oxide also would slow with time.

The oxide formed on Fe-26Cr is the same as the Cr_2O_3 formed on Cr except for a minor Fe content, and the oxidation rates are similar. Addition of 0.5% Si to Fe-26Cr leads to the formation of silica islands under the $(Fe,Cr)_2O_3$ layer but has no appreciable effect on the oxidation resistance. Fe-26Cr-1Mn and type 446, both containing Mn, form spinel layers as well as M_2O_3 and show greater weight gains. Mn is apparently deleterious in oxidation-resistant Fe-Cr alloys.

The oxidation of Fe-26Cr is highly sensitive to surface preparation. The initial rate is especially rapid after electropolishing. The three other Fe-26Cr alloys and Cr behave similarly. As a result the oxide layer blisters away from the metal surface, fails mechanically and a second layer forms below. Corresponding irregularities appear in the oxidation curves.

Moisture appears to have no effect on the oxidation resistance of Fe-26Cr except that it enhances the volatilization of Cr oxide thus thinning the layer and decreasing the weight gain but increasing the amount of metal consumed.

For best results in the utilization of high temperature alloys which rely on Cr for oxidation resistance it should be advantageous to prepare the metal surface carefully, arrange moderate oxidation conditions for the first exposure, and avoid gas flows that would aggravate oxide evaporation. Mn should be avoided; no doubt certain other alloying additives would be beneficial.

Acknowledgment

The authors are grateful to Mrs. Alma Harvey for skillful assistance with the oxidation experiments and Mr. P. E. Beaubien for the metallography.

Manuscript received Dec. 14, 1964. This paper was presented at the Washington Meeting, Oct. 11-15, 1964. Any discussion of this paper will appear in a Discussion Section to be published in the December 1965 JOURNAL.

REFERENCES

1. D. Caplan, A. Harvey, and M. Cohen, *Corrosion Science*, **3**, 161 (1963).
2. A. U. Seybolt, *This Journal*, **107**, 147 (1960).
3. A. U. Seybolt, *Advan. Phys.*, **12**, 1 (1963).
4. O. Kubaschewski and B. E. Hopkins, "Oxidation Metals and Alloys," p. 236, Butterworths, London (1962).
5. D. Lai, R. J. Borg, M. J. Brabers, J. D. MacKenzie, and C. E. Birchenall, *Corrosion*, **17**, 357t (1961).
6. G. C. Wood, *Corrosion Science*, **2**, 173 (1962).
7. D. Caplan, A. Harvey, and M. Cohen, *This Journal*, **108**, 134 (1961).
8. D. Caplan and M. Cohen, *ibid.*, **108**, 438 (1961).
9. R. K. Di Cerbo and A. U. Seybolt, *J. Am. Ceram. Soc.*, **42**, 430 (1959).
10. D. Caplan, P. E. Beaubien, and M. Cohen, submitted to the Metallurgical Society of AIME (1964).
11. D. Caplan and M. Cohen, *Corrosion Science*, **3**, 139 (1963).
12. D. Caplan and M. Cohen, *J. Metals*, **4**, 1057 (1952).
13. D. Caplan and M. Cohen, *Corrosion*, **15**, 141t (1959).

Studies on the Oxygen Gradients in Oxidizing Metals

III. Kinetics of the Oxidation of Zirconium at High Temperatures

J. P. Pemsler

Ledgemont Laboratory, Kennecott Copper Corporation, Lexington, Massachusetts

ABSTRACT

The oxidation of zirconium was studied in the temperature range 840°-1100°C. Film growth and oxygen solution processes were separated experimentally. Oxygen solution obeys diffusion kinetics and remains parabolic for sufficiently thick samples. Film growth does not obey normal rate laws; an exceedingly rapid initial rate is followed by a period of slower growth. The over-all weight gain curve is explained in terms of the separate film growth and oxygen solution processes. At temperatures $\geq$975°C voids form in the oxide; they act as diffusion blocks and promote formation of a duplex layer. The mechanism of void formation is discussed in terms of a condensation of oxygen vacancies. The effect of orientation, pressure, surface preparation, and initiation temperature are discussed.

The kinetics of the oxidation of zirconium has been extensively investigated over a wide range of temperatures. Authors variously report the rate as cubic transforming to linear or parabolic transforming to linear. There are relatively few measurements at high temperatures where oxygen dissolution in the metal represents a significant quantity of the total oxygen absorbed. The high-temperature data are for the most part of short duration and exhibit poor reproducibility from sample to sample. High-temperature studies have in general relied on thin coupons which are not amenable to long term observation of the kinetics for two reasons: (i) Spalling and cracking at the edges after relatively short times prevents accurate assessment of the weight gains; and (ii) the meeting of the oxygen gradients in the center of the sample alters the rate of dissolution of oxygen in the metal, so that the kinetic curve is dependent on the thickness of the sample.

There has been only one group of investigators which has attempted to separate quantitatively the contributions of film thickness and oxygen dissolution to the kinetics of the high-temperature process. Wallwork, Smeltzer, and Rosa (1) oxidized 2 mm-thick zirconium coupons for times up to 200 hr at 850°C. They report that both the oxide film and over-all weight gain conform to parabolic kinetics. Rosa and Smeltzer (2) oxidized similar samples for times up to 100 hr at 950°C. They report that after an initial deviation both oxide film thickness and total weight gain conform to parabolic kinetics.

In a recent investigation (3) the author has shown that the oxygen gradient beneath the oxide film on zirconium oxidized at high temperatures may be measured experimentally and is in good agreement with values from a theoretical expression involving the diffusivity, time, and oxide film thickness. Furthermore, it was noted that with coarse grained samples the oxide film thickness at 850°C did not conform to a parabolic rate of growth, but rather grew at a very rapid rate for the first several hours, and thereafter, at a greatly reduced rate.

It is the purpose of this work to attempt: (i) to obtain accurately and reproducibly kinetic data for the oxidation of zirconium at high temperatures for long periods of time; (ii) to separate quantitatively the film growth and oxygen dissolution processes; and (iii) to investigate the mechanism of the film growth process.

Experimental

The zirconium used in this investigation was obtained in the form of 1.9 cm diameter rod, and the analysis is given in Table I. Spheres of 1.74 cm diameter were machined from the rod with a tolerance of 25μ on the diameter. The spherical shape was chosen to eliminate the effects of edges and corners as a source of initiation of oxide failure and spalling. Furthermore, the spherical shape enables precise calcula-

Table I. Analysis of zirconium rod

Element	ppm
C	115
N	30
O	850
Fe	480
Cu	13
Ni	7
Cr	95
Mn	6

Table II. Vendor's analysis of oxygen

Element	ppm
Ar	15
CH_4	15
Kr	10
Xe	4
CO_2	7
H_2O	6
N_2	2

tion of the quantity of oxygen dissolved in the metal; the situation is far more complex with other sample shapes such as parallelopipeds where gradients from different directions overlap.

Spheres were etched in an aqueous solution of 50% nitric and 5% hydrofluoric acids, rinsed, dried, and suspended by a thin platinum wire in an Ainsworth continuous recording semi-microbalance of 0.01 mg sensitivity and 400 mg weight gain capacity. The balance was evacuated, and the sphere was annealed for 1 hr at the temperature at which the oxidation was to take place. After annealing, the furnace was removed and the sample allowed to cool to room temperature. High-purity grade oxygen whose analysis is given in Table II was then admitted to the sample tube and the furnace repositioned around the sample tube. A continuous record of the weight gain was obtained throughout the course of the oxidation. In the two runs of less than 1 hr at 910°C, the oxygen was admitted while the sample was at temperature in order to define the exposure time more precisely. At the conclusion of the oxidation run spheres were removed from the balance, imbedded in bakelite mounts, and machined to within 0.25 mm of the diameter. A final polish for 60 sec on a napless cloth was used to prevent rounding of the oxide film. Photographs of the oxide film were taken at suitable magnification at eight areas equidistant around the circumference of the circle of polish. The thickness of the oxide film at each area was obtained from the photographs by measuring the area of the oxide film with a planimeter.

Since the diffusion coefficient of oxygen in zirconium is highly temperature dependent, and at the temperatures under consideration in this study the quantity of oxygen dissolved in the metal represents a considerable portion of the total oxygen absorbed, it is necessary to control and measure the temperature accurately. The initial experiments at 840°C were performed using a rate-proportioning galvanometer controller. In this instance the temperature varied by ±2.5° from the control point. In subsequent experiments at higher temperatures, a 1 mv potentiometric controller with an external solid-state zero suppression reference together with a proportioning current adjuster were used to control the temperature of the furnace. A calibrated measuring thermocouple placed along side of the suspended zirconium sphere and read on a 670 μv full-scale potentiometric recorder was used to monitor the temperature continuously throughout the course of the oxidation. The controlling and recording thermocouples were led directly to an automatic ice-point reference system and thence to the controller and recorder. During the course of the oxidations temperatures were maintained constant to better than ±0.5°C.

Diffusion Equations

Below α/β transformation.—Calculation of the oxygen gradients beneath the film on oxidized metals necessitates the solution of a moving interface diffusion problem with the oxidation rate as a boundary condition. The solution to this problem for the case of alpha zirconium has been derived elsewhere (3, 4).

The oxygen concentration C at a distance x from the oxide/metal interface is given by the expression

$$C = C_s \frac{\operatorname{erfc}(x/2\sqrt{D_\alpha t})}{\operatorname{erfc}(s/2\sqrt{D_\alpha t})} \quad [1]$$

where C_s is the oxygen concentration in zirconium coexisting with ZrO_2, D_α is the diffusion coefficient of oxygen in zirconium at the experimental temperature, s is the distance of the oxide/metal interface from the position of the initial surface, and $x = x' + s$.

Integration of Eq. [1] gives the total quantity of oxygen present in the metal beneath the oxide film

$$M = 2C_s\sqrt{D_\alpha t}\left[\frac{\exp(-s^2/4D_\alpha t)}{\sqrt{\pi}\operatorname{erfc}(s/2\sqrt{D_\alpha t})} - \frac{s}{2\sqrt{D_\alpha t}}\right] \quad [2]$$

where M is the quantity of oxygen dissolved in the metal per unit area of surface.

The use of spherical samples necessitates the solution of the above case in spherical coordinates. In a sphere of radius a with an initial oxygen concentration of zero, the boundary conditions are

$$C = 0 \text{ at } r > 0, t = 0 \quad [3]$$

and

$$C = C_s \text{ at } r = a - s \quad [4]$$

where s is defined as above.

The concentration C at a distance r from the center of the sphere is given by

$$C = C_s \frac{1 + \frac{2a}{\pi r}\sum_{n=1}^{\infty}\frac{(-1)^n}{n}\sin\left(\frac{n\pi r}{a}\right)\exp\left[-\frac{D_\alpha n^2\pi^2 t}{a^2}\right]}{1 + \frac{2a}{\pi(a-s)}\sum_{n=1}^{\infty}\frac{(-1)^n}{n}\sin\frac{n\pi(a-s)}{a}\exp\left[-\frac{D_\alpha n^2\pi^2 t}{a^2}\right]} \quad [5]$$

Integration of Eq. [5] gives the total quantity of oxygen contained in the metal sphere of radius $a-s$ beneath the oxide film.

$$M = C_s \frac{\frac{4}{3}\pi(a-s)^3 + \sum_{n=1}^{\infty} 8\pi(-1)^n\left(\frac{a}{n\pi}\right)^3\left(\sin\frac{n\pi(a-s)}{a} - \frac{n\pi(a-s)}{a}\cos\frac{n\pi(a-s)}{a}\right)\exp\left[-\frac{D_\alpha n^2\pi^2 t}{a^2}\right]}{1 + \frac{2a}{\pi(a-s)}\sum_{n=1}^{\infty}\frac{(-1)^n}{n}\sin\frac{n\pi(a-s)}{a}\exp\left[-\frac{D_\alpha n^2\pi^2 t}{a^2}\right]} \quad [6]$$

The necessity of performing summations makes the equation most conveniently evaluated by computer methods.

The diffusion coefficient of oxygen in alpha zirconium has been measured by the author (5) and subsequently by several additional authors (6-9). The value in the alpha phase is considered to be known with high accuracy and expressed by

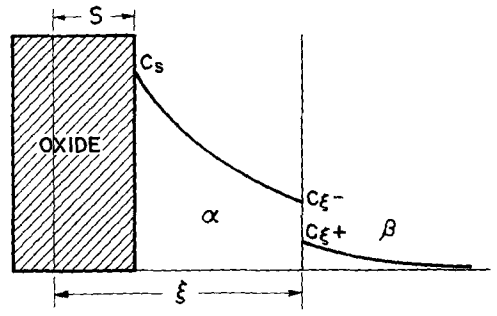

Fig. 1. Schematic diagram of zirconium oxidized at temperatures above the α/β transition temperature.

$$D_\alpha \text{cm}^2/\text{sec} = 5.2 \exp[(-50{,}800 \pm 870)/RT] \quad [7]$$

The saturation value of oxygen in alpha zirconium coexisting with zirconia was taken as $C_s = 0.456$ g/cm^3 (10, 11). The quantity of metal s consumed in generation of an oxide film of thickness l was taken as $s = 0.666l$.

For spheres of 1.74 cm diameter oxidized at 840°C, the value of M calculated for a sphere from Eq. [6] was about 4% less than values for a semi-infinite sample as calculated from Eq. [2].

Above α/β transformation.—Oxygen is a strong alpha stabilizer and at temperatures above the α/β transformation (862°C) a more complex situation exists, as shown in Fig. 1. Beneath the oxide film there exists a solution of oxygen in alpha zirconium for a distance ξ from the original metal interface, until an oxygen concentration of $C_{\xi-}$ is reached. At this position there is a plane of discontinuity where the concentration falls to $C_{\xi+}$, the saturation value of oxygen in the body centered cubic β zirconium. Thereafter, the concentration falls to a value of C_0, the initial oxygen content of the metal. The boundary conditions for a semi-infinite sample are expressed as

$$C = C_0 \text{ at } x > 0\ t = 0 \quad [8]$$

$$C = C_s \text{ at } x = s\ t > 0 \quad [9]$$

$$C = C_{\xi+} \text{ at } x = \xi - 0 \quad [10]$$

$$C = C_{\xi-} \text{ at } x = \xi + 0 \quad [11]$$

The particular integrals satisfying Eq. [8] through [11] are

$$C_\alpha = C_s + \frac{(C_s - C_{\xi-})\left[\text{erf}\left(\frac{s}{2\sqrt{D_\alpha t}}\right) - \text{erf}\left(\frac{x}{2\sqrt{D_\alpha t}}\right)\right]}{\text{erf}\left(\frac{\xi}{2\sqrt{D_\alpha t}}\right) - \text{erf}\left(\frac{s}{2\sqrt{D_\alpha t}}\right)} \quad [12]$$

and

$$C_\beta = \frac{C_{\xi+}\left[\text{erfc}\left(\frac{x}{2\sqrt{D_\beta t}}\right)\right]}{\text{erfc}\left(\frac{\xi}{2\sqrt{D_\beta t}}\right)} \quad [13]$$

The mass flow across the boundary ξ is given by

$$(C_{\xi-} - C_{\xi+})\frac{d\xi}{dt} = -D_\alpha\left(\frac{\partial C}{\partial x}\right)_{\xi-0} + D_\beta\left(\frac{\partial C}{\partial x}\right)_{\xi+0} \quad [14]$$

where D_α is the diffusion coefficient of oxygen in alpha zirconium and D_β is the diffusion coefficient in beta zirconium.

Setting $\gamma = \xi/2\sqrt{Dt}$ and $\phi = D_\alpha/D_\beta$, and integrating Eq. [14] we obtain

$$C_{\xi-} - C_{\xi+} = \frac{C_s - C_{\xi-}}{\left(\text{erf}\gamma - \text{erf}\frac{s}{2\sqrt{D_\alpha t}}\right)\gamma\sqrt{\pi}}\exp[-\gamma^2] - \frac{C_{\xi+} - C_0}{\gamma\sqrt{\pi\phi}\,\text{erfc}\,(\gamma\phi^{1/2})}\exp[-\gamma^2\phi] \quad [15]$$

from whence ξ can be calculated.

The total quantity of oxygen contained in the alpha and beta phases are obtained by integrating Eq. [12] and [13], respectively.

$$M_\alpha = C_s(\xi - s) + \frac{C_s - C_{\xi-}}{\text{erf}\left(\frac{\xi}{2\sqrt{D_\alpha t}}\right) - \text{erf}\left(\frac{s}{2\sqrt{D_\alpha t}}\right)}\left[(\xi - s)\,\text{erf}\left(\frac{s}{2\sqrt{D_\alpha t}}\right) - \xi\,\text{erf}\left(\frac{\xi}{2\sqrt{D_\alpha t}}\right) - \frac{2\sqrt{D_\alpha t}}{\sqrt{\pi}}\exp\left[-\frac{\xi^2}{4D_\alpha t}\right] + s\,\text{erf}\left(\frac{s}{2\sqrt{D_\alpha t}}\right) + \frac{2\sqrt{D_\alpha t}}{\sqrt{\pi}}\exp\left[-\frac{s^2}{4D_\alpha t}\right]\right] \quad [16]$$

$$M_\beta = \frac{C_{\xi+}\,2\sqrt{D_\beta t}}{\sqrt{\pi}}\,\frac{\exp\left[-\frac{\xi^2}{4D_\beta t}\right]}{\text{erfc}\left(\frac{\xi}{2\sqrt{D_\beta t}}\right)} - C_{\xi+}\xi \quad [17]$$

The increase in the quantity of oxygen in the metal during oxidation is then equal to the amount of oxygen in the alpha phase plus the amount in the beta phase minus the initial oxygen content.

$$M = M_\alpha + M_\beta - \frac{4}{3}\pi a^3 C_0 \quad [18]$$

No attempt was made to solve Eq. [16] directly for the spherical case. The oxygen content of the alpha phase M_α was evaluated for a semi-infinite sample from Eq. [16] and the result decreased by 4% (see above) to correct for spherical geometry. The evaluation of M_β for the sphere is analogous to the evaluation of M according to Eq. [6], where now s is replaced by ξ, and computer methods used.

Values of C_s, D_α, and s are obtained as in the preceding section. Values of D_β are obtained from the work of Mallett *et al.* (6).

$$D_\beta = 0.0453 \exp[(-28{,}200 \pm 2400/RT)] \quad [19]$$

and are known only to within about a factor of two.

Values of $C_{\xi-}$ were estimated from the phase diagram (10, 11) and are probably correct to within a 30% error. Since it was difficult to estimate values of $C_{\xi+}$ from the phase diagram, it was determined experimentally at one temperature. A cylinder 0.5 cm in diameter x 1.5 cm long was oxidized at 967°C for 64 hr, after which the oxygen concentration at the center was calculated to be $0.69C_{\xi+}$. The oxide film and alpha phases were machined from the sample and the remaining transformed β-phase analyzed for oxygen. The value of $C_{\xi+}$ at 967°C was obtained in this manner, and values at the other temperatures were estimated by assuming that values of $C_{\xi+}$ are linear with temperature near the transformation temperature (in agreement with the shape of the phase diagram). Values of D_β, $C_{\xi+}$, and $C_{\xi-}$ are listed in Table III.

Table III. Values used in diffusion calculations

Temp, °C	D_β, cm^2/sec	$C_{\xi+}$, g/cm^3	C_{ξ}, g/cm^3
910	2.80×10^{-7}	0.0105	0.0435
975	5.22×10^{-7}	0.0210	0.0790

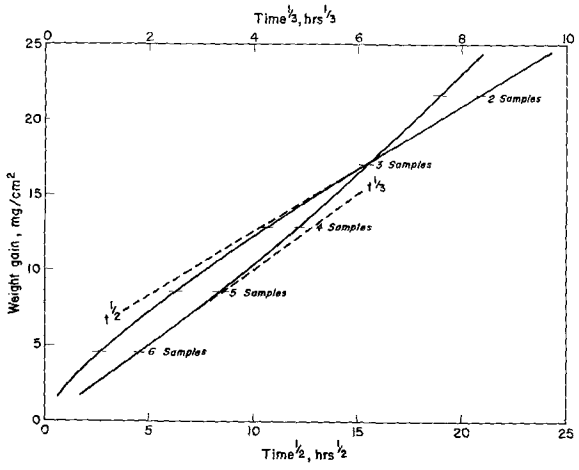

Fig. 2. Total weight gain of zirconium oxidized at 840°C

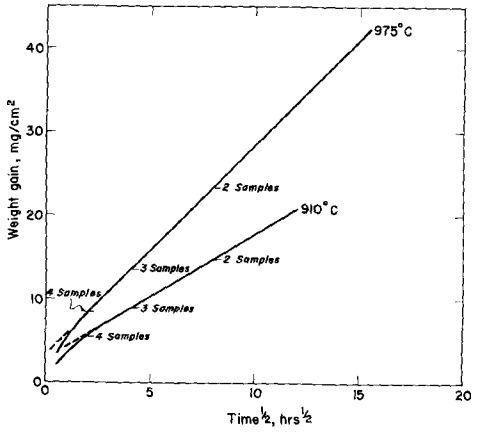

Fig. 3. Total weight gain of zirconium oxidized at 910° and 975°C

Results and Discussion

Weight gain.—Data for the total weight gain at 840°, 910°, and 975°C are given in Fig. 2 and 3. Data at 840°C are presented in the form of both parabolic and cubic plots. Solid lines indicate the continuous weight gain curves, and dashed lines represent extrapolation of parabolic and cubic portions. The reproducibility of the data was excellent, and all sample points fall within the breadth of the line representing the data. Since samples were to be used for further measurements, separate experiments were concluded at varying periods of time; therefore, the data presented in Fig. 2 are derived from seven samples for a duration of 7 hr, six samples for a duration of 40 hr, etc., as indicated on the figure. It is apparent from examination of this figure how a discrepancy may arise in reporting high-temperature kinetic data in terms of parabolic and cubic rates. The rate conforms quite well to a cubic relationship up to about 80 hr after which it bends off toward the ordinate, indicating that the weight gain rate is now more rapid than that represented by a cubic relationship. It should be noted that the cubic curve extrapolates well through the origin. Furthermore, if the data are plotted on logarithmic coordinates, which by their nature emphasize the early time data, a straight line is obtained whose slope equals 0.375, close to the cubic value. Investigators who performed experiments for times not far beyond 80 hr at this temperature would be inclined to report their data as conforming to a cubic relationship.

Examination of the parabolic plot indicates that there is a rapid initial weight gain which does not conform to the parabolic law, and only after about 150 hr does the weight gain increase parabolically. One would have to ignore a large initial portion of the curve to conclude that the weight gain data obeys a parabolic behavior. In any case further analysis will show that the total weight gain curve has little theoretical significance since the total weight gain curve is the sum of the film growth and oxygen dissolution processes which themselves have different rate behaviors.

Table IV. Oxide film thickness for various times at 840°, 910°, and 975°C

	Time, hr	$\Delta x_a \pm d_a$, μ	Min-Max, μ
840°C	7.0	20.1 ± 0.7	18-21
	40.0	29.8 ± 0.8	28-31
	113.0	38.0 ± 1.2	35-40
	234.0	44.9 ± 1.0	44-47
	435.0	52.7 ± 1.1	52-56
	601.5	59.8 ± 0.8	58-63
910°C	0.25	10.9 ± 0.3	9-13
	0.75	13.9 ± 0.3	12-15
	4.0	19.3 ± 0.3	17-21
	17.0	25.8 ± 0.4	23-28
	63.7	35.1 ± 0.5	33-38
	146.0	43.7 ± 0.7	42-47
975°C	4.0	25.9 ± 0.5	21-35
	16.7	30.7 ± 1.2	26-39
	63.7	42.8 ± 1.7	36-49
	237.5	67.1 ± 5.9	60-71

Δx_a is average oxide thickness; d_a is average deviation from mean; Min is minimum oxide thickness; Max is maximum oxide thickness.

Data at 910° and 975°C are also highly reproducible and are presented in Fig. 3 as parabolic plots. At these temperatures the region of conformity to cubic kinetics is small so that no cubic plot is given. After relatively short times, representing however considerable weight gains, the total weight gain curves conform closely to parabolic rates. The reason for this will become clear in the following sections where the separate processes are analyzed.

Oxidation behavior was also investigated at 1025°, 1050° and 1100°C, but no total weight gain curves were obtained since the capacity of the continuous weighing balance was exceeded after relatively short periods of time.

Film thickness.—Data for the growth of oxide films at 840°, 910°, and 975°C are presented in Table IV and Fig. 4. At 840° and 910°C the films are of relatively uniform thickness, differing by a maximum of 3-5μ at different areas. At 975°C the oxide/metal interface becomes irregular and the films differ in thickness by 10-15μ from point to point (see section on Metallography). Very little difference exists between the rate of growth of oxide at 840° and 910°C; however, at 975°C the film grows appreciably more rapidly than at 910°C.

Data at the two lower temperatures where the oxides appear dense and pore-free are presented in parabolic cubic, and quartic form in Fig. 5. The parabolic plot is inadequate at both short and long times; conformity begins at about 4 hr and ends at about 100 hr at these temperatures. The cubic plot fits the data quite well except for times less than about 4 hr. The quartic

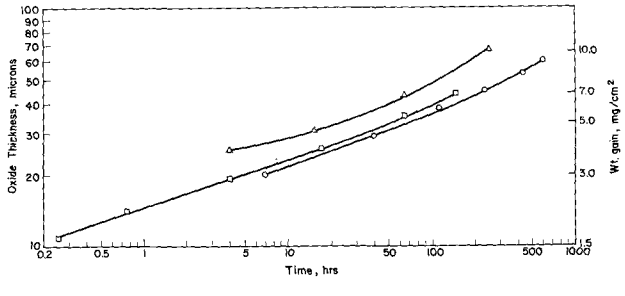

Fig. 4. Logarithmic plot of the oxide film growth on zirconium oxidized at 840° (○), 910° (□), and 975° (△).

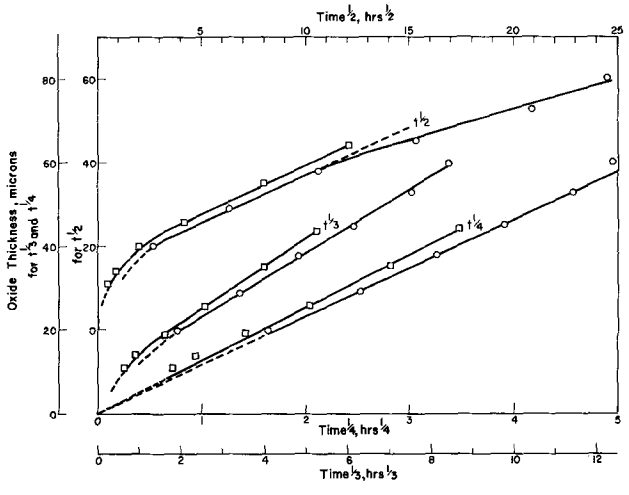

Fig. 5. Parabolic, cubic, and quartic plot of oxide film growth on zirconium oxidized at 840° (○) and 910°C (□).

plot appears to conform to the data rather well even at very short times with the exception of the last point at 840°C for 600 hr, which is slightly above the line. Figure 5 should however at this time remain an exercise in curve fitting, since quantitative information on the structure and transport properties through the oxide is necessary in order to understand, rather than rationalize, the data which does not conform to any established rate law. A qualitative explanation for the rapid initial growth followed by a slower growth will be offered in the section on Mechanism.

Data for growth at 1025°, 1050°, and 1100°C are presented in Table V. The rate of film growth continues to increase greatly at these higher temperatures. At 1025°C the oxide/metal interface becomes highly irregular and the oxide thickness varies by a factor of two to three from place to place. Little additional growth is observed between 16 and 77 hr. At 1050°C after the first 5 hr the film is of fairly uniform thickness, and irregularity commences by 18 hr. At 1100°C there was widespread localized attack in the vicinity of the platinum support wires. The thickness of the unaffected areas was relatively uniform.

Oxygen in the metal.—A knowledge of the total weight gain and measurement of the oxide film thickness enables the computation of the quantity of oxygen dissolved in the metal substrate beneath the oxide film. Furthermore, the latter quantity can be calculated according to Eq. [6] for temperatures below the α/β transformation and by Eq. [16], [17], and [18] above the α/β transformation. Calculated and experimental data for oxygen dissolved in the metal below the α/β transformation are plotted as a function of the square root of time in the lower curve in Fig. 6. Here the solid line represents calculated values, and separate experimental points are indicated in the figure. At 840°C

Table V. Oxide film thickness for various times at 1025°, 1050°, and 1100°C

	Time, hr	Δx_{Max}, μ	Δx_{Min}, μ
1025°C	4.0	90	45
	16.3	125	45
	77.2	125	60
1050°C	5.3	190	180
	18.5	380	250
	64.0	630	250
1100°C	31.0	650	610

Δx_{Max} is maximum oxide thickness; Δx_{Min} is minimum oxide thickness.

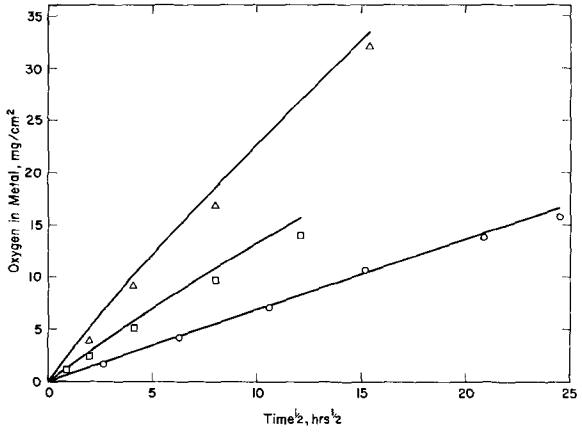

Fig. 6. Oxygen in solution in zirconium oxidized at 840° (○), 910° (□), and 975°C (△).

Fig. 7. Zirconium sphere oxidized for 17 hr at 975°C showing α/β phase boundary. Magnified approximately 60X; polarized light.

there is excellent agreement between calculated and observed oxygen content of the metal. Data are parabolic as demanded by diffusion theory.

Metallographic examination of samples oxidized above the α/β transition temperature clearly reveals the position of the α/transformed β boundary (Fig. 7). Measurement of the distance of the α/transformed β boundary from the oxide/metal interface and the previously evaluated oxide thickness enables calculation of the parameter ξ. It is also possible to calculate ξ from Eq. [15]. However, uncertainties in the values of $C_{\xi+}$, $C_{\xi-}$, and D_β do not permit the calculation of ξ with great accuracy, and a comparison of observed and calculated values of ξ is not too rewarding. For example, examination of a sample oxidized for 64 hr at 910°C gave an observed value of $\xi = 5.54 \times 10^{-2}$. Calculation using maximum and minimum estimates of $C_{\xi+}$, $C_{\xi-}$, and D_β gives values ranging from 4.88×10^{-2} to 5.60×10^{-2}.

Agreement between calculated and experimental data at 910° and 975°C as shown in Fig. 6 are not as good as at 840°C. This may be due to two factors: (*a*) As discussed above there are appreciable uncertainties in the values of the solubility parameters at the α/β interface and the diffusion coefficient of oxygen in the β-phase; and (*b*) the formation of voids at the metal/oxide interface (see section on Metallography) may act as discontinuities in the Zr/ZrO_2 diffusion couple so that the flow of oxygen to the metal is interrupted.

The calculated curve at 910°C is initially linear when plotted against $t^{1/2}$, and then curves downward toward the abscissa. This is due to the fact that after about 50 hr the gradients in the β-phase meet at the center of the sphere, thereafter slowing down the rate of ab-

sorption of oxygen into the β-phase. The calculated curve at 975°C is again initially linear with $t^{1/2}$ representing a maximum rate of diffusion. After a few hours at this temperature, the gradients begin to meet in the center of the sphere causing the line to bend toward the abscissa. Shortly thereafter, the β-phase becomes saturated with oxygen, and the rate again becomes parabolic representing the increase of oxygen in the α-phase.

Kinetics.—Having previously examined the film growth and oxygen diffusion kinetics, we are now in a position to understand the over-all weight gain curves as a summation of the two separate processes. In the initial stages the rapid film growth coupled with oxygen dissolution gives rise to an approximately cubic rate of growth. As the reaction proceeds, the rate of film growth decreases markedly, and the relative quantity of oxygen in the metal compared with oxygen in the film increases. Since the oxygen dissolution process is parabolic, it is not surprising that at longer times the over-all kinetics tends toward a parabolic process. Furthermore, the activation energy for the dissolution process is much higher than for oxide growth so that at the higher temperatures the oxygen dissolution process represents a larger part of the over-all weight gain. Consequently, the time necessary to approach parabolic kinetics decreases with increasing temperature.

It must be borne in mind that the depth of oxygen penetration into the sample is quite appreciable at these temperatures and the thickness and geometry of the specimen are exceedingly important in determining the shapes of the kinetic curves. A thin sample may rapidly become saturated with oxygen, and the film growth will then be paramount in determining the kinetics. Conversely, a thick sample will continue to dissolve oxygen at a parabolic rate, while the film growth will proceed comparatively slowly.

At the temperatures under consideration in this study the over-all kinetic curve is of little theoretical significance. The oxygen dissolves in the metal according to diffusion theory, and its contribution to the over-all kinetics is entirely predictable according to equations previously discussed. It remains then to understand the film growth law in terms of the structure and transport properties of the film.

Metallography.—The film formed at 840°C appears dense and adherent and exhibits a fine, columnar structure. In all samples except the one with the longest exposure time there was no evidence of cracking in the oxide or accelerated growth. However, the sample exposed for 601.5 hr developed several thin lines of white oxide around the circumference of the sphere. The fine cracks probably develop due to the accumulation of stresses caused by the oxide growth. This process may be enhanced by thermal cycling, and a specimen with a thick oxide film which has been rapidly cooled and reheated to temperature in oxygen shows a network of such cracks around the sample.

Careful examination of the structure of the sound film formed at 840°C indicates some difference in the structure of the oxide near the oxide/metal interface compared with the oxide further out toward the oxide/gas interface. In order to reveal this more clearly it is necessary to polish perpendicular to the fine columnar grains so that they are viewed in the direction of growth. This is best achieved on a spherical sample by polishing at the circumference through the oxide film until the metal is just reached. In addition, appreciable magnification of the oxide is achieved since this technique is similar to polishing a flat oxide at a low angle. Examination of the sample prepared in this manner indicates that the outer oxide consists of a somewhat coarser structure than the fine inner oxide.

The oxide film formed on samples exposed at 910°C is quite similar to that observed on the samples formed at 840°C. The oxide again appears dense and adherent. Differences in structures of the outer and inner oxide are more pronounced at 910° than at 840°C.

At 975°C the duplex nature of the scale becomes more pronounced than at lower temperatures. After the initial exposure (4 hr), voids are visible at the oxide/metal interface; at later times they become buried in the oxide by further growth, while new voids continue to originate at the metal/oxide interface (Fig. 8-11). These voids act as diffusion blocks preventing further oxidation of metal below them and necessitate that further oxidation occur around them. Voids also appear to enhance the tendency toward formation of the duplex oxide layer. Beyond the voids toward the oxygen/oxide interface, there are ovals of oxide with a milky white appearance under polarized light; the fine columnar structure is retained between the void and oxide/metal interface. The whitening of the oxide may be logically explained by the action of the void in preventing access of the oxide above it to the demand for oxygen from the oxide and metal below it. The nonstoichiometric oxide would then tend to be oxidized toward the stoichiometric composition by oxygen from the gas phase.

The presence of second phase particles in the metal enhances the formation of voids, and a Zr-0.5 w/o (weight per cent) B alloy containing particles of ZrB_2 exhibits void formation at temperatures as low as 840°C. At higher temperatures voids selectively nucleate at the second phase particles.

At 1025°C after the first exposure time of 4 hr the film is highly irregular and contains many voids. The duplex oxide layer becomes quite pronounced. By 16 hr the oxide whitens appreciably, and by 77 hr the entire oxide appears milky white.

At 1050°C after the first exposure of 5 hr, the film is quite uniform in thickness. There appears to be a distribution of fine voids throughout the oxide, but it

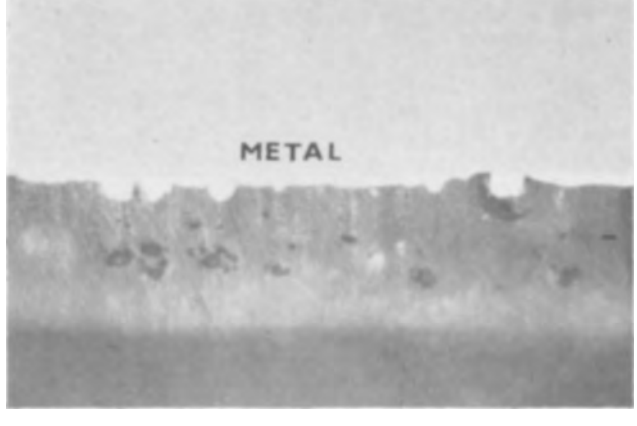

Fig. 8. Zirconium sphere oxidized for 64 hr at 975°C showing voids at metal/oxide interface and in the oxide. Magnified approximately 525X; bright light.

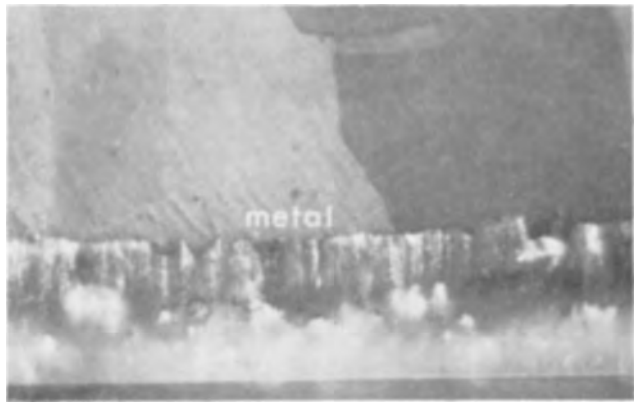

Fig. 9. Same as Fig. 8 but viewed under polarized light.

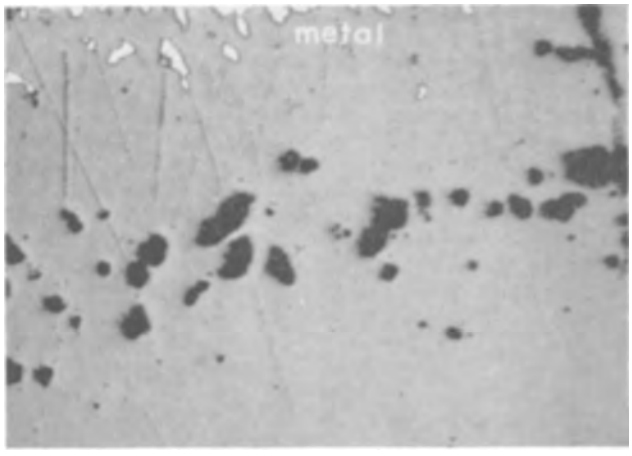

Fig. 10. Perpendicular taper section of sample in Fig. 8. Bright light. Areas of metal near the top of the picture are due to an irregular metal/oxide interface combined with a tapering polish.

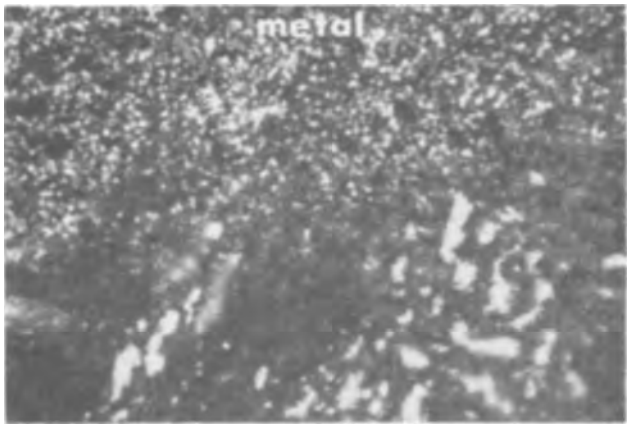

Fig. 11. Same as Fig. 10 but viewed under polarized light

is difficult to be certain of this due to the tendency of the columnar grains of oxide to be pulled out during polishing. There is no evidence of the development of the larger voids or the duplex layer characteristic of samples oxidized at lower temperatures. However, by 18.5 hr the oxide has become irregular, larger voids are forming at the metal/oxide interface, and there is a tendency toward the formation of a duplex layer. Several areas of accelerated oxidation due to gross cracking of the oxide were observed. After 64 hr areas of accelerated oxidation were widespread. In other areas the oxide consisted of a duplex oxide containing voids.

At 1100°C after an exposure of 31 hr, accelerated attack occurred in those areas where the sample was in contact with the platinum support wire. In other areas the oxide was uniform in thickness and as yet showed no tendency toward large void formation or a duplex layer.

Various authors have noted that the onset of accelerated oxidation at high temperatures is accompanied by the formation of a duplex layer. It appears on the basis of this work that the development of the duplex layer is gradual and dependent on time and temperature. At 840° and 910°C for the times investigated in this study, the duplex layer appears to be developing slowly. Voids are not observed, but their presence on a micro scale is not precluded and may even be inferred by the early stages of duplex layer development as observed. Accelerated corrosion at these temperatures appears to be due to gross cracks developing in the oxide film. At higher temperatures and simultaneous with the appearance of voids in the oxide film, the duplex layer undergoes a more rapid development. The development of stoichiometric ZrO_2 as an outer

Table VI. Effect of pressure on oxide thickness on ½ in. spheres oxidized for 64 hr at 910°C

Pressure, Torr	Average thickness and deviation, μ	Maximum, μ	Minimum, μ
1	35.5 ± 0.6	36.5	34.8
14	35.1 ± 0.6	36.0	34.0
100	36.3 ± 1.0	38.5	35.2
730	37.3 ± 0.7	39.2	35.9
730*	35.1 ± 0.5	36.0	34.4

* ¾-in. sphere.

layer is accompanied by an accelerated growth of the total oxide. It therefore appears that the outer stoichiometric layer becomes nonprotective.

Orientation effect.—The thickness of the oxide film formed on coarse grained zone refined zirconium oxidized at 910°C for 64 hr was found to vary somewhat from grain to grain. The variation of the oxidation rate of zirconium with orientation has been reported previously (3). Its persistence to the thick film region is noted in this study. Variation of thickness with orientation is much less pronounced for zirconium than for hafnium (12). In the latter case wide deviations from stoichiometry have been noted in those grains oxidizing more slowly. Thus, the oxidation rates may involve unequal rates of formation of vacancies from crystal faces of different orientations. This phenomenon is under further investigation in this laboratory using single crystal material.

Pressure.—One-half inch diameter spheres were oxidized at 910°C for 64 hr at pressures ranging from 1 to 730 Torr. Results of the oxide thickness measurements are given in Table VI which includes the average value, average deviation, and maximum and minimum values at each pressure. For comparison, data from the ¾ in. diameter sphere is listed. The variation in thickness from sample to sample appears to be within the experimental reproducibility, so that pressure in the range investigated does not affect the oxidation rate.

Surface preparation.—In order to determine the effect of surface preparation on film growth and total weight gain, spherical samples were oxidized in both the as-machined condition and as shot-blasted with fine-grit sand. Samples were oxidized at 840°C for 24 hr. The weight gain curve paralleled those of the chemically polished samples, but the ordinate was displaced higher by several per cent. Metallographic examination indicated that, with the exception of small protrusions at the surface, the oxide thickness was identical with that observed on chemically polished samples. The differences in weight gain must then be due to the small protrusions from the irregular surface which were oxidized during the initial stages of the oxidation. Therefore, at 840°C for times beyond the initial stages of the reaction, it does not appear that the surface treatment has any effect on the kinetics. However, the possibility cannot be excluded that at much later stages of oxidation the surface irregularities may act as sites for initiation of cracks in the film.

Initiation temperature.—Experiments were performed to determine whether there is an effect of exposing the sample to oxygen while at temperature as opposed to the technique used in nearly all of these experiments of allowing the sample to cool before admitting oxygen. At 840°C beyond the very early stages of the reaction (~15 min), the weight gain curves were identical.

Mechanism.—Zirconium dioxide exhibits a complex dependence of conductivity on oxygen partial pressure (13, 14). Conduction is considered to be largely ionic with n-type conductivity predominating at low oxygen partial pressures ($<10^{-20}$ atm) such as would exist within a sound oxide film growing on the metal substrate. Oxygen vacancies and possibly interstitials

are believed to be the mobile species. At higher oxygen partial pressures ($>10^{-8}$ atm) such as would be encountered in a cracked ZrO_2 film, the p-type oxide may predominate (14), and cation migration cannot be excluded.

The oxidation process is generally pictured as occurring by the formation of an oxygen ion vacancy at the metal/oxide interface

$$Zr_{(metal)} = Zr^{+4}{}_{(s)} + 2\square_{O}{}^{=} + 4e^{-}$$

where $Zr_{(metal)}$ represents a zirconium atom in the metal lattice, $Zr^{+4}{}_{(s)}$ represents a Zr^{+4} ion on a lattice site in the oxide, and $\square_{O}{}^{=}$ represents an oxygen ion vacancy in the oxide lattice. The electrons may be bound to the oxygen vacancy, present as a defect associated with $Zr^{+3}{}_{(s)}$ ions, or mobile in the lattice. In order for oxidation to proceed, $\square_{O}{}^{=}$ and electrons must diffuse through the oxide to the oxygen/oxide interface where they are consumed in the reaction

$$O_2 + 2\square_{O}{}^{=} + 4e^{-} = 2O^{=}{}_{(s)}$$

where $O^{=}{}_{(s)}$ is an oxygen ion in the oxide lattice.

It is suggested here that the formation of voids at the metal/oxide interface encountered during oxidation at the higher temperatures of this study ($\geqslant$975°C) may be considered to result from a condensation of oxygen vacancies. It is also possible that at 840° and 910°C voids are forming on a microscale too fine to be viewed with optical microscopy. These voids may act as diffusion blocks preventing the access of oxygen ions to the metal/oxide interface, thereby retarding the oxidation rate.

In the initial phase of oxidation the film is forming at an exceedingly rapid rate, leading to a highly defect-rich oxide. As time passes, the oxygen vacancies may cluster and eventually condense to form voids. This may occur most readily at the oxide/metal interface or at an inclusion if it is present to aid the nucleation. One then may consider oxidation to occur through an oxide containing blocked diffusion paths. At the higher temperatures where the voids occur on a gross scale, oxidation of the outer oxide toward the stoichiometric value becomes more complete, and the duplex layer more pronounced. The near stoichiometric outer layer is apparently nonprotective. This may be due to the fact that a p-n junction may develop within the oxide at the meeting of the two oxide layers. The outer scale may then allow migration of Zr^{+4} ions which could account for its lack of protectiveness.

Any theory explaining the oxidation of zirconium and hafnium must account for the orientation dependence of the oxidation rate in the thick film region. For this reason, studies using single crystal material have been initiated in this laboratory. Further work on the structure and transport within the oxide films is also in order.

Acknowledgment

The author is again indebted to J. K. Litchfield for experimental assistance and suggestions through the course of this study; thanks are expressed to E. J. Moreau for extensive metallography. Valuable discussions on the diffusion equations were held with Drs. A. L. Loeb, S. H. Gelles, and G. Kemeny, and on nonstoichiometry with Dr. G. G. Libowitz.

Manuscript received Nov. 12, 1964. This paper was presented at the Washington Meeting, Oct. 11-15, 1964.

Any discussion of this paper will appear in a Discussion Section to be published in the December 1965 JOURNAL.

REFERENCES

1. G. R. Wallwork, W. W. Smeltzer, and C. J. Rosa, *Acta. Met.*, **12**, 409 (1964).
2. C. J. Rosa and W. W. Smeltzer, *ibid.*, **13**, 55 (1965).
3. J. P. Pemsler, *This Journal*, **111**, 381 (1964).
4. J. P. Pemsler, *J. Nuclear Materials*, **7**, 16 (1962).
5. J. P. Pemsler, *This Journal*, **105**, 315 (1958).
6. M. W. Mallett, W. M. Albrecht, and P. R. Wilson, *ibid.*, **106**, 181 (1959).
7. M. Davis, K. R. Montgomery, and J. Standring, *J. Inst. Metals*, **89**, 172 (1961).
8. G. Sainfort, R. Jacquesson, and P. Laurent, "Colloquium on Diffusion in the Solid State," C. E. N. Saclay (1958), North Holland Publishing Co.
9. J. N. Chirigos, "The Use of Microhardness in the Determination of the Diffusivity of Oxygen in Alpha Zirconium," Report WAPD-TM-306 (1962).
10. R. F. Domagala and D. J. McPherson, *Trans. AIME*, **200**, 238 (1954).
11. E. Gebhardt, H.-D. Seghezzi, and W. Dürrschnabel, *J. Nuclear Materials*, **4**, 255 (1961).
12. J. P. Pemsler, *This Journal*, **111**, 1339 (1964).
13. P. Kofstad and D. J. Ruzicka, *ibid.*, **110**, 181 (1963).
14. N. M. Tallan, *J. Am. Ceram. Soc.*, **47**, 635 (1964).

Tantalum Films Deposited by Asymmetric A-C Sputtering

F. Vratny and D. J. Harrington

Bell Telephone Laboratories, Incorporated, Murray Hill, New Jersey

ABSTRACT

The new technique of asymmetric a-c sputtering has been evaluated for the deposition of tantalum films in argon, oxygen-argon, and nitrogen-argon gas mixtures. This method utilizes a lower sputtering potential on the tantalum substrate holder every half cycle compared to the potential on the tantalum cathode. At an optimum current ratio, tantalum films of three to five times that of bulk resistivity are obtained compared to twenty to forty times bulk resistivity for normal d-c glow discharge sputtering. The reactive sputtering experiments confirm that the normal high resistivity of sputtered tantalum films are caused by impurities gettered during the deposition and that the greater tolerance to reactive gas pressure with asymmetric a-c sputtering may be due to ion and electron bombardment during deposition. Further work is required to confirm this latter supposition.

Present methods for the deposition of tantalum films rely upon evaporation methods (1, 2), *i.e.*, electron beam evaporation, or d-c sputtering from a tantalum cathode (3-6). With some exceptions, the sputtering technique when used with initial background pressures of 10^{-6} Torr produces films with specific resistivities of 100 to 300 μ-ohm-cm and temperature coefficients of resistance in the range of $\pm$200 ppm/°C (7). The high resistivity in sputtered films is indicative of 5-10 a/o (atomic per cent) of oxygen impurity (6) assuming the latter is the prime component gettered during deposition. Evaporated films have been obtained with

values of 15 μ-ohm-cm and +3000 ppm/°C (1, 2, 3, 8) under conditions of ultra high vacuum and/or very high deposition rates. By careful control over sputtering variables it has been possible to obtain sputtered films with resistivities of only 50 μ-ohm-cm and temperature coefficients of +1500 ppm/°C (4, 6) although the basic criteria for obtaining such films routinely have not been rigorously established.

The advent of asymmetric a-c sputtering (9-11) offers the possibility of obtaining routinely tantalum films of high purity without the necessity of ultra high vacuum techniques. Frerichs (9-11) reported that superconducting tantalum films were obtained with a transition region from 4.45° to 4.3°K, compared to a value of 4.38°C for bulk tantalum. The purity of the film was ascribed to argon bombardment of the surface of the sample and a decrease in rate of incorporation of residual gases from the vacuum system.

The sputtering of tantalum has provided an important method of preparing thin film components and integrated circuits (12-14) especially when utilized with reactive gases to deposit a tantalum nitride film. The asymmetric a-c sputtering technique could provide a means of obtaining relatively pure films which would serve as a reproducible starting material for reactive sputtering, provided reactive gas molecules can be incorporated in the film under asymmetric a-c deposition conditions. A comparison of the properties of films prepared by reactive sputtering both with a normal d-c and the asymmetric a-c method should provide a pertinent test of the proposed method of purification.

Method

Asymmetric a-c sputtering is performed by applying a partially rectified 60 cycle a-c potential to two identical tantalum electrodes. The substrate is placed on the electrode with the lower bombarding potential. In anology with the geometry used for film deposition in normal d-c sputtering, the latter electrode, the substrate electrode, will be designated the anode in this paper. With a completely symmetrical voltage wave form, the anode and cathode collect equal numbers of energetic argon ions, and no net deposition occurs. However, by using a smaller average potential (E_2) at the substrate electrode (see Fig. 1) more tantalum arrives from the cathode than can be removed by ion bombardment at the anode. Concurrent with the ion motion in the plasma there is also electron transport. This is indicated by curve C which represents the inverse of curve B. Thus, if curve B represents the field affecting the ion density at the substrate and B' represents the field affecting the ion density at the cathode, then curve C represents, respectively, the field affecting the electron density at the cathode while C' represents the field affecting the electron density at the substrate. Frerichs (9) reported that a favorable degree of asymmetry is a cathode to anode current ratio of five to ten. To obtain a wide range of anode to cathode current ratio a supply was used with silicon rectifiers and a variable resistance (R) in one arm of a bridge network (Fig. 2). The output from a high-voltage transformer is placed across the anode and the current limiting network which in turn is connected to the cathode. The cathode current I_c, is controlled by the

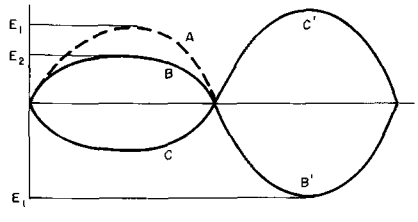

Fig. 1. A typical cathode wave form: (A) normal; (B) asymmetric, cathode potential, E_2 less E_1; (C) substrate potential.

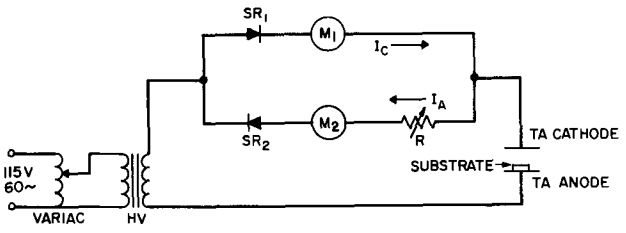

Fig. 2. Asymmetric a-c power supply. SR1, SR2, high voltage diodes; M1, Mw, milliammeter; R, variable resistance 2K to 1 meg; HV, high voltage transformer 10 kv.

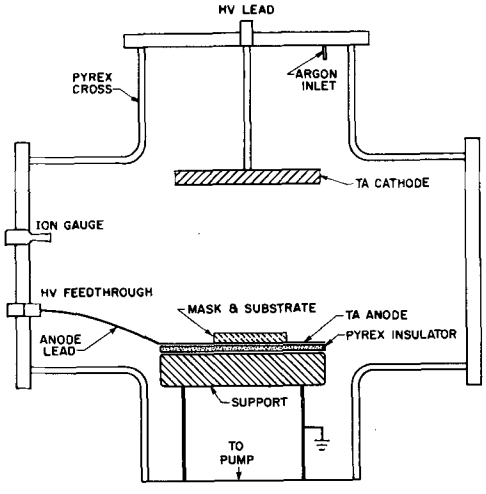

Fig. 3. Schematic of the sputtering chamber

plasma impedance and a small resistive drop across the diodes while the anode current, I_A, is diminished further by the resistance, R. By varying the resistance, R, a range of anode to cathode current ratios (I_A/I_c) is obtained of approximately 0.05 to 0.35.

The cathode and anode were high-purity tantalum plates 4 in. in diameter and ¼ in. thick. These were mounted in a 6 in. ID "Pyrex-cross" sputtering chamber (Fig. 3). The cathode was suspended from a high voltage feedthrough while the anode was mounted on a Pyrex spacer. All experiments were performed at a cathode potential of 4 kv and a cathode current density of 0.25 ma/cm^2 at an argon pressure of 20 x 10^{-3} Torr. Tantalum was deposited on 1 by 3 in. Corning 7059 glass through mechanical masks covered by a thin layer of tantalum. These substrates were cleaned by a succession of washes in detergents, water, hydrogen peroxide, and deionized water. They were dried in a nitrogen stream at 110°C and placed in the vacuum chamber. The system was evacuated by means of a 300 l/sec diffusion pump with a liquid nitrogen cooled baffle. An ultimate pressure of 2 x 10^{-6} Torr and a nominal leak rate of 0.05 1 atm/sec are typical for this machine. Tantalum films with specific resistivities of 150-200 μ-ohm-cm and temperature coefficients of resistance of ±200 ppm/°C are conventionally produced by d-c sputtering in this system

Results

In the process of asymmetric a-c sputtering argon ion bombardment occurs at both the cathode and anode. If we consider the two extreme cases, it is evident that for an identical potential at both electrodes there will be no deposition at the anode, yet due to the high intensity of ion bombardment this condition will produce the maximum cleaning at the surface. Correspondingly, for normal d-c cathode sputtering the deposition rate will be large at the anode, yet due to minimal bombardment, the substrate will be ineffectively cleaned. Between these two extremes there is a compromise of effective deposition and cleaning. To

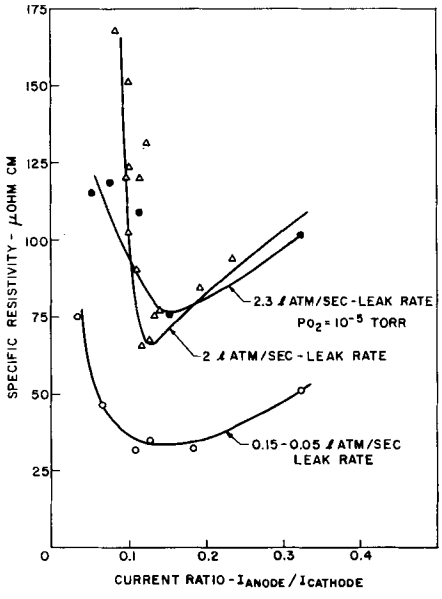

Fig. 4. Specific resistivity as a function of current ratio

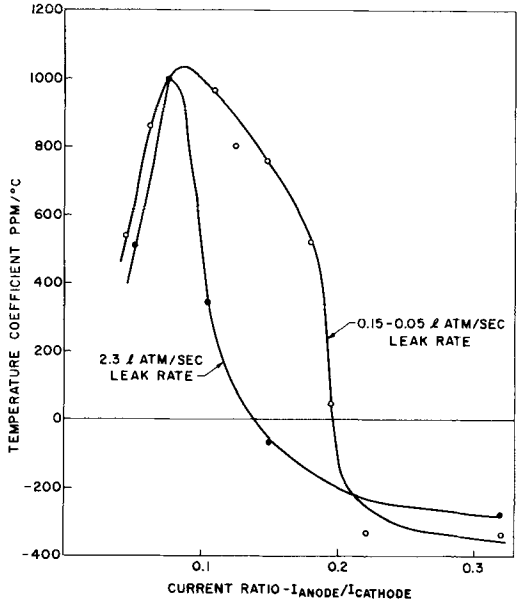

Fig. 5. Temperature coefficient of resistance as a function of current ratio.

explore this method of sputtering, the deposition rate, resistivity, and temperature coefficient of tantalum films were evaluated as a function of the current ratio to determine the optimum conditions. Due to the direct correlation between resistivity and impurity level (6) the specific resistivity can also be used as an indication of the purity of the deposited film.

The measured deposition rate, using a constant cathode potential of 4 kv (rms) was a direct function of the current asymmetry ratio. The sputtering pressure was 20μ while the pressure before sputtering was typically $\sim 2 \times 10^{-6}$ Torr. At an anode to cathode current ratio of 0.25 the deposition rate was ~30 Å/min, and at a current ratio of 0.1 it was ~60 Å/min. Further data indicated that a linear correlation exists between the deposition rate and the difference in power (Δw, in watts) supplied to the cathode and anode (Eq. [1]).

$$\text{Deposition rate (Å/min)} = 5.1\ (\pm 0.6)\ (\Delta w) - 100\ (\pm 10) \quad [1]$$

This equation shows that for a constant flux of tantalum atoms arriving from the cathode, less tantalum remains deposited on the substrate with increasing power supplied to the anode. This result tends to confirm that bombardment-sputtering occurs at the anode with increasing current ratio.

The increased bombardment at the anode reflects itself in increased purity of the resultant tantalum film as manifested in the resistivity and temperature coefficient of resistance despite the lower deposition rate. The resistivity drops to a minimum value with increasing current ratio from 0 to 0.15 (Fig 4) while further anode current beyond a ratio of 0.15 causes an increase in resistivity. The resistivity change at a background pressure of $\sim 2\text{-}5 \times 10^{-6}$ Torr (0.05 to 0.15 liter-atm/sec virtual leak) from 200 μ-ohm-cm for d-c sputtering to a minimum of ~37 μ-ohm-cm represents a change from ~10 a/o oxygen to ~3 a/o oxygen if the change in resistivity is due to this impurity (6). The increase in resistivity with anode current ratio above 0.15 will be discussed later.

The change in resistivity with increasing current ratio to ~0.15 exhibits a sensitivity to residual impurities in the vacuum system. At a leak rate of residual gases of ~2 liter-atm/sec the resistivity minimum corresponds to ~65 μ-ohm-cm while a deliberate oxygen leak rate of 10^{-5} Torr (2.3 liter-atm/sec) gives a nearly identical current ratio profile with a resistivity minimum at ~75 μ-ohm-cm. The temperature coefficient of resistance of these films similarly exhibits a sensitivity to the current ratio and gaseous impurity (Fig. 5). It is noteworthy that the maxima in the temperature coefficient curve occur at a lower current ratio than the minima in the resistivity curve. This difference indicates that the film properties that determine the resistivity and temperature coefficient have a different dependence on the anode-cathode current ratio.

It is evident that the ability to obtain low resistivity films by this technique is a function of the level of the residual gases in the system during sputtering. Thus, it is possible to sputter reactively by this method. The main advantage of this technique is that it provides a reproducible low resistivity film as a starting point for the controlled modification of its electrical properties. During reactive sputtering it would have the effect of diluting the contribution of undesired reactive gases in the system An evaluation of the process of reactive sputtering and a study of the quality of the resultant film components have been carried out. Gerstenberg (6) and Pendergast (15) have prepared tantalum nitride and tantalum oxide films. The tantalum oxide films exhibit a monotonic increase in resistivity with increasing oxygen content and a monotonic decrease in the temperature coefficient. The tantalum nitride films have a specific resistivity of 200 μ-ohm-cm which is nearly independent of the nitrogen partial pressure over a pressure range corresponding to the formation of the compound Ta_2N and TaN. In the same nitrogen partial pressure range, the temperature coefficient of resistance has a value of —50 to —100 ppm/°C. Due to the inherent leak rate of vacuum systems and other d-c deposition variables it has not been possible to completely reproduce the exact pressure dependence reported by Gerstenberg (6) although the Ta_2N and TaN phases always occur with approximately the same electrical properties.

Experiments were performed at varying nitrogen and oxygen partial pressure in argon to assess the suitability of the asymmetric a-c process for controlled deposition by reactive sputtering. Reactive sputtering was carried out at a current ratio of 0.13, a cathode potential of 4 kv and cathode current of 20 ma (~0.25 ma/cm^2) at an argon pressure of 20μ. Sputtering in oxygen-argon gas mixtures produced an increase in resistivity with increasing oxygen partial pressure (Fig. 6) for both the a-c and d-c technique. However, the resistivity is always lower at a given oxygen pressure in the a-c sputtering technique. As an example, at a background pressure of 2×10^{-6} Torr there is a re-

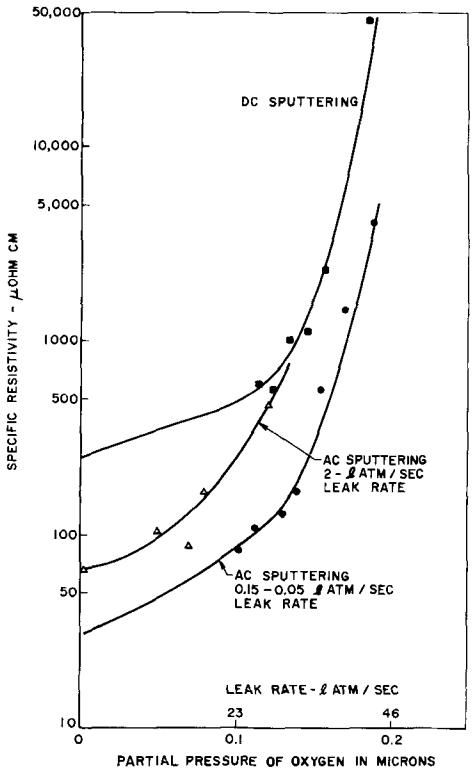

Fig. 6. Specific resistivity as a function of oxygen partial pressure

sistivity differential of ~200 μ-ohm-cm. This constitutes a decreased sensitivity to oxygen of 4-7 a/o (6). At higher oxygen pressures the curves tend to merge. This difference is also apparent in the temperature coefficient of resistance for these films. They are generally higher by 600 to 800 ppm/°C for the asymmetric a-c method (Fig. 7). Correspondingly, it was possible to sputter in argon-nitrogen gas mixtures and reproduce d-c results which were obtained only by using extreme care to control sputtering parameters and residual gases (see Fig. 8 and 9).

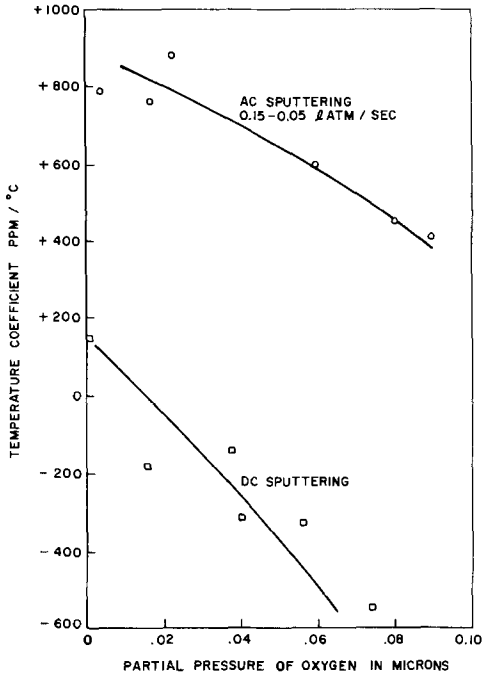

Fig. 7. Temperature coefficient of resistance as a function of oxygen partial pressure.

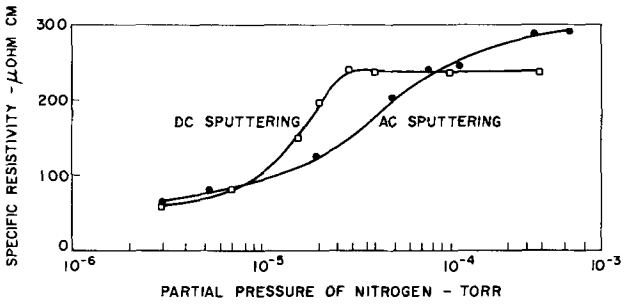

Fig. 8. Specific resistivity as a function of nitrogen partial pressure

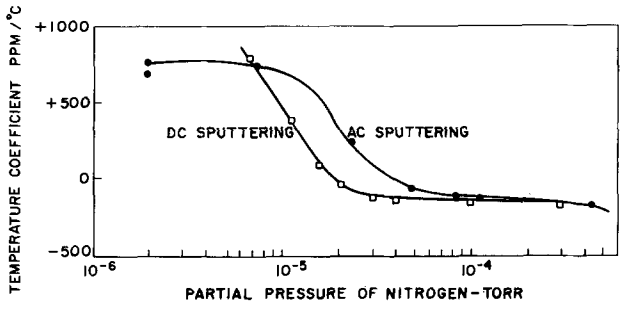

Fig. 9. Temperature coefficient of resistance as a function of nitrogen partial pressure.

Discussion

The basic model employed by Frerichs (9-11) to explain purification of films deposited by the asymmetric a-c sputtering technique is the argon ion bombardment of the film during deposition. The degree of cleaning given the depositing film on the anode is determined by the degree of current asymmetry. The latter factor establishes the ion flux to the surface while the energy and flux density of incident ions determines the probability of removal of matter from the film. An additional feature which we will consider below is the effect of electron bombardment of the substrate.

In considering a model of film cleaning by argon ion bombardment it is necessary to evaluate three factors: the probability of collision between the individual incident ions and impurity atoms; the fraction of energy available to an impurity atom as a result of collision; and the probability of desorption of an impurity atom. If we assume that an impurity atom has the same cross section as a tantalum atom, we can calculate the probability of collision between the incident ions and atoms on the surface. In this way we can obtain an estimate of the probability of reducing an impurity level (excluding secondary processes).

When tantalum is deposited at a rate of 50 Å/min, the arrival rate or the collision rate of tantalum is ~6 x 10^{14} at./sec/cm^2 while the impurity level at a background pressure of 10^{-6} Torr and 300°K is 3.6 x 10^{13} molecules/sec/cm^2 (taken for the case of oxygen[1]) with a sticking coefficient of 0.1. Although it is known that sticking coefficients can be as large as 1.0 for fresh reactive surfaces (17) and as small as 10^{-5} for dirty surfaces (18) or physically adsorbed states at high temperatures (19). For physically adsorbed states at modest temperatures or clean surfaces a sticking coefficient of 0.1 is a reasonable approximation (17, 19). For this sticking coefficient, the impurity level corresponds to about 12 a/o of monatomic oxygen which will be incorporated in the film. Thus, the total flux corresponds to 88% tantalum and 12% impurity. Since an impurity atom (as oxygen) which is present at low surface coverage will probably sit on a

[1] It is recognized that many residuals exist in conventional vacuum systems. In the system under consideration it is estimated that the residuals are made up of 20% oxygen, 60% nitrogen, 5% carbon as CH_4 and CO, 15% others. During deposition the oxygen level drops to a very low level, nitrogen drops by about 20% and the hydrogen level increases to ~10^{-6} Torr (16).

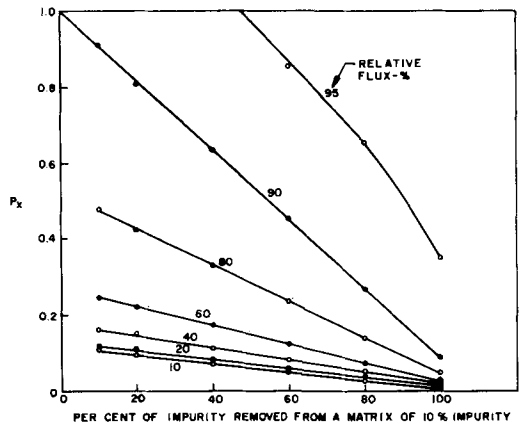

Fig. 10. Probability of surface cleaning as a function of relative incident flux.

tantalum lattice site there will be an equal probability of collision between an argon ion and either tantalum or oxygen assuming equal cross section. With the initial assumption that an impurity atom is the same size as a tantalum atom and occupies a random tantalum lattice site the probability of collision between an argon ion and surface impurity was calculated for a variable argon ion flux and for a constant surface density of 10% impurity atoms and 90% tantalum atoms (Fig. 10). The probability of collision between the argon ion flux and the surface density of impurity flux is large above a relative ion flux of 92% while the probability drops appreciably at lower flux densities. If the collision probability is interpreted in terms of removal then the probability of removal of 10% of the impurities, *i.e.*, reducing the total level from 10 to 9% is appreciable in the range of 95-100% relative ion flux, but decreases rapidly as the flux density decreases.

In addition to the collision probability it is necessary to consider the relative size of the impurity atom and tantalum as well as the probability of their removal. It is known that the relative cross section of oxygen and tantalum is quite different and that the cross section may vary with the energy of the incident ion (20). It may be estimated that at rest energy an oxygen ion has a larger relative cross section than tantalum by 5.45 (21). As a result, the collision probability would be larger by a proportionate factor. On impact, an argon ion is able to impart ~98% of its energy to an oxygen molecule while tantalum will receive roughly 59% of the energy of the incident argon ion as a result of momentum conservation in a diatomic collision. However, this energy is distributed in the lattice. It can be approximated that tantalum has a sputtering threshold between 25 and 30v (22) with reported values as large as 120v (23-25). The lattice surface displacement energy is ~4.79 ev (26) while oxygen on tantalum has a dissociation energy of roughly 9 ev (27). If the lattice energies and momentum conservation processes are interpreted in terms of sputtering yields, we can combine energy transfer and surface desorption effects and estimate (28) a relative sputtering ratio (S_O/S_{Ta}) of 0.78 with a range of 0.35 to 1.5 depending on the upper and lower limits of the threshold. If we include the relative cross section of oxygen and tantalum (5.45), we obtain a sputtering ratio S_O/S_{Ta} of 4.25 with a range from ~2.1 to 8.5, *i.e.*, oxygen desorption is more probable. When this is applied to the collision probability (Fig. 10) we may see that a 60% relative ion flux corrected by the above sputtering ratio will be as effective as 92% relative flux *i.e.*, a single projectile will be 4.25 times as productive on oxygen as on tantalum.

In establishing an argon ion flux to the sample, it is evident that argon can respond to the 60 cycle changes in the anode-cathode potential as it is able to traverse 8-16 cm (29-34) between these changes. The measured current ratio of anode current to cathode current then gives an indication of the relative degree of surface bombardment. In Fig. 4 we initially have 10 a/o impurities at a zero current ratio and 2-3 a/o at the resistivity minima or 70 to 80% removal of impurities. At this point the argon flux is ~1.5-3 x 10^{14} or 25-50% of the deposition flux. This corresponds to a collision probability with a 10% surface impurities coverage of ~0.1-0.42. When modified by the difference in sputtering yield this represents a probability of at least 0.2 but no more than 3 with a mean value of 0.8. This is a marginal proof of effective cleaning by argon bombardment for the most probable yield is less than one. Further, this model also requires a continuous improvement in resistivity at a higher asymmetry current ratio due to the enhancement of the argon ion density. However, we obtain an increase in the film resistivity at a higher anode current as seen by the rise in resistivity above a current ratio of 0.15.

Because of these anomalies we feel this deposition mechanism is inadequate. This may suggest a coexisting mechanism of argon incorporation at high argon ion flux density, for it is known that a bombarding particle will have an effective penetration depth from about 2 to 200 Å/kev (35). This produces incorporation of the neutralized species at a rate of 10^{14} to 10^{15} at./cm^2/kev (36) or between 1 and 10% of the deposition flux. Films analyzed for argon place the argon content in this range (37). This will reduce the effective electron mean free path and thus increase the resistivity and reduce the temperature coefficient. These factors are insufficient to explain the ability of the incident argon ion flux to clean the sample to the implied degree exhibited by the resistivity current-ratio profile of Fig. 4. An additional mechanism we wish to propose is the clean up by the presence of an intense electron flux at the substrate surface. It should be noted in Fig. 1 that as the potential alternates between the cathode and substrate the argon ion and electron flux density to the substrate also change. In the first half of the potential cycle, the argon ion flux to the substrate is low while the electron flux to the cathode is also low. In the latter half of the potential cycle the electron flux to the substrate is large while the argon ion flux to the cathode is also large. It is felt that the electron flux to the substrate contributes to an additional degree of cleaning. This phenomena has been observed by Peterman (38), Moore (39), and Redhead (40). Further work is in progress to clarify the deposition mechanism in asymmetric a-c sputtering (41).

Conclusions

Our results agree with earlier work which has demonstrated that deposition of thin films by asymmetrical a-c sputtering can lead to an improvement in film purity as demonstrated by the lower resistivity and higher temperature coefficients of resistance.

It was also pointed out that the background pressure has a pronounced effect on the ultimate purity of the deposited film. This was demonstrated by the variation in resistivity and temperature coefficient of resistance as a function of doping conditions.

It was proposed that the removal of these impurities is due to argon ion bombardment. This is suggested by the reduction in deposition rate which occurs at high anode currents. Secondary mechanisms are proposed to expand on this mechanism. One proposal was that the increase in resistivity at higher asymmetry ratio I_A/I_C is due to argon incorporation. A further proposal is that electrons which are generated in the plasma play a significant role in the deposition process.

It has been shown that deposition of thin films by a-c asymmetric sputtering can offer a reproducible base for controlled reactive sputtering. Evaluation of passive components prepared by this technique is presently in progress and appears to be favorable.

Manuscript received Sept. 29, 1964. This paper was presented at the Pittsburgh Meeting, April 15-18, 1964.

Any discussion of this paper will appear in a Discussion Section to be published in the December 1965 JOURNAL.

REFERENCES

1. J. F. Marchand and F. A. Venema, *Phillips Res. Repts.*, **14**, 427 (1959).
2. D. Gerstenberg and P. Hall, *This Journal*, **111**, 936 (1964).
3. R. W. Berry and D. J. Sloan, *Proc. IRE*, **47**, 1070 (1959).
4. C. Altman, 9th Proc. Amer. Vacuum Society (1962).
5. N. W. Silcox and L. I. Maisel, *This Journal*, **109**, 1151 (1962).
6. D. Gerstenberg and C. J. Calbick, *J. Appl. Phys.*, **35-2**, 402 (1964).
7. Landolt-Boernstein, Elektrische Eigenschaften I, Vol. II, No. 6, p. 4, Springer Verlag, Berlin (1959).
8. C. A. Neugebauer and R. A. Ekvall, *J. Appl. Phys.*, **35**, 547 (1964).
9. R. Frerichs, *ibid.*, **33**, 1898 (1962).
10. R. Frerichs and C. J. Kircher, Proc. 8th International Conf. on Low Temperature Physics, London, September, 1962.
11. C. J. Kircher, Late News Paper presented at the Pittsburgh Meeting of the Society, April, 1963; R. Frerichs and C. J. Kircher, *J. Appl. Phys.*, **34**, 3541 (1963).
12. D. A. McLean, *Wescon Conf. Proc.* 1959.
13. R. W. Berry and N. Schwartz, *Proc. Natl. Conv. Mil. Elect.*, **1960**, p. 214.
14. D. Gerstenberg and E. H. Mayer, *Proc. Elect. Comp. Conf.*, **1962**, p. 57.
15. W. Pendergast, Paper presented at the Pittsburgh Meeting of the Society, April 1963; Extended Abstracts.
16. J. Sosniak, Private communication
17. A. E. J. Eggleton, F. C. Tompkins, and D. W. B. Wanford, *Proc. Roy. Soc.*, **A213**, 266 (1952).
18. I. Langmuir, *J. Am. Chem. Soc.*, **37**, 1139 (1915).
19. Buritz, Varnerin, *Trans. Faraday Soc.*, 284 (1961).
20. J. B. Hasted, *Proc. Roy. Soc.*, **A205**, 421 (1951).
21. L. Pauling, "Nature of the Chemical Bond," Cornell University Press, (1959); *J. Am. Chem. Soc.*, **49**, 765 (1927); W. H. Achariasen, *Z. Krist.*, **80**, 137 (1931); M. L. Neuberger, *ibid.*, **83**, 1 (1936).
22. G. K. Wehner, Proc. 5th International Conf. on Ionization Phenomena in Gases, p. 1141 (1961).
23. G. K. Wehner, *Phys. Rev.*, **93**, 633 (1954).
24. G. K. Wehner, Sputtering Yield Data in the 100 to 600 e.v. Energy Range, General Mills Rept. #2309, July 15, 1962.
25. E. B. Henschke, *Phys. Rev.*, **121**, 1286 (1961).
26. R. L. Eager and D. B. Langmuir, *ibid.*, **89**, 911, (1953).
27. B. W. M. Trapnell, "Chemisorption P100," W. E. Garner, Editor, Butterworth (1957).
28. R. S. Pease, *Scuola Intern. Fisica Corso, XIII SETT*, 151 to 165 (1959).
29. M. A. Biondi and L. M. Chanin, *Phys. Rev.*, **94**, 910 (1954).
30. J. A. Hornbeck, *ibid.*, **84**, 615 (1951).
31. R. A. Nielsen, *ibid.*, **50**, 950 (1936).
32. L. Colli and U. Facchini, *Rev. Sci. Instr.*, **23**, 39 (1952).
33. H. D. Hagstrum and J. T. Tate, *Phys. Rev.*, **59**, 354 (1941); J. T. Tate and P. T. Smith, **39**, 270 (1932).
34. G. H. Kinchin and R. S. Pease, *Repts. Prog. in Phys.*, **18**, 1 (1955).
35. B. Johnson, J. L. Lineweaver, and J. T. Kerr, *J. Appl. Phys.*, **31**, 51 (1950).
36. J. S. Colligan, *Vacuum*, **11**, 5/6, 272 (1961).
37. Analysis performed by W. Guldner of this Laboratory, see: *Anal. Chem.*, **35**, 1744 (1963); Proc. 1964 Electronic Comp. Conf., p. 9-13, Washington, D. C., May 1964, Bell Telephone Monograph 4803.
38. L. A. Peterman, *Nuovo Aimento*, 1-2 suppl., p. 201 (1963); *Trans. Amer. Vac. Soc.* (1962).
39. G. E. Moore, *Trans. Amer. Vac. Soc.*, 16 (1959); *J. Appl. Phys.*, **32**, 124 (1961).
40. P. A. Redhead, *Appl. Phys. Letters*, **4-9**, 166 (1964); *Can. J. Phys.*, **42**, 886 (1964).
41. F. Vratny and N. Schwartz, Deposition of Tantalum Films by Substrate Electrode Bias Sputtering, 11th National Symposium of the American Vacuum Society, October 1, 1964.

Vapor Transport Reactions Related to Halophosphate Phosphor Formation

Jacob G. Rabatin and George R. Gillooly

Luminescent Materials Laboratory, General Electric Company, Cleveland, Ohio

ABSTRACT

A double crucible technique has demonstrated that the principal phosphor forming reactions may involve particle-particle interaction between $Ca_2P_2O_7$ and CaF_2 leading to direct formation of apatite and POF_3. The POF_3, or vapors of similar composition, react with $CaCO_3$ also forming apatite. The transport of vapors containing fluorine, phosphorus, oxygen, and antimony has been demonstrated. Activation of the phosphor above 1000°C occurs by a reaction of Sb_2O_4 vapor with apatite.

The ease of formation of apatites from solid-state reactants commonly used in the preparation of halophosphate phosphors belies the complexity of the system from which these products are derived. Some general reactions of the usual starting materials, investigated by the use of differential thermal analyses and thermogravimetric analyses, have been reported along with isolated chemical and x-ray diffraction studies (1-6). These data reveal such a multiplicity of possible intermediate reactions as to preclude interpretation of the kinetics or mechanism of apatite formation. Thus it is sometimes assumed that apatite formation and activation proceed by solid-state diffusion processes (7, 4).

Based on earlier studies (8, 9) it has been postulated that, with the usual starting material, $CaHPO_4$, $CaCO_3$, CaF_2, $CaCl_2$, etc., halophosphates form by a two-step solid-state process. In the first step, $Ca_3(PO_4)_2$ is formed by the reaction

$$Ca_2P_2O_7 + CaCO_3 \rightarrow Ca_3(PO_4)_2 + CO_2 \qquad [1]$$

It is further assumed that $CaCO_3$ dissociates to CaO before reaction [1] begins. The subsequent apatite-forming reaction is also a solid-solid type, namely;

$$3Ca_3(PO_4)_2 + CaF_2 \rightarrow [Ca_3(PO_4)_2]_3CaF_2 \qquad [2]$$

Mixed apatites can be obtained by varying any of the above ingredients (8, 9).

The possibility of vapor transport as a mechanism accelerating apatite formation was first indicated by the work of Daubree (10) who obtained apatite by passing vapor of phosphorus trichloride over red-hot lime. More recently, Montel (11) has studied in detail

the reaction between $Ca_2P_2O_7$ and CaF_2 showing that apatite and the vapor, POF_3, are the two products according to the reaction

$$18Ca_2P_2O_7 + 14CaF_2 \rightarrow 5 \text{ apatite} + 6POF_3 \quad [3]$$

Since both $Ca_2P_2O_7$ (formed by low-temperature decomposition of $CaHPO_4$) and CaF_2 are normally employed as solids in the manufacture of halophosphate phosphors, the presence of POF_3 or a vapor of similar composition may play a role during the synthesis. The present study further indicates that the vapor transport of P, O, Sb, and halogens does play an important part in the formation of halophosphate phosphors.

Methods

Two simple techniques were used for the studies reported herein. The first involved the use of a small crucible placed inside a larger covered crucible as is illustrated in Fig. 1. Firings were made at various temperatures and for several times. Appropriate mixtures were placed in each crucible, thus permitting reaction between crucible contents only by vapor transport mechanisms. As indicated by undisturbed surfaces, there was no evidence in any case of solid material transfer by gas entrainment. Further, in most cases no evidence for a liquid phase was found; thus any possibility of liquid creep from one vessel to another can be discounted.

After firing, the contents of each crucible were identified by standard x-ray diffraction methods using an XRD-5 GE x-ray diffraction apparatus. ASTM x-ray data file together with comparisons of original x-ray patterns were used to identify the various phases present. Although this technique is qualitative, since some vapor may escape, the appropriate choice of reactants and trapping materials enables definitive demonstration of vapor transport from one crucible to the other. Relative line intensities of the x-ray diffraction patterns were used to estimate the amounts of the products present.

The second technique makes use of a quartz tube with a constriction at the center which allows the flow of gas from one compartment to the other. A quartz wool plug was also placed in the constriction. Appropriate materials were placed in each compartment; then the tube was evacuated and sealed. Firings were also performed for various times and temperatures. After firing, the products were examined by x-ray diffraction and chemical methods. Since this is a closed system, quantitative data can be obtained about vapor transport and mechanisms.

Results and Discussion

Apatite Forming Reactions

Reaction of $Ca_2P_2O_7$ *with* CaF_2.—In order to confirm Montel's (11) work, several proportions of $Ca_2P_2O_7$ and CaF_2 were blended and fired at temperatures from 700° to 1100°C. The major product in every case was fluorapatite. When excess $Ca_2P_2O_7$ was used over that shown in reaction [3], x-ray diffraction showed the presence of $Ca_2P_2O_7$. When CaF_2 was used in excess of that shown in reaction [3], CaF_2 was present in the product.

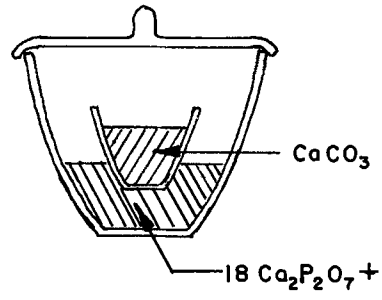

Fig. 1. Double crucible arrangement for vapor transport experiments

To show the presence of POF_3 (or vapors of similar composition) as one of the products of reaction [3] the following double crucible experiment was performed: The outer crucible contained Montel's mixture (reaction [3]); the inner crucible contained $CaCO_3$. After firing at 1000°C for 1 hr, the product in the outer crucible was fluorapatite. The products of the inner crucible were fluorapatite and CaF_2. It can be readily concluded that F, O, and P were all transported to the inner crucible where the most probable reaction was

$$18CaCO_3 + 6POF_3 \rightarrow [Ca_3(PO_4)_2]_3CaF_2 + 18CO_2 + 8CaF_2 \quad [4]$$

The product of the outer crucible was fluorapatite as expected from Montels' reaction (reaction [3]). If reactions [3] and [4] are combined and divided by 6 the following equation results.

$$3Ca_2P_2O_7 + 3CaCO_3 + CaF_2 \rightarrow \text{Apatite} + 3CO_2 \quad [5]$$

Reaction [5] has the usual proportions of reactants used in phosphor formulations.

When the mixture for reaction [5] was placed in the outer crucible and $CaCO_3$ was placed in the inner crucible, on heating 1 hr at 1000°C, the products in the inner crucible were CaO and a trace of CaF_2. These results indicate that, in an intimate mixture of the reactants, the vapors liberated by the solid-solid reaction of $Ca_2P_2O_7$ with CaF_2 will react quickly and completely with the nearest $CaCO_3$. Thus no vapor escapes to react with the $CaCO_3$ in the inner crucible.

Reaction of HF *with* $Ca_2P_2O_7$.—Since hydrolysis of POF_3 may occur to some extent and, thus, free HF and P_2O_5 may be reactants, the following double crucible experiment was performed. $Ca_2P_2O_7$ was placed in the outer crucible, and in the inner inverted crucible NH_4HF_2 (as a source of HF) was placed. The crucibles were heated for ½ hr at 900°C, and the products of the outer crucible were examined (the inner crucible was empty because of the volatility of NH_4HF_2). Both unreacted $Ca_2P_2O_7$ and fluorapatite were present. The following reaction is proposed.

$$5Ca_2P_2O_7 + 2HF \xrightarrow[\frac{1}{2} \text{ hr}]{900°C} \text{apatite} + 2P_2O_5\uparrow + H_2O \quad [6]$$

Vapor-solid reactions of this type would be expected to lead to a more rapid and complete dispersion of reactants than the usual solid-solid diffusion processes.

Reaction of P_2O_5 *with* CaF_2.—When the outer crucible containing CaF_2 and inner inverted crucible containing $(NH_4)_2HPO_4$ (as source of P_2O_5) were heated ½ hr at 900°C, the products of the outer crucible were fluorapatite and some unreacted CaF_2. The reaction leading to apatite formation is in balanced form

$$10CaF_2 + 6P_2O_5 \xrightarrow[\frac{1}{2} \text{ hr}]{900°C} \text{apatite} + 6POF_3\uparrow \quad [7]$$

This reaction along with [4] and [6] is of the gas-solid type. The liberation of POF_3 by this reaction would lead to a further repeat of reaction [4] whereever POF_3 came in contact with $CaCO_3$. The fact that a gaseous phosphorus-fluoride product did form according to reaction [7] was demonstrated by the use of a third small crucible containing $CaCO_3$ placed in the crucible setup mentioned above. After heating at 900°C for ½ hr, this third crucible now contained CaF_2 and $Ca_2P_2O_7$ with some apatite again illustrating the vapor transport of P and F.

Reaction of POF_3 *with* $Ca_3(PO_4)_2$.—Since there is a possibility that in a phosphor mix some $Ca_3(PO_4)_2$ may form according to reaction [1], the following double crucible experiment was performed. The outer crucible contained a mixture of $Ca_2P_2O_7$ and CaF_2 as a source of POF_3 (reaction [3]). The inner crucible con-

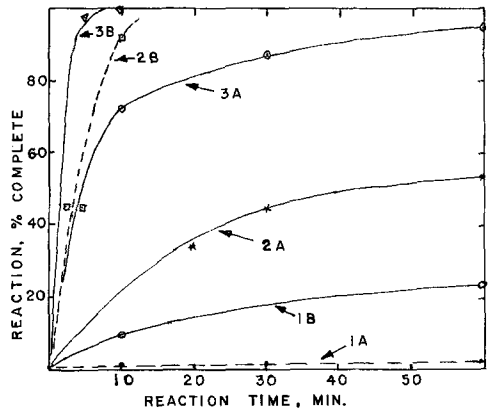

Fig. 2. Rate of formation of products at A, 800°C; B, 900°C for the reactions.

1. $Ca_2P_2O_7 + CaCO_3 \rightarrow Ca_3(PO_4)_2$
2. $3Ca_3(PO_4)_2 + CaF_2 \rightarrow$ apatite
3. $18Ca_2P_2O_7 + 14CaF_2 \rightarrow 5$ apatite

tained $Ca_3(PO_4)_2$. The setup was heated 1 hr at 900°C. The products of the inner crucible were fluorapatite and $Ca_2P_2O_7$. The probable reaction is

$$14Ca_3(PO_4)_2 + 2POF_3 \xrightarrow[1\text{ hr}]{900°C} 3\text{ apatite} + 6Ca_2P_2O_7 \quad [8]$$

These results once again illustrate the great tendency toward apatite formation whenever the ions Ca^{+2}, P^{+5}, $O^{=}$, and F^{-} are present.

Reaction Rates for Apatite Formation

It may be argued that reactions [3], [4], [6], [7], and [8] occur only under very special conditions, but that in actual practice apatite forms only by a stepwise process involving reactions [1] and [2]. To answer this more definitely, kinetic studies were performed on mixtures according to reactions [1], [2], and [3] at 800° and 900°C. Samples were heated in 5 ml crucibles at these temperatures for the desired times. The products were analyzed by standard x-ray diffraction techniques involving the measurement of line intensities. The completely reacted product line intensities were used for the 100% values of apatite for reactions [2] and [3], and β $Ca_3(PO_4)_2$ for reaction [1]. Although some error will arise due to line broadening for very small crystallites formed during the initial stages of reaction, the results are sufficiently accurate to determine relative rates of formation. Results are presented in Fig. 2. The data could not be fitted to either first order or parabolic rate curves. Thus only qualitative estimates of relative rates are indicated in the discussion.

The results demonstrate that at 800°C apatite formation by reaction [3] is much more rapid than its formation by the stepwise process involving reactions [1] and [2] since reaction [1] [formation of β $Ca_3(PO_4)_2$] is a relatively sluggish rate-determining step. Reaction [3] is several times more rapid than reaction [2] and about 100 times more rapid than reaction [1]. Even at 900°C reaction [3] is still the most rapid. Thus it can be concluded that in apatite mixes reaction [3] would be the dominant reaction.

Other Vapor Reactions

Reaction of apatite with Sb_2O_4.—During the formation of fluorescent apatites, solid solution of Sb^{+3} ions occurs in the apatite structure. To determine how apatite might react with antimony compounds, the following double crucible experiment was performed. The inner crucible contained a mixture of 10 fluorapatite + $2Sb_2O_4$. Antimony tetroxide was chosen because of its low volatility at high temperatures. The outer crucible contained $CaCO_3$. The system was heated at 1100°C for 1 hr and the products analyzed. The inner crucible contained a luminescent apatite (indicating the solid solution of Sb^{+3} ions in fluorapatite) plus a minor phase of $Ca(SbO_3)_2$. The outer crucible (originally $CaCO_3$) now contained CaF_2, $Ca_2Sb_2O_7$, and CaO. The proposed sequence of reactions to explain these results is as follows, (assuming a solid solution of 0.1 mole Sb^{+3} per mole of apatite).

The solid solution of antimony in apatite appears to require the removal of F^{-} and Ca^{++} ions from apatite. The Ca^{++} ions react with Sb_2O_4 to give $Ca(SbO_3)_2$. The F^{-} ions form an antimony halide, perhaps SbOF, as indicated in Eq. [9].

$$10[Ca_3(PO_4)_2]_3CaF_2 + 2Sb_2O_4 \xrightarrow[1\text{ hr}]{1100°C} 10[Ca_3(PO_4)_2]_3 0.9CaF_2 \cdot 0.1SbOF + Ca(SbO_3)_2 + SbOF\uparrow \quad [9]$$

The outer crucible trapped this vapor to give (in air)

$$3CaO + 2SbOF + O_2 \rightarrow Ca_2Sb_2O_7 + CaF_2 \quad [10]$$

Reaction of $Ca_2P_2O_7$ *with* $Ca(SbO_3)_2$.—According to Butler *et al.* (3) the Sb_2O_3 usually used as the starting antimony compound rapidly reacts to form $Ca(SbO_3)_2$. To determine how $Ca(SbO_3)_2$ may enter into phosphor formation, the system $Ca_2P_2O_7$ + $Ca(SbO_3)_2$ was studied at several temperatures together with the reaction of $Ca_3(PO_4)_2$ with Sb_2O_4. The results are as follows.

1. Below about 1100°C (in air)

$$Ca_3(PO_4)_2 + Sb_2O_4 + \tfrac{1}{2}O_2 \rightarrow Ca_2P_2O_7 + Ca(SbO_3)_2 \quad [11]$$

2. Above 1100°C (open crucibles)

$$Ca_2P_2O_7 + Ca(SbO_3)_2 \rightarrow Ca_3(PO_4)_2 + \text{volatile products} \quad [12]$$

Presumably Sb_2O_4 is the volatile product. Kinetic studies were performed on mixtures according to reaction [12] at temperatures of 1000°, 1100°, and 1200°C. Results are presented in Table I.

The theoretical weight loss for reaction [12] is 49.0%. Thus the results in Table I confirm that this reaction did occur above 1100°C. Since Sb_2O_4 is a product of this reaction, presumably as a vapor, it can now react according to reaction [9] leading to solid solution of Sb^{+3} in apatite.

Vapor transport of F *and* Cl *from apatites.*—To determine if high-temperature vapor transport of F^{-} and Cl^{-} ions may occur, possibly by means of a water cycle, the following sealed tube experiments were performed. Chlorapatite was placed in one compartment, fluorapatite in another. The systems were evacuated, sealed, and heated at 1200°C for 20 and 72 hr, respectively. Chemical analysis for chlorine was made on the products of each compartment. X-ray diffraction analyses of the products after 72 hr firings show the product of each compartment were fluorchlorapatites of almost identical patterns. The chloride analyses are listed in Table II. The results lead to the conclusion that both Cl^{-} and F^{-} ions were involved in a vapor transport mechanism, possibly through a water cycle as indicated.

$$[Ca_3(PO_4)_2]_3CaX_2 + 2HOH \rightleftarrows [Ca_3(PO_4)_2]_3Ca(OH)_2 + 2HX\uparrow \quad [13]$$

Table I. Weight losses for reaction of $Ca_2P_2O_7 + Ca(SbO_3)_2$

Reaction time, hr	% Wt loss 1000°C, %	1100°C, %	1200°C, %	Product at 1200°C
1	0	1.5	4.9	β $Ca_3(PO_4)_2 + Ca_2P_2O_7 + Ca(SbO_3)_2$
2	0	3.0	12.0	β $Ca_3(PO_4)_2 + Ca_2P_2O_7 + Ca(SbO_3)_2$
23	3.0	5.2	50.0	β $Ca_3(PO_4)_2$

Table II. Chloride content of sealed tubes fired at 1200°C

Compartment	Chloride Content Wt % 20 hr	72 hr
Fluorapatite	1.8	2.9
Chlorapatite	5.3	2.5

Table III. Decomposition of $CaCO_3$ at high pressures of CO_2

Mixture	Pressures of CO_2, psi	Temp, °C	% Wt loss	Theory wt loss %
$CaCO_3$	90	1100	15.0	44.0
$CaCO_3$	120	1000	1.2	44.0
$6CaHPO_4 + 3CaCO_3 + CaF_2$	120	700	15.2	15.6

By simple gaseous diffusion the hydrogen halides could diffuse to the opposite chamber resulting in the mixed fluorchlorapatites. At 1200°C the equilibration by direct vapor transport of $CaCl_2$ and CaF_2 might also be considered.

Vapor transport of CaF_2.—Measurable vapor pressure of CaF_2 at 1200°C has been reported (12). To determine if this vapor may react with β $Ca_3(PO_4)_2$, a sealed tube experiment was performed at 1200°C. One compartment contained CaF_2 and the other β $Ca_3(PO_4)_2$. After heating the system for 20 hr, the products were examined by x-ray diffraction. The $Ca_3(PO_4)_2$ compartment now contained a major phase of fluorapatite plus minor unreacted phases of $Ca_3(PO_4)_2$ and CaF_2. These results confirm that a vapor transport of F did occur. Although these results may be only of passing interest to the study of the usual processes for apatite formation, they do illustrate once again that unusual vapor transport phenomena can exist at high temperatures.

Apatite Formation under CO_2 Pressures

A pressure vessel similar to that previously described for DTA (13) was used to study the effect of pressure of CO_2 on the tendency for apatite formation. If it is assumed that the two-step process of apatite formation occurs according to reactions [1] and [2], then reaction [1] should be greatly depressed in a CO_2 atmosphere if free CaO is essential to the process as has been assumed by other authors (2, 6). Various mixtures were placed in the pressure vessel and heated for 1 hr at the indicated pressure and temperatures. Weight losses were determined on the cooled samples. The results are presented in Table III. The results in Table III clearly indicate that $CaCO_3$ dissociation can be greatly depressed in CO_2 even at 1100°C, yet apatite formation is essentially complete even at 700°C. It is highly unlikely therefore that the usual dissociation of $CaCO_3$ to CaO is necessary to apatite formation. This is additional evidence that the principal apatite forming reaction is pressure insensitive as would be expected from the reaction of $Ca_2P_2O_7$ with CaF_2 (reaction [3]). The second most important apatite forming reaction is between POF_3 and $CaCO_3$ (reaction [4]), which can be considered an acid-base-type reaction and therefore insensitive to CO_2 pressure.

High-Temperature X-ray Diffraction Studies of Halophosphate Mixes

Phosphor mixes composed of $CaHPO_4$, $CaCO_3$, CaF_2, $CaCl_2$, Sb_2O_3, and $MnCO_3$ in proportions used for phosphor manufacture were examined by high-temperature x-ray diffraction methods using the GE-XRD-5 unit together with a Tem-Press furnace assembly. X-ray diffractometer traces were made at various temperatures. The results are in general agreement with the thermogravimetric data of Wanmaker and Verheyke (2) namely that:

1. beginning at about 450°C
$$2CaHPO_4 \rightarrow \gamma Ca_2P_2O_7$$
2. beginning at about 500°C
$$Sb_2O_3 + \tfrac{1}{2}\, O_2 \rightarrow Sb_2O_4$$
3. beginning at about 650°C, fluorchlorapatite forms.

In no cases were any diffraction lines detected for $Ca_3(PO_4)_2$ to indicate its presence even in small amounts. These results also tend to indicate that in phosphor mixes apatite formation probably occurs primarily by reactions [3] and [4].

Summary

The present studies have permitted a simplification of the potential reactions involved in the preparation of halophosphate phosphors from the usual starting materials ($CaHPO_4$, $CaCO_3$, CaF_2, Sb_2O_3). The principal apatite forming reaction involves the interaction of $Ca_2P_2O_7$ particles with CaF_2 particles beginning at about 600°-700°C leading directly to formation of the apatite plus a vapor phase of POF_3 (11). The second most important apatite forming reaction is between POF_3 and $CaCO_3$ which also proceeds by a direct reaction that does not require free CaO, thus being pressure insensitive. These studies demonstrate that vapor transport plays a dominant role in the formation and activation of halophosphate phosphors.

Acknowledgments

The authors greatly appreciate the helpful comments and criticisms of Dr. H. C. Froelich and Dr. E. F. Apple.

Manuscript received Sept. 14, 1964; revised manuscript received Dec. 22, 1964. This paper was presented at the Toronto Meeting, May 3-7, 1964.

Any discussion of this paper will appear in a Discussion Section to be published in the December 1965 JOURNAL.

REFERENCES

1. W. L. Wanmaker, A. H. Hoekstra, and M. G. A. Tak, *Phillips Research Repts.*, **10**, 11 (1955).
2. W. L. Wanmaker and M. L. Verheyke, *ibid.*, **11**, 1 (1956).
3. K. H. Butler, M. J. Bergin, and V. M. B. Hannaford, *This Journal*, **97**, 117 (1950).
4. J. L. Ouweltjes and W. L. Wanmaker, *ibid.*, **103**, 160 (1956).
5. D. Robbins, ECS Electronic Division Extended Abstracts, **11**, 31 (1962).
6. S. Kamiya, *Electrochemistry, Japan*, **31**, 246 (1963).
7. W. L. Wanmaker and C. Bakker, *Proc. Symp. React. Solids*, 709 (1960).
8. G. Chaudron and R. Wallaeys, *Soc. Chim. France Bull. fasc.*, 3-4 mars-avrill, pp. 132-134 (1949).
9. G. Chaudron and R. Wallaeys, *Compt. rend.*, **230**, (1950).
10. A. Daubree, *ibid.*, **32**, 625 (1851).
11. G. Montel, Silicium, Schwefel, Phosphate, Colloq. Sek. Anorg. Chem. Intern. Union Reine U. Angew. Chem., Munster, 1954, pp. 178-183 (1955).
12. D. Schulz and A. Searcy, *J. Phys. Chem.*, **67**, 103 (1963).
13. J. Rabatin and C. Card, ECS Electronic Division Extended Abstracts, Abstract 90, 222-224 (1957).

Microstructures in CdS:Au Single Crystals

Arthur Dreeben

RCA Laboratories, Radio Corporation of America, Princeton, New Jersey

ABSTRACT

The incorporation of gold in CdS crystals grown from the vapor phase results in the formation of two types of precipitates. Type I, probably a CdAu phase, consists of small (2.5-7μ) hexagonally shaped platelets throughout the crystal oriented to reflect the CdS crystal symmetry. Type II are much larger hexagons (160μ) apparently of elemental gold in localized positions, and with an orientation rotated 30° with respect to the small ones. Type I precipitates have been found to decorate a unique, highly symmetrical network of dislocations associated only with Type II hexagons. The dislocations are generated in a critical strain field developed around hexagons of sufficient size. Strain birefringence has been observed around these hexagons in polarized light.

In a previous investigation (1), it was demonstrated that extraneous phases precipitate in CdS crystals containing the acceptor elements Cu, Ag, or Au. The precipitates involving Cu and Ag were thought to be sulfide phases, whereas gold was found to segregate as the element together with a CdAu phase. It was shown that each of the precipitates had a characteristic shape and crystallographic orientation. The sulfides formed needles, rods, or disks, but the gold phases formed hexagonal platelets.

In this paper, additional results of direct optical observations of precipitates in CdS:Au crystals are presented. The principal findings include the identification of two kinds of hexagonal platelets, which differ in size and crystallographic orientation, and the observation of a unique, decorated imperfection network associated with the larger hexagons.

Experimental

The crystals used in this work were cut from large boules of CdS:Au which were grown from the vapor phase, oriented, and polished as previously described (1). The powder charge from which the boules were produced, contained 5 mole % of gold as gold (III) sulfide prepared by precipitation from a solution of chloroauric acid, trihydrate. With this amount of gold, globules of the metal, formed by thermal decomposition of the sulfide during crystal growth, are found in contact with the boule. During growth, therefore, molten gold is present, and this condition promotes its incorporation in the crystal. The polished samples were examined under the polarizing microscope using transmitted, incident and dark field illuminations.

Observations

As previously noted (1), discrete hexagonal platelets lying in a (0001) basal plane had been found to segregate in CdS:Au crystals. In the present samples, the average size of this species (hereafter called type I) ranges from about 2.5 to 7μ. However, in Fig. 1A, some giant hexagons (hereafter called type II) up to 160μ across can also be seen in localized sites which are at various distances below the surface of the crystal. Transmitted polarized light disclosed a strain birefringence around these large precipitates clearly seen as the white areas radiating outward from the type II hexagons in Fig. 1B. The "specks" in these photomicrographs are the smaller, type I precipitates.

In addition to their size, type II hexagons are also distinguished by a surrounding array of unique, highly symmetrical, decorated dislocations. This network in the CdS crystal consists of two distinct patterns as seen in Fig. 2. One of these is superimposed over the hexagon in the form of an asterisk whose arms are directed through and extend beyond the vertices of the large hexagon. The other decoration is a peripheral, open hexagonal array with sides paralleling those of the precipitate at a distance of about 40-45μ. The asterisk and the peripheral hexagon both consist of many individual, aligned type I precipitates.

The photomicrograph in Fig. 2 was taken with the aperture diaphragm of the microscope condenser stopped-down to increase the depth of field, thereby showing all features of the arrays together. However, the type II hexagon and the two decorated patterns are not coplanar, the composite consisting of the separate parts shown in Fig. 3. In this typical crystal, 0.7 mm thick, incipient formation of the asterisk is visible close to the surface (Fig. 3A), but the fully developed pattern is first seen at 0.17 mm below the surface of the crystal. The asterisk continues in a three-dimensional array and is still clearly seen at a depth of 0.25 mm where distinct outlines of the peripheral, open hexagon also appear (Fig. 3B). In fact at this focus, elements of an inner pattern (I in 3B) and outer pattern (O in 3B) can be seen. The peripheral hexagon is at last sharply defined at a depth of 0.32 mm, while the decoration forming the asterisk is beginning to diminish (Fig. 3C). Both patterns essentially terminate at about 0.47 mm below the surface. Finally, the type II hexagonal precipitate is brought into focus at a depth of 0.57 mm (Fig. 3D). Below this hexagon, there is a somewhat less distinct repeat pattern of the peripheral figure and the asterisk.

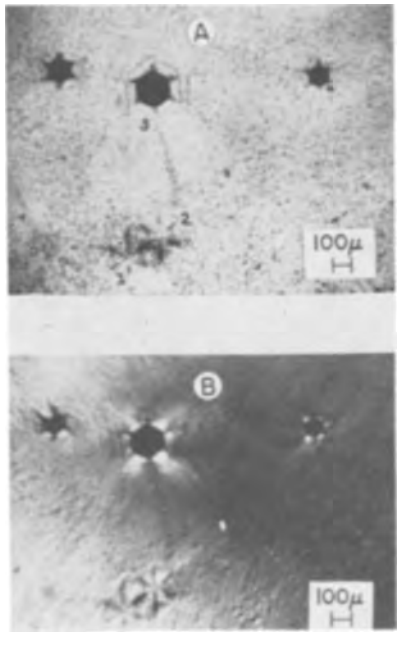

Fig. 1. Photomicrograph of CdS:Au single crystal showing (A) giant hexagons in transmitted light and (B) strain birefringence around the hexagons in polarized light.

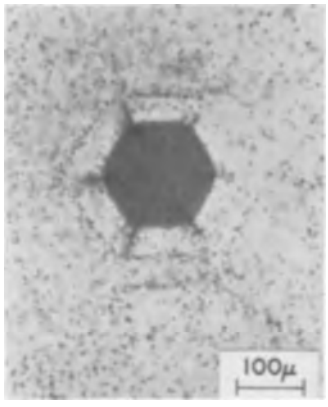

Fig. 2. Decorated dislocation arrays around hexagon No. 3 in Fig. 1

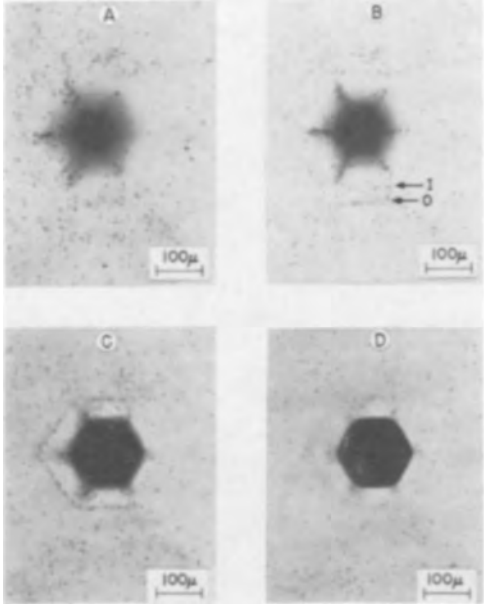

Fig. 3. Separate parts of the decorated array in Fig. 2, (A) near the crystal surface; (B) asterisk and outlines of peripheral rings, 0.25 mm below surface; (C) sharply defined ring, 0.32 mm below surface; and (D) type II hexagon, 0.57 mm below surface.

The interesting formation of the decorations above and below another type II hexagon is shown in Fig. 4. In this specimen, the asterisk and the peripheral hexagon (Fig. 4A) are seen above and essentially around the left side of the type II precipitate (Fig. 4B), while below the large hexagon, the patterns are around its right side (Fig. 4C). In Fig. 4D, a different portion of the peripheral hexagon appears at a level 0.07 mm below the position in Fig. 4C and also further away from the sides of the type II hexagon.

In the lower central portions of each illustration in Fig. 1, two asterisks (labelled 1 and 2 in 1A) can be seen without accompanying type II hexagons. Found at the surface of the crystal, they are the remnants of the typical systems already shown, but from which the other parts were removed during polishing. One of these is seen in greater detail in Fig. 5, which also clearly shows that these decorations consist of arrays of individual type I hexagons.

Crystallography of Precipitates

In (0001) planes, type I precipitates observed in many crystal slices from different boules always have the same orientation. They are bounded by $\{10\bar{1}0\}$ planes of the CdS with the a-axes directed through the vertices of the hexagons which have the same orientation as etch pits in the basal plane. This correspondence is shown in Fig. 6.

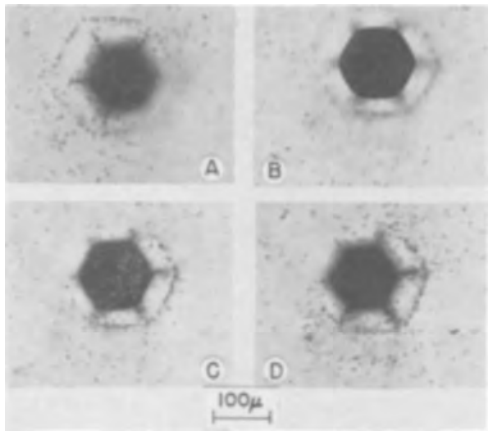

Fig. 4. (A) Dislocation array above hexagon; (B) type II hexagon; (C) dislocation array below hexagon; (D) 0.07 mm below field in (C), note outward displacement of peripheral ring.

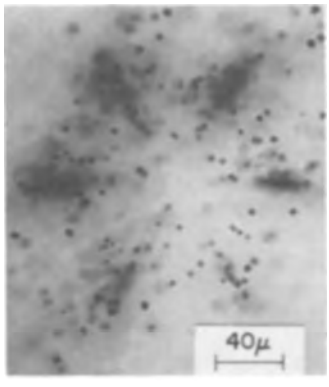

Fig. 5. Dislocation array after hexagon is removed. Note that decoration consists of individual type I hexagons.

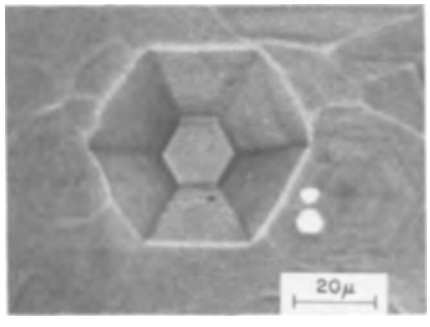

Fig. 6. Photomicrograph in incident light showing orientation of type I hexagons and etch pits in basal plane.

The large type II hexagons also have a self-consistent orientation, but it is different from that of type I. In Fig. 7, the outlines drawn around several of the type I precipitates make it readily apparent that the type II hexagon is rotated 30° with respect to the small ones. The relationship between the precipitates and the decorated dislocations with respect to the basal plane of CdS is summarized schematically in Fig. 8.

In all of the preceding photomicrographs, the precipitates have been seen as they are arranged in a basal plane. In Fig. 9 the arrangement in a (1010) plane is shown in transmitted, dark-field illumination. Type I hexagons appear as the short bright lines, while type II are the longer ones. X-ray methods established that the CdS C-axis ([0001] direction) is perpendicular to the lines in the plane of the picture and that the a-axis $[\bar{1}2\bar{1}0]$ is parallel to them. This illustration also shows arrays from asterisks and peripheral hexagons above and below the type II precipitates. However, the clear, undecorated regions directly around the pre-

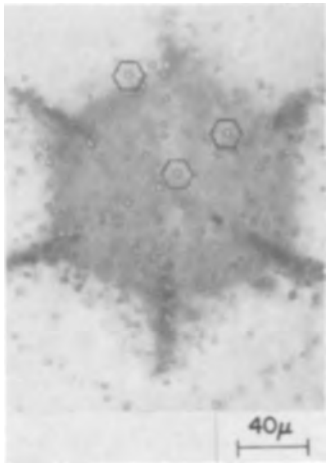

Fig. 7. Photomicrograph showing different orientations of type I (small) and type II hexagons.

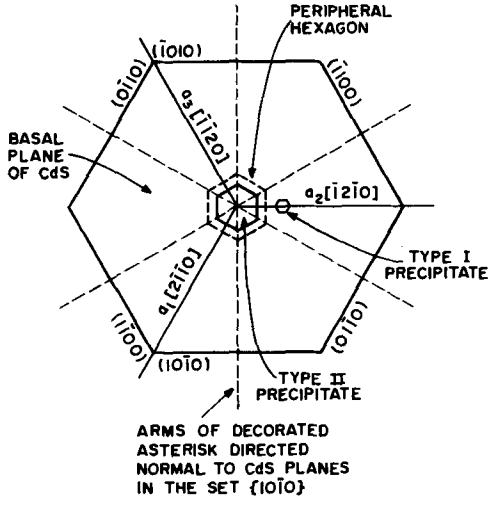

Fig. 8. Orientations of precipitates and decorated arrays with respect to the basal plane of CdS.

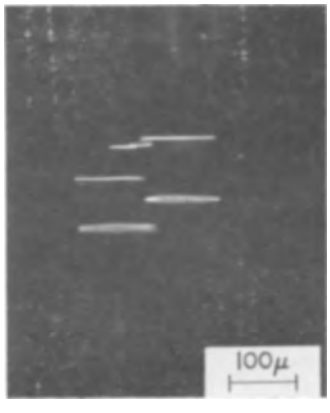

Fig. 9. Dark field illumination of hexagonal platelets in a (10$\bar{1}$0) plane of CdS. C-axis perpendicular and a-axis parallel to hexagonal "lines."

cipitates confirm the earlier observation that the decoration patterns terminate at some distance from the large hexagons.

Other Decorations

In addition to the dislocation arrays surrounding the type II precipitates, there are often decorated lines that emanate from the type II precipitates, one of which can be seen in Fig. 1A between the positions labelled 2 and 3. Similar lines are also shown in Fig. 10 where it will be noted that many type I precipitates

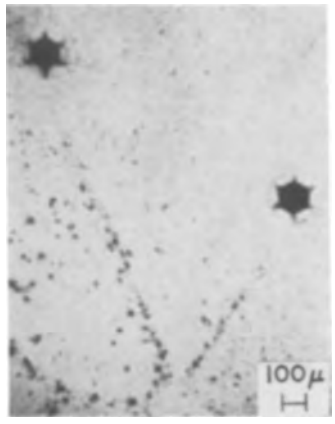

Fig. 10. Decorated boundaries emanating from type II hexagons

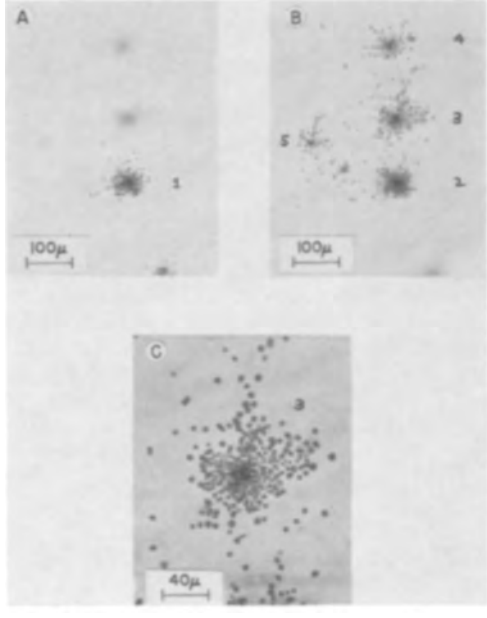

Fig. 11. Clusters of type I hexagons along boundaries shown in Fig. 10.

are grouped in clusters along and near the lines. The clusters, seen at higher magnification in Fig. 11, are arranged in a three-dimensional network. For example, group 1 in Fig. 11A is about 0.2 mm below the crystal surface, and the defocused outlines of other groups can also be seen. These appear in the same field, but at a depth of 0.4 mm as shown in Fig. 11B where the shadow of group 1 can be seen over group 2. Formations of this type are often associated with subboundaries.

Discussion

The two respective orientations of type I and type II precipitates suggest that they may be different chemical species. This is consistent with electron diffraction data indicating the presence of Au and CdAu phases in the CdS crystal. Gold has a face-centered cubic lattice and some CdAu phases have a hexagonal structure (2). In view of these structural differences, it is reasonable to expect the precipitates to have dissimilar epitaxial arrangements in the hexagonal CdS lattice. At present it has not been possible to obtain selected area electron or x-ray diffraction patterns of the precipitates. However, it is likely that the CdAu hexagonal structure would adopt the orientation bounded by the low index {10$\bar{1}$0} planes of hexagonal CdS and thereby reflect the crystal symmetry in the same way as the etch pits and type I precipitates shown in Fig. 6. On the other hand, the cubic Au, with {111} close packed planes, may well prefer the other ob-

served orientation of type II precipitates which are rotated at a 30° angle with respect to type I (see Fig. 7).

The different crystallographic orientations, and the probable separate identities of each precipitate, together with the fact that the dislocation arrays and boundaries are decorated with type 1 precipitates, suggest that different precipitation mechanisms are operating. One possible sequence for precipitation and decoration consistent with the observations is the following. Type II precipitates nucleate and grow at localized sites during the formation of the CdS boule while it is still at a high temperature. When these hexagons are sufficiently large, a critical strain field is established, and the symmetrical dislocation network is generated. In this connection it can be pointed out that the networks have never been observed around the small type I precipitates. In addition, the peripheral hexagonal loop is either very weakly defined or missing from type II precipitates well within the crystal, but which are less than about 100μ in size compared with 140μ for those associated with a complete array.

The CdAu phase, on the other hand, appears to have a greater solubility and remains in solution at or near the crystal growth temperature of CdS. As the crystal cools, type I hexagons precipitate randomly and on preferred sites for nucleation provided by the dislocations.

The decoration of sub-boundaries in the crystals was pointed out earlier (see Fig. 10 and 11). The other prominent dislocations in these crystals comprise the symmetrically decorated arrays around type II precipitates. The peripheral hexagons appear to be decorated prismatic loops (3) whose sides are on traces of $(11\bar{2}0)$ planes in the basal plane. It is also possible that the loop is part of a helical dislocation, an arrangement which could account for the displacement of the sides of the peripheral hexagon with respect to the type II precipitate as shown in Fig. 3B. 4C, and 4D. Two observations are of particular interest. One is that the network consisting of the precipitate, the asterisk, and the peripheral hexagon is not coplanar; the other is the situation shown in Fig. 4, wherein parts of hexagonal loops exist on opposite sides above and below a type II precipitate. The mechanisms leading to these formations are not yet completely known. However, the source of the dislocation network appears to be a type II precipitate of sufficient size to develop around it, a critical strain field which is observable in polarized light. The dislocation loops once formed may glide away from the source thereby tending to relieve the stresses and leave the precipitate relatively isolated (4).

Acknowledgment

The author is indebted to M. S. Abrahams for helpful discussions. W. M. Anderson ably assisted in preparing the materials, and G. Neighbor performed the x-ray analyses.

The research reported in this paper was sponsored by the Department of Defense, Advanced Research Projects Agency, Materials Sciences Office, under Contract No. SD-182.

Manuscript received Sept. 22, 1964. This paper was prepared for delivery before the San Francisco Meeting, May 9-13, 1965.

Any discussion of this paper will appear in a Discussion Section to be published in the December 1965 JOURNAL.

REFERENCES

1. A. Dreeben, *This Journal*, **111**, 174 (1964).
2. V. G. Rivlin, W. Hume-Rothery, and B. Ryder, *Acta Met.*, **10**, 1143 (1962).
3. F. Seitz, *Phys. Rev.*, **79**, 723 (1950).
4. K. B. Harvey, *Phil. Mag.*, **8**, 435 (1963).

Bourdon Gauge Determination of Chemical Equilibrium in the Ge-Cl_2 System

T. O. Sedgwick

Thomas J. Watson Research Center, International Business Machines Corporation, Yorktown Heights, New York

ABSTRACT

Bourdon gauge pressure measurements of samples of $GeCl_4(g)$ and $GeCl_4(g)$ plus Ge(s) have been made in the temperature range 300°-1300°K. The pressure change of pure $GeCl_4$ as a function of temperature indicates that it does not dissociate up to 1300°K. The pressure *vs.* temperature behavior of $GeCl_4(g)$ plus Ge(s) is described by the equilibrium

$$Ge(s) + GeCl_4(g) \rightleftarrows 2GeCl_2(g)$$

The standard enthalpy, ΔH°, and entropy, ΔS°, of reaction at 723°K were found to be 34.9 kcal and 46.7 eu, respectively.

In contrast to the Ge-H_2-I_2 and Si-H_2-Cl_2 epitaxial growth systems (1, 2) for which complete thermodynamic analyses have been made, there is insufficient thermodynamic data currently available for a similar analysis of the Ge-H_2-Cl_2 system. A complete thermodynamic description of this system would, for example, obviate the present speculation regarding the gas phase composition in $GeCl_4$ epitaxial growth and etching processes (3-5). As a first step toward this goal, the present work describes a quantitative determination of the equilibrium in the Ge-Cl_2 system using a Bourdon gauge.

As early as 1887 Nilson and Pettersson (6) noted the thermal stability of $GeCl_4$. By measuring the vapor density of $GeCl_4$ vapor they found that it was essentially undecomposed up to 1012°K at atmospheric pressure. In contact with solid Ge, however, it has been repeatedly postulated that an equilibrium with the dichloride obtains (3, 4, 7, 8)

$$Ge(s) + GeCl_4(g) \rightleftarrows 2GeCl_2(g)$$

Although both Dennis and Hunter (7) and Schwarz and Baronetzky (9) have obtained a solid reaction product with a Cl/Ge ratio of 2 from the action of gaseous $GeCl_4$ on solid Ge, it does not necessarily follow that the vapor phase species has either the same stoichiometry or the same degree of polymeric character (monomer *vs.* dimer, etc.). This is particularly true since it appears that the solid $(GeCl_2)_x$ phase is polymeric (10).

Although related Group IVA halide systems. *i.e.*, $Si-Cl_2$, $Ge-I_2$, $Ge-Br_2$, exhibit disproportionation type equilibria (11-13), there was the possibility that species other than $GeCl_2$ and $GeCl_4$ might be important in the present system. For example, both Ge_2Cl_6 and GeCl have been produced under nonequilibrium conditions in this system (9, 14-16).

Experimental

Bourdon gauge, pressure control, and measurement.—The Bourdon gauge (12) and furnace used in the present studies are shown in Fig. 1. Flag movements caused by pressure changes modulate a light beam passing through the light pipes. The resultant optical signal is used to actuate automatically the valves to both pressure and vacuum sources which control the pressure in the equalizing chamber to "null" the flag. The details of this automatic pressure control system have been described previously by Hochberg (17).

The pressure in the equalizing chamber was measured with a model FA 129 Wallace and Tiernan dial-type manometer which had been calibrated with a 13 mm diameter Hg manometer. Both the pressure control and accuracy are within ±0.2 mm Hg. The zero pressure point was checked frequently and, although its variation was normally within the above limits, an occasional deviation of 1-2 mm Hg was observed.

Chemical purity.—Sylvania "Special High Purity" semiconductor grade $GeCl_4$ was distilled under vacuum to remove all inert gases and transferred to the gauge in an all glass apparatus. Since 1-mg quantities of $GeCl_4$ were used, the glass apparatus was carefully cleaned and baked out before transfer of the $GeCl_4$. In sample 1, a 36 ohm-cm undoped Ge wafer was used. In samples 2 and 3, small wafers of 16 ohm-cm Ga doped Ge were used as the Ge solid phase. The wafers were etched in "white etch" and rinsed with deionized water and ethanol before use. The Bourdon gauge and wafer were baked out at 450°-700°C for more than 12 hr at a final pressure of 2×10^{-7} mm Hg (at the pump). The bake out tube (to vacuum) and the sample delivery tube were subsequently removed from sample chamber and are not shown in Fig. 1.

Experimental procedure.—The pressure of a total of four different samples was measured as a function of temperature. The pressure readings were taken over several cycles of increasing and decreasing temperatures. In the temperature region where a chemical reaction took place, it was necessary to wait for ½ hr ($T > 800$°K) to several days ($T < 600$°K) before chemical equilibrium was achieved, and no further change in pressure occurred as a function of time. The temperature was measured with a Pt-Pt 10 Rh or a Chromel-Alumel thermocouple both at the Ge wafer in the bottom of the sample chamber and at the top of the thermocouple well. The temperature in the furnace was adjusted so that the top of the Bourdon gauge was 2-10°C higher than the bottom (position of Ge wafer) to avoid condensation of solids on the spoon.

Results and Discussion

Thermal stability of $GeCl_4(g)$.—The pressure of a sample of gaseous $GeCl_4$ (59 mm Hg at 300°K) at constant volume was found to be a linear (within <1%) function of the temperature up to 1300°K. It was therefore concluded that $GeCl_4$ does not dissociate significantly over this range of temperature and pressure.

Equilibrium in the $GeCl_4$-Ge *system.*—The pressure *vs.* temperature data for three different samples of $GeCl_4(g)$ plus Ge(s) spanning a fivefold range in total pressure are shown in Fig. 2. In each sample the number of moles of solid Ge used was at least a factor of ten greater than the number of moles of gaseous $GeCl_4$. The presence of an excess Ge solid phase was confirmed visually up to ~800°K. During the measurements no solid phase other than Ge was observed with one exception.[1]

In all three samples the initial linear portion of the curves (up to ~570°K) is attributed to an ideal gas law pressure increase of $GeCl_4$ gas. From ~570°-950°K the increasing slope shows an increase in the number of gas molecules. In samples 1 and 3 the second linear region above ~950°K has a slope, P/T, twice the slope

[1] In one experiment using a different furnace arrangement, the sample temperature was dropped rapidly by cooling the bottom of the gauge with an air stream. In this case a yellow-green-gray solid was condensed on the chamber walls and the final pressure read 36 mm Hg instead of the expected 54 mm Hg. Presumably the color was due to a condensed chlorine containing phase similar to that described by Schwarz and Baronetzky (9). On recycling the system at a uniform temperature, the condensed phase disappeared, and the pressure returned to the expected value.

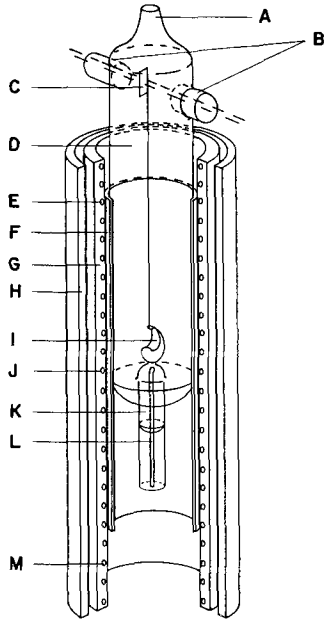

Fig. 1. Bourdon gauge and furnace arrangement: A, to pressure control; B, light pipes; C, flag; D, equalizing chamber; E, M, end windings; F, nickel pipe; G, quartz furnace; H, Morganite heat reflector; I, asymmetric spoon; J, center winding; K, sample chamber; L, thermocouple well.

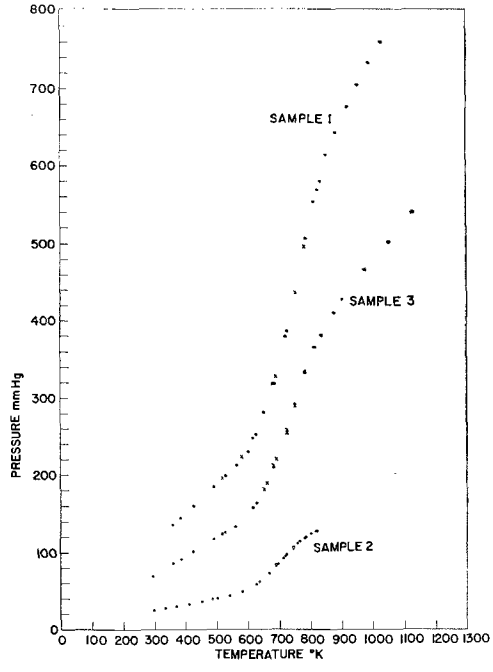

Fig. 2. Pressure *vs.* temperature data for three samples of $GeCl_4(g)$ plus Ge(s) at constant volume.

Table I. Slope of pressure vs. temperature curves for samples of $GeCl_4(g) + Ge(s)$

	(P/T) for $T < 570°K$	(P/T) for $T > 950°K$	$\frac{(P/T) \text{ for } T > 950°K}{(P/T) \text{ for } T < 570°K}$
Sample I	0.375 ± 0.001 [7]	0.742 ± 0.001 [4]	1.98
Sample II	0.240 ± 0.001 [8]	0.477 ± <0.001 [3]	1.98

The numbers in brackets indicate the number of data points averaged.

of the respective low temperature linear regions as indicated in Table I.

Postulation of an equilibrium model.—As possible models, we have considered all equilibria involving $GeCl_4(g)$, Ge(s), and the species $(GeCl_x)_y$ where $x = 1, 2, 3$ and $y = 1, 2$.

$y = 1$

$$3Ge(s) + GeCl_4(g) \rightleftarrows 4GeCl(g) \quad [1]$$

$$Ge(s) + GeCl_4(g) \rightleftarrows 2GeCl_2(g) \quad [2]$$

$$1/3Ge(s) + GeCl_4(g) \rightleftarrows 4/3GeCl_3(g) \quad [3]$$

$y = 2$

$$3Ge(s) + GeCl_4(g) \rightleftarrows 2Ge_2Cl_2(g) \quad [4]$$

$$Ge(s) + GeCl_4(g) \rightleftarrows Ge_2Cl_4(g) \quad [5]$$

$$1/3Ge(s) + GeCl_4(g) \rightleftarrows 2/3Ge_2Cl_6(g) \quad [6]$$

The observed doubling of the number of gas molecules in passing from low to high temperatures (see Table I), indicates that only the equilibria Eq. [2] and [4] are adequate models. In addition, there is a model involving two simultaneously operative equilibria, *i.e.*, Eq. [5] and [7], which is consistent with the observed doubling of molecules as discussed above.

$$Ge(s) + GeCl_4(g) \rightleftarrows Ge_2Cl_4(g) \quad [5]$$

$$Ge_2Cl_4(g) \rightleftarrows 2GeCl_2(g) \quad [7]$$

Although the three models Eq. [2], [4], and [5] and [7] are indistinguishable on the basis of Bourdon gauge measurements alone, the latter two models are considered unlikely since neither the species Ge_2Cl_4, Ge_2Cl_2, nor their analogs for any Group IVA-halide (carbon excepted) combination have ever been observed (18, 19). In the Ge-I_2 system, for instance, the complementary Bourdon gauge measurements of Lever (12) and weight-loss measurements of Jona *et al.* (13) specifically rule out the possibility that Ge_2I_2 and Ge_2I_4 are major constituents of the vapor phase. In the Ge-Cl_2 system Haq (20) has been able to observe only a single species which persists over the whole temperature range 473°-873°K (presumed to be $GeCl_2$). In the present study the onset of Ge etching has been observed visually to coincide with a measurable pressure increase, which indicates qualitatively that there is at most only a small concentration of Ge_2Cl_4 present. For the above reasons the model involving $GeCl_2$ has been chosen as the most probable description of the system, and the following analysis will be made on the basis of Eq. [2]

Test of the model.—In order to test the validity of the proposed model, Eq. [2], the functional dependence of the equilibrium constant, K_p, on temperature and pressure was determined.

$$K_p = \frac{P^2_{GeCl_2}}{P_{GeCl_4}} \quad [8]$$

The partial pressures of $GeCl_2$ and $GeCl_4$ were calculated by noting that

$$P_{total} = P_{GeCl_4} + P_{GeCl_2} \quad [9]$$

and since no chlorine containing solid phase was observed, the molecular conservation of chlorine in the vapor phase requires that

$$\frac{N_{Cl}RT}{V} = 4P_{GeCl_4} + 2P_{GeCl_2} \quad [10]$$

where N_{Cl} is the total number of moles of chlorine atoms in the gas phase.

Simultaneous solutions of Eq. [9] and [10] yield

$$P_{GeCl_4} = \frac{N_{Cl}RT}{2V} - P_{total} \quad [11]$$

$$P_{GeCl_2} = 2P_{total} - \frac{N_{Cl}RT}{2V} \quad [12]$$

The quantity $N_{Cl}R/V$ is a constant for each sample and was calculated from Eq. [11] for $T > 950°K$ where P_{GeCl_4} is essentially zero and from Eq. [12] for $T < 570°K$ where P_{GeCl_2} is essentially zero (see Table I).

The standard enthalpy $\Delta H°$, and entropy, $\Delta S°$, of reaction were obtained by the second law treatment using the relation

$$\log K_p = \frac{\Delta H°}{-2.303RT} + \frac{\Delta S°}{+2.303R} \quad [13]$$

where $\Delta H°$ and $\Delta S°$ are assumed independent of temperature.

Calculated values of $\log K_p$ *vs.* $1/T$ are shown in Fig. 3. The constancy of K_p with varying pressure at constant temperature and the linearity of the $\log K_p$ *vs.* $1/T$ are confirmation that the model Eq. [2] is a satisfactory description of the system. If significant quantities of GeCl, $GeCl_3$, or Ge_2Cl_3 were present, log

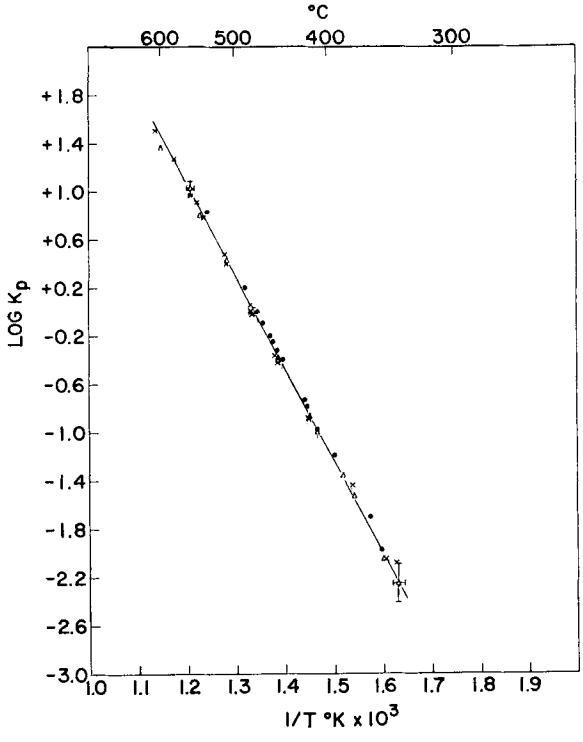

Fig. 3. log K_p *vs.* $1/T$ for the postulated equilibrium $Ge(s) + GeCl_4(g) \rightleftarrows 2GeCl_2(g)$. X, Sample 1; •, sample 2; △, sample 3.

Table II. Calculated thermodynamic properties of the reaction

	$Ge(s) + GeCl_4(g) \rightleftarrows 2GeCl_2(g)$	
	$\Delta H°_{723°K}$ (kcal)	$\Delta S°_{723°K}$ (eu)
Sample 1	34.1	45.6
Sample 2	35.5	47.7
Sample 3	35.0	46.7
Avg	34.9 ± 0.5	46.7 ± 0.7

Standard state 1 atm

K_p would not be constant with varying total pressure nor would it in general be linear with $1/T$.

Calculated values of $\Delta H°$ and $\Delta S°$ for each sample based on a least squares fit of Eq. [13] to the data are presented in Table II.

As a check on the experimentally determined value of $\Delta S°$, the entropy of reaction was calculated at 700°K from entropy values of Ge(s) and $GeCl_4(g)$ listed by Kelley (21, 22) and from a computed entropy of $GeCl_2(g)$ from estimated molecular constants and spectroscopic data described in Appendix I.

$$\Delta S°_{700} = 2S°_{GeCl_2(g)} - S°_{Ge(s)} - S°_{GeCl_4(g)}$$
$$\Delta S°_{700} = 2 \times 80.7 \pm 2 - 12.6 \pm 0.1 - 103.8 \pm 0.8$$
$$\Delta S°_{700} = 45.0 \pm 4 \text{ eu} \qquad [14]$$

The calculated value of 45.0 eu is in excellent agreement with the measured value of 46.7 eu and is well within the uncertainties in the entropy values indicated.

Acknowledgment

The author wishes to thank A. Reisman, R. Lever, and H. Leonhardt for many helpful discussions. He is particularly indebted to B. Agule who made most of the experimental measurements and calculations, and to G. Cheroff and F. Hochberg who designed, built, and tested the automatic pressure control system. This work was supported in part by AFCRL Contract No. AF19(628)-2468.

Manuscript received Nov. 2, 1964. This paper was presented at the Toronto Meeting, May 3-7, 1964.

Any discussion of this paper will appear in a Discussion Section to be published in the December 1965 JOURNAL.

REFERENCES

1. A. Reisman and S. A. Alyanakyan, *This Journal*, **111**, 1154 (1964).
2. R. F. Lever, *IBM J. Res. & Dev.*, **8** #[4], 460 (Sept. 1964).
3. J. J. Grossman, *This Journal*, **110**, 1065 (1963).
4. E. I. Giuargizov, *Fiz. Tverdogo Tela*, **5**, 1150 (1963).
5. K. J. Miller and M. J. Grieco, *This Journal*, **111**, 1099 (1964).
6. L. F. Nilson and D. Pettersson, *Z. Physik. Chem.*, **1**, 27 (1887).
7. L. M. Dennis and H. L. Hunter, *J. Am. Chem. Soc.*, **51**, 1151 (1929).
8. O. H. Johnson, *Chem. Rev.*, **51**, 441 (1952).
9. R. Schwarz and E. Baronetzky, *Z. anorg. u. allgem. Chem.*, **275**, 1 (1954).
10. C. W. Moulton and J. G. Miller, *J. Am. Chem. Soc.*, **78**, 2702 (1956).
11. H. Schafer and J. Nickl, *Z. anorg. u. allgem. Chem.*, **274**, 250 (1953).
12. R. F. Lever, *This Journal*, **110**, 775 (1963).
13. F. Jona, R. F. Lever, and H. R. Wendt, *ibid.*, **111**, 413 (1964).
14. D. Shriver and W. L. Jolly, *J. Am. Chem. Soc.*, **80**, (1958).
15. W. L. Jolly, C. B. Lindahl, and R. W. Kopp, *Inorgan. Chem.*, **1**, 958 (1962).
16. Jevons, Bashford, and Biscoe, *Proc. Phys. Soc. (London)*, **49**, 532 (1937).
17. F. Hochberg, Paper presented at the New York Meeting of the Society, Sept. 29-Oct. 3, 1963, Abstract 139.
18. T. Moeller, "Inorganic Chemistry," Chap. 16, John Wiley & Sons, Inc., New York (1952).
19. C. Eaborn, "Organosilicon Compounds," Chap. 3, Academic Press, New York (1960).
20. K. E. Haq and W. von Muench, Paper presented at the New York Meeting of the Society, Sept. 29-Oct. 3, 1963, Abstract 140.
21. K. K. Kelley and E. G. King, *Bur. Mines Bull. 592*, U. S. Gov't. Printing Office, Washington, D. C. (1961).
22. K. K. Kelley, *Bur. Mines Bull. 584*, U. S. Gov't. Printing Office, Washington, D. C. (1961).
23. "Tables of Interatomic Distances and Configuration in Molecules and Ions," Special Publication No. 11, The Chemical Society, London (1958).
24. R. K. Asundi, M. Karim, and R. Samuel, *Proc. Roy. Soc.*, **A50**, 581 (1938).
25. G. C. Sinke, "Thermodynamic Properties of Combustion Products." Dow Chemical Co., Midland, Mich. (April 1959).
26. G. Herzberg, "Molecular Spectra and Molecular Structure," p. 131, Van Nostrand, New York (1945).
27. "JANAF Thermochemical Data," Dow Chemical Co., Midland, Mich.

APPENDIX I

Calculation of the Entropy of $GeCl_2(g)$

The bond length of 2.1Å was taken to be essentially equal to the Ge-Cl bond length in $GeCl_4(g)$ (23). There is electron diffraction (23) and spectroscopic (24) evidence that the Group IV A dihalides are nonlinear. The bond angle of $GeCl_2$ was assumed to be the same as for $SiCl_2$ which was estimated by Sinke (25). The symmetric valence vibration frequency, ω_1, and the deformation vibration frequency, ω_2, for $GeCl_2$ were estimated by averaging the corresponding vibrational frequencies of $SnCl_2$ and $SiCl_2$ as measured by Asundi, Karim and Samuel (24). The asymmetrical valence vibrational frequency, ω_3, was estimated to be equal to 1.12 ω_1 since the nonlinear XY_2 molecules listed by Herzberg (26) in Table 37 exhibit on the average the property $\omega_3 \simeq 1.12\ \omega_1$.

Table III. Summary of the estimated and calculated molecular constants

Molecular weight	143.5g
Ge-Cl bond length	2.1Å
Cl-Ge-Cl angle	110°
Product of moments of inertia $I_AI_BI_C$	1.308×10^{-113} g²/cm⁶
Symmetry number	2
Vibrational levels [multiplicities]	
ω_1	450 cm⁻¹ [1]
ω_2	185 cm⁻¹ [1]
ω_3	505 cm⁻¹ [1]

The entropy was calculated from the data in Table III using the formulas given in the JANAF tables (27). Only the ground electronic state was assumed to be occupied in analogy to $SnCl_2$ and $SiCl_2$ (24, 25), and the usual assumptions of a rigid rotator and harmonic oscillator were made.

$$S°_{total} = S°_{electronic} + S°_{translation+rotation} + S°_{vibration}$$
$$= 0 + 72.6 + 8.1$$
$$S°_{total} = 80.7 \pm 2 \text{ eu} \qquad [15]$$

Deposition of Germanium Films by Sputtering

K. E. Haq

Thomas J. Watson Research Center, International Business Machines Corporation, Yorktown Heights, New York

ABSTRACT

Both n and p-type germanium films were deposited epitaxially by using asymmetric a-c sputtering. The quality of the films was found to be strongly dependent on the substrate temperature and the voltages during both the cleaning and the sputtering cycles. It was demonstrated that when the sputtering parameters were properly adjusted, the films deposited from n-type source material showed n-type conductivity, even when they were polycrystalline, indicating that the p-type conductivity observed previously in sputtered films was primarily due to impurities. Further, epitaxial films of the same type and conductivity and of approximately the same carrier concentration as the source material were deposited with substrate temperatures as low as 350°C.

There have been continuing efforts in the deposition of single crystal films of semiconducting materials epitaxially on various substrates. Considerable success has been achieved in obtaining good quality films by the halogen transport process. Although germanium and silicon films were deposited epitaxially by vacuum evaporation and sputtering techniques (1-5), the films, with the exception of a few cases, showed p-type conductivity, even though the source materials were heavily doped with n-type impurities. In those few instances (4-5) where the authors reported success in depositing n-type silicon films, the evaporations were conducted at a vacuum of 10^{-9} Torr. As for germanium there have been no reports of successful deposition of n-type films by either sputtering or evaporation. There has been considerable discussion in the literature as to why the films generally showed p-type conductivity (6-7). Some authors attributed this result to impurities, while others considered it to be due to imperfection in the crystalline structure of the films. Recently, it has been demonstrated in the case of silicon that the p character in conductivity is not entirely due to structural defects but due partially to contamination.

Frerichs (8) has reported that good quality superconducting metal films can be deposited by using asymmetric a-c sputtering. In the present investigation the same technique has been successfully used for the deposition of single crystal germanium films. It has been observed that even with the use of a system capable of obtaining vacuum in the high 10^{-6} range, both n- and p-type germanium films can be deposited on either type of germanium substrate, if the sputtering conditions are properly adjusted. In the present paper detailed conditions for depositing such films by sputtering and their properties will be reported.

Experimental

Apparatus.—The experimental apparatus consisted of a 14 in. glass bell jar system with a 2-in. oil diffusion pump and a liquid nitrogen trap. After overnight pumping, the system reached an ultimate vacuum of 7 x 10^{-6} mm Hg. The electrode geometry was as shown in Fig. 1. The electrodes were made of ¼ in. stainless steel rods surrounded with stainless steel shields. A spacing of 1/16 in. was maintained between the rod and the shield. A disk of polycrystalline germanium approximately 2 in. in diameter was used as a source material. It was prepared by casting pure germanium with a known amount of impurity. The disk rested on a molybdenum stage screwed to the top of the lower electrode. This arrangement precluded the use of any clips or screws for holding the source, and thus eliminated the problem of sputtering of undesirable impurities along with the source material. The germanium substrate was held with clips to a molybdenum disk which was screwed to the upper electrode with the substrate facing down towards the source.

One geometrical feature of the shields surrounding the source and the substrate should be pointed out. In the case of the source, the shield protruded approximately 1/16 in. beyond the level of the source. This arrangement confined the bombardment to the source alone, due to the repulsion of the positive ions by the shield. The substrate, on the other hand, protruded about the same distance beyond its shield. This configuration insured uniform bombardment of the substrate by the positive ions during the cleaning cycle.

The substrate heater consisted of a hollow doughnut shaped structure attached to the shield that surrounded the substrate holder. The heating of the substrate was accomplished by radiation. The temperatures of the substrate were determined in the following way: In an auxiliary experiment the temperatures of the substrate holder corresponding to different temperatures of the heater were measured by attaching one thermocouple to the heater and another to the substrate holder. A calibration curve was then plotted. During the actual run, the temperature of the heater was monitored. Using the calibration curve, the temperature of the substrate was determined.

An asymmetric 60 cycle a-c voltage was used for sputtering. The characteristics of the voltages applied to the source, the substrate, and the shields are shown in Fig. 2. Several features of the voltages should be

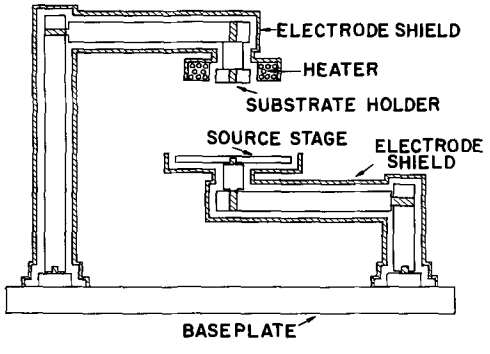

Fig. 1. Electrode geometry used for deposition of germanium film by sputtering.

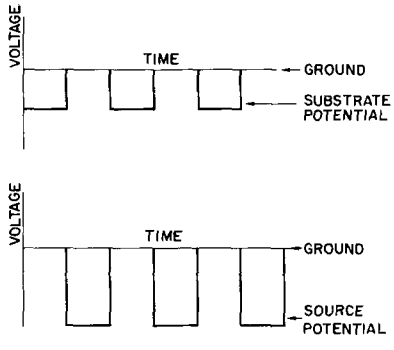

Fig. 2. Characteristics of voltages appearing on the source, substrate, and the shields during sputtering.

pointed out. First, the wave forms of the voltages appearing on the electrodes were square rather than sinusoidal. Second, when the source became negative, the substrate and the shields were at the ground potential. Similarly, when the substrate became negative, the source and the shields were at the ground potential. In this way, during sputtering the bombardment of all the undesirable parts of the system by positive ions was prevented. In the rest of the discussion, the negative voltages appearing on the source and the substrate will be referred to as the sputtering voltage and the cleaning voltage respectively.

Operational Procedure

The following procedure was used for the deposition of films. Germanium wafers, cut from a single crystal ingot, were first mechanically polished, and given a 5 min etch with CP_4. The wafer was then rinsed several times with deionized water and stored under alcohol until ready to be mounted. The source material was cleaned in the same way as the substrates. No further cleaning was done to the source between runs. After the source and the substrate were mounted, the system was evacuated to 7×10^{-6} Torr. The substrate heater was then turned on. Sufficient time was allowed for the substrate to come to a predetermined temperature equilibrium. A dynamic equilibrium pressure of approximately 45μ was then established in the bell jar by bleeding in ultra high purity argon through a needle valve, with the system open to the mechanical pump through a liquid nitrogen trap. It is essential that a cold trap be used between the bell jar and the mechanical pump to prevent the back-streaming of oil vapor from the mechanical pump. Experience has shown that unless such a precaution is taken, the properties of the film are adversely affected.

After the establishment of the argon pressure in the bell jar, both the source and the substrate were cleaned for 5 min with 1000v ions. At the end of the cleaning period, the source voltage was raised, while the substrate voltage was lowered to some predetermined values. The run was continued for a period of several hours, at the end of which time the system was opened to the diffusion pump and allowed to cool under vacuum before the film was exposed to air.

Results and Discussion

Since there has been considerable discussion in the literature as to why the evaporated and sputtered germanium films showed only p-type conductivity, part of the present investigation was devoted to determining the various deposition parameters which gave either n- or p-type films when n-type source material was used. After determining the conditions that gave reproducible n-type films, several such films were deposited on p-type substrates. The characteristics of the films and the p-n junction were then investigated. Germanium films were deposited on germanium substrates under various growth conditions. In all experiments the source to substrate distance was maintained constant at 2½ in. X-ray diffraction techniques were used to determine whether or not the films were epitaxial. The thickness of the films was determined by an interferometric method. The type of conductivity of the films was established from thermoelectric voltage measurements.

It has been observed that films deposited from a n-type source material show p-type conductivity unless several precautions are taken. First, after the system is pressurized with clean argon to a predetermined value, the sputtering must be immediately initiated. Second, the ion bombardment should be confined between the source and the substrate. Otherwise, impurities released from the electrodes and the fixtures during sputtering are incorporated in the film. Finally, the geometry of the electrodes should be such that uniform bombardment of the substrate during the cleaning cycle is insured. Otherwise, part of the film may show n-type conductivity, whereas the rest may be p-type. This phenomenon was observed during the early part of the investigation when proper precautions were not taken.

As the run proceeds the system slowly becomes heated and as a result, outgassing of the apparatus increases. If the run is continued for too long, the contamination from outgassed impurities may be so severe that the type of conductivity of the film may vary through the deposit thickness. It will be instructive, perhaps, to describe the result of a particular run, since it illustrates such an effect; and moreover, it gives an indication as to what might have been the chief reason for the general occurrence of p-type conductivity of sputtered and evaporated films deposited from n-type source material.

The experiment was designed to obtain a thick n-type film on a p-type substrate, therefore the run was continued for 8 hr, instead of the usual 3-4 hr. When examined, the film unexpectedly showed p-type conductivity. After a few upper layers were removed by flash etching, the film underneath was found to be n-type, indicating that the p-type impurity was incorporated in the layers that were deposited in the latter part of the run. We interpret this to be associated with system outgassing as the temperature of the supporting structures increases. This result would also imply that the chief cause of the generally observed p-type conductivity in films prepared by evaporation and sputtering from n-type sources is due to impurity rather than crystal defects. It should be noted that several of the deposited films during the present investigation showed n-type conductivity, even though they were found to be polycrystalline by x-ray analysis.

The crystalline quality of the films was found to be strongly dependent on sputtering parameters, namely substrate temperature, deposition rate (*i.e.*, the sputtering voltage) and the cleaning voltage. For a particular temperature of the substrate and cleaning voltage, the film may be epitaxial, polycrystalline, or amorphous, depending on the growth rate. At a low growth rate the film is epitaxial, while at an increasing growth rate the film becomes first polycrystalline and then amorphous. Similar dependence of crystalline properties of deposited films on substrate temperature and deposition rate was observed by Krikorian (9) in the case of d-c sputtering.

Films deposited from p-type source always showed p-type conductivity, whether or not the films were single crystal. On the other hand, the films deposited from an n-type source material showed p-type conductivity, unless the temperature and the voltage applied during the cleaning cycle were consistent with the sputtering voltage (*i.e.*, deposition rate). For example the films deposited with the substrate at 400°C and the cleaning voltage of 250v showed p-type conductivity when the sputtering voltage was 3000v. However, when the sputtering voltage was reduced to 2000v, the films deposited at the same substrate temperature and cleaning voltage showed n-type conductivity. Table I shows the highest sputtering volt-

Table I. Highest sputtering voltages at which n-type Ge films were obtained on p-type <111> oriented Ge substrates at various substrate temperatures and cleaning voltages

Substrate temp, °C	Cleaning voltage	Sputtering voltage	Deposition rate, μ/hr	Crystallinity
500	500	3700	1.0	Single
400	250	2000	0.32	Single
400	600	3000	1.1	Single
350	600	3000	0.9	Single
325	600	3000	1.5	Poly
300	600	3000	1.4	Poly

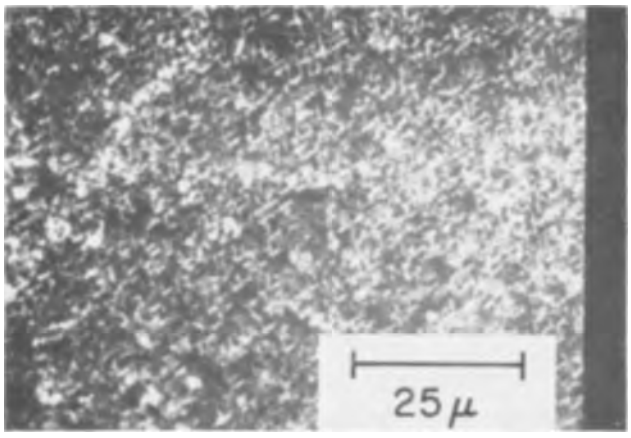

Fig. 3. Photograph of the "as grown" surface of the germanium epitaxial layer deposited by sputtering.

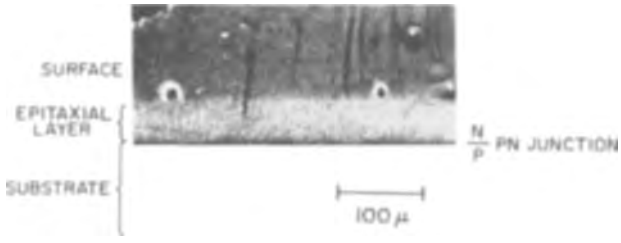

Fig. 4. Appearance of the junction after it was angle lapped and stained with copper.

ages at which n-type films were obtained at various substrate temperatures and cleaning voltages.

The films were examined in several ways to evaluate their properties. To do that, a polycrystalline n-type source doped with 2-3 x 10^{17} atoms/cc of antimony was prepared. Using this source, single crystal n-type films were deposited on p-type substrates.

Under microscopic examination, films deposited on substrates oriented in the <111> direction showed triangular pyramids, as can be seen in Fig. 3. From an n-type layer deposited on a p-type substrate containing 7-9.4 x 10^{18} atoms/cc of impurity, diodes were fabricated by mesa etching. The current voltage characteristics and the differential capacitance of the diodes were measured. A plot of $1/C^2$ *vs.* voltage showed a straight line indicating that the junction was abrupt. Further, from the slope of the straight line, the carrier concentration was estimated at 1.04 x 10^{17}/cc., which was approximately the doping level of the source material. The reverse bias breakdown voltage also agreed with the value calculated from the carrier concentration. To further examine the nature of the junction, a sample was angle lapped and stained with copper. The appearance of the junction at 250X, exhibited in Fig. 4, shows that the junction was fairly sharp. To determine the concentration and the mobility of the carriers, a sample was prepared by depositing n-type film on a 40 ohm/cm p-type germanium substrate oriented in the <111> direction. The previously described source material was used here also. The sputtering voltage, 3000v; substrate temperature, 360°C; cleaning voltage, 600v were used for deposition. A 100 mil square chip of the deposit was diced and contact was made at the four corners. The resistivity and the Hall voltage were measured at liquid nitrogen temperature by using the Van der Pauw method. The mobility and the carrier concentration, calculated from the above measurements were as follows:

$$\mu = 1930 \text{ cm}^2/\text{v sec}$$

$$N = 3 \times 10^{17}/\text{cc}$$

Thus the carrier concentration of the film is approximately equal to the doping level of the source material. This would indicate that in the sputtering process the transfer of material from source to substrate takes place without change of composition.

Fritzschi (10) made Hall voltage and resistivity measurements at liquid nitrogen temperatures on bulk samples with various carrier concentrations. The mobilities calculated from his data for carrier concentrations 2.7 x 10^{17}/cc and 1.3 x 10^{17}/cc are 1810 cm^2/v sec and 3230 cm^2/v sec, respectively, showing that the mobility of the carriers in the sputtered films is similar to that of the bulk material for the same range of carrier concentration. This would indicate that the films obtained by sputtering have fairly good crystalline quality.

Acknowledgment

The author expresses his appreciation to M. Cowher for making the Hall voltage and resistivity measurements and to Dr. F. Fang for differential capacitance data. He also thanks Dr. A. Reisman for his critical reading of the manuscript.

Manuscript received Dec. 2, 1964.

Any discussion of this paper will appear in a Discussion Section to be published in the December 1965 JOURNAL.

REFERENCES

1. G. A. Kurov, S. A. Semiletov, and Z. G. Pinsker, *Kristallografia*, **2**, 59 (1957).
2. O. Weinreich, G. Dermit, and C. Tufts, *J. Appl. Phys.*, **32**, 1170 (1961).
3. F. Reizman and H. Basseches, "Metallurgy of Semiconducting Material," J. B. Schroeder, Editor, Interscience Publishers, New York (1961).
4. E. T. Handelman and E. I. Povilonis, *This Journal*, **111**, 201 (1964).
5. I. G. Ptushinskii and I. A. Lupan, *Ukrain. Fiz. Zhur.*, **4** [1], 125 (1959).
6. G. A. Kurov, *Fiz. Tverdogo Tela*, **3**, No. 6 (1961).
7. D. S. Campbell, *Brit. J. Appl. Phys.*, **15**, (1964).
8. R. Frerichs, *J. Appl. Phys.*, **33**, 1898 (1962).
9. E. Krikorian and R. J. Sneed, Vac. Trans. Symposium 1963.
10. H. Fritzsche, J. Phys. Chem. Solids, Pergamon Press, Vol. 6 (1958).

On the Mechanism of the Deposition of Silica by Pyrolytic Decomposition of Silanes

Julius Klerer

Bell Telephone Laboratories, Incorporated, Murray Hill, New Jersey

ABSTRACT

The mechanism of formation of silica films produced by the thermal decomposition of ethyltriethoxysilane has been studied. It is proposed that the thermal decomposition of the silane results in the production of complex silicon-alkyl radicals which become chemisorbed on a hot surface and suffer further decomposition in order to form a silica film. Recombination of these radicals on a cold surface leads to the formation of organic polymers of silicon. A new technique for the production of thick silica films is also presented.

Thermal decomposition of organo-oxy-silanes has been reported to provide a method for the deposition of thin silica films. Jordan (1) used ethyltriethoxysilane vapor which was passed with argon as a carrier gas into a furnace at ≅ 700°C to accomplish film formation on a sample contained in the furnace at the same temperature. This is a closed tube technique. Klerer (2), utilizing the same experimental arrangement and conditions, allowed the gases from the furnace to contact a sample outside of the furnace in an open tube technique and obtained a film claimed to be silica.

The mechanism of formation of these films has been formulated and their properties measured. It is shown that the films produced by the technique of Jordan are probably pure silica and that those produced by the technique of Klerer are organic polymers of silicon.[1] A new technique for producing silica films is also presented.

Materials and Methods

Ethyltriethoxysilane was obtained from Union Carbide Silicones Division and redistilled to obtain the purified silane. This product was then used as the starting material for all of the investigations. Mass spectrographic analysis of the gases exiting from the furnace during the thermal decomposition of the silane was performed. Gases evolved on heating of the polymer film were also examined by the mass spectrograph. Infrared transmission spectra of both types of films were obtained. Density and refractive index of the films were determined by ellipsometric techniques.

Experiments and Results

Furnace films.—Utilizing the closed tube technique, argon was passed through ethyltriethoxysilane at 1 CFH and then through a furnace maintained at 725° ±5°C. A gas sampling tube was placed at the exit end of the furnace, and gases were allowed to pass through it for a period of 15 min; then the tube was sealed off. The composition of the gases were determined by the mass spectrograph. The principal gases observed and their relative amounts normalized to C_2H_4 were $CH_2 = CH_2$ [1], CH_4[0.75], CO [1], and H_2 [0.49]. Trace amounts of C_2H_6 and C_3H_8 [0.02] were also noted, and essentially no evidence of water was found.

Samples of chemically (CP-4) polished silicon (100 ohm-cm), when placed in the furnace at 725°C, were coated with a film. The infrared transmission spectra of these films were comparable to silica films produced by thermal (1200°C, dry O_2) and steam (975°C) oxidation of similar silicon wafers.

The furnace films, when heated to 825°C in air or in argon, appeared to become denser as evidenced by an increase in refractive index from 1.430 to 1.450. Similar results were reported by Pliskin *et al.* (3). Deposition of the furnace films at 825°C resulted in a silica film with a refractive index of 1.450, and further heat-treatment at 900°C did not result in any further change in the refractive index. Deposition of furnace films above 825°C resulted in cloudy films initially which were followed by whitish and grayish appearing films as the temperature was raised to 950°C.

One deficiency of the furnace films is that, unless they are properly annealed, cracking or crazing of the film occurs when the thickness exceeds 15,000-20,000Å (3). A new technique for depositing silica films was developed to overcome this difficulty. Wafers of silicon were placed on a hot stage at 900°C and ethyltriethoxysilane vapor, carried in a stream of nitrogen, was allowed to impinge on the heated silicon. Formation of a silica layer occurred. The refractive index was determined to be 1.455.

Further heating at higher temperatures did not change this value, and the infrared spectra agreed closely with that of thermally oxidized silicon. At a nitrogen flow rate of 2 CFH and a surface temperature of 800°C, 2000Å of silica were formed per minute. Clear and continuous layers up to 200,000Å have been formed which withstood temperature cycling from 900°C to liquid nitrogen temperature.

Polymer films.—A reinvestigation of the films produced by the open tube technique was initiated in order to characterize them with respect to the other silane decomposition techniques.

Table I. Infrared absorption bands of polymer films

Frequency, cm^{-1}	Intensity	Provisional assignment	Effect of heating on intensity, 300°C, air
3600	W	Free—OH	Appears on heating
3380	S	H_2O, Silanol, —OH	Diminishes
2960	M	$=CH_2$, $CH_2=CH_2$	No change
2880	W	$—CH_3$, $O—CH_3$	Diminishes
2240	M	Si—H	Diminishes
1637	VW	$CH_2=CH_2$, Opal	No change
1460	W	$R—CH_3$, CH Bend	Diminishes
1415	VW	$R—CH_3$, CH Bend	Diminishes
1395	VW	$R—CH_3$, CH Bend	Vanishes
1255	W	$Si—CH_3$, Si—C Bend	Diminishes
1170	SSh	≡Si—O—R, Opal	No change
1065	VS	Si—O stretch, Opal	No change
1013	WSh	Si—O—Si	No change
965	W	—OH deformation	Diminishes
940	W	—OH deformation	Vanishes
880	S	Si—C stretch Si—OH deformation	Diminishes
770	M	Si—O—C $Si—CH_3$	Diminishes and shifts to 800 cm^{-1}

VW, very weak; W, weak; M, medium; S, strong; VS, very strong; Sh, shoulder.

References: L. J. Bellamy, "The Infra-red Spectra of Complex Molecules" John Wiley & Sons, Inc., New York (1954); G. J. Janz and Y. Mikawa, *Bull. Chem. Soc. Japan*, 34, 1504 (1961); K. E. Lawson, "Infra-red Absorption of Inorganic Substances," Reinhold Publishing Corp., New York (1961); R. S. McDonald, *J. Phys. Chem.*, 62, 1168 (1958); F. A. Miller and C. H. Wilkins, *Anal. Chem.*, 24, 1253 (1952); M. Randic, *Spectrochim. Acta*, 18, 115 (1962); N. Wright and M. J. Hunter, *J. Am. Chem. Soc.*, 69, 803 (1947).

[1] Jordan's silica films will henceforth be called "Furnace" films and the films produced by Klerer will be called "Polymer" films.

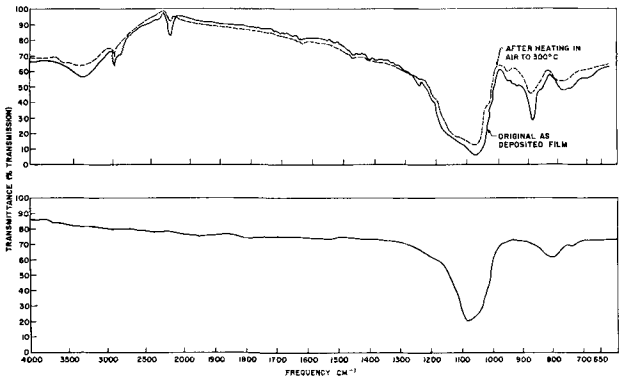

Fig. 1. Infrared spectra of polymer film before and after heat treatment (top) and typical spectra for a furnace produced (750°-825°C) film of silica. Perkins-Elmer model 221 with NaCl prism. Films were deposited on 100 μ-ohm-cm silicon wafers of 0.010 in. thickness. Film thickness was approximately 15,000Å.

Films produced by the open tube process in thicknesses below 3000Å had exhibited infrared transmission spectra similar to the furnace films (2). However, on examination of 15,000Å polymer films, absorption bands were readily observed indicating the presence of $\equiv Si-CH_3$, $\equiv Si-OCH_3$, $\equiv Si-OCH_2CH_3$, $\equiv Si-O-Si\equiv$, $\equiv SiOH$, $\equiv Si-H$, and $\equiv Si-CH=CH_2$ groups as well as bands similar to those in silica gel or opal. Heating of the polymer films above 175°C caused a decrease in magnitude of the absorption bands of $\equiv Si-OH$, $\equiv Si-OCH_3$, $\equiv Si-OCH_2CH_3$, $\equiv Si-H$ and $\equiv Si-CH_3$ with the appearance of some free —OH groups, the remainder of the infrared band structure being unaffected.

Table I lists the principal infrared absorption band positions and provisional assignments together with the change in intensity of the bands on heating of the polymer film to 300°C in air. The particular bands listed appear most frequently in the spectra of polymer films prepared under slightly differing conditions of gas flow and temperature. The principle changes in the spectra are in the different fine structure observed. Figure 1 presents the infrared absorption spectra of a typical polymer film (prepared at 720°C and gas flow of 1 CFH) before and after heat treatment as compared to the spectra obtained from a furnace deposited oxide.

Gases evolved on heating the polymer films were analyzed by the mass spectrograph. The principal gases found were CH_3CH_2OH, H_2, $CH_3CH_2CH_3$, and H_2O. The relative amounts of these gases varied from film to film. Since these gases differed from the thermal decomposition products obtained from the closed tube process, the question arose as to the influence of room air on the polymer film.

A long furnace tube was prepared in which a series wafer was placed from the center of the furnace (725°C) out to the cold exit end (95°C). To prevent back diffusion, the exit from the tube was arranged to bubble through silicone oil. On admitting the ethyltriethoxysilane and argon mixture, film formation was observed on those wafers in the temperature zone between 600°-725°C and on those wafers in the zone between 250°-95°C. The films formed at 600°-725°C were identical to the furnace films, and the films formed between 150° and 95°C were found similar to the polymer films by means of infrared spectral analysis and dissolution behavior in hydrofluoric acid solution. No film formation was observed on substrates in the temperature range between 250° and 600°C. The formation of polymer films in this controlled atmosphere indicated that the gases evolved on heating of the polymer film come from the structure of the film rather than the environment of deposition.

The effect of substrate temperature on the film formed utilizing the open tube technique was investigated. An open furnace was set up so that the gases exiting from the tube would impinge on substrates mounted on a hot stage. During the course of these experiments, the gas flow and temperature in the furnace were constant at 1 CFH and 720°C. Films were deposited on silicon wafers at room temperature to 700°C in 50° steps. No film deposition occurred in the temperature range 250° to 500°C. In addition, the rate of growth of the films decreased as the temperature of the substrate was raised to 250°C, no growth of the film occurred between 250° and 500°C, and then the rate of growth increased from 500° to 700°C. The films deposited in the range of room temperature to 250°C were identical to the polymer film, and the films deposited from 500° to 700°C were similar to the furnace coating.

One of the characteristics of the polymer film in contrast with the furnace film is that in thicknesses $>$ 20,000Å it will crack or spall off silicon or germanium surfaces when heated to $\cong$ 250°C. This can be attributed to a change in density and bonding characteristics upon heating the film to 250°C. Table II presents the results obtained on these films before and after heating together with data obtained for silica films produced by the different techniques.

Discussion of Results

Thermal Decomposition Mechanism

The thermal decomposition of metal alkyls of the type MR_X has been shown to result in the production of free radicals (6). In some cases, besides the normal formation of alkyl radicals, metal alkyl radicals have been proposed to explain the order of the reaction and to justify the end products of the decomposition. One such example is the thermal decomposition of silicon tetramethyl, $Si(CH_3)_4$, in which free radicals such as $Si(CH_3)_3$ and $Si(CH_3)_3CH_2$ have been proposed in the reaction mechanism.

A tentative mechanism for the thermal decomposition of ethyltriethoxysilane can be arrived at by a consideration of both the bond structure of the silane, $(CH_3CH_2)Si(OCH_2CH_3)_3$, and the gaseous products evolved during the decomposition; namely, C_2H_4, CO, CH_4, H_2, and traces of C_3H_8 and C_2H_6. The bond energies involved in the ethyltriethoxysilane would be as follows: Si—O (108 kcal); Si—C (60 kcal); C—O (86 kcal); C—C (83 kcal); C—H (96 kcal) (7). As the temperature is raised, it would be expected that initial bond rupture would occur in the group $\equiv Si-CH_2CH_3$ followed by attack on the group $\equiv Si-OCH_2CH_3$ to give the following possibilities: $(CH_3CH_2O)_3Si(CH_2CH_3)$

$$\rightarrow (CH_3CH_2O)_3Si + CH_3CH_2$$

$$\rightarrow (CH_3CH_2)Si(CH_3CH_2O)_2O + CH_3CH_2$$

$$\rightarrow (CH_3CH_2)Si(CH_3CH_2O)_2 + CH_3CH_2O$$

Table II. Properties of silica films prepared by different techniques*

Technique	Refractive index	Density	Dissolution rate in 1.8M HF, Å/sec
Thermal (dry O_2)	1.450	2.23 ± 0.02	3.3
Steam (high pressure)	1.475	2.32 ± 0.02	3.7
Anodic	1.362	1.80 ± 0.05	360.0
Furnace	1.430	2.14 ± 0.07	48.0
Furnace (after heating to 825°C)	1.450		12.0
Polymer	1.430	1.63 ± 0.04	550.0
Polymer after heating at 250°C	1.390	1.9 ± 0.02#	1200.0

* Measurements made by R. J. Archer and Miss R. E. Cox of these Laboratories.

Calculated from observed volume decrease of 30.6 ± 1.5% and weight decrease of 12.8 ± 4.1%.

Other conceivable reactions could, and quite possibly do, occur, but these shown are sufficient to justify the final products observed. The alkyl free radicals produced from the proposed reactions can then react further in the following well-known manner (6):

$$CH_3CH_2 \rightarrow CH_2{=}CH_2 + H$$

$$CH_3CH_2O \rightarrow CH_3CO + H_2$$

$$CH_3CO \rightarrow CH_3 + CO$$

$$CH_3 + H \rightarrow CH_4$$

$$2CH_3 \rightarrow CH_3CH_3$$

$$CH_3 + CH_3CH_2 \rightarrow CH_3CH_2CH_3$$

Although the formation of the gaseous products observed can be explained by these equations, the relative amounts found did not fit any stoichiometric relations that could be derived from these free radical processes.

The radicals such as R_3Si or R_2—Si—O where R can be CH_3CH_2— or CH_3CH_2O— should exist in the gas phase. These can combine with the radicals previously proposed or with themselves to condense out on cooler portions of the apparatus to form polymer films. This can be illustrated in the experiments, where a series of wafers were placed in the closed furnace. Polymer coatings were obtained at the cooler exit end of the furnace tube. In the hot zone of the furnace, the radicals were further decomposed, forming a silica coating.

The over-all reaction for the thermal decomposition of ethyltriethoxysilane can be simply stated as

$$(CH_3CH_2)Si(CH_3CH_2O)_3 \rightarrow \left[\begin{array}{l}\text{complex}\\ \text{silicon}\\ \text{alkyl radical}\end{array}\right] + CH_2{=}CH_2 + CH_4 + CO + H_2$$

Mechanism of Furnace Film Formation

In the hot zone of the furnace (600°-850°C) the complex silicon alkyl radicals in the gas phase can now proceed to build up silica layers. Radicals such as R_3Si or R_3Si—O can associate with a metal surface by attachment of the —O atom to the metal, or through the —Si atom coupling to a surface oxide by bonding with an oxygen atom. The organic fractions of the radical then can be thermally cracked to form new bonds to repeat the process, and film formation would continue to occur.

The changes in refractive index and etch rate of these films on heating suggest the presence of organic groups in the film. For films formed below 825°C, these groups can be removed by heating to >825°C. Deposition of the film at 825°C appears to result in organic free silica coatings. The presence of these organic groups in the silica films deposited below 825°C probably cause the crazing of the thicker films (>15,000Å), since they can alter the bonding characteristics and/or structural arrangement of the film. This can thus result in poor stress or strain release leading to discontinuous films. The thermal treatment of the film *in situ* (>825°C) results in producing thick craze-free films and is attributed to densification of the film (3).

The question of whether organic groups are occluded in the film or really part of the structure can be resolved by observations made on films which were deposited on the hot stage at ≧ 800°C. The hot stage technique illustrates direct thermal surface decomposition, with minimum chance for entrapment of gases. At temperatures below 800°C on the hot stage, films containing organic grouping were produced, implying that these organic groups are not occluded or entrapped in the film but are still attached to the silicon atom. If this is the case, it would lend supporting evidence to the existence of radicals such as those mentioned earlier in this section.

Mechanism of Polymer Film Formation

It is not surprising that the mechanism of film formation of the furnace and polymer films should differ. In one case, the silane is being thermally decomposed with simultaneous deposition on a hot surface, and in the other case the silane is being thermally decomposed and then deposited on a relatively cold surface. The difference in properties of these films is shown in Table II.

The behavior of the deposition rate of the polymer film on surfaces which were at different temperatures can be explained by the following mechanism.

The ethyltriethoxysilane is decomposed in the furnace to organic gas residues and the complex silicon alkyl radical. This radical emerges from the furnace tube and contacts a surface. There it undergoes physical adsorption and when another radical attachment occurs in its proximity, crosslinking can occur. Repetition of this process would lead to thicker and thicker layers. This process requires a finite time for the radical to remain on the surface until another radical approaches. As the temperature of the surface is raised, more kinetic energy is imparted to these radicals, and they tend to spend a shorter time on the surface, thus decreasing the probability of crosslinking with another radical landing nearby. Since there is probably a Boltzmann distribution of energy in the particles emerging from the open furnace, there should be a decrease in deposition rate as the temperature of the surface is raised because the more energetic particles spend less time on the surface. Ultimately, when the temperature is raised to a point such that the hot surface imparts sufficient kinetic energy to the least energetic radicals, sufficient physical adsorption on the surface cannot occur and deposition ceases. This situation remains in effect until 500°C is reached.

At this and higher temperatures, it is proposed that a chemisorption mechanism is initiated since there is now enough energy available so that bonding between the radical and the surface can occur. Initially, the more active sites on the surface react and then as the temperature is raised, more sites come into play until rapid formation of a coating occurs. After the first monolayer is complete, the other radicals can link up with this monolayer, etc. These coatings are similar to the furnace films, and essentially the same mechanism occurs there, namely, radical attachment to the surface and subsequent cracking of the radical to produce new bonds for further growth of the oxide.

The film layers deposited at the lower temperature must be organic polymers of silica. From the proposed mechanism presented on the thermal decomposition of ethyltriethoxysilane, the formation of a complex silicon alkyl radicals plus radicals such as CH_3CH_2, CH_3CH_2O, H, CH_3, and CH_3CO occurs in the heated zone of the furnace. As these radicals exit from the furnace, they can recombine on cooling on surfaces to form bonds such as ≡Si—CH_3, ≡SiOCH_3, ≡Si—OH and also to cross link on the surface to form polymers of varying lengths and linkages intermixed with small silica groupings. The low density and high dissolution rate of the polymer film demonstrates a fairly open network in the film. Its refractive index indicates that SiO_2 groupings are present in large concentration.

On heating, the film undergoes a shrinkage and rearrangement leading to a higher density. This shrinking and rearrangement are due to condensation and elimination reactions between neighboring silane groupings to eliminate H_2O, CH_3CH_2OH, H_2, and $CH_3CH_2CH_3$. The higher dissolution rate is due probably to increased porosity with change in structure. The decrease in refractive index serves to demon-

strate that a more open network was present. The films, however, remain coherent on heating at thicknesses less than 15,000Å, and their similarity in chemical properties to silica makes them an attractive coating for use in applications where high-temperature processing is not a factor.

Summary

It has been proposed that the thermal decomposition of ethyltriethoxysilane on a hot surface to form a continuous, amorphous, silica film is essentially a free radical process, involving an initial chemisorption on the surface. The chemisorbed radical suffers further thermal decomposition resulting in the formation of new bonds for attachment to other radicals, thus building up the layer.

Recombination of thermally produced radicals on a cold surface results in an organic polymer of silicon, which exhibits some of the properties of pure silica.

Thermal decomposition of silanes on a hot surface in air has been demonstrated and leads to a technique for growing thick films of pure silica.

Acknowledgment

Acknowledgment is due E. E. Francois for the mass spectrographic determinations and Miss D. M. Dodd for the infrared spectra measurements.

Manuscript received Nov. 10, 1964.

Any discussion of this paper will appear in a Discussion Section to be published in the December 1965 JOURNAL.

REFERENCES

1. E. Jordan, *This Journal*, **108**, 478 (1961).
2. J. Klerer, *ibid.*, **108**, 1070 (1961).
3. W. A. Pliskin and H. S. Lehman, Paper presented at the Toronto Meeting of the Society, Abstract No. 76, May 1964.
4. "Free Radicals," The Catholic University of America Press, Washington (1958).
5. R. B. Sosman, *Trans. Brit. Ceram. Soc.*, **54**, 655 (1955).
6. E. W. R. Steacie, "Atomic & Free Radical Reactions," Reinhold Publishing Co., New York (1954).
7. T. L. Cottrell, "The Strengths of Chemical Bonds," Butterworths Scientific, London (1953).

Solid and Liquid Phase Miscibility of Calcium Metal and Calcium Fluoride[1]

Barry D. Lichter[2] and M. A. Bredig

Chemistry Division, Oak Ridge National Laboratory, Oak Ridge, Tennessee

ABSTRACT

The solubility of Ca in solid CaF_2 was determined by vapor phase equilibration in the temperature range 1060°-1265°C in which it rises from 0.4 to approximately 2 mole %. This solubility is considered in an analysis of the melting point depression of CaF_2, which suggests that the ionization. $Ca^{++} = + 2e^-$, takes place in dilute solution. The equilibrium $2Ca^{++} + 2e^- \leftrightharpoons Ca_2^{++}$ is shifted toward the right, *i.e.*, molecule ion formation, by increasing metal concentration. Literature data for liquid solutions are reinterpreted in terms of complete miscibility of Ca and CaF_2 in the liquid state.

In studies of the phase equilibria and electrical conductance of one type of molten metal halide-metal system, the assumption has been made (1) that in dilute solutions the metal dissolves by being ionized in the ionic medium according to $M = M^{z+} + ze^-$. At higher concentrations, evidence was found (1, 2) in some systems of association of the electrons to form molecules or molecule ions such as Na_2 or $(Ca_2)^{2+}$. The latter species was thought by Rogers, Tomlinson, and Richardson (3) to exist even in dilute solutions of Ca in CaF_2; but in order to support this hypothesis, a heat of fusion of CaF_2 as high as 10 kcal/mole rather than 7.1 kcal/mole measured calorimetrically (4), as well as insolubility of calcium and of NaF (5) in solid CaF_2, has to be assumed. Since evidence for a rather unexpectedly high solubility of Ca in solid CaF_2 existed in the literature (6), determination of the true extent of such solid solution was made the objective of the work reported below.

Experimental Procedures and Results

Materials.—Calcium fluoride was in the form of large, high-purity, optical quality crystals (Harshaw).

Calcium metal (Nelco Metals, Inc.) was in the form of redistilled pellets (metallic impurities in ppm: 800 Mg, 5 Fe, 6 Mn, 40 Ni, and 10 Al). The calcium was kept under argon in a metal can with a tight-fitting lid. Attempts were made to select pellets having a minimum of surface oxide.

Armco iron crucibles (impurities in ppm: 80 C, 260 S, 90 P, 500 O, and 6 N) were used to contain Ca and CaF_2 during experimental runs.

High-temperature equilibration.—Experiments consisted of high-temperature annealing of CaF_2 crystals in an atmosphere of Ca vapor, followed by moderately rapid quenching to room temperature (100° min^{-1} initial cooling rate). The pressure of the Ca vapor was established as the equilibrium calcium vapor pressure of a saturated solution of CaF_2 in molten Ca metal at the experimental temperature.

Figure 1 shows the arrangement of materials in the iron crucible. The bottom compartment was charged

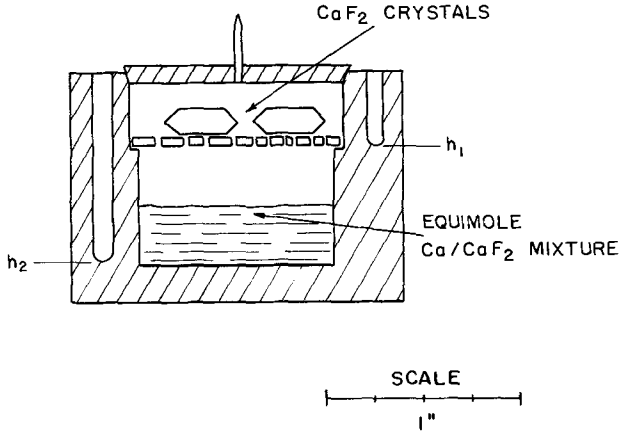

Fig. 1. Crucible assembly for high-temperature equilibrium.

[1] Research sponsored by the United States Atomic Energy Commission under contract with the Union Carbide Corporation.

[2] Present address: Division of Metallurgical Engineering, University of Washington, Seattle, Washington.

with a 2-3g approximately equimolar mixture of Ca pellets and CaF_2 powder. At the equilibration temperature, this mixture formed a saturated solution of CaF_2 in liquid Ca according to the phase diagram of Rogers, Tomlinson, and Richardson (3). The top compartment contained 2-5g of CaF_2 in the form of 2-8 mm thick platelets cleaved from a single crystal. The platelets were supported on a thin iron partition in which were drilled a number of small holes. The average composition of the combined systems varied in different runs from 0.2 to 0.5 mole fraction calcium, N_{Ca} = g atoms Ca/(g atoms Ca + moles CaF_2). Several experiments were attempted with the partition removed and the CaF_2 crystals in contact with the Ca-CaF_2 mixture. However, these experiments resulted in erroneously high values for the solubility of Ca, due to pitting-type attack of CaF_2 crystals by the melt. This phenomenon is discussed further below.

The lid was fusion-welded to the crucible in an inert gas dry box. The crucible was evacuated through a tube in the lid to a pressure of $<10^{-5}$ mm Hg, and the tube was crimped and welded shut. The crucible was contained in the furnace in a closed Inconel tube under 2 atm pressure argon, and the temperature was controlled with two Pt/Pt-10% Rh couples in series, using a L&N Micromax controller. The temperature was measured at positions h_1 and h_2 (Fig. 1) using Pt/Pt-10% Rh thermocouples. The variation of either couple during a run was $<\pm 1°C$. However, the measured temperature difference between h_1 and h_2 could not be reduced below $\pm 5°C$ at temperatures between 1060° and 1260°C.

The time to establish equilibrium was determined from results of duplicate runs and from results obtained with crystals of varying thickness in a given run.

Microscopic evidence for true solid solubility at elevated temperature.—Quenched CaF_2 crystals were translucent, appearing gray or rose-brown in color. However, crystals which were in contact with the melt were green. Microscopic examination under transmitted light revealed the following structures shown in Fig. 2:

(*a*) Metallic particles ranging from 1 to 10μ diameter were uniformly distributed in the crystal matrix.

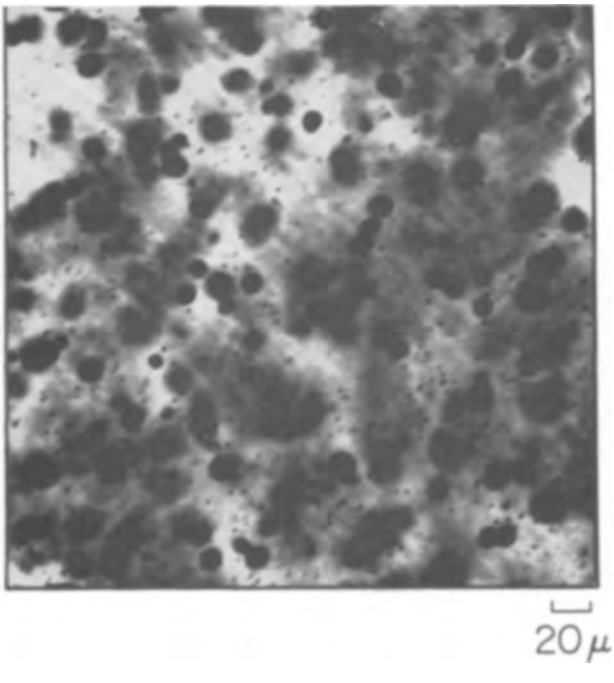

Fig. 2a. Structure of quenched CaF_2 crystals; Sample equilibrated through the gas phase.

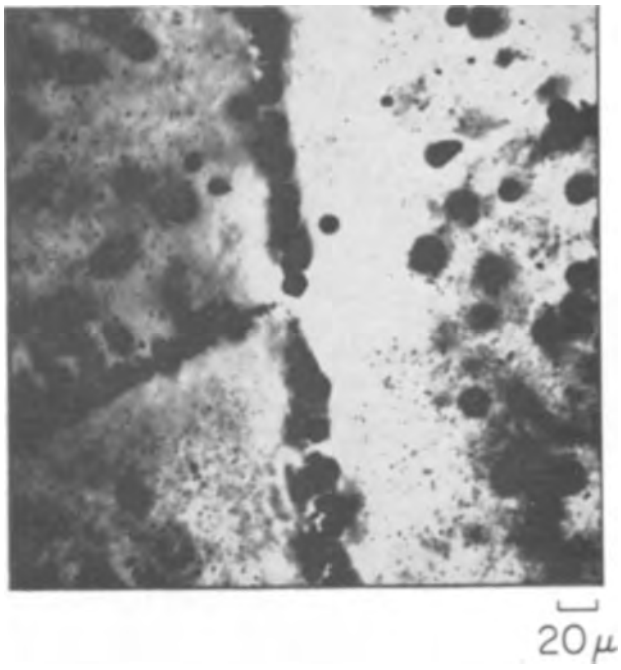

Fig. 2b. Sample equilibrated through the gas phase

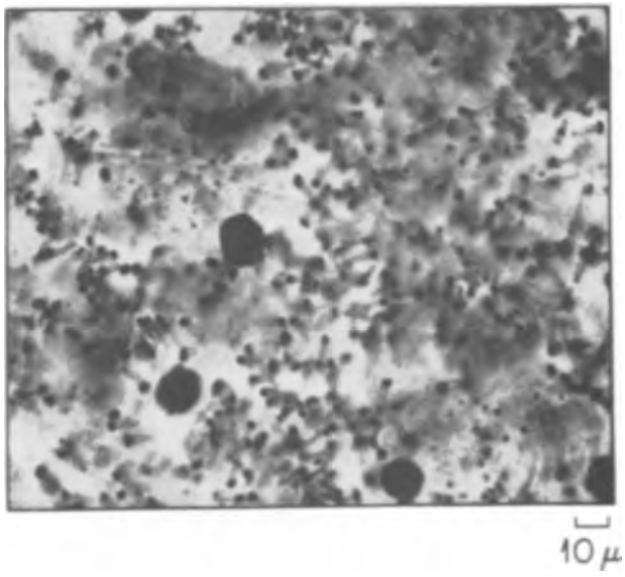

Fig. 2c. Sample in contact with the melt

The presence of submicroscopic colloidal particles was also indicated by the muddy appearance of the matrix.

(*b*) At certain locations in the crystal, presumably low-angle grain boundaries, the particle density was unusually high, while in immediately adjacent areas the particle density was low.

(*c*) Green crystals contained a larger amount of colloid as evidenced by lower transparency. In addition, a network of fine pits could be resolved at higher magnification.

The existence of isolated spherical particles in the single crystal matrix suggests that during quenching a true precipitation from saturated solid solution occurred, where the precipitating phase is a liquid. Areas of high particle density as shown in Fig. 2b are consistent with precipitation at preferential sites. However, for crystals in contact with the melt, dissolution of calcium in the crystal and dissolution of the crystal in the melt can occur simultaneously. Attack of the crystal presumably took place via the formation of small pits (Fig. 2c) which served to entrap excess calcium. The metallic content of green crystals was found to be about twice that of crystals equilibrated through the gas phase, and, in general, the results of

Table I. Solubility of calcium metal in solid CaF_2 between 1060° and 1265°C

Run No.	t, °C	N_{Ca} (s) × 100	Annealing time, hr	Sample thickness, mm
13	1265	1.70	42	8.2
12	1215	1.55	86	8.6
11	1175	1.00	51	6.4
2	1145	0.60	22	2.0
6	1080	0.52	96	2.2
14	1090	0.44	113	4.6
5	1060	0.42	65	7.4

calcium analysis were less reproducible for green crystals.

Determination of excess calcium in quenched CaF_2 *crystals.*—Quenched crystals were ground to a fine powder, leached with distilled water, and the resulting solutions titrated against standard HCl and NaOH solutions. The amount of metallic calcium present was calculated from the measured basicity of the solutions on the reasonable assumption that, with the moderate quenching rate used, a negligible amount of calcium remained in supersaturated solid solution at room temperature.

No basicity was detected in crystals used in control experiments for which calcium was omitted from the crucible during high-temperature annealing. Crystals from the control experiments were transparent, uncolored, and free of any precipitate. Several additional sources of error were considered and evaluated as follows:

(*a*) Chromatographic analysis of the gas evolved from a sample during leaching revealed only hydrogen, and the calculated calcium content agreed to within 5% with results from the titration, thus ruling out significant contamination from soluble impurities (P, S, N, and O).

(*b*) Before grinding, quenched crystals were washed in distilled water. Titration of the wash water revealed less than 1% of the calcium present in the crystal, thus ruling out errors from calcium condensed on the crystal surface during quenching.

(*c*) The major possible source of error was found to be incomplete dissolution of colloidal calcium during leaching. The procedure adopted was to grind the crystal in a known volume of standard HCl solution, back titrate the mixture with NaOH, reacidify, regrind the mixture, and repeat the titration. After 5-10 grindings no subsequent calcium dissolution was detected.

Results are summarized in Table I. The partial and total phase diagrams for the system CaF_2-Ca are shown in Fig. 3 and 4 which include most of the data of Rogers *et al.* (3).

Discussion

Comparison with previous studies of phase equilibria in the system CaF_2-Ca.—The existence of solid subhalides (*e.g.*, CaF) in alkaline earth metal-metal halide systems as reported by Wöhler and Rodewald (7) has not been confirmed by more recent investigations (3,8,9). In particular, the main features of the system CaF_2-Ca were recently determined by Rogers *et al.* (3), and the results pertinent to the present discussion are given in Fig. 3, 4, and 5. These authors did not determine the solubility of calcium in solid CaF_2; however, their observations do not support the exceptionally high solubility previously reported by Mollwo (6). Mollwo's results are based on (*a*) optical absorp-

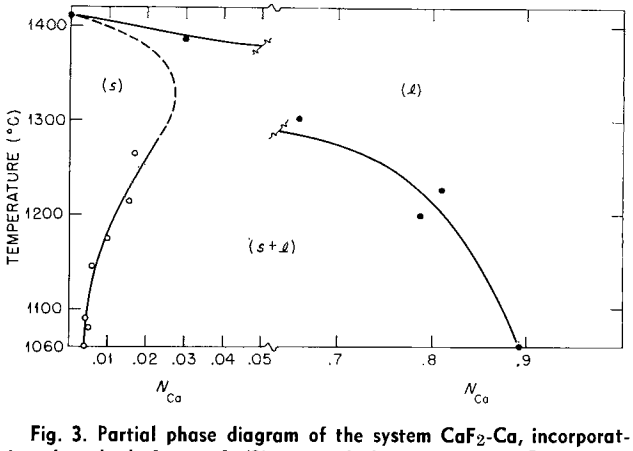

Fig. 3. Partial phase diagram of the system CaF_2-Ca, incorporating data both from ref. (3), •, and the present work, ○.

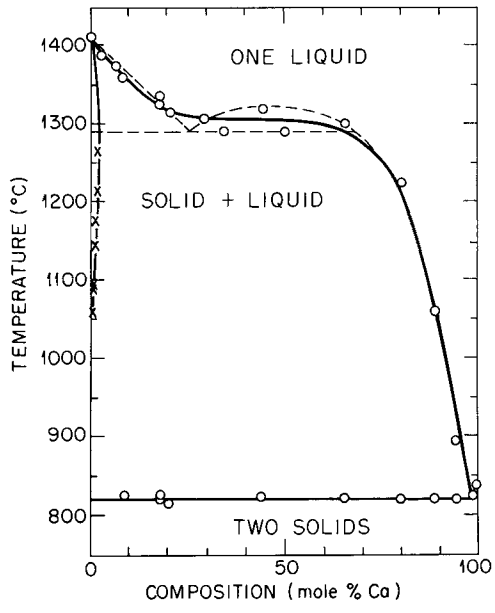

Fig. 4. Complete phase diagram of the system CaF_2-Ca, showing absence of monotectic reaction and of liquid-liquid phase equilibria. — — —, R., T., R. (in error); ———, Lichter and Bredig; ○, differential thermal analysis, R., T., R.; X, solubility, L and B.

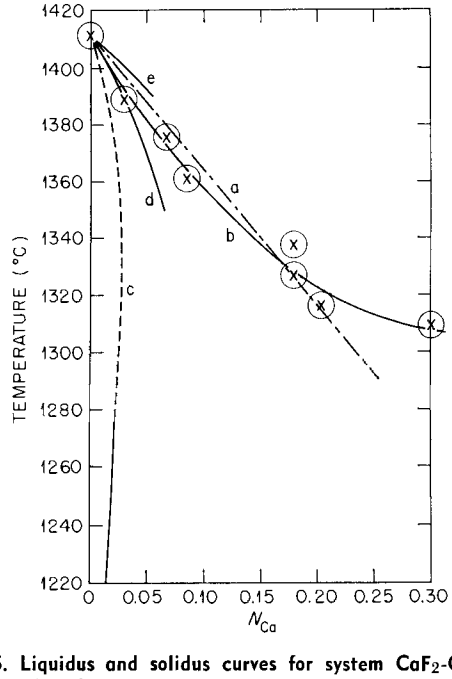

Fig. 5. Liquidus and solidus curves for system CaF_2-Ca: a, experimental liquidus, after Rogers, Tomlinson, and Richardson (3); b, experimental liquidus proposed by Lichter and Bredig for data of ref. (3); c, solidus; d, ideal liquidus, $T = T_m - (2\,RT_m^2/\Delta H_m)(N_{Ca}(l) - N_{Ca}(s))$ for $Ca \rightarrow Ca^{++} + 2e^-$; e, ideal liquidus, $T = T_m - (RT_m^2/\Delta H_m)(N_{Ca}(l) - N_{Ca}(s))$ for $Ca + Ca^{++} \rightarrow Ca_2^{++}$. Note identity of curves b and d for $N_{Ca}(l) < 0.02$ and increasing positive deviation of b from d at higher metal concentrations.

tion measurements of samples annealed in calcium vapor at 450°-600°C and then quenched; (b) measurements at 600° and 800°C of the velocity of color centers produced by application of a strong electric field; and (c) measurements of pycnometric density of samples annealed in calcium vapor at ~1000° and ~1100°C and then quenched. These results are an order of magnitude greater than the results of the present work which are felt to be accurate to ±10%. This disagreement is difficult to explain without further experimental details of Mollwo's measurements. In particular, microscopic observations of quenched samples used in optical absorption and density measurements are lacking, and the absence of colloidal calcium in quenched samples is not confirmed.

It will be noticed that in our diagrams we have rejected the notion of the existence in this system of a monotectic reaction and consequently of a consolute or critical solution temperature. The opposite conclusion reached by Rogers, Tomlinson, and Richardson, namely, that between 1290° ± 5° and 1322° ± 10°C equilibria between two liquid phases exist is not supported by their experiments. The new interpretation of these data is necessary because no thermal effect at the alleged monotectic temperature of 1290° was obtained for any of the six compositions below 20 mole % Ca that were studied. Particularly on heating, the differential thermal analysis would have shown a monotectic reaction, if present, even more distinctly than the liquidus. That the sensitivity of the method used was satisfactory is attested to by the appearance of the corresponding eutectic effects even in these mixtures containing relatively little Ca metal which also has a lower heat of fusion than CaF_2. Furthermore, the thermal effects which Rogers, Tomlinson, and Richardson reported for three compositions within the range of the alleged liquid-liquid reaction, namely, 29, 45, and 65 mole % Ca cannot possibly have been caused by this reaction which is characterized by a very small enthalpy change (or, more correctly, a very small change in the heating or cooling rate) while the far greater enthalpy change of a monotectic reaction remained unrecorded in these three and six additional compositions mentioned above. There can be no doubt that actually all five of the observed thermal effects within the alleged liquid-liquid separation range involved solid CaF_2 (liquidus curve), with a scattering of ±12°C which is actually less than two thirds the scattering (±20°) of the three points between 75 and 95 mole % Ca. (One notes that the scattering increased greatly in going from the salt-rich to the metal-rich ranges of the phase diagram, namely, from ±2° to ±20°. This may be at least partly connected with a parallel increase in the tendency to phase segregation during the quenching operation carried out by Rogers *et al.* before each differential thermal analysis run.)

The results reported by Rogers *et al.* as "solubility" from another series of experiments designed to preserve the alleged liquid-liquid equilibria by quenching are subject to grave doubt because of the inherent faults of the method that were pointed out by the authors themselves as well as one of us (Bredig); thus, they cannot be included in the discussion (two of the experimental solubilities, those at 1303°C, show deviations of as much as 16 and 31%).

With the new interpretation, the CaF_2-Ca system represents the first metal-halide pair outside of the alkali metal systems (Cs-CsX and Rb-RbBr) to exhibit complete salt-metal miscibility in the liquid state, *i.e.*, absence of liquid-liquid phase equilibria. In comparison with the other calcium metal-halide systems, this is to be ascribed principally to the high melting point of the fluoride. However, the shape of the liquidus is characteristic of a large deviation from Raoult's law and of a more than incipient tendency toward formation of two liquid phases.

Analysis of freezing point depression of CaF_2 by calcium.—The finding of limited solubility of calcium metal in solid CaF_2 gives rise to a modification of the interpretation of the liquidus curve advanced by Rogers *et al.* (3). In the other CaX_2-Ca systems (X = Cl, Br, I), Dworkin, Bronstein, and Bredig (1, 9) have interpreted the observed melting point depression of CaX_2 by Ca and the electrical conductivity of dilute solutions in terms of the dissociation (ionization) of Ca metal in the highly ionized medium which the molten salt represents, *i.e.*, according to $Ca = Ca^{++} + 2e^-$. The electrons are thought of as anion- or color-centerlike species (2, 10-12). With increasing metal (or electron) concentration, the reaction $2e^- + 2Ca^{++} = (Ca_2)^{++}$ was assumed to progress toward the right, *i.e.*, the formation of a molecule ion resembling somewhat in electronic structure the $(Cd_2)^{++}$ and $(Hg_2)^{++}$ ions and especially the Na_2 molecules proposed earlier for the NaX-Na systems (2). If one assumes that in dilute solutions Ca dissolves in the liquid phase in a similar manner as in solid CaF_2, namely, according to $Ca = Ca^{++} + 2e^-$, with electrons substituting in "ideal" mixtures for F^- ions, one obtains for the activity of CaF_2 in both the solid and liquid phases

$$a_{CaF_2} = X_{Ca++} \cdot X_{F-} \qquad [1]$$

where the Ca^{++} cation fraction = $X_{Ca++} = 1$ and the F^- anion fraction

$$X_{F-} = \frac{n_{F-}}{n_{F-} + n_{e-}} = \frac{2n_{CaF_2}}{2n_{CaF_2} + 2n_{Ca}} = N_{CaF_2}$$

Therefore

$$a_{CaF_2} = X^2_{F-} = N^2_{CaF_2} \qquad [2]$$

and the equation for the melting point depression becomes

$$T - T_m = \Delta T =$$

$$\frac{RT_m^2}{\Delta H_m} \cdot \ln \left(\frac{a^{(l)}_{CaF_2}}{a^{(s)}_{CaF_2}} \right) = \frac{RT_m^{\,2}}{\Delta H_m} \cdot 2 \ln \frac{N^{(l)}_{CaF_2}}{N^{(s)}_{CaF_2}} \qquad [3]$$

Thus, the melting point depression, ΔT, is proportional to twice the difference in the logarithms of the mole fractions of CaF_2 in the liquid and solid phases. At low concentration of Ca, $\ln N_{CaF_2} = (N_{CaF_2} - 1) = -N_{Ca}$, and Eq. [3] can be written

$$\Delta T = -\frac{2RT_m^2}{\Delta H_m} \left(N^{(l)}_{Ca} - N^{(s)}_{Ca} \right)$$

$$= -\frac{4 \times (1684)^2}{7100} (\Delta N_{Ca}) = -1600 \cdot \Delta N_{Ca} \qquad [4]$$

Figure 5 shows that it is possible at temperatures near T_m, *i.e.*, at small concentrations of calcium metal, to reconcile the experimental results obtained for the liquidus by Rogers *et al.* (3) and the estimated solidus from the present work with this equation: At T approximating T_m, curve d, the ideal liquidus corresponding to $Ca = Ca^{++} + 2e^-$ and to

$$T = T_m - \frac{2RT_m^2}{\Delta H_m} \left(N^{(l)}_{Ca} - N^{(s)}_{Ca} \right) \qquad [5]$$

with estimated $N_{Ca}(s)$ from curve c, approximates curve b, the curve drawn by us through the experimental point from ref. (3). At higher metal concentrations in the liquid phase, there occurs strong positive deviation from Raoult's law as one might expect with limited miscibility in the liquid phase and/or increasing reaction according to

$$2e^- + 2Ca^{++} = (Ca_2)^{++}$$

i.e., interaction and trapping of pairs of anion of F-centerlike electrons in the form of molecule ions.

Summary

1. Contrary to reports in the literature, solid CaF_2, in equilibrium with the calcium vapor over a saturated solution of CaF_2 in liquid calcium metal, dissolves near 1330°C a maximum of approximately 2.7 mole % calcium metal.

2. The depression of the melting point of CaF_2 by low concentration of Ca can be interpreted in terms of a solidus as estimated from the measurements and of the known calorimetric heat of fusion, with the assumption that the solution mechanism in the solid is the same as in the dilute liquid phase, namely, $Ca \rightarrow Ca^{++} + 2e^-$ (F centerlike electrons). With increasing metal concentration, the dissolution of calcium metal in molten CaF_2 follows $Ca + Ca^{++} \rightarrow (Ca_2)^{++}$, or $2Ca^{++} + 2e^- \rightarrow (Ca_2)^{++}$ to an increasing degree. The ionization according to $Ca \rightarrow Ca^{++} + 2e^-$ is thus believed to be similar to that in the calcium metal solutions in the three other CaX_2 melts (X = Cl, Br, I) where such ionization is supported by electrical conductance data.

3. The CaF_2-Ca system is the first metal-halide system outside of the alkali metal systems to exhibit complete metal-salt miscibility in the liquid state, *i.e.*, absence of liquid-liquid phase equilibria.

Acknowledgment

The authors wish to express their thanks to Messrs. G. Goldberg and G. R. Wilson for chemical analyses and to Mr. T. E. Willmarth for the microphotographs.

Manuscript received April 20, 1964; revised manuscript received Dec. 8, 1964.

Any discussion of this paper will appear in a Discussion Section to be published in the December 1965 issue of the JOURNAL.

REFERENCES

1. A. S. Dworkin, H. R. Bronstein, and M. A. Bredig, *Discussion Faraday Soc.*, **32**, 188 (1962); M. A. Bredig, *J. Chem. Phys.*, **37**, 914 (1962).
2. H. R. Bronstein and M. A. Bredig, *J. Am. Chem. Soc.*, **80**, 2077 (1958); and *J. Phys. Chem.*, **65**, 1220 (1961); M. A. Bredig and H. R. Bronstein, *J. Phys. Chem.*, **64**, 64 (1960).
3. P. S. Rogers, J. W. Tomlinson, and R. D. Richardson, "Proceedings of the International Symposium on Physical Chemistry of Process Metallurgy," Pittsburgh 1959, G. R. St. Pierre, Editor, p. 909, Interscience Publishers, New York (1961).
4. B. F. Naylor, *J. Am. Chem. Soc.*, **67**, 150 (1945).
5. A solubility of 4% NaF in solid CaF_2 [D. M. Roy and Rustum Roy, *This Journal*, **111**, 420 (1964)] reconciles the depression of the melting point of CaF_2 by NaF as observed by Rogers *et al.* (3) with the actual heat of fusion, 7.1 kcal.
6. E. Mollwo, *Nachr. Ges. Wiss. Gottingen*, II, New Series, **1**, 79 (1934).
7. L. Wöhler and G. Rodewald, *Z. anorg. u. allgem. Chem.*, **61**, 54 (1909).
8. See, *e.g.* M. A. Bredig, "Mixtures of Metals with Molten Salts" in "Molten Salt Chemistry," Milton Blander, Editor, Interscience Publishers, New York (1964).
9. M. A. Bredig *et al.*, To be published.
10. F. Seitz, *Revs. Modern Phys.*, **13**, 384 (1946); **26**, 7 (1954).
11. J. H. de Boer, *Rec. Trav. Chim. Pays-Bas*, **56**, 301 (1937).
12. K. S. Pitzer, *J. Am. Chem. Soc.*, **84**, 2025 (1962).

Some X-Ray and Thermoelectric Studies on Cubic Th_3X_4 Compounds

C. E. Price[1] and I. H. Warren

Department of Metallurgy, The University of British Columbia, Vancouver, British Columbia, Canada

ABSTRACT

Measurements of thermoelectric power and electrical conductivity have been made up to 950°C on Th_3P_4, Th_3As_4, Th_3Sb_4, and $Th_3(AsSb)_4$ solid solutions. Thermal conductivity data have been obtained near 30°C. X-ray and density measurements suggest that the compounds are stoichiometric.

A previous paper (1) indicated that Th_3As_4 may have interesting thermoelectric properties with a figure of merit comparable to the more widely investigated isostructural compound $Ce_{3-x}S_4$. It was shown that compounds having either n- or p-type properties could be prepared, and that appreciable quantities of Fe, Co, Ni, CaS, and BaS could be taken into solution. This investigation was limited by the purity of the thorium available (99%) and the presence of ThO_2 as a major contaminant in the products. The present study, using three grades of thorium metal and an improved preparational technique, reports thermoelectric and x-ray data on Th_3P_4, Th_3As_4, Th_3Sb_4, and $Th_3(AsSb)_4$ solid solutions.

Experimental

Materials.—Three grades of thorium were used: 99.0% metal from Dominion Magnesium Limited, 99.9% metal from Lindsey Chemical Corporation, and 99.99+% metal from Leytess Metal Corporation. All metals were received as fine powders; the Dominion and Leytess samples had been packed in sealed containers under an inert atmosphere. They were opened and stored in an inert gas glove box. A typical analysis quoted by the suppliers for Leytess metal, in ppm, was: oxygen, 30; nitrogen, 20; hydrogen, 5; carbon, 20; aluminum, 5; copper, 10; iron, 25; and all others, ±2. Iron was also the main metallic contaminant in the other thorium powders. Arsenic and antimony of 99.999% purity were obtained from Consolidated Mining and Smelting Company. The 99.9% purity phosphorus was from the Fisher Scientific Company.

Preparation of compounds.—The compounds Th_3P_4, Th_3As_4, and Th_3Sb_4 were prepared by heating the constituents together in sealed and evacuated Vycor or quartz capsules. Quantities of 20g were made at a time, the elements being weighed to within 0.002g of that required stoichiometrically by the formula. The heating rates were critical for a too rapid increase in temperature led to a violent exothermic reaction which fragmented the capsules. The samples of phosphide, arsenide, and antimonide were heated over a period of 100 hr to 450°, 620°, and 900°C, respectively. For the arsenide it proved essential to maintain the temperature below 350°C for the first 30 hr. No attack of the containers was observed. The capsules were opened, and the products (fine gray powders) stored in the

[1] Present address: Mackay School of Mines, University of Nevada, Reno, Nevada.

glove box. Attempts to prepare a compound Th_3Bi_4, isostructural to the known compound U_3Bi_4, were unsuccessful.

Fabrication.—Cylindrical compacts 0.9 cm in diameter and 1-2 cm long were prepared by hot pressing with induction heating, and under a helium atmosphere. Graphite dies and plungers were used, loading taking place in the glove box. During the heating cycle a pressure of 5000 psi was maintained continuously. The heating rates were approximately 150°/min. Temperature measurement was by a W- W/26% Re thermocouple placed down a 0.3 cm hole drilled almost to the bottom of the upper plunger. In some instances a molybdenum sleeve was used to separate the sample from direct contact with the carbon of the die. When solid solutions were prepared the powders were mixed beforehand in a mortar. Prior to the measurement of properties, the outer layers of the samples were ground away.

Analyses.—X-ray measurements, using a diffractometer in conjunction with a Geiger counter and chart recorder, were made on the powders and compacts. The powders were imbedded in a flat surface of vacuum grease to prevent oxidation. For angles greater than about 22° it was possible to separate the two peaks of the α_1-α_2 doublet in the CuK_α radiation used. Less than about 2% of ThO_2 (or a second phase) could not be detected by this method, but from metallographic examination it was estimated, through comparison with contaminated samples, that 0.1% of ThO_2 would be visible readily. In contaminated samples ThO_2 occurred as small white particles. Representative compacts were chemically analyzed to determine the thorium-arsenic ratios and carbon contents. Analyses for dissolved oxygen were not made because of ease of atmospheric contamination.

Property measurement.—Densities were measured by immersion in CCl_4. Thermal conductivity values (K) were obtained near room temperature by simultaneous absolute and comparative steady-state methods. Temperature gradients of near 10°, 20°, and 30°C were in turn maintained across the sample held under a vacuum of 10^{-5} mm Hg. Temperature measurements were made with copper-constantan thermocouples cleated into copper at each end of the sample. Indium amalgam was used to minimize thermal contact resistances (2). Agreement and reproducibility were to within 5%. Thermoelectric power (α) with reference to copper was determined from liquid nitrogen temperatures to near 1000°C *in vacuo*, using a 10°-20°C/cm temperature gradient. Electrical conductivity results (σ) of reproducibility to within 3% were obtained using stainless steel probes pressed against a side of the compact. These measurements have been described in more detail elsewhere (3).

Results and Discussion

The compacts which were all of a silver gray color tarnished very readily in air, dark surface films forming on antimonides and phosphides within 5 min. Although all measurements were done *in vacuo*, some exposure to air proved unavoidable during transfer and assembly. However, exposures of up to 1 hr appeared not to change the results. Samples placed clean and shiny in the apparatus showed a dark surface film after the high-temperature measurements. No reaction occurred with the copper end pieces. The materials were weakly diamagnetic.

Dense Th_3P_4 compacts could not be prepared, for on heating between 1200° and 1600°C the compound gradually decomposed giving the mono form. Th_3As_4 was stable up to 2050°C, densification started near 800°C and appeared to be complete by 1500°C. With Th_3Sb_4 a liquid phase appeared at about 1600°C, but dense compacts could be obtained at 1400°C.

X-ray measurements on the powders gave results, in Å ± 0.0005, of Th_3P_4 8.6530, Th_3As_4 8.8548, and Th_3Sb_4 9.3659. These figures differ slightly from the solely reported data of 8.617, 8.843, and 9.372, respectively, summarized by Pearson (4). Attempts to vary the 3Th:4X ratio of arsenide and antimonide compacts failed; monocompound formation or anion deposition on the fabrication container occurred with all arsenide and antimonide compacts exhibiting the same lattice spacing. With Th_3P_4 compacts the lattice spacing appeared to vary in the range 8.630-8.654Å; however, our inability to get dense compacts free of ThP precludes any conclusions in this instance. In the isostructural compound $Ce_{3-x}S_4$, however, the lattice size was reported to vary only slightly from 8.6250Å ($x = 0$) to 8.6347Å ($x = 1/3$), but this led to a density drop from 5.68 to 5.18 gm cc^{-1} as x went from 0 to 1/3 (5). As, in the present study, the lattice spacing was constant and the measured densities of arsenide and antimonide were within 1% of that required for a stoichiometric structure, it seems probable that departures from the formula Th_3X_4 are very small or nonexistent in these compounds. Chemical analyses gave carbon contents of 0.02-0.04% and thorium-anion ratios within 5% of ideal.

Table I. Thermoelectric data

Compact	Fabrication Time, min	Fabrication Temp, °C	α, $\mu V°C^{-1}$	σ, ohm-cm^{-1}	K, cals cm^{-1} sec^{-1} °C^{-1}	Density % theor.
Th_3P_4	15	1200	−223	1.5	0.0066	92
Th_3As_4	30	1900	−160	545	0.0130	100
Th_3Sb_4	15	1600	−52.5	3,370	0.0179	100

Thermoelectric data near room temperature for compacts based on the 99.99% purity thorium are summarized in Table I. The variation of thermoelectric power (α) and electrical conductivity (σ) with temperature for these materials are shown in Fig. 1 and 2. Changes in pressing temperatures between 1400° and 2000°C could shift by up to 50°C the temperature at which a given value of α was obtained. Thus, in Fig. 1 the temperature axis may be moved ± 25°C. As before (1) the trend was for a higher room temperature α with an increased pressing temperature. The reported electrical conductivities (Table I) were the highest obtained, lower pressing temperatures giving in some instances values down to 25% of these figures. The possibility of carbon contamination or inhomogeneity was considered by progressively grinding layers off some samples and remeasuring but no property changes were found.

Data for arsenide and antimonide compacts made from the less pure thoriums are shown in Fig. 3 and 4. The compacts were fabricated as for the purest metal and again α was found to be slightly influenced by pressing temperature. The impure compacts tend to maintain a positive α to a much higher temperature and in the case of the arsenides give subsequently a smaller negative value. As the major metallic impur-

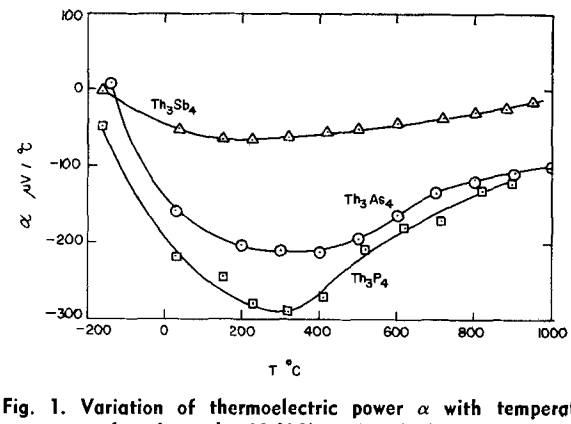

Fig. 1. Variation of thermoelectric power α with temperature for compacts based on the 99.99% purity thorium.

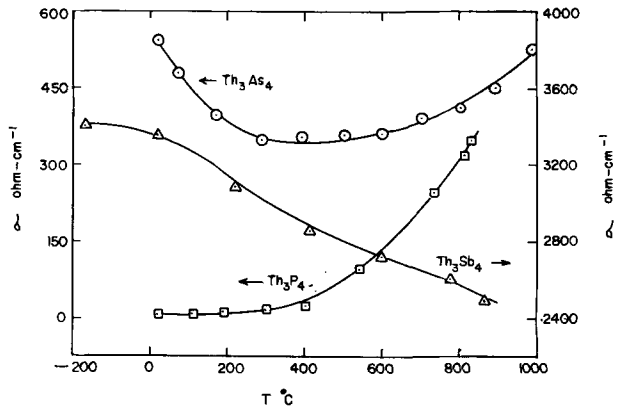

Fig. 2. Variation of electrical conductivity σ with temperature for compacts based on the 99.99% purity thorium.

ity in these compounds is iron it seems likely that the p-type behavior observed in these compounds is not intrinsic to the materials, but arises from the presence of iron and similar impurities providing acceptor levels at low temperatures. These impurity effects are very similar to those observed for metallic additions, nickel in particular, in the previous study.

One unexpected feature of this investigation concerned the behavior of Th_3As_4 compacts pressed in molybdenum lined dies, which were used to reduce the possibility of carbon contamination. Molybdenum diffused into samples pressed at 1800°-1900°C giving products which appeared to have partially melted. The properties of two specimens (using 99.99% metal) prepared in this way are shown in Fig. 5. One sample not only has a high p-type value near room temperature but, unlike any other compact studies here or previously (1), maintains a negative thermoelectric power

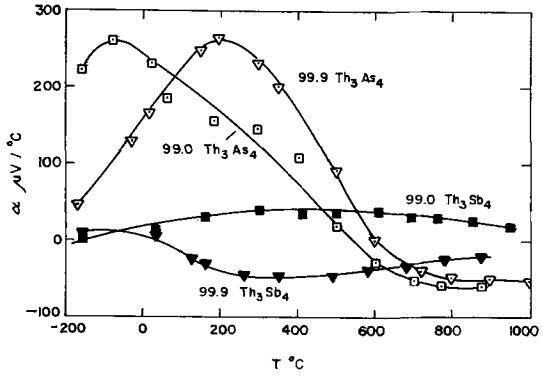

Fig. 3. Variation of thermoelectric power α with temperature for Th_3As_4 and Th_3Sb_4 compacts based on the 99.0 and 99.9% purity thoriums.

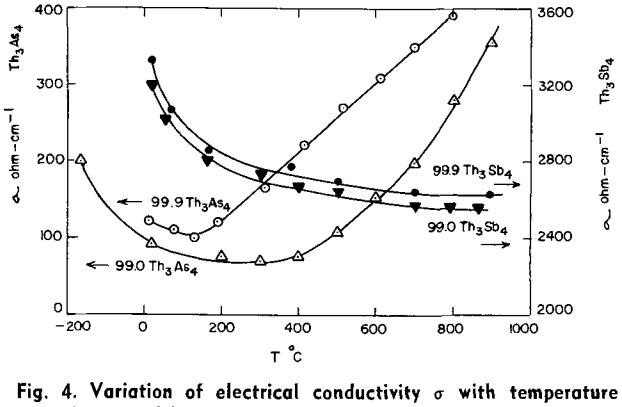

Fig. 4. Variation of electrical conductivity σ with temperature for Th_3As_4 and Th_3Sb_4 compacts based on the 99.0 and 99.9% purity thoriums.

Table II. Room temperature x-ray and thermoelectric data

Compact Th_3As_4 (proportion)	Th_3Sb_4 (proportion)	Lattice parameter Å	±	$\mu v°C^{-1}$	$(ohm\text{-}cm)^{-1}$	K, cals cm^{-1} sec^{-1} $°C^{-1}$	Density, g cc^{-1}
1.0	—	8.4383	0.0005	+170	270	0.0128	9.51
0.95	0.05	8.8638	0.0005	+203	120	0.0121	9.55
0.90	0.10	8.8813	0.0005	+53	93	0.0103	9.52
0.75	0.25	8.972	0.001	+36	260	0.0092	9.51
0.50	0.50	9.10	0.02	−36	570	0.0098	9.54
0.25	0.75	9.258	0.001	−40	950	0.0110	9.57
0.10	0.90	9.3292	0.0005	−10	1430	0.0130	9.48
0.05	0.95	9.3667	0.0005	−2	2010	0.0151	9.52
—	1.0	9.3840	0.0005	+8	3300	0.0178	9.51

in excess of 200 μv/°C from 500° to 1000°C. Chemical analysis of this sample showed 0.14 w/o (weight per cent) molybdenum; the x-ray pattern was unaltered from Th_3As_4. In this instance, due to the size and shape of the samples, the electrical conductivities could only be measured approximately, but appeared to be between 150 and 450 $(ohm\text{-}cm)^{-1}$ over the temperature range.

The examination of the Th_3As_4-Th_3Sb_4 solid solutions was undertaken using the 99.9% thorium metal which was plentifully available. In Table II room temperature x-ray and thermoelectric data are summarized. The lattice spacing of the middle alloys is only approximate for line broadening occurred. The compounds were all pressed between 1500° and 1600°C which was very near to the melting point for antimony rich alloys. Annealing compacts for 50 hr at 1400°C *in vacuo* had no effect on the properties. Figures 6 and 7 illustrate the variation of α and σ with temperature, intermediate properties occurring for those compounds not shown. The electrical conductivity peak with the 75% antimonide sample is not understood, but was reproduced on a second specimen. It appeared from these results that the arsenide rich compounds had the best thermoelectric properties, accordingly an alloy of composition $Th_3(0.9\ As, 0.1\ Sb)_4$ was fab-

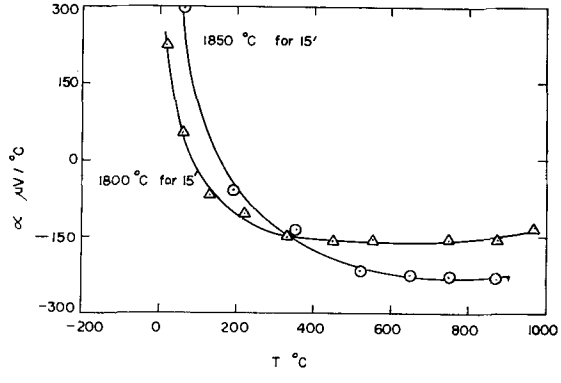

Fig. 5. Variation of thermoelectric power α with temperature for two molybdenum contaminated Th_3As_4 compacts, based on the 99.99% purity thorium.

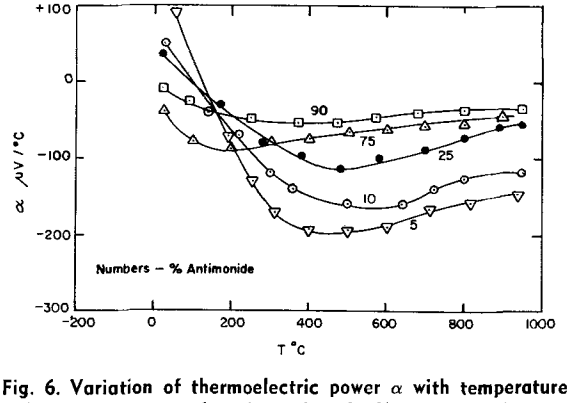

Fig. 6. Variation of thermoelectric power α with temperature for $Th_3(As\cdot Sb)_4$ compacts, based on the 99.9% purity thorium.

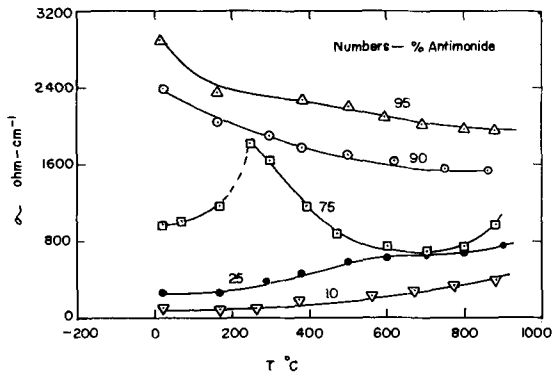

Fig. 7. Variation of electrical conductivity σ with temperature for $Th_3(As \cdot Sb)_4$ compacts, based on the 99.9% purity thorium.

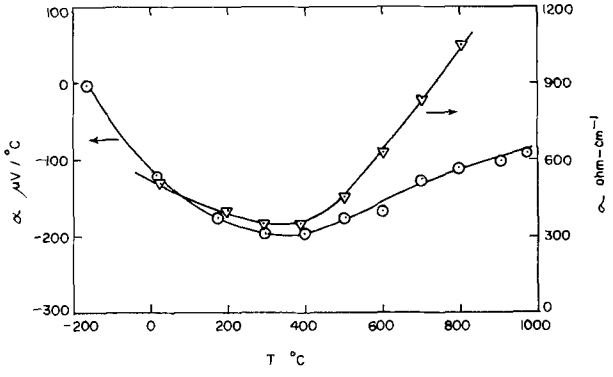

Fig. 8. Variation of thermoelectric power α and electrical conductivity σ with temperature for a $Th_3(0.9As, 0.1Sb)_4$ compact based on the 99.99% purity thorium.

ricated using the 99.99% thorium metal. α and σ data for this compact (pressed for 30 min at 1550°C) are shown in Fig. 8.

These Th_3As_4 base compounds have possibilities as high-temperature n-type thermoelectrics. Exact figures of merit (Z) cannot be calculated but if, as in InAs and GeTe (6), K is assumed to halve between 30° and 800°C, then approximate values can be computed. The best Z obtained at 800°C is 0.5 x 10^{-3} $°C^{-1}$ for the $Th_3(As_{0.9}Sb_{0.1})_4$ of Fig. 8. The other materials studied give maximum figures of 0.1-0.4 x 10^{-3} $°C^{-1}$ up to 900°C. These values, which are almost certainly not the ultimate obtainable, are somewhat lower than the Z of 0.6 x 10^{-3} $°C^{-1}$ for InAs at 800°C and 0.9 x 10^{-3} $°C^{-1}$ for GeTe at 600°C (6).

Interpretation of the data obtained in this investigation is clearly restricted by the polycrystalline nature and limited purity of the compacts. They are conventional in that the electronegativity differences (7) Th_{IV}1.4, P 2.1, As 2.0, Sb 1.8 are suitable for semiconducting properties (8) and the increasing metallic behavior with temperature is in the correct order Sb-As-P. The fortuitous molybdenum contaminated samples show that n-type conductors of high thermoelectric power up to at least 1000°C can be produced. Phase diagrams of thorium-Group VB compounds are not available but the isostructural uranium compounds U_3Sb_4 (9) and U_3Bi_4 (10) break down below their melting point to give the mono compound. Reference to these diagrams and the observations here with the phosphide suggest that it will be difficult to take the investigation any further for zone refining will be inapplicable and single crystal growth techniques not straightforward.

Acknowledgment

The program was supported by a grant from the Canadian Uranium Research Foundation.

Manuscript received Aug. 23, 1964; revised manuscript received Feb. 15, 1965.

Any discussion of this paper will appear in a Discussion Section to be published in the December 1965 JOURNAL.

REFERENCES

1. I. H. Warren and C. E. Price, To be published.
2. A. D. Stuckes and A. P. Chasmar, *Proc. London Phys. Soc.*, p. 119 (1957).
3. I. H. Warren and C. E. Price, *Can. Met. Q*, **3**, 183 (1964).
4. W. B. Pearson, "Lattice Spacings and Structures of Metals and Alloys," Pergamon Press, London (1958).
5. M. Cutler, R. L. Fitzpatrick, and J. F. Leavy, *J. Phys. Chem. Solids*, **24**, 319 (1963).
6. R. R. Heikes and R. W. Ure, Jr., "Thermoelectricity: Science and Engineering," pp. 429 and 435, Interscience Publishers, New York (1961).
7. W. Gordy and W. J. Orville Thomas, *J. Chem. Phys.*, **24**, 439 (1956).
8. C. H. L. Goodman, *J. Phys. Chem. Solids*, **6**, 305 (1958).
9. B. J. Beaudry and A. H. Daane, *AIME Trans.*, **215**, 199 (1959).
10. R. J. Teitel, *ibid.*, **215**, 131 (1959).

Some Considerations on the Use of Platinum Electrodes in Chloride Solutions

R. P. Frankenthal and H. W. Pickering[1]

Edgar C. Bain Laboratory for Fundamental Research,

United States Steel Corporation, Research Center, Monroeville, Pennsylvania

ABSTRACT

As part of some studies on the passivity of iron-chromium alloys, experiments were performed to determine under which conditions platinum pre-electrolysis electrodes and auxiliary electrodes will dissolve anodically in chloride solutions and cause interference with subsequent measurements due to the cathodic redeposition on the alloy of the dissolved platinum. For these experiments potential-current relationships were measured and thin foils of the alloy were examined by transmission electron microscopy and by selected-area electron diffraction for the presence of deposited platinum. Even when the anolyte and catholyte were separated by a fine-porosity fritted disk during pre-electrolysis, platinum subsequently deposited on the working electrode. Platinum will also dissolve anodically from the auxiliary electrode when a net cathodic current flows at the working electrode; if the electrochemical measurements are not sufficiently fast, the dissolved platinum will diffuse to the working electrode and deposit on it. The presence of dissolved platinum can usually be detected electrochemically. However, an examination of the material under study by transmission electron microscopy and electron diffraction is the most certain means to determine whether platinum will redeposit under the conditions of the experiment.

In the course of an investigation of the passivity of iron-chromium alloys, it was deemed necessary to investigate the effect of pre-electrolysis of the electrolyte solution. The need for pre-electrolysis in electrochemical studies has been well established, particularly by Bockris (1, 2). The usual procedure (3) is to perform the pre-electrolysis either between two electrodes of the metal under study or between two platinum electrodes and under conditions more stringent than those in the actual experiment, thereby, hopefully, eliminating the impurities that could affect the experiment.

In the work with iron-chromium alloys it was not possible to do the pre-electrolysis between two electrodes of this alloy, since at the current densities required for the pre-electrolysis the anode would assume a potential at which chromium is oxidized to dichromate ion; this ion would then interfere with the passivity experiment. It was, therefore, decided to use platinum electrodes. However, since some of the work was to be done in solutions containing NaCl and since it is well known (4-6) that a platinum anode will dissolve in a chloride medium to give either the chloroplatinite or the chloroplatinate ion, an investigation was conducted into the possible side effects of this anodic dissolution. From a combination of electrochemical measurements and observations by transmission electron microscopy, we have drawn certain conclusions concerning the use of platinum electrodes in chloride media.

Experimental

The working electrode for the electrochemical measurements and the foils for the electron microscope specimens were prepared from a laboratory vacuum melt of high purity Fe-24% Cr alloy. Cylindrical electrodes (1 in. high and ¼ in. in diameter) were machined with a threaded hole for electrical connection at one end. The material for the foils was cold rolled to 0.003 in. Immediately prior to use, the electrodes and the foils were electropolished in a mixture of glacial acetic acid and perchloric acid (5:1) at 35v, rinsed in reagent-grade methanol, dried, and immediately inserted into the cell. Electrical contact was made to the electrode by means of a brass screw that was isolated from the environments by a Teflon sleeve. To obtain electrical contact with the foil, a thin platinum wire, covered by a glass sleeve, was spot-welded to one end of the foil. The opening at the weld area, as well as the weld, was sealed with polyethylene.

The studies were conducted in three solutions: 1*N* H_2SO_4, 1*N* H_2SO_4 + 0.1*N* NaCl, 1*N* H_2SO_4 + 0.01*N* NaCl. These were made from reagent grade chemicals and doubly distilled water with a conductivity of 3×10^{-7} mho-cm. Pre-electrolysis, when performed, was conducted for 24 hr at a current density of 15 ma/cm^2 between two platinum electrodes, each 10 cm^2 in area. Experiments were conducted with the anode and cathode in the same compartment and also with the electrode compartments separated by a fritted-glass disk (fine porosity). In the latter case, the electrolyte to be used in the passivity experiments was in the cathode compartment. All solutions were purged with prepurified helium before and during use.

The cell was constructed completely of Pyrex. Both water-wetted glass stopcocks and Teflon stopcocks were used. A Luggin capillary connected the cell to the reference electrode via a salt bridge. The auxiliary electrode was a platinum cylinder (40 mm diameter), concentric with the working electrode to insure uniform current distribution. The working electrode was inserted through a ball joint, so that the electrode could be properly placed with respect to the Luggin capillary. A hydrogen reference electrode was used when the electrolyte was H_2SO_4; a saturated calomel reference electrode was used when chloride was present in the solution. All potentials are reported relative to the normal hydrogen electrode (NHE). Prepurified helium was swept through the cell at all times. The potential-current curves were obtained with a Wenking potentiostat and a motor-driven potentiometer. The potential sweep rate was normally 100 or 200 mv/hr.

Bulk specimens and the foils were treated electrochemically in an identical manner, and the potential-current curves were always similar. The following polarization treatments were used:

1. Immersion at +0.475v *vs.* NHE (passive region, see Fig. 1); holding at this potential until the electrode was passive; sweeping the potential to —0.165v,

[1] On leave until September 1965 at the Max Planck Institut für Physikalische Chemie, Göttingen, Germany.

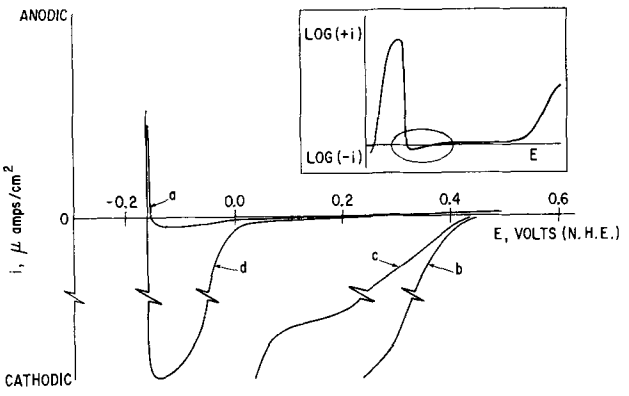

Fig. 1. Potential-current curves in the region of passivity and the Flade potential: (a) in 1*N* H_2SO_4 or in 1*N* H_2SO_4 + 0.1*N* NaCl with no interference from platinum; (b) in presence of large quantities of dissolved platinum; (c) in presence of intermediate amounts of dissolved platinum; (d) in presence of traces of dissolved platinum. Inset shows the over-all passivity curve; the circled area shows the portion plotted in main part of figure.

at which potential the anodic current is increasing sharply as passivity decays.

2. Immersion at —0.500v for 10 sec, at which potential hydrogen evolution proceeds vigorously, sudden switch to +0.475v, followed by the procedure outlined for treatment No. 1. This treatment should give an oxide-free surface prior to passivation.

3. Same as treatment No. 1, but potential is suddenly switched from +0.475 to —0.165v, instead of sweeping through this range.

When the foils reached the final potential, *i.e.*, —0.165v, they were pulled from the cell with the potential still applied, rinsed with reagent-grade methanol, and dried. Some foils were examined immediately in the electron microscope; others were stored in a desiccator until they were examined. There was no effect due to storage. Each foil was examined by transmission electron microscopy in a Siemens Elmiskop. In addition, selected-area electron diffraction allowed examination of regions of specific interest.

Solutions were chemically analyzed for platinum by evaporating the solution to a very small volume and adding a few drops of stannous chloride. A brownish-black precipitate indicated the presence of platinum.

Results and Discussion

Table I summarizes the experimental conditions for the various experiments.

Figure 1 summarizes the electrochemical findings in the form of potential-current curves for the alloy under the different conditions in the region of passivity and of the Flade potential ($E \approx -0.2$v). Curve a is for the series of experiments a_1 and a_2. In H_2SO_4 the potential-current relationship is essentially independent of pre-electrolysis, polarization sweep rate up to approximately 500 mv/hr, and polarization treatment. The cathodic loop has been explained by Edeleanu (7) and is due to hydrogen evolution prior to the breakdown of passivity. As soon as chloride is added to the solution, the other conditions become critical. In experiment a_2, conditions were such that the potential-current curve was the same as for experiment a_1, and the transmission electron micrographs of the foil showed no trace of platinum deposits.

Table I. Summary of experimental conditions

Experimental series	Solution composition	Pre-electrolysis	Polarization sweep rate, mv/hr	Polarization treatment
a_1	1*N* H_2SO_4	Yes, No	100-500	1, 2, and 3
a_2	1*N* H_2SO_4 + 0.1*N* NaCl	No	200	1
b	1*N* H_2SO_4 + 0.1*N* NaCl	Yes	200	1
c	1*N* H_2SO_4 + 0.1*N* NaCl	No	200	2
d	1*N* H_2SO_4 + 0.01*N* NaCl	No	100	1

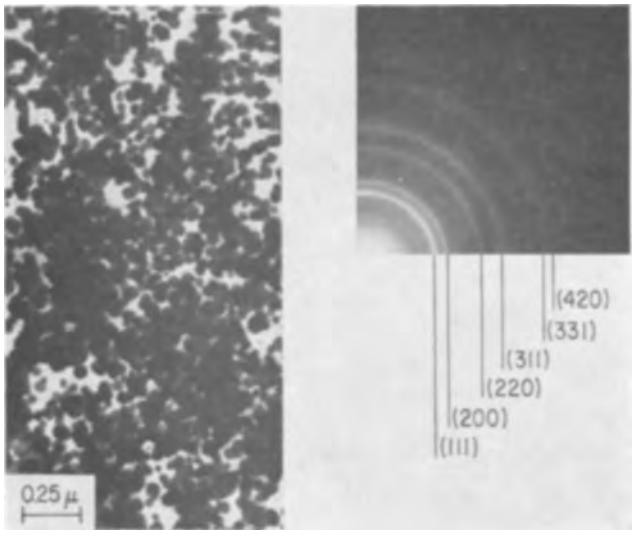

Fig. 2a. (Left) Transmission electron micrograph of platinum deposit at edge of foil after pre-electrolysis of chloride-containing solution between platinum electrodes. (b) (right) Selected-area electron diffraction pattern of area shown in (a) identifying the deposit as platinum.

In experiment b the same solution was used as in experiment a_2, but it was first pre-electrolyzed between two platinum electrodes in the same compartment; the potential-current relationship is given by curve b. It is obvious that a different cathodic reaction is occurring and that it is occurring at potentials corresponding to a strong oxidizing agent. Chemical analysis of the solution revealed the presence of platinum. A transmission electron micrograph (Fig. 2a) of an area at the edge of a foil that had been subjected to a sweep through this potential range shows a heavy deposit, which has been identified as platinum by selected-area electron diffraction (Fig. 2b).

Experiment c in which the alloy surface was initially cathodically reduced (polarization treatment 2) resulted in curve c. The initial cathodic current is again due to platinum deposition; a limiting current is observed, indicating that the concentration of dissolved platinum is considerably less than for the case represented by curve "b". The transmission electron micrograph (Fig. 3) of a foil shows deposits of platinum. The further increase in the cathodic current after the limiting current is due to hydrogen evolution. This hydrogen evolution begins at a potential about 100 mv more positive than that observed for case a. This results from a lowering of the hydrogen

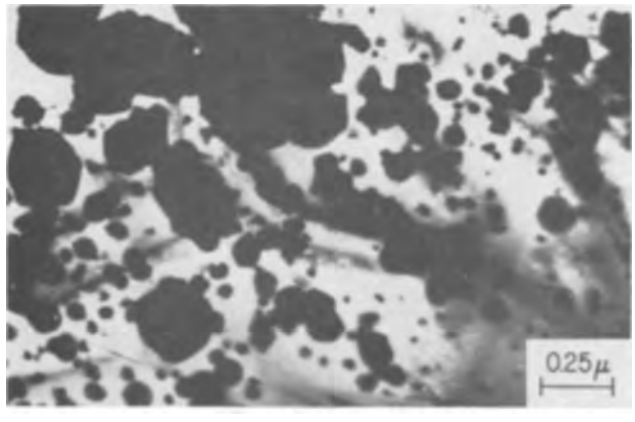

Fig. 3. Transmission electron micrograph of platinum deposit on a foil. Platinum dissolved from the auxiliary electrode during initial hydrogen evolution treatment to clean surface.

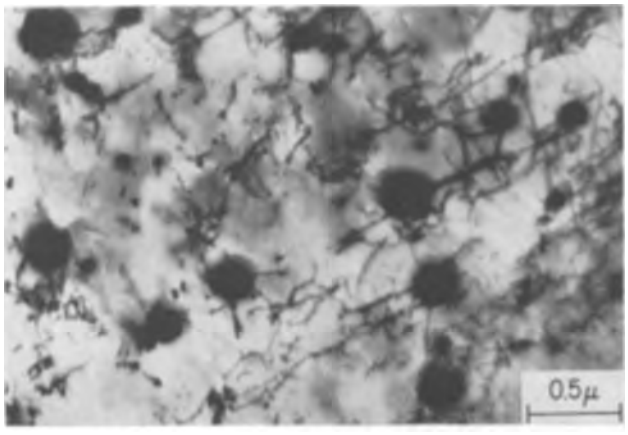

Fig. 4. Transmission electron micrograph of platinum deposit on a foil. Platinum dissolved from auxiliary electrode during potential sweep through cathodic loop. Lines in background are dislocations.

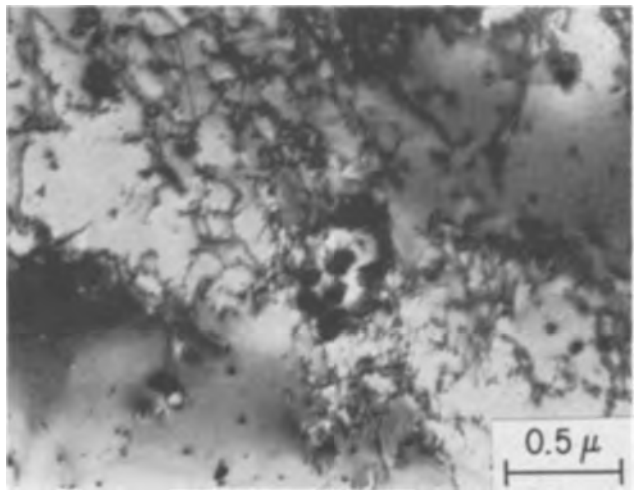

Fig. 5. Transmission electron micrograph showing deposit, which is presumably platinum, on foil exposed to H_2SO_4. Solution had been pre-electrolyzed between two platinum electrodes for 24 hr at 15 ma/cm^2. Foil was subjected to polarization treatment No. 1.

overpotential by the platinum deposit. Sweeping through the same potential range with a platinum electrode, the beginning of hydrogen evolution also occurred at the potential shown in curve c.

The deposition of platinum was also observed in experiment d in which more stringent precautions were taken to avoid the anodic dissolution of platinum and its redeposition, but in which a slower polarization sweep rate was used. A potential-current curve similar to a was expected. Instead, the potential-current curve showed a sharply increased cathodic current in the loop, as shown in curve d. The cathodic loop began at about the same potential as for curve a. A transmission electron micrograph (Fig. 4) of the foil shows deposits of platinum. The platinum, undoubtedly, came from the auxiliary electrode during the sweep through the cathodic loop, during which time this electrode had a net anodic current imposed on it. Because of the slow potential sweep rate, the dissolved platinum had time to diffuse to the working electrode, to deposit and to depolarize the hydrogen-evolution reaction. Integrating the area under the time-current curve (potential varied linearly with time) of the cathodic loop, it is estimated that the maximum amount of platinum that could have been dissolved is equivalent to ½ coulomb, assuming the complete absence of other anodic reactions such as chlorine evolution.

When the cathode and anode compartments were separated by a fine-porosity fritted disk during a 24-hr pre-electrolysis of a chloride-containing solution, sufficient dissolved platinum diffused through the disk to be detected qualitatively by chemical analysis. The presence of the dissolved platinum was also detected as a cathodic current when a platinum electrode was swept through the potential range from +0.5 to 0.0v in this solution. Although no foils were examined for this pre-electrolysis condition, the platinum undoubtedly would also have been found on them.

It has been determined that passivity curves in chloride solutions can best be measured by rapidly sweeping the sample through the desired potential range, a procedure which can lead to markedly distorted passivity curves (8), if the rate is too great, or by obtaining a point-by-point plot (polarization treatment No. 3), omitting regions in which the net current on the working electrode is cathodic; and by omitting pre-electrolysis and the initial cathodic reduction of air-formed oxide films. Work in H_2SO_4 showed no deleterious effects on the potential-current curves when pre-electrolysis and oxide reduction were omitted.

The authors are indebted to the reviewer for bringing to their attention the fact that platinum has been found to dissolve in H_2SO_4 (9). The dissolution of platinum by H_2SO_4 is also thought to have occurred in this work since micrographs of foils treated in H_2SO_4 showed deposits which looked like platinum (Fig. 5). This foil had been subjected to polarization treatment No. 1 after pre-electrolysis of the H_2SO_4 solution. Additional evidence in the form of electron diffraction data must be obtained before it may be unequivocally stated that platinum dissolves in H_2SO_4 under the conditions of our experiments. In this regard it should be noted that the test conditions were considerably more severe in the work of Hirano *et al.* (9) than they were in the work reported here. In their work an anodic current of 2 amp was imposed on a platinum wire (area, 5 cm^2) for 3 to 5 hr; analysis of the mercury cathode showed the presence of approximately 10 μg of platinum. If the deposits, such as those in Fig. 5, are platinum, it was not evident from the potential-current curves indicating that electron microscopy is a more sensitive technique.

The cathodic deposition of platinum appears initially as random deposits (Fig. 4), which grow with continued deposition; for the case in which large quantities of platinum are in solution, the deposits eventually impinge upon one another (Fig. 2a) to cover significant portions of the working electrode surface.

Conclusions

Great caution must be exercised when platinum electrodes are used in chloride-containing media. It has been shown that, whenever a platinum electrode is subjected to an anodic current, some dissolution will occur; if the electrochemical measurements are not sufficiently fast, the dissolved platinum will diffuse to the working electrode and deposit on it. The presence of dissolved platinum can usually be detected electrochemically. However, an examination of the material under study by transmission electron microscopy and electron diffraction is the most certain means to determine whether platinum does deposit under the conditions of the experiment. It has been determined that passivity curves in chloride media can best be measured by rapidly sweeping the desired potential range or by obtaining a point-by-point plot, omitting regions in which the net current on the working electrode is cathodic and by omitting pre-electrolysis and the initial cathodic reduction of oxide films.

Acknowledgments

The authors wish to express their thanks to the following members of this Laboratory: Dr. S. S. Brenner for editorial discussions while writing this paper; Mr. G. W. Momeyer for the chemical analyses; and

Drs. L. S. Darken and R. A. Oriani for their continuing encouragement.

Manuscript received Aug. 24, 1964.

Any discussion of this paper will appear in a Discussion Section to be published in the December 1965 JOURNAL.

REFERENCES

1. J. O'M. Bockris and B. E. Conway, *Trans. Faraday Soc.*, **45**, 989 (1949).
2. J. O'M. Bockris, "Modern Aspects of Electrochemistry," Vol. 1, p. 260, Butterworths Scientific Publications, London (1954).
3. J. O'M. Bockris, I. A. Ammar, and A. K. M. S. Huq, *J. Phys. Chem.*, **61**, 879 (1957).
4. A. Shluigin and A. Frumkin, *Acta Physicochim. U.R.S.S.*, **3**, 791 (1935).
5. B. Ershler, *ibid.*, **19**, 139 (1944).
6. J. Llopis and A. Sancho, *This Jounal*, **108**, 720 (1961).
7. C. Edeleanu, *J. Iron Steel Inst.*, **188**, 122 (1958).
8. N. D. Greene and R. B. Leonard, *Electrochim. Acta*, **9**, 45 (1964).
9. S. Hirano, A. Mizuike, and M. Saheki, *Bunseki Kagaku*, **8**, 827 (1959); *CA*, **57**, 1965g (1962).

On the Equilibrium Properties of Single Crystalline Copper Electrodes

Leslie H. Jenkins and Ugo Bertocci

Solid State Division, Oak Ridge National Laboratory, Operated by Union Carbide Corporation for the United States Atomic Energy Commission, Oak Ridge, Tennessee

ABSTRACT

It is shown that, when true equilibrium conditions exist in the aqueous system studied, no single crystal orientation exposed to solution spontaneously changes with time. Also, under these conditions no differences in equilibrium potential can be measured between different orientations. Data are offered which suggest that some previous measurements possibly were not the result of equilibrium properties, but rather were produced by kinetic phenomena.

Previous studies to determine the equilibrium shapes of copper crystals exposed to aqueous solutions and/or to explore the possibility of the existence of thermodynamically more stable orientations have been reported. Getman (1) observed that in $CuSO_4$ solutions single crystalline copper exhibited an equilibrium potential about 3.5 mv greater than that of copper amalgam electrodes. Leidheiser and Gwathmey (2) reported that in acidic copper sulfate solutions copper single crystals with surfaces oriented (100) were anodic to the (111) orientation by approximately 7 mv in solutions exposed to the atmosphere. This difference dropped to ~2 mv in solutions from which air had been removed previously by boiling and which were under a hydrogen atmosphere. Annealing the crystals in hydrogen before exposure to air-saturated solutions caused the (111) to become anodic to the (100) by about 3 mv. However, Tragert and Robertson (3) concluded that only the (111) orientation was stable and capable of producing a reversible cell, and that in time all other orientations approached the (111) since they were metastable in $CuSO_4$ solutions. Since these and other published data are not in complete agreement, it seemed worthwhile to establish and attempt to understand, if possible, the reasons for disagreement.

Materials

Three different types of 99.999% pure copper single crystals were used. Coupons ~10 x 20 x 1 mm with the preferred orientation on the large 20 x 10 mm area were prepared in a manner described previously (4). Coin shaped crystals, 25 mm diameter x 7 mm thick, were cut with an acid saw from larger single crystal cylindrical slugs which had been grown by a modified Bridgman technique. Spherical crystals ~12 mm in diameter also were grown by the latter technique. Copper sulfate solutions were prepared from reagent grade $CuSO_4 \cdot 5H_2O$ and H_2SO_4. These solutions were prepared and maintained in a rack reservoir by methods previously described. All solutions reported in this study were 0.2M in $CuSO_4$ with pH adjusted to ~1 with sulfuric acid. Also, at the time of removal from the storage rack and admission to the systems of interest, the solutions, free of dissolved oxygen, were under a hydrogen atmosphere and at equilibrium with copper metal.

Experimental Method

Following normal mechanical preparation (4), coupon crystals were electropolished in an acid copper phosphate bath, rinsed in dilute phosphoric acid, washed in distilled water, and dried in a jet of oxygen. They were then suspended from one of the four glass hooks of the insert thimble of the test cell, as shown in Fig. 1. The entire apparatus was attached to the reaction rack through the side-arm standard glass joints with o-ring seals. After repeated evacuation and filling with hydrogen, a heater was placed about the lower portion of the flask, and the crystals annealed at 450°C

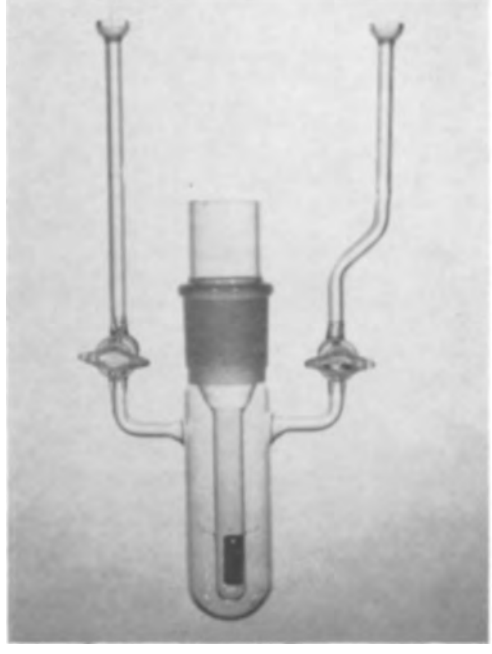

Fig. 1. Annealing cell for coupon crystals

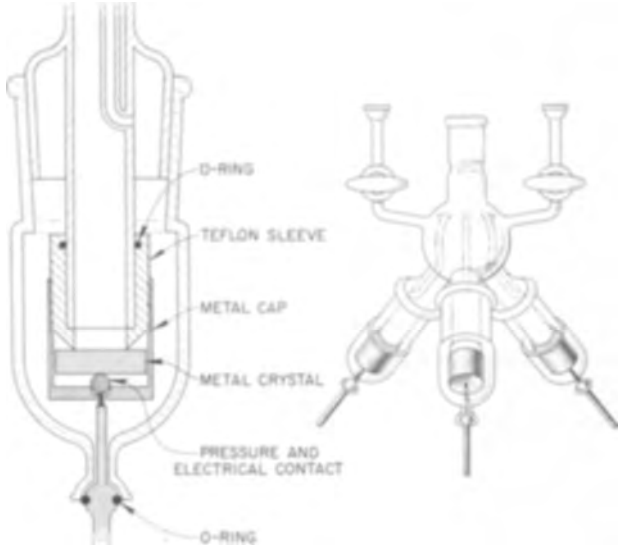

Fig. 2. Tripod cell permitting isolation of a single orientation

under H_2 for ~15 hr. When annealing had been completed and the crystals cooled to ambient temperature, the pre-equilibrated copper sulfate solution under a hydrogen atmosphere was admitted to the flask. The side-arm stopcocks were closed and the apparatus removed from the filling rack and immersed in a water bath at 25.04° ± 0.02°C. Periodic visual inspections could be made of the systems.

Cylindrical (coin shaped) crystals were first polished on a chemical polishing wheel to remove small surface irregularities introduced by the acid sawing process (5). The remainder of the polishing and washing procedure was identical to that given coupon crystals. After drying, the polished crystals were mounted on one of the three legs of a tripod cell in the manner shown in Fig. 2. A glass electrode which had been sealed vacuum-tight into a standard taper glass bushing with o-rings and epoxy resins was inserted in the standard taper joint at the top of the cell. Another entry port to the system, not shown in the illustration and hereafter referred to as the side port, was provided by a small standard taper joint located in the upper rear quadrant of the cell. A platinum wire sealed through the corresponding male member of the joint provided a means of electrical contact as well as a means of suspension of a polycrystalline 99.999% copper wire. When assembly was complete, this entire apparatus was also attached to the filling rack with o-ring seals at the standard joints on the side-arms of the cell. After repeated evacuations and filling with hydrogen, copper sulfate solution was admitted to the system and the side-arm stopcocks closed. Obviously, it was impossible to anneal the crystals. A constant temperature air bath, temperature 23.0° ± 0.1°C, was placed about the system and constant temperature maintained for the remainder of the experiment. Since the system was so massive, temperature fluctuations within the cell were small.

Potential differences between the glass electrodes and metal specimens were measured with a Beckman, model G, pH meter. Potentials between metal crystals were measured with a Cary, Model 31V, vibrating reed electrometer.

In all cases after experimentation was completed, the cells were opened quickly and the crystal hurriedly washed in distilled water, dried in a jet of oxygen, and examined with the optical microscope.

Experimental Results

Equilibrium Systems

Annealed crystals.—Four coupon crystals, oriented (100), (110), (111), and (321), respectively, were suspended from the glass hooks of the insert thimble. Systems were exposed to the copper sulfate solution for periods of 1, 3, 7, and 17 weeks. Visual inspection of the crystals showed no detectable changes in surface topography on all samples during this time. In every case, after removal from the cell, absolutely no evidence of change in surface structure could be observed microscopically. In one instance, rather than filling the flask to a level such that all samples were entirely immersed, as was normally done, only enough solution was admitted to cover half of each coupon. Upon opening, it was impossible to detect even where the solution level had been on these crystals. Also, determination of sample weights in two systems before and after exposure to solution showed no weight changes.

A spherical copper crystal[1] was suspended from a special insert thimble consisting of only one large vertical hook, annealed, and exposed to solution for two weeks in one case and four weeks in another. At the end of the indicated times no changes could be detected on any surface area in either case.

Nonannealed crystals.—To insure that the previous results were not due to the presence of undesired orientations on the edges of the coupon crystals, similar studies were conducted on cylindrical crystals in tripod cells since exposure to solution could be restricted to the orientation of interest. Coin shaped crystals with the large flat areas oriented (100), (110), and (111), respectively, were mounted one on each leg of the cell. After exposure to the copper sulfate solution at controlled temperature for periods varying from one week to four months, the cells were opened and the solution removed and saved for analysis. Examination of the crystal surfaces showed that in no case was there any detectable change in the surfaces exposed to the solutions.

Neither could a change be observed on any of these three orientations which in one system had been exposed to the solution for one year at ambient laboratory temperature, nor was any change in surface structure observed on a spherical crystal suspended from the glass electrode after a four months' exposure at controlled temperature of 23.0° ± 0.1°C.

Rest potentials.—The following observations were made only on nonannealed crystals in cells of the tripod type. It is difficult experimentally both to isolate an orientation and anneal the crystal, and it was judged to be unnecessary in this instance.

Immediately on admitting solution to the cells, a small initial potential difference (never exceeding 1.5 mv) could sometimes be measured between different orientations as well as a polycrystalline wire suspended through the side entry port. However, within 1 hr these differences had decreased to 0.2 mv, a value never exceeded during the remainder of the experiments and thought to be about the limit of experimental error in these systems. Since the magnitude and sign of both the initial and later potential differences varied from one orientation to another in different systems, they are not thought to be significant, and only one typical set of data are shown as system A, Table I.

Because the glass electrode had been subjected to vacuum treatment during preparation of the system, it usually required about 4 hr of exposure to solution before reliable results could be obtained. After that period a potential difference of ~300 mv was observed between the glass electrode and the copper crystals. The exact magnitude varied from one electrode and one system to another. Since aging and standardization of the electrode could not be accomplished after the vacuum treatment and prior to exposure to solutions, the absolute magnitude of the potentials observed is not significant. However, it is significant that other than the first few hours not only were no potential differences measured between crystals after one day or one year, but in every instance the potential measured

[1] Spherical 99.999% pure copper single crystals were kindly supplied by John V. Cathcart of this Laboratory.

Table I. Potential differences of various orientations

System	Potential of (100) mv vs. (110)	(111)	Time after solution admitted
(A)	0.75	0.62	0.1 hr
No O_2 leak	0.09	−0.27	1.0 hr
No residual O_2	0.02	−0.11	1.5 hr
	2.01	1.66	0.1 hr
(B)	2.26	2.01	1.0 hr
No O_2 leak	0.99	1.53	8.0 hr
Slight residual O_2	0.24	0.10	24.0 hr
	−0.10	0.14	48.0 hr
(C)	9.15	8.65	1 day
Constant O_2 leak	7.42	7.70	5 day
Equivalent to a corrosion current of ~10 μa/cm^2	5.98	6.84	15 day
	4.96	4.64	30 day
	4.48	3.47	60 day
	3.88	2.61	90 day

between the glass electrode and the crystals also did not change with time.

Nonequilibrium Systems

Since the experimental conditions described here were quite different from those of previous workers (1-3), it was understandable that the data were not in full agreement. However, a possible explanation of the cause(s) for disagreement was desirable. Fortunately, air inadvertently leaking slowly into a system under observation resulted in potential differences arising between electrodes and produced changes in surface topography which suggested a means of explaining these differences.

It has been shown (6) that surfaces being oxidized by oxygen dissolved in solution are attacked uniformly since the reaction rate is diffusion controlled. However, another reaction mechanism is possible in a system of copper metal exposed to a solution of its ions. If the system is originally at equilibrium, then the equilibrium constant of $\sim 10^{-6}$ is satisfied for the reaction

$$Cu^{2+} + Cu^{o} \leftrightharpoons 2Cu^{+} \quad [1]$$

If air slowly leaks into the system at a point far removed from the metal, equilibrium is destroyed by the reaction

$$2Cu^{+} + \tfrac{1}{2}O_2 + 2H^{+} \leftrightharpoons 2Cu^{2+} + H_2O \quad [2]$$

The equilibrium concentration of copper(I) ions can be restored only when copper metal is oxidized by copper(II) ions, as in reaction [1] proceeding to the right.

Controlled, constant leak rates in the systems could be obtained through faulty platinum-through-glass seals of the male standard joint at the side entry port. If a very limited reaction was desired, evacuation and flushing with hydrogen was limited so that a trace of air was retained in the system. The following data were all obtained using tripod cells.

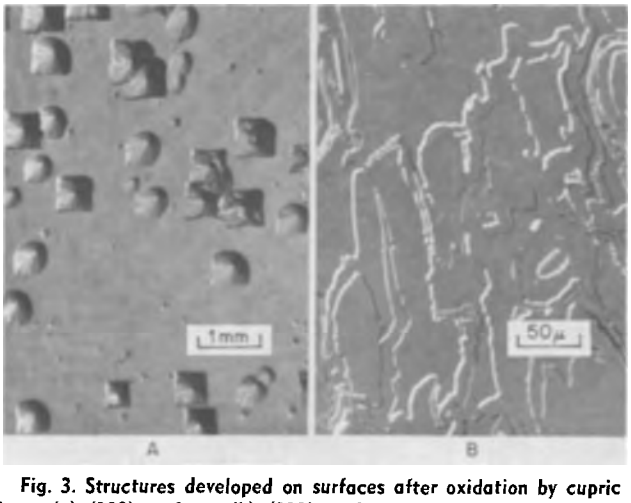

Fig. 3. Structures developed on surfaces after oxidation by cupric ions: (a) (100) surface; (b) (111) surface.

Figure 3 shows typical structures developed by cupric ion oxidation of the indicated surface. It is obvious that dissolution on the (100) and (111) occurred in highly restricted regions rather than uniformly over the entire surface. This phenomena was repeated in all systems at all reaction rates up to 30 μa/cm^2, the greatest rate studied. Facets developed on the (110) were more uniformly distributed, but their appearance and habit also were observed repeatedly in all systems not at equilibrium.

Table I records some typical potential differences measured in these systems. As previously stated, the first group of data in the table was collected from an experiment in which not only had the cell initially been well evacuated and flushed with hydrogen so that no residue of oxygen remained, but there was also no leak in the system. The experiment supplying the second group of data, System (B), had not been well evacuated and flushed so that a small residue of oxygen remained. However, there was no leak in the cell, and equilibrium was established within two days. Obviously the potential differences observed reflect the corrosion process occurring on the various orientations. Although the potentials are meaningful, when the system was opened and the surfaces examined the reaction generating the potentials had been so slight that surface changes could be detected only on the (100), and then only after extremely careful observation. Needless to say, no corrosion rate could be established since no detectable change in copper concentration occurred in solution.

System (C) in Table I had a constant leak of air into the system which resulted in a corrosion rate equivalent to approximately 10 μa/cm^2 geometric electrode area. The gradual decrease in potential differences reflects (among other things) changes in the crystal surfaces, for when the samples were removed after 111 days, very little of the original surface remained on any of the electrodes.

Discussion and Conclusions

The failure of all crystals (annealed or not; either coupon, spherical, or cylindrical) to develop facets spontaneously after exposure to oxygen-free copper sulfate solutions (initially at equilibrium with polycrystalline copper) for varying periods of time up to one year suggest that no crystal orientation is thermodynamically more stable than any other in the system studied. The data in Table I show that even small departures from equilibrium conditions generate a measurable and significant potential difference and suggest that, if at equilibrium a potential difference as little as ~1 mv existed between different orientations, facets of preferred orientation(s) would develop since mass transfer could occur.

Because equilibrium potentials were measured in a cell which did not permit annealing the crystals, it is probable that initial small potential differences sometimes observed between crystals was due primarily to the dissolution of oxide originally present on the electrode surface. Certainly in noncorroding systems no potential differences could be measured between unlike orientations or between the glass electrode and one orientation as compared with another. Therefore since any potential differences between orientations cannot be measured experimentally, and since spontaneous faceting does not occur over long periods of time, it is reasonable to conclude that no potential difference exists between different orientations under equilibrium conditions.

The nature of the pits developed on (100) surfaces and the formation of ledges on the (111), as well as the potential differences observed in cells containing dissolved oxygen, perhaps explain the variance of

these data with most of those in the literature. First of all, the physical dimensions of each leg of the tripod cell were equal, and geometric surface areas exposed to solution were the same for all crystals. It can be assumed then that over-all corrosion rates were equal in the legs of any one cell. The potential differences observed were not due to differences in corrosion rate, but reflect rather complex surface properties of the different crystals. These problems will be enlarged and treated in another paper.

None of the data discussed here was collected under conditions in which the corrosion current exceeded 30 μa/cm^2. Many observations were made on systems reacting at rates ~10 μa/cm^2, but most data were obtained with rates of 0.5-3 μa/cm^2. In all cases significant differences in potential could be measured, even at the slowest rates. The magnitude of the differences was generally proportional to the difference in corrosion rates from one system to another, and although the significance is not clear, the (100) was usually anodic with respect to the (111) and (110) in all corroding systems.

In summary, it has been shown that two conditions must be fulfilled before true equilibrium exists in a solution of copper sulfate exposed to copper metal: (*A*) No dissolved oxygen can be present or corrosion will occur as shown in Eq. [1] and [2]. (*B*) Even if no dissolved oxygen is present, the solution must be pre-equilibrated with copper metal before immersion of the test electrode, or reaction [1] will occur until equilibrium is established. It must be emphasized again that dissolution due to the latter cause is not inappreciable for the equilibrium concentration of copper(I) ions in solutions of copper (II) ions at unit activity is ~10^{-3}M. Finally, although not discussed here previously, Miller and Lawless (7) have shown that the *p*H of such systems is a factor in establishing equilibrium as defined by Eq. [1]. Their results need not be described at length, but clearly they demonstrate that, even in deaerated $CuSO_4$ solutions at all *p*H values above ~3.2, oxide films grew over the metal surfaces for periods of hours, and that in addition to the composition and growth forms of the films being complex, it was reasonable to assume that little, if any, metal surface is free of oxide under such conditions. Therefore, whatever the final equilibrium state in these latter systems, it is reached slowly, accompanied by a decreased *p*H of the solution, and certainly must involve some consideration of the presence of an oxide film. Obviously, in such a system an initial potential difference between electrodes which decreased with time possibly could be due only to the complex processes occurring on the surface rather than to differences in thermodynamic states of crystal orientations.

Then at the moment of immersion of a test electrode true equilibrium exists only in solutions which are free of dissolved oxygen, which have been pre-equilibrated with copper metal, and which exhibit a *p*H less than about 3.2. While the equilibrium results reported here were obtained under these conditions, the authors are unaware of any previous reports on the single crystal Cu-aqueous copper sulfate system in which all three requirements were satisfied. Therefore, it is possible that many previous measurements of others reporting crystallographic differences in equilibrium potentials were obtained from systems originally removed from equilibrium, and the potential differences observed were due to kinetic rather than thermodynamic phenomena.

Manuscript received Oct. 21, 1964; revised manuscript received Jan. 30, 1965.

Any discussion of this paper will appear in a Discussion Section to be published in the December 1965 JOURNAL.

REFERENCES

1. F. Getman, *J. Phys. Chem.*, **34**, 1454 (1930).
2. H. Leidheiser, Jr., and A. T. Gwathmey, *Trans. Electrochem. Soc.*, **91**, 97 (1947).
3. W. E. Tragert and W. D. Robertson, *This Journal*, **102**, 86 (1955).
4. L. H. Jenkins and J. O. Stiegler, *ibid.*, **109**, 467 (1962).
5. F. W. Young, Jr., and T. R. Wilson, *Rev. Sci. Inst.*, **32**, 559 (1961).
6. L. H. Jenkins, *This Journal*, **107**, 371 (1960).
7. G. T. Miller, Jr., and K. R. Lawless, *ibid.*, **106**, 854 (1959).

Studies of the Electrochemical Kinetics of Indium

II. System Indium + Indium Sulfate at Higher C.D.

V. Markovac and B. Lovrecek

Institute of Electrochemistry and Electrochemical Technology, Faculty of Technology, University of Zagreb, Zagreb, Yugoslavia

ABSTRACT

In a previous paper the kinetics of the deposition and dissolution of indium was studied by a galvanostatic method of single current pulses. At c.d. higher than 2.5 x 10^{-3} amp/cm^2 a change in the mechanism of the deposition and dissolution of indium was observed. To study the phenomenon, the cathodic and anodic polarization in solutions of indium sulfate with *p*H 2.5, *p*H 1.56, and *p*H 1.0 was investigated as well as the deposition of hydrogen at cathodic polarization in equivalent sulfate solution without indium. After cathodic polarization at chosen c.d.'s, the polarographic investigation of the indium sulfate solution was done. Analysis of the experimental data obtained by cathodic polarization in indium sulfate solution at higher c.d. points to the reaction step $In^{3+} + 2e_0^- \rightarrow In^{1+}$ as rate-determining. For anodic polarization one can conclude that a disproportionation reaction occurs with increasing c.d., and that the first anodic reaction step $In^o - e_0^- \rightarrow In^{1+}$ becomes rate-determining.

In a previous paper (1) the kinetics of deposition and dissolution of indium in sulfate solution was studied using a galvanostatic method of single square-wave pulses.

In that paper it was mentioned that experimental $\eta_A - \log_{10} i$ curves for c.d.'s higher than 2.5 x 10^{-3} amp/cm^2 do not follow Tafel linear relation as found for the region of lower c.d.'s, but show reproducible deviations. The phenomena indicate the existence of some other processes which interfere in the processes previously described (1) and point to changes in the mechanism of deposition and dissolution of indium at higher c.d.'s.

These phenomena were investigated by a slightly modified experimental method (1). The expressions

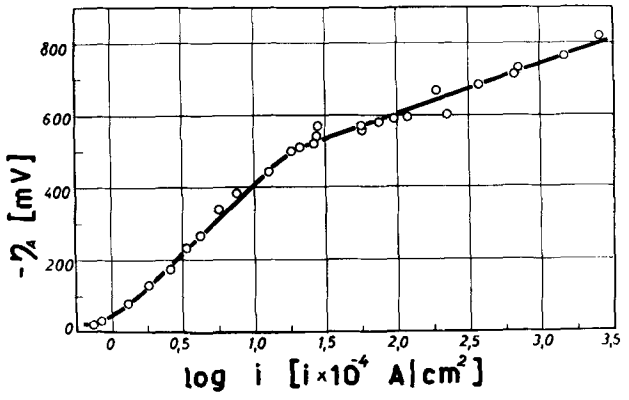

Fig. 1. η_A — log $_{10}i$ curve for cathodic polarization. Electrolyte: 0.116*N* $In_2(SO_4)_3$ + 0.5*N* K_2SO_4, *p*H 2.5.

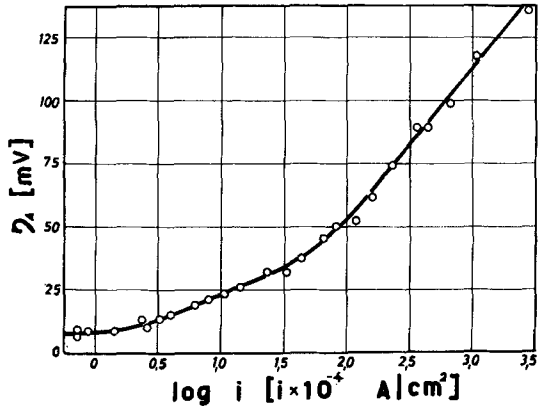

Fig. 2. η_A — $\log_{10}i$ curve for anodic polarization. Electrolyte: 0.116*N* $In_2(SO_4)_3$ + 0.5*N* K_2SO_4, *p*H 2.5.

for kinetics of "many steps" electrode reactions (2) were used.

Experimental

For cathodic and anodic polarization of indium (as 0.3% indium amalgam) with galvanostatic single pulses the same apparatus was used as described (1), with the exception that the electrolytical cell was placed in a wooden air thermostat provided with thermoregulator and ventilator that allows work at a constant temperature of 25° ± 1°C.

Polarization was carried out in the following electrolytes

0.116*N* $In_2(SO_4)_3$ + 0.5*N* K_2SO_4, *p*H 2.5

0.116*N* $In_2(SO_4)_3$ + 0.5*N* K_2SO_4, *p*H 1.56

0.116*N* $In_2(SO_4)_3$ + 0.5*N* K_2SO_4, *p*H 1.0

0.5*N* K_2SO_4, *p*H 2.5

Chemicals used were of analytical reagent grade and water was redistilled.

The experimental $\eta_t - t$ curves were obtained in the same way as previously described (1).

To test for the presence of ions of lower valency in the electrolyte after cathodic polarization, the electrolysis and polarography of indium sulfate solution were done in an analogous way as earlier (3).

Results

Activation overpotential-current density relationship.—The difference between the steady-state potential and the ohmic overpotential η_Ω represents the activation overpotential η_A (1).

When the values of activation overpotential (η_A) were plotted against the logarithms of c.d. ($\log_{10} i$), the curves (Fig. 1, 2) for cathodic and anodic polarization in 0.116*N* $In_2(SO_4)_3$ + 0.5*N* K_2SO_4 at *p*H 2.5 were obtained. Both curves are linear in the c.d. ranges 2.5 x 10^{-4} — 2.5 x 10^{-3} amp/cm² and 8.5 x 10^{-3} — 2.5 x 10^{-1} amp/cm².

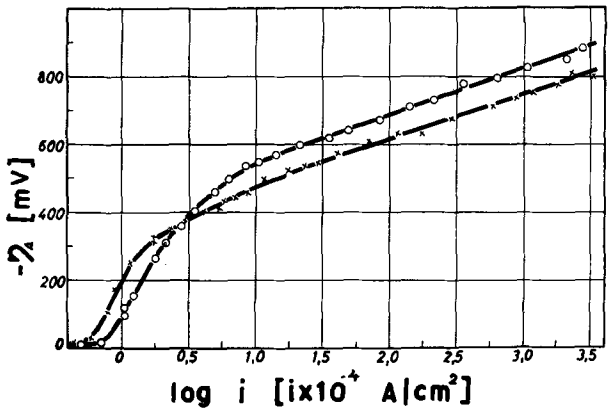

Fig. 3. η_A — $\log_{10}i$ curves for cathodic polarization. Electrolyte: 0.116*N* $In_2(SO_4)_3$ + 0.5*N* K_2SO_4; x, *p*H 1.0; ○, *p*H 1.56.

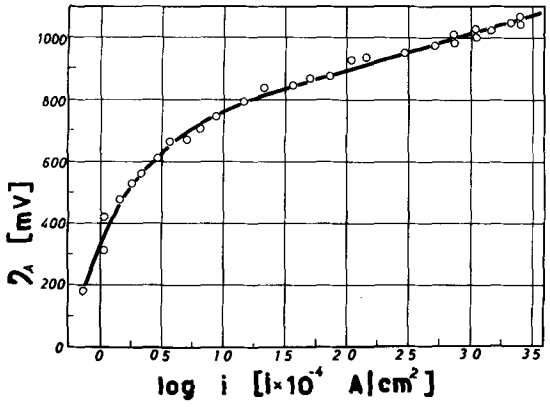

Fig. 4. η_A — $\log_{10}i$ curve for cathodic polarization. Electrolyte: 0.5*N* K_2SO_4, *p*H 2.5.

Figure 3 shows η_A — $\log_{10} i$ curves for cathodic polarization in 0.116*N* $In_2(SO_4)_3$ + 0.5*N* K_2SO_4 at *p*H 1.56 and *p*H 1.0, respectively. The curve corresponding to the solution with *p*H 1.56 is linear in the c.d. ranges 8.5 x 10^{-5} — 2.5 x 10^{-4} amp/cm² and 1.5 x 10^{-3} — 3.0 x 10^{-1} amp/cm² as is the curve in the solution with *p*H 1.0 in the c.d. ranges 7.0 x 10^{-5} — 1.2 x 10^{-4} amp/cm² and 1.5 x 10^{-3} — 3.0 x 10^{-1} amp/cm².

Figure 4 shows the η_A — $\log_{10} i$ curve for cathodic polarization in an electrolyte without indium (0.5*N* K_2SO_4 at *p*H 2.5). In the c.d. range 1.5 x 10^{-3} — 2.5 x 10^{-1} amp/cm² the experimental curve shows a marked linear relation with characteristics usual for the deposition of hydrogen. (Experimentally obtained parameters of Tafel-line are: $a = -0.666$v, $b = 0.114$v).

The linear parts of the experimental η_A — $\log_{10} i$ curves (Fig. 1, 2, 3, 4) that are in fact Tafel-lines are treated with a method earlier developed (2), using expressions for the slowest reaction step, *i.e.*, the rate-determining step.

$$\frac{\partial \log i_-}{\partial V} = -\frac{zF}{2.303\,RT}(n_c^* - \alpha) \qquad [1]$$

$$\frac{\partial \log i_+}{\partial V} = \frac{zF}{2.303\,RT}(n_a^* - 1 + \alpha) \qquad [2]$$

Since the left sides of Eq. [1] and [2] represent the slopes of the experimental Tafel-lines, it was possible to obtain from the experimental data n_c^*, n_a^*, and α.[1]

[1] n_c^* and n_a^* being the ordinal numbers of the slowest reaction step for the cathodic and anodic polarization (small integer), α the transfer coefficient ($0 < \alpha < 1$), and z the number of electrons involved in the slowest reaction step.

Table I. Kinetic parameters for cathodic polarization

Electrolyte	pH	Range of c.d., amp/cm²	$\partial \log_{10} i_{-}/\partial V$ #	α#	n_c*	z
0.116*N* $In_2(SO_4)_3$ + 0.5*N* K_2SO_4	2.5	2.5×10^{-4} to 2.5×10^{-3}	2.87	0.834	1	1
		8.5×10^{-3} to 2.5×10^{-1}	6.11	0.823	1	2
0.116*N* $In_2(SO_4)_3$ + 0.5*N* K_2SO_4	1.56	8.5×10^{-5} to 2.5×10^{-4}	1.44	0.917	1	1
		1.5×10^{-3} to 3.0×10^{-1}	7.20	0.792	1	2
0.116*N* $In_2(SO_4)_3$ + 0.5*N* K_2SO_4	1.0	7.0×10^{-6} to 1.2×10^{-4}	1.24	0.929	1	1
		1.5×10^{-3} to 3.0×10^{-1}	7.84	0.773	1	2
0.5*N* K_2SO_4	2.5	1.5×10^{-3} to 2.5×10^{-1}	8.74	0.494	1	1

Mean values derived from 2-7 complete experimental curves.

Table II. Kinetic parameters for anodic polarization

Electrolyte	pH	Range of c.d., amp/cm²	$\partial \log_{10} i_{+}/\partial V$ #	α#	n_a*	z
0.116*N* $In_2(SO_4)_3$ + 0.5*N* K_2SO_4	2.5	2.5×10^{-4} to 2.5×10^{-3}	48.0	0.803	3	1
		8.5×10^{-3} to 2.5×10^{-1}	14.99	0.869	1	1

Mean values derived from 4-7 complete experimental curves.

Results of the calculations are presented in Table I and Table II.

Polarographic investigations.—Figure 5 shows polarograms obtained before and after cathodic polarization of indium in sulfate electrolyte and a polarogram obtained in the corresponding sulfate electrolyte without indium. As it is seen (Fig. 5) there is no experimental curve with an anodic wave. Consequently after cathodic polarization it is not possible to prove the existence of ions of lower valency by polarography.

Discussion

Ohmic Overpotential

When the experimental values of the ohmic overpotential were plotted against the values of the current i, the linear relation was obtained with slope representing the resistance R (Fig. 6). The resistance R calculated on the ground of expression of Mattsson and Bockris (4) is in good accordance with values determined experimentally (Table III).

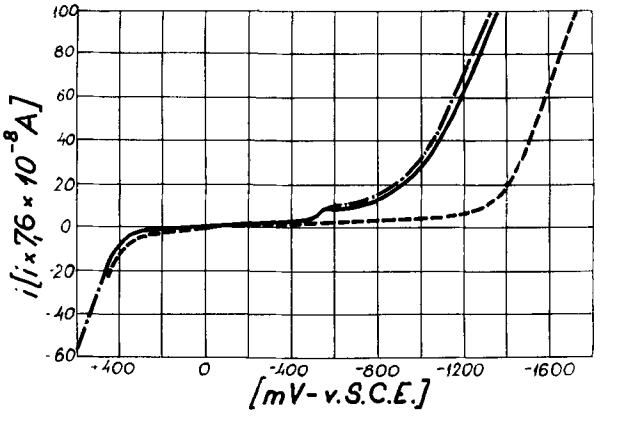

Fig. 5. Polarograms for electrolyte: 0.116*N* $In_2(SO_4)_3$ + 0.5*N* K_2SO_4, pH 2.5: —, before electrolysis; — · — · —, after electrolysis (i_c = 71.9 ma/cm², t = 10 min); — — — electrolyte without indium.

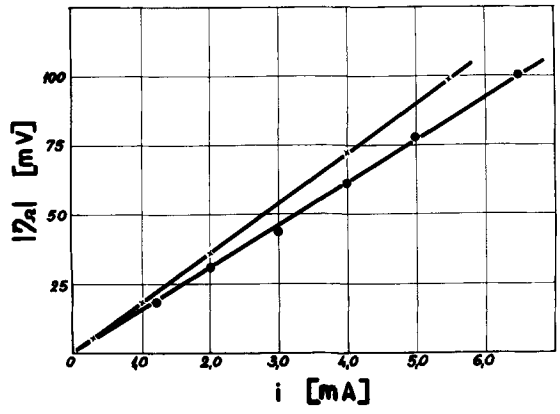

Fig. 6. $|\eta_\Omega|$ — i curves for electrolyte: 0.116*N* $In_2(SO_4)_3$ + 0.5*N* K_2SO_4; x, pH 1.56; O, pH 1.0.

Activation Overpotential-Logarithms of Current Density Curves

For the electrochemical deposition and dissolution of indium in the region of lower c.d.'s (Fig. 1, 2, Table I, II) it was found that the first step was the slowest one in the cathodic reaction and that the third step was the slowest one in the anodic reaction (1).

$$In^{3+} \xrightarrow[\text{slowest}]{+e_0^-} In^{2+} \xrightarrow{+e_0^-} In^{1+} \xrightarrow{+e_0^-} In^0 \qquad [3]$$

$$In^0 \xrightarrow{-e_0^-} In^{1+} \xrightarrow{-e_0^-} In^{2+} \xrightarrow[\text{slowest}]{-e_0^-} In^{3+} \qquad [4]$$

If the c.d. is increased over 2.5×10^{-3} amp/cm², η_A — $\log_{10} i$ curves do not follow earlier relations either at cathodic or at anodic polarization.

Cathodic curve at higher c.d.'s.—The curve for cathodic polarization shows a transition in the range of c.d.'s 2.5×10^{-3} — 8.5×10^{-3} amp/cm², but in the range of higher c.d.'s there exists again a linear relation with another slope (Fig. 1). Such an experimental fact points to the change in the mechanism of indium deposition at higher c.d.'s. To explain the significance of the linear part of the experimental η_A — $\log_{10} i$ curve at higher c.d.'s we have to consider the processes that might occur under given circumstances.

It might be assumed that the first step of the overall reaction, Eq. [3], at higher c.d.'s is so much accelerated that the over-all reaction is controlled eventually by the second or third cathodic step. The assumption is questionable because the linear part of the experimental curve has a slope that shows according to Eq. [1] that the first cathodic reaction step is the slowest one (Table I). Furthermore, after the cathodic polarization at chosen c.d.'s it was not possible to find oxidizable intermediates by polarography, *i.e.*, we did not succeed in recording the anodic wave (Fig. 5).[2]

[2] In an earlier investigation (3) it was possible to register ions of lower valency by polarography after anodic polarization.

Table III. Resistance calculated and experimentally determined for 0.116*N* $In_2(SO_4)_3$ + 0.5*N* K_2SO_4 at various pH values

pH	$R_{calc.}$	$R_{exp.}$
1.56	17.7	18.0
1.0	15.3	15.4

For corresponding data for electrolyte of pH 2.5 see ref. (1).

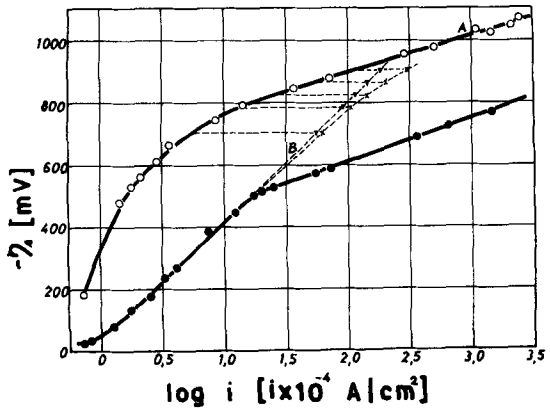

Fig. 7. •, cathodic η_A — $\log_{10} i$ curve for electrolyte: 0.116*N* $In_2(SO_4)_3$ + 0.5*N* K_2SO_4, *p*H 2.5. ○, Cathodic η_A — $\log_{10} i$ curve for electrolyte: 0.5*N* K_2SO_4, *p*H 2.5. ▾, Selected points at the lengthened linear part of curve of deposition of indium. x, Curve constructed by addition A and B.

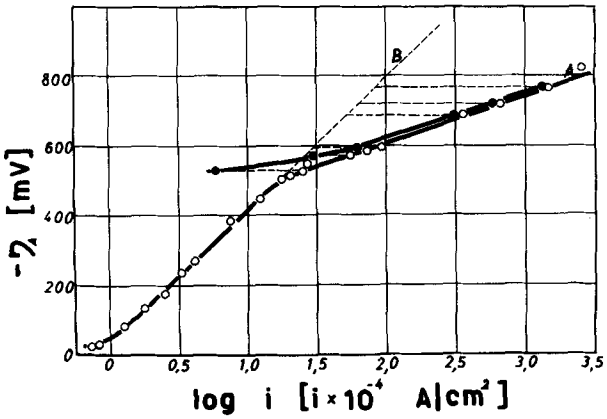

Fig. 8. ○, cathodic η_A — $\log_{10} i$ curve for electrolyte: 0.116*N* $In_2(SO_4)_3$ + 0.5*N* K_2SO_4, *p*H 2.5 •, Curve constructed by subtraction A and B.

According to other authors (5) it might be assumed that the deposition of hydrogen may influence the experimental curve at increased c.d.'s and low *p*H values. Actually, our experimental results (Fig. 3) show some changes with decreasing *p*H, although the general shape and characteristic slopes remain the same. To find the magnitude of the influence that hydrogen deposition might have at higher c.d.'s on the experimental η_A — $\log_{10} i$ curve, a parallel cathodic polarization was carried out using an equivalent electrolyte without indium. The curve obtained in such a way shows over a wide range a typical Tafel linear relation for hydrogen deposition as often reported in the literature.

To compare experimental η_A — $\log_{10} i$ curves at cathodic polarization in the presence and absence of indium, we applied the following procedure (Fig. 7). The linear part of the curve in the presence of indium at lower c.d.'s was lengthened, and at that part of the curve random points of c.d.'s were added to those of hydrogen discharge at the same overpotentials. In such a case, the constructed and experimental curve would coincide if the discharge of hydrogen is a simultaneous and parallel process to the deposition of indium at higher c.d.'s. However, this is obviously not the case (Fig. 7) and indicates that at higher c.d.'s some changes occur in the kinetics of deposition of indium itself, although under such conditions some deposition of hydrogen might be expected.

Let us therefore consider again the possible reaction steps of the over-all electrochemical process of deposition. There is no reason not to accept the possibility of the fusion of any two of the three possible reaction steps [3], especially in the range of higher c.d.'s; *i.e.*, the deposition of indium might proceed as follows:

$$In^{3+} \xrightarrow{+e_o^-} In^{2+} \xrightarrow{+2e_o^-} In^o \qquad [5]$$

$$In^{3+} \xrightarrow{+2e_o^-} In^{1+} \xrightarrow{+e_o^-} In^o \qquad [6]$$

Reaction [5] would hardly be possible because either the second cathodic step should be the slowest, or the linear part of the experimental curve at lower c.d.'s (Fig. 1) should have the same slope at higher c.d.'s too. However, the slope at higher c.d.'s does not show according to Eq. [1] that the second reaction step is the slowest one. It follows that only the reaction [6] may be considered as the possible ones.

Considering reaction [6], from the slope of the experimental curve at higher c.d.'s it can be calculated that the first cathodic reaction step is the slowest one (Table I). In addition, the reaction step

$$In^{1+} + e_o^- \rightarrow In^o \qquad [7]$$

was fast enough at lower c.d.'s too, and it would hardly be possible that the over-all reaction is influenced by it. In support of this is the fact that after cathodic polarization at chosen c.d.'s it was not possible to register oxidizable ions of lower valency by polarography.

On the basis of the shape of the experimental curve (Fig. 1) and earlier considerations it follows, that going from lower c.d.'s to higher ones, a change in the mechanism of the deposition of indium occurs. One mechanism is predominant at lower c.d.'s and the other at higher c.d.'s, while in the region between both processes are possible. The difference between the total experimental c.d. and the partial current of the interfering process is the c.d. to be used for the rate-determining process in the given range. Applying this principle in the higher c.d. range by subtracting the c.d. values of the lengthened Tafel-line (representing the rate-determining process at lower c.d.'s) from the c.d. values of the experimental curve at the same overpotential, one obtains a curve representing the rate-determining reaction step at higher c.d.'s. That curve differs very little from the experimental one in the range of higher c.d.'s (Fig. 8). From the slope of the constructed curve and Eq. [1] can be calculated that the first step is the slowest one of the over-all reaction [6]. All the mentioned facts and qualitative considerations point to the possibility of a reaction involving two electrons and one ion of In^{3+} at higher c.d.'s. Increasing the density of electrons at the cathode increases the probability of the simultaneous reaction of two electrons and one ion of In^{3+}, especially at higher concentrations of In^{3+} (concentration of the electrolyte) and low concentrations of In^{2+}. (In^{2+} was a product of the slowest reaction step at lower c.d.'s, and because of the faster subsequent reaction steps this ion would hardly be found near the cathode).

From these facts it can be concluded that the reaction

$$In^{3+} \xrightarrow[\text{slowest}]{+2e_o^-} In^{1+} \qquad [8]$$

is the slowest step in the cathodic polarization of indium in sulfate solutions at higher c.d.'s.

Anodic curve at higher c.d.'s.—At higher c.d.'s the experimental η_A — $\log_{10} i$ curve of the anodic polarization of indium does not follow the original Tafel linear relation. It changes slope. In the range of c.d.'s 8.5×10^{-3} — 2.5×10^{-1} amp/cm² it follows again a linear relation but with a different slope. The slope of this second part of the curve shows according to Eq. [2] that the first anodic step is now the slowest one

in the over-all electrochemical dissolution of indium (Eq. [4], Table II). That change in the mechanism of the dissolution of indium is possible to explain in following way: As the reaction step

$$In^{2+} - e_o^- \rightarrow In^{3+} \quad [9]$$

is the slowest one at lower c.d.'s, the ions of lower valency are accumulated as proved by polarography (3). By the accumulation of the ions less stable than In^{2+} there is the general possibility (6, 7) that they are removed by a disproportionation reaction as for instance

$$2In^{2+} \rightarrow In^{3+} + In^{1+} \quad [10]$$

An increase of c.d. increases the concentration of In^{2+} and therefore the disproportionation reaction [10] is accelerated. With such an accelerated disproportionation, the third step of the over-all electrochemical reaction of dissolution [4] has less and less influence. In addition, with the process accelerated according to reaction [10], other disproportionation reactions may be assumed, as of the type

$$3In^{1+} \rightarrow In^{3+} + 2In^{o} \quad [11]$$

In favor of reaction [11] are earlier observations (3) when small crystals of indium were found in electrolyte after anodic polarization.

Considering accelerated disproportionation reactions [10] and [11], it can be assumed that the over-all anodic reaction [4] is really controlled by the first reaction step

$$In^{o} - e_o^- \rightarrow In^{1+} \quad [12]$$

at higher c.d.'s as proved by the slope of experimental curve (Fig. 2, Table II).

Manuscript received June 9, 1964; revised manuscript received Feb. 1, 1965.

Any discussion of this paper will appear in a Discussion Section to be published in the December 1965 JOURNAL.

REFERENCES

1. B. Lovrecek and V. Markovac, *This Journal*, **109**, 727 (1962).
2. B. Lovrecek, *J. Phys. Chem.*, **63**, 1795 (1959).
3. Lj. Duić. Z. Kovac, and B. Lovrecek, *Croat. Chem. Acta*, **32**, 213 (1960).
4. E. Mattsson and J. O'M. Bockris, *Trans. Faraday Soc.*, **55**, 1586 (1959).
5. W. Kangro and Fr. Weingärtner, *Z. Elektrochem.*, **58**, 505 (1954).
6. J. Heyrovsky, *Discussion Faraday Soc. Electrode Processes*, 212 (1947).
7. K. J. Vetter and G. Manecke, *Z. Physik. Chem.*, **195**, 337 (1950).

Technical Notes

Preparation of Transition Metal Oxide-Metal Electrodes

Richard L. Every

Central Research Division, Continental Oil Company, Ponca City, Oklahoma

Recent interest has been evidenced in the formation of oxides on transition metals for various purposes. Electrodes of NiO on Ni are used in batteries (1) and fuel cells (2). Tantalum oxide on tantalum is used for electron emission (3), as an electrolytic rectifier (4), and for electrolytic capacitors (5-7). Titanium oxide on titanium has also been used as a capacitor (8). Oxides are used to protect the transition metals from corrosion and erosion (9, 10). Transition metal oxides have been used in catalysis (11) and electrochemistry (12-26). Various other workers have conducted miscellaneous studies of oxides on the transition metals, *i.e.*, Mo (27), W (28), Nb (29, 30), Nb and Zr (31), Zr (32), Ta (33), Ni (34-36), Pt (37-47), Pt and Pd (48), Pd (49, 50), Rh and Ir (51), Nb, Th, W, U, and Co (52), and Nb, U, V, Ti, Zr, and Ta (53).

The present study is concerned with the fabrication of metal oxide-metal electrodes of ZrO_2, α-Nb_2O_5, Nb_2O_5 (penta), Rh_2O_3, PdO, HfO_2, β-Ta_2O_5, Ta_2O_5 (penta), and PtO on their respective parent metals. (The α, β, and penta are ASTM designations.) The electrochemical characteristics of these electrodes are being studied and will be reported at a later date.

Experimental

All electrodes were about 0.038 x 1.3 x 3.8 cm. About two-thirds of the electrode (about 6.5 cm^2 of metal) was oxidized. The oxides formed were identified either by x-ray or electron diffraction.

The electrode metals were designated "commercially pure" by the manufacturer. All metals except platinum were abraded with fine emery cloth prior to each oxidation. X-ray diffraction patterns verified the removal of residual oxides with this treatment. The platinum electrode was preheated to redness for several seconds in order to remove residual oxides before depositing the platinum black (54). The oxides and the methods of formation are listed in Table I.

Many unsuccessful attempts were made to form the transition metal oxides before trying the general method of using the molten oxidizing salts with and without electrolysis. The exact temperature of the molten salt is apparently not critical in the formation of the oxide. As seen in Table I, typical temperature conditions range from 360° to 420°C. However, the use of electrolysis is important in the formation and growth of certain of the oxides.

To accomplish electrolysis, dry cell batteries were used in series with an ammeter and a rheostat. The current densities given in Table I represent maxima as controlled with the rheostat. The ability to maintain these maxima was limited. In each electrolysis the current density could be controlled for about 1 min before it slowly decayed to a minimum value. Using fresh batteries and established oxide films, these minimum current values could be repeated; this proved that the current decay was due to formation of the oxide film and was not due to the current drain on the battery.

Discussion

Films identified as the oxides were formed on Ta, Rh, and Hf without electrolysis. The thickness of the oxide films was increased with prolonged exposure to the molten salts. Upon microscopic examination of the films, the surface of the electrodes appeared slightly etched. Surprisingly, Ta was oxided in molten $KClO_3$ after only 30 min while it was apparently not oxidized after 3 hr in molten KNO_3.

Table I. Method of preparation of metal-metal oxide electrodes

Oxide	Condition	Appearance
ZrO_2	Anode in 400°C KNO_3 for 5 min with 6v. No current control.	Dark gray
α-Nb_2O_5 (high temp)	Anode in 360°-400°C KNO_3 or $KClO_3$ with 180v and current density controlled at a maximum of 31 ma/cm².	White
Nb_2O_5 (penta)	Anode in 360°-400°C KNO_3 or $KClO_3$ for 5 min with 90v and current density controlled at a maximum of 31 ma/cm². Electrode was then boiled in 96% H_2SO_4.	Silvery-gray
Rh_2O_3	Placed in 400°C KNO_3 or $KClO_3$ for 12 hr.	Dull
PdO	Anode in 400°C KNO_3 for 2 hr with 6v. No current control.	Gray
HfO_2	Placed in 400°C KNO_3 or $KClO_3$ for 1 hr.	Blue
Ta_2O_5 (penta)	Anode in 420°C $KClO_3$ for less than 5 min with 6-60v and current density controlled at a maximum of 2.3-23 ma/cm².	Yellow and blue-green
β-Ta_2O_5	Placed in 380°C $KClO_3$ for 30 min.	Dark blue
	Anode in 400°C KNO_3 or $KClO_3$ with 90v for 1 min. No current control.	Gray
PtO	Pt black (54) electrode placed in O_2 atmosphere at temperatures exceeding 465°C for several hours.	Black below 500°C; gray above 500°C.

Merely dipping the electrodes of Zr, Nb, and Pd into molten salt was not sufficient to form enough oxide for identification; however, the color of the Nb electrode did change to blue. This blue Nb had a few weak x-ray lines in common with Nb_2O_5 (ASTM Powder Diffraction File Card No. 5-0352), but the evidence was inconclusive.

The ZrO_2 formed in 400°C KNO_3 with 6v was a thick, gray coating and could be removed only with extreme difficulty. However, when Zr was made the anode in molten $KClO_3$ with 6v for 5 min, a white coating formed which flaked off and left a blue, deeply etched, and relatively oxide-free Zr surface.

The α-Nb_2O_5 (high temperature) formed as a thick, white adherent powder which could be scraped from the electrode with difficulty. The fact that it formed at 360°-400°C is a little surprising since the transition to the α structure is given as 1095°C (55). The electrical energy used to make this electrode may explain the unexpected appearance of the high-temperature form.

A somewhat less adherent gray coating with flecks of white was formed on Nb when the applied voltage was dropped from 180 to 90v. This coating was dissolved by placing it in hot H_2SO_4 for about 2 hr; this resulted in an etched Nb_2O_5 (penta) surface. The α-Nb_2O_5 was also dissolved by a similar treatment, but the resulting surface was severely eroded.

Niobium was also subjected to electrolysis in molten salts with 6 to 45v. The electrode color changed from blue to amber to gray as the voltage was increased. A study of the diffraction patterns indicated some Nb_2O_5 (penta) might have been present, but positive identification was doubtful.

Diffraction d-spacing values for Rh_2O_3 are not available from the ASTM data file. However, we were able to obtain 6 coincident peaks on comparison of x-ray diffraction patterns from commercial anhydrous Rh_2O_3 powder (Alfa Inorganic Inc.) and our own oxidation product.

When Pd was made the anode in 400°C $KClO_3$ with 6v, a heavy froth in the electrolyte forced the experiment to stop at the end of 5 min. A thick black coating had formed and was identified as PdO. The PdO formed in KnO_3 with 6v was a thick, gray adherent coating at the end of 2 hr. No problems with froth were experienced in KNO_3.

The forms of Ta_2O_5 are many, and as in the case of Nb_2O_5 the positive identification of any given structure is elusive. Ta_2O_5 (penta) (ASTM Card No. 7-231) was identified as the result of electrolysis in $KClO_3$ with 6v at a maximum current density (c.d.) of 2.3 ma/cm² and again with 60v at a maximum of 23 c.d. units. These thick adherent coatings were yellow and bluish-green to violet, respectively. Little success was realized in trying to form Ta_2O_5 (penta) with electrolysis in KNO_3. Some highly colored oxides were formed with various treatments, but identification was not positive.

β-Ta_2O_5 (ASTM Card No. 8-255) apparently may be fabricated in a number of ways. Thin films of this type were the result of heating Ta to redness in work preliminary to this study and also resulted from exposing Ta to molten $KClO_3$ for about 30 min. The β form was also obtained with electrolysis in both molten salts with 90v for about 1 min. This was an extremely adherent, thick gray coating. Under a microscope, it was found that scratches on the Ta surface had been smoothed over by the gray coating.

Mixed oxides of PtO_2 and PtO were identified spectrophotometrically from adherent films which were formed when Pt was placed in molten salts with and without electrolysis (56).

ASTM diffraction d-spacing values are also not available for PtO. It had been reported (57) that PtO should have the same structure as PdO. We found 7 coincident x-ray diffraction peaks on comparing our platinum oxide with ASTM data on PdO, and have therefore tentatively identified our product as PtO. The PtO made by exposing Pt black to O_2 at high temperatures is more tightly adherent than the original Pt black, but is still easy to remove by scraping.

Manuscript received Nov. 30, 1964; revised manuscript received Jan. 22, 1965.

Any discussion of this paper will appear in a Discussion Section to be published in the December 1965 JOURNAL.

REFERENCES

1. G. W. D. Briggs, E. Jones, and W. F. K. Wynne-Jones, *Trans. Faraday Soc.*, **51**, 1433 (1955).
2. F. T. Bacon, *Nature*, **186**, 589 (1960).
3. E. K. Smith, U. S. Pat. 2,565,004 (1951).
4. G. P. Zharikov, *Uch. Zap., Azerb. Gos. Univ., Ser. Fiz-Mat. i Khim. Nauk*, **1962**(3), 43 (1962); Via *C.A.* 60:2417h.
5. G. J. Kahan, U. S. Pat. 2,775,553 (1956).
6. M. J. Bolton and A. F. Torrisi, U. S. Pat. 2,785,-116 (1957).
7. J. Burnham, U. S. Pat. 2,871,425 (1959).
8. E. Wainer, U. S. Pat. 2,874,102 (1959).
9. U. R. Evans and J. Stockdale, *J. Chem. Soc.*, **1929**, 2651.
10. E. A. Gulbransen, *Ind. Eng. Chem.*, **41**, 1385 (1949).
11. D. A. Dowden, N. Mackenzie, and B. M. W. Trapnell, *Adv. in Cat.*, **IX**, 65 (1957).
12. M. Breiter, K. Hoffmann, and C. A. Knorr, *Z. Elektrochem.*, **61**, 1168 (1957).
13. H. A. Johansen, G. B. Adams, Jr., and P. Van Rysselberghe, *This Journal*, **104**, 339 (1957).
14. P. Van Rysselberghe and H. A. Johansen, *ibid.*, **106**, 355 (1959).
15. B. E. Conway and P. L. Bourgault, *Can. J. Chem.*, **37**, 292 (1959).
16. A. V. Byalobzheskii and V. D. Val'kov, *Doklady Akad. Nauk S.S.S.R.*, **134**, 121 (1960).
17. A. Kozawa, *Bull. Chem. Soc. Japan*, **35**, 1051 (1962).
18. D. M. Mohilner, W. J. Argersinger, Jr., and R. N. Adams, *Anal. Chim. Acta*, **27**, 194 (1962).
19. S. Uneri, *Commun. Fac. Sci. Univ. Ankara, Ser. B*, **10**, 7 (1962).
20. L. Lederer and N. D. Greene, *Electrochim. Acta*, **8**, 883 (1963).
21. M. W. Breiter, *ibid.*, **8**, 973 (1963).
22. S. Shibata, *Bull. Chem. Soc. Japan*, **36**, 525 (1963).

23. N. G. Bardina, *Zh. Fiz. Khim.*; **37**, 2688 (1963); Via *C. A.* 60:10203a.
24. J. J. Lingane and P. J. Lingane, *J. Electroanal. Chem.*, **5**, 411 (1963).
25. S. W. Feldberg, C. G. Enke, and C. E. Bricker, *This Journal*, **110**, 826 (1963).
26. J. S. Mayell and S. H. Langer, *ibid.*, **111**, 438 (1964).
27. H. A. Liebhafsky, *J. Appl. Phys.*, **17**, 901 (1946).
28. R. W. Schmidt, *Kolloid Zeits.*, **102**, 15 (1943).
29. J. V. Cathcart, J. J. Campbell, and G. P. Smith, *This Journal*, **105**, 442 (1958).
30. D. W. Aylmore, S. J. Gregg, and W. B. Jepson, *ibid.*, **107**, 495 (1960).
31. R. E. Salomon, G. B. Adams, and W. M. Graven, *ibid.*, **110**, 1163 (1963).
32. N. G. Bardina and P. D. Lukovtsev, *Z. Fiz. Khim.*, **37**, 57 (1963).
33. J. V. Cathcart, R. Bakish, and D. R. Norton, *This Journal*, **107**, 668 (1960).
34. H. K. Embaby and A. A. Moussa, *J. Chem. Soc.*, **1958**, 4027.
35. J. S. Anderson and D. F. Klemperer, *Proc. Roy. Soc.*, **258A**, 350 (1960).
36. A. U. MacRae, *Appl. Phys. Letters*, **2**, 88 (1963).
37. M. Becker and M. Breiter, *Z. Elektrochem.*, **60**, 1080 (1956).
38. F. C. Anson and J. J. Lingane, *J. Am. Chem. Soc.*, **79**, 4901 (1957).
39. H. A. Laitinen and C. G. Enke, *This Journal*, **107**, 773 (1960).
40. K. Nagel and H. Dietz, *Electrochim. Acta*, **4**, 1 (1961).
41. *Ibid.*, **4**, 141 (1961).
42. W. Boeld and M. Breiter, *ibid.*, **5**, 145 (1961).
43. F. C. Anson, *Anal. Chem.*, **33**, 934 (1961).
44. F. C. Anson and D. M. King, *ibid.*, **34**, 362 (1962).
45. D. G. Peters and J. J. Lingane, *J. Electroanal. Chem.*, **4**, 193 (1962).
46. A. I. Brodskii and V. A. Lunenok, Burmakina, *Doklady Akad. Nauk S.S.S.R.*, **151**, 1358 (1963).
47. V. E. Petrakovich, *Z. Analit. Khim.*, **18**, 1161 (1963).
48. J. K. Lee, R. N. Adams, and C. E. Bricker, *Anal. Chim. Acta*, **17**, 321 (1957).
49. D. Inman, *Nature*, **194**, 279 (1962).
50. Y. A. Mazitov, K. I. Rozental, and V. I. Veselovskii, *Z. Fiz. Khim.*, **38**, 151 (1964); Via *C. A.* 60: 11616b.
51. W. Boeld and M. Breiter, *Electrochim. Acta*, **5**, 169 (1961).
52. D. W. Aylmore, S. J. Gregg, and W. B. Jepson, *This Journal*, **106**, 1010 (1959).
53. J. S. L. Leach, *ibid.*, **110**, 680 (1963).
54. O. F. Steinbach and C. V. King, "Experiments in Physical Chemistry," p. 143, American Book Co., New York (1950).
55. F. Holtzberg, A. Reisman, M. Berry, and M. Berkenblit, *J. Am. Chem. Soc.*, **79**, 2039 (1957).
56. R. L. Every and R. L. Grimsley, *J. Electroanal. Chem.*, In press.
57. W. J. Moore and L. Pauling, *J. Am. Chem. Soc.*, **63**, 1392 (1941).

Cobalt Phthalocyanine as a Fuel Cell Cathode

Raymond Jasinski

Tyco Laboratories, Incorporated, Waltham, Massachusetts

One of the necessary characteristics of an oxygen electrode is that it chemisorb oxygen without degradation of the catalytically active surface. Reversible absorption has been observed in aqueous solution for some metal chelates, *e.g.*, bis (salicylal) ethylene diamine cobalt (II), heme, and cobalt (II) histidine (1). The possible application of these soluble compounds as fuel cell cathode catalysts would lead to a complicated engineering system, even if the oxygen-exchange kinetics were favorable.

A number of insoluble metal chelates will also chemisorb oxygen; the most chemically stable of these are the metal porphyrins and the metal phthalocyanines. The molecules are square planar complexes (2) with the metal atom symmetrically surrounded by four nitrogen atoms. These nitrogen atoms are each members of ring systems, which in turn are connected by carbon atoms (porphyrins) or nitrogen atoms (phthalocyanines). The details of crystal structure, chemical properties, and methods of preparation have been summarized recently (3).

A number of these compounds are insoluble in most common solvents, acid (8M H_2SO_4) and base (7*N* KOH). Concentrated sulfuric acid is required to solvate cobalt and copper phthalocyanine (CoPc, CuPc). CuPc is reported to be stable to thermal decomposition at 500°C. No decomposition of CoPc has been observed at 120°C under oxygen. Further stability can be achieved by partially chlorinating the compound or by polymerization (4).

Copper phthalocyanines (CuPc) have been reported to be active catalysts for hydrogen reactions such as o-p conversion and H_2-D_2 exchange (5-7). More relevant to the present work are the properties of copper and cobalt phthalocyanines as oxidation catalysts. For example, both compounds have been used in the air oxidation of mercaptan sulfur to disulfides for the "sweetening" of petroleum products (3,8). A preliminary appraisal of CoPc as a fuel cell cathode catalyst has been discussed in a recent note (9). In the present paper, CoPc is more fully evaluated in a practical electrode configuration, and its catalytic activity is compared to that of other known catalysts measured under identical experimental conditions.

Experimental

IR-free voltage measurements were made with the interrupter technique, employing a transistorized sine wave commutator (10). The test H_2/O_2 fuel cells had end-plates machined from Teflon; a Teflon O ring was employed to prevent uncontrolled evaporation of water. The use of Teflon components obviates problems which could arise from the oxidation and/or corrosion of metal end-plates.

A platinum wire imbedded in the end-plates served as the electrical lead. The contribution of the Pt wires to catalytic activity was found to be negligible; thus the electrodes were the only electrochemically active materials in the system.

An electrolyte of 35% KOH, immobilized in an asbestos membrane, was used. The anodes, 5 cm^2 disks, consisted of 9 mg Pt/cm^2 plastic-bonded to a nickel screen (American Cyanamid Corporation).

The cell temperature was 80°C unless otherwise noted. A thermocouple was placed in one of the Teflon plates and positioned above the cathode.

Only total cell voltages were measured since it was difficult to insert a probe into the test set-up described. Platinum cathodes were therefore run in the same cell to establish a point of reference. Data for H_2/O_2 cells are apparently self-consistent to $\pm$ 0.015v, as the reproducibility of the cell performances indicates. The flow rate of oxygen was adjusted to remove the water produced by the cell reaction; the hydrogen was "dead-ended." Both gas pressures were kept at 2.08 atm (16 psig).

In previous work (9) a cathode had been used which consisted of a porous nickel plaque onto which a coating of CoPc had been slurried. These structures were effective electrodes only if O_2 was passed through the CoPc coating. Impregnating porous plaques was difficult because of the limited solubility of CoPc in com-

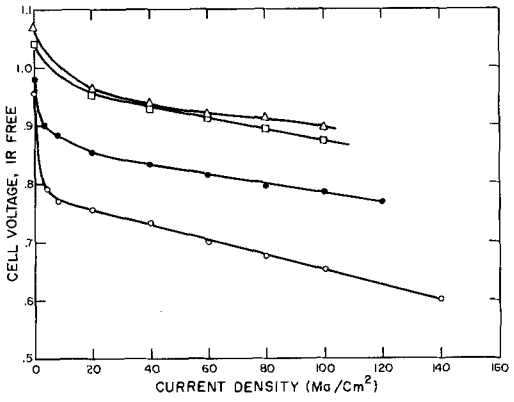

Fig. 1. Performances of H_2/O_2 fuel cells operating at 80°C with an electrolyte of 35% KOH, and a platinum black anode (9 mg/cm²). The cathodes are: 9 mg/cm² platinum (□); 40 mg/cm² silver (△); 14 mg/cm² CoPc (●); and 20 mg/cm² acetylene black (○).

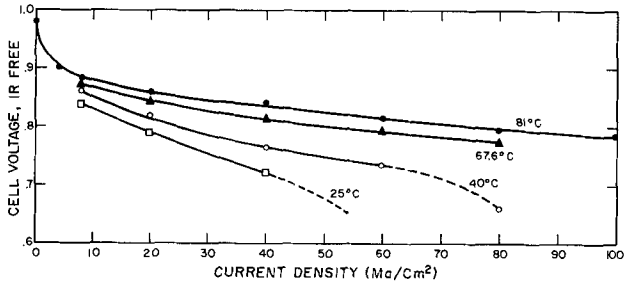

Fig. 2. Temperature dependence of the performance of H_2/O_2 fuel cells employing a CoPc cathode. The cell was operated with an electrolyte of 35% KOH and a platinum anode.

mon solvents. A more suitable electrode structure was formed by Teflon-bonding a mixture of 0.072g of CoPc and 0.048g of acetylene black to a 5 cm² nickel screen disk. Acetylene black cathodes were also prepared by Teflon-bonding 0.12g to nickel screen.

This method of electrode preparation is relatively independent of the particular material employed as the catalyst and has been used to investigate a variety of nonconductive metal chelates. After the electrode has been "activated" in the manner described below, a cell resistance of 0.022 ohm was obtained. This may be compared to a cell resistance of 0.018 ohm obtained for Teflon bonded platinum electrodes in the same cell. No attempt was made to reduce further the internal resistance.

Cobalt phthalocyanine, supplied by the National Aniline Division of Allied Chemical Corporation, was 99% pure and was used without further treatment.

Results

The chemical stability of CoPc under conditions approximating fuel cell operation was evaluated as follows. A sample was placed in 35% KOH and heated to 75°C. No discoloration of the liquid was noted. A second sample was placed in 30% H_2O_2. Again no discoloration occurred, although gas evolution was noted. Similar experiments with iron phthalocyanine resulted in considerable decomposition of the chelate, particularly in the presence of hydrogen peroxide.

Electrode activation.—The initial performance of CoPc cathodes was generally low, *e.g.*, 80 ma/cm² at 0.70v. However, it was found that if the cathode were polarized to H_2 evolution potentials, subsequent operation improved, *e.g.*, 80 ma/cm² at 0.81v. No decrease in output was noted after 10 hr of operation. The maximum performance which could be obtained is that shown in Fig. 1. The increase in electrochemical activity is accompanied by a change in appearance of the electrode. On dismantling the cell, it is found that the color of the catalyst mixture had changed from red-violet to brown-black. "Activation" also lowers the internal resistance of the cell. Typically, the resistance decreased from 0.05 to 0.02 ohm.

That this pretreatment is not a temporary charging effect is indicated by a comparison of the quantity of charge passed during activation with that passed on subsequent fuel cell operation. Activation is accomplished with 600 ma/cm² (3 amp), flowing for 2 min (0.05 amp-hr). Typically, the cell was then operated at 100 ma/cm² for 10 hr (5.0 amp-hr). This difference in charge of 10^2 can best be explained by postulating a permanent alteration in the structure of the catalyst.

Since activation was carried out at a current density of 600 ma/cm², significant IR heating occurred. Thus, the presence of oxygen and the generation of H_2 in the cathode cavity suggest at least five possible activation mechanisms: (i) the effect is electrochemical; (ii) the effect is thermal; (iii) the effect involves heat and O_2; (iv) the effect involves heat and H_2; (v) the effect involves an alteration of the physical structure of the electrode. *e.g.*, wetting characteristics.

Temperature measurements, made with the thermocouple placed above the cathode compartment, indicated that the cell temperature never rose above 90°C. Since heat transfer through Teflon is low, most probably the temperature at the electrode surface was somewhat higher during the current density flow of 600 ma/cm². To insure an adequate evaluation of the effect of temperature, the electrode was first heated to 350°C under argon before use in a cell. Since this did not activate the electrode, heating alone is not sufficient. Second, the electrode was heated in a hydrogen atmosphere up to 340°C. A number of inactive electrodes resulted, although the electrode had changed color to brown-black and the internal resistance was lowered. Therefore, mechanism (iv), IR heating plus H_2, is not the explanation. It should be noted that heating the electrode in H_2 at a higher temperature (370°C) did provide active cathodes. Activation under these conditions is presumed to be an alternate mechanism. Third, a cell was polarized so that O_2 was evolved at the CoPc electrode. Activation did not occur. Finally, activation was not noted for the acetylene black or the platinum black electrodes, indicating that the effect represented an alteration of CoPc.

Apparently the effect is electrochemical, indeed, an "arrest" in the time-potential curve is observed at a cell voltage of approximately — 1v. This occurs when activating the CoPc electrodes but not the acetylene black. The "arrest" was noted for only CoPc electrodes which were inactive initially, *i.e.*, those not activated by gaseous H_2 at 370°C. It is not possible with this limited data to offer a detailed description of the mechanism by which the electrochemically altered CoPc improves cathode performance.

Cell performance.—The performance of the CoPc cathode in a H_2/O_2 cell is compared in Fig. 1 to that for acetylene black, platinum black, and silver (40 mg/cm²). At a constant current density of 100 ma/cm² the cells performed as follows: CoPc cathode 0.79 ± 0.015v, acetylene black 0.65v, platinum black and silver 0.87v. Thus, it is apparent that CoPc functions as an oxygen electrode catalyst, although its performance is 0.08v poorer than that obtained with platinum black. This difference could be slightly greater if an equal loading, 15 mg/cm², of platinum were used. On the basis of relative cost, however, the use of CoPc becomes more favorable.

Cell performance as a function of temperature is summarized in Fig. 2. Some output is obtained at room temperature so that a fuel cell employing this catalyst could be considered as self-starting. An increase in temperature results in an increase in performance. The

temperature of 80°C was arbitrarily chosen as the operating point.

Discussion

It has been possible to form an oxygen electrode with a metal chelate, cobalt phthalocyanine, as the active catalyst. Sufficient electrical conductivity was achieved by mechanically blending the chelate with acetylene black. A stable electrode structure was formed by Teflon-bonding the mixture to a metal screen. Since a supported electrolyte was also used, no difficulty was noted due to variations in electrode uniformity across the face of the screen.

The electrochemistry (*e.g.*, activation, pretreatments) of the chelate compounds is different from that experienced with metal and oxide catalysts. The "activation" treatment, found with cobalt phthalocyanine, (which resulted in an increase in cell voltage of 0.1v at 100 ma/cm^2) was without noticeable effect when applied to acetylene black, platinum, and silver.

The activation step is a reductive procedure; chemical testing indicated the absence of free cobalt or cobalt oxide. A recent paper (7) on the activation of hydrogen by copper phthalocyanine has indicated three types of catalytically active sites: (*a*) the chelated metal atom, (*b*) unpaired electrons arising during heat treatments, (c) unpaired π electrons formed by the opening of double bonds. Furthermore, it is indicated that the hydrogen reaction rates are enhanced by catalyst polymerization due to an increase in the density and stability of unpaired electrons. It is possible that the electrochemical treatment induced polymerization and/or increased the density of unpaired electrons. It is also possible that Co(II) was reduced to Co (I). However, phthalocyanine complexes of monovalent metal atoms are generally unstable. A more rigorous explanation for this effect cannot be made until the mechanism for oxygen reduction is determined.

The current densities sustained with H_2/O_2 cells were sufficiently high (60-120 ma/cm^2), to be considered for application in practical fuel cell systems. The H_2/O_2 cell voltage is about 0.1v lower than can be obtained at present with either platinum or silver catalysts. Some metal phthalocyanines are relatively inexpensive and are employed commercially as dyes; for example, the copper compound is available at approximately $1.10/lb.

Acknowledgment

The author wishes to acknowledge the support of the Air Force Cambridge Research Laboratories under Contract AF 19 (628)-2845.

Manuscript received Sept. 22, 1964; revised manuscript received Jan. 18, 1965.

Any discussion of this paper will appear in a Discussion Section to be published in the December 1965 JOURNAL.

REFERENCES

1. J. C. Bailar, "Chemistry of the Coordination Compounds," p. 45, Reinhold Publishing Corp., New York (1956).
2. G. T. Byrne, R. P. Linstead, and A. R. Lowe, *J. Chem. Soc.*, **1934**, 4017.
3. F. Moser and A. Thomas, "Phthalocyanine Compounds," Reinhold Publishing Co., New York (1963).
4. M. Dahlen, *Ind. Eng. Chem.*, **31**, 839 (1939).
5. M. Calvin, E. Cockbain, and M. Polanyi, *Trans. Faraday Soc.*, **32**, 1436 (1936).
6. M. Calvin, D. Eley, and M. Polanyi, *ibid.*, **32**, 1443 (1936).
7. D. Eley and G. Acres, *ibid.*, **60**, 1157 (1964).
8. W. Gleim and P. Urban, U. S. Pat. 2,882,224 (1959).
9. R. Jasinski, *Nature*, **201**, 1212 (1964).
10. G. Pollnow and R. Kay, *This Journal*, **109**, 648 (1962).

Effect of Oxide Hydration on Surface Potential of Oxidized P-Type Silicon

A. B. Kuper[1] and E. H. Nicollian

Bell Telephone Laboratories, Incorporated, Murray Hill, New Jersey

The n-type tendency of silicon surfaces under thick oxide has been known since the first work of Atalla, Tannenbaum, and Scheibner (1). In the present paper experimental evidence is presented showing that an important cause of this tendency is hydration of the oxide and that the effect is reversible. Temperature-humidity history is thus important in establishing the silicon surface potential of passivated structures. This effect has practical significance for oxidized silicon device performance and reliability.

Atalla *et al.* (1) showed that fast (close to the interface) donor-type states were present and observed the n-type surface tendency on diodes oxidized after diffusion. Sah (2) reported the n-type tendency on diodes where oxidation was done before diffusion. Kahng (3) used high pressure steam oxidation after diffusion and also found n-type surfaces. Edagawa *et al.* (4) found the n-type tendency using grown junction silicon diodes oxidized in wet O_2, dry O_2, wet N_2, and wet H_2.

Water is expected to be present in silica films grown in steam or after exposure to steam as shown by Ligenza and Spitzer (5, 6) who studied the exchange of oxygen between silica and steam and by Moulson and Roberts (7) who observed infrared absorption due to water in silica.

Diodes in the present work were conventional n^+p planar junctions with no metal contacts. Oxidation preceded diffusion. Preoxidation cleaning was similar to that used by Atalla *et al.* (1).

Planar diodes 3.6 x 10^{-4} cm^2 in area, approximately 8 mils in diameter, were made by diffusion of phosphorus into chemically polished (Appendix A) boron-doped pulled crystal silicon. Resistivities from 0.5 to 5 ohm-cm were used. To make the diodes, the silicon was given a final boiling nitric acid, boiling water cleaning (Appendix B) and oxidized in atmospheric pressure steam (Appendix C) at 1050°C for 1 hr, which formed 6000Å of oxide. Photoresist masking was used and holes were etched in the oxide. Phosphorus doped layers 4μ deep with a sheet resistance of 50 ohm/sq were then formed in the etched areas by predifusion at 740°C for 40 min followed after glass removal by 1 hr at 1230°C in dry nitrogen — 10% oxygen. Diodes in this "dehydrated" state had reverse dark currents in the nanoampere range. Diode reverse current results were qualitatively the same when the oxide was grown in dry oxygen.

Diodes then oxidized in unpressurized steam at 1050°C with consequent "hydration" of the oxide had

[1] Currently on leave of absence at Case Institute of Technology, Cleveland, Ohio.

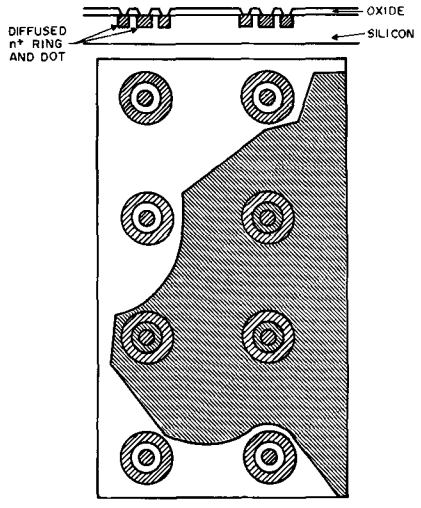

Fig. 1. Extent of n-channel under oxide after steaming ring and dot diodes 2 hr at 408°C. Silicon is 0.5 ohm-cm p-type. Shaded region indicates extent of channel measured by diode photoresponse. Outside diameter of devices is 15 mils, and center to center distance is 50 mils.

channel saturation currents in the milliampere range. If diodes were then heated for about 1 hr at 1000°C in dry ambient, reverse currents were reduced to the nanoamp range again. Dry air, oxygen, nitrogen, and argon as well as vacuum were found to be suitable for drying.

The channel that resulted when the oxide was hydrated was shown to be n-type extending over the p-region by measuring diode photoresponse using a small chopped light spot. The extent of one channel resulting from steaming a set of ring and dot diodes at 408°C for 2 hr is shown in Fig. 1. Here, hydration was stopped before the entire surface was inverted. The oxide was of uniform thickness. This patchy inversion (also suggested the spread of data in Fig. 2) suggests that localized conditions at the oxide-air or oxide-silicon interface may control the rate of inversion.

If the oxide were completely etched off in concentrated HF and the sample then rinsed thoroughly and dried, no channel was present, as has been reported (1). Results are summarized in Fig. 2. Hydrogen at 400°C also produced channels, in agreement with Blum *et al.* (8), but longer exposure time than with steam was required to produce a channel of the same strength. Exposure to other gases at 400°C did not produce channels as shown in Table I.

Reversible channeling was also seen by means of measurements of the diode capacity. In the dehydrated state for the case of 0.5 ohm-cm p-type there was negligible excess capacity. In the hydrated state, the presence of a channel was clearly indicated by excess capacity at low bias. This excess capacity went to zero at about the same reverse voltage at which the reverse current saturated.

Five ohm-cm p-type ($N_a = 2.5 \times 10^{15}$ cm^{-3}) silicon remained slightly inverted at the surface after 1000°C baking in dry nitrogen for 2 hr while 0.5 ohm-cm (4×10^{16} cm^{-3}) did not, suggesting that there was an effective donor concentration of the order of 10^{11} cm^{-2} in this experiment.

At 800°C, the current-voltage characteristic of the dehydrated state was found to reach equilibrium from the hydrated state in less than 1 min. Likewise, the heavily channeled state could be achieved at 1050°C in steam in less than 1 min. Reverse currents of diodes in the dehydrated state changed slowly when given wet-dry cycling at low temperatures as shown for 300°C in Fig. 3. Data of this kind generally indicated that hydration proceeded somewhat faster

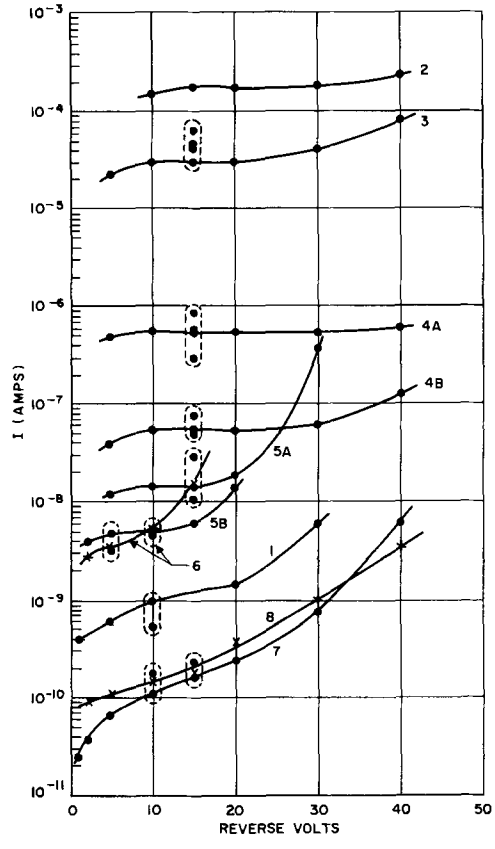

Fig. 2. Summary of reverse current vs. voltage on planar diodes from one diffused slab of 0.5 ohm-cm boron doped pulled crystal silicon. Each curve represents a group of diodes. Vertical box indicates the spread of current data. A and B refer to regions of a piece which showed a distinct grouping of currents after baking. Curve 1, initial state after phosphorus diffusion; curve 2, oxidized in 1 atm steam pressure at 1050°C for 1 hr after 1. Oxide over junction is approximately 8000Å thick; curve 3, baked 5 min in air at 460°C after curve 2; curve 4, baked 30 min in dry argon at 700°C after curve 2; curve 5, baked 30 min in dry argon at 750°C after curve 2; curve 6, baked 30 min in dry argon at 800°C after curve 2; curve 7, baked 1 hr in dry nitrogen at 1000°C after curve 2; curve 8, oxide etched off in concentrated HF after curve 2, dry nitrogen ambient. The "soft" characteristic of curves 5 and 6 is a typical result of heating an unclean sample and is not regarded as significant for this experiment.

than dehydration at the same temperature. Estimated relaxation times (time for reverse current to decrease by a factor 10) for baking temperatures between 200° and 700°C were consistent in many cases with the known rate of diffusion of water through silica glass (7).

The effect of water on diode reverse current observed in the present experiments is similar, except for longer relaxation times, to the effect of humidity at room temperature on diodes that have not been thickly oxidized. This suggests that the observed effects are due to water or a water-related species largely concentrated at the silicon-oxide interface.

To test this model, hydrated oxide was progres-

Table I. n^+p (1.5 ohm-cm) Planar diode aging

Aging temp, °C	Exposure time, hr	Gas at 1 atm	Saturation current, μa
390	64	Room air	No channel
390	64	Dry N_2	No channel
390	4	Dry CO_2	No channel
390	64	Dry He	No channel
390	17	Dry H_2	0.5
406	0.16	H_2O	16
406	0.5	H_2O	40
390	3.5	H_2O	2000

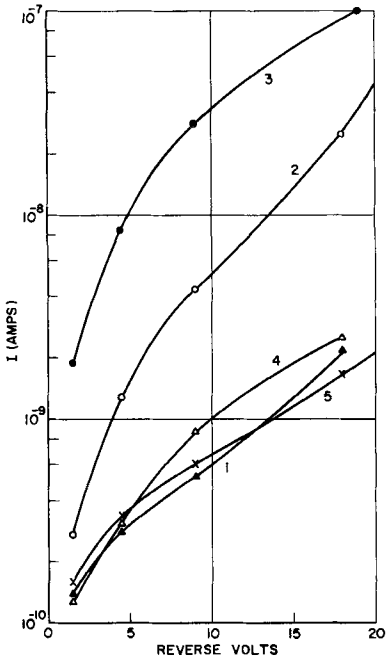

Fig. 3. Diode reverse characteristics. Low-temperature steam and bake cycle of a diode starting in the dehydrated state. The p-region resistivity is 0.5 ohm-cm. Oxide over junction is approximately 6000Å thick. Curve 1, start; curve 2, After 30 min in atmospheric pressure steam-oxygen mixture at 300°C; curve 3, after 52 min more as in curve 2; curve 4, after 40 min bake in air at 300°C after curve 3; curve 5, after 60 min more as in curve 4.

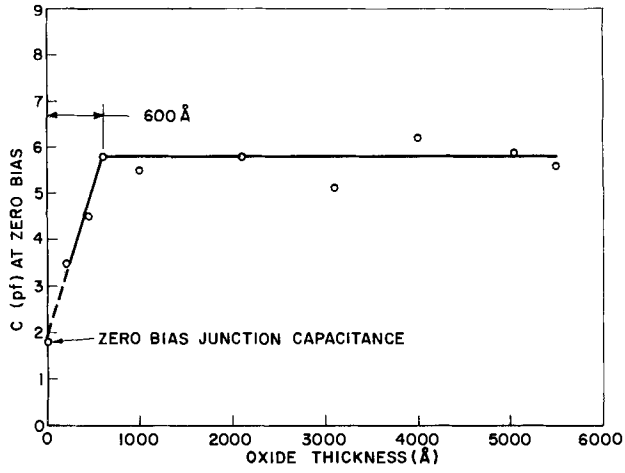

Fig. 4. Total zero bias capacitance of one channeled 0.5 ohm-cm diode measured at 100 kc as a function of oxide thickness on the inverted surface. Oxide thickness is measured by matching color to a standard whose thickness is known by ellipsometer measurement and is verified for each point by measuring the dielectric breakdown voltage of oxide on the slab.

sively etched off a channeled diode and the zero-bias capacity was measured. The result in Fig. 4 shows that the surface of the 0.5 ohm-cm silicon remained inverted until only a few hundred angstroms of hydrated oxide remained. (Oxide thickness less than 1000Å was obtained by controlled etching and checked by dielectric breakdown.) Figure 4 shows that a substantial number of ionized donors from hydration were in the oxide within 600Å of the silicon. The charge may be confined even closer because disappearance of the channel beginning at a thickness of 600Å may be a spurious result due to the fact that such thin oxide probably contains pinholes, and/or that states at the oxide-air interface become important.

The experiments suggest that hydration effects in steam depend on a water species acting as a donor localized on the oxide side of the oxide-silicon interface.

Manuscript received Jan 6, 1965. This paper was presented at the Washington Meeting, Oct. 11-15, 1964.

Any discussion of this paper will appear in a Discussion Section to be published in the December 1965 JOURNAL.

REFERENCES

1. M. M. Atalla, E. Tannenbaum, and E. J. Scheibner, *Bell Sys. Tech. J.*, **38**, 749 (1959).
2. C. T. Sah, *Proc. IRE*, **49**, 1623 (1961).
3. D. Kahng and M. M. Atalla, "Silicon-Silicon Dioxide Field Induced Surface Devices," IRE-AIEE Solid State Device Research Conference, Pittsburgh, Pa. (1960).
4. H. Edagawa, Y. Morita, S. Maekawa, and Y. Inuishi, *J. Phys. Soc. Japan*, **17**, 1190 (1962).
5. J. R. Ligenza and W. G. Spitzer, *J. Phys. Chem. Solids*, **14**, 131 (1960).
6. W. G. Spitzer and J. R. Ligenza, *ibid.*, **17**, 196 (1961).
7. A. J. Moulson and J. P. Roberts, *Nature*, **182**, 200 (1958); and T. Drury, G. J. Roberts, and J. P. Roberts, Sixth International Congress Glass, Washington, D. C. (1962).
8. J. Blum, R. Warwick, H. M. Pollack, and M. Genser, *This Journal*, **111**, 58C (1964) Abstract No. 55.
9. R. Lieberman, W. R. Bracht, D. L. Klein, *ibid.*, **111**, 62C (1964).

APPENDIX

(*A*) *Silicon surface preparation.*—(111) orientation silicon sawed into 0.020 in. slices. Both sides lapped with 12μ aluminum oxide to thickness of 0.0095 in. Diode side polished with 0.3μ aluminum oxide to 0.0085 in. Slice cleaned of grit by copper displacement (9). Both sides etched with 19:1 HNO_3:HF in rotating cup. Final thickness 0.0045 in.

(*B*) *Cleaning before oxidation.*—Degrease. 2 min in HF, 20 min in deionized water recirculator at 80°C; 15 min in HNO_3 at 80°C; 20 min in deionized water at 80°C again.

(*C*) *Steam oxidation* is done in an all-quartz system. Water is from recirculating deionizer and 0.2μ filter system in which conductivity is monitored at 0.05 μmho/cm.

The Minimum in Molar Conductance of $CdCl_2$ in Water-Methanol

D. O. Johnston

Department of Chemistry, David Lipscomb College, Nashville, Tennessee

and P. A. D. de Maine

Department of Chemistry, University of California, Santa Barbara, California

Molar conductances of $CdCl_2$ in methanol (1) and in ethanol (2, 3) have been measured. Golben and Dawson (3) proposed that in ethanol $CdCl_2$ dissociates in the most dilute range as an uni-univalent electrolyte. For CdI_2 in methanol (4, 5) conductance values show a maximum, but no maxima have been reported for the chlorides. Hartley and Raikes (6) have reported the ionic mobilities of Cd^{++}, Cl^-, and other ions in methanol.

Conductance minima have been reported for methanol-water systems containing KCl, KOH, NH_4Cl, or HCl (7). The minima for the KCl and KOH systems

Table I. Molar conductance values for $CdCl_2$ in methanol-water at 5°, 20°, and 45°C

Salt concn,* M/L	Water concentration in moles/liter																		
	0.000	0.001	0.005	0.010	0.400	1.010	1.510	2.020	3.030	3.550	4.060	4.570	5.090	5.660	6.200	7.680	9.240	12.89	15.51	20.74
@ 5°																				
0.0005	52.70	52.70	52.69	52.81	52.64	52.15	51.46	51.01	50.39	50.22	49.91	49.06	50.15	50.08	50.26	50.97	51.84	54.01	55.03	56.58
0.0010	45.25	45.59	45.59	45.76	45.89	45.80	45.58	45.15	44.86	44.81	44.28	43.74	43.87	43.94	43.90	44.43	44.63	46.55	47.58	49.90
0.0015	41.50	41.64	41.50	42.23	42.03	41.95	41.89	42.29	41.88	41.97	41.19	40.99	41.08	40.89	41.13	41.31	41.35	42.82	44.37	46.06
0.0020	38.31	38.04			38.69			38.62			38.99		38.90		39.07			39.79		44.67
0.0040	31.07	31.39			31.84			33.21			33.63		33.52		33.46			34.57		37.98
0.0100	22.65	22.57			23.14			24.32			25.61		26.06		26.38			27.84		29.93
@ 20°																				
0.0005	63.53	63.53	63.53	63.51	63.43	63.47	63.37	63.47	63.28	64.30	63.46	63.17	64.41	65.40	65.40	66.81	69.21	74.41	78.00	84.28
0.0010	52.72	53.40	53.17	53.63	54.00	54.85	55.28	55.42	55.76	56.16	56.10	56.00	56.72	56.87	57.09	58.57	59.56	63.99	67.02	73.46
0.0015	47.87	47.69	47.65	48.61	48.73	49.43	50.14	51.14	51.66	52.23	51.93	51.86	52.48	52.60	53.24	54.06	55.17	58.98	62.56	68.13
0.0020	43.62	43.55			44.61			46.65			49.33		48.96		50.41			54.93		65.30
0.0040	34.79	35.10			36.20			39.15			41.55		41.93		42.64			47.20		55.41
0.0100	25.13	25.03			25.78			28.27			30.93		31.90		32.85			37.54		43.55
@ 45°																				
0.0005	76.36	77.39	76.87	77.67	78.95	81.60	82.61	84.00	85.60	88.80	86.93	87.11	90.49	91.06	92.80	96.13	101.7	113.4	121.8	140.0
0.0010	61.45	62.03	61.74	62.65	64.18	67.04	69.08	70.48	72.63	74.62	75.85	76.63	78.40	79.01	80.15	83.64	86.8	97.1	105.9	121.2
0.0015	55.22	54.70	54.47	55.96	56.93	59.19	61.38	63.44	66.56	68.25	68.72	69.54	71.41	71.73	73.29	76.71	79.4	89.4	96.8	111.6
0.0020	49.09	49.07			51.90			57.33			64.56		65.85		69.75			82.9		107.0
0.0040	38.16	38.70			40.58			46.23			52.66		54.46		57.25			70.3		89.1
0.0100	27.49	27.42			28.63			32.84			38.09		40.12		42.28			54.6		69.6

* As this table is traversed to the right, the $CdCl_2$ concentration increases by 3% because of the nonideality of water-methanol.

occur between 40 and 60 mole % water which coincide with maxima in the viscosity. At 25°C water-methanol mixtures show a maximum in viscosity at 73 mole % water (8). The pronounced conductance minimum at 5°C for HCl-methanol-water at 20 mole % water has been ascribed by Gurney (9) to partial suppression of proton jumps by the water molecules capturing protons from methonium ions since the methonium ion has a proton level higher than that of the hydronium ion. As the water concentration is increased, the conductance increases because of proton jumps between water molecules.

Experimental

General techniques of preparing solutions and measuring resistances with a General Radio Company Impedance Bridge (Type 1650A) at 5°, 20°, and 45°C have been described elsewhere (1, 10). The Fisher Spectrograde methanol had a specific conductivity of 9×10^{-7} ohms^{-1} cm at 20°C. The anhydrous Fisher Certified Reagent $CdCl_2$ assayed 99.1% $CdCl_2$, and chloride analysis showed a maximum deviation of 0.52% from stoichiometry. The water, distilled in an all-glass apparatus, had a specific conductivity of 3.5×10^{-6} ohms^{-1} cm at 20°C.

In Table I concentrations of $CdCl_2$ and water are given. In calculation of $CdCl_2$ concentrations solvent densities reported by Mikhail and Kimel (8) were used. The solutions were stable for at least 24 hr. Resistance measurements on 29 duplicate samples in the area of the minimum showed that resistances could be measured reproducibly to within 1%.

Results

For constant $CdCl_2$ concentrations the molar conductances of $CdCl_2$-water-methanol systems decrease with an increase in water concentration to about 4.5M (17 mole %) (Table I). Conductances then increase for higher water concentrations. This effect was observed for $CdCl_2$ concentrations from 0.005 to 0.0015M at 5°, and 0.0005M at 20°C, but was not noted for salt concentrations equal to or greater than 0.0005M at 45°C. Table I contains some of the data which illustrate these statements. Concentrations near 9M in water are required to achieve the conductance value obtained in anhydrous methanol at 5°C.

Discussion

If water complexing with the salt is important, the high local dipole moment of the water molecules should enhance and not decrease ionization. It appears that solvolysis products may be important in producing the minimum. At 5°C the minimum for the $CdCl_2$-water-methanol system occurs between 16 and 18 mole % water, while for HCl-water-methanol the minimum is at 20 mole % water. Decreased mobility of the Cd species formed by hydrolysis together with diminished proton jumps would account for a decrease in conductance as water is added to the system. The increase at higher water concentrations would result from increased ionization of the salt and from increased proton jumps.

However, the lack of a conductance minimum at 45°C and at higher salt concentrations indicates that besides solvolysis there may be other important effects such as basic solvent structure. Viscosity studies (1, 8) indicate that water increases structure in a solution more than methanol. Increased solvent structure might offer sufficient resistance to ions to effect a conductance decrease until ionization effects offset the structural resistance. Then conductance increases with higher water concentrations. At 45°C water would not add a sufficient increase in structure to counteract the greater production of ions.

Acknowledgments

This research was supported by a grant from the Petroleum Research Fund, administered by the American Chemical Society. D.O.J. is appreciative of the National Defense Education Act Fellowship.

Manuscript received Oct. 9, 1964. This paper was taken from the Ph.D. thesis of one of the authors (D.O.J.), University of Mississippi, 1963.

Any discussion of this paper will appear in a Discussion Section to be published in the December 1965 JOURNAL.

REFERENCES

1. D. O. Johnston and P. A. D. de Maine, *J. Chem. Eng. Data*, **8**, 586 (1963).
2. M. Golben, Thesis, University of Kentucky (1960).
3. M. Golben and L. R. Dawson, *J. Phys. Chem.*, **64**, 37 (1960).
4. S. I. Sklyarenko, I. V. Smirnov, and M. G. Zhukova, *Zhur. Fiz. Khim.*, **26**, 1125 (1952).
5. V. S. Galinker, *Ukrain. Khim. Zhur.*, **20**, 626 (1954).
6. H. Hartley and H. R. Raikes, *Trans. Faraday Soc.*, **23**, 393 (1927).
7. T. Erdey-Gruz, E. Kugler, and A. Reich, *Magyar Kem. Folyoirat*, **63**, 242 (1957).
8. S. Z. Mikhail and W. R. Kimel, *J. Chem. Eng. Data*, **6**, 533 (1961).
9. R. W. Gurney, "Ionic Processes in Solution," pp. 75-8, 224-6, McGraw-Hill Book Co., New York (1953).
10. D. O. Johnston and P. A. D. de Maine, To be published.

Observation of Active Areas in Thin Films of Palladium

Steve Eisner

Materials Research Section, The Martin Company, Denver, Colorado

Active centers in catalysts have been attributed by other investigators to emergent dislocations (1, 2), and point defects (2). Other kinds of crystal imperfections may also function as active centers, such as stacking faults, sessile dislocations, and impurity atoms.

The palladium-hydrogen system was chosen for the further study of active catalytic centers because of the large amount of hydrogen sorbed (from 1000 to 3000 times the metal volume) by palladium at room temperature. Exposure of palladium to hydrogen yields an expansion of the palladium lattice of 0.2Å, *i.e.*, from 3.8Å to 4.0Å (3).

Experimental Methods

Films on thin transparent substrates.—Thin films were deposited in a vacuum chamber by vapor deposition of palladium on microscope cover glasses and on Mylar substrates. The glass substrate had previously been cleaned by glow discharge to provide adherent coatings.

The average thickness of the palladium deposit was measured by weight changes on known areas of substrate. Specimens having an average thickness of 570Å were chosen for the hydrogen experiments.

Before they were exposed to hydrogen, the coatings showed no palladium hydride lines in the x-ray diffraction pattern.

Films on iron crucibles.—Thin films were deposited on the outside of previously polished Armco iron analytical crucibles. The crucibles were then set up over a Unitron microscope so that changes in the surface films could be photographed as hydrogen diffused through the crucible and combined with the palladium.

The crucibles were filled with a 4% solution of H_2SO_4 containing As_2O_3 as a poisoning agent. A current of 1 amp/in.^{2} was passed through the electrolyte, the crucible being cathodic. Diffusion of hydrogen through the crucible to the palladium film on the underside was clearly evident in 2 hr by the formation of the rosettes on the film.

The relative rate of hydrogen sorption and desorption in both types of experiments was recorded by two methods: (a) by measuring the change in intensity of the palladium hydride x-ray diffraction lines during and after exposure to hydrogen; (b) by measuring the change in light transmitted through the glass substrate specimens during and after exposure to hydrogen.

Discussion

Changes in thin films on glass and Mylar substrates.—Hydrogen was passed over thin palladium films on Mylar and on glass. The formation of a palladium hydride was indicated by the curling of the palladium-coated Mylar, showing expansion of the films. Glass-based films crinkled as the film expanded with the formation of palladium hydride (Fig. 1).

Crinkling started from microscopically observable points or lines on the surface. With only 300X magnification, defect areas rather than individual defects were seen. Circular crinkle patterns developed around point areas and elliptical crinkle patterns around active line areas. Increase in the diameters of the circles or ellipses means that the hydrogen gas entered through the hydride phase or through the palladium at a highly stressed edge of the crinkled area.

When the hydrogen was shut off, visible uncrinkling began after a few minutes (Fig. 2). This continued until all crinkling disappeared.

More photographs (Fig. 3) were taken when the palladium film was exposed to hydrogen again, after the cycle of crinkling and uncrinkling shown in Fig. 1 and 2. Comparison of Fig. 1g and 3e shows that new active centers have been formed. Since no impurities have been added to the film, it is assumed that the new active areas are due to the cold work created by the crinkling process. [Recent work (2) has shown the relationship of cold work to catalysis in the case of ortho-para hydrogen conversion by nickel catalysts.]

After several cycles of crinkling and uncrinkling, the crinkling film changed its appearance from sharp-ridge crinkles to deformed or splayed-out crinkles, and occasional cracks also developed. This cracking, after frequent mechanical cycling, is reminiscent of fatigue cracking phenomena in metals.

Changes in films on iron substrates.—The effect of diffusing hydrogen by electrolysis for 2 hr through

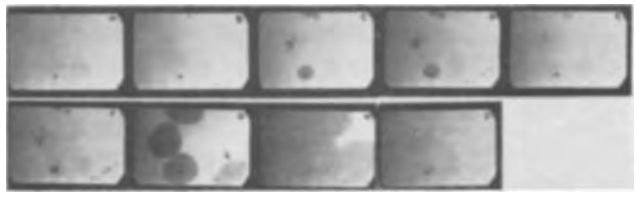

Fig. 1. (a through i). Approximately 160X micrographs taken 3 sec apart. Hydrogen gas was flowed over a palladium film evaporated on glass. Rosettes of crinkled area formed. When the flow was stopped (Fig. 1c) the rosettes disappeared. The flow was restarted again (Fig. 1e), and the rosettes grew until the entire surface was covered. It is interesting to note that active centers may be both in the form of points and lines (arrow).

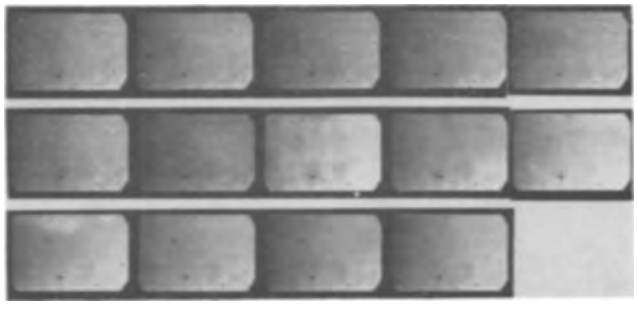

Fig. 2. Stream of hydrogen was stopped, and the crinkled surface was photographed every 3 sec. Uncrinkling was much slower than crinkling.

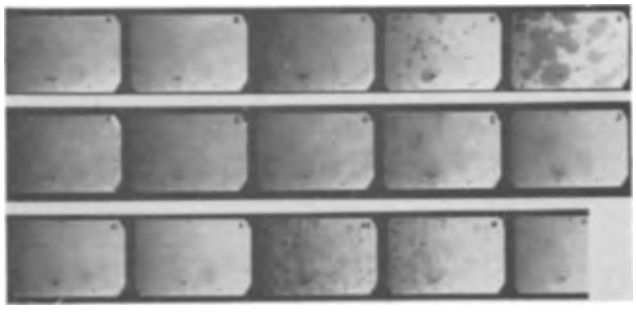

Fig. 3. (a through o). The flow of hydrogen was restarted. Figures 3c, 3d, and 3e show that new active centers are in evidence. These were generated by the cold work of the previous crinkling process. These centers are assumed to be crystal imperfections such as emergent dislocations or stacking faults. After several cycles of hydrogen pickup and release, the crinkles seem to lose their sharpness.

Fig. 4. Rosettes were formed on 500Å-thick palladium evaporated on an iron crucible which was hydrogen charged from the inside. Magnification 700X.

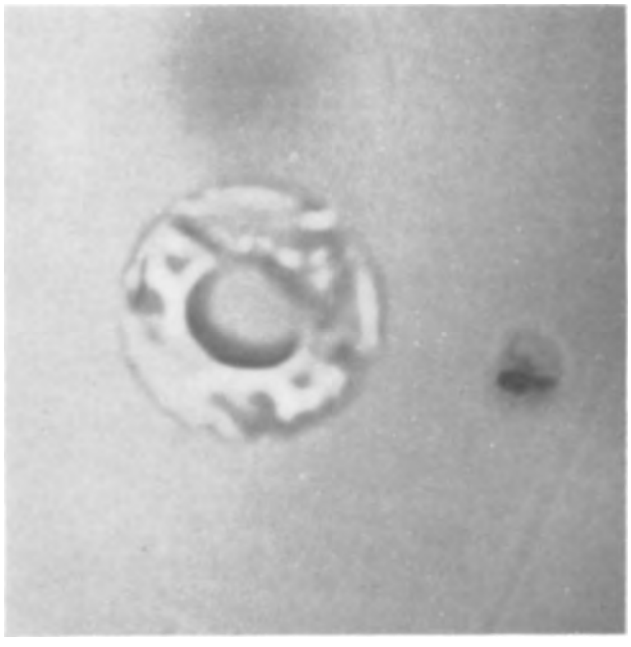

Fig. 5. Rosette shown in Fig. 4 deformed after a few hours. Magnification 700X.

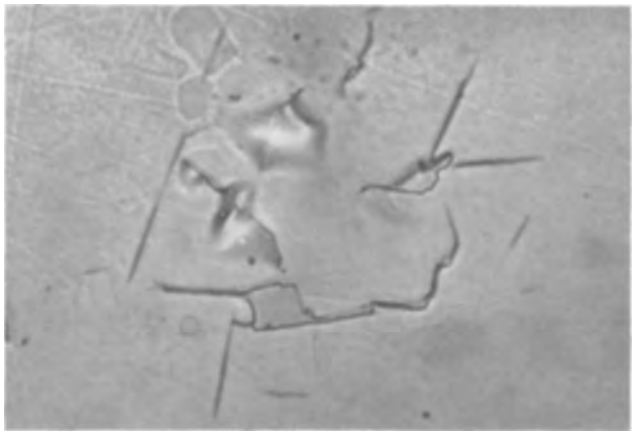

Fig. 6. Rosette shown in Fig. 5 and Fig. 6 cracked within 24 hr. Magnification approximately 800X.

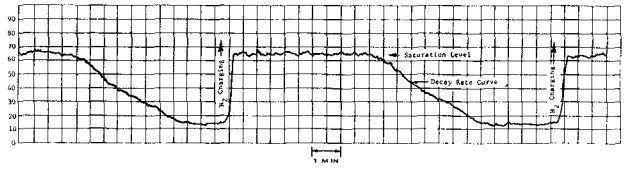

Fig. 7. Intensity of a single palladium hydride line changes with sorption and desorption of hydrogen. The sorption is quite rapid; the desorption is slow.

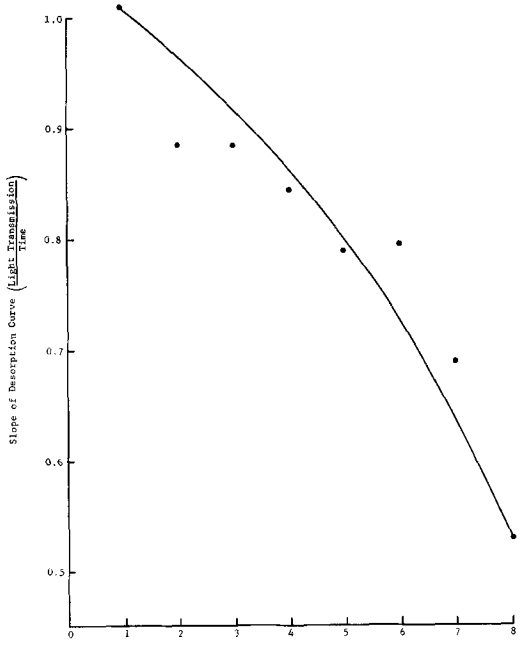

Fig. 8. Slope of the hydrogen desorption curve as measured by densitometry tends to decay with the number of charging cycles.

polished Armco iron crucibles was the creation of individual rosettes on the palladium film deposited on the outside of the crucibles (Fig. 4). The rosettes did not disappear with time as did the crinkles in palladium films on glass. Instead, the rosettes deformed (Fig. 5) and cracked (Fig. 6) within 24 hr.

Changes in x-ray diffraction line intensity.—The rapid increase and slow decay of x-ray diffraction line intensity (Fig. 7) for the palladium hydride lines can be related to the rapid crinkling and slow uncrinkling of the palladium film shown in Fig. 1 and 2. The rate of change in diffraction line intensity can also be related to the microcinematographs taken of the crinkling and uncrinkling phenomena. Saturation of the palladium film with hydrogen is indicated by the constant intensity level of the palladium hydride line (Fig. 7).

Densitometer readings.—Similar evidence was given by densitometer readings as light was transmitted through the thin palladium film during hydrogen sorption crinkling and desorption uncrinkling. The desorption curves have a smaller slope with each succeeding cycle of hydrogenation. The slopes of the desorption curves were obtained from the densitometer recordings.

The slopes of the desorption curves were measured from 0.1 to 1.0 min after hydrogen saturation of the palladium film, the curve being relatively straight during this time.

These slopes, when plotted against the number of hydrogenation cycles (Fig. 8), show a gradual decrease. This decrease in hydrogen escape from a thin palladium film with an increasing degree of cold work due to crinkling indicates that hydrogen traps are

formed by cold work. Such an assumption is not out of line with metallurgical investigations that show it is more difficult for hydrogen to diffuse through hard steels than through soft steels (4).

X-ray diffraction studies showed the rapid increase of palladium hydride line intensity under hydrogen exposure, but the slow decrease in this intensity after exposure. Visual confirmation was provided also in the rapid crinkling and slow uncrinkling of the palladium film by means of microcinematographs. Eventual saturation of the palladium film with hydrogen is indicated by the constant-intensity level of the palladium hydride line. The decrease of hydrogen escape shows that hydrogen traps are formed by cold work.

Conclusions

The following conclusions apply:

1. The active areas of the hydrogen-palladium thin film systems (as evidenced by mechanical crinkling) are due to impurities and/or crystal imperfections.
2. New active areas are created by cold working (due to crinkling) of thin palladium films. This indicates that the creation or interaction of dislocations is important in forming active areas.
3. Hydrogen traps are created by cold work in palladium thin films as shown by decay curves of palladium hydride lines in the x-ray diffraction pattern after repeated hydrogen exposure. Densitometer readings through the palladium film also support this conclusion.

Acknowledgment

This work was initiated at the Boeing Company.

Manuscript received Dec. 18, 1964. This paper was prepared for delivery before the San Francisco Meeting, May 9-14, 1965.

Any discussion of this paper will appear in a Discussion Section to be published in the December 1965 JOURNAL.

REFERENCES

1. I. Uhara, S. Yanagimoto, K. Tani, and G. Adachi, *Nature*, **192**, 867 (1961).
2. I. Uhara, S. Kishimoto, T. Hikino, Y. Kageyame, H. Hamada, and Y. Numoto, *J. Phys. Chem.*, **67**, 996 (1963).
3. J. N. Andrews and A. R. Ubbelohde, *Proc. Roy. Soc.*, **A253**, 6 (1959).
4. U. V. Bhat and H. K. Lloyd, *Iron and Steel*, p. 451 (November, 1950).

Brief Communications

Recrystallization of Thin Films of Germanium and Silicon

S. Nielsen

Ministry of Aviation, Royal Radar Establishment, Great Malvern, Worcestershire, England

Recent work on thin alloy zone crystallization processes (1) has suggested the possibility of recrystallizing thin films of semiconductors. We report here some progress in recrystallizing films of silicon and germanium deposited on insulating substrates and comment on some of the difficulties experienced with these processes.

Recrystallization has been attempted by forming a thin liquid alloy zone in the film and driving this zone across the film using a temperature gradient. For example a layer of germanium 1μ thick was evaporated onto a sapphire substrate at room temperature and a stripe of aluminum, 100μ wide, evaporated on top of the germanium layer. The layer was then subjected to a temperature gradient for 8 hr by placing the sapphire on a molybdenum strip heater in a vacuum system at 10^{-5} Torr. Thermocouples on the heater indicated a gradient of 150°C/cm across the 100μ wide aluminum-germanium alloy zone and a zone temperature of 650°C ± 10%. Under these conditions the zone did not move (Fig. 1), but certain regions of the film adjacent to the zone (appearing white in Fig. 1) had recrystallized. The crystallite size in these regions is ~0.05 mm (Fig. 2) compared to ~100Å before recrystallization. The crystallites showed no preferred orientation with respect to the substrate or zone and were confirmed as silicon by x-ray microprobe analysis. Larger gradients and longer times did not significantly increase the area recrystallized.

Silicon films, 1μ thick, deposited on sapphire by reduction of trichorosilane also showed recrystallized regions (Fig. 3) when treated in the same way. Figure 3 shows a region near an aluminum zone, which had

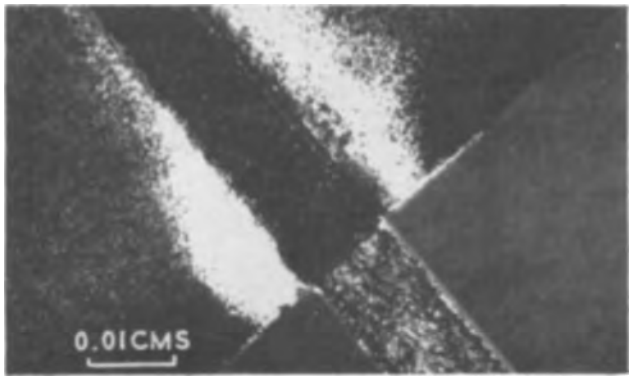

Fig. 1. Polycrystalline germanium film and aluminum alloy zone on sapphire substrate after heating for 8 hr in a temperature gradient of 150°C/cm.

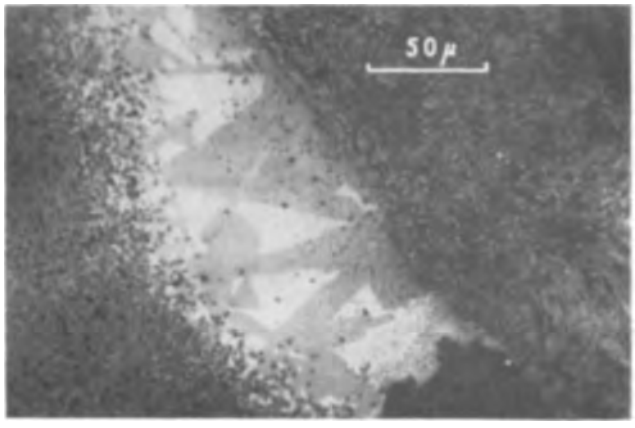

Fig. 2. Recrystallized region near aluminum alloy zone shown in Fig .1.

Fig. 3. Recrystallized region of a polycrystalline silicon film on sapphire.

been subjected to a temperature gradient of 100°C/cm at a zone temperature of 1000°C.

Zones of gold or tin alloys were used with germanium and silicon layers with various temperature gradients, but no zone movement was observed. In all cases the gold or tin diffused rapidly away from the zone, but produced no recrystallization. Attempts were also made to drive the gold or tin zones using an electric current (2); this produced very irregular movement of alloy, but again gave no recrystallization.

Experiments on the epitaxial deposition through thin liquid alloy layers (3) showed that epitaxy is possible through gold or tin alloy layers but not through aluminum layers. We attributed this to a coherent oxide skin over the surface of the aluminum alloy, the alloy then not being able to accept silicon from the vapor. We think that the recrystallization observed with aluminum zones in the above experiments is due to the removal of oxide from grain boundaries enabling the alloy to interact with the silicon crystallites. The gold or tin alloys do not remove this oxide and hence diffuse along grain boundaries without affecting the crystallites.

We conclude therefore that considerable recrystallization of silicon or germanium films by thin alloy zone crystallization processes is possible, but that difficulties are to be expected over the zone movement. These difficulties are probably enhanced by oxide contamination and must be overcome either by use of an oxide getter or perhaps by use of very steep temperature gradients such as is possible with electron beam processes.

Acknowledgment

This paper is published by permission of the Controller H. M. Stationery Office.

Manuscript received Jan. 22, 1965.

Any discussion of this paper will appear in a Discussion Section to be published in the December 1965 JOURNAL.

REFERENCES

1. D. T. J. Hurle, J. B. Mullin, and E. R. Pike, *Solid State Communications*, **2**, 201 (1964).
2. D. T. J. Hurle, J. B. Mullin, and E. R. Pike, *Phil. Mag.*, **9**, 473 (1964).
3. J. D. Filby and S. Nielsen, *This Journal*, **112**, 535 (1965).

Low-Temperature Epitaxy of Silicon by Sublimation onto Thin Alloy Layers

J. D. Filby and S. Nielsen

Ministry of Aviation, Royal Radar Establishment, Great Malvern, Worcestershire, England

The work of, for example, Carman *et al.* (1) on the regrowth of silicon from a silicon-gold eutectic, of Wagner and Ellis (2) on their V.L.S. process, and of Hurle *et al.* (3) on thin alloy zone crystallization processes, suggested that it would be possible to epitax silicon at low temperatures by evaporation onto a thin alloy layer. Results from recent experiments indicate that this is true, epitaxy of silicon having been obtained as low as 300°C.

The apparatus used is illustrated in Fig. 1. Silicon was sublimed from the source by heating it to 1300°C using induction heating. The substrate was heated by radiation from the source. The substrate temperature and the deposition rate were determined by the source-to-substrate distance and varied from 1100°C and 5 μ/hr to 500°C and ½ μ/hr. The substrate temperature was calibrated against the source temperature and source-substrate distance by using thermocouples in a blank run. At the start of each run the source temperature was determined with an optical pyrometer and the substrate temperature derived from it. This substrate temperature may be in error by ±50°C. The apparatus was pumped by a 10 l/sec ion pump which maintained a pressure of 5 x 10^{-8} Torr during the sublimation.

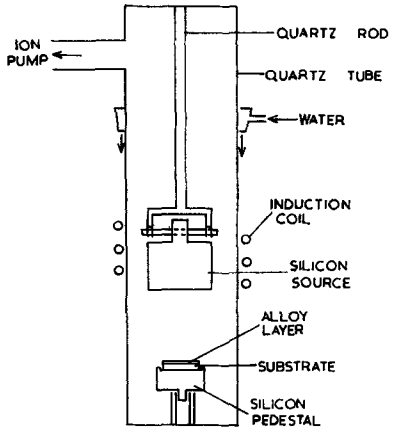

Fig. 1. Schematic diagram of sublimation apparatus

The substrate used in these experiments was a (111) silicon wafer which had been mechanically polished, degreased, and freed from oxide in HF. Before putting the substrate in the apparatus, a layer of metal 1-10μ thick was evaporated over part of the surface, the surface being near room temperature during the evaporation. The metal then alloyed with the silicon substrate to form a thin liquid layer at the deposition temperatures. Layers of gold, silver, copper, indium, and tin were alloyed in this way. After deposition, the layers were examined before and after removal of the alloy layer, and after bevel and vertical sectioning and etching, using optical microscopy and electron diffraction techniques.

The results from these experiments indicated that epitaxial silicon could be prepared by deposition through the liquid alloy layer. However, certain difficulties were experienced. First, the alloy layer showed a tendency to break up, the area covered by it

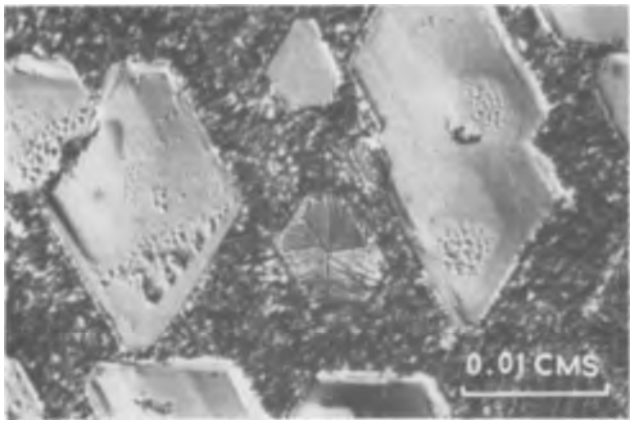

Fig. 2. Cellular silicon growth obtained under a gold alloy layer

depending on the constituents used and on the temperature. With gold alloy layers, for example, the layer broke up into droplets of 10-100μ diameter at temperatures above 1000°C. If radial temperature gradients were present, these droplets moved across the surface. At lower temperatures the droplet size increased, and at 700°C or lower the layer was substantially stable. Second, the silicon deposit underneath the alloy layers was often irregular. Figure 2 shows an example of this; a gold alloy layer has been removed and an irregular cellular type of growth revealed. This type of growth was observed under gold, silver, indium, and tin, but not copper alloys. The surface area of cells varied with the alloy and with the deposition temperature from 100 μ^2 to 0.5 mm^2. Sections through layers showing cellular growth also often revealed droplets of alloy trapped at the interface. We attribute this cellular growth to an irregular alloying caused by impurity on the substrate surface.

A polycrystalline deposit was observed on the surface of aluminum alloy layers; this we attribute to silicon depositing onto a coherent skin of oxide on the surface of the alloy.

Etching studies showed that the silicon deposited in the cells was usually more perfect than that deposited between them. A stacking fault density of 10^6/cm^2 within the cells was typical. An exception was the case of gold where no stacking faults were observed in the grown material unless a substrate with a heavily oxidized surface was used. For copper, where cellular growth was not observed, stacking fault densities of 10^3/cm^2 were obtained underneath alloy globules and in their immediate surroundings. We think that the stacking fault density is related to the oxygen concentration in the alloy.

One advantage of the sublimation process is that the temperature gradient through the alloy layer is such that the temperature of the alloy vapor interface is higher than that of the alloy substrate interface, the significance of this having been stressed recently by the authors (4).

So far our work has shown that epitaxial growth of silicon on silicon can be obtained at 850°, 800°, 500°, 400°, and 300°C using silver, copper, tin, gold, and indium alloys, respectively.

Acknowledgment

This paper is published by permission of the Controller, H. M. Stationery Office.

Manuscript received Jan. 22, 1965.

Any discussion of this paper will appear in a Discussion Section to be published in the December 1965 JOURNAL.

REFERENCES

1. J. N. Carman, P. E. Stello, and C. A. Bittman, *J. Appl. Phys.*, **25**, 543 (1954).
2. R. S. Wagner and W. C. Ellis, *Appl. Phys. Letters*, **4**, 89 (1964).
3. D. T. J. Hurle, J. B. Mullin, and E. R. Pike, *Solid State Communic.*, **2**, 201 (1964).
4. J. D. Filby, S. Nielsen, and G. J. Rich, C.V.D. Conference on Electronic Materials, Birmingham, England, 1964.

Microampere Multiple Constant Current Power Supply

Joseph B. Story[1] and Robert D. Wales

Materials Sciences Laboratory, Lockheed Missiles and Space Company, Palo Alto, California

A number of the more interesting anodic oxide thin films can be grown to potentials exceeding 100v. If it is desired to carry out this growth at a constant current, there is a problem in obtaining a suitable constant current source. The simple unit that is used for many purposes involves the use of a very large resistance in series with the cell, and a correspondingly high voltage across the combination. This makes the change in voltage across the cell small compared with the total and results in a correspondingly small change in the current. The voltage required for this apparatus is inconveniently large for use in thin film studies.

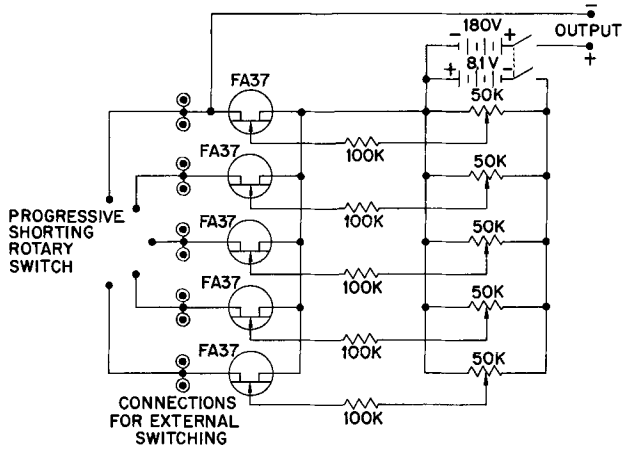

Fig. 1. Field effect transistor constant current power supply

One solution to this problem has been presented by one of the authors (1), who utilized the properties of a photomultiplier tube. It has now been found that a supply with smaller drift can be constructed using one or more field effect transistors in parallel (each individually adjustable). In addition, this arrangement offers the possibility of switching rapidly through a series of constant currents by using the transistors in various combinations. This rapid switching has been used by one of the authors (2) in investigating the mechanism of anodic germanium oxide film formation.

A circuit diagram of the power supply is shown in Fig. 1. The most critical factor involved is the stability of the biasing potential. For this purpose, six Mallory RM-42R mercury batteries (1.35v each) were used in series. It appears that a partial discharge of the batteries increases the stability. The FA 37 field effect transistors were of Amelco manufacture. Beckman

[1] Present address: University of Arkansas, Graduate Institute of Technology, Fayetteville, Arkansas.

precision potentiometers (50K) were used for adjusting the biasing potential.

Each of the FA 37 transistors is useful for currents up to 75 μa. The paralleling of transistors permits proportionately higher currents. It should also be possible to increase the current range by the selection of a different field effect transistor.

After a warm-up of 1½ hr, the drift over a period of 6 hr was 0.6% for currents up to 75 μa for one transistor. During this time there was usually a period of several hours during which the drift was about 0.01%. When the load is varied such that the voltage across it varies from zero to 100v, the current drops by 3.6%, 2.3%, and 1.8% for initial currents of 25 μa, 50 μa, and 75 μa, respectively.

Manuscript received Jan. 7, 1965.

Any discussion of this paper will appear in a Discussion Section to be published in the December 1965 JOURNAL.

REFERENCES

1. R. D. Wales, *This Journal*, **110**, 946 (1963).
2. J. B. Story, To be published.

Errata

On page 417 of the April 1965 issue of the Journal in the paper by Joseph B. Kushner "Relationship between Deposit Thickness and Current Density during the Early Stages of Electrodeposition," Eq. [8a], [9a], and [10a] should read

$$T_1 (I_1)^{3p/2} = T_2 (I_2)^{3p/2} = \text{constant} \quad [8a]$$

$$t_1 (I_1)^{(3p+2)/2} = \text{a constant} \quad [9a]$$

$$T_1/T_2 = t_1/t_2^{3p/(3p+2)} \quad [10a]$$

Manuscripts and Abstracts for Fall 1965 Meeting

Papers are being solicited for the Fall Meeting of the Society, to be held at the Statler-Hilton Hotel in Buffalo, N. Y., October 10, 11, 12, 13, and 14, 1965. Technical sessions probably will be scheduled on: Batteries (including Symposia on Charging Characteristics of Batteries and Characteristics of Electrodes during Charging), Corrosion, Electrodeposition (including Symposium on Thin Film Technology), Electronics-Semiconductors, Electrothermics and Metallurgy (including a Symposium on Zirconium and Its Alloys).

To be considered for this meeting, **triplicate copies of the usual 75-word abstract, as well as of an extended abstract of 500-1000 words** (see notice on page 121C of this issue), must be received at The Electrochemical Society, 30 East 42 St., New York, N. Y., 10017, *not later than May 17, 1965.* (Papers solely sponsored by the Corrosion Division **do not** require an extended abstract.) *Please indicate on 75-word abstract for which Division's symposium the paper is to be scheduled, and underline the name of the author who will present the paper.* No paper will be placed on the program unless one of the authors, or a qualified person designated by the authors, has agreed to present it in person. Clearance for presentation of a paper at the meeting should be obtained before the abstract is submitted. An author who wishes his paper considered for publication in the JOURNAL or ELECTROCHEMICAL TECHNOLOGY should send triplicate copies of the manuscript to the Managing Editor of the appropriate publication 30 East 42 St., New York, N. Y., 10017. Concerning papers to be published in the JOURNAL, see notice on per page charge on page 122C of this issue.

Presentation of a paper at a technical meeting of the Society does not guarantee publication in the JOURNAL or ELECTROCHEMICAL TECHNOLOGY. However, all papers so presented become the property of The Electrochemical Society, and may not be published elsewhere, either in whole or in part, unless permission for release is requested of and granted by the Editor. Papers already published elsewhere, or submitted for publication elsewhere, are not acceptable for oral presentation except on invitation by a Divisional program Chairman.

The Effect of Oxygen Pressure on the Oxidation of Zone-Refined Iron

W. E. Boggs, R. H. Kachik, and G. E. Pellissier

Applied Research Laboratory, United States Steel Corporation, Monroeville, Pennsylvania

ABSTRACT

The rate of oxidation of pure iron increases with decreasing oxygen pressure in the temperature range of 220°-450°C and the pressure range 100-0.01 Torr. Fe_3O_4 forms initially on the surface of the iron, and subsequently Fe_2O_3 nucleates in the surface of the Fe_3O_4. As the Fe_2O_3 layer becomes continuous, diffusion through the Fe_3O_4 layer is reduced, resulting in a substantial reduction of the oxidation rate. At low oxygen pressures (0.01 Torr), the rate of nucleation of Fe_2O_3 is low, resulting in relatively thick films of Fe_3O_4 and high oxidation rates, whereas at high oxygen pressures (100 Torr), the rate of nucleation of Fe_2O_3 is high, resulting in thinner Fe_3O_4 films, and lower over-all oxidation rates.

The technical literature contains more reports of investigations of the oxidation of iron and its alloys than of any other metal system (1, 2), presumably because of the great commercial and technological importance of ferrous materials. In the majority of studies reported, rates of oxidation of fairly pure commercial iron in oxygen or clean air have been determined for ranges of temperature and exposure time at a single gas pressure. Because of the greater practical interest in oxidation at higher temperatures, considerably more research has been devoted to the oxidation behavior of iron and its alloys at temperatures above about 600°C, where relatively thick oxide layers or scale form in a short time. The most recent information concerning the low temperature oxidation of relatively pure iron (200°-470°C and oxygen pressures of about 20 Torr) has been reported in a series of papers by Cohen and co-workers (3-8).

Some time ago, an investigation of the low temperature oxidation behavior of iron was undertaken by the present authors to provide background information for a larger research program directed toward obtaining a better understanding of the oxidation and corrosion behavior of commercially important alloy steels. The experimental pattern established in a recently completed study of the oxidation of tin (9-11) was followed, in that the effect of oxygen pressure as well as temperature was explored, and the constitution and morphology of the resulting oxide films were examined at various stages of film formation and growth. In an initial series of experiments carried out under oxygen pressures of 100, 10, 1, 0.1, and 0.01 Torr, at 270°C, it was found that the thickness of the resulting oxide films, for a given exposure time, increased quite substantially as the oxygen pressure was lowered. This unexpected finding prompted a more comprehensive study of the effects of pressure, temperature, and time of exposure on the oxidation kinetics and on the constitution and microstructure of the oxide films. The results are presented in this paper together with a proposed model for the mechanism of oxidation that appears to account satisfactorily for the experimental observations.

Materials and Experimental Work

Specimen purity.—Zone-refined iron was used in this investigation. According to the analysis provided by the source, Battelle Memorial Institute, the purity of the iron was about 99.99%, Table I. After the iron had been reduced to foil and electropolished in preparation for the oxidation experiments, it was analyzed by solid mass spectrometry and vacuum fusion. According to these analyses the purity of the iron foil was 99.94%, Table I.

Table I. Purity of the iron used in the oxidation study

Impurity	Battelle analysis of bulk, ppm	Mass spectrometric analysis of foil, ppm	Vacuum fusion analysis of C, N, and O, ppm
Aluminum	4	**	
Antimony	<10 N.D.*	N.D.	
Arsenic	<10 N.D.	13	
Beryllium	<5 N.D.	**	
Boron	<5	12	
Cadmium	<50 N.D.	N.D.	
Calcium	1	2.5	
Carbon	10	**	14
Chlorine		12	
Chromium	1	19	
Cobalt	10	53	
Copper	1	102	
Gallium	<50 N.D.	50	
Germanium		30	
Hydrogen	<0.1 N.D.	**	
Lead	<1	N.D.	
Magnesium	2	5	
Manganese	1	20	
Molybdenum	10		
Nickel	4	42	
Nitrogen	<2	**	3
Oxygen	27	**	19
Phosphorus	<5	55	
Potassium		<20	
Silicon	10	101	
Sodium		<20	
Sulfur	<10	34	
Tin	1	N.D.	
Tungsten	<1 N.D.	N.D.	
Vanadium	<10 N.D.	N.D.	
Zinc		2.5	
All others		<0.2-0.7	
Maximum Purity	99.992% Fe	99.941% Fe	

* N.D. means none detected. Detection limits are given.
** Not determinable by solids mass spectrometer in an iron matrix.

Specimen preparation.—Half-inch-thick wafers of the zone refined iron were cold-rolled to a thickness of about 6 mils. Specimens of the rolled material were electropolished to clean and smooth the surface, vacuum-annealed at 10^{-6} Torr and 950°C for 4 hr, and then slowly cooled to room temperature (2°C/min). After this treatment, the foils contained relatively large grains (1 mm average diameter) that were free of deformation.

Surface preparation.—Great care must be taken in surface preparation prior to oxidation experiments. Ideally, the metal surface should be atomically flat and clean. Since mechanical polishing tends to distort and strain the surface layers, electropolishing is often employed to produce the desired smooth surfaces. Unfortunately, the resulting metal surfaces are usually covered by thin oxide films as a consequence of the electropolishing mechanism (12). The problem of removal of this electropolishing residue has not been solved satisfactorily. In the case of iron, hydrogen reduction is employed quite often, but it leaves

a residue of reduced iron and may result in surface rearrangement (12). Despite these anticipated disadvantages, electropolishing, followed by hydrogen reduction, was the method of surface preparation chosen for this investigation.

The following specimen preparation was found to yield fairly reproducible oxidation data. Specimens of the cold-rolled and vacuum-annealed iron foil were electropolished in a solution of 15% perchloric acid and 85% glacial acetic acid, washed, and dried. The foils were then transferred to a vacuum microbalance system and, after evacuation to 10^{-7} Torr, were reduced in pure hydrogen at a pressure of 10 Torr and a temperature of 400°C for 1 hr. The microbalance system was again evacuated to 10^{-7} Torr, the temperature was adjusted, and the system allowed to equilibrate; then pure oxygen was introduced to initiate an oxidation experiment.

Electron microscopic examination revealed that these electropolished and hydrogen-reduced iron surfaces were very smooth. There was no evidence of the gross surface rearrangement, such as faceting, that may occur in the course of hydrogen reduction at higher temperatures (12). A weight loss of the specimen corresponding to an iron oxide film 25-30Å thick was observed during the reduction.

To determine the nature of the electropolishing residues and the effectiveness of the hydrogen reduction, electropolished specimens were examined by reflection electron diffraction both before and after hydrogen reduction. The diffraction patterns (Fig. 1) consisted of elongated spots characteristic of the reflection electron diffraction patterns usually obtained from electropolished surfaces (13). Both patterns were identified as diffraction patterns of α-iron. Since available information suggests that a layer of contamination 25-50Å thick would completely obscure the low-angle diffraction maxima of a flat metal surface (14-16), the observed reflection diffraction pattern of iron, with marked refraction streaking and low background scatter, tended to confirm that the electropolishing treatment resulted in a film only 25-30Å thick on the iron surface. As is shown in Fig. 1, the refraction streaks are longer, and the background is lower, in the diffraction pattern of the hydrogen-reduced specimen than in the pattern of the electropolished specimen. Thus, it was concluded that the hydrogen reduction treatment had effected some cleaning of the surface. The physical condition of the iron produced by the reduction of the oxide film is not known.

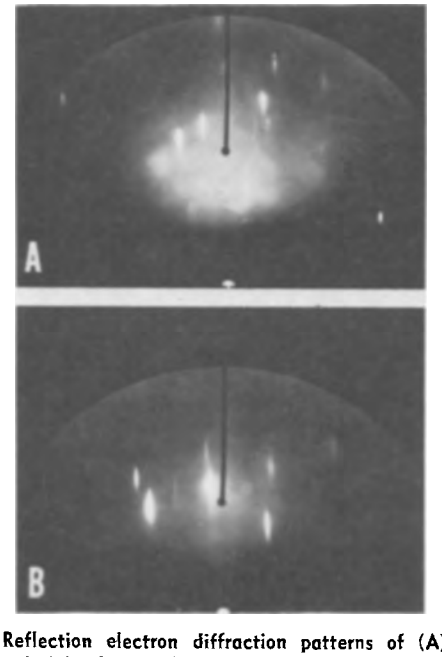

Fig. 1. Reflection electron diffraction patterns of (A) electropolished, and (B) electropolished and hydrogen-reduced surfaces of zone-refined iron.

Vacuum microbalance.—The Gulbransen-type vacuum microbalance (17) used in this investigation had been used in a previously reported study of the oxidation of tin (9). Because of radiometric and buoyancy effects (18), which are pressure and temperature dependent, it was necessary to apply corrections to the data obtained from the vacuum microbalance in the course of kinetic studies. These corrections involved making the initial and final measurements of the balance deflection while the specimen was at the oxidation temperature in high vacuum (9). Since the relative proportion of Fe_3O_4 in an oxide film containing both Fe_3O_4 and α-Fe_2O_3 will increase during evacuation at elevated temperatures at the expense of the α-Fe_2O_3 (19), it has been necessary to modify this procedure to obtain representative specimens of the oxide films for x-ray and electron-diffraction analysis and electron-microscopic examination. Separate specimens of iron were oxidized and then allowed to cool rapidly to room temperature before evacuation, to minimize the change in the composition of the oxide film. Thus, the kinetic data and the x-ray analytical data were obtained from the oxidation of separate specimens of iron foil.

Analysis of Iron oxide.—X-ray diffraction techniques were used in the estimation of the compositions of the stripped iron oxide films reported in this paper. These techniques are only qualitative. A minor constituent, comprising as much as 10% of the total film, might not be detected. Furthermore, it is difficult to distinguish between the two cubic oxides, Fe_3O_4 and γ-Fe_2O_3. In this work, all cubic oxide is reported as Fe_3O_4, and only the rhombohedral oxide, α-Fe_2O_3, is reported as a separate phase, although it is to be expected from the studies of Sewell and Cohen (8) that γ-Fe_2O_3 may form between the Fe_3O_4 and α-Fe_2O_3 phases.

Electron microscopy.—Specimens of oxide were removed from the metal using a dry stripping method which is a modification of the two-layer, plastic-replication technique used throughout the earlier studies of tin oxidation (10). The oxidized iron foil specimens were coated with a thin layer of formvar followed by a thick layer of parlodion. After the plastic was dry, the edges of the specimen were sheared, loosening the adjacent oxide; the plastic backing together with most of the oxide film was then peeled from the iron surface. After the thick parlodion film was dissolved in amyl acetate, the oxide, supported on formvar, was ready for examination by transmission electron microscopy and diffraction, or by x-ray diffraction. The disadvantage of the technique was that iron oxide films of thickness less than about 100Å adhered too tightly to the iron surface, and could not be stripped. Therefore, the earlier stages of iron oxide formation were not investigated. However, the metal surface at the oxide-metal interface could be replicated and examined after the oxide had been removed, since the metal surface was not damaged by the dry stripping technique. In most instances scattered fragments of the oxide remained attached to the metal after stripping. Replicas of these partially stripped surfaces were used to study simultaneously the topography of the top surface of the oxide and that of the metal at the oxide-metal interface. Replicas of the bottom surface were prepared by evaporating carbon on the underside of the stripped oxide, and then dissolving the plastic backing layer in amyl acetate. Much of the oxide was washed from the carbon replica when the plastic backing was being dissolved. Replicas of the interfaces were shadowed with platinum before examination in an electron microscope. The average film thicknesses calculated from the microbalance data were verified by measuring the

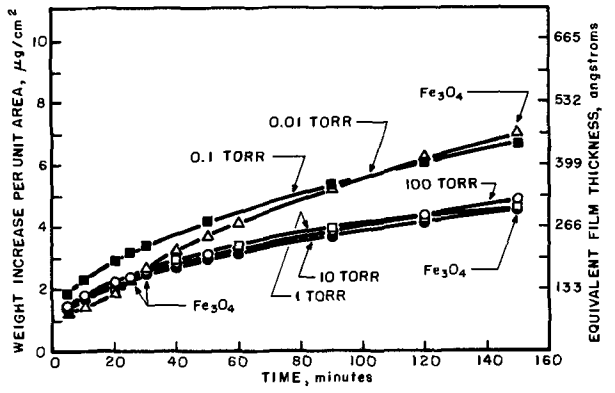

Fig. 2. Effect of oxygen pressure on the oxidation of zone-refined iron at 220°C, linear plot.

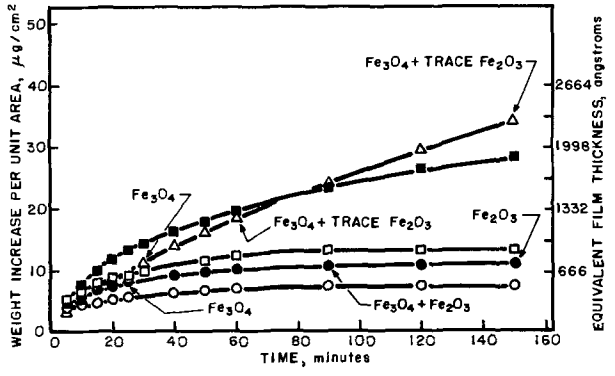

Fig. 3. Effect of oxygen pressure on the oxidation of zone-refined iron at 270°C, linear plot. △, 0.01 Torr; ■, 0.1 Torr; □, 1 Torr; ●, 10 Torr; ○, 100 Torr.

length of the shadows cast by the oxide fragments on the replicas of the oxide-metal interface.

Experimental Results

Kinetic Data

Plots of the microbalance data obtained from the oxidation of iron for 150 min at 220°C and oxygen pressures of 0.01, 0.1, 1, 10, and 100 Torr, respectively, are shown in Fig. 2. The data obtained at 1, 10, and 100 Torr are coincident, within the limits of experimental error. However, the data obtained at 0.1 and 0.01 differ significantly from the data obtained at the higher oxygen pressures. Thus, there appears to be an increase in the oxidation rate with decreasing oxygen pressure at 220°C. Another interesting feature of these data is that, although the curves for the iron oxidation at 0.1, 1, 10, and 100 Torr are either coincident or essentially parallel, the rate curve for the oxidation at 0.01 Torr goes through an induction period before crossing the other curves and proceeding at the highest rate.

Figure 3 is a plot of the microbalance data for the oxidation of iron for 150 min at 270°C, and oxygen pressures of 0.01, 0.1, 1, 10, and 100 Torr, respectively. Here, the effect of external oxygen pressure on the kinetics is clearly evident. The total weight increase was much greater at the low oxygen pressures than at the higher oxygen pressures. Again, the data obtained from the oxidation at 0.01 Torr exhibit an induction period, and then the reaction proceeds at the highest rate.

The effect of oxygen pressure on the rates of oxidation at 350°C is shown in Fig. 4. The greatest differences in the amounts of oxide formed at the different oxygen pressures were observed at this temperature. The oxidation appears to proceed in two stages: (i) an initial period of high oxidation rate, followed by

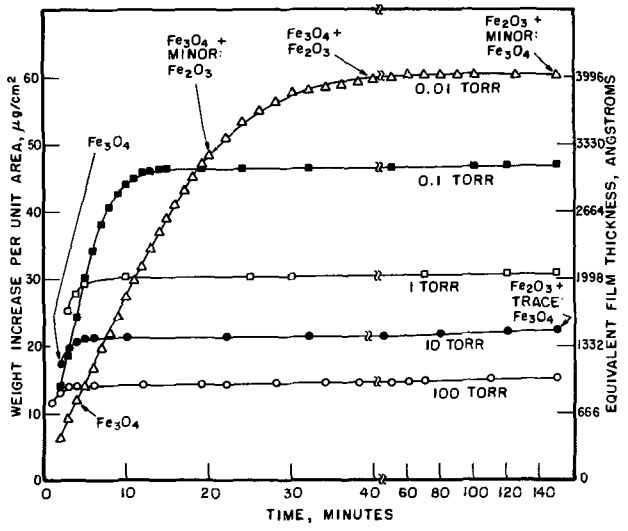

Fig. 4. Effect of oxygen pressure on the oxidation of zone-refined iron at 350°C, linear plot.

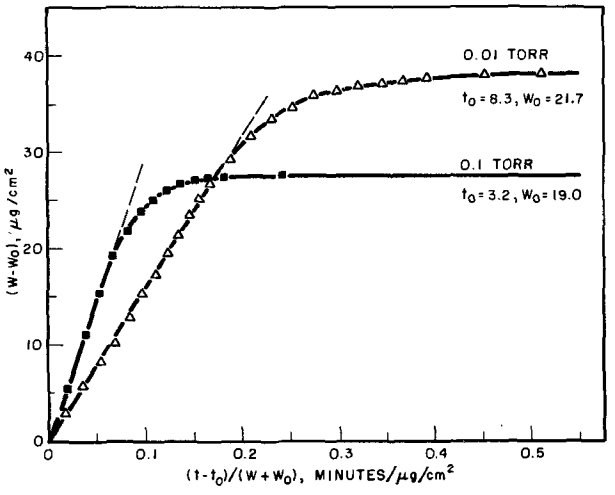

Fig. 5. Parabolic plot of data from the first stage of oxidation at 350°C, 0.1 and 0.01 Torr.

(ii) a rather sharp transition into a period of lower oxidation rate. The duration of the first stage, the period of high oxidation rate, was strongly dependent on oxygen pressure. However, the plots of the data obtained in the second stage of the oxidation are essentially parallel, an indication that there is very little oxygen pressure dependence in the second stage. The plot of the data obtained at 0.01 Torr crosses that obtained at the other pressures, as was observed at the lower temperatures.

These data, plotted in a parabolic manner, are shown in Fig. 5. The data from the first stage of the oxidation at 0.1 and 0.01 Torr, respectively, at 350°C, appear to conform to a parabolic rate law. The duration of this first stage at the higher oxygen pressures was too short to yield data that could be tested for this conformity. It appears likely that the early stage of the oxidation at 1, 10, and 100 Torr may also conform to a parabolic rate law. At the end of the first stage, oxidation proceeds through a transition period, and eventually enters a parabolic region having a much lower rate constant, Fig. 6.

The data obtained from the oxidation of iron at 450°C and at oxygen pressures of 0.01, 0.1, 10, and 100 Torr, respectively, are shown in Fig. 7. It is evident that the external oxygen pressure has very little effect on the oxidation rate at this temperature. The first parabolic region exists for a very short time, if at all, and the microbalance data shown in these

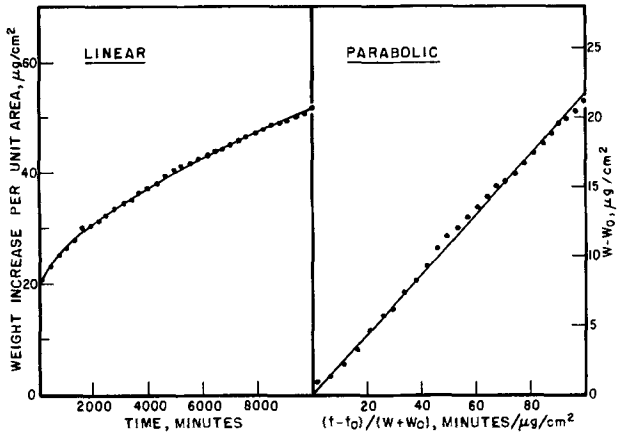

Fig. 6. Linear and parabolic plots of data from the second stage of oxidation at 350°C and an oxygen pressure of 10 Torr; w_o = 29 μg/cm²; t_o = 1500 min.

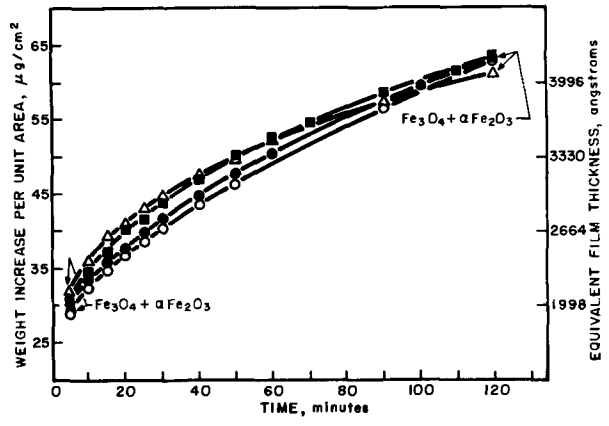

Fig. 7. Effect of oxygen pressure on the oxidation of zone-refined iron at 450°C, linear plot. ○, 100 Torr; ●, 10 Torr; ■, 0.1 Torr; △, 0.01 Torr.

plots represent only the second region of the oxidation process.

X-ray Diffraction Analyses

The approximate crystalline constitution of the oxide films formed at 0.01 Torr and at 10 Torr and at temperatures of 220°, 270°, 350°, and 450°C, as estimated by x-ray diffraction analyses of the stripped oxide, are shown on the curves of Fig. 2, 3, 4, and 7, respectively. At 220°C, Fe_3O_4 was the only oxide phase detected during 150-min reaction time. At 270°C, Fe_3O_4 was the only phase detected after 30-min exposure at either oxygen pressure. As the reaction progressed at 10 Torr, increasing amounts of α-Fe_2O_3 were detected, until at 150 min the amount of Fe_3O_4 remaining in the stripped film was scarcely detectable. In contrast, Fe_3O_4 continued to be the major oxide phase formed at an oxygen pressure of 0.01 Torr, even after 150 min of oxidation.

As shown in Fig. 4, the rate curves for the oxidation of iron at 350°C are divided into an initial region of high oxidation rate and a later region of lower oxidation rate. The major oxide phase found in the first region was Fe_3O_4. Toward the end of this region of high oxidation rate, the α-Fe_2O_3 phase began to appear. As the reaction rate began to diminish, increasing amounts of α-Fe_2O_3 were detected, until after 150 min of oxidation, α-Fe_2O_3 was the major oxide phase found in the films. The weight gain, from the end of the period of high oxidation rate until the termination of the experiments at 150 min, corresponded approximately to the amount of oxygen that would be required to completely convert the Fe_3O_4 phase to α-Fe_2O_3.

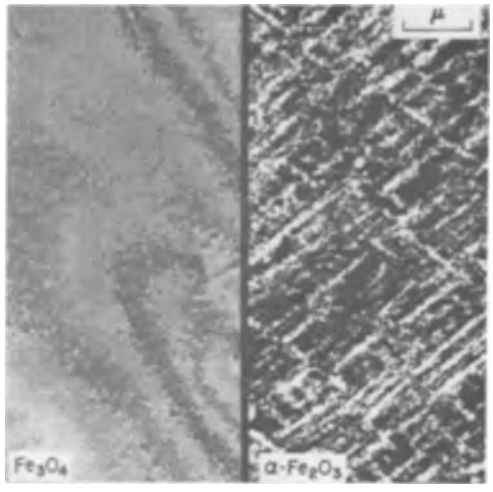

Fig. 8. Transmission electron micrographs showing the fine mottled texture typical of Fe_3O_4 films and the coarse "herringbone" texture typical of α-Fe_2O_3 films.

These data suggest that the initial region of high oxidation rate corresponds mainly to the growth of the Fe_3O_4 layer, whereas the later region of lower oxidation rate corresponds mainly to the growth of the α-Fe_2O_3 phase. The duration of the period of Fe_3O_4 growth appears to be strongly dependent upon the external oxygen pressure. This period of time was short at high oxygen pressures, and became longer as the oxygen pressure was decreased.

Approximately equal amounts of both oxide phases were detected in the oxide films formed at 450°C, irrespective of the external oxygen pressure. Evidently, the initial period of unhindered Fe_3O_4 formation was very short (or perhaps nonexistent).

Morphology of Iron Oxide Films

Electron micrographs of typical Fe_3O_4 and α-Fe_2O_3 films are shown in Fig. 8A. The Fe_3O_4 layer (Fig. 8A) has a very fine-grained texture as though it were composed of very small crystallites. Single-crystal electron-diffraction patterns were always obtained from these films. Thus, if the observed texture is indicative of a polycrystalline film, all crystals are very nearly of the same orientation. The typical α-Fe_2O_3 film has a rather coarse-grained, "herringbone" texture. Electron diffraction patterns of these films usually indicated that the α-Fe_2O_3 crystals occurred in several orientations. However, completely random orientation in this layer was seldom observed. The influence of temperature and oxygen pressure on the texture, or crystallite size, of the α-Fe_2O_3, as a function of oxidation time, is illustrated in Fig. 9, 10, and 11.

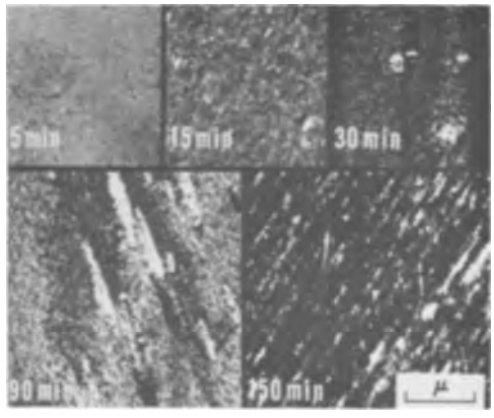

Fig. 9. Electron micrographs of the oxide formed on zone-refined iron at 270°C and an oxygen pressure of 10 Torr.

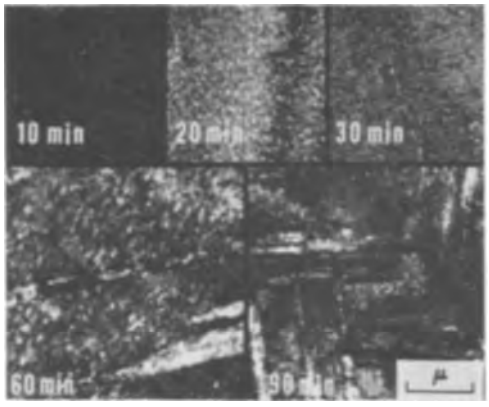

Fig. 10. Electron micrographs of oxide formed on zone-refined iron at 270°C and an oxygen pressure of 0.01 Torr.

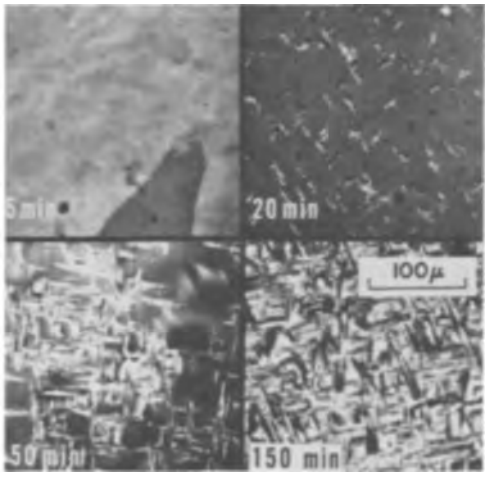

Fig. 11. Optical micrographs of oxide formed on zone-refined iron at 350°C and an oxygen pressure of 0.01 Torr.

Electron micrographs of stripped oxide films that had formed upon exposure at 270°C and an oxygen pressure of 10 Torr, for different times, are shown in Fig. 9. After 5 min, the oxide consisted of a fairly uniform fine-grained layer, typical of Fe_3O_4. After 15 min, a few irregularities (bright spots) appeared in the oxide film. These spots were better defined after 30 min, and after 90 min they had developed into small parallel acicular platelets. The film appeared to be composed almost completely of these platelets in the typical "herringbone" texture of an α-Fe_2O_3 film, after reaction with oxygen for 150 min.

Electron micrographs of the oxide films that had formed upon exposure at 270°C and an oxygen pressure of 0.01 Torr, for different times, are shown in Fig. 10. Little change from the typical fine-grained texture of Fe_3O_4 was apparent until the reaction had progressed for 60 min. After this time, the acicular platelets were observed growing in the surface of the Fe_3O_4 matrix, but they were fewer in number, larger, and farther apart than the platelets formed at 10 Torr in the same length of time. Even after 90 min of reaction, large areas of Fe_3O_4 remained between the platelets in the oxide formed at 0.01 Torr. Beyond 90 min of oxidation the oxide became opaque to the 50 kv electron microscope beam.

The oxide film formed at 350°C became too thick for examination by transmission electron microscopy in 5 to 10 min of oxidation. However, the changes in oxide morphology, as the films became richer in α-Fe_2O_3, could be observed by light microscopy at lower magnifications. A series of light micrographs of oxide films in situ that had formed upon exposure at an oxygen pressure of 0.01 Torr are shown in Fig. 11.

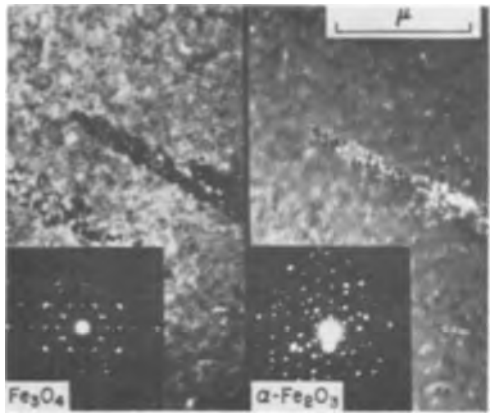

Fig. 12. Bright-field (left) and dark-field (right) electron micrographs and diffraction patterns of Fe_3O_4 matrix and α-Fe_2O_3 platelets.

After 5 min of oxidation, the film was composed mainly of Fe_3O_4, and very little microstructural detail was evident. After 20 min, the acicular platelets were visible in the Fe_3O_4, and these became quite profuse in some grains after 50 min of oxidation. Finally, after 150 min of oxidation, the oxide film consisted of a profusion of closely interlocked platelets, arranged in a Widmanstätten pattern. This type of structure in iron oxide films has been observed by other investigators (20-22).

A detailed study of these oxide films using both bright-field and dark-field contrast electron microscopy, coupled with selected-area electron diffraction analysis, revealed that the acicular crystals were composed of α-Fe_2O_3, apparently nucleated in the surface of the Fe_3O_4 layer. This is demonstrated by the electron micrographs and diffraction patterns of Fig. 12. An α-Fe_2O_3 crystal appears as the diagonal dark platelet in the mottled gray background of the bright-field micrograph. The electron-diffraction pattern of Fe_3O_4 in the inset was obtained from the matrix area surrounding the platelet. The same crystal appears in bright contrast in the dark-field micrograph. This dark-field electron micrograph was obtained by using the (100) reflection of the α-Fe_2O_3 electron diffraction pattern shown in the inset. The orientation of these α-Fe_2O_3 platelets is believed to be related to the crystallographic orientation of the iron substrate through the lattice of the intervening Fe_3O_4 layer. For example, a Widmanstätten pattern consisting of rectangles and squares probably indicates that the substrate iron was oriented with a (100) plane parallel to the surface (20, 21).

Replicas of partially stripped surfaces revealed the topography of both the metal surface at the oxide-metal interface and the oxide at the oxide-gas interface, and provided an independent means of estimating the thickness of the oxide. For example, the average thickness of the oxide film formed on a specimen of iron in 150 min at 350°C and 10 Torr was estimated to be 1525Å from the length of shadows on a replica of the partially stripped iron surface. The thickness of this film calculated from the microbalance data was 1460Å. Similarly, the thickness of an oxide film formed in 60 min at 350°C and 0.01 Torr was estimated to be 4051Å by the shadow-casting method, compared to 4289Å obtained by calculation from the microbalance data.

Figure 13 is an electron micrograph of such a replica obtained from an iron specimen oxidized at an oxygen pressure of 10 Torr and a temperature of 350°C for 5 min. The iron surface (A) remained relatively smooth, whereas slight changes in the topography of the top surface of the oxide (B) were observed, which corresponded to α-Fe_2O_3 crystals. The

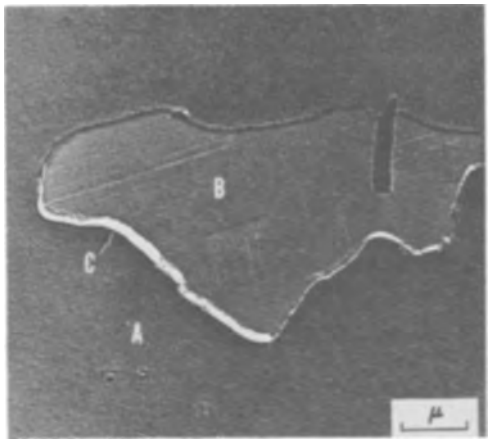

Fig. 13. Electron micrograph of platinum-shadowed replica of (A) metal at oxide-metal interface and (B) oxide at oxide-oxygen interface after oxidation for 5 min at 350°C and a pressure of 10 Torr, showing shadow (C) used for calculation of oxide thickness.

thickness of this oxide film, as calculated from the length of the shadow (C), is 1150Å, whereas a thickness of 1250Å was calculated from the weight-gain measurements. The oxide surface at the oxide-metal interface (not shown) was about as smooth as the metal surface (A) shown in Fig. 13.

A roughening of both surfaces occurs with further oxidation, but the oxide-metal interface remains much smoother than the oxide-oxygen interface. Figure 14 is an electron micrograph of a replica of a partially stripped iron surface that had been oxidized at 10 Torr and 350°C for 120 min. Striations in the replica of the metal surface (A) appear to correspond to striations in the replica of the top surface of the oxide (B). The locations of the replica shadows relative to these striations indicate that the striations represent indentations (grooves) in the oxide at the oxide-oxygen interface, or ridges in the metal at the oxide-metal interface. The grooves in the top surface of the oxide appear to correspond to the earliest formed segments of α-Fe_2O_3 platelets. Thus, the ridges in the metal, and the grooves in the oxide, may be evidence of a decreased transport of iron from the metal substrate into and through the oxide, in the area immediately beneath the spreading α-Fe_2O_3 platelets.

The change from a predominantly Fe_3O_4 to a predominantly α-Fe_2O_3 surface texture, upon oxidation at 350°C and an oxygen pressure of 0.01 Torr, is illustrated by the electron micrographs of surface replicas shown in Fig. 15 and 16. Both the surface of the metal

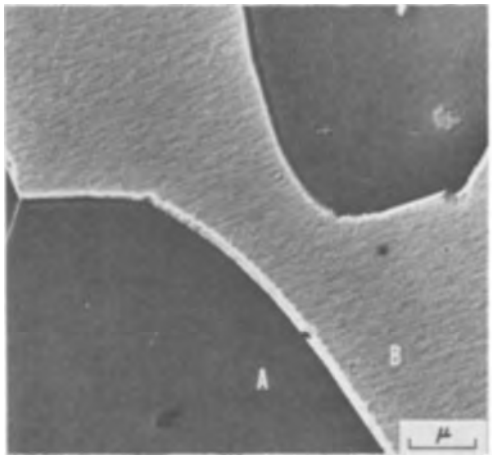

Fig. 14. Electron micrograph of platinum-shadowed replica of (A) iron at the oxide-metal interface, and (B) oxide at the oxide-oxygen interface after oxidation for 120 min at 350°C and a pressure of 10 Torr.

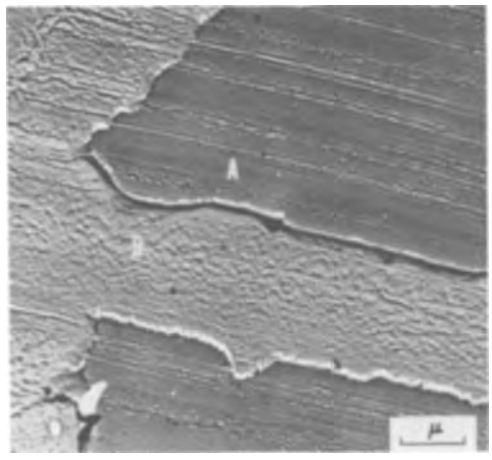

Fig. 15. Electron micrograph of platinum-shadowed replica of (A) metal at oxide-metal interface, and (B) oxide at oxide-oxygen interface after oxidation for 5 min at 350°C and a pressure of 0.01 Torr.

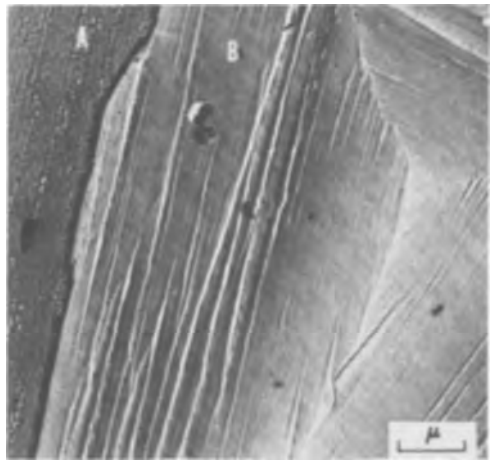

Fig. 16. Electron micrograph of platinum-shadowed replica of (A) metal at oxide-metal interface, and (B) oxide at oxide-oxygen interface after oxidation for 120 min at 350°C and a pressure of 0.01 Torr.

at the oxide-metal interface (A), and the surface of the oxide (Fe_3O_4) at the oxide-gas interface (B), are very smooth after oxidation for 5 min. In contrast, after 150 min of oxidation (Fig. 16), the surface of the metal (A) remained relatively smooth, but the surface of the oxide (B) at the oxide-gas interface became quite rough, and assumed the typical α-Fe_2O_3 "herringbone" texture. These observations suggest that the α-Fe_2O_3 platelets formed first at the oxide-oxygen interface, and grew inward toward the oxide-metal interface, since evidence of the platelets was found much earlier in the replicas of the oxide-oxygen interface than in the replicas of the oxide-metal surface. It is believed that local "masking" of the Fe_3O_4-oxygen interface, with respect to oxygen access, by the spreading α-Fe_2O_3 platelets, is sufficient to cause the observed changes in the topography of the oxide-metal interface.

Discussion

It is evident from the foregoing experimental information that the oxidation rates decreased sharply as the proportion of α-Fe_2O_3 in the oxide film increased. Wagner (23) has suggested that a low oxidation rate would result if a continuous layer of α-Fe_2O_3 existed at the outer surface of the Fe_3O_4 phase, whereas a higher rate of oxidation would result if the Fe_3O_4 phase was directly and continuously exposed to gaseous oxygen. At low oxygen pressures, the rate of formation of α-Fe_2O_3, in the surface of a previously

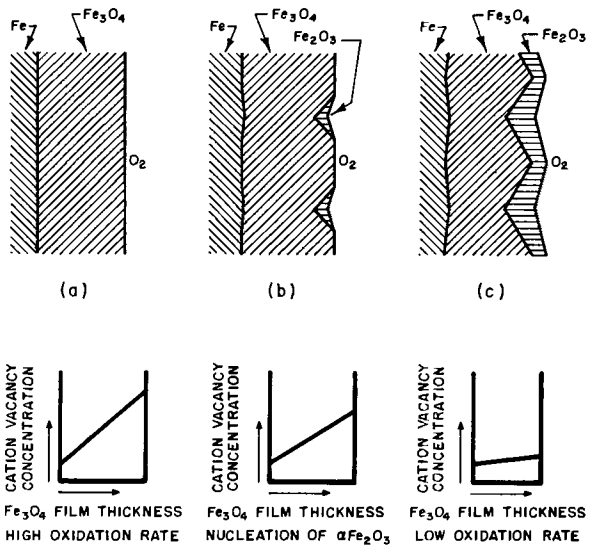

Fig. 17. Schematic diagram illustrating the effect of oxygen pressure.

existing layer of Fe_3O_4, might be low and the coverage discontinuous, whereas at high oxygen pressures, the rate of α-Fe_2O_3 formation might be high and the coverage more continuous. Two limiting cases: (*a*) a film consisting entirely of Fe_3O_4, and (*c*) a film of Fe_3O_4 covered by a film of α-Fe_2O_3 are sketched in Fig. 17, together with an intermediate case (*b*) wherein the α-Fe_2O_3 has nucleated and grown in the Fe_3O_4 film, but not to the extent that it forms a continuous outer layer.

Fe_3O_4 is a p-type, cation-deficit, semiconductor oxide (24). The following equations, based on defect equations suggested by Hauffe (24), represent the phase-boundary reactions that may occur in a layer of Fe_3O_4 in direct contact with adsorbed oxygen at the oxide-gas interface [1] and with iron at the oxide-metal interface [2]:

$$2\,O_2 \rightleftarrows Fe_3O_4 + (Fe\,\square'' + 2Fe\,\square''' + 8\,\oplus)_{\text{in } Fe_3O_4} \quad [1]$$

$$3Fe + (Fe\,\square'' + 2Fe\,\square''' + 8\,\oplus)_{\text{in } Fe_3O_4} \rightleftarrows Null_{Fe_3O_4} \quad [2]$$

where $Fe\,\square''$ and $Fe\,\square'''$ are cation vacancies in the Fe_3O_4 lattice sites normally occupied by Fe^{++} and Fe^{+++} ions respectively, and $\oplus$ are positive holes, that is, missing electrons elsewhere in the oxide lattice. The cation vacancies serve as carriers for iron ions moving outward through the oxide from the metal to the gas interface. The defect equations indicate that the cation vacancies are produced at the Fe_3O_4-O_2 interface, when oxygen is incorporated in the Fe_3O_4 crystal lattice. A change in the concentration of vacancies in the oxide lattice, produced by a change in oxygen pressure, will produce a similar change in the flux of iron ions moving outward through the oxide, and a change in the amount of iron reaching the outer surface of the oxide will produce a proportionate change in the observed oxidation rate.

According to Birchenall (25), α-Fe_2O_3 is an n-type, anion-deficit, semiconductor oxide. The following defect equations are suggested, representing the phase-boundary reactions (after a layer of α-Fe_2O_3 has formed at the outer surface of an Fe_3O_4 film) at the Fe_2O_3-O_2 interface

$$\tfrac{1}{2}\,O_2\,(g) + (O\,\square^{\cdot\cdot} + 2\,\ominus)_{Fe_2O_3} \rightleftarrows Null_{(Fe_2O_3)} \quad [3]$$

Where $O\square^{\cdot\cdot}$ is an oxygen ion vacancy and $\ominus$ is an extra lattice electron. The reactions at the Fe_2O_3-Fe_3O_4 interface are as follows

$$2Fe_3O_4 \rightleftarrows 3Fe_2O_3 + (O\,\square^{\cdot\cdot} + 2\,\ominus)_{Fe_2O_3} \quad [4]$$

$$12Fe_2O_3 \rightleftarrows 9Fe_3O_4 + (Fe\,\square'' + 2Fe\,\square''' + 8\,\oplus)_{Fe_3O_4} \quad [5]$$

The reaction at the Fe_3O_4-Fe interface is the same as given before in Eq. [2]. Thus, the boundary reactions at the α-Fe_2O_3-Fe_3O_4 interface would produce the ion and electron carriers for both types of oxide, and the external oxygen pressure should have no effect on the carrier concentration in either oxide when the Fe_3O_4 phase is covered by a continuous layer of α-Fe_2O_3.

In the temperature range in which this model is valid, a continuous layer of α-Fe_2O_3 will reduce the oxygen pressure at the outer surface of the Fe_3O_4 by many orders of magnitude to the dissociation pressure of α-Fe_2O_3 ($\sim 2 \times 10^{-34}$ Torr at 350°C). The concentration of cation vacancies will be reduced, and, in consequence, the flux of iron ions through the Fe_3O_4 layer needed to support the growth of the Fe_3O_4 layer will be reduced. After the α-Fe_2O_3 layer has become continuous, the additional weight gain of the iron specimen may be attributed mainly to the reaction of Fe_3O_4 with oxygen to produce more α-Fe_2O_3.

The proposed model for the mechanism of oxidation appears to explain the effect of oxygen pressure observed at 220°, 270°, and 350°C. Although α-Fe_2O_3 was not detected by x-ray diffraction analysis of the films formed in 150 min at 220°C and 10 or 100 Torr, this oxide phase was detected after increased reaction times under these same oxidizing conditions. Thus, an α-Fe_2O_3 layer too thin for x-ray detection, but sufficient to suppress the oxidation rate, probably was formed also at the higher oxygen pressures at 220°C.

In contrast, little or no pressure effect was observed at 450°C, and the proportions of the two oxide phases apparently did not change with increasing reaction time or with change of external oxygen pressure. Roughly equal amounts of Fe_3O_4 and α-Fe_2O_3 were found in the films formed at all pressures. Thus, it appears that the diffusion of iron outward through the Fe_3O_4 layer balances the diffusion of oxygen inward through the α-Fe_2O_3 layer, so that the process results in a dynamic equilibrium that maintains approximately equal amounts of the two oxide phases throughout the course of the oxidation at this temperature.

Conclusions

The amount of oxide formed on pure iron in a given length of time at temperatures of 220°-350°C increases as the oxygen pressure is decreased from 100 to 0.01 Torr. The oxidation kinetics are characterized by an initial, pressure-dependent period of high rate followed by a pressure-independent period of relatively low rate. The major oxide phase formed in the initial period of high oxidation rate is Fe_3O_4. As the proportion of the α-Fe_2O_3 phase in the oxide film increases, the oxidation rate decreases. The rates of nucleation and growth of the second phase, α-Fe_2O_3, appear to be pressure dependent. At high oxygen pressures, a layer of α-Fe_2O_3 quickly forms in the surface of the Fe_3O_4 film; it is believed that the presence of this layer reduces the rate of formation of cation vacancies in the Fe_3O_4 film, thereby decreasing the flux of cations through the film and lowering the oxidation rate. More time is required at low oxygen pressures for the α-Fe_2O_3 layer to form, and, consequently, the initial high rate of oxidation persists longer, and results in a thicker oxide film, than is formed at higher oxygen pressures.

Acknowledgment

The authors gratefully acknowledge the suggestions of Professor Carl Wagner in the deduction of a mechanism to explain the observed pressure effect.

Manuscript received Sept. 24, 1964. This paper was presented at the Washington Meeting, Oct. 11-15, 1965.

Any discussion of this paper will appear in a Discussion Section to be published in the December 1965 JOURNAL.

REFERENCES

1. O. Kubaschewski and B. E. Hopkins, "Oxidation of Metals and Alloys," Second Edition, pp. 108, Academic Press, Inc., New York (1962).
2. U. R. Evans, "The Corrosion and Oxidation of Metals," p. 24, St. Martin's Press, New York (1960).
3. P. B. Sewell, C. D. Stockbridge, and M. Cohen, *Can. J. Chem.*, **37**, 1813 (1959).
4. E. J. Caule, K. H. Buob, and M. Cohen, *This Journal*, **108**, 829 (1961).
5. C. D. Stockbridge, P. B. Sewell, and M. Cohen, *ibid.*, **108**, 928 (1961).
6. P. B. Sewell, C. D. Stockbridge, and M. Cohen, *ibid.*, **108**, 933 (1961).
7. P. B. Sewell and M. Cohen, *ibid.*, **111**, 501 (1964).
8. P. B. Sewell and M. Cohen, *ibid.*, **111**, 508 (1964).
9. W. E. Boggs, R. H. Kachik, and G. E. Pellissier, *ibid.*, **108**, 6 (1961).
10. W. E. Boggs, P. S. Trozzo, and G. E. Pellissier, *ibid.*, **108**, 13 (1961).
11. W. E. Boggs, *ibid.*, **108**, 124 (1961).
12. P. B. Sewell, E. G. Brewer, R. Ramasubramanian, and M. Cohen, Fifth International Congress for Electron Microscopy, Vol. 1, Abstract GG-8, Academic Press, New York (1962). See also *J. Phys. Chem.*, **67**, 2008 (1963).
13. W. Kranert, K. H. Leise, and R. Raether, *Z. Physik*, **122**, 248 (1944).
14. G. I. Finch, *J. Chem. Soc.*, 1137 (1938).
15. L. N. D. Lucas, *Proc. Phys. Soc.* (London), **A64**, 943 (1951).
16. H. Raether, *J. Phys. Radium*, **11**, 11 (1950).
17. E. A. Gulbransen, *Trans. Electrochem. Soc.*, **81**, 327 (1942).
18. "Vacuum Microbalance Techniques," Vol. I, M. J. Katz, Editor, pp. 111-150, Plenum Press, Inc., New York (1961).
19. E. J. Caule and M. Cohen, *This Journal*, **108**, 834 (1961).
20. J. B. Wagner, Jr., K. R. Lawless, and A. T. Gwathmey, *Trans. AIME*, **221**, 257 (1961).
21. J. V. Laukonis and R. V. Coleman, *J. Appl. Phys.*, **30**, 1364 (1959).
22. P. B. Sewell, E. G. Brewer, and M. Cohen, Fifth International Congress for Electron Microscopy, Vol. 1, Abstract C-8, Academic Press, New York (1962).
23. Carl Wagner, Max-Planck-Institut für Physikalische Chemie, Private communication.
24. K. Hauffe, "Reaktionen in und an Festen Stoffen," p. 506, Springer-Verlag, Berlin, Gottingen, Heidelberg (1955).
25. M. H. Davies, M. T. Simnad, and C. E. Birchenall, *J. Metals*, **3**, 889 (1951); **5**, 1250 (1953).

Electrochemical Measurements on Zirconium and Zircaloy-2 at Elevated Temperatures

II. 200°-300°C[1]

A. L. Bacarella and A. L. Sutton

Oak Ridge National Laboratory, Oak Ridge, Tennessee

ABSTRACT

Rates of film growth in oxygenated dilute sulfuric acid have been measured on zirconium and Zircaloy-2 at temperatures from 200° to 300°C using electrochemical methods. The resulting rate-time plots were analyzed according to logarithmic and cubic kinetics. The kinetic constants obtained from these results, and those of other investigators, were correlated with respect to temperature. The calculated activation energy for the cubic rate constant was 29.7 kcal/mole. The reduction of oxygen was studied as a function of film thickness. The results showed two polarization regions, a high current region with a Tafel slope about 3-5 (2.3 RT/F) and a low current region with a Tafel slope decreasing with film thickness from 4 (2.3 RT/F) to 1.4 (2.3 RT/F). The oxygen evolution reaction was also studied at 295°C. The observed Tafel slope ranged between 0.8 to 1.0 (2.3 RT/F). The anodic process in the over-all corrosion reaction was postulated to be a field-dependent ionic transport of oxygen ions. The Tafel slope for this process increased with film thickness from 4 (2.3 RT/F) to 16 (2.3 RT/F). At 295°C, a steady-state anodic rate independent of potential was observed. This result suggests that at steady-state the film dissolution rate is equal to the rate of film formation. The weak-field approximation to the conventional anodizing equation is postulated for the film formation reaction. The film dissolution reaction is not postulated.

In recent years an increasing number of studies of redox processes on passive electrodes have been made. From these studies attempts have been made to assess the role of the passive oxide film in the kinetics of the redox processes. These studies, however, are being made on very thin films, 50-100Å. Here are reported kinetic results on films from 200 to 3000Å thick. It is hoped that the results obtained on these "thick" films and at temperatures of 200°-300°C will provide further insight into the role the passive film plays in determining the mechanism of redox processes.

The film-growth reaction involves the transport of ionic species through the film. Studies of anodic film growth have been made on valve metals (Zr, Ta, Al). These investigations, however, concern the kinetics of film growth at high field strength. Few electrochemical studies have been made concerning film growth at low field strengths.

Here, electrochemical techniques are employed to study film-growth kinetics at temperatures from 200° to 300°C. Film-growth rates based on polarization resistance measurements have been previously reported (1, 2). The polarization resistance is defined as the derivative, $(dE/dI)_{E \to E_o}$, where I is the net current flowing through the electrode at the measured potential E, and E_o is the open-circuit corrosion potential. Theoretical justification for the correlation between the polarization resistance and corrosion rate was provided by Stern and Geary (3) and Posey (4). Stern

[1] Research sponsored by the United States Atomic Energy Commission under contract with the Union Carbide Corporation.

and Weisert (1) made an extensive investigation of the literature and demonstrated the general applicability of the method. They have shown that the experimental range of the Tafel slopes, $b = dE/d\log I$, is limited, and a simple measurement of the polarization resistance, $(dE/dI)_{E\to E_o}$, provides an estimate of the corrosion rate within a factor of 2. Although the systems investigated by Stern and Weisert were two-phase corrosion systems, metal/solution, its more general applicability to systems forming a passive oxide, metal/oxide/solution, was demonstrated by Stern (6), Meyer (1), and Bacarella (2).

In the experiments reported here, current-voltage measurements were made as a function of time. The measurements were interpreted according to logarithmic polarization behavior, and the rates were determined from the polarization resistance measurements and from the extrapolation of the Tafel-lines to the open-circuit potential. The rates were calculated from the polarization resistance using Eq. [1],

$$I_{corr} = \left(\frac{dI}{dE}\right)_{E\to E_o} \times \frac{RT}{F} \times \frac{1}{(\alpha_a Z_a) + (\alpha_c Z_c)} \quad [1]$$

where I_{corr} is the corrosion rate in amp/cm^2. The quantities $\alpha_a Z_a$ and $\alpha_c Z_c$ were obtained from the Tafel slopes, $b = dE/d\log I$, for the anodic and cathodic reactions, respectively, where

$$\alpha Z = \frac{2.3\,RT}{F} \times \frac{1}{b} \quad [2]$$

Experimental

The measurements were made on Zircaloy-2 rod-type specimens (electrodes) in 0.05*M* H_2SO_4 which was saturated with 250 psi O_2 at 25°C. The solutions were prepared using C.P. H_2SO_4 and triply distilled water, two distillations of which were obtained from a two-stage all quartz commercial still.

Rate measurements as a function of time were made at 206°, 260°, and 295°C. The experiments were performed in a titanium reaction cell, Fig. 1, designed to contain approximately 175 cc of aqueous acid at 300°C and 2000 psi. The reaction cell was mounted in a vertical position and contained five convenience ports, four at the top and one at the bottom. Solution entered the cell from the bottom and exited from one of the top ports. At temperature, solution flowed through the cell at about 0.5 cc/min. The other three ports provided positions for a thermocouple well and the two electrodes, at Pt reference electrode and the Zircaloy-2 test electrode. Teflon cones were used to insulate these electrodes from the reaction cell and to provide a pressure seal. At 260°-300°C, it was necessary to air cool the Teflon cones to maintain the pressure seal. This was accomplished by providing two titanium tube extensions which were air cooled at a rate such that the temperature at the Teflon seal position was *ca.* 60°-90°C, and approximately independent of temperature changes in the reaction cell. For measurements at 295°C the Pt reference electrode was positioned entirely in the air-cooled portion of the titanium tube extension, giving a "reference" potential independent of temperature changes in the reaction cell. Side arm outlets on the titanium tube extensions provided for solution flow past the "stem" portion of the electrode. A drawing of the reaction cell, electrodes, and fittings is shown in Fig. 1 and 2.

Measurements were performed on several electrodes fabricated from different Zircaloy-2 stock, and with different surface preparations. The electrodes were machined in one piece to the shape shown in Fig. 2. For some of the initial measurements an air-formed film (360°C, 3 days) or an anodized film (180v, 1.0M Na_2SO_4, 0.05M H_2SO_4) was put on the electrode stem before exposure to the environment. The film was put on the stem to minimize the corrosion from this portion of the electrode which was at an unknown and decreasing temperature up to the air-cooled Teflon seal position. This pretreatment, however, resulted in some white oxide formation at the high-temperature region of the stem. Because of this white oxide formation subsequent measurements were made on electrodes without a pre-formed film on the stem.

The same specimen was used repeatedly, and before immersion into the cell, the oxide film formed in the previous experimental exposure was removed by polishing with No. 0 emery cloth. The polished electrode was rinsed thoroughly in distilled H_2O and then immersed in a H_2O-HNO_3-HF chemical polishing bath long enough (~2 min) further to remove several mils of metal. The electrode was then rinsed with triply

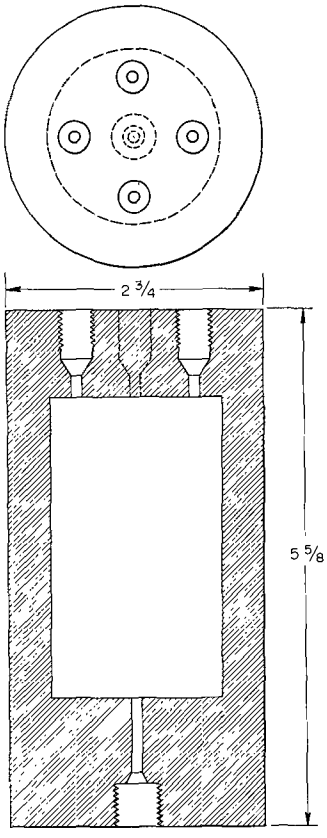

Fig. 1. Titanium reaction cell

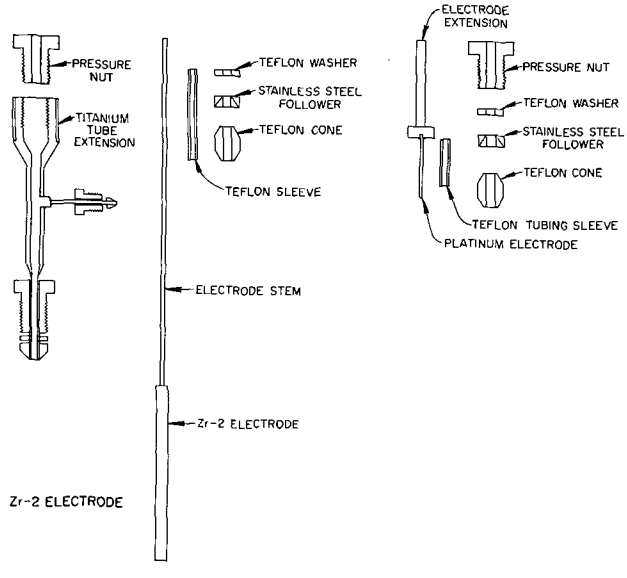

Fig. 2. Zircaloy-2 electrode and fittings

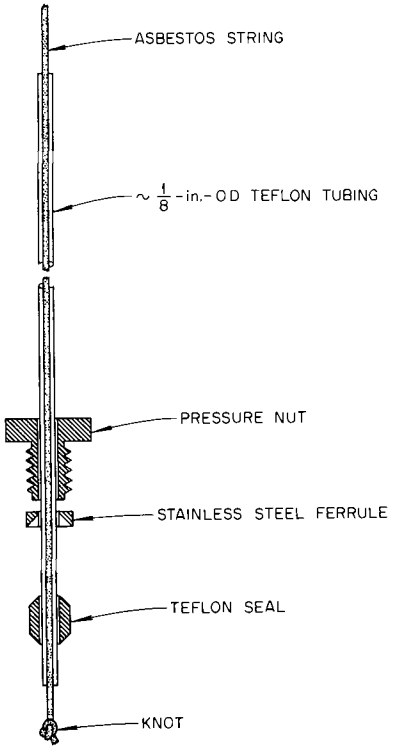

Fig. 3. Salt bridge for external reference

distilled water by rapid transfer from beaker to beaker, with a final transfer to a beaker of boiling triply distilled water for 2 min. With this surface preparation the electrode showed no areas of preferential white oxide growth. However, after long exposure at 295°C (>15,000 min) a uniform distribution of white oxide was observed to form in the high-temperature region of the electrode.

Using the apparatus and the procedures previously described (2), the solution in the reaction cell was brought to within ±5°C of operating temperature in 4-5 min and to ±1°C in 20-30 min.

Using galvanostatic and potentiostatic techniques, current-voltage measurements were made as a function of time. Rates were determined from linear polarization resistance measurements and from the extrapolation of Tafel lines to the open-circuit potential.

Voltages were measured with a L&N RIE meter, and currents were measured by recording the voltage drop across precision resistors in series in the polarizing circuit.

In some of the experiments reported here an external calomel reference electrode at 25°C and 1 atm was used. Bridging this electrode into the high temperature and pressure in the reaction cell was accomplished as shown in Fig. 3. An asbestos string was presaturated with the experimental solution and pulled tightly through Teflon "spaghetti." The asbestos string was knotted at the high-pressure and temperature end to prevent its expulsion through the Teflon spaghetti. The Teflon spaghetti and asbestos string were sealed into the cell with a Teflon cone pressure seal. The bridge entered the cell only to the air-cooled portion of the titanium tube extension since the asbestos string decomposed at high temperature.

Results

Typical current-voltage behavior, at long exposure times, for Zircaloy-2 in the oxygenated dilute sulfuric acid environment is presented in Fig. 4. Here, the measurements were made on an electrode (fabricated from plate stock) which had been exposed at 295°C and at a constant anodic potential, —0.200v *vs.* Pt/O_2 (90°C), for 28,000 min. For the last 18,000 min

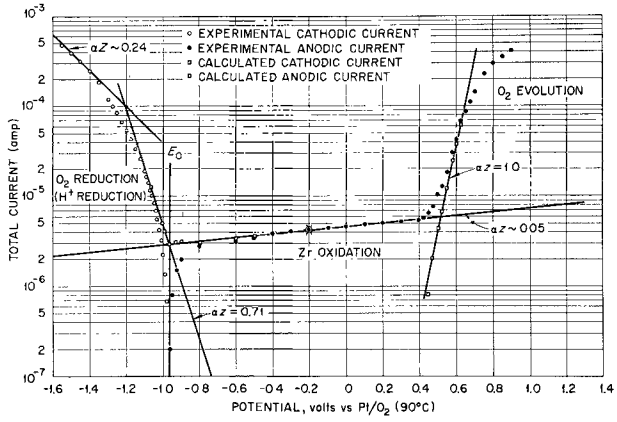

Fig. 4. Current-voltage measurements for Zircaloy-2 in O_2 saturated 0.05M H_2SO_4 295°C, after 25,000 min at —0.200v *vs.* Pt/O_2 (90°C).

at this potential the anodic rate was at a steady-state value of 4.4×10^{-6} amp or 7.3×10^{-7} amp/cm^2.

Three current-voltage regions are observed: the cathodic region from —1.600v *vs.* Pt/O_2 (90°C) to the open-circuit corrosion potential at —0.963v *vs.* Pt/O_2 (90°C), the anodic region from —0.963v to about +0.400v *vs.* Pt/O_2 (90°C), and the region of the oxygen evolution reaction at potentials above +0.400v *vs.* Pt/O_2 (90°C).

Values of the electrochemical transfer coefficient, (αZ), reported in Fig. 4, were obtained from expanded plots of the data. Other measurements, at long exposure time ($t > 2800$ min), gave values between 0.66-0.75 for the low-current cathodic ($\alpha'_c Z'_c$) and values from 0.23-0.29 for the high-current cathodic ($\alpha'_c Z'_c$). The anodic ($\alpha_a Z_a$) values ranged from 0.035-0.07 at these exposure times. The transfer coefficient for the O_2 evolution reaction ranged from 1-1.25.

Initially, the rate is changing rapidly with time, and Tafel measurements are difficult to obtain. However, from such measurements made as a function of time it was observed, for the results at 295°C, that the low-current cathodic ($\alpha'_c Z'_c$) increased from 0.25 at about 80-100 min to 0.72 at 2800 min and was then constant throughout further exposure. The value of the transfer coefficient in the high-current region of the cathodic reaction was constant at about 0.25 throughout exposure. The anodic transfer coefficient, for the oxidation of zirconium decreased from 0.17 at 100-120 min, to 0.06 at about 1000 min, and was then constant throughout further exposure.

At 268°C, ($\alpha'_c Z'_c$) increased from 0.25 to 0.60 while ($\alpha'_a Z'_a$) decreased from 0.20 to 0.10.

At 206°C, ($\alpha'_c Z'_c$) went from 0.25 to 0.45, while ($\alpha'_a Z'_a$) decreased from 0.25 to 0.10.

On the basis of these measurements, the rates at the open-circuit corrosion potential were obtained from the linear polarization resistance measurements using Eq. [1]. At 206°C, the sum of the αZ's was approximately constant at $\Sigma\alpha Z = 0.45$ throughout the experiment. At 260°C, $\Sigma\alpha Z$ was approximately 0.45 for the first 300 min, increasing linearly from 0.45 to 0.70 to 3600 min, then remaining constant at 0.70 throughout further exposure. At 295°C the sum of the αZ's was approximately constant at 0.40 for 500 min. From 500 to 2800 min a linear increase from 0.40 to 0.76 was used, and then a constant value at 0.76 throughout further exposure.

Typical rate-time data obtained from such measurements, on electrodes exposed to oxygenated 0.05M H_2SO_4 are shown in Fig. 5. Curve (a), 293°C, and curve (b), 258°C, were obtained on specimens fabricated from rod stock. Curve (c), 206°C, was obtained on a specimen fabricated from plate stock. Measurements were also made at 295°C on speci-

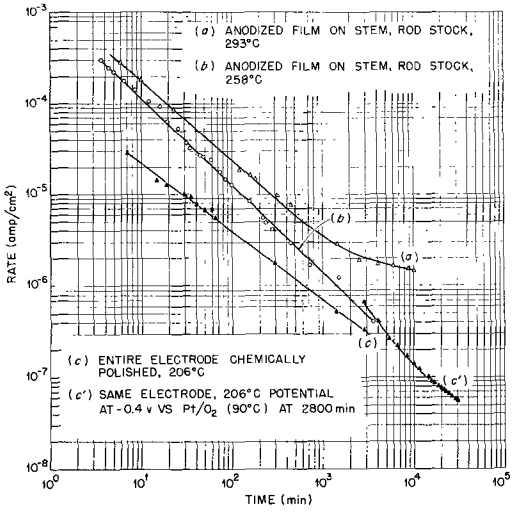

Fig. 5. Corrosion rate of chemically polished Zircaloy-2 in O_2 saturated 0.05M H_2SO_4.

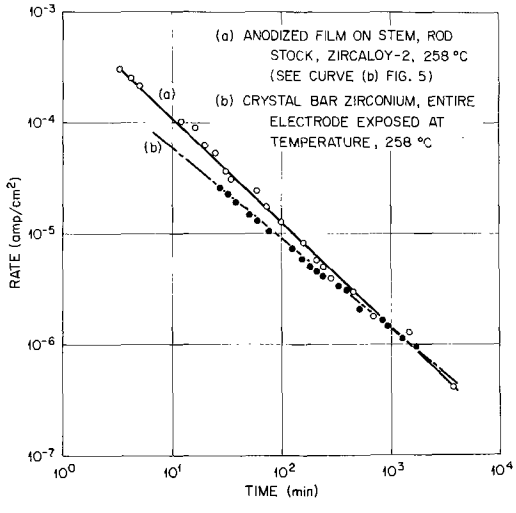

Fig. 6. Corrosion rate of zirconium and Zircaloy-2 in O_2 saturated 0.05M H_2SO_4 at 258°C.

mens fabricated from plate stock. The results are similar to those represented as curve (a).

In Fig. 6, measurements on crystal-bar zirconium at 258°C are compared with those obtained on Zircaloy-2 at 258°C [Fig. 5, curve (b)]. For the measurements on crystal-bar zirconium, the entire electrode was exposed at temperature. These results show that there is little difference between the corrosion of zirconium and Zircaloy-2, and that the "stem" portion of the Zircaloy-2 electrode does not affect the corrosion behavior.

The rate-time results shown in Fig. 5 and 6 were obtained on electrodes exposed at the open-circuit corrosion potential. The result at 293°C, represented by curve (a) in Fig. 5 shows the rate levelling off to an apparent steady-state value. At 10,280 min, the rate at the open-circuit potential, —0.900v *vs.* Pt/O_2 (60°C), is 1.3 x 10^{-6} amp/cm². The potential at this time was made anodic (700 mv) to —0.200v *vs.* Pt/O_2 (60°C), and the rate at this potential, initially ~ 3.5 x 10^{-6} amp/cm², decreased to a steady-state value of 1.1 x 10^{-6} amp/cm². Current-voltage measurements performed after anodization at this potential, Fig. 7, curve (1), showed that the rate at the open-circuit potential decreased from 1.3 x 10^{-6} to 4.8 x 10^{-7} amp/cm², and the open-circuit potential went cathodic to —0.980v *vs.* Pt/O_2 (60°C) from —0.900v *vs.* Pt/O_2 (60°C).

The potential was then made anodic an additional 500 mv to +0.300v *vs.* Pt/O_2 (60°C) and the rate

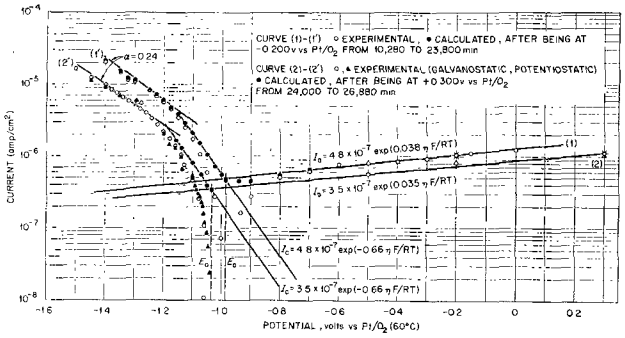

Fig. 7. Current-voltage measurements for Zircaloy-2 in O_2 saturated 0.05M H_2SO_4, 298°C for electrode (A) in Fig. 5.

again initially about 3.5 x 10^{-6} amp/cm², decreased with time to the same steady-state value, 1.1 x 10^{-6} amp/cm². Current-voltage measurements, curve (2), Fig. 7, showed the rate at the open-circuit potential decreased further to 3.5 x 10^{-7} amp/cm², and the open-circuit potential went cathodic another 55 mv to —1.035v *vs.* Pt/O_2 (60°C).

Additional evidence for a steady-state rate at this temperature was provided by the results shown in Fig. 4. Here the rate at —0.200v *vs.* Pt/O_2 (90°C) was constant at 7.3 x 10^{-7} amp/cm² for 18,000 min.

Steady-state rates were not observed for measurements at 206°and 258°C. In the experiment at 206°C, curve C, Fig. 5, the potential was made anodic at —0.400v *vs.* Pt/O_2 (90°C) at 2800 min. The anodic rate at this potential was observed to decrease continuously until the experiment was terminated at 28,000 min.

It was further observed from current-voltage measurements that both the anodic and cathodic currents were a function of film growth, Fig. 7 and 8. The anodic current decreased continually with film growth, until steady state at 295°C, while the cathodic current decreased initially for 2800 min, remained essentially constant for a further period of film growth, and then increased slightly until steady state was approached at 295°C.

From Fig. 8, the anodic reaction is apparently diffusion controlled, $\alpha Z \sim 0.0$. Other measurements made at times near to 80 min (100-120 min) have yielded Tafel-lines for the anodic reaction, with a calculated transfer coefficient about 0.17. However, at 295°C the Tafel slope increases rapidly and at 1000 min the transfer coefficient $\alpha = 0.06$, and is constant throughout further exposure.

Discussion

The reliability of the rate measurements must be demonstrated before any discussion can be attempted.

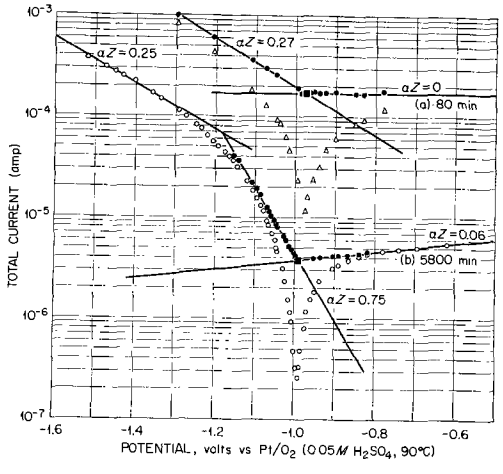

Fig. 8. Current-voltage behavior on Zircaloy-2 in O_2 saturated in 0.05M H_2SO_4 at 295°C as a function of film thickness.

Electrochemical measurements at these temperatures have not been performed by other investigators, and a comparison from the point of view of the electrochemical factors is therefore not provided.

A satisfactory basis for demonstrating the reliability of the measurements on a quantitative basis can be made by an analysis of the data according to rate laws already postulated for zirconium. The kinetic constants obtained can then be compared with those of other investigators.

Various kinetic expressions have been proposed for the corrosion of zirconium and "mechanisms" have been postulated in support of these kinetic expressions. Indeed the same data have at various times been used by different investigators to demonstrate different kinetic expressions.

The confusion demonstrates that the data are not adequate for distinguishing between cubic and logarithmic rate expression and, also, that a simple rate expression does not adequately describe the corrosion behavior over the entire period of film growth.

Here an analysis of the rate data for the initial (first 300 min) corrosion period is made according to logarithmic and cubic rate laws, and a satisfactory correlation of the data on both bases is made.

When the reported weight gain data (7) for zirconium and Zircaloy-2 are analyzed according to the empirical rate law

$$w = kt^n \qquad [3]$$

it is found that the slope of the logarithm of the weight gain *vs.* the logarithm of the time give values for the exponent n, in Eq. [3], ranging between 0.25 and 0.33. Here w is the weight gain, t is the time, and k and n are constants. A value of $n - 0.33$ represents a cubic rate law. If the derivative of Eq. [3] is taken, a relation between the rate (R) and time is obtained

$$\frac{dw}{dt} = R = nkt^{(n-1)} \qquad [4]$$

and the slope of the logarithm of the rate *vs.* the logarithm of the time give values for $(n - 1)$. With the value of n ranging between 0.25 to 0.35, the values of $(n - 1)$ range between —0.75 to —0.65. For a parabolic rate law the value of $(n - 1)$ would be —0.5.

The slopes of the log/log plots of the rate-time data reported here range between —0.67 to —1.0, with most values near —0.75. Consequently, the shape of the rate-time data, provided by the exponent $(n - 1)$ in Eq. [4], are similar to those obtained from weight gain measurements of other investigators (7). Parabolic kinetics is not observed on this basis.

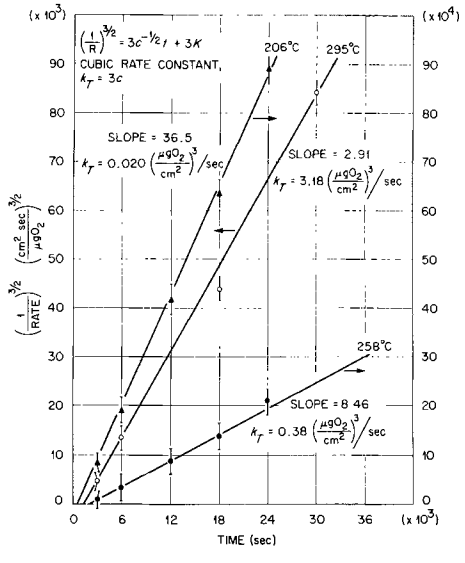

Fig. 9. Plot of $(1/rate)^{3/2}$ *vs.* time from cubic formulation of rate-time data.

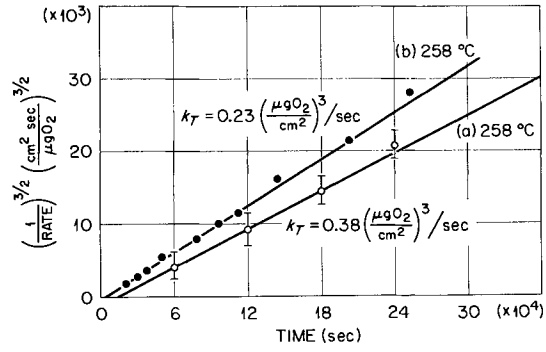

Fig. 10. $(1/rate)^{3/2}$ *vs.* time from cubic formulation of rate-time data, for zirconium and Zircaloy-2.

To obtain a quantitative comparison with other workers, the data for the first 300 min were analyzed first according to cubic kinetics, $n = 0.33$ in Eq. [3] or $(n - 1) = -0.67$ in Eq. [4].

In Fig. 9, are plotted $(1/R)^{3/2}$ *vs.* time (t) in seconds for the three temperatures here reported. The results for crystal-bar zirconium (Fig. 6) are plotted in Fig. 10. The rates, R, are expressed in weight gain units, $\mu g\ O_2/cm^2 sec$, where 1 amp/cm² = 80 $\mu g\ O_2/cm^2 sec$. It can be shown that the cubic rate constant k_T in the cubic rate law expressed as

$$w^3 = k_T t + k \qquad [5]$$

is related to the slope of the line in Fig. 9 and 10 by the relation

$$k_T = \frac{27}{(S)^2} \qquad [6]$$

where S is the slope of $(1/R)^{3/2}$ *vs.* t plot.

In Fig. 11 the calculated cubic rate constants are compared with the data of Mallet, Albrecht, and Ben-

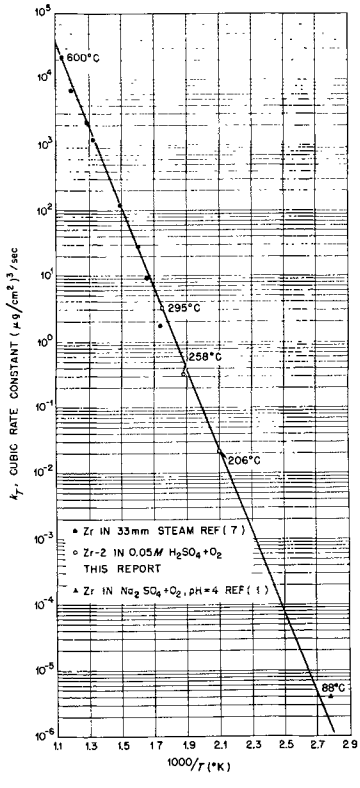

Fig. 11. Arrhenius plot of cubic rate constant for zirconium and Zircaloy-2 in steam and aqueous electrolyte.

nett (7) for crystal-bar zirconium in 33 mm steam obtained as weight gain data and with the data of Meyer (1) for crystal-bar zirconium in oxygenated Na_2SO_4, pH = 4 at 88°C, obtained using electrochemical methods. Here a correlation is provided over ten orders of magnitude in the rate constant, k_T, and over a 500°C temperature range. The calculated activation energy from these data is 29.7 kcal/mole.

This correlation provides a quantitative tie-in between the rates obtained from electrochemical measurements (88°-300°C) and those obtained as weight gain data (300°-600°C).

A further correlation with weight gain measurements is provided by the analysis of the data according to the logarithmic rate law. This correlation of the data was suggested by Jenks (8) who made an extensive analysis of the corrosion data for zirconium and Zircaloy-2 according to the logarithmic rate law.

The logarithmic law is expressed by

$$R = Ae^{-Bx} \qquad [7]$$

where R is the rate, x is the film thickness and A and B are constants. It can be shown that the logarithmic expression between the rate and film thickness (Eq. [7]) becomes the hyperbolic relation between the rate and time

$$1/R = 1/A + Bt \qquad [8]$$

where R is the rate, t is time, and A and B are the same constants appearing in Eq. [7].

In Fig. 12 are plotted the reciprocal rate *vs.* time for the data previously correlated on the cubic rate law basis. The slope of the line in Fig. 12 gives the value of B in the logarithmic rate law.

In Fig. 13 these data are compared with the data of Mallet, Albrecht, and Bennett (7) for zirconium and with the data of Cox (9) for zirconium and Zircaloy-2 in 15 psi steam at 300°C. The B values from the weight gain data are obtained from Jenks (8).

Here again quantitative agreement with weight gain data is obtained. The calculated activation energy for the parameter $1/B$ is 9.0 kcal/mole.

From similar observations, other workers (10) have postulated an initial logarithmic oxidation rate followed by a cubic rate law.

Cox (9) has postulated a double logarithmic rate expression: the initial logarithmic corrosion being con-

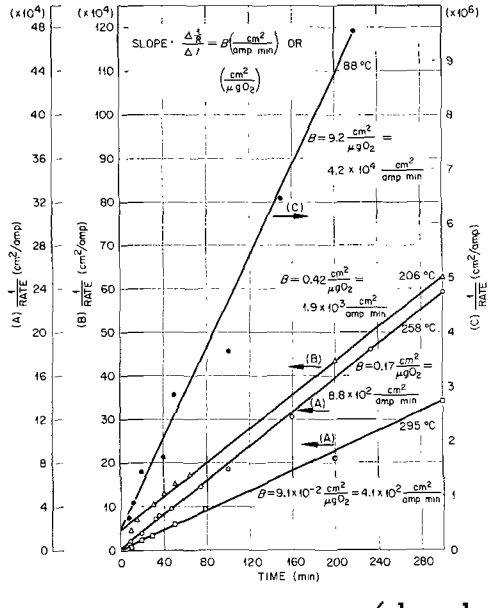

Fig. 12. Hyperbolic plot of rate-time data $\left(\frac{1}{R} = \frac{1}{A} + Bt\right)$ at several temperatures.

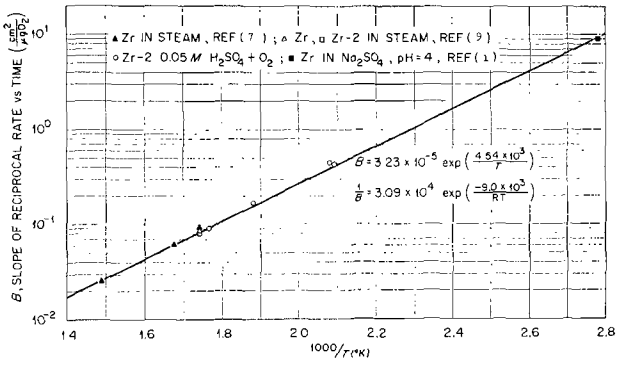

Fig. 13. Arrhenius plot of hyperbolic rate constant, B, $\left(\frac{1}{R} = \frac{1}{A} + Bt\right)$ for Zr and Zr-2 steam and aqueous electrolyte environment.

trolled by the electron flow from metal to oxide through a space-charge region in the oxide, a process suggested by Uhlig (11), with a simultaneous corrosion by easy diffusion paths, also a logarithmic rate process. This latter process is analogous to a mechanism proposed by Evans, Davies, and Agar (12).

Using electrochemical concepts, Meyer (2) has derived theoretical expressions to account for the variation in the shapes of the rate-time curves. A rate law in reasonable agreement with experiment was derived on the assumption that both ion transport (the anodic process) and the reduction of oxygen were rate determining. The assumption was made that the anodic process was controlled by a field-dependent rate-determining process within the film, analogous to the anodizing equation (13, 14), $i = A \exp(BF)$, where F is the field strength within the film and A and B are constants. The reduction current was proportional to $\exp(-\alpha_c Z_c V_f/RT)$ where V_f is the potential across the film. The resulting rate expression was roughly hyperbolic in rate-time, but did not permit an exact analytic expression.

A similar model is possible for the rate of film growth at the temperatures investigated here. The assumption that the anodic process is controlled by a field-dependent rate-determining process within the film has been more difficult to accept for the film thicknesses obtained at these temperatures. However, in studies of the anodic film growth on valve metals (Al, Zr), Charlesby (13, 14) has argued that the anodic current is an hyperbolic sine function of the field strength

$$i = A[\exp(BF) - \exp(-BF)] = 2A \sinh(BF) \qquad [9]$$

Here F is the field strength, and A and B are constants. On the basis of this equation he has shown that the particular rate law relating film thickness to time (t) will depend on the portion of the range (t) studied. In an application of this model to the thermal oxidation of zirconium, Polling and Charlesby (15) have concluded that the growth of the oxide layer is a logarithmic function of time up to temperatures of about 260°C, cubic at 300°C, and at higher temperatures tends toward a quadratic function of time. They have argued on the basis of Eq. [9] and Mott's (16) theory of oxidation, that the relation between oxide thickness and time depends on the value of the parameter Z, equal to the product of the electric field F, ion charge q, and barrier width a, divided by kT, [$Z = (qaF/kT)$]. For low temperatures when $Z > 3$ the growth should be an approximately logarithmic function of time. At higher temperatures, when Z is about equal to one, the growth should be approximately

cubic, while for lower values of Z, (at still higher temperatures) the growth is parabolic. An estimate of $(qa/kT) = 3.4 \times 10^{-6}$ cm/v was made by Charlesby (13) in a study of anodic film growth on zirconium. This value was based on $\epsilon = 20$ for the dielectric constant. In a later publication, Polling and Charlesby (17) have shown $\epsilon = 28$ on the basis of weight increase and oxygen liberated during film formation. Assuming then that the dielectric constant is about 30, (qa/kT) becomes $(30/20) \times 3.4 \times 10^{-6} = 5.1 \times 10^{-6}$ cm/v. Further, assuming qa/kT is independent of temperature, as was found for Ta (18-20), an estimate of $Z = qaV/kT\delta$, can be made. A value of $V = 2$v can be assumed for the potential drop across the film for zirconium corrosion. The film thickness δ, after 300-400 min at 250°C, is approximately 1000Å; consequently $Z \sim 5.1 \times 10^{-6} \times 2/1 \times 10^{-5} \sim 1.0$, and the film growth kinetics is cubic. In this report, the data for the first 300-400 min corrosion were analyzed according to both the logarithmic and cubic rate laws, and it is not unreasonable then to argue that the anodic process is controlled by a field-dependent rate-determining process within the film, analogous to the weak-field anodizing equation, $i = 2A \sinh Z$, where $Z = qaF/kT$. For corrosion at open circuit, however, the cathodic current as well as the anodic current can be assumed to be rate determining. The cathodic current may be represented by an expression of the form, $i_c = K_c f(C_e) \exp(-\alpha_c Z_c VF/RT)$, where K_c contains the potential independent part of the specific rate constant and $f(C_e)$ is some function of the electron concentration, C_e. The electron concentration is included in the cathodic rate expression since the cathodic current is also initially a function of film thickness and is presumably related to the trapping of electrons at anion vacancy sites. Since the Tafel slope for the anodic reaction increases rapidly with film growth, the over-all rate rapidly comes under anodic control, and to a first approximation the rate-time behavior can be interpreted primarily in terms of the anodic partial process.

Another factor which is sometimes considered in anodic film growth is the question concerning the effective force acting on an ion in the film. There is evidence (21, 22) that the effective force is the Lorentz force, $q(\epsilon + 2)F/3$, rather than the Maxwell force, qF. Here q is the charge on the ion and F is the average field, V_f/δ, where V_f is the potential across the film, and δ is the film thickness.

Meyer (23, 24) has studied reduction processes on passive zirconium in Na_2SO_4 solutions at 25° and 75°C. He has shown two Tafel regions for the oxygen reduction reaction, a low-current region with a transfer coefficient $\alpha'_c \sim 0.67$ to 0.72, $b = 1.4$ $(2.3\ RT/F)$ and a high-current region with a transfer coefficient $\alpha'_c \sim 0.25$ to 0.30, $b = 4$ $(2.3\ RT/F)$. Intermediate values of the transfer coefficient, $0.25 < \alpha'_c < 0.72$, which are observed here, are not discussed. The dual barrier model was also used to explain the unusual Tafel slopes obtained for the reduction of cupric ion on passive stainless steel in aerated 0.10M H_2SO_4 (25). Bockris and Srinivasan (26) have reported high Tafel slopes for H^+ reduction on Si and on W (contaminated with C) in 0.5M NaOH. MacDonald and Conway (27) have used Meyer's (23) theory to explain the high Tafel slopes they observed in the oxygen evolution reaction of Au. Makrides (28) employed a different mechanism to explain the high Tafel slope observed for the anodic oxidation of Fe^{+2} to Fe^{+3} in studies of the Fe^{+2}/Fe^{+3} redox kinetics on passive Ni, Fe, Fe-Cr alloys, and Ti.

A low-current region and a high-current region are also observed for the cathodic reduction of O_2 in the systems studied here, Fig. 4, 7, and 8. The high-current region is independent of film thickness, and $\alpha'_c \sim 0.23$ to 0.29, $b \sim 4(2.3\ RT/F)$. For the low-current region, however, an apparent continual increase in the transfer coefficient from $\alpha'_c = 0.26$ to 0.76 is observed. The Tafel slope decreases from $b = 4$ $(2.3\ RT/F)$ to $b = 1.3$ $(2.3\ RT/F)$.

Equations accounting for these observations can be derived and are based on a model which considers the semiconductor aspects of the film in conjunction with the dual barrier model. Here, it is assumed that with an increase in film thickness the oxide behaves more like a semiconductor, and the transfer coefficient, α_f, for electron transport through the film barrier approaches unity. The rate of charge transfer through the film barrier can be represented as

$$r_f = K_f \exp(-\alpha_f FV_f/RT) \qquad [10]$$

where r_f, if the rate, K_f, contains the potential independent part of the specific rate constant and concentrations, V_f is the potential drop across the film barrier, and α_f, the transfer coefficient, is a function of film thickness.

For the electrochemical charge transfer reaction at the oxide/solution interface, the postulated mechanism (23) is

$$O_2 + e = O_2^- \quad \text{slow} \quad 1$$

$$O_2^- + H^+ = HO_2 \quad \text{fast} \quad 2$$

$$HO_2 + e = HO_2^- \quad \text{fast} \quad 3$$

$$HO_2^- + H^+ = H_2O_2 \quad \text{fast} \quad 4$$

with step 1 the slow step. With step 4 the slow step, the rate equation is

$$r_s = Fk_4 \cdot \frac{k_3}{k_{-3}} \cdot \frac{k_2}{k_{-2}} \cdot \frac{k_1}{k_{-1}} [O_2][H^+][1-(\theta_1+\theta)] \exp\frac{-4\alpha_s FV_s}{RT} \qquad [11]$$

where r_s is the rate of the electrochemical charge transfer reaction, the k's, are the potential independent part of the specific rate constants, θ_1 and θ_2 are coverage terms for HO_2 and HO_2^-, V_s is the potential drop across the oxide/solution barrier, and α_s is the transfer coefficient. For a symmetrical barrier, $\alpha_s = 1/2$ and the apparent transfer coefficient becomes $4\alpha_s = 2$. With step 1 as the slow step the transfer coefficient is $\alpha_s = 1/2$.

In the high-current region, step 1 is rate determining. In the low-current region step 4 is rate determining. With values of the transfer coefficient (α_s, α_f) for the separate reactions, the dual barrier model predicts the measured transfer coefficient $\alpha_t = \frac{\alpha_s\alpha_f}{\alpha_s+\alpha_f}$, in terms of the measured potential $V_t = V_s + V_f$. Consequently, the measured transfer coefficient α_t increases in the low-current region from $\alpha_t = \frac{2 \cdot 1/2}{2+1/2} = 0.4$ for "thin" films, $(\alpha_f = 1/2)$, to a value $\alpha_t = \frac{2 \cdot 1}{2+1} = 0.67$ for "thick" films, $(\alpha_f = 1)$. In the high-current region, with $\alpha_s = 1/2$, and α_f again increasing with film thickness from 1/2 to 1, $\alpha_t = \frac{1/2 \cdot 1/2}{1/2+1/2} = 0.25$ for thin films and increases to $\alpha_t = \frac{1/2 \cdot 1}{1/2+1} = 0.33$ for thick films.

The oxygen evolution reaction was also studied, Fig. 4, and Tafel slopes ranging from $b = 0.8$ $(2.3\ RT/F)$ to $b = 1.0$ $(2.3\ RT/F)$ were observed. The value 4/5 $(2.3\ RT/F)$ was observed by MacDonald and Conway (27) for the O_2 evolution reaction on Au. Also at the higher current densities, a diffusion current plateau similar to the reaction on Au was observed. The measurements have not been extended to the higher current densities where the dual barrier model predicts the value $b = 4$ $(2.3\ RT/F)$ observed by MacDonald and Conway.

The observation of a steady-state rate independent of potential at 290°-300°C may be compared to observations made for the anodic film growth on iron in 1*N* H_2SO_4 at 25°C (29), and to the dissolution of zirconium in aqueous HF solutions at 25°C (30). These observations were explained by assuming a continuous formation and dissolution of film on the surface of the metal. The conventional anodizing equation is postulated for the film formation reaction in both the iron and zirconium experiments. The dissolution reaction for zirconium in the aqueous HF environment is controlled by the rate of mass transfer of undissociated HF to the surface of the film. For the dissolution reaction of iron, a purely chemical process not involving the transfer of charge across the interface was first postulated (29, 31). Vetter (32), however, postulated that the constancy of the corrosion current with potential, and its variation with *p*H could be explained if the dissolution involved the transfer of ferric ions from the oxide into solution under the action of a field at the oxide/solution interface. The field is established by the reaction, O^{2-} (oxide) + $2H^+ = H_2O$ which maintains the potential difference across the oxide interface at an equilibrium value for each *p*H.

Equilibrium between the film growth reaction and the film dissolution reaction is also postulated for zirconium at 290°-300°C. The film growth reaction involves the field-dependent ionic transport of oxygen ions (presumably via an anion vacancy mechanism) through the film. The dissolution reaction however has not been studied. Zirconium is found in solution in quantity sufficient to account for the steady-state rate. However, other mechanisms are not excluded. The appearance on nonprotective white oxide or the dissolution of oxide in the zirconium metal phase can also lead to a steady-state rate. The rate of the latter process (33) is great enough at 300°C to account for the observed steady-state rate, 5×10^{-7} to 1×10^{-6} amp/cm^2.

Acknowledgment

The authors greatly appreciate the kind encouragement and helpful discussions with Drs. R. E. Meyer, F. A. Posey, and G. H. Jenks.

Manuscript received Oct. 29, 1964. This paper was presented in part at the New York Meeting, Sept. 29-Oct. 3, 1963.

Any discussion of this paper will appear in a Discussion Section to be published in the December 1965 JOURNAL.

REFERENCES

1. R. E. Meyer, *This Journal*, **106**, 930 (1959).
2. A. L. Bacarella, *ibid.*, **108**, 331 (1961).
3. M. Stern and A. L. Geary, *ibid.*, **104**, 56 (1957).
4. F. A. Posey, *ibid.*, **106**, 571 (1959).
5. M. Stern and E. D. Weisert, Proc. Am. Soc. Testing Materials, **59**, 1280 (1959).
6. M. Stern, *This Journal*, **106**, 376 (1959).
7. M. W. Mallet, W. M. Albrecht, and R. E. Bennett, *ibid.*, **104**, 349 (1957).
8. G. H. Jenks and A. L. Bacarella, Oak Ridge National Laboratory, ORNL-3417, 72 (1963).
9. B. Cox, *This Journal*, **108**, 24 (1961).
10. I. I. Karobkhaw, D. V. Ignatov, A. I. Yevstyukhim, and V. S. Yemelyanov, Second U.N. Int. Conf. on Peaceful Uses of Atomic Energy, A/Conf. 15/P/2054, August 1958.
11. H. H. Uhlig, *Acta Met.*, **4**, 541 (1956).
12. U. R. Evans, *Trans. Electrochem. Soc.*, **91**, 547 (1947).
13. A. Charlesby, *Acta Met.*, **1**, 340 (1953).
14. A. Charlesby, *Proc. Phys. Soc. London*, **B66**, 317 (1953).
15. J. J. Polling and A. Charlesby, *Acta Met.*, **2**, 667 (1954).
16. N. F. Mott, *Trans. Faraday Soc.*, **43**, 429 (1947).
17. J. J. Polling and A. Charlesby, *Proc. Phys. Soc., London*, **B67**, 201 (1954).
18. D. A. Vermilyea, *Acta Met.*, **1**, 282 (1953).
19. L. Young, *Trans. Faraday Soc.*, **50**, 153 (1954).
20. J. F. Dewald, *This Journal*, **102**, 1 (1955).
21. R. J. Maurer, *J. Chem. Phys.*, **9**, 579 (1941).
22. J. R. Tessman, A. H. Kahn, and W. Shockley, *Phys. Rev.*, **92**, 890 (1953).
23. R. E. Meyer, *This Journal*, **110**, 167 (1963).
24. R. E. Meyer, *ibid.*, **107**, 847 (1960).
25. F. A. Posey, G. H. Cartledge, and R. P. Yaffe, *ibid.*, **106**, 582 (1959).
26. J. O. M. Bockris and S. Srinivasan, *Electrochim. Acta*, **9**, 31 (1964).
27. J. J. MacDonald and B. E. Conway, *Proc. Roy. Soc.*, **A269**, 419 (1962).
28. A. C. Makrides, *This Journal*, **111**, 392, 400 (1964).
29. U. F. Franck and K. G. Weil, *Z. Elektrochem.*, **568**, 14 (1952).
30. R. E. Meyer, *This Journal*, **111**, 147 (1964).
31. L. Young, "Anodic Oxide Films," pp. 234 *et seq.*, Academic Press, London and New York (1961).
32. K. J. Vetter, *Z. Phys. Chem.*, **202**, 1 (1953).
33. M. Davis, K. R. Montgomery, and J. Standring, *J. Inst. Met.*, **89**, 172 (1961).

The Reaction of Zirconium with Carbon Dioxide and Carbon Monoxide at 850°C

R. J. Hussey[1] and W. W. Smeltzer

Department of Metallurgy and Metallurgical Engineering, McMaster University, Hamilton, Ontario, Canada

ABSTRACT

An investigation has been made of the kinetics, the chemistry, and the solid-state processes for the reaction of zirconium with carbon dioxide and carbon monoxide at 850°C. In carbon dioxide at 10 cm Hg pressure, the kinetic curve showed an initial decreasing rate, an intermediate increasing rate, and a final decreasing rate. The ratio of carbon to oxygen uptake by zirconium in carbon dioxide was dependent on time and varied from 0.19 to 0.04 over a period 1-48 hr. Carbon produced in the early stages of reaction was incorporated into the oxide and led to formation of a needle-like phase of a ternary lower oxide or a solid solution at the metal/oxide interface. Due to a high ratio of carbon to oxygen uptake in carbon monoxide, this phase developed to a distinct intermediate layer between the oxide scale and metal substrate. The kinetic curves in this gas exhibited a continuously decreasing oxidation rate; eventually breakaway occurred, possibly due to the presence of the secondary phase at the metal-oxide interface. In the range of parabolic oxidation for both carbon dioxide and carbon monoxide, the rates were similar in magnitude to that found in oxygen. Comparison of oxygen gradients demonstrated that the extent of oxygen solution in the metal was the same for oxidation in these gases.

There has been little published work on the reaction of zirconium with carbon dioxide at elevated temperatures (1-6). Some preliminary studies were made by Hayes, Roberson, and Robertson (1) at temperatures in the range 600°-1000°C. They showed the presence of both zirconium carbide and zirconium dioxide in the reaction product. A more detailed investigation was carried out by O'Driscoll, Tyzack, and Raine (2) on the oxidation of zirconium and zirconium alloys at temperatures in the range 400°-800°C. Long-term kinetic data showed that initially the rate relationship was between parabolic and cubic and subsequently it was linear, followed by breakaway. The influence of change of pressure from 1 to 8 atm on the reaction rate was shown to be slight.

More recently Debuigne and Lehr (3) have shown that zirconium oxidizes in carbon dioxide according to a parabolic rate equation up to 90 hr at 750°C. Subsequent work by Guerlet and Lehr (4) at temperatures in the range 600°-850°C indicates that the kinetics up to 25 hr obey a rate relationship intermediate between cubic and parabolic. The main reaction was believed to be dissociation of the carbon dioxide into carbon monoxide and oxygen at the gas-oxide interface and the formation of an adherent oxide film of monoclinic zirconia and concurrent solution of oxygen in the metal. The reaction leading to the formation of carbon was believed to contribute to less than 1% of the total weight gain of an oxidized specimen. Maekawa (5) also found no evidence for carbon uptake at temperatures in the range 650°-850°C.

Contrary to these findings from the latter two investigations there is evidence which demonstrates that carbon composes about 2% of the total weight gain of a specimen for oxidation in carbon dioxide in the temperature range 550°-750°C (6). Furthermore, the kinetic results indicate that there is an initial period of relatively small weight gain and decreasing rate followed by a period of rapidly increasing rate, which occurs after only 2 hr at 750°C and about 6 hr at 550°C.

In the light of the contradictory evidence in the literature, a systematic investigation has been made of the kinetics, the chemistry, and the solid-state processes occurring for the reaction of zirconium with carbon dioxide at 850°C. Since carbon monoxide is a reaction product, experiments were also carried out on the oxidation of zirconium in this gas. The results obtained are to be compared with the corresponding results for oxidation in oxygen in order that the influence of carbon, if present in the reaction product, on the various relative phenomena may be determined.

Experimental

Both the vacuum microbalance (7) and a spiral spring were used to obtain kinetic data. Carbon consumption during oxidation was determined by means of an analysis apparatus attached to the microbalance case. The analysis technique was based on the use of carbon-14 as a tracer element. A study of the solid-state processes was facilitated by using metallographic techniques, x-ray diffraction analyses, and autoradiographic techniques.

The zirconium was of the same batch as that used previously (7). Specimens were cut from both 1 and 2 mm sheet to sizes of 1.5 x 1 and 1 x 0.75 cm. Carbon dioxide, 99.99% pure, was dried by passage over phosphorus pentoxide. The carbon monoxide had a minimum purity of 99.6%; it was further purified by passage over ascarite and Linde 5A molecular sieves and finally through a trap immersed in liquid air. Radioactive carbon dioxide was prepared as described previously (8) and was dried by passage over magnesium perchlorate and phosphorus pentoxide. It was solidified at liquid air temperature and outgassed at 10^{-6} mm Hg for 6 hr prior to storage in sealed Pyrex bulbs. The activity of the gas was 0.25 μc/ml at N.T.P.

Prior to oxidation all specimens were outgassed in a vacuum of 10^{-6} mm Hg for 12 hr at room temperature and then heated in vacuum for 75 min at 850°C. Kinetic results were obtained using a microbalance of sensitivity 4.69 μg/division for short term experiments and a Ni-Span C spiral spring of sensitivity 36.0 μg/division for long term experiments. Additional weight gain data were obtained from individual specimens, which were oxidized for successively increasing times in a quartz reaction tube.

The analysis apparatus, attached to the microbalance case, enabled the gas to be sampled from the system during a kinetic experiment without interruption of oxidation. The gas was analyzed for carbon monoxide

[1] Present address: School of Metallurgy, University of New South Wales, Kensington, Australia.

($C^{14}O$) after removing carbon dioxide ($C^{14}O_2$) by freezing in liquid air. The residual gas pressure was determined by means of an end-window Geiger-Muller tube (20th Century Electronics Type EW3Hb), where the number of pulses received per second was proportional to the pressure of the gas at constant temperature (the half-life of carbon-14 is 5600 yr). The gas was returned to the balance case after analysis, which required a period of 2 hr. From a knowledge of the balance case volume and the volume of the sampling apparatus the partial pressure of the carbon monoxide was evaluated. Using this value and the total weight gain of the specimen at the moment the gas was sampled, the weight of carbon consumed by the specimen was calculated. The pressure in the balance case was not altered by more than 5% during a sampling cycle.

After oxidation the specimens were prepared for metallographic examination by abrading through 240 to 600 mesh grit SiC wet papers, polishing for 3-5 min on a 1μ diamond lap and finally for several hours on a Syntron vibratory polisher using a water slurry of 0.3μ γ-Al_2O_3 on a Selvyt cloth. Hardness profiles in the metal substrate beneath the oxide layer were determined with a Vickers microhardness indenter using the standard 124° diamond under a 20g load.

Autoradiographs, showing the presence and distribution of carbon on specimens oxidized in carbon dioxide ($C^{14}O_2$), were obtained by placing strips of Ilford Industrial G x-ray film in contact with such specimens and exposing them for periods of 1-3 weeks.

Structures of the oxidation products formed on the specimens were determined by means of x-ray reflection diffraction. Oxidized specimens were mounted on microscope slides and fitted to the stage of a Norelco diffractometer and, using CuKα radiation with a nickel filter, diffraction patterns were obtained over the range $2\theta = 30°$-$70°$.

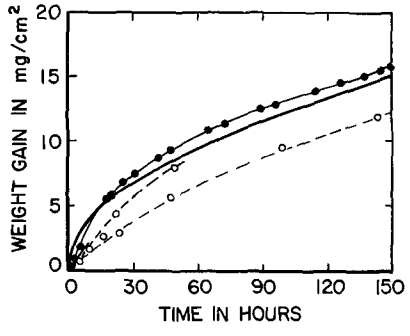

Fig. 1. Oxidation of zirconium at 850°C in carbon dioxide at 10 cm Hg pressure (•, spiral spring; ○, individually oxidized specimens). The present results are compared with the corresponding kinetic curve (continuous line) for oxidation of zirconium at 850°C in oxygen at 40 cm Hg pressure.

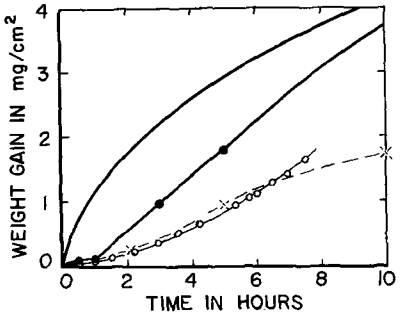

Fig. 2. Oxidation of zirconium at 850°C in carbon dioxide at 10 cm Hg pressure (•, spiral spring; ○, microbalance; ×, individually oxidized specimens) showing initial kinetics. The present results are compared with the corresponding curve (continuous line) for oxidation of zirconium at 850°C in oxygen at 40 cm Hg pressure.

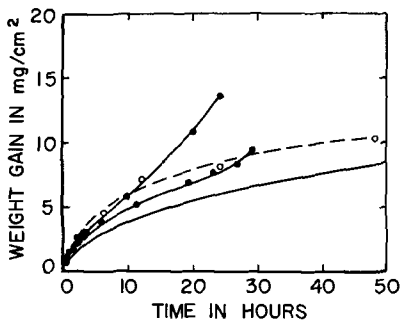

Fig. 3. Oxidation of zirconium at 850°C in carbon monoxide at 10 cm Hg pressure (•, spiral spring; ○, individually oxidized specimens with rounded edges). The present results are compared with the corresponding kinetic curve (continuous line) for oxidation of zirconium at 850°C in oxygen at 40 cm Hg pressure.

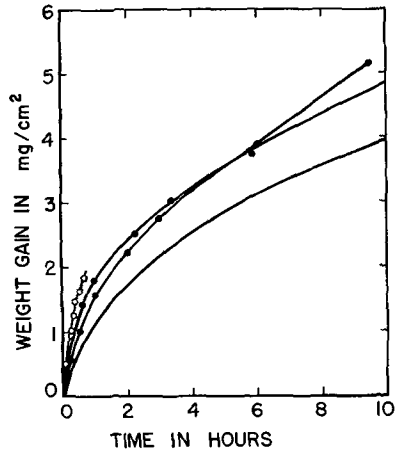

Fig. 4. Oxidation of zirconium at 850°C in carbon monoxide at 10 cm Hg pressure (•, spiral spring; ○, microbalance) showing initial kinetics. The present results are compared with the corresponding curve (continuous line) for oxidation of zirconium at 850°C in oxygen at 40 cm Hg pressure.

Results

Oxidation kinetics—carbon dioxide and carbon monoxide.—Kinetic curves for oxidation in carbon dioxide at a pressure of 10 cm Hg are plotted as weight gain in mg/cm² *vs.* time in hours (Fig. 1). More detailed curves showing the early stages of reaction up to 10 hr are shown in Fig. 2. The kinetic curves given here and subsequently comprise all the data obtained. The curves may be divided into three sections. Initially there is a period lasting about 30 min during which the oxidation rate decreases. Subsequently there is a region of increasing rate until after about 10 hr the stage is again reached where the rate decreases with time up to 149 hr. Comparison of these curves with a corresponding kinetic curve for oxidation in oxygen (9) (Fig. 1) shows that initially the rate is much slower in carbon dioxide. Eventually, however, a stage is reached when the rates at a given time in both carbon dioxide and oxygen become approximately the same.

Kinetic data obtained for oxidation in carbon monoxide at 10 cm Hg pressure are plotted as weight gain in mg/cm² *vs.* time in hours (Fig. 3). The initial behavior is shown in detail in Fig. 4. At the outset the rate is more rapid than that observed for oxidation in carbon dioxide (Fig. 2). Moreover, the rate decreases until at a certain time, which varies from specimen to specimen, the rate begins to increase. Comparison again with the corresponding rate curve for oxidation in oxygen (Fig. 3) shows that the oxidation rates at a given time in these two gases are approximately of the same magnitude prior to the onset of breakaway.

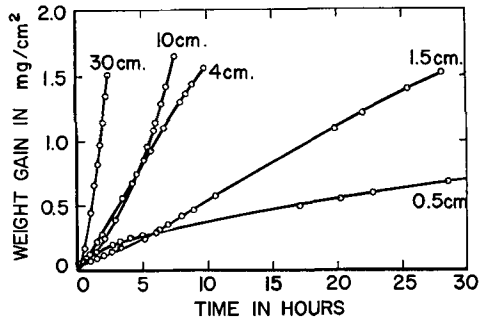

Fig. 5. Oxidation of zirconium at 850°C in carbon dioxide at various pressures.

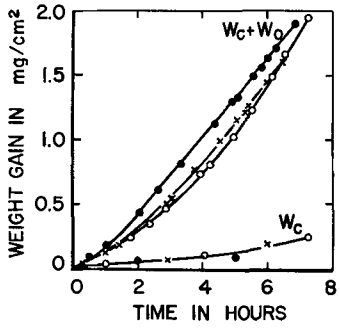

Fig. 6. Oxidation of zirconium at 850°C in carbon dioxide at 10 cm Hg pressure; $w_c + w_o$ represents total weight gain, and w_c represents weight gain due to carbon.

Influence of pressure on the oxidation kinetics.—In order to determine the effect of pressure on the oxidation rate in carbon dioxide a series of specimens were oxidized at pressures from 0.5 to 30 cm Hg. The kinetic results obtained are summarized in Fig. 5. The weight gain at a given time decreased markedly with decreasing pressure. Furthermore, there is a significant difference in rates over this pressure range during the stage of increasing rate of oxidation.

Kinetics of carbon consumption.—The rate of carbon consumption was determined by oxidizing three specimens in radioactive carbon dioxide ($C^{14}O_2$) on the microbalance at 10 cm Hg pressure. The gas was sampled periodically, and values for the amount of carbon consumed by the specimen or lost from the gas phase were obtained (Table I). These results are compared with the kinetics curves in Fig. 6. The shape of the curve for carbon uptake by the specimens was similar to that for the kinetic curves, which represent the total uptake due to carbon and oxygen consumption.

To determine whether the rate of carbon consumption decreased at longer times, an additional experiment was performed in which the amount of carbon monoxide in the gas phase was determined after a specimen had been oxidized in carbon dioxide ($C^{14}O_2$) for 48 hr. The value for the weight of carbon removed

Table I. Amount of carbon consumed by zirconium oxidized in carbon dioxide at 850°C

Pressure, cm Hg	Time, hr	Total weight gain, $(w_c + w_o)$, $\mu g/cm^2$	Weight gain of carbon (w_c), $\mu g/cm^2$	$w_c/w_c + w_o$
10	1	124	23	0.19
	2	417	66	0.16
	3	555	57	0.10
	4	802	110	0.14
	5	1286	90	0.07
	6	1438	182	0.13
	7¼	1955	246	0.13
	48	8114	344	0.04
1.5	1	120	3	0.02
	4¾	409	66	0.16
	9¾	806	111	0.14
	25½	1694	133	0.08

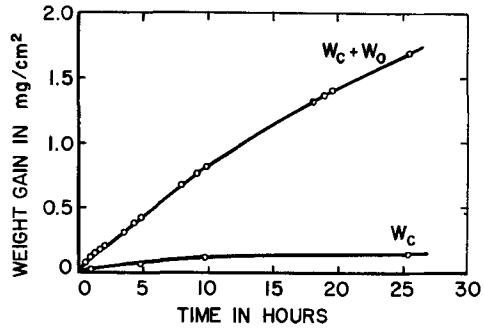

Fig. 7. Oxidation of zirconium at 850°C in carbon dioxide at 1.5 cm Hg pressure; $w_c + w_o$ represents total weight gain, and w_c represents weight gain due to carbon.

from the gas phase (Table I) shows that indeed a stage of decreasing carbon consumption is reached at this time, corresponding to that observed for the total weight gain curves. If the data are expressed as the ratio of the weight gain due to carbon (w_c) to the total weight gain ($w_c + w_o$), where w_o is the weight increase due to oxygen, the percentage of carbon formed decreased with time from 19% at 1 hr to 4% at 48 hr (Table I). The error in the values of w_c was ± 1.5%

Since there was a pronounced pressure effect on the kinetics the effect of pressure change on the rate of carbon uptake was determined. A sample was oxidized in carbon dioxide ($C^{14}O_2$) at a pressure of 1.5 cm Hg, and the gas was sampled at times from 1 to 25½ hr. The weight of carbon and the total weight gain were determined (Table I) and the corresponding curves are shown in Fig. 7. As found for the results at the higher pressure the kinetic curve in both cases is of the same form. Further apart from the initial value the ratio $(w_c/w_c + w_o)$ decreases with increasing time, and is of the same order as those values found at 10 cm Hg pressure.

Chemistry of the reaction.—In order to establish whether reaction occurred between carbon dioxide and carbon during oxidation, two experiments were devised. In the first a specimen was oxidized in 10 cm Hg pressure carbon dioxide ($C^{14}O_2$) for 12 hr in order to deposit radioactive carbon in the specimen. The radioactive gas was then pumped off and replaced by inactive carbon dioxide to the same pressure as before and oxidation allowed to proceed for a further 6 hr. If reaction took place as

$$C^{14} + C^{12}O_2 = C^{12}O + C^{14}O$$

then the carbon monoxide would be radioactive. No activity was found in the residual gas, and hence the reaction in the forward direction was negligible.

It was possible to demonstrate, however, by the second experiment that the dissociation of carbon monoxide into carbon dioxide and carbon does occur. The residual gas after oxidation of zirconium in carbon monoxide at 10 cm Hg pressure for 48 hr was sampled and analyzed for carbon dioxide. There was about 12% carbon dioxide in the gas phase. Consequently, considerable dissociation of carbon monoxide occurred during oxidation of zirconium since the formation of carbon dioxide and carbon from disproportionation of carbon monoxide at 850°C is only 0.4%.

Metallographic examination.—Several samples were oxidized for successively increasing lengths of time in carbon dioxide and in carbon monoxide at 10 cm Hg pressure to allow metallographic examination to be made at the various stages of oxidation. A mean curve is drawn through the weight gains of the various samples, as shown in Fig. 1 and 3.

During the initial stage of oxidation in carbon dioxide the specimens were covered with oxide films exhibiting interference colors. The total maximum weight gain at this stage was generally of the order of 150

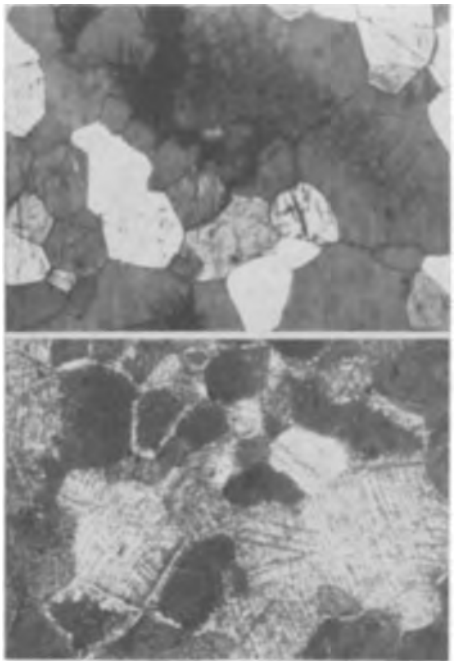

Fig. 8. Photomicrograph showing needles of an additional phase after (a) (top) 10 hr; (b) (bottom) 48 hr. Magnification approximately 160X.

$\mu g/cm^2$. Since this weight gain represents both oxide formation and oxygen solution in the metal and since at this temperature the relative amount of oxygen present as solution in the metal is likely to be large (9), the weight gain of oxygen due to oxide film formation would be much less than 150 $\mu g/cm^2$ and would correspond to a film thickness consistent with the observed interference colors. Corresponding to that portion of the curve which showed an increasing rate, areas of dark gray oxide began to appear at the edges of a specimen. As time proceeded, gray oxide also appeared on selected grains of the flat surface, and it gradually spread to cover the entire specimen.

Microscopic examination of the surfaces of specimens exposed for periods up to 2 hr in carbon dioxide showed that certain metal grains oxidized preferentially. During the stage of increasing rate of oxidation small needles of a new phase were observed on those grains covered with the thicker oxide layer. These needles appeared to nucleate at the metal grain boundaries and occasionally within the grains. Much of this phase grew across grains in directions mutually at about 60° to one another (Fig. 8a) and eventually spread across the entire grain. The number of grains on which the needles were found increased with time. Concurrently the oxide film associated with such grains thickened rapidly until only the outline of the needles became visible (Fig. 8b). Apparently the new phase nucleated and grew initially on those grains which have a preferred orientation, as indicated by a common growth direction. Adjacent grains only showed needle growth and concurrent gray oxide formation at a later stage. The needles were not of sufficient thickness to be detected on microscopic examination of sectioned specimens. Examination of those specimens oxidized over the range of pressures 0.5-30 cm Hg for periods to 25 hr revealed that the amount of new phase formed decreased as the pressure decreased until, at 1.5 and 0.5 cm Hg, needles were not detected.

In the early stages of oxidation in carbon monoxide, the specimens were covered with a gray-black glossy scale. The occurrence of cracked oxide at the specimen edges became evident after 12 hr. After oxidation for 24 and 48 hr, the oxide on the surface showed blisters of either gray or white oxide. The growth of large amounts of oxide at edges was delayed by rounding the specimen edges. As illustrated in Fig. 3, the specimen, whose edges had been rounded, showed breakaway at a later stage. Thus breakaway for the small rectangular specimens was associated with gross oxidation at edges and contributed a relatively large amount to the over-all weight gain. Larger specimens, such as those oxidized individually for 24 and 48 hr (Fig. 3), did not show a breakaway rate to any marked extent, since oxidation at edges even after 48 hr contributed only a relatively small amount to the over-all weight gain. Formation of the new phase consisting of needles was only observed during the first few minutes of oxidation, but detailed examination of their growth was obscured by the rapid growth of the scale.

Sections of specimens oxidized in carbon dioxide and in carbon monoxide after long times showed the oxide to be gray, adherent, and columnar in structure when viewed under polarized light. Scales formed in carbon dioxide were uneven due to different thicknesses of oxide on individual metal grains. The oxide layer formed on those samples oxidized in carbon monoxide, however, were generally fairly uniform. Although specimens which had been oxidized in carbon monoxide for a few hours or more did not show evidence of needles, an additional phase was found at the metal-oxide interface (Fig. 9a). This phase was more heavily concentrated at the specimen edges, where there was considerable oxide cracking (Fig. 9b). It was pale yellow in color and had a hardness of the order of 1400 DPN, which was considerably harder than the metal beneath it (maximum hardness about 1100 DPN).

Oxidized specimens showed a region of metal beneath the oxide layer, which was much harder than the pure metal. Three microhardness traverses were made on sectioned specimens, which had been oxidized for periods of 24 and 48 hr in carbon dioxide and on sectioned specimens, which had been oxidized in carbon monoxide for periods of 6 and 48 hr. As illustrated in Fig. 10, the hardness gradients, expressed as DPN (20g load) *vs.* distance from the metal-oxide interface in microns,

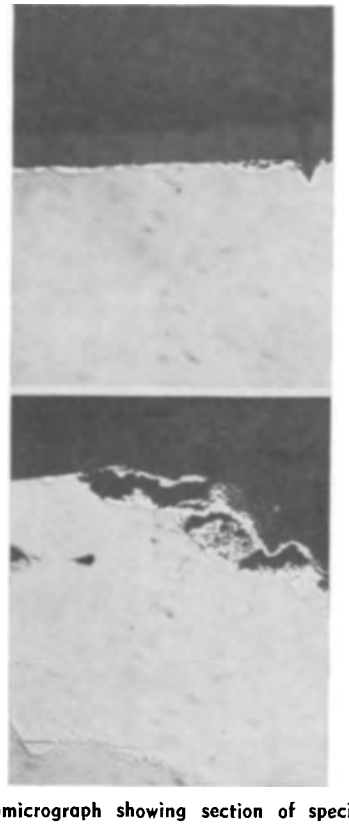

Fig. 9. Photomicrograph showing section of specimen oxidized in carbon monoxide (a) (top) surface of specimen; (b) (bottom) edge of specimen.

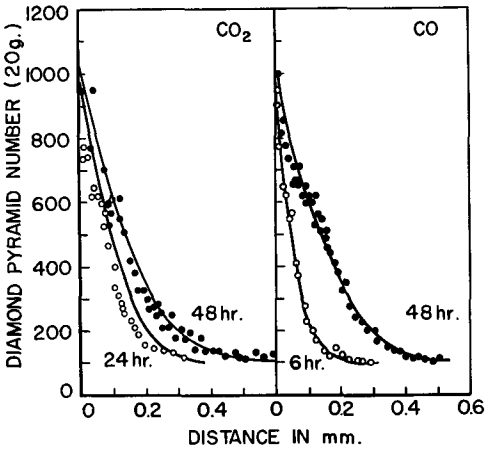

Fig. 10. Hardness gradients on specimens oxidized at 850°C at 10 cm Hg pressure. Points represent experimental determinations, and full lines represent calculated gradients.

extended to a considerable depth into the metal and the penetration distance (10) increased markedly with time.

Autoradiography.—Autoradiographs obtained from the surfaces of specimens, which had been oxidized in carbon dioxide for times from 1 to 144 hr, confirmed that there was consumption of carbon. The carbon distribution varied quite markedly as shown by the light (higher carbon concentration) and dark (lower carbon concentration) areas (Fig. 11). The carbon distribution became more uniform with long exposures, but even after 144 hr there was still a variation in concentration. Unfortunately, it was not possible to detect from the autoradiographs whether the needles had a relatively higher carbon content than the metal grains on which they were growing. Nevertheless, it was found that the areas of gray oxide were associated with a relatively higher carbon content.

Autoradiographs taken of cross sections of two specimens oxidized for 48 and 144 hr showed that the carbon consumed was confined almost entirely to the oxide and very little, if any, was present in the metal.

X-ray analyses.—Reflection x-ray diffraction patterns were obtained from two specimens, one of which had been oxidized in carbon dioxide for 22 hr at 10 cm Hg pressure, and the other which had been oxidized in carbon monoxide for 12 hr also at this pressure. Monoclinic zirconia and α-zirconium only were found to be present. There was no evidence for zirconium carbide.

Since, however, film thicknesses were such that the x-ray beam was not able to penetrate sufficiently deeply into the metal substrate, the oxide was polished back until some of the underlying metal was exposed. For the specimen oxidized in carbon dioxide the relative intensities of all the lines increased and, in particular, the metal lines. Again there was no evidence for the presence of the carbide phase. In the case of the specimen oxidized in carbon monoxide, however, besides an over-all enhancement of the diffraction lines, three extra lines were found, which were not identifiable with the metal, the oxide, or the carbide. These lines appeared at diffraction angles of $2\theta = 30°\ 50'$, $39°\ 50'$ and $48°\ 10'$. One of these lines corresponded to a very weak line ($2\theta = 48°\ 10'$) observed in the pattern for this specimen prior to polishing back the oxide. Since a new phase was observed at the metal-oxide interface after several hours (Fig. 9) it seems likely that the extra diffraction lines were associated with this phase.

In order to determine whether zirconium dioxide can take up carbon, zirconia powder was outgassed at room temperature for 12 hr and at 850°C for 75 min in a vacuum of 10^{-6} mm Hg and then heated in carbon monoxide. There was an initial rapid increase in weight, which decreased gradually until, after 120 hr, the weight gain became zero. Analysis of the gas after oxidation revealed that it contained 6% carbon dioxide. The relative increase in weight of the specimen was 0.018%. From these considerations the formula assigned to the solid solution thus formed was $ZrO_{1.993}C_{0.018}$. The zirconia powder was found to have turned gray, possibly due to either carburization by the carbon monoxide and/or nonstoichiometry by loss of oxygen. An x-ray diffraction pattern of this substance was identical to the corresponding pattern for zirconia.

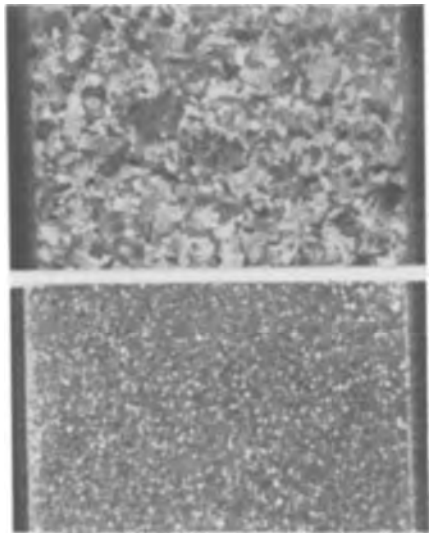

Fig. 11. Autoradiographs of surface of specimens oxidized in carbon dioxide for (a) (top) 2 hr; (b) (bottom) 48 hr. Magnification approximately 160X.

Discussion

Thermodynamics.—When zirconium reacts with carbon dioxide and with carbon monoxide at 850°C several reactions are thermodynamically feasible and may occur as represented by the equations given in Table II. These reactions, however, do not account for the oxidation mechanism, because the free or combined carbon reacts with the oxide scale or the underlying zirconium-oxygen solid solution to form compounds or solid solutions for which no thermodynamic or structural data are available. For example, it has been shown that carbon combines with zirconium dioxide and that a new phase is formed beneath the oxide scale (Fig. 8 and 9).

Mechanism and chemistry—Reaction with carbon dioxide.—Oxidation led to the formation of oxide, carbon monoxide, and carbon. If the oxide grew by the inward diffusion of oxygen via anion vacancies, carbon, formed at the gas-oxide interface may be incorporated into the growing oxide layer and diffuse inward. Evidence for carbon in the oxide was shown from examination of the autoradiographs of sectioned oxidized specimens and by its absorption in the oxide on heating in carbon monoxide.

Although zirconium carbide could be formed by reactions [3] and [4], the experimental evidence demonstrated that these reactions did not occur, since zirconium carbide was not found. Thus it is concluded that

Table II. Standard free energy changes for the system zirconium-carbon dioxide

	Reaction	$\Delta G°$ (1123°K), kcal/mole
[1]	$Zr + 2CO_2 = ZrO_2 + 2CO$	−139.3
[2]	$Zr + CO_2 = ZrO_2 + C$	−133.3
[3]	$Zr + C = ZrC$	−41.6
[4]	$2Zr + CO_2 = ZrO_2 + ZrC$	−174.9
[5]	$CO_2 + C = 2CO$	−6.0
[6]	$Zr + 2CO = ZrO_2 + 2C$	−127.3
[7]	$3Zr + 2CO = ZrO_2 + 2ZrC$	−168.9

reactions [1] and [2] occur, leading to the formation of carbon monoxide and to incorporation of carbon. The reaction of carbon dioxide with the carbon formed, reaction [5], was shown not to occur.

The value of the ratio $w_c/(w_c + w_o)$ (Table I), assuming reaction [2] took place exclusively, is 0.273. From the experimental values, it was calculated that the percentage of reaction [2] occurring decreased from 62 to 11% from 1 to 48 hr, respectively, at a pressure of 10 cm Hg. Thus the extent to which this reaction occurred decreased from a relatively large proportion initially to a much smaller value at longer times.

Hayes, Roberson, and Robertson (1) have suggested that zirconium carbide is formed during oxidation and that it could be distinguished from that present in the unoxidized carbon-melted metal. Zirconium carbide in such carbon-containing zirconium is largely unattacked during oxidation in both oxygen (11) and carbon dioxide (2). The present results show, however, that the carbide could not be detected. Although Maekawa (5) and Guerlet and Lehr (4) were not able to detect carbon as a reaction product at temperatures in the range 650°-850°C, the use of the radioactive tracer carbon-14 has shown that carbon was formed during the oxidation at 850°C. Moreover, previous work (6) has proved that carbon was a product of reaction at temperatures in the range 550°-750°C.

Mechanism and chemistry—Reaction with carbon monoxide.—The main reaction products in this system are solids. In contrast to the corresponding reaction with carbon dioxide, where the ratio $w_c/(w_c + w_o)$ may vary between zero and 0.273, carbon and oxygen are formed simultaneously (reaction [6]) and the ratio is 0.429. It is assumed by comparison with the corresponding reaction mechanism for carbon dioxide that carbon is deposited initially at the gas-oxide interface and then migrates inward through the oxide scale. Reactions [3] and [7] are precluded because there was no evidence for zirconium carbide. The reverse of reaction [5] was shown to occur with the formation of carbon dioxide and concurrent deposition of carbon.

Kinetics and metallography—Carbon dioxide.—The kinetic curve obtained at 10 cm Hg pressure exhibited three distinct parts: an initial decreasing rate, an intermediate rapidly increasing rate, and a final decreasing rate. Earlier work at temperatures in the range 650°-750°C and at this pressure (6) agrees with the general shape of the reported curves. Previous results (3,4) at a pressure of 76 cm Hg show agreement to both parabolic and cubic-parabolic rate relationships, with no evidence for an increasing rate of oxidation at short times. The weight gain at a given time at 76 cm Hg pressure is greater than that found at the highest pressure of 30 cm Hg employed in this investigation. Any period of increasing oxidation rate which may have occurred at 76 cm Hg pressure was possibly obscured because of the relatively high oxidation rate or by the method of weight gain determination used.

During the initial stages, the oxidation rate was very much less than that in oxygen (Fig. 2). Possibly the oxidation rate was controlled by the dissociation rate of carbon dioxide. When the oxide film is thin migration of oxygen and carbon through it might be expected to be a relatively rapid process.

During the range of increasing oxidation rate, a needle-like phase was observed at the metal-oxide interface. On many grains these needles grew laterally at 60° to one another and appeared to have nucleated principally at grain boundaries. It is believed that the carbon concentration set up at the metal-oxide interface was sufficient for carbon to dissolve to a limited extent in the zirconium-oxygen solid solution. When this solution reached a critical concentration of carbon, the new phase was precipitated and grew in the form of needles. The required carbon content was probably quite low, since carbon is only slightly soluble in zirconium (12). Precipitates of this type were observed by Bailey (13) when zirconium foil was oxidized in the electron microscope. Bailey was of the opinion that these needles constitute a lower oxide of zirconium. It is possible, then, that in the present work, where the needles are visible in the optical microscope, they consist of a lower oxide of zirconium, stabilized by small amounts of carbon.

A specific reason cannot be advanced for the increasing rate region in the kinetic curves. The more rapid rate could be associated with the dependence of the carbon dioxide dissociation rate on surface properties of the oxide, which vary with film thickness or alternatively with the lateral growth of the needle-phase along the metal-oxide interface, causing the oxide to crack, leading to easier access of the reactants to the metal beneath. It has been shown for the iron system that the first consideration is valid (14, 15). In support of the latter consideration, Bailey (13) has suggested that growth of a lower oxide leads to cracking of the oxide film. Both of the above considerations would account for the large effect of carbon dioxide pressure over the range 0.5-30 cm Hg on the kinetics. If the chemisorption consideration accounted for the initial reaction rates, eventually diffusion of oxygen across the oxide layer would become a rate-determining step on establishment of a concentration gradient. On the other hand, this concentration gradient could be established even though the oxide was initially cracked, provided the cracks healed themselves.

The oxidation rate at a given time in carbon dioxide after about 25 hr was about the same as the corresponding rate in oxygen. When plotted in parabolic form (Fig. 12), the data show a reasonable fit to this plot and indicate that the parabolic rate constants in each case were approximately the same. Since autoradiographic results showed that carbon did not penetrate into the metal to any appreciable extent, the hardness gradients in the metal substrate were due to oxygen solution. Using the value of the diffusion constant for oxygen in α-zirconium at 850°C and the error function equation for oxygen diffusion given previously (9) the hardness profiles were calculated, assuming that hardness was proportional to oxygen concentration. These profiles represented the experimental results to a good approximation (Fig. 10). Accordingly, the oxidation mechanism may approximate to the corresponding model for oxidation in oxygen, namely, a diffusion process of oxygen in both the oxide and the metal leading to a parabolic rate of oxidation (9).

Kinetics and metallography—Carbon monoxide.—The oxidation kinetics were in the form of a continuously decreasing rate curve. No period of initial decreasing rate followed by an increasing rate was observed. However, small needles were observed on most grains during the first minute of oxidation, but were subsequently obscured by the rapidly thickening oxide film. It was possible that a period of increasing rate did

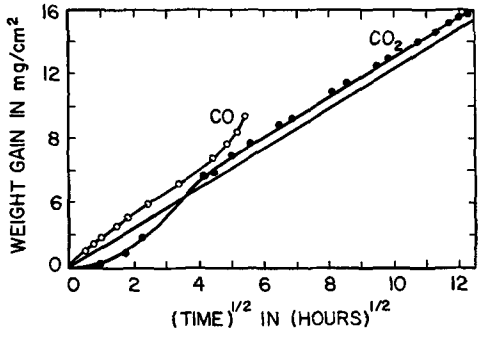

Fig. 12. Oxidation of zirconium at 850°C in carbon dioxide and carbon monoxide at 10 cm Hg pressure. Present results are compared with the corresponding curve (continuous line) for oxidation of zirconium at 850°C in oxygen at 40 cm Hg pressure.

exist, but was not detectable because of the very rapid oxidation.

During the early stages of oxidation, the ratio of carbon to oxygen from carbon monoxide is fixed at 0.429 (reaction [6]). The relatively large carbon potential would lead to a rapid carbon build-up at the metal-oxide interface and gives rise to the formation of a new phase, which was observed at this interface (Fig. 9). No evidence was found to suggest that this phase differs in structure from the needle-like phase. This second phase was not zirconium carbide and, in fact, did not correspond to any known substance. It was found to a larger extent at the edges where there was a large amount of oxide cracking and at blisters and cracks in the compact film. Possibly the presence of this phase led to eventual cracking of the oxide film, due to the stresses set up at the metal-oxide interface.

The kinetics before onset of breakaway oxidation (Fig. 12) indicate that the rate at a given time approximated to the corresponding rate found in oxygen and in carbon dioxide. On calculating the hardness gradients in the metal in the same way as for the specimens oxidized in carbon dioxide, they show good agreement with the experimental plots at 6 and 48 hr (Fig. 10). All these findings support the conclusion that oxygen dissolves in the metal during oxidation to essentially the same degree in oxygen, carbon dioxide, and carbon monoxide.

Acknowledgments

The authors were indebted to G. R. Purdy and G. R. Wallwork for helpful discussions. This work forms part of a research project sponsored by the U.S. Air Force Office of Scientific Research, Office of Aerospace Research and the Defence Research Board, Ottawa, Canada.

Manuscript received Nov. 16, 1964. This paper was presented at the Washington Meeting, Oct. 11-15, 1964.

Any discussion of this paper will appear in a Discussion Section to be published in the December 1965 JOURNAL.

REFERENCES

1. E. T. Hayes, A. H. Roberson, and R. H. Robertson, *This Journal*, **97**, 316 (1950).
2. W. G. O'Driscoll, C. Tyzack, and T. Raine, 2nd U.N. International Conf. Peaceful Uses of Atomic Energy, Paper No. 1450 (1958).
3. J. Debuigne and P. Lehr, *Mem. Sci. Rev. Metallurg.*, **50**, 911 (1963).
4. J. P. Guerlet and P. Lehr, *C. R. Acad. Sci. Paris*, **258**, 930 (1964).
5. T. Maekawa, *Nippon Kinzoku Gakkaishi*, **24**, 608 (1960).
6. S. J. Gregg, R. J. Hussey, and W. B. Jepson, *Corrosion*, **17**, 575t (1961).
7. R. J. Hussey and W. W. Smeltzer, *This Journal*, **111**, 564, (1964).
8. N. Zwiebel, J. Turkevitch, and W. W. Miller, *J. Am. Chem. Soc.*, **71**, 376 (1949).
9. G. R. Wallwork, W. W. Smeltzer, and C. J. Rosa, *Acta Met.*, **12**, 409 (1964).
10. R. J. Hussey and W. W. Smeltzer, *This Journal*, **111**, 1221 (1964).
11. B. Cox, *Corrosion*, **16**, 188t (1960).
12. C. J. Smithells, Metals Reference Book, Vol. 1, 3rd ed. (1962).
13. J. E. Bailey, *J. Nucl. Mat.*, **8**, 259 (1963).
14. W. W. Smeltzer, *Trans. AIME*, **218**, 674 (1960).
15. F. Pettit, R. Yinger, and J. B. Wagner, Jr., *Acta Met.*, **8**, 617 (1960).

Diffusion Coefficients and Anion Vacancy Concentrations for the Zirconium-Zirconium Dioxide System

Tennyson Smith

North American Aviation Science Center, Thousand Oaks, California

ABSTRACT

Experiments have been carried out at 386°C to determine the concentration of anion vacancies at the metal-oxide interface and the diffusion coefficients for anion vacancies in zirconium dioxide films on zirconium by the "interruption kinetic technique." The conditions for which this technique is valid are discussed. The anion vacancy concentration in the oxide at the oxide-metal interface (386°C) proved to be $(7 \pm 0.7) \times 10^{-3}$ g atom/cm^3 as compared to $(2.2 \pm 2) \times 10^{-3}$ calculated from the phase diagram. Diffusion coefficients can be expressed as

$$D = 0.9 \times 10^{-3} e^{-\frac{28{,}700 \pm 600}{RT}} \quad \text{cm}^2/\text{sec}$$

Theoretical calculation of the entropy of vacancy formation and values of D_o are made assuming three models. It is concluded that electrons are trapped at anion vacancies or impurity centers, rather than act as Fermi-electrons in the conduction band.

As pointed out by Rosenburg (1), measurement of the parabolic rate constant yields values for the product DC, where D is the diffusion coefficient and C is the concentration of the diffusing defect. Independent measurements of D or C are required in order to separate D and C. These measurements are not only difficult to make but are inconclusive unless differences in sample structure and purity are demonstrably negligible. Rosenburg (1) describes a technique that will yield accurate and simultaneous determination of D and C from reaction rates alone.

Debuigne and Lehr (2) and Douglass (3) have reported values of D as a function of temperature for oxygen diffusion in pure zirconium dioxide powder. Kingery *et al.* (4) have reported values of D for oxygen diffusion in stabilized zirconia sintered pellets. Domagala and McPherson (5) have studied the equilibrium between oxygen gas-zirconium metal-zirconium dioxide. From their data one can calculate values for C at the metal-oxide interface. The diffusing defects (6), in the case of zirconium dioxide, are anion vacancies which have been created by dissolution of oxygen into the metal at the metal-oxide interface.

It is the purpose of this article, to report results for D and C, using Rosenburg's (1) interrupted anneal technique; to discuss results obtained, which did not satisfy the prescribed experimental conditions; to

compare results with those obtained by independent measurements reported by the authors mentioned above; and to compare results with theoretical values. The theoretical value of D depends on the choice of one of three models; (*a*) that the two electrons (which must be associated with each anion vacancy for electrical neutrality) are trapped at the anion vacancy; (*b*) these electrons are trapped at cation sites; or (*c*) these electrons can be considered as Fermi-electrons in the conduction band of the oxide. It has been estimated in a previous paper (7) that the concentration of electrons in the conduction band is of the order of 10^{-15} mole/cm^3, as compared to a vacancy concentration of the order of 10^{-5} mole/cm^3 for a zirconium dioxide powder. It is predicted therefore that model (c) will not be involved. We wish to distinguish between models (*a*), (*b*), and (*c*), if possible.

Experimental

Crystal bar zirconium samples about 1½ in. long by ¼ in. in diameter were machined to have hemispherical ends. They were mechanically polished on a lathe with No. 3/0 emery paper and then by 3-μ diamond dust, and were then cleaned in anhydrous ether followed by another cleaning in pure alcohol. Samples were sealed in quartz or Vycor sample holders and attached to a vacuum furnace system. The samples were first annealed at 700°C under vacuum to remove any oxide film (dissolved into sample) and then they were brought to the desired temperature. Oxidation was followed by continuously recording the oxygen pressure change in the constant volume system with a thermistor manometer, (10^{-5} to 1 Torr). The system also contained a strain gauge pressure transducer for work in the pressure range 1-1000 Torr. A constant temperature bath was built into the system to control the temperature of the thermistor and transducer to ± 0.02°C. High-purity research grade oxygen (Matheson Company) was used as-received. Maximum limits of possible impurities were listed in mole per cent as $CO_2 < 0.1$, $CO < 0.01$, $He < 0.01$, $N_2 < 0.01$, and $H_2 < 0.01$. The film thickness was calculated from the oxygen pickup and the value always checked with that obtained by comparison of the sample color with an interference-color step gauge.

Anion vacancy concentration and diffusion coefficients.—Application of Rosenburg's "interruption kinetic technique" was used to determine the diffusion coefficient D and the concentration of defects C (anion vacancies) which are involved in the oxidation of zirconium as follows.

Figure 1 shows the general situation for various defect possibilities during the oxidation of a metal.

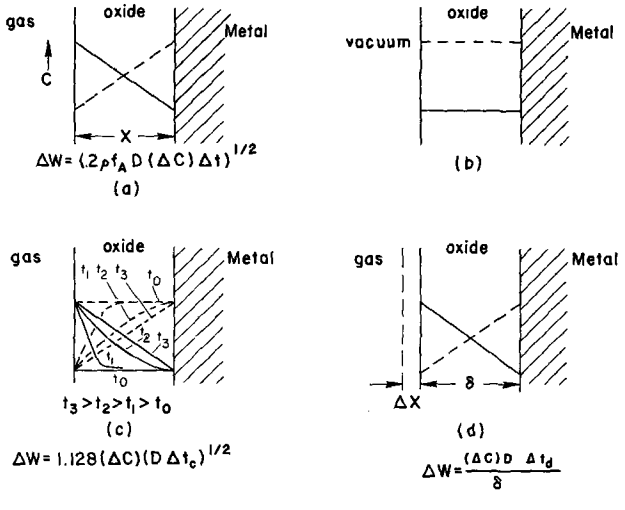

Fig. 1. Defect concentration profile: (a) during oxidation, (b) at equilibrium, after oxygen removal, (c) during semi-infinite media diffusion, (d) steady-state diffusion.

Figure 1a shows the assumed concentration profile of the diffusing defects during film growth. The solid line across the oxide in Fig. 1a represents the concentration of interstitial anions (atoms or molecules) or cation vacancies, whichever the case may be. The dashed line represents the concentration of interstitial cations (or atoms) or anion vacancies. The type of defect cannot be determined by kinetic experiments alone, but must be established by some other suitable method such as chemical analysis, marker experiments, etc. It has been found that in most cases only one type of defect is predominantly involved in any given system.

Figure 1b represents the equilibrium concentration profile after the oxidizing gas has been evacuated from the system. On admitting gas to the system again, the film acts as a semi-infinite medium for diffusion for a time, illustrated by Fig. 1c. The curves designated t_0, t_1, t_2, and t_3 represent the profile at various times between equilibrium and steady state diffusion.

Figure 1d shows the profile when steady state is reached after the interruption (film growth, Δx, is small with respect to the thickness δ). Following this, oxidation resumes as in Fig. 1a again.

By solving Fick's second law, with the appropriate boundary conditions, Rosenburg reports two limiting forms of the equation relating the number of defects crossing unit area in time t. For the case of oxidation of zirconium these limiting forms can be expressed

$$W_c = 1.128\, C\, [Dt_c]^{1/2} \quad (t << \delta^2/D) \qquad [1]$$

and

$$W_d = DCt_d/\delta + \delta C/3 \quad (t > \delta^2/2D) \qquad [2]$$

where W is the gram atoms of oxygen/cm^2 of zirconium sample, C is the anion vacancy concentration (gram atom/cm^3) at the oxide-metal interface, D is the diffusion coefficient for anion vacancies, t is the time starting at reexposure to oxygen, δ is the film thickness, and subscripts refer to the period (of Fig. 1) for which the equation is valid.

We add the third limiting equation, that of film growth during period a (Fig. 1) where no interruption is made

$$W_a = (\rho f DCt_a/8)^{1/2} \qquad [3]$$

where ρ is the oxide film density, f is the weight fraction of the oxide that is oxygen. Equation [3] is derived from the parabolic growth equation

$$dW/dt = DC/\delta \qquad [4]$$

where

$$\delta = 16W/\rho f \qquad [5]$$

and 16 is the atomic weight of oxygen. As pointed out by Rosenburg, Eq. [1] and [2] are valid only if the following conditions are met: (*a*) D is independent of C; (*b*) the oxide surface is flat (roughness factor unity); (*c*) $\Delta X << \delta$; (*d*) no initial reaction (such as adsorption) contributes appreciably to W; (*e*) $t << \delta^2/D$, Eq. [1]; (*f*) $t > \delta^2/2D$, Eq. [2]. For diffusion by a vacancy mechanism condition (*a*) should be a good assumption. Condition (*b*) is difficult to ascertain accurately. Rosenburg considered his chemically polished InSb to have a roughness factor of $F = 1.3$. An estimate of the roughness factor for the zirconium samples used in this study is $F = 1.5 \pm 0.5$, from electrical capacitance measurements. Condition (*c*) is easily met, except for very thin films. Condition (*d*) is usually not met but can be corrected for. If for any reason (perhaps due to initial adsorption) the intercept of Eq. [1] is not zero, the value of the intercept, designated Z, can be treated as an additive constant. Any expression containing W must be corrected by the value Z. In order to satisfy conditions (*e*) and (*f*), order of magnitude values of D must be known in advance, or as will be shown later order of magnitude values of C must be known in advance.

The experimental data can be expressed by the following equations

$$W_c = r_c t_c^{1/2} + Z \quad (t << \delta^2/D) \qquad [6]$$

$$W_d = r_d t_d + W_o \quad (t > \delta^2/2D) \qquad [7]$$

$$W_a = r_a t_a^{1/2} \quad \text{no interruption} \qquad [8]$$

where r is the slope of a plot of W *vs.* t or $t^{1/2}$, and W_o and Z are the intercepts.

Since the values for W, r, and Z can be obtained from a single interruption experiment, we now have four equations and two unknowns. The equations for the diffusion coefficient and vacancy concentration are

$$D = [1.128\, r_d \delta / r_c]^2 \qquad [9]$$

$$D = [1.128 \times 8 r_a^2 / \rho f r_c]^2 \qquad [10]$$

$$C = 3[W_o - Z]/\delta \qquad [11]$$

$$C = [r_c/1.128]^2/r_d\delta \qquad [12]$$

$$C = [r_c/1.128 r_a]^2\, \rho f/8 \qquad [13]$$

$$C = 8[r_a r_c/1.128 r_d \delta]^2/\rho f \qquad [14]$$

Although Eq. [10], [13], and [14] are analytically correct, they are less useful than Eq. [9], [11], and [12] because very accurate values for r_a are needed (Eq. [10] and [14] are to the fourth power in r).

Results

Oxidation of zirconium at 386°C.—A sample of crystal bar zirconium was oxidized in pure oxygen at temperature (period a, Fig. 1a) until the oxide thickness was 280Å, at which point the oxygen was pumped out of the system and the sample annealed (period b, Fig. 1b).

It should be mentioned that, because of the large equilibrium constant in favor of zirconium oxidation, no vacuum system is good enough to reduce the oxygen pressure to a value that oxidation would cease. It is only because the rate-determining step becomes diffusion of oxygen in the gas phase, which at low enough pressure is slow with respect to diffusion in the solid, that equilibrium such as illustrated in Fig. 1b can be approached.

After the anneal the oxygen was re-admitted to the system and the reaction followed by recording the pressure drop with a very sensitive thermistor manometer. When normal oxidation had been re-established (periods c and d, Fig. 1c and d) and the film had thickened to 418Å, the same procedure was repeated and so on for various thicknesses up to 4850Å.

Figure 2a shows a plot of the experimental data for a film that had been annealed in vacuum for 41 hr. The question arises as to which time the slope of the curve should be taken. It is seen in Fig. 2b that between $t^{1/2} \sim 8$ and 32 the data fall close to a straight line but becomes concave up beyond $t^{1/2} \sim 32$. The slope of the line (Fig. 2b) between $t^{1/2} \sim 8$ and 32 is r_c and the intercept is Z. When oxidation approaches the condition just prior to the interruption, the slope of the line (W *vs.* $t^{1/2}$) will approach r_a. From Eq. [12] we obtain

$$r_a/r_c = (\rho f/8C)^{1/2}/1.128 \qquad [15]$$

and it is predicted that the curve (following r_c period) will be concave up if $C < 0.1\,\rho f$ and concave down if $C > 0.1\rho f$. In the case of zirconium oxidation $\rho f = 1.5$ ($\rho = 5.83$ g/cm^3, $f \approx 0.26$) and as will be shown later $C \sim 10^{-2}$ to 10^{-3} g at./cm^3 from the phase diagram, so that $r_a > r_c$ and the curve should be concave up as seen ($t^{1/2} > 32$) in Fig. 2b. From Eq. [3] and [8], [an experimental value of r_a (at 386°C) is 2.2 x 10^{-8} g at./cm^2 sec$^{1/2}$] and the order of magnitude value of $C \sim 5 \times 10^{-3}$ g/cm^3 we obtain $(\delta^2/2D) \sim 10^3$ sec. It should be noted that $t \sim 10^3$ ($t^{1/2} \sim 33$) is just where the curve in Fig. 2b begins to curve up. In order to satisfy conditions (c) and (f), it follows that r_d should be taken as the slope (Fig. 2a) at t just greater than 10^3.

The slope of the line between 1000 and 2000 sec (Fig. 2a) yields the value $r_d = 0.75 \times 10^{-10}$ g at. O/cm^2 sec, the intercept yields $W_o = 1.12 \times 10^{-7}$ g at. O/cm^2. The slope of the line between $t^{1/2} = 10$ and 32 (Fig. 2b) yields the value $r_c = 4.8 \times 10^{-9}$ g at. O/cm^2 sec$^{1/2}$ and the intercept yields $Z = 0.34 \times 10^{-7}$ g at. O/cm^2. From Eq. [9] and $\delta = 3.13 \times 10^{-5}$ cm the diffusion coefficient is calculated to be $D = 3.1 \times 10^{-13}$ cm^2/sec; from Eq. [11], $C = 0.75 \times 10^{-2}$ g at./cm^3 and from Eq. [12], $C = 0.76 \times 10^{-2}$ g at./cm^3. With the more accurate value of D we see that conditions (c), (*e*), and (*f*) have been satisfied. By taking r_d from the curve (Fig. 2a) between 2000 and 3000 sec [where condition (*c*) is less likely to be met] we obtain values of $D \sim 2.1 \times 10^{-13}$, C (Eq. [11]) $\simeq 0.98 \times 10^{-2}$ and C (Eq. [12]) $\simeq 0.93 \times 10^{-2}$. This shows that values for D and C are not extremely sensitive to condition (*c*).

Rosenburg (1) solved the diffusion equation by numerical analysis and gives a table (his Table I) which can be used to predict W *vs.* t if the correction for Z is made. The solid lines in Fig. 2 are the theoretical curves determined with the aid of Table I (1).

Figure 3 shows data for which condition (*f*) was not satisfied, *i.e.*, the time of the experiment was too short to allow $t_d > \delta^2/2D$. It is seen that, although r_c is of the right order of magnitude (3.7×10^{-9} at 380°C as compared to 4.8×10^{-9} at 386°C in Fig. 2), the

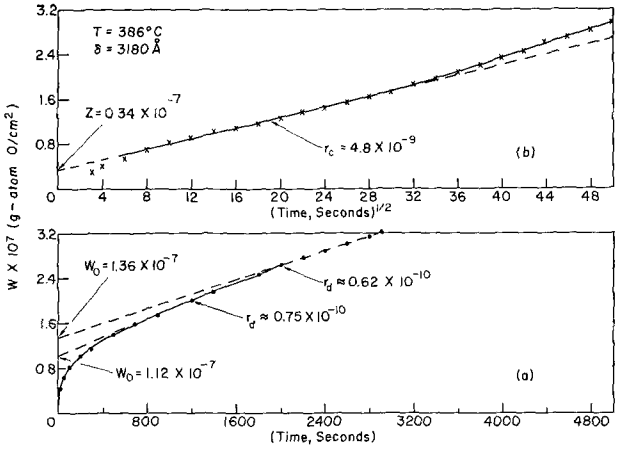

Fig. 2. Oxygen pickup by a zirconium sample after annealing the previously formed oxide layer to equilibrate the anion vacancy concentration throughout the film. The oxygen pickup is given as a function of time (a) and the square root of time (b curve).

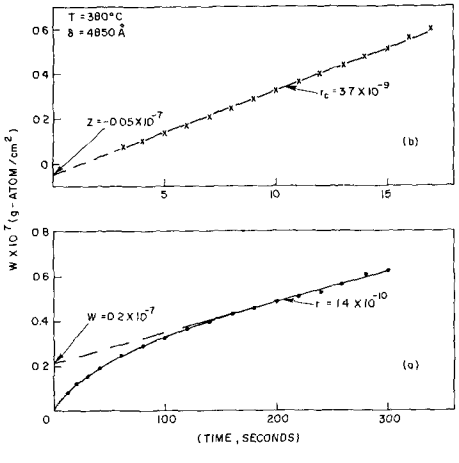

Fig. 3. Oxygen pickup by a zirconium sample after annealing the previously formed oxide layer to equilibrate the anion vacancy concentration throughout the film. The oxygen pickup is given as a function of time (a) and the square root of time (b). Apparent values for r_d and W are wrong because the condition that $t > \delta^2/2D$ was not satisfied.

Table I. Values for the diffusion coefficient and the anion vacancy concentration from kinetic data

Experimental conditions						Results		
Anneal time, hr	Temperature, °C	Film thickness, δ Å (cm × 10^8)	$\frac{\delta^2}{2D}$, sec	$t(r_d)$, sec	$\Delta t(r_c)$, sec	D Eq. [9] cm^2/sec ×10^{13}	C Eq. [11] g-at./cm^3 ×10^2	C Eq. [12] g-at./cm^3 ×10^2
	Conditions (a-f) satisfied			($t > \delta^2/2D$)	($t << \delta^2/D$)			
16	386	2650	1170	1200	64-900	3.2	0.76	0.74
7	386	2900	1400	1600	250-900	3.0	0.60	0.58
41	386	3130	1600	1700	100-400	3.1	0.75	0.76
	Condition (f) not satisfied			($t > \delta^2/2D$)	($t << \delta^2/D$)			
48	380	4850	3900	300	10-200	53	0.12	0.13
	Condition (e) not satisfied			($t > \delta^2/D$)	($t << \delta^2/D$)			
14	386	2040	690	800	200-1300	1.3	2.1	2.1
	Condition (c) not satisfied			$\Delta\delta << \delta$				
5	250	280	1300	1400	100-400	0.03	3.2	2.8

value of r chosen as r_d is a factor of two higher. Values of D, C (Eq. [11]) and C (Eq. [12]) prove to be 53 x 10^{-13} cm^2/sec, 0.12 x 10^{-2} and 0.13 x 10^{-2} g at./cm^3, respectively. It should be noted that in spite of the fact that r_d was measured at $t \sim 300$ sec rather that $t > (\delta^2/2D \sim 3900$ sec), the experimental data are predicted with Rosenburg's Table I, e.g., the solid lines in Fig. 3 are theoretical if the values $D = 53 \times 10^{-13}$ and $C = 0.12 \times 10^{-2}$ are used. It should also be noted that C (Eq. [11]) checks with C (Eq. [12]) regardless of the value of t at which r_d is measured. It is concluded that prediction of the data [with the Table I (1)] and close correlation between C (Eq. [11]) and C (Eq. [12]) are necessary but not sufficient to establish accurate values for D and C. Care must be taken to see that all of the conditions (a-f) are satisfied.

In Table I, experimental conditions and calculated values of D, C (Eq. [11]) and C (Eq. [12]) are given. If the roughness factor is greater than unity, it is seen from Eq. [9]-[14] that values for D, calculated with the assumption that F is unity, should be multiplied by $1/F^2$. That is, any term calculated from a value of W (r_d, r_c, r_a, and δ) must be divided by F. If F is taken as 1.5 for the zirconium samples, the values of D in Table I should be multiplied by the factor 0.4. It can be seen from Eq. [9]-[14] that calculated values of C are independent of F, since F cancels in each case. The experiments represented in the top group of Table I, satisfy the conditions (a-f). The average value of D at 386°C is 3.1 x 10^{-13} cm^2/sec (if $F = 1$), an average value of C is (7.0 ± 0.7) x 10^{-3} g at./cm^3. The results for the lower group in Table I shows that high values for D result if condition (f) is not satisfied, high values of C result if condition (e) is not satisfied, and high values of C result if condition (c) is not satisfied. In the bottom group the correlation between C (Eq. [11]) and C (Eq. [12]) is within about 3%, even though the limiting conditions have not been met.

Effect of temperature.—Experiments were carried out at various temperatures without interruption. Figure 4a shows data for oxidation at 365° and 418°C. It is seen from Fig. 4b that the parabolic rate law was obeyed. Values for DC are calculated from Eq. [3] and [8] and are plotted as open circles in Fig. 6. In another experiment a sample with a 1500Å film was oxidized at various temperatures with resultant small changes in δ. It is seen from Eq. [4] that except for small curvature due to the small change in δ, that approximately straight lines should result. The slope of these lines multiplied by the average value of δ should yield values for DC. The results from Fig. 5 are plotted in Fig. 6 as solid points. The solid line is a least squares fit of the experimental points. Expressing the product $r\delta$ [where $r = (dW/dt)_\delta$] as a function of temperature we have

$$r\delta \cong DC \approx 1.5 \times 10^{-4} e^{-\frac{31{,}100 \pm 600}{RT}} \quad \text{(g at. O/cm}^2\text{-sec)} \quad [16]$$

In order to express D as a function of temperature we need C as a function of temperature.

Calculation of anion vacancy concentration from equilibrium data.—Domagala and McPherson (5) have studied the equilibrium between oxygen gas-zirconium metal-zirconium dioxide, from 500°C to above 1900°C. Oxygen forms a solid solution with zirconium up to 6.75 w/o (weight per cent) [29 a/o (atomic per cent)] at which point nonstoichiometric (oxygen deficient) zirconium dioxide precipitates. This saturation concentration (29 a/o) is constant with temperature

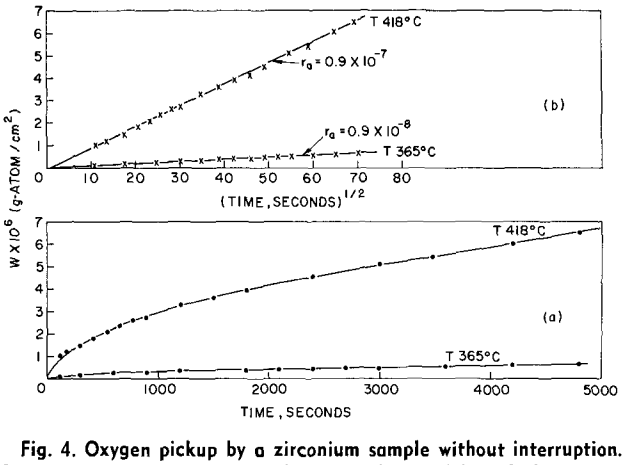

Fig. 4. Oxygen pickup by a zirconium sample without interruption. Oxygen pickup is given as a function of time (a) and the square root of time (b) at two temperatures (365° and 418°C).

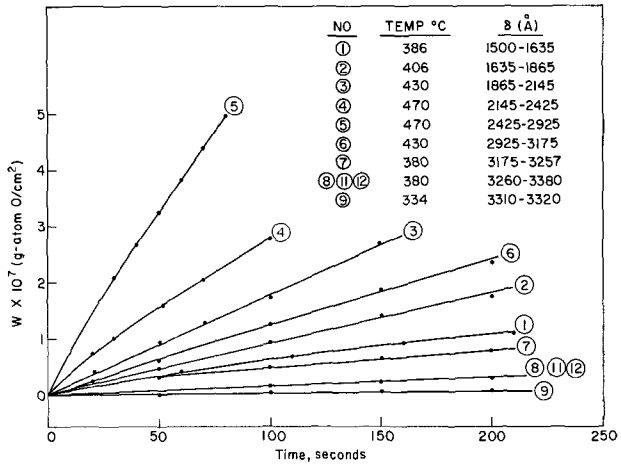

Fig. 5. Oxygen pickup by a zirconium sample at approximately constant film thickness as a function of temperature.

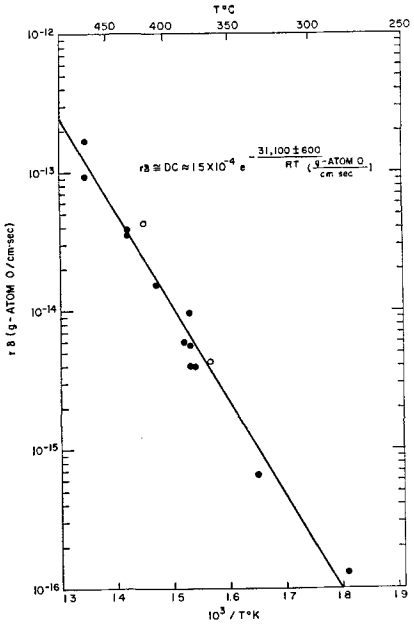

Fig. 6. An Arrhenius plot of ln $R\delta$ vs. $1/T$ for oxidation of zirconium from Fig. 5 (•). The open circles are from the curves in Fig. 4.

up to approximately 1900°C. The oxygen concentration in the zirconium dioxide is 25 w/o (65.5 a/o) at 700°C and decreases in a linear fashion to 23 w/o (63 a/o) at 1900°C. Most investigations to date have indicated that nonstoichiometric ZrO_2 has an anion deficit structure. From the above information, the concentration of oxygen ions at 700°C is

$$(25/16)/(100/5.83) = 0.091 \text{ g at. } O^{=}/cm^3$$

For stoichiometric oxide (26 w/o oxygen), the oxygen ion concentration is 0.095 g at. O/cm^3. Therefore, the anion vacancy concentration is 0.095 − 0.091 = 0.004 g at. $\square/cm^3$. A similar calculation for 1900°C yields $C(1900°C) = 0.011$ g at. $\square/cm^3$. The resulting empirical equation relating the concentration of anion vacancies and temperature is

$$C \cong 5.8 \times 10^{-6} T \qquad [17]$$

where T is in °C and C is in g at. $\square/cm^3$.

From Eq. [17] and the reported (5) experimental error of ± 0.5 w/o, at 386°C

$$C = (2.2 \pm 2) \times 10^{-3} \text{ g at. } \square/cm^3 \qquad [18]$$

as compared to

$$C = (7.0 \pm 0.7) \times 10^{-3} \text{ g at. } \square/cm^3 \qquad [19]$$

for the top group of Table I.

The above concentrations represent 2.3 and 6.7% of the oxygen ions missing, respectively, or nonstoichiometric $ZrO_{1.977}$, $ZrO_{1.926}$. At 386°C the diffusion of oxygen into zirconium metal is very slow so that the equilibrium concentration of oxygen is certainly not attained throughout the bulk metal. It is expected that the equilibrium concentration would be approached at the metal-oxide interface, but a lower than equilibrium oxygen concentration in the metal interface would tend to increase vacancy concentration as found. To test these possibilities further, experiments should be carried out on nearly oxygen saturated zirconium with oxide films about 2000Å thick.

To obtain Eq. [17] in exponential form, we make the following analysis. Consider the reaction at the ZrO_2-Zr interface to be

$$Zr_i + O^{=} \rightleftarrows \square O^{=} + 2e^{-} + O_i \qquad [20]$$

where Zr_i represents interstitial positions in the zirconium lattice, $O^{=}$ represents the oxygen ions in the ZrO_2 lattice, $\square O^{=}$ represents the anion vacancies created when oxygen ions give up two electrons e^{-}, and enter the zirconium metal as atoms, O_i, in interstitial positions. At equilibrium the chemical potential (partial molar free energy) of the species in each phase will be equal. The equilibrium constant K_v can be expressed

$$K_v = \frac{a_{\square}\, a_{e^-}{}^2\, a_{O_i}}{a_{Zr_i}\, a_{O^=}} \qquad [21]$$

where $a_{\square}$, a_{e^-}, a_{O_i}, a_{Zr_i}, and $a_{O^=}$ represent the activities of $\square$, $\square_{O^=}$, e^{-}, O_i, Zr_i, and $O^{=}$, respectively. We choose as standard states the concentration of each of the species at equilibrium at 386°C. Therefore, at 386°C, the activities are each unity and, consequently, K_v is unty. Since a_{O_i} and $a_{O^=}$ are essentially independent of temperature and since for every vacancy two electrons are promoted into the ZrO_2, $C_{e^-} = 2C$.

From Eq. [21], at any temperature

$$K_v \approx a_{\square}\, a_{e^-}{}^2 = \left[\frac{C(T)}{C(386°C)}\right]^3 \qquad [22]$$

and from Eq. [17]

$$K_v \cong \left[\frac{T}{386}\right]^3 \qquad [23]$$

Now from thermodynamics

$$\Delta\bar{F}° = \Delta\bar{H}° - T\Delta\bar{S}° = -RT\ln K_v \qquad [24]$$

where $\Delta\bar{F}°$, $\Delta\bar{H}°$, and $\Delta\bar{S}°$ are the partial molar free energy, enthalpy, and entropy changes for the reactant and products in their standard states. A plot of ln K_v *vs* $1/T$°K reveals $\Delta\bar{H}°$ to be approximately 7.1 ± 0.3 kcal/mole in the temperature range 300°-800°C. At 386°C (659K°) K_v is unity, so $\Delta\bar{F}° = 0$ and the experimental entropy change is

$$\Delta\bar{S}° = \frac{\Delta\bar{H}°}{T} \cong \frac{7100}{659} \approx 11 \pm 0.3 \text{ e.u.} \qquad [25]$$

The anion vacancy concentration can be expressed in exponential form as

$$C(T) = C(386°C)K_v^{1/3} \approx C(386°C)\, e^{\frac{\Delta\bar{S}°}{3R}}\, e^{-\frac{\Delta\bar{H}°}{3RT}} \qquad [26]$$

Equation [26] can be expressed as

$$C(T) \approx 1.4 \times 10^{-2}\, e^{-\frac{2{,}400}{RT}} \text{ g at./cm}^3 \qquad [27]$$

with $C(386°C)$ from Eq. [18] (from equilibrium studies) and

$$C(T) \approx 4.4 \times 10^{-2}\, e^{-\frac{2{,}400}{RT}} \text{ g at./cm}^3 \qquad [28]$$

with $C(386°C)$ from Eq. [19] (from oxide film studies).

The most accurate relation between D and temperature would result from the best value for the temperature coefficient and an accurate value of D at a particular temperature. It follows from Eq. [16] and [28] that the activation energy for D is (31.1 − 2.4 = 28.7) kcal/mole. If we use 28.7 kcal/mole as the best value and 3.1 x 10^{-13} cm^2/sec as an accurate value for D at 386°C we obtain the equation for D for oxide films on zirconium as a function of temperature

$$D = 0.9 \times 10^{-3}\, e^{-\frac{28{,}700 \pm 600}{RT}} \text{ cm}^2/\text{sec} \qquad [29]$$

Douglass (3) measured the diffusion coefficient of oxygen in zirconia sintered pellets. He considered the anion vacancy concentration to be constant during his experiments and obtained the equation

$$D = 5.5 \times 10^{-2} e^{-\frac{33{,}400 \pm 3{,}100}{RT}} \quad [30]$$

From the formula $ZrO_{1.994}$ (for his pellets) the constant concentration that he used, must have been equivalent to 2.8×10^{-4} g at. (vacancies)/cm^3. Douglass reported that some oxygen-saturated alpha zirconium was present in the sintered pellets. Consequently the vacancy concentration may not have been constant, but could probably best be expressed by Eq. [27]. If this is so, with Eq. [27], Eq. [30] should be written

$$D \approx (C'/C) \times 5.5 \times 10^{-2} \times e^{-\frac{33{,}400 \pm 3{,}100}{RT}} \approx 1.1 \times 10^{-3} e^{-\frac{3{,}100 \pm 3{,}100}{RT}} \quad [31]$$

where $C' = 2.8 \times 10^{-4}$.

Debuigne and Lehr (2) also report the diffusion coefficient for oxygen diffusion as a function of temperature as do Kingery *et al.* (4). From a comparison of the experimental data in Table II, it is seen that a good correlation exists between results for the oxidation of zirconium. Correlation with measurements on sintered $ZrO_{1.994}$ pellets is fair if Eq. [31] is used. A good correlation is not expected with the stabilized zirconia because of the added calcium and the different lattice structure (cubic rather than monoclinic).

Theoretical check on D.—To see if one of the models, (*a*) electrons trapped at anion vacancies, (b) electrons trapped at cation sites, or (c) Fermi-electrons in the conduction band, can be supported and the others rejected, the following analysis is made.

For vacancy diffusion in the oxide there are approximately four positions that an oxygen ion could jump into in an adjacent plane if it were vacant. Therefore, from diffusion theory

$$D \approx 4 \lambda^2 N_v P_v \quad [32]$$

where λ is the jump distance from one lattice site to another, N_v is the probability that a neighboring anion site will be vacant (just the fraction of sites that are vacant) and P_v is the probability that a jump can be made if the neighboring site is vacant.

Since $P_v = \nu e^{-\Delta F^\ddagger/RT}$, where ν is the frequency of the diffusant and $\Delta F^\ddagger$ is the activation free energy for diffusion and from Eq. [22], $N_v = \frac{C(T)}{C_{O=}} = 0.023\ K_v^{1/3}$ (where $C_{O=}$ is the total concentration of anions), then

$$D \approx (4 \lambda^2 (0.023)\ \nu \left[e^{\left(\frac{\Delta \bar{S}^\circ}{3} + \Delta S^\ddagger\right)/R} \right] e^{-\left(\frac{\Delta \bar{H}^\circ}{3} + \Delta H^\ddagger\right)/RT} \quad [33]$$

and

$$D_o \approx 0.09 \lambda^2 \nu \left[e^{\left(\frac{\Delta \bar{S}^\circ}{3} + \Delta S^\ddagger\right)/R} \right] \quad [34]$$

According to Zener (12)

$$\Delta S^\ddagger \approx \beta \frac{\Delta H^\ddagger}{T_m} \quad [35]$$

where $\Delta H^\ddagger$ is the activation enthalpy for diffusion, T_m is the melting temperature of the medium of diffusion and

$$\beta = \frac{d(\mu/\mu_o)}{d(T/T_m)} \quad [36]$$

In Eq. [36], μ and μ_o are the appropriate elastic constants at temperature T and at absolute zero, respectively. For most metals and oxides β varies between 0.35 and 0.45. By plotting Young's modulus as a function of temperature for ZrO_2 from the data of Ryschkewitsch (13) and extrapolating to 0°K, a value of β proves to be 0.4. Then since $\Delta H^\ddagger \approx 30$ kcal/mole and $T_m = 2970$°K, it follows from Eq. [35] that $\Delta S^\ddagger \approx 4$ e.u. The jump distance in the ZrO_2 lattice for oxygen ions is about 3Å. The frequency of the diffusant has been calculated in Eq. [16A] (Appendix A) to be about 3×10^{12} sec^{-1}. This frequency should also be close to that calculated with the characteristic Debye temperature.

$$\nu_{max} \approx \frac{\theta_D k}{h} = 7 \times 10^{12}\ \text{sec}^{-1} \quad [37]$$

where the Debye temperature for ZrO_2 is approximately (14) $\theta_D = 345$°K. Estimated values for the thermodynamic entropy of vacancy formation $\Delta \bar{S}^\circ$ are calculated in Appendix A for the three models. With the estimated values for the parameters in Eq. [34], we calculate the following values for D_o:

Table II, experimental	$D_o \approx 0.1 \times 10^{-2}$
$\Delta \bar{S}^\circ \sim 11$ (exp.),	$D_o \sim 1 \times 10^{-2}$
$\Delta \bar{S}^\circ \sim 14$ (model, a),	$D_o \sim 2 \times 10^{-2}$
$\Delta \bar{S}^\circ \sim 16$ (model, b),	$D_o \sim 3 \times 10^{-2}$
$\Delta \bar{S}^\circ \sim 25$ (model, c),	$D_o \sim 12 \times 10^{-2}$

Only order of magnitude values can be expected from the theoretical calculation, and it is seen that models *a* and *b* yield an order of magnitude value for D_o whereas model *c* does not. These results, along with those in Appendix A, confirm the prediction of a previous paper (7), that electrons are trapped at vacancies or impurity centers. This conclusion is in agreement with others (3, 4) (from electrical measurements).

Conclusions

Accurate values of the diffusion coefficient and concentration of the diffusing defect can be obtained with the "interruption kinetic technique." The values obtained for D and C are of the same order of magnitude as reported in the literature for oxide powders and sintered pellets, but are considered to be more accurate for oxide films on zirconium. Good correlation between calculated values for C from Eq. [11] and [12], and prediction of experimental data are not sufficient to establish that D and C values are valid. Correct values can be obtained only if all of the restricting conditions are met. It is concluded from a theoretical analysis that the electrons (associated with anion vacancies) are trapped at vacancies or cation sites rather than in the conduction band of the oxide.

Table II. Experimental diffusion coefficients for oxygen in zirconium dioxide
$D = D_o e^{-Q/RT}$

Temperature range, °C	C (anion vacancy) g at./cm^3 ×10^3	D_o, cm^2/sec ×10^3	Q, kcal/mole	D (at 386°C) cm^2/sec ×10^{13}	Remarks and reference
380-386	7 ± 0.7	0.9	28.7 ± 0.6	3.1 ± 0.1	Oxide on Zr. This work
400-900	—	1.0	29.3	2.2	Oxid. on Zr (2)
700-1000	0.28	1.1	31.0 ± 3.1	(0.07-7.0)	Sintered $ZrO_{1.994}$ (3)
700-1100	7.1	10	28.1	55	Sintered $Zr_{0.85}Ca_{0.15}O_{1.85}$ (4)

The results in the paper point up the importance of measuring defect concentrations during the actual oxidation study rather than rely on measurements made during independent studies on different source material. Rate constants reported in the literature for the oxidation of metals involve the product of the diffusion coefficient and diffusing defect concentration gradient. These cannot usually be separated unless one or the other has been measured independently. There is a large probability that independent measurements will involve parameters different than those during the oxidation experiment so that absolute values of D or C may not represent the values that exist during the oxidation experiment. However, it is much more likely that coefficients of temperature and pressure, etc., would correlate well.

Manuscript received Oct. 6, 1964.

Any discussion of this paper will appear in a Discussion Section to be published in the December 1965 JOURNAL.

REFERENCES

1. A. J. Rosenburg, *This Journal*, **107**, 795 (1960).
2. J. Debuigne and P. Lehr, "Corrosion of Reactor Materials," International Atomic Energy Agency, Vienna, **2**, 105 (1962).
3. D. L. Douglass, "Corrosion of Reactor Materials," International Atomic Energy Agency, Vienna, **2**, 224 (1962).
4. W. D. Kingery *et al.*, *J. Am. Ceram. Soc.*, **42**, 393 (1959).
5. R. F. Domagala and D. S. McPherson, *J. Metals*, **6**, 238 (1954).
6. J. Chirigos and D. E. Thomas, WAPD-53 (1952).
7. T. Smith, *This Journal*, **111**, 1020 (1964).
8. L. Pauling, *J. Am. Chem. Soc.*, **69**, 542 (1947).
9. T. L. Hill, "An Introduction to Statistical Thermodynamics," p. 444, Addison-Wesley Publishing Co., Inc., London (1960).
10. H. B. Huntington *et al.*, *Phys. Rev.*, **99**, 1085 (1955).
11. K. K. Kelley, Bulletin 584 B.M.
12. C. Zener, *J. Appl. Phys.*, **22**, 372 (1951).
13. E. Ryschkiwitsch, "Oxydkeramik der Einstoffsystem," p. 227, Springer-Verlag (1948).
14. K. K. Kelley, *Ind. and Eng. Chem.*, **36**, 377 (1944).

APPENDIX A

Theoretical and Experimental Entropy of Vacancy Formation

We have considered the anion vacancy concentration at the oxide-metal interface calculated from kinetic and equilibrium studies. It is of interest next to compare theoretical values with experimental values for the entropy of the reaction at the oxide-metal interface, in terms of the three models suggested in the introduction.

The positive entropy change of Eq. [25] is associated with the increase in freedom of the electrons, interstitial oxygen atoms and anion vacancies. The entropy change for reaction [20] can be expressed in terms of the individual species:

$$\Delta\bar{S}^\circ = \bar{S}^\circ(\square O^=) + 2\bar{S}^\circ(e^-) + \bar{S}^\circ(O_i) - \bar{S}^\circ(O^=) - \bar{S}^\circ(Zr_i) \qquad [1A]$$

where $\bar{S}^\circ(\square O^=)$, $\bar{S}^\circ(e^-)$, $\bar{S}^\circ(O_i)$, $\bar{S}^\circ(O^=)$, and $\bar{S}^\circ(Zr_i)$ are the partial molar entropies of the anion vacancies electrons, interstitial oxygen atoms, anions in the ZrO_2 lattice and empty interstitial positions in the zirconium lattice, respectively. The individual entropies can be expressed in terms of their configurational and vibrational entropies as follows.

Configurational Entropy

Since α zirconium is hexagonal close packed, there are two tetrahedral and one octahedral interstices for every zirconium atom. The radius of the tetrahedral interstices are $0.225\ r_{zr} = 0.36$Å since the metallic radius (8), r_{zr}, of zirconium is 1.60Å. The radius of the octahedral interstices is approximately $0.414\ r_{zr} = 0.66$Å. Since the metallic radius r of an oxygen atom is 0.66Å, it is assumed that oxygen atoms enter only octahedral interstices. Therefore, for (29 ± 1) a/o oxygen in α zirconium, $n = 0.02$ moles/cm^3, $N = 0.071$ moles/cm^3, $n/N = 0.28$ and the configurational entropy is

$$\bar{S}^\circ_{oi}(\text{conf}) = -R \ln\left(\frac{n/N}{1 - n/N}\right) \approx 1.8 \pm 0.1 \text{ e.u.} \qquad [2A]$$

A similar argument is valid for the distribution of anion vacancies among the anion lattice positions in ZrO_2. From Domagala and McPherson's (5) equilibrium data

$$C = (2.2 \pm 2) \times 10^{-3} \text{ moles } \square/\text{cm}^3 \text{ and}$$
$$(C_{O^=}) = 0.095 \text{ moles } O^=/\text{cm}^3$$

so in this case $n/N = C/(C_{O^=}) = (2.3 \pm 2) \times 10^{-2}$ and

$$\left(\bar{S}^\circ_{\square O^=}\right)(\text{conf}) = -2 \ln\left(\frac{2.3 \times 10^{-2}}{1 - 2.3 \times 10^{-2}}\right) = 7.5 \pm 2.8 \text{ e.u.} \qquad [3A]$$

Now the electrons that leave oxygen ions are probably promoted to positions in the vicinity of zirconium ions (Zr^{+3}) in the ZrO_2. Some of the electrons can be excited into the conduction band and move freely throughout the oxide. However, if the large majority of electrons are associated with cations, the entropy of the electrons will be primarily configurational. The concentration of electrons is just twice the vacancy concentration and the cation concentration is $C_{Zr+4} = 0.0475$. Therefore, for electrons, $n/N = 0.004/0.0475 = 0.084 \pm 0.08$ and

$$\bar{S}^\circ_{e^-} = -2 \ln\left(\frac{0.084}{1 - 0.084}\right) = 4.76 \pm 4 \text{ e.u.} \qquad [4A]$$

If, however, the electrons are trapped at the vacancies, each anion vacancy has four nearest neighbor zirconium cations which can act as sites for the extra electrons. There are two electrons associated with each vacancy for electrical neutrality, so that $n/N \approx 0.5$.

Therefore,

$$\bar{S}^\circ_{e^-} \approx -2 \ln\left(\frac{0.5}{1 - 0.5}\right) = 0 \qquad [5A]$$

If the majority of the electrons were promoted into the conduction band of the oxide and acted as a Fermi-Dirac gas, an approximate equation for the entropy (9) is

$$\bar{S}^\circ_{e^-} \cong \frac{2\pi mkT}{h^2} \cdot 2\pi Nk\left(\frac{\pi V}{3N}\right)^{2/3} \qquad [6A]$$

Since

$$\frac{2\pi mkT}{h^2} \approx 10^{13}$$

and

$$\left(\frac{\pi V}{3N}\right)^{2/3} \approx 10^{-13}$$

$$\bar{S}^\circ_{e^-} \approx 2\pi R \approx 12 \text{ e.u.} \qquad [7A]$$

Vibrational Entropy

The interstitial oxygen atoms have three vibrational modes, each (assumed equal) of frequency ν_{oi}. The vibrational frequencies of the eight nearest neighbors to the interstitial oxygen atoms will be increased (from ν_{Zri} to $\nu_{Zr,oi}$) due to the presence of the oxygen atom. Therefore,

$$\bar{S}^\circ(oi) - \bar{S}^\circ(Zr_i) = 3R\left(\ln\frac{kT}{h\nu_{oi}} + 1\right) + 8R \ln\frac{\nu_{Zri}}{\nu_{Zr,oi}} \qquad [8A]$$

Removal of an oxygen anion from the oxide lattice allows the four nearest neighbor zirconium ions to relax away from the vacancy center while the next nearest neighbor anions relax toward the vacancy center.

Table IA. Comparison of theoretical values for the entropy of vacancy formation with the experimental value

Model	$\Delta S°$ e.u. Eq. [18] $C = 2.2 \pm 2$	Maximum estimated error	Eq. [19] $C = 7 \pm 0.7$	Maximum estimated error
Experimental	11	± 0.3	11	±0.3
(a) Electrons trapped at anion vacancies	15	± 8	14	±5
(b) Electrons trapped at cation sites	25	±16	16	±6
(c) Fermi-electrons in conduction band	39	$\begin{pmatrix}+96\\-23\end{pmatrix}$	25	±6

As a result

$$\bar{S}°(\square O^{=}\text{ vib}) - \bar{S}°(O^{=}\text{ vib}) = 4R \ln \frac{\nu_{Zr,O^{=}}}{\nu_{Zr,\square}} + 6R \ln \frac{\nu_{O^{=}}}{\nu_{O^{=},\square}} - 3R\left\{\ln \frac{kT}{h\nu_{O^{=}}} + 1\right\} \quad [9A]$$

where $\nu_{Zr,O^{=}}$ and $\nu_{Zr,\square}$ are the frequencies of the four nearest neighbor zirconium ions before and after the anion is removed, and $\nu_{O^{=}}$ and $\nu_{O^{=},\square}$ are the frequencies of the six next nearest neighbor anions before and after the vacancy is formed. The total vibrational entropy change for reaction [20] can be expressed

$$\Delta\bar{S}°(\text{vib}) = R \ln \left[\frac{\nu_{Zri}}{\nu_{Zr,oi}}\right]^{8} \left[\frac{\nu_{Zr,O^{=}}}{\nu_{Zr,\square}}\right]^{4} \left[\frac{\nu_{O^{=}}}{\nu_{O^{=},\square}}\right]^{6} \left[\frac{\nu_{O^{=}}}{\nu_{oi}}\right]^{3} \quad [10A]$$

Values for ν_{Zri}, $\nu_{Zr,O^{=}}$, and $\nu_{O^{=}}$ can be estimated for the normal lattice without vacancies or interstitials with the Einstein relation

$$\nu_{max} = \frac{k\theta_D}{h} \quad [11A]$$

where θ_D is the Debye temperature.

It is more difficult to estimate values for $\nu_{Zr,oi}$, $\nu_{Zr,\square}$, $\nu_{O^{=},\square}$, and ν_{oi} after defect formation.

To avoid some of the more difficult calculations, we will assume that, as shown by Huntington *et al.* (10) for interstitial copper in copper, that

$$\bar{S}°(oi) - \bar{S}°(Zr_i) \approx R \quad [12A]$$

and concentrate on Eq. [9A].

To obtain values for $\nu_{Zr,O^{=}}$ and $\nu_{O^{=}}$ for the normal ZrO_2 lattice, we will assume that at 386°C the equipartition of energy exists and that we can consider the ZrO_2 lattice as an ensemble of equivalent harmonic oscillators.

From thermodynamic literature (11) the experimental entropy of ZrO_2 at 386°C is 24 e.u. Since there are 3 g at./mole of ZrO_2 and each atom has three vibrational modes (one for each of the X, Y, and Z directions), there are $9N$ harmonic oscillators per mole of ZrO_2. It follows that

$$\bar{S}°(ZrO_2) = 9R\left(\ln \frac{kT}{h\nu} + 1\right) \approx 24 \quad [13A]$$

and that

$$(\nu_{Zr,O^{=}}) \approx (\nu_{O^{=}}) \approx 10^{13}\ \text{sec}^{-1} \quad [14A]$$

We can estimate a value for $(\nu_{O^{=},\square})$ with Zener's (12) equation

$$\nu \approx \left(\frac{\Delta H‡}{2m\lambda^2}\right)^{1/2} \quad [15A]$$

where $\Delta H‡$ is the activation energy (expressed in ergs) for diffusion, m is the mass of the diffusant, and λ is the jump distance.

The frequency calculated in Eq. [15A] is that of the vibrating particle just before passing over the barrier and this should correspond with $\nu_{O^{=},\square}$ for vacancy diffusion of oxygen in ZrO_2. Therefore, since the activation energy for oxygen diffusion in ZrO_2 is about 30 kcal/mole (see Table II) and since the jump distance is approximately 3Å

$$\nu_{O^{=},\square} \approx \left(\frac{33 \times 10^{10}}{2 \times 16}\right)^{1/2} \frac{1}{3 \times 10^{-8}} \cong 3 \times 10^{12} \quad [16A]$$

We expect a slight increase in $\nu_{Zr,O^{=}}$ as it goes to $\nu_{Zr,\square}$ [*i.e.*, $(\nu_{Zr,\square}) > (\nu_{Zr,O^{=}})$], but we will assume for the sake of simplicity that $(\nu_{Zr,\square}) \approx (\nu_{Zr,O^{=}}) \approx 10^{13}$ (see Eq. [14A]). It follows from Eq. [9A] that

$$\bar{S}°(\square, O^{=}, \text{vib}) - \bar{S}°(O^{=}_{\text{lattice}}\text{ vib}) \approx 5.2\ \text{e.u.} \quad [17A]$$

Finally, Eq. [1A] can be expressed as

$$\Delta\bar{S}° = [\bar{S}°(\square, O^{=}, \text{vib}) - \bar{S}°(O^{=}\text{ vib})] + [\bar{S}°(oi, \text{vib}) - \bar{S}°(Zr_i\text{ vib})] + \bar{S}°(\square, O^{=}, \text{conf}) + 2\bar{S}°(e^{-}\text{ conf}) + \bar{S}°(oi\text{ conf}) \quad [18A]$$

The values we have calculated for these terms are summarized as follows:

$$[\bar{S}°(\square, O^{=}, \text{vib}) - \bar{S}°(O^{=}\text{ vib})] \approx 5.2 \quad [19A]$$

$$[\bar{S}°(oi, \text{vib}) - \bar{S}°(Zr_i\text{ vib})] \approx 2 \quad [20A]$$

$$\bar{S}°(\square, O^{=}\text{ conf}) \approx 7.5 \quad [21A]$$

$$2\bar{S}°(e^{-}, \text{conf}) \approx \begin{cases}0 \text{ trapped at vacancies}\\9.6 \text{ trapped at cations}\\24 \text{ Fermi electrons}\end{cases} \quad [22A]$$

$$\bar{S}°(oi, \text{conf}) \approx 0.7 \quad [23A]$$

Table IA gives values for $\Delta\bar{S}°$ for the three models along with an estimated maximum error for each calculation. It is seen that the best correlation is obtained by assuming model (a). However, due to the large error inherent in such calculations model (b) cannot be rejected. In spite of the large error, model (c) can be rejected because values used to estimate $\Delta\bar{S}°$ would have to be off by a factor of 10^3 in order to correlate with the experimental value.

Cathode Overpotential and Surface-Active Additives in the Electrodeposition of Copper

I. Effects of Some Carboxyl and Amino Compounds

H. Schneider, A. J. Sukava, and W. J. Newby

Department of Chemistry, The University of Western Ontario, London, Ontario, Canada

ABSTRACT

Additives containing carboxyl and amino groups increase the overpotential of a copper cathode during electrolysis in an acid sulfate electrolyte, the amino group being more effective than the carboxyl. At a given additive concentration the overpotential increment apparently depends on the adsorptivity and size of the additive molecule. The adsorptivity in turn depends on the number and kind of polar functional groups, the structural relation between electron-donating atoms, and the lattice dimensions of the copper deposit. It is suggested that the behavior of a chemisorbed additive can be understood in terms of two effects, (i) the complete blockage of growth sites by chemisorption bonds and (ii) the partial blockage of adjacent sites by the physical bulk of the adsorbed molecule.

It is generally believed that the effect of addition agents on cathode overpotential (or polarization) during electrodeposition of metals arises primarily because of adsorption of the additive on the cathode surface (1-9). Possible coordination with the metal ions in solution might also have an effect (6-8, 10-14). In addition, the ability of the additive to impede metal-ion transport in the cathode film could play a more minor role (15).

This paper deals with the effects on cathode overpotential during electrodeposition of copper of a number of additives containing carboxyl and amino groups, the object being a better understanding of the correlation between cathode overpotential increments and the constitution and structure of surface-active additive molecules. The data are interpreted in accordance with the expected adsorption behavior of the compounds used.

Experimental

To facilitate comparison with published data, our experimental methods and conditions were much the same as those used in other studies (8, 16, 17). The Haring cell method was selected as the means of overpotential measurement because of simplicity and convenience. Precise control of cathode surface variables was not necessary for our purposes.

All experiments were made with 150 ml of electrolyte containing 125 g/l $CuSO_4 \cdot 5H_2O$ and 100 g/l H_2SO_4, both reagent grade. The apparent current density was 2 amp/dm^2 and the temperature was 25° (±0.5) °C. Some of the additives were Eastman's "white label" grade and others were "standardized" amino acids from the Nutritional Biochemicals Corporation. The water was distilled from alkaline permanganate in all-glass apparatus.

For each experiment the cathode was first brought to a reproducible standard state (18) by electrodeposition from standard electrolyte (which contained no additive) at 3 amp/dm^2 for about 30 min and then at 2 amp/dm^2 until a steady-state overpotential of 100 (±5) mv was attained (8, 18). The latter step usually required 1 or 2 hr.

After the standard surface was formed, the standard electrolyte was discarded and solution containing the addition agent was poured into the cell. Just as in other studies (8), a contact time of 5 min was normally allowed before closing the electrolysis circuit. This was in order that initial overpotential values in the presence of additives might be at least roughly compared and related to comparable conditions at the beginning of electrolysis.

The rapid initial changes in total overpotential during the first few seconds of electrolysis were followed in many experiments with a du Mont type 324 cathode-ray oscilloscope (C.R.O.). Thereafter more accurate measurements of the slowly changing and steady-state overpotentials were made at intervals of 5 and 15 min with a L & N K-2 potentiometer. A Nesco JY-120 recorder was used in some experiments to follow the overpotentials up to about 8 hr. For all measurements during the build-up of overpotential, the C.R.O. sweep frequency and sweep length were adjusted to give one 2-in. sweep per second.

The mechanically polished copper cathodes could be used repeatedly if they were first coated with a thin film of paraffin before the standard surface was deposited (19). The entire deposit could then be removed by peeling with a knife. The polished copper strip was attached with paraffin to the Lucite mounting block of the Haring cell and then dipped into 50% nitric acid to etch and clean the exposed surface. After rinsing and drying, the assembly was dipped into a 0.5% solution of paraffin in ether. Evaporation of the ether left the desired film on the cathode face. The standard surface was deposited over the film, followed in turn by the experimental deposit in the presence of additive. Brittle deposits were easily removed after first heating the cathode and deposit to redness and then quenching in cold water.

The paraffin film obviously prevented strong bonding between the deposit and substrate surface, but without measurable effect on overpotential values. The reason might be that submicroscopic surface protrusions provide regions of high charge density sufficient to initiate deposit nucleation without providing sufficient contact area for bond formation.

Results

A number of simple carboxyl and amino compounds were studied to determine their relative effectiveness in increasing the cathode overpotential. The purpose was to examine the effect of: (*a*) the number and kind of functional groups present in the additive molecule; (*b*) variation in the size of the hydrocarbon portion of the molecules when the functional groups are in the same structural relationship; and (c) variation in the structural relationship between the same functional groups. The compounds studied were: ethylamine, propionic acid, malonic acid, glycine, α-alanine, β-alanine, γ-aminobutyric acid, leucine, β-phenylalanine, and aspartic acid. The data for some of these cover a wide range of concentration in reasonable detail. Others are less complete. The number

of experiments varied from four with propionic acid to about forty with α-alanine.

All overpotentials in this paper are the total values. In particular, no attempt is made to consider concentration overpotential separately. Some experiments suggest that the concentration component is not significantly affected by our additives and that it is probably no greater than 10 mv under our experimental conditions. The effects of different additives can therefore be reasonably compared by reference to total overpotentials only.

Typical overpotential-time relations in Fig. 1 show that a steady state is attained in all cases after about 2 hr. The dependence of steady-state overpotentials on additive concentration is shown in Fig. 2, where the curves represent the best averages of overpotentials reproducible to within ±5 and ±10 mv at the low and high concentrations respectively. The maximum at 10 or 20 min (Fig. 1) follows an earlier maximum and minimum at about 0.01 and 0.5 sec, some values of which are shown along with the steady-state overpotentials in Table I.

The data are in general agreement with other results (4, 17). The greater the number of functional groups in the additive molecule, the greater the overpotential

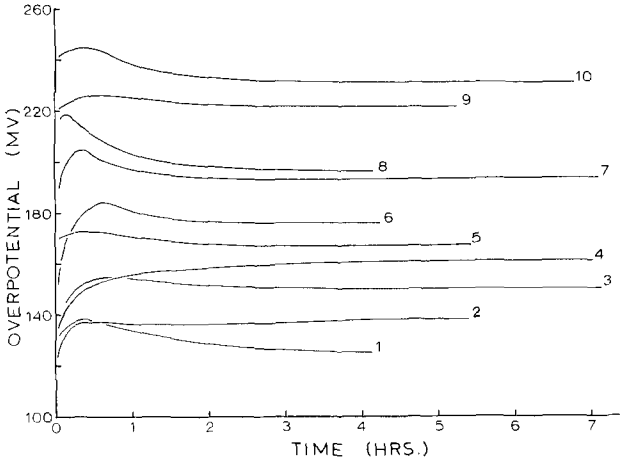

Fig. 1. Variation of total overpotential with time: curve 1, 5.0 x 10^{-3}M γ-amino butyric acid; curve 2, 4.0 x 10^{-2}M propionic acid; curve 3, 2.0 x 10^{-4}M β-alanine; curve 4, 7.5 x 10^{-5}M aspartic acid; curve 5, 1.5 x 10^{-3}M leucine; curve 6, 5.0 x 10^{-2}M ethylamine; curve 7, 5.0 x 10^{-3}M α-alanine; curve 8, 5.0 x 10^{-2}M malonic acid; curve 9, 2.8 x 10^{-3}M β-phenylalanine; curve 10, 2.0 x 10^{-2}M glycine.

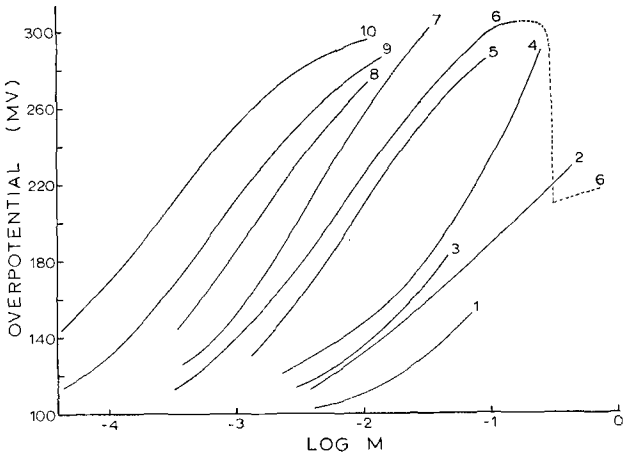

Fig. 2. Total steady-state overpotential as a function of additive concentration: curve 1, propionic acid; curve 2, ethylamine; curve 3, γ-amino butyric acid; curve 4, malonic acid; curve 5, glycine; curve 6, α-alanine; curve 7, leucine; curve 8, β-phenylalanine; curve 9, β-alanine; curve 10, aspartic acid.

Table I. Typical steady-state and initial maximum and minimum total overpotentials

Additive	Concentration, m/l	η_{max}, mv	η_{min}, mv	$\eta_{steady\ state}$, mv
β-alanine	9.0 x 10^{-4}	116	115	205
	9.6 x 10^{-3}	120	115	278
Aspartic acid	1.5 x 10^{-3}	142	135	262
	7.5 x 10^{-3}	175	171	291
Leucine	5.0 x 10^{-3}	150	147	225
	8.0 x 10^{-3}	165	158	245
β-phenylalanine	2.8 x 10^{-3}	118	113	228
Malonic acid	3.3 x 10^{-1}	(no detectable max.-min. behavior)		312
	6.6 x 10^{-1}	145	140	335
Ethylamine	1.0 x 10^{-1}	130	127	190

increment. The greater effectiveness of the amino group over the carboxyl is shown by the data for ethylamine and propionic acid, and the importance of the structural relation between functional groups is seen on comparing α-alanine, β-alanine, and γ-aminobutyric acid. In addition, when other factors are equal, the overpotential is increased by an increase in size of the hydrocarbon part of the molecule.

Apart from some experiments with α-alanine, no detailed study of the high-concentration region was attempted. The data for α-alanine at concentrations above about 3 x 10^{-1}M showed poor reproducibility, but on the average the overpotential decreased by about 90 mv when this concentration was exceeded. This is shown by the broken portion of the overpotential-log M curve in Fig. 2, where M is the molarity. The deposit surfaces showed no particular roughening that might have caused a supposed decrease in true current density to account for the overpotential drop.

Discussion

Because of the greater effectiveness of the amino group as compared with the carboxyl in increasing the overpotential (Fig. 2), it may be suggested and assumed that, since this group is undoubtedly protonated in the acid solution, deprotonation probably occurs in the adsorption with the formation of competitive chemisorption bonds by the nitrogen atom. The generally greater effectiveness of compounds containing two functional groups in probably due to greater adsorptivity resulting from two-point chemisorption bonding, in a manner suggested before for dicarboxylic acids (20). Similarly, a trifunctional molecule might be expected to adsorb by three-point bonding if the electron-donating atoms can take appropriate positions relative to copper atoms on the cathode surface. The effect of functional group multiplicity therefore depends on structural relations since changes in structure may either increase or decrease adsorptivity. The overpotential attributable to the hydrocarbon part of the molecule appears to depend only on effective size.

Effect of structure.—The data for α- and β-alanines in Fig. 2 are an example of the effect of the structural relation between the same functional groups. Both compounds appear to be stable during electrolysis, as shown by the steady states in Fig. 1, and the difference in effectiveness may therefore be attributed to different adsorptivities of the normal molecules. This difference can be understood if it is assumed that two-point nitrogen-oxygen attachment is involved at different but adjacent copper atoms.

Estimates of the range of nitrogen-oxygen internuclear distances, made with Dreiding stereomodels, show that this distance varies with bond rotation from about 2.7 to 3.6Å with α-alanine, and from about 2.1 to 4.9Å with β-alanine. Comparison of these numbers with the three shortest internuclear distances in the copper lattice, 2.55, 3.6, and 5.1Å, suggests that β-alanine is better able to form strain-free nitrogen-oxygen attachments with a copper surface since it can more easily straddle at least the two shortest copper-copper distances. Therefore, without considering bond angles or orientation (which would also be necessary

for a detailed picture of the adsorbed state), the greater effectiveness of β-alanine can be expected.

The relatively small overpotential effect of γ-aminobutyric acid requires further study. However, the fact that this compound readily undergoes ring closure to form the γ-lactam on thermal decomposition suggests the possibility that sufficient cyclization might occur in acid solution too, possibly by hydrogen bonding between the amino and carboxyl groups, to restrict its adsorption on copper mainly to one-point attachments. The weaker chemisorption could then account for the small overpotential increments.

The greater effectiveness of aspartic acid compared with β-alanine can be expected because this compound is a structural combination of α- and β-alanines with a common amino group. The variation with bond rotation of the relative positions of the amino and carboxyl groups in relation to copper atoms in the lattice suggests that aspartic acid can probably adsorb by three-point attachment, although only to a limited extent because any two-point bonding by one end might be expected to restrict the bonding capabilities of the other.

Effect of molecule size.—The data for the four α-amino acids, glycine, α-alanine, leucine, and β-phenylalanine (Fig. 2) show the increase in overpotential with increased size of the hydrocarbon part of the molecule. Because the tendency to chemisorption is undoubtedly the dominant force in adsorptivity, it can be assumed as a first approximation that the adsorptivities of all four compounds are about the same since each has the same structural arrangement of the same electron-donating groups. The overpotential attributable directly to the chemisorption bonds would be approximately the same with each compound at the same concentration, and the different overpotentials with the different compounds would be due to different size alone. This implies two distinct overpotential effects or causes, the complete blockage of some growth sites by chemisorption bonds and the partial blockage of other adjacent sites by the actual bulk of the adsorbed molecule. The bond effect would be expected to cause a simple increase in true current density, and therefore an increase in activation overpotential according to the Tafel relation, depending on the fraction of growth sites blocked by the bonds at any given time in the dynamic adsorption process. (The steady-state overpotentials in Fig. 1 mean that a dynamic equilibrium is necessarily established with respect to any additive adsorption.) The bulk or screen effect can be regarded as a superimposed hindrance against copper ion movement to adjacent growth sites, and probably as a further effect on true current density, but depending on effective molecule size.

Behavior of α-alanine at high concentration.—The drop in overpotential with α-alanine at concentrations above about 3×10^{-1}M (Fig. 2) means a reduction in the energy required for electrodeposition at the experimental rate. It seems therefore that the chemisorption of this additive undergoes a change to a weaker form under these conditions, possibly by thermal disorientation of the initial monolayer in a manner suggested by Conway and co-workers in another context (21). It might be assumed that the initial monolayer is virtually complete at about 3×10^{-1}M and that a predominant two-point chemisorption is involved with the nitrogen and oxygen atoms adjacent to the copper surface. With the disorientation arising from increased concentration, the attachment would change to one-point, possibly accommodating a greater number of molecules in the adsorbed phase. The total screen effort would be expected to increase, but the dominant bond effect could conceivably be less, with decreased overpotential the net result.

The poor reproducibility of the data above about 3×10^{-1}M was evident in that a few experiments gave overpotential values that appeared to be a continuation of the main curve (Fig. 2), while most showed the drop. This could mean that the disorientation of the monolayer is probably sensitive to minor variations in surface structure.

Manuscript received Sept. 19, 1963; revised manuscript received Feb. 1, 1965. This paper is a contribution from the Department of Chemistry, University of Western Ontario, London, Ontario, with financial assistance from the National Research Council, Ottawa.

Any discussion of this paper will appear in a Discussion Section to be published in the December 1965 JOURNAL.

REFERENCES

1. H. Fischer, *Z. Elektrochem.*, **49**, 342, 376 (1943).
2. W. Gauvin and C. A. Winkler, *Can. J. Research B*, **21**, 125 (1943).
3. M. A. Loshkarev, *Doklady Akad. Nauk S. S. S. R.*, **72**, 729 (1950).
4. C. C. Roth and H. Leidheiser, *This Journal*, **100**, 553 (1953).
5. A. I. Levin, E. A. Ukshe, and V. S. Kolevatova, *Zhur. Fiz. Khim.*, **28**, 116 (1954).
6. L. L. Shreir and J. W. Smith, *Trans. Faraday Soc.*, **50**, 393 (1954).
7. E. H. Lyons, *This Journal*, **101**, 376 (1954).
8. A. J. Sukava and C. A. Winkler, *Can. J. Chem.*, **33**, 961 (1955).
9. E. J. Duwell, *This Journal*, **109**, 1013 (1962).
10. G. Fuseya and K. Murata, *Trans. Am. Electrochem. Soc.*, **50**, 235 (1926).
11. E. H. Lyons, *This Journal*, **101**, 363 (1954).
12. E. H. Lyons, J. C. Bailar, and H. A. Laitinen, *ibid.*, **101**, 410 (1954).
13. Z. A. Solov'eva and O. A. Abrarov, *Zhur. Fiz. Khim.*, **31**, 1248 (1957).
14. I. K. Rusnak, *Nauch. Doklady Vysshei Shkoly, Khim. Tekhnol.*, **1958**, 646.
15. H. Fischer, *Kolloid-Zeit.*, **106**, 50 (1944).
16. B. I. Parsons and C. A. Winkler, *Can. J. Chem.*, **32**, 581 (1954).
17. S. Adamek and C. A. Winkler, *ibid.*, **32**, 931 (1954).
18. W. Gauvin and C. A. Winkler, *Can. J. Research A*, **21**, 37 (1943); *ibid., B*, **21**, 81 (1943).
19. H. F. Collins, "The Metallurgy of Lead," 2nd ed., p. 453, C. Griffin and Co., London (1910).
20. Yu. Yu. Matulis and A. I. Bodnevas, *Izvest. Akad. Nauk S.S.S.R., Otdel. Khim. Nauk*, **1954**, 577.
21. B. E. Conway, R. G. Barradas, and T. Zawidzki, *J. Phys. Chem.*, **62**, 676 (1958).

Cathode Overpotential and Surface-Active Additives in the Electrodeposition of Copper

II. Effects of Compounds Containing Divalent Sulfur

A. J. Sukava, H. Schneider, D. J. McKenney, and A. T. McGregor

Department of Chemistry, The University of Western Ontario, London, Ontario, Canada

ABSTRACT

The sulfur-containing compounds, cystine, cysteine, methionine, and dimethyldisulfide, cause greater increments in the overpotential of a copper cathode in acid sulfate electrolyte than do related compounds containing carboxyl and amino groups only. Their effectiveness is presumably due to strong chemisorption involving the sulfur atom directly. These compounds appear to undergo slow chemical change during electrolysis. At low concentrations the large cystine molecule is more effective than the smaller dimethyldisulfide, but at high concentrations this order is reversed. The large molecules in high concentration are probably subject to mutual hindrance in the adsorbed phase, while smaller molecules with the same sulfur-group content and at the same concentration are able to block growth sites more effectively by forming a higher percentage of chemisorption bonds. Steady-state overpotential increments after sufficiently prolonged electrolysis indicate that surface-active additives are not necessarily removed from the solution by electrolysis and codeposition. The mobile, dynamically adsorbed additive might give rise to excess weight because of physical enclosure of solution in interstitial spaces within the deposit. The volume percentage of such spaces probably increases the more the additive causes continual nucleation and greater polycrystallinity.

In general, sulfur-containing amino acids like cystine and methionine cause greater increments in the overpotential of a copper cathode in acid copper sulfate electrolyte than do the related nonsulfur compounds, glycine and aspartic acid (1, 2). The divalent sulfur atom evidently imparts to these molecules a special potency in their additive function. This paper presents the results of a more detailed study of the overpotential effects of some sulfur compounds, with emphasis on their possible chemisorption behavior on the copper surface.

Experimental

The experimental procedure was in all respects the same as that in part I of this series (3).

Results

The variation of overpotential with time and the effect of additive concentration on the steady-state overpotential were studied in some detail with cystine, cysteine, methionine, and dimethyldisulfide. Data with ethyl mercaptan and β-mercaptopropionic acid were limited by low solubility in the standard electrolyte. Most of the data for cystine are taken from a previous study (2, 4) and some are published here for the first time.[1] The monofunctional dimethyldisulfide was chosen partly to isolate and emphasize the additive function of the disulfide group in cystine. As before (3), comparisons are made on the basis of effects on total overpotential only.

All of these sulfur compounds increased the overpotential at all concentrations. Their effectiveness is generally much greater than that of compounds containing only carboxyl and amino groups, and to some extent they appear also to differ from the latter in their mode of action. Typical overpotential-time data in Fig. 1 and steady-state overpotential-concentration relations in Fig. 2 may be compared with the effects of nonsulfur compounds (3).

Roughly quantitative observations with the cathode-ray oscilloscope showed the same initial overpotential-time pattern with each sulfur additive. An early maximum and minimum occurred at about 0.01 and 0.5 sec (Table I), followed by a second maximum and then a slow decrease to an ultimate steady state (Fig. 1). The initial maximum-minimum difference was much more pronounced than that found with additives containing no sulfur (3). The second maximum and steady state were both attained earlier the higher the concentration.

It seemed likely that the decrease in overpotential after the second maximum, as shown best by dimethyldisulfide at low concentrations, reflects either a gradual roughening of the surface with a consequent decrease in true current density or some slow chemical change in the additive during electrolysis. To decide this point, several experiments were made in which the additive-containing electrolyte that remained at steady state after a few hours of electrolysis was re-used in another cell with a new standard cathode surface. The results showed that cystine, cysteine, and dimethyldisulfide undoubtedly undergo some change during the first electrolysis up to the time that the steady state

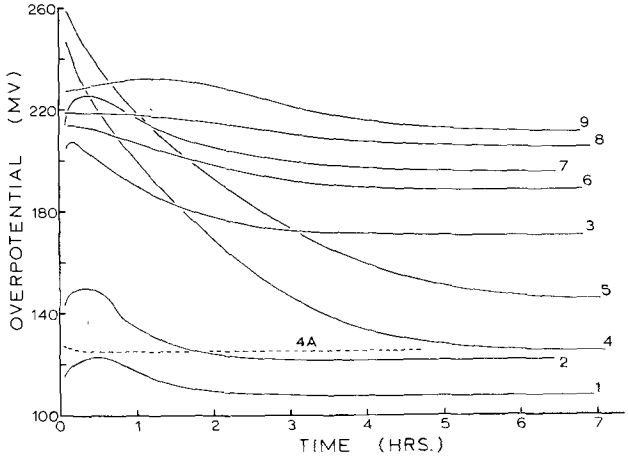

Fig. 1. Variation of total overpotential with time: curve 1, 4.1 x 10^{-7}M cysteine; curve 2, 8.2 x 10^{-7}M cysteine; curve 3, 8.2 x 10^{-6}M cysteine; curve 4, 2.33 x 10^{-6}M dimethyldisulfide; curve 4A, repeat electrolysis with solution from 4; curve 5, 3.30 x 10^{-5}M dimethyldisulfide; curve 6, 1.30 x 10^{-5}M methionine; curve 7, 1 x 10^{-6}M β-mercaptopropionic acid; curve 8, 2.0 x 10^{-5}M cystine; curve 9, saturated ethyl mercaptan.

[1] The authors thank Dr. C. A. Winkler, McGill University, for the use of these data.

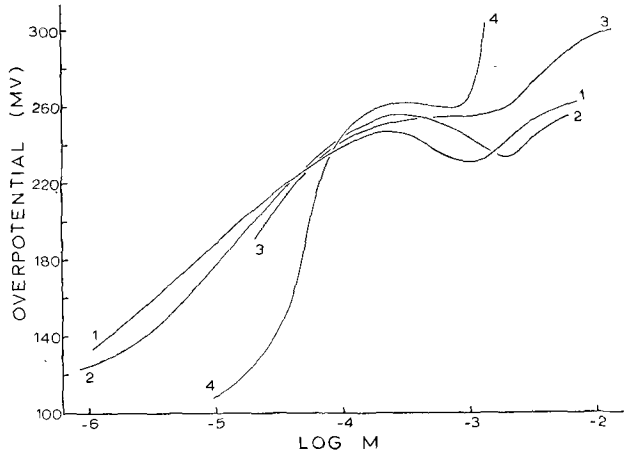

Fig. 2. Total steady-state overpotential as a function of additive concentration: curve 1, cystine; curve 2, cysteine; curve 3, methionine; curve 4, dimethyldisulfide.

is attained. This is obvious from curve 4A in Fig. 1 for a typical repeated electrolysis with dimethyldisulfide. The high second maximum was not obtained and the steady state was attained earlier at the original value. (No experiments of this kind were made with methionine.)

The steady-state overpotential-concentration curves in Fig. 2 show that the order of effectiveness of the sulfur additives is reversed at about 1 x 10^{-4}M. The smaller the molecule, the less the overpotential increment at low concentrations and the greater the increment at high concentrations. A maximum and subsequent minimum occur at roughly the same concentrations with cystine and cysteine (Fig. 2). The curve for dimethyldisulfide shows the same behavior although less well-defined, while the curve for methionine shows only general similarity.

Discussion

The variation of overpotential with time was of interest for two reasons. It has been suggested that protonation of the additive in the acid solution causes the initial maximum and minimum overpotentials because of cataphoretic surge of positively charged additive particles toward the cathode surface when the circuit is first closed (2, 5). Also, adsorption of additive on the cathode has been thought to give rise to occlusion of the additive in the growing deposit, with its supposed depletion in the solution causing a steady decrease in overpotential with time (2).

Initial maxima and minima.—The suggestion that the initial behavior shown in Table I is attributable at least in part to protonation of the additive might be readily accepted when the additive is a reasonably strong base like an amino compound. On the other hand, compounds like β-mercaptopropionic acid or dimethyldisulfide cannot be sufficiently protonated despite their Lewis-base structure and despite the high acidity of the solution at the cathode surface. When the initial overpotentials in Table I are compared with those found for nonsulfur compounds (3), and when the effect of the divalent sulfur is noted, it seems certain that the over-all behavior is governed largely by adsorption of additive on the cathode prior to electrolysis. (The free energy of this adsorption and the rate of diffusion of the additive might also be important, as might the possible dipole properties and polarizability of the additive molecules in the cathode field.) Some preliminary experiments have shown that the maximum-minimum difference with sulfur additives is increased by an increase in the period of contact between cathode and solution prior to electrolysis, but with nonsulfur carboxyl and amino compounds this variable seems to have no effect. Possibly, and in agreement with similar suggestions by others (6), such nonsulfur compounds are not appreciably adsorbed before current flow begins.

Table I. Typical steady-state and initial maximum and minimum total overpotentials

Additive	Concentration, m/l	η_{max}, mv	η_{min}, mv	$\eta_{steady\ state}$, mv
Cystine	2.08 × 10^{-5}	124	109	205
	4.16 × 10^{-5}	142	113	220
	4.16 × 10^{-4}	202	140	242
	6.24 × 10^{-4}	219	145	235
Cysteine	8.25 × 10^{-6}	115	102	176
	8.25 × 10^{-5}	141	108	237
	8.25 × 10^{-4}	182	130	243
	2.48 × 10^{-3}	204	129	235
Methionine	1.35 × 10^{-5}	110	97	190
	3.37 × 10^{-5}	132	90	212
	1.35 × 10^{-4}	222	115	245
	3.37 × 10^{-4}	248	150	255
β-mercaptopropionic acid	1 × 10^{-6}	120	109	195
Ethyl mercaptan	1 × 10^{-5} approx. (saturated)	270	165	260
	(saturated, concentration not determined)	150	116	210
Dimethyldisulfide	7.75 × 10^{-6}	150	120	105
	1.10 × 10^{-5}	170	120	115
	2.33 × 10^{-5}	165	115	125
	3.30 × 10^{-5}	195	107	146
	1.16 × 10^{-4}	240	130	

Steady-state overpotential and excess deposit weight.—The significance of Fig. 1 is that all our additives gave rise to an apparently true steady-state overpotential, after sufficiently prolonged electrolysis, down to the lowest effective concentrations. This is well illustrated by the curve for cysteine at 4.1 x 10^{-7}M. It is therefore certain that no appreciable reduction in the concentration of these additives occurs by any kind of bonded occlusion in the growing deposit, which means that the adsorption of additive must be sufficiently dynamic and the adsorbate phase sufficiently mobile to enable the copper lattice to grow without covering the additive molecules, except perhaps by mere entrapment of solution in interstitial spaces in the deposit.

Since electrolysis does not cause a decrease in additive concentration by codeposition, the excess deposit due to surface-active additives (7-11) might be attributed to physically entrapped solution in interstitial spaces rather than to adsorbed additive. (The excess deposit is the weight of deposit obtained in the presence of an additive in excess of that obtained in the absence of additive with the same amount of charge flow.) It may be noted that a correlation has been found between the polycrystallinity of the deposit and the excess weight (7, 8, 11); the finer the deposit, the greater the excess weight. This would mean that a greater volume percentage of interstitial spaces occurs as the deposit becomes more polycrystalline with the more extensive nucleation caused by adsorbed additive.

Chemical change.—The results of repeated electrolyses as typified by curve 4A in Fig. 1 are evidence of some chemical change during electrolysis such that the effectiveness of the additive in increasing the overpotential is reduced. This is substantiated in part by literature statements that cystine and thiourea form copper II sulfide at the cathode (12) and by similar claims for sulfur additives in the electrodeposition of nickel (13, 14). The formation of a dark anode "mud" whenever such additives are present during copper electrolysis suggests that anode effects might be an additional factor.

The marked decrease in overpotential after the second maximum leads to the conclusion that the chemical change involves a high percentage of additive when it is present in low concentration. The long-term overpotentials would then be true steady-state values caused by relatively stable reaction products or equilibrium mixtures. The equally reasonable conclusion follows that the same change must take place at high concentrations too, but that the fraction of additive undergoing change in a given period of time is less the higher the concentration. The so-called steady

states obtained with high concentrations of sulfur additives are therefore steady only because the percentage rate is small, and the overpotentials under these conditions are caused primarily by the unchanged form of the additive.

Steady-state effects.—The data in Fig. 2 show that at high concentrations the ability of sulfur additives to increase the overpotential increases with a decrease in molecule size. This can be understood if it is assumed that strong sulfur-copper chemisorption bonds are formed with a sufficiently greater contribution to overpotential than that due to the rest of the molecule. The marked difference in the ability of sulfur and nonsulfur additives to increase the overpotential can then also be explained.

It seems reasonable from the overpotential values that concentrations of sulfur additives in excess of about 1×10^{-4}M (Fig. 2) are approximately sufficient to complete the initial monolayer on the cathode surface. A given area of the surface could accommodate in this layer a greater number of the small dimethyldisulfide molecules than would be possible with cystine, since the larger nonsulfur portion of an adsorbed cystine molecule could prevent the bonding of another cystine molecule at an adjacent copper atom. The effect would be the blockage of a higher percentage of growth sites by chemisorption bonds with dimethyldisulfide than with cystine, and therefore a greater overpotential increment.

Since reaction products and unchanged sulfur additives are presumably responsible for the increments in steady-state overpotential at low and high concentrations, respectively, it would be expected that a change in the order of effectiveness might occur with change in concentration, as is shown in Fig. 2, although the complete reversal would not necessarily follow. Because of the chemical change, the data do not reliably show the relative effects of dimethyldisulfide and cystine at the lowest concentrations, with only a small fraction of the surface covered, although the larger cystine molecule can be expected to have the greater effect under such conditions, and the crossing of the overpotential-concentration curves should be found even if no chemical change occurred.

The decrease in overpotential with increase in additive concentration above about 2.5×10^{-4}M (Fig. 2) might reflect a decreased bonding effect as a result of thermal disorientation similar to that suggested previously for α-alanine (3). Since sulfur additives are evidently much more strongly adsorbed than α-alanine, it is not surprising that the maximum overpotential occurs at a much smaller concentration. The data in the region of all these maxima showed poor reproducibility, which supports the view that the cause of the maximum might be the same with both kinds of additive.

It is worth noting that the two adjacent sulfur atoms in dimethyldisulfide and cystine do not impart to these compounds a markedly greater ability to increase the overpotential than that due to the single sulfur in cysteine and methionine. The probability of sulfur-copper bonding might be greater with a disulfide, but the actual chemisorption presumably cannot involve both sulfurs simultaneously. This might be expected from the pertinent internuclear distances, 2.04Å for the sulfur-sulfur distance in the disulfide and the minimum 2.55Å between copper atoms in the lattice. With this in mind, it seems unlikely that thermal disorientation of the initial monolayer could satisfactorily account for the overpotenital drop with dimethyldisulfide at 2.5×10^{-4}M (Fig. 2), or even for the plateau if the curve is so interpreted, the reason being that dimethyldisulfide can presumably adsorb in only one regularly oriented manner by one-point attachment at one of the sulfur atoms.

A previous suggestion that cystine is probably reduced to cysteine at the cathode (2) is obviously not supported by our more detailed study. The fallacy in this view, which was based on the close similarity of the overpotential effects at low concentrations, has been noted before (15).

Manuscript received Sept. 19, 1963; revised manuscript received Feb. 1, 1965. This paper is a contribution from the Department of Chemistry, University of Western Ontario, London, Ontario, with financial assistance from the National Research Council, Ottawa.

Any discussion of this paper will appear in a Discussion Section to be published in the December 1965 JOURNAL.

REFERENCES

1. S. Adamek and C. A. Winkler, *Can. J. Chem.*, **32**, 931 (1954).
2. A. J. Sukava and C. A. Winkler, *ibid.*, **33**, 961 (1955).
3. H. Schneider, A. J. Sukava, and W. J. Newby, *This Journal*, **112**, 568 (1965).
4. A. J. Sukava, Ph.D. Thesis, McGill University (1955).
5. B. I. Parsons and C. A. Winkler, *Can. J. Chem.*, **32**, 581 (1954).
6. S. I. Khotyanovich, O. K. Gal'dikene, and Yu. Yu. Matulis, *Tr. Soveshch. po Vopr. Vliyaniya Poverkhn. Aktiv. Veshchestv na Elektroosazhdenie Metal.*, **1956**, 25.
7. G. Fuseya and K. Murata, *Trans. Am. Electrochem. Soc.*, **50**, 235 (1926).
8. G. Fuseya and M. Nagano, *ibid.*, **52**, 249 (1927).
9. C. Marie and A. Buffat, *J. Chim. Phys.*, **24**, 470 (1927).
10. R. Taft and H. E. Messmore, *Trans. Kansas Acad. Sci.*, **32**, 42 (1929); *J. Phys. Chem.*, **35**, 2585 (1931).
11. M. Kikuchi and H. Toyoda, *J. Chem. Soc. Japan, Ind. Chem. Sect.*, **52**, 33 (1949); *Repts. Govt. Chem. Ind. Research Inst. Tokyo*, **49**, 31 (1954); *ibid.*, **49**, 36 (1954).
12. D. R. Turner and G. R. Johnson, *This Journal*, **109**, 798 (1962).
13. A. V. Pamfilov and R. M. Morgart, *Ukrain. Khim. Zhur.*, **23**, 684 (1957).
14. R. M. Morgart and O. E. Panchuk, *Zhur. Priklad. Khim.*, **32**, 833 (1959).
15. J. Llopis, J. M. Gamboa, and L. Arizmendi, *Publs. inst. quim. fis. "Antonio de Gregorio Rocasolano,"* **10**, 224 (1956).

Structure of Electrodeposited Lead Dendrites

F. Ogburn, C. Bechtoldt, J. B. Morris,[1] and A. de Koranyi

National Bureau of Standards, Washington, D.C.

ABSTRACT

Electrodeposited lead dendrites were grown and examined by x-ray diffraction and metallographically. Their structure was essentially that of two crystals having a twist relation about a common [111] pole which was normal to the flat surface of the two-dimensional dendrites. Each dendrite contained many small voids or channels. The direction of growth was either about halfway between a <211> direction of one crystal and a neighboring <211> direction of the second crystal or halfway between <110> directions.

Electrodeposited dendrites[2] have been described and reviewed extensively by Wranglen (1). He examined dendrites of lead, tin, silver, cadmium, and copper microscopically and by x-ray diffraction and described them as single crystals. Faust and Johns (2) examined electrodeposited dendrites of lead, silver, copper, gold, and aluminum, and by metallography found at least one grain boundary in each of the dendrites growing in <211> or <110> directions, but not in dendrites growing in a <100> direction.

The lead dendrites, as shown by Wranglen, are of two main types: those that are flat and growing in a <110> direction and those that are three dimensional and growing in a <100> direction. The growth of <100> dendrites is favored by conditions of solution depletion, and they are branched at right angles. The <110> dendrites have been described as monocrystalline, branched at 60°, and growing with the plane of the dendrite parallel to a {111} plane. The lead dendrites examined by Faust and Johns were of the <110> type with "twin planes."

As part of a program of investigating the growth and character of metal crystals grown by electrodeposition, we had occasion to grow and examine some lead dendrites. We had hoped to use these as seeds for growing larger crystals, and we wished to know something about the quality of the crystals. Wranglen had considered only morphology and x-ray diffractometer measurements, and Faust and Johns had made only a very limited metallographic examination. All in all very little was known about the lead dendrites which are extremely easy to grow.

We grew numerous dendrites of lead by electrodeposition. In many respects they appeared to be the <110> dendrites of Wranglen, but were neither twinned in the usual sense nor single crystals. The apparent difference is probably attributable to the use of more powerful tools for their examination. Certainly these were not unusual growths inasmuch as they were obtained consistently and to the virtual exclusion of other types.

Growth of Dendrites

The dendrites were grown by electrodeposition in a 0.5M solution of lead acetate and 2M ammonium acetate with a lead anode and cathode. Reagent grade chemicals and distilled water were used without any purification steps.

The plating cell consisted of a 100 ml beaker filled with electrolyte and covered with a rubber stopper. The lead anode was supported at one side of the beaker through a hole in the stopper. On the other side, a glass tube 4 mm in diameter, was inserted in a hole in the stopper and positioned so that one end was in the electrolyte about a centimeter from the bottom of the beaker. The cathode was inserted in this tube so that one end was a few millimeters above the submerged end of the open tube. For some of the experiments the cathode was a long sliver of lead, and at other times it was a short cylinder of lead cast around the end of a copper wire which served to support the lead and to make an electrical connection. With this arrangement, the dendrites' growth was confined by the tube and controlled so that only one or two dendrites grew in a predetermined direction. This facilitated the measurement of growth rate and the subsequent isolation of a single dendrite for metallographic or x-ray examination. The electrolysis was carried out galvanostatically using a high resistance in series with the cell.

A scale was mounted near to and parallel to the tube so that it and the tip of the growing dendrite could be observed simultaneously through a telescope. This permitted measurement of the rate of growth or elongation of the dendrite.

The first stages of growth were usually marked by the appearance of numerous minute needles or trees. Most of these ceased to grow at a very early stage, and usually only one or two grew to lengths of more than a millimeter. This is a selective process in which the surviving dendrites are those which grow most readily and which are favorably oriented with their growth directions nearly parallel to the tube axis. As deposition was continued, the rate of advance of the tip, the growth rate, was measured. At the end of the experiment, the dendrite was recovered and examined.

A number of dendrites were grown in this manner at rates varying from 0.001 to 1 mm/min. The corresponding current densities calculated from rates of advance of the tips would be 18-18,000 ma/cm^2. The currents per unit area of tube cross section were 0.5-40 ma/cm^2.

It is of incidental interest to note here the relation between the quantity of lead in the dendrites and in the solution in the tube. The solution contained 1.3 mg of lead per millimeter length of the tube and dendrites grown at the rate of 0.3 mm/min contain an average of about 0.35 mg/mm length. Hence, dendrite growth did not depend on diffusion of lead ions from the open end of the tube. This is readily predictable without experiment, although it may not be realized by the experimenter. The deposition conditions are such that ion diffusion is more closely characterized by spherical diffusion than by linear diffusion which could not support the rapid dendritic growth. The concentration gradient for lead ions is confined to a short distance from the rapidly advancing tip.

Appearance of Dendrites

As had been observed by Wranglen (1), the dendrites were flat (Fig. 1). Their thickness ranged between 15 and 90μ. While growing, the flat surfaces were highly lustrous, but became rather dull after drying in air. Branching was close to 60° to the main stalk for some dendrites. Very often, the angles were not sufficiently well defined to measure meaningfully.

Although the dendrites were always to be described as flat, they almost always had short projections at an angle to the over-all plane of the dendrite.

[1] Present address: Howard University, Washington, D. C.

[2] As used in this paper, dendrite refers to the external form of the growth and not to its internal structure.

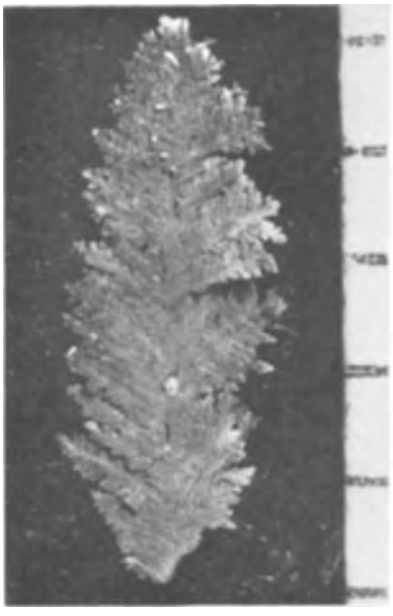

Fig. 1. Lead dendrite grown at 0.6 mm/hr; 1 div = 1 mm

These projections accounted for only a small portion of the total mass, but might account for some extra reflections of low intensity found in the diffraction patterns.

Also, a truly flat dendrite was seldom, if ever, isolated. The extreme fragility of these dendrites was such that they were difficult to handle without deformation. Some of the misalignment observed by x-ray diffraction and grain boundaries found metallographically could be and, perhaps, should be attributed to strain and deformation induced after the dendrite was formed.

X-ray Diffraction Examination

Several lead dendrites were examined by the x-ray diffraction techniques employing Laué, precession, and Weissenberg cameras. The transmission Laué patterns always indicated more than one orientation with misalignment in each. The method used by Wranglen (1) would indicate the dendrites to be single crystals.

Precession camera photographs were very informative. These were made with the axis of precession perpendicular to the flat side of the dendrite. Zero level (111) photographs of the dendrite shown in Fig. 1 show twelve pronounced {220} reflections with sixfold symmetry. The first level (111) photograph (Fig. 2) with the same setting shows two sets of pronounced {111} reflections with threefold symmetry with another double set of very weak {111} reflections displaced 60° from the primary orientations. This pattern can be accounted for if the lead is present in two primary orientations with a (111) plane common to both orientations and parallel to the plane of the dendrite with a slight amount of lead in a "twin relationship" to each of these two positions. One primary orientation is rotated 33° relative to the other and about the common [111] pole. Because of the inherent sixfold symmetry of the zero level (111) photographs, first level (111) photographs are required for determining the true angle of twist and the presence of normal twin growth, if any.

Figure 3 is a precession photograph of a dendrite with three orientations 30° and 60° apart (one pair has a twin relation). An equitorial Weissenberg photograph of the same dendrite confirms the zero level precession photograph and also clearly shows misalignment about the growth axis of the dendrite. All the diffraction methods showed considerable dispersion about the two orientations. As indicated earlier, some of this dispersion may be due to handling of the specimen.

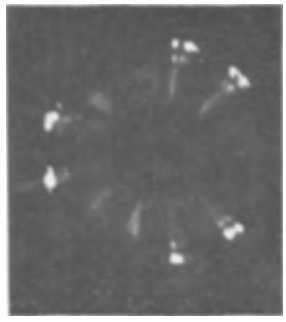

Fig. 2. First level (111) precession photograph of dendrite of Fig. 1. Pronounced (111) reflections are from material with two orientations, 33° apart. Weak (111) reflections are displaced 60° from intense reflections.

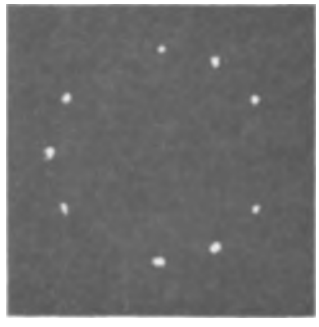

Fig. 3. First level (111) precession photograph of dendrite. (111) reflections from material with 3 different orientations, 30° and 60° apart.

The precession patterns appear to be representative of the dendrite inasmuch as patterns were made at random positions along the length and width of some of the dendrites with no significant differences observed in the appearance of the patterns. Precession patterns were also made with the plane of the dendrite parallel to the x-ray beam. While of poor quality they indicate one surface of the dendrite to be of one orientation and the opposite surface of the other orientation. Because of physical factors and the density of lead, the part of the pattern which results from reflection from the surface of the platelet is greatly enhanced over that part which depends on transmission. The two surface effects are recorded on opposite sides of the pattern (3).

Table I summarizes the angular relationship observed. The angles recorded have a precision to within about ½° insofar as they represent the angle occurring most frequently. There is, however, a spread of up to as much as ±10° from the model value.

Determination of Direction of Growth

The direction of growth of a dendrite was assumed to be parallel to the long axis of the dendrite and was measured as the angular displacement from the axis of the goniometer supporting the dendrite, after alignment for the precession photographs. This measurement could well involve an uncertainty of 2 or 3 degrees. The <110> and <112> directions were deter-

Table I. Twist angle between crystals of lead dendrites

Rate of growth, mm/min	Twist angle*
0.001	50°
0.002	20°
0.01	31°
0.2	30°, 30°, 60°
0.3	27°, 33°, 60°
0.3	33°, (27°), (60°)
0.6	27°, (33°), (60°)

* Angles for weak reflections are shown in parenthesis.

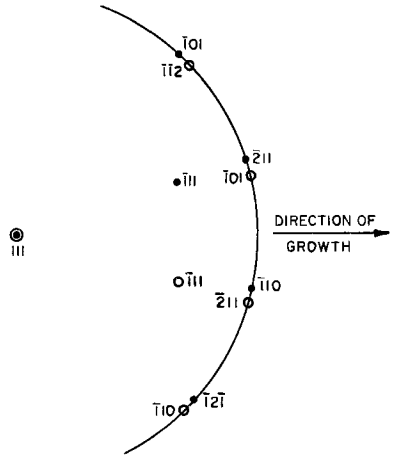

Fig. 4. Stereographic projection showing orientations of material in dendrite of Fig. 1 and 2; ○, projections of one orientation; ●, projections of other orientation.

mined from the {220} reflections of the zero level precession photographs and the {111} reflections of the first level, in terms of the angular displacement from the axis of the goniometer head. In this manner, the direction of growth was determined to be half-way, within 3° or 4°, between the $<\bar{2}11>$ directions of the two crystals (Fig. 4). The two $<\bar{2}11>$ directions were 33° apart. Also a dendrite with a twist of 27° was found to have grown in a direction half-way between two $<\bar{2}11>$ directions. Both of these dendrites, however, gave precession photographs showing weak reflections for twist angles of 60°. Another dendrite, with a twist angle of 31°, had an apparent growth direction half-way between two $<10\bar{1}>$ directions.

A fourth dendrite, with 3 orientations and twist angles of 27°, 33°, and 60°, was of interest. It grew half-way between the two $<\bar{2}11>$ directions of the two crystals 33° apart and simultaneously half-way between the two $<10\bar{1}>$ directions of the two crystals 27° apart. This simultaneous relationship is possible wherever the two twist angles total 60°.

Metallographic Examination of Cross Sections

Figure 5 is a micrograph of a portion of the cross section of a dendrite. It is immediately evident that the dendrite contains voids or channels. The dark areas are the plastic mounting material which flowed into the voids during curing.[3]

Since the voids did fill with the mounting plastic, it is evident that they were not closed off from the outside, but must have a wide opening or at least two openings. Successive polishing of the section of one dendrite revealed that any given void did not extend more than about a tenth of a millimeter along the stalk or branch.

All of the dendrites have two layers. Sometimes the voids are much less evident, and occasionally one layer is absent over a portion of the cross section. Other portions might have a third layer, as shown in

[3] Epon 815 with diethylaminpropylamine was used to mount the lead dendrites. This cures over a two-day period at room temperature. Other mounting materials tried did not fill the voids, and successful polishing and etching were not achieved.

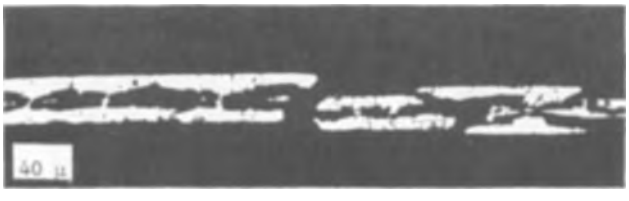

Fig. 5. Cross section micrograph of dendrite of Fig. 1, 2, and 4. Magnification approximately 200X.

Fig. 6. Cross section micrograph of lead dendrite. Magnification approximately 400X.

Fig. 6 and 5. Figure 5 shows boundaries within a layer, and we have observed cross sections with a twin boundary within a layer and parallel to the plane of the layer or dendrite.

Discussion

Pertinent to any consideration of the growth mechanism of these dendrites are the circumstances in which they were grown. The initial nuclei were numerous and oriented in many different directions, probably with many forms or combination of twin and twist boundaries and crystal imperfections. Of those present initially only those that grew the most rapidly along the axis of the restraining tube survived. This is a highly selective process, and it means that the kinds of dendrites described were faster growing, but were not the only kinds that grew. It also means that the structure favorable for the most rapid growth may not always have been the one to survive since orientation is also involved in the selection process.

The diffraction patterns and the cross-section micrographs show the dendrites to be essentially of two layers, each a layer of different orientation separated by a twist boundary. Some dendrites had 3 and/or 4 orientations with a common [111] pole. The third (and fourth) orientation always had a twin relation to one of the other orientations. The true relationship of these interfaces cannot be determined from the diffraction patterns. But is seems reasonable to think of these dendrites as having a twin and a twist boundary parallel to the plane of the dendrite. To have two twist boundaries with the twist angles totalling 60° would seem too fortuitous.

Since each dendrite observed, except for the normal twin relationship mentioned before, consisted of essentially two crystals, it seems reasonable to say that some interaction between the two crystals is responsible for rapid growth, more rapid than possible if each grew independently. It has been shown that for rapid two-dimensional growth of some dendrites with diamond, zinc blende, and closest packed cubic structure, twin lamellae are required to provide suitable re-entrant angles (4). The dendrites grown in this investigation appear to have grown by another mechanism. Such an interaction is provided by a re-entrant angle mechanism similar to that suggested by Price (5) for some cadmium crystals grown from the vapor. Figure 7 (similar to Fig. 16 of Price) shows re-entrant angles that might be formed by the two layers of the lead

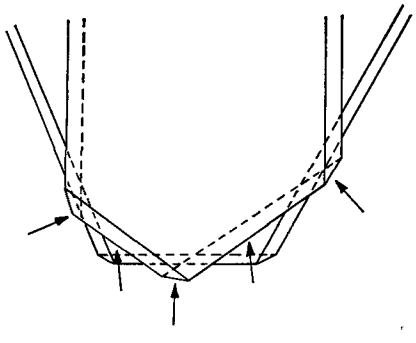

Fig. 7. Diagram showing re-entrant angles formed by overlapping crystal. Each crystal is bounded by (111) facets.

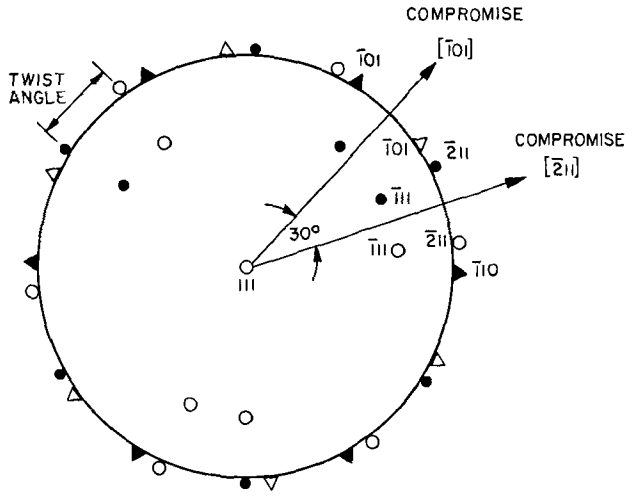

Fig. 8. Diagram showing directional orientations within plane of dendrite.

dendrites. This model assumes that all bounding surfaces are {111}.

If the two surfaces of the re-entrant angle are the same crystallographically, then one would expect no differentiation during the deposition process and, hence, the crystal boundary would not be planar and the surfaces would not remain planar. This appears to lead to complications which can be avoided by saying that the bounding surfaces, excepting the composition plane, are other than {111}; for example: {110} or {100}.

The twist angle may be determined by the relative stability associated with each possible angle. Price (5) has discussed this in terms of coincident hexagonal nets. The twist angles observed in the lead dendrites do not agree exactly with those predicted by Price on the basis of nearest neighbor considerations, but we cannot say that our results are at variance with his.

It is also possible that the twist angle is more dependent on the optimum growth directions for each crystal with the actual growth direction of the composite dendrite being a compromise. This leads to the question of what determines the growth direction and what is the growth direction.

We found growth directions that were either a compromise <$\bar{2}$11> or <$\bar{1}$01> direction. Consideration of Fig. 8 shows that although completely equivalent crystallographic directions are 120° apart for either a single or composite crystal, partially equivalent directions are 60° apart and suggest branching at 60° to the main stalk. Now if both [$\bar{1}$01] and [$\bar{2}$11] compromise directions occur we would expect branching to occur at 30° since these compromise directions are 30° apart. Since this branching angle has not been observed, it seems likely that growth occurs in only one of the two compromise directions. Now the dendrites having three or more orientations, including the material giving weak x-ray reflections, all included a twist displacement of 60°. As indicated earlier, this is a situation in which both compromise directions occur simultaneously, and either one can be controlling. Of the dendrites measured for growth direction, one gave x-ray reflections for only two orientations, and the growth direction appeared to be a compromise [$\bar{1}$01] direction.

Price (5) reported that for similar cadmium dendrites (hexagonal system) he observed the compromise direction of growth to be between two <10$\bar{1}$0> directions. This is equivalent to growth between two <$\bar{2}$11> directions for face-centered cubic systems. Our results indicate that the compromise direction of growth could also be between <$\bar{1}$01> directions.

One can conceive of mechanisms to account for growth in the compromise [$\bar{1}$01] direction, or for the compromise [$\bar{2}$11] direction. We lack, however, the knowledge to predict the growth direction.

Acknowledgment

The authors are indebted to the Advanced Research Projects Agency, Department of Defense, which helped support the work described.

Manuscript received Dec. 28, 1964; revised manuscript received Feb. 1, 1965. This paper was presented at the Washington Meeting, Oct. 11-15, 1964.

Any discussion of this paper will appear in a Discussion Section to be published in the December 1965 JOURNAL.

REFERENCES

1. G. Wranglen, *Trans. Royal Inst. Tech.*, No. 94 (1959).
2. J. W. Faust, Jr., and H. E. Johns, *This Journal*, **108**, 109 (1961); **110**, 463 (1963).
3. M. J. Buerger, "Crystal-structure Analysis," p. 227, John Wiley & Sons, Inc., New York.
4. N. Albon and A. E. Owen, *J. Phys. Chem. Solids*, **24**, 899 (1963); H. F. John and J. W. Faust, Jr., "Metallurgy of Elemental and Compound Semiconductors," Interscience Publishing Co., New York (1961); J. W. Faust, Jr., and H. F. John, *This Journal*, **108**, 855 (1961); R. S. Wagner, *Acta Met.*, **8**, 57 (1960); D. R. Hamilton and R. G. Seidensticker, *J. Appl. Phys.*, **31**, 1165 (1960).
5. P. B. Price, *Phil. Mag.*, **4**, 1229 (1959).

Epitaxial Growth of ZnSe on GaAs

Alexander Baczewski

General Telephone & Electronics Laboratories Inc., Bayside, New York

ABSTRACT

Zinc selenide has been grown epitaxially on the gallium plane of gallium arsenide substrates. The overgrowth has the <111> orientation of the seed and exhibits an unambiguous Laue pattern. The vapor species was transported to the substrate in a gas stream consisting of argon, hydrogen, hydrogen chloride, and ammonium iodide. Growth rates of 5 μ/hr were usual, and thicknesses of 200μ were attained.

Recent developments in the field of injection luminescence have stimulated an interest in the preparation of single crystals of II-VI compounds and of epitaxially grown crystals using crystals of III-V compounds as a basis. This paper deals with the epitaxial growth of ZnSe on GaAs as a substrate. This combination was chosen because both compounds crystallize in the cubic zinc sulfide system and have very similar lattice spacings: GaAs 5.653 (1), ZnSe 5.667 (2). This small difference should minimize strain, particularly since intermediate layers of solid solutions of the compounds occur during deposition and further heat treat-

ment. The existence of such compounds and their continuous miscibility have been proven by the investigations of Goryunowa *et al.* (3). The high melting point of ZnSe (1515° ± 20°C) (4) and the dissociation of the vapors make it extremely difficult to prepare crystals of this material, either from the melt or from the vapor phase. Fischer (5) overcame the experimental difficulties by constructing a furnace in which a modified Bridgeman-Stockbarger growth arrangement pulls ZnSe growing epitaxially upon ZnTe under argon. In other experiments, Fischer used very high pressures of Se or Zn to prevent the dissociation of zinc selenide during zone melting.

Confronted with similar problems in the preparation of GaAs and GaP, Ing and Minden (6) adopted an open-tube synthesis system. Gallium and arsenic or phosphorus were placed in boats inside a heated quartz tube and transported toward the cooler end by reacting the metal with gaseous hydrogen chloride and by distilling the As or P at the same time. Similar methods have been described by Schaefer (7) and by Holonyak (8). The technique described in this paper makes use of the reaction of zinc selenide with hydrogen chloride at elevated temperature and the dissociation of the volatile compounds at lower temperature in an open tube system. Gallium arsenide wafers positioned in the deposition zone afford sites for epitaxial growth. The severe corrosive action of the transporter gases is reduced by the admixture of a volatile iodine compound. Nongrowth areas of the substrates are also protected by a nonreactive coating.

Experimental

Vapor transport experiments were carried out in a quartz tube (55 cm long, 44 mm ID) inside a 45-cm-long tubular furnace wound with Nichrome wire. To obtain the desired temperature profile, taps were connected with resistors. To afford another hot zone near the entrance of the furnace a heater tape was wound around the tube controlled to 200°C by a variable resistor. Another heater tape was wound around the tube between the first tape and the gas inlet. It was kept at 300°C in order to prevent back sublimation of the volatile iodide. A chromel-alumel thermocouple monitoring the temperature was enclosed in a small quartz tube attached to the reaction tube, since it had been found that a reentering tube served as a heatsink drawing all the crystal growth away from the substrate.

Another thermocouple inside the reaction tube controlled the input to the heater tapes. A rectangular quartz plate throughout the whole length of the growth tube served at one end as a support for a quartz wool plug saturated with source material. At the other end, slots were ground into the plate for holding the targets. Electronic grade zinc selenide (60-mesh) was used as the source material. The substrates were cut (0.5 x 0.5 x 0.01 cm) from undoped gallium arsenide single crystals in the (111) direction. The gallium faces were polished to half-wave flatness having a surface finish of one-quarter micron. The transport gases were prepurified hydrogen, pure argon, and hydrogen chloride (99.9% min. pure). Catalytic units removed oxygen from hydrogen and argon. Hydrogen chloride was bubbled through concentrated sulfuric acid to remove water. Teflon tubing was used for all connections. Figure 1 indicates the experimental arrangement.

A typical growth experiment was run thus: ZnSe was powdered onto a mat of quartz wool which was then rolled and enclosed in a wrapper made from woven quartz that was previously fired to remove organic substances. This arrangement ensures intimate contact between the carrier gases and source. The wrapper was fastened to the quartz plate with quartz fibers. The substrates were glued on their arsenide face with sodium silicate onto freshly cleaved and cut mica and, after a Freon spray, placed into the grooves of the quartz plate. The plate was introduced into the quartz

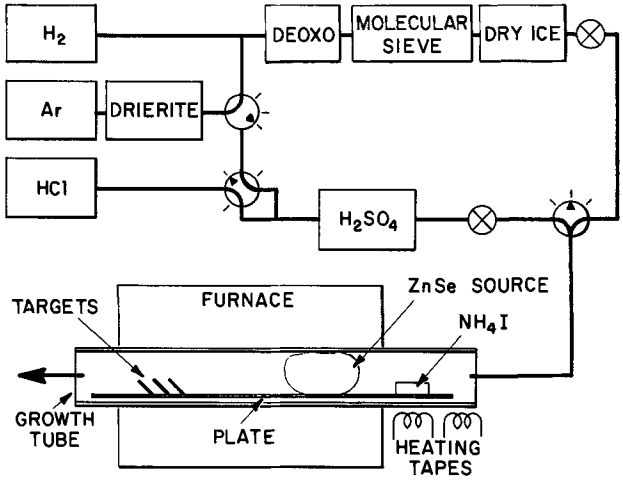

Fig. 1. Apparatus for the epitaxial deposition of zinc selenide

tube. A quartz boat containing an ammonium halide was positioned into the tube in the vicinity of the furnace. While the furnace was heated up (300°C for the first tape, 200°C for the halide, 600°-740°C for the source, 570°-610°C for the substrates) and for the following 16 hr, a flow of 20 ml hydrogen per minute and 20 ml argon per minute was maintained. Then, 1 ml hydrogen-chloride gas per minute was added to the stream. After another 24 hr, the hydrogen chloride flow was increased to 10 ml/min. Most runs were terminated after 96 hr. The assembly was cooled in a stream of hydrogen and argon.

Results

Epitaxial single crystals of ZnSe, tightly adhering to the (111) plane of GaAs, have been grown at rates from 1 to 5 μ/hr. Thicknesses of 200μ were attained. Figure 2 shows a single crystal of ZnSe removed from the GaAs substrate, and Fig. 3 shows a cross-section of a well-adhering epitaxial growth. The lower layer is the gallium arsenide substrate, the upper layer is zinc selenide. An x-ray scan proved single crystallinity. The crystals showed no visible u.v. fluorescence at room temperature and strong red fluorescence at 77°K.

Discussion

In a vapor phase transport system the probability of a reaction of the substrate with the carrier gas has to be taken in account. It is impossible to expose germanium to acidic vapors. Gallium arsenide is also severely etched under the conditions of the zinc sele-

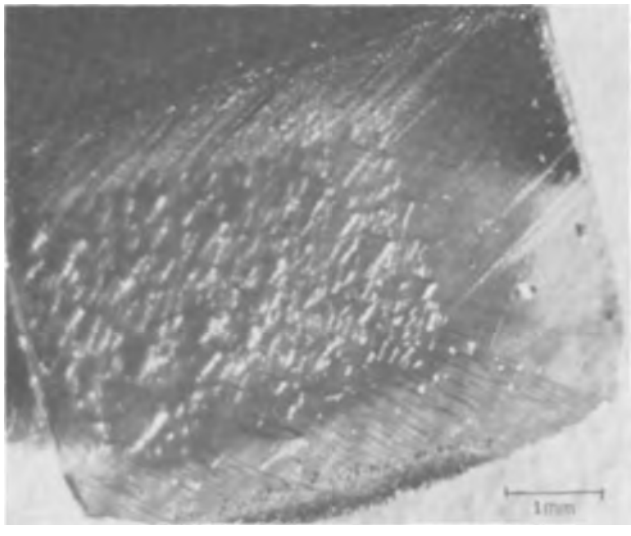

Fig. 2. Zinc selenide crystal. (111) Zinc face faces the viewer. Gallium arsenide substrate removed.

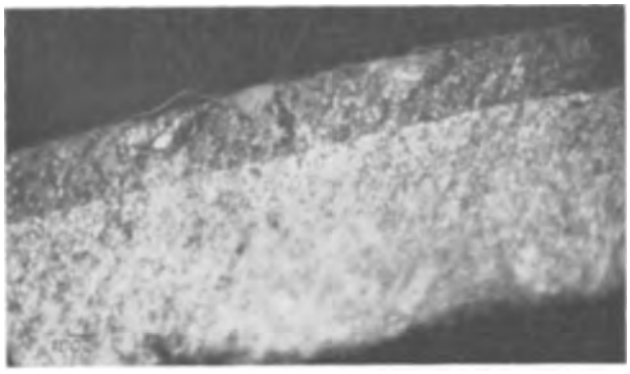

Fig. 3. Cross section of zinc selenide (dark), grown epitaxially upon (111) gallium plane of gallium arsenide substrate.

nide vapor transport in gaseous HCl. This is not to be expected because it is not soluble in concentrated aqueous hydrochloric acid unless an oxidizing agent is present. It also is only very slightly heat etched at the temperature of the substrate in the absence of hydrogen chloride. This effect may be explained by the fact that hydrogen chloride always contains small amounts of chlorine and that the chlorine content increases under the influence of heat. Experiments to enclose sacrificial amounts of GaAs in the growth tube between the source and the substrate met with no success. A simple way to remove the chlorine within the reaction tube is by a displacement reaction, *e.g.*

$$Cl_2 + 2NH_4I = 2NH_4Cl + I_2$$

Iodine as an oxidizing agent is less active than chlorine and therefore reduces the etching action of the carrier. It was introduced as volatile ammonium iodide and the above reaction occurred in the gaseous phase. Experiments proved that it prevented etching even at steeply increasing amounts of hydrogen chloride.

Very small amounts of oxygen also increase the rate of reaction of GaAs with HCl. Therefore great pains were taken to exclude it by adding catalytic deoxygenizing units to the gas purification train and by always keeping the equipment under positive pressure.

An aqueous solution of sodium silicate had been used at first for adhering the back of the substrate in order to facilitate handling and positioning. Then it had been noticed that single crystals occasionally grew although most of the substrate disappeared during the growth period. Every time the spot only remained where the adhesive had been applied. It is likely that epitaxial growth occurred in the initial stages of the experiment at the crystallite-substrate interface before the corrosive gases could etch away all of the substrate. This experience suggested the coating of all non-growth areas with a sodium silicate solution.

The initial growth of single crystals depends on the lateral mobility of growth centers which arrange themselves as a continuation of the substrate lattice. It is very important that no foreign molecules be present on the surface. Various conventional cleaning methods were tried but none was capable of rendering the surface free of contamination as ascertained by the atomizer test.[1] A method to vaporize the contaminants by the action of heat and hydrogen has been worked out. This method served also to remove and volatilize any volatile and reactive constituents of the sodium silicate adhesive. The substrates were placed into the growth tube without any special cleaning aside from a Freon spray to remove fingerprints. It was proved by the atomizer test that the substrate became wettable after 16 hr of this treatment. A similar observation has been made recently by Pizzarello (11) who increased the temperature of his substrates for a short time to improve the quality of their surfaces. He used a closed system, however, where the contaminants cannot be ultimately removed.

Gaseous hydrogen chloride reacts with ZnSe at elevated temperatures and the volatile reaction products re-form the solid in a cooler zone

$$2HCl(g) + ZnSe(s) \rightleftharpoons ZnCl_2(g) + H_2Se(g)$$

The reaction is so rapid that it has been found advantageous to dilute the hydrogen chloride with hydrogen and argon. At the temperature chosen, ZnSe has a vapor pressure of approximately 0.05 mm (9), a fact which demonstrates the advantages of vapor transport over sublimation methods. The dissociation of H_2Se at that temperature which might cause deposition of selenium upon the substrate is almost negligible and is further reduced by the presence of hydrogen.

Crystals grown at a faster rate displayed more irregularities than the ones grown at slower rates. Those grown at a 1 ml/min flow of hydrogen chloride had smooth surfaces (Fig. 2), whereas those grown at a 11.5 ml/min flow showed regular arrays of (111)-oriented pyramids (Fig. 4). Similar surface defects have been observed by Newman and Goldsmith (12) in their investigation of the vapor growth of gallium

Fig. 4. Zinc selenide deposited upon (111) gallium face of gallium arsenide at high flow rates.

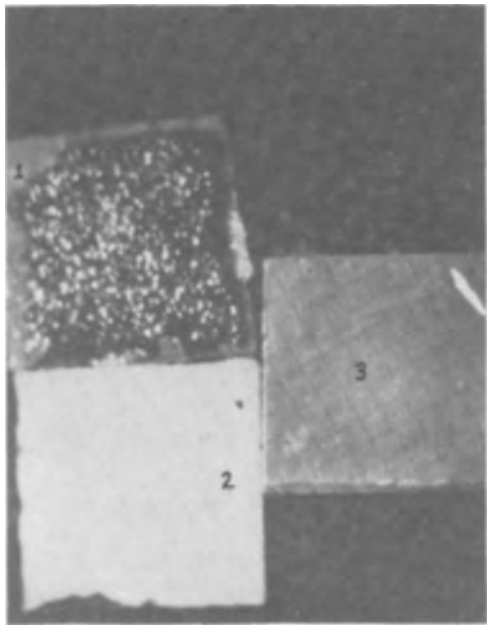

Fig. 5. Substrates plus overgrowths upon (111) gallium plane that has been exposed at different temperatures (see text).

[1] A fine mist of water is sprayed under standard conditions against the sample. If the surface is clean a continuous film of water is obtained. This test is capable of detecting 8×10^{-8}g of water shedding contaminant per square centimeter. Freshly cleaved mica serves as a standard for cleanliness (10).

arsenide. The reactive deposition of zinc selenide in a gas stream occurs over a wide temperature range in contradistinction to the equilibrium conditions in a closed system (8). Crystallization has been observed in a zone ranging from 620° to 520°C. The habit, however, changes as a function of temperature, the optimum for single crystal growth lying above 585°C. Figure 5 shows three substrates that had been exposed to different temperatures. Number one (591°C) shows a clear epitaxial layer, number two (568°C) has a multicrystalline deposit which appears white on the photograph and number three (538°C) had a multicrystalline layer which spalled off when the sample was removed from the tube. It therefore shows the shiny surface of gallium arsenide.

Acknowledgments

The author gratefully acknowledges helpful discussions with Dr. Lewis J. Bodi, and the patient and diligent assistance of Mr. Mark Goetzler who performed most of the laboratory work. He also wishes to thank Mr. Paul Lublin for the x-ray diffraction studies.

Manuscript received Dec. 28, 1964. This paper was presented at the Toronto Meeting, May 3-7, 1964.

Any discussion of this paper will appear in a Discussion Section to be published in the December 1965 JOURNAL.

REFERENCES

1. Handbook of Chemistry and Physics, 42nd edition, 1960.
2. P. M. Bethke and P. B. Barton, Jr., U. S. Geol. Surv. Paper No. 424 B, 266 (1961).
3. N. A. Goryunowa and N. N. Fedorova, *Sov. Phys. Sol. State*, **1**, 307 (1959) (English trans).
4. A. G. Fischer, *This Journal*, **106**, 838 (1959).
5. A. G. Fischer, Electrochemical Society Meeting, Pittsburgh, April 15-18, 1963.
6. S. W. Ing and H. T. Minden, *This Journal*, **109**, 995 (1962).
7. H. Schaefer, Chemische Transportreaktionen, Verlag Chemie, 1962.
8. N. Holonyak, Jr., D. C. Jillson, and S. F. Devacqua, "Metallurgy of Semiconductor Materials," Metallurgical Society Conferences, Vol. 15, pp. 49-60, New York (1962).
9. I. V. Korneeva, V. V. Sokolov, and A. V. Novoselova, *Zhur. Neorg. Khim.*, **5**, 241 (1960).
10. H. B. Linford and E. B. Saubestre, ASTM Bull. No. 190, p. 47 (TP 73), May (1953).
11. F. A. Pizzarello, *This Journal*, **110**, 1059 (1963).
12. R. L. Newman and N. Goldstein, *ibid.*, **108**, 112 (1961).

X-Ray Diffraction Topographs of Imperfections in Gallium Arsenide by Anomalous Transmission of X-Rays

E. D. Jungbluth

General Telephone & Electronics Laboratories, Incorporated, Bayside, New York

ABSTRACT

Imperfections in single crystals of GaAs grown by the Czochralski and horizontal gradient freeze method have been observed by the anomalous transmission of x-rays. Slip occurs equally on the three octahedral (111) planes in the Czochralski pulled ingot. Radial slip predominates in crystals grown by the gradient freeze technique. The variation in the distribution of dislocations in crystals grown by both techniques is observed and compared. Large inclusions of tin and tin arsenide have been detected in heavily doped GaAs. The formation of SiO diffusion masks on single crystal GaAs causes large strains when the sample is heat-treated under diffusion conditions.

The interest in gallium arsenide as the subject of research in the semiconductor industry has been heightened in the last two years by the emergence of the injection laser. One of the parameters influencing the electrical performance of a semiconductor material is the occurrence of structural imperfections. The prominent role that dislocations play in affecting electrical characteristics has been the subject of several papers which include the influence of dislocations on the electrical conductivity in metals (1), microplasma phenomena in silicon p-n junctions (2,3), and the distribution of dislocations in relation to voltage distribution and photoconductive response in gallium arsenide (4).

The observation of dislocations in gallium arsenide has heretofore been limited, for the most part, to the identification of etch pit sites, on major crystallographic planes, with emergent dislocations (5-7). The limitations of analyzing dislocation networks by means of surface topography is obvious. Moreover, the high dislocation densities present in commercially available GaAs complicate the use of x-ray diffraction microscopy. In respect to the control of dislocation densities the state of the art in gallium arsenide crystal growth is in its infancy compared with growth of silicon or germanium crystals.

X-ray diffraction microscopy can be used to produce topographs which effectively map the geometrical distributions of a variety of crystalline imperfections. The extinction-contrast technique has been applied successfully to materials exhibiting low x-ray absorption (8, 9). Thus, images of dislocations, segregation, precipitation and stacking-fault phenomena have been observed in silicon. For materials with high x-ray absorption, a complementary technique utilizes the Borrmann effect to record imperfections (10-12). Both techniques have the advantage over etching in being nondestructive. This paper reports on the direct observation of imperfections in single crystals of gallium arsenide by use of the Borrmann effect, *i.e.*, the anomalous transmission of x-rays.

Experimental Techniques

The technique employed in this study is based on the parallel-beam method of Barth-Hosemann (13). A standard copper x-ray diffraction tube, operated at 20 kv and 20 ma, was utilized. The images were recorded on 50μ Ilford nuclear plates with about a 12-hr exposure. Only the diffracted image is presented in subsequent figures, which are photographic negatives, *i.e.*, the diffraction contrast is reversed relative to the nuclear plates.

The crystals, which are grown by both Czochralski and horizontal gradient freeze methods, were oriented optically and sectioned in 1-mm-thick wafers. Sections were cut normal to the growth axis, along (111) planes, parallel to the growth axis along (112) planes, and at 19°21′ to the growth axis along one of the octahedral (111) planes. In the boat-grown samples, which were not seeded, the axis of the (111) plane that lies

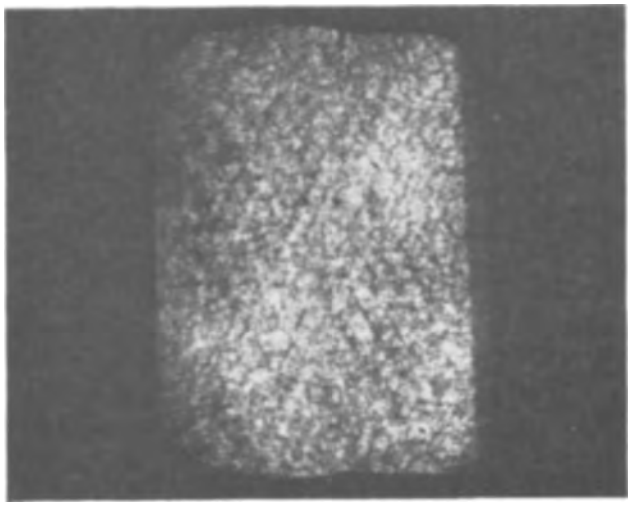

Fig. 1. Radial distribution of dislocations in GaAs; {220} reflection. Czochralski growth technique.

closest to the long dimension of the crucible is arbitrarily considered to be the growth axis. The wafers were chemically polished in a 1:2:3 solution of $HF:HNO_3:H_2O$ to remove surface damage.

Results

Distribution of dislocations.—It is well known that the dislocation densities vary both across the diameter and along the length of Czochralski-grown semiconductor crystals. Orders of magnitude variation have been observed in both cases. Figure 1 is an x-ray topograph of one of our GaAs wafers oriented normal to the growth axis and sectioned from an ingot grown by the Czochralski method. The variation of the diffraction contrast across the slice is indicative of variation in the dislocation density. The darker areas correspond to imperfect regions. An order of magnitude difference in dislocation density is estimated from the center to the edge of the crystal and was confirmed by etch pit techniques to vary from 10^4 to 10^5 dislocations/cm^2. Individual dislocations are difficult to resolve at this dislocation density due to the strong interaction of strain fields surrounding each dislocation. The threefold symmetry of the dislocation patterns, which is evident in the original topograph, suggests slip in the octahedral (111) planes.

The variation of the dislocation density along the length of the crystal is obvious in Fig. 2. This section was oriented along a (112) plane. Thermal stresses that arise due to temperature fluctuations complicate the growth of defect-free material. Slip mechanisms

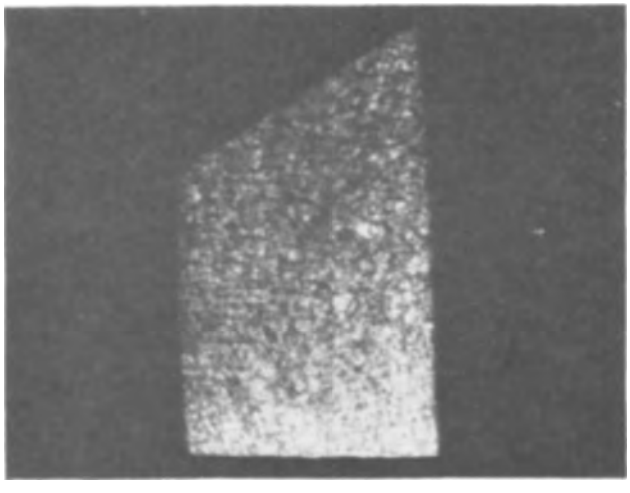

Fig. 2. Axial distribution of dislocations in GaAs; {220} reflection. Czochralski growth technique.

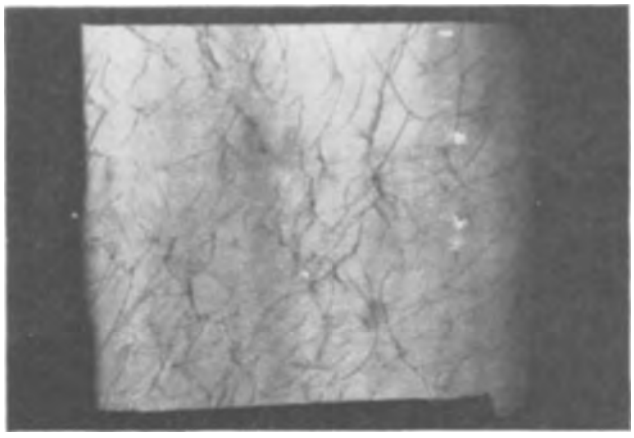

Fig. 3. Low-dislocation-density GaAs; {220} reflection. Horizontal gradient freeze technique.

during the growth process are influenced by thermal stresses, which could be responsible for the observed variation in dislocation density. Compounding this problem is the motion of the melt through the temperature zone in the Czochralski technique. The radial and axial thermal variations associated with this growth method tend to vary the localized stresses and consequently slip is easily induced.

The horizontal gradient freeze method circumvents some of the problems associated with the Czochralski method. The melt itself remains stationary, while solidification occurs due to a movement of the temperature gradient along the ingot. Hence, it is only necessary to control the temperature profile, since the melt itself is not moving. Therefore, crystals may be grown with a rather low defect structure.

Figure 3 is a typical example of the high perfection available in GaAs crystals grown by the gradient freeze method. This crystal is n-type, resistivity 0.13 ohm-cm, and has an etch pit density of about 200 per cm^2. The section is oriented along a <111> direction closest to the long dimension of the boat. The distribution of dislocations appears random, and no preferred concentration of dislocations was observed. Although the dislocations in most cases were curvilinear, a tendency to align near the <110> directions was observed. Most of the dislocations appear with the same resolution along their entire length. This indicates that the dislocations lie in the plane of the wafer and suggests that slip is principally in a radial direction. The mechanical constraint imposed on growth by the confining walls of the crucible boat apparently imposes less difficulties in the way of the growth of good crystals than do the thermal gradients of the Czochralski technique.

Figure 4 is a {220} reflection of a section of gallium arsenide grown by the gradient freeze method. This

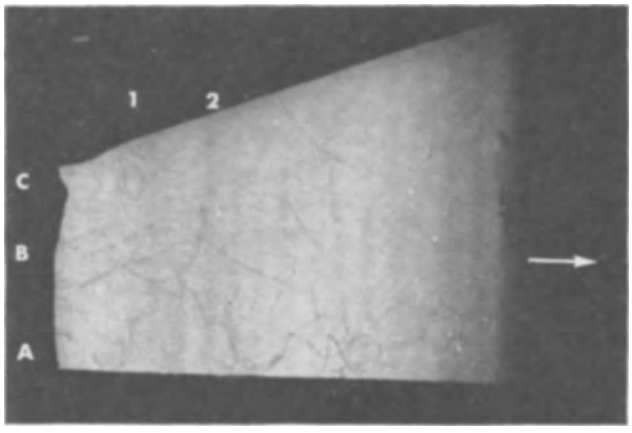

Fig. 4. {220} reflection of a GaAs wafer; A side facing beam; the direction of the diffraction vector is indicated.

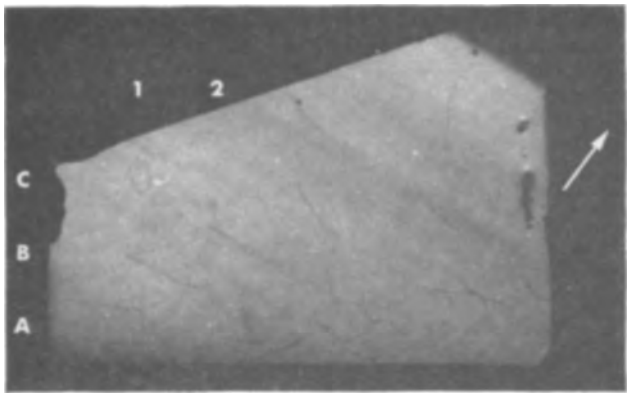

Fig. 5. {202} reflection of the same wafer as Fig. 4; A side facing beam.

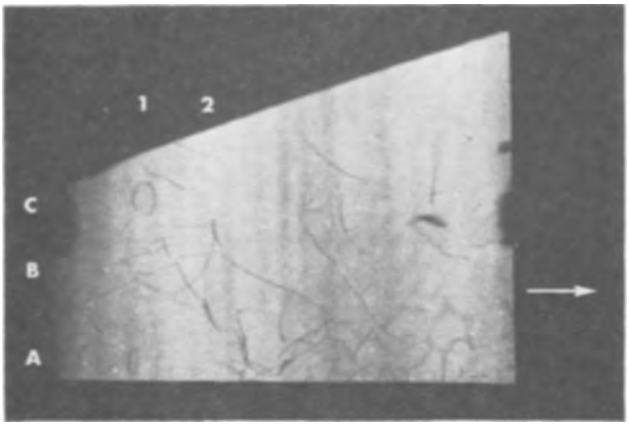

Fig. 6. {220} reflection of same wafer as Fig. 4; B side facing beam.

section is oriented along an octahedral (111) plane, A face toward the beam side. This crystal was zinc doped to a concentration of about 1.7 x 10^{18} at./cm^3. The dislocation group at B-1 appears well resolved, but runs from the A to B surface of the crystal. Vestiges of other dislocations are seen, but with decreased contrast and resolution due to the unfavorable contrast conditions in this reflection. In the {202} reflection of Fig. 5, the same dislocation group, B-1, has a minimum of contrast. The directions of the diffraction vectors are indicated in the micrographs. The dislocation group B-1 must therefore have a strong Burgers vector component in the <220> direction and have a strong component lying in the {202} planes. If the crystal is remounted, so that the B side faces the beam, then several new dislocations appear for the same {220} reflection as in Fig. 4. The ring dislocation at C-1 is observable in both Fig. 4 and 6, while a new ring at A-1 becomes visible in Fig. 6. In addition, an improved sharpness of several of the dislocations is apparent in Fig. 6. This is a consequence of the spreading of the beam within the crystal lattice and could lead to misinterpretations involving the perfection of any given wafer (14). This is interpreted to mean that the ring dislocation at A-1 lies closer to the A surface of the crystal. The ring at C-1 must lie approximately midway between the A and B surfaces since it is visible in both reflections. By considering the geometry of the wafer, it has been determined that the dislocation ring at A-1 must lie approximately 300μ from the A surface. There was no evidence for segregation or precipitation in crystals grown by the gradient freeze method and doped with zinc to the order of 10^{18} at./cm^3.

Impurity traces.—The anomalous transmission x-ray method has been used for impurity trace analysis for arsenic in germanium and oxygen in silicon (15). The electron probe is being used extensively to trace the chemical species of inclusions in a variety of host matrices. Lublin has identified the formation of tin and

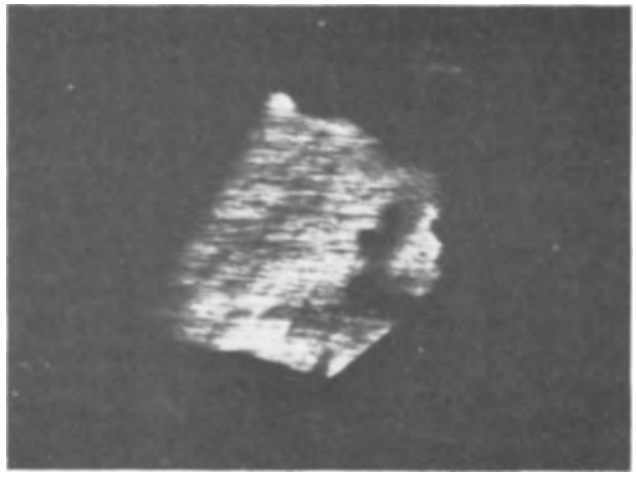

Fig. 7. X-ray topograph of heavily tin doped GaAs; precipitation of tin complexes appear as large dark spots.

tin arsenide inclusions, of sizes up to 200μ, in heavily doped GaAs using the electron probe (16). Figure 7 is an x-ray topograph of a section of Czochralski grown GaAs doped with tin to an average concentration of 10^{18} at./cm^3. The large dark spots are not reflection dependent, indicating the presence of an insoluble foreign species. The largest spot was in the order of 200μ size and is attributed to the presence of a precipitated species of tin. Probe analysis revealed an inhomogeneous concentration of impurity varying from 10^{18} to 10^{20} at./cm^3. The precipitates consisted of two phases, pure tin and tin arsenide. The formation of large precipitates due to doping beyond the solubility limits could actively participate in the degradation of the electrical characteristics of active devices.

Selective masking effects.—Silicon monoxide is known to be an effective mask against the diffusion of zinc and cadmium in GaAs (17). The creation of densely dislocated regions under SiO masks on germanium occurs as the substrate approaches plastic deformation temperature (18). In order to ascertain the effect of SiO masks on the perfection of GaAs substrates, samples were prepared in the following way. Circular masks (5 mm diameter) of SiO were deposited on substrates similar to that of Fig. 3. The deposits were 840Å thick and bonded to the substrate at 500°C. The sample was subsequently zinc diffused at 1100°C for 3 min. Figure 8 is a topograph of the resulting dislocation pattern. High x-ray absorption, indicative of severely disturbed lattices, occurs in the region under the mask. In the surrounding regions, which are unmasked, dense dislocation networks may be resolved. The dislocation networks in the unmasked portion are due to the in-diffusant of high concentrations of substitutional zinc (19). Heat-treatment of similar samples, but unmasked, at elevated temperatures did

Fig. 8. Zinc diffusion through a circular SiO mask.

not generate any additional imperfections. No change in the topograph was observed after SiO deposition but prior to diffusion. The strain associated with the oxide mask extends 300μ below the surface of the mask. The difference in the x-ray absorption between masked and unmasked areas must be due to inherent stresses set up by the dissimilar thermal expansion coefficients which activate slip systems at elevated temperatures.

Acknowledgments

The author wishes to thank R. J. Modena for assisting in the experimental work and J. Black who was responsible for the SiO on GaAs sample. He also wishes to thank D. J. Bracco for his advice and encouragement in this and other projects.

Manuscript received July 20, 1964. This paper was presented at the Toronto Meeting, May 4-7, 1964.

Any discussion of this paper will appear in a Discussion Section to be published in the December 1965 JOURNAL.

REFERENCES

1. Z. Basinski, J. Dugdale, and A. Howie, *Phil. Mag.*, **8**, 1989 (1963).
2. A. Chynoweth and G. Pearson, J. *Appl. Phys.*, **29**, 1103 (1958).
3. R. Haitz, A. Goetzberger, R. Scarlett, and W. Shockley, *ibid.*, **34**, 1581 (1963).
4. P. Thornton, *Solid-State Electron.*, **6**, 677 (1963).
5. H. Gatos and M. Lavine, *This Journal*, **107**, 427 (1960).
6. J. Richards and A. Crocker, *J. Appl. Phys.*, **30**, 611 (1959).
7. H. Schell, *Z. Metal.*, **48**, 158 (1957).
8. A. R. Lang, *J. Appl. Phys.*, **30**, 1748 (1959).
9. J. B. Newkirk, *Phys. Rev.*, **110**, 1465 (1958).
10. G. Borrmann, W. Hartwig, and H. Imler, *Z. Naturforsch*, **13a**, 792 (1958).
11. H. Barth and R. Hosemann, *ibid.*, **13a**, 792 (1958).
12. G. Schwuttke, *J. Appl. Phys.*, **33**, 2760 (1962).
13. Barth and Hosemann, *op. cit.*
14. V. Gerold and F. Meier in "Direct Observation of Imperfections in Crystals," p. 509, J. Newkirk and J. Wernick, Editors, Interscience Publishers, Inc., New York (1962).
15. Schwuttke, *op. cit.*
16. P. Lublin, Private communication.
17. T. Yeh, *This Journal*, **110**, 341 (1963).
18. P. A. Schumann, Jr., and A. J. Rideout, *Solid-State Electron.*, **7**, 849 (1964).
19. J. Black and E. D. Jungbluth, To be published.

High-Temperature Oxidation

II. Molybdenum Silicides

Joan B. Berkowitz-Mattuck

Arthur D. Little, Inc., Cambridge, Massachusetts

and R. R. Dils

Advanced Materials Research & Development Laboratory, Pratt & Whitney Aircraft, North Haven, Connecticut

ABSTRACT

The oxidation of $MoSi_2$, Mo_5Si_3, and Mo_3Si has been studied at temperatures of 1300°-2000°K, and at oxygen partial pressures of 2-20 Torr. Below 1970°K, at oxygen pressures around 10 Torr, measurements of the rate of total oxygen consumption *vs.* time show an initial period of high linear rate, an intermediate region where the rate declines sharply with time, and a final plateau region of virtually zero oxidation rate. For each of the silicides, the total oxygen consumed prior to the attainment of the plateau decreases with temperature, and under given experimental conditions is largest for Mo_3Si, less by a factor of about six for Mo_5Si_3, and less by another factor of six for $MoSi_2$. The oxidized samples display a smooth glassy outer oxide layer that bridges across the tops of the cracks in the alloys and an inner oxidized zone, consisting of several irregular phases. Electron microprobe analysis and x-ray photomicrographs of the oxidized specimens show that the outer protective oxide is pure SiO_2, within the limits of detectability, *i.e.*, the outer oxide contains less than 0.1% Mo. The inner oxide layer contains SiO_2, molybdenum rich phases, including the terminal solid solution phase, and the original alloy phase. Evidence is presented that suggests that the oxide layers grow by inward diffusion of oxygen to the oxide/alloy interface where preferential oxidation of silicon occurs. The excellent oxidation resistance of the molybdenum silicides derives from the formation of this continuous layer of pure silica. Above 1970°K, at oxygen pressures above 10 Torr, an increased oxidation rate is observed due to formation of SiO(g) at the alloy/oxide interface, which causes rupture of the protective oxide. Below 1970°K, at oxygen pressures near 2 Torr, the rate of oxidation of $MoSi_2$ is linear at all times since the oxygen partial pressure is insufficient to maintain a protective SiO_2 layer on the alloy surface.

The remarkable oxidation resistance of molybdenum disilicide at temperatures between 1200° and 1970°K has been recognized for many years and has been ascribed to the formation of a self-healing coating of high silica content glass (1-11). Oxidation resistance measurements have generally been limited to net weight change after a specified period in oxygen or air, and apart from the initial survey of Kieffer and Cerwenka (2), work has concentrated on $MoSi_2$ to the virtual exclusion of the lower silicides Mo_5Si_3 and Mo_3Si.

Quantitative weight change data on the oxidation of $MoSi_2$ is fragmentary and contradictory. At 1270°K (1) the net weight change was reported to be negative for the first 25 min in oxygen and positive for the next 40 min. At 1380°K (4) small net weight losses were observed in 75 and 150 hr. Between 1470° and 1770°K net weight gains were found in two laboratories (1-5), but the values reported after 300 hr at 1470°K differ by a factor of ten. Also at 1470°K, a single publication (1) includes two weight change *vs.* time curves that differ by orders of magnitude in both rate of oxidation and absolute value of the weight change in a 1-hr period. At 1840°K, Long (5) measured net weight losses of 4×10^{-4} g/cm^2 in periods of 100 and 135 hr. From the available experimental evi-

dence it has been deduced that the products of oxidation of $MoSi_2$ must be $Mo_5Si_3 + SiO_2$ and/or a ternary Mo-Si-O glass (9). It has also been suggested (9) that in the early stages of oxidation of Mo_5Si_3, evolution of $MoO_3(g)$ predominates over Mo_5Si_3 or ternary oxide formation and that the composition of the oxidation product layer is thus shifted toward higher silica content.

The present study was undertaken to obtain a systematic comparison of the oxidation behavior of the three silicides, Mo_3Si, Mo_5Si_3, and $MoSi_2$, above 1000°C at oxygen partial pressures below 20 Torr. Continuous measurements of total oxygen consumption rate *vs.* time, as well as metallographic and electron probe analysis of the oxide films, are reported. The total oxygen consumed was measured rather than the more usual net weight change, since during the oxidation of molybdenum silicides, net weight change is compounded of a weight gain due to the formation of $SiO_2(c)$ and a weight loss due to vaporization of molybdenum oxides. Total oxygen consumption is a direct sum of the amounts of oxygen in all of the product oxides, volatile and nonvolatile, and hence is more directly related to alloy oxidation rates. Metallographic and electron probe microanalyses of the oxide films show that the protective oxide on the molybdenum silicides is pure SiO_2 containing less than 0.1% of molybdenum. In addition, for all of the silicides, an enhancement of the molybdenum content of the alloy at the alloy/oxide interface is observed. It is suggested that $SiO_2(c)$ and gaseous molybdenum trioxide are produced simultaneously in the initial stages of silicide oxidation, that the silica flows laterally to cover the alloy surface, and the reaction continues at an exceedingly slow rate by the preferential oxidation of silicon at the alloy/oxide interface. On this basis, the observation of a net weight gain or weight loss should be very sensitive to precise experimental conditions.

Experimental Method

Samples in the form of ingots about 10 cm long and 0.7 cm in diameter were synthesized from du Pont semiconductor grade silicon and General Electric high-purity molybdenum powder by cold pressing, low-temperature sintering, and zone melting of the sintered compact with a moving induction coil (12). Products were analyzed for crystal structure, stoichiometry, and purity by standard electron probe, x-ray, chemical, and spectrographic analytical methods. Synthesis of each silicide resulted in polycrystalline material within 1% of stoichiometric composition. Due to vaporization of silicon, all samples were on the molybdenum-rich side of stoichiometry, the Mo_3Si contained a small amount of second-phase terminal solid solution; Mo_5Si_3 samples were single phase; $MoSi_2$ samples contained a small amount of second phase material Mo_5Si_3. In all cases the volume percentage of second phase detected was less than 1%. Impurities included C, Al, O, and B in the ppm range.

The experimental procedure for determination of the oxidation rate has been described in detail in Part I of this series (13). A thermal conductivity cell of the type employed in vapor phase chromatography was used to compare the oxygen concentration in a helium stream before and after removal of some of the oxygen by reaction with the heated samples. In the present experiment samples approximately 0.3 cm long were cut from the zone melted bars described above, polished through diamond dust, and cleaned with acetone and distilled water. The samples were then mounted by three-point contact with Al_2O_3 support rods and degassed at 2100°K in helium prior to oxidation. Samples prepared in this manner were enclosed in a Pyrex and quartz flow system, and heated inductively; the rate of total oxygen consumption was monitored continuously with the thermal conductivity cell. All of the oxidation measurements were made in atmospheres of helium and oxygen flowing at about 95 cc/min with a total pressure of 760 Torr. A linear gas velocity of approximately 3 cm/sec was maintained in the neighborhood of the samples.

Oxidized samples were sectioned, mounted, and polished for optical examination and electron probe microanalysis. Standard static and scanning electron probe microanalysis techniques were used to determine concentrations near the oxidized surface and to provide backscattered electron and x-ray micrographs of the oxidized samples. The instrument (Cambridge Instrument Company, Ltd.) incorporated an incident electron beam and 20° x-ray take-off angle. An electron accelerating voltage of 15-40 kv and an electron beam current of 0.5 to 1 x 10^{-7} amp were used; the electron beam diameter was approximately 1μ. The molybdenum content was determined by analysis of the MoKα and MoLα characteristic x-rays; the silicon content was determined by analysis of the SiKα characteristic x-rays.

The data obtained were corrected for x-ray absorption effects using the data of Green (14) and absorption coefficients from a recently published compilation (15). Fluorescence effects are of negligible importance in this particular system (16-17) when the SiKα and MoLα characteristic x-rays are employed. No correction for electron deceleration effects was included since such a correction would be limited by incomplete quantitative data on the electron behavior in the alloys and the elemental standards (17); however, this effect is not expected to alter the results substantially.

Experimental Results

Oxidation behavior.—The majority of the oxidation experiments were conducted between 1300° and 1970°K in atmospheres maintaining an oxygen partial pressure of near 10 Torr. For such low oxygen partial pressures, the thermal conductivity technique measures rates of total oxygen consumption, dQ/dt, directly and continuously. The curves of total oxygen consumption, Q, *vs.* time for Mo_3Si, Mo_5Si_3, and $MoSi_2$ were obtained by integration of the experimental rate curves from time zero to selected times and are shown in Fig. 1. In general, the data show an initial period of rapid linear oxidation, a short intermediate period when the rate of oxidation diminishes with time, and a final region in which the oxidation rate is exceedingly slow.

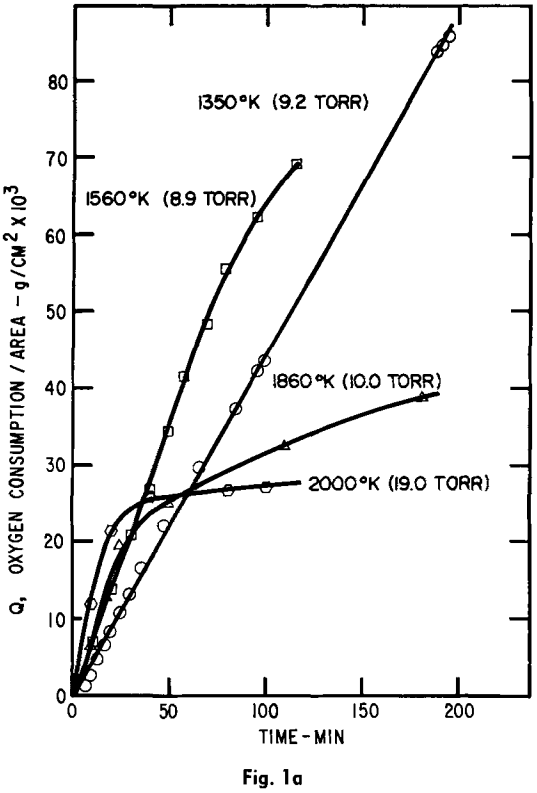

Fig. 1a

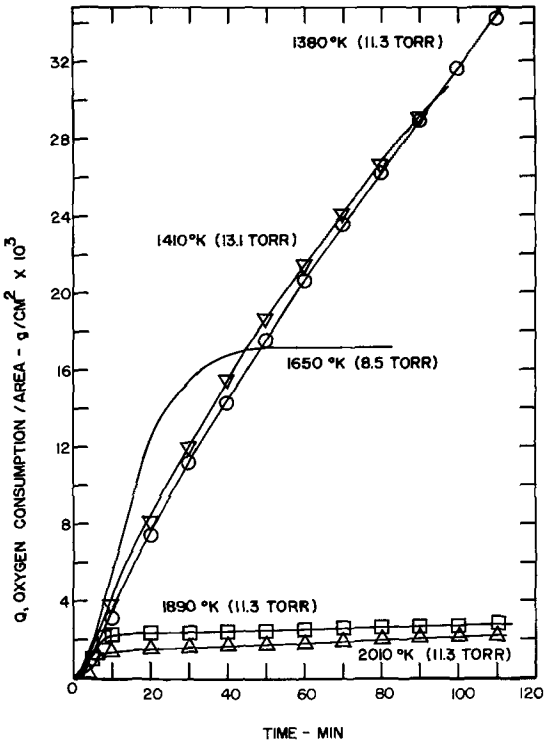

Fig. 1b

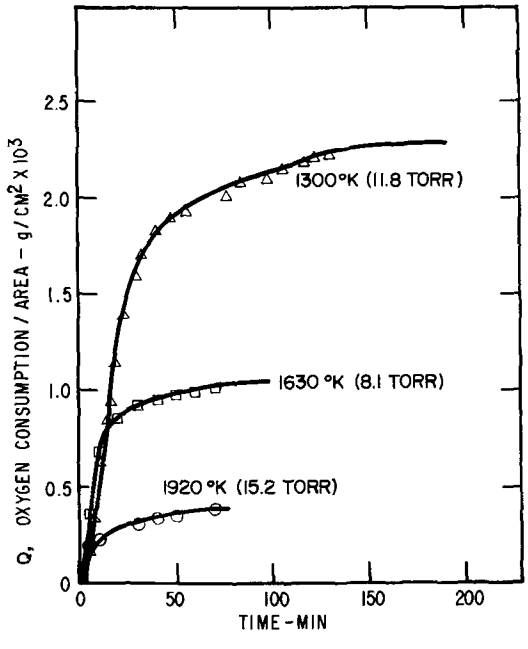

Fig. 1. Oxygen consumption *vs.* time curves: a, Mo_3Si; b, Mo_5Si_3; c, $MoSi_2$.

Mo_3Si oxidized at 1350°K displays no final plateau region, although the rate of oxidation as measured by the thermal conductivity curve was observed to decrease slowly with time. At 1560°K, a distinct decrease in oxygen consumption rate is seen after about 80 min; at 1860°K the decrease in rate occurs earlier, and at 1960°K, a definite plateau region is observed (Fig. 1a). For Mo_5Si_3, a limiting rate is not seen over the period of observation at 1380° or 1410°K, but a plateau region is prominent at the higher temperatures (Fig. 1b). In the case of $MoSi_2$, the final oxidation rates are very slow in every experiment (Fig. 1c).

The oxidation rates observed, once a limiting rate has been reached, are of the same order for all of the molybdenum silicides. However, the total depth of alloy oxidized prior to the plateau region is greatest for Mo_3Si, less by a factor of about six for Mo_5Si_3, and less by another factor of six for $MoSi_2$. For all three silicides, the asymptotic value of net oxygen consumption, Q_o, decreases with increasing temperature between 1300° and 2000°K. This decrease is not necessarily in contradiction to the customary increase in the rates of chemical reactions with temperature, since at least two steps are required for the attainment of a limiting oxidation rate. Both volatile molybdenum trioxide and condensed $SiO_2(c)$ are formed in the early stages of oxidation. The rate-limiting step leading to the plateau might be the lateral flow of SiO_2 to form a continuous boundary layer. The higher the temperature, the earlier the rate-limiting process takes over, thus leading to lower values of total oxygen consumption with temperature.

The total oxygen consumption Q, *vs.* time, t, plots can be fitted approximately by two parameter equations of the form $Q = Q_o\,[1 - \exp(-\alpha t)]$, as suggested earlier by Jaenicke (10) where Q_o and α depend on temperature, pressure, and surface composition. However, Q, the total oxygen consumed, is a composite quantity representing the sum of the amount of oxygen in each of the product oxides. Since at least two oxides are formed during the course of oxidation of molybdenum silicides, such curve fittings tend to obscure the complexity of the basic oxidation mechanism, and will not be employed here.

Above 1970°K, there is a change in the mechanism of oxidation of $MoSi_2$ that results in an irregular final region of the oxidation curves. For example, a portion of a typical recorder tracing for the oxidation of $MoSi_2$ at a temperature of 2000°K and an oxygen partial pressure of 9 Torr is shown in Fig. 2. The ordinate is proportional to rate of total oxygen consumption, the abscissa is proportional to time. The initial behavior is similar to that at lower temperatures, a period of high oxidation rate that diminishes with time to a low value. The plateau region is interrupted, however, by short periods of increased oxygen consumption, which are associated with small protrusions of SiO(c) found in the oxide film on cooling and identified by x-ray diffraction analysis. Figure 3 shows the total oxygen consumption *vs.* time curve constructed by integration of the experimental rate curve, part of which is reproduced in Fig. 2. The small irregularities apparent in the rate curve are not seen in the integrated plot. However, in both figures it is clear that the oxidation rate drops rapidly to a low value, rises sharply, and then drops once more, as the protective oxide film is ruptured by evolution of SiO(g) and then heals. As the experiment continues, repetitions of this process occur. At similar temperatures and oxygen partial pressures, Mo_3Si and Mo_5Si_3 do not display this behavior (Fig. 1a and 1b), probably, as discussed below, because of the lower activity of silicon in the alloys.

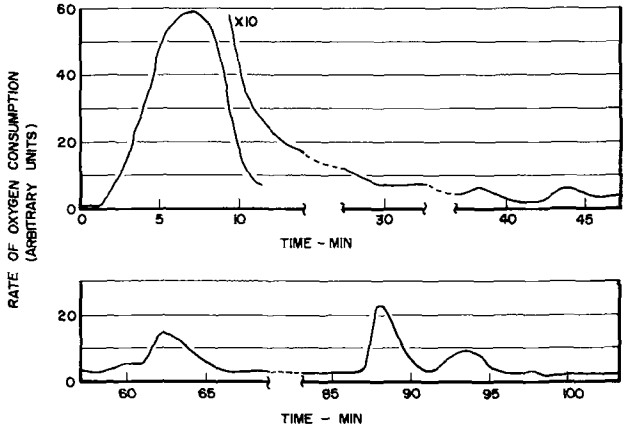

Fig. 2. Thermal conductivity curve for oxidation of $MoSi_2$ under conditions leading to film rupture.

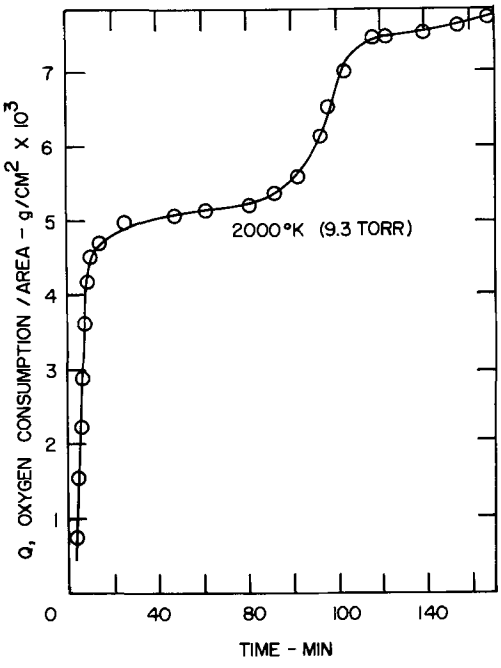

Fig. 3. Oxygen consumption vs. time curve for $MoSi_2$ under conditions leading to film rupture.

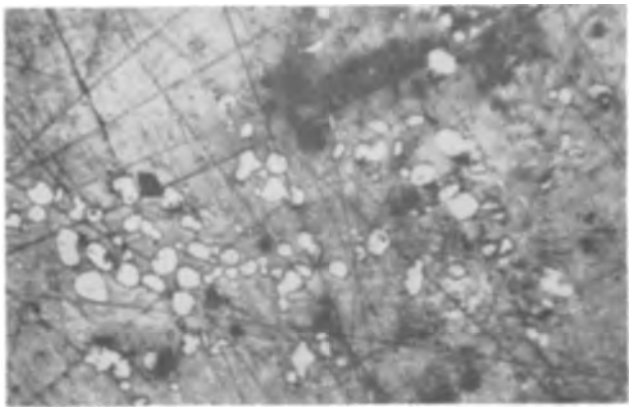

Fig. 4. Photomicrograph of Mo_3Si surface prior to oxidation. Magnification 60X.

At temperatures below 1970°K and oxygen partial pressures near 2 Torr the oxidation of $MoSi_2$ is linear, and no decrease in the oxidation rate occurs even when the total oxygen consumption exceeds the high-pressure asymptotic value for the given temperature. In one experiment conducted at 1950°K and oxygen partial pressure of 1.6 Torr, linear oxidation was allowed to proceed for an hour, after which the oxygen partial pressure was raised to 13 Torr. The oxidation rate decreased immediately, and the customary final plateau region described above was observed.

Oxide film examination.—Specimens oxidized in the temperature range 1300°-1970°K as described above were subjected to optical examination and electron probe microanalysis. Figure 4 is a photomicrograph of a typical sample of Mo_3Si prior to oxidation. The distribution of round second-phase inclusions of the α-solid solution of silicon in molybdenum is to be noted. Figure 5 shows a cross section of a similar sample after oxidation at 1860°K at an oxygen partial pressure of 10 Torr. A smooth gray outer oxide and a partially oxidized inner layer can be seen. It is also observed that the α solution phases available in the original material are enveloped by oxide, indicating significant diffusion of oxygen into the bulk silicide. Thus the terminal solid solution served as an inert marker as it was not oxidized. Another area of this

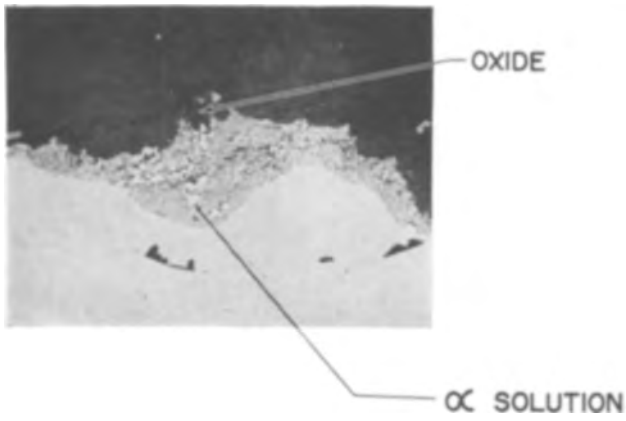

Fig. 5. Photomicrograph of a cross section of Mo_3Si after oxidation at 1860°K and 10 Torr. Magnification approximately 90X.

oxidized specimen is shown in Fig. 6. Figure 6a is an optical micrograph of the oxide film; Fig. 6b is a back-scattered electron micrograph of the same field of view. In such a micrograph, areas of higher density appear light due to the larger electron backscattering coefficient of these areas. It is observed that the outer oxide is less dense than the original silicide and that the inner oxide consists of phases which are more and less dense than the silicide. Figures 6c and 6d are SiKα and MoLα x-ray micrographs of the same field of view. In Fig. 6c, areas of high molybdenum content are dark and areas of high silicon content are light; in Fig. 6d the situation is reversed. Thus, the outer layer is a region of high silica concentration; the in-

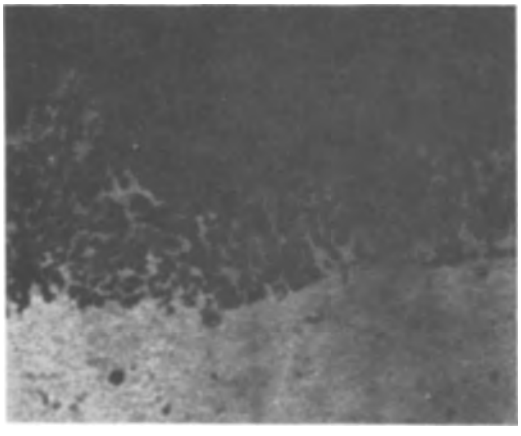

Fig. 6. Cross section of Mo_3Si oxidized under the conditions given in Fig. 7: a, photomicrograph.

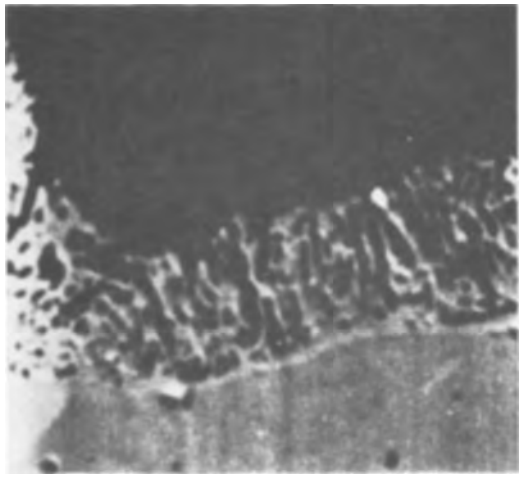

Fig. 6b. Back-scattered electron micrograph. Magnification 740X

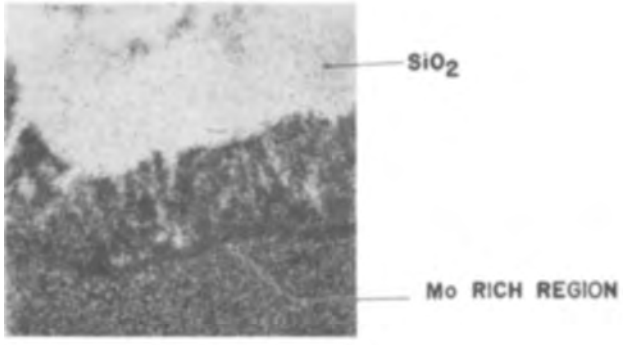

Fig. 6c. X-ray micrograph taken with SiKα radiation

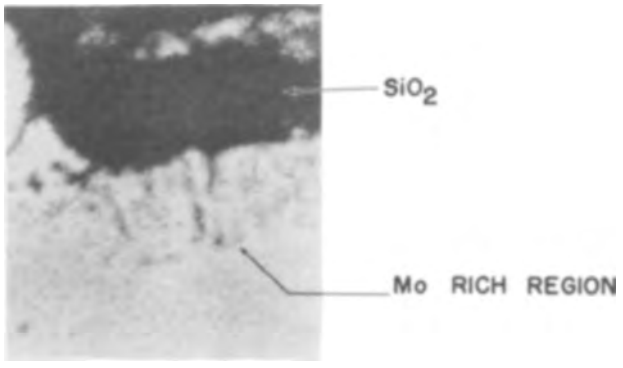

Fig. 6d. X-ray micrograph taken with MoLα radiation

ner oxide layer consists of areas of high molybdenum content and areas of high silicon content. In addition, a narrow region of high molybdenum content separates the unoxidized silicide from the oxidized layers.

Quantitative analyses of the various oxide products were achieved by a series of static beam analyses. The results, presented in Table I, show that the outer oxide is SiO_2 containing less than 0.1% molybdenum. To confirm this observation, oxidized samples were annealed overnight at 1370°K in an argon atmosphere; it was observed by x-ray diffraction techniques that the outer oxide layer was transformed to β-crystobalite. Due to the irregularity of the inner oxide region, exact chemical analyses of the phases were not possible; however, the silicon-rich areas contained less than 2% molybdenum, and the molybdenum-rich areas were at least 95% molybdenum. It appears therefore that the inner oxide consists of SiO_2 and terminal solid solution molybdenum phases. The narrow region of high molybdenum content observed between the unoxidized silicide and the oxide layers contained from 96 to 100% molybdenum and is the terminal solid solution molybdenum phase.

A cross section of an Mo_5Si_3 pellet after oxidation at 1890°K in an atmosphere with an oxygen partial pressure of 5 Torr is presented in Fig. 7. Again a smooth gray outer oxide and an inner partially oxidized region was observed. It is noted that the oxide bridges across the top of cracks that intersect the surface to the same depth as in the surrounding alloy. This is an example of the self-healing tendency of the oxide which contributes to the low oxidation rates of all the molybdenum silicides. Electron probe microanalyses of the oxidation products show that the same type of reactions occur in both the Mo_5Si_3 and Mo_3Si specimens. The outer oxide is SiO_2; the inner oxide region consists of SiO_2 and molybdenum-rich phases, including terminal solid solution molybdenum phases. Mass balance is preserved by the existence of a molybdenum gradient across the alloy/oxide interface.

The oxide developed on $MoSi_2$ specimens was too thin to allow electron probe microanalysis to be performed; however, it is probable that the oxidation products are similar to those observed on the lower silicides.

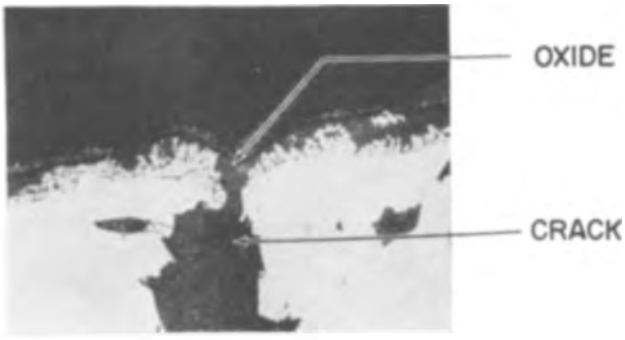

Fig. 7. Photomicrograph of cross sections of Mo_5Si_3 after oxidation at 1885°K and 5 Torr, 267X. a, Oxide in the neighborhood of a crack.

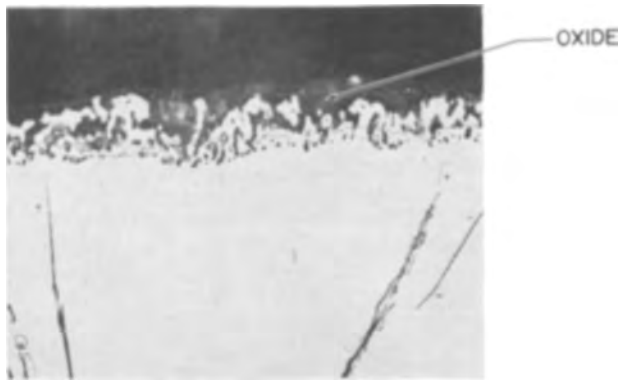

Fig. 7b. Normal oxide layer

Discussion

Oxidation products.—As a first approximation the oxidation of an alloy is expected to yield the oxides

Table I. Results of quantitative electron probe microanalysis of Mo_3Si

Sample description	Analyzed area	Experimental compositions* Mo, %	Si, %	Material	Theoretical composition Mo, %	Si, %
Mo_3Si; oxidized at 1860°K and 10 Torr	1. Matrix	90.2 ± 0.5	—	Mo_3Si	91.1	—
	2. Mo rich layer between Mo_3Si and inner oxide	95-100	—	γMo	≈100	—
	3. Inner oxide					
	a, high Si phase	<2	>40	SiO_2	0	47
	b, high Mo phase	>95	—	γMo	≈100	—
	4. Outer oxide	<0.1	49 ± 1	SiO_2	0	47

* Error indicated represents standard counting error. 3 σ.

of the component elements. Preferential oxidation of one constituent may occur for thermodynamic or kinetic reasons. The free energies of formation of $MoO_3(g)$ and $SiO_2(c)$ at 1500°K are −95 (18) and −154 (19) kcal/mole, respectively. Thus, although molybdenum is somewhat more noble than silicon, both oxides are sufficiently stable so that neither can be excluded on thermodynamic grounds. $MoO_2(c)$ with a free energy of formation of −77 kcal/mole (20) at 1500°K and $SiO(g)$ with $\Delta F_{f,1500} = -52$ kcal/mole (19) are also thermodynamically possible products.

The work reported above established that the outer solid oxide layer formed on the molybdenum silicides is pure SiO_2, containing not more than 0.1% molybdenum. In addition, at the end of every oxidation experiment, $MoO_3(c)$ was found condensed on the cool walls of the reaction chamber. It is therefore suggested that the principal products of oxidation of molybdenum silicides in the 1300°-2000°K range at oxygen pressures around 10 Torr are a volatile molybdenum oxide and $SiO_2(c)$. While extrapolation of mass spectrometric data on the products of oxidation of molybdenum at low oxygen pressures (21) suggests that under the conditions of the present experiments the vapor might be expected to contain $MoO_3(g)$, $(MoO_3)_2(g)$, and $(MoO_3)_3(g)$, the precise vapor composition is not important to the subsequent discussion, and for simplicity, the molybdenum species will be assumed to be $MoO_3(g)$.

Oxidation behavior.—The specific oxidation behavior observed in these tests is determined by kinetic considerations. On the basis of the data presented, it is possible to outline the phenomena involved in the oxidation of the molybdenum silicides. Let us first consider the behavior of specimens oxidized below 1970°K at high oxygen partial pressures. In the initial period of rapid linear oxidation rate, we postulate that $MoO_3(g)$ and $SiO_2(c)$ are formed simultaneously in proportion to the concentrations of molybdenum and silicon in the alloy surface. $MoO_3(g)$ should evaporate as rapidly as it forms, while $SiO_2(c)$ should nucleate and grow on the silicide surface. The growth of $SiO_2(c)$ will decrease the surface area directly available for reaction with the atmosphere and therefore the rate of oxygen consumption will diminish with time. At the temperatures of the present experiments, the SiO_2 will flow and eventually form a continuous protective layer. Subsequently, the rate of oxidation will be determined by diffusion through this barrier and will be negligible. As temperature is increased, flow of the SiO_2 occurs more rapidly; the resultant decrease in the exposed silicide surface area limits the total oxygen consumption.

Once a continuous layer of silica has formed, subsequent oxidation can continue only by diffusion of reactive components through the film barrier. It is clear from the very low final rates of total oxygen consumption observed and from the electron probe results that vaporization of MoO_3 cannot continue once a protective film of $SiO_2(c)$ has formed. If $MoO_3(g)$ evolved at the $SiO_2(c)$-alloy interface below 1970°K, it would rupture the silica film, and irregularities would be seen in the oxygen consumption rate curves as the protective film was broken and healed. Such periodic increases in oxidation rate were not observed at these temperatures. At the $SiO_2(c)$-gas interface, $MoO_3(g)$ could only form if molybdenum migrated from the alloy through the silica film. In this case molybdenum should have been detected in the outer oxide film. No molybdenum was detected in the oxide; in addition, the alloy immediately adjacent to the oxide layer was distinctly enriched in molybdenum compared to the bulk alloy.

In fact, the metallographic results indicate that the oxide layer grows at least in part by inward diffusion of oxygen. The electron probe results show that silicon is oxidized preferentially at the oxide-terminal solid solution interface, and that successive layers of increasing molybdenum content are produced between the bulk alloy and the oxide. The stability of a high molybdenum content phase between the bulk alloy and the oxide suggests that the oxygen activity at the alloy-oxide interface is very low. It is therefore likely that inward diffusion of oxygen through silica and outward diffusion of silicon through the alloy and molybdenum-rich phases occur to a significant extent during the final stage oxidation.

The process occurring in the plateau region of the curves in Fig. 1-3 is postulated to be oxidation of silicon at the silicide/oxide phase boundary. The rate-controlling step in this region might be either the rate of diffusion of oxygen through $SiO_2(c)$, diffusion of silicon through the terminal solid solution, or the chemical reaction at the phase boundary.

It is difficult to determine the exact rate-controlling process. The activation energy for permeation of oxygen through vitreous silica at 1200°-1350°K is about 20 kcal/mole, and the diffusing species is thought to be molecular oxygen (22). High-temperature oxidation experiments on silicon metal (23, 24) suggest an activation energy which is even higher, about 40 kcal/mole, and relates to motion of oxygen ions (25). The rate of oxidation of the molybdenum silicides in the final region is so low that it is difficult to determine an activation energy with any accuracy or to decide whether the reaction is linear or parabolic. Nevertheless, the activation energy does appear to be less than 20 kcal, and reactions at the silicide/oxide phase boundary and/or diffusion of the silicon through the terminal solution must be considered as possible rate-controlling steps.

Applying data of Norton on the migration of oxygen through silica to the present experiments, one may calculate the oxygen partial pressure at the terminal solid solution/oxide interface. At an ambient oxygen pressure of 12 Torr the effective oxygen pressure at the terminal solid solution/oxide interface, for a silica film thickness of 1 mm, would be less than 10^{-12} Torr at 1300°K and 10^{-10} Torr at 2000°K. Since the limiting film thickness for all of the molybdenum silicides is greater than 10^{-3} mm, the oxygen pressure at the interface is less than 10^{-7} Torr in every case. At this pressure, by extrapolation of the data of Berkowitz *et al.* (26), the rate of oxidation of molybdenum should be less than 10^{-10} g/cm²-min of oxygen at all temperatures. Silicon will thus be oxidized preferentially, but its low concentration at the interface under steady-state conditions will contribute to the low oxidation rates observed in the final plateau region.

On the basis of the above discussion it is possible to understand why some workers have observed net weight losses and others have observed net weight gains in the high-temperature oxidation of $MoSi_2$. The stoichiometric oxidation of a molybdenum silicide of formula $MoSi_x$ to $MoO_3(g)$ and $xSiO_2(c)$ would result in a net weight loss unless x were greater than three. Once a continuous film of $SiO_2(c)$ has formed, and possibly even before, silicon is oxidized preferentially and loss of molybdenum from the alloy ceases; hence a net weight gain becomes possible. The oxidation of the molybdenum-rich alloys, Mo_5Si_3 and Mo_3Si, always results in net weight losses. The oxidation of $MoSi_2$ can result in net weight losses or weight gains, depending on the molybdenum concentration at the surface, the surface topography, and the precise conditions of temperature, pressure, and flow.

Above 1970°K, at high oxygen pressures, the rate of oxidation of $MoSi_2$ was observed to increase markedly. Samples quenched from the high temperature were covered with brown protrusions, identified by x-ray as $SiO(c)$. The breakdown of the protective silica film has been ascribed (6) to the formation of $SiO(g)$ at the alloy-oxide interface by the reaction

$$Si(alloy) + SiO_2(c) = 2SiO(g) \qquad [1]$$

For silicon at unit activity, the equilibrium pressures of $SiO(g)$ calculated for reaction [1] are 3.6×10^{-1} Torr at 1500°K and close to 1 atm at 2000°K (19). At

the higher temperature, the pressure is sufficient to rupture the protective oxide film. The decreased silicon activity of the lower silicides, Mo_5Si_3 and Mo_3Si, should result in lower equilibrium SiO(g) pressures and hence in a silica film stable to higher temperatures. This was found by Fitzer (10) and in the present investigation.

At 1950°K at a low oxygen partial pressure, 1.6 Torr, oxidation was found to be linear, and a solid oxide failed to form on the surface of $MoSi_2$. This behavior may be explained by a mechanism first proposed by Wagner (26) in connection with the oxidation of pure silicon. The oxygen partial pressure may be considerably less at the solid surface than in the bulk gas due to a slow rate of diffusion across a boundary layer of gaseous SiO(g) formed via reaction [1]. Hence, the oxygen pressure at the surface may be insufficient to maintain a layer of SiO_2(c). The activity of silicon over the two-phase system $MoSi_2$-Mo_5Si_3 at 1960°K is about 0.1. The Wagner theory predicts that, under the experimental conditions described, an oxygen partial pressure of 20 Torr in the bulk gas is required for formation of SiO_2(c). Experimentally, a silica film was formed on an $MoSi_2$ surface at an oxygen pressure of 13 Torr but failed to form at 1.6 Torr, in excellent agreement with the theory.

Summary

Continuous measurements of total oxygen consumption *vs.* time were made for Mo_3Si, Mo_5Si_3, and $MoSi_2$ in the range 1300°-2000°K at oxygen pressures around 10 Torr. The results for all of the silicides investigated in this temperature and pressure range show an initial region of rapid linear oxidation, an intermediate region of declining oxygen consumption rate, and a final region of small oxidation rate.

In the initial period, SiO_2(c) nucleates and grows at silicide surface sites and MoO_3(g) evaporates as rapidly as it forms.

In the intermediate region of declining oxidation rate, the reactive surface area is decreasing due to the growth of SiO_2(c).

The final region is attained when a continuous layer of SiO_2 has formed on the alloy surface by growth and lateral flow. In the final region, silicon is oxidized preferentially at the alloy/oxide interface at a slow rate, which is controlled either by diffusion of the reactive components or by a phase boundary reaction.

The resultant outer oxide layer is pure SiO_2(c) containing less than 0.1% of molybdenum; mass balance near the surface of the silicides is preserved by the establishment of layers of increasing molybdenum content between the bulk alloy and the outer oxide.

Above 1970°K, at oxygen partial pressures of 10 Torr, an increased oxidation rate of $MoSi_2$ is encountered due to the formation of SiO(g) at the oxide alloy interface which causes rupture of the protective oxide.

Below 1970°K, at oxygen partial pressures near 2 Torr, the rate of oxidation of $MoSi_2$ is linear at all times since the oxygen partial pressure is insufficient to maintain a protective SiO_2 layer on the alloy.

Finally, it is important to note a significant difference between the oxidation of bulk molybdenum silicides and the oxidation of silicide coatings on molybdenum (27). The coatings are not in thermodynamic equilibrium with the metal, and silicon can diffuse away from the coating into the substrate, with a deleterious effect on coating performance (28).

Manuscript received Oct. 23, 1964; revised manuscript received Feb. 22, 1965. This research was supported in part by the United States Air Force under Contract No. AF 33(616)-6154, monitored by the Air Force Materials Laboratory, Research and Technology Division, Wright-Patterson Air Force Base, Ohio.

Any discussion of this paper will appear in a Discussion Section to be published in the December 1965 JOURNAL.

REFERENCES

1. E. Fitzer, "Plansee Proceedings, 1955," Pergamon Press, London (1956); note Fig. 1 and 13.
2. R. Kieffer and E. Cerwenka, *Z. Metallk.*, **43**, 101 (1952).
3. E. Fitzer, *Metall.*, **9**, 1062 (1955).
4. W. A. Maxwell, NACA RM E9601 (1949).
5. R. A. Long, NACA RM E50F22 (1959).
6. E. Fitzer, "Plansee Proceedings, 1958," Pergamon Press, London (1959).
7. E. Fitzer, *Berg- u. Hüttenmänn. Monatsh. montan. Hochschule Leoben*, **97**, 81 (1952).
8. R. Kieffer, F. Benesovsky, and K. Konopicky, *Ber.*, **31**, 223 (1954).
9. A. W. Searcy, *J. Am. Ceram. Soc.*, **40**, 431 (1957).
10. E. Fitzer, "Passivierende Filme und Deckschichten," Springer-Verlag (1956).
11. E. A. Beidler, C. F. Powell, I. E. Campbell, and L. F. Yntema, *This Journal*, **98**, 21, 511 (1951).
12. G. Feick, Tech. Doc. Rept. No. ASD-TDR-62-204, Part I, Aeronautical Systems Div., Wright-Patterson Air Force Base, Ohio, April, 1962.
13. J. B. Berkowitz-Mattuck, *This Journal*, **111**, 908 (1964).
14. M. Green, "X-ray Optics and X-ray Microanalysis," H. H. Pattee, V. E. Cosslett, and A. Engstrom, Editors, p. 361, Academic Press, N. Y. (1963).
15. Norelco Reporter, May-June 1962.
16. D. B. Wittry, Univ. Southern California Rept. (84-204) 1962.
17. R. R. Dils, L. Zertz, and R. A. Huggins, "X-ray Optics and X-ray Microanalysis," H. H. Pattee, V. E. Cosslett, and A. Engstrom, Editors, p. 341, Academic Press, New York (1963).
18. R. P. Burns, G. DeMaria, J. Drowart, and R. T. Grimley, *J. Chem. Phys.*, **32**, 1363 (1960).
19. JANAF Tables of Thermochemical Data, Dow Chemical Co., Midland, Mich.
20. E. G. King, W. W. Weller, and A. U. Christensen, U. S. Bur. Mines Rept. Invest. No. 5664 (1961).
21. F. J. Norton, *Nature*, **191**, 701 (1961).
22. J. B. Ligenza and W. G. Spitzer, *J. Phys. Chem. Solids*, **14**, 131, (1960).
23. J. T. Law, *J. Phys. Chem.*, **61**, 1200 (1957).
24. P. J. Jorgensen, *ibid.*, **37**, 874 (1962).
25. J. B. Berkowitz-Mattuck, A. Büchler, J. L. Engelke, and S. N. Goldstein, *ibid.*, **39**, 2722 (1963).
26. C. Wagner, *J. Appl. Phys.*, **29**, 1295 (1958).
27. R. A. Perkins, L. A. Riedinger, and S. Sokolsky, *Space and Aeronautics*, **39**, 107 (1963).
28. R. W. Bartlett, P. R. Gage, and P. A. Larssen, "Investigation of Mechanisms for Oxidation Protection and Failure of Intermetallic Coatings for Refractory Metals," Sixth Quarterly Progress Report under Contract No. AF 33(657)-9170 between Philco and ASD, Wright-Patterson Air Force Base, Ohio, Jan. 15, 1964.

Prevention of Oxidation in a Glow Discharge Environment with Sputtered Permalloy Films as an Example

Eric Kay

IBM San Jose Research Laboratory, San Jose, California

ABSTRACT

Problems associated with the elimination of significant amounts of oxygen inclusions in sputtered thin films grown in a plasma environment are discussed. In particular data are presented to show that a plasma environment can easily be produced in which the concentration of ground state, excited and ionic oxygen containing species is sufficiently low so that no discernible effects on the magnetic properties of sputtered Permalloy films due to antiferromagnetic inclusions can be detected. Experimental evidence is also given to show that neither the energy of bombarding ion species at the cathode nor the inevitable electron bombardment of the substrate need influence the inducement of a truly uniaxial anisotropy into the NiFe film provided independent temperature control of the film during its growth can be achieved. A comparison between d.c. and asymmetric a.c. as well as substrate biasing with respect to the plasma is made with particular reference to the substrate environment.

The presence of very small concentrations of oxygen in the environment in which a thin film grows has in the past more often than not been considered detrimental to the attainment of well controlled physical properties of the resultant film. This has been largely due to the fact that the theoretical significance of such small concentrations of oxygen incorporated, often in a structurally undefined way, in the thin film is difficult to ascertain.

More recently well controlled small partial pressures of oxygen in the film growth environment have been used to advantage. Herrick (1) has shown that intentional burial of oxygen gas in the film condensate during growth, estimated at 10^{19} atoms/cc, can greatly retard or even arrest the grain boundary motion in semiconducting CuI films. Recent examples (2, 3) of technological significance in the production of microcircuits might be the significant extension of sheet resistance per square while maintaining reasonably low temperature coefficients in refractory metal films by trapping small amounts of oxygen during film growth.

In studies of magnetic thin films very little has been reported on such deliberate introduction of very small concentrations of reactive species in the system during film growth. The significance of inadvertently incorporated impurity sites has, however, been the subject of numerous publications. Several authors have attempted to correlate the "inevitable" presence of small amounts of oxides in NiFe films to their magnetic behavior (4-8). In particular the explanation of magnetic properties of thin sputtered and evaporated Permalloy films as reported by Francombe (9) and Prosen (10) respectively invoke the presence of significant amounts of oxides as determined by electron diffraction. It is the purpose of this paper to show that oxidation of sputtered Permalloy films grown in a d-c glow discharge environment need not be a significant problem at any stage during film growth. Data will be presented indicating that neither the usual ultrahigh vacuum bakeout techniques nor deliberate high energy ion bombardment of the growing film during deposition, as first suggested by Frerichs' (11) asymmetric a-c sputtering technique for "oxygen free" film growth, are necessary to obtain uniaxial sputtered NiFe films with low coercivity, H_c, and magnetic anisotropy field, H_K. It will also be shown that such magnetic properties can be obtained independent of the cathode fall potential used in the discharge provided independent control of the substrate temperature is maintained.

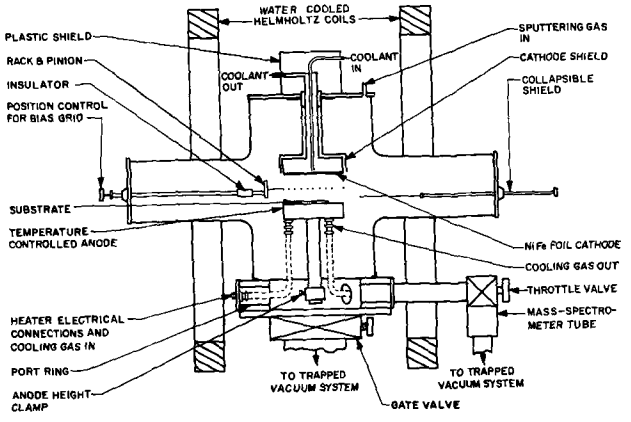

Fig. 1. Schematic of a d-c glow discharge apparatus

Experimental

The configuration of the glow discharge sputtering apparatus is shown schematically in Fig. 1. Ultrahigh vacuum facilities requiring time consuming high temperature bakeout procedures were deliberately excluded from our apparatus. Instead, a method of film preparation as described in detail in our earlier publication (12) involving inert gas ion bombardment of the entire apparatus, including the substrate surface, just before the NiFe deposition and continuous precleaned inert gas flushing was used as a means of reducing contaminants in the system. This precleaning approach was based on findings of atomically clean crystal surfaces obtained by ion bombardment in much more idealized systems (13), as well as promising results reported on glass by several authors (14-17) in a glow discharge system. An ultimate pressure of 1 x 10^{-7} Torr was routinely attained. Our mass spectrometer data were obtained using a Diatron 20 spectrometer tube which continuously monitored the effluent gases leaving the discharge chamber. The Diatron was operated at a 10^{-5} Torr level while the discharge chamber during sputtering was at a pressure in the 10^{-1} to 10^{-2} Torr region. The gas analysis runs were obtained with all the effluent gases going through the 2 in. mass spectrometer pumping system. The actual film preparation runs were made with all the gas going through the 4 in. pumping station right below the discharge chamber.

Most of the significant structural, chemical, and magnetic property changes occur during the first 2000Å

of film growth; which, therefore, was the thickness range in which most of our film measurements were made. Metal and glass substrate preparation and temperature control as well as standard magnetic property evaluation and actual discharge procedures were described in detail earlier (12).

The oxide content of the sputtered films was cross checked by several standard methods as follows. Reflection electron diffraction to distinguish film surface[1] oxidation from film bulk oxidation; high resolution surface replication using Pt-C replicas to allow correlation of the reflection diffraction data with the surface topography. High resolution transmission electron diffraction to check for film bulk oxide formation in excess of approximately 1% and transmission microscopy to observe the effect of possible oxidation on crystal shape, size, and continuity of the NiFe films.

A gravimetric microchemical method of film analysis was used for films which could not be stripped off the metal or glass substrates for subsequent transmission electron diffraction. A large body of experimental data indicated that an accurate total weight of the film can be more reliably and certainly more conveniently determined by the use of a Rodder quartz ultramicrobalance, than by an indirect method of film thickness and density measurement. The capacity of the microbalance is 200 mg. The sensitivity is 0.06 μg and the accuracy is ± 0.5 μg.

The accurately weighed films were dissolved in dilute HNO_3 and analyzed in solution by well-established spectrophotometric methods using o-phenanthroline for iron and 8-dimethylglyoxime for nickel. By comparing the amounts determined independently in this way with the total weight of the original sample, quantitative estimates of the purity of NiFe films could be made. The accuracy of this spectrophotometric method of analysis for Fe deteriorates when the sample weight is less than approximately 150 μg of which only 30 μg is Fe in an 80:20 NiFe sample. To check recovery for very thin films larger substrate areas and consequently larger film weights must be used.

In some cases the effect of positive ion bombardment of the growing NiFe film during deposition on subsequent magnetic properties of these sputtered films was examined. The positive ion bombardment to the exclusion of negative ion or electron bombardment was accomplished by inserting a bias grid as shown in Fig. 1. This grid was grounded and the entire substrate assembly biased negative with respect to the grid. Good temperature control during these film ion bombardment runs was possible only because the substrates were in excellent thermal contact with the entire temperature controlled anode assembly.

Results and Discussion

It has been well recognized that oxidation during film synthesis can occur in several stages. The first and most difficult to ascertain can be caused by the presence of oxidizing agents, such as adsorbed or dissolved gases on or near the surface of the substrate. The second stage can occur from bombardment of the film during deposition by oxidizing species, and the third stage could be oxidation of the film surface after deposition. All three of these oxidation possibilities have been invoked by several authors to account for deviations from the predicted behavior of pure NiFe films. These oxidation sources will be examined here, particularly as they pertain to a glow discharge environment as encountered in this work.

Oxidation at the substrate-film interface.—Substrate surface oxidation would be expected to reflect itself particularly during the very early stages of film growth. Our sputtered films less than 100Å thick which were occasionally successfully stripped off our glass substrates showed no evidence of oxide formation using high resolution electron diffraction as a criterion. This is in sharp contrast to Prosen *et al.* (10) results for their thermally evaporated "normal" NiFe films deposited onto glass substrates in a 10^{-6} Torr environment. They report finding an initial layer of about 100Å thickness consisting of αFe_2O_3 and $NiFe_2O_4$ as determined by electron diffraction. Their substrates were precleaned by ion bombardment (no details given). Also contrary to Prosen's findings our films could always be dissolved completely in 0.3M HNO_3 as determined visually as well as by ultramicrobalance weighings of the resultant substrate and comparing it with its original weight. Spin wave pinning experiments as described by Kooi *et al.* (18) are being considered as an additional analytical approach to establish the presence or absence of antiferromagnetic inclusions, *e.g.*, oxides at the substrate-film interface.

It should be remembered that during the initial stages of film deposition, in the argon d-c discharge environment, the dielectric glass substrate is immersed in the negative glow, and its surface will, therefore, float at a negative potential with respect to the plasma as soon as the substrate shielding arrangement is removed. Therefore, besides the deliberate high energy ion bombardment of the substrate before film deposition in which the anode table is temporarily made the cathode of the system, the film is again inevitably subject to low energy ion bombardment (2-3 ev) due to the negative space charge build-up at the dielectric glass surface as soon as it is exposed to the plasma to initiate film deposition. Judging from purity of our $<$100Å NiFe films, this low energy inert gas ion bombardment may remove weakly bonded contaminants throughout film growth. It certainly cannot be responsible for sputtering in the usual sense. Threshold energies for detectable momentum transfer sputtering are of the order of 20 ev.

Unquestionably the mechanism involved in this substrate cleaning procedure is quite different to the many more or less sophisticated chemical procedures described in the literature. The effective removal of surface contaminants on glass by chemical means is particularly complex because the chemistry involved is not clearly understood. The existence of dissolved gases, such as H_2O, CO_2, and O_2, has been reported by many authors. In addition, several authors (19) have postulated the existence of a silica gel layer of several thousand angstroms on the surface of glass. Some of the commonly used chemical "cleaning" reagents can be absorbed by this gel, and evidence exists (20) that the cationic components of glass can diffuse into this gel from below and react with the absorbed chemicals to form a surface, the composition of which is complex.

Low energy ion bombardment of the substrate in glow discharge environment must undoubtedly be included in any mechanism describing the well-established general observation that the substrate to metal film bond is much stronger for sputtered films than for similar films condensed onto glass substrates in a high vacuum environment. This stronger bond need not necessarily be accounted for by assuming an oxide layer at the interface, as has been suggested several times in the literaure.

Oxidation during film growth.—All our high resolution transmission electron diffraction patterns for thick films up to 1500Å could be accounted for entirely by fcc NiFe alloy as demonstrated by a typical example in Fig. 2a.

Since, in contrast to evaporated films, it is usually difficult to strip sputtered NiFe films off glass substrates, it was often unavoidable to get transmission diffraction data off carbon coated copper electron microscope grids which were placed next to the glass substrates. This is a commonly used practice and is sometimes justifiable from the point of view of crystal structure studies where an amorphous C film substrate can be assumed to be similar to an amorphous glass surface. However, it is well to remember the limitations of this practice when problems of oxidation are of interest. First, it is very difficult to say to what

[1] "Film surface" does not refer to a monolayer, since such can only be selectively analyzed by low energy electron diffraction techniques and not by "reflection" diffraction, as used here

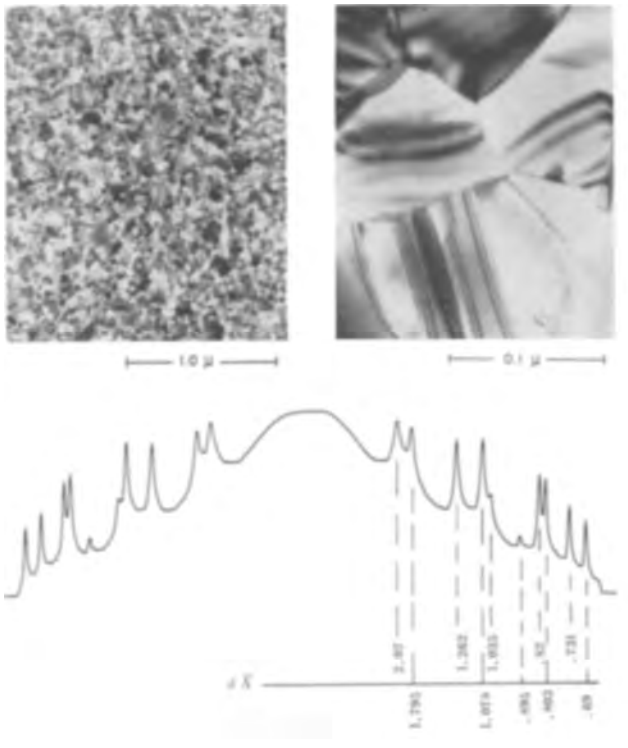

Fig. 2a. Typical transmission electron micrographs of a 700Å sputtered NiFe film made in a precleaned system showing continuous platelet structure at two magnifications, and a densitometer trace of the electron diffraction pattern of this film.

degree the surface temperature of a carbon film on a conducting Cu grid approximates the surface temperature of a dielectric, such as glass, when these are placed on an anode assembly immersed in a plasma. Second, the surface contaminants of glass cannot be assumed to be the same as those on a carbon film. Within these limitations, however, the transmission diffraction data from sputtered NiFe films on C should be indicative of the degree of oxidation or lack thereof during stage two; *i.e.*, oxidation due to reaction with oxidizing species in the plasma during film growth.

Since no oxide patterns developed in our films to film thicknesses up to 1500Å, we find our results again in conflict with diffraction results by Prosen who finds a stratified oxide composition throughout his thick films if prior to film deposition in a 10^{-6} Torr environment the glass substrate were exposed to a 10^{-3} Torr O_2 environment. Furthermore, on our thick films all of the film weight as determined with the ultramicrobalance was accounted for spectrophotometrically as Ni and Fe to within $\pm 1\%$, except in those cases in which the precleaning procedure was deliberately excluded. In these latter cases the electron diffraction data clearly showed oxide structure and the "gravimetric" Ni and Fe analysis showed less than 100% recovery of the original film weight. The electron micrographs of such films were discontinuous with large holes clearly visible as shown in Fig. 2b. As anticipated the coercivity in such films increased and the saturation magnetization decreased. No systematic magnetic study of partially oxidized NiFe films was made, since the aim in this work was to avoid oxidation.

Oxidation after film deposition.—Reflection electron diffraction patterns of many of the films examined during this study showed a complete absence of any oxide patterns. In view of the independently studied surface morphology of these films, these reflection diffraction patterns are interpreted as indicating that if surface oxides were formed either during examination of the film in the Kerr magnetic optic apparatus or during subsequent examination in the electron microscope then such oxides could only have been present as one or two monolayers or as amorphous oxides. If the latter were the case then the magnetic and microchemical data indicate less than 1% of amorphous surface oxide. Also, the lack of incoherent scattering contributing to the background of the reflection diffraction patterns suggests the absence of significant amounts of amorphous oxide (see Fig. 2c).

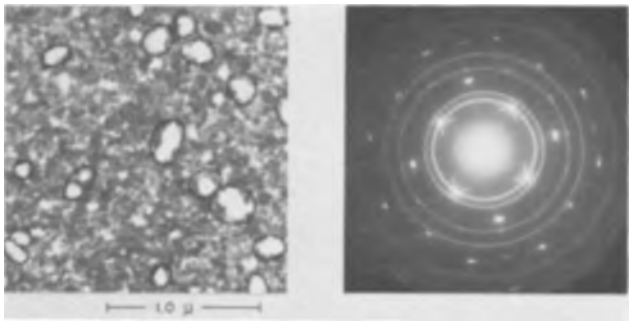

Fig. 2b. Transmission electron micrograph and electron diffraction pattern of 700Å sputtered NiFe film made in a "dirty" system. Circled areas are holes in the film.

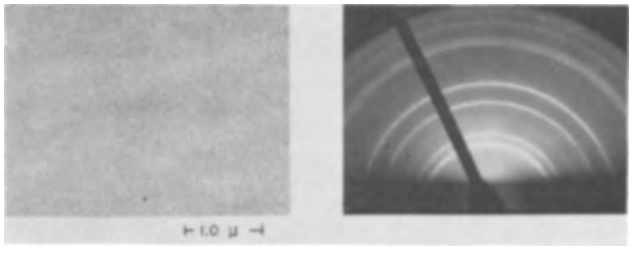

Fig. 2c. Pt-C replica and reflection electron diffraction pattern of a 700Å NiFe film made in a carefully cleaned system.

The absence of oxide structure together with the magnetic stability for many months indicates that surface oxidation was insignificant with respect to magnetic properties. As expected, every NiFe film which showed no evidence of any oxide formation also had exactly similar saturation magnetization values. Verification of this can be seen from the equal heights of the typical B.H. loops of films shown in Fig. 3, all three of which were of identical thickness.

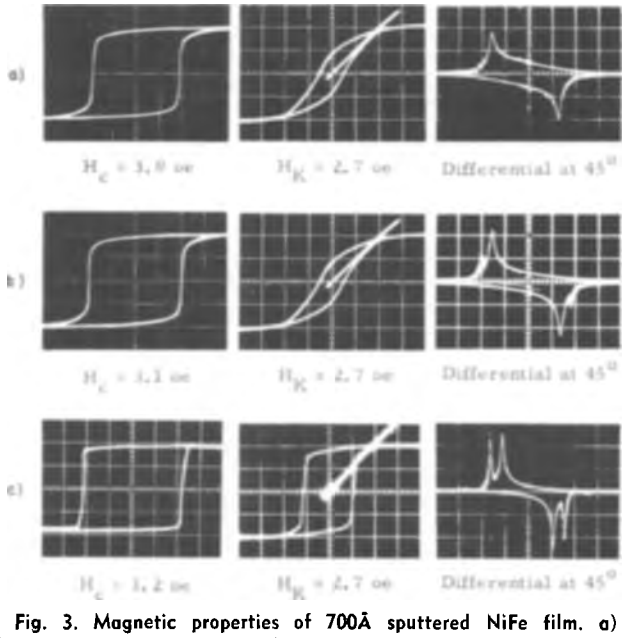

Fig. 3. Magnetic properties of 700Å sputtered NiFe film. a) Substrate at ground potential, cathode potential at —2000v. b) Substrate at —100v with respect to plasma, cathode potential at —2000v. c) Substrate at ground potential, cathode potential at —3500v.

From the results discussed so far it would appear that significant amounts of oxidizing species were not present in our glow discharge system during film growth. Monitoring the partial pressures of gas species as they leave the discharge chamber was used as a diagnostic technique to determine what types of gases were being created or removed from the vapor phase during consecutive stages of film preparation. It must be pointed out that this is not to be interpreted as an analysis of the actual species which exist in the plasma in the immediate vicinity of the growing film. It is well-known that a variety of relatively long-lived electronically excited, free radical and ionic species exist in various regions of the d-c discharge which would not show up as such in the exit gas of the discharge system. Knewstubb and Tickner (21) have recently shown that in an argon discharge in which water was estimated to be present at a partial pressure of 10^{-6} Torr, H_3O^+ is the only oxygen containing positive ion species that can readily be detected by mass spectrometry in the negative glow region. It is pertinent to note that the concentration of this particular molecule ion, like others, drops very sharply at different distances from the cathode, depending on the presence of small amounts of other impurity gases such as H_2. The mass spectrometric analysis by Lunt and Gregg ((22) on a 3 x 10^{-2} Torr oxygen d-c discharge further illustrates the point that different species exist in well-defined regions of the discharge. They found no negative ions in the negative glow region, yet 50% of the negative current carriers in the positive column were O^- ions. Our films are grown on substrates held in the negative glow region.

Mass spectrometric data presented in Table I clearly show that the amount of hydrogen leaving our discharge chamber increased by almost two orders of magnitude as soon as the discharge was initiated. Since the water signal only decreased by a factor of less than two, it is clear that the water decomposition in the discharge cannot account for the hydrogen increase. The decomposition of hydrocarbon in the discharge was considered a more likely mechanism whereby H_2 is produced because of the fact that methane fragments increased significantly as soon as the discharge was turned off. After lengthly pumping the CH_4 peaks fell to their original low value. These observations are tentatively interpreted as indicating that as soon as the discharge is turned on, low amu hydrocarbons are produced, some of which are further decomposed to H_2 and some are gettered by the walls and the film deposit. As soon as the discharge is turned off, the production of H_2 ceases and the gettered hydrocarbons are desorbed and show up as CH_4 in the exit gas. The 32 peak was barely detectable and remained essentially unchanged throughout. The mass spectrometer ion currents listed in Table I are uncorrected for relative ionization efficiency and pumping effects, etc., and can, therefore, be used only to determine the relative increase or decrease of the partial pressure of a given mass number during the various stages of film preparation.

Table I. Residual gas composition before and during sputtering in a dynamic flow system. All effluent gases through Diatron at 1 x 10^{-5} Torr. Sputtering chamber at 10^{-1} Torr argon.

amu	Diatron collector current, picoamps: Before sputtering	During sputtering	Directly after sputtering	Species
2	0.17	15.6	7.8	H_2
12	0.01	<0.01	0.03	C
13	0.01	<0.01	0.07	CH
14	0.15	0.03	0.18	N, CH_2
15	0.25	0.15	1.14	CH_3
16	0.09	0.14	1.29	CH_4, NH_2
17	0.42	0.18	0.23	OH, NH_3
18	1.8	1.1	1.0	H_2O
28	1.8	0.31	0.57	CO, N_2, C_2H_4
32	0.12	0.09	0.09	O_2
44	0.39	0.12	0.15	Organics

The degree to which the presence of H_2 and CH_4 during film deposition was responsible for the lack of discernible amounts of Fe-Ni-oxide must remain conjectural.

Effect of cathode fall potential and substrate biasing on magnetic properties of NiFe *films.*—It has been reported earlier that (23) low coercivity (<4 oe) sputtered NiFe films having a well-defined uniaxial anisotropy could not be prepared at ion energies ~ <3000 ev bombarding the NiFe cathode. Such was also our experience at the beginning of this study. Isotropic films with H_c values in excess of 10 oe were common on glass substrates. A more pronounced deviation from the zero magnetostriction composition leaving the cathode than that observed at 3500v (12) was considered a distinct possibility during the early stages of sputtering, which could account for the high H_c films. However, x-ray fluorescence analysis of NiFe films which were made at a cathode potential of 2000 ev in this laboratory showed no significant variation in the NiFe ratio throughout film growth and was equal to 4.0.

Two possibilities remained that had not previously been resolved which could account for high coercivity films. First, that in a 2000 ev cathode potential run electron bombardment of the substrate placed on the grounded anode does not raise its temperature sufficiently to get into the critical temperature region shown (12) necessary to obtain low wall motion threshold energies. Second, that although the physical location of the substrate with respect to the cathode was the same for these 2000 ev runs as for that previously reported at 3500 ev, the electron temperature profile along the discharge is significantly displaced at this lower energy. This could result in larger concentrations of reactive ionized oxygen containing species being formed in the immediate vicinity of the substrate where the film is growing, thereby increasing the possibility of introducing a more significant amount of antiferromagnetic inclusions in our films than was the case at 3500 ev. Two sets of runs were made to distinguish between temperature and increased ion concentration effects.

Any direct correlation between coercivity, H_c, at a given thickness and film temperature can only be ascertained unequivocally if the film temperature remains constant throughout the film growth. Large temperature profiles during film growth reflect themselves crystallographically especially in particle size and defect structure as demonstrated earlier (12). This in turn is related in different ways to the domain wall energy as one goes from thin films to thicker films, as discussed by Middelhoek (24) and can be expected to reflect itself in the H_c values.

With the use of a special substrate temperature control system to be described elsewhere, the substrate temperature was maintained within ± 1°C throughout film deposition. The temperature chosen was 350°C which was shown in our previous publication to be ideal for uniaxial anisotropy sputtered NiFe films. One set of experiments was run with cathode fall potential at 2000 ev and with the metal substrates held at ground potential and at a temperature of 350° ± 1°C. The resultant films had a well-defined uniaxial anisotropy and had low coercivity values. Typical magnetic data is shown in Fig. 3a. As can be seen these films were inverted, *i.e.*, $H_c > H_K$, and were similar to those prepared at 3500 ev, Fig. 3c.

All the high coercivity, isotropic NiFe films on glass which we obtained at the beginning of this study at cathode potentials of 2000 ev undoubtedly resulted from low substrate temperatures during film growth. Since independent temperature control of the substrate was not available at that time large temperature profiles from room temperature to several hundreds of degrees during a 100 sec run was the inevitable situation as originally described by Francombe *et al.* (9), who obtained magnetically isotropic films at low cathode potentials. From their data it is evident that at

2000 ev the temperature of glass substrates barely reached 200°C which is apparently inadequate (12) to induce a uniaxial anisotropy into these films.

In a second set of runs the effect of deliberate positive ion bombardment and rejection of negative ions from the film during deposition was examined. This was accomplished by biasing the entire anode assembly including the metal substrate 100v negative with respect to the grounded ring structure or grid which was introduced into the negative glow region above the "anode" assembly. We have shown previously (25) that this type of configuration rejects from the substrate most of the electrons and any negative ions which may be present. However, part of the positive ions which diffuse through the negative glow region will be continually accelerated into the substrate across this 100v gradient. The rest will drift toward the Crookes dark space and be accelerated into the cathode. A certain degree of analogy to Frerich's asymmetric a-c sputtering technique is obvious. The temperature of the substrate was again controlled throughout deposition at 350° ± 1°C. The structural and magnetic properties of the films prepared in this manner were essentially identical to those in the unbiased configuration (see Fig. 3b). We interpret this to show that the rejection of electrons and negative ions (if present) and bombardment by 100 ev positive ions on the growing NiFe film played no discernible role in determining magnetic properties in our system.

These data, therefore, suggest that low coercivity, H_c, and low anisotropy field, H_K, films having low dispersion of the easy axis direction of magnetization can be made in a d-c discharge at any voltage provided the critical substrate temperature is maintained throughout film growth and the oxidizing species in the discharge environment are minimized by appropriate precleaning procedures.

Manuscript received Jan. 27, 1964; revised manuscript received Jan. 4, 1965.

Any discussion of this paper will appear in a Discussion Section to be published in the December 1965 JOURNAL.

REFERENCES

1. C. S. Herrick, Electrochemical Society Meeting, April 15-18, 1963, Pittsburgh, Pa., Abstract No. 70.
2. L. Maissel, J. Simmons, and M. Casey, IRE Trans. Component Pts. CP8, 70 (1961).
3. W. J. Pendergast, Electrochemical Society Meeting, April 15-18, 1963, Pittsburgh, Pa., Abstract No. 61.
4. W. L. Roth and G. A. Slack, *J. Appl. Phys.*, **31**, 352*S* (1960).
5. J. Lommel and C. D. Graham, Jr., *ibid.*, **32**, 83*S* (1961).
6. C. P. Bean, "Structure and Properties of Thin Films," C. A. Neugebauer, Editor, p. 331, John Wiley & Sons, New York (1959).
7. R. D. Heidenreich, E. A. Nesbitt, and R. D. Burbank, *J. Appl. Phys.*, **30**, 995 (1959).
8. M. Prutton, Transactions of 9th National Vacuum Symposium, Oct. 31-Nov. 2, 1962, Los Angeles, p. 59.
9. M. H. Francombe and J. A. Noreika, Symposium on Electrical and Magnetic Properties of Thin Metallic Layers, Louvain, Belgium, Sept. 4-7, 1961; *J. Appl. Phys.*, **33**, 1119 (1962).
10. R. J. Prosen *et al.*, *J. Appl. Phys.*, **33**, 1150*S* (1962).
11. R. Frerichs, *ibid.*, **33**, 1898 (1962).
12. E. Kay, *ibid.*, **35**, 2936 (1964).
13. H. D. Hagstrum, *ibid.*, **32**, 1015 (1961).
14. L. Holland, *Advances in Vacuum Sci. and Technol.*, **2**, 755 (1960).
15. R. L. Hines, *J. Appl. Phys.*, **28**, 587 (1957).
16. N. A. Florescu, *Vacuum*, **8**, 46 (1958).
17. A. F. Fray and S. Nielsen, *Brit. J. Appl. Phys.*, **12**, 603 (1961).
18. C. F. Kooi *et al.*, *J. Phys. Soc. Japan*, **17**, Supplement B-1, 599 (1961).
19. G. Koranyi, *J. Soc. Glass Technol.*, **43**, 438*T* (1959).
20. S. Tsuchikaski *et al.*, *J. Ceram. Ass. Japan*, **66**, (754), 233 (1958).
21. P. F. Knewstubb and A. W. Tickner, *J. Chem. Phys.*, **38**, 464 (1963).
22. R. W. Lunt and A. H. Gregg, *Trans. Faraday Soc.*, **36**, 1062 (1940).
23. M. H. Francombe and A. J. Noreika, *J. Appl. Phys.*, **32**, 978 (1961).
24. S. Middelhoek, Thesis, University of Amsterdam, The Netherlands, 1961.
25. E. Kay, *J. Appl. Phys.*, **34**, 760 (1963).

Trace-Ion Diffusion in Molten Alkali Carbonates

P. L. Spedding and R. Mills

Diffusion Research Unit, Research School of Physical Sciences, Australian National University, Canberra, Australian Capital Territory

ABSTRACT

Tracer-diffusion coefficients have been measured for Na^+ and $CO_3^=$ ions in the pure Na_2CO_3 melt and of Na^+, K^+, and $CO_3^=$ ions in a eutectic mixture of lithium, sodium, and potassium carbonates. The open-ended capillary method was used for these measurements. In the Na_2CO_3 melt, agreement with the Nernst-Einstein equation is found at 910°C, but at 1050° there is a discrepancy of 22%. The experimental activation energies for diffusion of the ions in both the pure Na_2CO_3 melt and the eutectic mixture are the same within ±1 kcal.

In recent years the alkali carbonate melts have been studied extensively with regard to many of their physical and transport properties by Janz and coworkers (1-3). However, diffusion measurements in these systems are either scant or lacking. We have therefore instituted a program of tracer-diffusion studies and initially investigated two kinds of systems, the pure sodium carbonate melt and an eutectic mixture of sodium, potassium, and lithium carbonates.

The sodium carbonate system was chosen because tracer-diffusion measurements, in conjunction with existing conductivity data, allow both testing of the Nernst-Einstein equation and the calculation of friction coefficients. In addition, diffusion measurements previously reported in this system by Djordjevic and Hills (4) appear to be anomalous. The eutectic mixture of alkali carbonates was studied both from interest in the fundamental structure of eutectics and from its importance as an electrolyte in high-temperature fuel cells. With regard to this latter factor, it is possible that transport data of this type will be useful in evaluating sources of energy loss in actual fuel cell systems.

Experimental

Apparatus.—The apparatus, which is illustrated in Fig. 1, consisted of a furnace and its ancillary shields, enclosing a diffusion cell. The furnace, A, was capable

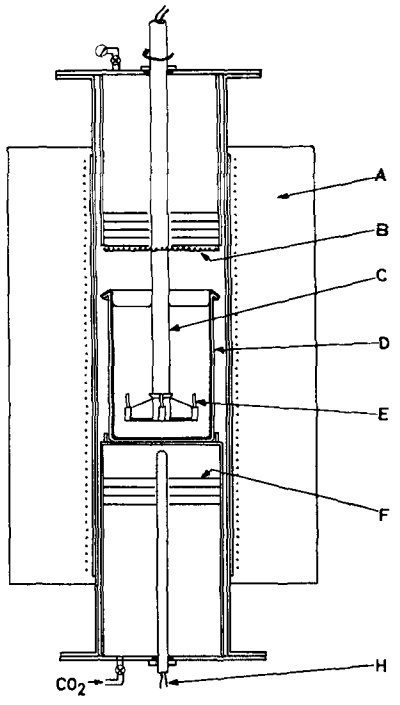

Fig. 1. Cross-sectional view of the furnace and capillary diffusion apparatus: A, furnace; B, auxiliary heater; C, hollow capillary holder containing measuring thermocouple; D, salt bath contained in a 80% Au-20% Pd lined stainless steel pot; E, capillaries; F, heat shields; H, sensing thermocouple for saturable reactor control.

of operation up to 1000°C and a saturable reactor-type control maintained the temperature of the diffusion zone in the furnace to within ± 0.3° at the 700°C point. The measuring thermocouple was calibrated to ± 0.2° up to 500°C with a platinum resistance thermometer, and also with the primary and secondary fixed points for S, Ag, Au and Zn and Al. Originally the furnace relied on the heat shields, F, to maintain the temperature vertically through the furnace, but it was found that at the higher temperatures this was not sufficient to prevent a negative temperature gradient being set up through the diffusion zone. This resulted in convectional currents in the capillaries, and to overcome this effect an auxiliary heater, B, was provided which enabled any desirable temperature gradient to be applied. The furnace was normally operated so that a positive gradient was just measurable. It was also found to be necessary to cool the saturable reactor core by means of a small fan to prevent slow temperature drifts particularly in the lower temperature range.

The diffusion cell consisted of a large bath of salt, D, into which the holder containing the diffusion tubes, E, could be lowered. The holder assembly, C, was capable of rotation so that the speed at the capillary mouth could be varied up to 325 mm/sec. In addition the holder could also be given vertical travel at a rate depending on its speed of rotation. At maximum rotation speed the vertical movement was 2 cm/hr. This provision was made to ensure that there was no build-up of radioactive material in the path of travel of the capillary mouth. Subsequently, tests showed this to be unnecessary so, for the majority of determinations, the holder was rotated in the one horizontal plane. In order to test for immersion effects, provision was made to open and close the capillary mouth by means of a sliding mechanism.

All metal components of the apparatus contacting the molten carbonate were made from palau: an 80% wt. gold-20% wt. palladium alloy. This alloy has been reported to be resistant to carbonate attack (1). Actual measurements at 1000°C for 94 hr have shown this alloy to be essentially unaffected by carbonate, despite the development of a blue-gray surface discoloration at between 350°-660°C.

The alloy diffusion tubes had thick walls both to provide sufficient mechanical strength to allow them to be handled by tongs without damage and also to impart sufficient thermal inertia to allow them to be transferred to the main furnace without solidification of the melt. The actual length of the capillaries (nominally 3.5 cm) was measured on a travelling microscope at 20°C and corrected to the temperature of the particular determination by using accurate thermal expansion data for the alloy (5).

Materials.—Analytical reagent grade lithium, sodium, and potassium carbonates were used for the salt bath and as a dilutant for the labelled material. The carbonates for the bath were dried at 120°C to constant weight before use whereas those for radioactive material dilution were melted under a carbon dioxide atmosphere and stored in a desiccator until use. The long-lived radioactive sodium carbonates were obtained from the Radiochemical Centre, Amersham, England; one being labelled with Na^{22} and the other with C^{14}. The short-lived Na^{24} and K^{42} carbonates were obtained from the Australian Atomic Energy Commision, Lucas Heights, New South Wales.

Procedure.—The diffusion tubes were filled in a small auxiliary furnace using a manually operated filling capillary and were then quickly transferred to the tube holder in the main furnace. The filling temperature was about 100°-200°C above the melting point of salt. The tubes were almost completely immersed and equilibrated for 3 hr under a positive carbon dioxide pressure. The temperature gradient was carefully controlled at the start of diffusion to ensure that the tube temperature was the same as the environment into which it was lowered. If the slide was used, it was run onto the top of the tube just before immersion and slowly removed immediately afterwards to give the start of the diffusion run. Normally, a medium-sized drop of radioactive salt on the top of the tubes was sufficient to minimize immersion effects at the start of diffusion. At the end of a diffusion run the temperature of the furnace was dropped to within 100°C of the melting point before removing the tubes from their holder for analysis.

The radioactive salt was removed from the diffusion tubes into aqueous solution by vibratory drilling. For Na^{22} diffusion the resulting solution was made up by weight in a counting vial and counted by standard techniques using a Franklin linear amplifier and a RIDL scaler. The C^{14} was counted with the same apparatus using standard liquid scintillation procedures. The scintillator solution used consisted of 1-4 dioxane as solvent and the following solutes: 50 g/l of naphthalene, 4 g/l of 2-5 diphenyloxazole and 0.1 g/l of 1-4-di-2-(5-phenyloxazole)-benzene. A 10 ml aliquot of this dioxane-scintillator solution was admitted to the counting bottle together with a 5 ml aliquot of the radioactive solution which had been made up to 25 ml in a volumetric flask.

The general design of the apparatus was initially tested by determining the diffusion coefficient of Na^{22} in 0.3M NaCl solution at 25°C. This work established first that there was no measurable difference between the use of a large drop of solution on the top of the diffusion tube or the use of the slide to minimize immersion effects. Second, it showed that there was need for tube-holder rotation, but that no measurable difference existed between rotation in the one horizontal plane or in a changing horizontal plane. The extension of these aqueous experimental conditions to molten salts is discussed later.

Auxiliary Measurements

Comparison with previous work.—As a check on the apparatus and procedure, the tracer-diffusion coefficient of Na^{22} in $NaNO_3$ was measured and compared with the values of Dworkin *et al.* (6). This system has

Table I. Diffusion of Na^{22} in $NaNO_3$ melt

T, °C	D^*, cm²/sec $\times 10^5$ (This work)	D^*, cm²/sec $\times 10^5$ (Dworkin *et al.*)	D^*, cm²/sec $\times 10^5$ (Angell and Tomlinson)
368	2.62	2.61	—
	2.64	—	—
365	2.53	2.55	—
	2.56	—	—
348	—	2.29	2.25
328	—	2.00	1.97

also been used for checking by Angell and Tomlinson (7). As shown in Table I, our agreement with the above workers is good.

End effects.—Errors in diffusion measurements due to end-effects associated with the open-ended capillary method, have been the subject of much enquiry and discussion. Two sources of error are involved and are usually termed the "immersion effect" and the "Δl" effect. The nature of these effects has been described in detail by, among others, Mills and Kennedy (8), Wang (9), Berne and Berggren (10), and Angell and Tomlinson (7). It is fairly well established that the immersion error is negligible if a large drop of active solution remains on the capillary face just prior to immersion and if reasonably long times of diffusion are used. As these conditions pertained to this study, this type of error needs no further discussion. In aqueous solutions the Δl effect can be made negligible as a source of error. Mills (11) has shown that if a flow of liquid of controlled velocity (in the range 1-3 mm/sec) was passed over the capillary faces in his apparatus then the measured diffusion coefficients coincided with those accurately determined with the diaphragm cell. It was concluded from this that the effect must be minimized under these conditions. In molten salts, there are no independent data against which a flow rate can be tested to give the magnitude of the Δl effect. In consequence, two indirect approaches to the treatment of the problem can be distinguished.

In one approach, an attempt is made to select flow conditions (usually by rotation of the capillaries in the melt) under which the Δl effect will be minimal. A flow rate approximately in the region 1-3 mm/sec as specified by Mills (11) for aqueous solution has been used by some investigators (6, 7). It will be realized of course that this flow rate will give conditions which will vary with such parameters as the capillary dimensions and the fluid viscosity so that the Reynold's number is the more basic consideration. Fortunately in many of the above cases, the geometry of the system and the physical properties of the molten salts have given Reynold's numbers overlapping the range used by Mills (11). The approach can be criticized in the respect that conditions applicable to aqueous solutions do not necessarily apply to molten salts even with identical Reynold's numbers. Experimental control of temperature and flow are much less rigorous in the latter case. However, the absence of end errors greater than the over-all experimental error has been verified by using capillaries of differing lengths or by using different diffusion times (6, 7). The two errors are comparable (±1-3%) so that studies where the Δl effect is not recognizable serve to put an upper limit on its magnitude.

The alternative approach adopted by Bockris and co-workers (12, 13) has been to find a plateau in the rotation rate *vs.* diffusion coefficient curve (usually at higher Reynold's numbers than those used above), employ a flow in this region and then estimate the Δl produced and correct for it. In these studies, the effect has been related to physical parameters by an empirical equation established for aqueous dye solutions. Use of this formula in molten salts is criticizable for the same reasons as the approach above. A more serious criticism is that rather large corrections of unknow accuracy may be involved, of the order of 10-20%, which affect the accuracy of the corrected experimental values correspondingly.

In this study we have adopted the first approach and used low flow rates of 1-3 mm/sec. (Reynold's numbers 5-16). This procedure will give, in our opinion, in the final analysis, the more accurate diffusion coefficients. As a first test of the apparatus, studies were carried out in aqueous solution using a dye system. Flow rates below Re=5 allowed a definite build-up of material at the tube mouth while rates above Re=16 disturbed the solution at the trailing edge of the capillary mouth within the observed boundary layer. Further studies were carried out using Na^{22} trace-ion diffusion in an aqueous 0.3M NaCl solution as the calibrating system. It was found that within the above flow conditions the measured coefficients were on an average within 0.6% of the diaphragm cell values (11). As the flow rate was increased beyond this range the measured coefficients increased steadily. Trace-ion diffusion of Na^{22} in the molten carbonate eutectic at 685°C showed that the coefficients varied in a more pronounced way with flow rate. The measured diffusion coefficients rose sharply by 7% from nonstirred to stirred conditions (Re=5-16) and then continued to rise slowly with increasing flow rate until at Re = 140, it increased by a further 5.3%. Measurements in the chosen flow rate range (Re=5-16) with tubes of different lengths gave the same diffusion coefficients within the usual experimental errors. It seems apparent therefore that under these flow conditions the Δl effect will be minimal.

Diffusion coefficients were determined also for sodium ion in the eutectic at several different temperatures using tubes of different diameter. Tubes with diameters of 1.0 mm or below gave virtually identical results and were therefore used for all determinations.

Isotope effects.—The qualifying assumption is made when determining diffusion coefficients using isotope tracers that there is no observable isotope effect. This was checked by determining diffusion coefficients in the carbonate eutectic during the same run, using Na^{22} and Na^{24} tracers (Table II).

There is obviously no difference observable above experimental error among the diffusion coefficients. The Na^{22} (calculated) figures are taken from the equations in the main body of the results.

Expansion coefficient.—Practically no data exist for the thermal expansion of the 80% gold-20% palladium alloy. Values were therefore determined up to 1000°C using standard techniques (5) (Table III).

Dissociation pressures.—In order to ensure that the composition of the carbonate melts remained constant they were maintained under carbon dioxide at a pressure well in excess of their respective dissociation pressures. The actual dissociation pressures were determined using a static method and in the case of sodium

Table II. Na^{22}, Na^{24} diffusion coefficients in the carbonate eutectic

Temp, °C	$D^*_{Na^{22}}$ cm²/sec	$D^*_{Na^{22}}$ (calc.) cm²/sec	$D^*_{Na^{24}}$ cm²/sec
729	3.12×10^{-5}	3.16×10^{-5}	3.10×10^{-5}
			3.21×10^{-5}
730	3.16×10^{-5}	3.18×10^{-5}	3.09×10^{-5}
			3.16×10^{-5}
			3.25×10^{-5}

Table III. Linear expansion coefficient of palau

Temp, °C	cm/cm °C $\times 10^{-6}$ e
0	—
100	13.20
200	13.42
300	13.64
400	13.87
500	14.09
600	14.34
700	14.59
800	14.84
900	15.12
1000	15.40

Table IV. Dissociation pressures of carbonate melts

Temp, °C	Na_2CO_3, mm Hg	Li/Na/KCO_3, (43.5:31.5:25.0 mole %) mm Hg
700	—	—
750	—	10.5
800	—	24
850	—	46
900	—	72
950	9	108

Table V. Tracer-diffusion in Na_2CO_3 melt

Temp, °C	$D^*_{Na^+} \times 10^5$ cm²/sec	Temp, °C	$D^*_{CO_3^=} \times 10^5$ cm²/sec
910	5.52	901	3.07
	5.75		3.05
	5.63		2.99
944	6.39	932	3.36
	6.63		3.30
	6.57		3.50
	6.69	984	4.11
	6.59		3.98
982	7.64		4.09
	7.68	1062	5.25
	7.75		5.29
1043	9.53		5.20
	9.58		
	9.49		
897	(19.2)[a]		(27.9)[a]

[a] Values of Djordjevic and Hills (4).

$$D^*_{Na^+} = (1.00 \pm 0.05) \times 10^{-2} \exp - \frac{12{,}170 \pm 130}{RT}$$

$$D^*_{CO_3^=} = (2.86 \pm 0.10) \times 10^{-3} \exp - \frac{10{,}620 \pm 180}{RT}$$

Table VI. Tracer-diffusion in Li/Na/K, CO_3 eutectic melt

(43.5:31.5:25.0 mole %)

Temp, °C	$D^*_{Na^+} \times 10^5$ cm²/sec	Temp, °C	$D^*_{K^+} \times 10^5$ cm²/sec	Temp, °C	$D^*_{CO_3^=} \times 10^6$ cm²/sec
561	1.05	612	1.15	420	1.06
	1.03		1.09	484	1.89
672	2.35	697	2.08		1.89
	2.20		1.98	588	4.60
	2.20		2.05		4.33
		730	2.50	610	4.93
876	6.00		2.58		5.20
	5.93		2.53	651	6.33
	6.00	771	3.21		6.39
770	3.90		3.19	730	10.29
	3.87		3.17		10.17
	3.89	842	4.52	748	11.48
			4.48		11.33
			4.58	792	13.84
			4.52		13.67
				861	17.77
					16.50

$$D^*_{Na^+} = (8.06 \pm 0.32) \times 10^{-3} \exp -(11{,}035 \pm 75)/RT$$
$$D^*_{CO_3^=} = (1.58 \pm 0.07) \times 10^{-3} \exp -(10{,}070 \pm 75)/RT$$
$$D^*_{K^+} = (9.73 \pm 0.55) \times 10^{-3} \exp -(11{,}880 \pm 67)/RT$$

carbonate they were in reasonable agreement with previous workers who used this method (14, 15) (Table IV).

Results

Tables V and VI list data for tracer-diffusion of various ions in the two melts investigated. The constants in the equations were calculated by the method of least squares (16). Figure 2 illustrates how the diffusion rates of the ions compare in the pure melt and in the eutectic.

Discussion

Examination of Figure 2 shows that in both media the smaller the individual ion the higher its diffusion rate. It may also be noted that the effect of the eutectic is to slow down the $CO_3^=$ ion but speed up the Na^+ ion.

Trace-ion diffusion data for the pure Na_2CO_3 system together with the values of Djordjevic and Hills (4) are reported in Table V. There are large discrepancies between the two sets of values. However, the fact that

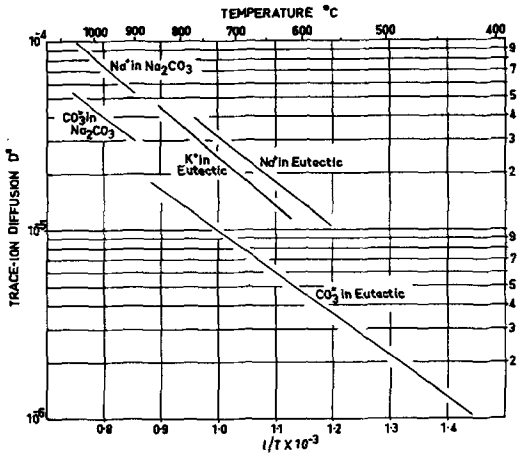

Fig. 2. Tracer diffusion coefficients of Na^+ and $CO_3^=$ in pure Na_2CO_3 and of Na^+, K^+, and $CO_3^=$ in the ternary eutectic plotted against the reciprocal of the absolute temperature.

in our study the diffusion rate of the small cation is greater than that of the large anion, as well as a much better correlation with the Nernst-Einstein equation would lead to the assumption that the open-ended capillary values are more correct.

The Nernst-Einstein equation for Na_2CO_3 is of the form

$$\mu_{Na_2CO_3} = (2F^2/RT)(D^*_{Na^+} + D^*_{CO_3^=}) \quad [1]$$

where μ is the molar conductance. This equation can be used to calculate values of μ at various temperatures, and these can then be compared with the experimental values from conductance studies. We have used the data of Janz and Lorenz (1), and the temperature variation of the observed and calculated molar conductances are shown in Fig. 3. Previous investigators have found that values of μ calculated from tracer-diffusion data are generally greater (10-40%) than those obtained from conductance studies. It has also been found that the deviation becomes smaller as the temperature decreases. In our study the deviation at 1050°C is +22% and with decrease in temperature it reaches zero at 910°C and −2% at about 900°C. The reality of the negative deviation at 900°C is questionable as the compounding of errors by the addition of the diffusion coefficients, would give a maximum total error of several per cent in the calculated values. It is tempting to attribute this negative deviation, if real, to the Bardeen-Herring correlation factor (17) which has been applied to the corresponding calculation in ionic solids. However, the application of

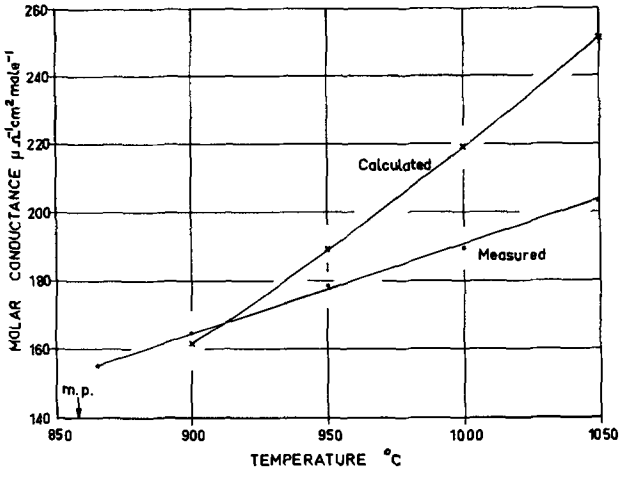

Fig. 3. Molar conductance of Na_2CO_3 as measured by Janz and Lorenz (1) and as calculated from the Nernst-Einstein equation using the measured tracer diffusion coefficients.

such a concept about 42° above the melting point is very arguable.

An explanation advanced for the positive deviation of conductances calculated from tracer-diffusion data is the presence of ion pairs or neutral molecules in the melt. Janz and Lorenz (3) have recently summarized evidence for the existence of ion pairs of the form $[M^+CO_3^=]^-$ in alkali carbonate melts. If such ion pairs move as a kinetic unit, they could act as a vehicle for the movement of the tracer species but because of the masking of charge, contribute little to conductance. However, Janz and Lorenz (1) suggest that rotation of such ion pairs as in a Grotthus-type mechanism may be the rate-determining process in conduction. We would expect that such a mechanism should be equally effective in promoting tracer-diffusion. The temperature dependence of the deviation from the Nernst-Einstein equation could then be explained by postulating that at lower temperatures the rotational mechanism of transport is predominant. As conduction and tracer-diffusion are equally affected the Nernst-Einstein equation is obeyed. With increasing temperature, the translational mode becomes more important, favoring tracer-diffusion so giving the observed positive deviation.

An alternative method of treating conductance and diffusion data is to calculate the friction coefficients for interaction among the various species. The basic formulations for this type of description have been given by Klemm (18) and Laity (19).

In Table VII, we give a summary of these friction coefficients at four temperatures and for comparison the values for $NaNO_3$ as calculated from the data of Van Artsdalen *et al.* (20) by Djordjevic and Hills (4). A fairly close correspondence at the lower temperatures between the values for $NaNO_3$ and Na_2CO_3 is evident. Plots of $d \ln r/d\ 1/T$ are found to be linear as has been similarly found for $NaNO_3$ by Laity (19). However, it seems that little information can be gleaned from this approach at the present stage.

A more informative approach is to compare the experimental activation energies for the various transport processes both in the pure Na_2CO_3 melt and the carbonate eutectic mixture. These are shown in Table VIII.

Examination of Table VIII shows that the experimental activation energy for viscous flow in pure Na_2CO_3 ($E_{vis} = 25.7$) is much larger than that for conductance ($E_\Lambda = 4.23$). Such a difference is usual for molten salts although this case is one of the most marked examples. The qualitative explanation which is normally offered to explain these differences is that in conduction, the current is carried mainly by the small ions, (Na^+ in the case of Na_2CO_3), which can migrate through the lattice without appreciable disturbance and thus have an associated low activation energy. In viscous flow on the other hand the observed high activation energy is attributed to the necessity to displace the large anions relative to one another. However, the activation energy for tracer-diffusion for the $CO_3^=$ ion ($E_{D^*CO_3^=} = 12.2$) is much lower than E_{vis}, and yet in the diffusion process these large anions must again be displaced. The first salient fact that we must seek to explain therefore is the high value of E_{vis} for pure Na_2CO_3.

It is suggested that the high value of E_{vis} is due to an additional factor which affects viscous flow to a much greater degree than the other transport processes. Most models of molten salts assume that their chief structural characteristic is the existence of interpenetrating anion and cation lattices which do not have the long-range order of the crystalline state, yet are sufficiently real to the extent that each ion has, on the average, more nearest neighbors of opposite than of its own charge. When a velocity gradient is imposed on an ionic liquid the associated shearing force has to distort this lattice, and there will therefore be a restoring force opposing flow. There will therefore be an electrostatic increment added to the viscosity and in this respect the effect is distantly analogous to the Falkenhagen effect in dilute electrolytes. The effect would also be greater for multiply charged ions. In the eutectic however, where E_{vis} is only 10.7 kcal/mole, the presence of three ions of widely different size would distort the lattice considerably so that the required shearing force is much less. The much lower values of the activation energies for conduction and diffusion can then be attributed to the ability of the ions to migrate through the lattice without appreciable disturbance.

A second point of considerable interest in Table VIII is that the activation energies for diffusion of anions and cations both in the pure Na_2CO_3 and in the eutectic are all very similar. This is in accord with nearly all other tracer-diffusion measurements in molten salts. One conclusion that can be drawn from this practical equivalence is that some sort of cooperative act is involved in the diffusion process. The coupled-vacancy concept suggested by Borucka, Bockris, and Kitchener (21) is one possibility. The predominant diffusing species for Na_2CO_3 could then be the $[Na^+CO_3^=]^-$ ion pair whose existence was postulated by Janz and Lorenz (3) and which has already been invoked above to explain deviations from the Nernst-Einstein equation. On this model, the low value for E_Λ could then be explained in terms of a predominant contribution to conductance of the migration of free Na^+ ions.

Although the explanations offered above give an approximate qualitative accord with the observed data, there are obvious points of criticism. For example, the movement of free Na^+ ions would also contribute to tracer diffusion, and one might therefore expect the over-all activation energy, for diffusion of Na^+ ions to be less than that for $CO_3^=$ ions. In fact $E_{D^*Na^+}$ is slightly higher than $E_{D^*CO_3^=}$. It should also be emphasized that these experimental activation energies in Table VIII which are obtained from plots of experimental data are not necessarily equivalent to the theoretical activation energies, such as for instance given by Eyring's rate process theory, and caution must be used in interpreting the smaller trends among them.

Attention has also been drawn to the fact that the equivalence of cation and anion experimental activation energies in tracer diffusion is in accord with the theory of Cohen and Turnbull (22). The basic concept of this theory as far as diffusion is concerned is that

Table VII. Friction coefficients for Na_2CO_3 melts at various temperatures

T, °C	$r_{1-} \times 10^{-8}$	$r_{--} \times 10^{-8}$	$r_{1+} \times 10^{-8}$
	(watt sec² cm⁻² eq⁻¹)		
900	3.40	2.94	0.99
950	3.16	2.10	0.69
1000	2.95	1.48	0.47
1050	2.77	1.00	0.30
	$NaNO_3$		
348	3.63	3.53	0.87

Table VIII. Experimental activation energies of transport in alkali carbonate melts

Component	Medium	E_Λ, kcal/equiv.	E_{vis}, kcal/mole	E_D^*, kcal/mole	
$(Na_2CO_3)/2$	Na_2CO_3	4.23[a]			
Na_2CO_3	Na_2CO_3		25.7[b]		
Na^+	Na_2CO_3			12.2	
$CO_3^=$	Na_2CO_3			10.6	
$(Na_2CO_3)/2$	Li/Na/K CO_3	6.46[c]			
Na_2CO_3	Li/Na/K CO_3		10.7[b]		±0.4
Na^+	Li/Na/K CO_3			11.0	
K^+	Li/Na/K CO_3			11.9	
$CO_3^=$	Li/Na/K CO_3			10.1	

[a] Janz and Lorenz, *This Journal*, **108**, 1052 (1961).
[b] Janz and Saegusa, *ibid.*, **110**, 452 (1963).
[c] Ward and Janz, *Electrochim. Acta*, In press.

molecular transport occurs by the movement of molecules into voids, with a size greater than some critical value, formed by the redistribution of free volume. Although originally intended for simple molecular liquids, it has been found to be applicable also to molten salts. The equation of interest in this context is

$$D^* = ga^*u \exp \frac{(-\gamma v^*)}{(\bar{v}_m \alpha T)} \quad [2]$$

where g is a geometric factor, a^* the approximate ionic diameter, u the gas kinetic energy, γ a numerical factor to correct for overlap of free volume, v^* the critical void volume, $\bar{v}_m$ the mean molecular volume, and α the coefficient of thermal expansion. It is readily seen that

$$\frac{E_{D^*}}{R} = \frac{\gamma v^*}{\alpha \bar{v}_m} \quad [3]$$

Lunden (23) has stated that $\gamma v^*/\alpha \bar{v}_m$ is fairly close to unity for both anion and cation for all halides and nitrates which are nearly completely ionized. It is probable that similar considerations apply to the alkali-metal carbonates.

Acknowledgment

Grateful acknowledgment is made to the Reserve Bank of Australia for a grant for fuel cell research, part of which has been used to finance the above study.

Manuscript received Dec. 7, 1964.

Any discussion of this paper will appear in a Discussion Section to be published in the December 1965 JOURNAL.

REFERENCES

1. G. J. Janz and M. R. Lorenz, *This Journal*, **108**, 1052 (1961).
2. G. J. Janz and M. R. Lorenz, *J. Chem. Eng. Data*, **6**, 321 (1961).
3. G. J. Janz and F. Saegusa, *This Journal*, **110**, 452 (1963).
4. S. Djordjevic and G. J. Hills, *Trans. Faraday Soc.*, **56**, 269 (1960).
5. P. L. Spedding, *J. Less Common Metals*, **7**, 395 (1964).
6. A. S. Dworkin, R. B. Escue, and E. R. Van Artsdalen, *J. Phys. Chem.*, **64**, 872 (1960).
7. C. A. Angell and J. W. Tomlinson, *Discussion Faraday Soc.*, **32**, 237 (1961).
8. R. Mills and J. W. Kennedy, *J. Am. Chem. Soc.*, **75**, 5696 (1953).
9. J. H. Wang, *ibid.*, **74**, 1182 (1952).
10. E. Berne and J. Berggren, *Acta Chem. Scand.*, **14**, 428 (1960).
11. R. Mills, *J. Am. Chem. Soc.*, **77**, 6116 (1955).
12. S. B. Tricklebank, L. Nanis, and J. O'M. Bockris, *J. Phys. Chem.*, **68**, 58 (1964).
13. J. O'M. Bockris, S. Yoshikawa, and S. R. Richards, *ibid.*, **68**, 1838 (1964).
14. J. T. Howarth and W. E. S. Turner, *J. Soc. Glass Tech.*, **14**, 394 (1930); **15**, 360 (1931).
15. P. Lebeau, *Ann. Chim. Phys.*, **6**, 422 (1905).
16. H. Margenan and G. M. Murphy, "The Mathematics of Physics and Chemistry," p. 519, 2nd ed., D. Van Nostrand & Co., N. J. (1957).
17. J. Bardeen and C. Herring, "Imperfections in Nearly Perfect Crystals," W. Shockley, Editor, John Wiley & Sons, Inc., New York (1952).
18. A. Klemm, *Z. Naturforsch.*, **8a**, 397 (1953).
19. R. W. Laity, *Ann. N. Y. Acad. Sci.*, **79**, 997 (1960).
20. E. R. Van Artsdalen, D. Brown, A. S. Dworkin, and F. J. Miller, *J. Am. Chem. Soc.*, **78**, 1772 (1956).
21. A. Z. Borucka, J. O'M. Bockris, and J. A. Kitchener, *Proc. Roy. Soc.*, **A241**, 554 (1957).
22. M. H. Cohen and D. Turnbull, *J. Chem. Phys.*, **31**, 1164 (1959).
23. A. Lundén, *Discussion Faraday Soc.*, **32**, 264 (1961).

The Coverage of Platinized Platinum Electrodes with Simple Organic Species

P. R. Johnson[1] and A. T. Kuhn

Chemistry Department, University of Pennsylvania, Philadelphia, Pennsylvania

ABSTRACT

The adsorption of formic acid, formaldehyde and the "reduced CO_2" species on platinized platinum electrodes was studied. A simultaneous determination of the number of coulombs and the number of chemical equivalents involved in the reduced CO_2 species, showed it to be a two-electron reduction product. Analysis of the solution failed to reveal any desorbed products.

Of the many possible methods available for the measurement of adsorbed species (1) on the surface of an electrode, one first described by Pavela (2), was used in this work. Although this method (which is described below) has certain inherent limitations and involves certain assumptions, it is simple to use where it is applicable.

In this method, the electrode at open circuit is immersed in the electrolyte containing the adsorbing species. After a period of time, it is withdrawn, rinsed with distilled water, and replaced in another cell containing a similar electrolyte. Galvanostatic transient measurements may then be made without any danger of readsorption from the bulk of the solution during the measurement period. The limitations of the method are mainly that it can be used to measure adsorption only at the open-circuit potential. Several objections to the method are listed by Breiter (3). The results of this author (4), however, indicate that at higher adsorbent concentrations certainly, results obtained by Pavela are in excellent agreement with those obtained by galvanostatic or potentiostatic transient methods. A further objection to the method, which does not appear to have been previously made, is the possibility of oxidation of the adsorbed material, either directly by the oxygen in the air, or by a simultaneous anodic and cathodic process, in which the oxygen is electrochemically reduced. In spite of all these objections, the work of Breiter cited above, and certain of the measurements described below, indicate that the method is a valid one.

The purpose of the work was threefold. First, it was felt that only by a simultaneous correlation of coulombs and chemical equivalents of CO_2, could the reduced CO_2 species recently described by Giner (1), be better characterized. Second, working with formic acid, it was hoped to confirm a recent result of Breiter (4), in which he shows formic acid adsorption to be both one and two site in nature. Last it was felt

[1] Present address: O. M. B. Werke, Trottheim-Weser, Germany.

that some knowledge of formaldehyde coverage might be useful.

The only recent references in the literature concerning the reduction of CO_2 are due to Van Ryssselberghe (5) and Jordan (6). However, both of these workers used mercury electrodes and very high cathodic overpotentials. That the former of these two authors reported almost quantitative formation of formic acid from CO_2 under these conditions may or may not be relevant to the experiments described here, which were all done on platinum electrodes at potentials close to zero on the N.H.E. scale. Cohen and Jahn (7), however, reported (in a very early work) traces of formic acid with a large number of different electrodes including platinum.

Experimental Technique

The cell used in this work was a conventional three compartment cell, with the counterelectrode separated from the working electrode compartment by a fine glass frit. The reference electrode was the "dynamic hydrogen" electrode, recently described by Giner (8). All quoted potentials are in the same solution. The supporting electrolyte was $2N$ H_2SO_4, and all measurements were made at 25° ± 1°C except when otherwise stated. The working electrode consisted of two superimposed circular disks of platinized platinum gauze, 55 mm in diameter. The potential scans were made with a Wenking potentiostat, at the rate of 90 mv/min. Current was recorded on an Esterline Angus recorder.

Results

The first set of experiments was designed to test the validity of Pavela's method. The reduced CO_2 was formed on the electrode in the manner described by Giner (1), by holding the electrode potentiostatically at 0.0v for 15 min while passing CO_2 through solution. After formation, the species was anodically oxidized with the potential sweep, both with and without transfer and washing of the electrode. During the oxidation, a stream of prepurified nitrogen was passed through the electrolyte. In both cases, an oxidation peak was observed at 650 mv. The number of coulombs under the peak was measured, having first subtracted the small but measurable current recorded in a blank run where no reduced CO_2 was formed. The area under the peak was found to be 8.57 coulombs, ±0.4 coulombs, irrespective of whether the electrode had been washed and transferred or not. The appearance and shape of the peak were identical in both cases. It was felt that these results constituted a test of the method, and that its further use was justified.

Reduced CO_2 species.—The procedure used here was to alternate two types of experiments. In the first case, having formed the reduced CO_2 in the manner previously described, the electrode was transferred and

Table I. Results

(i) Potential scans

Adsorbing species	Coulombs in H_2 region*	Coulombs in organic region**
Hydrogen	9.9 ± 0.3	0.0
Reduced CO_2	4.0 ± 0.2	8.57 ± 0.15
Formic acid	0.0	11.1 ± 0.5
Formaldehyde	0.0	22 to 13 (decreasing with time)

(ii) Titration experiments
Chemical analysis of reduced CO_2

Difference between end points of phenolphthalein and methyl red titres
In experiments: 0.45 cc, 0.45 cc, 0.45 cc of $0.137N$ H_2SO_4.
In blank runs: 0.15 cc, 0.15 cc, 0.15 cc of $0.137N$ H_2SO_4.

* Potential range 0.0 to 0.3v.
** Potential range 0.5 to 0.85v.

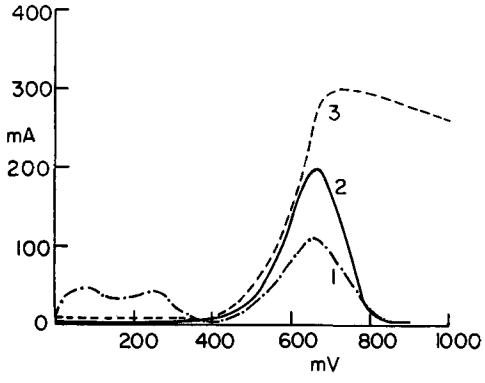

Fig. 1. Current-voltage scans following transference and rinsing of the electrode. Curve 1, Reduced CO_2; curve 2, formic acid 1M; curve 3, formaldehyde 1M; scan rate 90 mv/min; $2N$ H_2SO_4.

washed and placed in a cell containing $2N$ H_2SO_4. The 90 mv/min potential scan was then applied, the current being recorded. In the second case, having formed the reduced CO_2 species, the electrode was transferred to a cell containing 50 ml of $50N$ NaOH. It was found simpler, in this case, to perform a galvanostatic oxidation, and an anodic current of 100 ma was passed for 3 min. At the end of this time, the electrode was removed and washed, with the washings decanted back into the cell. The contents of the cell were then titrated with $0.137N$ H_2SO_4, using first phenolphthalein and then methyl red as indicators. The difference between the two titres gives the amount of carbonate present in solution. A set of dummy runs was made, identical to the above in all respects, except that the reduced CO_2 was not formed in the first place. These experiments enabled a small correction to be made for losses in washing, aerial carbon dioxide etc. Results are shown in Table I and in Fig. 1.

Coverage with formic acid.—A 1M solution of formic acid was used in $2N$ H_2SO_4. The electrode was transferred with washing as previously described, and the potential scan was applied. Results again are shown in Table I and in Fig. 1.

Coverage with formaldehyde.—A 40% aqueous solution of formaldehyde, free from added preservative was used and diluted down to give a 1M solution in $2N$ H_2SO_4. The current-voltage curves obtained after washing and transfer, using the potential scan, were very different from those previously encountered. In the first place, the maximum current was, initially at least, some two times larger than those in the previous experiments with formic acid, etc. Second, contrary to the good reproducibility of these experiments, the currents in the formaldehyde experiments were irreproducible by a factor of 100%. Third, the current-voltage curve did not show a peak but rather a plateau, beginning at 650 mv and extending beyond 1.00v into the oxide region (see Fig. 1). The last difference was observed after the electrode had stood for several hours in distilled water. A white flocculence was observed on and close to the surface of the electrode, which was assumed to be a formaldehyde polymer. No further quantitative experiments were attempted.

From Table I, it may be seen that the number of chemical equivalents of reduced CO_2 formed (from the titration) are

$$(0.45 - 0.15) \times 10^{-3} \times 1.37 \times 10^{-1} = 4.11 \times 10^{-5}$$

From the potential scan measurements, the number of equivalents is $8.57/nF$, where F is the Faraday, n the number of electrons involved in the reduction. This term is thus 4.44×10^{-5}, if $n = 2$ is assumed, which agrees with the titration value within the limits of experimental error.

Analysis of cell solutions.—Experiments were made to see whether any of the reduced CO_2 might desorb

from the electrode into solution, and there be identifiable. In the apparatus described above, three runs were made, each one of 24-hr duration. During this time, CO_2 was slowly bubbled into solution, while the electrode was potentiostatically held at 0.0v. Two of these runs were made at 25°C, while the third was made at 80°C, since the work of Giner (1) shows that the reduction process is faster at this temperature. All three solutions, plus a control solution to check the presence of possible impurities, were tested as follows.

The chromotropic acid test for formaldehyde and formic acid was applied, first on a portion of each solution, then after the solution had been shaken with magnesium shavings, to reduce formic acid to formaldehyde. These tests were all negative, although the sensitivity of the test, using known dilute formic acid solutions, was better than 1 ppm of formic acid. The Schiff test for aldehydes gave negative results. The final test was for carbon monoxide, where (in a separate 24-hr run at 25°C) the carbon dioxide was not bubbled through the cell, but the cell was presaturated with CO_2 and sealed. This was to avoid expulsion of any CO formed by the CO_2 stream. The cell was then purged with pure nitrogen, the effluent gas being passed through a commercial CO detection kit with a threshold sensitivity of 50 ppm. No coloration was observed. This experiment was repeated, using the same electrode and solution, after one week, since the results of Gilman (see the Discussion section) indicate that the desorption of CO is an extremely slow process. Again no coloration was reported. The conclusion was reached that none of the substances tested for was present in detectable amounts.

Discussion

Reduced CO_2

If the foregoing results are accepted, it must be assumed that two electrons are involved in the reduction of each carbon dioxide molecule. This at once eliminates a large number of species and leaves such compounds as C=O, HCOOH as virtually the only simple molecules corresponding to CO_2, twice reduced. Two other possibilities cannot be ruled out. The first of these is the compound OHC-COOH, glyoxal. This is the only other compound both reasonably simple and also complying with the stoichiometric requirements outlined above. It has further interest, being speculatively mentioned as a possible "blocking species" or "poison product," in a recent paper on the electro-oxidation of formic acid by Brummer and Makrides (9). The second alternative is that the species being investigated here, the reduced CO_2, is incapable of existing in free solution, just as the hydrogen atom can exist only in the adsorbed state, and not in solution. This last possibility would mean that the reduced CO_2 could never be identified by conventional chemical means, since it would either not desorb, or else, in so doing, would react either with a similar molecule or with water to form a stabler species. So the final choice lies between these alternatives.

As described in the Results section, no formic acid was found in solution, nor any formaldehyde, nor (by the Schiff test) any aldehyde. Furthermore, we know, from the work of Breiter (4) both the shape of the formic acid adsorption isotherm, and we have some idea of the time required for equilibrium to take place. Thus, from Fig. 6 in this work (4), we see that a θ value similar to the one observed for reduced CO_2 in this work would correspond to a high and easily detectable concentration of formic acid in the bulk solution.

The blank Schiff test would seem to preclude the glyoxal compound unless, like CO, it is a compound only slightly desorbed. Further evidence against this compound is seen in Table II where its coverage is compared with other species.

Table II. Compared coverages

Species	Work	Q_H/Q_x
Reduced CO_2	Giner (1)*	0.7:1
Reduced CO_2	This work	0.7:1
Carbon monoxide (1 atm)	Gilman (10)	0.7:1
Formic acid 1M	Breiter (4)	0.8:1
Formic acid 1M	This work	0.9:1
Glyoxal	Brummer and Makrides (9)	1:1 (approx.)

* Value not quoted directly, obtained from published data by curve weighing.

A meaningful way of comparing coverages, especially when collating values of different authors and different species, is to express the coulombic equivalent of the coverage as a function of the hydrogen coverage for the same electrode Q_H. Table II sets out to do this. It is thus seen that the coverage of the electrode with reduced CO_2 matches the figure quoted by Gilman for 1 atm of CO. The desorption of CO may also be seen from the work of Gilman. He found a CO coverage of 0.5 mC/cm^2 on the electrode, in the presence of 1 atm of the gas. When he waited for approximately 15 min and swept the solution with argon during this time, he found a CO coverage of 0.42 mC/cm^2. From these figures, we may say that carbon monoxide does not, to all intents and purposes, desorb, for if the desorption found by Gilman is expressed as a current, it comes to the order of 1.0×10^{-7} amp/cm^2, which is the order of magnitude of impurity currents found in even the most scrupulously clean experiments. It is thus not possible to say whether the CO was desorbed or electrooxidized. In either case, this result suffices to show why, if the reduced CO_2 is in fact carbon monoxide, its detection in solution is so difficult. Furthermore, the very "poisoning" nature of carbon monoxide ensures that once the electrode is so covered, little further reaction can proceed.

Formic Acid Results

The results of the formic acid coverage experiments with platinized platinum, obtained by a method different from that of Breiter for bright platinum and supporting his results, confirm the inhomogeneity of formic acid adsorption, showing both one and two site adsorption to be possible.

There must be a considerable difference in the electrochemical behavior of these two types, and consideration of the two site adsorbed formic acid as the "blocking species" is in many ways more attractive than the invocation of such species as glyoxal which have been neither observed nor suspected as intermediates in the electrooxidation of formic acid.

Breiter has shown (11) that the adsorption of 10% of oxygen on an electrode surface inhibits the electroorganic oxidation reaction by almost an order of magnitude. In the same way, the current decay at constant potential reported by so many observers, in potential regions where oxygen adsorption is not considered possible, is also of similar magnitude. In both cases, it is possible that certain "preferred sites" are lost, either by oxygen or formic acid coverage. Equally it is known that severe oxidation or reduction will replace these sites in circulation until they are removed once more.

Formaldehyde Results

The anomalous and irreproducible behavior of this compound, together with the observation of a white flocculent and insoluble polymer, is less surprising when the polymerisability of the substance is taken into account.

Similar behavior has been observed in the anodic oxidation of cyclohexadiene (12) which coated the electrode with a glassy polymer. The implications of the present work seem to be that reactions in which formaldehyde is an intermediate or starting product

may be poisoned by a polymer which was observed in these experiments on account of a higher formaldehyde concentration than that used by most other workers, in the presence of a large platinized platinum electrode.

Conclusions

The main conclusions arising from this work are as follows. First, the reduced CO_2 is a doubly reduced species. Second, from negative tests and from a comparison of coverages, this species is most probably carbon monoxide. Third, a polymer formation is reported for the first time in the electrooxidation of formaldehyde. Last, the inhomogeneous adsorption of formic acid is confirmed.

Manuscript received May 13, 1964; revised manuscript received Oct. 26, 1964.

Any discussion of this paper will appear in a Discussion Section to be published in the December 1965 JOURNAL.

REFERENCES

1. J. Giner, *Electrochim. Acta*, **8**, 857 (1963).
2. T. O. Pavela, *Ann. Acad. Sci. Fenn., Ser. II, A Chem.*, **59** (1954).
3. M. W. Breiter, *This Journal*, **7**, 622 (1962).
4. M. W. Breiter, *Electrochim. Acta*, **8**, 450 (1963).
5. T. E. Teeter and P. Van Rysselberghe, Proc. CITCE Meeting, 1954.
6. J. Jordan, *Proc. Chem. Soc.*, **1960**, 257.
7. A. Cohen and S. Jahn, *Ber.*, **37**, 2837 (1904).
8. J. Giner, *This Journal*, **111**, 376 (1964).
9. S. Brummer and A. Makrides, *J. Phys. Chem.*, 1448 (1964).
10. S. Gilman, *ibid.*, 2657 (1962).
11. M. W. Breiter, *This Journal*, **109**, 1100 (1962).
12. B. J. Piersma, Private communication.

Oxygen Overvoltage Measurements on Bright Platinum in Acid Solutions

I. Bright Platinum

James P. Hoare

Research Laboratories, General Motors Corporation, Warren, Michigan

ABSTRACT

Overvoltage measurements were made on bright platinum in sulfuric acid solutions both for the anodic evolution and the cathodic reduction of oxygen. It has been found that the experimental data are compatible with a kinetic equation of the type

$$i = i_o' \frac{A'}{A} \left[e^{-z'\alpha'(E - E'_o)F/RT} - e^{z'(1-\alpha')(E - E'_o)F/RT} \right] - i_o'' \frac{A''}{A} \left[e^{z''(1-\alpha'')(E - E''_o)F/RT} - e^{-z''\alpha''(E - E''_o)F/RT} \right]$$

which was derived from a consideration of a polyelectrode model. By using the proper boundary conditions, this equation reduces to more familiar forms in certain regions. The Tafel slopes were found to be 0.122 for anodic and 0.095 for cathodic overvoltage. The i_o is 1.3×10^{-9} amp/cm^2. At the rest potential of 1.06v, a value of 0.32 μa/cm^2 was calculated for the corrosion current density, i_m, using the derived rate equation. This value agrees well with those estimated in the literature. It is suggested that the rate-determining step for anodic evolution of oxygen is

$$(H_2O)_{ads} \rightarrow (OH)_{ads} + H^+ + e$$

and for cathodic reduction

$$(O_2)_{ads} + e \rightarrow (O_2^-)_{ads}$$

The reversible oxygen potential can be observed only on a completely covered surface, and the over-all electrochemical process is

$$O_2 + 4H^+ + 4e \rightleftharpoons 2H_2O$$

in either direction. Peroxide is formed as an intermediate in the reduction of oxygen, but at the steady state concentration of 10^{-5} M this does not disturb the over-all kinetics.

From a series of investigations of the nature of the rest potentials observed on noble metal electrodes in oxygen saturated acid solutions (1, 2), it has been suggested that the metal-oxygen systems are not simple ones but involve more than one electrochemical process occurring on the same metal surface. Such systems are referred to as polyelectrodes (3) and the rest potentials are mixed potentials (4). In order to understand the mechanism of the oxygen electrode, the system must be polarized. In the literature, most attention has been paid to the evolution of oxygen (5), whereas less work seems to have been done on the reduction of oxygen (6). A contributing factor may be the fact that peroxide builds up as a complicating intermediate in the reduction of oxygen. In either case, anodic or cathodic overvoltage, steady potentials were not generally obtained at low current densities (7); only at the higher current densities could steady potential values be obtained. A satisfactory interpretation of these observations may be made in terms of a polyelectrode. It is the purpose of this work to interpret some overvoltage measurements on the noble metals from such a view point. This report will record the investigation of the Pt/O_2 electrode.

Experimental

The measurements were made on small beads (0.04-0.05 in. in diam) melted at the end of Pt wires (99.99% pure). All purification techniques were the same as before (1). Tight-fitting clear Teflon spaghetti was

slipped over the Pt wire leads and pressed up against the Pt bead so that only the bead was exposed to the solution. Polyethylene was not used in the test compartment of the cell, since it was feared that the presence of peroxide, produced in the reduction of oxygen, might attack the polyethylene and contaminate the electrode surface just as was cautioned in the use of concentrated HNO_3 (2). A dual Teflon cell (1) was used and an α-Pd-H reference electrode (8) was mounted in the left-hand compartment. Three test beads as checks were mounted in the right-hand compartment.

Because the i_o for the oxygen reaction on Pt in acid solutions is quite low, about 10^{-9} amp/cm^2 (9, 10), overvoltage measurements must be made at very low current densities (μa/cm^2). This may be done in two ways; (*a*) by using very large electrodes such as those of Watanabe and Devenathan (11) with an ordinary current supply, or (*b*) by using small electrodes with very large resistors in series with the current supply. The second method was chosen because the large electrodes in the first method require large cells and great quantities of solution to be cleaned, and hence, increase enormously the chances for contamination of the system with impurities. The series resistance box was made up of 10-, 50-, and 100- megohm resistors, having a total resistance of 670 megohms. In addition to this, a very large resistor was made by drawing a pencil line on a strip of Mylar with contacts at various points along the strip. The current was determined by measuring the potential drop across a standard resistor with a General Radio Electrometer, Model 1230A. By means of a switch, this meter could be removed from the circuit when the cell potentials were measured. The potential drop between the test electrode and the reference electrode was measured with a second General Radio Electrometer in series with a standard cell to buck the measured potential so that a low scale could be used on the meter. In this way, the potential could be read within $\pm$0.5 mv. An electronic current interrupter (12) was used to determine the solution iR drop between the test and reference electrodes. It was found that, up to a current density of 1 ma/cm^2, the iR correction was less than a millivolt.

The partial pressure of oxygen, P_{O_2}, was varied by diluting the oxygen flow with nitrogen. A rough determination of the P_{O_2} was obtained from the rotameter readings and the final one from a Beckman Oxygen Analyzer. All experiments were carried out at a temperature of 25° $\pm$ 1°C in 2*N* H_2SO_4 solutions. To minimize contributions to the potential by concentration polarization, the system was stirred with gas flows of at least 350 cc/min. At this rate of stirring, there was not any dependence of the potential on stirring rate over the complete range of current density values studied.

In general, the following procedure was used in determining the current-potential curves after the Pt/O_2 electrode had come to a steady rest potential. In some experiments (Fig. 1) in which the region in the neighborhood of the rest potential was to be investigated, the electrode was polarized at the lowest current densities first. In others, (Fig. 2 and 3) the system was polarized either anodically or cathodically at the highest current density to be investigated until the potential became steady (when the change in potential with time was less than 1 mv over an interval of 10 min). Then, the current density was lowered stepwise to the lowest current density to be investigated, after which it was raised again stepwise. The steady potential (potential change was less than 0.5 mv over an interval of 120 sec) was recorded at each current step, and the plotted curves represent the data obtained from at least three, and in some cases from as many as six or seven, complete cycles of decreasing and increasing current density. As seen in the next section, there is usually a transition region between the data at low current densities and that at the higher ones in which steady potential measurements could not be obtained. To get reproducible results, the data in Fig. 1 must be obtained before that in either Fig. 2 or 3. Oxygen overvoltage, defined as

$$\eta = E_{O_2} - E_{rev}$$

where η is the overvoltage and E_{O_2} is the potential of the oxygen electrode at a given current density, i, was determined by using a value of 1229 mv (13) for the reversible oxygen potential, E_{rev}.

Results

A plot of the potential against the apparent current density at very low current densities is given in Fig. 1. The complete oxygen overvoltage curves as a function of the logarithm of the apparent current density are given in Fig. 2 for the cathodic reduction of oxygen and in Fig. 3 for the anodic evolution of oxygen on bright platinum. In Fig. 4, the overvoltage data are plotted such that the i_o's for the two overvoltage curves can be determined. Finally, Fig. 5 is the plot of the overvoltage as a function of the partial pressure.

In general, it may be seen from Fig. 2 that the cathodic overvoltage curve consists of three parts. If the Pt/O_2 electrode is polarized from the steady state rest potential at current densities no greater than about 1 μa/cm^2, a linear potential-current curve is obtained in which the points may be reproduced within $\pm$0.5 mv. Beyond this point, the curve becomes logarithmic and, provided a current density of about 100 μa/cm^2 is not exceeded, a reproducible curve with a slope of about 0.070 is obtained. At high current densities (in the neighborhood of 1 ma/cm^2) a limiting current is reached, and the system is polarized to the discharge of H^+ ions. After polarizing the system at high current densities, the potential follows the upper

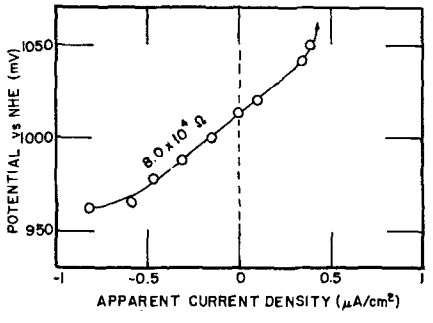

Fig. 1. Polarization data for bright Pt at low current densities in the vicinity of $E = E_{rev}$.

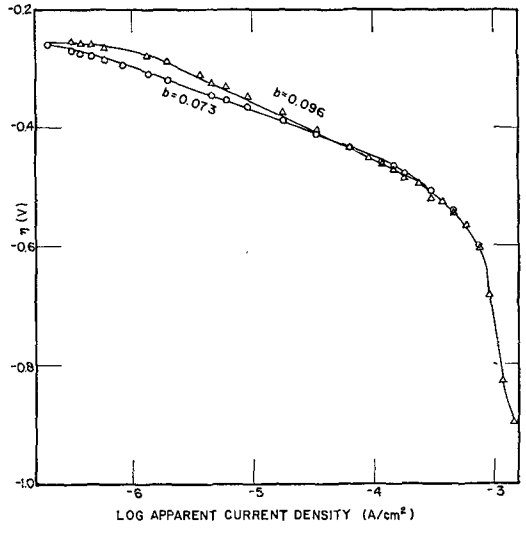

Fig. 2. Oxygen cathodic overvoltage curves on a bright platinum bead. Circles represent data of first cycle of polarization and triangles that averaged over four additional cycles.

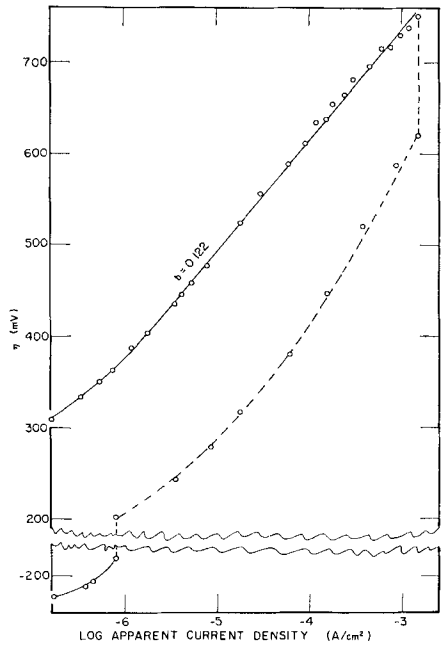

Fig. 3. Oxygen anodic overvoltage curves on a bright platinum bead. The dashed line represents non-steady state points obtained for increasing anodic currents from the rest potential, E_m. At the highest current, the system was permitted to drift to a steady state condition represented by the vertical dashed line. The solid line is the average of three cycles of anodic polarization and represents steady state points.

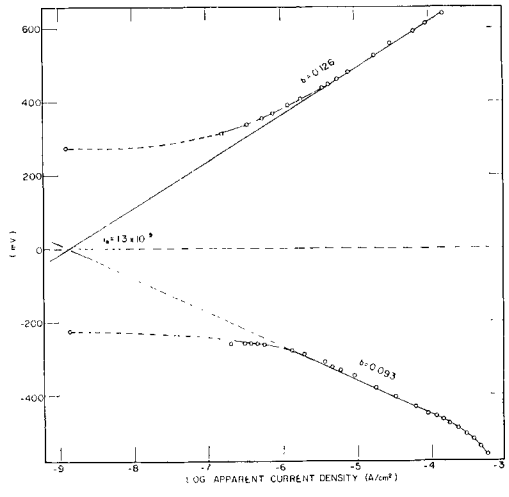

Fig. 4. Plot of the anodic and cathodic overvoltage for bright platinum. The extrapolated Tafel slopes cross at zero overvoltage or a potential of 1.229v.

curve in Fig. 2 when the current is decreased (the slope changes from 0.073 to 0.096). If the Pt/O_2 electrode is polarized initially at the highest current density studied until a steady state is reached, after which the overvoltage curve is obtained, a logarithmic curve with a slope of 0.095 ± 0.003 (from 10 observations) is found (upper curve of Fig. 2). The points in Fig. 2 were averaged from four cycles of decreasing and increasing current density over the whole range with a deviation from the mean within ±6 mv.

At very low anodic current densities, a linear, $E - i$, curve is obtained with the same slope as the cathodic curve which passes through the rest potential as shown in Fig. 1. The slope is 6.0 ± 2.0 x 10^4 ohms (10 observations). At higher current densities the points are no longer time-invariant and drift to more noble values, as shown by the dotted line in Fig. 3. As the current was increased, the points on the dashed curve were not steady. Finally, at the highest current density, the

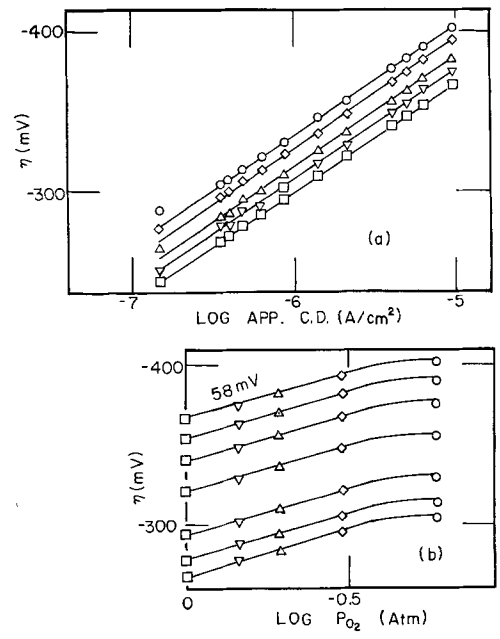

Fig. 5. (a) Plot of oxygen overvoltage as a function of the partial pressure of oxygen, P_{O_2} · P_{O_2} = 1, □; 0.688, ▽; 0.518, △; 0.331, ◇; 0.167, ○. (b) Plot of oxygen overvoltage against the log of P_{O_2}. A slope of 58 mv indicated a one-electron rate-determining step.

system was maintained under these conditions until the potential did become steady (as indicated by the dotted line). Now, the anodic overvoltage curve was obtained as shown by the full line in Fig. 3. The points are averaged from three cycles of polarization, and the deviation from the mean was within ± 5 mv. The slope of this curve is 0.122 ± 0.006 (4 observations).

In Fig. 4 are given the anodic and cathodic overvoltage curves taken on the same bead with the cathodic curve taken first and the anodic second. In both cases, the electrode was polarized at the highest current density studied until the potential became steady, after which the overvoltage curve was determined. The points are the average of three cycles of polarization. It may be seen that the slopes of these lines intersect at zero overvoltage; the i_0 is 1.3 x 10^{-9} amp/cm².

A plot of the overvoltage for different values of P_{O_2} is shown in Fig. 5a where the points are the average of three or four cycles of polarization over the indicated current density range. The deviation from the mean was within ±2 mv. Points taken from these curves were used to plot the overvoltage as a function of log P_{O_2} in Fig. 5b at the given current densities. The slope of these lines is 58 mv. There appears to be some flattening of the curves at the low values of P_{O_2}.

Discussion

The general electrode kinetic equation may be written as

$$i = \vec{k}C_r e^{-z\alpha EF/RT} - \overleftarrow{k}C_o e^{z(1-\alpha)FE/RT} \qquad [1]$$

where i is the current density, $\vec{k}$ and $\overleftarrow{k}$ are the specific rate constants for the forward and back reactions, C_r and C_o are the concentrations of the reductant and the oxidant in the bulk of the solution, z is the number of electrons exchanged in the rate-determining step, α is the symmetry factor which gives the fraction of the total electrode potential which drives the forward reaction (often its value is close to 1/2), E is the potential, F the Faraday, and R and T have their usual significance. At the equilibrium potential, E_o, the rates of the forward and back reactions are equal,

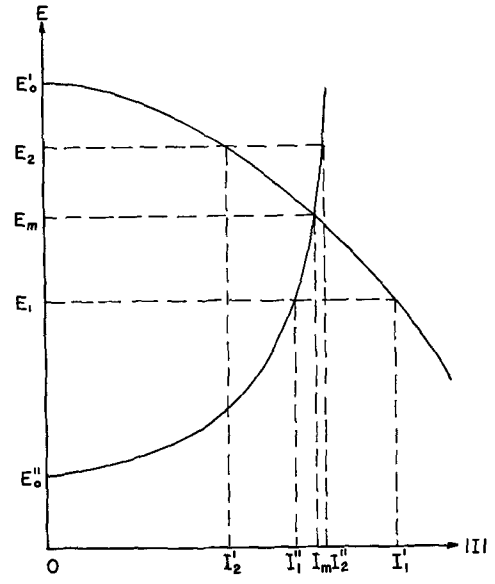

Fig. 6. Schematic diagram of the local cell polarization curves of the two half-reactions of the polyelectrode system, Pt/Pt-O/O_2. Potential vs. NHE is plotted along the ordinate while the absolute value of the local cell current is plotted along the abscissa. At $E = E_m$, $I_m = I' = I''$; at all other potentials, $I = I' - I''$. See text for details.

and so the anodic and cathodic current densities are equal

$$i_o = i_c = i_a = \vec{k}C_r e^{-z\alpha FE_o/RT} = \overleftarrow{k}C_o e^{z(1-\alpha)FE_o/RT} \quad [2]$$

It may be shown (14) that the rate equation in the cathodic direction may be written as

$$i_c = i_o\,[e^{-z\alpha\eta F/RT} - e^{z(1-\alpha)\eta F/RT}] \quad [3]$$

and in the anodic direction

$$i_a = i_o\,[e^{z(1-\alpha)\eta F/RT} - e^{-z\alpha\eta F/RT}] \quad [4]$$

where η, the overvoltage is defined as $\eta = E - E_o$.

These are the kinetic equations for activation overvoltage at a simple electrode. In the case of a polyelectrode, the system is not at equilibrium but at a steady state, since a local cell current, I, is always flowing. There are two electrode reactions and two i_o's. Since the mixed potential, E_m, is between the equilibrium potentials, E'_o and E''_o of the two reactions, the system with the more noble E_o, E'_o, will be cathodically polarized, while the other, E''_o will be anodically polarized. The equations are

$$[i' = i'_o\,e^{-z'\alpha'(E-E'_o)F/RT} - e^{z'(1-\alpha')(E-E'_o)F/RT}] \quad [5]$$

and

$$[i'' = i''_o\,e^{z''(1-\alpha'')(E-E''_o)F/RT} - e^{-z''\alpha''(E-E''_o)F/RT}] \quad [6]$$

At the mixed potential, E_m, as shown in the diagram in Fig. 6, the local cell current, I, is related to the currents of the two component reactions, I' and I'', by

$$I = I' = I'' \quad [7]$$

In Fig. 6 E'_o is 1229 mv for the O_2/H_2O reaction, $O_2 + 4H^+ + 4e \rightleftharpoons 2H_2O$, and E''_o is 880 mv for the Pt/Pt-O reaction. Pt-O $+ 2H^+ + 2e \rightleftharpoons$ Pt $+ H_2O$. It has been suggested (1), from a study of rest potentials, that the shapes of the polarization curves are similar to those shown in Fig. 6. When the system is polarized away from E_m, the observed current is $I = I' - I''$. From [5] and [6] the kinetic equation becomes $i = i'A'/A - i''A''/A$, or

$$i = i'_o\frac{A'}{A}\,[e^{-z'\alpha'(E-E'_o)F/RT} - e^{z'(1-\alpha')(E-E'_o)F/RT}]$$

$$-i''_o\frac{A''}{A}\,[e^{z''(1-\alpha'')(E-E''_o)F/RT} - e^{-z''\alpha''(E-E''_o)F/RT}] \quad [8]$$

Here, A' is that part of the surface area on which the O_2/H_2O reaction takes place, A'' is that on which the Pt/Pt-O reaction takes place, and $A = A' + A''$. For the condition that

$$RT/F < |(E - E'_o)| \text{ and } |(E - E''_o)| \quad [9]$$

Eq. [8] reduces to the following, since the second term in each bracket drops out.

$$i = i'_o\frac{A'}{A}e^{-z'\alpha'(E-E'_o)F/RT} - i''_o\frac{A''}{A}e^{z''(1-\alpha'')(E-E''_o)F/RT} \quad [10]$$

If the system at an open-circuit potential of $E = E_m$ is galvanostatically cathodized, a given current, I, is maintained and, since the electrode surface is an equipotential surface, the potential will shift from E_m to E, where

$$I_1 = I'_1 - I''_1 = i'_1A' - i''_1A'' = i_1A \quad [11]$$

in a similar fashion, one obtains the following if the system is anodically polarized to E_2

$$I_2 = I'_2 - I''_2 = i'_2A' - i''_2A'' = i_2A \quad [12]$$

At $E = E_m$, $I_m = I' = I''$, or

$$i'_oA'e^{-z'\alpha'(E_m-E'_o)F/RT} = i''_oA''e^{z''(1-\alpha'')(E_m-E''_o)F/RT} = I_m \quad [13]$$

Let the polarization at the very low current densities be defined as

$$p = E - E_m \quad [14]$$

Eliminating E between Eq. [10] and [14] and using the definition of I_m from Eq. [13], one obtains

$$i = \frac{I_m}{A}\,(e^{-z'\alpha'pF/RT} - e^{z''(1-\alpha'')pF/RT}) \quad [15]$$

For very low current densities, the exponentials may be expanded in a series and only the first two terms are kept. This gives

$$i = \frac{I_m}{A}\{1 - z'\alpha'pF/RT - [1 + z''(1-\alpha'')pF/RT]\}$$

$$i = \frac{I_m}{A}\frac{pF}{RT}\,[-z'\alpha' - z''(1-\alpha'')] \quad [16]$$

This shows that the polarization is a linear function of the current density in this region as demonstrated in Fig. 1. The quantity, p, may be positive or negative and the slope, $di/dp = \dfrac{I_mF}{ART}\,[-z'\alpha' - z''(1-\alpha'')]$. Assuming that $\alpha' = \alpha'' = \frac{1}{2}$, and that $z' = z'' = 1$, since it is generally believed that only one electron is transferred at a time

$$I_m = -(di/dp)\frac{ART}{F} \quad [17]$$

Taking $-di/dp = 1.25 \times 10^{-5}$ mhos (see Fig. 1), $I_m/A = 3.2 \times 10^{-7}$ amp/cm^2, the local cell current density, i_m, at $E = E_m$. This value agrees quite well with the value (0.2 μa/cm^2) found by Vetter and Berndt (15) for i_m on bright Pt in 1N H_2SO_4 solution.

In general, A' and A'' are functions of the potential. In the case where the surface is covered by a layer of adsorbed oxygen (anodic polarization at high current densities), the Pt/Pt-O reaction is virtually eliminated and $A' \rightarrow A$. Here, the A-term drops out and reproducible, steady potential data are obtained. Similarly, at high cathodic polarization, only the reduction

of oxygen contributes to the current and again, $A' \rightarrow A$. In the region of E_m steady values of the potential are obtained because the values of the change in potential, $E - E_m$, were very small, and the nature of the surface did not change appreciably. However, in the transition region between these extreme cases A' and A'' varied, and as noted above, drifting potentials and hysteresis phenomena were observed.

As the electrode is polarized in the cathodic direction, further away from $E = E_m$, Eq. [16] no longer holds, i is no longer a linear function of the potential, and Eq. [10] must be used to describe the system. From Fig. 6, it is assumed that $i'_o >> i''_o$, because the Pt/Pt-O reaction is more easily polarized than the O_2/H_2O reaction. Then, the second term of Eq. [10] drops out; also, $A' \rightarrow A$. Since now the system is determined by the cathodic reduction of oxygen, the overvoltage is described by the equation

$$\eta_c = \frac{RT}{z\alpha F} \ln i_o - \frac{RT}{z\alpha F} \ln i_c \qquad [18]$$

as demonstrated by the data presented in Fig. 2. Here the system is no longer a polyelectrode system, but a simple one with only one i_o. At a current density of about 10^{-3} amp/cm^2, a limiting current sets in, and the system is polarized to the discharge of hydrogen ions. Figure 2 shows that the reduction of oxygen is the rate-controlling process, since the polarization curve is continuous over the entire range of current densities up to the limiting current density. This is not true for the anodic polarization curve, as shown in Fig. 3.

As one polarizes the system anodically from $E = E_m$, Eq. [16] no longer holds and Eq. [10] must be considered. In this case, as E becomes more noble, it approaches E'_o, and the condition $RT/F < |(E - E'_o)|$ no longer holds. The exponential in the first bracket becomes very small and, consequently, $i'' > i'$. Now the current is determined by the Pt/Pt-O reaction, which is at a limiting current condition, as seen in Fig. 6. Therefore, for a given constant anodic current, the potential drifts with time as observed experimentally until a new system is reached. This situation is described by the dashed curve in Fig. 3. It is suggested that the new system, for which steady state polarization data are obtained, is the anodic evolution of oxygen on a complete layer of adsorbed oxygen about a monolayer thick. The potential drift is produced under anodic polarization conditions by the slow formation of a monolayer of oxide which according to Lingane (16) contains a large amount of PtO_2. Once this layer is formed, which does not build up much beyond a monolayer thick (17), steady-state measurements may be made. In this case, the O_2/H_2O reaction contributes virtually all the anodic current since oxide formation virtually ceases, and Eq. [8] transforms to Eq. [4]. In this region, the overvoltage is described by the relationship

$$\eta_a = -\frac{RT}{z(1-\alpha)F} \ln i_o + \frac{RT}{z(1-\alpha)F} \ln i_a \qquad [19]$$

Again, the system is no longer a polyelectrode, and a single i_o may be assigned to the system. Since the surface of the electrode, now, is quite different from that when the potential was E_m, the system does not return to $E = E_m$ on open circuit but to a point about 270 mv more noble than the reversible potential of 1229 mv, as shown in Fig. 4. This was also observed by Bockris and Huq (9). With time, such a potential drifts to less noble values, indicating that a complete layer of adsorbed oxygen is unstable in acid solutions as found before (2).

From Fig. 4, it is seen that the extrapolated slopes of the cathodic and the anodic overvoltage curves cross at the reversible potential of 1229 mv. Similar observations were made by Hoar (10) and by Bockris and Huq (9). These data indicate that the O_2/H_2O reaction does proceed on a Pt/O_2 electrode and that the reversible potential could be observed if the surface could be maintained inert and electronically conducting. This, in effect, occurs on the Pt surface at high cathodic current densities and on the conducting monolayer of adsorbed oxygen on Pt at high anodic current densities. In general, these conditions are not met on open circuit. It has been shown that, if the Pt surface is passivated by treatment with concentrated nitric acid (2), a conducting, chemically inert layer is formed. In this case, the reversible potential of 1229 mv was observed on open circuit.

The difference in the values of the slopes of the anodic and cathodic curves most likely represents the difference in the paths over which the anodic and cathodic processes take place. In the absence of a peroxide stabilized system [H_2O_2 added to the electrolyte in such systems as those investigated by Yeager (18) and Berl (19)] the evolved oxygen comes from adsorbed water. Kaganovich and co-workers (20) have shown that the anion participates in the reaction at very high current densities and very high concentrations. However, in the present case, the water molecule is probably oriented with the oxygen next to the chemically inert, conducting layer of adsorbed oxygen on the electrode surface. An electron is transferred to the electrode to form an adsorbed OH group, and a hydrated H^+ ion migrates into the solution. When two OH groups are adsorbed on neighboring sites, an activated complex composed of two adsorbed OH groups is formed. With the transfer of two more electrons, this complex falls apart to give an adsorbed O_2 molecule, (which can then desorb) and two hydrated H^+ ions. Peroxide need not be involved because an O-O bond is not broken but formed. Rozental and Veselovski (21), using O^{18} techniques, have shown that the adsorbed oxygen layer, Pt-O, does not participate in the electrode reaction but only serves as the surface on which the reaction proceeds. Breiter (22) has come to similar conclusions.

For the case of the reduction of oxygen, however, the O-O bond must be broken. In all cases, after polarization, peroxide can be detected. There is some evidence (23) that with continued polarization the H_2O_2 concentration builds up to a steady state value. The data in Fig. 2 support this, since after the first one or two cycles of cathodic polarization a reproducible overvoltage curve is obtained. From the tests made with $TiSO_4$ reagent (24), this steady-state concentration of H_2O_2 is between 10^{-6} and 10^{-5}M for Pt/O_2 electrodes. What determines the value of this steady-state concentration is the ability of the electrode surface to decompose the H_2O_2 formed. Bockris (9) found that concentrations of H_2O_2 less than 10^{-4}M do not interfere with the cathodic Tafel slope. This concept seems to be supported by the data in Fig. 4.

From the data presented in Fig. 5, it may be seen that the rate-determining step in the reduction of oxygen must depend on the partial pressure of oxygen and must be a one-electron step (59 mv per decade of the log P_{O_2}). Suppose that molecular oxygen is adsorbed on the Pt-O layer, then the rate-determining step could be the discharge of one electron to form O_2^-. The second electron could be transferred more rapidly to form $O_2^=$ which would combine with two hydrated H^+ ions to form the relatively stable intermediate H_2O_2. This intermediate builds up to a steady-state concentration ($\sim 10^{-5}$M) because of the catalytic decomposition of the H_2O_2 to H_2O and O_2. The resulting O_2 can undergo the transfer of two more electrons so that effectively a 4-electron process has taken place. The decomposition of H_2O_2 may occur chemically or electrochemically as proposed by Gerischer (25), but such processes do not contribute current to the external circuit since the electrochemical decomposition proceeds through a local cell mechanism in which the local cell current is lost to the external circuit.

Although it is not advisable to use the Tafel slope alone as a diagnostic criterion for the electrode kinetics of such a complicated electrode process as the oxygen electrode, the slopes of the anodic and cathodic curves,

0.122 and 0.095, respectively, are close to the value of $2RT/F$ which Bockris (26) finds for a slow-discharge-of-an-electron step. Therefore, for the anodic evolution of oxygen on an adsorbed layer of Pt-O, the rate-determining step may be

$$(H_2O)_{ads} \rightarrow (OH)_{ads} + H^+ + e \qquad [20]$$

For the cathodic reduction of oxygen on platinum, it may be

$$(O_2)_{ads} + e \rightarrow (O_2^-)_{ads} \qquad [21]$$

In both cases, the over-all reaction involves the transfer of four electrons so that the over-all reaction is

$$O_2 + 4H^+ + 4e \rightleftharpoons 2H_2O$$

as suggested by the data in Fig. 4.

The data in Fig. 4, also, provide a value of the stoichiometric number equal to $3 < \nu < 4$, which appears to be inconsistent with the proposed mechanisms. In the anodic evolution of oxygen, ν should be 2 since two OH radicals must be formed from two molecules of water. Also, a value of 2 would be expected in the reduction of oxygen since the transfer of an electron to $(O_2)_{ads}$ occurs a second time from the O_2 liberated by the decomposition of the peroxide formed in the first steps. However, as pointed out by Parsons (27), ν cannot be determined from the slopes of the anodic and cathodic overvoltage curves if the activated complex in the rate-determining steps for the anodic and cathodic processes is not the same. It is quite likely that such is the case from a consideration of the reactions given by Eq. [20] and [21]. This could provide an explanation for the anomalous values of ν obtained from the data in Fig. 4.

From the analysis of the Pt/O_2 electrode presented here, it is important to realize that reproducible steady state data can only be obtained when there is some hope of characterizing the nature of the surface on which the electrode process is taking place. If this is not done, drifting potentials and hysteresis effects are observed as demonstrated in the transition region between the data obtained at low and at high current densities.

Acknowledgments

The author wishes to express his gratitude to Professor B. E. Conway of the University of Ottawa and Dr. Raymond Thacker and Dr. J. L. Griffin of the General Motors Research Laboratories for their interesting comments and suggestions.

Manuscript received Nov. 6, 1964.

Any discussion of this paper will appear in a Discussion Section to be published in the December 1965 JOURNAL.

REFERENCES

1. J. P. Hoare, *This Journal*, **109**, 858 (1962).
2. J. P. Hoare, *ibid.*, **110**, 1019 (1963).
3. E. Lange and H. Göhr, *Z. Elektrochem.*, **63**, 74 (1959); E. Lange and P. Van Rysselberghe, **105**, 420 (1958).
4. C. Wagner and W. Traud, *Z. Electrochem.*, **44**, 391 (1938).
5. K. J. Vetter, "Elektrochemische Kinetik," p. 506, Springer Verlag, Berlin (1961).
6. K. J. Vetter, *ibid.*, p. 513.
7. A. Hickling and S. Hill, *Disc. Faraday Soc.*, **1**, 236 (1947).
8. D. J. G. Ives and G. J. Janz, "Reference Electrodes," p. 112, Academic Press, New York (1961); J. P. Hoare, *G. M. Eng. J.*, **9**, No. 1, 14 (1962).
9. J. O'M. Bockris and A. K. M. S. Huq, *Proc. Roy. Soc.*, **A237**, 277 (1956).
10. T. P. Hoar, *ibid.*, **A142**, 628 (1933).
11. N. Watanabe and M. A. V. Devenathan, *This Journal*, **111**, 615 (1964).
12. S. Schuldiner and R. E. White, *ibid.*, **97**, 433 (1950).
13. W. H. Latimer, "Oxidation Potentials," Prentice-Hall, New York (1952).
14. E.g. J. O'M. Bockris, "Modern Aspects of Electrochemistry," Chap. 4, Academic Press, New York (1954).
15. K. J. Vetter and D. Berndt, *Z. Elektrochem.*, **62**, 378 (1958).
16. J. J. Lingane, *J. Electroanal. Chem.*, **2**, 296 (1961).
17. W. Böld and M. Breiter, *Electrochim. Acta*, **5**, 145 (1961).
18. M. O. Davies, M. Clark, E. Yeager, and F. Hovorka, *This Journal*, **106**, 56 (1959).
19. W. G. Berl, *Trans. Faraday Soc.*, **83**, 253 (1943).
20. R. I. Kaganovich, M. A. Gerovich, and E. Kh. Enikeev, *Dok. Akad. Nauk SSSR*, **108**, 107 (1956).
21. K. I. Rozental and B. I. Veselovski, *ibid.*, **111**, 637 (1956).
22. M. W. Breiter, *Electrochim. Acta*, **9**, 441 (1964).
23. G. Bianchi, F. Mozza, and T. Mussini, *ibid.*, **7**, 457 (1962).
24. F. D. Snell and C. T. Snell, "Colorimetric Methods of Analysis," p. 882, New York (1959).
25. R. Gerischer and H. Gerischer, *Z. Physik. Chem. N. F.*, **6**, 178 (1956).
26. J. O'M. Bockris, *J. Chem. Phys.*, **24**, 817 (1956).
27. R. Parsons, *Trans. Faraday Soc.*, **47**, 1332 (1951).

Oxygen Overvoltage Measurements on Bright Platinum in Acid Solutions

II. Bright Platinum in H_2O_2 Stabilized Acid Solutions

James P. Hoare

Research Laboratories, General Motors Corporation, Warren, Michigan

ABSTRACT

Oxygen overvoltage measurements were made on a Pt/O_2 electrode in H_2O_2-stabilized acid solutions. The concentration of H_2O_2 was 0.1M. It was found that the rest potential did not reach the reversible O_2/H_2O_2 potential (682 mv), and was independent of the H_2O_2 concentration and of the partial pressure of oxygen. These findings are explained in terms of a polyelectrode model in which the rest potential is a mixed potential composed of the half reactions

$$H_2O_2 \rightarrow O_2 + 2H^+ + 2e$$

and

$$H_2O_2 + 2H^+ + 2e \rightarrow 2H_2O.$$

From the polarization data, it is concluded that the mixed potential and the electrode kinetics are controlled by the reaction

$$O_2 + 2H^+ + 2e \rightleftharpoons H_2O_2$$

The system acts as though it were a reversible O_2/H_2O_2 electrode with an E_o of 810 mv. A value of 1.13×10^{-3} mho is calculated for the rate of the electrode reaction. The rate-determining step both in the anodic and the cathodic directions involves the discharge of the first electron.

In general, it is found that the presence of H_2O_2 may be detected in any system in which the reduction of oxygen takes place. Berl (1) found that oxygen is reversible to the HO_2^- ion in alkaline electrolytes at inert electrodes, and Yeager and co-workers (2) obtained reproducible results from their work on oxygen electrodes in alkaline solution when the system was "stabilized" by adding H_2O_2 to the system. For very dilute concentrations of peroxide in acid solutions, it was found (3) that the rest potential was shifted to less noble values with increasing H_2O_2 concentrations. For larger concentrations of H_2O_2, however, the rest potential did not reach the reversible value of 682 mv (4) quoted for the O_2/H_2O_2 reaction but became independent of the H_2O_2 concentration and dependent on the *p*H, as observed by Bockris and Oldfield (5) and by Gerischer (6). Apparently H_2O_2 is always present in the reduction of oxygen because the O-O bond is so strong that a stable peroxide intermediate is formed. Tracer experiments carried out by Yeager and coworkers (7) in alkaline H_2O_2 solutions indicate that the O-O bond is never broken.

The present report is concerned with oxygen overvoltage experiments carried out on Pt electrodes in acid solutions to which peroxide had been added.

Experimental

The cell, electrode, solution preparations, and experimental techniques are the same as those described before (3, 8). In most cases, the electrode was allowed to come to a steady state in oxygen saturated 2*N* H_2SO_4 solution. Then, the required amount of H_2O_2 was added to the solution with a hypodermic syringe after which polarization measurements were made. All potentials are referred to the normal hydrogen electrode (NHE). The solutions were stirred with purified oxygen at a rate of about 275 cc/min at which rate all observed potentials were independent of stirring. The work was carried out at a temperature of 25° ± 1°C.

Results

A plot of the polarization curves at low current densities obtained on Pt, Au, and Rh electrodes in O_2-saturated 2*N* H_2SO_4 solution which is 0.1M in H_2O_2 is presented in Fig. 1. The cathodic overvoltage curve, Fig. 2, and the anodic overvoltage curve, Fig. 3 [determined from the rest potential value rather than from the reversible oxygen potential (4) of 1229 mv], were obtained on bright Pt on O_2-saturated 2*N* H_2SO_4 which is also 0.1M in H_2O_2. Figure 4 gives the partial pressure of oxygen (P_{O_2}) data.

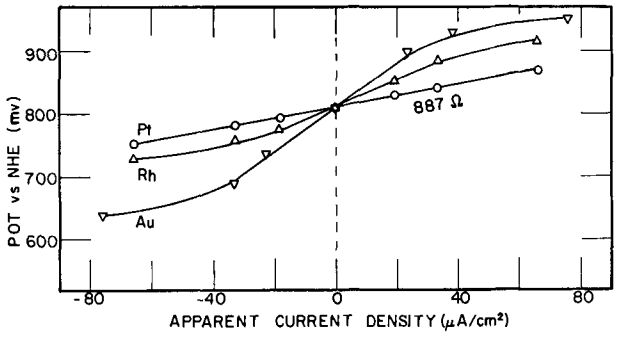

Fig. 1. Polarization of Au, Rh, and Pt electrodes at low current densities in 0.1M H_2O_2 acid solution (2*N* H_2SO_4). All electrodes have the same rest potential (810 mv) but different rates of reaction ($-di/d\eta$).

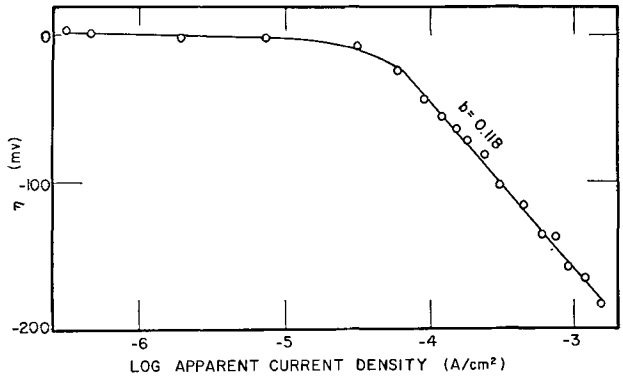

Fig. 2. Overvoltage measurements for the cathodic reduction of oxygen on bright Pt in 0.1M H_2O_2 acid solution (2*N* H_2SO_4). The overvoltage was determined from the rest potential instead of 1229 mv.

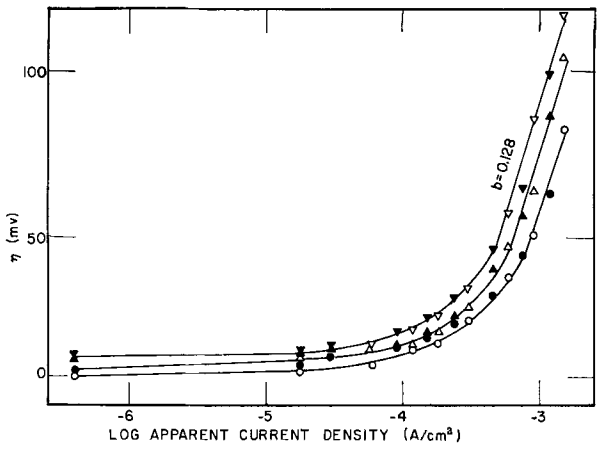

Fig. 3. Overvoltage measurements for the anodic evolution of oxygen on bright Pt in 0.1M H_2O_2 acid solution (2N H_2SO_4). The overvoltage was determined from the rest potential. Open symbols represent data for increasing polarization and filled symbols that for decreasing values. Three cycles of polarization are presented, the polarization increasing with each cycle. The slope of 0.128 does not change.

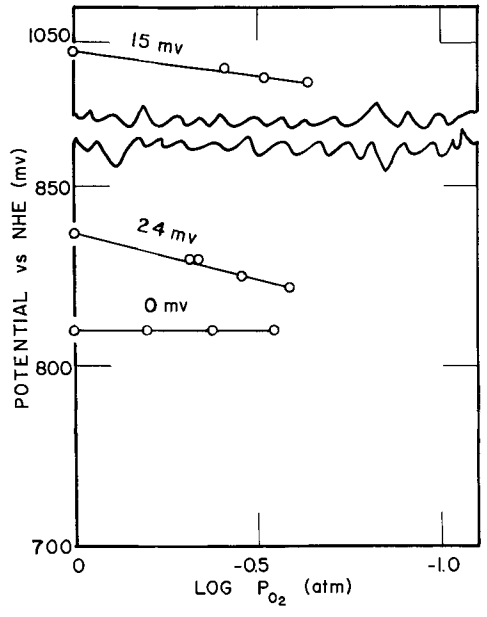

Fig. 4. A plot of the rest potential as a function of the partial pressure of oxygen for bright Pt in acid solutions containing different amounts of H_2O_2. The top curve contains no H_2O_2; the middle, 4 x 10^{-6}M H_2O_2; the bottom, 0.1M H_2O_2.

When H_2O_2 was added to the system, the rest potential fell rapidly to less noble values, and, as seen in Fig. 1, the steady rest potential was the same on the three different metals. However, the rate of the electrochemical reaction is different for each metal as shown by the different slopes. The points in Fig. 1 represent the average value of at least three complete cycles of polarization through the rest potential; the deviation from the mean was within ±2 mv.

It was found that the polarization of a platinum electrode in H_2O_2 stabilized acid solution was very low, as shown in Fig. 2 and 3. With cathodic polarization a reproducible curve was obtained after one or two cycles of polarization. The reproducible curve on which the points represent the average values of at least three cycles of polarization is presented in Fig. 2. These points could be reproduced within ±6 mv. A Tafel slope of 0.118 was obtained. In contrast, the anodic curves were not reproducible from one cycle to another but drifted progressively to larger overvoltage values at the higher current densities. A constant slope of 0.128 was observed.

The fact that the rest potential at high H_2O_2 concentrations is independent of the P_{O_2} has also been observed by other investigators (5, 6, 9). In addition, the overvoltage is independent of P_{O_2} in acid solutions of about 0.1M H_2O_2. The top curve in Fig. 4 is a Pt/O_2 electrode in H_2O_2-free solution; the middle curve, in a solution 4 x 10^{-6}M in H_2O_2; the bottom curve, in a solution 0.1M in H_2O_2.

Discussion

As H_2O_2 is added to a system in which a Pt/O_2 electrode is at rest in O_2-saturated acid solution, the rest potential is shifted to less noble values, and the slope of a plot of the potential as a function of the P_{O_2} deviates from a value of 15 mv towards one of 30 mv (see Fig. 4). Yet, as the H_2O_2 concentration increases, the potential becomes independent of the H_2O_2 concentration and does not reach the reversible potential of 682 mv (4) for the O_2/H_2O_2 reaction

$$O_2 + 2H^+ + 2e \rightleftharpoons H_2O_2, \qquad E_o = 682\,\text{mv} \qquad [1]$$

Since the rest potential also becomes independent of P_{O_2} at this point, it must be a mixed potential (10) because the Nernst equation is not obeyed. Giner (9) also came to this conclusion. The observed rest potential in strong H_2O_2 solutions is 810 ± 5 mv [in good agreement with the value obtained by Bockris (5) at pH = 0] and is independent of the electrode material in striking contrast to the systems in which peroxide is absent (11). This behavior indicates that the mixed potential does not involve a metal/metal oxide reaction.

The data in Fig. 4 show the influence of a 2-electron, potential-determining reaction. Therefore, in all probability one of the half-reactions determining the mixed potential is the O_2/H_2O_2 reaction, Eq. [1]. The other half-reaction could either be the O_2/H_2O reaction

$$O_2 + 4H^+ + 4e \rightleftharpoons 2H_2O, \qquad E_o = 1229\,\text{mv} \qquad [2]$$

or the H_2O_2/H_2O reaction

$$H_2O_2 + 2H^+ + 2e \rightleftharpoons 2H_2O, \qquad E_o = 1770\,\text{mv} \qquad [3]$$

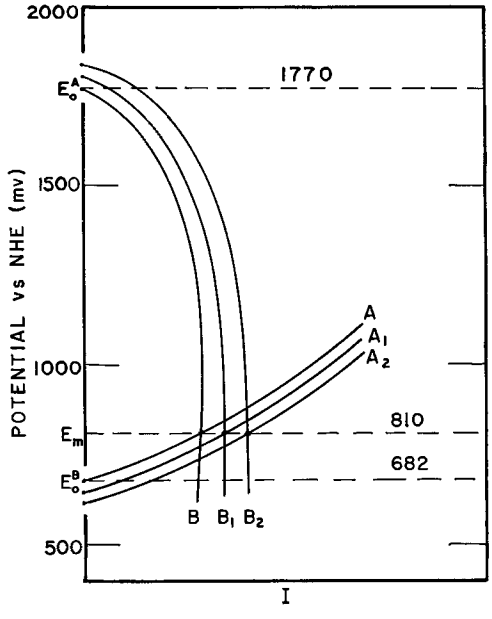

Fig. 5. Schematic diagram of the local cell polarization curves for a Pt electrode in 0.1M H_2O_2 acid solution (2N H_2SO_4). The A-curves represent the reaction $O_2 + 2H^+ + 2e \rightleftharpoons H_2O_2$; the B-curves, $H_2O_2 + 2H^+ + 2e \rightleftharpoons 2H_2O$. The curves A to A_2 and B to B_2 sketch the change in shape for increasing P_{O_2}. Since the mixed potential, E_m, is the same for each pair of curves, the observed rest potential is independent of P_{O_2}.

In the presence of high concentrations of H_2O_2, Eq. [3] is favored as the other half-reaction. For low H_2O_2 concentrations, the potential is probably determined by a complicated interaction of all three of the above reactions plus, no doubt, a metal/metal oxide reaction. This conclusion is supported by the lack of a simple relationship between potential and P_{O2} in this region in solutions with varying concentrations of H_2O_2 as observed here and by Giner (9).

Figure 5 is a sketch of the mixed potential diagram for a Pt/O_2, H_2O_2 electrode for high concentrations of H_2O_2. The A-curves are those for the O_2/H_2O_2 reaction for increasing concentrations of H_2O_2; and the B-curves, for the H_2O_2/H_2O reaction. Since the rest potential is so much closer to the E_o of the O_2/H_2O_2 reaction than the E_o of the H_2O_2/H_2O reaction, the H_2O_2/H_2O reaction must be strongly polarized down to the O_2/H_2O_2 reaction by the local cell action, as shown in the diagram. Because the O-O bond is so strong, the rate of the H_2O_2/H_2O reaction, as well as the i_o, should be small. Such a picture agrees with Yeager's findings (7) that the O-O bond is not broken easily.

The local cell is set up such that Eq. [3] is driven in the cathodic direction while Eq. [1] is driven in the anodic direction. Both reactions depend on the peroxide concentration, but $E^A{}_o$ is inversely dependent whereas $E^B{}_o$ is directly dependent on it. As a result, the corresponding pairs of curves cross at the same potenital producing the observed effect that the rest potential, E_m, is independent of the H_2O_2 concentration.

In the presence of H_2O_2, there will be competition between O_2 and H_2O_2 molecules for available adsorption sites on the electrode surface. For large concentrations of H_2O_2, the competition may become so strong that the surface is mostly covered with adsorbed peroxide and very sparsely covered with adsorbed oxygen. For ordinary values of P_{O2} the surface is saturated with adsorbed oxygen because, here, an oxygen saturated surface is only sparsely covered with oxygen. If this were the case, the potential would not respond to changes in P_{O2}, as observed experimentally.

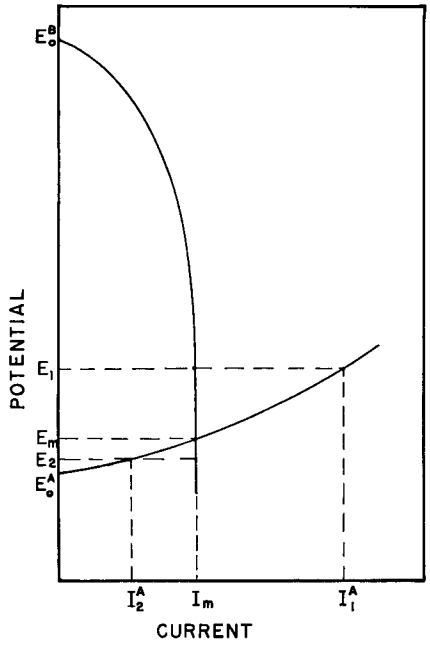

Fig. 6. Schematic diagram of the polarization of the local cell set up at a Pt electrode in 0.1M H_2O_2 acid solution (2N H_2SO_4). At the mixed potential, E_m, the H_2O_2/H_2O reaction is in a virtual limiting current condition. Changes in the local cell current, $I = I^A - I^B$, produced by anodic (E_1) or cathodic (E_2) polarization, are made up chiefly by I^A since $I^B \sim I_m$, the local cell current at open circuit. The kinetics, then, are controlled by the O_2/H_2O_2 reaction.

When the system is polarized galvanostatically, the potential is shifted to a point where the demanded current, I, equals the difference between the partial currents, I^A and I^B, as shown in Fig. 6. It may be seen that virtually all of the anodic current is contributed by the O_2/H_2O_2 reaction because the H_2O_2/H_2O reaction is in a condition of a virtual limiting current at $E = E_m$, that is, $I^B = I_m$. In like manner, the cathodic current, I_2, is controlled by $I^A{}_2$. This explains the linear curve in Fig. 1 which passes through the rest potential without a change of slope. As far as the polarization data are concerned, the system behaves like a reversible O_2/H_2O_2 electrode with an E_o of 810 mv. This is why the overvoltage data presented in Fig. 2 and 3 were determined from the rest potential value rather than from 1229 mv. When the system is polarized to potentials less noble than $E^A{}_o$ in Fig. 6 (682 mv), the reduction of oxygen according to Eq. [1] controls the electrode kinetics, since the H_2O_2/H_2O reaction (Eq. [3]) is in a limiting current density region. In this case, the system behaves like a single electrode system with only one i_o important to the kinetics. Consequently, the overvoltage curve, Fig. 2, obeys a Tafel relationship. Similarly, the curves in Fig. 3 have Tafel regions.

From the slope of the curve in Fig. 1, the rate (12) of the O_2/H_2O_2 reaction of Pt ($-di/d\eta$) is 1.13 x 10^{-3} mho. The i_o obtained from Fig. 2 is 3.98 x 10^{-5} amp/cm^2. If the overvoltage is calculated from 1229 mv, the i_o is 7.76 x 10^{-9} amp/cm^2. It is not possible to determine an i_o from Fig. 3 because the value changes with each cycle of polarization. For such a complicated system as the oxygen electrode, it may be better to use the linear slope of the E-i curve, $-di/d\eta$, at very low current densities (see Fig. 1), rather than i_o, for comparison of the catalytic activity of various electrode surfaces. This is suggested because the choice of values for $-di/d\eta$ is less than those for i_o. Using the equation for the corrosion current density, i_m, derived before (8),

$$i_m = -(di/dp)\left(\frac{RT}{F}\right)$$

one obtains a value of 2.9 x 10^{-5} amp/cm^2 for i_m. Because of the direction of the local cell action, H_2O_2 is consumed. This relatively large corrosion current explains the high rate of the catalytic decomposition of H_2O_2 as compared to the homogeneous decomposition reaction (6).

The overvoltage curves in Fig. 2 and 3, together with the data in Fig. 1, indicate that the anodic and cathodic reactions are the reverse of one another. Reproducible curves are obtained in the cathodic reduction of oxygen because peroxide is produced and a steady-state concentration of H_2O_2 can be maintained. In the anodic evolution of oxygen, however, the H_2O_2 is consumed and the overvoltage increases with each cycle of polarization. The anodic slope of 0.128 suggests that an electron discharge step is rate-controlling, probably the first electron discharge step

$$(H_2O_2)_{ads} \rightarrow (HO_2^-)_{ads} + H^+ + e \qquad [4]$$

A slope of 0.118 for the cathodic reduction of oxygen suggests that the rate-determining step for the reduction of oxygen at a Pt/O_2, H_2O_2 electrode may also be an electron discharge step

$$(O_2)_{ads} + e \rightarrow (O_2^-)_{ads} \qquad [5]$$

even though the overvoltage is independent of P_{O2}. This may be so because the surface is saturated with adsorbed oxygen.

It may be seen, then, that the concept of a polyelectrode (14) successfully explains the behavior of the rest potential of a Pt/O_2, H_2O_2 electrode in strong solutions of H_2O_2. The overvoltage curves indicate that the anodic and cathodic reactions are the reverse of one another, since the reaction

$$O_2 + 2H^+ + 2e \rightleftharpoons H_2O_2$$

controls both the mixed potential and the electrode kinetics. Such a scheme is in agreement with Yeager's finding that the O-O bond is very difficult to break and that a peroxide stabilized Pt/O_2 electrode is a good reversible oxygen electrode.

Manuscript received Nov. 6, 1964.

Any discussion of this paper will appear in a Discussion Section to be published in the December 1965 JOURNAL.

REFERENCES

1. W. G. Berl, *Trans. Faraday Soc.*, **83**, 253 (1943).
2. R. R. Whitherspoon, H. Urbach, E. Yeager, and F. Hovorka, Tech. Rpt. 4, ONR Contract No. Nonr 581(00) (1954).
3. J. P. Hoare, *This Journal*, **109**, 858 (1964).
4. W. H. Latimer, "Oxidation Potentials," Prentice-Hall, New York (1952).
5. J. O'M. Bockris and L. F. Oldfield, *Trans. Faraday Soc.*, **51**, 249 (1955).
6. R. Gerischer and H. Gerischer, *Z. Physik. Chem. N. F.*, **6**, 178 (1956).
7. M. O. Davies, M. Clark, E. Yeager, and F. Hovorka, *This Journal*, **106**, 56 (1959).
8. J. P. Hoare, *ibid.*, **112**, 602 (1965).
9. J. Giner, *Z. Elektrochem.*, **64**, 491 (1960).
10. C. Wagner and W. Traud, *ibid.*, **44**, 391 (1938).
11. J. P. Hoare, *This Journal*, **111**, 988 (1964).
12. P. Dolin, B. Ershler, and A. Frumkin, *Acta Physicochim. URSS*, **13**, 782 (1940).
13. E. Lange and H. Göhr, *Z. Elektrochem.*, **63**, 75 (1959).

Determination of the Composition of Complexes and Their Instability Constant by Calorimetry

I. The Cuprocyanide Complexes

Abner Brenner

National Bureau of Standards, Washington, D. C.

ABSTRACT

The calorimetric method for determining the chemical formula and the instability constant of a complex ion involves the determination of the partial molal heat effects resulting from the separate addition of increments of each of the constituents of the complex to a complete range of mixtures of the constituents. The general mathematical derivations necessary for the utilization of the method have been developed, and the complex copper cyanides have been used as an example. The instability constants for the $Cu(CN)_3^{--}$ and the $Cu(CN)_4^{---}$ ions were found to be 1.0×10^{-5} and 2.3×10^{-3}, respectively.

The determination of the composition of complexes and of their instability constants is an important aspect of chemistry. With the resurgence of inorganic chemistry during the past two decades, these subjects have taken on an increased interest. Treatises (1) dealing with the methods of determining the composition of complexes and tabulation (2) of the instability constants of over a thousand complexes have appeared recently.

The composition of stable complexes offers no problem, because the compounds can be isolated and analyzed, or their composition can be established by a titration, as for example, the composition of the argentocyanide ion by the titration of a silver salt with cyanide ion. However, complexes which have relatively large instability constants, for example 10^{-3}, may dissociate too much to be determined in that manner, and special procedures must be used. One of the most used methods is Job's method of continuous variation (3) which involves preparation of a complete series of mixtures of the two constituents of the complex, each mixture having the same number of moles; for example, 0.9 mole of A with 0.1 mole of B, and 0.8 mole of A with 0.2 mole of B, 0.7 mole of A with 0.3 mole of B, etc. Job showed that certain properties of the series of solutions, for example the absorption of light or the heat of reaction, were a maximum or minimum at the stoichiometric composition. Another general method of establishing the composition of complexes is thermometric titration.

After the chemical formula of a complex ion has been established, the instability constant may be determined by a variety of means. For example, known concentrations of the two reactants are brought together in a system, and the concentration of the complex which is formed is determined by spectrophotometry. The necessary information is then at hand for using the mass action expression for calculating the instability constant.

The calorimetric method, which is reported in this paper, for determining the chemical formula and the instability constant of a complex ion involves the determination of the partial molal heat effects resulting from the separate addition of increments of each of the constituents of the complex to a complete range of mixtures of the constituents. The general mathematical derivations necessary for the utilization of the method have been developed, and the complex copper cyanides have been used as an example. The method is of general applicability. It has not been reported previously in the literature.

In the following treatment, concentrations are used instead of activities. This is permissible, since the early work on the law of mass action has shown that many systems yield a reasonably satisfactory constant, if concentrations are used in the mass action expression. In this presentation the instability constant is used instead of the stability constant. Since the former is a small number for the cases considered here, some of the derivations are simplified by showing that some terms containing the constant can be neglected owing to its smallness.

Principle of the Calorimetric Method Illustrated by the Cuprocyanide Complexes. Qualitative Discussion

Consider the formation of a complex compound, A_mB_n, from the two reactants A and B. The calorimetric method consists in measuring the heat evolved by the reaction of a small increment (for example 1g) of one of the reactants (A or B) with a mixture of a large amount (for example several hundred grams) of A and B. The heat effect, Δh, is a function of the composition of the reaction mixture, that is, of the ratio

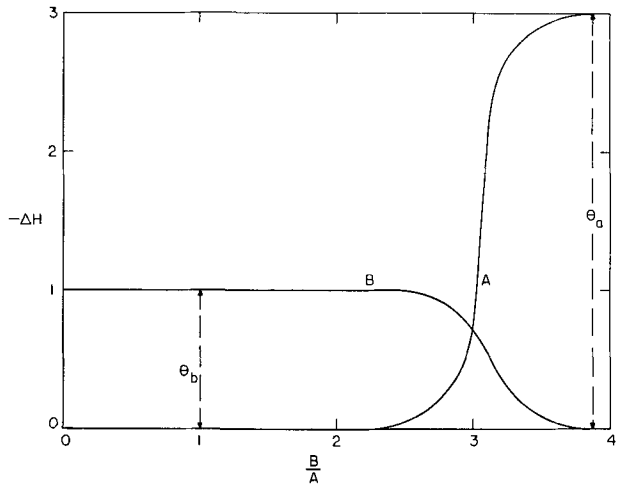

Fig. 1. Schematic representation of the partial molal heat effects occurring with a system of two components, A and B, which produce only one complex, AB_3. Curves A and B represent the heat effects obtained on adding increments of A and B, respectively, to mixtures initially containing A and B in various proportions. Note that the two curves cross at the stoichiometric composition. θ_a and θ_b are the maximum partial molal heat effects representing complete conversion of the increment to complex.

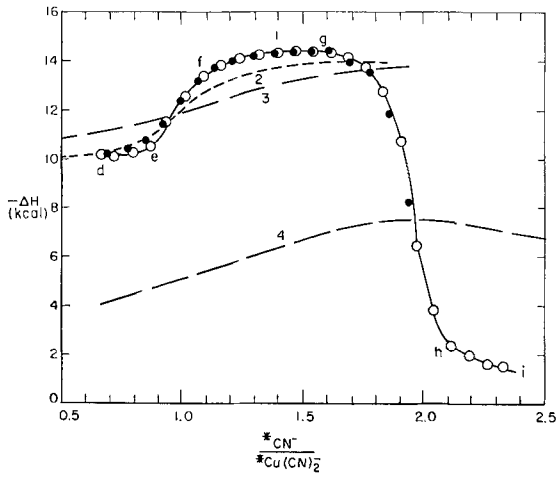

Fig. 2. Curve 1. Experimental data representing the addition of increments of solid sodium cyanide to a system initially consisting of a solution of the cuprocyanide ion, $Cu(CN)_2^-$. The open and solid circles represent the data of duplicate experiments.

The mass action equations are:

$$\text{I.}\ \frac{[Cu(CN)_2^-]\,[CN^-]}{[Cu(CN_3^{--})]} = k_1$$

$$\text{II.}\ \frac{[Cu(CN)_3^{--}]\,[CN^-]}{[Cu(CN)_4^{---}]} = k_2$$

Reactions I and II both occur in the region d-e-f and mainly reaction II in the region g-h-i. Curves 2 and 3 represent the determination of the constant k_1 by the graphical method for the region d-e-f-g. Curves 2 and 3 represent assumed values of k_1 of 10^{-5} and 10^{-4}, respectively, with $k_2 = 10^{-3}$. Curve 4 represents the integral heat effects that would have been obtained by Job's method, if various proportions of $Cu(CN)_2^-$ and CN^- were mixed, the sum of the two constituents always being 1 mole. On the abscissa, $*Cu(CN)_2^-$ represents the initial number of moles of $Cu(CN)_2^-$, that is, the number of moles of copper in the system. $*CN^-$ represents moles of cyanide initially added to the $*Cu(CN)_2^-$ solution.

of B to A. The heat effects are reported as a partial molal quantity, ΔH, where $\Delta H = \Delta h/dM$, and dM represents the fraction of a mole of increment added to the reaction mixture. The value of ΔH will vary from zero to some maximum value. The latter value is obtained by adding an increment of one salt to a large quantity of the other salt in the unadulterated state, as this results in virtually complete reaction of the increment. The experimentally determined ΔH can be better envisioned as the heat obtained by adding one mole of a reactant to an infinite amount of the mixture.

Figure 1 shows a diagrammatic representation of the partial molal heat effects accompanying the formation of a single complex from increments of A or B. The partial molal heat effect is plotted against the composition of the mixture. Two curves are shown, as increments of either A or B can be added to the reaction mixture. Curve B for increments of reactant B shows that, on adding the latter to mixtures rich in A, a constant value of ΔH is obtained initially. This is because virtually the whole increment of B reacts. This value of ΔH representing complete reaction of the increment is given the symbol θ. Near the stoichiometric point, the value of ΔH rapidly decreases and then becomes virtually zero, because virtually all of the A in the mixture is already combined and the effect of more B in shifting the equilibrium farther toward a more complete reaction is small. A similar train of events, represented by curve A, takes place on adding increments of A to reaction mixtures comprising the range of composition from pure B to pure A. It will be noted that curves A and B cross at the stoichiometric point. In this example the sharpness of the curve serves to indicate the stoichiometric composition of the complex, but this indication cannot be depended on in general.

The calorimetric method will be referred to in this publication as the method of increments.

The data for the cuprocyanide system, shown in Fig. 2, were obtained by adding increments of solid sodium cyanide, about 1g, to a solution containing 0.6 moles of copper as cyanide, the initial composition of the solution approximated the composition corresponding to the $Cu(CN)_2^-$ ion. An ordinary Dewar vessel calorimeter was used in a thermostatted oil bath.

Temperatures were measured with a platinum resistance thermometer. Much of the equipment was the same as that used by Sherfey and Brenner (4) in their studies of electrochemical calorimetry. The interpretation of the data is as follows. The addition of sodium cyanide to the initial system which contained $Cu(CN)_2^-$ resulted in the formation of $Cu(CN)_3^{--}$ ion. The partial molal heat was constant and (equal to 10 kcal/mole CN^-) during this reaction, as the curve shows a plateau extending from d to e. When this reaction was about completed, the heat effect rapidly changed to a larger value, representing the formation of the $Cu(CN)_4^{---}$ ion. During the formation of this latter ion from the $Cu(CN)_3^{--}$ ion the partial molal heat effect was sensibly constant, as shown by the plateau extending from f to g. The large decrease in heat effect between g and h represents virtually the disappearance of $Cu(CN)_3^{--}$, hence, the heat effect falls toward that of the heat of solution of sodium cyanide ($\Delta H = 0.26$ kcal/mole), but does not attain it.

Since solid sodium cyanide was used, the heat effect also involved the heat of solution of this salt, and this heat effect should be subtracted from the heat of reaction of an increment. This necessity could have been avoided by adding the increments in the form of a solution. Since the heat of solution of the sodium cyanide (a cooling effect) was only 0.26 kcal cal, which was about the size of the experimental error involved in the determinations of the partial molal heat effects, no corrections were made.

If copper cyanide were added in increments to a solution initially consisting only of sodium cyanide solution, a similar curve with two plateaus would be obtained, representing first the formation of the $Cu(CN)_4^{---}$ ion and next the formation of $Cu(CN)_3^{--}$.

The sharp breaks in the curve corresponding to a ratio of $\frac{*CN^-}{*Cu(CN)_2^-}$ of 1 and 2 shows unambiguously

the composition of the two complexes which have been formed. Here $*Cu(CN)_2^-$ represents the initial composition of the solution, hence, also the copper concentration; and $*CN^-$ represents the cyanide ion added subsequently as increments. Since the slope of such curves may not always be sharp enough to indicate the composition of a complex, a general method for determining the composition from the maximum partial molal heats of reaction, θ, is given in a later section.

The following treatment of the method of increments is divided into several sections. The treatment of a system of reactants which form only one complex is considered first. Under this heading there are two general subjects: (A) the determination of the composition of the complex from the maximum partial molal heat effects, θ, and (B) the determination of the instability constant from calorimetric data such as shown in Fig. 2. Item (B) has two parts, representing the use of two different methods of reporting concentrations. For aqueous solutions molar concentrations are most convenient, but for fused salt systems, mole fraction is more convenient; hence, the derivations for a system of a single complex were done for both types of concentration. The treatment of systems forming two or more complexes comes after the simple system as with the latter there are two general parts A and B. The treatment of the calculation of instability constants for systems of two or more complexes is more involved than for a system of a single complex and the obtaining of explicit algebraic formulas for the constants may not be possible. For that reason, a graphical method which is of a general applicability is also given.

Method of Increments Applied to System of One Complex

Determination of composition of complex.—Before the method of increments can be applied to the determination of the instability constant, the composition of the complex must be established. This is easily accomplished for a system of reactants, A and B, which form only one complex, A_mB_n. Two calorimetric measurements are required:

1. The maximum partial molal heat effect, θ_a, is obtained by the addition of an increment of A to unadulterated B. Since there is a large excess of B, A is virtually completely converted into the complex

$$mA + nB \rightarrow A_mB_n \qquad [1]$$

The heat of this reaction forming a mole of A_mB_n is $m\theta_a$.

2. Similarly, an increment of B is added to a large excess of A to yield the maximum partial molal heat effect, θ_b. The heat of this reaction forming a mole of A_mB_n is $n\theta_b$.

Since $m\theta_a$ must equal $n\theta_b$

$$m/n = \theta_a/\theta_b \qquad [2]$$

Since m and n must be integers, the ratio θ_a/θ_b establishes the composition of the complex.

Determination of the instability constant.—Instability constant based on molar concentrations.—General derivation.—The first step in determining the instability constant is to set up the mass action expression for the formation of the complex. In this section the expression will be based on molar concentrations. The general expression for the formation of the complex represented by Eq. [1] is

$$\frac{(C_y)^m\,(C_x)^n}{C_a} = k \qquad [3]$$

where C_y is the concentration of constituent A, C_x is the concentration of constituent B, and C_a is the concentration of the complex in a mixture which is in equilibrium, and k is the instability constant.

For purposes of calculation, the expression is rewritten in terms of the initial amounts of A and B used in preparing a mixture. These amounts are expressed as concentrations in moles per liter and will be represented by y and x, respectively, and the concentration of the complex by $\bar{a}$. The concentrations of A and B after $\bar{a}$ has been formed will be, respectively, $y - m\bar{a}$ and $x - n\bar{a}$, and the mass action expression is

$$(y - m\bar{a})^m \cdot (x - n\bar{a})^n = k\bar{a} \qquad [4]$$

The following derivation deals with increments of B which are added to various mixtures of A and B, prepared from a fixed amount of A. To determine k in Eq. [4], the concentration of $\bar{a}$ must be derived from the calorimetric data. This is done by first finding an algebraic expression for $\bar{a}$ in terms of the partial derivatives, $\bar{a}'$ and $\bar{a}''$, of $\bar{a}$ with respect to x. Later it is shown how the values of $\bar{a}'$ and $\bar{a}''$ are readily obtained from partial molal heat effects, ΔH.

The derivation is clearer if the physical meaning of $\bar{a}'$ is made evident. Instead of considering it as the ratio of two differentials, consider it as the fraction of a mole of complex, A_mB_n, formed by adding 1 mole of B to an infinite amount of reaction mixture of A and B of various compositions. For example, in Eq. [4], if n were 1, then the maximum amount of complex which could be formed from 1 mole of B (in an infinite amount of mixture) would be 1 mole. If the mixture already contained more than the stoichiometric ratio of B, the amount of complex formed from the additional amount would be small. Thus, in this example, $\bar{a}'$ is a number which expresses the fraction of reaction of the increment and varies between unity and zero. If the value of n in Eq. [4] were 2, then the value of $\bar{a}'$ would vary between the limits of zero and 0.5. In general, $\bar{a}'$ is a fraction varying between the values of zero and $1/n$ and represents the number of moles of complex formed by adding one mole of reactant to an infinite amount of mixture.

Differentiation of $\bar{a}$ in Eq. [4] with respect to x gives

$$m(y - m\bar{a})^{m-1} \cdot (-m\bar{a}')\,(x - n\bar{a})^n + n(y - m\bar{a})^m(1 - n\bar{a}')\,(x - n\bar{a})^{n-1} = k\bar{a}' \qquad [5]$$

Dividing Eq. [5] by Eq. [4] gives

$$\frac{-\bar{a}'m^2}{y - m\bar{a}} + \frac{n(1 - n\bar{a}')}{x - n\bar{a}} = \frac{\bar{a}'}{\bar{a}} \qquad [6]$$

A further simplification is introduced if the value of $\bar{a}'$ is calculated only for the stoichiometric point, that is, where $x/y = n/m$. This relation is best introduced into the equation by using a new variable, z, such that

$$x = nz,\ y = mz \qquad [7]$$

Equation [6] then becomes

$$\frac{-m\bar{a}'}{z - \bar{a}} + \frac{1 - n\bar{a}'}{z - \bar{a}} = \frac{\bar{a}'}{\bar{a}} \qquad [8]$$

Solving Eq. [8] for $\bar{a}$

$$\bar{a} = \frac{\bar{a}'z}{\bar{a}'(1 - m - n) + 1} \qquad [9]$$

when $x/y = n/m$

If the partial differentiation of $\bar{a}$ in Eq. [4] had been made with respect to y instead with respect to x, the final equation would have been the same as Eq. [9], except that $\bar{a}'$ would be with respect to y. Since at the stoichiometric point, $\bar{a}$ would have the same value for both equations, this means that

$$\frac{\partial\bar{a}}{\partial x} = \frac{\partial\bar{a}}{\partial y} \qquad [10]$$

when $(x/y) = (n/m)$.

Physically, this relation means that curves A and B of Fig. 1 must cross at the stoichiometric point, because as shown later, the partial derivatives are proportional to ΔH, the ordinate of the curve.

The intersection of the two curves would be a very precise method of obtaining the composition of the complex, if the partial molal heat effects for both $\bar{a}$ and b could be obtained experimentally.

An expression for the instability constant k is obtained by substituting in the original mass action expression of Eq. [4] the values of x, y, $z - \bar{a}$, and $\bar{a}$, as given in Eq. [7]-[9]. At the stoichiometric point Eq. [4] has the form

$$m^m n^n (z - \bar{a})^{m+n} = \bar{a}k \qquad [11a]$$

and

$$k = \left[\frac{z(1 - \bar{a}'m - \bar{a}'n)}{\bar{a}' - \bar{a}'m - \bar{a}'n + 1}\right]^{m+n} \cdot \frac{m^n \cdot n^n(\bar{a}' - \bar{a}'m - \bar{a}'n + 1)}{\bar{a}'z} \qquad [11b]$$

for values of the variables at the stoichiometric point.

Experience with this equation showed that it was not suitable for calculating k because the expression in the parenthesis, $(1 - \bar{a}'m - \bar{a}'n)$ is a small number, if k is small, and it appeared that $\bar{a}'$ could not be calculated (see following section) with sufficient accuracy from the experimental data to give the parenthesis a meaningful value. For example, if m and n were both unity, $\bar{a}'$ would be very nearly 0.5, and the value of the parenthesis would be nearly zero. If the data were not precise, its value might even appear to be negative, which is obviously erroneous.

It was felt intuitively, that there should be a relation between the instability constant and the steepness of the curves, A or B (Fig. 1), where they passed through the stoichiometric point, and this suggested that the differentiation be carried a step further. The following treatment shows that the introduction of the second derivative, $\bar{a}''$, makes the calculation of k practicable.

Equation [6], which does not explicitly involve k, is chosen for partial differentiation of $\bar{a}$ and $\bar{a}'$ with respect to x.

$$\frac{(y - m\bar{a})(-m^2\bar{a}'') + m^2\bar{a}'(-m\bar{a}')}{(y - m\bar{a})^2} + \frac{(x - n\bar{a})(-n^2\bar{a}'') - n(1 - n\bar{a}')^2}{(x - n\bar{a})^2} = \frac{\bar{a}\bar{a}'' - (\bar{a}')^2}{\bar{a}^2} \qquad [12]$$

For the stoichiometric point where $x = nz$ and $y = mz$, the equation simplifies to

$$\frac{m\bar{a}''}{(z - \bar{a})} + \frac{m(\bar{a}')^2}{(z - \bar{a})^2} + \frac{n\bar{a}''}{(z - \bar{a})} + \frac{(1 - n\bar{a}')^2}{n(z - \bar{a})^2} = \frac{-\bar{a}''}{\bar{a}} + \left(\frac{\bar{a}'}{\bar{a}}\right)^2 \qquad [13]$$

This equation is simplified by use of Eq. [8] and [9] and leads to an expression for $z - \bar{a}$

$$z - \bar{a} = \frac{\bar{a}'}{\bar{a}''n} \cdot [\bar{a}'n(m + n - 1)(\bar{a}'m + \bar{a}'n - 2) + n - 1] \qquad [14]$$

On substituting in the mass action expression of Eq. [4] or Eq. [11a] for x, y, and for $z - \bar{a}$ as given by Eq. [14] and $\bar{a}$ as given by Eq. [9], a general expression for k is obtained for values of the variables at the stoichiometric point:

$$k = \left[\frac{\bar{a}'}{\bar{a}''n}\right]^{m+n} \cdot \frac{m^m n^n(\bar{a}' - \bar{a}'m - \bar{a}'n + 1)[\bar{a}'n(m + n - 1)(\bar{a}'m + \bar{a}'n - 2) + n - 1]^{m+n}}{\bar{a}'z} \qquad [15]$$

In Eq. [15] $\bar{a}'$ and $\bar{a}''$ represent partial derivatives with respect to x. To obtain the equation which is valid for adding increments of y to a reaction mixture, interchange m and n and let $\bar{a}'$ and $\bar{a}''$ be the partial derivatives with respect to y.

Equation [15] appears to be more cumbersome than it is in reality. For example, if m and n were both unity, the equation would be

$$k = \frac{4[\bar{a}'(1 - \bar{a}')]^3}{(\bar{a}'')^2 z} \qquad [16]$$

when $(x/y) = (n/m)$.

It will be noted that this equation does not contain small differences between large numbers. The value of $1 - \bar{a}'$ involves no difficulty since the value of $\bar{a}'$ is close to 0.5.

Before illustrating the use of Eq. [16] with the cuprocyanide system, it is necessary to show the relation between the partial derivatives, $\bar{a}'$ and $\bar{a}''$, in the equation and the experimentally determined partial molal heat effects.

Relation between partial molal heat effects and the partial differentials.—The following discussion shows that the partial differential, $\bar{a}'$ is proportional to the partial molal heat effect, ΔH. Figure 1 shows that the partial molal heat effect corresponding to the complete reaction of an increment of B is θ_b. Where ΔH has a value less than θ_b, this indicates that only a fraction of the increment has reacted. More specifically, the fraction of the increment that has reacted and been converted to the complex is equal to $\Delta H/\theta_b$. The discussion at the beginning of this section showed that the moles of complex, A_mB_n, formed from the complete reaction of a mole of B added to an infinite system was $1/n$. In the case of incomplete reaction of an increment, the moles of complex formed would be $(1/n)(\Delta H/\theta_b)$. This expression is the same as $\bar{a}'$, which was shown (at the beginning of the previous section) to represent the number of moles of complex formed by adding one mole of reactant to an infinite amount of mixture of A and B.

$$\bar{a}' = \Delta H/n\theta_b \qquad [17]$$

Here $\bar{a}'$ refers to partial differentiation with respect to x, which latter represents the reactant B.

Differentiation of Eq. [17] with respect to x gives an expression for $\bar{a}''$

$$\bar{a}'' = \frac{1}{n\theta_b}\frac{\partial(\Delta H)}{\partial x} \qquad [18]$$

Thus, $\bar{a}''$ is proportional to the slope, $\partial(\Delta H)/\partial x$, of the curves, such as shown in Fig. 1, if the abscissa reads directly in terms of the variable x. However, the value of the partial molal heat effect, ΔH, is usually plotted against the composition, $f(x,y)$, of the mixture of A and B, for example against the ratio x/y or the ratio $x/(x + y)$, so that the stoichiometric compositions can be more readily seen from the figure. The slope of the curve is $\partial(\Delta H)/\partial f(x, y)$. The derivative of ΔH with respect to x is then obtained by the following relation

$$\frac{\partial(\Delta H)}{\partial x} = \frac{\partial(\Delta H)}{\partial f(x, y)} \cdot \frac{\partial f(x, y)}{\partial x} \qquad [19]$$

If the abscissa represents the ratio x/y, Eq. [19] becomes

$$\frac{\partial(\Delta H)}{\partial x} = \frac{1}{y}(\text{Slope}) \qquad [20]$$

If the abscissa represents the mole fraction $x/(x+y)$, Eq. [19] becomes

$$\frac{\partial(\Delta H)}{\partial x} = \frac{y}{(x+y)^2}\,(\text{Slope}) \qquad [21]$$

Example of the cuprocyanide system.—As an example of the method of increments, the value of k is calculated for the formation of the complex cuprocyanide ion, $Cu(CN)_4^{---}$ from $Cu(CN)_3^{--}$. In this system two complexes can be obtained from the $Cu(CN)_2^-$ ion as already discussed.

$$Cu(CN)_2^- + CN^- \rightleftarrows Cu(CN)_3^{--} \qquad [22]$$

$$Cu(CN)_3^{--} + CN^- \rightleftarrows Cu(CN)_4^{---} \qquad [23]$$

At the first slope, e-f, shown in Fig. 2, the $Cu(CN)_2^-$ ion is being converted into both $Cu(CN)_3^{--}$ and some $Cu(CN)_4^{---}$ ion, and the considerations of the preceding derivation do not apply without modification. However, at the slope, g-h, only an insignificant concentration of the $Cu(CN)_2^-$ can be present, as indicated by the constancy of the heat effect in the neighborhood of g, hence, the reaction involves only the formation of a single complex, $Cu(CN)_4^{---}$ according to Eq. [23].

The mass action expression for Eq. [23] is

$$\frac{(y-\bar{a})(x-\bar{a})}{\bar{a}} = k \qquad [24]$$

where x and y represent, respectively, the initial concentrations expressed in moles per liter, of CN^- and $Cu(CN)_3^{--}$; and $\bar{a}$ represents the concentration of $Cu(CN)_4^{---}$. The value of the instability constant, k, is given by Eq. [16]. The curve gives $\bar{a}' = 0.5$ (according to Eq. [17]) at the stoichiometric point where $x/y = 1$ $\left(\text{or}\ \frac{*CN^-}{*Cu(CN)_2^-} = 1\right)$. The slope of the curve in the figure at the stoichiometric point is $\frac{\partial \Delta H}{\partial(x/y)}$, and equals −56,500. The concentration of copper as complex was 0.6M. The value of $\bar{a}''$ is obtained from Eq. [18] and [20]

$$\bar{a}'' = \frac{1}{n\theta_b}\cdot\frac{1}{y}\,(\text{Slope}) = \frac{1}{14{,}000}\cdot\frac{1}{0.6}\,(-56{,}500) = -6.7$$

Substitution in Eq. [16] of $\bar{a}'' = -6.7$, $\bar{a}' = 0.5$, and $z = my = 0.6$ gives

$$k = 0.0023 \qquad [25]$$

Derivation of expressions for calculating k when the mass action expression is written in terms of mole fractions.—For fused salt systems, concentrations expressed in terms of mole fractions are easier to use than molarities, since mole fractions depend only on the weight of each component, whereas molarities require also a knowledge of the densities of the mixtures, data for which are not, in general, available. It will be assumed that the mass action law will yield a constant with concentrations expressed as mole fractions, although this constant will not necessarily be numerically equal to that obtained with molar concentrations.

For the purpose of the mathematical derivation, the mass action law is expressed in this section in terms of mole fractions. However, for experimental purposes and for the subsequent calculation, it is more convenient to express the magnitude of the initial additions, x and y, to the mixture and of the increments directly in terms of moles. Thus, the derivatives of the product, $\bar{a}$, with respect to x or y will also be in terms of moles. The reaction to be discussed is

$$rA + sB \rightleftarrows ArBs \qquad [26]$$

Let y and x in this discussion represent the moles of reactants, A and B, initially used to make up the mixture and let $\bar{a}$ represent the moles of product, ArBs, formed. The moles of A and B present at equilibrium are $y - r\bar{a}$ and $x - s\bar{a}$, respectively. The total number of moles, f, present in the reaction mixture is: $(x - s\bar{a}) + (y - r\bar{a}) + \bar{a} = y + x + \bar{a}(1 - r - s) = f$. The mass action law expressed in mole fractions is

$$\frac{\left[\frac{y-r\bar{a}}{f}\right]^r\left[\frac{x-s\bar{a}}{f}\right]^s}{\frac{\bar{a}}{f}} = k \qquad [27]$$

For greater ease in calculating the partial derivative of $\bar{a}$ with respect to x, the equation is rearranged to a more convenient form

$$\left[\frac{y+x+\bar{a}(1-r-s)}{y-r\bar{a}}\right]^{r-1}\left[\frac{y+x+\bar{a}(1-r-s)}{x-s\bar{a}}\right]^s = \frac{y}{k\bar{a}} - \frac{r}{k} \qquad [28]$$

$$\left[1+\frac{x+\bar{a}-s\bar{a}}{y-r\bar{a}}\right]^{r-1}\left[1+\frac{y+\bar{a}-r\bar{a}}{x-s\bar{a}}\right]^s = \frac{y}{k\bar{a}} - \frac{r}{k} \qquad [29]$$

Differentiation of Eq. [29] and rearrangement of terms gives

$$\left\{\left[\frac{y+x+\bar{a}(1-r-s)}{(y-\bar{a}r)^{r-1}(x-\bar{a}s)^s}\right]^{r+s-2}\right\}\left[\frac{s(\bar{a}'x-\bar{a}'rx-y-\bar{a}'ys-\bar{a}+\bar{a}r)}{x-\bar{a}s} + \frac{(r-1)(y+\bar{a}'y-\bar{a}'ys-\bar{a}r+\bar{a}'rx)}{y-\bar{a}r}\right] = \frac{-y\bar{a}'}{k\bar{a}^2} \qquad [30]$$

The first term of Eq. [30] on the left, indicated by the braces, can be replaced by substituting from Eq. [28], to give an equation which does not contain k

$$\frac{y-\bar{a}r}{y+x+\bar{a}(1-r-s)}\cdot\left[\frac{s(\bar{a}'x-\bar{a}'rx-y-\bar{a}'ys-\bar{a}+\bar{a}r)}{x-\bar{a}s} + \frac{(r-1)(y+\bar{a}'y-\bar{a}'ys-\bar{a}r+\bar{a}'rx)}{y-\bar{a}r}\right] = \frac{-y\bar{a}'}{\bar{a}} \qquad [31]$$

The next step is to find the value of this expression at the stoichiometric point where $x/y = s/r$, and this is done most conveniently by introducing the variable, z, such that $x = sz$ and $y = rz$.

On making this substitution in Eq. [31], the following simple expression is obtained for the relation between $\bar{a}$ and $\bar{a}'$

$$\bar{a} = z\bar{a}'(r+s) \qquad [32]$$

If the differentiation of $\bar{a}$ had been done with respect to y instead of x, the same Eq. [32] would have been obtained except that a' would be the derivative of $\bar{a}$ with respect to y. This equality indicates that the two partial derivatives are equal and that the two curves such as shown in Fig. 1 must cross at the stoichiometric composition. This was the same result as that obtained in the derivation based on molar concentrations.

An expression for k now can be obtained by substituting the expression for $\bar{a}$, as given in Eq. [32], into the original mass action expression, Eq. [27]

$$\frac{r^r \cdot s^s (1 - \bar{a}'r - \bar{a}'s)^{r+s}}{(r+s)\bar{a}'[(r+s)(1 + \bar{a}' - \bar{a}'r - \bar{a}'s)]^{r+s-1}} = k \quad [33]$$

This equation is not recommended for calculation of k for the same reason as that given in the previous discussion dealing with molar concentrations; namely, the factor $(1 - \bar{a}'r - \bar{a}'s)$ represents a small difference and cannot be determined accurately. Therefore, as in the prior discussion in an earlier section, it is necessary to obtain an equation for k based on the second derivative of $\bar{a}$.

In order to differentiate the cumbersome expression in Eq. [31], it was rewritten in the following form

$$(r-1)(y + \bar{a}'y - \bar{a}'ys - \bar{a}r + \bar{a}'rx) + \frac{s(y - \bar{a}r)(\bar{a}'x - \bar{a}'rx - y + \bar{a}'ys - \bar{a} + \bar{a}r)}{x - \bar{a}s} = \frac{-y\bar{a}'(y+x)}{\bar{a}} - y\bar{a}'(1 - r - s) \quad [32]$$

Differentiation of Eq. [32] gives

$$(r-1)(\bar{a}''y - \bar{a}''ys + \bar{a}''rx) + \frac{s(y - \bar{a}r)(\bar{a}''x - \bar{a}''rx + \bar{a}''ys)}{x - \bar{a}s} + s(\bar{a}'x - \bar{a}'rx - y + \bar{a}'ys - \bar{a} + \bar{a}r)\left[\frac{(x - \bar{a}s)(-\bar{a}'r) - (y - \bar{a}r)(1 - \bar{a}'s)}{(x - \bar{a}s)^2}\right] = \frac{-y\bar{a}'}{\bar{a}} + y(y+x)\cdot\left[\frac{-\bar{a}\bar{a}'' + (\bar{a}')^2}{\bar{a}^2}\right] - y\bar{a}''(1 - r - s) \quad [33]$$

The value of Eq. [33] is computed for the stoichiometric point by substituting $x = sz$, $y = rz$, and substituting for $\bar{a}$ and $\bar{a}'$ as necessary and, also using Eq. [32]. Equation [33] then simplifies to

$$z - \bar{a} = \frac{\bar{a}'_x r(\bar{a}'_x r + \bar{a}'_x s - \bar{a}'_x - 1)}{\bar{a}''_x s} \quad [34]$$

If the differentiations had been done with respect to y, the equation would be the same except for the interchanging of r and s

$$z - \bar{a} = \frac{\bar{a}'_y s(\bar{a}'_y r + \bar{a}'_y s - \bar{a}'_y - 1)}{\bar{a}''_y r} \quad [35]$$

The terms $\bar{a}''_x$ and $\bar{a}''_y$ refer to differentiation with respect to x and y, respectively.

Division of Eq. [34] by Eq. [35] leads to the result

$$\frac{\bar{a}''_x}{\bar{a}''_y} = \frac{r^2}{s^2} \quad [36]$$

This shows that the slopes of the curves for increments of x and y at the stoichiometric point are inversely proportional to the square of the coefficients of B and A in the chemical reaction.

An expression for k is obtained for values of the variables at the stoichiometric point by substituting Eq. [34] into the original expression Eq. [27] and letting $x = sz$ and $y = rz$.

$$k = (-1)^{1-s-r} \cdot \left[\frac{\bar{a}'r}{\bar{a}''_x z(r+s)}\right]^{r+s} \cdot \left(\frac{r}{s}\right)^r \cdot \frac{(\bar{a}'r + \bar{a}'s - \bar{a}' - 1)}{\bar{a}'} \quad [37]$$

If r and s were both unity, the equation for k would simplify to

$$k = \left[\frac{\bar{a}'}{2\bar{a}''z}\right]^2\left[\frac{\bar{a}' - 1}{\bar{a}'}\right] \quad [38]$$

Thus far, no utilization has been made of Eq. [37] for fused salt systems. However, an investigation of the complexes present in a mixture of molten potassium chloride and cadmium chloride is in progress in our laboratory and is well toward completion. This system will be interpreted by the use of Eq. [37].

Derivation of the Composition of Complexes and of the Instability Constant for Reactants Forming Two or More Complexes

The discussion of the previous section showed that, for two reactants which form only one complex, the composition of the complex and the instability constant can be easily obtained by the method of increments. The investigation of a system of two reactants which form two or more complexes is no more difficult to deal with experimentally than a system of a single complex, except that similar data must be collected for each of the complexes. The calculations, however, are considerably more involved because two complexes may be formed simultaneously. The partial molar heat effect, ΔH, would then be a composite of two different heats of reaction.

Determination of the composition of the complexes.— The first subject to consider is the determination of the stoichiometric composition of the complexes from the maximum partial molal heat effects. In the case of the copper cyanide system, as already mentioned, the breaks in the curve are sharp enough to indicate the composition of both complexes, but this is not a general method, as such steep slopes in the curves do not occur unless the instability constants are small, for example 10^{-3}.

Figure 3 represents a schematic diagram of a system of three complexes. The horizontal portions of the curves are evidence of the existence of a different complex on each side of the plateau. As increments of B are added to mixtures starting with pure A and progressing through all ranges of composition to pure B, the initial complex formed contains the highest ratio of A to B and the subsequent complexes contain a successively lower ratio of A to B. Similarly, if increments of A were added to mixtures which were initially high in B and then proceeded through all ranges of composition to pure A, the initial complex would contain the highest proportion of B to A. However, the same series of complexes must be formed whether the increments are made with A or B. These qualitative ideas assist in understanding the sets of equations used for deriving the composition of the complexes from the partial molal heat effects.

To illustrate the method, the composition of complexes will be derived for the particular situation in which three complexes are successively formed from A and B. The partial molal heat quantities of interest in this derivation are the maximum partial molal heat effects, θ, corresponding to the plateaus as shown in Fig. 3.

On adding increments of constituent B to a complete series of mixtures three maximum partial molal heat effects, θ_1, θ_2, and θ_3, would be obtained experimentally, if there were three complexes.

$$rA + sB \rightleftarrows A_rB_s\,;\ \Delta R_1 = s\theta_1 \quad [39]$$

$$tA_rB_s + (rv - st)\,B \rightleftarrows rA_tB_v\,;\ \Delta R_2 = (rv - st)\,\theta_2 \quad [40]$$

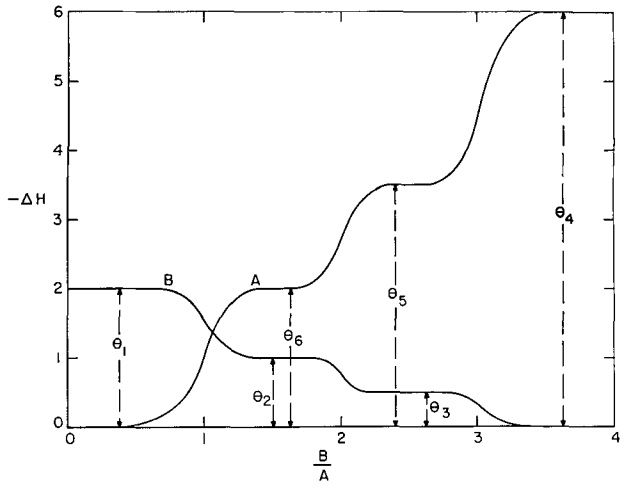

Fig. 3. Schematic representation of the partial molal heat effects for a system of two components which produce three complexes, AB, AB_2, and AB_3.

$$mA_tB_v + (nt - mv)\,B \rightleftarrows tA_mB_n\,;\,\Delta R_3 = (nt - mv)\,\theta_3 \quad [41]$$

ΔR refers to the heat effect for the equation as written, that is, for the formation of 1 mole of product in Eq. [39], r moles of product in Eq. [40], and t moles of product in Eq. [41].

However, for calculating the composition of the complexes, the equations for the reactions must be in the simple form of Eq. [39], that is, show the heat effect for the formation of the complex directly from A and B. Hence, Eq. [40] and [41] for the formation of A_tB_v and A_mB_n must be modified.

The equation for the direct formation of A_tB_v is obtained by multiplying Eq. [39] by t, adding to Eq. [40] and dividing by r. The final result is

$$tA + vB \rightarrow A_tB_v\,;\,\Delta R_{2a} = \frac{st(\theta_1 - \theta_2) + rv\theta_2}{r} \quad [40A]$$

Similarly, the equation for the direct formation of complex A_mB_n from A and B is obtained by multiplying Eq. [40A] by m and adding to Eq. [41] to give the following equation:

$mA + nB \rightarrow A_mB_n\,;\,\Delta R_{3a} =$

$$\frac{mrv(\theta_2 - \theta_3) + mst(\theta_1 - \theta_2) + nrt\theta_3}{rt} \quad [41A]$$

To permit the calculation of the coefficients, m and n, r and s, t and v, three additional equations, similar to Eq. [39], [40A], and [41A] must now be obtained for the addition of increments of A to a range of mixtures starting with pure B

$$mA + nB \rightleftarrows A_mB_n\,;\,\Delta R_4 = m\theta_4 \quad [42]$$

$$vA_mB_n + (nt - mv)\,A \rightleftarrows nA_tB_v\,;\,\Delta R_5 = (nt - mv)\,\theta_5 \quad [43]$$

$$sA_tB_v + (rv - st)\,A \rightarrow vA_rB_s\,;\,\Delta R_6 = (rv - st)\,\theta_6 \quad [44]$$

Since the coefficients are small integers, the ratios of m/n, t/v, and r/s are adequate to determine them. To determine the ratio, r/s, Eq. [44] is multiplied by r/s and added to Eq. [40], giving the result

$$\frac{r(rv - st)}{s}A + (rv - st)B \rightleftarrows \frac{(rv - st)}{s}A_rB_s$$

$$\Delta R_{2,6} = (rv - st)\,\theta_2 + \frac{r(rv - st)\,\theta_6}{s} \quad [45]$$

Simplifying, the equation becomes

$$rA + sB \rightleftarrows A_rB_s\,;\,\Delta R_{6a} = s\theta_2 + r\theta_6 \quad [46]$$

To obtain the ratio, s/r, the heat effect, ΔR_{6a}, of Eq. [46] is equated to the heat effect, ΔR_1, of Eq. [39]

$$s\theta_1 = s\theta_2 + r\theta_6 \quad [47]$$

This equation leads to the result that

$$s/r = \theta_6/(\theta_1 - \theta_2) \quad [48]$$

To obtain the ratio, t/v, multiply Eq. [43] by t/v and add to Eq. [41], giving the result

$$\frac{t(nt - mv)}{v}A + (nt - mv)B \rightleftarrows \frac{(nt - mv)}{v}A_tB_v$$

$$\Delta R_{3,5} = (nt - mv)\,\theta_3 + \frac{t(nt - mv)}{v}\theta_5 \quad [49]$$

Simplifying, this gives

$$tA + vB \rightleftarrows A_tB_v\,;\,\Delta R_{5a} = v\theta_3 + t\theta_5 \quad [50]$$

Equate the heat effect, ΔR_{5a}, of Eq. [50] to the heat effect R_{2a} of Eq. [40A]

$$v\theta_3 + t\theta_5 = \frac{st(\theta_1 - \theta_2) + rv\theta_2}{r} \quad [51]$$

This equation is solved by making a substitution for for s/r given in Eq. [48], to give the result

$$t/v = (\theta_2 - \theta_3)/(\theta_5 - \theta_6) \quad [52]$$

To obtain the ratio, n/m, equate the heat effect, ΔR_{3a}, of Eq. [41A] to the heat effect, ΔR_4, of Eq. [42].

$$m_{\theta 4} = \frac{mrv(\theta_2 - \theta_3) + mst(\theta_1 - \theta_2) + nrt\theta_3}{rt} \quad [53]$$

This equation is solved by making a substitution for s from Eq. [48] and a substitution for v, using Eq. [52], to yield the following result

$$n/m = \frac{(\theta_4 - \theta_5)}{\theta_3} \quad [54]$$

Equations [48], [52], and [54] give the compositions of the three complexes in terms of the maximum partial molal heat effects, θ, which latter are determined experimentally under conditions that result in essentially complete reaction of the increment. If more than three complexes are formed, the procedure which has been illustrated can be extended. If only two complexes, A_rB_s and A_tB_v, were formed, the two equations for the addition of increments of B would be the same as Eq. [39] and [40]. The equations for the addition of increments of reactant A would be similar to those of Eq. [42] and [43]

$$tA + vB \rightleftarrows A_tB_v\,;\,\Delta R_3 = t\theta_3$$

$$sA_tB_v + (rv - st)\,A \rightleftarrows vA_rB_s\,;\,\Delta R_4 = (rv - st)\,\theta_4 \quad [55]$$

The formula for determining their composition would be

$$\frac{s}{r} = \frac{\theta_4}{\theta_1 - \theta_2} \text{ and } \frac{v}{t} = \frac{\theta_3 - \theta_4}{\theta_2} \quad [56]$$

Calculation of instability constants when two complexes are formed.—Derivation for a system with one and two ligands added.—The instability constant was derived in an earlier section for equilibria involving only one complex, and a formula was applied to the copper cyanide system, shown in Fig. 2, for the reaction of $Cu(CN)_3^{--}$ with CN^- to form $Cu(CN)_4^{---}$. The equations could not be similarly applied to the sloping portion of the curve, e-f, because two equilibria were involved. Along the slope the addition of CN^- to a mixture containing $Cu(CN)_2^-$ ion resulted in the formation of both $Cu(CN)_3^{--}$ ion and $Cu(CN)_4^{---}$ ion.

To determine the instability constant for the formation of $Cu(CN)_3^{--}$, the constant for the formation of $Cu(CN)_4^{---}$ must also be taken into consideration.

The method of calculating the instability constant for the equilibria involving the $Cu(CN)_3^{--}$ ion is done in the following sections in two ways. The first method is an analytic one involving the derivation of a formula for calculating k. The formula is applicable only to a system of reactions in which one complex is derived from the other by addition of only one additional ligand. The other method of calculation is a graphical one and the procedure can be applied generally. For pedagogic purposes the specific calculation of the instability constant of the cuprocyanide system

$$Cu(CN)_2^- + CN^- \rightleftarrows Cu(CN)_3^{--} \qquad [22]$$

will be carried through first. The extension to a general procedure will then appear simpler.

Two reactions take place simultaneously when increments of cyanide ion are added to mixtures consisting of $Cu(CN)_2^-$ and $Cu(CN)_3^{--}$. Depending on the composition of the mixture, $Cu(CN)_3^{--}$ and $Cu(CN)_4^{---}$, both can be formed, or only $Cu(CN)_4^{---}$ at the expense of both $Cu(CN)_2^-$ and $Cu(CN)_3^{--}$. The mass action expressions are

$$\frac{[Cu(CN)_2^-][CN^-]}{[Cu(CN)_3^{--}]} = k_1 \qquad [57]$$

$$\frac{[Cu(CN)_3^{--}][CN^-]}{[Cu(CN)_4^{---}]} = k_2 \qquad [58]$$

The ratio of k_2 to k_1 will be used in the following derivations. The value of k_2 was calculated earlier; see Eq. [25].

$$\frac{k_2}{k_1} = K \qquad [59]$$

K is a number larger than unity, when the instability constant, k_1, for the formation of the first complex is smaller than that for the succeeding complexes.

In terms of concentrations, Eq. [57] and [58] are written as follows

$$(y - \bar{a} - b)(x - \bar{a} - 2b) = \bar{a}k_1 \qquad [60]$$

$$\bar{a}(x - \bar{a} - 2b) = bk_2 \qquad [61]$$

where y = moles of $Cu(CN)_2^-$ initially used, expressed as mole/liter; x = moles of CN^-, initially added to the $Cu(CN)_2^-$, and expressed as moles/liter; $\bar{a}$ = molar concentration of $Cu(CN)_3^{--}$ formed; b = molar concentration of $Cu(CN)_4^{---}$ formed. Note that the formation of 1 mole of $Cu(CN)_3^{--}$ removes only one mole of $Cu(CN)_2^-$ and one mole of CN^-, whereas the formation of one mole of $Cu(CN)_4^{---}$ removes two moles of CN^-.

Equations [60] and [61] involve three unknowns, $\bar{a}$, b, and k_1 (k_2 is known); and at least one more equation is required for calculating them.

Two additional equations are derived from the first and second derivatives of $\bar{a}$ or b with respect to x.

Divide Eq. [60] by Eq. [61] to give Eq. [62], which does not contain x

$$(y - \bar{a} - b) = \frac{\bar{a}^2}{bK} \qquad [62]$$

Equation [62] is differentiated with respect to x, considering both $\bar{a}$ and b as dependent variables

$$-\bar{a}' - b' = \frac{bK(2\bar{a}\bar{a}') - \bar{a}^2 b'K}{b^2K^2} \qquad [63]$$

This equation is simplified using Eq. [62] and the approximate relation

$$-\bar{a}' = 2b' - 1 \qquad [63A]$$

to give an equation involving b'

$$b' = \frac{2\bar{a} + bK}{\bar{a}(4 - K) + Ky} \qquad [64]$$

Equation [63A] is obtained by differentiating Eq. [61]

$$1 - \bar{a}' - 2b' = k_2\left[\frac{\bar{a}b' - b\bar{a}'}{\bar{a}^2}\right] \qquad [65]$$

Since the instability constant, k_2, is a small number, for example 0.002, $1 - \bar{a}' - 2b'$ can be considered as equal to zero. This involves no appreciable error, since $\bar{a}'$ and b' cannot be determined from the experimental data with this precision.

The use of the approximation gives equations which do not fit the part of the reaction indicated by the portion of the curve g-h-i in Fig. 2. An equation for b' which does not involve the approximation and, hence, is valid for all of curve 1, was derived, but no use is made of it in this treatise.

$$b' = \frac{\bar{a}^2(2\bar{a} + bK)}{(\bar{a}k_2 + 2\bar{a}^2)(2\bar{a} + bK) - K(y - \bar{a} - 2b)(bk_2 - \bar{a}^2)} \qquad [64A]$$

With Eq. [64], three simultaneous equations are available for solving for the three unknowns. In addition an equation for b'' is obtained by differentiating Eq. [64]. After making the differentiation, the expression for b'' is simplified by use of Eq. [63A] and [64]

$$b'' = \frac{2b'(b' - 1)(4 - K) + 2}{\bar{a}(4 - K) + Ky} \qquad [66]$$

The expression in the numerator of Eq. [66] occurs frequently, hence, it will be represented by the symbol, α. Equation [66] then becomes

$$b'' = \frac{\alpha}{\bar{a}(4 - K) + Ky} \quad \text{with} \quad \alpha = 2b'(b' - 1)(4 - K) + 2 \qquad [67]$$

Equations [60], [61], [64], and [66] or [67] comprise a system of four simultaneous equations in three unknowns. These equations will next be solved for K, the ratio of k_2 to k_1. The plan of attack is to use Eq. [64] as the basis for substitutions. Values of $\bar{a}$ and b are obtained as functions of K so that the substituted equations contain only one variable, K.

The variable, b, can be obtained as a function of $\bar{a}$ and K by solving Eq. [62]

$$b = \frac{K(y - \bar{a}) \pm \sqrt{K^2(y - \bar{a})^2 - 4\bar{a}^2K}}{2K} \qquad [68]$$

The value of b from Eq. [68] is substituted into Eq. [64] and the equation is simplified to give the following

$$2b' - 1 = \frac{\sqrt{K^2(y - \bar{a})^2 - 4\bar{a}^2K}}{\bar{a}(4 - K) + Ky} \qquad [69]$$

Note that this equation contains two unknowns: K and $\bar{a}$. The value of $\bar{a}$ in terms of K is determined from Eq. [67] and substituted into Eq. [69], as follows.

First note that the denominator of Eq. [69] is readily obtained from Eq. [67]

$$\bar{a}(4 - K) + Ky = \frac{\alpha}{b''} \qquad [70]$$

Equation [70] also leads at once to an equation for $\bar{a}$ which contains only the unknown, K

$$\bar{a} = \frac{\alpha - b''Ky}{b''(4 - K)} \qquad [71]$$

Also, for substituting into Eq. [69], the value of $y - \bar{a}$ is readily obtained from Eq. [71]:

$$y - \bar{a} = \frac{4b''y - \alpha}{b''(4 - K)} \qquad [72]$$

Substitution of the values from Eq. [70], [71], and [72] into Eq. [69] gives after some simplification

$$2b'-1=\frac{\sqrt{K^2(4b''y-\alpha)^2-4K(\alpha-b''Ky)^2}}{\alpha(4-K)} \quad [73]$$

Further simplification yields

$$(2b'-1)\alpha=\sqrt{\frac{K(4b''^2y^2K-\alpha^2)}{4-K}},$$

$$\alpha=2b'(b'-1)(4-K)+2 \quad [74]$$

The value of b' is not restricted by Eq. [74], and we can select the point on the curve where $b'=0.5$. However, the value of b'' must also be taken for this same point. With $b'=0.5$, Eq. [74] takes the following simple form

$$K=16(b''y)^2 \quad [75]$$

The following discussion shows the method of evaluating b' and b'' from calorimetric data for a reaction involving the formation of two complexes. The method is similar to that given earlier for a single complex.

Relations between partial molal heat effects and the partial derivatives.—In a reaction involving the formation of two complexes by adding increments, dx, of the ligand B, part of the increment goes to form one complex and part goes to form some of the higher complex. It is assumed that a significant amount of a third complex is not simultaneously formed; hence, only the situation involving two complexes needs to be treated.

The following equations for the formation of the complexes are not given in the most general form, such as those of Eq. [39] and [40], but they are more suitable for pedagogic purposes.

$$mA+nB\rightleftarrows A_mB_n; \qquad \Delta R_1=n\theta_1 \quad [76]$$

$$A_mB_n+rB\rightleftarrows A_mB_{n+r} \text{ or } A_mB_s,\ s=n+r;\ \Delta R_2=r\theta_2 \quad [77]$$

According to the discussion in an earlier section and Eq. [17], the value of ΔH for the reaction of Eq. [76] is

$$\Delta H_1=n\theta_1\bar{a}' \quad [78]$$

where $\bar{a}'=\partial A_mB_n/\partial x$

The value of ΔH_2 for the formation of complex A_mB_s consists of two terms. The complex is considered as being formed from A and B through the intermediary of the formation of A_mB_n. The value of ΔH_2 is, therefore

$$\Delta H_2=b'(n\theta_1+r\theta_2),\ b'=\partial A_mB_s/\partial x \quad [79]$$

The total partial molal heat effect is the sum of Eq. [78] and [79].

$$\Delta H=\Delta H_1+\Delta H_2=\bar{a}'n\theta_1+b'(n\theta_1+r\theta_2)$$

In a later section, a relation is shown between $\bar{a}'$ and b' (Eq. [95]) according to which, $\bar{a}'=(1-sb')/n$

On substituting for $\bar{a}'$ in Eq. [80], the final result for the relation between the partial molal heat effect, ΔH, and b' is

$$\Delta H=\theta_1+rb'(\theta_2-\theta_1) \quad [81]$$

The value of b'' can be obtained by differentiating Eq. [81] and using the slope of the curve in the same manner as described earlier for a single complex.

Numerical calculation for the cuprocyanide system.—The equations for the cuprocyanide system were given by Eq. [22] and [23], and they correspond to Eq. [76] and [77] with $m=n=r=1$.

Since $\theta_1=10{,}000$ cal and $\theta_2=14{,}000$ cal, the value of ΔH corresponding to $b'=0.5$ is readily obtained from Eq. [81].

$$\Delta H=10{,}000+4{,}000\ b'=12{,}000 \quad [82]$$

This value of ΔH is at the midpoint of the slope.

The value of b'' is next obtained by differentiating Eq. [81].

$$\frac{\partial\Delta H}{\partial x}=rb''(\theta_2-\theta_1) \text{ or}$$

$$b''=\frac{1}{4000}\cdot\frac{\partial\Delta H}{\partial x}=\frac{1}{4000}\cdot\frac{1}{y}\text{ (Slope)} \quad [83]$$

The slope of the curve at the midpoint is 15,600 and $y=0.6$. Hence, $b''=\frac{1}{4000}\cdot\frac{1}{0.6}(15{,}600)=6.5$

Substituting this value for b'' in Eq. [75] gives

$$K=16(b''y)^2=16(6.5\times0.6)^2=243 \quad [84]$$

$$k_1=k_2/K=0.0023/243=9.5\times10^{-6} \quad [85]$$

Calculation of the instability constant by graphical means when two complexes are formed.—The algebraic solution of a set of simultaneous equations such as those presented by Eq. [60] and [61] of the previous section becomes too difficult when the concentrations are raised to a power, and a graphical method of solution is more convenient. The procedure is actually a kind of curve fitting. The instability constant, considered as a parameter, is given a series of values, and for each value a curve is calculated, representing ΔH as a function of the initial composition of the mixtures. By successive calculations a curve can be found that fits the experimental one as closely as desired. The equations for a general case are derived, but the example of the copper cyanide complexes is used to illustrate the numerical procedure.

Let the reaction of the ligand B with A be as represented in Eq. [76] and [77]. As in the previous derivations, y and x represent the concentrations of A and B expressed as molar concentrations. The following are the mass action equations

$$(y-m\bar{a}-mb)^m\ (x-n\bar{a}-sb)^n=\bar{a}k_1 \quad [86]$$

$$\bar{a}(x-n\bar{a}-sb)^r=bk_2 \quad [87]$$

In this discussion, k_2 is assumed to be known, since it can be obtained as described in the section on Relation between partial molal heat effects without the interference of the reaction of Eq. [86].

To obtain an equation not containing x, each side of Eq. [86] is multiplied by itself r times and each side of Eq. [87] is multiplied by itself n times.

$$[y-m(\bar{a}+b)]^{mr}(x-n\bar{a}-sb)^{nr}=(\bar{a}k_1)^r \quad [88]$$

$$\bar{a}^n(x-n\bar{a}-sb)^{nr}=(bk_2)^n \quad [89]$$

$$\text{Let, } (k_1)^r/(k_2)^n=1/K \quad [90]$$

Divide Eq. [88] by Eq. [89] to eliminate the expression containing x

$$\frac{[y-m(\bar{a}+b)]^{mr}}{\bar{a}^n}=\frac{(\bar{a}k_1)^r}{(bk_2)^n}=\frac{\bar{a}^r}{Kb^n} \quad [91]$$

$$Kb^n[y-m(\bar{a}+b)]^{mr}=\bar{a}^s,\ n+r=s \quad [92]$$

Differentiation with respect to x and substituting $[y-m(\bar{a}+b)]=Z$

$$nb^{n-1}b'KZ^{mr}-Km^2b^nb'rZ^{mr-1}-Km^2\bar{a}'b^nrZ^{mr-1}=\bar{s}\bar{a}'\bar{a}^{s-1} \quad [93]$$

A relation between b' and $\bar{a}'$ is obtained by differentiating Eq. [87] with respect to x

$$r(x-n\bar{a}-sb)^{r-1}(1-n\bar{a}'-sb')=k_2\frac{d(b/\bar{a})}{dx} \quad [94]$$

Since k_2 is small and the parenthesis $(x-n\bar{a}-sb)$, which represents unreacted x, is also small, then

$1 - n\bar{a}' - sb'$ can be set equal to zero. This approximation is legitimate, since the error made by this approximation in calculating the heat of reaction would not be as large as that involved in the experimental calorimetric determination, which is probably several per cent.

$$1 - n\bar{a}' - sb' = 0 \text{ or } \bar{a}' = \frac{(1 - sb')}{n} \qquad [95]$$

On substituting the expression for $\bar{a}'$ from Eq. [95] and $\bar{a}^s$ from Eq. [92] into Eq. [93] and simplifying, an expression for b' is obtained

$$\frac{1}{b'} = \frac{\bar{a}n(nZ - m^2br)}{b(sZ + m^2\bar{a}r)} + s \qquad [96]$$

The procedure of calculating a series of curves is as follows. Take a value of y which will be held constant for the whole series of curves. The variation of the composition of the solution is obtained by letting x vary. Assume a value of k_1 for a given curve. The value of k_2 is assumed known. Give b a series of values and calculate the corresponding values of $\bar{a}$ from Eq. [92] which does not contain x. Calculate the values of x from Eq. [89], using the values of $\bar{a}$ and b which have been determined. The moles per liter of the initial additions used to form the solution are now known. The value of b' is obtained from Eq. [96]. The last step is to calculate the value of the heat of reaction, ΔH, from the series of values of b' and plot a curve of ΔH *vs.* the ratio of x to y.

Examples of the graphical method applied to the copper cyanide system are given in Table I and graphed as curves 2 and 3 in Fig. 2. For the sake of simplicity, k_2 was taken as equal to 10^{-3}. The value of y (initial concentrations of $Cu(CN)_2^-$) was taken as 0.6M and considered as a constant. For given values of b, the value of $\bar{a}$ was calculated from the following equation which was obtained from Eq. [90] to [92] with $m = n = r = 1$ and $s = 2$: $\bar{a} = \frac{1}{2}[-bK + \sqrt{bK(bK - 4b + 4y)}]$. The values of x were obtained from Eq. [89] using it in the form: $x = bk_2/\bar{a} + \bar{a} + 2b$. The value of b' was calculated next, using Eq. [64]:

Table I. Illustration of the graphical method for addition of increments of CN^- to a cuprocyanide solution. Computation of curves showing the relation between partial molal heat effect, ΔH, and the $*CN^-/*Cu(CN)_2^-$ ratio of the bath

k_1^β	K^β	x	$\frac{x}{y}$	$\bar{a}$	b^β	$\bar{a}'$	b'	ΔH, kcal
10^{-5}	100	0.264	0.44	0.260	0.002	0.96	0.02	10.08
10^{-5}	100	0.4365	0.728	0.4165	0.01	0.817	0.092	10.4
10^{-5}	100	0.5097	0.85	0.4697	0.02	0.606	0.197	10.76
10^{-5}	100	0.6001	1.00	0.5	0.05	0	0.50	12.0
10^{-5}	100	0.6774	1.13	0.4772	0.10	−0.54	0.77	13.1
10^{-5}	100	0.7928	1.32	0.3923	0.20	−0.88	0.942	13.75
10^{-5}	100	0.8981	1.49	0.2971	0.30	−0.94	0.97	13.9
10^{-5}	100	1.10	1.83	0.099	0.50	−0.994	0.997	14.00
10^{-4}	10	0.294	0.49	0.255	0.02	0.682	0.159	10.63
10^{-4}	10	0.431	0.71	0.331	0.05	0.42	0.29	11.15
10^{-4}	10	0.567	0.94	0.3663	0.10	0.09	0.46	11.85
10^{-4}	10	0.743	1.24	0.343	0.20	−0.36	0.68	12.7
10^{-4}	10	0.876	1.46	0.275	0.3	−0.62	0.81	13.2
10^{-4}	10	1.16	1.94	0.05	0.55	−0.96	0.98	13.9

Data which are known: Initial $*Cu(CN)_2^-$ concentration of the bath (represented by y) was 0.6M. Instability constant, k_2, for reaction: $Cu(CN)_4^{---} \rightleftarrows Cu(CN)_3^{--} + CN^-$ was taken to be 1.0×10^{-3}, and the heat of reaction $\Delta H = -14{,}000$ cal. k_1 is the instability constant for the reaction: $Cu(CN)_3^{--} \rightleftarrows Cu(CN)_2^- + CN^-$ with the heat of reaction $\Delta H = -10{,}000$ cal.

The columns marked with β indicate values of the variables which have been assumed for purposes of calculation. The data in the other columns represent values calculated as indicated in the text.

For definition of the other variables, see text: $K = k_2/k_1$; x = initial concentration of CN^- (moles/l) used in the solution; $\bar{a}$ = concentration $Cu(CN)_3^{--}$, moles/l; b = concentration $Cu(CN)_4^{---}$, moles/l; $\bar{a}' = \frac{\partial \bar{a}}{\partial x}$; $b' = \frac{\partial b}{\partial x}$.

$$b' = \frac{2\bar{a} + bK}{4\bar{a} + K(y - \bar{a})}$$, which can be derived from Eq. [96] with the help of Eq. [92] and the relation: $Z = y - m(\bar{a} + b)$. Finally, the values of ΔH were calculated from Eq. [81] which had the form: $\Delta H = 10{,}000 + 4{,}000\ b'$. Curve 2 with the assumed value of 10^{-5} for k_1 comes closer to the experimental curve than curve 3 with $k_2 = 10^{-4}$. No attempt was made to make a closer approximation with the graphical method as the purpose here was primarily for demonstration.

Discussion

The calorimetric method for determining the composition of complexes and their instability constants is more general than any of the other methods because heat is always involved in a reaction. The method can be applied to aqueous solutions, fused salt systems, and even to gaseous systems. Not enough experience has been obtained with it to know its limitations and precision.

In comparison with Job's method of continuous variation, which is much used for determining the composition of complexes, it has a wider applicability because it can be used for systems in which more than one complex is formed. Job's method cannot in general be applied to systems which form more than one complex. This was recognized by Job himself (3b). Nevertheless, Vosburgh and Cooper (5) showed that under some circumstances information on the existence and even the composition of more than one complex in a solution could be obtained by measurements of light absorption, using light of various wavelengths. However, Job's method used in conjunction with calorimetric measurements would not show the existence of more than one complex. For example, application of Job's method to the copper cyanide system would lead to only one maximum. This is illustrated by curve 4 in Fig. 2 which shows the results that would have been obtained by Job's method. These data were obtained by calculation from the data of the method of increments.

The calorimetric method bears a resemblance to thermometric titrations. There are some differences in the experimental procedures, but the main difference is in the analysis of the data. In both methods successive increments of one of the reactants are added to the reaction mixture. However, the thermometric method is actually an integral method, because the datum which is plotted is the extent of the temperature rise that has occurred since the initiation of the experiment with the addition of the first increment. In the calorimetric method, a difference of temperature is measured, and the ideal is to keep the system at almost constant temperature by adding a small increment; furthermore, the system must be allowed to return to its initial temperature before another increment is added. The variation of the heat effects are opposite in the thermometric and calorimetric methods. Consider the addition of increments of a strong acid reactant to a system consisting initially only of a strong alkali, until neutralization is accomplished. In the thermometric method, the plot of temperature against additions would show a steeply rising curve until the neutralization point were reached, beyond which the curve would be constant. In the calorimetric method, the curve of partial molal heat effect against composition would be horizontal until the neutralization point was reached, beyond which point, the curve would sharply fall to zero.

The following values of 25°C of the instability constants of the complex cyanide ions were obtained with the method of increments

$$\frac{[Cu(CN)_2^-][CN^-]}{[Cu(CN)_3^{--}]} = k_1 = 1.0 \times 10^{-5}$$

$$\frac{[Cu(CN)_3^{--}][CN^-]}{[Cu(CN)_4^{---}]} = 2.3 \times 10^{-3}$$

Penneman and Jones (6) obtained similar values, $k_1 = 1.5 \times 10^{-5}$ and $k_2 = 5.7 \times 10^{-3}$, for 25°C by observing the infrared absorption spectra of the compounds in order to establish their concentration in solution. Rothbaum (7) obtained the following values for 20°C by measurement of the electrode potentials of copper in cyanide solutions

$$k_1 = 1 \times 10^{-5} \text{ to } 5 \times 10^{-5} \qquad k_2 = 5 \times 10^{-2}$$

Of these methods, the measurement of electrode potentials is the least satisfactory, as there is doubt that the potential is reversible and that it actually represents the assumed reaction. The method of Penneman and Jones required that various complex compounds be prepared so that their absorption spectra could be obtained. The detection of the $Cu(CN)_2^-$ ion was not feasible because of its low relative absorption coefficient, and the concentration of this ion and also of the cyanide ion had to be obtained by difference. In comparison, the method of increments did not require the isolation of any of the complexes.

Acknowledgment

The author wishes to acknowledge the assistance of J. M. Sherfey who did the laboratory work on the calorimetric measurements of the cuprocyanide system, and the interest and support of Fielding Ogburn in the calculations. The author also wishes to thank the Division of Research, Chemistry Branch, Atomic Energy Commission, for their continuing support of the project on electrochemical calorimetry of which project this research is a byproduct.

Manuscript received Aug. 17, 1964; revised manuscript received Nov. 9, 1964.

Any discussion of this paper will appear in a Discussion Section to be published in the December 1965 JOURNAL.

REFERENCES

1. F. J. C. Rossotti and H. Rossotti, "The Determination of Stability Constants and other Equilibrium Constants in Solution," McGraw-Hill Book Co., New York (1961); H. L. Schläfer, "Complex Formation in Solution. Methods for the Determination of the Composition and Stability Constants of Dissolved Complex Compounds," Springer, Berlin (1961).
2. K. B. Yatsimirskii and V. P. Vasil'ev, "Instability Constants of Complex Compounds," Pergamon Press, Oxford, New York (1960); Stability Constants. Part II, Inorganic Ligands, J. Bjerrum, G. Schwarzenbach, L. G. Sillen. Special Publication No. 7, The Chemical Society, Burlington House, London W.1.
3a. P. Job, *Ann. Chim.*, [10] **9**, 113 (1928); Compt. rend., **180**, 928 (1925).
3b. *Ann Chim.*, [11] **6**, 97 (1936).
4. J. M. Sherfey and A. Brenner, *This Journal*, **105**, 660 (1958).
5. W. C. Vosburgh and G. R. Cooper, *J. Am. Chem. Soc.*, **63**, 437 (1941).
6. R. A. Penneman and L. H. Jones, *J. Chem. Phys.*, **24**, 293 (1956).
7. H. P. Rothbaum, *This Journal*, **104**, 682 (1957).

The Utilization of Thermogalvanic Cells for Studying the Freezing of Electrolytic Solutions and Ion Migration in Ice

Minas Ensanian

Physical Chemistry Group, Bell Aerosystems Company, Buffalo, New York

ABSTRACT

Ion transport during the freezing of electrolytic solutions to dry ice temperatures has been followed by means of a thermogalvanic cell. The low-temperature limit of an operating cell depends primarily on ion size and polarizability. Unexplained low-temperature changes in electrode polarity as well as spontaneous outbursts of energy have been observed. The technique offers a method for studying the ion-rejection process at an advancing ice-liquid interface as well as ion migration through ice.

With respect to the demineralization of saline water by the freezing method it is known that an ion-rejection process (1, 2) is in operation at the advancing solid/liquid interface. Although a number of studies have appeared in related areas such as the electrical conductivity of ice, etc. (3-20) the literature with respect to this problem is severely limited and the mechanisms and phenomenon poorly understood.

This communication summarizes an exploratory examination of beryllium, aluminum, iron, copper, magnesium, zinc, tin, and lead thermogalvanic cells in which the electrolyte surrounding one of the electrodes is gradually frozen. The principle objective was to ascertain the feasibility of using a thermocell as a tool for the investigation of ion migration during the freezing of electrolytic solutions and subsequently in the resulting doped ice.

In spite of difficulties that are inherent in the study of any nonequilibrium system the experimental results, although preliminary, are nevertheless of such a nature as to strongly demonstrate the potential of the thermocell approach.

Experimental Procedure

The thermogalvanic cells consisted simply of a very large Pyrex U-tube which contained about 400 ml of electrolyte and at whose ends were two identical electrodes partially immersed in the electrolyte. The metal electrodes approximately (1/64 x 1/2 x 3 in.) were made from available sheet materials and cleaned by standard procedures. In one case the electrode was placed against a thin tipped glass tube containing a chromel-alumel thermocouple and positioned in the center of the arm with a minimum distance slightly more than ¼ in. from the glass wall.

The other electrode which remained at ambient temperature was attached in a similar manner to a mercury thermometer. Temperature measurements were made at the tips of the electrodes which were 34 in. apart.

All emf's were measured by L&N null and thermocouple potentiometers and precautions were taken to insure against metallic thermocouple effects.

The cold arm of the U-tube was surrounded by a polyethylene jacket which extended about ½ in. above and 2½ in. below the level of the electrode and which was kept firmly packed with powdered dry ice. The electrolytes were 0.1M solutions of reagent grade beryllium, aluminum, iron(ic), copper(ic), magnesium and zinc sulfates except for tin(ous) chloride and lead nitrate. In the case of the tin salt a well mixed 400 ml suspension of an equivalent amount of material was

used although a large part of the suspension settled at the bottom of the U-tube, no such settling was observed with the nonacidified iron salt which appeared to be in solution. No acids were added to these solutions which along with the electrodes were newly made for each experiment.

An experiment would commence on packing the jacket (about 30 min after insertion of the electrodes) with about 2500g of powdered dry ice. Due to factors such as dry ice evaporation and recrystallization repacking was necessary during the course of an experiment, and since it was important to standardize the freezing rate the problem was minimized by a slow continuous packing and it was found that the vibrational effects in so doing had no effect on the potentials. Minor temperature variations as a result of this purely mechanical (packing) factor are not serious unless they occur at what may be termed "cut-off" (T_o) or "transition temperatures" (T_t) and although difficult to reproduce may be defined as follows. (T_o) denotes that temperature at which the output potential and current become zero, *i.e.*, the thermocell is no longer operative so long as the cold electrode is at that temperature or lower. The latter term (T_t) refers to that temperature at which a polarity change is observed, *i.e.*, when both the potential and current drop to zero and then rise again; however, in so doing the polarity of the cold and hot electrodes of the cell have changed with respect to their original connections with the positive and negative posts of the potentiometer.

Experimental Results

Some experimental results are shown, and in Tables I and II the values represent the average of three experiments.

During a 4-hr period the ambient temperatures (T_2) never varied more than ±2°C. The polarity for the cold and hot arms of the cell refers to the positive and negative terminals of the potentiometer prior to any low temperature transitions where such occurred. At times, as the electrodes were placed in the solution, one or two polarity changes would occur, and although the solutions were not made acidic, these were probably due to invisible gas films or local cell effects on the metal surfaces, since experiments conducted, *e.g.*, with magnesium in very weak acid solutions, displayed polarity changes (as a result of some gas evolution) which were almost oscillatory in nature while the temperature differential maintained between the electrodes was negligible.

However, the polarity would immediately stabilize after the jacket was packed with dry ice. For the systems studied the average time to freeze was 19 min and the average freezing temperature was 7°C.

At temperatures below —30°C both beryllium and tin were found to be quite sensitive to minor temperature variations (± 2°C). Tin exhibits numerous outbursts of energy if the freezing operation is interrupted, *i.e.*, if the temperature is held constant for several minutes then followed by a 1° or 2° rise. Plots of output voltage *vs.* temperature for both metals under these circumstances are almost periodic with pronounced dampening in the beryllium curve.

For example, if the emf of the tin thermocell at —34°C is 90 mv, then temperature stabilization will produce a rapid decay and reduce the voltage to zero. When this is followed by a slight rise in temperature several minutes later, the emf suddenly exceeds 0.1v and again decays to zero on temperature stabilization. This has been tested at lower temperatures and confirmed in view of profound experimental difficulties associated with temperature control. However, if freezing proceeds uninterrupted (continuous packing of the dry ice is necessary) the cell voltage is reasonably stabilized approximately up to the apparent cut-off temperature.

Under the experimental conditions described here great difficulty was encountered in attempting to cool the tin cell below —70°C, and it is quite possible that the system will continue to operate at considerably lower temperatures; the same may be true of beryllium.

Another interesting factor is that when a system is "thermally shocked," *i.e.* by a sudden removal of the dry ice when the thermocell is at a low temperature (see Shock Temperature in Table III), the established zero potential state or the absence of any voltage may persist from 2-25 min, after which the voltage suddenly switches back on. Although there is no strong evidence as yet, there seems an indication that except perhaps for iron and tin (whose duration is short) the duration of the zero potential state is remarkedly uniform, *viz.*, around 15 min. However, a longer period is generally required to attain the voltages and respective temperatures shown in Table III. As a result of thermal shocking one of two things may occur, *viz.*, the high voltage may persist through the phase transition or it may begin to decay within 10° or 20° of the freezing point and finally cut-off near 0°C followed by a polarity change, although producing negligible voltage.

In this respect the iron thermocell has on several occasions exhibited an extraordinary behavior in that,

Table I. Observed polarity, cut-off, and transition temperatures for the systems studied

Electrode system	Radii of ion, A	(T_o) °C	(T_t) °C	Polarity Cold elect.	Polarity Hot elect.	Function of the cold electrode
Beryllium (2+)	0.34	−70	−38 −60	+	−	Cathode
Aluminum (3+)	0.57	−63		+	−	Cathode
Iron (3+) (2+)	0.67 0.83	−60	−41 −60	+	−	Cathode
Copper (2+)	0.70	−45	−33 −45	−	+	Anode
Magnesium (2+)	0.78	−22		−	+	Anode
Zinc (2+)	0.83	−9		−	+	Anode
Tin (2+)	1.12	−70		−	+	Anode
Lead (2+)	1.20	−29	−7	−	+	Anode

Ionic radii are taken from Goldschmidt (21). Ambient temperatures were generally 25°C. Be, Fe, and Cu systems displayed two low-temperature polarity transitions.

Table II. Magnitudes of potentials before and after freezing

Electrode system	Maximum observed potential before freezing, mv	Temp, °C	Highest observed potential after freezing, mv	Temp, °C
Be	100	12	100	12
Al	275	9.5	375	−12
Fe	7	12	50	−28
Cu	9	7.5	21	−27
Mg	40	9	40	9
Zn	9	12	13	6.3
Sn	9	8.5	90	−34
Pb	2	9	27	−23

Table III. Thermal shock temperatures and potentials

Electrode system	Shock temp, °C	Voltage, mv	Temp, °C
Be	−69	>100	−10
Al	−78	500	−8.5
Fe	−74	100	−7
Cu	−37	13	−8
Mg	−30	60	0
Zn	−30	14	0.5
Sn	−70	14	−8.8
Pb	−50	14	−1.2

under conditions of thermal shock (which induces defects within the crystal lattice and thus facilitates diffusion), the polarity transition has occurred almost at the same temperature as when the heating rate was considerably slower, *i.e.*, during the initial cooling. During thermal-shock experiments no unusual colorations were noticed in ice in the region of the electrode at the time the dry ice was removed, except for a dark blue color of short duration in an isolated case with copper; however, the possibility exists. Likewise it was not possible to determine the effects of the cracking (noise resulting from expansion) on the potential in the absence of an automatic recording device.

Discussion

Neglecting for the moment any chemical factors associated with the phenomena of impurity accommodation within the ice lattice, one may expect some correlation between (T_o) and the ionic radii as is shown in Table I. The behavior of beryllium and tin are to be expected in view of beryllium's small size and tin's very high polarizability.

The relatively low cut-off temperature for lead (as compared with magnesium and zinc) is also a reflection of polarization phenomena.

On the assumption that cation-migration through ice is somehow related to the ionic-potential (after Cartledge) (22) then (T_o) should decrease in the same order as the electrode metals are listed, with beryllium having the lowest cut-off temperature and lead the highest. This would be true if migration depended solely on the ability of the cation to polarize the susceptible O^{2-} ion and might help to explain the rather close proximity of beryllium, aluminum, and iron in Table I.

One may draw an analogy between ice and quartz on the assumption that ice has a quartz-like structure, *i.e.*, by substituting the oxygen atoms for the silicon in quartz although the hydrogens do not bond the oxygens in the same rigid manner. The comparative role of ionic potential for rigid and nonrigid oxygen bonding may be shown by comparing this work with that of Gibson and Vogel (23) who found that Li^+ moves much more easily through crystalline quartz than do Na^+ and Cu^+, while Mg^{2+}, although smaller than Na^+, scarcely moves at all.

The fact that the cells are operative at low temperature would seem to indicate the existence of discrete water molecules (24) in the ice.

Again on the basis of ionic potential in this investigation, copper, magnesium, and zinc fall into the proper order.

When negligible current is drawn the total voltage (E_t) produced by a thermogalvanic cell is given by (dE/dt) (T_2-T_1) and therefore, the output should increase with an increase in the temperature differential. However, on the assumption that the freezing process will interfere with ion migration and the formation of ice (via the ion-rejection mechanism) will deplete ion concentration, one would expect a potential drop (during the freezing cycle) just prior to solidification, but this is not always the case. In fact, the stability of the voltage during the phase transition (liquid to solid) is at times remarkable and particularly in the case of beryllium and tin the experimental voltages are greater at the freezing point than the theoretical based on the above expression. The magnitudes of the potentials before and after freezing are shown in Table II.

With respect to hysteresis (reversibility of emf, temperature plots) the reproducibility of a transition temperature (polarity change) ordinarily could only be expected (during a warm-up period) if the heating and freezing rates were equal in view of the residual entropy of ice, since the crystal can exist in any one of a large number of configurations, each corresponding to certain orientations of the water molecules.

In view of the scarcity of data truly characteristic of the systems studied, the results are too complicated for a ready interpretation of the mechanism of the observed low-temperature polarity transitions.

A polarity transition denotes a change in the sign of the current transporting species (analogous to the sign of the Hall constant of a semiconductor) and the phenomena may be a reflection of elastic relaxation in the crystalline material resulting in a molecular reorientation and therefore, in spite of steric factors (ionic radii) the possibility of "anionic conduction" exists.

Quartz and lead iodide, for example, display anisotropy in their conductivity, and in the latter the anisotropy is several powers of ten at low temperatures and is temperature dependent.

If the observed transitions are due to processes at the electrode surface or are interfacial in nature, then they might be associated with the bursting of surface films or some type of semiconductor phenomena at the interface (metal/doped ice) irrespective of the multiplicity of the low temperature polarity transitions, *e.g.*, at −38° and −60°C for beryllium.

In an isolated incident a copper thermocell, after being at (T_o) for about 5 min displayed an outburst of energy exceeding by a factor of 10 any previously recorded voltage with this system in this investigation.

The origin of the factor responsible for the observed transitions may possibly be ascertained by the symmetry of voltage-temperature plots in the transition region, *i.e.*, whether the curves are parabolic. This would entail refined automatic recording equipment as well as means for greater temperature control.

The iron and copper curves in the transition region, although plotted from limited and preliminary data, appear to exhibit symmetry, and on this basis one may conclude that the phenomena resides within the ice.

Numerous questions however remain to be answered, *viz.*, the effects of degassing the electrolyte and the use of an inert gas atmosphere, characterization of the metals and their surfaces, changes as a result of varying the anion of the salt, pH, the effects of variations in the length of the ice below the electrode and thermal gradients and concentration gradients.

With respect to these considerations and the fact that the experimental work was carried out under conditions where temperature regulation and the measurement of potential and temperature was done manually, the experimental error may be considerable. Nevertheless, in terms of the desired objective, the value of the approach has been demonstrated. It is possible that, if the freezing and heating rates are extended to periods of several days or longer and with a fair degree of temperature control, one may reasonably expect data that will lead not only to a better understanding of the phenomena involved during the freezing of electrolytic solutions, but perhaps to the nature of the ion rejection as well. There is no reason to believe that with some ingenuity, perhaps entailing a high-pressure electrode, even hydrogen ion migration through ice cannot be investigated by this technique.

Returning to the problem of the desalination of sea water by the freezing process, if the observed outbursts of energy reside in the bulk of the ice, then with regard to the large-scale demineralization of salt water, the remote possibility arises of recovering some of the spent energy by taking advantage of the thermoelectric properties of ice. After all, thunderstorm electricity (25) is somehow associated with the freezing of water droplets, thermal gradients, and charge separation.

Conclusion

1. These experiments indicate that the thermocell approach can be developed into a method for studying the freezing of electrolytes and ion migration in ice.

2. Thermogalvanic action in dilute electrolytes has been shown to persist near dry ice temperatures, ion size and polarizability being important.
3. Although the evidence is limited it appears that low-temperature polarity transitions are a bulk rather than a surface phenomena.
4. Outbursts of energy at low temperatures may be indicative of cooperative relaxation processes in ice.
5. The observed increase in ion migration as the result of a slight temperature rise in the doped ice seems reconcilable with the known fact that water from aged arctic ice is potable, the older ice having experienced two or more warm-up periods.
6. Future refinements of this work must consider the nature of the electrode surface with regard to nucleation and growth of ice crystals.

Acknowledgment

The author is grateful to Robert T. Foley for his introduction to the subject of thermogalvanic potentials. This study has proceeded only because of his complete cooperation and that of Robert E. Salomon and William Rogers, Jr. Suggestions from Alfonso R. Gennaro and André J. de Bethune are gratefully acknowledged. The author is indebted to C. Roland Eddy for an interesting discussion concerning the origin and nature of the observed polarity changes and to the Leeds & Northrup Company for the loan of a potentiometer, and lastly, Charles Counts for assistance in the laboratory.

The initial phase of this work was done at Melpar, Incorporated, and Temple University.

Manuscript received June 2, 1964; revised manuscript received Nov. 23, 1964.

Any discussion of this paper will appear in a Discussion Section to be published in the December 1965 JOURNAL.

REFERENCES

1. T. G. Thompson and K. H. Nelson, *Sears Foundation J. Marine Research*, **13**, 2 (1954).
2. J. P. Lodge, M. L. Baker, and J. M. Pierrard, *J. Chem. Phys.*, **24**, 716 (1956).
3. E. J. Workman and S. E. Reynolds, *Phys. Rev.*, **78**, 3 (1950).
4. R. S. Bradley, *Trans. Faraday Soc.*, **53**, 687 (1957).
5. F. Heinmets, *Nature*, **188**, 925 (1960).
6. E. J. Murphy, *Phys. Rev.*, **79**, 203 (1950).
7. N. V. Cohan, M. Cotti, J. V. Iribarne, and M. Weissmann, *Trans. Faraday Soc.*, **58**, 490 (1962).
8. A. Spernol, *Z. Elektrochem.*, **59**, 31 (1955).
9. E. W. B. Gill and G. F. Alfrey, *Brit. J. Appl. Phys. Suppl.*, **2**, S. 16 (1953).
10. L. Onsager and M. Dupuis, "Thermodynamics of Irreversible Processes," p. 294, "The Electrical Properties of Ice," Rendiconti della Scuola Internazionale di Fisica Enrico Fermi, Corso X. Bologna: Zanichelli (1960).
11. Ad. Steinmann, *Helv. Phys. Acta*, **30**, 581 (1957).
12. F. Humbel, F. Jona, and P. Scherrer, *ibid.*, **26**, 17 (1953).
13. J. C. Decroly, H. Gränicher, and C. Jaccard, *ibid.*, **30**, 465 (1957).
14. C. Jaccard, *ibid.*, **32**, 89 (1959).
15. M. Eigen, L. De Maeyer, and H. Ch. Spatz, *Ber.*, **68**, 19 (1964).
16. J. D. Dunitz, *Nature*, **197**, 860 (1963).
17. B. Cleaver, E. Rhodes, and A. R. Ubbelohde, *Discussion Faraday Soc.*, **32**, 210 (1961).
18. S. A. Rice, *ibid.*, **32**, 181 (1961).
19. A. Klemm, *ibid.*, **32**, 203 (1961).
20. A. S. Dworkin, H. R. Bronstein, and M. A. Bredig, *ibid.*, **32**, 188 (1961).
21. V. M. Goldschmidt, *Chem. Ber.*, **60**, 1263 (1927).
22. G. H. Cartledge, *J. Am. Chem. Soc.*, **52**, 3076 (1930).
23. G. Gibson and R. C. Vogel, *J. Chem. Phys.*, **18**, 1094 (1950).
24. L. Pauling, *J. Am. Chem. Soc.*, **57**, 2680 (1935).
25. J. Latham, *Nature*, **200**, 4911 (1963).

Technical Notes

Improved Techniques for Acid Polishing and Forming Etch Pits at Dislocations on the (100) Face of Copper Crystals

Lawrence D. Dyer

Research Laboratories, General Motors Corporation, Warren, Michigan

The purpose of this note is to report two useful improvements in the methods of surface preparation and characterization of copper single crystals. The first is an addition of phosphoric acid to the cupric chloride polishing solution of Young (1). This improvement gives a surface sufficiently smooth to reduce the electropolishing time to as little as ½ min. The second is an electrochemical technique for forming excellent dislocation etch pits on the (100) face. The etching is carried out in the same phosphoric acid solution in which the crystal is electropolished, thereby avoiding the possibility of contamination in transferring the crystal from one vessel to another.

Sample Preparation

The test samples were single crystals of copper in the shape of bars ½ x ¾ x 2½ in. cemented to ⅛ in. thick glass slides with a commercial cyanoacrylate resin. They contained 1.5 to 3 x 10^4 dislocation sites/cm^2 on their (100) working surfaces (2). Prior to electropolishing, the orientation of the (100) planes of each crystal was determined to within 0.01° relative to the actual surface of the sample (3). Then each crystal was polished to this (100) orientation in an acid polishing machine (4), and the final smoothing was done electrolytically in a bath of 60% orthophosphoric acid.

Acid Polishing Improvement

During the initial polishing, it was sometimes necessary to remove a wedge of material up to 0.10 in. thick in order to obtain a surface of the desired orientation. To accomplish this in a reasonable time, concentrated hydrochloric acid saturated with $CuCl_2 \cdot 2H_2O$ was used. At this stage the surfaces of the crystals were rather rough and would require 20-40 min elec-

tropolishing to reach a usable smoothness. It was found empirically that a particularly smooth surface could be obtained in all subsequent acid polishing of a given sample by using an acid polishing solution of 70 g/liter $CuCl_2 \cdot 2H_2O$ in a 2:1 mixture of concentrated hydrochloric acid and 85% orthophosphoric acid. This solution removes material about 1/3 as fast as the concentrated solution. Either solution is continually depleted in cupric ion concentration as polishing proceeds, but the proper cupric ion concentration may be restored by additions of 30% H_2O_2 (5). After acid polishing with the solution that is more dilute in copper, the surface of the crystal in the electropolishing bath becomes bright very quickly and is usable at 30 sec elapsed time. However, we usually continue the electropolishing for a total of 3 min to allow additional smoothing to occur. The reduction in electropolishing time from the former 30 min to the present 3 min is particularly important when it is desired to reduce the rounding of edges and the amount of removed material.

Formation of (100) Etch Pits

The advantages of electrochemical methods for forming etch pits at dislocations have been described by Bertocci, Hulett, and Jenkins (6), who reported success with such a method for the (111) face of copper using acid chloride-bromide solutions. Some dislocation etch pits were also observed for (100) and (110) surfaces, but the occurrence of random faceting with the chloride-bromide solutions made interpretation difficult. In the process of trying to make these solutions work better on the (100) face, the present electrochemical method was discovered. It was noticed that in certain circumstances dislocation etch pits appeared even in the phosphoric acid electropolishing bath before subjecting them to the acid chloride-bromide electrochemical etch. A necessary condition was that the phosphoric acid polishing bath be quite low in copper concentration. While etching at a single voltage gave satisfactory etch pits, the background roughness was always unacceptable. However, it was discovered that a proper sequence of two voltages and etching times eliminated the objectionable background roughness while producing satisfactory etch pits. This method is reminiscent of the transient electroetching technique originally used by Young (7) for revealing dislocations in impure copper crystals. Optimum combinations of voltages and times were established at $v_1 = 0.3$-0.5v, t_1, 50-60 sec, and $v_2 = 1.0$-1.3v, $t_2 = 30$-45 sec depending on the size of pits desired. This set of voltages and times depends slightly on the concentration of cupric ion in the phosphoric acid polishing bath and on the rate of stirring, if any. The method fails to work entirely when the bath becomes more concentrated than 0.05M in cupric ion, in agreement with the work of Bertocci, Hulett, and Jenkins (6) on the (111) face in acid chloride-bromide solutions. The pits are similar to those observed on LiF by Gilman (8), fresh dislocations appearing as small, shallow but sharp pyramids. Aged dislocations appear as large deep pyramids. Flat-bottomed pits of both kinds appear and can probably be interpreted as dislocations that have moved or no longer have a component perpendicular to the (100) surface (9). Since the crystal is not transferred from the electropolishing bath to a separate etching solution in this method, it has the advantage of avoiding the possibility of picking up a film of contaminant from the atmosphere or from the surface of either solution. With this method, some background etching occurs and some nondislocation etch pits form around large pits, but these can be distinguished from those at fresh dislocations; the former are extremely shallow compared with the other types, and the latter are arranged in flow patterns downstream from the large pits. The new method gave pits that were smaller and more uniform than those obtained with the ferric chloride etch so that the newer method has a greater resolution of fine details. Etch pit counts on several crystals by the two methods gave the same results.

In practice it has been possible to start with a solution of 0.01M copper in 60% orthophosphoric acid and to use it for extended periods for both dislocation etching and electrolytic polishing. When the solution becomes about 0.04M in copper, it may be reduced to 0.01M by replacing ¾ of it with 60% orthophosphoric acid.

Manuscript received Jan. 7, 1965.

Any discussion of this paper will appear in a Discussion Section to be published in the December 1965 JOURNAL.

REFERENCES

1. F. W. Young, Jr., and T. R. Wilson, *Rev. Sci. Instr.*, **32**, 559 (1961).
2. L. D. Dyer, *J. Appl. Phys.*, In press.
3. L. D. Dyer, *Rev. Sci. Instr.*, Submitted for publication.
4. L. D. Dyer, *ibid.*, **34**, 1114 (1963).
5. F. W. Young, Jr., Private communication.
6. J. Bertocci, L. D. Hulett, and L. H. Jenkins, *This Journal*, **110**, 1190 (1963).
7. F. W. Young, Jr., *J. Appl. Phys.*, **28**, 787 (1957).
8. W. G. Johnston and J. J. Gilman, *ibid.*, **30**, 129 (1959).
9. F. W. Young, Jr., *ibid.*, **32**, 1815 (1961).

Note on Single Crystalline Calcium-Aluminate, $Ca_{12}Al_{14}O_{33}$

L. H. Brixner

Pigments Department, Experimental Station, E. I. du Pont de Nemours & Company, Wilmington, Delaware

In the CaO/Al_2O_3 phase diagram shown by Lea (1) the compound $6CaO \cdot 7Al_2O_3$ is listed as the one with the lowest melting point, about 1450°C. This is a temperature at which the Czochralski crystal growing technique should be particularly suitable if the composition melts congruently and has no disruptive phase changes between the melting point and room temperature. The fact that, according to Swanson (2), $Ca_{12}Al_{14}O_{33}$ is cubic should also make it an interesting novel host crystal for lasers if indeed good-sized single crystals could be grown.

We set out, therefore, to study the growth characteristics of this compound as well as the fluorescent emission of some rare earth ions incorporated in $Ca_{12}Al_{14}O_{33}$. Valence compensation can be achieved according to $Ca^{+2}{}_{12-2x}Ln^{+3}{}_xNa^{+1}{}_xAl_{14}O_{33}$. The fact that Cr^{+3} might also substitute for Al^{+3}, as in $Ca_{12}{}^{+2}Al_{14-x}{}^{+3}Cr_x{}^{+3}O_{33}$ makes this host especially interesting, particularly in view of the fact that Kiss (3) has just demonstrated a cross pumped laser using an yttrium aluminum garnet crystal doubly doped with Cr^{+3} and Al^{+3}. However, both garnets, $Ln_3Al_5O_{12}$, and simple rare earth aluminates of the type $LnAlO_3$ melt considerably higher than $Ca_{12}Al_{14}O_{33}$ and generally require the Verneuil technique for the preparation of large crystals.

Single crystal growing experiments with $Ca_{12}Al_{14}O_{33}$ were carried out with a 25 kw Westinghouse radio-frequency generator (450 kc/sec) as a power source. An automatic radio-frequency voltage controller regulating to 2.5% was used in conjunction with the generator. The melt was contained in a pure Ir crucible

of 40-mil wall thickness. The melting point as observed with an optical pyrometer was 1470°C, which is probably 20°-30°C low. The vapor pressure at the melting point is low and crystals up to 4 or 5 in. in length and ½ in. in diameter were readily pulled at speeds from ½ to 1 in. an hour. At slow rotation rates of about 10-60 rpm, the cross section of the crystals had essentially triangular symmetry, whereas at high rotation speeds it was almost round.

Crystals were invariably slightly orange or greenish in color, and to date we have not been able to grow completely colorless crystals, although Linde's best grade of Al_2O_3 and Baker and Adams Special Reagent grade $CaCO_3$ were used as starting materials. Since the Al_2O_3 is of a quality which produces colorless sapphire, we suspect that the source of impurities is associated with the $CaCO_3$, and further purification of this chemical seems necessary. Since the growth rates so far employed for the preparation of the single crystals have been fairly rapid (½-1 in./hr) an alternate explanation for the coloration would be defects generated to minimize any produced strain.

Laue back reflection photographs confirmed the single crystal nature of the pulled rods and the lattice parameter of 11.984Å derived from an x-ray powder diagram is in good agreement with the data given in (2). X-ray fluorescence analysis gave 48.63% CaO, 51.30% Al_2O_3 (calc. 48.53% CaO; 51.47% Al_2O_3). Semiquantitative spectrographic analysis showed Si (300 ppm), Ba (20 ppm), Fe (100 ppm), and V (50 ppm) in detectable quantities. Of these, Fe or V particularly could have been the source of the coloration of the crystals.

The thermal conductivity of single crystalline $Ca_{12}Al_{14}O_{33}$ was measured by an absolute technique and found to be 28.6 mw/cm-deg in the growth axis direction. The hardness, measured with a Reichert microhardness tester, was 6.9 on Mohs scale. Fluorescent emission (excited with 2537Å uv radiation) as a function of activator concentration was determined for the $Ca_{12-2x}Tb_xNa_xAl_{14}O_{33}$ and $Ca_{12-2x}Eu_xNa_xAl_{14}O_{33}$ systems. The typical green Tb^{+3} emission occurred in three lines centered around 485, 538, and 573 mμ, with the 538 mμ line being the most intense. Optimum quantum yields were observed at $x = 3$, which corresponds to 28.2 w/o (weight per cent) Tb, an exceptionally high optimum activator concentration for Tb. The europium emission centered around 590 mμ and 610 mμ with the shorter emission being more intense. Optimum emission occurred with the composition $Eu_3Na_3Ca_6Al_{14}O_{33}$, which contains 27.2% Eu.

More work with these systems seems indicated, particularly in view of the close structural and compositional relationship between the garnets such as $Y_3Al_5O_{12}$ ($a_o = 12.01$Å) and $Ca_{12}Al_{14}O_{33}$ ($Ca_4Al_{3.66}O_{11}$) with an a_o of 11.98Å.

Acknowledgment

The assistance of Mr. F. Walls in growing the single crystals is greatly appreciated.

Manuscript received Feb. 18, 1965.

Any discussion of this paper will appear in a Discussion Section to be published in the December 1965 JOURNAL.

REFERENCES

1. F. M. Lea, C. H. Desch, "The Chemistry of Cement and Concrete," 2nd ed., p. 52, Edward Arnold Co., London.
2. ASTM File Card #9-413, Ref. *Natl. Bur. Standards Circ. 539*, **9** (1959).
3. Z. T. Kiss and R. C. Duncan, *Appl. Phys. Letters*, **5**, 200 (1964).

Chromium Fluorescence in the $LaAlO_3$-$LaGaO_3$ System

R. Mazelsky and R. Ohlmann

Research Laboratories, Westinghouse Electric Corporation, Pittsburgh, Pennsylvania

A careful structural examination has been made of the rare earth perovskite-type compounds, ABO_3, where the oxidation state of the A and B ions are three. Of particular interest in this paper are $LaAlO_3$ and $LaGaO_3$. Geller (1, 2) has examined these compounds and has found that, at room temperature, they are rhombohedral and orthorhombic, respectively. It has been reported (3-5) that $LaAlO_3$ is a suitable matrix for examining the fluorescent properties of the rare earth and transition metal ions, such as neodymium and chromium since they can be incorporated substitutionally over a large concentration range. In this paper the fluorescence of chromium ions in $LaAlO_3$, $LaGaO_3$, and in solid solutions of the two is reported with emphasis on the variation of fluorescence as the Al/Ga ratio is changed.

The compounds were prepared from 99.99% Lindsay La_2O_3 and Linde optical grade Al_2O_3. The Ga_2O_3 was prepared from 99.9999% gallium metal purchased as the oxide from Alcoa. The materials were prepared from the powders by firing intimate mixtures at 1400°-1500°C. In all cases, within the limits of the sensitivity of x-rav powder diffraction, the materials were single phase. Lattice parameters were calculated from the high-angle reflections and were uncorrected for absorption. The fluorescence spectra were obtained using a one-meter Jarrell-Ash Company spectrometer, the samples being excited by an AH-6 mercury lamp with a $CuSO_4$ solution filter. All optical measurements were made on samples in which 0.5% of the B site ions were replaced by chromium.

The variation of the cube root of the volume with composition is shown on the upper curve of Fig. 1. There is a linear dependence until the composition reaches approximately 80% $LaGaO_3$ at which point there is an anomalous expansion. The lower section of Fig. 1 shows the fluorescence maxima splitting and line shape of the R-lines as a function of composition. There is a regular increase of the energy of the fluoresence peak as the concentration of gallium increases. $LaGaO_3$ and $LaAlO_3$ show twin fluoresence peaks at 77°K, but the splitting is not clearly resolved in the solid solutions due to the much broader line widths occurring than those in the "pure" compounds. This is in agreement with results reported by Tolstoy and Shun-Fu (6) who reported on the Al_2O_3-Ga_2O_3 system doped with chromium.

Chromium activated $CeAlO_3$ was also prepared. The powder photograph was conveniently indexed as orthorhombic, $a = b = 3.762$Å, $c = 3.794$Å. This would calculate to a volume intermediate between $LaAlO_3$ and $PrAlO_3$ as expected. Only weak chromium fluorescence was observed, which is perhaps due to quenching by the trivalent cerium.

In both $LaAlO_3$ and $LaGaO_3$ there is little question that chromium shows a strong preference for the B (Al or Ga) site. This is both because of the relative sizes of the ions (La/Al or Ga≈2) and the coordination number of 12 for lanthanum as opposed to 6 for aluminum and gallium. In both materials the chromium would be in a slightly distorted oxygen octahedron. In $LaAlO_3$ the lattice symmetry is rhombohedral while

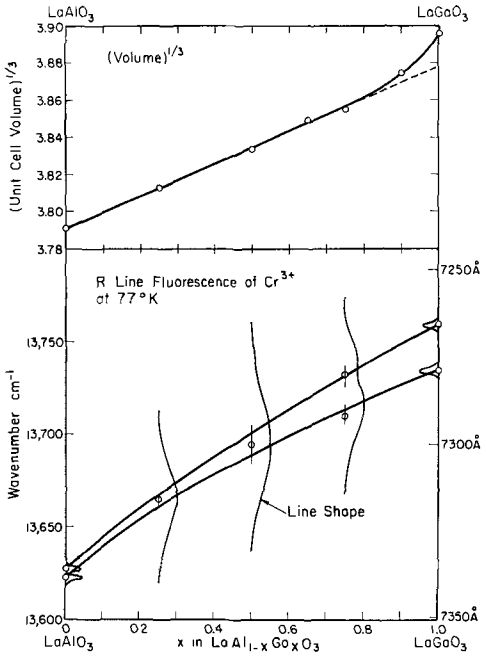

Fig. 1. Upper curve, (unit cell volume)$^{1/3}$ for various solid solutions of $LaAlO_3$ — $LaGaO_3$. Lower curve, fluorescence in the R-lines of Cr^{+3} in $LaAlO_3$ — $LaGaO_3$ solutions at 77°K.

in $LaGaO_3$ the symmetry is orthorhombic although in both cases there are relatively small deviations from the cubic lattice (1, 2). The lattice parameters shown in Fig. 1 show a smooth variation with composition. In the series there is a transformation from the rhombohedral to the orthorhombic lattice as $LaGaO_3$ is added to $LaAlO_3$, but it is not easily detectable from powder x-ray analysis. However, there should be only small changes in the oxygen ion environment around the chromium throughout the series.

As $LaGaO_3$ is added to $LaAlO_3$ the volume of the unit cell increases. This is consistent with the ionic radii reported by Geller (7) for Al^{+3} (0.558Å), Ga^{+3} (0.613Å). The ionic radius for Cr^{+3} in the perovskite lattice is calculated by Geller to be 0.608Å. This would indicate that chromium is somewhat "squeezed" in $LaAlO_3$ and in an appropriately sized site in $LaGaO_3$. The net effect would be for the Cr^{+3} - O^{-2} distance to increase as the solid solution ranges from $LaAlO_3$ to $LaGaO_3$.

The R-line from Cr^{3+} in octahedral surroundings is due to transitions between the ^2E excited state and the $^4A_2$ ground state (8). The splitting of the R-line arises from a trigonal distortion of the symmetry combined with the spin-orbit coupling in $LaAlO_3$. The R-line may be split by the orthorhombic distortion in $LaGaO_3$, but it is likely the spin-orbit interaction also is important in this crystal. To first order, the energy difference between ^2E and $^4A_2$ does not depend on the crystalline field but only on the exchange energy caused by the electrostatic electron repulsion. However, this energy, which is measured by fitting Racah parameters B and C to experimentally determined energy levels, is always calculated to be lower for Cr^{3+} in crystals than for free ions because of the neglect of the interactions with the ligand orbitals and higher energy states (9). There is also a 30% variation in these parameters between various hosts (10). The approximations present in existing theories prevent a meaningful theoretical correlation between the 9% increase in the ^2E - $^2A_2$ energy difference and the 2.6% increase in the lattice parameter from $LaAlO_3$ to $LaGaO_3$. In fact, for Cr^{3+} in the garnet structure, the energy of this transition decreases in going from $Y_3Al_5O_{12}$ to $Y_3Ga_5O_{12}$ (9), just the opposite of what was found in the present case.

The 24 cm^{-1} splitting of the R-lines in $LaGaO_3$ compared to 5.4 cm^{-1} in $LaAlO_3$ may be qualitatively understood as due to the greater distortion of the Cr^{3+} site from octahedral symmetry in $LaGaO_3$ compared to $LaAlO_3$ (1, 2), although in both cases the distortion is small. The broad line widths of the fluorescence observed from the solid solutions is likely to be an inhomogeneous broadening arising from the individual Cr^{3+} ions being in somewhat different surroundings from each other. This suggests that the Al and Ga distribute themselves at random in the various B sites. The line shape may be expected to be Gaussian, but the presence of a pair of lines made this difficult to verify.

Manuscript received Feb. 3, 1965.

Any discussion of this paper will appear in a Discussion Section to be published in the December 1965 JOURNAL.

REFERENCES

1. S. Geller and V. B. Bala, *Acta Cryst.*, **9**, 1019 (1956).
2. S. Geller, *ibid.*, **10**, 243 (1957).
3. F. Forrat, R. Jansen, and P. Trevoux, *Compt. rend.*, **256**, 1271 (1963).
4. R. C. Ohlmann, *Bull. Am. Phys. Soc.*, **9**, 281 (1964).
5. J. Murphy, R. C. Ohlmann, and R. Mazelsky, *Phys. Rev. Letters*, **13**, 135 (1964).
6. N. A. Tolstoy and L. Shun-Fu, *Optics and Spectros*, **14**, 202 (1963).
7. S. Geller, *Acta Cryst.*, **10**, 248 (1957).
8. J. S. Griffith, "Theory of Transition Metal Ions," Cambridge University Press, London (1961).
9. C. E. Schäffer and C. K. Jorgensen, *J. Inorg. Nucl. Chem.*, **8**, 143 (1958).
10. D. L. Wood, J. Ferguson, K. Knox, and J. F. Dillon, Jr., *J. Chem. Phys.*, **39**, 890 (1963).

Growth Rate and Defect Structure of Gel-Grown Crystals

H. K. Henisch, J. I. Hanoka, and J. Dennis

Materials Research Laboratory, Pennsylvania State University, University Park, Pennsylvania

In the course of previous work (1), it was shown that large and well-ordered crystals of a variety of materials, suitable for solid-state experimentation, can be grown at or near room temperature in gels. The method is specially valuable for crystals which by virtue of their low dissociation temperatures or low solubilities cannot be grown from the melt, from the vapor, or directly from solution.

From observations of the growth process, it was tentatively concluded that there exists in the immediate neighborhood of the crystal surface a supersaturation which remains constant during growth. A direct test of this hypothesis would involve microanalytic procedures which, in the prevailing circumstances, would be very difficult to apply. It is, however, possible to devise an indirect test by reference to theories of crystal growth (2-4) which concern themselves specifically with stagnant solutions. In particular, Frank (3) has developed equations which give a description of diffusion-controlled growth rates for several different idealized geometries. In the ordinary way, stagnancy in solutions is hard to achieve, but in a gel system it is

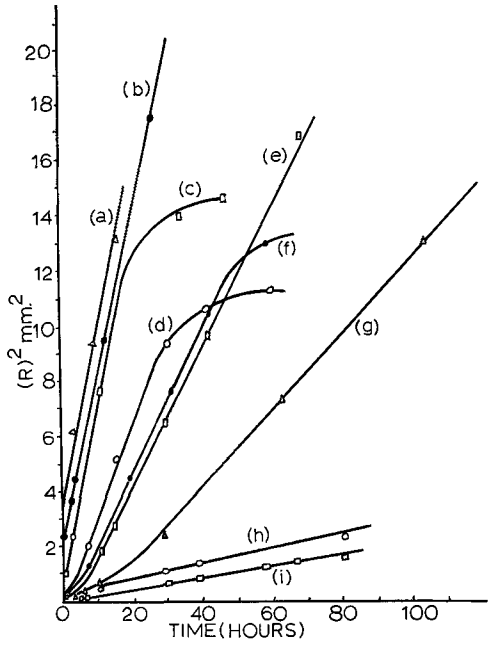

Fig. 1. Time-size relations of gel-grown crystals: (a), (c), sodium tartrate; (b), (e), (g), calcium tartrate; (d), (f), strontium tartrate; (h), (i), sodium oxalate.

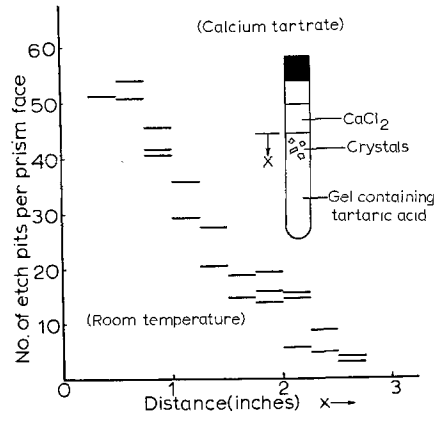

Fig. 2. Etch pit counts as a function of distance from diffusion interface. Etch pit numbers averaged over four nearly equal faces; each line represents measurements on one crystal.

completely assured. Such systems therefore provide new opportunities for applications of the theory, all the more since the essential correctness of the model has already been confirmed by means of multiple-beam interferometry (5).

The growth rates calculated by Frank involve the "reduced radius" s which, for a spherical system, is defined as $rD^{-1/2}\,t^{-1/2}$, where r is the radius of the crystal, D the diffusivity, and t the time. A constant value of s implies a constant solute concentration at the crystal surface, and vice versa. It is a simple matter to check whether s is indeed constant during growth, and results of this kind are given below. Since the starting time is not known, it is the relationship between r^2 and t which must be tested for linearity.

Two limitations must be borne in mind: one arising from the initial transient period during which steady-state concentrations are established, and one arising from exhaustion of the available solute. Both factors must give rise to nonlinearity. The duration of the first is not easy to calculate, but the second can be estimated without difficulty from the original reagent concentrations in the gel and from the distance between the crystal under observation and its nearest neighbor. In addition, there may be smaller difficulties due to departures from the simple geometry envisaged by Frank, although various linear projections used for R in Fig. 1 gave consistent results.

Using the techniques already described (1), several types of crystals have been grown, some in systems which involve only simple crystallization in the presence of the gel and some which involve a chemical reaction resulting in the formation of the solute. Linear r^2 *vs.* t relationships have been observed in both cases, suggesting that the chemical reaction as such was not the rate-determining process in crystal growth. Results are shown in Fig. 1. In each case, departures from linearity set in during the later stages of growth at times which could reasonably be associated with the onset of interaction between the diffusion regions surrounding neighboring crystals. The appearance of distinct linear regions may be taken as a confirmation of the constant surface supersaturation hypothesis.

It has already been reported (1) that the color of calcium tartrate crystals growing in waterglass depends on the illumination during growth. These color changes were traced to varying iron contamination, iron being a common impurity in waterglass. The same effects can be reproduced in sodium metasilicate gels by making a small amount of iron available. Since effective segregation coefficients generally depend on the speed of crystal growth, it was of interest to examine whether irradiation of the growing crystals changes the growth rate as well as the iron content. No growth rate changes were detected. The mechanism whereby light inhibits the inclusion of iron impurity thus remains unclear. The observations do, however, support the conclusion that we are dealing with systems in which the growth rate is controlled by the diffusion process in the gel and not by the detailed mechanism of crystal growth.

In systems which depend on the diffusion of one reagent through a gel charged with another, the average crystal growth rate is greatest near the top of the diffusion column where the concentration gradients are high, and small near the bottom where the gradients are likewise small. Corresponding to this distribution of growth rates, there is also a distribution in the number of etch pits on any crystal face, as shown in Fig. 2. If the occurrence of etch pits is accepted, in the most general terms, as a measure of disorder, then Fig. 2 and the arguments above suggest strongly that the growth rate itself determines the number of defects built into the crystal, even in the absence of foreign impurities. Such a process had already been envisaged by Jagodzinski (6) and Washburn (7) and is, presumably, linked with the low surface mobility of molecules at the growth temperature. The average etch pit densities observed on gel-grown crystals of the kind listed in Fig. 1 are comparable with those found on good germanium crystals, *i.e.*, 10^3 to 10^4 pits/cm^2. Occasionally, crystals are found which have lower etch pit densities by an order of magnitude.

It is plausible to suppose that the constant surface supersaturation maintained in the gel system is responsible for the high degree of order. The surface diffusion coefficients are expected to increase (8) with increasing temperature, leading to greater perfection and thus to fewer etch pits. A small but significant effect of this kind has been observed on calcium tartrate over the practical range of growth temperatures (20°-65°C).

Manuscript received Jan. 25, 1965. This work was supported by a grant from the Advanced Research Projects Agency.

Any discussion of this paper will appear in a Discussion Section to be published in the December 1965 JOURNAL.

REFERENCES

1. H. K. Henisch, J. Dennis, and J. I. Hanoka, *J. Phys. Chem. Solids*, **26**, 493 (1965).
2. C. W. Bunn, *Discussions Faraday Soc.*, **5**, 132 (1949).
3. F. C. Frank, *Proc. Roy. Soc.*, **A201**, 586 (1950).
4. A. Seeger, *Phil. Mag.*, **44**, 1 (1953).

5. F. S. A. Sultan, *ibid.*, **43**, 1099 (1952).
6. H. Jagodzinski, "Crystallography and Crystal Perfection," p. 177, G. N. Ramachandran, Editor, Academic Press, New York (1963).
7. J. Washburn, "Growth and Perfection of Crystals," p. 342, R. H. Doremus, B. W. Roberts, and D. Turnbull, Editors, John Wiley & Sons, Inc., New York (1958).
8. P. G. Shewmon, "Diffusion in Solids," p. 185, McGraw-Hill Book Co., New York (1963).

The Viscosity of Some Molten Lead Compounds

C. B. Oliver

Central Research Laboratories, The General Electric Company Limited, Wembley, England

Although melts in the lead fluoride-lead oxide system are commonly used as solvents for growing crystals of refractory oxides by the fluxed-melt method [e.g., White (1)], very few physical data have been published for these liquids. As part of an investigation into fluxed-melt growth processes, a fairly rapid survey of the viscosities of melts in the lead-fluoride-lead oxide system was made using a rotating crucible viscometer. This work was not designed to yield viscosity values of high absolute accuracy, but to determine quickly the relative magnitudes of viscosities of different compositions.

Apparatus

The method is essentially that of Margules (2) and Lillie (3), in which a crucible containing the liquid is rotated at constant speed, and the viscous torque on a bob suspended in the liquid is measured.

The crucible was of platinum to reduce chemical attack by the liquids and was 50 mm deep and 50 mm in diameter. It was supported inside a Kanthal electric furnace (maximum operating temperature 1250°C) by an alumina tube which could be rotated about a vertical axis at several speeds between 2 and 20 rpm, selected by a gear-box.

The liquids used evaporated fairly rapidly, changing the liquid depth appreciably in a few hours. The platinum bob was therefore in the form of a disk 2 mm thick and 40 mm in diameter, which was totally immersed and suspended by a platinum rod 2 mm in diameter. The viscous drag on the rod was relatively small so that small variations in liquid depth had a negligible effect on the total viscous torque.

The platinum rod projected above the furnace and was suspended by a steel wire 7 ft in length. The crucible was rotated in each direction alternately, and the difference between the equilibrium positions of the bob was measured with an optical lever 2 meters long. At equilibrium the torque exerted on the bob by the rotating liquid was balanced by the elastic torque of the suspension, and the deflection of the optical lever from the rest position provided a measure of the viscosity.

Vertical adjustment of the disk position to within about 0.05 mm was effected with a micrometer screw. This was used in setting up, and also to measure the liquid depth, the point at which the disk touched the crucible bottom or the liquid surface being determined visually with a mirror.

A Pt-Pt/13%Rh thermocouple was dipped into the liquid to measure its temperature to within ±3°C between each viscosity measurement. Reproducible curves of viscosity against temperature were obtained by making measurements while the liquid temperature slowly changed through about 100°C, thus avoiding the need for elaborate temperature control. The rotation of the crucible provided adequate stirring. About five minutes was required for each viscosity measurement, during which time the temperature change was negligible. Observations were made during periods of up to 30 hr in some cases. The depth of the liquid was measured and samples taken for chemical analysis at frequent intervals.

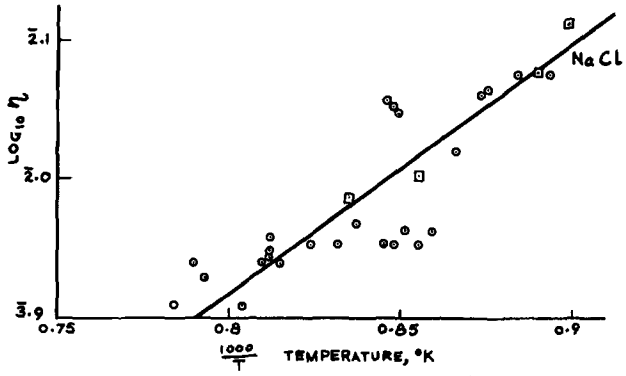

Fig. 1. Graph of log η against the reciprocal of the absolute temperature for sodium chloride. (Ω = 13 and 18.6 rpm, d = 3.7 cm.) ○, This work; □, Lorenz (1912).

The apparatus was partially enclosed and ventilated to remove harmful vapors.

Calibration

The viscometer was calibrated with water at 19°C, at which temperature the viscosity of water is 0.01030 poise (4).

The lower surface of the disk was held 10 mm above the crucible bottom throughout this work. At this height the deflection was found to be insensitive to small variations in the disk position.

The relation between viscosity and the apparatus variables was found to be

$$\eta = \frac{k\theta}{\Omega f(d)} \qquad [1]$$

where η is the viscosity in poise; k = 0.2 and was a constant for the apparatus; θ is the deflection of the optical lever from its rest position, in cm; Ω is the rotation speed of the crucible in rpm; and $f(d) = 5.56\ (d - 1.2)^{1/2} + 15$, where d is the liquid depth in cm.

The height of liquid above the top surface of the disk was $(d - 1.2)$ cm, and the expression for $f(d)$ implied that the viscous torque exerted on the disk by the liquid around and below it is independent of the height of liquid above the disk, as might be expected.

Equation [1] was found to be valid for speeds below 20 rpm; above that speed inertial effects became significant. All the variables were measured with an accuracy of ± 1% or better, but the accuracy of k, the

Table I

Material	E, kcal/mole	A, poise
$52PbO:48PbF_2$	5.4 ± 1.1	0.0026 ± 0.0005
PbO	8.5 ± 1.7	0.001 ± 0.002
$Pb(BO_2)_2$	17.3 ± 3.4	0.0001 ± 0.00002
NaCl	8.3 ± 1.7	0.0003 ± 0.00006

5. F. S. A. Sultan, *ibid.*, **43**, 1099 (1952).
6. H. Jagodzinski, "Crystallography and Crystal Perfection," p. 177, G. N. Ramachandran, Editor, Academic Press, New York (1963).
7. J. Washburn, "Growth and Perfection of Crystals," p. 342, R. H. Doremus, B. W. Roberts, and D. Turnbull, Editors, John Wiley & Sons, Inc., New York (1958).
8. P. G. Shewmon, "Diffusion in Solids," p. 185, McGraw-Hill Book Co., New York (1963).

The Viscosity of Some Molten Lead Compounds

C. B. Oliver

Central Research Laboratories, The General Electric Company Limited, Wembley, England

Although melts in the lead fluoride-lead oxide system are commonly used as solvents for growing crystals of refractory oxides by the fluxed-melt method [e.g., White (1)], very few physical data have been published for these liquids. As part of an investigation into fluxed-melt growth processes, a fairly rapid survey of the viscosities of melts in the lead-fluoride-lead oxide system was made using a rotating crucible viscometer. This work was not designed to yield viscosity values of high absolute accuracy, but to determine quickly the relative magnitudes of viscosities of different compositions.

Apparatus

The method is essentially that of Margules (2) and Lillie (3), in which a crucible containing the liquid is rotated at constant speed, and the viscous torque on a bob suspended in the liquid is measured.

The crucible was of platinum to reduce chemical attack by the liquids and was 50 mm deep and 50 mm in diameter. It was supported inside a Kanthal electric furnace (maximum operating temperature 1250°C) by an alumina tube which could be rotated about a vertical axis at several speeds between 2 and 20 rpm, selected by a gear-box.

The liquids used evaporated fairly rapidly, changing the liquid depth appreciably in a few hours. The platinum bob was therefore in the form of a disk 2 mm thick and 40 mm in diameter, which was totally immersed and suspended by a platinum rod 2 mm in diameter. The viscous drag on the rod was relatively small so that small variations in liquid depth had a negligible effect on the total viscous torque.

The platinum rod projected above the furnace and was suspended by a steel wire 7 ft in length. The crucible was rotated in each direction alternately, and the difference between the equilibrium positions of the bob was measured with an optical lever 2 meters long. At equilibrium the torque exerted on the bob by the rotating liquid was balanced by the elastic torque of the suspension, and the deflection of the optical lever from the rest position provided a measure of the viscosity.

Vertical adjustment of the disk position to within about 0.05 mm was effected with a micrometer screw. This was used in setting up, and also to measure the liquid depth, the point at which the disk touched the crucible bottom or the liquid surface being determined visually with a mirror.

A Pt-Pt/13%Rh thermocouple was dipped into the liquid to measure its temperature to within ±3°C between each viscosity measurement. Reproducible curves of viscosity against temperature were obtained by making measurements while the liquid temperature slowly changed through about 100°C, thus avoiding the need for elaborate temperature control. The rotation of the crucible provided adequate stirring. About five minutes was required for each viscosity measurement, during which time the temperature change was negligible. Observations were made during periods of up to 30 hr in some cases. The depth of the liquid was measured and samples taken for chemical analysis at frequent intervals.

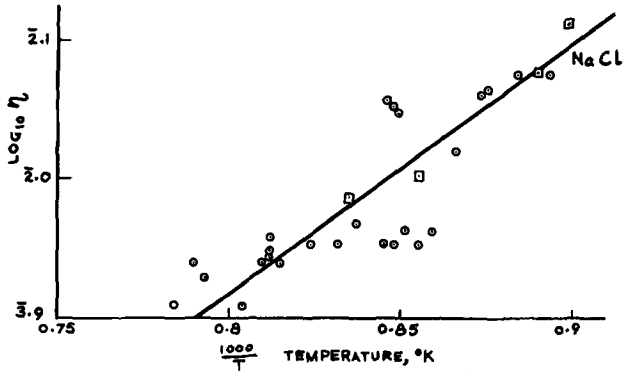

Fig. 1. Graph of log η against the reciprocal of the absolute temperature for sodium chloride. (Ω = 13 and 18.6 rpm, d = 3.7 cm.) ○, This work; □, Lorenz (1912).

The apparatus was partially enclosed and ventilated to remove harmful vapors.

Calibration

The viscometer was calibrated with water at 19°C, at which temperature the viscosity of water is 0.01030 poise (4).

The lower surface of the disk was held 10 mm above the crucible bottom throughout this work. At this height the deflection was found to be insensitive to small variations in the disk position.

The relation between viscosity and the apparatus variables was found to be

$$\eta = \frac{k\theta}{\Omega f(d)} \qquad [1]$$

where η is the viscosity in poise; k = 0.2 and was a constant for the apparatus; θ is the deflection of the optical lever from its rest position, in cm; Ω is the rotation speed of the crucible in rpm; and $f(d) = 5.56\ (d - 1.2)^{1/2} + 15$, where d is the liquid depth in cm.

The height of liquid above the top surface of the disk was $(d - 1.2)$ cm, and the expression for $f(d)$ implied that the viscous torque exerted on the disk by the liquid around and below it is independent of the height of liquid above the disk, as might be expected.

Equation [1] was found to be valid for speeds below 20 rpm; above that speed inertial effects became significant. All the variables were measured with an accuracy of ± 1% or better, but the accuracy of k, the

Table I

Material	E, kcal/mole	A, poise
$52PbO:48PbF_2$	5.4 ± 1.1	0.0026 ± 0.0005
PbO	8.5 ± 1.7	0.001 ± 0.002
$Pb(BO_2)_2$	17.3 ± 3.4	0.0001 ± 0.00002
NaCl	8.3 ± 1.7	0.0003 ± 0.00006

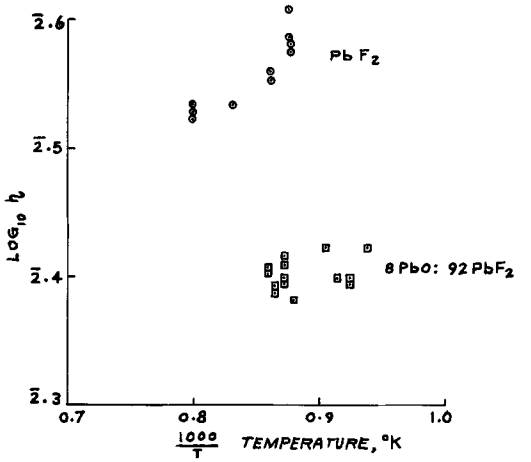

Fig. 2. Graph of log η against $1/T$ for: ○, lead fluoride (Ω = 9.3 rpm, d = 3.5 cm); □, 8 mole % lead oxide —92% lead fluoride mixture (Ω = 4.65 rpm, d = 2.4 cm).

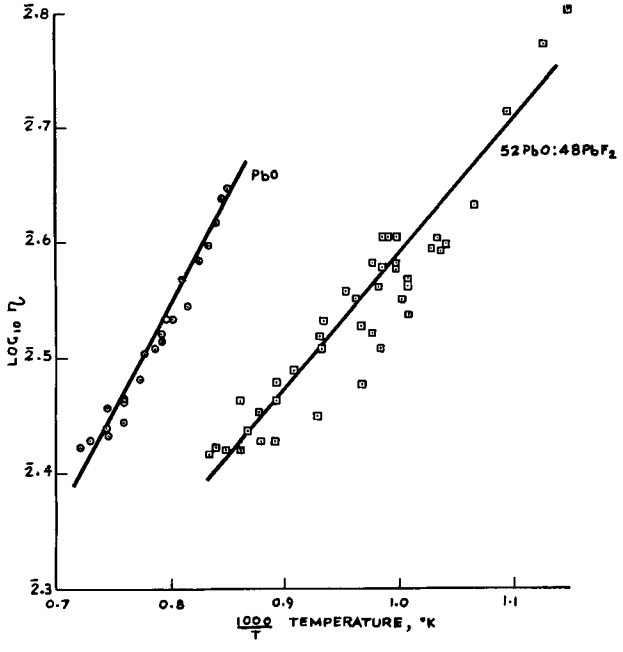

Fig. 3. Graph of log η against $1/T$ for: ○, lead oxide (Ω = 4.65 rpm, d = 2.4 cm); □, 52 mole % lead oxide —48% lead fluoride mixture (Ω = 4.65 rpm, d = 1.5 and 2.5 cm).

calibration constant, was only about ± 10%. No correction was made for thermal expansion at the working temperature, as the experimental accuracy did not warrant it.

The calibration was checked, using sodium chloride. The logarithm of viscosity is shown as a function of the reciprocal of the absolute temperature in Fig. 1, and it can be seen that the results are consistent with those of Lorenz (5). The activation energy for viscous flow was calculated from the slope of the graph according to the usual equation (6, 7).

$$\eta = A \exp (E/RT) \qquad [2]$$

where η is the viscosity in poise; T is the absolute temperature; E is the activation energy for viscous flow; R = 1.99 cal/°C, is the gas constant per mole; and A is a constant for a given liquid over a small temperature range. The values of E and A for NaCl, given in Table I, are somewhat inconsistent with values given by Murgulescu and Zuca (8) for other alkali halides (E = 4 to 7 kcal/mole and A = 0.0005 to 0.0012

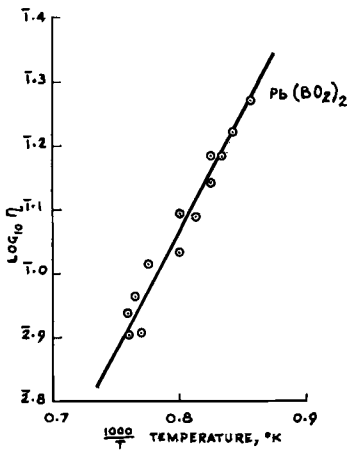

Fig. 4. Graph of log η against $1/T$ for lead borate (Ω = 2.3 rpm, d = 2.9 cm).

poise) but the agreement is sufficiently close to confirm the validity of Eq. [1].

Results

Figures 2, 3, and 4 show log η as a function of the reciprocal of the absolute temperature for four compositions in the PbF_2-PbO system and also for lead borate. The speed of rotation of the crucible and mean depth of the liquid are also given in each case.

The lead fluoride was an extra pure grade from British Drug Houses Ltd., with total impurities of less than 0.1%. All other reagents were of Analar grade.

Results for lead fluoride and the 8 mole % lead oxide-lead fluoride mixture are of low accuracy, because only the observations made at low temperatures and during the first 5 hr after melting were reproducible. At higher temperatures or after longer periods the composition of the melt changed due to the reaction of the lead fluoride with atmospheric water vapor to produce lead oxide. Results are only presented for melts for which chemical analysis of samples showed less than 1% change from the normal composition. Values of E and A for these compositions were not derived, but it is clear from Fig. 2 that the viscosity of the 8 mole % lead oxide mixture is lower than that for pure lead fluoride at the same temperature.

Results for lead oxide and the 52 mole % lead oxide-lead fluoride mixture, shown in Fig. 3, are more reliable and the accuracy of the values of E and A in Table I is about ± 20%. It will be seen that at a given temperature the viscosities of the mixture are appreciably lower than those of the individual components.

The effects of modifying the viscosity of lead oxide by adding other materials were briefly investigated. The results for lead borate are shown in Fig. 4. The accuracy is again estimated at ± 20%. The results show that the addition of a large amount of boric oxide increases the viscosity of lead oxide, as was anticipated from the high viscosity of boric oxide itself.

It was not possible to determine the effect on viscosity of the addition of sodium chloride to lead oxide because the liquids were immiscible and the platinum was rapidly attacked at the interface between the two liquids.

Manuscript received Dec. 15, 1964; revised manuscript received Feb. 9, 1965.

Any discussion of this paper will appear in a Discussion Section to be published in the December 1965 JOURNAL.

REFERENCES

1. E. A. D. White, *Quart. Revs.*, **15**, 1 (1961).
2. M. Margules, *Sitz. Ber. Akad. Wiss. Wien.*, **83**, 588 (1881).
3. H. R. Lillie, *J. Am. Ceram. Soc.*, **12**, 505 (1929).

4. R. Hosking, *Phil. Mag.*, **18**, 260 (1909).
5. R. Lorenz, *Z. phys. Chem.*, **79**, 63 (1912).
6. E. N. da C. Andrade, *Phil. Mag.*, **17**, 497 (1934).
7. S. Glasstone, K. J. Laidler, and H. Eyring, "The Theory of Rate Processes," McGraw-Hill Publishing Co., New York (1941).
8. I. G. Murgulescu, and S. Zuca, *Z. phys. Chem.*, **218**, 379 (1961).

Purification and Crystal Growth of Gold

Paul H. Schmidt

Bell Telephone Laboratories, Incorporated, Murray Hill, New Jersey

A prerequisite for electronic band structure studies of a metal is a high resistance ratio, a measure of the electronic quality and "purity" of a metal. Past attempts to purify gold to achieve a high resistance ratio have been relatively unsuccessful. At best, resistance ratios, $R_{300°K}/R_{4.2°K}$, approaching 400 have been recorded on zone refined and vacuum melted gold. This note describes a technique which has been developed for producing single crystals of gold on which resistance ratios to 6040 have been measured.

During manufacture and previous crystal growing and purification operations the container material primarily used has been graphite. However, according to Hansen (1), carbon is soluble in gold up to 0.3 wt % (2). It is therefore logical to suspect carbon as one of the primary elements associated with the low resistance ratios of high-purity (metallic) gold. Studies were therefore initiated to investigate the variation of resistance ratios with crystals grown in different container materials and gases.

Crystal Growth

The Bridgman method of crystal growth was selected for crystal fabrication. Single crystals of gold were grown in graphite, single crystal sapphire, and boron nitride crucibles.[1] Crystals grown in graphite crucibles were lowered through the furnace in a sealed and evacuated (5×10^{-6} Torr) fused silica container. Sapphire and boron nitride crucibles were lowered through the furnace in flowing dry oxygen in a sintered alumina sleeve, Fig. 1. All containers were prefired at a temperature several hundred degrees higher than the working temperature to vaporize impurities which might otherwise contaminate the gold. The temperature of the furnace in the hot zone was maintained at 1150° ± 1°C, approximately 100°C above the metal's melting point, to insure complete melting and prevent stray nuclei formation. The drop rate in all cases was 0.5 in./hr across a 20°-30°C/0.1 in. temperature gradient. Crystals up to 3½ in. long and ⅝ in. diameter have been made by this method and were limited in size only by the dimensions of the containers. The usual growth direction of these Bridgman grown crystals, as confirmed by optical and x-ray methods, was parallel to a <211> direction. It was observed that very careful handling and support of these crystals was required to avoid plastic deformation and strain. Crystals were easily removed from the graphite containers. Crystals grown in boron nitride containers were also easily removed although some sticking occurred due to the boric oxide binder. Crystals were easily removed however by either peeling off the crucible or immersing it in hot water for 15 to 30 min. Sapphire containers were very difficult to remove and had to be broken away from the crystal. Most sticking was observed at the tail end (end freezing last) of the crystal.

[1] Graphite crucibles were made from high-purity AUC grade graphite supplied by the National Carbon Company. Sapphire crucibles were supplied by Linde Air Products. Boron nitride crucibles were supplied by High Temperature Materials, Inc.

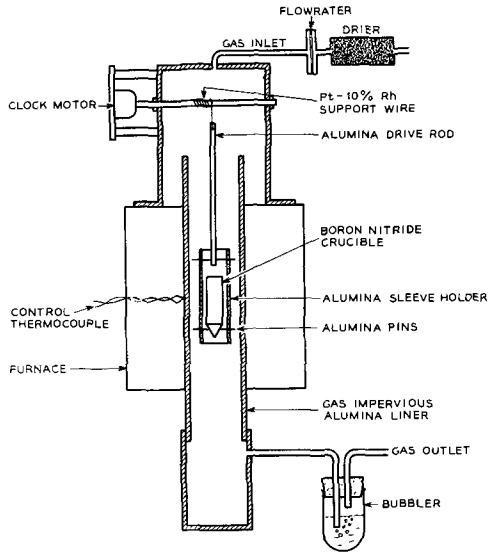

Fig. 1. Crystal growth apparatus

Table I

Container	Atmosphere	Supplier	Raw material resistance ratio	Melted material resistance ratio	Remarks
Graphite	Vac. 1×10^{-5} Torr	Sigmund Cohen Co. 99.999% rod	366	tip 230 tail 596	Crystal easily removed
Graphite	Vac. 1×10^{-5} Torr	American Smelting and Refining Co. 99.999% rod	69	~100	Crystal easily removed
Sapphire	Flowing dry oxygen	Sigmund Cohen Co. 99.999% rod	366	4000	Gold wet container in spots —difficult to extract
Boron nitride	Flowing dry oxygen	Sigmund Cohen Co. 99.999% powder	366	6040	Easily removed by peeling off container
Boron nitride & B_2O_3 cover flux	Air	Sigmund Cohen Co. 99.999% rod	366	686	Easily removed by peeling off container
Electron beam float zone	~1×10^{-6} Torr vacuum	Johnson Mathey 99.999% powder	—	28	Difficult to carry zone ⅛" diameter
Radio frequency float zone	~1×10^{-6} Torr vacuum	Sigmund Cohen Co. 99.999% rod	366	—	Could not carry zone due to low surface tension of gold

Some small diameter crystals of gold were also made by float zone refining techniques. The low surface tension of gold however, made application of these techniques unattractive for future crystal growth and purification, Table I.

Results and Conclusions

The above experiments revealed that crystals grown in sapphire or boron nitride crucibles in the presence of oxygen displayed higher resistance ratios than crystals grown in graphite containers in vacuum, Table I.

The mechanism believed to be responsible for purification is

$$\text{Au} + \text{carbon Impurity in raw material} \xrightarrow[1150°\text{C}]{\text{Oxygen atm}} \text{Au} + \text{CO/CO}_2$$

A carbon-oxygen reaction and the formation of carbon monoxide/carbon dioxide gas is presented as the mechanism for purification. Removal of carbon monoxide/carbon dioxide from the system is effected with the flowing oxygen carrier. Some improvement in resistance ratio was also observed along the boule axis and can be easily justified by segregation due to the mechanism of normal freezing.

It appears therefore that single crystals of gold of high electronic quality and purity can be grown by the Bridgman method. Use of boron nitride containers in the presence of an oxygen atmosphere was the prerequisite for successful purification. Although boron nitride was found to be a very satisfactory container material, it was not unique. It further appears that this method would be applicable to several other metals. However, slight modification of the procedure outlined for gold might be required. These modifications would include the use of different atmospheres, cooling of the melt in vacuum, and subsequent vacuum degassing. The crystals grown for this study are presently being used for electronic band structure studies and therefore sampling for analysis is impossible at this time.

Acknowledgments

The author wishes to thank F. Sorentino for his assistance on furnace operation and A. Von Neida for the use of his facilities.

Manuscript received Jan. 22, 1965.

Any discussion of this paper will appear in a Discussion Section to be published in the December 1965 JOURNAL.

REFERENCES

1. M. Hansen, "Constitution of Binary Alloys," 189-90 (1958).
2. W. Hempel, *Z. angew. Chem.*, **17**, 324 (1904).

The Calcium Chloride-Calcium Oxide Fused Salt Electrolytic System: Solubilities, Metal Contents, and Freezing Points

W. D. Threadgill

Department of Engineering, School of Engineering, Vanderbilt University, Nashville, Tennessee

During an investigation (1) of the production of metallic calcium by electrolysis of calcium oxide dissolved in molten calcium chloride in a modified moving cathode type cell, related investigations of solubility of the oxide, freezing points, and metal content of the electrolyte were made. Electrolytes of calcium chloride and calcium oxide-calcium chloride mixtures were used.

Raw materials used were A.C.S. analytical reagent grade, anhydrous calcium chloride and calcium oxide, N. F. IX, lumps. The calcium chloride was used as received. The oxide was kept at a temperature of 980°C for a period of 7 hr before use to decompose any carbonate that might be present.

Freezing temperature as a function of composition is shown in Fig. 1. The solid line portion of the graph represents the data for fourteen mixtures in which a definite plateau was observed on the cooling curve as an indication of the freezing point. The dashed line represents the data obtained for twelve mixtures in which no definite plateau occurred in the cooling curve, but the slope of the curve changed at the temperature taken as the freezing point.

Three mixtures exhibited a second freezing point at 593°, two at 596°, one at 602°C. This suggests the possibility of an eutectic mixture with a freezing point in the range 593°-602°C. Furthermore, a mixture with a calcium oxide concentration of 16.9% by weight exhibited only one freezing point, 593°C, suggesting that this is possibly the composition of the eutectic. Concentrations greater than 18.8% by weight were not used because at this high concentration the melt was very viscous, and it was questionable whether the oxide that was not dissolved would settle out or remain in suspension.

The anhydrous calcium chloride, which had an oxide concentration of 0.1% due to hydrolysis, exhibited a freezing temperature of 766°C. Extrapolation of the freezing point curve to zero oxide concentration gives a freezing temperature of 768°C for the calcium chloride used.

According to data contained in the International Critical Tables (2), from the work of Sackur (3), for calcium chloride freezing at 765°C addition of 5.72% oxide reduced the freezing temperature to 742°C. A mixture containing 10.23% calcium oxide was reported to have a freezing point of 727°C. Frary (4) found the freezing point of a mixture containing 6.24% oxide and 3.38% carbonate to be 705°C and noted that additional oxide gave partial freezing at about 770°C. The freezing temperature of the chloride he used was 766°C. The melting point of pure calcium chloride is reported as 773.9° and 744°C (5-7).

Early experimenters (8, 9) who worked with fused salt electrolytes noted a black coloration after elec-

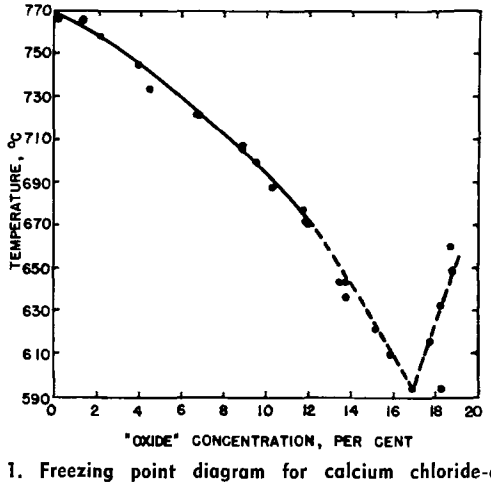

Fig. 1. Freezing point diagram for calcium chloride-calcium oxide system.

trolyzing for some time. It is the consensus of opinion of most investigators that the metal is suspended in the melt as fine particles and that no subsalt of calcium is formed, although calcium subchloride has been prepared by Guntz and Bassett (10) and Wohler and Rodewald (11) at temperatures of 1000°C or above.

In order to determine the metal content of the electrolyte, samples were obtained at intervals during electrolysis and analyzed for metallic calcium by a volumetric procedure based on measurement of the volume of hydrogen gas evolved by the reaction of calcium metal with water. Particular attention was given to the sampling procedure so that the sample would not be obtained in regions of strong convection currents since this would probably give a high metal content.

At 816°C the metal content (weight per cent) of the chloride electrolyte varied from 0.02 to 0.04% with the average for seven different determinations being 0.03%. This electrolyte had not previously been subjected to electrolysis. In comparison, Kunitomi (12) found 0.14% metal at this temperature. At 795°C, the metal content varied from 0.02 to 0.05% with the average for six different determinations being 0.03%. In comparison, Kunitomi (12) found 0.1% metal at this temperature.

At 816°C, the metal content of a calcium chloride-calcium oxide electrolyte containing 0.7% by weight oxide averaged 0.02% for five different determinations. At 830°C and an oxide concentration of 1% by weight, the metal content of the mixed electrolyte varied from 0.02 to 0.03% with the average of six different determinations being 0.02%. In comparison, Kunitomi (12) found 0.16% metal in a chloride electrolyte at this temperature.

The over-all average of thirteen different determinations with the electrolyte of calcium chloride alone was 0.03%. The over-all average of eleven different determinations with the chloride-oxide electrolyte was 0.02%.

In all cases, the metal content of the electrolyte during this investigation was markedly below that found by Kunitomi (12). A probable explanation of this discrepancy lies in difference in operating and sampling techniques. Kunitomi (12) used a much higher current density, 516 amp/in.^{2}, than was used in this case, approximately 300 amp/in.^{2}. This increase in current density possibly resulted in much stronger convection currents in his apparatus even though he was using approximately twice the quantity of electrolyte used here. These stronger currents would cause a higher degree of bath agitation and tend to sweep more metal away from the cathode. Samples taken from regions in which these currents were present would be expected to contain a higher concentration of metal than the less agitated regions.

Lorenz (9) stated that is was possible to lower the "metallic fog" content of the electrolyte by adding other substances which had an inhibiting action on its formation; however, no specific substances were mentioned. In this investigation, calcium oxide exhibited this inhibitory effect since the current used in each case was the same and operating conditions and techniques were maintained identical as nearly as possible.

Manuscript received Aug. 25, 1964.

Any discussion of this paper will appear in a Discussion Section to be published in the December 1965 JOURNAL.

REFERENCES

1. W. D. Threadgill, Ph.D. Thesis, University of Missouri (1954).
2. *International Critical Tables*, **4**, 40 (1928).
3. O. Sackur, *Z. physik. Chem.*, **78**, 568 (1910).
4. F. C. Frary and W. L. Badger, *Trans. Am. Electrochem. Soc.*, **16**, 185 (1909).
5. Wilhelm Plato, *Z. physik. Chem.*, **58**, 362 (1907).
6. *International Critical Tables*, **5**, 131, 1926.
7. Kurt Arndt, *Z. Elektrochem.*, **12**, 337 (1906).
8. Richard Lorenz, *Trans. Am. Electrochem. Soc.*, **6**, 160 (1904).
9. A. R. Johnson, *ibid.*, **18**, 125 (1910).
10. M. Guntz and Henry Bassett, Jr., *Bull. Soc. Chim. Paris*, **35**, 404 (1906).
11. Paul Wohler, *J. Chem. Soc.*, **88**, Part 2, 708 (1905).
12. Minoru Kunitomi, *J. Chem. Soc. Japan, Pure Chemistry Section*, **71**, 40 (1950).

Ageing Effects in Thin Anodic Oxide Films on Au in $HClO_4$

S. B. Brummer

Tyco Laboratories, Inc., Waltham, Massachusetts

In a previous paper (1) it was shown that the properties of thin oxide films on Au depend strongly on the potential, E_a, at which they are formed. Thus, as the potential is increased the amount of oxide on the electrode increases, being a monolayer at about 1.45v *vs.* H_2/H^+ in the same solution. In addition, the reduction of a potentiostatically preformed oxide becomes more difficult at higher potentials of formation, although the reduction is still quantitative (2). In this paper, some experiments are reported which indicate that the properties of the anodically formed films are sensitive also to the time for which they are formed, τ_a. In effect, the oxide is growing slowly even at long times of formation and becomes harder to reduce. Ageing effects of this kind are well known for thick oxide films (3), but very little is known about the ageing of very thin films. Frumkin (4) reports such effects for anodically formed films on Pt; however, there appears to have been no quantitative investigation of this phenomenon.

Experimental Procedure

Oxides were formed at each potential by means of a Wenking fast rise potentiostat. To measure the extent of oxidation, Q_a, the oxides were usually reduced galvanostatically at ~300 μa/cm^2. Switching of the counterelectrode from the potentiostatic to the galvanostatic circuit was achieved with a Hg-wetted relay. The potential-time transient was followed on an oscilloscope via a high impedance voltage follower (Philbrick P2 amplifier used as electrometer). The method of determining from the oscilloscope traces the amount of oxide and the potential of reduction of the oxide has been described previously (1). Usually, a large part of the oxide is reduced at a constant potential. However, at short times of formation and/or at low potentials of formation and/or with large reduction currents, the oxide reduction curve (chronopotentiogram) shows a sloping portion rather than a flat plateau. In these cases, the first potential at which the oxide starts to be reduced was used in assessing the reduction potential of the oxide at the given current density. This is illustrated in Fig. 1. For reduction experiments with linear potential sweeps, an Exact Electronics function generator (Model 250) was used to generate the potential ramp, and the potential across a decade resistance box (General Radio Company, 0.05%) was recorded with an oscilloscope. In some

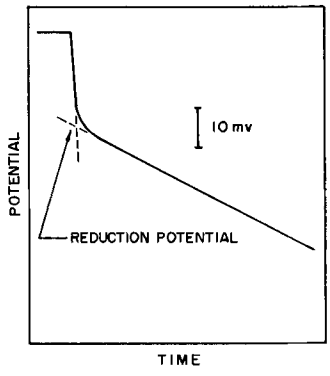

Fig. 1. Estimation of the reduction potential from chronopotentiograms when the oxide reduction takes place over a range of potentials.

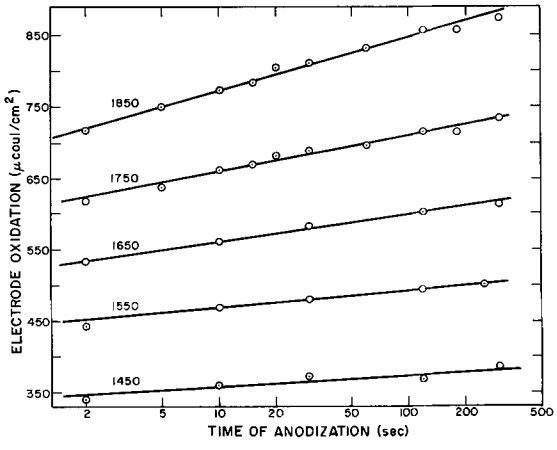

Fig. 2. Growth of oxide at various potentials (mv vs. R.H.E.) as a function of time.

cases, two plug-in units were used in the oscilloscope, allowing an X-Y presentation.

In other respects, the methods and procedures are as previously described (1). It is to be emphasized that the counterelectrode should also be of Au; if Pt is used, the working electrode is contaminated with what appears to be about a monolayer of Pt. Experiments were carried out in 1*N* $HClO_4$ at room temperature (23° ± 2°C). A hydrogen reference electrode was used, and potentials are reported against Pt, H_2/H^+ in the test solution.

Results and Discussion

Growth of the oxide.—Figure 2 shows some results during the latter stages of the oxide growth for the extent of the electrode oxidation as a function of time at each potential. Growth of the oxide appears to follow a semi-logarithmic relationship, *i.e.*,

$$Q_a = a + b \log \tau_a \qquad [1]$$

where a and b are constants. At the shortest anodization times used here, 2 sec, most of the oxide has already formed. Thus, at 1.85v, the oxide is already at 82% of its 5-min value after 2 sec of formation and, at 1.45v, it is 88% of its 5-min value. However, it appears from information available in the literature for the growth of thin oxide films on Pt (5, 6), particularly from the data of Gilman (6), we may have considerable confidence in the applicability of Eq. [1] to the earlier stages of the oxide growth. If these oxides are considered as adsorbed layers rather than as distinct compounds (7), then Eq. [1] would follow from the application of the Temkin adsorption isotherm, sometimes known as Elovich kinetics (8). We may estimate a monolayer of oxide as 400 (1) or 450 (9), or 650 (9) μcoul/cm², but whichever of these is the most

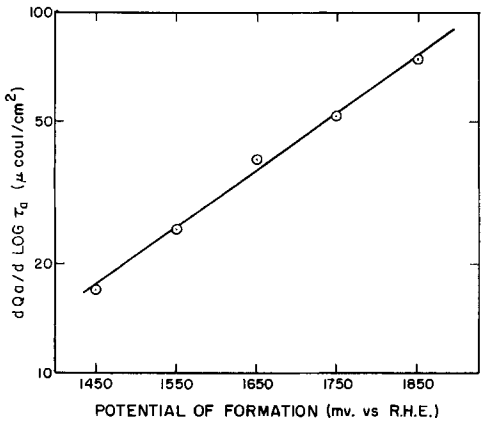

Fig. 3. Semi-logarithmic expression of the growth-rate constant *b* as a function of potential.

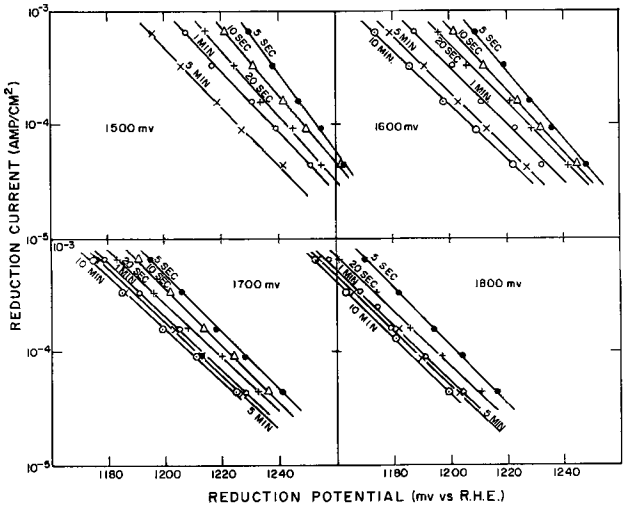

Fig. 4. Current-potential curves for the reduction of oxides, as a function of time and potential of formation.

reasonable, the present data extend from less than a monolayer to considerably above a monolayer. Despite this, there is a smooth variation of the parameter b of Eq. [1] with E_a (Fig. 3).

As expected, the growth rate of the oxide is higher, in absolute terms, at the higher potentials of formation, and also, as indicated above, the fractional growth (2 sec to 5 min) is more at the higher potentials. Although the growth rate is relatively slow even at the highest potentials (Fig. 2), the equating previously (1) of the 5-min value of Q_a with its infinite time value does involve small errors in the Q_a values presented, as does the procedure used by Laitinen and Chao (10). For example, at 1.85v the 5-min values should perhaps be about 8% less than the 1-hr value of Q_a. However, it is unlikely that the oxide thickens indefinitely, for as has been observed at the higher potentials (1, 2), the oxide has a finite rate of dissolution; hence the error in selecting the 5-min values of Q_a would be less than this. In fact very little difference was found between the 5-min and 20-min values of Q_a (1).

Reduction of the oxide.—The reduction kinetics of the oxide are shown in Fig. 4 as a function of E_a and τ_a. It is seen that at a given potential of formation the oxide becomes progressively harder to reduce with longer times of formation. At any potential of formation, the general effect is a shift of the Tafel line for the reduction of the oxide (slope 39-41 mv) to lower potentials. At the shorter times of formation, however, the slope tends to be less than the usual value, par-

ticularly at the lower potentials. As has been noted, reduction potentials in this region are the least reliable as the chronopotentiogram has the least satisfactory plateau.

The time variation of the oxide reduction kinetics is more pronounced at the lower potentials of formation. The oxides stabilize much more rapidly at their ultimate (5 or 10 min) properties at higher potentials of formation; this is despite the fact that the oxide, at the higher potentials, is much "thicker" (if "thickness" is the relevant term for $\sim 0.8 \leq$ layer thickness ≤ 2 layers) and, thus, presumably, any transport processes through the film would be more difficult. On the other hand, the higher field resulting from the higher potential would help to counteract this for ion migration processes through the film. So, although there is both relatively and absolutely a much larger change in the quantity of oxide formed during the range of τ_a, 2 sec to 5 min, at the higher potentials of formation, the properties of the oxide change much more, during this time, at the lower potentials of formation.

Use of triangular potential sweeps for oxide reduction.—It is clear from the data presented here that triangular sweeps are to be employed for studies of oxide reduction only with extreme caution. In the method of Will and Knorr (11), the oxide is formed over a range of potentials, and not only is this likely to lead to an inhomogeneous oxide *per se* (1), but also the oxide has only a fraction of a second to "age." Consequently, we would not expect the results obtained on the cathodic sweep of the triangles to be quantitatively significant. This is apparent from the curves shown in Fig. 5. These represent the current potential curves for the reduction of oxide formed under various conditions. Curve A is the current-potential curve for the reduction of oxide formed for 5 min (*i.e.*, $\simeq$ infinite time) at 1500 mv. A full description of such curves will be given later. Curves B and C represent the reduction of oxide formed during the anodic part of a 0.14 v/sec triangular wave. In B, the triangle was terminated at 1500 mv, in C at ~1600 mv. As expected, A and B are not comparable, relatively little oxide being formed in B. C was chosen such that $Q_A = Q_C$. We note that the oxide in C is more easily reduced and, also, is reduced over a wider range of potential (*i.e.*, the peak is shorter and squatter). A comparison of B and C indicates that a considerable part of Q_C is formed between 1500 and 1600 mv, *i.e.*, at a higher potential than the top potential of A. From the previous work (1) it would, therefore, be supposed that the oxide in C would be harder to reduce than that in A. Thus, the main reason why curve C indicates an oxide which is misleadingly easy to reduce is because the oxide has not had enough time to "age." The broadness of the peak in C would indicate that the oxide is unusually inhomogeneous compared with A. The reduction curves obtained after various times of formation at a fixed potential (Fig. 6) do not indicate that unaged oxide is usually more inhomogeneous than the aged material; for example, the width of the reduction peak at the current corresponding to half the maximum current is the same for each time of formation, about 80 mv in this instance. Thus the inhomogeneity of the oxide in C, which is too large to be associated solely with the formation of oxide over a range of potential *per se* (1), must result mainly from the "freezing-in" of oxide configurations formed at short times at the lower potentials. These configurations will not have "aged" out in the short time before the cathodic sweep. In order to avoid such errors, say to keep the reduction potential at a given current to less than 5 mv with respect to the 5 min values, we would have to allow at least 2 min at 1600 (cf. Fig. 4). This involves extremely slow sweep rates and clearly indicates that the method of Will and Knorr (11) is not suitable to study such reactions quantitatively.

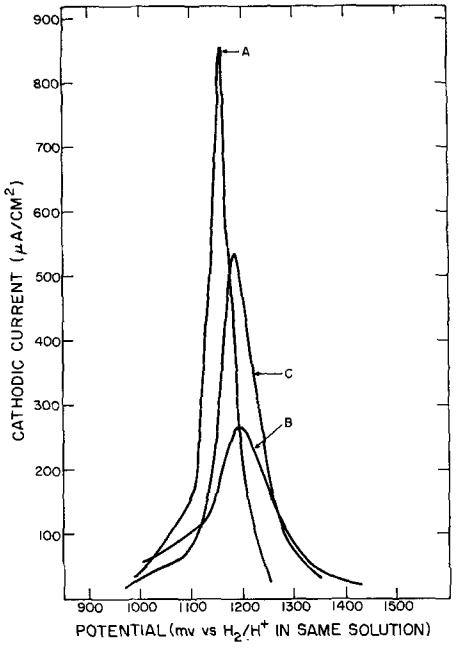

Fig. 5. Current-potential curves for the reduction of oxides, made with linear potential sweeps of 0.14 v/sec. Curve A, oxide reduced after 5 min at 1500 mv; curve B, oxide formed and reduced during triangular potential sweep, reversed at 1500 mv; curve C, triangular sweep reversed at ~ 1600 mv, such that $Q_A = Q_C$.

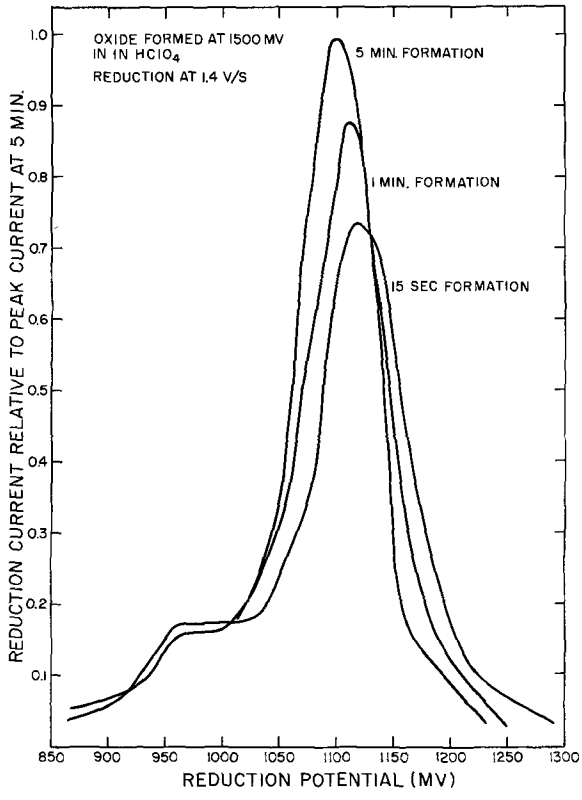

Fig. 6. Current-potential curves for the reduction of oxides, made with linear potential sweeps of 1.4 v/sec, as a function of time of formation at 1500 mv.

Summary

1. The properties of anodic oxide films on Au in 1*N* $HClO_4$ have been studied as a function of time (2 sec to 5 min) and of potential of formation (1450 to 1850 mv *vs.* Pt, H_2/H^+ in the same solution).

2. Over the range observed (10-20% of the total oxide), the oxide grows slowly with time, apparently according to Elovich kinetics, although the constants are potential-dependent.

3. Oxides formed at longer times at a given potential are harder to reduce.
4. This "ageing" effect is greatest at the lower potentials of formation, despite the greater thickness of the oxide at the higher potentials and despite the larger change in the amount of oxide at the higher potentials.
5. Because of these ageing effects, the triangular sweep method of Will and Knorr is not suitable to study these films.

Acknowledgments

It is a pleasure to acknowledge the skillful experimental assistance of Mrs. M. J. Turner. This work was supported by the Office of Naval Research under contract Nonr 3765(00).

Manuscript received Dec. 22, 1964. This paper was presented at the Toronto Meeting, May 3-7, 1964.
Any discussion of this paper will appear in a Discussion Section to be published in the December 1965 JOURNAL.

REFERENCES

1. S. B. Brummer and A. C. Makrides, *This Journal*, **111**, 1122 (1964).
2. K. J. Vetter and D. Berndt, *Z. Elektrochem.*, **62**, 378 (1958).
3. L. Young, "Anodic Oxide Films," Academic Press, London (1961).
4. A. N. Frumkin, "Advances in Electrochemistry and Electrochemical Engineering," Vol. 3, p. 305, John Wiley & Sons, Inc., New York (1963).
5. S. W. Feldberg, C. G. Enke, and C. E. Bricker, *This Journal*, **110**, 826 (1963).
6. S. Gilman, *Electrochim. Acta*, **9**, 1025 (1964).
7. D. A. Vermilyea, "Advances in Electrochemistry and Electrochemical Engineering," Vol. 3, John Wiley & Sons, Inc., New York (1963).
8. S. Yu. Elovich and G. M. Zhabrova, *Zh. Fiz. Khim.*, **13**, 1761 (1939).
9. A. Hickling, *Trans. Faraday Soc.*, **42**, 518 (1946).
10. H. A. Laitinen and M. S. Chao, *This Journal*, **108**, 726 (1961).
11. F. G. Will and C. A. Knorr, *Z. Elektrochem.*, **64**, 270 (1960).

The Kinetics of the Stannous/Stannic Redox Reaction at Carbon Electrodes

H. Lerner and L. G. Austin

Department of Fuel Technology, College of Mineral Industries, The Pennsylvania State University, University Park, Pennsylvania

As part of an experimental study to determine the effects of a porous diffusion electrode on the over-all kinetics of an electrochemical reaction (1,2), it was desired to employ a redox couple having a relatively low exchange current and a fairly simple reaction mechanism. A study of the literature (3) showed that the Sn^{2+}/Sn^{4+} redox couple in HCl might meet these requirements. Vetter (4) concluded, as a result of some steady-state cathodic polarization measurements at mercury and platinum electrodes, that this redox couple reacted fairly irreversibly according to the mechanism

$$Sn^{2+} \rightleftarrows Sn^{3+} + e^- \quad \text{Step r}$$
$$Sn^{3+} \rightleftarrows Sn^{4+} + e^- \quad \text{Step o}$$
$$\overline{Sn^{2+} \rightleftarrows Sn^{4+} + 2e^- \quad \text{Over-all reaction}} \qquad [1]$$

The rate equation for this mechanism is given by (4, 5),

$$i = 2i_{o,r}e^{\alpha_r F\eta/RT}\frac{[(1 - i/i_{L,R}) - (1 + i/i_{L,O})e^{-2F\eta/RT}]}{[1 + (i_{o,r}/i_{o,o})e^{-(1-\alpha_r+\alpha_o)F\eta/RT}]} \qquad [2]$$

where $i_{o,r}$, $i_{o,o}$, α_r, α_o are the exchange currents and transfer coefficients for steps r and o, respectively, $i_{L,R}$ and $i_{L,O}$ the limiting currents for Sn^{2+} and Sn^{4+}, respectively, and F, η, R, T, and i have their usual significance. Equation [2] was derived on the assumption that the concentration of Sn^{3+} would be very small so that any mass transport effects involving this species could be neglected. The terms involving i_L reflect the use of the Nernst diffusion layer theory to account for mass transport effects involving Sn^{2+} and Sn^{4+}. When $i_{o,r}/i_{o,o} >> 1$ and $i_{o,r}/i_L << 1$ three distinct irreversible regions of the mechanism can be obtained during steady-state measurements of voltage *vs.* current. The regions are:

1. *Step o rate controlling*

$$[e^{-2F\eta/RT} << 1 << (i_{o,r}/i_{o,o})e^{-(1-\alpha_o+\alpha_r)F\eta/RT}, i/i_L << 1]$$
$$i = 2i_{o,o}e^{(1+\alpha_o)F\eta/RT} \qquad [3]$$

For example, if $i_{o,r}/i_{o,o}$ is about 10^3 and $\alpha_r \simeq \alpha_o$, this Tafel region would extend from η equal to about 30 mv to about 120 mv.

2. *Step r rate controlling*

$$[(i_{o,r}/i_{o,o})e^{-(1-\alpha_o+\alpha_r)F\eta/RT} << 1 \text{ and } i/i_L << 1]$$
$$i = 2i_{o,r}e^{\alpha_r F\eta/RT} \qquad [4]$$

For the figures given before, this Tafel region starts at η about 240 mv and the upper limit will occur at about $i = 0.1\ i_L$.

3. *Step r and mass transport rate controlling*

$$[(i_{o,r}/i_{o,o})e^{-(1-\alpha_o+\alpha_r)F\eta/RT} << 1 \text{ and } i/i_L \text{ tending to one}].$$
$$i = 2i_{o,r}e^{\alpha_r F\eta/RT}(1 - i/i_L) \qquad [5]$$

The lower limit of η will be the same as for Eq. [4] while η becomes large as $i \rightarrow i_L$.

The only anodic polarization measurements reported by Vetter used Hg electrodes, but since Hg could be expected to react at the anodic potentials required for the oxidation of Sn^{2+}, this work is suspect (although it agreed with the results of cathodic polarization measurements). In the study reported here, pyrolytic carbon electrodes were used to establish with greater certainty the mechanism and form of the anodic rate equation for the Sn^{2+}/Sn^{4+} couple at a solid electrode. The results obtained from the steady-state and galvanostatic measurements discussed below supported the mechanism of Eq. [2].

Experimental

The water used throughout the experimental work was prepared by deionizing tap water with an Ilco research model ion-exchange column, stirring it for 48 hr with a spectrographic grade of graphite powder (SP-1, National Carbon Company), filtering, and distilling. The purpose of the graphite treatment was to reduce the amount of adsorbable organic impurities in the water. The specific resistance of the water was greater than 10^6 ohms. Hydrochloric acid was pre-

pared by distilling the concentrated reagent grade material (Fisher) after it had been diluted to approximately the constant boiling mixture concentration (~6.1M). The distillate, which was a middle cut, was then diluted to 4M. The HCl was considered acceptable for use when its polarographic current was equal to, or less than 0.2 μa ($m^{2/3}t^{1/6} \sim 2.5$) at —0.72v *vs.* a SCE. Two methods were used to prepare the 4*N* HCl solution of the Sn^{2+}/Sn^{4+} couple. The first consisted of dissolving reagent grade (Fisher) $SnCl_7 \cdot 2H_2O$ and $SnCl_4 \cdot 5H_2O$ in 4*N* HCl, stirring the solution with graphite for two days and filtering. In the second method, 4*N* HCl was stirred with graphite for two days, filtered and electrolyzed at a Hg cathode with the evolution of hydrogen ($i \sim 0.5$ ma/cm^2). Nitrogen (passed through a purification train containing an HCl solution of VCl_2, a charcoal trap in a dry ice-acetone bath and suitable saturators) was used to stir the HCl. After three days of electrolysis some of the HCl was removed from the electrolysis cell (with the current still flowing) and placed in the test cell. Reagent grade tin (Fisher) was then added to the HCl and dissolved by heating. The resulting $SnCl_2$ solution was then stirred in the presence of air to obtain an approximately equimolar solution of $SnCl_2$ and $SnCl_4$. The concentrations of the redox couple were determined by a potentiometric method, with the $SnCl_4$ being determined following its reduction to $SnCl_2$ with a lead reductor. No significant difference was found in results obtained from the solutions prepared by the two methods.

The test cell was a 250 ml glass beaker which had been cleaned with hot chromic acid solution and preconditioned with 4*N* HCl for at least a week. The cell cover was made of Lucite and contained holes for the pyrolytic carbon electrode (area = 0.25 cm^2), the platinum counter electrode (area = 12.8 cm^2), the salt bridge of the saturated calomel reference electrode and a nitrogen inlet tube. The carbon test electrode was made from a piece of pyrolytic graphite (~½ x ½ x 3 in.) which had been machined into a cylinder with the long dimension parallel to the basal plane. One end of this cylinder (edge plane) was machined perpendicular to the axis, and a piece of Alphex shrinkable tubing (FIT-275) was used to mask off the sides. This tubing, made of irradiated polyolefin, shrinks to a predetermined size on heating. This gave a tight, leak-proof fit. The cell was maintained at 25.0° ± 0.03°C in a water bath, and the solution was stirred with a magnetic stirrer.

The circuit for the steady-state measurements was of conventional design, providing an input impedance of about 10^{11} ohms for the voltage measurements and an accuracy and reproducibility of better than 1%. The galvanostatic measurements utilized a regulated voltage supply (Harrison, #800A-2), a relatively large series resistor and a mercury relay (Western Electric, #275-B). With appropriate circuitry (6) it was possible to obtain a constant current pulse of variable duration with a rise time of less than 5 μsec. The voltage-time traces were recorded using an oscilloscope and a Polaroid camera.

All of the measurements were performed following deaeration of the system overnight. In the steady-state measurements a small amount of negative hysteresis was obtained at the lower current densities. It was found, however, that, if the system was brought to $i/i_L \simeq 0.7$ prior to a measurement, completely reproducible results were obtained over the entire polarization curve. A galvanostatic technique was used to correct for IR effects in the steady-state measurements of η.

Results and Discussion

Figure 1 shows the steady-state values of polarization *vs.* log current for the oxidation of a solution of 0.104M $SnCl_2$ and 0.081M $SnCl_4$ in 4M HCl at the pyrolytic carbon electrode. The polarization (η) was obtained from the relationship, η = measured voltage-

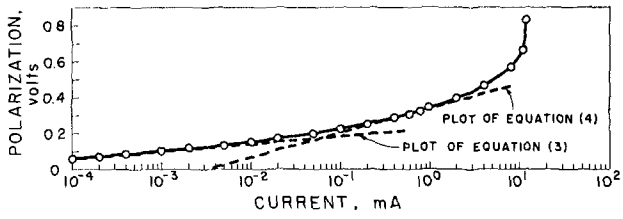

Fig. 1. Experimental plot of polarization vs. log current for steady-state oxidation of 0.104M $SnCl_2$ and 0.081M $SnCl_4$ in 4*N* HCl at pyrolytic carbon electrode (area = 0.25 cm^2). Solid line, experimental results; dashed line, extrapolations of results according to Eq. [3] and [4].

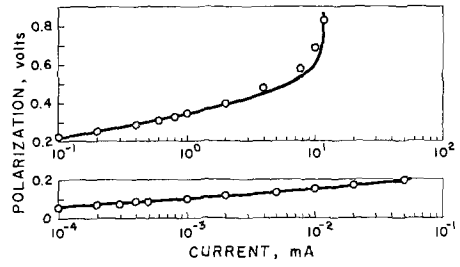

Fig. 2. Fit of experimental results of Fig. 1 to Eq. [2]

open circuit voltage, where the open-circuit voltage (—0.127v *vs.* SCE) was taken as the reversible voltage. [This open-circuit voltage was extremely reproducible over long periods of time, independent of any measurement sequence and insensitive to changes in stirring rates. The value given by Vetter (4) is 0.16v *vs.* NHE for 1M HCl, but the potential of this couple is dependent on the HCl concentration, decreasing as the concentration of HCl increases (7). In addition a liquid junction potential of about 30 mv (8) existed between the saturated KCl solution of the reference electrode and the 4M HCl solution containing the redox couple. The corrected open-circuit potential for the Sn^{2+}/Sn^{4+} couple was therefore about 0.15v *vs.* NHE, in reasonable agreement with Vetter's value.] Figure 1 also contains plots of the experimental data according to Eq. [3] and [4], from which the kinetic constants were obtained. These plots gave good straight lines with the values, $\alpha_o = 0.41$, $i_{o,o} = 8.0 \times 10^{-6}$ ma/cm^2, $\alpha_r = 0.43$ and $i_{o,r} = 7.0 \times 10^{-3}$ ma/cm^2.

Figure 2 shows the fit of the experimental data of Fig. 1 to Eq. [2]. Equation [2] was plotted using a value of $i_L = 11.5$ ma and the values of the kinetic constants that were obtained from Fig. 1. Excellent agreement was obtained over the first four decades of current, but in the final decade where the value of current approaches the limiting current, the agreement was not as good and some deviation of the experimental results from Eq. [2] can be observed. A similar deviation was obtained with a different concentration of the redox couple at the pyrolytic carbon electrode (which showed it was not due to a variation of the activity coefficient with concentration), and also for several porous carbon electrodes. To account for this deviation a number of possibilities were considered.

The possibilities of impurities in the system or errors in the measurements were rejected because: (i) the deviation was very reproducible and was found in all of the systems studied; (ii) the voltage and current measuring sections of the apparatus were carefully calibrated prior to all of the measurements; (iii) no hysteresis effects were observed in this current region; and (iv) impurity effects usually occur only in the low current region, whereas, this deviation occurred at relatively large currents. The results were reproducible when the position and shape of the counter electrode were changed, which showed that the effect was not due to nonuniformity of current distribution. Another possibility was that there existed some chemical step in the mechanism which preceded the electron transfer

Table I. Consistency of $i\tau^{1/2}$ as a function of i for $Sn^{2+} \rightarrow Sn^{4+} + 2e^-$ at a pyrolytic carbon electrode*

i, ma	τ, s·c	$\tau^{1/2}$, $sec^{1/2}$	$i\tau^{1/2}$, ma $sec^{1/2}$
1.44	45.3	6.73	9.68
2.39	15.6	3.95	9.44
4.80	4.07	2.02	9.70
5.80	2.86	1.69	9.80
7.48	1.74	1.32	9.87
13.4	0.55	0.74	9.92

* 0.0675M $SnCl_2$ and 0.0945M $SnCl_4$ in 4*N* HCl; area of electrode = 0.25 cm^2.

steps (*e.g.*, dissociation of $SnCl_4^{2-}$ to Sn^{2+}). If this chemical step were slow enough to control the rate of the reaction partially at higher currents, the current would be less than that predicted by Eq. [2]. This possibility was investigated with the galvanostatic technique by measuring $i\tau^{1/2}$ as a function of i for the oxidation of Sn^{2+}, see Table I.

It is clear that $i\tau^{1/2}$ is constant within the limits of experimental error, and therefore (9) a slow preceding chemical step is not present.

Since the deviation occurred only in the region where the rate of mass transport of Sn^{2+} to the electrode was partially controlling the rate of the reaction, it was considered that the deviation was probably due to a breakdown of the simple Nernst diffusion layer theory. It is well known that this theory is at best only a good approximation (10). One reasonable explanation for the breakdown of this theory for the system used in this study is the density change which would be expected to occur in the diffusion layer region as a result of the buildup in concentration of $SnCl_4$ as $i \rightarrow i_L$ [(dens. of $SnCl_4$)/(dens. of $SnCl_2$) > 1 for equimolar concentrations]. This would lead to a corresponding increase in the mass transport coefficient and give rise to the observed deviation between Eq. [2] and the experimental results.

Figure 3 compares the experimental data of Fig. 1 with experimental results obtained for a lower concentration of the redox couple (0.0120M $SnCl_2$ and 0.0088M $SnCl_4$ in 4*N* HCl). The ratio of the limiting currents for the two concentrations of $SnCl_2$ is 9.2 which is approximately the same as the ratio of their concentrations, 8.7. At any given current in the regions of Eq. [3] and [4] the approximately tenfold change in concentration of the redox couple results in a change in η of approximately 0.040 and 0.10v, respectively. This is in fairly good agreement with the expected values (assuming first-order kinetics) of $\Delta\eta = 0.040$v and $\Delta\eta = 0.12$v, respectively.

Summary and Conclusions

From the results of steady-state and galvanostatic measurements on the edge-atom plane of a pyrolytic carbon electrode, and from previous results reported in the literature for Hg and Pt electrodes, it appears that the mechanism for the redox reaction $Sn^{2+} \rightleftarrows Sn^{4+} + 2e^-$ consists of two consecutive one-electron transfer steps (reaction [1]), where the intermediate Sn^{3+} has a very small concentration. The second step in the anodic process has the lower exchange current, and at low currents it is rate controlling. At sufficiently large currents the first step becomes rate controlling and the rate equation assumes a simple Tafel form with a slope of 2.3 $RT/\alpha_T F$. The values of the kinetic parameters on the edge-atom plane of pyrolitic graphite were $i_{o,r} = 7.0 \times 10^{-3}$ ma/cm^2, $i_{o,o} = 8.0 \times 10^{-6}$ ma/cm^2, $\alpha_r = 0.43$ and $\alpha_o = 0.41$, based on the open-circuit potential of —0.122v *vs.* a SCE. The double layer capacity of the edge plane was 127 $\mu Fd/cm^2$, so that the geometric exchange current densities given above are probably about 6 or 7 times larger than the values for a smooth surface.

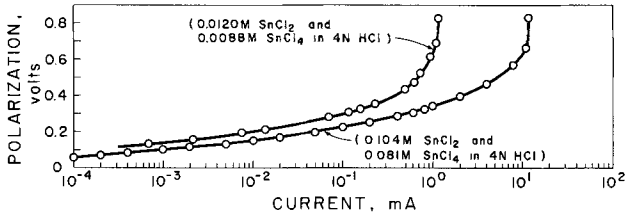

Fig. 3. Comparison of experimental polarization *vs.* log current results for two different concentrations of the $SnCl_2/SnCl_4$ couple.

Manuscript received Nov. 24, 1964; revised manuscript received Feb. 12, 1965.

Any discussion of this paper will appear in a Discussion Section to be published in the December 1965 JOURNAL.

REFERENCES

1. L. G. Austin and H. Lerner, *Electrochim. Acta*, **9**, 1469 (1964).
2. H. Lerner and L. G. Austin, In preparation, see "Experimental Confirmation of the Theory of Polarization at Flooded Porous Diffusion Electrodes;" Extended Abstracts of Theoretical Division, Toronto Meeting of the Society, **2**, 21 (1964).
3. H. Lerner, Ph.D. Thesis, pp. 36 and 77, Pennsylvania State University (1964).
4. K. J. Vetter, "Elektrochemische Kinetik," pp. 129 and 379, Springer-Verlag, Berlin (1961).
5. Ref. (3), p. 30.
6. Ref. (3), p. 100.
7. C. S. Huey and H. V. Tartar, *J. Am. Chem. Soc.*, **56**, 2585 (1934).
8. E. C. Potter, "Electrochemistry," p. 96, Cleaver-Hume Press Ltd., London (1956).
9. P. Delahay, "New Instrumental Methods in Electrochemistry," p. 199, Interscience Publishers, Inc., New York (1954).
10. P. Delahay, *ibid.*, p. 226.

On the Potential/pH Diagrams of the $Cu\text{-}NH_3\text{-}H_2O$ and $Zn\text{-}NH_3\text{-}H_2O$ Systems

H. E. Johnson[1] and J. Leja

Department of Mining and Metallurgy, University of Alberta, Edmonton, Alberta, Canada

One of the most promising developments in the study of the stress corrosion cracking of alpha brass in aqueous ammonia environments has been Mattsson's (1) correlation of the pH dependence of cracking with certain features of the potential/pH diagrams for the $Cu\text{-}NH_3\text{-}H_2O$ and $Zn\text{-}NH_3\text{-}H_2O$ systems. These diagrams were based on the thermodynamic data published by Latimer (2) in 1952. In the course of extending the stress corrosion studies to define more precisely the effect of various copper ammine complexes (3), it

[1] Present address: Esso Production Research Company, Houston, Texas.

appeared that the diagrams proposed by Mattsson might be improved by the inclusion of intermediate copper-ammine and zinc-ammine complexes (containing less than four ammonia ligands per coordinating metal ion), and by re-locating the regions of stability of the solid phases CuO, Cu_2O, and $Zn(OH)_2$. Since both Mattsson (1) and Hoar (4) have correlated the Cu_2O region with the tarnish formation on alpha brass undergoing stress corrosion cracking, it is important that the corrected potential/pH diagrams be considered in any further investigation of this type.

Construction of Diagrams

The principles of construction of potential/pH diagrams are well known (5) but it is useful to reiterate the two main conventions (5a) that are observed in setting up the equations from which the graphs are constructed. Considering the general reaction

$$aA + bB + cH_2O + mH^+ + ne^- = 0 \qquad [I]$$

Convention I. For reactions without oxidation ($n = 0$), the coefficients a and m are taken as positive. The substance A is then the more basic of the compounds involved, and therefore appears to the right of substance B in the diagram.

Convention II. For reactions with oxidation ($n \neq 0$), a and n are taken as being positive, so that substance A is the more highly oxidized of the compounds involved, and thus appears above substance B in the diagram.

The data used in the construction of the corrected diagrams are given in Table I: they do not differ significantly from those used by Mattsson (1).

Figures 1a, 2a, and 3a are taken from Mattsson's (1) work (the line numbers refer to his equations); the diagrams have been re-drawn to the same scale as the corrected diagrams which are presented in Fig. 1b, 2b, and 3b. The line numbers in the "b" diagrams refer to the following chemical reactions and the corresponding potential/pH equations:

$$Cu^{++} + e^- = Cu^+$$
$$E = 0.153 + 0.0591 \log [Cu^{++}]/[Cu^+] \qquad [1]$$

Table I. Constants used in pH/potential equations

1. Oxidation potentials

		Reference
$Cu^{++} + 2e^- = Cu$	$E^\circ = +0.337V$	(2)
$Cu^+ + e^- = Cu$	$E^\circ = +0.521V$	
$Cu^{++} + e^- = Cu^+$	$E^\circ = +0.153V$	
$Zn^{++} + 2e^- = Zn$	$E^\circ = -0.763V$	

2. Equilibrium constants — Reference

$$\beta_n = \frac{[ML_n]}{[M][L]^n}$$

where M is the metal and L the ligand.

Complex	$\log \beta_n$	
$Cu(NH_3)^+$	5.93	(6)
$Cu(NH_3)_2^+$	10.86	
$Cu(NH_3)^{++}$	4.18	(7)
$Cu(NH_3)_2^{++}$	7.71	
$Cu(NH_3)_3^{++}$	10.63	
$Cu(NH_3)_4^{++}$	12.79	
$Zn(NH_3)_3^{++}$	7.28	
$Zn(NH_3)_4^{++}$	9.42	

$pK_{NH_4^+} = 9.614$ @ 22°C (in 2M NH_4NO_3)

3. Molar standard chemical potentials, kcals @ 25°C

Substance	State	μ°	Reference
H^-	aq	0	(2)
NH_3	aq	−6.36	
NH_4^+	aq	−19.00	
NH_4OH	aq	−62.86	
Cu^+	aq	+12.01	
Cu^{++}	aq	+15.53	
CuO	Solid	−30.4	
Cu_2O	Solid	−34.98	
Cu	Solid	0	
Zn	Solid	0	
Zn^{++}	aq	−35.184	
ZnO	Solid	−76.05	
H_2O	aq	−56.56	(5)
$Cu(NH_3)^+$	aq	−2.45	Calculated from equilibrium constants
$Cu(NH_3)_2^+$	aq	−15.54	
$Cu(NH_3)^{++}$	aq	+3.47	
$Cu(NH_3)_2^{++}$	aq	−7.71	
$Cu(NH_3)_3^{++}$	aq	−18.05	
$Cu(NH_3)_4^{++}$	aq	−27.36	
$Zn(NH_3)_3^{++}$	aq	−64.20	
$Zn(NH_3)_4^{++}$	aq	−73.48	

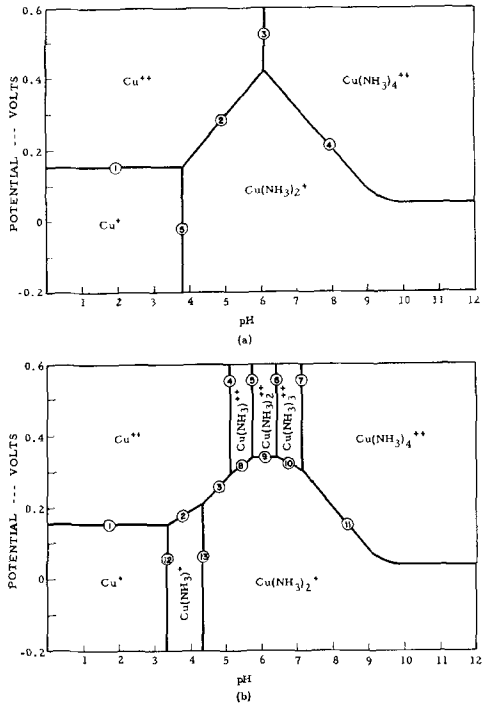

Fig. 1. Potential/pH diagrams for the homogeneous Cu-NH_3-H_2O system. (a) After Mattsson (1), (b) present work. [25°C, total dissolved Cu = 0.05M, total ($NH_3 + NH_4^+$) = 1.0M.]

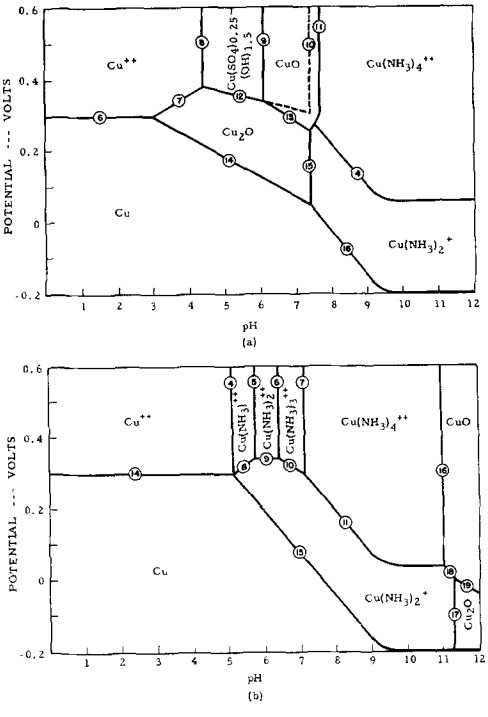

Fig. 2. Potential/pH diagrams for the heterogeneous Cu-NH_3-H_2O system. (a) After Mattsson (1), (b) present work.

$$Cu^{++} + NH_4^+ + e^- = Cu(NH_3)^+ + H^+$$
$$E = -0.044 + 0.0591\,pH + 0.0591 \log [NH_4^+] + 0.0591 \log [Cu^{++}]/[Cu(NH_3)^+] \qquad [2]$$

$$Cu^{++} + 2NH_4^+ + e^- = Cu(NH_3)_2^+ + 2H^+$$
$$E = -0.301 + 0.118\,pH + 0.118 \log [NH_4^+] + 0.0591 \log [Cu^{++}]/[Cu(NH_3)_2^+] \qquad [3]$$

$$Cu(NH_3)^{++} + H^+ = Cu^{++} + NH_4^+$$
$$pH = 5.09 - \log [NH_4^+] + \log [Cu(NH_3)^{++}]/[Cu^{++}] \qquad [4]$$

$$Cu(NH_3)_2^{++} + H^+ = Cu(NH_3)^{++} + NH_4^+$$
$$pH = 5.74 - \log [NH_4^+] + \log [Cu(NH_3)_2^{++}]/[Cu(NH_3)^{++}] \qquad [5]$$

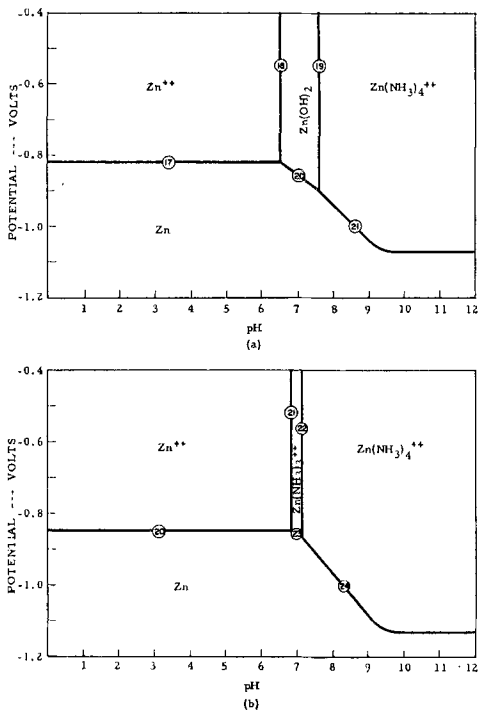

Fig. 3. Potential/pH diagrams for the heterogeneous Zn-NH_3-H_2O system. (a) After Mattsson (1), (b) present work. [25°C, total dissolved Zn = 0.001M, total (NH_3 + NH_4^+) = 1.0M.]

$$Cu(NH_3)_3^{++} + H^+ = Cu(NH_3)_2^{++} + NH_4^+$$
$$pH = 6.35 - \log [NH_4^+] + \log [Cu(NH_3)_3^{++}]/[Cu(NH_3)_2^{++}] \quad [6]$$

$$Cu(NH_3)_4^{++} + H^+ = Cu(NH_3)_3^{++} + NH_4^+$$
$$pH = 7.11 - \log [NH_4^+] + \log [Cu(NH_3)_4^{++}]/[Cu(NH_3)_3^{++}] \quad [7]$$

$$Cu(NH_3)^{++} + e^- + NH_4^+ = Cu(NH_3)_2^+ + H^+$$
$$E = 0.0591\, pH + 0.0591 \log [NH_4^+] + 0.0591 \log [Cu(NH_3)^{++}]/[Cu(NH_3)_2^+] \quad [8]$$

$$Cu(NH_3)_2^{++} + e^- = Cu(NH_3)_2^+$$
$$E = 0.339 + 0.0591 \log [Cu(NH_3)_2^{++}]/[Cu(NH_3)_2^+] \quad [9]$$

$$Cu(NH_3)_3^{++} + e^- + H^+ = Cu(NH_3)_2^+ + NH_4^+$$
$$E = 0.715 - 0.0591\, pH - 0.0591 \log [NH_4^+] + 0.0591 \log [Cu(NH_3)_3^{++}]/[Cu(NH_3)_2^+] \quad [10]$$

$$Cu(NH_3)_4^{++} + e^- + 2H^+ = Cu(NH_3)_2^+ + 2NH_4^+$$
$$E = 1.135 - 0.118\, pH - 0.118 \log [NH_4^+] + 0.0591 \log [Cu(NH_3)_4^{++}]/[Cu(NH_3)_2^+] \quad [11]$$

$$Cu(NH_3)^+ + H^+ = Cu^+ + NH_4^+$$
$$pH = 3.33 - \log [NH_4^+] + \log [Cu(NH_3)^+]/[Cu^+] \quad [12]$$

$$Cu(NH_3)_2^+ + H^+ = Cu(NH_3)^+ + NH_4^+$$
$$pH = 4.34 - \log [NH_4^+] + \log [Cu(NH_3)_2^+]/[Cu(NH_3)^+] \quad [13]$$

$$Cu^{++} + 2e^- = Cu$$
$$E = 0.337 + 0.0295 \log [Cu^{++}] \quad [14]$$

$$Cu(NH_3)_2^+ + 2H^+ + e^- = Cu + 2NH_4^+$$
$$E = 0.974 - 0.118\, pH - 0.118 \log [NH_4^+] + 0.0591 \log [Cu(NH_3)_2^+] \quad [15]$$

$$CuO + 4NH_3 + 2H^+ = Cu(NH_3)_4^{++} + H_2O$$
$$pH = 10.30 + 2 \log [NH_3] - 0.5 \log [Cu(NH_3)_4^{++}] \quad [16]$$

$$Cu_2O + 4NH_3 + 2H^+ = 2Cu(NH_3)_2^+ + H_2O$$
$$pH = 9.99 + 2 \log [NH_3] - \log [Cu(NH_3)_2^+] \quad [17]$$

$$CuO + 2NH_3 + 2H^+ + e^- = Cu(NH_3)_2^+ + H_2O$$
$$E = 1.257 - 0.118\, pH + 0.118 \log [NH_3] - 0.0591 \log [Cu(NH_3)_2^+] \quad [18]$$

$$2CuO + 2H^+ + 2e^- = Cu_2O + H_2O$$
$$E = 0.669 - 0.0591\, pH \quad [19]$$

$$Zn^{++} + 2e^- = Zn$$
$$E = -0.763 + 0.0295 \log [Zn^{++}] \quad [20]$$

$$Zn(NH_3)_3^{++} + 3H^+ = Zn^{++} + 3NH_4^+$$
$$pH = 6.83 + 0.333 \log [Zn(NH_3)_3^{++}]/[Zn^{++}] - \log [NH_4^+] \quad [21]$$

$$Zn(NH_3)_4^{++} + H^+ = Zn(NH_3)_3^{++} + NH_4^+$$
$$pH = 7.13 - \log [NH_4^+] + \log [Zn(NH_3)_4^{++}]/[Zn(NH_3)_3^{++}] \quad [22]$$

$$Zn(NH_3)_3^{++} + 3H^+ + 2e^- = Zn + 3NH_4^+$$
$$E = -0.156 - 0.089\, pH - 0.089 \log [NH_4^+] + 0.0295 \log [Zn(NH_3)_3^{++}] \quad [23]$$

$$Zn(NH_3)_4^{++} + 4H^+ + 2e^- = Zn + 4NH_4^+$$
$$E = 0.055 - 0.118\, pH - 0.118 \log [NH_4^+] + 0.0295 \log [Zn(NH_3)_4^{++}] \quad [24]$$

The lines represented by Eq. [1]-[24] were plotted in Fig. 1b, 2b, and 3b by substituting the following concentrations in the appropriate equations: 0.05M total dissolved copper, 0.001M total dissolved zinc, and 1.0M total dissolved ammonia (NH_3 plus NH_4^+). The copper and ammonia concentrations correspond to the approximate composition of solutions used in stress corrosion cracking tests (1, 3, 4) on alpha brass (copper added as copper sulfate; ammonia added as ammonium hydroxide and/or ammonium sulfate). The zinc concentration was determined analytically in the course of (or at the conclusion of) such tests; Mattsson's Zn-NH_3-H_2O diagram (Fig. 3a) is based on a zinc concentration of 0.01M, whereas Fig. 3b was calculated for 0.001M Zn, which is more representative of the actual zinc concentration (3).

Discussion

A comparison of the diagrams shows the following important differences:

(a) Fig. 1a has been modified as shown in Fig. 1b to indicate the stepwise addition of NH_3 ligands (our Eq. [4], [5], [6], [7], [12], and [13]); Mattsson's diagram is not incorrect in this respect, but does not clearly show the regions where intermediate complexes are formed. These regions are very important in the stress corrosion cracking of brass, since rapid cracking times have been correlated (3) with the presence of copper-ammine complexes containing an average of 1.5-3.0 NH_3 ligands per copper ion originally present in test solutions.

(b) In Fig. 2a, Mattsson shows a region of stability for the solid phase $Cu(SO_4)_{0.25}(OH)_{1.5}$, which precipitated from his test solutions during storage. We have not observed a similar aging phenomenon if CO_2 dissolved in distilled water was removed by boiling or purging with N_2 and consequently have not included this substance in Fig. 2b.

(c) Fig. 2a shows a stability region for Cu_2O which appears to be incorrectly located. Mattsson's equation No. (15) was written as

$$0.5Cu_2O + 2NH_4^+ = Cu(NH_3)_2^+ + H^+ + 0.5H_2O \quad [II]$$

which may be re-written as

$$2Cu(NH_3)_2^+ + 2H^+ + H_2O = Cu_2O + 4NH_4^+ \quad [III]$$

to give a negative free energy change of −23.2 kcal/mole Cu_2O. The reaction can also be written as

$$Cu_2O + 4NH_3 + 2H^+ = 2Cu(NH_3)_2^+ + H_2O \quad [IV]$$

with a free energy change of −27.4 kcal/mole Cu_2O (which is our Eq. [17]). Equations [III] and [IV] appear contradictory since, according to Convention I, Cu_2O is more basic than $Cu(NH_3)_2^+$ and should appear to the right of $Cu(NH_3)_2^+$ if Eq. [IV] is considered, and vice versa, $Cu(NH_3)_2^+$ is more basic than Cu_2O if Eq. [III] (or [II]) is considered. Obviously, one of these two reactions is inapplicable. Reaction [IV] can be justified as taking precedence over reac-

tion [III] because its free energy change is greater than that for reaction [III]. Further, careful tests (10) with pure copper in ammoniacal solutions of pH 6-8 have established no formation of Cu_2O tarnish in the Cu_2O region indicated in Mattsson's diagram, Fig. 2a. Therefore, we have concluded that reaction [IV] is the correct one, and represented the Cu_2O stability region to the right of $Cu(NH_3)_2^+$ region, as in Fig. 2b.

(d) For reasons analogous to those discussed above, the region for the stability of CuO in Fig. 2a appears also incorrectly placed. Mattsson's re-written equation No. (11)

$$Cu(NH_3)_4^{++} + 2H^+ + H_2O = CuO + 4NH_4^+; \Delta G^\circ = -22.4 \text{ kcal/mole CuO}$$

was compared by us with its paradoxical counterpart

$$CuO + 4NH_3 + 2H^+ = Cu(NH_3)_4^{++} + H_2O; \Delta G^\circ = -28.2 \text{ kcal/mole CuO}$$

which is represented by line 16 in Fig. 2b, after concluding that it is the more favored one.

Halpern (8) has published a diagram of the Cu-NH_3-H_2O system in which the CuO region is located far to the right as we have shown in Fig. 2b; his diagram is calculated for dissolved copper concentrations of 10^{-6} M, so the absolute positions of the lines differ from those in Fig. 2b, but the relative positions of the CuO and $Cu(NH_3)_4^{++}$ regions are in accordance with our considerations.

(e) Finally, in Fig. 3a, the region of stability of $Zn(OH)_2$ appears to be incorrectly predicted, again for the same reasons as discussed before. Mattsson's equation No. (19) written as

$$Zn(OH)_2 + 4NH_4^+ = Zn(NH_3)_4^{++} + 2H^+ + 2H_2O$$

(which has a free energy change of +21.74 kcal/mole) was compared with the reaction

$$Zn(OH)_2 + 4NH_3 + 2H^+ = Zn(NH_3)_4^{++} + 2H_2O; (\Delta G^\circ = -28.82 \text{ kcal})$$

which is not shown in Fig. 3b because the line separating the $Zn(OH)_2$ and $Zn(NH_3)_4^{++}$ regions occurs at a pH of 13.

(f) The stepwise formation of the zinc-ammine complexes is not ignored in Fig. 3b, but the uptake of the first three NH_3 ligands occurs over such a narrow pH range that the separate regions could not be shown on the pH scale used. For this reason, only line 21 is included in the diagram.

(g) Because of the different assumptions regarding the dissolved zinc content of test solutions, the absolute positions of lines separating solid and dissolved substances are lower in Fig. 3b than in 3a. This does not affect the relative positions of the various stability regions.[3]

The blue-black tarnish which develops in brass exposed to copper-ammonia solutions in the pH range 6.0-8.0 was tentatively identified as Cu_2O by Mattsson (1) (on the basis of microscopic examination) and by Forty and Humble (9) on the basis of ring patterns obtained during electron diffraction of tarnish flakes (that had been damaged by mishandling or by heating and curling in the electron beam). Johnson and Leja (3) confirmed this identification by means of x-ray diffraction patterns obtained on tarnished brass strips and on tarnish powder scraped from the brass, and by polarographic analysis of tarnish powder. Since Mattsson's potential/pH diagram for the heterogeneous system Cu-NH_3-H_2O system (Fig. 2a) shows a stability region for Cu_2O over the pH range 4-7.5, it is natural that both Mattsson (1) and Hoar (2) correlated the tarnish appearance with the potential/pH diagram. However, there are two important points that have been overlooked in making this correlation:

(i) The potential/pH diagrams in Fig. 2 are calculated for pure copper, and it has been shown (10) that the solutions of pH 6-8 which rapidly tarnish brass do not produce a tarnish on pure copper (as predicted by Fig. 2a).

(ii) The tarnish penetrates the brass substrate and does not loosely deposit on the surface (9, 10) from the bulk solution. This indicates that the Cu_2O tarnish is produced and stabilized by localized reactions at the brass/solution interface. Since the equation for the line separating the stability regions of $Cu(NH_3)_2^+$ and Cu_2O (Eq. [17], Fig. 2b) is

$$pH = 10.03 - \log \frac{[Cu(NH_3)_2^+]}{[NH_3]^2} \qquad [V]$$

the stability of Cu_2O in a brass-cupric ion-ammonia system at a pH as low as 6, for example, can be explained if the ratio in the log term of Eq. [V] is greater than 10^4. It has been shown (3) that there is no drastic increase in the pH at the brass/solution interface (as compared to the pH in the bulk solution) therefore the above condition for Cu_2O stability at low pH must be realized by the preferential formation of $Cu(NH_3)_2^+$ as a result of the reaction

$$2Cu(NH_3)_2^{++} + Zn = 2Cu(NH_3)_2^+ + Zn^{++}$$

[3] According to Dr. Pourbaix, a potential/pH equilibrium diagram for the system Zn-NH_3-H_2O was prepared about 10 years ago by F. Jolai (Paris), no reference of publication is available.

Acknowledgments

The authors wish to acknowledge the financial support of the National Research Council of Canada for this work.

Manuscript received March 9, 1964; revised manuscript received Nov. 16, 1964.

Any discussion of this paper will appear in a Discussion Section to be published in the December 1965 JOURNAL.

REFERENCES

1. E. Mattsson, *Electrochim. Acta*, **3**, 279 (1961).
2. W. M. Latimer, "Oxidation Potentials," 2nd Ed., Prentice-Hall, Englewood Cliffs (1952).
3. H. E. Johnson and J. Leja, To be published.
4. T. P. Hoar, *Corrosion*, **19**, 331t (1963).
5. M. J. N. Pourbaix, "Thermodynamics of Dilute Aqueous Solutions," (a) p. 54, Edward Arnold, London (1949).
6. "Stability Constants, Part II: Inorganic Ligands," The Chemical Society, London (1958).
7. J. Bjerrum, "Metal Ammine Formation in Aqueous Solution," P. Haase and Son, Copenhagen (1957).
8. J. Halpern, *Trans. AIME*, **9**, 280 (1957).
9. A. J. Forty and P. Humble, *Phil. Mag.*, **8**, 247 (1963).
10. H. E. Johnson, Ph.D. Dissertation, University of Alberta (1964).

Brief Communications

Hexavalent Fluorides of Tantalum and Niobium

G. W. Mellors and S. Senderoff

Development Department, Parma Research Laboratory, Union Carbide Corporation, Parma, Ohio

It has been found that hexavalent compounds of tantalum and niobium can be prepared by the electrolysis of solutions of the pentavalent tantalum and niobium fluorides dissolved in molten alkali fluorides with any suitable conducting cathode and an inert anode such as graphite. It is known that similar electrolysis of molten chlorides, mixed chlorides and fluorides, and mixed fluorides and oxides does not produce these higher valence tantalum and niobium compounds, but instead produces chlorine or oxygen at the anode. Only in the case of an essentially pure fluoride system does one observe that no gas is produced at the anode, but that instead, the higher valence tantalum or niobium fluoride is formed. It is noteworthy that copious fluorine evolution occurs at the anode when the molten alkali fluoride mixture alone is electrolyzed with a graphite anode. On addition of a few per cent of either K_2TaF_7 or K_2NbF_7 gas evolution instantly ceases, and formation of the hexavalent compounds takes place.

For example, a solution used for plating tantalum (1) containing 14.2 w/o (weight per cent) K_2TaF_7 dissolved in Flinak[1] was electrolyzed in an argon atmosphere with a graphite anode and copper cathode at 770°C and anode and cathode current densities of 100 ma/cm² for 21 hr to convert 71% of the contained tantalum to the hexavalent state. This was confirmed by titrating the oxidized form with a known weight of tantalum metal according to the reaction

$$5Ta^{6+} + Ta^0 \rightarrow 6\,Ta^{5+}$$

Nb^{5+} was oxidized to Nb^{6+} in a similar system in which K_2NbF_7 replaced the K_2TaF_7. The completeness of the conversion, however, could not be established in this case because niobium metal reacts with Nb^{5+} as well as with Nb^{6+} so the titration is ambiguous. In the tantalum case it is known that tantalum metal does not react with Ta^{5+} in these systems under the given conditions.

Identification of the valency state.—The valence state of the compounds was established by means of chronopotentiometry using a Ni/NiF_2, Flinak|| reference electrode as described elsewhere (2). Figure 1 shows the anodic chronopotentiograms for the oxidation of K_2TaF_7 dissolved in Flinak and for the solvent alone. It is clear that the solvent and graphite electrode are clean anodically below 0.7v and the plateau in Fig. 1 which starts near 0.2v results from the oxidation of the added Ta^{5+}. The average $E_{1/4}$ for this oxidation obtained from 10 chronopotentiograms is 0.19 ± 0.01v noble to the Ni/NiF_2, Flinak|| reference electrode. Figure 2 shows the anodic-cathodic chronopotentiogram on the K_2TaF_7 solution and the $\tau_{cathode}/\tau_{anode}$ is seen to be 0.33. This indicates that the product of the anodic reaction is a soluble compound (3). The difference of nearly 0.1v in potential of the cathodic and anodic steps indicates a little irreversibility even after correction for the IR drop.

Figure 3 shows a plot of the potential-time characteristics of a typical chronopotentiogram such as that in Fig. 1. For a reversible oxidation to yield a soluble product this plot should be a straight line with a slope of 2.3 $RT/n\mathbf{F}$ where n is the number of electrons involved in the oxidation. The data shown by the circles

[1] Flinak is the eutectic mixture of KF, NaF, and LiF.

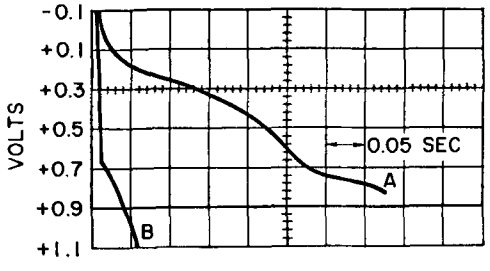

Fig. 1. Anodic chronopotentiograms. A, solution of K_2TaF_7 in Flinak; current density, 0.0139 amp/cm²; concentration, 3.6 x 10^{-5} mole/cm³; temperature, 750°C; anode, graphite. B, Flinak solvent only; current density, 0.015 amp/cm²; temperature, 750°C; anode, graphite.

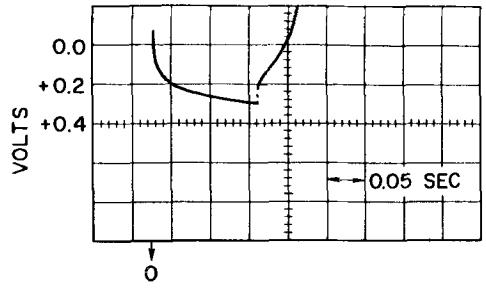

Fig. 2. Anodic-cathodic chronopotentiogram of K_2TaF_7 in Flinak; anodic cycle on left, cathodic on right; current density, 0.015 amp/cm²; temperature, 750°C; concentration, 3.6 x 10^{-5} mole/cm³; electrode, graphite.

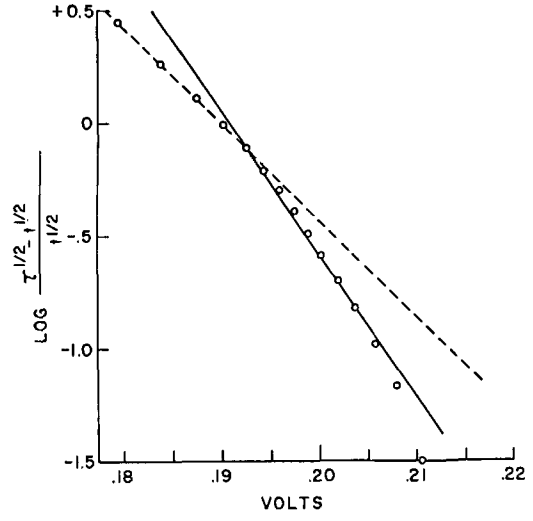

Fig. 3. Electron number for oxidation of K_2TaF_7 in Flinak from E vs. $f(t)$ plot.

do not give a straight line, and alternative plots for irreversible reactions or insoluble products (3) depart much further from straight lines. If one draws the solid line through the data points for times longer than $\tau_{1/4}$ (ordinate = 0) the slope yields a value of 1.0 for n. If one draws the dotted line through the other extreme using only the initial points for $t < \tau_{1/4}$ the slope of the line still gives a value of n of only 1.4. One may reasonably conclude from this that the oxidation is a one-electron oxidation and the small departure observed in the initial part of the curve results from some interaction between the graphite electrode and the pentavalent tantalum in the electrolyte. This may account for the small degree of irreversibility indicated in Fig. 2. Finally, the value of $i\tau^{1/2}$ for the oxidation at two concentrations of K_2TaF_7 gives a diffusion coefficient for $[TaF_7]^{-2}$ of 1.5 x 10^{-5} at 750°C if one takes n as 1.0 in the equation

$$\frac{i\tau^{1/2}}{c} = \frac{1}{2}\pi^{1/2} n\mathbf{F}D^{1/2} \quad (4)$$

This diffusion coefficient is identical to that found for the heptafluotantalate ion from the chronopotentiometry of its 3-electron reduction (2).

Similar chronopotentiograms and their analysis for the oxidation of fluoniobate show that it is also a one-electron oxidation, slightly irreversible, with the hexavalent niobium fluoride completely soluble in the Flinak at 770°C. The $E_{1/4}$ value for the oxidation is 0.25v noble to the nickel reference electrode.

It is realized that until these compounds are isolated and their structure determined by spectroscopy or other means, they cannot be unambiguously characterized as hexavalent metal fluorides. However, these data show unambiguously that a new oxidation state has been produced by a one-electron oxidation of heptafluotantalate ion in a fluoride medium, and that the ion being oxidized has the same diffusion coefficient as $[TaF_7]^=$. It might be suggested that the formation of a F_2^- ion (analogous to peroxy compounds) and its coordination with the $[TaF_7]^=$ could be consistent with the data. While this cannot be disproved at this time, it seems unlikely that such a compound would be thermally stable at the temperature of these experiments or that $2F^- \rightarrow F_2^- + e$ would occur at only 0.2v noble to nickel when the estimated potential for $F^- \rightarrow 1/2\ F_2^0 + e$ is 2.7v *vs.* the same Ni/Ni^{2+}, Flinak|| reference half-cell.

Properties of the hexavalent niobium and tantalum fluorides.—The compounds are indefinitely stable in molten Flinak between 700° and about 850°C. On cooling they decompose with the evolution of fluorine to form the pentavalent compounds, but it is possible that by rapid quenching the hexavalent material might be preserved at lower temperatures. They are strong oxidizing agents as shown by their $E_{1/4}$ potentials which are more than 1v noble to the $E_{1/4}$ potentials for the reduction of the pentavalent tantalum and niobium compounds (2). They rapidly dissolve their respective metals as well as the refractory lower fluorides such as TaF_2 which are insoluble in molten Flinak solution.

Acknowledgment

The authors are indebted to W. J. Reinhart, who made the chronopotentiometric measurements, R. L. Zupancic, who operated the electrolysis cells, and Professor H. A. Laitinen for his valuable discussion and criticism.

This work is the subject of patent applications filed in the United States and elsewhere and further studies on the electrochemistry and chemistry of these compounds are continuing.

Manuscript received Jan. 22, 1965.

Any discussion of this paper will appear in a Discussion Section to be published in the December 1965 JOURNAL.

REFERENCES

1. G. W. Mellors, S. Senderoff, Canadian Pat. No. 688, 546 (1964); *This Journal*, **110**, 180C (1963).
2. S. Senderoff, G. W. Mellors, and W. J. Reinhart, *ibid.*, To be published.
3. W. H. Reinmuth, *Anal. Chem.*, **32**, 1514 (1960).
4. P. Delahay, "New Instrumental Methods in Electrochemistry," Chap. 8, Interscience Publishers, New York (1954).

Anodic Oxide Films on Vanadium

R. G. Keil and R. E. Salomon

Department of Chemistry, Temple University, Philadelphia, Pennsylvania

The growth of anodic oxide films on aluminum, tantalum, zirconium, and hafnium has been investigated by a number of workers (1). Films exhibiting sharp interference colors which are characteristic of thickness can be prepared by anodization in a variety of aqueous electrolytes. Attempts to extend these studies to other metals, such as vanadium, are complicated by the appreciable solubility of the oxidation product in aqueous media. If such films could be grown, however, a direct quantitative chemical analysis of them would be quite feasible.

Young (2) suggests the use of partly nonaqueous electrolytes as media for the growth of water soluble anodic oxide films. Anhydrous organic solvents dissolve only small quantities of salt and cannot be made highly conductive. Furthermore, these solutions when used as anodization media often lead to unusual oxidation states (2).

It has been found that the anodic oxidation of vanadium in anhydrous acetic acid that has been saturated with $Na_2B_4O_7 \cdot 10H_2O$ leads to films which exhibit well-defined interference colors characteristic of formation voltage and thickness. The growth of these films is rather sensitive to the water-borate ratio although the total borate present is not of major significance.

Samples of vanadium in rod form, 99.4% pure, were wet polished with aluminum oxide powders, etched in 6.7*N* nitric acid, and then washed with glacial acetic acid. The specimens were placed in a thermostated anodization cell containing a Ag/AgAc reference electrode and a platinum foil cathode. Provisions for purging and stirring the solution with dry nitrogen were made. Electrolyte was added to the cell and the electrode was anodized at constant voltage for periods of from 10 to 15 min. The current was followed by means of a recorder.

After anodization the films were washed in glacial acetic acid and allowed to dissolve into distilled water. The resulting solution was analyzed quantitatively for vanadium by a colorimetric method (3).

Film growth could be inferred by the observation of the changing interference colors. The current, which initially appeared to be limited by the electrolyte resistance, decreased monotonically and approached a limiting value of the order of 0.50 ma/cm^2 in a few minutes. The interference colors were found to be characteristic of formation voltages for potentials up to 25v whereas breakdown occurred above this point. The solution obtained by dissolving a known area of the film in distilled water was found to contain pen-

Table I. Relation between formation voltage, film color, and amount of vanadium (V)

Formation voltage, v	Film color	Total vanadium (V) moles $cm^{-2} \times 10^7$
7.0	Light yellow	
9.0	Yellow	1.00
11.0	Dark yellow	1.08
12.0	Reddish yellow	
13.0	Purple	1.15
15.0	Blue	1.23
22.0	Green	

tavalent vanadium in an amount that was linearly related to the formation voltage. Results are shown in Table I.

Blank runs showed that correction of the data due to dissolution of the bare metal in distilled water were unnecessary. Several other electrolytes such as anhydrous acetic acid saturated with sodium metaborate, absolute methanol saturated with $NaNO_3$, $NaNO_2$, $Na_2B_4O_7 \cdot 10H_2O$, Na_2CO_3, $Na_2C_2O_4$, H_3BO_3, and acetic acid saturated with Na_2SO_4 and small amounts of water were tried and found to be unsatisfactory.

The results suggest that small quantities of water are necessary and that this water should be tied up by hydration to reduce the solubility of the oxide film. Specular reflectance measurements on the thicker oxides permit tentative identification of the film as nonstoichiometric V_2O_5 (4).

Acknowledgment

This work was supported by the United States Atomic Energy Commission.

Manuscript received Nov. 20, 1964; revised manuscript received Feb. 15, 1965.

Any discussion of this paper will appear in a Discussion Section to be published in the December 1965 JOURNAL.

REFERENCES

1. L. Young, "Anodic Oxide Films," Academic Press, New York, 1961.
2. *Ibid.*, p. 187.
3. N. A. Talvitie, *Anal. Chem.*, **25**, 604 (1953).
4. A. L. Companion and R. E. Wyatt, *J. Phys. Chem. Solids*, **24**, 1025 (1963).

Correction

In the paper by Willem van Hees "A Bacterial Methane Fuel Cell" which was published in the March 1965 issue of the Journal, the last reaction in column 2, page 260, should read

$$E = E_o' - RT/2f \ln ([AH_2]/[A])$$
$$= E_o' - 0.03 \log 10^c = E_o' - 0.03c$$

Discussion Section

This Discussion Section includes discussion of papers appearing in the JOURNAL of The Electrochemical Society, Vol. 110, No. 8 (August 1963) and Vol. 111, No. 5, 7, 8, 9, 11, and 12 (May-December 1964). Discussion not available for this issue will appear in the Discussion Section of the December 1965 JOURNAL.

A Technique for the Evaluation of Hydrogen Embrittlement Characteristics of Electroplating Baths

M. A. V. Devanathan, Z. Stachurski, and W. Beck
(pp. 886-690, Vol. 110, No. 8)

M. A. V. Devanathan,[1] Z. Stachurski, and W. Beck[2] (Additional comments by the authors of the paper): The paper which Dr. Dubpernell discusses is one of a series of three papers[3-5] devoted to interrelated problems. Investigated in the three papers were: diffusion of hydrogen through palladium,[3] iron and steel,[4,5] the mechanism of hydrogen evolution on iron,[4] and hydrogen embrittlement of steel during electroplating.[5] The answer to most of Dubpernell's questions can be found in the cited papers. The principle of the method used in all three papers has already been discussed in a reply by Dr. Beck.

The method was based on certain assumptions. These are:

1. Adsorption of atomic hydrogen takes place on the test membrane while hydrogen is evolved on the "cathodic side" of the membrane.
2. Atomic hydrogen diffuses to the other side of the membrane, the potential of which is maintained anodic with respect to hydrogen.
3. Ionization of hydrogen on the "anodic side" of the membrane is a source of current which is monitored and called permeation current.
4. The rate of diffusion of atomic hydrogen through the membrane under the given conditions is proportional to the hydrogen coverage on the cathodic side.

The validity of the above assumptions was carefully checked by us.[3,4] The questions asked by Dubpernell indicate that it is necessary to describe again briefly how this was done.

The authors' first experiments were run on palladium membranes. It was found that the variation of the permeation currents with time corresponds to that predicted by diffusion theory. The diffusion coefficient was found to be independent of the thickness of the membrane and corresponded to extrapolated values of gas penetration at elevated temperatures. The anodic side of the membrane never became passive in experiments with electrolytically evolved hydrogen. The reason is that its potential was negative *vs.* reversible potential of α-Pd in alkaline solution and was positive *vs.* reversible potential of hydrogen in the same solution. Only in the one case when we filled one cathodic compartment with H_2 instead of electrolyte did the anodic side become completely passivated. The penetration current in this particular case was initially about 100 times larger than during any experiment with electrolytic evolution of hydrogen conducted by us. This large penetration current fell irreversibly to nearly zero. Passivation was in this case probably associated with the formation of β-Pd.

In the authors' work on hydrogen evolution on iron[4] they always covered the anodic side of the iron membrane with a very thin layer of palladium. This "protected" it against anodic passivation and did not impede hydrogen penetration. They also found that annealing of Armco iron prior to experiments led to reproducible results. Without annealing, no steady-state penetration could be obtained and blistering was frequent.

On palladium-coated annealed iron membranes the variation of penetration with time also was as predicted by diffusion theory. The diffusion time lag was proportioned to the square of the thickness of the membrane; the diffusion coefficient was reasonably independent of membrane thickness. The reciprocal of the permeation rate increased linearly with the membrane thickness. The diffusion coefficient again was found to be in agreement with one extrapolated from high-temperature permeation measurements. The mechanism of hydrogen evolution from acids was found (from changes in coverage of atomic hydrogen) to be slow discharge, in accordance with Frumkin. This seems to be sufficient evidence that what was measured was really hydrogen penetration and not any "side reaction" as postulated by Dubpernell.

The third phase of the experiment[5] was the application of the above method to the problem of hydrogen embrittlement of steel during electroplating. The principal point of this work was that the electroplated coating was the controlling factor with respect to the quantity of hydrogen, penetrating the steel. This is due to the very low permeation rate of hydrogen through coatings (mainly Cd). The entire discussion of Dubpernell of "damage due to excessive pretreatment" is therefore pointless. Steel served merely as the support for the coatings. The amount of hydrogen which penetrated during the formation of a coating could be measured by the method described. This was then compared with the extent of embrittlement of another sample of steel which was plated from the same type of bath and tested mechanically in independent experiment. The correlation was presented.[5]

As a last point of the discussion, Dubpernell insists that it is molecular rather than atomic hydrogen which diffuses through the membrane. With respect to palladium, it was long ago found by means of paramagnetic susceptibility measurements that dissolved hydrogen gives electrons to the d-band of palladium.[6] It is therefore entirely ionic. A similar situation seems to prevail with iron. Bryan and Dodge[7] determined the diffusion coefficient of hydrogen for penetration from the gaseous phase. Extrapolation of their values for footnote 3 to room temperature gives values in close agreement with our data.[8] The particles diffusing must be therefore the same at room temperature and at elevated temperature.

Furthermore, the work by Sieverts *et al.*[9] has shown that the diffusing species is not molecular hydrogen. He found that the solubility of gaseous hydrogen in iron was proportional to the square root of the pressure of H_2. He concluded that H_2 dissociates and dissolves in α-Fe in the form of atoms.

There is moreover no difference between penetration through polycrystalline iron and through monocrystals.

[1] Present address: Central Electrochemical Research Institute, Karaikudi-3, Madras, India.

[2] Present address: Dept. of the Navy, Office of Naval Research, Branch Office, London, Navy 100, Box 39, F.P.O., New York, N. Y.

[3] M. A. V. Devanathan and Z. Stachurski, *Proc. Roy. Soc.*, A, 270, 90 (1962).

[4] M. A. V. Devanathan and Z. Stachurski, *This Journal*, 111, 619 (1964).

[5] M. A. V. Devanathan, Z. Stachurski, and W. Beck, *This Journal*, 110, 886 (1963).

[6] N. F. Mott and H. Jones, "The Theory of the Properties of Metals and Alloys," p. 200, Dover Publications, New York (1958).

[7] W. L. Bryan and B. F. Dodge, *A. I. Ch. E. Journal*, 9, 223 (1963).

[8] J. McBreen, Thesis, University of Pennsylvania, 1964.

[9] A. Sieverts, W. Krumbhaar, and E. Juresch, *Z. Phys. Chem.*, 77, 591 (1911).

For penetration from the gas phase this was checked by Smithels and Ransley[10] and for electrolytically evolved hydrogen by McBreen.[8] Shwed and Sharpenko[11] have shown that introduction of hydrogen in iron reduces its work function. The explanation is that hydrogen is in the ionized or partially ionized state.

The above facts seem to the authors' to establish an adequate basis for their experimental method.

G. Dubpernell[12]: The additional comments from Stachurski are of interest but fail to be convincing. It is still felt that the proposed method is not a measure of either hydrogen diffusion or hydrogen embrittlement. A few inaccuracies appear to warrant further comment.

Stachurski states that the anodic side of the membrane never became passive (with but one exception). However, the publication in question states that "Whenever the permeation currents were large the anodic side of the palladium showed a tendency to passivate with formation of visible oxide films," and refers further on to ". . . the formation of visible oxide films on the anodic side of the membrane. . . ." These statements were taken to indicate a not infrequent formation of visible oxide films on palladium.

Reference is made to the coating of the anodic side of iron membranes with a very thin layer of palladium, but the thickness of these layers is not given. It is stated that these layers ". . . did not impede hydrogen penetration," but this is not considered to be true. Rather thin membranes of sound palladium metal have been found to be impermeable to hydrogen; they are then considered to be "poisoned," or in need of "cleaning" or "activation," but it is felt by the writer that solid palladium does not normally permit hydrogen diffusion at room temperature and that the adsorption of hydrogen which occurs should be classed as some type of compound formation between hydrogen and palladium, rather than diffusion.

Stachurski states that without annealing no steady-state penetration of the Armco iron membranes could be obtained. How would he explain the lack of diffusion without annealing?

Stachurski is not correct when he says that Dubpernell insists that it is molecular rather than atomic hydrogen which diffuses through the membrane. It is felt that sound, solid, undamaged membranes do not permit any diffusion whatsoever at room temperature, whether they be of palladium or iron. It is only when the electrolyte is able to penetrate a pore or capillary in the metal that the current enters and may cause hydrogen or oxygen evolution within the metal or on the back side of a membrane, according to whether it is charged cathodically or anodically.

The statement of Mott and Jones in 1936 appears to relate to compound formation between hydrogen and palladium and is not believed to have any bearing on the question of diffusion.

Bryan and Dodge studied the diffusion of hydrogen through iron at 126°-693°C, using hydrogen pressurers of 0.033-300 atm. In agreement with many other investigations they showed that hydrogen is insoluble in iron at room temperature. Stachurski should accordingly not try to apply any of their data to room temperature measurements.

The reference to Sieverts is also to high-temperature work which likewise shows that hydrogen is insoluble in iron at room temperature, and does not seem to contain any discussion of the possible dissociation of hydrogen in iron at high temperatures. Several other papers by Sieverts[13,14] do discuss this point, but Sieverts considers it of doubtful validity, since the solubility of sulfur dioxide in copper also varies as the square root of the pressure and yet the sulfur dioxide is not dissociated.

Smithels and Ransley also worked at high temperatures (100°-1600°C); while they did fail to find any difference between polycrystalline iron and a single crystal, they also showed that hydrogen is insoluble in iron at room temperature.

The thesis by McBreen has not yet been published and is unavailable for comment. Likewise the paper by Shwed and Sharpenko is not available to the writer.

The work of at least nine or ten other investigators has also shown the apparent insolubility of hydrogen in iron at room temperature. An excellent summary is given by Blake, Jordon, and Pumphrey.[15] It is this very lack of solubility of hydrogen in iron at room temperature which is probably one of the causes of hydrogen embrittlement. Solubility of even part of the hydrogen in the iron would probably be quite helpful or even eliminate embrittlement. Hewitt[16] concludes that ". . . hydrogen in solid low alloy steel remains in interstitial solution only above about 130°C. Below this temperature it seems to precipitate rapidly into traps associated with dislocations. . . ."

It may be of interest that Martin and Rummel in a mass spectral study[17] were unable to detect any monatomic hydrogen diffusing in the inside of a palladium tube 0.003 in. thick. Even above the ionization potential of hydrogen they only obtained large yields of both masses 2 and 3.

In summary, the proposed method for the determination of hydrogen permeation and for the evaluation of hydrogen embrittlement, seems of doubtful validity.

The Reaction at the Iron Alkaline Electrode

A. J. Salkind, C. J. Venuto, and S. U. Falk (pp. 493-495, Vol. 111, No. 5)

P. B. Mee[18]: Salkind, Venuto, and Falk found that in the discharged condition, the iron active material contained αFe, Fe $(OH)_2$, and Fe_3O_4, although Fe_3O_4 was found only when the material had been previously washed in a reducing solution. They also reported the presence in their x-ray diffraction patterns of a minor peak at 2.22Å which appeared whenever strong patterns of αFe were observed. Salkind *et al.* did not however provide any hypothesis as to the origin of this peak.

Such a peak has also been observed in this Laboratory during the examination of iron active material, and has been attributed to the presence of $\alpha Fe_2O_3 \cdot H_2O$, which is stoichiometrically equivalent to 2FeOOH. The material used in this Laboratory's examination was prepared by conventional Edison-type processes and was supplied by Alkaline Batteries Ltd., Redditch, England. One specimen was examined in the as-prepared powdered condition and the second after forming in the following manner. Thirteen grams of as-prepared iron active powder were compressed into a conventional pocket, fully charged using four positive tube electrodes at 600 ma for 15 hr, and then discharged at the same current until the cell voltage had fallen to 1v. (Four positive tube electrodes were used to ensure that discharge was under negative electrode control.) The cycle was repeated three times, and after the final discharge, the cell was short circuited for half an hour. The pocket was finally washed in distilled water and allowed to dry before examination.

[10] C. J. Smithels and C. E. Ransley, *Proc. Roy. Soc.*, A, **150**, 172 (1935).

[11] M. Shwed and G. Sharpenko, Vester. Akad Nauk SSR Inst. *Machinoved i Automatiki*, 2, 159 (1963).

[12] M&T Chemicals, Inc., Detroit 20, Mich.

[13] A. Sieverts, *Z. Elektrochem.*, **16**, 707 (1910).

[14] A. Sieverts, *Z. Metallkude.*, 21, 37 (1929).

[15] P. D. Blake, M. F. Jordon, and W. I. Pumphrey, Iron and Steel Institute (London), Special Report 73, Hydrogen in Steel, p. 76 (1961).

[16] J. Hewitt, Iron and Steel Institute (London), Special Report 73, Hydrogen in Steel, p. 83 (1961).

[17] T. W. Martin and R. E. Rummel, *Science*, 143, 797 (1964).

[18] Development and Research Dept., The International Nickel Co. (Mond) Ltd., Wiggins St., Birmingham, England.

Table I. X-ray reflections from iron-negative active material comparison of experimental data with ASTM standards

ASTM standards						Experimental data	
α Fe	Fe_3O_4	$Fe(OH)_2$	α $Fe_2O_3 \cdot H_2O$	δ Fe_2O_3	FeO	As-prepared	As-formed (discharged)
d, Å : I/I_1			4.97 (60)				4.91
	4.85 (40)						
		4.597 (100)					
			4.18 (100)				4.17
			3.36 (60)				3.34
	2.97 (70)					2.96	2.96
		2.82 (80)					
			2.69 (70)				2.69
			2.58 (55)				
	2.53 (100)			2.53 (80)		2.53	2.53
					2.49 (80)		
			2.48 (40)				2.46
			2.44 (80)				
	2.42(10)						
		2.40 (100)					
			2.30 (10)				
			2.25 (60)				2.22
				2.19 (100B)			
			2.18 (60)				
					2.15 (100)		
			2.14 (10)				
	2.10 (70)					2.10	2.09
			2.09 (15)				
2.03 (100)						2.03	2.03
			2.01 (20)				

In Table I the x-ray reflections observed from the iron negative active materials are recorded in comparison with ASTM standard data, showing that, in agreement with Salkind *et al.*, the as-prepared material consisted of αFe and Fe_3O_4. The as-formed and discharged material in the present experiment contained αFe, $\alpha Fe_2O_3 \cdot H_2O$, and Fe_3O_4.

During our analysis considerable x-ray line broadening was evident, as shown by the traces of Fig. 1;

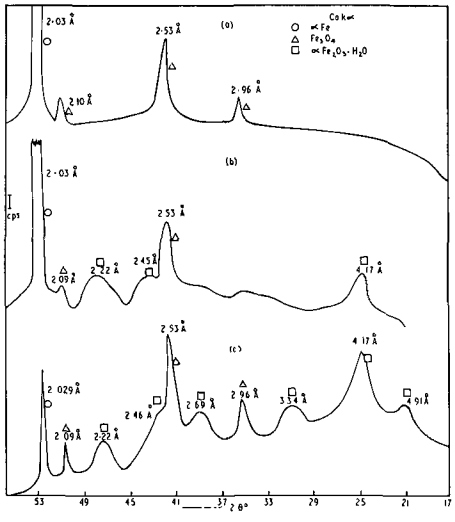

Fig. 1. X-ray diffraction traces from (a) as-prepared material, (b) as-formed material, and (c) as-formed material after dissolution of α Fe in $FeCl_3$ solution.

the lines varied widely in sharpness indicating a possible platelike particle shape. Assuming the line broadening to be due entirely to crystallite size effects, analysis of the x-ray patterns indicates that the mean crystallite sizes of αFe and Fe_3O_4 in the as-prepared material were > 1500 and 600-700Å, respectively. Similarly it was found in the as-formed and discharged material that $D_{\alpha Fe} > 1500$Å, $D_{Fe_3O_4} \sim 200/300$Å, and $D_{\alpha Fe_2O_3 \cdot H_2O}$ (110) $\sim$ 65Å in the orthorhombic lattice.

Examination in a type EM6 electron microscope indicated that the as-prepared material consisted of particle agglomerates and very thin flakes of Fe_3O_4, whereas the as-formed material had an irregular particle shape and wide particle size range, 500 → 25000Å, with the majority in the range 500 → 7000Å. Electron diffraction patterns were consistent with the presence of $\alpha Fe_2O_3 \cdot H_2O$. Marked shape anisotropy would, of course, lead to deviation from the theoretical relative intensities of the lines in the x-ray diffraction pattern and might thus explain why only one of the lines of $\alpha Fe_2O_3 \cdot H_2O$, *i.e.*, at 2.22Å, was observed by Salkind *et al.* A further possibility would arise however if insufficient filtration had been used in that the line could then be the Kβ reflection of α Fe (110).

A. J. Salkind, C. J. Venuto, and S. U. Falk: We are very interested in the work of Mr. Mee in examining the oxide states of iron and we are pleased to observe that he has substantiated much of the data which we reported.

In his discussion he mentioned two possibilities for the existence of the reflection at 2.22Å which appears in our work and which we did not identify at that time. The first is the possibility of $\alpha Fe_2O_3 \cdot H_2O$ and the second a line due to stray radiation caused by the insufficient filtration of the Cr x-ray beam.

From the data presented by Mr. Mee it appears that he does have $\alpha Fe_2O_3 \cdot H_2O$ in the material prepared in his experiments. We believe his latter suggestion however, is the cause of the 2.22Å reflection in our experiments for the following reasons:

1. We never obtained the 2.22Å peak unless the αFe was very intense.
2. We obtained it in the pattern for Armco iron indicating it is not necessarily a battery reaction product.
3. This could not be $\alpha Fe_2O_3 \cdot H_2O$ because all other lines were identified as αFe and or Fe_3O_4 *vs.* $Fe(OH)_2$ in our patterns. None of the other $\alpha Fe_2O_3 \cdot H_2O$ lines were recorded.
4. We believe that the 2.22Å peak is probably due to CrKβ radiation reflected from the (110) plane of αFe. 2θ angle calculated on the basis using CrKβ = 2.08479 and a d-value for the (110) plane of α-Fe gave an angle 61.9°. This compares favorably with the 2θ of 62° where the 2.22Å line was recorded on our charts.

Since our original work we have x-rayed the high αFe samples with chromium radiation and increased Vanadium filtration and also with copper radiation using a monochromator. In both instances the 2.22Å peak was eliminated.

We do not doubt that Mr. Mee is correct in that he produced $Fe_2O_3 \cdot H_2O$ under his particular experimental conditions. We suggest that this is being caused by the reaction of air oxygen with his iron active material.

A Kinetic Study of The System Si-$SiCl_4$

R. R. Monchamp, W. J. McAleer, and P. I. Pollak
(pp. 879-881, Vol. 111, No. 7)

S. E. Craig, Jr.[19]: In their article on the etch rates of silicon by $SiCl_4$, Monchamp, McAleer, and Pollak follow established tradition by noting that mass transport is, or may be, important and then completely

[19] Arizona State University, Tempe, Ariz.

omitting mass transport considerations from their analysis. Apparently the authors join many researchers in the epitaxial field who believe that "true kinetic" analyses are somehow more noble or more general than analyses which involve mass transport considerations. Certainly mass transport solutions are general. Once developed for a particular geometry, they apply to reactors of that geometry for any reaction whether the reaction is mass transfer controlled or not. On the other hand, the true kinetic and equilibrium relationships apply to particular reactions regardless of reactor type. In any practical case, the equilibrium and kinetics of the reactions couple with the transport phenomena in the reactor to produce the observed overall kinetics. Any analysis must therefore give adequate consideration to all three of these phenomena.

This general lack of attention to mass transport considerations is somewhat surprising since in most of the operational epitaxial reactors, mass transport is of major importance, while in many, it is the rate controlling phenomenon. Monchamp's work may be a classic example of how attempts to circumvent mass transport considerations can lead to erroneous conclusions.

The sealed reactor used by Monchamp would have very slow mass transfer; hence, we would not be surprised to find the kinetics limited by the rate of gas phase transport. Monchamp concluded that mass transport was not important because he measured an apparent activation energy of 49,100 cal/mole. A large activation energy usually indicates a reaction where mass transport is unimportant, but this is not always the case as shown below.

Since the reactor contains $SiCl_4$ in great excess, the kinetics could not be limited by the rate of transport of $SiCl_4$ to the surface, but the kinetics could be limited by the rate at which $SiCl_2$ is transported from the surface. This can be expressed in terms of a mass transport coefficient, k_p, and the partial pressure difference between the surface, p_{SiCl_2}, and the bulk gas phase, $p^o_{SiCl_2}$

$$r = k_p\,(p_{SiCl_2} - p^o_{SiCl_2}) \qquad [1]$$

Equation [1] applies whether the reaction is mass transport controlled or not. When "true kinetic" data are being sought, this equation is used to calculate the true partial pressure at the interface. If the equilibrium constant is small, the partial pressure of $SiCl_2$ in the bulk gas will be essentially zero while the partial pressure of $SiCl_4$ at the interface will be essentially the total measured pressure, p_{SiCl_4}. If the reaction rate is mass transport controlled, equilibrium will exist at the interface. Under these conditions, as Monchamp points out

$$K = \frac{(p_{SiCl_2})^2}{p_{SiCl_4}} \qquad [2]$$

From a combination of [1] and [2], the exact equivalent of Monchamp's Eq. [8] is obtained

$$r = k_p\,K^{1/2}\,P_{SiCl_4}{}^{1/2} \qquad [3]$$

If k_p is independent of pressure, then the 0.49 power rate dependence on P_{SiCl_4} is fully explained. In open tube, flow reactors mass transport coefficients based on partial pressure driving forces are inversely proportional to the total pressure. However, in the reactor design reported, the mass transport is mainly dependent on the rate of natural convection caused by the difference in density of the gases at the hot zone and cold zone. Since the densities of the gases are directly proportional to the total pressure, it is not unlikely that the net result is a k_p independent of pressure. Experimental verification of this point is needed.

When we take natural logarithm of Eq. [3], and differentiate the result with respect to the reciprocal of the absolute temperature at constant pressure we obtain

$$\frac{d(\ln R)}{d(1/T)} = \frac{d(\ln k_p)}{d(1/T)} + \frac{1}{2}\frac{d(\ln K)}{d(1/T)} \qquad [4]$$

or

$$-\frac{\Delta E_o}{R} = -\frac{\Delta E_m}{R} - \frac{1}{2}\frac{\Delta H^o}{R} \qquad [4a]$$

The left side of Eq. [4] is the slope of the straight line in Fig. 3 of Monchamp's paper and is equal to minus the apparent over-all activation energy, ΔE_o, divided by the ideal gas constant, R. The first term on the left of Eq. [4] is minus the apparent activation energy for mass transport, ΔE_m, divided by R. From thermodynamics, the last term in Eq. [4] is minus one-half of the standard enthalpy of reaction, ΔH^o, divided by R.

For open tube flow type reactors, ΔE_m is generally quite small and ranges from 0 to about 5 kcal/mole. However, for the reactor used by Monchamp, the mass transport depends on the natural convective currents which depend on the temperature difference between the cold zone and the hot zone. Hence, for this case we would estimate an abnormally high ΔE_m of from 5 to 10 kcal/mole. Again, this requires experimental verification.

There is considerable uncertainty in the standard enthalpy of reaction in the range of temperatures used by Monchamp. From the available literature,[20-25] $\Delta H^o_{1383°K}$ is calculated to be between 66.12 and 81.64 kcal/mole.

From Eq. [4a] and the above data, the apparent activation energy of the reaction would be between 38.12 and 50.82 kcal/mole for reaction kinetics which are fully mass transfer controlled. These values are in satisfactory agreement with Monchamp's reported value of 49.10 kcal/mole.

Since Monchamp's measured activation energy is apparently the sum of equilibrium and mass transport effects, it cannot be considered a true activation energy in the sense of Eyring[26]. Thus it is meaningless for Monchamp to speculate on the kinetics of reaction being controlled by the rate of desorption. All of the observed phenomena could be fully explained by simple mass transport and equilibrium.

Whether the data reported by Monchamp really represent true kinetic data or not can only be resolved by a critical experiment. Had he used a flow-type reactor, the experiment would have consisted of varying the total flow rate while keeping the feed gas composition, temperature, and pressure constant. If this does cause a change in reaction rate, mass transport is important and must be considered. Such a simple test cannot be used on Monchamp's closed system. However, he could vary the reactor diameter to produce a change in the mass transfer coefficient. A more critical test would be deliberately to increase the rate of natural convection by installing a cold gas return line as shown in Fig. 1. If this had an effect on the rate of deposition, mass transport would definitely be an important consideration in this reaction.

[20] G. C. Sinke, "Thermodynamic Properties of Combustion Products," Dow Chemical Co., Report No. AR-1S-59, April 1959, Contract AF 33(616)6149, AD 214587.

[21] L. Brewer, "The Chemistry and Metallurgy of Miscellaneous Materials—Thermodynamics," ed. by L. L. Quill, 1st Ed., McGraw-Hill Book Co., New York (1950).

[22] C. Cerny and E. Erdos, *Collection Czechoslov. Chem. Communs.*, 19, 646 (1954).

[23] B. Schneider and J. Pliva, *Collection Czechoslov. Chem. Communs.*, 19, 653 (1954).

[24] H. Schäefer and J. Nickl, *Z. anorg. allgem. Chem.*, 274, 250 (1953).

[25] H. Schäefer, H. Jacob, and K. Etzel, *Z. anorg. allgem. Chem.*, 286, 27 (1956).

[26] S. Glasstone, K. J. Laidler, and H. Eyring, "The Theory of Rate Processes," Chapter III, McGraw-Hill Book Co., New York (1941).

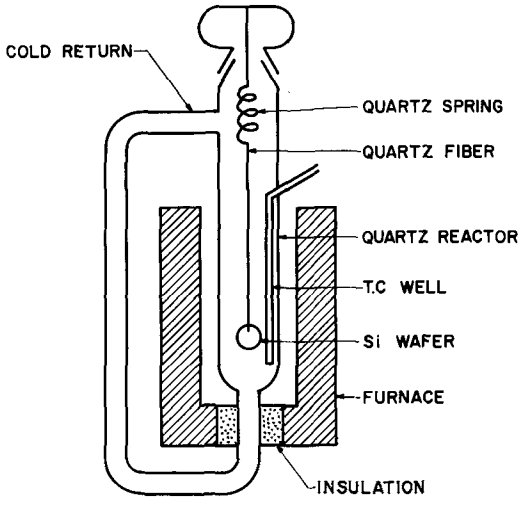

Fig. 1. Suggested modification of Monchamp's reactor to test for the significance of mass transport.

R. R. Monchamp[27], W. J. McAleer[28], and P. I. Pollak[29]: We have enjoyed reading Professor Craig's comments and, in general, are in full agreement with his concern for the part that is played by mass transport phenomena in gas systems. However, some of his comments lead us to believe that perhaps he had misunderstood several of our statements and, of course, he could not know the details of some of the negative type results we had obtained. In addition to technical reasons stated in our paper, we purposely did not want to work in a dynamic flow system since we knew that Dr. Thomas, with whom we had correspondence at that time, was examining such a system. His work has now been published.[30] Having been major commercial producers of epitaxial silicon, we were quite aware of the fact that the system under investigation was not an operational epitaxial reactor. We purposely designed it in this manner to simplify the experimentation.

We don't agree with Professor Craig that our conclusions are necessarily erroneous, since we took what we considered adequate precautions to assure ourselves that we were operating in a kinetic regime which was mass transport independent. The general agreement of the experimental findings of Alstrup and Thomas with our published results bears witness to this fact. Based on their results, in which a dynamic flow system was used, Alstrup and Thomas also arrived at a surface adsorption or desorption mechanism as the rate-controlling step rather than a mass transport controlled phenomena, as suggested by Professor Craig. Apart from this, we are very happy with Professor Craig's analysis and agree that many more experiments could have been carried out to satisfy his criticism. This is usually true for all research publications in the literature, and we would be stunned indeed if no improvement over our work would be possible. Unfortunately, we are no longer in a position to examine some of the questions raised by Professor Craig, and we suggest that he carry out the ultimate experimental and theoretical analysis of this system instead.

Aside from its technical significance, if our paper has accomplished nothing but to generate an interest and increased activity in the study of the $SiCl_4$-Si-H_2 kinetics, then we feel quite successful. We might further point out that this etching reaction was to be a starting point in a study of the entire $SiCl_4$, $SiCl_{4-x}H_x$, H_2, Si system. Judging from the confliction of opinions and interpretations of data for this first step, it is apparent that there is room for many more investigations and that it will be some time before the kinetics of the entire system are resolved.

[27] Present address: Airtron, A Division of Litton Industries, Morris Plains, N. J.

[28] Present address: Merck Sharp & Dohme Research Laboratories, Division of Merck & Co., Inc., West Point, Pa.

[29] Present address: Merck Sharp & Dohme Research Laboratories, Division of Merck & Co., Inc., Rahway, N. J.

[30] O. Alstrup and C. O. Thomas, *This Journal*, 112, 319 (1965).

Oxidation of Aluminum by Carbon Dioxide in the Presence of Cryolitic Electrolyte

S. Gjerstad and B. J. Welch (pp. 976-980, Vol. 111, No. 8)

W. B. Frank[31]: Gjerstad and Welch have presented convincing evidence that the rate-determining step in the oxidation of aluminum by carbon dioxide in the system cryolitic melt-molten aluminum is the "transfer of the dissolved metal or reacting species, from the melt-metal interface to, or near the melt-gas interface." There also appears to be evidence in their paper and elsewhere that the reacting species is predominantly dissolved sodium rather than aluminum or aluminum monofluoride.

Sodium has been identified in the vapors above the fused cryolite-aluminum system.[32] The sodium pressure is a function of melt composition,[33] increasing with sodium fluoride content and decreasing in acid (aluminum fluoride rich) melts. The appreciable solubility of sodium in sodium halide fusions has been reported by Bredig.[34]

Aluminum monofluoride pressures resulting from the aluminum-melt reaction have also been measured spectroscopically[33] and found to be much lower than those of sodium near the cryolite composition. Only in highly acid bath does the aluminum monofluoride pressure approach that of sodium.

Aluminum monofluoride and sodium can be thought of as being generated independently by aluminum-melt reactions. The sodium producing reaction can be written

$$Al + 6NaF\left\{\begin{matrix}\text{melt}\\\text{species}\end{matrix}\right\} \rightleftarrows Na_3AlF_6\left\{\begin{matrix}\text{melt}\\\text{species}\end{matrix}\right\} + 3Na \qquad [1]$$

The appreciable activity of sodium fluoride in cryolite-base melts results from the partial dissociation[35-37] of cryolite. The free energy change for the above reaction is +7 kcal at 980°C. Thus, this reaction is more favored thermodynamically than reaction (B) of Gjerstad and Welch.

The free energy change for the aluminum monofluoride producing reaction

$$2Al + Na_3AlF_6\left\{\begin{matrix}\text{melt}\\\text{species}\end{matrix}\right\} \rightleftarrows 3NaF\left\{\begin{matrix}\text{melt}\\\text{species}\end{matrix}\right\} + 3AlF \qquad [2]$$

is +50 kcal at 980°C The relative values for the free energy changes of reactions [1] and [2] and the melt activities resulting from the partial dissociation of cryolite are qualitatively consistent with the spectroscopically observed pressures of Na and AlF.

The decreased reactivity of the liquid Cu-Al alloy from that of pure aluminum appears to substantiate sodium as the major species oxidized by carbon dioxide. The ratio of the reactivities of the 50 mole % Al alloy to that of pure aluminum was observed by

[31] Aluminum Co. of America, Alcoa Research Labs., New Kensington, Pa.

[32] J. J. Stokes, Jr., and W. B. Frank, Proc. AIME Symposium on Extractive Metallurgy of Aluminum, Vol. 2, p. 3 (1962).

[33] J. J. Stokes, Jr., Unpublished Work, Alcoa Research Laboratories.

[34] M. A. Bredig, "Molten Salt Chemistry," ed. by M. Blander, p. 367, Interscience Publishers, New York 1964.

[35] J. Brynestad, K. Grjotheim, and S. Urnes, *Metallurgia ital.*, 52, 495 (1960).

[36] W. B. Frank and L. M. Foster, *J. Phys. Chem.*, 64, 95 (1960).

[37] M. Rolin and M. Bernard, *Bull. soc. chim. France*, 429 (1962).

Gjerstad and Welch as 0.58. On the basis of the electrochemical measurements of Grube and Hantelmann[38] the aluminum activity in a 50 a/o (atomic per cent) Al-Cu alloy at 980°C is indicated to be 0.28. From reaction [1] it is seen that the sodium activity is proportional to the cube root of the aluminum activity of the metal phase. Thus if sodium is the dominant oxidizable species, the ratio of reactivities should be $(0.28)^{1/3}$ or 0.66, in reasonable agreement with the observed ratio of Gjerstad and Welch of 0.58.

The increased reduction of CO_2 to CO by the NaF-AlF_3 melt-aluminum system with increased sodium fluoride content reported by Thonstad[39] is also consistent with the concept of sodium as the dominant species oxidizable by CO_2.

It is interesting to note that the diffusion rate of dissolved metal in the melt appears to be anomalously high, based on the measured rate of reaction and estimates of the solubility of either sodium or aluminum. The observed reaction rate of 7.8×10^{-6} moles $CO_2/cm^2/min$ at 980°C is equivalent to 2.6×10^{-7} g atoms $Na/cm^2/sec$ or 8.7×10^{-8} g atoms $Al/cm^2/sec$. These figures are in good agreement with Thonstad's[39] reported "total reactivity" for aluminum. Assuming the aluminum concentrations to be zero at the melt-gas interface and the saturation solubility of 0.1 w/o (weight per cent)[40] at the melt-metal interface, a diffusion coefficient of 2×10^{-3} cm^2/sec is calculated from Fick's law of diffusion. An even higher diffusion coefficient is calculated for sodium on the basis of an estimate of sodium solubility. Diffusion coefficients for ionic species in fused salts are generally in the range of 10^{-5} to 10^{-4} cm^2/sec.[41] No measurements of diffusion coefficients of metals dissolved in molten salts are reported in the literature.

S. Gjerstad and B. J. Welch: We agree with Dr. Frank that the experimental data published since this paper went to press[42-44] tend to support the sodium alternative as the more probable mechanism. In our discussion we were not concerned with the origin of the solvated species, but mechanism of its oxidation. The calculations of Frank indeed give added support to the sodium alternative, and if the more recent aluminum activity determined by Wilder[45] (0.265) is used, the agreement becomes even better. Angell and Tomlinson[46] have measured diffusion coefficients of Cd dissolved in $CdCl_2$ and obtained values of the same order of magnitude as those reported for ionic species in fused salts. Since Nanis and Bockris[47] have shown that the magnitude of diffusion coefficients in fused salts is dependent only on the melting temperature and the absolute temperature, the calculated values of diffusion based on measured Al solubilities are unreasonably high. This would therefore tend to support further the sodium alternative. In our opinion the question that is to be resolved is what is the nature of the solvated species—free sodium, or Na_2^+ as suggested by Thonstad.[44]

[38] G. Grube and P. Hantelmann, *Z. Elektrochem.*, **48**, 399 (1942).

[39] J. Thonstad, *This Journal*, **111**, 955 (1964).

[40] H. Nozaki and K. Miyanchi, *J. Chem. Soc. Japan*, (Ind. Chem. Sec.), **51**, 3 (1948).

[41] "Fused Salts," ed. by B. R. Sundheim, p. 224, McGraw-Hill Book Co., New York 1964.

[42] J. J. Stokes, Jr., and W. B. Frank, Proc. AIME Symposium on Extractive Metallurgy of Aluminum, Vol. 2, p. 3 (1962).

[43] "Fused Salts," ed. by B. R. Sundheim, p. 224, McGraw-Hill Book Co., New York 1964.

[44] J. Thonstad, *This Journal*, **111**, 955 (1964).

[45] T. C. Wilder, "The Thermodynamic Properties of the Liquid Aluminum-Copper System," Paper presented at the Chicago Meeting, AIME, February 1965.

[46] C. A. Angell and J. W. Tomlinson, *Discussions Faraday Soc.*, **32**, 237 (1961).

[47] L. Nanis and J. O'M. Bockris, *J. Phys. Chem.*, **67**, 2856 (1963).

Use of Index of Refraction Liquid for the Measurement of the Refractive Index of Thin Transparent Films on Silicon

A. E. Lewis (pp. 1007-1009, Vol. 111, No. 8)

R. H. Muller[48]: It is interesting to see that the time-honored immersion method for the determinaiton of refractive indices has found a new application for transparent solid films. One of the limitations of the method described is due to the necessity of a well-observable light interference such as saturated interference colors in the film before immersion. This requires, as stated by the author A. E. Lewis, equal reflectivities of the air-oxide and oxide-metal interfaces at normal incidence. An extension of the present technique, using particular angles of incidence[49] and polarized light should alleviate this situation.

As reported earlier,[50] "optimum" angles of incidence $\phi||$ and $\phi\perp$ exist for light polarized parallel and normal to the plane of incidence,[51] respectively, under which the amplitudes of the reflections from the air-film and film-metal interfaces are equal. This results in easily observable interference phenomna, even under conditions where the difference in reflectivity precludes any observation at normal incidence. Typical values of these optimum angles of incidence have been computed for silicon covered by transparent dielectric films of the reported refractive index of the oxide and adjacent values. The results are given in Table I together with those for two other base-metals. Numerical values used for the complex refractive index of the metals $n_2(1 - i\kappa_2)$ are also listed in Table I.

Table I. Optimum angles of incidence ϕ for light interference in transparent dielectric films on metal surfaces

Film refractive index n_1			1.30		1.45		1.60	
Angle of incidence			$\phi\|\|$	$\phi\perp$	$\phi\|\|$	$\phi\perp$	$\phi\|\|$	$\phi\perp$
Metal	Optical constants n_2	κ_2						
Si	4.05	0.01	76°	68°	76°	63°	76°	57°
Ni	1.75	1.95	84°	71°	84°	65°	84°	59°
W	3.46	0.94	82°	70°	82°	63°	82°	57°

In the modification of the immersion technique, suggested here, the reflection coefficient[52] of the film-liquid interface is a much steeper function of the refractive index difference between the two phases than under normal incidence (Fig. 1). Thus, the sensitivity of the method is improved in addition to making observation of the film interference easier. The use of polarization normal to the plane of incidence will in general be preferable to that parallel to the plane of incidence because the observations are possible at a lower angle of incidence which is often more convenient. As shown in Fig. 1, for an angle of incidence of 75°, which represents an average of the desirable values listed in Table I, the polarization normal to the plane of incidence also is associated with a somewhat better sensitivity.

It must be borne in mind that the immersion method presupposes a sharp boundary between homogeneous dielectrics. It is therefore strictly valid only for non-absorbing films. Computations for the reflection on absorbing media carried out according to Koenig[53] in-

[48] Lawrence Radiation Laboratory, University of California, Inorganic Materials Research Division, Berkeley, Calif.

[49] Defined as the angle between incident beam and normal to the surface.

[50] R. H. Muller, *J. Opt. Soc. Amer.*, **54**, 419 (1964). R. H. Muller, Lawrence Radiation Laboratory Report UCRL-10963.

[51] Defined as the plane containing incident and reflected beams.

[52] Defined as the ratio of the incident and reflected amplitudes.

[53] W. Koenig, "Elektromagnetische Lichttheorie," In Handbuch der Physik, Edited by H. Geiger and K. Scheel, Vol. 20, p. 242, Springer, Berlin (1928); R. H. Muller, Lawrence Radiation Laboratory Report UCRL-11813.

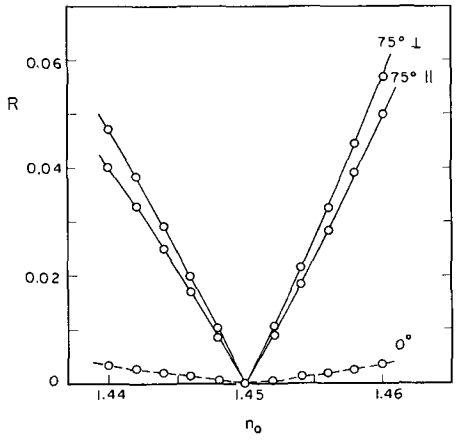

Fig. 1. Reflection coefficients R for dielectric medium (n_1 = 1.45) in contact with another dielectric of variable refractive index n_0. Angles of incidence 75° and 0°, polarization parallel (||) and normal ($\perp$) to the plane of incidence.

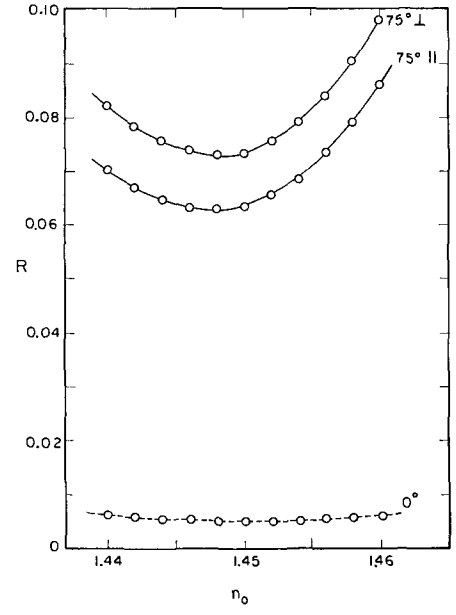

Fig. 2. Reflection coefficients of a slightly absorbing medium (n_1 = 1.45, κ_1 = 0.01) in contact with a dielectric of variable refractive index n_0. Angles of incidence 75° and 0°, polarization parallel and normal to the plane of incidence.

dicate that even for very slightly absorbing films (absorption index $\kappa_2 < 0.05$), the minimum in reflectance at the liquid-film interface, which occurs instead of the zero reflectance for a dielectric, gives only an approximate value of the real part of the complex film refractive index (Fig. 2).

A. E. Lewis: An increase in the intensity of the interference color obtained from a thin film is obtained by increasing the angle of incidence as shown by Muller[54] for a thin nonabsorbing film on a reflecting substrate in air. An examination of Fresnel's laws of reflection shows that this is expected because of the refraction occurring at the air-film interface. The angle of incidence increases faster than the angle of refraction as the angle of incidence is increased. The reflectance of the air-film interface therefore increases faster than the reflectance of the substrate. As the reflectance of the air-film interface increases relative to that of the substrate, the two reflectances become more equal and the intensity of the interference color increases.

This condition does not apply to the measurement of the index of refraction of a film using liquids. In this

[54] R. H. Muller, *J. Opt. Soc. Amer.*, 54, 419 (1964).

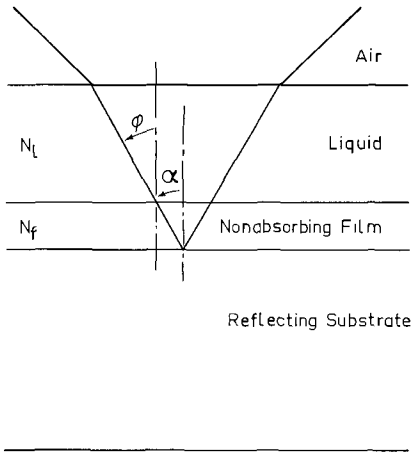

Fig. 1. Refraction of light in liquid covered film where $n_l \approx n_f$

method a "thick" liquid is applied to the film as shown in Fig. 1. Because the refractive index of the film and the liquid are almost equal, *i.e.*, $\Delta n = 0.005$, the angle of refraction (α) is only slightly different from the angle of incidence (ϕ), and although the reflectance of both the film and the substrate increase with increasing angle of incidence, there is no observable differential increase of the film reflectance relative to the substrate.

The conclusion that no increase in the sensitivity of the method is obtained by varying the angle of incidence in either polarized or nonpolarized light has been confirmed by observations made as a result of this discussion.

There is no statement in the paper that observable interference colors require equal reflectances of the air-film and film-substrate interfaces at normal incidence. The only requirement is that the reflectances must yield an observable interference color. This condition is fulfilled for very unequal reflectances and for angles of incidence other than zero. The technique found most suitable is to observe a film-step immersed in a liquid without a microscope or other optical aid. Immersed steps can be seen by this technique that can not be seen under a microscope.

As stated by Muller and also in the paper the method is applicable to nonabsorbing films. Films not strictly nonabsorbing such as SiO (index of refraction as high as 2.1) have, however, been measured without difficulty using this method. Such films are brown and obviously absorbing even in thicknesses less than a micron.

A High Performance Propane Fuel Cell Operating in the Temperature Range of 150-200°C

W. T. Grubb and C. J. Michalske (pp. 1015-1019, Vol. 111, No. 9)

G. H. J. Broers[55]: The authors, on page 1018 (Discussion and Results), mention four factors that may affect the steady state rate of oxidation: (i) mass transport of fuel or water to the electrocatalyst sites. (ii) . . . . . adsorption . . . . . (iii) . . . . . surface reactions . . . . (iv) rate of mass transport of CO_2 away from the reaction sites.

Then it is concluded that (i) and (iv) will not be rate determining, since the observed polarization curves are well removed from the limiting current region.

In my opinion this conclusion does not hold with regard to (iv). Considering reaction

$$C_3H_8 + 6H_2O = 3CO_2 + 20\,H^+ + 20\,e^- \qquad [1]$$

the theoretical influence of CO_2 mass transport on the Nernst potential E of the anode is of the form

$$\Delta E(CO_2) = (3RT/20\,F)\ln(1 + i/i_o) \qquad [a]$$

[55] Central Technical Institute, T.N.O., 198 Hoogte Kadijk, Amsterdam, Netherlands.

where R, T, and F have their usual significance, i is the current density and i_o is a constant; i_o is associated with the effective diffusion layer thickness δ, the effective diffusion constant D and the concentration c_o of CO_2 at the reaction sites when $i = 0$:

$$i_o = 20\ FDc_o/3\delta \qquad [b]$$

The + sign in [a] is typical for mass transport of reaction products: away from the reaction sites. Generally this mode of transport does not yield limiting currents (unless the electrode becomes blocked completely by the product), but will give rise to a pseudo Tafel behavior whenever $i >> i_o$.

In that case the linear plot of ΔE *vs.* i according to [a], yields a polarization curve of a shape similar to that of "activation controlled processes," that is, similar to the curves shown in, *e.g.*, Fig. 6 on page 1018.

Since very little will be known about δ, D, and c_o under the experimental conditions, an *a priori* neglection of mass transport effects of type (iv) might not be justified.

Of course, Grubb and Michalske's discussion on the factors (ii) and (iii) need not be ruled out by the present argument on (iv).

W. T. Grubb and C. J. Michalske: It is agreed that CO_2 mass transport could affect the rate under Broers' conditions without showing a limiting current behavior. Experimental evidence to show whether Broers' conditions apply to the present case is lacking. There is evidence that the performance of saturated hydrocarbon anodes in phosphoric acid at 150°C is a rather strong function of the structure of the fuel molecule.[56] We therefore favor the hypothesis that the fuel molecule is involved in one or more rate-determining steps and that mass transport of CO_2 away from the anode is not rate determining under the conditions of our experiments.

Mechanical Stresses during the Oxidation of Copper and Their Influence on Oxidation Kinetics. III

W. Jaenicke, S. Leistikow, and A. Stadler
(pp. 1031-1037, Vol. 111, No. 9)

U. R. Evans[57]: The authors have used the derivation of the logarithmic equation put forward by Davies, Agar, and myself in 1954 in interpreting their results. They are right in saying "one has to be cautious stating and interpreting oxidation laws;" but their observations on stress in the film certainly do seem to confirm the interpretation of the laws which we then put forward to explain our results on iron.

I appreciate also their reference to my "indirect evidence" of stresses in films published in this JOURNAL in 1947. In the same year I reported some much more direct evidence, but my paper,[58] presented at a symposium, escaped general notice. Those who have access to the symposium report may care to study my photographs (especially Fig. 3, 4, 7, 8, and 10), which are probably more convincing than any verbal description. For those who have no access, I attempt a summary.

Rectangles of nickel foil were heated along one edge to give wedge-shaped films producing interference colors. cemented to glass by means of petroleum jelly (vaseline), after which the nickel was removed anodically, leaving the films clinging to the glass, but now showing complementary colors. Had the films been stress-free they would have remained flat, but in fact the thicker parts of the films developed wrinkles, showing that while attached to the metal they must have been unnaturally compressed, although only after the removal of the nickel, were they free to assume a relatively unconstrained state by wrinkling, thus relieving the compressional stresses. Very instructive was one case (Fig. 10), where an island of metallic nickel had escaped anodic attack, and the film remained anchored to it, so that the wrinkles somewhat recalled the ridges of a mountain radiating from a central peak.

While the thicker films suffered wrinkling, an indication of fairly uniform stress, the thinner films curled up into tight rolls, indicating a stress gradient; one area was photographed by reflected light (Fig. 7) and by transmitted light (Fig. 8), and it is seen that the roll includes about 2½ convolutions, showing that the stress on this thin film must have been much higher at one face than the other.

The thinnest films of all failed in some cases either to wrinkle or curl, but remained flat. This was not because there was no stress, but because, when the thickness is sufficiently small, the decrease of strain energy accompanying curling or wrinkling will be less than the energy needed to deform the vaseline or to detach the film. When the vaseline was weakened by warming, these very thin films broke into contorted shapes.

The thicknesses at which these different phenomena passed into one another depended on the mechanical pretreatment of the nickel, but the following generalization was based on the study of over 100 tranfers:

"In the thick region, the film is strongly wrinkled . . . . The wrinkles usually come closer together as the films become thinner . . . Below a certain thickness (probably about 1000Å on nickel abraded with 2/0 emery), slits or holes appear in the film; at the edge of the gaps, the films tend to curl . . . At still lower thicknesses (about 500Å) the whole film is broken up into fragments . . . . which become smaller and more numerous as the thin region is approached, and then tend to curl up into rolls. Films too thin to give colors often curl into such tight rolls that the greater part of the vaseline surface is left bare. The tendency to curl increases as the thickness diminishes . . . The number of convolutions seen within the rolls increases as the film becomes thinner, showing that the stress gradient must increase as thickness diminishes. Observation is assisted if lines are drawn on the surface (before heating with heat-resistant pastel, or after heating with a lead pencil); the lines are clearly visible after transfer . . . The cause of the wrinkles in the thick film is found in the fact that the nickel oxide occupies, at its natural density, 1.6 times the volume of nickel destroyed in producing it . . . Wrinkling cannot be explained by differential thermal expansion, since the coefficient of expansion of nickel is too low, even if that of the oxide is neglected; moreover, similar wrinkling has been observed in the films formed on iron without heating by anodic treatment in sulphuric acid.[59]"

The explanation offered in 1947 for the stress (based essentially on the Pilling-Bedworth mechanism) is only valid for a film formed by movement of oxygen inward, not of metal outward. It is today generally believed that on nickel there are two layers, one produced by oxygen moving inward and the other by nickel moving outward. At first sight, this would seem to account for the curling, since the inner part only would be in compressional stress. Unfortunately, the curling is observed to take place in the wrong direction, and it must frankly be confessed that, although the observations provide convincing proof of stress in the films, they leave the origin of that stress still in doubt. The curling may represent a stress gradient produced in the metal by abrasion or other treatment and inherited by the oxide.

W. Jaenicke, S. Leistikow, and A. Stadler: We are glad, that in the foregoing remark Dr. Evans has again brought the attention to his ingeneous experiments of

[56] W. T. Grubb and C. J. Michalske, Proc. 18th Annual Power Sources Conference, Atlantic City, p. 17.

[57] 19, Manor Court, Grange Road, Cambridge, England.

[58] U. R. Evans, "Influence of Residual Stress on Chemical Behavior:" Symposium on Internal Stresses in Metals and Alloys, Organized by the Institute of Metals in London, 1947. Report published 1948, p. 291.

[59] U. R. Evans, *Nature*, 126, 130 (1930).

1947. They demonstrate, that on Ni similar effects happen as on Cu, in spite of the much higher reaction temperatures, which could cause plasticity of the oxide, as we have found at 500°C with copper. Evans has dissolved the metal to make visible the stress gradients within the oxide, while in some of our experiments the layer was reduced and by this way a dilatational stress within the metal could be measured. It is difficult however to understand the wrinkling of the thicker films if this is due only to stress relieving of strained homogeneous films because one has to consider new compressions at the concave parts and dilatations at the convex parts of the NiO.

We are pleased that also in Dr. Evans' opinion a simple volume effect like the Pilling-Bedworth rule does not cause permanent stresses in the interior of oxide layers if they grow by metal-ion transport. We wish to go farther and we believe, that this rule is of no importance also if the place of reaction is an inner phase boundary as long as the metal surface is flat. Such surfaces of course are seldom maintained during the reaction, especially if polycrystalline material or alloys are oxidized.

The Oxidation of Pyrolytic Graphite at Temperatures of 1400°-1800°F and at Air Velocities of 25-100 cm/sec.

M. Levy and P. Wong (pp. 1088-1091, Vol. 111, No. 9)

D. E. Rosner[60] and H. D. Allendorf[61]: The recent paper of Levy and Wong raises several interesting questions concerning the true high-temperature kinetics of pyrolytic graphite oxidation and the effects of diffusional limitations on the apparent kinetics of such highly exothermic heterogeneous chemical reactions. We wish to call attention here to aspects of practical and/or theoretical interest, some of which are currently under investigation at this laboratory.

Departures from Arrhenius behavior.—As noted by Levy and Wong, the fact that they, as well as many other investigators, have observed the transition from chemical to diffusion control to occur at surface temperatures in the 1100°-1200°K range is a reflection of the similarity of the reaction systems employed, especially as regards grade of carbon, specimen size, pressure level, and flow rate. However, in many aerospace applications (*e.g.*, leading edges for lifting Earth reentry vehicles [62] transport conditions are such that the transition is delayed to much higher surface temperatures (above 1400°K). The true specific reactivity of pyrolytic graphite at elevated surface temperatures is therefore of particular interest.

While it is tempting to make a simple straight line extrapolation (of kinetic regime data) on the Arrhenius plane, such a procedure would be unrealistic for the following reason.[63] If one casts the kinetic data of Levy and Wong in the form of a dimensionless reaction probability, ϵ, (*e.g.*, the probability that a carbon atom will be removed per O_2 strike) one finds that, in the kinetic region investigated, ϵ has a locally Arrhenius temperature dependence $\epsilon_0 \exp(-E/RT)$ with a pre-exponential term ϵ_0 that greatly exceeds unity. Since ϵ (as defined above) cannot exceed 2 (if each O_2 strike leads to the formation and desorption of 2 CO molecules) it is obvious that the Arrhenius temperature dependence (*i.e.*, constant activation energy) cannot be maintained at indefinitely high surface temperatures. Indeed, the kinetic data of Levy and Wong reveal that a leveling off of the true specific reactivity must occur somewhere below about 2400°K (a surface temperature well below the sublimation threshold). Maxima in the high-temperature oxidation probability of graphite in O_2 have been reported in the past[64] and have recently been observed at about 1600°K by the discussors in preliminary work with both diatomic and atomic oxygen.[63] As a corollary to these remarks, it is clear that an observed reduction in apparent activation energy is not a sufficient condition for invoking external diffusional limitations to explain experimental observations. One must (as Levy and Wong have done) investigate other effects, such as the dependence of reaction rate on flow rate, to rule out true kinetic departures from simple Arrhenius behavior.

Kinetics of the attack of graphite by atomic oxygen[63].—In the aerospace environment cited above[62,65,66] oxygen atoms are formed behind shock waves by thermal dissociation of O_2. Moreover, it is unlikely that there will be adequate time for homogeneous oxygen atom recombination in the cooler regions of the gas flow adjacent to the solid surfaces.[65,66] Consequently, the true kinetics of the attack of high-temperature pyrolytic graphite by atomic oxygen is a subject of current importance and one for which apparently no experimental data exist. Indeed, it remains to be seen whether pyrolytic graphite will display significantly improved oxidation resistance over ordinary commercial graphite in such an environment. Our preliminary experiments on the attack of commercial graphite (Speer Company, Grade 580) by atomic oxygen[63] in the surface temperature range 1100°-2000°K reveal that O-atom strikes are considerably more effective (a factor between 6 and 80 times) than O_2 in removing carbon atoms from the lattice. We hope to extend this work to other forms of graphite using experimental techniques similar to those employed in footnotes 63, 67.

Diffusional effects for exothermic surface reactions[68].—In discussing the transition from chemical to transport control one usually expects a monotonic dependence of reaction rate parameters (apparent activation energy, reaction order, *etc.*). However, it should be pointed out that for strongly exothermic, temperature sensitive surface reactions (such as graphite oxidation) this transition can display rather intriguing (certainly not monotonous!) behavior.[68] For example, in the intermediate regime the observed activation energy, reaction order, and sensitivity to flow velocity changes need not lie between the limits set by reaction rate and diffusion control. (Specifically, the apparent activation energy can exceed the true activation energy and the reaction rate can, locally, decrease with an increase in flow velocity.[69]) For a reaction of a prescribed kinetic order, in a system in which radiative heat transfer is negligible, these "overshoots" are largely determined by the magnitude of the product[68]

$$\alpha \equiv r_D \cdot \frac{Y_{O_2,\infty} Q}{\bar{c}_p T_\infty} \cdot \frac{E}{RT_\infty}$$

where r_D is the recovery factor for chemical energy, dependent on the ratio of the Fick coefficient for O_2 diffusion through the gas mixture to the mean thermal diffusivity of the mixture (r_D is a number of order unity); $Y_{O_2,\infty}$ is the oxygen mass fraction in the oxidiz-

[60] AeroChem Research Laboratories, Inc., Princeton, N. J.; Subsidiary of Pfaudler Permutit Inc.

[61] AeroChem Research Laboratories, Inc., Princeton, N. J.; Subsidiary of Pfaudler Permutit Inc.

[62] S. M. Scala and L. M. Gilbert, General Electric Co., MSD Space Sciences Lab., Report TIS R63 SD 89. November 1963.

[63] D. E. Rosner and H. D. Allendorf, "High Temperature Kinetics of Graphite Oxidation by Dissociated Oxygen," AeroChem TP-105, November 1964; *AIAA J.*, Submitted.

[64] J. S. Binford, Jr., "Kinetics of the Oxidation of Graphite," Literature of the Combustion of Petroleum, American Chemical Soc., Advances in Chemistry Series, No. 20, pp. 39-48, February 1958.

[65] D. E. Rosner, "Radiation Cooling of Aerodynamically Heated Surfaces at High Mach Numbers," in "Supersonic Flow, Chemical Processes and Radiative Transfer," pp. 439-483, Pergamon Press, London (1964).

[66] D. E. Rosner, *AIAA J.*, **1**, 1550 (1963).

[67] D. E. Rosner and H. D. Allendorf, *J. Chem. Phys.*, **40**, 3441 (1964).

[68] D. E. Rosner, *AIAA J.*, **2**, 593 (1964).

[69] There is a suggestion of such behavior in the 1400° and 1500°F data reported in Fig. 3 of the paper, although additional points in the velocity range 25-50 cm/sec would be required to verify this.

ing gas; Q, the heat of oxidation (combustion) per unit mass of oxygen; $\bar{c}_p$, the mean specific heat of gas mixture; T_∞, the temperature of oxidizer stream; E, the true activation energy of the surface reaction; and R, the universal gas constant.

For graphite oxidation in air under the conditions investigated by Levy and Wong, even assuming CO(g) to be the dominant reaction product (which underestimates Q), this parameter appears to be large enough to produce significant effects on the nature of the transition from reaction rate-to-diffusion control. We would therefore like to ask if the authors of the paper have observed any evidence of this type. If not, perhaps radiative heat transfer in the furnace environment suppresses this interesting class of transition phenomena. This may also explain their observation that the graphite surface temperature never exceeded the furnace temperature by more than 20°K, whereas simple theory[68] would have predicted a temperature excess ΔT_{max}, given by

$$\Delta T_{max} = r_D Y_{O_2,\infty} Q/\bar{c}_p$$

(which amounts to more than 100°K in the present system).

Finally, Levy and Wong made reference to the concept of resistance additivity in discussing the transition from chemical to diffusion control. While this concept has been of undeniable qualitative value, we would like to emphasize that it should not be quantitatively applied to situations in which the interfacial mass flux $\dot{m}''$ associated with the oxidation process has a significant effect on the local boundary layer profiles.[70,68] This point, which has also been considered by Welsh and Chung,[72] is specifically illustrated in Fig. 1 for the case of graphite ablation in air at a forward

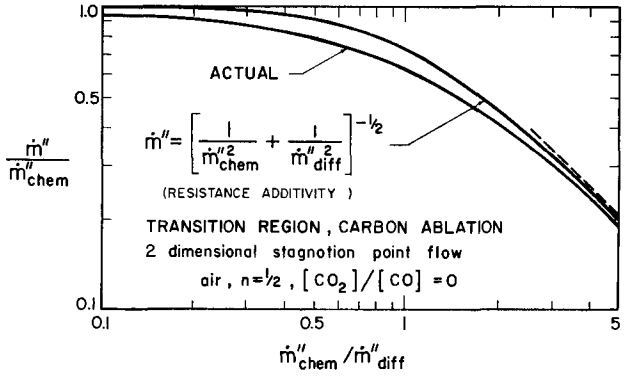

Fig. 1 Failure of the method of resistance additivity for the ablation of graphite in air.

stagnation point. In making these illustrative predictions we have assumed that the true reaction order is ½ and CO(g) is the dominant reaction product. At surface temperature levels such that primary CO_2 is formed in appreciable amounts the shape of the transition is also expected to exhibit a marked dependence on the relation between the primary CO/CO_2 ratio and local O_2 partial pressure.[72]

This discussion is based on work carried out under Air Force (Office of Scientific Research, Propulsion Div.) support, Contracts AF 49 (638) 1138 and AF 49 (638)-1195.

[70] This is especially true for the oxidation of tungsten or molybdenum in non-vitiated air at surface temperatures such that the metal oxides are volatile. [71]

[71] D. E. Rosner and H. D. Allendorf, Discussion of "Oxidation of Molybdenum, 550°C-1700°C," *This Journal*, **111**, 759 (1964).

[72] W. E. Welsh and P. M. Chung, "An Analysis of the Effect of Heterogeneous Reaction Kinetics on the Combustion of Graphite at the Stagnation Region of a Blunt Body in Hypersonic Flow," Aerospace Corp. (El Segundo, Calif.), Report TDR-169(3230-12) TN-6; SSD-TDR-63-40, February 1963.

M. Levy and P. Wong: We wish to thank Dr. D. E. Rosner and H. D. Allendorf for their interesting discussion.

We acknowledge the importance of the reaction of pyrolytic graphite with atomic oxygen but not at the temperature (1033°-1255°K) and low air velocities considered in our paper. Equilibrium constants for the reaction $\frac{1}{2}\ O_2(g) \rightleftarrows O(g)$ indicate that the dissociation of oxygen molecules becomes appreciable above 1473°K.

Regarding conditions where the apparent activation energy can exceed the true activation energy and the reaction rate can, locally, decrease with an increase in flow velocity, we have not observed this phenomenon in the transition region.

The Transmission of Electrolytically Deposited Hydrogen Through a Palladium Membrane Electrode

G. W. Castellan, R. A. La Pietra, and P. L. Damour

(pp. 1273-1283, Vol. 111, No. 11)

G. Dubpernell[73]: The difficulty with the work presented in these papers is that it is predicated on the assumption that electrolytically evolved hydrogen can diffuse through a palladium diaphragm freely and easily at room temperature. If the investigator assumed that hydrogen cannot diffuse through solid palladium at room temperature, he would have little difficulty in proving his point, as this is believed to be the case actually, even though not the widely accepted view. It is felt that adsorption of hydrogen and compound formation between hydrogen and palladium should not be regarded as synonymous with diffusion through a membrane.

It is postulated that the observed effects are due to porosity of the membranes and to the direct evolution of hydrogen on the back of the membrane through the pores. Little effort seems to have been made to check for such porosity of the membranes, even though a simple means has been suggested.[74]

Thus La Pietra and Castellan found it necessary to "clean" their palladium membranes by a 12 hr anodic treatment in 2*N* H_2SO_4 at 69.5 ma/cm^2, although they do not state what was present to require such prolonged anodic cleaning. They ". . . were plagued by the lack of reproducibility . . ." which could not be eliminated by anodic activation of the entrance side of the foil between each series of measurements. In his dissertation[75] La Pietra notes that even with the prolonged anodic cleaning about one in every four experiments gave anomalous results in that the percentage transmission of hydrogen was very much lower, and it was decided to reject all such runs. He also actually noted the appearance of "leaks" in some of his palladium diaphragms, and when he tried to test for leaks with acid indicator paper on the back of the diaphragm, found that this cut the transmission of hydrogen by more than half, and such a procedure had to be discontinued. It is also worthy of note that the results with the thinnest foil, 0.001 in. thick, were extremely erratic and consequently were not reported.

It appears likely that the prolonged anodic treatment in 2*N* H_2SO_4 could corrode holes through the palladium diaphragms. Palladium is not as resistant to corrosion as many of the other platinum metals and is known to corrode under these conditions.[76]

It would appear to have been in order to determine the weight loss or change in thickness of the palladium diaphragms, but they do not seem to have been examined after the tests.

[73] M&T Chemicals, Inc., Detroit 20, Mich.

[74] G. Dubpernell, *This Journal*, **103**, 704 (1956).

[75] R. A. La Pietra, "An Electrochemical Study of the Passage of Hydrogen Atoms through A Diaphragm Cathode," 58 pages, The Catholic University of America Press, Washington, D. C. (1961).

[76] M. Pourbaix, "Atlas D'Equilibres Electrochimiques á 25°C," p. 361, Gauthier—Villars and Cie, Paris (1963).

Damour and Castellan anodized their palladium membranes at 100 ma for 30 min. It appears from Damour's dissertation[77] that the exposed area on each membrane was 1 cm in diameter, so the current density of anodization would have been about 127 ma/cm^2. In this work the preliminary cleaning of the membrane by flaming in a gas flame (Meker burner) as used by La Pietra was questioned, and a hydrogen-oxygen gas flame was used instead. Nevertheless, "poisoning" of the surface of the palladium was appreciable, and many times no gas would diffuse through the foils.

It seems evident that much more is involved here than a simple diffusion of hydrogen through palladium, and that a re-evaluation and a new approach would be in order. It is felt that much can be learned from a more painstaking study of thin, undamaged membranes handled with extreme care, and that if such membranes fail to permit any diffusion, they should not be regarded as poisoned, or in need of surface activation or cleaning.

G. W. Castellan, R. A. La Pietra, and P. L. Damour: The principal purpose of the prolonged anodic treatment of the cell system was not so much to clean the electrodes as to purify the electrolytic solution. The 12 hr electrolysis in Part II was replaced in Part III with a 30 min anodization to activate the electrode but in Part III the sulfuric acid solution was pre-electrolyzed for 12 hr in a flask outside the system.

We did not check the membranes specifically for porosity after using them. However, we attribute our inability to obtain satisfactory results with the thinnest (0.001 in.) membrane to the development of punctures in the membrane. If the pores are produced by anodic corrosion we think that our experiments would not have been as reproducible as they were.

On the general question of whether hydrogen diffuses through the bulk of the metal or through pores, we do not thing that the experiments in the set of papers in question here provide evidence on either side of this question. We have assumed in the interpretation that the hydrogen diffuses through the bulk of the metal. Other experiments, notably those in which the resistance of palladium is measured as a function of hydrogen content,[78,79] indicate strongly to our minds that hydrogen does diffuse through bulk palladium at room temperature.

As far as the question of compound formation is concerned, again the experiments in question here do not yield evidence on either side. And, at least within this limited scope we think one can take either side as a legitimate point of view.

We agree that the system deserves further examination using a number of different approaches. The situation with regard to "poisoning" is particularly unsatisfactory.

The Density and Surface Tension of Molten Fluorides, II. The System NaF-LiF-ZrF_4

G. Mellors and S. Senderoff (pp. 1355-1357, Vol. 111, No. 12)

H. M. Scholberg[80]: The authors have shown break points at low concentrations of ZrF_4 in the mixed fluoride solvents used for Fig. 4 and 5, which are not justified because of the following reasons. Gibbs equation suggests that the curves of Fig. 4 and 5 should be concave downward; otherwise, if it were drawn as a series of straight lines, as the authors have done, the force-area curve that would be obtained would be a step curve. Certainly, within the precision indicated by the authors, there appears to be no reason for discarding a smooth force-area curve in favor of a stepped curve. The break at high concentration shown in Fig. 5 is probably real as it has its counterpart in similar curves of organic surface active substances in water, where the break point is usually interpreted as the point of micelle formation.

A calculation of the surface excess at high concentration using Fig. 4 gives the value 3.90 x 10^{14} molecules/cm^2. This compares rather well with the value of 8.15 x 10^{14} calculated by means of the perfect gas law for surfaces. In view of the high pressures involved it is reasonable to expect that this sort of agreement would indicate that activity would not change the situation significantly.

It is possible, as I have shown in an article[81] to correlate surface tension and viscosity data to determine molecular structure parameters for solutions. I believe that it would be extremely interesting to apply that method to this problem.

G. W. Mellors and S. Senderoff: We do not accept the contention that the breaks at low concentration in Fig. 4 and 5 are less justified than the break at higher concentrations in Fig. 5, since there is no evidence for formation of solid phases at the temperatures studied at any concentration. If, however, micelle formation is equivalent to what we have called "clustering" or "ordering" in the liquid state, this may occur at both high and low concentrations.

There is no basis for the statement that the Gibbs equation curves must, *a priori*, result in curves concave downward. In fact, one cannot predict theoretically what shape curves will be obtained in a system such as this in which the identity of the solute species changes with composition as a result of interaction with the solvent. It will be noted in Fig. 5 that the Gibbs plots (lower curves) are concave downward at low concentration and concave upward at high concentration. This fact is strong evidence that the solvent species has changed from one complex ion $[ZrF_7]^{=}$ to another $[ZrF_5]^{-1}$.

M. A. Bredig[82]: Proof for the existence of complexes in molten salt mixtures is generally hard to come by. Thus, one is not readily persuaded that in Fig. 4 and 5 proposed "sharp breaks" actually exist as evidence for the occurrence of complex ions ZrF_7^{-3} and ZrF_5^{-} and for "clustering" or "ordering" corresponding to compositions Na_3ZrF_7 and K_3ZrF_7. The scattering of the experimental points, most pronounced in the top (enthalpy) curve in Fig. 4, seems much too large to justify drawing straight-line segments such as those shown in these figures. A gradual curvature over the whole range is actually indicated such as the authors present in Fig. 3 by the one smooth curve with which Fig. 4 showing the same data are not consistent. Furthermore, it is very improbable that clustering to a composition Na_3ZrF_7 (or K_3ZrF_7) would occur at 800°C, well above the melting point: Segregation of Na and Li does not take place even in the far more sensitive solid state at as low a temperature as the ternary eutectic (590°) where not pure Na_3ZrF_7 as stated by the authors but the solid solution phase $(Na, Li)_3ZrF_7$ forms, very rich in lithium (approximating just the Na:Li ratio 2:3 that was present in the measurements; cf. "Phase Diagrams of Nuclear Reactor Materials," R. E. Thoma, Editor, Oak Ridge National Laboratory, November 20, 1959, ORNL-2548, Table and Fig. 3.37, page 60/61; in press, *J. Chem. Eng. Data*, July 1965).

G. W. Mellors and S. Senderoff: We do not agree that the data shown in Fig. 4 and 5 would be correctly represented by smooth curves.

There is no inconsistency between Fig. 3 and 4. The logarithmic plot of Fig. 4, by magnifying the low con-

[77] P. L. Damour, "The Effect of Temperature and Pressure on the Maximum Diffusion Rate of Hydrogen Through Palladium," 54 pages, University Microfilms, Inc., Ann Arbor, Michigan (1962).

[78] R. J. Fallon and G. W. Castellan, *J. Phys. Chem.*, **64**, 4 (1960).

[79] T. B. Flanagan, *J. Phys. Chem.*, **65**, 280 (1961).

[80] 120 Juniper Drive, North Kingston, R. I.

[81] H. M. Scholberg, *J. Phys. Chem.*, To be published.

[82] Chemistry Division, Oak Ridge National Laboratory, Oak Ridge, Tenn.

centration portion, makes the inflections in this region clearly evident. In the linear plot of Fig. 3 these inflections are less clearly defined, but departures of points from the curve may be observed near 10 and 25 mole% ZrF_4.

Our statement that "Na_3ZrF_7 ($\sim$ 11.7 mole % ZrF_4) is a solid phase found in equilibrium with the melt at the 604° eutectic temperature" is correct according to ORNL-2548 cited by MAB which is also our ref. (3). There is no special significance to the 590° eutectic cited by MAB since, in fact, the solvent composition we used falls between that of these two eutectic mixtures.

Plasma Anodized Aluminum Oxide Films

G. J. Tibol and R. W. Hull (pp. 1368-1372, Vol. 111, No. 12)

W. A. Pliskin[83]: The authors stated, "For very thick films, the method of Pliskin and Conrad,[84] using three wavelengths, provides an extension of this simple nondestructive method into the micron range." The original published paper[84] on the Vamfo technique (which is the name we had given this method) showed that it can be used for the measurements of film thicknesses from several hundred angstroms to several microns. The thicknesses of films thicker than a micron can be measured with use of only one interference filter. Also, the thicknesses of films in the range of 800Å to a micron and of known refractive index can be measured accurately using only one filter if the order of approximate thickness is already known or determined as described in Section b, p. 47, of ref. 84. The three or more filter technique described on p. 46 of ref. 84 is intended for those cases where both the approximate film thickness is not known and the thickness is less than 1μ. It is only one of several Vamfo variations described in that paper. The variation which we have used most commonly for thickness measurements is based on Eq. [2] (see p. 44 and end of Section b on p. 47 of ref. 84) with $d = N\lambda/2\mu \cos r$.

G. J. Tibol and R. W. Hull[85]: Pliskin describes in Ref. 84 several variations of a technique he calls "Vamfo" in which monochromatic interference fringes are observed as the sample is tilted, so that the film thickness follows the equation he states above. The thickness d is determined only when the refractive index μ is known. If μ is unknown, an additional measurement must be made. In Pliskin and Conrad's paper it is shown that a step measurement at normal incidence may be used as the second measurement.

When examining capacitor dielectric films, Tibol and Hull have found capacitance to be a very useful second measurement. The rapid change of dielectric constant with deviations from full film density magnifies the precision of the film thickness determination. We considered it to be significant that the thickness and dielectric constant determinations could be made on the actual samples to be electrically measured without any prior assumption of film structure.

[83] IBM Components Division, Poughkeepsie, N. Y.

[84] W. A. Pliskin and E. E. Conrad, *IBM J. Research and Development*, 8, 43 (1964).

[85] Basking Ridge, N. J.

Call for Papers for Cleveland Meeting, May 1966

Papers are being solicited for the Spring Meeting of the Society, to be held at the Sheraton-Cleveland Hotel in Cleveland, Ohio, May 1, 2, 3, 4, and 5, 1966. Technical sessions probably will be scheduled on: Electric Insulation, Electronics (including Luminescence and Semiconductors), Electrothermics & Metallurgy, Industrial Electrolytic, and Theoretical Electrochemistry.

To be considered for this meeting, **triplicate copies of the usual 75-word abstract, as well as of an extended abstract of 500-1000 words** (see notice on page 121C of the May issue), must be received at The Electrochemical Society, 30 East 42 St., New York, N. Y., 10017, *not later than December 15, 1965. Please indicate on 75-word abstract for which Division's symposium the paper is to be scheduled, and underline the name of the author who will present the paper.* No paper will be placed on the program unless one of the authors, or a qualified person designated by the authors, has agreed to present it in person. Clearance for presentation of a paper at the meeting should be obtained before the abstract is submitted. An author who wishes his paper considered for publication in the JOURNAL or ELECTROCHEMICAL TECHNOLOGY should send triplicate copies of the manuscript to the Managing Editor of the appropriate publication 30 East 42 St., New York, N. Y., 10017. Concerning papers to be published in the JOURNAL, see notice on per page charge on page 133C of this issue.

Presentation of a paper at a technical meeting of the Society does not guarantee publication in the JOURNAL or ELECTROCHEMICAL TECHNOLOGY. However, all papers so presented become the property of The Electrochemical Society, and may not be published elsewhere, either in whole or in part, unless permission for release is requested of and granted by the Editor. Papers already published elsewhere, or submitted for publication elsewhere, are not acceptable for oral presentation except on invitation by a Divisional program Chairman.

Design of Primary and Secondary Cells

II. An Equation Describing Battery Discharge

C. M. Shepherd

U. S. Naval Research Laboratory, Washington, D. C.

ABSTRACT

A discussion is given of the derivation and application of an equation which gives an excellent description of a wide variety of cell and battery discharges. This equation gives the cell potential during discharge as a function of discharge time, current density, and certain other factors. It makes possible a complete description of cell discharge characteristics, using a minimum of experimental data and at the same time pinpointing experimental errors. It can also be used to describe cell charges, capacities, power evolution, and to predict capacities. A description is given of a simple numerical method for fitting this equation to a particular set of battery discharge curves. A graphical method is described for comparing characteristics of various types of cells.

This paper is one of a series whose ultimate goal is to determine procedures for designing batteries having optimum properties such as minimum weight or minimum volume. In particular, the derivation and application of an equation describing cell discharge will be discussed. The equation can be used to locate variations in the discharge data due to experimental error, uncontrolled variables, etc., thus minimizing the amount of experimental data needed and cutting the costs of evaluation. A complete set of discharge curves can be described by a single equation, making it possible to present in less space a more detailed description of cell characteristics than has been customary in many battery papers.

Derivation and Determination of the Discharge Equation

The mathematical analysis given here is based on the assumption that the following conditions are applicable: (*A*). The anode and/or cathode have porous active materials. (*B*). The electrolyte resistance is constant throughout discharge. (*C*). The cell is discharged at a constant current. (*D*). The polarization is a linear function of the active material current density.

When ionic discharge is the slow or rate determining process, the relationship between steady-state current density and activation overpotential at an electrode in a constant concentration electrolyte is usually written as

$$i = i_o e^{\alpha\eta ZF/RT} - i_o e^{-(1-\alpha)\eta ZF/RT} \qquad [1]$$

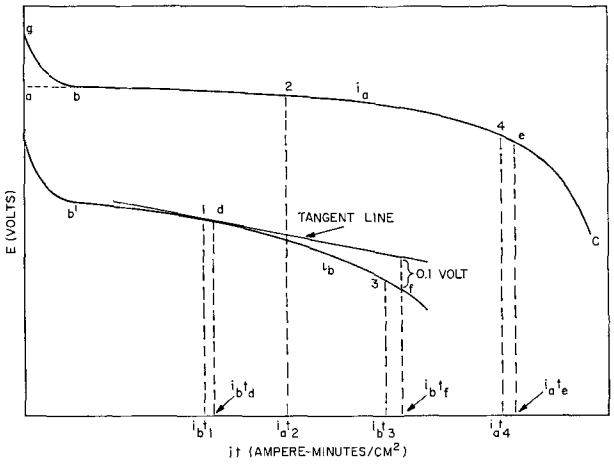

Fig. 1. Typical discharge curves used in equation fitting

where i is the apparent current density in amperes per square centimeter, i_o is the apparent exchange current density in amperes per square centimeter, α is the transfer coefficient ($0 \leq \alpha \leq 1$), Z is the number of electrons transferred in the rate-determining step, F is the Faraday, R is the gas constant, and T is the temperature in °K. The steady-state activation overpotential, η, is positive for the deposition of cations.

When the exponential terms are expanded as a series, powers greater than one can be neglected if η is sufficiently small and Eq. [1] becomes

$$\eta = \left(\frac{RT}{ZFi_o}\right) i \qquad [2]$$

thus establishing a linear relationship between η and i which is fairly accurate up to the values of η equal to approximately 0.03v. If Eq. [1] is applicable to a cell, the variation of η with change in i can be fitted by a straight line within approximately 0.02-0.04v up to values of η equal to about 0.2-0.4v. A potential drop of this magnitude would cover the major portion of the polarization that occurs during most battery discharges.

In Fig. 1, two solid curves, i_a and i_b, are shown which represent typical battery discharges. The potential in volts is plotted as a function of (it), the quantity of electricity that has been obtained from the battery at time t. It is assumed in the derivation that follows that the polarization is linear to the right of point b and b'. If all factors except polarization are ignored, then E_c, the cathode potential during discharge, is defined as

$$E_c = E_{sc} - K_c i_{am} \qquad [3]$$

where E_{sc} is a constant potential, K_c is the cathode coefficient of polarization per unit active material current density, and i_{am} is the active material current density. The successful use of Eq. [3] as a fundamental equation in the derivation that follows does not necessarily imply that the theoretical factors associated with Eq. [1] apply to most battery discharges even though both equations are linear.

In the case of a porous electrode the active material current density i_{am} is defined as being inversely proportional to the amount of unused active material and is also equal to i at the beginning of the discharge. Consequently

$$i_{am} = \left(\frac{Q_c}{Q_c - it}\right) i \qquad [4]$$

where t is the time at any point during the discharge and Q_c is the amount of available cathode active material expressed in units such as ampere hours per unit area.

When Eq. [4] is substituted in Eq. [3]

$$E_c = E_{sc} - K_c\left(\frac{Q_c}{Q_c - it}\right)i \qquad [5]$$

Similarly

$$E_a = E_{sa} - K_a\left(\frac{Q_a}{Q_a - it}\right)i \qquad [6]$$

where the subscripts a and c denote the anode and cathode values for the constants, respectively. A sign convention is used here which makes the value of the potential terms positive.

If Q_a is approximately equal to Q_c, as it generally is in a well designed cell, Eq. [5] and [6] can be summed to give

$$E = E_s - K\left(\frac{Q}{Q - it}\right)i \qquad [7]$$

where $E = E_a + E_c$ is the potential of the cell (neglecting the internal resistance) at any time t during the discharge; $E_s = E_{sa} + E_{sc}$ is a constant potential; $K = K_a + K_c$ is the polarization coefficient in ohm cm^2; and $Q = Q_a = Q_c$ is the available amount of active material in coulombs or similar units per unit area.

If Q_a is appreciably larger than Q_c, then the numerical increase in the value of the last term in Eq. [6] will be small compared to the numerical increase in the value of the last term of Eq. [5] as (it) approaches Q_c in value. Consequently, the second term of Eq. [6] can be considered to be approximately constant and the sum of Eq. [5] and [6] will still have approximately the form shown in Eq. [7]. Under these conditions the approximate values of K, Q and E_s will be $K = K_c$, $Q = Q_c$, and $E_s = E_{sa} + E_{sc} - K_a i$. If Q_c is appreciably larger than Q_a, then the approximate values of K, Q, and E_s will be $K = K_a$, $Q = Q_a$, and $E_s = E_{sa} + E_{sc} - K_c i$. Thus Q is determined by the amount of available active material on the controlling electrode which is the one that fails first. A similar argument will show that the same type of equation will be approximately true when several cells are connected in series to form a battery.

When the potential drop due to internal resistance is considered, Eq. [7] becomes

$$E = E_s - K\left(\frac{Q}{Q - it}\right)i - Ni \qquad [8]$$

where N, the internal resistance per unit area, is measured in ohm cm^2 or other suitable units.

When Eq. [8] is evaluated mathematically, a set of curves is obtained, one of which, plotted in Fig. 1, is a dotted line from a to b and a solid line from b to c. The initial drop in potential at the beginning of a cell discharge is not included in Eq. [8]. Consequently another term must be added to correct for the difference between the dotted line potential calculated from Eq. [8] and the solid line gb that represents the actual discharge potential. It has been found that the expression $A\exp(-BQ^{-1}it)$, where A and B are empirical constants, gives an excellent estimate of the initial potential drop in virtually every case. When this term is added to Eq. [8], the final equation

$$E = E_s - K\left(\frac{Q}{Q - it}\right)i - Ni + A\exp(-BQ^{-1}it) \qquad [9]$$

is obtained. In a number of cases the initial drop in potential was too rapid to be included in the observed experimental data and consequently, the value of $A\exp(-BQ^{-1}it)$, being negligible, could be ignored.

That portion of the discharge curve that lies to the right of point b in Fig. 1 could be predicted from Eq. [9] if the numerical values of E_s, K, Q, and N were known, providing the basic assumptions were true. However, the labor involved in determining these values would be so large that it probably would be easier, and certainly more accurate, to determine discharge curves experimentally. However, Eq. [9] can be fitted numerically to experimental discharge data, thus determining empirical values of E_s, K, Q, N, A, and B. Such a numerical equation gives an accurate description of the cell or battery discharge and can be used to describe energy evolution, cell capacity, and can be used in predicting cell capacities. Despite its successful applications, it must be considered to be an empirical equation since the numerical values of K, Q, and N that are determined in this manner will vary considerably at times from their true values as defined in the basic assumptions.

There are a number of methods that can be used to determine the numerical values of E_s, K, Q, N, A, and B in Eq. [9] from experimental discharge data, most of which are unsuitable. The least squares solution is particularly involved and time-consuming. The following approach is easily applied, rapid, reasonably accurate and is used in fitting Eq. [9] to discharge curves obtained at a number of current densities. In Fig. 1, four points, labeled 1, 2, 3, and 4 have been selected on two discharge curves which were obtained at the moderately low current density, i_a, and the moderately high current density, i_b. The values of E and (it) at points 1, 2, 3, and 4 are E_1, E_2, E_3, and E_4 and i_bt_1, i_at_2, i_bt_3, and i_at_4, respectively. These four points are chosen to the right of the initial potential drop. Thus the value of $A\exp(-BQ^{-1}it)$ is negligible and the potential at point 2 is found from Eq. [9] to be approximately

$$E_2 = E_s - K\left(\frac{Q}{Q - i_at_2}\right)i_a - Ni_a \qquad [10]$$

Similarly

$$E_4 = E_s - K\left(\frac{Q}{Q - i_at_4}\right)i_a - Ni_a \qquad [11]$$

Subtracting Eq. [11] from Eq. [10] gives

$$E_2 - E_4 = Ki_a\left(\frac{Q(i_at_4 - i_at_2)}{(Q - i_at_1)(Q - i_at_2)}\right) \qquad [12]$$

The equation for $E_1 - E_3$ is obtained in a similar manner and is divided into Eq. [12] to give

$$\frac{E_2 - E_4}{E_1 - E_3} = \frac{i_a}{i_b}\,\frac{(i_at_4 - i_at_2)}{(i_bt_3 - i_bt_1)}\,\frac{(Q - i_bt_3)(Q - i_bt_1)}{(Q - i_at_4)(Q - i_at_2)} \qquad [13]$$

When numerical values of E, i, and (it) are taken from the discharge data in Fig. 1 and substituted in Eq. [13], a quadratic equation in Q is obtained which is solved to give a numerical value of Q. This value of Q is substituted in Eq. [12] and solved to obtain a numerical value of K. When these values of Q and K are substituted in Eq. [10] and a similar equation for E_1, two simultaneous equations are obtained which may be solved to give numerical values for E_s and N. When these values of E_s, N, K, and Q are substituted in Eq. [9], E is obtained as a specific function of (it). The calculation of Q by use of Eq. [13] can generally be simplified by choosing point 2 in a manner such that i_at_2 equals either i_bt_3 or i_bt_1.

The two discharge curves, i_a and i_b, that are chosen as a basis for these calculations should be representative of the complete set of discharge curves and should show no obvious visual discrepancies that would indicate variations not present in the other curves. They are selected in the following manner. If (it) is held constant, Eq. [9] shows that the potential E to the right of point b in Fig. 1 may be stated as a linear function of the current density, i, in the form

$$E = E_s - B_1 i \qquad [14]$$

where B_1 is a constant equal to $K\left(\frac{Q}{Q - it}\right) + \mathrm{N}$

A fairly good fit to Eq. [14] is shown in Fig. 2 where E has been plotted as a function of i for five values of

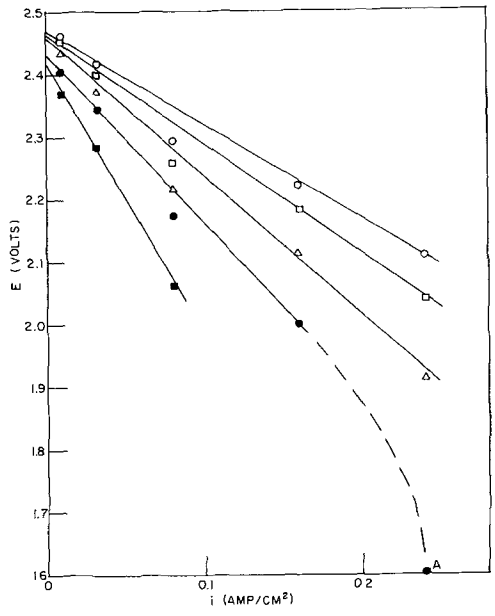

Fig. 2. Potential during cell discharge *vs.* current density for constant values of (*it*). The *it* values in amp-hr/cm²: ○, 0.00266; □, 0.00532; △, 0.00798; ●, 0.01063; ■, 0.01329.

(*it*) using the discharge data for the lead-zinc cell shown in Fig. 4g. The potentials, E at the current density, $i = 0.0798$ amp/cm², were considerably lower than the straight lines drawn through the corresponding values of (*it*), thus showing that this particular discharge was out of agreement with the remainder of the data. Variations this large were not observed as a rule. The remaining four values of i gave good straight line fits in Fig. 2. Either of the two low values of i could be used for i_a and either of the two high values could be used for i_b. As a rule a plot of E *vs.* i for each of two values of (*it*) will be sufficient to select satisfactory values of i_a and i_b. Points such as A which were taken past the knee of the discharge curve should not be used in making up these charts of E *vs* i. Very low values and very high values of i are avoided if feasible in selecting i_a and i_b since these extreme values have a tendency to be less accurate. With a little experience, i_a and i_b often can be selected on the basis of judgment without drawing up a chart such as that shown in Fig. 2.

If Eq. [9] is a perfect fit for the discharge data, then the plot of E *vs.* i as illustrated in Fig. 2 would consist of straight lines intersecting on the E axis at $E = E_s$. If the plot of E *vs.* i gives lines that do not intersect on the E axis or if they are curves, then Eq. [9] does not describe the discharge data perfectly. However, Eq. [9] is so adaptable that it can describe such cases with good accuracy and it has not been necessary to reject any data on this account. Discharge data were not accepted for study here whenever they were so erratic and full of error that a plot of E *vs.* i did not give some semblance of a smooth curve. It was found that all of the data that were acceptable on this basis could be fitted by Eq. [9]. Virtually all of the room temperature discharge data taken from the literature were found to be acceptable. At low temperatures the available data were more erratic and less acceptable.

The points 1, 2, 3, and 4 used to calculate the numerical values of the parameters K, Q, and N are selected in the manner illustrated in Fig. 1. A tangent is drawn to the high current density discharge curve at point d and point f is selected to be 0.1v below the tangent line. Point d is determined by eye by laying a transparent plastic straight edge tangent to the curve and adjusting the point of tangency until $i_b t_d$ equals 0.5 $i_b t_f$. This method is rapid and sufficiently accurate. Point e is located in a manner similar to f. The value of E for point 3 is approximately 0.03v

Table I. Values of ΔE in volts

	(*i t*)						
i	2	5	10	20	30	50	65
2	0.116	0.106	0.091	0.068	0.045	0.019	0.007
10	0.133	0.118	0.088	0.057	0.037	0.013	0.002
20	0.145	0.123	0.087	0.050	0.032	0.008	0.000
40	0.144	0.120	0.084	0.048	0.027	0.006	0.000
60	0.141	0.117	0.087	0.056	0.030	0.008	0.002
80	0.140	0.115	0.086	0.056	0.031	0.003	0.001
100	0.143	0.123	0.085	0.049	0.026	0.009	0.003
120	0.153	0.118	0.085	0.049	0.025	0.010	0.000
Avg.	0.139	0.118	0.087	0.054	0.032	0.0095	0.0018

greater than it is for point f. The value of E for point 4 is approximately 0.02v greater than it is for point e. Point 1 is chosen so $i_b t_1$ equals approximately 0.5 $i_b t_3$. If $i_b t_f / i_a t_e$ is less than 0.7, point 2 is chosen directly above point 3 so that $i_a t_2$ will equal $i_b t_3$. If $i_b t_f / i_a t_e$ is greater than 0.7, point 2 is chosen directly above point 1 so that $i_a t_2$ will equal $i_b t_1$. This procedure gives an approximate location of the points which supply the numerical data to substitute in Eq. [12] and [13], and make possible the calculation of numerical values of K, Q, N, and E_s which can be substituted in Eq. [9] along with values of A and B to give a fairly good numerical description of the discharge data. Values of E *vs.* (*it*) for different discharge rates can be calculated from this numerical equation and compared to the actual discharge data. If the agreement is not good enough, it can be improved by the method of successive approximations. A new calculation can be made using slightly different locations for one or more of the four points on the two discharge curves, i_a and i_b. If the calculated points were too far away from the measured results in the area to the left of some point such as 4, it could be corrected by selecting a new location for point 4 which would be slightly to the left of the old location and calculating a new numerical equation. The points calculated by this new equation to the right of point 4 would be a little farther away from the actual discharge data as a rough rule than those calculated from the first equation. A fairly good fit should be obtained with the first calculated equation. If it is at all possible, a very good fit will have been obtained by the third calculation. Each calculation should take less than one hour of time.

The calculations thus far are sufficient to give a numerical evaluation of Eq. [8], which is plotted in Fig. 1 as a dotted line from a to b and a solid line from b to c. The difference in potential, ΔE, between this calculated dotted line of Eq. [9] and the true discharge potential shown by the solid line gb in Fig. 1 is approximated by the term $A \exp(-BQ^{-1}it)$ in Eq. [10]. In Table I values of ΔE *vs. it* are given for each discharge curve of the Edison cell shown in Fig. 4a. The average values of ΔE *vs.* (*it*) in Table I are plotted on semi log paper in Fig. 3 and fitted by a straight line

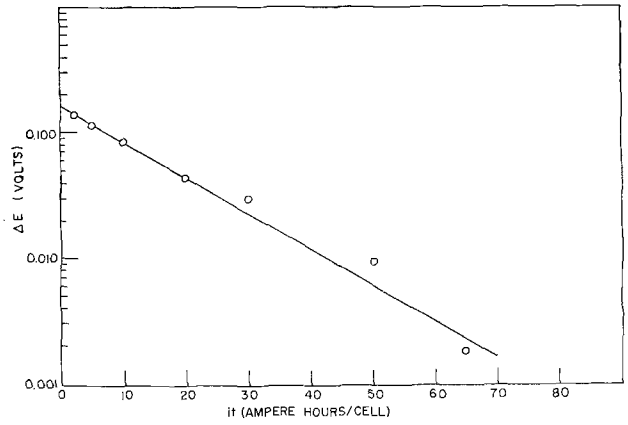

Fig. 3. Determination of ΔE from numerical data

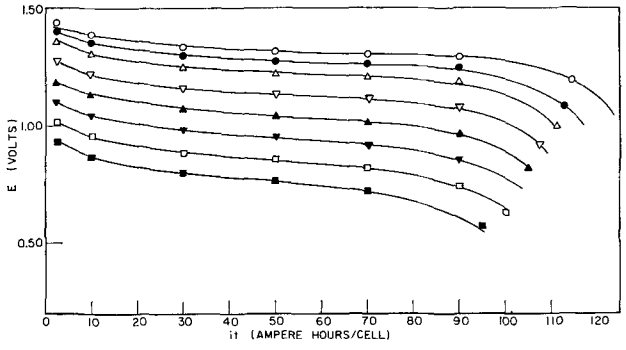

Fig. 4a-g. Comparison of points calculated from discharge equations with solid lines representing actual discharges at various current densities. a. Edison cell, NiOOH-Fe-KOH. Calculated points, amp/cell: ○, 2; ●, 10; △, 20; ▽, 40; ▲, 60; ▼, 80; □, 100; ■, 120.

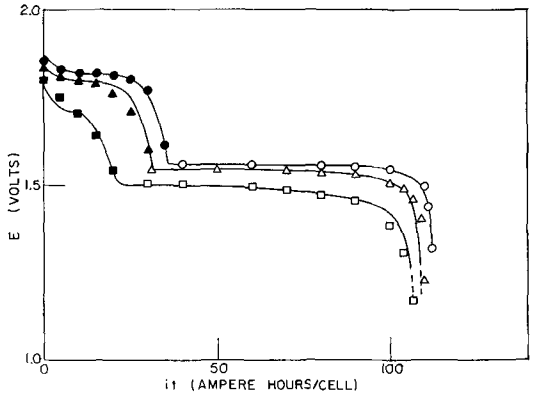

Fig. 4b. Silver cell, AgO-Zn-KOH. Calculated points, amp/cell: ●—○, 2.5; ▲-△, 10; ■-□, 60.

whose equation is $\Delta E = A\exp(-BQ^{-1}it)$. The intercept on the ordinate gives the numerical value of A. The numerical value of B/Q can be calculated from the slope or from a single point taken on the straight line. In nearly all cells the value of ΔE is much less at high values of it/Q than in the example shown in Fig. 3 where $\Delta E = 0.006$v at it equals 50 or it/Q equals 0.433. In most cells ΔE would be less than 0.006v at a value of it/Q equal to 0.10 and would be close to zero in value at it/Q equals 0.15. If points 1 and 2 were chosen in Fig. 4a at $it = 50$ then a correction of $\Delta E = 0.006$v should be subtracted from the values of E_1 and E_2 to be used in calculating the constants in Eq. [9]. This value of ΔE could not be estimated accurately until after the first calculation had been made.

Discussion of the Equation and its Applications

Experimental discharge data for a number of different types of batteries have been plotted as solid lines in Fig. 4 (1, 2, 3, 4, 5). The potential E is shown for various current densities, i, as a function of (it) which is expressed in ampere hours per square centimeter or ampere hours per cell where the area is not known. Equation [9] has been fitted numerically to each set of discharge data thus obtaining a different numerical equation for each chart in Fig. 4. The numerical values of the constants for each of these equations are shown in Table II and are dependent on the unit of time, t, and also on the unit of area used in defining the current density. Since the area is unknown in most cases, the area of the entire cell is

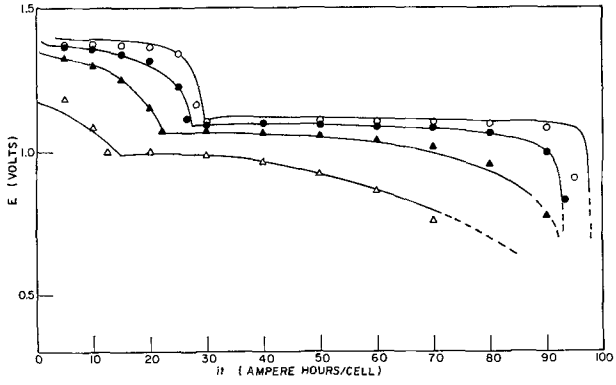

Fig. 4c. Silver cadmium cell, AgO-Cd-KOH. Calculated points, amp/cell: ○, 0.625; ●, 2.5; ▲, 10.0; △, 40.0.

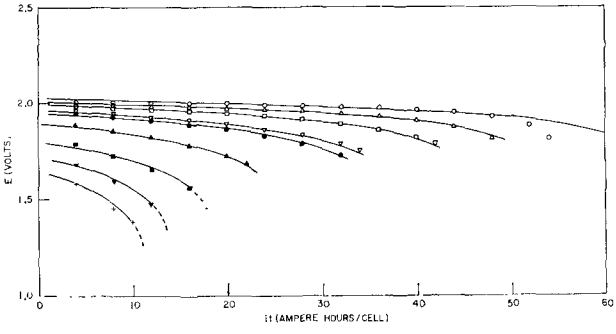

Fig. 4d. Lead acid cell, PbO_2-Pb-H_2SO_4. Calculated points, amp/cell: ○, 0.8; △, 2; □, 4; ▽, 8; ●, 10; ▲, 20; ■, 40; ▼, 60; +, 80.

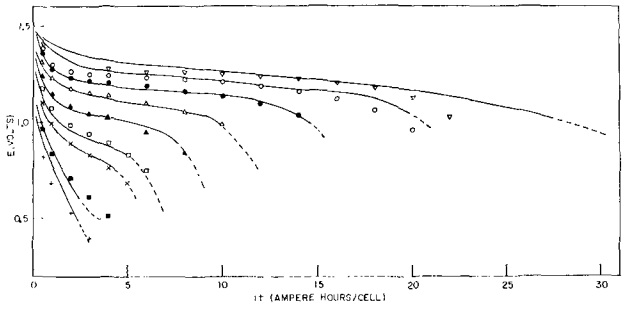

Fig. 4e. Dry cell. Calculated points, amp/cell: ▽, 0.125; ○, 0.25; ●, 0.5; △, 1.0; ▲, 2.0; □, 3.0; X, 4.0; ■, 6.0; +, 8.0.

Table II. Values of the parameters in Eq. [9] for various types of cells

Type cell	Fig. No.	E_s, v	K, ohm cell*	Q, amp-hr/cell*	N, ohm cell*	A, v	B/Q Cell*(amp-hr)$^{-1}$	Temp, °C	Ref.
Edison	4a	1.3080	0.0003936	115.4	0.00390	0.165	0.06564	Room	1
Silver-zinc	$4b_1$	1.8310	0.005138	37.06	−0.00388	0.020	0.60	27	2
	$4b_2$	1.5567	0.00040	112.0	0.00067			27	2
Silver-cadmium	$4c_1$	1.3733	0.00831	28.68	−0.00543			27	
	$4c_2$	1.0990	0.00260	95.75	−0.000965			27	
Lead acid	4d	2.0030	0.0189	58.31	−0.0150			25	3
Dry cell	4e	1.2743	0.3343	25.61	−0.269	0.360	2.197	25	
Ni-Cd	4f	1.2021	0.001358	74.67	−0.000241	0.080	0.1386	−18	4
Lead-zinc	4g*	2.4607	0.9722	0.01737	0.3589			27	5

* The word cell is defined as the electrode area of the entire cell. It is replaced in 4g by cm². Since the area terms cancel out in Eq. [9], it is not necessary to know the numerical value of the area.

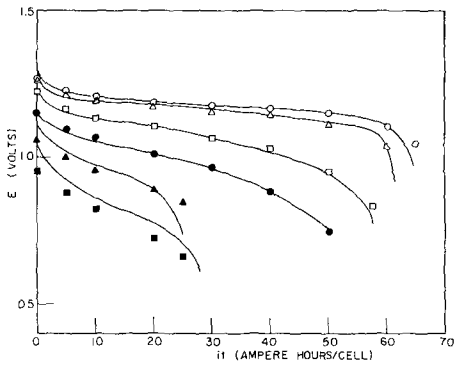

Fig. 4f. Sintered nickel cadmium cell, NiOOH-Cd-KOH, —18°C. Calculated points, amp/cell: ○, 15; △, 24; □, 65; •, 120; ▲, 200; ■, 300.

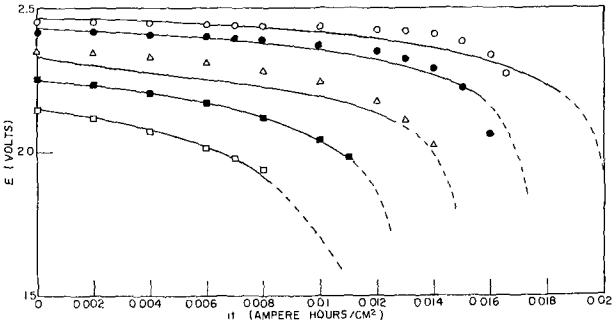

Fig. 4g. PbO_2-Zn-H_2SO_4 reserve cell. Calculated points, amp/cm²: ○, 0.00957; •, 0.0319; △, 0.0798; ■, 0.1595; □, 0.2393.

taken as the unit area and the current density is defined as the amperes per cell and is equal in value to the total discharge current. The points in Fig. 4 are calculated from these equations. It can be seen that the calculated points give good fits in every case to the solid lines that represent the actual discharge data. Thus the information in Table II is sufficient to give an excellent description of the discharge data in Fig. 4 at a considerable savings in space. Equation [9] was applied to a wide variety of discharge data from various types of physically constructed batteries for each of the common battery systems. The examples selected for Fig. 4 were in each case the one which covered the widest range of current densities. Equation [9] was also fitted successfully to discharge data from the following systems: PbO_2-Cd-H_2SO_4, HgO-In-KOH, air cell-air-Zn-KOH, AgCl-Zn-NaCl, PbO_2-Pb-$HClO_4$, CuO-Zn-NaOH, NiOOH-Zn-KOH, Cl_2-Zn-$ZnCl_2$, PbO_2-Sn-$HClO_4$, PbO_2-Pb-HBF_4, HgO-Zn-KOH. No individual curves were omitted in any case. The poorest fit obtained in all the cases studied was with the dry cell data which is shown in Fig. 4e. Most of the data was taken from the literature and was selected to cover as wide a range of current densities as possible. Unfortunately, the amount of low temperature discharge data was limited and some of it had to be rejected as erratic when tested by the method illustrated in Fig. 3.

In Fig. 4b and 4c the discharge took place in two steps and it was found that a separate equation could be fit to each step. The first step in each case is indicated by the subscript 1 on the figure number in Table II. For example, the equation for the silver cell in Fig. 4b would be

$$E = 1.8310 - 0.005138\left(\frac{37.06}{37.06 - it}\right) i + 0.00388\, i + 0.020 \exp(-0.60\, it)$$

or

$$E = 1.5567 - 0.0004\left(\frac{112}{112 - it}\right) i - 0.00067\, i$$

whichever is higher in value.

Whenever the calculated values of E_s, K, Q, and N are the true or defined values and are not affected by the choice of the four points, Eq. [9] fits that particular discharge data theoretically. Whenever the calculated values of E_s, K, Q and N are not the true or defined values and are affected by the choice of points 1 to 4, Eq. [9] is fitting that particular discharge data empirically. In this latter case, there are a number of specific combinations of numerical values of E_s, K, Q and N which will give good fits to a particular set of discharge curves. Among these combinations E_s and Q will be fairly constant while K and N may vary somewhat, N becoming smaller as K becomes larger. For example, two individuals fitting Eq. [9] to a particular set of discharge curves might get two different equations, each of which fit the data quite well even though they had appreciably different values for K and N.

As a very rough rule, a closer approach to a theoretical fit is generally found in the presence of one or more of the following conditions: the discharge data covers a narrow range of current densities, the potential drop due to polarization is low, the electrolyte does not change in composition during discharge, the slope of the discharge curves before the knee is relatively small, the ratio $(it)/Q$ is fairly large and covers a relatively narrow range of values of (it), and the calculated value of N is not negative. Most of these conditions can be observed in Fig. 4a.

In any case, Eq. [9] is so adaptable that wide variations in its constants, particularly K and N, enable it to be fitted with good accuracy to a very wide range of discharge data. A large increase in the numerical value of K will be accompanied by such a large decrease in the value of N that N will often be negative in value as can be seen in Table II. Since N is the internal resistance in the original derivation and theoretically cannot be negative in value, it is obvious that Eq. [9] must be considered to be empirical in most of its curve fitting applications and there is no reason to believe that it should have to describe fully the discharge of every type of battery.

In Fig. 2 the measured potential is low for the points at i equals 0.0798 amp/cm². In Fig. 4g the measured potential at this current density is appreciably lower than the calculated potential thus indicating the very strong likelihood of an error in this data. When there are only three discharge curves and two of them are correct, it is not possible to tell by this method which one of the three is in error without collecting more data. A fourth discharge made at a different current density will, if correct, determine which of the other three curves contains the error.

An examination of all of the data fitted by Eq. [9] shows that the differences between the calculated and the measured results are often larger at the highest current densities than they are at intermediate current densities. This larger variation can be attributed to the high relative dispersion of the data; the fact that the highly simplified calculation methods given here tend to give the poorest fit at high current densities; and the fact that the poorest fit is often obtained at the extreme limits when fitting equations to measured data. There is also a tendency for a very few of the calculated curves at the lowest current density to have less slope and a smaller capacity than the observed data. This condition is most noticeable in Fig. 4g and seems to be most generally associated with batteries whose electrolytes change appreciably in concentration during discharge. As a rough empirical approximation, it is assumed that the drop in potential in a battery is directly proportional to the change in electrolyte concentration during discharge, assuming all other factors are neglected. Equation (9) can then be written as

$$E = E_s - K\left(\frac{Q}{Q - it}\right) i - Ni + A \exp(-BQ^{-1}it) - Cit \quad [15]$$

where C is a constant.

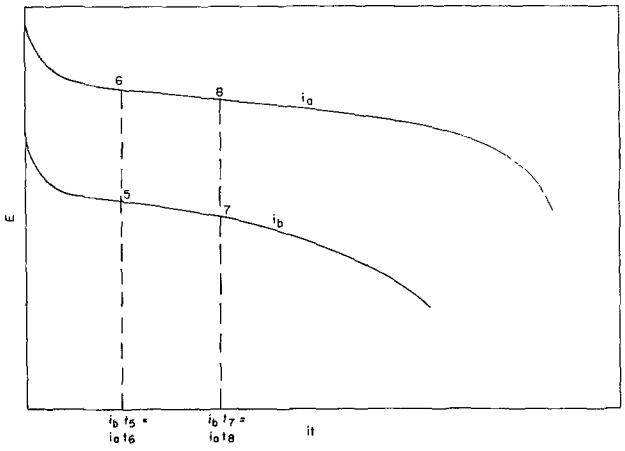

Fig. 5. Typical discharge curves to be used in numerical calculation of C.

To determine the numerical value of C select four points as shown in Fig. 5 which are far enough past the initial potential drop for the exponential term to be negligible. From Eq. [15]

$$E_5 = E_s - Ki_b\left(\frac{Q}{Q - i_b t_5}\right) - Ni_b - Ci_b t_5 \quad [16]$$

and

$$E_7 = E_s - Ki_b\left(\frac{Q}{Q - i_b t_7}\right) - Ni_b - Ci_b t_7 \quad [17]$$

Subtracting Eq. [17] from Eq. [16] gives

$$E_5 - E_7 = Ki_b\left[\left(\frac{Q}{Q - i_b t_7}\right) - \left(\frac{Q}{Q - ibt_5}\right)\right] + C(i_b t_7 - i_b t_5) \quad [18]$$

Similarly

$$E_6 - E_8 = Ki_a\left[\left(\frac{Q}{Q - i_b t_7}\right) - \left(\frac{Q}{Q - ibt_5}\right)\right] + C(i_b t_7 - i_b t_5) \quad [19]$$

From Eq. [18] and Eq. [19]

$$C = \frac{i_b(E_6 - E_8) - i_a(E_5 - E_7)}{(i_b - i_a)(i_b t_7 - i_b t_5)} \quad [20]$$

Numerical values of C are calculated from Eq. [20] and substituted in Eq. [15].

Let $E' = E + Cit$.

Then $E_1' = E_1 + Ci_b t_1$, $E_2' = E_2 + Ci_a t_2$, $E_3' = E_3 + Ci_b t_3$, and $E_4' = E_4 + Ci_a t_4$. If E_1', E_2', E_3', and E_4' are substituted for E_1, E_2, E_3, E_4, respectively, in Eq. [10] to [13], they can be used to calculate numerical values of Q, K, N, and E_s in the manner previously described.

Numerical values of Eq. [15] were determined in this manner for the lead-zinc cell shown in Fig. 4g and found to be

$$E = 2.4775 - 0.9237\left(\frac{0.0181}{0.0181 - it}\right)i - 0.4295\,i - 4.25\,it$$

Calculated points from this equation are shown in Fig. 6 to give a better fit to the experimental data than was obtained by the use of Eq. [9].

If the basic assumptions are assumed to be true during the charge of a cell, then the following equation would hold for the potential during charge

$$E = E_s + K\left(\frac{Q}{Q - it}\right)i + Ni - A\exp(-BQ^{-1}it) \quad [21]$$

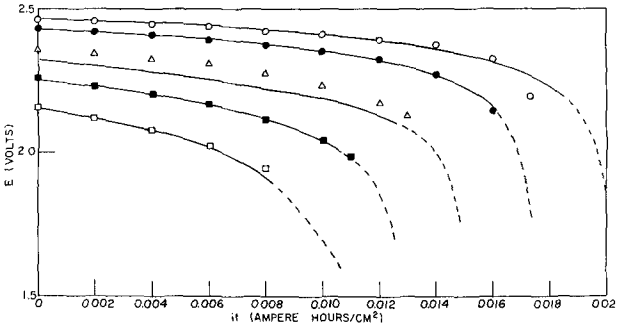

Fig. 6. Comparison of points calculated from the discharge equation with solid lines representing actual discharges at various current densities. PbO_2-Zn-H_2SO_4 reserve cell. Calculated points, amp/cm²: ○, 0.00957; ●, 0.0319; △, 0.0798; ■, 0.1595; □, 0.2393.

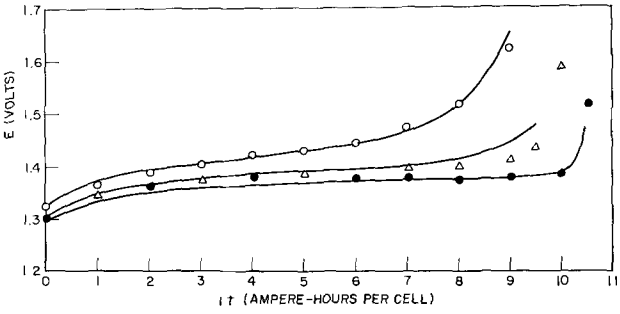

Fig. 7. Comparison of the charge data of a Ni-Cd cell with the calculated results for various current densities. Nickel cadmium cell, Ni-OOH-Cd-KOH. Calculated points, amp/cell: ○, 16.0; △, 2.5; ●, 0.16.

Equation [21] can be obtained from Eq. [9] by reversing the signs of the last three terms. Equation [21] has been fitted to the charge of a Ni-Cd cell in Fig. 7. The solid lines represent the actual data and the points are calculated from the equation

$$E = 1.379 + 0.0024\left(\frac{1}{1 - 0.095\,it}\right)i - 0.00116\,i - 0.08\exp(-0.693\,it)$$

The use of Eq. [21] in describing the charging of a cell has been tested on a very limited amount of data. Consequently, it is not yet certain to what extent it can be successfully applied.

The total energy W_t that has been evolved from the beginning of the discharge up to time t is defined by the equation

$$W_t = \int_o^t i\,E\,dt$$

Substituting Eq. [8]

$$W_t = \int_o^t\left[E_s i - K\left(\frac{Q}{Q - it}\right)i^2 - Ni^2 + Ai\exp(-BQ^{-1}it)\right]dt \quad [22]$$

$$W_t = [E_s\,it + KQi\ln(Q - it) - Ni^2t - AQ/B\exp(-BQ^{-1}it)]_o^t \quad [23]$$

$$W_t = E_s it - KQi\ln(1 - it/Q)^{-1} - Ni^2t + AQ/B(1 - \exp(-BQ^{-1}it)) \quad [24]$$

The constants from an equation describing the discharge of a Ni-Cd cell at 27°C were substituted in Eq. [24] and the total energy evolved at time t was found to be

$$W_t = 1.25\,it - 0.0238\,i\ln(1 - 1.05\,it)^{-1} - 0.006\,i^2t + 0.0248\,[1 - \exp(-3.83\,it)] \quad [25]$$

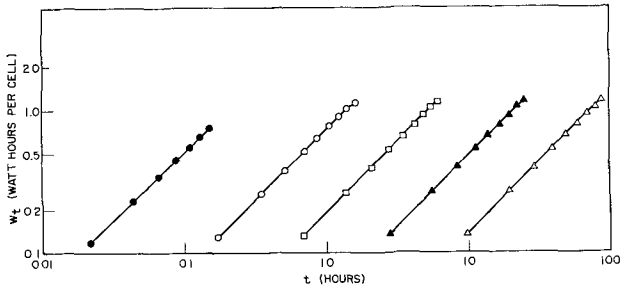

Fig. 8. Comparison of the energy evolved during the discharge of a Ni-Cd cell with the calculated results for various current densities. Sealed nickel cadmium cell, NiOOH-Cd-KOH, 27°C. Calculated points, amp/cell: •, 4.5; ○, 0.56; □, 0.14; ▲, 0.035; △, 0.010.

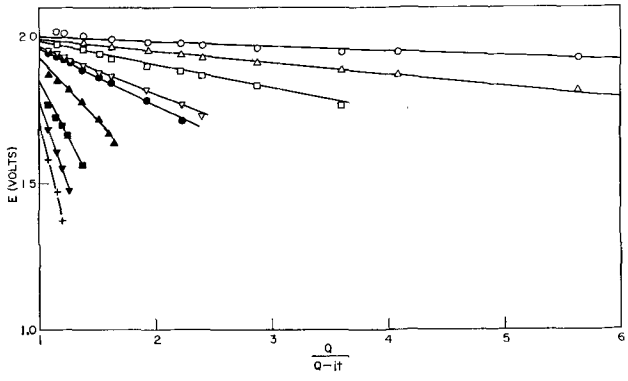

Fig. 9. Discharge curves showing the potential as a function of $Q/Q\text{-}it$ for various current densities. Lead acid cell, PbO_2-Pb-H_2SO_4. Current density, amp/cell: ○, 0.8; △, 2; □, 4; ▽, 8; •, 10; ▲, 20; ■, 40; ▼, 60; +, 80.

In Fig. 8, W_t in watt hours per cell for a Ni-Cd battery has been plotted as a function of t in hours for various values of the cell current in amperes. The solid lines are obtained from calculations based on numerical integration of the actual discharge data. The points are calculated from Eq. [24]. The agreement between the calculated and the measured results in such cases depends entirely upon how well Eq. [9] can be fitted to the original discharge data.

Once the discharge is past the initial potential drop, the exponential term becomes negligible and Eq. [9] can be written as

$$E = E_s - Ni - \left(\frac{Q}{Q - it}\right)Ki \qquad [26]$$

which shows the potential E to be a linear function of $Q/(Q - it)$ with slope $-Ki$ for any given current density, i. Actual discharge potentials were taken from the lead acid battery discharge data in Fig. 4d and plotted in Fig. 9 against $Q/(Q - it)$ for each of nine current densities. Straight lines gave good fits to these plotted points. The average value of the K's, determined from the slopes of each of these nine lines was 0.0195 as compared to the calculated value of 0.0189 given in Table II.

In Fig. 9 the values of E for $Q/(Q - it)$ equals one can be seen from Eq. [26] to be

$$E = E_s - (N + K)i \qquad [27]$$

which shows E here to be a linear function of i with slope, $-(N + K)$, and intercept, E_s. Values of E for $Q/(Q - it)$ equals one were taken from Fig. 9 and plotted in Fig. 10 to give a straight line. The numerical values of E_s and N determined from this straight line were 1.998 and −0.0155 as compared to the calculated values of 2.003 and −0.0150 given in Table II. The values of E_s, K, and N determined by the two methods are virtually identical and show that the graphical

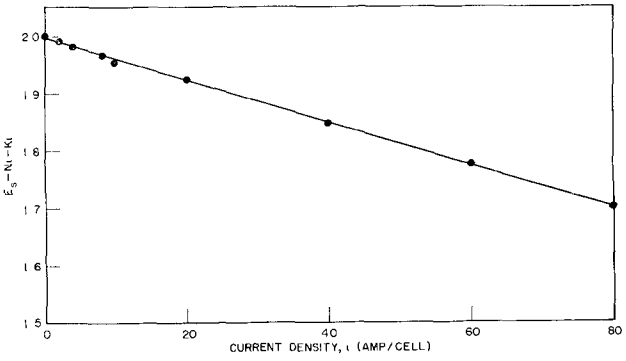

Fig. 10. E_s-Ni-Ki plotted as a function of current density

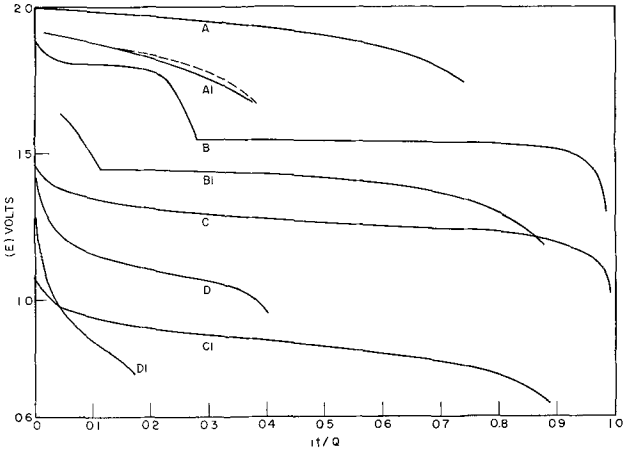

Fig. 11. Discharge curves showing the cell potential during discharge as a function of the fraction of active material used up at any given time.

	Rate Q/i
A, Lead acid	11 hr 14.6 hr
A1, Lead acid	1 hr 2.8 hr
B, Silver zinc	11 hr 11.2 hr
B1, Silver zinc	1 hr 1.14 hr
C, Edison	11 hr 11.3 hr
C1, Edison	1 hr 1.12 hr
D, Dry cell	11 hr 25.6 hr
D1, Dry cell	1 hr 6.4 hr

method of Fig. 9 and 10 can be used in fitting Eq. [9] to discharge data whenever the value of Q is known. If the basic assumption holds true, then Q can be calculated from the amount of active material on the controlling electrode and the graphical method is applicable. In the more empirical applications, such as the lead acid battery just shown, the calculated value of Q will be somewhat less than the value determined from the amount of active material and the graphical method would not be accurate. Almost all of the available discharge data gave no information on the amount of active materials and consequently the feasibility of using this graphical method for fitting Eq. [9] to discharge data has not yet been determined.

Presentation of Discharge Data

A study of Eq. [9] suggests the possibility of plotting battery discharge data against dimensionless quantities in a manner that would make possible more direct comparisons between various types of cells. In Fig. 11 the potential during discharge is plotted as a function of it/Q where it/Q is the fraction of active material used up at time, t. Discharge data are shown here at the 1-hr and the 11-hr rate for four common types of cells. The value of it/Q at the end of the discharge is the efficiency of utilization of the active material. In each case, the discharge was assumed

to be ended when E equalled $E_s - Ki - Ni - 0.25$v. Thus in Fig. 1, curve i_a, the end voltage would be 0.25v below the voltage at point a. A drop of more than 0.25v would have precluded the use of much of the available data. In Fig. 4 the discharge curves are shown as dotted lines wherever they extended past this assumed end point.

Here in Fig. 11 is a method of comparing at equal discharge times such factors as efficiencies, potentials, variations of potentials with time, potential drops due to internal resistance, etc., for various types of constructions of cells. The two curves at A1 represent two different sizes and constructions of lead acid cells. Although the difference in discharge characteristics is small between these two cells, it could, in many cases, be quite large and could be readily demonstrated on a chart of this type. Other things being equal, the cell size is not important here, since each cell is being discharged at a particular value of Q/i that is held constant with change in cell size, which is equivalent to saying n times the current would be drawn from a cell n times as large. The values of Q/i given in Fig. 11 represent the time each cell would have taken to discharge 100% of the active material on the controlling electrode at the particular current density, i. The discharge characteristics of the four cells in Fig. 11 could have been compared by plotting E *vs.* it/Q at a constant value of Q/i such as 10 hr, thus giving a slightly different graph. A number of other variations can be made of this chart. The vertical axis could be the ratio of the discharge potential to the theoretical potential. In this case the area under the curve would be the theoretical watt hour efficiency. If the vertical axis were the ratio of the discharge potential to the average charge voltage, E_c, the area under the curve would be the watt hour efficiency defined by the ratio of the output in watt hours to the input in watt hours. The equation for this latter curve can be obtained by dividing E_c into Eq. [9] to give

$$\left(\frac{E}{E_c}\right) = \left(\frac{E_s}{E_c}\right) - \left(\frac{K}{E_c} i\right)\left[\frac{1}{1 - (it/Q)}\right] - \left(\frac{N}{E_c} i\right) + \left(\frac{A}{E_c}\right)[\exp(-BQ^{-1})(it)] \quad [28]$$

where each quantity in brackets or parentheses is dimensionless. In Fig. 11 the values of it/Q were taken from Table II and are empirical to a certain extent. If Q had been calculated from the actual amounts of active material on the controlling electrode, its value would have been slightly larger and the discharge curves in Fig. 11 would be changed slightly. Values of (it) per unit weight of active material or per unit cell weight, or watt hour efficiencies could have been used in place of it/Q for the abscissa in Fig. 11. The important thing in each of these cases is that the use of some form of dimensionless quantity, or factor closely related thereto, as either or both of the coordinates enables a quantitative, visual study and comparison to be made of the characteristics of certain types of equivalent discharges, either for different types of cell systems, or different constructions of the same cell system, or both. As shown in Eq. [28], the equation for each of these cases can be obtained easily from Eq. [9].

Manuscript received Feb. 4, 1965. This paper was presented at the Boston Meeting, Sept. 16-20, 1962.

Any discussion of this paper will appear in a Discussion Section to be published in the June 1966 JOURNAL.

REFERENCES

1. C. F. Anderson, *This Journal*, **99**, 244C (1952).
2. C. P. Wales, NRL Rpt 5167, 11 Aug. 1958.
3. E. A. Hoxie, *Trans.*, AIEE, Part II Applications and Industry, **73**, 17 (1954).
4. G. B. Ellis, H. Mandel, and D. Linden, *This Journal*, **99**, 250C (1952).
5. W. J. Schlotter, *ibid.*, **99**, 205C (1952).

GLOSSARY

A	Numerical value of Δe at $(it) = 0$ (v)
α	Transfer coefficient (dimensionless)
B	Constant parameter (dimensionless)
C	Constant parameter (volt cm^2 amp^{-1} sec^{-1})
E	Cell potential during discharge (v)
E_a	Anode potential during discharge (v)
E_c	Cathode potential during discharge (v)
E_s	A constant potential parameter (v)
ΔE	Initial potential drop (v)
η	Steady-state activation overpotential (v)
F	Faraday (coulombs equiv.$^{-1}$)
i	Apparent current density (amp cm^{-2})
i_{am}	Active material current density (amp cm^{-2})
i_o	Apparent exchange current density (amp cm^{-2})
K	Coefficient of polarization (ohm cm^2)
K_a	Coefficient of polarization for anode (ohm cm^2)
K_c	Coefficient of polarization for cathode (ohm cm^2)
N	Internal resistance of cell (ohm cm^2)
Q	Amount of active material on controlling electrode as coulombs (coulombs cm^{-2})
Q_a	Amount of active material on anode as coulombs (coulombs cm^{-2})
Q_c	Amount of active material on cathode as (coulombs cm^{-2})
R	Gas constant (amp volt sec deg^{-1} mole^{-1})
T	Temperature (deg)
t	Time (min or hr)
W_t	Energy evolved during cell discharge (amp volt sec cm^{-2})
Z	Number of electrons transferred in rate determining step (dimensionless)

The Electrode Potential of the Semiconductor CuS in Solutions of Copper Ions and Sulfide Ions

P. Ruetschi[1] and R. F. Amlie

The Carl F. Norberg Research Center, The Electric Storage Battery Company, Yardley, Pennsylvania

ABSTRACT

The electrode potential of cupric sulfide was measured in aqueous acidic solutions of cuprous chloride and cupric chloride, as well as in alkaline solutions of sulfur and sulfide ions. The redox couples Cu^{++}/Cu^{+} and S/S^{--} exhibit high reversibility on this electrode material. Nonstoichiometric excess sulfur in CuS behaves energetically like free elemental sulfur. The reason for the voltage increase observed when elemental sulfur is added to a cuprous chloride electrode is explained by the mechanism that the electrode reaction changes from $e^{+}CuCl \rightleftarrows Cu + Cl^{-}$ to a redox mechanism, $e + CuCl_2 \rightarrow CuCl + Cl^{-}$ at the $CuS^{=}$ solution interface, whereby cupric chloride is generated by the chemical reaction $2CuCl + S \rightleftarrows CuCl_2 + CuS$. The principle of coupling a chemical reaction with an electrochemical reaction in a closed cycle is shown to be of considerable advantage for the construction of certain types of battery electrodes.

As a result of the discovery that electrodes of cuprous chloride in magnesium chloride electrolyte show an increased electrode potential when the cuprous chloride is intimately mixed with elemental sulfur (1), an investigation was undertaken to elucidate the mechanism responsible for this phenomenon. It had been observed previously that cuprous chloride and sulfur mixtures, when suspended in a chloride electrolyte, reacted to form cupric sulfide. This reaction does not take place with mixtures of the dry materials in the absence of aqueous electrolytes, even when heated to the melting point of sulfur, but it proceeds when these mixtures are immersed in acidic aqueous magnesium chloride solutions according to

$$2\,CuCl + S \rightarrow CuS + CuCl_2 \text{ (dissolved)} \qquad [1]$$

The precipitation of CuS was confirmed experimentally by x-ray analysis, and the formation of $CuCl_2$ in solution by colorimetry. As early as 1889 Vortmann and Padberg (2) described this reaction qualitatively.

In view of reaction [1], it was considered desirable to determine the effect of cupric ion concentration on the potential of a cupric sulfide electrode. The present investigation also includes a study of the cupric sulfide electrode in solutions containing both cupric and cuprous ions, and further in solutions containing sulfide ions.

Electrochemical Properties of Metal Sulfides

An investigation of metal sulfide electrodes in aqueous solutions was carried out by Wrabetz, in collaboration with Noddack and Herbst (3-5). According to Wrabetz *et al.* the electrochemical behavior of heavy metal sulfide electrodes in aqueous solutions is influenced by the presence of nonstoichiometric excess sulfur in these materials. The sulfide electrodes differ from a normal electrode system of the first or second kind in that only a minute Faradaic current can flow without a complete exhaustion of the available excess sulfur and a corresponding alteration in the composition of the electrode surface. It was observed that many metal sulfide electrodes, in contact with solutions containing the corresponding cations, establish a reversible potential. It was also found that the metallic sulfides, in aqueous solutions containing the respective cation, have their own electrochemical potential series which is more noble than that of the respective parent metals. Many of the metal sulfides, studied in solutions containing different concentrations of the cation, showed the electrode potentials to be determined by the solute activity in accordance with the Nernst relationship. Only one measurement with a cupric sulfide electrode was described in the work of Wrabetz, and its potential was approximately 0.24v positive to that of copper in the cell system $Pt/CuS/CuSO_4$ (0.1m)/Cu. The potentials were unstable due to high resistance between the loose cupric sulfide powder and the platinum wire used for making contact.

Wrabetz *et al.* (3) were the first workers to systematically study the electrochemistry of metal sulfide electrodes in aqueous solutions; prior investigations lack quantitative data and are thus of limited value. However, a study by Trumpler (6) is pertinent since he measured the potentials of a series of metallic sulfide semiconductors in solutions containing the respective cations. He also studied metal sulfide electrodes in solutions containing sulfide ions and dissolved sulfur (*i.e.*, polysulfide ions), and came to the conclusion that sulfide electrodes exhibited the same potentials as an inert metallic electrode such as platinum.

Cupric sulfide is usually obtained as a lustrous, blue-black salt which is insoluble in water and cold dilute strong acids, although it dissolves readily in hot, moderately dilute nitric acid. Copper(II) sulfide is converted to Cu_2S at elevated temperature in the presence of air, and at lower temperatures in a hydrogen atmosphere. It is slowly oxidized by moist air. Copper(II) sulfide is a semiconductor showing an exceptionally high electronic conductivity, having a specific resistance in the order of 10^{-4} ohm-cm. Badecker (7) reports 1.25×10^{-4} ohm-cm and Fischbeck and Dorner (8) give 4×10^{-5} ohm-cm, which may be compared with 1.7×10^{-6} ohm-cm for copper metal. Cupric sulfide is reported as crystallizing in both the hexagonal and monoclinic systems (9). Remy describes the crystal structure as hexagonal with the lattice constants $a_o = 3.972$Å, $c_o = 16.344$Å.

Experimental

The electrochemical study of copper (II) sulfide in chloride solutions of copper ions, sulfide ions, or polysulfides was carried out by measuring electrode potentials both under equilibrium conditions and during current flow. The experiments were performed in Pyrex glass cells, one of which together with the electric circuit, is depicted in Fig. 1. All electrode potential measurements with chloride electrolytes were made by means of saturated calomel reference electrodes (0.241v *vs.* NHE), with the liquid junction established in the interconnecting capillary tube. In addition to the reference electrode capillary, the cell of Fig. 1 was also provided with a connection to the counter elec-

[1] Present address: LeClanche, S.A., Yverdon, Switzerland.

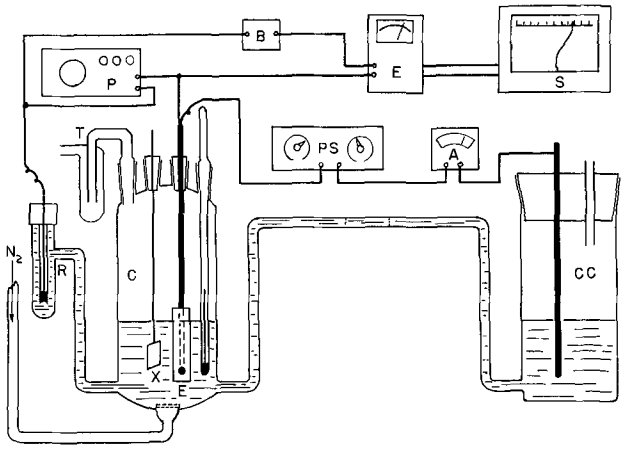

Fig. 1. Schematic of apparatus. C, Pyrex test cell: auxiliary Pt electrode; E, sample electrode; R, reference electrode; CC, counter electrode cell; P, potentiometer; B, bias box; E, electrometer-amplifier; S, strip chart recorder; PS, power supply; A, ammeter.

trode compartment and with a gas inlet. Effective purging of dissolved oxygen was realized by the continuous introduction of a finely divided stream of prepurified nitrogen gas ($O_2 < 8$ ppm) introduced through a fritted-glass disk. The nitrogen was purified by passing it through a heated column of copper turnings. The counter electrode was a 0.6 cm diameter graphite rod in a separate compartment, which was connected to the test cell by an electrolyte bridge approximately 25 cm in length. A porous filter paper plug was inserted into the electrolyte bridge to reduce convection between compartments. The top section of the test cell was provided with four standard taper joints which held the sample electrode, the platinized platinum electrode, a gas exit bubble trap, and a thermometer. All experimental data were taken at 25°C.

Potentials were measured by means of both a Rubicon portable potentiometer (±0.0002v) and a General Radio type 1230-A DC Electrometer-Amplifier used to drive a Honeywell recorder. A bias box was included in the electrometer input to avoid switching of the electrometer polarity during discharge. A multirange constant current supply provided well regulated currents over the desired range.

Cupric sulfide electrode samples were retained in a 0.63 cm diameter cavity, drilled into a rectangular epoxy block as shown in Fig. 2. The epoxy block encapsulated a graphite rod of spectrographic purity, 0.63 cm in diameter, to provide contact with the electrode material in the cavity. The cupric sulfide was compacted into the cavity at pressures in the order of 3000 psi (150 lb total force) which was usually sufficient for cohesive compaction and could not be greatly exceeded due to the limited mechanical strength of the cast epoxy. Loosening of the pellet was only observed after prolonged immersion in acidic electrolytes, and this difficulty was eliminated by the addition of a few per cent of powdered Teflon to the CuS powder prior to compaction. Fisher Certified Reagent CuS used in this study was further purified by allowing it to remain in contact with a large quantity of 4% HNO_3 for 24 hr with intermittent shaking to achieve good dispersion. The acid solution acquired a faint blue color during this treatment due to the removal of copper. The sample was filtered, washed with distilled water, and dried at 100°C in air. Electrode potentials were measured during periods up to 3 days to insure that the stable equilibrium values had been obtained.

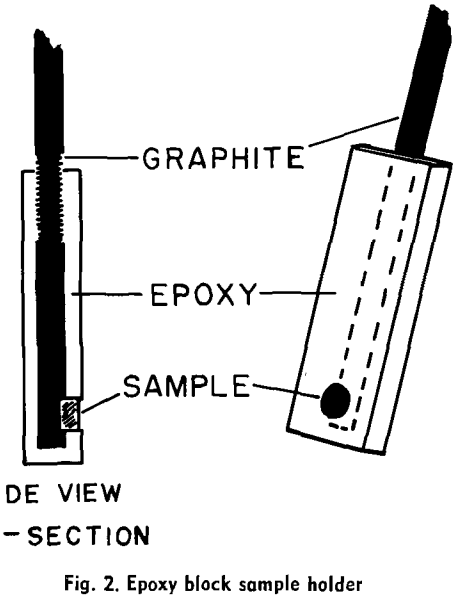

Fig. 2. Epoxy block sample holder

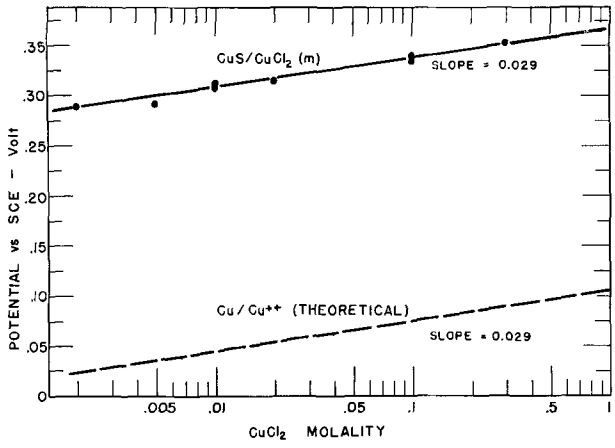

Fig. 3. Cupric sulfide potential as a function of $CuCl_2$ concentration. 1.0M HCl, 2M total (Cl^-). Theoretical Cu/Cu^{++} couple plot assumes $\gamma Cu^{++} = 1$.

Results and Discussion

Effect of $CuCl_2$ *concentration on the* CuS *electrode potential.*—The dependence of the cupric sulfide potential (*vs.* saturated calomel) on the concentration of cupric chloride is shown in Fig. 3. In addition to the molal $CuCl_2$ concentration indicated, the solutions were 1*M* in HCl, with an addition of KCl adjusted to give a total chloride concentration of 2*M*. The *p*H values of the solutions were maintained essentially constant by this procedure, and the extent of complexing of cupric chloride ions was maintained constant (10). The cupric chloride concentration was varied by more than two orders of magnitude while the ionic strength changed only from 2.0 to 2.3. Under these conditions the mean activity coefficient of cupric chloride can be expected to remain nearly constant throughout the series of measurements. The results show that the CuS electrode in a $CuCl_2$ electrolyte obeys the theoretically expected relationship for a divalent ion. The electrode responds to the Cu^{++} activity in a reversible manner, and the potential-log concentration plot of Fig. 3 has a slope 0.029 which is in agreement with that predicted by the Nernst relationship

$$E = E_{o(CuS/CuCl_2)} + (2.3\,RT/2F) \log [CuCl_2] \quad [2]$$

at 25°C. The theoretical behavior for the Cu/Cu^{++} electrode couple is also included in this graph for comparison, in order to illustrate that the sulfide electrode is about 0.260v more positive. This potential increase of the sulfide electrode can be explained by the supposition that the nonstoichiometric cupric sulfide, containing excess sulfur in the crystal lattice, can promote the following potential determining reaction

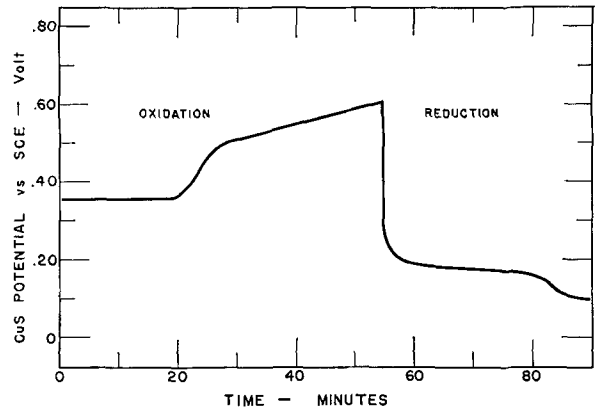

Fig. 4. Chronopotentiometric curve of CuS polarization during charge (oxidation) and discharge. 5 ma (16 ma/cm^2); 0.1*M* $CuCl_2$, 1.0*M* HCl, 2*M* total (Cl^-).

$$2e^- + Cu^{++} + S_{(CuS)} \rightleftarrows CuS \qquad [3]$$

or

$$2e^- + Cu^{++} + \square_{(CuS)} \rightleftarrows CuS \qquad [4]$$

where $S_{(CuS)}$ represents excess sulfur and $\square_{(CuS)}$ is a copper ion deficiency in the CuS lattice. Subtracting from [3] or [4] the equation

$$2e^- + Cu^{++} \rightleftarrows Cu$$

one obtains

$$S_{(CuS)} + Cu \rightleftarrows CuS \qquad [5]$$

or

$$\square_{(CuS)} + Cu \rightleftarrows CuS \qquad [6]$$

The free energies of Eq. [5] and [6] determine the voltage difference between the CuS/Cu^{++} electrode and the Cu/Cu^{++} electrode. The experimental value of 0.26v, corresponding to a free energy increase of $\Delta G = -nFE = -11.9$ kcal, is very close to the free energy of formation of CuS from elemental copper and sulfur, namely −11.7 kcal (11). The excess sulfur in CuS is therefore shown to be essentially "free" sulfur.

Cupric sulfide can phenomenologically be considered as a "dilute copper metal," analogous to a metal amalgam. The "dissolved" Cu^{++} ions in CuS are able to equilibrate with Cu^{++} ions in solution and are able to support limited forward and backward electrochemical reactions. It is evident that deposition of Cu^{++} ions into the sulfide can only proceed as long as there is excess sulfur (or deficiency of copper) in the CuS structure. Dissolution of copper can proceed until the surface is so rich in sulfur that conductivity is impaired and strong polarization begins.

Polarization curves at constant current charge and discharge are illustrated in Fig. 4. The CuS/Cu^{++} couple is relatively easily polarized with slight current flow. No metallic copper is formed during cathodic polarization since (Cu^{++}) ions are discharged into the CuS crystal where they combine with excess sulfur or cation vacancies. During anodic polarization Cu^{++} ions are dissolved out of the CuS lattice, leaving excess sulfur or cation vacancies. On continued cathodic polarization, as the excess sulfur is depleted (or the Cu^{++} vacancies filled), the CuS electrode potential becomes polarized to more negative potentials and the reduction of cupric ions to cuprous ions becomes the predominant reaction. The corresponding reduction step is clearly indicated in Fig. 4.

The CuS *electrode in solutions of* Cu^+ *and* Cu^{++} *ions.*—A study was made on the behavior of the CuS electrode in solutions containing both Cu^+ and Cu^{++} ions. Figure 5 shows a plot of the potential (measured *vs.* a saturated calomel electrode) against the molal ratio of cupric chloride to cuprous chloride. The cupric chloride concentration was maintained at 0.1*M*, whereas the cuprous chloride concentration was varied between 0.003 and 0.30 moles per 1000g of water. These solutions also contained 1*M* HCl to maintain a constant pH and the requisite quantity of KCl to bring the total chloride concentration of the solutions up to 2*M* (12-15).

Cuprous chloride powder, dried at 100°C in an inert atmosphere, was added to the cell electrolyte after removal of dissolved oxygen, and a constant stream of purified nitrogen was maintained to prevent contact of the solution with air. Both the cupric sulfide electrode and a platinized platinum electrode reached the same stable potential after equilibration in a given solution. The results of the experiments shown in Fig. 5 demonstrate that the CuS electrode functions as the inert part of the redox electrode

$$e^- + Cu^{++} \rightarrow Cu^+ \qquad [7]$$

with

$$E = E_{o(CuCl_2/CuCl)} + (2.3\,RT/F)\log([CuCl_2]/[CuCl])$$

Anodic and cathodic polarization measurements showed that this redox reaction exhibited excellent reversibility at the solid CuS surface. High current densities could be supported in the forward and reverse directions with only small potential changes. To cite one example, in a solution 0.10*M* in both cuprous and cupric chloride, with an apparent current density of 3.2 ma/cm^2, the potential decreased 15 mv during reduction and increased 15 mv during oxidation, after 20 min. The corresponding polarizations for platinized Pt were about 380 mv and 60 mv, respectively. The reversibility of the redox reaction at the CuS electrodes was therefore better than that at the platinized platinum electrode. From Fig. 5 it is seen that the CuS electrode potential in solutions containing both monovalent and divalent copper ions is more negative than in solutions of cupric ions only, and that the potential is dominated by redox reaction [7]. The same potentials were realized with a platinized platinum electrode as with a CuS electrode which substantiates that the measured potentials were reversible redox values.

This important result provides a clear explanation of the mechanism of a cuprous chloride electrode, containing sulfur, in a water-activated battery (1). Wetting of the electrode initiates the reaction between cuprous chloride and sulfur, producing CuS and $CuCl_2$ according to reaction [1]. The cupric ions generated in this manner are reduced in a subsequent electrochemical step, according to Eq. [7], which has been shown to be very fast. The excellent reversibility of this redox reaction makes possible a relatively high discharge current and also dictates that the redox couple will determine the electrode potential. The reaction of cuprous ions with sulfur replenishes the cupric ion concentration and maintains the Cu^{++}/Cu^+ ratio essentially constant. In this manner, cuprous chloride and sulfur are consumed to form cupric sulfide and chloride ions as the end-products of the discharge reaction. CuS has been identified as the end-product in discharged electrodes by x-ray diffraction analysis. This mechanism explains how elemental sulfur appears to be readily reducible with little polarization, and how the high positive voltage level is attained. The $Cu/CuCl/Cl^-$ potential in 2*M* chloride solution at pH 0 is about −0.10v against the saturated calomel reference electrode. The $Cu^{++}/(Cu^+)$ redox potential, as measured by the CuS electrode at very low (Cu^+) concentrations, is in the vicinity of 0.35v (*vs.* SCE), as may be seen from Fig. 5. It is evident that a potential increase of about 0.45v can therefore be attained. This increase has actually been realized during activation and discharge of cuprous chloride-magnesium batteries by the addition of sulfur to the cuprous chloride active material (1). It is thus evident that the addition of sulfur can provide a substantial benefit by increasing the energy output of this battery system.

From a thermodynamic standpoint, the maximum available voltage increase is given by the difference in free enthalpy between the reactions

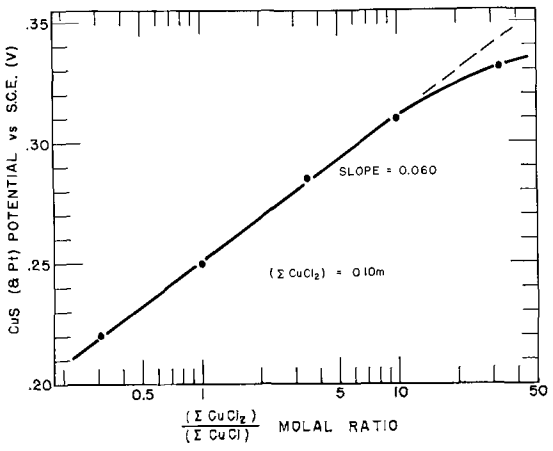

Fig. 5. Cupric sulfide (and platinized Pt) potential as a function of the $CuCl_2/CuCl$ molal ratio. 0.1M $CuCl_2$, 1.0M HCl, 2M total (Cl^-).

$$e^- + CuCl \rightleftarrows Cu^+ Cl^- \qquad [8]$$

and

$$e^- + CuCl + S \rightleftarrows CuS + Cl^- \qquad [9]$$

From the difference in free enthalpy one obtains $\Delta E = -\Delta G/nF = 11.7/23.06 = 0.506$v.

Experimental results given in reference (1) indicate that this theoretical upper limit can be approached rather closely. This would mean that the reaction of sulfur according to Eq. [1] proceeds to nearly the saturation concentration of $CuCl_2$ in solution, such as to render the free energy of reaction [1] equal to zero. According to Latimer, reaction [1] has a positive free energy of 2.7 kcal if all the reactants and products are in the crystalline state and does thus not proceed spontaneously. However, for dissolved $CuCl_2$ at 1M concentration the free energy is −2.5 kcal. Thus, the equilibrium cupric chloride concentration for reaction [1] is close to the saturation value of about 5.8M.

The potential of CuS was also briefly investigated in solutions containing only cuprous chloride, but no cupric chloride. Oxygen was removed carefully from these solutions to avoid oxidation and metallic, oxide-free copper powder was stirred into the solution to remove any cupric ions present by the reaction $Cu^{++} + Cu \rightarrow 2\ Cu^+$. The electrode potentials were erratic and not reproducible. This is apparently due to a lack of an exchange between cupric ions in solution and in the solid. The hypothetical reaction $e^- + Cu^+ + S_{(CuS)} \rightleftarrows CuS$ does not seem to proceed because the excess free sulfur $S_{(CuS)}$ reacts preferably with CuCl according to reaction [1], producing cupric ions which become potential determining according to reaction [7].

There is however one additional reaction which deserves attention in this connection. If an electrode of CuS is immersed in a solution of CuCl which is free of $CuCl_2$, the potential remains considerably higher than that of copper in a solution of CuCl. Solutions free of $CuCl_2$ are conveniently prepared by removal of oxygen and reacting the CuCl solutions with clean metallic copper powder. The reaction

$$Cu + CuCl_2 \rightarrow 2\ CuCl$$

removes all traces of divalent copper.

The electrode potential of CuS in CuCl solution is maintained at nearly the same level even after applying small currents in the cathodic direction. It was established experimentally that the following reaction proceeds

$$e^- + CuCl + CuS \rightarrow Cu_2S + Cl^- \qquad [10]$$

The product Cu_2S was identified by x-ray analysis. Up to one third of the capacity of CuS could be utilized in this manner. In a 0.3M solution of CuCl (1M HCl + 1M KCl) the open circuit voltage of the electrode was +0.156v *vs.* Hg_2Cl_2, which is 0.271v above the potential of the Cu/CuCl couple. Theoretically, one calculates for the couple $CuS/Cu_2S/CuCl/Cl^-/CuCl/Cu$ a voltage of 0.385v.

Reaction [10] therefore constitutes a further reserve capacity of electrodes containing cuprous chloride and sulfur. After exhaustion of the sulfur according to reaction [1] and formation of CuS, the cuprous chloride can further react according to Eq. [10], at a slightly reduced voltage level.

Response of the CuS electrode to sulfide ions.— Sodium sulfide solutions varying in concentration between 0.001 and 0.5M were prepared with 0.5M sodium chloride as the supporting electrolyte, and the potential of the CuS electrode measured in these solutions, using a saturated calomel reference electrode. The *p*H values increased with increasing Na_2S concentration, attaining 13.1 in the 0.5M Na_2S + 0.5M NaCl solution. Sodium sulfide is extensively hydrolyzed in these solutions

$$Na_2S + H_2O \rightleftarrows NaHS + NaOH$$

with

$$HS^- \rightleftarrows H^+ + S^{--};\ K = 10^{-14}$$

From this one calculates for the concentration of $[HS^-]$

$$[HS^-] \rightleftarrows [H^+]\ [S_t^{--}]/([H^+] + 10^{-14}) \qquad [11]$$

where S_t^{--} is the total concentration of divalent sulfur present ($S^{--} + HS^-$). The electrode potentials of CuS in sulfide ion solutions are shown in Fig. 6. At very low sulfide ion concentrations the potential rises to a positive and constant value which must represent an adsorption potential by chloride ions.

The potential decreases sharply as the Na_2S concentration is increased above 0.003M and follows subsequently a straight line on the logarithmic plot, with a slope of about 30 mv.

If the reaction at the sulfide electrode is written in the form

$$2e^- + S_{(CuS)} + H_2O \rightleftarrows HS^- + OH^- \qquad [12]$$

and at the mercurous chloride reference electrode as

$$2e^- + HgCl_2 \rightleftarrows 2Hg + 2Cl^- \qquad [13]$$

the over-all reaction becomes

$$S_{(CuS)} + 2Hg + 2Cl^- + H_2O \rightleftarrows Hg_2Cl_2 + HS^- + OH^- \qquad [14]$$

where $S_{(CuS)}$ is the excess sulfur in CuS. One would then expect the following potential dependence

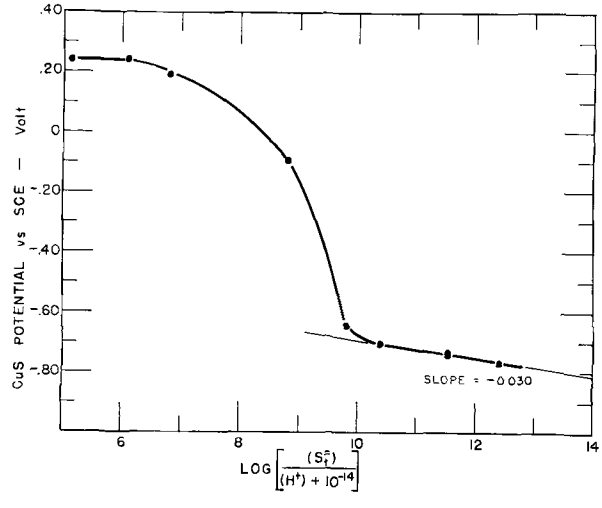

Fig. 6. Cupric sulfide potential as a function of log $[(S_t^{--})/(H^+ + 10^{-14})]$ where (S_t^{--}) = total Na_2S concentration. 0.5M NaCl.

$$E = E_{o(CuS/S_t^{--})} - (2.3\,RT/2F)\log \{[S_t^{--}]/([H^+] + 10^{-14})\} \quad [15]$$

since (Cl^-) concentration was maintained constant. This would predict a slope of —0.029v, when the potential is plotted against the logarithmic term. The experimental results of Fig. 6 agree well with this prediction.

The deviation between the experimental and theoretical slope is due to a dissolution of sulfur and the presence of polysulfides in the more concentrated sulfide solutions, as shown below in greater detail.

The standard potential of the couple

$$2e^- + S \rightleftarrows S^{--}$$

at pH 14 is —0.72v *vs.* calomel according to Latimer.

This value checks well with the experimentally measured value extrapolated with the help of reference (15), from the data of Fig. 6, to a concentration of 1*M* at pH 14, which is another indication that the excess sulfur in CuS is essentially "free."

It has been pointed out that sulfur readily dissolves in alkaline solutions. Hickling (16) has studied the behavior of solutions containing both dissolved sulfur and sodium sulfide, on inert electrodes. He found that the dissolved sulfur species were able to support a reversible redox potential and high currents in the forward and backward direction. Also Gerischer (17) reports that the electrochemical oxidation of sulfide to sulfur can proceed with high efficiencies. It was of interest to measure the redox couple

$$2e^- + S_{(dissolved)} + H_2O \rightleftarrows HS^- + OH^- \quad [16]$$

on CuS electrodes.

Solutions containing sulfur and sulfide in varying concentrations were prepared, and the voltage of CuS in these solutions measured against a calomel reference electrode. The potentials showed extreme reversibility and were established with ease. Forward and backward electrochemical reactions could be maintained with very small polarization. It was discovered that on CuS the redox couple was even more reversible than on platinized platinum.

According to Eq. [16] one obtains for the potential

$$E = E_{o(S/SH^-)} - (2.3\,RT/2F)\log [[S_t^{--}]/\{[S]([H^+] + 10^{-14})\}] \quad [17]$$

Figure 7 confirms this behavior; the slope checks excellently with the theoretical value. These results are in agreement with the data reported by Hickling and, moreover show that Eq. [17] can be applied to solutions of different pH values.

Conclusions

1. Cuprous chloride reacts with sulfur in acidic aqueous chloride solution to produce cupric sulfide and dissolved cupric chloride; the latter reaches an equilibrium concentration close to saturation.

2. The increase in voltage observed when sulfur is added to a cuprous chloride electrode in acidic magnesium chloride solution is caused by the fact that the electrode mechanism changes from

$$e^- + CuCl \rightarrow Cu + Cl^-$$

to

$$e^- + CuCl_2 \rightarrow CuCl + Cl^-$$

where the cupric chloride is generated by chemical reaction between cuprous chloride and sulfur:

$$2CuCl + S \rightarrow CuCl_2 + CuS$$

If the cupric chloride reaches the equilibrium concentration, the total free energy of formation of CuS (11.7 kcal) can be utilized as electrical energy and the over-all process can be written in the form

$$e^- + CuCl + S \rightarrow CuS + Cl^-$$

resulting in a theoretical voltage increase of 0.506v. Further capacity could be delivered by the electrode through the reaction

$$e^- + CuCl + CuS \rightarrow Cu_2S + Cl^-$$

with a theoretical electrode potential increase of 0.38v.

3. The discovery of this phenomenon is of practical importance to the technology of cuprous chloride-magnesium batteries.

4. Potential measurements of CuS in solutions containing either cupric ions or sulfide ions indicate that the nonstoichiometric excess sulfur in CuS acts essentially as "free" sulfur.

5. In solutions containing both dissolved sulfur and sulfides, CuS exhibits the characteristics of a very reversible redox electrode

$$2e^- + S \text{ (dissolved)} \rightarrow S^{--}$$

$$S^{--} + H^+ \rightleftarrows HS^-$$

6. While Wrabetz (3) showed that nonstoichiometric micro-quantities of excess sulfur in metal sulfides are responsible for the high electrode potential of these materials in solutions of their cations, the present investigation showed that similar over-all effects can be achieved with stoichiometric macro-quantities of elemental free sulfur, mechanically admixed with cuprous chloride to form the electrodes, whereby the sulfur regenerates continuously the higher oxidation state of the electrode couple from the lower oxidation state and large current outputs at an increased voltage become possible.

7. The utilization of a purely chemical step in the production of electrical energy according to the scheme

$$\begin{array}{ccccccc} A & + & B & \xrightarrow{\text{chemical reaction}} & C & + & D \\ \uparrow & & & & & & \\ \text{electrochemical reaction} & & & & & & \end{array}$$

may have considerable merit in the construction of various types of battery electrodes.

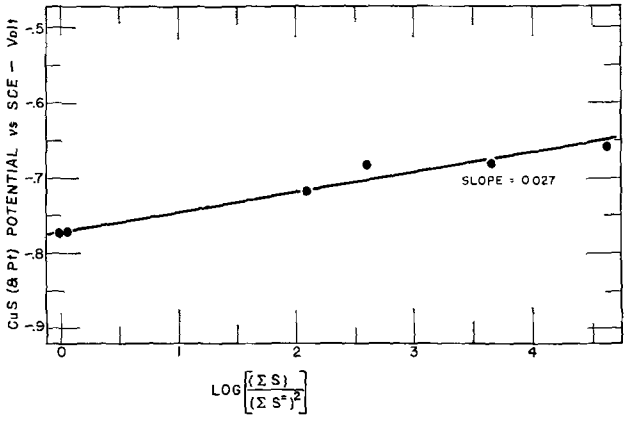

Fig. 7. Cupric sulfide (and platinized Pt) potential as a function of log $(\Sigma S)/(\Sigma S^=)^2$ Total sulfide concentration, $(\Sigma S^=)$, corrected hydrolysis by $[H^+]\ [S^=]/[HS^-] = 10^{-14}$; 0.5*M* NaCl.

Manuscript received Nov. 30, 1964.

Any discussion of this paper will appear in a Discussion Section to be published in the June 1966 JOURNAL.

REFERENCES

1. H. N. Honer, R. F. Amlie, and P. Ruetschi, To be published.
2. G. Vortmann and C. Padberg, *Chem. Ber.*, **22**, 2642 (1889).
3. W. Noddack and K. Wrabetz, *Z. Electrochem.*, **59**, 96 (1955).
4. W. Noddack, K. Wrabetz, and W. Herbst, *ibid.*, **59**, 752 (1955).

5. K. E. Wrabetz, *ibid.*, **60**, 722 (1956).
6. G. Trumpler, *Z. Physik. Chem.*, **99**, 9, (1921).
7. K. Badeker, *Ann. Phys.*, (4) **22**, 749 (1907).
8. K. Fischbeck and O. Dorner, *Z. anorg. allgem.. Chem.*, **181**, 372 (1929).
9. H. Remy, "Treatise on Inorganic Chemistry," Vol. II, p. 390, Elsevier Publishing Co., New York (1956).
10. D. F. C. Morris and E. L. Short, *J. Chem. Soc.*, 2672 (1962).
11. W. M. Latimer, "Oxidation Potentials," p. 184, Prentice Hall Inc., New York (1952).
12. A. A. Noyes and M. Chow, *J. Am. Chem. Soc.*, **40**, 739 (1918).
13. F. Fenwick, *ibid.*, **48**, 860 (1926).
14. O. Gatty and E. C. R. Spooner, "The Electrode Potential Behavior of Corroding Metals in Aqueous Solutions," Oxford University Press (1938).
15. Tor Hurlen, Special Scientific Report No. 3, Jan. 1961, Central Institute for Industrial Research, Blindern, Oslo, Norway, ASTIA AD-252811.
16. P. L. Allen and A. Hickling, *Trans. Faraday Soc.*, **53**, 1626 (1957).
17. H. Gerischer, *Z. Elektrochem.*, **54**, 540 (1950).

Effect of Surface Treatment on the Corrosion of Stainless Steels in High-Temperature Water and Steam

M. Warzee, J. Hennaut, M. Maurice, C. Sonnen, and J. Waty

Société d'Etudes, de Recherches et d'Applications pour l'Industrie "S.E.R.A.I.", Bruxelles, Belgium

and Ph. Berge

EURATOM, Bruxelles, Belgique

ABSTRACT

The corrosion behavior of AISI 304 and 410 steels as well as 23.5 Cr-21.5 Ni steels in superheated steam at temperatures between 400° and 600°C was found to be influenced markedly by preliminary surface treatments: electrolytic polishing, mechanical polishing, milling, lathe-turning, grinding. The treatments accompanied by cold-working reduced the corrosion rate, the effect being retained for long times (at least 2000 hr for AISI 304 steel at 450°C). This enhanced corrosion resistance is attributed to the presence of cold-worked surface layers which were detected by measurement of x-ray line broadening. Electron microprobe analyses of the oxide layers and of the underlying metal showed that the oxide is enriched and the metal depleted in chromium and manganese. These elements thus seem to diffuse through the cold-worked layer toward the oxide. In water, at 300°C and below, the phenomena are more complex and not yet fully understood.

The corrosion of stainless steels in water and steam at high temperature has been studied extensively in recent years in connection with nuclear reactor construction (1). One of the factors liable to modify the corrosion rate is the initial surface treatment of the metal. The studies carried out previously, however, scarcely enable the importance of this corrosion factor to be evaluated and, above all, to be understood.

Fowler, Douglas, and Zyzes (2) consider that the initial surface treatment does not have an important effect on the corrosion of stainless steels in pressurized water between 250° and 320°C. On the other hand, Friend (3) thinks that roughness is disadvantageous, and Roebuck, Breden, and Greenberg (4) recommend actual machine finishing or pickling in order to obtain good corrosion resistance under these conditions. Nevertheless, they consider that the favorable effect of these treatments diminishes greatly during long-term tests. Videm and Aas (5) show that the surface treatment of stainless steels has considerable influence on their behavior in water at high temperature, but do not give details of the favorable treatments. Tolstaya *et al.* (6) show that electrolytic polishing decreases the corrosion rate by a factor of 2, while Rockwell and Cohen (7) put the factor at about 10. On the other hand, Ruther and Greenberg (8) found that electrolytic polishing had a disastrous influence on the behavior of stainless steels in steam at 650°C. Stiefel (9) indicates that a finely machined surface behaves much better in steam at 650°C than a nonmachined surface, but does not specify the type of machining.

In order to try to evaluate and understand the role played by the surface treatment, we endeavored to distinguish the three characteristics of the surface of a metal, as defined by Jacquet (10):

1. Microgeometric characteristics (roughness).
2. Chemical characteristics. Pollution and, particularly, the presence of an oxide film are the most important.
3. Physical or structural characteristics. Disturbances in the metallic lattice, either at the microscopic, submicroscopic, or atomic levels, caused by the surface treatments. Hardness changes and internal stresses in the surface layers are possible consequences of these structural disturbances.

One of the aims of this study was to see which of these characteristics could have an influence on the corrosion of stainless steels in water and steam over a fairly wide temperature range.

Preliminary Experiments and Objectives

The first part of the study, published elsewhere (11), concerned AISI 304 stainless steel. The curves in Fig. 1 reproduce the results obtained in autoclaves in pressurized water at 300°C and in steam at 400°C and 200 atm pressure with specimens which have been subjected to various mechanical surface treatments or to

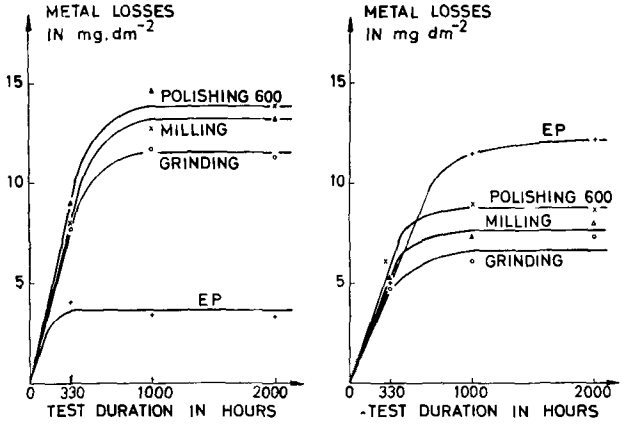

Fig. 1. Corrosion of AISI 304 in autoclaves: (a) (left), water at 300°C; (b) (right), steam at 400°C, 200 kg/cm².

electrolytic polishing. Details of these treatments are given in the experimental section of this paper. The values reported are averages over many tests, each involving a large number of specimens which made it possible to study statistically the significance of the results. It was found that electrolytic polishing appreciably improved the corrosion behavior in water at 300°C as compared with the three mechanically treated states. In steam at 400°C, the mechanically treated samples behaved better than in water at 300°C and became better than the electrolytically polished specimens.

The preliminary studies suggested that the following areas should be investigated: (*a*) to discern if the differences observed in water at 300°C and in steam at 400°C were due to a change in the physical state of the water or to the rise in temperature; (*b*) to cover a wider temperature range; (c) to investigate whether the surface treatment affected only the initial phase of oxidation or whether this effect persisted to longer times. The very slight corrosion of stainless steels under these conditions did not make it possible to study by autoclave tests the corrosion rate after 1000 hr with sufficient accuracy; (*d*) to ascertain whether other stainless steels behave similarly; (*e*) to discern what surface state characteristic is responsible for the observed effects.

Experimental

Specimen preparation.—The material used for this investigation was mainly AISI 304 stainless steel. Some additional tests were made using AISI 410 steel and also with a steel containing 23.5% Cr and 21.5% Ni.

Prior to the corrosion tests, the surface of the specimens was treated in a standardized manner. Three different mechanical treatments were used: (i) mechanical polishing through 600 grit paper, (ii) machine grinding with carborundum (grain size 80), and (iii) milling. A fourth type of treatment was electrolytical polishing in a perchloric-acetic acid bath. These treatments were followed by a chemical conditioning of the resulting surfaces. The standard method was immersion for 2 min in boiling water. Occasionally, conditioning techniques were tried in order to check if this step in the preparation of the specimens might alter the corrosion behavior. Alternate treatments were as follows: (*a*) exposure during 8 days in an air-conditioned room at 20°C and 50% humidity; (*b*) immersion for 2 min in nitric acid of density 1.33 at 20°C; (*c*) pickling during 25 min in a bath composed of 10% HNO_3, 3% HF, and 87% H_2O at 30°C (a layer of 6μ was dissolved by this treatment). Some of the mechanically treated specimens were heated under H_2, A, or in vacuum at 1050°C followed by quenching. The specimens were then chemically conditioned by the standard method (2 min in boiling water).

The surface of the treated specimens was examined by various methods: the roughness of the surface was measured with a profilograph Talysurf model 3 (Taylor-Hobson); the results are expressed in terms of the "central line average," henceforth designated as C.L.A. which is defined as the mean absolute deviation of the profile from the center line. Results of these measurements are given in Table I.

The oxide films formed on stainless steel in various media were compared by coulometric reduction in

Table I. Effect of surface treatment on roughness values of AISI 304 steels

Surface treatment	C.L.A. in microns	
	Parallel*	Perpendicular*
Milling	11	11
Grinding	3	5.2
Mechanical polishing	1	8
Electrolytic polishing	1.6	1.6

* The roughness profiles were measured parallel and perpendicular to the direction of mechanical surface treatment.

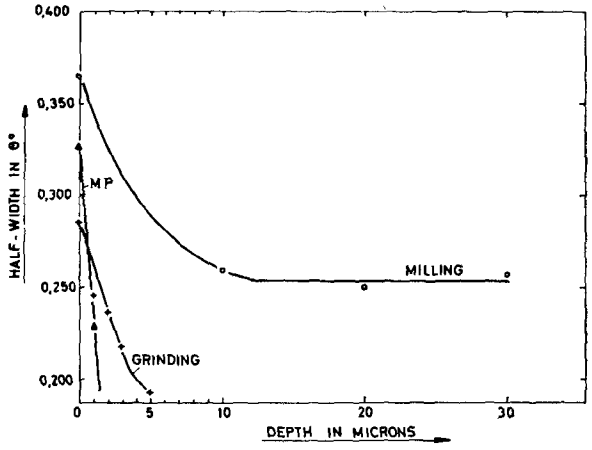

Fig. 2. Measure of the surface cold work of AISI 304 using the half-width of the (111) austenite line. Depth for which the ray profile is similar to that of the electrolytic polished state; grinding, 5-6μ; mechanical polishing, 1-2μ.

sulfuric acid. This method, as described previously (12), makes it possible to evaluate the number of coulombs required to reduce the passivation oxides of stainless steels as well as the exchange current, expressing slow oxidation in sulfuric acid (13). This last value may therefore indicate the protection conferred by the oxide independently of its thickness. The exchange current values obtained with these different chemical treatments vary greatly (13).

In order to evaluate the thickness of the layers affected by the various mechanical treatments, the broadening of the (111) austenite line in the x-ray diffraction pattern of the specimen was measured. For this purpose, the method for the study of surface layers by grazing emergence of the diffracted beam, described by Legrand (14), was adapted to an asymmetrically mounted focusing camera. The Kα line of copper, obtained from a bent quartz crystal monochrometer was used. Figure 2 shows the variation in the half-peak width of the (111) line measured on the photometric recordings. It can be seen that the depths of the cold-worked layer depend greatly on the mechanical treatment. The method reveals no further surface cold-work for specimens polished through 600 grit paper, after 2μ have been dissolved, whereas 6μ are to be removed from ground specimens, and milled specimens are still thoroughly cold-worked at a depth of 30μ.

Autoclave tests.—This technique has been described previously (15). The water used in all of the experiments was extremely pure (resistivity reading 20 Mohm-cm and oxygen content below 15 x 10^{-6} g/liter).

Measurement of the diffused hydrogen.—When a metal is oxidized in oxygen-free water, hydrogen is produced. If the specimen under study is in the shape of a small capsule containing water or steam, the hydrogen formed diffuses through the walls. Bloom *et al.* (16) have shown that it is possible to plot the corrosion-*vs.*-time curve by measurement of the quantity of evolved hydrogen. A longitudinal section through the capsules used is shown in Fig. 3. They are small cylinders of 20 mm diameter and 38 mm length. After annealing, all inside surfaces are subjected to the specified treatments. Bottom and top are then sealed by electron beam welding. The required quantity of water is added through the filling tube which is then pinched off and sealed by spot welding. The sealed capsules are placed in a gas collecting rig, a flow sheet of which is shown in Fig. 4. The rig is made of Pyrex glass and can hold ten capsules which are placed in ten gas collecting chambers heated individually by electric furnaces. The gas accumulated in each collecting chamber is periodically swept into a gas chromatograph for measurement. Because of the high precision

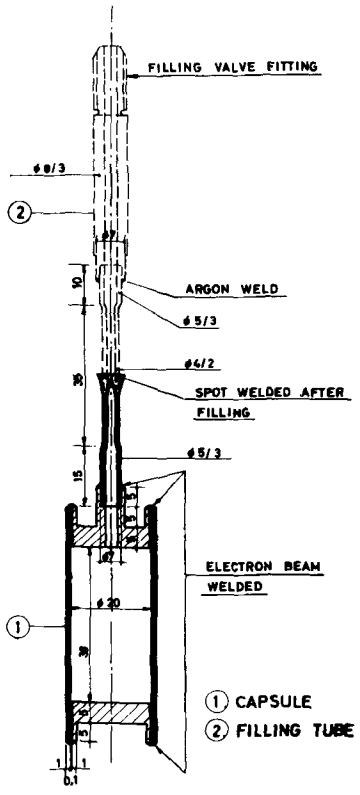

Fig. 3. Hydrogen diffusion test capsule

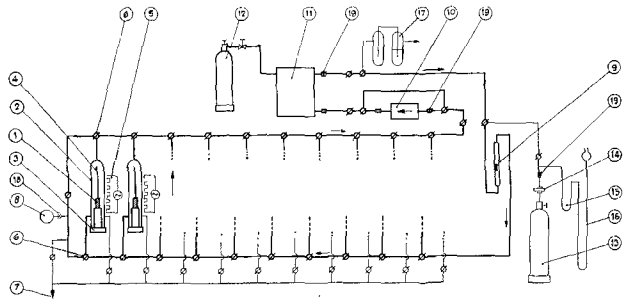

Fig. 4. Flow sheet of experimental rig for hydrogen diffusion measurements: 1, test capsule; 2, gas collecting chamber; 3, bottom closure of chamber; 4, thermometer; 5, electric furnace; 6, three-way stopcocks; 7, to vacuum line; 8, Penning vacuum gauge; 9, flow meter; 10, sealed circulating pump; 11, gas chromatograph; 12, bottle for calibration gas mixture; 13, argon bottle; 14, high-purity pressure reducer; 15, liquid air trap; 16, mercury manometer; 17, exit gas bubble counter with no return safety device; 18, conical ground joint; 19, glass to metal seals.

of hydrogen determination by gas chromatography, this method makes it possible to measure accurately the low corrosion rate of AISI 304 steel at 300°C after 1000 hr. This was not possible with autoclave measurements.

Results and Discussion

The corrosion was evaluated after reduction of the oxide layer in a stream of pure hydrogen at 800°C. It was always assumed that the metal to oxygen ratio was that of magnetite. However, for high corrosion rates, i.e., for electrolytically polished specimens at temperatures above 450°C, the results are given by simple measurement of the weight gain, as reduction in hydrogen and descaling have proved unsatisfactory. The values obtained are thus slightly below the real total corrosion values since the metal lost as detached scale in the autoclave is not taken into account.

In order to examine the oxide layers microscopically, polished cross sections were prepared after protecting the oxide by a layer of cobalt deposited electrolytically.

Variations in composition of the oxide and the underlying metal were determined with the electron microprobe. Specimens oxidized in steam for 1000 hr were used for these measurements.

Table II shows the total corrosion values from 1000-hr experiments in autoclaves at different temperatures in pressurized water and superheated steam for the electropolished and mechanically treated states. As the three mechanically treated states give very close corrosion values, the corrosion results for the milled and the electropolished specimens only are indicated. The corrosion rate at 500°C is sufficiently high for the autoclave measurements to indicate the oxidation

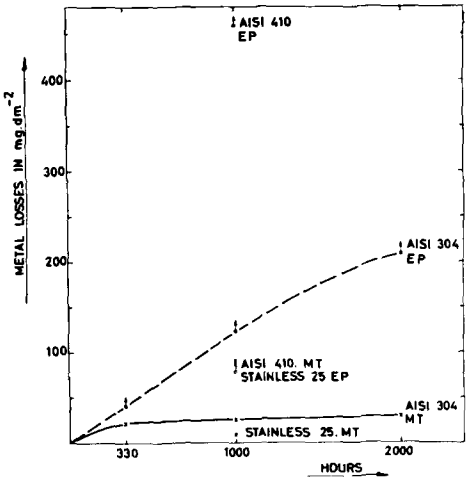

Fig. 5. Corrosion of stainless steels in superheated steam at 500°C, 70 kg/cm^{-2} (autoclaves).

Table II. Total corrosion values in mg dm^{-2} after 1000 hr in autoclaves

Stainless Steel Compositions, %				Surface treatment	Water				Superheated steam					
					Temperature, °C				Temperature and pressure					
									250°C	350°C	400°C	450°C	500°C	600°C
					200	250	300	350	15 kg/cm²	35 kg/cm²	70 kg/cm²	70 kg/cm²	70 kg/cm²	70 kg/cm²
	AISI 304													
C	0.04	Si	0.5	Milled	12.4	13.4	12.9	5.1	3.0	4.5	7.5	27.2	34.2	18.7
Ni	11.0	Mn	1.1	Electro-polished	6.9	4.7	3.4	3.3	3.1	4.5	11.4	78	>160	>1100
Cr	18.8													
	Stainless 25 (Uddeholm)			Milled	—	—	3.3	—	—	—	3.8	—	8.4	—
C	<0.075	Si	<2.0											
Ni	21.5	Mn	<2.0	Electro-polished	—	—	>7.5	—	—	—	>5	—	>79	—
Cr	23.5	P	<0.03											
S	<0.025													
	AISI 410			Milled	—	—	30.5	—	—	—	6.8	—	83	—
C	0.07	Cr	13.4											
Mn	0.38	Si	0.32	Electro-polished	—	—	30.1	—	—	—	55	—	>460	—
P	0.021	S	0.006											

Table III. Corrosion rates of AISI 304 steel in mg dm^{-2} hr^{-1} measured by hydrogen diffusion

Measured at time, hr	Treatment	Corrosion rates* Water, 300°C	Superheated steam, 300°C 50 kg/cm²	Superheated steam, 450°C 70 kg/cm²
1000	Electropolished	0.003	0.003	0.045
	Lathe-turned	0.008	0.003	0.005
2000	Electropolished	—	—	0.040
	Lathe-turned	—	—	0.003

* For the calculation of the corrosion rates, the metal to oxygen ratio was assumed to be that of magnetite.

kinetics, even after 1000 hr (Fig. 5). This is not so at 300°C.

The corrosion rates of AISI 304 steel measured by hydrogen diffusion are shown in Table III.

These results show that:

1. The adverse influence of a mechanical surface treatment noted for AISI 304 in water at 300°C did not occur in superheated steam at the same temperature. In saturated steam, however, the results were similar to those obtained in water. Below the critical temperature, the physical state of water must thus be considered as an essential factor of the behavior. Between 250° and 350°C, the corrosion in superheated steam was independent of the surface state and was generally lower than in water.

The fact that the corrosion of electropolished specimens in water was higher at 200° than at 250°C and 300°C is due to the larger quantity of metal in solution in the water at 200°C. It is probable that the transformation of more soluble ferrous hydroxide into magnetite is slower at 200° than at 300°C (1, 17).

2. The curves in Fig. 6 summarize the results of AISI 304 corrosion after 1000 hr in superheated steam at various temperatures. The corrosion in this medium, which was independent of the surface state up to 350°C, was dependent on this factor above 400°C. A mechanical surface treatment improved the behavior of the specimens above that temperature; this improvement increased with temperature. At 600°C, the total corrosion rate of electropolished specimens in 1000 hr was more than 50 times greater than that of mechanically treated specimens.

3. The hydrogen diffusion data (Fig. 7 and 8) and also the 500°C autoclave curves (Fig. 5) clearly demonstrate that the effect of the surface treatment is not a short-term effect; under the conditions employed in our experiments, the oxidation kinetics in steam from 400°C upwards and for exposure times up to 2000 hr

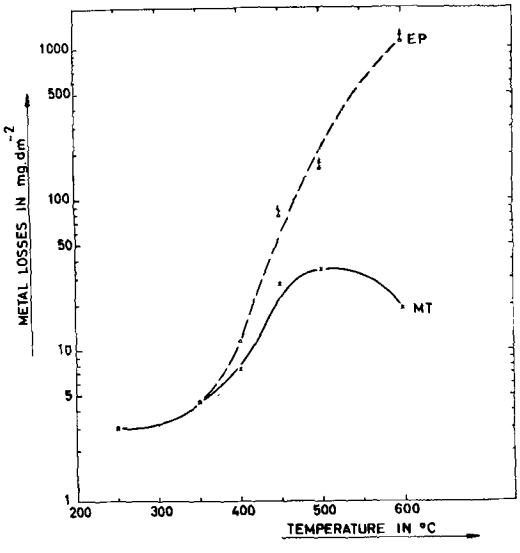

Fig. 6. Total corrosion of AISI 304 in 1000 hr in superheated steam (autoclaves).

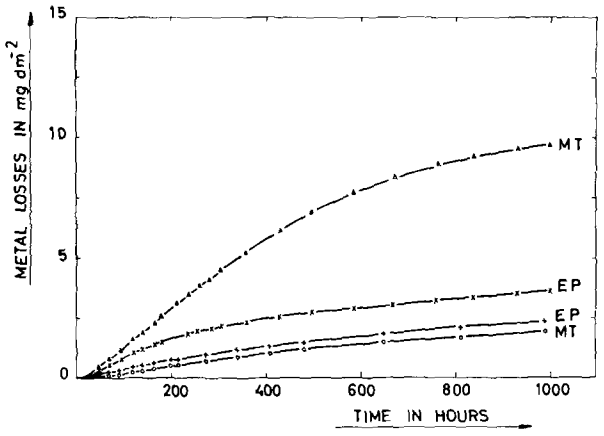

Fig. 7. Total corrosion of AISI 304 at 300°C measured by hydrogen evolution. △, X, Water 300°C; +, ○, superheated steam at 300°C.

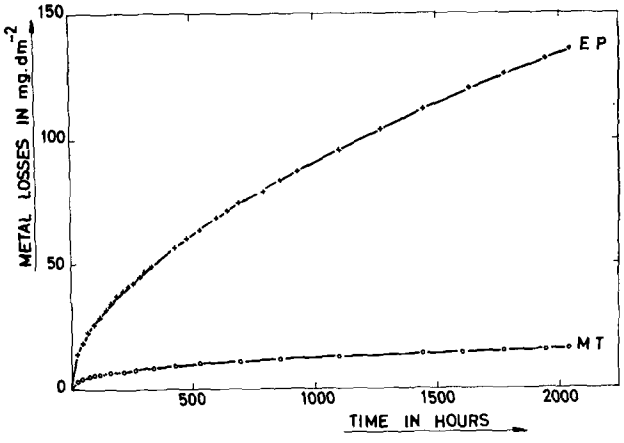

Fig. 8. Total corrosion of AISI 304 in superheated steam at 450°, 70 kg/cm², measured by hydrogen evolution.

are considerably altered by mechanical treatment. The favorable effect of electrolytic polishing on corrosion in water at 300°C was retained after 1000 hr.

4. The favorable effect of a mechanical surface treatment on corrosion in steam at high temperature is the same for AISI 410 and 23.5 Cr-21.5 Ni steels as for AISI 304 steel. On the other hand, electrolytic polishing imparts no noticeable improvement on these steels in water at 300°C.

5. The various roughness values obtained by the different mechanical treatments do not alter appreciably the corrosion behavior of AISI 304 steels in water and steam. Furthermore, the different methods of chemical conditioning of the surface did not bring about noticeable effects. The pickling of a previously electropolished specimen also did not change the corrosion behavior of the surface in water and steam at high temperature. It is thus impossible to relate the behavior of electrolytically polished specimens in this medium to the presence of an oxide film formed during polishing as was the case in the corrosion of iron-chromium alloys oxidized in oxygen (18).

The influence of cold-work on the corrosion behavior was shown by the specimens which had been pickled in the nitric-hydrofluoric acid bath after the four surface treatments. Only the milled specimen which had been cold-worked to a depth greater than 6μ, maintained a low corrosion rate at 500°C after pickling, whereas the three other surface treatments produced corrosion rates similar to that of the electropolished specimen. All the specimens which were quenched from 1050°C behaved similarly in steam at 500°C to the electropolished specimens.

Fig. 9. Section of an AISI 304 sample marked with a diamond point and oxidized for 1000 hr in steam at 500°C.

Figure 9 shows a section of an electropolished specimen of AISI 304 steel on which a mark was scribed with a diamond point under constant load. The specimen was oxidized during 1000 hr in steam at 500°C. It can be seen that the oxide layer on the area cold-worked by the diamond point is distinctly thinner than on the remainder of the surface. These results show that the improvement in the behavior in steam at high temperature observed after mechanical treatment is due to the presence of a cold-worked layer several microns thick.

The electron microprobe analysis of cross sections of mechanically treated specimens was not possible because after 1000 hr at 500°C in steam the oxide films are too thin (0.4μ). However, surface analysis of a specimen was carried out, the depth of penetration of the beam being about 3μ. The results obtained were therefore only qualitative, but a very marked enrichment of the oxide layer in chromium and in manganese was observed. This is shown in Table IV.

The microscopic study of oxides formed on electropolished specimens has shown that they consist of two layers separated by the initial surface of the metal. The outside layer is highly crystallized magnetite, free of chromium and nickel, whereas the inside layer probably resulted from an internal oxidation of chromium in a nickel-rich austenite matrix (19). The chromium content of the metal under the oxide layer is given in Table V.

It may be ascertained that no chromium concentration gradient is formed in the metal of the electropolished sample, whereas with the mechanically treated samples a depletion of the chromium content is found in the neighborhood of the oxide, which itself is rich in chromium. It is therefore probable that the diffusion rate of the chromium is higher in the layer affected by the mechanical treatments because of the increased number of dislocations in the crystal lattice.

The film initially formed on the cold-worked surfaces would be greatly enriched in chromium as a result of this diffusion and might thus afford a greater degree of protection against later oxidation of the iron. A similar mechanism has been suggested by Poulignier *et al.* (20) to explain the favorable effect of superficial cold-work on the oxidization of Cr-Ni-Co-Mo alloys in air.

Table IV. Electron microprobe analysis of a milled specimen of AISI 304 steel oxidized for 1000 hr in steam at 500°C

Analyzed layer	Concentrations in %				
	Fe	Cr	Ni	Mn	Si
Original metal	69	18	11	1.5	0.9
Oxide	59.6	23.6	10	6.2	0.6

Table V. Chromium content of the metal under the oxide layer of AISI 304 steel specimens oxidized for 1000 hr at 500°C

Thickness of the metal consumed by corrosion	Milled 0.4μ	Ground 0.4μ	Electropolished Approx. 2μ
Depth under oxide layer, μ	Chromium contents in %		
2	17.3	17.3	18.0
5	17.4	17.6	18.0
10	17.7	17.9	18.0
20	17.7	18.1	18.0
30	18.1	18.1	18.0
200	18.1	18.1	18.0

Conclusions

The corrosion rate of stainless steel in superheated steam at high temperature is greatly affected by the initial surface treatment of the metal. The essential factor was found to be cold-work which reduces considerably the corrosion rates. Definition of the surface state in terms of its roughness is totally inadequate. Pickling or electrolytic polishing are also insufficient to define a surface state, because the cold-worked surface layers may not have totally disappeared.

In water at 300°C and below, more complex phenomena seem to be involved in which the physical state of the water, the temperature, and the surface state of the metal as well as its composition contribute in a manner which is not yet fully understood. The investigation of these mechanisms is more difficult because of the low corrosion values obtained.

It should be possible to make use in nuclear power plants of the considerable improvement in corrosion behavior in superheated steam produced by suitable surface treatments.

Acknowledgment

This work was supported by the Commission of the European Atomic Energy Community. The authors thank for the permission to publish this paper. Thanks also due to Mr. Hochmann, Director of Research of the Company "Ateliers et Forges de la Loire," for his kindness to permit the electron microprobe analyses to be carried out in his laboratories.

Manuscript received Oct. 2, 1964. This paper was presented at the Washington Meeting, Oct. 11-15, 1964.

Any discussion of this paper will appear in a Discussion Section to be published in the June 1966 JOURNAL.

REFERENCES

1. Corrosion and Wear Handbook for Water Cooled Reactors," D. J. De Paul, Editor (1957).
2. R. Fowler, D. L. Douglas, and F. C. Zyzes, KAPL-1248 (1954).
3. W. Z. Friend, *Proc. Amer. Power Conf.*, **18**, 613 (1956).
4. A. N. Roebuck, C. R. Breden, and S. Greenberg, *Corrosion*, **13**, 87 (1957).
5. K. Videm and S. Aas, Kjeller Report, No. 39 (1963).
6. M. A. Tolstaya, G. N. Gradusov, and S. V. Bogatyreva, AEC-tr-4698 (1960).
7. T. Rockwell and P. Cohen, *Prog. Nuclear Energy*, Series IV, **1**, p. 281 (1956).
8. W. E. Ruther and S. Greenberg, *This Journal*, **111**, 1116 (1964).
9. W. Stiefel, *Rev. Tech. Sulzer*, No. 3, 21 (1961).
10. P. A. Jacquet, *Met. Rev.*, **1**, 157 (1956).
11. M. Warzee, Ph. Berge, M. Maurice, and J. Waty, *Compte rend. Acad. Sc. Paris*, **256**, 5566 (1963).
12. Ph. Berge, *Compte rend.*, **245**, 1239 (1957).
13. M. Cunha Belo, Ph. Berge, J. Montuelle, and G. Chaudron, *Corrosion et Anticorrosion*, **12**, 297 (1964).
14. C. Legrand, *Bull. Soc. Franç. Minéral. Crist.*, **74**, 20 (1951).
15. M. Warzee, M. Maurice, C. Sonnen, J. Waty, and Ph. Berge, *Rev. Met.*, **61**, 593 (1964).
16. M. C. Bloom, M. Krulfeld, W. A. Fraser, and P. N. Vlannes, *Corrosion*, **13**, 297 (1957).
17. U. R. Evans, "The Corrosion and Oxidation of Metals," p. 438, Edward Arnold, London (1960).
18. D. Caplan, A. Harvey, and M. Cohen, *This Journal*, **108**, 134 (1961).
19. M. Warzee, J. Hennaut, M. Maurice, and Ph. Berge, *Mém. Sci. Rev. Mét.*, **62**, 239 (1965).
20. J. Poulignier and P. A. Jacquet, *Rev. Mét.*, **49**, 541 (1952); J. Poulignier, *Corrosion et Anticorrosion*, **11**, 466 (1963).

The Migration of Metal and Oxygen during Anodic Film Formation

J. A. Davies, B. Domeij, J. P. S. Pringle, and F. Brown

Research Chemistry Branch, Chalk River Nuclear Laboratories,

Atomic Energy of Canada Limited, Chalk River, Ontario, Canada

ABSTRACT

Beta-ray spectroscopy and radiotracer techniques have been used to study the transport of metal and oxygen during anodic oxidation. Both species are mobile during oxide film growth on Al, Nb, Ta, and W, but in Zr and Hf only oxygen transport is observed. Radiotracer measurements showed that the amount of metal dissolving in the electrolyte was usually less than 1% of the total oxidized, but that for Al it could be as high as 40%, depending on the current density and electrolyte used.

Although the anodic oxidation of metals has been studied extensively in recent years, the nature of the mobile species within the growing oxide film has not been clearly established. Experimental evidence has been presented in Al, for example, to suggest that anodic oxidation proceeds by metal ion migration (1, 2), by oxygen ion migration (3), or by a combination of both processes (4, 5).

To resolve such discrepancies, a "transport number" experiment is required in which a thin surface layer is tagged with a completely immobile marker atom, whose position is then followed during the subsequent anodic oxidation. If the metal ions alone are mobile, new oxide will be formed at the oxide/electrolyte interface on top of the tagged layer, and so the marker will become buried. On the other hand, if oxygen ions are the only mobile species, the new oxide forms at the metal/oxide interface underneath the tagged layer, and so the marker remains close to the outer surface throughout the oxidation.

The ideal marker atoms for such a transport experiment should be (i) uncharged, so that they do not migrate under the influence of the applied electric field; (ii) large in size, so that they do not diffuse significantly within the oxide lattice; (iii) present in trace amount, so that the macroscopic properties of the tagged oxide remain unaltered; and (iv) such that their depth beneath the surface can be determined *in situ*, without damaging or destroying the oxide layer. Previous investigations (1, 6) have not fulfilled these criteria.

Radioactive isotopes of the heavier inert gases should approximate the ideal marker closely. Of all the possible atomic markers, the inert gases are the most likely to remain uncharged within the oxide lattice. The heavier gases are much bigger than either metal or oxygen ions and, if radioactive, can be used in trace amounts. Furthermore, the radioisotopes Xe^{125} and Rn^{222} decay with the emission of monoenergetic conversion electrons and α particles respectively, and so their depth beneath the surface of a solid can be measured *in situ* by means of high precision nuclear spectroscopy (7, 8).

Our earlier experiments on the anodic oxidation of Al and Ta in aqueous solution (3) showed that the Xe^{125} markers in anodic Al_2O_3 remained very close to the outer surface. We also noted that an appreciable amount of aluminum went into solution during anodizing, which suggested that aluminum ions might be mobile but were not building oxide at the outer surface. Subsequent experiments (4,5) showed that the final location of the marker atoms within the aluminum oxide layer depended markedly on the current density used and also on the nature of the electrolyte. At higher current density we observed an appreciable burying, which shows that metal transport is responsible, at least in part, for oxide growth. We have now found that the amount of aluminum going into solution during anodizing also varies with the current density; obviously, this loss must be considered in assessing the relative importance of cation mobility in the growing oxide.

Consequently, it was decided to carry out a more detailed radiochemical investigation of the anodizing behavior of Al and Ta. Two types of experiments have been used: (i) transport number experiments using Xe^{125} marker atoms as in the previous work (3, 5); and (ii) experiments with neutron-activated metals in order to determine the amount of metal ion dissolving during the anodic oxidation. The effect of current density was studied in both sets of experiments, and for Al the nature of the electrolyte was varied. In addition, the anodic behavior of zirconium, niobium, hafnium, and tungsten was studied.

Experimental Procedure

Xe^{125} *depth measurements.*—In these experiments, trace amounts of Xe^{125} were incorporated in a thin anodic oxide layer on the surface of a metal foil. After measuring the mean depth of the Xe^{125} atoms, the foil was anodized further to produce a thick oxide film, and the mean depth of the Xe^{125} atoms was again determined. The difference in the Xe^{125} depths, divided by the thickness increment of the oxide, gave the fraction of the anodic oxide formed outside the Xe^{125} layer.

A previous paper from this laboratory (9) has described the use of an isotope separator for injecting Xe^{125} into solid targets. The Xe^{125} ions strike one tenth of the area of the target, 3.5 x 1.0 cm, as a line 3.5 cm long and 0.1 cm wide; the total number of Xe^{125} was always less than $10^{12}/cm^2$, and so the atomic concentration of Xe^{125} in the tagged layer did not exceed 20 ppm. A relatively low injection energy, either 3 or 5 kev, was used to keep the depth of the tagged layer small. The Xe^{125} could have been injected directly into the oxide layer, and a very narrow Xe^{125} depth distribution would have resulted (10). Because of the possibility that radiation damage to the oxide might affect its anodizing behavior, we preferred to put the Xe^{125} into the metal, and then anodize to convert the surrounding metal to oxide. As the distribution of embedded Xe is known for Al (9) and W (11), it is possible to calculate the anodizing voltage required to oxidize just this depth, and suitable voltages for the other metals could be inferred. This procedure does not eliminate the possibility that radiation damage in the metal may affect the anodic oxidation, but it has previously been shown that this is negligible for Al (12).

With the Xe^{125} atoms in a very thin layer of oxide, the target was inserted into the source chamber of the Chalk River $\pi\sqrt{2}$ β-spectrometer and the shapes of the

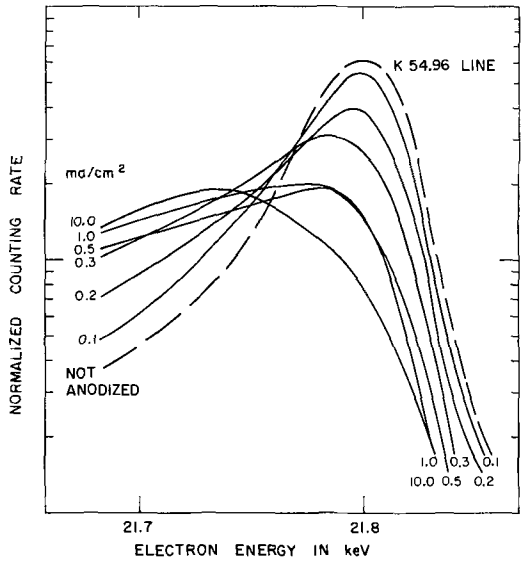

Fig. 1. The K54.96 conversion electron spectra from Xe^{125} atoms in anodic Al_2O_3; 3 kev Xe^{125} in Al subsequently anodized to 125v. The effect of current density is shown.

21.79 and 155.2 kev electron peaks, arising from K conversion of the 54.96 and 188.4 kev nuclear transitions, respectively, were measured. The target was then removed, anodized under the desired conditions, replaced in the spectrometer, and the peaks remeasured. Further anodizing and peak measurements were carried out as needed. The depth of the Xe^{125} layer after anodizing was found from the conversion electron spectra by comparing the observed attenuation of the 21.79 kev peak with that produced by absorbers of known thickness (7). The 155.2 kev peak is not significantly attenuated by the absorber thicknesses involved in the present work; it was measured to provide a normalizing factor for eliminating variations in source strength, geometrical efficiency, etc., in the spectrometer. Sample K54.96 spectra are shown in Fig. 1 for the anodization of Al in aqueous citrate.

A detailed description of this β-spectroscopic method for measuring small penetration depths has been given elsewhere (7). In the article, the method had been calibrated against known thicknesses of Al and Au absorbers; it was necessary for the present purpose to extend these calibrations to anodic oxides. Accordingly, anodized Al and W targets were bombarded with monoenergetic Xe^{125} ions of 1, 40, and 160 kev energy, and the Xe^{125} conversion electron spectra measured. The mean penetration depth, $\bar{R}$, of Xe^{125} in anodic Al_2O_3 and WO_3 is known accurately as a function of incident energy from the work of Domeij *et al.* (10), and the targets were anodized sufficiently (70v for W, 125v for Al) to ensure that essentially all the Xe^{125} was stopped in the oxide layer. Comparison of $\bar{R}$ against the normalized K54.96 peak height, N, in Fig 2 shows that N decreases exponentially with $\bar{R}$ as observed previously for Al and Au. Strictly, the mean "exponential" depth, $\bar{x}$, defined in the previous article (7) should be used for comparison with N, but the discrepancy between $\bar{R}$ and $\bar{x}$ is small provided that the thickness of the Xe^{125} layer is also small, as is the case in these oxides.

Xenon penetration depths are not known experimentally for the other anodic oxides; it was assumed that the electron stopping powers of HfO_2 and Ta_2O_5 were the same as that of WO_3. To provide a calibration for ZrO_2 and Nb_2O_5, the mean penetration depths of 80 kev Xe^{125} ions in these oxides were calculated from the theory of Lindhard (13) and used with the experimentally observed K54.96 peak height to construct the calibration shown in Fig. 2. These theoretical pene-

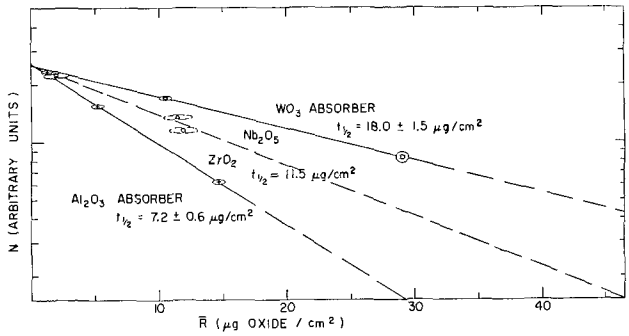

Fig. 2. Calibration of N, the normalized counting rate at the natural peak position of the K54.96 line, against the mean depth, $\bar{R}$, of the Xe^{125} atoms in anodic oxides.

tration depths, 11.9 $\mu g/cm^2$ for ZrO_2 and 11.5 $\mu g/cm^2$ for Nb_2O_5 are estimated to have an error of about 10%; it was assumed that the calibration for these two oxides was the same.

Dissolution of metal during anodizing.—A neutron activation technique was used to measure the extremely small amounts of metal ion that dissolve during anodic oxidation. Metal targets identical to those used above were irradiated in the NRX reactor at a flux of 2 x 10^{13} n cm^2/sec until a specific activity of ~10 mc/g was attained. No suitable radioisotope of Nb is produced by neutron activation, and the short half life of Al^{28} makes it necessary to start with a much higher specific activity (approximately 1000 mc/g) in order to have sufficient time to carry out the anodic oxidation. The irradiated targets were anodized at constant current to various voltages, and the amount of metal dissolved was determined by comparing with a standard. The latter was prepared by dissolving a known weight of the irradiated metal in an identical volume of etching solution.

Target preparation.—The targets were high-purity metal foils of dimensions 3.5 x 1.0 x 0.02 cm. Apart from W, all targets were polished either chemically or electrochemically in order to remove the mechanically damaged surface region using the following reagents:

(*a*) For Nb and Ta: chemically polished with a 5:2:2 mixture of concentrated H_2SO_4:HNO_3:HF acids.
(*b*) For Zr and Hf: chemically polished in a 45:4:51 mixture of concentrated HNO_3:concentrated HF:H_2O.
(*c*) For Al: electrochemically polished in perchloric acid-acetic anhydride.
(*d*) For W: not polished; the same material was used as in ref. (11).

Immediately prior to use, targets of Al and W were given a final pre-anodizing treatment, which consisted of the successive formation and dissolution of several anodic oxide layers approximately 1000Å thick. Unfortunately, no suitable reagent for dissolving the anodic oxides of Zr, Nb, Hf, and Ta without attacking the underlying metal is known to us, and so this pre-anodizing treatment could not be applied.

Anodizing procedure.—The anodic oxidations were all carried out at constant current, using the following electrolytic solutions:

(*a*) For Nb and Ta: 0.1M Na_2SO_4 in water.
(*b*) For Zr, Hf, and W: 0.4M KNO_3 + 0.04M HNO_3 in water.
(*c*) For Al: (i) Vermilyea's solution A (6), *i.e.*, sodium tetraborate (50 g/l) in 95% ethylene glycol—5% water; (ii) ammonium dihydrogen citrate (30 g/l) in water. The electrolyte temperature was always 25°C.

Results

Mobility of metal and oxygen.—Before discussing the behavior of individual metals, it is necessary to establish the significance of the experimental results. For

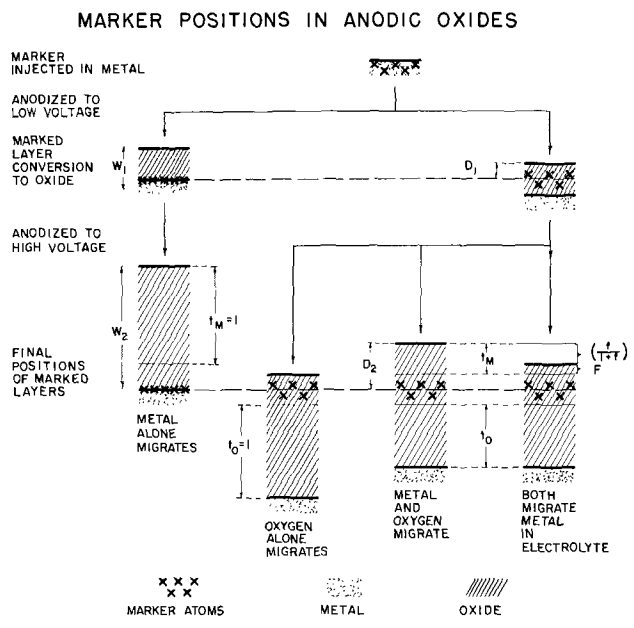

Fig. 3. Effect of metal and oxygen migration on the final position of an inert marker in an oxide film.

this purpose, the oxide is assumed to grow on a plane surface, to be of effectively uniform thickness at all times, and to be free of flaws; it is also assumed that the marker is present in negligible concentration and is truly immobile. There are then three possibilities for oxide growth; either the metal alone moves, or the oxygen alone, or they both move. The effect of metal and oxygen mobility on the final marker position is illustrated in Fig. 3.

If metal ion migration is solely responsible for film growth, the fresh oxide layers will be formed at the oxide/electrolyte interface on top of the marked layer. The situation is complicated, however, by the fact that the metal layers consumed during the oxidation must be replaced by oxide if the film is to remain in contact with the metal. Since the oxygen is, by definition, immobile, the oxide film must adjust itself to the metal surface by some process of plastic flow deformation; under these circumstances, the marker atoms will be trapped at the oxide/metal interface. Such markers would, therefore, appear buried by the full depth of the oxide film, but no practical example of this has yet been found.

If the oxide grows entirely by the inward movement of oxygen ions, migrating either directly through the oxide or by a series of replacement events, then the fresh oxide layers will be formed at the metal/oxide interface underneath the marked layer. The latter will, therefore, remain close to the oxide/electrolyte interface, and no burying of the marker will be observed.

If both metal and oxygen move, the marker atoms will be found somewhere in the middle of the film, the exact position depending on the relative mobilities of the metal and oxygen. Since all the metal ions migrating across the marked layer give rise to oxide above it, and all the oxygen ions migrating inward to oxide below, it is evident that the final position of the marked layer within the oxide can be used as a measure of the ionic transport fractions of metal and oxygen. Denoting these fractions by t_m and t_o, such that $t_m + t_o = 1$, it follows that t_m is equal to F, the fractional burying of the marked layer.

So far, it has been assumed that fresh oxide is formed only at the surfaces of the existing oxide. This is where it must occur if either the metal or the oxygen is the sole mobile species. If, however, both are mobile, the possibility arises that fresh oxide can be formed at points within the existing oxide, as suggested by Cheseldine (14). Growth of new oxide within the existing oxide does not appear to occur under the conditions of the present experiments, for if it did the Xe^{125} distribution would tend to broaden; the experiments with Rn^{222} show that no significant broadening takes place (4).

For the practical determination of t_m, account must be taken of the finite depth of the Xe^{125} markers in the initial oxide film. Accordingly, differential experiments were carried out in which the Xe^{125} depth, D_1, was measured in the low voltage oxide of thickness W_1. After anodizing to high voltage to produce an oxide film of thickness W_2, the depth, D_2, of the Xe^{125} was again measured. The fraction F was then obtained from

$$F = \frac{D_2 - D_1}{W_2 - W_1}$$

The cationic transport fraction, t_m, is equal to F only if no metal dissolves in the electrolyte; if metal does dissolve, say a fraction, f, of that giving rise to oxide, then

$$t_m = \frac{F + f}{1 + f}$$

Niobium, tantalum, and tungsten (*Fig.* 4).—After bombardment with Xe^{125}, samples of these three metals were anodized to low voltage in order to incorporate the Xe^{125} in the oxide layer, and then reanodized to a much higher voltage. No Xe^{125} was lost from any of these oxides during the oxidation process, and only trace amounts of metal were found in the electrolyte; less than 0.1% for Ta, and less than 0.5% for W. No information could be obtained for Nb as no suitable radioisotope was available. Oxide thicknesses were extracted from the appropriate information in Young's book (15). The increase in the Xe^{125} depth divided by the increase in the total oxide thickness gave the fractional burying, F, of the Xe^{125}; with such a small loss of metal to the solution, F approximates the cationic transport fraction t_m very closely.

As can be seen from Table I, t_m is close to 0.30 for all three metals, and so the oxygen mobility is about twice that of the metal. The error in each determination is probably about ± 0.03, due to uncertainties in the Xe^{125} depth; variations in the individual errors quoted for the latter are due to differing counting rates in the samples measured. The Xe^{125} depths in Nb_2O_5 are less reliable because of the larger uncertainty in the calibration; Ta_2O_5 has been assumed to have the same

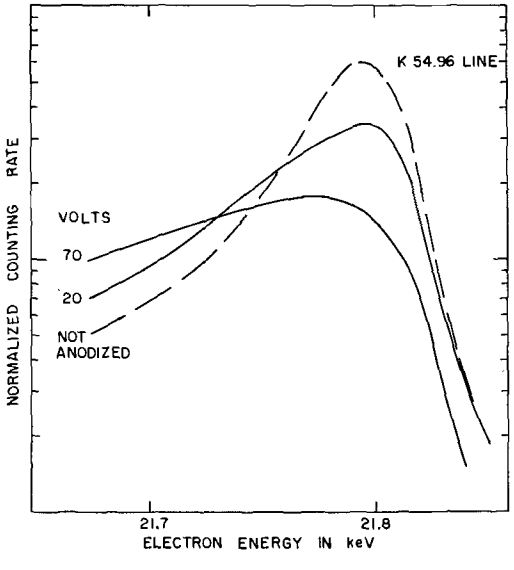

Fig. 4. The K54.96 conversion electron spectra from Xe^{125} atoms in anodic WO_3; 5 kev Xe^{125} in W subsequently anodized at 0.1 ma/cm².

Table I. Niobium, tungsten, and tantalum

Current density, ma/cm²	Final voltage, v	Total oxide formed, μg/cm²	Xe^{125} depth, μg/cm²	Change in oxide thickness, μg/cm²	Change in Xe^{125} depth, μg/cm²	Fractional burying, $F = t_m$
Niobium						
0.1	10	11.3	5.7 ± 1.0			
0.1	125	141	34 ± 6	130	28	0.22
1.0	10	10.5	4.5 ± 1.0			
1.0	60	63	18.5 ± 3	52.5	14	0.27
10.0	10	8.8	(5)			
10.0	125	110	38 ± 4	101	33	0.33
Tantalum						
0.1	10	13.4	3.5 ± 1.5			
0.1	60	82.8	21.5 ± 1.0	69	18	0.26
1.0	10	12.9	6.0 ± 1.0			
1.0	60	77.4	25.7 ± 1.5	64.5	20	0.31
10.0	10	12.1	7.7 ± 1.0			
10.0	125	151	48 ± 2	139	40	0.29
Tungsten						
0.1	20	26.8	16.8 ± 1.0			
0.1	70	93.8	37 ± 3	67	20	0.30
1.0	10	12.3	13.5 ± 1.0			
1.0	60	73.8	36.5 ± 1.5	61.5	23	0.37

calibration as WO_3. No value for the Xe^{125} depth in Nb anodized at 10 ma/cm² to 10v was measured, and so a value of 5 μg/cm² was chosen. In the light of these errors, no significant variation of t_m with current density or oxide thickness is observed in these metals.

Zirconium and hafnium (Fig. 5).—As can be seen from Table II, the fractional burying, F, of the Xe^{125} in these metals was very small at all the current densities used. Substantial amounts of Xe^{125} were lost during the anodizing process, together with a small loss of metal; we have no data for Hf, but about 0.6% of the Zr appeared in the electrolyte. As is well known, the anodizing behavior of these two metals is much more variable than that of the metals already discussed; there is a marked tendency to evolve oxygen, with resulting lower current efficiency for the formation of oxide. Accordingly, the oxide thicknesses were calculated from a fixed rate of 20 Å/v (15), using a density of 5.5 g/cm³ for ZrO_2 and 9.7 g/cm³ for HfO_2 (16); the errors in these thicknesses could easily reach 25%.

The amount of metal appearing in solution corresponds to approximately 1.0 μg/cm² of oxide, and this loss is nearly sufficient to account for the magnitude of the Xe losses. If the Xe^{125} tagged layers nearest the surface are removed, the depth distribution of the remaining Xe^{125} will change in such a way that the measured mean depth increases. This effect could account for at least part of the apparent burying; certainly t_m is not greater than 0.05. Accordingly, the thickening of the anodic oxide in these metals must proceed almost entirely by oxygen migration.

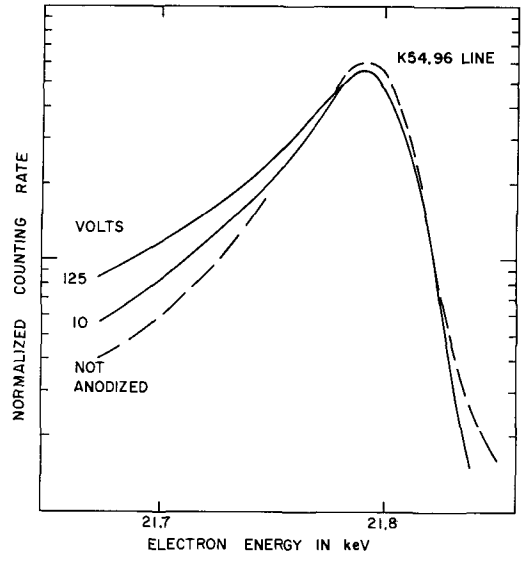

Fig. 5. The K54.96 conversion electron spectra from Xe^{125} atoms in anodic ZrO_2; 3 kev Xe^{125} in Zr subsequently anodized at 1.0 ma/cm².

Table II. Zirconium and hafnium

Current density, ma/cm²	Final voltage, v	Oxide formed, μg/cm²	Xe^{125} depth, μg/cm²	Xe^{125} retained, %	Change in oxide thickness, μg/cm²	Change in Xe^{125} depth, μg/cm²	Fractional burying, $F = t_m$
Zirconium							
1.0	10	11	3.4 ± 1.0	82			
1.0	125	138	3.2 ± 1.0	69	127	−0.2	0
4.0	10	11	(3)				
	125	138	8 ± 1.5	64	127	5	0.04
10.0	10	11	(3)	81			
	113	124	8 ± 1.5	59	113	5	0.05
Hafnium							
1.0	10	19	3.7 ± 1.0	93			
1.0	57	110	8.5 ± 1.0	86	91	5	0.05

Aluminum.—In solution A.—The results obtained on anodizing Al to 125v in solution A (50 g/l sodium tetraborate in 95% ethylene glycol, 5% water) are given in Table III. The Xe^{125} is completely retained in the oxide at all current densities and occurs at the same depths, 31 μg/cm², within the experimental error of 3 μg/cm². Some 2% of the metal appears in the electrolyte, the amount decreasing with increasing current density. The mean value of t_m calculated from these results is 0.58 ± 0.04; the error in the individual results is greater than this at 0.06, arising largely from uncertainty in the Xe depth.

In these experiments with Al, the preliminary anodization to low voltage was omitted, and t_m was calculated by a different method. The mean range, $\overline{R}$, of 3 kev Xe^{125} projectiles in polycrystalline Al foil is known to be 2.9 μg/cm² (9), which corresponds to 5.5 μg/cm² of Al_2O_3. This value was then substituted for D_1 and W_1 in the formula already given for F. Oxide thicknesses were calculated from the weight gains recorded by Bernard and Cook (17) at constant current in an ammonium pentaborate/glycol electrolyte; reasonable agreement with a constant voltage calibration made in solution A is observed.

In ammonium citrate (Fig. 1).—The results obtained on anodizing Al to 125v in 3% aqueous ammonium citrate are shown in Table IV, and are substantially different from those obtained in solution A. In order to relate t_m to the observed Xe^{125} depth in the oxide, two other factors must be taken into account; the first is the dissolution of the Al in the electrolyte, and the second is the loss of Xe^{125}.

Although the amount of Al appearing in the electrolyte decreases with increasing current density as in solution A, the fraction f is nearly twenty times as great at the same current density. It was observed that this dissolution occurs only during anodizing; if the oxide is immersed in the electrolyte without an applied field for a time comparable to the anodizing time, the dissolution is negligible. Similarly, if the applied voltage (100v) was less than that used to form the oxide (125v), no dissolution occurred either. These results confirm Hoar and Mott's hypothesis (18) that the dissolution of the Al is field assisted.

The Xe^{125} is all retained in the oxide except at very low current densities, where for 0.2 ma/cm², the loss of 8% is insufficient to affect the mean Xe^{125} depth very much. The 69.5% loss at 0.1 ma/cm², however is in a very different category, because the observed Xe^{125} depth is then a measure of the Xe^{125} remaining, which may have a very different depth distribution from the original. Two extreme possibilities can be considered. The Xe^{125} layer can be removed completely from 69.5% of the surface, the remaining 30.5% being untouched and thus retaining its original depth distribution. Under these circumstances, the measured depth corresponds to that measured at other current densities, although the significance of the resultant t_m is open to question. Alternatively, the Xe^{125} layer may

Table III. Aluminum

Aluminum anodized to 125v	In solution A				
Experimental results					
Current density (ma/cm²)	0.1	0.3	0.5	1.0	10
Observed Xe^{125} depth (μg/cm²)	30.0 ± 3	30.5 ± 3	33.5 ± 3	32.0 ± 3	29.5 ± 3
Observed Xe^{125} retention (%)	100	100	100	100	100
Al fraction in electrolyte, F*	[0.03]	0.02_3	[0.02]	0.01_6	0.00_8
Calculations					
(i) Oxide formed (μg/cm²)	46.9	45.6	45.1	44.2	42.4
(ii) Oxide equivalent in electrolyte (i) × F (μg/cm²)	1.4	1.0	0.9	0.7	0.3
(iii) Corrected Xe^{125} depth Observed + (ii) − 5.5 (μg/cm²)	25.9	26.0	28.9	27.2	24.2
(iv) corrected oxide thickness (i) + (ii) − 5.5 (μg/cm²)	48.3	46.6	46.0	44.9	42.7
(v) Cationic transport fraction t_m = (iii)/(iv)	0.54	0.56	0.63	0.60	0.57

* Values of F in brackets have been interpolated for the purpose of calculation.

be removed uniformly across the surface, leaving 30.5% of the Xe^{125} behind at all points. In polycrystalline Al, 30.5% of the 3 kev Xe^{125} projectiles penetrate more than 2.8 μg/cm², which corresponds to 5.3 μg/cm² of Al_2O_3. The net burial of the Xe^{125} atoms is then 5.5-5.3 μg/cm² or 0.2 μg/cm², not 5.2 μg/cm² as observed. Both values have been used in the calculations for Table I to give the possible range for t_m.

The oxide film thickness was calculated from data available in the literature, as no experimental calibrations were available for the constant current conditions used here. For aqueous borate electrolytes, Young (15) has given an equation relating the current density to the field strength across the oxide, from which angstrom per volt increments can be obtained for any current density. Young, however, measured his oxide thicknesses by a method which included the charge to form the films as a parameter and apparently assumed 100% current efficiency for oxide formation. This is not so; as with aqueous citrate, substantial amounts of Al pass into the borate electrolyte. If Young's values are corrected for the loss of Al to solution, they become very similar to those obtained by Bernard and Cook (17) in ammonium pentaborate/glycol; the latter have therefore been used to compute the oxide thicknesses in aqueous citrate as well as in solution A.

Calculations of Table IV show that in aqueous citrate, t_m does vary with current density, from about 0.37 at 0.1 ma/cm² to 0.72 at 10 ma/cm². The experimental error in each value is about 10%, arising both from uncertainty in the Xe^{125} depth and in the fraction of Al going into solution; errors in the total oxide thickness have relatively little effect, except at high current density. The value of 0.72 recorded at 10 ma/cm² may not therefore be significantly greater than 0.58, but the variation of t_m with current density in aqueous citrate definitely is significant.

Although there does not appear to be any chemical difference between the oxides formed in aqueous and nonaqueous electrolytes (15, 17), it has long been known that Al tends to give duplex films in the former. The outer layer, that next to the electrolyte, has a low resistance to the passage of ionic current and is porous (19), whereas the inner "barrier" layer is continuous and has a high resistance. It is questionable whether the films produced here contain pores, as pore formation has only been observed, for neutral electrolytes like ammonium citrate, on prolonged anodizing at about 0.01 ma/cm² (19, 20), which is one tenth of the lowest current density used here. The agreement between the oxide thicknesses formed in aqueous and nonaqueous electrolytes is additional evidence against the presence of a porous layer. Nevertheless, these citrate films do show similarities to porous films, particularly as regards the solution of Al in the electrolyte.

No direct measure of the Al dissolving in the electrolyte appears to have been made under conditions in which the anodic films are known to be porous, but values of f can be calculated from data on the amount of Al remaining in the oxide (21, 22). Thus on anodizing in 15% H_2SO_4 at 21.1°C for 30 min, the fraction f ranges from 0.57 at 13 ma/cm² to 0.44 for 78 ma/cm². This variation is qualitatively similar to that observed in the citrate electrolyte, but the f values are somewhat greater. It seems possible, therefore, that the variation in t_m is related to the onset of porous oxide formation.

Discussion

The differing results reported in the literature for oxygen and metal mobility in these oxides stem from incomplete interpretation of the experimental data. This arises first from a belief that either the metal or the oxygen can move, but not both (2), and second from a tacit assumption that the foreign atoms used as

Table IV. Aluminum

Aluminum anodized to 125v	In 3% aqueous ammonium citrate					
Experimental results						
Current density (ma/cm²)	0.1	0.2	0.3	0.5	1.0	10
Observed Xe^{125} depth (μg/cm²)	5.2 ± 1.5	9.6 ± 1.0	13.0 ± 2	22.5 ± 2	21.0 ± 3	30.0 ± 4
Observed Xe^{125} retention (%)	30.5	92	100	100	100	100
Al fraction in electrolyte, F*	0.43 ± 0.02	[0.41]	0.40 ± 0.02	[0.35]	0.31 ± 0.02	0.19 ± 0.01
Calculations						
(i) Oxide formed (μg/cm²)	46.9	46.0	45.6	45.2	44.2	42.4
(ii) Oxide equivalent in electrolyte (i) × F (μg/cm²)	20.2	18.9	18.2	15.8	13.7	8.1
(iii) Corrected Xe^{125} depth Observed + (ii) − 5.5 (μg/cm²)	20.4-25.4†	23.0	25.7	32.8	29.2	32.6
(iv) Corrected oxide thickness (i) + (ii) − 5.5 (μg/cm²)	61.6	59.4	58.3	55.4	52.4	45.0
(v) Cationic transport fraction t_m = (iii)/(iv)	0.33-0.41	0.39	0.44	0.59	0.56	0.72

* Values of F in brackets have been interpolated for the purpose of calculation.
† See text for correction applied.

markers are themselves immobile. To illustrate, the work of Lewis and Plumb (1) will be discussed.

These workers anodized aluminum at 50v in 3% ammonium tartrate and then briefly at 52v in radioactive 0.1% $H_2S^{35}O_4$ electrolyte; analysis of the oxide by slow dissolution in 5% H_3PO_4-2% CrO_3 at 50°C showed that almost all the radioactivity was removed in the first 4 min. The reverse experiment, 15v in the $S^{35}O_4^{--}$ electrolyte first followed by 50v in tartrate, was also performed, whereupon the bulk of the radioactivity dissolved between the eighth and fourteenth minutes in the stripping solution. Lewis and Plumb concluded that the oxide applied first was removed last and, hence, that fresh oxide was being formed at the oxide-electrolyte interface. However, these workers had apparently no means of knowing when their oxide was completely dissolved, and consequently, in the reverse experiment, they had no means of knowing whether any oxide was being formed underneath the radioactive layer due to oxygen migration. Furthermore their interpretation rests on the assumption that the $S^{35}O_4^{--}$ is a truly immobile marker. Were the sulfate ion mobile, it would, from its charge, tend to move in toward the metal-oxide interface, and these experiments could then be interpreted solely on the basis of oxygen migration.

Similar experiments have been performed with tantalum, using the film formed in concentrated sulfuric acid as the marker layer. Such films dissolve much more rapidly in HF than do films formed in dilute aqueous electrolytes, and this property has been used to analyze the duplex films. Vermilyea (6) anodized first in dilute aqueous sulfate, and then in concentrated sulfuric acid, and found that the faster dissolving layer was on the outside of the final oxide film. Like Lewis and Plumb, he concluded that metal was the mobile species. Franklin, as reported by Young (15), carried out the reverse experiment, using concentrated sulfuric acid first and dilute acid second, and found that the faster dissolving layer was in the middle of the final oxide. Very recently, Cheseldine (14) has repeated this last experiment almost exactly, forming his marker layer in formic acid rather than concentrated sulfuric. His observations were the same as Franklin's, and he concluded that both the metal and the oxygen were mobile. His value for t_m, 0.48, is however rather larger than that reported here.

It is quite clear that in these experiments on Ta, the marked layer has different properties from the rest of the oxide, and the same may be true of the $S^{35}O_4^{--}$ experiments on Al. In an effort to avoid the complications of chemically different layers, Amsel and Samuel (2) have used O^{18} as the tracer during the anodization of Al, and determined its position in the final oxide by means of nuclear spectroscopy. The introduction of a marker that is part of the oxidation system in principle increases the information that may be obtained from the experiment, for the final depth distribution of the O^{18} is a function not only of the oxygen mobility, but of the method by which it moves. Difficulty in determining the O^{18} distribution with sufficient accuracy, however, limits the information that can be obtained by this nuclear method.

Amsel and Samuel found that a thin O^{18} layer put on first remained essentially in contact with the metal/oxide interface during subsequent anodization to high voltage in an O^{16} electrolyte. They therefore concluded that either the oxygen was immobile, or that it moved in single jumps from one lattice plane to the next, so that the order of the oxygen atoms in the oxide was conserved. The mixing of the O^{16}/O^{18} layers predicted on the basis of the second assumption was not observed, but even with 100% oxygen transport, it would only have been three times the experimental limit of detection. Amsel and Samuel's results are not therefore in conflict with the present observation of about equal metal and oxygen transport in Al.

The results obtained from previous experiments are not therefore in conflict with those reported here, provided that the usual assumption is made; that the Xe^{125} markers are immobile. The Xe^{125} could move in these oxides for one of two reasons; it could diffuse, or it could move under the influence of the applied field because it has a net charge. Since no experimental evidence can be presented on the second point, it will be assumed, for the purposes of the present paper, that the Xe is not charged.

The absence of Xe^{125} diffusion in these oxides is well established. Except for injection energies below 5 kev, all the Xe^{125} striking the surface of anodic Al_2O_3 and WO_3 remains in the oxide (10). This behavior exactly parallels that of the corresponding metals, where the low sticking factor at low bombardment energies was ascribed to failure of the ions to penetrate to a sufficient depth in their initial impact (12). Furthermore, experiments in this laboratory by Kelly have shown that on heating anodic Al_2O_3, no Xe^{125} is released below 600°C, even when the Xe^{125} is injected directly into the oxide at such low energy, 1 kev, that it must be very close to the surface. And finally, the range and the range straggling of injected Xe^{125} ions in anodic Al_2O_3 and WO_3 agrees well with that expected from the theory (13) of Lindhard *et al.* on the range of energetic particles in amorphous solids.

Although the Xe^{125} does not diffuse appreciably in the static oxide, there remains the possibility that it could diffuse in the growing oxide. If so, the distribution of the Xe^{125} markers in the oxide should broaden. The β-ray spectrometry method used here provides no information on the depth distribution of the Xe^{125}, but in a similar experiment using the closely related isotope Rn^{222}, it was shown, by α-particle spectrometry, that no appreciable broadening of the distribution occurs (4).

Manuscript received Dec. 21, 1964.

Any discussion of this paper will appear in a Discussion Section to be published in the June 1966 JOURNAL.

REFERENCES

1. J. E. Lewis and R. C. Plumb, *This Journal*, **105**, 496 (1958).
2. G. Amsel and D. Samuel, *J. Phys. Chem. Solids*, **23**, 1707 (1962).
3. J. A. Davies, J. P. S. Pringle, R. L. Graham, and F. Brown, *This Journal*, **109**, 999 (1962).
4. J. A. Davies and B. Domeij, *ibid.*, **110**, 849 (1963).
5. J. P. S. Pringle and J. A. Davies, Paper presented at the Pittsburgh Meeting of the Society, April 1963, Abstract No. 167.
6. D. A. Vermilyea, *Acta Met.*, **2**, 482 (1954).
7. R. L. Graham, F. Brown, J. A. Davies, and J. P. S. Pringle, *Can. J. Phys.*, **41**, 1686 (1963).
8. B. Domeij, I. Bergström, J. A. Davies, and J. Uhler, *Arkiv fysik*, **24**, 399 (1963).
9. J. A. Davies, F. Brown, and M. McCargo, *Can. J. Phys.*, **41**, 829 (1963).
10. B. Domeij, F. Brown, J. A. Davies, and M. McCargo, *ibid.*, **42**, 1624 (1964).
11. M. McCargo, J. A. Davies, and F. Brown, *ibid.*, **41**, 1231 (1963).
12. F. Brown and J. A. Davies, *ibid.*, **41**, 844 (1963).
13. J. Lindhard, M. Scharff, and H. E. Schiøtt, *Kgl. Danske Videnskab. Selskab., Mat.-Fys. Medd.*, **33**, 1 (1963).
14. D. M. Cheseldine, *This Journal*, **111**, 1128 (1964).
15. L. Young, "Anodic Oxide Films," Academic Press, New York (1961).
16. Handbook of Chemistry and Physics, Chemical Rubber Publishing Co., 43rd ed., (1961-2).
17. W. J. Bernard and J. W. Cook, *This Journal*, **106**, 643 (1959).
18. T. P. Hoar and N. F. Mott, *J. Phys. Chem. Solids*, **9**, 97 (1959).
19. M. S. Hunter and P. F. Towner, *This Journal*, **108**, 139 (1961).
20. T. A. Renshaw, *ibid.*, **108**, 185 (1961).
21. R. B. Mason and P. E. Fowle, *ibid.*, **101**, 53 (1954).
22. R. B. Mason, *ibid.*, **102**, 671 (1955).

Magnetic Properties and Corrosion Behavior of Thin Electroless Co-P Deposits

J. S. Judge, J. R. Morrison, D. E. Speliotis, and G. Bate

Systems Development Division, International Business Machines Corporation, Poughkeepsie, New York

ABSTRACT

Thin magnetic films of Co-P were prepared in two somewhat different electroless cobalt solutions. The magnetic properties and the corrosion behavior of these films as a function of thickness was studied. The films exhibited high coercivities with a maximum of about 1000 oe at a thickness of 600Å. The magnetic moment of these films was found to decrease on exposure to high humidity and moderate temperatures (40°-70°C); this was used as a means of studying the extent of corrosion. The extent of corrosion was found to vary as the 2/3 power of the thickness of the film.

Advances in information storage have created an increasing demand on the capacity of the storage media. For very high density applications, the thinness of the recording surface is of the utmost importance. A thin recording medium not only facilitates the writing of sharper transition regions by the recording transducer, but is also better able to resist demagnetization. Metallic surfaces of chemically deposited Co-P have been investigated as recording media (1, 2). However, the thickness region below 4000Å, which is of far greater importance for high density recording, has not been investigated. It is primarily this region that is the subject of our study.

Two thickness series, produced in somewhat different solutions, were examined. The structural and magnetic properties of these deposits were investigated. Furthermore, the magnetic moment of the deposits was found to decrease on exposure to relatively mild conditions of humidity and temperature. This phenomenon was utilized to study the corrosion behavior of the deposits.

Preparation

The films were deposited on Mylar substrates which were presensitized with the usual $SnCl_2$-$PdCl_2$ treatments (3). Prior to this, the Mylar substrate had been rendered hydrophilic by a two-step process involving immersion first into a hot chromic-sulfuric acid solution, and then into a hot sodium hydroxide solution.

Two somewhat different electroless cobalt solutions were used, a sulfate and a chloride solution. The composition and conditions of the plating solutions were:

Sulfate		Chloride	
$CoSO_4$	0.11M	$CoCl_2$	0.13M
NaH_2PO_2	0.19M		
$(NH_4)_2SO_4$	0.50M	$NH_4H_2PO_2$	0.18M
Na_3(citrate)	0.12M	$(NH_4)_2H$(citrate)	0.155M

Temp.: 80°C; pH: 8.7 at 50°C (pH adjusted with NH_4OH); no agitation.

Thickness, Composition, and Structure

Figure 1 shows the dependence of the weight of the deposit on plating time for the two solutions. From the slope of these curves, the plating rates were measured to be 1.35 $\mu g/cm^2$/sec for the deposits from the sulfate solution, and 1.12 $\mu g/cm^2$/sec for the deposits from the chloride solution. These weights were determined by x-ray fluorescence measurements.

The weight of phosphorus deposited was also determined in this way. The dependence of the weight of phosphorus deposited on the total weight of the deposits is shown for the deposits from both solutions in Fig. 2. It can be seen from this plot that there is no apparent change in per cent phosphorus (within the precision of the data) over this thickness range. The average phosphorus content obtained from the slope of the plots of Fig. 2 is 5.8 ± 0.35% and 5.0 ± 0.2% for the deposits from the sulfate and chloride solutions, respectively.

Assuming a density similar to bulk cobalt of 8.9 g/cm^3, these films cover a thickness range from 200 to 5000Å.

The structure of the films was examined by x-ray diffraction, and was found to be hcp, with crystallite

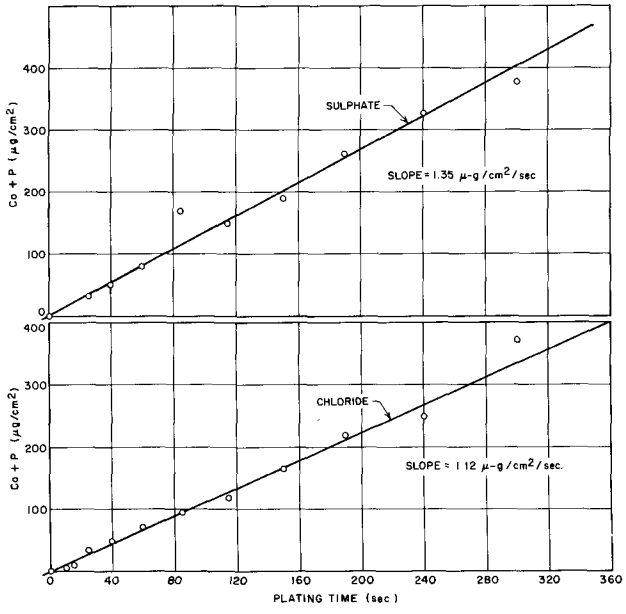

Fig. 1. Weight of deposits vs. plating time.

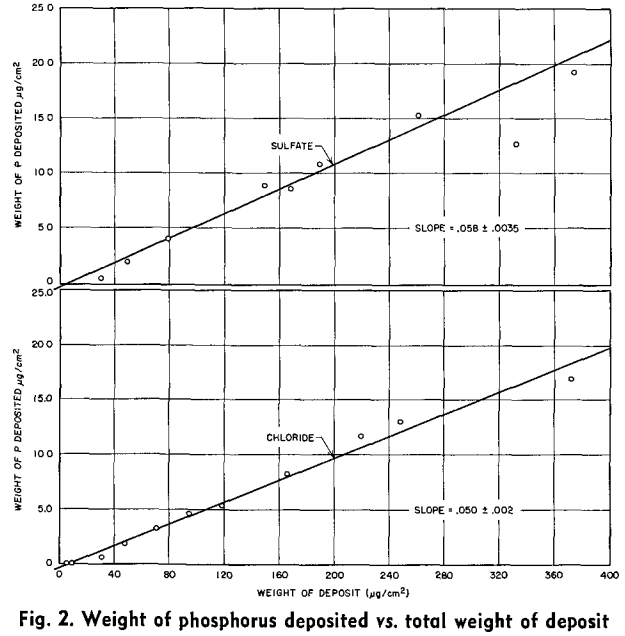

Fig. 2. Weight of phosphorus deposited vs. total weight of deposit

size ranging from 200 to 700Å. This technique gave no evidence of the whereabouts of the phosphorus.

The films had a residual compressive stress of ~20,000 psi. This stress was estimated from the curvature of a sample with plating on only one side (4).

Magnetic Properties

Magnetic measurements were performed using a vibrating sample magnetometer and a very sensitive torsion balance magnetometer (5). The variation of coercivity with thickness is shown in Fig. 3; both curves rise quickly from zero to a maximum coercivity at a thickness of 600-700Å, and then decrease more gradually, tending to a constant coercivity of approximately 400 oe at very large thicknesses. Referring to Fig. 3, we distinguish three different regions of the dependence of coercivity on thickness. Region a (less than 200Å) is dominated by a large number of superparamagnetic regions, resulting in coercivities increasing rapidly with increasing particle size. Region b (300-1000Å) is characterized mostly by a single domain region with very high coercivity. It is interesting to note that this thickness range corresponds to the size of the crystallites. Finally, region c (>1000Å) corresponds to the growth of multidomain regions. Further support to this interpretation can be derived from Fig. 4, where the ratio of remanent to saturation moments is plotted as a function of the thickness of the deposit. In region a, one would expect very low squareness due to the presence of superparamagnetic regions. Region b is characteristic of individual single domain regions with increasing interactions. Finally, region c, with relatively high squareness, is characteristic of strongly coupled and multidomain areas.

The magnetic moment density of the deposits was found to be 111 emu/g for samples prepared in the sulfate bath, and 116 emu/g for samples prepared in the chloride bath, and independent of the thickness of the deposit. The calculated magnetic moment densities, assuming the phosphorus to exist in the films as the nonferromagnetic Co_2P, were 120 emu/g and 125 emu/g for the films from the sulfate and chloride baths, respectively. The discrepancy between the measured and calculated values of the magnetic moment of the deposits may be attributed to the presence of some cobalt oxide or an amorphous cobalt phase (6).

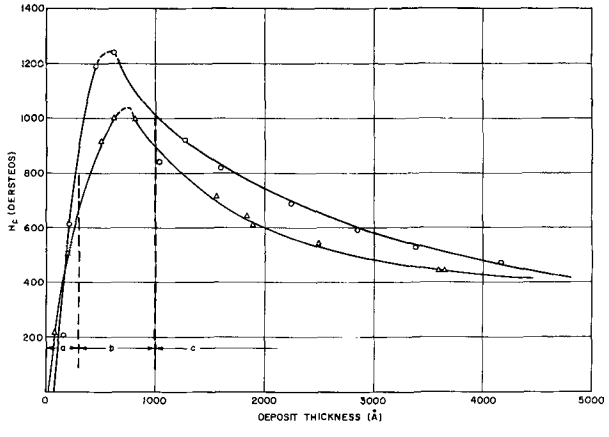

Fig. 3. Coercivity *vs.* thickness; △, chloride; ○, sulfate

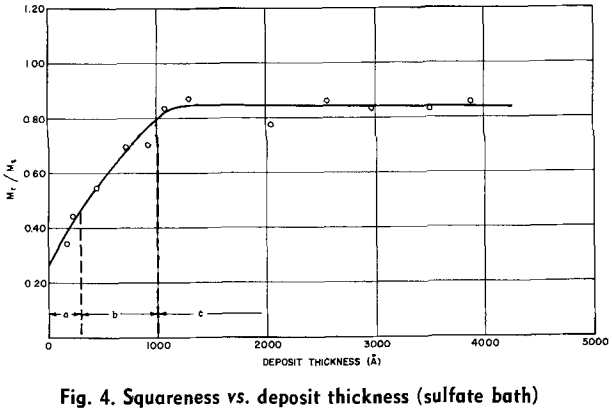

Fig. 4. Squareness *vs.* deposit thickness (sulfate bath)

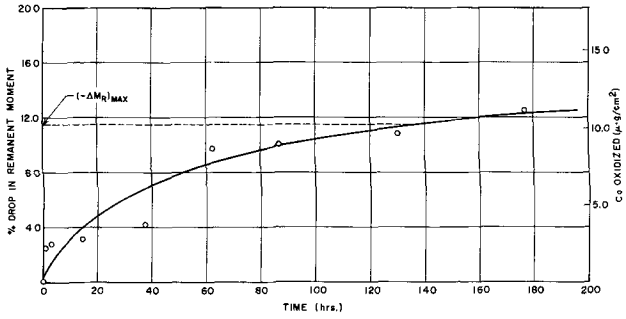

Fig. 5. Per cent decrease in remanence with time due to corrosion

Corrosion Behavior

The corrosion behavior of these deposits was followed by periodically measuring their magnetic moments as they were exposed to high humidity and temperature. Apparently, because of the thinness of these films, and their consequently high surface to volume ratio, relatively large percentage changes in their magnetic moments occurred

A torsion balance magnetometer (5) was used in these studies This instrument had the necessary sensitivity for measurements of small changes in remanent moment. Sensitive measurements of saturation moments were too time consuming to obtain and since there was no apparent change in squareness with corrosion and since the greater sensitivity of the torsion balance was necessary, all the corrosion data are based on changes in remanent moments

The sample used was a disk of 1 cm diameter. These disks were placed in a constant temperature-humidity cabinet and periodically removed for measurements of M_r.

Ten samples plated in an identical manner to a nominal thickness of 1000Å were subjected to this test at 43.5° ± 1.5°C and 80 ± 5% relative humidity. A typical curve of per cent drop in remanent moment *vs.* time is shown in Fig. 5.

The remanent moment, M_r, is related to the amount of ferromagnetic (unoxidized cobalt) by the following relationship

$$M_r = Sq.\ M_s$$

where M_s is the saturation moment of the sample and $Sq.$ the squareness of the sample.

$$M_s = \sigma_s\left(\frac{W}{A}\right)A = \sigma_s\, XA$$

where W is the weight of unoxidized cobalt, A the

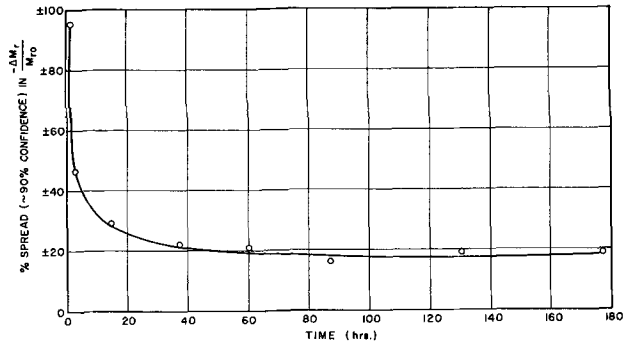

Fig. 6. Per cent deviation from the average change in ten samples

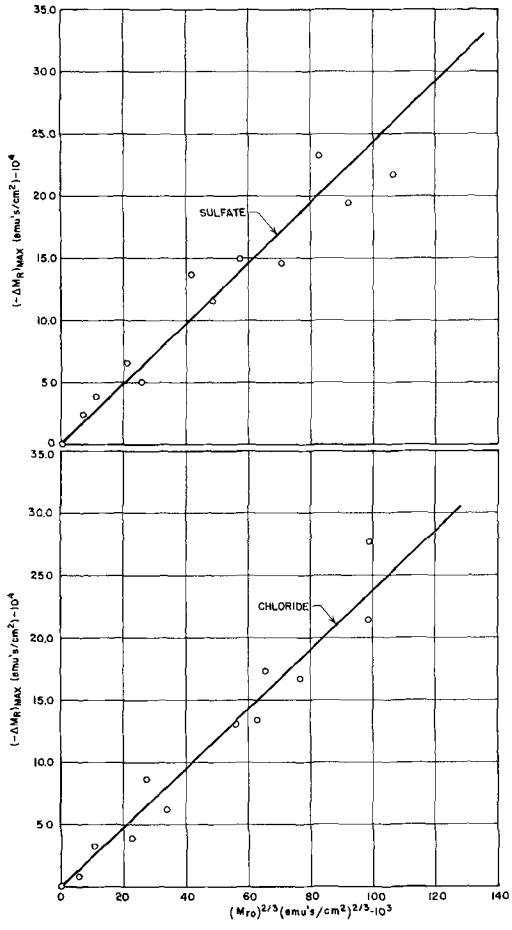

Fig. 7. Dependence of extent of corrosion on initial moment

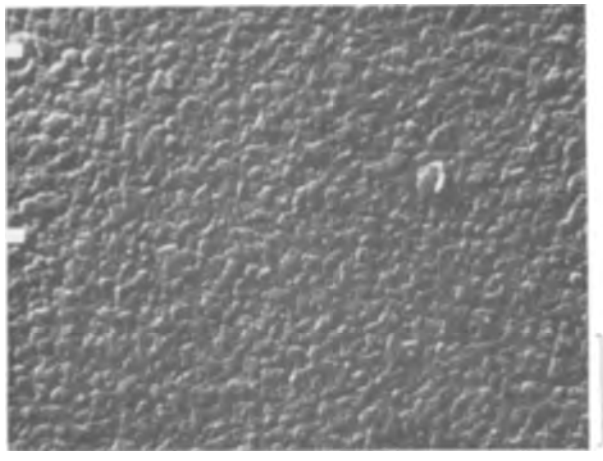

Fig. 8. Electron micrograph of electroless cobalt on Mylar

area of the sample, $X = W/A$, σ_s the saturation moment per gram

$$M_r = Sq.\ \sigma_s XA$$

$$\text{or the fraction of cobalt oxidized} = \frac{-\Delta X}{X_o} = -\Delta M_r/M_{ro}$$

then $-\Delta X = -\Delta M_r X_o/M_{ro}$ = weight per unit area of cobalt oxidized. The weight per unit area of oxidized cobalt for the 1000Å film has been indicated on the right hand ordinate of Fig. 5.

The reproducibility was evaluated by plotting the per cent spread (90% confidence level) in the value of the percentage corrosion as a function of time. This is plotted in Fig. 6; it shows that "identical" samples level out to within ±20% of the same final value of

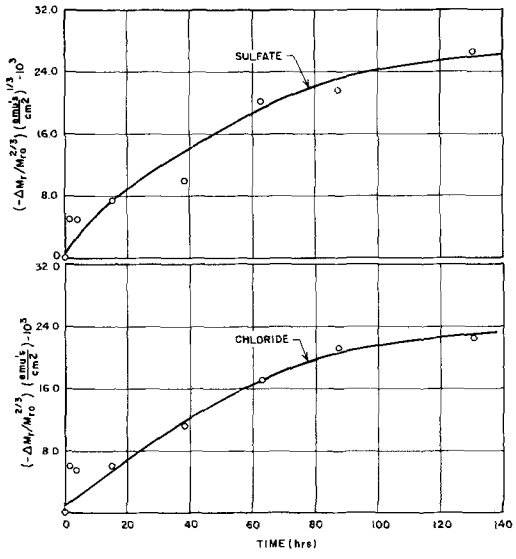

Fig. 9. Corrosion *vs.* time; temperature, 43.5°C; relative humidity, 80%.

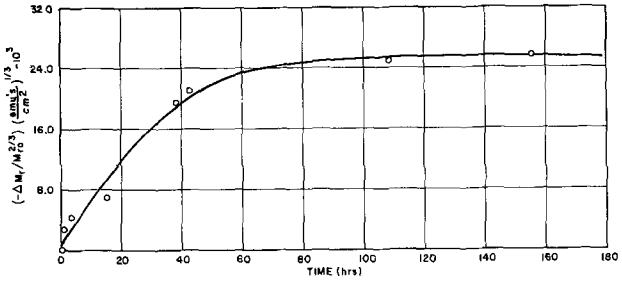

Fig. 10. Corrosion *vs.* time; temperature, 65°C relative humidity, 80%.

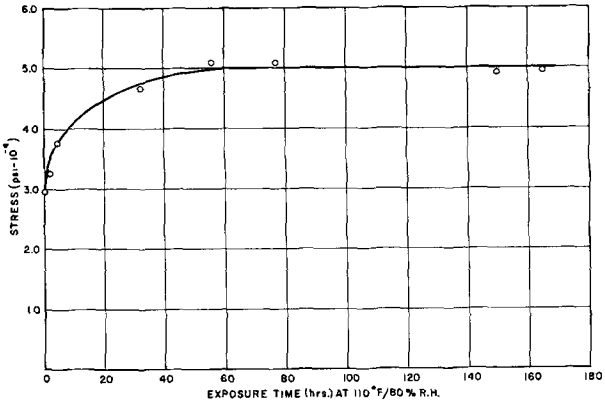

Fig. 11. Deposit stress *vs.* corrosion time

corrosion. The necessity of considering the average behavior of a number of samples is apparent.

When the two thickness series previously described were subjected to these conditions (43.5°C, 80% R.H.), it was found that the change in remanent moment increased with increasing thickness. This effect is particularly apparent, considering only the maximum drop in remanent moment after sufficiently long exposure (*i.e.*, a value at times greater than 100 hr; for these purposes $(-\Delta M_r)_{Max}$ is $-\Delta M_r$ after 140 hr exposure, see Fig. 5). The dependence of $(-\Delta M_r)_{Max}$ on sample thickness was found to best fit an $M_{ro}^{2/3}$ dependence. This dependence is shown in Fig. 7 for samples from both solutions. This dependence would result if the film were composed of hemispherical clumps

the surface area of which increased as the 2/3 power of their thickness. Electron micrographs of similar samples lend support to this interpretation (see Fig. 8).

As a consequence of this thickness dependence, the average value of the thickness independent quantity $-\Delta M_r/M_{ro}^{2/3}$ has been plotted against time for these samples in Fig. 9. These curves show a parabolic or logarithmic (the data does not enable one to distinguish) dependence typical of the formation of a protective oxidation product. It is interesting that despite the difference in early environment (*i.e.*, the plating solution), magnetic properties, and composition of the samples from the sulfate solution and the chloride solution, they exhibit almost identical corrosion behavior. The behavior for both series at 65.5°C and 80% relative humidity is shown in Fig. 10. In this case, the curve levels out at the same value of $-\Delta M_r/M_{ro}^{2/3}$ but rises to this value in about half of the time.

The residual compressive stress of the deposits increased in a manner similar to that of the decrease in remanent moment. The average stress (estimated by the bent strip method) as a function of exposure time at 43.5°C, 80% R. H. is shown in Fig. 11. This result indicates the formation of a corrosion layer of greater specific volume than the metal, again indicative of a protective product (6).

Reflection electron diffraction indicates that the corroded surface is mainly Co_3O_4. Furthermore, an estimate of the thickness of the corrosion film from electron diffraction data agrees fairly well with the 12% measured from the magnetic data for the 1000Å film.

Assuming the product is completely Co_3O_4, the parabolic rate constant in terms of oxygen pick-up can be estimated. This yields the following results for a 1000Å film

	43.5°C	65.5°C
K (g/cm²)²/sec	$3.6 \cdot 10^{-17}$	$4.7 \cdot 10^{-17}$

Conclusion

The magnetic properties of electroless cobalt deposits of variable thickness prepared in different solutions (a sulfate and a chloride solution) were found to be very similar. Furthermore, the variations of the magnetic properties with thickness are related to the crystallite size growth of the deposits. Magnetic moment measurements were used successfully as a very sensitive means of studying the corrosion of magnetic deposits. The amount of corrosion increased with increasing thickness, indicating that the deposits became rougher at increased thickness, *i.e.*, their surface area increased. The advantages of very thin metallic films for magnetic recording must be contrasted with the danger of significant atmospheric corrosion when their surface to volume ratio becomes large. In addition, magnetic and recording studies of such materials must be undertaken with precautions lest significant corrosion occurs during the sometimes extended period of investigation of specific samples.

Manuscript received Sept. 22, 1964; revised manuscript received March 12, 1965.

Any discussion of this paper will appear in a Discussion Section to be published in the June 1966 JOURNAL.

REFERENCES

1. R. D. Fisher and W. H. Chilton, *This Journal*, **109**, 485 (1962).
2. L. D. Ransom and V. Zentner, *ibid.*, **111**, 1423 (1964).
3. E. A. Bergstrom, U. S. Pat. No. 2,702,253.
4. L. Serota, *Metal Finishing*, p. 77, May (1961).
5. G. Bate, D. Schofield, and W. Sucksmith, *Phil. Mag.*, **46**, 621 (1965).
6. J. S. Sallo and J. M. Carr, *J. Appl. Phys.*, **34**, 1309 (1963).
7. N. B. Pilling and R. E. Bedworth, *J. Inst. Met.*, **29**, 529 (1923).

Rotating Disk Study of the Dissolution of Zirconium in HF-HNO_3

R. E. Meyer

Chemistry Division, Oak Ridge National Laboratory, Oak Ridge, Tennessee

ABSTRACT

The rotating disk electrode system was used to determine the rate constants of the reaction of zirconium with HF in solutions of HNO_3 and HF. The reaction was found to be first order with respect to HF, and the rate constants decreased slightly as the potential became more anodic. Possible mechanisms explaining the role of HF in the dissolution reaction are discussed.

When zirconium dissolves in aqueous solutions containing HF, the over-all rate of the reaction is controlled by the rate of mass transfer of undissociated HF molecules to the surface of the electrode (1, 2). An investigation in detail of the kinetics of this reaction requires that the concentration of HF be precisely controlled and determined at the reaction interface. A rotating disk electrode was therefore selected to study this system; for, as Levich (3) has emphasized, this system provides a uniformly accessible surface, *i.e.*, it provides a uniform, determinable concentration of the migrating species along the surface of the electrode. If this condition of uniform accessibility were not met, as would be the case if ordinary methods of stirring were employed, the overpotential would vary across the surface, and complicated current-voltage behavior would be observed.

The dissolution of zirconium in solutions containing HF appears to be complicated in that in some, and perhaps in all cases the reaction proceeds by the continuous formation and dissolution of a film (2). The study of the over-all reaction, therefore, involves the study of both the dissolution and film formation reactions. Some aspects of the kinetics of the film formation reaction were reported previously (2), but the dissolution reaction could not be studied until the mass-transfer conditions were better defined. In the work described here, the rotating disk was used to determine the rate constants of this surface reaction and the dependence of this rate constant on the potential and concentration. All measurements were carried out at potentials sufficiently anodic so that the rate of the hydrogen evolution reaction was negligible.

The derivations of the equations describing the rotating disk electrode system have been summarized by Levich (3). In this reference, it is shown that the flux of a neutral particle is given to within a few per cent by the expression

$$j = 0.62\, D^{2/3} \nu^{-1/6} \omega^{1/2} (C_B - C_i) \qquad [1]$$

where j is the flux, D is the diffusion coefficient, ν is the kinematic viscosity, ω is the angular velocity in

radians per second, C_B is the concentration in the bulk of the solution, and C_i is the concentration of the reactant at the interface. If the migrating species is neutral, or if the species is charged and there is a large excess of inert electrolyte (at least 100 to 1), then the current will be given by

$$I = 0.62\, nFSD^{2/3}\nu^{-1/6}\omega^{1/2}(C_B - C_i) \qquad [2]$$

where nF is the charge that is transferred per mole of the migrating species, and S is the area of the electrode.

In many cases of interest, the rate of the surface reaction is comparable to the rate of mass transfer. The reaction rate at the surface may be expressed by the equation

$$I = n'FkSC_i^m \qquad [3]$$

where k is the rate constant, C_i is the concentration of the reactant at the interface, and m is the order.[1] In the steady state

$$I = nFAS(C_B - C_i)\omega^{1/2} = n'FkSC_i^m \qquad [4]$$

where $A = 0.62\ D^{2/3}\nu^{-1/6}$. If $m = 1$, these equations may be solved with the elimination of C_i to give

$$\frac{1}{I} = \frac{1}{n'FkSC_B} + \frac{1}{nFASC_B\omega^{1/2}} \qquad [5]$$

A plot of I^{-1} *vs.* $\omega^{-1/2}$ should therefore be linear for a first order reaction, and the rate constant can be determined by extrapolation of the line to infinite frequency of rotation ($\omega^{-1/2} \rightarrow 0$). From the slope of the line, the expression nFA can be calculated, and n can be determined if the value of D is known (or D can be determined if n is known). If the order is not unity, the determinations of the order and the constants are less straightforward, but various techniques have been devised for treating the data (3, 4).

If the rate constant k is large so that the rate of the surface reaction is fast compared to the rate of mass transfer, then C_B will be much greater than C_i in Eq. [2] and the limiting current will be given by

$$I = nFASC_B\omega^{1/2} \qquad [6]$$

and a plot of I^{-1} *vs.* $\omega^{-1/2}$ will go through the origin.

In this work, a series of determinations were made of the current as a function of angular velocity, potential, and solution composition at several potentials anodic to the open-circuit potential. The rate constant k was determined, and n was calculated using estimates of the value of D.

Experimental

In the design of the experiment, the conditions assumed in the solution of the convective-diffusion equation must be maintained. The flow of the solution over the surface of the electrode must be laminar, and the dimensions of the electrode must be large compared to the diffusion and hydrodynamic boundary layers and small compared to the dimensions of the cell (3, 5, 6). In practice, the correct conditions are best determined empirically by varying the pertinent dimensions of the cell until reasonable results are obtained. The conditions depend on the degree of precision desired. If it is desired to determine diffusion coefficients, great care must be taken, for the slopes of plots of Eq. [5] are quite sensitive to the hydrodynamic conditions. If rate constants of surface reactions are desired, then the requirements are relaxed slightly as long as reasonable extrapolations can be carried out.

[1] In Eq. [3], the n is primed because it does not necessarily have the same value as the n in Eq. [2]. In the mass transfer expression, Eq. [2], n refers to the number of Faradays transported for every mole of HF that reacts with the zirconium at the surface. This number would therefore depend on the ratio of zirconium to HF in the complex that forms at the surface. The n' in Eq. [3] is the number of Faradays transported across the interface for every mole of zirconium that reacts and would therefore normally have a value of four.

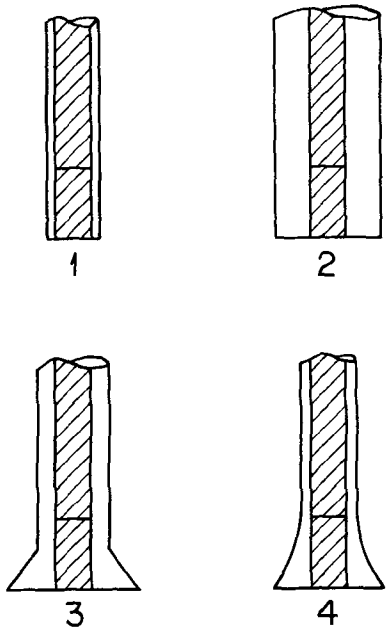

Fig. 1. Electrode shapes used in rotating disk experiments. The outer sections are Teflon.

The electrode shapes shown in Fig. 1 were tried. In each of these configurations, the working surface was the end of a cylindrical electrode ¼ in. in diameter, which was carefully machined perpendicular to the axis of rotation. The electrode was then threaded to a holder which was mounted so that the eccentricity of rotation was less than 0.0015 in. The cylindrical surfaces of the electrode were insulated with a lacquer, and Teflon sleeves of various shapes were fitted about the electrode. All of these configurations gave the same results, and most of the experiments were conducted with No. 1 and 4 of Fig. 1. The cell was made of Teflon with an outer steel liner for reinforcement, and it had an internal diameter of 2¾ in. and a depth of 4 in. Varying the depth of the solution and varying the position of the electrode did not affect the results. Gas inlets and exits were made by leading ⅛ in. diameter Teflon "spaghetti" tubing through holes in the Teflon cell just large enough to insure a tight fit. The saturated calomel reference electrode was also bridged into the solution with the Teflon spaghetti tubing. Varying the position of the tip of the tubing did not affect the results. The solutions contained the required amount of HF plus 1.2M HNO_3. The nitric acid served to minimize IR drop, to act as an inert electrolyte, and to suppress ionization of HF.

Speed control was effected by a General Radio 1701-AK Variac speed control driving a 1/15 hp d-c motor. This unit gave excellent regulation from about 100 rpm to 4000 rpm. The angular velocity was determined with a General Radio Strobotac.

During the experiments, the electrodes were held at constant potential with a potentiostat. Currents were recorded by measuring the potential drops across precision resistance with a Hewlett-Packard 425 AR DC Microvolt-Ammeter coupled to a Brown recorder. In some of the experiments, temperatures were maintained at 25°C with a water bath, but since the temperature coefficient of the reaction was quite small, many of the experiments were conducted at 25° ± 1°C with the room thermostat.

Results

The experimental apparatus was tested by investigating the reduction of oxygen on platinum in the limiting current region where Eq. [6] should be valid. For this purpose, a platinum disk electrode whose exposed surface area was identical to that of the zirco-

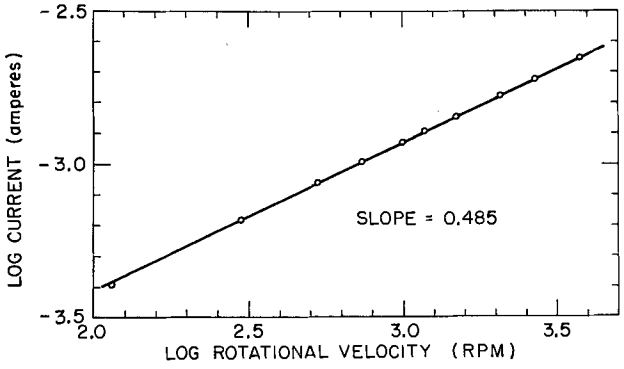

Fig. 2. Reduction of oxygen on rotating platinum disk electrode 0.1M Na_2SO_4, O_2-saturated, electrode area = 0.316 cm².

nium electrodes was used. Figure 2 shows a plot of log I *vs.* log ω for this system. The slope of the line is 0.485, which is very close to the theoretical 0.5. A few additional experiments were performed in which a large glass beaker was substituted for the Teflon container, and crystals of $KMnO_4$ were placed in the bottom. The flow pattern characteristic of rotating disks (3) was observed as the $KMnO_4$ dissolved.

Plots of I^{-1} *vs.* $\omega^{-1/2}$ are shown in Fig. 3 and 4 for two separate runs. According to Eq. [5], the extrapolations of these lines determine the fraction $1/n'FkSC_B$, *i.e.*, the reciprocal current at infinite frequency of rotation. The rate constant, k, was then calculated for each experiment, and values of the rate constant are recorded in Table I.

If the reaction were precisely first order with respect to the concentration of HF, the values of k would be independent of concentration. Instead they tend to decrease slightly as the concentration is reduced to 0.005N HF, and then they decrease more sharply as the concentration is reduced to 0.001N. Possible explanations for this effect are discussed below. The deviations from first order in an individual run did not appear to be large enough to affect the validity of the extrapolation to infinite frequency, for, as shown in Fig. 2 and 3, the deviations from linearity are not apparent.

The tendency for the apparent order to be slightly greater than unity can also be shown by calculating the concentration at the interface by using the following equation, obtained from Eq. [4]

$$C_i = C_B - \frac{I}{nFAS\omega^{1/2}} \qquad [7]$$

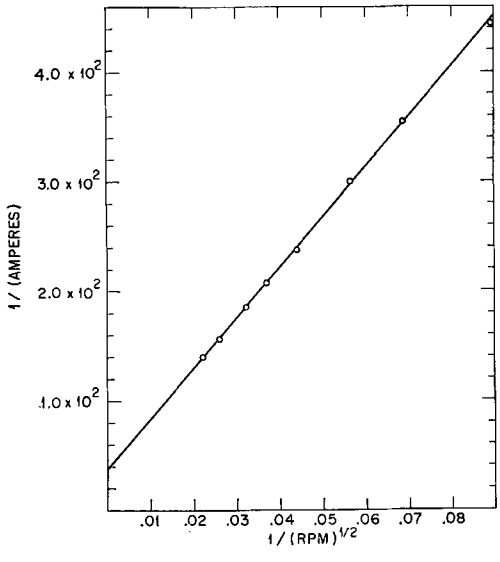

Fig. 3. Rotating disk plot of I^{-1} vs. $(\text{rpm})^{-1/2}$ for zirconium in 0.0213M HF and 1.2M HNO_3, 25°C, —500 mv *vs.* SCE, electrode area = 0.316 cm².

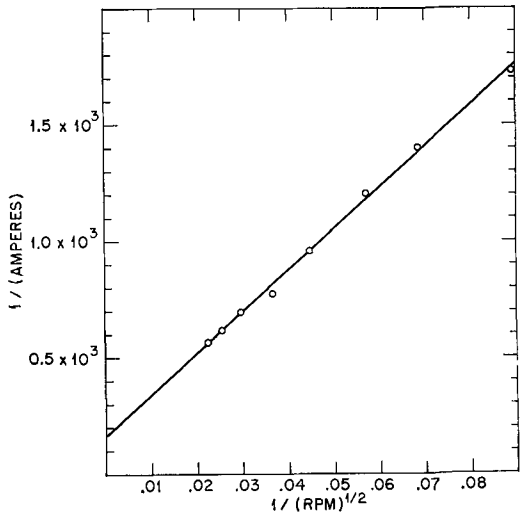

Fig. 4. Rotating disk plot of I^{-1} vs. $(\text{rpm})^{-1/2}$ for zirconium in 0.00535M HF and 1.2M HNO_3, 25°C, —500 mv vs. SCE, electrode area = 0.316 cm².

The numerical or effective order can be determined from a plot of log I *vs.* log C_i, since the slope of this plot is numerically equal to the order. The quantity nFA was obtained from the slope of the plots of $1/I$ *vs.* $1/\omega^{1/2}$ (Eq. [5]) for each run. The average value of nFA for all of the runs in 1.2M HNO_3 is 32.5. In this computation, the units of concentration were moles per cubic centimeter and the units of ω were rpm. An example of a plot of log I *vs.* log C_i is shown in Fig. 5 where an order of 1.17 was found. For most of the runs, the orders found were slightly above unity; values between 1.1 and 1.2 were most common.

The value of the quantity nFA was checked by another method of evaluation which took advantage of the fact that as the stirring rate tends to zero, the concentration at the interface also tends to zero. Therefore, if a plot of I *vs.* $\omega^{1/2}$ is extended to the origin, the slope of the tangent drawn to the line at the origin will be given by Eq. [8] [cf. ref. (4)].

$$\frac{dI}{d\omega^{1/2}} = nFASC_B \qquad [8]$$

This method is illustrated in Fig. 6 where it is estimated that nFA equals 33.7. This value agrees well with the values found above.

The value of n in the product nFA can be determined if the diffusion coefficient and the viscosity are known, as shown by Eq. [1]. The viscosity will be given to a

Table I. First order rate constants for zirconium dissolving in 1.2M HNO_3 and varying concentrations of HF

Concentration of HF, mole/liter	k in cm sec⁻¹			
	−600 mv	−500 mv	−400 mv	−300 mv
0.0426	0.0197	0.0110	0.0195	—
0.0426	—	0.0146	0.0176	0.0126
0.0213	0.0104	0.0105	0.00961	0.00826
0.0200	0.0101	0.00940	0.00886	0.00855
0.0200	0.0104	0.00948	0.00868	0.00826
0.0100	0.00977	0.00870	0.00806	0.00785
0.0100	0.00948	0.00914	0.00863	0.00762
0.00532	0.0108	0.00958	0.00800	0.00658
0.00532	0.00943	0.00834	0.00697	0.00640
0.00500	0.00914	0.00720	0.00642	0.00596
0.00500	0.00806	0.00684	0.00627	0.00598
0.00500	0.00876	0.00782	0.00787	—
0.00213	0.00526	0.00495	0.00456	0.00417
0.00213	0.00376	0.00358	0.00329	0.00409
0.001065	0.00324	0.00290	0.00267	0.00242
0.00100	0.00321	0.00298	0.00311	0.00275
0.00100	0.00313	0.00332	—	0.00254
0.001065*	0.00471	0.00438	0.00399	0.00368
0.001065**	0.00414	0.00376	0.00339	0.00316
0.001065**	0.00391	0.00386	0.00347	0.00342

* 0.12M HNO_3.
** 0.12M HNO_3 + 1.1M $NaNO_3$.

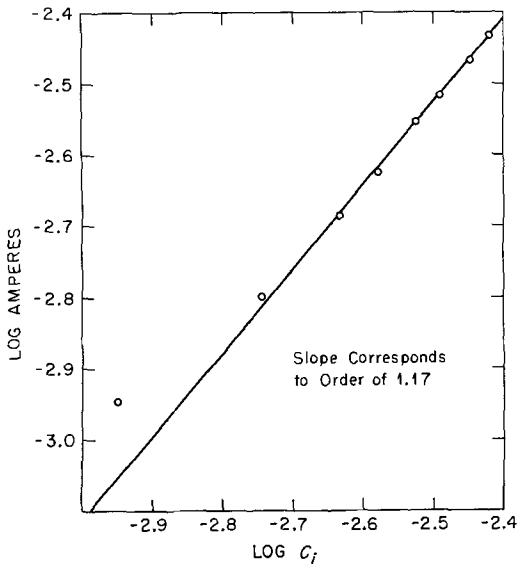

Fig. 5. Determination of order of reaction for zirconium in 0.010M HF, 1.2M HNO_3, 25°C, —300 mv vs. SCE, electrode area = 0.316 cm^2.

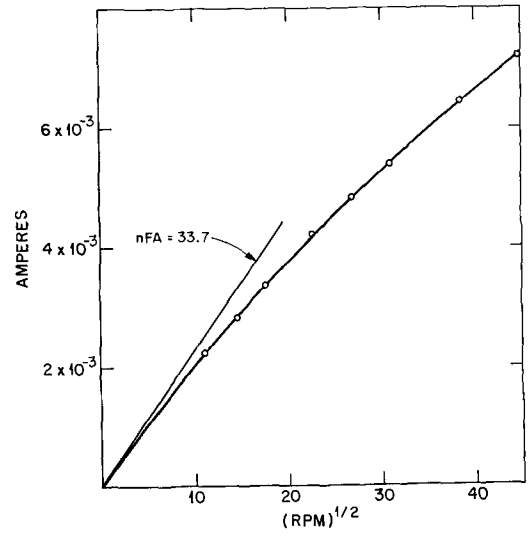

Fig. 6. Rotating disk plot of I vs. $(rpm)^{1/2}$ for zirconium in 0.0213M HF, 1.2M HNO_3, 25°C, —500 mv vs. SCE, electrode area = 0.316 cm^2.

good approximation by the viscosity of the appropriate concentration of HNO_3. Since the viscosity enters as the 1/6 power, it need not be known precisely. To the author's knowledge, the diffusion coefficient of HF has not been determined experimentally. Further, it is difficult to make a reliable estimate of D because the degree of the interaction of HF with the water is unknown. However, because all known values of D in aqueous solutions are of the order of magnitude of 10^{-5} cm^2/sec, such a value would be expected. From the known values of nFA, the product $nD^{2/3}$ is calculated to be 7.6×10^{-4}. Therefore, if D is 2×10^{-5}, n is about 1, and if D is 10^{-5}, n is 1.65. If n would be 4, D would be 2.6×10^{-6}, a value that is probably too low. A value of D between 10^{-5} and 2×10^{-5} seems reasonable for HF and would be consistent with a complex containing from 2.5 to 4 fluoride ions per zirconium ion. The charge on the zirconium ion is assumed to be four.

Discussion

The essential results may be summarized as follows: (*A*) The reaction rate constant, k, is almost potential independent. (*B*) The reaction at the surface is first order with respect to HF. (*C*) The over-all reaction occurring at or very near the surface is $Zr + bHF \rightarrow ZrF_b^{4-b} + bH^+ + 4e^-$ where b probably has a value from 2.5 to 4. (*D*) There is an effect which tends to decrease the rate constants as the concentration of HF is reduced.

If the dissolution reaction were a simple electrochemical reaction with a normal potential dependence, then the rate constant, k, should increase as the potential becomes more anodic. Furthermore, if normal values of the Tafel slope are assumed, the current would increase by at least two orders of magnitude in the 300 mv potential region that was investigated. Instead, values tended to decrease slightly as the potential became more anodic. This effect is understandable if the potential at the film solution interface where the dissolution takes place remains essentially unchanged as the over-all potential between the metal and the solution is changed. The potential change would then occur primarily across the film or the film-metal interface. This would be in accord with a model, previously proposed (2), in which the dissolution reaction occurs by the continuous dissolution and formation of the film. In this model, the zirconium is oxidized to form a film of oxide on the surface, and the dissolution proceeds by the action of HF on the zirconium ions at the interface between the film and the solution. This is also similar to the case of passive iron (7) where it is observed that the rate of dissolution of the film is potential independent over a wide potential range. In the case of iron, it was assumed that the potential at the interface stays constant and is determined by the equilibrium $2H^+ + O^{=}_{lattice} \rightleftharpoons H_2O$. A similar equilibrium might also be proposed for the case of zirconium.

The following scheme seems reasonable for the reaction mechanism at the interface between the film and the solution

$$Zr^{+4}_{lattice} + HF \rightarrow ZrF^{+3} + H^+$$
$$ZrF^{+3} + HF \rightarrow ZrF_2^{+2} + H^+$$
$$\text{- - - - - - - - - - - - - -}$$
$$Zr_{b-1}^{4-(b-1)} + HF \rightarrow ZrF_b^{4-b} + H^+$$

The intermediate complexes may either be solution complexes at or near the surface, or they may be surface complexes in that they are bonded to the film. If the first reaction is rate-determining, then the rate of the reaction will be given by the expression

$$r = k_1(HF) \qquad [9]$$

where k_1 is the rate constant for the first reaction. If the succeeding complexing reactions occur rapidly in the solution at or very near the interface, a value of n in agreement with the results could be obtained. The complexing reactions must occur in a distance small compared to the width of the diffusion boundary layer so that the complexing affects the value of the concentration of HF at the interface. If the complexing reactions occurred in the bulk of the solution, then the value of n found experimentally would be four, because four units of charge (the Zr^{+4} ion) would be removed from the interface for every reacting HF molecule. The actual value of n is probably from 1 to 1.65 as shown above. Therefore, Eq. [9] could represent the correct mechanism if the complexing occurs at or near the interface.

A similar kinetic equation would result if some or all of the complexing reactions occurred with surface atoms as in the following scheme

$$Zr^{+4}_{lattice} + HF \rightarrow ZrF^{+3}_{lattice} + H^+$$
$$ZrF^{+3}_{lattice} + HF \rightarrow ZrF_2{}^{+2}_{lattice} + H^+$$
$$\text{- - - - - - - - - - - -}$$
$$ZrF_{b-1}{}^{4-(b-1)}{}_{lattice} + HF \rightarrow ZrF_b^{4-b} + H^+$$

In this scheme, all but the last complex is formed on the surface of the film. The expressions for the rates of these reactions are

$$r_1 = k_1(HF)\left(1 - \sum_{n=1}^{b-1} \theta_n\right) \qquad [10]$$

$$r_2 = k_2\,(\mathrm{HF})\,\theta_1 \qquad [11]$$

$$\cdots\cdots\cdots$$

$$r_b = k_b\,(\mathrm{HF})\,\theta_{b-1} \qquad [12]$$

In these equations, the θ's represent the coverages of the various complexes on the surface.

In the steady state, the r's are equal and

$$k_1(\mathrm{HF})\left(1 - \sum_{n=1}^{b-1}\theta_n\right) = k_2(\mathrm{HF})\,\theta_1 = \ldots = k_b(\mathrm{HF})\,\theta_{b-1} \qquad [13]$$

or

$$k_1\left(1 - \sum_{n=1}^{b-1}\theta_n\right) = k_2\,\theta_1 = \ldots k_b\,\theta_{b-1} \qquad [14]$$

Since there are $(b-1)$ equations in $(b-1)$ unknowns (the values of θ_n), this set of equations may be solved to give any of the values of θ_n in terms of the rate constants. Therefore, the resulting current expression will have the form

$$I = nFKS(\mathrm{HF}) \qquad [15]$$

where K is a combination of rate constants.[2] This has the same form as Eq. [9], and unfortunately, there seems to be no way of distinguishing between these two possibilities.

As noted above, the reaction is not exactly first order, but the effective order is slightly greater than unity. According to the above mechanisms, one would expect an exact first order. A possible clue to this behavior is provided by the experiments in 0.12M HNO_3. Although the concentration of HF is essentially unchanged, the rates are greater than the rates at the same concentration of HF and 1.2M HNO_3. It may be that the nitrate ion, which is present in large relative quantities, competes with the HF molecules at the interface. At high ratios of HNO_3 to HF, the reaction may be slightly inhibited. The ratio of HNO_3 to HF is decreased as the stirring rate is increased, and the rate would then increase faster than if a normal first order mechanism were operating.

Another possibility is that at the lower concentrations of HF, a thicker film may be formed on the surface [cf. ref. (2)]. Relatively thick films may be more resistant to the action of HF as compared to the very thin films formed in the more concentrated solutions. Therefore, as the HF concentration at the interface is changed by varying the rotational velocity, the film may vary in thickness, and, if the thicker films are more resistant, the effect would be to increase the order slightly above first order. This effect would also explain the slight decrease in rate at constant concentration as the potential is made more anodic, for at the more anodic potentials, thicker films are formed (2).

It is also possible that the above systems of equations do not describe this system correctly, and that a more complex mechanism leading to an order of 1.2 occurs. However, the mechanisms described above seem to be the simplest that will describe the data.

[2] If, for example, b equals three, then $K = (k_1k_2k_3)/(k_1k_2 + k_1k_3 + k_2k_3)$.

Manuscript received Nov. 19, 1964; revised manuscript received Feb. 23, 1964. This paper was presented at the Washington Meeting, Oct. 11-15, 1964. The research was sponsored by the United States Atomic Energy Commission under contract with Union Carbide Corporation.

Any discussion of this paper will appear in a Discussion Section to be published in the June 1966 JOURNAL.

REFERENCES

1. T. Smith and G. R. Hill, *This Journal*, **105**, 117 (1958).
2. R. E. Meyer, *ibid.*, **111**, 147 (1964).
3. V. G. Levich, "Physico-Chemical Hydrodynamics," pp. 72-78, Prentice-Hall, Englewood Cliffs, N. J. (1962).
4. A. N. Frumkin and G. Tedoradse, *Z. Elektrochem.*, **62**, 251 (1958).
5. D. Jahn and W. Vielstich, *This Journal*, **109**, 849 (1962).
6. D. P. Gregory and A. C. Riddiford, *J. Chem. Soc.*, 3756 (1956).
7. K. J. Vetter, *Z. Elektrochem.*, **58**, 230 (1954).

Electronic Paramagnetic Resonance Study of the Thermal Decomposition of Dibasic Calcium Orthophosphate

J. A. Parodi, R. L. Hickok, W. G. Segelken, and J. R. Cooper

Lighting Research Laboratory, Lamp Division, General Electric Company, Cleveland, Ohio

ABSTRACT

Electronic paramagnetic resonance (EPR) spectra of trace quantities of Mn^{+2} in solid solution in $CaHPO_4 \cdot 2H_2O$, $CaHPO_4$, γ-$Ca_2P_2O_7$, β-$Ca_2P_2O_7$, and α-$Ca_2P_2O_7$ are given. The utility of EPR in following phase changes is demonstrated. The transition from β-$Ca_2P_2O_7$ to α-$Ca_2P_2O_7$ is established as occurring within the temperature range, 1171°-1179°. The results of hydrothermal experiments indicate that γ-$Ca_2P_2O_7$ is a metastable phase. It is established by EPR that the amorphous gel formed as an intermediate in the dehydration-recrystallization of $CaHPO_4 \cdot 2H_2O$ is in dynamic equilibrium with the solution phase.

Although electronic paramagnetic resonance (EPR) has been used extensively in physics research and free radical chemistry (1, 2) since it was discovered by Zavoyskiy (3) in 1944, it has had rather limited use in the study of solid-state chemical reactions. It has been used to study the effect of pressure (4) and also of impurities (5) on the hexagonal to cubic phase transformation of ZnS, and to follow the course of the synthesis of calcium fluorophosphate (6). Phase changes were followed by observing the EPR spectrum of manganous ion introduced in solid solution in the concentration range of 0.005-0.05% by weight.

In the following paper the EPR of Mn^{+2} is used to follow the thermal decomposition of dibasic calcium orthophosphate dihydrate, beginning with the dehydration to $CaHPO_4$ and followed by pyrolysis to γ-$Ca_2P_2O_7$ with subsequent inversions to β-$Ca_2P_2O_7$ and α-$Ca_2P_2O_7$.

The mechanism of dehydration of $CaHPO_4 \cdot 2H_2O$, which has been studied by Vol'fkovich and Urusov (7), Boullé and Dupont (8-10), and Rabatin, Gale, and Newkirk (11), is dependent on the partial pressure of water vapor in contact with the salt and on the method of preparation. Dehydration is favored by high hu-

midity; indeed the recrystallization of $CaHPO_4 \cdot 2H_2O$ to $CaHPO_4$ goes to completion very readily above 75° in water (10). Chiola and Vanderpool (12) state that $CaHPO_4$ is formed by the dehydration of $CaHPO_4 \cdot 2H_2O$ in aqueous medium over the temperature range 65°-104°. The question of whether or not there is an exchange with the solution during recrystallization is taken up in this paper.

The thermal decomposition of dibasic calcium orthophosphate to γ-$Ca_2P_2O_7$ is apt to be rather complex depending on whether $CaHPO_4 \cdot 2H_2O$ or crystalline $CaHPO_4$ is the starting material and whether the ambient atmosphere is dry or humid (8-11). The highest reported temperature at which γ-$Ca_2P_2O_7$ is formed is about 475° (11). When γ-$Ca_2P_2O_7$ is fired at a somewhat higher temperature β-$Ca_2P_2O_7$ is produced. Temperatures reported for this phase transition are 555° (13), 700°-750° (14), and 850° (15). The transition temperature for the inversion of β-$Ca_2P_2O_7$ to α-$Ca_2P_2O_7$ is given as 1140° (16), 1270° (17), 1130° (18), and 1220° (15). The latter two inversions (γ to β and β to α) appear to be straightforward and will be used to illustrate the utility of the EPR method in following phase transformations.

Experimental

Preparation of materials.—The refractive indices and x-ray diffraction patterns of all preparations described below were in agreement with the literature.

1. $CaHPO_4 \cdot 2H_2O$, brushite

Dibasic calcium orthophosphate dihydrate was prepared by two methods. The first of these procedures, described by St. Pierre (19), produces high-purity crystals. It was not possible to introduce manganese into solid solution by this method, but incorporation of manganese was achieved by the second procedure described below.

A solution containing 0.4M $Ca(NO_3)_2$, 0.4M H_3PO_4, and 0.004M $Mn(NO_3)_2$ was slowly neutralized with dilute NH_4OH at 53°. The product was washed with 10^{-3}M H_3PO_4 to insure that no adsorbed Mn would remain. Although it is desirable to carry out this precipitation at low temperature in order to minimize hydrolysis, it was possible to incorporate manganese only at 53° and above.

2. $CaHPO_4$, monetite

Anhydrous dibasic calcium orthophosphate containing trace concentrations of divalent manganese was prepared in two ways: (*a*) by the dehydration-recrystallization of $CaHPO_4 \cdot 2H_2O$ (10, 12) and (*b*) by a homogeneous precipitation procedure (20, 21) in which a solution of the cation salts and phosphoric acid is very slowly neutralized by ammonia liberated during the hydrolysis of urea. The preparative details for the former method are given further on in this paper. Typical conditions for some of the preparations made by the latter method are given in Table I.

Chemical analysis of the recrystallized $CaHPO_4$ gave a Ca/PO_4 mole ratio of 1.023 and an ignition loss of 7.54%, indicating the presence of minor amounts of basic hydrolysis products. On the other hand chemical analysis of homogeneously precipitated $CaHPO_4$ (*e.g.*, Ca/PO_4 = 0.983 and ignition loss = 7.25%) suggests contamination with a small quantity of a more acidic phosphate, even though microscopic examination showed the crystals to be free of included impurity phases.

Table I. Homogeneous precipitation of $CaHPO_4$

Concentrations of chemicals used to make solution, and other conditions of preparation

Preparation No.	1 and 2	3	4
$Ca(NO_3)_2$	1.2M		
$CaCO_3$		0.1M	0.2M
$Mn(NO_3)_2$	2×10^{-3}M	10^{-4}M	2×10^{-4}M
H_3PO_4	1.5M	1.0M*	1.0M*
Urea	1.5M	0.4M	0.6M
Temperature	83°	85°-90°	85°-90°
Time	5 days	8 hr	1 hr
pH at end of precipitation	2.5	<3.0	2.3

* Actual hydrogen ion concentration is somewhat less than indicated, because acid was used to neutralize $CaCO_3$.

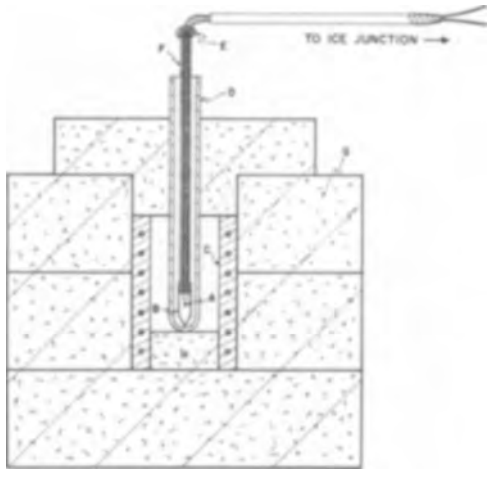

Fig. 1. Furnace for phase transition experiments. A, Pt, Pt-10% Rh thermocouple; B, Pt sample tube; C, heating element; D, mullite tube; E, epoxy cement; F, alumina thermocouple tube; G, alumina fire brick; H, alumina fire brick plug.

3. Calcium Pyrophosphate $Ca_2P_2O_7$

All of the calcium pyrophosphates were obtained from the pyrolysis of monetite or brushite. Gamma calcium pyrophosphate was obtained both by prolonged heating in a vacuum (*e.g.*, 8 days at 275°) and by firing for 4 hr at 500°. β-$Ca_2P_2O_7$ was prepared by firing at 1050° for 1 hr or by hydrothermal treatment: 4 hr at 450° and 30,000 psi. Alpha calcium pyrophosphate was prepared by ignition at 1250° for 1 hr. In addition to using dibasic orthophosphates containing manganese in solid solution, traces of manganese were incorporated in the beta and alpha polymorphs by slurrying the material to be ignited in acetone containing a manganous salt, drying, and firing.

Temperature of the phase transitions, γ-$Ca_2P_2O_7 \rightarrow \beta$-$Ca_2P_2O_7$ and β-$Ca_2P_2O_7 \rightarrow \alpha$-$Ca_2P_2O_7$.—The temperatures of the indicated phase transitions were determined by inserting a thermocouple directly into the center of the sample as shown in Fig. 1. The weight of the sample was about 0.2g. The thermocouple was calibrated both before and after the experiments against a standard thermocouple certified by the National Bureau of Standards. There was no change in calibration with use. The output of the thermocouple was read from a precision potentiometer.

Samples were fired from 16 to 20 hr, and the resulting structures were determined by x-ray diffraction and EPR (Mn^{+2} present in the approximate concentration, $Mn/Ca = 10^{-3}$).

Electronic paramagnetic resonance.—Electronic paramagnetic resonance of the polycrystalline calcium phosphate was measured on a Varian Associates V-4500 EPR spectrometer with a resonant frequency of 9480 Mc/s and a modulation frequency of 200 cps. Approximately ¾ in. of sample at one end of a fused quartz sample tube 4 mm OD x 3 mm ID x 4 in. or more in length was used. The EPR spectra reproduced in this paper are potentiometric recorder tracings of the first derivative of absorption of microwave energy versus the magnetic field, which increases from left to right in the figures.

Results and Discussion

EPR spectra of divalent manganese in $CaHPO_4 \cdot 2H_2O$, $CaHPO_4$, γ-$Ca_2P_2O_7$, β-$Ca_2P_2O_7$, and α-$Ca_2P_2O_7$ are presented in Fig. 2. All EPR spectra of a given compound, irrespective of method of preparation, are identical. This indicates that the local symmetry of the

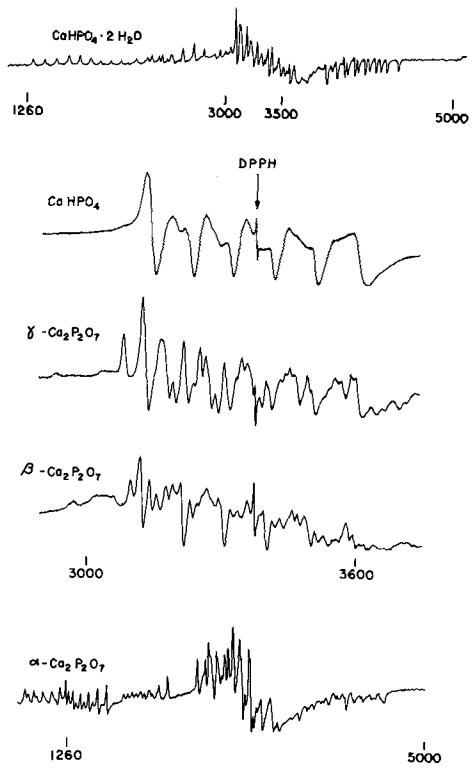

Fig. 2. EPR spectra of Mn^{++} in solid solution in the indicated dibasic orthophosphates and pyrophosphates of calcium. The field marker diphenyl picryl hydrazyl, g = 2.0036, is indicated by DPPH.

crystalline field about the manganous ion (assumed to substitute for Ca^{+2} in these structures) is not affected by minor deviations from stoichiometry which may exist (22, 23).

The high-temperature polymorph, α-$Ca_2P_2O_7$:Mn, has an EPR spectrum which, although unique, is similar to that of $CaHPO_4 \cdot 2H_2O$:Mn in broad outline. Further, both extend over a wide range of magnetic field, about 4100 gauss for the former and 3300 gauss for the latter. The crystalline field interaction with Mn^{+2} is, thus, quite intense for these two structures. On the other hand the effect of the crystalline field on Mn^{+2} in $CaHPO_4$, γ-$Ca_2P_2O_7$, and β-$Ca_2P_2O_7$ appears to be much less, because the range of all three spectra is only about 600 gauss. In the case of powdered samples, however, one cannot discount the possibility that the angular dependence of the spectral lines is such that lines which would appear at large separation in spectra of single crystals are washed out in spectra of powders, and therefore that the fine structure splitting constant is actually larger than it appears to be.

Recrystallization of $CaHPO_4 \cdot 2H_2O$

During the dehydration-recrystallization of $CaHPO_4 \cdot 2H_2O$ in an aqueous slurry the formation of an amorphous gel intermediate was observed. Nucleation and growth of the $CaHPO_4$ crystals occurs in and from this intermediate. One of the questions arising from this observation was whether equilibrium was established between this intermediate phase and the ions in solution. To answer this question experiments were conducted in which EPR measurements were used to follow the course of Mn^{+2} during the transformation.

$CaHPO_4 \cdot 2H_2O$, both with and without incorporated Mn^{+2}, was slurried at 82°C in water and in 0.01M H_3PO_4. For the latter starting material the solutions were also 1.44×10^{-4}M in $Mn(NO_3)_2$. In every case EPR showed that Mn^{+2} was incorporated in the recrystallized $CaHPO_4$.

To eliminate the possibility that incorporation of Mn^{+2} in $CaHPO_4$ had occurred after crystallization, $CaHPO_4$ was equilibrated in 0.01M $Mn(NO_3)_2$ at 90°-100°C for two weeks. EPR showed no trace of Mn^{+2} incorporation.

Table II. Determination of transition temperature, β-$Ca_2P_2O_7 \rightarrow$ α-$Ca_2P_2O_7$

Firing range, °C	Firing time, hr	EPR result	X-ray result
1170.1-1171.2	22	β	β
1172.8-1173.6	17½	α + small amt. β	α + small amt. of some other phase
1174.3-1175.4	17½	α + trace β	α
1177.3-1179.0	15½	α	α

The β-$Ca_2P_2O_7$:2×10^{-3} Mn used for this experiment was made by firing $CaHPO_4 \cdot 2H_2O$ plus manganous acetate at 1050° for 90 min. The $CaHPO_4 \cdot 2H_2O$ was made by the procedure described by St. Pierre (19).

The conclusion reached from these experiments is that the amorphous gel formed as an intermediate in the dehydration-recrystallization of $CaHPO_4 \cdot 2H_2O$ is in dynamic equilibrium with the solution phase. Exchange of ions appears to be rapid.

It is interesting that β-$Ca_2P_2O_7$ and not γ-$Ca_2P_2O_7$ is the result when dibasic calcium orthophosphate undergoes pyrolysis at 450° and 30,000 psi. This temperature is well below that reported for the transition of γ-$Ca_2P_2O_7$ to β-$Ca_2P_2O_7$. As a matter of fact the purpose of carrying out the original hydrothermal pyrolysis at 450° was to prepare well crystallized γ-$Ca_2P_2O_7$. Subsequent experiments in which $CaHPO_4$ was fired overnight or longer at 30,000 psi water pressure and at various temperatures over the range 300°-450° yielded only the starting material, $CaHPO_4$, or β-$Ca_2P_2O_7$. Products were identified by EPR and x-ray diffraction. Temperature and pressure were quenched simultaneously at the conclusion of each experiment. The transition from $CaHPO_4$ to β-$Ca_2P_2O_7$ occurred at 410° ± 15°. When β-$Ca_2P_2O_7$ was similarly treated at 398° and 376° the reverse reaction did not proceed. From these experiments it is concluded that γ-$Ca_2P_2O_7$ is a metastable phase. Mesmer and Irani (15) have shown that the transition from γ- to β-$Ca_2P_2O_7$ is exothermic and therefore also have concluded that the γ-phase must be metastable.

Temperature of the Phase Transition, β-$Ca_2P_2O_7$ *to* α-$Ca_2P_2O_7$

The transition from beta calcium pyrophosphate to alpha calcium pyrophosphate occurs over a narrow range of no greater than 8°. As is seen by reference to Table II the transition begins at a temperature of 1171° or greater. The upper limit of the transition is, according to x-ray results, 1175°; whereas according to EPR it is between 1175° and 1179°. The EPR interpretation is based on a small difference in relative intensity of three pairs of lines. Referring to Fig. 3, the line intensity ratios, A/B, C/D, and E/F, increase on going from the beta to the alpha pyrophosphate. In all samples ignited at 1179° and above the corresponding intensity ratios are the same, whereas for the sample fired at 1174°-1175° the ratios are all a little less than the respective ratios in the former samples. This indicates that perfection of the α-$Ca_2P_2O_7$ structure is not quite complete at 1175° and that at some temperature in the interval, 1175°-1179°, the transformation is complete. It should be emphasized that the temperatures given here are those of the thermocouple at a point within the sample and that there is bound to be some temperature variation along the ¾ in. length of the sample, which might account for the observed temperature range for the phase transition.

The data in Table II were obtained from a sample of β-$Ca_2P_2O_7$:2×10^{-3} Mn prepared by firing $CaHPO_4 \cdot 2H_2O$ to which manganous acetate was added prior to ignition. The same results were obtained with β-$Ca_2P_2O_7$:Mn prepared by the pyrolysis of $CaHPO_4$:Mn precipitated from homogeneous solution. This indicates that the transition is independent of the history of the

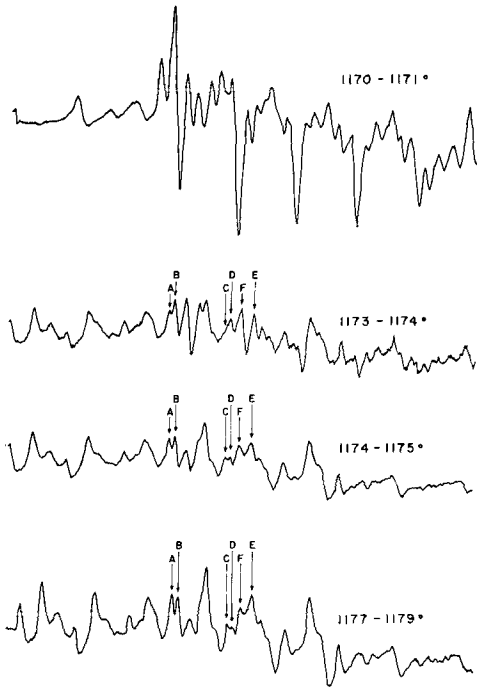

Fig. 3. EPR spectra of $Ca_2P_2O_7$:2 x 10^{-3} Mn fired overnight at indicated temperatures. A progressive change from the beta to the alpha polymorph is evident as the firing temperature increases.

starting material. Furthermore, inasmuch as the method of St. Pierre (19), which was used to prepare the brushite, is known to give very high-purity material, the results also indicate that the quantity and kind of impurities present in the homogeneously precipitated monetite have a negligible effect on the phase transition.

The transition temperature of 1175° ± 4° given here for the above materials is intermediate between the temperatures reported by Hill, Faust, and Reynolds (16) and Mesmer and Irani (15), 1140° and 1220°, respectively.

A point that perhaps should be brought up is the irreversibility of the above structure transformation under normal conditions of preparation for relatively pure material. If the structure change were reversible, quenching would have been necessary to preserve the high-temperature form. The phase transition is so irreversible, as a matter of fact, that α-$Ca_2P_2O_7$ has been prepared by firing at 1250° and annealing overnight in the range 1150° ± 20°, which it is seen is just below the transition range.

Temperature of the Phase Transition, γ-$Ca_2P_2O_7$ to β-$Ca_2P_2O_7$

The transition from γ-$Ca_2P_2O_7$ to β-$Ca_2P_2O_7$ is rather sluggish and poorly defined. Roughly, the temperature range in which the phase change occurs lies between 680° and 740°, in approximate agreement with McIntosh and Jablonski (14), but this appears to be partially dependent on the history of the sample. Results are summarized in Table III.

It is seen that for one starting material, A, there is practically a one to one correspondence between EPR and x-ray diffractometer results. The one exception is for the sample fired at 729°-730°: EPR indicates that conversion to β-$Ca_2P_2O_7$ is not quite complete whereas x-ray results indicate that the conversion is complete. The EPR interpretation is based on the disappearance of a line due only to γ-$Ca_2P_2O_7$:Mn and the appearance and subsequent growth of a line due only to β-$Ca_2P_2O_7$:Mn. As seen in Fig. 4, at 729°-730° there is still a trace of the γ-$Ca_2P_2O_7$:Mn line showing in the EPR spectrum.

Table III. Determination of transition range, γ-$Ca_2P_2O_7$ → β-$Ca_2P_2O_7$

Starting material	Run No.	Firing range, °C	Firing time, hr	EPR result	X-ray result*
A	1	689	16	γ	γ
	2	696	17½	γ + trace β	progressive change toward β
	3	701-702	16	γ + small amt. β	
	4	721	18	β + small amt. γ	
	5	729-730	19	β + trace γ	β
	6	737-739	17	β	β
B	7	685-687	7	γ + trace β	
	8	697-700	17	γ + β	
	9	704-705	21	β + small amt. γ	
	10	706	19	β + small amt. γ	
	11	711	19	β + trace γ	
C	12	686-687	17½		γ
	13	691-692	16½		γ + β
	14	700-704	15½		γ + β
	15	707-708	15½		β

Note: The EPR spectrum of Run No. 7 was identical to that of No. 2 and the EPR of No. 11 was the same as that of No. 5. Thus by comparison with starting material A, the estimated maximum transition range of B is 680°-720°. Starting materials: A, prepared by firing $CaHPO_4$:Mn 1 hr at 500°; B, prepared by firing $CaHPO_4$:Mn 18 hr at 500°; C, prepared by firing $CaHPO_4 \cdot 2H_2O$ 2-3 hr at 600°. $CaHPO_4 \cdot 2H_2O$ prepared by addition of calcium sucrate solution to a dilute solution of phosphoric acid (19).

* For group A the x-ray diffractometer was used; for group C the x-ray powder camera was used.

Summary

The thermal decomposition of dibasic calcium orthophosphate was studied by electron paramagnetic resonance (EPR) and x-ray diffraction. EPR spectra of trace amounts of manganous ion in solid solution in $CaHPO_4 \cdot 2H_2O$, $CaHPO_4$, γ-$Ca_2P_2O_7$, β-$Ca_2P_2O_7$, and α-$Ca_2P_2O_7$ are presented. The utility of EPR in following phase changes is demonstrated. The investigations of the phase transitions, γ-$Ca_2P_2O_7$ to β-$Ca_2P_2O_7$ and β-$Ca_2P_2O_7$ to α-$Ca_2P_2O_7$, delineate the fact that EPR is often more sensitive than x-ray diffraction in detecting phase changes.

Some results of the above study which are of possible interest to lamp phosphor technology are given below.

1. It is established by EPR that the amorphous gel formed as an intermediate in the dehydration-recrys-

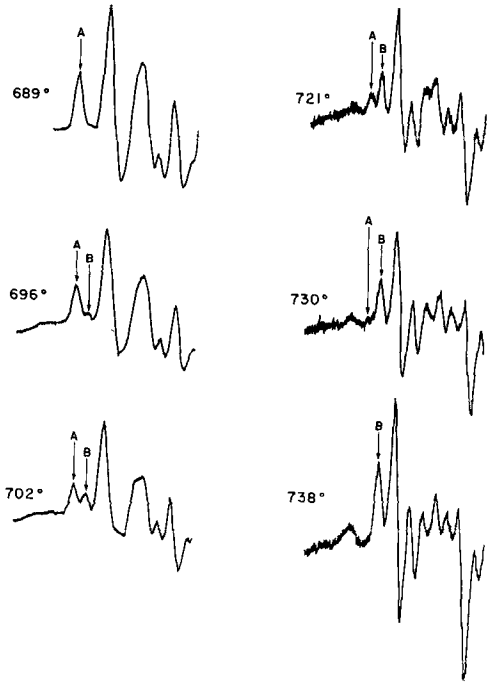

Fig. 4. Portion of EPR spectrum of $Ca_2P_2O_7$:Mn showing change from γ- to β-$Ca_2P_2O_7$:Mn as the firing temperature is increased. Peak A is due to γ-$Ca_2P_2O_7$:Mn and peak B is due to β-$Ca_2P_2O_7$:Mn.

tallization of $CaHPO_4 \cdot 2H_2O$ is in dynamic equilibrium with the solution phase.

2. The transition from β-$Ca_2P_2O_7$ occurs within the temperature range 1171°-1179°.

3. The phase change from γ-$Ca_2P_2O_7$ to β-$Ca_2P_2O_7$ is very sluggish and poorly defined, proceeding roughly between 680° and 740°.

4. When $CaHPO_4$ is heated over the temperature range, 300°-450°, under 30,000 psi water pressure only $CaHPO_4$ or β-$Ca_2P_2O_7$ is produced, the transition occurring at 410° ± 15°. This indicates that γ-$Ca_2P_2O_7$, which under normal atmospheric pressure is the product of the pyrolysis of $CaHPO_4$ in the approximate temperature range of 300°-700°, is a metastable phase.

Acknowledgment

The authors are greatly indebted to Dr. J. F. Sarver for his help in both the implementation and interpretation of the hydrothermal experiments.

Manuscript received Oct. 14, 1964; revised manuscript received March 9, 1965.

Any discussion of this paper will appear in a Discussion Section to be published in the June 1966 JOURNAL.

REFERENCES

1. S. A. Al'tshuler and B. M. Kozyrev, "Electron Paramagnetic Resonance," C. P. Poole, Jr., Translation Editor, Academic Press, New York (1964).
2. D. J. E. Ingram, "Free Radicals as Studied by Electron Spin Resonance," Academic Press, New York (1958).
3. Ye. K. Zavoyskiy, Doctor's Dissertation, Moscow, FIAN, 1944; *J. Phys. USSR*, **9**, 245 (1945).
4. J. S. van Wieringen, *Physica, s'Grav.*, **19**, 397 (1953).
5. M. Aven and J. A. Parodi, *J. Phys. Chem. Solids*, **13**, 56 (1960).
6. P. H. Kasai, *J. Phys. Chem.*, **66**, 674 (1962).
7. S. I. Vol'fkovich and V. V. Urusov, *Izvest. Akad. Nauk S.S.S.R., Otdel. Khim. Nauk*, **4**, 341 (1951).
8. A. Boullé, *Compt. rend.*, **226**, 1617 (1948).
9. A. Boullé and M. Dupont, *ibid.*, **240**, 860 (1955).
10. A. Boullé and M. Dupont, *ibid.*, **241**, 42 (1955).
11. J. G. Rabatin, R. H. Gale, and A. E. Newkirk, *J. Phys. Chem.*, **64**, 491 (1960).
12. V. Chiola and C. D. Vanderpool, Canadian Pat. No. 673, 681, Nov. 5, 1963.
13. E. J. Fox and K. G. Clark, *Ind. Eng. Chem.*, **35**, 1264 (1943).
14. A. O. McIntosh and W. L. Jablonski, *Anal. Chem.*, **28**, 1424 (1956).
15. R. E. Mesmer and R. R. Irani, *J. Chem. Engr. Data*, **8**, 530 (1963).
16. W. L. Hill, G. T. Faust, and D. S. Reynolds, *Am. J. Sci.*, **242**, 457 (1944).
17. W. F. Bale, J. F. Bonner, H. C. Hodge, H. Adler, A. R. Wreath, and R. Bell, *Ind. Eng. Chem., Anal. Ed.*, **17**, 491 (1945).
18. G. Trömel, H. J. Harkort, and W. Hotop, *Z. anorg. Chem.*, **256**, 253 (1948).
19. P. D. S. St. Pierre, *J. Am. Chem. Soc.*, **77**, 2197 (1955).
20. L. Gordon, M. L. Salutsky, and H. H. Willard, "Precipitation from Homogeneous Solution," John Wiley & Sons, Inc., New York (1959).
21. R. W. Mooney and M. A. Aia, *Chem. Revs.*, **61**, 433 (1961).
22. B. Bleaney and K. W. H. Stevens, *Rept. Progr. Phys.*, **16**, 108 (1953).
23. K. D. Bowers and J. Owen, *ibid.*, **18**, 305 (1955).

APPENDIX

The following x-ray diffraction powder pattern was obtained for gamma calcium pyrophosphate made by the pyrolysis of both $CaHPO_4 \cdot 2H_2O$ and $CaHPO_4$ preparations described earlier. It is compared here with the earlier determination of McIntosh and Jablonski (14). It is seen that the two patterns are essentially in agreement, but that there are minor differences. The differences are probably accounted for, however, by the techniques used. The present data were taken on a modern goniometer with larger dispersion and better resolution than the film technique of McIntosh and Jablonski.

X-ray powder pattern of gamma calcium pyrophosphate

This paper* dÅ	This paper* I/I_1	M. and J. dÅ	M. and J. I/I_1	This paper* dÅ	This paper* I/I_1	M. and J. dÅ	M. and J. I/I_1
4.51	5	4.55	7	1.951	5	1.96	8
		4.19	5	1.880	<5	1.88	5
3.35	30	3.35	42	1.859	5	1.86	11
3.23	10	3.25	13	1.830	<5		
3.092	65	3.11	65	1.810	10	1.82	35
3.050	45	3.06	35	1.776	5	1.79	27
2.978	5			1.737	<5	1.74	9
2.924	100	2.94	100			1.70	5
2.820	5			1.661	<5	1.67	17
2.788	5	2.78	7	1.638	<5		
2.758	10			1.620	<5		
		2.70	17	1.606	<5		
2.688	5			1.592	<5		
2.544	5	2.56	9	1.567	<5	1.57	13
2.402	<5	2.42	7	1.504	<5	1.51	13
2.359	<5			1.489	<5		
				1.465	<5	1.47	11
2.336	<5	2.34	7			1.40	5
2.268	<5			1.375	<5	1.38	5
2.247	<5			1.336	<5	1.34	5
2.218	15	2.24	35	1.305	<5	1.31	7
2.161	5	2.18	27			1.28	5
2.135	<5	2.15	7			1.27	5
2.113	<5					1.22	4
2.090	15	2.10	23			1.20	4
2.027	<5	2.02	7			1.12	5
1.999	<5					1.09	5
1.979	<5						

* Data taken on G.E. goniometer using copper radiation through nickel filters.

Erratum

The Brief Communication "Recrystallization of Thin Films of Germanium and Silicon" which was published on pages 534 and 535 of the May 1965 issue of the JOURNAL has two authors J. D. Filby and S. Nielsen. Mr. Filby's name was omitted in error.

The Solidification of PbTe-SnTe Alloys under the Influence of Ultrasonic Agitation

H. E. Bates and Martin Weinstein

Tyco Laboratories, Incorporated, Waltham, Massachusetts

ABSTRACT

The previously described technique for the solidification of thermoelectric materials by ultrasonic agitation of a freezing melt has been applied to the solid solution 0.7 PbTe-0.3 SnTe. The material prepared by this technique is fine-grained, dense, and chemically homogeneous. The thermoelectric properties of lead telluride-tin telluride have been measured as a function of temperature. The room temperature figure of merit is approximately $0.6 \times 10^{-3}/°K$. Compressive-flow strength and ductility are improved by ultrasonic agitation; 0.7 PbTe-0.3 SnTe prepared in this study showed 35% reduction in length at an ultimate compressive stress of over 16,000 psi, compared to an ultimate compressive strength of 7,500 psi and 10% reduction in length for unagitated material. Precipitation in the PbTe-SnTe system is discussed. In particular the effects of ultrasonic irradiation on the precipitation phenomenon are described in detail.

Interest in the use of thermoelectric materials for power generation and refrigeration has led to important research into the fundamental nature of thermoelectric phenomena and the means of optimizing thermoelectric properties by alloying and doping (1). Of equal or greater importance to the designer of practical thermoelectric devices are what Klein (2) terms "the auxiliary properties": melting point, vapor pressure, coefficient of expansion, mechanical strength, etc. While the first three properties are quite insensitive to any manipulation of the material other than appreciable changes in composition, which may be incompatible with the desired thermoelectric properties, the possibility does exist of improving the mechanical properties without affecting the composition.

Because of the predominantly covalent nature of most thermoelectric materials, they tend to be highly susceptible to cleavage and brittle failure. The simplest way to decrease brittle fracture in any material is to decrease the grain size, that is, to interpose as many barriers (grain boundaries) as possible to the propagation of micro- and gross cracks. The irradiation of solidifying ingots with ultrasound as a means of producing a fine-grained, equiaxed structure has been studied extensively in the USSR and to a lesser extent in this country (3, 4). An entirely satisfactory mechanism for the refinement of grain structure by ultrasonic vibration has yet to be advanced, but there is general agreement that refinement is caused through decreasing the critical nucleus size by increasing the pressure at certain points in the liquid (3, 5) and/or disrupting the advancing solid-liquid interface by cavitation (4, 6).

The application of ultrasonic irradiation to PbTe-SnTe alloys can be expected to yield several benefits: a fine grained, equiaxed structure with good mechanical strength, free of inclusions and porosity; a chemically homogeneous material free of the gross and microsegregation which occurs under normal freezing conditions. Because of the tendency of doping elements to segregate during normal freezing, most commercial thermoelectric materials have been prepared by cold pressing and sintering or extrusion. The purpose of this investigation was to prepare crystalline, homogeneous alloys with satisfactory thermoelectric properties and mechanical properties superior to those of materials prepared by other techniques.

Experimental

The experimental equipment and procedures here outlined have been described in detail elsewhere (1). Figure 1 shows the assembly used to solidify a melt under ultrasonic agitation. A charge of 50-75g was sealed under vacuum in the quartz tube. A Pt-wound resistance furnace was lowered over the tube and heated until the charge melted, as indicated by a thermocouple attached at the base of the tube. At this point the piezoelectric transducer, epoxied to the base of the quartz pedestal, was energized. Shortly after agitation began, the furnace was raised by a motorized hoist so that solidification proceeded from the bottom of the ingot upward at a rate defined by the rate of removal of the furnace. As the freezing interface moved upward, the input frequency to the PZT crystal was varied to maintain a resonant condition. The input power was also increased gradually to compensate for attenuation of the ultrasonic waves in the solidified portion of the ingot.

Ingots of 0.7 PbTe-0.3 SnTe were solidified under agitation of 19-21 kc at approximately 50w nominal input power and 33-35 kc at 35w. Directional solidification was begun with the base of the melt at approximately 910°C. Growth rate in both cases was about 1.1 in./hr. Faster growth rates tended to diminish grain refinement.

A calorimetric technique was devised to measure the ultrasonic energy input to the melt. The heat capacity of a gallium melt of the same volume as an ordinary ingot was measured in the agitation assembly (Fig. 1), using a thermocouple and a small resistance heater immersed in the melt. The gallium melt was then agitated at various levels and frequencies. The energy absorbed by the melt during agitation was calculated from the known heat capacity and the temperature increase during the application of the ultrasound. The results of these measurements are shown in Fig. 2; the nominal power input refers to the electrical input to the transducer. It can be seen from Fig. 2 that the efficiency of the system is highest when operation takes place in the vicinity of the natural frequency of the transducer (36 kc). Efficiencies of over 35% were achieved at the 34.4 kc resonance. Inputs producing more than 10 w/cm^2 fractured the quartz tube at the tube-pedestal joint.

Results

Employing the process variables noted above, ingots of 0.7 PbTe-0.3 SnTe were produced 0.7 in. in diameter and over 1 in. long which were fine-grained, dense, and chemically homogeneous.

Microstructure.—The solidification of 0.7 PbTe-0.3 SnTe under the influence of ultrasonic agitation resulted in a microstructure (Fig. 3) free of inclusions, porosity, columnar grains, and the segregation asso-

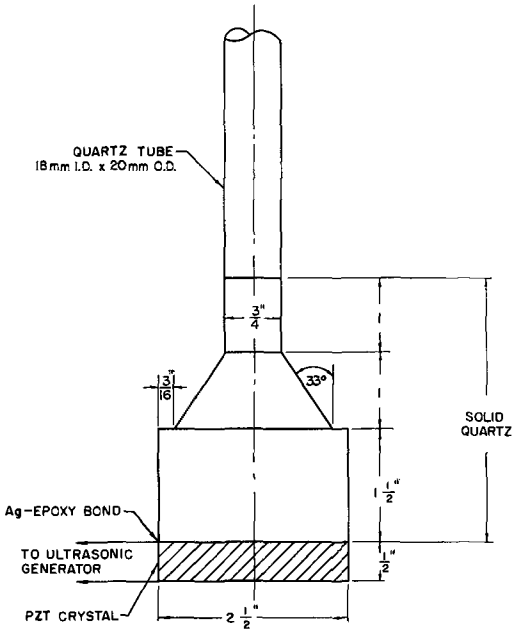

Fig. 1. Piezoelectric transducer, quartz concentrator, and crucible assembly.

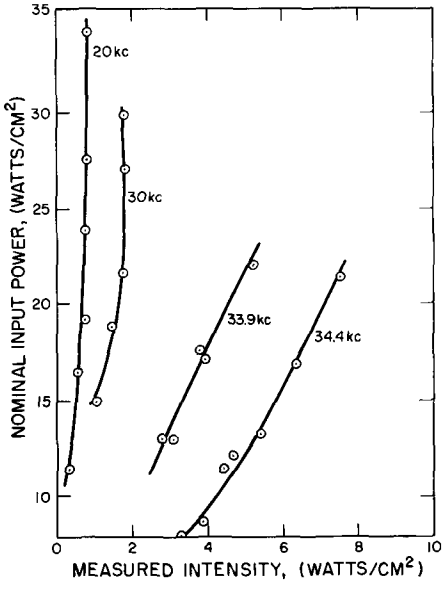

Fig. 2. Ultrasonic energy conversion efficiency for four resonant frequencies.

ciated with normal freezing. Directionally solidified ingots ordinarily consist of five or six columnar grains running the length of the ingot. The surfaces of unagitated ingots usually show considerable porosity and roughness, a feature which is eliminated by the ultrasonic agitation. The microstructure of a water-quenched 0.7 PbTe-0.3 SnTe ingot, with dendritic structure and extensive microsegregation characteristic of this treatment, is shown in Fig. 4. Annealing of this structure below the melting point for 2 hr produced spheroidization of the intergranular segregated phase with little accompanying recrystallization and grain growth. Evidence for the chemical homogeneity produced by ultrasonic agitation is shown in Fig. 5, where the room temperature resistance of p-type 0.7 PbTe-0.3 SnTe is plotted as a function of distance for an agitated and an unagitated ingot. Variations of this sort are even more pronounced in doped alloys where segregation of the dopant produces a quite abrupt variation in properties in the final portion of the ingot to freeze.

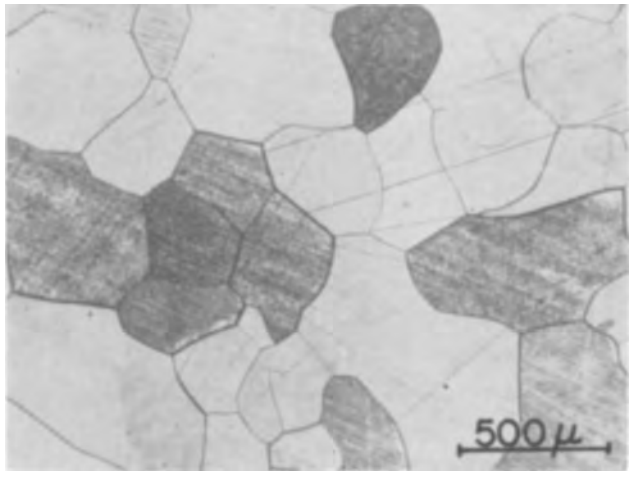

Fig. 3. Microstructure of 0.7 PbTe-0.3 SnTe ingot solidified under ultrasonic agitation. Magnification approximately 42X.

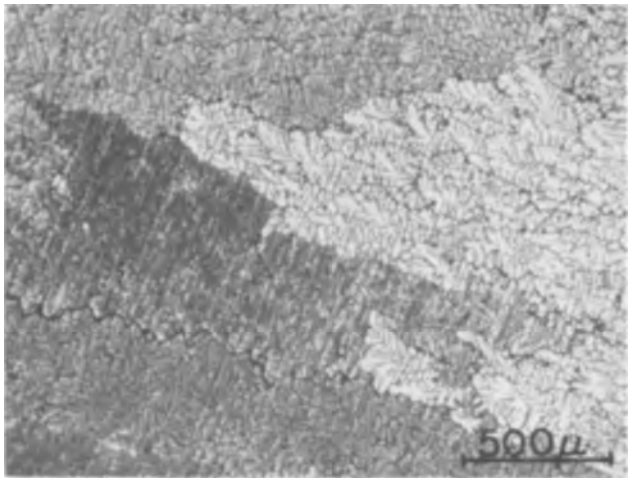

Fig. 4. Microstructure of water-quenched 0.7 PbTe-0.3 SnTe ingot. Magnification approximately 42X.

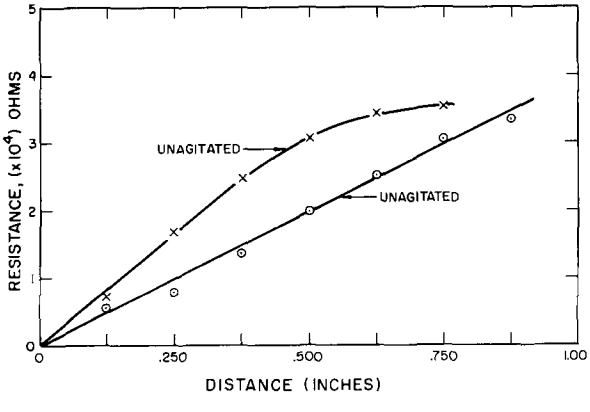

Fig. 5. Room temperature resistance as a function of distance along agitated and unagitated 0.7 PbTe-0.3 SnTe ingots.

Thermoelectric properties.—The figure of merit $Z = \alpha^2/K\rho$ provides a means of comparing the efficiencies of different thermoelectric materials. In the above expression α is the Seebeck coefficient in volts per °C, K is the thermal conductivity in watts/cm/°C, and ρ the electrical resistivity in ohm-centimeters. The Seebeck coefficient and resistivity of cast, directionally solidified, and ultrasonically agitated 0.7 PbTe-0.3 SnTe ingots were measured as a function of temperature.

1. Seebeck Coefficient.—The variation of Seebeck coefficient with temperature is shown in Fig. 6. The ultrasonically agitated material contained a slight excess (0.3 at. %) of Te. The recent investigation by

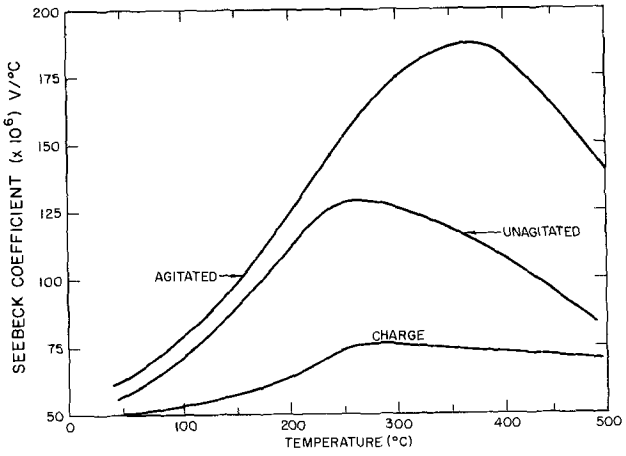

Fig. 6. Seebeck coefficient as a function of temperature of 0.7 PbTe-0.3 SnTe.

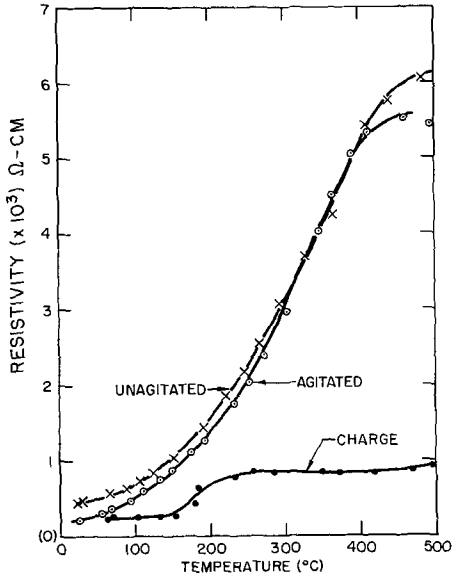

Fig. 7. Resistivity as a function of temperature of 0.7 PbTe-0.3 SnTe.

Machonis and Cadoff (7) which employed cation-rich single crystals of nominal composition 0.7 PbTe-0.3 SnTe showed a slightly different Seebeck behavior, giving a maximum Seebeck coefficient of 190 μv/°C at 180°C. Both the Te-rich and cation-rich specimens are p-type. The low value of the Seebeck coefficient for the directionally solidified material is probably due to segregation and inhomogeneities of the kind discussed by Cosgrove *et al.* (8). The directionally solidified, unagitated ingot also contained 0.3 a/o (atom %) excess Te. Metallographic examination of the cast material showed that the peculiar behavior of the Seebeck coefficient, and of the resistivity, was caused by melting of the interdendritic phase, probably Pb-Sn eutectic (eutectic temperature $\approx$ 185°C). Melting was evidenced by spheroidization of the phase in the pre-existant segregation pattern.

2. Resistivity.—The variation of resistivity with temperature is shown in Fig. 7. The difference between agitated and unagitated ingots is negligible. The resistivity as a function of temperature given by Machonis and Cadoff (7) for cation-rich 0.7 PbTe-0.3 SnTe varied from 0.9 x 10^{-3} ohm-cm at room temperature to 10 x 10^{-3} ohm-cm at 500°C.

3. Electrical Efficiency.—The electrical efficiency factor α^2/ρ is shown in Fig. 8 as a function of temperature. The low values of the directionally solidified material are due to lowering of the Seebeck coefficient by inhomogeneous distribution of excess constituents.

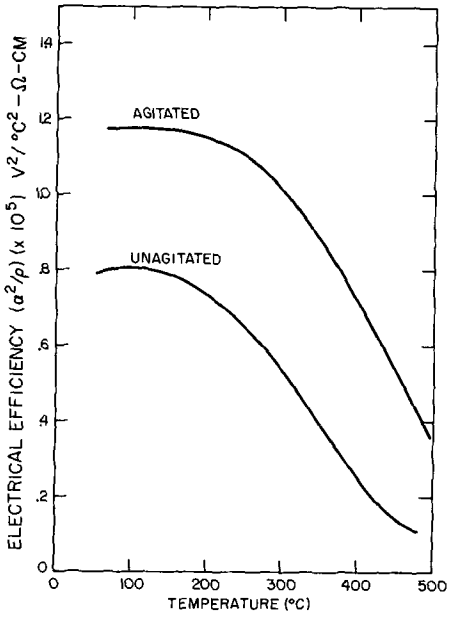

Fig. 8. Electrical efficiency factor as a function of temperature of 0.7 PbTe-0.3 SnTe.

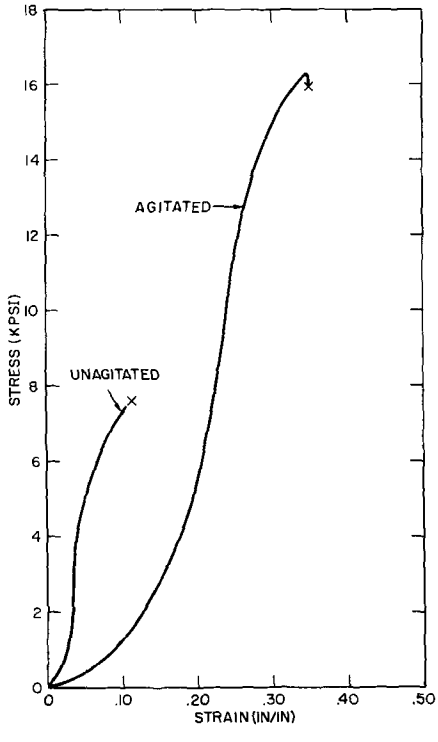

Fig. 9. Stress-strain behavior in compression of 0.7 PbTe- 0.3 SnTe prepared by directional solidification, and directional solidification with ultrasonic agitation.

The total thermal conductivity of 0.7 PbTe-0.3 SnTe has been estimated, in the absence of any measurements, as 0.02 w/cm °K at room temperature. It is probably actually lower, the data of Machonis and Cadoff indicate $k_T \approx$ 0.015 w/cm °K at 300°K; however, using 0.02 w/cm °K the room temperature figure of merit, Z, of ultrasonically prepared 0.7 PbTe-0.3 SnTe is approximately 0.6 x 10^{-3}/°K.

Mechanical properties.—The stress-strain characteristics in compression of 0.7 PbTe-0.3 SnTe prepared by directional solidification, with and without ultrasonic agitation, were measured. Rectangular specimens about 0.4 in. square by 0.3 in. long were compressed in a Hounsfield Tensometer, Type W. Strain rate was

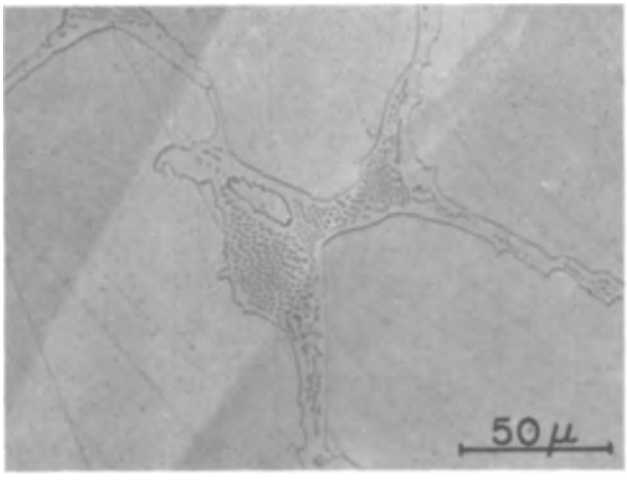

Fig. 10. Sn-Pb eutectic in grain boundaries of stoichiometric 0.7 PbTe-0.3 SnTe ingot. Magnification approximately 420X.

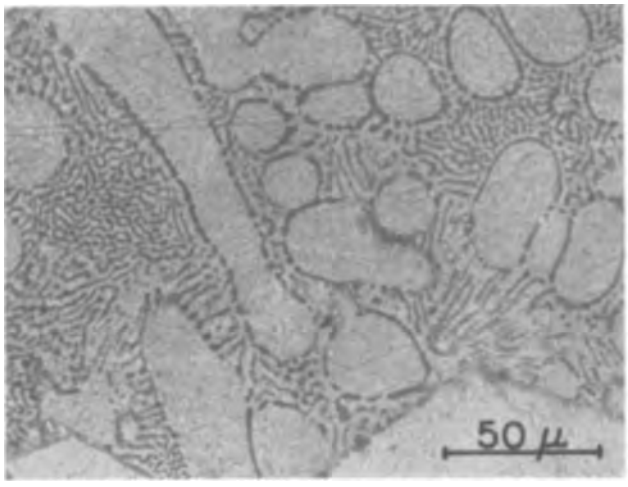

Fig. 11. Eutectic structure in last portion to freeze of unagitated ingot of 0.7 PbTe-0.3 SnTe +0.3 a/o Te. Magnification approximately 420X.

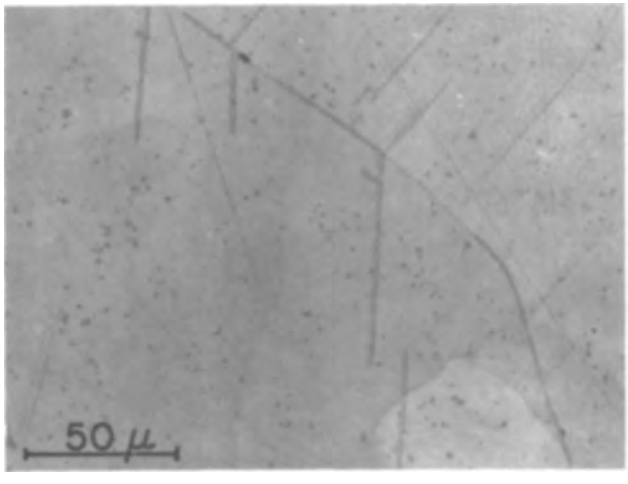

Fig. 12. Precipitation of excess Sn as stringers and spheroids in ultrasonically agitated 0.7 PbTe-0.3 SnTe. Magnification approximately 420X.

approximately 5 %/min. Results of these measurements are presented in Fig. 9. Compression was parallel to the direction of solidification in both cases. The unagitated material showed 30-40% lower strength when compressed perpendicular to the growth axis, while the agitated ingots were isotropic. The considerable improvement in strength and ductility of the agitated

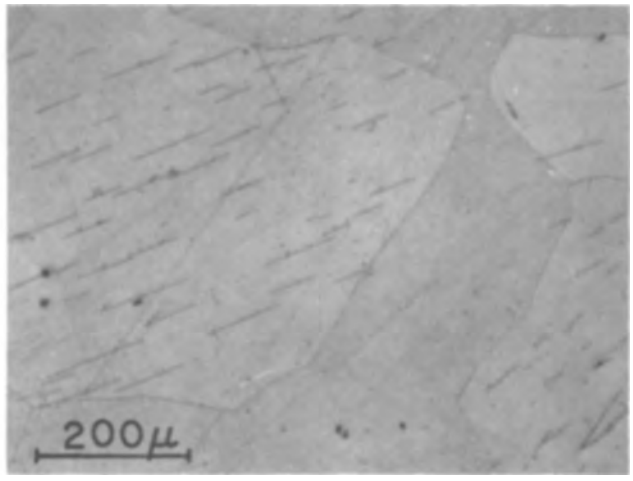

Fig. 13. Precipitation of excess Sn on slip lines in grains of ultrasonically agitated 0.7 PbTe-0.3 SnTe. Magnification approximately 85X.

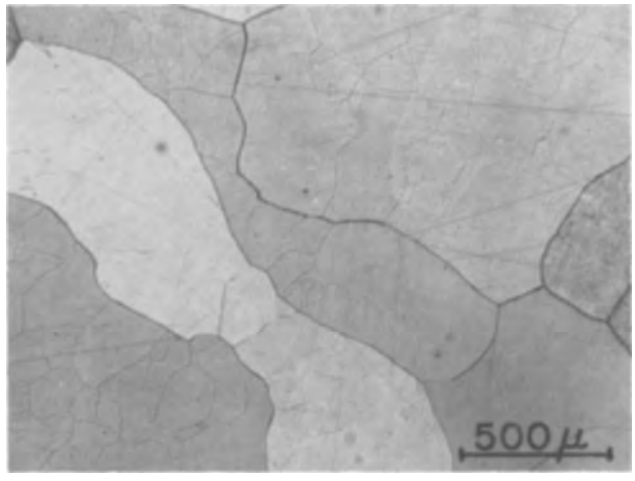

Fig. 14. Extensive subgrain array in bottom portion of ultrasonically agitated ingot of 0.7 PbTe-0.3 SnTe. Magnification approximately 42X.

material can be attributed, as in the case of PbTe in the previous study (1), to the production of a fine-grained, equiaxed structure free of inclusions and porosity. It is interesting to note that in both systems, PbTe and 0.7 PbTe-0.3 SnTe, the agitated material has twice the ultimate strength and three times the ductility of the unagitated.

Precipitation phenomena.—Some interesting observations of second phase precipitation were made during this investigation. Some ingots of 0.7 PbTe-0.3 SnTe when agitated with fairly high sound intensities (8-10 w/cm^2 at 35 kc) showed extensive intergranular porosity in the bottom third of the ingot. In the solid portion of the ingot there was an almost continuous network of eutectic phase (Fig. 10). These ingots were made with the stoichiometric amounts of Sn and Te. Due to the deviation from stoichiometry in SnTe (9, 10), a stoichiometric melt will contain an excess of Sn on solidification. It is felt that this eutectic is of Sn-Pb, which, because of its low ($\approx$185°C) melting point appeared in the grain boundaries as liquid and was then forced out by the ultrasonic irradiation and concentrated in the top of the ingot. To eliminate this problem, ingots were prepared with excess Te and the intensity of the ultrasound was slightly reduced. Addition of 0.3 a/o excess Te effectively eliminated precipitation of Sn. In the unagitated ingot a small amount of eutectic which is thought to be Te-PbTe was found in the last portion to freeze (Fig. 11). The interesting aspect of the precipitation of excess Sn in stoichiometric ingots was that moderate intensi-

ties of ultrasound resulted in a regular array of parallel stringers and tiny, random spheroids of Sn in the bulk of the grains, with very little precipitation in the grain boundaries. Figure 12 shows the intersection of the needle-like Sn with a grain boundary. Figure 13 shows the regularity of this structure and the virtual absence of Sn precipitated at the grain boundaries. It is felt that these precipitates occur on slip lines in the grains; the regularity of the array, the change in orientation from one grain to the next, the appearance of competing orientations intersecting the predominant one, (Fig. 13) and particularly the observation of subgrain formation in agitated ingots (Fig. 14) indicate deformation of the grains by the ultrasonic process. Lane, Cunningham, and Tiller (11) also observed decoration of slip lines by carbide precipitates in an Fe-Mn-Cr alloy with ultrasonic agitation of the solidifying ingot.

Silverstein *et al.* (12) found evidence of increased stress in the grain boundaries of ultrasonically agitated weldments in Ta, but in the present investigation the evidence from precipitation of excess Sn indicates that although the grain boundaries remain regions of high strain, the ultrasonic irradiation has effected a redistribution of the strain in the aggregate such that precipitation is now favored in the bulk.

Conclusions

1. Fine-grained, homogeneous p-type 0.7 PbTe-0.3 SnTe has been prepared by ultrasonic agitation of directionally solidified ingots.
2. The ultrasonic irradiation of solidifying 0.7 PbTe-0.3 SnTe produced material with twice the compressive strength and three times the ductility of directionally solidified 0.7 PbTe-0.3 SnTe.
3. The thermoelectric properties and efficiency of p-type 0.7 PbTe-0.3 SnTe (Te-rich) prepared by ultrasonic agitation are superior to those of directionally solidified unagitated material.
4. Ultrasonic agitation promotes the precipitation of excess Sn from 0.7 PbTe-0.3 SnTe in the bulk of the grains along slip planes, rather than at the grain boundaries.

Acknowledgments

The authors wish to thank Mr. E. J. Sherwin for aid in the experimental segment of the program. The financial support of the Bureau of Ships, Department of the Navy, under contract No. NObs-86015 is gratefully acknowledged.

Manuscript received Dec. 1, 1964; revised manuscript received March 10, 1965. This paper was presented at the Washington Meeting, Oct. 11-15, 1964.

Any discussion of this paper will appear in a Discussion Section to be published in the June 1966 JOURNAL.

REFERENCES

1. M. Weinstein, *Trans. AIME*, **230**, 321 (1964).
2. P. H. Klein, in "Thermoelectric Materials and Devices," p. 56, I. B. Cadoff and E. Miller, Editor, Reinhold Publishing Co., New York (1960).
3. J. R. Wallace, *J. Metals*, **15**, 5372 (1963).
4. J. G. Kura and H. W. Mishler, Defense Metals Information Center, Battelle Memorial Institute, AD Report No. 410538, Air Force Contract No. AF 33(616)-7747, May 1963.
5. R. G. Garlick and J. F. Wallace, *AFS Trans.*, **67**, 366 (1959).
6. I. G. Polotskii and G. I. Levin, *Sb. Nauchn. Rabot. Inst. Metallofiz. Akad. Nauk UKrSSR*, **13**, 176 (1961).
7. A. A. Machonis and I. B. Cadoff, *Trans. Met. Soc. AIME*, **230**, 333 (1964).
8. G. J. Cosgrove, J. P. McHugh, and W. A. Tiller, *J. Appl. Phys.*, **32**, 621 (1961).
9. J. Umeda, M. Jeong, and T. Okada, *Japan. J. Appl. Phys.*, **1**, 277 (1962).
10. R. F. Brebrick, *J. Phys. Chem. Solids*, **24**, 27 (1963).
11. D. H. Lane, J. W. Cunningham, and W. A. Tiller, *Trans. Met. Soc. AIME*, **218**, 985 (1960).
12. S. M. Silverstein, J. N. Antonvich, R. P. Sopher, and P. J. Rieppel, *Metal Prog.*, **80**, 6 (1960).

Donor Diffusion into GaAs from Group VI Compounds

R. G. Frieser

Bell Telephone Laboratories, Incorporated, Murray Hill, New Jersey

ABSTRACT

A simple and reproducible technique is presented for diffusing donors into p-type GaAs using binary sulfides, selenides, or tellurides as donor sources. Using compound sources, the effective vapor pressure of the donor impurity is reduced, thereby limiting troublesome surface erosion of the wafers during diffusion. Either a sealed or a "closed box" system is suitable. With Al_2S_3 as a doping source, observed junction depth in zinc or in cadmium doped GaAs varied linearly with the square root of time. The diffusion coefficient of sulfur is given by $D = 2.6 \times 10^{-5} \exp(-1.86/kT)$ in Zn doped GaAs. Anomalous results were obtained in Cd doped substrates at higher temperatures where higher values of the effective diffusion coefficients were observed.

Donors such as S, Se, Te, or Sn have been diffused into GaAs by several investigators (1-4). In all reported cases the donor sources were the elements themselves. Reported difficulties with this technique were alloying and formation of sulfides during diffusion which produced severe surface erosion. At diffusion temperatures both donor elements and arsenic are not only quite reactive, but volatilize to an appreciable extent (5, 6). Furthermore, in the presence of sulfur the transport problem of arsenic and gallium from the surface of the GaAs wafers is enhanced, presumably by the formation of volatile compounds (5).

The present work was directed toward employing group VI compounds (sulfides, selenides, or tellurides) as donor sources, thus reducing the vapor pressure of donor elements during diffusion. This report describes a simple and reproducible technique, using compounds as donor sources for diffusion into GaAs. The effective diffusion coefficient of sulfur has been determined and will be discussed.

Experimental

Exploratory work indicated that a practical and useful donor diffusion system for GaAs should incorporate the following features: (*a*) a minimum temperature gradient across the diffusion system to prevent surface erosion caused by transport and redeposition of material elsewhere in the system; (*b*) an oxygen-free source of arsenic to satisfy the equilibrium arsenic pressure in the system; and (*c*) a source providing a constant and low concentration of donor atoms.

These conditions were approximated in the following manner. Sealed quartz tubes were used for the major portion of this work; however, equally good results

were obtained with a "closed box" system for the diffusions (7). The temperature gradient across the sealed diffusion tube was 3°C or less during the diffusion, thereby reducing surface erosion. Crushed undoped GaAs was placed in the system to limit arsenic as well as gallium loss from the slice to be diffused (5). Sulfides were chosen as donors since the concentration of donors over these compounds in a closed system is constant and only a function of the dissociation pressure, which is uniquely determined by the temperature. A wide range of surface concentrations and junction depth is therefore possible by merely choosing a sulfide with an appropriately low vapor pressure of sulfur and a suitable diffusion temperature and time. The same argument applies to selenides and tellurides as well. One limitation on the choice of source is that the second component of the source should not form a stable arsenide at diffusion conditions.

Materials.—Table I lists the properties of the GaAs used in this work as supplied by the manufacturer on the basis of Hall and resistivity measurements. All crystals were cut into slices perpendicular to their growth direction, <111> within 5°, and ~0.38 mm thick. The slices were lapped and then chemically polished (8) on the arsenic-rich side prior to diffusion. All donor compounds came from commercial sources and were used without further treatment.

To provide the partial vapor pressure of arsenic in the diffusion system, crushed undoped GaAs (B18) (Table I) was acid washed [70 ml H_2SO_4 (95%), 15 ml H_2O_2 (30%), 15 ml H_2O] (9), rinsed with deionized water, acetone, and dried. Table II is a list of all the compounds examined on an exploratory basis as donor sources. Diffusion temperature was 900°C except for those compounds in Table II marked with an asterisk for which it was 800°C. Diffusion time was 2 hr.

Primarily because of their melting points and because little surface erosion and good junctions were obtained, the following compounds were chosen for more detailed consideration as donor sources: As_2S_3, GeS, Ga_2S_3, and Al_2S_3. Aluminum sulfide provided the bulk of the data of this work.

Procedure.—Quartz tubes (9 mm ID, 1 mm wall) were thoroughly cleaned (HF, NH_4OH, DI water) and dried at 100°C in an oven. Precisely weighed amounts of crushed GaAs (1000-4000 μg), the donor source (100-1000 μg) and one or two wafers (of different zinc concentration) were placed into the bottom of a tube. The weight of the wafers ranged from 10,000 to 80,000 μg. This tube was evacuated to ~1 Torr, heated for about 5 min at 300°C to remove any moisture, oxygen, or free sulfur, if present, and sealed while still under vacuum and hot. For donor sources other than Al_2S_3 the temperature was 150°C. Diffusions were carried out in a high-temperature furnace operated in the range of 800° to 1100° for ½ to 16 hr. The sealed diffusion tubes were placed in a heavy stainless steel jacket. Temperature gradients of 3° ± 0.5°C or less in a 12 cm temperature zone were observed during diffusions. To prevent surface deterioration after diffusion and during cooling the following procedure was found to be best. The steel jacket with the tube inside was removed from the furnace and ~¼ in. of the tube was exposed to room air for ~1 min until the steel jacket reached ~750°C (cherry red). The ampoule was then completely withdrawn from the steel jacket and the end opposite the wafer was quenched.

Evaluation.—The diffused wafers were examined microscopically (37x — 235x) for etch pits and other signs of erosion. Also, each GaAs slice was checked for weight loss following each diffusion run. Most Zn doped and many of the Cd doped wafers exhibited blemish-free surfaces after diffusion. Pitting in spots was occasionally observed. Wafers which showed weight loss in excess of 0.3% were discarded.

Films that deposited occasionally on GaAs during the quenching operation were removed by boiling the wafers in CS_2 followed by boiling in dilute (1:1) HCl, (etch rate ~100 Å/min.).

The diffused wafers were angle lapped and stained. The staining solution[1] when applied to a junction under illumination darkens the p-region with respect to the n-region or decorates the n-region preferentially with copper, depending on the conductivity difference between the two sides of the junction. Junction depths were obtained by both the standard technique (10) and by interference microscopy (11) with a general accuracy of ±0.3μ.

Table I. GaAs substrate

GaAs crystals Designation	Impurity	Impurity conc per cm³	Resistivity ohm-cm
M15	Zn	8.1×10^{16}	3.2×10^{-1}
M16	Zn	5.6×10^{17}	5.8×10^{-2}
M10	Zn	4.2×10^{18}	1.2×10^{-2}
M21	Cd	5.6×10^{17}	5.8×10^{-2}
B10	Cd	9.2×10^{17}	5.6×10^{-2}
B25	Cd	2.8×10^{17}	6.5×10^{-2}
B18	Undoped	—	—

Table II. Donor sources investigated at 900°C in crystal B25

Junctions were obtained with the following compounds	
Al_2S_3	GeS_2
Al_2Se_3	In_2S_3*
Al_2Te_3	MoS_3
As_8S_2	$MoSe_2$
As_2S_3	PtS*
As_2Se_3	P_2S_6*
As_2Se_5	SnS
Ga_2S_3	NH_4SCN
GeS	NH_2CSNH_2*
No junctions were obtained with the following compounds	
HgS*	SnS_2
MoS_2	Tl_2S
$MoTe_2$	WS_2
P_4S_3	ZnS

Results

Table III indicates that higher concentrations of sulfur can be obtained with the lower melting sulfides employed in this study. Junctions were obtained in low resistivity GaAs using As_2S_3 as a donor source while Al_2S_3 produced a junction only at higher temperatures in the same material. The highest melting donor sources did not produce a junction at 900°C in the high conductivity GaAs.

Using Al_2S_3 as the donor source the presence of either elemental arsenic or crushed GaAs resulted in the same junction depth. This observation is in contrast with Vieland's results (2). He found that the junction depth of sulfur in GaAs depended on the arsenic pressure below 1 atm. The equilibrium pressure in the present system was presumably satisfied from the lapped side of the GaAs, since only one side of the wafer was polished. That this contention is justified is supported by the following observation. In some cases the wafers exhibited weight losses (2%) without any structural changes on the polished side of the GaAs wafer. Presumably the material was lost from the lapped rather than the polished side.

Zinc out-diffusion appeared not to have been very significant in this study, although it cannot be completely ruled out. A series of experiments was performed at 900°, 1000°, and 1100°C for 2- and 4-hr

[1] Staining solution: solution A: 10g $CuSO_4 \cdot 5H_2O$ + 50 ml H_2O; solution B (8, 9): 35 ml conc. H_2SO_4 + 5 ml H_2O + 5 ml H_2O_2 (30%); stain: 1 ml of solution B + 50 ml solution A.

Table III. Comparison of junction depth as a function of mp and bp of sulfides

Wafer acceptor conc, cm⁻³	Diffusion Time, hr	Diffusion Temp, °C	Junction depth, μ	Source material	Source MP, °C	Source BP, °C
Zn 8.1×10^{16}	2	900	None	Ga_2S_3	1225	—
Zn 8.1×10^{16}	2	900	1.6	Al_2S_3	1100	1550
Zn 4.2×10^{18}	1	1100	1.6	Al_2S_3	1100	1550
Zn 4.2×10^{18}	1	900	None	Al_2S_3	1100	1550
Zn 4.2×10^{18}	1.5	900	0.2	As_2S_3	300	700

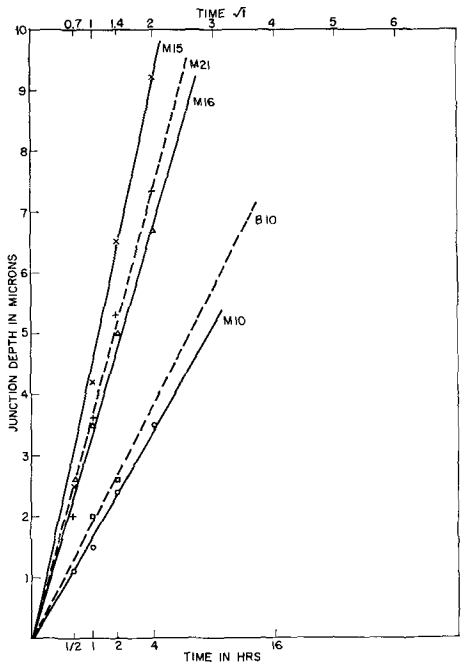

Fig. 1. Sulfur diffusion into GaAs at 1100°C
M15 x——x Zn 8.1 x 10^{16} M16 △——△ Zn 5.6 x 10^{17}
M10 ○——○ Zn 4.2 x 10^{18} M21 +——+ Cd 5.6 x 10^{17}
B10 □——□ Cd 9.2 x 10^{17}

diffusions into zinc-doped GaAs samples of two different acceptor concentrations within the same ampoule. The observed junction depths were found to be independent of the number of wafers in the diffusion capsule and the presence of wafers of other acceptor concentrations. Even though crushed undoped GaAs was present in all capsules, noticeable differences in the junction depth might have been expected if out-diffusion had been significant. Comparable experiments were not performed using the Cd doped series.

Figures 1-3 are plots of the average junction depth in microns as a function of the square root of diffusion

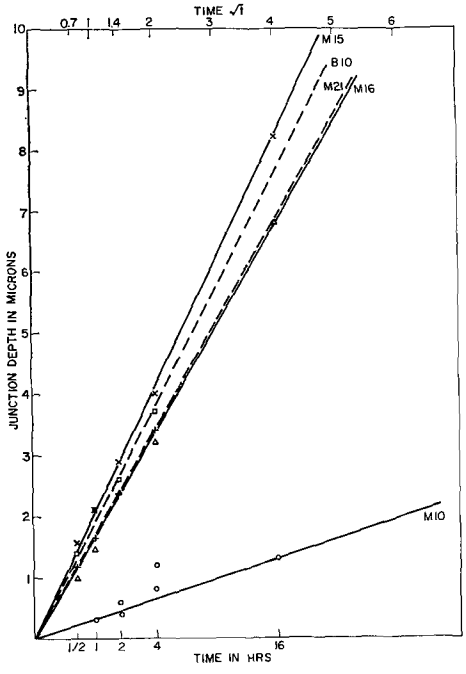

Fig. 2. Sulfur diffusion into GaAs at 1000°C
M15 x——x Zn 8.1x 10^{16} M16 △——△ Zn 5.6 x 10^{17}
M10 ○——○ Zn 4.2 x 10^{18} M21 +——+ Cd 5.6 x 10^{17}
B10 □——□ Cd 9.2 x 10^{17}

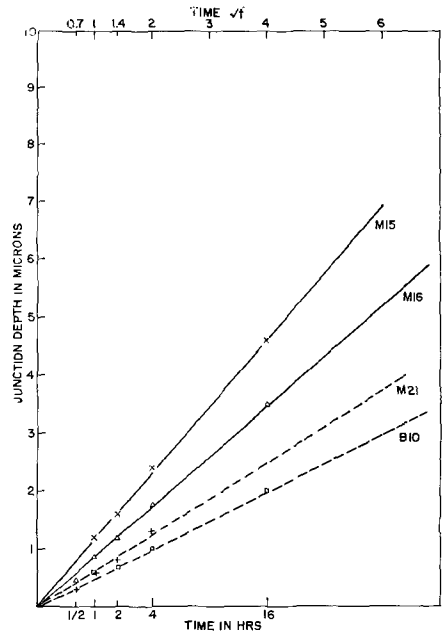

Fig. 3. Sulfur diffusion into GaAs at 900°C
M15 x——x Zn 8.1 x 10^{16} M16 △——△ Zn 5.6 x 10^{17}
M21 +——+ Cd 5.6 x 10^{17} B10 □——□ Cd 9.2 x 10^{17}

time for the various wafers using Al_2S_3 as the donor source. It is assumed, since no junction was observed for sample M10, that the maximum concentration of electrically active sulfur was $<4 \times 10^{18}$ cm^{-3} at 900°C. Because erosion problems were encountered in the Cd runs, the precision of these data is not as high as that of the Zn runs. For that reason the Cd data will be discussed separately. Figure 4 shows photomicrographs (90X) of representative junctions obtained in M15 (900°C, 16 hr) using Al_2S_3 as a donor source and in two samples of M15 (1100°C, 1 hr) using GeS and As_2S_3.

Estimation of apparent diffusion coefficients.—Although neither the surface concentration nor the dis-

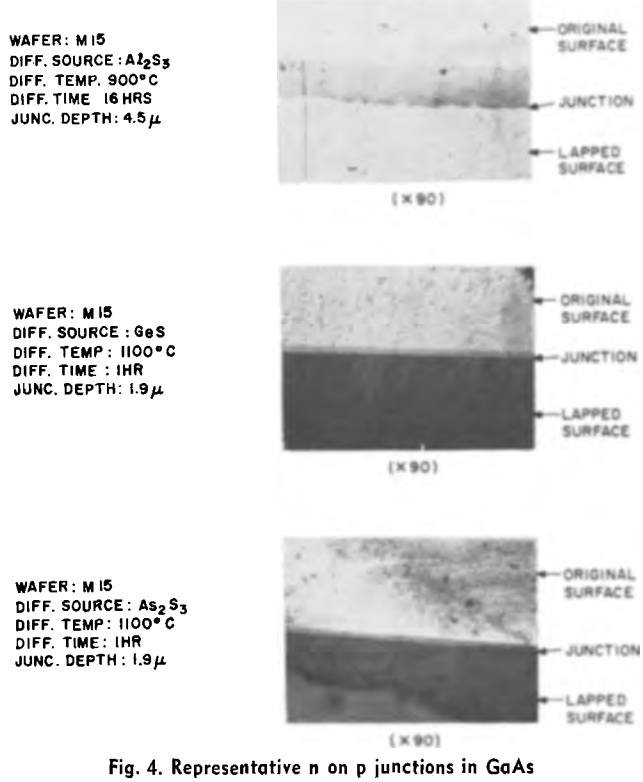

Fig. 4. Representative n on p junctions in GaAs

Table IV. Calculated diffusion coefficients in cm^2/sec

Wafer pairs		GaAs—1100°C 2 hr	4 hr
(a)	M15	3.9×10^{-12}	3.9×10^{-12}
	M10	4.2×10^{-12}	3.2×10^{-12}
(b)	M15	4.0×10^{-12}	4.1×10^{-12}
	M16	3.8×10^{-12}	3.9×10^{-12}
(c)	M10	3.8×10^{-12}	4.0×10^{-12}
	M16	3.8×10^{-12}	3.9×10^{-12}

$D_{1100} = 3.9 \pm 0.2 \times 10^{-12}$; $D_{1000} = 1.1 \pm 0.2 \times 10^{-12}$; $D_{900} = 2.9 \pm 0.2 \times 10^{-13}$.

tribution profile of sulfur in these wafers was known, effective diffusion coefficients were estimated, using a modification of a method employed by Fuller (12). The following assumptions had to be made:

1. At a given temperature the same effective donor concentration exists above Al_2S_3 in all capsules.
2. All wafers have the same surface concentration of donors, under the same diffusion conditions.
3. The diffusion coefficient is independent of the donor and the acceptor concentration (a frequent, although not necessarily correct assumption).
4. The supply of donors is essentially unlimited in the diffusion system.
5. Sulfur diffusion in GaAs follows a complementary error function distribution.

On the basis of these assumptions, the surface concentrations are the same for a given temperature and the following equation is applicable

$$\frac{N_1}{N_2} = \frac{\text{Erfc } (X_1/2\sqrt{Dt})}{\text{Erfc } (X_2/2\sqrt{Dt})} \qquad [1]$$

X is the junction depth in cm, D the diffusion coefficient in cm^2/sec, t the diffusion time in seconds, and N_1 and N_2 are the Zn concentrations in the two crystals chosen (Table I). Using paired values of the observed junction depth in GaAs samples of different acceptor concentrations the diffusion coefficients of sulfur were calculated by a technique of successive approximations (curve fitting) (12). Table IV shows the values obtained by this technique for Zn doped wafers at 1100°C as well as the averages for 1000° and 900°C.

These values are plotted in Fig. 5 and, within experimental error, lie on a straight line. The activation energy for sulfur diffusing into GaAs computed from these data is 1.86 ± 0.01 ev. The diffusion coefficient can be thus described by the equation $D = 2.6 \times 10^{-5} \exp(-1.86/kT)$.

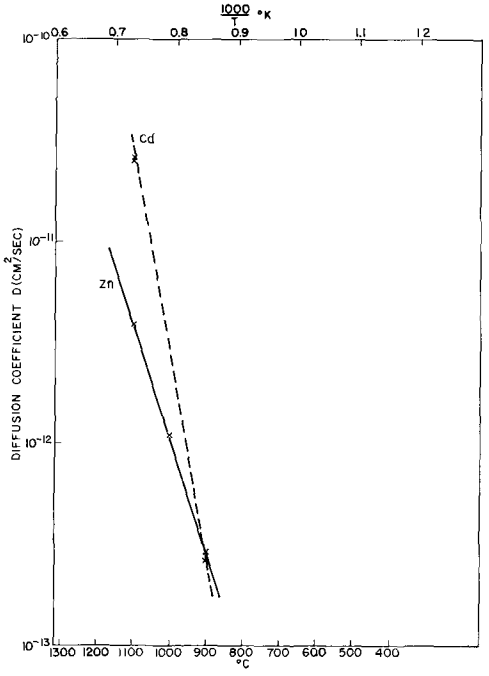

Fig. 5. Diffusion constants of sulfur in GaAs. The variation of the calculated D with $1/T$ for the Zn and Cd experiments is attributed partially to the effects of out diffusion. The Zn data (solid line) are considered more reliable (see text).

Zn doped
$D_{900} = 2.9 \pm 2.0 \times 10^{-13}$
$D_{1000} = 1.1 \pm 0.2 \times 10^{-12}$
$D_{1100} = 3.9 \pm 0.2 \times 10^{-12}$
$D = 2.6 \times 10^{-5} e^{-1.86/KT}$

Cd doped
$D_{900} = 3.6 \times 10^{-13}$
$D_{1100} = 2.6 \times 10^{-11}$
$D = 4.4\ e^{-3.06/KT}$

Discussion

The straight line relationship between the junction depth and $(\text{time})^{1/2}$ indicates that Fick's law is obeyed in these experiments. Out-diffusion of zinc was found to be small, if not negligible, on the basis of special experiments. The activation energy obtained in this study agrees closely with that reported by Vieland (2) who based his value on junction migration studies. The present value is about one half that reported by Goldstein (1) from his radiotracer studies. Table V summarizes the literature values and those of this study.

Fane and Goss, studying the diffusion of Sn and Se in GaAs (3), have observed that junction depths are consistently less than penetration depth when determined by radiotracer techniques. Tannenbaum had observed that the phosphorous concentration in silicon determined by radiotracer techniques was larger than that determined by electrical measurements (13) and concluded that not all impurity atoms in a semiconductor contribute to the conductivity.

It may be appropriate to consider the Cd data plotted as dashed lines on Fig. 1-3. Even though these data were not as reliable as the Zn data the points which could be determined lie on straight lines passing through the origin and, therefore, deserve consideration. The diffusion coefficients could only be calculated at 900° and 1100°C which yielded values of $D_{900} = 3.6 \pm 0.1 \times 10^{-13}$ and $D_{1100} = 2.6 \pm 0.1 \times 10^{-11}$. This is equivalent to an effective activation energy of 3.06 ev and a $D_o = 4.4$. As discussed previously, out-diffusion did not appear to play an important role in the zinc experiments. Unfortunately, even less is known about the out-diffusion of Cd. While it is possible that the effects observed here are due to some extent to Cd out-diffusion, this cannot be resolved on the basis of the present work. However, it is possible that the difference is due partially to another effect. Certain anomalies exist in the data as plotted in Fig. 1-3. Sulfur diffusion into Zn or Cd doped GaAs of the same acceptor concentration might be expected to yield data giving comparable slopes. This is observed for diffusions at 1100° and 1000°C, but not at 900°C (Fig. 1-3, M16 and M21). The relative position of the lines with respect to each other should be the same at each diffusion temperature. This is found to be the case for Zn doped GaAs. For Cd doped GaAs a reversal of this order takes place at 1000°C. While there is a large uncertainty in the precision of the Cd points, it appears that the general relationship of these lines to each other is real.

There appears to be a correlation between the relative position of these lines and the intrinsic temperature. GaAs is extrinsic at the indicated temperatures if the impurity concentration exceeds the values shown in Table VI. With the data of this table applied to the experimental findings, the following picture emerges.

Table V. Sulfur diffusions into GaAs

	E, ev	D_o, cm^2/sec*	$D_{1100°C}$, cm^2/sec
This work	1.86 ± 0.01	2.6×10^{-5}	3.9×10^{-12}
Vieland (2)	1.8 ± 0.8	—	—
Goldstein (1)	4.04	4×10^{3}	6.0×10^{-12}

*$D_T = D_o \exp - E/kT$.

Table VI. Intrinsic-extrinsic conditions of GaAs at diffusion temperatures

Intrinsic carrier concentration (14)
WAFERS

Desig-nation	Type	Acceptor conc, cm^{-3}	Condition at diff. temp. 1100°C 1.7×10^{18}	1000°C 7×10^{17}	900°C 3×10^{17}
M10	Zn	4.2×10^{18}	ex.	ex.	ex.
M15	Zn	8.1×10^{16}	int.	int.	int.
M16	Zn	5.6×10^{17}	int.	int.	ex.
M21	Cd	5.6×10^{17}	int.	int.	ex.
B10	Cd	9.2×10^{17}	int.	ex.	ex.

Table VI shows that M21, M16, and B10 are intrinsic at 1100° and extrinsic at 900°C. Figures 1 and 3 show that at these temperatures the slope of these respective lines increases regularly as the acceptor concentration of the wafer to be diffused decreases. Differences in the slope of M21 and M16 may reflect out-diffusion at these temperatures. At 1000°C (Fig. 2) the slope of B10 is steeper than that of M21 and M16. At this temperature, however, B10 is extrinsic whereas both M21 and M16 are intrinsic (Table VI). This may suggest an influence of the electric field on donor diffusions into GaAs and the possibility that the activation energy for the diffusion of sulfur into GaAs is dependent not only on the presence but on the type of acceptor (*i.e.*, Zn or Cd) as well. Further work to investigate these anomalies is required before definite conclusions can be drawn.

It should be pointed out, too, that defects in the crystal structure, which are known to affect the diffusion coefficient (4) were not taken into account in this study.

Summary

A simple and reproducible technique is described for the donor diffusion into GaAs using group VI compounds as sources. This technique limits surface erosion and permits control over the donor concentration. Junction migration studies have provided values for the effective activation energies for the diffusion of S in Zn-doped GaAs comparable to those in the literature. Discrepancies observed in Cd doped wafers could partially be attributed to out-diffusion. It is, however, suggested that the sulfur diffusion into GaAs may also be affected by the presence or absence of an electric gradient in the GaAs during the diffusion. This effect if present, appears to be impurity dependent.

Acknowledgment

The author wishes to thank C. S. Fuller, J. M. Whelan, J. Klerer, and Mrs. E. Handelman for their helpful discussions and advice, and L. J. Boccia for technical assistance.

Manuscript received Jan. 19, 1965. This paper was presented at the Toronto Meeting, May 3-7, 1964.

Any discussion of this paper will appear in a Discussion Section to be published in the June 1966 JOURNAL.

REFERENCES

1. B. Goldstein, *Phys. Rev.*, **121**, 1305 (1961).
2. L. J. Vieland, *J. Phys. Chem. Solids*, **21**, 318 (1961).
3. R. W. Fane and A. J. Goss, *Solid-State Electronics*, **6**, 383 (1963).
4. L. R. Weisberg, *Trans. Met. Soc. AIME*, **230**, 291 (1964).
5. L. R. Weisberg, Editor, Scientific Rep. No. 7, High Temp. Semicon. Res. (RCA), April-June 1961, p. 34.
6. J. van Den Boomgaard and K. Schol, *Philips Research Repts.*, **12**, 127 (1957).
7. L. A. D'Asaro, *Solid-State-Electronics*, **1**, 3 (1960).
8. M. V. Sullivan and G. A. Kolb, *This Journal*, **110**, 585 (1963).
9. T. A. Cunnel, J. T. Edmond, and W. R. Harding, *Solid-State Electronics*, **1**, 97 (1960).
10. C. S. Fuller and J. A. Ditzenberger, *J. Appl. Phys.*, **27**, 544 (1956).
11. N. L. Bond and F. M. Smits, *Bell System Tech. J.*, **35**, 1209 (1956).
12. C. S. Fuller, *Phys. Rev.*, **86**, 136 (1952).
13. E. Tannenbaum, *Solid-State-Electronics*, **2**, 123 (1961).
14. Scientific Rep. No. 7A, Application of Tunneling to Active Diode (GE), January 1962, Fig. 10.

Photovoltaic Effects at Rectifying Junctions to Deposited CdS Films

M.Bujatti[1] and R. S. Muller

College of Engineering, University of California, Berkeley, California

ABSTRACT

The photovoltaic response of blocking contacts to deposited CdS films has been measured in the wavelength range 0.3-1.3μ. Film properties as deduced from these measurements are compared with inferences drawn from photoconductivity behavior and with information on film treatment. Although evidence for photoemission of electrons from the rectifying contacts was sought, none was found. An interesting interference phenomenon was observed in thicker films. The phenomenon can be traced to standing-wave patterns in the films.

The photovoltaic effect at rectifying contacts made to vapor deposited CdS thin films has been studied. The CdS films were deposited using the technique described by Zuleeg and Senkovits (1). The quality of the CdS films deposited was found to depend critically on the temperature of the substrate with respect to the temperature of the source; films deposited on a cold substrate were dark orange or black and conductive, while those deposited on a properly heated substrate were lemon yellow and highly resistive. These characteristics are believed to be related to differing amounts of excess Cd present in the films.

The metals used to make contacts to the CdS films were Al, Cu, Te, and Au. Of these, only Al formed an ohmic contact; Cu, Te, and Au formed rectifying contacts. The photovoltaic effect at the junction was detected as a function of light intensity and wavelength. The dependence on light intensity was found to be linear. The dependence on wavelength varied slightly with the metal involved. Some common features were observed:

1. The photovoltage *vs.* wavelength plots achieved a maximum value beginning at a wavelength which varied with the metal involved and ending at approximately 0.5μ (which corresponds energetically to the CdS band gap).
2. The lower wavelength limits corresponded to photon energies varying linearly with the work function of the metal forming the junction.
3. In addition to the main response these photovoltage plots consistently exhibited a weak maximum (between 10^{-1} to 10^{-2} times weaker than the main peak) at a wavelength of 850 mμ. At this wavelength value a peak was observed both in the absorption and in the photoconductivity measurements on the CdS films. The peak at 850 mμ is therefore attributed to a transition internal to the CdS.
4. No evidence of photoemission from the metal was found. No simple relation holds between the response in the long wavelength region and the thickness of the metal layer or the metallic work function. The weak response which was detected at long wavelengths was probably due to the presence of impurity states in the CdS band gap.

Fabrication of the Samples

The structure of the diodes used in the experiments is shown in Fig. 1. The three differing geometries shown in Fig. 1 were adopted to determine if anisotropy in the properties of the films might affect photovoltage measurements. In fact, all diode structures behaved in substantially the same way. Two sources provided the CdS which was used to make the diodes: (*a*) CdS powder (mat 33-C-291) from RCA Laboratories;[2] (*b*) CdS powder of an ultra-high purity grade from Eagle Picher Company. The resistivity of the material was measured by compressing the powder in a ceramic cylinder between a copper plate and a screw tightened to the cylinder. The value of the resistivity as obtained from this measurement was of the order of 10^7 ohm-cm. The over-all electrical results obtained with either material (*a*) or material (*b*) were substantially the same.

The films were deposited on glass substrates which were heated to temperatures ranging from 150° to 350°C. A source similar to that described by Zuleeg and Senkovits (1) was used. The color of the films deposited ranged from a dark orange for substrate temperatures near 150°C to yellow for the higher temperatures. The resistivity varied correspondingly from 1 ohm-cm to approximately 10^4 ohm-cm in the dark. The films evaporated on warm substrates were all photosensitive to some degree, with the sensitivity depend-

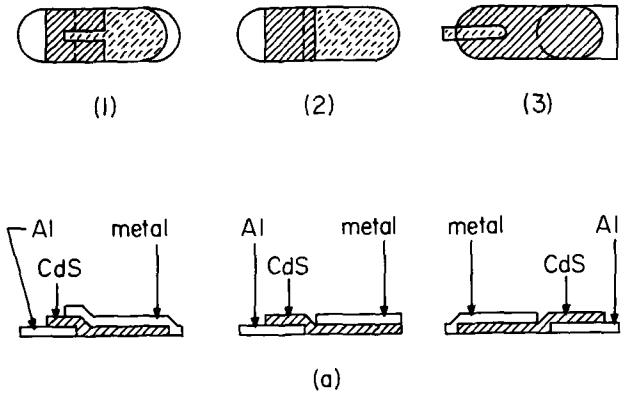

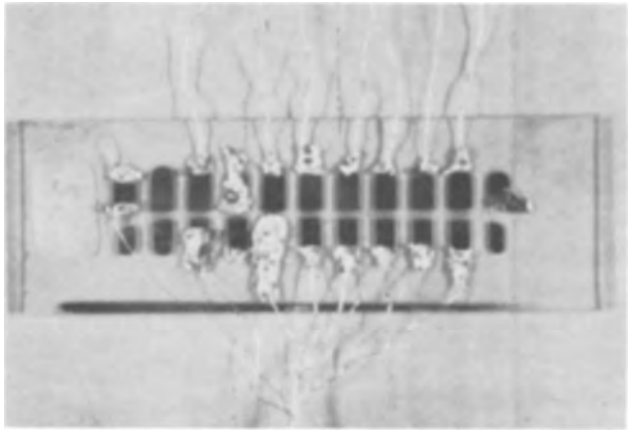

Fig. 1. Different shapes adopted for the diodes. An example of type I is shown in (b) (bottom) in actual size.

[1] Present address: Facoleta di Ingegneria, Universita di Roma, Italy.

[2] Kindly supplied by Dr. P. K. Weimer of the RCA Laboratories, Princeton, New Jersey.

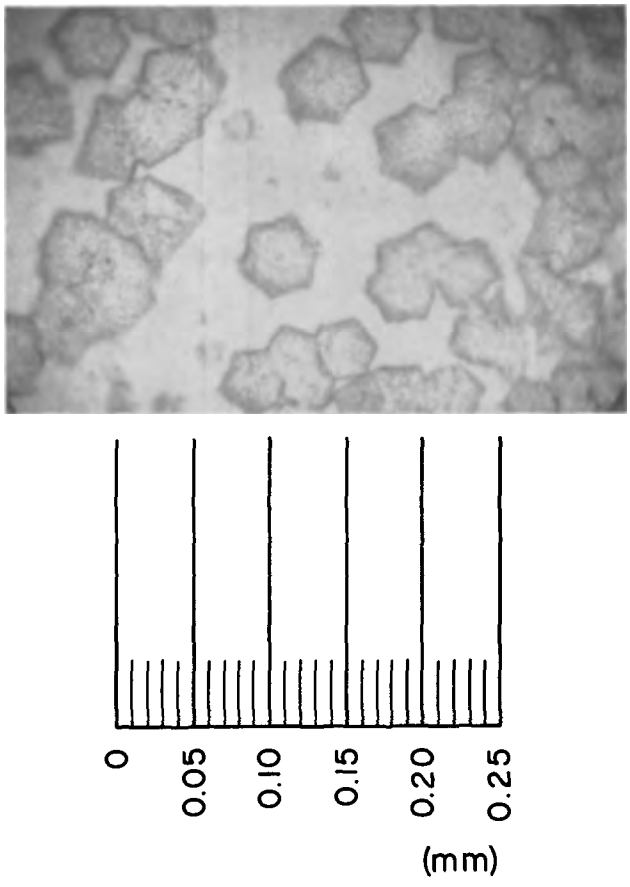

Fig. 2. Etch patterns on a CdS film deposited on a substrate warmed at 150°C.

ing on the temperature of the substrate. Ratios of dark to room-light resistivities of 2:1 or 3:1 were typical. When the temperature of the substrate reached or exceeded 300°-350°C, the deposition became slow and re-evaporation was observed. An optimum substrate temperature seems to be about 200°C when the source temperature is around 750°-800°C. The composition of the films also varied with the thickness of the deposit; thinner films showed higher conductivity than thicker ones for the same temperature of evaporation.

The crystallographic structure of the CdS films was studied via x-ray examination. Diffraction patterns from the films contained only one strong line corresponding to the (002) direction of the hexagonal structure. The line corresponding to the (101) direction (the strongest line for randomly oriented powders) was much weaker in the pattern from the films and was of the same order as the line corresponding to the (004) direction (*i.e.*, the second-order diffraction in the direction of the principal hexagonal axis). The intensity ratio between the (002) and (101) lines was approximately 10^4, while a randomly oriented sample would give a ratio 59/100 for these lines. Two weak lines corresponding to CdO were detected on the x-ray pattern from a sample deposited on a cold substrate and baked in air at 350°C.

Some of the samples were etched by exposure to warm vapors of concentrated HCl. Under microscopic examination at 200 magnification, no crystalline pattern was detectable on the samples evaporated on a cold substrate, postbaked or not. On films deposited on a warm substrate, hexagonal patterns ranging in size up to 40-50μ were observed (Fig. 2). These patterns may either be $CdCl_2$ precipitates or else actual etch pits. Recent work on this question will soon be published. The Al and CdS layers were deposited in a two-step evaporation, without opening the bell jar in order to avoid oxidation of the Al layer. The counter electrode (Cu, Au, or Te) was then deposited in a straight-forward manner. The metal-CdS diode cells fabricated in this laboratory and discussed in this paper belong to five sets of samples. Table I summarizes the fabrication data for these samples.

Table I. Sample fabrication properties

Slide No.	Structure	Evaporation pressure,* Torr	Temp. substr, °C	Temp. source, °C	Thickness of CdS, μ**	Dark resistivity, ohm-cm
51	Al-CdS-Au	1.9×10^{-7}	300	780	0.098	4.9×10^3
54	Al-CdS-Te	3×10^{-7}	250	780	0.243	5.8×10^2
55	Al-CdS-Cu	3×10^{-7}	275	770	0.164	6.6×10^3
56	Al-CdS-Cu	3.5×10^{-7}	250	760	0.115	2.3×10^3
59	Al-CdS-Au	1.2×10^{-7}	285	780	0.140	3.1×10^3

* The pressure was measured at the throat of the chamber just before the evaporation started; during evaporation, the pressure typically reached 2 or 3×10^{-6} Torr.

** The thickness was measured by using a Normarski-type interferometer.

Experimental Results

No appreciable bulk photovoltage was detected across CdS films deposited on warm substrates, the connections being made through In-soldered ohmic contacts. (In a few cases photovoltages which never exceeded a few microvolts were obtained at such junctions under very concentrated visible illumination.[3]) Somewhat larger bulk photovoltages were obtained on some CdS samples deposited on substrates at lower temperatures. The maximum value of the bulk photocurrent detected was 0.2 nA (1 Mohm meter resistance). This was measured on a 1μ thick sample having a resistivity of 2.75 ohm-cm. The bulk-generated photocurrent varied quite irregularly when a concentrated beam of light was moved along test samples which consisted of ohmic contacts made to the opposite edges of films 1.2 cm in length. This photocurrent probably stemmed from a nonuniform distribution of impurity states in the film, which gave rise to a nonuniform conductivity. Potential barriers at the microcrystal boundaries could also be responsible for the detected photoeffect. In all cases, however, and particularly in the case of the films deposited on warm substrates, the bulk photovoltage was negligible in magnitude when compared to the photovoltages measured at metal blocking contacts to the CdS films.

A Bausch and Lomb monochromator with a coil-filament tungsten bulb was used as a light source. Photovoltaic response was measured in a range of wavelengths extending from 0.325 to 1.6μ, obtained by using two different diffraction gratings (0.325-0.800μ and 0.700-1.600μ). The intensity of illumination at each

[3] G. O. Müller has reported measurements of ohmic-contact photovoltage responses. *Phys. Stat Solidi*, 3, 523 (1963).

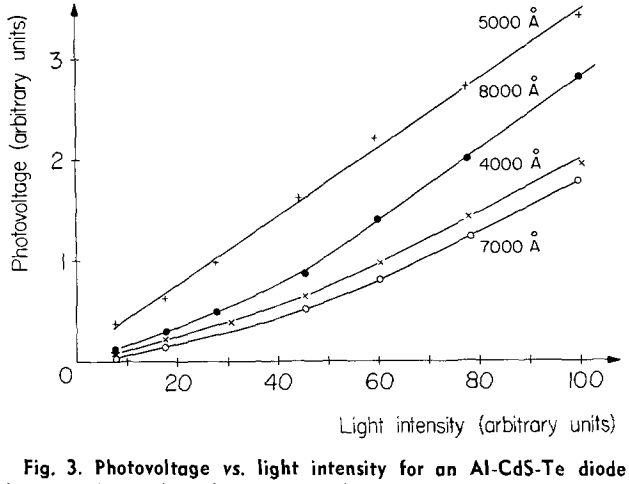

Fig. 3. Photovoltage vs. light intensity for an Al-CdS-Te diode (unit 54.3) at five different wavelengths. The polarity of the photovoltage was such as to make the blocking contact positive.

wavelength was varied by adjusting the monochromator supply voltage with a variac. The measured photovoltage depended linearly on the intensity, and was of a polarity to make the blocking contact positive. A typical curve of photovoltage *vs.* light intensity for an Al-CdS-Te sample is shown in Fig. 3.

Figure 4 shows typical curves of the measured photovoltage versus wavelength for three different metal-CdS rectifying contacts. Several features common to all three curves are easily understood.

1. The measured photovoltage drops in each case all three curves are easily understood.

ev, this energy is near to values reported for the CdS band gap at room temperatures (2).

2. In each case the photovoltage becomes appreciable at a short wavelength which varies with the metal used to make the blocking contact.

3. A much smaller peak is detectable for a wavelength of about 850 mμ.

In order to investigate further the nature of the peaks detected in the photovoltaic response, both the photoconductive response and the absorption spectrum of the CdS films were also measured. Curves obtained from these measurements are shown in Fig. 5 and 6. Finally, the photovoltage measurements obtained on the diodes fabricated in this laboratory were compared with the measurements made on samples supplied by R. Zuleeg of the Hughes Microelectronics Division, Newport Beach, California. Measurements on the Hughes units are plotted in Fig. 7 for a typical cell. The Hughes samples were Au-CdS diodes with different thicknesses of the Au-layer, deposited in the structure described by Zuleeg (1). The CdS powder used by Zuleeg was supplied by Harshaw Chemical Company.

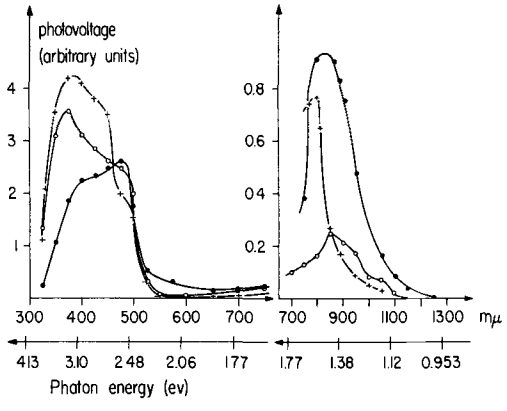

Fig. 4. Photovoltage *vs.* wavelength for three CdS diodes: +, Al-CdS-Te; •, Al-CdS-Cu; ○, Al-CdS-Au.

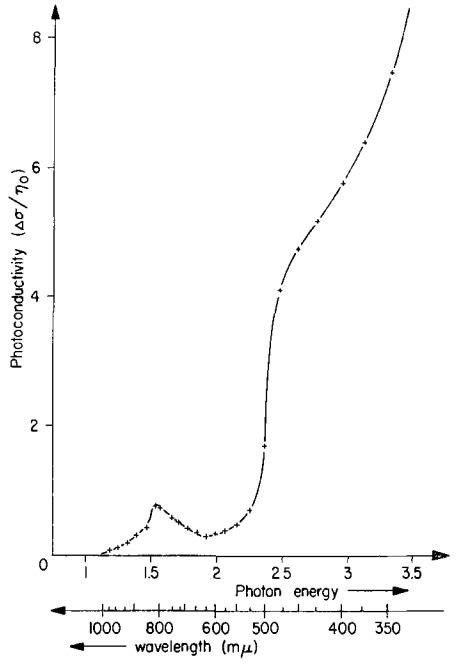

Fig. 5. Photoconductive response *vs.* photon energy for a deposited CdS film.

Discussion of Results

It is found that evaporation in a vacuum of roughly 10^{-6} Torr leads to dark-colored low-resistivity films when the substrate temperature is roughly 150°C or less (with a temperature of about 850°C for the source). At temperatures below 150°C the vapor pressure of free Cd is less than 10^{-5} Torr, and hence free Cd condensation is likely. Free S has a vapor pressure more than four orders of magnitude higher than free Cd in this range of temperatures, so that excess S is not likely to be present in the evaporated films. The dark color and low resistivity can thus be plausibly connected with the presence of Cd excess, either by virtue of S vacancies in the lattice, or else because of interstitial Cd atoms. Recent work with radioactive tracers by Woodbury (3) has indicated that interstitial Cd is very unlikely in CdS crystals.

It was possible to alter the resistivity of the films, which were deposited on a cold substrate by baking them in an open tube under a H_2 atmosphere for roughly 30 min at 350°C. During this heat-treatment, the films changed color from dark orange to pale yel-

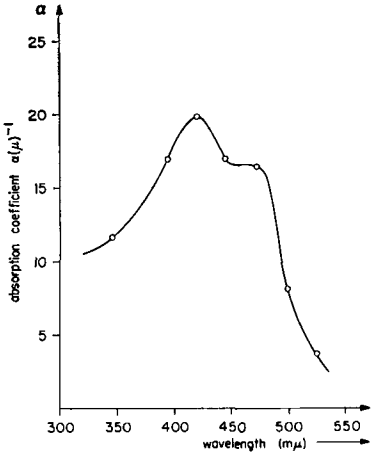

Fig. 6. Absorption spectrum for a deposited CdS film

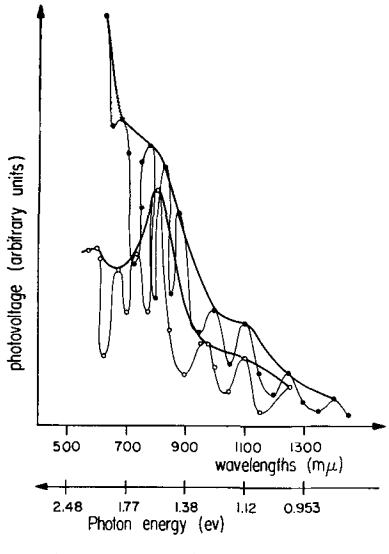

Fig. 7. Photovoltage *vs.* wavelength for two Al-CdS-Au diodes showing interference phenomena: ○, thinner Au layer (a); •, thicker Au layer (b).

low and simultaneously increased in resistivity by as many as six orders of magnitude from their as-deposited condition. By contrast, it was found that air-baking in an open tube of samples for times comparable to the hydrogen bake resulted in a much smaller resistivity change while preserving the striking color change. The increased resistivity is thought to stem from the elimination of the excess Cd at the crystallite surfaces. The comparative ineffectiveness of air baking may be a result of the oxidation of the Cd at the material surface; which may act to inhibit further Cd diffusion. (CdO was observed in the x-ray spectrum of air-baked samples.) Berger *et al.* (4) have explained measurements on CdS films which were heat treated in vacuum by postulating the presence of two competing processes. The first is the diffusion of excess Cd to the surface where it is vaporized, and the second is the creation of sulfur vacancies near to the crystal surface owing to CdS dissociation. The increase in resistivity and color changes which we have observed suggest that the elimination of excess Cd predominates at low temperatures outside of vacuum. Somorjai and Jepsen (5) argue that the relatively fast diffusion which adjusts the resistivity of annealed CdS films is due to sulfur-vacancy migration from the Cd-rich interior to the surface. The diffusion constant for substitutional Cd (3) is far too low to be effective for the annealing times and temperatures that we have used. The sulfur-vacancy diffusion constant, while not known in detail, appears to have a value of about 10^{-5} at 800°C and a very low, but as yet undetermined, activation constant. A diffusion constant of this order would fit the relatively rapid change in resistance which we have observed on annealing.

The energy levels associated with Cd or S vacancies or with interstitial Cd are not known exactly, although there is general agreement in the literature that S vacancies result in electronic energy levels located roughly 0.2 ev below the conduction band, if doubly charged, and 0.5 ev below the conduction band, if singly charged (6).

In order to interpret the photovoltaic response data, we first discuss the photoconductivity and transmission data of Fig. 5 and 6. The photoconductive response curve in Fig. 5 is a plot of $\Delta\sigma/n_o$ *vs.* photon energy where $\Delta\sigma$ is the increase in photoconductivity and n_o is the photon flux. The expected large photoconductive response for photon energies near and above the band gap is evident. Also present in the photoconductivity data is a smaller peak in the neighborhood of 1.5 ev (830 mμ). Evidence for energy absorption at 1.5 ev was also obtained from transmission measurements.

The general character of the observed photovoltage *vs.* wavelength curves (Fig. 4) is seen to be approximated fairly closely by the spectral absorption curves of Fig. 6. Minor variations in the curve shapes with varying metallic electrodes can be partly understood in terms of differing reflectivities by the contacts themselves. In the short-wavelength region, the photovoltage *vs.* wavelength curves drop more rapidly than does the absorption coefficient curve. The short wavelength decrease in photovoltage occurs at different wavelengths depending on the metal forming the junction. The photon energies which correspond to the point at which the curves drop are proportional to the work function of the metal, as is evident in Fig. 8. Although too many factors are unknown for an exact quantitative analysis, the proportionality between work function and photovoltage decrease may be caused by the dependence of space-charge layer thickness on surface-barrier height. The short free-hole diffusion length in CdS would confine all photovoltaic effects to the space-charge layer, and hence any photoresponse would be a sensitive function of the depletion layer width, which, in turn, is dependent on the electrode metal's work function.[4]

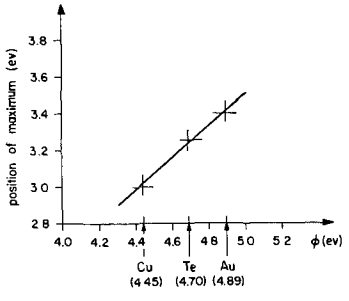

Fig. 8. Position of the first peak in the low wavelength region of the photovoltaic response as a function of the work function of the metal forming the junction.

No evidence is found in any of the samples of the presence of photoemission of electrons from the metal as found by Williams and Bube (7). There is in all the curves a background which could be interpreted according to Williams and Bube's theory, but no simple relation has been found between the responses obtained from samples with differing thicknesses of the metal layer and between the metal forming the junction and the shape of the curve. In the long wavelength region, where metallic photoemission should be observed under the Bube and Williams hypothesis, both the photoconductivity response and the transmission spectrum show evidence of transitions inside the CdS. The photoconductivity increases and the transmission shows many weak absorption and emission peaks. These points seem to suggest that the response in the region considered is probably due to the presence of distributed impurity and imperfection levels in the CdS. The peak at 850 mμ appears in all diodes studied and is therefore certainly due to a transition internal to the CdS.

Results quite similar to those obtained for the diodes fabricated in this laboratory were also measured on the diodes fabricated by the Hughes Semiconductor Division. Since the CdS layers in the Hughes diodes were almost ten times thicker than the CdS layers deposited in this laboratory, the response for energies higher than the band gap was nearly completely nulled by photon absorption in the CdS layer, when illuminating from the Al side of the Hughes diode. The response obtained with illumination from the Au side was quite similar to that obtained from the units fabricated in this laboratory. Also, for the Hughes diodes the response at higher wavelengths could be due both to photoemission and to distributed trapping levels in the CdS. Here we do not have any data on the CdS transmission and photoconductivity to be compared with the photovoltaic response. Again there is no evidence for photoemission from the metal, as no simple relation is found between the back and the front responses and between the responses of two units having differing thicknesses for the Au layer (Fig. 7). A rigorous comparison is not possible owing to the presence of superimposed oscillations in photovoltage *vs.* wavelength due to an interesting interference phenomenon in the CdS layer.

To prove the validity of an interference hypothesis in explaining these oscillations in measured photovoltage, we have compared the wavelength of the incident light corresponding to the maxima in the photovoltage oscil-

[4] This mechanism was suggested by Professor A. C. English.

Table II. Measured and calculated wavelengths at photovoltage maxima

m	$2nd/m$, μm, calc	Maxima, μm, meas.
6	1310	1250
7	1125	1100
8	990	1000
9	878	875
10	790	775
11	716	725
12	660	670
13	607	600

lations with the wavelength values obtained by assuming the effect to be caused by standing wave patterns formed from reflections at the Au and Al surfaces. If standing wave patterns are present one can predict the maxima to occur for $2nd = m\lambda$, where n is the refractive index of the CdS (2.5), $d = 1.58\mu$ is the thickness of the CdS layer, and m is an integer. In Table II the wavelengths of the maxima of sample a measured on Fig. 7 are compared with those calculated from the theory just proposed. A similar comparison holds for unit 6 of Fig. 7 which had a CdS layer 2.05μ thick.

It can be seen that the agreement between theory and measurements is quite reasonable. The presence of the interference phenomenon makes it difficult to detect clearly the position of any maxima in the long-wavelength region that may result from other physical mechanisms. The interference phenomenon is not present in the diodes fabricated in our laboratory because of the difference in structure and of the semitransparent metal layer.

Conclusion

CdS films obtained by evaporation with both the temperature of the substrate and the temperature of the source opportunely controlled show a microcrystalline structure, having a high degree of orientation. The pale-yellow color and the high resistivity of the films indicate that large amounts of excess Cd are not present. Metal junctions to these films show a photovoltaic effect when illuminated with light in the wavelength region between 350 and 500 mμ; the first limit depending on the metal involved. No evidence for photoemission in the long-wavelength region has been detected.

Manuscript received Jan. 28, 1965. This report was prepared by the University of California, Electronics Research Laboratory under USAF Contract No. AF-33(616)-7553 and AF-33(615)-1045.

Any discussion of this paper will appear in a Discussion Section to be published in the June 1966 JOURNAL.

REFERENCES

1. R. Zuleeg and E. J. Senkovits, Abstract 95, Paper presented at the Pittsburgh Meeting of the Society, April 15-18, 1963.
2. R. H. Bube, "Photoconductivity of Solids," p. 233, J. Wiley & Sons, Inc., New York (1960).
3. H. H. Woodbury, *Phys. Rev.*, **134**, A492 (1964).
4. H. Berger, E. Gutsche, W. Kahle, and G. Lebmann, *Phys. Stat. Sol.*, **3**, 265 (1963).
5. G. A. Somorjai and D. W. Jepsen, *J. Chem. Phys.*, September 1964.
6. R. H. Bube and L. A. Barton, *RCA Rev.*, **20**, 565 (1959).
7. R. Williams and R. H. Bube, *J. Appl. Phys.*, **31**, 968 (1960).

A Novel Crystal Growth Phenomenon: Single Crystal GaAs Overgrowth onto Silicon Dioxide

F. W. Tausch, Jr., and A. G. Lapierre, III

Engineering Department, Sylvania Semiconductor Division, General Telephone and Electronics, Incorporated, Woburn, Massachusetts

ABSTRACT

Epitaxial growth of GaAs in windows on SiO_2-masked GaAs substrates has been studied and found to yield smooth-surfaced single crystal epitaxial layers. Single crystal overgrowth onto the SiO_2 films, initiating from the windows and growing out laterally over the SiO_2, has also been observed to occur in many instances. Studies of growth habits and patterns, inspection of cleaved sections, x-ray studies, and crystallographic considerations have led to a proposed growth mechanism which is not only consistent with the experimental window growth and overgrowth observations, but also indicates that the processes are highly controllable; it has been shown that overgrowth can be virtually inhibited, and it is concluded that with proper mask geometry single crystal overgrowth can occur over large areas almost without restraint.

In the course of investigating the SiO_2-masked epitaxial growth of GaAs in windows, which has never been reported in the literature, it was observed that not only window growth of excellent quality was obtained, but that the epitaxial layer frequently grew out laterally from the windows in the SiO_2 mask, resulting in an area of sandwich structure with the single crystal epitaxial GaAs layer separated from the GaAs substrate by the amorphous SiO_2 film (*e.g.*, see Fig. 6 and 7). This behavior is quite different from that reported for growth of silicon in windows [*e.g.*, ref. (4)], where lateral overgrowth has not been reported. Since this phenomenon of overgrowth appears to be not only novel but also potentially useful for device fabrication, it has been further investigated. This paper includes some preliminary results and conclusions derived from study of growth in windows and overgrowth.

Experimental

Substrates used in the work reported here were heavily doped (tellurium) n-type GaAs, cut and polished within 3° of the $(\bar{1}\bar{1}\bar{1})$ As faces. Essentially similar results were obtained on the (111) Ga faces. SiO_2 films of 100-10,000Å thickness were deposited conventionally

Fig. 1. Photomicrograph of L-shaped mask used in early work. Dark areas represent SiO_2 removal to GaAs substrate. Stripes are one-half mil wide and 13 mils long. Magnification approximately 95X.

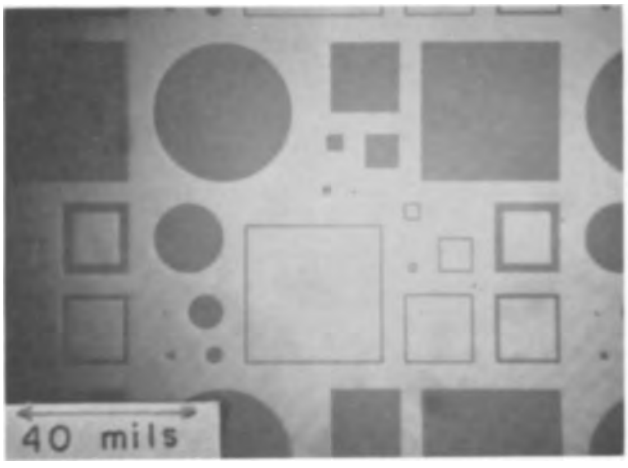

Fig. 2. Photomicrograph of specially designed mask for overgrowth study. Dark areas represent SiO_2 removal to GaAs substrate. Windows range from one-half to 32 mils over-all. Magnification approximately 25X.

by pyrolysis of tetraethyl orthosilane, and windows were opened in the SiO_2 by standard photolithographic techniques. Figure 1 shows the simple window pattern used in early work, consisting of an L-shape with legs 13 mils long and one-half mil wide, and with a 3 by 3 mil square in the center. Figure 2 shows a more elaborate pattern which was designed for study of overgrowth and which incorporates both round and square windows of various sizes (½-32 mils over-all) as well as frames of various sizes (2-32 mils over-all) and frame widths (½-2 mils). Masks were not intentionally aligned along specific crystallographic planes unless noted.

Epitaxial layers up to about 10μ thick were deposited on these slices in a conventional quartz vertical vapor transport reaction system, similar to that reported by Williams and Ruehrwein (1), utilizing an undoped GaAs source and either HCl or $AsCl_3$, in hydrogen, as the transport agent. Growth rates normal to the surface were generally 0.5-2.0 μ/min. The source temperature was 900°C, and the deposition temperature was from 710° to 730°C.

Results

Figures 3 and 4 show typical growths of about 10μ thickness obtained using the two masks previously described. It should be mentioned that most of the gross imperfections apparent in these growths are due to imperfect photolithographic work, incomplete removal of oxide, or imperfect cleaning of substrate surface. Laue back-reflection x-ray photographs confirm the single crystallinity of both growth in windows and

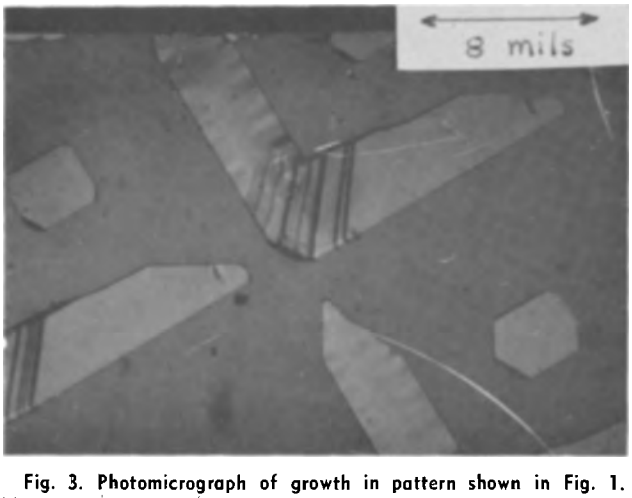

Fig. 3. Photomicrograph of growth in pattern shown in Fig. 1. Magnification approximately 125X.

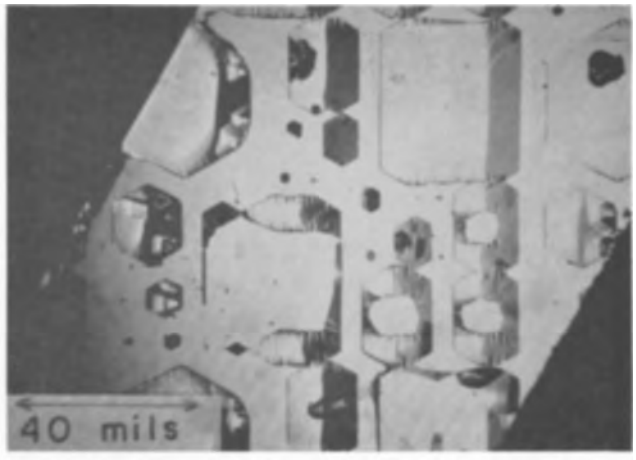

Fig. 4. Photomicrograph of growth in mask shown in Fig. 2. Magnification approximately 25X.

overgrowths, except where obvious polycrystallinity exists.

Comparison of Fig. 3 with Fig. 1 shows that lateral overgrowth of several mils has occurred from the one-half mil wide stripes, although growths of the central squares has tended to form hexagons and then virtually stop. Similarly, comparison of Fig. 4 with Fig. 2 shows that growth in all of the windows except the largest of the squares has formed hexagons, and that even the largest of the squares tend toward hexagons, and that the three smallest frames (2, 4, and 8 mils over-all) have been filled by overgrowth. Figures 5A, B, and C show an 8-mil frame before overgrowth, after almost complete overgrowth, and after complete overgrowth; these pictures not only demonstrate the development into the hexagonal shape, but also show that practically no growth occurred on two sides. It may be noted that the pattern is still faintly visible through the overgrowths of Fig. 5B and C. Finally, Fig. 5D and E show examples of better quality overgrowths of 2 and 4 mil frames, achieved by growing at a slower rate (*i.e.*, closer to 0.5 μ/min normal to the surface, rather than 1.0 or 2.0 μ/min).

A number of other features apparent in Fig. 3 and 4 may deserve comment here. For example, spurious nucleation occurred on a few places on the SiO_2 in some cases, especially at high growth rates, but was generally not a problem. Also, it can be seen that less perfect areas frequently occur wherever advancing growth fronts intersect; these may result in low-angle

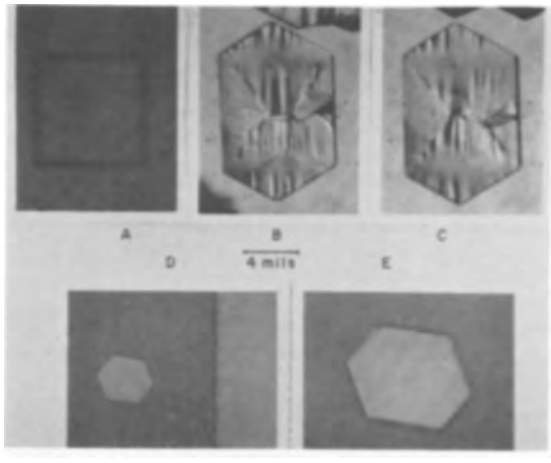

Fig. 5A. Photomicrograph (250X) of 8-mil frame before growth. Figure 5B and 5C. Same as Fig. 5-A except after almost complete overgrowth (5-B) and after complete overgrowth (5-C). Figure 5D. Photomicrograph (350X) of high quality overgrowth in 2-mil frame. Figure 5E. Photomicrograph (350X) of high quality overgrowth in 4-mil frame.

grain boundaries, which were observed in some x-ray photographs of these areas, although low-angle grain boundaries were also detected in some substrates. In any event, it will be shown later that the problem of intersecting growth fronts can be avoided by proper choice of mask geometry.

Identification of Faces

As previously mentioned, all growths reported here were carried out on the polished (111) surfaces of GaAs. The flat top surfaces of completed hexagons were in several instances measured to be oriented three degrees from the polished substrate surface by interferometry. Subsequent x-ray determination of the substrate orientation of these slices showed that the polished substrate surface was itself three degrees off the (111) plane in the corresponding direction. These observations not only indicate that the top surface tends to grow into a (111) facet, but also further support the single-crystallinity evidence of the growths. The tendency toward (111) facet formation may also explain some of the stepping which is apparent in Fig. 3 and 4, especially in large areas where not enough vertical growth has occurred to result in a single (111) facet across the entire top surface of the window.

In order to identify the slow-growing crystallographic planes bounding the growth figures, samples were cleaved along the {110} cleavage planes and inspected from the side; {110} cleavage was confirmed in several instances by x-ray orientation. It should be noted that there are three {110} cleavage planes, sixty degrees apart, perpendicular to any {111} face.

Referring again to Fig. 4, this is a top view of a sample twice cleaved along parallel {110} planes. It can be seen that these cleavage lines are perpendicular to one set of sides of any completed hexagon, and hence generally reveal the crystallography of the corresponding advancing growth front. A side view of such a cleavage through a completed hexagon invariable reveals a structure such as that sketched in Fig. 6A and 6B, and shown in photomicrograph 6C. The faces shown, at approximately 70° from the (111) plane, correspond to other {111} planes (see Table I). Consideration of the crystallography involved leads to the conclusion that the overhanging facet is chemically the same {111}

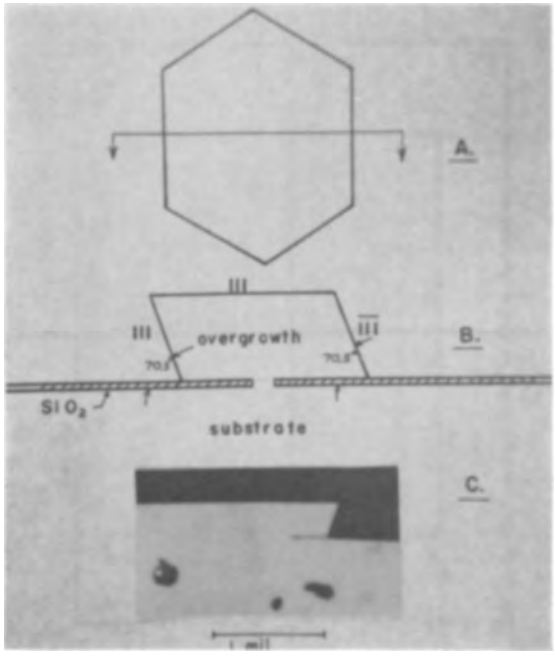

Fig. 6. Sketch of (110) cleavage of completed (grown) hexagon. Figure 6B. Side view of above cleavage through completed hexagon, showing opposing (111) facets. Figure 6C. Photomicrograph (1000X) of typical cleavage as above.

Table I. Angles between (111) and x planes along 110 zone

It may be mentioned that the difference between the two columns, as referred to in the text, is that one always refers to upward sloping faces while the other always refers to downward sloping faces; hence in a cleavage which reveals two upward sloping faces, both planes will appear in the same column, while if the cleavage reveals both on upward and a downward sloping face, one will appear in each column.

x		x	
$\bar{1}\bar{1}2$	90° 0′	111	−0° 0′
337	85° 57′	332	−10° 2′
$\bar{1}\bar{1}3$	79° 58′	553	−12° 16′
$\bar{1}\bar{1}4$	74° 12′	331	−22° 0′
115	70° 32′	551	−27° 13′
117	66° 9′	771	−29° 30′
$\bar{1}\bar{1}9$	63° 40′	110	−35° 16′
001	54° 44′	$77\bar{1}$	−41° 2′
119	45° 48′	$55\bar{1}$	−43° 19′
117	43° 19′	$33\bar{1}$	−48° 32′
115	38° 56′	$55\bar{3}$	−58° 15′
114	35° 16′	$33\bar{2}$	−60° 30′
113	29° 30′	$11\bar{1}$	−70° 32′
337	23° 31′	335	−84° 57′
112	19° 28′	$11\bar{2}$	−90° 0′
335	14° 25′		
557	9° 27′		
111	0° 0′		

plane (*i.e.*, either gallium or arsenic) as the top (111) face, while the upward sloping facet is chemically the same {111} face as the bottom ($\bar{1}\bar{1}\bar{1}$) face of the substrate wafer. In any of the top-view photographs the upward sloping facets appear dark due to the illumination, while the downward sloping facets are not visible. From the photomicrograph in Fig. 6C of the cross section of a completed hexagon can be seen the flat top (111) plane of the growth in the window, the 70° overhanging {111} side facet, and the small amount of overgrowth which has resulted from the formation of that facet. The SiO_2 masking can be seen in this photograph as the dark line separating the overgrown layer from the substrate. Cleavages across overgrown L-shaped patterns such as in Fig. 2, as well as across frames and windows where the hexagonal shape has not yet developed, frequently reveal leading edges at angles as shown in Fig. 7B. Referring again to Table I, the facet at about 35° to the (111) appears to correspond to a {110}, and that at about 55° appears to correspond to a {100}; usually the two facets have been of approximately equal magnitudes, as indicated by

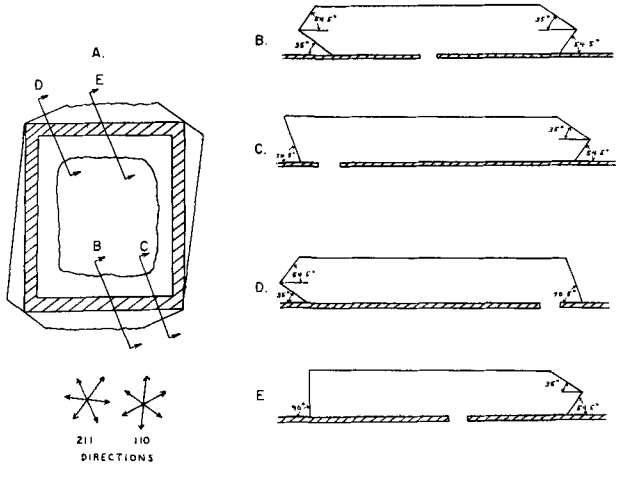

Fig. 7A. Partially overgrown frame with four cleavages indicated, for use with Fig. 7B through 7E. Figure 7B. Sketch of cleavage revealing both (100) over (110), and (110) over (100) double facets. Figure 7C. Cleavage revealing both a (111) facet and a (110) over (100) combination facet, also indicating relative lateral growth rates. Figure 7D. Cleavage revealing the other possible combination, with (111) and (100) over (110) facets. Figure 7E. Cleavage across a (110) perpendicular facet. (Note that vertical dimensions in side view sketches, Fig. 7B through 7E are exaggerated for clarity).

the sketches. Cross sections showing leading edges consisting of the {110} and {100} double facet on one edge and a {111} facet on the opposite edge have also been observed, as in Fig. 7C and 7D. The discovery of these combinations of facets is important in corroborating the identification of all the faces, since consideration of the crystallography involved (and reference to Table I) leads to the conclusion that the combinations pictured are the only ones consistent with the observed angles.

The above-mentioned existence of combination {110}-{100} faces deserves comment since it would be expected (2) that a (111) layer spreading over a substrate {111} surface in opposed [211] directions should result in a step along a {110} plane in one direction and a step along a {100} plane in the other direction. Similarly for the layer spreading over the chemically opposite (111) surface the {100} step should form in the first direction and the {110} step in the other. The distinctive feature of overgrowth, however, is that the (111) layer is effectively spreading over both (111) and $(\bar{1}\bar{1}\bar{1})$ faces simultaneously since the layer is growing over an SiO_2 substrate rather than a {111} oriented substrate; the combination growth front involving both {110} and {100} steps is thus not too surprising. It might be mentioned that epitaxial overgrowth is, in many respects, similar to dendritic growth.

Another facet frequently found on cleavage has been one at 90° to the (111) plane, as sketched in Fig. 7E. Although the {211} plane is in the {110} zone, and is 90° from the (111) plane (see Table I), it is not likely to form facets on GaAs (3). On checking the top view of these cleavages it was found that the cleavage {110} planes were not perpendicular to the growth front, as was true in Fig. 7A through 7D. Rather, the front was 60° from the cleavage plane, advancing in a direction 30° from any [211] direction. These directions are the [110] directions and, indeed, the 90° face is probably the {110} face. Note that in Fig. 4 the planes forming the interiors of the three 16-mil frames are 30° from the exterior {111} hexagonal facets and are probably these perpendicular {110} facets.

Facets at angles corresponding to other crystallographic planes have also been observed, but have not been identified with any degree of certainty.

Proposed Growth Mechanism

Considering now the factors which determine the growth pattern obtained, it is clear that the amount of overgrowth obtained with each possible facet as a leading edge will vary, and the {111} facets will advance most slowly (*i.e.*, at the same rate as the top (111) face).

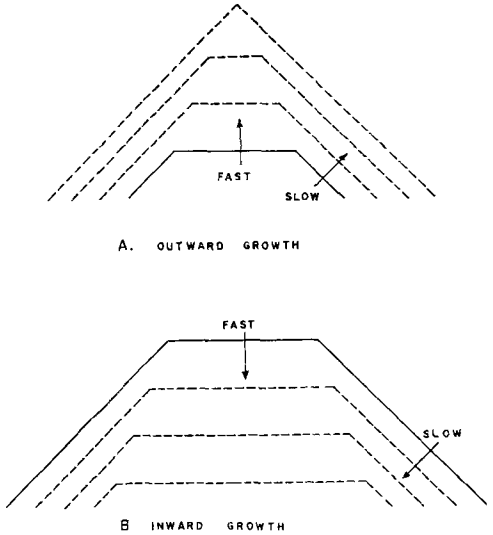

Fig. 8A. Sketch of effect of relative facial growth rates on habit of diverging growth front (outward growth). Figure 8B. Sketch of effect of relative facial growth rates on habit of converging growth front (*i.e.*, inward growth).

The factor determining which growth front forms is whether the growth front is diverging or converging. First consider the case where the growth front diverges, *i.e.* Fig. 8A. The length of the slow growing front increases at the expense of the fast growing front, and the final form is recognizable as the circumscribed {111} hexagonal facets to which all mask shapes tend to overgrow in the outward direction.

Considering next growth along a converging front, i.e., Fig. 8B, it is now the fast growing facets which tend to survive and predominate. For example, the interior overgrowths in the 16-mil frames of Fig. 4 appear to be forming facets which are aligned 30° from the {111} exterior facets, and hence are believed to be the relatively fast growing {110} perpendicular faces. The fact that fast growing faces are not self-annihilated in this case makes possible controlled rapid overgrowth of a converging growth front. The relatively extensive inward growth apparent in the L-shaped areas of Fig. 3 may be explained in terms of growth steps initiated at the inside corner.

It is interesting and informative to speculate briefly on some of the techniques by which overgrowths could be controlled, in the light of the previously developed mechanism. For example, by proper orientation of a hexagonal mask pattern, *i.e.*, with sides parallel to {111} faces, it should be possible to inhibit completely rapid overgrowth and thereby limit growth in all directions (including normal to the surface) to the slow {111} face growth rate; growth in circular windows approaches this condition. As another example, overgrowth over large areas should be possible by exploiting a geometry which avoids {111} facet formation, *i.e.*, straight lines or concave curvatures (see Fig. 8B). It may be noted that the problem of defects caused by intersecting growth fronts is avoided along straight or gently curving window openings.

Conclusions

It has been shown that single crystal epitaxial growth occurs in windows, and that the growth tends to rapidly overgrow the SiO_2 until a hexagonal figure bounded by {111} facets is formed. The overgrowth is itself single crystal, and rather extensive (several mils) overgrowths of good appearance have so far been achieved. A mechanism of overgrowth has been proposed which is not only consistent with the experimental observations, but also indicates that the overgrowth process is highly controllable; by proper geometrical relationship between the mask and the substrate crystallography overgrowth can be virtually inhibited, and it is concluded that overgrowth can also be made to occur over large areas almost without restraint. The integrity of the isolating SiO_2 film has been established since it is visible on sectioning and after the overgrown GaAs has been chipped away.

Acknowledgment

The authors would like to thank R. W. Berkstresser for x-ray analysis and for assistance in crystallographic determination.

Manuscript Feb. 1, 1965.

Any discussion of this paper will appear in a Discussion Section to be published in the June 1966 JOURNAL.

REFERENCES

1. F. V. Williams and R. A. Ruehrwein, *This Journal*, **108**, 177C (1961).
2. R. C. Sangster, in "Compound Semiconductors," Vol. 1, p. 249, Willardson and Goering, Editors, Reinhold Publishing Corp., New York.
3. *Ibid.*
4. A. F. McKelvey, Proceedings of the Third Annual Microelectronics Symposium, pp. II-B-1 to II-B-6, St. Louis, April 1964.

Kinetics of Epitaxial Silicon Deposition by a Low Pressure Iodide Process

John E. May

Semiconductor Products Department, General Electric Company, Auburn, New York

ABSTRACT

This report is primarily a study of the factors which control the vapor transport process of silicon in a modified closed tube low pressure cyclic iodide process. The kinetics of transport from the source to the substrate are examined and are found to agree with a diffusion controlled mechanism. The model is useful for estimating the deposition rate under a variety of conditions. The process is found capable of depositing silicon on silicon substrates at relatively high deposition rates. Impurity doping with this process is accomplished by incorporating the desired impurity into the source silicon.

Vapor phase transport-closed tube processes are of considerable interest for epitaxial deposition of semiconductor materials (1-4). Essentially, the process involves incorporating into a closed tube the substrate, the source of material to be deposited, and a carrier gas. By heating the source and substrate to different temperatures, the carrier gas reacts with the source material to form a volatile compound which then migrates to the substrate. Decomposition and deposition occurs at the substrate. The decomposition products may then travel back to the source to pick up more material. In the silicon-iodine system studied by Wajda and Glang (4), for instance, the substrate is maintained at about 950°C, the source at 1100°C, and iodine pressure at 20 atm. With a source to substrate distance of 10 to 15 cm they observe deposition rates of the order of 10 μ/hr. The dominant transport mechanism in this case is thermal convection.

Dash and Taft (5) on the other hand have used a low pressure silicon iodine cyclic process and have brought the source much closer to the substrate. The source and substrate can be heated inductively to different temperatures to achieve a steep temperature gradient. The close space geometry has been also used by Sirtl (6) and by Nicoll (7).

This paper shows that the combination of close spacing and low pressure lead to a substantially more rapid deposition rate, and that the process is diffusion controlled.

Preliminary Analysis

In this report we expand the initial work of Dash and Taft (5) on the cyclic iodide process, investigating further the effect of pertinent variables which control the transport and deposition processes. In addition, the kinetics and mechanism of transport are examined and estimates are made of the deposition rate as a function of the experimental variables.

An important feature of this process is the relatively small distance between the source and substrate. This distance is maintained by placing the substrate between two slabs of silicon which are separated by means of a quartz ring. Two arrangements are shown schematically in Fig. 1. One piece of silicon acts as the source of material and the other is the heater for the substrate. Transport from source to substrate is accomplished in an iodine atmosphere by heating the source to temperature T_1 and the substrate to temperature T_2 where $T_1 < T_2$. The iodine reacts with the source silicon to form a volatile iodide with an equilibrium partial pressure at the source greater than its equilibrium partial pressure at the substrate. This supersaturated iodide at the substrate drives the original reaction in the reverse direction leaving elemental silicon on the substrate. A concentration gradient of silicon iodide is therefore established between the source and substrate. At an average temperature of 1100°C and 1 mm of iodide pressure the mean free path is about 10^{-2} cm. We would expect then that a diffusion controlled process would operate down to spacer distances between source and substrate of the order of a millimeter.

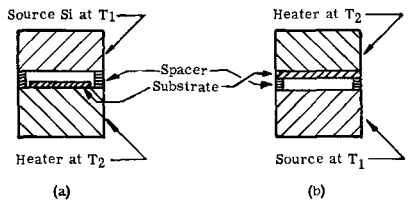

Fig. 1. Schematic of heater, substrate, and source assembly

For a diffusion controlled process the flux of material passing between the source and substrate is given by

$$J = -D\,\partial C/\partial X$$

where D is the gaseous interdiffusion coefficient of the iodide and $\partial C/\partial X$ is the equilibrium concentration gradient between the source and substrate. Since $C = n/v = p/RT$, the maximum growth rate (G) of the deposit is given by

$$G = D\,M\Delta p/\rho\,RT_a\,d \qquad [1]$$

where M is the atomic weight of Si, Δp is the difference in equilibrium iodide pressure between the source and substrate, ρ is the density of Si, R is a gas constant, T_a is the average temperature, and d is the distance between the source and substrate. Since Δp is a function of the iodine temperature and the temperature of the source and substrate, and D is a function of temperature and iodine pressure, we now have an expression containing the variables which influence the deposition rate. This approach is similar to that used by Schäfer *et al.* (8), in their study of metal-halide transport reactions.

This model assumes that there is no barrier to nucleation and growth of silicon on the substrate and that equilibrium iodide partial pressures are maintained at the source and substrate interfaces.

One important feature of silicon-iodine chemistry is that by varying the iodine pressure, silicon can be made to deposit in either the high or low temperature region (9). High pressures favor migration of silicon from the high temperature region to the low temperature region by means of the reaction

$$SiI_4 + Si \rightleftharpoons 2SiI_2 \qquad [2]$$

However (at low pressures) the additional reaction

$$SiI_4 \rightleftharpoons Si + 4I \qquad [3]$$

can occur, which in combination with reaction [2] will give the net reaction

$$SiI_2 \rightleftharpoons Si + 2I \qquad [4]$$

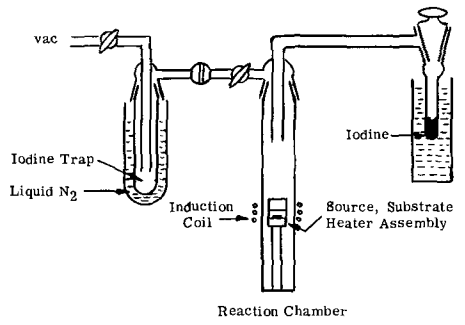

Fig. 2. Apparatus for epitaxial deposition by cyclic iodide process

Depending on whether reaction [3] or [4] is dominating, we would have

$$\Delta p \propto p^4_I \quad [5]$$

or

$$\Delta p \propto p^2_I \quad [6]$$

Another pressure sensitive term is the interdiffusion coefficient D. This varies as

$$D \propto T^n/P \quad [7]$$

where P is the pressure, T the temperature, and n a constant of about 1.5 to 2. Equations [5] or [6] in combination with Eq. [7] and [1] predict the rate of deposition to be proportional to the iodine pressure if SiI_2 is the dominant carrier species and proportional to p^3_I if SiI_4 is the dominant species. This dependence should be obeyed so long as the process is diffusion controlled, that is, when the source to substrate distance is about ten times the mean free path. At appreciably less than 1 mm iodine pressure, we would expect a departure from a diffusion controlled process with a source to substrate distance of 1 mm.

In the next sections we determine the effect of variables on the deposition rate and compare the results with those expected from the analysis.

Experimental

The apparatus used in this experiment is shown in Fig. 2. It is a demountable vacuum system consisting of a quartz reaction chamber with a tapered joint connected to an iodine source vessel and a liquid nitrogen trap to prevent the iodine from entering the vacuum pump. The source and substrate assembly which was used for most of this work is that shown in Fig. 1 (b) and consists of two Si rods (⅞ in. diameter x 1 in. long) of predetermined impurity content separated by a notched quartz ring. The source and substrate heater temperatures are established by positioning an induction coil at the appropriate elevation around the source and heater. The apparatus is enclosed by a box in which the interior can be heated above the iodine source temperature.

The operating procedure consists of pumping the system down to about 10^{-6} mm with the iodine source open to the liquid nitrogen trap. Once the desired temperatures of source and substrate are established the reaction chamber is closed off from the cold trap and vacuum pump, but the iodine source is kept open to the reaction chamber.

Temperatures were measured with an optical pyrometer by sighting on the periphery of the source and heater just above and below the quartz ring. The optical temperatures were corrected for emissivity (10) and true temperatures are reported here.

The iodine vapor pressure used here is that reported in the Handbook of Chemistry & Physics (11).

The substrates used here were 25 ohm-cm-N-type Si with (111) sufaces which were cleaned and then chemically polished with a solution of 100 cc HF, 180 cc acetic acid, 300 cc of HNO_3, and 0.35g of iodine. Immediately prior to loading in the reaction chamber they were immersed in HF and rinsed in deionized water.

The source silicon for this work was 0.01 ohm-cm P-type. Evaluation of deposit thickness was made by polishing a 6° bevel on the coated surface and staining the P region with HF-HNO_3 1000:1. The width of the P region was measured with a microscope and eye piece micrometer. This thickness was checked against the thickness determined from stacking fault measurements in order to determine whether a significant amount of diffusion of doping impurities into the substrate had occurred.

The deposition rates were obtained by dividing the deposit thickness by the total elapsed time starting after the desired temperatures were established and the cold trap was closed. Deposition rates determined in this manner could possibly be on the low side. Experiments have shown that it takes several minutes to achieve a linear growth rate. The total time of the run was therefore scheduled to be long compared with the time to achieve steady state conditions.

Results

Since Δp is a function of ΔT (the difference in temperature between the substrate and the silicon source), we shall present the deposition rate data *vs.* ΔT and then infer the proper iodide species from this and other data. The relationship between deposition rate and Δp will then be shown.

Dependence of epitaxial deposition rate on source and substrate temperatures.—In this experiment the substrate heater temperature was kept constant at 1290°C true temperature and the source temperature was varied. The iodine vapor pressure was maintained at 0.7 mm and the source to substrate distance was 1 mm. The data so obtained are shown in Fig. 3.

Dependence of deposition rate on iodine vapor pressure.—In this series of experiments the deposition rates were determined as a function of iodine pres-

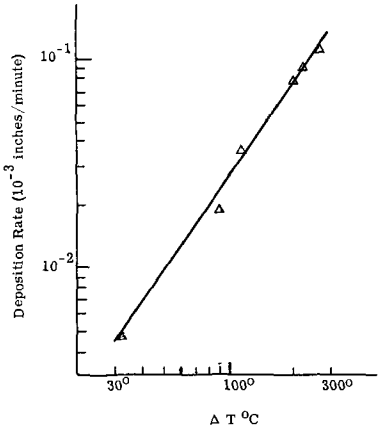

Fig. 3. Variation of deposition rate with ΔT. Iodine pressure, 0.7 mm Hg; separation, 1 mm; substrate temperature, 1290°C; source temperature, varied.

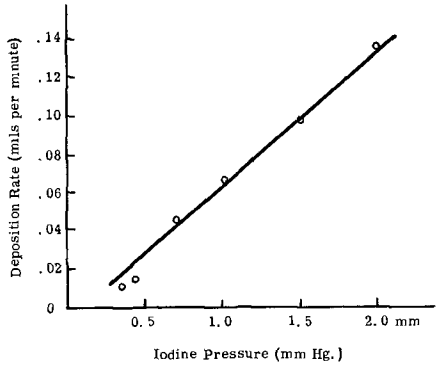

Fig. 4. Variation of deposition rate with iodine pressure. Substrate temperature, 1300°C; source temperature, 1150°C; separation, 1 mm.

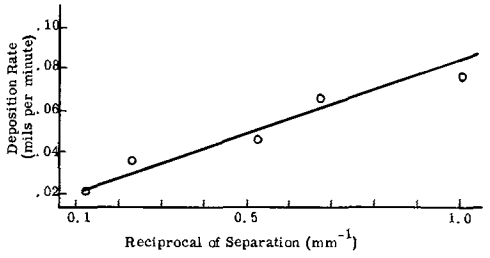

Fig. 5. Effect of source to substrate distance on deposition rate. Substrate temperature, 1300°C; source temperature, 1090°C; iodine pressure, 0.7 mm Hg.

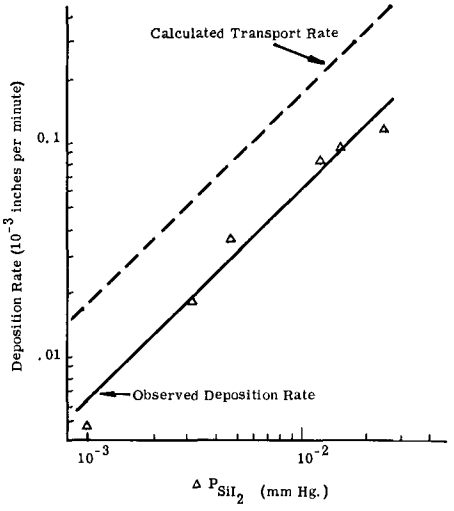

Fig. 6. Variation of deposition rate with ΔP_{SiI_2} and comparison with theory. Iodine pressure, 0.7 mm Hg; separation, 1 mm; substrate temperature, 1290°C; source temperature, varied.

sure over the range 0.3-2 mm. The source and heater were kept at 1150° and 1300°C, respectively, while the spacer distance was 1 mm. The results are shown in Fig. 4.

Effect of source to substrate distance on deposition rate.—The dependence of deposition rate on the distance between the source and substrate was studied with a source temperature of 1090°C, substrate heater temperature of 1300°C, and an iodine pressure of 0.7 mm. Quartz spacers of 1-9 mm were used. It was found that as the spacing increased, the uniformity of the deposit decreased. The data plotted in Fig. 5 indicates that the deposition rate is roughly proportional to the reciprocal of the distance.

Discussion and Results

The results of the study of the variation of deposition rate with iodine pressure indicates that the deposition rate is directly proportional to the iodine pressure at least within the limited range reported here. As discussed in the Preliminary Analysis, the result indicates that SiI_2 is the dominant species. This is in accordance with thermodynamic calculations. The slightly lower deposition rates at the lower iodine pressures are probably caused by the evaporation of silicon which becomes significant compared with the deposition rate.

With evidence that SiI_2 is the major transport species we can re-plot Fig. 4 ($G = f\Delta T$) as $G = f(\Delta p)_{SiI_2}$. For the net reaction

$$SiI_2 \rightleftharpoons Si + 2I \qquad [8]$$

we calculate from Schäfer and Morcher (9) the silicon diiodide pressure in equilibrium with iodine and silicon. This is given by

$$\log (P^2I/P\ SiI_2)_{mm} = 7.447 - 8256/T \qquad [9]$$

The experimental relationship G (exp) $= f(\Delta p)$ is shown in Fig. 6 and is interpreted to indicate that the deposition rate is directly proportional to Δp_{SiI_2}, in qualitative agreement with Eq. [1].

Comparison of calculated and observed deposition rates.—It is of interest now to compare quantitatively the observed results with those predicted from Eq. [1]. It is important first to consider the geometry of our system. We have relatively hot silicon connected to a distance source of iodine maintained at millimeter pressures. The wall temperature of the apparatus is about 75°C, which is lower than the silicon temperature but higher than the iodine source temperature. We assume that the pressure of iodine in the space between the silicon source and substrate is about the same as the equilibrium iodine pressure maintained at the iodine source. At these pressures and silicon temperatures the iodine is practically completely dissociated.

The coefficient of interdiffusion of SiI_2 in iodine may be estimated from kinetic theory (12, 13). (See Appendix.) Combining Eq. [1] and [A-1] and evaluating the constants, we obtain the following expression for the maximum rate of deposition

$$G = 23.5\ (T_a)^{1/2}\ \Delta p\ SiI_2\ (atm)/d\ (cm)\ \Sigma P_{mm} \qquad [10]$$

G is in mils per minute, ΣP is the total gas pressure in mm, and $\Delta p\ SiI_2$ is computed from Eq. [9].

The results calculated from Eq. [10] are compared in Fig. 6 with the experimental results. We see that the calculated transport rates are about three times the observed deposition rates. However, with an apparatus modified to permit hydrogen cleaning of the substrate and source surfaces, we have observed deposition rates quite close to the calculated maximum rates. For instance, with the source at 1150°C, substrate at 1300°C, and iodine pressure at 3.5 mm, we have observed on occasion deposition rates of 0.35 and 0.47 mil/min which compare with a calculated rate of 0.5 mil/min. No doubt the rate at which gases enter the system during the deposition period is a variable. It increases ΣP which has not been taken into consideration in the calculation, and one which we have not determined. The formation of more stable gas-silicon compounds will also decrease the deposition rate. Considering the assumptions and estimates which have been made in the calculation then, the agreement between observed and calculated maximum deposition rates is good.

Acknowledgments

The author gratefully acknowledges the discussions of the cyclic iodide process with E. A. Taft, Jr. and Dr. W. C. Dash at an early stage in his investigation. Dr. F. H. Horn, R. E. Hysell, and F. E. Gentry reviewed the report and H. Sheldon, J. B. Crooks, and Mrs. M. Bestard assisted in various phases of the experimental work.

Manuscript received Nov. 23, 1964; revised manuscript received March 17, 1965.

Any discussion of this paper will appear in a Discussion Section to be published in the June 1966 JOURNAL.

REFERENCES

1. J. C. Marinac, *IBM Journal*, **4**, No. 3, 248 (1960).
2. E. S. Wajda, B. W. Kippenhan, and W. H. White, *ibid.*, **4**, 288 (1960).
3. R. Glang and B. W. Kippenhan, *ibid.*, **4**, No. 3, 299 (1960).
4. E. S. Wajda and R. Glang, "Metallurgy of Elemental & Compound Semiconductors," R. O. Grubel, Editor, p. 229, Interscience Publishers, New York (1961).
5. W. C. Dash and E. A. Taft, Private communication.
6. E. Sirtl, *J. Phys. Chem. Solids*, **24**, 1285 (1963).
7. F. H. Nicoll, *This Journal*, **110**, 1165 (1963).
8. H. Schäfer, H. Jacob, and K. Etzel, *Z. anorg. u. allgem. Chem.*, **286**, 27 (1956).
9. H. Schäfer and B. Morcher, *ibid.*, **290**, 279 (1957).
10. F. G. Allen, *J. Appl. Phys.*, **28**, 1510 (1957).

11. "Handbook of Chemistry and Physics," Thirty First Ed., Chemical Rubber Publishing Co., Cleveland (1948).
12. S. Dushman, "Scientific Foundations of Vacuum Technique," John Wiley and Sons, New York (1949).
13. E. H. Kennard, "Kinetic Theory of Gases With an Introduction to Statistical Mechanics," McGraw-Hill Book Co., New York (1938).

APPENDIX

The interdiffusion coefficient was calculated from the theory of Maxwell, Chapman, and Enskog [see Dushman (12) p. 75, or Kennard (13) p. 194], and is given by

$$D_{12} = \frac{(v^2_1 + v^2_2)^{1/2}}{3\pi\, n_{12}\, \sigma_{12}^2} \qquad [A1]$$

where v_1 and v_2 are the average velocities $\left(\frac{8}{\pi}\frac{RT}{M}\right)^{1/2}$ of species 1 and 2, $n_{12} = n_1 + n_2$ = number of molecules/cm^3 of species 1 and 2 and $\sigma_{12} = \frac{\sigma_1 + \sigma_2}{2}$ where σ is the molecular diameter of species 1 and 2. Using values of $\sigma_I = 2.8 \times 10^{-8}$ cm and $\sigma_{SiI2} = 7.2 \times 10^{-8}$ cm we compute $D_{12} = 5.6 \times 10^2$ cm^2/sec at Ta = 1498°K and P = 0.7 mm.

The Anodic Synthesis of CdS Films

William McNeill, Leonard L. Gruss, and Dorsey G. Husted

Pitman-Dunn Institute for Research, Frankford Arsenal, Philadelphia, Pennsylvania

ABSTRACT

Cd is shown to behave as a typical "valve anode" in solutions of $Na_2S \cdot 9H_2O$ in ethanol and becomes covered with a film which acts as an electrical barrier, exhibits interference colors, increases in thickness as voltage is increased, and gives rise to sparking at voltages in excess of 150 V. Voltage-time curves, film thickness and electrical resistance, and x-ray diffraction analyses showing the films to be CdS are presented. The thickness-voltage ratio based on interference colors is 26 Å/v.

The synthesis and properties of anodic oxide barrier films on metals such as Al and Ta are well known and have been described in detail by Young (1). Among important properties of films of this type are: the approximate linear increase of thickness with formation voltage for nonporous films at constant current density (2); the appearance of interference colors during film growth (3); and the ability to sustain very large electric fields (4). The majority of papers on this subject deal with films which are composed mainly of oxides of the anode metal, although some work has been reported on non-oxide films such as AgCl (5, 6).

In this paper we describe the anodic behavior of Cd in electrolytes which contain sulfide ions.

Experimental

Electrolytes.—The anodic reaction of Cd was studied with a number of electrolytes, and "valve anode" properties were observed in solutions of Na_2S in dimethylformamide, liquid NH_3, CH_3OH, C_2H_5OH, and $Na_2S \cdot 9H_2O$ in C_2H_5OH. In all cases, anodic reaction products included CdS as shown by powder x-ray diffraction analyses. All further studies reported here were carried out in solutions of $Na_2S \cdot 9H_2O$ in C_2H_5OH. Reagent grade chemicals were used throughout.

The solutions of $Na_2S \cdot 9H_2O$ in C_2H_5OH were subject to slow air oxidation which resulted in formation of S_8^0 (rhombic), Na_2SO_3 and $Na_2SO_4 \cdot 10\,H_2O$ all of which were identified by powder x-ray diffraction. The stated concentrations of these solutions are therefore nominal and refer to conditions at the start of an experiment. Also, a yellow color, presumed due to polysulfide formation appeared in the solution during anodization.

Anodes.—Anodes were round Cd rods of 1.27 or 0.63 cm diameter. These were reagent grade Cd of 99.9% purity. Anodes used for study of voltage-time characteristics and determination of film structure and composition were machined to approximate hemispheric shape on one end, inserted in tight-fitting Teflon sleeves and chemically polished by alternate immersion in a 60:40 conc. HNO_3, glacial acetic acid solution, and water. This was followed by a 5 to 8 second immersion in a solution containing 32g CrO_3 and 6g Na_2SO_4 in 100 ml H_2O. The polishing solution was removed by washing in H_2O and the anode was given a final rinse in dry C_2H_5OH.

Anodes used for study of film thickness were embedded in polymethylmethacrylate blocks. These were subsequently cut and polished. In the polishing procedure a series of abrasive papers was employed through grit size No. 600. The specimens were then lapped on a gamal cloth wheel using first Al_2O_3 and finally a reagent grade MgO.

Anodic reaction.—Anodic reactions of Cd were studied at current densities of 0.0155, 0.0775, and 0.155 amp/cm^2 in 0.1*N* and in 0.05*N* $Na_2S \cdot 9H_2O$ in C_2H_5OH. Three replications were made for each set of conditions and the maximum cell voltages were reproducible within ±5%. Cell voltages are plotted as functions of time in Fig. 1. These curves exhibit the characteristic

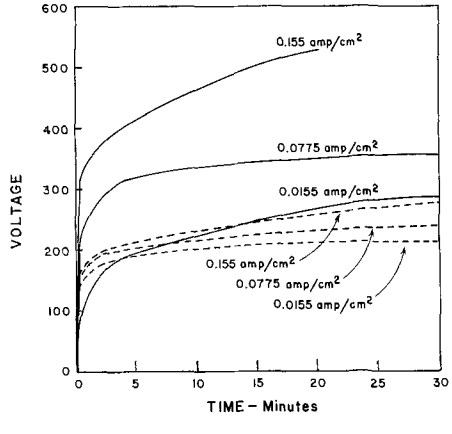

Fig. 1. Voltage-time curves for Cd anodized in solutions of $Na_2S \cdot 9H_2O$ in C_2H_5OH. Solid lines are for 0.05*N* solutions.

Table I. Electroluminescence and spark initiation voltages for anodic films on Cd in $Na_2S \cdot 9H_2O$ in C_2H_5OH

Conc. of $Na_2S \cdot 9H_2O$	Current density, amp/cm²	Electro-luminescence, v	Spark voltage, v
0.05*N*	0.155	40	230
0.05*N*	0.077	30	230
0.05*N*	0.015	35	200
0.10*N*	0.155	50	200
0.10N	0.075	30	170
0.10*N*	0.015	45	155

shape that is associated with the growth, breakdown, and sparking of anodic barrier films (7, 8). In the initial stage of the anode reaction, up to about 100v, the voltage rises very rapidly and is accompanied by the appearance of a film which exhibits a sequence of interference colors corresponding to increasing thickness. As the anodic film increases in thickness, its characteristic bright yellow color becomes more pronounced. In some cases, especially when films were grown at constant voltage, there was a tendency for films to be somewhat cloudy or opaque. The origin of this behavior is not clear as yet, but we assume it arises from contaminants in the electrolyte or in the anode, or from excessive current densities causing premature breakdown of the film. In the absence of such deleterious effects, it was usually possible to grow films to voltages in excess of 100v with no appreciable loss in transparency. In these cases gas evolution was observed starting at about 150v.

Electroluminescence and sparking were observed for the experimental conditions listed above, and the voltages at which these effects became visible are given in Table I. It is difficult to give precise voltages for the occurrence of these effects, but in replicate experiments the ranges for appearance of electroluminescence and sparking were approximately 5v and 10v respectively.

Films or coatings produced above the spark potential were all yellow or orange and opaque. The spark reaction products were normally adherent after completion of the anode reaction, but products of the same composition were ejected from the anode surface during the spark reaction.

Film and coating composition.—Qualitative chemical tests and powder x-ray diffraction analyses were used to determine film composition and structure.

Treatment of unsparked films with dilute HCl resulted in dissolution of the film, evolution of H_2S, and formation of a clear solution. No change in the appearance of smooth films, produced at 50v, was observed after immersion for two hours in CS_2. Some change such as pitting or erosion of the film would have been expected if elemental surfur had been present.

The results of powder x-ray diffraction analyses of anodic film samples obtained at different formation voltages is presented in Table II. The x-ray patterns were made on a Norelco x-ray unit using Ni filtered K_α radiation of Cu. Samples were exposed in a Debye-Scherrer camera for approximately 15 hr, with the beam at 18 ma and 40 kv.

The powder samples were prepared by scraping the film from the Cd anode after anodic formation and washing in C_2H_5OH. The Cd present in the 50 and 70v samples is introduced during the scraping and is not present in the samples of thicker coatings obtained at 90, 110, and 130v. Cd is present again in coatings formed at voltages in excess of 220v. All of the latter coatings were produced in the presence of sparking which may have been sufficiently energetic to dislodge metal from the anode. Attempts to obtain x-ray data from thin (50v) films *in situ* with the wide angle goniometer were unsuccessful and there was no evidence for either crystal structure or preferred orientation.

Electrical resistance.—The d-c electrical resistance was calculated from current and voltage values for films

Table II. X-ray diffraction analysis of films on Cd produced by anodic treatment in 0.05*N* $Na_2S \cdot 9H_2O$ in C_2H_5OH

Anodic formation voltage	Products determined by x-ray diffraction
50	Cd
70	Cd
90	CdS 3 diffuse lines
110	CdS 5 diffuse lines
130	CdS 10 diffuse lines
220 (sparking)	CdS 24 lines, Cd 20 lines
315 (sparking)	CdS 23 lines, Cd 11 lines
500 (sparking)	CdS 27 lines, Cd 8 lines
750 (sparking)	CdS 21 lines, Cd 15 lines

in contact with the electrolyte at various stages of formation. In this experiment the anodes were 1.27 cm diam Cd rods, 25 cm in length which were machined and chemically polished to produce smooth surfaces. These were masked with bands of a pressure-sensitive tape so that the anode surfaces prior to electrolytic treatment consisted of series of exposed areas 1.27 cm wide and separated by masked areas of equal width. The anodization procedure was to insert the anode to its full length in 0.05N $Na_2S \cdot 9H_2O$ in C_2H_5OH, anodize at predetermined constant voltage for periods of 10 and 45 min, and after each period of anodization to raise a section of the anode out of the electrolyte and increase the voltage to the next desired level. The data are plotted in Fig. 2. The resistance values are at least two orders of magnitude larger than the resistance of the solution in the anodic cell (which has a specific resistivity of approximately 1100 ohm cm), and thus the electrolyte contribution to the measured resistance is very small and may be neglected. The decrease in the resistance *vs.* formation voltage curves as shown in Fig. 2 at the higher voltages may be related to the development of crystal structure which the x-ray data in Table II show to occur to an increasing degree as formation voltage is increased.

A series of resistance measurements was also made with a film formed on Cd for 16 hr at 100v in 0.05*N* $Na_2S \cdot 9H_2O$ in C_2H_5OH. After forming under the above conditions, the circuit was opened and a 10 $K\Omega$ resistor was placed in series with the anode. The voltage drop across this resistor was measured with a vacuum tube voltmeter in order to calculate current flowing in the cell as voltage applied to the cell was raised in approximate 10v increments. At each voltage setting, current readings were taken over a period of time, sufficient for decay of transients, and the current density was plotted as a function of voltage on the film. These values are shown in Fig. 3. It is apparent from this plot that the current passing through the CdS film is nonlinearly dependent on the applied voltage.

Film thickness.—Film thicknesses were estimated from interference colors for samples prepared by anodizing in 0.05*N* $Na_2S \cdot 9H_2O$ in C_2H_5OH. The anodes were Cd rods mounted lengthwise in polymethylmethacrylate blocks and polished mechanically to expose a flat sur-

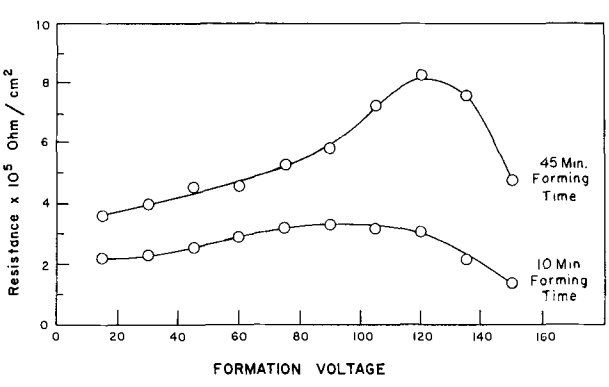

Fig. 2. Electrical resistance of anodic CdS films, formed and measured in 0.05*N* $Na_2S \cdot 9H_2O$ in C_2H_5OH at 25°C.

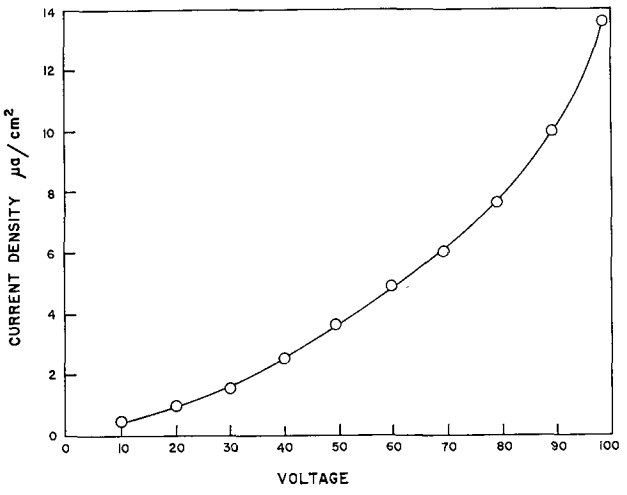

Fig. 3. Current density-voltage relation for CdS film: formed 16 hr; 100v; 0.05*N* $Na_2S \cdot 9H_2O$ in C_2H_5OH.

face measuring 0.7 x 2.4 cm. The film was prepared by anodizing at a current density which ranged between 0.3 to 2.5 ma/cm² as the applied voltage was increased from 0 to 200v at the rate of 2.4 v/min. The anode was simultaneously withdrawn from the electrolyte by means of a clock drive at a rate of 0.19 mm/min. Thus, a film increasing in thickness from 0 to that corresponding to 200v was displayed over a length of anode surface measuring 1.6 cm. There was some uncertainty as to the position of the first fringe but in the range 0 to 195v, fringes could be observed in sodium light (λ = 5893Å) and were found to be equally spaced, occurring at intervals of 45v. The last two fringes at about 150 and 195v were in a film that was slightly cloudy and it appears that in this voltage range, film growth and film breakdown occur simultaneously. Film thickness increase was calculated as a function of voltage with the aid of the expression cited by Booker and Benjamin (9)

$$d = r\frac{\lambda}{2n}$$

in which d is film thickness, r is the number of fringes, λ is the wavelength of incident light, and n is the refractive index. This latter value is assumed to be the same for the film as for bulk CdS in which n is 2.5 measured with light of the above wavelength (10). The film thickness difference between fringes is calculated at 1178Å and since this corresponds to a voltage interval of 45v, the thickness/voltage ratio is determined as 26Å/v.

Discussion

The experimental study, described in the preceding sections, of the anodic behavior of Cd in $Na_2S \cdot 9H_2O$ solutions in C_2H_5OH is of interest due to the barrier nature of the films which are produced, and the scientific and technical areas which appear as subjects for further investigation.

The barrier which forms on the Cd anodes consists of a thin film which sustains large electric fields as is shown by the appearance of interference colors, electroluminescence, and dielectric breakdown accompanied by sparking at elevated anodic voltages. Nearly all the voltage applied to the electrolysis cell is accounted for by the film since the solution resistance can account for only about 1% of the cell resistance. One can therefore estimate that fields in these films are of the order of 4 x 10^6 v/cm.

The question of composition of the films is not completely answered by the measurements made thus far, but it is clear that CdS is present in films obtained above 90v. The even spacing of interference fringes in films grown as wedges of uniformly increasing thickness, indicates that the refractive index of the film does not change appreciably over the voltage range 50 to 200v, and this would indicate that gross changes in film composition do not occur in this voltage range.

The ability to control anodic film composition and properties is of interest in connection with possible applications in electronic devices. We have prepared films similar to those described above on Cd anodes in which small quantities of Al, Cu and Mn were present as alloy constituents. Also, exploratory studies have shown that Cl can be incorporated in the CdS anodic films via anion deposition if NH_4Cl is added to the electrolyte.

The anodic formation of CdS films opens several areas of research which should yield useful results. Other Group II-IV and Group III-V compounds can probably be prepared in this form. It is also reasonable to expect that some of the compounds of Group V and VI elements with transition and inner transition metals will be accessible via anodic processes.

Acknowledgments

The authors are indebted to Dr. W. J. Kroeger of Frankford Arsenal, and to Dr. J. V. R. Kaufmann, of the U.S. Army Munitions Command, for encouragement and support of this work. Thanks are also due to Doctors F. Verderame, J. Varimbi, and H. Gisser for helpful discussions and review of the manuscript.

Manuscript received Dec. 17, 1964; revised manuscript received March 22, 1965. This work was supported by the Army Materiel Command, Project No. OMS 5010.11.838, "Basic Research in the Physical Sciences."

Any discussion of this paper will appear in a Discussion Section to be published in the June 1966 JOURNAL.

REFERENCES

1. L. Young, "Anodic Oxide Films," Academic Press, New York (1961).
2. G. Hass, *J. Opt. Soc. Amer.*, **39**, 532 (1949).
3. D. A. Vermilyea, *Acta Met.*, **1**, 282 (1953).
4. A. Guntherschulze and H. Betz, *Z. Physik*, **91**, 70 (1934).
5. W. Jaenicke, R. P. Tischer, and H. Gerischer, *Z. Elektrochem.*, **59**, 448 (1955).
6. A. Guntherschulze, *Ann. Physik*, **26**, 372 (1908).
7. L. L. Gruss and W. McNeill, *Electrochem. Tech.*, **1**, 283 (1963).
8. A. Guntherschulze and H. Betz, *Z. Physik*, **107**, 347 (1937).
9. G. R. Booker and C. E. Benjamin, *This Journal*, **109**, 1206 (1962).
10. J. E. Powderly, R. H. Fabrig, K. E. Beam, S. J. Rodrique, and W. E. Medcalf, "Research in Purification of CdS Crystals," Prog. Rpt. 7116, Contract No. AF33(6166203).

Conductivity Anomalies of Dimethyl Sulfone

Erik Kissa

Jackson Laboratory, Organic Chemicals Department,

E. I. du Pont de Nemours and Company, Wilmington, Delaware

ABSTRACT

The electrical conductivity of dimethyl sulfone has been measured while cooling it from 130° to 30°C at a rate of 0.5°C/min. Unlike diphenyl sulfone or chlorotriphenylmethane, dimethyl sulfone exhibited conduction anomalies attributable to proton conduction and interfacial polarization.

The chemical electret (1) was formed by solidifying a mixture of carnauba wax, resin, and beeswax in an electric field (2). Various substances have been shown to form electrets (3, 4). Unlike the classical electret, dimethyl sulfone exhibits long-lasting voltage reminiscence when a strong electric field is applied after freezing (5). Considering proton conduction and phase changes as possible causes, the conductivity-temperature relationship of dimethyl sulfone was studied.

Experimental

Purification.—Dimethyl sulfone was purified by neutralization of its acidic impurities and recrystallization from chloroform and from ethanol, dried *in vacuo* over metallic sodium, and sublimed twice. M.p. 108-109°C. Anal. Calc'd: C, 25.5; H, 6.4; S, 34.1. Found: C, 25.5; H, 6.4; S, 34.0.

Diphenyl sulfone was sublimed twice, M.p. 128°C. Anal. Calc'd: C, 66.0; H, 4.6; S, 14.7: Found: C, 66.1; H, 4.7; S, 14.7.

Chlorotriphenylmethane was recrystallized from a mixture of benzene and petroleum ether. M.p. 112-113°C. Anal. Calc'd: Cl, 12.7. Found: Cl, 12.6.

The purified compounds were stored and handled under anhydrous conditions.

Conductivity measurements.—The conductivity cells were 20 x 40 mm Pyrex vials equipped with a Teflon plug through which an inlet tube for dry argon, a thermocouple well, and two platinum wire electrodes, 10 mm apart, were introduced. The upper part of the electrodes was covered with a glass tubing, leaving a 10-mm long portion exposed.

The conductivity cells were charged with molten samples and cooled slowly to room temperature. After standing 16 hr they were heated to 130°C and cooled in an oil bath at a rate of 0.5°C/min. A General Radio impedance bridge was used at 1 kc frequency for measuring resistances up to 10^7 ohms. For higher resistances, a General Radio type 1862-B megohm-meter was used, by applying two 1-sec long d-c pulses of opposite polarity.

On heating from 28° to 130°C, dimethyl sulfone, diphenyl sulfone, and triphenylmethane did not exhibit conduction anomalies: the apparent conductivities increased gradually with the increasing temperature until melting occurred with a sharp conductivity increase.

Typical conductivity curves obtained by cooling the molten compounds from 130° to 30°C are shown in Fig. 1. The conductivity minimum slightly below the freezing point was present also with carbon electrodes or when switching from one pair of platinum electrodes to another pair arranged crosswise.

The conductivity of molten dimethyl sulfone changed only by 20% rel. when subjected to the (about 1-v a.c.) output of the impedance meter for 3 hr. However, an application of 50v d.c. increased the conductivity of molten dimethyl sulfone 2.7 times in 3 hr, and an acidic electrolysis product had formed.

Dielectric properties.—Dielectric measurements were carried out in the frequency range betwen 200 and 6000 cps with a General Radio Type 716-C capacitance bridge equipped with a Balsbaugh cell. The dielectric constant-temperature curve of cooling dimethyl sulfone exhibited a peak which was frequency-dependent and weakened with time. It was very strong at 200 cps and disappeared at 6000 cps (Fig. 2). The peak in the dissipation factor-temperature curve was also time- and frequency-dependent; at 200 cps (Fig. 2) it was too high to be measured.

Discussion

The conduction anomalies of dimethyl sulfone can be explained by accumulation of space charges associated with proton conduction and coexistence of two phases with different conductivities, already observed in long-chain alcohols (6). Frosch (7) explained the rise in dielectric constant of n-octadecanol by interfacial polarization, caused by the coexistence of liquid and solid phases. Hoffman and Smyth (8) believed this to be improbable and concluded that two solid phases formed on freezing. The highly conductive α phase, in which proton transfer was facilitated by molecular rotation, changed via a nonconductive β_1 form to the stable β_2 form.

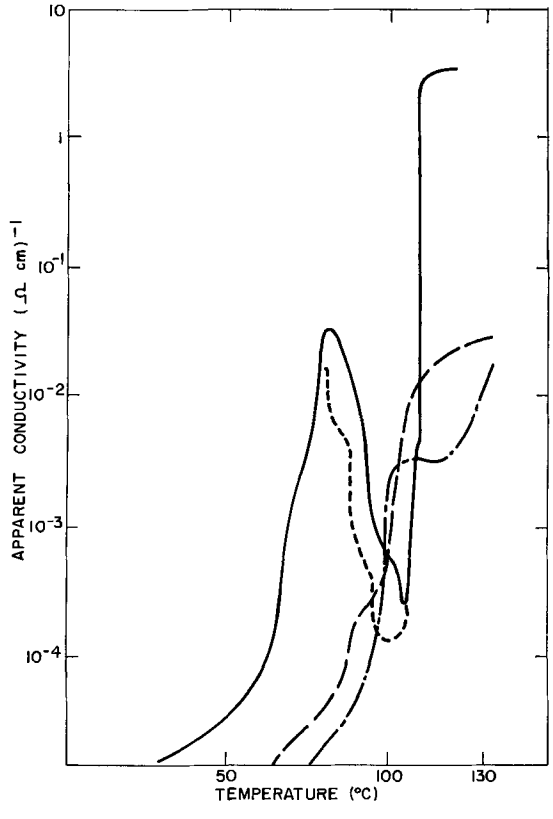

Fig. 1. Apparent conductivities of dimethyl sulfone, diphenyl sulfone, and chlorotriphenylmethane during cooling of their melts. ——, $CH_3SO_2CH_3$; — — —, $CH_3SO_2CH_3$ reversed direction; — - —, $C_6H_5SO_2C_6H_5$; —— ——, $(C_6H_5)_3$ CCl.

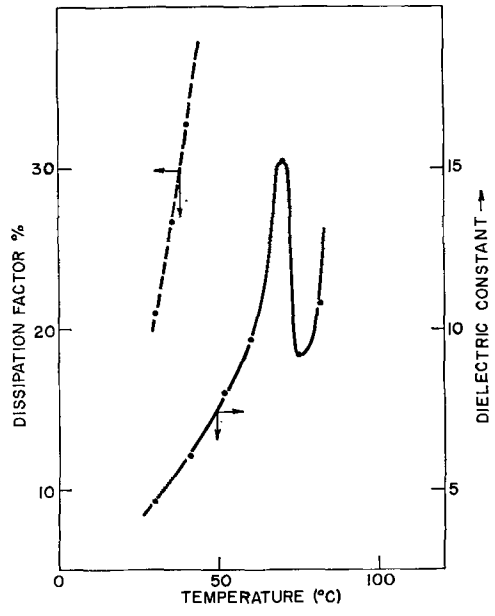

Fig. 2. Temperature dependence of the dielectric constant and the dissipation factor at 200 cps.

The conductivity minimum of freezing dimethyl sulfone appears with the formation of first crystals on the electrodes and is associated with interfacial polarization. With progressing solidification a conductive pseudo-solid is formed, in which molecular rotation may permit a proton transfer. On further cooling the metastable amorphous phase transforms into the stable crystalline form which does not permit molecular rotation, and the resistance increases again.

The release of protons in dimethyl sulfone under electric stress is indicated by its dielectric properties and by the formation of acidic electrolysis products. The somewhat acidic nature of hydrogen in dimethyl sulfone has been demonstrated by Hochberg and Bonhoeffer (9) who observed hydrogen-deuterium exchange in alkaline D_2O. Activation of hydrogen by the sulfonyl group is shown also by metalation with a Grignard reagent (10, 11).

Diphenyl sulfone and chlorotriphenylmethane cannot provide protons and do not show conductivity anomalies.

Measurements of electric conductivity change during phase transitions may provide a method for structure determination and identification of compounds which release a proton under electric stress.

Acknowledgment

The author is indebted to Dr. M. R. Kegelman for measurements of dielectric properties.

Manuscript received July 23, 1964; revised manuscript received Nov. 16, 1964.

Any discussion of this paper will appear in a Discussion Section to be published in the June 1966 JOURNAL.

REFERENCES

1. O. Heaviside, Electrical Papers #1.
2. M. Eguchi, *Phil. Mag.*, **49**, 178 (1925).
3. F. Gutmann, *Rev. Mod. Phys.*, **20**, 457 (1948).
4. C. P. Smyth, "Dielectric Behavior and Structure," McGraw Hill Co., New York (1955).
5. F. C. Chromey and E. Kissa, Unpublished work.
6. C. P. Smyth, "Dielectric Phenomena," in "Physics and Chemistry of the Organic Solid State," D. Fox, M. M. Labes and A. Weissberger, Editors, Vol. I, Interscience Publishers, New York (1963).
7. E. Frosch, *Ann. Physik*, **42**, 254 (1942).
8. J. D. Hoffman and C. P. Smyth, *J. Am. Chem. Soc.*, **71**, 431 (1949).
9. J. Hochberg and K. F. Bonhoeffer, *Z. Physik Chem.*, **A184**, 419 (1939).
10. W. E. Truce and K. R. Buser, *J. Am. Chem. Soc.*, **76**, 3577 (1951).
11. L. Field and J. M. McFarland, *ibid.*, **75**, 5583 (1953).

Hydrogen Overvoltage on Rhenium and Niobium Electrodes

M. J. Joncich[1] and L. S. Stewart[2]

Department of Chemistry, University of Tennessee, Knoxville, Tennessee

and F. A. Posey

Chemistry Division, Oak Ridge National Laboratory, Oak Ridge, Tennessee

ABSTRACT

Polarization curves of the hydrogen evolution reaction are presented for rhenium and niobium electrodes in dilute hydrochloric acid solutions as a function of temperature. The Tafel reaction is the rate-determining step in the hydrogen evolution reaction on rhenium. The behavior of niobium electrodes is much more complicated. The presence of the passive oxide layer on niobium produces an ohmic contribution to the total overvoltage. The corrected activation-overvoltage curves for niobium show a change of Tafel slope which is consistent with a Volmer-Tafel mechanism if certain assumptions are made about the distribution of potential at the interface. Activation energies of the hydrogen reaction are computed for both rhenium and niobium electrodes.

Comparatively few studies on the electrochemical behavior of rhenium and niobium electrodes have been reported. Pecherskaya and Stender (1) measured hydrogen overvoltage on rhenium. Hydrogen overvoltage on niobium was studied by Bockris (2), by Kononchuk and Barmashenko (3), and by Rotinyan and Kozhevnikova (4). The use of Nb as a pH-responsive electrode was investigated by Jensovsky (5) and by Galinker (6). An electrode potential-pH diagram for rhenium was constructed from available thermodynamic data by Pourbaix (7). Anodic oxidation of rhenium was studied by Lavrenko (8), while the anodic behavior of niobium has been the subject of a number of investigators (9-22).

Here we present data for hydrogen overvoltage on rhenium and niobium electrodes in dilute hydro-

[1] Present address: Department of Chemistry, Northern Illinois University, DeKalb, Illinois.

[2] Present address: Department of Chemistry, Rutgers University, New Brunswick, New Jersey.

chloric acid solutions. Current densities from 10^{-6} to 10^{-2} amp/cm^2 were used and measurements were made over the temperature range, 5°-45°C. Conclusions are drawn about the mechanism of the hydrogen evolution reaction on rhenium and niobium under these conditions and the apparent activation energies of the reactions are calculated.

Experimental

The experimental cell was similar to that described by Ammar and Awad (23) except for certain modifications which facilitated cleaning and equalization of hydrogen pressure in the three cell compartments. Teflon stopcocks were used throughout the apparatus. A platinum electrode of large area was employed as a polarizing electrode, and the current density at this electrode was kept low enough so that no significant oxygen evolution occurred (24).

The hydrogen reference electrode was constructed of 30-gauge platinum wire and checked frequently against a standard calomel electrode. Cathodes for pre-electrolysis were made of the same metal as the electrodes used in the experiments. Rhenium electrodes were constructed from wires fabricated from 99.99% pure rhenium powder by Sylvania Electric Products Inc. Spectroscopic analysis of this material showed Ca, 0.01-0.1%; Fe, 0.01%; and Si, 0.1%. Niobium metal was obtained from a sheet cold-pressed at 40 tons/in.^{2} and purified by a zone-refining method. Spectroscopic analysis of the niobium showed O, 0.01%; N, 0.018%; C, 0.010%; Zr, 0.04%; and Ta, 0.14% by weight. Rhenium and niobium electrodes were mounted in Teflon holders, cleaned by immersion in hydrochloric acid, and rinsed repeatedly with distilled water and with conductance water.

Electrolytic tank hydrogen was purified by passage through a train consisting of an alkaline solution of potassium permanganate, cocoanut charcoal, silica gel, Anhydrone, Hopcalite, Ascarite, DeOxy Catalytic Purifier, and silica gel. A gas washer located between the purification train and the cell was used to saturate the hydrogen gas with the test solution. Temperature control was accomplished by use of an insulated air bath; temperature was constant to within ± 0.1°C.

Hydrochloric acid solutions were prepared by dilution of a constant-boiling distillate of reagent grade hydrochloric acid and conductance water. Pre-electrolysis was conducted for a minimum of 50 hr with a current of 4-5 ma. Several hours were allowed for the establishment of temperature equilibrium. A L&N pH Indicator was used to measure both potentials and currents. Current was supplied from a bank of batteries and regulated by use of variable resistors. Electrode potentials were measured by the direct method within a few minutes after application or change of polarizing current as recommended by Schuldiner (25). Potentials measured in this manner were stable and polarization curves were reproducible. Stirring by hydrogen gas was continued during the measurements.

Results

Tafel plots of data for hydrogen overvoltage on rhenium electrodes in 0.037*N* and 0.145*N* HCl are shown in Fig. 1 and 2. Resistance overvoltage due to IR drop in the solution phase between the electrode surface and the tip of the reference electrode capillary contributes significantly to the measured overvoltage at the higher current densities. The resistive contribution was subtracted from the measured overvoltage values by a series of successive graphical approximations. Use of this correction, together with a correction due to the rate of the anodic reaction near the equilibrium potential, leads to the dashed Tafel lines in Fig. 1 and 2. The exact value of the resistance correction varied with each series of measurements because of unavoidable differences in the placement of the reference electrode capillary. Values of the resistance corrections for the data of Fig. 1 are 13.9, 13.7, 8.7, and 12.3 ohm-cm^2 at

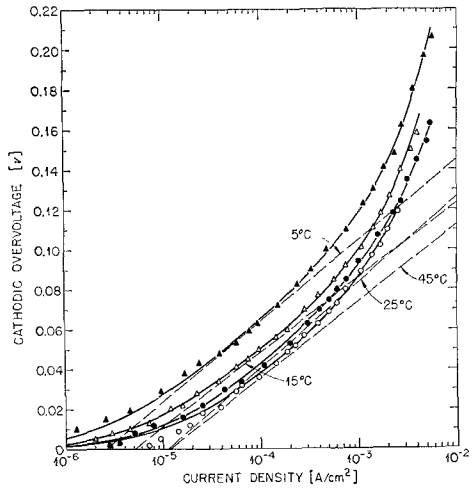

Fig. 1. Hydrogen overvoltage on rhenium in 0.037*N* HCl as a function of temperature; temperature in °C: ▲, 5; △, 15; •, 25; ○, 45. Solid lines are calculated polarization curves; dashed lines are cathodic Tafel lines corrected for resistance overvoltage and the rate of the anodic reaction.

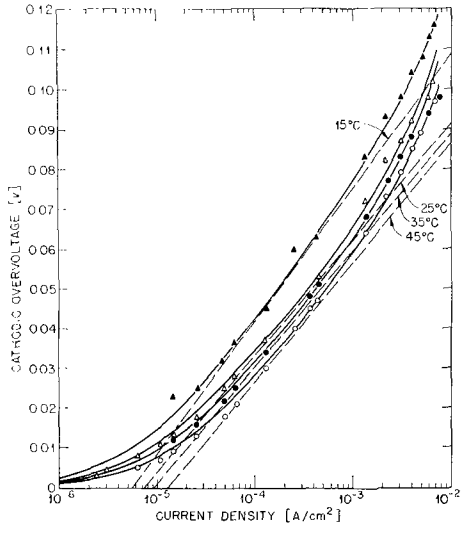

Fig. 2. Hydrogen overvoltage on rhenium in 0.145*N* HCl as a function of temperature; temperature in °C: ▲, 15; △, 25; •, 35; ○, 45. Solid lines are calculated polarization curves; dashed lines are cathodic Tafel lines corrected for resistance overvoltage and the rate of the anodic reaction.

5°, 15°, 25°, and 45°C, respectively. Corrections for resistance overvoltage for the data of Fig. 2 are similar, except that resistance values are only one-fourth as large as those necessary to correct the data of Fig. 1 because the solution concentration is approximately four times greater.

Tafel plots of the anodic reaction, calculated from the difference between the experimental data points and the dashed Tafel lines in Fig. 1 and 2 in the region near the equilibrium potential, show that the rate of this reaction is independent of the overvoltage. Use of this fact, taking into account the resistance overvoltage, leads to Eq. [1] for the total overvoltage. In Eq. [1], $|\eta|$ (V) is the absolute value of

$$|\eta| = |b| \log \left(1 + \frac{|j|}{j_o}\right) + |j|R_s \qquad [1]$$

the overvoltage, $|b|$ (V/decade of current) is the absolute value of the Tafel slope, $|j|$ (amp/cm^2) is the absolute value of the applied current density, j_o (amp/cm^2) is the exchange current density, and R_s (ohm-cm^2) is the resistance between the electrode surface

Table I. Parameters for hydrogen overvoltage on rhenium electrodes in dilute hydrochloric acid solutions

Solution	Temperature, °C	a, v	b($\times 10^3$), v	j_o, (amp/cm²)
0.037*N* HCl	5	−0.226	−40.5	2.65×10^{-6}
	15	−0.198	−37.5	5.1×10^{-6}
	25	−0.213	−43.0	1.14×10^{-5}
	45	−0.189	−38.4	1.18×10^{-5}
0.145*N* HCl	15	−0.176	−33.5	5.7×10^{-6}
	25	−0.150	−29.2	7.3×10^{-6}
	35	−0.147	−29.3	9.3×10^{-6}
	45	−0.147	−30.0	1.3×10^{-5}

and the reference electrode capillary tip.[3] Table I presents values of the Tafel a and b constants as well as values of the exchange current density calculated from the Tafel lines in Fig. 1 and 2. The a and b constants are defined conventionally by Eq. [2], which is Tafel's equation. Values of j_o, b, and R_s

$$\eta = a + b \log |j| \qquad [2]$$

were used with Eq. [1] to calculate the solid lines in Fig. 1 and 2; these theoretical lines fit the data very well.

Data for hydrogen overvoltage on niobium electrodes in 0.145*N* HCl are shown in Fig. 3. In this case, a large correction for resistance overvoltage is necessary; this correction was made in the same manner as that used for the data of Fig. 1 and 2. Resistive corrections in the case of the rhenium electrode in 0.145*N* HCl (cf. Fig. 2) average approximately 2.5 ohm-cm², which is consistent with the conductivity of the solution and the placement of the tubulus of the reference electrode, whereas those for the niobium electrode average approximately 216 ohm-cm². We suggest that, during the time necessary for the measurement of the overvoltage, no significant change occurs in the thickness of the oxide layer on the surface of the niobium electrodes. The poor electronic conductivity of the passive layer then accounts for the large resistive contribution to the measured overvoltage. Since the electronic conductivity of the passive oxide layer on niobium in solution is not known accurately, no reliable estimate can be given, in the absence of capacity measurements, of the film thickness on the electrodes used here. The resistive correction for the ohmic behavior of the film in this case may be defined by Eq. [3]

[3] Equation [1] is essentially Hammett's relation (26) for the Tafel mechanism of the hydrogen evolution reaction. In this case the exchange current density (j_o) is equal to j_r, the limiting current density of the Tafel reaction, which is independent of electrode potential.

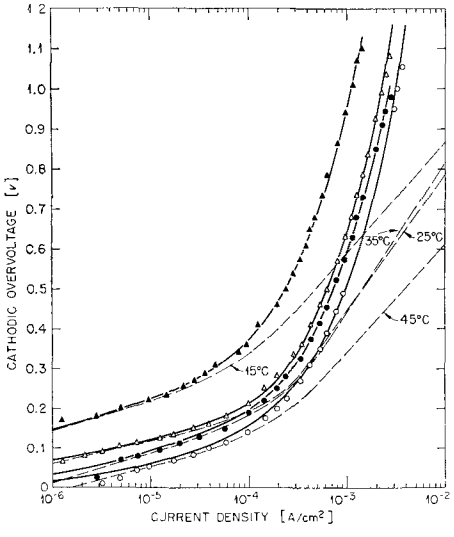

Fig. 3. Hydrogen overvoltage on niobium in 0.145*N* HCl as a function of temperature; temperature in °C: ▲, 15; △, 25; ●, 35; ○, 45. Solid lines are calculated polarization curves; dashed lines are cathodic Tafel lines corrected for resistance overvoltage and the rate of the anodic reaction.

$$R_{ox} \equiv \Delta\phi_{ox}/j = l/\sigma_{ox} \qquad [3]$$

where R_{ox}(ohm-cm²) is the resistivity correction, $\Delta\phi_{ox}$ is taken to be the potential difference across the oxide layer, j is current density, l is the thickness of the layer, and σ_{ox} is the specific conductance of the layer. For $R_{ox} = 200$ ohm-cm², σ_{ox} would have a value between 10^{-9} and 10^{-7} ohm^{-1} cm^{-1} if the film thickness were between 20 and 2000Å. This order of magnitude of specific conductance for the Nb_2O_5 layer at the temperatures of this study is not unexpected in view of the results obtained elsewhere on the specific conductance of sintered and single crystal Nb_2O_5 specimens as a function of departure from stoichiometry and of temperature (27-29).

Correction of the data of Fig. 3 for the ohmic contribution leads to the dashed Tafel lines shown in the graph. In this case, a change of Tafel slope occurs, corresponding to a change in the identity of the rate-determining step in the hydrogen evolution reaction. The corrected overvoltage data are described well by an expression of the form of Eq. [4]

$$j_c = \frac{j_{o,1}\, j_{o,2} \exp\left[-2.303\left(\frac{1}{b_1}+\frac{1}{b_2}\right)\eta\right]}{j_{o,1} \exp\left[-2.303\eta/b_1\right] + j_{o,2} \exp\left[-2.303\eta/b_2\right]} \qquad [4]$$

where j_c is the current density of the cathodic process, $j_{o,1}$ and $j_{o,2}$ are the exchange current densities obtained by extrapolation of the two Tafel regions to zero overvoltage, and b_1 and b_2 are the corresponding Tafel slopes (cf. Eq. [2]).[4] Values of parameters for the overvoltage in this case are given in Table II. The solid lines in Fig. 3 are theoretical polarization curves calculated by use of Eq. [4] and the data of Table II together with the correction for the ohmic behavior of the passive layer and for the rate of the anodic reaction near the equilibrium potential.

Estimated exchange current densities from the data of Fig. 1, 2, and 3 are plotted as a function of temperature in Fig. 4 and 5. In the case of the rhenium electrode, exchange current densities are essentially independent of the concentration of hydrogen ions, and the line shown in Fig. 4 is a least squares fit of all the data. The slope of the line is equivalent to an apparent enthalpy of activation of 5.96 kcal/mole. The apparent enthalpy of activation of the rate-determining process in the low current region on niobium is found from Fig. 5 to be 31.4 kcal/mole. The corresponding value for the process which determines the rate at larger overvoltages is 11.3 kcal/mole. Both values were determined by least squares fit of a simple Arrhenius-type equation to the available data.

Discussion

The data of Pecherskaya and Stender (1) for hydrogen overvoltage on rhenium were obtained in 2*N*

[4] Equation [4] is a generalized form for the cathodic polarization curve of the hydrogen evolution reaction in the case of a dual mechanism with small surface coverage of adsorbed hydrogen atoms. With $j_{o,1} = j_o^V/2$, $j_{o,2} = j_r$, $b_1 = 2.303\ RT/(1-\alpha_V)F$, and $b_2 = 2.303\ RT/2F$, Eq. [4] is a form of the Hammett equation (30) for the Volmer-Tafel mechanism of the hydrogen evolution reaction. In this case, j_o^V is the exchange current density of the Volmer reaction, j_r is the limiting current density of the Tafel or recombination reaction, and α_V is the transfer coefficient of the Volmer reaction. However, for $j_{o,1} = 2j_o^V$, $j_{o,2} = 2j_o^H$, $b_1 = 2.303\ RT/(1-\alpha_V)F$, and $b_2 = 2.303\ RT/(2-\alpha_H)F$, Eq. [4] is a form of Vetter's relation (31) for the Volmer-Horiuti reaction sequence. In this case, j_o^V and j_o^H are the exchange current densities of the Volmer and Horiuti reactions, respectively, and α_V and α_H are the corresponding transfer coefficients.

Table II. Parameters for hydrogen overvoltage on niobium electrodes in 0.145*N* HCl

Temperature, °C	a_1, v	b_1($\times 10^3$), v	$j_{o,1}$, (amp/cm²)	a_2, v	b_2($\times 10^3$), v	$j_{o,2}$, (amp/cm²)
15	−0.700	−71	9.4×10^{-9}	−1.429	−280	7.9×10^{-6}
25	−0.402	−57	8.8×10^{-8}	−1.472	−343	5.1×10^{-5}
35	−0.461	−75	7.0×10^{-7}	−1.569	−376	6.7×10^{-5}
45	−0.373	−64	1.5×10^{-6}	−1.153	−271	5.6×10^{-5}

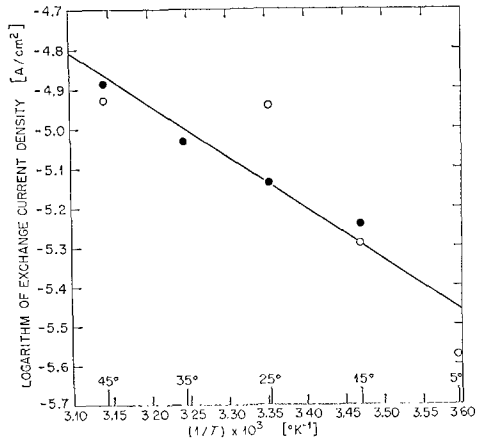

Fig. 4. Variation of the exchange current of the hydrogen reaction on rhenium with temperature. ○, 0.037*N* HCl; ●, 0.145*N* HCl.

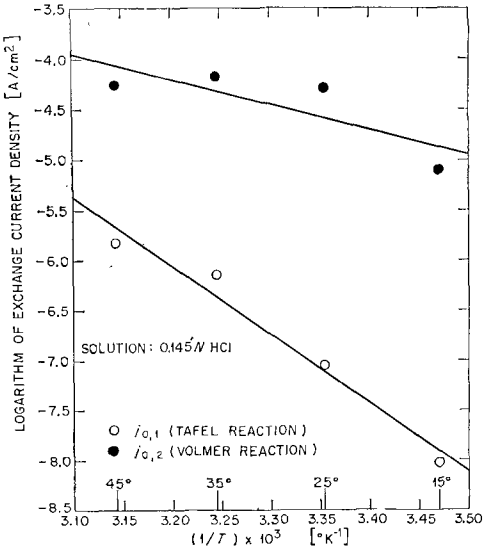

Fig. 5. Variation of the calculated exchange current densities of the hydrogen reaction on niobium with temperature. Solution, 0.145*N* HCl; ○, $j_{0,1}$ (Tafel reaction); ●, $j_{0,2}$ (Volmer reaction).

H_2SO_4 at 25°C. These authors reported an exchange current density of approximately 10^{-3} amp/cm² in the medium studied and a Tafel slope of $b = 0.14$v. Their data are not extensive, and only one data point is in very good agreement with this work. Pecherskaya and Stender report a cathodic overvoltage of 0.09v at a current density of 5 x 10^{-3} amp/cm²; this value compares favorably with the corrected Tafel lines of Fig. 1 and 2. Hydrogen overvoltage on rhenium is quite low; it is comparable to that found for iridium and rhodium (32).

We find that the Tafel slopes for the hydrogen evolution reaction on rhenium in dilute hydrochloric acid are close to 30 mv/decade (cf. Table I). The Tafel slopes obtained in 0.037*N* HCl are somewhat higher than this value, but double layer effects are probably important here, and the resistive correction is less certain in the more dilute solution. Calculations of the rate of the anodic reaction near the equilibrium potential show that the rate of this reaction is independent of potential, and the exchange current densities obtained by extrapolation of the Tafel lines are insensitive to the concentration of hydrogen ions in solution. These facts suggest that the Tafel reaction, $2H_{(ads.)} = H_{2(aq.)}$, determines the rate of the hydrogen evolution reaction on rhenium. This conclusion is supported by values of the stoichiometric numbers obtained from the polarization resistances and the estimated exchange current densities. All calculated stoichiometric numbers are near unity, ranging from 0.8 to 1.3.

Our value of the Tafel slope (30 mv/decade) may still be consistent with that of Pecherskaya and Stender (140 mv/decade) if a transition in the nature of the rate-determining step occurs near current densities of 10^{-2} amp/cm². In this case, an increase in cathodic polarization would increase the surface coverage of adsorbed atomic hydrogen to the point where the Tafel reaction would be essentially in equilibrium, and the rate of the over-all reaction would then be controlled by the Volmer reaction, $H^+_{(aq.)} + e^- = H_{(ads.)}$ (33). The apparent activation energy at the equilibrium potential of the hydrogen reaction on rhenium, obtained from Fig. 4 as 5.96 kcal/mole, refers in this case to the mean enthalpy of activation of the forward and reverse steps of the Tafel reaction.

The data on hydrogen overvoltage on niobium of Bockris (2) in 0.1*N* HCl and of Kononchuk and Barmashenko (3) in 1*N* H_2SO_4 are fragmentary, and the Tafel slopes do not agree with those observed here. The reason for this discrepancy is not known; it is possible that their measurements were influenced by the presence of impurities which could exert an important effect on the results in such a polarizable system. The measurements of Rotinyan and Kozhevnikova (4) are more extensive, and their observations resemble ours to a greater extent. These authors measured hydrogen overvoltage on niobium in 0.01-10.0*N* H_2SO_4 at temperatures from 25° to 55°C. They found nonlinear Tafel plots in the region 10^{-5}-10^{-4} amp/cm², whereas linear Tafel plots were obtained for current densities greater than 10^{-4} amp/cm². In addition, deviations from linearity were observed in dilute solutions for current densities greater than about 2 x 10^{-3} amp/cm² at 25°C.

The results of Rotinyan and Koshevnikova are understandable on the basis of the data in Fig. 3. The Tafel plot in the range, 10^{-5}-10^{-4} amp/cm², is nonlinear because of the effect of the anodic reaction and because the change in Tafel slope occurs in this range of current densities. Above approximately 10^{-4} amp/cm², linear Tafel plots could then be obtained in concentrated acidic solutions; under these conditions the thickness of the oxide layer on the surface of the niobium electrode and thus the ohmic contribution to the total overvoltage should be much less than in dilute acids. However, in dilute acids the ohmic properties of the passive oxide layer should contribute significantly to the total overvoltage, and in this case one should expect nonlinear Tafel plots, as found by Rotinyan and Kozhevnikova.

The Tafel slopes observed in the two linear regions of the polarization curves in Fig. 3 average $b_1 = 67$ mv and $b_2 = 318$ mv, respectively. Transitions in Tafel slope are expected for the hydrogen evolution reaction on electrodes with no superficial oxide layers for the Volmer-Tafel and the Volmer-Heyrovsky mechanisms (33). The Volmer-Tafel mechanism involves a transition in Tafel slope from 29 to 116 mv/decade at 25°C for normal values of the transfer coefficients, whereas Tafel slopes of the Volmer-Heyrovsky mechanism should show a transition from 39 to 116 mv/decade. Although the transition in Tafel slopes is observed on niobium, values of the slopes are roughly twice those expected at an interface with no passive oxide layer.

Unusual values of Tafel slopes for oxidation-reduction reactions on passive electrodes have been discussed by Posey, Cartledge, and Yaffe (34), Meyer (35), MacDonald and Conway (36), and Makrides (37). The dual-barrier model and its variations used by these authors account for high values of Tafel slopes which are frequently found on passive metals. In this model, the distribution of potential at the passive interface is recognized to be complex; only that part of the total potential difference between metal and solution which exists at the oxide-solution interface affects the rate of electrochemical charge-transfer steps

of oxidation-reduction reactions. For cases where transfer of charge must occur across two energy barriers, both of which are affected by changes in the total interfacial potential difference, the Tafel slope of the over-all reaction is given by Eq. [5], where

$$b_{(\text{dual barrier})} = 2.303 \frac{(\beta_1 + \beta_2)RT}{\beta_1 \beta_2 F} \quad [5]$$

β_1 and β_2 are the transfer coefficients of the separate energy barriers (34). If $\beta_1 = \beta_2 = 1/2$, then the Tafel slope will be 2.303 ($4RT/F$) instead of 2.303 ($2RT/F$) for a simple reaction in a system involving a single barrier. The Tafel slopes of Fig. 3 can be understood on this basis. The dashed lines are corrected for the ohmic behavior of the passive layer, so that only the potential differences at the metal-oxide interface and at the oxide-solution interface need be considered. If both of these potential differences can vary with cathodic current, then the dual-barrier model and the formula of Eq. [5] should be applicable. The ratio of Tafel slopes for regions of high and low current density in the case of the Volmer-Tafel reaction is 4; that for the Volmer-Heyrovsky reaction is 3. The ratio of the average Tafel slopes of Fig. 3 is 4.7, although that for the results at 15° and at 45°C is 3.9 and 4.2, respectively. We conclude tentatively that the Volmer-Tafel mechanism of the hydrogen evolution reaction operates on niobium in dilute hydrochloric acid solutions and that the high Tafel slopes observed are a consequence of the existence of a passive layer which is described to a first approximation by a dual-barrier model.

Activation energies calculated from the plot of exchange current densities as a function of temperature in Fig. 5 are 31.4 kcal/mole for the Tafel reaction on the niobium surface and 11.3 kcal/mole for the Volmer reaction. These values represent the mean enthalpies of activation of the forward and reverse steps of the respective reactions. The value of 11.3 kcal/mole for the Volmer reaction is comparable to the value of 10.5 kcal/mole calculated by Rotinyan and Kozhevnikova from their data in the range from 10^{-4} to 10^{-2} amp/cm^2. Extrapolation of the lines in Fig. 5 to their point of intersection shows that the exchange current densities of the Volmer and Tafel reactions should be equal in the vicinity of 90°C. Therefore at temperatures higher than about 90°C, the Volmer reaction alone should govern the over-all rate of the hydrogen evolution reaction and no change of Tafel slope should be observed in the cathodic polarization curve of niobium.

Acknowledgment

Partial support of this project was provided by the Rhenium Fund of the University of Tennessee.

Manuscript received June 22, 1964; revised manuscript received Nov. 16, 1964. This paper was presented at the Los Angeles Meeting, May 6-10, 1962. A portion of this work was taken from a thesis submitted by one of the authors (L.S.S.) to the University of Tennessee in partial fulfillment of the requirements for the MSc degree; another portion was sponsored by the United States Atomic Energy Commission under contract with the Union Carbide Corporation.

Any discussion of this paper will appear in a Discussion Section to be published in the June 1966 JOURNAL.

REFERENCES

1. A. G. Pecherskaya and V. V. Stender, *Zhur. Fiz. Khim.*, **24**, 856 (1950).
2. J. O'M. Bockris, *Trans. Faraday Soc.*, **43**, 417 (1947).
3. T. I. Kononchuk and I. B. Barmashenko, *Ukrain. Khim. Zhur.*, **26**, 25 (1960).
4. A. L. Rotinyan and N. M. Kozhevnikova, *Zhur. Fiz. Khim.*, **37**, 1818 (1963).
5. L. Jensovsky, *Coll. Czech. Chem. Comm.*, **16**, 127 (1951).
6. V. S. Galinker, *Izvest. Vysshikh Ucheb. Zavedenii, Khim. i Khim. Tekhnol.*, **4**, 189 (1961).
7. M. Pourbaix, *Z. Elektrochem.*, **62**, 670 (1958).
8. V. O. Lavrenko, *Zhur. Fiz. Khim.*, **35**, 198 (1961).
9. L. Young, *Trans. Faraday Soc.*, **52**, 502, 515 (1956).
10. L. Young, *Acta Met.*, **4**, 101 (1956).
11. D. A. Vermilyea, *This Journal*, **104**, 427 (1957).
12. Yu. M. Valokobinskii, *Dokl. Akad. Nauk S.S.S.R.*, **113**, 1023 (1957).
13. G. B. Adams and T. Kao, *AECU-3769* (1957), U.S.A.E.C. Tech. Inf. Div., Oak Ridge, Tennessee.
14. L. Young, *Can. J. Chem.*, **38**, 1141 (1960).
15. W. M. Graven, R. E. Salomon, and G. B. Adams, *TID-6514* (1960), U.S.A.E.C. Tech. Inf. Div., Oak Ridge, Tennessee.
16. G. B. Adams and T. Kao, *This Journal*, **107**, 640 (1960).
17. L. Young, "Anodic Oxide Films," p. 186, Academic Press, London (1961).
18. A. Yu. Shatalov and T. P. Bondareva, *Dokl. Akad. Nauk S.S.S.R.*, **147**, 1137 (1962).
19. A. Yu. Shatalov, T. P. Bondareva, and L. E. Tsygankova, *Zhur. Priklad. Khim.*, **36**, 588 (1963).
20. A. Yu. Shatalov and T. P. Bondareva, *Zhur. Fiz. Khim.*, **37**, 868 (1963).
21. R. E. Salomon, G. B Adams, and W. M. Graven, *This Journal*, **110**, 1163 (1963).
22. P. H. G. Draper, *Electrochim. Acta*, **8**, 847 (1963).
23. I. A. Ammar and S. A. Awad, *J. Phys. Chem.*, **60**, 837 (1956).
24. S. Schuldiner, *This Journal*, **101**, 426 (1954).
25. S. Schuldiner, *ibid.*, **99**, 488 (1952).
26. L. P. Hammett, *J. Am. Chem. Soc.*, **46**, 7 (1924).
27. E. H. Greener, D. H. Whitmore, and M. E. Fine, *J. Chem. Phys.*, **34**, 1017 (1961).
28. E. H. Greener and W. M. Hirthe, *This Journal*, **109**, 600 (1962).
29. R. F. Janninck and D. H. Whitmore, *J. Chem. Phys.*, **37**, 2750 (1962).
30. L. P. Hammett, *Trans. Faraday Soc.*, **29**, 770 (1933).
31. K. J. Vetter, *Z. Elektrochem.*, **59**, 435 (1955).
32. J. P. Hoare and S. Schuldiner, *J. Chem. Phys.*, **25**, 786 (1956).
33. K. J. Vetter, "Elektrochemische Kinetik," pp. 410 ff, Springer-Verlag, Berlin (1961).
34. F. A. Posey, G. H. Cartledge, and R. P. Yaffe, *This Journal*, **106**, 582 (1959).
35. R. E. Meyer, *ibid.*, **107**, 847 (1960).
36. J. J. MacDonald and B. E Conway, *Proc. Roy. Soc. (London)*, **269A**, 419 (1962).
37. A. C. Makrides, *This Journal*, **111**, 392, 400 (1964)

Conduction Properties of Valve Metal-Oxide Systems

I. A New Theory

M. J. Dignam

Department of Chemistry, University of Toronto, Toronto, Ontario, Canada

ABSTRACT

A theory of cooperative ion transport in anodic oxide films on valve metals has been developed on the basis of a dielectric mosaic model. The oxide, which is "amorphous," is considered to be composed of very small crystallites or polymeric units. Ion transfer from one such unit to another is strongly influenced by the distribution of ions within these units since the field assisting the transfer will be a function of the polarization of the dielectric oxide medium. Transient ionic conduction phenomena and anomalous charging currents arise as a result of the slow adjustment of the polarization of the medium to new conditions. Two mechanisms for the rate of change of the polarization are employed, one involving thermally activated ion migration, the other being associated with the large energies dissipated during an ion transfer event. The equations arising from this model have been solved for a number of particular experimental conditions.

Recent data (1-8) concerning the anodic oxidation of the valve metals have revealed serious limitations in all previous quantitative theories dealing with the growth mechanism for these oxides. The purpose of this paper is to present a new theory which is in accord with the facts now available. In the following paper this theory is compared with previous theories, the principal one being the high field Frenkel defect theory (9), in relation to most pertinent data.

It seems likely that the main fault of previous theories lies in their failure to allow for cooperative phenomena associated with ion migration through the film. Although the possibility of such phenomena has been mentioned by Young (9) no attempt has been made previously to allow quantitatively for them. According to the high field Frenkel defect theory, transient conduction phenomena arise as a result of a slow readjustment of the concentration of ionic current carriers following a change in the field strength or current density. In the present theory the transients are ascribed to cooperative transport phenomena, the concentration of current carriers being essentially independent of field strength and current density. The detailed model, which rests on time dependent dielectric polarization phenomena, can be regarded at the very least as an "incorrect model" which nevertheless leads to the correct form for the cooperative phenomena, and at most a satisfactory approximation to the "true model."

The paper is divided into five sections with this section followed by Outline of Theory and Summary and Discussion providing the descriptive development of the theory. The detailed mathematical development has been confined to the remaining two sections. The major support for the theory is presented in the following paper (10) in which excellent agreement between the present theory and data is demonstrated.

Outline of Theory

In the present theory the oxide is treated as a nonuniform dielectric, being composed of very small crystallites or polymeric "molecular" units. Since the bonding possesses a considerable covalent character (11), the intra-"molecular" bonding will be stronger than the inter-"molecular" bonding. This will lead to regions of low density, or quasi gaps, between adjacent molecular units. The low density found for these oxides compared with their bulk densities is consistent with the above model.

Two simultaneous rate-controlling processes for ion transport through such an oxide must be considered. The one is associated with the transfer of ions from one molecular unit to the next, and the other with ionic migration within the molecular units. We shall focus attention initially on the former.

Because of the discontinuous nature of the dielectric medium, the electric field, E_e, assisting this ion transfer process will depend on the polarization of the oxide, P, so that we may write

$$E_e = E + \delta P/\mathcal{E}_o \qquad [1]$$

where E is the applied field, $\mathcal{E}_o$ the permittivity of free space, and δ a geometric factor of the order of unity introduced since the detailed geometry of these quasi gaps is unknown.

In order to take account of ion migration within the molecular units, the polarization term is separated into two terms, $P = P_1 + P_2$, where P_1 is considered to arise from conventional inertial and electronic polarization processes and P_2 from ion transport within the individual molecular units. The ordinary polarization, P_1, will have a small relaxation time and may be considered to follow the applied field in the normal manner

$$P_1 = \mathcal{E}_o \chi_1 E \qquad [2]$$

where χ_1, the electric susceptibility of the oxide measured at sufficiently high frequencies, say 1 kc, is to a good approximation independent of field and time. The ion transport polarization, P_2, however, since it involves mass transport, will have a large relaxation time so that it will vary linearly with the applied field only under steady-state conditions of constant field and current density.

In attempting to predict the variation of the transport polarization, P_2, with the field strength, time, and current density, there are several factors which should be borne in mind. If the effective field strength, E_e, is sufficiently high to cause a significant number of ion transfer events per unit time per unit volume, then the energy imparted to the molecular units as a result of these events will be very important and must be taken into account. From the available kinetic data (12) one can estimate that the energy imparted to a molecular unit receiving a charged species will be, for example, about 5 ev or more for a tantala film, which in relation to the estimated diameter of a molecular unit, 9Å (10), represents a very considerable energy density. Indeed such a unit will possess about 10^3 degrees of freedom, giving an impact energy per degree of freedom of about 0.2 kt at room temperature, or about ½ the mean thermal energy. The impact energy will be highly localized initially, making its effect greater than the above estimate would suggest. Under conditions where the collision process will be important, that is for ion current densities which are

not too small, it is to be expected that the rate of change of the transport polarization, P_2, is controlled almost solely by the collision density per unit time, the rate associated with conventional thermally activated processes being negligible by comparison. For sufficiently low ion current densities, however, thermally activated polarization processes must predominate.

A possible mechanism for the collisionally activated polarization process follows: Immediately following an ion transfer event, the donor and acceptor molecular units will be depolarized or perhaps even acquire a dipole moment in the opposite direction. To re-establish their previous dipole moments or acquire their equilibrium dipole moments, ion migration in each is required. The high impact energy involved in the ion transfer event should be more than enough to produce both defects and sufficient vibrational excitation to establish in a short time the local equilibrium dipole moment for both the donor and acceptor molecular units.

To complete the outline of the theory, some statement as to how the ion current density varies with E_e and time is required. At any given moment it is apparent that certain of the molecular units will have a net electrostatic charge by virtue of their possessing an excess or deficit of the mobile species involved in the ion transfer process. Provided that the number density of these charged molecular units is independent of E_e at fixed temperature, the ion current density can be represented as a function of E_e and temperature only, the functional form being very similar to the exponential relationship conventionally used to interpret steady-state anodic oxidation data. Accepting this provision for the moment, we see that, for the present model, transient ionic conduction phenomena arise entirely from the time dependent polarization phenomena within the oxide film. The most critical tests of this model will therefore involve the measurement of transients, although certain unique predictions concerning steady-state anodic oxidation can also be subject to verification.

Mathematical Development of Model

In this section the model outlined will be used to obtain first a specific equation relating the ion current density to the effective field strength, then a differential equation for the variation with time of the dielectric polarization, and finally solutions of these equations for certain special cases.

Dependence of ion current on the effective field strength.—We shall assume, in accord with normal practice, that only one species bearing a charge rZe is involved in the ion transfer process and further that the majority of the molecular units are electrostatically neutral (where Z is the absolute value of the oxidation state of the species, e the charge on the proton, and $r = 1$ or -1 according to the sign of the charge on the species). The small contribution to kinetic processes made by units possessing a charge which differs from zero or $\pm Ze$ will be neglected.

From the above it is sufficient to consider the following four types of ion transfer processes:

1. Transfer from a neutral species to an adjacent neutral species, with a transfer probability, p_o
2. Transfer from a species with a charge rZe to an adjacent neutral species, with a transfer probability, $p_{+r} >> p_o$.
3. Transfer from a neutral species to an adjacent species with a charge $-rZe$, with a transfer probability, $p_{-r} >> p_o$.
4. Transfer from a species with a charge rZe to an adjacent species with a charge $-rZe$, with a transfer probability $>> p_{+r}$ or p_{-r}.

In a previous publication (12) it was shown that the net activation energy, $W'(E_e)$, for the transfer of a charged species across a potential energy barrier in the presence of a high electrostatic field, E_e, is given by

$$W'(E_e) = \phi' - E_e\mu^{*\prime}(1 - E_e\mu^{*\prime}/C'\phi')$$

where ϕ' is the zero field activation energy, $\mu^{*\prime}$ the zero field "activation dipole" (*i.e.*, effective charge times activation distance for the ion transfer process), and C' a dimensionless parameter the value for which depends on the shape of the potential energy barrier.[1] The transfer probability per unit time from a given molecular unit will therefore be given by

$$p_o = N'\nu \exp\{-[\phi' - E_e\mu^{*\prime}(1 - E_e\mu^{*\prime}/C'\phi')]/kT\} \quad [3]$$

Associating Eq. [3] with process 1 and assuming that a charge rZe on a molecular unit will change the transfer probability to or from this unit simply by contributing a constant additional field term, $\mathcal{E}_r$, to the effective field which would exist in the absence of such a charge, we may write

$$p_{+r} = N'\nu \exp\{-[\phi' - [E_e + \mathcal{E}_{+r}]\mu^{*\prime}(1-[E_e + \mathcal{E}_{+r}]\mu^{*\prime}/C'\phi')]/kT\} \quad [4]$$

or

$$p_{+r} = \kappa_{+r}p_o \quad [5]$$

where

$$\kappa_{+r} = \exp\{\mathcal{E}_{+r}\mu^{*\prime}[1-(2E_e + \mathcal{E}_r)\mu^{*\prime}/C'\phi']/kT\} \quad [6]$$

A corresponding set of equations is obtained for p_{-r} from the above by replacing $+r$ with $-r$. The terms $\mathcal{E}_{+r}$ and $\mathcal{E}_{-r}$ will be positive and represent the constant field contributed by the net charge on one of the molecular species. From geometric considerations, it follows that $\mathcal{E}_{+r} > \mathcal{E}_{-r}$ and hence that $\kappa_{+r} > \kappa_{-r}$. If the quadratic term in the field in the net activation energy did not exist (*i.e.*, $1/C' = 0$), then κ_{+r} and κ_{-r} would be strictly independent of E_e. The presence of the quadratic term introduces a variation in κ_{+r} and κ_{-r} with E_e which is negligible compared with the variation of p_o with E_e provided that $\mathcal{E}_{+r}\mu^{*\prime}/C'\phi' << 1$, a statement in accord with the values obtained experimentally for aluminum (10). Associating the ion current (*i.e.*, the current leading to film growth) i, with the ion transfer processes 1 to 4, we may write

$$i = Zed[n_op_o + n_{+r}\kappa_{+r}p_o + n_{-r}\kappa_{-r}p_o + (\kappa_{+r} + \kappa_{-r})p_od(f\sigma')n_{+r}n_{-r}] \quad [7]$$

where d is the mean dimension of a molecular unit along the field direction and n_o, n_{+r}, and n_{-r} the volume concentrations of molecular units which bear changes of zero, $+rZe$ and $-rZe$, respectively. The final term within the square brackets of Eq. [7] requires some explanation. It represents the rate of annihilation of charged molecular units by transfer process 4, which has been treated as a "collision" annihilation with a "capture" cross-sectional area ($f\sigma'$), which should be about equal to or somewhat greater than the mean cross-sectional area, σ' ($=1/Nd$, where N is the volume concentration of molecular units), of the molecular units in a plane normal to the applied field. In an analogous manner, the net rate of formation of charged molecular units is given by

$$\frac{dn_{+r}}{dt} = \frac{dn_{-r}}{dt} = n_op_o - (\kappa_{+r} + \kappa_{-r})p_od(f\sigma')n_{+r}n_{-r} \quad [8]$$

If at some time steady-state concentrations prevail (*i.e.*, $dn_{+r}/dt = 0 = dn_{-r}/dt$) it follows from Eq. [8] that any subsequent changes in the field, E_e, under isothermal conditions, will have a negligible effect on n_{+r}, n_{-r}, and n_o (since the variation of κ_{+r} and κ_{-r} with E_e is negligible). The equation

$$dn_{+r}/dt = dn_{-r}/dt \simeq 0$$

will therefore be satisfied even under conditions of rapidly changing field. Thus Eq. [8] reduces to

$$n_{+r}n_{-r} = n_o/(\kappa_{+r} + \kappa_{-r})d(f\sigma')$$

[1] It is probably more correct to regard ϕ' and $\mu^{*\prime}$ as extrapolated values, the extrapolation to $E_e = 0$ being based on the behavior at high fields only (12).

$$\simeq n_o^2/(\kappa_{+r} + \kappa_{-r})f$$

since for

$$n_o >> n_{+r} \text{ and } n_{-r},\ d\sigma' \simeq 1/n_o$$

In the bulk of the film, remote from the interfaces, the mean space charge will be essentially zero, so that we may set $n_{+r} = n_{-r}$. Under these conditions Eq. [7] and [9] yield

$$i = \frac{Ze}{\sigma'}\left[2 + \left(\frac{\kappa_{+r} + \kappa_{-r}}{f}\right)^{1/2}\right] p_o \qquad [10]$$

Equation [10] will only be valid remote from the interfaces. To allow for space charge phenomena, Eq. [7] and [9] must be solved in conjunction with Poisson's equation. For the present, however, we shall assume that the films involved are thick enough that Eq. [10] may be used without serious error.

It is now convenient to write Eq. [10] in the following form

$$i = (Ze/\sigma)\kappa^{1/2} p_o \qquad [11]$$

where

$$\sigma = \sigma'\left[2 + \left(\frac{\kappa_{+r} + \kappa_{-r}}{f}\right)^{1/2}\right] \Big/ \kappa^{1/2}$$

and κ is identically κ_{+r} or κ_{-r}, whichever is the greater. (From previous discussion, $\kappa_{+r} > \kappa_{-r}$.) κ is therefore given by

$$\kappa = \exp\{\mathcal{E}\mu^{*\prime}[1-(2E_e + \mathcal{E})\mu^{*\prime}/C'\phi']/kT\} \qquad [12]$$

where the subscript, r, has been omitted for brevity. It follows from our earlier assumption, $n_o >> n_{\pm r}$, that $\kappa^{1/2} >> 1$. Since f probably lies between about 1 and 2, we may set the following limits on σ, $\sqrt{2} \geqq \sigma/\sigma' \geqq 1/\sqrt{2}$. Furthermore, from the equations for κ_{+r} and κ_{-r} it is easily shown that σ/σ' will vary not more than 0.15% for a 1% change in absolute temperature. Its variation with the effective field, E_e, will be totally negligible. It follows, therefore, that $\sigma \simeq \sigma'$ and is for all practical purposes independent of both temperature and field strength (provided of course σ' is independent of these).

Combining Eq. [3], [11], and [12], the desired relationship is obtained

$$i = i_o \exp\{-[\phi - E_e\mu^* (1 - E_e\mu^*/C\phi)]/kT\} \qquad [13]$$

where

$$i_o = ZeN'\nu/\sigma \qquad [14]$$

$$\phi = \phi'\left[1 - \frac{\mathcal{E}\mu^{*\prime}}{2\phi'} + \frac{1}{2C'}\left(\frac{\mathcal{E}\mu^{*\prime}}{\phi'}\right)^2\right] \qquad [15]$$

$$\mu^* = \mu^{*\prime}\left[1 - \mathcal{E}\frac{\mu^{*\prime}}{C'\phi'}\right] \qquad [16]$$

$$C = C'\left[1 - \frac{\mathcal{E}\mu^{*\prime}}{C'\phi'}\right]^2 \Big/ \left[1 - \frac{\mathcal{E}\mu^{*\prime}}{2\phi'} + \frac{1}{2C'}\left(\frac{\mathcal{E}\mu^{*\prime}}{\phi'}\right)^2\right] \qquad [17]$$

From the space charge data for the anodic oxidation of aluminum, one can estimate that $\mathcal{E}\mu^{*\prime}/C'\phi' \simeq 0.07$ (10). Using this value and setting $C' \simeq 3.6$ (12) we have for this system

$$(\phi' - \phi)/\phi' \simeq 0.12$$
$$(\mu^{*\prime} - \mu^*)/\mu^{*\prime} \simeq 0.07$$
$$(C' - C)/C' \simeq 0.02$$

Experimentally determined values for ϕ', μ^*, and C will provide, therefore, reasonably good estimates of the more fundamental primed parameters.

Rate of change of the dielectric polarization.—In determining the rate of change of the dielectric polarization, and hence of E_e, as a function of the appropriate variables, it is convenient to work with the dipole moments of the individual molecular units. For conditions of uniform polarization of the oxide, the dipole moment per unit volume will be the same throughout the oxide, so that the dipole moment associated with a given molecular unit will be proportional to its volume. Since the volume of a molecular unit might vary from one unit to the next, the dipole moment per molecular unit appears at first to be a poor parameter with which to work. However, since the ultimate form of the equations involves a simple linear summation over all the molecular units, mean values for the dipole moments and polarizabilities may be used at the outset without it introducing an approximation in the final equations.

Accordingly, we shall define the following parameters:

- E_e field effective in assisting the ion transfer process
- E_p field effective in polarizing a given molecular unit
- N number of molecular units per unit volume
- μ dipole moment per molecular unit
- μ_1 dipole moment per molecular unit associated with the fast polarization process.
- μ_2 dipole moment per molecular unit associated with the slow, ion transport, polarization process
- α_s static polarizability associated with μ (*i.e.*, $\alpha_s = \mu/E_p$ for static conditions)
- α_1 differential polarizability associated with μ_1 (*i.e.*, $\alpha_1 = (\partial\mu_1/\partial E_p)_{\mu_2}$)
- α_2 static polarizability associated with μ_2 (*i.e.*, $\alpha_2 = \mu_2/E_p$ for static conditions)
- i ion current density associated with the growth of film (as opposed to charging current)
- Ze absolute magnitude of the charge transferred during an ion transfer process
- d mean dimension of a molecular unit along the applied field direction
- σ' mean cross-sectional area of a molecular unit in a plane normal to the applied field direction, $= 1/Nd$

Using these parameters, Eq. [1] becomes

$$E_e = E + \delta N\mu/\mathcal{E}_o \qquad [18]$$

where δ is a factor of the order of unity which allows for the uncertainty as to the precise contribution of the polarization of the medium to the effective field strength, E_e. Similarly, we have

$$E_p = E + \delta' N\mu/\mathcal{E}_o \qquad [19]$$

where δ' is a factor analogous to δ, introduced for the same reason. By definition, we also have

$$\mu = \mu_1 + \mu_2 \qquad [20]$$

For μ_2 constant, $(\partial\mu_1/\partial E_p)_{\mu_2} = \alpha_1$. However, the presence of μ_2 introduces a depolarization field proportional to μ_2 ($\gamma\mu_2/\alpha_2$ say), acting in the opposite direction to E_p. We may therefore write

$$\mu_1 = \alpha_1[E_p - \gamma\mu_2/\alpha_2] \qquad [21]$$

where $1 \geqq \gamma \geqq 0$, since for steady-state conditions, $\mu_2/\alpha_2 = E_p$.

From Eq. [20] and [21] it follows that

$$\alpha_s = \alpha_1(1 - \gamma) + \alpha_2 \qquad [22]$$

The principal equation now lacking is that for the rate of change of μ_2 with time, in accordance with the collisionally induced and thermally activated polarization processes discussed previously. We shall treat the collisionally induced process first.

The ion transfer frequency per unit volume of oxide is clearly given by i/Zed. In accordance with our previous assumption, ion transfer processes type 2 and 3 will predominate so that the effect of processes 1 and 4 on the rate of change of polarization will be neglected. This approximation amounts to neglecting $\kappa^{-1/2}$ compared with unity. Immediately before an ion transfer event, the uncharged molecular unit taking part in the event will have, on the average, a dipole moment nearly equal to the average of the di-

pole moments for all units. Following the ion transfer process, the dipole moment will be the equilibrium value, $\alpha_2 E_p$, so that the contribution to the change in $N\mu_2$ per collision made by the initially uncharged molecular unit is on the average $(\alpha_2 E_p - \mu_2)$.

The contribution made by the charged molecular unit must be calculated differently. Being few in number, a charged molecular unit will have been involved in a collision process much more recently on the average than the uncharged unit and hence will have, in general, a dipole moment differing appreciably from the average value. The contribution to the change in $N\mu_2$ made by the initially charged molecular unit can be represented approximately by $\alpha_2(dE_p/dt)\,\Delta t$ where $(dE_p/dt)\Delta t$ approximates the change in E_p between consecutive ion transfer processes involving the unit in question, Δt being an appropriately weighted average lifetime for a charged unit. For a molecular unit of charge rZe, the average lifetime is $1/p_{+r}$, while for a charge $-rZe$ it is $1/p_{-r}$. The combined average lifetime, weighted according to transfer frequency, is therefore given by

$$\begin{aligned}\Delta t &= [p_{+r}/(p_{+r}+p_{-r})]\,(1/p_{+r}) + \\ &\quad [p_{-r}/(p_{+r}+p_{-r})]\,(1/p_{-r}) \\ &= 2/(p_{+r}+p_{-r}) = 2/p_0(\kappa_{+r}+\kappa_{-r}) \\ &\simeq ZeNd/i\kappa^{1/2}\end{aligned}$$

where the last step involves Eq. [10].

Multiplying the ion transfer frequency per unit volume by the total change in $N\mu_2$ per transfer process, we now obtain the following equation

$$\left(\frac{d(N\mu_2)}{dt}\right)_c = \frac{i}{Zed}\,[\alpha_2 E_p - \mu_2] + \frac{N}{\kappa^{1/2}}\,\alpha_2\,\frac{dE_p}{dt}$$

or

$$\left(\frac{d\mu_2}{dt}\right)_c = \frac{i\sigma'}{Ze}\,[\alpha_2 E_p - \mu_2] + \frac{\alpha_2}{\kappa^{1/2}}\,\frac{dE_p}{dt} \qquad [23]$$

where the subscript, c, denotes that it is the collisionally induced component of $(d\mu_2/dt)$. Ultimately, it will be shown that the term in dE_p/dt can be neglected, so that the approximations involved in obtaining it are of little consequence. This is fortunate since this term is too large for sufficiently small i. (For $i = 0$ this term should be zero.)

The thermally activated component of $d\mu_2/dt$ will be equal to the ion current per molecular unit within the molecular units arising most probably as a result of surface ion transport. Assuming a single ionic species to predominate in this transport process, we may write

$$\frac{d\mu_2}{dt} = \frac{i\sigma'}{Ze}\,[\alpha_2 E_p - \mu_2] + \frac{\alpha_2}{\kappa^{1/2}}\,\frac{dE_p}{dt} + 2Z'ebv'n'\left[\exp\left(-\frac{Q}{kT}\right)\right]\sinh\left[\frac{w^{*\prime}\theta}{kT}\left(E_p - \frac{\mu}{\alpha_s}\right)\right] \qquad [24]$$

where the new symbols are defined as follows:

- $Z'e$ absolute magnitude of the charge associated with the ionic species
- b mean jump distance for the ionic species (*i.e.*, mean distance travelled per activation)
- ν' vibrational frequency along the reaction coordinate associated with the ionic species
- n' number of ionic species per molecular unit in preferred sites for migration
- Q zero field activation energy for migration of ionic species from preferred sites
- $w^{*\prime}$ activation dipole associated with Q (*i.e.*, activation distance times effective charge)

The first two terms of Eq. [24] come directly from Eq. [23], the final term being that for conventional ion transport allowing for the possibility of high field strengths (13). The internal field effective in assisting the ion transport will be proportional to $E_p - \mu/\alpha_s$. (This clearly has the correct form for $\mu = 0$ and also for $\mu = \alpha_s E_p$, *i.e.*, $d\mu_2/dt = 0$ for $\mu = \alpha_s E_p$.) The proportionality constant, θ, would appear to be somewhat greater than unity.[2] The quadratic term in the field strength, such as introduced in Eq. [3] (*i.e.*, the term containing C'), should be entirely negligible in the present case since $E_p - \mu/\alpha_s$ is at least a factor of 10 less than E_e for a given applied field, E. This statement can be verified readily from the equations presented in the remainder of this section and from empirical values for the constants presented in the following paper (10). However, the nature of the model would suggest a range of values for the parameters Q and $w^{*\prime}$, so that the hyperbolic sine function term in Eq. [25] can only be regarded as a rather rough approximation.

Elimination of E_p, μ_1, μ_2, and α_2 from Eq. [19], [20], [21], [22], and [24], and replacing $w^{*\prime}\theta$ with $w_e^{*\prime}$ yields

$$\begin{aligned}\frac{d\mu}{dt} + \left(\frac{1-\delta' N\alpha_s/\mathcal{E}_0}{1-\delta' N\alpha_1'/\mathcal{E}_0}\right)\frac{i\sigma'\mu}{Ze} &= \left(\frac{\alpha_1'}{1+\delta' N\alpha_1'/\mathcal{E}_0}\right)\frac{dE}{dt} \\ &+ \left(\frac{\alpha_s}{1-\delta' N\alpha_1'/\mathcal{E}_0}\right)\frac{i\sigma'}{Ze}E + \left[\frac{\alpha_s-\alpha_1}{\alpha_s-\alpha_1(1-\gamma)}\right] \\ &\left[\frac{2Z'ebv'n'}{1-\delta' N\alpha_1'/\mathcal{E}_0}\right]\left[\exp\left(-\frac{Q}{kT}\right)\right] \\ &\sinh\left[\frac{we^{*\prime}}{kT}\left(E - \frac{\mu}{\alpha_s}\left\{1 - \frac{\delta' N\alpha_s}{\mathcal{E}_0}\right\}\right)\right] \qquad [25]\end{aligned}$$

where $\alpha_1' = \alpha_1 + \dfrac{\alpha_s - \alpha_1}{\kappa^{1/2}}$. Assuming, as before, that $\kappa^{1/2} >> 1$, one may neglect $(\alpha_s - \alpha_1)/\kappa^{1/2}$ compared with α_1, thus eliminating this term as previously mentioned.

Equation [25] may be simplified considerably by introducing the dynamic and static electric susceptibilities, χ_1 and χ_s, respectively, defined as follows

$$\chi_1 = \frac{N}{\mathcal{E}_0}\,\underset{\dot{E}\to\infty}{\text{Limit}}\,\frac{d\mu}{dE} \qquad [26]$$

$$\chi_s = \frac{N}{\mathcal{E}_0}\,\underset{\dot{E}\to 0}{\text{Limit}}\,\frac{d\mu}{dE} \qquad [27]$$

From Eq. [25]

$$\chi_1 = N\alpha_1'/\mathcal{E}_0(1-\delta' N\alpha_1'/\mathcal{E}_0) \qquad [28]$$

$$\chi_s = N\alpha_s/\mathcal{E}_0(1-\delta' N\alpha_s/\mathcal{E}_0) \qquad [29]$$

Eliminating α_1' and α_s from Eq. [25], [28], and [29] and substituting $\mu = P/N$ where P is the polarization of the oxide, we obtain the desired equation

$$\frac{dP}{dt} = \mathcal{E}_0\chi_1\frac{dE}{dt} + Bi[\mathcal{E}_0\chi_s E - P] + i_{co}[\exp(-Q/kT)]\sinh[w_e^{*\prime}(E - P/\mathcal{E}_0\chi_s)/kT] \qquad [30]$$

where

$$B = \left(\frac{1+\delta'\chi_1}{1+\delta'\chi_s}\right)\frac{\sigma'}{Ze},$$

$$i_{co} = \frac{(\chi_s-\chi_1)(1+\delta'\chi_1)2Z'ebv'\eta'N}{\chi_s - \chi_1[1-\gamma(1+\delta'\chi_s)]}$$

Alternatively, eliminating $P = N\mu$ from Eq. [18] and [30], an equation for the effective field strength, E_e, is obtained

[2] For the simple electrostatic model in which the crystallites are treated as dielectric spheres in a uniform field, E_p, the internal field assumed to be the Lorentz field, and γ assumed to be unity, it can be shown that $\theta = (1 - \alpha_1/\alpha_s)^{-1}$. A more general treatment of the problem suggests a somewhat smaller value for θ.

$$\frac{dE_e}{dt} + BiE_e = (1 + \delta\chi_1)\frac{dE}{dt} + Bi(1 + \delta\chi_s)E + (\delta i_{co}/\mathcal{E}_o)[\exp(-Q/kT)] \sinh\left\{\frac{w_e^{*\prime}}{kT}\left[\frac{(1 + \delta\chi_s)E - E_e}{\delta\chi_s}\right]\right\} \quad [31]$$

To complete the development of the basic equations for the model, we note that the current flowing in the external circuit, I, will be given by

$$I = i + i_c + i_e \quad [32]$$

where i is the ion current leading to film growth, given by Eq. [13]; i_c is the total charging current, $d[P + \mathcal{E}_o E]/dt$, and i_e the current arising from electronic conduction through the film, which we shall assume to be zero. From Eq. [18] and [30], the charging current is given by

$$i_c = \mathcal{E}_o K_1 \frac{dE}{dt} + \frac{Bi\mathcal{E}_o}{\delta}[(1 + \delta\chi_s)E - E_e] + i_{co}[\exp(-Q/kT)] \sinh\left\{\frac{w_e^{*\prime}}{kT}\left[\frac{(1 + \delta\chi_s)E - E_e}{\delta\chi_s}\right]\right\} \quad [33]$$

where $K_1 = 1 + \chi_1$ is the dynamic dielectric constant for the oxide.

Elimination of E_e, i_c, and i from Eq. [13], [31], [32], and [33] leads to a differential equation which may in principal be solved to obtain I as a function of time, given E as a function of time and a suitable boundary condition. In the following sections we shall use these equations to obtain I as a function of E or t for a number of special cases, thus providing equations which are readily amenable to experimental verification. In general, however, digital computer methods are required.

Particular Solutions of Basic Equations

For simplicity, no case will be considered for which the rate of change of the polarization brought about by collision is of the same magnitude as that brought about by thermally activated ionic conduction. The discussion of transient phenomena will therefore be classified according to i large (*i.e.*, collision process dominant) and i small (*i.e.*, thermally activated process dominant). We shall begin, however, by obtaining the steady-state solution.

Steady-state solution.—For steady-state conditions ($dE/dt = di/dt = 0$) it follows from Eq. [13] and [31] that $E_e = (1 + \delta\chi_s E)$ and hence from Eq. [32] and [33] that $I = i$. Substituting these results into Eq. [13], we obtain the desired solution

$$I = i_o \exp\left\{-\left[\phi - E\mu_s^*\left(1 - \frac{E\mu_s^*}{C\phi}\right)\right] \Big/ kT\right\} \quad [34]$$

where $\mu_s^* = (1 + \delta\chi_s)\mu^*$. We note that, apart from space charge effects, four parameters, i_o, ϕ, μ_s^*, and C are sufficient to define the steady-state behavior according to this model.

It is convenient to define the steady-state reciprocal Tafel slope, β_s, as follows

$$\beta_s = \underset{\dot{E} \to 0}{\text{Limit}} \frac{d \ln I}{dE} \quad [35]$$

from which we have

$$\beta_s = \frac{\mu_s^*}{kT}\left[1 - \frac{2\mu_s^* E}{C\phi}\right] \quad [36]$$

General transient behavior for i large.—For i sufficiently large, the collisionally activated polarizing process will dominate so that the final term in Eq. [31] and [33] may be neglected. Equation [31] can then be written

$$\frac{d(\mu^* E_e)}{dt} + Bi(\mu^* E_e) = \mu_1^* \frac{dE}{dt} + Bi\mu_s^* E \quad [37]$$

where $\mu_1^* = (1 + \delta\chi_1)\mu^*$. From Eq. [32] and [33], and setting $[K_1 + (1 - \delta)/\delta] \simeq K_1$, we obtain

$$I - \mathcal{E}_o K_1 \frac{dE}{dt} = i\left[1 + B\mathcal{E}_o K_1\left(\frac{\mu_s^* E - \mu^* E_e}{\mu_1^*}\right)\right] \quad [38]$$

For both alumina and tantala the term in B does not exceed about 0.05 for any realizable experiment (10) so the above approximation should normally be a satisfactory one, particularly since one would expect δ to be close to unity and K_1 is large compared to unity.

Eliminating $\mu^* E_e$ and i from Eq. [13], [37], and [38], it is seen that apart from K_1, which is readily determined independently, only two parameters, μ_1^* and B, are required in addition to the steady-state parameters to define transient behavior for i large. Unfortunately, the solution of even this equation generally requires the use of a digital computer, although two important exceptions are for the cases $\dot{E}$ very large and $\dot{E} = 0$.

Transient behavior for i and $\dot{E}$ large.—In considering this case, it is convenient to define the transient reciprocal Tafel slope, β_1, as follows

$$\beta_1 = \underset{\dot{E} \to \infty}{\text{Limit}} \frac{d \ln I'}{dE} \quad [39]$$

where $I' = I - \mathcal{E}_o K_1 \, dE/dt$ can be obtained readily from the experimental measurements. Using the boundary condition that at $t = 0$, $E = E_o$, and $\mu^* E_e = \mu_s^* E_o$ (*i.e.*, steady-state conditions prevailed immediately before commencing the rapid change in field) Eq. [13], [37], [38], and [39] yield

$$\beta_1 = \frac{\mu_1^*}{kT}\left[1 - \frac{2\mu_s^* E_o}{C\phi} - \frac{2\mu_1^* \Delta E}{C\phi}\right] + B\mathcal{E}_o K_1\left[\frac{\mu_s^* - \mu_1^*}{\mu_1^*}\right] \quad [40]$$

where $\Delta E = E - E_o$ and the approximation

$$1 >> B\mathcal{E}_o K_1\left(\frac{\mu_s^* - \mu_1^*}{\mu_1^*}\right)\Delta E$$

has been made. The final term in Eq. [40] contributes less than 3% to β_1 for both alumina and tantala (10) so may usually be neglected. The integrated form of Eq. [39] and [40] can be written

$$\frac{1}{\Delta E}\ln\frac{I'}{I_o} = \frac{\mu_1^*}{kT}\left[1 - \frac{2\mu_s^* E_o}{C\phi} - \frac{\mu_1^* \Delta E}{C\phi}\right] + B\mathcal{E}_o K_1\left[\frac{\mu_s^* - \mu_1^*}{\mu_1^*}\right] \quad [41]$$

$$\simeq \beta_1 \text{ for } \Delta E \text{ small}$$

where I_o is the steady-state current density before effecting the rapid change in E. It is noteworthy that the variation of β_1 with E_o is closely related to the variation of β_s with E (Eq. [36]), a prediction which can readily be checked (10).

Constant field transients for i large.—From Eq. [37], on setting $\dot{E} = 0$, we obtain

$$\frac{d(\mu^* E_e)}{dt} = Bi(\mu_s^* E - \mu^* E_e) \quad [42]$$

Also, from Eq. [13] and [34], respectively, we have

$$kT \ln (i/A) = \mu^* E_e - (\mu^* E_e)^2/C\phi \quad [43]$$

$$kT \ln (I_s/A) = \mu_s^* E - (\mu_s^* E)^2/C\phi \quad [44]$$

where $A = i_o \exp(-\phi/kT)$ and I_s is the steady-state current density for the field, E, in question.

From Eq. [42], [43], and [44], the following equation may be readily verified

$$\frac{d \ln i}{dt} = Bi \ln (I_s/i) + \frac{(\mu_s^* E - \mu^* E_e)^2}{kT\, C\phi} \quad [45]$$

Solving for $\mu^* E_e$ and $\mu_s^* E$ from Eq. [43] and [44], respectively, we obtain

$$\mu_s^* E - \mu^* E_e = \frac{C\phi}{2} \left[\left(1 - \frac{4kT}{C\phi} \ln \frac{i}{A} \right)^{1/2} - \left(1 - \frac{4kT}{C\phi} \ln \frac{I_s}{A} \right)^{1/2} \right] \quad [46]$$

It is readily proven that for $a_1 < 1$ and $a_2 < 1$, $(1 - a_1)^{1/2} - (1 - a_2)^{1/2} = \frac{1}{2}(a_2 - a_1)/(1 - \xi)^{1/2}$ for some ξ in the interval (a_1, a_2), the first approximation value for ξ being $(a_1 + a_2)/2$.[3] Equation [46] can therefore be written

$$\mu_s^* E - \mu^* E_e = (kT/z^{1/2}) \ln (I_s/i) \quad [47]$$

where

$$z = 1 - (4kT/C\phi) \ln (i_*/A) \quad [48]$$

and i_* is some current in the interval (I_s, i), a first approximation for which is given by: $i_* \simeq (I_s i)^{1/2}$. An alternative expression for z can be obtained by replacing I_s in Eq. [44] by i_s (to avoid confusion of symbols), solving for $\mu_s^* E$ and evaluating $dE/d \ln i_s$

$$\frac{dE}{d \ln i_s} = \frac{1}{\beta_s(i_s)} = (kT/\mu_s^*)[1 - 4(kT/C\phi) \ln (i_s/A)]$$

where $\beta_s(i_s)$ is the steady-state reciprocal Tafel slope for a current density i_s. We may therefore write

$$z^{1/2} = kT\, \beta_s(i_*)/\mu_s^* \quad [49]$$

From Eq. [45] and [47] we now have

$$\frac{d \ln i}{dt} = Bi \ln (I_s/i) \left[1 + \frac{kT}{zC\phi} \ln (I_s/i) \right] \quad [50]$$

Eliminating $\mu_s^* E - \mu^* E_e$ from Eq. [38] and [47] we obtain

$$I = i \left[1 + B\mathcal{E}_0 K_1 \frac{kT}{\mu_1^* z^{1/2}} \ln (I_s/i) \right] \quad [51]$$

Recalling that the term in B is small compared with unity, we may write

$$\ln (I_s/i) = \ln (I_s/I) \left[1 + B\mathcal{E}_0 K_1 \frac{kT}{\mu_1^* z^{1/2}} \right] \quad [52]$$

Since $1 + B\mathcal{E}_0 K_1\, kT/\mu_1^* z^{1/2}$ varies only slowly with z, and z in turn varies only slowly with I, we may set

$$\frac{d}{dt} (1 + B\mathcal{E}_0 K_1\, kT/\mu_1^* z^{1/2} \simeq 0$$

and obtain from Eq. [52]

$$\frac{d \ln i}{dt} \simeq \frac{d \ln I}{dt} \left[1 + B\mathcal{E}_0 K_1 \frac{kT}{\mu_1^* z^{1/2}} \right] \quad [53]$$

Eliminating $d \ln i/dt$, i and $\ln (I_s/i)$ from Eq. [50] using Eq. [53], [51], and [52], respectively, we obtain

$$\frac{d \ln I}{dt} = BI \ln (I_s/I)[1 + a \ln (I_s/I)] \quad [54]$$

where

$$a = \frac{kT}{zC\phi} \left[1 - \frac{B\mathcal{E}_0 K_1 C\phi z^{1/2}}{\mu_1^*} \right] \left[1 + B\mathcal{E}_0 K_1 \frac{kT}{\mu_1^* z^{1/2}} \right]$$

Fortunately, for both aluminum and tantalum (10), $a \simeq 10^{-2}$ for typical conditions. It appears, therefore, that the term in a may usually be neglected. Accordingly, integration of Eq. [54] gives

$$\frac{1}{I} \simeq \frac{1}{I_o} - B \int_o^t \ln \frac{I_s}{I}\, dt \quad [55]$$

where I_o is the value of I at $t = 0$. An alternative integrated form of Eq. [54] may be written (neglecting the term in a)

$$\ln (I_s/I) = [\ln (I_s/I_o)] \exp (-Bq) \quad [56]$$

where

$$q = \int_o^t I\, dt$$

is the charge passed per unit area. We note that for a fixed value of I_s/I_o, $\ln (I_s/I)$ is a function of q only, being independent of both the steady-state current density and the temperature. The duration of these transients will of course depend on the current density.

The approximations made in deriving Eq. [55] and [56] should be valid within experimental error for $|\log I_s/I| \leq 2$. If approximate values for the various constants are known, a may be calculated as a function of I and the correction term included. In general, however, other sources of error will be more important.

It is perhaps worthwhile pointing out that the term in a in Eq. [54] arises as a result of two effects, the quadratic term in the field in the net activation energy (Eq. [3]), and the ionic contribution to the charging current. The two effects tend to cancel one another.

General transient behavior for i small.—For i sufficiently small so that the collisionally activated contribution to the polarization process may be neglected, Eq. [30] becomes

$$\frac{dP}{dt} = \mathcal{E}_0 \chi_1 \frac{dE}{dt} + i_{co} \left[\exp \left(-\frac{Q}{kT} \right) \right] \sinh \left[\frac{w_e^{*\prime}}{kT} \left(E - \frac{P}{\mathcal{E}_0 \chi_s} \right) \right] \quad [57]$$

For both alumina and tantala near 25°C Eq. [57] is a reasonable approximation only when i is vanishingly small, that is when $I = i_c$ (10). For other metal-oxide systems, however, or for alumina and tantala at sufficiently high temperatures, it is possible that $i_{co} \exp (-Q/kT)$ will be sufficiently large that Eq. [57] would apply even for reasonably large values of i. Before limiting the discussion to the case $i \approx 0$, therefore, the case where $i \gtrsim i_c$, yet is sufficiently small for the present approximation to be valid, will be considered.

Constant field transients for i small.—Making the substitutions

$$y = \frac{w_e^{*\prime}}{kT} \left(\frac{P}{\mathcal{E}_0 \chi_s} - E \right)$$

and

$$g = w_e^{*\prime} i_{co} [\exp (-Q/kT)]/\mathcal{E}_0 \chi_s\, kT$$

Eq. [57] becomes, for $\dot{E} = 0$,

$$dy/\sinh y = -g\, dt$$

which on integration gives

$$\ln [\tanh (y_o/2)] - \ln [\tanh (y/2)] = gt \quad [58]$$

or

$$-y = 2\tanh^{-1} [De^{-gt}]$$

where

$$D = \tanh (-y_o/2)$$

and

$$y = y_o \text{ at } t = 0$$

We may replace y by $(w_e^*/\mu_s^*)(\mu^* E_e - \mu_s^* E)/kT$ where $w_e^* = (1 + 1/\delta\chi_s) w_e^{*\prime} \simeq w_e^{*\prime}$ and obtain

$$\left(\frac{\mu_s^* E - \mu^* E_e}{kT} \right) = \frac{2\mu_s^*}{w_e^*} \tanh^{-1} [De^{-gt}] \quad [59]$$

and

$$g \simeq w_e^* i_{co} [\exp (-Q/kT)]\, \mu_1^*/\mu_s^*\, \mathcal{E}_0 K_1\, kT$$

[3] Defining $F(\xi) = (1 - \xi)^{1/2}[(1 - a_1)^{1/2} - (1 - a_2)^{1/2}] - \frac{1}{2}(a_2 - a_1)$, by substitution we have $F(\alpha_1) = -F(\alpha_2)$, so that $F(\xi)$, which is continuous in the interval (a_1, a_2), changes sign in the interval and hence is zero for some ξ in (a_1, a_2). Also, since $F(a_1) = -F(a_2)$, linear interpolation gives $\xi \cong (a_1 + a_2)/2$.

Eliminating $\mu^* E_e$ from Eq. [47] and [59] the following result is obtained

$$\ln (I_s/i) = 2z^{1/2} (\mu_s^*/w_e^*) \tanh^{-1} [De^{-gt}] \quad [60]$$

Since z varies only slowly with i, we may to a first approximation set it equal to the mean of the extreme values of z, given approximately by (see Eq. [48] and [49])

$$\bar{z} \simeq 1 - (4kT/C\phi) \ln \left(\frac{i_o I_s^3}{A^4} \right)^{1/4} = (kT \bar{\beta}_s/\mu_s^*)^2$$

where $i = i_o$ at $t = 0$ and $\bar{\beta}_s$ is the steady-state reciprocal Tafel slope for a current density equal to $(i_o I_s^3)^{1/4}$. Equation [60] therefore becomes

$$\ln (I_s/i) \simeq (2kT \bar{\beta}_s/w_e^*) \tanh^{-1} [De^{-gt}] \quad [61]$$

where $D \simeq \tanh [(w_e^*/2kT\bar{\beta}_s) \ln (I_s/i_o)$. Because of the complex form of the equation (derived in the next section) for the charging current, interpretation of data in terms of Eq. [61] will only be feasible for $I \simeq i$ (*i.e.*, $i >> i_c$).

We note that Eq. [61] predicts $\ln (I_s/i)$ to be a function only of time for i_o/I_s and temperature fixed. The duration of these transients is therefore independent of the steady-state current density, but is highly dependent on the temperature, since g contains a Boltzmann factor. This behavior is in marked contrast to that for constant field transients at high ion currents (cf. Eq. [56]). The two cases can therefore be readily distinguished experimentally.

Charging current for i small.—For i sufficiently small, we may combine Eq. [57] with the relation

$$i_c = d[P + \epsilon_o E]/dt$$

and obtain

$$i_c' = A_c \sinh \left[\frac{w_e^*}{kT} \left(\frac{\mu_s^* - \mu_1^*}{\mu_s^*} \right) \left(E - E_* - \frac{q_c'}{\mathcal{E}_o(\chi_s - \chi_1)} \right) \right]$$

or setting

$$1 + \chi_s \simeq (1 + \chi_1)(1 + \delta\chi_s)/(1 + \delta\chi_1) = K_1 \mu_s^*/\mu_1^*$$

$$i_c' \simeq A_c \sinh \left\{ \frac{w_e^*}{kT} \left[\left(\frac{\mu_s^* - \mu_1^*}{\mu_s^*} \right) (E - E_*) - \frac{\mu_1^*}{\mu_s^*} \frac{q_c'}{\mathcal{E}_o K_1} \right] \right\} \quad [62]$$

where $i_c' = i_c - \mathcal{E}_o K_1 \, dE/dt$ is the ionic contribution to the charging current; $A_c = i_{co} \exp(-Q/kT)$, $q_c' = \int_o^t i_c' dt$, $E_* = (P_o/\mathcal{E}_o - \chi_1 E_o)/(\chi_s - \chi_1)$ and P_o and E_o are the values of P and E at $t = 0$. For a fully annealed film, the ionic contribution to the polarization will be zero at $t = 0$ (*i.e.*, $P_o = \mathcal{E}_o \chi_1 E_o$) so that $E_* = 0$ for this case. If equilibrium polarization conditions prevail at $t = 0$ (*i.e.*, $P_o = \mathcal{E}_o \chi_s E_o$) then $E_* = E_o$.

The analysis of data in terms of Eq. [62] requires numerical integration to obtain q_c'. If we consider the special case of constant field, the charging current may be obtained as an explicit function of time. Accordingly, differentiation of Eq. [58] with respect to time yields

$$i_c = 2DA_c e^{-gt}/(1 - D^2 e^{-2gt}) \quad [63]$$

where

$$D = \tanh \left[\frac{w_e^*}{2kT} \left(\frac{\mu_s^* - \mu_1^*}{\mu_s^*} \right) (E_o - E_*) \right]$$

and E = a constant $= E_o$. An equation somewhat more convenient for fitting to empirical data is obtained by solving for e^{gt} and taking logarithms. The resulting equation is

$$\ln \left[\frac{|i_c/A_c|}{(1 + i_c^2/A_c^2)^{1/2} - 1} \right] = gt - \ln |D| \quad [64]$$

Summary and Discussion

A theory of cooperative ion migration in valve metal oxide films has been developed on the basis of a dielectric mosaic model of the film. The cooperative phenomena arise then as a result of time dependent polarization properties of the oxide film. Thus the ion current leading to film growth depends not only on the applied field strength and temperature but also on the polarization of the medium. The transient conduction properties of these systems are therefore determined by the kinetics of the polarization processes.

In addition to conventional "fast" polarization processes, for this model a "slow" polarization process, associated with ionic migration within a single mosaic component (crystallite or polymeric unit) must exist. Two independent mechanisms for the kinetics of the slow polarization process have been proposed; the "high ion current mechanism" in which the change in the slow component of the polarization is induced by the transfer of ions from one polymeric unit to the next and the "low ion current mechanism" in which the ionic migration within the polymeric units takes place by a conventional high field ionic conduction process. The terms "high" and "low" are of course only relative, implying correctly that at sufficiently high ion current densities, for a given temperature, one mechanism will predominate, while the other will predominate at sufficiently low ion current densities. For a given range of ion current densities, the low ion current mechanism should predominate at sufficiently high temperatures, and vice-versa.

In discussing the model it is convenient to consider steady-state and high ion current conditions separately from low ion current conditions.

For steady-state conditions, the following kinetic parameters are required to define the behavior of the system: a pre-exponential factor, i_o, an activation energy, ϕ, an effective charge-activation distance product, μ_s^*, and a parameter, C, to allow for the nonlinear dependence of the net activation energy on the field strength. A precisely analogous set of parameters is required for the high field Frenkel defect theory (14). For high ion current transient experiments, the present model required an additional two parameters; another effective charge-activation distance product, μ_1^*, and a constant, B, related to the cross-sectional area of a polymeric unit. For similar experiments, the high field Frenkel defect theory requires three additional parameters; parameters analogous to μ_1^* and B, plus an additional parameter similar to C of the present model (5).

As the high field Frenkel defect model does not predict anything analogous to the low ion current phenomena predicted by the present model, comparison in this area is not really possible. However, in order to predict conduction phenomena associated with annealing experiments (4, 5), the Frenkel defect theory requires a knowledge of an additional activation energy and another exponential factor. The present model is extended to cover these phenomena and also phenomena relating to low ion currents by the addition of three new parameters; a pre-exponential factor, i_{co}, an activation energy, Q, and an effective charge-activation distance product, w_e^*. The present model therefore involves, in total, the same number of disposable constants as does the Frenkel defect theory, so that agreement with data is not achieved simply by introducing more disposable constants. As most of the data presently available in fact are concerned with high ion current conditions (10), the present theory generally involves one less disposable constant.

Apart from the obvious tests which can be applied to most theories (*i.e.*, that they lead to functional forms in agreement with data and to reasonable values for the parameters) the present model offers two additional checks for internal consistency. The parameter, C, can be determined from both steady-state (Eq. [36]) and transient (Eq. [41] Tafel slope measurements. The parameters μ_s^* and μ_1^* can be evaluated from high ion current measurements (Eq. [36] and [41], respectively), with the ratio μ_s^*/μ_1^* also being obtainable from charging current measurements, since

$\mu_s^*/\mu_1^* \simeq K_s/K_1$, the ratio of the static to dynamic dielectric constant.

The parameters i_o, ϕ, μ_s^*, and C are most readily obtained from steady-state measurements (Eq. [34]); the parameter μ_1^* from high ion current measurements for conditions of rapidly changing field (Eq. [41]); and the parameter B from constant field transients for high ion current conditions (Eq. [55] or [56]). The remaining three parameters, i_{co}, Q, and w_e^* can be obtained from charging current measurements for fields sufficiently low so that the ion current is essentially zero (Eq. [62] and [64]).

In the following paper (10) the model is discussed in relation to existing theories and presently available data.

Acknowledgments

The author wishes to express his appreciation to Dr. J. P. Valleau for reading the manuscript and for many useful discussions.

Manuscript received Nov. 24, 1964. This paper was presented in part at the Pittsburgh Meeting, April 15-18, 1963.

Any discussion of this paper will appear in a Discussion Section to be published in the June 1966 JOURNAL.

REFERENCES

1. B. Verkerk, P. Winkel, and D. G. de Groot, *Philips Research Repts.*, **13**, 506 (1958).
2. G. Amsel and D. Samuel, *J. Phys. Chem. Solids*, **23**, 1707 (1962).
3. J. A. Davies and B. Domeij, *This Journal*, **110**, 849 (1963).
4. D. A. Vermilyea, *ibid.*, **104**, 427 (1957).
5. L. Young, *Proc. Roy. Soc.*, **A263**, 395 (1961).
6. M. J. Dignam, *This Journal*, **109**, 184 (1962).
7. P. J. Ryan and M. J. Dignam, *Can. J. Chem.*, **40**, 1875 (1962).
8. M. J. Dignam and P. J. Ryan, *ibid.*, **41**, 3108 (1963).
9. L. Young, "Anodic Oxide Films," Chap. 3, Academic Press, London (1961).
10. M. J. Dignam, *This Journal*, **112**, 729 (1965).
11. A. F. Wells, "Structural Inorganic Chemistry," p. 37, 2nd ed., Oxford University Press (1952).
12. M. J. Dignam, *Can. J. Chem.*, **42**, 1155 (1964).
13. F. S. Stone, "Chemistry of the Solid State," Chap. 2, Edited by W. E. Garner, Butterworth's Scientific Publications (1955).
14. L. Young, *Proc. Roy. Soc.*, **A258**, 496 (1960).

Conduction Properties of Valve Metal-Oxide Systems

II. Comparison of Data with New Theory

M. J. Dignam

Department of Chemistry, University of Toronto, Toronto, Ontario, Canada

ABSTRACT

Data from the literature for the anodic oxidation of a number of the valve metals have been analyzed in terms of the dielectric polarization theory of ionic transport, developed in Part I, and previous theories. The unique predictions of this theory were found to be in excellent accord with the data.

In the preceding paper (1) a theory of cooperative ion transport has been developed and equations appropriate to various experimental conditions derived. The purpose of the present paper is to test this theory against available data and compare its predictions with those of other theories. In respect to the latter, special attention will be paid to the high field Frenkel defect theory, proposed originally by Bean, Fisher, and Vermilyea (2) as this is the only other theory capable of describing, even qualitatively, most of the observed phenomena. Very briefly, in this theory the transient ionic conduction phenomena are attributed to a slow adjustment of the field dependent population of Frenkel defects to a change in the field. A detailed description of this model and others can be found elsewhere (3).

The theory and available data will be discussed under the headings: Steady-State Data, Tafel Slope Data, Constant Field Transients, and Space Charge Effects.

Examination of Available Data

Steady-state data.—The conventional empirical equation used to fit steady-state ionic conduction data can be written

$$I = \alpha \exp \beta E \qquad [1]$$

where α contains the Boltzmann factor for the zero field activation energy. In most previous theoretical treatments, β is predicted to have the form aq/kT where a is an activation distance or mean activation distance for the field assisted displacement of an ion of charge q.

In relation to Eq. [1], three kinds of anomalous behavior have been observed:

1. For zirconium, the parameters α and β have been found by Young (4) to depend on the thickness of the anodic film. The data for tantalum (5), aluminum (6), niobium (7), bismuth (8), and titanium (9) show no such anomaly for films thicker than about 100Å.

2. The Tafel slope, $(d \ln I/dE)_T$, has been found to vary more slowly with the absolute temperature than predicted by setting $\beta = aq/kT$, for both tantalum (5, 10) and niobium (7). For titanium, β appears to decrease more rapidly than $1/T$ with increasing temperature. Sufficiently accurate data are not available for other valve metals to check the temperature dependence of β.

3. For both tantalum (5) and aluminum (6) a variation of the Tafel slope with field strength at a given temperature has been observed. The data for other valve metals are not sufficiently precise to allow this observation to be made.

With regard to the first anomaly, zirconium appears to be unique among the valve metals in displaying film thickness dependent kinetic behavior for films thicker than about 100Å. This suggests either that additional complicating factors are present (for example film inhomogeneity) or that a different mechanism is involved. Young has suggested (4), and indeed it appears not unreasonable, that zirconium oxidizes anodically in accord with Dewald's two barrier model (11). The difficulty with this model, however, is that it requires no less than six disposable constants to define steady-state behavior, while Young's generalization of the model involves at least seven disposable constants (12). With such flexibility, agreement between data of limited scope, such as steady-state data, is almost guaranteed regardless of the validity of the model. Nevertheless, this model must be regarded as a possibility in connection with the anodic oxidation of zirconium.

Dewald's model has also been applied to the steady-state anodic oxidation of tantalum (10, 13) and niobium (14) with the purpose of explaining the Tafel

slope anomalies mentioned above. With the exception that the dependence on thickness predicted by this model has never been detected, the Tafel slope anomalies were accounted for quantitatively. Once again, however, it must be emphasized that this improvement over Eq. [1] is gained by introducing three new parameters, for a total of six. By contrast, Eq. [13] of the previous paper (1), reproduced below for convenience, is also able to account for the Tafel slope anomalies for the above metals and for aluminum (15) with the addition of only one positive parameter, C.

$$I = i_o \exp\left\{ - \left[\phi - E\mu_s^* \left(1 - \frac{E\mu_s^*}{C\phi} \right) \right] / kT \right\} \quad [2]$$

An equation of the form of [2] was first suggested by Young (5) on empirical grounds. He later justified the presence of a quadratic term in the field on the basis of a postulated variation of activation energy with the condenser pressure (16). In a recent paper by the author (15) it is pointed out that the condenser pressure effect is probably too small to explain the observed phenomena. Further, it is shown that the quadratic term arises quite naturally from a more detailed consideration of ion transfer processes at high electrostatic fields. Specifically, it was shown that not only the form of Eq. [2], but also the empirical values for C for Ta, Nb, and Al are predicted correctly by assuming that the interaction potential between the mobile ion and its immediate surroundings can be represented by a Morse function for small displacements. If one accepts the Morse function postulate, C is not an independent constant, so that the Tafel slope anomalies for Ta, Nb, and Al may be explained quantitatively without increasing the number of disposable constants above three. It would appear, therefore, that Eq. [2] represents a far more satisfactory explanation for the Tafel slope anomalies than does Dewald's model, at least in the cases of Ta, Nb, and Al, particularly since Dewald's model does not lend itself readily to explaining even qualitatively the transient conduction phenomena observed for the anodic oxidation of these metals.

It should be emphasized at this point that Eq. [2] cannot be regarded as specific to the theory developed in the preceding paper. An essentially identical equation can be expected for the Mott-Cabrera theory (17), the high field Frenkel defect theory, or Verwey's theory (18). The only way in which the present theory can be regarded as in any way unique in relation to Eq. [2] is that a Morse function interaction potential is more in accord with the new theory than it is with the other theories mentioned. Indeed, the ion transfer process from one molecular unit to the next would appear to be not unlike the dissociation of a diatomic molecule.

The Tafel slope anomaly for titanium cannot be interpreted in the same way as that for Ta, Nb, and Al, since the effect, being in the opposite direction, requires a negative value for C. A negative value for C can be explained in terms of a range or distribution of values for the activation energy and activation distance, as outlined by Young (5). However, an equally probable explanation of the titanium results would be that the current efficiency for formation of the film decreases with increasing temperature and decreasing current density. A further explanation is that the theory of the previous paper is applicable, but that μ_s^* decreases with increasing temperature as a result of a variation of χ_s, the static electric susceptibility, with temperature. A re-examination of titanium using the optical techniques developed by Young should resolve this uncertainty.

The situation is, therefore, that Ta, Nb, and Al give data in agreement with Eq. [2] where the values of C are in accord with that predicted on the basis of a Morse interaction potential; the data for Bi (8) are also consistent with this equation although of insufficient precision to verify the term in C; the data for Ti are uncertain since the current efficiency for film formation is unknown; and finally, the data for Zr are definitely not in accord with this equation. Accordingly, in this paper we shall be concerned primarily with the behavior of Ta and Al, for which the major amount of data are available, and to a lesser extent Nb and Bi. The data for other metals or semimetals which exhibit valve metal film forming properties are not sufficiently complete or precise to distinguish between alternative mechanisms.

A brief comment on the magnitude of the parameters found experimentally is relevant at this point. For Ta, Young (5) obtained a value for μ_s^* (qa in his notation) of 35 eÅ which on choosing the maximum possible effective charge on the mobile ion, + 5e gives an effective activation distance of 7Å, an extremely large value. If we assume a value for C for the anodic oxidation of Bi of the same order as that found for Ta, Nb, and Al (*i.e.*, about 3.3) then a value of 129 eÅ for μ_s^* may be calculated from Young's data (8). In this case, the value for the effective activation distance is no less than 43Å. Even without making any allowance for the covalent bonding in these oxides (which would be expected to lead to effective changes appreciably less than +5e and + 3e, respectively) it is seen that these values for μ_s^* are very much too large to be equated to the product of a charge and activation distance. The other valve metals also give high values for the steady-state effective activation dipole, μ_s^*. These high values are immediately explained in terms of the new theory, since $\mu_s^* = (1 + \delta\chi_s)\mu^*$ where μ^* is the "true" activation dipole, χ_s the static electric susceptibility of the oxide, and δ a geometric factor of the order of unity. A more quantitative consideration of this matter will be reserved for the following section. At this point, however, it is worth noting that the suggestion that the field effective in causing ion migration is greater than the applied field is by no means a new one. Indeed in 1941, Maurer (19) explained the temperature dependence of the ionic conduction of glasses on the assumption that the effective field was given by the static dielectric constant times the applied field. The point was first raised in connection with anodic oxide films by Young (20) in 1954. Until now, however, this concept has received very little attention.

Perhaps the most serious limitation of all previous theories lies in their failure to account for the recent data (21-25) regarding anionic and cationic transport in certain valve metal oxides. I wish to draw particular attention to the excellent work of Davies and colleagues (21-23) in which using β-spectroscopy in conjunction with Xe^{125} and Rn^{222} marker experiments, they were able to evaluate the transport numbers appropriate to the anodic oxidation of Al, W, Ta, and Zr. The anionic transport numbers were found to be (23) for Al_2O_3 0.45 ± 0.5; for WO_2 and Ta_2O_5 0.65 ± 0.04; and for ZrO_2 0.99 ± 0.01. In addition the transport numbers for Al_2O_3 were found to be independent of current density over the range 10^{-4} to 10^{-2} amp/cm^2, with a similar result found for WO_2 and ZrO_2. The effect of current density on transport numbers for Ta_2O_5 had not been investigated at the time this paper was prepared.

For previous theories to be compatible with these data, one must first assume that the activation dipole for anionic and cationic defects present in the film are nearly identical, since the transport numbers are independent of field strength. Next, since pre-exponential factors will be comparable for all defects, one must assume that the zero field activation energies for migration of the anionic and cationic defects are nearly the same. Such postulates if proposed to explain the results for only a single metal-oxide system should be regarded with great scepticism and must be considered entirely out of the question when required to explain the data for more than one metal oxide system. Indeed, if any of the previous theories are to be ac-

cepted even tentatively, one is forced to reject the validity of the transport number data.

Let us now examine the data of Davies and collaborators in terms of the newly proposed theory. The transport numbers will be determined largely by the fraction of the charge carried through the individual molecular units by anions and cations, respectively, since the gap between molecular units is presumably quite small compared with the dimensions of such units. Immediately following an ion transfer event, the donor and acceptor molecular units will be depolarized. To re-establish their equilibrium dipole moments, ion migration in each is required. In general one would expect both anionic and cationic defects to be produced in a somewhat random manner in the two molecular units by the highly exoenergetic ion transfer process. As the impact energy for ion transfer will be very nearly independent of current density, no significant dependence on current density would be expected. From this model we deduce, therefore, transport behavior, in accord with the above data. The theory is also in accord with the transport data presented in a recent paper by Amsel and Samuel (25) and an earlier paper by Verkerk, Winkel, and Groot (24).

Tafel slope data.—Two kinds of Tafel slope determinations have been made on a number of the valve metal-oxide systems: steady-state Tafel slopes, evaluated from the steady-state relation between current and field strength, and transient Tafel slopes, obtained from the relation between current and field strength when the field (or current) is changed very rapidly. The steady-state and transient reciprocal Tafel slopes, β_s and β_1, respectively, are given by Eq. [36] and [40] (or [41]) of the previous paper

$$\beta_s = \underset{\dot{E} \to 0}{\text{Limit}} \frac{d \ln I}{dE} = \frac{\mu_s^*}{kT}\left[1 - \frac{2\mu_s^* E}{C\phi}\right] \qquad [3]$$

$$\beta_1 = \underset{\dot{E} \to \infty}{\text{Limit}} \frac{d \ln I'}{dE} \simeq \left(\frac{\Delta \ln I'}{\Delta E}\right)_{\Delta t \to 0} \simeq \frac{\mu_1^*}{kT}\left[1 - \frac{2\mu_s^* E_o}{C\phi}\right] \qquad [4]$$

where the approximations amount to neglecting $\mu_1^* \Delta E / C\phi$ compared with unity and a further small term, cf (1) Eq. [40] and following.

From the excellent data of Young (5, 26), the field dependence of the Tafel slopes for the tantalum system are represented by the following equations

$$\beta_s\, kT = 34.98\ (1 - 9.58E)\ e\text{Å} \qquad [5]$$

$$\beta_1\, kT = 11.15\ (1 - 9.50\, E_o)\ e\text{Å} \qquad [6]$$

The manner in which β_1 was determined was such that $\Delta E << E$ so that the approximations contained in Eq. [4] are justified in this instance. We now note that the empirical coefficients of E and E_o in the above expressions are the same well within experimental error, as predicted by Eq. [3] and [4]. The same agreement within experimental error has been found for aluminum from recent data obtained in this laboratory (6, 27). Unfortunately, however, we have as yet been unable to obtain the coefficient of E_o in the expression for the transient Tafel slope any more accurately than ± 30%. Data of sufficient precision to test this prediction for other value metals are lacking at present.

On the basis of previous theories, and in particular the high field Frenkel defect theory, the agreement between the coefficients of E and E_o (Eq. [5] and [6]) must be regarded as entirely fortuitous, whereas it is a specific prediction of the present theory.

It is of interest at this point to show how χ_s may be estimated from Tafel slope data. If complete data are available, μ_s^* and μ_1^* can be determined from β_s and β_1 *vs.* E and E_o, respectively, from which one obtains $(\delta\chi_s + 1)/(\delta\chi_1 + 1) = \mu_s^*/\mu_1^*$ or assuming $\chi_s >> (1/\delta - 1)$ and $\chi_1 >> (1/\delta - 1)$,

$$\mu_s^*/\mu_1^* \simeq K_s/K_1 \qquad [7]$$

where K_s and K_1 are the static and dynamic dielectric constants. Using standard a-c capacitance data at sufficiently high frequencies (1000 cps would appear to be sufficiently high) the dynamic dielectric constant can be calculated and thence an estimate of the static electric susceptibility, χ_s, or static dielectric constant, K_s, obtained from μ_s^*/μ_1^*. If data for the variation of the Tafel slopes with field strength are not available, then for measurements such that $E \simeq E_o$ and ΔE small, it follows that

$$\beta_s/\beta_1 \simeq \mu_s^*/\mu_1^* \simeq K_s/K_1$$

To date, no independent determinations of K_s are available to test the validity of Eq. [7].

One of the more fundamental predictions of the present theory is that the transient Tafel slope and conventional dynamic dielectric constant are related, since

$$\mu^* = \mu_1^*/(1 + \delta\chi_1) \quad \text{or} \quad \delta\mu^* = \mu_1^*/(1/\delta + \chi_1) \simeq \mu_1^*/K_1$$
$$[\text{for } K_1 >> (1/\delta - 1)]$$

If oxygen ions are the ones involved in the ion transfer process for all the valve metal systems, then $\delta\mu^*$ should not differ greatly from one system to the next, so that μ_1^*/K_1 will be approximately a constant. The variation in ionic character, bond strength, and structure will of course introduce some variation in μ_1^*/K_1. The real justification for assuming oxygen ion transport between crystallites is, of course, that this postulate is in accord with the results. However, a reasonable case can be made for this postulate simply on the basis of the proposed model. Since the oxides are partially ionically bonded, the radius of the oxygen species will be appreciably larger than that of the metal species. The oxygen "ions" will therefore stand out from the surface of the crystallites, in relation to the metal "ions," so that the effective field at the oxygen ions should be somewhat higher. The higher polarizability of the anionic species should also favor oxygen ion transport between crystallites rather than cation transport.

Table I lists values of μ_1/K_1 for the systems tantalum, aluminum, niobium, and bismuth and their respective oxides. Young's values for μ_1^* (26) and K_1 (28) for Ta_2O_5 are reported, along with the corresponding values for Al_2O_3 obtained recently in the author's laboratory (27). In a previous publication (15) Young's data (7) for Nb_2O_5 were used to calculate μ_s^*. Combining this result with Young's value for K_1 (29) and Vermilyea's (30) determination of $\mu_s^*/\mu_1^* = 2.1$ ($q\lambda$ effective/$q\lambda$ initial, in his terminology) gives the required values of μ_1^* and K_1 for Nb_2O_5. Young's data for Bi_2O_3 (8) provides values for β_s, β_1, ψ, and K_1. Since the quadratic parameter, C, is nearly the same for Ta_2O_5, Nb_2O_5, and Al_2O_5 (15), μ_1^* for Bi_2O_3 was calculated from Eq. [4] and [5] assuming $C \simeq 3.3$.

As predicted, the values of μ_1^*/K_1 in Table I show much less variation than do the values of either μ_1^* or K_1 individually. Furthermore, the variation in $\mu_1^*/K_1 \simeq \delta\mu^*$ can be explained qualitatively on the assumption that it is due primarily to a variation in the effective charge on the oxygen "ion" from oxide to oxide. Thus the oxides in which the metal is in an

Table I. Relation between transient activation dipole and dynamic dielectric constant

Oxide	μ_1^* eÅ	K_1	$\mu_1^*/K_1 \simeq \delta\mu^*$ eÅ
Ta_2O_5	11.1$_5$	27.6	0.40
Nb_2O_5	16	41.4	0.39
Al_2O_3	7.8	8.8$_5$	0.88
Bi_2O_3	40	62	0.65

oxidation state of +3 should involve a higher proportion of ionic *vs.* covalent bonding than those involving a metal oxidation state of + 5, so that μ^* for Al_2O_3 and Bi_2O_3 should be appreciably greater than μ^* for Ta_2O_5 and Nb_2O_5. Between Ta_2O_5 and Nb_2O_5, according to the usual variation with ionic size, Ta_2O_5 should be slightly more ionic (31). The argument favoring more ionic bonding for Al_2O_3 than for Bi_2O_3 rests on the fact that the first ionization potential for Al is 1.3 ev lower than that for Bi (32).

Finally, as a check on the reasonableness of the magnitudes of the kinetic parameters μ_1^* and μ_s^*, we shall attempt to estimate the magnitude of the effective activation distance. From the crystal lattice parameters, Wells (33) estimates that the bonding in α Al_2O_3 is about 50% ionic. Assuming about the same proportion of ionic bonding is involved in the anodically formed oxide, we may estimate the effective charge on the oxygen species in Al_2O_3 to be about 1e. This leads to an effective activation distance at zero field strength of about $0.9/\delta$ Å, which for $\delta \simeq 1$ is an eminently reasonable value. It is tempting to suggest that this calculation justifies choosing a value for δ of about unity, however, the assumptions involved in this estimate are sufficiently bold to make such a proposition somewhat hazardous. Nevertheless, the calculation does indicate that the values of μ_1^* are of the correct magnitude.

In summary, the Tafel slope data for Ta, Nb, Al, and Bi are in complete accord with the theory presented in the previous paper. It would be very difficult to rationalize the data of Table I on the basis of any previous theory.

Constant field transients.—Measurements of transient conduction phenomena under conditions of very nearly constant field strength have been made by Young (26) on tantalum and in the author's laboratory on aluminum (27). Typical examples of these data are reproduced in Fig. 1 and 2. Young's data were obtained by heating a previously anodized sample to 100°C for a few minutes then returning it to the cell, applying suddenly an appropriate constant voltage and recording the current for the first few seconds. Our measurements were made following thermal treatment both for 1 hr at 60°C and for a few minutes at room temperature. The voltage was not applied suddenly but increased to its final value at a rapid linear rate, as shown in Fig. 2.

There are several points of interest in these curves which we shall discuss primarily with reference to Fig. 2. The initial upswing in the current during the

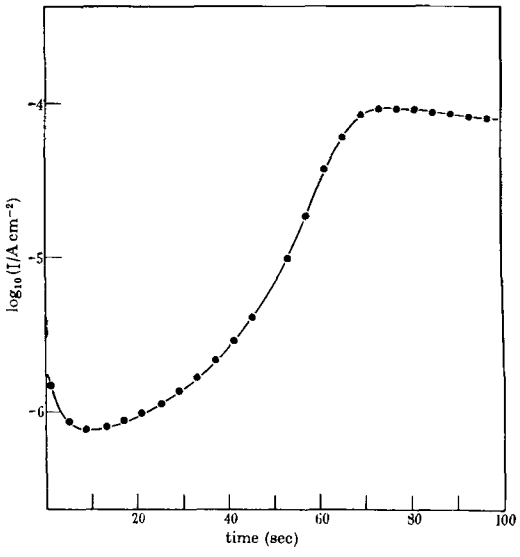

Fig. 1. Young's data for tantalum (26). Logarithm of the current density, *I*, as a function of time on reapplication of a fixed anodic potential.

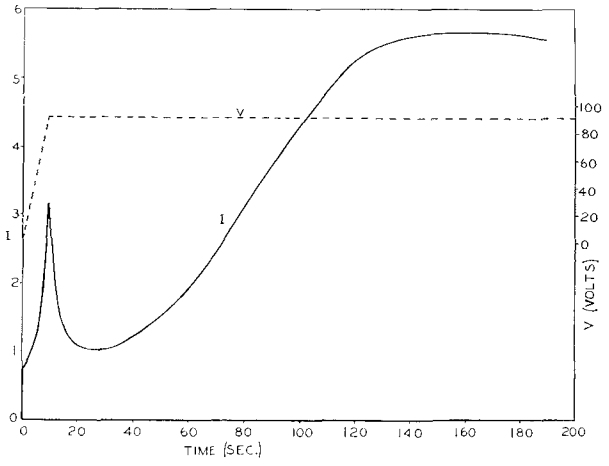

Fig. 2. Current density, *I* (μa cm^{-2}) as a function of time for aluminum on reapplication of anodic potential, *v*, as illustrated.

voltage build-up stage and the fall in current immediately after the voltage becomes constant cannot be explained by any previous theory, except by postulating fissures in the anodic film as Young has done (26). On the present theory, such charging currents are to be expected and represent strong evidence in support of an anomalous polarizing process which we have referred to as the transport polarization process.

A second point of interest is the fact that, apart from the present theory, there exists no quantitative theory even for the shape of the curves beyond the point where the anomalous charging currents will make a significant contribution. The high field Frenkel defect theory predicts a curve shape (log *I vs. t* or *I vs. t*) which is at all times concave downward, as pointed out by Young (26), whereas experimentally (Fig. 1 and 2) the curves are at first distinctly concave upward. It has previously been suggested to the author that effects such as these are likely brought about as a result of structural changes during thermal treatment, but all these same features have been observed in the author's laboratory for aluminum samples which have been merely held at room temperature and zero applied voltage for a minute before re-applying the voltage. Such an explanation, therefore, seems improbable.

Before attempting a quantitative fit of these transient measurements to the present theory, it is worthwhile to give a qualitative description, in terms of the present theory, of the processes occurring over the various regions of Fig. 2.

On applying the linearly increasing voltage, the conventional charging current rapidly achieves its constant value of $\mathfrak{S}_0K_1(dE/dt)$, giving rise to the initial current jump. This is then followed by the more sluggish build-up of the "anomalous" charging current, dP_2/dt, under conditions where the growth current, i, is negligible, so that the collision process is not contributing to dP_2/dt. This initial build-up of the charging current should be given by Eq. [62] of the previous paper, from which we see that the current should rise approximately according to a hyperbolic sine function of the voltage, in qualitative agreement with the observed shape. When the voltage rise is stopped, the polarization of the medium is still well below the equilibrium value for the applied field, so that E_e is still too small to produce a significant number of ion transfer events. The total current observed is therefore still only the charging current, which should drop abruptly by an amount $\mathfrak{S}_0K_1(dE/dt)$, equal to the initial abrupt rise, then decay approximately as a negative exponential of the time, according to Eq. [63] of the previous paper. Unfortunately, the slow response of the recorder used did not permit the resolution of the initial fast drop from the subsequent decay.

Up to about 200 sec, therefore, the polarization of the medium, and hence the effective field, E_e, has been increasing almost exclusively by the thermally activated polarization process, the effective field being too small to cause a significant number of ion transfer events to take place. Somewhat after 20 sec, however, the growth current starts to become of significance, so that by 30 sec the rate of increase of the growth current effected by the increasing polarization of the medium has more than overcome the rate of fall of the thermally activated component of the charging current. From about 30 sec onward, the thermally activated polarization process becomes negligible compared with the collision induced process and the charging current small compared with the growth current, i. As the growth current increases, it increases the rate of change of the polarization of the medium, and hence of E_e, thus increasing the rate of increase of i and producing the concave upward portion of the curve from 30 to 80 sec. Ultimately, this "autocatalytic" process is overcome as the polarization of the medium approaches its steady-state value, leading to the rounding off from 80 to 140 sec. The decrease in current beyond 160 sec is caused by the slow fall in the applied field resulting from the slow film growth.

The data relating to the charging current are not sufficiently accurate to warrant quantitative treatment. Measurements are now being undertaken in this laboratory to test this aspect of the theory. We shall at present analyze quantitatively only that part of the data for which the thermally activated component of the charging current can be neglected. The correct equation for these conditions, Eq. [55] of (1), is recorded below

$$1/I = 1/I_o - B\int_o^t \ln(I_s/I)\,dt \qquad [8]$$

where I_o is the current density at $t = 0$, and I_s is the steady-state current density.

In Figure 3, the data for aluminum are plotted according to Eq. [8] for the experimental points lying between about 30 and 150 sec. In order to illustrate more clearly the quality of the agreement between the data and Eq. [8], the data for tantalum have been plotted in Fig. 4 according to a rearranged form of Eq. [8], *viz.*

$$F = [1/I - B\int_o^t \ln(I/I_o)\,dt] = 1/I_o - [B\ln(I_s/I_o)]t \qquad [8']$$

Both these sets of data are in excellent accord with Eq. [8] and hence with the present theory. The values of B calculated from the slopes are 8.0 x 10^3 cm^2/coulomb for tantalum and 11.4 x 10^3 cm^2/coulomb for aluminum. A number of values for aluminum have been obtained which are in agreement to about ± 5%. From the theory we have

$$B = (\sigma'/Ze)\,(1 + \delta'\chi_1)/(1 + \delta'\chi_s) \simeq (\sigma'/Ze)\,(\mu_1^*/\mu_s^*)$$

since

$$(1 + \delta'\chi_1)/(1 + \delta'\chi_s) \simeq (1 + \delta\chi_1)/(1 + \delta\chi_s) = \mu_1^*/\mu_s^*$$

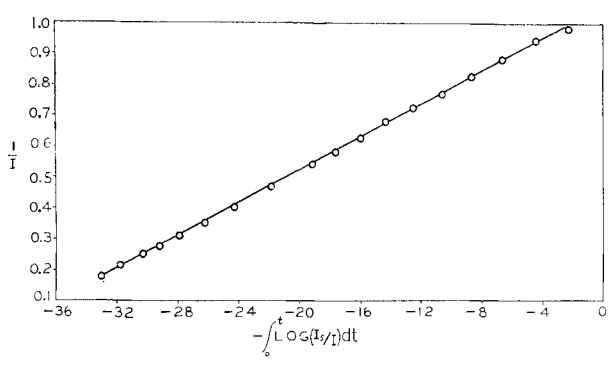

Fig. 3. Data of Fig. 2, plotted according to Eq. [8] (I in μa cm^{-2}, t in sec).

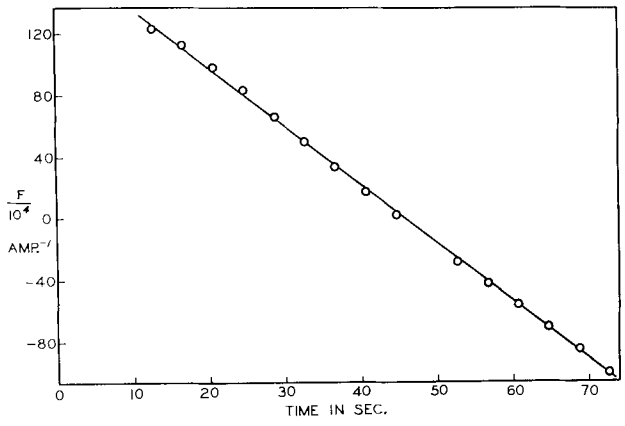

Fig. 4. Data of Fig. 1 plotted according to Eq. [8']

for $\chi_1 >> 1/\delta'$ and $1/\delta$, or $\delta' \simeq \delta$. Setting $Z = 2$ we then obtain $\sigma'^{1/2} = 8.9$Å for tantala and 11Å for alumina. On the reasonable assumption that the crystallites should contain at least one unit cell and be sufficiently small to give rise to the observed diffuse diffraction patterns, $\sigma'^{1/2}$ should lie between about 4 and 20Å, in excellent accord with the above values.

From the experimental value for the pre-exponential factor for the tantalum system, $i_o = 1.7_4$ x 10^8 amp/cm^2 (5), and the theoretical form for i_o, cf. Eq. [14] in (1), it follows that

$$1.7_4 \text{ x } 10^8 \text{ (amp/cm}^2) = ZeN'\nu/\sigma \simeq N'\nu\mu_1^*/\mu_s^* B$$

On substituting the empirical values for μ_1^*/μ_s^* and B we obtain $N'\nu \simeq 4$ x 10^{12} sec^{-1}, an eminently reasonable result since N', the number of charged species per molecular unit located at suitable sites for transfer to the next molecular unit, would be expected to be close to unity.

Since B contains a molecular unit dimension parameter, it is entirely possible that it will vary somewhat with film formation conditions. A thorough investigation to look for such an effect has not as yet been carried out but the present results (27) indicate that a variation in B of 20% or more can be effected by the choice of formation current density.

As stated previously, the data relating to the "anomalous" charging current are not sufficiently accurate to warrant quantitative treatment. A computer calculation to generate the entire experimental curve shown in Fig. 2, starting from Eq. [1], [13], [30], and [32] of the previous paper, has, however, been carried out. The result of this calculation was good qualitative, but not quantitative agreement with the experimental data. The failure to achieve a quantitative fit was traced to the form chosen for the "anomalous" charging current, dP_2/dt, *i.e.*, final term Eq. [30] of (1) or final term Eq. [24] of (1). It appears that the variation of dP_2/dt with E is in accord with Eq. [30] of (1) since the initial build-up of the charging current could be fitted well and for reasonable values of the parameters ($w_e^* \simeq 1.6$ eÅ and $Q \sim 0.8$ ev). The decrease of dP_2/dt from the peak under conditions of constant E, however, are not in accord with Eq. [30] of (1). The present equations appear to predict the wrong functional dependence of the anomalous charging current on P_2 or P. In view of the approximations made in deriving the equation for the thermally activated polarization process, this is not too surprising. It is felt, however, that this aspect of the theory can be substantially improved without altering the basic model. Efforts in this direction are now under way.

Influence of space charge on steady-state anodic oxidation.—As mentioned in the previous paper, Eq. [10] and hence Eq. [19] of the previous paper are only valid in a region of the film where the space charge is negligible. We shall now investigate the influence of

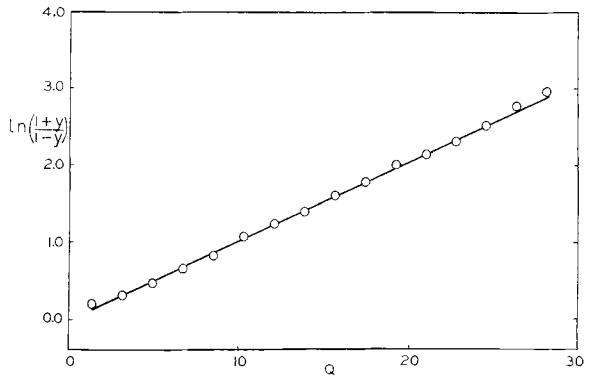

Fig. 5. Space charge data for aluminum (34) plotted according to Eq. [15]. (Q is charge passed in mcoul/cm^2).

space charge for steady-state anodic oxidation conditions.

From Eq. [7] and [9] of the previous paper and Poisson's equation, and assuming $\kappa_{+r} >> \kappa_{-r}$ we may write

$$i = ZedN + r\kappa p_o \quad [9]$$

$$n_{+r}n_{-r} = n_o^2/f\kappa = n_\infty^2 \quad [10]$$

$$dE/dx = (n_{+r} - n_{-r})Ze/\mathcal{E} \quad [11]$$

where $\kappa \simeq \kappa_{+r}$, $\mathcal{E}$ is the permittivity of the oxide ($K_s\epsilon_o$ for steady-state conditions), n_∞ the value of n_{+r} and n_{-r} beyond the space charge zone and x the distance into the oxide measured from the interface away from which the species of charge rZe move. The assumption $\kappa_{+r} >> \kappa_{-r}$ (or the converse) is required to obtain agreement with the data and would appear to be justified providing the molecular units are sufficiently small. Since $\sigma' \simeq 100$Å^2, we may assume a radius for a molecular unit of about 5Å and a nuclear separation between surface oxygen species on adjacent molecular units of about 2Å. The ratio of the two field terms (1), $\mathcal{E}_{+r}$ and $\mathcal{E}_{-r}$, should then be given approximately by $(\mathcal{E}_{+r}/\mathcal{E}_{-r}) \sim (5 + 2)^2/5^2 \simeq 2$. Therefore for $\kappa_{+r} \simeq 10^6$ (the value consistent with the experimental data reported below), $\kappa_{-r} \sim (10^6)^{1/2} = 10^3$ so that $\kappa_{+r}/\kappa_{-r} \sim 10^3$.

Returning to Eq. [9] to [11], we can write

$$dE/dx = (y - 1/y)Zen_\infty/\epsilon \quad [12]$$

where $y = p_{o\infty}/p_o$ and $p_{o\infty}$ is the value of p_o beyond the space charge zone. Since we shall consider only steady-state conditions y is given by

$$y = \frac{\exp\left[E_\infty\mu_s^*(1 - E_\infty\mu_s^*/C\phi)/kT\right]}{\exp\left[E\mu_s^*(1 - E\mu_s^*/C\phi)/kT\right]}$$

or

$$y = \exp\left[\bar{\beta}_s(E_\infty - E)\right] \quad [13]$$

where

$$\bar{\beta}_s = \frac{\mu_s^*}{kT}\left[1 - \frac{(E_\infty + E)\mu_s^*}{C\phi}\right]$$

and E_∞ is the field beyond the space charge zone, $\bar{\beta}_s$ is the steady-state reciprocal Tafel slope for thick films (*i.e.*, thicker than the space charge zone) measured at a field strength $(E_\infty + E)/2$ (see Eq. [3]). Since the small variation in the Tafel slope with field strength is only just detectable, taking $\bar{\beta}_s$ independent of field will be a satisfactory approximation for E close to E_∞.

Using the above expression for y and making the approximation that $\bar{\beta}_s$ is constant, Eq. [12] can be written

$$dy/dS \simeq (1 - y^2)/2 \quad [14]$$

where

$$S = (2\bar{\beta}_s Zen_x/\mathcal{E})x$$

Integrating this equation we obtain

$$\ln[(1 + y)/(1 - y)] = S + S_o \quad [15]$$

where S_o is the integration constant, so that a plot of $\ln[(1 + y)/(1 - y)]$ *vs.* distance from the appropriate interface should yield a straight line of slope $(2\bar{\beta}_s Zen_\infty/\mathcal{E})$. The space charge data previously published for aluminum (34) is plotted in Fig. 5 according to Eq. [15]. Differential field strengths as a function of charge passed were calculated from measurements of the time derivative of the anodic overpotentials as a function of charge passed. Details of the experimental procedure and assumptions involved in interpreting these data can be found in the original paper. However, it is worth pointing out that the assumptions are consistent with the present model.

As can be seen, the data fall on an excellent straight line. In the original paper it was shown that the slope of such plots was independent of current density, a result in conflict with the basic postulate of the high field Frenkel defect model and probably in conflict with any model which predicts a significant dependence of the bulk defect concentration on current density. Such a result, however, is in accord with the predictions based on the present model.

The slope of the graph was found to be $1.0_4 \times 10^2$ coulomb^{-1}, which for an oxide density of 3.2 g/cm^3 (35) corresponds to $1.8_6 \times 10^6$ cm^{-1}. Comparing this with the theoretical slope and setting $\bar{\beta}_s = 4.8 \times 10^{-6}$ cm/v (35), $\mathcal{E} = K_s\mathcal{E}_o \simeq (\beta_s/\beta_1)K_1\mathcal{E}_o \simeq 25.8\,\mathcal{E}_o$ (27), and $Z = 2$, we obtain $n_\infty = 1.4 \times 10^{18}$ cm^{-3}. Estimating n_o as follows: $n_o \simeq (\sigma')^{-3/2} \simeq 1.3 \times 10^{21}$ cm^{-3}, we have $n_\infty/n_o \simeq 10^{-3}$, a reasonable result.

We can obtain an estimate of $\mathcal{E}_r = \mathcal{E}$ in the following manner. From Eq. [10], $\kappa = (n_o/n_\infty)^2/f \simeq 10^6$. From Eq. [12], [15], [16], and [17] of the previous paper, it can be shown that

$$\ln\kappa \simeq \frac{\mathcal{E}\mu^*}{kT}\left[1 - \frac{2E_e\mu^*}{C\phi}\left(1 - \frac{4\mathcal{E}\mu^*}{C\phi}\right)\right] \quad [16]$$

where terms of the order of $(\mathcal{E}\mu^*/C\phi)^2$ have been neglected in comparison with unity. Assuming steady-state conditions and setting $(1 + \delta\chi_1) \simeq \delta K_1$ Eq. [16] can be written

$$\ln\kappa \simeq \frac{\mathcal{E}\beta_1}{\delta K_1} + \frac{8E\mu_s^*}{K_1^2kT}\left(\frac{\mathcal{E}\mu_1^*}{\delta C\phi}\right)^2 \quad [17]$$

where the term in $\mathcal{E}^2$ is fairly small compared to that in $\mathcal{E}$. Using previously reported values (*i.e.*, $\mu_s^* \simeq 23.5$ eÅ (15), $C\phi \simeq 7.8$ ev (15), $\mu_1^* \simeq 7.8$ eÅ, $K_1 \simeq 8.8_5$, and setting $E \simeq 8.5 \times 10^6$ v/cm. and $\kappa \simeq 10^6$, we calculate $\mathcal{E}/\delta \simeq 5 \times 10^7$ v/cm. (From this value, $\mathcal{E}\mu^*/C\phi \simeq \mathcal{E}\mu_1^*/\delta K_1 C\phi = 0.07$, a result consistent with the approximation made, *i.e.*, $(\mathcal{E}\mu^*/C\phi)^2 << 1$.) The value of $\mathcal{E}$ estimated in this way appears to be of the correct order, although a reliable independent estimate based on electrostatic considerations is difficult to make.

Summary

In the previous sections, selected data from the literature have been examined in the light of the newly proposed theory. The theory has by no means been applied, however, to the majority of the vast amount of data available in this field, an undertaking which lies outside the scope of the present paper. The principal features of the steady-state and transient behavior of electrodes formed by anodic oxidation of Ta, Al, Nb, and Bi have been examined and found to be in excellent accord with the theory. Specifically, the present theory is the only one to provide a reasonable explanation for: (*a*) the transport number data (Ta, Al); (*b*) the correlation between the field dependence of the transient and steady-state Tafel slopes (Ta, Al); (*c*) the correlation between the transient charge-activation distance product and the dielectric constant (Ta, Nb, Al, Bi); and (*d*) the form of constant field transients (Al, Ta). In addition, the theory provides a quantitative interpretation of space charge phenomena for thin films (Al). Again, all of the parameters deduced on the basis of this model are

of precisely the expected magnitude. Even the apparently discrepant behavior of Zr, mentioned earlier, can be reconciled with the present model. In this regard, the most obvious assumption to make is that the metal-oxide interface plays a major role in the conduction process.

Much additional data are required to properly test this theory. At present, however, it is the only quantitative theory which accounts for most of the observed conduction properties for these systems.

Manuscript received Nov. 29, 1964. This paper was presented in part at the Pittsburgh Meeting, April 15-18, 1963.

Any discussion of this paper will appear in a Discussion Section to be published in the June 1966 JOURNAL.

REFERENCES

1. M. J. Dignam, *This Journal*, **112**, 722 (1965).
2. C. P. Bean, J. C. Fisher, and D. A. Vermilyea, *Phys. Rev.*, **101**, 551 (1956).
3. L. Young, "Anodic Oxide Films," Chap. 3, Academic Press, London (1961).
4. L. Young, *Trans. Faraday Soc.*, **55**, 632 (1959).
5. L. Young, *Proc. Roy. Soc. Series A*, **258**, 496 (1960).
6. M. J. Dignam, D. G. W. Goad, and M. Sole, *Can. J. Chem.*, **43**, 800 (1965).
7. L. Young, *Trans. Faraday Soc.*, **52**, 502 (1956).
8. L. Masing and L. Young, *Can. J. Chem.*, **40**, 903 (1962).
9. W. Mizushima, *This Journal*, **108**, 825 (1961).
10. H. G. Draper and P. W. M. Jacobs, *Trans. Faraday Soc.*, **59**, 2888 (1963).
11. J. F. Dewald, *This Journal*, **102**, 1 (1955).
12. L. Young, *Can. J. Chem.*, **37**, 276 (1959).
13. A. R. Bray, P. W. M. Jacobs, and L. Young, *Proc. Phys. Soc.*, **71**, 405 (1958).
14. L. Young, *Trans. Faraday Soc.*, **52**, 515 (1956).
15. M. J. Dignam, *Can. J. Chem.*, **42**, 1155 (1964).
16. L. Young, *This Journal*, **110**, 589 (1963).
17. N. Cabrera and N. F. Mott, *Rept. Progr. Phys.*, **12**, 163 (1949).
18. E. J. W. Verwey, *Physica*, **2**, 1059 (1935).
19. R. J. Maurer, *J. Chem. Phys.*, **9**, 579 (1941).
20. L. Young, *Trans. Faraday Soc.*, **50**, 159 (1954).
21. J. A. Davies, J. P. S. Pringle, R. L. Graham, and F. Brown, *This Journal*, **109**, 999 (1962).
22. J. A. Davies and B. Domeij, *ibid.*, **110**, 849 (1963).
23. J. A. Davies, Private communication.
24. P. Verkerk, P. Winkel, and D. G. Groot, *Philips Research Repts.*, **13**, 506 (1958).
25. G. Amsel and D. Samuel, *J. Phys. Chem. Solids*, **23**, 1707 (1962).
26. L. Young, *Proc. Roy. Soc. Series A*, **263**, 395 (1961).
27. M. J. Dignam and P. J. Ryan, In preparation.
28. L. Young, *Proc. Roy Soc.*, **A244**, 41 (1958).
29. L. Young, *Can. J. Chem.*, **38**, 1141 (1960).
30. D. A. Vermilyea, *This Journal*, **104**, 427 (1957).
31. L. Young, "Anodic Oxide Films," p. 186, Academic Press, London (1961).
32. W. M. Latimer, "The Oxidation States of the Elements and their Potentials in Aqueous Solutions," Prentice-Hall, Inc., New York (1952).
33. A. F. Wells, "Structural Inorganic Chemistry," 2nd ed., p. 37, Oxford University Press (1952).
34. M. J. Dignam and P. J. Ryan, *Can. J. Chem.*, **41**, 3108 (1963).
35. W. J. Bernard and J. W. Cook, *This Journal*, **106**, 643 (1959).
36. L. Young, "Anodic Oxide Films," Chap. 11, Academic Press, London (1961).

A Method for the Dynamic Measurement of Capacity at Electrode Interfaces

C. C. Krischer and R. A. Osteryoung

North American Aviation Science Center, Thousand Oaks, California

ABSTRACT

A potentiostatic method to permit determination of double layer capacity of electrodes under dynamic conditions has been developed. Small potential pulses are superimposed on a d-c sweep and the capacity is determined from the magnitude of current changes observed at the initiation and cessation of the pulse. Further, a method utilizing a transistor is described which permits rapid switching of a potentiostat from galvanostatic to potentiostatic operation.

Although several methods for the dynamic measurement of double-layer capacity have been reported, they appear to suffer from certain disadvantages. Breiter (1) utilized an a-c impedance technique to obtain qualitative curves at solid electrodes.

Boddy and Sundburg (2) developed a simple method of measuring the capacity continuously and rapidly. The authors used a current sweep which had superimposed short duration current pulses. The analysis of the resulting potential-time transients, properly displayed on a cathode ray tube, gave the value of the capacity over the whole length of the sweep. The disadvantage of this method is that the potential change, dE/dt, is not constant with time for a linear current sweep. dE/dt varies depending on the current-potential characteristic of the electrode. To keep dE/dt approximately constant these authors used a nonlinear sweep.

A potentiostatic method would be more convenient and is reported here. A linear d-c sweep voltage is applied directly to the electrode via a potentiostat. Superimposed on this potentiostatic sweep are low amplitude potential pulses. The pulse is short compared to the RC time constant of the electrode network.

In the first part of this paper it is shown how the electrode capacity can be calculated from the current transient that is caused by a potential pulse.

The advantage of using a linear potential sweep rather than a linear current sweep is quite evident if one recalls that the differential capacity curve that one is interested in lies in a potential region where dE/di of the indicator electrode has a maximum. Employing a galvanostatic method, the potential region of interest is passed rapidly if a linear current sweep is used.

In carrying out our work on germanium electrodes (3) we desired and devised a method to permit rapid switching of the cell from a potentiostatic mode to a galvanostatic mode of operation which is reported in the second part of this paper.

Dynamic Potentiostatic Measurement of Electrode Capacity

The electrical equivalent of the impedance of an indicator electrode in the potentiostatic circuit is shown in Fig. 1. It consists of a resistor, R, representing all series resistances in the circuit such as uncompensated resistance in the electrolyte, in the indicator electrode, etc., a resistor, R_p, representing the

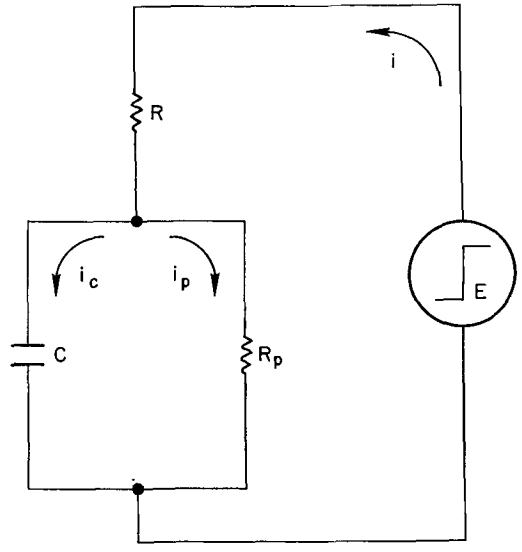

Fig. 1. Electrical equivalent circuit for the application of a potential step (potentiostatic operation) at a metal (or semiconductor) electrolyte interface.

impedance of the faradaic reaction and a capacitor, C, the capacitance of the double layer. [In the case of a germanium electrode, C represents the capacitance due to a space charge layer within the germanium (4).] The potentiostat is a potential source of effectively zero internal impedance. If it delivers a positive potential step of the magnitude, E, a current, i, will flow through the circuit. At $t=0$ the capacitor acts as a short circuit of R_p and an initial current

$$i_o = E/R \qquad [1]$$

will flow. The charging current i_c decays exponentially

$$i_c = \frac{E}{R}\exp\left(-\frac{t}{R'C}\right) \qquad [2]$$

where $R' = \dfrac{RR_p}{R+R_p}$. Simultaneously a current i_p starts to build up exponentially

$$i_p = \frac{E}{R+R_p}\left[1-\exp\left(-\frac{t}{R'C}\right)\right] \qquad [3]$$

The total current i is the sum of the two

$$i = i_c + i_p = \frac{E}{R}\exp\left(-\frac{t}{R'C}\right) + \frac{E}{R+R_p}\left[1-\exp\left(-\frac{t}{R'C}\right)\right] \qquad [4]$$

The initial slope of this curve is given by

$$\left(\frac{di}{dt}\right)_{t\to 0} = -\frac{E}{R^2C} \qquad [5]$$

At $t = \Delta t$ a negative step of the same amplitude, $-E$, is delivered (the sequence of the two steps is a rectangular pulse, Δt is the pulse width). At the beginning of the negative step the current changes by $-E/R$, followed by an exponential current-time behavior analogous to the one expressed in Eq. [4]. If the pulse width

$$\Delta t << R'C \qquad [6]$$

Eq. [5] can be approximated by

$$\Delta i = -\frac{\Delta t E}{CR^2} \qquad [7]$$

where Δi is the change in current during the time interval of the pulse. In this equation C and R are unknown; but according to Eq. [1], $R = E/i_o$ so the unknown capacity C becomes

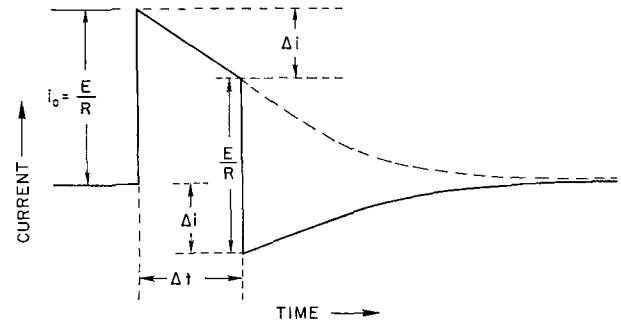

Fig. 2. Schematic of the current time behavior that results by application of a potential pulse in the circuit of Fig. 1 for $R_p >> R$. The line from which i_o rises represents the d-c level.

$$C = \frac{\Delta t}{E}\frac{i_o^2}{\Delta i} \qquad [8]$$

From this relationship it is seen that one can calculate C if at a known pulse width Δt and amplitude E the quantities i_o and Δi are measured. Figure 2 represents a schematic of the current transient that is caused by a potential pulse. The dashed line indicates the current decay that would occur if the negative step were missing. Note that the quantities i_o and Δi which are needed for the calculation of the capacity are the maximum positive and negative amplitudes of the transient.

In order to measure the capacity potential curve in a dynamic manner a single (or repetitive) linear potential sweep with superimposed short duration pulses is applied to the electrode. The duration of the pulses has to be sufficiently short so that the sweep d-c level may be considered constant over the interval of the pulse. The current transient which results as a consequence of this polarization is characteristic for the electrode impedance-potential curve. Figure 3 gives an example. The line with maximum intensity represents the d-c current through R_p of Fig. 1. This trace corresponds to the base line from which i_o rises, see Fig. 2. As the potential sweep is linear with time, this curve represents a conventional current potential plot. The envelope curves of low intensity above and below the most intense line are caused by the current excursions due to the superimposed pulses. Since there are 250 pulses of 3 μsec duration per horizontal division in Fig. 3, the current transients, one of which is

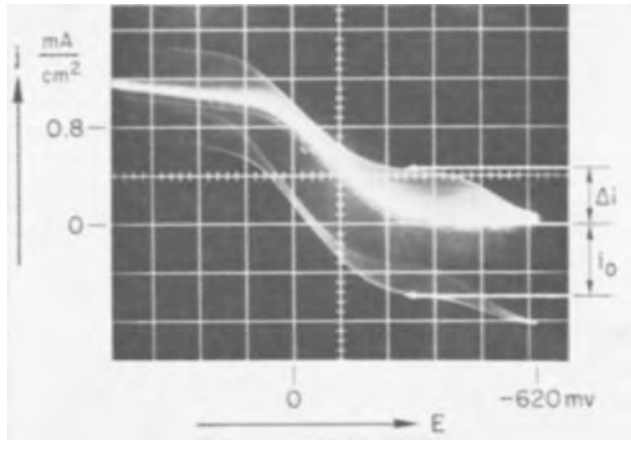

Fig. 3. Example of a current potential curve obtained potentiostatically with a single d-c sweep of 0.24 v/sec which had superimposed negative pulses of 100 mv amplitude and 3 μsec width. Repetition rate of the square wave pulse generator: 500 sec^{-1}. Electrode: 10 ohm cm n-Ge. Electrolyte 0.5M $NaClO_4$ 0.1M buffer pH 7, unstirred. The intense line (d-c voltage curve) within the trace became wider during the course of reproduction; it should be as narrow as in the left side of the figure. The arrows indicate typical current-transient amplitudes, see Fig. 2 and text.

shown in Fig. 2, merge together to yield an area of low intensity compared to the intensity of the main current-potential curve resulting from the voltage sweep. If the intensity of the oscilloscope beam is sufficient to permit observation of the current transients resulting from the voltage pulses, the main current potential trace from the voltage sweep is brighter and diffuse because of its longer duration relative to the transients. This problem, which affects the accuracy of the measurement, may be partially solved by intensifying the beam during appropriate portions of the trace. The deviations on either side of the d-c current trace directly represent the current amplitudes i_o and Δi, compare Fig. 2 and 3. With Eq. [8] one can then calculate C at any desired potential. From Fig. 3 it is seen that the condition $\Delta i << i_o$ is in most potential regions not fulfilled. Therefore, the exponential is at $t = \Delta t$ no longer near linear, condition [6] is not strictly fulfilled. Equation [8] then yields capacity values which are larger than in the case of validity of condition [6]. This error is however partly compensated by another effect. The rise time of the potentiostat tends to round off edges of the current transient: i_o will be measured smaller than it should be. These two errors tend to cancel each other. We found the accuracy to be within ±20%. The systematic error for one particular system will, however, be constant so that relative changes are easily detectable. In ref. (3) capacity potential curves are reported which are in good agreement with the calculated curves.

Intermittent Galvanostatic Switching of a Potentiostat

For the purpose of studying the surface of electrodes it may be desirable to polarize the electrode by a known amount of charge prior to the measurement of the characteristic. Most conveniently the charging is carried out under constant current conditions for a given time interval, *i.e.*, in a galvanostatic mode of operation. In order to minimize changes of the resulting state of the electrode before the capacity measurement is initiated, rapid switching to the potential where the capacity measuring sweep starts is required. A versatile, yet simple circuit is described which meets this requirement.

A transistor is placed in series with the cell. A voltage, E, is applied from the potentiostat to cause a potential drop, E_{trans}, across the transistor sufficient to drive it well into its limiting current region (reverse bias), (see Fig. 4). This results in the current through the cell being controlled by the limiting current characteristics of the transistor. The limiting current can be selected by appropriate transistor base current input (see Fig. 5). Changes in the voltage across the cell have little effect on the current through the system provided that such changes occur within the limiting current region of the transistor. When the voltage, E, is such as to result in a potential drop across the transistor which brings it into the forward biased region, there is little potential drop across the transistor. The current through the transistor can change appreciably with little change in potential drop across the transistor.[1]

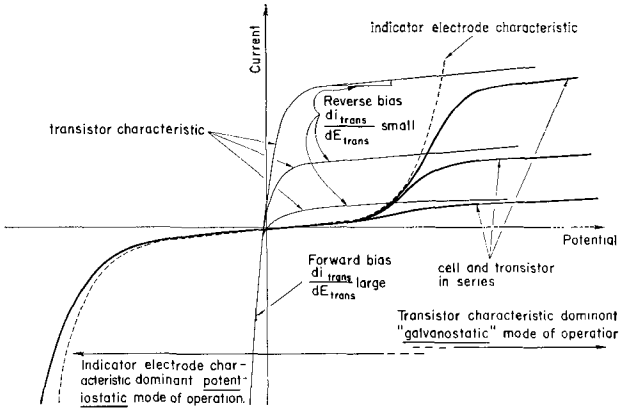

Fig. 4. Current potential behavior of a series combination of cell and transistor. The voltage drops as a function current are: dashed, of the indicator electrode; thin, of the transistor with three different base currents; and bold, of the cell and the transistor with three different base currents in series.

It was found (3) that in steep portions of the transistor characteristic (forward bias) the transistor capacity was much larger than the capacity of a germanium electrode in the flat part of its current potential curve. In this potential region, in which the potentiostatic mode prevails, the transistor capacity does not introduce a significant error in the measurement of the electrode capacity. Figure 4 represents a schematic construction of the current potential curves that result if a transistor with three different base currents is placed in series with an electrode which has an activation controlled current-potential characteristic. It is seen that the introduction of the transistor yields current clamping in one direction. It is in the potential region of small currents where the differential capacity curve is measured potentiostatically.

To summarize, placing the transistor in series with the indicator electrode serves the purpose of controlling the current through the cell. This is accomplished by applying a voltage that brings the transistor into reverse bias. The transistor characteristic then dominates. Under forward bias of the transistor, the indicator electrode characteristic prevails, and the transistor introduces only a slight perturbation on the indicator electrode characteristic. The base current, which has to be supplied by a current source other than the potentiostat, has two functions: (i) it determines the limiting current during the galvanostatic period, and (ii) it diminishes the interference of the transistor during the potentiostatic period. The perturbation of the indicator electrode characteristic during this period may be kept small by injecting a large base current, top curve in Fig. 4.

The design of the electrical circuit has to fulfill two requirements: short rise time of the potentiostat and versatility in the input system. The latter is needed in order to provide well-defined galvanostatic prepolarization followed by potentiostatic capacity measurement. We therefore employed the Wenking potentiostat in the adder configuration (6) rather than in the conventional differential mode. An oscilloscope with a delayed sweep capability is a convenient source of prepolarizing pulse and measuring sweep. The time base of such oscilloscopes may deliver two sawtooth and square wave voltages. One couple of sawtooth and square wave voltages corresponds to the normal or delaying sweep, the other to the delayed sweep. The voltages are of fixed amplitude and polarity. Attenuation and in some cases inversion is needed. The durations of the wave forms are calibrated and variable within a wide range. The beginning of the delayed sweep with respect to the normal sweep (and normal gate) is determined by the setting of the calibrated delay time potentiometer.

The details of the experimental arrangement are shown in Fig. 5. The response of the circuit is demonstrated in Fig. 6. It represents a photograph of a typical current transient that is caused by a rectangular potential pulse. The rise time is a little less than one μsec.

[1] Since the transistor is in series with the cell,

$$i_{trans} = i_{cell} = i(E_{trans})$$

and

$$E_{trans} = E - E_{cell}$$

$$\frac{di}{dE_{cell}} = \frac{di_{trans}}{dE_{trans}} \cdot \frac{dE_{trans}}{dE_{cell}} = -\frac{di_{trans}}{dE_{trans}}$$

$$di = -\frac{di_{trans}}{dE_{trans}} \cdot dE_{cell}$$

In the region of reverse bias, di_{trans}/dE_{trans} is very small (*ca.* 10^{-6} ohm^{-1}) so that a change in the cell voltage does not change i. In the forward bias region di_{trans}/dE_{trans} is very large, there is very little potential drop across the transistor, and dE_{cell} is unaffected by changes in i.

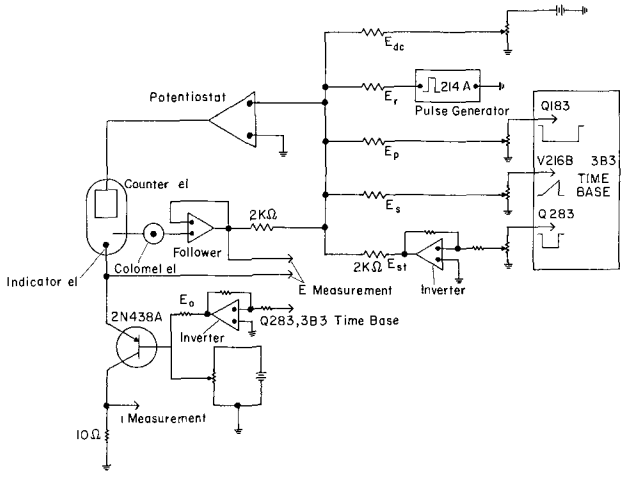

Fig. 5. Schematic representation of the electrical circuit for galvanostatic prepolarization followed by rapid potentiostatic measurement of the current and capacity-potential curve. The amplifiers are Philbrick, type P65A. The 3B3 time base is a Tektronix module, the numbers refer to the switching diagram of the time base manual. The pulse generator is a Hewlett-Packard product, type 214A. The potentiostat is a Wenking model.

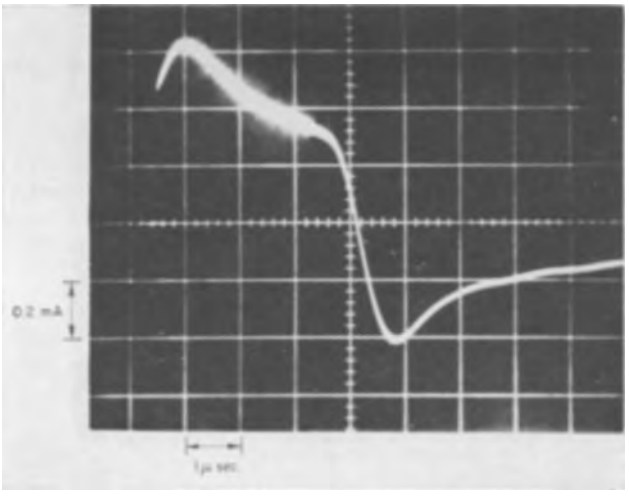

Fig. 6. Typical current time behavior that results upon application of a rectangular potential pulse to the following, not standard circuit elements: 150 ohm resistance in series with a 4 x 10^{-8}F capacitor which has a 10K ohm resistor in parallel. Pulse amplitude was 75 mv, duration 3 μsec. From the figure the series resistor is calculated to 125 ohm (instead of 150) and the capacitor to 3.6 10^{-8}F (instead of 4.10^{-8}F). The *R'C* network is similar to a 1 cm² Ge-electrolyte interface at the potential of the capacity minimum.

For studies of the germanium-electrolyte interface we were interested in pretreating the electrode with known amounts of cathodic charge prior to the impedance measurement. Therefore, in the circuit of Fig. 5 a n-p-n transistor was used to limit the cathodic current. For anodic pretreatment a p-n-p transistor would be chosen. Both current directions can also be limited if two transistors, n-p-n and p-n-p, with appropriate base currents, are placed in series.

Three waveforms of the timebase combined with two other voltage sources are used. The task of the individual potential sources is as follows:

1. Prior to the polarizing cycle the potential has to be set at a d-c level, $E_{d\text{-}c}$, which yields a reproducible steady state of the surface.

2. For the capacity measurements free running short duration rectangular pulses are needed. We used a Hewlett Packard 214A pulse generator.

3. To drive the transistor into its limiting current region in order to prepolarize, a high amplitude prepolarizing pulse, E_p, is applied. We chose the square wave of the normal or delaying sweep of the time base.

4. Furthermore, the measuring linear sweep, E_s, is needed. The sawtooth of the delayed sweep is used. The delay time of this delayed sweep with respect to the beginning of the normal sweep thereby determines the duration of the prepolarizing pulse.

5. In order to initiate the sweep at any desired potential, an additional pulse, E_{st} is required. Without this pulse the linear sweep would start in the limiting current region. The changeover from galvanostatic to potentiostatic mode would be gradual instead of abrupt. The gate of the delayed sweep which occurs simultaneously with the sawtooth can be used for E_{st} advantageously.

As indicated in Fig. 5, this latter pulse source, *i.e.*, the timebase, is also utilized to increase the transistor base current. Thereby a transistor characteristic is selected which causes the least interference of the indicator electrode characteristic at small current densities, compare Fig. 4. For further experimental details see Fig. 5 and its legend.

Figure 7 is a schematic representation of the waveform that appears at the output of the potentiostat by application of voltages 1-5 as listed above.

Listed below are some polarization cycles that can easily be obtained with the circuit of Fig. 5.

Prepolarization, anodic sweep (PA).—The cycle of Fig. 7 is described above in detail in which the voltage is increasing with time. This sweep will be called an anodic sweep. Decreasing voltage with time is called a cathodic sweep.

Prepolarization, cathodic sweep (PC).—If the same potential region as in Fig. 7 should be measured with a cathodic sweep, the amplitude of E_{st} is increased by the amount of E_s and E_s itself is inverted.

Anodic sweep (A).—If anodic sweep without galvanostatic prepolarization is desired one can (i) make the transistor limiting current very small by omitting the base current and making the delay time $\sim$ 0 or (ii) E_p is omitted and an inverted gate, $-E_{st}$, brings the sweep to a potential, $E_{d\text{-}c} - E_{st}$, which is desired as the sweep starting potential.

Cathodic sweep (C).—If cathodic sweep and no prepolarization is desired, the cathodic sweep is simply initiated at $E_{d\text{-}c}$. E_p and E_{st} are omitted.

Although our original interest in devising this procedure was focused on the studies of the germanium-electrolyte interface the technique is applicable to other electrodes such as metal electrodes and the dropping mercury electrode. For example, we have examined the differential capacity at a dropping mercury electrode in various electrolytes by this method and obtained agreement with literature results. Because a dropping mercury electrode has a longer time constant *R'C* than a germanium interface, the pulse dura-

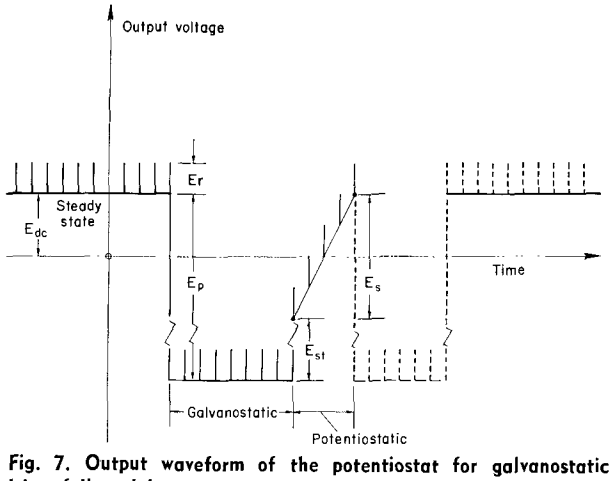

Fig. 7. Output waveform of the potentiostat for galvanostatic pulsing followed by a potentiostatic sweep. The voltages are with reference to Fig. 5. The dashed part following the sweep represents the termination of the galvanostatic pulse.

tion was chosen longer than in the case of germanium. Adjusting the pulse width to the particular RC network of the electrochemical system is necessary to obtain reasonable accuracy.

For low values of the time constant $R'C$ of the indicator electrode the method may be used up to high sweep rates $v = dE/dt$. At germanium electrodes sweep rates up to 300 v/sec were employed (3). For convenience we chose a combination of square wave and sawtooth voltages for the prepolarization and potential variation. The circuit described above allows, however, the use of other wave forms as well, such as a triangular or a sine wave. An application of this method to the study of germanium electrodes will be reported (3).

Summary

A dynamic capacity measuring method is devised. It is based on the analysis of current transients that are caused by short duration potential pulses. The dynamic variation of the potential is achieved with a linear potential sweep on which the pulses are superimposed. An oscilloscope serves as a sweep generator. The charge flow during the measurement of the capacity potential curve may be kept very small (in the order of a few μa sec/cm^2) if appropriate values of the sweep starting potential and the sweep rate $v = dE/dt$ are chosen.

This method may be employed advantageously in connection with a novel technique of switching the cell from the normal potentiostatic into a galvanostatic mode, as is also described in this paper. A transistor, placed in series with the indicator electrode, represents the fast switching element. The galvanostatic mode serves to charge the electrode surface to a known extent. The same oscilloscope (with delayed sweep capability) that delivers the sweep controls also the prepolarization time. With the method described above one is able to measure the electrochemical characteristic of a prepolarized electrode, since its state remains practically undisturbed in the course of the measurement. The galvanostatic prepolarization may be chosen in the cathodic, anodic or both current directions.

Manuscript received Jan. 25, 1965.

Any discussion of this paper will appear in a Discussion Section to be published in the June 1966 JOURNAL.

REFERENCES

1. M. W. Breiter, *J. Electroanal. Chem.*, **7**, 38 (1964).
2. P. J. Boddy and W. J. Sundburg, *This Journal*, **110**, 1170 (1963).
3. C. C. Krischer and R. A. Osteryoung, *ibid.*, To be published.
4. K. Bohnenkamp and H. J. Engell, *Z. Electrochem.*, **61**, 1184 (1957).
5. W. Guggenbuhl, M. J. O. Strutt, and W. Wunderlin, "Halbleiter Bauelemente," I, Birkhauser Verlag, Basel, Stuttgart (1962).
6. George Lauer, Helmar Schlein, and R. A. Osteryoung, *Anal. Chem.*, **35**, 1789 (1963).

The Effect of Dislocations and Orientation on the Electrical Double Layer Capacity of Silver Surfaces

R. G. Rein, C. M. Sliepcevich, and R. D. Daniels

University of Oklahoma, Norman, Oklahoma

ABSTRACT

This study was undertaken in an attempt to obtain a better understanding of the effects of dislocations, crystal orientation, and surface imperfections on the catalytic activity of metals. Relative surface areas of pure silver crystals were determined from measurements of double layer capacities for {110}, {111}, and {211} planes with dislocation densities ranging from 10^6 to 10^8 cm^{-2}. Care was taken to insure that clean, oxide-free surfaces were used during measurements. Although it was found that the relative areas of {110} and {211} planes were proportional to the log of dislocation density, the relative area of {111} planes was found to be independent of dislocation density. The behavior of the double layer capacity as influenced by abrasion, cracks, notches, grain boundaries, and dislocations is discussed in terms of changes in physical area and changes in effective area resulting from additional dislocations. Models of metal surfaces and knowledge about the structure of the double layer are inadequate, at present, to allow positive conclusions to be drawn about the effect of dislocations on double layer capacity. The double layer capacity of mercury in 0.2N H_2SO_4 was experimentally determined to be 19.4 $\pm$ 2.2 μf/cm^2 which agrees favorably with values reported recently.

Crystal imperfections and surface orientation, particle geometry and surface irregularities are factors which can influence the activity of catalysts (1-3). The effectiveness of a metallic catalyst has been found to be dependent on the crystal face exposed to the reactants (4-8). In addition, Liedheiser and Gwathmey have found that {100} planes of copper become roughened while catalyzing the reaction of oxygen and hydrogen; whereas {111} planes remained smooth (6). Introducing imperfections into a crystal has also been reported to influence catalytic activity (9-12). Barnes and Mazey (13) show a change in surface area with irradiation, a common method for disturbing a metal lattice.

Although the BET area has been used frequently in correlating kinetic data for catalytic reactions, in most cases the superficial area, or some equivalent, is used without giving any consideration to surface conditions. Since it is possible that significant information can be masked if differences in surface area between crystal planes and differences in area due to crystal imperfections are not considered, this investigation was undertaken to determine changes in area as influenced by dislocation density and crystal orientation.

The many methods for determining surface areas have been summarized by Adamson (14), Brunauer (15), and Gregg (16). Of the methods mentioned, only the various adsorption methods, such as the well-known BET technique and the double layer capacity method are generally applicable. Gas adsorption techniques are not satisfactory in the case of metals because of their small area to volume ratio. The relative decrease in pressure or volume of the adsorbed gas is too small, for a reasonable size sample, to allow accurate analysis. For this reason the double layer capacity method first proposed by Bowden and Rideal (17) was used to determine the effective surface areas of the silver crystals employed in this study.

Throughout this paper three different area terms will be used: (*a*) superficial area, which is determined by the gross dimensions of the sample; (*b*) physical

area, which takes into account all mechanical surface irregularities such as roughness, notches, cracks, misorientation at grain boundaries, regardless of the scale of dimensions; and (c) effective area, which is determined by the double layer capacity measurement and which may be influenced both by the physical area as defined above and by energy factors associated with crystal surface orientation and crystal defects.

The double layer capacity method as originally conceived was based on the assumption that the double layer capacities of metal electrodes with equal physical areas are the same and independent of the metal being investigated. However, it is conceivable that the double layer capacity measurement considers not only the physical area but also area affects arising from crystal orientation and defects. Consequently, an attempt was made to isolate these latter factors by taking special precautions to maintain a constant physical area while varying only the dislocation density and crystal orientation.

The measured double layer capacity is given by

$$\left(\frac{\partial \Gamma}{\partial E}\right)_{T,\,P,\,\text{etc.}} = C \text{ (at time} = 0) \qquad [1]$$

where Γ is the charge in coulombs on the double layer per unit superficial area, E is the potential in volts across the double layer, and C is the differential capacity applicable for short durations of time (time < 0.10 sec) in farads per unit superficial area. The units of superficial area are hereafter denoted by an asterisk $(cm^2)^*$. Thus, $\partial\Gamma/\partial E$ represents the instantaneous measured value of the capacity at time equal zero.

If the superficial area of a metal and the effective area for capacity determination are identical, $\partial\Gamma/\partial E = C'$ will have the units of (farads/effective area in cm^2). The assumption is made for a mercury electrode that the effective area for capacity determinations is identical to its superficial area. Therefore the capacity of any metal electrode, C, divided by the capacity of a mercury electrode, C', gives the effective area of the metal electrode relative to its superficial area.

$$CAR = \frac{C}{C'}\,\frac{(cm^2)}{(cm^2)^*} \qquad [2]$$

The abbreviation, *CAR*, refers to the capacity area ratio and will be used throughout the paper. It is an indication of the effective area.

In these measurements care must be taken to eliminate concentration and ohmic polarization, which would distort the value of the potential applicable to the double layer. For reproducibility and accuracy of measurement, care must also be exercised to eliminate impurities on the electrode surface and in the electrolytic solution as impurities also tend to affect the capacity of the double layer (14, 17, 18).

Procedure

Apparatus and General Considerations

The effective areas of silver specimens were measured by the double layer capacity first proposed by Bowden and Rideal (17). The electrical circuit is shown in Fig. 1.

The oscilloscope (O) was used in conjunction with an oscilloscope camera to record the potential E (t) of the silver electrode. The integrated current through the cell Γ (t) was obtained from readings on the recorder (R) of the voltage across the capacitor. The output of the signal generator (SG) was a square wave of frequency 0.05 cps and supplied the polarizing current for the cell. The steady-state current density through the cell was 10^{-4}-10^{-3} amp/$(cm^2)^*$.

Since the signal generator output was from plus volts to minus volts and the desired output was from zero to plus volts, the circuit SGB was used to bias out the undesired negative output.

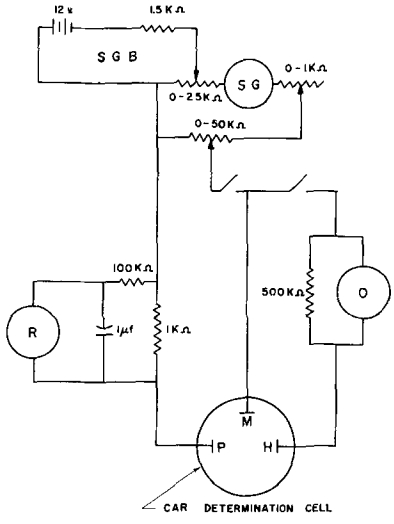

Fig. 1. Electrical circuit

(H) is a standard hydrogen electrode, (P) a platinum electrode, and (M) the metal electrode whose effective area is being determined.

The effects of ohmic polarization were minimized by putting the electrodes near each other (at the corners of an equilateral triangle of side 4 cm). Hydrogen bubbling from the hydrogen electrode agitated the solution to eliminate concentration polarization.

The electrolyte was $0.2N$ H_2SO_4 which had been freed from dissolved oxygen by heating under a slight vacuum for 1-2 hr and cooled to room temperature in a hydrogen atmosphere.

Although Bowden and Rideal (17) state that the determinations may be made either during polarization or depolarization of the double layer, the larger part of the data were obtained during polarization; however some data, which agreed with that obtained by polarization, were obtained during depolarization. All data were obtained at temperatures between 75° and 80°F.

Crystal Preparation

The silver single crystals used for effective area determinations were grown in the laboratory (19). The crystals were oriented by the Laue back-reflection x-ray technique and cut with a standard, water-cooled cut-off machine, so as to expose either {211}, {111}, or {110} planes. The desired surfaces were then mechanically polished with successively finer grit polishing disks, the final treatment being with a 600C disk. The crystals were then deformed to introduce a controlled number of dislocations. Two methods of deformation were used: (a) The crystals were bent to a U shape by either a 1.00 or a 4.00 cm radius plunger-die combination (see Fig. 2a); the deforming force was applied normal to the surface whose area was to be measured.

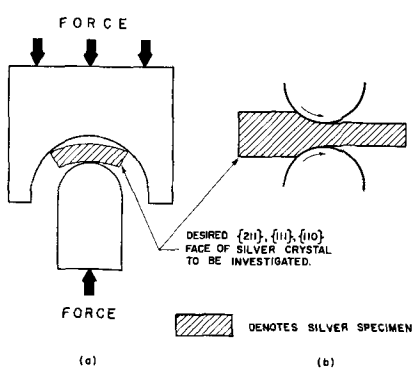

Fig. 2. Methods of crystal deformation

(b) The crystals were cold-rolled to a given reduction; the applied force again was normal to the surface whose area was to be measured (see Fig. 2b).

The crystals, after deformation were electropolished in a 5 w/o (weight per cent) KCN solution. This treatment lasted for 3-6 min at 1-2 amp/cm^2. The electropolished surfaces appeared bright, shiny, and free from microscratches as determined by microscopic examinations at 300X. The surfaces were also strain-free as evidenced by the distinct poles rather than smears obtained on a Laue back-reflection pattern of a sample prepared in this manner.

A thermal-etching technique applicable to silver (19, 20) was used to determine the dislocation density. The samples were annealed at 600°-615°C for 45-90 min in an argon atmosphere, etched 10-15 min in a 10% oxygen-90% argon mixture, and cooled to room temperature in an argon atmosphere. Etch pits were counted at magnifications of 1500-2500X on a metallograph. Figure 3 is representative of the etch pit observations. The macroscopic dimensions of the specimens were then measured with a micrometer and used to calculate the superficial area.

After thermal etching, an electrical lead was connected to the sample by an alligator clip and the sample was mounted in Koldmount. The face which was to be subjected to *CAR* determinations was protected by a strip of fiberglass tape during mounting. After mounting, the tape was removed, and the surface cleaned with methanol to remove traces of adhesive and fingerprints.

To insure the absence of any oxide layer either of two final surface preparations was used: (a) The samples were again electropolished for 15-20 sec, washed with distilled water, and then placed in the *CAR* determination apparatus, a technique found acceptable by Wisdon and Hackerman for iron (21). (b) The samples were subjected to 2-4 hr of electrolytic reduction to reduce any oxide layer (22, 23). For this treatment the sample served as the cathode, oxygen-free 0.2N H_2SO_4 as the electrolyte and platinum as the anode. A steady-state current density was passed through the cell; the range of densities used was between 5-15 μa/cm^2*. After this pretreatment the samples were immediately placed in the *CAR* apparatus. The double layer capacity, and hence the *CAR*, was found to be independent of the two techniques used for final surface preparation.

To isolate the dependence of *CAR* on undesirable effects, the following exceptions were made to the general procedure mentioned: (a) Sample *E*, an undeformed sample: the final polish was with a 240C polishing disk, instead of electropolishing, to determine the effect of scratches on the *CAR*. (b) Sample F, deformed 62% by rolling: it completely recrystallized during the annealing treatment. (c) Samples I and J: the *CAR* was measured after use of these samples as catalysts for the decomposition of formic acid. The surface of sample J was not cleaned prior to the *CAR* tests, while sample I was subjected to 4 hr of electrolytic reduction. (d) Sample K: the thermal etching treatment and determinations of dislocation density were made after the *CAR* tests to minimize possible recrystallization effects.

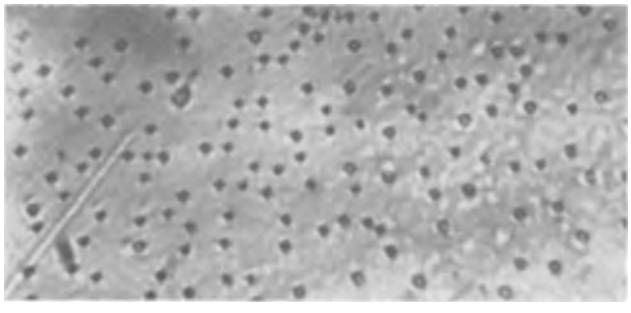

Fig. 3. Etch pits on a {211} plane of silver (2000X and 1.2 x 10^7 dislocations/cm^2).

Table I. Capacity area ratio (*CAR*) Data

Sample	Crystal face exposed	Dislocation density	Double layer capacity f/(cm^2)*	*CAR*	Number of determinations
A	211	3.2×10^6	52.6 ± 1.6	2.71	11
B	211	1.0×10^7	68.5 ± 2.6	3.53	16
C	211	1.7×10^7	67.2 ± 2.3	3.46	19
I[a]	211	3.2×10^6	50.3 ± 1.6	2.59	9
J[b]	211	3.2×10^6	59.6 ± 3.2	3.07	7
S	211	7.3×10^7	73.3 ± 6.2	3.78	14
U	211	1.1×10^7	66.0 ± 2.6	3.40	15
K	110	7.1×10^7	76.9 ± 3.8	3.97	13
L	110	3.2×10^6	56.3 ± 6.4	2.90	13
W	110	1.3×10^7	68.3 ± 3.5	3.52	17
M	111	7.3×10^5	71.2 ± 4.0	3.67	29
N	111	1.3×10^6	69.6 ± 5.9	3.59	24
O	111	3.0×10^6	64.9 ± 3.4	3.34	14
T	111	3.4×10^6	69.0 ± 5.8	3.56	15
V	111	6.0×10^7	71.1 ± 4.5	3.66	9
F[c]	110	1.0×10^8	83.8 ± 2.6	4.22	12
E[d]	211	Scratched	128.1 ± 4.9	6.60	10
Hg	—	—	19.4 ± 2.2	1.00	18

[a] *CAR* determined after sample was used to catalyze the decomposition of formic acid. Surface cleaned prior to determination.
[b] *CAR* determined after sample was used to catalyze the decomposition of formic acid. Surface not cleaned prior to determination.
[c] Sample recrystallized.
[d] Final surface preparation was with 240C polishing disk.

It is possible that the cold work used to introduce dislocations into the specimens could cause recrystallization of the samples during the annealing and thermal etching treatment. The grain boundaries thus formed could also affect the area measurements. To determine the extent of recrystallization, if any, several specimens were etched in an ammonium persulfate-sodium cyanide solution. Sample F (noted above) was the only one which exhibited recrystallization.

To determine the double layer capacity of the mercury, a fresh pool of mercury was placed in a plastic tube; electric contact was made via a copper disk connected to a lead in the bottom of the tube. The tube was immediately placed in the cell and the necessary data were obtained. Sufficient holes and slots were cut in the tube to eliminate the possibility of concentration polarization.

Results

The results of this investigation are shown graphically in Fig. 4-7, and are given in tabular form in

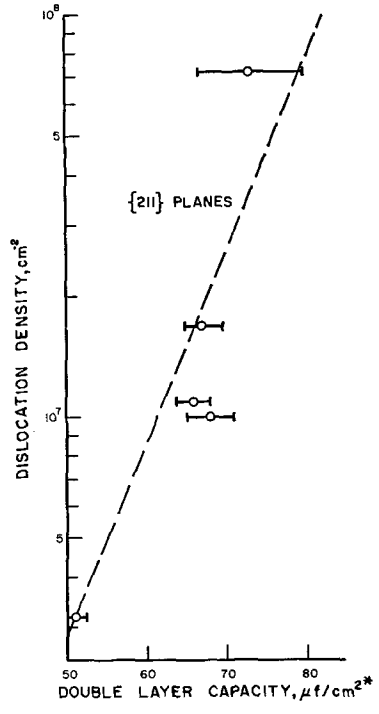

Fig. 4. Dislocation density vs. double layer capacity {211} planes

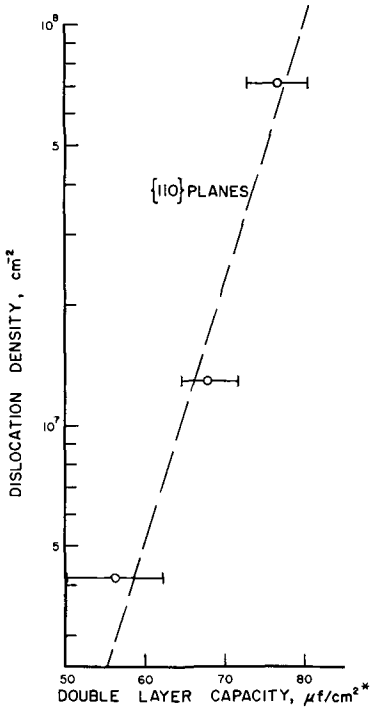

Fig. 5. Dislocation density *vs.* double layer capacity {110} planes

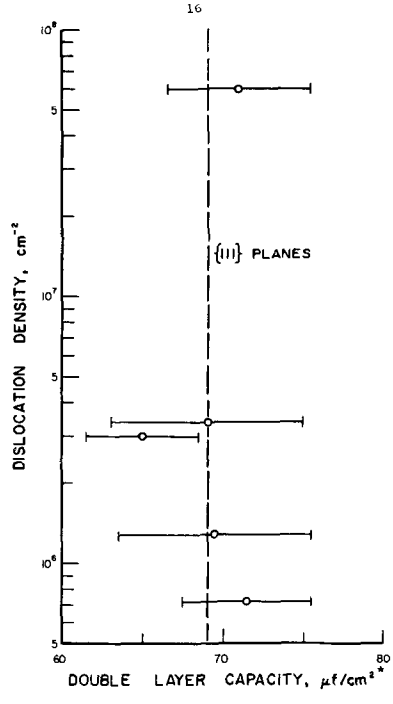

Fig. 6. Dislocation density *vs.* double layer capacity {111} planes

Table I. Since there is no theoretical correlation available, the data are represented by straight lines rather than resorting to curve fitting. Figures 4-6 are plots of log dislocation density in units of surface intersections per square centimeter for various crystal planes *vs.* double layer capacity (within 95% confidence limits). Double layer capacity, as noted earlier, has been assumed to be a measure of the effective area which takes into account both physical area and energy factors. However, since precautions were taken to keep the physical area constant, the changes in double layer capacity are attributed to energy effects arising from changes in crystal surface orientation and dislocation density. In Fig. 7 the previous results are condensed on a single graph to illustrate the influence

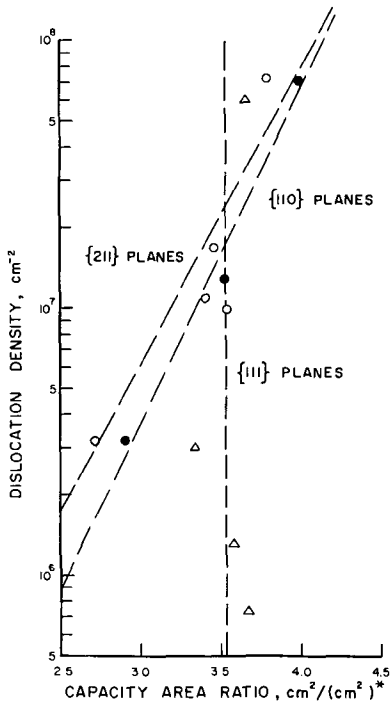

Fig. 7. Dislocation density *vs.* capacity area ratio for various planes: △, values for {111} planes; ○, values for {211} planes; ●, values for {110} planes.

of planar orientation on the effective area. In this figure double layer capacity is converted to *CAR*.

As indicated by Fig. 4-6, the *CAR* of {211} and {110} planes, which are the double layer capacities of these planes divided by that of mercury, appear to be sensitive to changes in dislocation density, while the *CAR* of {111} planes is insensitive to these changes. From Fig. 7, the effective area of {111} planes is about 3½ times the superficial area, while for {211} and {110} planes it changes from approximately 2½ times the superficial area at low dislocation densities to 4 times at higher densities.

In Table I notice that the effective area of sample E is 2½ times as great as that for undeformed, smooth {211} surfaces (samples A and I). This result is to be expected since the final surface preparation of sample E involved polishing with a 240C disk instead of electropolishing.

Comparison of data for samples A and I, with clean surfaces, and sample J, with a contaminated surface, indicates the necessity of clean surfaces.

As mentioned earlier, the *CAR* is merely the double layer capacity of the silver surface divided by that of a mercury surface. The capacity of mercury surfaces was found, within 95% confidence limits, to be 19.4 ± 2.2 μf/cm² (Table I).

Discussion

The value of 19.4 ± 2.2 μf/cm² for the double layer capacity of mercury in $0.2N$ H_2SO_4 obtained in this investigation agrees favorably with other recently determined values (24-27) and serves to confirm the reliability of the results obtained in this study.

Referring again to Table I, sample E was not electropolished after mechanical polishing with a 240C disk. In this case the double layer capacity of the single silver crystal was 128 ± 4.9 μf/(cm²)* or 6½ times that of mercury. It is assumed that this increase in effective area is indicative of an increase in physical area due to surface roughening. A comparable value was given by Bowden and Rideal (17) for a silver specimen which was polished with "flour" sandpaper. The value is 100 ± 10 μf/(cm²)*. The agreement is acceptable considering that the degree of mechanical polishing of the specimen used by Bowden and Rideal

is not accurately known. Furthermore, it is not known whether their specimen was polycrystalline or a single crystal.

In Table I, the double layer capacity for sample F which was electropolished, but was polycrystalline, was found to be 83.8 $\mu f/(cm^2)$*. This value is in the range of the double layer capacity for other polycrystalline metal surfaces in H_2SO_4; 70 $\mu f/(cm^2)$* having been observed for copper (28) and 85.5 $\mu f(cm^2)$* for a 10μ zinc coating on aluminum (29). These values are somewhat higher than those for the electropolished, single crystals and can possibly be attributed to increased area due to grain boundaries in the metals. In addition, surface irregularities in the substrate for the zinc coating could cause an increase in the area.

Figures 4-6 indicate that the precision involved in these measurements is not great, as evidenced by the spread of 95% confidence limits. Data of Bowden and Rideal (17) exhibit a similar lack of precision, which they attribute to the very small quantities being measured. Regardless of the precision involved, it appears that the *CAR* of {211} and {110} faces (Fig. 4 and 5) tends to increase with increasing dislocation density, while that of {111} faces (Fig. 6) does not. In addition, successive determinations of *CAR* on the same sample (constant dislocation density) gave a random spread of results, indicating that the silver surface did not become roughened during the measurements.

In considering the effect of dislocations on double layer capacity, and thus on the *CAR*, it is believed that the tendency of the double layer capacity to increase with increasing dislocation density (as in the cases of {110} and {211} planes) is not due to an increasing physical area since the intersection of dislocations with a surface which has been electropolished leads to no change in the physical area of that surface. In addition, since the specimens were not recrystallized the apparent change in double layer capacity or effective area is not produced by the introduction of grain boundaries. It appears that the *CAR* or effective area is influenced by something other than changes in physical area. This additional contribution to the effective area is assumed to be caused by the energy of dislocations intersecting the surface. However, present theoretical models of metal surfaces are inadequate quantitatively to analyze this effect; a more atomistic model is needed to characterize the surface in regions of defects and distortion.

In summary:

1. The double layer capacity for abraded metal electrode surfaces is significantly greater than that for electropolished surfaces; the difference is attributed to the increased physical area due to abrasion.

2. The double layer capacities of electropolished polycrystalline metal electrode surfaces are greater than those of electropolished single crystal surfaces, but far less so than those of abraded surfaces. Part of this difference in effective area is probably due to an increased physical area caused by grain boundaries. However, a portion of the change in effective area is thought to be caused by dislocations.

3. The double layer capacity of electropolished single crystal silver electrodes increases with increasing dislocation density on the {211} and {110} planes but not on the {111} planes.

Acknowledgment

This work was supported in part by the Office of Naval Research. The valuable suggestions of T. D. Perkins and W. R. Upthegrove in the experimental phases of this work are acknowledged.

Manuscript received Aug. 24, 1964; revised manuscript received March 15, 1965.

Any discussion of this paper will appear in a Discussion Section to be published in the June 1966 JOURNAL.

REFERENCES

1. G. C. Bond, "Catalysis by Metals," p. 468, Academic Press, New York (1962).
2. R. H. Griffith and I. D. F. Marsh, "Contact Catalysis," 3rd Edition, p. 129, Oxford University Press, London (1957).
3. S. M. Walas, "Reaction Kinetics for Chemical Engineers," p. 153, McGraw-Hill Book Co., New York (1959).
4. A. J. Crocker and A. J. B. Robertson, *Trans. Faraday Soc.*, **54**, 931 (1958).
5. R. E. Cunningham and A. T. Gwathmey, *Adv. in Catalysis*, **10**, 89 (1957).
6. H. Liedheiser, Jr. and A. T. Gwathmey, *J. Am. Chem. Soc.*, **70**, 1200 (1948).
7. H. Liedheiser, Jr. and A. T. Gwathmey, *ibid.*, **70**, 1206 (1948).
8. H. M. C. Sosnovsky, *J. Chem. Phys.*, **23**, 1486 (1955).
9. J. Eckell, *Z. Electrochem.*, **39**, 433 (1933) as discussed by L. E. Cratty and A. V. Granto in *J. Chem. Phys.*, **26**, 96 (1957).
10. H. E. Farnsworth and R. F. Woodcock, *Adv. in Catalysis*, **9**, 123 (1956).
11. J. W. Hall and H. F. Rose, *Industrial and Engineering Chemistry Fundamentals*, **3**, 158 (1964).
12. H. M. C. Sosnovsky, *J. Phys. Chem. of Solids*, **10**, 308 (1959).
13. R. S. Barnes and P. J. Mazey, *Proc. Roy. Soc. (London)*, **A275**, 47 (1963).
14. A. W. Adamson, "Physical Chemistry of Surfaces," Chap. 10, Interscience Publishers, Inc., New York (1960).
15. S. Brunauer, "The Adsorption of Gases and Vapors," Chap. 9, Oxford University Press, London (1945).
16. S. J. Gregg, "The Surface Chemistry of Solids," 2nd Edition, Reinhold Publishing Corp., New York (1961).
17. F. P. Bowden and E. K. Rideal, *Proc. Roy. Soc. (London)*, **A120**, 59 (1928).
18. J. A. V. Butler, "Electrical Phenomena at Interfaces," p. 47, Methuen and Co., Ltd., London (1951).
19. T. D. Perkins, Ph.D. Thesis, University of Oklahoma (1963). Also Final Report, Office of Naval Research Contract Nonr 982-(08), Task No. NR 051-418, March 1, 1963.
20. A. A. Hendrickson and E. S. Machlin, *Acta Met.*, **3** (1955).
21. N. E. Wisdon and N. Hackerman, *This Journal*, **110**, 319 (1963).
22. J. A. Allen, *Trans. Faraday Soc.*, **48**, 273 (1952).
23. F. W. Salt and J. G. N. Thomas, *Nature*, **178**, 434 (1956).
24. I. M. Barclay and J. A. V. Butler, *Trans. Faraday Soc.*, **36**, 128 (1940).
25. F. P. Bowden and K. E. W. Grew, *Faraday Soc. Disc.*, **1**, 93 (1947).
26. V. E. Past and Z. A. Iofa, *Zhur. Fiz. Khim.*, **33**, 13 (1959).
27. M. Proskurin and A. Frumkin, *Trans. Faraday Soc.*, **31**, 110 (1935).
28. J. O'M. Bockris and B. E. Conway, *J. Chem. Phys.*, **28**, 707 (1958).
29. A. M. Yampol'shii, *Zhur. Priklad. Khim.*, **33**, 1967 (1960).

Technical Notes

Molybdenum Oxidation Kinetics at High Temperatures

R. W. Bartlett[1]

Aeronutronic Applied Research Laboratories, Philco Corporation, Newport Beach, California

Oxidation of molybdenum results in condensed oxides at moderate temperatures and evaporation of gaseous oxide species at temperatures above approximately 700°C. Seven oxidation rate studies have been made at temperatures in excess of 1000°C (1-7). The recent investigation by Gulbransen *et al.* (6), was carried to the highest temperature, 1700°C. These studies have been conducted in air and oxygen but over narrow pressure ranges. The present study was conducted between 1380° and 2470°C (molybdenum mp 2625°C) and over a wider oxygen pressure range, 1 x 10^{-6} atm to 1 atm.

The experimental technique employed a 24-in. diameter cold wall furnace chamber. This permitted free convection around the sample without apparatus constraints on gas mixing or oxygen diffusion within the boundary layer formed by molybdenum oxide vapors diffusing outward from the sample. Polycrystalline molybdenum rods, 0.125-in. initial diameter, were used as samples and heated electrically. The furnace chamber was maintained at the appropriate oxygen pressure by controlling the flow of dry oxygen through the system. Oxidation rates were determined by measuring the sample diameter at suitable intervals using an optical technique. Temperatures were measured with either a color-ratio optical pyrometer or a disappearing filament pyrometer corrected for the emissivity of molybdenum. The apparatus and procedures are described more completely in a previous paper concerning oxidation of tungsten (8). Commercially pure molybdenum was used. The major impurities determined by spectrographic analysis were silicon 0.12%, iron 0.22%, and nickel 0.089%.

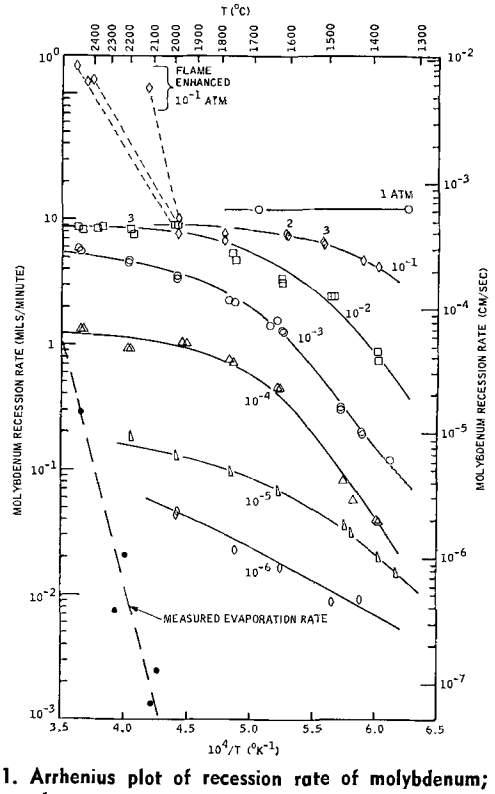

Fig. 1. Arrhenius plot of recession rate of molybdenum; isobars at indicated system oxygen pressure.

The surface recession data conformed with a linear rate law. This condition is consistent with either a surface reaction or transport within the gas boundary film acting as the rate controlling step. An Arrhenius plot of the rate data is shown in Fig. 1. Evaporation rates measured at a total pressure below 1 x 10^{-7} atm are plotted in the lower left-hand corner of Fig. 1. These data show that evaporation of molybdenum was not affecting the oxidation rates in Fig. 1.

Oxidation products were transported away from the sample and deposited on the chamber walls. X-ray diffraction analysis of several samples of this powder residue indicated MoO_3 to be the principal constituent. Variable amounts of Mo_9O_{26}, always below 30%, were also present in these samples.

The oxidation behavior of molybdenum at high temperatures is similar to the oxidation behavior of tungsten (8). The rate has an exponential temperature dependence at lower temperatures that is typical of chemical systems. Since the activation energy is too high for gaseous diffusion, an activation energy barrier at the surface is indicated. Above 1700°C the oxidation rates become less sensitive to temperature. Near the melting point the rate is independent of temperature provided the oxygen pressure is above 10^{-5} atm. The bends in the oxidation rate isobars plotted in Fig. 1 occur in the same temperature range as for tungsten. However, because of the lower melting point of molybdenum, an extended temperature region in which the rate was independent of temperature was not observed. The molybdenum oxidation rates are slightly lower at high pressures and considerably higher at low pressures than the corresponding tungsten oxidation rates. The change in temperature dependence of the rate suggests a transition in rate-controlling step from a chemically activated process to a gas kinetic process at high temperatures. For both processes, the boundary layer present at higher pressures probably affects the results by lowering the oxygen partial pressure at the surface compared with the oxygen pressure beyond the boundary layer. Although a boundary layer analysis was not attempted, the rate results are valid for any free convection application of molybdenum.

Comparisons with other investigators are difficult because of the variable effects caused by different experimental systems on the boundary layer. Gulbransen *et al.* (6) measured molybdenum oxidation rates in 0.1 atm of oxygen. Their samples were oxidized in a closed end tube which probably restricted oxygen input and oxide vapor purging. This system complicates the boundary layer analytical problem, but it makes the rate more sensitive to gas flow at moderate

[1] Present address: Stanford Research Institute, Menlo Park, California.

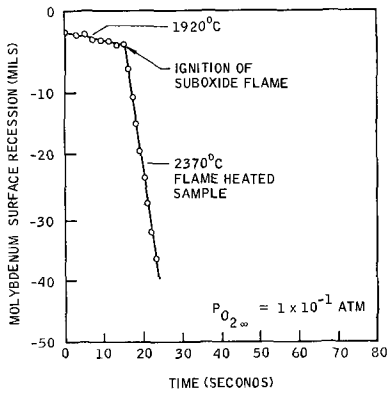

Fig. 2. Transition in the oxidation rate of molybdenum caused by ignition of the suboxide diffusion flame at 15 sec.

velocities than an open system. Their fastest rate data are consistent with the rate data at equivalent temperatures and pressures (10^{-1} atm) from this study. Rosner and Allendorf (7) measured the oxidation rate in an oxygen partial pressure of 3 x 10^{-2} Torr (4 x 10^{-5} atm) and reported molybdenum/oxygen molecule reaction probabilities. Their data were converted to equivalent slab recession rates, assuming a gas temperature of 300°K. An extrapolation of these rates to 1400°C joins the 1 x 10^{-4} atm Arrhenius isobar of Fig. 1, which is fair agreement. The molybdenum oxidation rates observed by Modisette and Schryer (4) in slow moving air above 1400°C vary between 1.3 and 2.8 mils/min. This rate is about 1/5 the oxidation rate in pure oxygen of the same partial pressure, 0.21 atm, observed in the present study. A lowered rate in air is expected because nitrogen impedes diffusion of oxygen in the boundary layer.

The most interesting aspect of oxidizing molybdenum at high temperatures and pressures is a large discontinuous increase in rate observed at oxygen pressures near 1 atm. This change in rate was accompanied by a sudden rise in temperature even when external heating was removed. Furthermore, the samples were surrounded by a typical gas flame, indicating the combustion of fuel in the gas phase rather than on the surface of the metal rod. Although oxidation of tungsten at 10^{-1} atm and 1 atm was self-supporting at high temperatures once initiated, the flame phenomena and discontinuous increases in rate were not observed with tungsten (8). The transition in behavior associated with flame ignition was easily distinguished. Rods burning normally without an accompanying flame appeared as bright incandescent objects. The surrounding cloud caused by condensation of molybdenum oxide particles could only be detected by reflected light. After flame ignition the reverse in light intensity occurred. The incandescent rod could not be visually distinguished from the flame surrounding it unless filters were used. Prior to ignition, temperature could not be detected by optical pyrometry within the vapor cloud. After ignition, the color temperature of the flame, measured by a color ratio optical pyrometer, varied from 2200° to 2500°C in 0.1 atm of oxygen and between 2700° and 2800°C in 1 atm of oxygen. These temperatures were recorded using fields of view which excluded the sample. The high flame temperature associated with an oxygen pressure of 1 atm caused the sample to melt within a few seconds after ignition of the flame.

Sample diameters were measured photographically using filters. A typical rate curve resulting from gas flame enhanced oxidation is shown in Fig. 2. Oxidation of the sample continued to obey a linear rate law after ignition but proceeded at a much faster rate. The flame enhanced oxidation rates at 0.1 atm were included in the Arrhenius plot, Fig. 1; average values are listed in Table I.

Table I. Effect of the diffusion flame on molybdenum recession rates at high temperatures (temperature independent region) and high oxygen pressures

	P_{O_2} = 0.1 atm	P_{O_2} = 1 atm
Avg. rate without flame	9 mils/min	12 mils/min
Avg. rate with flame	133 ± 25 mils/min	470 mils/min*

* Burn out prevented accurate rate data acquisition on four other samples.

In experiments conducted at both 0.1 atm and 1 atm oxygen pressures, ignition of the flame did not occur unless a temperature above approximately 1900°C was used. This temperature corresponds with the temperature at which the suboxide, $MoO_2(g)$, becomes appreciably more prevalent than $MoO_3(g)$ as the oxidation product determined by Berkowitz-Mattuck *et al.* (10), using mass spectrometric methods. This relation indicates that the flame results from the outward diffusion of the $MoO_2(g)$ and the subsequent reaction of $MoO_2(g)$ with oxygen to produce $MoO_3(g)$. Polymerization reactions are also strongly exothermic in this system. The heat released by these chemical reactions can account for the gaseous diffusion flames observed. The reactions are summarized as follows: neglecting the small amount of $MoO_3(g)$ produced at the metal surface, the primary surface oxidation reaction is formation of the molybdenum dioxide monomer

$$Mo + O_2 \rightarrow MoO_2(g)$$

The net secondary reaction in the gas phase, including oxidation and polymerization to the dominant equilibrium species $(MoO_3)_3(g)$, is

$$\frac{3}{2} O_2 + 3MoO_2(g) \rightarrow (MoO_3)_3(g)$$

$$\Delta H^\circ = -598 \text{ kcal/mole of product}$$

This reaction is 50% more exothermic than the equivalent reaction in the tungsten system (11, 12)

$$\frac{3}{2} O_2 + WO_2(g) \rightarrow (WO_3)_3(g)$$

$$\Delta H^\circ = -405 \text{ kcal/mole}$$

This difference in released heat provides a possible explanation for the presence of the diffusion flame with molybdenum under conditions where it was not observed with tungsten.

The casual relation between the adjacent diffusion flame and the increased metal surface oxidation rate is uncertain. The increased turbulence and temperature in the boundary layer caused by the flame may explain the rate increase. Analysis of mass transfer in turbulent boundary layers and flames is complex and was not attempted.

Acknowledgment

This research was sponsored by the Air Force Materials Laboratory, Research and Technology Division, Air Force Systems Command, U. S. Air Force. The author is indebted to Dr. W. M. Fassell, Jr., and Mr. J. P. Pope for assistance in conducting this investigation.

Manuscript received Nov. 16, 1964; revised manuscript received Feb. 16, 1965.

Any discussion of this paper will appear in a Discussion Section to be published in the June 1966 JOURNAL.

REFERENCES

1. C. R. Wilks, "Effects of Temperature, Pressure and Mass Flow on Oxidation of Molybdenum," SAMPE Eastern Division Meeting, MIT, Cambridge, Mass., May 1960.
2. E. S. Bartlett and D. N. Williams, *Trans. AIME*, **212**, 280 (1958).
3. North American Aviation, Inc., "High Temperature Oxidation of Molybdenum Under High Altitude

Conditions," Air Force Contract AF 33(600)-28469, ASTIA No. 147839, NAA Rept. No. AL-2617, Sept. 1957.
4. J. L. Modisette and D. R. Schryer, "An Investigation of the Role of Gaseous Diffusion in the Oxidation of a Metal Forming a Volatile Oxide," NASA Tech. Note D-222, March 1960.
5. J. W. Semmel, Jr., "High Temperature Materials," pp. 510-19, J. Wiley & Sons, Inc., New York (1959).
6. E. A. Gulbransen, K. F. Andrew, and F. A. Brassart, *This Journal*, **110**, 952 (1963).
7. D. E. Rosner and H. D. Allendorf, *J. Chem. Phys.*, **40**, 3441 (1964).
8. R. W. Bartlett, *Trans. AIME*, (in press).
9. R. B. Bird, W. E. Stewart, and E. L. Lightfoot, "Transport Phenomena," Chap. 16, J. Wiley & Sons, Inc., New York (1960).
10. J. B. Berkowitz-Mattuck, A. Büchler, J. L. Engelke, and S. N. Goldstein, *J. Chem. Phys.*, **39**, 2722 (1963).
11. P. E. Blackburn, M. Hoch, and H. L. Johnston, *J. Phys. Chem.*, **62**, 769 (1958).
12. J. Berkowitz, W. A. Chupka, and M. G. Inghram, *J. Chem. Phys.*, **27**, 85 (1957).

Effect of Concentration on the Fluorescence of Samarium in Cerium Dioxide

Michael Kestigian, Ronald H. Curry, and Fredric D. Leipziger
Sperry Rand Research Center, Sudbury, Massachusetts

This note is concerned with the effect of concentration on the fluorescence of samarium in cerium dioxide. A study of the spectral properties of rare earth phosphors was recently carried out by Ropp (1). This investigation was concerned with rare earth sesquioxide systems. The existence of a samarium-activated cerium-dioxide phosphor was first reported by Tomaschek (2).

Experimental Procedure

Cerium-dioxide samples in which the molar concentration was 0.01% or less were prepared by the addition of appropriate amounts of a solution of samarium ion to cerium dioxide. These preparations were completely dried, ground in an agate mortar, and calcined in platinum vessels at 1350°C in oxygen for 12 hr. On removal from the furnace, the specimens were cooled, reground, and the calcination procedure repeated. An oxygen atmosphere was used in the calcination process to ensure the formation of stoichiometric cerium dioxide. Cerium-dioxide samples in which the molar concentration of samarium was greater than 0.1% were prepared from the oxides. These preparations were ground under ethanol, dried, and calcined as outlined above. The cerium dioxide used was prepared from the oxalate by decomposition in an oxygen atmosphere (3). The chemicals were all reported to be 99.9+% pure.

The fluorescence was measured using a Jarrell-Ash 82-00 monochromator equipped with a 15,000 lpi grating, a fixed-slit width of 100μ, and a slit height of 5 mm. An EMI-9558A photomultiplier tube (S-20) was used as a detector. Standard amplification and recording techniques were applied. The excitation radiation used to record the samarium fluorescence was 3600Å. The intensity of the fluorescence observed with 2537Å excitation was insufficient for quantitative recording of the spectrum.

The samarium content of the cerium-dioxide samples was analyzed by a mass spectrograph using an AEI-MS7 spark-source instrument. The powdered specimens were mixed with equal weights of pure graphite powder and pressed into ⅛ x ¾ in. electrodes. The electrodes were sparked for a sufficient length of time to produce sensitivities of 1 in 10^{-8}. Analysis for samarium was performed by measuring the lines produced by the Sm^{147} and Sm^{149} isotopes. These lines were free of interference from other rare earth metals and rare earth oxides. Ilford Q-II plates were used to record the spectra and were developed and measured using standard techniques.

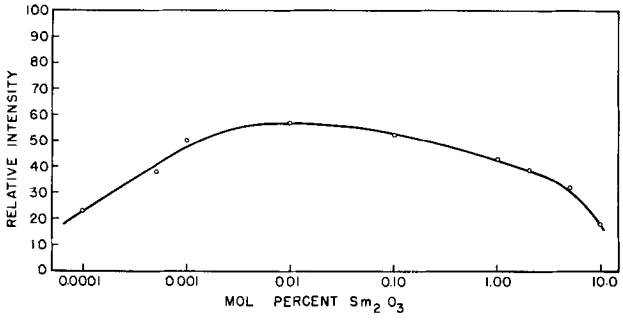

Fig. 1. Plot of fluorescence intensity vs. concentration

Experimental Results

Spectrographic studies indicated that four peaks were present in the fluorescence spectra of samarium-activated cerium dioxide. These were located at 573, 607, 615, and 621 mμ. Only the 573 and 615 mμ peaks were strong enough to be studied quantitatively. The decision to study the concentration dependence of samarium in cerium dioxide by investigation of the 573 mμ line was made because of the better signal-to-noise ratio of the photoelectric instrument described above. This fluorescence (573 mμ) was observed at concentrations as low as 10^{-4} mole % Sm_2O_3. A plot of fluorescence intensity versus concentration is shown in Fig. 1. Referring to the figure, it can be seen that the fluorescence intensity shows a slow increase with increased samarium-oxide concentration to a broad maximum at about 0.01 mole % followed by a decrease to a concentration of about 10 mole % Sm_2O_3. The fluorescence was not detectable at concentrations above 10 mole % Sm_2O_3. It was surprising that the maximum in the fluorescence-intensity curve occurred at so low a concentration. In most examples of concentration quenching, the effect does not become significant until concentrations of the order of 1% are reached. To what extent these anomalies are due to the use of finely divided powders or truly represent intrinsic material properties is not clear at this point.

In the course of this investigation, it was observed that numerous high-purity cerium compounds exhibited the same fluorescence described above. The fluorescence was observed in some cerium-dioxide samples in the "as-is" condition, while in other cerium-dioxide and cerium containing raw materials the fluorescence became visible only after calcination at high temperature. These samples were all found to be contaminated with other rare earths in concentrations ranging from 0.05 to 100 ppm. Samarium was present as an impurity in all cerium-dioxide samples which exhibited the fluorescence. The level of samarium ranged from 5 to 50 ppm ±50%.

Summary

The fluorescence of samarium as a function of concentration in a cerium-dioxide matrix has been investigated. Fluorescence is observed when only a few

ppm Sm are present in CeO_2. The fluorescence intensity increases with concentration until 0.01 mole % Sm_2O_3 has been added, after which concentration quenching sets in and the fluorescence intensity decreases with increased Sm concentration.

Acknowledgment

The authors gratefully acknowledge Dr. Roger Newman for helpful discussions and comments.

Manuscript received Nov. 12, 1964.

Any discussion of this paper will appear in a Discussion Section to be published in the June 1966 JOURNAL.

REFERENCES

1. R. C. Ropp, *This Journal*, **111**, 311 (1964).
2. R. Tomaschek, *Z. Elektrochem.*, **36**, 737 (1930).
3. A. Glasner and M. Steinberg, *Bull. Research Council, Israel*, **8A**, 174 (1959).

Epitaxial Growth of GaAs Through Cracks in SiO_2 Masks

M. Michelitsch

International Business Machines Corporation Laboratories, Boeblingen, Germany

SiO_2 layers several thousand Ångströms thick on GaAs wafers have shown excellent masking characteristics against epitaxial growth and diffusion (1, 2). Such films are commonly produced by pyrolytic decomposition of gaseous $Si(C_2H_5O)_4$ on GaAs wafers at several hundred degrees centigrade. About 5000Å can easily be obtained within 30 min.

Figure 1 shows the epitaxial growth apparatus. It consists of three quartz tubes, 20 mm in diameter. Two of these contain the separate source materials As and Ga (and if desired a dopant such as Se), the third one the GaAs wafer (seed). The source tubes are connected with the seed tube by capillaries 1 mm in diameter. To prevent deposition on the outer wall of the seed tube it is lined with a separate removable tube, which is surrounded by a H_2 counter flow. By changing the direction of the H_2 counter flow "growth" or "no growth" can be obtained. For no growth, the reaction gases pass through only the source tubes (HCl/H_2 in the Ga tube, H_2 in the As tube), and the reaction at the source materials can reach a steady state. The gases leave the system through valves A and B. Because of a hydrogen counter flow through the seed tube and the capillaries to the source tubes, no growth can occur. For growth, valves A and B are closed and valve C is opened. The reacted gases from the source tubes enter a mixing chamber through both capillaries near the quartz observation window. From there the gas mixture passes over the seed and leaves the system through the liner tube and valve C.

Each tube is heated by a separate furnace with three heating zones each. The observation window (mixing chamber) is heated by a separate small furnace to prevent GaAs deposition there. By means of a long focus microscope it is possible to observe the growth process while it occurs.

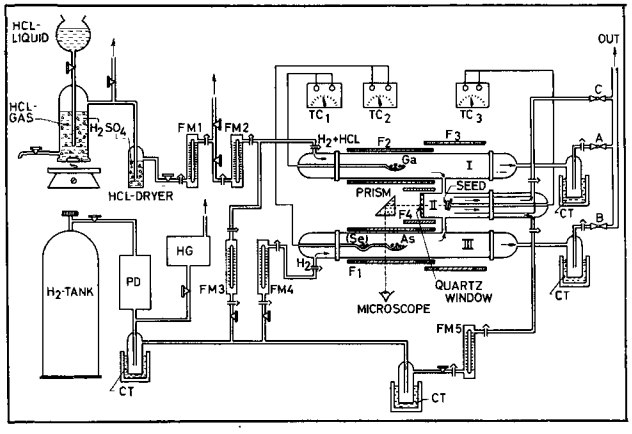

Fig. 1. Ga-As-HCl-H_2 synthesis system: FM, flow meters; TC, thermocouples and millivoltmeters; CT, cold traps (liquid nitrogen); PD, puridrier; HG, hygrometer; F_i, furnaces; I, Ga-tube; II, seed tube; III, As tube; A, B, C, valves.

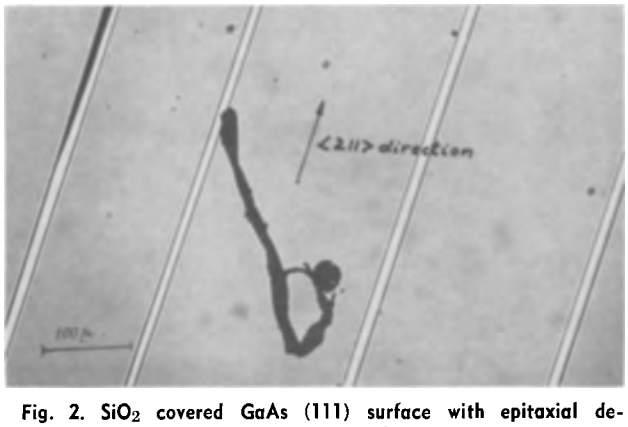

Fig. 2. SiO_2 covered GaAs (111) surface with epitaxial depositions through <211> oriented cracks.

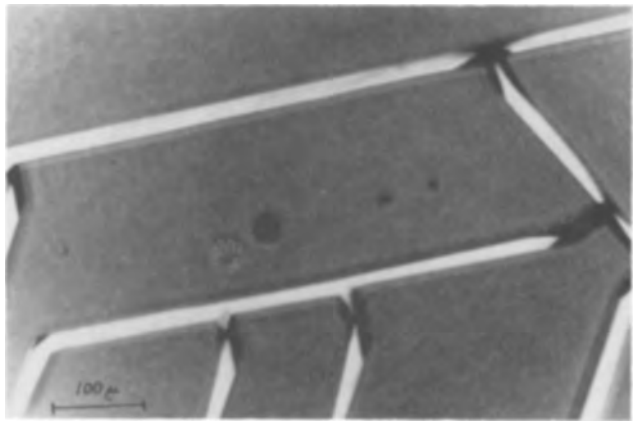

Fig. 3. Epitaxial deposition through <211> oriented cracks intersecting at 60°.

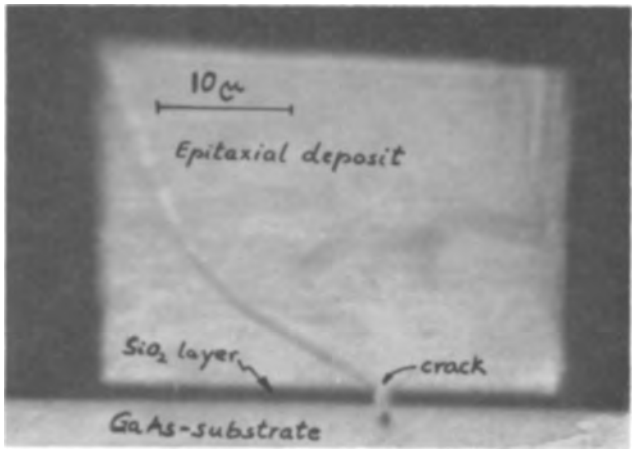

Fig. 4. Cross section (cleaved) of a crack with epitaxial overgrowth.

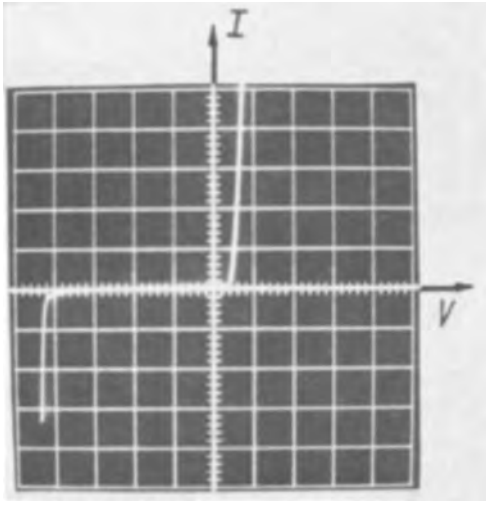

Fig. 5. I-V characteristic of a "crack diode" (substrate approx. 10^{18} cm^{-3} Zn-doped, epitaxy 5 x 10^{17} cm^{-3} Se-doped). Vertical, 0.1 ma/div; horizontal: 2v/div.

Typically the temperature at the Ga boat was 500°C, at the As boat 450°C, at the mixing chamber 900°C, and at the seed 780°C. The flow rates were 10 and 70 cm^3/min HCl and H_2, respectively, in the Ga tube, and 70 cm^3/min in the As tube.

During investigations of the epitaxial growth of GaAs on partially SiO_2 masked GaAs (111)-substrates, cracks in the SiO_2 layers were frequently observed during heat-up, which were due to differential thermal expansion of the SiO_2 and GaAs. Cracking occurs if the SiO_2 layer is thicker than about 5000Å. The cracks described in the following were about 0.5-1μ wide, several millimeters long, and parallel to <211> directions in the (111) oriented substrate. The bottoms of the cracks serve as nucleation sites for epitaxial growth. Once the cracks are filled up with epitaxial material, the growth spills over the SiO_2 layer (Fig. 2, 3, 4). Overgrowth 25μ high was produced in 2 min. Although the growth rate is rather high, it is consistent with rates obtained on uncoated substrates under similar conditions, and the material grown through the cracks which was examined by electron diffraction was shown to be monocrystalline having the same orientation as the substrate.

As the cleavage planes in GaAs are {110}, the line of intersection of the cleavage planes with a (111) surface lies in the <211> direction. It is therefore possible to produce long and narrow GaAs bars by cleaving. If the epitaxial layer has the opposite conductivity type to the substrate, GaAs diodes with long but extremely narrow junctions can be obtained. The electrical characteristics (Fig. 5) of such narrow vapor growth junctions are usually better than those of junctions grown on chemically cleaned GaAs substrates. This is due to the extreme cleanliness of GaAs surface in the cracks, which are not formed until the heat-up, just prior to deposition.

With proper doping this method should be useful for producing laser diodes. Other structures, such as, for example, narrow heterojunctions are possible.

Acknowledgments

The author wishes to thank Dr. G. Hellbardt for suggesting the design of the vapor growth furnace, Mr. K. Brack for performing the electron diffraction measurements, Miss H. Leistikow for performing the SiO_2 masking of the GaAs wafers, and Mr. C. E. Kelly for preparing Fig. 3.

Manuscript received Nov. 22, 1964.

Any discussion of this paper will appear in a Discussion Section to be published in the June 1966 JOURNAL.

REFERENCES

1. S. W. Ing, Jr., and W. Davern, *This Journal*, **111**, 120 (1964).
2. S. R. Shortes, J. A. Kanz, and E. C. Wurst, Jr., *Trans. Met. Soc. AIME*, **230**, 300 (1964).

Transpiration Studies of the Gallium-Hydrogen Iodide-Hydrogen System

V. J. Silvestri

International Business Machines Corporation, Watson Research Center, Yorktown Heights, New York

The transport of gallium by means of hydrogen iodide is of interest because of its importance in gallium arsenide synthesis and epitaxial growth systems (1). In addition, hydrogen iodide has been useful for transporting gallium as a dopant during the epitaxial growth of germanium (2).

In a recent thermodynamic evaluation of the Ga-HI-H_2 system, the conditions of temperature and pressure under which the efficient transport of gallium occurs were discussed (3). The application of these data to an experimental flow system requires that equilibrium be assured at the gallium bed. It was therefore the purpose of this investigation to determine gas flow conditions under which a hydrogen iodide-hydrogen mixture comes into equilibrium with a gallium source. The measurements also served to check the validity of the thermodynamic data employed in the evaluation of the system.

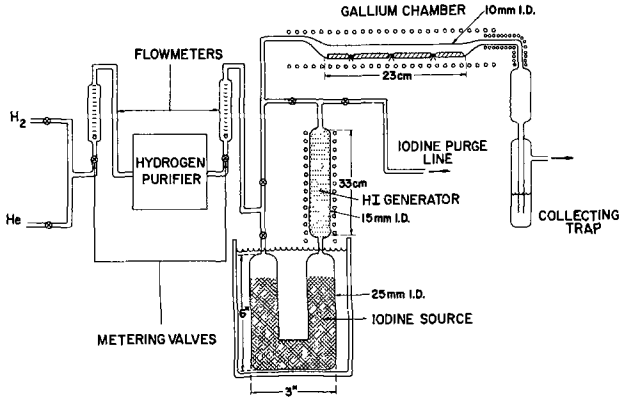

Fig. 1. Schematic representation of the flow system employed for transpiration studies.

Apparatus and Experimental Procedure

Figure 1 depicts schematically the flow system used. It consists of an iodine chamber followed by a hydrogen iodide generator, a gallium bed, and a collecting trap. The gases used were purified with molecular sieves,[1] to remove oxygen, primarily to avoid oxidation of the gallium. The latter presented a surface area of approximately 23 cm^2 to the flowing gas stream.

[1] J. Mickel Associates.

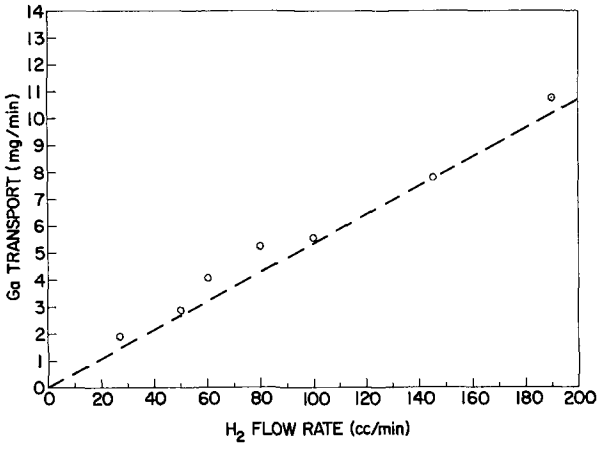

Fig. 2. Gallium transport as a function of hydrogen flow rate. Pressure of HI, 21.4 Torr; gallium temperature 433.4°C. Broken line represents the thermodynamically predicted gallium transport; ⊙, experimental values.

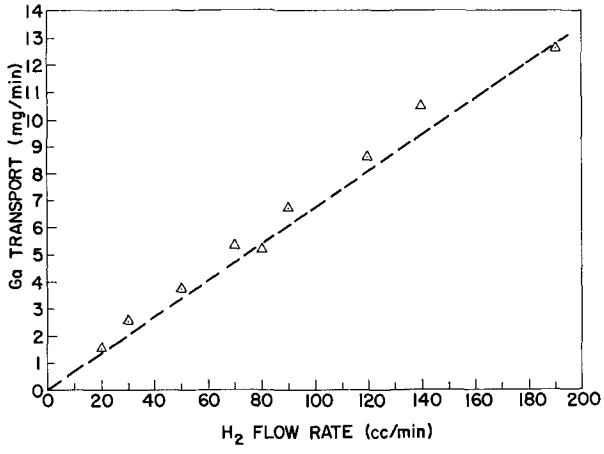

Fig. 3. Gallium transport as a function of hydrogen flow rate. Pressure of HI, 34.4 Torr; gallium temperature 408.8°C. Broken line represents the thermodynamically predicted gallium transport; △, experimental values.

For the experiments, monitored flows of hydrogen were passed through calibrated flow meters into the iodine source. The iodine bed was designed on the basis of previous iodine evaporation studies (4) such that vapor saturation would be achieved in this chamber. The temperature at the iodine source was controlled to ±0.5°C in a thermostated water bath. The catalysis of the reaction between hydrogen and iodine was effected by the platinum wool at 300°C, and the effluent from this column was then carried into the gallium bed. Here the following reactions to form gallium iodides occurred:

$$Ga(l) + 3HI(g) \rightleftarrows GaI_3(g) + 3/2H_2(g)$$
$$2Ga(l) + GaI_3(g) \rightleftarrows 3GaI(g) \quad (5)$$

The resulting iodides were collected in the two sectioned trap shown at the end of the system in Fig. 1. Condensation of the iodides occurred for the most part in the upper portion of the cold trap. The lower section contained a 6*N* KOH solution where any products escaping the freezeout zone were dissolved. The contents of both regions were then analyzed, using wet chemical techniques, for gallium and iodine.

Two different hydrogen iodide input pressures (21.4 and 34.4 Torr) were used at two different gallium bed temperatures (433.4° and 408.8°C), respectively, and for each set of conditions the amounts of gallium and iodine collected were determined for various flow rates. Experimental pressures and temperatures were chosen on the basis of thermodynamic calculations

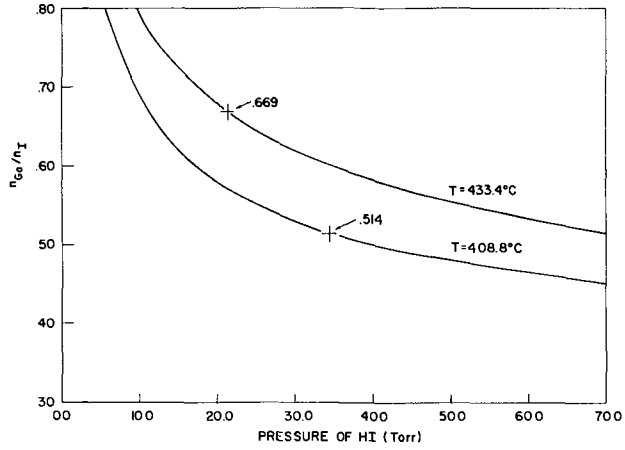

Fig. 4. Equilibrium data extracted from ref. (3) showing the predicted molar gallium to iodine ratio as a function of an initial pressure of HI entering a gallium bed at the indicated temperatures.

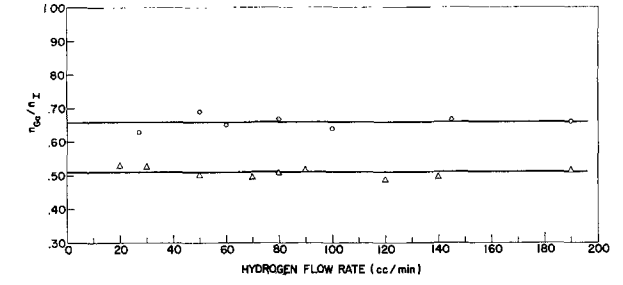

Fig. 5. Experimentally determined gallium to iodine molar ratios plotted as a function hydrogen flow rate: ⊙, pressure of HI, 21.4 Torr, gallium temperature 433.4°C; △, pressure of HI, 34.4 Torr, gallium temperature 408.8°C.

made specifically for a gallium arsenide flow system (1).

Results and Discussion

In order to determine whether equilibrium is achieved the data may be plotted in several ways. A comparison of either the gallium transport rate or the gallium to iodine ratio with those predicted thermodynamically may be made. Data as given below provide both comparisons.

In Fig. 2 and 3 the gallium transport rate has been plotted as a function of hydrogen flow rate for the two experimental conditions previously described. The agreement of the experimentally obtained values with the theoretical rates shows equilibrium was achieved for all flow rates.

In Fig. 4 the predicted (3) gallium to iodine molar ratios have been plotted for the two temperatures under consideration as a function of the initial pressure of hydrogen iodide entering a gallium source. For the experimental hydrogen iodide pressures employed, the indicated predicted ratios in Fig. 4 are obtained. Figure 5 presents the experimentally determined molar gallium to iodine ratios as a function of hydrogen flow rate. As would be expected from Fig. 2 and 3 the ratio is constant and the values are in close agreement with the predicted values in Fig. 4.

Acknowledgment

The author wishes to thank B. L. Olsen of IBM's analytical group for his part in the work and to acknowledge the helpful discussions with H. Leonhardt, A. Reisman, and S. A. Alyanakyan.

Manuscript received Jan. 15, 1965. This paper was presented at the Washington Meeting, Oct. 11-15, 1964. The work was supported in part by AFCRL Contract No. AF19(628)-2468.

Any discussion of this paper will appear in a Discussion Section to be published in the June 1966 JOURNAL.

REFERENCES
1. H. R. Leonhardt, *This Journal*, **112**, 237 (1965).
2. A. Reisman, Private communication.
3. A. Reisman and S. A. Alyanakyan, *This Journal*, **111**, 1154 (1964).
4. A. Reisman, M. Berkenblit, and S. A. Alyanakyan, *ibid.*, **112**, 241 (1965).
5. V. J. Silvestri and V. J. Lyons, *ibid.*, **109**, 963 (1962).

Theoretical Electromotive Forces for Cells Containing a Single Solid or Molten Fluoride, Bromide, or Iodide

Walter J. Hamer, Marjorie S. Malmberg,[1] and Bernard Rubin[2]

National Bureau of Standards, Washington, D. C.

In a previous paper (1) an electromotive force series for solid and molten chlorides was presented for temperatures ranging from 25° to 1500°C. This series was based on the Gibbs energy (free energy) of formation of the respective solid and molten chlorides and corresponded to the reversible emfs of cells of the type

metal | metallic chloride | chlorine gas [1]

It was also shown that it was unnecessary for practical purposes to divide the emfs into separate anodic and cathodic potentials, although one could assume that the potential of the chlorine electrode is zero (2) for each solid or molten chloride; the potential of each metal would then be, by convention, equal to the emf of the whole cell [1].

In this paper similar series are given for solid and molten fluorides, bromides, and iodides. These are given, respectively, in series arrangement, in Tables I, II, and III. A heavy vertical line in the tables indicates that the values to the left of the line are for solid halides while those to the right are for molten halides. When a sublimation, vaporization, or decomposition temperature is given in parenthesis, the emf directly above it is for that temperature rather than for the one heading the column. These potentials are given a positive sign here to be consistent with the procedure followed in the previous paper (1) on the chlorides. The emfs, therefore, correspond to the Gibbs energy of formation of the respective halides. If the Stockholm convention (3) were followed the opposite sign would be used and the emfs would correspond to the Gibbs energy of decomposition of the halides. As was done previously the Gibbs energies used were those published by Brewer (4) or the National Bureau of Standards (5) and the heat capacities used were those published by Kelley (6). In some cases the necessary heat capacity data were not available. In those cases the values were estimated using either the Kelley rule (7), namely, 7.0 thermochemical calories per degree C and mean gram-atom for solid compounds, 8.0 for liquid compounds, 7.3 for solid metals, and 7.5 for liquid metals, or the Shomate method (8) using the enthalpy and heat capacity data given by the National Bureau of Standards (5). Other compilations of thermochemical data are available, for example, the "Janaf Thermochemical Tables," Dow Chemical Company, Midland, Michigan, Loose Data Sheets, 1960—. Although these new compilations are undoubtedly in a better state of revision than NBS Circular 500 the latter source was adhered to here so that the fluoride, bromide, and iodide series, here presented, would be internally consistent with the chloride series previously published (1). The necessary equations and the sequence of the calculations for obtaining the emfs at different temperatures were given in the previous paper and need not be repeated here.

The uncertainties in emf listed in the tables for the solid cell at 25°C correspond to the uncertainties in the enthalpy of formation of the halides at 25°C quoted by Brewer; these uncertainties were assumed to apply also to the data in the National Bureau of Standards Circular (5) since these values agree closely with those of Brewer and the sources of the two sets of data are nearly the same. The uncertainties in entropy values are generally small compared to those in enthalpy values and accordingly the uncertainties in emf here listed are based on uncertainties in enthalpy rather than Gibbs energies of formation. In addition, the authors are more concerned with the order of the respective halides in any one series than with the actual values and these orders will probably remain the same whether the uncertainties are based on enthalpies or Gibbs energies.

It is emphasized here, as in the previous paper on the chlorides, that these emfs are for theoretical cells, *i.e.*, for ones in which there is no interaction between the metals or the halogen with the halides, no solubilities of the metals in the halides, or vice versa, or any other factors that would lead to deviations of the metals, the halides, or the halogens from their standard states. These emfs nevertheless have value in serving to indicate if deviations from the ideal state are present in actual cells.

In each table the values for the aqueous cell at 25°C are given for comparison (9). Since for these solid and molten systems at high temperatures, bromine and iodine exist as gases, the data for the aqueous system in these cases are for the gaseous state even though the stable state at this temperature is the liquid and solid, respectively. The emfs for liquid bromine and solid iodine for aqueous systems at 25°C would be 0.016v and 0.100v lower, respectively, than those given in the tables. In each case it may be noted that the order of the elements does not parallel that of the aqueous system. Furthermore, the orders for the solid and molten fluorides, chlorides (1), bromides, and iodides are not the same, *i.e.*, there is not a constant difference between any two halide series. Relative reducing power of an element, magnesium for example, must be confined to a single halide series. For example, if lithium were placed in fused barium fluoride it would displace the barium (1) with the formation of lithium fluoride, thus

$$2Li + BaF_2 \rightarrow 2LiF + Ba$$

However, in fused bromides or iodides the reverse would occur, namely

$$Ba + 2LiBr \text{ (or LiI)} \rightarrow BaBr_2 \text{ (or } BaI_2) + 2Li$$

Manuscript received Nov. 4, 1964.

Any discussion of this paper will appear in a Discussion Section to be published in the June 1966 JOURNAL.

REFERENCES
1. W. J. Hamer, M. S. Malmberg, and B. Rubin, *This Journal*, **103**, 8 (1956).
2. R. W. Laity, "Reference Electrodes," D. J. G. Ives

[1] Present address: Department of Chemistry, University of Maryland, College Park, Maryland.
[2] Present address: AF Cambridge Research Laboratories, Office of Aerospace Research, L. G. Hanscom Field, Bedford, Massachusetts.

and G. J. Janz, Editors, Chap. 12, Academic Press, New York (1961).
3. J. A. Christiansen and M. Pourbaix, *Compt. rend. conf. union intern. chim. pure et appl., 17th Conf., Stockholm*, p. 83 (1953).
4. L. Brewer, "The Chemistry and Metallurgy of Miscellaneous Materials, Thermodynamics," L. L. Quill, Editor, McGraw-Hill Book Co., Inc., New York (1950).
5. "Selected Values of Chemical Thermodynamic Properties," *Nat. Bur. Standards, Circ.* 500 (1952); also Series III (1948-1953).
6. K. K. Kelley, *U. S. Bur. Mines, Bull.* 383(1935), 393(1936), 476(1949), 584(1960).
7. Ref. 6, *Bull.* 476, p. 206.
8. C. H. Shomate, *J. Am. Chem. Soc.*, **66**, 928 (1944).
9. W. M. Latimer, "The Oxidation States of the Elements and Their Potentials in Aqueous Solutions," 2nd ed., Prentice-Hall, Inc., New York (1952).

Table I. Standard electromotive forces for single, solid, or molten metallic fluorides*

Order 25°C	Metal ion	E° 25°C (aqueous) v	25°C (solid) v	Uncertainty (25°C) v	100°C v	200°C v	300°C v	350°C v	400°C v	450°C v	500°C v	550°C v	600°C v	800°C v	1000°C v	1500°C v
1	Eu^{+2}	6.266	6.234	±0.15	6.167	6.080	5.996	5.955	5.914	5.874	5.834	5.795	5.756	5.602	5.453 |	5.101
2	Li^{+1}	5.911	6.054	±0.09	5.981	5.881	5.775	5.722	5.669	5.617	5.564	5.512	5.461	5.256 |	5.071	4.495
3	Ca^{+2}	5.736	6.021	±0.01	5.953	5.864	5.776	5.732	5.689	5.646	5.603	5.560	5.517	5.350	5.182 |	4.785
4	Sm^{+2}	<6.03	6.017	±0.15	5.950	5.863	5.779	5.738	5.698	5.657	5.617	5.578	5.539	5.385	5.236	4.884
5	Sr^{+2}	5.756	6.012	±0.002	5.943	5.854	5.768	5.726	5.684	5.643	5.602	5.562	5.522	5.364	5.203 |	4.768
6	Ba^{+2}	5.766	5.952	±0.02	5.885	5.797	5.712	5.670	5.629	5.588	5.547	5.507	5.468	5.310	5.154 |	4.803
7	Ra^{+2}	5.786	5.941	±0.07	5.871	5.781	5.694	5.651	5.608	5.566	5.524	5.483	5.442	5.277	5.111	4.566
8	La^{+3}	5.386	5.811	±0.10	5.743	5.656	5.571	5.530	5.489	5.448	5.408	5.368	5.329	5.174	5.020	4.648
9	Ce^{+3}	5.346	5.739	±0.10	5.671	5.584	5.499	5.457	5.416	5.376	5.335	5.295	5.255	5.097	4.938	4.555
10	Pr^{+3}	5.336	5.710	±0.10	5.645	5.563	5.483	5.444	5.405	5.367	5.329	5.291	5.254	5.109	4.965	4.621
11	Nd^{+3}	5.306	5.652	±0.10	5.584	5.496	5.411	5.369	5.327	5.286	5.245	5.204	5.164	5.004	4.843	4.458
12	Pm^{+3}	5.286	5.637	±0.10	5.573	5.490	5.410	5.370	5.332	5.294	5.256	5.218	5.181	5.035	4.894	4.560
13	Na^{+1}	5.580	5.607	±0.01	5.534	5.429	5.325	5.273	5.221	5.170	5.119	5.068	5.017	4.818	4.529	3.781
14	Sm^{+3}	5.276	5.594	±0.10	5.530	5.447	5.367	5.328	5.289	5.250	5.213	5.175	5.138	4.992	4.850	4.517
15	Gd^{+3}	5.266	5.580	±0.10	5.515	5.433	5.352	5.313	5.274	5.236	5.198	5.161	5.123	4.977	4.836	4.504
16	K^{+1}	5.791	5.525	±0.02	5.446	5.338	5.230	5.176	5.123	5.070	5.017	4.965	4.913	4.674	4.355	3.630
17	Tb^{+3}	5.256	5.522	±0.10	5.457	5.375	5.295	5.255	5.217	5.178	5.140	5.103	5.065	4.920	4.778	4.447
18	Dy^{+3}	5.216	5.493	±0.10	5.429	5.346	5.266	5.226	5.188	5.149	5.111	5.074	5.036	4.891	4.749	4.419
19	Y^{+3}	5.236	5.478	±0.10	5.414	5.331	5.251	5.212	5.173	5.135	5.097	5.059	5.022	4.876	4.735	4.407
20	Ho^{+3}	5.186	5.449	±0.10	5.385	5.302	5.222	5.183	5.144	5.106	5.068	5.030	4.993	4.847	4.706	4.376
21	Mg^{+2}	5.236	5.438	±0.02	5.369	5.278	5.188	5.144	5.100	5.056	5.013	4.969	4.926	4.746	4.567	3.994
22	Rb^{+1}	5.791	5.421	±0.04	5.348	5.250	5.153	5.105	5.057	5.009	4.961	4.913	4.865	4.583	4.274 |	3.670
23	Lu^{+3}	5.116	5.407	±0.10	5.342	5.259	5.179	5.140	5.100	5.062	5.025	4.987	4.950	4.804	4.662	4.336
24	Er^{+3}	5.166	5.406	±0.10	5.342	5.259	5.179	5.140	5.101	5.063	5.025	4.987	4.950	4.804	4.662	4.333
25	Eu^{+3}	5.276	5.392	±0.10	5.327	5.245	5.164	5.125	5.086	5.048	5.010	4.973	4.935	4.790	4.648	4.316
26	Tm^{+3}	5.146	5.392	±0.10	5.327	5.245	5.164	5.125	5.086	5.048	5.010	4.973	4.935	4.789	4.648	4.320
27	Cs^{+1}	5.789	5.217	±0.01	5.140	5.037	4.935	4.884	4.833	4.783	4.733	4.682	4.632	4.367	4.055 |	3.677
28	Yb^{+3}	5.136	5.175	±0.10	5.111	5.028	4.948	4.908	4.870	4.831	4.793	4.756	4.719	4.573	4.431	4.104
29	Sc^{+3}	5.946	5.059	±0.10	4.999	4.921	4.845	4.809	4.772	4.736	4.701	4.666	4.631	4.495	4.363	4.076
30	Th^{+4}	4.766	4.925	±0.11	4.864	4.786	4.710	4.673	4.637	4.600	4.565	4.529	4.494	4.355	4.220	3.962
31	Zr^{+3}	—	4.813	±0.36	4.753	4.676	4.601	4.565	4.529	4.493	4.458	4.424	4.389	4.255	4.123	3.825
32	Be^{+2}	4.716	4.705	±0.11	4.652	4.586	4.524	4.494	4.464	4.435	4.407	4.379	4.352	4.247	4.073 |	4.058
33	Zr^{+4}	4.396	4.586	±0.33	4.527	4.452	4.380	4.345	4.310	4.276	4.242	4.208	4.175	4.045	3.964 (903S)	
34	U^{+4}	4.366	4.564	—	4.505	4.430	4.357	4.322	4.287	4.252	4.217	4.183	4.149	4.015	3.881 |	3.626
35	Hf^{+4}	4.566	4.477	±0.43	4.419	4.344	4.271	4.236	4.202	4.168	4.134	4.100	4.067	3.939	3.860 (927S)	
36	Ti^{+3}	ca 4.076	4.329	±0.22	4.274	4.204	4.137	4.104	4.072	4.040	4.009	3.978	3.947	3.828	3.712	3.499
37	$(Al^{+3})_2$	4.526	4.250	±0.07	4.188	4.107	4.026	3.986	3.946	3.906	3.867	3.828	3.789	3.629	3.471	3.275
38	V^{+3}	4.086	3.896	±0.43	3.841	3.771	3.704	3.671	3.639	3.608	3.577	3.546	3.516	3.398	3.284	3.087
39	Mn^{+2}	4.046	3.881	±0.11	3.828	3.760	3.695	3.663	3.632	3.601	3.570	3.540	3.510	3.391	3.289	3.044
40	Ti^{+4}	—	3.794	±0.22	3.741	3.673	3.619 (284V)									
41	Cr^{+2}	3.771	3.708	±0.07	3.655	3.587	3.523	3.492	3.461	3.430	3.400	3.371	3.341	3.227	3.115	2.883
42	V^{+2}	ca 4.046	3.664	±0.43	3.606	3.531	3.460	3.425	3.391	3.358	3.325	3.292	3.260	3.133	3.011	2.754
43	Cr^{+3}	3.606	3.601	±0.07	3.543	3.471	3.401	3.366	3.333	3.300	3.267	3.234	3.202	3.076	2.954 |	2.742
44	Zn^{+2}	3.629	3.591	±0.07	3.535	3.465	3.397	3.365	3.332	3.299	3.265	3.231	3.198	3.068	2.912	2.439
45	Ga^{+3}	3.496	3.440	±0.14	3.376	3.292	3.211	3.171	3.132	3.093	3.055	3.017	2.980	2.923 (952S)		
46	Fe^{+2}	3.306	3.417	±0.04	3.362	3.291	3.223	3.191	3.158	3.126	3.094	3.062	3.030	2.905	2.780	2.529
47	Cd^{+2}	3.269	3.356	±0.02	3.303	3.234	3.169	3.135	3.101	3.068	3.035	3.002	2.969	2.826	2.605	2.109
48	In^{+3}	3.208	3.353	±0.04	3.289	3.206	3.123	3.083	3.043	3.003	2.964	2.925	2.887	2.736	2.589 |	2.447
49	V^{+4}	—	3.307	±0.43	3.253	3.186	3.121	3.104 (327D)								
50	Co^{+2}	3.143	3.231	±0.02	3.177	3.110	3.045	3.014	2.983	2.952	2.922	2.892	2.862	2.746	2.631	2.391
51	Ni^{+2}	3.116	3.226	±0.02	3.169	3.096	3.026	2.992	2.958	2.924	2.890	2.857	2.825	2.697	2.573	2.338
52	Pb^{+2}	2.992	3.221	±0.04	3.155	3.082	3.011	2.975	2.938	2.901	2.865	2.829	2.793	2.654	2.525 |	2.350
53	Mn^{+3}	2.583	3.209	±0.07	3.152	3.079	3.009	2.975	2.941	2.908	2.875	2.842	2.810	2.682	2.557 |	2.383
54	Fe^{+3}	2.902	3.166	±0.19	3.109	3.036	2.966	2.932	2.899	2.865	2.832	2.800	2.767	2.640	2.513 |	2.354
55	Sb^{+3}	—	2.946	—	2.898	2.839 |	2.782	2.758	2.746 (376S)							
56	Bi^{+3}	—	2.891	—	2.834	2.761	2.690	2.652	2.615	2.578	2.542	2.506	2.470 |	2.381 (1027V)		
57	V^{+5}	—	2.706	±0.17	2.657 |	2.652 (111V)										
58	Tl^{+1}	3.202	2.602	±0.22	2.549	2.481	2.416 |	2.385	2.359	2.333	2.308	2.284	2.260	2.234 (655V)		
59	Cu^{+2}	2.529	2.526	±0.09	2.471	2.400	2.333	2.301	2.269	2.237	2.206	2.176	2.145	2.028 |	1.922	1.693
60	Co^{+3}	3.288	2.472	±0.14	2.415	2.342	2.273	2.239	2.205	2.172	2.139	2.107	2.075	1.949 |	1.826	1.670 (1327V)
61	Tl^{+3}	2.145	2.306	±0.14	2.250	2.180	2.113	2.078	2.044	2.011	1.978 |	1.945	1.918	1.815	1.718 (927V)	
62	Pd^{+2}	1.879	2.212	±0.22	2.158	2.091	2.026	1.995	1.964	1.934	1.904	1.874	1.845	1.741 |	1.660	1.574
63	Rh^{+3}	2.066	2.081	±0.29	2.025	1.952	1.882	1.849	1.815	1.782	1.750	1.717	1.684	1.554	1.424 |	1.099 (1427S)
64	Ag^{+1}	2.067	1.917	±0.04	1.871	1.815	1.762	1.736	1.711 |	1.690	1.674	1.660	1.646	1.597	1.551	1.509
65	Hg^{+2}	2.012	1.800	±0.22	1.735	1.653	1.574	1.535	1.476	1.414	1.353	1.293	1.233 |	1.180 (647D)		(1147V)
66	Pd^{+3}	—	1.518	±0.29	1.457	1.380	1.360 (227D)									
67	Au^{+3}	1.366	1.243	±0.43	1.194	1.131	1.071	1.042	1.014	0.986	0.958	0.931	0.904 |	0.809	0.734	0.555 (1197V)
68	Au^{+2}	<1.381	1.019	±0.43	0.966	0.899	0.834	0.803	0.772	0.742	0.712	0.683	0.654 |	0.538	0.421	0.144 (1252V)
69	Au^{+1}	1.186	0.607	±0.17	0.565	0.513	0.464	0.440	0.415	0.391	0.367	0.342 |	0.318	0.220	0.123	−0.121 (1202V)

S, sublimation; V, vaporization; D, decomposition.
* Values listed at the sublimation, vaporization, or decomposition temperatures obviously apply to cells with the solid or molten electrolyte, that is, slightly below the sublimation, vaporization, or decomposition temperature.

Table II. Standard electromotive forces for single, solid, or molten metallic bromide*

Order 25°C	Metal ion	E° 25°C (aqueous) v	25°C (solid) v	Uncertainty (25°C) v	100°C v	200°C v	300°C v	350°C v	400°C v	450°C v	500°C v	550°C v	600°C v	800°C v	1000°C v	1500°C v
1	Cs^{+1}	4.004	3.988	±0.01	3.918	3.824	3.730	3.683	3.637	3.590	3.544	3.498	3.452	3.204	2.903	2.468 (1300V)
2	Ra^{+2}	4.001	3.957	±0.07	3.890	3.803	3.718	3.676	3.635	3.594	3.553	3.513	3.473	3.310	3.154	2.667
3	K^{+1}	4.006	3.946	±0.01	3.874	3.775	3.677	3.628	3.580	3.532	3.485	3.438	3.391	3.187	2.904	2.385 (1383V)
4	Rb^{+1}	4.006	3.936	±0.04	3.866	3.773	3.681	3.635	3.589	3.543	3.497	3.452	3.407	3.151	2.852	2.348 (1352V)
5	Ba^{+2}	3.981	3.814	±0.01	3.750	3.669	3.590	3.552	3.514	3.476	3.438	3.401	3.364	3.216	3.084	2.791
6	Sm^{+2}	<4.24	3.708	±0.15	3.649	3.572	3.498	3.462	3.426	3.391	3.355	3.321	3.286	3.165	3.062	2.822
7	Sr^{+2}	3.971	3.621	±0.01	3.559	3.479	3.402	3.363	3.326	3.288	3.251	3.214	3.178	3.053	2.930	2.595
8	Na^{+1}	3.795	3.613	±0.02	3.544	3.445	3.348	3.299	3.251	3.203	3.156	3.108	3.061	2.889	2.667	2.107 (1392V)
9	Li^{+1}	4.126	3.569	±0.09	3.514	3.441	3.363	3.324	3.287	3.249	3.212	3.176	3.147	3.040	2.940	2.798 (1310V)
10	Ca^{+2}	3.951	3.416	±0.02	3.357	3.280	3.206	3.170	3.134	3.099	3.064	3.028	2.994	2.861	2.740	2.447
11	La^{+3}	3.601	3.122	±0.04	3.061	2.983	2.907	2.870	2.833	2.797	2.761	2.725	2.690	2.553	2.438	2.167
12	Ce^{+3}	3.561	3.050	±0.04	2.989	2.911	2.835	2.798	2.761	2.724	2.688	2.652	2.616	2.482	2.363	2.085
13	Pr^{+3}	3.551	3.011	±0.04	2.951	2.874	2.799	2.763	2.727	2.691	2.655	2.620	2.585	2.462	2.354	2.092
14	Nd^{+3}	3.521	2.986	±0.04	2.928	2.852	2.778	2.742	2.706	2.670	2.634	2.599	2.564	2.441	2.327	2.060
15	Pm^{+3}	3.501	2.934	±0.04	2.877	2.803	2.732	2.697	2.662	2.628	2.594	2.561	2.527	2.413	2.314	2.086
16	Sm^{+3}	3.491	2.891	±0.10	2.833	2.760	2.689	2.653	2.619	2.585	2.551	2.517	2.484	2.372	2.328 (887D)	
17	Gd^{+3}	3.481	2.862	±0.04	2.805	2.731	2.660	2.625	2.590	2.556	2.522	2.488	2.455	2.329	2.227	1.998 (1487V)
18	Tb^{+3}	3.471	2.819	±0.04	2.761	2.688	2.616	2.581	2.547	2.512	2.478	2.445	2.412	2.282	2.177	1.950 (1487V)
19	Dy^{+3}	3.431	2.775	±0.04	2.714	2.636	2.560	2.522	2.485	2.448	2.412	2.376	2.341	2.201	2.079	1.829 (1477V)
20	Y^{+3}	3.451	2.761	±0.04	2.700	2.621	2.545	2.508	2.471	2.434	2.398	2.362	2.326	2.187	2.062	1.815 (1467V)
21	Ho^{+3}	3.401	2.746	±0.04	2.686	2.607	2.531	2.493	2.456	2.420	2.383	2.347	2.312	2.172	2.047	1.805 (1467V)
22	Er^{+3}	3.381	2.717	±0.04	2.657	2.578	2.502	2.464	2.427	2.391	2.354	2.318	2.283	2.143	2.013	1.774 (1457V)
23	Eu^{+3}	3.491	2.689	±0.10	2.631	2.558	2.486	2.451	2.417	2.382	2.348	2.315	2.282	2.164	2.120 (887D)	
24	Tm^{+3}	3.361	2.689	±0.04	2.628	2.549	2.473	2.435	2.398	2.362	2.325	2.289	2.254	2.114	1.984	1.755 (1437V)
25	Lu^{+3}	3.331	2.645	±0.04	2.584	2.506	2.429	2.392	2.355	2.318	2.282	2.246	2.211	2.071	1.940	1.726 (1407V)
26	Mg^{+2}	3.451	2.606	±0.01	2.548	2.474	2.403	2.368	2.333	2.299	2.265	2.232	2.199	2.078	1.980	1.824 (1227V)
27	Zr^{+2}	—	2.528	±0.43	2.471	2.397	2.326	2.292	2.257	2.224	2.190	2.157	2.124	1.992	1.860	1.710 (1227V)
28	Sc^{+3}	3.161	2.506	±0.01	2.446	2.367	2.291	2.253	2.216	2.180	2.143	2.107	2.072	1.932	1.846 (929S)	
29	Zr^{+3}	—	2.433	±0.29	2.373	2.296	2.222	2.186	2.150	2.115	2.080	2.044	2.010	1.875	1.857 (827 dp)	
30	Yb^{+3}	3.351	2.428	±0.10	2.368	2.289	2.213	2.175	2.138	2.102	2.065	2.029	1.994	1.854	1.726 (ca 1000D)	
31	U^{+3}	2.881	2.397	—	2.342	2.272	2.205	2.171	2.138	2.106	2.073	2.041	2.009	1.889	1.793	1.569
32	Th^{+4}	2.981	2.378	±0.11	2.318	2.241	2.164	2.127	2.090	2.053	2.017	1.981	1.945	1.820	1.788 (857V)	
33	Hf^{+4}	2.781	2.201	±0.32	2.142	2.066	1.993	1.977 (322S)								
34	U^{+4}	2.581	2.060	—	2.003	1.929	1.858	1.823	1.789	1.755	1.721	1.691	1.663	1.573 (ca 766V)		
35	V^{+2}	ca 2.261	2.016	±0.43	1.958	1.883	1.810	1.775	1.740	1.706	1.672	1.639	1.605	1.476	1.374	1.269 (1227V)
36	Zr^{+4}	2.611	2.006	±0.22	1.948	1.873	1.801	1.766	1.761 (357S)							
37	Ti^{+2}	2.711	1.995	±0.22	1.940	1.869	1.801	1.768	1.735	1.703	1.671	1.639	1.608	1.511	1.424	1.331 (1227V)
38	Mn^{+2}	2.261	1.908	±0.04	1.854	1.786	1.719	1.687	1.654	1.623	1.591	1.560	1.529	1.422	1.334	1.322 (1027V)
39	Be^{+2}	2.931	1.869	±0.11	1.818	1.755	1.695	1.666	1.638	1.610	1.584	1.581 (527V)				
40	Ti^{+3}	ca 2.281	1.843	±0.14	1.788	1.717	1.649	1.615	1.582	1.550	1.518	1.486	1.454	1.331 (927 dp)		
41	$(Al^{+3})_2$	2.741	1.761	±0.03	1.707	1.649	1.617 (257V)									
42	Tl^{+1}	1.417	1.738	±0.02	1.686	1.619	1.553	1.517	1.480	1.444	1.416	1.391	1.367	1.275	1.267 (819V)	
43	Ti^{+4}	—	1.731	±0.11	1.710	1.687	1.680 (230V)									
44	In^{+1}	ca 1.331	1.717	±0.22	1.659	1.582	1.156	1.487	1.458	1.429	1.401	1.374	1.347	1.318 (662V)		
45	Zn^{+2}	1.844	1.624	±0.02	1.567	1.494	1.424	1.390	1.357	1.329	1.301	1.272	1.245	1.192 (702V)		
46	Cr^{+2}	1.985	1.539	±0.11	1.486	1.418	1.353	1.321	1.289	1.258	1.227	1.197	1.167	1.049	0.954	0.900 (1127V)
47	Cd^{+2}	1.484	1.537	±0.02	1.475	1.395	1.318	1.278	1.238	1.198	1.159	1.120	1.085	0.944	0.876 (863V)	
48	Ge^{+4}	—	1.409	±0.16	1.364	1.316 (189V)										
49	Pb^{+2}	1.207	1.366	±0.02	1.309	1.234	1.160	1.122	1.089	1.059	1.031	1.003	0.976	0.876	0.823 (914V)	

Table II (Continued)

Order 25°C	Metal ion	E° 25°C (aqueous) v	25°C (solid) v	Uncertainty (25°C) v	100°C v	200°C v	300°C v	350°C v	400°C v	450°C v	500°C v	550°C v	600°C v	800°C v	1000°C v	1500°C v
50	$(Si^{+3})_2$	—	1.344	±0.14	1.298	1.245	1.213 (240V)									
51	Sn^{+2}	1.217	1.331	±0.02	1.280	1.215	1.153	1.122	1.093	1.063	1.036	1.008	0.981	0.960 (639V)		
52	In^{+3}	1.423	1.321	±0.04	1.264	1.189	1.114	1.078	1.062 (371S)							
53	Ga^{+3}	1.611	1.297	±0.01	1.244	1.183 (314V)										
54	Fe^{+2}	1.521	1.247	±0.01	1.194	1.127	1.062	1.030	0.999	0.968	0.937	0.907	0.876	0.780	0.730 (927V)	
55	V^{+4}	—	1.225	±0.43	1.183	1.131	1.108 (247V)									
56	Co^{+2}	1.358	1.149	±0.02	1.097	1.030	0.965	0.934	0.902	0.872	0.841	0.811	0.781	0.684	0.635 (927V)	
57	Ni^{+2}	1.331	1.106	±0.04	1.049	0.977	0.907	0.872	0.838	0.804	0.771	0.738	0.705	0.576	0.527 (877V)	
58	Cu^{+1}	0.560	1.049	±0.03	1.000	0.939	0.881	0.853	0.826	0.799	0.774	0.754	0.736	0.667	0.605	0.494 (1318V)
59	Ag^{+1}	0.282	1.011	±0.01	0.966	0.911	0.860	0.836	0.814	0.795	0.781	0.767	0.754	0.706	0.659	0.520
60	Si^{+4}	—	0.999	±0.01	0.953	0.922 (153V)										
61	Sn^{+4}	1.074	0.987	±0.01	0.939	0.880	0.877 (207V)									
62	$(Hg^{+1})_2$	0.292	0.942	±0.01	0.871	0.779	0.690	0.646	0.582	0.573 (407D)						
63	Fe^{+3}	1.117	0.888	±0.06	0.836	0.769	0.716	0.692	0.669	0.647	0.625	0.604	0.583	0.571 (627V)		
64	Sb^{+3}	—	0.831	—	0.776	0.719	0.672 (288V)									
65	Bi^{+3}	—	0.824	—	0.774	0.710	0.657	0.630	0.604	0.578	0.573 (461V)					
66	B^{+3}	—	0.773	±0.06	0.742 (91V)											
67	Hg^{+2}	0.227	0.737	±0.01	0.663	0.566	0.483	0.469 (319V)								
68	Cu^{+2}	0.744	0.662	±0.02	0.609	0.541	0.476	0.459 (327D)								
69	As^{+3}	—	0.636	—	0.597	0.551	0.542 (221V)									
70	Mo^{+2}	—	0.585	±0.15	0.538	0.477	0.419	0.391	0.363	0.336	0.309	0.283	0.257	0.198 (727D)		
71	Rh^{+1}	0.481	0.564	±0.12	0.521	0.468	0.418	0.394	0.370	0.347	0.324	0.301	0.279	0.224 (727D)		
72	Mo^{+3}	1.281	0.520	±0.07	0.467	0.399	0.333	0.301	0.270	0.253 (427D)						
73	Rh^{+3}	0.281	0.506	±0.04	0.452	0.384	0.318	0.286	0.254	0.223	0.192	0.176 (527D)				
74	Pd^{+2}	0.094	0.492	±0.06	0.441	0.376	0.314	0.284	0.254	0.225	0.196	0.167	0.139	0.061	0.028 (927V)	
75	Ir^{+1}	—	0.477	±0.12	0.435	0.382	0.332	0.308	0.285	0.262	0.240	0.217	0.196	0.184 (627D)		
76	Mo^{+4}	—	0.434	±0.04	0.381	0.314	0.249	0.221 (347V)								
77	Pt^{+4}	—	0.390	±0.04	0.337	0.268	0.203	0.185 (327D)								
78	Ir^{+2}	−0.019	0.369	±0.07	0.315	0.247	0.182	0.150	0.119	0.088	0.071 (477D)					
79	W^{+2}	—	0.369	±0.15	0.321	0.260	0.202	0.174	0.146	0.126 (437D)						
80	In^{+3}	−0.069	0.361	±0.07	0.308	0.240	0.174	0.142	0.110	0.094 (427D)						
81	W^{+4}	—	0.325	±0.05	0.272	0.203	0.138	0.120 (327S)								
82	Os^{+2}	0.231	0.325	±0.11	0.277	0.217	0.159	0.131	0.103	0.076	0.049	0.023	−0.003	−0.094	−0.162	−0.202 (1127V)
83	W^{+5}	—	0.321	±0.13	0.271	0.207	0.149	0.134 (333V)								
84	Ru^{+3}	—	0.289	±0.04	0.236	0.168	0.102	0.085 (327D)								
85	Pt^{+3}	—	0.289	±0.10	0.236	0.167	0.101	0.069	0.037	0.035 (405D)						
86	Pt^{+2}	ca −0.119	0.282	±0.07	0.228	0.160	0.094	0.063	0.031	0.025 (410D)						
87	W^{+6}	—	0.275	—	0.267 (37D)											
88	Pt^{+1}	—	0.260	±0.13	(dp)											
89	Au^{+1}	−0.599	0.169	±0.04	0.125	0.069	0.063 (212D)									
90	Au^{+3}	−0.419	0.153	±0.07	0.106	0.053 (187D)										

S, sublimation; V, vaporization; D, decomposition; dp, disproportionates.

* Values listed at the sublimation, vaporization, or decomposition temperatures obviously apply to cells with the solid or molten electrolyte, that is, slightly below the sublimation, vaporization, or decomposition temperature.

Table III. Standard electromotive forces for single, solid, or molten iodides*

Order 25°C	Metal ion	E° 25°C (aqueous) v	25°C (solid) v	Uncertainty (25°C) v	100°C v	200°C v	300°C v	350°C v	400°C v	450°C v	500°C v	550°C v	600°C v	800°C v	1000°C v	1500°C v
1	Cs^{+1}	3.559	3.557	±0.01	3.491	3.397	3.303	3.257	3.211	3.164	3.119	3.073	3.028	2.791	2.500	2.080 (1280V)
2	Rb^{+1}	3.561	3.474	±0.04	3.406	3.315	3.224	3.179	3.134	3.089	3.045	3.000	2.956	2.705	2.406	1.967 (1304V)
3	K^{+1}	3.561	3.441	±0.01	3.369	3.269	3.171	3.122	3.074	3.026	2.979	2.931	2.884	2.686	2.387	1.923 (1324V)
4	Ra^{+2}	3.556	3.350	±0.07	3.283	3.195	3.110	3.068	3.027	2.986	2.945	2.905	2.865	2.713	2.578	2.111
5	Eu^{+2}	4.036	3.231	±0.15	3.172	3.095	3.021	2.985	2.948	2.913	2.878	2.846	2.819	2.712	2.613	2.384
6	Ba^{+2}	3.536	3.187	±0.01	3.124	3.042	2.963	2.924	2.886	2.848	2.811	2.773	2.737	2.598	2.479	2.205
7	Sm^{+2}	<3.80	3.122	±0.15	3.063	2.987	2.913	2.876	2.840	2.805	2.769	2.738	2.710	2.604	2.504	2.269
8	Na^{+1}	3.350	3.035	±0.01	2.967	2.871	2.776	2.729	2.682	2.636	2.589	2.544	2.498	2.353	2.135	1.703 (1304V)
9	Sr^{+2}	3.526	3.014	±0.01	2.953	2.874	2.797	2.759	2.722	2.685	2.648	2.617	2.589	2.480	2.370	2.063
10	Li^{+1}	3.681	2.914	±0.09	2.860	2.788	2.712	2.675	2.639	2.603	2.572	2.541	2.511	2.398	2.292	2.208 (1171V)
11	Ca^{+2}	3.506	2.845	±0.01	2.784	2.705	2.628	2.591	2.554	2.517	2.480	2.444	2.407	2.272	2.150	2.015 (1227V)
12	La^{+3}	3.156	2.486	±0.01	2.423	2.341	2.261	2.222	2.184	2.146	2.108	2.070	2.033	1.891	1.770	1.535 (1402V)
13	Ce^{+3}	3.116	2.457	±0.01	2.398	2.321	2.246	2.209	2.173	2.137	2.101	2.066	2.031	1.897	1.779	1.560 (1397V)
14	Pr^{+3}	3.106	2.414	±0.01	2.352	2.272	2.194	2.156	2.118	2.081	2.044	2.007	1.971	1.836	1.720	1.507 (1377V)
15	Nd^{+3}	3.076	2.371	±0.01	2.309	2.229	2.151	2.113	2.075	2.037	2.000	1.962	1.925	1.782	1.657	1.440 (1367V)
16	Pm^{+3}	3.056	2.327	±0.02	2.266	2.188	2.111	2.074	2.037	2.000	1.964	1.928	1.892	1.752	1.639	1.443 (1367V)
17	Sm^{+3}	3.046	2.284	±0.10	2.220	2.138	2.058	2.019	1.980	1.942	1.904	1.866	1.829	1.682 (820D)		
18	Gd^{+3}	3.036	2.201	±0.01	2.138	2.056	1.977	1.938	1.900	1.861	1.824	1.787	1.749	1.603	1.470	1.282 (1337V)
19	Tb^{+3}	3.026	2.183	±0.03	2.118	2.035	1.953	1.913	1.874	1.835	1.796	1.758	1.719	1.570	1.430	1.240 (1327V)
20	Dy^{+3}	2.986	2.154	±0.01	2.090	2.007	1.927	1.887	1.848	1.810	1.771	1.733	1.696	1.548	1.409	1.228 (1317V)
21	Y^{+3}	3.006	2.139	±0.03	2.077	1.995	1.916	1.878	1.839	1.801	1.764	1.727	1.690	1.545	1.404	1.237 (1307V)
22	Ho^{+3}	2.956	2.110	±0.01	2.046	1.962	1.881	1.841	1.801	1.762	1.723	1.685	1.647	1.497	1.351	1.174 (1297V)
23	Er^{+3}	2.936	2.096	±0.01	2.034	1.954	1.876	1.837	1.800	1.762	1.725	1.688	1.652	1.509	1.370	1.212 (1277V)
24	Tm^{+3}	2.916	2.067	±0.01	2.006	1.926	1.849	1.812	1.774	1.737	1.701	1.664	1.628	1.487	1.350	1.207 (1257V)
25	Eu^{+3}	3.046	2.038	±0.10	1.974	1.890	1.809	1.769	1.729	1.691	1.651	1.613	1.575	1.425	1.369 (877D)	
26	Zr^{+2}	—	2.038	±0.43	1.980	1.905	1.833	1.798	1.763	1.733	1.709	1.685	1.661	1.571	1.484	1.473 (1027V)
27	Lu^{+3}	2.886	1.995	±0.01	1.932	1.851	1.772	1.733	1.695	1.657	1.619	1.582	1.545	1.400	1.259	1.137 (1207V)
28	Mg^{+2}	3.006	1.951	±0.01	1.893	1.819	1.747	1.712	1.676	1.643	1.609	1.575	1.542	1.423	1.353 (927V)	
29	Zr^{+3}	—	1.922	±0.29	1.861	1.781	1.704	1.683 (327 dp)								
30	Sc^{+3}	2.716	1.908	±0.01	1.847	1.768	1.692	1.655	1.617	1.581	1.544	1.508	1.473	1.333	1.257 (909S)	
31	Yb^{+3}	2.906	1.807	±0.10	1.742	1.659	1.577	1.538	1.498	1.459	1.420	1.382	1.344	1.194	1.048	1.029 (1027D)
32	U^{+3}	2.436	1.767	—	1.714	1.647	1.581	1.549	1.517	1.486	1.455	1.424	1.393	1.270	1.146	0.837
33	Hf^{+4}	2.336	1.648	±0.32	1.586	1.507	1.430	1.392	1.355	1.335 (427S)						
34	Th^{+4}	2.536	1.496	±0.11	1.435	1.356	1.279	1.241	1.203	1.166	1.129	1.093	1.060	0.939	0.918 (837V)	
35	Zr^{+4}	2.166	1.496	±0.22	1.438	1.363	1.290	1.255	1.220	1.199 (431S)						
36	U^{+4}	2.136	1.467	—	1.410	1.336	1.265	1.230	1.195	1.160	1.126	1.092	1.058	0.923	0.788	0.383
37	V^{+2}	ca 1.816	1.453	±0.43	1.399	1.331	1.266	1.235	1.203	1.172	1.142	1.112	1.083	0.970	0.915 (927V)	
38	Ti^{+2}	2.266	1.409	±0.22	1.351	1.277	1.205	1.169	1.135	1.100	1.066	1.033	0.999	0.894	0.799	0.787 (1027V)
39	Mn^{+2}	1.816	1.388	±0.04	1.333	1.263	1.196	1.163	1.130	1.098	1.066	1.034	1.002	0.903	0.890 (827V)	
40	Tl^{+1}	0.972	1.388	±0.02	1.334	1.264	1.196	1.159	1.122	1.087	1.059	1.032	1.005	0.902	0.890 (823V)	
41	Cr^{+2}	1.541	1.279	±0.15	1.226	1.157	1.091	1.059	1.027	0.995	0.964	0.933	0.903	0.784	0.771 (827V)	
42	Ti^{+3}	ca 1.846	1.250	±0.14	1.194	1.122	1.052	1.020 (347 dp)								
43	Ti^{+4}	—	1.212	±0.11	1.159	1.094	1.037	1.010	0.995 (377V)							

Table III (Continued)

Order 25°C	Metal ion	E° 25°C (aqueous) v	25°C (solid) v	Uncertainty (25°C) v	100°C v	200°C v	300°C v	350°C v	400°C v	450°C v	500°C v	550°C v	600°C v	800°C v	1000°C v	1500°C v
44	Be^{+2}	2.486	1.203	±0.11	1.150	1.084	1.020	0.990	0.960	0.930	0.910 (487V					
45	Zn^{+2}	1.399	1.185	±0.01	1.130	1.060	0.993	0.960	0.928	0.895	0.868	0.841	0.815	0.750 (727V)		
46	$(Al^{+3})_2$	2.296	1.184	±0.01	1.129	1.057	0.999	0.971	0.952 (386V)							
47	In^{+1}	ca 0.886	1.171	±0.22	1.107	1.020	0.931	0.887	0.853	0.819	0.785	0.752	0.720	0.650 (715V)		
48	Cd^{+2}	1.039	1.141	±0.02	1.086	1.016	0.949	0.914	0.882	0.860	0.839	0.819	0.799	0.711 (796V)		
49	Ge^{+2}	0.636	1.084	±0.33	1.031	0.962	0.905	0.879	0.854	0.829	0.805	0.781	0.758	0.724 (677V)		
50	Ge^{+4}	—	1.019	±0.16	0.963	0.896	0.838	0.810	0.795 (377V)							
51	Pb^{+2}	0.762	1.008	±0.01	0.944	0.870	0.799	0.763	0.726	0.696	0.670	0.644	0.620	0.532	0.504 (872V)	
52	In^{+3}	0.978	0.911	±0.04	0.860	0.793	0.738	0.713	0.687	0.663	0.639 (500V)					
53	Ga^{+3}	1.166	0.853	±0.01	0.797	0.725	0.665	0.638 (349V)								
54	Sn^{+2}	0.772	0.849	±0.07	0.794	0.725	0.652	0.612	0.589	0.550	0.520	0.491	0.462	0.396 (714V)		
55	Cu^{+1}	0.115	0.821	±0.04	0.771	0.707	0.645	0.615	0.586	0.557	0.528	0.500	0.474	0.396	0.324	0.244 (1207V)
56	Ag^{+1}	−0.163	0.788	±0.01	0.743	0.696	0.659	0.641	0.624	0.607	0.590	0.574	0 563	0.528	0.496	0.401
57	Fe^{+2}	1.076	0.759	±0.04	0.706	0.639	0.574	0.542	0.511	0.480	0.449	0.418	0.390	0.306	0.295 (827V)	
58	$(Hg^{+1})_2$	−0.153	0.677	±0.02	0.609	0.521	0.444 (290D)									
59	Co^{+2}	0.913	0.646	±0.02	0.596	0.531	0.469	0.439	0.409	0.379	0.350	0.326	0.306	0.229	0.219 (827V)	
60	Hg^{+2}	−0.218	0.607	±0.01	0.542	0.459	0.387	0.358	0.355 (354V)							
61	B^{+3}	—	0.549	±0.07	0.510	0.464	0.460 (210V)									
62	Ni^{+2}	0.886	0.542	±0.02	0.487	0.415	0.346	0.312	0.278	0.245	0.212	0.179	0.147	0.053 (747S)		
63	Si^{+4}	—	0.452	±0.01	0.399	0.335	0.282 (288V)									
64	Sb^{+3}	—	0.452	—	0.403	0.341	0.288	0.263	0.238	0.225 (427V)						
65	Bi^{+3}	—	0.441	—	0.386	0.315	0.244	0.207	0.170	0.164 (408D)						
66	Mo^{+2}	—	0.369	±0.15	0.315	0.247	0.182	0.150	0.119	0.088	0.058	0.027	−0.004	−0.127	−0.249	−0.555
67	Rh^{+3}	−0.164	0.361	±0.14	0.308	0.239	0.174	0.156 (327D)								
68	Pd^{+2}	−0.351	0.325	±0.17	0.272	0.203	0.138	0.106	0.074	0.046	0.021	−0.002	−0.026	−0.082 (827V)		
69	Rh^{+1}	0.036	0.325	±0.13	0.277	0.217	0.159	0.132	0.104	0.090 (427D)						
70	As^{+3}	—	0.318	—	0.268	0.209	0.157	0.132	0.108	0.101 (414V)						
71	Ir^{+1}	—	0.304	±0.12	0.261	0.208	0.159	0.135	0.111	0.088	0.065	0.054 (527D)				
72	Mo^{+4}	—	0.304	±0.04	0.253	0.187	0.120	0.086	0.053	0.038 (422V)						
73	Ir^{+2}	−0.464	0.217	±0.07	dp											
74	Pt^{+3}	—	0.217	±0.10	0.160	0.086	0.032 (277D)									
75	Pt^{+4}	—	0.206	±0.04	0.150	0.078	0.024 (277D)									
76	Pt^{+2}	ca −0.564	0.195	±0.07	0.142	0.073	0.008	−0.010 (327D)								
77	Au^{+1}	−1.044	0.194	±0.04	0.165	0.138 (177D)										
78	Ir^{+3}	−0.514	0.152	±0.07	0.060	−0.059	−0.176	−0.233	−0.290	−0.321 (427D)						
79	W^{+2}	—	0.130	±0.15	0.077	0.009	−0.009 (227V)									
80	Rh^{+2}	0.036	0.108	±0.11	dp											
81	Pt^{+1}	—	0.108	±0.13	0.061	0.000	−0.058 (300 dp)									
82	W^{+4}	—	0.108	±0.11	0.055	0.029 (137D)										

S, sublimation; V, vaporization; D, decomposition; dp, disproportionates.
* Values listed at the sublimation, vaporization, or decomposition temperatures obviously apply to cells with the solid or molten electrolyte, that is, slightly below the sublimation, vaporization, or decomposition temperature.

Hydrogen Peroxide Reactions on Gold Electrodes

A. K. M. S. Huq[1] and A. C. Makrides

Tyco Laboratories, Incorporated, Waltham, Massachusetts

Studies of the kinetics of oxygen reduction on metal electrodes are generally complicated by the formation of surface oxides which are stable in the potential range of interest (1). Frequently, both the two-electron and four-electron reductions occur, with the result that the kinetics are further complicated by reactions involving hydrogen peroxide (2). The difficulties introduced by surface oxide films are absent with gold electrodes; in this case, the oxide film is reduced at potentials above 1.0v (3,4) so that oxygen reduction and the peroxide reactions can be studied on an oxide-free metal electrode over a relatively wide potential range.

The hydrogen peroxide reactions on platinum and gold electrodes have been examined by a number of authors (5-8). The suggested mechanisms assume either a surface saturated with adsorbed hydroxyl radicals (6), or postulate reactions with either adsorbed hydrogen or oxygen atoms on the electrode (7). Some results, presented below, on the H_2O_2 reactions on Au show that the mechanisms suggested so far are not correct. A more detailed discussion of the reaction mechanisms is given elsewhere.

The standard experimental procedure and precautions for electrochemical measurements were followed. The electrolytic cell was a three-compartment, Pyrex vessel and was cleaned in chromic-sulfuric solution. The test electrodes, gold cylinders of spectroscopic purity,[2] were electropolished in a cyanide bath and were mounted so that only Teflon and the electrode were exposed to solution (9). The test electrodes were cleaned either in chromic-sulfuric or in hot, concentrated nitric acid and rinsed with distilled water and test solution before use. Both cleaning procedures gave the same results. The counterelectrode was platinized platinum or gold and the reference electrode was saturated calomel. The cell was thermostated at 30.0° ± 0.1°C.

Triply distilled water, one distillation being from $KMnO_4$, was used to make up solutions of H_2SO_4 (C. P. reagent). *p*H measurements were carried out both before and after a run with a Beckman *p*H meter. The solution was de-aerated either with a stream of nitrogen or of argon.

The steady-state, current-potential curves were established potentiostatically with a Wenking potentiostat. After a rest potential was established, the electrode was subjected to the following cycle: the potential was decreased stepwise (50 or 100 mv per step) to 0.0v *vs.* a reversible H^+/H_2 in the same solution; then it was increased stepwise through the rest potential to about 1.2v *vs.* a reversible H^+/H_2 in the same solution, and then back to the rest potential. Any number of cycles could be traced in this fashion with reproducible results.

Current densities are expressed in amp/cm² of geometric area. The electrode area (~1 cm²) was determined for each run. Reported current densities can be converted to current densities per true cm² by dividing by a roughness factor of about 1.1. All potentials are expressed *vs.* the standard hydrogen electrode (S.H.E.).

The rest potential.—The rest potential of Au in H_2O_2 solutions is essentially independent of the concentration of H_2O_2 (0.05- 2.1 M/l) at constant *p*H (0.4). The *p*H dependence of the rest potential is shown in Fig. 1; it follows the relation

Rest potential = 0.816 — 0.052 *p*H at 30°C

This is in fair agreement with the results of Bockris and Oldfield (6) who found

Rest potential = 0.842 — 0.059 *p*H at 25°C

Electrochemical reduction and oxidation.—The overall reactions for the electrochemical reduction and oxidation of H_2O_2 are

$$H_2O_2 + 2e^- + 2H^+ \rightarrow 2H_2O$$

and

$$H_2O_2 \rightarrow O_2 + 2H^+ + 2e^-$$

Typical Tafel curves for reduction and oxidation are given in Fig. 2. The main point which we wish to emphasize in this communication is that the reaction rate at a fixed potential increases directly with peroxide concentration both for oxidation and for reduction (Fig. 2). Thus, the electrochemical orders of both reactions are unity with respect to H_2O_2.

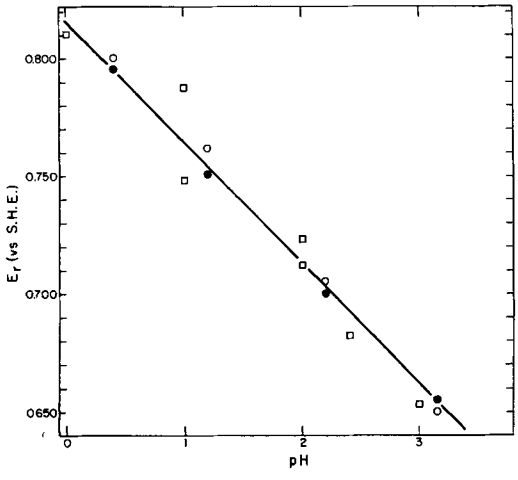

Fig. 1. Rest potential of gold in H_2O_2 solutions as a function of *p*H. Squares show values given by Bockris and Oldfield (6); open circles and solid circles are from this work.

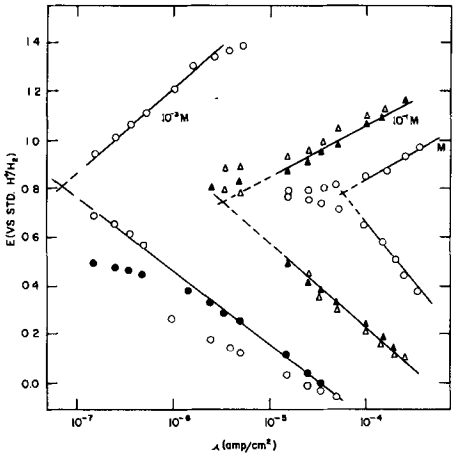

Fig. 2. Polarization curves for gold in H_2O_2 solutions. The solution was 0.1*N* H_2SO_4 in this instance. Open points are for increasing and full points for decreasing current densities.

[1] Present address: Atomic Energy Center, Dacca, Pakistan.
[2] Supplied by Johnson, Matthey & Company, Ltd., London.

These experimental results are not consistent with the mechanism advanced by Bockris and Oldfield (6) to account for the pH dependence of the rest potential. These authors suggested that the rest potential is determined by the activity of adsorbed OH radicals and that at even small H_2O_2 concentrations, the surface is saturated with OH radicals. This mechanism implies a zero order of reaction with respect to H_2O_2 which is contrary to observation.

Bianchi and collaborators (7) proposed that peroxide decomposes by a chemical, rather than electrochemical, process. According to these authors, peroxide decomposition takes place on cathodic polarization by reaction with atomic hydrogen adsorbed on the electrode surface, *i.e.*,

$$H_2O_2 + 2H_{ads} \rightarrow 2H_2O$$

A substantial cathodic current ($>10^{-5}$ amp/cm^2) was observed on gold at 0.5v *vs.* H^+/H_2. At this potential, no adsorbed hydrogen is detectable on gold. Therefore, this mechanism is not tenable. Furthermore, this mechanism does not account for the Tafel slope.

According to Bianchi *et al.* (7), H_2O_2 decomposes anodically by reacting with a surface metal oxide according to

$$M(0) + H_2O_2 \rightarrow M + H_2O + O_2$$

This mechanism does not account for the Tafel slope observed here on anodic polarization. It is of interest to note that in experiments with $C_{H_2O_2} = 10^{-1}$M, the anodic overpotential increased sharply at 1.4v *vs.* H^+/H_2, *i.e.*, at the potential where appreciable oxide formation takes place (4). Thus, contrary to the suggestion of Bianchi *et al.* (7), oxide formation may actually inhibit the electrochemical oxidation of H_2O_2 on gold electrodes.

It is apparent that the electrochemical reactions of H_2O_2 on gold are complicated. They are similar in some respects to those on platinum. For example, Gerischer and Gerischer (8) found Tafel behavior on Pt and a first order dependence on $C_{H_2O_2}$, but a highly complicated pH dependence: The coefficient $(\partial \log i/\partial \text{ pH})_E$ was a function of pH and changed from —0.3 at pH = 1 to —0.6 at pH = 5, while for anodic polarization this coefficient varied from 0.6 to 0.2 in the same pH range. No mechanism was advanced by these authors which explained these observations (8).

Finally, the suggestion that platinum or gold electrodes are reversible with respect to hydrogen ion in solutions containing H_2O_2 (2, 6), and that their operation does not depend on the activity of H_2O_2, provided some small amount is present (2, 6), are also not borne out by these studies. The relatively simple dependence of the rest potential on pH and its independence on the H_2O_2 activity are essentially accidental: they arise from summing up partial reactions which are not reversible and which have fairly complicated mechanisms.

Acknowledgment

The authors are grateful to Mrs. M. J. Turner for her skillful experimental assistance. This work was supported by the Harry Diamond Laboratories of the U. S. Army under Contract No. DA-49-186-AMC-136(D).

Manuscript received June 4, 1964.

Any discussion of this paper will appear in a Discussion Section to be published in the June 1966 JOURNAL.

REFERENCES

1. M. Breiter in "Advances in Electrochemistry and Electrochemical Engineering," Vol. I, p. 123, P. Delahay, Editor, Interscience, New York (1961).
2. "Reference Electrodes," Chap. 7, D. J. G. Ives and G. J. Janz, Editors, Academic Press, New York (1961).
3. H. A. Laitinen and M. S. Chao, *This Journal*, **108**, 726 (1961).
4. S. B. Brummer and A. C. Makrides, *ibid.*, **111**, 1122 (1964).
5. J. Weiss, *Trans. Faraday Soc.*, **31**, 668, 1547 (1935).
6. J. O'M. Bockris and L. Oldfield, *ibid.*, **51**, 249 (1955).
7. G. Bianchi, F. Mazza, and T. Mussini, *Electrochim. Acta*, **7**, 457 (1962); G. Bianchi, G. Caprioglio, S. Malaguzzi, F. Mazza, and T. Mussini, AFOSR TN 60-299, May 1960.
8. R. Gerischer and H. Gerischer, *Z. physik. Chem. (N.F.)*, **6**, 178 (1956).
9. M. Stern and A. C. Makrides, *This Journal*, **107**, 782 (1960).

Brief Communication

Etching Characteristics and Light Figures of the {111} Surfaces of GaAs

Isamu Akasaki and Hiroyuki Kobayasi

Matsushita Research Institute Tokyo, Inc., Ikuta, Kawasaki, Japan

Because of various interesting properties and practical importance, the physical, chemical, and electrical properties of GaAs have been extensively investigated (1-3). GaAs has a zinc-blende structure and exhibits crystallographic polarity along the <111> directions (4), that is, the outermost atom layer in each {111} face consists of either Ga or As atoms which are triply bonded to the lattice. Conventionally (4) the former is designated as A(111) and the latter B($\bar{1}\bar{1}\bar{1}$). These two {111} faces are physically and chemically different.

In this paper, the differences in orientations of etch pits and light figures of both the {111} faces are described. An explanation for this will also be given in terms of the relative reactivities of some principal planes and the structural properties of GaAs. On the basis of these differences both types of {111} faces are easily distinguished.

Orientations of Etch Pits and Light Figures

To determine the crystallographic indices of facets developed on a crystal surface by grinding or chemical etching, the light figure method was used. The sample was cut from a GaAs single crystal in the form shown in Fig. 1. The base and both sides were ground within a few degrees parallel to the planes ($2\bar{1}\bar{1}$), Ga(111), and As($\bar{1}\bar{1}\bar{1}$), respectively. Figure 2 illus-

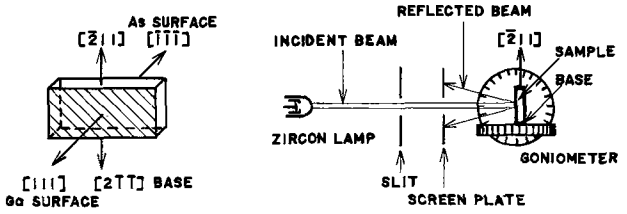

Fig. 1 (left). Form and orientations of sample. Fig. 2 (right). Light figure apparatus and arrangement of sample.

trates the light figure apparatus in which the sample was arranged with the [2̄11] direction up, and with a narrow beam of light (about 1 mm in diameter) normal to the {111} faces and the screen plate. The compositions of etchants and etching times used are similar to those summarized by Faust (2) (see Table I).

Ga *surface.*—Figure 3 shows a photomicrograph and a light figure of Ga(111) face ground with No. 500 emery powder. The light figure consists of threefold symmetrical arrows pointing in the [2̄11], [12̄1], and [112̄] directions. As seen in Fig. 4 and 5, upon the A-1 etching, the mechanically damaged layer was gradually removed, the <2̄11> arrows of the light figure becoming faint and giving way to three <211̄> arrows in opposite positions. This change of light figure is schematically depicted in Fig. 6. Similar light figures pointing in <211̄> directions were also obtained by the A-2 etching.

As *Surface.*—Optically the ground As(1̄1̄1̄) face resembled that of the Ga(111)) face, Fig. 3(a). The light figure from a ground As surface was also similar to that from a ground Ga surface, Fig. 3(b), and correspondingly pointed in [21̄1̄] directions. Since surface grinding introduces a center of symmetry, the resulting Laue symmetry m3m is that of the diamond structure. A light figure from the Ga(111) face of threefold symmetry with the arrows pointing in the [2̄11], [12̄1], and [112̄] directions, respectively, corresponds to a related light figure from the As(1̄1̄1) face with the arrows of the threefold symmetry pointing in the three opposite directions [21̄1̄], [1̄21̄], and [1̄1̄2], respectively.

Figure 7 shows a photomicrograph and a light figure of an etched As(1̄1̄1̄) face with the B-1 etchant. The vertices of the triangular etch patterns and the arrows of the light figure point in the [21̄1̄], [1̄21̄], and [1̄1̄2] directions. B-2 etchant produces the more complex light figure seen in Fig. 8. The form of the light figure has not yet been analyzed, but the arrows also point in <211̄> directions. Contrary to the case of Ga surface, these light figures from ground and etched As surfaces are always oriented in the same directions.

Etching Rate Measurement

Since the incident beam is normal to the {111} faces, the arrow parts of the light figures show reflectograms of many oblique facets developed on the surfaces. Accordingly the directions of arrows give the crystallographic indices of the facets; for example in the case of Ga surface, the <2̄11> arrows indicate that the oblique micro-facets may be {1̄11} or {110} planes assuming that only low index planes are developed. In surface grinding, {110} planes seem important, since these planes are predominantly developed in the microcleavage of GaAs (1, 2).

The directions of the light figure shown in Fig. 5 are the same as those of the Ga surface etched with Schell etchant, and the latter orientations were the [21̄1̄], [1̄21̄], and [1̄1̄2] directions as reported by Abrahams *et al.* (5). Therefore the side facets of the etch pits appearing on Ga surface with HNO_3-H_2O etchants may be {100} planes. An explanation for this is given by the relative reactivities of some principal planes with the etchant, because pits developed by etching are generally bounded by planes of minimum reactivity. Samples (about 5 x 10 x 1 mm in size) were cut from undoped n-type single crystal GaAs with carrier concentration of about 10^{17} cm^{-3} and were polished by Br_2-CH_3OH solution (6) previously to remove the mechanically damaged layers. One large surface of each sample within a few degrees parallel to Ga(111), (110), (100), or As(1̄1̄1̄) was prepared, and the remaining surfaces were completely coated with Apiezon

Table I. Compositions of etchants and etching times for production of light figures

Etchant				
Notation	Composition	Volume ratio	Etching time	Surface
A-1	$HNO_3 : H_2O$	1 : 1	7 min	Ga
A-2	$HNO_3 : H_2O$	2 : 1	10 sec	Ga
B-1	$HF : H_2O_2 : H_2O$	2 : 1 : 8	50 min	As
B-2	$HF : HNO_3 : H_2O$*	3 : 1 : 2	7 min	As

Concentration (wt %) : HNO_3, ~60; HF, 46; H_2O_2, 30.
H_2O : deionized water.
* Several drops of 1% $AgNO_3$ are added in mother solution of about 30 ml.

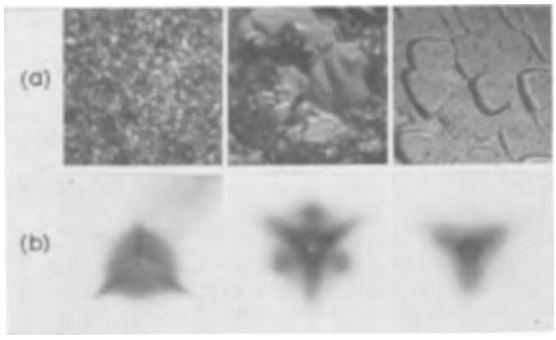

Fig. 3-5, 7, 8. In each figure, (a) shows photomicrograph (magnification 490X) of surface and (b) light figure. Fig. 3 (left) Ga surface ground with No. 500 emery powder; Fig. 4 (center) and 5 (right). Ga surface which had been ground and then etched with A-1 etchant for about 3 min (Fig. 4) and for about 7 min (Fig. 5).

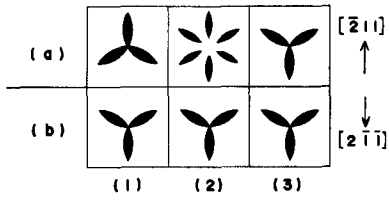

Fig. 6. Schematic illustration of orientations of various light figures from Ga surface (a) and As surface (b). 1, ground surface; 2, ground and slightly etched surface; 3, etched surface.

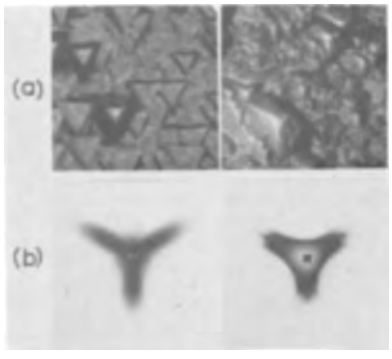

Fig. 7 (left) and 8 (right). As surface etched with B-1 etchant for about 50 min (Fig. 7) and with B-2 for about 7 min (Fig. 8).

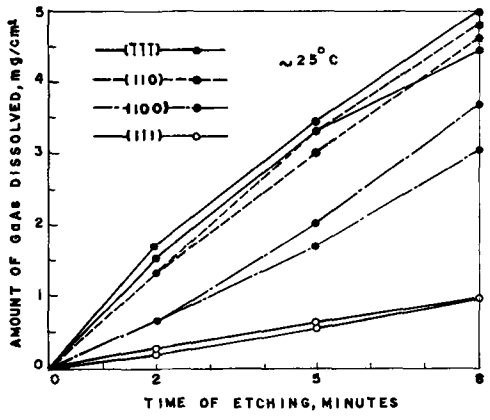

Fig. 9. Amount of GaAs dissolved with A-1 etchant as a function of orientation.

wax to protect them from the etchant. The etching rates of the respective planes were determined from weight losses of the samples which were simultaneously immersed in the A-1 etchant. The temperature of the etchant was kept at about 25°C. The results of Fig. 9 show that the etching rate decreases in the following order: As{$\bar{1}11$}>{110}>{100}>Ga{111}, which differs from the order in InSb for the etchants reported in (7). Since the {$\bar{1}11$} planes developed on Ga(111) face consist of As atoms only (4), it is not necessary to take account of the reactivity of Ga{$1\bar{1}\bar{1}$} planes. It appears that the pits obtained on the Ga(111) face by the A-1 etching are bounded by {100} planes which are more stable than the others.

On the other hand, the results of Fig. 6 suggest that the side facets of pits appearing on the As($\bar{1}\bar{1}\bar{1}$) face by chemical etching may be represented by either planes {$\bar{1}\bar{1}0$} or {$1\bar{1}\bar{1}$}. The etching rate of the four crystallographic planes with the B-1 etchant is in this order: As{$\bar{1}11$}$\simeq${110}$\simeq${100}>Ga{111}, which is in agreement with the results obtained by the A-1 etching. In this case, the reactivity of the Ga{$1\bar{1}\bar{1}$} planes must be compared with that of the {$\bar{1}\bar{1}0$} planes. Thus these side facets are thought to be the most stable Ga{$1\bar{1}\bar{1}$} family planes.

It is of interest that the side facets of etch pits appearing on the Ga surface may be {100} planes, whereas on the As surface {111} planes are predominantly revealed by these etchants. The former type of etch pit corresponds to the positive trigon pit and the latter to the negative trigon pit,[1] as observed in Ge (8). This relation differs from the case that etch pits on A surfaces of two kinds of III-V compounds. namely, GaP and InAs, are positive and negative trigon pits, respectively (2). As shown in Fig. 6, the light figures from the ground and etched Ga surfaces are oppositely oriented, while those of the As surface are in the same directions. These relations easily lead to the differentiation of both the {111} faces. From the orientations of light figures,[2] any crystallographic orientation of a sample can be readily determined with considerable accuracy.

Acknowledgment

The authors would like to express their thanks to Dr. Y. Koike and to Dr. K. Miyaji for their interests in this work. This experiment was greatly assisted by Messrs. T. Hara and M. Hashimoto.

Manuscript received Jan. 4, 1965; revised manuscript received April 12, 1965.

Any discussion of this paper will appear in a Discussion Section to be published in the June 1966 JOURNAL.

REFERENCES

1. C. Hilsum and A. C. Rose-Innes, "Semiconducting III-V Compounds" in "International Series of Monographs on Semiconductors," H. K. Henisch, Editor, Vol. 1, Pergamon Press, New York (1961).
2. "Preparation of III-V Compounds" in "Compound Semiconductors," R. K. Willardson and H. L. Goering, Editors, Vol. 1, Reinhold Publishing Corp., New York (1962).
3. O. Madelung, "Physics of III-V Compounds," Translated by D. Meyerhofer, John Wiley & Sons, Inc., New York (1964).
4. H. C. Gatos and M. C. Lavine, *This Journal*, **107**, 427 (1960).
5. M. S. Abrahams and L. Ekstrom, "Properties of Elemental and Compound Semiconductors," H. C. Gatos, Editor, Metallurgical Society Conferences, Vol. 5, p. 225, Interscience Publishers, New York (1960).
6. C. S. Fuller and H. W. Allison, *This Journal*, **109**, 880 (1962).
7. M. C. Lavine, A. J. Rosenberg, and H. C. Gatos, *J. Appl. Phys.*, **29**, 1131 (1958).
8. T. Arizumi and I. Akasaki, *Japan. J. Appl. Phys.*, **2**, 143 (1963).
9. Unpublished results.

[1] The pits developed on both the Ga(111) and As($\bar{1}\bar{1}\bar{1}$) faces of GaAs by iodine vapor at higher temperatures were found to be oriented in <$\bar{2}11$> and <$2\bar{1}\bar{1}$> directions, respectively, indicating that they were negative trigon pits (9).

[2] All photographs of light figures lack the detail and sharpness of the direct view on the screen plate.

A Transmission Electron Microscope Study of the Breakdown of Passivity on Fe-24% Cr

H. W. Pickering[1] and R. P. Frankenthal

Edgar C. Bain Laboratory for Fundamental Research,

United States Steel Corporation, Research Center, Monroeville, Pennsylvania

ABSTRACT

The application of transmission electron microscopy and of selected area electron diffraction together with potentiodynamic techniques is described in a study of the nature of the breakdown of passivity on Fe-24% Cr. When the potential is slowly swept from the passive region to the Flade region, local breakdown of the passive film occurs, followed by pitting of the substrate. Physical or chemical inhomogeneities in the passive film not associated with dislocation termini or grain boundaries in the alloy appear to be the most probable sites for the breakdown. However, the influence from multi-atomic steps in the alloy cannot be eliminated. On the other hand, if the rate of potential change from the passive region into the Flade region is rapid, general reduction of the film occurs followed by general etching of the alloy surface instead of pitting. In this case the effect of the inhomogeneities in the film is lost.

It has been shown that the size of the pits can be calculated assuming an equal and uniform current density on all the pit surfaces; this current density has been calculated to be slightly less than the critical current density for passivation. The observed pitting is discussed in relation to crystallographic etch pitting of dislocations on close-packed planes, the passive film acting to retard the lateral motion of steps. The results also show that an "aggressive anion" is not necessary for the initiation and initial propagation of pitting to occur if other conditions are fulfilled. Finally, the observed data appear to agree best with the theory of passivity that envisions a sequence of steps starting with the adsorption of an oxygen species and ending with the formation of an oxide.

The passivity of metals and alloys and its breakdown have been studied primarily by well-known electrochemical techniques, such as the amperostatic and the potentiostatic determination of polarization curves (1-3). Such studies usually measure an average current density. They give little information about the local current distribution, the nature and thickness of the passive film, or its distribution over the surface. To obtain such information nonelectrochemical techniques must be used. For example, some optical microscope examinations have been made of the pitting that occurs during the breakdown of passivity in certain media (4), ellipsometry has been applied to the measurement of the thickness of passive films (5, 6), and electron diffraction has been used to identify the passive films on iron (7). The work on iron (5, 7) has shown the passive film to be approximately 20Å thick so that it would be very difficult to see even in the electron microscope, Recently Kruger (5) has observed the sites of film breakdown on iron by optical and by transmission electron microscopy. His technique involved placing the passivated iron in a dilute copper sulfate solution until passivity decayed, as indicated by potential measurements. Copper deposited at the cathodic sites during the subsequent attack on the iron. Discrete, noncontinuous cathodic sites were observed, and it was determined indirectly that the breakdown depended on properties of the film, which in turn were affected by the metal substrate since surface orientation influenced the number of breakdown sites. However, no effect due to emergent dislocations in the alloy surface could be found.

In this work transmission electron microscopy and selected area electron diffraction have been applied to study the breakdown of passivity on an Fe-24% Cr alloy in H_2SO_4 by observing the sites of attack on the alloy at which the passive film had been reduced. It is assumed that those sites at which film breakdown occurs will be anodic to the areas still covered by the passive film and thus will preferentially dissolve. The advantage of this technique over Kruger's is that one observes the metal directly rather than observing copper decoration. On the other hand, by our technique it is necessary to allow the attack of the substrate to proceed to a point at which one can observe this attack by electron microscopy. In this work the passivation and breakdown thereof were controlled electrochemically by a potentiostat. An iron-chromium alloy was chosen primarily because this alloy system has been studied extensively (8-15) and because the alloy does not oxidize appreciably when exposed to air at room temperature; thus no complications arise during the transfer of the sample from the electrolytic cell to the electron microscope. It will be shown that when the potential of the specimen is changed slowly from the passive region to the Flade region, crystallographic pitting of the substrate alloy is observed, whereas when the change in potential is very rapid, a general etching of the alloy surface is observed. The observed data permit one to extend the theory of pitting corrosion and to discuss the nature of the film that causes passivity.

Experimental

The working electrode for the electrochemical measurements and the foils for the electron microscope specimens were prepared from a vacuum melt of high-purity Fe-24% Cr alloy which has the following analysis: Cr-23.8%; C-0.0075%; N-0.0068%; O-0.050%; P-<0.005%; S-0.004%; Si-<0.01%; Al-<0.005%; Cu-<0.01%; Mg-<0.001%; no other elements were detected. This is a bcc alloy. The bulk alloy was vacuum-annealed at 760°C for 64 hr and quenched in brine. Cylindrical electrodes (1 in. high and ¼ in. in diameter) were machined with a threaded hole for electrical connection at one end. The material for the foils was cold-rolled to 0.003 in. The electrodes and foils were then re-annealed in vacuum at 760°C for 40 hr and quenched in brine. Some foils were used in the annealed state and others were elongated up to 4% in a tensile machine. Immediately prior to use, the elec-

[1] On leave until September 1965 at the Max-Planck-Institut für Physikalische Chemie, Göttingen, Germany.

trodes and the foils were electropolished in a mixture of glacial acetic acid and perchloric acid (5:1) at 35v, rinsed in reagent-grade methanol, dried, and immediately inserted into the cell. Electrical contact was made to the electrode by means of a brass screw that was isolated from the environment by a Teflon sleeve. To obtain electrical contact with the foil, a thin platinum wire, covered by a glass sleeve, was spot-welded to one end of the foil. The opening in the sleeve at the weld area, as well as the weld, was sealed with polyethylene.

The studies were conducted in 1*N* H_2SO_4 made from reagent-grade acid and doubly distilled water with a conductivity of 3 x 10^{-7}mho-cm. The results obtained with pre-electrolysis of the solution for 24 hr at a current density of 15 ma/cm^2 between two platinum electrodes, each 10 cm^2 in area, did not differ from those obtained without pre-electrolysis. All solutions were purged with prepurified helium before and during use.

The cell was constructed completely of Pyrex. Both water-wetted stopcocks and Teflon stopcocks were used. A Luggin capillary connected the cell to the reference electrode via a salt bridge. The auxiliary electrode was a platinum cylinder (40 mm diameter), concentric with the working electrode to insure uniform current distribution. The working electrode was inserted through a ball joint, so that the electrode could be properly placed with respect to the Luggin capillary. A hydrogen reference electrode was used and all potentials are reported relative to the normal hydrogen electrode (NHE). Prepurified helium was swept through the cell at all times. The potential-current curves were obtained with a Wenking potentiostat and a motor-driven potentiometer. The rate of variation of potential was normally 100 or 200 mv/hr; this is referred to below as the slow sweep rate. The potential could also be switched rapidly from any one value to another. Current-time transients were observed on an oscilloscope and photographed with a Polaroid camera. When the bulk specimens and the foils were treated electrochemically in an identical manner, the potential-current curves were always similar. All work was done at 25° ± 1°C.

After a foil had been subjected to its specific polarization treatment, it was pulled from the cell with the potential still applied, rinsed with reagent-grade methanol, and dried. Some foils were examined immediately in the electron microscope; others were stored in a desiccator until they were examined. There was no effect due to storage. Each foil was examined by transmission electron microscopy in a Siemens Elmiskop. In addition, by selected area electron diffraction it was possible to obtain crystallographic data of specific interest. When thickness fringes were used for quantitative measurements, it was necessary to tilt the specimen until it was oriented in the exact Bragg condition (16).

Results

A potential-current curve for the alloy is shown in Fig. 1a. The potential region from —0.3 to +0.5v was measured by starting at +0.5v and sweeping the potential to —0.3v at 200 mv/hr. The transpassive region was measured by sweeping the potential from +0.5 to +1.8v at 200 mv/hr. A small cathodic loop is observed prior to the breakdown of passivity. This has been explained by Edeleanu (3) and is due to the beginning of hydrogen evolution prior to the breakdown. Figure 1b shows the anodic loop in greater detail.

Figures 2a and 2b show foils with electropolished surfaces. In Fig. 2a the smoothness of the surface is indicated by the uniform breadth of the thickness fringes at the edge of the foil and at the grain boundary. Figure 2b shows a typical dislocation distribution for this alloy after annealing followed by a 2% elongation.

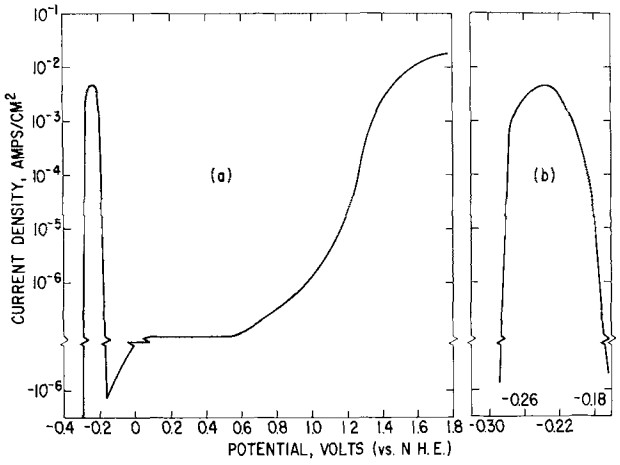

Fig. 1. Potential-current curve for Fe-24% Cr in 1*N* H_2SO_4; sweep rate, 200 mv/hr. (a) From hydrogen evolution to oxygen evolution; (b) anodic loop only.

If a specimen is passivated without going through the anodic loop, its appearance will be identical with those of Fig. 2a and 2b. This can be done by either immersing the sample directly at any potential in the passive potential range or by first immersing it at a potential more negative than —0.28v (hydrogen evolution range) and then switching the potential into the passive region. No differences are observed between the two methods.

When an electropolished and passivated foil is subjected to a slow potential sweep from +0.5v into the Flade region (—0.17v to —0.24v) and then examined by transmission electron microscopy, one typically observes crystallographic pits such as shown in Fig. 3-6. This type of pitting has been found on the following surfaces: {001}, {111}, {121}, {021}, {221}, {133}, {135}, and {231}. The morphology of the pits is a function of substrate orientation. However, the number of micrographs obtained were insufficient to evaluate

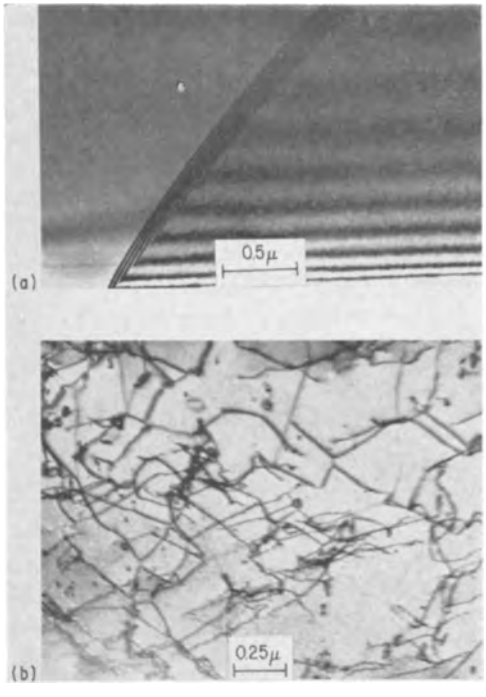

Fig. 2. Transmission electron micrographs of electropolished and/or passivated foils. (a) Smooth and uniform thickness fringes at edge of foil and at grain boundary indicate smoothness of foil surface; (b) smooth and undistorted image of dislocations in a foil annealed and elongated 2% indicates a polished foil surface.

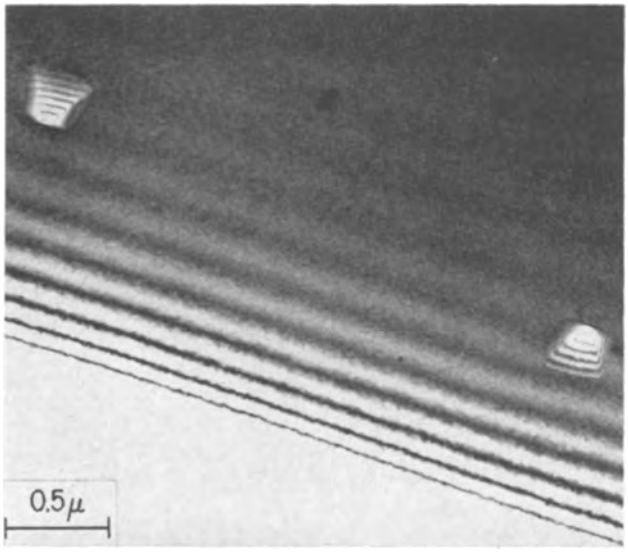

Fig. 3. Transmission electron micrograph of a foil with {121} surface on which passivity was slowly destroyed producing crystallographic pitting. Smooth thickness fringes at edge of foil indicate that no etching has occurred.

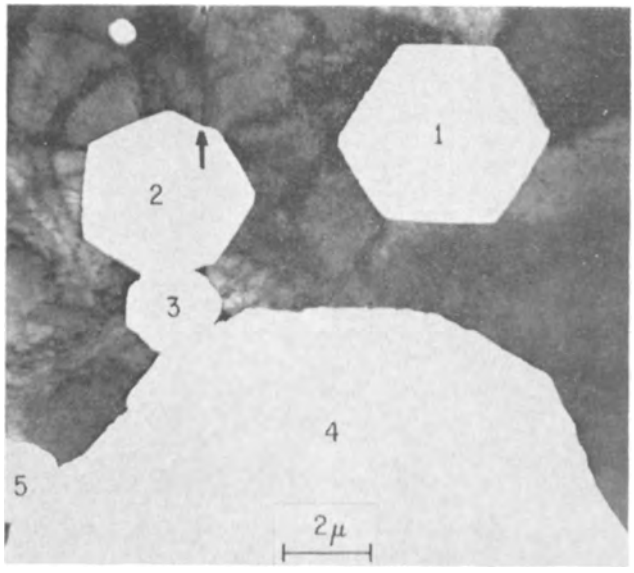

Fig. 4. Transmission electron micrograph of a foil with a {221} surface on which passivity was slowly destroyed producing crystallographic pitting. Arrow shows grain boundary.

whether or not the frequency of pitting, *i.e.*, film breakdown, is also a function of substrate orientation. It has also been established that pitting does not occur preferentially at dislocations, either present after the anneal or produced by plastic deformation, or at grain boundaries in the alloy. This was readily determined since the pits, dislocations, and grain boundaries could be observed simultaneously; this observation is consistent with previous electron microscopic observations (17) of pitting of metals and alloys covered by protective films. The effect of multi-atomic steps on the alloy cannot, however, be ruled out since examination of bulk specimens at low magnification (1900X, optical microscope) indicates possible mutual alignment of some of the pits.

The foil shown in Fig. 3 was swept from +0.5v to −0.19v. In this micrograph one sees pits with thickness fringes along their sides giving an indication of their angle with the surfaces. Selected area electron diffraction established that the pits are on a {121} surface and that the two sides of each pit which appear parallel to each other form <101> traces with the surface. The traces can be associated with the intersection of low-index planes with the surface; however, the traces of the other two sides do not correspond to low-index planes. The smoothness of the thickness fringes at the edge of the foil indicates that there has been little, if any, general etching of the foil surface. Crystallographic pitting and a lack of general etching were typical of all the experiments in which the breakdown of passivity occurred during slow potential sweeps.

The foil shown in Fig. 4 was swept from +0.5v to −0.24v. The pits are hexagonal in shape. A grain boundary runs through pits 2, 3, and 4 and the sides of the pits in the right-hand grain are rotated approximately 20° across the boundary from the sides in the left-hand grain. Equivalent sides of pits in the same grain are parallel. Although the sharp sides have been rounded off in pit 4, as is typical for later stages of pit growth, the basic shape of the hexagon can still be discerned, and the sides are parallel to the equivalent sides on the other pits. The left-hand grain has a {221} surface. The orientation of the right-hand grain was not established, but from the shape of the pits, it presumably also has a {221} surface. Surface traces for these pits could not be positively identified, but quite likely are in each case one of two possible traces, both of which lie within the error of the measurement

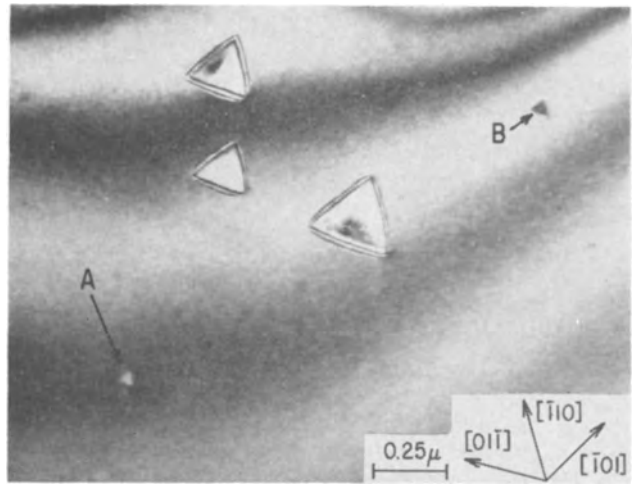

Fig. 5. Transmission electron micrograph of a foil with a (111) surface on which passivity was slowly destroyed producing crystallographic pitting. Vectors shown correspond to pit traces.

and both of which could be formed by low index planes.

In Fig. 5 one observes triangular pits on a {111} surface that was swept to −0.18v. The faces of the pits make <110> traces with the foil surface identifying them as probably belonging to one or more of the low-index planes. Taking a reasonable value for the extinction distance of 300Å in this alloy for the operating 110 reflection, it is possible to estimate the slope of the sides from the number and separation of the thickness fringes seen at the borders of each pit. A slope of greater than 60° but less than 90° is obtained indicating that of the low index planes only the {111} planes could be parallel to the pit sides. Furthermore, from contrast considerations, it may be deduced that the bottoms of the pits must be nearly flat and closely parallel to the surface and therefore must also be {111} planes. This is indicated by the observations that there are an equal number of thickness fringes at the borders of each pit and that for those pits lying fully within the bend contours (pit A, Fig. 5) or fully out of the bend contours (pit B), the contrast does not change within the pit.

Figure 6 shows an example of the rounding-off of a crystallographic pit as it gets large. It is obvious from

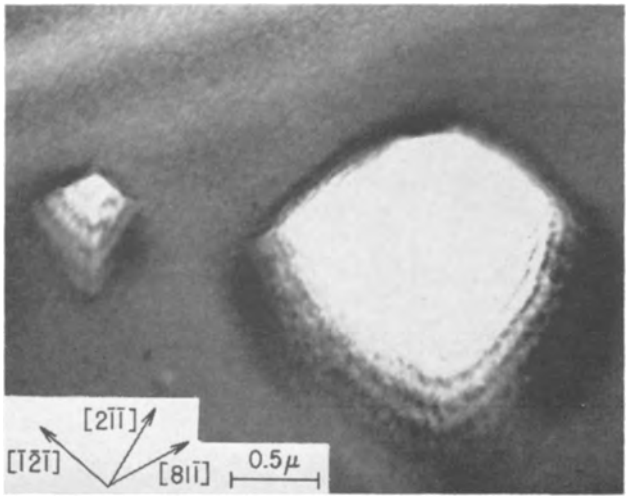

Fig. 6. Transmission electron micrograph of a foil with a (1$\bar{3}$5) surface demonstrating rounding of a pit at advanced stage of growth. Vectors shown correspond to pit traces.

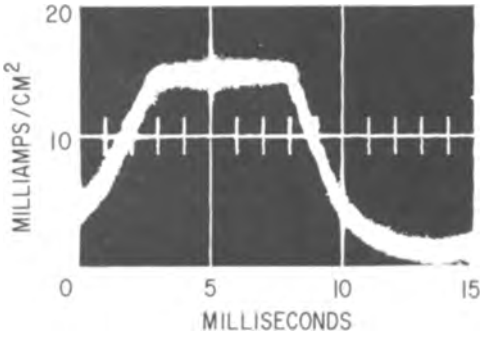

Fig. 7. Current-time transient. Potential switched from —0.18 to —0.19v.

this picture that the large pit had the same geometry as the smaller one before it started to become rounded. These pits have formed on a {135} surface and from electron diffraction data appear to have had sides parallel to {110} before rounding. Rounding was typical of all pits at later stages of growth. Also it appears that within each grain there might be groups of pits that have the same size. For example, in Fig. 4 pits 1 and 2 are about the same size, as are pits 3 and 5; in Fig. 3 the pits are of equal size; in Fig. 5 one observes three sizes for the five pits: one large, two slightly smaller, and the two very small. Similar results have been seen on other foils.

To determine whether the pitting attack was related to the aging, i.e., growth or thickening, of the initial passive film during lengthy periods at a passive potential, some foils were treated to the slow potential sweep after the foil was essentially, but not completely, passive. In this case, the current had decayed to approximately two to three times the value it has when complete passivity has been achieved. The same crystallographic pitting was observed as when the foil was passivated for extended times.

To help elucidate the mechanism of the observed pitting, current-time transients were observed when the potential was rapidly switched in the Flade region. For example, a specimen was held at —0.18v until the current density had reached a steady-state value of 4 ma/cm^2. The potential was then switched to —0.19v and the transient shown in Fig. 7 was observed. The new steady-state current density after some minutes was 6 ma/cm^2.

Figures 8 through 10 show the appearance of the foil when its potential is rapidly switched from the passive region into the Flade region. Similar results

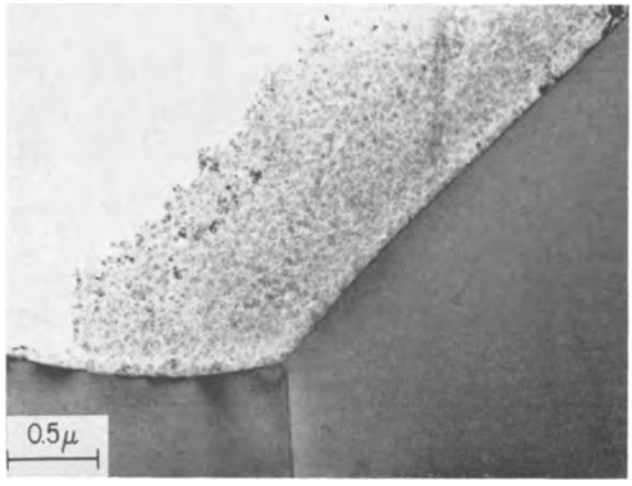

Fig. 8. Transmission electron micrograph of a foil on which passivity was rapidly destroyed resulting in anisotropic etching of the surface.

are also obtained when the potential of the foil is switched from the hydrogen evolution range ($E <$ —0.28v) into the Flade region. In all cases over-all etching of the surface is observed and pitting is never seen. Figure 8 shows a typical example at a fairly early state of etching. The potential was switched to a value at which the final current after 30 sec was approximately 0.3 ma/cm^2. It is seen that large variations in the initial rate of etching occur from grain to grain. The lighter grain is heavily etched, whereas the two darker grains have been etched to only a very slight degree. This anisotropy of etching was evident for all experiments in which the etching was stopped at a sufficiently early stage. At later stages the anisotropy of etching was no longer evident. Although Fig. 8 shows the severely etched grain at the edge of the foil, severe etching was also observed in grains which

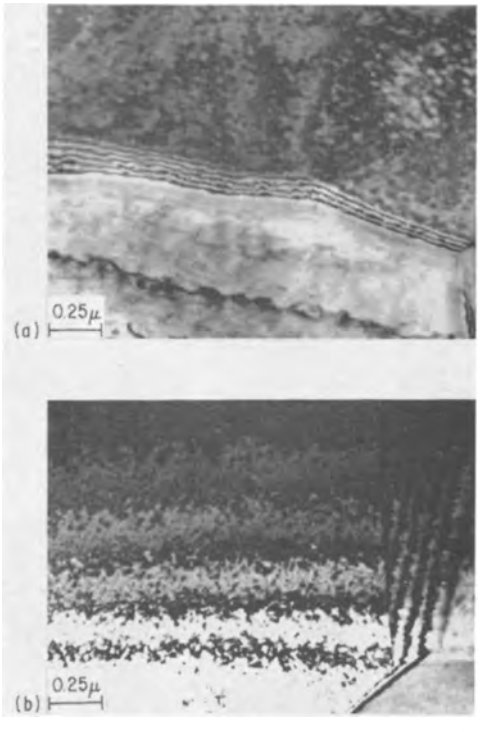

Fig 9. Transmission electron micrograph of a foil on which passivity was rapidly destroyed resulting in etching of the surface. (a) Roughening of surface is indicated by wavy thickness fringes at grain boundary and by the presence of thickness fringe patterns on grains; (b) severe roughening of surface is indicated by nonuniform ragged thickness fringes at edge of foil and at grain boundary.

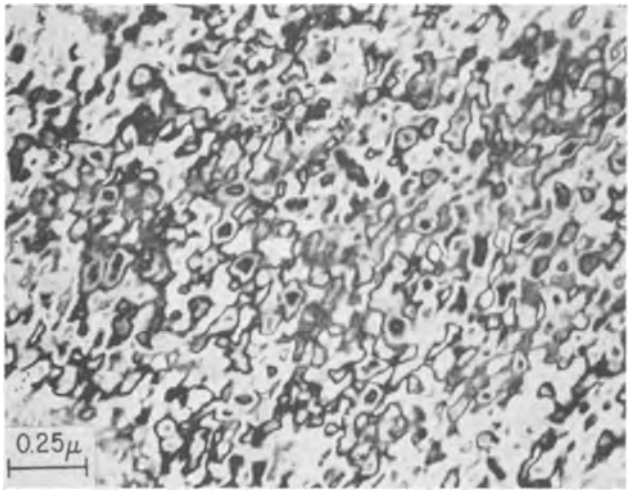

Fig. 10. Transmission electron micrograph of a foil on which etching is demonstrated by thickness fringes from which surface roughening can be measured as indicated in text.

were not at the foil's edge. In Fig. 9a and 9b the etched condition of the surface is shown by the raggedness of the thickness fringes at grain boundaries, within the grains, and at the edge of the foil. The uneven nature of the attack becomes more apparent when the condition of the fringes in these micrographs is compared to that of a foil with an electropolished surface (Fig. 2a). Figure 10 is a micrograph showing thickness fringes which effectively produce a relief map of an etched surface and can be used to give an indication of surface roughness. The thickness fringes show that the surface consists of many mounds and shallow depressions. Taking 300Å as a reasonable value of the extinction distance in this alloy for the operating 110 reflection, Fig 10 is then contoured in steps of this height. An average of 1 thickness fringe was observed at each depression, indicating a total depth of approximately 300Å. From measurements of the diameter of the thickness fringes, it is estimated that the average diameter of the depressions is of the order of ten times their depth.

Discussion

Nature of breakdown of passive film.—The most definitive observation is that as passivity breaks down the mode of attack of the alloy substrate is a function of the rate of potential sweep. When it is sufficiently slow, *e.g.*, 200 mv/hr, crystallographic pitting of the alloy occurs, presumably at the sites at which the film has been destroyed, and no etching of the surface is visible. When the rate of potential change is sufficiently fast, *i.e.*, when the potential is switched from the passive range into the Flade region, the surface is etched into mounds and depressions and no pitting is observed.

It is thought that the nature of the sites for the initiation of breakdown of passivity during a slow potential sweep must be connected with local changes in some property of the passive film or of the alloy (it will be argued below that it probably is the passive film). However, when the potential is suddenly switched from the passive region into the Flade region, the driving force for film breakdown is so great that the local differences, which come into play during the slow potential sweep, are completely masked, an over-all reduction of the passive film occurs, and the entire alloy surface undergoes a general etching attack.

Local breakdown of passivity during slow potential sweep.—When the alloy is subjected to a potential in the passive region, it becomes covered by a protective film that essentially stops all corrosion but that which is equivalent to the small passive current density. As the potential is slowly swept into the Flade region, the film is destroyed locally; this is followed by pitting of the substrate at these local sites. From Fig. 4 to 6 it is seen that size variations exist among pits on the same grain, indicating that film breakdown prior to pitting was nucleated at different times, hence at different potentials. It is concluded that the nucleation of film breakdown is heterogeneous and must occur at physical or chemical defects in the film. These defects may be solely the property of the film or they may result from defects in the substrate.

With respect to the effect of the substrate, it has been found that dislocation termini and grain boundaries must be unimportant because pitting did not occur preferentially at these sites. Since monoatomic surface steps and kink sites have a close geometric similarity with a dislocation site, they too are probably unimportant as sources for the local film breakdown (17). Further, since pitting has been observed on many crystallographic planes of the alloy, the nucleation of film breakdown is independent of substrate orientation. Effects of the substrate arising from multiatomic steps cannot be ruled out since an indication of possible mutual alignment of some of the pits does exist. Also the effect of chemical inhomogeneities in the alloy on the film is not known, except that it would not be unreasonable to expect variations in the composition of the film to be associated with variations in the composition of the substrate.

Sources of local fluctuations in the passive film not related to the substrate would depend on the nature of this film. If it is a crystalline oxide, then any defect in the crystal structure, such as dislocations, grain boundaries, chemical fluctuations, etc., could provide sites for breakdown. If the film is either an amorphous oxide or an adsorbed layer, then pores, other physical defects, or chemical fluctuations could be the sites of attack. Chemical fluctuations could consist of nonstoichiometry such, as suggested by Caplan *et al.* (12) for films on Fe-26% Cr, by Sewell *et al.* (7) and by Pryor and Evans (18) for films on iron, or of impurity segregation which occurs during growth of the film (17).

As a particular potential peculiar to a specific defect is reached during the slow potential sweep, breakdown of the film followed by pitting of the alloy occurs. If it is assumed that for a particular surface orientation growth conditions are the same for all pits, then it follows that the larger the pit the more positive was the potential at which it was initiated.

It was reported that within each grain there appear to be groups of pits that have the same diameter. If this observation on further testing proves to be valid, it would appear to support the oxide film theory of passivity more than the adsorbed film theory, since it is easier to visualize numerous types of discrete local variations (chemical and physical) associated with an oxide film than with an adsorbed layer in the absence of preferential attack at dislocations and grain boundaries in the substrate.

Kinetics and morphology of pitting.—The kinetics of the pitting reaction must be consistent with the overall electrochemical behavior of the system and with the shape and size of the resulting pits. Since the crystallography of the pits shown in Fig. 5 is known, it is possible to calculate their size at any time, t, assuming that the current density is uniform and equal on all surfaces of the pit.

As previously stated, the sides and the bottom of the pits appear to be {111} surfaces. Since {111} surfaces intersect at 71° angles, the dimensions of the pit are related by

$$a = b + 3h(\tan 19°)\ (\sec 30°) \qquad [1]$$

where h is the pit depth normal to the foil surface, a is the length of a pit side on the foil surface, and b is the length of a pit side on the bottom surface. Assuming that all the sides dissolve continuously at the same rate, k

$$a = 2\sqrt{3}\,kt \sec 19° \quad [2]$$

and

$$h = kt \quad [3]$$

where t is measured from the time the pit is nucleated. Thus

$$h = \frac{a}{2\sqrt{3}} \cos 19° \quad [4]$$

and the dimensions of the pit may be calculated from the measured value of a and Eq. [1] and [4]. The largest pit in Fig. 5 is 3000Å on a side and the calculated depth is 820Å, in good agreement with the depth estimated from the thickness fringes at the edges of the pit to be between 750 and 900Å. Similarly the depth of the two smallest pits was calculated from the measured a and estimated from contrast considerations to be approximately 150Å. This good agreement supports the assumption of a uniform and equal current density on all surfaces of pits.

The dissolution rate, k, can be obtained from Eq. [2]. Assuming that the largest pit in Fig. 5 was nucleated at the potential at which passivity first started to break down, the growth time was 325 sec and $k = 2.5 \times 10^{-8}$ cm/sec. The equivalent current density, as calculated from the lattice parameter for the alloy and assuming an average valence of 2.25 (iron dissolves as ferrous ion and chromium as chromic ion), is 8×10^{-4} amp/cm^2.

To understand why the pitting reaction is stable, consider the transient behavior of the alloy when the bare metal surface is first exposed (Fig. 7). The limiting current density is most likely diffusion controlled by a precipitated corrosion product (8, 19, 20). The diffusion-controlled state is unstable and repassivation occurs within milliseconds, accounting for the fact that this phenomenon has not previously been reported for Fe-Cr alloys with Cr > 3%. The current-time relationship shown in Fig. 7 represents an average over the entire electrode surface. For the case of localized pitting, the build-up of the corrosion products within the confines of the pit is much greater than on an open surface (21, 22), resulting in a lower value for the limiting current density which persists. For the current density to remain constant during pitting, a steady state must be established between the rate of formation and rate of dissolution of the diffusion-hindering layer. The good agreement between the experimentally determined and the calculated pit depth, the reasonable value of the calculated current density for pitting, and the results of the current-transient experiments indicate that the dissolution reaction occurs at the same rate on all pit surfaces and that this rate, *i.e.*, current density, is constant over the period of time and potential investigated. That pitting does occur at a constant current density has been shown by Edeleanu (23).

When the pit has penetrated through the foil and the diameter-to-depth ratio becomes sufficiently large, the pit becomes rounded (Fig. 4 and 6). This must be due to a change in the kinetics and/or mechanism of the dissolution process. Additional work is required to elucidate the factors involved.

The results presented here also give a better understanding of the phenomenon of pitting corrosion. Since the foils that can be examined by transmission electron microscopy are normally 1000-2000Å thick, comments can only be made about the initiation and the initial growth of pits. It has been believed (22) that pitting corrosion can occur only in the presence of certain "aggressive anions," *e.g.*, chloride, the action of which has been explained in several ways (22, 24). Our work shows that the initiation and the initial propagation of pitting corrosion does not require an "aggressive anion," but only that under the experimental conditions the defects in the passive film are preferentially attacked and that anodic dissolution can proceed by the mechanism detailed above.

The observed crystallographic pitting resembles crystallographic etch pitting (c.e.p.) controlled by step nucleation normally used to etch dislocations on close-packed planes (25, 26), but differences exist. The pits in this work do not occur preferentially at emerging dislocation as in c.e.p. Furthermore, the pits here have been observed on many surface orientations and are not limited to close-packed planes. In c.e.p. the sides of the pits have been reported usually to consist of discrete steps of low-index planes. The pitting reported here appears to produce smooth planes on the sides.[2] Qualitatively, this may be seen from the thickness fringes in the pits in Fig. 3. If the sides were stepped, then statistically a thickness fringe must occasionally coincide either with the flat portion of the step or with the riser, resulting in fringes of variable width. Examination of fringes within many pits has never shown this. Also direct observation in the electron microscope has never shown any steps within the limit of resolution of the microscope (~20Å).

In c.e.p. the pit develops because the lateral motion of steps is retarded by a poison in the etchant permitting the nucleation of many steps before the first have moved appreciably from their source. In this work the principal agent that retards the lateral motion of steps is the passive film which is present on the surface of the foil but not on the walls of the pit. The sides will dissolve to expose the low-index planes and thus produce the observed crystallographic symmetry. The smoothness of the sides is consistent with the absence of any film that would retard step motion.

Etching of surface resulting from rapid breakdown of passivity.—The general etching shown in Fig. 8 through 10 always occurs when the potential of the specimen is rapidly switched from the passive range into the Flade region. This has been observed at potentials at which the breakdown of the passive film is just commencing, as well as at potentials in the high-current region. It has been established that the etching is not an advanced state of pitting. For example, in Fig. 8 the two darker grains have been etched slightly,[3] yet no pit is seen on either grain. Numerous other grains, with degrees of etching ranging down to almost none, have been examined and pitting was never observed. Thus it appears that under these conditions the passive film is reduced uniformly, at least over each grain, and etching can proceed through the thinned film. The anisotropy in the degree of etching (Fig. 8) must then be explained either on the basis of varying thickness of the film on different grains or on the basis of the anisotropy of corrosion rates on different crystal faces. Insufficient data exist at present to differentiate between these mechanisms.

From the experiments in which general etching was also observed when the potential was switched from the hydrogen-evolution region ($E < -0.28$v) into the Flade region, it appears that the low-index surfaces are consistently more etched than the higher-index surfaces.[4] This is in disagreement with the known anisotropy of corrosion rates in which low-index planes normally corrode more slowly than the higher index ones. The results, however, are understandable if the first step in passivation is the adsorption of some form of oxygen. Then less adsorption, and hence more etching, would be expected on the low-index planes since they make fewer nearest-neighbor bonds with the adsorbate and hence adsorb less strongly.

This suggestion coupled with the earlier one that the passive film after complete passivation may most likely be an oxide, would be in closest agreement with the theory of Hackerman (28).

[2] This is not meant to imply that a steady-state concentration of steps and kinks, analogous to the equilibrium concentration discussed by Burton, Cabrera, and Frank (27) does not exist.

[3] Although the etching is not obvious in this micrograph, it was evident in the microscope when the specimen was tilted at a different angle.

[4] This etching cannot be associated with the short time required to desorb and/or oxidize surface hydrogen and to form the initial surface film, because the same processes do not result in visible etching when the potential is jumped from the hydrogen-evolution range into the passive range (+0.5v).

Acknowledgments

The authors wish to thank Doctors S. Barnartt, S. S. Brenner, N. P. Louat, R. A. Oriani, and P. R. Swann for helpful discussions; Dr. J. K. Hurwitz and Mr. G. W. Momeyer for spectrographic and chemical analysis, respectively; and Mr. A. D. Damick for much help in setting up the experimental apparatus.

Manuscript received Feb. 23, 1965. This paper was presented in part at the Washington Meeting, Oct. 11-15, 1964.

Any discussion of this paper will appear in a Discussion Section to be published in the June 1966 JOURNAL.

REFERENCES

1. U. F. Franck, *Z. Naturf.*, **4a**, 378 (1949).
2. J. H. Bartlett, *Trans. Electrochem. Soc.*, **87**, 521 (1945).
3. C. Edeleanu, *Nature*, **173**, 739 (1954); *Iron and Steel Inst.*, **188**, 122 (1958).
4. H. J. Engell and N. D. Stolica, *Arch. Eisenhüttenwesen*, **30**, 239 (1959).
5. J. Kruger, *This Journal*, **110**, 654 (1963).
6. V. V. Andreeva, *Corrosion*, **20**, 35t (1964).
7. P. B. Sewell, C. D. Stockbridge, and M. Cohen, *This Journal*, **108**, 933 (1961).
8. R. Olivier, "Passiviteit van Ijzer en Ijzer-Chroom Legeringen," Dissertation, Leiden, 1955; *Proc. Sixth Meeting CITCE*, 1954, p. 314, Butterworths Scientific Publications, London.
9. M. Prazak, V. Prazak, and V. Cihal, *Z. Elektrochem.*, **62**, 739 (1958).
10. G. M. Florianovich and Y. M. Kolotyrkin, *Doklady Akad. Nauk S.S.S.R.*, **130**, 585 (1960).
11. T. Heumann and R. Schürmann, *Werkstoffe u. Korrosion*, **9**, 560 (1961).
12. D. Caplan, A. Harvey, and M. Cohen, *This Journal*, **108**, 134 (1961).
13. Y. M. Kolotyrkin, G. V. Golovina, and G. M. Florianovich, *Doklady Akad. Nauk S.S.S.R.*, **148**, 1106 (1963).
14. T. Heumann and H. S. Panesar, *This Journal*, **110**, 628 (1963).
15. G. Aronowitz and N. Hackerman, *ibid.*, **110**, 633 (1963).
16. G. Thomas, "Transmission Electron Microscopy of Metals," John Wiley & Sons, Inc., New York (1962).
17. H. W. Pickering and P. R. Swann, *Corrosion*, **19**, 373t (1963).
18. M. J. Pryor and U. R. Evans, *J. Chem. Soc.*, **1949**, 3330.
19. U. F. Franck, *Werkstoffe u. Korrosion*, **9**, 504 (1958).
20. N. Sato and G. Okamoto, *This Journal*, **110**, 605 (1963).
21. H. H. Uhlig, *Trans. AIME*, **140**, 411 (1940).
22. Y. M. Kolotyrkin, *Corrosion*, **19**, 261t (1963).
23. C. Edeleanu, *J. Inst. Metals*, **89**, 90 (1960-61).
24. T. P. Hoar, *Trans. Faraday Soc.*, **45**, 683 (1949).
25. F. W. Young, Jr., and L. D. Hulett, "Metal Surfaces: Structure, Energetic and Kinetics," ASM Monograph 1962, pp. 375-400.
26. J. J. Gilman, W. G. Johnston, and G. W. Sears, *J. Appl. Phys.*, **29**, 747 (1958).
27. W. K. Burton, N. Cabrera, and F. C. Frank, *Phil. Trans. Roy. Soc.*, **243A**, 299 (1959).
28. N. Hackerman, *Z. Elektrochem.*, **62**, 632 (1958).

The Absorption of Electrolytically Generated Hydrogen

Fujio Matsuda and Thomas C. Franklin

Chemistry Department, Baylor University, Waco, Texas

ABSTRACT

A study has been made of the absorption of electrolytically generated hydrogen by iron wires and the migration of hydrogen through iron membranes. The data are in agreement with the assumption that the rate of absorption is proportional to the amount of adsorbed hydrogen. It was also indicated that the amount of hydrogen absorbed at equilibrium was governed by an equilibrium between the amount of adsorbed and absorbed hydrogen.

As a part of a series of correlation studies on the effect of hydrogen on different processes at solid metal electrodes and the effect of additives on these processes (1-3), a study was made of the effect of additives in solution on the rate of migration of hydrogen into iron and the resulting effect on the embrittlement of the iron. Much work has already been reported in this area as indicated by the early review of Buzzard and Cleaves (4) and by the recent symposium of the American Electroplaters Society (5).

A study of the migration of hydrogen through iron membranes has recently been completed by Devanathan (6).

Experimental

The iron electrodes were prepared by sealing varying lengths (1-8 cm) of Baker Analyzed Reagent Grade iron wire in glass. The electrodes were dipped in 6M nitric acid and rinsed with distilled water before using.

The coulometric techniques previously used (1-3) in studies of hydrogen at solid electrodes were used in this study. This is similar in principle to the coulometric technique described by Devanathan *et al.* (7, 8) for the determination of surface coverage by hydrogen. In this technique the iron reactions are subtracted graphically while Devanathan treated them mathematically. It has been experimentally checked as a method of measuring absorbed hydrogen in palladium (9) and iron (10) wires. Hydrogen was generated on the iron electrode for varying lengths of time at a constant current density and for varying current densities at constant times by connecting the cell to the batteries. The cell was then connected to the polarograph and the hydrogen was electrolytically oxidized. The nonpolarizable electrode was a large platinum gauze electrode. The solution was 2*N* sodium hydroxide.

The embrittlement of the iron was measured by a simple bend test. Each wire was usually long enough for three or four such tests, and the average results were reproducible within one-third of a bend.

The studies of penetration of hydrogen through iron membranes were made with a series of different cells. Figure 1 shows a typical cell. The electrical connections immersed in the water bath were coated with RTV-11 silicone rubber. In many of the runs the membrane was at the bottom of the generation cell to prevent bubbles from blocking the electrode. The iron membranes were prepared by etching shim steel sheet with 1M nitric acid. Both generation side and the diffusion side contained a 2*N* sodium hydroxide solution. Hydrogen was generated electrolytically on the iron electrode in the generation cell. Anodic current voltage curves were run on both the generation and diffusion sides by shifting the large platinum gauze electrode and using it as the nonpolarizable electrode.

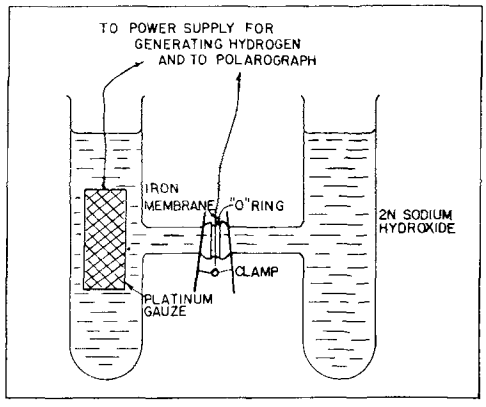

Fig. 1. Cell for iron membrane experiments

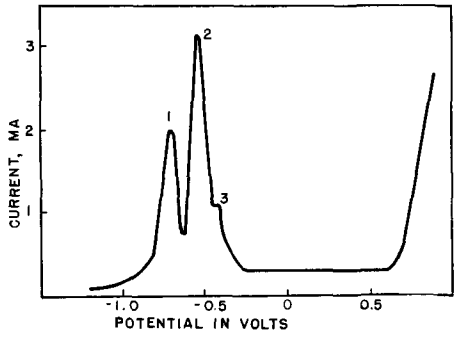

Fig. 2. Current-voltage curve for the oxidation of hydrogen on iron

In the quantitative penetration experiments hydrogen was generated on the electrode overnight before measuring the penetrated hydrogen. Therefore, the measurements were made with iron saturated with hydrogen. In order to study the effect of additives sodium sulfide was added to the generation side. The times recorded are the times of hydrogen generation after the surface hydrogen on the diffusion side of the membrane was removed by electrolytic oxidation.

In all cases the reagents were the purest available commercially. The temperature of the cells were maintained at 25° ± 0.5°C.

Data and Discussion of Results

Figure 2 is a typical current-voltage curve for the oxidation of an iron electrode on which hydrogen has been electrolytically generated. Above this potential region one obtains two pronounced maxima indicating oxide formation. As can be seen in the graph there are three maxima, indicating that there are three substances, presumably three different forms of hydrogen, being oxidized. The existence of various forms of hydrogen on platinum has been shown by a number of workers (2, 11-15). The existence of two different mechanisms of absorption of hydrogen by iron, indicative of two different forms of hydrogen, has been shown by the work of Le Boucher (16). The first two peaks were shown to be due to the oxidation of hydrogen by membrane experiments such as those run by Schuldiner and Hoare (17). After electrolytically generating hydrogen on one side of the iron membrane current voltage curves were obtained on both the generation and diffusion sides of the membrane. The two peaks were obtained at the same potentials on both sides of the membrane. If these are caused by hydrogen, then the area under each peak (since the voltage is increasing linearly with time) is a measure of the amount of hydrogen present in each form. The first form is oxidized very rapidly by air and potassium permanganate, while the second and third forms are oxidized more slowly by the chemical oxidizing agents, therefore it was concluded that the first peak was

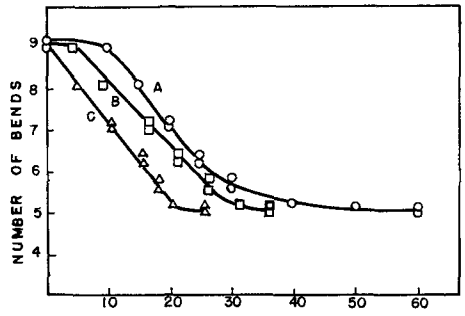

Fig. 3. Curve A, effect of generating time on number of bends needed to break iron wire; curve B, effect of total area under the curve on number of bends needed to break iron wire; curve C, effect of area of second and third maxima on the number of bends needed to break iron wire.

caused by the oxidation of adsorbed hydrogen at the surface of the electrode while the second and third peaks are caused by the oxidation of hydrogen in the interior of the iron. The two peaks in current potential curves obtained in the membrane experiments also behaved in a manner consistent with the interpretation that the first peak is caused by hydrogen on the surface of the iron and the second peak is caused by hydrogen absorbed in the iron. On the generation side the first peak builds in area with time, essentially reaches a constant value, and then, the second peak forms. On the diffusion side the second peak builds up first. The area of the second peak measured from either side was essentially the same. The third peak was not investigated to any extent since it forms only at high charging current densities or long charging times.

A further indication that the second peak was caused by absorbed hydrogen was obtained from embrittlement studies. It has been repeatedly observed that if one plots the number of bends necessary to break a specimen, or some similar measurement, against the charging time or charging current density one obtains a curve with a marked delay in it similar to A in Fig. 3. If one plots the total area under the curve in place of the charging time, one obtains a similar curve (curve B) with a delay in it. However, if one plots the area under the second peak against the number of bends needed to break the wire, one eliminates the delay entirely (curve C). There is still some curvature at the lower end of the graph because it has been impossible experimentally to separate the third form of hydrogen from the second absorbed form and the third form is produced in this lower region.

Figures 4 and 5 show the variation of the total area under the maximum with charging time and charging current density. Examination was made of these curves along with an examination of the original current-voltage curves and a visual examination of the electrode during the charging process. These indicated that

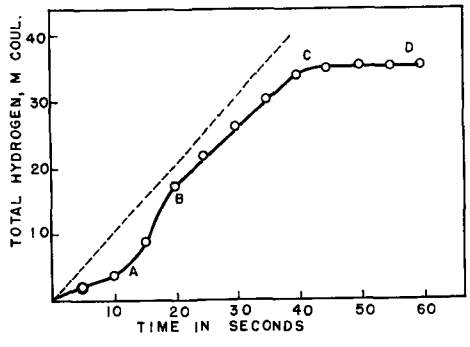

Fig. 4. Effect of time of generation on total area under the maxima (current density, 0.83 ma/cm^2). - - - -, Total hydrogen generated on the electrode; o——o——o, measured area under the curves.

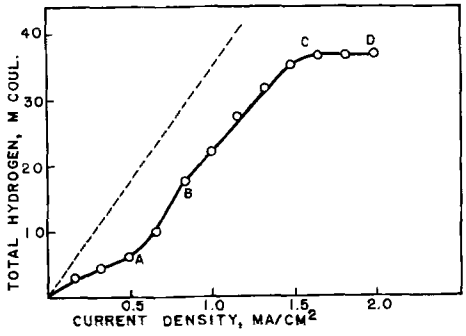

Fig. 5. Effect of generating current density on total area under the maxima (time of generation, 30 sec). - - - -, Total hydrogen generated on the electrode; ○———○———○, measured area under the maxima.

up to the region of point A no hydrogen was visibly desorbed and only the first maximum was found. Therefore, it was concluded that the charging current was being used to reduce oxides and form adsorbed hydrogen. In the next region, AB, the second peak began to form, and in the straight line portion of the curve, BC, the surface was presumably saturated with hydrogen, since the first peak stopped growing, and the major process occurring was the migration of hydrogen into the interior of the metal. A small amount of desorption of hydrogen was observed in this region. Likewise, it is seen that the two curves drop off slightly from the theoretical slope. The fact that the curves approach the theoretical indicates once again that the area under the curve is a quantitative measure of the amount of hydrogen oxidized at the electrode, the drop off from theoretical being due to the small amount of hydrogen being visibly desorbed. At the upper end the rate of growth of the second peak slowed down and the third peak formed. In the final portion of the curve where the curve is parallel to the abscissa the electrode was saturated with hydrogen and all the hydrogen generated was desorbed.

From these observations it was concluded that the slope of BC was a measure of the rate of absorption of hydrogen by the iron from a surface saturated with adsorbed hydrogen under these conditions. It was also concluded that from the final height of the curve one can calculate the total amount of hydrogen present in the electrode at saturation.

Figures 6, 7, 8, and 9, show the effect of acetonitrile, 2, 7-disodium naphthalene disulfonate, sodium sulfide, and arsenious oxide on the rate of migration of the hydrogen into the iron (the slope of BC). The acetonitrile and disulfonate caused a decrease in the slope. The sulfide and arsenious oxide caused a decrease in slope at very low concentrations, but at higher concentrations the slope increased.

The generally accepted theory of migration of hydrogen into iron involves migration from an adsorbed

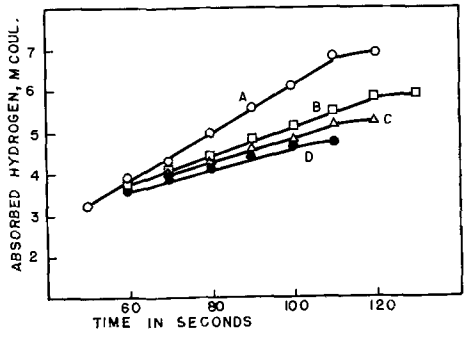

Fig. 6. Effect of acetonitrile on area under second maximum. Curve A, no acetonitrile; B, 2 X 10^{-3}M acetonitrile; C, 6 X 10^{-3}M acetonitrile; D, 8 X 10^{-3}M acetonitrile.

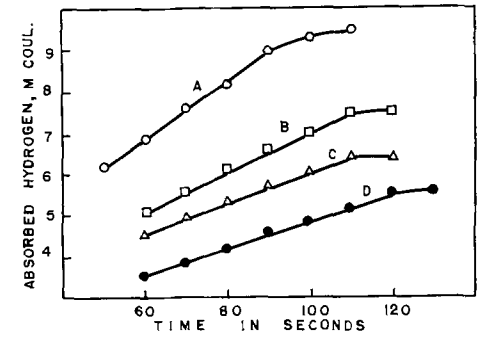

Fig. 7. Effect of disodium 2,7-naphthalenedisulfonate on area under second maximum. Curve A, no sulfonate; B, 0.5 X 10^{-3}M sulfonate; C, 1.0 X 10^{-3}M sulfonate; D, 4.0 X 10^{-3}M sulfonate.

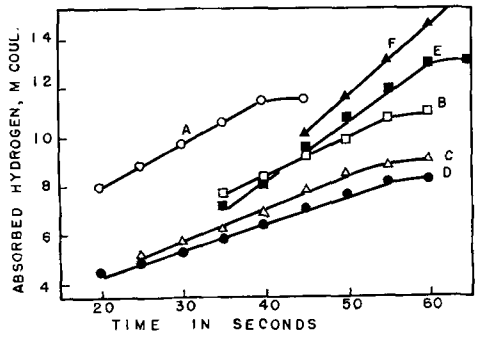

Fig. 8. Effect of sodium sulfide on area under second maximum. Curve A, no sulfide; B, 10^{-8}M; C, 10^{-7}M; D, 10^{-6}M; E, 10^{-5}M; F, 10^{-4}M.

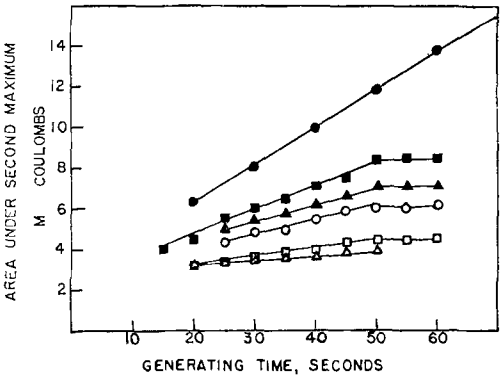

Fig. 9. Effect of arsenious oxide on area under second maximum: •, 10^{-4}M, arsenious oxide; ■, no arsenious oxide; ▲, 10^{-5}M arsenious oxide; ○, 10^{-8}M arsenious oxide; □, 10^{-6}M arsenious oxide; △, 10^{-7}M arsenious oxide.

layer of hydrogen on the surface. Figure 10 shows plots of the slope of BC (the rate of adsorption of hydrogen) against the amount of adsorbed hydrogen on the electrode surface as measured by the area under the first peak. In agreement with prediction it is a straight line. The differences in slope of these four lines can be attributed to differences in surface area of the electrode in these four experiments. It can be seen that the curves do not go through the origin. This is because of a consistent error in taking the residual. Since hydrogen is generated, the amount of hydrogen in solution in the vicinity of the electrode changes, causing changes in the residual. It is seen that the effect of the additive in solution is to change the area under the first peak (the amount of adsorbed hydrogen). This in turn changed the rate of absorption of the hydrogen.

Similar results were obtained using iron membranes. Figure 12 shows a plot of the area under the first peak on the diffusion side as a function of time of hydrogen

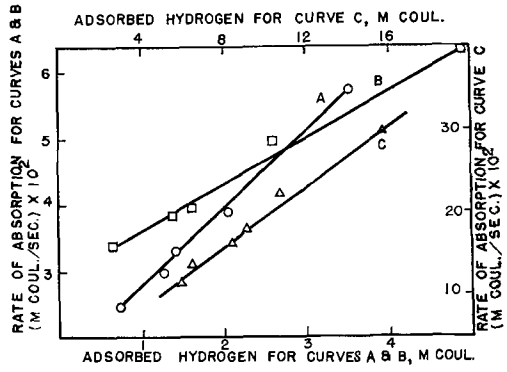

Fig. 10. Variation of rate of increase of area with area under first maximum: curve A, acetonitrile; curve B, disodium, 2,7-naphthalenedisulfonate; curve C, sodium sulfide.

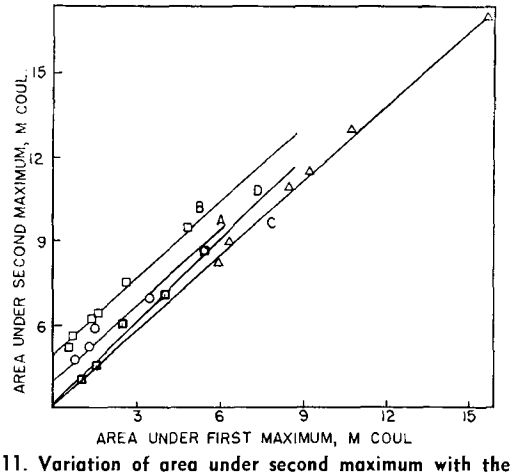

Fig. 11. Variation of area under second maximum with the area under the first maximum: curve A, acetonitrile; curve B, disodium 2,7 naphthalene disulfonate; curve C, sodium sulfide; curve D, arsenious oxide.

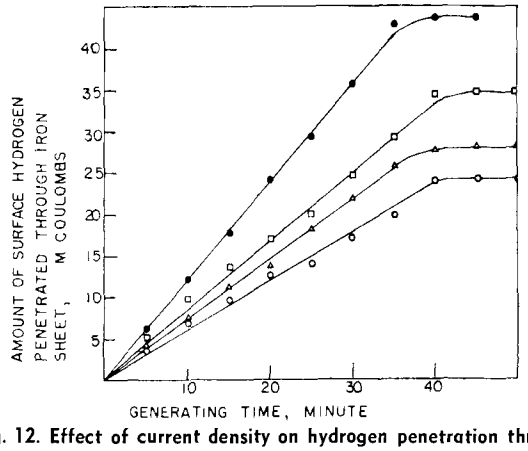

Fig. 12. Effect of current density on hydrogen penetration through iron membranes; thickness of iron sheet—3.0 X 10^{-3}cm. ●, 2.50 ma/cm²; □, 1.88 ma/cm²; △, 1.25 ma/cm²; ○, 0.63 ma/cm².

generation at different current densities. It is seen that the area builds up linearly with time and then eventually levels off. Similar results are obtained if one varies the concentration of sulfide on the generation side (Fig. 13). In both cases, if one plots the area under the first peak on the generation side as a function of the rate of buildup of area on the diffusion side one obtains straight lines (Fig. 14). All of this is consistent with the viewpoint that the areas are proportional to the surface hydrogen on the respective sides and that the rate of diffusion of hydrogen through the saturated membrane is proportional to the amount of hydrogen on the surface on the generation side. This is further indicated since the rate of diffusion should be inversely proportional to the thickness of the iron membrane and the slope of the two straight

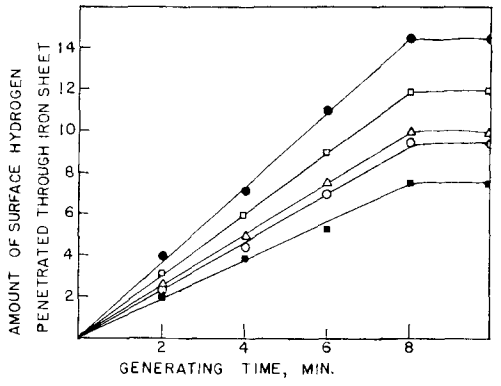

Fig. 13. Effect of sulfide on hydrogen penetration through iron membranes; thickness, 2.5 X 10^{-3}cm; current density, 0.63 ma/cm². ●, 8 X 10^{-4}M sulfide; □, 6 X 10^{-4}M sulfide; △, 4 X 10^{-4}M sulfide; ○, 2 X 10^{-4}M sulfide; ■, no sulfide.

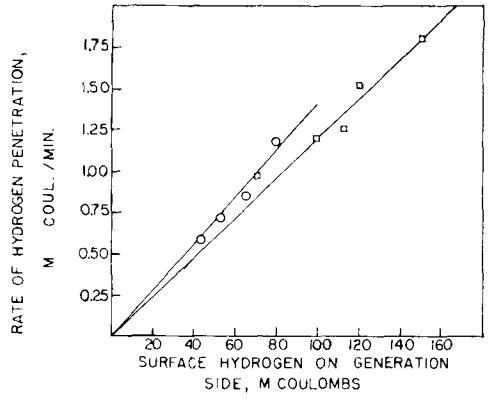

Fig. 14. Effect of area under first peak on the generation side on the rate of increase of area on diffusion side: ○, data from current density experiments; □, data from sulfide experiments.

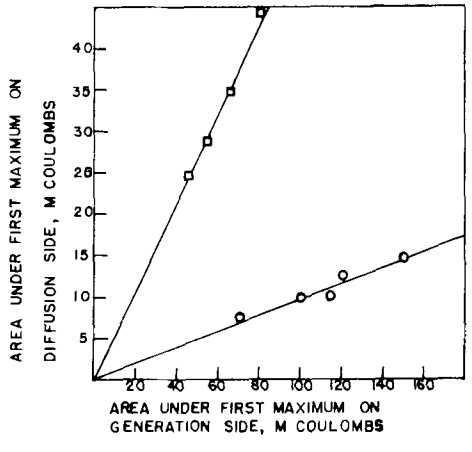

Fig. 15. Effect of area under first peak on generation side on the area under the first peak on the diffusion side under steady-state conditions: □, data from current density experiments; ○, data from sulfide experiments.

lines in Fig. 14, one obtained by variation in current density and the other by use of an additive, multiplied by the thickness of the membrane are 4.3 x 10^{-5} and 4.8 x 10^{-5} cm/in., respectively. These two figures are, within experimental error, identical.

Figure 15 shows that there is a linear relationship between the areas under the curves obtained on the two sides of the membrane in the final steady-state portion of the curves in Fig. 12 and 13. This is consistent with a steady state in which the rate of diffusion of hydrogen through the membrane equals the rate of desorption of hydrogen on the diffusion side.

Table I. Effect of electrode length on the third form of hydrogen

Electrode length, cm	Third peak area, m coulombs	Intercept, m coulombs
5	4 to 5	5.09
4	3 to 4	4.23
2	2 to 4	3.40

$$\left(\frac{dH_{II}}{dt}\right)_{diffusion} = -\left(\frac{dH_{II}}{dt}\right)_{desorption}$$

$$\left(\frac{dH_{II}}{dt}\right)_{diffusion} = kH_I \; ; -\left(\frac{dH_{II}}{dt}\right)_{desorption} = kH_{II}$$

$(H)_I$ is the hydrogen on the surface on the generation side, and $(H)_{II}$ is the hydrogen on the surface on the diffusion side. Therefore

$$k(H)_I = k'(H)_{II}$$

The two experimental slopes are not equal and should not be expected to be equal because the desorption mechanism is sensitive to the presence of impurities in the solution.

As previously observed (Fig. 6-9) the additives also affected the amount of hydrogen absorbed at equilibrium. Figure 11 shows the relationship between the amount of hydrogen absorbed at equilibrium and the amount of hydrogen adsorbed on the surface.

Although these curves have essentially the same slope they do not pass through the origin. This is because the final equilibrium area includes both the second and the third forms of absorbed hydrogen. It was not possible to accurately measure the amount of area under the third peak. It was possible to get the range of this area. In Table I this is tabulated along with the intercept, and it is seen that the intercept corresponds to the experimental value of the third area.

The average slopes of all four lines is 0.91 with the average deviation of the mean being 0.07. In all four cases then the amount of hydrogen absorbed at equilibrium is governed by an equilibrium constant of the following form

$$K_{eq} = \frac{H_{II\,eq}}{H_{I\,eq}}$$

It might well be assumed that the first and third peaks are caused by oxidation of two surface forms of hydrogen in line with previous reports on platinum. However, chemical oxidation does not attack the hydrogen rapidly in the third peak. Another interpretation would be that the third form of hydrogen is hydrogen in voids in the metal. However, so far the studies have not established the nature of the third form of hydrogen.

Acknowledgment

The research reported in this paper has been sponsored by the Geophysics Research Directorate of the Air Force Cambridge Research Laboratories, Office of Aerospace Research, under Contract AF 19(604)-8414.

Manuscript received March 19, 1962. This paper was presented at the Detroit Meeting, Oct. 1-5, 1961.

Any discussion of this paper will appear in a Discussion Section to be published in the June 1966 JOURNAL.

REFERENCES

1. T. C. Franklin and R. D. Sothern, *J. Phys. Chem.*, **58**, 951 (1954).
2. T. C. Franklin and S. L. Cooke, Jr., *This Journal*, **107**, 556 (1960).
3. T. C. Franklin and J. R. Goodwyn, *ibid.*, **109**, 288 (1962).
4. R. W. Buzzard and H. E. Cleaves, NBS Circular 511, 1951.
5. *Tech. Proc. Am. Electroplaters' Soc.*, **47**, 110 (1960).
6. M. A. V. Devanathan and Z. Stachurski, *This Journal*, **111**, 619 (1964).
7. M. A. V. Devanathan, J. O'M. Bockris, and W. Mehl, *J. Electroanal. Chem.*, **1**, 143 (1959).
8. M. A. V. Devanathan and M. Selveratham, *Trans. Faraday Soc.*, **56**, 1820 (1960).
9. T. C. Franklin and N. F. Franklin, *J. Electroanal. Chem.*, **6**, 242 (1963).
10. T. C. Franklin and N. F. Franklin, *ibid.*, In Press.
11. A. Eucken and B. Weblus, *Z. Elektrochem.*, **55**, 114 (1951).
12. M. Breiter, C. A. Knorr, and V. Volkl., *ibid.*, **59**, 681 (1955).
13. M. Breiter, H. Kammermaier, and C. A. Knorr, *ibid.*, **60**, 37 (1956).
14. *Ibid.*, **60**, 119 (1956).
15. S. Schuldiner and R. M. Roe, *This Journal*, **110**, 332 (1963).
16. B. Le Boucher, *Rev. Inst. Petrol. (France)*, **18**, 1-66 (1963).
17. S. Schuldiner and J. P. Hoare, *Can. J. Chem.*, **37**, 228 (1959).

The Anomalous Codeposition of Iron-Nickel Alloys

H. Dahms and I. M. Croll

IBM Watson Research Center, Yorktown Heights, New York

ABSTRACT

The dependence of the anomalous codeposition of iron-nickel alloys on the pH at the cathode surface is investigated. An equation is derived to evaluate the surface pH as a function of bulk pH, rate of hydrogen evolution, buffer concentration, and diffusion conditions. The results obtained on rotating disk electrodes show that anomalous codeposition is due to a suppression of nickel discharge and that suppression occurs only when the surface pH is high enough to cause hydroxide formation. A type of mechanism is proposed by which the adsorption of ferrous hydroxide suppresses the deposition of nickel but permits a high rate of iron discharge. Experimental results which support this mechanism are discussed. This type of mechanism could be of general importance for other systems exhibiting anomalous codeposition.

In the electrodeposition of iron-nickel alloys from noncomplexing solutions the rate constant of iron deposition is higher than that of nickel, although the reverse order is observed when iron and nickel are deposited separately from their respective baths. This phenomenon of "anomalous codeposition" (1) has been reported under a wide variety of conditions in iron-nickel plating (2-6). Analogous anomalies, the preferential deposition of the less noble metal, have been encountered frequently in the electroplating of other alloys of the iron-group metals (7).

Several attempts to interpret this phenomenon have been made. Glasstone and Symes (2) suggested that "the presence of iron retards the change from metastable to stable nickel." No evidence for a metastable form of nickel has been given. Vagramyan and Fatueva

(4) discuss several possible causes in a rather general way. Sysoeva and Rotinyan (6) ascribe the shift in deposition rates to a shift in the zero charge potential. Their theory, which fits only their limited data, is, however, not in accord with our present knowledge of the dependence of reaction rates on zero charge potentials (8,9). Brenner (10) has developed an "addition agent theory" to account for the anomalous codeposition of zinc with the iron-group metals. He points out that the discharge of nickel is sensitive to the adsorption of addition agents and postulates that the addition agent is produced by the cathode reaction only when the current density is sufficiently high to raise significantly the pH of the cathode diffusion layer. In summary it can be said that the mechanism of anomalous codeposition is little understood. This fact has been stated clearly by Brenner (11) in his recent comprehensive survey on alloy deposition.

In the present investigation emphasis will be placed on the evaluation of the role of the pH at the cathode surface and its effect on codeposition. It has been shown recently at the dropping mercury electrode (12) that an increase in the pH at the interface and subsequent hydrolysis effects cause anomalies in the deposition of iron group metals which are analogous to those observed in the plating of iron-nickel alloys. In order to control the pH at the interface the diffusion to and from the electrode has to be well defined. For this purpose rotating disk electrodes (13) are used in this study.

Theory

The pH changes at the cathode surface are due to the over-all reactions

$$2H_3O^+ + 2e = H_2 + 2H_2O \qquad [1]$$

and

$$2H_2O + 2e = H_2 + 2\,OH' \qquad [2]$$

Both processes take place at iron (14) and nickel (15) electrodes. Diffusion processes will tend to compensate for these pH changes at the interface. The diffusion of the following species has to be considered: hydrogen ions, hydroxyl ions, and buffers. Any species reacting with H_3O^+ or OH' has buffering action. This buffering involves reactions of the type $nH^+ + A^- = H_nA$ as well as hydrolysis reactions $Me^{n+} + mOH' = Me\,OH_m^{(n-m)+}$. The diffusion of all buffering species can be treated in the same way taking into account the different direction of diffusion. In the treatment below, the species H_nA, therefore, represents hydrolysis products as well.

For the steady state in planar diffusion normal to the electrode we can write[1]

$$\frac{j_H}{F} = D_H\frac{\partial C_H}{\partial x} - D_{OH}\frac{\partial C_{OH}}{\partial x} + nD_{HA}\frac{\partial C_{HA}}{\partial x} \qquad [3]$$

where j_H is the current density of hydrogen evolution due to reactions [1] and [2]; F is Faraday's constant; $D_H'D_{OH}'$, D_{HA} are diffusion coefficients of hydrogen ions, hydroxyl ions, and buffer H_nA, respectively; C is the concentration of these species; and x is distance normal to the electrode. We can substitute C_{OH} and C_{HA} in Eq. [3] by using the relations

$$C_HC_{OH} = K_W \qquad [4]$$

$$C_H{}^nC_A = K_H \times C_{HA} \qquad [5]$$

and

$$C = C_{HA} + C_A \qquad [6]$$

where K_W is the ionization constant of water; K_H the dissociation constant of buffer; C, total concentration of buffer components; C_{HA}, concentration of undissociated buffer acid; C_A, concentration of buffer anion.

[1] The influence of migration is not taken into account. Migration is, however, negligible as long as the transport number of H^+, OH', and buffers is small; *e.g.*, in our case the transport number of HSO_4' (in 1M $MeSO_4$, 10^{-2}M H_2SO_4 solution) is about 0.02, *i.e.*, an error of 2% is introduced by neglecting migration. Similar arguments would hold for most plating baths.

We then obtain from Eq. [3]

$$\frac{j_H}{F} = D_H\frac{\partial C_H}{\partial x} + \frac{D_{OH}K_W}{C_H{}^2}\frac{\partial C_H}{\partial x} + n^2D_{HA}\frac{C\,C_H{}^{n-1}K_H}{(K_H + C_H{}^n)^2}\frac{\partial C_H}{\partial x} \qquad [7]$$

Equation [7] has to be integrated over the distance between electrode surface ($x = 0$, $C_H = C_H$) and the thickness of the "diffusion layer" ($x = \delta$, $C_H = C^o{}_H$). For the rotating disk electrode the thickness of the diffusion layer is given by (13)

$$\delta = 1.62\left(\frac{D}{\nu}\right)^{1/3}\left(\frac{\nu}{\omega}\right)^{1/2} \qquad [8]$$

where ν is the kinematic viscosity of the solution; $\omega = 2\pi f$ (f, number of rotations per second).

It follows from Eq. [8] that the thickness of the diffusion layer depends on the diffusion coefficient of the particular species. However, we have to assume an identical diffusion layer thickness for all species in order to integrate Eq. [7]. Using this approximation[2] we obtain by integrating Eq. [7]

$$\frac{j_H}{F}\delta = D_H(C^o{}_H - C_H) + D_{OH}K_W\frac{C^o{}_H - C_H}{C_HC^o{}_H} + nD_{HA}K_HC\frac{C^o{}_H{}^n - C_H{}^n}{(K_H + C_H{}^{o^n})(K_H + C_H{}^n)} \qquad [9]$$

It is interesting to note that in Eq. [9] the diffusion current consists only of additive terms although the equilibria among the species during diffusion have been taken into account. Ruetschi and Truempler (16) have derived an anologous additive expression for polarographic conditions on the basis of a simplified model allowing for equilibria only in the bulk and in the "reaction zone."

From Eq. [9] the hydrogen ion concentration at the surface, C_H, can be evaluated since all other quantities are experimentally amenable. An example is given in Fig. 1.

[2] Since in general the diffusion coefficients do not differ greatly the error involved is not too serious; *e.g.*, in our case with $D_{HSO_4'} = 1.1 \times 10^{-5}$, and $D_{Ni^{++}} = 0.69 \times 10^{-5}$ cm sec^{-1} (17) the thickness of the diffusion layer varies by ±6%.

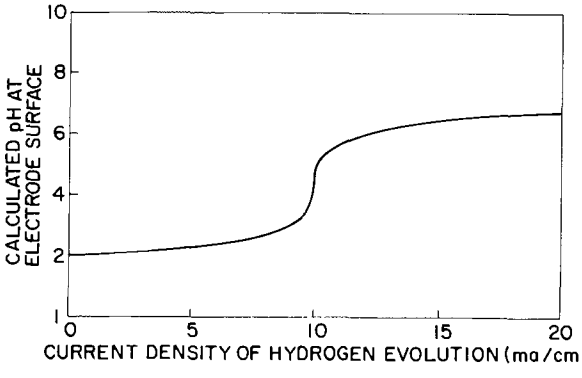

Fig. 1. Example of relation between current density and surface pH calculated from Eq. [9]. Solution: 0.5M $NiSO_4$, 0.5M $FeSO_4$, 10^{-2}M H_2SO_4. Quantities used for the calculation are: $\delta = 2.1 \times 10^{-3}$ cm [experimentally obtained for I_3' reduction in agreement with literature (18)], $D_{HSO4'} = 1.1 \times 10^{-5}$ cm^2 sec^{-1}; the second term of Eq. [9] can be neglected here since $C_H > 10^{-7}$ moles/l; the third term expressing the contribution of the hydrolysis reaction $Me^{++} + 2H_2O \rightleftarrows Me(OH)_2 + 2H^+$ yields a surface pH of 6.8 [calculated for a hydrolysis constant of $Ni(OH)_2$ $K = 1.6 \times 10^{-16}$ (20) and an activity coefficient of $NiSO_4$ $f = 0.042$ (24)]. Experimental determination of the pH in the presence of $Ni(OH)_2$ yielded pH = 6.7. The diffusion of species such as $NiOH^+$ and $FeOH^+$ have not been taken into account since their contribution is negligible due to their hydrolysis constants (21-23).

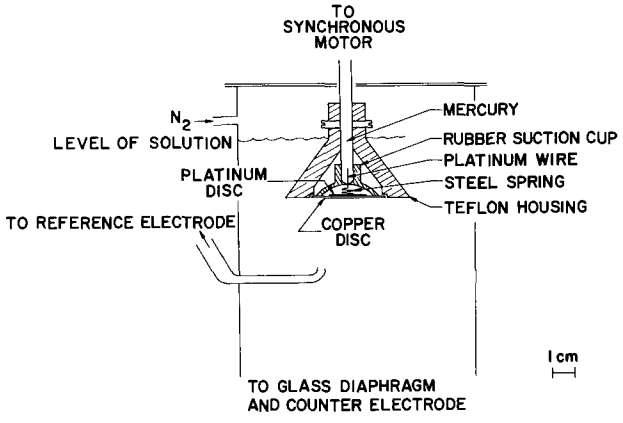

Fig. 2. Diagram of experimental arrangement

Experimental

Rotating copper disk electrodes with areas of 0.64 and 5.1 cm^2 were used. A schematic sketch of the larger electrode is given in Fig. 2. The disk is mounted simply by pressing it on the suction cup. Then the Teflon ring is adjusted so that disk and ring are in the same plane. This arrangement permits fast changing of the plated samples which are subsequently subjected to analysis. The electrical contact to the disk was satisfactory (resistance less than 0.1 ohm). The electrode was rotated by a synchronous motor at 10 rps. The performance of the whole arrangement was checked by measuring the diffusion limiting current of the reaction $I_3^- + 2e \rightarrow 3I^-$ which has been reported in the literature (18). Agreement within ± 5% was obtained.

The distance between electrode plane and probe of the reference electrode (a saturated calomel electrode) was kept constant. The potential drop due to ohmic resistance between cathode and reference electrode was determined by means of an oscilloscope from the decay of the electrode potential with time after switching off the current (19). All experiments were carried out under potentiostatic conditions at 22° ± 1°C. A Wenking potentiostat (rise time 10^{-5} sec) was used.

The electrolysis cell was U-shaped. The counter electrode was separated from the cathode compartment by two glass disks in order to avoid contamination by anode products.

The solutions were made up of analytical grade chemicals and conductivity water. Recrystallization and pre-electrolysis were used for further purification. Nitrogen was swept through the solution for at least 15 min prior to experiments. The mounted electrode disks were degreased in acetone, etched in warm nitric acid (diluted 1:1) for 30 sec, and then rinsed carefully in conductivity water. The samples were plated for 300 or 600 sec. The current was recorded on a fast-response recorder (0.1 sec full-scale deflection).

The electrodeposits were analyzed by x-ray fluorescence or by standard colorimetric techniques after dissolving the metal deposit. From these data and the knowledge of the total current passed the partial current due to hydrogen evolution was calculated. From the hydrogen evolution current the *p*H of the surface of the electrode was then evaluated on the basis of Eq. [9]. An example of the relation between hydrogen evolution current and surface *p*H is given in Fig. 1. Similar plots were constructed for other experimental conditions and the surface *p*H read off.

Results

The lower part of Fig. 3 shows Tafel plots of the separate deposition of iron and nickel compared to the deposition rates in alloy formation. It can be seen that the deposition of iron is hardly affected by the presence of nickel. The deposition of nickel is changed little at very low current densities, but is suppressed strongly

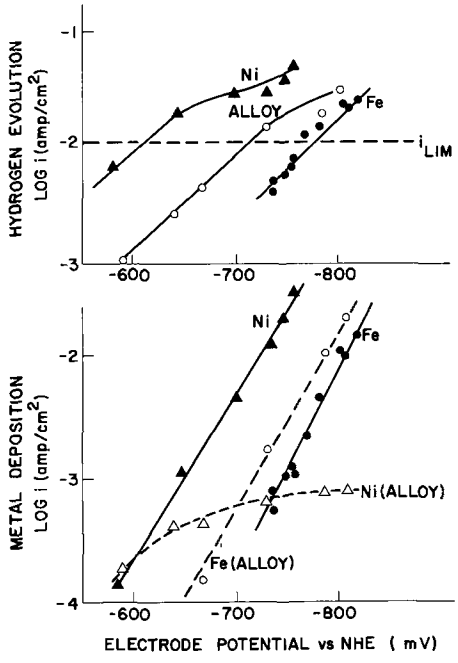

Fig. 3. Lower part: Tafel plots of iron-and-nickel deposition as separate metals and as alloys: ▲, nickel deposition from 0.5M $NiSO_4$, 0.01M H_2SO_4; ●, iron deposition from 0.5M $FeSO_4$, 0.01M H_2SO_4; △, nickel deposition from 0.5M $NiSO_4$, 0.5M $FeSO_4$, 0.01M H_2SO_4; ○, iron deposition from 0.5M $NiSO_4$, 0.5M $FeSO_4$, 0.01M H_2SO_4. Upper part: Tafel plots of hydrogen evolution under the same conditions.

at more negative potentials. The suppression of nickel discharge starts as soon as metal hydroxides are formed at the electrode, *i.e.*, at about the same potential at which the rate of hydrogen evolution exceeds the diffusion limited current of hydrogen ions i_{lim} (upper part of Fig. 3). Evaluation of the surface *p*H on the basis of Eq. [9] shows that this potential coincides with the rise of the surface *p*H from that of the bulk

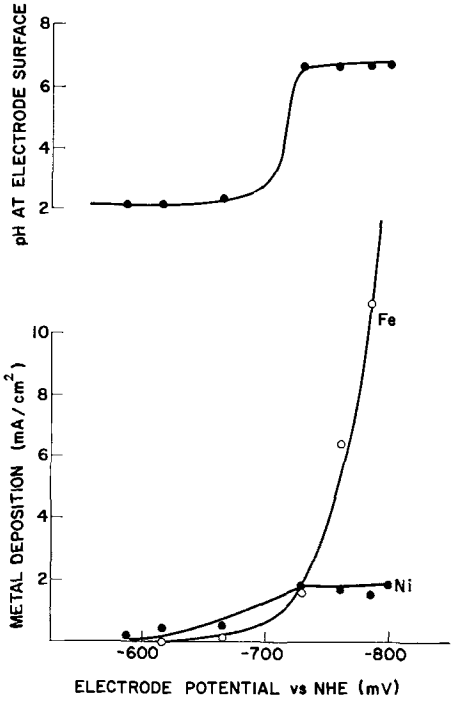

Fig. 4. Lower part: current-voltage curves of iron and nickel deposition from 0.5M $NiSO_4$, 0.5M $FeSO_4$, 0.01M H_2SO_4 solution. Upper part: *p*H at electrode surface calculated from partial current of hydrogen evolution.

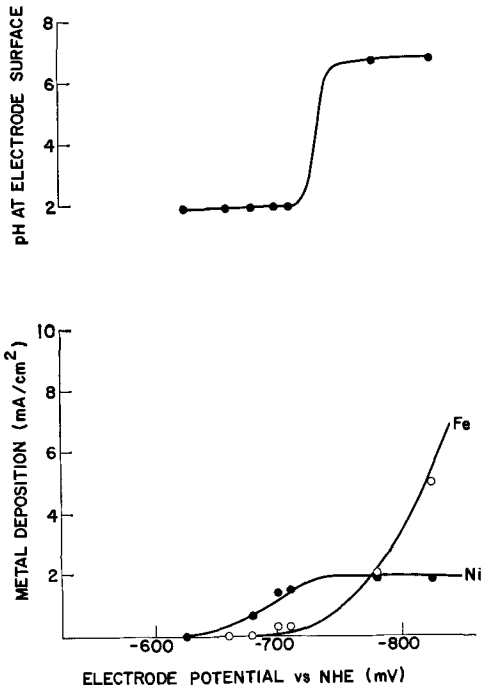

Fig. 5. Lower part: current-voltage curves of iron and nickel deposition from 0.5M $NiSO_4$, 0.5M $FeSO_4$, 0.02M H_2SO_4 solution. Upper part: pH at electrode surface calculated from partial current of hydrogen evolution.

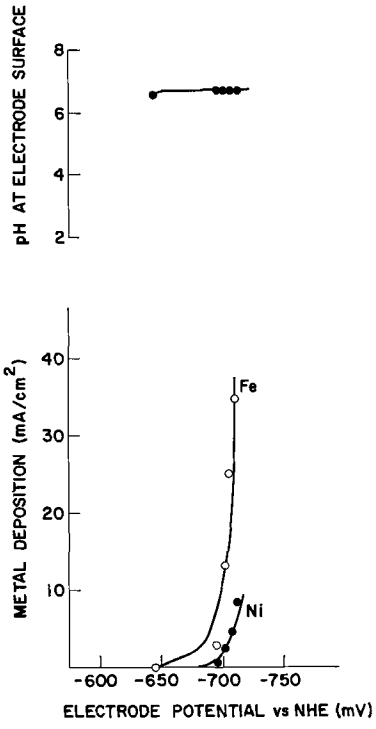

Fig. 6. Lower part: current-voltage curves of iron and nickel deposition from 0.5M $NiSO_4$, 0.5M $FeSO_4$, 0.001M H_2SO_4 solution. Upper part: pH at electrode surface calculated from partial current of hydrogen evolution.

to values sufficient for the formation of metal hydroxides. The dependence of plating rates on the surface pH is plotted in Fig. 4 and 5.

At higher bulk pH values (Fig. 6) the rate of hydrogen ion diffusion is so low that metal hydroxides are formed over the whole deposition range. It can be seen that under these conditions anomalous codeposition occurs throughout.

Figure 7 shows the influence of the iron ion concentration on the deposition rates. These measurements were done in a supporting electrolyte of 0.5M Na_2SO_4 in order to keep the activity coefficients and the ohmic voltage drop in the solution approximately constant. It can be seen that there is no noticeable increase in deposition rate with increasing iron concentration. Although there is some deviation from the averaged Tafel slope, no systematic trend to higher or lower deposition rates with increasing ferrous ion concentration is to be seen.

As hydrolysis appears to be responsible for the suppression of nickel discharge, and since ferric ions already hydrolyze at a pH of $\sim$ 3-4 (20), it was of interest to investigate the influence of traces of ferric ions present in the solution. Figure 8 shows the results of this study. No effect of ferric ions on the mechanism could be detected.

Discussion

The experimental results (Fig. 3-6) show a close relation between surface pH [3] and deposition rates: anomalous codeposition occurs when the surface pH is high enough to cause the formation of hydroxides. As long as the surface pH stays close to that of the bulk there are no anomalies in the deposition rates. In previous work (2-6) observations have been confined mainly to the region of anomalous codeposition (high surface pH) because no particular attention was paid to provide a sufficient rate of diffusion of hydrogen-ion-containing species to the electrode surface. Glasstone and Symes (2) used buffered solutions in order to maintain the bulk pH at the cathode surface. However, it can be calculated from their diffusion-limited deposition of iron (their Fig. 3, 4) that the maximal rate of diffusion of buffer acid was lower than the rate of hydrogen evolution observed (their Table I) in most of their experiments. It is interesting to note that at very low current densities, *i.e.*, at low hydrogen evolution currents, the authors do observe a sudden change to nickel-richer deposits. This is in qualitative agreement with the present work.

Since anomalous codeposition occurs only when metal hydroxides are formed in the cathode layer, the role of the hydroxides in deposition and codeposition has to be considered. It is clear that hydroxides of both iron and nickel ions are formed when the diffusion limited current of hydrogen ions is exceeded in all cases, in the deposition of single metals as well as in codeposition. However, since the anomalous suppression of the rate of nickel deposition occurs only during

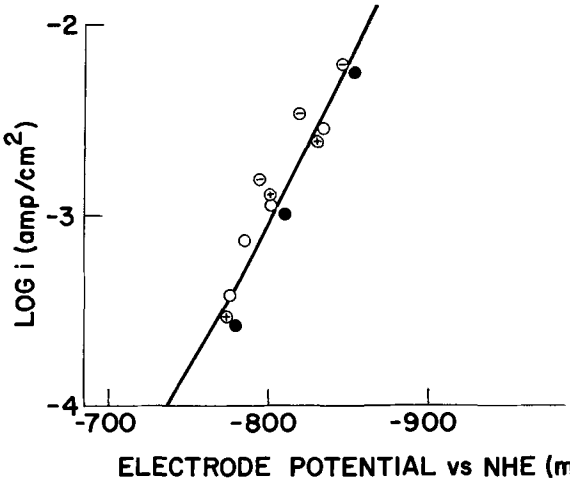

Fig. 7. Tafel plot of iron deposition as a function of ferrous ion concentration from solution of 0.5M Na_2SO_4, 0.01M H_2SO_4, 0.1M $NiSO_4$, xM $FeSO_4$. ○, x = 0.015M; ⊖, x = 0.03M; ⊕, x = 0.06M; ●, x = 0.1M.

[3] Recent direct measurements of the surface pH in nickel deposition [J. Matulis and R. Slizys, *Electrochim. Acta*, 9, 1177 (1964)] are in good agreement with our values calculated from Eq. [9].

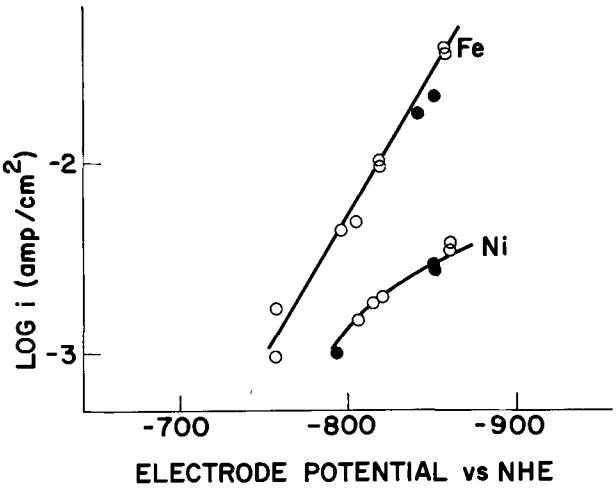

Fig. 8. Influence of Fe^{3+} content on deposition of iron-nickel alloys from a solution of 0.5M $FeSO_4$, 0.5M $NiSO_4$, 0.01M H_2SO_4. ○, Fe^{3+} less than 5 x 10^{-5}M; ●, Fe^{3+} — 5 x 10^{-3}M.

codeposition but not during deposition of nickel alone (Fig. 3) this effect must be attributed to the formation of ferrous hydroxide. The suppression of nickel discharge in the presence of ferrous hydroxide can be accounted for by assuming preferential absorption of ferrous hydroxide at the electrode which blocks the deposition of nickel.

This view is supported by the observation that preferential adsorption of ferrous hydroxide in the presence of nickel ions and subsequent suppression of nickel discharge occurs at the mercury electrode under analogous conditions (12).

Although the preferential adsorption of ferrous hydroxide in the presence of nickel cannot be interpreted on the basis of the hydrolysis constants [$Fe(OH)_2$: $K = 1.8 \times 10^{-15}$; $Ni(OH)_2$: $K = 1.6 \times 10^{-16}$], a higher rate of hydrolysis, rate of adsorption, or free energy of adsorption could account for the experimentally observed preferential adsorption. Another possibility is that ferric ions [hydrolysis constant $K = 6 \times 10^{-38}$ (20)] could form the first hydroxide layer. Figure 7 shows, however, that the addition of ferric ions has no effect on the anomalous codeposition. This result does not exclude the possibility that traces of ferric ions could form an initial monolayer of hydrolysis products.

The preferential adsorption of ferrous hydroxide would explain the fact that, although the rate of nickel discharge is suppressed, a high rate of iron discharge is maintained since the adsorbed ferrous hydroxide can provide the discharging species for iron deposition. The results shown in Fig. 7 support this point of view. It can be seen that the rate of iron discharge is independent of the concentration of ferrous ions in solution. This result means that the rate-determining step in iron deposition (in the presence of nickel) involves an adsorbed species, the surface concentration of which does not change with the ferrous ion concentration in solution.

On the basis of the discussion given above, the following type of mechanism can be proposed

$$2\,H_2O + 2e \rightarrow H_2 + 2\,OH' \qquad [1]$$

$$Fe^{++} + 2\,OH' \rightleftarrows Fe(OH)_{2,ads}\,(\theta_{Fe(OH)_2} \rightarrow 1) \qquad [2]$$

$$\text{At } \theta\text{: } Fe(OH)_{2,ads} + Fe(OH)_n^{(2-n)+} + 2e \rightarrow Fe + Fe(OH)_{2,ads} + n\,OH' \qquad [3]$$

$$\text{At } 1-\theta\text{: } (Ni(OH)_n^{(2-n)+} + 2e \rightarrow Ni + n\,OH' \qquad [4]$$

where θ is surface coverage with ferrous hydroxide.

Since anomalous codeposition is observed primarily in the electrodeposition of alloys containing one or more ions which are susceptible to hydrolysis (Fe, Co, Ni, Zn) (7), the type of mechanism given above could be of general importance in anomalous plating. It explains the two most characteristic features of anomalous codeposition: (i) the sudden change of systems from normal to anomalous codeposition with increasing current density which is caused by the equally sudden change of the *p*H at the electrode surface; (ii) the strong influence of temperature which effects the rate of evolution of hydrogen and the rate of diffusion to the electrode.

Acknowledgment

The authors wish to thank Mrs. J. D. Olsen for her skillful experimental assistance.

Manuscript received Nov. 20, 1964; revised manuscript received April 21, 1965. This paper was presented at the Washington Meeting, Oct. 11-15, 1964.

Any discussion of this paper will appear in a Discussion Section to be published in the June 1966 JOURNAL.

REFERENCES

1. A. Brenner, "Electrodeposition of Alloys," Vol. I, p. 77, Academic Press (1963).
2. S. Glasstone and T. E. Symes, *Trans. Faraday Soc.*, **23**, 213 (1927); **24**, 370 (1928).
3. A. Brenner, *loc. cit.* Vol. II, p. 239 (literature reviewed up to 1960).
4. A. T. Vagramyan and T. A. Fatueva, *This Journal*, **110**, 1030 (1963).
5. N. V. Korovin, *Zhur. Neorg. Khim*, **2**, 2259 (1957).
6. V. V. Sysoeva and A. L. Rotinyan, *Doklady Akad. Nauk USSR*, **144**, 1098 (1962).
7. A. Brenner, loc. cit., Vol. II, p. 191.
8. P. Delahay and M. Kleinerman, *J. Am. Chem. Soc.*, **82**, 4509 (1960).
9. L. I. Antoproff, "Kinetics of Electrode Processes and Null Points of Metals," New Delhi (1960).
10. A. Brenner, *loc. cit.*, Vol. II, p. 222.
11. A. Brenner, *loc. cit.*, Vol. II, p. 193.
12. H. Dahms, *J. Electroanal. Chem.*, **8**, 5 (1964).
13. V. G. Levich, "Physicochemical Hydrodynamics," Prentice Hall (1962).
14. J. O'M. Bockris, A. Drazic, and A. Despic, *Electrochim. Acta*, **4**, 325 (1961).
15. J. O'M. Bockris and E. C. Potter, *J. Chem. Phys.*, **20**, 614 (1952).
16. P. Ruetschi and G. Truempler, *Helv. Chem. Acta*, **35**, 1021 (1952).
17. I. M. Kolthoff and J. J. Lingane, "Polarography," 2nd ed., p. 52, Interscience, New York (1952).
18. E. A. Hogge and M. E. Kraichmann, *J. Am. Chem. Soc.*, **76**, 1431 (1954).
19. K. J. Vetter, "Elektrochemische Kinetik," p. 313, Springer Verlag (1961).
20. W. M. Latimer, "Oxidation Potentials," 2nd ed., Prentice Hall, New York (1952).
21. F. Lindstrand, *Svensk. Kem. Tid.*, **56**, 282 (1944).
22. B. O. Hedstroem, *Arkiv. Kemi*, **5**, 457 (1953).
23. F. Achenza, *Ann. Chem. (Rome)*, **49**, 624 (1959).
24. B. E. Conway, "Electrochemical Data," Elsevier (1952).

Rare Earth Activated Phosphors Based on Yttrium Orthovanadate and Related Compounds

Frank C. Palilla, Albert K. Levine, and Maija Rinkevics

General Telephone & Electronics Laboratories, Inc., Bayside, New York

ABSTRACT

The adoption of YVO_4:Eu as a new red-emitting primary in color television has stimulated investigation of a new class of phosphors obtained by appropriate substitutions in YVO_4:Eu. Substitution of Y^{3+} by Gd^{3+} and Lu^{3+} provides equally efficient hosts for Eu^{3+} with no significant spectral differences. Substitution of Y^{3+} by La^{3+} leads to a less efficient host with important differences in the emission characteristics of Eu^{3+}. Use of rare earth activators other than Eu^{3+} provides a series of phosphors which emit over most of the visible range. Spectral data and preferred concentration ranges are presented as well as the effect of temperature on the fluorescent emission intensities.

The cathodoluminescent response of YVO_4:Eu has recently been described (1, 2) and, in particular, attention has been drawn to it because of its wide adoption as the new red-emitting primary in color television. The ultraviolet excited emission from this phosphor has been reported by Van Uitert *et al.* (3, 4), and more recently by Levine and Palilla (5) who have shown it to be extremely efficient under this mode of excitation. The notable properties of YVO_4:Eu has stimulated investigation of a new class of phosphors obtained by appropriate cation substitution in YVO_4, and by use of rare earths other than europium as activators.

Lanthanum, Gd, and Lu were investigated as host cations replacing Y. All four elements have the same valence electron configuration (d^1s^2) and are optically inert. Their ionic radii in the trivalent state are 1.14, 0.97, 0.85, and 0.92Å, respectively (6); the ionic radii of all the other trivalent rare earths lie within this range. In their trivalent state Y, La, Gd, and Lu possess spherically symmetrical electronic structures and are characterized by considerable stability: Y^{3+} and La^{3+} have a noble gas electronic structure (f^0), Lu^{3+} possesses a complete 4f shell (f^{14}), and Gd^{3+} has a half-filled shell (f^7). Such configurations provide the basis for effective host crystal structures because of the absence of lower lying energy levels by way of which excitation energy might be dissipated. Moreover, when combined with proper anions these cations form matrices which exhibit no absorption in the visible region and hence are white in body color. Reference to the similar properties of Y^{3+} and Gd^{3+} as host cations for luminescence has already been made by several investigators (3, 7, 8).

The elements Tm, Er, Ho, Dy, Tb, and Sm in the trivalent state were selected as the activators. All fluoresce when excited and their emissions cover most of the visible range. Their similarity in ionic size and valence state to the selected host cations permits incorporation into the selected hosts without the complications of charge compensation. Furthermore, in common with Y^{3+}, Gd^{3+} and Lu^{3+}, they all crystallize in the tetragonal system with the xenotime structure (9-12). It is particularly desirable that the host and activator cations form isostructural compounds when the activator concentrations may be high, as is the case in this class of compounds. Lanthanum, because of its larger ionic radius, provides an exception and crystallizes in a different system from the rest of the lanthanides.

Experimental Procedure

The rare earth orthovanadates were prepared by blending the mixed oxides or the coprecipitated oxalates of the rare earths with an appropriate compound of vanadium and then firing the mixture in a silica or platinum crucible at 900°C or higher.

The arrangement for recording the excitation and emission spectra of the powders is indicated in Fig. 1. The phosphor sample is packed in a flat plaque with a quartz window and centered in the bottom of a dewar having observation ports at 90° to one another. Excitation radiation enters by one port and the sample fluorescence is observed through the other. Room temperature data are obtained before the liquid nitrogen is added to the dewar for the low-temperature observations. This procedure makes both sets of traces quantitatively comparable. Excitation is provided by a 200-w d-c xenon lamp, whose output is passed through a Leiss quartz prism monochromator, to select the desired wavelength, and then focused on the sample.

Fluorescence from the sample is focused on the entrance slit of a Jarrell-Ash 0.5-meter Ebert grating monochromator, and that portion reaching the exit slit is detected by a 6255B-EMI photomultiplier (S-13 surface). Either monochromator may be scanned automatically: the prism monochromator provides excitation spectra; the grating monochromator emission spectra. The integrated luminous output of the samples under 253.7-nm excitation was measured with a Photovolt photometer Model 520-M using a 1P21 photomultiplier as a detector in conjunction with a Wratten 106 filter.

Results and Discussion

The orthovanadates of Y^{3+}, Lu^{3+}, and Gd^{3+}, prepared as above, consist of well-formed crystallites. The powders give sharp x-ray patterns which confirm that these compounds crystallized in the tetragonal system with the xenotime structure, and that secondary phases are absent. In this structure the vanadium atoms are tetrahedrally coordinated with oxygen atoms, while

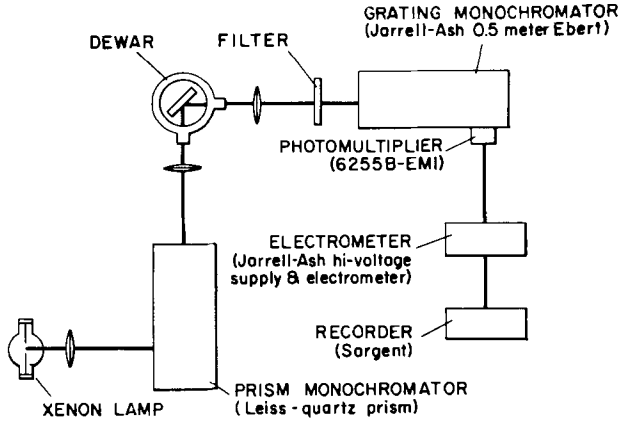

Fig. 1. Experimental arrangement for determining excitation and emission spectra.

each rare earth ion is surrounded by eight oxygen neighbors arranged in the form of two distorted tetrahedra. Lanthanum orthovanadate crystallizes in the monoclinic system with the monazite structure.

Under u.v. excitation the unactivated vanadates of Y^{3+}, Lu^{3+}, and Gd^{3+} exhibit broad-band blue-white luminescence which gives a peak in the photomultiplier response near 450 nm (Fig. 2). Since the response of the S-13 surface is reasonably flat between 400 and 500 nm, the corrected peak for this host fluorescence also lies near 450 nm. The difference in fluorescence intensity between liquid nitrogen temperature and room temperature indicates that lattice vibrations lead to dissipative transitions as the temperature is raised. The multiplets which are superimposed on the YVO_4 host emission are due to Dy^{3+} (481 and 576 nm) and Tm^{3+} (477 nm) impurities in the Y_2O_3 source material. The emission spectrum of $GdVO_4$ is very similar to that of YVO_4 except that it shows multiplets at 619 and 595 nm due to Eu^{3+} impurity in the Gd_2O_3. The same broad fluorescence at 450 nm is observed with $LuVO_4$. In the case of $LaVO_4$ no host emission was detected. Brixner and Abramson (13) recently reported weak broad-band host emission centered at 475 nm from YVO_4, $GdVO_4$ and $LaVO_4$ at room temperature. Careful examination of their spectra indicates that the peak near 475 nm is probably due to Tm^{3+} and/or Dy^{3+} impurities, which probably account also for the multiplets at 480 nm. The multiplets reported at 525 and 555 nm should be attributed to Er^{3+}, that at 575 nm to Dy^{3+}, and those at 595 and 618 nm to Eu^{3+}. This argument is supported by the data presented immediately below.

When selected lanthanides are incorporated into these vanadates they function as activators and introduce characteristic emission and absorption lines. Furthermore they are effective in quenching the host luminescence. From Fig. 2 it is seen that when activators are added to YVO_4, the host luminescence is almost completely quenched at room temperature, but remains pronounced at reduced temperature. The apparent exception in the case of Eu^{3+} is due to its high concentration (5 mole %) as compared with the others (0.5 mole %). When the Eu^{3+} concentration is reduced below 1 mole % the host emission at −196°C begins to become prominent. The emission lines due to the activators are sharp and occur in groups characteristic of each particular rare earth. In the cases of Er^{3+} and, particularly, Ho^{3+} sharp absorption lines are superimposed on the host emission at −196°C. These lines are due to transitions from the ground states of the ions followed, at least in part, by nonradiative processes. The nonradiative processes of excited Er^{3+} and Ho^{3+} in YVO_4 probably limit the emission intensity at room temperature also. The lines at 576 nm which appear in most of the spectra are due to Dy^{3+}, an impurity generally found with Y^{3+}. In those cases where the relative photomultiplier response as shown in Fig. 2 is small, the spectral details shown were verified by measurements made at higher gain. Table I presents a summary of the principal groups of emission lines, relative luminosity under 253.7-nm excitation, and preferred concentration ranges of activators in YVO_4. It should be noted here that activation by Dy^{3+} gives the most luminous phosphor. However, activation by Eu^{3+} gives a phosphor of almost equal luminance despite the fact that its emission is in a region where the luminosity function is smaller. In terms of radiant energy output Eu^{3+} is the most efficient of the rare earth activators for YVO_4. The weak emission with Tb^{3+} as activator is not consistent with the correspondence suggested by Dieke and Hall (14) between fluorescence efficiency and the magnitude of the energy gap between excited and low-lying levels of the rare earth ions. The poor fluorescence of Tb^{3+} in YVO_4 may be attributable to inefficient energy transfer from the crystal lattice. The fluorescence from terbium in $GdVO_4$ and $LaVO_4$ is also weak.

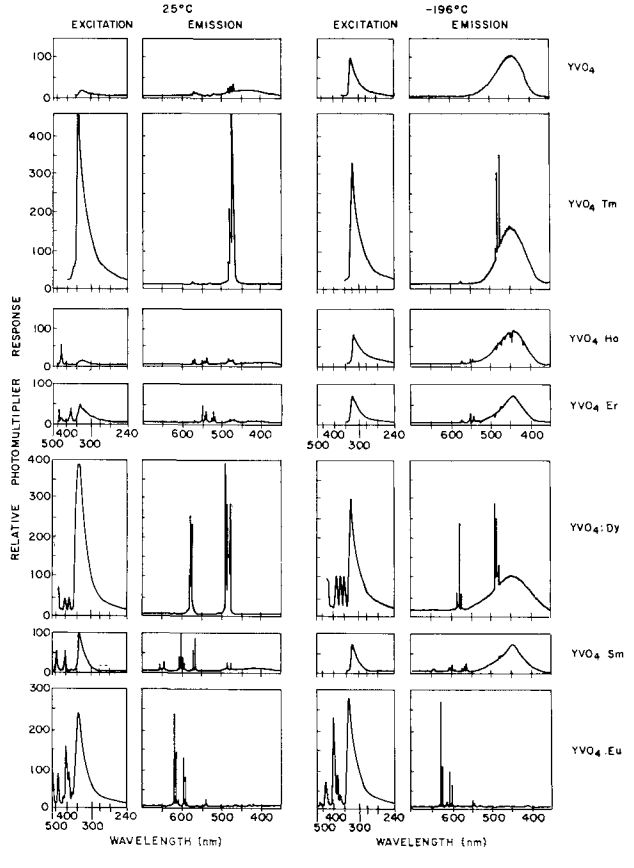

Fig. 2. Emission and excitation spectra of YVO_4 and YVO_4:Ln at 25° and −196°C. Ln = Tm^{3+}, Ho^{3+}, Er^{3+}, Dy^{3+}, Sm^{3+}, and Eu^{3+}. The excitation spectra are for the emission peak in each case and terminate when the excitation wavelength coincides with the emission being monitored. Similar spectra are obtained when Gd^{3+} and Lu^{3+} are substituted for Y^{3+}. Relative response refers to 6255B-EMI photomultiplier.

Table I. Summary of principal groups of emission lines, relative luminosity, and preferred concentration ranges of activators

Phosphor	Preferred conc. range of activator, mole %	Principal emission line groups, nm	Visual emission color	Relative luminosity, 253.7 nm excitation
YVO_4:Tm	0.5-1.0	477	Blue	12.2
YVO_4:Tb	—	—	Green	<1.0
YVO_4:Ho	0.1-1.0	545	Green	8.8
YVO_4:Er	0.4-0.8	553, 525	Green	20.5
YVO_4:Dy	0.3-0.7	576, 481	Yellow-white	130.0
YVO_4:Sm	0.1-1.0	650, 606, 569	Orange-red	63.0
YVO_4:Eu	3.0-10.0	619, 595, 698	Red	100.0

Figure 2 also shows that the excitation spectra of rare earth activated yttrium vanadates are similar for all the rare earths, except that beyond 330 nm each of the activator ions exhibits the narrow excitation bands characteristic of its own direct absorptions. These direct absorption bands are in most cases considerably weaker than the broad u.v. excitation band which has the same general character as in the unactivated vanadates. The rare earth activated orthovanadates of gadolinium and lutetium also give essentially identical excitation spectra. When corrected for the variation of output intensity with wavelength of the excitation source (discussed in the following paragraph) the excitation spectrum is intense over a wide range (Fig. 3). Because this excitation band is independent of the host cation or activator species, it must be considered as associated with the vanadate ion in this structure.

The vanadate-associated excitation band was determined by the method of Eby (15) which gives corrected spectra. This method employs a deuterium arc lamp in conjunction with a 0.5-meter Seya-Namioka

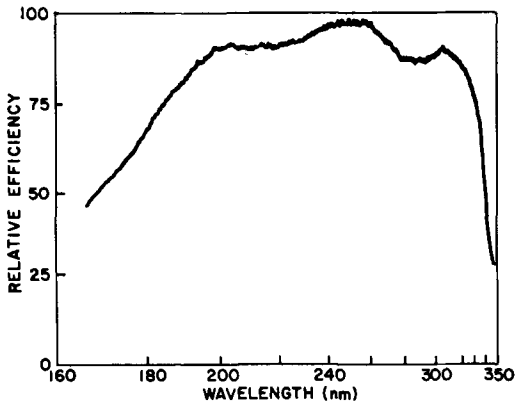

Fig. 3. Excitation spectrum typical of RVO_4 and RVO_4:Ln. R = Y, Lu, Gd, and La.

type of vacuum grating monochromator. Most of the radiation from the monochromator is used to excite the phosphor, but a portion of the beam is intercepted and measured by a monitoring system which leads to corrections for the variation of light output with wavelength. The resulting spectra are thus corrected for the various instrumental effects. Figure 3 shows the spectrum obtained with YVO_4:Eu. Several of the systems described above were studied in this way; all were found to give similar excitation spectra. The host-associated excitation spectrum is seen to be unusually broad. Furthermore the excitation efficiency is uniformly high from 180 to 330 nm, a property which indicates the potential of this phosphor system in mercury discharge lamps.

Comparison between the orthovanadates of the isostructural Y, Lu, and Gd compounds and $LaVO_4$ as hosts was made using europium ion as activator. Under 253.7 nm excitation YVO_4:Eu, $GdVO_4$:Eu, and $LuVO_4$:Eu exhibit almost equal emission intensity, and are about four times more intense than $LaVO_4$:Eu. Figure 4 gives the excitation and emission spectra of these compounds. With Gd, Lu, and Y hosts, the Eu^{3+} emission at 619 nm was monitored; with La, the Eu^{3+} emission at 615 nm was monitored. It is apparent that only minor differences exist between the isostructural orthovanadates, but important differences appear in the case of $LaVO_4$:Eu. In addition to the weaker fluorescence intensity of Eu^{3+} in $LaVO_4$, there is a pronounced alteration of the relative intensities of the principal emission lines, which appear at the same wavelengths. For example, within the structurally sensitive electric dipole $^5D_0 \rightarrow {}^7F_2$ transition, the 615 and 612.5 nm emissions in $LaVO_4$:Eu are considerably more

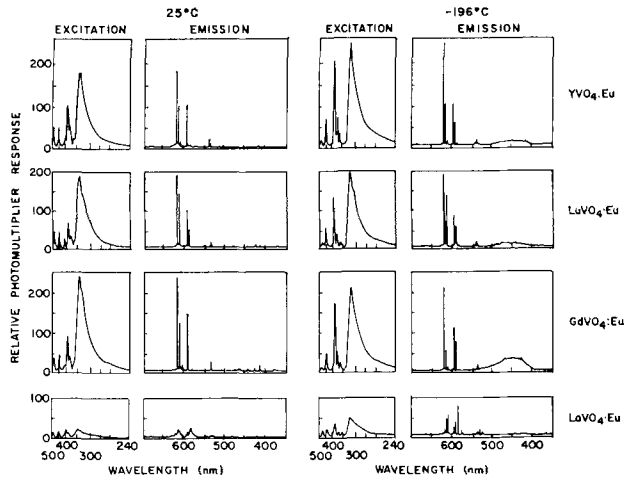

Fig. 4. Emission and excitation spectra of RVO_4:Eu at 25° and —196°C. Relative response refers to 6255B-EMI photomultiplier.

intense with respect to the 619 nm emission than is the case with the other orthovanadates. These results are consistent with previous observations (1, 5) pertaining to crystal field effects on Eu^{3+} emission from Y_2O_3 and YVO_4, two hosts which present substantially different environments. Also, in the Y, Lu, and Gd orthovanadates activated with Eu^{3+}, the preferred transitions by far are those involving $^5D_0 \rightarrow {}^7F_2$ levels, while in $LaVO_4$, the transitions originating from the $^5D_0$ excited level and terminating at the $^7F_1$ multiplets occur to a greater extent, when allowance is made for the photomultiplier response. The former transitions correspond to the emissions centered between 612 and 619 nm, while the latter correspond to those near 595. The prominence of these emissions in $LaVO_4$:Eu represents an example of an increase in the probability of an allowed magnetic dipole transition ($^5D_0 \rightarrow {}^7F_1$) with decrease in environmental symmetry. The lines evident in the $LaVO_4$:Eu emission at about 587 (the most pronounced emission at —196°C) and 579 nm were not detected in the spectra from $GdVO_4$:Eu, $LuVO_4$:Eu, and YVO_4:Eu. These emissions appear to correspond to an additional $^5D_0 \rightarrow {}^7F_1$ component and to the $^5D_0 \rightarrow {}^7F_0$ transition, respectively. It should be noted also that although the Eu^{3+} emission intensity is little affected by a reduction of temperature in YVO_4, $GdVO_4$, and $LuVO_4$, the effect in $LaVO_4$ is pronounced. In contrast to the differences observed in the fluorescence of Eu^{3+} in these hosts little difference, except for intensity, is detectable in the excitation spectra. This constitutes further confirmation that the principal absorption of energy occurs by way of the vanadate

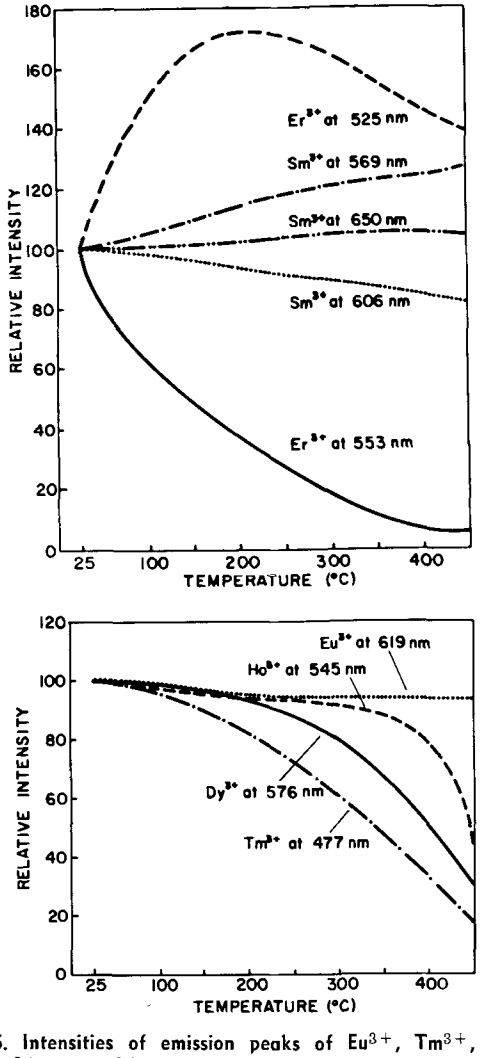

Fig. 5. Intensities of emission peaks of Eu^{3+}, Tm^{3+}, Ho^{3+}, Dy^{3+}, Sm^{3+}, and Er^{3+} in YVO_4 with temperature relative to their intensities at 25°C.

ligand. In all cases, there is a small shift in peak excitation intensity toward shorter wavelength with decrease in temperature to —196°C.

Figure 4 also shows that in all the systems activated with Eu^{3+}, little line sharpening occurs as the temperature is reduced from 25° to —196°C. This indicates that there is negligible dissipative interaction between the Eu^{3+} and the crystal lattice of these hosts. This temperature relationship continues, so that even at elevated temperatures YVO_4:Eu emits quite strongly. Figure 5 indicates that there is no appreciable temperature quenching up to at least 400°C. This, together with its excellent response, evident from Fig. 3, to the principal lines from both low- and high-pressure mercury discharges indicates the potential of YVO_4:Eu as a red color-correcting component in mercury lamps.

Not all activators in YVO_4 behave similarly, as is shown in Fig. 5. Unless otherwise stated, only the relative intensities of the major emission groups are plotted. It is seen that Dy^{3+} and Ho^{3+} fluoresce strongly from room temperature up to about 200°C, beyond which strong temperature quenching occurs. With Tm^{3+} a continuous decrease with increasing temperature above room temperature is found. On the other hand, Sm^{3+} shows a continuous, but small increase in intensity of its emission at 650 nm, a steady decrease in its shorter wavelength emission at 606 nm, and a continuous increase in its minor emission at 569 nm. Finally Er^{3+} exhibits a sharp and steady decrease in its emission at 553 nm, while its emission at 525 nm reaches a peak intensity at 200°C. Quantitative and detailed measurement of the different behavior with temperature of the various activators in YVO_4 should provide valuable data for fundamental studies of the mechanism of energy transfer and emission processes in this system of phosphors.

Acknowledgments

Grateful acknowledgment is made to B. O'Reilly for his assistance in the preparation of many of the phosphors, to V. Brophy for much of the spectral data, and to J. Eby for the investigation of the excitation characteristics in the short wavelength u.v. region. The authors also wish to express their thanks to F. Avella, L. Bodi, C. Brecher, and C. Wiggins for helpful discussions and suggestions.

Manuscript received April 22, 1965. This paper was presented at the San Francisco Meeting, May 9-13, 1965.

Any discussion of this paper will appear in a Discussion Section to be published in the June 1966 JOURNAL.

REFERENCES

1. A. K. Levine and F. C. Palilla, *Appl. Phys. Letters*, **5**, 118 (1964).
2. A. K. Levine and F. C. Palilla, *Trans. N. Y. Acad. Sci.*, **27**, 517 (1965).
3. L. G. Van Uitert, R. C. Linares, R. R. Soden, and A. A. Ballman, *J. Chem. Phys.*, **36**, 702 (1962).
4. L. G. Van Uitert, R. R. Soden, and R. C. Linares, *ibid.*, **36**, 1793 (1962).
5. A. K. Levine and F. C. Palilla, Paper presented at the San Francisco Meeting of the Society, May 9-13, 1965, Abstract No. 40. Submitted for publication in the Journal.
6. L. H. Ahrens, *Geochim. et Cosmochim. Acta*, **2**, 155 (1952).
7. K. A. Wickersheim and R. A. Lefever, *This Journal*, **111**, 47 (1964).
8. R. C. Ropp, *ibid.*, **111**, 311 (1964).
9. E. Broch, *Z. Physik. Chem.*, **20B**, 345 (1932).
10. W. O. Milligan, L. M. Watt, and H. H. Rachford, Jr., *J. Phys. Chem.*, **53**, 227 (1949).
11. J. R. Gambino and C. J. Guare, *Nature*, **198**, 1084 (1963).
12. H. Schwarz, *Z. Anorg. u. allgem. chem.*, **323**, 44 (1963).
13. L. H. Brixner and E. Abramson, *This Journal*, **112**, 70 (1964).
14. G. C. Dieke and L. A. Hall, *J. Chem. Phys.*, **27**, 465 (1957).
15. J. E. Eby, Paper presented at the Toronto Meeting of the Society, May 3-7, 1964, Abstract No. 27.

Laser Characteristics of Niobium Compensated $CaMoO_4$ and $SrMoO_4$

P. A. Flournoy and L. H. Brixner

Engineering Physics Laboratory and Pigments Department, respectively,

E. I. du Pont de Nemours and Company, Inc., Wilmington, Delaware

ABSTRACT

The niobium-compensated $CaMoO_4$ and $SrMoO_4$ systems have been found to be excellent host materials for rare earth ions. A discussion is given of pertinent crystal properties, fluorescence spectra, laser output wavelengths, thresholds for stimulated emission, and other parameters of importance in practical utilization of these materials for pulsed and CW lasers. A comparison with the sodium compensated $CaWO_4$:Nd^{3+} system is given where data are available.

Laser action has been observed in several single crystal materials containing trivalent neodymium ions (1). Of particular interest is the calcium tungstate host lattice (2), which was the first to provide a continuously operating solid-state laser at room temperature. Neodymium-doped calcium and strontium molybdates were first demonstrated to lase by Johnson (3), but he observed high thresholds due to poor crystal properties. Brixner (4) developed a procedure for purifying and stabilizing these materials to improve their growing characteristics and produce large single crystals of excellent optical quality. In the present study, the fluorescence and stimulated emission characteristics of neodymium-doped calcium and strontium molybdate are presented, and where possible compared to calcium tungstate as a host.

Crystal Properties

Although rare earth ions can be introduced into the scheelite lattice without a secondary compensating ion (creating a defect lattice), valence compensation by a second ion is generally preferred since it simplifies the fluorescent emission spectrum and lowers the threshold for laser action. The most common scheme, as outlined by Nassau (2), is to compensate with Na^+ for each Ca^{2+} ion replaced by a rare earth ion. Although the structural match for these ions is nearly perfect, sodium presents problems because of its vola-

Table I. Crystal properties

	$CaMoO_4$	$SrMoO_4$	$CaWO_4$[a]
Typical composition	$(NdNb)_{0.013}(CaMo)_{0.987}O_4$	$(NdNb)_{0.012}(SrMo)_{0.988}O_4$	$Ca_{0.96}No_{0.02}Nd_{0.02}WO_4$
Segregation coefficient	1.3 ± 0.1	1.0 ± 0.1	0.40
Thermal conductivity, mw/cm °C	39.5 (a-axis) (295°K) 38.2 (c-axis)	40.4 (a-axis) (295°K) 41.6 (c-axis)	30.0 (295°K)
Heat capacity, cal/g °C	0.165	0.148	0.104
Melting point	1480°C	1490°C	1595°C
Refractive index	1.997 (a-axis) 1.996 (c-axis)	1.940 (a-axis) 1.940 (c-axis)	1.91

[a] K. Nassau, Proc. Symposium Optical Masers, p. 451, Brooklyn Polytechnic Press, New York (1963).

tility at high melt temperatures and its relatively low segregation coefficient. Therefore, in the work reported here, we balanced in the Mo^{6+} site by introducing the same amount of Nb^{5+} for each Ca^{2+} or Sr^{2+} ion being replaced by Nd^{3+}. Compared with sodium containing compositions, niobates are considerably more stable, and no losses are experienced at melt temperature. Moreover, the segregation coefficient is much more favorable, being close to unity.

Brixner (4) recently published a detailed study of the niobium compensated calcium molybdate, its Czochralski crystal-growth characteristics, crystal structure, and fluorescent properties. Additions of rare earth niobate as small as ½ mole % stabilize $CaMoO_4$ and keep it from losing oxygen and turning deep blue. Other workers (1) had difficulty eliminating this blue coloration on direct growing and have had to anneal under oxygen. Since the molybdates can be grown at 1480°-1490°C (100°C lower than calcium tungstate), fewer impurities are introduced from the melt container. Using a Jarrell Ash 3.4m grating plane spectrograph, semiquantitative analysis of singly pulled $CaMoO_4$ of our own preparation and $CaWO_4$ grown from Sylvania "crystal grade" feed gave the following results:

	Na	Mg	Zn	Pb	Mn	Ni	Co	Al	B	Si
$CaMoO_4$	<100	~20	<100	<100	<10	<100	<100	<10	<10	~80
$CaWO_4$	<100	~100	<100	~100	~10	<100	<100	~10	<10	~100

Although most of the elements analyzed were below the limit of detection, the results reflect the higher quality of the $CaMoO_4$ feed.

A comparison of some important crystal properties of $CaMoO_4$, $SrMoO_4$, and $CaWO_4$ is given in Table I. The average segregation coefficient for $NdNbO_4$ in $CaMoO_4$ based on the analytical evaluation of over 50 crystals is 1.31. The $CaO:MoO_3$ ratio never deviates more than 1% from unity. If equal starting quantities of Nd_2O_3 and Nb_2O_5 are used, excellent charge compensation over the length of the crystals is obtained without the need for stoichiometric correction. The neodymium concentration varies linearly along the length of the crystal on the order of 3%/in. The segregation coefficient for $NdNbO_4$ in $SrMoO_4$ was found to be unity within the accuracy of the measurement, and variations of the neodymium concentration along the length of 6-in. crystals were too small to measure. On the other hand, variations in neodymium concentration as large as 20-30% per inch are typical for sodium compensated $CaWO_4$ unless large excesses of sodium are used.

Fluorescent Properties

Fluorescence spectra of Nb^{5+}-compensated $CaMoO_4$ and $SrMoO_4$ containing 1.3 mole % Nd^{3+} were recorded with a Bausch & Lomb two-meter-grating spectrograph using Kodak 1-Z infrared sensitive spectroscopic plates. The samples were placed in a quartz dewar containing liquid N_2. Fluorescence emission was excited by a Gates HBO 100 W/2 high-pressure mercury arc through a Corning 4600 filter.

The $4F_{3/2} \rightarrow 4I_{11/2}$ emission from niobium compensated $CaMoO_4:Nd^{3+}$ is shown in Fig. 1, as obtained from a microdensitometer scan of the original spectroscopic plate. The emission line widths are approximately 12Å at 295°K and 5Å at 77°K. Stimulated emission is observed for the lines indicated by arrows under the conditions discussed below. The spontaneous emission lifetime for neodymium in the $CaMoO_4$ host at 295°K was observed to vary nearly linearly with concentration over the range from 0.5 to 2.0 mole % $NdNbO_4$ as shown in Fig. 2. Fluorescence yield measurements as a function of rare earth concentration indicate an optimum Nd^{3+} concentration of 1.3 mole %. The fluorescence yield determined in this way is, of course, a function of the absorption coefficient, and no attempt was made to correct the data for this effect. Therefore the "optimum" values of concentration are usually slightly lower than that required for optimum laser performance.

Fluorescent emission from the strontium host is shown in Fig. 3. The data are similar to that of Fig. 1, but shifted by 20-30Å to the short wavelength side with a significant change in the intensity distribution among the stronger bands. Line widths vary from 35

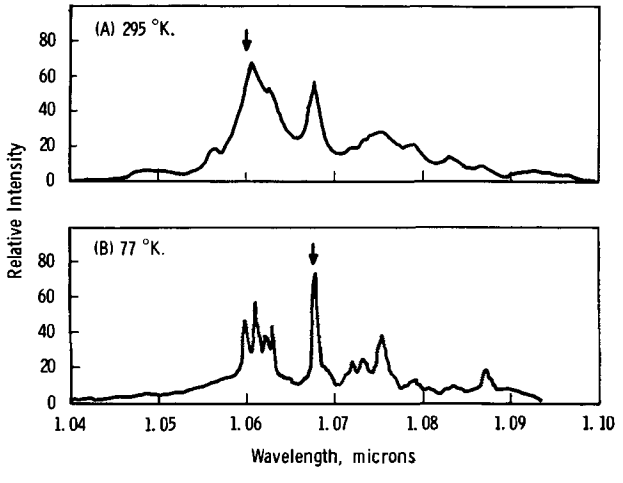

Fig. 1. $4F_{3/2}$ $4I_{11/2}$ emission in $CaMoO_4:Nd^{3+}$ with Nb^{5+} compensation: (a) 295°K, (b) 77°K. Observed laser lines are indicated.

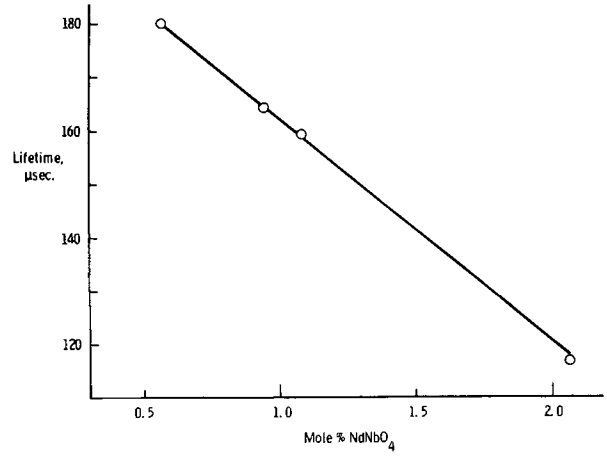

Fig. 2. Spontaneous emission lifetimes for $NdNbO_4$ in $CaMoO_4$ as a function of concentration; $T = 295$°K.

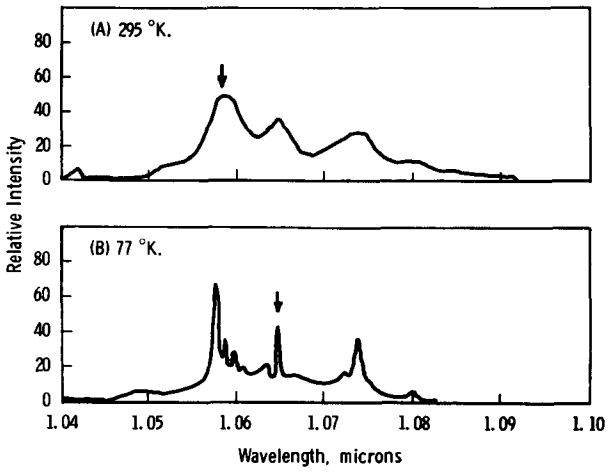

Fig. 3. $4F_{3/2}$ $4I_{11/2}$ emission in $SrMoO_4:Nd^{3+}$ with Nb^{5+} compensation: (a) 295°K, (b) 77°K. Observed laser lines are indicated.

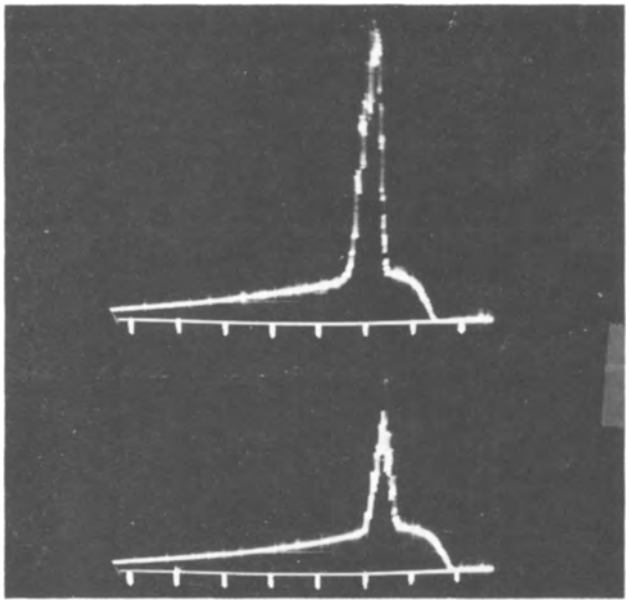

Fig. 4. Light output of a $CaMoO_4:Nd^{3+}$ crystal at 1.060μ with $T = 134$°K. Upper trace: 12% above threshold; lower trace: 8% above threshold; time scale is 100 μsec/div.

to 40Å at 295°K to 6 to8Å at 77°K. Room temperature lifetimes for this host are longer by approximately 20 μsec for 1% neodymium. Fluorescence yield measurements show an optimum Nd^{3+} concentration of 1.2 mole %.

Laser Experiments

Single crystal boules were cut and ground into cylindrical rods ¼ in. diameter and 3 in. long. The cylindrical surfaces were left rough and the ends polished to form a Fabry-Perot resonator. Silver was evaporated onto the end surfaces; one end was 5% transmissive and the other completely opaque.

Laser characteristics were measured under pulsed illumination in a Lear-Siegler LS-3 laser head with a Kemlite FT100B helical xenon flash lamp. Temperature from 135° to 295°K was controlled by placing the laser crystals in precooled flowing nitrogen gas. The lamp was flashed by discharging a 5-μf condenser charged to 2000v. Light from the laser rods was detected with a Dumont K1485 photomultiplier through a 3-mm silicon filter. Figure 4 shows a typical laser emission just above threshold for $CaMoO_4$. For 2 or 3 in. long rods, thresholds invariably less than 10 joules have been observed at 135° and 295°K under these conditions. In a more efficient setup, Duncan (5) reported thresholds as low as 0.6 joules at 77°K and 1.0 joules at 300°K on our $CaMoO_4$:Nd crystals.

The spectral distribution in the output was recorded on Kodak 1-Z spectroscopic plates by focusing the emitted radiation into a Bausch & Lomb 2-meter grating spectrograph. At room temperature, stimulated emission is observed at 1.0595μ in $CaMoO_4$ and 1.0573μ in $SrMoO_4$. The line width decreases to ~0.8Å in both cases. At 134°K, the same transitions are observed with the output wavelength decreasing by 4Å in $CaMoO_4$ and 7Å in $SrMoO_4$. However, at 77°K the lowest thresholds are observed for the 1.067μ line in $CaMoO_4$ and 1.064μ line in $SrMoO_4$.

Continuous operation of the $NdNbO_4$:$CaMoO_4$ system at both 77°K and room temperature has been achieved and is reported elsewhere (5). The niobium compensated $CaMoO_4$ can also be readily "Q-spoiled" (6).

Summary

The niobium-compensated $CaMoO_4$ and $SrMoO_4$ systems show promise as excellent, active materials for lasers. The thermal stability of the rare earth niobates combined with the favorable segregation coefficients allows the growth of uniform crystals of excellent optical quality. In addition low melting points minimize contamination from the melt container. The fact that Duncan (5) observed continuous laser operation at room temperature with $CaMoO_4$:Nd crystals clearly indicates the high optical perfection necessary for continuous oscillations and makes this particular composition only the second scheelite-type host after $CaWO_4$:Nd (7) to do so. The principal practical advantage we see in the $CaMoO_4$ over the $CaWO_4$ host is the appreciably higher thermal conductivity which will greatly alleviate cooling problems during operation, since heat will be dissipated much faster. While the difference in refractive indices is not very great, it certainly constitutes a further small advantage for $CaMoO_4$. The fluorescence of Nd^{3+} in $CaMoO_4$ has a narrower line width and simpler emission spectrum than Nd^{3+}-doped $CaWO_4$, which also is rather desirable since it results in lower thresholds.

In conclusion, we can state that $CaMoO_4$ as a solid-state laser host has come a long way since the original experiments by Johnson (1) and can now be considered at least equivalent to the corresponding tungstate and further, more detailed studies seem indicated.

Manuscript received March 17, 1965.

Any discussion of this paper will appear in a Discussion Section to be published in the June 1966 JOURNAL.

REFERENCES

1. L. F. Johnson, *J. Appl. Phys.*, **34**, 897 (1963).
2. K. Nassau and A. M. Broyer, *ibid.*, **33**, 3064 (1962).
3. L. F. Johnson and R. R. Soden, Unpublished work.
4. L. H. Brixner, Paper presented at the New York Meeting of the Society, Sept. 29, 1963; *This Journal*, **3**, 690 (1964).
5. R. C. Duncan, *J. Appl. Phys.*, **36**, 874 (1965).
6. R. B. Clay, Private communication.
7. L. F. Johnson, G. D. Boyd, K. Nassau, and R. R. Soden, *Phys. Rev.*, **126**, 1406 (1962).

Solubility and Electrical Behavior of Zinc, Sulfur, Selenium, and Tellurium in Gallium Phosphide

F. A. Trumbore, H. G. White, M. Kowalchik, R. A. Logan, and C. L. Luke

Bell Telephone Laboratories, Incorporated, Murray Hill, New Jersey

ABSTRACT

A thermal gradient technique was used to grow GaP crystals at ~1040°C from gallium solutions doped with zinc, sulfur, selenium, or tellurium. The solid solubilities of the donor impurities appear to vary linearly with the melt concentrations at the lower doping levels and with the square root of the melt concentration at higher doping levels, all in the extrinsic range. This behavior contrasts with that of zinc, for which the solid solubility varies only as the square root of the melt concentration as expected for a singly ionized acceptor dissolving in an extrinsic semiconductor. The excess donor or acceptor concentrations were significantly lower than the impurity concentrations at the higher doping levels.

In an earlier paper (1) we discussed the solid solubility and electrical behavior of tin, an amphoteric group IV impurity, in GaP. In this paper we present the results of similar studies on GaP crystals grown from gallium solutions containing the group VI donors sulfur, selenium, or tellurium or the group II acceptor zinc. Of particular interest here is the variation of doping level and electrical activity as a function of impurity concentration in the liquid at constant temperature. We shall see that, while the behavior of zinc is relatively simple, the donor behavior does not appear to be completely consistent with models previously suggested for the incorporation of group VI impurities in III-V compounds.

Experimental

The crystals were grown from gallium solutions contained in sealed, evacuated vitreous silica tubes by using a thermal gradient method described previously (1, 2). Seventeen crystals were grown at 1040° ± 20°C in a single run lasting five weeks. The thermal gradient in the furnace was ~15 to 20 deg/cm. Large grained polycrystalline ingots weighing about 2g were obtained.

Values of $|N_D - N_A|$, the excess donor or acceptor concentration, were obtained from surface barrier capacitance measurements as described previously (1, 3). As will be evident from the results, the agreement between duplicate capacitance measurements on different parts of the crystals varied considerably from crystal to crystal, presumably due to variations in the quality of the crystal (freedom from micro-occlusions, grain boundaries, etc.). In seeking evidence of precipitation of the dissolved impurities some samples were heated to ~1000°C for periods of 1-8 min and then quenched either in a jet of nitrogen or in a silicone oil. After etching to avoid any surface effects the samples were remeasured.

The impurity concentrations were determined by using spectrophotometric techniques. Prior to analysis the samples were crushed and digested for a day or more in hot concentrated hydrochloric acid to insure removal of any occluded gallium or other phases containing the impurity in question. The tellurium- and selenium-doped samples were also digested briefly (~5 to 15 min) in aqua regia. Rods were cut from ten samples (doped with zinc, selenium, or tellurium) for mass spectroscopic analysis. The principal contaminant was found to be silicon, generally at levels of about 1×10^{17} atoms/cc or lower.

Results and Discussion

The results of the chemical analyses and of the capacitance measurements on the quenched and as-grown crystals are summarized in Table I.

Table I. Results of chemical analyses, capacitance measurements and quenching experiments on GaP crystals grown at 1040°C*

Dopant	C_L (a/o)	C_S (atoms/cc) (Chemical)	$\lvert N_D-N_A\rvert$ (cm^{-3}) (Capacitance) As-grown	After quench
Zn	9.0	$(1.5_0,1.5_4)\times10^{19}$	$(5.0,5.5)\times10^{18}$	[Too lossy to measure]
Zn	0.92	$(3.0,4.6)\times10^{18}$	$(2.4,2.1)\times10^{18}$	[(~1-2)×10^{19}]
Zn	0.092	$(1.3_5,1.6_0)\times10^{18}$	$(5.3,6.6,5.8,12)\times10^{17}$	—
Zn	0.0092	4.5×10^{17}	$(3.3,3.4)\times10^{17}$	$(3.2,3.5)\times10^{17}$
S	0.47	$(5.6,6.0)\times10^{19}$	$(5.0,6.2)\times10^{18}$	[(~1-2)×10^{19}]
S	0.095	$(2.9,3.1)\times10^{19}$	$(3.7,4.6)\times10^{18}$	—
S	0.010	$(3.1,3.9)\times10^{18}$	$(3.2,5.4)\times10^{18}$	—
S	0.00087	$(1.6,7.0,7.8)\times10^{17}$	$(3.1,8.0)\times10^{17}$	—
Se	0.48	4.1×10^{19}	$(6.6,7.2)\times10^{18}$	$(4.1,9.5)\times10^{18}$
Se	0.098	$(1.8,2.0)\times10^{19}$	$(5.0,6.3)\times10^{18}$	—
Se	0.0092	$(4.1,4.1)\times10^{18}$	$(3.2,5.2)\times10^{18}$	—
Se	0.0010_5	$(4.9,5.5)\times10^{17}$	$(0.4,1.0)\times10^{18}$	$(2.6,3.3)\times10^{17}$
Se	0.00012	—	$(6.0,8.6)\times10^{16}$	—
Te	4.8 (1050°C)	$(1.2,1.5_5)\times10^{19}$	5.9×10^{18}	—
Te	0.48	$(5.0,5.4)\times10^{18}$	$(2.3,2.8)\times10^{18}$	$(3.3,4.4)\times10^{18}$
Te	0.092	$(1.9_1,2.3_8)\times10^{18}$	$(1.5,1.6)\times10^{18}$	—
Te	0.0093	—	$(1.4,2.1)\times10^{17}$	$(1.2,1.2,1.7,2.1,5.0)\times10^{17}$
Te	0.0049	—	$(4.6,6.4)\times10^{16}$	$(0.6,1.0,1.1,1.1,1.4,1.5,1.8,1.8,1.8,2.1)\times10^{17}$

* One crystal, as indicated in the table, was grown at 1050°C; the temperatures are uncertain to ~±20°C, largely because of the high thermal gradient which was measured outside the sample tubes. The individual results of the chemical analyses, performed on different portions of the crushed sample, and capacitance measurements are tabulated in order to give a measure of the reliability of the data especially with regard to the elimination of occluded impurity. Values of $|N_D-N_A|$ in brackets are not to be trusted as much as the other values and may be in error by a factor of two or more; this is due to the fact that certain junctions were very lossy at high doping levels and the necessary size of the evaporated gold dots, on which the capacitance is measured, was prohibitively small.

Zinc.—The solid solubility data for zinc at 1040°C are plotted in Fig. 1 along with some data at 800°C obtained by Chang and Pearson (4) from radiotracer diffusion measurements. Also included is the solid solubility at 1040°C corresponding to the pseudobinary solidus point interpolated from Chang and Pearson's data. It is seen that, at the lower melt concentrations (≲ 10 atom % zinc), both sets of data are fit very well by a straight line with a slope of ½.

The usual model for describing the incorporation of a singly ionized acceptor, A, in a III-V compound, *e.g.*, GaP, involves the following equations and equilibrium constants:

$$A(l) + V_{Ga} = A_{Ga}^- + e^+;\ K_1 = (A_{Ga}^-)p/(A_L)(V_{Ga}) \quad [1]$$

$$Ga(l) + V_{Ga} = Ga_{Ga};\ K_2 = (Ga_L)(V_{Ga}) \quad [2]$$

$$0 = e^+ + e^-;\ K_i = n_i^2 = np \quad [3]$$

$$(A_{Ga}^-) + n = p \quad [4]$$

where the quantities in parentheses represent concentrations of the respective entities, n and p are the

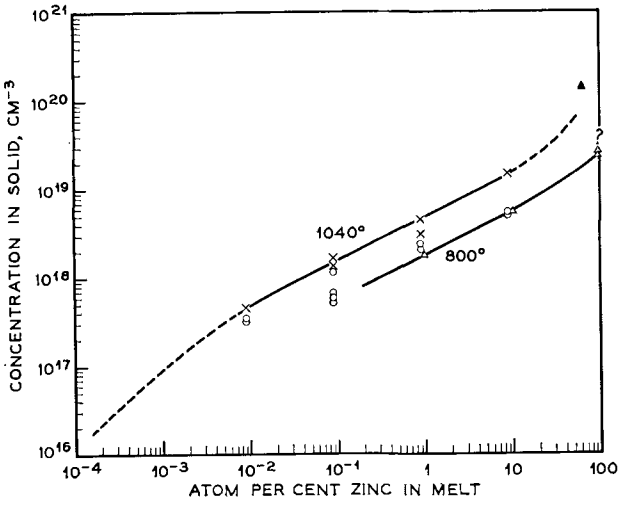

Fig. 1. Zinc and excess acceptor concentrations in GaP crystals as a function of the concentration of zinc in gallium solution at 1040°C. Also included are some data of Chang and Pearson (4) from diffusion experiments at 800°C and a point on the solidus curve at 1040°C from their work. The dashed curves are extrapolations of the data as discussed in the text. The question mark indicates that the liquidus curve for the pseudobinary Zn-GaP system is unknown at 800°C. X, Zinc concentration at 1040°C, ○, N_A-N_D at 1040°C; △, zinc concentration at 800°C (Chang and Pearson); ▲, zinc concentration at 1040°C (Chang and Pearson).

free electron and hole concentrations, and n_i is the intrinsic carrier concentration. Ideal dilute solution behavior is assumed. In an intrinsic semiconductor, where $(A_{Ga}^-) << n_i$, it follows from Eq. [1] that

$$(A_{Ga}^-) = \left\{ \frac{K_1(V_{Ga})}{n_i} \right\} (A_L) \equiv K_5(A_L) \text{ (intrinsic)} \quad [5]$$

In the extrinsic case where $(A_{Ga}^-) = p >> n_i$ one obtains

$$(A_{Ga}^-) = [K_1(V_{Ga})]^{1/2} (A_L)^{1/2} \equiv K_6(A_L)^{1/2} \text{ (extrinsic)} \quad [6]$$

where it has been assumed that (V_{Ga}) is constant, *i.e.*, the solutions are dilute enough so that (Ga_L) is constant (see Eq. [2]). If it is assumed further that the acceptor is completely ionized, then $(A_{Ga}^-) = (A_S)$, the total concentration of acceptor in the solid. The fact that, at 1040°C, (Zn_S) is proportional to $(Zn_L)^{1/2}$ down to a level of $\sim 5\times10^{17}$ cm^{-3} indicates that $n_i < 5\times10^{17}$ cm^{-3} which is consistent with the expected value of $\sim 2\times10^{17}$ cm^{-3}.[1] Extrapolation of the zinc solubility to lower doping levels assuming $n_i = 2\times10^{17}$ cm^{-3} is shown in Fig. 1 by the lower dashed curve.

An estimate of the solubility of zinc at higher concentrations, where (Ga_L) and (V_{Ga}) are changing significantly, may be obtained from the more exact form of the equilibrium constant in Eq. [1]

$$(A_S) = K_7 \left\{ \frac{\gamma_A{}^L(A_L)}{\gamma_{Ga}{}^L(Ga_L)} \right\}^{1/2} \quad [7]$$

where $\gamma_A{}^L$ and $\gamma_{Ga}{}^L$ are the activity coefficients in the liquid phase. By using available thermodynamic data for $\gamma_{Zn}{}^L$ and $\gamma_{Ga}{}^L$ for the binary Ga-Zn system (5) extrapolated to 1040°C a first approximation can be made as shown by the upper dashed curve in Fig. 1. In this approximation it is assumed that the values of $\gamma_{Ga}{}^L$ and $\gamma_{Zn}{}^L$ are the same in the ternary system as in the binary system, *i.e.*, they are unaffected by the presence of phosphorus. Preliminary work by Panish (6) indicates approximately 60 a/o (atom per cent) zinc for the pseudobinary liquidus point at 1040°C. This value leads to a predicted solid solubility of $7\text{-}8\times10^{19}$ atoms/cc compared with the solidus point of $1\text{-}1.5\times10^{20}$ atoms/cc obtained by Chang and Pearson (4) and by Allison (7).

It should be noted that no account has been taken of the presence of neutral zinc atoms, especially at the higher doping levels, as discussed by a number of authors (8-10). This might increase the predicted solubility by a factor of two or more; however uncertainties in the effective masses, degeneracy factors, and other parameters make this calculation sufficiently uncertain so that it is not deemed worthwhile in this paper.

Turning to the capacitance measurements, the data in Table I show that for the most lightly doped sample, containing 4.5×10^{17} atoms/cc of zinc, the value of $(N_A—N_D)$ was precisely the same before and after quenching (3.3×10^{17} cm^{-3}). Aside from experimental error, the difference between (Zn_s) and $(N_A—N_D)$ is consistent with the probable presence of $\sim1\times10^{17}$ atoms/cc of silicon, acting as a donor impurity.

At higher zinc concentrations there is a significant difference between $(N_A—N_D)$ and (Zn_S); for example, at a doping level of 1.5×10^{19} atoms/cc of zinc, $(N_A—N_D)$ is a factor of three lower in the as-grown crystal. The surface barrier junction on the quenched sample was too lossy to measure, indicating a higher $(N_A—N_D)$ value and suggesting the presence of precipitation. Precipitation of zinc in GaP has been observed previously by Gershenzon and Mikulyak (11). Thus, it appears that the zinc in solid solution is electrically active. This is consistent with the behavior of zinc in GaAs as reported by Black (12), who found that for zinc diffused into GaAs the free carrier concentration is equal to (Zn_S) within ±20%.

The variation of (Zn_S) as a function of either the zinc pressure, p_{Zn}, or of the zinc concentration in a liquid phase has been studied previously in a number of III-V compounds, *e.g.*, in GaAs (4,13) GaSb (14), InSb (15), and GaP (4). In three cases (13-15) where a wide doping range was studied, (Zn_S) varied linearly with p_{Zn} or (Zn_L) at low values of (Zn_S) and at higher concentrations was proportional to a lower power of p_{Zn} or (Zn_L). A change from a linear to a square root dependence of (Zn_S) on P_{Zn} or (Zn_L) is the normal behavior expected for a singly ionized acceptor as shown in Eq. [5] and [6]. However, in each of these three cases the change from linear behavior was found to occur at doping levels much greater than the values of n_i extrapolated from low temperature n_i data. McCaldin (13) discusses these results in detail. For example, Hall and Racette (16) quote an extrapolated value at the melting point of GaAs for n_i of 5×10^{18} cm^{-3} which is inconsistent with the value of 4×10^{18} cm^{-3} at 1000°C deduced by McCaldin from the zinc solubility data. There is obviously a need for reliable data on n_i at high temperatures. In the case of GaP the data in Fig. 1 are consistent with the predicted value of n_i, as mentioned earlier.

Selenium, sulfur, and tellurium.—The results of the chemical analyses and the capacitance measurements are plotted in Fig. 2, 3, and 4. The most extensive and precise data were obtained in the case of selenium. The results of the chemical analyses indicate the existence of a linear dependence of (Se_S) on (Se_L) at concentrations below $\sim5\times10^{18}$ atoms/cc and a square root dependence at concentrations above 10^{19} atoms/cc. The square root dependence of the doping level in the crystal on the melt concentration at higher doping levels is also consistent with the chemical data for sulfur and tellurium. Unfortunately, the analytical technique for tellurium was not sufficiently sensitive for the most lightly doped samples and for sulfur the scatter in the data at the lowest doping level was quite large so that the evidence for a linear dependence at lower concentrations is not as clear cut as for selenium. If we accept the square root dependence as the true behavior at high doping levels it is seen that the inflec-

[1] This figure was calculated assuming density of states effective masses of $m_p^* = 1.1\ m_o$ and $m_n^* = 0.9\ m_o$, where m_o is the free electron mass, and an energy gap given by $E_{Gap} = 2.39 - 5.5 \times 10^{-4}T$ ev (M. Gershenzon, private communication).

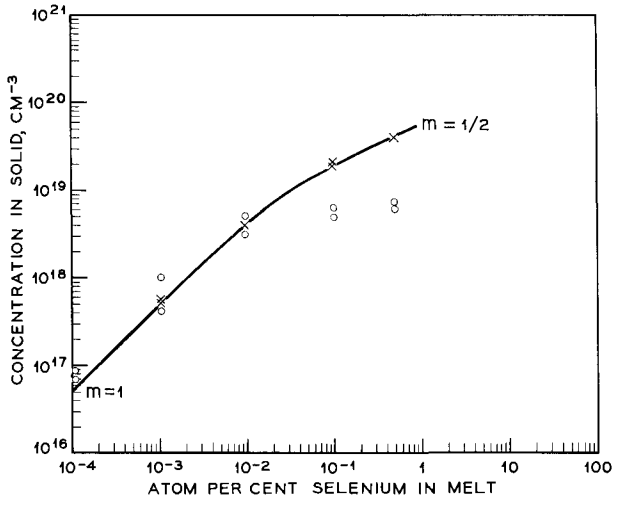

Fig. 2. Selenium and excess donor concentrations in GaP crystals as a function of the concentration of selenium in gallium solution at 1040°C. X, Selenium concentration; ○, N_D-N_A.

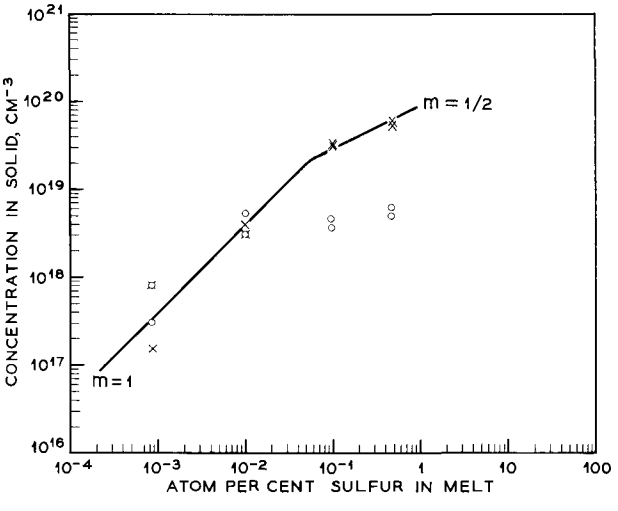

Fig. 3. Sulfur and excess donor concentrations in GaP crystals as a function of the concentration of sulfur in gallium solution at 1040°C. X, Sulfur concentration; ○, N_D-N_A.

tion point, presumably to linear behavior, occurs at different doping levels for the three donor impurities with a spread of an order of magnitude between sulfur and tellurium. Also, the inflection points occur at doping levels appreciably above the expected value of 2×10^{17} cm^{-3} for n_i.

The situation is complicated further by the results of the capacitance measurements which, as in the case of zinc, indicate agreement of the donor concentration with (N_D-N_A) values at low concentrations within the precision of the data. However, as seen in Table I, there is little or no evidence from the quenching experiments for precipitation, at least for the selenium, although (N_D-N_A) is as much as a factor of four or five lower than (Se_S) at the high doping levels. In the case of tellurium there is a relatively small difference between (N_D-N_A) and (Te_S) and the quenching experiments indicate that precipitation may be responsible for at least part of the difference. Whether or not the apparent increases in (N_D-N_A) as a result of quenching are real, especially for the most lightly doped sample, could be determined only by more extensive work on better quality crystals. Only two quenching experiments were performed on sulfur-doped samples, including one sample which was not analyzed chemically. The results on the latter sample indicated, as in the case of selenium, that no change occurred in (N_D-N_A) on quenching.

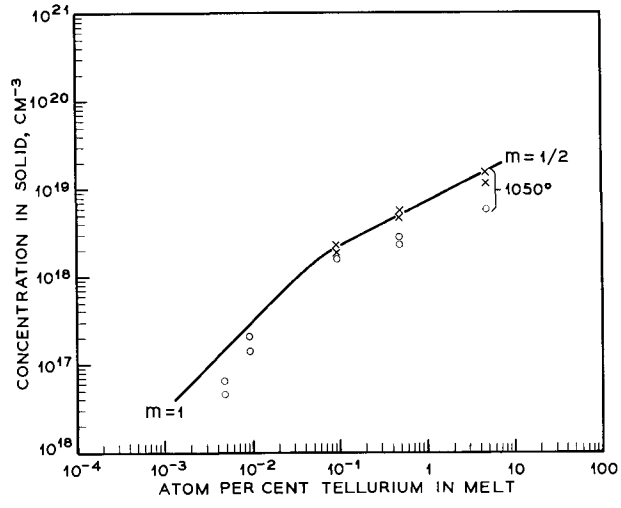

Fig. 4. Tellurium and excess donor concentrations in GaP crystals as a function of the concentration of tellurium in gallium solution at 1040°C. X, Tellurium concentration; ○, N_D-N_A.

Summarizing the situation for the donor impurities, a successful model for the incorporation of a group VI donor, D, in GaP grown from solution apparently must explain the following: (*i*) a linear dependence of (D_S) on (D_L) at low concentrations and a square root dependence at higher concentrations, all at doping levels above the expected value of n_i, (*ii*) inflection points in the (D_S) *vs.* (D_L) plots at different doping levels for the three impurities, (*iii*) relatively high concentrations of electrically inactive or compensated donor impurities at the higher doping levels, and (*iv*) the fact that the (N_D-N_A) values for all three donors appear to depart from the (D_S) values at doping levels of $\sim2\text{-}5\times10^{18}$ cm^{-3}, suggesting the presence of some "intrinsic" interaction common to all three donors.

There has been considerable work on the properties of other III-V compounds doped with group VI donor impurities. For detailed references and discussions of this previous work, see the recent papers of Black and Lublin (17) and Wooley and Blazey (18). Of particular interest here is the work of Vieland and Kudman (19) on the behavior of selenium in GaAs grown near the melting point of GaAs. They observed a linear dependence of (Se_S) on (Se_L) over a doping range well above and below the "accepted" value of n_i of $\sim5\times10^{18}$ cm^{-3}, in contrast to our square root dependence of (Se_S) on (Se_L) at the higher doping levels in GaP.

A number of workers have observed electrically inactive or compensated group VI donors in III-V compounds such as GaAs (17-21). Both Vieland and Kudman and Black and Lublin report a cube root dependence of free carrier concentration on (Se_S) [and in the latter case, (Te_S)] in GaAs at high doping levels. This finding is not inconsistent with our results for GaP as illustrated in Fig. 5. Black and Lublin pointed out that, in view of the work of Fuller and Wolfstirn (22) on reversible control of free carrier concentration in Se- and Te-doped GaAs by suitable heat treatment and quenching, the cube root behavior might be fortuitous and simply a result of similarity in growth conditions. In contrast to the GaAs studies, our crystals were grown over 400° below the melting point of GaP and still appear to show the same cube root behavior. Also, our quenching experiments yield little evidence of precipitation.

In order to account for their results and to explain some anomalous optical absorption data, Vieland and Kudman (19) invoked the formation of a neutral complex involving a gallium vacancy and three selenium atoms. This appears to be a reasonable assumption since the II-VI compounds Ga_2S_3, Ga_2Se_3, and Ga_2Te_3 all have defect zincblende structures with 1/3 of the gallium sites vacant. A number of III-V and II-VI

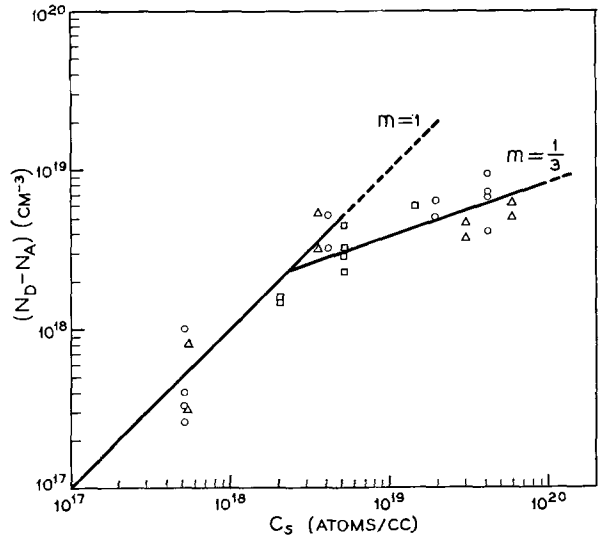

Fig. 5. Plot of excess donor concentration as a function of doping level in the solid for sulfur, selenium, and tellurium in GaP. Here the individual capacitance measurements are plotted while the photometric analyses were averaged to give a single point. As seen in Table I, only in the case of the most lightly sulfur-doped sample do the duplicate photometric analyses differ appreciably. The capacitance data for as-grown and quenched samples are included in this plot. ○, Selenium; □, tellurium; △, sulfur.

compounds form a continuous series of solid solutions (23) and the incorporation of one vacancy for every three selenium atoms, for example, into the III-V compounds is certainly to be expected as the concentration of selenium increases.

A second model is the one proposed by Gasson *et al.* (24), to explain their results on $(InAs)_{3(1-x)} - (In_2Te_3)_x$ solid solutions and related systems. They considered the gallium vacancy to be a compensating triply charged acceptor and only for very heavily doped material did they consider the formation of complexes involving a gallium vacancy and one, two, or three tellurium atoms. Vieland and Kudman, however, point out that for their selenium doped GaAs crystals the electron mobilities are higher than for silicon-doped (compensated) crystals with comparable carrier concentrations. This argues against compensation of the group VI impurity by a triply charged vacancy. Other variations of these models are discussed by Kröger (25).

A third suggestion concerning the presence of inactive donors in certain III-V compounds is that of Woolley and co-workers. For example, in the case of InSb it was postulated (26) that as more and more tellurium or selenium is added the electrons start filling up broader conduction band minima and are not detected by Hall effect measurements, even though the tellurium and selenium still behave as donors. In the case of GaP, however, the data are based on capacitance measurements which presumably would not be affected by such band structure considerations.

The various equilibria can be written for the models involving charged vacancies, complexes, etc. (19, 24, 25). However, none of the models is completely consistent with our GaP data. For example, the triply charged vacancy model does predict a cube root dependence of n on the doping level of the group VI impurity at high doping levels. However, it is also predicted that in this range, $(D_S) \propto (D_L)^{3/4}$ which is not in agreement with either our square root or Vieland and Kudman's linear dependence of (D_S) on (D_L). The latter authors' vacancy complex model predicts that $n \propto (D_L)^{1/6}$ [not as $(D_L)^{1/3}$ as stated in their paper] which may not be inconsistent with the GaAs or GaP results considering the scatter in the data. However, the dependence of (D_S) on (D_L) in this treatment is not clear since Vieland and Kudman invoke the presence of Se and Ga_2Se_3 species in the liquid phase and one must know the appropriate equilibrium constants in order to carry out the calculation. At any rate, the behavior of selenium in GaP and GaAs differ markedly insofar as the dependence of (D_S) on (D_L) is concerned and it seems unlikely that a simple model could explain both cases.

In conclusion, there is one point that should be stressed. This is that most of the various proposed models involve the assumption of equilibrium conditions; if the crystal growth conditions depart significantly from equilibrium, agreement with theory would not be expected. The diffusion coefficient of zinc in GaP is large enough so that equilibrium conditions should be closely approached. Although very slow growth rates prevailed in these experiments, the situation with regard to the slower diffusing donor impurities is not so definite, and facet effects could play a role.

Acknowledgments

The authors are indebted to C. D. Thurmond and R. A. Logan for helpful discussions and to A. J. Ahearn and D. L. Malm for the mass spectrometric analyses.

Manuscript received Jan. 14, 1965.

Any discussion of this paper will appear in a Discussion Section to be published in the June 1966 JOURNAL.

REFERENCES

1. F. A. Trumbore, M. Kowalchik, H. G. White, R. A. Logan and C. L. Luke, *This Journal*, **111**, 748 (1964).
2. F. A. Trumbore, C. R. Isenberg, and E. M. Porbansky, *J. Phys. Chem. Solids*, **9**, 60 (1959).
3. H. G. White and R. A. Logan, *J. Appl. Phys.*, **34**, 1990 (1963).
4. L. L. Chang and G. L. Pearson, *J. Phys. Chem. Solids*, **25**, 23 (1964).
5. R. Hultgren, R. L. Orr, P. D. Anderson, and K. K. Kelley, "Selected Values of Thermodynamic Properties of Metals and Alloys," p. 747, John Wiley and Sons, New York (1963).
6. M. B. Panish, Private communication.
7. H. W. Allison, *J. Appl. Phys.*, **34**, 231 (1963).
8. F. A. Trumbore, E. M. Porbansky, and A. A. Tartaglia, *J. Phys. Chem. Solids*, **11**, 239 (1959).
9. C. D. Thurmond, in "Properties of Elemental and Compound Semiconductors," H. C. Gatos, Editor, p. 121, Interscience Publishers, New York (1960).
10. K. Lehovec, *J. Phys. Chem. Solids*, **23**, 695 (1962).
11. M. Gershenzon and R. M. Mikulyak, *J. Appl. Phys.*, **35**, 2132 (1964).
12. J. Black, *This Journal*, **111**, 924 (1964).
13. J. O. McCaldin, *J. Appl. Phys.*, **34**, 1748 (1963).
14. U. Merten and A. P. Hatcher, *J. Phys. Chem. Solids*, **24**, 1064 (1963).
15. U. Merten and A. P. Hatcher, *ibid.*, **23**, 533 (1962).
16. R. N. Hall and J. H. Racette, *J. Appl. Phys.*, **35**, 379 (1964).
17. J. Black and P. Lublin, *ibid.*, **35**, 2462 (1964).
18. J. C. Woolley and K. W. Blazey, *This Journal*, **111**, 951 (1964).
19. L. J. Vieland and I. Kudman, *J. Phys. Chem. Solids*, **24**, 437 (1963).
20. R. W. Fane and A. J. Goss, *Solid-State Electronics*, **6**, 383 (1963).
21. O. V. Emel'yanenko, T. S. Lagunova, and D. B. Nasledov, *Soviet Phys., Solid State*, **2**, 176 (1960).
22. C. S. Fuller and K. B. Wolfstirn, *J. Appl. Phys.*, **34**, 2287 (1963).
23. J. C. Woolley, in "Compound Semiconductors, Volume I. Preparation of III-V Compounds," R. K. Willardson and H. L. Goering, Editors, Chap. 1, Reinhold Publishing Corporation, New York (1962).
24. D. B. Gasson, I. C. Jennings, J. E. Parrott, and A. W. Penn, Proc. Int. Conf. on Physics of Semiconductors, Exeter, p. 681 (1962).
25. F. A. Kröger, "Chemistry of Imperfect Crystals," Chap. 16, North Holland Publishing Co., Amsterdam (1964).
26. J. C. Woolley and E. W. Williams, *This Journal*, **111**, 210 (1964).

Electrochemical Behavior of Grown Oxide Films on Silicon

Frank C. Collins

Department of Chemistry, Polytechnic Institute of Brooklyn, Brooklyn, New York

ABSTRACT

The large shifts in surface potential which are observed after biasing oxidized silicon surfaces at elevated temperatures may be explained in terms of a simple ionic polarization effect. The electrostatic potential and the ionic concentration profiles and the ionic surface density are calculated in terms of the known bias potential and the measured surface potential of the semiconductor. Exact solutions are found for the limiting case of zero ionic flux, using the Poisson-Boltzmann relation. First order approximate solutions are found for the case of small ionic flux in a final polarized steady state. The several mechanisms which have been proposed to account for the film polarization are examined.

Thermally grown silicon dioxide films have often been used to passivate exposed p-n junctions in diode and transistor structures and as active elements in insulated gate field effect transistors. Polarization of these films and the appearance of built-in fields at the silicon-silicon dioxide interface are accordingly of technical importance.

Some previously reported studies of the electrical properties of these films have employed a metal-oxide-semiconductor (MOS) structure formed by evaporating small contacts of aluminum or other metal on the surface of the oxide. Capacitance measurements of these structures after various treatments have been particularly useful. The MOS capacitance as a function of applied voltage is well understood (1-3). The reciprocal of the total measured capacitance is the sum of the reciprocals of the constant capacitance of the oxide dielectric film and the potential-dependent semiconductor surface capacitance. The capacitance C_s per unit area of an n-type semiconductor is given by (2) $C_s = q\ (\epsilon n/kT)^{1/2}$ when the surface and bulk electrostatic potentials of the semiconductor are equal, corresponding to the flat band condition. (The symbols in the equation have conventional significance. The equation may be appropriately modified for a p-type semiconductor.) In the MOS structure, the flat band condition is established in the semiconductor if the work function difference between the metal and the semiconductor is equal and opposite to the applied potential difference, providing that no surface states exist and no built-in potential difference exists in the oxide film. If either exist, the applied potential must be correspondingly altered in order to establish the flat band condition. If surface states are absent, the required change in the applied potential will be equal and opposite to the built-in potential of the oxide film, plus the work function difference.

It has long been known that silicon dioxide films are electrically unstable under bias at elevated temperatures. In order to study this instability, there have been several investigations which have involved the application of a bias under elevated temperatures, in the neighborhood of 200°C, for times up to 1 hr followed by the measurement at room temperature of the voltage dependence of the MOS capacitance (4-6).

The initial built-in potential before the temperature-bias treatment may be of the order of −5 to −40v in terms of the sign and magnitude of the potential which must be applied to the metal contact in order to restore the flat band condition in the semiconductor surface (4). A bias of the order of ±20v is applied to the metal contact in the temperature-bias treatment. Only a small change of the built-in potential of the film is observed if a negative bias is applied in the temperature-bias treatment. Under the positive bias-temperature treatment, the built-in potential of the film becomes more strongly negative. Built-in potential shifts of −80v and more have been observed after temperature bias treatments in the cases where the film has been thermally grown in wet oxygen (4). Much smaller initial built-in potential shifts occur in the case of film grown in dry oxygen (5).

Studies of the conduction of the film under temperature-bias treatment show that the integral of current flowing with the metal contact positive is of the right order of magnitude to account for the observed degree of film polarization (4, 6. 7). It is considerably larger than the integral of the current flowing with the metal contact negative, particularly in the case of wet-grown films (8). The current decays in the time of about an hour to a final saturation value corresponding to a small residual steady current. Only a very small part of the decaying portion of the current time curve is accounted for by the displacement current, the time dependence of which is determined by the RC constant for the circuit. The remainder of the time-dependent current brings about the observed polarization of the film. This part of the current may be recovered as a reverse current on removing the applied bias (8). The charge reversibly transferred in the temperature-bias treatment appears to result from the field migration of ionic constituents of the film under the applied bias.

Thomas and Young (9) have related the experimental shift in the surface potential of the semiconductor to an arbitrarily chosen distribution of positive charge in the oxide film. In this paper, the calculations are extended to an ionic distribution which obeys the Poisson-Boltzmann relation. An exact solution is obtained for a limiting case of zero ionic flux after polarization of the film and a first order solution for the case that the residual ionic fluxes are nonzero but small. The solutions enable the ionic concentration and the ionic surface density in the film to be calculated directly in limiting cases.

There are two possible extreme situations which cannot be distinguished on the basis of presently available experimental information: (i) the charge consists of cation only, and (ii) the charge consists of equal numbers of anions and cations summing to a net charge of zero within the film. The potential and ionic concentration distributions and the ionic surface density are obtained in closed form for the first case, which is also that treated by Thomas and Young (9). An approximate solution is developed for the second case on the basis of symmetry arguments.

Where a final residual ionic flux exists in the film, the Poisson-Boltzmann equation cannot be used. A perturbation treatment of the problem is presented using the Poisson equation and Fick's law. The first order term is integrable, and expressions in closed form are obtained for the potential profile and the surface ionic density. The magnitude of the perturbation term in the surface ionic density is such that it probably may be neglected over the range of observed final currents. Neither the identity of the diffusing ions

nor the mechanism of the transport of the final residual current across the film are yet established.

The plausibility of the various proposals which have been advanced for the electrochemical mechanisms of these processes are reviewed and related to the quantitative calculations presented in the first section of this paper.

Calculation of the Polarization of the Film

The number fluxes of the several species which may be present are given by

$$J_i = -D_i \frac{dc_i}{dx} \mp \frac{D_i \alpha_i q}{kt} c_i \frac{dV}{dx} \qquad i = 1,2,... \quad [1]$$

where J_i is the flux rate for the ith species, D_i, c_i, and $\alpha_i q$, respectively, its diffusion constant, concentration and electric charge, and V is the electrostatic potential. Where the species is nonionic, $\alpha_i = 0$, and only the free diffusion term remains. The remaining symbols have conventional significance. The negative sign applies to cations and the positive to anions. In the final steady state of current flow, the fluxes J_i must all be constant. They will be zero only in the case that the mechanism of the final residual charge transport through the film is purely electronic. We shall treat both cases, beginning with the simpler case of zero flux.

Where all $J_i = 0$, Eq. [1] may be immediately integrated and, with the boundary conditions $V(O) = 0$, and $c_i(0) = c_{io}$, (the origin being taken at the silicon-silicon dioxide interface) assume the form

$$c_i(x) = c_{io} \exp [\mp \alpha_i q V/kT] \qquad i = 1,2,... \quad [2]$$

where the ambiguity in sign has the same meaning as before.

If the concentrations of electrons and holes are small compared to those of the major ionic species, Poisson's law takes the form

$$\frac{d^2V}{dx^2} = -\frac{\rho}{\epsilon} = -\sum_i \frac{\alpha_i q}{\epsilon} c_{io} [\exp \mp \alpha_i q V(x)/kT] \quad [3]$$

where the sum is over all ionic species present in the film. Multiplying the last equation by $2(dv/dx)$ transforms it into a readily integrable form. By use of the previous boundary conditions and the additional one, $(dV/dx)_{x=o} = \mathcal{E}_o$, we obtain

$$\left(\frac{dV}{dx}\right)^2 = \mathcal{E}_o^2 \mp \sum_i \frac{2c_{io}kT}{\epsilon} (1 - e^{\mp \alpha_i qV/kT}) \quad [4]$$

For further integration, Eq. [4] is rearranged as follows

$$dx = \left[\mathcal{E}_o^2 \mp \sum_i \frac{2kT}{\epsilon} c_{io} (1 - e^{\mp \alpha_i qV/kT}) \right]^{-1/2} dV \quad [5]$$

Equation [5] is well-known and arises in a number of situations involving electrolytes. MacDonald (10) has made a critical review of the literature of solutions of it under various conditions. The case of a single ionic species is of particular interest here and does not appear to have been previously handled. Where only one species of ion is present, the integration may be carried out in closed form. Following Thomas and Young (9), we shall suppose that the species is cationic. Equation [5] may then be put into the form

$$dx = (a + b\, e^{-mV})^{-1/2}\, dV \quad [6]$$

where

$$a = \mathcal{E}_o^2 - \frac{2kT}{\epsilon} c_o$$

$$b = \frac{2kT}{\epsilon} c_o$$

$$m = \frac{\alpha q}{kT}$$

The integral of Eq. [6] with the boundary conditions $V = 0$ at $x = 0$ is (11)

$$x = \frac{V}{a^{1/2}} + \frac{2}{ma^{1/2}} \ln \frac{a^{1/2} + (a + b\, e^{-mV})^{1/2}}{a^{1/2} + \mathcal{E}_o} \quad [7]$$

The integral may assume a different form if $2kTc_o/\epsilon > \mathcal{E}_o^2$, but this condition does not arise in this problem. The known quantities are the potential difference $V(X)$ across the film under which the film was polarized and the field $\mathcal{E}_o$ in the oxide at the semiconductor boundary. Here X is the outer surface of the oxide film. The potential difference $V(X)$ differs from the bias between metal and semiconductor by the amount of the band bending in the semiconductor which is small at the temperatures under which the temperature-bias treatments are conducted. The field $\mathcal{E}_o$ is determined from the bias dependence of the metal-oxide-semiconductor capacitance at room temperature (see Appendix A). This involves the assumption that the ionic distribution is frozen when it is quenched from the temperature at which the polarization was effected.

Except in the immediate vicinity of the silicon interface, $x = 0$, $mV >> 1$, Eq. [7] takes the limiting form

$$\lim_{mV >> 1} x = \frac{V}{a^{1/2}} + \frac{2}{ma^{1/2}} \ln \frac{2a^{1/2}}{a^{1/2} + \mathcal{E}_o} \quad [7a]$$

Thus in most of the thickness of the film

$$dV/dx = a^{1/2}$$

so that the electrostatic field is constant in this region and is, in fact, very little less than ideal dielectric field $V(X)/X$ where X is the value of x at the outer surface of the film. This enables a simple evaluation of the constant $a^{1/2}$ from Eq. [7a], after substitution of the boundary condition $V(X) = V_X$, by the method of successive approximations. The first approximation is

$$a^{1/2} = \frac{V_X}{X} + \frac{2}{mX} \ln \frac{2V_X/X}{X_X/X + \mathcal{E}_o} \quad [7b]$$

The error involved in taking the first approximation only is smaller than the usual errors of the measurements.

Having an approximate value of $a^{1/2}$, the boundary value of the concentration c_o may be evaluated in terms of the known quantities by making use of the definition of a. Table I gives values of the limiting field $a^{1/2}$ and the boundary concentration c_o for se-

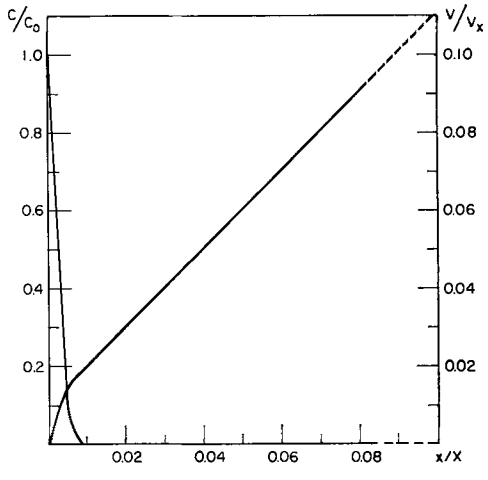

Fig. 1. Electrostatic potential and ionic concentration profiles in 5000Å thick silicon dioxide film under 200v bias at 200°C ($V_R = -80$v).

Table I. Values of the limiting field $a^{1/2}$, the boundary ionic concentration c_o, and the ionic surface density, σ, calculated for various values of the applied bias, V_x, and resulting potential shift, V_R, and boundary field $\mathcal{E}_o$ in temperature-bias treatments at 200° and 225°C of silicon dioxide films of various thicknesses

V_x, v	X, Å	V_R, v	$\epsilon_o \times 10^{-6}$, v/cm	$(V_x/X) \times 10^{-6}$, v/cm	$a^{1/2} \times 10^{-5}$, v/cm	$c_o \times 10^{-20}$, cm^{-3}	$\sigma \times 10^{-12}$, cm^{-2}
				200°C			
10	3000	−20	1.00	0.333333	3.3145	0.2594	1.5901
		−50	2.00		3.2992	1.1343	3.9721
		−140	5.00		3.2768	7.2368	11.113
	7000	−60	1.00	0.142857	1.4124	0.2857	2.0425
		−130	2.00		1.4051	1.1602	4.4226
		−340	5.00		1.3949	7.2818	11.5602
20	3000	−10	1.00	0.666666	6.6606	0.1622	0.7942
		−40	2.00		6.6478	1.0372	3.1757
		−130	5.00		6.6273	7.1595	10.3157
	5000	−30	1.00	0.400000	3.9908	0.2451	1.4292
		−80	2.00		3.9821	1.1198	3.8097
		−230	5.00		3.9688	7.2416	10.9480
	7000	−50	1.00	0.285714	2.8477	0.2679	1.7011
		−120	2.00		2.8410	1.1425	4.0811
		−330	5.00		2.8312	7.2641	11.2186
30	3000	−30	2.00	1.00000	9.9890	0.8751	2.3810
		−60	3.00		9.9812	2.3331	4.7613
		−120	5.00		9.9701	6.9977	9.5207
	7000	−110	2.00	4.28571	4.2736	1.1128	3.7404
		−180	3.00		4.2695	2.5704	5.3688
		−320	5.00		4.2642	7.2345	10.8778
				225°C			
20	3000	−10	1.00	0.666666	6.6601	0.1541	0.7944
		−40	2.00		6.6408	0.9854	3.1774
		−130	5.00		6.6245	6.8002	10.3164

lected values of the experimental variables over a range of these parameters.

Equations [7] and [2] enable the calculation of the electrostatic potential and concentration profiles in the film. Figure 1 illustrates the results for a typical set of experimental parameters. The forms of the curves do not differ appreciably for other choices of the values of the experimental parameters. Some observations are noteworthy: The ionic concentration is negligible except within a very short distance of the silicon interface. This is in agreement with the finding of Kuper and Nicollian (5) that film polarization persisted when etched away to a few hundred Angstroms of the silicon interface. As the electrostatic field $a^{1/2}$ differs but little from the ideal dielectric field V_X/X in most of the thickness of the oxide film, the polarization of the film does not affect the field migration of the ions. This in contrast to the model of Thomas and Young (9).

The foregoing analysis permits the total ionic surface density to be readily calculated. This is given by

$$\sigma = \int_o^X c(x)\,dx$$

$$= \int_o^X c(V)\,\frac{dx}{dV}\,dV \qquad [8]$$

Insertion of Eq. [2] and [6] into [8] followed by integration yields

$$\sigma = \frac{\epsilon}{q}\left[\mathcal{E}_o - (a + b\,e^{-mV_X})^{1/2}\right] \qquad [9]$$

which simplifies to

$$\sigma = \frac{\epsilon}{p}\,(\mathcal{E}_o - a^{1/2}) \qquad [9a]$$

for the case that $mV_X >> 1$.

Values of the surface densities σ corresponding to various values of the experimental variables are also given in Table I. The calculated surface densities correspond roughly to an ion fraction of 0.001 in the interfacial layer of atoms.

Several significant conclusions may be drawn from the calculated quantities tabulated in Table I. The potential shifts V_R and the boundary field $\mathcal{E}_o$ are very roughly proportional to the ionic densities c_o and σ. The temperature dependence of the relation between the ionic concentrations c_o and σ and the boundary field $\mathcal{E}_o$ is quite small, c_o decreasing only a few per cent for a given $\mathcal{E}_o$ in the interval 200°-225°C. A given ionic content σ produces a larger potential shift V_R in the thicker films.

Another case of interest is that where no net charge excess exists in the film so that the charge distribution is that of a pure dipole. An exact solution for this problem has been obtained by Jaffé (12) in terms of elliptic functions and by an approximate solution by MacDonald (13). Another excellent approximation may be obtained for the special case of a symmetrical electrolyte if $qV(X) >> 2kT$. Equation [5] takes the form

$$dx = \left[\mathcal{E}_o^2 + \frac{2kT}{\epsilon}\,c_{+o}\,(1 - e^{-\alpha qV/kT}) - \frac{2kT}{\epsilon}\,c_{-o}\,(1 - e^{\alpha qV/kT})\right]^{-1/2} dV$$

As the problem is completely symmetrical relative to the axis at $X/2$, the following relations hold

$$V(X/2) = V(X)/2$$

$$c_+(X/2) = c_-(X/2)$$

and

$$c_{-o} = c_{+o}\,e^{-\alpha qV(X)/kT}$$

Further, if $\alpha qV(X/2) >> kT$, $c_+(x)$ is completely negligible for all values of $x > X/2$ and $c_-(x)$ is similarly negligible for $x < X/2$. The problem is then reduced to the calculation of the distribution of a single ionic component in the region 0 to $X/2$. This problem has already been solved for the interval 0 to X. It will be seen that solution for the pure dipole case amounts only to the introduction of the scale factor 1/2 into the variables V and x. It is to be particularly noted that it leaves the field $\mathcal{E}_o$ at the boundary unchanged. Thus the existence of a given value of the field $\mathcal{E}_o$ under the applied bias $V(X)$ across the film at the semiconductor boundary is consistent with either the excess charge or pure dipole case. The presence or absence of anions in the outer region of the oxide film can only be determined by outer surface potential measurements.

It is probable that the residual current flowing in the film in the final steady state is due to ionic transport, rather than purely electronic processes, and thus involves redox reactions occurring at the semiconductor interface and at the metal electrode at the outer surface of the film. The foregoing treatment is invalid in this case.

No exact method exists for the calculation of the potential and ionic concentration profiles for the single ion case under the condition of nonzero flux rate. Fromhold (14) has developed numerical solutions to the problem, but it is not easy to extract from his data values for the potential and ionic concentration profiles corresponding to arbitrary values of the bias potential $V(X)$ and the boundary field $\mathcal{E}_o$ appropriate to the present situation. In the following a method of successive approximations will be developed for the case that the flux J is small compared to the other terms in Eq. [1]. While this is not generally valid for all values of $x < X$, it will be true in the important regions near the boundaries of the film which are the only ones contributing significantly to the various integrals arising in the treatment. We shall here confine attention to the simpler case in which only cations are present in the film.

Equation [1] for the steady-state case takes the form

$$J = -D\,\frac{dc}{dx} - \frac{D\alpha q}{kT}\,c\,\frac{dV}{dx} \qquad [10]$$

which may be rearranged as follows

$$d \ln c = -mdV - \frac{J}{Dc}\frac{dx}{dV}dV \qquad [11]$$

where m has the previous significance of $m = \alpha q/kT$.

While Eq. [11] is not readily integrable, a first order approximation in a method of successive approximations may be integrated in closed form. We assume that in the limit of small J, the last term of the right hand side of Eq. [11] is small compared to the first and make use of the $J = 0$ solutions for c and dx/dV as zeroth order approximations in this term. The integral of Eq. [11] is

$$c = c_o e^{-mV - JK/Dc_o} \qquad [12]$$

where

$$K = \int_o^V \frac{e^{mV}dV}{(a + b\,e^{-mV})^{1/2}} = \int_o^V \frac{dK}{dV}dV$$

$$= \frac{1}{ma}[e^{mV/2}(a\,e^{mV} + b)^{1/2} - (a+b)^{1/2}]$$

$$-\frac{b}{ma^{3/2}}\ln\frac{a^{1/2}e^{mV/2} + (a\,e^{mV}+b)^{1/2}}{a^{1/2} + (a+b)^{1/2}} \qquad [13]$$

and where a and b have the same meaning as before and the derivative of K has been formally introduced for future reference. The procedure used in the integration is given in the Appendix (B). For the purposes of later manipulation, it is desirable to rearrange Eq. [13] as follows

$$K = \frac{1}{ma}[e^{mV}(a + b\,e^{-mV})^{1/2} - (a+b)^{1/2}] - \frac{b}{2a}X^o(V) \qquad [14]$$

It will be observed that substitution of reasonable experimental values into Eq. [14] will lead to the condition $JK/D\ c_o > mV$ in Eq. [12] for larger values of mV. However, this situation is not serious if the range of admissibility of the treatment is explicitly taken to apply only in the region of small values of x. It is only in this region that $c(x)$ is appreciably larger than zero.

In order to make further progress it is necessary to make use again of the assumption that the last term on the right-hand side of Eq. [11] is small compared to the first. We expand Eq. [12] as follows with neglect of terms beyond first order

$$c = c_o e^{-mV}(1 - JK/Dc_o) \qquad [15]$$

The last equation may now be inserted into Poisson's equation, Eq. [3]

$$\frac{d^2V}{dx^2} = -\frac{\alpha q c_o}{\epsilon}e^{-mV}(1 - JK/Dc_o) \qquad [16]$$

The last equation may be integrated by the same methods earlier used in the $J = 0$ case and we obtain

$$\frac{dx}{dV} = (a + b\,e^{-mV} + Q)^{-1/2} \qquad [17]$$

where

$$Q = \frac{aqJ}{D\epsilon}\int_o^V e^{-mV}K(V)\,dV \qquad [18]$$

In the limiting case of small J, $a + b\exp(-mV)$ is much larger than Q in the region of V where the values of the integrand of Eq. [17] contributes significantly in the integration of x. Thus Eq. [17] may be expanded by use of the binomial theorem and we obtain

$$x = \int_o^V (a+b\,e^{-mV})^{-1/2}\left[1 - \frac{1/2\,Q(V)}{a+b\,e^{-mV}}\right]dV$$

$$= x^o - \frac{1}{2}\int_o^V \frac{Q(V)\,dV}{(a+b\,e^{-mV})^{3/2}} \qquad [19]$$

where $x^o = x^o(V)$ denotes the solution of x for the $J = 0$ case.

The integrations indicated in Eq. [18] and [19] are not difficult. Integrating Eq. [18] by parts and making use of the definition of $K(V)$ in Eq. [13] yields

$$Q = \frac{\alpha q}{\epsilon}\frac{J}{D}\left\{-\frac{1}{m}e^{-mV}K\,\Big|_o^V + \frac{1}{m}\int_o^V e^{-mV}\frac{dK}{dV}dV\right\}$$

$$= \frac{\alpha q}{\epsilon}\frac{J}{D}\left\{-\frac{1}{m}e^{-mV}K(V) + \frac{1}{m}\int_o^V \frac{dV}{(a+b\,e^{-mV})^{1/2}}\right\}$$

$$Q = \frac{\alpha q J}{Dm\epsilon}[x^o(V) - e^{-mV}K(V)] \qquad [20]$$

The final integration is then

$$x = x^o(V) + \frac{\alpha q J}{Dm\epsilon}\left\{\int_o^V \frac{x^o(V)\,dv}{(a+b\,e^{-mV})^{3/2}} - \int_o^V \frac{e^{-mV}K(V)\,dV}{(a+b\,e^{-mV})^{3/2}}\right\} \qquad [21]$$

The details of the integration of Eq. [21] are somewhat lengthy and are given in the Appendix (C). The final results are

$$x = x^o(V) + \frac{\alpha q J}{\epsilon D m}\left\{\frac{x^{o2}(V)}{2a} - \frac{x^o(V)}{2m\,a^2}\left[\frac{3}{(a+b\,e^{-mV})^{1/2}} - \frac{1}{(a+b)^{1/2}}\right] - \frac{V}{2\,ma^2} + \frac{1}{2\,m^2a^2}\ln\frac{a+b\,e^{-mV}}{a+b} + \frac{2}{m^2\,a\,b}\left[\frac{(a+b)^{1/2}}{(a+b\,e^{-mV})^{1/2}} - 1\right]\right\} \qquad [22]$$

Equation [22] is approximately valid only for small values of x and V. Accordingly, it may not be used in conjunction with the boundary condition $V(X) = V_X$ in order to determine the value of a as was done with Eq. [7a]. However, in the former case, it was found that $a^{1/2}$ differed but very little from the ideal dielectric field V_X/X. The value of a calculated from Eq. [7a] could be used in Eq. [22] to obtain an approximate potential profile. This has not been pursued because it appears from the following calculation of the ionic surface density that the perturbation term may be small over the range of experimental variables actually encountered.

The calculation of the ionic surface density is initiated by combining Eq. [8], [15], and [17] which yields

$$\sigma = \int_o^V \frac{c_o e^{-mV}(1 - JK/Dc_o)}{(a+b\,e^{-mV} + Q)^{1/2}}dV \qquad [23]$$

On expanding the denominator by use of the binomial theorem, the following is obtained after neglect of higher order terms in QJK

$$\sigma = \int_o^V c_o e^{-mV}(a+b\,e^{-mV})^{-1/2}\left[1 - \frac{Q}{2(a+b\,e^{-mV})} - \frac{JK}{Dc_o}\right]dV \qquad [24]$$

The upper limit of the integral will be set after examination of convergence.

The first term in Eq. [24] is the same as that appearing in Eq. [8] and is immediately integrable. The remaining two terms are integrated after some analysis. However, the integrals and techniques involved

are quite analogous to those employed in the integration of Eq. [21] and will not be reproduced here. The final results are

$$\sigma = \sigma^0 - \frac{4\,c_0 \alpha q J}{bm\epsilon d}\left\{ \frac{2(a+b)^{1/2}}{m^2 ab}\left[(a+b\,e^{-mV})^{1/2} - (a+b)^{1/2}\right] + \frac{x^0}{ma}\left[(a+b\,e^{-mV})^{1/2} - (a+b)^{1/2}\right] \right\}$$

$$- \frac{2\,c_0 \alpha q J}{bm\epsilon D(a+b\,e^{-mV})^{1/2}} \frac{2}{m^2 a}\left\{ \left[(a+b)^{1/2} - (a+b\,e^{-mV})^{1/2}\right] + \frac{b\,e^{-mV}}{2\,ma} x^0 + \frac{1}{m} x^0 \right\}$$

$$- \frac{J}{D}\left\{ \frac{2(a+b)^{1/2}}{m^2 ab}\left[(a+b\,e^{-mV})^{1/2} - (a+b)^{1/2}\right] + \frac{x^0}{ma}\left[(a+b\,e^{-mV})^{1/2} - (a+b)^{1/2}\right] \right\} \qquad [25]$$

where σ^0 is the solution for the zero flux case, Eq. [9], and x^0 has analogous significance. It will be seen that Eq. [25] is convergent for large values of mV and in fact reduces to the comparatively simple form for $x = X$

$$\sigma = \sigma^0 - \frac{2c_0 \alpha q J}{bm\epsilon D}\left[\left(\frac{2}{m^2 a^{3/2}} - \frac{4\mathcal{E}_0}{m^2 ab} - \frac{2x^0}{ma}(\mathcal{E}_0 - a^{1/2}) + \frac{x^0}{ma^{1/2}}\right] + \frac{J}{D}\left[\left(\frac{2\mathcal{E}_0}{m^2 ab} + \frac{x^0}{ma}\right)(\mathcal{E}_0 - a^{1/2})\right] \qquad [25a]$$

where note has been taken that $a + b = \mathcal{E}_0^2$.

The approximate magnitudes of all quantities appearing in Eq. [25a] are known, thus enabling the order of magnitude of the difference $\sigma - \sigma_0$ to be calculated. The final residual current density αqJ for oxide film of 7000Å thickness grown in a wet oxygen process is of the order of 3×10^{-11} amp/cm^2 at 200°C under a potential bias of 20v (8, 15). The diffusion constant D and its temperature coefficient for the migrating ionic species in the film have been calculated from measurements of polarization rate and high-frequency conductivity at 300°C (16). The value of D extrapolated to 200°C is 1.8×10^{-10} cm^2/sec. The remaining quantities required for the numerical calculation may be obtained from Table I. The relative magnitude of the first order term compared to that of zeroth order thus calculated is $(\sigma - \sigma_0)/\sigma_0 = 0.01$. This indicates that the deviation from the Poisson-Boltzmann distribution is quite small and may be neglected entirely over the range of experimental variables examined in this work.

Qualitative Considerations

There appears to be little question that the polarization under bias occurs because of diffusion of ions in the film. Among the questions remaining to be resolved are those of the species of ions involved in the diffusion and the nature of the charge transport process in the final steady-state flow of current after the polarization has been effected. These questions may be related if the final irreversible current arises from ionic motion rather than by purely electronic processes.

The impurities involved in the film polarization are probably cationic. This is supported by the observed fact that very little current flows and very little film polarization occurs when a negative bias is applied to the film in the given temperature range (8). With negative bias, the impurity cations are swept away from the semiconductor interface, but some minor polarization must however remain. The silicon is now anodic with respect to the oxide layer and any oxidation would be attended by the formation of oxide ion vacancies at the interface which would migrate away more slowly than they are formed. The field at the semiconductor boundary would then remain positive as actually observed instead of becoming negative.

The identity of the cationic species remains in question. It has been suggested by Thomas and Young (9), and by Seraphim, Brenneman, d'Heurle, and Friedman (17) that the cation responsible for the polarization may be an oxide ion vacancy in the oxide film. This explanation no longer seems plausible in view of the recent measurements of the diffusion constant and diffusion activation energy for the ionic species responsible for polarization of the film (16). These are $D = 1.8 \times 10^{-10}$ cm^2/sec and $E = 0.62$ ev at 200°C, which indicate a more easily diffusing species than an oxide ion vacancy.

In conductivity studies on bulk quartz (18), current transport has been ascribed to ionic carriers, including sodium, the magnitude of the conductivity agreeing roughly with the measured impurity content. In the present system, however, current transport by protons may be significant in view of the strong dependence of the magnitude of the degree of polarization of the film on the presence or absence of water vapor during growth (5).

In the ionic migration bringing about the polarization of the film, it is necessary that the cathodic reaction involving these ions be at least partially blocked. Otherwise, the cations diffusing up to the silicon interface would be discharged and polarization at this surface would not occur. Electrode processes involving the ions in question are probably fairly reversible under the conditions of the experiment. However, high concentrations of the reduced species could be built up at the silicon interface as a result of the electrolytic reduction. The resulting unchanged species would diffuse away only by field-free diffusion instead of by field drift, which brought the cations up to the surface. The resulting unfavorable ratio of the activities of reduced species to the cations at the interface would thermodynamically lower the electrode potential sufficiently so that the interface would become a partially blocking electrode with resulting polarization of the film.

The explanation of film polarization on the basis of a blocked electrode effect predicts decreased polarization of the film when it is biased at temperatures which are significantly higher than 200°C. This is because outward diffusion of the reduced species from the semiconductor interface will occur more rapidly as the temperature is raised. The consequent lowering of the thermodynamic potential of the reduced species at the cathode then will unblock this electrode, permitting electron transfer and the depolarization of the oxide film.

Acknowledgment

The author is indebted to Dr. Donald P. Seraphim, Dr. Harold L Friedman, and Dr. Donald R. Young for helpful discussions of the problem and to Messrs. Morton Schrager and Robert Poignant who checked the integrations and numerical calculations.

The research was supported in part under the Office of Naval Research Contract Nonr-839(38).

Manuscript received Jan. 4, 1965; revised manuscript received April 14, 1965.

Any discussion of this paper will appear in a Discussion Section to be published in the June 1966 JOURNAL.

REFERENCES

1. R. H. Kingston and S. F. Neustadter, *J. Appl. Phys.*, **26**, 718 (1955).
2. D. R. Frankl, *Solid State Electronics*, **2**, 71 (1961).
3. D. R. Kerr, *IBM J. Res. and Dev.*, **8**, 385 (1964).
4. D. R. Kerr, J. S. Logan, P. J. Burkhardt, and W. A. Pliskin, *ibid.*, **8**, 376 (1964).

5. A. B. Kuper and E. H. Nicollian, Paper presented at the Washington Meeting of the Society, Oct. 11-15, 1964.
6. E. H. Snow, A. S. Grove, B. E. Deal, and C. T. Sah, *ibid.*
7. M. Yamin and F. L. Worthing, Paper presented at the Toronto Meeting of the Socety, May 3-7 (1964).
8. E. Bassous, Private communication.
9. J. E. Thomas, Jr., and D. R. Young, *IBM J. Res. and Dev.*, **8**, 368 (1964).
10. J. R. MacDonald, *J. Chem. Phys.*, **40**, 3735 (1964).
11. B. P. Pierce, "Short Table of Integrals," Ginn and Co., p. 54, No. 412 (1929).
12. G. Jaffe, *Ann. Physik*, **16**, 217 (1933).
13. J. R. MacDonald, *J. Chem. Phys.*, **22**, 1317 (1954).
14. A. T. Fromhold, Jr., *J. Chem. Phys.*, **38**, 282 (1963); **39**, 2278 (1963); *J. Phys. Chem. Solids*, **24**, 1081 (1963).
15. A. E. Brenneman, Private communication.
16. J. S. Logan, Private communication.
17. D. P. Seraphim, A. E. Brenneman, F. M. d'Heurle, and H. L. Friedman, *IBM J. Res. and Dev.*, **8**, 400 (1964).
18. S. W. Strauss, D. G. Moore, W. N. Harrison, and L. E. Richards, *J. Res. Nat. Bur. Standards*, **56**, 135 (1956).
19. B. P. Pierce, *loc. cit.* p. 22, No. 156.
20. H. B. Dwight, "Tables of Integrals and Other Mathematical Data," p. 42, No. 202.01, MacMillan, New York (1934).

APPENDIX

A. *Relation of the "flat-band" potential to the boundary field $\mathcal{E}_0$ under temperature bias.*—The boundary field $\mathcal{E}_0(V_X)$ corresponding to the saturation condition under the applied bias $V(X) = V_X$ is readily calculated from the value of the reverse bias V_R necessary to produce the capacitance corresponding to zero field at the surface of the semiconductor. Assuming that the ionic distribution is frozen in on quenching to room temperature and the absence of surface states, the boundary field prevailing when the bias is removed is given by

$$\mathcal{E}_0(0) = \mathcal{E}_0(V_X) - V_X/X$$

To obtain zero field at the boundary $x = 0$, we must apply the reverse potential V_R so that

$$\mathcal{E}_0(0) + V_R/X = 0$$

Then

$$\mathcal{E}_0(V_X) = (V_X - V_R)/X$$

where V_R will be in general negative.

B. *Integration of Eq. [13].*—In order to effect this integration, the equation is first rearranged as

$$K = \int_0^V \frac{e^{3mV/2}\,dV}{a^{1/2}[e^{mV} + (b/a)]^{1/2}} \qquad [A\text{-}1]$$

and the substitution $y = \exp(mV/2)$ is introduced. Equation [A-1] then becomes the standard form (20)

$$K = \int_1^{e^{mV/2}} \frac{2y^2\,dy}{ma^{1/2}[y^2 + (b/a)]^{1/2}}$$

which, after substitution of the limits, becomes the second part of Eq. [13].

C. *Integration of Eq. [21].*—The first of the integrals appearing in Eq. [21] may be integrated by parts after noting that

$$\int \frac{dV}{(a + b\,e^{-mV})^{3/2}} = \int \frac{e^{3/2\,mV}\,dV}{a^{3/2}[e^{mV} + (b/a)]^{3/2}} \qquad [A\text{-}2]$$

which may be converted to a readily integrable form (19) by making the substitution $y = \exp(mV/2)$ and becomes

$$\frac{2}{ma^{3/2}}\left\{-\frac{a^{1/2}}{(a + b\,e^{-mV})^{1/2}} + \frac{mV}{2} + \ln\left[\frac{a^{1/2} + (a + b\,e^{-mV})^{1/2}}{a^{1/2}}\right]\right.$$

The second operation required in the integration by parts is simply

$$\frac{dx^o}{dV}\,dV = \frac{dV}{(a + b\,e^{-mV})^{1/2}}$$

The integral in question after integrating by parts as above indicated becomes

$$\int_0^V \frac{x^o(V)\,dV}{(a + b\,e^{-mV})^{3/2}} = \frac{x^{o^2}(V)}{a} - \frac{2x^o(V)}{ma(a + b\,e^{-mV})^{1/2}} + \frac{2}{ma}\int_0^V \frac{dV}{(a + b\,e^{-mV})} - \frac{1}{a}\int_0^V x^o(V)\,\frac{dx^o}{dV}\,dV \qquad [A\text{-}3]$$

The last two integrals are easily reduced and we obtain

$$\int_0^V \frac{x^o(V)\,dv}{(a + b\,e^{-mV})^{3/2}} = \frac{x^{o^2}(V)}{2a} - \frac{2x^o(V)}{ma(a + b\,e^{-mV})^{1/2}} + \frac{2V}{ma^2} + \frac{2}{m^2a^2}\ln\frac{a + b\,e^{-mV}}{a + b} \qquad [A\text{-}4]$$

After the introduction of Eq. [16], the last integral of Eq. [21] becomes

$$\int_0^V \frac{e^{-mV}K(V)\,dV}{(a + b\,e^{-mV})^{3/2}} = \frac{1}{ma}\int_0^V \frac{dV}{(a + b\,e^{-mV})} - \frac{(a + b)^{1/2}}{ma}\int_0^V \frac{e^{-mV}\,dV}{(a + b\,e^{-mV})^{3/2}} - \frac{b}{4a}\int_0^V \frac{x^o(V)\,e^{-mV}\,dV}{(a + b\,e^{-mV})^{3/2}} \qquad [A\text{-}5]$$

The first two integrals on the right hand side of Eq. [A-5] are well-known forms. The last is integrated by parts making use of the relations

$$\int \frac{e^{-mV}\,dV}{(a + b\,e^{-mV})^{3/2}} = \frac{2}{bm}\,(a + b\,e^{-mV})^{-1/2}$$

$$\frac{dx^o}{dV}\,dV = \frac{dV}{(a + b\,e^{-mV})^{1/2}}$$

On carrying out these operations, Eq. [A-5] takes the form

$$\int_0^V \frac{e^{-mV}K(V)dV}{(a + b\,e^{-mV})^{3/2}} = \frac{1}{ma}\left[\frac{V}{a} + \frac{1}{ma}\ln\frac{a + b\,e^{-mV}}{a + b}\right] - \frac{1}{m^2ab}\left[\frac{(a + b)^{1/2}}{(a + b\,e^{-mV})^{1/2}} - 1\right] - \frac{x^o(V)}{2ma}\left[\frac{1}{(a + b\,e^{-mV})^{1/2}} - \frac{1}{(a + b)^{1/2}}\right] \qquad [A\text{-}6]$$

Equation [22] results from the introduction of Eq. [A-4] and [A-6] into Eq. [21].

Growth and Morphology of Silicon Ribbons

S. N. Dermatis,[1] J. W. Faust, Jr., and H. F. John

Research and Development Center, Westinghouse Electric Corporation, Pittsburgh, Pennsylvania

ABSTRACT

Ribbons of silicon were grown from a supercooled melt and examined by various techniques. From the morphology of the ribbons, dislocation patterns, twin structures, and microsegregation traces, it was shown that the basic growth sequence is similar to that given for germanium. Some differences are found, however, and these are described. Microsegregation traces were used to elucidate the growth sequence of degenerate ribbons.

Germanium and indium antimonide can be pulled under controlled conditions from a supercooled melt in the form of long ribbons (1, 2). The ribbons are very uniform and have flat faces that approximate {111} planes (3). It has been shown that at least two twin planes parallel to and approximately midway between the flat faces are necessary for continuous ribbon growth (4, 5), and that the growth of the ribbons involves two propagation mechanisms, one for lengthwise growth and one for lateral growth (6). The obvious usefulness of material in ribbon form and the greater interest in silicon devices focused attention immediately on ribbon growth of silicon. It is the purpose of this paper to discuss the growth and morphology of silicon ribbons, and to compare the observations with the extensive data available on germanium ribbons.

Examination Techniques

In this investigation the morphology, internal structure, and perfection of the seeds, buttons, and ribbons were studied. Table I gives a summary of the techniques used and the sample preparation for each technique. In some cases other etchants can be used, but those listed here were found to give the best results. The morphology of the buttons and ribbons was examined with a binocular and a standard metallurgical microscope. In the pulling experiments, the seeds were oriented by means of the etch pits produced by the NaOH etch (see Table I). The furnace used is described elsewhere (7). The twin spacing of the seeds and ribbons was measured by fracturing (8) while those in the button were measured by potting the button, cutting a cross section, polishing, and etching. The etchants used are given in Table I. To reveal the growth history by microsegregation striations (6, 9), special ribbons were pulled from highly doped melts. The dopants used were boron and aluminum. To obtain the best results several different concentrations of dopant were investigated over the range from approximately 10^{17} to 10^{20} carriers per cc. Microsegregation striations were revealed by examination of etched main faces, potted and etched cross sections, and also some fractured cross sections. The etchants used for this purpose are also given in Table I.

Dislocations on the main faces could be revealed by several etchants, two of which are given in Table I. Dislocations intersecting the cross sections were revealed on fractured cross sections by the two etchants listed or on polished cross sections by the Dash etch.

[1] Present address: Center for Materials Science and Engineering, Massachusetts Institute of Technology, Cambridge, Massachusetts.

Table I. Techniques for studying silicon ribbons

Reason	Surface	Etchant
To study twin and button structures	1. Fractured 2. Potted and polished	CP_4*
To reveal dislocation	Natural surface or fractured cross section	Dash** Chromic acid†
To reveal segregation traces		
(a) on faces	Natural surface	CP_4*
(b) on cross sections	Potted and polished or fractured cross section	CP_4* Chromic acid†
To orient seeds	Natural face	Hot NaOH‡

* HNO_3:HF:acetic acid (5:3:5).
** HNO_3:HF:acetic acid (3:1:10).
† CrO_3:HF:H_2O (2:4:4).
‡ Triangles point in <111> directions.

Results and Discussion

When it was attempted to use a furnace similar in design to that used for germanium, it was found that in order to get enough supercooling in the center of the melt, the silicon at the sides of the crucible was also supercooled. This supercooling plus reaction of the silicon with the crucible walls resulted in nucleation and growth from the sides of the crucible quickly stopping the controlled growth of the ribbon. Although this problem could be reduced by a crucible material that would not be wet by the silicon, no materials were found that met these requirements. The problem was overcome by the use of a heat shield (10). It was found that in the modified furnace any of the materials ordinarily used for pulling silicon could be used as a crucible, such as quartz, boron nitride, or silicon carbide. Supercoolings between 5° and 20° were used; the pulling speed ranged to 12 ipm (inches per minute); however, ribbons have been pulled as fast as 20 ipm.

Seeds.—As in the case of germanium ribbons, seeds are of the utmost importance for controlled dendritic growth. The initial seeds were primitive dendrites obtained in the normal fashion (1, 4). That is, a single crystal or a crystal containing one twin plane oriented in the directions given for germanium (1, 4), was plunged into a supercooled melt. After growth commenced, the resulting mass was withdrawn at a rapid rate, the order of 12 ipm.

General features of buttons and dendrites.—Several growth masses from which primitive dendrites were obtained were examined and then potted, polished,

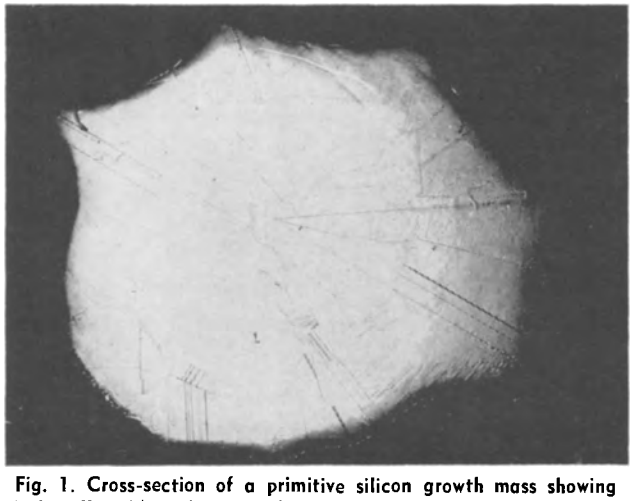

Fig. 1. Cross-section of a primitive silicon growth mass showing twin lamellae. Magnification 6X.

and etched. It was found that the number of primitive dendrites found on each growth mass varied. Figure 1 shows the cross section of a growth mass of silicon. The width of the twin lamellae varied from less than 1μ to several hundred microns. This is to be compared with germanium where the maximum width of the twin lamellae reported in the growth mass was about 70μ and the widest twin spacing found for primitive dendritic growth was 35μ (4).[2]

The protuberance in Fig. 1 shows where primitive dendrites grew from the growth mass. Figure 2 shows one of these protuberances at a higher magnification. Since the melt was highly doped, the core structures of two primitive dendrites that propagated downward can be seen (these are marked by arrows in Fig. 2). Comparing silicon and germanium primitive growth masses, many more twin lamellae are found in the silicon. This observation is consistent with the fact that with single twin seeds of silicon it was relatively easy to generate additional twin planes.

When seed, properly oriented (4) were used for controlled dendritic growth, faceted buttons resulted (see Fig. 3). The buttons, although similar to those found in germanium, were not as well formed. In the button of Fig. 3 a ribbon grew from each wing. Only one ribbon could be made to continue growing by suitable adjustment of pulling speed and/or temperature. The ribbons grew in the $<2\bar{1}\bar{1}>$ directions as long thin ribbons and were faceted along the sides by {111} planes. The side facets can be seen on Fig. 4 for a narrow ribbon.

The two main faces were essentially atomically flat {111} planes. Microscopic examination of the unetched main faces showed that they contained growth steps as shown in Fig. 4. Booker (12) has measured these steps and found them to be ramps of varying height; on good ribbons the step heights were usually not greater than 500 to 1000Å, although growth steps as high as 10,000Å were measured on some ribbons. This height is greater than those reported for germanium by about a factor of two. He also reported some reverse steps on these ribbons which were not found on ribbons of germanium. Under the best growth conditions these steps were spaced far enough apart so that the thickening of the ribbon over a foot length was not greater than 1 mil. The formation of growth steps which takes place at the meniscus (3) is one thickening process for ribbons. It is more difficult to keep under control for silicon than for germanium. Another thickening process, that of degenerate growth below the surface of the melt, will be mentioned later.

[2]Hamilton and Seidensticker have reported wider twin spacings, but the rate of propagation of their ribbons was greatly reduced (11).

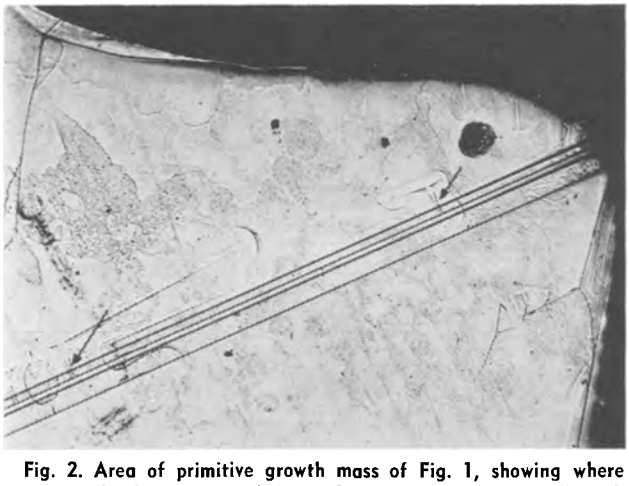

Fig. 2. Area of primitive growth mass of Fig. 1, showing where primitive dendrites grew (cores of dendrites are marked with arrows). Magnification approximately 60X.

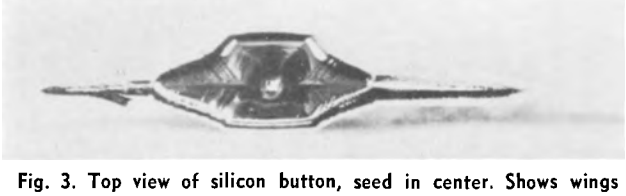

Fig. 3. Top view of silicon button, seed in center. Shows wings and facets.

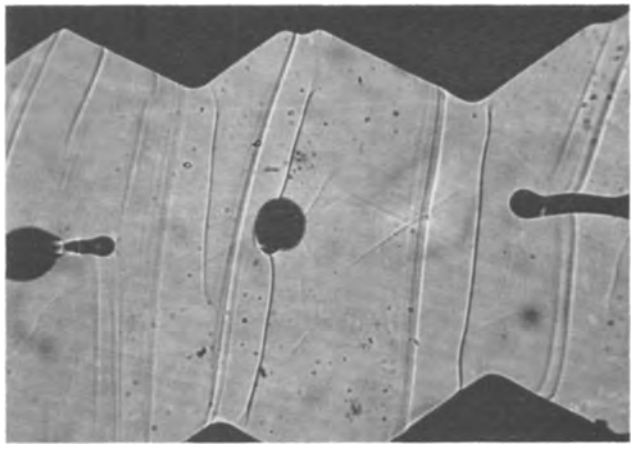

Fig. 4. Growth steps and slip patterns on a natural face of silicon ribbon. Magnification approximately 80X.

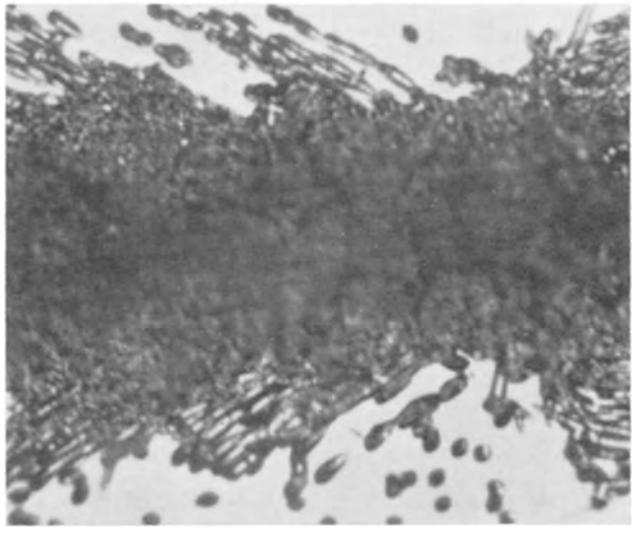

Fig. 5. Dislocations in central strip of natural face. Magnification 200X.

Dislocation studies.—The crystal perfection of the ribbons varied greatly. The dislocations were limited to the three general areas given previously for germanium ribbons (13). In most cases slip patterns (see Fig. 4) were found along the central part of the main faces. This central stripe of slip patterns was shown to consist of patches with a very high density of dislocations, Fig. 5 [area I dislocations (13)]. The fast etching rate of the Dash etch along a dislocation gave an elongated slot instead of the two pits at the end of dislocation half loops as obtained for germanium (13). The slip and dislocations have been shown to arise from small pockets of liquid which became trapped, subsequently froze, and expanded to deform the surrounding material (13). An entrapped droplet can be seen in Fig. 8. Dislocation loops radiate in all possible slip directions from the entrapped droplets. They can be revealed on polished and etched cross sections as seen in Fig. 6. The entrapped droplet shows a high density of dislocations on one side of this two twinned

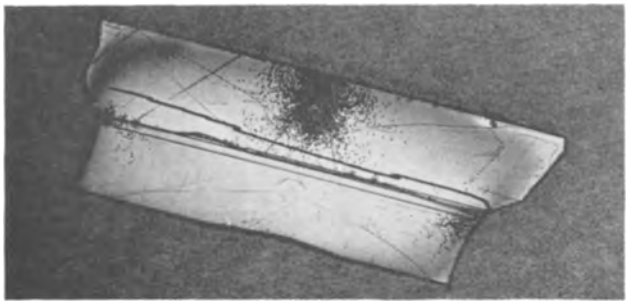

Fig. 6. Cross section of silicon ribbon showing dislocations and microsegregation traces. Magnification approximately 75X.

ribbon, while the other side is relatively free of dislocations.

Random dislocations were found along one or both edges of the main faces [area II dislocations (13)]. Pockets of dislocations were found, but only rarely, on the cross sections running parallel to the twin lamellae near one or both edges [area III dislocations (13)]. In the case of germanium ribbons (13), it was suggested that the area III dislocations arise from stresses set up by a mechanism similar to that for the slip and dislocations in area I. In area III, the liquid became trapped by freezing taking place across the extremities of the H-arm. The term H-arm will be more evident later; they can be seen quite clearly in Fig. 8 and 11. The rare occurrence of dislocations in this area in silicon suggests that this is not taking place, and that the growth between the H-arms takes place more uniformly from the core and the inner part of the H-arm.

Pulling experiments.—Ribbons with an even number of twin planes grew in any one of six <211> directions; however, once a ribbon started to grow in the vertical direction, it usually continued to grow in that direction without branching. Ribbons with three twin planes were grown in both the "right" and "wrong" directions [this terminology is explained elsewhere (1, 4)] as determined by the etch pits from the NaOH etch (see Table I). When the seed was used in the right direction (*i.e.*, the $<2\bar{1}\bar{1}>$ direction), a single ribbon resulted growing vertical to the melt.

These findings are the same as those reported for germanium (1, 4). When the three-twin seed was used in the wrong direction (*i.e.*, the $<\bar{2}11>$ direction), ribbons preferred to grow normal to the melt rather than at 60° to the vertical as was reported for germanium (1, 4). Some 60° growth was found, however. On examination of the flat faces and cross sections of highly doped ribbons that grew normal to the melt, the slip pattern on the main faces and the core of the ribbon on the cross sections was found to be in the center. Ribbons that grew 60° to the vertical, *i.e.*, those with an odd number of twin planes growing in the wrong direction or 60° branches of ribbons with an even number of twin planes, have the central slip pattern and the core of the ribbon displaced to the warmer edge of the ribbons. This asymmetric growth was also obtained when ribbons were purposely pulled from a position close to the crucible walls rather than in the center which is, of course, the center of thermal symmetry.

Segregation studies.—The addition of dopants to the melt from which ribbons were grown proved invaluable in elucidating the growth mechanism of the germanium ribbons (4, 6). Boron or aluminum was added to the silicon melts for similar studies; however, the boron proved more effective with the etchants listed in Table I. Etching was carried out on the main flat face, the potted polished and etched cross sections, and on fractured cross sections to bring out the microsegregation traces. Figure 7 shows the main flat face; both the A and the B traces [this terminology is explained elsewhere (9)] are visible as is the "backbone," or core, of the ribbon. Figure 8 shows a polished and etched cross section of a three-twinned silicon ribbon; two of the three twins do not extend all the way across the cross section. Here the central core is clearly visible as are the B traces going out to form the H-arm structure. The outside of the H-arms are concave and have been filled in by parallel {111} overgrowth while the area between the H-arm shows little structure. It is this area where any macrosegregation is found (6). Some of the melts were so highly doped that excessive macrosegregation was observed as shown by the stained cross section in Fig. 9. The microsegregation studies show that the growth mechanism for silicon ribbons is the same as that given for germanium (4, 6, 14).

The traces around the core of the dendrite are particularly interesting. For the most part the general features of this cross section are similar to those found in germanium ribbons (6); however, the core area is different. Figure 10 is an enlargement of the core area of this cross section; the accompanying sketch

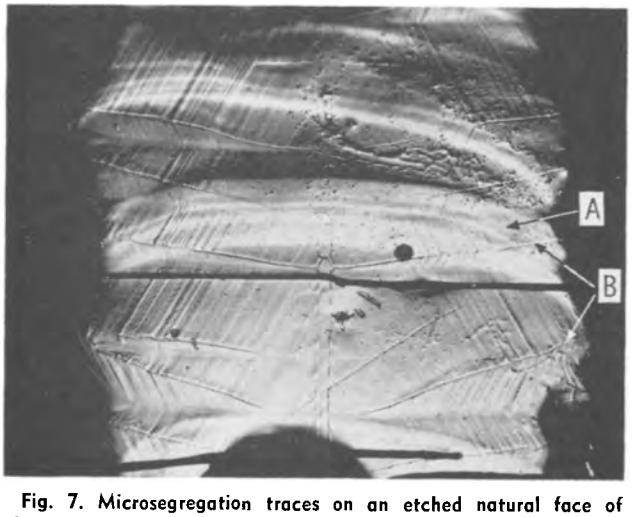

Fig. 7. Microsegregation traces on an etched natural face of silicon. A and B refer to types of traces (see text). Magnification approximately 75X.

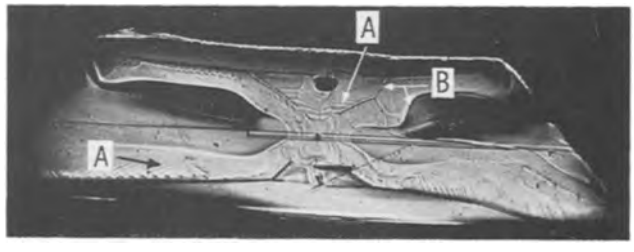

Fig. 8. Cross section of heavily doped silicon ribbon etched to reveal microresistivity striations. Magnification approximately 60X.

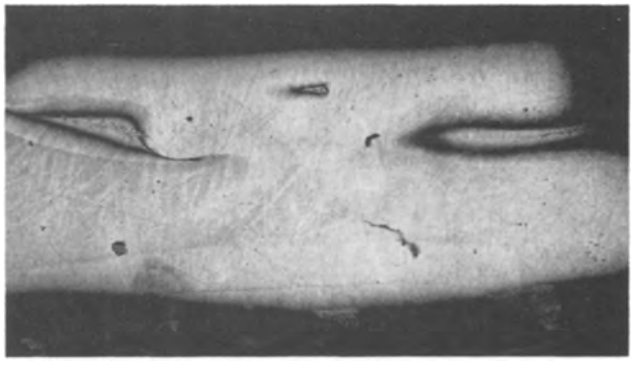

Fig. 9. Cross section of heavily doped silicon ribbon stain-etched to show areas of larger segregation. Magnification approximately 150X.

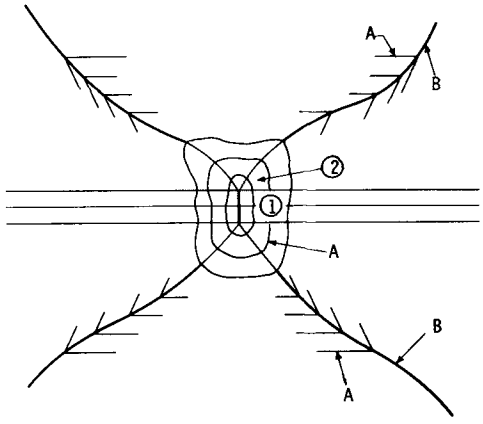

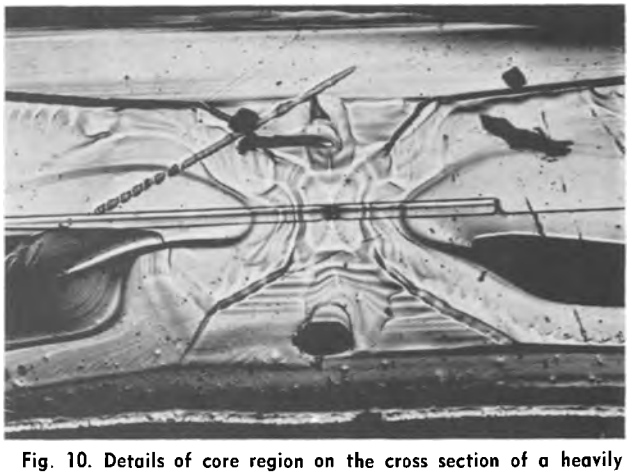

Fig. 10. Details of core region on the cross section of a heavily doped silicon ribbon. Magnification approximately 150X.

is included to aid in interpretation of the cross section. In the case of germanium well-defined A and B traces were found from the core outward. Here, however, it is noted that the B traces are poorly defined in the immediate vicinity of the core (area 1). The A traces, instead of being straight along {111} planes, are curved entirely around the core. This suggests that the core itself is highly faceted, as in the case of germanium, but that just behind the core the ribbon is not highly faceted. Farther out one can see A traces outlining the {111} planes and the B traces that are the intersection of the growth fronts indicating that good faceting exists once again. Figure 11, although not exhibiting all of the A and B traces of Fig. 6, shows the displacement of the core to the side for a ribbon grown at 60° to the melt; the H-arm growth is clearly visible as is the core. In general it was not as easy to reveal the microsegregation traces in silicon ribbons as it was in germanium ribbons (6).

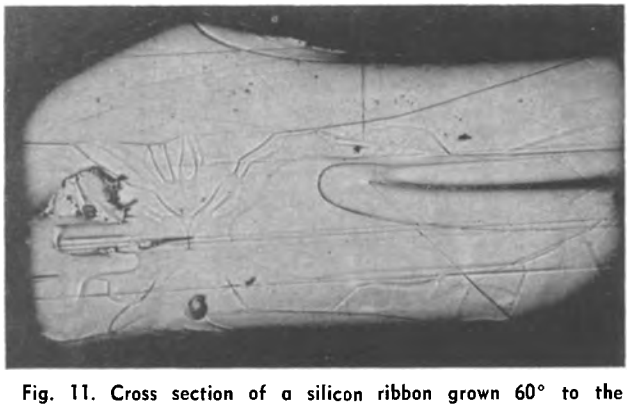

Fig. 11. Cross section of a silicon ribbon grown 60° to the vertical. Magnification approximately 75X.

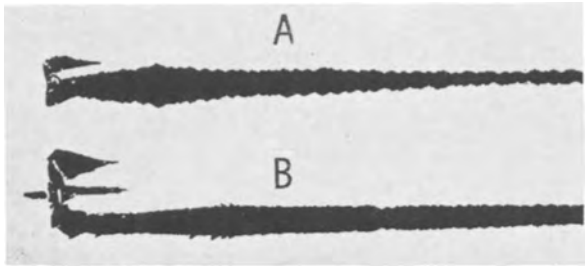

Fig. 12. Silicon ribbons: (a) degenerate; (b) nondegenerate.

Degenerate growth.—Although, as is evidenced from the above, the silicon ribbons are similar in appearance and growth to germanium ribbons, there is one growth problem that is almost exclusively peculiar to silicon ribbons. When a ribbon is pulled, it invariably at the beginning is wide with excellent surfaces, but in many cases degenerates within the first inch or two into a thick narrow ribbon with highly faceted edges and with very irregular main faces, *i.e.*, large growth steps and deep pits instead of slip patterns. An example of such a ribbon is shown in Fig. 12a. How this degeneration takes place can be found by studying the cross sections of various regions of the ribbons. Figure 8 shows the good ribbon with the well developed H-arm growth. Figure 13 shows an intermediate region where one can note the concave and the convex nature of the B traces going out to the corners of the ribbon and the A traces ending at a concave line. This suggests a considerable degeneration of the previously good H-arm growth. Figure 14, on the other hand, shows the cross section of a completely degenerate ribbon. Here one can see that the B traces go out to the corners, and the A traces go from it to convex B traces. Such a phenomenon suggests that degeneration occurs in the earliest stages of the core development at a time well before any growth at the meniscus (*i.e.*, growth steps) could influence the morphology of the ribbons. This degeneration could be caused by changing thermal conditions at the tip or by impurity influenced modification of nucleation and layer completion. Actually, by the time the growing ribbon has reached the meniscus it has assumed its maximum width (6); thus, the observed narrowing could not

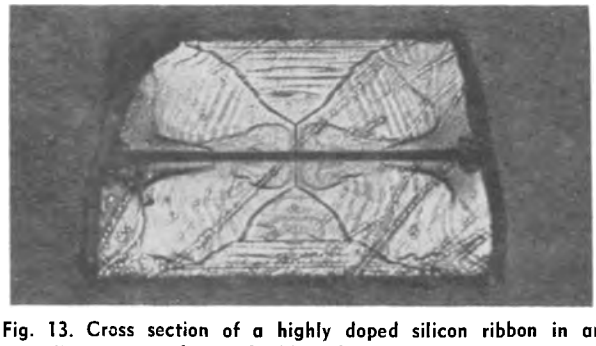

Fig. 13. Cross section of a highly doped silicon ribbon in an intermediate stage of growth. Magnification 200X.

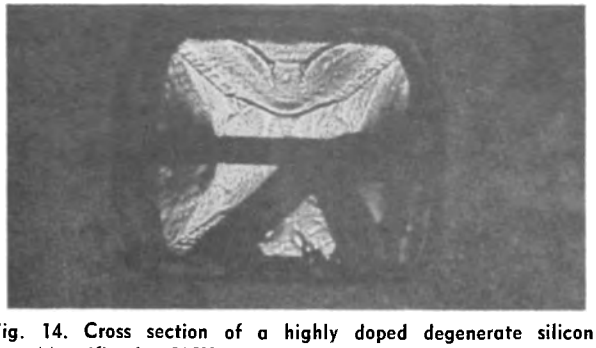

Fig. 14. Cross section of a highly doped degenerate silicon ribbon. Magnification 200X.

take place at the meniscus. Although the relative importance of thermal conditions at the growing tip and impurity effects on core development have not been determined, the development of improved thermal shielding systems, which give a more nearly isothermal melt but which may also cut down on impurity transfer from the outside, have made it possible to grow long lengths of ribbons without degeneration or excessive thickening, see Fig. 12b.

Spikes (*i.e.*, incipient branching) occasionally show up at low pulling speeds. From the length of the spikes one can say that this growth initiates between the growing tip and the meniscus, possibly in the area where the faceting is not pronounced. Although the effects of various twin spacings on the growth morphology have not been extensively studied, it does seem that the spikes show up more frequently at the larger twin spacings.

Further improvement in the technique for growing silicon ribbons has been made much less important by the development of the web technique (10) which yields a more versatile material. It is of relatively little importance whether the side dendrites in the web material are degenerate or not.

Summary

The general morphology of the buttons and ribbons, the location of the dislocations, and particularly the growth history as shown by microsegregation traces suggest that the basic growth mechanism of silicon ribbons is the same as that for germanium. There are, however, differences between the growth of silicon and germanium ribbons. These differences are:

1. Difficulty in obtaining 60° silicon ribbons when a seed containing an odd number of twins is used in the "wrong" direction.
2. Less highly faceted area of the silicon ribbons just behind the growing tip.
3. Tendency of the silicon ribbons to become degenerate.
4. Tendency of the silicon ribbons to spike, especially at low pull rates or wide twin spacings.
5. Easier to generate additional twin planes in silicon.
6. Less difference in the core faceting between silicon ribbons grown in the "right" and the "wrong" direction with three twinned seeds.
7. Higher growth steps on silicon ribbons.

Items 2, 3, and 6 suggest perturbations to the basic growth mechanism of germanium. The other differences are in control of the growing technique. The tendency of the ribbons to degenerate has been reduced by the addition of heat shields.

Acknowledgments

The authors wish to express their gratitude to Mrs. H. Larson and Mrs. S. Hillbeck for preparing the ribbons for examination.

Appreciation also is expressed to the Air Force Logistics Command, Aeronautical Systems Center, Wright Patterson Air Force Base, for their partial support of this work.

Manuscript received Feb. 10, 1965. This paper was presented at the Houston Meeting, Oct. 9-13, 1960.

Any discussion of this paper will appear in a Discussion Section to be published in the June 1966 JOURNAL.

REFERENCES

1. A. I. Bennett and R. L. Longini *Phys. Rev.*, **116**, 53 (1959).
2. H. Nicholson and J. W. Faust, Jr., *This Journal*, **110**, 940 (1963).
3. R. L. Longini, A. I. Bennett, and W. J. Smith, *J. Appl. Phys.*, **31**, 1204 (1960).
4. J. W. Faust, Jr., and J. F. John, *This Journal*, **108**, 855 (1961).
5. D. R. Hamilton and R. Seidensticker, *J. Appl. Phys.*, **31**, 1165 (1960).
6. J. W. Faust, Jr., and H. F. John, *This Journal*, **108**, 860 (1961).
7. S. N. Dermatis, To be published.
8. J. W. Faust, Jr., and H. F. John, *This Journal*, **107**, 562 (1960).
9. J. W. Faust, Jr., H. F. John, and S. O'Hara, in "Metallurgy of Semiconductor Materials," J. B. Schroeder, Editor, p. 181, Interscience Publishers, New York (1962).
10. S. N. Dermatis and J. W. Faust, Jr., *I.E.E.E. Trans. on Communications and Electronics*, **65**, 94 (1963).
11. D. R. Hamilton and R. Seidensticker, *J. Appl. Phys.*, **34**, 1415 (1963).
12. G. R. Booker, *This Journal*, **107**, 188C (1960).
13. J. W. Faust, Jr., and H. F. John, *ibid.*, **108**, 864 (1961).
14. G. F. Bolling and W. A. Tiller, in "Metallurgy of Elemental and Compound Semiconductors," R. Grubel, Editor, p. 97, Interscience, New York (1961).

Electrical Properties of Copper Segregates in Silicon P-N Junctions

J. E. Lawrence

Fairchild Semiconductor, Division of Fairchild Camera & Instrument Corporation, Palo Alto, California

ABSTRACT

The electrical properties of segregated copper are greatly influenced by the structure of the lattice disorder to which the impurity precipitates. Two crystal defects, the sessile fault and the lattice void, act as precipitation sites for the copper impurities discussed in this work. Copper which precipitates at a small sessile fault will acquire a platelet distribution within the limits of the newly formed disorder. The copper platelet will cause a P-N junction to exhibit a soft reverse characteristic if the platelet is in the depletion region of the junction. Copper which precipitates at a lattice void will redistribute to form loosely packed {110} arrays. These {110} copper segregates contribute a constant multiplier to a copper-free P-N junction's electrical I-V trace.

Segregated copper impurities near a planar diffused P-N junction will contribute irregular reverse bias characteristics to the electrical junction in semiconductor crystals. The physical and electrical behavior of nonsegregated copper in silicon and germanium has been the topic of many publications in the last decade. Copper is reported to diffuse interstitially as a single charged positive ion (1). Interstitial copper ions combine with vacancies in the silicon lattice to create a substitutional impurity. Substitutional copper has been

identified as a triple acceptor in both silicon and germanium crystals by Hall and Racette (2), who also report the diffusivity, solubility, and electrical charge values for copper impurities in silicon, germanium, and gallium arsenide.

Copper has a strong temperature-dependent solid solubility in silicon which causes supersaturation and the formation of precipitates during a crystal's cooling from an annealing treatment. The Cottrell interaction energy relating interstitial copper impurities to regions of lattice distortion is favorable to the formation of precipitates during a thermal treatment. Dash (3), Schwuttke (4), and Thomas (5) have provided experimental evidence of the interaction of copper impurities with crystal disorders in the silicon lattice. Schwuttke discusses the influence of oxygen on the precipitation of copper. Early work by Goetzberger and Shockley (6) identified precipitated metallic impurities as contributing to excessive reverse currents below avalanche breakdown. However, they did not associate a specific distribution of metallic impurities with particular electrical characteristics.

Structure of the Copper Precipitation Site

In this work, the behavior of copper at a crystal defect was investigated at a sessile fault and a lattice void. Both of these crystal disorders form near the surface of silicon wafers during a thermal treatment.

The silicon wafers used in this investigation initially contained either antimony, boron, or phosphorus bulk dopant impurities at dopant concentrations from 4 x 10^{14} to 4 x 10^{18} atoms/cm^3. The wafers contained a known dislocation density varying from less than 10 to greater than 10^5/cm^2. Thermal treatments were conducted at temperatures between 1000° and 1260°C in atmospheres of dry oxygen, steam, or nitrogen. The thermal treatments varied from 5 min to 10 hr while the quenching times varied from 30 sec to 10 min.

The sessile faults are formed during the recovery of a plastically deformed surface. The deformation was introduced by mechanically polishing silicon wafers. These mechanically worked wafers were annealed to permit the recovery of the distorted surface. The sessile faults which form at the crystal's surface grow in size in a direct relationship to the annealing time and temperature. The sessile faults described here develop along the inclined {111} planes and thus distort the exposed (111) surface along the $<\bar{1}10>$ directions. This crystal disorder has a half-hexagonal configuration in its inclined $(\bar{1}11)$ plane as shown in Fig. 1. The peripheral distribution of lattice strain of this crystal defect has been delineated on a cleaved $(\bar{1}11)$ plane by copper decoration and Sirtl etching. Copper precipitates will resist brief periods (less than 60 sec) of etching with the Sirtl solution (7).

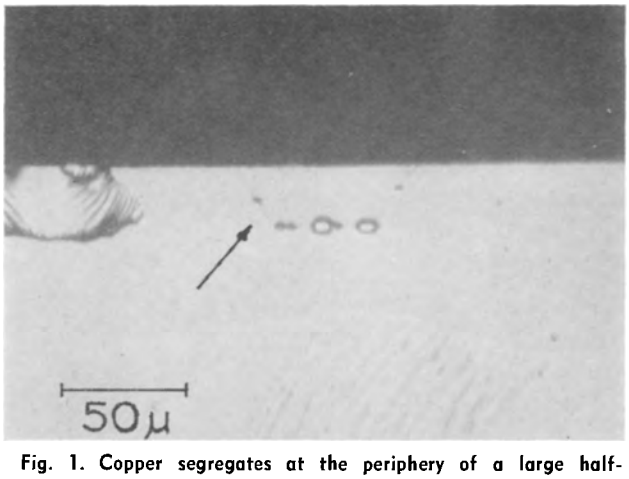

Fig. 1. Copper segregates at the periphery of a large half-hexagonal sessile fault delineated on a cleaved $(\bar{1}11)$ face by Sirtl etching.

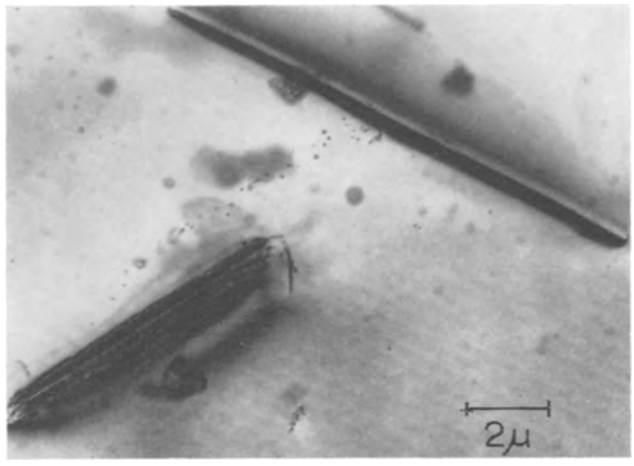

Fig. 2. Two sessile faults. Electron transmission micrograph

This plastic deformation induced crystal defect was identified as a sessile fault from an analysis of the defect's electron transmission properties. Such analysis was aided by the development of a quick and reliable technique for preparing uniform films 1000Å thick and greater than 2 mm in diameter (8). The extinction contrast fringes in the crystal disorders shown in Fig. 2 identified the imperfections as being two dimensional sessile faults such as twin faults or stacking faults. These are very likely stacking faults for they do not contribute to a twin diffraction pattern when analyzed by selective area electron diffraction. Also, a single planar slip at the surface, producing a stacking fault, will form more readily during the recovery of a plastically deformed lattice than will a double slip which produces a twin lamalla. Thomas (5) investigated a similarly formed crystal defect by the selective area electron diffraction technique and drew the same conclusion.

A large amount of crystal disorder develops near the surface of "strain free" wafers during high temperature annealing treatments. This structural disorder does not form in crystals containing a high degree of initial lattice strain from bulk dislocations or surface faults. The silicon wafers prepared for analysis of this thermally induced disorder contained less than one hundred dislocations per square centimeter and had 150μ of material removed from each lapped wafer face by chemical polishing. The electron transmission micrographs in Fig. 3a and 3b show the structural order of the silicon surface before and after a thermal treatment at 1200°C for 1 hr in a dry nitrogen ambient. The interference fringes in Fig. 3a and 3b

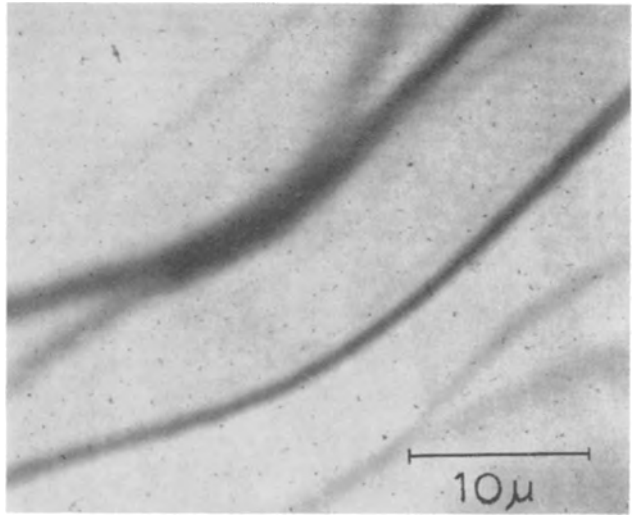

Fig. 3a. Electron transmission micrograph: defect free lattice before thermal treatment.

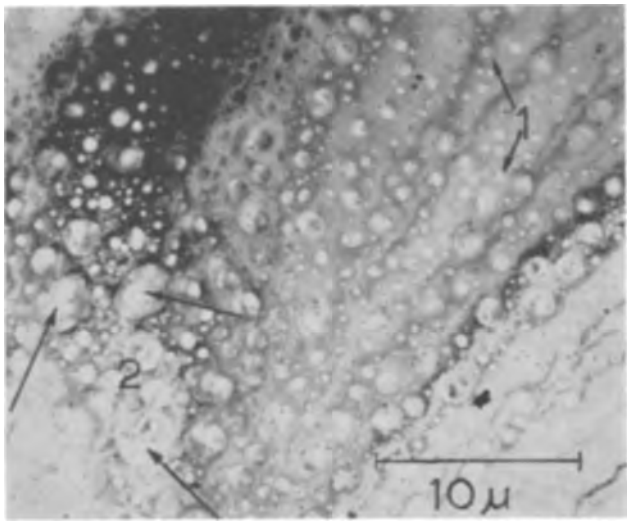

Fig. 3b. Electron transmission micrograph: surface lattice voids formed during thermal treatment.

provide a sensitive means of identifying lattice disorders and slight variations in film thickness. The micrograph in Fig. 3a illustrates a surface free of lattice distortion which is characteristic of the nonheat-treated material used in this investigation. The transmission micrograph in Fig. 3b identifies the structure of the thermally induced crystal disorders.

Several stages in the development of this crystal imperfection may be interpreted from the disorders in Fig. 3b. The disorders initially appear as flat disk-like structures in the (111) plane (No. 1 in Fig. 3b). These disk structures, as a unit, are immobile; however, they can grow by acquiring some unidentified unit such as a vacancy and by expanding into a neighboring disorder of similar formation. Large thermally induced disorders can combine with adjacent disorders that do not lie in the same (111) layer. The large disorders (No. 2 in Fig. 3b) possess irregular configurations which suggest they have developed by a recent combination.

These thermally induced disorders do not appear to be dislocations or sessile faults for they do not have a Burgers vector that can be resolved by the extinction contrast technique of the electron microscope. These disorders are volume discontinuities in the silicon lattice, such as voids. This identification seems probable since their formation is only a function of the structural order of the initial material and the treatment temperature and not a function of the annealing ambient. The subject imperfection is not an impurity inclusion for the disorders do not have unique electron transmission or diffraction properties. Recent work by Booker and Stickler (9) discusses a similar disorder that is reported to be of amorphous material, probably an oxide.

Incomplete work by the author has lead to the belief that the fundamental unit of a thermal lattice void, the vacancy, is created at a crystal surface by a wafer's dopant impurity forming a Schottky vacancy. (Thermal voids form more readily in highly doped material than lightly doped materials.) The slow quenching of a low dislocation density material would produce a supersaturation of vacancies. In the absence of a readily accessible vacancy sink such as a surface or dislocation, many vacancies could combine to initiate a void in this treatment environment.

The formation of a Schottky defect and the diffusivity of a vacancy in germanium reported by Goldberg (10) supports the author's preliminary model for vacancy formation. The interaction of vacancies to form clusters, a primary unit of a void, has been recognized as possible by Melngailis and O'Hara (11) and Elbaum (12). The existence of surface lattice voids in thermally treated low dislocation density germanium crystals has been reported by Tweet (13).

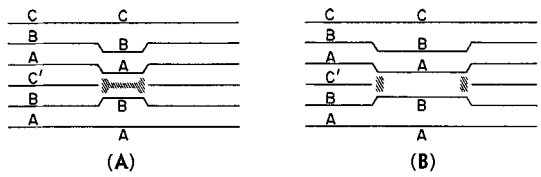

Fig. 4. Schematic diagrams: (A) Copper platelet in small newly formed sessile fault. (B) Copper segregation in large sessile fault.

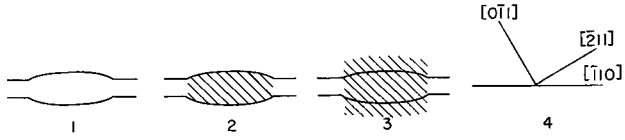

Fig. 5. Formation model for copper segregate at lattice void: diagram 1, copper free void; diagram 2, copper impurities saturate void; diagram 3, copper impurities supersaturate void; diagram 4, copper redistributes to form {110} planar arrays.

The Distribution of Precipitated Copper

Copper was introduced to the test wafers in a manner that allowed reference wafers to be exposed to the thermal treatment at the same time without being exposed to the metallic impurity. This was accomplished by placing two test wafers 8 in. apart on a furnace carriage with a copper-plated silicon wafer between them. The carriage was then passed into a furnace which was continually flushed with fresh oxygen. Different temperature zones in the furnace allowed tests to be conducted at temperatures between 1000°C and 1260°C.

The distribution of segregated copper at a sessile fault is dependent on the size of the lattice disorder and the amount of copper available to precipitate. Diagrams representing the distribution of copper at sessile faults, when a limited amount of the impurity is available for precipitation, is presented in Fig. 4a and 4b. The lines identified by the letters in the schematics represent ($\bar{1}$11) planes of atoms at their intersection with the (111) wafer surface. The discontinuous "C'" rows represent simplified sessile faults. The cross-hatched lines represent the manner in which copper impurities prefer to segregate in a small sessile fault (Fig. 4a) and a similarly formed fault which has grown in size during a prolonged thermal treatment (Fig. 4b).

Copper impurities appear to seek a platelet distribution in small newly formed sessile faults. This is graphically represented by the uninterrupted cross-hatch lines in Fig. 4a. Experimental evidence of the platelet distribution of segregated copper was achieved

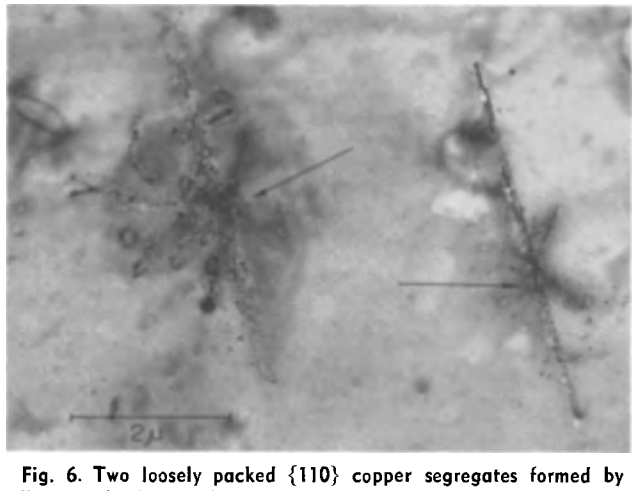

Fig. 6. Two loosely packed {110} copper segregates formed by collapsing lattice void precipitation sites.

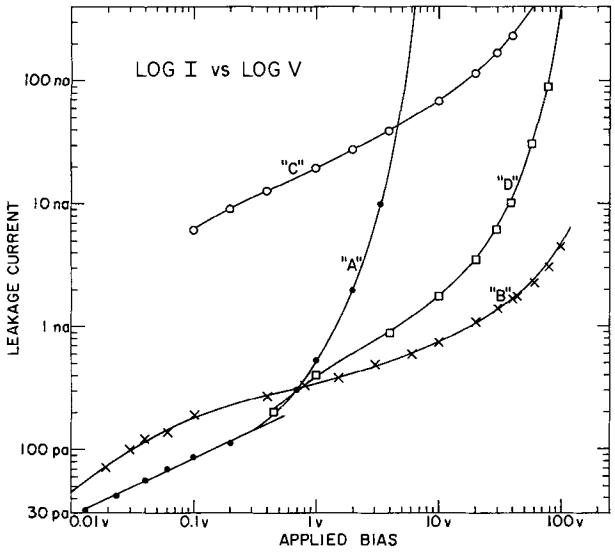

Fig. 7. Log I *vs.* log V electrical traces of deep diffused P-N junctions with "A" sessile fault copper platelet, "B" copper-free, "C" loosely packed {110} copper segregates, "D" copper-free surface lattice voids.

by cleaving a wafer containing many copper decorated sessile faults and observing the distribution of segregated copper at several exposed lattice faults. Copper platelets possessing half-hexagonal configurations and occupying the entire region within the limits of newly formed sessile faults have been delineated.

The region of greatest lattice distortion of a large sessile fault is along its subsurface perimeter. Copper impurities are, thus, more likely to segregate to the periphery of large sessile faults as represented graphically in Fig. 4b and illustrated in the micrograph shown in Fig. 1. This micrograph also indicates that the copper does not achieve a uniform distribution along the total perimeter of the large sessile fault, but rather segregates into localized regions.

A model for the development of a copper segregate at a thermally induced lattice void is graphically illustrated in Fig. 5. Diagram 1 in this figure represents the structure of a simplified lattice void. Copper is initially attracted to the crystal void because of its lattice distortion and free electrical bonds. The cross-hatched lines in diagram 2 represent copper impurities that have precipitated at the lattice void. It is reasonable to assume that copper impurities prefer to precipitate at existing segregates rather than to nucleate a new site. Therefore, copper impurities will continue to be attracted to a lattice void long after it has become saturated with copper atoms. Diagram 3 represents the precipitated impurities as extending beyond the limits of the crystal void. The lattice surrounding the crystal void cannot accept the acquired supersaturated concentration of copper. Therefore, the copper precipitates are forced to redistribute along low energy crystal planes. Diagram 4 illustrates the (111) intersection of three of these planes of segregated copper.

Copper is redistributed to form a loosely packed array of secondary precipitates along specific {110} planes following the collapse of a lattice void precipitation site. The redistribution planes were identified as {110} by determining the direction at which individual copper segregate planes intersected the (111) wafer surface and a $(\bar{1}11)$ cleaved face. The planes of segregated copper which intersected one {111} plane at a $<\bar{2}11>$ direction, also intersected the other {111} plane at a $<\bar{1}10>$ direction. The distribution of copper following the collapse of a lattice void was determined by analyzing electron transmission micrographs, such as that shown in Fig. 6. This micrograph illustrates two loosely distributed arrays of secondary precipitates, which resulted from a forced redistribution of copper impurities at two collapsed lattice void precipitation sites. The widely separated secondary precipitates appear as well defined dark dots in Fig. 6. These two collapsed void segregates appeared in a silicon wafer into which a low concentration of copper impurities had been introduced.

Copper impurities in the silicon lattice precipitate during thermal treatments above 1000°C and not solely during the cooling from the annealing temperature. This was determined by studying the configuration of oxide irregularities which develop over copper decorated surface lattice disorders. The oxide irregularities are aligned to the same $<\bar{2}11>$ or $<\bar{1}10>$ directions as the copper segregates on which they develop. They alter the uniform topography of the oxide film by nearly one tenth the thickness of the silicon dioxide layer. The copper impurities could not have segregated during a 30 sec quenching period and still contributed to the oriented oxide irregularities.

Electrical Behavior of Segregated Copper

As mentioned earlier, the electrical behavior of segregated copper is governed by the structure of the precipitated impurities in the silicon lattice. Copper which segregates to form a tightly packed platelet, *e.g.*, at a small newly formed sessile fault, will exhibit a different electrical behavior from copper which segregates to form a loose distribution of secondary precipitates, *e.g.*, following the collapse of a lattice void precipitation site.

A copper platelet in the space charge region of a reverse biased P-N junction will emit visible light from a pair of oriented microplasmas and alter the I-V characteristics of the electrical junction. It has been reported (14) that small points of emitted light (microplasmas) carry essentially all of a reverse biased P-N junction's premature breakdown current. The intensity of an individual point of emission is proportional to the carrier recombination multiplication factor, which, is, in turn, proportional to the field strength at the small localized point of emission (15). The detection of a $<\bar{1}10>$ aligned pair of microplasmas with a separation of approximately 10μ identified an electrically active copper platelet and the principal location of premature junction breakdown for the diodes prepared in this investigation. The localized points of emission coincide with the crystal surface intersection of a copper platelet's edges at low voltage (10-50v). Additional emission occurs at the subsurface corners of the platelet at higher voltages (50-100v). The diameter of the microplasmas increases from 0.5 to 1μ with an increase in the reverse bias.

The depletion layer that encounters a copper platelet appears to envelope the impurity aggregate, thus creating a band of very high field strength along the periphery of the platelet. The field reaches its greatest strength at the four corners (see Fig. 1) of the half hexagonal platelet. Assuming a platelet width of 10Å, the field intensity could be substantially above 10^6 v/cm. On the other hand, copper impurities in the depletion region which have formed a loosely distributed {110} array of secondary segregates following the collapse of a lattice void precipitation site do not emit visible light.

The structure of the segregated metal impurity located in the depletion region of a P-N junction greatly effects the electrical behavior of the junction. The log I *vs.* log V traces of several planar deep-diffused diodes are shown in Fig. 7 to illustrate the electrical effects of two structures of segregated copper. Curve "A" illustrates the reverse characteristics of a P-N junction containing a single active sessile fault copper platelet near the surface. The copper platelet, 8μ long and a small fraction of a micron wide, contributes to a soft I-V characteristic at low voltages and an ohmic slope at high voltages. Only the low voltage portion of the characteristic trace is shown in

Fig. 7. The voltage dependent field strength at the periphery of the platelet dominates the spreading resistance factor at low voltages, thus contributing the soft slope. However, at high voltages, the spreading resistance factor is dominant, thus the ohmic slope. Essentially all of the electrically active copper in the 12μ of silicon nearest the surface was confined to the first 3μ, the depth of the copper platelet. The diode's I-V trace gradually changed from the initial slope shown at "A" to that shown at "B" as the surface lattice was removed in graduated steps by chemical polishing. Curve "B" illustrates the electrical characteristic of a copper free P-N junction.

Curve "C" identifies the reverse characteristics of a P-N junction containing over one hundred separate loosely packed {110} arrays of secondary copper precipitates. (The distribution of the secondary precipitates following the collapse of a lattice void was shown in Fig. 6.) The parallel displacement between curves "B" and "C" indicates that reverse current in the loosely packed metal precipitates case is larger than the reverse current of a copper-free P-N junction by a constant factor of nearly 70.

The slope of curve "D" is characteristic of the deep diffused P-N junctions created in very low dislocation density material when foreign metallic impurities were absent. The difference in slope between curves "B" and "D" could be caused by thermally induced surface lattice voids acting as recombination centers. This assumption seems reasonable since dislocations have been shown to act as recombination centers for electrons and holes (16).

Conclusions

The foregoing discussion has established certain qualitative conclusions about the behavior of copper segregates at sessile faults and surface lattice voids produced in silicon by heat treatments at 1200°C.

1. Copper impurities acquire a half-hexagonal platelet configuration within the limits of small newly formed sessile faults.
2. Copper impurities which precipitate at surface lattice voids are redistributed to form loosely packed {110} arrays of secondary precipitates.
3. The platelet distribution of copper contributes to a soft electrical characteristic at low voltage, and an ohmic I-V slope at high voltages.
4. The loosely packed {110} distribution of copper contributes a constant multiplier to a P-N junction's leakage current on a log I *vs.* log V plot.

Acknowledgment

The author wishes to acknowledge Dr. R. N. Tucker for his stimulating suggestions during the development of the work summarized in this paper. The assistance of H. Koehler, R. Dyck, and G. Daughters on this work is greatly appreciated.

Manuscript received Feb. 9, 1965. This paper was presented at the Washington Meeting, Oct. 11-15, 1964.

Any discussion of this paper will appear in a Discussion Section to be published in the June 1966 JOURNAL.

REFERENCES

1. F. Van Der Maesen and J. A. Brenkman, *This Journal*, **102**, 229 (1955).
2. R. N. Hall and J. H. Racette, *J. Appl. Phys.*, **35**, 379 (1964).
3. W. C. Dash, *ibid.*, **27**, 1193 (1956).
4. G. H. Schwuttke, *This Journal*, **108**, 163 (1961).
5. D. J. D. Thomas, *Phys. Stat. Sol.*, **3**, 2261 (1963).
6. A. Goetzberger and W. Shockley, *J. Appl. Phys.*, **31**, 1821 (1960).
7. E. Sirtl and A. Adler, *Z. Metallkunde*, **52**, 529 (1961).
8. J. E. Lawrence and H. Koehler, *J. Sci. Instruments*, **42**, 270 (1965).
9. G. R. Booker and R. Stickler, To be published, *Phil. Mag.*
10. Colman Goldberg, *Phys. Rev.*, **88**, 920 (1952).
11. J. Melngailis and S. O'Hara, *J. Appl. Phys.*, **33**, 2596 (1962).
12. C. Elbaum, *Phil Mag.*, **5**, 669 (1960).
13. A. G. Tweet, *J. Appl. Phys.*, **30**, 2002 (1959).
14. A. G. Chynoweth and K. G. McKay, *ibid.*, **30**, 1811 (1959).
15. R. H. Haitz, A. Goetzberger, R. M. Scarlett, and W. Shockley, *ibid.*, **34**, 1581 (1963).
16. S. Roy Morrison, *Phys. Rev.*, **104**, 619 (1956).

Doped Anodic Oxide Films for Device Fabrication in Silicon

II. Diffusion Sources of Controlled Composition, and Diffusion Results

P. F. Schmidt,[1] T. W. O'Keeffe, J. Oroshnik, and A. E. Owen[2]

Westinghouse Research Laboratories, Pittsburgh, Pennsylvania

ABSTRACT

Control of sheet resistance and surface concentration subsequent to diffusion was achieved by controlling the doping level in the oxide. The ternary system diethylphosphate (DEP)-nitrite-tetrahydrofurfuryl alcohol was found suitable for producing doped oxide films that can be used for base or collector diffusions. The correlation between concentration of DEP in the solution and amount of phosphorus incorporated into the oxide was determined by tracer experiments with P-32 tagged DEP. The more dilute solutions were found to be sensitive to temperature and current density during anodization. Incorporation of alkali ions into the anodic oxide film can be avoided if the number of anodizations in the same batch of solution is limited. The out-diffusion of phosphorus from the doped oxide source can be suppressed by placing a non-doped anodic oxide over it. Reproducibility data for the diffusion results are given. The fabrication of simple device structures and the electrical performance of such devices are described.

Part I of this communication (1) dealt with the doping of anodic oxide films on silicon by incorporation of phosphorus. The emphasis in Part I was on achieving very heavy doping levels and on studying the properties of the oxide film itself. Part II deals with the utilization of these novel diffusion sources. The emphasis is therefore on (*a*) the reproducibility of the doping level in the oxide at those doping levels suitable for emitter, base, and collector diffusions, (*b*) on the reproducibility of the diffusion results,

[1] Present address: Bell Telephone Laboratories, Inc., Allentown, Pennsylvania.

[2] Present address: Dept. of Glass Technology, University of Sheffield, Sheffield, England.

and (c) on the actual fabrication of simple device structures.

Choice of Anodizing Solution

The use of a 15 v/o solution of pyrophosphoric acid in tetrahydrofurfuryl alcohol was described in the previous communication (1). This solution yields a very heavily doped oxide and is being used for emitter diffusions. When stored under complete exclusion of moisture, it appears to be stable over periods of months. On the other hand, its viscosity and hygroscopicity pose handling problems, and it is not so well suited for the preparation of anodizing solutions for base or collector diffusions where a greater degree of control is required.

An anodizing solution useful for these purposes was found in the ternary system diethylphosphate-alkali nitrite-tetrahydrofurfuryl alcohol. The concentration of nitrite is kept fixed at 1.50g NO_2^-/100 ml tetrahydrofurfuryl alcohol (THF), while varying the ratio of diethylphosphate (DEP) to nitrite in decade steps. The ratio of DEP to nitrite determines the amount of phosphate incorporated into the oxide, while the nitrite at the same time serves to maintain the conductivity of the solution at a more or less constant value and contributes only oxygen to the electrode reaction. The THF does not seem to participate in the anodic electrode reaction to an appreciable extent in the presence of the DEP and nitrite.

Initially, sodium nitrite was used until it was found that under certain conditions sodium ions are incorporated into the oxide film, and are diffused subsequently into the silicon, resulting in uncontrolled N-type doping. Substitution of potassium nitrite eliminated this trouble. Potassium can also be incorporated into the oxide film (compare below under tracer run with K-42), but apparently to a much lesser extent than sodium. The use of ammonium nitrite is not feasible because ammonium nitrite is not stable chemically. Apart from this consideration, it is doubtful that it would be useful for the anodization process; the electronic leakage current during the formation of anodic oxide films on silicon in solutions of ammonium nitrate is intolerably large and results in inferior oxide quality. Perhaps hydrogen is getting into the oxide during formation, as has been claimed in the case of beryllium (2).

Nitrite is used rather than nitrate because of its good solubility in organic solvents, and because it also gives lower leakage currents than nitrate. No chemical instability of the nitrite-DEP-THF solutions has been noticed. The electrical conductivity (approximately 1 k-ohm-cm) of these solutions hermetically sealed into a conductivity cell remained unchanged for months.

Pure DEP and distilled THF was obtained from Distillation Products Industries, Rochester, New York. Analytical grade sodium or potassium nitrite by Fisher was used without further purification. Anodizations were in general carried out at 6 ma/cm^2 to 150v and the leakage current was then permitted to decay at constant voltage for ½ hr, after which time further changes in leakage current become very small. At constant voltage a 10-min decay proved sufficient to reach constancy of the count from wafers anodized in radiotracer solution; increase in oxide thickness[3] after 10 min at constant voltage is apparently negligible.

In order to investigate the correlation between concentration of DEP in the solution and concentration of phosphorus in the oxide, a tracer run was carried out in which the DEP was tagged with P-32.

Relationship between Ratio DEP/NO_2^- in anodizing Solution, and Concentration of Phosphorus in Oxide

P-32 tagged DEP with a specific activity of 10.4 mc/ml DEP was obtained from Nuclear Chicago Co. The DEP was diluted with a solution of 1.80g $NaNO_2$ in 100 ml THF in a 1:1 ratio by volume. This master solution was then used to prepare more dilute solutions in which the DEP/NO_2^- ratio was varied in decade steps. The volume of each batch of radioactive solution was about 7 cm^3, so that stirring of the solutions would have been very difficult to accomplish. Anodizations were therefore carried out in unstirred solutions but under rigorous exclusion of moisture.

The solutions most concentrated with respect to DEP showed instability with time; the amount of phosphorus incorporated kept decreasing with a time constant of days. The more dilute solutions did not show this behavior. No analogous behavior is observed with nonradioactive, concentrated DEP solutions, as shown by the fact that diffusion results obtained on Si wafers anodized in these solutions did not depend on the age of the solution. The most plausible explanation is that the radioactivity of the sample caused radiolysis of the solution, perhaps accompanied by the formation of water, and that the chemical change caused by the radiolysis is responsible for the decrease in the amount of phosphorus that is incorporated into the oxide by anodization.

Anodizations in the radioactive solutions of different strength were carried out in rapid succession on the same day; thus the results obtained are not falsified by the above mentioned instability of the more concentrated solutions. Chemically polished P-type silicon bars of resistivity 2 ohm-cm were used. The bars were approximately 6 x 0.5 x 0.1 cm in size, and their large surfaces were <110>, <100>, or <121> oriented.

After anodization the samples were thoroughly rinsed with methanol and with water to remove adherent liquid and after drying were inserted in tight fitting plexiglas holders and placed in a lead shield underneath the window of a Geiger-Muller counter. The holders exposed a 1 cm length of the top surface of the samples. The region located near the meniscus of the solution during anodization was shielded by a lid in order to ensure uniformity of the sample surface to be counted. The procedure for measuring the P-32 concentration in the oxide or in the silicon has been described in Part I of this paper (1).

Counts from radioactive oxide films are sensitive to the surface roughness factor of the sample. For this reason the same wafers were used again[4] for subsequent anodizations, with the same side up during counting. Since anodization is known to result in smoothing of the surface, some decrease in surface area during a series of runs was unavoidable. However, the surface roughness factor of chemically polished silicon wafers is generally accepted to be 1.3, and can therefore not vary much, in view of the fact that a chemically polished surface shows no asperities but only long-range undulation.

[4] After stripping of the oxide film in HF.

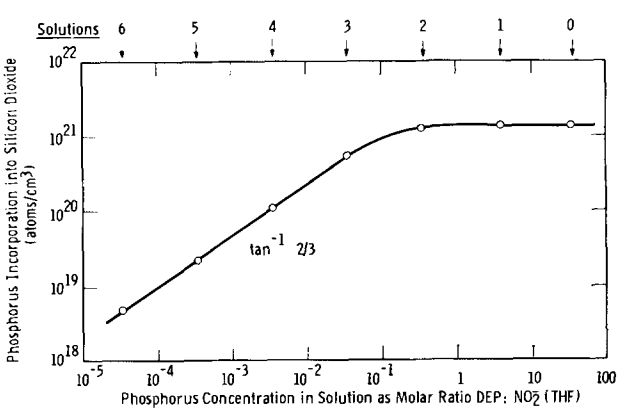

Fig. 1. Relation between phosphorus incorporation and molar ratio DEP:NO_2^- in the solution. Solution temperature, 25°C; current density, 6 ma/cm^2.

[3] The oxide thickness after anodization to 250v (at constant voltage for 30 min) in the KNO_2-THF solution was determined both by ellipsometry and from the reflectance minimum as a function of wavelength in the ultraviolet. The thickness/voltage increment was found to be 5.6 Å/v. The refractive index was found to be 1.48 at the mercury green line.

Figure 1 shows the relationship between the DEP/NO_2^- ratio in the anodizing solution, and the resulting concentration of phosphorus in the oxide. The NO_2^- concentration in all solutions was 1.5g/100 in THF. The amount of phosphorus incorporated saturates quite sharply at a molar ratio of 0.3. This is, however, not the upper limit to which phosphorus can be incorporated. Concentrations of 4.1 x 10^{21} atoms P/cm^3 SiO_2 have been obtained by anodization in solutions of pyrophosphoric acid in THF, and even higher concentrations can be achieved by anodization in the pure acid. The reason why the amount of phosphorus incorporable from DEP solution saturates at a molar DEP:NO_2-ratio of 0.3 may be that either the dissociation of the DEP molecule or its adsorption to the electrode surface reaches a limiting value at this concentration. Formation of water at the anode due to oxidation of the ethyl radical is another possibility.

At lower DEP/NO_2^- ratios there is a simple 2/3 power relationship; this linear portion (on a log-log plot) probably extends to even lower DEP/NO_2^- ratios, but these have not been investigated. The simplest explanation for this 2/3 slope would be to assume that the concentration of DEP at the oxide surface is related to the bulk concentration of DEP in the solution by a 2/3 power law. Nitrite and phosphate ions contribute to oxide growth in a proportion determined by their concentration at the oxide surface and by the given electrode potential.

No indication of incorporation of the ethyl radical into the oxide has been observed; it is known from other experiments with glycerine as the solvent that incorporation of organic matter into the oxide can occur and will result in severe degradation of the oxide during the heat treatment necessary for diffusion. No degradation of oxides grown in the DEP-NO_2^--THF solution has been observed subsequent to diffusion. Conclusive proof, one way or the other, could be obtained by using C-14 tagged DEP, but this was not available. If incorporation of the ethyl radical does not occur, then it must be postulated that the DEP molecule dissociates at the oxide surface during the electrode reaction. However, the composition of the phosphorus-oxygen complex incorporated into the oxide by the electrode reaction (P_xO_y) is not known.

Figure 2 shows the average sheet conductivity after diffusion. The actual points of measurement are shown. The spread of the data would be determined by the inaccuracies of measuring sheet resistances and junction depths (compare below). Figure 3 shows the surface concentration calculated from the data in Fig. 2 and from the junction depths shown in Fig. 4. It can be seen that the electrical data, obtained independently from the tracer experiments, parallel the tracer information quite closely. It should be noted that the surface concentrations shown in Fig. 3 refer only to

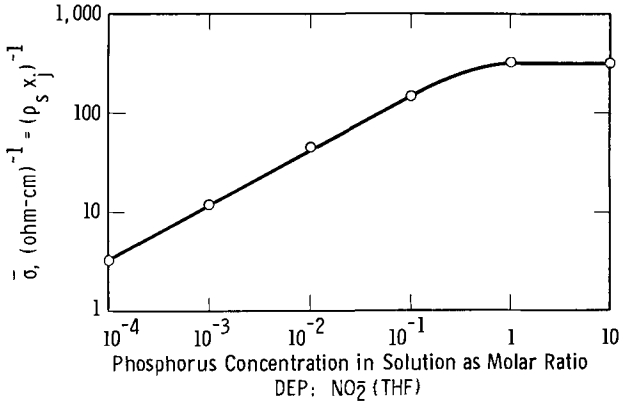

Fig. 2. Relation between average sheet conductivity after diffusion and molar ratio DEP:NO_2^- in the solution. Material, 5 ohm-cm p-Si; anodization temperature, *t*, 25°C; diffusion temperature, *T*, 1200°C; diffusion time, τ, 1 hr.

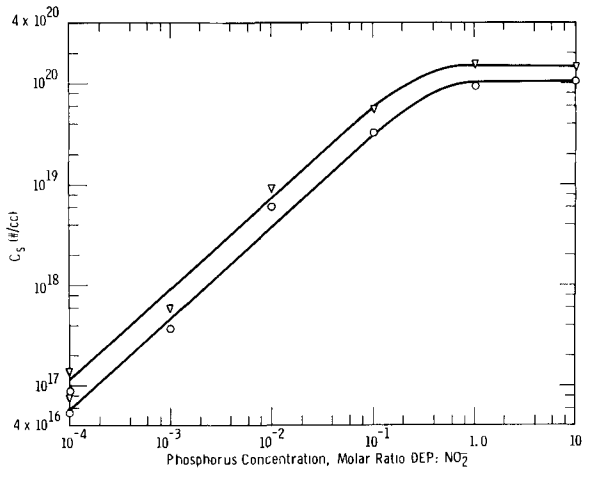

Fig. 3. Surface concentrations after 1 hr diffusion at 1200°C *vs.* molar ratio DEP:NO_2^- in the solution. ▽, Erfc distribution; ○, Gaussian distribution; material, 5 ohm-cm p-Si; anodization temperature, *t*, 25°C; diffusion temperature, *T*, 1200°C; diffusion time, τ, 1 hr.

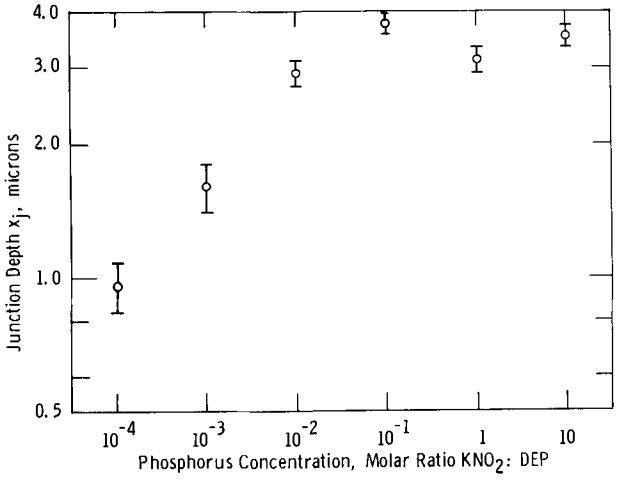

Fig. 4. Junction depths after 1 hr diffusion at 1200°C *vs.* molar ratio DEP:NO_2^- in the solution. Material, 5 ohm-cm p-Si; anodization temperature, *t*, 25°C; diffusion temperature, *T*, 1200°C; diffusion time, τ, 1 hr.

electrically active phosphorus and do not allow for the fact that the diffusion of phosphorus at very high concentrations does not follow a complementary error function (erfc) distribution (3). The nontracer data of Fig. 2-4 were obtained on <111> oriented Si disks, 2 ohm-cm resistivity, so that any effects due to formation of SiP precipitates were minimized (4).

Temperature and Current Density Effects on Amount of Phosphorus Incorporated into Oxide

Table I, top half, shows the effect of the temperature of anodization on the amount of phosphorus incorporated into the oxide at a constant current density of 5.6 ma/cm^2.

It can be seen that the temperature sensitivity of the solution increases with its dilution. The existence of this effect indicates that the amount of DEP adsorbed to the oxide surface decreases with increasing temperature and is approximately in equilibrium with the concentration of the DEP in the bulk of the solution at the current densities here employed.

Table I, bottom half, shows the effect of current density on amount of phosphorus incorporated at two different temperatures, and in solutions of three different concentrations of DEP. It can be seen that the amount incorporated increases consistently with in-

Table I. Effect of current density and temperature on amount of phosphorus incorporated

Solution No.	25°C	0°C	
Temperature effect at constant current density of 5.6 ma/cm²			
1	4.2×10^{21} cm^{-3}	4.6×10^{21} cm^{-3}	10% increase
4	3.0×10^{20} cm^{-3}	4.6×10^{20} cm^{-3}	53% increase

Current density effect at different temperatures

Solution No.	Temp, °C	4.7 ma/cm²	5.6 ma/cm²	7.1 ma/cm²	12.0 ma/cm²
1	0	4.2×10^{21} cm^{-3}	4.6×10^{21} cm^{-3}		
4	0		4.6×10^{20} cm^{-3}	5.0×10^{20} cm^{-3}	
5	25		5.7×10^{19} cm^{-3}		8.4×10^{19} cm^{-3}

creasing current density. In view of the fact that the solutions were of relatively high resistivity (in the 1 k-ohm-cm range) and that it was not possible to stir them mechanically, it is clear that the silicon anode was at a higher temperature than the external water bath, especially at the higher current densities. Since the effects of current density and temperature are in opposite directions, the current density effect is probably more pronounced than indicated by Table I.

Table II provides essentially the same information on the temperature effect, but by way of the electrical data after diffusion from oxides anodized at the different temperatures in nontracer solutions. Also shown in Table II are data for the pyrophosphoric acid/THF system. As expected for a solution very concentrated with respect to phosphate ions, the temperature effect is small. As reported previously (1), no current density effect could be observed in the $H_4P_2O_7$-solution in the range 3-5 ma/cm². The $\overline{C_s}$ values in Table II were taken intermediate between the values calculated from either a Gaussian or an erfc distribution.

The above discussion shows that anodization cells must be thermostated and that the current density must be carefully controlled if good reproducibility is to be obtained; the more dilute the solution with respect to DEP, the more stringent this requirement. It is also advisable to stir the solutions in order to improve heat exchange between the interior of the anodization vessel and the thermostating solution; Teflon-coated magnetic stirrers have been found very satisfactory for this purpose.

Surface Roughness Factor and Reproducibility of Doping Level in Oxide

The oxide diffusion source follows the surface of the sample in every detail. There is less of a smoothing-out effect than occurs by penetrating a small distance into the silicon when predepositing phosphorus from the gas phase. It is therefore necessary to control the surface roughness of the silicon samples rather carefully. Confirmation of this hypothesis was obtained when counting opposite sides of the same Si bar after anodization in the tracer solution. While the reproducibility of the amount of phosphorus incorporated into the oxide was in general better than 1%, the two surfaces of the sample usually had distinctly different counts, each fully reproducible.

Table III. Tracer data on reproducibility of phosphorus incorporation

Anodization carried out in solution of $H_4P_2O_7$ in THF

Sample No.	Phosphorus concentration in oxide (150v film)
1	3.1×10^{21} cm^{-3}
2	3.2×10^{21} cm^{-3}
3	3.1×10^{21} cm^{-3}
4	3.1×10^{21} cm^{-3}

Note: Tracer data are sensitive to surface roughness of individual wafers.

Table III shows the kind of reproducibility obtained by successive anodizations in the same batch of pyrophosphoric acid/THF solution. The same kind of data also were obtained with the most concentrated DEP/NO_2^--THF solutions. No attempt was, however, made to establish reproducibility data by tracer experiments with the more dilute solutions because of the temperature effect and the practical impossibility of stirring these solutions. Reproducibility data with the more dilute solutions were obtained therefore from the diffusion results with doped oxides grown in nontracer solutions (thermostated and stirred). Figure 5 shows these results for the 10^{-3}:1 DEP/NO_2^-/THF solution. These data represent, so to say, the "worst possible cases," since 16 consecutive anodizations were carried out in the same batch of solution, the series spanning a period of 36 days. Normally, solutions would be discarded after a much smaller number of anodizations. In addition, the statistical error inherent in the diffusion procedure enters into the results. In view of these additional factors the reproducibility of the average sheet conductivity, calculated on the assumption of an error of $\pm$ 0.2μ in junction depth, and $\pm$ 10% in sheet resistance measurement is considered satisfactory at this level (about 26 ohms/square) of sheet resistance.

Loss of Phosphorus from Doped Oxide During Diffusion

Unprotected films.—During the earlier phases of this work nondoped anodic oxide films of sufficiently good quality to prevent out-diffusion of phosphorus from the doped oxide underneath were not available. For this reason the doped oxide was not covered by a nondoped film, and the tracer runs were carried out in sealed quartz tubes. Considerable loss of phos-

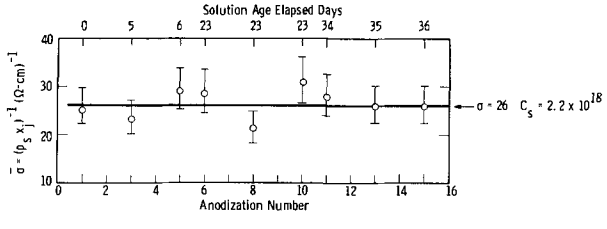

Fig. 5. Average sheet conductivity after diffusion for 2 hr at 1200°C *vs.* the number of anodizations in the same batch of 10^{-3}:1, DEP:NO_2^- solution. Material, 2 ohm-cm p-Si; phosphorus concentration: DEP: $NO_2^- = 10^{-3}$; anodization temperature, t = 25°C; diffusion temperature, T, 1200°C; diffusion time, τ, 2 hr.

Table II. Effect of temperature on amount of phosphorus incorporated from electrical data

Anodizing solution \ Anodization temp.	25°C X_j, microns	25°C s, ohms/sq	25°C (ohm-cm)$^{-1}$	25°C C_s, atoms cm^{-3}	0°C X_j, microns	0°C s, ohms/sq	0°C (ohm-cm)$^{-1}$	0°C C_s, atoms cm^{-3}
Pyrophosphoric acid in THF	7.22	5.5	251.—	8.0×10^{19}	8.02	4.7	265	8.6×10^{19}
DEP:NO_2^- = 10^{-4} in THF	3.48	447.—	6.4	1.6×10^{17}	4.41	111.—	20.4	1.3×10^{18}

P-type Si, 2 ohm-cm ($C_b = 7 \times 10^{15}$ atoms cm^{-3}). Anodization voltage doped oxide: 150v, covered by nondoped oxide anodized to 350v. Diffused for 2 hr at 1200°C in flowing nitrogen. Solution 10^{-4}:1, DEP:NO_2^-.

Table IV. Loss of phosphorus from unprotected doped oxide films as a function of time at 1175°C in sealed quartz tube with argon backfill

Sample number	Time at 1175°C, min	P in oxide source, %	P in silicon, %	P on walls of tube, %
1	5	47	26	27
2	10	36	34	30
3	15	29	41	30
4	20	30	34	36
5	45	13	40	47
6	60	18	37	45

phorus to the surroundings during the first few minutes at high temperature was observed, as well as some back-indiffusion of phosphorus into the oxide during longer diffusion times. Due to the density of quartz the diffusion of phosphorus into the quartz walls is slow, so that the surface concentration of phosphorus at the surface of the wall remains high. When the anodic oxide source becomes depleted due to diffusion into the silicon, phosphorus from the quartz walls diffuses back into the anodic oxide and from there into the silicon. Table IV gives some semiquantitative data. It has been established that the losses of phosphorus to the surroundings are even greater in an open flow system.

It was also observed that heavily phosphorus-doped anodic films disintegrated when heated to high temperatures in high vacuum. A background pressure of 0.025 ± 0.005 Torr of oxygen was required to stabilize an anodic oxide film with about 10 w/o (weight per cent) P_2O_5 for 2 hr at 1170°C under continuous pumping. Anodic oxide films grown in a nitrite/THF solution (no phosphorus) showed no deterioration at oxygen pressures as low as 0.01 Torr under the same conditions. The background pressure of oxygen required for stabilization is presumably a function of the phosphorus concentration of the film.

Protected films.—All of the diffusion results presented here (with the exception of Table IV) were obtained from silicon samples on which the doped oxide had been anodized to 150v, and a nondoped oxide grown to a total of 250v in a solution of 1.5g nitrite in 100 ml THF. The nondoped oxide grows on top of the doped oxide because anodic oxide growth on silicon, in all electrolytes tested so far, occurs by cation migration (1). It was found that the quality and thickness of the oxide grown in the nitrite-THF solution was sufficient to practically eliminate out-diffusion of phosphorus from the sample for about ½ hr at 1200°C in the case of very heavily doped oxide films and for correspondingly longer times in the case of more weakly doped oxide films. The diffusivity of phosphorus in SiO_2 is strongly concentration dependent (5). Since heavily doped oxide films are used for shallow emitter diffusions and do not require more than 20-30 min at 1200°C, these anodic oxide covers can be used for emitter, base, and collector diffusions. It is therefore possible to cover anodic oxide diffusion sources on silicon with a nondoped anodic oxide film, and to diffuse the sample in an open tube without contaminating the furnace tube or unprotected regions of the surface. This is an important aspect to be considered when fabrication of complementary device structures (6) by simultaneous diffusion of boron and phosphorus is undertaken. It also should enable considerable simplification of the diffusion apparatus. Table V shows the losses of phosphorus from the doped oxide during anodization to a higher voltage in the nitrite/THF solution, as well as the subsequent losses from the Si-SiO_2 system during subsequent diffusion at 1200°C. It can be seen that the losses in either case are quite small. It is not certain that there is any loss of that phosphorus which is incorporated into the doped oxide, when the sample is anodized to a higher voltage in the nitrite/THF solution. It is known that phosphate is tenaciously adsorbed to the oxide surface subsequent to anodization in phosphate solution

Table V. Tracer data on loss of phosphorus from doped oxide films during subsequent anodization to deposit protecting oxide, and during diffusion for 2 hr at 1200°C in flowing nitrogen

Counts/sec from silicon bars anodized in DEP^{32}-$NaNO_2$-THF solution, normalized to standard date: (a) after anodization to 150v in tracer solution; (b) after coating with additional SiO_2 (anodic or pyrolytic); (c) after diffusion for 2 hr at 1200°C in flowing N_2, flow rate 1500 cc/min, 1 in. Φ tube.

Coating method	Sample	Solution No.	Anodization temp, °C	Current density	Counts after depositing a) Doped oxide	b) Undoped SiO_2 Anodic	Pyrolytic	c) Counts after diffusion
1	C*	4	0	7.1	195	185		178
1	V	4	0	5.5	179	172		170
2	Q	2**	25	5.8	197	195		185
2	I	2**	25	6.2	202	193		188
3	O	4	0	5.8	173	171	164	156
4	K	4	0	5.9	176	—	No data	180
1	Y***	$H_4P_2O_7$	25	6.0	No data	3390		2930

* Sample C was diffused for 3 hr at 1200°C.

** These anodizations were carried out at a time when solution No. 2 had already deteriorated by radiolysis and the amount of phosphorus incorporated had dropped drastically.

*** Sample Y has an emitter type doped oxide, which normally would be diffused only for 20-30 min. The prediffusion phosphorus concentration in the oxides of samples C through K was of the order 1.5×10^{20} atoms P/cm³ SiO_2. The prediffusion concentration of phosphorus in the oxide of sample Y was 3.2×10^{21} atoms P/cm³ SiO_2.

Legend for the different coating methods:
1. Additional nondoped anodic oxide film equivalent to 150v (900Å).
2. Additional nondoped anodic oxide film equivalent to 200v (1200Å).
3. 5000Å pyrolytic SiO_2 on top of nondoped oxide (type 1 coating).
4. 5000Å pyrolytic SiO_2 directly on top of doped anodic oxide.

(1), and cannot be removed completely by rinsing with various solvents. It may be this chemisorbed phosphorus which shows up as a "loss" during anodization to a higher voltage in the nitrite/THF solution. Also shown in Table V is sample Y, anodized in $H_4P_2{}^{32}O_7$ in THF solution (*i.e.*, an "emitter anodization"). It can be seen that this sample suffered an 11% loss during the 2 hr diffusion.

An unexpected effect, recorded in Table VI, was noticed when the effectiveness of oxide films of different thicknesses and of different methods of deposition, in suppressing the out-diffusion of phosphorus during heat treatment, was investigated. The ratios shown in Table VI were obtained by counting the oxide covered Si wafers in situ, the stripping the oxide in HF, and recounting the wafers in situ. The HF solutions also were evaporated to dryness and measured as an additional check. It can be seen that thicker oxide films cause a greater percentage of the original total phosphorus present in the oxide source to diffuse into the silicon. The density of the oxide film may also be involved. Since in every case not more than about 5% of the phosphorus was lost to the surroundings during heat treatment, there is no obvious explanation for this effect.

Contamination of Anodic Oxide with Sodium or Potassium Ions. Tracer Run with K-42

The early work with the DEP-nitrite-THF system was done with sodium nitrite. It had been established

Table VI. Effect of additional nondoped oxide on percentage of phosphorus driven from the oxide into the silicon by diffusion for 2 hr at 1200°C

Kind and thickness of oxide coating	Ratio $\frac{\text{Phosphorus in Si}}{\text{Phosphorus in Si} + SiO_2}$, %
1. 150v doped oxide + additional 100v of undoped anodic oxide	42
2. 150v doped oxide + additional 200v of undoped anodic oxide	65
3. 150v doped oxide + additional 150v undoped anodic oxide, followed by 5000Å of pyrolytic oxide (deposition temperature 750°C)	68
4. 150v doped oxide + additional 5000Å of pyrolytic oxide (deposition temperature 750°C)	75

that 5 ohm-cm p-type silicon, anodized in a sodium nitrite/THF solution and then diffused at 1200°C gave no indication of the presence of an n-type dopant (sodium ions) in the anodic oxide film. During the course of the work unexplained n-type doping to a depth of a couple of microns was observed on silicon surfaces protected with this type of anodic oxide, especially if the oxide had been grown at 0°C instead of at room temperature. Substitution of potassium nitrite for sodium nitrite solved the difficulty from the point of view of device fabrication. It was felt desirable to investigate whether potassium is at all incorporated into the anodic oxide film, and what precautions have to be observed to prevent incorporation. A tracer run with K-42 was therefore carried out.

Since $K^{42}NO_2$ is not available commercially, and its synthesis would have posed considerable difficulties, a small quantity of $K^{42}NO_3$ was obtained from Oak Ridge National Laboratories, and was diluted 10:1 with nonradioactive KNO_2. The specific activity after dilution was 200 mc/g potassium. While in general, it is not desirable to have nitrate ions present during anodization, because of the increase in electronic leakage current, it was expected that nitrate ions could be tolerated at the 10:1 dilution. Anodizations in the tracer solution (0.22g "KNO_2"/10 ml THF) showed no anomalous behavior. The half-life of K-42 is only 12.5 hr. The experiments therefore had to be carried out essentially without control runs, and the results should be considered only as qualitative.

It was found that the anodic SiO_2 film formed in the tracer solution showed an appreciable activity but that 2/3 of this activity could be removed by anodization to a slightly higher voltage in nontracer KNO_2/THF solution. It is not known whether the amount of K-42 that could be removed was only chemisorbed to the surface of the oxide or some of the potassium ions were sufficiently mobile to be extracted by the anodic bias. The incorporation of protons into anodic oxide films grown in aqueous solutions is by now well documented (7). A model has been proposed (8) according to which protons diffuse into the oxide film when the anodic field strength opposing such diffusion, is lowered below a certain critical value. Due to the relatively large size of the potassium ion this explanation for the removal of 2/3 of the radioactive potassium appears unlikely but cannot be disregarded altogether. In any case, only 1/3 of the potassium initially present was incorporated into the anodic oxide in immobile form. This amount corresponded to 1.06×10^{-3} w/o K_2O.

A sample treated in this way was diffused at 1200°C for 2 hr in a sealed quartz tube with argon backfill. The amount of K-42 on the sample was then found to have decreased appreciably. It is not known whether this decrease is due to out-diffusion only, or whether isotopic exchange with nonradioactive potassium on the walls of the quartz tube may also be involved. 80% of the K-42 which had remained on the sample had remained in the oxide film, since it could be removed from the sample by a dip in concentrated HF. The remaining 20% had diffused into the silicon, confirming the suspected n-type contamination by alkali ions. The activity on the Si sample was too low to attempt establishment of a diffusion profile.

Next experiments were carried out to measure the effects of current density and temperature of the anodizing solution on the amount of potassium incorporated into the oxide. While such effects may exist, they were completely overshadowed by another effect; the amount of potassium incorporated into the oxide increased with each additional anodization in the same batch of solution, and eventually reached a value about 100 times larger than that observed during the first anodization. It thus appears that the passage of current through the solution causes a chemical change in composition which favors the incorporation of alkali ions. Since the volume of the tracer solution was very small, the effect would be very pronounced.

Enough DEP was then added to the K-42 tracer solution to arrive at the over-all composition of solution No. 1 (see Fig. 1). Anodization in this solution seemed to indicate that the amount of potassium incorporated into the oxide had decreased due to the presence of DEP in the solution; the data on this particular point are questionable, due to the statistical error involved in counting the activity. The more surprising result, however, was that after diffusion at 1200°C all of the potassium present on the sample had been transferred into the silicon. No activity could be detected when the anodic oxide, after diffusion, was dissolved in HF, the solution evaporated to dryness and the residue counted.

The above observations explain why n-type doping by alkali ions had been observed only in sporadic fashion when the sodium nitrite/THF solution was used; the number of anodizations in one and the same batch of solution (for a given volume of solution) is of great importance.

Device Fabrication

Phosphorus-diffused diodes.—Many diodes were fabricated in a preliminary attempt to show the feasibility of producing good junction characteristics. Sharp reverse breakdowns in the range of 60-80v on 2 ohm-cm p-type substrate were typical. The breakdown voltage is less than expected from the resistivity of the substrate. This is probably an impurity effect since the diodes had not been gettered (9).

Phosphorus and boron.—The availability of localized, phosphorus-doped diffusion sources opens the way to the simultaneous, side by side, diffusion of n-type and p-type dopants. Since boron and phosphorus have very nearly equal diffusivities in silicon and because the diffusion of boron into silicon is masked by SiO_2, it is possible to obtain nearly identical diffusion profiles for n-type and p-type dopants in this manner, and to fabricate complementary integrated devices on the same chip of silicon. Figure 6 shows a complementary pnp-npn pair [Fig. 3 of reference (6)] in which the n-type diffusions were carried out from phosphorus-doped anodic oxide films. The diffusion data, obtained on simultaneously diffused control chips, are shown in Table VII.

Figure 7 shows the collector characteristics of an npn double diffused planar transistor. The n-type silicon substrate of 1 ohm-cm resistivity served as collector, the base was produced by conventional diffusion of boron from the gas phase, and the emitter was diffused from a phosphorus-doped anodic oxide. Figure 8 shows the performance of a pnp transistor in which the collector was produced by conventional diffusion of boron into 1 ohm-cm n-type silicon. The base region was produced by diffusion of phosphorus from a doped oxide, and the emitter by conventional boron diffusion. It must be stressed that these devices have not yet been optimized as to their base widths, since the goal was merely to show feasibility; nor has any gettering procedure been applied. The general

Fig. 6. Complementary npn-pnp transistor pair produced by phosphorus diffusion from doped anodic oxide films.

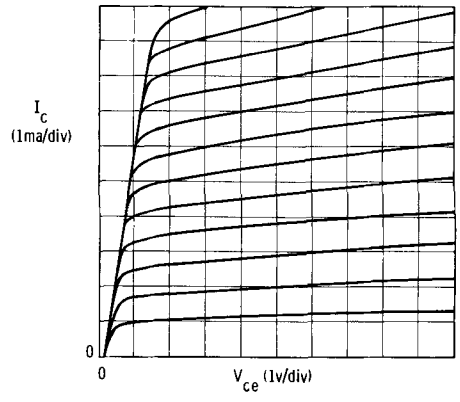

Fig. 7. Collector characteristics of an npn double diffused planar transistor produced by electrochemical techniques. I_b = 0.01 ma/step; h_{fe} = 85.

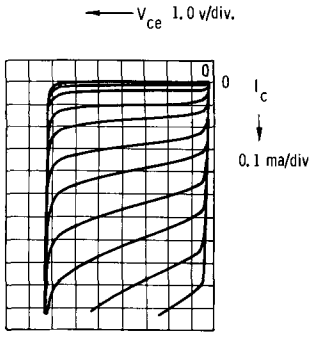

Fig. 8. PNP common emitter transistor characteristics: i_b = 0.01 ma/step; h_{fe} = 12.

method of fabricating complementary npn-pnp transistor structures on the same silicon substrate is described elsewhere (6).

Phosphorus and gallium or aluminum.—If a p-type dopant is used which penetrates SiO_2 masks easily, and which diffuses faster in silicon than does phosphorus, then the fabrication of npn mesa type transistors, or of 4-layer npnp power switches, by a single heat treatment is possible. Gallium and aluminum satisfy this requirement.

Phosphorus-gallium simultaneous double diffusions have been carried out using sealed quartz tubes with argon backfill. The silicon samples (30 ohm-cm n-type) were anodized to either 100 or 150v in the pyrophosphoric acid-THF solution, but were not given a protective oxide coating. During diffusion the silicon was kept at 1175°C, the metallic Ga source at 900°C by means of a two-zone furnace. All junctions produced were perfectly planar. Table VIII lists the values obtained in separate experiments for surface concentrations and diffusion constants after gallium diffusions from the gas phase and phosphorus diffusion from the anodic oxide source under the specified conditions. The diffusion constant for Ga was found experimentally to lie between the values given by Fuller and Ditzenberger (11) and by Kurtz and Gravel (12). The values found for phosphorus under the given special conditions will be discussed in more detail in Part III of this paper (10). Table VIII also shows the junction depths predicted by using the values obtained from the single diffusion experiments, while the last column gives the experimentally measured junction depths of the npn structures produced. There is apparently no large interaction between the two diffusants for these experimental conditions.

Table IX is analogous to Table VIII for an aluminum-phosphorus double diffusion. The whole system (Si + anodic oxide source + metallic aluminum sources) was held at 1175°C in this case. The silicon samples had been anodized only to 60v in the pyrophosphoric acid-THF solution. The measured value of D for aluminum from the single diffusions agreed with that of Fuller and Ditzenberg. Again the agreement between the experimental and predicted junction depths is good, somewhat better than 10% in this case.

A TRINISTOR was also fabricated from one of the phosphorus-aluminum double diffused structures, with a breakover voltage of 800v at room temperature.

Table VII. Diffusion profile data on complementary pnp-npn transistor pair of Fig. 6

Surface concentrations, concentrations at junctions, and junction depths

PNP Transistor	C_s Emitter	1.4×10^{20} atoms cm^{-3}	C_s Base	8.4×10^{18} atoms cm^{-3}	C_s Collector	2.8×10^{17} atoms cm^{-3}
	C_j Emitter Base	3.5×10^{18} atoms cm^{-3}	C_j Base Collector	2.1×10^{17} atoms cm^{-3}	C_j Collector Substrate	5.5×10^{15} atoms cm^{-3}
	ρ_s Emitter	17.7 ohms/square	ρ_s Base	57 ohms/square	ρ_s Collector	289.5 ohms/square
	x_j Emitter	1.2μ	x_j Base	2.4μ	x_j Collector	9.9μ
NPN Transistor	C_s Emitter	2.3×10^{20} atoms cm^{-3}	C_s Base	5.7×10^{18} atoms cm^{-3}	C_s Collector	5.5×10^{15} atoms cm^{-3}
	C_j Emitter Base	4.3×10^{18} atoms cm^{-3}	C_j Base Collector	5.5×10^{15} atoms cm^{-3}		
	ρ_s Emitter	19.7 ohms/square	ρ_s Base	163.0 ohms/square		
	x_j Emitter	0.7μ	x_j Base	3.2μ		

Geometrical data

Emitter areas	2.2×2.2 mils^2	Base areas	5.0×6.4 mils^2	Collector area pnp	11.0×11.0 mils^2
Distance from center pnp to center npn areas	17.6 mils			Collector area npn	Substrate

Note: All concentrations have been calculated on the assumption of a Gaussian diffusion profile. The Gaussian is a good approximation both for diffusion from the phosphorus doped oxide, and for the boron under the given experimental conditions (predep. + drive-in).

Table VIII. Simultaneous diffusion of phosphorus and gallium into Si

Dopant	Single diffusion Profile	Co cm^{-3}	D × 10^{12} cm^2/sec	Time (hr)	Substrate, ohm cm-type	Predicted double diffusion $X_j(\mu)$ E/B	$X_j(\mu)$ B/C	Sample	Expt. results $X_j(\mu)$ E/B	$X_j(\mu)$ B/C
P	Gaussian	5×10^{19}	0.75							
Ga	erfc	5×10^{18}	1.25	1-1/2	30-n	4.0	4.8	60*	4.4	4.8
Fuller & Ditzenberger			2.8					61*	4.6	5.2
Kurtz & Gravel			1.0	5-1/6	30-n	4.2	8.9	62*	6.5	9.6

* Samples No. 60 and 61: 100v doped oxide; sample No. 62: 150v doped oxide.

Table IX. Simultaneous diffusion of phosphorus and aluminum into Si

Dopant	Single diffusion Profile	Co cm^{-3}	D × 10^{12} cm^2/sec	Time (hr)	Predicted double diffusion Substrate, ohm cm-type	$X_j(\mu)$ E/B	$X_i(\mu)$ B/C	Sample	Expt. results $X_j(\mu)$ E/B	$X_j(\mu)$ B/C
P	Gaussian	5 × 10^{19}	0.75	21	100-n	14	37	1	13	38
Al	erfc	3 × 10^{18}		21	100-n			2	13	38
Fuller and Ditzenberger			10	21	100-n			3	13	39
				31	20-n	17	38	4	16	41

Conclusions

It has been shown that electrochemical techniques can be employed for the fabrication of phosphorus-doped diffusion sources on silicon. Sufficient control can be exercised over the amount of phosphorus incorporated into the diffusion source, and its out-diffusion into the surroundings practically eliminated by means of a protective nondoped oxide film, to make the technique useful for all phases of device fabrication (emitter, base, and collector diffusions). Diodes, transistors, and some trinistors fabricated in this way had acceptable characteristics.

Acknowledgments

This work was jointly supported by the Electronics Development Laboratory, Aeronautical Systems Division, Wright-Patterson Air Force Base, Dayton, Ohio, and by Westinghouse Electric Corporation. Thanks are due to Professor J. O'M. Bockris, of the University of Pennsylvania, for a helpful discussion, and to Mr. A. Knopp, of the Westinghouse Semiconductor Division, Youngwood, for the aluminum diffusions. The untiring help of N. Roney and J. Moyles with the experiments is gratefully acknowledged.

Note added to revise manuscript: The authors are indebted to the reviewer for drawing their attention to ref. (13), which deals with the diffusion of impurities from doped SiO_2 films prepared by co-sputtering into GaAs.

Manuscript received Jan. 25, 1965; revised manuscript received April 20, 1965.

Any discussion of this paper will appear in a Discussion Section to be published in the June 1966 JOURNAL.

REFERENCES

1. P. F. Schmidt and A. E. Owen, *This Journal*, **111**, 682 (1964).
2. K. E. Heusler, *Ber. Bunsengesellschaft*, **67**, 943 (1963).
3. E. Tannenbaum, *Solid State Electronics*, **2**, 123 (1961); S. Maekawa, *J. Physical Soc. Japan*, **17**, 1592 (1962); J. J. Chang, *IEEE Trans. on Electron Devices ED-10*, 357 (1963).
4. P. F. Schmidt, T. W. O'Keeffe, and R. Stickler, *This Journal*, **111**, 1188 (1964); **112**, 878 (1965).
5. J. Tsai, Thesis, Ohio State University, 1960.
6. I. M. Mackintosh, P. F. Schmidt, and M. W. Larkin, *Proc. IEEE*, **52**, 1447 (1964).
7. G. M. Krembs, *This Journal*, **110**, 938 (1963).
8. T. P. Hoar and N. F. Mott, *J. Phys. Chem. Solids*, **9**, 97 (1959); T. P. Hoar and J. Yahalom, *This Journal*, **110**, Sec. II, 614 (1963).
9. A. Goetzberger and W. Shockley, *J. Appl. Physics*, **31**, 1821 (1960); S. W. Ing, R. E. Morrison, L. L. Alt, and R. W. Aldrich, *This Journal*, **110**, 533 (1963).
10. A. E. Owen, T. W. O'Keeffe, and P. F. Schmidt, To be published as Part III of this series.
11. C. S. Fuller and J. A. Ditzenberger, *J. Appl. Phys.*, **27**, 544 (1956).
12. A. D. Kurtz and C. L. Gravel, *ibid.*, **29**, 1456 (1958).
13. S. R. Shortes *et al.*, Extended Abstract 151, Electronics Division, ECS New York Meeting, 1963.

Interstitial-Substitutional Diffusion in a Finite Medium, Gold into Silicon

G. J. Sprokel

Systems Development Division, International Business Machines Corporation, Endicott, New York

ABSTRACT

A differential equation describing interstitial-substitutional diffusion is derived. Boundary conditions are selected pertinent to diffusion into a finite medium. Laplace's tranformation is used to solve the differential equation. The result is plotted as a relation between dimensionless quantities. The quantities D_1 and C_{01} can be calculated from the intercept and the initial slope, respectively. The theory is applied to the diffusion of gold into silicon wafers of varying thickness.

Interstitial-substitutional diffusion was proposed by Frank and Turnbull (1) to explain the diffusion of copper in germanium. The idea was used by Dash (2) and by Wilcox and LaChapelle (3, 4) for the diffusion of gold in silicon. More recently, this same idea was used by Weisberg and Blanc (5) to describe the diffusion of zinc in GaAs and by Pumper and Prostoserdova (6) for zinc in InSb.

Briefly, it is assumed that the diffusing species occupies interstitial positions in the host lattice; however, as it approaches sufficiently close to a lattice vacancy it may convert to a substitutional position by occupying that vacancy. Substitutional diffusion is not ruled out, but it is assumed that interstitials diffuse several orders of magnitude faster than either substitutionals or vacancies.

The continuity equation for this model is

$$\frac{\partial c_i}{\partial t} = D_i \frac{\partial^2 c_i}{\partial x^2} - k' c_i c_v \qquad [1]$$

The first term on the right describes the diffusion of interstitials into the volume element. The second term is the decrease in the local interstitial concentration caused by the conversion of interstitials to substitutionals. Since each conversion requires one vacancy, the rate is proportional to the local concentrations of

interstitials (c_i) and vacancies (c_v). The rate constant is k'.

The general solution of Eq. [1] is derived below. In order to illustrate its use in calculating D_i, the solution is applied to the diffusion of gold in silicon. Sufficient data for this system were available. Some consequences of the model are also discussed. The solution is an application of Laplace transformation theory; this approach has not been taken in earlier publications.

General Solution of the Diffusion Equation

The boundary requirements to be imposed on Eq. [1] must reflect the experimental conditions. The boundary conditions are

$$c_i(0,t) = c_0 \quad t > 0 \qquad [2]$$

$$c_i(x,0) = 0 \quad 0 \leq x \leq w \qquad [3]$$

$$\left(\frac{\partial c_i}{\partial x}\right)_{x=w} = 0 \quad t > 0 \qquad [4]$$

Equation [2] is the supply equation; it requires that the concentration of interstitials at the surface $x = 0$ be constant throughout the experiment. The quantity c_0 is interpreted as the solubility of interstitials, and w is the wafer thickness. Equation [3] is self evident. Equation [4] states that the gradient be zero at the opposite surface of the wafer, $x = w$. Experience indicates that fast diffusing impurities penetrate through the entire wafer during a normal diffusion run. The boundary condition merely states that the diffusant shall not leave the wafer at the opposite side. It excludes any interaction between the surface and the diffusing impurity.

The solution of Eq. [1], subject to the boundary conditions, determines $c_i(x,t)$ everywhere. However, the experimentally observed concentration at a point x is the sum of the local interstitial and substitutional concentrations. The two terms cannot be determined independently. During the experiment, the rate at which substitutionals are formed is given by the second term on the right in Eq. [1]. Thus

$$\frac{\partial c_s}{\partial t} = k' c_i c_v \qquad [5]$$

Equation [5] is assumed to be valid until the lattice becomes saturated with substitutionals. Once $c_i(x,t)$ is found, $c_s(x,t)$ can be obtained by integration. The sum $c_m = c_i + c_s$ is the experimentally observed concentration.

In solving Eq. [1], as well as in carrying out the integration [5], it is assumed that c_v is independent of t. To solve Eq. [1], let

$$\bar{c}(x,p) = \int_0^\infty c_i(x,t)\, e^{-pt}\, dt \qquad [6]$$

Equation [1] transforms to

$$\frac{\partial^2 \bar{c}}{\partial x^2} - \frac{p+k}{D_i}\bar{c} = 0 \qquad [7]$$

in which $k = k'c_v$.

The general solution of Eq. [7] is

$$\bar{c} = A\, e^{+\sqrt{\frac{p+k}{D_i}}\,x} + B\, e^{-\sqrt{\frac{p+k}{D_i}}\,x} \qquad [8]$$

Equations [2] and [4] transform to

$$\bar{c}(0,p) = \frac{1}{p} c_0 \qquad [9]$$

$$\left(\frac{\partial \bar{c}}{\partial x}\right)_{x=w} = 0 \qquad [10]$$

Inserting Eq. [9] and [10] into Eq. [8], one obtains expressions for A and B. Inserting these back into Eq. [8] one arrives at

$$\bar{c} = c_0 \frac{\cosh \sqrt{\frac{p+k}{D_i}} \cdot (x-w)}{p \cosh \sqrt{\frac{p+k}{D_i}} \cdot w} \qquad [11]$$

The inverse transform is [8], [9]

$$\frac{c_i}{c_0} = \frac{\cosh \sqrt{\frac{k}{D_i}}\,(w-x)}{\cosh \sqrt{\frac{k}{D_i}}\,w} - 2\sum_0^\infty (-1)^n \frac{(2n+1)\frac{\pi}{2} \cos (2n+1)\frac{\pi}{2}\left(1-\frac{x}{w}\right)}{\left\{(2n+1)\frac{\pi}{2}\right\}^2 + \frac{kw^2}{D_i}} e^{-\left[\left\{(2n+1)\frac{\pi}{2}\right\}^2 + \frac{kw^2}{D_i}\right]\frac{D_i t}{w^2}} \qquad [12]$$

In view of Eq. [5], c_s is obtained from

$$\frac{c_s}{c_0} = k \int_0^t \frac{c_i(x,\tau)}{c_0} \cdot d\tau \qquad [13]$$

$$\frac{c_s}{c_0} = \frac{kt \cosh \sqrt{\frac{k}{D_i}}\,(w-x)}{\cosh \sqrt{\frac{k}{D_i}}\,w} - 2\sum_0^\infty (-1)^n \frac{(2n+1)\frac{\pi}{2}\cdot\frac{kw^2}{D_i} \cos (2n+1)\frac{\pi}{2}\left(1-\frac{x}{w}\right)}{\left[\left\{(2n+1)\frac{\pi}{2}\right\}^2 + \frac{kw^2}{D_i}\right]^2} \cdot \left\{1 - e^{-\left[\left\{(2n+1)\frac{\pi}{2}\right\}^2 + \frac{kw^2}{D_i}\right]\frac{D_i t}{w^2}}\right\} \qquad [14]$$

Finally, the sum of Eq. [12] and [14] can be written as follows

$$\frac{c_m}{c_0} = 2\frac{kw^2}{D_i}\cdot\frac{D_i t}{w^2} \sum_0^\infty (-1)^n \frac{(2n+1)\frac{\pi}{2} \cos (2n+1)\frac{\pi}{2}\left(1-\frac{x}{w}\right)}{\left\{(2n+1)\frac{\pi}{2}\right\}^2 + \frac{kw^2}{D_i}} + 2\sum_0^\infty (-1)^n \frac{\left\{(2n+1)\frac{\pi}{2}\right\}^3 \cos (2n+1)\frac{\pi}{2}\left(1-\frac{x}{w}\right)}{\left[\left\{(2n+1)\frac{\pi}{2}\right\}^2 + \frac{kw^2}{D_i}\right]^2} \left\{1 - e^{-\left[\left\{(2n+1)\frac{\pi}{2}\right\}^2 + \frac{kw^2}{D}\right]\frac{D_i t}{w^2}}\right\} \qquad [15]$$

Equation [3] was used to express the cosh in terms of a cos series. This simplifies the numerical calcu-

Table 1. Numerical values of c_m/c_0 for $x/w = 1$, D_it/w^2 from 0.1 to 50 and kw^2/D_i from 0 to 10 as given by Eq. [15]

D_it/w^2	kw^2/D_i 0	0.05	0.15	0.2	0.3	0.4	0.5	1	2	3	4	5	6	7	8	9	10
0.1	0.00	0.00	0.00	0.00	0.00	0.00	0.00	0.00	0.00	0.00	0.00	0.00	0.00	0.00	0.00	0.00	0.00
0.2	0.21	0.21	0.21	0.21	0.21	0.20	0.20	0.20	0.18	0.06	0.04	0.01	0.00	0.00	0.00	0.00	0.00
0.4	0.50	0.50	0.50	0.50	0.49	0.49	0.49	0.47	0.44	0.41	0.38	0.17	0.12	0.07	0.02	0.00	0.00
0.6	0.68	0.68	0.68	0.68	0.68	0.68	0.68	0.67	0.65	0.62	0.59	0.56	0.24	0.16	0.09	0.01	0.00
0.8	0.79	0.80	0.80	0.81	0.81	0.82	0.82	0.84	0.84	0.82	0.79	0.75	0.71	0.25	0.16	0.06	0.00
1.0	0.86	0.86	0.86	0.90	0.91	0.92	0.93	0.98	1.01	1.01	0.99	0.95	0.90	0.34	0.22	0.10	0.00
2.0	0.96	1.00	1.05	1.14	1.22	1.29	1.36	1.61	1.91	2.00	1.99	1.93	1.85	0.81	0.57	0.33	0.09
3.0	0.97	1.06	1.15	1.31	1.48	1.62	1.75	2.23	2.77	2.95	2.97	2.90	2.76	2.65	0.91	0.55	0.20
4.0	0.97	1.11	1.24	1.49	1.73	1.93	2.13	2.86	3.64	3.92	3.96	3.86	3.72	3.53	1.25	0.78	0.30
5.0	0.96	1.16	1.33	1.67	1.98	2.26	2.51	3.48	4.51	4.90	4.96	4.85	4.66	4.42	1.60	1.00	0.41
10	0.97	1.40	1.79	2.54	3.22	3.86	4.43	6.59	8.88	9.74	9.92	9.74	9.37	8.90	3.32	2.12	0.93
20	0.97	1.86	2.71	4.29	5.73	7.07	8.26	12.8	17.6	19.4	19.8	19.5	18.8	17.9	6.75	4.36	1.98
30	0.97	2.34	3.63	6.05	8.23	10.3	9.82	19.0	26.3	29.1	29.8	29.3	28.2	26.8	10.2	6.60	3.02
40	0.97	2.81	4.56	7.80	10.7	13.5	16.0	25.2	35.1	38.8	39.7	39.1	37.6	35.7	13.6	8.84	4.07
50	0.97	3.28	5.48	9.55	13.2	16.7	19.8	31.5	43.8	48.5	49.6	48.8	47.0	44.7	17.0	11.1	5.12

lations slightly. As noted previously, Eq. [15] is valid up to the saturation concentration of substitutionals.

Equation [15] is the desired solution. It is expressed as a relation between the dimensionless quantities c_m/c_0 and $(x/w, D_it/w^2, kw^2/D_i)$. Numerical values of c_m/c_0 can be calculated in terms of these three parameters, although the absolute values of D_i, c_0, and k are as yet unknown. Values of x/w were selected in increments of 0.1 from 0.01 to 1. For each value of x/w, the quantity c_m/c_0 was calculated as a function of D_it/w^2 and kw^2/D_i. A Fortran program[1] was written to perform these calculations. In certain cases, *viz.*, $D_it/w^2 >> 1$ and $x/w = 1$, the series converges rapidly, and manual calculation becomes feasible. For the sake of brevity, numerical values of c_m/c_0 for $x/w = 1$ only, are listed in Table I. However, these are sufficient for calculation of D_i.

Figure 1 illustrates the function c_m/c_0 (Dt/w^2) for kw^2/D_i from 0 to 10. The function has a maximum for $kw^2/D_i \approx 3.5$ and the curves beyond this maximum are indicated as broken lines for purposes of clarity. First, consider the family of curves for which kw^2/D_i is far below 3.5. For this group, $c_m/c_0 \approx 0$ for $D_it/w^2 < 0.2$. As a first approximation this can be regarded as an intercept and an estimate of D_i can be made independent of c_0 or kw^2/D_i. As D_it/w^2 increases from approximately 0.2 to 1, c_m/c_0 increases rapidly and almost independently of kw^2/D_i. A first estimate of c_0, independent of kw^2/D_i, can be made from this section of the curve. Finally, beyond $D_it/w^2 \approx 1$, the slope of the curve is determined mainly by kw^2/D_i, and an estimate of k is obtained from this part of the curve. Once approximate values of D_i, c_0, and k are known, further refinement is achieved by iteration. The amount of labor involved is not excessive.

The physical interpretation of the shape of these curves is quite evident. It takes a finite interval of time before the diffusing impurity reaches the opposite end of the wafer. This time lag is mainly determined by the diffusion constant. At the surface $x = w$, most of the impurity is initially in the interstitial mode, and the rate of increase is nearly proportional to c_0. Later on, the interstitial concentration is close to its maximum value, c_0, and is practically constant. The substitutional concentration now increases at a constant rate which is proportional to k.

Consider the curves for which kw^2/D_i is larger than 3.5. These graphs are straight lines and the sharp rise after the initial time lag has disappeared. A large ratio of k/D_i means that the rate at which interstitials change to substitutionals is large compared to the diffusion of interstitials and the interstitial concentration is small everywhere. Thus, the increase in c_m becomes smaller as k/D_i increases.

Inspection of experimental data reveals which case is applicable. For example, if gold is diffused in silicon, the concentration at the surface $x = w$ increases rapidly for short diffusion times and much slower thereafter [ref. (7), Fig. 3 and 4]. Thus, for this system it is probable that $kw^2/D_i < 1$.

[1] This program has not been released and is not available.

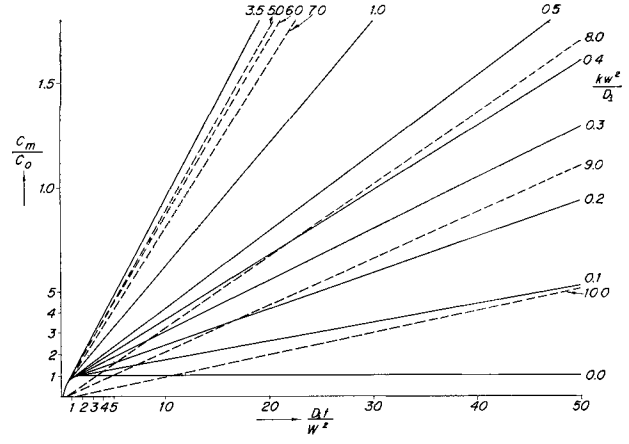

Fig. 1. Graphical presentation of Eq. [15]. c_m/c_0 vs. D_it/w^2 with kw^2/D_i as a parameter. The function has a maximum for $kw^2/D_i \approx 3.5$.

Experimental Data on the Diffusion of Gold in Silicon

Tables II and III summarize data on the diffusion of gold in silicon at 1000° and 1100°C, respectively. The data at 1000°C were taken from the earlier paper (7). The experimental quantities listed in the tables are: the diffusion time; the thickness, w, of the wafer; and the observed gold concentration, c_m, at the surface $x = w$.

The experimental procedures involved have been described before. Briefly, one side of the wafer $(x = 0)$ is plated with gold doped with Au 199. The plated

Table II. Summary of diffusion data at 1000°C*

Diffusion time, hr	Wafer thickness, in.	t/w^2, cm^{-2} sec	c_m, at./cm³	D_it/w^2 for $D_i = 2 \times 10^{-6}$	c_m/c_0 for $c_0 = 7 \times 10^{34}$
1/3	0.060	5.2×10^4	2×10^{13}	0.1	0.03
1/2	0.0265	4.0×10^5	5×10^{14}	0.8	0.72
2	0.0275	1.5×10^6	1×10^{15}	3.0	1.4
4-1/2	0.0275	3.3×10^6	1.4×10^{15}	6.6	2.0
12	0.0273	9.0×10^6	2.3×10^{15}	18	3.3
28	0.0270	2.2×10^7	4.0×10^{15}	44	5.7

* Data from ref. (6).

Table III. Summary of diffusion data at 1100°C

Diffusion time, hr	Wafer thickness, in.	t/w^2, cm^{-2} sec	c_m, at./cm³	D_it/w^2 for $D_i = 2 \times 10^{-6}$	c_m/c_0 for $c_0 = 9 \times 10^{35}$
1	0.0780	9.2×10^4	2.9×10^{15}	0.46	0.32
2-1/3	0.0781	2.1×10^5	9.2×10^{15}	1.07	1.02
1/2	0.0287	3.4×10^5	$\sim 7 \times 10^{15}$	1.69	~0.8
2	0.029	1.3×10^6	$\sim 8 \times 10^{15}$	6.50	~0.9
3-3/4	0.040	1.3×10^6	1.2×10^{16}	6.50	1.33
24	0.0772	2.2×10^6	1.4×10^{16}	11.2	1.55
13	0.0401	4.5×10^6	2.2×10^{16}	22.6	2.45
24	0.040	2.7×10^6	3.0×10^{16}	43.2	3.33
12	0.0262	9.8×10^6	$\sim 2.2 \times 10^{16}$	49.6	~2.5

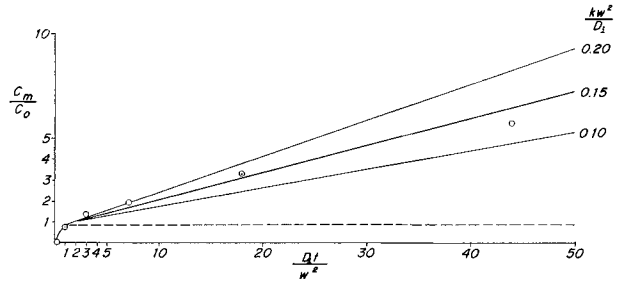

Fig. 2. Graph of Eq. [15] for $kw^2/D_i = 0.15$. Data points are for Au diffused into Si at 1000°C calculated with $D_i = 2 \times 10^{-6}$ cm² sec and $c_o = 7 \times 10^{14}$ cm^{-3}. The broken line represents c_i/c_o for $kw^2/D_i = 0.15$. For $D_i t/w^2 < 1$ $c_i \approx c_m$.

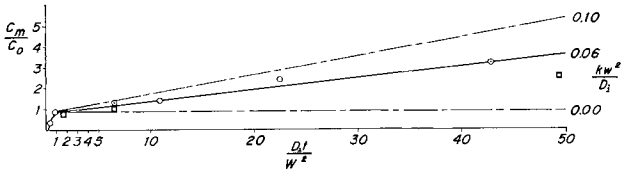

Fig. 3. Graph of Eq. [15] for $kw^2/D_i = 0.06$. Data points are for Au diffused into Si at 1100°C calculated with $D_i = 5 \times 10^{-6}$ cm² sec and $c_o = 9 \times 10^{15}$ cm^{-3}. Data marked (□) from ref. (7). The graph of c_i/c_o for $kw^2/D_i = 0.06$ coincides for all practical purposes with the graph of c_m/c_o for $kw^2/D_i = 0$ and was therefore omitted.

wafer is heated either in an argon atmosphere or in an evacuated capsule. After diffusion, thin slices are etched off sequentially starting at the surface $x = w$. The amounts of gold and silicon in the etchant are determined and concentration profiles are constructed from these data. It was found that the gold concentration was nearly constant throughout most of the wafer. Close to the surface, at $x = w$, c_m is slightly higher. This is a surface effect which was discussed in the earlier paper (7), but is ignored here.

In the last two columns of the tables the values of c_m/c_o and $D_i t/w^2$ are listed for each experiment. D_i and c_o are calculated from the intercept and initial slope of a graph of c_m *vs.* t/w^2 and refined by iteration as discussed above. Figures 2 and 3 represent graphically Eq. [15] for $x/w = 1$ and kw^2/D_i as indicated. The experimental data fall on these curves to within the experimental uncertainty (estimated at 10%). Thus, it is concluded that the model, differential Eq. [1], adequately accounts for the experimental observations. Table IV lists the numerical values of D_i, c_o, and kw^2/D_i.

Wilcox and LaChapelle published (4) values for the diffusivity and the activation energy of gold diffusing in silicon. From these data, one calculates:

$$D_i = 3.2 \text{ to } 15.5 \times 10^{-6} \text{ (at 1000°C)}$$

$$D_i = 4.3 \text{ to } 9.0 \times 10^{-6} \text{ (at 1100°C)}$$

which is in good agreement with the results presented here.

Discussion

The gold diffusion mechanism.—In Fig. 4, c_m/c_o is plotted against x/w for values of $D_i t/w^2$ and kw^2/D_i which are within the range of interest for the gold diffusion problem. For $D_i t/w^2 \geq 1$, the concentration is nearly constant throughout the wafer; for $D_i t/w^2 < 1$, c_m/c_o decreases from approximately 1 to 0. Experimental data on diffusion are usually presented as c_m *vs.* x, but in this case such graphs are not suitable for calculations. Experimental gold concentration profiles were found to conform with Fig. 4 throughout most of the wafer. Data for $x/w < 0.1$ are uncertain because of alloying at the plated surface; whereas for $x/w > 0.9$ the effects of the opposite surface are noticeable. In this region an increase in c_m is observed. This was attributed to an increase in the vacancy concentration near that surface (7).

Table IV. Numerical values

	1000°C	1100C°
D_i in cm² sec^{-1}	2×10^{-6}	5×10^{-6}
c_o in at. cm^{-3}	7×10^{14}	9×10^{15}
kw^2/D_i	0.15	0.06

In Fig. 5, c_i/c_o is plotted against x/w for values of $D_i t/w^2$ and kw^2/D_i as in Fig. 4. If Fig. 4 and 5 are compared, it is seen that for $D_i t/w^2 \leq 1$, $c_i \approx c_m$ everywhere and for $D_i t/w^2 > 1$, $c_i \approx c_o$. Initially and up to diffusion times such that $D_i t/w^2 \approx 1$, gold is present almost exclusively as interstitials. For longer diffusion periods, the interstitial concentration has reached its maximum value, c_o. Further diffusion into a volume element is limited by the rate at which substitutionals are formed. The substitutional gold concentration increases throughout the wafer as $c_o kt$ until saturation is reached.

There is a practical consequence to this. The data in Table IV indicate that c_o increases strongly with diffusion temperature, but k remains constant. Therefore, to obtain a large ratio of c_s/c_i, it is better to diffuse at lower temperature and for a longer time interval. In Fig. 2 and 3, c_i/c_o is also plotted and the ratio c_s/c_i can be obtained from these curves. Note that for an average diffusion run c_s/c_i is still less than 10.

Effect of vacancy concentration.—For the average gold diffusion experiment, $D_i t/w^2 > 1$ (for a 0.010 in. wafer $t = 5$ min at 1000° and 2 min at 1100°C) and, therefore, the parameter k is important. The experiments at 1100°C were performed with wafers obtained from two suppliers. The two kinds of samples do not show a significant systematic difference. It may be assumed that the data in Table IV hold for any carefully grown silicon crystal, in particular, for the average crystal $kw^2/D \approx 0.1$. The parameter k was defined as

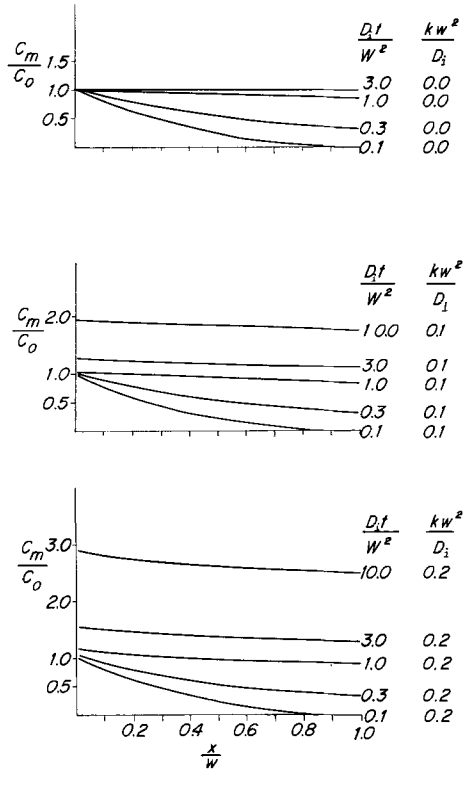

Fig. 4. c_m/c_o *vs.* x/w for $D_i t/w^2$ and kw^2/D_i in the range of interest for gold diffusion (Eq. [15]).

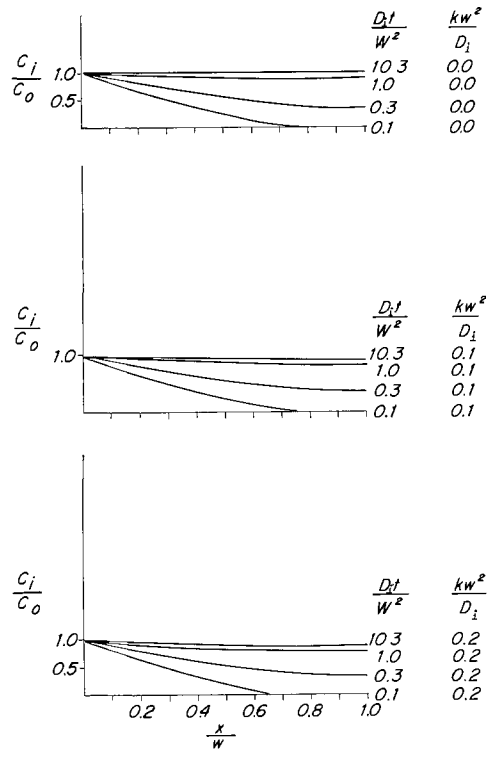

Fig. 5. c_i/c_0 vs. x/w for $D_i t/w^2$ and kw^2/D_i as in ref. (4) (Eq. [12]).

$k = k'c_v$. A local increase in c_v, as expected near a dislocation, results in a proportional increase in kw^2/D_i and therefore in c_m/c_0 (see Fig. 1). The effect is quite large. Take for example a local c_v, 10 times larger than the average. The local gold concentration must then increase about 8 times faster than the average. The diffusion process imposes no limit on c_m, but in practice saturation is soon reached. From the solubility of gold in silicon, as determined by Collins (10) and from the data in Table IV, it follows that at saturation c_m/c_0 is about 18 at 1000° and about 4 at 1100°C. A relatively small local increase in c_v is sufficient to cause an increase in c_m until saturation is reached. Since interstitial gold is still diffusing into the wafer, gold must precipitate out. Dash (2) observed that gold precipitates out at dislocations and discussed this in terms of the interstitial-substitutional mechanism. This is confirmed here in a more quantitative manner.

Comments on the Model

The model, Eq. [1], requires only that the conversion of interstitials is first order in c_i. In particular, no assumptions are made as to the magnitude of c_0 or the value of the ratio c_s/c_i at saturation. If the supply of gold is sufficient, the interstitial and substitutional concentrations will eventually attain their saturation values and these are determined from the experiments. At any point in the wafer the interstitial concentration reaches its maximum (c_0) long before the substitutional. It would be of interest to keep the gold supply below the amount needed to saturate the sample. According to the model, all gold atoms would eventually be incorporated as substitutionals and one could search for any differences in the electrical behavior of the gold. It is questionable whether such experiments can ever be performed (7).

In a sense then, the existence of interstitials is caused by the experimental conditions, and this is a flaw in the model. A different model can be formulated in which one accounts for the generation of interstitials from substitutionals as Frenkel defects. Interstitial gold is properly a cation (11) and as such will tend to react with charged vacancies

$$Au_i^+ + V^- \leftrightarrows [Au_s] + V^o$$

$$V^o \leftrightarrows V^- + \oplus$$

$$[Au_s] + \ominus \rightleftarrows Au_s^- \qquad \text{acceptor center}$$

$$[Au_s] \leftrightarrows Au_s^+ + \ominus \qquad \text{donor center}$$

The continuity equation is

$$\frac{\partial c_i}{\partial t} = D_i \frac{\partial^2 c_i}{\partial t^2} - \alpha c_i + \beta c_s \qquad [1a]$$

which is Eq. [1] with the additional βc_s term describing the generation of interstitials from substitutionals. Equation [1a] cannot be integrated at once; further assumptions are necessary, some of which are briefly discussed below.

If the reverse reaction is allowed, it is tantamount to assuming that equilibrium exists or is eventually reached. Application of chemical reaction kinetics (1, 5) leads to a relation between c_s and c_i. If this relation is linear, as it would be in this case, substitution of it into Eq. [1a] leads to an equation which is of the same form as Eq. [1] except for the factor multiplying c_i. Only the numerical value of this factor is found from the diffusion experiments, but more information is not available. For the reactions outlined above this factor would contain the hole concentration. Wilcox *et al.* (4) found that the diffusion of Au in Si did not depend on the hole concentration which suggests that the correction is not important in this case. However, in other cases (5) such considerations can be quite important.

Formal application of reaction kinetics is questionable, since a substitutional atom does not "react with" a vacancy. The procedure must be regarded as an attempt to arrive at some relation between c_i and c_s which makes Eq. [1a] integrable. Justification lies in the agreement with experimental results.

Diffusion of substitutionals is not ruled out, but the net transport is assumed to be negligible compared to that of interstitials. In a recent article by Kucher (13), no attempt was made to establish a relation between c_i and c_s. Two continuity equations, one for interstitials and the other for substitutionals (each with their own boundary conditions), are solved simultaneously. The rate constants are assumed to be proportional to their respective equilibrium concentrations (solubilities). An expression is obtained for $D_s << D_i$, $c_s^o >> c_i^o$, and $\alpha >> \beta$ (in the terminology of Eq. [1a]). Direct comparison with Eq. [15] is not possible because Kucher assumes the specimen to be infinitely thick even for the fast diffusing species. If the ratio D_s/D_i is indeed of the order 10^{-3} or 10^{-4} (Kucher), the concentration profiles would be given by the sum of a nearly straight line (c_i) and a function which is approximately erfc $x/2\sqrt{D_s t}$ for a diffusion experiment such that $D_i t/w^2 > 1$ but $D_s t/w^2 << 1$. The effect of the erfc term should be largest for small x/w. The experimental data are uncertain near $x/w = 0$ and definite conclusions are not possible. Near $x/w = 1$, still for a short diffusion time, only the interstitial component is important and Kucher's model is arbitrarily close to the one discussed in this paper. Experimental results are available over a range in t/w^2 of nearly 10^3. For long periods the effect of the D_s term should be noticeable throughout a substantial portion of the wafer. However, it was not observed because the concentration profiles remain essentially straight lines (7).

A final comment on Eq. [15] should be made. The series converges slowly and therefore calculations are cumbersome if a computer is not available. The inverse transform of Eq. [11] can be determined by another method. If the cosh term is expanded, a series is obtained which can be transformed term-by-term [ref. (12) lists the appropriate transform]. The series obtained in this way often converge faster; however, the final answer (after solving integral [13]) turned

out to be more involved than Eq. [15]. Therefore, it was decided to program Eq. [15] instead. A complete set of tables for c_m/c_0 and c_i/c_0, for x/w between 0.01 and 1, in increments of 0.1 is available on request.

Conclusion

The diffusion of gold in silicon can be described quite well by an interstitial-substitutional mechanism. Initially and up to the diffusion period, $D_i t/w^2 \approx 1$, gold is present almost exclusively as interstitials. Toward the end of this period the interstitial concentration has become constant throughout the wafer. Further diffusion is limited by the rate at which substitutionals are formed. The gold concentration remains constant throughout the wafer and increases linearly with time until the maximum solubility is reached. Dissociation of substitutionals is not excluded, but information on the equilibrium between interstitials and substitutionals is not available from the diffusion data. A local increase in the vacancy concentration results in an accumulation of substitutional gold in that area.

Acknowledgment

The cooperation of Dr. A. J. Lavin and Dr. A. L. Jones of the Mathematical Science Department is gratefully acknowledged. Mr. J. H. Ramsey at the Scientific Computation Laboratory wrote the Fortran II program.

Manuscript received March 5, 1965. This paper was presented at the San Francisco Meeting, May 9-13, 1965.

Any discussion of this paper will appear in a Discussion Section to be published in the June 1966 JOURNAL.

REFERENCES

1. F. C. Frank and D. Turnbull, *Phys. Rev.*, **107**, 617 (1956).
2. W. C. Dash, *J. Appl. Phys.*, **31**, 2275 (1960).
3. W. R. Wilcox and T. J. LaChapelle, *ibid.*, **35**, 240 (1964).
4. W. R. Wilcox, T. J. LaChapelle, and D. H. Forbes, *This Journal*, **111**, 1377 (1964).
5. L. R. Weisberg and J. Blanc, *Phys. Rev.*, **131**, 1548 (1963).
6. E. Y. Pumper and I. V. Prostoserdovo, *Sov. Phys. Solid State*, **6**, 692 (1964).
7. G. J. Sprokel and J. M. Fairfield, *This Journal*, **112**, 200 (1965).
8. J. Crank, "The Mathematics of Diffusion," Oxford (1957).
9. R. V. Churchill, "Operational Mathematics," McGraw Hill Book Co., New York (1958).
10. C. B. Collins, R. O. Carlson, and C. J. Gallagher, *Phys. Rev.*, **105**, 1168 (1957).
11. B. I. Boltaks, G. S. Kulikov, and R. S. Malkovich, *Sov. Phys. Solid State*, **2**, 2134 (1961).
12. J. Crank, *op. cit.*, p. 328, No. 19.
13. T. I. Kucher, *Sov. Phys. Solid State*, **6**, 623 (1964).

The Etching and Polishing Behavior of Ge and Si with HI

A. Reisman and M. Berkenblit

IBM Watson Research Center, Yorktown Heights, New York

ABSTRACT

Studies of the etching and vapor polishing behavior of Ge with HI as a function of temperature, linear gas stream velocity, etch rate, and etchant concentration, indicate that temperature is the most significant parameter affecting the smoothness of the etched surfaces. A less pronounced effect is the occurrence of microscopic pitting above a critical etchant concentration. The other parameters did not appear to affect surface characteristics. Less detailed studies of the HI etching of Si have been used to define practical conditions for the vapor polishing of Si. A qualitative analysis of the requirements for a usable vapor polish and the experimental conditions necessary to quantitatively define the kinetics of solid-gas etching reactions are presented.

During the past few years, several reports have been issued on the etching kinetics and polishing behavior of Ge and Si in anhydrous HCl at elevated temperatures (1-5). Analogous studies using HBr and HI have not been reported during this period, perhaps due to the unavailability of these reagents in pure enough form.

Recently, a method for instantaneously and continuously generating HI of high purity in a noncorrosive system was described in conjunction with its use in a Ge disproportionation transport system (16). Since the possible effects of contamination are minimized with this HI source, and because the use of HI as an in situ polishing agent is compatible with open tube vapor growth schemes, investigation of its etching and polishing behavior with Ge, Si, and GaAs was begun. The present report describes the results of studies with Ge and presents some less extensive Si data. From the observed etching characteristics as a function of the several experimental parameters examined, specific requirements for deriving kinetic data from open tube experiments are indicated.

Experimental Procedure

Semiconductor preparation.—As starting materials, two different 0.01 ohm cm p-type Ge crystals pulled in the <111> direction were cut into circular wafers 1.39 cm^2 with their surfaces perpendicular to the <211> direction. When suitable vapor polishing conditions were established, other common orientations and a range of resistivities of both n- and p-type wafers were also studied with comparable polishing results to those on <211> surfaces being obtained. The quantitative etching and polishing data to be described, however, were all obtained on <211> surfaces.

The sawed wafers were chemically polished with NaOCl solutions (7) in order to remove surface damage introduced during sawing and lapping procedures. Final wafer thicknesses were from 18-20 mils.

Chemical reagents.—The HI generator described in ref. (6) was charged with Gallard-Schlesinger Ultrapure I_2, and during the course of the studies two separate charges were used without any resultant differences in etching behavior. Matheson Ultra High Purity H_2 (10 ppm maximum impurity) and Matheson Commercial He (100 ppm maximum impurity) were employed as carrier and flushing gases, respectively, without further purification. A number of bottles of each gas were used without any differences observed among them insofar as etching results were concerned. The Pt wool catalyst tower at the output side of the iodine bed was maintained at between 400° and 450°C, and gas flow rates were monitored with wet test meter calibrated ball flow meters.

Apparatus and etching procedure.—Figure 1 is a schematic representation of the apparatus employed.

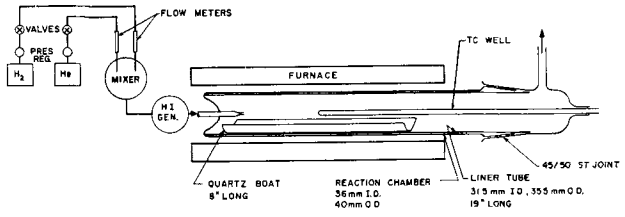

Fig. 1. Schematic representation of III etching apparatus

It consists of the HI generator and a resistance wound furnace surrounding an etching chamber. Close fitting liner tubes of known bore were used to facilitate cleaning after each etching experiment, and nests of these liners could be used to vary linear gas stream velocities without altering the quantity of etchant passing over the wafer in a defined time.

A wafer, after being x-ray analyzed to verify the exactness of orientation subsequent to chemical polishing, was placed horizontally into a quartz open ended boat and loaded into the liner of the etching chamber. In this position, the wafer made contact with the boat at only two points, being essentially suspended in the gas stream. The system was flushed for 15 min in H_2 flowing at 177 cm/min at room temperature (1380 cm³/min input flow rate). The furnace, monitored by a moveable Pt-10% Rh thermocouple encased in a quartz well along the furnace axis, was then brought to temperature. The etchant mixtures were fed into the system at different velocities, at different concentrations and for different time periods, depending on the conditions being evaluated. When the flow of etchant was terminated, the system was flushed with H_2 for 30 min at the flow rate employed, then for 5 min at 1380 cm³/min after which time the furnace was turned off. The gas flow was continued while the furnace cooled.

Results

Figure 2 presents graphs of Ge etch rate in mg loss/defined time/defined area as a function of linear gas stream velocity at each of four etching temperatures. The data when multiplied by the factor 0.144 are converted to mg/cm²/min. The design of the HI generator is such that the H_2 carrier gas passing through it becomes saturated with iodine at the flow rates required to generate the linear velocities specified; therefore, for a given iodine source temperature, the mole fraction of HI in the gas input to the etching chamber was constant for the temperatures and linear gas stream velocities shown. For the data used to define the curves of Fig. 2, the iodine source was maintained at 95°C providing an HI mole fraction of 0.0927. Weight losses for these and subsequent etching experiments were reproducible to ±1 mg, at least three determinations being made for each piece of data.

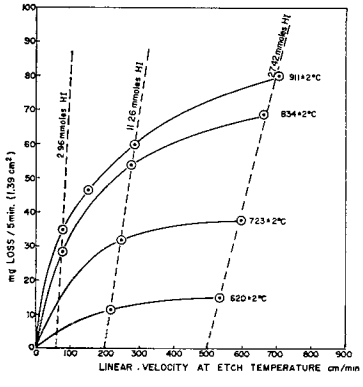

Fig. 2. Variation of etch rate with linear velocity at different etch temperatures; <211> 0.01 ohm-cm P pulled Ge; NaOCl prepolished; I_2 source 95°C.

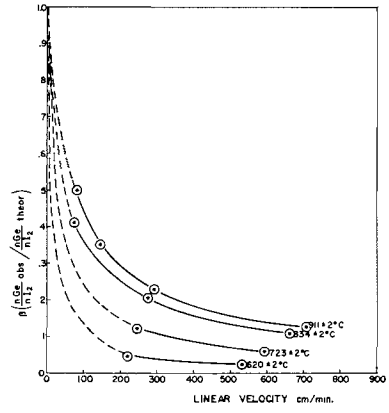

Fig. 3. Plot of efficiency *vs.* linear velocity; <211> 0.01 ohm-cm P pulled Ge, NaOCl prepolished; I_2 source 95°C.

It is seen from Fig. 2 that each of the curves exhibits a sharp initial slope and then tends to level off. The dashed lines connecting the different isotherms represent lines of constant etchant flux. Since at a given input flow rate of hydrogen, the linear velocity in the etching chamber will increase with increasing temperature due to gas expansion, these constant flux lines exhibit a finite positive slope. Consequently, under conditions of constant HI input mole fraction, constant system geometry, and constant HI flux, the average residency time of an etchant particle in the vicinity of the wafer decreases with increasing temperature. The temperature interval covered by the curves of Fig. 2 was specifically chosen because the theoretical amount of Ge brought into the vapor phase per mole of I_2 introduced as HI at each of the temperatures is essentially the same (8). Thus at 620° the thermodynamic vapor phase Ge/I_2 mole ratio is 0.64, and at 723°-911° it is 0.65. It is seen, therefore, from Fig. 2 that at constant HI flux the efficiency increases with increasing temperature. Fig. 3 presents efficiency *vs.* linear velocity graphs for the data of Fig. 2. The efficiency, β, is the fraction of the theoretical (thermodynamic) quantity of Ge removed from the sample.

Under the etching conditions leading to the data of Fig. 2, the appearance of wafers after treatment was found to be independent of linear gas stream velocity at any particular etching temperature. There were, however, marked differences in the appearance of wafers from temperature to temperature, these surface effects being shown in Fig. 4 and 5. Starting at 834° the wafers began to give evidence of nonselectivity of

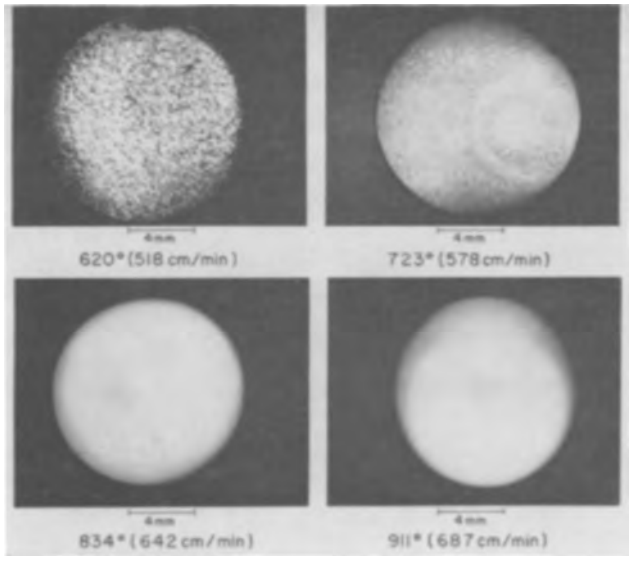

Fig. 4. Variation of surface characteristics with etch temperature

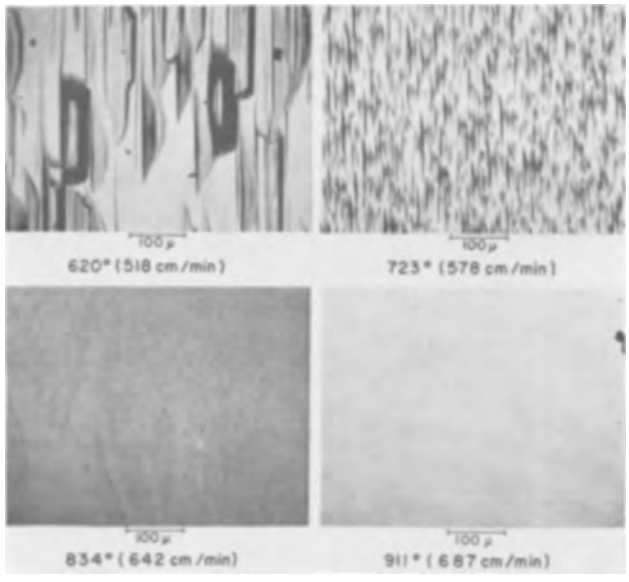

Fig. 5. Variation of surface characteristics with etch temperature

surface etching, and at 911° etching appeared to be completely surface nonselective. Although some edge rounding was observed on polished wafers, there was little tendency for the lead edge of the wafer to etch faster than the tail end. The significance of this observation will be discussed subsequently.

Figure 6 shows plots of the variation of etching rate with source iodine pressure at three different temperatures. The data for each of the curves was taken at constant input flow rate of H_2 (1380 cm³/min). Consequently, the linear velocity at each etching temperature is different as noted in Fig. 6. In addition, a small variation in linear velocity occurs along each curve due to the variation of HI mole fraction. The linear velocities given were calculated by considering only the H_2 input flow rate and the etching temperature.

With increased iodine pressure it is seen that the curves tend to level off, this leveling off being more pronounced at the lowest etching temperature. In addition, it is seen that at low I_2 source pressures, the effect of source temperature on the etch rate becomes small as the temperature of etching is increased. Figure 7 demonstrates this behavior more effectively. The data for Fig. 7 were acquired by determining the variation of etch rate with variation of etching temperature at three different iodine source temperatures. Again each of the curves was evaluated at a constant H_2 input flow rate of 1380 cm³/min. Consequently, the linear velocity in each of the curves varies along the curve, this time because of temperature variation. Relative to the lowest etching temperature on each curve, T_1, the fraction variation with increasing temperature, T_2, is given by $(T_2 - T_1)/T_1$. In addition, at

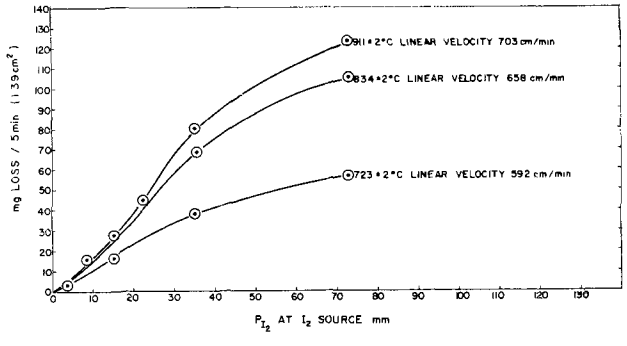

Fig. 6. Variation of etching rate with iodine source pressure at different etching temperatures. <211> 0.01 ohm-cm P pulled Ge, NaOCl prepolished; input flow rate of 1380 cm³/min.

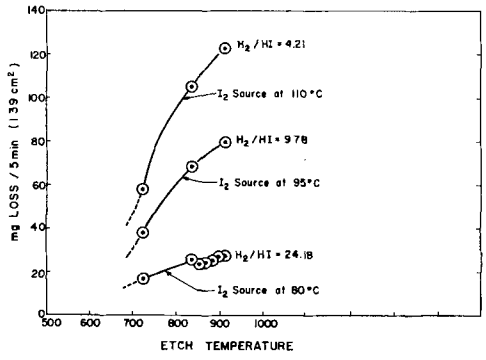

Fig. 7. Variation of etching rate with etching temperature at different I_2 source temperatures. <211> 0.01 ohm-cm P pulled Ge, NaOCl prepolished; input flow rate 1380 cm³/min.

any given temperature, the linear velocity for each curve is slightly different due to the effect of different HI mole fractions being present.

The macroscopic polish quality as a function of iodine source pressure was essentially independent of etchant concentration, evidence for good polishing becoming noticeable at 834°, and superior polishing being detected at 911° at all etchant concentrations. However, a less pronounced effect at 911° due, it appears, to etchant concentration was observed. Thus, the surfaces showed few microscopic pits at an iodine source pressure of *ca.* 15 mm (I_2 source at 80°), a higher density of pits at *ca.* 35 mm (I_2 source at 95°), and a still larger pit density at 73 mm (I_2 source at 110°). These effects are shown in Fig. 8. The polish quality as a function of T at an 80° iodine source temperature became excellent at 890° and above, which is coincident with the plateau for the 80° iodine curve of Fig. 7.

Finally, Fig. 9 presents etch rate *vs.* linear velocity data for an iodine source at 15 mm (I_2 source at 70°). These conditions are the ones currently employed by us in vapor polishing Ge.

Discussion

Effect of experimental parameters on polishing.—The results of the experiments depicted in Fig. 2-9 indicate that absolute etch rate is unimportant in achieving good polishing. Furthermore, variation of etch rate at a

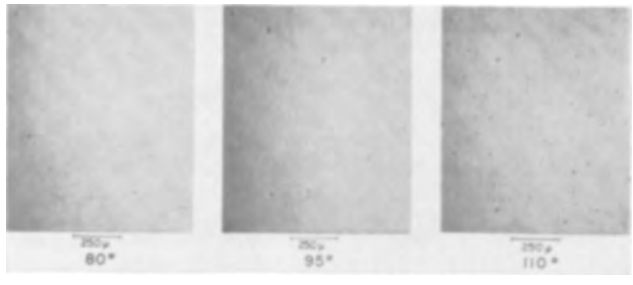

Fig. 8. Variation of polish quality with iodine source temperature

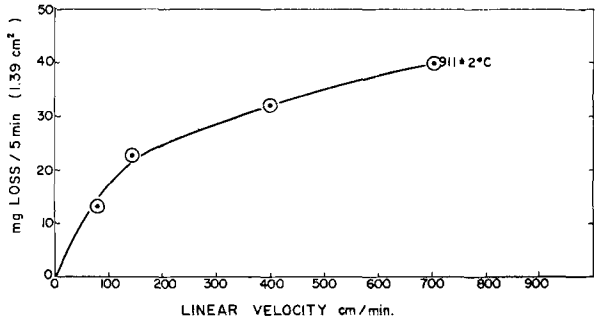

Fig. 9. Plot of etch rate *vs.* linear velocity for iodine source at 15 mm. <211> 0.01 ohm-cm P pulled Ge, NaOCl prepolished; I_2 source at 70°C.

given temperature, by varying etchant flux via a variation in linear gas stream velocity, did not result in variation in surface characteristics for the temperature in question. In addition, for the constant etchant concentration conditions of Fig. 2 identical etch rates again achieved by varying the gas stream linear velocity and, therefore, etchant flux resulted in different surface characteristics at different etch temperatures. As noted above, variation in etchant concentration which represents another way of changing etchant flux and etch rate does appear to cause a second order effect, namely pitting, when the mole fraction of HI exceeds approximately 0.09. Thus, we may conclude that of all the parameters considered the only one which markedly affects surface characteristics during etching is the temperature.

There are, however, certain practical reasons for operating within defined linear velocity and etchant concentration ranges as can be seen from the data. Thus, from Fig. 2 it is evident that if polishing is effected at high linear gas stream velocities, the variation of etch rate with linear gas stream velocity is small, making possible precise control of etch rate without precise control of linear gas stream velocity. Similarly, from Fig. 6 and 7 it is observed that at lower etchant concentrations, the variation of etch rate with temperature is small, again making possible precise control of etch rates without very precise control of temperature. Specifically, the lowest HI partial pressure employed in which etch rate variation with temperature in the polishing range is small, also represents the concentration at which the formation of microscopic etch pits was no longer observed.

Kinetic model to explain polish behavior.—If we visualize the surface as comprised of protrusions and depressions, successful polishing of a rough surface is possible only if the protrusions tend to etch at a faster rate than do the depressions. Conversely, if we begin with a polished surface and desire to retain this polish as the surface is stripped, the process must proceed either by a uniform removal or in a step wise fashion where, after a step forms it tends to be preferentially etched. Starting with polished surfaces, therefore, the expected crystallographic variation in etch rate would tend to result in development of depressions and protrusions. The generated protrusion heights must remain small via preferential etching of them after a certain height is attained in order that the polish remain usable. Thus, beginning with a very smooth surface in which damage is minimal, it is to be expected that vapor polishing will tend to result in some degradation depending on the ability to minimize surface controlled processes.

If the prepolished surface is relatively uniformly damaged, as is probably the case for a mechanically polished surface, crystallographic specificity should be minimized, due to the effects of the damage. In this instance the etching is expected to proceed via a more or less uniform stripping procedure. The use of mechanically damaged surfaces has been utilized frequently in the HCl-Si polishing technique, and the reason for the latter's success may in part be due to the above explanation.

The following rather simplified and idealized models may be invoked to discern the roles of temperature, etchant concentration, and linear gas stream velocity in achieving surface smoothness.

We have assumed that because of position, because of greater turbulence around the apex of a protrusion, and because of a mean free path considerations at 1 atm pressure, protrusions present themselves more frequently to fresh etchant than do depressions. Under the most favorable conditions, where every etchant molecule strikes a protrusion apex on encountering the surface, the maximum reduction in protrusion height, h_p, occurs if the etchant molecule reacts immediately. Actually, one expects an etchant molecule to travel along the surface a distance, d, before reaction occurs. The greatest reduction in protrusion height that would result on the average under the most favorable conditions, therefore, is given by h_p-d. This difference, h_p-d, would increase if the value d decreases, and the resultant surface would acquire enhanced smoothness. The effects of temperature in decreasing the value of d are evident. In general, therefore, we seek an etchant with a very high specific reaction rate constant, and we want the effects of crystallographic orientation to be minimized.

As one increases the etchant concentration in the system, the etchant collision frequency at any given site on the surface begins to increase. If the time interval between successive collisions with a site begins to approach either the residency time of etchant at the site, or of a reaction product species at the site, enhanced replenishment in depressions will increase because the reaction distance d will in effect increase. This undesirable occurrence implies an advantage is to be accrued from operation at lower etchant pressures.

If we now consider the following proposed model of the kinetics of a usable gas-solid polishing reaction, the effects of linear velocity on etch rate, but not on polish quality become evident. This picture also serves to point out the nature of the problems attendent with conducting definitive kinetic experiments of solid-gas reactions under steady state conditions.

From our studies of the HI-Ge polishing behavior it has been found within experimental limits, that for the wafer size employed, the entire surface was found to etch at a uniform rate. This evidence is further supported by the fact that edge rounding, which may indicate that the edges are more damaged than the surface, is uniform around the perimeter. Since the wafer surface extends in the direction of the gas stream drift velocity, one may conclude that the average etchant pressure over the entire wafer surface, and reasonably therefore at least one diameter distance radially, is constant. The indication of uniform etchant partial pressure axially over the wafer in our experiment does not, however, simultaneously imply that this pressure is equal to the input pressure P_i of reactant or that no gradient existed radially, one diameter removed from the sample, for the following reason: Assuming that the etch rate for the forward reaction of the defined system is given by an equation of the form $R = kP^n$ where R is the rate, k the specific rate constant, and P the pressure of HI over the wafer, the rate will be maximum only when P is the input HI pressure in our system.[1] Examination of Fig. 2, however, reveals that such was not the case over the velocity range examined. For if indeed the apparent uniform pressure over our wafer was the input pressure, the etch rate would have reached a maximum immediately after the equilibrium velocity range was exceeded. We know, however, from calculations of the observed efficiencies, and the fraction these are of the thermodynamically predicted values, that under the conditions described by Fig. 2 no regions of equilibrium were actually observed. This is demonstrated in Figure 3 for the data of Fig. 2.

The value β represents

$$\frac{\left(\dfrac{\text{Ge etch rate in moles/defined time defined area}}{\text{I}_2\text{ input rate moles/defined time defined area}}\right)}{(\text{Ge}/\text{I}_2)_{\text{theoretical}}}$$

Since in the range of temperatures used $(\text{Ge}/\text{I}_2)_{\text{theoretical}}$ is constant, *i.e.*, 0.64 at 620° to 0.65 at 723°-911°, the curves of Fig. 3 are all on the same efficiency scale. That the etchant pressure was axially uniform, but not equal to the input pressure and that a radial gradient was present was experimentally demonstrated as follows. For the experiment used to define the curves of Fig. 2 further studies were conducted at 911° and 723° in which a nest of liner tubes was used in place of the

[1] This is true of course only if $n > 0$. If the value of n were zero, it is evident that in our plots of etch rate vs. linear velocities, following an initial transpiration region as velocities approach zero, the curves would level off.

single linear tube used in deriving the data of Fig. 2. Since the input flow rate used was the same as for the highest velocities shown in this figure for the two temperatures in question, the effect of using a nest of liner tubes was to increase the linear gas stream velocities over the wafers, but not to change the number of etchant molecules/unit time passing the wafer. In other words the number of etchant molecules remained constant but their residency time decreased. For the case cited, the linear gas stream velocities were 1164 cm/sec at 911° rather than 703 cm/sec and 979 cm/sec rather than 592 cm/sec at 723°. In both instances the etch rate increased, *i.e.*, 92 mg *vs.* 80 mg/defined time/defined wafer area at 911° and 42 mg *vs.* 38 mg/defined time/defined wafer area at 723° and the etch proceeded uniformly over the wafer. A reasonable explanation for an enhanced etch rate accompanying a decreased residency time at constant flux is that in addition to uniform axial pressure distribution being maintained when the radial distance between the wafer and the chamber walls was decreased, the radial pressure gradient also decreased. In other words more complete mixing occurred radially. Since the partial pressure of etchant at the chamber wall is expected to be greater than the partial pressure at the wafer surface, the increase in etch rate accompanying the radial distance decrease implies that the effective etchant pressure more nearly approximated the input pressure when the etching chamber diameter was decreased, due to more complete mixing of the gas in a radial direction.

Relating our Fig. 2 curves with our model then, we see that as our flows tend toward zero, the system tends toward equilibrium, and the etch rate *vs.* linear velocity curves tends toward linearity. In this region the rate of the forward and reverse reactions approach one another. As the transpiration region is exceeded, the rate of the forward reaction becomes greater than the reverse reaction. This is caused by an increase in the actual HI partial pressure over our wafer which results in an over-all etch rate increase. With further increase in gas stream velocity, the average pressure immediately in the vicinity of the wafer continues to increase until it is effectively equal to the input pressure. At this point the etch rate becomes constant since the input pressure determines the maximum rate that can be observed.

Thus, in order to define the kinetics of the process, it is seen that the pressure dependency of etch rate must be evaluated in the plateau linear velocity region. At lower linear velocities two uncertainties are present; (*a*) the value of the pressure that exists at the surface; (*b*) the effect on the forward rate caused by the back reaction.

In a closed system, the same problems obtain and may presumably be overcome by measuring the instantaneous weight-time or pressure-time change at the start of the reaction or by creating turbulence throughout the chamber by rapid stirring.

The effect, however, of uniform, but less than input etchant pressure in the surface vicinity, while a barrier to quantitatively describing the kinetics does assist in achieving good polishing. For example, if we consider the protrusions and depressions separately in terms of turbulence in each area, we see that the average etchant pressure around the apex of a protrusion will tend to be greater than the average etchant pressure in the depression. This will result in faster removal of protrusion regions. Again, with increasing linear velocity, this microscopic removal rate difference will serve to enhance removal rate, but will not particularly affect polish quality. This because, at both slow and fast velocities, the turbulence effect will diminish as the protrusions disappear and both regions will begin to see the same effective pressure. At this point the quality of polish becomes solely a function of the specific reaction rate constant and the latter's tendency toward variation in different crystallographic directions.

Conditions for Polishing Si

Based on the results obtained with Ge and the suggested model, studies have been initiated to determine the feasibility of using HI as a vapor polish for Si, and ultimately to compare the HCl-Si and HI-Si reactions. Al_2O_3 lapped <111> oriented 10 ohm cm "p" type Si was tried using the etching temperature as the sole parameter. The I_2 source pressure was arbitrarily chosen as 35 mm and the linear velocity of the H_2 input was chosen equally arbitrarily at 1380 cm^3/mm. At 1175° the polish quality showed first indications of improvement. In the range 1220°-1250°C superior polishes to those obtained by conventional chemical solution means were observed.

Acknowledgment

The authors wish to thank Drs. H. Leonhardt and T. Sedgwick of this group for their many stimulating discussions and suggestions. This work was in part supported by AFCRL Contract No. AF19(628)-2468.

Manuscript received Oct. 15, 1964; revised manuscript received Feb. 12, 1965.

Any discussion of this paper will appear in a Discussion Section to be published in the June 1966 JOURNAL.

REFERENCES

1. J. A. Amick, E. A. Roth, and H. Gossenberger, *RCA Rev.*, **24**, 473 (1963).
2. G. A. Lang and T. Stavish, *ibid.*, **24**, 488 (1963).
3. K. Bean and P. Gleim, 124th Meeting Electrochemical Society, New York City, Sept. 29-Oct. 3, 1963, RNP No. 17.
4. K. J. Miller and M. J. Grieco, *ibid.*, RNP No. 18.
5. W. N. Whitten, Jr., 125th Meeting Electrochemical Society, Toronto, May 4-7, 1964, Abs. No. 66.
6. A. Reisman and M. Berkenblit, *This Journal*, **112**, 315 (1965).
7. A. Reisman and R. Rohr, *ibid.*, **111**, 1425 (1964).
8. A. Reisman and S. A. Alyanakyan, *ibid.*, **111**, 1154 (1964).

Tetragonal Germanium Dioxide and Equilibria in the Ge-O-H System

M. M. Faktor and J. I. Carasso

Post Office Reserach Station, Dollis Hill, London, England

ABSTRACT

The thermodynamic stability of tetragonal germanium dioxide has been characterized by measurements of the equilibrium H_2/H_2O ratios in the temperature range 830°-1020°K. Results are extrapolated to 298°K using estimated heat capacities, to give the standard thermal parameters, and to the tetragonal-hexagonal transition point to give the free energy of formation of both modifications at that temperature. Hence, using published entropy and specific heat data for hexagonal germanium dioxide, the standard thermal parameters of this modification are computed. Sizeable crystals of tetragonal GeO_2 have been grown by vapor transport under near-equilibrium conditions.

The aims of this paper are to establish the energy relationships of the solid modifications of germanium dioxide. There are two crystalline allotropes, hexagonal and tetragonal, and there is also a glassy form, all of which persist at room temperature and atmospheric pressure. Some of the physical properties of the three forms are summarized in Table I.

Inspection of Table I reveals a major difference in density and in chemical reactivity between the allotropes, brought about by the change from 4:2 to 6:3 coordination. The solubilities given in Table I unambiguously characterize the stability sequence of the three forms and suggest a value of at least 4 kcal $mole^{-1}$ for the standard free energy of the transformation reaction

$$GeO_2(hex,s) \rightarrow GeO_2(tetr,s) \qquad [1]$$

but they do not afford a reliable estimate of the free energy difference for reasons which we have discussed previously (6). The enthalpy of formation of hexagonal germania has been measured by a number of workers; the results (given in Table II), show serious disagreement.

No thermodynamic parameters for tetragonal germania have appeared in the literature explicitly. In this paper we report measured equilibrium constants for the reaction

$$Ge(s) + 2H_2O(g) \rightarrow GeO_2(tetr,s) + 2H_2(g) \qquad [2]$$

and other derivable thermochemical parameters of interest. The results, when manipulated by standard thermochemical procedures, allow us to reject as spurious some of the values for the enthalpy of formation of the hexagonal modification listed in Table II [including a recent, authoritative measurement (14), and to confirm some of the other values (11, 13)].

Observations on the interconversion and crystal growth of these materials under quasi-equilibrium conditions in the presence of water vapor are also reported.

Table II. Published values of the enthalpy of formation of hexagonal germania

Enthalpy of formation, kcal $mole^{-1}$	Method	Reference
-128.1 ± 0.6	Oxygen combustion	(7)
-128.6 ± 0.5	Oxygen combustion	(8)
-141	Not indicated	(9)
(-129.2 ± 2.0)	Dissolution calorimetry	(10)
-132.6 ± 2.0	Above, corrected	(11)
~ -136.9	Dissolution calorimetry	(10)
-141.8	Equilibrium, dynamic	(12)
-132.3 ± 1.0	Equilibrium, static	(13)
-129.08 ± 0.13	Oxygen combustion	(14)
-132.2 ± 1.2	Dissolution calorimetry	(11)
-133.0 ± 0.5	Computed for hexagonal GeO_2	This work

The unusually large difference in free energy between the allotropes suggested the feasibility of growing the stable modification under conditions of absolute instability of hexagonal germanium dioxide. Since tetragonal germania films can be expected to show desirable stabilizing and diffusion masking properties (unlike the other forms), the controlled production of these films could have interesting repercussions in device technology. Reactions producing germania under conditions thermodynamically compatible with all the forms have hitherto invariably yielded either the hexagonal or the glassy form, and the extreme sluggishness of the transformation to the stable tetragonal allotrope under "clean" conditions, *i.e.*, in the absence of mineralizing catalysts or high-pressure hydrothermal conditions, has been stressed frequently (1, 15, 16).

Experimental

Materials.—Elementary germanium: monocrystalline, zone-levelled, 2 ohm-cm n-type germanium was ground in an agate mortar to a fine powder.

Hexagonal germania: semiconductor grade (Johnson Matthey) germania was dried in a muffle at 700°C for 30 min. This oxide, although exceptionally low in

Table I. Properties of germanium dioxide

	Modification		
	High temperature	Low temperature	Amorphous
Crystal system	Hexagonal	Tetragonal	Glass
Type	Quartz	Rutile	
Density at 25°C (1)	4.228	6.239	3.637
Ge-O bond length in Å	1.737 (2)	1.86 (3)	
Transition point in °C	1033 ± 5	1033 ± 5	
Solubility at 25°C g/$liter^{-1}$ of water	4.53 (4)	<0.005 (5)	~5.18 (1)
Melting point, °C (1)	1116 ± 4	1086 ± 5	
Action of hydrofluoric acid (1)	Dissolves very rapidly	None detected	Dissolves very rapidly
Action of hydrochloric acid (1)	Dissolves rapidly	None detected	Dissolves rapidly
Action of 5*N* sodium hydroxide (1)	Dissolves rapidly	Dissolves very slowly	Dissolves rapidly

metallic impurities, is known to contain chlorine (0.075% by weight was found after drying). The oxide was soluble in 40% aqueous hydrofluoric acid with a negligible residue, confirming that it was the pure hexagonal modification.

Tetragonal germania: previously suggested fluxes (1) for the conversion to the tetragonal form were thought unsuitable. The catalyst used was lithium germanate, prepared from equimolar quantities of hexagonal germania and lithium carbonate by heating the mixture slowly to 1250°C in a platinum dish. The melt was cooled and ground to a fine powder in an agate mortar. Hexagonal germanium dioxide was mixed with 0.1% of the lithium germanate and heated in a muffle in a covered platinum dish at 900°C for 24 hr. The progress of the reaction was followed by taking samples for x-ray powder analysis, which can detect hexagonal germania down to ~0.1%. After 12 hr the allotropic transformation reaction was complete. Attempts to decrease the amount of catalyst by a factor of 10, with a corresponding increase in heating time, led to only ~5% conversion and were not pursued. However, spectrographic analysis of the final product revealed the presence of only 20 ppm of lithium as well as 4 ppm of chromium. No other metallic impurities were detected above the 1 ppm level. The material showed a faint pink coloration.

Measurement of allotropic transformation temperature.—The temperature of the tetragonal-hexagonal GeO_2 transformation was redetermined in a commercial (Netsch) thermal analysis apparatus, using the differential dynamic calorimetry assembly with a cylindrical liner of sheet platinum to minimize thermal gradients. The reference crucible contained a small gold ingot (mp 1063°C). An endothermic peak (corresponding to the allotropic transformation) was observed at a temperature 28° ± 5° below the fusion point of the gold in the reference crucible. Thus the transformation temperature is 1035° ± 5°C.

Measurement of specific heat.—The room temperature specific heat of tetragonal GeO_2 was measured by the cooling time-constant method in an apparatus designed to give a precision of better than 1% with powdered samples of low thermal conductivity. A thin-walled copper calorimeter (1 cm diameter x 5 cm long), filled with the dried powder, was heated to 35°-40°C, and allowed to cool in a double-walled glass tube (2 mm air gap) immersed in a water thermostat set at 25°C. The cooling curve was plotted using very fine copper-constantan thermocouples (5 junctions) to measure the temperature of the copper calorimeter. The cold junctions were kept at the thermostat temperature, and the temperature difference (ΔT) was measured on a d-c potentiometer with an electronic balance detector sensitive to 1 μv, giving a discrimination of 0.005° in the measurement of ΔT. The cooling was rigorously Newtonian ($\Delta T = \Delta T_o e^{-t/\tau}$) for values of ΔT between 5° and 0.5°. The cooling time-constant τ was calculated from the slope of plots of log ΔT against time; the thermal resistance was obtained by calibration with water. The reproducibility of heat capacity measurements was of the order of 0.05% at the 95% confidence level. No significant systematic errors were observed when the calibration was repeated with standards having widely different thermal conductivity and heat capacity.

High-temperature equilibrium measurements (static method).—Most of the measurements of the H_2/H_2O ratio in equilibrium with Ge and GeO_2 at 800°-1025°K were made in a "constant water-vapor pressure" apparatus in which the H_2O pressure was clamped at 13.3 mm Hg by a pool of liquid water kept at 15.7° ± 0.05°C, thus enabling the H_2/H_2O ratio to be measured simply by monitoring the total pressure. As a check, some measurements were also made in a "constant total pressure" apparatus not including a liquid water phase, in which gas-phase compositions had to be determined by gas analysis. The results of the latter experiment had to be corrected for thermal diffusion by the empirical formula for H_2/H_2O mixtures derived by Shibata and Kitagawa (28)

$$\log\left(\frac{P_{H_2O}}{P_{H_2}}\right)_{T_2} = \left(1 + 0.065 \log\frac{T_2}{T_1}\right) \log\left(\frac{P_{H_2O}}{P_{H_2}}\right) - 0.205 \times 10^{-3} (T_2 - T_1)$$

This correction was unnecessary in the former experiment, because the gas phase was recirculated past the solid phase in a closed loop by means of a diaphragm pump. The agreement between the two experimental approaches was satisfactory. However, only the constant water-vapor pressure results were used in the calculations because their precision was significantly higher.

Constant water-vapor pressure apparatus.—The apparatus (Fig. 1) was built round a fused silica tube inserted in a horizontal, Kanthal-wound, furnace, fitted with water-cooled brass end-plates. The sample (crushed Ge + tetragonal GeO_2, ~50g) is contained in a fused quartz cell 1 of 250 cc capacity provided with a small effusion orifice. (The desirability of thus restricting the flow of vapor to and from the sample is discussed under "Procedure.") The apparatus can be evacuated to 10^{-2} mm Hg by a two-stage rotary pump. By suitable manipulation of the taps, the distilled water in bulb 2 can be thoroughly degassed and partly transferred to the horizontal Liebig condenser 3 which is maintained at 15.7° ± 0.05°C by circulating water from a thermostat. (Room temperature was not allowed to fall below this temperature at any time during the work.) The total pressure in the system is measured by a differential oil manometer via a glass spoon gauge 4 fitted with a galvanometer mirror 5 of one-meter focal length. The sensitivity of the

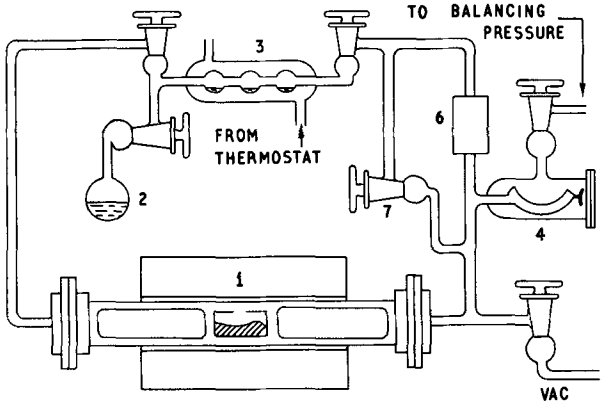

Fig. 1. Apparatus for measuring H_2/H_2O ratios in equilibrium with Ge + GeO_2 tetragonal (constant water vapor pressure).

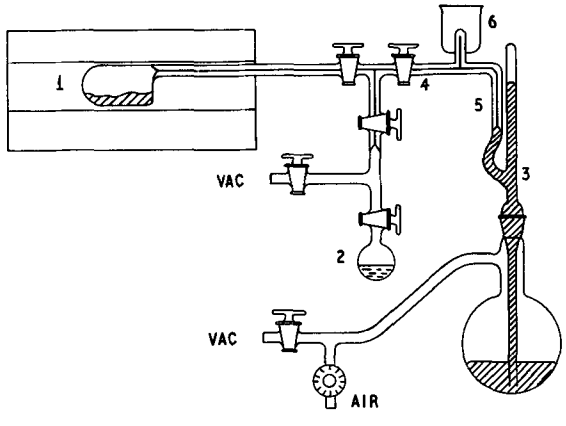

Fig. 2. Apparatus for measuring H_2/H_2O ratios in equilibrium with Ge + GeO_2 tetragonal (constant total pressure).

spoon gauge was matched to that of the oil manometer, giving an over-all discrimination of the order of 0.05 mm Hg in the reading of total pressure. The gas mixture is recirculated past the hot solids by diaphragm pump 6, provided with a shunting tap 7 for controlling the flow. The dead volume of the apparatus was reduced from 3 to 1 liters by inserting two well fitting quartz "sausages" into the furnace tube. The time constant of the approach to equilibrium under these conditions was about 1 hr at 650°C.

Constant total pressure apparatus (Fig. 2).—The solid sample of crushed Ge + GeO_2 (~10g) was held in a 25-ml fused quartz bulb 1 with a long capillary tubulation of 2 mm bore extending beyond the mouth of the furnace. The small flask 2 contains a few milliliters of distilled water. The required pressure of water vapor is introduced into the system and measured in the constant volume mercury manometer 3 by means of a cathetometer. The composition of the gas phase is measured by isolating a fixed volume of the gas between tap 4 and reference mark 5, and measuring its pressure before and after freezing out the water at liquid-nitrogen temperature in cold finger 6. Dead volumes are kept small by using capillary connections and taps. Uniformity of gas composition can be checked by discarding the stagnant gas in the connecting tubes.

Procedure

The design of these experiments was strongly influenced by the significant vapor pressure of the lower oxide, GeO (18) at the temperatures in question. The reactions are

$$Ge + H_2O = GeO + H_2; \frac{P_{H_2} P_{GeO}}{P_{H_2O}} = K_1 \quad [3]$$

$$GeO_2 + H_2 = GeO + H_2O; \frac{P_{H_2O} P_{GeO}}{P_{H_2}} = K_2 \quad [4]$$

Germanous oxide can also be formed by the proportionation reaction

$$Ge + GeO_2 = 2\,GeO \quad [5]$$

but this solid-solid reaction is not expected to proceed at a rate comparable with the rates of the reactions involving gaseous species. Unless the tendency of GeO to sublime to the cooler parts of the furnace is checked, the steady-state pressure of this compound in the reaction zone will be significantly lower than its equilibrium value. This, in turn, will force the H_2/H_2O partial pressure ratio to take on spuriously high or spuriously low values, according to whether reaction [3] or reaction [4] is the faster.

Experimentally, we found that the H_2/H_2O ratio in the constant water-vapor pressure apparatus decreased as the orifice size was decreased, pointing to the pressure being determined by reaction [3]. Adequate Knudsen conditions were obtained with orifice areas of 4 mm^2 or less. Measurements were made with an orifice of ~0.4 mm^2. In the constant total pressure apparatus, Knudsen conditions were provided by the long capillary connection.

In some of the runs, equilibrium was approached from the reduction (instead of from the oxidation) side by starting with a hydrogen-rich mixture produced in a previous run at a lower temperature. The agreement between oxidation and reduction runs was entirely satisfactory (see Table III). It should be stressed, however, that this is not a sufficient test of true equilibrium conditions as had been previously implied (13), and that very serious errors may arise if the partial pressure of a volatile intermediate species is allowed to depart significantly from its equilibrium value. The steady-state hydrogen-water ratio observed with the sample in an open boat at 650°C could be reproduced exactly, whether it was approached from the oxidation or from the reduction side, but this was shown to be a false equilibrium by working under Knudsen conditions, which gave quite a different value for the equilibrium H_2/H_2O ratio.

Table III. Data for reaction [2]

Temperature, °K	P_{H_2}/P_{H_2O}	log K	$\Delta G°$, cal $mole^{-1}$	Direction of approach to equilibrium
831	2.780	0.8880	−3375	Reduction
848	2.658	0.8490	−3226	Oxidation
873	2.459	0.7816	−3121	Oxidation
873	2.345	0.7402	−2956	Reduction
886	2.288	0.7188	−2913	Reduction
921	1.525	0.3664	−1544	Reduction
923	1.508	0.3568	−1506	Oxidation
923	1.485	0.3436	−1451	Oxidation
923	1.464	0.3294	−1391	Oxidation
948	1.376	0.2772	−1202	Oxidation
963	1.286	0.2184	−962	Oxidation
973	1.202	0.1598	−711	Reduction
1021	0.959	−0.0364	+170	Oxidation

Transformation of a metastable solid phase into the stable modification is another possible source of error. We attempted to check Yokokawa's results (13) for the hexagonal form of GeO_2 in our apparatus, and we observed a drift of the "equilibrium" gas-phase composition toward the value for tetragonal GeO_2. The drift was barely significant at temperatures below 600°C, but should in principle be guarded against by extrapolating to zero time when dealing with a metastable phase. At 650°, approximately 15% conversion of hexagonal to tetragonal GeO_2 took place in times of the order of a day, and the gas composition plateau drifted from $\frac{P_{H_2}}{P_{H_2O}} = 1.00$ to $\frac{P_{H_2}}{P_{H_2O}} = 1.16$ (cf. ref. (13) and Table III).

Results and Discussion

Experimental results are shown in Table III together with the computed equilibrium constants and free-energy changes for reaction [2]. The last column of Table III indicates the direction of approach to equilibrium.

The results in column four of Table III were linearized by least squares, yielding the equation

$$\Delta G_T^o = -20800 + 20.7\,T \text{ cal } mole^{-1} \quad [6]$$

for the free-energy change of reaction [2] in the temperature range 830°-1020°K. By combining the experimental values obtained above (Table III) with the corresponding free energies of formation of water (19) we find the free energies of formation attending reaction [7].

$$Ge(s) + O_2(g) \rightarrow GeO_2 \text{ (tetr,s)} \quad [7]$$

Least-squares linearization then allows us to express the free energy of formation of tetragonal germania as

$$\Delta G_T^o = -139970 + 47.6\,T \text{ cal } mole^{-1} \quad [8]$$

in the same temperature range. Both the above linearization procedures are admissible over our narrow temperature range because the curvature caused by specific heat differences between reactants and products is small compared with other experimental inaccuracies.

Allowance for ΔCp terms is important, however, when the results are projected downwards to 298°K or upward to the transition point. The specific heat of tetragonal germania, not previously reported, was measured at room temperature by the cooling method and found to be 11.2 ± 0.1 cal deg^{-1} $mole^{-1}$. The temperature dependence of the specific heat was estimated assuming a linear behavior up to the metastable melting point of tetragonal GeO_2 where its value should be indistinguishable from that of hexagonal germania (20). A purely empirical procedure (21) led to the same result

$$Cp\ (GeO_2, \text{tetr}) = 9.1 + 7 \times 10^{-3} T \text{ cal } deg^{-1} \text{ } mole^{-1}$$

This was combined with the corresponding equations for gaseous oxygen and crystalline germanium (22, 29) to yield the specific heat change involved in reaction [7] as a function of temperature, with adequate precision by the linear equation

$$\Delta Cp = -3.7 + 4.6 \times 10^{-3}T \text{ cal deg}^{-1} \text{ mole}^{-1} \quad [9]$$

If we assume that Eq. [8] is strictly applicable at the mid-point of the temperature range studied, then for reaction [7]

$$\Delta H^\circ_{298} = -139970 - \int_{298}^{925} (-3.7 + 4.6 \times 10^{-3}T)\, dT$$
$$= -139400 \text{ cal mole}^{-1} \quad [10]$$

$$\Delta S^\circ_{298} = -47.6 - \int_{298}^{925} \left(-\frac{3.7}{T} + 4.6 \times 10^{-3} \right) dT$$
$$= -46.3 \text{ cal deg}^{-1} \text{ mole}^{-1} \quad [11]$$

The standard entropy change computed above, coupled with the standard entropies for oxygen gas (22) (49.0 cal deg^{-1} mole^{-1}) and for crystalline germanium (22) (7.4 cal deg^{-1} mole^{-1}), yields $S^\circ_{298} = 10.1$ cal deg^{-1} mole^{-1} for tetragonal germania, for which we estimate an uncertainty of not more than ±2 entropy units. Standard entropies derived from "second law" measurements by extrapolation to room temperature are notoriously inaccurate: in the absence of "third law" values, their reasonableness should be scrutinized. At first sight, the difference of 3 cal deg^{-1} mole^{-1} in standard entropy between hexagonal germania (23) and the value calculated above for tetragonal germania seems startlingly large for a solid-solid transformation. Yet, some of the best semi-empirical methods for estimating the entropy of solids (24) suggest an even lower value for S°_{298} (GeO_2, tetr). Thus, Venner's (25) plot of the logarithm of formula weight *vs.* the entropy, and Karapetyants' (26) linear plot of room-temperature specific heat *vs.* the entropy, for a related family of isomorphous crystals, both lead to 8 cal deg^{-1} mole^{-1} for the standard entropy of tetragonal germanium dioxide on the basis of the value for tetragonal tin dioxide and lead dioxide. These semiempirical methods have been well tested and found to be reliable to ±2 cal deg^{-1} mole^{-1}. Our second-law value of 10.1 ± 2 cal deg^{-1} mole for S°_{298} (GeO_2, tetr) therefore is not unreasonable.

The transition temperature of tetragonal to hexagonal germania was redetermined and found to be 1308°K ± 5° in excellent agreement with Laubengayer and Morton's (1) but not with a more recent value (16, 27).

Extrapolation of the values in Eq. [8] to the transition temperature, which must take into consideration the enthalpy and entropy of fusion at the melting point of germanium (14), enables us to obtain the free energy of formation of both modifications at the transition point

$$\Delta H_{1308} = -139970 - 7600 + \int_{925}^{1308} (-3.7 + 4.6 \times 10^{-3}T)dT$$
$$-147000 \text{ cal mole}^{-1} \quad [12]$$

and

$$\Delta S_{1308} = -47.6 - 6.3 + \int_{925}^{1308} \left(-\frac{3.7}{T} + 4.6 \times 10^{-3} \right) dT$$
$$= -53.4 \text{ cal deg}^{-1} \text{ mole}^{-1} \quad [13]$$

which, when combined by the Gibbs-Helmholtz relation, yield the free energy of formation of germania at the transition temperature

$$\Delta G_{1308} = -147000 + 53.4 \times 1308$$
$$= -77100 \text{ cal mole}^{-1} \quad [14]$$

The entropy of hexagonal germania has been measured as a function of temperature (20, 23), and the entropy change on formation of hexagonal germania from the elements has been computed as a function of temperature (29, 30). Using these literature data we derive the standard enthalpy of formation of hexagonal germania as

$$\Delta H^\circ_{298} = -133000 \pm 500 \text{ cal mole}^{-1}$$

the free energy of formation of hexagonal germania as

$$\Delta G^\circ_{298} = -120100 \pm 500 \text{ cal mole}^{-1}$$

and the enthalpy of formation of hexagonal germania at the transition temperature as

$$\Delta H^\circ_{1308} = -138500 \pm 500 \text{ cal mole}^{-1}$$

From the above and Eq. [12] the enthalpy of transformation at the transformation temperature is

$$\Delta(\Delta H)_{1308} = -8500 \pm 1000 \text{ cal mole}^{-1}$$

and thus the entropy of transformation is

$$\Delta(\Delta S)_{1308} = 6.5 \text{ cal deg}^{-1} \text{ mole}^{-1}$$

The free energy of formation of tetragonal GeO_2 between 298°K and 1308°K is described by the three-term equation

$$\Delta G^\circ(GeO_2, \text{tetr}) = -138.5 + 6.3 \times 10^{-3}\, T \log T$$
$$+ 27.3 \times 10^{-3} T \text{ kcal mole}^{-1}$$

In view of the experimental and computational uncertainties of the present work, no useful purpose would be served by introducing further terms into the free energy equation.

The computational procedure is summarized in Fig. 3.

Growth of Tetragonal Germania

This communication is not concerned explicitly with the rates of the reactions considered. However, in view of the technological interest in the preparation of tetragonal germanium dioxide as a protective film on germanium, or in single crystal form, a few general comments on the reaction rates may not be out of place.

The significant conversion of hexagonal to tetragonal germania observed in the course of this work, and the time scale involved, have already been mentioned in the experimental section. This suggests that the growth of tetragonal germania is promoted by participation of the gaseous transporting agents appearing in Eq. [3] and [4].

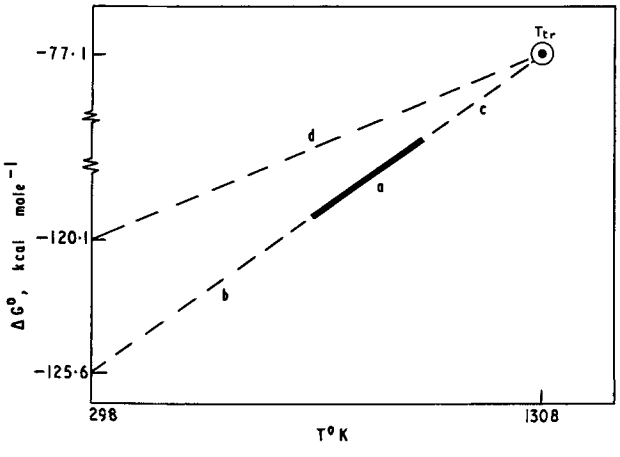

Fig. 3. Free energy of formation of germanium dioxide (not to scale): (a) measured for tetragonal GeO_2 (830°-1020°K); (b) projection to 298°K, using the slope of (a) and measured room temperature specific heat; (c) projection of (a) to the transition point T_{tr} by the same procedure; (d) projection from T_{tr} to 298°K for hexagonal GeO_2, using published entropy and specific heat values.

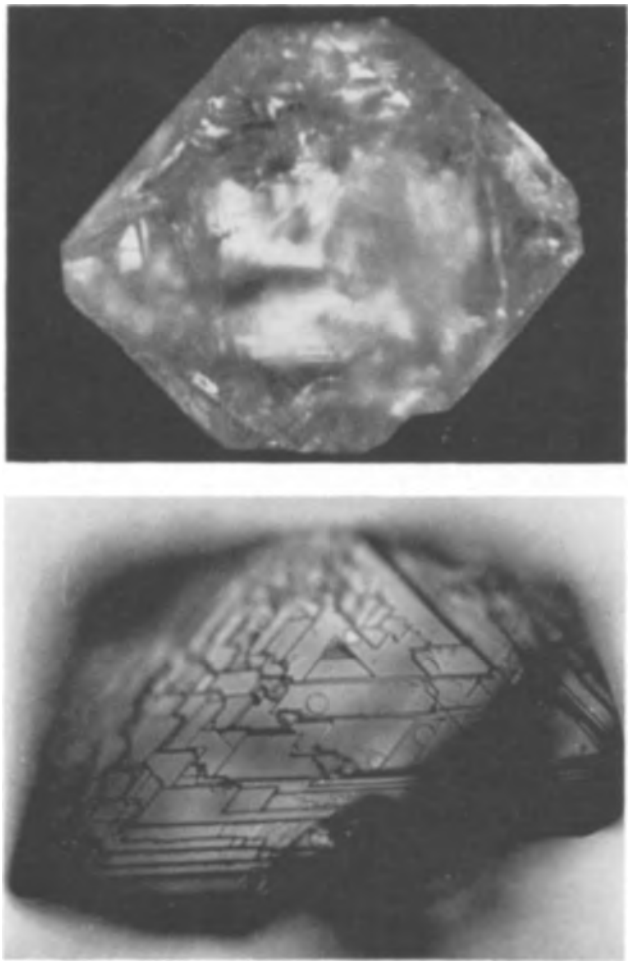

Fig. 4. Tetragonal GeO_2, grown by the transport reactions [3] and [4]: (a) (top) crystal habit, 200X; (b) (bottom) surface topography, 1000X.

This possibility was further tested as follows. A 25 cc silica tube was charged with 5g of hexagonal germania and 25 mg of elementary germanium. It was then evacuated to 5μ pressure, filled with saturated water vapor from liquid water at 22°C, and sealed off. After 30-hr heating at 700°C, the charge was examined by x-ray powder analysis, which revealed complete conversion to the tetragonal modification.

In an attempt to grow some sizeable crystals, a small silica boat containing 5g of germania glass and 10 mg of Ge was placed in a 25 cc silica capsule which was pumped out (to 5μ) and back-filled with water vapor saturated at room temperature. Then the capsule was sealed off and placed in a furnace with a temperature gradient so that the end containing the charge was at 700°C while the other end was at 660°C. After 40 hr the capsule was removed from the furnace. Some 10% of the charge had been transferred to the cold end, where it had grown as small well-developed crystals (Fig. 4). X-ray analysis of these, and of the remainder of the charge, revealed the presence of tetragonal germania only.

Summary

The numerical values measured and derived in this investigation, and their estimated uncertainty limits, are summarized below.

The parameters derived for the formation of tetragonal germania are

$$\Delta H^\circ_{298} \text{ kcal mole}^{-1} — 139.4 \pm 1.0$$

$$\Delta G^\circ_{298} \text{ kcal mole}^{-1} — 125.6 \pm 1.6$$

$$S^\circ_{298} \ (GeO_2, \text{tetr}) \ 10.1 \pm 2.0 \text{ cal deg}^{-1} \text{ mole}^{-1}$$

and

$$\Delta G_T = -138.5 + 6.3 \times 10^{-3} T \log T + 27.3 \times 10^{-3} T \text{ kcal mole}^{-1}$$

(in the temperature range 300°-1350°K)

The parameters derived for the formation of hexagonal germania are

$$\Delta H^\circ_{298} \text{ kcal mole}^{-1} — 133.0 \pm 0.5$$

$$\Delta G^\circ_{298} \text{ kcal mole}^{-1} — 120.1 \pm 0.5$$

The free energy of formation of both allotropes at the transition point is

$$\Delta G^\circ_{1308} \text{ kcal mole}^{-1} — 77.1 \pm 0.5$$

The parameters for the transformation reaction at the transition point are

$$\Delta H^\circ_{1308} \text{ kcal mole}^{-1} — 8.5 \pm 1.0$$

$$\Delta S^\circ_{1308} \text{ cal deg}^{-1} \text{ mole}^{-1} \ 6.5 \pm 1.0$$

The experimentally determined free energy of the reaction

$$Ge(s) + 2H_2O(g) = GeO_2(s, \text{tetr}) + 2H_2(g)$$

is

$$\Delta G^\circ_T = -20800 + 20.7T \pm 250 \text{ cal mole}^{-1}$$

in the temperature range 830°-1020°K.

Acknowledgment

The authors are grateful to G. R. Newns for much helpful discussion and for redetermining the allotropic transition point, and to A. K. Chatterjee for experimental assistance. Acknowledgment is due to the Engineer-in-Chief of the British Post Office for permission to publish this paper.

Manuscript received Jan. 6, 1965; revised manuscript received April 5, 1965. This paper was prepared for delivery before the Washington Meeting, Oct. 11-15, 1964.

Any discussion of this paper will appear in a Discussion Section to be published in the June 1966 JOURNAL.

REFERENCES

1. A. W. Laubengayer and D. S. Morton, *J. Am. Chem. Soc.*, **54**, 2303 (1932).
2. G. S. Smith and P. B. Isaacs, *Acta Cryst.*, **17**, 842 (1964).
3. E. R. Lippincott, A. van Valkenburg, C. E. Weir, and E. N. Bunting, *J. Research Natl. Bur. Standards*, **61**, 61 (1958).
4. W. Pugh, *J. Chem. Soc.*, **1929**, 1537.
5. J. H. Müller and C. H. Gulezian, *J. Am. Chem. Soc.*, **54**, 3142 (1932).
6. J. I. Carasso and M. M. Faktor, "The Electrochemistry of Semiconductors," p. 205, P. J. Holmes, Editor, Academic Press, London, New York (1962).
7. G. Becker and W. A. Roth, *Z. phys. Chem.*, **A161**, 69 (1932).
8. H. Hahn and R. Juza, *Z. anorg. Chem.*, **244**, 120 (1940).
9. W. M. Latimer "Oxidation Potentials," Prentice Hall, New York (1952).
10. W. L. Jolly and W. M. Latimer, *J. Am. Chem. Soc.*, **74**, 5757 (1952).
11. J. L. Bills and F. A. Cotton, *J. Phys. Chem.*, **68**, 802 (1964).
12. K. Ono, Y. Inada, and I. Konno, *Bull. Res. Inst. Mineral Dressing Met.*, **11**, 159 (1959).
13. T. Yokokawa, M. Koizumi, M. Shimoji, and K. Niwa, *J. Am. Chem. Soc.*, **79**, 3365 (1957).
14. A. D. Mah and L. H. Adami, *U. S. Bur. Mines Bull., Rept of Investigation* 6034 (1962).
15. Y. Kotera and M. Yonemura, *Trans. Faraday Soc.*, **59**, 147 (1963).
16. J. F. Sarver, *Am. J. Sci.*, **259**, 709 (1961).
17. O. Kubaschewski and E. Ll. Evans, "Metallurgical Thermochemistry," 3rd ed., Pergamon Press (1958).

18. W. L. Jolly, "Some Problems in the Chemistry of Germanium," Radiation Lab., University of California, 1952, USAEC. LICHL-1638, Technical Information Service, Oak Ridge, Tenn. See also W. L. Jolly and W. M. Latimer, *J. Am. Chem. Soc.*, **74**, 5757 (1952).
19. "Termodinamicheskie Svoistva Individual'nykh Veshchestv" (Thermodynamic Properties of Individual Substances) Vol. II, Izd. Akad. Nauk SSSR, Moscow (1962).
20. A. U. Christensen and K. K. Kelley, *U. S. Bur. Mines, Rept Investigation* 5710 (1961).
21. H. M. Goodwin and H. P. Kalmus, *Phys. Rev.*, **28**, 1 (1909).
22. K. K. Kelley and E. G. King, Contributions to the Data on Theoretical Metallurgy. XIV. Entropies of the Elements and Inorganic Compounds: U. S. Bur. Mines Bull. 592, 1961.
23. E. G. King, *J. Am. Chem. Soc.*, **80**, 1799 (1958).
24. Ref. (19), Vol. I, p. 143.
25. R. Venner, "Termokhimicheskie Raschety," (Thermochemical Calculations), Inostr. Lit., Moscow, 1950.
26. M. Kh. Karapetyants, *Zhur. fiz. Khim.*, **30**, 593 (1956); **32**, 1763 (1958).
27. J. F. Sarver and F. A. Hummel, *J. Am. Ceram. Soc.*, **43**, 336, (1960).
28. Z. Shibata and H. Kitagawa, *J. Fac. Sci. Hokk. Univ. Ser. III*, **2**, 223 (1938).
29. K. K. Kelley, U. S. Bur. Mines Bull 584 (1960).
30. F. X. Hassion, C. D. Thurmond, and F. A. Trumbore, *J. Phys. Chem.*, **59**, 1076 (1955).

Electrical Conductance of Alkali Germanate Melts at 1300°C

E. F. Riebling and S. D. Gabelnick[1]

Research and Development Laboratories, Corning Glass Works, Corning, New York

ABSTRACT

Electrical conductance data are presented for a series of binary alkali germanate melts containing from zero to 30 mole % M_2O (where M = Li, Na, K). The equivalent conductance at 1300°C and the activation energies for conductance change rather sharply (increase and decrease respectively) with the addition of less than 2 mole % of alkali oxide. Equivalent conductance is related to cation-oxygen attraction forces while activation energy is related to cation volume. Some of the specific deviations can be explained in terms of the presence of GeO_6 octahedra. Results are compared with similar data for alkali silicate melts, molten salts, and alkali germanate glasses.

Previous viscosity and density studies have shown that the addition of alkali oxides to molten GeO_2 causes germanium(IV) to change from tetrahedral to octahedral coordination (1, 2). The maximum stability of octahedrally coordinated germanium(IV) at 1300°C appears to occur for melts containing from 15 to 30 mole % M_2O. A rapid return to tetrahedral coordination takes place for most germanate melts as the alkali oxide content is increased above 30 mole %. This sequence of events is radically different from that observed by Bockris and co-workers for similar alkali silicate melts (3).

Bockris *et al.* (3) have shown that electrical conductance (or cation mobility) can also be of value in interpreting the structure of molten oxides. They found that the equivalent conductance tended to increase as the molten silica network was altered. This suggested the possibility that cation mobility would be altered in a slightly different fashion by the unusual structure changes that occur during breakup of the molten germania network.

This paper presents electrical conductance results for alkali germanate melts at 1300°C (200°C above the melting point of the network forming species) that contain from 0 to 30 mole % M_2O. Similar information is not available for alkali silicate melts containing less than 20 mole % M_2O. The data will be compared with similar results for alkali germanate glasses (4).

Experimental

The preparative techniques and chemical analysis procedures for most of these samples have been previously described (1). Individual melts were prepared in several cases. Eagle Picher Electronic Grade GeO_2 and Baker reagent-grade analyzed Li_2CO_3, Na_2CO_3, and K_2CO_3 were used to prepare the melts.

A dipping electrode arrangement was used to measure the melt resistances. It consisted of a pair of parallel Pt·40 % Rh wires imbedded in a partially split mullite rod. Each melt was contained in a 37 mm diameter by 50 mm high platinum crucible under an air atmosphere. A General Radio Company Impedance Bridge (Type 1650-A) was used in conjunction with a Cenco Audio Oscillator to measure resistance as a function of frequency. All leads were shielded. Temperatures were measured with calibrated Pt·6 % Rh *vs.* Pt·30 % Rh thermocouples and a Rubicon Potentiometer (Model No. 2745). A 24 in. Pt·30 % Rh alloy wound alumina muffle furnace was used as the heat source. Details of the instrument and its unusual calibration procedures are described in greater detail elsewhere (5).

Resistances were measured at 10 kc for an electrode immersion depth of 8 mm. Any contributions to the total impedance by capacitive reactances in the melt were negligible at that frequency. Indeed, capacitive effects were rather small between 1 and 10 kc.

Results

The individual specific conductance values (κ) were calculated from the experimental resistances with the aid of log κ *vs.* log Ω calibration equations that were developed for each electrode arrangement. All of the specific conductance data observes the relationship:

$$\kappa = C \exp(-\Delta H^{\neq}_{\kappa}/RT) \quad [1]$$

or

$$\log \kappa = a - b\,[10^4/T(°K)] \quad [2]$$

This allowed the use of a least squares treatment of the individual specific conductance values that were obtained in the temperature range 1075°-1350°C. Table I gives the least squares constants of the log κ equations for all of the alkali germanate compositions as well as for a sample of pure GeO_2.[2]

The equivalent conductances (Λ) were calculated for the purpose of determining to what extent network alteration contributes to cation mobility. The following equation was used

$$\Lambda = 100\,\kappa M/\rho n Z X \quad [3]$$

[1] Present address: Department of Chemistry, University of California, Berkeley, California.

[2] Emission spectroscopy showed that this sample contained from 0.001 to 0.01 w/o (weight per cent) Na_2O as the chief alkali impurity both before and after the run. This impurity level is slightly higher than the level encountered during a previous viscosity study of pure GeO_2 (1).

Table I. Specific conductance equations for alkali germanate melts

Composition, mole %	$\log \kappa = a - b \times 10^4/T(°K)$ a	b
GeO_2*	1.4736	0.8295
0.56 % LiO_2	0.5457	0.4032
2.48	1.4002	0.3995
8.02	2.0661	0.3855
9.59	2.1732	0.3843
17.68	2.1997	0.3414
31.79	2.4677	0.3150
0.24 % Na_2O	0.7552	0.5376
0.72	1.0543	0.5023
1.53	1.7192	0.5266
4.29	1.8816	0.4602
7.79	2.4289	0.4702
12.8	2.2522	0.3952
21.7	1.9535	0.3102
29.9	1.6684	0.2144
0.47 % K_2O	3.0922	0.9115
1.95	3.1653	0.8145
4.58	2.8476	0.6561
7.41	2.8199	0.5933
16.69	1.9959	0.3691
28.07	1.5559	0.2381

* Contained 0.001 to 0.01 w/o Na_2O as chief impurity.

where M is the molecular weight of M_xO_y, ρ is the melt density (g/cc), n the w/o M_xO_y, Z the charge on M, and X the number of M atoms per molecule of M_xO_y. The equivalent conductance so calculated is that due to one gram equivalent per cc and is free of concentration effects. Equation [3] is valid only when the network forming species does not contribute significantly to conductance (6). As will be seen, this is a justifiable assumption in this case. A composition dependent increase in the observed Λ values can therefore be associated with an increased cation mobility.

Figure 1 shows the equivalent conductance isotherms for 1300°C as a function of composition for the zero to 30 mole % alkali oxide region. The rather sharp increases are significant in that even small amounts of alkali oxide cause large cation mobility changes. Figure 2, drawn on a large scale, depicts the Λ isotherms for the 0 to 5 mole % alkali oxide region.[3] Equivalent conductance at infinite dilution values (Λ_0) can be obtained from this plot. This was not possible with the available molten alkali silicate conductance data.

The composition dependence of the activation energy for electrical conductance ($\Delta H^{\neq}_{\kappa}$) is depicted for each series of melts in Fig. 3. Small amounts of either Na_2O or Li_2O appear to have a more pronounced influence than do similar amounts of K_2O. It is possible to use $\Delta H^{\neq}_{\kappa}$ for comparative purposes because $\Delta H^{\neq}_{\kappa} \approx \Delta H^{\neq}_{\Lambda}$ for melts with small expansion coefficients. The two energies differ by only a few tenths of a kilocalorie for the melt with the largest expansion coefficient (~30 mole % K_2O).

Discussion

Analysis of equivalent conductance results.—The most likely phenomenon that could be responsible for enhanced cation mobilities (Fig. 1) would involve network alteration. Previous viscosity and density results (1, 2) for these systems are indicative of extensive network alteration that accompanies small additions of alkali oxide to molten germania. The trends of these equivalent conductance isotherms thus generally agree with the previously developed model for the structure of these alkali germanate melts.

The general order of Λ ($Li^+ > Na^+ > K^+$) for all compositions at 1300°C is similar to that observed for simple molten salts and is therefore what one would expect if ionic field strength strongly influenced cation mobility. Isocomposition plots of Λ_{1300} *vs.* cation volume are not linear. However, similar plots of Λ_{1300} *vs.* I {where $I = 2z/(r_+ + r_-)^2$ = cation-oxygen attraction force} exhibit a closer adherence toward linearity (Fig. 4). These plots are completely linear for the zero, 1, 20, and 30 mole % M_2O lines at 1300°C. This linear dependence appears to be related to composition in that it becomes more pronounced (by ~3x) as the alkali oxide content is increased from infinite dilution to 30 mole %.

One can assume that the $\Delta\Lambda_0/\Delta I$ slope (for the case of infinite dilution in Fig. 4) represents a norm because the current carriers are essentially isolated from each other while migrating through a somewhat unperturbed O-Ge-O network. If this assumption is correct, then Λ_{K^+} is less than expected for the 5 to 15 mole % K_2O region. This conclusion is supported by the fact that the $\Delta\Lambda/\Delta I$ slope for the Na^+ to Li^+ region increases in a fairly regular fashion as the alkali content is increased. It would thus appear that the field

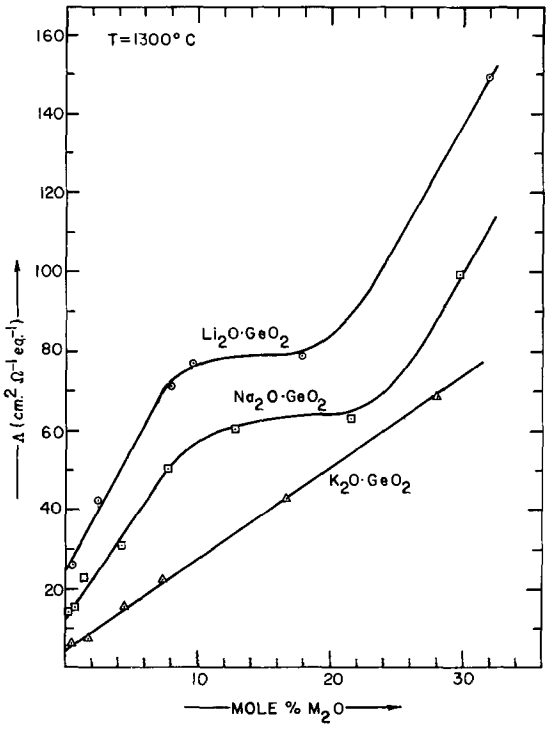

Fig. 1. Equivalent conductance isotherms for alkali germanate melts as a function of composition at 1300°C.

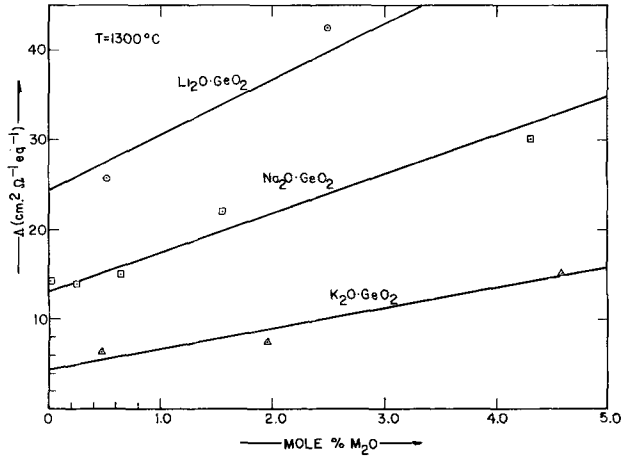

Fig. 2. Large-scale plot of equivalent conductance isotherms (1300°C) for GeO_2 rich alkali germanate melts.

[3] The conductance point for the lowest Na_2O content in Fig. 2 (pure GeO_2 containing 0.001-0.01 w/o Na_2O impurity) was calculated with Eq. [3], 0.01 w/o Na_2O assumed. This point falls close to the Na_2O isotherm and is within the deviation experienced by the other data points. This offers a possible explanation of the fact that the present value of κ_{1300} for GeO_2 is 1.59×10^{-4} ohm^{-1} cm^{-1}. Essentially the same value was obtained for a second sample run in a dry O_2 atmosphere. It is slightly higher than Mackenzie's value of 6.8×10^{-5} ohm^{-1} cm^{-1} (7) for a sample that contained 0.1 w/o CaO and less than 0.001 w/o Na_2O, MgO, and SiO_2.

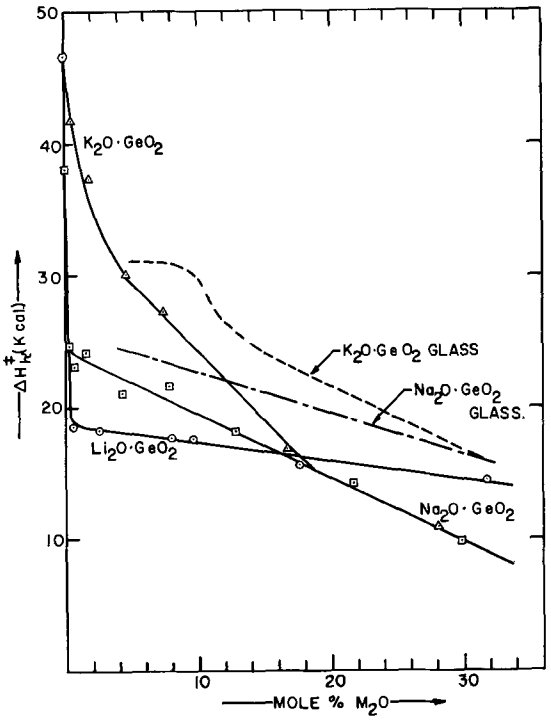

Fig. 3. Activation energy for electrical conductance as a function of composition for alkali germanate melts.

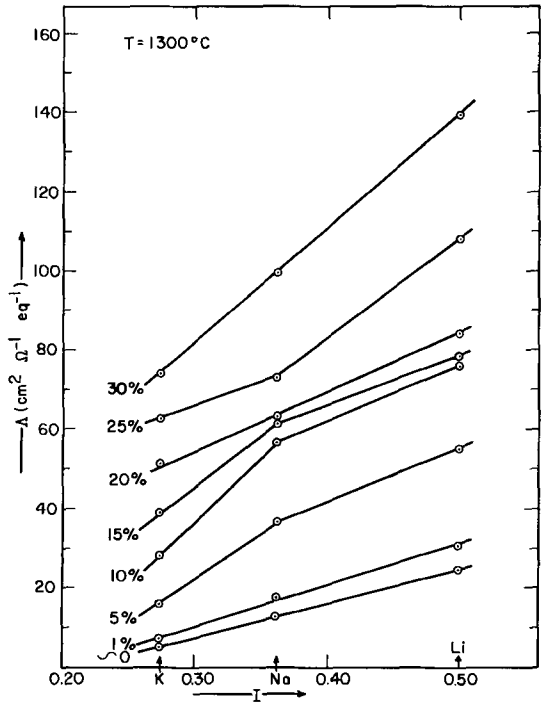

Fig. 4. Isocomposition plots of equivalent conductance at 1300°C as a function of *I*, the cation-oxygen attraction force.

strength of K^+ is not large enough to dominate mobility completely in the 5 to 15 mole % K_2O region.

It is now suggested that (*a*) the aforementioned change of Λ_{1300} dependence on *I* and (*b*) the apparent Λ_{1300} deviations experienced by K^+ are both indirectly associated with the gradual formation of clusters of GeO_6 octahedra. The appearance of clusters of edge shared GeO_6 octahedra can lead to small, local regions of order that are randomly dispersed throughout the O-Ge-O liquid. Instead of a silica like situation, there would be a different distribution of hole sizes that could conceivably lead to a greater dependence of cation mobility (under conditions of an applied electric field) on field strength.

The coordination change for germanium(IV) is accompanied by a slightly more voluminous packing of oxygens around the Na^+ and K^+ ions (2). This could superimpose a volume restriction on the field strength factor for the mobility of the relatively large potassium containing polyhedra at 1300°C.

The general trend for each cation at 1150°C is similar to those observed at 1300°C. However, small differences do occur. The Λ_{1300} plateaus for Li^+ and Na^+ (Fig. 1) tend toward slight Λ_{1150} maxima at about 10 mole % M_2O and Λ_{1150} minima at about 20 mole % M_2O, while Λ_{1150} for K^+ curves slightly as it approaches infinite dilution at pure GeO_2. A collective comparison of the three Λ_{1150} isotherms reveals one reversal. Thus, $\Lambda_{K^+} > \Lambda_{Na^+}$ for the 19 to 25 mole % M_2O region. Clearly, cation mobility at 1150°C (just 35°C above the melting point of pure GeO_2) is not the reasonably simple or linear function of *I* that it appears to be at higher temperatures. The fact that these additional irregularities are found in a composition region where extensive GeO_6 octahedra formation occurs suggests a possible relationship.

Activation energies.—The large activation energy decreases that are discontinuous functions of composition (Fig. 3) indicate a possible change of conductance mechanism, especially for small concentrations (less than 1 mole % M_2O) of Li^+ and Na^+ ions. The general trend of $\Delta H^{\neq}_K$ for the zero to 15 mole % M_2O region ($K^+ > Na^+ > Li^+$) is similar to that observed for simple alkali halide molten salts (which possess much smaller $\Delta H^{\neq}_K$ values).

The activation energies for these alkali germanate melts are not linearly dependent on *I*. However, they are linearly dependent on cation volume (Fig. 5) for compositions in the 0 to 15 mole % M_2O region. The fact that this dependence gradually decreases and finally becomes nonexistent at 17 mole % M_2O suggests that network alteration proceeds in such a fashion as

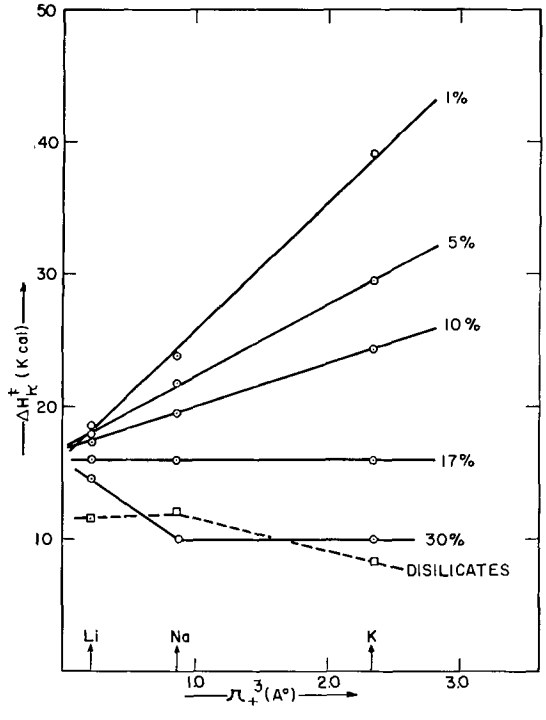

Fig. 5. Isocomposition plots of activation energy for electrical conductance ($\Delta H^{\neq}_K$) as a function of cation volume.

to produce a similar energy barrier for electrical conduction when an alkali germanate melt contains a mixture of GeO_6 and GeO_4 polyhedra.

It is suggested that since $\Delta H^{\neq}_{\kappa}$ is initially related to cation volume, hole size plays a role in the conductance mechanism. Apparently, the critical hole size for the 0 to 10 mole % M_2O region lies between the sizes of the Na^+ and K^+ ions, K^+ being a trifle too large. This could explain the absence of an immediate rather sharp decrease of $\Delta H^{\neq}_{\kappa}$ with increase of K_2O content (Fig. 3).

Comparison with alkali silicate melts.—No conductance data are available for molten binary alkali silicate systems containing less than 20 mole % alkali oxide. Extrapolation of the silicate data from the 20 mole % M_2O region to pure SiO_2 would be risky because of the sharp property changes to be expected. However, comparisons are possible for melts close to the 33 mole % M_2O composition.

Figure 6 reveals a marked difference in the field strength dependence of Λ for the 30 mole % M_2O germanate melts at 1150°C and the 33 mole % M_2O silicate melts at 1750°C. Although the temperatures are different, each isocomposition line represents a temperature region just above the melting point of the respective network forming species. Cation mobility in the silicate melts is clearly not a simple function of ion-oxygen attraction. This is an additional indication that (*a*) the molten germania network is altered in a fashion that is different from that suggested by Bockris *et al.* (3, 6) and (*b*) the structure of these germanate melts differ from that postulated for the corresponding silicates.

The interpretation of the cation volume dependencies observed for $\Delta H^{\neq}_{\kappa}$ in the 30 mole % M_2O region (Fig. 5) is not as simple as for the lower alkali concentration melts. Although the trends are not exactly similar for the two network formers, the relative values for $\Delta H^{\neq}_{\kappa}$ in each cation system suggest that they possess similar conductance mechanisms at about 33 mole % M_2O.

Bockris *et al.* developed the following equation for the calculation of the entropy of activation ($\Delta S^{\neq}_{\Lambda}$) for molten alkali silicate melts (6). They used Eyring's theory of absolute reaction rates

$$\Lambda = 3.26 \times 10^{19}\, zd^2 \exp(\Delta S^{\neq}_{\Lambda}/R) \exp(-\Delta H^{\neq}_{\Lambda}/RT) \quad [4]$$

where z is the ion charge and d the 1.5Å (jump distance).[4] The free energy of activation ($\Delta F^{\neq}_{\Lambda}$) can then be calculated from

$$\Delta F^{\neq}_{\Lambda} = \Delta H^{\neq}_{\Lambda} - T\,\Delta S^{\neq}_{\Lambda} \quad [5]$$

The conduction model for Eq. [4] involves cation movement from one interstitial hole in the oxide network to the next. The calculation of $\Delta S^{\neq}_{\Lambda}$ and $\Delta F^{\neq}_{\Lambda}$ in such a fashion is at best approximate. These quantities have been calculated for the present alkali germanate melts solely for the purpose of comparing them with the alkali silicate values.

Figure 7 depicts $\Delta S^{\neq}_{\Lambda}$ and $\Delta F^{\neq}_{\Lambda}$ as functions of melt composition for the alkali germanate systems. Comparison of the $\Delta S^{\neq}_{\Lambda}$ values with the $\Delta H^{\neq}_{\Lambda}$ curves of Fig. 3 shows that $\Delta H^{\neq}_{\Lambda} >> T\Delta S^{\neq}_{\Lambda}$ for all of these germanate melts (usually by a factor of 3 to 7 x greater). It would appear that the enthalpy (or energy barrier) predominates over any steric factor in the activated complex during cation displacement.[5] This predominance of $\Delta H^{\neq}_{\Lambda}$ is manifest in the slight $\Delta F^{\neq}_{\Lambda}$ trends (Fig. 7) where $K^+ > Na^+ > Li^+$ for all germanate compositions studied.

Bockris *et al.* (6) reported more negative entropies of activation and slightly smaller enthalpies of activation (by about 4 kcal at 20 mole % M_2O) for the alkali silicates at 1750°C. This reveals the larger relative role of a steric factor in the activated complex for silicates when compared to germanates. The trend toward more negative entropies of activation for the alkali rich germanate melts (Fig. 7) is one that suggests a slight similarity with the higher temperature silicate analogues.

Although it would appear that similar cation jumping mechanisms occur in the 20-30 mole % M_2O region for both network formers, there are differences of detail that can be related to melt structural differences.

Comparison with molten salts.—Figure 6 compares the Λ *vs.* I plots of 30 mole % M_2O germanate melts at 1150°C with similar data for a comparable series of alkali disilicate melts at 1750°C and with a series of alkali chloride melts at $T = 1.05$ (T_{MP}) {temperature range 650°-890°C}. Two facts stand out: (*a*) the Λ *vs.* I trend for the alkali germanates is similar to the trend for alkali chlorides, and (*b*) cation mobility is higher in the alkali chloride melts than in either of

[4] A dielectric constant of 5 was assumed for the silicate melts. The same value has been assumed for the corresponding germanate melts.

[5] This observation reinforces the significance of the dependence of $\Delta H^{\neq}_{\Lambda}$ on cation volume for the 0 to 20 mole % M_2O region.

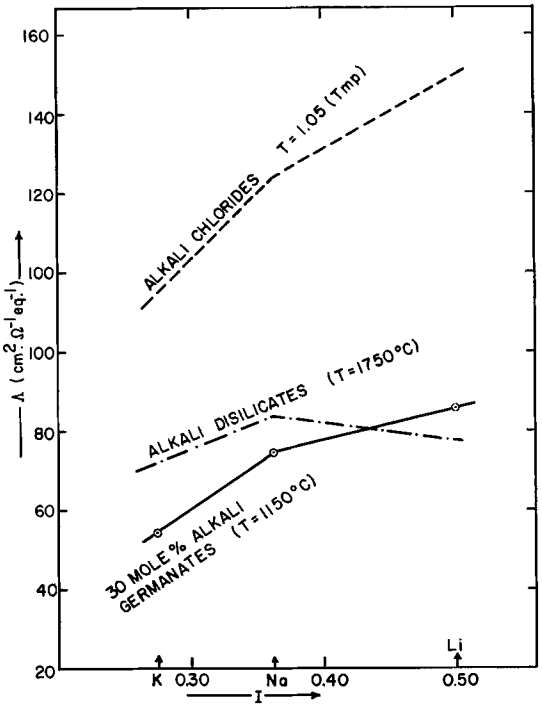

Fig. 6. Equivalent conductance *vs.* I for a series of selected molten salts, molten silicates, and molten germanates.

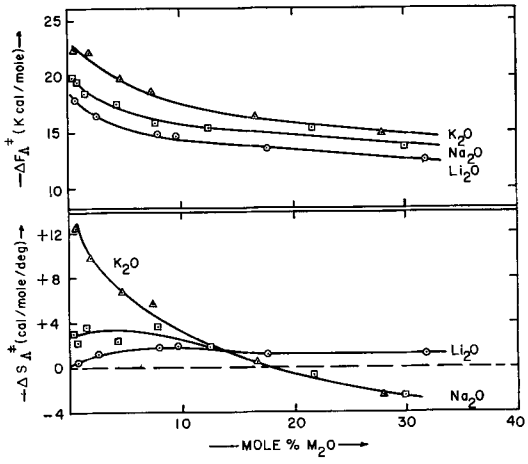

Fig. 7. Free energy of activation ($\Delta F^{\neq}_{\Lambda}$) at 1300°C and entropy of activation ($\Delta S^{\neq}_{\Lambda}$) as a function of composition for a series of alkali germanate melts.

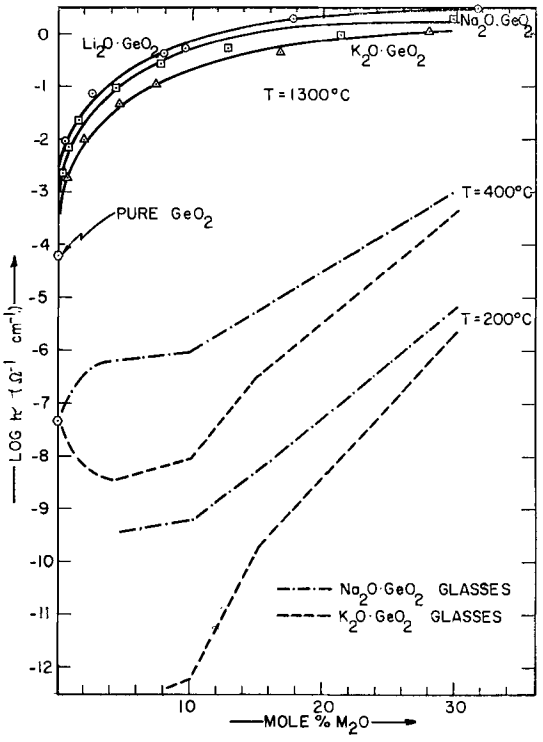

Fig. 8. Specific conductance *vs.* composition for alkali germanate melts and alkali germanate glasses: — • — • —, $Na_2O \cdot GeO_2$ glasses; — — —, $K_2O \cdot GeO_2$ glasses.

the oxide liquids at much higher temperatures {for $T \sim 1.05$ (T_{MP}) of the network former}.[6]

Thus, although the cation mobilities are reasonably large in a 30 mole % alkali germanate melt, they are still only one-half the value experienced in a simple chloride melt. The mixture of holes produced by the presence of GeO_6 and GeO_4 polyhedra in the anionic portion of the liquid obviously does not enhance cation mobility to the same extent as the holes in a simple chloride ion matrix.[7]

Comparison with alkali germanate glasses.—The specific conductances of the sodium germanate melts at 1300°C are from 10^3 to 10^5 times higher than the values reported by Ivanov (4) for the analogous glasses at 400°C (Fig. 8). These differences are even larger for the potash compositions. This is indicative of a greatly reduced charge carrier mobility for the glassy state and is to be expected. These conductance differences reach a maximum at an alkali oxide content of about 10 mole % M_2O (Fig. 8) and are followed by a continuous decrease as far as measured (to about 30 mole % M_2O).

It appears that cation mobility in the glass is altered in a slightly different fashion with change of composition than that encountered for melts at 1300°C.[8] The specific conductance in the 0 to 15 mole % M_2O region appears to be more steeply dependent on ion field strength for a given glass than for its corresponding liquid.

The $\Delta H^{\neq}_{\kappa}$ differences between melt and glass (Fig. 3) are not nearly as pronounced as those just discussed for specific conductance. The glass state values reported by Ivanov (4) are always larger than the melt values reported herein, but only by about 1-5 kcal. Also, $\Delta H^{\neq}_{\kappa}$ for K^+ is generally larger than $\Delta H^{\neq}$ for Na^+ for both glass and melt. However, $\Delta H^{\neq}_{\kappa}$ in the glasses is independent of ion type (for K^+ and Na^+) at about 30 mole % M_2O compared to 17 mole % M_2O for the melts.

In conclusion, the similarity of energy barriers for alkali germanate glasses and melts suggests that the same activated process or mechanism of electrical conduction holds for both condensed states.

Acknowledgment

The authors would like to thank Dr. S. D. Stookey for his encouragement and P.C. Logel for assistance with the experiments.

Manuscript received Feb. 11, 1965. This paper was presented at the San Francisco Meeting, May 10-13, 1965.

Any discussion of this paper will appear in a Discussion Section to be published in the June 1966 JOURNAL.

REFERENCES

1. E. F. Riebling, *J. Chem. Phys.*, **39**, 1889 (1963).
2. E. F. Riebling, *ibid.*, **39**, 3022 (1963).
3. H. Bloom and J. O'M. Bockris, "Molten Electrolytes," in "Modern Aspects of Electrochemistry," J. O'M. Bockris, Editor, Vol. 2, Academic Press Inc., New York (1959).
4. A. O. Ivanov, *Soviet Physics-Solid State*, **5**, 1933 (1964). Translated from Fizika Tverdogo Tela, **5**, 2647 (1963).
5. E. F. Riebling and P. C. Logel, *Rev. Sci. Instr.*, **36**, 425 (1965).
6. J. O'M. Bockris, J. A. Kitchener, S. Ignatowicz, and J. W. Tomlinson, *Trans. Faraday Soc.*, **48**, 75 (1952).
7. J. D. Mackenzie, *J. Chem. Phys.*, **29**, 605 (1958).
8. N. N. Greenwood and I. J. Worrall, *J. Chem. Soc.*, 1680 (1956).
9. E. F. Riebling and C. E. Erickson, *J. Phys. Chem.*, **67**, 307 (1963).
10. K. S. Evstropiev and A. O. Ivanov in "Advances in Glass Technology," F. R. Matson and G E. Rindone, Editors, Part 2, p. 79, Plenium Press, New York (1963).
11. A. O. Ivanov and K. S. Yevstropov, *Doklady Akad. Nauk S.S.S.R.*, **145**, 797 (1962).
12. M. K. Murthy and J. Ip, *J. Am. Ceram. Soc.*, **47**, 328 (1964).
13. M. K. Murthy and J. Aguayo, *ibid.*, **47**, 444 (1964).
14. M. K. Murthy and J. Ip, Paper No. 36-B-64, presented at American Ceramic Society Meeting, Chicago, April 1964.

[6] The temperature coefficients (or activation energies) are largest for the alkali germanate melts.

[7] Disruption of a simple anion lattice also appears to account for the conductance decreases that occur during the melting of α-AgI and the addition of Ga^+ to either molten Ga_2Cl_4 (8) or molten Ga_2I_4 (9).

[8] Examination of Eq. [3] might suggest that significantly different density changes with composition between glass and melt might be responsible. This is not the case. Other studies have shown (10-14) that the density *vs.* composition plots for most of the alkali germanate glass systems exhibit maxima similar to those reported for the high-temperature melts (2). This justifies the use of κ in the above comparison.

Vacuum Deposited Molybdenum Films

R. A. Holmwood and R. Glang

IBM Components Division, East Fishkill Facility, Hopewell Junction, New York

ABSTRACT

Vacuum evaporation of molybdenum with an electron bombardment source on oxidized silicon wafers produces films whose properties depend on the condensation temperature. At 600°C or above, the films have resistivities comparable to molybdenum wire, satisfactory adhesion, and tolerable stress. They are potentially useful as interconnections for silicon devices and monolithic circuits. All films are polycrystalline with (110) fiber texture. Other crystallite orientations appear above 500°C, while simultaneously the intrinsic film stress becomes decreasingly tensile and, at 625°C, compressive. Film stress and preferred orientation are considered to result from the interaction of lattice defects during the entire growth process and not merely from lattice distortions at the film substrate interface.

Vacuum deposited metal films are finding increasing application in silicon devices and monolithic circuits. At present aluminum films are widely used for contacts and interconnections. However, these films are easily scratched and tend to corrode when exposed to moisture. Among alternative metals, molybdenum is attractive because its coefficient of thermal expansion is closer to that of silicon than any other metal except tungsten. Furthermore, it is harder than aluminum, while its resistivity is only about twice as high. However, the vapor pressure of molybdenum is less than 10^{-2} Torr at 2530°C, which has long been an obstacle in attempts to produce evaporated coatings (1). Recently, the development of electron bombardment sources has made possible the evaporation of refractory metals (2, 3). In this investigation, electron bombardment has been used to evaporate molybdenum, and the properties of the resulting films have been studied to evaluate their applicability in microelectronic circuits on silicon substrates.

Experimental Techniques

The molybdenum films were prepared in a commercial vacuum system equipped with a 4 in. oil diffusion pump and a liquid nitrogen trap located directly over a water-cooled baffle. A schematic diagram of the vacuum chamber is shown in Fig. 1. It consists of an 18 in. open end stainless steel bell jar with aluminum top plate and dutchman collar. The insertion of a liquid nitrogen shroud greatly improved the ultimate pressures obtainable. Molybdenum was evaporated from a work-accelerated electron beam source shown in Fig. 2.

The source material was vacuum zone purified molybdenum rod with a specified purity of 99.999% (4). The weight of a charge varied from 4 to 9g. The charge was placed on a water-cooled copper pedestal at ground potential. A heated tungsten filament surrounding the charge and enclosed by a tantalum deflection shield served as an electron source. Filament and shield were at —5 kv relative to the charge. The power supplied to the source was adjusted by varying the temperature of the tungsten filament. About 500w were required to initially melt the charge, and 1.5 kw to produce a deposition rate of 10 Å/sec. During evaporation, some molybdenum was deposited on the tungsten filament thus lowering its resistance. Similarly, the increasing thermal contact between the melting charge and the cooled pedestal as well as the gradually decreasing size of the melt necessitated continuous power adjustments to maintain a constant deposition rate.

The deposition rate was monitored by a quartz crystal oscillator operating at 4.1 mc. A programmed cam opened a shutter exposing the crystal to the evaporant for 10 sec, and then closed the shutter for another 10 sec. Just prior to opening again, the frequency was measured and printed on tape. The frequency difference between intervals was converted to an average rate for the exposed time. The conversion factor was obtained by an initial calibration, after which the crystal remained fixed in relation to source and substrates. The resonant frequency becomes temperature sensitive when the crystal exceeds approximately 100°C. To avoid unnecessary radiant heating from the substrate holder and to facilitate faster temperature stabilization after exposure to the source, the crystal was placed in a water-cooled copper holder. This mode of operation provided thickness and rate control with an accuracy of ± 10%.

The substrate heater assembly consisted of a stainless steel cylinder with a closed bottom suspended from the top plate. Three cartridge heaters embedded

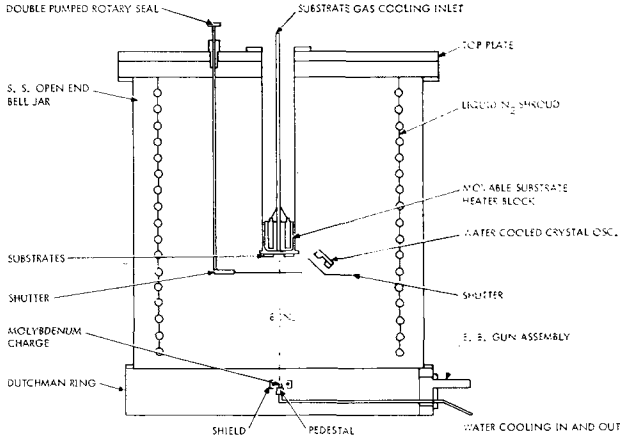

Fig. 1. Schematic diagram of vacuum chamber

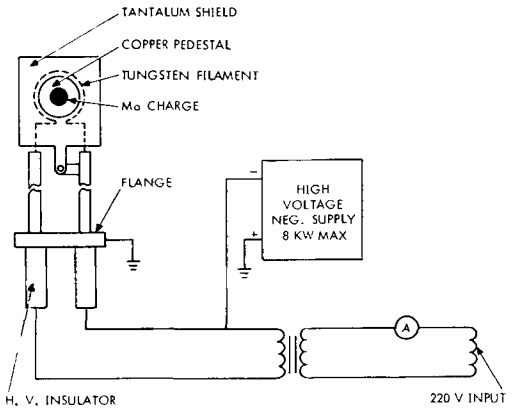

Fig. 2. Schematic diagram of Mo evaporation source

in a nickel block with a gas cooling tube attached were inserted into the steel cylinder as shown in Fig. 1. Thus, heat supply to the substrates was regulated external to the vacuum chamber. Inside of the vacuum chamber, a molybdenum plate was fastened to the bottom of the steel cylinder. This plate had three circular recesses to accommodate 1 in. diameter silicon substrates, which were held in place by ring shaped clamps. Good thermal contact between the substrates and the molybdenum holder was achieved by applying gallium metal to the interface. The temperature was monitored by a thermocouple attached to the molybdenum holder. Comparison measurements with thermocouples silver soldered to the front surfaces of silicon wafers showed the substrate temperatures to be within 5°C of the holder temperature. However, at substrate temperatures above 600°C, gradual loss of thermal contact occurred because the gallium alloyed with the molybdenum. Consequently, substrate temperatures higher than 600°C may be in error as much as 20°C. By adjusting heater current and gas flow manually, the substrate temperatures were maintained within ± 5°C.

The chamber was evacuated while the substrates were heated to 400°C and with liquid nitrogen circulating through the shroud. The ultimate pressure prior to energizing the source and with the substrates at deposition temperature was always below 1.10^{-7} Torr. When the molybdenum was melting, some outgassing occurred bringing the pressure temporarily up to about 2.10^{-6} Torr. During the evaporation, the pressure remained below 2.10^{-7} Torr.

Film Properties

Early evaporation experiments demonstrated that molybdenum film properties are most sensitive to the deposition temperature. Other experimental conditions were held constant. All films were approximately 1μ thick and deposited at 10 ± 1 Å/sec. The substrates were 0.006-0.008 in. thick silicon wafers, cut from (111) oriented single crystalline rods. They had been lapped, chemically etched, and thermally oxidized. The oxide was approximately 6000Å thick. Prior to deposition, the wafers were cleaned ultrasonically in detergent solution, demineralized water, and acetone and stored in a vapor degreaser containing isopropanol.

All measurements on films were made after the samples had been removed from the vacuum system. The thickness was determined with a stylus instrument (5) after a step had been etched into the film. Reproducibility was about ± 4%. Control measurements were made on parallel monitor slides using interferometric techniques. Thickness data of both methods agreed within the error limits of the stylus method.

Resistivities.—The sheet resistances of the molybdenum films ranged from 0.05 to 0.55 ohm/sq at room temperature. Measurements were made with a commercial instrument containing four probes in a linear array. For comparison, voltage drop measurements were performed on subtractively etched film patterns of known geometry. The four point probe data were always about 4% lower than the voltage drop values. The room temperature resistivity of molybdenum films as a function of the deposition temperature is shown in Fig. 3.

The resistivity of etched film patterns was measured from 25° to 100°C in 5° intervals. These data were evaluated by the method of least squares to determine the temperature coefficient α and the resistivity at 0°C, ρ_0, as defined by the equation

$$\rho(T) = \rho_0 + \rho_0 \cdot \alpha \cdot T \qquad [1]$$

Results are shown in Table I along with the ratio of resistivities at liquid nitrogen temperature and 0°C. Resistivity data are a good indication of the combined effects of chemical impurities and physical defects on

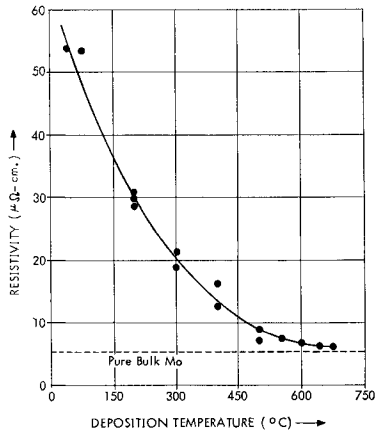

Fig. 3. Room temperature resistivity of molybdenum film vs. deposition temperature.

the mean free path of electrons (6). For a transition metal such as molybdenum, size effects on the mean free path need not be considered for films 1μ thick (7, 8), particularly since the structure of these films must be expected to be highly defective. In evaporated chromium films, for example, the mean free path of electrons has been estimated to be about 30Å (9), and in films of tantalum and tungsten the resistivity becomes independent of thickness from 300 to 400Å on (3).

The resistivity curve shown in Fig. 3 indicates increasing film purity and decreasing structural defects with increasing deposition temperature. At 600°C the film resistivity and its temperature coefficient approach the values of the bulk metal and are similar to those of drawn pure molybdenum wire (10). Mattiessen's rule holds with fair approximation as shown in column V of Table I. Thus, the magnitude of the residual resistivity of high-temperature films can be explained with the assumption of stress and a moderate concentration of point defects. Examples of electrical properties of heavily deformed wire in Table I show that stress contributes relatively little to the residual resistivity. Therefore, low-temperature films must have a large number of scattering centers. The highest film resistivities observed cannot be attributed merely to lattice defects, but indicate chemical impurities. The large deviations from Mattiessen's rule suggest the presence of a second phase. Molybdenum is known as an effective getter material for many gases including oxygen (11). The lower molybdenum oxides are thermodynamically stable in the pressure-temperature range in question. Although data for this temperature interval are not available, it is known that 1545°C are required to produce a total sublimation pressure of 0.25 Torr over MoO_2+Mo (12). Furthermore, oxide formation has been observed to occur at the grain boundaries if molybdenum was annealed in vacuum containing minute quantities of oxygen (13).

Table I. Resistivity data of molybdenum films prepared at various deposition temperatures

Deposition temp, °C	Resistivity at 0°C	ρ, μohm-cm, at 25°C	Temp. coeff. α, degree^{-1}	$\alpha \cdot \rho$, 10^{-10} ohm-cm deg^{-1}	$\frac{\rho_{-196}}{\rho_0}$
85	53.7	54.6	0.00066	361	0.796
200	29.7	30.7	0.00140	430	0.710
200	27.6	28.8	0.00152	436	0.693
400	15.5	16.4	0.00226	370	0.550
400	12.5	13.1	0.00220	289	0.520
600	6.02	6.60	0.00387	255	0.284
600	6.02	6.59	0.00378	249	0.274
Pure Mo (4)	5.00	5.57	0.00482	268	0.097
Mo wire (10)		ρ_{20}	α	$\alpha \cdot \rho_{20}$	—
Cold drawn to 500μ		6.10	0.00423	262	—
Cold drawn to 100μ		6.75	0.00387	261	—
Cold drawn to 30μ		7.25	0.00371	269	—
Annealed at 700°C		6.30	0.00405	255	—

Therefore, the presence of grain boundary oxide in molybdenum films deposited at low temperatures is quite possible. The assumption can be reconciled with a positive temperature coefficient of resistivity such as observed if the grain boundary phase merely constricts the conductive paths between grains, but does not form a coherent barrier layer.

The process of oxide formation during film deposition must be preceded by chemisorption of oxygen atoms. With increasing substrate temperature, the probability of desorption of adatoms increases, and fewer oxide nuclei will form. Some adatoms are trapped before desorption or incorporation into an oxide nucleus occurs, thus forming impurity scattering centers. The latter must also decrease with increasing substrate temperature as desorption becomes more complete.

In conclusion, the mechanisms suggested to interpret the resistivity *vs.* temperature curve of molybdenum films attribute the greatest contributions toward residual resistivities to grain boundary oxide and impurity scattering. Both effects decrease with deposition temperature due to increasing desorption of adatoms. At the highest temperatures, the residual resistivity is small enough to be explained largely on account of lattice defects and stress.

Adhesion.—The adhesion of the molybdenum films to the substrates varied with the deposition temperature. Films prepared below 100°C did not adhere well and sometimes peeled off on exposure to air. The best adhesion was achieved between 200° and 500°C; these films could not be torn off the substrates by repeated attempts with adhesive tape (14). Films prepared at 100°-200°C or above 500°C adhered firmly enough to withstand the application of photosensitive lacquer, chemical etching, and similar process steps, but could be partially removed with adhesive tape.

Crystalline structure.—The films were investigated by x-ray diffraction techniques using CuK_α radiation and a pulse height analyzer. All films were polycrystalline and showed diffraction peaks associated with bcc molybdenum lattice. The relative peak intensities indicated a fiber texture typical for bcc metals with the lattice plane of greatest packing density, (110), parallel to the substrate surface (15). This texture has been reported before for evaporated molybdenum films (16). The only other orientation consistently present was (211). Crystallites with planes of higher indices parallel to the surface appeared regularly at or above 500°C deposition temperature. In this range, the intensities of (211) peaks increased slightly, but (110) still remained the strongest peak.

It has been attempted to determine the average grain size from the width of the diffraction peaks. Due to the absence or weakness of most peaks, it was not possible to apportion line broadening accurately to grain size and random lattice distortion effects. Estimated grain sizes of films deposited between room temperature and 400°C are in the range of 250-500Å. At deposition temperatures of 600°C or higher, the diffraction peaks are very sharp, and the average grain size must be greater than 1000Å. For several films, the lattice constant in the direction perpendicular to the film surface has been calculated. Although these data are not very accurate, they indicate tensile strain of 0.10 to 0.25% parallel to the surface for all films. This is the same order of magnitude which was obtained by separate stress measurements discussed below.

Film stress.—Stresses of considerable magnitude have been observed in evaporated films (17-19), and various measuring techniques have been reported (20, 21). If the films are attached to a thin substrate, the latter experiences an elastic deformation which can be used to determine the stress. A modification of this technique was applied to evaluate the stress in molybdenum films. It can be shown that a circular substrate wafer assumes a parabolic curvature resulting from the presence of a stressed film (22). The curvature can be measured and expressed by the parameter (ϵ) of the parabola $\delta = \epsilon \cdot r^2$, δ being the upward deflection of the substrate at a distance r from the center. The film stress parallel to the surface (σ) is given by

$$\sigma = \frac{E}{3(1-\nu)} \cdot \frac{t_{Si}^2}{t_{Mo}} \cdot \epsilon \text{ [dynes/cm}^2\text{]} \qquad [2]$$

where t_{Si} and t_{Mo} are the thicknesses of substrate and film. The proportionality factor includes Young's modulus and Poisson's ratio for (111)-oriented silicon wafers; its numerical value is $10^{12}/1.30$. Stress data obtained by this method are accurate within about $\pm$ 10%.

All films were found to be under tensile stress, and depending on the deposition temperature, their values ranged from $2.5 \cdot 10^9$ to $7.5 \cdot 10^9$ dynes/cm^2. This is the same order of magnitude published by Hoffman *et al.* for thin films of Ni, Fe, and Co (18). The tensile strength of sintered or cast molybdenum ingots is typically 3 to $5 \cdot 10^9$ dynes/cm^2, but may increase to $1.7 \cdot 10^{10}$ dynes/cm^2 after cold deformation (23). Because of the highly defective structure, the strength of evaporated films is probably similar to cold deformed bulk material. Besides, the tensile strength of films even several microns thick often exceeds the strength of bulk material due to pinning of dislocations at the surface, particularly if the metal forms oxide films which further impede the motion of dislocations (24). It is therefore safe to conclude that the stress values observed are below the fracture strength of the films. Indeed, microscopical investigation of slightly etched molybdenum films over oxidized silicon surface has never revealed the presence of cracks. This is not true for films on bare silicon surfaces, where solid-state diffusion at 600°C produces molybdenum silicide phases which are brittle and subject to cracking.

The stress data quoted for molybdenum films have been measured after cooling the substrates to room temperature. Therefore, part of this total stress is due to the difference between coefficients of expansion of molybdenum and the silicon substrate. This portion of the stress can be subtracted to arrive at the intrinsic stress, which is a more meaningful quantity in regard to the film condition at the deposition temperature (25). For purposes of this discussion, the total stress (σ) has been converted into total strain (Δl) parallel to the substrate surface

$$\Delta l = \frac{1-\nu}{E} \cdot \sigma \qquad [3]$$

where $\nu = 0.324$ and $E = 3{,}17 \cdot 10^{12}$ dynes/cm^2 are Poisson's ratio and Young's modulus of elasticity for molybdenum (26). The strain contribution of differential thermal expansion ($\Delta l_{d.e.}$) has been calculated from expansion data of both materials. Dilatometer measurements on 1 x 0.1 x 0.1 in. bars of zone purified molybdenum and of silicon, the latter cut from a (111)-oriented single crystal wafer, have been performed in the same apparatus to ensure that the data are comparable. The measured values were in excellent agreement with published data for silicon (27) and molybdenum (23, 28-32). Finally, the intrinsic strain (Δl_i) was calculated according to

$$\Delta l = \Delta l_{d.e.} + \Delta l_i \qquad [4]$$

The three types of strain are shown as a function of temperature in Fig. 4. Between room temperature and 500°C, the intrinsic strain is tensile and nearly constant. Above 500°C, there is a gradual decrease and finally a reversal to compressive strain at about 625°C.

Discussion

It could be argued that the amorphous SiO_2 films may become plastic at the higher temperatures and thus allow the molybdenum films to relieve part of

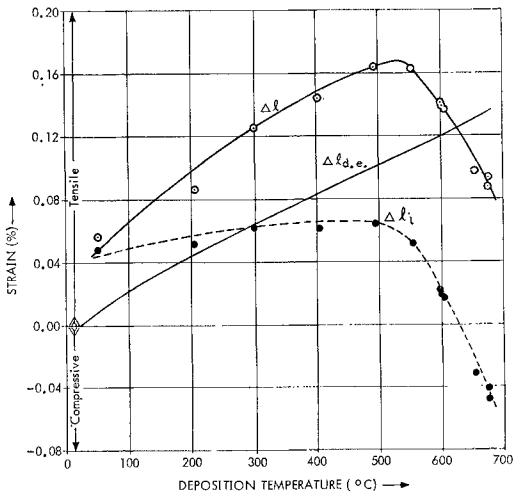

Fig. 4. Strain in evaporated molybdenum films vs. deposition temperature.

the intrinsic stress. If this were the case, the total strain curve would approach the differential expansion curve but not cross it as observed. Similarly, stress relief by contraction of the molybdenum film alone is not possible since this requires movement relative to the SiO_2 film and thus total loss of adhesion. Finally, the possibility of a permanent plastic deformation of the silicon wafer itself must be excluded since the shape of several substrates has been examined closely before film deposition and after its removal without finding any changes. Therefore, the effect of decreasing intrinsic tensile stress and reversal to compression above 500°C must be real.

It is interesting to note that the change in stress behavior occurs in the same temperature range where the films begin to show a trend toward random crystallite orientation. While there is not sufficient information to postulate a detailed mechanism for the origin of intrinsic stress in thin films, experimental results may be interpreted within the concepts of Hoffman and coworkers (18, 19, 25). These authors assume that imperfections formed during deposition undergo change shortly after being trapped by succeeding layers of deposited metal. This rearrangement of atoms, for instance, the conversion of dislocations into vacancies, or vice versa, produces a change in lattice volume and thus causes intrinsic stress. If the mobility of atoms is high enough, the lattice defects may consolidate by forming grain boundaries. The results of this investigation suggest that from 500°C on, lattice defects have sufficient mobility to interact by forming crystallites of orientations other than (110), and that this process is coupled with some relief of tensile stress. At the lower temperatures, the lower atomic mobility or the presence of grain boundary oxide or both of these factors confine the interaction of defects to individual crystallites which maintain their orientation and remain highly stressed.

This does not explain the occurrence of compressive intrinsic stress above 600°C. There may be another defect interaction mechanism at the higher temperatures with the effect of increasing rather than reducing the lattice volume. Another possible cause for compressive stress is the presence of residual gas atoms in solid solution (21). However, additional assumptions have to be made to explain why the compressive effect of dissolved gases should be observed only at higher temperatures.

The question of stress as determined by the SiO_2-Mo film interface has also been investigated. Cabrera (33) has discussed stress in epitaxial films under the aspect of lattice mismatch between substrate and film. Although thermal SiO_2 is not crystalline, it consists of a distorted network of cross-linked tetrahedrons with

Table II. Effect of low-temperature nucleation on film strain

Run No.	Total strain, % Film prenucleated at 400°C	"Pure" 650°C film
115	0.117	0.081
120	0.118	0.100
122	0.128	0.116

an average Si-Si distance of 3.2Å (34). The atomic distances in various molybdenum lattice planes are 3.15Å for (001), 2.76 and 3.15Å for (110), 2.76 and 4.46Å for (211), and 4.46Å for (111). Consequently, the mismatch of spacing between substrate molecules and molybdenum atoms should produce tensile film stress for (110) and compressive stress for (111) crystallites. The experimental data do not contradict this concept, but are certainly not conclusive. However, it has been investigated whether the structure and stress of the films are determined by the conditions prevalent during nucleation, *i.e.*, by the mismatch at the interface.

Two silicon wafers were loaded into the vacuum system, and one of them was exposed to receive 500-1200Å of molybdenum at 400°C while the other was shielded by a shutter. After raising the temperature to 650°C, a molybdenum film of 10,000Å was deposited over both wafers. If the lattice mismatch at the interface determines the character of the film, the samples prenucleated at 400°C should continue to grow at the higher temperature without changing their (110) orientation and thus maintain the high stress typical for low-temperature films. Considering the difficulties of close temperature control at high temperatures, the "pure" 650°C film should show a total strain of 0.08-0.12%, while a 400°C film would vary between 0.14-0.15%. The results of three pairs of samples are shown in Table II.

The data indicate that the prenucleated films are consistently more strained than the "pure" 650°C films, but not as high as a "pure" 400°C film. Furthermore, all samples show x-ray diffraction peaks of (200), (310), (222), and (321) crystallites typical for high-temperature films in addition to (110) and (211). Consequently, the structure and stress situation of the prenucleating layer does not propagate throughout the entire 650°C film. While the slightly higher stress values may be indicative of a gradual transition, the high-temperature mechanism of defect interaction dominates, causing reorientation of small crystallite regions and partial stress relief. In conclusion, these results, too, support a stress generation and relief mechanism effective during the entire film growth as suggested by Hoffman and, at least for these polycrystalline films, contradict the concept of stress being determined exclusively by lattice distortions at the substrate interface.

Summary and Conclusions

A vacuum evaporation process for molybdenum with a 2 kw work accelerated electron gun has been developed. Thickness control for films of about 1μ may be accomplished within ± 10% by a shielded and water-cooled quartz crystal oscillator. The properties of molybdenum films condensed on oxidized silicon wafers are determined by the substrate temperature. To achieve resistivities of 10 μ ohm-cm or less, condensation temperatures above 450°C are required. Resistivities comparable to molybdenum wire are obtained at or above 600°C. At these temperatures, the adhesion to thermal SiO_2 is weaker than in the interval 200°-500°C but still sufficient for subsequent device fabrication processes. All films have tensile stresses close to the fracture strength of bulk molybdenum. However, this is not considered to be critical since the tensile strength of thin films is usually higher than for the same material in bulk form; accordingly, film cracking has not been observed. Consequently, molyb-

denum films are compatible with passivated silicon substrates and may be used for integrated circuit interconnections. In contact with bare silicon, the applicability is temperature limited on account of the formation of brittle molybdenum silicides through solid-state reaction. The films exhibit an interesting stress behavior insofar as the intrinsic component is nearly constant up to a deposition temperature of 500°C, then decreases and changes from tensile to compressive stress at 625°C. This is accompanied by a transition from almost pure (110) to more random crystallite orientation in the same temperature interval. A casual relationship between the two phenomena is suggested in accordance with concepts about the origin of stress proposed by Hoffman *et al.* The increased atomic mobility at the higher temperatures allows consolidation of lattice defects by reorienting small regions of material and simultaneously reducing tensile stresses. It is also shown that crystallite orientation and generation of stress are not determined by the first layer of deposit attached to the substrate, but are subject to change during the entire film growth if temperature conditions are altered.

Acknowledgment

The authors would like to thank Mrs. C. Walter for stress measurements, Messrs. B. L. Graves for sample preparation, B. Narken for expansion measurements, E. J. Taschler for valuable help in the assembly of the vacuum system and evaporation source, Ch. H. Ma, J. S. Makris, and N. R. Stempel for x-ray diffraction work.

Manuscript received Feb. 17, 1965; revised manuscript received April 2, 1965. This paper was presented at the San Francisco Meeting, May 9-14, 1965.

Any discussion of this paper will appear in a Discussion Section to be published in the June 1966 JOURNAL.

REFERENCES

1. "The Metal Molybdenum," p. 200, J. Harwood, Editor, American Society for Metals, Cleveland (1958).
2. J. C. Kelly, *J. Sci. Instr.*, **36**, 89 (1959).
3. N. J. Maskalick and C. W. Lewis, *Trans. 8th Nat. Vac. Symp.*, **2**, 874 (1961), Pergamon Press, 1962.
4. R. A. Holmwood and R. Glang, to be published. *J. Chem. and Engng. Data.*
5. N. Schwartz and R. Brown, *Trans. 8th Nat. Vac. Symp.*, **2**, 836 (1961).
6. J. E. Kunzler, in "Ultra-High-Purity Metals," p. 171, Am. Soc. for Metals, Metals Park, Ohio (1962).
7. J. Bardeen, *J. Appl. Phys.*, **11**, 88 (1940).
8. H. Mayer, "Structure and Properties of Thin Films," p. 225, John Wiley & Sons, Inc., New York (1959).
9. I. G. Young and C. W. Lewis, *Trans. 10th Nat. Vac. Symp.*, p. 428, MacMillian Company (1964).
10. W. Geiss and J. A. M. vanLiempt, *Z. Physik*, **41**, 867 (1927).
11. R. W. Roberts and T. A. Vanderslice, "Ultrahigh Vacuum and its Applications," p. 27, Prentice Hall, Inc., Englewood Cliffs, N. J. (1963).
12. P. E. Blackburn, M. Hoch, and H. L. Johnston, *J. Phys. Chem.*, **62**, 769 (1958).
13. R. E. Maringer and A. D. Schwope, *J. Metals*, March 1954, p. 365.
14. L. Holland, "Vacuum Deposition of Thin Films," p. 99, John Wiley & Sons, Inc., New York (1958).
15. C. S. Barrett, "Structure of Metals," p. 444, McGraw-Hill Book Co., Inc., New York (1952).
16. I. R. Landau, "Metals and Alloys," Vol. 9, 73, 100 (1938).
17. R. E. Thun, in "Physics of Thin Films," Vol. 1, p. 226 Academic Press, New York (1963).
18. R. W. Hoffman, R. D. Daniels, and E. C. Crittenden, Jr., *Proc. Phys. Soc., London*, **B67**, 497 (1954).
19. J. D. Finegan and R. W. Hoffman, *Trans. 8th Nat. Vac. Symp.*, **2**, p. 935, Pergamon Press, New York (1961).
20. J. W. Menter and D W. Pashley in "Structure and Properties of Thin Films," p. 111, Proc. Int. Conf., Bolton Landing, 1959, John Wiley & Sons, Inc., New York.
21. H. Blackburn and D. S. Campbell, *Trans. 8th Nat. Vac. Symp.*, **2**, p. 943, Pergamon Press, New York (1961).
22. R. Glang, R. Holmwood, and R. L. Rosenfeld, *Rev. Sci. Instr.*, **36**, 7 (1965).
23. J. Harwood, "The Metal Molybdenum," p. 10, American Society for Metals, Cleveland (1958).
24. J. W. Menter and D. W. Pashley, *l.c.*, p. 137.
25. H. S. Story and R. W. Hoffman, *Proc. Phys. Soc. London*, **B70**, 950 (1957).
26. H R. Clauser, "The Encyclopedia of Engineering Materials and Processes," p. 430, Reinhold Publishing Corp., New York (1963).
27. L. Maissel, *J. Appl. Phys.*, **31**, 211 (1960).
28. *Physikalisch-Technisches Reichsamt, Z. Instr.*, **40**, 156 (1920).
29. J. Disch, *Z. Physik*, **5**, 173 (1921).
30. P. Hidnert and W. B. Gero, *Sci. Pap. Bur. Stand.*, **19**, 429 (1924).
31. R. S. Archer in "Rare Metals Hand Book," p. 291, 2nd ed., Reinhold Publishing Corp., New York (1961).
32. Climax Molybdenum Co., "Molybdenum Metal," Climax, Ohio, 1960.
33. N. Cabrera, p. 42/43 in "Structure and Properties of Thin Films," Proc. of an Intern. Conf. at Bolton Landing, New York, 1959.
34. H. A. Robinson, *J. Phys. Chem. Solids*, **26**, 209 (1965).

Contact Potential Difference between Silver Nitrate and Silver

James L. Copeland[1] and Ralph L. Seifert

Department of Chemistry, Indiana University, Bloomington, Indiana

ABSTRACT

The silver nitrate-silver contact potential was determined from 190° to 280°C by the Zisman dynamic condenser method. At the melting point of the salt the contact potential of liquid silver nitrate relative to silver is —530 mv, with a temperature coefficient of 0.14 mv/deg, and that of the solid salt is —608 mv. The discontinuity of 78 mv at the melting point is attributed primarily to a greater excess surface concentration of silver ions in the liquid than in the solid salt.

Of the various methods that have been used to measure contact potential between two dissimilar substances, only the electron beam deflection method (1), the Kelvin variable condenser method (2, 3), and the Zisman dynamic condenser method (4) do not involve ions and/or electrons impinging on the test surfaces during part of the procedure. Therefore these methods are most acceptable for study of the contact potential of a metal and its salt, either molten or in solution. The Zisman dynamic condenser method was

[1] Present address: Department of Chemistry, Kansas State University, Manhattan, Kansas 66504.

used in this study because it permits greatest precision of measurement.

One plate of the dynamic condenser is vibrated relative to the other. If there is a difference in the Volta (or outer) potentials of the facing surfaces, the periodic change in capacitance of the condenser produces an alternating current in a high resistance in the circuit joining the plates. The a-c potential across the resistor is amplified. A variable emf source between one plate and the resistor permits equalization of the Volta potentials as indicated by zero a-c signal. This balancing emf at zero signal equals the contact potential between the substances of which the plates are made if there is no net thermal emf in the external circuit and the error due to fringing field (5) is avoided. To the extent that any net error from these two sources can be held constant in two successive series of measurements, the error can be cancelled out by using one condenser plate as a reference surface, determining the apparent contact potential of each of the two desired substances relative to the reference plate (6), and calculating the contact potential of the two substances.

To determine the contact potential between silver and silver nitrate in contact with the silver, a silver vibrating plate was used as a reference. Its contact potential was determined relative to the surface of a stationary silver plate and then relative to silver nitrate covering the stationary silver plate.

Experimental

Materials.—Reagent grade silver nitrate (Baker Analyzed) was used without purification other than drying. Helium used as an inert atmosphere had a stated impurity content of 0.01%.

The two plates comprising the dynamic parallel-plate condenser were fabricated from silver with a purity of 999+ fine as quoted by the Baker Platinum Division of Engelhard Industries, Inc. Before all runs the plates were abraded with No. 1 steel wool and boiled successively in the following concentrated aqueous solutions for about 30 min each, with intervening rinsings in distilled water: (*a*) ammonium hydroxide, (*b*) hydrochloric acid, and (*c*) potassium cyanide. After thorough washing in distilled water, the plates were treated as above but in reverse order for the solutions, rinsed in distilled water, heated in air at 500°-600°C for approximately 4 hr, and then transferred to a desiccator while still hot. During and following this treatment the plates were handled only with clean tongs or surgical latex gloves, care being taken not to touch the active surfaces.

Apparatus.—The vibrating condenser was mounted inside a cubic brass vacuum chamber, designed to permit all operations during a run to be performed without opening the chamber. Viewing ports were provided in the front of the chamber, and three adjustable supports permitted leveling the chamber to insure that the lower surface of the upper condenser plate would be parallel to the surface of the molten silver nitrate. Details of construction are given in ref. (7).

The silver plates of the dynamic condenser are shown in Fig. 1, with the mounting assembly and heater for the vibrating plate. Upper plate (G) was vibrated at a frequency of 40 cps, with an amplitude of 2 mm, by means of a drive shaft which linked connector (A), through a Sylphon bellows, to an external ⅛ hp synchronous motor, geared to deliver 2400 rpm. Heater (C) was supported by its heavy copper leads and did not touch any part of the vibrating plate assembly.

Silver cylinder (H), serving as stationary plate, was mounted above a leveling platform by three silica tubes and a transite ring. The leveling platform could be raised and lowered through a distance of 3.2 cm from outside the vacuum chamber. When (H) was in its lower position a rectangular stainless steel salt pan could be moved between the condenser plates. A

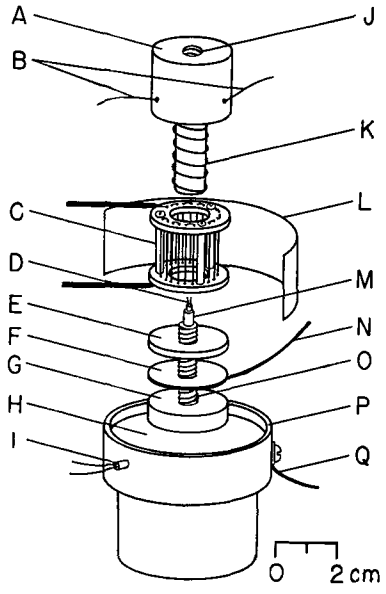

Fig. 1. Plates of dynamic condenser and exploded view of the mounting assembly and heater for the vibrating upper plate: (A) boron nitride connector; (B) leads from thermocouple (D); (C) heater, No. 26 nichrome wire on boron nitride frame; (D) chromel-alumel thermocouple in alumina insulator; (E) alumina washer; (F) silver washer; (G) vibrating silver plate of dynamic condenser; (H) stationary plate of dynamic condenser, upper surface of solid silver cylinder; (I) insulated chromel-alumel thermocouple; (J) threaded hole for reciprocating drive shaft; (K) grounded shield wire; (L) silver foil reflector (unwrapped); (M) quartz thermocouple well; (N) silver wire lead to vibrating plate; (O) ¼-28 thread on extension from silver condenser plate, for screwing into holder (A); (P) rim of cavity for holding silver nitrate; (Q) silver wire lead to stationary plate.

stud on the sliding bottom of the pan caught on rim (P), dumping silver nitrate into the plate cavity as the pan was pushed over it. The lower portion of cylinder (H) was surrounded by a small cylindrical furnace positioned inside the three silica supports but not touching the cylinder. Thermocouple (D) extended to within 4 mm from the lower surface of plate (G), and thermocouple (I) was about 0.8 mm below the center of the top surface of cylinder (H).

Storage batteries were used for heater current during measurements. Alternating current was used during prolonged periods when measurements were not being made. One side of each electrode heater circuit and of each thermocouple circuit was grounded. A grounded wire shield between each plate and its heater eliminated an observed change in measured contact potential which was proportional to the d-c heater current. The shields also reduced the slight dependence of measured contact potential on mean plate separation to less than the random error in the measurements. This dependence of apparent contact potential on plate separation (5) had already been greatly diminished by making the vibrating plate smaller than the stationary one.

For balancing the contact potential between the plates a K-2 potentiometer was connected by a reversing switch to the vibrating plate and to ground. The off-balance 40-cycle signal was passed through a 50 megohms input resistor of a high-gain amplifier with a band-pass filter tuned to 40 cps. The amplified signal was displayed on an oscilloscope. Although shielded wires were used throughout the circuit for signal-carrying leads and batteries were used for the heaters and amplifier, a small amount of 60-cycle pickup was present in the amplified signal.

Procedure.—To detect a very small amplitude 40 cps signal in the presence of the 60 cps pickup, use was made of the fact that the combined signal was repeti-

tive every 1/20 sec. With oscilloscope triggered by a 60 cps signal and set at a sweep rate of 0.1 msec/cm, a 40 cps component in the input signal produced three almost linear and parallel traces, with vertical displacement proportional to the amplitude of the 40 cps component. The null point, at which a single trace was observed, could be detected within ± 0.2 mv. However, over periods of 2-5 min, the applied potential necessary to obtain a null signal was observed to exhibit random fluctuations, sometimes as large as 3.5 mv but for the majority of experimental points less than 0.8 mv.

With the system evacuated to less than 0.1 mm Hg, the plates were heated for 1 hr at about 300°C. The decomposition pressure of silver oxide at 300°C is 19.8 atm (8). Helium was then admitted to about 50 mm Hg above atmospheric pressure. Contact potential measurements were made at regular intervals until the values became constant. To establish a blank curve for the contact potential of the silver surface of the stationary plate relative to the vibrating reference plate, measurements were then made at plate temperatures comparable to those at which measurements were later to be made with silver nitrate on the stationary plate.

Helium was chosen as ambient gas because studies by Mignolet (9) showed that helium, with the lowest polarizability of any gas, should have undetectable effect on the measured contact potentials of metals. Since its dielectric constant of 1.0000684 at S.T.P. is the smallest of any gas, it would best approximate the dielectric properties of a vacuum while decreasing the rate of loss of salt by vaporization. At no time during the course of a complete run was the condenser chamber opened or the ambient gas altered (except for hydrogen treatment in the last run).

After completion of measurements for the blank curve, the stationary plate was lowered, and silver nitrate was placed in the plate cavity and melted before the plate assembly was raised to measuring position. The dynamic condenser was now composed of the reference plate and the surface of the liquid silver nitrate in contact with the silver surface for which the blank curve had been established. Contact potential measurements were made at a temperature near 250°C until a constant value was attained, and then at different temperatures. For all the silver nitrate measurements, except those in run 3 near the melting point [209.7°C (10)], the temperature of the vibrating reference plate was held 10° ± 1°C above that of the stationary plate to preclude possible condensation of vapor from the molten salt. From 199° to 214°C in the third silver nitrate run some measurements were made with a temperature difference of only 2°, but the average difference was about 3.5°C. Many runs were terminated before constant values were attained at 250°C, owing to such factors as loss of salt by creepage and possibly evaporation, failure of electrical connections within the housing, and electrical shorting by the creeping salt. Generalizations concerning behavior during the blank measurements are therefore based on many more runs than those associated with the three completed salt runs.

In the final run the bare plates were heated in hydrogen as well as helium before constant values were obtained. Prior to this run the stationary plate had been contaminated by silver chloride, which permeated the surface. Since the thermocouple channel was exposed when the contaminated surface was cut away, the plate cavity was refurbished with molten silver and subsequently faced-off and polished prior to routine plate preparation. Since molten silver dissolves more than 20 times its own volume of oxygen (S.T.P.) and solid silver just below its melting point dissolves its own volume (11), the oxygen content of the surface stratum of the refurbished plate must have been considerably greater than that in earlier runs. This was borne out by the initial silver-silver contact potential of about —75 mv at 300°C,[2] which did not change for several days. The helium was then replaced by dry electrolytic hydrogen, whereupon the contact potential abruptly changed polarity and then remained fairly constant at about 100-130 mv. This positive potential of the stationary plate surface, relative to the smaller vibrating plate, could result from reaction of hydrogen with the greater concentration of oxygen diffusing to the surface of the more massive silver cylinder, forming transiently adsorbed water molecules with the positive end of their dipoles outward. On replacement of the hydrogen by helium, the contact potential became even more negative than before, possibly owing to accelerated depletion of oxygen from the small reference plate by the hydrogen treatment. A second hydrogen treatment gave the same behavior, but to less extent. When stability in the vicinity of zero contact potential was finally attained, the system was evacuated at less than 0.1 mm Hg for 24 hr, flushed with electrolytic hydrogen, again evacuated for 24 hr, and then flushed and filled with helium. The plates were aged therein for 48 hr at about 500°C. Subsequent agreement of measurements in this run with the two earlier completed runs indicates that any effect that oxygen may have had on the earlier completed runs was very small.

The silver-silver contact potential measurements in each blank run indicated the time when both plates had aged adequately to nearly identical states, and provided a correction curve for application to the silver nitrate data to compensate for possible temperature-dependent voltages appearing elsewhere in the circuit.

Results

Condenser stabilization.—Figure 2 is a plot of observed contact potential *vs.* time for a typical blank during its stabilization period and illustrates the long time required to attain constant values as well as the tendency to proceed from negative values to zero or slightly positive ones. Since the concentration of oxygen absorbed during the preliminary plate treatment would decrease relatively rapidly in the small reference plate, the slowly diminishing negative contact potential must have resulted from continuing diffusion of oxygen to the surface of the massive silver cylinder forming the stationary plate. The final constant contact potentials obtained in practically all the blank runs were close to zero, indicating that the two silver surfaces were finally almost identical.

Each dynamic condenser composed of silver nitrate surface and vibrating reference plate required two to three weeks to attain constant contact potential at constant temperature. The variation of observed values with time did not display a qualitatively reproducible trend. The general tendency was to begin at negative values, to rise with time to less negative values, and to fall back eventually to a constant value near the ini-

[2] The sign of the contact potential is taken as the sign of the potential applied to the vibrating reference plate to achieve a null point, *i.e.*, the contact potential is the Volta potential of the stationary plate (silver or silver nitrate) relative to that of the vibrating reference plate.

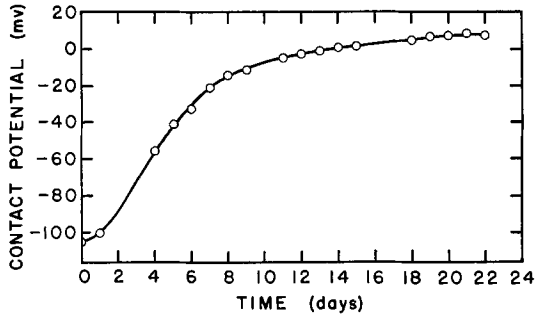

Fig. 2. Typical variation of contact potential between silver plates during stabilization at 280°C for blank run.

tial values. However, plots of the data were erratic, with numerous maxima and minima.

Contact potentials.—Results obtained in the three completed runs are shown in Fig. 3, 4, and 5. Each plotted point represents the average of at least three readings taken over a period of several minutes at the given temperature, which is that for the stationary plate. Time intervals between points at different temperatures varied from 30 min to several hours. After the initial stabilization period, each of the blank runs required two days for completion, and the three silver nitrate runs required three, six, and two days, respectively. Reproducibility of both blank and salt runs was verified by taking data both with descending and ascending temperatures—circles and dots, respectively, in Fig. 3, 4, and 5.

The lower curves in Fig. 3, 4, and 5 give the contact potential, or difference in Volta potential, between the silver nitrate surface and the surface of the reference plate. Subtraction of the potential of the stationary silver plate relative to the reference plate at each temperature (upper curves) gives the desired contact potential, which is the Volta potential of the surface of the silver nitrate, ψ_{AgNO_3}, minus the Volta potential of the silver plate in contact with the salt, ψ_{Ag}. This difference in Volta potentials is given as a function of temperature in Fig. 6, as determined from the smoothed curves in Fig. 3, 4, and 5.

The curvature observed above 214°C in run 1 (Fig. 3) for both the blank and silver nitrate data was unusual, being observed in neither the other two completed runs nor in the numerous sets of blank measurements made in incompletable runs. This curvature must have resulted from some temperature-dependent voltage bias not connected with the silver and silver nitrate surfaces of the stationary plate, since it cancelled out in the calculation of the silver-silver nitrate contact potential, giving a resultant curve similar to those of runs 2 and 3, as shown in Fig. 6. This illustrates the advantage of using a reference plate.

Above about 217°C the blank and silver-nitrate

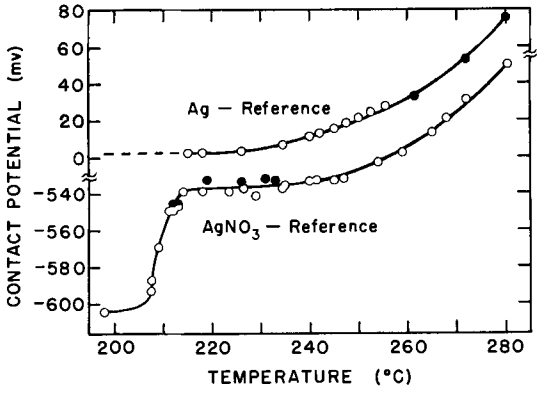

Fig. 3. Large temperature dependence of contact potential observed only in run 1.

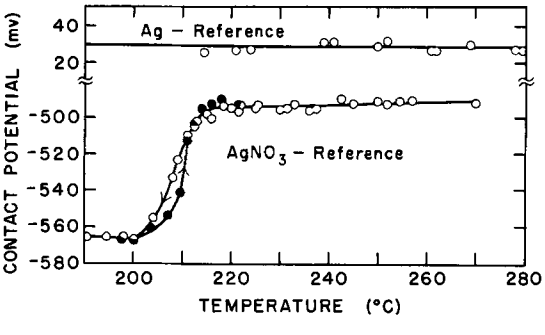

Fig. 4. Contact potentials obtained in run 2. Ten degrees temperature difference between plates for all points.

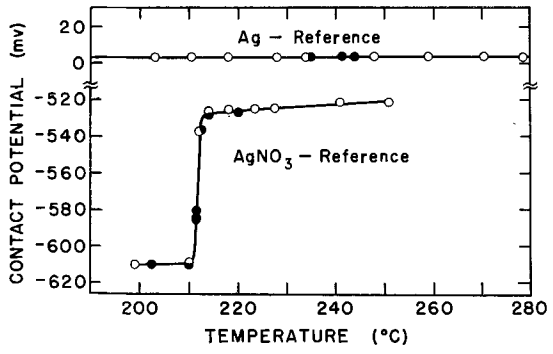

Fig. 5. Contact potentials obtained in run 3. Temperature difference between plates only 2°-5°C for salt data between 199° and 214°C.

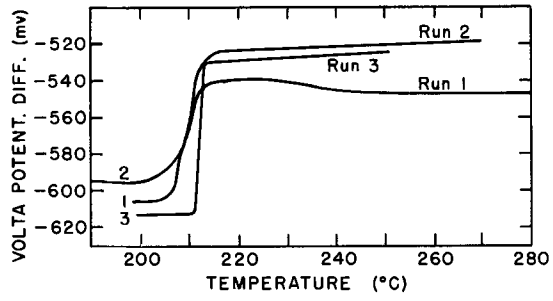

Fig. 6. Volta potential of silver nitrate surface minus that of silver in contact with silver nitrate.

curves for runs 2 and 3 are linear within experimental error. The best linear equation was determined by the method of least squares for each of the four sets of data and the equations for the blank and salt measurements in each run were combined to give the following:

Run 2: $\psi_{AgNO_3\ (l)} - \psi_{Ag} =$

$$-(541.9 \pm 11.5) + (0.085 \pm 0.046)t \qquad [1]$$

Run 3: $\psi_{AgNO_3\ (l)} - \psi_{Ag} =$

$$-(563.2 \pm 5.8) + (0.155 \pm 0.025)t \qquad [2]$$

where t is temperature in °C at the position of the thermocouple in the stationary plate. Equation [1] is based on salt data for t = 218°-270°C and Eq. [2], 218°-251°C. The error terms are standard deviations calculated for the least squares evaluations of the constants. Standard deviations of experimental points from the calculated equations for the blank and salt measurements were, respectively, for run 2, 2.3 and 1.9 mv, and for run 3, 0.12 and 0.74 mv.

Corresponding calculations for linear portions of the curves below the melting point of silver nitrate gave:

Run 2: $\psi_{AgNO_3\ (s)} - \psi_{Ag} =$

$$-(570.5 \pm 19.8) - (0.127 \mp 0.096)t \qquad [3]$$

Run 3: $\psi_{AgNO_3\ (s)} - \psi_{Ag} =$

$$-(622.0 \pm 11.9) + (0.043 \pm 0.058)t \qquad [4]$$

Standard deviations of experimental points for the solid salt measurements were 0.73 mv for run 2 and 0.56 mv for run 3.

If values given by Eq. [1] to [4] are weighted by the reciprocal of their variance, the following average values are obtained. At the melting point of pure silver nitrate, 209.7°C (10), the Volta potential of the liquid salt relative to silver is about —530 mv, with a temperature coefficient of about 0.14 mv/deg, and that of the solid salt relative to silver is about —608 mv, with a temperature coefficient of —0.003 mv/deg. In each phase the silver nitrate is saturated with silver,

helium at about 800 mm Hg, and nitrogen dioxide and oxygen at their decomposition pressures for the silver-saturated solution.

Discussion

Temperature gradients in silver nitrate.—Vertical and radial temperature gradients in the melt resulted from the higher temperature of the reference plate and the cooling of the edge of the stationary plate by convection currents in the helium. Resulting convection currents in the melt may have produced transient local variations in the liquid salt surface during the stabilization period. Mixing by convection may have accelerated the approach to near steady states for processes occurring in the melt, although temperature dependent states would continue to be affected slightly by the temperature gradients.

Silver-silver nitrate interface.—The surface of the stationary plate after a run had the same appearance as following its initial preparation, except that small adherent crystals of silver formed on the inner surface of the cavity rim (P in Fig. 1) at approximately the position of the initial molten salt surface. They were formed in this region of lowest temperature by crystallization of dissolved silver and/or by electrochemical deposition resulting from the radial temperature gradient in the silver. Some localized solution and recrystallization of silver may have occurred at all parts of the interface due to the different work functions of different crystallographic faces. It proved to be impossible to remove the last trace of silver nitrate from the stationary plate by creepage and evaporation before the creeping salt caused electrical leakage inside the condenser chamber. Therefore no measurements were made of the contact potential of the final silver surface relative to the reference plate. If it were different than the value obtained initially, all the calculated contact potentials would be in error by approximately the same small value. The magnitude of the observed discontinuity near 210°C would not be influenced significantly.

Solutes in silver nitrate.—After the long stabilization period the melt must have been saturated, at the stabilization temperature, with helium, silver dissolved from the stationary plate and formed from decomposition of the melt, and the nitrogen dioxide and oxygen from decomposition of the melt. No determinations of solubilities of these substances in silver nitrate have been made.

Since the final stabilized contact potential for the salt runs was always close to the values obtained at the beginning of the stabilization period, the less negative values for the intervening period were caused either by transient effects such as unknown trace impurities in the silver nitrate diffusing to the surface and eventually vaporizing, or by differing rates of increase of the effects due to decomposition of melt, solubility of silver and helium, and electrochemical solution and deposition of silver at the salt-metal interface. If the latter, the influences of the different effects on the final equilibrium state approximately cancelled each other. After a steady state was finally achieved at the stabilizing temperature, any further changes with temperature of effects influencing contact potential must have been reversible and have occurred rapidly enough to be completed by the time the plate temperatures were stabilized, since only small random changes were observed during the 2-5 min periods that measurements were made at each experimental temperature. Any changes occurring more slowly and any irreversible temperature dependent changes must have had no effect on contact potential in view of the observed reproducibility of measurements with ascending and descending temperatures. Thus the presence of any nitrogen dioxide and oxygen from decomposition of the melt must not have influenced the measurements significantly. Reported decomposition pressures (12) increase from 7 mm Hg at 248°C, which is near the stabilization temperatures for the three runs, to 80 mm Hg at 280°C, the highest temperature at which contact potential measurements were made. If the pressure of decomposition products in the condenser chamber increased during high-temperature measurements and these products did affect the measured contact potential, values determined initially at the stabilization temperatures would not have been reproduced later.

Discontinuity of contact potential at the melting point of silver nitrate.—Because of the radial temperature gradient in the silver nitrate, its temperature below the center of the vibrating plate was higher than that near the edge. Therefore, contact potentials obtained near the melting point were influenced by the fraction of the salt surface that had solidified with descending temperatures and the fraction that had melted with ascending temperatures. During run 2 (Fig. 4) thirty minutes elapsed between the measurements at 203.5°, 207°, and 209.5°C, made with ascending temperatures. This was twice the time allowed for stabilization between descending temperatures. Therefore the lower curve must represent a closer approach to equilibrium. When a still closer approach to uniform temperature was achieved near the melting point in run 3 by reducing the temperature difference between plates and waiting about an hour for stabilization at each temperature, the resulting data (Fig. 5) indicated that there must be a discontinuity in the contact potential at the melting point. As measured by the stationary plate thermocouple, the temperature at the sharp rise in Fig. 5 is about 2°C above the melting point of pure silver nitrate (10). This is the combined error resulting from temperature gradients and use of an uncalibrated small-wire thermocouple.

The observed discontinuity in value of the contact potential indicates that the surface potentials of solid and liquid salt at the helium interface differ by about 78 mv. The observed difference may result from the influence of surface concentrations of the solutes discussed above, which would be different for the two phases, and/or from preferential concentration of silver ions in the surface of the melt to a greater degree than in the solid and/or a similar concentration of nitrate ions in the surface of the solid. The concentrations of gases in the melt must have been small and were probably exceeded by the concentration of silver. Since solidification of the silver nitrate progressed toward the warmer reference plate, any silver forced out of solution would tend to collect on the surface of the salt under the reference plate. This would cause a discontinuity in the opposite direction from that observed. Therefore it is concluded that the major cause of the observed discontinuity in the contact potential is a larger concentration of Ag^+ ions than NO_3^- ions in the free surface of the melt.

Acknowledgment

The authors wish to express their thanks to the Directorate of Chemical Sciences, Air Force Office of Scientific Research and to the Atomic Energy Commission for their support of the research reported in this paper.

Manuscript received Oct. 27, 1964; revised manuscript received April 19, 1965.

Any discussion of this paper will appear in a Discussion Section to be published in the June 1966 JOURNAL.

REFERENCES

1. B. J. Rothlein and P. H. Miller, Jr., *Phys. Rev.*, **76**, 1882 (1949).
2. Lord Kelvin, *Phil. Mag.*, **46**, 82 (1898).
3. W. E. Meyerhof and P. H. Miller, Jr., *Rev. Sci. Instr.*, **17**, 15 (1946).
4. W. A. Zisman, *Rev. Sci. Instr.*, **3**, 367 (1932).
5. K. W. Bewig, "Improvements in the Vibrating Condenser Method of Measuring Contact Potential Difference," Naval Research Lab., Report 5096, Feb. 4, 1958; Document PB131530, O.T.S., U. S. Dept. of Commerce, Washington, D. C.

6. K. W. Bewig and W. A. Zisman, *J. Phys. Chem.*, **67**, 130 (1963).
7. J. L. Copeland, "The Contact Potential Difference between Metallic Silver and Molten Silver Salts," Ph.D. thesis, Indiana University, Bloomington, Ind. (1962). Available from University Microfilms, Ann Arbor, Mich., order no. 625022.
8. F. G. Keyes and H. Hara, *J. Am. Chem. Soc.*, **44**, 479 (1922).
9. J. C. P. Mignolet, *Discussions Faraday Soc.*, **1950** (8), 105, 326; *J. Chem. Phys.*, **21**, 1298 (1953).
10. K. J. Macleod and F. E. W. Wetmore, *Ann. N. Y. Acad. Sci.*, **79**, 873 (1960). [C. Sinistri and P. Franzosini, *Ric. Sci. Rend. Sez*, **A3** (4), 419 (1963) give the value 209.4° ± 0.2°C]
11. J. W. Laist, "Copper, Silver, and Gold," Vol. II of "Comprehensive Inorganic Chemistry," M. C. Sneed, J. L. Maynard, and R. C. Brasted, Editors, p. 141, D. van Nostrand Co., Inc., New York (1954).
12. M. Centnerszwer and M. Blumenthal, *Bull. intern. acad. polon. sci., Classe sci. math. nat.*, **1936A**, No. 8-9, 482.

The Anodic Reaction Mechanism in Fused Silver Nitrate

Nirmal Gupta[1] and Benson R. Sundheim

Department of Chemistry, New York University, New York, New York

ABSTRACT

The oxidation of the nitrate ion at a Pt anode in molten $AgNO_3$ has been studied by steady-state and fast-sweep voltammetry. Two mechanisms are found, both leading to $NO_2 + \frac{1}{2} O_2$. The first is susceptible to transport control and has an $n\alpha$ value of 1.17 at 238°C. It is postulated that this mechanism involves the preliminary dissociation of the nitrate ion to form $NO_2^+ + O_2^=$, the latter (possibly bound as orthonitrate) being the electroactive species. The second mechanism is not subject to transport control and has an $n\alpha$ value of 0.90. This is thought to involve the formation of NO_3 radical followed by its decomposition to form the products. If the E_o values of 0.357v and 1.25v (*vs.* Ag/Ag^+) are adopted, the two mechanisms are characterized by exchange current densities of 2.4×10^{-3} and 0.14 amp/cm², respectively. The corresponding values calculated for k_o, the heterogeneous rate constant, are 1.3×10^{-7} and 1.1×10^{-7} cm/sec.

The objective of this study is to devise and test a mechanism for the electrochemical oxidation of a nitrate ion on a platinum electrode in molten silver nitrate. The information obtained from the preliminary investigation of potential *vs.* current curves in the steady-state condition led to the exploration of the possibility of there being more than one reaction mechanism in different potential regions.

Experimental Procedures

Reference electrode.—A 1 cm² piece of silver metal dipping in the molten silver nitrate was used as a reference electrode. In a preliminary test a current voltage curve wherein the potential of a silver cathode was measured with respect to a resting silver reference electrode was carried out over a considerable range of current densities. A graph of current *vs.* observed potential showed a straight line corresponding to an apparent resistance of 0.53 ohm. On this basis, it was concluded that the reference electrode showed no noticeable polarization and therefore could be used safely. The stability of the potential of two such silver electrodes with respect to one another over a period of time was excellent.

Instrumentation.—The temperature of the cell was maintained at an arbitrarily selected temperature of 238.6° in a large pot melting furnace fitted with temperature regulating and stirring equipment. An equimolar mixture of sodium nitrite and sodium nitrate was used as the melt. The assembly was capable of maintaining the temperature to within 0.02 of a degree of the desired temperature. Since the temperature measured in these experiments was actually that of the bath and not of the silver nitrate, the cells were allowed to remain in the melt for at least 2 hr in order to attain the correct temperature before any measurements were made.

Preparation of silver nitrate.—Silver nitrate of analytical quality (Baker Analyzed) was melted in a cell and subjected to continuous evacuation by a mechanical vacuum pump for several hours. During this time, gases, mostly water vapor, were evolved. Two electrodes of platinum and silver, respectively, and of 3.5 cm² geometrical surface area were then inserted in the melt and an electrolysis carried out for 48 hr under vacuum at a current density of 4.5 ma/cm². This pre-electrolysis procedure was found to be necessary in order that the current *vs.* potential measurements be reproducible. Presumably, heavy metal ions were removed by this procedure. The silver nitrate thus obtained was transparent and colorless and could be subjected to a number of melting and solidification cycles in the presence of light under vacuum without any perceptible change in color. Figure 1 shows a Pyrex cell for potential *vs.* current measurements fitted with a multiple pulley which was used to rotate at various speeds, the large platinum electrode having a geometrical surface area of 3.45 cm². The two silver electrodes were placed symmetrically with respect to the rotating platinum electrode. All three of the electrodes were completely immersed in the molten silver nitrate during the experiment. It was found that reproducible results could be obtained only if the cell was continuously evacuated. A satisfactory rotating seal was made by choosing the glass tube and bottom glass joint for a snug fit. Both of the joints had the same inner diameter. Such a contact could be used with mercury at speeds up to 2000 rpm. At higher rotation speeds, the glass tube was coated with a thin layer of platinum in place of the tungsten spiral around the glass tube. Number 8 cup grease was used as a lubricant between the cup and the glass tubing. For rotating the platinum microelectrode at speeds greater than 1200 rpm, a Bodine synchronous motor was used at 1800 rpm. The armature of this motor was connected to a gear arrangement with a 1:1 ratio. One of these gears had a hollow center shaft which was used to hold the platinum microelectrode. The rotating contact was established by inserting copper wire in the mercury pool.

Analysis of reaction products.—The cell shown in Fig. 2 was used to collect the reaction products. The cell had one platinum electrode and one silver electrode. Break seals in the side arm were used to col-

[1] Present address: Institute of Gas Technology, Chicago, Illinois 60616.

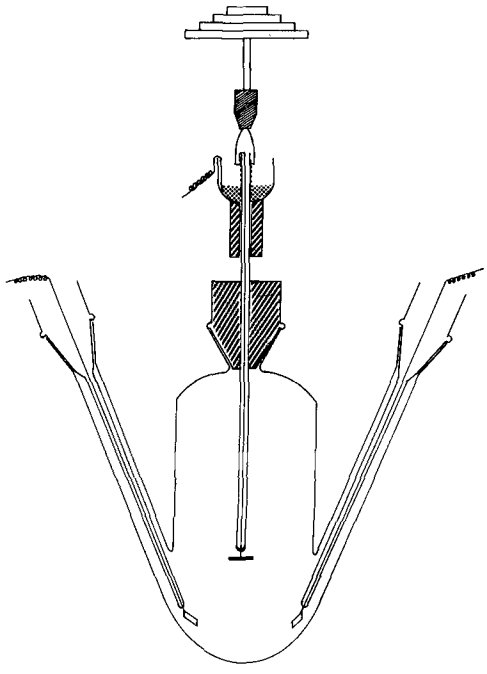

Fig. 1. Cell for voltammetry with rotating electrode

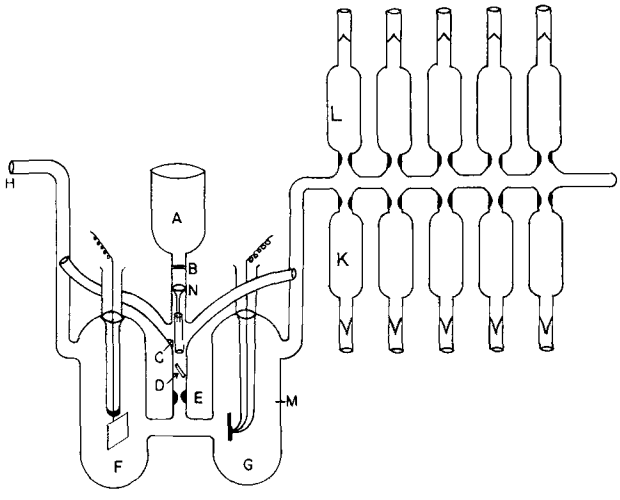

Fig. 2. Arrangement for analysis of products of electrolysis. Liquid pre-electrolyzed $AgNO_3$ is transferred to A. Suction at H causes it to flow through the sintered disk B up to the level M. The magnet D is manipulated so as to adjust N and C to prevent $AgNO_3$ from touching the walls near the seal-off. The remaining $AgNO_3$ in A is allowed to solidify and the tube C allowed to drop to E. The outer tube is cut just below the ring seal N and sealed off. After electrolysis between the silver electrode F and the platinum electrode G, the accumulated products are sealed off in, say, L. The open end of the break seal in K is joined to the vacuum system and the cell evacuated. The apparatus is sealed and the procedure continued.

lect successive samples for mass spectrographic analysis.

Electrodes.—The platinum microelectrode was made from a number 40 B and S gauge platinum wire by sealing it in lead glass tubing to make a vacuum tight seal. The end was ground and polished to a fine finish exposing only the crosssection of the wire. This was subjected to boiling hydrochloric acid for 5 min, washed with distilled water, and dried at 160°C. The large platinum electrode consisted of a circular platinum disk, 2 cm in diameter and 2 mm thick with a center shaft (2 in. in length) made out of 0.5 mm diameter platinum wire. This wire was spot welded to tungsten wire, and a junction was placed in a long Pyrex tube, the sleeve encasing the tungsten, giving a vacuum tight joint. The cleaning treatment was the same as in the case of the platinum microelectrode. Silver electrodes were made in two ways. A silver wire of B and S gauge 14 was spot welded to tungsten wire and both were enclosed in Pyrex tubing as in the case of the large platinum electrode. A piece of 1 cm^2 silver was then welded to the bare silver wire. A second method was to clean B and S gauge 24 silver wire by dipping it in concentrated ammonium hydroxide solution for 30 min and then carefully melting a fine Pyrex capillary over it with a small flame. A thick Pyrex tube was sealed on to the thin capillary. This was then subjected to an annealing process. Liquid tight Pyrex-silver seals could be made in this fashion. Current voltage curves were measured with a Sargent model XV Polarograph or with a combination of a Fluke differential voltmeter model 801 BR and a Greiback model 700 expanded scale milliammeter as appropriate. The programmed potentiostat was synthesized from the type O Plug-in Preamplifier unit and the type 545A oscilloscope (Tektronix Corporation). This preamplifier contains two stabilized differential amplifiers as well as a d-c preamplifier. It is capable of dealing with time constants down to 10 μsec and currents up to 1 ma. The circuit was arranged as shown in Fig. 3. The first operational amplifier served as a potentiostat and the second as a current-to-voltage converter. The program for the potentiostat was obtained from the oscilloscope (saw-toothed for single sweeps) or from a Hewlett Packard signal generator (triangular waves for cyclic voltammetry). A suitable bias was added when necessary from a battery and resistance network. The output voltage of the second operational amplifier, being proportional to the current, was connected to the vertical plate preamplifier of the oscilloscope and the program to the horizontal amplifier. In this way, the display on the oscilloscope was current *vs.* electrode potential. The traces were photographed using a Beattie-Coleman oscilloscope camera fitted with a Polaroid back. Voltage and time calibrations of the scales and circuits were made periodically.

Experimental Results

The effect of the speed of rotation of the platinum electrode on the steady-state potential *vs.* current density curves is shown in Fig. 4. All of these measurements were taken at one temperature only, *i.e.*, 238.6°C. No change in the potential *vs.* current density curves was noted at speeds greater than 1200 rpm. This was therefore considered to be a rotation speed sufficient to reduce the diffusion overpotential at these current densities and hence effectively to separate the activation overpotential from the diffusion overpotential. Figure 5 shows the potential *vs.* current density curves in the range 0-420 $\mu a/cm^2$, both when the platinum electrode was kept stationary and also when it was

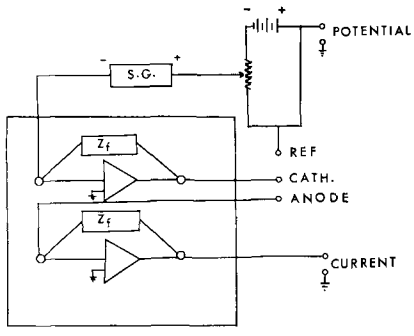

Fig. 3. Arrangement for oscillographic voltammetry. For this purpose the upper amplifier serves as a potentiostat with $Z = \infty$ and the lower one as a current to voltage converter with $Z =$ 0.1M.

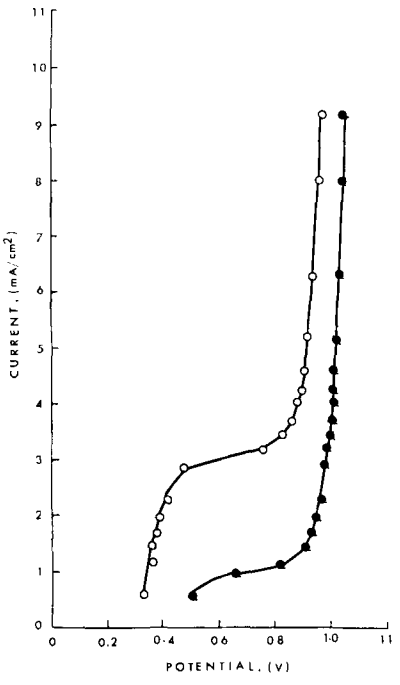

Fig. 4. Current density as a function of potential (with respect to Ag/Ag^+) for a Pt anode in $AgNO_3$ at 238.6°C; ○, 1100 rpm; ●, 0 rpm.

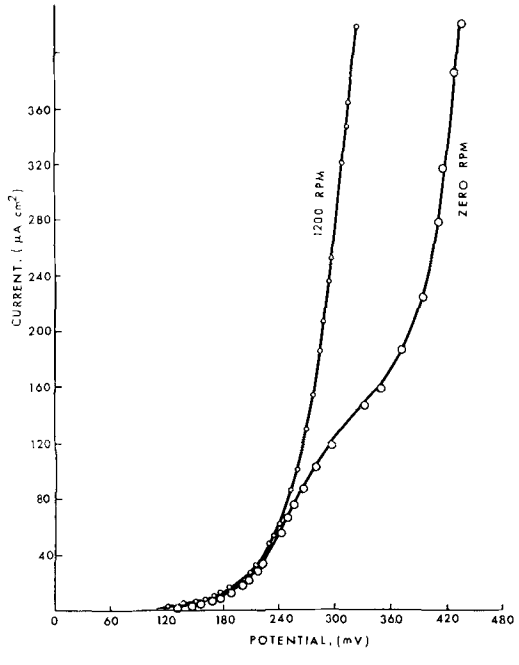

Fig. 5. Current density as a function of potential (with respect to Ag/Ag^+) for a Pt anode in $AgNO_3$ at 238.6°C.

rotated at speeds of 1200 rpm or more. Thus these curves represent the continuation of Fig. 4 into the lower current density region. The over-all curve shows two distinct reactions. The first occurs below +0.5v and the second near 0.95v. The process taking place below +0.5v seems to be transport controlled while the one near 0.95v is essentially independent of transport.

Table I shows the results of the mass spectrographic analysis of the reaction products collected by electrolyzing pre-electrolyzed molten silver nitrate at 238.6°C using platinum as the anode and silver as the cathode. Variations with current density (or equivalently with electrode potential) are not significantly different for various regions of the current potential curve.

Table I. Anodic reaction products

Current density, ma/cm²	% NO	% O_2	% NO_2
1.3	43.8	56.2	0.00
0.06	45.0	55.0	0.00
0.013	44.0	56.0	0.00

Table II. n and α as functions of temperature

Temp, °C	$n\alpha$	if n is	then α is
238.6	1.17	2	0.59
246.5	1.25	2	0.62
255.0	1.26	2	0.63

In Table II the values of n and α calculated from the Tafel lines as plotted in Fig. 6 are given. The exchange current density cannot be obtained from this graph since the value of E_o for this reaction has not yet been evaluated.

Cyclic voltammetry.—These experiments were carried out at 256°C using a platinum microelectrode of area 1.167×10^{-3} cm². It is observed that a slow sweep gives rise to a potential *vs.* current curve which resembles the steady state. As the sweep rate is increased to values greater than 10 cps, a separation of anodic and cathodic curves is noted which increases with increasing sweep rate. At frequencies equal to or greater than 50 cps a sharp peak near +0.5 appears. Above 500 cps another peak is observed near +0.9v but only in the cathodic curve. In addition, a small loop due to the reversible dissolution of silver from the platinum electrode is seen near 0 potential. As the potential becomes greater than 1v, very large currents are obtained, the curves being strongly distorted by gas bubbles.

In order to identify the source of these peaks, current-potential curves were determined on systems to which additions of potassium nitrite and of water were made. It was observed that the presence or absence of either of these substances had no effect on the details of the curve. Controlled potential pre-electrolysis at 0.5v produced no change in the peaks.

Discussion

The standard electrode potential for the over-all reaction $AgNO_3 = Ag^o + NO_2 + \frac{1}{2} O_2$ is calculated (1, 2) to be 0.357v at 238°C. These products are favored by 87 mv over NO + O_2 at this temperature. The dissociation of NO_2 is a relatively slow reaction, at least in the gas phase (3). A recent study (4) has shown that a reversible electrode with the expected potential is established in molten $AgNO_3$ by bubbling NO_2 + O_2 over a Pt bristle. It was noted that the electrode polarized readily but depolarized rapidly. The

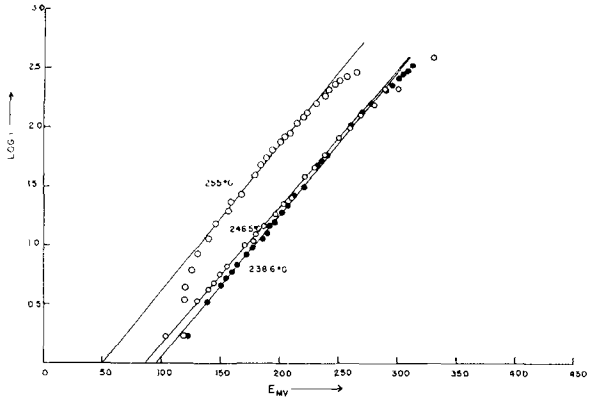

Fig. 6. Tafel diagram for the lower potential reaction. Logarithm of current density (μa/cm²) *vs.* potential. Platinum electrode rotated at 1200 rpm.

stability of the $NO_2 + O_2$ mixture in the melt was verified by analysis of the effluent gases.

The experimental results clearly indicate that there are two reactions. The Tafel graphs (Fig. 6) for the first (lower potential) reaction lead to $n\alpha$ values of 1.17 at 238°C so that $n \neq 1$. Furthermore, this reaction is susceptible to transport control and is limited long before the products break into free bubbling (as occurs for the second reaction). In order to account for these facts, we postulate that the electrode reaction involves the preliminary dissociation of the nitrate ion

$$NO_3^- = NO_2^+ + O^=$$
$$O^= = O + 2e$$
$$O + O = O_2$$
$$NO_2^+ + NO_3^- = [N_2O_5] = 2NO_2 + \tfrac{1}{2}O_2 \qquad \text{(i)}$$

If the last reaction is not too rapid, depletion of the electroactive species, $O^=$, from the vicinity of the electrode produces the concentration polarization. The species NO_2^+ by now is well known. Duke and Yamamato (5) concluded that chemical redox equations suggest that the equilibrium dissociation of the nitrate ion into the nitronium and oxide ions takes place to a significant extent in fused alkali nitrates. Raman studies have suggested (6) that there may be more than one species of nitrate ion in molten silver nitrate. (It might well be that the oxide ion is actually solvated as NO_4^{3-}, the orthonitrate ion.) The oxide ion has also been postulated as an intermediate in the oxidation of the $CO_3^=$ in molten carbonates.

This hypothesis may be tested by making use of the acidic nature of the pyrosulfate ion in nitrate melts.

$$S_2O_3^= + NO_3^- = NO_2^+ + 2SO_4$$
$$NO_2^+ + O^= = NO_3^- \qquad \text{(ii)}$$

That is, the addition of $Na_2S_2O_3$ to the $AgNO_3$ melt may be expected to suppress the oxide ion. Current-voltage curves were taken on successive additions of $Na_2S_2O_3$ and show (Fig. 7) that the expected effect is indeed produced, namely, that the overpotential is substantially increased.

These data may be used to obtain an approximate value for the dissociation constant of NO_3^- as follows:

For curves 1 and 2 in Fig. 7 the increase in potential is about 0.013v at 253.5°C when 1g of potassium pyrosulfate is added to 100g of silver nitrate. Assuming that all of the pyrosulfate reacts at once with NO_3^- ions to produce NO_2^+ in equivalent proportions and that the whole of this NO_2^+ stays in the $AgNO_3$, we can proceed with the calculation. The pertinent reactions are

$$NO_3^- \underset{k}{\rightleftharpoons} NO_2^+ + O^= \qquad [1]$$

$$S_2O_7^= + NO_3^- \rightarrow 2SO_4^= + NO_2^+ \qquad [2]$$

where k is the equilibrium constant for reaction [1].

We set X equal to the unknown concentration of $O^=$ or NO_2^+ ions before addition of the $S_2O_7^=$ and set Y equal to the concentration of NO_2^+ according to Eq. [1] but after the addition of S_2O_7. The latter is also equal to the concentration of $O^=$ after the $S_2O_7^=$ addition.

$$[NO_2^+]_o = X = [O^=]_o \qquad [3]$$
$$k = [O^=][NO_2^+] \qquad [4]$$
$$[NO_2^+] = Y\,[S_2O_7^=] \qquad [5]$$
$$[O^=] = Y \qquad [6]$$

Rearrangement of these equations leads to the relation

$$k = Y(Y + [S_2O_7^=]) = X^2 \qquad [7]$$

According to the Nernst equation, the overpotential before, E_o', and after E_f', the addition of $K_2S_2O_7$ one respectively

$$E_o' = E_o^o + [2.303\,RT/2F]\,\log \text{products}/X \qquad [8]$$
$$E_f' = E_o^o + [2.303\,RT/2F]\,\log \text{products}/Y \qquad [9]$$

Therefore, $2.303\,RT/2F \log (X/Y) = 0.013$v or $\log (X/Y) = 0.2474$; $Y = X/1.768$; $X = 1.94 \times 10^{-2}$; $k = 3.76 \times 10^{-4}$.

Similar calculations for the 0.024v rise in overpotential on the addition of a total of 2g of $K_2S_2O_7$ to 100g of $AgNO_3$ yield the value of the equilibrium constant k as 1.4×10^{-4} (m^2/l^2). The smaller value of k on the addition of larger amounts of pyrosulfate suggests that the assumption that the concentration of NO_2^+ after the addition of $S_2O_7^=$ is increased by equivalent amounts is not quite correct because of the gradual spontaneous evolution of NO_2 gas.

$$NO_2^+ + NO_3^- \rightleftharpoons [N_2O_5] \rightarrow 2NO_2 + \tfrac{1}{2}\,O_2 \qquad [10]$$

The faster this reaction takes place the greater is the error introduced in the evaluation of k, the error being in a direction to make the calculated value too large.

If we accept the value of E^o for the reaction at 238° to be 0.357v (2, 3), then a value of i_o can be found from the Tafel curve. This value for i_o is found to be 1.4×10^{-4} amp/cm².

We turn now to the second reaction and recall that it shows no evidence of transport control until free bubbling occurs at the surface. In fact, if the electrode is strongly polarized and then open circuited, it is found that a potential of approximately 1.25v is established within a few milliseconds of the current interruption. This potential is independent of the applied current density over wide limits. (The details of the later decay depend on the applied current density.) The current-potential curves must first be corrected for the limiting current (1.1 ma) from the first reaction. After this correction is made a graph of the logarithm of the current *vs.* the applied potential is found to give a reasonably straight line (Fig. 8). If

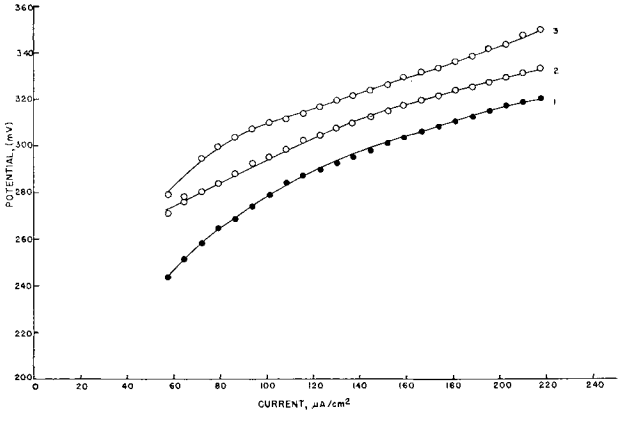

Fig. 7. Effect of successive additions of $Na_2S_2O_7$, 253.5°C

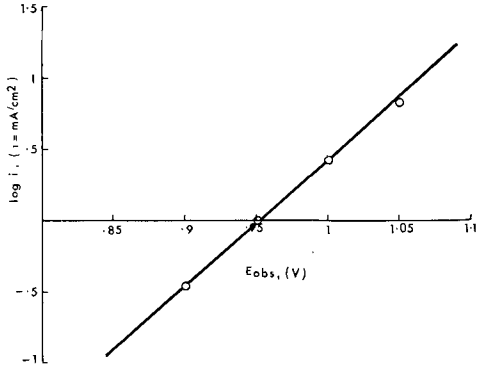

Fig. 8. Tafel diagram for the higher potential reaction. (The limiting current density from the lower potential reaction has been subtracted from the observed current density.)

we assume that the usual exponential relationship between current and voltage applies to reactions very far from the equilibrium, then the Tafel slope of this is found to be 0.90 corresponding to possible values of $n = 2$, $\alpha = 0.45$ or of $\alpha = 0.90$, $n = 1$. If we assume that the value of E° (for the continuous reaction) at this potential is 1.25v, then a value for i_o is computed as 2.4×10^{-3} amp/cm^2.

The definitions of i_o and E_o in systems of this sort need special attention. The general question is discussed elsewhere (7). Here it is sufficient to say that the equilibrium potential between reactants and products in their solid states is chosen for E_o when this is known. In the case where it is not known but the reaction is found to proceed reversibly, then the experimental value of E in the steady-state condition with reactants and products in their standard state (here sufficiently well achieved at the point of free bubbling of gaseous products) can be used. It is possible that this reversibility refers to some relatively short lived state which is an intermediate, but whose concentration never becomes large at reasonable current densities. The element of arbitrariness in the definition of E_o for a system which is irreversible under the conditions of the experiment and for which no thermodynamic potential is known means that there is no real significance to be attached to the comparison of this i_o with that of other reactions in the absence of auxiliary assumptions. In the present case, it is not clear whether the higher potential reaction is reversible at all. The appearance of a reverse potential at 1.25v may be due to reasons other than a back reaction, such as the concentration overpotential from the first reaction which no longer can be stirred away when the products bubble freely over the electrode. The higher potential reaction might well consist of the oxidation of nitrate ion to a short lived nitrate radical, which then rapidly and irreversibly decomposes.

Finally, we note that heterogeneous rate constants for the low potential and high potential reactions can be formally calculated by use of the calculated concentration of oxide ion in the one case and that of nitrate ion in the other case (assuming unit activity of the products). The values obtained in this way are 1.3×10^{-7} and 1.1×10^{-7} cm/sec, respectively.

Acknowledgment

It is a pleasure to acknowledge the assistance to this work of the Office of Naval Research (Contract 285-37 with New York University).

Manuscript received March 11, 1965. This paper was abstracted from a thesis submitted to the Graduate Faculty of Arts and Science, New York University in partial fulfillment of the requirements for the Ph.D. degree. This paper was presented at the San Francisco Meeting, May 9-13, 1965.

Any discussion of this paper will appear in a Discussion Section to be published in the June 1966 JOURNAL.

REFERENCES

1. National Bureau of Standards Circular 500 (1952).
2. K. K. Kelley, U. S. Bureau of Mines, Bulletin 584 (1950).
3. W. A. Rosser and H. Wise, *J. Chem. Phys.*, **24**, 493 (1956).
4. J. A. A. Ketelaar and A. Dammers-DeKlark, *Receuil*, **83**, 322 (1964).
5. F. R. Duke and S. Yamamato, *J. Am. Chem. Soc.*, **81**, 6378 (1959).
6. G. E. Walrafen and D. E. Irish, *J. Chem. Phys.*, **40**, 911 (1964).
7. B. Sundheim, In preparation.

The Electrodeposition of Coherent Deposits of Refractory Metals

II. The Electrode Reactions in the Deposition of Tantalum

S. Senderoff, G. W. Mellors, and W. J. Reinhart

Development Department, Parma Research Laboratory, Union Carbide Corporation, Parma, Ohio

ABSTRACT

The reduction of pentavalent tantalum to tantalum metal in molten LiF-NaF-KF eutectic mixture has been studied by chronopotentiometry between 650° and 850°C. It is a two-step reduction apparently involving a three-electron step followed by a two-electron step. The first step is diffusion controlled, and the diffusion coefficient of the reacting species is 1.5×10^{-5} cm^2/sec at 750°C and its activation energy 8.5 kcal/mole.

In a previous paper (1) the electrodeposition of coherent deposits of refractory metals, alloys, and compounds from molten fluoride electrolytes was described. In order to improve our understanding of the mechanism of metal deposition in these systems, a study of the electrode processes by means of chronopotentiometry was undertaken. In this paper the mechanism for the deposition of tantalum from the solution of K_2TaF_7 in the KF-LiF-NaF eutectic mixture is discussed.

Experimental

Solvent preparation.—The solvent was the eutectic mixture LiF-NaF-KF (46.5-11.5-42 mole % mp 454°C), and was prepared from analytical reagent grade salts. These were fused in a graphite crucible with 15 w/o (weight per cent) NH_4HF_2 to prevent hydrolysis, allowed to cool to a temperature just above the freezing point and poured into a nickel crucible, transferred to a nickel purification apparatus and sparged with H_2 for 48 hr at 750°C to remove the NH_3 and HF remaining from the decomposition of NH_4HF_2 and to reduce to metallic nickel the NiF_2 formed by attack on the crucible. During the last 4 hr of sparging the melt was electrolyzed between two graphite electrodes at 5 ma/cm^2 with a total current of 100 ma. This purification procedure resulted in $i\tau^{1/2}$ values for the solvent of less than 1×10^{-3} amp cm^{-2} sec$^{1/2}$ at a current density of 0.04 amp/cm^2 and −1.2v *vs.* a Ni/Ni^{+2} reference electrode.

Solutes.—Recrystallized potassium fluotantalate (K_2TaF_7) was obtained from the Kawecki Chemical Company and dried under vacuum at 150°C. The NiF_2 used for the reference electrodes was prepared using the method of Priest (2) except that ClF_3 was used instead of F_2.

Furnace.—The furnace for the chronopotentiometric cell was constructed around two well insulated Hevi-Duty semicylindrical heating elements type 5712-KSP. The temperature was controlled with a chromel-alumel thermocouple and a Model 402 Wheelco controller.

Chronopotentiometric circuit.—A conventional chronopotentiometric circuit was used with a pulsing mechanism and voltage cut-off switch similar to that de-

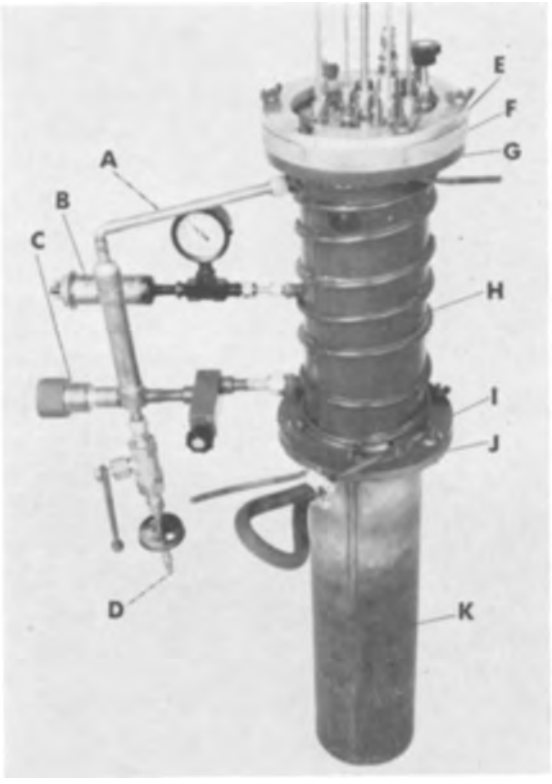

Fig. 1. Chronopotentiometric cell: A, gas exit line; B, vacuum gauge; C, vacuum or gas inlet line; D, gas exit bubbler tip; E, steel flange; F, Plexiglas cover disk; G, steel flange; H, water-cooled stainless steel can; I, steel flange; J, steel flange; K, Hastelloy alloy X can.

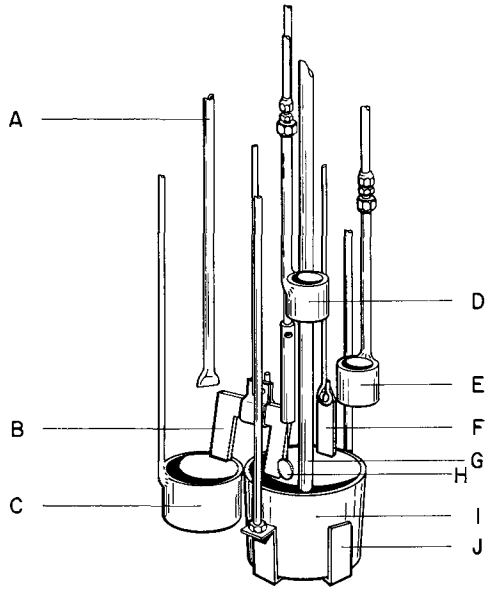

Fig. 2. Internal components of chronopotentiometric cell: A, gas inlet tube; B, salt bridge, usually alumina; C, nickel crucible for reference electrode; D, sampling cup; E, addition cup, F, counter electrode; G, thermowell; H, indicator electrode; I, crucible (nickel or molybdenum) for electrolyte under study; J, nickel cradle.

scribed by Senderoff, *et al.* (3), except that an automatic current reversing switch was added. The constant current source was a 200-375v power supply, and its current output was measured by feeding the voltage from a precision resistor to a Sargent Recorder No. S-72150. The potential between the indicating electrode and reference electrode was fed into a Tektronix 535A oscilloscope with type D plug-in. The resulting chronopotentiograms were photographed with an attached Polaroid camera.

Chronopotentiometric cell.—The cell bottom (K) (Fig. 1) was an 18 in. high, 4⅞ in. OD can constructed from 1/16 in. Hastelloy alloy X sheet and a ½ in. steel flange. The cell top (H) was a 12 in. high, 4⅞ in. OD cylinder constructed from 1/32 stainless steel sheet and two steel flanges. The flange of the can (J), and the upper flange of the cell top (G), were fitted with "O" ring grooves, and the cell top and flanges of the cell bottom were water cooled with ⅛ in. copper tubing to protect the "O" rings and Plexiglas cover (F). Fittings on the side of the cell top provided for a vacuum line (C), vacuum gauge (B), and a gas exit tube (A), through a paraffin bubbler (D).

Cell components.—Containers for the test melt were molybdenum cups (I), 6 cm wide by 4 cm deep, No. Q14792-A from the Fansteel Metallurgical Corporation (see Fig. 2). The reference electrode cups (C), the addition cup (E), and sampling cup (D) were machined from nickel rod. The addition cup had a small hole drilled through the bottom to permit molten salts (but not solids) to pass through. The molybdenum cup was suspended by means of a nickel hanger (J), the reference electrode cups by means of nickel rods joined by welding.

Insulation problems.—At 700°-800°C recrystallized alumina insulators acquired appreciable conductivity in the presence of the vapors of the fluorides and led to electrical leaks from the anode through the test melt container to the grounded metal electrolysis can giving rise to abnormally long transition times. The only effective means of electrical isolation has been to support all of the cell components from separate nickel rods leading from the cold zone of the cell where they are held by Swagelok fittings on the Plexiglas cover. There are no contacts among any of the components of the cell or with the walls of the can below the Plexiglas cover.

Electrodes.—Disk indicating electrodes were stamped from tantalum or platinum sheet (5 mil) and spot welded to either tantalum or platinum wire (15 mil). Counter electrodes were strips cut from ⅛ in. tantalum sheet. All of the electrodes were cleaned with concentrated HNO_3 and distilled H_2O. Both platinum and tantalum indicating electrodes with areas ranging from 0.49-1.67 cm^2 were successfully used, yielding identical results, although the majority of the experiments were carried out with platinum electrodes having an area of about 0.9 cm^2.

Reference electrode.—Approaches to reference electrodes in molten fluorides have been reported by Grjotheim (4), Manning (5), Coriou (6), and Crouthamel (7), but our most successful approach was a half-cell similar to Grjotheim's in which a solution of 1 mole % NiF_2 in KF-LiF-NaF was contained in a nickel crucible which acted as the electrode. The NiF_2 solutions were obtained as dip samples from a 1000g, 1 mole % NiF_2/KF-LiF-NaF bath. Contact between the reference and experimental electrolyte was made with the porous alumina bridge described below.

Salt bridge.—The salt bridges (Fig. 2B), were cut from Norton Company alumina filter disks (RA-98 coarse particle size). They were leached in concentrated HNO_3 for 24 hr, continuously washed with distilled H_2O for ½ hr, immersed in boiling H_2O for 1 hr, and vacuum dried at 400°C. They were saturated with purified molten KF-NaF-LiF bath under argon, cooled, and stored in closed bottles in a dry box. Bridges so prepared had a resistance of less than 10 ohms at 750°C, but on long contact with the molten fluorides they introduced impurities into the melt which were reduced at —1.5v and at —0.5v. Introduction of the impurity at —0.5v could be avoided by immersing the bridge in the melt only during the recording of the chronopotentiogram. The impurity reduced at —0.5v is probably iron and the less noble one reduced at —1.5v is aluminum.

Procedure.—The apparatus was assembled and evacuated to less than 5μ overnight, while held at 600°C. The cell was then cooled, vented to argon, and the reference electrode slug, solvent slug and salt bridge inserted followed by evacuation at 400°C overnight. The salts were fused under vacuum at 600°C for 2 to 3 hr, the system vented to argon, and the furnace temperature elevated to 750°C. After equilibrium had been attained the transition time of the solvent was recorded. The tantalum-bearing salts contained in a nickel addition cup in the cold zone of the cell were then plunged into the melt. The usual procedure for recording chronopotentiograms was followed. At a given concentration and temperature, runs at a number of current densities were recorded. The temperature was then changed, allowed to become constant, and recordings at another group of current densities were made. When the appropriate temperature and current density range had been completed a sample for analysis was taken and the run terminated. Another experiment was then performed in the same way with a new solution at another concentration.

Results

Chronopotentiograms were run at concentrations of K_2TaF_7 ranging from 0.02 to 0.1 millimoles cm^{-3}, at current densities which varied from 0.05 to 0.25 amp/cm^2 and at temperatures of 640°-860°C. In Fig. 3 is illustrated a typical chronopotentiogram showing the two reduction steps with $E_{1/4}$ values at about 1.0 and 1.2v. In Fig 4 is shown the relationship among transition time, τ, current density, i, and concentration, C, at 750°C for the first plateau. Each of the points represents the average of about 10 chronopotentiograms and includes the maximum practical current density range for that concentration. The average value for $[E_1]_{1/4}$ for this set is 1.03 ± 0.05v for the first plateau. The average value of the $[E_2]_{1/4}$ for the second plateau is 1.26 ± 0.06v. The transition time of the second plateau is on the average about 80% longer than that of the first plateau. Tables I and II summarize the data obtained at 750°C.

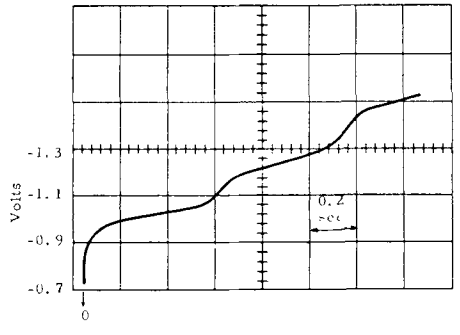

Fig. 3. Cathodic chronopotentiogram for K_2TaF_7 dissolved in KF-LiF-NaF, eutectic mixture (Flinak); concentration = 8 x 10^{-5} moles/cm^3; current density = 0.113 amp/cm^2; temp. = 750°C; cathode, platinum.

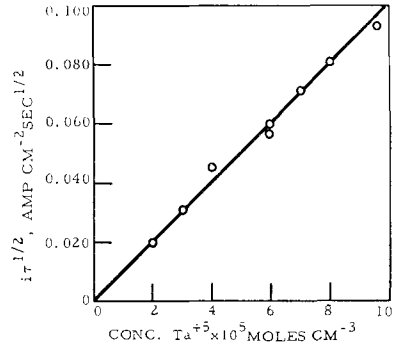

Fig. 4. Transition time, current, concentration relationship from cathodic chronopotentiograms of K_2TaF_7 in Flinak at 750°C.

Table I. Chronopotentiometric data for the reduction of K_2TaF_7 in Flinak at 750°C

Conc. K_2TaF_7 (moles cm^{-3}) × 10^5	C.D. (amp/cm^2) Min.	Max.	$[E_1]_{1/4}$ (v) Avg.	Std. dev.	$[E_2]_{1/4}$ (v) Avg.	Std. dev.	$i\tau_1^{1/2}$ (amp $sec^{1/2}$ cm^{-2}) Avg.	Std. dev.	No. of runs
2.0	0.056	0.110	1.04	0.025	1.24	0.057	0.020	0.0025	10
3.0	0.075	0.230	1.02	0.024	1.24	0.031	0.031	0.0029	11
4.0	0.065	0.115	1.06	0.056	1.28	0.052	0.045	0.0015	11
4.4	0.092	0.142	1.05	0.025	1.29	0.040	—	—	3
4.5	0.092	0.158	1.08	0.033	1.34	0.022	—	—	4
5.9	0.050	0.250	—	—	—	—	0.060	0.0015	5
5.9	0.045	0.246	0.97	0.038	1.18	0.020	0.057	0.0028	11
7.0	0.050	0.180	—	—	—	—	0.071	0.0030	12
8.0	0.061	0.240	0.97	0.052	1.18	0.064	0.081	0.0024	7
9.6	0.113	0.151	1.07	0.017	1.31	0.021	0.093	0.0036	7
Over-all average			1.03	0.054	1.26	0.060			

$i\tau_1^{1/2}/C$ (amp $sec^{1/2}$ cm $mole^{-1}$) × 10^{-3} Avg.	Std. dev.
1.01	0.05

Table II. Transition time of the second plateau for the reduction of K_2TaF_7 in Flinak at 750°C

Conc.	τ_2/τ_1 Avg.	Std. dev.	$i\tau_2^{1/2}$ (amp $sec^{1/2}$ cm^{-2}) Avg.	Std. dev.	$i\tau_2^{1/2}/C$ (amp $sec^{1/2}$ cm $mole^{-1}$) × 10^{-3}	No. of runs
2.0 × 10^{-5}	2.9	1.1	0.036	0.010	1.80	9
3.0	2.3	0.8	0.044	0.005	1.47	5
4.0	0.91	0.07	0.044	0.006	1.10	11
5.9	1.5	0.02	0.068	0.013	1.15	11
8.0	2.1	0.02	0.118	0.052	1.47	7
Over-all average	1.8	0.7				

In Fig. 5 is shown the chronopotentiogram for the solvent only, indicating the absence of anything significant below the alkali metal reduction potential near 2v.

In Fig. 6 is shown the result for successive cathodic and anodic chronopotentiometry on the system. The ratio $\tau_{anodic}/\tau_{cathodic} = 0.83$.

Discussion

Precision of Data

An over-all precision of about 5% in the value of $[E_1]_{1/4}$ for the first plateau is indicated by the data in Table I. This corresponds to a standard deviation of about 50 mv in the potential, and at least 20 mv of this can be ascribed to the instability of the reference electrode. Additional work on a reference electrode for molten fluoride systems is required. $E_{1/4}$ is independent of concentration and of current density.

The transition time constant $i\tau_1^{1/2}/C$ for the first plateau also has a standard deviation of about 5%. Since the graphical determination of τ_1 is rendered imprecise by the slope of the plot between the two plateaus (Fig. 3) the major portion of this deviation in the transition time constant is ascribable to the irreversibility of the second step. Within this degree of accuracy $i\tau_1^{1/2}/C$ is independent of both current density and concentration.

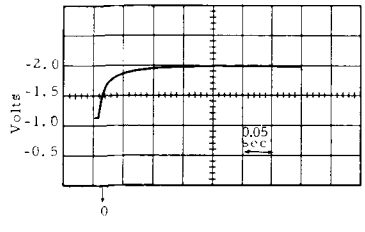

Fig. 5. Cathodic chronopotentiogram of Flinak solvent only; current density, 0.0336 amp/cm^2; temp, 750°C; cathode, tantalum.

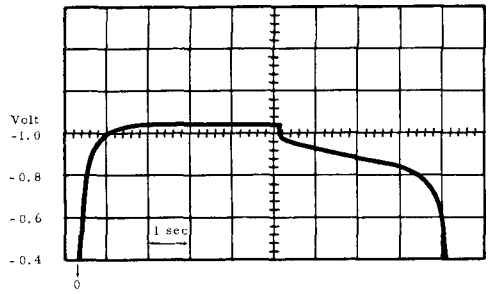

Fig. 6. Cathodic-anodic chronopotentiogram of K_2TaF_7 dissolved in Flinak. Cathodic portion on left, anodic on right: current density, 0.00964 amp/cm^2; temp, 750°C; cathode, platinum.

In Table II it is seen that while the $[E_2]_{1/4}$ values are only slightly less precise than the $[E_1]_{1/4}$ values the quantities associated with the transition times are very much less precise. Also, except for the highest concentration, the transition time constant for the second step, $i\tau_2^{1/2}/C$, is not constant, but decreases with increasing concentration. This lack of precision and constancy in transition time data arises from the fact that the second step is not diffusion controlled, but has rather complex kinetics which will be discussed below.

It will be noted in Tables I and II that the standard deviation of the $E_{1/4}$ values for each concentration is generally less than that of the over-all average. This suggests that the stability of the reference electrode during one experiment on one electrolyte is better than its reproducibility from experiment to experiment. In the case of the transition time constants, however, the per cent standard deviations for the individual experiments are about the same as the over-all value, but the deviations for the individual experiments decrease with increasing $i\tau_1^{1/2}$ values. The absolute values, however, show no consistent variation with concentration or $i\tau_1^{1/2}$ and suggest, therefore, that there is an absolute error in the measurement which is independent of the concentration, current, or any of the variables. This absolute error is most likely the graphical measurement of the transition time which becomes smaller percentagewise as the transition time increases.

Kinetics of the Electrode Reaction

Figure 3, when compared with Fig. 5, shows three steps at 1, 1.2, and 1.5v not associated with the solvent. The last of these arises from aluminum introduced from the salt bridge and is eliminated when a boron nitride salt bridge is used instead of the alumina. Boron nitride salt bridges could not be used easily, however, since they frequently disintegrated in the melt. The two steps then, at 1 and 1.2v, are associated with the reduction of the fluotantalate to tantalum metal. The most interesting properties to elucidate regarding the kinetics of this reduction are the electron change for each step, the rate-controlling process, and the nature of the reactants and products of the reactions. The easiest to establish is the final product, tantalum metal, which may be identified on the electrodes and which on a macroscopic scale is produced at 100% current efficiency (calculated on an over-all 5-electron reduction) at the cathode under a wide range of operating conditions.

The nature of the first step.—In a diffusion-controlled reaction (8)

$$i\tau^{1/2} = \frac{1}{2} nCD^{1/2} F\pi^{1/2} \qquad [1]$$

where i is the current density, τ the transition time, n the number of electrons in the reduction, C the concentration of the reacting species, D the diffusion coefficient of the reacting species, and F the Faraday constant.

Table III. Transition time ratios for various values of n

τ_2/τ_1	n_1	n_2
0.56	4	1
1.8	3	2
5.3	2	3
24.0	1	4

This requires that the transition time constant, $i\tau^{1/2}/C$, be independent of current density and concentration, and that $i\tau^{1/2}$ plotted against C be linear and extrapolate to zero at zero concentration. Examination of Fig. 4 and Table I confirms that these requirements are all met. The independence of current density, although implied, is not explicitly shown, but it is demonstrated without qualification in the data of the 81 runs from which Table I and Fig. 4 were prepared. It is, therefore, reasonable to presume that the first step is diffusion controlled and that the n in Eq. [1] represents the over-all number of electrons in the first reduction and D the diffusion coefficient of the reacting species of the first step.

The reactant for the first step is easily definable. It is undoubtedly an ion containing the pentavalent tantalum which is added to the bath. The valence of the tantalum in the operating solution has never been found to be other than 5.0, and thus it is established that no lower valence states are significant. Finally, it has been established by J. S. Fordyce, of our laboratory, that the tantalum exists in the melt as the $[TaF_7]^{-2}$ ion and that this ion is exceptionally stable under the conditions of operation. The studies of the infrared spectra of the tantalum plating systems on which this conclusion is based will be published separately. It may be concluded, then, that the reducible species which is the reactant in the first step is the heptafluotantalate (V) ion. There remains to be established the intermediate which is the product of the first step. This can be done by determining the value of n for the first step. There are two ways by which this can be accomplished.

(*A*) In stepwise, diffusion-controlled reductions such as occur in this case, it has been shown that (8)

$$\frac{\tau_2}{\tau_1} = \frac{2n_2}{n_1} + \left(\frac{n_2}{n_1}\right)^2 \qquad [2]$$

where τ_2 and τ_1 are transition times for the second and first step, respectively, and n_2 and n_1 are the corresponding electron numbers for each step. In Table III are shown the values of the ratio τ_2/τ_1 for the various possible values of n_2 and n_1 considering that $n_1 + n_2$ equals 5. The measured average value of $\tau_2/\tau_1 = 1.8 \pm 0.7$ for the 43 chronopotentiograms listed in Table II. The imprecision results largely from the variation in the value of τ_2 and is associated with some departure from diffusion control conditions for the second step of the reaction. However, the electron numbers suggested by this data are 3 and 2, for the first and second step, respectively. The close agreement of the τ_2/τ_1 ratio with the theoretical value must nevertheless be considered fortuitous since Eq. [2] applies strictly only when both steps are diffusion controlled.

(*B*) A method of obtaining the n number for a chronopotentiometric reduction which is independent of the second step depends on the shape of the potential-time curve of the first step only. It has been shown that when the reactants and products of a reversible reaction are soluble substances (8, 9)

$$E = E'_0 + \frac{RT}{nF} \ln \frac{\tau^{1/2} - t^{1/2}}{t^{1/2}} \qquad [3]$$

so that a plot of E *vs.* log $[\tau^{1/2} - t^{1/2}]/t^{1/2}$ is a straight line of slope 2.3 RT/nF where n is the desired electron number, and E, the potential at time t in the chronopotentiogram. If the product is an insoluble substance

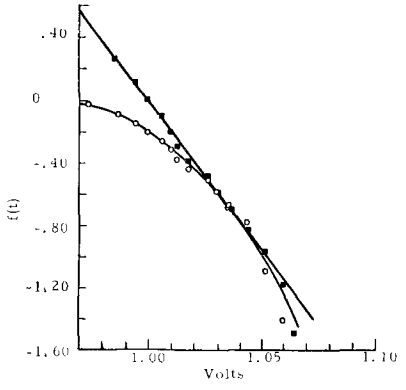

Fig. 7. Instantaneous cathode potential as a function of time during a chronopotentiometric run: ■, E vs. log $(\tau^{1/2} - t^{1/2})/t^{1/2}$; ○, E vs. log $(\tau^{1/2} - t^{1/2})$. Concentration, 5.9 x 10^{-5} mole/cm^3; current density, 0.045 amp/cm^2; temp, 750°C.

deposited on the cathode, the appropriate relation is (9)

$$E = E'_0 + \frac{RT}{nF} \ln (\tau^{1/2} - t^{1/2}) + \text{constant} \qquad [4]$$

and a linear plot of E *vs.* log $(\tau^{1/2} - t^{1/2})$ results. In Fig. 7 both these plots are shown for a typical chronopotentiogram of the first step of the reduction. It is evident that Eq. [3] applies. The slopes of the lines obtained by plotting 38 chronopotentiograms according to Eq. [3] gave an average value for n of 3.3 with a standard deviation of 0.8. Again the precision is insufficient to establish unequivocally $n = 3$, but in both cases $n = 3$ seems to be favored, and when this is coupled with the fact that occasionally sludges containing insoluble divalent tantalum fluorides are found in the operating solutions, there is good reason to believe that the first reduction step is a three-electron reduction to produce a divalent tantalum species.

There is some question regarding the nature of this divalent species. The linearity of the plot of Eq. [3] and the invariance of $E_{1/4}$ with concentration point to the divalent material as a soluble product. However, if it were soluble $\tau_{anode}/\tau_{cathode}$ in Fig. 6 should be 0.33 (9). It is found to be 0.83 at 9.64 ma/cm^2, 0.88 at 45.4 ma/cm^2, and 0.90 at 79.5 ma/cm^2. For a totally insoluble product the ratio of anodic to cathodic transition times should be unity since all that is cathodically produced at the electrode remains there to be oxidized in the anodic cycle (9). This would indicate that the product of the first reduction is only slightly soluble, that some of it dissolves and diffuses away, but that the faster the cathodic reduction is accomplished the less of it escapes from the electrode before the reoxidation step. This is confirmed by the occasional presence of an insoluble sludge consisting mostly of divalent tantalum fluorides in macroscopic electrolyzed solutions. The behavior of the E *vs.* t relationship and the constancy of $E_{1/4}$ can be explained by suggesting that through most of the time, τ, and certainly well beyond $\tau_{1/4}$, one is dissolving the product in the cathode layer, and only near the end of time, τ, is saturation reached. The departure of the last two points from the straight line of Fig. 7 may be a result of this saturation effect. The anodic cycle then oxidizes what is finally deposited as a solid on the electrode as well as whatever is available of the material in solution. It appears, therefore, that the final product of the first reduction step is slightly soluble TaF_2 and the first reduction step may be written

$$[TaF_7]^{-2} + 3e \rightarrow TaF_2(s) + 5F^-$$

The rate of the reaction is controlled by the rate of diffusion of the fluotantalate ion in the mixed alkali fluoride solvent.

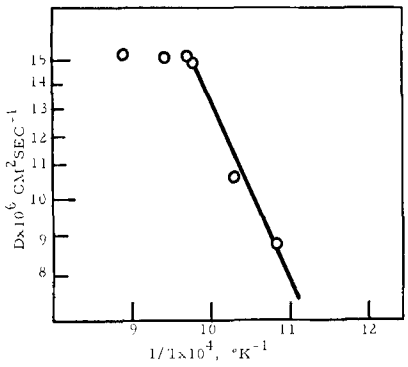

Fig. 8. Activation energy for diffusion of fluotantalate ion in molten Flinak.

Once one has established the electron number, n, as 3, one may use Eq. [1] to calculate the diffusion coefficient of the reacting species. This was done at various temperatures, and the results are shown in Fig. 8. The plot is linear between 650° and 800°C and corresponds to an activation energy for diffusion of 8.5 kcal/mole. The departure from linearity which is observed above 800°C occurs near the upper temperature limit for satisfactory plating (10). It may result from the thermal decomposition of the reacting species at this temperature with resultant decrease in its concentration, or may be an effect of increasing cathode surface area due to the unsatisfactory nature of the deposit at this temperature.

The activation energy may be compared with those obtained chronopotentiometrically by Thalmayer, Bruckenstein, and Gruen (11) who found an activation energy of 5.8 kcal/mole for diffusion of Ag^+ in molten KCl-LiCl; Cd^{2+}, 6.5; Pb^{2+}, 7.9; Bi^{3+}, 9.8; and U^{4+}, 7.72 kcal/mole. Senderoff, Klopp, and Kronenberg (3) measured diffusion coefficients by tracer diffusion from a capillary and reported 6.9 kcal/mole for Ag^+ in molten KCl-LiCl and 5.8 kcal/mole for sulfate ion in the same solvent.

The diffusion coefficient of the pentavalent tantalum species at 750°C is 1.5 x 10^{-5} cm^2/sec. This compares with 7.6 x 10^{-5} for Ag^+ in KCl-LiCl (3) at the same temperature. If one extrapolates the values in Fig. 8 to 400°C one obtains a diffusion coefficient of 1.2 x 10^{-6} which compares with those of Thalmayer *et al.* (11), for the same temperature of 24.7 x 10^{-6} for Ag^+, 12.1 x 10^{-6} for Cd^{2+}, 8.9 x 10^{-6} for Pb^{2+}, 7.2 x 10^{-6} for Bi^{3+}, and 4.89 x 10^{-6} for U^{4+} in molten KCl-LiCl.

The decreasing diffusion coefficient and increasing activation energy for diffusion with increasing valence is probably a result of the increasing complexity and size of the diffusing species as suggested by Laitinen and Ferguson (12). That the Ta^{5+} species falls well into line on this basis is additional corroboration that a highly complexed ion such as $[TaF_7]^{-2}$ is the active species at the cathode. At 750°C the diffusion coefficient is 1/5th of that measured for Ag^+ in KCl-LiCl which suggests a high degree of coordination of the transported tantalum ion since the viscosity of the fluoride melt is only twice that of the chloride melt at this temperature.

The nature of the second step.—The product of the second step has been shown to be tantalum metal. The reactant for this step is the product of the first one and is almost certainly solid TaF_2 or a saturated solution of this compound in molten Flinak. The reaction is not diffusion controlled as is shown by the decrease of $i\tau_2^{1/2}/C$ with increasing concentration. The study of the details of the kinetics of this reduction is made difficult by the imprecision of the data for this step. It is believed that the lack of reproducibility results from varying degrees of saturation of the electrolyte around the cathode and from uncontrollable partition of the current between the solid and dissolved species.

It is probable that potentiostatic measurements may be more suitable than chronopotentiometric studies for the elucidation of the mechanism of the final reduction step. Further, while Fig. 6 shows that the first step is highly reversible, cathodic-anodic chronopotentiometry on the second step shows a wide divergence between the anodic and cathodic potentials. This probably indicates additional electrochemical complications requiring further study.

Macroscopic observations which emphasize the importance of the sparingly soluble intermediate, TaF_2, are (*a*) tantalum metal is essentially unattacked in contact with K_2TaF_7 in molten Flinak between 650° and 850°C; this is in contradistinction to the rapid attack on niobium metal in contact with K_2NbF_7 in the same solvent. (*b*) the solution of fluotantalate in contact with the metal or after electrolysis always has an apparent valence of 5.0, while that of fluoniobate has a valence less than 5.0 and after prolonged electrolysis it approaches 4.0. This demonstrates the existence of a soluble reduced niobium fluoride and shows that the tantalum is inert in its pentavalent salt only because it is protected by the insoluble difluoride.

Summary

The electrodeposition of tantalum from K_2TaF_7 dissolved in a molten alkali fluoride solvent occurs in two steps. The first may be written

$$[TaF_7]^{-2} + 3e \rightarrow TaF_2(s) + 5F^-$$

and the second

$$TaF_2(s) + 2e \rightarrow Ta + 2F^-$$

The first step is a diffusion controlled, highly reversible reaction and the diffusion coefficient of the pentavalent tantalum species is 1.5×10^{-5} cm²/sec at 750°C. The activation energy for diffusion between 650° and 800°C is 8.5 kcal/mole. The low value of diffusion coefficient and high activation energy are consistent with a highly coordinated reducible species such as the $[TaF_7]^{-2}$ ion. The second step is not diffusion controlled and only poorly understood. Its kinetics probably involve the reduction of both solid and dissolved TaF_2 and it is highly irreversible.

Acknowledgment

The authors are grateful for the valuable discussion and criticism by Professor H. A. Laitinen throughout the course of this work.

Manuscript received Jan. 1, 1965; revised manuscript received April 19, 1965. This paper was presented at the Washington Meeting, Oct. 11-15, 1964.

Any discussion of this paper will appear in a Discussion Section to be published in the June 1966 JOURNAL.

REFERENCES

1. G. W. Mellors and S. Senderoff, *This Journal*, **112**, 266 (1965).
2. H. F. Priest in "Inorganic Synthesis," Vol. III, L. F. Audrieth, Editor-in-Chief, McGraw-Hill Book Co., New York (1950).
3. S. Senderoff, E. M. Klopp, and M. L. Kronenberg, Final Report Contract NOrd-18240, Part II, Sept. 15, 1962.
4. K. Grjotheim, *Z. Physik. Chem., N. F.*, **11**, 150 (1957).
5. D. L. Manning, *J. Electroanal. Chem.*, **6**, 227 (1963).
6. H. Coriou, J. Dirian, and J. Huré, *J. chim. Phys.*, **52**, 479 (1955).
7. (a) M. S. Foster, C. E. Crouthamel, D. M. Gruen, and R. L. McBeth, *J. Phys. Chem.*, **68**, 980 (1964); (b) M. S. Foster, S. E. Wood, and C. E. Crouthamel, *Inorg. Chem.*, **3**, 1428 (1964).
8. P. Delahay, "New Instrumental Methods in Electrochemistry," Chap. 8, Interscience, New York (1954).
9. W. H. Reinmuth, *Analyt. Chem.*, **32**, 1514 (1960).
10. G. W. Mellors and S. Senderoff, Can. Pat. 688,546 (1964).
11. C. E. Thalmayer, S. Bruckenstein, and D. M. Gruen, *J. Inorg. Nucl. Chem.*, **26**, 347 (1964).
12. H. A. Laitinen and W. S. Ferguson, *Analyt. Chem.*, **29**, 4 (1957).

Automation of the Measurement and Processing of Voltammetric Data

M. W. Breiter

Research Laboratory, General Electric Company, Schenectady, New York

ABSTRACT

An assembly for the measurement of voltammetric current-potential curves and of the ohmic and capacitive components of the impedance of the interphase electrode/solution by voltammetry with superimposed a-c voltage is described. The analog to digital recording equipment which records the electrochemical data on paper tape is discussed. The main features of three computer programs required for the data processing by computer are outlined. The time for data processing is reduced to about a tenth of the value of the usual procedures, thus allowing time to evaluate more experimental points than previously. The feasibility of the set-up is demonstrated by two examples.

Information on the electrochemical formation or removal of adsorbed layers (1-3) and oxides (4) at solid electrodes, on the adsorption of ions (5, 6) or organic molecules (7), and on the kinetics of electrode reactions with adsorbed species (8, 9) may be obtained by voltammetric measurements. Two different types of measurements have been used successfully. (*a*) Potentiostatic current-potential curves: either a periodic voltage of triangular shape (1, 3) or a single ramp (2) are applied to the test electrode at different sweep rates, and the current is recorded as a function of potential; (*b*) voltammetry with superimposed alternative current: the ohmic and capacitive component of the interfacial impedance are measured (6) as a function of potential for a given frequency at small and intermediate sweep rates up to 100 mv/sec.

While the taking and recording of voltammetric data are automated the processing of the data has been cumbersome since a large number of experimental points has been involved in most cases. So far the experimental curves have been recorded by recorders or photographed from the screen of oscilloscopes. Any evaluation of the data required the tedious job of determining them manually point by point from the graphs or enlargements of films. Then the data were converted mainly by slide rules into the correct units and plotted immediately or put together

in a table for further computations, perhaps by computer. The time for data processing has been cut considerably in many fields of science by the use of high-speed computers. It appeared desirable to apply similar techniques in order to eliminate the manual procedure of determining voltammetric data from graphs or films. Now these data are printed out in table form and plotted, if requested, for any potential scale with constant increments in the potential range of the measurements. The time for processing is reduced to about a tenth of the value of the manual procedure. A larger number of experimental points may be evaluated than previously. In addition, the smoothing of experimental data by simplified least square procedures is easily carried out. Instrumentation and programming are described subsequently.

Assembly for Electrochemical Measurements

The assembly for which a block diagram is presented in Fig. 1 is an improved version of a set-up reported previously (6). It consists of a potentiostatic circuit for the application of the potential sweep and a galvanostatic circuit for the impedance measurements. Both circuits are connected to a cell of conventional design. All the electrodes are in the same solution and at the same temperature. Pretreatment of the electrodes and purification were as discussed (10).

The potentiostatic circuit is shielded by a suitable choke L from the a-c circuit. It allows sweep rates from about 3 mv/sec to 300 mv/sec. The range of the function generator was extended to lower frequencies by internal alterations. The voltage of triangular shape between K and ground is applied between test electrode and a large hydrogen electrode (platinized Pt-foil). The large hydrogen electrode is polarized little by cathodic currents up to 100 ma. It was dimensioned such that anodic currents up to 10 ma do not produce a noticeable polarization. If larger currents than 1 ma are required, a d-c power supply modified into an amplifier with small output impedance is inserted at point K. The decade resistor R_4 serves for the measurement of the current. The electrode potential is measured between A and B.

The a-c current generated by a low-frequency oscillator flows through three parallel branches. Resistors R_1, R_2, and R_3 are chosen such that each of them is at least 300 times larger than any other impedance in the respective branch. A voltage of 10 mv_{eff} is maintained across the 10 ohm resistor between A and E. Reference voltages for the resolved component indicators are produced from this voltage. The a-c current which flows between a platinum wire spiral and the test electrode is equal to R_3/R_1 in ma_{eff}. The resistor, R_2, is taken such that the voltage between A and D becomes equal to the ohmic potential drop across the electrolytic resistance R_{El} which is measured as part of the ohmic component of the interfacial impedance in a series circuit. A method of determining R_{El} was developed (6) and verified (9) for platinum electrodes. The a-c voltage between B and D ($\tilde{U}_{signal}$) is kept smaller than 2.5 mv_{eff}. The ohmic and capacitive part of $\tilde{U}_{signal}$ are measured separately by two resolved component indicators by connecting G to D and H to B. The two reference voltages ($\tilde{U}_{reference}$) have a phase shift of 90° against each other. They are made nearly equal by selecting appropriate values of C_2. The a-c assembly is calibrated and corrected for small phase shifts at each frequency before the actual measurements by connecting H to F and G to A. The phase shift is compensated by adjusting the dial of one of the analyzers slightly until the reading of the capacitive component on the meter is zero. The reading of the ohmic component achieves a maximum when the phase shift is zero. Then it corresponds to 2.5 mv_{eff}. The meters are disconnected during the actual measurements since their response time is slow. The measurements of $\tilde{I}$ and $\tilde{U}_{signal}$ are made with the same analyzer (input G and H). Different connections are established by a suitable switch.

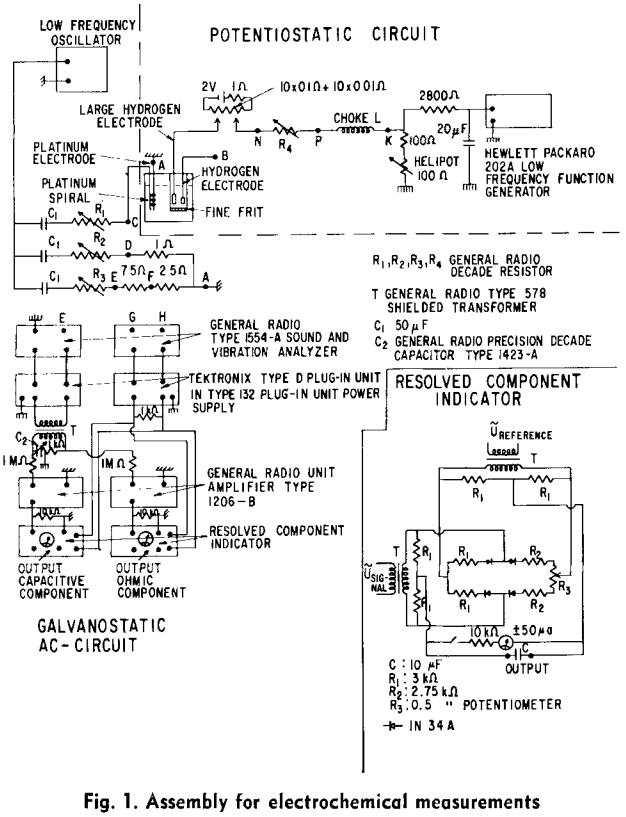

Fig. 1. Assembly for electrochemical measurements

A discussion of the circuit of the indicator (see Fig. 1) and a mathematical treatment was given by Geyger (11). The indicator is balanced at $\tilde{U}_{signal} = 0$ for zero output by the potentiometer R_3. The long-time stability of this adjustment was improved considerably over the previous design (6) by introducing the transformer T. Impedance measurements were made between 100 and 20,000 cps with transformers type 578-A. An extension to 20 cps is planned with type 578-B. The reference voltage has to be much larger than the signal voltage that the d-c voltage across the capacitor C is independent of the reference voltage and proportional to the ohmic or capacitive part, respectively, of $\tilde{U}_{signal}$. A ratio of ten was satisfactory here. The accuracy of the readings of the ohmic and capacitive component is 1% of full-scale value.

Analog to Digital Recording Equipment

A high-speed computer requires a rapid feeding of the data to be processed. Since voltammetric measurements at small and intermediate sweep rates are slow, the experimental data are punched on paper tape in digital form by the recording unit. When sufficient data are accumulated, they are transferred to magnetic tape by the tape reader in a format suitable for programming in Fortran. Finally, they are read into the computer from magnetic tape and processed. The G.E. 225 computer and tape reader were used.

The analog to digital recording equipment was designed and constructed by the Design Engineering and Instrumentation Unit of the General Electric Research Laboratory in collaboration with Dr. T. W. Hickmott, Research Laboratory, and the author. Essentially it is a multichannel recorder. Up to ten signals may be recorded independently. The signal fed to the input of channel 1 is recorded first, then the signal of channel 2, etc. One complete cycle of input readings requires 18 msec times the number of channels being used. In the "one cycle" mode the sequence stops after the last of the input channels has been recorded. Another cycle is initiated by the trigger signal of the

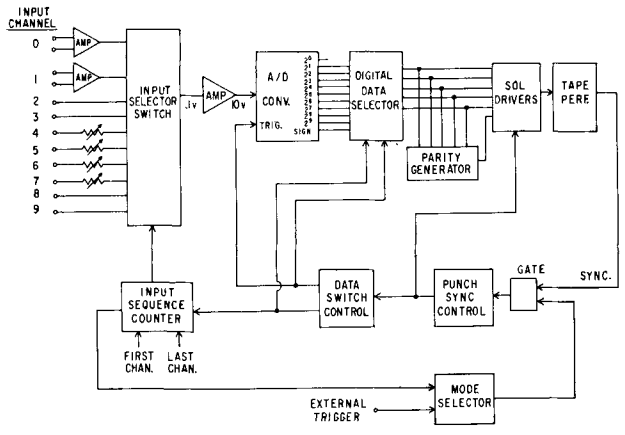

Fig. 2. Block diagram of the analog to digital recording equipment

external generator. The maximum rate of recording per channel corresponds to 55/(number of channels) data per second and may be used continuously in the "continuous" mode. In the one step mode the first external trigger leads to the recording of channel 1, the second trigger to that of channel 2, etc.

A functional block diagram is shown in Fig. 2. There are 10 d-c voltage inputs available. Two of these inputs lead to differential d-c amplifiers with input scaling switches to cover the range 1 mv to 10v full scale in 9 steps. Four of the other inputs are supplied with divider networks covering the range 100 mv to 300v full scale in eight steps. Four of the inputs are direct to the input selector switch at 100 mv full scale. The input selector switch connects the inputs one at a time to the common amplifier which raises the level to 10v full scale for the analog to digital converter. The output of the converter is ten binary bits and sign. These digital data are punched by the tape perforator in two punch cycles (6 bits per cycle). The code used is unique to this equipment. Odd parity is generated for each punch cycle. Manual settings allow any number of input channels to be sequenced, beginning with any selected channel.

The time sequence of events for one cycle of input readings is as follows. External trigger opens gate. Next synchronous pulse from perforator triggers synchronizing control. Data switch control is set to first half of data at the digital data selector and A/D converter is triggered. A conversion is performed in 100 μsec giving 10 binary bits and sign. The solenoid drivers are gated on for 4.5 msec to record the first half of data. Synchronous pulses from the perforator are at 9 msec intervals. The second synchronous pulse sets the data switch control for second half of data and input sequence counter is advanced to the next channel. The solenoid drivers are gated on for 4.5 msec to record the second half of data. The third synchronous pulse from the perforator returns data switch control to the first half of data and triggers the A/D converter to convert the input voltage of the second channel. This cycling continues according to the mode chosen.

Three rotary switches allow the insertion of a coding in the first block on the paper tape to identify up to 199 run numbers by supplying different negative voltages to the converter in the "Run Number" position of the selector switch. The run number is punched as many times in the first block as channels are used. A network for the automatic recording of the range settings of the six channels with divider network is connected to the range setting switches of the respective channels. Different positive voltages are given to the converter and recorded as binary numbers that are interpreted by the program as scale factors. If the scale factors are not changed during one run it is sufficient to record them once in the second block on paper tape. If the scale factors have to be changed during the measurements, up to four scale factors may be recorded during each cycle of input readings in the one cycle or continuous mode by the use of the four channels without divider network. Provisions are made on the rear of the chassis panel for this arrangement. The sequence of the recording of the current-potential measurements described subsequently was as follows: potential, current, scale factor potential, scale factor current. A similar sequence was utilized for the impedance measurements. The measurements of the electrochemical variables can be considered simultaneous for sweep rates below 100 mv/sec.

On the paper tape a single punch in punch position 8 of the perforator represents the "end of block" character. The introduction of such a character allows the program to find synchronization errors. The end block character may be recorded after 2^N blocks of data by the use of the "End of Block Spacing" control. The inputs without divider network may also serve to trim d-c output voltages of many standard laboratory instruments with the aid of voltage dividers to a full scale of 100 mv for an extension of the recording system. A voltage is created and connected to the inputs of all channels when the input selector switch is in the "Test" position. After conversion the following data bits are punched: sign, 2^8, 2^6, 2^4, 2^2 and a code bit in the same perforator channel as 2^6 to designate the simple test pattern. Since the bit 2^1 represents 0.2% of full scale an increase of 0.2% will cause a punch of the bit 2^1 and also of the parity bit. At a decrease of 0.2% the bit 2^2 will not be punched and the bit 2^1 will be punched. The voltage for the test pattern is taken from the same source as that for the run numbers. Thus a correct pattern is evidence that the A/D converter is correct within $\pm$ 0.2% and that the run number should be recorded properly.

The output of the common amplifier is connected to a panel meter which allows a 1% reading of voltages which are constant or slowly changing. The state of the input sequence counter is indicated as an aid for the initial setting by four lamps. This counter may also be advanced manually by a button to connect any input to the system so that an indication is seen on the panel meter. The output of the converter may be read from ten small lamps corresponding to 2^0, 2^1, — — — 2^9 and two sign lamps on the panel.

The accuracy of the recording unit was found to be 0.4% of full-scale values for the eight inputs which are ground referenced. It is 1% for the differential amplifiers for full-scale values equal or larger to 100 mv. At smaller values it is about 3%. In the case of voltammetric data the accuracy of the potential measurement determines the meaningful spacing of the cycles of input readings. A frequency of 5 cps was chosen for the triggering signal at a sweep rate of 30 mv/sec.

Programming

Three programs in Fortran were written for the processing of voltammetric data. The first program is always required for the transfer of the data from paper tape to magnetic tape as fixed point numbers. The second program handles the processing of I-U data from magnetic tape. The third program processes the impedance measurements. Since these programs are long and unique for the recording unit and the specific measurements, only their main features will be discussed here. The computer programs will be made available to readers on request.

Program 1 looks first for the run number and then the numbers representing scale factors. It is necessary that this information appears in this order. The number of channels is determined from the first block on paper tape. The number of characters between end blocks is counted by the tape reader and compared to the number of channels being used. Any block of data containing the wrong count is not recorded on magnetic tape, and a diagnostic is printed out. The first record on magnetic tape contains the following information: run number, number of

blocks in one record on magnetic tape. The number of blocks per record varies with the number of channels and is derived by program 1 in such a way as to maintain the same Fortran format on the tape (126 words/record). If required, the same dummy number is filled in several times at the end of a record. The run number is the first word in any record besides the last one which consists only of the dummy words and designates the end of a run. The scale factor numbers are recorded in the second record. Data are in the subsequent records which are counted and numbered. The record number is the second piece of information on the records with data. The total number of records with data in one experimental run is printed out at the end. The tape reader interprets about two inches of blank paper tape as the end of a run. Program 1 is applicable whether the scale factors are recorded only once in the second block on paper tape or are recorded together with the electrochemical data.

Programs 2 and 3 for the processing of data from magnetic tape differ somewhat whether the scale factors are variable or constant during the measurements. Both programs create the scale factors in the beginning and assign them during the execution to the scale factor numbers picked up from magnetic tape. One data card is read for each run with additional information. For program 2 these are: electrode area, temperature, increment for the potential scale chosen, number of increments, first value of potential scale, maximum permissible increment between two subsequent measurements of potential, positive or negative fixed point number deciding for or against plotting of data. In addition there are on the data card in the case of program 3: frequency, electrolytic resistance R_{El}(R_{El} = 0 if correction is not required), R_3/R_1 instead of R_4, a second fixed point number determining if the impedance is considered as a series or parallel circuit of resistance and capacitance. The electrochemical data in each record are converted into the correct units successively. If two subsequent measurements of potential differ more than the permissible value prescribed on the data card, all the electrochemical variables pertaining to the second potential reading are discarded. Such a precaution is necessary since errors occur by chance during the taking of hundreds

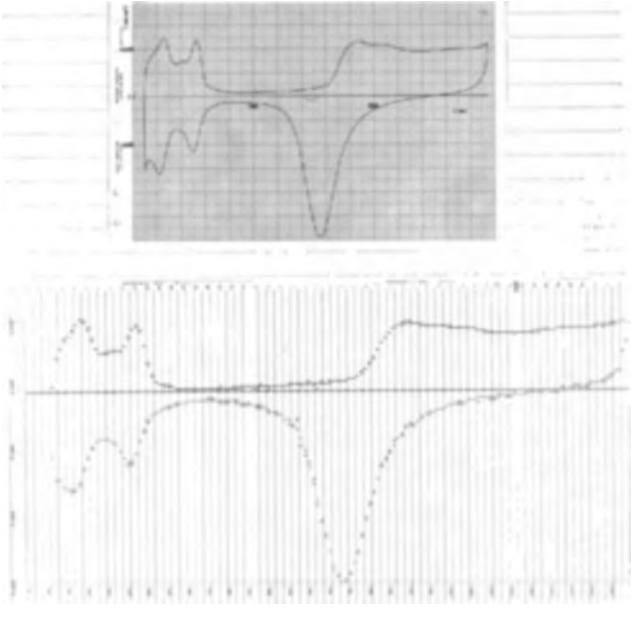

Fig. 3. Upper I-U curve on platinum in N H_2SO_4 is recorded by X-Y recorder; Lower I-U curve is plotted by printer. 1,3: interpolated values of current density. 2,4: smoothened values of current density.

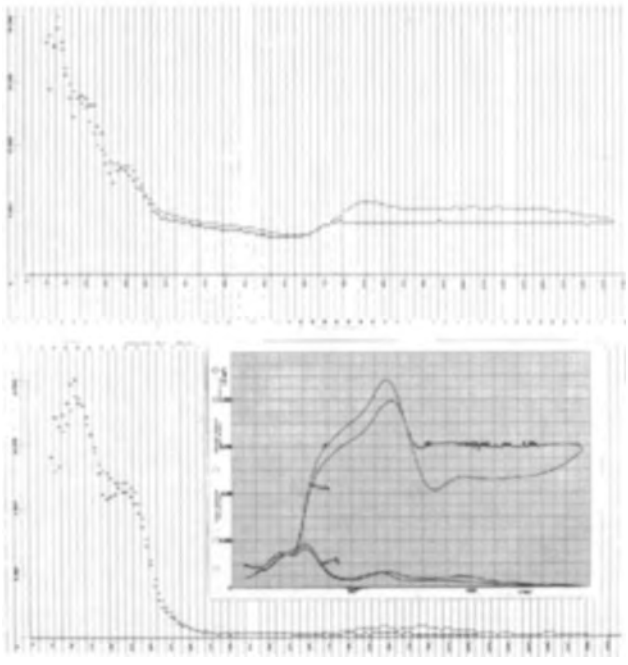

Fig. 4. Ohmic and capacitive components of the impedance on platinum in N H_2SO_4 are recorded by X-Y recorder on graph paper in a series circuit. Upper computer plot: capacitive component in parallel circuit; Lower computer plot: ohmic component in parallel circuit. 1: anodic sweep; 2: cathodic sweep.

of points. An arbitrary potential scale with constant increments as requested by the data card is established for the potential range of the measurements. The programs compute either the values of the current density or those of the ohmic and capacitive components according to this potential scale by linear interpolation from the experimental data and store them in memory, distinguishing between anodic and cathodic sweep. The capacity is derived from the capacitive component by program 3. Each of the interpolated values is smoothened by a simplified least square procedure (12) involving seven points in its vicinity. The values of the electrochemical variables are printed out subsequently according to the potential scale for the anodic and cathodic sweep. Interpolated and smoothened values are given. If requested on the data card, a plot is produced by the high-speed printer. The choice between a series or a parallel analog circuit for the impedance in program 3 simplifies the interpretation of these measurements which can only be made in a series circuit (see Fig. 1). The first data recorded in the case of impedance measurements correspond to 2.5 mv_{eff} applied during the calibration procedure for the resolved component indicators. Program 3 averages and computes the calibration factor.

It is simple to add program extensions, for instance the integration of parts of the I-U curves, as subroutines to programs 2 or 3. Similarly, the data tabulated may be obtained easily on punch cards in a format suitable to further computations. However, direct further processing is not considered since an intermediate judgement of the experimental data by the scientist is thought necessary.

Examples

A current-potential curve on smooth platinum in N H_2SO_4 at 30 mv/sec and 30°C with its typical shape (1, 3) is shown twice in Fig. 3. The quiescent solution was saturated with helium before the measurements. The upper curve was recorded with the Varian F80 X-Y recorder. The lower curve was plotted by the printer of the G.E. 225 computer, the

scales being adjusted by program 2. During the anodic sweep the symbol 1 stands for the values of the current density which were obtained by interpolation from the measured values while the symbol 2 represents the results of the smoothening of the interpolated values. The same statements hold for symbols 3 and 4 during the cathodic sweep. Values derived by interpolation and subsequent smoothing coincide if only one symbol appears. It is clear from a comparison that the accuracy of the recording unit is equivalent to that of the X-Y recorder. The data plotted in the lower curve were also printed out in a table which, however, is omitted here to avoid duplication.

The ohmic and capacitive component of the interfacial impedance of smooth platinum were measured in N H_2SO_4 at 10,000 cps in a series circuit. The sweep rate was 30 mv/sec. R_{El} was compensated. The curves as obtained in successive runs and recorded by the X-Y recorder are shown on the graph paper in Fig. 4. A discussion of their shape was given elsewhere (6). The upper and lower plots made by the printer represent the capacitive and ohmic component respectively of the impedance in a parallel circuit. The capacative component is proportional to the capacity here. Both components reflect (9) the heterogeneity of the platinum surface with respect to the Volmer reaction in the potential range of hydrogen adsorption. The impedance is practically capacitive above 0.5v in the so-called double layer region and oxygen region.

Acknowledgments

The author acknowledges gratefully the assistance of Doctors B. McCarrol and G. M. White during the programming and that of Mr. J. Sicko and E. Underkoffler in technical problems concerning the Digital to Analog Recording Unit.

Manuscript received March 17, 1965.

Any discussion of this paper will appear in a Discussion Section to be published in the June 1966 JOURNAL.

REFERENCES

1. F. G. Will and C. A. Knorr, *Z. Elektrochem.*, **64**, 258 (1960).
2. T. C. Franklin and S. L. Cooke, Jr., *This Journal*, **107**, 556 (1960).
3. Ya. Kolotyrkin and A. N. Chemodanov, *Doklady Akad. Nauk S.S.S.R.*, **134**, 128 (1960).
4. J. L. Weininger and M. W. Breiter, *This Journal*, **111**, 707 (1964).
5. M. W. Breiter, *Electrochim. Acta*, **8**, 925 (1963).
6. M. W. Breiter, *J. Electroanalyt. Chem.*, **7**, 38 (1964).
7. M. W. Breiter, *Electrochim. Acta*, **8**, 973 (1963).
8. M. W. Breiter and S. Gilman, *This Journal*, **109**, 622 (1962); **110**, 449 (1963).
9. M. W. Breiter, *J. Phys. Chem.*, **68**, 2249 (1964). (1964).
10. M. W. Breiter, *J. Electroanalyt. Chem.*, **8**, 230 (1964).
11. W. Geyger, *Arch. Tech. Messen*, Z., 52-7, Z. 52-8 (1948).
12. A. Savitsky and M. J. E. Golay, *J. Analyt. Chem.*, **36**, 1627 (1964).

Oxygen Overvoltage Measurements on Bright Platinum in Acid Solutions

III. Nitric Acid-Passivated Bright Platinum

James P. Hoare

Research Laboratories, General Motors Corporation, Warren, Michigan

ABSTRACT

Oxygen overvoltage measurements were made on platinum electrodes which had been passivated in nitric acid. It was demonstrated that the reversible oxygen electrode may be obtained. Apparently, the treatment with HNO_3 significantly changes the nature of the platinum surface, and it is suggested that the Pt surface is converted to a Pt-O alloy. The Pt-O-alloy surface not only is a better peroxide decomposing catalyst than Pt, but also accelerates the adsorption of oxygen and the electron transfer step. Although the overvoltage is independent of the partial pressure of oxygen for large values of P_{O_2}, the rate-determining step is considered to be the discharge step

$$(O_2)_{ads} + e \rightleftharpoons (O_2^-)_{ads}$$

The rate of reduction of oxygen is increased by two orders of magnitude on Pt-O-alloy electrodes from that on Pt electrodes, and the overvoltage is reduced by at least 200 mv.

In a previous report (1) it was suggested that the reversible oxygen potential, 1.229v (2), was not observed because platinum is not inert to the reactants of the electrode reaction. As a result, the Pt/O_2 electrode is a polyelectrode (3), and since the system is always polarized by a local cell current, it never reaches equilibrium but only a steady state. The steady-state potential is a mixed potential (4). It was further suggested (1) that, if the electrically conducting layer of adsorbed oxygen on the platinum surface could be maintained complete, the reversible potential should be observed. Effectively, this is accomplished at high polarization, as shown by the fact that the extrapolated Tafel curves for anodic and cathodic overvoltage cross at the reversible oxygen potential (5-7).

It was shown in a second report (8) that a complete layer of adsorbed oxygen, which is electronically conducting and chemically inert, can be produced on a Pt surface by treatment with concentrated nitric acid. The reversible potential was observed for periods of time exceeding 24 hr.

In this report the polarization data taken on HNO_3 passivated Pt electrodes are presented.

Experimental

As before (8), small beads (0.02-0.03 in. in diameter melted at the end of platinum (99.99% pure) wires were passivated in concentrated HNO_3 in a Teflon cell for at least 72 hr. Afterwards, the beads were washed in triply distilled water and mounted in the right-hand side of a dual Teflon cell (1)

filled with $2N$ H_2SO_4 solution. The use of polyethylene was avoided, since HNO_3 attacks it. An α-Pd-H reference electrode (9) was used in the left-hand compartment of the cell. All cell and electrode preparations and all purification techniques were the same as those described before (1, 7, 8). The electrodes were polarized and the overvoltage determined in the same manner as that described in the previous report (7). All measurements were made at 25° ± 1°C and at a P_{O_2} of 1 atm (except the data shown in Fig. 6).

Results

Two systems are to be distinguished; type I, in which the HNO_3 passivated platinum electrode exhibits the reversible oxygen potential, and type II, in which it exhibits a potential from 100 to 150 mv less noble than the reversible potential. Type II electrodes are produced from type I electrodes when such electrodes have been strongly cathodized or anodized.

In Fig. 1, the polarization data taken at low current densities are presented for a type I electrode and in Fig. 2, for a type II electrode. The cathodic overvoltage curves for both types of electrodes are given in Fig. 3. Anodic overvoltage data for a type I electrode are plotted in Fig. 4 and for a type II electrode in Fig. 5. The dependence of the overvoltage on the partial pressure of oxygen (P_{O_2}) is presented in Fig. 6 for a type II electrode.

The data presented in Fig. 1 give a slope of 700 ohms which is nearly two orders of magnitude different from that (6 x 10^4 ohms) obtained on untreated bright platinum (7). These points were the average of at least three cycles of increasing and decreasing polarization over the current density range indicated and could be reproduced within ±2 mv. It is of interest to note that the linear curve

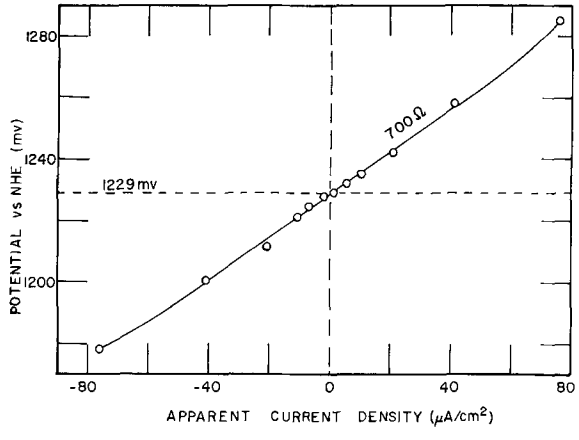

Fig. 1. Polarization data for the reversible oxygen electrode on bright platinum at low current densities.

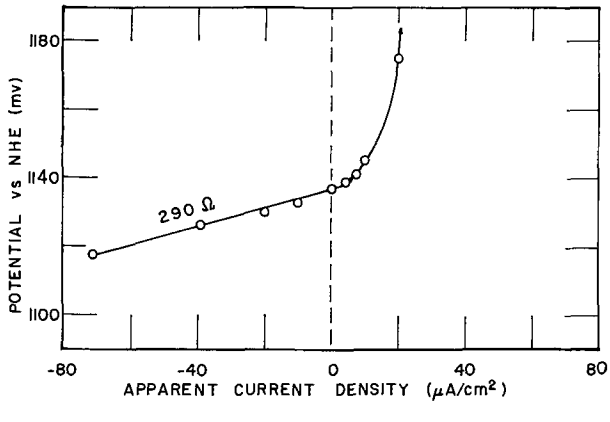

Fig. 2. Polarization data for a Pt-O-alloy electrode at low current densities.

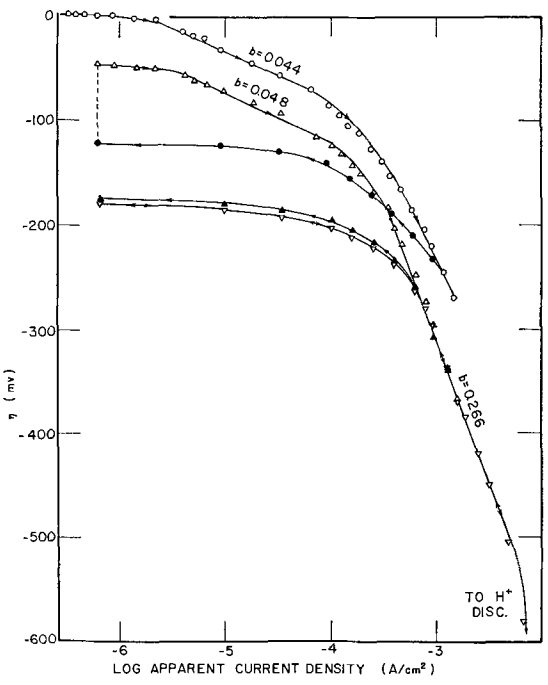

Fig. 3. Cathode overvoltage data on HNO_3-treated Pt electrodes. Arrows indicate direction of polarization. ○, ●, First cycle of polarization; △, ▲ = second; ▽ = final reproducible polarization curve. See text for details.

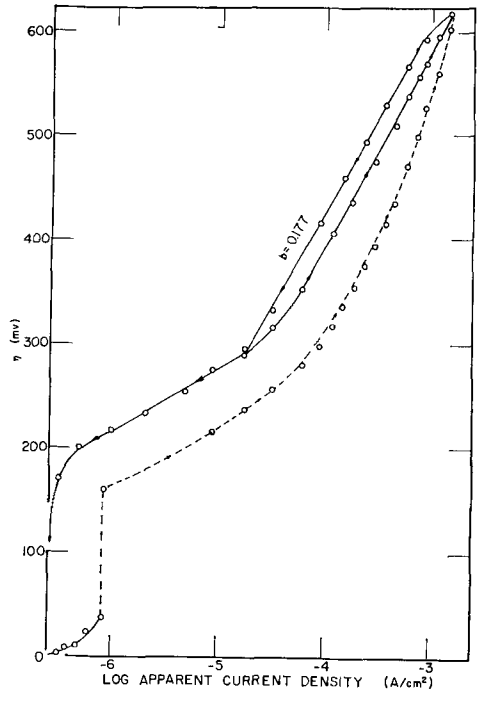

Fig. 4. Anodic overvoltage data on HNO_3-treated Pt electrode. Dashed curve contains nonsteady-state points; solid curve is reproducible curve. Arrows indicate direction of polarization.

passes through the reversible oxygen potential at open circuit without a change in slope.

When a type I electrode is cathodically polarized beyond the current density range given in Fig. 1, the curve is not retraced on the decreasing part of the polarization cycle as indicated in Fig. 3 by the arrows. If the circuit is opened and the system permitted to come to a steady state (indicated by the dashed part of the curve in Fig. 3), a second polarization curve may be obtained which is displaced from the first by about 50 mv. Both of these curves exhibit

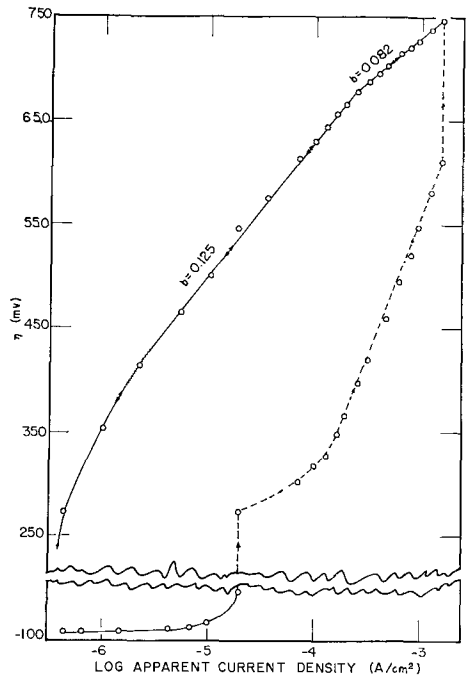

Fig. 5. Anodic overvoltage data on a Pt-O-alloy electrode. Dashed curve contains nonsteady-state points; solid curve is reproducible curve. See text for details.

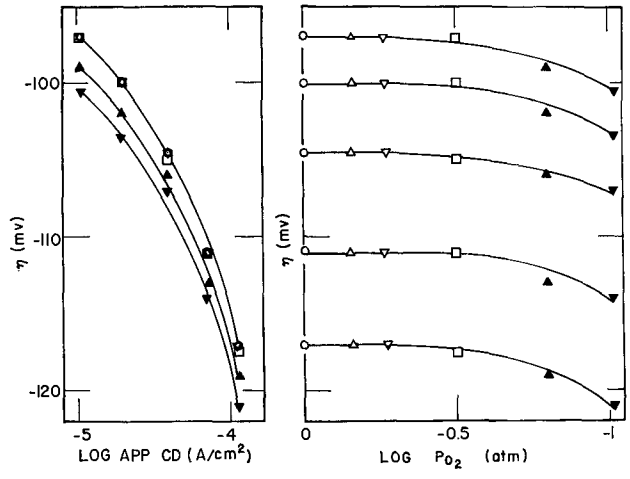

Fig. 6. Oxygen overvoltage as a function of P_{O_2} on a Pt-O-alloy electrode. P_{O_2} values are: ○, 1; △, 0.71; ▽, 0.54; □, 0.32; ▲, 0.16; ▼, 0.091. Data for the η-log P_{O_2} curves were taken from the η-log apparent current density curves.

a slope of about 0.045 with a break at about 10^{-4} amp/cm² and a change of slope to much higher values (>0.200) at the higher current densities. Now, if the system is polarized through several cycles without opening the circuit, a reproducible curve (indicated by double headed arrows) is obtained. The points on this curve are the average of three cycles with the greatest deviation from the mean being ±5 mv. It is to be noted that the slope of 0.045 cannot be detected and that all of the curves run together at high current densities with the very high Tafel slope of 0.266. A limiting current is reached near 10^{-2} amp/cm² and the system goes to hydrogen ion discharge. It is interesting to compare these results with those obtained on untreated Pt (7). The limiting current density is increased by an order of magnitude, and the overvoltage at a given current density, say 10^{-4} amp/cm², is decreased by 250 mv by the treatment of a Pt bead electrode with HNO_3.

When the circuit is opened, the steady rest potential is about 100-150 mv less noble than the reversible potential. It is seen, then, that a type I electrode has been converted to a type II electrode by cathodic polarization. Such an electrode, brought to the hydrogen potential (—50 mv *vs.* α-Pd-H) by replacing the O_2-stirring with H_2-stirring or by cathodizing for 2 min, or both, still gave the same type of polarization curves for the type II electrode (Fig. 3) instead of those for bright Pt [Fig. 2 of ref. (7)]. The i_o for the first cycle of polarization (type I electrode) in Fig. 3 is 1.8 x 10^{-6} amp/cm², three orders of magnitude greater than the i_o for untreated Pt (1.3 x 10^{-9} amp/cm²). However, the slope of 0.266 found on the type II electrode gives an i_o of 7.2 x 10^{-5} amp/cm². This higher reactivity is reflected in the low value (290 ohms) of the slope of the low current density curve given in Fig. 2.

When a type I electrode is polarized anodically, reproducible points may be obtained up to a point about 100 mv more noble than the rest potential. Above this point, the potential drifts to more noble values as shown by the dashed curve in Fig. 4. Succeeding cycles of polarization produce curves with the same slope, but with a hysteresis as shown. When this system is open circuited, the potential falls to the rest potential of a type II electrode within 2 hr. It may be seen that a type I electrode is converted to a type II electrode by anodic polarization also.

The anodic overvoltage of type II electrode is given in Fig. 5. For increasing polarization, the points are not steady, but drift with time toward more noble values. At the highest current density studied, the electrode was polarized until a steady potential was obtained. This behavior is described by the dashed curve. Now, a reproducible curve (solid lines) may be obtained. The points are the average of four cycles of polarization and deviate within ±4 mv of the mean. This curve exhibits two slopes, a lower one of 0.125 and a higher one of 0.082. The lower slope gives an i_o of 1.7 x 10^{-9} amp/cm².

In all cases, the platinum electrodes before and after a run were smooth and mirror bright.

It is interesting that the cathodic overvoltage of a type II electrode is independent of P_{O_2} for large values of P_{O_2} (1-0.3 atm). For P_{O_2} values below about 0.3 atm, the overvoltage becomes dependent on the P_{O_2} with a coefficient of about 5-10 mv/log P_{O_2} (see Fig. 6).

Discussion

Although treatment with concentrated HNO_3 is assumed to produce a chemically inert, electronically conducting layer of adsorbed oxygen, a more deep-seated change in the platinum surface apparently takes place. From double layer capacity measurements made on treated and untreated Pt electrodes (10), it appears that a certain amount of oxygen is more intimately associated with the platinum than the oxygen adsorbed in the monolayer of Pt-O. This oxygen cannot be removed easily by reduction in H_2 nor by cathodization, but only by heating in an H_2 flame to white heat. It is proposed that this oxygen actually dissolves in the surface layers of the platinum metal to form a Pt-oxygen alloy. It has been found (11) that oxygen will dissolve in massive Pt. Such an alloy could have the properties of a metal, be difficult to reduce in H_2 or by cathodic polarization, and lose oxygen by heating to a white heat. Since the solution of oxygen may require molecular or atomic rearrangements, the process would be quite slow. Such a mechanism could explain why Pt must be in contact with concentrated HNO_3 for at least 72 hr to form a complete passivating layer (8).

Basically, the treatment of Pt with HNO_3 produces an electrode material different from that of the original untreated Pt metal. In addition to producing a different electrode surface, the HNO_3 treatment also forms a complete layer of electronically conducting adsorbed oxygen as shown by the reversible characteristics of the data presented in Fig. 1. This com-

plete layer is unstable in acid solutions (8), however, and degenerates to an incomplete layer. Then the rest potential is no longer a reversible potential but a mixed potential. As demonstrated in Fig. 3 and 4, strong anodic or cathodic polarization destroys this complete protective film. In this case the exposed sites are not bare Pt sites as those in the untreated Pt case but are Pt-O-alloy sites. Therefore, a type I electrode is a Pt-O-alloy surface covered by a complete layer of adsorbed oxygen while a type II electrode is a Pt-O-alloy surface covered by an incomplete layer of adsorbed oxygen. Most likely, these layers are not much thicker than a monolayer.

Apparently, the Pt-O-alloy is a better catalyst for the oxygen reaction than is the pure Pt. Supporting data for this concept are found in the data of Fig. 2 in which the slope is much lower than that for the corresponding data [see Fig. 1 of ref. (7)] of the untreated Pt. Frumkin (12) has shown that the slope, $-di/d\eta$, of the linear curve at low current densities may be taken as the rate of the over-all electrode reaction. Using this concept, it is seen that the rate of the oxygen reaction on the treated Pt surface, 3.4 x 10^{-3} mho, is about two orders of magnitude greater than that on the untreated Pt surface, 1.7 x 10^{-5} mho. This higher reactivity is reflected in the considerably lower oxygen overvoltage on a Pt-O-alloy cathode than on a Pt cathode [compare Fig. 3 with Fig. 2 of ref. (7)].

It is interesting to note that the anodic overvoltage curve on a Pt-O-alloy electrode, Fig. 5, is nearly the same as that found on the Pt electrode [Fig. 3 of ref. (7)]. One outstanding difference is the fact that, in the low current density range (below 10^{-5} amp/cm^2), the overvoltage curve bends downward below the extrapolated Tafel line on the Pt-O-alloy electrode (Fig. 5) but flattens out above the extrapolated Tafel line on the Pt electrode [Fig. 3 of ref. (7)]. If the anodic reaction occurs on a complete layer of platinum oxide, as suggested before (7), one would expect to observe the same kinetic parameters for both kinds of electrodes, since the basis metal is no longer the catalyst for the electrochemical reaction.

Because the greatest difference in electrochemical properties of a Pt and a Pt-O-alloy electrode appears in the cathodic reduction of oxygen, it is possible that the Pt-O-alloy surface is a much better peroxide decomposing catalyst. This concept may be used to explain the difference in the anodic polarization at very low current densities on these electrodes. In the Pt-O-alloy case, as open-circuit conditions are approached, the metal peroxide linkages such as PtO_2 are quickly broken, and the system returns to the partial monolayer of Pt-O. Here, the data would fall below the extrapolated Tafel line. In the Pt case, this does not happen as quickly, and the metal peroxides formed in the anodic process maintain the potential at the more noble values. Under these conditions, one would expect the data to remain above the extrapolated Tafel line. As a check on this suggestion, a Pt-O-alloy electrode was cathodized at about 1 ma/cm^2 for 7.25 hr. The overvoltage value was steady at —292 mv for the final 6 hr. At the end of the polarization run, a sample of solution was tested for the presence of H_2O_2 with $TiSO_4$ reagent (13). Since the test was negative, this means that the concentration of peroxides was below 10^{-6}M. On a Pt electrode cathodized under similar conditions, peroxide is easily detected. These data support the contention that a Pt-O-alloy surface is a much better peroxide decomposing catalyst than a Pt surface.

The rest potential on a Pt-O-alloy electrode is higher ($E_m \sim 1100$ mv) than on a Pt electrode ($E_m \sim 1060$). This should be expected because the data of Fig. 2 and 3 show that the polarization is much lower on a Pt-O-alloy electrode. Considering the mixed potential diagram of Fig. 6, ref. (7), the O_2/H_2O reaction would be much flatter in the case of a Pt-O-alloy electrode and the Pt/Pt-O curve would cut it at a point, E_m, closer to E_o'. Consequently, a greater cathodic current density range should be found on a Pt-O-alloy electrode over which the boundary condition (7)

$$RT/F < |(E - E_o')| \text{ or } |(E - E_o'')|$$

and the linear relationship hold, as shown by Fig. 2. A calculation of the local cell current density i_m, using Eq. [21] of ref. (7) and a value of $-di/dp = 3.4 \times 10^{-3}$ from Fig. 2, gives the value of 8.7×10^{-5} amp/cm^2. The higher corrosion current agrees with the picture of a more active surface in the Pt-O-alloy case. When the system is polarized anodically, the system comes under the control of the Pt/Pt-O reaction quickly, which is even nearer to a limiting current condition than on the Pt electrode (7). As seen in Fig. 2, the anodic branch of the curve is quite short, and the potential rises quickly with increasing anodic current density. An interesting point is the fact that at the high anodic current densities (Fig. 5)) there is a change in slope from 0.125 to 0.082. This behavior implies a change of mechanism. Contrary to what is generally found in most electrochemical systems, the slope changes to a lower value. This may mean that the surface has become a better catalyst for the electrode reaction. Such an observation is not incompatible with the findings that metal peroxide linkages such as PtO_2 are detected in this potential range (14) and that such electrodes make more reversible indicator electrodes than those not preanodized (15, 16).

The observation that the overvoltage was independent of the partial pressure of oxygen at the higher values of P_{O_2} was unexpected. Suppose that the reduction of oxygen proceeds through the following steps. The dissolved oxygen in solution which is in equilibrium with the P_{O_2} above the solution is first adsorbed on the electrode surface.

$$(O_2)_{aq} \rightleftharpoons (O_2)_{ads} \quad [1]$$

An electron is transferred

$$(O_2)_{ads} + e \rightleftharpoons (O_2^-)_{ads} \quad [2]$$

followed by the reaction with a hydrated hydrogen ion

$$(O_2^-)_{ads} + H^+ \rightleftharpoons (HO_2)_{ads} \quad [3]$$

A second electron is transferred

$$(HO_2)_{ads} + e \rightleftharpoons (HO_2^-)_{ads} \quad [4]$$

and reaction with a second hydrogen ion follows

$$(HO_2^-)_{ads} + H^+ \rightleftharpoons (H_2O_2)_{ads} \quad [5]$$

The adsorbed peroxide may desorb into solution or undergo catalytic decomposition to H_2O and O_2

$$2(H_2O_2)_{ads} \overset{cat}{\rightleftharpoons} H_2O + (O_2)_{ads} \quad [6]$$

Reaction [6] is not a simple step and may go by an electrochemical mechanism (17) or by a purely chemical decomposition path. In any event, the liberated oxygen can then undergo steps [2] to [5] so that, effectively, four electrons may be liberated.

In the untreated Pt case (7), the experimental evidence indicates that step two is rate-controlling and that the H_2O_2 (ads) desorbs into solution until the concentration becomes about 10^{-5}M in H_2O_2. Yet, in the Pt-O-alloy case, step two may still be rate-controlling even though the overvoltage is independent of P_{O_2} for the following reason. According to the polarization data, the Pt-O-alloy surface is quite reactive to oxygen, and the surfaces could very well be saturated with adsorbed oxygen even at values of P_{O_2} down to 0.2 atm. Although the layer of adsorbed oxygen is in equilibrium with the partial pressure of oxygen above the solution, the rate could not be increased by increasing P_{O_2} above 0.2 atm because the surface cannot adsorb any more oxygen. In effect, a limiting current

with respect to P_{O_2} has been reached at 0.2 atm. Below a P_{O_2} value of 0.2 atm, the surface is no longer saturated with adsorbed oxygen and the rate becomes dependent on the P_{O_2}. In addition, reaction [6] occurs so fast on Pt-O-alloy surfaces that the peroxide concentration in solution cannot build up to a detectable amount. If the P_{O_2} becomes low enough, a point may be reached where enough oxygen cannot get to the surface to support the demanded current density. In this case, step one begins to influence the rate and may become rate-determining. This change in the rate-determining step may be seen in the P_{O_2} data of Fig. 5b of ref. (7) for an untreated platinum electrode. Here, the slope of the η-log P_{O_2} curve deviates from a 58-mv value to lower ones at low values of P_{O_2}.

Most likely the hysteresis effects noted in the first cycles of polarization reflect the results of changes in the system produced by the polarization procedure. After a time, the system comes to a steady state and reproducible overvoltage curves may be obtained. For the anodic curves the change is caused chiefly by the formation of a complete layer of adsorbed oxygen much of which is in the form of PtO_2. On the other hand, the chief cause for hysteresis effects in the cathodic curves is the building up of a steady-state concentration of peroxide in the solution. It was shown (1) that the rest potential was lowered by small changes in the peroxide concentration in the low concentration range. This would lower the first part of the cathodic curve, as observed.

These data support the conclusion that the treatment of Pt with HNO_3 produces a significant change in the nature of the metal surface. It is suggested that this change takes the form of a Pt-O alloy. The Pt-O-alloy surface not only is a much better peroxide decomposing catalyst than Pt, but also it greatly facilitates the adsorption of oxygen from solution and the electron transfer to the adsorbed oxygen. This is reflected in the observation that the rate of the oxygen reaction is two orders of magnitude greater, that the overvoltage is significantly lowered on Pt-O-alloy electrodes, and that the overvoltage is independent of the P_{O_2} for large values of P_{O_2}.

Acknowledgments

The author wishes to express his gratitude to Professor Paul Delahay of the Louisiana State University and to Dr. Raymond Thacker and Dr. John L. Griffin of the General Motors Research Laboratories for their interesting comments and suggestions.

Manuscript received Feb. 3, 1965.

Any discussion of this paper will appear in a Discussion Section to be published in the June 1966 JOURNAL.

REFERENCES

1. J. P. Hoare, *This Journal*, **109**, 858 (1962).
2. W. H. Latimer, "Oxidation Potentials," Prentice-Hall, New York (1952).
3. E. Lange and H. Gohr, *Z. Elektrochem.*, **63**, 75 (1959).
4. C. Wagner and W. Traud, *ibid.*, **44**, 391 (1938).
5. T. P. Hoar, *Proc. Roy. Soc.*, **A142**, 628 (1933).
6. J. O'M. Bockris and A. K. M. S. Huq, *ibid.*, **A237**, 277 (1956).
7. J. P. Hoare, *This Journal*, **112**, 602 (1965).
8. J. P. Hoare, *ibid.*, **110**, 1019 (1963).
9. D. J. G. Ives and G. J. Janz, "Reference Electrodes," Academic Press, New York (1961), p. 112; J. P. Hoare, *G. M. Eng. J.*, **9** [1], 14 (1962).
10. J. P. Hoare, *Nature*, **204**, 71 (1964).
11. T. V. Kalish and R. K. Burshtein, *Doklady Akad. Nauk SSSR*, **88**, 863 (1953); V. I. Luk'yanycheva and V. S. Bagotskii, *ibid.*, **155**, 160 (1964).
12. P. Dolin, B. Ershler, and A. Frumkin, *Acta Physicochim. URSS*, **13**, 782 (1940).
13. F. D. Snell and C. T. Snell, "Colorimetric Methods of Analysis," Vol. II, 3rd ed., D. Van Nostrand Co., New York (1949).
14. J. J. Lingane, *J. Electroanal. Chem.*, **2**, 296 (1961).
15. D. T. Sawyer and L. V. Interrante, *ibid*, **2**, 310 (1961).
16. D. G. Davis, *Talanta*, **3**, 335 (1960).
17. R. Gerischer and H. Gerischer, *Z. Physik. Chem. N. F.*, **6**, 178 (1956).

Potential of a Platinum Electrode at Low Partial Pressures of Hydrogen or Oxygen

Theodore B. Warner and Sigmund Schuldiner

U. S. Naval Research Laboratory, Washington, D. C.

ABSTRACT

The open-circuit potential on bright platinum in 1M H_2SO_4 was measured as a function of oxygen or hydrogen partial pressure from 10^{-2} to 10^{-7} atm. The very low rates of H_2 or O_2 flow which were required were produced by a special gas generator. Potentials predicted by the Nernst equation for the H^+/H_2 couple were not observed below 10^{-4} atm H_2 partial pressure. A Nernst relation with a slope of 0.06 v/decade of oxygen partial pressure was found. The oxygen leak into the closed system used was found to be about 10^{-7} atm. Based on the assumption that the resultant dissolved O_2 decreases the dissolved H_2 concentration in the solution at the electrode surface, an equation was developed for obtaining the effective H_2 partial pressure.

The Nernst equation relating hydrogen partial pressure and potential of a platinum electrode in acid solution has been experimentally verified previously for hydrogen partial pressures ranging from hundreds of atmospheres down to 0.01 atm (1). It is often assumed to be valid at much lower hydrogen pressures. One purpose of this study was to check this assumption and to determine the conditions under which normal Nernst behavior prevails. The potential behavior of platinum in acid solutions equilibrated with oxygen at partial pressures ranging down to less than 10^{-6} atm was also determined.

Previous work at this Laboratory (2, 3) had shown that substantial amounts of oxygen and hydrogen could dissolve in the "skin" of a Pt electrode and affect its catalytic activity (and also appear as an unexpected participant in chemical reactions). We differentiate here between solution of a gas into the bulk of the metal in the usual sense of the word "solution," and a kind of rapid selective absorption of gas atoms into a relatively few atomic layers of metal immediately below the surface atomic layer. This layer immediately below the surface we shall call the "derma" of the metal, by analogy to biological usage. This type of absorption can then be termed "dermasorption." These experiments were designed to give additional information on the ways gases absorb in platinum, particularly on the time required to sorb

and desorb them, and the effects of sorbed gases on open-circuit potentials.

For meaningful measurements in electrochemical systems having small exchange current densities, conditions inside the cell must be rigorously controlled. The system utilizing Pyrex pipe recently built in this Laboratory (4-6) gave such control. Being gas-tight, it permitted effective exclusion of air and other atmospheric contaminants.

Experimental

Apparatus.—The electrochemical cell (6) contained a miniature glass reference electrode, a Pt bead electrode of about 0.17 cm^2 apparent area, a Pt wire electrode 5 cm long with a 0.064 cm diameter, and a Pt gauze electrode of very large area. The surface-to-volume ratios of the bead, wire, and gauze were 26, 62, and 450 cm^{-1}, respectively. The electrolyte was 1M H_2SO_4 maintained at 25° ± 1°C. The helium purification train was identical with that described previously (5) except that an improved electrolytic H_2/O_2 generator replaced the conventional design previously used. Hydrogen was treated as before in a Serfass Hydrogen Purifier, saturated with water, and introduced into the gas train between the H_2/O_2 generator and the cell. Kern High Vacuum Greaseless stopcocks (Viton A diaphragm) at the ends of a T-connection between the helium and hydrogen lines were used to block the flow of either gas. The hydrogen line was always back-flushed (from cell to Serfass) with helium and left filled with pure He when not in use.

The H_2/O_2 generator[1] shown in Fig. 1 was used to generate pure H_2 or O_2 at low rates. We shall describe this device as an H_2 generator with the understanding that the same principles also apply to the oxygen case. For our purposes, it was important that H_2 added to the helium stream not be contaminated with trace amounts of O_2, so the generator used was designed to avoid crossdiffusion of electrode products while retaining the advantages of electrolytically generated gas.[2] Crossdiffusion is impeded in four ways: (*a*) a very long path, including a glass frit, separates the two compartments; (*b*) buffer compartments act very much like plates in a conventional condenser, hydrogen diffusing downward from the working electrode is stripped by the incoming pure He, while in the upper chamber, the He + H_2 stream coming from the electrochemical cell creates an H_2-rich region below the oxygen-rich counter electrode compartment; (*c*) hydrogen-rich gas bubbles flowing over the Pd-tube counter electrode impede oxygen bubble formation; and (*d*) H_2 gas introduced on the inside (*i.e.*, the room side) of the Pd tube dissolves into the Pd and the anodic reaction is largely $H \rightarrow H^+ + e$ (7). In practice, visible bubble formation at the counter electrode is only seen at currents in excess of 20-50 ma. Hydrostatic pressure difference between the two chambers automatically compensates for the pressure drop through the cell and associated bubblers.

[1] Figure 1 shows an improved design and differs from the generator employed in this study in one respect; instead of using the circular disks shown, baffles in the lower buffer compartments were formed by pushing in the sides of the glass walls as is commonly done in vapor condensers.

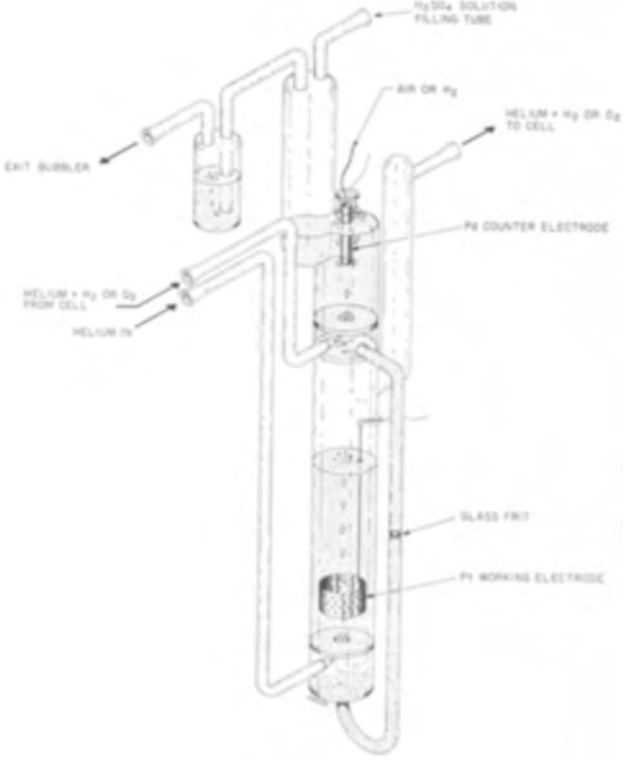

Fig. 1. Electrolytic H_2 or O_2 generator

Perhaps the greatest advantage of this design is that at very low H_2 or O_2 generation rates no gas is formed at the counter electrode at all. The anodic reaction at the counter electrode is the oxidation of H (dissolved in Pd) to H^+; a steady supply of H(dissolved) is provided by H_2 introduced inside the tube. The cathodic reaction at the counter electrode is the reduction of H^+ to H, this hydrogen dissolves in the Pd tube, diffuses to the inside surface and reacts with the oxygen there (in this case the inside of the Pd tube is open to air) to form H_2O.

Procedure.—Glassware was cleaned with boiling HNO_3 followed by 12-15 rinses with triply distilled water and/or by heating to the annealing temperature. Preliminary solution pre-electrolysis and calibration of the glass reference electrode in 1 atm of H_2 were carried out as before (6), the H_2 line was backflushed and filled with He, and the desired partial pressure of H_2 or O_2 in He (known to ±5%) was obtained by generating gas at the required rate. Helium flow was always 88 ± 4 cc/min, pressure within the cell was 13 Torr over atmospheric, and open circuit potentials of the three electrodes were measured with a Keithley 603 electrometer and reported *vs.* the normal hydrogen electrode (NHE), as before (6).

Although the experimental system was gas tight, there is no question but that a minute amount of leakage of oxygen from air[3] took place by diffusion through Viton-A O-rings connecting the various sections of glass pipe. This leakage was unimportant as long as the partial pressure of oxygen or hydrogen was more than 10^{-5} atm. However, at partial pressures of these gases approaching 10^{-6} atm and lower, the leak rate of O_2 from the air was significant and was taken into account. Since the He flow was constant, for convenience leak rates will be discussed frequently in terms of the net partial pressure of gas resulting.

Results and Discussion

Experimental results.—The experimental results are shown in Fig. 2. Values were obtained with increasing and decreasing gas partial pressures and were accepted after a steady state potential had been attained at an electrode (usually within ±10 mv). Results for oxygen pressures above 10^{-4} atm confirm previous work from this Laboratory (6). Potentials under H_2 at partial pressures $<10^{-4}$ atm deviate markedly from those predicted for the reversible H^+/H_2 couple by the Nernst potential equation. Before interpreting these data, however, the response time, extent, and probable effects of O_2 leaking into the system from its surroundings must be considered.

[2] A conventional H-cell generator cannot be used for partial pressures below 10^{-4} to 10^{-5} atm because of effects due to crossdiffusion of the gases produced.

[3] It should be pointed out that the air in the laboratory was purified by constant recirculation through an absolute filter to remove aerosols and through a carbon bed to remove gases and vapors. Smoking was not permitted in the laboratory.

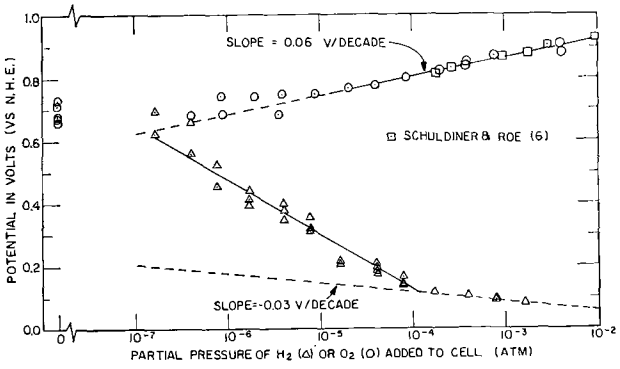

Fig. 2. Effects of H_2 and O_2 partial pressure on platinum rest potentials. The points are experimental results. In the hydrogen region, the dashed line gives reversible H^+/H_2 potentials as predicted by the Nernst equation. In the oxygen region, the dashed line is an extrapolation of the linear region found at higher pressures.

Response time.—The time required to come to a true steady state was variable, depending on the H_2 or O_2 partial pressure, the previous gas partial pressure at which the electrode was equilibrated, and the surface-to-volume ratio of the electrode. The time increased as the surface/volume ratio decreased, as partial pressure decreased, and as the change from previous pressure increased. Periods of several days were required at the lowest pressures and three or more days for open circuit potentials under pure helium (*i.e.*, helium containing only that oxygen leaking into the system). False, apparently steady state, potentials were often observed for many hours. They were always between the last potential obtained and the new one being approached.

The above behavior could consistently be interpreted by assuming that for an open-circuit potential to represent truly steady state conditions, the amount of H_2 or O_2 dissolved in the platinum must be allowed to come to equilibrium with the amount at the surface. The long times required for this, and the surface/volume effect, imply that the partition must ultimately be between gas dissolved in the bulk of the metal and gas on the surface. If sufficient time was allowed, all three electrodes invariably came to the same mean potential within 5 mv. These results, then, coupled with earlier results (2), suggest that dermasorbed gases can exchange relatively rapidly with the surface, and that gases dissolved in the bulk of the metal must exchange slowly with the dermasorbed layer (and thus with the surface).

Effect of oxygen leakage.—For the case of O_2 added to the He, any O_2 leak adds to the partial pressure of O_2 actually in the system. The case of O_2 leaking into a system to which H_2 is being added is more complex. Very little is known about the effects of trace amounts of O_2 in H_2 on the potential of a Pt electrode, but an estimate may be made by assuming that any O_2 at the Pt surface will react with H_2 until only an effective net excess of H_2 remains. Since reaction of H_2 with O_2 could take place only at the platinum surface, the H_2 concentration would be reduced only at or very near to the platinum-solution interface. An "effective" H_2 partial pressure, *i.e.*, the pressure that would result in the same electrode potential in the absence of a leak, was calculated by assuming Henry's law and complete reaction of O_2 and H_2 present in solution at the interface. The net excess concentration of H_2 in solution was used to calculate the pressure of H_2 in the gas phase that would be in equilibrium with it in the absence of any leak, and this pressure was used as the effective H_2 partial pressure.

$$(P_{H_2})_{\text{effective}} = \frac{\alpha_H (P_{H_2})_{\text{added}} - 2\alpha_O (P_{O_2})_{\text{leak}}}{\alpha_H} \quad [1]$$

Table I. Polarization of the hydrogen electrode by oxygen

P_{O_2}[a] in gas phase, atm	(P_{H_2})[b] effective calculated, atm	E (mv *vs.* NHE) Exp.	Calc.[c]
0.0092	0.97	0.8	0.4
0.0161	0.94	1.3	0.8
0.0252	0.89	1.9	1.5
0.0547	0.77	3.8	3.4
0.100	0.59	7.1	6.9

[a] Lorch (9), mixture with hydrogen, total pressure 1 atm.
[b] Calculated using Eq. [1].
[c] Calculated from the Nernst equation, $E = -0.0295 \log (P_{H_2})_{\text{effective}}$.

where α_H and α_O are the solubilities of H_2 and O_2 in 1M H_2SO_4 at 25°C, taken as 0.0149 and 0.023 std. cc/ml H_2SO_4, respectively (8). (At H_2 generation rates lower than the O_2 leak rate a net excess of O_2 resulted.)

Lorch (9) studied chemical polarization of the hydrogen electrode by oxygen, and his experimental data were used to check the assumptions implicit in Eq. [1]. The results, given in Table I, show agreement within 0.5 mv for H_2 partial pressures near 1 atm. In the next section we assume that this model also applies at very low partial pressures of both O_2 and H_2.

Extent of oxygen leakage.—The potential behavior of the platinum electrode was a sensitive indicator of the background O_2 concentration. The fact that addition of H_2 to the He stream sufficient to give a partial pressure of 4×10^{-7} atm H_2 caused the potential to drop ~0.1v indicated that the P_{O_2} could not have been much larger than this. Furthermore, plotting effective H_2 pressures *vs.* observed potential under the assumption of O_2 leaks of 10^{-6} and 10^{-7} atm (Fig. 3 and 4) gives an unreasonable picture when 10^{-6} atm[4] is as-

[4] For example, the corrections made in Fig. 3 compress potential values between 0.45 and 0.75v into the range of partial pressures between 0.85 and 1.00×10^{-6} atm. In this region the individual points should have been erratic, but in fact, they were very steady and fairly reproducible as shown in Fig. 2.

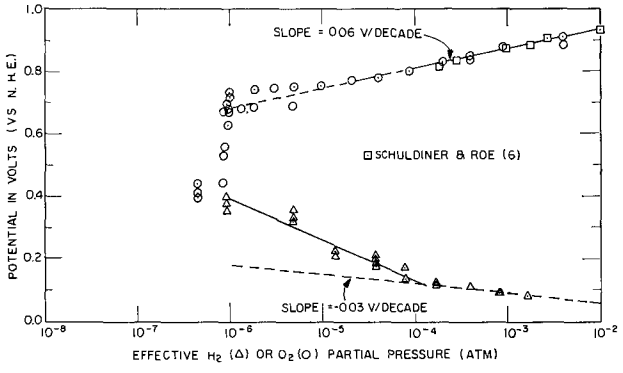

Fig. 3. Platinum rest potentials *vs.* H_2 or O_2 partial pressures corrected for an assumed oxygen leak of 1×10^{-6} atm using Eq. [1].

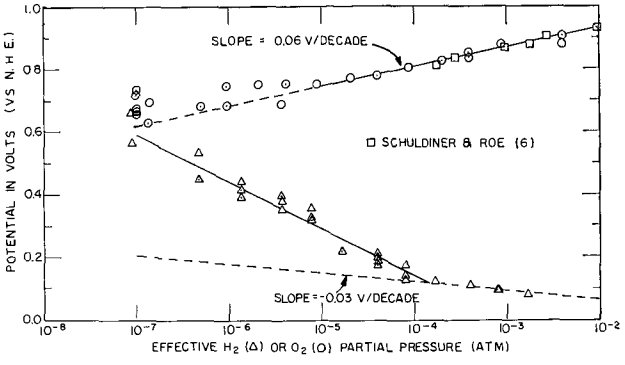

Fig. 4. Platinum rest potentials *vs.* H_2 or O_2 partial pressures corrected for an assumed oxygen leak of 1×10^{-7} atm using Eq. [1].

sumed and organizes the data coherently when 10^{-7} atm is assumed.

The above estimate based on electrochemical evidence is in reasonable agreement with the 10^{-6}-10^{-8} atm oxygen partial pressure due to leaks that would be estimated *a priori* within such a flowing system, since Viton-A O-rings are suitable for use in vacuum systems operating in the 10^{-6} Torr region. It was also confirmed by analyses using a modified CED 21-103c Mass Spectrometer that indicated that O_2 concentration in the nominally pure He flowing through our system was less than 1 ppm.[5]

Platinum rest potentials vs. P_{H_2} or P_{O_2}.—The preceding discussion indicates that Fig. 4 most closely represents the potential behavior of these systems. Clearly, a reversible H^+/H_2 couple cannot control electrode potential below 10^{-4} atm hydrogen. What does control potential is, at present, a moot question. It seems quite unlikely that an oxygen leak of the order of 10^{-7} atm could be responsible for this potential behavior at hydrogen partial pressures several orders of magnitude larger, providing that at this low partial pressure all of the oxygen which gets to the Pt surface does react readily with hydrogen.

Schuldiner (10) showed that the relationship between exchange current density i_o and P_{H_2} was

$$i_o = 1.43 \times 10^{-3} P_{H_2}(1-\theta_o)^2 \qquad [2]$$

where θ_o is the fraction of available Pt surface covered with atomic hydrogen at P_{H_2}. At low hydrogen partial pressures, θ_o will undoubtedly be very small compared to unity and for all practical purposes $(1-\theta_o)^2$ will approach one. Hence, at $P_{H_2} = 10^{-4}$ atm, $i_o \approx 1.4 \times 10^{-7}$ a/cm^2, and at $P_{H_2} = 10^{-7}$ atm, $i_o \approx 1.4 \times 10^{-10}$ a/cm^2. If a mixed potential involving H^+/H_2 and, say, the O_2/HO_2 (7) reactions were potential determining, i_o for the O_2/HO_2 reaction would have to be of the same order of magnitude as the H^+/H_2 reaction. It is very unlikely that the O_2/HO_2 or any other possible potential-determining reaction involving O_2 at 10^{-7} atm would have an i_o comparable to the H^+/H_2 reaction. All literature indications are that any equilibrium reactions on Pt involving O_2 at 1 atm have i_o values of not more than 10^{-10} a/cm^2.

It is also unlikely that these potentials are caused by polarization by the electrometer (10^{14} ohms shunted by 10 $\mu\mu F$), for then one would expect an even more marked effect on the presumably more easily polarized Pt/O_2 system. In addition, electrometer measurements were the same for electrodes which were not permanently connected and for which potential measurements were made in a few minutes after connecting the electrometer circuit.

It should be stressed that the unexpected relation between potential and hydrogen partial pressure below 10^{-4} atm is an experimental fact and does not depend on any assumptions about how hydrogen may interact with oxygen. The same kind of behavior would be expected in any real system from which oxygen is imperfectly excluded. It is believed that the deviation from Nernst behavior may be due to the rather complex sorption of hydrogen on platinum (5), where even at 1 atm of H_2 there are only a relatively small number of weakly bonded H atoms which are in rapid equilibrium with H_2 and H^+ (10, 11).

It is interesting that the Pt/O_2 system fits a Nernst relation at substantially lower O_2 partial pressures than does Pt/H_2. The oxygen rest potential follows the same Nernst relation previously obtained at this Laboratory (6). These results similarly indicate a potential-determining equilibrium

$$O_2 + H^+ + e = HO_2 \qquad [3]$$

assuming a constant activity of HO_2 adsorbed on the Pt surface.

The open circuit potentials for "pure" He, *i.e.*, at 10^{-7} atm O_2 in Fig. 4, are somewhat scattered. This may be the result of an extremely long time being required for establishment of true equilibrium between absorbed, dermasorbed, and chemisorbed O_2 at such low partial pressures. Also, small variations in the O_2 leak from time to time are possible. These values differ from the previously reported values of 0.2-0.4v (6). The reason for the discrepancy may be that in the previous work a Pd tube electrode at about 50 mv (NHE) was present in the cell. We have observed that at very low oxygen partial pressures such a Pd electrode will cause the Pt electrode to become less positive. The Pd may have either contributed a small amount of H_2 to the cell or acted as an effective O_2 getter to give O_2 partial pressures virtually equal to zero. A combination of these two effects is also possible. The effect of hydrogen-containing Pd at very low O_2 partial pressures requires further investigation.

[5] Such a concentration is at or below the lower detection limit of the instrument. The amount of O_2 was determined from repeated measurements and blanks, with due consideration of wall effects. Interestingly, the mass spectrometer data giving an N_2/O_2 ratio of about three supported the view that O_2 entering the system did so by diffusion through the Viton O-rings, where unequal diffusion rates of N_2 and O_2 are reasonable. The N_2/O_2 ratio in the helium as received was about six, and inadequate helium purification would have given at least that value. If a gross leak existed, the ratio would have been four or larger.

Acknowledgments

We gratefully acknowledge the assistance of Dr. F. E. Saalfeld, who carried out the mass spectrometer analyses, and Mr. G. J. Bergen, who fabricated much of the glassware, including the H_2/O_2 generator.

Manuscript received Jan. 8, 1965; revised manuscript received April 5, 1965. This paper was presented at the San Francisco Meeting, May 9-13, 1965.

Any discussion of this paper will appear in a Discussion Section to be published in the June 1966 JOURNAL.

REFERENCES

1. D. J. G. Ives and G. J. Janz, "Reference Electrodes," p. 119, Academic Press, New York (1961).
2. S. Schuldiner and T. B. Warner, *This Journal*, **112**, 212 (1965).
3. S. Schuldiner and T. B. Warner, *Anal. Chem.*, **36**, 2510 (1964).
4. T. B. Warner and S. Schuldiner, *This Journal*, **111**, 992 (1964).
5. S. Schuldiner and R. M. Roe, *ibid.*, **110**, 332 (1963).
6. S. Schuldiner and R. M. Roe, *ibid.*, **110**, 1142 (1963).
7. S. Schuldiner, *ibid.*, **106**, 440 (1959).
8. "International Critical Tables," **3**, 271 (1928).
9. A. E. Lorch, *Trans. Electrochem. Soc.*, **70**, 401 (1936).
10. S. Schuldiner, *This Journal*, **106**, 891 (1959).
11. S. Schuldiner, *ibid.*, **108**, 384 (1961).

Electrical Conductance in Acidic, Aqueous Solutions

R. A. Horne

Arthur D. Little Inc., Cambridge, Massachusetts

ABSTRACT

Protonic conduction occurs by the Grotthuss mechanism. Below about 0.001M HCl, the lengths of the Grotthuss chains are determined by the temperature, but over the range of 0.001M to about 0.5M, the chains are principally disrupted by other protons. In this range the chain length and the equivalent conductance depend on the cube root of the concentration. An Arrhenius-type equation is developed for describing the concentration dependence of the conductance which yields values in agreement with experiment to within 1% over the range 5°-65°C and up to 0.4M. The activation energy which appears in the chain-terminating terms of this equation is that of "hole" formation in the solvent water.

Elsewhere (1, 2), we have pointed out that the Onsager-Fuoss (3) and similar equations for the concentration dependence of the electrical conductivity of ionic solutions based on consideration of the electrophoretic and relaxation effects may not be applicable to acidic, aqueous solutions or any other systems in which the Grotthuss mechanism makes a conductive contribution (4). The purpose of the present study is to indicate some of the directions which the derivation of a conductivity equation applicable to protonic conduction might take.

Throughout this discussion, we will be concerned with only the Grotthuss component of protonic conduction. Although the Grotthuss mechanism dominates protonic conduction, protons also conduct by the "normal" process of hole formation and this latter process may account for as much as 20% of the total conductance at 1 atm and 25°C.

Viscosity

At 1 atm rotation of water molecules is the rate-determining step of the Grotthuss mechanism (5, 6). Although its value is less, the activation energy of protonic conduction in aqueous solutions above 10°C varies in the same way with temperature as does that for the electrical conductivity of strong 1:1 salts such as KCl, thereby suggesting that energetically "hole" formation in water and rotation of water molecules are similar processes. The velocity of the translational movement for a sphere of radius, a, in a medium of viscosity η is given by Stokes' law

$$v = F/6\pi\eta a \qquad [1]$$

where F is the applied force, while the angular velocity, ω, of a sphere rotating in a viscous medium is given by

$$\omega = \tau/8\pi\eta a^3 \qquad [2]$$

where τ is the applied torque. Notice that the translational movement depends on the first power of the radius whereas the rotational movement depends on the third power. The application of hydrostatic pressure breaks up the order in liquid water and reduces the effective radius of hydrated ions in aqueous solution (7-9). Consequently, one expects the pressure dependence of the relative conductance to be greater for HCl solutions than for KCl solutions. Figure 1 shows such to be the case. In fact, HCl shows a greater pressure dependence than anticipated. The explanation of this is discussed later.

Both Eq. [1] and [2] contain the first power of the viscosity of the medium. Pressure, but not temperature, alters the sizes of hydrated ions (see above) and this may give rise to an apparent higher power dependence on viscosity, but as long as the solution is sufficiently dilute so that the ions do not have to compete for waters of solvation, changing the concentration of the electrolyte should not affect the sizes of the hydrated ions.

The dielectric relaxation time of water decreases with increasing electrolyte concentration (10, 11). If the speed of rotation of water molecules, the rate-determining step of the Grotthuss mechanism, behaves in like manner, then protonic equivalent conductance should increase with increasing concentration which is contrary to observation.

The introduction of ions alters the extent of structure in liquid water and gives rise to changes in the macroscopic viscosity. The proton has a positive viscosity B-coefficient (see Eq. [3]) of 0.070, indicating that it is a structure-forming ion (12). Qualitatively then, one might expect it to order the solvent, hinder the rotation of water molecules, and thus impede Grotthuss conduction as observed. An obvious attack on the present problem of deriving an expression for the concentration-dependence of protonic conductivity is to express the conductance as some function of the limiting conductance and the viscosity as given by the relation of Jones and Dole (13).

$$\eta = \eta^0 (1 + A\sqrt{C} + BC) \qquad [3]$$

where η^0 is the viscosity of pure water, C the concentration of electrolyte, and A and B are constants. Unfortunately, the effect of electrolyte concentration on viscosity is much too small to account for the observed effect on the equivalent conductance. Thus for 0.01M HCl, the relative viscosity at 25°C is only 1.0008, while the reciprocal of the relative equivalent con-

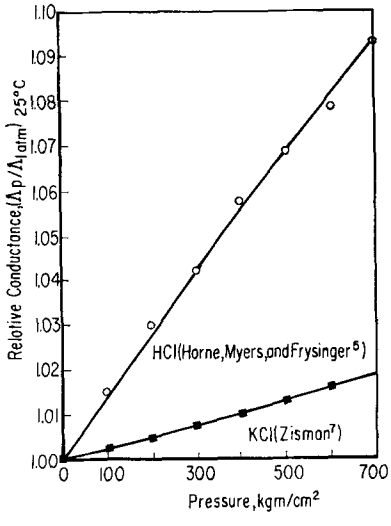

Fig. 1. Pressure dependence of the relative electrical conductances of aqueous acid and salt solutions.

Table I. Thermal termination of Grotthuss chains and structural parameters

Temp, °C	$(\Lambda^\circ/\Lambda^\circ_{0°C})^{-1}$	Λ°/Λ^*	$\eta/\eta_{0°C}$	$H/H_{0°C}$	$S/S_{0°C}$
0	1.00	—	1.00	1.00	1.00
18	0.84	—	0.65	0.88	0.66
25	0.63	0.99	0.58	0.86	0.57
35	0.54	0.99	0.50	0.82	0.47

ductance $(\Lambda/\Lambda^\circ)^{-1}$ is 1.03. In other words, the viscosity changes by only 0.08%, whereas the conductance changes by more than 3%.

In summary, the approach of estimating the retardation of water rotation from structural changes in liquid water as reflected by the macroscopic viscosity does not appear to be an attractive one.

While the concentration of electrolyte has much less effect on the macroscopic viscosity than on the conductance, the reverse is true in the case of temperature as illustrated by Table I which compares conductance ratios (based on "International Critical Tables" data) for HCl with the relative viscosity.

The above conclusion should not be taken to mean that conductivity, viscosity, and the degree of structure in liquid water are unrelated. On the contrary, Table I illustrates that they all have similar temperature dependencies (14). This table compares the reciprocal of the limiting conductance relative to 0°C, the ratio of the limiting conductance Λ°, to that, Λ^*, obtained by the extrapolation Λ *vs.* $C^{1/3}$ to 0°C; the relative viscosity $\eta/\eta_{0°C}$; the relative number of unbroken hydrogen bonds, $H/H_{0°C}$; and the relative size of the water clusters, $S/S_{0°C}$.

The latter two parameters are calculated from the estimates of Nemethy and Scheraga (15). This table indicates that the changes in the structural parameters are much larger than the changes in Λ°/Λ^*. Notice, however, the good parallel between the relative viscosity and the relative cluster size.

Grotthuss Chain Termination

Electrical conduction by the Grotthuss mechanism occurs only in the interstitial or "free" water between the fluctuating clusters in liquid water (16). This is not an unreasonable assumption inasmuch as (*a*) water molecules within the clusters are less free to rotate; (*b*) a cluster represents a closed Grotthuss propagative circuit; and (c) the only entity undergoing dipole orientation in water is the simple H_2O molecule and not polymeric forms (17). Also, the formation of small water polymers is not favored (15, 18).

If the protonic conductance involves only the "free" or monomeric water molecules, then the equivalent conductance should be proportional to the monomer concentration. Figure 2 shows such to be the case.

The proton flips propagate along transient chains of H-bonded water molecules in the free solvent. In pure water or in very dilute solutions, the length of these chains will depend for the most part on temperature; this is normal or thermal chain termination (TCT). The introduction of a second proton into a chain will be dependent on the concentration and as the concentration increases should become the dominant chain-terminating factor (CCT). Let the concentration of protons in a unit cube be C; let us assume for the sake of simplicity that a proton is "proceeding" along a chain along the edge of the unit cube,[1] then the distance which it can "move" without encountering a second proton will depend on $C^{-1/3}$. This distance is the "lattice length" discussed by Frank and Thompson (19), and they note that "it makes no particular difference what kind of a lattice is assumed —it is the $C^{1/3}$ dependence that counts." Protonic conduction should depend on the cube root of the proton concentration.

Figure 3, based on the data of Owen and Sweeton (20), exhibits the concentration-dependence of the equivalent conductance of aqueous HCl solutions at different temperatures and, indeed, Λ_{HCl} *vs.* $C^{1/3}$ is linear over a broad concentration range, roughly 0.001 to 0.5M. The departure from linearity above 0.5M is not surprising, for this represents a concentrated solution. Of greater significance are the departures below 0.001M.

In very dilute HCl solutions (below 0.001M) the conductance depends on $C^{1/2}$ (21). On the basis of this experimental finding the conductance at infinite dilution can be estimated by an extrapolation of a plot of Λ *vs.* $C^{1/2}$ to $C = 0$, without making any commitment as to the correctness of various theories of conductance which predict a $C^{1/2}$ dependence. Hence

[1] When the electrical potential is applied, the direction of a proton's apparent movement ceases to be random.

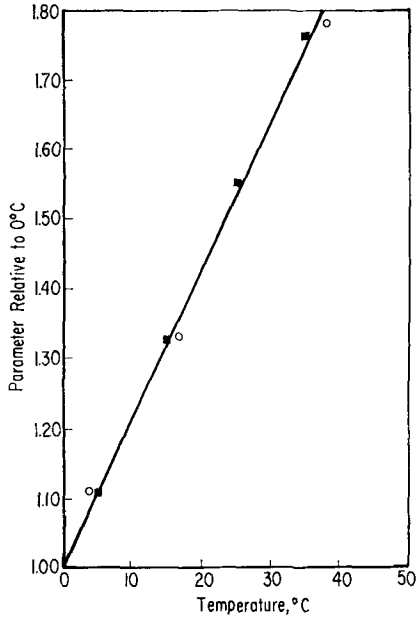

Fig. 2. Relation between proton conductance and water-monomer concentration. Parameters: ○, fraction of monomeric water relative to 0°C, $N_T/N_{0°C}$ where N is the number of monomers per 100 water molecules [I. R. Rao, Proc. Roy Soc. London, 145A, 489 (1934)]; ■, protonic limiting equivalent conductance relative to 0°C, $\Lambda^\circ_T/\Lambda^\circ_{0°C}$ [Robinson and Stokes (17)].

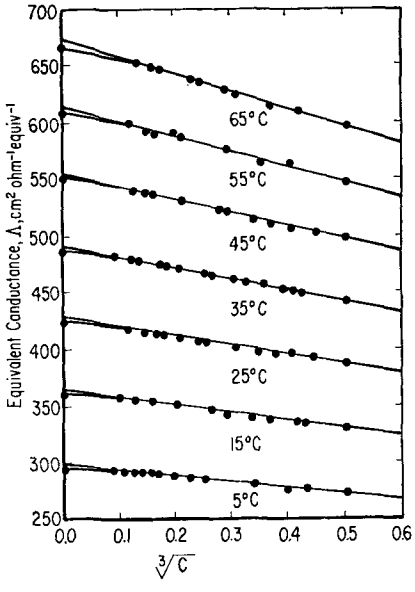

Fig. 3. Concentration dependence of the conductivity of aqueous HCl solutions [based on data of Owen and Sweeton (20)].

Table II. Properties of the Λ vs. $C^{1/3}$ plots

Temp, °C	Limit equiv. cond. (17), $\Lambda°$, cm²-ohm⁻¹ equiv⁻¹	Λ^*, cm²-ohm⁻¹ equiv⁻¹	$\Lambda^*-\Lambda°$, cm²-ohm⁻¹ equiv⁻¹	Slope
5	297.6	300	2.4	53
15	362.1	365	3	68
25	426.2	430	3.6	82
35	489.2	493	4	98
45	550.3	555	5	117
55	609.5	615	6	134
65	666.8	675	7	157

the conductances at infinite dilutions are taken to be the limiting conductances, $\Lambda°$, as given by Owen and Sweeton (20). The introduction of the concept of limiting conductance as commonly defined is of interest because physical significance can be assigned to the difference between

$$\Lambda^* = \lim_{C\to 0} \Lambda \text{ vs. } \sqrt[3]{C} \text{ and } \Lambda° = \lim_{C\to 0} \Lambda \text{ vs. } \sqrt{C}$$

If the linear segments of the curves in Fig. 3 are extrapolated down to infinite dilution of electrolyte, the values obtained, Λ^*, are greater than the limiting conductances, $\Lambda°$. Λ^* may be interpreted as the conductance corresponding to indefinitely long Grotthuss chains. But in this low proton concentration region, the chains are not indefinitely long. They are thermally terminated. The lengths of the chains decrease with increasing temperature, thus the difference between Λ^* and $\Lambda°$ should increase with increasing temperature. Table II shows such to be the case. The differences and slopes in Table II are obtained from replots (not shown) of Fig. 3 on a much-expanded scale. The conductance may be represented by an equation of the form

$$\Lambda_{T,C} = \Lambda^* - \text{TCT} - \text{CCT} \qquad [4]$$

where TCT and CCT are thermal chain termination and concentration chain termination terms respectively. The former term is related to the difference $\Lambda° - \Lambda^*$. If the logarithm of this difference is plotted *vs.* the reciprocal of the absolute temperature (Fig. 4), a reasonably linear Arrhenius plot is obtained. There is some deviation from linearity below 25°C, but the deviation amounts to only about 10% of the value of $\Lambda° - \Lambda^*$ even at 5°C. The activation energy calculated from the slope of the linear part of this curve (25°-65°C) by the integrated form of the Arrhenius equation is 3.53 kcal/mole. Figure 4 also shows an Arrhenius plot of the limiting conductance of aqueous KCl solutions from data quoted

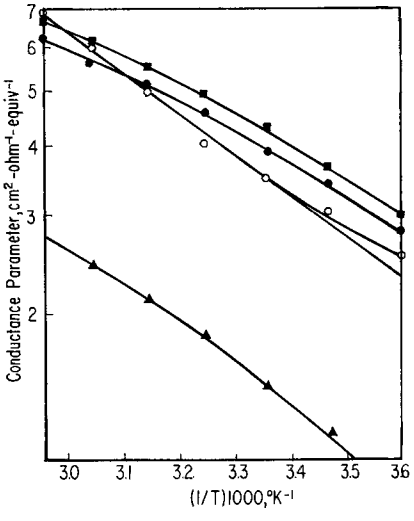

Fig. 4. Arrhenius plots of conductance parameters: ○, $\Lambda^*_{T,\,0,\,HCl} - \Lambda°_{HCl}$; ■, $\Lambda_{0.5M\ HCl}/100$; ●, $\Lambda^*_{T,\,0,\,HCl}/100$; ▲, $\Lambda°_{KCl}/100$.

by Robinson and Stokes (17). The curve is not linear, indicating that the activation energy of conductance, E_a, is temperature dependent. Over the temperature range 5°-65°C, its value varies from 3.02 to 3.77 kcal/mole. The rate-controlling step of normal conduction in aqueous solutions involves the formation of a hole in the solvent (22). Thermal rupture of a Grotthuss chain is equivalent to the formation of a one-dimensional hole, therefore one finds that E_a for thermal chain termination is nearly the same as for hole formation (that is to say for normal ionic conduction).

The slopes of Λ *vs.* $C^{1/3}$ in the linear part of the curves in Fig. 4 are also temperature dependent (Table II) and an Arrhenius plot of these slopes is linear over the entire temperature range 5°-65°C and its slope corresponds to an activation energy of 3.38 kcal/mole, the same value as for normal conduction as expected. Thus Eq. [4] becomes

$$\Lambda_{T,C} = \Lambda^*_{T,0} - \phi\, 1.32 \times 10^3 e - 3530/RT - 2.39 \times 10^4 e - 3380/RT \sqrt[3]{C} \qquad [5]$$

where T is the absolute temperature. The term ϕ has been introduced because as concentration chain termination becomes more frequent, the probability of a chain being thermally terminated decreases. The value of ϕ is given by

$$\phi = (1.32 \times 10^3 e^{-3530/RT}) / (1.32 \times 10^3 e^{-3530/RT} + 2.39 \times 10^4 e^{-3380/RT} \sqrt[3]{C}) \qquad [6]$$

The constants in Eq. [5] and the activation energies have been calculated from the data of Owen and Sweeton (20). The numerical difference between the E_a's is small; in actuality they probably should be the same value. This enables Eq. [5] to be rewritten in the form

$$\Lambda_{T,C} = K_1 e^{-E_{a,r}/RT} - (\phi K_2 + K_3 \sqrt[3]{C})\, e^{-E_{a,h}/RT}$$

where the K's are constants and $E_{a,r}$ and $E_{a,h}$ are the activation energies for the rotation of water molecules and hole formation in water, respectively.

An Arrhenius plot of Λ^* is shown in Fig. 4. Inspection shows that it parallels that of $\Lambda_{0.5M\ HCl}$ and that its value is less than for normal conduction. Again this is to be expected for the rate-determining step in protonic conduction involves the rotation of water molecules (5), and E_a for this process is less than that for hole formation.

Values of conductance, calculated from values of Λ^* given in Table II and from Eq. [5] are given in Table III along with the experimental values of Owen and Sweeton (20). The agreement is satisfactory (less than 1% deviation) over a very wide temperature and concentration range.

Returning now to Fig. 1, a_{KCl} represents the hydrated radii of K^+ and Cl^- and its value decreases with increasing pressure; however, the interpretation of a_{HCl} is less clear. The species rotating are single water molecules (see above), not clusters; hence pressure cannot alter their size significantly. The pressure dependence of the relative conductance of HCl solutions (Fig. 1), therefore, cannot be explained in terms of the a^3 term in Eq. [2]. Protonic conduction is confined to the free water. The application of pressure increases the ratio of free to clustered water, and this effect gives rise to the observed increase in conductivity by increasing the relative amount of the conductive medium.

Salt Electrolytes

We have shown above that, due to the operancy of a special conductive mechanism, over the concentration range 0.001 to nearly 0.5M the conductance of HCl solutions depends on the cube root of the concentration of electrolyte. A puzzling difficulty now arises, namely, the conductance of a great many 1:1 salts (and their diffusion coefficients and log $f\pm$ as

Table III. Comparison of experimental and calculated results

Temp, °C	Concentration	Λ_{calc}	Λ_{obs}	$\Delta\Lambda$
5	0.000000	298	298	0
	0.000776	294	295	−1
	0.00106	294	295	−1
	0.00164	293	294	−1
	0.00197	293	293	0
	0.00279	293	293	0
	0.00429	292	292	0
	0.00562	291	291	0
	0.00880	290	290	0
	0.0125	288	288	0
	0.0168	286	286	0
	0.0389	282	282	0
	0.0695	279	298	+1
	0.0834	277	277	0
	0.124	274	274	0
	0.440	261	258	+3
	0.812	252	243	+9
	1.089	186	233	−47
15	0.00000	362	362	0
	0.00106	358	358	0
	0.00228	356	356	0
	0.00459	354	354	0
	0.00909	351	351	0
	0.00946	351	351	0
	0.0191	348	347	+1
	0.0262	346	345	+1
	0.0406	343	342	+1
	0.0525	341	340	+1
	0.0695	339	337	+2
	0.0732	338	337	+1
	0.0819	337	335	+2
	0.124	333	331	+2
	0.440	316	312	+4
	0.812	306	243	+63
	1.089	299	233	+66
25	0.00000	426	426	0
	0.00207	419	420	−1
	0.00344	416	418	−2
	0.00507	415	416	−1
	0.00589	415	415	0
	0.00987	413	412	+1
	0.0149	410	409	+1
	0.0179	409	408	+1
	0.0289	405	404	+1
	0.0426	402	401	+1
	0.0549	399	398	+1
	0.0675	397	396	+1
	0.0864	395	393	+2
	0.124	390	389	+1
	0.440	370	365	±5
	0.812	357	343	+14
	1.089	351	328	+23
35	0.00000	489	489	0
	0.00095	483	484	−1
	0.00112	482	483	0
	0.00229	480	481	−1
	0.003222	479	479	0
	0.00522	475	477	−2
	0.00642	474	475	−1
	0.00980	472	473	−1
	0.0170	468	468	0
	0.0206	467	467	0
	0.0307	864	862	+2
	0.0366	462	461	+1
	0.0450	460	458	+2
	0.0549	457	456	+1
	0.0621	456	454	+2
	0.0695	455	453	+2
	0.124	446	444	+2
	0.440	422	417	+5
	0.812	406	392	+14
	1.089	399	376	+23
45	0.00000	550	550	0
	0.00207	540	541	−1
	0.00345	537	538	−1
	0.00470	536	536	0
	0.00938	530	531	−1
	0.00995	530	531	−1
	0.00215	523	523	0
	0.00242	522	522	0
	0.0393	516	516	0
	0.0508	513	513	0
	0.0546	511	511	0
	0.0903	508	509	−1
	0.124	499	498	+1
	0.440	410	467	+3
	0.812	451	437	+12
	1.089	443	421	+22
55	0.00000	609	609	0
	0.00183	597	599	−2
	0.00381	594	595	−1
	0.00445	593	594	−1
	0.00772	588	589	−1
	0.00996	585	586	−1
	0.0241	576	577	−1
	0.0244	576	576	0
	0.0454	567	568	−1
	0.0471	567	567	0
	0.0635	562	562	0
	0.0701	560	560	0
	0.124	549	549	0
	0.440	515	514	+1
	0.812	493	485	+8
	1.089	480	464	+16
65	0.00000	667	667	0
	0.000983	660	662	−2
	0.00250	657	658	−1
	0.00477	647	648	−1
	0.00517	645	647	−2
	0.0128	637	638	−1

Table III. (Continued)

Temp, °C	Concentration	Λ_{calc}	Λ_{obs}	$\Delta\Lambda$
	0.0138	637	637	−1
	0.0249	628	629	−1
	0.0300	625	626	−1
	0.0505	615	617	−2
	0.0554	614	616	−2
	0.0715	612	610	+2
	0.124	595	598	−3
	0.440	556	559	−3
	0.812	529	527	+2
	1.089	515	506	+9

well) also exhibit a linear dependence on $C^{1/3}$ (19) even although, as we have seen, their conductance mechanism is entirely different from that of acids. However, data quoted by Robinson and Stokes (17), shows that KCl departs far more from linearity than does HCl. Normal ionic conduction depends on successive hole-formation determining the ion's path through the medium whereas protonic conduction depends on successive rotations of water molecules. A second ion may obstruct the former process as well as the latter. At 25°C the slope of the linear part of Λ *vs.* $C^{1/3}$ is very nearly the same and has a value of −50 for NaCl, KCl, and LiCl (19), while the corresponding value of HCl is −92, or nearly twice as great. If we compare the concentration dependence of the relative conductance of HCl and KCl solutions, we see that the latter falls off more rapidly with concentration. Apparently it is more difficult for successive hole-formations to circumvent an obstructing ion than it is for successive water rotations, a conclusion compatible with the observation that the activation energy of electrical conduction of KCl is higher than that for HCl (5).

Acknowledgment

This work was supported in part by the Office of Naval Research.

Manuscript received Nov. 25, 1964; revised manuscript received April 1, 1965.

Any discussion of this paper will appear in a Discussion Section to be published in the June 1966 JOURNAL.

REFERENCES

1. R. A. Horne and R. A. Courant, *J. Chem. Soc.* (London), 3548 (1964).
2. R. A. Horne, *J. Chem. Phys.*, **40**, 2064 (1964).
3. L. Onsager and R. M. Fuoss, *J. Phys. Chem.*, **36**, 2689 (1932).
4. See also E. Yaeger, J. Booker, and F. Hovorka in "The Structure of Electrolytic Solutions," W. J. Hamer, Editor, p. 95, John Wiley & Sons, Inc., New York (1959).
5. R. A. Horne, B. R. Myers, and G. R. Frysinger, *J. Chem. Phys.*, **39**, 2666 (1963).
6. B. E. Conway, J. O'M. Bockris, and H. Linton, *ibid.*, **24**, 834 (1956).
7. W. A. Zisman, *Phys. Rev.*, **39**, 151 (1932).
8. R. A. Horne, *Nature*, **200**, 418 (1963).
9. R. A. Horne and R. A. Courant, *J. Geophys. Res.*, **69**, 1971 (1964).
10. D. M. Riston, J. B. Hasted, and C. H. Collie, *Compt. rend.*, **225**, 285 (1947).
11. G. H. Haggis, J. B. Hasted and T. J. Buchanan, *J. Chem. Phys.*, **20**, 1452 (1952).
12. R. W. Gurney, "Ionic Processes in Solution," p. 168, McGraw-Hill Book Co., New York (1953).
13. G. Jones and M. Dole, *J. Am. Chem. Soc.*, **51**, 2950 (1929).
14. See also Figure 3 in R. A. Horne and R. A. Courant, *J. Phys. Chem.*, **68**, 1258 (1964).
15. G. Nemethy and H. A. Scheraga, *J. Chem Phys.*, **36**, 3382 (1962).
16. R. A. Horne and E. H. Axelrod, *ibid.*, **40**, 1518 (1964).
17. R. A. Robinson and R. H. Stokes, "Electrolyte Solutions," 2nd ed., p. 12, Butterworths Scientific Publications, London (1959); *Vide* R. P. Marchi and H. Eyring, *J. Phys. Chem.*, **68**, 221 (1964).

18. H. S. Frank and W. Y. Wen, *Disc. Faraday Soc.*, **24**, 133 (1957).
19. H. S. Frank and P. T. Thompson, in "The Structure of Electrolyte Solutions," W. J. Hamer, Editor, pp. 113-134, John Wiley & Sons, Inc., New York (1959).
20. B. B. Owen and F. H. Sweeton, *J. Am. Chem. Soc.*, **63**, 2811 (1941).
21. R. H. Stokes, *J. Phys. Chem.*, **65**, 1242 (1961).
22. S. Glasstone, K. J. Laidler, and H. Eyring, "The Theory of Rate Processes," Ch. IX and X, McGraw-Hill Book Co., New York (1941).

Electrochemical Studies of NO^+ and NO_2^+ in Concentrated H_2SO_4

L. E. Topol, R. A. Osteryoung, and J. H. Christie[1]

North American Aviation Science Center, Thousand Oaks, California

ABSTRACT

Linear sweep voltammetric and chronopotentiometric studies were made on solutions of NO_2^-, NO_3^-, NO, and $NO_2(N_2O_4)$ in 18*F* sulfuric acid. It was found that the electroactive species in both NO_2^- and NO solutions is NO^+ and the NO-H_2SO_4 reaction is slow. In contrast the NO_2-H_2SO_4 reaction to yield NO_2^+ is extremely rapid. The NO-NO^+ couple appears to be reversible on clean Pt or Au but the NO_2-NO_2^+ couple is not. Some anodization results with Pt and Au in H_2SO_4 are also described.

Raman spectroscopy (1, 2, 3) has been used to demonstrate that the nitrosonium ion NO^+ and the nitronium (nitryl) ion NO_2^+ are formed by dissolution of nitrite and nitrate, respectively, in concentrated H_2SO_4

$$NO_2^- + 3H_2SO_4 \rightarrow NO^+ + 3HSO_4^- + H_3O^+ \quad [1]$$

$$NO_3^- + 3H_2SO_4 \rightarrow NO_2^+ + 3HSO_4^- + H_3O^+ \quad [2]$$

Both these species are formed by the reaction of NO_2 (or N_2O_4) with concentrated H_2SO_4

$$2NO_2 + 3H_2SO_4 \rightarrow NO_2^+ + NO^+ + 3HSO_4^- + H_3O^+ \quad [3]$$

It has been reported that NO also reacts with concentrated H_2SO_4 but there has been disagreement about the products of the reaction (4,5).

Although it is known that NO_2^+, and probably NO^+ also, play important roles in the dissolution of metals in HNO_3 and that NO^+ and NO_2^+ are attacking electrophiles in organic nitrosations, deaminations, and nitrations, the electrochemical behavior of these species has been the subject of only two polarographic studies (6, 7). Only one report on the electrochemical behavior of nitrogen oxides dissolved in H_2SO_4 has appeared (8).

In the present work linear sweep voltammetry and chronopotentiometry with Pt and Au electrodes have been applied to the study of solutions on NO_2^-, NO_3^-, NO, and NO_2 in 18*F* H_2SO_4. Solutions of NO_2^- and NO_3^- with H_2SO_4 < 15*F* are unstable and evolve oxides of nitrogen (6).

Experimental

Baker and Adamson reagent grade H_2SO_4 (96%), $NaNO_2$, and $NaNO_3$, and Matheson NO (99% pure) and NO_2 (99.5% pure) were used without further purification.

The current-voltage curves were obtained with the potential sweep apparatus described previously (9). The chronopotentiometric setup, using a John Fluke Model 351A constant current supply, was conventional. The linear sweep voltammetric and chronopotentiometric curves were recorded on a Moseley Model 2D X-Y recorder or a Tektronix Type 564 storage oscilloscope.

The Pyrex cell consisted of three compartments with the outer two connected to the center one by coarse-porosity fritted disks. The reference half-cell was Hg/Hg_2SO_4 (satd.), H_2SO_4 (18*F*) [saturated mercuric sulfate electrode (SMSE)] which has a potential of +0.22v *vs.* the saturated calomel electrode (10). The counter electrode was Pt. The Au and Pt wire or foil indicator electrodes were cleaned mechanically or by cathodization in H_2SO_4. It was found that reproducible waves in NO^+ solutions resulted after such treatment. The solutions were deaerated in the usual manner by passing argon gas through them; Ar was also bubbled through the solution between measurements to destroy concentration gradients. Chronopotentiometric transition times were measured by the method of Voorhies and Furman (11).

[1] Present address: Chemistry Department, California Institute of Technology, Pasadena, California.

Results

The Nitrosonium ion.—Voltage sweeps on clean Pt or Au electrodes taken in solutions prepared either by dissolving $NaNO_2$ or NO in 96% H_2SO_4 appear to be identical. One cathodic peak at +60-80 mv *vs.* SMSE and one anodic peak at +125-150 mv were observed (Fig. 1). The average peak separation of 65 mv is in reasonable agreement with the theoretical value of 56 mv for a reversible one-electron process (12). Since it is known that the stable N(III) species in 96% H_2SO_4 is NO^+, the reduction process must be

$$NO^+ + e \rightarrow NO \quad [4]$$

and the oxidation process, the reverse. The single electron reduction is in agreement with the results of

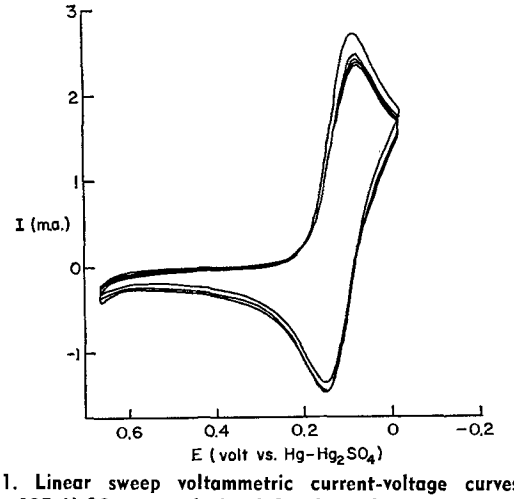

Fig. 1. Linear sweep voltammetric current-voltage curves of NO^+ in 18*F* H_2SO_4 on cathodized Pt electrode.

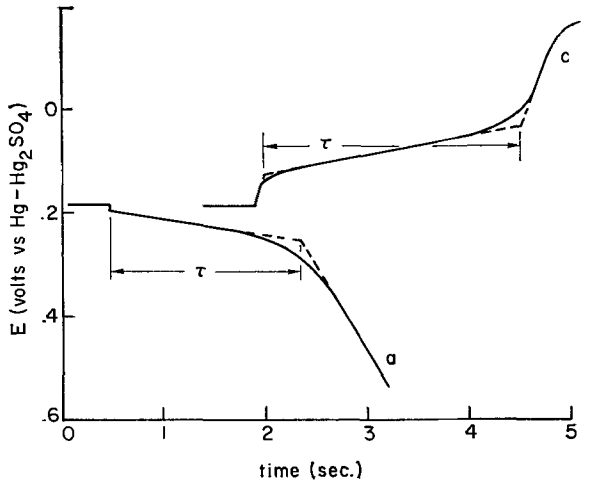

Fig. 2. Chronopotentiometric waves showing transition times τ for NO and NO^+ in H_2SO_4. (a) NO — e → NO^+, anodic (for NO)-current = 0.200 ma; (c) NO^+ + e → NO, cathodic (for NO^+)-current = 1.200 ma.

Masek (6, 7) for 18*F* H_2SO_4. If the linear potential sweep is cycled between 0.0 and +0.4v, a steady state is approached in which the ratio of the cathodic peak current to the anodic peak current is slightly greater than unity but is independent of sweep rate.

Chronopotentiometry with clean Pt or Au electrodes in solutions of nitrite or nitric oxide gave similar cathodic waves (Fig. 2, curve c). Values of $i\tau^{1/2}$ for these waves were fairly constant over a wide range of current density for both NO and NO_2^- solutions (Table I). The slight increase of $i\tau^{1/2}$ with τ may be due to the effects of nonlinear diffusion and/or convection (13). For $NaNO_2$ solutions $i\tau^{1/2}/C$ was constant over a concentration range of 2 to 30 m*F* $NaNO_2$. Plots of E *vs.* log $[(\tau/t)^{1/2} - 1]$ were linear for both NO_2^- and NO solutions with a slope of 53-60 mv, corresponding to a reversible one-electron process, and with $E_{1/4} = +0.110$-0.120v *vs.* SMSE. Current-reversal chronopotentiometry for $NaNO_2$ solutions (Fig. 3) yielded ratios of the forward electrolysis time t_f to the reverse (anodic) transition time τ_r which varied from the theoretical ratio $t_f/\tau_r = 3$, the ratio increasing with increasing t_f (Table II). If an anodic chronopotentiogram was taken immediately after bubbling NO through the solution in the cell, an oxidation wave, identical to that observed on current reversal after the NO^+ reduction wave is found (Fig. 2, curve a). This wave must correspond to the reverse of reaction [4].

It was noted that the current-voltage curves observed after the Pt electrode had been anodized at potentials more anodic than +1.4v *vs.* the SMSE differed markedly from those observed on "clean"

Table I. $i\tau^{1/2}$ Values on Au electrode for $NaNO_2$ (16.7mF) in 18*F* H_2SO_4

i(ma)*	τ(sec)	$i\tau^{1/2}$(ma-sec)$^{1/2}$
0.700	25.5	3.54
0.800	19.3	3.52
1.000	11.24	3.36
1.200	7.81	3.36
1.400	5.66	3.34
1.600	4.22	3.29
1.800	3.25	3.25
2.000	2.58	3.22
2.200	2.09	3.18
2.400	1.72	3.15
2.4	1.81	3.23
2.6	1.58	3.27
3.0	1.16	3.23
3.5	0.835	3.20
4.0	0.650	3.16
5.0	0.415	3.22

* The data for i = 0.700 to 2.400 ma were taken on an X-Y recorder. The data for i = 2.4 to 5.0 ma were taken on an oscilloscope.

Table II. Ratio of forward* to reverse times for chronopotentiometric waves on Au electrode in 16.7mF $NaNO_2$-H_2SO_4 solution

i = 1.00 ma			i = 0.50 ma		
τ_f(sec)	τ_r(sec)	τ_f/τ_r	τ_f(sec)	τ_r(sec)	τ_f/τ_r
1.66	0.61	2.72	10	3.1	3.2
3.68	1.32	2.79	20	6.6	3.0
5.64	1.92	2.94	30	9.0	3.3
7.66	2.56	2.99	40	11.2	3.6
10.66	3.40	3.13	55.2	12.6	4.4

* Forward wave is cathodic.

(cathodized) electrodes (see Fig. 4). The most striking difference was the great decrease of the anodic peak. Upon cycling the potential between 0 and +0.4v, the anodic peak grew in slowly while the cathodic peak decayed rapidly. The cathodic peak was also broader than with previously cathodized electrodes.

Chronopotentiometry with a previously anodized electrode showed little difference in the cathodic wave, but only a very small wave, if any, was observed on current reversal. Similar experiments with anodized Au electrodes showed similar results, but the differences were not so striking as with Pt electrodes.

It appears that the reduction of NO^+ to NO occurs on anodized as well as on cathodized electrodes but that the subsequent reoxidation of NO does not readily take place on anodized electrodes. It was thought that this might be due to a blockage of the surface for the NO oxidation by anodically formed oxide on the surface of the electrode.

The anodic behavior of Pt and Au electrodes in pure 18*F* H_2SO_4 was studied to find out whether there was an anodically formed oxide which was not removed at potentials at which NO oxidation should take place.

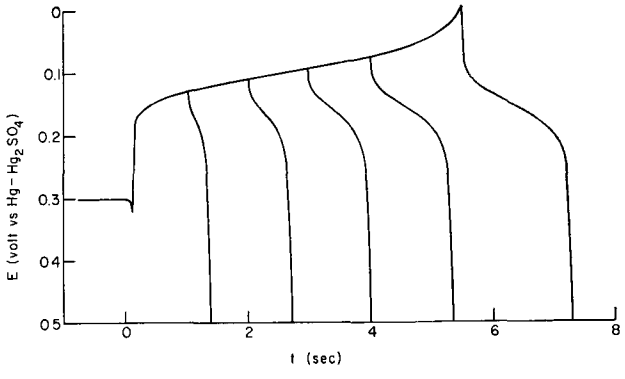

Fig. 3. Current-reversal chronopotentiometric waves for NO^+ solutions. (Forward wave is cathodic.)

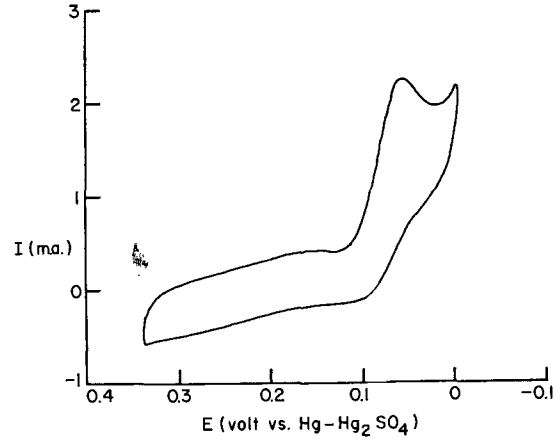

Fig. 4. Linear sweep voltammetric current-voltage curve for NO^+ in H_2SO_4 on anodized Pt electrode.

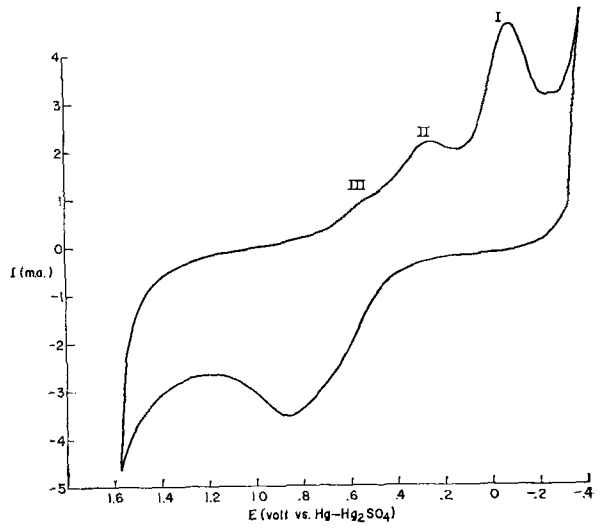

Fig. 5. Linear sweep voltammetric current-voltage curve of 18F H_2SO_4 on anodized Pt.

Figure 5 shows the current-potential behavior of a Pt electrode in pure H_2SO_4. There is only one broad anodic peak (at ~ +0.85v *vs.* SMSE) before depolarization by the solvent at +1.6v. Three cathodic peaks at +0.50(III), +0.25(II), and −0.10v(I) are apparent; these peaks also occur if the solution is stirred during the experiment, indicating that they are due to the reduction of material on the surface of the electrode.

A clean Pt electrode was then potentiostated at various anodic potentials for 30 sec and swept cathodic. After anodization at +0.68v only peak I is apparent, but with successive anodizations at increasingly anodic potentials, peaks II and III appear and finally after anodization at the most anodic potentials (>1.4v), peaks I and II coalesce to form one broad peak.

After this procedure the electrode was cleaned by cathodization and again anodized in 18*F* H_2SO_4 as above. After anodization the electrode was transferred to a 6 m*F* $NaNO_2$ solution and current-voltage curves were taken (+0.4-0.0v). The current-voltage curves were "normal" if the electrode had been subjected to anodization conditions less severe than +1.6v for 120 sec, and even in this case the behavior returned to normal within a few cycles. In contrast, anodization at +1.6v for 30 sec in the nitrite solution itself results in a complete absence of the NO oxidation peak and a large broadening of the NO^+ peak.

The voltage sweep behavior of Au in 18*F* H_2SO_4 is shown in Fig. 6. Peak I in Fig. 6 appears to be due to

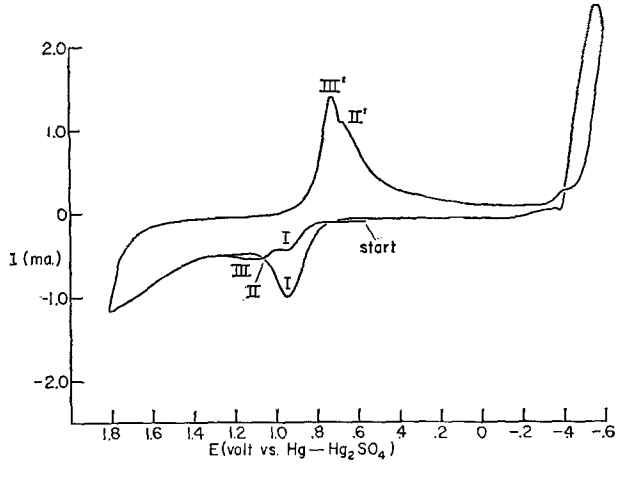

Fig. 6. Linear sweep voltammetric current-voltage curve for 18F H_2SO_4 on Au.

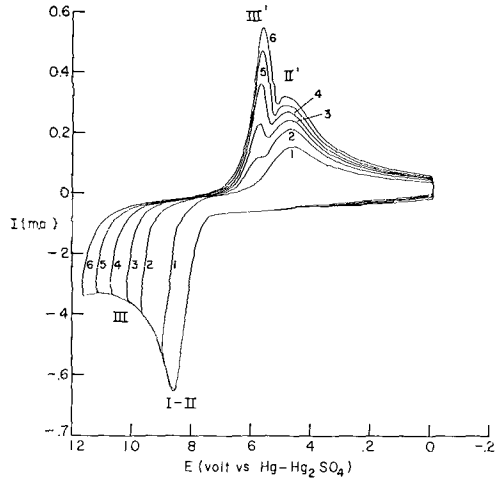

Fig. 7. Cyclic voltammetry of 18M H_2SO_4 between 0 and 1.2v (*vs.* Hg-Hg_2SO_4) on Au.

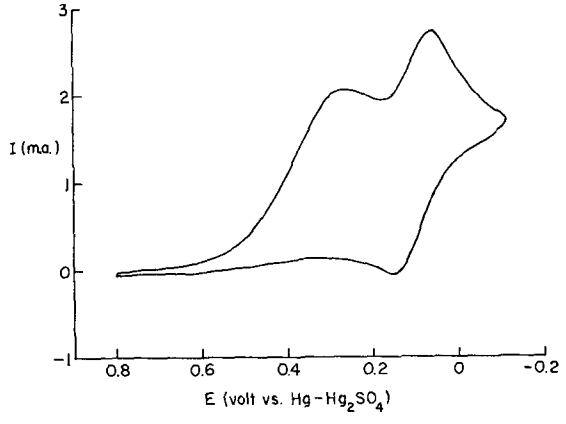

Fig. 8. Linear sweep voltammetric current-voltage curve of NO_2^+ in H_2SO_4. Potential span velocity is 0.9 v/sec.

the oxidation of material formed in the cathodic solvent decomposition. The reduction peaks II′ and III′ are associated with the anodic peak II and the region III (Fig. 7). If the solution is stirred while the experiment is being carried out, peak II′ is absent but peak III′ still occurs.

The nitronium ion.—Solution of both $NaNO_3$ and NO_2 in 18*F* H_2SO_4 yield similar linear sweep voltammograms (Fig. 8). Two cathodic peaks are present, the second corresponding to reaction [4] found in NO^+ solutions. There is only one anodic wave which occurs at the same potential as the oxidation of NO. There is no anodic wave corresponding to the reoxidation of the product of the first reduction wave. In addition, no anodic peak corresponding to the oxidation of NO_2 is found even immediately after NO_2 gas is bubbled through the solution.

Chronopotentiometry of NO_2^+ solutions at both Pt and Au electrodes yields two reduction waves, the second of which corresponds to that for NO^+ reduction. If the current is reversed after the second wave, only the wave corresponding to NO oxidation is found. The product $i\tau_1^{1/2}$ for the first wave as well as $i(\tau_1 + \tau_2)^{1/2}$ are approximately constant over a wide range of current density. In addition, the ratio of the transition time τ_2 for the second wave to the transition time τ_1 for the first has the value $\tau_2/\tau_1 = 1.5$-1.7. The ratio of the transition times for a two electron process followed by a one electron process should be 1.25 (14).

The rest potential of an electrode standing in contact with an NO_2^+ solution drifts anodic with time and an electrode that has been in contact with the solution for several minutes gives cathodic chronopotentiograms which are more poorly defined and which have

longer transition times than those obtained immediately after the electrode is put into the solution. It is apparent that the electrode is attacked chemically by the NO_2^+, presumably with the formation of oxides on the surface.

Linear sweep voltammetric curves of the above solutions for sweep rates of 25 to 1000 mv/sec were reproducible and yielded essentially linear plots of peak current *vs.* (sweep rate)$^{1/2}$ for both waves. The potential of the peaks did not vary to any extent with sweep rate.

Discussion

The similarity of electrochemical behavior between solutions formed by dissolving $NaNO_2$ and NO in H_2SO_4 indicates that the NO must react to give NO^+ as a product. The reaction is

$$2NO + 5H_2SO_4 \rightarrow 2NO^+ + SO_2 + 2H_3O^+ + 4HSO_4^- \quad [5]$$

as has been verified by subsequent studies in this laboratory (15) The ocurrence of this reaction would suggest that the reduction of NO^+ should be catalytic, *i.e.*, the NO formed should react with the solvent to regenerate NO^+. The electrochemical results do not indicate that this is the case. (The slight increase of $i\tau^{1/2}$ with $\tau^{1/2}$ in Table I for the reduction of NO^+ is probably due to nonlinear diffusion.) If the forward rate of reaction [5] is very slow, no catalytic effect will be observed. The fact that NO remains in solution for several minutes after exposure of the solution to NO gas indicates that the reaction is indeed slow. Preliminary kinetic studies (15) have yielded results consistent with second-order kinetics with a rate constant of 0.22 liter/mole-sec. This rate would give an effect on the transition time well within the experimental error.

The reaction of NO_2 with H_2SO_4 is very rapid as can be verified by exposing H_2SO_4 to NO_2 gas at a known pressure and observing the very rapid decrease in pressure. The chronopotentiometry of NO_2^+ solutions indicates that the first process is a two electron reduction of NO_2^+ to NO^+, followed by the one electron reduction [4]. Masek (6) has proposed the following mechanism for this process

$$2(N(V) + e \rightarrow N(IV)) \quad [6a]$$

$$2N(IV) \rightarrow N(III) + N(V) \quad [6b]$$

$$N(III) + e \rightarrow N(II) \quad [6c]$$

The chronopotentiometric behavior for such a second order disproportionation following the electrochemical reaction has been treated by Feldberg and Auerbach (16). If the disproportionation reaction is sufficiently fast, the over-all process would simply appear to be

$$N(V) \xrightarrow{2e} N(III) \xrightarrow{e} N(II) \quad [7]$$

It is therefore impossible to tell from our data whether the first reduction proceeds by Masek's mechanism or by a direct two-electron reduction to NO^+.

Bianchi *et al.* (8) recently have reported polarization curves for Pt electrodes in 45-85% H_2SO_4 (approximately 6-12*F*) through which nitrogen oxides were passed. Their results are in disagreement with Masek's results (6, 7), of which they seem to be unaware, as well as ours. Bianchi reports two reduction waves.

$$NO^+ + e \rightarrow NO \quad [8]$$

and

$$2NO + 2H^+ + 2e \rightarrow H_2N_2O_2 \quad [9]$$

Masek has shown that the final reduction product is hydroxylamine and that this reduction occurs cathodic to the potential for H_2 evolution on Pt.

Bianchi *et al.* also report three oxidation waves which they attribute to the processes

$$NO - e \rightarrow NO^+ \quad [10]$$

$$2NO^+ + 2H_2O - 2e \rightarrow N_2O_4 + 4H^+ \quad [11]$$

$$N_2O_4 + H_2O - 2e \rightarrow N_2O_5 + 2H^+ \quad [12]$$

The last two waves were found to be absent in $H_2SO_4 < 73\%$ and this was attributed to the disproportionation of N_2O_4 in the more dilute acid to give NO^+ and HNO_3. We find that it is impossible to oxidize NO^+ in 96% acid and that the disproportionation of NO_2 (or N_2O_4) is very rapid. It seems unlikely that the disproportionation of N_2O_4 should take place in 96% acid and with acid less than 73% but not at intermediate concentrations. An attempt to observe reaction [11] in an 80% H_2SO_4 solution containing $NaNO_2$ also failed. No explanation for the discrepancies between our results and those of Bianchi seems to be available.

Acknowledgments

We wish to thank Mr. George Lauer for his help with experimental problems. This work was supported in part by the U.S. Atomic Energy Commission.

Manuscript received Dec. 22, 1964; revised manuscript received April 14, 1965.

Any discussion of this paper will appear in a Discussion Section to be published in the June 1966 JOURNAL.

REFERENCES

1. C. K. Ingold, D. J. Millen, and H. G. Poole, *J. Chem. Soc.*, **1950**, 2576.
2. D. J. Millen, *ibid.*, **1950**, 2600.
3. W. R. Angus and A. H. Leckie, *Nature*, **134**, 575 (1934); *Proc. Roy Soc.*, **A149**, 327 (1935).
4. J. W. Mellor, "A Comprehensive Treatise on Inorganic and Theoretical Chemistry," Vol. VIII, John Wiley and Sons, Inc., New York (1962).
5. E. Berl and K. Winnacker, *Z. anorg. allgem. Chem.*, **208**, 124 (1932).
6. J. Masek in "Advances in Polarography," I. S. Longmuir, Editor, Vol. I, p. 340, Pergamon Press, New York (1960).
7. J. Masek and H. Przewlocka, *Collection Czech. Chem. Commun.*, **28**, 670 (1963).
8. G. Bianchi, T. Mussini, and C. Traini, *Chim. Ind.* (Milan), **45**, 1333 (1963).
9. G. Lauer, H. Schlein, and R. A. Osteryoung, *Anal. Chem.*, **35**, 1789 (1963).
10. A. A. Vlcek, *Collection Czech. Chem. Commun.*, **16**, 230 (1951).
11. J. D. Voorhies and N. H. Furman, *Anal. Chem.*, **30**, 1656 (1958).
12. P. Delahay, "New Instrumental Methods in Electrochemistry," p. 137, Interscience Publishers, Inc., New York (1954).
13. P. J. Lingane, *Anal. Chem.*, **36**, 1723 (1964).
14. Ref. 12, p. 192.
15. L. E. Topol and R. G. Adler, To be published.
16. S. W. Feldberg and C. Auerbach, *Anal. Chem.*, **36**, 505 (1964).

The Preparation and Thermodynamic Properties of a Palladium-Hydrogen Electrode

M. J. Vasile and C. G. Enke

Frick Chemical Laboratory, Princeton University, Princeton, New Jersey

ABSTRACT

The potential of a palladium-hydrogen electrode prepared by electrolytic methods was studied as a function of the composition of the electrode, temperature, and pH. The objective of these studies was to prepare a palladium hydrogen reference electrode which can be used in hydrogen free solutions. The potential was found to be a function of the electrode composition in the α phase, and β phase, and independent of composition in the $\alpha + \beta$ phase region. Equations were derived starting from fundamental thermodynamics which fit the potential *vs.* composition data in the α phase, and in the $\alpha + \beta$ phase region, as well as the temperature dependence for such an electrode. The procedure for preparing a palladium hydrogen reference electrode by electrolytic methods is given.

The absorption of gaseous hydrogen from aqueous solutions by palladium and the subsequent potential of the Pd-H/H_2 system has been studied extensively in recent years (1-4). Reference electrodes based on the Pd-H system have been used by several workers (5-7). Ives and Janz (8) have reviewed the literature on the palladium-hydrogen system up to 1961. At that time, differences in the experimental results and their interpretation were apparent; these differences still persist. One of the main points in contention is the potential determining mechanism for the observed +50 mv plateau of the Pd-H electrode.

Hoare (1) found that palladium will absorb hydrogen from aqueous acid solutions up to the atom ratio H/Pd = 0.03, or approximately to the limit of the α-phase.[1] He attributes the steady potential of +50 mv to the (Pd-H)α mixture. To explain the continuity of the +50 mv potential up to the concentration H/Pd = 0.36, a mixed potential was postulated due to the simultaneous presence of the α and β phases, with the α phases predominating (1). Equations were derived to show that the +50 mv plateau is due to the pure α phase at its maximum concentration, H/Pd $\cong$ 0.03.

Flanagan and Lewis (2) have found that the absorption of hydrogen from acid solutions does not stop at the α phase limit, but proceeds on the $\alpha + \beta$ region, and finally to the pure β phase [later work by Hoare (9) also confirms this fact]. They attribute the +50 mv plateau to the presence of the two-phase region, and the subsequent drop to zero volts to the pure β phase. The drop in potential from the initial value to the +50 mv plateau is attributed to the presence of the pure α phase. Both Flanagan and Lewis and Hoare and coworkers used relative resistance measurements to determine the H/Pd ratio.

Cathodically charged palladium-hydrogen electrodes have been studied by several workers (10-12). Their general conclusions or implications are that the potential remains constant over the entire two-phase ($\alpha + \beta$) region, and is a function of composition in the pure α and pure β regions. More recent work on the palladium-hydrogen system has been done by Aben and Burger (3) using polycrystalline x-ray diffraction to detect the phase present at the surface of the palladium after absorption of H_2 from aqueous acid solutions. Their work supports the view that the potential is dependent on composition in the pure α and β phases, but is independent of composition in the mixed $\alpha + \beta$ phase region.

[1] The phases of the palladium-hydrogen alloy are determined by the amount of distention in the lattice parameter of pure palladium. The lattice parameter of pure Pd is 3.883Å, while that of the α phase is 3.886Å, and that of the β phase is 4.032Å.

The pressure *vs.* composition isotherms and heats of solution for hydrogen gas in equilibrium with palladium metal have been determined most reliably by Gillespie and coworkers (13, 14). A successful theoretical treatment of this system which supports the idea that hydrogen forms a homogeneous solid solution with palladium has been given by Lacher (15).

The object of the following study was to prepare a palladium hydrogen reference electrode by cathodic occlusion of hydrogen. Such reference electrodes have been prepared by absorption of gaseous hydrogen from acid solutions, and were given the name α-Pd reference electrodes (5, 16). The attempts to prepare such an electrode electrolytically led to a re-examination of the potential *vs.* composition relationship for this system. In this study a gas chromatograph was used to analyze for the hydrogen content in the palladium. The work was then extended to include potential *vs.* temperature measurements for palladium-hydrogen alloys produced by cathodic charging, and also by absorption of gaseous hydrogen from acid solutions.

Apparatus

The cell used was a simple H-type cell with the two compartments separated by a fine porosity glass frit. Nitrogen or helium was supplied both above and below the solution level in the compartment that contained the Pd test electrode. A presaturator for the hydrogen supplied to the H_2/Pt reference electrode was used. The entire apparatus was immersed in a thermostatically controlled temperature bath at 24.8° ± 0.1°C. The electrolyte was 1*N* perchloric acid, made up with water from a Barnstead high-purity distillation apparatus and 70% perchloric acid (G. F. Smith and Company). For potential *vs.* composition measurements, the palladium electrodes were made using 0.0125 in. diameter wire (Engelhard Industries) spot welded to platinum leads of 0.025 in. diameter at both ends. These platinum leads were then inserted through a rubber septum (injection gasket) up to the Pt to Pd spot welds, giving a palladium loop electrode with two contacts. The septum was then force fitted into the end of a glass sleeve which contained the lead that connected the palladium electrode to the testing apparatus. For the temperature dependence measurements and reference electrode experiments, a palladium wire approximately 4 cm long and 0.0125 in. in diameter was spot welded to a platinum lead at one end. The platinum lead was then sealed in soft glass, up to, and just including, the spot weld. The straight, exposed palladium wire was then sheathed in a glass capillary which could serve as a luggin capillary.

The measuring instruments used were as follows: for potential difference measurements, a Keithley elec-

trometer (±0.5 mv) as well as a potentiometer capable of reading ±0.1 mv; for quantity of hydrogen in palladium an Aerograph A-90-P2 gas chromatograph capable of detecting less than 1 μl of gaseous H_2 in a carrier stream of nitrogen. The palladium in the loop electrodes was weighed to the nearest tenth milligram on a Mettler grammatic balance. A constant-current source was made by using a Philbrick R100B power supply (+300v, —300v) in series with precision resistors.

Procedure

Potential vs. composition measurements.—The palladium loop electrodes were charged with hydrogen by cathodizing them at a constant current of either 30 or 150 μa (current densities of approximately 60 and 300 μa/cm^2). Between 60% and 90% of the hydrogen liberated by this cathodization was occluded in the palladium lattice. The potential of the electrode thus charged was measured in nitrogen swept solution *vs.* a normal hydrogen electrode. After the potential was tested, the electrode was removed from the cell, rinsed in distilled water as rapidly as possible, and the septum holding the Pd loop was then pried out of the glass sleeve. The septum was then inserted in a specially made injection port on the gas chromatograph, and 6v a.c. was applied across the platinum leads after they had been lowered sufficiently to avoid heating the septum. The 6v a.c. was enough to cause the palladium loop to glow red and eject its hydrogen into the carrier gas stream.

Various methods of pretreatment of the palladium electrodes were tried. They included annealing in a gas-air flame, annealing by electrical heating, immersion in boiling concentrated nitric acid, and anodization.

It has been observed that charging the palladium electrodes electrolytically leads to higher concentrations of hydrogen at the surface than in the bulk (2). To minimize this possibility, low current densities were used, and an anodization procedure was developed which depends on the diffusion of the bulk hydrogen to the surface to relieve concentration gradients. The anodization procedure simply involves reversing the current for a short time interval followed by a measurement of the rest potential. This process was repeated until no change in potential occurred with the anodization.

Temperature dependence measurements were carried out by first getting an electrode to exhibit the +50 mv plateau, at 25°C, and then raising or lowering the bath temperature in 5°C steps. The system was allowed to remain at each temperature at least ½ hr after achieving a steady potential. The temperature bath was thermostatically controlled at all values to ±0.1°C. The stability of the electrode was tested prior to variations in the temperature by leaving the electrode on open circuit in solutions swept with inert gases for periods of 8-10 hr. After the whole temperature range from 25° to 50°C and from 25° to 0°C was examined, the temperature was returned to 25°C, and the potential and hence stability of the electrode were again checked. The temperature dependence of the plateau potential was also measured for electrodes of the configuration described previously, while absorbing gaseous hydrogen from solution at pressure equal to 1 atm. In these investigations, no long-term stability tests were made prior to variation of the temperature. The electrode potential was allowed to reach a steady state with hydrogen gas at 1 atm pressure, and temperature variations were started promptly.

To test the electrode response to solutions at different hydrogen ion concentrations the electrode was removed from the cell (capillary included) and the electrolyte in the cell was thoroughly flushed out and replaced with electrolyte of different hydrogen ion concentration. While the electrolyte in the cell was being changed, the palladium-hydrogen electrode was rinsed thoroughly with and stored in the new solution.

Platinization of the Pt/H_2 reference electrode was carried out according to a procedure described by Ives and Janz (8). The current density used for platinization was approximately 15 ma/cm^2. Palladization of the palladium electrodes, when done, was carried out at current densities of approximately 30 ma/cm^2. Palladizing solution was prepared according to a procedure given by Bates (17).

Discussion and Experimental Results

The potential of +50 mv for a Pd-H electrode in the two-phase region requires a thermodynamic explanation. It is held in the presence of dissolved hydrogen ($P = 1$ atm) and in the absence of dissolved hydrogen. It is evident that the Pd-H alloy supplies its own hydrogen for the potential determining reaction at the activity prescribed by the phase or phases present.

Flanagan and Lewis (2) propose the following half reactions for the system when absorbing hydrogen from solution.

$$x\mathrm{H}{:}y\mathrm{Pd} + \mathrm{H}^+ + e^- \rightarrow (\mathrm{x}+1)\mathrm{H}{:}y\mathrm{Pd}\ \text{Pd electrode} \quad [1]$$

$$1/2\ \mathrm{H_2} \rightarrow \mathrm{H}^+ + e^-\ \text{Pt electrode} \quad [2]$$

They give as the net reaction, the sum of these two half reactions.

$$x\mathrm{H}{:}y\mathrm{Pd} + 1/2\ \mathrm{H_2} \rightarrow (x+1)\mathrm{H}{:}y\mathrm{Pd} \quad [3]$$

They then go on to compare the free energies for the net reaction with the free energy change calculated from the equilibrium gas phase isothermal data of Gillespie (13, 14). However, the equilibrium pressure of hydrogen gas in contact with palladium at 25°C is 0.0202 atm, and the only term that involves hydrogen gas in Eq. [3] is that which derives from the hydrogen reference electrode, which is at P = 1 atm. The connection between ΔG as calculated from the gas phase data of Gillespie and the net reaction Eq. [3] given by Flanagan and Lewis is not quite clear.

An alternate, and more precise method of treating this system is to arrive at a Nernst equation based on Eq. [3]. This equation will be accepted as the potential determining mechanism, regardless of the phase or phases present at the surface of the Pd-H alloy.

For the net reaction, Eq. [3], ΔG may be written

$$\Delta G = (x+1)\mu_{\mathrm{H}}{}^{(m)} + y\mu_{\mathrm{Pd}}{}^{(m)} - \tfrac{1}{2}\mu_{\mathrm{H_2}}{}^{(g)} - y\mu_{\mathrm{Pd}}{}^{(m)} - x\mu_{\mathrm{H}}{}^{(m)} \quad [4]$$

according to $\Delta G = \Sigma n_i\mu_i$ prod. $- \Sigma n_j\mu_j$ react. The symbols are: $\mu_{\mathrm{H}}{}^{(m)}$ = chemical potential of H atoms in the Pd lattice; μ_{Pd} = chemical potential of Pd atoms; and $\mu_{\mathrm{H_2}}{}^{(g)}$ = chemical potential of H_2 in the gas phase. Upon subtracting terms

$$\Delta G = \mu_{\mathrm{H}}{}^{(m)} - \frac{1}{2}\mu_{\mathrm{H_2}}{}^{(g)} \quad [5]$$

which clearly indicates the H atoms in the Pd lattice as a part of the potential determining mechanism. It remains to find an expression for $\mu_{\mathrm{H}}{}^{(m)}$. There is good reason to believe that a reaction of the type

$$y\mathrm{Pd}{:}x\mathrm{H} = y\mathrm{Pd}{:}(x-2)\mathrm{H} + 2\mathrm{H}$$
$$2\mathrm{H} = \mathrm{H_2}$$

takes place at the surface of the Pd-H alloy (18). The Pd-H alloy would then be in equilibrium with H_2 only when the pressure of hydrogen is given by the isotherms determined by Gillespie. These facts lead to an expression for $\mu_{\mathrm{H}}{}^{(m)}$ since by conditions for equilibrium the following relationships must be satisfied

$$\mu_{\mathrm{H}}{}^{(m)} = \mu_{\mathrm{H}}{}^{(g)} \quad [6]$$

where $\mu_{\mathrm{H}}{}^{(g)}$ = chemical potential of hydrogen atoms in the hydrogen gas in equilibrium with the Pd-H alloy.

$$\mu_{\mathrm{H}}{}^{(g)} = \tfrac{1}{2}\mu_{\mathrm{H_2}}{}^{(g)} \quad [7]$$

and $\mu_{H_2}^{(g)}$ is the chemical potential of hydrogen gas at the equilibrium pressure, $P = P'_{H_2}$. This pressure is 1 atm only when the atom ratio H/Pd = 0.69.

Now

$$\mu_{H_2}^{(g)} = \mu_{H_2}^{o} + RT\ln P'_{H_2} \quad [8]$$

Therefore, by equating Eq. [6] and Eq. [7]

$$\mu_H^{(m)} = \tfrac{1}{2}\mu_{H_2}^{(g)} \quad [9]$$

and finally, by substituting Eq. [8] in Eq. [9],

$$\mu_H^{(m)} = \frac{\mu^o_{H_2}}{2} + \frac{RT}{2}\ln P'_{H_2} \quad [10]$$

For the net reaction, ΔG may now be written explicitly

$$\Delta G = \frac{\mu^o_{H_2}}{2} + \frac{RT}{2}\ln P'_{H_2} - \frac{\mu_{H_2}^o}{2} - \frac{RT}{2}\ln P_{H_2} \quad [11]$$

or

$$\Delta G = \frac{RT}{2}\ln (P'_{H_2}) - \frac{RT}{2}\ln P_{H_2} \quad [12]$$

The last term in Eq. [12] refers to the normal hydrogen reference electrode. When corrected for the partial pressure of water, Eq. [12] reads

$$\Delta G = \frac{RT}{2}\ln (P'_{H_2}) - \frac{RT}{2}\ln\left(\frac{P_{BAR} - P'_{H_2O}}{760}\right) \quad [13]$$

where P_{BAR} is the barometric pressure, and P'_{H_2O} is the partial pressure of water, both in mm Hg.

Since $\Delta G = -nFE$, we get the Nernst equation

$$E = -\frac{RT}{2F}\ln P'_{H_2} + \frac{RT}{2F}\ln\left(\frac{P_{BAR} - P'_{H_2O}}{760}\right) \quad [14]$$

or alternately written

$$E = -\frac{RT}{F}\ln (P'_{H_2})^{1/2} + \frac{RT}{F}\ln\left(\frac{P_{BAR} - P'_{H_2O}}{760}\right)^{1/2} \quad [15]$$

where E refers to the potential difference between the palladium-hydrogen electrode and the normal hydrogen reference electrode. In this derivation, the gas-solid equilibrium data were used only as a means to calculate an expression for $\mu_H^{(m)}$. Gas-solid equilibrium does not exist in the experimental conditions employed in this study, or in other studies, except when the H/Pd ratio reaches 0.69, at a hydrogen pressure of 1 atm. The establishment of the steady potential relies upon the exchange of hydrogen atoms in the lattice with hydrogen ions in solution, according to Eq. [1]. The activity of the hydrogen in the palladium, as derived by the preceding thermodynamic route, was found to be a constant in the two phase region.

From Eq. [15] it is possible to derive equations predicting the temperature dependence of the plateau potential and the dependence of the potential on composition of the electrode in the α phase at a given temperature. These equations are developed in the following sections and are compared with experimental results.

Potential as a function of composition.—Figure 1 shows the potential *vs.* composition curve for a palladium-hydrogen electrode in the pure α region at 25°C. The potential is decidedly a function of the atom ratio, H/Pd, and approaches a value of + 52 to + 53 mv, as the limit of the α phase is reached. Previous methods of measuring the atom ratio were not capable of such accuracy, presumably because the lifetime of the α phase is so short when the palladium is charged by absorption of gaseous hydrogen. X-ray analysis (3) has established the presence of the α phase during the descent to +50 mv, but the bulk H/Pd ratio was not obtained by this method.

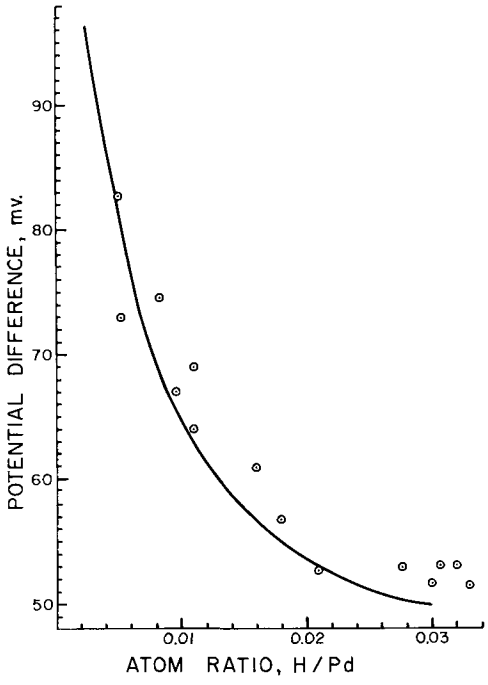

Fig. 1. Potential difference between a normal hydrogen electrode and a palladium-hydrogen electrode as a function of composition, to the limit of the α phase. ○, Experimental points; solid line predicted by Eq. [22] (temperature, 25°C).

The atom ratio was calculated as the bulk H/Pd ratio, with a propagated relative error of ±1.5%, at worst. The samples used in determining this segment of the curve were charged at a current density of ~ 60μ amp/cm^2 which should ensure a small concentration gradient between the surface and the interior of the metal.

Equation [15] can be expanded to show the potential as a function of composition if one knows how the pressure varies as a function of composition in the α phase. Tables of equilibrium hydrogen pressure as a function of composition at 30°C are given by Gillespie and Hall (13), but Moon (19) gives a phenomenological treatment which allows one to calculate the equilibrium pressure as a function of temperature and composition. These equations, which are valid only in the α phase region, are

$$\log\left(\frac{P^{1/2}}{r}\right) = -\log K + \beta r \quad [17]$$

$$\log K = -4.200 + 521.9/T \quad [18]$$

$$\beta = -926/(T - 215) \quad [19]$$

K is the equilibrium constant for the reaction

$$\tfrac{1}{2}H_2^{(g)} + \left(\frac{1}{r}\right)Pd^{(s)} = Pd_{(1/r)}\,H^{(s,\alpha)}$$

where P = equilibrium pressure of hydrogen, in mm Hg, and r = atom ratio, H/Pd. Converting to pressure in atmospheres yields

$$\log K_{atm} = -2.760 + 521.9/T \quad [20]$$

By substituting Eq. [19] and [20] into Eq. [17], an equation for the equilibrium pressure of hydrogen results. For $T = 298$°K

$$\log P^{1/2}{}_{atm} = 1.009 - 11.15\,r + \log r \quad [21]$$

Equation [21] may now be substituted into Eq. [15], the right-hand side of Eq. [21] replacing the term $\ln (P'_{H_2})^{1/2}$ in Eq. [15], after changing the base of the logarithm in the latter term. The resulting equation is

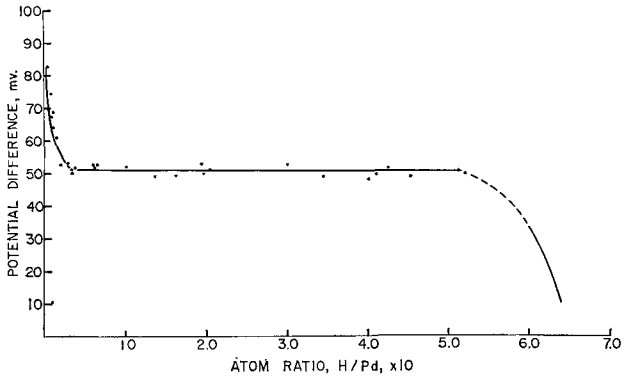

Fig. 2. Complete potential vs. composition curve for a palladium-hydrogen electrode (temperature, 25°C).

$$E = -0.05916(1.009\text{-}11.15\,r + \log r) + 0.5916 \log \left(\frac{P_{BAR} - P'_{H2O}}{760} \right)^{1/2} \quad [22]$$

for $T = 298°K$. In Fig. 1, the solid curve is the plot of Eq. [22] for values of r in the interval 0.0025 to 0.03.

The agreement between the observed values and those predicted by Eq. [22] is good, and provides substance to the thermodynamic arguments advanced. At the limit of the α phase Eq. [22] predicts a value of $E = +49.8$ mv. The value for E in the two-phase region calculated by using Eq. [15] is also + 49.8 mv. Thus, the two equations predict the same value of E at the point where the physical situation demands that their mathematical descriptions coincide.

The complete potential-composition curve is shown in Fig. 2. The potential was found to be constant in the two-phase region up to the concentration H/Pd = 0.52. The tolerance in the potential values was taken to be 50 ± 2 mv, in accord with previous workers (2, 3).

Equation [15] predicts a constant potential over the entire two phase ($\alpha + \beta$) region. At constant temperature, the only variable to appear in this equation is P'_{H_2}, which was found to be constant in the two-phase region by Gillespie and Hall (13). The pressure of hydrogen gas in equilibrium with a palladium-hydrogen alloy in the two-phase region at 25°C can be found from Eq. [23], due to Gillespie. Substitution of this value of the equilibrium pressure into Eq. [15] yields a value of + 49.8 mv as the potential in the two-phase region at 25°C.

For some experimental points beyond the ratio H/Pd = 0.4 it was necessary to anodize the electrodes to remove excess surface hydrogen. The anodization was done for convenience, since, if one is willing to wait long enough, the simultaneous process of inward diffusion of hydrogen, and diffusion of hydrogen into the electrolyte will result in a surface concentration which is very close to the bulk concentration. In order to achieve H/Pd ratios of 0.4 or greater, the current density was increased to 300 $\mu a/cm^2$.

To justify quantitatively the anodization technique, solutions for the diffusion of hydrogen in palladium were worked out. The boundary conditions contain the assumption that the anodization removed all the hydrogen from the metal to a radius consistent with the total number of anodic coulombs passed. A diffusion equation for the system, and the diffusion coefficient for hydrogen in palladium may be readily found (20). A solution of the equation for a typical case yielded the time necessary for the surface concentration to reach 99% of the bulk concentration to be of the order of magnitude of 10^{-1} sec. Thus, the anodization procedure can be justified on the grounds that the bulk H/Pd ratio establishes itself very rapidly at the surface after the cessation of anodic current.

The breaking point for the two phase limit was not determined, but points which lie in the pure β phase were found. In Fig. 2, the last point found in the two-phase region (H/Pd = 0.52) was joined by a smoothly descending curve (shown by the dotted line) with the three points found in the β phase only for the sake of continuity. It was found to be difficult to charge samples to a H/Pd ratio greater than 0.64 at the current densities employed. A probable explanation for this fact is that hydrogen in the metal is lost during the time interval between cessation of the cathodic current and analysis of the sample. The anodization technique was not used when studying the β phase potential behavior.

In these experiments the solution in which the palladium electrode was tested was constantly swept with nitrogen. There was effectively no means of preventing hydrogen dissolved in the palladium from establishing its equilibrium concentration in the electrolyte solution. This process manifested itself in a very slow rise in potential with time for electrodes that were in the β phase. Therefore, it is not necessary to invoke reasons for β phase instability in cathodically charged palladium hydrogen when no hydrogen is dissolved in the solution, since transport processes are sufficient to explain the loss of hydrogen.

The general conclusions drawn from the potential-composition data are that the potential is dependent upon the composition of the electrode in the pure α and pure β phase, and independent of composition in the $\alpha + \beta$ region. These conclusions agree with those of other workers, most recently Aben and Burger (3), and Flanagen and Lewis (2).

Potential as a function of temperature.—Figure 3 shows the temperature dependence of the cathodically charged palladium hydrogen electrodes. The experimental behavior is very close to being linear, with a slope of — 0.65 mv/°C. The data of Ratchford and Castellan (21) are included in Fig. 3. Their temperature dependence measurements were performed while the palladium was absorbing hydrogen from solution, and the temperature range studied was from 20° to 60°C. By use of their empirical equation $E = 0.06309 - 0.0005057(T\text{-}273.16)$ their values may be extended to 0°C.

It is evident that the slopes of the two different determinations do not agree. To test the possibility that electrode construction may have been responsible for this difference in slope, gas-phase absorption experiments in aqueous solution were carried out. Results

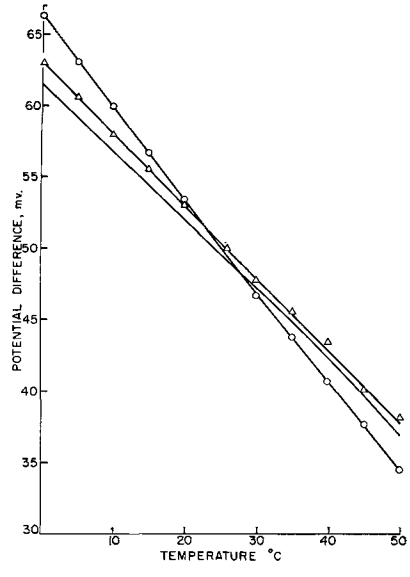

Fig. 3. Potential as a function of temperature for a palladium hydrogen electrode. ○, Experimental, electrolytically charged; △, data of Ratchford and Castellan; solid line predicted by Eq. [24].

are shown in Fig. 4. The slopes of the straight lines are in good agreement, and the potential values at any given temperature are within 1 mv of the predicted curve.

The temperature dependence of the potential of a two-phase palladium hydrogen electrode can be derived from Eq. [15]. Gillespie and Galstaun (14) give an equation which fits the two-phase equilibrium pressures for the palladium hydrogen system as a function of temperature.

$$\log P_{atm} = 4.6018 - 1877.82/T \qquad [23]$$

Substitution of this expression into Eq. [15] yields

$$E = -\frac{2.303\,RT}{2F}(4.6018 - 1877.82/T) + \frac{RT}{2F}\ln\left(\frac{P_{BAR} - P'_{H_2O}|}{760}\right) \qquad [24]$$

Inspection shows that this is a linear equation in T, with the exception of the term that involves the partial pressure of water.

Values calculated from Eq. [24] are plotted in Fig. 3 as a comparison with the various experiments. In the range $25° < T < 50°C$, the agreement between Eq. [24] and experiment is quite good for the case where palladium was absorbing hydrogen dissolved in solution. The agreement between Eq. [24] and the data of Ratchford and Castellan gets poorer as the temperature progresses to 0°C. According to Gillespie and Galstaun, the equation that gives the equilibrium pressure of hydrogen in the two-phase region is in error below 30°C. The error becomes larger as the temperature gets lower since their straight line approximates a curve in this region. The equilibrium pressure equation predicts 4.05 mm Hg for 0°C, and the observed equilibrium pressure was 3.56 mm Hg. If this experimentally observed pressure is substituted into Eq. [15]. the predicted value of E is + 63.14 mv. Ratchford and Castellan's empirical equation has + 63.09 mv as its 0°C value. The agreement here is excellent.

The thermodynamic arguments advanced have been remarkably successful in accounting for the temperature dependence of the palladium-hydrogen electrode while it is absorbing gaseous hydrogen. The agreement between theory and experiment is not quite as good for the case of cathodically charged palladium-hydrogen electrodes, although it is far from a failure. It is quite probable that the discrepancies between the two experimental situations are due to nonreversibility in the desorption process which must take place in order to have the cathodically charged electrodes establish a potential. Phenomena such as rift occlusion of hydrogen and hysteresis effects in the pressure *vs.* temperature relationship of the palladium-hydrogen alloy are possible sources of nonreversible behavior (22) which may alter the temperature dependence of the potential for cathodically charged electrodes. These phenomena would have a less pronounced effect for an electrode that is absorbing hydrogen from the gas phase.

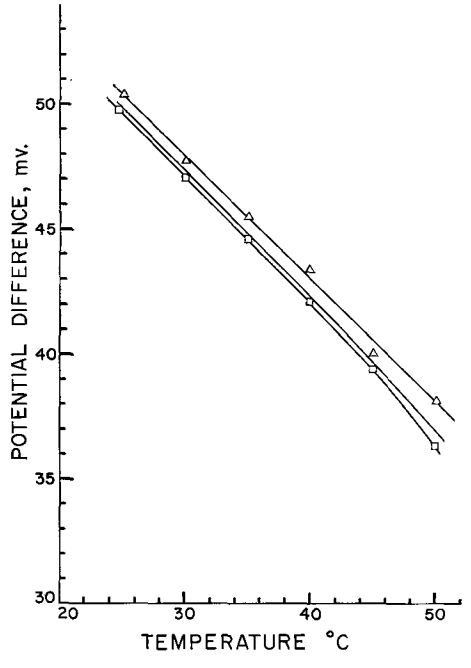

Fig. 4. Potential as a function of temperature for a palladium-hydrogen electrode while absorbing hydrogen from a solution. □, This study; △, data of Ratchford and Castellan; solid line predicted by Eq. [24].

No *p*H dependence could be found for two-phase palladium hydrogen electrodes when tested against a hydrogen electrode. Electrolytes that were tested were 2*N*, 1*N*, 0.1*N*, and 0.001*N* perchloric acid.

The Palladium-Hydrogen Reference Electrode

The preceding work was done with the object of developing a palladium-hydrogen reference electrode by electrochemical means. Other workers (5, 16) have made such an electrode by gas charging methods. It has been called the α-palladium reference electrode, since the +50 mv potential is characteristic of the concentration limit of the α phase. In practice, the "α-palladium" reference electrode actually has a composition in the two-phase region where the potential is essentially independent of the H/Pd ratio.

The electrode was constructed exactly the same way as those used for the temperature dependence measurements. Hydrogen was supplied to the palladium by constant current electrolysis of current density 75 μa/cm^2. These electrodes were palladized at a current density of 15 ma/cm^2 for 2 min, prior to charging with hydrogen.

If the electrodes displayed potentials lower than +50 mv after charging for a period of time necessary to give a H/Pd ratio of 0.5 (based on current-sorption efficiency of 60%), they were anodized according to the procedure described previously. Anodization, if necessary, re-established the +50 mv plateau potential, and the electrode was then inserted into a capillary sheath to minimize the loss of hydrogen by diffusion.

Such an electrode could be kept for periods of 24 hr in nitrogen swept solutions with only negligible changes in potential. For longer periods of time the potential was found to drift one or 2 mv but it could be restored to +50 mv by cathodization at the same current density required for charging.

Two disadvantages of the palladium hydrogen reference electrode as described here are:

1. Preparation: long electrolysis times are necessary due to such low currents.

2. Imprecision in the potential value. (Some workers have reported a value of +49.5 mv, and others a value of +50.4 mv.) For work that does not require such great accuracy, the potential may be taken as 50 ± 1 mv. It is also necessary to check the initial potential value against a normal hydrogen electrode, or some suitable reference electrode.

The prime advantage of this electrode is that it has the same *p*H response as a Pt/H_2 electrode, but may be used in hydrogen free solutions. There are several experimental situations where dissolved molecular hydrogen must be kept out of a test electrode compartment and elaborate methods and apparatus design are usually necessary to accomplish this. The use of a two-phase palladium-hydrogen electrode in a luggin capillary would eliminate the need of separating the reference electrode compartment from the test electrode compartment, and therefore greatly simplify cell designs.

Acknowledgment

This work was in part supported by the Directorate of Chemical Sciences, Air Force Office of Scientific Research, under Grant AFOSR-151-63. The authors also wish to thank The Electrochemical Society for its support in the form of the Electrochemical Society Summer Fellowship, (1964).

Manuscript received Jan. 19, 1965; revised manuscript received April 1, 1965.

Any discussion of this paper will appear in a Discussion Section to be published in the June 1966 JOURNAL.

REFERENCES

1. S. Schuldiner, G. Castellan, and J. P. Hoare, *J. Chem. Phys.*, **28**, 16 (1958).
2. T. B. Flanagen and F. A. Lewis, *Trans. Faraday Soc.*, **55**, 1409 (1959).
3. P. C. Aben and W. G. Burger, *ibid.*, **58**, 1989 (1962).
4. J. P. Hoare and S. Schuldiner, *J. Phys. Chem.*, **61**, 399(1957).
5. J. P. Hoare, *This Journal*, **110**, 245 (1963).
6. M. Fleischmann and H. Thirsk, *Trans. Faraday Soc.*, **51**, 71 (1955).
7. S. Schuldiner and J. P. Hoare, *Can. J. Chem.*, **37**, 228 (1959).
8. D. J. Ives and G. J. Janz, "Reference Electrodes," Academic Press, New York (1961).
9. J. P. Hoare, *J. Phys. Chem.*, **64**, 1780 (1960).
10. A. Frumkin and N. Aladjalova, *Acta Physicochem. URSS*, **19**, 1 (1944).
11. P. Nylen, *Z. Elektrochem.*, **43**, 915 (1937).
12. A. Frumkin, *Discussions Faraday Soc.*, **1**, 137 (1947).
13. L. J. Gillespie and P. Hall, *J. Am. Chem. Soc.*, **48**, 1209 (1926).
14. L. J. Gillespie and L. S. Galstaun, *ibid.*, **48**, 1209 (1926).
15. J. R. Lacher, *Roy Soc. London, Proc.*, **161**, 25 (1937).
16. J. P. Hoare, *Gen. Motors Eng. J.*, **9** [7], 14 (1962).
17. R. G. Bates, "Electrometric pH Determinations," John Wiley & Sons, Inc, New York (1954).
18. T. B. Flanagen and F. A. Lewis, *Trans. Faraday Soc.*, **56**, 363 (1960).
19. K. A. Moon, *J. Phys. Chem.*, **60**, 502 (1956).
20. W. Jost, "Diffusion," Academic Press, New York (1960).
21. R. J. Ratchford and G. W. Castellan, *J. Phys. Chem.*, **62**, 1123 (1958).
22. D. P. Smith, "Hydrogen in Metals," p. 95, University of Chicago Press, Chicago (1948).

Technical Notes

A Potentiometric Determination of Sodium in Amalgams

J. A. LeDuc, C. Lurie, and J. Kourilo

Electrochemical Research Section, Research and Development Department, M. W. Kellogg Company, New Market, New Jersey

The need for a rapid, accurate method for determining sodium concentration in a flowing amalgam stream was realized during a recent investigation of the ability of the sodium amalgam-oxygen fuel cell to recover power consumed during electrolysis of brine in mercury cells. A potentiometric method was decided on and involved measuring the potential between an amalgam half cell and a Hg/HgO reference cell

$$Na(Hg), Na^+ \,|\, NaOH(50\%) \,|\, HgO, Hg \qquad [1]$$

The relationship between cell potential and sodium concentration was determined at 20°C using a series of amalgam samples containing 0.01-0.53 w/o (weight per cent) sodium. The measuring system used is depicted in Fig. 1. The amalgam to be measured was admitted to the measuring cell H through the stopcock at G. After the potential across the system was read the amalgam was drained from the measuring cell H through a stopcock and another sample introduced through G. Reagent grade sodium metal and mercury purified in a laboratory-designed fractionating still were used. Sodium concentration was determined by reacting the amalgam with an aliquot of hot hydrochloric acid of known concentration and titrating the excess acid. The potentiometric measurements were made with a Gray Instrument Company Model E-3040-H potentiometer. The curve in Fig. 2 was fitted by the method of least squares. Analysis of the data reveals that the curve can be expressed as two linear relationships

$$\log [Na] = (E - 1.662)/0.105 \quad \text{for } E > 1.559v \qquad [2]$$

$$\log [Na] = (E - 1.624)/0.0636 \quad \text{for } E < 1.559v \qquad [3]$$

where E is the potential across [1]. The break in the Nernst equation plot is believed to be real within experimental uncertainty. Solution of Eq. [2] and [3] indicates that the sodium concentration at that point corresponds to $NaHg_{114}$.

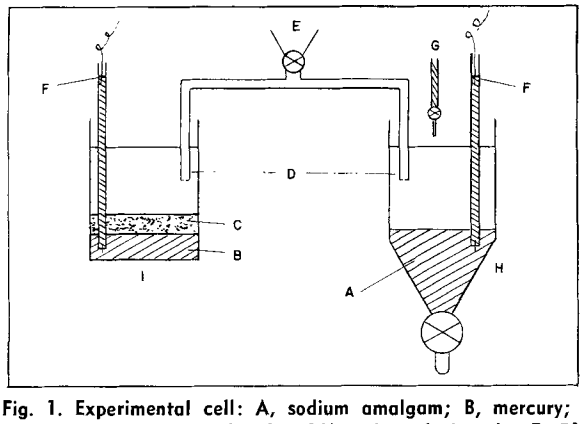

Fig. 1. Experimental cell: A, sodium amalgam; B, mercury; C, mercury and mercuric oxide; D, 50% sodium hydroxide; E, 50% sodium hydroxide salt bridge; F, leads to potentiometer; G, amalgam source; H, measuring cell, I, reference cell.

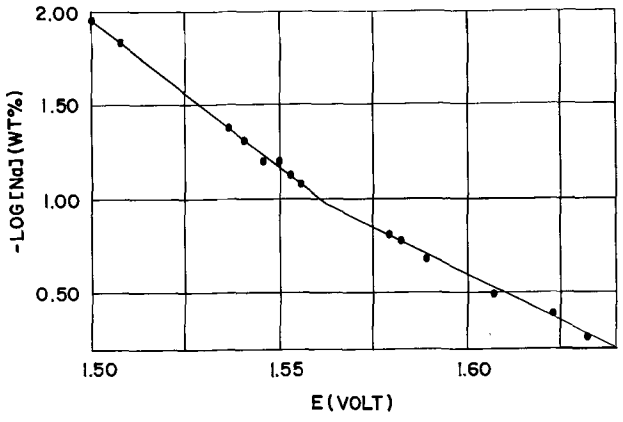

Fig. 2. Concentration-potential calibration curve

Measurements made with amalgams containing less than 0.01 w/o sodium were not reproducible. This uncertainty may be explained in terms of the reaction of the sodium in the amalgam with the electrolyte, *e.g.*, sodium corrosion. Sodium corrosion appears to be greater in more concentrated amalgams; however, the slope of the cell potential-sodium concentration curve near the origin must be considered. The rate at which the sodium corrosion decreases with decreasing sodium concentration is less than the rate at which the slope of the cell potential-sodium concentration curve increases. The Nernst equation shows that for very low sodium concentrations the slope is very steep and that

$$\left.\frac{dE}{d[\mathrm{Na}]}\right|_{\mathrm{Na}=0} = \infty$$

Sodium corrosion may be expressed as

$$\left.\frac{d[\mathrm{Na}]}{dt}\right|_{\mathrm{Na}=0} = 0$$

where t is time. For very low values of sodium concentration

$$\frac{d}{d[\mathrm{Na}]}E >> \frac{d}{d[\mathrm{Na}]}\frac{d[\mathrm{Na}]}{dt}$$

The conclusion is drawn that the effect of sodium corrosion on the cell potential is significant at very low sodium concentrations and that this technique is not suitable for determinations in that range. This method can be used for continuous evaluation of sodium concentration in flowing amalgam streams subject to the concentration limit indicated.

Manuscript received July 8, 1964.

Any discussion of this paper will appear in a Discussion Section to be published in the June 1966 JOURNAL.

Notes on the Chemical Polishing of Gallium Arsenide Surfaces

R. D. Packard

Honeywell Radiation Center, Boston, Massachusetts

In chemical etching and polishing of semiconductors, the surface undergoes a chemical change. Only those reactions which do not deposit insoluble impurities on the surface are generally useful. Such etches are usually aqueous solutions containing reagents which react with the semiconductor to form reaction products which are soluble. Occasionally, one reagent will serve the two purposes of reactant and solvent. Gaseous and molten salt etchants are also employed, but will not be considered here.

When compound semiconductors are chemically polished, a combination of etchants is generally necessary. Gallium arsenide is such a compound. Most of the commonly used etches contain either nitric acid or hydrogen peroxide as an oxidant for the arsenic. For polishing, HF or HCl is generally added, with or without extra water (1-5). Strong oxidizing agents act on arsenides to form a soluble arsenic acid, rather than an insoluble oxide as in the case of antimonides.

Gallium is rather reactive, being close to zinc and iron in the electromotive series, and is converted in acid solution to the soluble nitrate or fluoride. Sulfuric acid has been added as a complexing agent and to increase the viscosity of the etchant solution for chemical polishing (6). Nitric acid alone has been used; however, Kyser and Millea (7) show some disadvantages in this etch. Sullivan and Kolb (8) obtained highly polished surfaces in bromine-methanol solutions.

A brief discussion of etching solution viscosity is useful. A stagnant liquid film always exists immediately adjacent to the semiconductor, its thickness dependent on the degree of agitation of the solution. If the viscosity of the solution is increased, the diffusion rates of the reactant etch solution and product molecules across the film decrease since

$$\frac{dN}{d\theta} = -DA\frac{dC}{dX}$$

where N is moles diffused; θ, is time, sec; D, diffusion coefficient of the species concerned in the media, cm^2/sec; A, area through which diffusion occurs, cm^2; C, concentration, $moles/cm^3$; and, X, distance in the direction of diffusion, cm. Rearranging, $D = \dfrac{-dN/d\theta}{A(dC/dX)}$, the negative sign indicating that diffusion occurs in the direction of decreasing concentration. Increasing the solution viscosity increases the shear resistance which the diffusing component must overcome in order to travel through the film and thus decreases $dN/d\theta$ and the diffusion coefficient. The viscosity of the liquid is an index of its resistance to flow and diffusion.

High-viscosity etchants are preferred for chemical polishing because the reaction with the semiconductor tends to be concentrated at the high points (projections) on the surface. The etchant forms stagnant pools in the low regions (valleys) where in-diffusion of reactant acid molecules and out-diffusion of etch products occur very slowly because of the small concentration gradient due to the thick stagnant layer. Thus, the reaction rate increases at high points and decreases at low points, which eventually results in a smooth surface. High etch solution viscosity drops the etch rate in valleys to nearly zero.

At 70°F, the viscosity of 60% aqueous H_2SO_4 is 6 cp (centipoises), while that of 98% H_2SO_4 is 22 cp (9). By contrast, pure glycerine has a viscosity of 1375 cp at 70°F (10). As glycerine is added to an aqueous etching solution, the solution viscosity may rise ultimately to over 1000 cp at room temperature. The etch-acid concentrations simultaneously decrease, creating a very slow etchant.

Experimental work reported here consists of etching GaAs samples in various solutions of aqueous HCl and HNO_3 and glycerine. The acids were "Baker analyzed"

analytical reagents, 38% HCl and 70% HNO_3, respectively.[1]

The most satisfactory polishing etches were composed of approximately 1:1 volumetric mixtures of HCl and HNO_3, with relatively large amounts of glycerine.

Kyser and Millea (7) found that nitric acid etching of GaAs resulted, under certain circumstances, in a precipitation of foreign material on the GaAs surface. These precipitates were identified as As_2O_3 by x-ray diffraction and were explained as follows. Nitric acid dissolves the GaAs by oxidizing the As and forming a soluble Ga compound. As_2O_3 is not soluble in concentrated HNO_3 but is soluble in water to the extent of 2g per 1000 ml at room temperature. Thus, diluted HNO_3 is necessary to keep the As_2O_3 in solution. Excess glycerine, therefore, serves two purposes: that of increasing the viscosity of the etching solution, and keeping the nitric acid concentration sufficiently low so that the arsenic trioxide dissolves in the etchant rather than precipitates on the semiconductor surface.

Specifically, a mixture of 5 parts HCl, 5 parts HNO_3, and 40 parts glycerine, by volume, gave a highly polished, bright GaAs surface with an etch rate of 0.37 mg/cm^2/min. It is preferable to suspend the GaAs in the etchant solution and to agitate just enough to avoid retention of bubbles on the semiconductor surface. The Monsanto GaAs used in the experimental work had a {111} crystal orientation. It was 0.13 ohm cm n-type.

Since gallium chloride is soluble in benzene, an etching solution consisting of small volumes of HCl and HNO_3, benzene, and glycol or alcohol to make the components miscible is also effective as a chemical polishing agent. The highly polar HCl, however, is limited in solubility in the higher molecular weight glycols/alcohols, so care must be exercised to keep the mixture homogenous throughout the etching cycle. Glycol, in contrast with an alcohol, increases the etchant viscosity.

To summarize, etching solutions possessing higher viscosities than water are useful to produce highly polished GaAs surfaces. They function by slowing the rate of material removal, particularly in surface valleys, which exist only on nonflat surfaces, allowing microscopic surface projections to be brought down level with a minimal total semiconductor loss.

[1] The acids used for etching were low in copper content (0.0003 and 0.0001%, respectively) to avoid thermal conversion in GaAs during subsequent heat treatment.

Manuscript received March 23, 1965.

Any discussion of this paper will appear in a Discussion Section to be published in the June 1966 JOURNAL.

REFERENCES

1. F. A. Cunnell, J. T. Edmonds, and W. R. Harding, *Solid-State Electron.*, **1**, 97 (1960).
2. J. G. Harper and M. S. Astor, Electrochem. Soc. Electronics Div. Extended Abstracts, **8**, 161 (1959).
3. J. L. Richards, *J. Appl. Phys.*, **31**, 600 (1960).
4. J. L. Richards and A. J. Crocker, *ibid.*, **31**, 611 (1960).
5. H. A. Schell, *Z. Metallk.*, **48**, 158 (1957).
6. M. V. Sullivan and L. A. Pompliano, *This Journal*, **108**, 60C (1961).
7. D. F. Kyser and M. F. Millea, *ibid.*, **111**, 1102 (1964).
8. M. V. Sullivan and G. A. Kolb, *ibid.*, **110**, 585 (1963).
9. "Chemical Engineer's Handbook," J. H. Perry, Editor, pp. 372-3, 3rd ed., McGraw-Hill Book Co., New York (1950).
10. "Handbook of Chemistry and Physics," C. D. Hodgman, Editor-in-chief, p. 2025, Chemical Rubber Publishing Co., Cleveland (1955).

Etching and Crystal Growth in the GaAs-Sn System

M. F. Millea and W. R. Wilcox

Electronics Research Laboratory, Aerospace Corporation, El Segundo, California

The absence of a center of symmetry in the crystal structure of III-V compounds has been found to result in a large number of polarity effects (1). Minamoto and Malafi (2) have investigated the significance of crystallographic polarity on the alloy etching of GaSb by Sn. They found that the p-n junction formed by alloying on Sb{111} faces was planar, while the alloy junction on Ga{111} faces was curved. Better tunnel diodes were obtained when the alloying was performed on the Sb{111} face. Grimmeiss and Scholz (3) observed superior GaP diodes when Sn was alloyed to the P{111} face. The p-n junction obtained by alloying Sn to the P{111} of GaP was planar and parallel to the crystal surface.

The purpose of the present investigation is to develop an understanding of the effect of polarity on alloy etching and subsequent regrowth of GaAs by Sn. Because of similar polarity effects reported on the GaSb-Sn and GaP-Sn systems, one might expect the alloy etching and regrowth of all III-V compounds with Sn to be similar.

Experimental Procedure

Three techniques were used in this investigation. Most of our experiments were performed by alloying small cubes of Sn to mechanically polished As{111} and Ga{111} surfaces under an argon atmosphere. Various heating and cooling rates were used. The metallic region after alloying was chemically removed with dilute HCl and the morphology of the surface examined with an optical microscope.

The relative dissolution rates of the Ga{111} and As{111} were determined by dissolving both surfaces of a {111} wafer in pure Sn. In this experiment the GaAs wafer was placed in 10g of Sn at slightly above its melting point. The wafer was rotated at 1 cps with the direction of rotation being reversed every 30 sec and the bath was heated at 3°C/min. At 500°C the GaAs wafer was withdrawn from the molten Sn, and the metal adhering to the wafer was chemically removed with dilute HCl. The Ga{111} and As{111} surfaces were examined microscopically and the relative rates of dissolution observed.

The relative regrowth rates on the Ga{111} and As{111} faces were measured as follows. Ten grams of Sn were saturated with GaAs in a quartz tube. The solution was quenched, and a p-type {111}GaAs wafer and then a quartz rod were inserted into the tube. The solution was heated to slightly above its melting point, the GaAs wafer was submerged in it by the quartz rod, and the quartz tube was sealed off under vacuum. This ampoule was then heated to 600°C in an electric furnace and cooled to room temperature at 2°C/hr while being held in a vertical position. The GaAs was removed from the Sn, and the relative rates of regrowth on the Ga{111} and As{111} surfaces were determined by angle-lapping and staining.

Experimental Results

Dissolution.—When small cubes of Sn were alloyed on the As{111} of GaAs under a rapid-heating, rapid-

cooling cycle,[1] a planar alloy interface was observed. The same morphology was observed when Sn was alloyed to As{111} under a slow-heating, rapid-cooling cycle. This was identical to observation by others (2, 3). They reported that, when Sn is alloyed to the (111) face of p-type GaSb and GaP, a planar p-n junction results.

The morphology of the alloy interface on the Ga{111} is dependent on the heating rate. When small cubes of Sn were alloyed to the Ga{111} under rapid-heating, rapid-cooling conditions, a rounded noncrystallographic alloy interface was formed. This observation is similar to that of Minamoto and Malafi (2) on the alloy interface on the Ga{111} of GaSb. When Sn is alloyed to the Ga{111} under slow-heating, rapid-cooling conditions, triangular alloy pits were observed, as shown in Fig. 1a. The alloyed Ga{111} surface shown in Fig. 1a was etched for 5 min in 1 part HNO_3, 2 parts HgO to reveal dislocations (4). The result is reproduced in Fig. 1b. As can be seen in this microphotograph, a chemical-etch pit occurred at the center of each alloy-etch pit.

The relative dissolution rates of the As{111} and Ga{111} were determined by the second experimental procedure described in Experimental Procedure. The thickness of the dissolved region on the As{111} was 50×10^{-4} cm, while on the Ga{111} the thickness was 15×10^{-4} cm, except in the alloy etch pits. The distance from the original surface to the bottom of the alloy etch pits on the Ga{111} was approximately 50×10^{-4} cm. This experiment indicates that the dissolution rate of the As{111} is greater than that of the Ga{111}.

Regrowth.—The regrowth of GaAs from a Sn-GaAs solution also shows a polarity effect. When small cubes of Sn were alloyed to the Ga{111} under a rapid-heating, slow-cooling cycle, the interface reproduced in Fig. 2a was observed. Slow cooling rates were used to promote regrowth on the GaAs wafer. The regrowth on the As{111} alloyed under similar conditions is illustrated in Fig. 2b. It can be seen in Fig. 2b that the regrowth on the As{111} proceeds in a lateral manner starting from the sides of the dissolved depression. Both lateral and perpendicular regrowth are observed on the Ga{111}.

The As{111} regrowth morphology illustrated in Fig. 2b is similar to the dissolution morphology of the As{111}.

The regrowth rates were determined with the third experimental procedure described in the preceding section. In this experiment the starting GaAs wafer

[1] The rapid cooling rate served to avoid regrowth on the GaAs wafer.

Fig. 1a. Photomicrograph of pits formed on Ga {111} surfaces of GaAs during dissolution by Sn under conditions of slow heating. Wafer quenched to prevent regrowth.

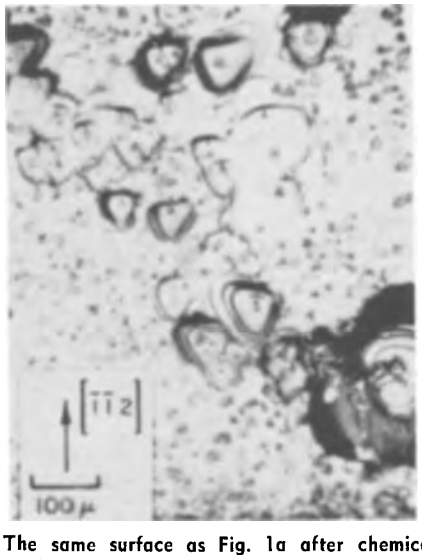

Fig. 1b. The same surface as Fig. 1a after chemical etching to produce dislocation etch pits. Note coincidence of some of these with Sn pits.

Fig. 2a. Photomicrograph of regrowth pyramids on Ga {111} surface of GaAs in Sn by slow cooling. Edge of dissolution hole in upper left hand corner showing lateral regrowth.

Fig. 2b. Photomicrograph of lateral regrowth from undissolved islands on As {111} surface.

was p-type so that the thickness of the regrowth layer (n-type) could be measured by conventional angle-lapping and staining techniques. The GaAs was submerged in the Sn solution to minimize lateral regrowth. If the specimen were not submerged, the regrowth on the As{111} proceeded in a lateral manner starting from the solid-liquid-vapor interface. It was determined from this experiment that the n-type region on the Ga{111} was twice as thick as on the As{111}. Several large growth hillocks were observed on the As{111}.

Discussion

The etching process in which a small mass of Sn is alloyed to GaAs is fundamentally identical to internal dissolution experiments (5, 6) and to the formation of "negative crystals" (7). In those experiments a cavity in a crystal is filled with solvent, and dissolution is permitted to occur. If the dissolution proceeds slowly, the shape of the cavity becomes faceted and approaches the equilibrium shape identical to that expected for the ordinary slow convex crystal growth of the same material in the same solution. The internal dissolution experiments and the present alloying experiments possess the common feature of increasing crystal surface area with time, in contrast to ordinary external (convex) dissolution in which the surface continually decreases.

Therefore our result that the morphology of the As{111} alloy interface is independent of heating rate indicates that the As{111} is a singular plane at equilibrium. That is, the prime determinant of the morphology of the As{111} alloy interface is probably the surface energy *vs.* orientation function, As{111} being located at a cusped minimum (8). The macroscopic morphology of the Ga{111} alloy interface indicates that the Ga{111} is not located at a cusp on the Wulff plot, *i.e.*, it is diffuse. Crystal growth experiments using a variety of techniques showed the same results and so tend to support these conclusions (9, 11).

The different rates of dissolution and regrowth on the As{111} and Ga{111} can be explained by considering the rate-controlling step in dissolution and growth. Experimentally it has been observed that the dissolution rate of the As{111} is faster than the dissolution rate of the Ga{111}. On the other hand, the rate of regrowth perpendicular to the Ga{111} is greater than the regrowth perpendicular to the As{111}. It should be noted that the Ga{111} is also reported to grow faster than the As{111} in crystal growth from the melt (9-11) and from the vapor (12-15). In the case of growth perpendicular to the {111}, the rate-limiting step is the addition of atoms of opposite type from those triply-bonded to the face (1), *i.e.*, Ga to As(111) and As to Ga(111). The rate-limiting step in dissolution would be the removal of the triply-bonded atom, *i.e.*, arsenic from As{111} and gallium from Ga{111}. Arsenic would be expected to add or dissolve more easily than gallium since arsenic is present in solution predominately as molecules (16-18) and gallium is present only as atoms. Hence an As_4 molecule could easily deposit on the Ga{111} surface, as suggested by Pizzarello for epitaxial vapor growth (19). In dissolution, As_4 molecules could be removed from the As{111}, or groups of arsenic atoms in solution could combine with an arsenic atom in the crystal surface to aid in its removal. One could therefore expect the As{111} dissolution rate to be greater than the Ga{111} dissolution rate and the Ga{111} perpendicular regrowth rate to be greater than the corresponding As{111} rate. Similar results would be expected for other III-V compounds containing P or Sb, since these atoms also are associated in solution and in the vapor (16, 17).

The alloy-etch pits observed on the Ga{111} during slow alloy etching (Fig. 1) are believed to be due to dislocations. This indicates, in agreement with the preceding paragraphs, that the gallium surface is attacked slowly and that a particular type or array of dislocations allows dissolution to proceed more rapidly in their vicinity. Higher over-all dissolution rates produce no alloy-etch pits, as would be expected.

Acknowledgments

The authors wish to thank A. B. Chase for valuable discussions, E. L. Nealy, M. M. Edgren, and L. D. Fullmer assisted in several of the experiments.

Manuscript received Jan. 4, 1965; revised manuscript received April 12, 1965. This work was supported by the U. S. Air Force under Contract No. AF04(695)-469.

Any discussion of this paper will appear in a Discussion Section to be published in the June 1966 JOURNAL.

REFERENCES

1. R. C. Sangster, "Compound Semiconductors," Vol. 1, Chap. 28, Reinhold Publishing Corp., New York (1962).
2. M. T. Minamoto and H. T. Malafi, *J. Appl. Phys.*, **34**, 1876 (1963).
3. H. G. Grimmeiss and H. Scholz, *Physics Letters*, **8**, 233 (1964).
4. M. S. Abrahams and L. Ekstrom, "Properties of Elemental and Compound Semiconductors," p. 225, Interscience Publishers, Inc., New York (1960).
5. H. E. Buckley, "Crystal Growth," p. 305, John Wiley & Sons, Inc., New York (1951).
6. R. Gross, F. Koref, and K. Moers, *Z. Physik*, **22**, 317 (1924); *C. A.*, **18**, 2093 (1924).
7. E. J. Gubelin, "Inclusions as a Means of Gemstone Indentification," Gemological Institute of America (1953).
8. N. Cabrera and R. V. Coleman, "The Art and Science of Growing Crystals," Ch. 1, John Wiley & Sons, Inc., New York (1963).
9. A. Steineman and V. Zimmerli, *Solid State Electr.*, **6**, 597 (1963).
10. S. G. Ellis, *J. Appl. Phys.*, **30**, 947 (1959).
11. K. F. Hulme and J. B. Mullin, *Solid State Electr.*, **5**, 211 (1962).
12. A. J. Crocker, *J. Appl. Phys.*, **33**, 2840 (1962).
13. N. Goldsmith and W. Oshinsky, *R.C.A. Rev.*, **28**, 546 (1963).
14. San-Mei Ku, *This Journal*, **110**, 992 (1963).
15. T. Okada, *Japan. J. Appl. Phys.*, **2**, 206 (1963).
16. D. Richman, *J. Phys. Chem. Solids*, **24**, 1131 (1963).
17. K. Weisner, "Compound Semiconductors," Vol. 1, p. 471, Reinhold Publishing Corp., New York (1962).
18. W. A. Latimer and J. H. Hildebrand, "Reference Book of Inorganic Chemistry," pp. 211, 213, The Macmillan Co., New York (1940).
19. F. A. Pizzarello, *This Journal*, **110**, 1059 (1963).

Three-Point Probe Calibration for GaAs

M. H. Norwood[1]

Texas Instruments Incorporated, Dallas, Texas

The three-point probe is a useful and necessary instrument for determining properties of p on p+ or n on n+ layers of semiconductor materials. Brownson (1) described the technique and showed calibration curves for breakdown voltage, V_B, as a function of resistivity for n-type silicon. Dobbs and Kovacs (2) also show details of equipment and calibration curves for silicon. Gardner, Hallenback, and Schumann (3) compared the performance of the three-point probe with the spreading resistance technique and the control slice method and concluded that the latter two were inferior to the three-point method.

This note describes similar data for both p-type and n-type GaAs for free carrier concentrations between 10^{15} cm^{-3} and 10^{19} cm^{-3}. This quantity is more closely related to breakdown voltage than the resistivity when mobility varies from sample to sample. Actually, breakdown depends more fundamentally on the difference between donor and acceptor concentrations. If shallow levels are assumed, the free carrier concentrations are a measure of this difference.

The probe tip used in this work was ground to a 30° angle from a ⅛ in. diameter tungsten carbide rod. A diamond wheel was used for rough grinding, and the tip was polished to shape on a glass plate with a fine grinding compound by rotating the rod in a ¼ in. hand drill. This tip has been in use more than a year and more than 30,000 breakdown measurements. Tungsten wire tips are not nearly so durable. The radius of the tip is 9 mils, and the probe force is about 200 dynes. This force is reproduced by using an ohmmeter to determine first contact, then compressing a spring of known compliance a known distance.

A high current pulse generator with a 60 cycle repetition rate and a 5% duty cycle was used rather than an a-c source for biasing the point diode in order to avoid heating effects. Breakdown is observed from the voltage-time display on the scope instead of the I-V curve. Pulse shape is not a critical factor.

Conventional six-contact Hall bar samples were used as calibration standards. Relatively homogeneous bars were chosen by comparing the two longitudinal resistance values and the two transverse Hall voltages. If the two comparable measurements differed by more than 10%, the bar was rejected. All breakdown measurements were performed in the rectangular area between the side contacts of the Hall bar. The surfaces were etched to a smooth finish.

Figure 1 shows the values of V_B as a function of free carrier concentration for 5 p-type and 17 n-type samples. The error bars show the range (considerably larger than the standard deviation) of 10 breakdown measurements, and the dots are average values. To some extent, the range correlates with degree of inhomogeneity, indicating that the probe is somewhat more repeatable than it first appears. Profiles of angle lapped epitaxial layers and bulk samples have been made with very fine increments (10μ), and these indicate considerable inhomogeneity within small areas. Therefore, part of the scatter in the data is attributable to the samples rather than to the instrument.

Occasional highly compensated samples do not fit the data pattern, possibly because of the more complicated dependence of free carrier concentration on donor and acceptor concentrations with the presence of appreciable numbers of deep levels. The data shown are therefore not representative of all GaAs samples, but have been useful and reliable in most cases. For epitaxial layers, apparent differences between Hall and three-point probe measurements of carrier concentration have been explained by profiling the angle-lapped incline. In some cases the carrier concentration varies enough through the layer to cause considerable differences between a surface measurement and an averaged bulk measurement, such as the Hall technique.

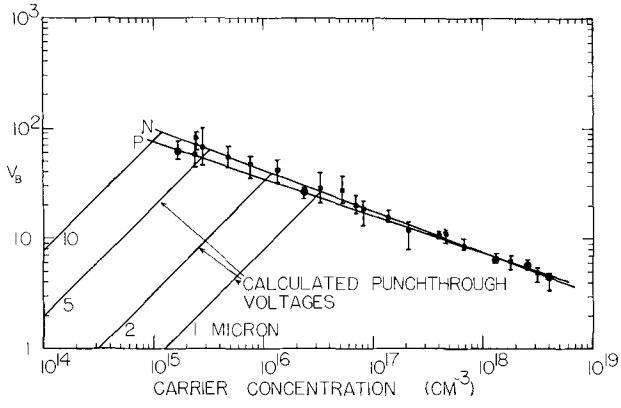

Fig. 1. Values of point contact breakdown voltage as a function of free carrier concentration for p- and n-type samples of GaAs; ■, n-type; ●, p-type.

The p-type and n-type data have been fitted by a least squares line. The results are

$$V_{Bn} = 100\ (n/10^{15})^{-0.372}$$

$$V_{Bp} = 75\ (p/10^{15})^{-0.338}$$

The exponents are smaller than for silicon (1) or for GaAs p-n junctions (4, 5). This may indicate that breakdown mechanisms other than avalanche are occurring. No attempt is made to explain these smaller exponents.

Figure 1 also shows calculated curves for voltages at which the depletion region thickness is equal to layer thickness. This effect, called "punchthrough," was described by Brownson (1). In the present work, most layers were too thick or highly doped to observe this alternate phenomenon, so none were observed.

Manuscript received Nov. 6, 1964; revised manuscript received April 12, 1965.

Any discussion of this paper will appear in a Discussion Section to be published in the June 1966 JOURNAL.

REFERENCES

1. J. Brownson, *This Journal*, **111**, 919 (1964).
2. P. J. H. Dobbs and F. S. Kovacs, *Solid State Technol.*, **7**, 8 (1964).
3. E. E. Gardner, J. F. Hallenback, Jr., and P. A. Schumann, Jr., *Solid State Electronics*, **6**, 311 (1963).
4. H. Kressel and N. Goldsmith, *RCA Review*, **24**, 182 (1963).
5. H. Kressel, A. Blicher, and L. H. Gibbons, Jr., *Proc. IRE*, **50**, 2493 (1962).

[1] Present address: National Engineering Science Company, Pasadena, California.

Hall Mobilities in Heavily Doped N-Type Gallium Arsenide

Forrest V. Williams

Monsanto Company, Saint Louis, Missouri

The amphoteric nature of the group IV elements as impurities in the III-V compounds has been fairly well documented. Germanium and silicon in gallium arsenide (1-5) and tin in gallium phosphide (6) have been studied in detail. As expected, the group IV element may substitute on either a group III lattice site or a group V lattice site and behave as a donor or an acceptor, respectively. The distribution of a given group IV element between the two sites in a III-V compound has been treated thermodynamically by Scott and Fredericks (7). It was concluded that covalent bond energies, strain energies, and equilibrium vapor pressures of the elements of the III-V compound are the chief factors determining the distribution.

It might be anticipated that the group VI elements, such as selenium and tellurium, would behave as normal donors in the III-V compounds. In this case, a donor level would be introduced for each group VI atom which is incorporated into the III-V lattice at a group V site. Actually, the experimental evidence which has been obtained suggests that the behavior of group VI elements in III-V compounds is complex, especially at high dopant concentrations. The behavior of selenium in Bridgman grown crystals of GaAs has been studied by Vieland and Kudman (8) By comparing the results of chemical analyses and Hall coefficient measurements, these workers showed that above a concentration of about 4×10^{18} at./cm^3 a considerable fraction of the Se dissolved in the crystal must be either un-ionized or electrically compensated. By comparison of the mobilities of the heavily selenium doped crystals with the mobilities of silicon doped crystals (compensated), it was concluded that compensation was not a factor and that selenium introduced no acceptor levels in GaAs. Their data were interpreted as evidence for a neutral gallium vacancy-selenium complex, $[V_{Ga}Se_3]$.

Electrical measurements on GaAs doped with selenium and with tellurium have been reported recently by Black and Lublin (9). These workers, in agreement with Vieland and Kudman, noted free carrier concentrations for both selenium and tellurium far below those expected from the chemically analyzed doping levels. In addition, Trumbore and co-workers (10) concluded that selenium is either compensated or electrically neutral in heavily doped crystals of solution grown GaP.

Two important points are evident in the results reported by Black and Lublin (who reported that their results were in agreement with those of Vieland and Kudman). First, the mobilities of their heavily doped selenium crystals of GaAs are not in complete agreement with the values reported by Vieland and Kudman for crystals with the same net carrier concentration. Second, there was a significant difference in the mobilities of single crystals doped to the same level with selenium and with tellurium, although Black and Lublin did not point out this difference.

It is the purpose of this communication to report some electrical properties which have been measured on epitaxial layers of GaAs which have been heavily doped with selenium, tellurium, and tin.

The preparative technique by which these epitaxial layers were grown has been described in detail (11). Briefly, the method utilizes the vapor transport of GaAs with HCl in a flow system. The reactions which are involved are

$$GaAs + HCl \rightleftarrows GaCl + \tfrac{1}{4}As_4 + \tfrac{1}{2}H_2$$

$$3GaCl + \tfrac{1}{2}As_4 \rightleftarrows 2GaAs + GaCl_3$$

The epitaxial layers were doped by the use of a separate reservoir of the doping element in the vapor transport system. As has been reported earlier (12), it is possible to obtain single crystal epitaxial layers of GaAs with net carrier concentrations greater than 1×10^{19} at./cm^3. All of the layers were grown on high resistivity ($>10^3$ ohm-cm) substrate oriented on the <100> plane. Owing to the insulating nature of the substrate, resistivities and Hall coefficients of the epitaxial layers could be measured directly. All measurements were made at room temperature. The Hall effect was measured at magnetic field strengths of 5000G, and the free-carrier concentration was calculated from the relation $n = 1/R_H e$. Owing to the small quantity of epitaxial material (most layers were on the order of 15-25μ thick) on the substrate, it was not possible to determine the total concentration of dopant in the epitaxial layers.

The results of this investigation, along with some pertinent data from the work of Vieland and Kudman (8) and Black and Lublin (9), are shown in Table I. The data reported in this work and the data reported by Vieland and Kudman for selenium doped crystals are plotted in Fig. 1.

Several points are evident from these tabulated results. It will be observed that the mobility values obtained in this investigation for tin doped crystals of GaAs are about 40% lower than the mobility values of crystals of GaAs doped with tellurium to the same net carrier concentration. This would indicate that a considerable portion of the tin substitutes for arsenic when in solid solution in GaAs. Trumbore and co-workers (6) have reported that about 25% of the tin in solid solution in GaP is substituted at the phosphorus lattice sites. Considering the tetrahedral covalent radii of the phosphorus and arsenic, a higher distribution of tin on group V lattice sites might be expected in the case of GaAs.

The mobility values obtained in this investigation for the tellurium doped crystals of GaAs are in excellent agreement with the single published value of Black and Lublin for crystals doped to the same carrier concentration. However, the mobility values obtained both in this study and by Black and Lublin for the selenium doped crystals are slightly lower than the values reported by Vieland and Kudman.

Table I. The free carrier concentration η and Hall mobility μ of GaAs doped with Te, Se, and Sn

$\eta = \frac{1}{R_H e}$ (cm^{-3})	μ(cm^2/v-sec) Te	Se	Sn
1.9×10^{19}	830	680	—
1.7×10^{19}	1070	670	—
1.5×10^{19}	1090	620	—
1.3×10^{19}	1210	710	—
1.1×10^{19}	1270	730	860
9.7×10^{18}	1370	—	820
9.6×10^{18}	1360	—	840
9.5×10^{18}	—	950*	—
9.3×10^{18}	—	1240**	810
9.0×10^{18}	1380	—	—
8.9×10^{18}	—	790	890
8.7×10^{18}	1440	—	810
8.5×10^{18}	1300*	—	—
8.4×10^{18}	1460	—	960
7.9×10^{18}	—	1090	890
4.0×10^{18}	1380	1380	—
3.0×10^{18}	1570	—	1490
1.7×10^{18}	2080	1720	—

* Black and Lublin, ref. (9).
** Vieland and Kudman, ref. (8).

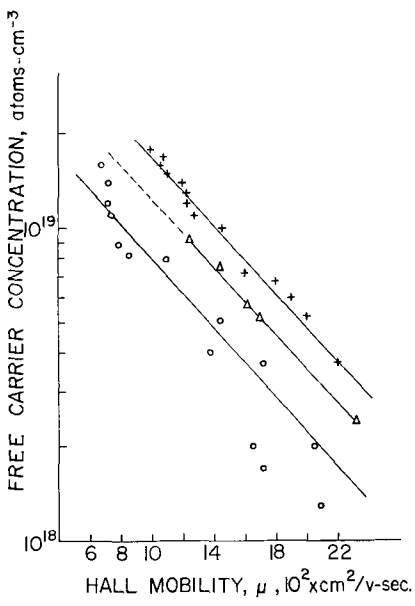

Fig. 1. Data for selenium and tellurium doped crystals: △, selenium doped Bridgmann crystals (5); ○, selenium doped epitaxial crystals, this work; +, tellurium doped epitaxial crystals, this work.

The interesting feature of the results obtained in this study, and confirmed by the data of Black and Lublin, is the difference in mobility between tellurium and selenium doped crystals of GaAs. The same effect is noted, to a greater degree, in the mobilities of Czochralski single crystals doped with sulfur and with tellurium. These mobility differences tend to disappear at doping levels below about 10^{18} at./cc The same phenomenon has been observed for selenium and tellurium dissolved in gallium antimonide (13). It was concluded that the character of the donor impurities, in addition to the two band model for GaSb, plays an important role in determining the electrical properties of n-type GaSb. The Hall mobilities of both germanium (14) and silicon (15) doped with phosphorus, arsenic, and antimony have been reported. As in the case of both GaAs and GaSb, the highest mobility values were obtained with the donor impurity with the largest atomic weight. However, the mobility values of phosphorus doped silicon and germanium are intermediate between those of arsenic and antimony doped samples. This result may seem surprising since the donor impurities with the smallest atomic weights have tetrahedral covalent radii which more nearly match the radii of the group IV or group V lattice site. It may be significant that the order of the effect in GaAs appears to be S > Se > Te.

No detailed explanations have been given for any of these observed differences in the electrical behavior of donor impurities at high concentrations. Holonyak *et al.* (15) have discussed the effect for the case of Ge in terms of modification of the conduction band, the degree of modification depending on the impurity involved. Strauss (13) speculated that the effect, in GaSb, may be due to impurity conduction. Regardless of the interpretation, evidence is accumulating that specification of the kind of impurity is necessary when discussing the electrical properties of heavily doped semiconductors.

Acknowledgment

The author wishes to thank Dr. M. A. Gilleo of this laboratory for many helpful discussions.

Manuscript received Dec. 16, 1964; revised manuscript received May 3, 1965.

Any discussion of this paper will appear in a Discussion Section to be published in the June 1966 JOURNAL.

REFERENCES

1. C. Kolm, S. A. Kulin, and B. L. Averbach, *Phys. Rev.*, **108**, 965 (1957).
2. J. M. Whelan, J. D. Struthers, and J. A. Ditzenberger, *Proceedings of the International Conference on Semiconductor Physics, Prague, 1960*, p. 943; also "Properties of Elemental and Compound Semiconductors," p. 146, H. C. Gatos Editor, Interscience Publishers, Inc., New York (1960).
3. J. O. McCladin and R. Harada, *J. Appl. Phys.*, **31**, 2065 (1960).
4. R. Solomon, R. Newman, and N. R. Kyle, *This Journal*, **108**, 716 (1961).
5. L. J. Vieland and T. Seidel, *J. Appl. Phys.*, **33**, 2414 (1962).
6. F. A. Trumbore, M. Kowalchik, H. G. White, R. A. Logan, and C. L. Luke, *This Journal*, **111**, 748 (1964).
7. A. B. Scott and W. J. Fredericks, *J. Phys. Soc. Japan*, **18**, Supplement II, 136 (1963).
8. L. J. Vieland and I. Kudman, *J. Phys. Chem. Solids*, **24**, 437 (1963).
9. J. Black and P. Lublin, *J. Appl. Phys.*, **35**, 2462 (1964).
10. F. A. Trumbore, H. G. White, M. Kowalchik, R. A. Logan, and C. L. Luke, Electronics Division Abstracts, Electrochemical Society, Vol. 13, No. 2, p. 62 (1964).
11. R. L. Newman and N. Goldsmith, *This Journal*, **108**, 1127 (1961); F. V. Williams and R. A. Ruehrwein, *ibid.*, **108**, 177C (1961).
12. F. V. Williams, *Solid State Electronics*, **7**, 833 (1964).
13. A. J. Strauss, *Phys. Rev.*, **121**, 1087 (1961).
14. Y. Furukawa, *J. Phys. Soc. Japan*, **16**, 687 (1961); *ibid.*, **15**, 730 (1960); W. G. Spitzer, F. A. Trumbore, and R. A. Logan, *J. Appl. Phys.*, **32**, 1822 (1961).
15. R. A. Logan, J. F. Gilbert, and F. A. Trumbore, *J. Appl. Phys.*, **32**, 131 (1961).
16. N. Holonyak, I. A. Lesk, R. N. Hall, J. J. Tiemann, and H. Ehrenreich, *Phys. Rev. Letters*, **3**, 167 (1959).

Crystallographic Dependence of SiP Precipitates in Diffused Silicon

T. W. O'Keeffe, P. F. Schmidt,[1] and R. Stickler

Westinghouse Research and Development Center, Pittsburgh, Pennsylvania

The formation of SiP precipitates in the surface layers of silicon diffused from doped anodic oxide films has been reported before (1). The existence of SiP precipitates was suggested by tracer data utilizing the P^{32} isotope and was confirmed on {110} oriented diffused silicon by transmission electron microscopy and by electron diffraction.

These tracer data showed the loss of a large fraction of the total phosphorus incorporated into the silicon by diffusion, when the silicon was subsequently anodized in nontracer solution for diffusion profile determination by the Tannenbaum method (2). The silicon samples used in the previous experiments were flat oblong bars cut along the length of the ingot, the large surface of the bar being {110} oriented.

It has now been shown by tracer evidence that no precipitates are found on {111} surfaces for diffusion times of about 1 hr or longer at 1200°C, the diffusion source being a doped anodic oxide film, *i.e.*, not an infinite source. For short diffusion times the precipitates are also found on the {111} surfaces if the initial phosphorus content of the oxide source is high enough. A striking difference in the behavior of the different surfaces is thus observed only for longer diffusion times. On the {110} surfaces the precipitates were still present after 16 hr of diffusion at 1175°C.

Whereas substitutional phosphorus is not lost to the anodizing solution but is incorporated into the oxide formed by anodization, both SiP and elemental phosphorus would be removed by anodization. Silicon phosphide also hydrolyzes in contact with acids, producing phosphine gas, PH_3, whereas elemental phosphorus is inert to nonoxidizing acids. The formation of PH_3 when the sample is in contact with HF solution can therefore be taken as an indication for the presence of silicon phosphide, but does not rule out the simultaneous presence of elemental phosphorus.

Experimental

Table I presents the data for 2-hr diffusion runs at 1200°C for two {111} oriented disks and for {110} oriented bars. As in the previous experiments (1), the samples were etched in CP-8 prior to anodization to remove all mechanical damage. Columns 2, 3, and 4 specify the diffusion conditions. "Clad" means that a nondoped anodic oxide film, 600Å thick, had been grown in potassium nitrite-tetrahydrofurfuryl alcohol solution (3) on top of the doped oxide in order to eliminate out-diffusion of phosphorus. The doped oxide film had been grown to 150v at constant voltage and was therefore approximately 900Å thick (4).

Column 5 of Table I gives the prediffusion concentration of phosphorus in the doped oxide source Column 6 gives the amount of phosphorus lost from the diffused sample when removing the source oxide by a quick dip in cold HF, column 7 the amount of phosphorus recovered when evaporating this HF solution to dryness; the latter two values refer to the concentration of phosphorus averaged over the combined thickness of source oxide plus oxide cladding. Column 8 gives the percentage of the total prediffusion phosphorus that was found in the silicon after stripping the oxide source in HF. Thereafter the silicon was anodized in a nontracer solution, and column 9 gives the loss to the anodizing solution during this first anodizing step. Columns 10 and 11 give the surface concentration of phosphorus in the silicon, either extrapolated from the tracer profile or calculated from the electrical resistivity profile.

In the case of the {111} surfaces the full amount of phosphorus lost from the disks when the oxide source is dissolved in HF, is recovered in the HF solution.[2] This can be taken as good evidence that no SiP precipitates were present, since these would hydrolyze to some extent when in contact with HF, and the phosphine gas evolved would not be recovered when evaporating the HF solution to dryness. This behavior is indeed shown by the bar type samples in the lower two columns. The

[1] Present address: Bell Telephone Laboratories, Inc., Allentown, Pennsylvania.

[2] The apparent discrepancy that on disks 3 and 4 more phosphorus is recovered from the HF solution than was lost from the Si sample during etching in HF is due to the fact that the counting in these two cases had to be carried out under completely different geometrical conditions. The discrepancy therefore reflects mostly the uncertainty in the conversion factors employed to convert the two counts to absolute amounts of phosphorus.

Table I. Diffusion and tracer data for 120 min diffusions

Sample	Clad.	Diffusion conditions: Temp, °C	Diffusion conditions: Time, min	Oxide concentration (cm^{-3}): Prediffusion	Post diffusion: Activity lost	Post diffusion: Collected	% in Si	% Loss 1st anod.	Silicon surface concentration, cm^{-3}: Tracer profile	Cond. profile	from ρ_s & x_j
1	2	3	4	5	6	7	8	9	10	11	12
Disk 4	Yes	1200	120	2.1×10^{21}	3.3×10^{20}	3.8×10^{20}	66	0	8×10^{19}	8×10^{19}	1.0×10^{20}
Disk 3	Yes	1200	120	1.6×10^{21}	3.6×10^{20}	4.0×10^{20}	56	0	6×10^{19}	7×10^{19}	9×10^{19}
BAR EE	Yes	1200	120	3.1×10^{21}	4.8×10^{20}	2.7×10^{19}	72	76	3.4×10^{19}	—	—
BAR V	Yes	1200	120	3.1×10^{21}	4.7×10^{20}	6.7×10^{19}	73	81	$\sim 3 \times 10^{19}$	—	—

Table II. Diffusion and tracer data for 20 min diffusions

Sample	Clad.	Diffusion conditions: Temp, °C	Diffusion conditions: Time, min	Oxide concentration (cm^{-3}): Prediffusion	Post diffusion: Activity lost	Post diffusion: Collected	% in Si	% Loss 1st anod.	Silicon surface concentration, cm^{-3}: Tracer profile	Cond. profile	from ρ_s & x_j
1	2	3	4	5	6	7	8	9	10	11	12
Disk 1	Yes	1200	20	2.3×10^{21}	6.6×10^{20}	—	45	30	1×10^{20}	9×10^{19}	1.4×10^{20}
Disk 2	Yes	1200	20	2.5×10^{21}	5.1×10^{20}	—	58	47	1×10^{20}	1.2×10^{20}	1.5×10^{20}
BAR F	No	1175	20	8.8×10^{20}	1.1×10^{20}	2.0×10^{19}	46	33	3×10^{19}	5×10^{19} (Na)	—
BAR H	No	1175	20	8.9×10^{20}	1.7×10^{20}	4.8×10^{19}	58	38	2.7×10^{19}	—	—

zero loss to the anodizing solution in the case of the {111} surfaces may therefore be safely attributed to the absence of SiP precipitates. The bar-type samples, on the other hand, show an enormous loss to the anodizing solution during the very first anodization step, 76-81% of the total phosphorus present in the silicon.

Table II is laid out in the same manner as Table I, but refers to 20-min diffusions at 1200° or 1175°C. It can be seen that there must now be SiP precipitates also on the {111} surfaces, as indicated by the loss to the anodizing solution. Electron transmission micrographs on these {111} oriented disks confirmed the existence of precipitates, but these were too small for identification by electron diffraction. It is noteworthy that the loss to the anodizing solution of the bar-type samples, diffused for 20 min at 1175°C, is distinctly less than the loss from the bar-type samples, diffused for 120 min at 1200°C. It seems that high temperature and long diffusion times favor the formation of SiP precipitates on the bar type samples.

In examining the data two facts were noted: (*A*) the extrapolated surface concentration of the tracer diffusion profile, as established by multiple anodizations, was always significantly higher on the {111} oriented disks, as compared to the bar-type samples, even though the prediffusion concentration of phosphorus in the doped oxide was the same. Apparently the phosphorus bound in the SiP precipitates on the {110} surfaces is not as available for diffusion even at the diffusion temperature of 1200°C. (*B*) All bars tested had been cut from the same 2 ohm-cm p-type silicon ingot (float-zoned), on which no dislocation count had been carried out.

In order to check the possible effect of dislocations preexistent in the silicon crystal on the formation and stabilization of SiP precipitates, two extreme conditions were compared and are shown in Table III. Bar BB had a dislocation count of 350/cm^2, and was accurately {110} oriented (the other bars were ± two degrees off their nominal orientation, as evidenced by x-ray diffraction). Disk 7, {111} oriented, was only mechanically but not chemically polished; its surface was therefore badly dislocated. It can be seen that some SiP precipitates are now present on the {111} surface even after a 2-hr diffusion at 1200°C, whereas relatively few precipitates have persisted on the {110} surface.

Bar DD is included in Table III to show that for short diffusion times high surface concentrations can be reached also on surfaces other than {111}. Both bar DD and disk 5 showed some anomalous behavior, and the results obtained on these two samples are questionable.

Table IV shows once more the surface concentration on all samples for which the electrical data are available [on bar F these were falsified by accidental contamination with sodium ions which were incorporated into the anodic oxide and had then diffused in the silicon (3)]. Column 5 shows again the C_o extrapolated from the tracer profile, column 6 the C_o calculated from the surface conductivity profile obtained during multiple anodizations assuming a mobility of 80 cm^2/v sec. Column 7 gives C_o values calculated from sheet resistance and junction depth when assuming a Gaussian phosphorus distribution, and column 8 when assuming a complementary error function distribution (5). The junction depths in microns are given in column 9. It can be seen that there is a tendency for the junction depths to be greatest when SiP precipitates are absent. The tendency for samples with SiP precipitates to show a relatively high C_o value, as calculated from sheet resistance and junction depth, while at the same time showing a small junction depth, may be due to deviations of the diffusion profile from a Gaussian or erfc distribution. There is no obvious explanation for the unusually great junction depth on bar BB.

Errors

Most of the data presented are based on the activity of the P^{32} enriched phosphorus incorporated into the samples. Where absolute values of the phosphorus concentration are quoted, an error associated with the uncertainty of the absolute activity of the original tracer, as received, is involved (±3%). The various conversion factors necessary to extract the absolute phosphorus concentration from the raw count data involve possibly another 10%. It might be mentioned that for all the data tabulated the statistical errors associated with the radioactivity phenomenon itself were always made insignificant by sufficiently long counting times. The most serious errors in the results for comparative purposes are purely experimental. In the case of the counts taken from the samples themselves (columns 5 through 10, excluding 7), the exact replacement of the sample in the same position was most important.

Table III. Diffusion and tracer data for low dislocations, {110} oriented bar BB, and for high dislocations, {111} oriented disk 7, 20-min diffusions on {110} oriented bars showing high C_o

Sample	Clad.	Diffusion conditions: Temp, °C	Diffusion conditions: Time, min	Oxide concentration (cm^{-3}): Prediffusion	Oxide concentration (cm^{-3}): Post diffusion: Activity lost	Oxide concentration (cm^{-3}): Post diffusion: Collected	% in Si	% Loss 1st anod.	Silicon surface concentration, cm^{-3}: Tracer profile	Silicon surface concentration, cm^{-3}: Cond. profile	Silicon surface concentration, cm^{-3}: from ρ_s & x_j
1	2	3	4	5	6	7	8	9	10	11	12
BAR BB	Yes	1200	120	1.5×10^{21}	2.9×10^{20}	2.5×10^{20}	52	6.2	2.7×10^{19}	8.5×10^{19}	6.5×10^{19}
Disk 7	Yes	1200	120	1.7×10^{21}	2.7×10^{20}	2.4×10^{20}	66	12	1.6×10^{20}	1.7×10^{20}	1.1×10^{20}
BAR DD	Poor	1200	20	4.2×10^{21}	5.4×10^{20}	3.8×10^{20}	22	30	8.1×10^{19}	1.2×10^{20}	1.2×10^{20}
Disk 5	Yes	1200	20	9.2×10^{20}	2.2×10^{20}	2.7×10^{20}	52	53	4.2×10^{19} (dubious)	8.5×10^{19} (dubious)	8×10^{19}

Note: BAR BB, Low dislocation material; Disk 7, Mechanically polished only.

Table IV. Summary of surface concentration and junction depth data

Sample	Diffusion temp, °C	Diff. time, min	SiP precip	Silicon surface concentration, atoms P/cm^{-3}: Tracer profile	Cond. profile	Gaussian	ERFC	Junction depth xj, μ	
1	2	3	4	5	6	7	8	9	
Disk 4	1200	120	None	8×10^{19}	8×10^{19}	1.0×10^{20}	1.4×10^{20}	5.3	
Disk 3	1200	120	None	6×10^{19}	7×10^{19}	9×10^{19}	1.2×10^{20}	4.5	
Disk 1	1200	20	Many	1×10^{20}	9×10^{19}	1.4×10^{20}	2.1×10^{20}	2.4	
Disk 2	1200	20	Many	1×10^{20}	1.2×10^{20}	1.5×10^{20}	2.3×10^{20}	2.1	
Bar BB	1200	120	Few	2.7×10^{19}	8.5×10^{19}	6.5×10^{19}	1.0×10^{20}	6.1	
Disk 7	1200	120	Few	1.6×10^{20}	1.7×10^{20}	1.1×10^{20}	1.5×10^{20}	4.1	
Bar DD	1200	20	Many	8.1×10^{19}	1.2×10^{20}	1.2×10^{20}	1.9×10^{20}	3.3	dubious
Disk 5	1200	20	Many	4.2×10^{19}	8.5×10^{19}	8×10^{19}	1.2×10^{20}	2.3	dubious

This source of error led to uncertainties of ±2% for the disk-shaped samples and ±1.2% for the bar-shaped samples. Counts from trays containing nonvolatile remains of dissolved oxides after evaporation were only reproducible to within ±10%, presumably due to uneven distribution of the material in the bottom of the trays.[3]

Most of the columns in the tables were actually obtained from counting rate difference values so that the increase in error involved in such procedure is large. A list of the errors involved in each of the columns follows (excluding those involved in determining the absolute phosphorus content):

Column	5, %	6, %	7, %	8 & 9, %	10, %
Error on disk	2	6	10	±3	6* (Disks 3 & 4; 50% disks 1 & 2)
Error on bar	1.2	6	10	±2	50

* Disks 3 and 4 were investigated in great detail; the statistical error on disks 1 and 2, and on the bars is much larger because too few measurements were taken.

Column 11 involves the surface conductance data and probably is accurate to ±20% assuming the value of 80 cm^2/v sec taken as the average electron mobility for a layer 0.1μ thick at the surface. Column 12 is the result for x_j, ρ_s measurements using Irvin's curves assuming a Gaussian distribution and involves the usual uncertainties inherent in such determinations.

Discussion

The data indicate that several factors are affecting the nucleation, growth, and stabilization of SiP. Crystal orientation and perfection appear as the most important factors, but conditions of heat-treatment, cooling rate, etc., may also be involved.

In the previous study (1) it was found that SiP precipitated in {110} oriented Si bars in the form of flat rods, lying in the {111} planes and elongated along <110 directions> (6). In {110} oriented samples the SiP particles are thus formed predominantly parallel to the sample surface, the Si/SiO_2 interface being the most likely location for the precipitates because conditions at the interface are favorable for the development of large crystals.[4] It is significant that {110} oriented, phosphorus diffused samples showed a large loss of phosphorus in the form of PH_3, due to the hydrolysis of SiP, when the doped oxide was removed in HF after diffusion treatment. Unless the SiP crystals are located directly at the interface, such a large loss of phosphorus would not be likely to occur during a short exposure to cold HF. The orientation relationship indicated above predicts that the rod-shaped SiP particles in diffused {111} oriented wafers would intersect {111} surface at larger angles so that only the small cross section of the rods would be exposed at the surface. The observation that SiP particles remain small in {111} oriented samples of normal crystal perfection can be explained as presumably due to unfavorable growth conditions.

[3] There is also another possible but less likely explanation: if the phosphorus incorporated into the oxide by anodization did not occur in the highest valence only (+5), then on dissolution of the oxide in HF and heating of the HF solution, the phosphorus present in a lower valence state would disproportion to give phosphoric acid and phosphine gas; the latter would be lost from the trays.

[4] One could also think of a stabilization of the SiP crystals by an increased oxygen content if they are located directly at the Si/SiO_2 interface.

In a low dislocation crystal, vacancy clusters or small dislocation loops were observed in germanium (7, 8) and were found to lie in {110} planes. It was found that heat-treatment and impurity concentration are very critical for the formation of the loops. It might be expected, therefore, that these parameters are also sensitive factors for the nucleation of SiP in silicon.

Another possibility for the creation of nucleation sites close to the wafer surface was recently pointed out by Barson *et al.* (9). According to these authors a fast oxidation treatment at somewhat lower temperatures can cause pile-up of phosphorus from the bulk of the (phosphorus doped) sample resulting in formation of vacancy loops near the oxide/silicon interface. These loops, then, can act as nucleation sites for the precipitates. The results with the mechanically polished, {111} oriented disk 7 shows that dislocations can also act as nucleation sites for SiP precipitates. From the tracer data it could be deduced that SiP precipitates must be present on this sample, and subsequent transmission electron microscopy did indeed confirm their presence. On this mechanically damaged (10) sample, the SiP precipitates had grown to micron size.

It is known that thick oxide layers formed on silicon surfaces can create high stresses which then are relieved by plastic strain (11). The slip dislocation formed in this way will intersect the crystal surface along the intersection of the slip plane, for instance, for {111} surfaces along <110> directions. In this case the particles precipitating during a diffusion treatment might be expected to be concentrated along these slip traces.

Acknowledgment

The authors are indebted to Mr. N. Roney for his meticulous care in the performance of the tracer experiments. This work was jointly sponsored by the Electronic Technology Laboratory, Aeronautical Systems Division, Wright-Patterson Air Force Base, Ohio, under contract AF 33-(657)-9897, and by Westinghouse Electric Corporation.

Manuscript received Jan. 25, 1965; revised manuscript received April 27, 1965.

Any discussion of this paper will appear in a Discussion Section to be published in the June 1966 JOURNAL.

REFERENCES

1. P. F. Schmidt and R. Stickler, *This Journal*, **111**, 1188 (1964).
2. E. Tannenbaum, *Solid State Electronics*, **2**, 123 (1961).
3. P. F. Schmidt, T. W. O'Keefe, J. Oroshnik, and A. E. Owen, *This Journal*, **112**, 800 (1965).
4. P. F. Schmidt and A. E. Owen, *This Journal*, **111**, 682 (1964).
5. J. C. Irvin, *BSTJ*, **41**, 387 (1962).
6. R. Stickler and T. J. Phillips, To be published.
7. G. R. Booker and R. Stickler, AIME Technical Conference on Semiconducting Materials, Los Angeles 1961, Interscience, New York (1962).
8. G. E. Brock and C. F. Aliotta, *IBM J. Res. Devel.*, **6**, 372 (1962).
9. F. Barson, W. J. Armstrong, and W. E. Mutter, *This Journal*, **111**, 1263 (1964).
10. R. Stickler and G. R. Booker, *Phil. Mag.*, **8**, 859 (1963).
11. W. Czaja, Private communication.

Preferential Vaporization of Carbon from Hafnium Carbide

R. L. Hansler

Lamp Research Laboratory, General Electric Company, Nela Park, Cleveland, Ohio

It has been reported (1) that when hafnium carbide vaporizes it loses carbon and hafnium at the same rate. This is in disagreement with an experiment reported here in which hafnium carbide, most certainly nearer to stoichiometric than the hafnium carbide studied by the previous authors, clearly lost carbon preferentially. In this work, it has also been shown that electrical resistivity is a more sensitive indicator of composition changes in hafnium carbide than is lattice constant.

For nearly stoichiometric HfC the rate of loss of carbon increases with temperature and with the amount of carbon in the carbide. A filament of hafnium carbide was prepared by heating hafnium to approximately 2800°K in an atmosphere of argon (99.9%) containing about 5 Torr of methane (99.9%). A steady-state condition was ultimately obtained. The hafnium carbide lost carbon at a rate equal to the rate at which it gained carbon by decomposition of the methane.

It was then heated to approximately 2800°K in pure argon at constant voltage (31v) for 2 min during which time the current dropped from 7.05 to 6.67 amp. The resistance of the wire at room temperature before and after this treatment was 1.95 and 2.75 ohm, respectively. When the same filament was recarburized by heating in methane and argon as had been done previously, the hot and cold resistance both returned to the previous values. This experiment shows clearly that carbon was preferentially lost from the hafnium carbide prepared, as described, for this study.

The room temperature resistance of hafnium carbide changes rather rapidly with composition near stoichiometry, but the lattice constant (2) changes comparatively slowly. Comparable resistance and lattice data are tabulated for four filaments of the same size which were carburized to different degrees by heating in different argon methane mixtures. Because of the small sample size no chemical analyses were possible. The lattice constants were determined in the usual fashion by x-ray diffraction.[1]

$R_{298°K}$, ohms	a_0 (Å)
1.576	4.6450 ± 0.0005
1.94	4.6424
3.09	4.6422
3.38	4.6410

[1] These measurements were kindly provided by Miss J. R. Cooper.

Manuscript received Nov. 11, 1964; revised manuscript received April 20, 1965.

Any discussion of this paper will appear in a Discussion Section to be published in the June 1966 JOURNAL.

REFERENCES

1. J. A. Coffman, G. M. Kibler, T. F. Lyon, and B. D. Acchione, WADD-TR-60-646, Part II, Jan. 1963 (AD 297 946).
2. R. G. Avarbe, A. I. Avgustinik, Iu. N. Vilk, Iu. A. Omelchanko, and S. S. Ordanian, *Zhur. Priklad. Khim.*, **35**, 1976 (1962).

Page Charge Adopted for the JOURNAL

Increased costs of publication have made it necessary for The Electrochemical Society to institute a per page charge for publication in the JOURNAL.

At the Meeting of the Board of Directors held in New York on September 29, 1963 a charge of $35.00 per printed page was established by the Board of Directors, on recommendation of the Publication and Finance Committees, for papers published in the JOURNAL. This action becomes effective for papers received after February 1, 1964.

A 10% reduction in the page charge will apply to papers authored by one or more members of The Electrochemical Society and/or by one or more employees of Patron or Sustaining Members of the Society.

Papers are accepted for publication on the basis of merit by established practices of review. Acceptance of future papers for publication will not be dependent on payment of this invoice. Where funds are not available for payment of this charge it will be waived by The Electrochemical Society.

Discharge and Recuperation of the Vanadium Pentoxide Electrode

Naola V. Watson and Allen B. Scott

Department of Chemistry, Oregon State University, Corvallis, Oregon

ABSTRACT

The pH dependence of the potential of V_2O_5 electrodes, at 25°C, was found to be 0.0602 v/pH unit. Only those cathode reactions yielding an insoluble oxide or oxyhydroxide are consistent with this result. Polarization was assumed to result from solid solution of the product in V_2O_5. A theory of recovery previously applied to MnO_2, involving the diffusion of the product into the solid oxide electrode, was applied with qualitative agreement in a limited region of pH and current density. The theory appears to be in need of modification to account quantitatively for the behavior of V_2O_5.

Vanadium pentoxide bears a resemblance to manganese dioxide as a cathode in electrochemical cells. The oxide is a semiconductor and is easily reduced in aqueous solution. We have found that a moderate polarization occurs during cathodic discharge; after a partial discharge a gradual recuperation occurs so that the potential returns in time to a value nearly that of the oxide before discharge. These similarities between MnO_2 and V_2O_5 have led us to believe that the mechanisms of discharge and recuperation in the two oxides may be much the same. Vanadium pentoxide has some distinct advantages over MnO_2 as research material. It is low melting (670°C), can be cast in any desired massive form, and single crystals can be prepared. Further, it is transparent in the orange and red, so that some indication of impurity or imperfection content may be given by optical measurements in the region of the fundamental absorption edge.

This paper describes the first of several investigations into the electrochemical properties of V_2O_5. In addition to providing some understanding of the behavior of this oxide, which itself has some promise as a cathode material (1), we expect the results to be of interest in the study of MnO_2 and oxide cathodes in general.

Coleman (2) proposed that the polarization of MnO_2, at least in certain regions of current density and electrolyte pH, resulted from an accumulation of oxyhydroxide on the surface, with recuperation taking place as the oxyhydroxide diffused into the solid MnO_2. He suggested that the diffusing species was the proton, accompanied by electrons moving through conduction levels of the crystal. This view was also adopted by Scott (3), who showed that the form of the polarization and recuperation curves, *e.g.*, those of Ferrell and Vosburgh (4), for MnO_2 could be satisfactorily accounted for by means of equations based on the diffusion equation for continuous flux on the surface of a semi-infinite solid, followed by a period of zero flux. Kornfeil (5) showed that the shape of the recuperation curve can be calculated from constants derived from the polarization curve, at a solution pH of 7.5, and an apparent current density of 0.15 ma/cm^2 and less.

Here we attempt to show that the product of the electrode reaction in V_2O_5 is an insoluble oxide or oxyhydroxide, and to account for the polarization and recovery on the basis of the theory applied to MnO_2.

Experimental

Preparation of the electrodes.—To form the electrodes, reagent grade vanadium pentoxide was melted around a strip of platinum foil in a Pyrex tube. The tube was then cooled, and the glass was broken away from the solid. The resulting cylindrical electrode had an apparent surface area of about 2.8 cm^2.

Analysis of the discharge product.—Electrodes were made the cathode for periods up to 72 hr in solutions saturated at pH 2 with V_2O_5 (about 4 x 10^{-3} mole V_2O_5/liter), to which was added about 0.1 mole/liter NH_4Cl to increase the conductivity. The pH was adjusted to values between 1 and 8 by additions of HCl and NH_3. At pH > 2 the solutions were no longer saturated with respect to V_2O_5, but dissolution of the electrodes was extremely slow. Currents ranged from 1.5 to 30 ma. The extent of reduction of the electrode and of material in solution around the electrodes was determined by potentiometric titration with ceric ammonium sulfate. The electrodes were dissolved in 100 ml of 2*N* H_2SO_4 for analysis.

X-ray powder diffraction patterns for the original electrode materials and for the electrode material after discharge were obtained by means of a North American Philips Company diffraction spectrometer.

Effect of pH on electrode potential.—Solutions used were McIlvaine's standard buffer solutions, saturated at 25°C with V_2O_5. The pH of each solution was measured by means of a Beckman Model G pH meter, and the potential of a V_2O_5 electrode immersed in the solution was measured, with reference to the saturated calomel electrode, by means of a Varian Model G 14 recording potentiometer. The temperature was 25° ±0.2°C.

Two types of electrodes were used in these experiments. The first type consisted of freshly prepared electrodes which had been allowed to stand in a saturated vanadium pentoxide solution until all the electrodes had attained the same potential. The other type consisted of electrodes which had been discharged for several hours. These latter electrodes were then allowed to stand in the discharge solution for 2 to 3 hr until they all attained the same potential.

Polarization and recuperation measurements.—The electrodes were discharged in well-stirred 0.5M KCl solutions saturated with V_2O_5, having pH's between 2 and 5. An external source of emf was used, and platinum foil was used as an anode. The apparent current density was in the range 0.12-0.35 ma/cm^2. A saturated calomel electrode was used as the reference, with the vanadium pentoxide cathode placed in direct contact with the tip of the reference electrode tube. A recording potentiometer automatically traced the polarization and recovery of the V_2O_5 potential. Polarization, or recovery, occurring within 10^{-2} sec after making, or breaking, the circuit was taken as the height of an apparently vertical voltage step on the trace of a Tektronix Type 502 oscilloscope having a frequency response of 1 Mc and using a sweep rate of 0.5 cm/sec. This polarization, about 10 mv, was essentially of the same magnitude on either making or breaking the circuit and was thought to be largely ohmic; it was sub-

tracted in all cases from the recorded polarization to give the slowly occurring and recovering component.

Results and Discussion

Product of the discharge.—The product, or products, of the electrolytic reduction of V_2O_5 is unknown. The number of oxides and oxyhydroxides, in which the oxidation number of vanadium is less than +5, is large. Anderson (6) identified 11 oxides of definite composition ranging from that of VO to that of V_2O_5. The following oxyhydroxides are known: VO(OH) (montroseite), $VO(OH)_2$ (duttonite), a second modification of $VO(OH)_2$ (7), and $V_3O_5(OH)_4$ (7). In addition, a mineral believed to have the formula $V_2O_3(OH)$ has been described (8). Dissolved ions which may result from the discharge include VO^{2+}, $HV_2O_5^-$, HVO_2^+, V^{3+}, VOH^{2+}, and VO^+. Of these, $HV_2O_5^-$ and HVO_2^+ occur only in solutions of pH > 5.3.

On discharge, the electrodes changed from purple or brown to jet black. The site of reduction was clearly seen, on sectioning discharged electrodes, to be at the solution-V_2O_5 interface rather than at the Pt-V_2O_5 interface, establishing the fact that charge transport through the V_2O_5 is electronic. It was impossible to separate mechanically the black material from the remaining V_2O_5 in the neighborhood of the surface. Many of the reduced oxides and oxyhydroxides, particularly those of oxidation state near +4, are reported to be black or blue-black.

The x-ray diffraction pattern of the surface material of an electrode discharged at an apparent current density $i = 7$ ma/cm^2 for 5 hr was compared with that of reagent grade V_2O_5 which had been melted, cooled, and crushed in a mortar. The pattern of the latter was identical to that of the original V_2O_5 powder, except for a difference in the intensity of several lines, arising undoubtedly from a preferential orientation of certain planes in the masses of small needle-shaped crystals which were still present in the frozen crushed sample.

Table I gives the result of the diffraction analysis. The pattern of the discharged electrode material was nearly the same as that of the undischarged V_2O_5, there being some differences in line intensities, some slight displacements, and three weak new lines. The product evidently was present either in solid solution, or in a proportion insufficient to give a distinct powder pattern, or in both. An estimate of the proportion of reduced form can be made on the basis of chemical analysis provided a formula for the product is assumed. In electrodes reduced to the extent of 35 ma hr cm^{-2}, it was found by titration of the electrode material with ceric ammonium sulfate that the proportion of product, based on the entire mass of the electrode, was generally in excess of 20%, if the formula of the product was assumed to be $V_3O_5(OH)_4$, or in excess of 5%, if the formula was assumed to be VO_2. Since only the surface portions were removed for x-ray analysis, it then appears likely that the product is present in a proportion considerably higher than 5%. The new lines could not be matched with the powder patterns of any of the 13 lower oxides or oxyhydroxides reported in the "X-Ray Powder Data File." We cannot yet draw any conclusions regarding the formula of the reduction product, but it appears probable that the product forms a solid solution with V_2O_5, whose diffraction pattern is thereupon only slightly modified.

Table I. Comparison of x-ray diffraction patterns of the discharge product and V_2O_5

Discharge product		V_2O_5	
Interplanar spacing, d	Relative intensity, I/I_1	Interplanar spacing, d	Relative intensity, I/I_1
7.43	11	—	—
5.79	36	5.79	17
4.87	16	—	—
4.39	100	4.39	100
4.10	85	4.11	59
3.49	9	3.50	6
3.42	13	3.42	24
3.13	9	—	—
2.89	40	2.89	39
2.77	10	2.77	15
2.620	5	2.623	10
2.189	95	2.191	49
1.922	10	1.925	11
1.902	22	1.905	20
1.831	6	1.868	6

Dependence of electrode potential on p*H.*—The cathodic discharge of V_2O_5 may occur according to one or more of the following types of reactions:

1. Solid reactant + ne + $n'H^+$ + pH_2O = solid product + qH_2O where either p or q = 0 and where n and n' are equal. This type of reaction is exemplified by the equations

$$V_2O_5 + 2e + 2H^+ + H_2O = 2VO(OH)_2 \quad (a)$$

$$V_2O_5 + 2e + 2H^+ = V_2O_4 + H_2O \quad (b)$$

2. Solid reactant + ne + $n'H^+$ = soluble ion + qH_2O where $n \neq n'$. This type of reaction is illustrated by

$$V_2O_5 + 6H^+ + 2e = 2VO^{2+} + 3H_2O \quad (c)$$

3. Soluble ion + ne + $n'H^+$ = soluble ion + qH_2O where $n = n'$. This is illustrated by

$$H_3V_2O_7^- + 2H^+ + 2e = HV_2O_5^- + 2H_2O \quad (d)$$

4. Soluble ion + ne + $n'H^+$ = soluble ion + qH_2O where $n \neq n'$, such as

$$VO_2^+ + 2H^+ + e = VO^{2+} + H_2O \quad (e)$$

According to the Nernst equation, the electrode potential is given by

$$E = E_o - \frac{RT}{nF} \ln \frac{(a_{\text{prod.}})^b (a_{H_2O})^q}{a_{\text{react.}} (a_{H_2O})^p (a_{H^+})^{n'}} \quad [1]$$

where $a_{\text{react.}}$ is the activity of solid vanadium pentoxide or its soluble ion, $a_{\text{prod.}}$ is the activity of the reduced form, and b is its coefficient.

If the activity of the water is taken as the activity of pure water, and if the activity ratio of the reactant and product vanadium compounds does not change as the p*H* is changed, then at 25°C

$$E = E_o' - \frac{n'}{n} (0.0591)\, p\text{H}$$

E_o' includes constant terms in addition to E_o. The slope of the curve of electrode potential *vs.* p*H* is just $-0.0591\ (n'/n)$.

Since reaction (d), above, is the only known reaction between ions in solution in which the ratio of electrons to hydrogen ions is unity, and this reaction occurs only at pH > 5.3, the dependence of electrode potential on p*H* in the range p*H* 2 to p*H* 5 will differentiate between a reaction involving two solids and reactions involving one or more vanadium ions in solution. The reaction must be one between two solids if $n = n'$ and if the assumption made concerning the activities of the vanadium compounds is valid. If the solids are present as pure phases, the validity of the assumption is assured. If they exist as a solid solution, equilibration with solutions of variable p*H* might conceivably alter the solid concentration ratio. However, in these experiments, the V_2O_5 was present in large excess so that its concentration could not be much affected by changes in solubility, and, further, the electrodes were allowed to come to equilibrium in solutions of low p*H* and then placed in solutions of increasing p*H* for the measurements. The solubility of the discharge product was found, by chemical analysis, to decrease with increasing p*H*, so that its activity in a solid solution should also have been unaffected by the change in p*H*.

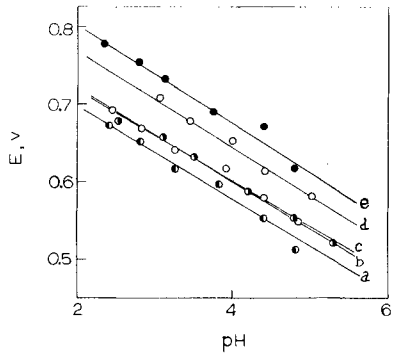

Fig. 1. Dependence of V_2O_5 electrode potential (with respect to the standard hydrogen electrode) on pH. Open and half-shaded circles, partially reduced V_2O_5; solid circles, V_2O_5.

Figure 1 gives the results of five different determinations of the dependence of the electrode potential on the solution pH. Curve e is for the pure vanadium pentoxide electrodes which were allowed to stand in the various buffer solutions for 30 min. Curves a, c, and d are for the partially reduced vanadium pentoxide electrodes which were allowed to stand in the buffer solutions 30, 60, and 60 min, respectively. Curve b is for partially reduced electrodes which were allowed to stand for 15 min in buffer solutions, which had been saturated with both vanadium pentoxide and the discharge product. The average slope of the curves was —0.0607v per pH unit; this value is nearly the theoretical slope for the case $n = n'$, indicating that both the reactant and product of discharge are solids.

Polarization and recuperation.—The foregoing results have led us to postulate that the cathodic polarization of V_2O_5 is due to an accumulation of a reduced compound in solid solution, which lowers the activity of V_2O_5 on the electrode surface. Recuperation may be the result of one or more of the following processes: (*a*) dissolution of the product, (*b*) diffusion of the product into the body of the electrode material, or (c) oxidation of the product by oxygen present in solution.

No special attempt was made to eliminate oxygen so that as yet we can make no statement concerning the role of direct oxidation in recuperation. We can, however, provide some indication of the importance of processes (*a*) and (*b*).

In Fig. 2 are shown typical curves of the polarization of the V_2O_5 electrode in solutions of varying acidity at 25°C. The apparent current density was in all cases about 0.25 ma/cm². After 10 min, the current was broken and the electrode potential recovered. The extent of polarization at 10 min clearly increases with increasing pH. So also does the polarization remaining at 20 min. Since chemical analysis showed the solubility of the reduced form to increase with decreasing pH, it is reasonable to conclude that at least a portion of the depolarization and recovery which occurs at low pH is the result of dissolution.

On the other hand, even at pH 7.7, the recovery was still remarkably rapid and leads us to the supposition that diffusion of the product into the solid oxide is the chief cause of recovery.

We now attempt to apply to theory previously given for MnO_2.

At constant pH, Eq. [1] reduces to

$$E = E_o'' - \frac{RT}{nF} \ln \frac{(a_{\text{prod.}})^b}{a_{V_2O_5}}$$

where the activities are those characteristic of the electrode surface, and E_o'' is the potential when $(a_{\text{prod.}})^b = a_{V_2O_5}$. If $b = 1$, if the activities are taken to be the respective concentrations, and if the concentration of vanadium atoms remains constant, the equation given by Kornfeil (5) applies, namely

$$E = E_o'' + k \log \left(\frac{A}{t^{1/2} - (t - T)^{1/2}} - 1 \right) \quad [2]$$

Here k should be 2.3 RT/F; A involves the rate of formation of product per unit surface area, the initial surface concentration of the oxidized form, and the diffusion coefficient for the product in the solid electrode; t is the time following the start of discharge at constant current; and T is the time at which discharge stops and recovery begins. The constants A and k may be obtained from the discharge portion of the curve, taking $t - T = 0$. For MnO_2, the recovery portion, calculated using constants so obtained, agrees well with observation (5).

If $b \neq 1$, Eq. [2] requires modification. In view of our limited knowledge of the electrode reaction, it does not seem worthwhile to test a variety of modifications based on assumed values of b, although in principle this may provide a means of discerning which of several processes may actually occur.

Instead, we have attempted to apply Eq. [2] to a series of discharges at varying current density, all at pH 3 and 25°C. The results are shown in Fig. 3. The constants used are given in Table II. Kornfeil (5)

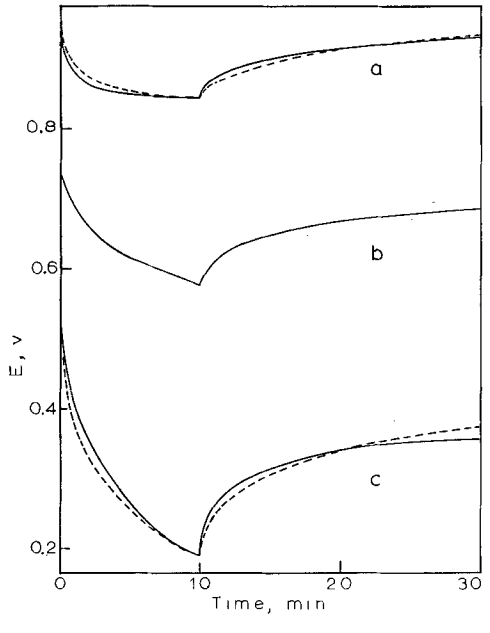

Fig. 2. Discharge and recovery of V_2O_5 electrodes at current density 0.25 ma/cm². pH: a, 1.5; b, 3.0; c, 7.7; E given with respect to the standard hydrogen electrode; solid lines, observed; broken lines, calculated (see Table II).

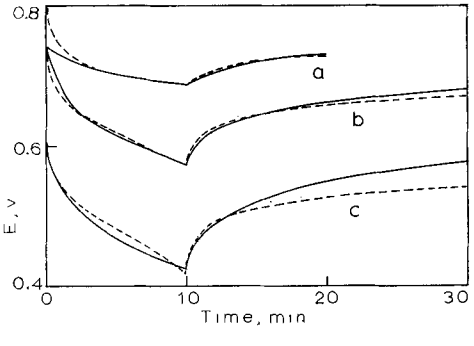

Fig. 3. Discharge and recovery of V_2O_5 electrodes at pH 3.0. Current density, ma/cm²: a, 0.12; b, 0.25; c, 0.35. Add 0.10v to ordinates of curve c. E given with respect to the standard hydrogen electrode; solid lines, observed; broken lines, calculated (see Table II).

Table II. Constants of Eq. [2] and [2']

Curve	pH	Current density, ma/cm²	E_o, v	k, v	A, min$^{1/2}$	c, v/min
Fig. 3, a	3	0.12	0.622	0.10	12.0	
b	3	0.25	0.634	0.10	4.2	
c	3	0.35	0.602	0.10	3.6	
Fig. 2, a	1.5	0.25	0.798	0.10	8.4	0.002
c	7.7	0.25	0.090	0.30	10.0	

found A and k from the slope of the discharge curve at two values of t; however, we found this process to be unsuccessful since, even at best, Eq. [2] fits the discharge portion only in the later stages where the slope is nearly constant. Rather, a single value of k, which should be current-density independent, was chosen such that all the curves could be roughly fit, both in the discharge and recovery portion by a suitable choice of the constant A. For these curves, k = 0.10v; best values of A and E_o were then found at each current density by trial.

At the two lower current densities, agreement between the observed curves (full lines) and those calculated from Eq. [2] (broken lines) was satisfactory. At the highest current density, with k = 0.10v, even the best value of A gave poor agreement with the observed curve. The value of k was significantly higher than the Nernst equation value, and, while the constant A decreased with increasing current density as it should, it was not inversely proportional to the current density. For MnO_2, k was found to be 0.068v at 25°C, and A varied inversely with current density (5).

Returning to the results obtained in solutions of variable pH, Fig. 2, we attempt again to apply Eq. [2].

Difficulties are to be anticipated here, since variations in pH affect not only the solubilities of the reactant and product, but may also alter the electrode reaction. In this regard, it must be emphasized that Eq. [2] has been applied successfully to MnO_2 only in a narrow range both of pH and current density.

At pH 7.7, qualitative agreement only was obtained, using k = 0.30v. This value is inconsistent with any conceivable polarization process which operates reversibly via activity changes in the reactants and products. At pH 1.5, no agreement between Eq. [2] and the observed curve could be obtained. However, if a term linear in the time was included, so that

$$E = E_o'' + k \log\left(\frac{A}{t^{1/2} - (t - T)^{1/2}} - 1\right) + ct \quad [2']$$

where c is a constant, a fair fit was obtained, using the constants given in Table II. The linear term in [2'] clearly tends to reproduce the effect of dissolution on polarization and recovery.

The variation of E_o'' with pH is considerably greater than 0.059 v/pH unit, which suggests that the reduction reaction may change between pH 1.5 and pH 3.0, and again between pH 3.0 and pH 7.7.

It may be concluded that, while the polarization and recovery of the V_2O_5 electrode is qualitatively similar to that of MnO_2 and rough agreement with the diffusion theory, applied successfully to MnO_2, was found at pH 3 and current density of 0.25 ma/cm² and less, the analogy with MnO_2 is far from perfect. The high value required for k and the failure of the inverse proportionality between A and current density at pH 3 may arise from any of several causes, including among other possibilities (a) dissolution of the product, (b) failure of the condition b = 1, and (c) oxidation of the product by dissolved oxygen.

Acknowledgment

This work was supported in part by the Office of Naval Research. The assistance provided by a National Science Foundation fellowship is gratefully acknowledged by Mrs. Watson.

Manuscript received March 23, 1965; revised manuscript received May 5, 1965. This paper was presented at the Washington Meeting of the Society, Oct. 11-15, 1964, and is based on the Ph.D. thesis of one of the authors (N.V.W.).

Any discussion of this paper will appear in a Discussion Section to be published in the June 1966 JOURNAL.

REFERENCES

1. D. V. Louzos, British Pat. 795,910 (1958).
2. J. J. Coleman, *Trans. Electrochem. Soc.*, **90**, 545 (1946).
3. A. B. Scott, *This Journal*, **107**, 941 (1960).
4. D. T. Ferrell and W. C. Vosburgh, *ibid.*, **100**, 451 (1951).
5. F. Kornfeil, *ibid.*, **109**, 349 (1962).
6. G. Andersson, *Acta Chim. Scand.*, **8**, 1599 (1954).
7. O. Glemser and E. Schwarzmann, *Z. anorg u. allgem. Chem.*, **278**, 249 (1955).
8. H. T. Evans, Jr., and M. E. Mrose, *Am. Mineral.*, **40**, 861 (1955).

Theory of Organic Corrosion Inhibitors

Adsorption and Linear Free Energy Relationships

Francis M. Donahue and Ken Nobe

Department of Engineering, University of California, Los Angeles, California

ABSTRACT

By considering adsorption processes of organic compounds as being determined by the electronic distribution in the "anchoring" group of an adsorbate, a correlation has been derived between adsorption measurements and Hammett-like substituent constants through the use of Linear Free Energy Relations (LFER). The analysis is extended to corrosion inhibitors by assuming that the mechanism of inhibition by organic molecules is chemisorption and that the energetics of the corrosion process *per se* are unaffected by the addition of substituents on the parent compound.

In a series of reviews and experimental papers Hackerman and co-workers (1-8) have discussed the effects of structural changes in organic compounds on corrosion inhibition. Each of the experimental papers (5-8) was a systematic study of the "structure-inhibition" relationship found among nitrogen-containing organics. In two reviews (3, 4) a strong implication was present that the key to the metal-organic interaction might be found using a physical organic approach. The present paper is an extension of this thought which endeavors to determine to what extent Linear Free Energy Relationships (LFER) may be used to correlate adsorption phenomena in general and corrosion inhibition in particular.

Theory.—Kinetic and equilibrium processes in organic chemistry have been found to fit an empirical equation proposed by Hammett (9) and discussed and extended by Jaffe (10) and Taft (11). The family of relationships thus obtained is a form of LFER usually designated as the Hammett relation and is given by

$$\log k/k_0 \text{ or } \log K/K_0 = \rho\sigma \quad [1]$$

where the k's are rate constants, K's are equilibrium constants, the zero subscripts refer to parent or reference compounds and the ρ and σ are the reaction and substituent constants which will be discussed below. The origin of the relation is derived from the observed regularity of the reactivity of substituted benzoic acids when compared with their respective pK's, *i.e.*

$$\log k = m(pK) + \text{const} \quad [2]$$

When the expression for benzoic acid itself was used as a reference (denoted with a zero subscript), the relation became

$$\log k/k_0 = m(pK - pK_0) \quad [3]$$

By setting the slope, m, equal to $+1.000$, for the ionization of substituted benzoic acids, the relation was further simplified to yield

$$\log k/k_0 = (pK_0 - pK) = \log K/K_0 = \sigma \quad [4]$$

This equation is then taken as the definition of the substituent constant, σ, *i.e.*, a substituent is given a numerical value which is dependent on its effect on the pK of the substituted benzoic acid compared to benzoic acid. From this definition, H has a σ of 0.00. Those substituents which increase ionization (*i.e.*, weaken the O-H bond) have positive values of σ, and those which decrease ionization (*i.e.*, strengthen the O-H bond) have negative values. From a simple electrostatic picture, substituents promoting ionization should attract electrons from the reaction center which in this case is the oxygen atom bonded to the acidic hydrogen. This result is borne out from qualitative experience in organic processes. By the same reasoning and experience, negative values of σ are associated with electron providing substituents. Electron withdrawal is a term introduced by the organic chemist to explain a decrease in the electronic charge density at an atom in a molecule due to the addition of a substituent. Likewise, electron provision is a term used to explain an increase in the electronic charge density at an atom due to the addition of a substituent.

Therefore, σ is a measure of the electron density or distribution at an atom. This measure of the electron density or distribution at a specific atom, in the molecule, is justified on the basis of quantum-mechanical calculations of electron charge density (q_i) of individual atoms within a molecular orbital structure [for example, see ref. (12), p. 58, and an application of this approach to nucleophilic and electrophilic substitution at azulene, *ibid.*, p. 94]. Such a concept should be very useful in studies where the electron density plays a dominant role. However, one must keep in mind the assumptions implicit in the Hammett treatment. The original approach assumed that all entropy effects were absent or so small as to be considered absent. However, Leffler (13) has shown that this stipulation is not necessary and that a linear relationship between enthalpy and entropy still gives the desired relationship. Steric effects have not been considered since Hammett correlated only meta and para substituents. The failure of the theory to describe the behavior of ortho substituents and aliphatic systems caused Taft to develop the σ^* scale (11). Further refinements of the technique have been developed and are discussed in review articles (10, 11, 14), but will not be treated here. In general these lead to rate or equilibrium equations which are due to structural changes

$$\log K/K_0 \text{ or } \log k/k_0 = [\rho\sigma] \quad [5]$$

where the brackets denote "the appropriate choice of parameter σ." By this it is meant that for aliphatic compounds or ortho-substituted ring compounds, the Taft constant σ^* would be appropriate and not, for example, the Hammett constant. Other substituent constants for particular molecular types have been devised and may be found in the aforementioned reviews.

From this discussion it is seen that ρ is an empirical constant, *i.e.*, it is the slope of the log rate or equilibrium-σ plot. The sign of ρ indicates whether a process is stimulated or inhibited by either electron withdrawal or electron providing at the reaction center.[1] The magnitude of ρ is a relative measure of the sensitivity of the process under study to electronic effects.

The applicability of the Hammett relation to purely organic processes has been demonstrated frequently (9-11, 14). The application to systems of electrochemical import has recently been shown (15, 17). From adsorption studies on alumina from pentane the free energy of adsorption of a number of compounds related to corrosion inhibitors has been correlated with the Hammett constant (18).

Consider an adsorption process

$$\mathrm{R\,Y} + \mathrm{M} \rightleftarrows \mathrm{R\,Y\text{------}M} \quad [6]$$

where R is some organic substituent group, Y is some organic functional group, M is a surface site, and R Y------M represents a chemisorbed species with some sort of electronic interaction between the functional group and the surface site. As a first approximation, the nature of the surface site has not been considered. In addition the electronic interaction has been scrupulously localized to M and Y and no suggestion is made as to which species functions as the Lewis base (electron donor). The process has an equilibrium constant K_a such that

$$K_a = \frac{\theta}{1-\theta} \quad [7]$$

which is related to the free energy of adsorption in the usual manner. The quantity θ is the fraction of the surface covered by the chemisorbed species. By an analogous treatment, the adsorption process of "reference substituent group," R_o, with equilibrium constant, K_{ao}, and surface coverage, θ_o, may be described. The effect of structure on the adsorption process is revealed by the relative change in the free energies

$$\Delta\Delta G_a^\circ = \Delta G_a^\circ - (\Delta G_a^\circ)_o = -RT \ln (K_a/K_{a,o}) \quad [8]$$

where the ΔG_a°'s are the standard free energies of adsorption. Comparing Eq. [8] and [5]

$$\Delta\Delta G_a^\circ = -[\rho'\sigma] \quad [9a]$$

where

$$\rho' = 2.303\,RT\,\rho \quad [9b]$$

Equations [9a], [8], and [7] lead to

$$[\rho'\sigma] = \log \frac{\theta(1-\theta_o)}{\theta_o(1-\theta)} \quad [9c]$$

From Eq. [9a] it is seen that the free energy of adsorption should exhibit a linear dependence with the appropriate σ. The parameter ρ should exhibit a temperature dependence (13). Although the derivation was for an adsorption process, the analysis would be similar for other changes of a physical parameter related to a comparable free energy change; for example, correlations with polarographic half-wave potentials should be anticipated, etc.

In substance, Eq. [9a] and [9c] show that the relative coverages in a hypothetical competitive chemisorption process will depend on the electronic distribution at the adsorption (reaction) center in the or-

[1] Reaction center is defined as that part of an organic molecule which is directly participating in the reaction. In the case of adsorption it is that part (adsorption center) which interacts with the surface.

ganic molecules. An alternate approach to viewing the phenomenon is to note that the relationship shows the relative tendency of one adsorbed species to be displaced (desorbed) when a second adsorbable species is present.

If one considers the kinetics of any surface reaction occurring with simultaneous adsorption of an inactive species, the rate is given by

$$r = \kappa\,(1 - \theta')\,\exp\,[-\Delta G^{\ddagger}/RT] \qquad [10]$$

where r is the rate of the reaction, κ is a constant, θ' is the surface coverage of the inactive (inhibiting) species, and $\Delta G^{\ddagger}$ is the free energy of activation. If one considers a family of organic compounds, where the functional group is held constant and the substituent is varied, the rate of the surface reaction in the presence of any member of this family compared to that of the parent compound is

$$\frac{r}{r_o} = \frac{1 - \theta'}{1 - \theta'_o}\quad \exp -\left[\frac{\Delta G^{\ddagger} - \Delta G_o^{\ddagger}}{RT}\right] \qquad [11]$$

In order to correlate the rates with the previously derived adsorption relationship, a simplifying assumption must be made.

$$\log\frac{1 - \theta}{1 - \theta_o} \cong \log\frac{1 - \theta'}{1 - \theta'_o} \qquad [12]$$

That is, the ratio of the surfaces not covered by the organic compounds is approximately the same whether considering a "purely" adsorption or an inhibiting process. Therefore, taking the log of [11], substituting [12] and [9] and rearranging

$$\log\frac{r}{r_o} = -\,[\rho\sigma] + \log\frac{\theta}{\theta_o} - \left[\frac{\Delta G^{\ddagger} - \Delta G_o^{\ddagger}}{2.3\,RT}\right] \qquad [13]$$

If the activation process for the reaction is unaffected by changing substituents on the organic compound (this assumes that the organic compounds alter the reaction rate solely by blocking the surface and not by "deactivating" other neighboring surface sites), Eq. [13] reduces to

$$\log\left(\frac{r}{r_o}\right) = -\,[\rho\sigma] + \log\frac{\theta}{\theta_o} \qquad [14]$$

When the relative coverages for the "pure adsorption" process are such that $\log\,(\theta/\theta_o) < [\rho\sigma]$,[2] a Hammett relation

$$\log\left(\frac{r}{r_o}\right) = -\,[\rho\sigma] \qquad [15a]$$

is obtained. This result indicates that the relative rate of the inhibited reaction is dependent on the electronic properties of the adsorbate.

Most corrosion inhibition data are given in the form of corrosivity (inhibited rate/uninhibited rate) or in per cent protection, I'. The corrosivity is $(1 - I)$ where $I = I'/100$. Equation [15] expressed in terms of the more familiar corrosion parameter, corrosivity then becomes

$$\log\frac{(1 - I)}{(1 - I)_o} = -\,[\rho\sigma] \qquad [15b]$$

In the foregoing no restriction has been made as to whether the adsorption is from solution or the gas phase or whether the surface reaction is on a solid or a liquid. Therefore, the treatment should be entirely general, and, more significantly, it suggests that gas phase adsorption measurements may be correlated with aqueous corrosion inhibition [this suggestion was implicit in the recent papers by Yao (20)] or electrocapillary data may be correlated with corrosion inhibition as suggested by Blomgren and Bockris (21).

Since Eq. [15a] is derived directly from Eq. [9c], a comparison of Eq. [15a] and [9a] where the ρ's are correlated by Eq. [9b] yields

$$\Delta\Delta G_a^{o} = 2.3\,RT\log\frac{r}{r_o} \qquad [16]$$

However, correlations of adsorption and corrosion inhibition data with the substituent constants, σ, shown later in this paper indicate that the ρ's are not equal. Therefore, subscripts "a" and "i" are used to identify the ρ's determined from adsorption and inhibition measurements, respectively. Equations [9a], [9c], and [15a] lead to relations which enable the direct correlation of adsorption and inhibition data

$$\Delta\Delta G_a^{o} = \frac{\rho'_a}{\rho_i}\log\frac{r}{r_o} \qquad [17]$$

and

$$\log\frac{\theta(1 - \theta_o)}{\theta_o(1 - \theta)} = -\frac{\rho_a}{\rho_i}\log\frac{r}{r_o} \qquad [18]$$

Although the aim of this paper is toward corrosion inhibition, other forms of inhibition of surface reactions are not precluded.

Discussion

Two simplifying assumptions are made in the present work, *viz.*, that one atom in the molecule may be considered as the "anchoring group" and that the electron density at that atom uniquely determines the adsorbability of the molecule as a whole. In the light of both experience and intuition, the assumptions oversimplify the problem. The former assumption constrains the researcher to focus on a single functional group during the course of a structure-inhibition evaluation. Such a practice was indeed followed in past inhibition studies, (5-8) and, hence, has been a traditional first approximation. The assumption that the electron density at the "anchoring group" uniquely determines the adsorbability still allows the possibility of π-interactions provided that such interactions are assumed to vary in the same qualitative manner as the electron density at the functional group under consideration. The reasonableness of this assumption cannot be determined *a priori*, but may be ascertained from experimental data (see below).

The theory herein derived offers a starting point for the consideration of a semi-quantitative approach to the structure-adsorption relationship of organic compounds on metals. By utilizing Hammett-like substituent constants, the problem of ascribing electronic charge densities determined from solutions of the LCAO-MO (Linear Combination of Atomic Orbitals-Molecular Orbital) method (12) is circumvented, and the experimentalist may, even with a limited organic chemistry background, use the tabulated "σ" values (10, 11, 14) in correlations.

Snyder (18) has calculated the free energy of adsorption of a number of organic chemicals which are structurally related to corrosion inhibitors by a technique based on experimental chromatographic retention volume measurements (see Eq. [2] in ref. 18). With a second technique, he calculated the free energy of adsorption by assuming a "localization" of the adsorbate-adsorbent interaction (see Eq. [5] in ref. 18). These latter calculations were shown to correlate well with the Hammett constant for "nonortho" substituents on pyridine, aniline, indole, and quinoline.

Figure 1 is a plot of the free energies of adsorption of a number of substituted pyridines calculated from the retention volume measurements of Snyder (18) against Hammett-like substituent constants. The free energies plotted are actually the differences between a substituted molecule and the parent compound, pyridine. Hammett σ values were used for the 3- and 4-substi-

[2] Hackerman and Cook (19) have shown that the amount of chemisorption does not vary much when the substituent is changed. There are, however, differences (as suggested by Eq. [9c]). These differences are suppressed by the scale which those authors used to represent their total adsorption data.

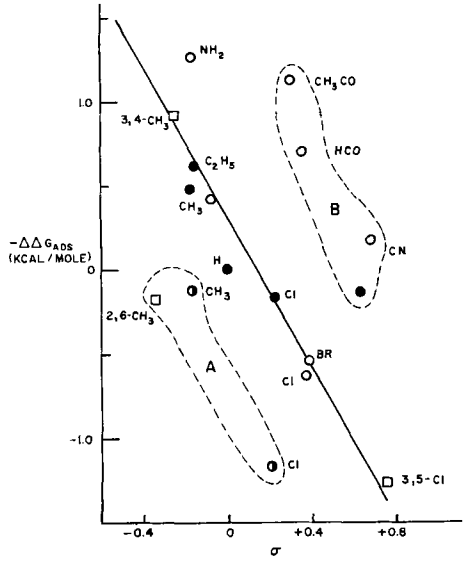

Fig. 1. Free energy of adsorption of substituted pyridines (18) compared to a Hammett-like substituent constant: solid circles represent substitution in the 4-position; open circles, in the 3-position; half-filled, in the 2-position; and squares, as shown.

tuted molecules, Taft σ^* values for the 2-substituted, and the sum of the appropriate σ's for multiple substituted molecules. The solid line is a least squares fit of all points (excluding those denoted by regions A and B). The correlation coefficient of this line was 0.95. The points making up the fit have a similar characteristic in terms of their contribution to the π-system. All of the substituents tend to donate electrons in resonance, *i.e.*, enrich the charge density of the π-system (22). On the basis of this observation, it would seem that the species which donate electrons in resonance do not affect the fit of the simple theory. However, such an observation is not universally true. The most interesting aspect of Fig. 1 is the failure of the substituents in region B to give a fit. These substituents tend to attract electrons in resonance and, thereby, decrease the electron density of the π-system. From the slope, *i.e.*, ρ' in Eq. [9a] of the observed fit, adsorption is increased by electron provision to the nitrogen on pyridine. However, on the basis of the substituents in region B, a diminution of electron density of the π-system gives a more favorable condition for adsorption for a given value of σ. It would have been instructive to use the Taft-Lewis treatment (17) to ascertain whether the observed effect was primarily due to resonance or inductive effects. However, insufficient data were available from the reference (18) for such an analysis.

The region denoted as A should not yield a correlation since the substituents are ortho to the reaction center, and consequently, can contribute a steric effect not allowed for in the simple Hammett treatment. The "ortho" substituents are quite well behaved, *i.e.*, they demonstrate that for a given electronic contribution the steric contribution is sufficient to diminish the tendency toward adsorption. The presence of a steric effect would tend to rule out a completely π-interaction as the mode of adsorption since an orientation of the molecule parallel to the substrate surface would be indifferent, sterically, to the location of the substituent. In summary, the correlation predicted by Eq. [9a], although not as all inclusive as would be desired, is satisfactory.

Ayers and Hackerman (8) have studied the inhibition of methyl pyridines on iron. Their results may be used to test Eq. [15b]. The methyl pyridines do not allow a test of the anomalies observed in Fig. 1 since the alkyl groups tend to donate electrons in resonance. However, an opportunity presents itself to note the effect of steric interactions in the vicinity of the nitrogen in the pyridine skeleton. Figure 2 shows a plot

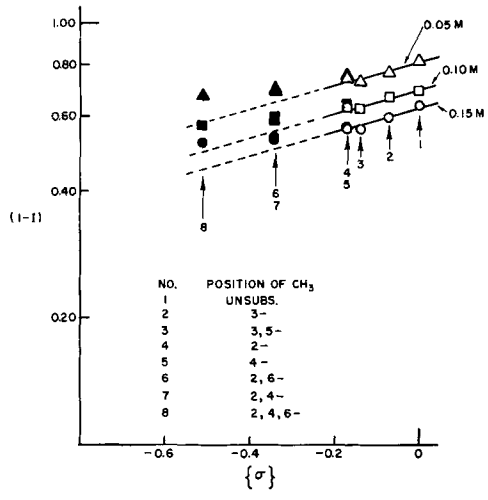

Fig. 2. Relative corrosivity of methyl-substituted pyridines (8) compared to Hammett-like substituent constants: open points should be collinear; filled points should not; position of the methyl group and concentration of the inhibitors are as shown.

of the data according to [15b]. For the 2-substituted pyridines, the Taft σ^* constant was used. The remainder of the σ's were the Hammett constants, and the σ's used for multiple substituents were the sum of the appropriate σ's. On the basis of the theory herein derived the open points, *i.e.*, those devoid of steric complications, should be collinear which indeed they seem to be. However, a single substitution in a 2-position fits the data just as well. The 2,4-disubstituted product shows a lesser deviation than that for the 2, 6-product and suggests that steric effects were really acting. However, the difference between the two corrosivities is not very great. Therefore, the observation made concerning the orientation of the molecules on alumina cannot be made in the inhibition work since the results are inconclusive. The qualitative correlation by Ayers and Hackerman between inhibition and ionization potential is in qualitative agreement with the approach developed in the present work since ionization potential and σ are qualitatively related.

A further test of theory is the fit of Eq. [17] shown in Fig. 3. Here five compounds which were included in the studies of both Snyder (18) and Ayers and Hackerman (8) may be examined. From the foregoing, three of the compounds (open symbols) should be collinear

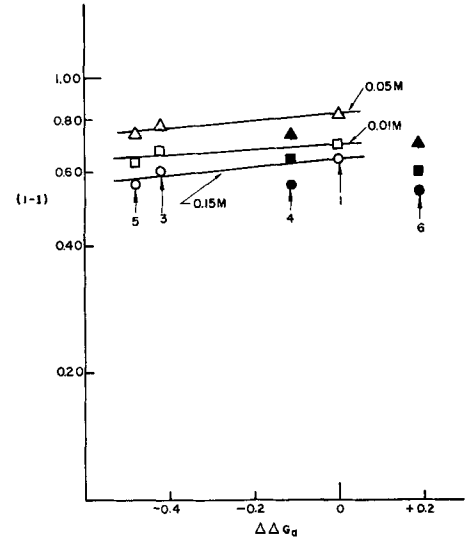

Fig. 3. Relative corrosivity data compared to adsorption measurements for substituted pyridines: open points should give a fit by Eq. [17]; filled points should not; concentrations of the inhibitors are as shown. For the identity of the compounds, see Fig. 2.

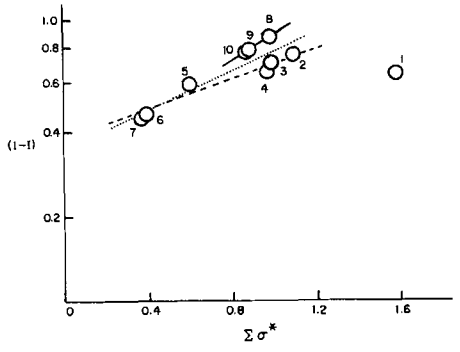

Fig. 4. Corrosivity of alkyl and alkyl-aryl amines (7) *vs.* Taft substituent constants: solid line joins alkyl amines; dashed line, alkyl-aryl amines. 1, aniline; 2, N-methyl aniline; 3, N-ethyl - -; 4, N-n-propyl - -; 5, N,N-dimethyl - -; 6, N,N-diethyl - -; 7, N,N-di-n-propyl - -; 8, methylamine; 9, ethylamine; 10, n-propylamine.

while the other two (filled symbols) should show varying degrees of deviation from the fit. The results substantiate the premise that direct comparison can be made between seemingly unrelated phenomena by an analysis based on LFER.

Alkyl and aryl-alkyl amines, *i.e.*, N-alkyl substituted anilines, have been studied by Kaesche and Hackerman (7). They have reported data on the maximum inhibition achieved by twelve such compounds. Figure 4 shows ten of these compounds plotted in terms of the sum of the Taft substituent constant (11). The other two, *viz.*, toluidines, were ring substituents and were not, therefore, amenable to the particular approach being used here. At the present level of sophistication it is not known whether the theory is actually applicable to the direct comparison of primary alkyl amines with secondary and tertiary alkyl-aryl amines (note the dotted line). Therefore, the internal correlations of alkyl amines (solid line) and the aryl-alkyl amines (dashed line) are shown as well. The lone point is that for aniline (a primary aryl amine) suggesting that substitution on the nitrogen changes the energetics of the adsorption process to such an extent that the internal correlations mentioned are probably a better representation of the fit. This conclusion derives from the observation that the removal of a methyl group from N-methylaniline causes a decrease in the corrosivity well below that predicted by the dashed-line correlation. This tends to suggest a steric interaction resulting on N-substituted anilines. In addition, the alkyl primary amines do not correlate at all with the aryl primary amine (aniline). From studies of amine-boron addition compounds, Taft has shown that secondary and tertiary amines have much larger steric strains than corresponding primary amines (23). Therefore, intuition suggests that the proximity of the primary alkyl amines to the aryl-alkyl amines is fortuitous and should not be taken seriously at this time. Indeed, the apparent fit of the secondary and tertiary amines may also be fortuitous.

The present analysis and the demonstration of its applicability has been somewhat hampered by insufficient data in the literature. Ring-substituted anilines have been studied both in terms of adsorption (18) and corrosion inhibition (24) quite extensively. Although a good correlation has been effected between oxidation potentials and Brown-Okamoto substituent constants (17), Snyder's "experimental" data for the adsorption of substituted anilines (18) were not as well behaved. Besides the -R groups which had failed to fit the simple theory (see above), the halo-substituents showed a nearly constant value of the free energy of adsorption independent of position or nature of the halogen. A comparison of the data of Every and Riggs (24) with that of Fox *et al.* (17) shows a displacement from the anticipated straight line (where oxidation potentials replace free energies of adsorption in Eq. [17]) for most of the halo-substituents. A similar trend is noted when the inhibition data (24) are plotted against the Hammett σ (assuming, that in the absence of substituent complications, [15b] is obeyed by such substituents as H, CH_3, and NH_2, which will be denoted as "inactive" substituents, *i.e.*, those which introduce no new resonance or inductive effects for substituted anilines). This is an area of investigation which is quite well suited to the Taft-Lewis treatment [see ref. (17) and the references therein] to discriminate between inductive and resonance contributions to electron density at a functional group. An extremely interesting group of compounds is the substituted benzenethiols which, although scarcely reported, show better inhibitive powers than the corresponding substituted anilines (24, 25). In addition, they have a ρ value of opposite sign from that of the anilines (26) suggesting a drastically different mechanism of inhibition and adsorption, as noted previously (25).

Summary

A theory has been advanced which now makes tractable the systematic study of the structure-inhibition relationships for organic compounds. The system is based on the electronic effects of substituents on the adsorption (reaction) center of an organic compound. A quantitative scale of values may be ascribed to substituents in terms of the appropriate Hammett-like substituent constant [see ref (9)-(11), (14)]. In addition, a correlation has been shown between adsorption measurements and corrosion inhibition through the substituent constant.

At present, the theory has had only token examination. It remains to ascertain the scope of the applicability by further, more detailed experimentation. For a complete analysis of a family of compounds [*e.g.*, see ref. (17)], meta and para-substituents must both be studied. In particular, "inactive" substituents, *e.g.*, alkyl groups, should be studied as well as cross-referencing, *i.e.*, if halogen substituents are used, then a number of experiments using halogen functional groups should be performed, etc.

Acknowledgment

This work was supported by NASA NsG 237-62. Partial support has been received from the University of California sea water desalination program and the Corrosion Research Council project 14.

Manuscript received Oct. 12, 1964; revised manuscript received March 31, 1965. This paper was presented at the Washington Meeting, Oct. 11-15, 1964.

Any discussion of this paper will appear in a Discussion Section to be published in the June 1966 JOURNAL.

REFERENCES

1. N. Hackerman and A. C. Makrides, *Ind. Eng. Chem.*, **46**, 523 (1954).
2. N. Hackerman and R. M. Hurd, "1st Intl. Congr. on Metallic Corr., London" p. 166, Butterworths, London (1962).
3. N. Hackerman, *Corrosion*, **18**, 322t (1962).
4. N. Hackerman, Comptes Rendus du Symposium European sur les Inhibiteurs de Corrosion, Ferrara (Italie) 1960, p. 99.
5. N. Hackerman, R. M. Hurd, and R. R. Annand, *Corrosion*, **18**, 37t (1962).
6. H. F. Finley and N. Hackerman, *This Journal*, **107**, 259 (1960).
7. H. Kaesche and N. Hackerman, *ibid.*, **105**, 191 (1958).
8. R. C. Ayers, Jr., and N. Hackerman, *ibid.*, **110**, 507 (1963).
9. L. P. Hammett, "Physical Organic Chemistry," McGraw-Hill Book Co., New York (1940).
10. H. H. Jaffe, *Chem. Revs.*, **53**, 191 (1953).
11. R. W. Taft, Jr., in "Steric Effects in Organic Chemistry," M. S. Newman, Editor, p. 559 cf., J. Wiley & Sons, Inc., New York (1956).
12. J. D. Roberts, "Molecular Orbital Calculations," Benjamin, New York (1962).
13. J. Leffler, *J. Org. Chem.*, **20**, 1202 (1955).

14. P. R. Wells, *Chem. Revs.*, **63**, 171 (1963).
15. W. F. Little *et al.*, *J. Am. Chem. Soc.*, **1964**, 1376.
16. W. F. Little *et al.*, *ibid.*, **86**, 1382 (1964).
17. I. Fox, R. W. Taft, Jr, and J. M. Schempf, Technical Report No. 22, Office of Naval Research, Contract Nonr 656 (05) Project NR055-328, June 1959.
18. L. R. Snyder, *J. Phys. Chem.*, **67**, 2344 (1963).
19. N. Hackerman and E. L. Cook, *ibid.*, **55**, 549 (1951).
20. Y. Yao, *ibid.*, **67**, 2055 (1963); **68**, 101 (1964).
21. E. Blomgren and J. O'M. Bockris, *ibid.*, **63**, 1475 (1959;) E. Blomgren *et al.*, *ibid*, **65**, 2000 (1961).
22. E. S. Gould, "Mechanism and Structure in Organic Chemistry," chap. 7, p. 199, Henry Holt & Co., New York (1959).
23. R. W. Taft, Jr., *J. Am. Chem. Soc.*, **75**, 4534 (1953).
24. R. L. Every and O. L. Riggs, *Materials Protection*, **3**, [9], 46 (1964).
25. O. L. Riggs and R. L. Every, *Corrosion*, **18**, 262t (1962).
26. F. M. Donahue and K. Nobe, Unpublished results.

Chemically Deposited Cobalt-Phosphorus Films for Magnetic Recording

Y. Moradzadeh

Systems Development Division, Development Laboratory,

International Business Machines Corporation, San Jose, California

ABSTRACT

Thin magnetic films of cobalt-phosphorus chemically deposited from a modified Brenner bath are reported in this paper. Detailed data are presented to demonstrate the role of deposition conditions on thickness, phosphorus content, and magnetic properties of the films. The films are much thinner than have been reported previously and exhibit a coercivity range of approximately 80 to 900 oe with a coercivity-thickness relation $H_c = At^{-2/5}$. This is similar to that reported by Fisher and Chilton for much thicker films. Some of the variables which control the magnetic properties of the deposited film are shown to be: film thickness, bath *p*H, hypophosphite concentration, and bath temperature; the first two are the dominant factors and overshadow any influence that the codeposited phosphorus may have. An account of the apparatus used for precise and automatic control of the bath *p*H is given. Well-adherent mirror-like films which are suited for conventional high-density magnetic recording, as well as Kerr magneto optical readouts, are obtained

Thin metallic films of cobalt-phosphorus, chemically deposited on the surface of a properly treated substrate, offer a wide range of controllable magnetic properties. These properties are suitable for conventional recording applications which require improved magnetic media (1). They are particularly suited for high-density recording due to their high coercivity and relative low film thickness. If the films are properly deposited on a glass substrate, they also provide a desirable medium for Kerr magneto-optical readouts (2).

The method of preparing cobalt-phosphorus film on Mylar, along with the influence of many variables on its magnetic properties, is described in this paper. The bath used in this investigation is similar to the one suggested by Brenner (3). Although Brenner reports the appearance of the deposit to be "dull," for this particular composition, very bright films are obtained by slight modification of this bath and also by depositing thinner films.

Pretreatment of the Mylar substrate is also simplified to a great extent from that reported by Fisher and Chilton (1), *i.e.*, no adhesive layer is applied to the Mylar surface. Although there is a good deal of agreement between this investigation and the work of Fisher and Chilton (1), it must be stressed that the bath composition used by them is somewhat different from the one reported here. In addition bath variables such as *p*H, temperature, and hypophosphite concentration are dealt with in greater detail. Furthermore, the deposited films are much thinner than those reported by Fisher and Chilton, hence resulting in higher obtainable coercivity ranges.

Experimental Procedures

Film preparation.—Mylar (du Pont type D) was used as the substrate throughout this investigation. The substrate was rendered hydrophilic by immersing it in a hot (95°C) solution of 25% NaOH which contained a few drops of a surface active agent (Tergitol 08, $C_4H_9CH(C_2H_5)CH_2SO_4Na$). After a 5-min immersion, the Mylar sample was rinsed with de-ionized water followed by a hot (80°C) rinsing in de-ionized water to remove all the sodium hydroxide. Alkali etching proved to be a desirable means of surface preparation; it not only created the necessary hydrophilic surface, but further increased the eventual cobalt-phosphorus film-to-Mylar adhesion without causing surface roughness. After the alkali treatment, the sample was immersed in an acidic solution of stannous chloride: $SnCl_2 \cdot 2H_2O$ (Mallinckrodt grade), 30g; HCl (concentrated), 50 ml; water (de-ionized), 1000 ml. Length of the immersion time was 30 sec. This process (sensitization) was followed by dipping the sample in hot de-ionized water (80°C) and immediately immersing for 30 sec in a palladium chloride bath having the following composition: $PdCl_2$ 0.1g; concentrated HCl, 10 ml; de-ionized water, 1000 ml.

The Mylar, thus treated, was then immersed in the deposition bath. The composition of the bath, unless otherwise indicated, was as follows

Cobalt chloride, $CoCl_2 \cdot 6H_2O = 27.1$ g/l

Sodium hypophosphite, $NaH_2PO_2 \cdot H_2O = 9$ g/l

Sodium citrate, $Na_3C_6H_5O_7 \cdot 2H_2O = 90$ g/l

Ammonium chloride, $NH_4Cl = 45.3$ g/l

Alkali for *p*H adjustment = NH_4OH

All of the materials were reagent grade. The bath temperature was kept constant to ±0.5°C; most of the experiments were conducted at 75°C, except when the temperature was a variable. The bath *p*H, as will be seen, played a critical role and therefore was controlled to within ±0.02 *p*H. Such control over the bath *p*H was made possible by using plating apparatus with

automatic pH recorder-controller. The pH of the bath is detected by an expanded-scale pH meter through a high-temperature glass and reference (AgCl, KCl) electrode. All the pH readings in this paper should be interpreted at the designated temperature. The pH meter was standardized with Beckman Buffer No. 14049 at 75°C. The pH of this buffer varies with temperature in the following manner;

Temperature, °C	pH
25	9.18
70	8.92
90	8.85

A decrease as small as 0.02 pH causes the controller to open the solenoid valve through a relay, permitting the release of enough ammonium hydroxide to readjust the pH to a preset level. This on-off pH-control process is monitored by a recorder. No thermal compensator is used since bath temperature is kept constant. The bath container is a conventional Pyrex reaction vessel; the lid is modified to hold in position the glass and reference electrodes, a thermometer, condenser, and a sample holder. It also provides entrance for ammonium hydroxide.

The bath was not agitated in this investigation. Bath volume was kept at 1100 cc; the size of the Mylar sample was 10 x 2 cm and 7.62 x 10^{-3} cm thick (3 mil). All water used for preparation and rinsing purposes was de-ionized, having a resistivity greater than 1 megohm-cm. Samples, thus prepared, were air dried and cut into ¼ x 2½ in. pieces for magnetic measurements, thickness measurements, and chemical analysis.

Magnetic measurements.—Samples (¼ x 2½ in.) were placed vertically into the center of the sensing coil of a 60-cycle B-H loop tracer having a maximum driving field of approximately 1400 oe. From the hysteresis loop displayed on the cathode ray tube of a Tektronix Type RM-503 oscilloscope, coercivity (H_c), squareness ratio (B_r/B_m), and retentivity (B_r) were calculated. Reproducibility of the coercivity readings is 1% for higher coercivities and 5% for lower coercivities (of the order of 100 oersteds).

Thickness measurements.—Two methods were applied: (*A*) determination of amount of cobalt and phosphorus by polarography and spectrophotometry, respectively. By assuming a bulk density of 8.9 and also surface uniformity, film thickness with 5% expected accuracy was obtained. (*B*) Standard two-beam interferometric method (4); the interference tester in conjunction with the "Reicharts Universal Camera Microscope MeF" was used; special masking and dissolution was applied to create a sharp step. The thickness measurement was reproduced to within ±0.5 μin. by this method.

Phosphorus analysis.—Phosphorus content was determined spectrophotometrically, using the heteropoly blue method (5). Total errors for phosphorus content was about 2%.

Experimental Results

Effect of deposition time.—The influence of deposition time on the film thickness is illustrated in Fig. 1, where an almost linear relation is observed. The slope is pH dependent. As will be seen later, this relationship is temperature and hypophosphite dependent also. The dependence of film coercivity on the deposition time is illustrated in Fig. 2. Here we see that film thickness (deposition time) has significant influence on the coercivity of the deposited film, particularly at higher pH ranges. A plot of log H_c *vs.* log thickness results in a straight line (Fig. 3) with a slope of 0.4. Hence, $H_c = At^{-2/5}$.

Another noteworthy influence of increased deposition time or film thickness is a decrease in the phosphorus content of the deposit (Fig. 4). It appears that a good portion of the phosphorus is codeposited in the initial stages of the reaction. The phosphorus content for the majority of the samples reported in this paper ranged up to about 4%.

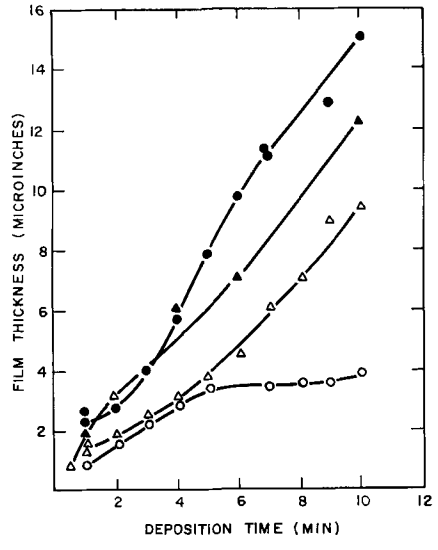

Fig. 1. Film thickness of cobalt-phosphorus *vs.* deposition time at various pH: ●, 8.42; △, 8.37; △, 8.20; ○, 7.66; bath temperature, 75°C.

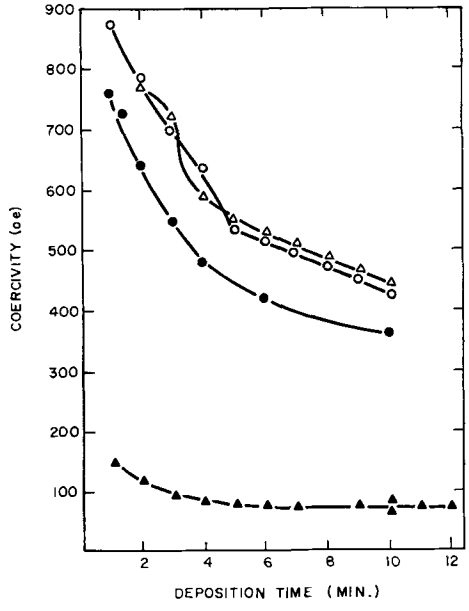

Fig. 2. Coercivity of cobalt-phosphorus films *vs.* deposition time for various pH: △, 8.70; ○, 8.42; ●, 8.37; ▲, 7.66; bath temperature, 75°C.

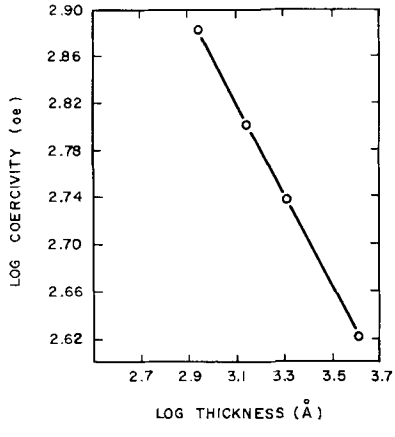

Fig. 3. Log of coercivity *vs.* log of thickness for cobalt-phosphorus depositions; slope, 0.40; bath temperature, 75°C; pH, 8.37.

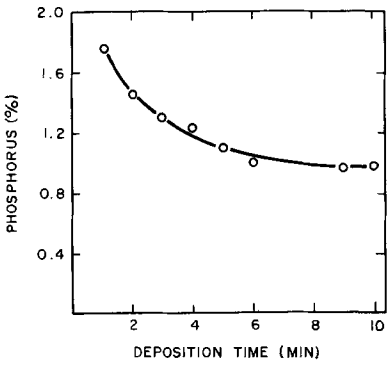

Fig. 4. Per cent phosphorus vs. deposition time for chemically deposited cobalt-phosphorus films; bath temperature, 75°C; pH, 8.42; thickness, 2.2-15 μin.

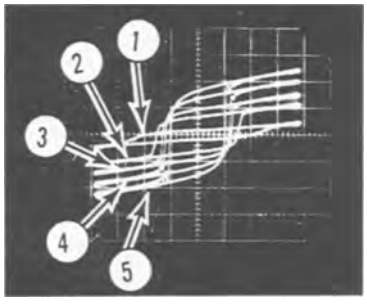

Fig. 5. Effect of deposition time at constant pH 8.2; temperature, 75°C: 1, 1 min; 2, 4 min; 3, 6 min; 4, 8 min; 5, 10 min.

The effect of deposition time on the shape of superimposed hysteresis loops is seen in Fig. 5 in which the decrease in H_c with simultaneous increase in B_m is observed. Squareness ratios ranging from 0.75 to 0.95, with B_r values from 7 to 10 kilogauss (also occasional higher and lower values) were observed.

Effect of bath pH.—Bath pH provides another significant tool in controlling the magnetic properties of cobalt-phosphorus films. Increasing the bath pH (in the alkaline range) increases the speed of deposition to a limit. This not only increases the thickness of the deposit, as seen in Fig. 6, but it apparently causes some structural changes which influence the magnetic properties. According to Fig. 6, a film thickness of 2 to about 14 μin. is obtained as the pH is varied from 7.7 to 8.3 at constant deposition time (10 min). The influence of pH on film coercivity is illustrated in Fig. 7.

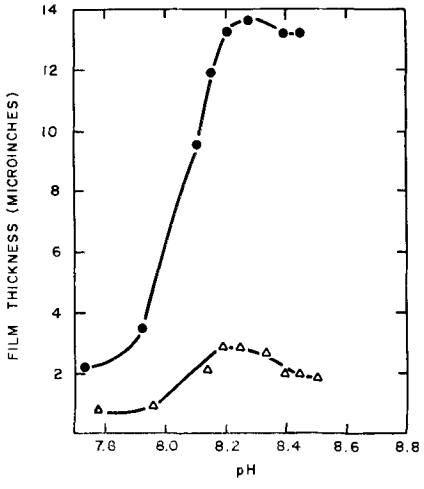

Fig. 6. Thickness of cobalt-phosphorus films vs. bath pH for various deposition times: ●, 10 min; △, 2 min; bath temperature, 75°C.

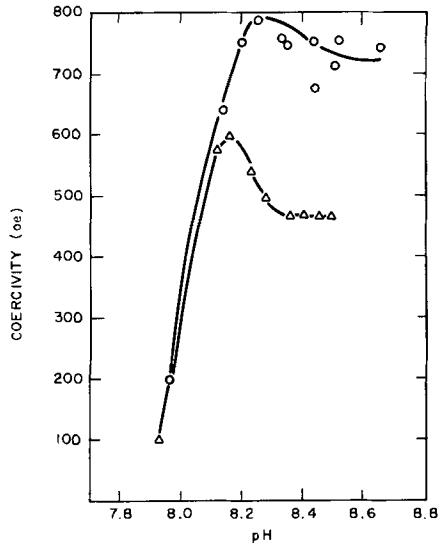

Fig. 7. Coercivity of cobalt-phosphorus films vs. bath pH for various deposition times: ○, 2 min; △, 10 min; bath temperature, 75°C.

Observe that as the pH increases there is a sudden initial increase in H_c, followed by a maximum and, finally, a reversal of the trend. This trend was also observed in Fig. 2, which is the result of a different set of experiments.

Table I helps to explain Fig. 7. The pH and thickness effects are separated in Table I, clearly demonstrating the H_c-pH dependence at constant film thicknesses of 2 and 4 μin. A gradual increase in pH causes sharp increases in coercivity, creating an order-of-magnitude increase in coercivity as the pH is increased by approximately 0.8. Therefore, the initial and sudden H_c increase of Fig. 7 is due solely to the increasing pH of the bath overshadowing the increasing thickness effect. The phosphorus content of the deposited film in general appears to decrease with increasing bath pH, as is illustrated in Table II.

The superimposed hysteresis loops pertaining to the pH effect are shown in Fig. 8. Note again the dominating effect of pH on coercivity in Fig. 8, where deposition time (film thickness) has been kept small. No definite correlation seems to exist between B_r and bath pH. The B_r/B_m does show a tendency to increase as the bath pH increases (see Fig. 9).

Table I. Effect of pH on coercivity of CoP film at various constant film thickness; temperature, 75°C

pH	Coercivity, oe
2 μin.	
7.67	120
8.37	760
8.41	800
9.44	875
4 μin.	
7.67	75
7.93	100
8.37	450
8.45	700

Table II. Influence of bath pH on phosphorus content and film coercivity of cobalt-phosphorus films

pH	Thickness, μin.	% P	H_c, oe
7.78	0.8	3.10	—
7.96	0.9	2.41	210
8.14	2.2	2.05	640
8.24	2.9	1.97	800

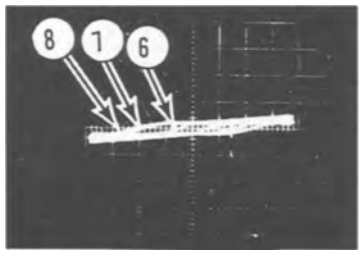

Fig. 8a. Effect of bath *p*H at 2-min deposition time: 6, *p*H 7.96; 7, 8.14; 8, 8.24.

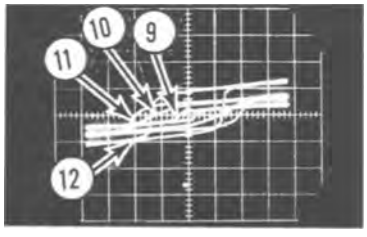

Fig. 8b. Effect of bath *p*H at 2-min deposition time: 9, *p*H 7.97; 10, 8.22; 11, 8.41; 12, 8.65.

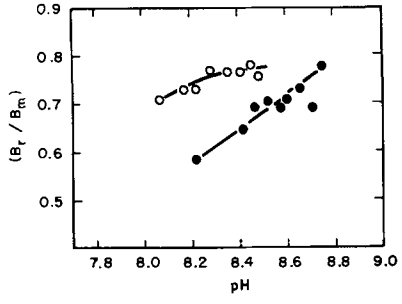

Fig. 9. Squareness ratio *vs.* bath *p*H for cobalt-phosphorus films: ●, 5 min; ○, 10 min; bath temperature 75°C.

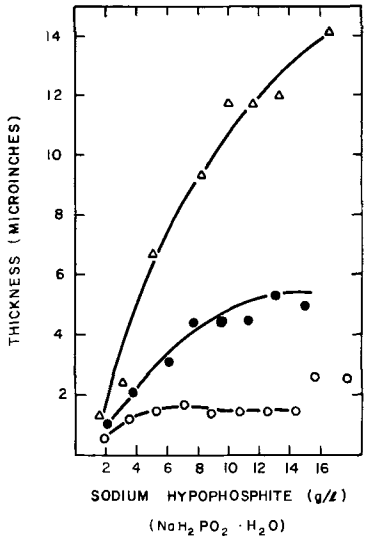

Fig. 10. Film thickness of cobalt-phosphorus *vs.* sodium hypophosphite: *p*H: △, 8.5; ●, 8.13; ○, 7.78; bath temperature, 75°C; deposition time, 5 min.

Effect of sodium hypophosphite.—Sodium hypophosphite is an essential component of the bath in that it reduces the cobalt ion to metallic cobalt.

Aside from its part as a reducing agent, sodium hypophosphite influences the speed of deposition. This effect is shown in Fig. 10, where deposition time and temperature were kept constant. Note that at a higher *p*H level (8.45) an increase in the sodium hypophosphite content of the bath from 2 to 14 g/l causes an increase of 12 μin. in the film thickness. Such an increase is less pronounced when the bath *p*H is kept at lower levels (7.78).

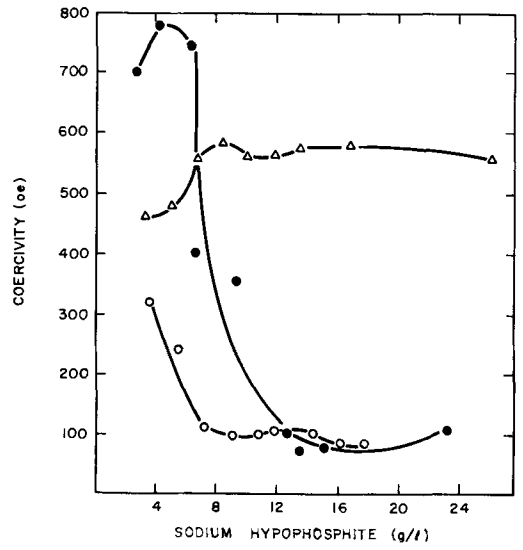

Fig. 11. Coercivity of cobalt-phosphorus films *vs.* sodium hypophosphite at various bath *p*H: △, 8.45; ●, 8.13; ○, 7.78; bath temperature, 75°C; deposition time, 5 min.

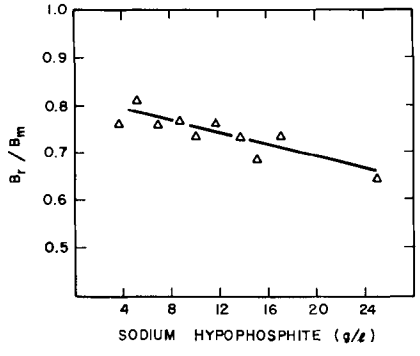

Fig. 12. Squareness ratio of cobalt-phosphorus film *vs.* sodium hypophosphite content of the bath: △, *p*H, 8.45; bath temperature, 75°C; deposition time, 5 min.

The influence of sodium hypophosphite content on the film coercivity is illustrated in Fig. 11. At low and moderate *p*H an increase in sodium hypophosphite causes a reduction in coercivity; at higher *p*H no sharp changes are observed. Fig. 11, in reality, represents three different effects: *p*H, film thickness, and sodium hypophosphite. The *p*H effect is separated from the other two by conducting three isolated experiments, keeping *p*H levels constant. Therefore, changes of film coercivity shown in Fig. 11 seem to be the result of an increase in the film thickness which is caused by sodium hypophosphite. Thus, the true influence of sodium hypophosphite is masked by the thickness effect.

Sodium hypophosphite content of the bath seems to have a negative influence on the B_r/B_m ratio of the deposition. In one particular case, as shown in Fig. 12, the B_r/B_m value drops from 0.8 to 0.65 as the sodium hypophosphite content is increased about 20 g/l.

Effect of bath temperature.—A strong dependency of film thickness and coercivity on bath temperature was observed as the bath temperature was changed from 70° to 95°C. Deposition took place at temperatures as low as 57°C, and, although this is a convenient temperature, the deposition rate is too slow for practical consideration.

The relation between bath temperature and film thickness is illustrated in Fig. 13 for two different *p*H levels. The amount of the deposit nearly doubles as

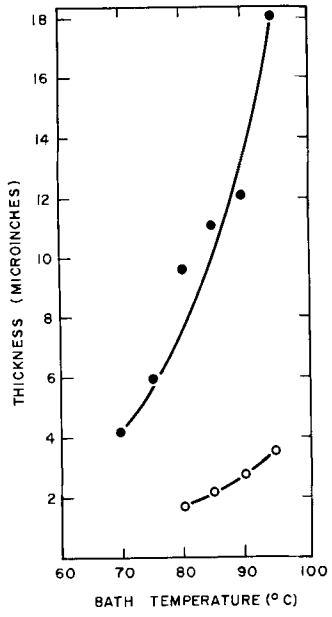

Fig. 13. Thickness of cobalt-phosphorus films *vs.* bath temperature; deposition time, 5 min; ○, *p*H 7.45; ●, *p*H 8.02.

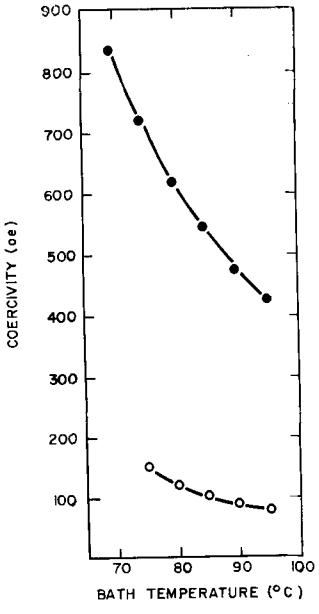

Fig. 14. Coercivity of cobalt-phosphorus deposition *vs.* bath temperature; deposition time, 5 min; ○, *p*H 7.45; ●, *p*H 8.02.

the temperature is increased from 70° to 80°C. As the temperature is raised to 95°C, film thickness increases to 18 μin. for a deposition time of 5 min. This tendency is *p*H dependent as is evident from Fig. 13.

The influence of bath temperature on the magnetic properties of deposition is illustrated in Fig. 14. A careful analysis of this figure shows that the reduction of H_c as a function of temperature is truly due to the increase in the film thickness which is caused by the increase in bath temperature (Fig. 13). Briefly, it appears to be the thickness which governs the coercivity rather than temperature. To demonstrate precisely the effect of the temperature, independent of film thickness, a new set of experiments is needed in which the thickness of the deposit is kept constant.

The magnitude of B_r/B_m for this series was within the range of 0.75-0.9; this range seems to be representative for most cobalt-phosphorus deposition.

Discussion

The pretreatment and posttreatment conditions play a significant part in the nature of the deposited film and its adhesion to the Mylar substrate. The alkali etching treatment proved to be much more satisfactory than a sodium dichromate-sulfuric acid treatment. The latter caused microscopic cracking of the substrate. The alkali etching approach suggested here should be a much more desirable method of rendering Mylar surface hydrophilic than the use of an adhesive as suggested by Fisher and Chilton (1). A more acidic sensitizer bath (compared to the activator bath) proved significant to a more uniform and consistent deposition. A few minutes heating cycle at 110°C after the deposition step causes a large increase in the adhesion value of Co-P to the Mylar surface.

The coercivity of the deposit which appears to be one of the most structure-sensitive characteristics, can be conveniently controlled by deposition time. Further control of coercivity, particularly for higher ranges, is achieved by the *p*H element or hypophosphite concentration.

The dependence of coercivity on film thickness is not new; it was first predicted by Néel (6) to be

$$H_c = At^{-4/3}$$

Fisher and Chilton (1) report a value of —1/3 for the exponent which agrees well with the empirical relation $H_c = At^{-2/5}$ reported in this paper. It should be noted, however, that the thickness-coercivity dependency can be overshadowed if other factors are not kept constant. Bath *p*H, for example, affects film coercivity noticeably even at the same film thicknesses (Table I); hence the above empirical relation is valid only when all other bath variables have been kept constant. It is very likely that the increase in bath alkalinity brings about some structural changes, as well as changes in the internal stresses, of the deposit; the latter is known to affect the coercivity of electro-deposited cobalt films (7).

The influence of phosphorus content on the magnetic property of the film is not clear. In one set of experiments, a linear increase in H_c as a function of per cent phosphorus was observed; however, the film thickness effect obscures any definite conclusion. In a second case, where *p*H is the main variable (Table II), a trend between per cent phosphorus and H_c is observed, which again is overshadowed by strong H_c-*p*H dependency. There is a need for more intensive investigation to determine the true influence of codeposited phosphorus.

The effect of hypophosphite is noticeable at low and moderate *p*H; bath temperature provides another tool for controlling the thickness, hence affecting the coercivity. In order to produce a film with desired film thickness and coercivity the four major factors, *i.e.*, deposition time, bath *p*H, temperature, and hypophosphite concentration, must be taken into consideration simultaneously.

Although the B_r/B_m ratio is not as sensitive to various changes it does increase with increasing film thickness and bath *p*H. Sodium hypophosphite, on the other hand, seems to have a decreasing effect on B_r/B_m.

The B_r values for the majority of the experiments remained between 7 to 10 kilogauss with occasional lower and higher values.

In conclusion the results of the study have served to provide the means for preparing thin, optically reflective magnetic recording media with a wide range of magnetic properties. These properties are suited particularly for high-density magnetic recording and Kerr magneto-optical readout.

Acknowledgments

The author wishes to acknowledge Mr. E. B. Moore, R. J. Cappell, and Dr. I. Barlow for their excellent assistance in thickness measurements, chemical analysis, and x-ray work, respectively. Thanks are also due to Dr.

J. T. Smith, and Mr. O. Kornei for their continued interest in this work, to Mr. N. Erez for his assistance in performing the experiments, to Mr. F. Stryker for earlier help in the substrate etching, and to Dr. J. R. Werning, Dr. G. Bate, and Mr. J. Judge for their comments in reviewing this paper.

Manuscript received Dec. 21, 1964; revised manuscript received May 19, 1965. (Work completed in 1962.)

Any discussion of this paper will appear in a Discussion Section to be published in the June 1966 JOURNAL.

REFERENCES

1. R. D. Fisher and W. H. Chilton, *This Journal*, **106**, 486 (1962).
2. B. R. Edwards, Private Communication.
3. A. Brenner, *Metal Finishing*, November-December (1954).
4. Osterreishisher Maschinenmarkt Mit Electrowirtschaft, VII, 5/6 (1963).
5. D. F. Boltz and M. G. Mellon, *Anal. Chem.*, pp. 873-877 (November 1947).
6. L. Néel, *J. Phys. Radium*, **17**, 250 (1956).
7. R. D. Fisher, *This Journal*, **106**, 479 (1962).

Determination of the Density and Dielectric Constant of Thin Ta_2O_5 Films

Julius Klerer

Bell Telephone Laboratories, Incorporated, Murray Hill, New Jersey

ABSTRACT

The density of anodically formed Ta_2O_5 thin films on sputtered tantalum has been measured *in situ*. The method used is the measurement of the average density of the assemblage tantalum-tantalum oxide and subsequent separation of the contributions of each component to this measured density. From a knowledge of the stoichiometry of the reaction, both the thickness and the angstrom per volt values (thickness of oxide formed per volt) can be determined for the oxide. Application of the capacitance formula for a parallel-plate capacitor leads to a value for ϵ. The values obtained are: Density; 8.00 g/cm^3 ± 2.4%; anodization constant, 16.0Å/v ±3.2%; dielectric constant, 21 ± 3.3% at 1 kcps.

The use of anodic Ta_2O_5 films for capacitor fabrication can be aided by a precise knowledge of the density and dielectric constant of these films. Reported densities have ranged from 7.93 g/cm^3 (1) to 8.74 g/cm^3 (2), and dielectric constant values reported range from 22 to 27.6 (3). Most of the values of these constants have been obtained from bulk oxides or from anodized tantalum foil.

This study represents an attempt to determine these values for the oxide anodically formed on sputtered tantalum. The density of the oxide is measured *in situ* by an independent method. From this value of density, the thickness of the film is obtained by a determination of the anodization constant (Å/v). The dielectric constant can then be evaluated by application of the ordinary formula for capacity.

Theoretical

Density.—The average density of the assemblage, tantalum-tantalum oxide can be defined as

$$D = \frac{\overline{M}}{\overline{V}} \qquad [1]$$

where $\overline{M}$ is total mass and $\overline{V}$ total volume.
Now by definition

$\overline{M}$ = mass of tantalum remaining (m_{Ta}) after anodization + mass of oxide formed during (m_o) anodization

$\overline{V}$ = volume of tantalum (v_{Ta}) after anodization + volume of oxide (v_o) formed during anodization.

The average density can then be redefined as

$$\overline{D} = \frac{m_{Ta} + m_o}{v_{Ta} + v_o}$$

By definition

$$V_{Ta} = \frac{m_{Ta}}{d_{Ta}};\ v_o = \frac{m_o}{d_o}$$

where d_{Ta} is the density of tantalum and d_o the density of tantalum pentoxide. Substituting for v_{Ta} and v_o and rearranging the equation to solve for d_o produces the expression

$$d_o = \frac{\overline{D} d_{Ta} m_o}{d_{Ta}(m_{Ta} + m_o) - D m_{Ta}} \qquad [2]$$

During the anodization process, two moles of tantalum are required for each mole of Ta_2O_5 formed. In order that stoichiometry be preserved, the mass of tantalum consumed (Δm_{Ta}) to form m_o grams of Ta_2O_5 is

$$\Delta m_{Ta} = m_o \frac{2M_{Ta}}{M_{Ta_2O_5}}$$

where M_{Ta} equals the atomic weight of tantalum and $M_{Ta_2O_5}$ equals the molecular weight of tantalum pentoxide. Thus, the original mass (P) of the tantalum before anodization is

$$P = m_{Ta} + m_o \cdot \frac{2M_{Ta}}{M_{Ta_2O_5}} \qquad [3]$$

By a previous definition

$$\overline{M} = m_{Ta} + m_o \qquad [4]$$

Solving Eq. [3] and [4] for m_o and m_{Ta} and placing the values of the atomic weight of tantalum and the molecular weight of Ta_2O_5 in the equations results in the following

$$m_o = 5.524\ \Delta M \qquad [5]$$

$$m_{Ta} = \overline{M} - 5.524\ \Delta M \qquad [6]$$

where $\Delta M = \overline{M} - P$

Combining Eq. [5], [6], and [2], a final working equation is obtained

$$d_o = \frac{5.524 \overline{D} d_{Ta} \Delta M}{M(d_{Ta} - D) + 5.524 D \Delta M} \qquad [7]$$

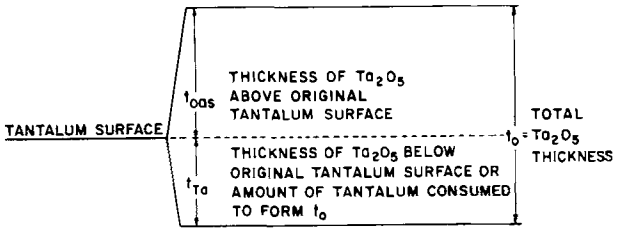

Fig. 1. Schematic structure of oxide film growth by anodization

All of the quantities on the right-hand side of this equation can be determined experimentally. The density of tantalum is taken as 16.6 g/cm³ (7).

Determination of the anodization constant.—As tantalum is anodized, the oxide grows above and below the original surface of the tantalum to give rise to the schematic structure shown in Fig. 1 where the volume of the oxide is greater than the volume of the metal displaced.

By definition

$$t_o = t_{oas} + t_{Ta} \qquad [8]$$

and assuming, for the moment, that the thickness is proportional to the applied field

$$t_o = k_1 V \qquad [8a]$$

$$t_{oas} = k_2 V \qquad [8b]$$

$$t_{Ta} = k_3 V \qquad [8c]$$

where V is the voltage applied and k the respective anodization constants. The t_{Ta} consumed to form t_o can be related by the ratio of densities

$$\frac{t_{Ta}}{t_o} = \frac{(2)\ (M_{Ta})\ (d_o)}{(M_{Ta_2O_5})\ (d_{Ta})} = B$$

or

$$t_{Ta} = Bt_o \qquad [9]$$

Substituting Eq. [9] into Eq. [8] and rearranging

$$t_o = \frac{t_{oas}}{(1 - B)} \qquad [10]$$

Eq. [8a], [8b], and [10] produce

$$k_1 = \frac{k_2}{1 - B} \qquad [11]$$

From Eq. [8b], a plot of t_{oas} *vs.* the applied voltage, V, yields a straight line whose slope equals k_2. Placing this value of k_2 in Eq. [11] determines k_1 and since $k_1 = k_2 + k_3$, the value of k_3 is likewise determined. The constant B is dependent on the determination of the density of the Ta_2O_5.

Determination of the dielectric constant of Ta_2O_5.—The capacitance of a parallel plate capacitor is defined as

$$C = \frac{0.0885A\epsilon}{t_o} \qquad [12]$$

where ϵ is the dielectric constant, A the area (cm²), t_o the thickness (cm), and C the capacitance (pf).

The thickness, t_o of the Ta_2O_5 film formed is proportional to the anodization voltage from Eq. [8a] and substituting into Eq. [12] produces

$$C = \frac{0.0885\epsilon A}{k_1 V}$$

If C is plotted as a function of $1/V$, a straight line is obtained with the slope $= (0.0885\epsilon A)/k_1$. On rearrangement

$$\epsilon = \frac{(\text{slope})\ (k_1)}{0.0885A} \qquad [13]$$

The value of the dielectric constant rests on the determination of k_1 from the previous section. The geometrical area can be measured directly.

Table I. Density determination

Slide No.	Average thickness of tantalum, Å	Average, ρ (μ-ohm-cm)	$\bar{D}$, g/cc	d_o, g/cc	Formation voltage, v
1	3449	49.7	13.15	7.95	130
2			12.96	5.85	130
3	3217	70.1	12.88	8.42	130
4			13.05	7.83	130
5	3573	50.4	13.15	7.67	130
6			13.34	7.99	130
7	3600	52.2	13.35	7.89	130
8			13.28	8.11	130
9	3309	259	13.02	7.58	130
10			13.13	8.30	130
11	3450	203	13.10	8.36	130
12			13.24	8.26	130
13	2842	46.5	10.58	8.01	250
14			10.54	7.86	250
15	3361	201	11.89	8.10	200
16			11.86	7.90	200
17	3460	213	13.85	7.91	100
18			13.84	7.79	100
19	3713	191	14.50	7.84	75
20			14.61	8.26	75

Average $d_o = 8.00 \pm 0.19$
$\pm 2.4\%$

Experimental

The tantalum utilized was sputtered through a mask to define a definite area onto Corning No. 7059 1 x 3 in. glass slides. The cathode was separated a distance of 5.25 cm from the work. At an argon pressure of 20 x 10^{-3} Torr and a potential of 4 kv, the current density was maintained at 0.35 ma/cm². The deposition rate was approximately 110 Å/min. Anodization of these slides was carried out at room temperature in aqueous 0.01% citric acid solution as follows: The current was maintained at a current density of 1 ma/cm² until the desired constant voltage was attained. Anodization was continued at the desired formation voltage for an additional hour. Capacitors were fabricated by the vacuum evaporation of gold counterelectrodes, the other contact being the underlying tantalum.

Weighing of the slides was performed on a Mettler type M5 Microbalance with a precision of ± 0.001 mg. Area determinations both for counterelectrode area and the area involved in the volume determinations were made with the Nikon Model 6 Shadowgraph with a precision of ± 0.001 cm².

Density determination.—Table I contains a summary of the data utilized for the density determination. $\bar{D}$ is obtained from the weight of the tantalum and tantalum oxide after anodization ($\bar{M}$) and measurement of the volume ($\bar{V}$) of the tantalum and tantalum oxide. The geometrical area is defined by the masked sputtered area and the thickness was obtained by Talysurf[1] measurements of the height of the tantalum and tantalum oxide. The use of the Talysurf measurements is more clearly illustrated in the next section.

$\bar{D}$ can be used as a measure of the ratio of tantalum to tantalum oxide. In order to vary this ratio, the formation voltage was changed to detect any influence upon the sensitivity of the method used for the density determination. The low value obtained for d_o for slide 2 in Table I is attributed to its being chipped during anodization. The density values obtained were computed using Eq. [7] and an average density and average error were calculated to be 8.00 g/cm³ ± 2.4%.

Determination of the anodization constant.—Figure 2 is a plot of the height of the oxide above the original tantalum surface (t_{oas}) as a function of the voltage. The height was determined by Talysurf measurements and the curve fitted by the method of least squares. The slope was computed to be 9.67 Å/v with a probable error of ± 2.2%

[1] Taylor-Hobson Ltd. Model 3 Talysurf with a straight line datum attachment.

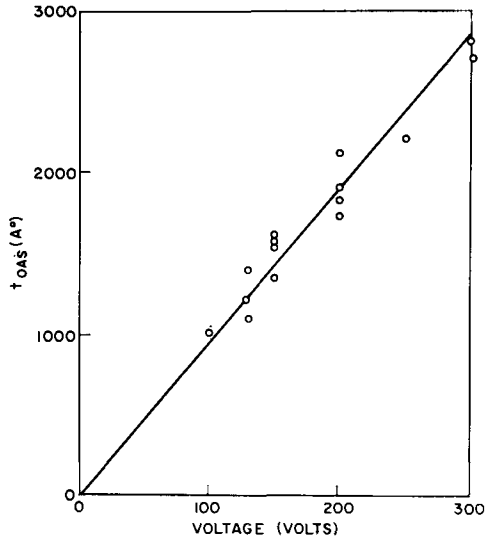

Fig. 2. Height of tantalum oxide film above original tantalum surface (t_{oas}) as a function of voltage; slope equals 9.67 Å/v.

Utilizing the formulas [8] to [11], the following values were determined

$$t_{Ta} = 0.3948\, t_{oxide}$$

Anodization constant (k_1)
= 16.0 Å/v ± 3.2% for Ta_2O_5

Anodization constant (k_3)
= 6.3 Å/v ± 3.2% for tantalum

Determination of the dielectric constant.—Sputtered tantalum slides were anodized as previously described to voltages between 100 and 300v and gold counterelectrodes were vacuum evaporated and the capacitance measured at 1 kc on a parallel capacitance bridge with a maximum error of ±0.5%. Figure 3 shows the curve obtained by plotting capacitance *vs.* reciprocal voltage. Each point represents the average of approximately 90 capacitors at each voltage. The curve was fitted by the method of least squares and the slope calculated to be 1.40 x 10^6 with a probable error of ±0.2%. From this value, the value of k_1, (16.0 Å/v) and the measured counterelectrode area (0.121 cm^2) the dielectric constant was calculated by application of Eq. [13]. The

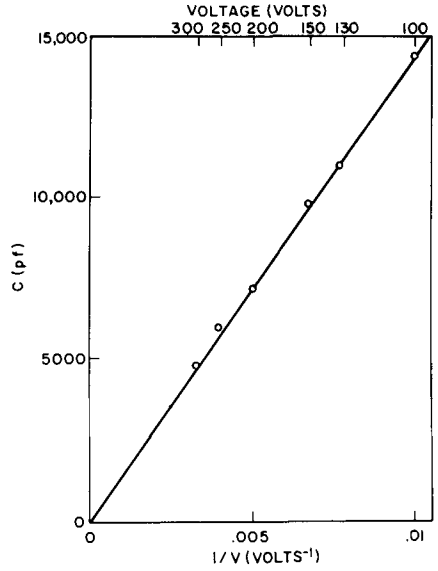

Fig. 3. Capacitance of tantalum oxide films as a function of voltage^{-1}; slope equals 1.40x10^6.

dielectric constant determined was ϵ = 21.2 with a maximum error of 3.3%.

Discussion

The determination of the density, anodization constants, and dielectric constant presented in this work, as well as in other papers to be cited, rests on the validity of several assumptions. One is that the density of the sputtered tantalum film is known and is constant throughout the film. Foreign gases in the field should change the density as has been shown in gas doping experiments (9).

The films utilized in this work were sputtered with no known addition of foreign gas. Talysurf measurements of the thickness of some of these sputtered tantalum films, combined with the geometrical area and weight, resulted in values of density of 16.5 g/cm^3. This agrees closely with reported values for bulk density, 16.6 g/cm^3. Resistivity measurements of the films used in this work also indicate that the tantalum was comparable to that normally obtained by sputtering. The question as to whether the resistivity of the tantalum as a function of thickness remains constant throughout the film is still debatable. It is believed, in general, that there is a graduation in resistivity in the sputtered tantalum film, particularly if a shutter is not utilized for presputtering. This gradation in resistivity has not, as yet, been shown to affect the density of the tantalum.

Another assumption is that the anodization reaction is 100% efficient. This has been confirmed by Vermilyea (6) and Young (3). Basic to this determination is the fact that the oxide formed is Ta_2O_5 and that the oxide is stoichiometric. These conditions appear to be realized within the limits of experimental error. In the present case, the determination of the density of the oxide did not seem to depend on the ratio of oxide to tantalum thickness nor on the resistivity of the tantalum, again implying that the density of the oxide was constant throughout and that stoichiometry was preserved.

The density of bulk Ta_2O_5 is reported to be 8.74 g/cm^3 in the Handbook of Chemistry and Physics (1). Reisman *et al.* report the density of the low-temperature crystalline form as 8.18 g/cm^3 and that of the high-temperature form to be 8.37 g/cm^3 (4). King *et al.* determined densities of 8.41 g/cm^3 and 8.63 g/cm^3 for the low- and high-temperature forms, respectively (5). All of the above values have been determined from bulk tantalum pentoxide, and it might be expected that these values would differ from the density obtained for a thin film of Ta_2O_5 on sputtered tantalum.

Young (1) determined the density of thin anodic films of Ta_2O_5 formed in 1% H_2SO_4 on chemically polished foil by the Archemedian displacement method to be 7.93 g/cm^3 ± 3%. This agrees closely with the present determination of a density of 8.00 + 2.4% for anodically formed Ta_2O_5 on sputtered tantalum. The validity of the newly proposed measurement technique devised is also supported.

This measurement technique requires that a large number of samples be used since the average surface area for the individual sample is ≅ 15 cm^2. The maximum error expected from a consideration of the probable errors in the variables was of the order of 4%. However, careful technique and probable cancellation of some of the expected errors occurs leading to the average error obtained. The reproducibility of the individual determination is low, as can be seen in Table I.

In contrast is the determination of the density of the oxide formed on sintered tantalum anode sets with a combined surface area of ~ 1600 cm^2 by the utilization of only three separate samples (7). A greater accuracy was expected and reported. The values obtained for the density were 8.039 ± 0.005 g/cm^3 for films formed in 0.01% HNO_3; 7.87 ± 0.01 g/cm^3 for films formed in 50% H_2SO_4; and 8.03 ± 0.04 g/cm^3

for films formed in 0.1% H_3PO_4. The accuracy of these values in leading to the speculation that the forming electrolyte has an influence on the density merits further confirmation. A more important point to be gathered from this study and the other determinations of density is that the oxide anodically formed on sintered tantalum, tantalum foil, and sputtered tantalum has essentially the same density.

Vermilyea (6) computed the anodization constant for Ta_2O_5 films on tantalum foil to be 14.95 Å/v using weight measurements and 15.27 Å/v using Faraday's law. The thickness of the oxide was measured by a calibrated color step gauge, and the density value for Ta_2O_5 was assumed to be 8.74 g/cm^3. If the density value determined in this work is used to recalculate Vermilyea's results, the anodization constant for Ta_2O_5 becomes 16.29 Å/v and 16.64 Å/v, respectively. This is to be compared with the value obtained experimentally in this work, 16.0 Å/v for the oxide. Vermilyea anodized his films in 1% Na_2SO_4 at an initial current density of 2 ma/cm^2 and held them at constant voltage until a current density of 0.1 ma/cm^2 was reached.

Patterson and White (8) using ellipsometric techniques determined the anodization constant of the oxide to be 14.1 Å/v for sputtered tantalum films on glass substrates and 16.6 Å/v on glazed alumina. The anodization was carried out in a phosphoric acid, water, and ethylene glycol solution. The voltage was raised at a rate of 2 v/min to a constant voltage and held till a current of 25 μma was reached. The difference in anodization constant on the two substrates was attributed to either a "secondary substrate" effect influencing the tantalum surface or to differences in the tantalum film, since separate sputtering runs were used for each substrate.

All of the values obtained correspond closely. The difference that might be present can possibly be attributed to the anodization techniques and/or film quality. The techniques used in this work measures gross effects and are not as dependent on the uniformity of the film. The measurements reported in the present work have only the error involved in the individual Talysurf measurements which appear to be small when the data has been compensated for in the least squares determination of the curve of t_{oas} *vs.* voltage.

The value of 21.2 at 1 kcps obtained for the dielectric constant is lower than has been reported. Young (9) reports values of dielectric constant from 23 to 25 for tantalum oxide anodically formed on tantalum foil previous to his own determination which is 27.6 ± 5% at 1 kcps (2). The differences in the dielectric constant might be attributable to the type of tantalum utilized and/or the anodization conditions utilized. The point has been made that electrolyte species can be incorporated into the growing oxide (7), and quite possibly an influence on the dielectric constant might be expected.

Conclusions and Summary

In this study, the sputtered tantalum used has been assumed to be as pure as can be produced at the present state of the art. The homogeneity of the oxide appears to be such that the validity of the determined density can be used with assurance. The derived values of the other constants, within error, appear to be valid. The theoretical derivations and the techniques utilized have been justified and can be used as a general technique for the study of the growth of oxide films. The limitation of these techniques lies in the fact that the stoichiometry of the oxide formed must be known.

In summary, the values obtained from this study are

$$d_o = 8.00 \pm 2.4\%$$
$$t_{Ta} = 0.3948\, t_{oxide}$$
Anodization constant (Ta_2O_5) = 16.0 Å/v ± 3.2%
Anodization constant (Ta) = 6.3 Å/v ± 3.2%
Dielectric constant (Ta_2O_5) = 21.2 ± 3.3%

Acknowledgment

The assistance of Miss Dolores Farrell in some of these experiments and the Talysurf measurements of the film thicknesses by R. Brown are greatly appreciated.

Manuscript received Jan. 28, 1965; revised manuscript received April 20, 1965. This paper was presented at the San Francisco Meeting, May 9-13, 1965.

Any discussion of this paper will appear in a Discussion Section to be published in June 1966 JOURNAL.

REFERENCES

1. L. Young, *Proc. Royal Soc.*, **A244**, 41 (1958).
2. C. D. Hodgman, Editor, "Handbook of Chemistry & Physics," Chemical Rubber Publishing Co. (1958).
3. L. Young, "Anodic Oxide Films," Academic Press, New York (1961).
4. A. Reisman, F. Holtzberg, M. Berkenblit, and M. Berry, *J. Am. Chem. Soc.*, **78**, 4514 (1956).
5. B. W. King, J. Schultz, E A Durbin, and W. H. Duckworth, Battelle Mem. Inst. Rep. BMI-1106 (1956).
6. D. A. Vermilyea, *Acta Met.*, *I*, 282 (1953).
7. A. J. Schrijner and A. Middelhoek, *This Journal*, **111**, 1167 (1964).
8. W. E. Patterson and C. L. White, "Thin Films Formed by Electrochemical Process," Texas Instrument Co., final report, June 1, 1962-January 31 1963, AD417100.
9. D. Gerstenberg and C. J. Calbick, *J. Appl. Phys.*, **35**, 402 (1964)

Inversion of Oxidized Silicon Surfaces by Alkali Metals

J. R. Mathews, W. A. Griffin, and K. H. Olson

Bell Telephone Laboratories, Incorporated, Laureldale, Pennsylvania

ABSTRACT

The effects of alkali-metals on the behavior of the oxide protected silicon surfaces has been investigated using a p-n structure. Examination of diode characteristics and photoresponses on controlled samples revealed the manner of alkali-metal electrolysis through the oxide and the formation of donor-type surface states at the $Si-SiO_2$ interface.

Investigations have been performed to determine the effects of alkali-metals on oxide protected semiconductor surfaces. The emission of glass modifiers, among them the alkalies, has been observed from glass to metal seals in semiconductor device packages (1). Since the use of such seals is a widespread practice in the semiconductor industry, knowledge of the behavior of alkalies and their effects on semiconductor surfaces is of importance. Figures 1 and 2 illustrate the degradation of aging stability and radiation resistance caused by alkali contamination of diodes. The figures represent data from diodes sealed in miniature glass packages

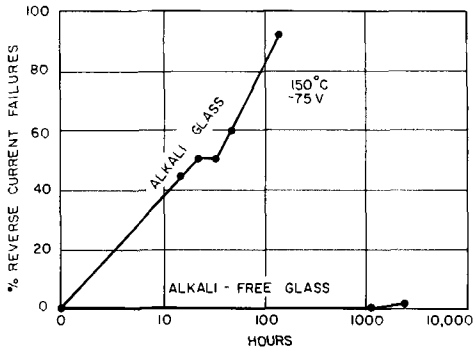

Fig. 1. Temperature-reverse voltage aging data

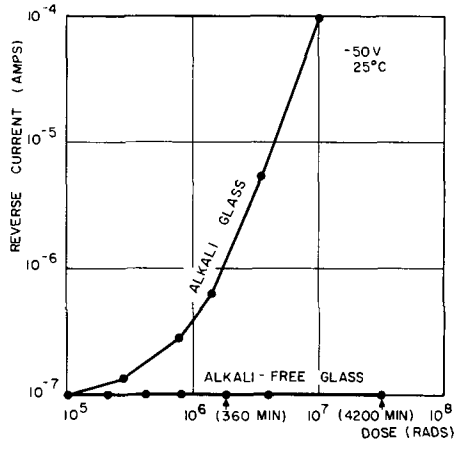

Fig. 2. Gamma irradiation-reverse voltage aging data

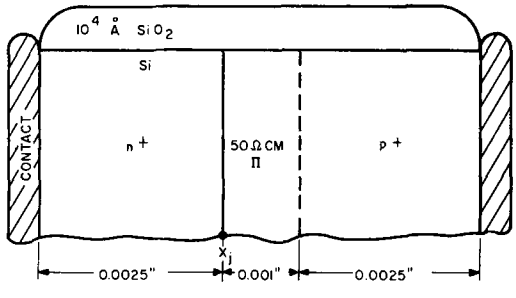

Fig. 3. Test wafer used during the investigation

using both alkali-containing and alkali-free glass cylinders.

Experimentation and Results

The structure used in the investigation was a silicon pπn diode with a high-pressure steam-grown SiO_2 protective film shown in Fig. 3. The gold-doped chip was 23 mils square with a 50 ohm-cm π layer. The encapsulation used as a source for alkali-metal contamination in some of the experimentation was the simple cylindrical structure shown in Fig. 4. Contamination of unpackaged device structures was obtained using the apparatus of Fig. 5. With the devices at room temperature, the metallic sodium was heated with a burner, and a small amount of O_2 was introduced. This procedure deposited a very fine sodium peroxide dust on the wafers down stream.

Surface effects on the contaminated devices were observed after the following treatments: (i) heating the devices for a few seconds in the range 600° to 700°C and above; (ii) reverse biasing the devices at temperatures between 100° and 200°C for times as short as a few hours; (iii) Irradiating the devices with gamma rays at room temperature with reverse bias for dosages as low as 2×10^5 rads.

When heated above the range 600°-700°C the contaminated devices became unstable and ambient sensitive. When reverse biased either at elevated temperature or under irradiation the devices exhibited characteristics of the types shown in Fig. 6. Excess reverse currents ranged from a few hundred nanoamperes to several milliamperes. Those devices whose excess reverse current began at zero bias were designated A. Those which exhibited no excess current below some threshold voltage were designated B. The threshold voltage of B devices was always less than the aging reverse bias. Double, occasional triple B, and combinations of A and B devices were observed.

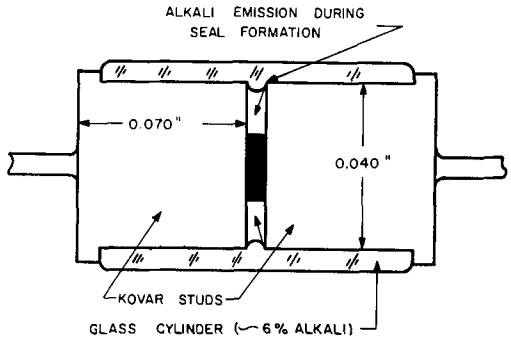

Fig. 4. Encapsulation used as the contamination source

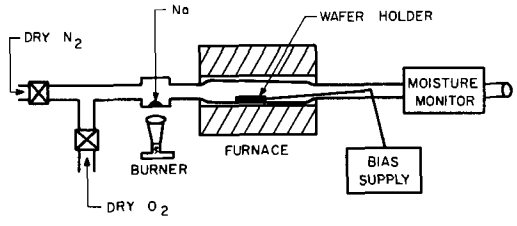

Fig. 5. Sodium contamination apparatus

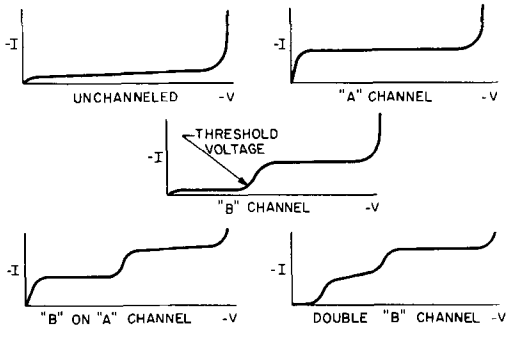

Fig. 6. Typical inverted diode characteristics

Reverse characteristics of these types are normally called channels and are associated with surface inversion. Etching and light-probe measurements were performed to determine the extent and nature of the inverted region. The protective oxide on inverted devices was etched in stages to determine the location of the surface states in the oxide. Device excess currents disappeared only when the last of the oxide had been removed.

The photoresponses were measured on devices which exhibited the various V-I characteristics shown in Fig. 7 and 8. By comparison with the uncontaminated diode, it can be seen in Fig. 7 that the B diode exhibited no excess reverse current below a voltage of about 25v. Above 25v a positive curvature exists and then the typical reverse characteristic of a channeled diode. Diodes b and d exhibited excess current starting at zero voltage as can be seen from the low-voltage insert. Notice that curve d exhibited the characteristic positive curvature of a B diode at low voltages. Those devices which exhibited excess reverse current starting at zero voltage also exhibited excess forward current as shown in Fig. 8, whereas the threshold voltage devices did not.

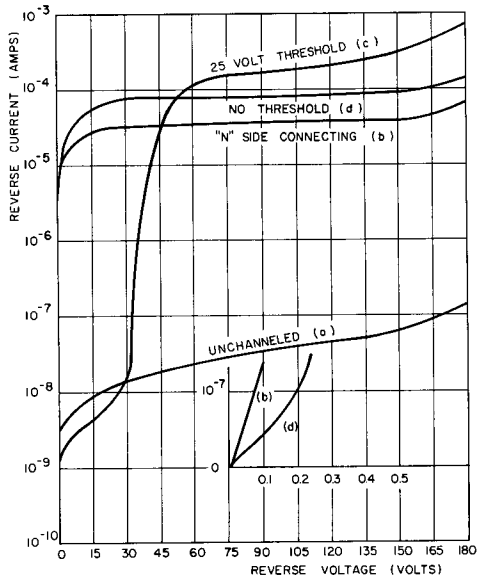

Fig. 7. Reverse characteristics

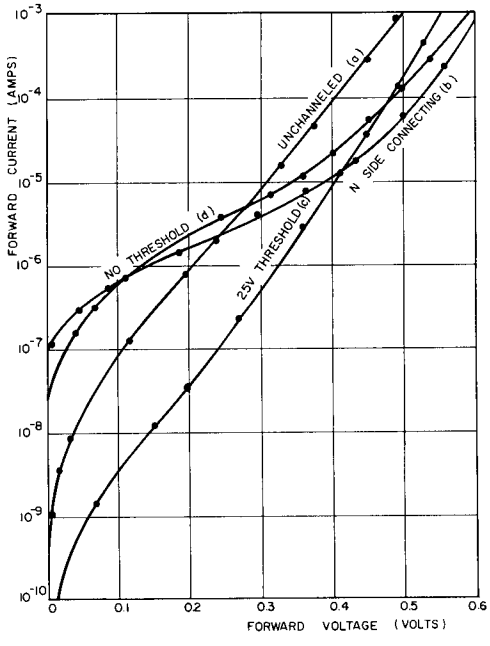

Fig. 8. Forward characteristics

A metallurgical microscope and a battery-operated electrometer were used for the photoresponse measurements. An aperture was mounted in a holder which fitted in the illuminator filter slot such that it was located at the objective image plane. This way both the sample and the light spot were in focus simultaneously. The spot size obtained with a 50μ aperture was approximately 8μ. Since the π layer width was approximately 30μ, the 8μ spot was sufficient to give adequate detail.

The photoresponse curves corresponding to the devices of Fig. 7 are shown in Fig. 9. The predominant characteristics of these curves are:

1. Diode b did not exhibit the large photoresponse peak at the p-n junction.
2. The peak in diode d was significantly smaller than the peak of diode a or c.
3. Diodes b, c, and d, exhibited a plateau in the photo response over the π layer.
4. No plateau existed in the noninverted device.

Inversion of the device π region after contamination from the glass-metal seal under conditions of elevated

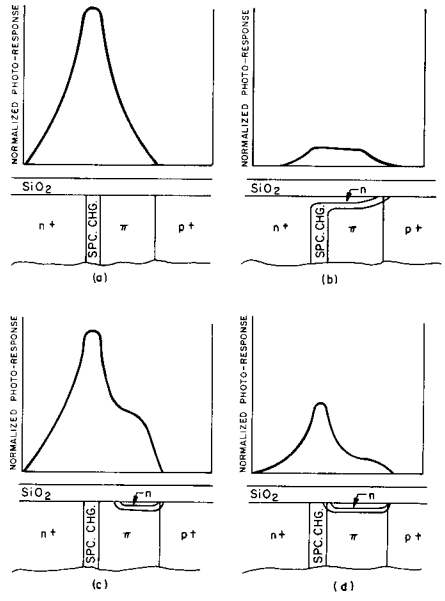

Fig. 9. Photoresponse of inverted diodes

temperature and reverse bias was observed to be delayed by more than an order of magnitude in time when a thin film of P_2O_5 or B_2O_3 glass was deposited over the SiO_2 protective film.

Discussion

The degrading effects of alkali metal contamination on oxide protected devices can be explained by two processes:

1. At temperatures in the range 600°-700°C and above, the alkali metals react visibly with the protective SiO_2 to form regions of alkali glass and devitrification. On cooling, differences in expansion coefficients cause cracking around the reacted area (1).
2. When alkali-metal contamination of the SiO_2 occurs at temperatures below approximately 600°C no visible reaction occurs. However, under conditions of either temperature or irradiation with reverse bias, electrolysis of the alkalies through the protective SiO_2 film occurs.

A model of this latter process for the pπn structure can be proposed with the aid of Fig. 10. Alkali ions are electrolyzed from the oxide surface to the interface along the fringing field lines and are deposited on the π side immediately adjacent to the expanded p-n junction depletion layer. They can then migrate down the interface covering the π region. As the inversion layer grows to the right, it accepts a portion of the diode bias depriving the junction depletion region of that voltage and causing it to recede near the surface. Actually, the depletion region in the vicinity of the p-n junction depletion-layer edge may remain the same, but the portion which is supported by the p-n junction recedes while the portion supported by the increased (positive) ionized charge-density of the surface states expands. The charge in the depletion region to the right of line a-a in Fig. 10 is compensated by the ionized surface donor states, that portion to the left is compensated by the ionized bulk donors of the p-n junction. The result is the establishment of short electric field lines to the left, as illustrated in Fig. 10. In this way the inversion layer can grow to the left, and the distance grown to the left will depend, for the most part, on the π layer resistivity and width, the alkali concentration, and electrolysis and migration rates.

When the diode is removed from the aging conditions, the p-n junction depletion layer recedes to its zero bias width. It may leave behind a noninverted region of the π layer surface (see Fig. 11). On reapplication of reverse bias, no excess current will flow until

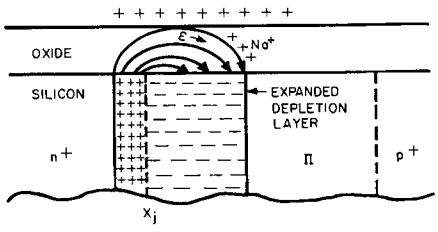

Fig. 10. Schematic representation of initiation and growth of an inversion layer by the process of alkali electrolysis: 10a. Initial stage of electrolysis.

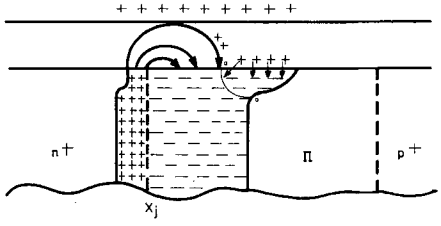

Fig. 10b. Initial stage of surface depletion

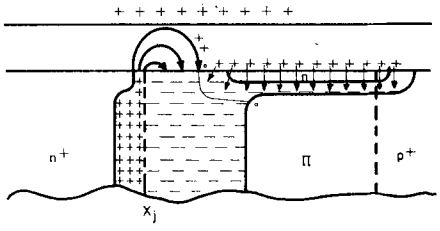

Fig. 10c. Final stage of surface inversion

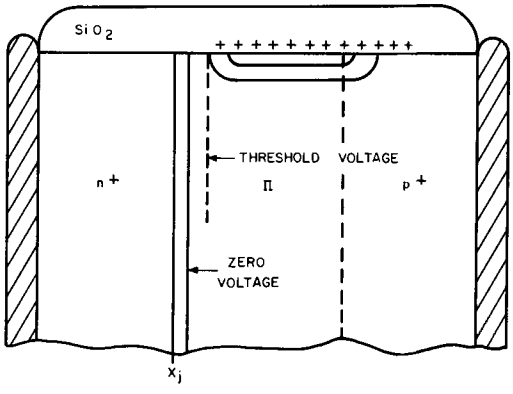

Fig. 11. "B" inversion layer geometry

a threshold voltage where the depletion region contacts the channel completing a current path. There is no reason to expect the noninverted π layer width to be uniform around the wafer perimeter. If the expanding depletion layer contacts the inversion layer in two isolated positions at different voltages, a double B characteristic would result. It is easy to see from this model how triple B and combinations of A and B devices could be created.

This surface inversion process explains why the device threshold voltages were always below the aging voltage and why the B devices exhibited no excess current in the forward direction. The device of curve d in Fig. 7 and 8 was one in which the inversion layer had grown sufficiently close to the p-n junction that it contacted the p-n junction depletion layer at zero reverse voltage but did not extend all the way to the p-n junction. Hence the model predicts that this device should be expected to exhibit the observed positive curvature at very low reverse voltages, and excess current at low forward voltages. Device b in Fig. 7 and 8 possessed an inversion layer which had contacted the metallurgical p-n junction thus creating a connection between the inversion layer and the diode's n side. This device should not be expected to exhibit positive curvature at low reverse voltage but should possess excess current at low forward voltage. Device c, the threshold device, possesses an inversion layer which does not contact the p-n junction depletion layer at zero bias and should not, therefore, possess excess current in the forward characteristic.

The photoresponse curves of Fig. 9 clearly reveal the inversion layer geometries of the various devices. The plateau in the photoresponses of all except the noninverted device locates the inversion layer on the π layer surface. The existence of the large photo-voltage peak in devices a, c, and d reveal the emergence of the p-n junction depletion layer at the surface, indicating that the inversion region did not connect with the diode's n side isolating the junction depletion layer from the surface as occurred with device b which shows no photo-voltage peak. Partial isolation of the junction depletion layer is indicated by the subdued peak in the photo response of diode d.

Electrolysis of the alkalies through the SiO_2 film is indicated by the resulting inversion layer geometries and the fact that the surface states were located at the Si-oxide interface as revealed by successively etching the oxide.

By depositing a thin film of P_2O_5 or B_2O_3 glass over the SiO_2 layer, the rate of inversion layer formation was drastically reduced. Extensive measurements were not performed on this system. The explanation, at present, appears to be a low alkali electrolysis rate in the P_2O_5 and B_2O_3 films.

Conclusion

Surface degradation of semiconductor devices from alkali-metal contamination is of importance in the semiconductor industry since glasses containing alkalies are used for surface passivation and for insulators in device packages where direct seals are made to metal parts.

Degradation of oxide protected alkali-metal contaminated pπn diodes can be attributed to:

1. Formation of alkali-glass and devitrification regions in the oxide at temperatures in the range 600°-700°C and above with subsequent cracking during cooling.
2. Surface inversion of the π layer caused by electrolysis of the alkalies through the protective oxide under conditions of (*a*) elevated temperature and reverse bias, and (*b*) irradiation and reverse bias.

Manuscript received April 12, 1965. This paper was presented at the Washington Meeting, October 11-14, 1964.

Any discussion of this paper will appear in a Discussion Section to be published in the June 1966 JOURNAL.

REFERENCE

1. R. T. Borawski, Paper presented at the Washington Meeting of the Society, October 1964.

The Controlled Sublimation Technique and Its Utilization for the Crystal Growth of Hexamine

G. E. Gottlieb

RCA Laboratories, Princeton, New Jersey

ABSTRACT

A technique has been developed for the growth of large single crystals of hexamine from the vapor. The method is based on sublimation, with modifications that allow stringent control over the process. A single nucleation is induced at a localized cold spot, produced by a fine tipped temperature-controlled copper rod, in contact with the wall of the growth ampoule. Another modification is the presence of four separate temperature zones. Single crystals of hexamine $\sim$ 2 cm^3 in volume were produced. The as-grown crystals exhibited considerable strain because they were in contact with quartz during growth. A significant improvement in the mechanical and electrooptic properties was observed after annealing the crystals. The best electrooptic coefficient (r_{41}) obtained was 4.18 x 10^{-10} cm/v; this corresponds to a half-wave voltage ($V_{\lambda/2}$) of 15 kv (width/length). The technique described here should be applicable for the crystal growth of many other materials. It could be extended to low vapor pressure materials by utilizing chemical transport instead of sublimation.

As a result of the advent of lasers, and the consequent effort to develop optical communication systems having bandwidths of thousands of megacycles, a need has arisen for wideband laser modulators and demodulators. The materials used for this purpose have been potassium dihydrogen phosphate and ammonium dihydrogen phosphate, along with cuprous chloride, which exhibit the electrooptic effect found in crystals that do not possess a center of symmetry. A good electrooptic material should have low loss tangent, large electrooptic coefficient, transparency over a wide spectral range, and a transverse as well as longitudinal electrooptic effect. The above mentioned materials lack some of these desirable properties. The molecular crystal hexamine (hexamethylenetetramine), a body-centered cubic possesses a linear electrooptic coefficient, a low loss tangent, and is transparent over a large spectral range. A comparison of electrooptic materials (1), manifests some of the advantages of hexamine for certain electrooptic applications.

Often with electronic materials, the utilization of a particular physical phenomenon has awaited the development of a technique for the preparation of large single crystals of the required perfection. The interesting electrooptic properties of hexamine, and the absence of a method of growing large single crystals has given impetus to the present work. Hexamine melts at 263°C; however the rapid decomposition encountered at this temperature precludes the utilization of melt techniques for the crystal growth of this material. Hexamine is very soluble in water, alcohol, and acetone, so that solution growth has been used to produce crystals. However, trapped solvent is usually included in these crystals. This leaves growth from the vapor as the most applicable crystal growth technique. Fortunately, hexamine has a high enough vapor pressure to make vapor growth or controlled sublimation a practicality (2).

Honigmann and Heyer (3) grew crystals of hexamine from the vapor, using a copper thermostat in an oven. Elaborate temperature controls were required in order to maintain conditions at the most desirable temperature (100°C). Veigele (4) reports a vapor growth technique in which a copper plate attached to a copper rod makes contact with a sealed ampoule in a beaker of boiling water. Nucleation occurs in the area in contact with the copper plate. The method to be discussed here is based on controlled sublimation, and can be used to grow large single crystals of hexamine.

Growth from the Vapor

For vapor growth of crystals, a source of vapor and a growth area are required. In the process of sublimation, an evaporating source at temperature T_1 may produce many nucleations in an area at a lower temperature T_2. In order to grow large single crystals, the number of nucleations in area T_2 must be limited. To avoid extensive nucleation, low supersaturation ratios are used. This means that small differences in temperature between the source and growth areas must be utilized.

The use of as high an average temperature as practical is desirable for several reasons: the rate of growth increases with the absolute vapor pressure at the growing surface; the crystallinity is also improved at higher temperatures, due to the higher surface mobility. Therefore crystals grown at high temperatures tend to be more perfect, and also growth can proceed at a reasonable rate.

The fact that the growth of single crystals from the vapor as described is essentially sublimation under controlled conditions explains why very pure crystals can be obtained by this technique. Of course, substances that have similar vapor pressures, cannot be removed by sublimation.

Experimental Procedure

The technique reported in this paper is characterized by four temperature zones denoted T_1, T_2, T_3, and T_4, respectively, as shown in Fig. 1; material vaporizes in region T_1, becomes supersaturated in region T_2, nucle-

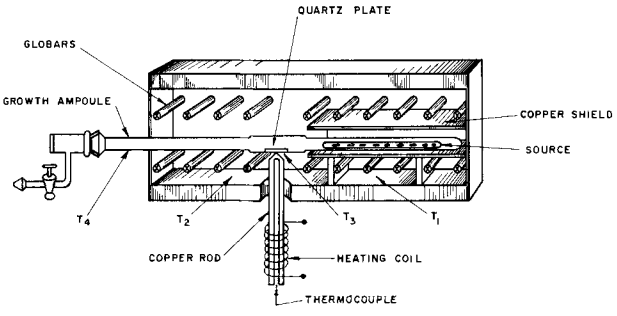

Fig. 1. Controlled sublimation apparatus with the four temperature regions: T_1, source temperature; T_2, growth zone temperature; T_3, temperature at tip of copper rod; T_4, ambient temperature.

ates and grows at localized cold spot T_3 with the excess crystallizing in region T_4. The ampoule itself extends through the furnace into the surrounding ambient. A copper rod, with a thermocouple extending to within an eighth of an inch of its bottom, rests on a flat area of the ampoule, in the colder temperature zone. This provides a localized cold spot. A heater wound directly on the copper rod controls the heat flow through the rod, and therefore the temperature of the cold spot. In order to produce a uniform temperature distribution, the source area is encased in a copper sleeve.

The growth ampoule containing hexamine powder is pumped down to a vacuum of 10^{-6} mm Hg and placed in the furnace; the cold zone and the copper rod, resting on the ampoule, are brought to the growth temperature. The hot zone, containing the source material, is then raised to the growth temperature. Hot zone temperatures of 100°-110°C, producing a vapor pressure of approximately 0.2 mm, were usually utilized (2). Cold zone temperatures 5°-10°C less than the hot zone were found to be satisfactory. The temperature of the copper rod is decreased until nucleation occurs in the area immediately under the rod. The temperature of the rod is then raised several degrees, to prevent the growth from proceeding too rapidly. This is necessary because greater supersaturation ratios are required for nucleation than for growth. The rod temperatures utilized were usually 65°-75°C. The reason for the apparently large temperature difference between the rod and T_2 is that heat must be conducted through two thicknesses of quartz. It is therefore probable that the actual temperature at the nucleation/growth area above the rod is only 2°-3°C below the cold zone temperature.

Growth onto a seed has also been utilized. In this case a flat quartz plate, with a small, well-formed hexamine crystal on it, is placed in the growth ampoule. The copper rod is then placed in contact with the flat area above or below the seed, and growth conditions rather than nucleating conditions are established.

When the crystal has grown to a usable size, it must be cooled. The cooling procedure is complicated by the relatively high vapor pressure of hexamine, and by the sensitivity to thermal shock which manifests itself in the extreme case by cracking the crystal, and more commonly by introducing varying amounts of strain. Because strain rotates the plane of polarization of the light entering the crystal, it seriously limits the usefulness of the material as an electrooptic modulator. In order to minimize the strain, a very slow rate of cooling must be used. However, the high vapor pressure, coupled with the long cooling time, would tend to sublime away part of the crystal during cooling. To eliminate this problem, the source area is kept 5° hotter than the crystal area during the cooling process. The source thereby provides sufficient vapor pressure to prevent sublimation of the crystal; the temperature difference between source and substrate is small enough so that no observable new growth occurs during cooling. The copper rod is also removed prior to cooling, so that the crystal is no longer a local cold spot. A cooling rate of 5°-10°C/hr, with the above conditions, has produced crack-free crystals.

In order to produce a crystal useful for electrooptic modulation, residual strain must be removed. It was found that this can be done by annealing the crystals after growth. Crystals were removed from the plates on which they were grown, and were sealed into an ampoule packed with hexamine powder. The ampoule was heated at 105°C for 3 hr and was then cooled slowly. Examination of the crystals with polarized light indicated that the strain originally present in the crystals was almost completely removed. This finding was corroborated by an increased electrooptic effect after annealing. This is shown in Table I. Crystals grown on quartz and on polyethylene, which originally had widely differing amounts of strain (polyethylene grown had less strain than quartz grown crystals) were both found to have little or no strain after annealing.

Table I. Electrooptic data

Crystal No.	Max. effect, % (I/I_o, 10 kv)	$V_{\lambda/2}$, kv (W/L)	r_{41}, cm/v	Crystal dimensions (mm) Width	Length
RH2	40	60	1.3×10^{-10}	$1.7 \times 1.9 \times 4.9$	
RH3	48	81	0.96×10^{-10}	$1.5 \times 1.9 \times 5.8$	
RH7	45	45	1.7×10^{-10}	$4.1 \times 4.1 \times 8.6$	
RH7 (after annealing)	59	37	2.1×10^{-10}	$4.1 \times 4.1 \times 8.6$	
RH10	—	15	4.18×10^{-10}	$3.2 \times 3.2 \times 2.7$	
RH37 (annealed)	60	41	1.9×10^{-10}	$2.6 \times 2.5 \times 5.9$	
RH38 (annealed)	40	30	2.6×10^{-10}	$1.9 \times 2.4 \times 11.5$	
RH39	27	57	1.36×10^{-10}	$5 \times 10 \times 10$	
RH40 (annealed)	45	32	2.66×10^{-10}	$10 \times 5 \times 15$	

RH7 and RH39 are cut from the same crystal. RH37, 38 and 40 are cut from the same crystal. Measurements were made at 6328Å, with a He-Ne gas laser source. I = Transmitted intensity (crossed polarizers) for a 10 kv field. I_o = Transmitted light intensity (parallel polarizers) for zero field. W = width. L = length.

Results

Spontaneous nucleation.—Large single crystals of 2 cm^3 volume have been obtained by allowing the hexamine to nucleate on a controlled cold spot on a flat wall of an ampoule. In order to obtain a useful, well-formed crystal, nucleation must occur very slowly; irregularities or malformations cannot be tolerated in this initial nucleation. The crystals produced from defect-free nucleations were hemispheric in appearance, approximately 1 in. in diameter with 6-8 flat faces evident. These faces were found to be [110], by Laue patterns. A representative crystal is shown in Fig. 2. The crystals produced are clear, with only a few inclusions. In order to produce such material, an extremely slow growth rate is required (0.1-0.2 g/day). Rapid growth produces imperfections, defects, and ultimately polycrystallinity.

As crystal growth proceeds, it becomes exceedingly difficult to retain the flat faces; the crystal tends to become completely hemispherical. However, the faces can be retained if the copper rods are changed periodically in order to always have a copper rod equal to or slightly smaller in diameter than the growing crystal.

Growth onto a seed.—(i) *Seed mounted on a quartz plate.*—A well-formed hexamine crystal approximately

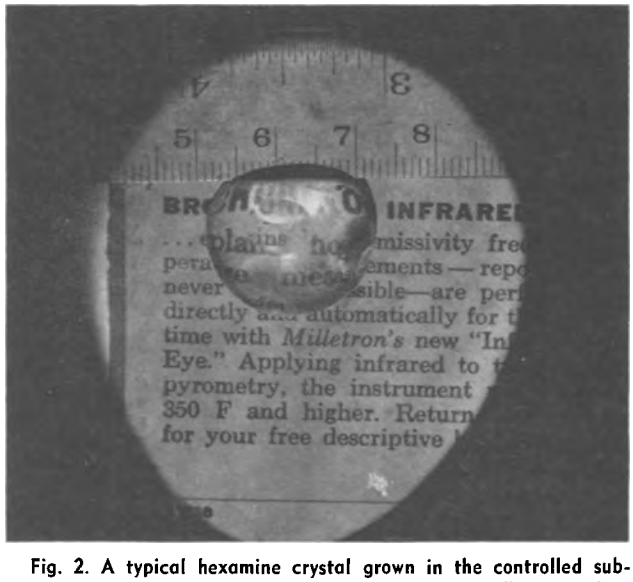

Fig. 2. A typical hexamine crystal grown in the controlled sublimation apparatus. The flat faces or "growth flats" are evident as nondistorted regions. The distortion in the crystals is due to the rounded surface.

1 mm on edge is placed on a quartz plate, and held in place with a small amount of "Torrseal," a high vacuum resin. The plate is then placed against the flat area of the ampoule, using silicone grease as the adhesive. Large single crystals, comparable to those previously described, were obtained by this technique. No unusual growth effects were observed. (ii) *Seed mounted on a polyethylene sheet.*—Crystals grown on quartz, either by seeding or by direct nucleation exhibit considerable strain. This strain was present regardless of the cooling cycle utilized. It is probably due to the large mismatch between the thermal expansion coefficient of hexamine and quartz. Therefore a thin sheet of polyethylene was mounted on a quartz plate with stopcock grease, and a seed was mounted on the polyethylene with the resin previously mentioned. Crystals produced in this manner exhibited reduced strain, compared to crystals grown on quartz. However, it was found that growth on polyethylene is more difficult than growth on quartz. This is due to the low surface energy of the polyethylene, resulting in low energy nucleation sites. The problem was resolved by initiating the growth process extremely slowly, using very small temperature differences.

Effect of vacuum bake.—In order to investigate the effects of volatile impurities on the growth process, several ampoules were baked at 85°C for several hours at 10^{-5} mm Hg prior to growth. The remainder of the growth procedure was similar to that described previously. The baked material sublimed at a slower rate than nonbaked material, necessitating source temperatures of 120°-130°C (10°-20°C higher than normal) in order to obtain a usable growth rate. The above facts indicate that baking removes a volatile impurity, possibly water vapor or alcohol.

Occasional growth defects were observed in the crystals. Microscopic examination showed these defects to be rectangular holes or voids. It was suspected that these defects were due to the presence of water vapor, but they were also encountered in the baked material. Therefore, the cause of these voids is not clear.

Electrical properties.—The electrooptic data obtained from representative crystals produced in this study, are presented in Table I. The electrooptic measurements were made by placing the crystals between crossed polarizers, and applying at 10 kv field. A He-Ne gas laser with an output at 6328Å was used for the light source. The change in the transmitted light intensity (I/I_o) was then measured, and the electrooptic coefficient was calculated using the following equation

$$I/I_o = \sin^2 \frac{\Gamma}{2}$$

where the retardation Γ is given by

$$\Gamma = \frac{2\pi l n_o^3 r_{41} E}{\lambda}$$

in which l is the path length of the light, n_o is the index of refraction, r_{41} is the electrooptic coefficient, E is the applied transverse field, and λ is the wavelength.

The half-wave voltage $V_{\lambda/2}$ is related to the electrooptic coefficient by the equation

$$V_{\lambda/2} = \lambda/2\, n_o^3\, r_{41}$$

The best experimental electrooptic coefficient (r_{41}) was 4.18 x 10^{-10} cm/v; this compares with a theoretical value (1) of 13.2 x 10^{-10} cm/v, and an experimental value of 7.3 x 10^{-10} cm/v, determined by McQuaid (5) on solution grown hexamine. However, recent work (6) indicates a half-wave voltage of 93 ± 9 kv for material prepared by a technique similar to McQuaid's. The difference between the experimental and theoretical values reported here is probably due to crystal imperfection, *i.e.*, inclusions, impurities, misorientation, and strain. Table I also manifests a size effect: the smaller crystals possess better properties than the larger ones. This is especially noticeable when small and large sections cut from the same boule are compared. This size effect is due to the imperfections mentioned above, and also apparently to crystal inhomogeneity. Table I also illustrates the considerable improvement in the electrooptic effect usually produced by the annealing process.

Discussion

The method described here differs from those previously described in the literature in several important respects. First, the ampoule projects into the room temperature ambient, providing an extra temperature zone. Second, the copper rod allows growth to occur only at a localized cold spot, and third, a pregrown seed can be mounted in the apparatus, thereby eliminating the difficult and time consuming nucleation process.

By allowing the ampoule to project through the furnace into the room temperature ambient a zone T_4 at a considerably lower temperature than the growing crystal is obtained and therefore any excess material above that required by the equilibrium conditions of the growing crystal continues to the coldest area. It was found that approximately 50% of the vaporized source material grew into single crystals, with the other 50% condensing at T_4. This is in contrast to a two-zoned situation in which the source temperature is extremely critical because of the control it exercises over the growing crystal. (Single crystals could not be grown in a two-zoned apparatus.) The degree of control inherent in this technique is demonstrated by the fact that spontaneous nucleation does not occur with temperature differences as large as 30°C; (supersaturation ratios of approximately 10).

The advantage of the copper rod, and its separate heater is that growth is limited to a localized cold spot, thereby eliminating multiple nucleations and also increasing the over-all control over the crystal growth parameters.

The use of pregrown seeds eliminates the tedious nucleation process. The seeds used were usually small, well-formed crystals that nucleate spontaneously in the cooler regions of the growth ampoules. The advantage of seeding is the additional control, and the over-all simplification that results.

The crystals grown under differing supersaturation conditions were examined via Laue patterns, and all were found to be of the cubic system; however, those grown with extremely high supersaturation ratios were needle-like ~ 3 mm on edge and 2 cm long. Crystals grown under more moderate conditions were circular and platelike as described previously. This is in agreement with the work of Ibuki (7), who found that the crystal habit of CdS varied with the supersaturation ratio.

The flat faces of the hexamine crystals were in all cases found to be [110]. This indicates that the nucleation process remains constant under differing conditions.

Conclusions

A technique for crystal growth via controlled sublimation has been developed. The process, characterized by four separate temperature zones, has been utilized to produce large crystals of hexamine for electrooptic modulation. In order to maximize the electrooptic effect, crystalline strain must be minimized by annealing the crystals after growth. The best electrooptic coefficient (r_{41}) obtained experimentally was 4.18 x 10^{-10} cm/v; this corresponds to a half-wave voltage ($V_{\lambda/2}$) of 15 kv (width/length). The effect of several parameters on the growth process were also studied. The technique should be applicable for the crystal growth of many materials, especially those possessing vapor pressures >0.1 mm at reasonable temperatures.

Acknowledgment

The author wishes to acknowledge the extremely capable technical assistance of J. F. Corboy, Jr., and

C. A. Goldsborough in performing these experiments. Thanks are also due to P. G. Herkart for useful discussions and suggestions. The author is indebted to G. H. Heilmeier for stimulating discussions, and to H. J. Kishi and W. Gorkiewicz for performing the electrooptic measurements.

Manuscript received March 15, 1965; revised manuscript received May 15, 1965.

Any discussion of this paper will appear in a Discussion Section to be published in the June 1966 JOURNAL.

REFERENCES

1. G. H. Heilmeier, *Appl. Opt.*, **3**, 1281 (1964).
2. I. Stranski in collaboration with others, Proceedings of the International Congress on Catalysis, Philadelphia, Pa., 1956; "Advances in Catalysis," Vol. IX, p. 406, Academic Press Inc., New York (1957).
3. B. Honigmann and H. Heyer, *Z. Krist.*, **106**, 199 (1955).
4. W. M. Veigele, *Am. J. Phys.*, **31**, 598 (1963).
5. R. McQuaid, *Appl. Opt.*, **2**, 320 (1963).
6. C. F. Buhrer and L. Ho, *Appl. Opt.*, **3**, 1500 (1964).
7. S. Ibuki, *J. Phys. Soc. Japan*, **14**, 1181 (1959).

Solid Solution in the GeTe-InTe System

J. C. Woolley

Physics Department, University of Ottawa, Ottawa, Ontario, Canada

ABSTRACT

Standard x-ray powder photograph techniques have been used to investigate the phases occurring in alloys of the GeTe-InTe section and also in some general alloys of the ternary systems Ge-In-Te which lie in the composition range bounded by GeTe-In_2Te_3-InTe-Ge. The conditions when the alloys are water quenched from the melt and when annealed to equilibrium at 400°C have been investigated. In the GeTe-InTe section, the water-quenched alloys show a single-phase condition in the range 0-75 mole % InTe, this phase having a rock salt-type structure over the range 8-75 mole % InTe and the GeTe-type structure at lower InTe content. The lattice parameter variation of this phase is compared with that for the similar PbTe-InTe and SnTe-InTe systems and correlated with the occupation by the indium atoms of octahedrally and tetrahedrally coordinated interstices in the tellurium lattice. When the alloys are annealed at 400°C, this long composition range for single phase behavior is lost, and in the region of the ternary diagram investigated, three three-phase fields have been determined.

Although the compound InTe has the B37 type structure (1), extensive solid solubilities of InTe in both of the rock salt-structure compounds PbTe and SnTe have been observed (2). It is found (2) that the limiting mole fractions x of the solute in the rock salt-type a phase have the values $x \sim 0.35$ and $x \sim 0.53$ for the $(PbTe)_{1-x}(InTe)_x$ and $(SnTe)_{1-x}(InTe)_x$ systems, respectively. This relatively large solubility of InTe in the rock salt structure can be correlated with the fact that a form of InTe with this structure [InTe(II)] can be produced by the effects of high pressure (3). InTe(II) is metastable at room temperature and atmospheric pressure and has a lattice parameter a_o of 6.154Å. In the systems $(PbTe)_{1-x}(InTe)_x$ and $(SnTe)_{1-x}(InTe)_x$, the lattice parameter is found to vary linearly with x and extrapolation to $x = 1$ [*i.e.*, to InTe(II)] gives values of 6.24 and 6.21Å, respectively, for the PbTe and SnTe alloys. The difference in these three values for a_o can be attributed to the fact that in the alloys some of the indium atoms occupy sites which are tetrahedrally coordinated by tellurium atoms (*i.e.*, sites equivalent to those in a zinc blende structure) rather than replace lead (or tin) atoms in sites octahedrally coordinated by tellurium. This results in the alloy in a lattice parameter larger than that which would occur if all indium atoms occupied octahedrally coordinated sites by substitution. From this lattice parameter data, and assuming a lattice parameter of a hypothetical zinc blende crystal of InTe as 6.38Å (from the atomic radii of tetrahedrally coordinated indium and tellurium), Rosenberg and Wald (4) have estimated that for the PbTe alloys about one third of the indium atoms enter the tetrahedral sites, and two thirds replace lead atoms substitutionally. A similar calculation for the SnTe alloys indicates that in that case a little less than a quarter of the indium atoms occupy tetrahedral sites in the rock salt lattice.

In the case of GeTe, this compound shows a rhombohedrally distorted rock salt structure at room temperature with $a_o = 5.973$Å and $\alpha = 88° 16'$ (5). However with increased temperature the rhombohedral distortion is reduced, and above 430°C (6) the cubic rock salt structure is observed. Since both GeTe and InTe can show the rock salt structure under suitable conditions, it was of interest to observe the solid solubility of InTe in GeTe. This study led to a consideration of ternary alloys of the Ge-In-Te diagram away from the GeTe-InTe section.

Experimental Procedures

All specimens were prepared from elements of 99.999% purity. For those lying in the GeTe-InTe section, the compounds GeTe and InTe were prepared first and then the ternary alloys prepared from these compounds. The other ternary alloys were prepared directly from the elements. The samples were sealed in evacuated quartz tubes and melted. They were held at 1100°C (*i.e.*, at a temperature well above the liquidus value for any alloy) for approximately 30 min, being agitated continually to give good mixing, and were then quenched in water. X-ray powder photographs were taken to establish the quenched condition. The specimens were then resealed and annealed at an appropriate temperature (normally 400°C) until an equilibrium condition was attained, as indicated by x-ray powder photographs. In all cases annealing for four days was found to be sufficient, and in the final work a standard four day annealing time was used.

Results

It should be noted here that the x-ray data obtained for the quenched samples need not in general represent any equilibrium state of the alloys. However data on the quenched condition are useful in that, as is shown below, metastable single phase solid solution is obtained, and the behavior of this metastable phase could be of interest in studies of semiconductivity and superconductivity of intermetallic alloys. The quenched

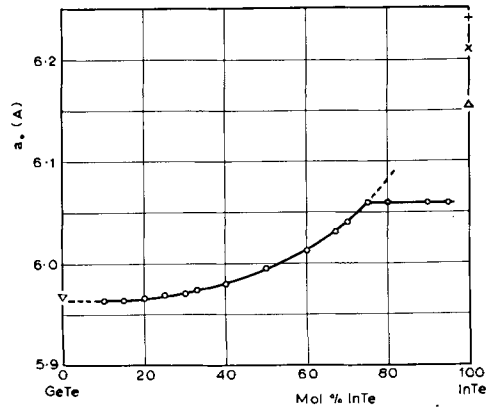

Fig. 1. Variation of lattice parameter a_0 of rock salt-type phase as a function of composition in the GeTe-InTe section. +, Value for InTe by extrapolation from PbTe-InTe data (1); ×, value for InTe by extrapolation from SnTe-InTe data (1); △, value for InTe(II) (2); ▽, value for GeTe by extrapolation from high temperature data (6).

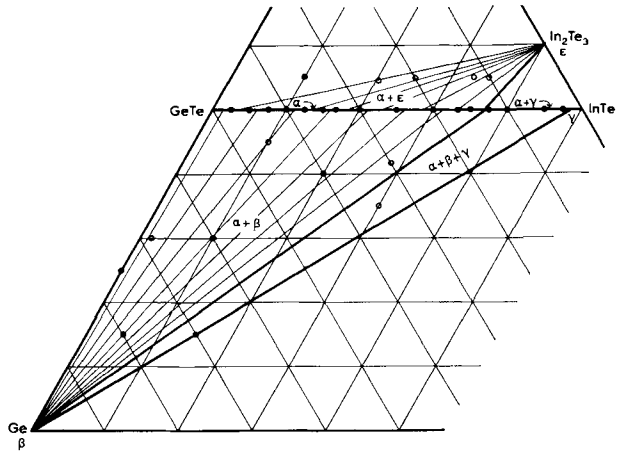

Fig. 2. Diagram showing conditions of alloys water quenched from the melt.

conditions have therefore been considered in some detail. The data on the annealed samples give, of course, a standard 400°C isothermal section of the phase diagram.

The GeTe-InTe *section.*—It was found that over a considerable range of composition the quenched specimens were single phase with a rock salt-type structure, although for alloys near the limit of the single phase range, *i.e.*, 60-75 mole % InTe, the higher angle x-ray lines were blurred. The alloy with 95 mole % GeTe content showed the rhombohedral GeTe-type structure rather than the rock salt structure even with the most rapid quench from the melt, *i.e.*, as with GeTe itself it was impossible to quench in at room temperature the high-temperature cubic phase. However the 95 mole % GeTe alloy had lattice parameter a_0 slightly larger than that of GeTe and lattice angle α nearer to 90°, *i.e.*, showing a transition toward a cubic form with increased InTe content. Figure 1 shows the variation of the rock salt-type lattice parameter a_0 as a function of composition, the point for GeTe itself being the extrapolated room temperature value from data by Mazelsky *et al.* (7). The graph shows a typical pseudobinary behavior, with the limit of single phase solid solution in the rock salt-type structure at 74-75 mole % InTe. The alloys containing 80, 90, and 95 mole % InTe show a second phase of an InTe type. However the lattice parameter of this phase is slightly smaller than that for InTe, showing a limited solid solution of GeTe in the InTe structure. Since in the 95 mole % InTe alloy, the rock salt-type lines are still visible, this range of solid solution must be less than 5 mole % GeTe, but no attempt has been made to determine this value more accurately.

When these alloys were annealed at 400°C, the pseudobinary behavior was no longer observed, and general three-phase conditions were found to apply. These results therefore are discussed below together with those for alloys not on the GeTe-InTe section.

Ge-In-Te *diagram.*—The alloys investigated were limited to those of composition inside the region GeTe-In_2Te_3-InTe-Ge. The diagram giving the quenched condition of the alloys is shown in Fig. 2. As indicated above, this is not an isothermal section of a ternary diagram, but gives a convenient method of presenting the conditions of the alloys in the quenched state. All alloys investigated showed the rock salt-type phase α (or the equivalent GeTe-type phase at large GeTe concentrations). Two two-phase fields ($\alpha + \beta$) and ($\alpha + \epsilon$) are observed where β is germanium and ϵ is In_2Te_3, and a three-phase field ($\alpha + \beta + \gamma$) where γ is the limiting InTe phase discussed above. Lattice parameter measurements confirmed that in the two-phase fields the tie lines ran as shown in the figure. The small region of the diagram between InTe and In_2Te_3 was not investigated.

When the alloys were annealed at 400°C, the pseudobinary behavior of the GeTe-InTe section and the resulting two-phase fields were lost. Specimens in the range 10-67 mole % InTe became three phase, the phases present being germanium (β), In_2Te_3(ϵ), and a rock salt-type phase (α). Comparison of the lattice parameter of the α phase with the data in Fig. 1 gave a value of approximately 92 mole % GeTe-8 mole % InTe as the composition of the phase. An accurate determination of this composition from lattice parameter data is difficult because of the small variation in lattice parameter with composition in this range. However the equilibrium α phase had a lattice parameter slightly smaller than the quenched 10 mole % InTe alloy, while the 5 mole % InTe alloy showed a rhombohedral GeTe-type structure after annealing, thus confirming that the equilibrium α phase lies between these two compositions. Thus the range of solid solution in the GeTe-InTe section is reduced to 0-8 mole % InTe, and for alloys in this range, when annealed at 400°C and then x-rayed at room temperature, there is a transition with increased InTe content from the rhombohedral pseudocubic GeTe structure to a cubic rock salt-type structure.

For well annealed specimens in the ($\alpha + \beta + \epsilon$) field, ordering lines were observed corresponding to the ordered structure of In_2Te_3.

The x-ray photograph of the annealed 30 mole % GeTe-70 mole % InTe alloys showed a very complicated pattern of lines, but in which the lines of none of the phases GeTe, InTe, In_2Te_3 or germanium could be observed. GeTe-InTe alloys in the composition range 75-95 mole % InTe showed this pattern of lines plus InTe lines, and the results for alloys off the GeTe-InTe section are consistent with there being a new δ phase very close to the 70 mole % InTe alloy. In the diagram shown here this new phase has been assumed to be at 70 mole % InTe. The InTe (γ) phase has the same lattice parameter as in the quenched state, indicating the retention of some limited solid solution (less than 5 mole %) of GeTe in the InTe structure.

The 400°C isothermal section is shown in Fig. 3. As indicated, there is a narrow two-phase field ($\alpha + \beta$) close to the Ge-Te boundary and three three-phase fields ($\alpha + \beta + \epsilon$), ($\beta + \delta + \epsilon$), and ($\beta + \gamma + \delta$). Again the region between In_2Te_3 and InTe was not investigated.

The transition temperatures at which the rock salt-type phase becomes unstable have not been determined accurately. The blurring of the high angle x-ray lines for quenched specimens containing 60-75 mole % InTe perhaps would indicate that the transition temperature is higher for these than for alloys of lower InTe content. For specimens in the range 30-50 mole %

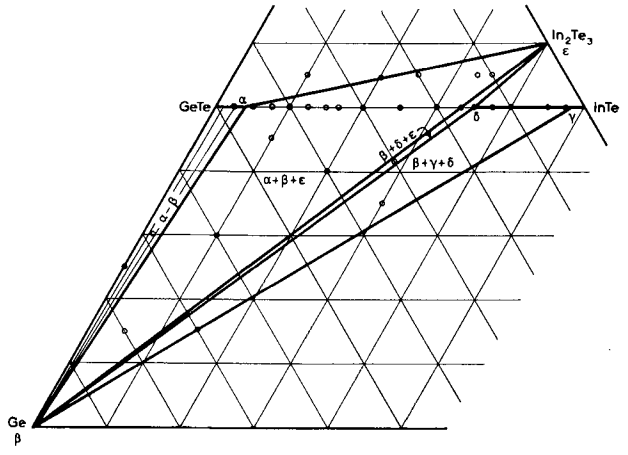

Fig. 3. Diagram showing 400°C isothermal section

InTe, the annealing results indicate a transition temperature in the vicinity of 450°C.

Discussion

Although neither GeTe or InTe show the rock salt-type structure in their equilibrium room temperature states, the quenched alloys of the GeTe-InTe section show a rock salt-type structure (although metastable) over a larger composition range than that for the corresponding PbTe-InTe and SnTe-InTe alloys. While however the lattice parameter varies linearly with composition in the two latter cases, Fig. 1 shows that this is not the case for the GeTe-InTe alloys. Hence here, an extrapolation to determine the effective rock salt-type parameter for InTe is difficult. In Fig. 1, the extrapolated values from the PbTe-InTe and SnTe-InTe systems are shown together with the value for InTe(II) given by Banus *et al.* (3). The extrapolation of the GeTe-InTe data appears to be closer to the other extrapolated values than to the InTe(II) result. As indicated at the beginning of this paper, this implies once again that some of the indium atoms are occupying tetrahedrally coordinated sites in the tellurium sublattice. However, the curvature of the a_o *vs.* composition line would indicate that here the ratio of tetrahedrally coordinated to octahedrally coordinated indium atoms is not constant with indium content. Thus in the range 0-20 mole % InTe it would appear that all of the indium atoms are in octahedrally coordinated sites. However if the value of lattice parameter for the hypothetical zinc blende InTe as given by Rosenberg and Wald (4) is assumed, the slope of the a_o *vs.* composition line at 70 mole % InTe indicates that three out of every four added indium atoms are entering tetrahedrally coordinated sites at this composition. The limit of single phase solid solution at 74 mole % InTe is thus not unexpected.

Acknowledgments

The author wishes to thank Mr. P. J. Montford-Azmier and various final year students at the University of Ottawa for assistance in the work of preparation and x-raying of specimens.

Manuscript received April 15, 1965.

Any discussion of this paper will appear in a Discussion Section to be published in the June 1966 JOURNAL.

REFERENCES

1. W. B. Pearson, "Handbook of Lattice Spacings and Structures of Metals and Alloys," p. 94. Pergamon Press, New York (1958).
2. A. J. Rosenberg, R. Grierson, J. C. Woolley, and P. Nikolic, *Trans Met. Soc. AIME*, **230**, 342 (1964).
3. M. D. Banus, R. E. Hanneman, M. Strongin, and K. Gooen, *Science*, **142**, 662 (1963).
4. A. J. Rosenberg and F. Wald, Tyco Labs. Technical Memorandum No. 1 (1964).
5. J. C. Woolley and P. Nikolic, *This Journal*, **112**, 82 (1965).
6. K. Schubert and H. Fricke, *Z. Metallk.*, **44**, 457 (1953).
7. R. Mazelsky, M. S. Lubell, and W. E. Kramer, *J. Chem. Phys.*, **37**, 45 (1962).

The Depth of Mechanical Damage in Gallium Arsenide

Charlie E. Jones and A. Ray Hilton

Texas Instruments, Incorporated, Dallas, Texas

ABSTRACT

A technique for the determination of the depth of damage induced into the surface of doped n-type gallium arsenide by sawing, grinding, and polishing is described. The infrared reflectivity in the 20-60μ region was used for this measurement. The relationship between the optical constants of GaAs and reflectivity is reviewed briefly. The extent of the damage is shown to be about equal to the diameter of the final grinding particles. The mechanical treatments produce defect states in the surface which serve as electron traps. This technique is not applicable in the study of p-type or undoped material.

The condition of the surface of semiconductors has taken on added significance with the advent of epitaxial techniques. The surface of a substrate on which an epitaxial layer is to be deposited should be as much like the bulk of that substrate as possible. Mechanical treatment of a substrate can produce damage which is propagated into a deposited layer (1). There is also evidence that defect states can be mechanically induced (2, 3).

Reflection and optical constants.—The normal incident reflectivity, the ratio of reflected radiation to incident radiation, is dependent on the optical constants (4)

$$R = \frac{(n-1)^2 + k^2}{(n+1)^2 + k^2} \qquad [1]$$

where n and k are the real and imaginary parts, respectively, of the complex index of refraction. The absorption coefficient, α, is related to k by (5)

$$\alpha = 4\pi k/\lambda \qquad [2]$$

The surface layers may be assumed to be very similar to the bulk when the measured reflectivity is the same as the reflectivity calculated from the optical constants of the bulk.

There are two absorption processes that cause significant changes in the reflection spectrum, at wavelengths greater than the band edge, of III-V compounds. They are lattice absorption and free carrier absorption. These absorption processes have been studied by many investigators (6-9). The calculated

curves presented in this report, Fig. 1, 2, 3, and 9, were derived using equations given by Lyden (8).

$$n^2 - k^2 = \epsilon_\infty - \frac{Ne^2}{m_c\epsilon_0\omega^2}\frac{\omega^2\langle\tau\rangle^2}{(1+\omega^2\langle\tau\rangle^2)} + \left[\frac{\epsilon_\infty+2}{3}\right]^2\frac{N_lQ^2}{M\epsilon_0}\left[\frac{(\omega_t^2-\omega^2)\tau_l^2}{\omega^2+(\omega_t^2-\omega^2)^2\tau_l^2}\right] \quad [3]$$

$$2nk = \frac{Ne^2}{m_c\epsilon_0\omega^2}\frac{\omega\langle\tau\rangle}{(1+\omega^2\langle\tau\rangle^2)} + \left[\frac{\epsilon_\infty+2}{3}\right]^2\frac{N_lQ^2}{M\epsilon_0}\left[\frac{\omega\tau_l}{\omega^2+(\omega_t^2-\omega^2)^2\tau_l^2}\right] \quad [4]$$

where ϵ_∞ is the relative dielectric constant of the medium in the absence of any contribution from free carriers at very high frequencies; N the free carrier concentration; e the electronic charge; m_c the conductivity effective mass; ϵ_0 the permittivity of free space; ω the angular frequency of the infrared radiation; $\langle\tau\rangle$ the relaxation time averaged over all the free current carriers; N_l the concentration of atom pairs AB; Q the effective charge; M the reduced atomic mass; τ_l the relaxation time related to the damping of the lattice vibration; ω_t the angular frequency of the traverse lattice vibration. The equations were programmed in Fortran IV on the IBM 7040 and the resultant curves were plotted using a Calcomp plotter.

Lattice absorption in GaAs.—A strong absorption band, at long wavelengths, occurs in GaAs due to the resonant vibration between the gallium and arsenic atoms. This absorption gives rise to high values of k (Equation [1]) and causes the reflectivity to rise and peak at about 36μ. This peak in reflectivity is referred to as the Reststrahlen band and is common in diatomic crystals. The optical constants and reflectivity of undoped GaAs in the region of the lattice absorption are shown in Fig. 1. The parameters specific to GaAs, used in calculating curves 1, 2, 3, and 9, were obtained from Hass (10), Moss (4), and Burstein (9).

The absorption process begins to cause significant changes in the optical constants at about 30μ. The real part of the index of refraction (n) first decreases, then rises to a maximum at a wavelength just past the resonant frequency, and finally levels off to a near constant value. The imaginary part (k) rises rapidly as the absorption process increases, reaches a maximum then rapidly drops to very small values. The reflection spectrum shows a minimum at 34μ, the Reststrahlen band peaking at 36μ, and constant values at wavelengths well past the absorption band.

Free carrier absorption in GaAs.—The free carrier absorption process has been thoroughly analyzed by Moss (6). Radiation, which has a wavelength greater than the absorption edge, may be absorbed by interaction with free carriers in the material under study. These free carriers may be supplied by the n-type dopant in GaAs. Figure 2 shows the effect on the optical constants and reflectivity of free carrier absorption (and free carrier alone) in doped 1 x 10^{18} cm^{-3} GaAs in the 20-60μ range. As the energy is absorbed by the free carriers, the value of n decreases to a minimum around 35μ, then slowly increases. The value of k increases as the absorption increases. The reflection spectrum shows a minimum at 27μ and rises smoothly to a maximum which is maintained at larger wavelength.

Lattice and free carrier absorptions actually occur at the same time, therefore, both effects must be considered together. The reflectivity of GaAs with various carrier concentrations is plotted in Fig. 3. The reflection minimum moves to shorter wavelength as the carrier concentration increases. The maximum stays about the same, and the long wavelength reflection increases. The position of the minimum is actually a good measure of the carrier concentration of the material being measured. Figure 4 is a plot of carrier concentration *vs.* position of the minimum in the reflection spectrum. The curve was drawn from experimental points taken in our laboratory. Values from Spitzer and Whelan (11) as well as calculated values are included for com-

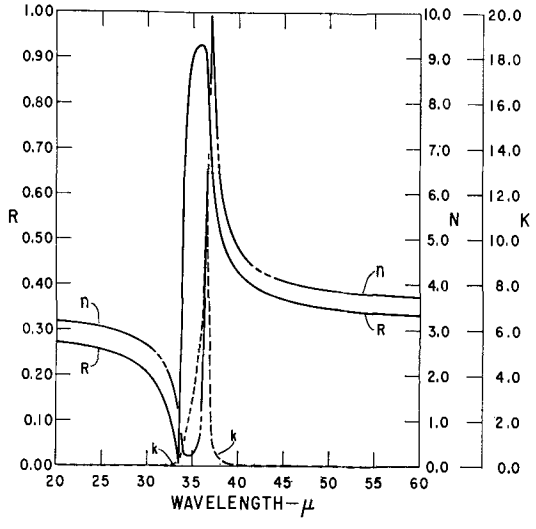

Fig. 1. Optical constants and reflectivity of undoped GaAs

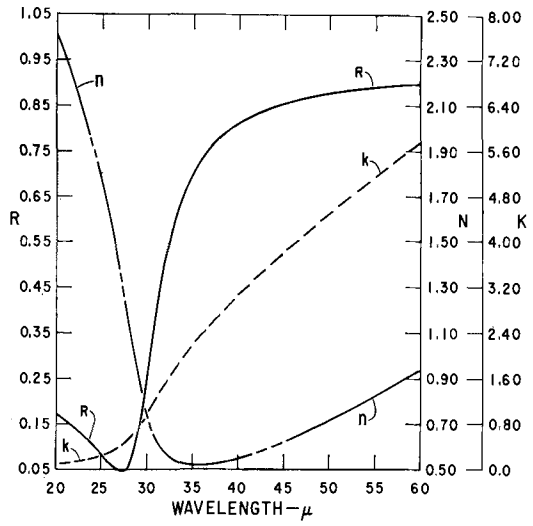

Fig. 2. Free carrier absorption in 1 x 10^{18} n-type GaAs

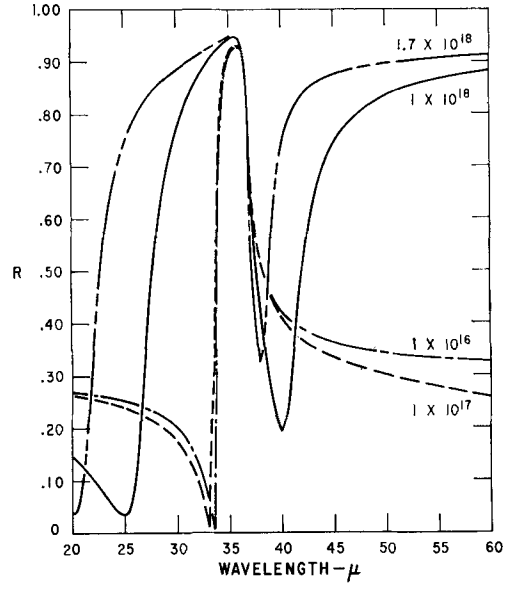

Fig. 3. Reflectivity of doped GaAs

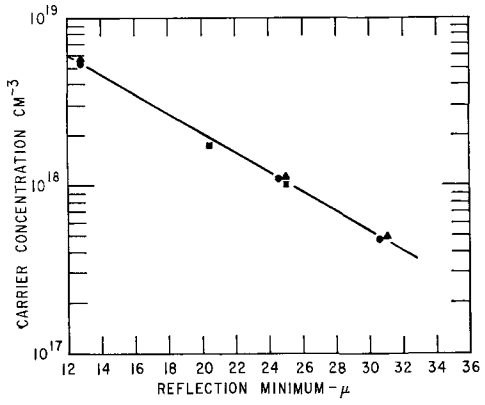

Fig. 4. Reflection minimum and carrier concentration: •, measured this laboratory; ■, calculated from Lydens' equations; ▲, Spitzer and Whelan.

parison. The relationship is linear over the range 5 x 10^{17} to 6 x 10^{18} cm^{-3} carriers. The calculated curves, Fig. 3, can be used to ascertain when measured reflection curves are the result of a surface that has the same optical constants that the bulk carrier concentration level demands.

Experimental Procedure and Results

The work described in this paper was carried out using n-type GaAs, Te doped $\approx$ 1.7 x 10^{18} cm^{-3} grown in the <111> direction, sliced parallel to the (111) plane. The reflection was measured from the B face. The study was carried out in this sequence: treat the surface mechanically, weigh, measure the reflectivity in the 20-60μ region, etch away an increment from the surface, weigh, measure reflectivity, etch away another increment, weigh, measure reflectivity, etc. This sequence was repeated until no significant change occurred in the reflection spectrum as more sample was etched away. The measured reflectivity was also compared to the theoretical reflectivity to be sure the final surface was actually about 1.7 x 10^{18} cm^{-3} GaAs. A H_2SO_4:H_2O_2:H_2O B face etch was used. The thickness removed by each etch was calculated from the sample weight loss, the surface area, and the density of GaAs. The area under the curve was used as a measure of the sample's over-all reflectivity. The result of one such sequence may be seen in Fig. 5. The polishing compound used in this case was 1200 grit (particle diameter $\approx$ 10μ). The reflectivity of the sample after it had been polished with the 1200 grit abrasive is marked with the solid dots. The reflectivity increased as the damaged layers were removed. At the end of the fourth etch a total of 13μ had been removed from the surface of the sample and the reflectivity (marked with open triangles) had reached a maximum. The reflection spectrum does not change as more surface is etched away and is equivalent to the reflectivity of a bulk

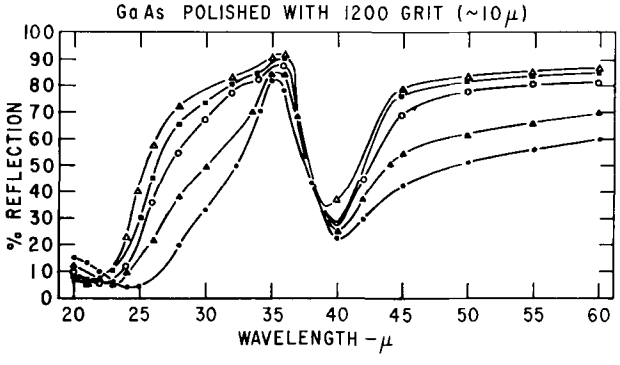

Fig. 5. GaAs polished with 1200 grit (~ 10μ). μ Removed: △, 13.0, 18.0, 25.0; ■, 5.8; ○, 2.2; ▲, 0.9; •, 0.0.

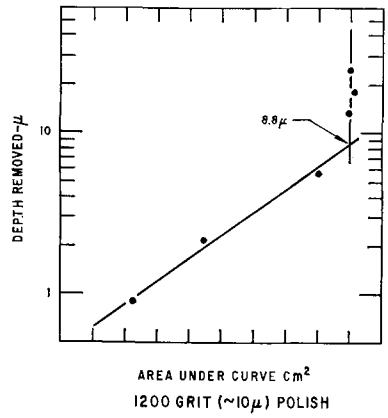

Fig. 6. 1200 grit polish

sample with a carrier concentration of 1.6 x 10^{18} cm^{-3}. This is in reasonable agreement with the estimated carrier concentration, 1.7 x 10^{18} cm^{-3}. Figure 6 is a plot of the observed relationship between the area under each reflection curve and the depth of the material removed. The area under the curve increases as more surface is removed until the surface shows the same optical constants as the bulk. No change occurs after the damaged layers have been removed because the layers being removed are just like the bulk. The curve changes slope at about 9μ. We then conclude that the 10μ particles damaged the surface to a depth of about 9μ.

Surfaces that were abraded by lapping compounds which had particle diameters of 3, 50, and 65μ were also treated in the same manner as described above. The results from the grinding and polishing part of this study are shown in Fig 7. The damage depth is approximately equal to the diameter of the abrasive particle. The results of Warekois, Lavine, and Gatos (12), using an x-ray technique, are included for comparison.

The grinding and polishing results agree satisfactorily with Warekois *et al.* (12) in the region of small particle damage, but do differ in the large particle region. Since the area of interest is the damage by small particles, no effort has been made to reconcile the differences in the large particle region.

The depth of the damage induced by sawing can also be measured by this technique. Figure 8 shows that a surface is damaged only about 8μ deep with a Hamco Dia-Saw.

Discussion

The described infrared reflection technique serves acceptably as a measure of the depth of damage in-

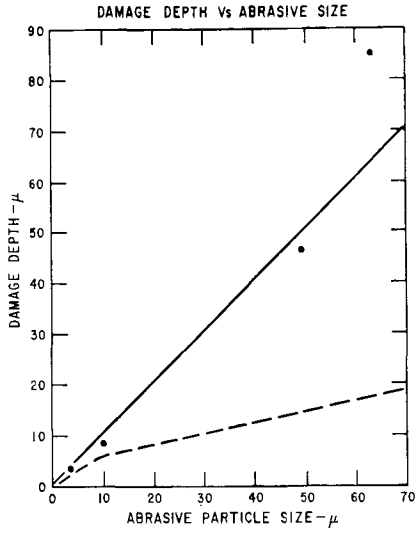

Fig. 7. Damage depth and abrasive size

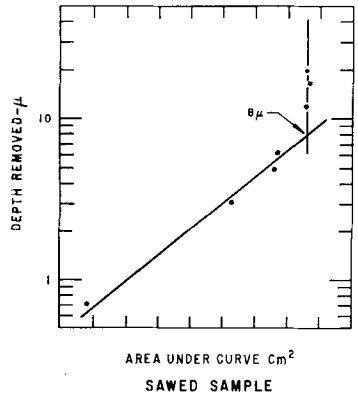

Fig. 8. Sawed sample

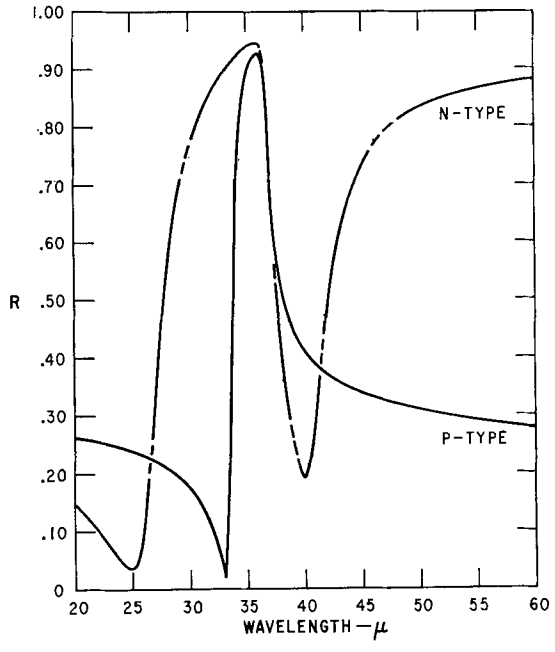

Fig. 9. Reflectivity: n-type (1 x 10^{18}) and p-type (1 x 10^{18}) GaAs

duced into doped n-type GaAs by mechanical treatment. When the surface has the same optical properties as the bulk, the damaged layers have been removed.

The data also lead to a better understanding of the type of damage produced by the saw and fine grit polishes. In Fig. 5 it should be noted that the point of minimum reflection moves to shorter wavelength as the damaged layers are removed. This suggests that the defects are serving as electron traps and lowering the number of free carriers available to absorb radiation. The free carriers are lower by about 10^{18} cm^{-3}; therefore, the concentration of defects must be at least the same order of magnitude.

The described method was not found to be useful, in the wavelength range of this report, for p-type GaAs with carriers 10^{18} cm^{-3} or less. It is evident from Fig. 9 that the effects due to free holes in p-type GaAs does not have the significance of the free carrier effects in n-type. This is true because of the effective mass of the hole is much larger than that of the electron. The effective mass value enters, as a squared term, into the denominator of free carrier equation (8).

Conclusions

The reflection technique described can be used to determine the depth of mechanically induced damage in doped n-type GaAs. GaAs is damaged by mechanical polishing to a depth about equal to the diameter of the abrasive particle. The damage produced by sawing and polishing appears to serve as electron traps causing the surface to contain fewer free carriers than the bulk material.

Acknowledgments

The authors wish to thank Dr. George Cronin for supplying the material used in this study, Mrs. Marilyn White for her efforts on the computer program, and Mr. Jim Parker for making the reflection measurements.

Manuscript received March 12, 1965; revised manuscript received June 5, 1965. This paper was presented at the Southwest Regional Meeting of the American Chemical Society, Shreveport, Louisiana, December 1964.

Any discussion of this paper will appear in a Discussion Section to be published in the June 1966 JOURNAL.

REFERENCES

1. W. N. Whitten, Jr., and J. E. McNamara, Paper presented at the Toronto Meeting of the Society, May 1964.
2. A. R. Hilton and F. Gamble, *J. Appl. Phys.*, **33**, 2398 (1962).
3. G. K. Walters and T. L. Estle, *ibid.*, **32**, 1854 (1961).
4. T. S. Moss, "Optical Properties of Semiconductors," p. 6, Academic Press, New York (1959)
5. *Ibid.*, p. 2.
6. *Ibid.*, p. 29
7. M. Born and K. Huang, "Dynamical Theory of Crystal Lattice," Oxford Press, London (1954).
8. H. A. Lyden. *Phys. Rev.*, **134A**, 1106 (1964).
9. E. Burstein, To be published.
10. M. Hass and B. W. Henvis, *Phys. and Chem. Solids*, **23**, 1099 (1962).
11. W. G. Spitzer and J. M. Whelan, *Phys. Rev.*, **114**, 59 (1959).
12. E. P. Warekois, M. C. Lavine, and H. C. Gatos, *J. Appl. Phys.*, **31**, 1302 (1960).

Effect of Fast Cooling on Diffusion-Induced Imperfections in Silicon

M. L. Joshi

Systems Development Division, International Business Machines Corporation, Poughkeepsie, New York

ABSTRACT

Misfit dislocations in phosphorus-diffused silicon are shown to suffer rearrangement on fast cooling. These dislocations extend in specific directions and act as centers of phosphorus precipitates. There are also other areas of precipitation where the particles are of irregular shape and size. The motion of dislocation network in the depths of the diffusion profile is mainly by glide, although a less dominant climb motion is observed.

The generation of misfit dislocations in silicon by solute concentration gradients imposed by diffusion of large dopant concentration has been demonstrated by the observation of etch pits (1) and slip lines revealed by chemical etching (2), x-ray microscopy (3), and the electron probe (4). Formation of dislocation networks on (111) orientation Si was reported by Jaccodine (5) and was later supported by the authors (6) in more detailed study through the technique of transmission electron microscopy. Thomas *et al.* (7) observed square grid of dislocations on (100) orientation through the same technique.

The study of phosphorus-induced imperfections (6) as a function of the depth in the diffusion profile shows that the dislocation network on (111) oriented wafer, with 2μ junction depth, exists only up to about $1/3\mu$ depth in the diffused layer. Penetration of the network in the diffusion profile was shown to have occurred from glide on the {111} planes inclined to the (111) plane of the wafer. Impurity precipitates, believed to be phosphorus precipitates, were also found throughout the diffusion profile in the same study. The detailed analysis of thin phosphorus-diffused layers in p-type silicon by Tannenbaum (8) shows that with high concentration of phosphorus ($>10^{20}/cm^3$) there is a significant difference between the profile determined by sheet resistivity and that by radiotracer measurements. This difference was interpreted to mean that part of the phosphorus might be in the form of precipitates. The actual detection of these precipitates (6, 9) corroborated the precipitation model.

Tannenbaum's diffusion data analysis (8) also indicated the importance of the rate of cooling down from the diffusion temperature. Precipitates of irregular size and shape were observed in a sample dropped from the furnace into an oil bath, in contrast to well-developed crystalline precipitates observed (6, 9) in a sample pulled from the diffusion furnace and allowed to cool slowly in air on a quartz platform. Dislocations generated during diffusion are also shown to be sites of enhanced precipitation. Rapid cooling may also cause basic dislocations in the silicon lattice, corresponding to {111} <110> slip, to extend in specific directions, due to the introduction of uniform stress field. Dislocation interactions are shown to be highly influenced by the energy processes that pull the dislocations into <110> alignment. Dislocation movement by "climb" is also shown to exist, although it may not be the dominant mechanism.

Experimental

Diffusion and quenching.—Three 10-mil thick and 1-in. diameter wafers were cut parallel to (111) from a Czochralski-grown Sb-doped (10^{15} cm^{-3}) silicon crystal. The wafers were lapped on both sides and chemically polished to remove any surface damage. The dislocation density of one of the wafers was found to be less than $10^3/cm^2$ by the etch pit technique. Two of the wafers were symmetrically diffused with phosphorus (junction depth 2μ) at a temperature of 1150°C with the P_2O_5 source held at 300°C. The surface concentration of phosphorus measured with a four-point probe was found to be 3×10^{21} at./cc. The wafers were removed from the furnace and quenched in oil. The significant rate of quenching is that which occurs during the first 400°C (approximately) where the process of diffusion can affect the precipitation. This significant rate could not be measured. However, the estimated average quenching rate (from 1150°C to room temperature) is about 0.5×10^3°C/sec.

The third wafer was not diffused and was used as a test wafer for the quenching process. The wafer was quenched from 1150°C in the same way (as in the case of the diffused wafer) to check whether any plastic deformation had occurred from the thermal stresses during the necessarily inhomogeneous cooling (12).

Specimen preparation.—One of the wafers was used for determination of the junction depth which was found to be 2μ. The other was cut into strips about ⅛ in. wide; these were subjected to anodic oxidation on the side to be studied. The appropriate depth in the solute profile was reached by successive removal of the oxide layers through HF. The thickness of the removed silicon layer through sectioning was determined from a comparison of the silicon oxide color to a standard film thickness gauge. Each strip was cut into ⅛ x ⅛ in. samples to be observed in a Philips electron microscope (100B), using a standard specimen holder with a slightly enlarged specimen receptacle.

The procedure for thinning the sample to obtain transparency to the electron beam is essentially the same as described in an earlier paper (6).

Experimental Observations

No significant generation of dislocations could be observed by the etching pit technique or by transmission electron microscopy in the test wafer. Occasionally regular, but mostly irregular, dislocation networks are found on the surface of the (111) oriented phosphorus diffused samples quenched in oil, Fig 1, in accordance with previous findings (5, 6). The dislocations are considered to be generated by the lattice parameter mismatch caused by the impurity gradient. Unlike the dislocations in the strictly hexagonal grids with <112> alignment (pure edge characteristic), we see many parallel dislocations whose axes are oriented in <110> directions, Fig. 2. These dislocations seem to lie almost entirely on the plane of the foil which is also the most active glide plane. They are 60° Read dislocations possessing a screw character in part. These long dislocations also show jogs. Such jogs are related to the quenching process which is expected to give rise to climb forces due to nonequilibrium concentrations of interstitials or vacancies. The jogged dislocations were found near the surface only (0μ depth). About 0.13μ deep in the diffused sample we find interactions between the dislocations, Fig. 3 and 4. Again, dislocation axes

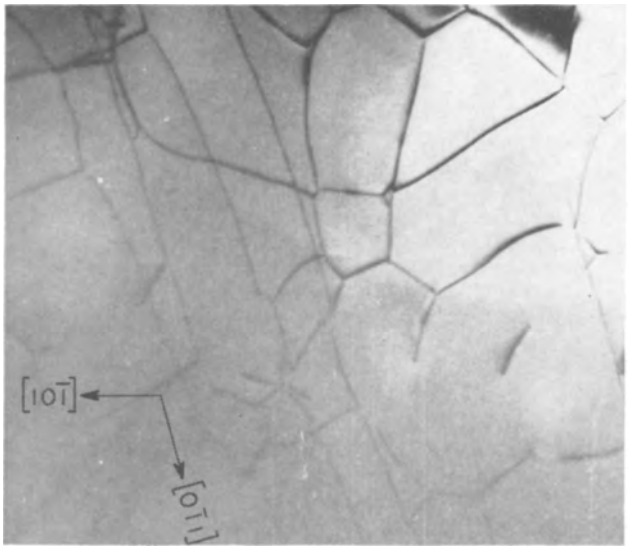

Fig. 1. Misfit dislocation network on the surface (0μ depth). Magnification approximately 17,330X.

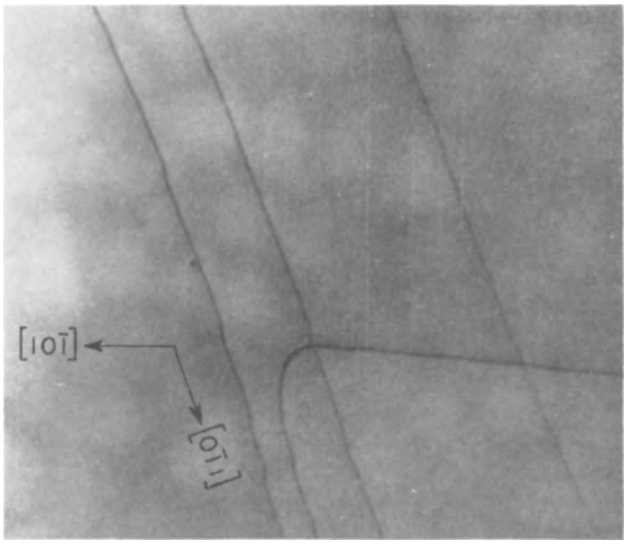

Fig. 2. Rectilinear dislocations in <110> directions with jogs in the surface (0μ depth). Note the elbow dislocation. Magnification approximately 17,330X.

in these figures are all in <110> directions and lie in the foil plane. Figure 5, however, indicates that all the dislocations are not on the same glide planes. Consequently a threefold node would not have 120° angles among its dislocations. This phenomenon also signifies that the transfer of dislocations to this depth on the film plane has occurred by glide. A possible reaction (Fig. 5) could be written as

$$\tfrac{1}{2}[011] + \tfrac{1}{2}[\bar{1}\bar{1}0] = \tfrac{1}{2}[\bar{1}01]$$

$$\text{on}(\bar{1}\bar{1}1) \quad \text{on}(\bar{1}11) \quad \text{on}(111)\text{—(plane of the film)}$$

The possible reaction for the dislocations in Fig. 3 and 4 could be written on the basis that they all have the same glide plane

$$\tfrac{1}{2}[\bar{1}10] + \tfrac{1}{2}[0\bar{1}1] = \tfrac{1}{2}[\bar{1}01]\text{—(all on the foil surface)}$$

The threefold nodes in these reactions should have their angles between interacting dislocations, rearranged to balance tension. However, we see 60°T joints at O and P in Fig. 3b (idealized diagram of Fig. 3 or 4), indicating that either the glide plane of intersections C and L may not be the same as that of the other dislocations, or that there exists processes which keep the dislocations in <110> alignment and lower their

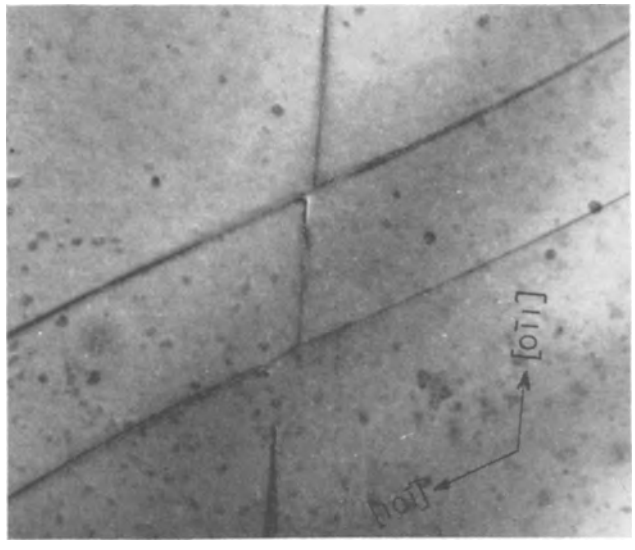

Fig. 3a. Threefold nodal interactions of dislocations lying in the foil plane and in <110> directions; the plane of observation is a 0.13μ depth in the sample. Note the incipient nodal reactions and the preservation of <110> alignment. Magnification approximately 6600X.

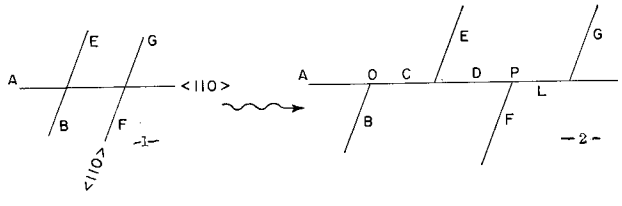

Fig. 3b. Idealized representation of Fig. 3a

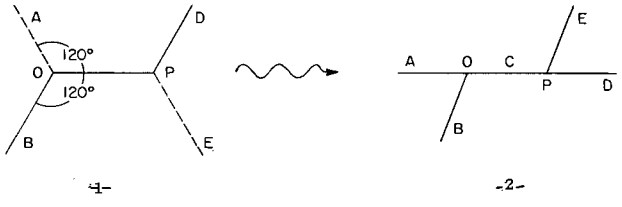

Fig. 3c.-1- Equilibrium configuration of two interacting dislocations with the same glide plane. -2- The observed configuration.

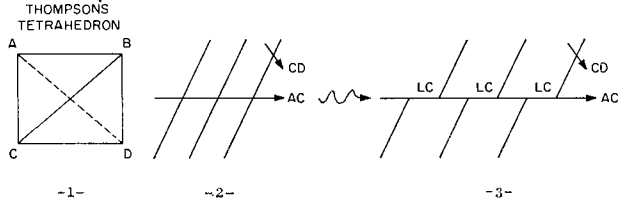

Fig. 3d. -1- Thompson tetrahedron of Burgers vectors as observed in <100> direction. -2- Interaction of a screw with a group of parallel dislocations belonging to the same family of Burgers vectors. -3- Formation of Cottrell locks.

configuration energy. Since these dislocations are misfit dislocations, it is reasonable to assume the latter case, which requires dislocations to have their Burgers vectors lie in the same plane as the diffusion plane. T joints and elbows have been observed in germanium under tension tests (13). The polygonal dislocations are shown also to exist in the quenched specimen, Fig. 6. Formation of an elbow is shown in Fig. 2. This is indicative of reduction of the line energy while maintaining <110> alignment. Impurity segregation along

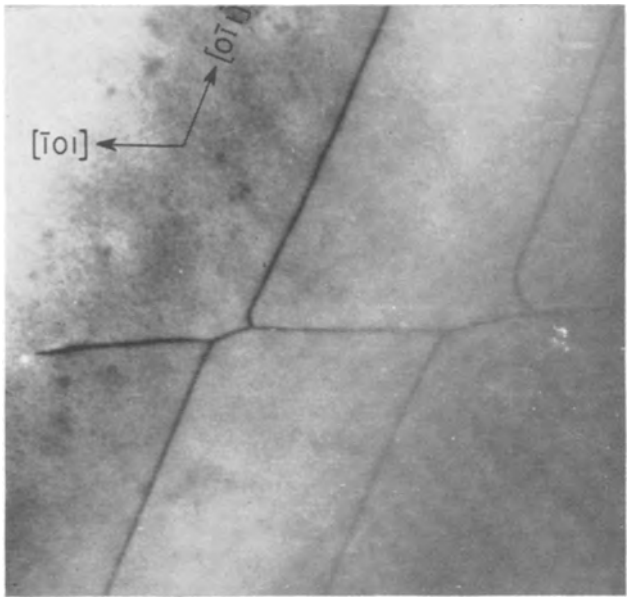

Fig. 4. The same as Fig. 3a except that the dislocation segments generated at the nodes after interaction are longer and the plane of observation is at 0.3μ. Magnification approximately 17,330X.

the dislocation lines is seen in Fig. 6. We also see there a diffused spotty contrast which can be attributed to general precipitation. Dark field imaging shows that the spots are structurally inherent to silicon. No well-developed crystalline hexagonal or square shapes were observed in the quenched specimen throughout the examined profile. The density of dislocations was reduced substantially ($<10^6$ cm/cm^3) below 0.4μ depth of the diffusion profile, which is in agreement with previous findings.

Discussion

An inhomogeneous temperature gradient is always accompanied by stresses which, if they are large, could cause plastic flow by relieving part of the stresses at the cost of the formation of a number of dislocations in the material in excess of those introduced by the impurity gradient (12). The failure to observe significant dislocation in the quench test wafer indicates that the majority of the dislocations observed in the diffused samples owe their origin to the diffusion gradient of phosphorus.

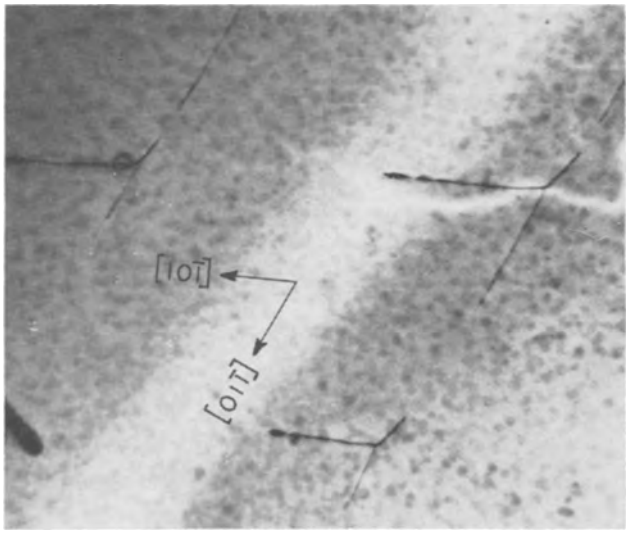

Fig. 5. Threefold nodal interaction of dislocations, all of which are not in the foil plane. The diffused spots are impurity clusters, and the plane observation is 0.13μ deep in the sample. Magnification approximately 17,330X.

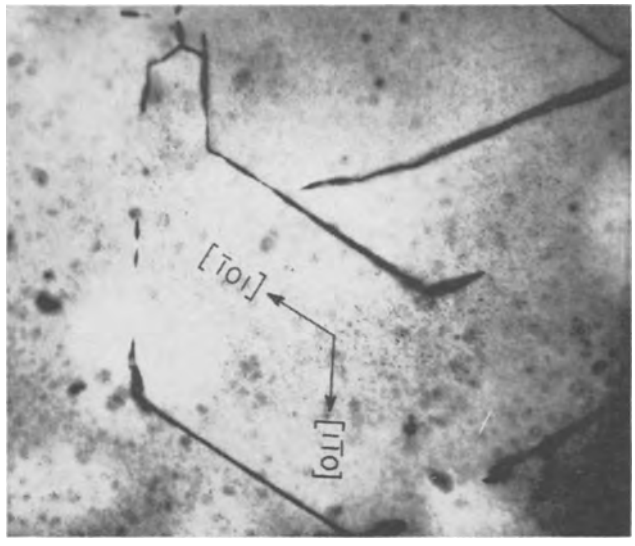

Fig. 6. Polygonal dislocations and the impurity atmosphere at 0.13μ depth. Magnification approximately 17,330X.

It is generally assumed that in cooling rapidly from diffusion temperature to room temperature a supercooled solution is obtained with substantially all the phosphorus frozen into substitutional positions. At high concentrations, however, precipitation can occur on cooling from diffusion temperatures, depending on the rate of cooling. It is also found that basic dislocation types corresponding to {111} <110> slip extend in specific directions if they are produced during uniform stress applications (10, 13).

Tannenbaum's (8) analysis of her diffusion data indicating the existence of phosphorus precipitates was supported by the observation of well developed crystallites believed to be phosphorus precipitates in the sample slowly cooled down from diffusion temperature. In the present experiment, no such precipitates were observed. The quenching, however, seems to have given rise to diffuse impurity precipitation in the matrix with some enhancement of impurity along dislocation lines. This again corroborates the precipitation model in the case of large amounts of phosphorus diffusion. The impurity segregation along dislocation lines could be due to both the Cottrell atmosphere (involving reduction in elastic energy) and the negative charge of dislocation lines (in n-type semiconductors) having coulombic attraction for positively charged impurities. One of the important consequences of these impurities would be the pinning of the dislocations. Even with very pure semiconductors, there are enough impurity atoms to saturate the dislocations present. The density of locking sites (14) in pulled crystals would be about $10^4/4 \times 10^{-8} \approx 10^{11}$/cm^3, where the numerator is the dislocation density and the denominator is the Burgers vector. The impurities in our experimental example could surely contribute this number of locking sites. The Cottrell model is known to be applicable in the case of Si (14-16).

A majority of the dislocation axes in the electron micrographs are oriented in <110> directions. Since the relief of the strain on the diffusion plane implies that the Burgers vectors should lie on the (111) plane of the wafer, these dislocations are 60° Read dislocations. The rectilinearity seems to have been caused by the uniform stresses probably produced during the rapid cooling. The <110> alignment of the dislocations has been shown to be inexplicable on the basis of anisotropy of elastic constants (17, 18). Hassen (19), however, has pointed out that the bonds opposite an extra half plane in the 60° dislocation are severely strained and, from consideration of the yield stress, it may be that they are broken, *i.e.*, there is a crack on the edge of the extra half-plane. The stress necessary to set the dislocation in motion must also be sufficient to move

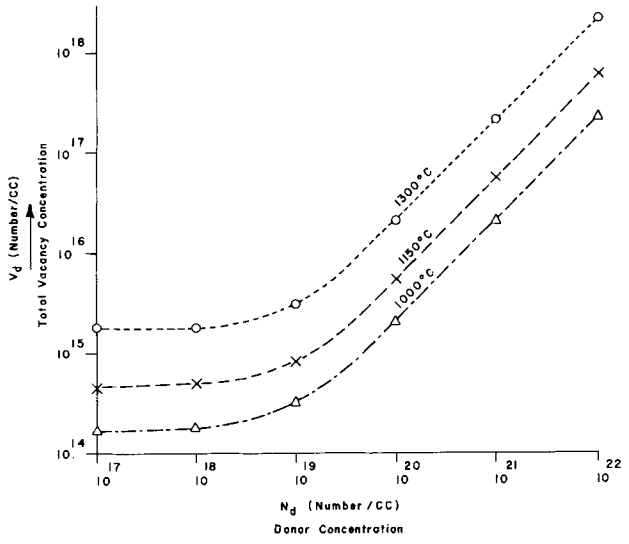

Fig. 7. Total vacancy concentration vs. donor concentration at different temperatures.

the broken bonds, *i.e.*, the cracks, along with it by diffusion. In other words, the 60° dislocation has a high Peirels-Nabarro friction arising from the periodic nature of the lattice and the breaking and remaking of new bonds as it moves.

The jogs in the wall aligned <110> dislocations will cause the mean dislocation line not to lie in the exact <110> crystallographic direction. These jogs could be formed either by tension or compression forces parallel to the foil plane (which is also a slip plane) or by climb. The climb mechanism, however, seems to be a reasonable explanation, in the light of the quenching treatment of the sample. The total vacancy concentration (*i.e.*, the sum of the neutral and the charged vacancies) estimated for $10^{21}/cm^3$ donor concentration at 1150°C is about $10^{18}/cm^3$ (see Appendix and Fig. 7). From the diffusion profile analysis (8), however we know that impurity atoms in the order of $10^{20}/cm^3$ exist in sites other than substitutional. The jogs, then, may be considered primarily due to the nonequilibrium concentration of the interstitials, giving rise to the climbing forces.

The double nature of the (111) extra half-planes requires the absorption or rejection of pairs of interstitials or vacancies. The movement of dislocations by jogs is energetically expensive. The dominant process of the transfer of dislocations to equalize strains in the diffusion profile is the glide process on the {111}<110> slip system, as illustrated in Fig. 5. Our own work (6) on (111) orientation and that of Washburn *et al.* (7) had postulated this mechanism, for which we have obtained herein the necessary evidence. The dislocation interactions in Fig. 3a and 4 are informative from the point of view of the junction reactions. Figure 3b idealizes the dislocation configurations in Fig. 3a. In Fig. 3b, A and L are in <110> direction, and junction dislocations C and D follow the same course of A and L without substantial attempt to balance the tensions at the threefold nodes, o and p. The study of triple nodes at equilibrium provides a measurement of line tensions. One can check in this way whether the line tension measure $K\mu b^2$ $(1 - \nu \cos^2 \alpha)$ is a sufficient criterion, where K is a numerical constant, μ the modulus of elasticity, ν Poisson ratio, and α is the angle between the dislocation line and Burgers vector. Knowing that the Fig. 3b-2- configuration is the result of the interaction in the sets of dislocations both lying in <110> direction and in the plane of the foil, it is imperative for the equilibrium condition that the dislocations at node O rearrange with 120° angles between them, as shown in Fig. 3c. Evidently the resultant reaction is the low energy configuration. Assuming isotropic line tensions and neglecting long-range interactions between dislocations, the change in elastic energy involved between these two configurations can be calculated. The decrease in energy (ΔE) involved in pulling OA from the —1— configuration into the —2— configuration, can be shown by a simple calculation to be

$$\frac{\Delta E}{E} \approx 0.5$$

where E is the isotropic line tension. For stability of the 60°T joint at O, then ΔE is the energy that must be derived from some energy-lowering source that maintains <110> alignment of the dislocations even after interaction with others. The source of this energy can be conceived to be the Peierls-Nabarro trough for a 60° Read dislocation and the pinning points, provided by impurity atoms. Another possibility is that, if we interpret the dislocation reaction with assumption that A is a screw dislocation, then the short segments C and L might not have the same glide plane as the foil plane has. If the intersected dislocations with Burgers vector CD are on the foil plane BCD and the intersecting screw dislocation on plane ABC with Burgers vector AC, then the interaction is AC + CD = AD (Fig. 3d). The resulting dislocation lying in the direction CB is capable of gliding on the (100) plane only. This is the undissociated Cottrell-Lomer lock (LC in Fig. 3d). Since this is sessile and cannot glide in the plane of the foil, it lies in the <110> direction, and it should appear as a straight line on the micrograph (20). This is in agreement with what is observed. The same interpretation has been given by Jenkinson and Lang for similar interactions among dislocations in floating-zone grown silicon (21). However, whether C and L are Cotrell locks, it cannot be said with certainty.

Conclusions

This study has shown that quenching produces precipitates of irregular size and shape, in contradistinction to the well-developed crystalline precipitates observed in slow cooling from the diffusion temperature. The dislocations act as centers of extra precipitation. The motion of the dislocation network in the depths of the diffusion profile is by glide, although a less dominant climb motion seems to exist.

Acknowledgments

The author is pleased to thank Professor G. Thomas, Department of Mineral Technology, University of California, and Dr. B. H. Kear of the Pratt-Whitney Research Laboratories, New Haven, Connecticut, for very helpful comments in the interpretation of this work. He also wishes to thank E. S. Wajda, J. N. Ramsey, J. G. Christ, and F. Wilhelm for their valuable help and encouragement and are grateful to S. Mader for help in experimental and theoretical matters. Thanks are due to W. J. Armstrong for carefully reviewing the manuscript and giving critical comments.

Manuscript received March 23, 1965.

Any discussion of this paper will appear in a Discussion Section to be published in the June 1966 JOURNAL.

REFERENCES

1. S. Prussin, *J. Appl. Phys.*, **32**, 1876 (1061).
2. H. J. Queisser, *ibid.*, **32**, 1776 (1961).
3. G. H. Schwuttke and H. J. Queisser, *ibid.*, **33**, (1962).
4. J. J. Landes, H. Schreiver, Jr., T. M. Buck, and J. R. Mathews, *Appl. Phys. Letters.* **3**, 206 (1963).
5. R. J. Jaccodine, *ibid.*, **4**, 114 (1964).
6. M. L. Joshi and F. Wilhelm, *This Journal*, **112**, 185 (1965).
7. J. Washburn, G. Thomas, and H. J. Queisser, *J. Appl. Phys.*, **35**, 1909 (1964).
8. E. Tannenbaum, *Solid State Electronics*, **2**, 123 (1961).

9. P. F. Schmidt and R. Stickler, *This Journal*, **111**, 1188 (1964).
10. W. C. Dash, *J. Appl. Phys.*, **29**, 705 (1958).
11. W. Bollman, *Phil. Mag.*, **7**, 1513 (1962).
12. H. G. Van Bueren, "Imperfections in Crystals," p. 277, North Holland Publishing Co., Amsterdam (1961).
13. D. B. Holt and A. E. Danger, *Phil. Mag.*, **8**, 1921 (1963).
14. R. G. Rhodes, "Imperfections and Active Centres in Semiconductors," p. 109, Pergamon Press Book (1964).
15. W. Kaiser, D. H. Keck, and C. F. Lange, *Phys. Rev.*, **101**, 1264.
16. G. L. Pearson. W. T. Read, and W. L. Feldman, *Acta Meta.*, **5**, 181.
17. A J. E. Foreman, *ibid.*, **3**, 322 (1955).
18. D. B. Holt, *J. Phys. Chem. Solids*, **23**, 1353 (1962).
19. P. Haasen, *Acta Met,*, **5**, 598 (1957).
20. M. J. Whelan, *Proc. Roy. Soc.*, **A249**, 114 (1958).
21. A. E. Jenkinson and A. R. Lang, "Direct Observation of Imperfections in Crystals," p. 471, J. B. Newkirk and J. M. Wernick, Editors, Interscience Publishers, N. Y. 1961 (AIME Conf., Mssouri).
22. M. F. Millea, ASTIA Document No. AD 215 265.
23. R. A. Swalin, "Thermodynames of Solids, "John Wiley & Sons, Inc., pp. 243-271 (1961).
24. R. A. Swalin, *J. Appl. Phys.*, **29**, 670 (1958).
25. E. Kooi, *This Journal*. **111**, 1383 (1964).

APPENDIX

Let us calculate the equilibrium concentration of vacancies in a highly doped n-type silicon crystal, following the line of argument given by Millea (22).

A fraction of the vacancies will be negatively charged since they are electron acceptors. The concentration of filled acceptor sites may be determined by Fermi-Dirac statistics. Therefore, we have, at a given temperature, the total number of vacancies in an intrinsic crystal

$$V_i = V^o + V^- \qquad [1]$$

where V^o is the number of neutral vacancies and V^- the number of charged vacancies. We will assume V^o to be constant, on the basis that the part of V^o converted to V^- at a given temperature will be replenished to its original concentration by diffusion of vacancies into the crystal from the crystal surface and from the dislocations. Then it is easy to see that a change in electron concentration introduces a proportional change in V^- and, consequently, a simple manipulation will show that the ratio (to a first approximation) of vacancies in a crystal doped with donors V_d, to the vacancies in an intrinsic crystal, V_i, is

$$\frac{V_d}{V_i} = \frac{n_d}{n_i} \qquad [2]$$

where n_d and n_i refer to electron concentrations in a doped and in an intrinsic crystal. The concentration of electrons as a function of doping can be found from the usual charge balance relation:

$$N_d + \frac{n_i^2}{n_d} = N_a + n_d \qquad [3]$$

where N_d is the number of donors, N_a the number of acceptors, and n_d the electron concentration in the conduction band. Combining [2] and [3], we obtain for predominant donor doping

$$\frac{V_d}{V_i} = \frac{N_d + (N_d^2 + 4n_i^2)^{1/2}}{2n_i} \qquad [4]$$

where

$$V_i = V^o\{1 + 2\exp[(E_{Fi} - E_A)]/kT\} \qquad [5]$$

where, again, E_{Fi} is the intrinsic Fermi level, E_A the energy level of the fraction of negatively charged vacancies which act as acceptors, T is temperature (absolute units), and k is Boltzmann's constant. For silicon, we use the figures given by Swalin (23, 24) $E_{Fi} = 0.545$ ev; $E_A = 0.16$ ev (below conduction band) and the enthalpy of formation of neutral vacancy, $\Delta H_v = 2.32$ ev. Figure 7 gives the calculated curves of total vacancy concentration as a function of donor concentration at different temperatures. The phosphorus surface concentration measured with four-point probe in our experimental wafer is about 3×10^{21} at./cc. The actual concentration of phosphorus, however, as measured by tracer technique (25) in a similar case has been shown to be about 10^{22} at./cc in the surface layer which is thinner than 1000Å. This indicates that the total vacancy concentration at 1150°C prior to quenching is about 10^{18} at./cc, or a little less.

The Oxidation Mechanism of Pure Uranium in Carbon Dioxide Between 350° and 650°C

J. J. Stobbs

Materials Division, Berkeley Nuclear Laboratories,

Central Electricity Generating Board, Berkeley, Gloucestershire, England

ABSTRACT

Weight gain/time curves obtained on a thermobalance are related to metallographic observations of the oxide. It is found that the oxide is initially protective, but as a result of nonuniform oxidation and cracking the oxidation rate accelerates until finally a linear rate law is obeyed. In the early stages of oxidation a separate layer of oxide grows at the oxide-gas interface, but soon attains a limiting thickness of a few thousand Angstroms and does not influence the over-all oxidation behavior. Carbon monoxide formed from the reaction between uranium and carbon dioxide reacts further in the cracks in the oxide.

The oxidation behavior of uranium in carbon monoxide and carbon dioxide is important when considering the consequences of can leaks in the current British and French type of gas-cooled nuclear power reactors. A large amount of empirical data relating to the behavior of reactor grade uranium in carbon dioxide of various purities has been obtained, although with few exceptions little success in understanding the scientific aspects of the system has been achieved. Recent work at the Berkeley Nuclear Laboratories of the Central Electricity Generating Board on the examination of failed fuel elements (1) and the development of an oxidation resistant coating for uranium fuel bars (2, 3) has indicated the need for a more fundamental understanding of the reactions between uranium and carbon monoxide and dioxide.

The work described here is part of a systematic investigation to determine the oxidation mechanism of uranium in these gases under a comprehensive range of experimental conditions.

Experimental

Specimens.—Uranium was obtained from the Centre d'Etudes Nucléaires de Saclay in ingot form and contained the following impurities (in ppm): Ag, < 0.5; Al, < 10; B, < 0.1; Be, < 0.5; C, 12; Cd, < 0.5; Cr, 6; Cu < 10; Fe, 19; H, < 1; K, < 20; Li, < 2; Mg, < 10; Mn, < 1; Na, 5; Ni, < 3; O, 13; P, ≤ 50; Pd, < 3; and Si, 15. The levels of the impurities are thus considerably lower than in British reactor grade uranium which contains 600-1000 ppm C, ~ 700 ppm Al and ~ 250 ppm Fe as its major impurities. Specimens 14 x 13 x 2 mm thick were used to investigate oxidation kinetics, and small pieces 5 x 5 x 2 mm thick were used to follow oxidation metallographically. All specimens were vacuum annealed at 950°C for 4 hr and then 660°C for 5 hr to give a stable α grain structure before oxidation. Kinetic specimens were mechanically polished to a ¼μ diamond finish on all faces; those for the qualitative metallographic studies were polished only on one face.

Oxidation.—Carbon dioxide was purified by passing it through successive columns of copper (prepared by the hydrogen reduction of wire form cupric oxide) at 350°C, magnesium perchlorate and phosphorus pentoxide. The purified gas contained ≤ 7 vpm oxygen and ≤ 3 vpm water vapor, nitrogen (~ 50 vpm) and carbon monoxide (≤ 25 vpm) being the only other impurities detected.

Rates of oxidation were measured in carbon dioxide at 1 atm pressure flowing at 50 cc/min on a Stanton "Massflow" vacuum thermobalance (Model MF — L5). During oxidation, each specimen was suspended inside an alumina crucible on a platinum wire. The specimen was brought to temperature (and cooled) in flowing carbon dioxide, this process taking between 25 and 35 min depending on the oxidation temperature. Oxidations were carried out at 350°, 450°, 550°, and 650°C (to ± 5°C), the temperature being measured with a chromel-alumel thermocouple in the gas stream adjacent to the specimen.

Both adherent and nonadherent oxide were analyzed for carbon and their structures determined by x-ray powder diffraction.

The metallographic features of oxidation were mainly followed by oxidizing specimens in a simple tube furnace with an observation port in one side so that the polished face could be examined with a binocular microscope (maximum magnification about 60X) during oxidation. At suitable intervals the furnace was cooled and the specimens removed for more detailed examination at higher magnifications.

Results

Weight gain measurements.—The oxidation rate at 350°C was too slow to be measured with the present apparatus. Weight gain/time curves typical of the other temperatures investigated are shown in Fig. 1-3; the original geometrical surface area of the specimens

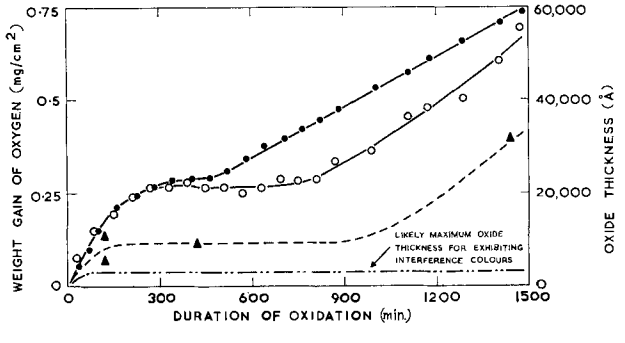

Fig. 1. Early stages of oxidation at 400° and 450°C. Weight gain data: •, run a; ○, run b (both present work, 450°C); ▲, Hayfield et al., 400°C (5). Oxide thickness data: — - - — Hayfield et al., 400°C (5).

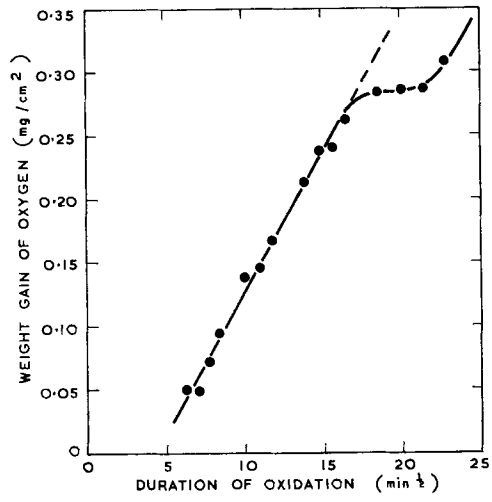

Fig. 2. Parabolic plot of the early stages of oxidation at 450°C

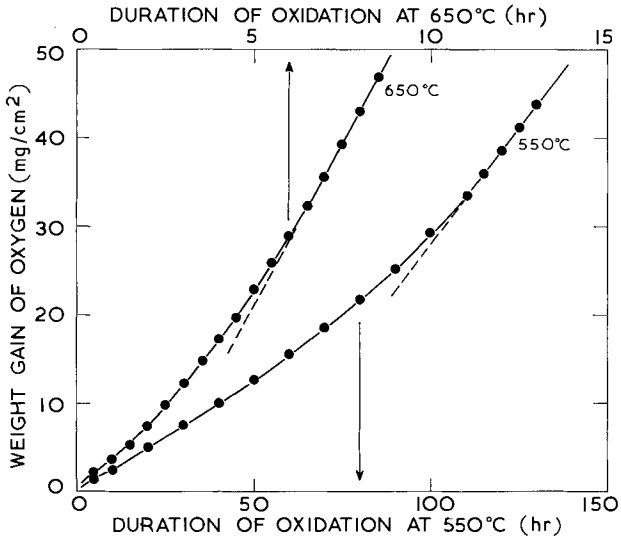

Fig. 3. Long-term oxidation behavior at 550° and 650°C

was used to calculate the weight gain per unit area.

It was evident that the oxidation behavior could be divided into four stages, the importance of which was influenced by temperature. The stages were:

(i). The parabolic growth of a uniform oxide layer to a thickness of ~ 2μ at 450°C and ~ 10μ at 550°C (a weight gain of 1.0 mg/cm² corresponds to an 8μ thick layer of crack-free UO_2); at 650°C it was not possible to decide if a parabolic rate law was obeyed since the form of the rapid initial oxide growth was obscured by the heat-up period.

(ii). A period when the oxidation rate remained very low, varying from 120 to 540 min at 450°C, to ~30 min at 550°C, and to zero time at 650°C.

Table I. Data relating to parabolic oxidation

Oxidation temperature, °C	Time to completion of parabolic oxidation, min	Weight gain at end of parabolic oxidation, mg/cm²	Parabolic rate constant, mg²/cm⁴ min
450(a)	256	0.28	4.8×10^{-4}
450(b)	256	0.27	4.2×10^{-4}
550(a)	182	1.37	2.8×10^{-2}
550(b)	180	1.25	2.2×10^{-2}
650(a)*	20	1.50	—
650(b)*	20	1.50	—

* Data refers to end of period when rate decreased with time.

Table II. Data relating to linear oxidation

Oxidation temperature, °C	Time to onset of linear oxidation, hr	Weight gain at onset of linear oxidation, mg/cm²	Linear rate constant, mg/cm² hr
450(a)*	>120	>3	>0.018
450(b)*	>300	>5	>0.018
550(a)	90	31	0.56
550(b)	110	33	0.51
650(a)	6.9	35	7.63
650(b)	6.6	30	7.11

* Linear oxidation rates were not attained in the times studied.

(iii). A gradual acceleration in the oxidation rate that increased with temperature.

(iv). A final linear oxidation rate that was attained sooner and was faster the higher the temperature.

Tables I and II summarize details of parabolic and linear oxidation.

Metallographic studies.—Several orders of interference colors appeared in rapid succession, individual grains showing different shades or different colors as a result of some dependence of the oxidation rate on the orientation of the underlying metal. The disparity in the thickness between thicker and thinner oxides became more marked with time, and a locally thicker oxide often appeared around surface discontinuities such as twin bands, scratches, and grain boundaries.

On further oxidation the thicker oxide spread laterally to cover the entire surface (Fig. 4). At the same time cracks appeared on the surface of the thicker oxide, and the whole surface eventually became a network of cracked oxide (Fig. 5). The cracks increased in size with time and, although small pieces of the outer layers of oxide often broke away, the oxide was generally adherent (see Table III).

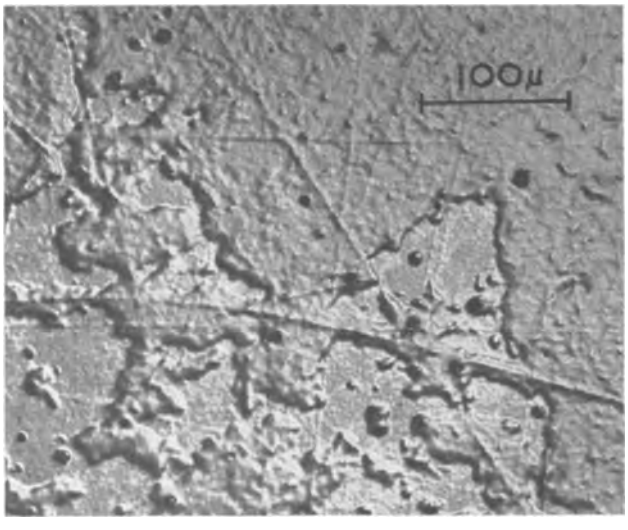

Fig. 4. Lateral growth of thicker oxide over the surface after 350 hr at 350°C.

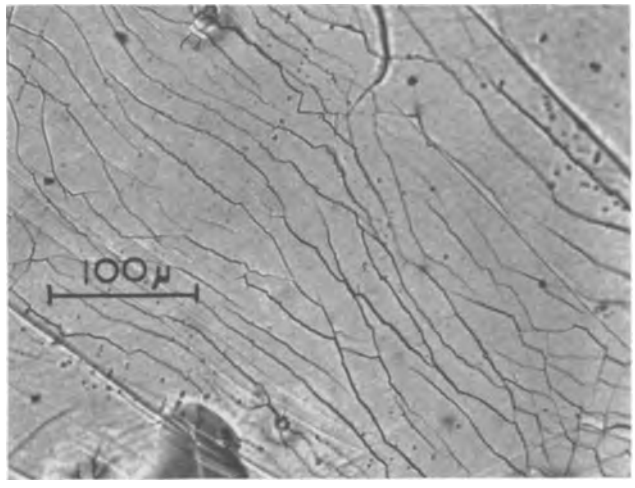

Fig. 5. Cracked oxide after 145 hr at 450°C

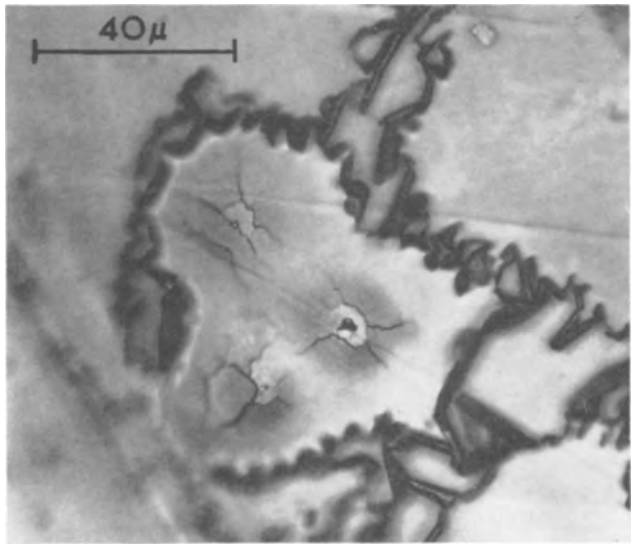

Fig. 6. Coiled thin layers of oxide on the surface after 7 hr at 550°C.

In some regions, prior to thicker oxide growth and cracking, very thin layers of oxide became partly detached and curled up on the surface (Fig. 6).

Cross sections of the oxides also showed the extensive cracking at the oxide-gas interface, but, although these cracks extended almost to the metal-oxide interface in many places, there was always a continuous layer of compact oxide next to the metal (Fig. 7 and 8).

A second phase was clearly visible at 550°C and in even greater amounts at 650°C, located near cracks in the oxide (*e.g.*, Fig. 8). Supplementary oxidation experiments were made at 650°C in static carbon dioxide in a sealed system (volume 500 cc) starting at 1 atm pressure, where the carbon monoxide produced

Table III. Data from the kinetic specimens relating to the form and composition of the oxide

Oxidation temperature, °C	Duration of oxidation, hr	Form of the adherent oxide	Form of the nonadherent oxide	% of nonadherent oxide*	Carbon content of the oxide (ppm by weight ±25%) Nonadherent	Adherent
450(a)	118	Thin, adherent, shiny, purple/gray film	Powder	1.4	—	—
450(b)	312	Thin, adherent, shiny, purple/gray film	Small flakes	10.4	1200	—
550(a)	123	Undulating, fairly adherent, shiny gray film	Small flakes	1.4	1400	2800
550(b)	140	Undulating, fairly adherent, shiny gray film	Small flakes	1.0	1700	—
650(a)	9	Undulating, cracked but fairly adherent, shiny gray film	Small flakes + powder	4.5	1300	—
650(b)	11	Undulating, cracked but fairly adherent, shiny gray film	Small flakes + powder	1.3	1600	2500

* The majority of loose oxide came from the edges of the specimens.

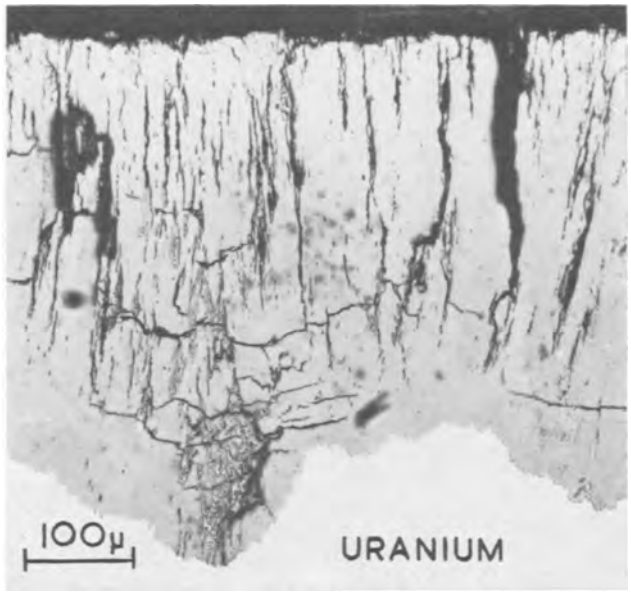

Fig. 7. Cross section of the oxide formed after 140 hr at 550°C

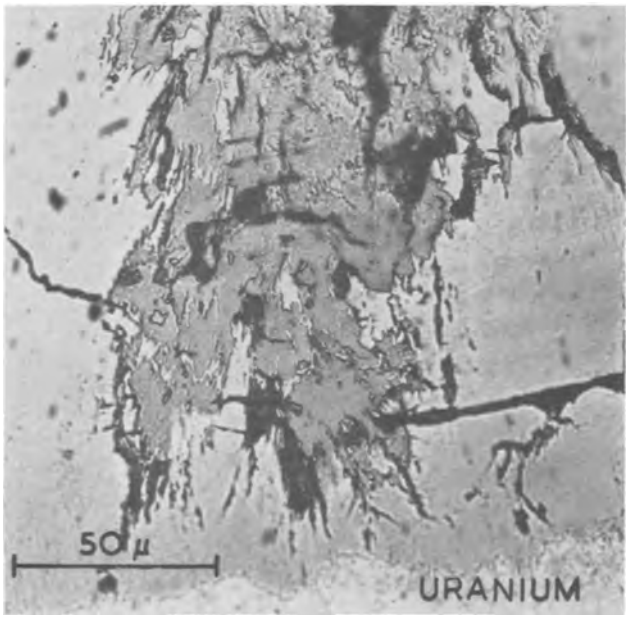

Fig. 8. Cross section of the oxide formed after 9¼ hr at 650°C showing the continuous oxide layer and the association of the second phase with cracks.

from the uranium-carbon dioxide reaction could accumulate and react with the uranium. It was evident that reaction with carbon monoxide led to a marked increase in the amount of the second phase. Further, if oxide formed at 650°C in flowing carbon dioxide was vacuum annealed at 800°C for several hours, the amount of this second phase could be increased by at least 50%.

X-ray diffraction.—At 550° and 650°C lines for uranium dioxide only were observed. At 450°C, in addition to uranium dioxide, traces of U_3O_8 were just detectable.

The room temperature lattice parameters of the oxides formed at 550° and 650°C were equivalent to that of stoichiometric UO_2 within the limits of experimental error, *i.e.*, 5.4705 ± 0.0005Å compared with a value of 5.4705Å derived by Lynds, Young, Mohl, and Libowitz (4). The extremely diffuse nature of the lines at 450°C precluded lattice parameter measurements at this temperature.

Carbon analysis.—Since the uranium contained only 12 ppm carbon, carbon analyses of the oxides listed in Table III indicate that significant quantities of carbon were incorporated from the gas stream. However, since even the highest carbon level corresponded to < 1% of the weight gain no correction need be made to the weight gain measurements. The amount of carbon incorporated from the gas appeared to be independent of temperature over the range investigated.

Discussion

It is evident from both the metallographic and kinetic results that oxidation can be broadly divided into an initial period when a crack-free protective oxide is formed, stages (i) and (ii), and a subsequent period when nonuniform oxidation and cracking of the oxide occurs, (stages (iii) and (iv).

Uniform oxidation.—At temperatures in the range 350°-550°C, qualitative oxide thickness assessments from interference colors (present investigation) and using the Drude-Tronstad polarimeter (5) show that a thin uniform oxide film rapidly builds up to a thickness of a few thousand Angstroms and thereafter thickens at a very slow rate (*e.g.*, Fig. 1). On the other hand, the weight gain studies suggest that the oxide continues thickening for a significantly longer period of time and attains a much greater thickness. Since the level of gaseous impurities in all experiments was similar, and the influence of any minor differences in surface preparation would be slight (6), i would seem that the two approaches have measured different quantities, and two layers of oxide must have been formed, the optical techniques measuring a thin outer layer of oxide. The observation of the thin curled up films of oxide (Fig. 6) is direct evidence for this.

By analogy with the low-temperature (<300°C) oxidation of uranium dioxide in oxygen (7, 8) it seems likely that the layers are of higher oxide such as UO_{2+x} or U_3O_7. As these oxides are structurally similar to the dioxide their detection is not simple. Thus from the present experiments the composition of the outer layers remains uncertain.

It is probable that the over-all growth of the uniform oxide is controlled by inward diffusion of O^{--} ions through uranium dioxide, since the activation energy for oxidation derived from the parabolic rate constants (45 kcal/mole, Fig. 9) falls within the range of that for the diffusion of O^{--} ions through slightly nonstoichiometric uranium dioxide and is significantly lower than the value for U^{4+} ion diffusion (9). This is consistent with data from inert marker and other techniques (10, 11).

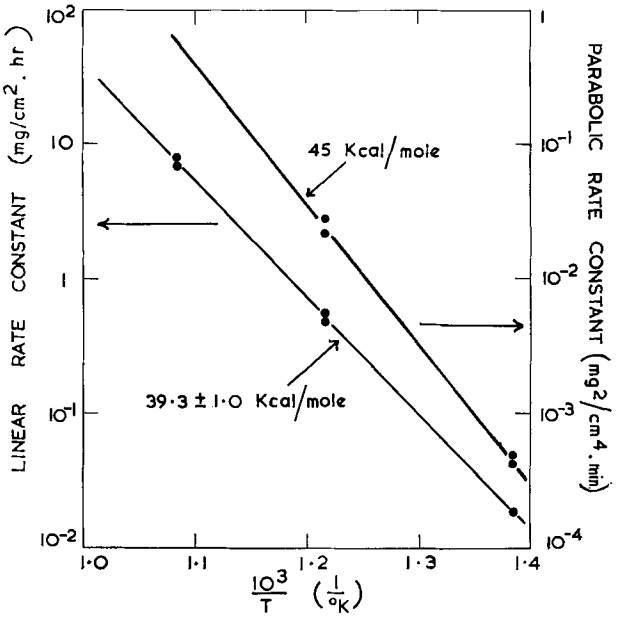

Fig. 9. Arrhenius plot of the parabolic and linear rate constants

Nonuniform oxidation.—The accelerating oxidation rate occurring in stage (iii) is due initially to the incidence of localized oxidation at grain boundaries, etc., then to the lateral growth of thicker oxide and the accompanying cracking.

This lateral growth must be the result of the high volume ratio of UO_2: U of 1.98. If the oxide were not restrained by the underlying metal it would cover a larger area, and is consequently under considerable compressive stress. At the thick oxide-thin oxide boundary the thick oxide will grow in a lateral direction where there is least resistance, to reduce the compressive stresses, and this will occur when the oxide step becomes sufficiently great, causing cracking in the adjacent thin oxide region. As the driving force for the process (the high stress in the oxide) is always maintained, the thicker oxide continues to propagate over the surface. The cracking of these thicker oxides is also a result of the compressive stresses in the oxide.

As oxidation proceeds the cracks propagate through the oxide until a linear oxidation rate is established [stage (iv)]. The activation energy for oxidation derived from the linear rate constants was 39.3 ± 1.0 kcal/mole which is very close to the value existing during uniform oxidation (Fig. 9), indicating that rate control remained by the diffusion of O^{--} ions through uranium dioxide. Thus linear oxidation must correspond to the state when the rate of crack propagation through the oxide equals the rate of oxide growth at the metal-oxide interface, with the oxidation rate controlled by diffusion across the thin compact layer of oxide between the tips of the cracks and the metal surface. Since it is not possible to measure the thickness of this layer, it is not possible to decide if the increase in linear rate with temperature is due entirely to faster diffusion rates or whether the uncracked oxide thickness also varied with temperature.

The weight gain at the onset of linear oxidation is similar at 550° and 650°C and significantly greater than the likely value at 450°C. This supports the x-ray evidence (more diffuse patterns at 450°C) and particle size measurements of Lyons and Popple (12) for there being some change in the physical properties of the oxide between 450° and 550°C.

This type of paralinear oxidation behavior where the oxide is initially protective, but breaks down to form porous outer layers of oxide, is well established for uranium in oxygen at low temperatures [*e.g.*, (13), (14)] and in many other systems (15). However, previous representations of the oxidation behavior of impure grades of uranium in carbon dioxide have almost always been in terms of one or more linear rates, frequently from zero time [*e.g.*, (16), (17)], although in most instances data could be as easily represented by an accelerating rate usually leading to a single final linear rate. The present interpretation enables the results to be more simply explained since theories based on multiple linear rate behavior are difficult to justify.

Carbon deposition.—It is evident from the carbon analyses of the oxides that the reaction occurring between uranium and carbon dioxide cannot be completely represented by the over-all equation

$$U + 2CO_2 \rightarrow UO_2 + 2CO \quad [1]$$

as also shown by Feron (18). The latter obtained similar carbon levels which were also independent of temperature. However, his assumption that carbon deposition results from the reaction

$$U + CO_2 \rightarrow UO_2 + C \quad [2]$$

is not wholly justified on the experimental evidence, and it seems more likely that the reaction leading to carbon deposition is

$$U + 2CO \rightarrow UO_2 + 2C \quad [3]$$

from the carbon monoxide produced by reaction [1]. As deposition of carbon on uranium dioxide from carbon monoxide only occurs when the carbon dioxide content of the gas is $< 1\%$ (19), the most likely site for reaction [3] will be within the cracks in the oxide, which constitute stagnant regions where the carbon dioxide content will be low; the association of the second phase (which has been shown to be directly connected with the carbon monoxide reaction) with cracks in the oxide supports this view. And the existence of a lower carbon content in the nonadherent oxide is also consistent since this oxide would consist of the outer layers that were near the widest parts of the cracks where the carbon dioxide content of the gas would be higher and the carbon deposition rate consequently low. Further, as cracking of the oxide became more extensive the carbon content should increase with time; this appears to be verified by the present results (Table III).

Although none of the known carbon containing uranium compounds were detected after oxidation in carbon dioxide, in agreement with the majority of previous workers, it seems possible from a comparison with oxidation in carbon monoxide (18) that the second phase corresponds to the compound UC_2, but is present in quantities too small for detection in the present experiments. An alternative explanation is that at the oxidation temperature some of the deposited carbon is taken into solution in the uranium dioxide. On cooling to room temperature the dissolved carbon in excess of the room temperature solubility limit (which may be zero), precipitates as free carbon in the oxide and appears as the second phase (oxide + precipitated carbon). The fact that the amount of the second phase can be increased by vacuum annealing the oxide as more free carbon is taken up from the cracks supports either mechanism.

Conclusions

1. The oxide initially formed on pure uranium in pure carbon dioxide in the temperature range 350°-650°C is protective, and nonuniform oxidation and cracking then occur leading to a gradual acceleration of the oxidation rate until eventually linear kinetics are obeyed. At this stage the rate of crack propagation through the oxide equals the rate of oxide growth, and the rate of oxidation remains controlled by the diffusion of O^{--} ions through a thin layer of uncracked uranium dioxide of constant thickness next to the metal.

2. Comparison with optical techniques for measuring oxide growth rate has shown that in the early stages of oxidation at 450° and 550°C a separate layer, probably of some higher oxide, grows at the oxide-gas interface, but soon attains a limiting thickness of a few thousand Angstroms and does not influence the over-all oxidation behavior.

3. Carbon monoxide produced from the reaction

$$U + 2CO_2 \rightarrow UO_2 + 2CO$$

reacts according to the equation

$$U + 2CO \rightarrow UO_2 + 2C$$

This latter reaction probably exclusively occurs in the cracks in the oxide, some of the deposited carbon either forming UC_2 or going into solution in the oxide.

Acknowledgment

The author wishes to acknowledge the valuable discussions and useful suggestions given by Dr. J. H. Buddery, the assistance of I. Whittle in preparing the paper, the experimental assistance of B. L. Bullock and Mrs. M. E. Gerrish, and the Central Electricity Generating Board for permission to publish the work.

Manuscript received Jan. 22, 1965; revised manuscript received May 26, 1965.

Any discussion of this paper will appear in a Discussion Section to be published in the June 1966 JOURNAL.

REFERENCES
1. V. J. Haddrell, Unpublished work.
2. A. T. Churchman, J. H. Buddery, B. Edmondson, G. W. Greenwood, R. V. Hesketh, and G. K. Williamson, Proceedings of the Third International Conference on the Peaceful Uses of Atomic Energy, P/156, Vol. 9, United Nations (1965).
3. J. H. Buddery, M. E. Clark, R. J. Peace, and J. J. Stobbs, *J. Nucl. Mater.*, **13**, 169 (1964).
4. L. Lynds, W. A. Young, J. S. Mohl, and G. G. Libowitz, "Nonstoichiometric Compounds," p. 62, American Chemical Society, Washington, D. C. (1963).
5. P. C. S. Hayfield, R. L. Graham and G. Ramshaw, "Uranium and Graphite," p. 29, Institute of Metals, London (1962).
6. L. Leibowitz, J. G. Schnizlein, J. D. Bingle, and R. C. Vogel, *This Journal*, **108**, 1155 (1961).
7. H. R. Hoekstra, A. Santoro, and S. Siegel, *J. Inorg. Nucl. Chem.*, **18**, 166 (1961).
8. B. Belbeoch, C. Piekarski, and P. Perio, *J. Nucl. Mater.*, **3**, 60 (1961).
9. J. Belle, A. B. Auskern, W. A. Bostrom, and F. S. Susko, "Reactivity of Solids," p. 452, Elsevier Publishing Corp., Amsterdam (1960).
10. J. G. Schnizlein, J. D. Woods, J. D. Bingle, and R. C. Vogel, *This Journal*, **107**, 783 (1960).
11. A. F. Bessonov and V. G. Vlasov, *Fiz. Metalli. Metallov*, **12** [5], 775 (1961).
12. M. R. J. Lyons and L. A. Popple, Unpublished work.
13. D. Cubicciotti, *J. Am. Chem. Soc.*, **74** [4], 1079 (1952).
14. J. Loriers, *Compt. rend.*, **234**, 91 (1952).
15. O. Kubaschewski and B. E. Hopkins, "Oxidation of Metals and Alloys," p. 64, Butterworths, London (1962).
16. J. E. Antill and K. A. Peakall. *J. Less Common Metals*, **1**, 227 (1959).
17. J. Paidassi, M. L. Pointud, R. Caillat, and R. Darras, *J. Nucl. Mater.*, **3**, [2], 162 (1961).
18. G. Feron, Report CEA-R2429 (1964).
19. L. E. J. Roberts, A. J. Walter, and V. J. Wheeler, *J. Chem. Soc.*, **1958**, 2472.

A New Assemblage for Hydrogen Electrodes

G. Bianchi, A. Barosi, G. Faita, and T. Mussini

Laboratory of Electrochemistry and Metallurgy, University of Milan, Milan, Italy

ABSTRACT

A new assemblage for hydrogen electrodes is presented which makes use of a support of porous graphite activated with platinum-black catalyst and which does not require a continuous flowing of hydrogen. At 25°C its exchange current measured in different environments is in the range of 11 to 30 ma/cm^2; bias potential is 0.03 mv; stability is better than 0.01 mv when the electrode is aged for some days. These essential characteristics render such an electrode convenient for precision measurements; moreover, in many cases this electrode enables one to avoid difficulties which arise from liquid junction potentials verified with some commonly used reference electrodes.

From the first simplest Hildebrand electrode (1) until the more recent types, the hydrogen electrode has undergone considerable modifications (2) to improve its performances for accurate measurements in the area of the electrochemical thermodynamics and kinetics (3).

Quite recently, Giner (5) presented a "polarized" hydrogen electrode, having a number of advantages when used for kinetic studies on strongly acid or alkaline environments, and Zaitsev and Bulgakova (6) applied a hydrogen electrode assemblage to determinations of partial pressures of hydrogen in inert gas mixtures.

New opportunities are now provided by the use of activated porous electrodes (7).

This investigation concerns the obtainment of a new hydrogen electrode assemblage, which is reasonably simple and at the same time satisfies the requirements of stability, reproducibility, and so on, by making use of a support consisting of porous graphite activated with noble metal catalysts.

Experimental

Figure 1 shows in detail the structure of the hydrogen electrode according to the present realization. The triple contact electrode-solution-gas occurs at the upper part of porous graphite disk A, covered by a thin layer of platinum black catalyst (see also enlarged detail in Fig. 1) and immersed in the solution up to about 2/3 of its thickness. The solution moves upward through the pores of the graphite disk by capillarity and moistens the catalyst layer. A thin network of sintered Teflon drops (TD) protects the catalyst from mechanical crumblings (7) and prevents the formation (during operation) of a gauze of solution on the activated surface of the electrode, without screening the catalyst itself. This way, the contact electrode-solution-gas is highly satisfactory, and neither the solution level nor the porosity degree of graphite are critical parameters. The catalyst is platinum-black Johnson & Matthey whose specific surface is 9.8 m^2/g.

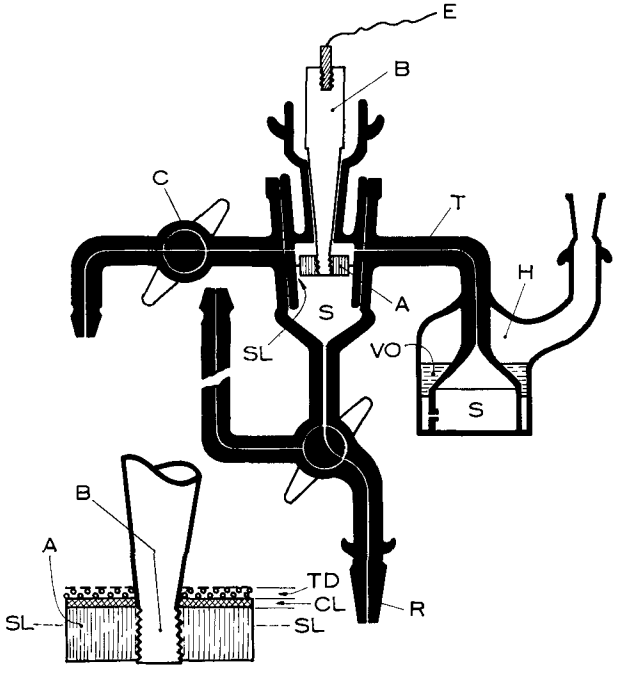

Fig. 1. Structure of the hydrogen electrode: A, porous graphite disk; B, screw stem of impermeabilized graphite; C, gas inlet stopcock; CL, catalyst layer; E, electrical connection; H, hydraulic seal; R, to second half-cell; S, solution; SL, solution level; T, tube connecting to hydraulic seal; TD, Teflon drop network; VO, vacuum oil layer on solution.

The porous graphite disk A is of the type PC 57 H Stackpole Carbon Company; it is 0.5 cm thick, 1.5 cm in diameter. The rate of applied catalyst is about 10 mg/cm^2. The real working surface is actually about 900 fold the geometrical surface, as it was determined according to the method of Laitinen and Enke (13).

A type-30 du Pont Teflon dispersion has been used to get sintered-drop networks on the catalyst layer, according to the technique described by Bianchi (7) and derived from that previously indicated by Elmore and Tanner (8). The porous graphite disk is kept in position by means of a screw stem (B) made of impermeabilized graphite which also acts as a support for electrical connections. The form of the glass vessel is such that the volume of gas and solution is reduced to a minimum; thus, equilibrium between solution and gas phase is more quickly reached and both temperature and pressure response are improved. The gas and vapor dilatations which occur following changes of temperature are compensated by a little hydraulic seal (H). This hydraulic trap obviously serves to keep the inside of the electrode at atmospheric pressure at any temperature and to prevent the entrance of air and foreign gases. In view of this purpose it is filled up to about half its volume with the same solution as in the porous electrode compartment: between this solution and external atmosphere a floating layer of high vacuum silicone oil is interposed (VO). The solution in this trap serves to quickly reach the vapor saturation in the tube (T) connecting the trap with the electrode compartment, when temperature must undergo any change.

If a graphite disk has been freshly activated and assembled as previously described, it is recommendable to keep it at a temperature in the order of 60°-70°C for about half a day under a moderate circulation of hydrogen, once for all; this way the last traces of adsorbed and dissolved gases are removed. In fact, the correct electrode behavior can be affected by nitrogen because it lowers the hydrogen partial pressure, while the last adsorbed oxygen traces are unimportant due to the rapid catalytic combination with hydrogen. If these points are considered in setting up the electrode, by a previous filling of the vessel and a deaeration of solution with hydrogen, the best satisfactory electrode behavior is obtained.

When preliminary operations have been carried out one can stop the hydrogen inlet with the appropriate stopcock (C) and now the hydrogen electrode is ready for use. Such as it is, it can be used at various temperatures, obviously taking into account appropriate corrections for vapor pressure of the solution.

No further hydrogen circulation is necessary during many weeks, and such an electrode can be easily handled as the most usual and popular reference electrodes.

Reversible emf measurements have been carried out with the aid of a type K3 L & N potentiometer with a type 610 B Keithley electronic millivoltmeter as a null-point detector, the input-impedance of the latter being higher than 10^{14} ohms. Accuracy of emf measurements is within ± 0.01 mv. The highest input impedance of such null-point detector enabled us to measure emf's keeping the stopcock connecting the two half-cells in the closed position.

Solutions were made up with doubly distilled water and Merck products, reagent grade. Hydrogen was used with total oxygen less than 5 ppm. Analysis and checking of solutions and other substances were done according to the conventional technique. Temperature of the cell was regulated to ± 0.01°C by means of an air thermostat.

Table I. Exchange currents according to Eq. [2]

Environment	Exchange current, ma/cm^2 at 25°C
1*M* HCl	16.2
6.06*M* HCl (=20% azeotropic HCl)	30.3
0.5*M* H_2SO_4	12.8
3.75*M* H_2SO_4	26.5
1*M* $HClO_4$	11.2

Results and Discussion

Stability.—The stability of the hydrogen electrode just described has been tested at 25° and 40°C by coupling it with an electrolytic-type silver-chloride electrode and taking reversible emf measurements of the resulting cell

$$\text{Pt/graphite-Pt black/}(H_2\ 1\ \text{atm})\text{/HCl}(1\ M)\text{/AgCl/Ag/Pt} \qquad [1]$$

all characteristics concerning the silver-chloride half-cell being already known accurately as outlined in the recent and exhaustive review by Ives and Janz (9). Cell 1 was controlled thermostatically at the appropriate temperature for twenty days, and emf measurements were made at intervals of about 12 hr. Both at 25° and at 40°C the emf of such cells verified a 0.03 mv total shift during the first eight days, but kept its value constant during the remaining twelve days of the experiment: this constant value in both cases was 0.01 mv less than the value which results from taking into account activity coefficients of HCl (11, 12) and correction to 760 mm Hg pressure of hydrogen. With regard to the activity coefficients of HCl, it is to be pointed out that the effect of AgCl solubility in HCl solutions is quite negligible when the HCl concentration is lower than 3*M*, as indicated by the data of Akerlöf and Teare (4). Besides, since we worked with 1*M* HCl and we kept the stopcock closed between the two half-cells any danger of hydrogen electrode poisoning by diffusing AgCl was avoided.

Since electrolytic-type silver-chloride electrodes are characterized by bias potentials in the range of 0.02 mv and generally constant to ± 0.005 mv (9) the stability of the present hydrogen electrode is 0.03 mv when the electrode is freshly prepared, being better than 0.01 mv when the electrode is 8 days old.

Bias potentials.—The intercomparison potential was determined on 5 identically prepared electrodes; one of them was characterized by a 22-day aging and was chosen as the basis for comparison, a second one had a 10-day aging, the others being freshly prepared. Measurements were taken at 25°C during 15 days: the resulting bias potential was 0.03 mv for newly prepared electrodes, but it reduced to 0.01 mv for aged electrodes.

Reversibility.—The reversibility of the present hydrogen electrode has been tested by evaluating exchange currents in polarization experiments. Exchange current actually is an important and critical parameter for reference electrodes, as has been pointed out adequately elsewhere (10). In the present case exchange currents have been determined by considering polarization curves related to cathodic discharge and to anodic ionization of hydrogen in various media. An identical hydrogen electrode was used as a reference electrode: thus, liquid junction potentials were avoided. These curves, at the lowest overpotentials (less than 10 mv) clearly showed a linear relationship between overpotential and current, so that exchange currents have been evaluated graphically according to the equation

$$i_o = \frac{RT}{2F}\frac{di}{d\eta} \qquad [2]$$

where i_o is exchange current, i is polarizing current, and η is the overpotential.

Exchange currents at 25°C, determined according to Eq. [2] and related to the apparent geometrical area of the electrode, are given in Table I.

From the order of magnitude of exchange currents in Table I it is apparent that this hydrogen electrode presents a high degree of reversibility.

Conclusions

A new and convenient assemblage for the hydrogen electrode has been presented which is easy to handle and widely applicable for measurements concerning electrochemical thermodynamics and kinetics.

Such an electrode is characterized by a high degree of reversibility, as shown by the range of exchange currents measured in different environments (11-30 ma/cm^2 at 25°C). Bias potential is 0.03 mv at 25°C. Stability tests against a Ag/AgCl/HCl electrode have been made at 25° and 40°C: thus, the stability of the present hydrogen electrode has been shown to be better than 0.01 mv when working with electrodes aged for some days.

The reference electrode may be realized with solutions of different compositions, and in many cases it helps overcome difficulties arising from liquid junction potentials observed with usual reference electrodes connecting to concentrated acid solutions.

Acknowledgment

This investigation has been carried out with the financial support of the "Consiglio Nazionale delle Ricerche," Rome, Italy.

Manuscript received Jan 25, 1965; revised manuscript received May 22, 1965.

Any discussion of this paper will appear in a Discussion Section to be published in the June 1966 JOURNAL.

REFERENCES

1. J. H. Hildebrand, *J. Am. Chem. Soc.*, **35**, 847 (1913).
2. W. M. Clark, "The Determination of Hydrogen Ions," p. 151, Williams & Wilkins, Baltimore (1923).
3. D. J. G. Ives and G. J. Janz, "Reference Electrodes," p. 71, Academic Press, New York (1961).
4. G. Akerlöf and J. W. Teare, *J. Am. Chem. Soc.*, **59**, 1855 (1937).
5. J. Giner, *This Journal*, **111**, 376 (1964).
6. O. S. Zaitsev and T. I. Bulgakova, *Russian J. Phys. Chem.*, **38**, 583 (1964).
7. G. Bianchi, *This Journal*, **112**, 233 (1965).
8. G. V. Elmore and H. A. Tanner, *ibid.*, **108**, 669 (1961).
9. D. J. G. Ives and G. J. Janz, "Reference Electrodes," pp. 188 and 204, Academic Press, New York (1961).
10. D. J. G. Ives and G. J. Janz, *ibid.*, p. 17.
11. R. G. Bates and V. E. Bower, *J. Research Nat. Bur. Standards*, **53**, 282 (1954).
12. S. R. Gupta, G. J. Hills, and D. J. G. Ives, *Trans. Faraday Soc.*, **59**, 1882 (1963).
13. H. A. Laitinen and C. G. Enke, *This Journal*, **107**, 773 (1960).

The Bubbling Gas Electrode

I. Instrumentation and Applications

Wayne J. Subcasky

Aeronutronic Division, Philco Corporation, Newport Beach, California

ABSTRACT

The bubbling gas electrode technique for studying electrochemical reactions at solid electrodes is described. This technique gave reproducible concentration gradients at the electrode surface by intermittently stirring the electrolyte in the vicinity of the electrode by means of electronically pulsed gas bubbles. Under the proper conditions current-voltage curves could be recorded automatically with a polarograph and interpreted in a manner similar to polarograms. The method has been found to be controlled by semi-infinite linear diffusion. Analytical applications and studies of catalyzed electrochemical reactions involving oxygen are discussed.

The use of solid electrodes for electrochemical systems has been reviewed by Adams (1). One of the major problems associated with solid electrodes has been the variation in manner and rate at which material is transported to and from the electrode. One solution to this problem uses a "dipping" electrode in which an inert gas is bubbled around the tip of a solid electrode. Such an electrode was first described by Lyalikov and Karmazin for use in fused salts (2). Flengas (3) used this technique in molten nitrates. Hills and co-workers (4) described a similar system for use in various solvent systems. The bubbling gas electrode (BGE) as herein described is an extension of the dipping electrode to aqueous solutions with electronic control of the rate of bubbling.

Experimental

In the BGE technique an electronically pulsed gas bubble was used to stir the solution intermittently in the immediate vicinity of the electrode. In this manner, the interval between stirring was accurately and reproducibly controlled, and the electrode was isolated from the solution only momentarily.

Figure 1 is a block diagram of the experimental arrangement used for these BGE studies. The function generator (Hewlett-Packard 202A) produced a square wave whose period could be varied from about 1 sec to 100 sec. This square wave controlled the bubble monitor circuit which in turn produced pulses of a few millisecond duration at intervals determined by the period of the function generator. The pulses produced by the bubble monitor circuit actuated the solenoid valve in the gas supply and allowed a small volume of gas to flow to the mantle surrounding the electrode in the cell. This gas stirred the electrolyte in the

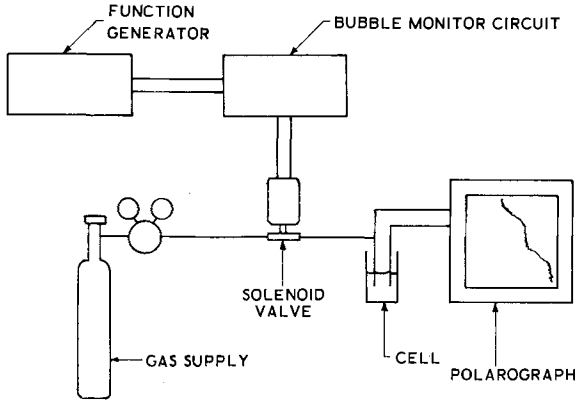

Fig. 1. Experimental arrangement for BGE studies

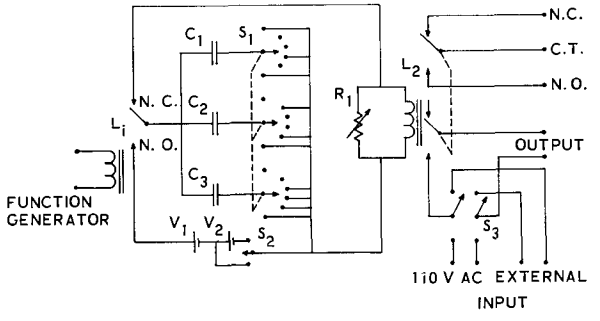

Fig. 2. Bubble monitor circuit. Components: C_1, 10 mfd; C_2, 20 mfd; C_3, 30 mfd; L_1, L_2, 5000 ohm DPDT d-c relays; R_1, 10 kohms; S_1, 3 pole 6 position rotary switch; S_2, SPST switch; S_3 DPDT switch; V_1, V_2, 45v battery.

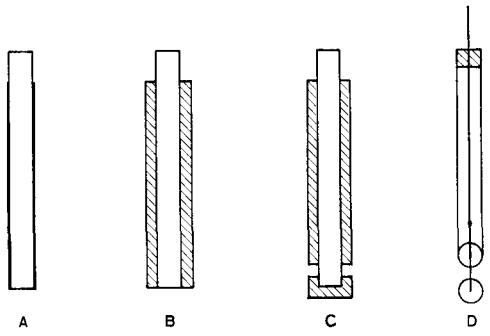

Fig. 4. Electrodes: A, graphite planar electrode insulated with paraffin; B, graphite planar electrode insulated with plastic; C, graphite cylindrical electrode insulated with plastic; D, platinum cylindrical electrode.

immediate vicinity of the test electrode. The current-potential curve of the solid test electrode was automatically recorded by the polarograph (Sargent Model XV).

Figure 2 is a schematic diagram of the bubble monitor circuit. The square wave from the function generator actuated relay L_1. The contacts of this relay alternately charged the condensers, C, from the batteries, V, and then discharged the condensers through the coil of the second relay, L_2. Actuation of L_2 momentarily closed the circuit to supply power to the solenoid valve. With this bubble monitor circuit, the interval between pulses and hence the interval between bubbles (the bubble time, τ) was determined by the period of the function generator. The length of the pulses was determined by the combination of the voltage used to charge the condensers, the size of the condensers, and by the effective resistance of the relay coil and parallel resistor, R. With the particular components used in this study the pulse width could be varied from about 30 msec to one-half of the pulse period.

Figure 3 shows the electrolytic cell and mantle bubble tube used in this study. An external saturated calomel electrode could be electrolytically connected to the test solution through an agar-KCl salt bridge. A mantle which surrounded the test electrode was used to disturb the concentration gradient. The pulse of gas released by the solenoid valve forced electrolyte down away from the electrode and out of the mantle. A small bleeder valve in the gas supply line to the mantle permitted the return of the electrolyte when the solenoid valve closed. This mantle bubble tube was easy to assemble and gave reproducible results.

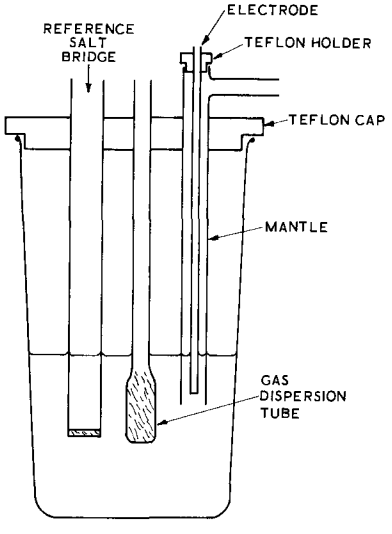

Fig. 3. Electrolytic cell

Various electrodes with different geometries were used. These are shown in Fig. 4. The graphite electrodes were prepared from spectrographic rods (United Carbon Company, Bay City, Michigan) and have a nominal diameter of 0.120 in. All graphite electrodes were first impregnated with molten paraffin to reduce the porosity. The two types of planar electrodes differed only in the manner of insulation. Some electrodes after impregnation with paraffin were given a heavier coating of wax. Before use a cross section of the graphite was exposed by abrasion with fine emery paper followed by polishing with bond paper. Other planar electrodes were insulated by covering the wax impregnated electrode with a heat shrinkable plastic sleeve (Ray Chemical Corporation, Redwood City, California). The lower part was polished as before. This latter method of sealing was preferable because the electrodes could be handled without danger of breaking of the wax coating.

Graphite cylindrical electrodes were prepared by completely covering a wax impregnated graphite rod with the heat shrinkable plastic. While the plastic was still warm the lower end was pinched together to form a tight seal. After the plastic was cooled, a narrow portion was cut away to expose a definite amount of the graphite. Platinum cylindrical electrodes were prepared by sealing B & S Gauge No. 20 platinum wire in soft glass and applying a bead of glass to the lower end.

Reduction of Copper

The supporting electrolyte for all studies with copper was approximately 1*M* NH_4Cl-1*M* NH_4OH. The supporting electrolyte was deaerated with nitrogen before any current-potential curves were determined. The nitrogen was first passed through a prebubbler containing the supporting electrolyte to minimize changes in the ammonia concentration. During the experimental runs the supporting electrolyte was blanketed with nitrogen. The electrodes were given a precathodic treatment at about —1.5v (SCE) to remove any oxides and/or adsorbed oxygen which might be present on the electrode. The pretreatment was particularly important with the graphite electrodes because of the large amount of adsorbed oxygen.

A large area saturated calomel electrode connected to the electrolysis cell through an agar-KCl salt bridge was used as the reference electrode. The voltage span of the polarograph was 0 to —1.0v, and the scan rate was 100 mv/min unless otherwise noted. In these preliminary studies no attempts were made to thermostat the cell, although the temperature of the supporting electrolyte varied less than 0.5°C during any particular experiment.

Residual current curves were always run to determine the completeness of removal of dissolved and adsorbed oxygen. These curves were run at the same sensitivity as the curves where copper was present. All curves run with the BGE technique used nitrogen

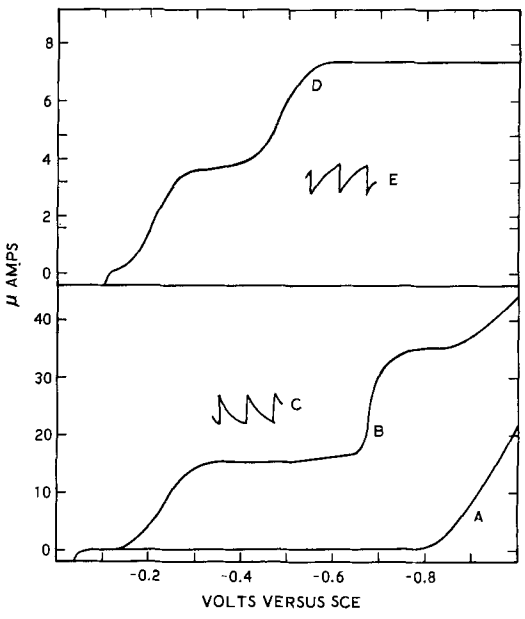

Fig. 5. Comparison of BGE and DME. Reduction of 1.04 *m*M Cu(II) in approx. 1*M* NH_4OH-1*M* NH_4Cl. BGE characteristics Pt cylindrical electrode, 0.205 cm^2, bubble time 4.06 sec. Curve A, residual current; B, in the presence of Cu(II); C, current-time behavior between individual bubbles. DME characteristics m = 1.702 mg/sec, t = 5.37 sec at —0.70v (SCE); curve D, polarogram in presence of Cu(II); E, current-time behavior of individual drops.

as the stirring gas. A bubble time of 4.06 sec was used for most of the curves. Copper was added to the deaerated supporting electrolyte as definite volumes of a stock solution containing a known amount of copper in the supporting electrolyte.

Figure 5 shows a comparison of the current-potential and current-time curves for the BGE and the DME. The solution used was 1.04 m*M* $CuSO_4$ in 1*M* NH_4OH-1*M* NH_4Cl. The characteristics of the DME were m = 1.702 mg/sec and t = 5.37 sec at —0.70v (SCE). The polarogram shows the typical two equal wave structure characteristic of the reduction of copper (II) in this supporting electrolyte. The first wave represents the one electron reduction of $Cu(NH_3)_4^{+2}$ to $Cu(NH_3)_2^{+}$ and the second wave the one electron reduction of $Cu(NH_3)_2^{+}$ to copper amalgam. The maximum in the current-time curve occurs at the end of each drop of mercury. The current increases as each mercury drop grows because the increase in area and the expansion of the Hg drop into the concentration gradient of the electrolyte more than compensates for the increasing thickness of the diffusion layer.

The current-potential curve for the BGE was obtained in the same solution as that used for the polarogram. The characteristics of the BGE were a platinum cylindrical electrode with a geometric area of 0.204 cm^2 and a bubble time of 4.06 sec. The first wave had the same shape and occurred at the same potentials for both the DME and the BGE. The second wave with the BGE occurred at more negative values and showed a sharp increase in current at the start of the wave rather than the S-shaped curve characteristic of polarograms. Both of these differences were due to the nature of the product of the second wave. With the DME, the product was copper amalgam. Hence the copper was deposited at less than unit activity, and the deposition occurred at less negative potentials. Also the activity of copper in the amalgam was constantly varying thereby giving a curvature to the lower portion of the wave (Heyrovsky-Ilkovic behavior). With the BGE the reduction product of the second wave was metallic copper at unit activity. As a result the deposition occurred at more negative potentials. As soon as a monomolecular layer of copper was present, the activity of copper did not vary and consequently the current increased rapidly with potential (Kolthoff-Lingane behavior). Similar curves were obtained with the various graphite electrodes with the exception that no hydrogen evolution was observed even at —1.0v (SCE). The geometry of the electrode did not seem to affect the shape of the curves. The only differences were in the magnitudes of the currents observed. These differences were proportional to the various areas for electrodes of different geometry. No statistically significant difference was found for currents recorded with linearly increasing potentials and for currents measured by holding the electrode at various constant potentials.

The reduction of $Cu(NH_3)_4^{+2}$ to $Cu(NH_3)_2^{+}$ was found to be reversible on both platinum and graphite. Figure 6 shows the plot of potential *vs.* log $i/(i_d - i)$ for a platinum cylindrical electrode. The slope as determined by the method of least squares was found to be 60.7 mv as compared to a theoretical valve of 59.1 mv at 25°C. A "*t*" test at the 95% confidence limit showed no significant difference between these two values. The half-wave potential was found to be —0.225v (SCE) as compared to a value of —0.24v normally reported for a 1*M* NH_4OH-1*M* NH_4Cl supporting electrolyte. The difference is probably due to a slightly lower concentration of ammonia in the supporting electrolyte.

No log plot was made to determine the reversibility of the second wave for reduction of $Cu(NH_3)_2^{+}$ to Cu^0. Deposition of metallic copper on the electrode changes the electrode area and makes interpretation of the log plot difficult. However when the direction of the potential scan was reversed no displacement along the potential axis was noted when the current passed from cathodic to anodic values due to the anodic stripping of the copper. This is commonly accepted as a sign that the couple is reversible.

With the BGE, the current decreased with time and reached a minimum just before the solution was stirred by a bubble (see Fig. 5). This was to be expected for diffusion to a stationary electrode. The theory for semi-infinite linear diffusion predicts that the diffusion limited current should decrease with the square root of time, *i.e.*, the product of the current and the square root of the time should be a constant. Table I shows this current-time product for the first wave in the reduction of copper on a graphite planar electrode. The currents listed are the averages of at least ten determination at each bubble time. The geometric area of the electrode was 7.30×10^{-2} cm^2 and the solution was 1.20 m*M* in Cu(II). The lack of constancy in the $i\tau^{1/2}$ product for small τ's was found to be due principally to the slow response time (10 sec for full-scale travel) of the polarograph recorder. Other experiments, with a faster recorder or an oscilloscope, showed that the constancy extended to bubble times as short as 1 sec in most cases.

To substantiate further the conclusion that the BGE with a planar electrode was a linear diffusion electrode the value of $i\tau^{1/2}$ was calculated from the known concentration of Cu(II) present, the measured geometric area, and the diffusion coefficient as measured by po-

Table I. Variation of current with bubble time for reduction of 1.20 m*M* $CuSO_4$ in 1*M* NH_4OH-1*M* NH_4Cl at —0.5v (SCE) with graphite planar electrode, 7.30×10^{-2} cm^2

τ, sec	i, μa	$i\tau^{1/2}$, μa-sec$^{1/2}$
1.00	19.74	19.74
2.00	13.04	18.44
3.00	9.72	16.84
4.00	8.44	16.88
5.00	7.66	17.13
6.00	6.99	17.12
7.00	6.518	17.32
8.00	6.100	17.25
9.00	5.740	17.22
10.00	5.372	16.98
20.00	3.948	17.66
		Average 17.15 ± 0.24

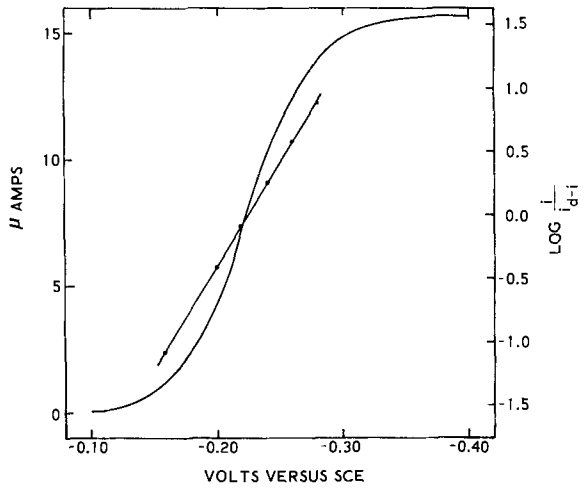

Fig. 6. Current-potential and log plots for reduction of Cu(II) to Cu(I). 1.04 mM $CuSO_4$ in approx. 1M NH_4OH-1M NH_4Cl. Platinum cylindrical electrode, 0.205 cm^2, bubble time 4.06 sec.

larographic techniques (5). The calculated value was 14.9 μa-sec$^{1/2}$ as compared with an experimental value of 17.15 μa-sec$^{1/2}$. The agreement is considered to be good considering the uncertainties present in determining the area of a solid electrode which might be somewhat porous.

The analytical possibilities of the BGE were determined by measuring the diffusion limited current as a function of the amount of Cu(II) added. Figure 7 shows this current-concentration relationship for a planar, graphite electrode. The current for the first wave was measured at —0.5v (SCE) and for the second wave at —0.9v (SCE). The points on the curve are the averages of at least three determinations. The curve shown for the second wave was determined from the total wave height. The proportionality constant for the second wave was slightly larger than twice that of the first wave because the electrode area had been increased slightly by deposition of metallic copper. The values of the constant, i/C, were found to be 7.50 $\pm$ 0.34 and 16.12 $\pm$ 0.52 μa/mM for the first and second waves, respectively.

For analytical applications of the BGE, determination of concentrations by the method of standard addition or by the method of a pilot ion might be simpler and more accurate. Either of these methods would minimize difficulties associated with changes in temperature, electrode area, bubble time, and extent of stirring which might occur from one determination to another.

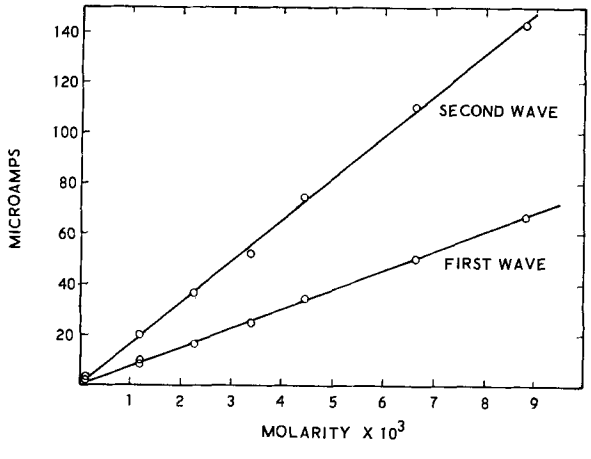

Fig. 7. Variation of diffusion current with concentration of $CuSO_4$ in 1M NH_4OH-1M NH_4Cl. Graphite planar electrode 7.30x10^{-2} cm^2, bubble time 4.00 sec.

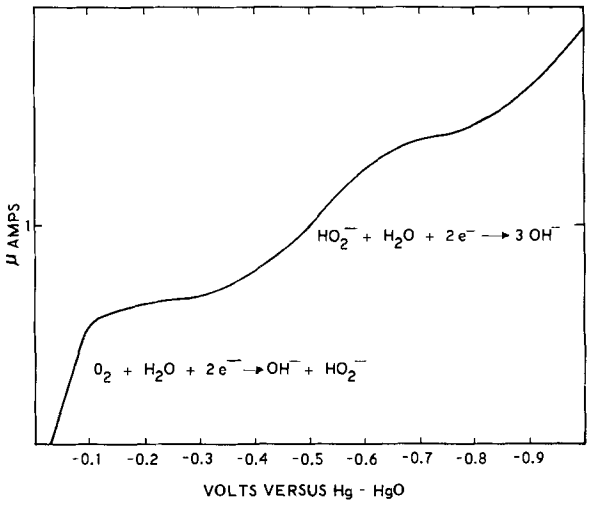

Fig. 8. Reduction of oxygen on uncatalyzed graphite. 25% by weight NaOH; graphite planar electrode, area 7.30 x 10^{-2} cm^2, bubble time 4.00 sec.

Reduction of Oxygen

The BGE technique was also used to study the reduction of oxygen at graphite electrodes in alkaline solution. For this work the supporting electrolyte was 25% by weight sodium hydroxide with oxygen as the bubbling gas. Solutions were not deaerated except where a residual current curve was desired. The graphite electrodes were precathodized for 1 min at —0.7v *vs.* the Hg pool to remove oxygen initially adsorbed on the electrode. If the precathodization step was eliminated, the current decreased with time even on the diffusion limited portion of the current voltage curve. An internal mercury pool was used as the reference and auxiliary electrode. The potential of the mercury pool in this alkaline solution was within a few millivolts of that of the normal hydrogen electrode.

The current-potential curve for the reduction of oxygen on an uncatalyzed graphite electrode is shown in Fig. 8. The curve is similar in shape to that obtained with a dropping mercury electrode. Two distinct waves are evident before the final current rise due to hydrogen evolution. The first wave corresponds to the nearly reversible two electron reduction of oxygen to hydrogen peroxide ions

$$O_2 + H_2O + 2e^- \rightarrow OH^- + HO_2^-$$

and the second wave to the totally irreversible reduction of hydrogen peroxide ions to hydroxide ions

$$HO_2^- + H_2O + 2e^- \rightarrow 3\ OH^-$$

The current of the first wave was slightly larger than that of the second. Even a so-called uncatalyzed graphite electrode caused some decomposition of the hydrogen peroxide ions

$$2HO_2^- \rightarrow 2\ OH^- + O_2$$

The oxygen produced by this catalytic decomposition enhances the height of the first wave. The first wave then corresponds to slightly greater than a two electron reduction and the second wave to slightly less than two electrons.

The effect of catalyzing the graphite electrode is shown in Fig. 9 and 10. The silver catalyzed electrode was prepared by electrodeposition of silver from a nitrate solution. The enhanced decomposition of hydrogen peroxide ions is readily apparent in the increased height of the first wave at the expense of the second wave. It was found experimentally that by increasing

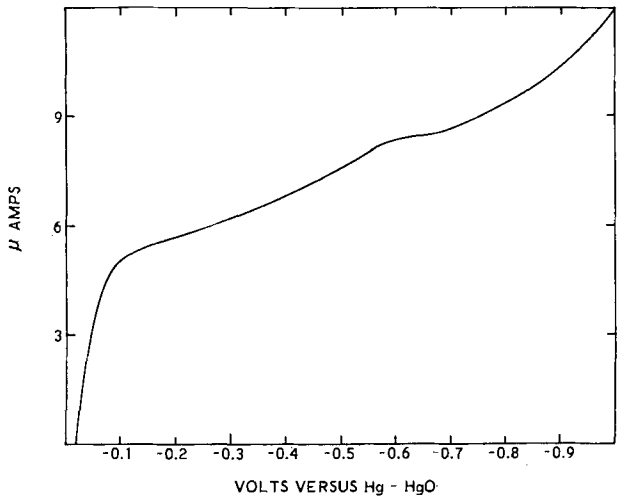

Fig. 9. Reduction of oxygen on silver catalyzed graphite. 25% by weight NaOH; graphite planar electrode plated with silver from $AgNO_3$, bubble time 4.00 sec.

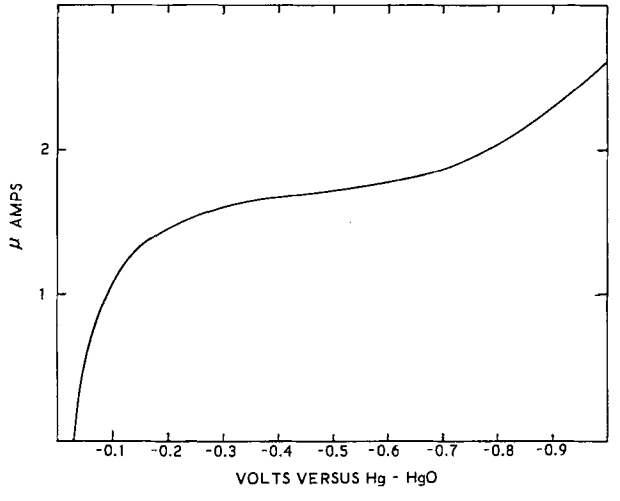

Fig. 10. Reduction of oxygen on spinel-type catalyzed graphite. 25% by weight NaOH; spinel formed by thermal decomposition of Co and Al nitrates, bubble time 4.00 sec.

the amount of silver on the electrode either by longer electrodeposition times or by thermal decomposition of silver nitrate deposited on the graphite electrode, the second wave could be made to disappear altogether indicating complete catalytic decomposition of the hydrogen peroxide ions.

In many experiments a high current peak was observed at potentials considerably positive to that observed for the reduction of oxygen. However, this current decreased rapidly with time when the electrode was held at constant potential. This decaying current at a potential of approximately +0.20v *vs.* NHE suggested that it was due to the electrochemical reduction of silver (I) oxide formed chemically by the reaction between silver and oxygen in the alkaline solution

$$2Ag + \tfrac{1}{2} O_2 \rightarrow Ag_2O$$

$$Ag_2O + H_2O + 2e^- \rightarrow Ag + 2\,OH^-$$

In some instances an apparent correlation was found between the area under the current peak and the length of time the electrode had been exposed to the alkaline solution containing oxygen. With the method used to deposit silver, the chemical oxidation of silver by dissolved oxygen was much slower than the electrochemical reduction of silver oxide and hence the current decayed with time.

Figure 10 shows the reduction of oxygen on a graphite electrode catalyzed with a cobalt-aluminum spinel type of material. The electrode was prepared by evaporation of a solution of cobalt and aluminum nitrates of the stoichiometric proportions and then thermally decomposing the nitrates at a red heat. This catalyst was sufficiently active that no second wave appeared. The decomposition of hydrogen peroxide ions was complete enough that no electrochemical reduction of peroxide ion was evident. A similar type of behavior has been reported for the reduction of oxygen on platinum (6).

Conclusion

The BGE technique has been found to be a rapid and simple method for studying electrochemical reactions at solid electrodes. Intermittent stirring of the electrolyte in the vicinity of the electrode by electronically pulsed gas bubbles gave reproducible concentration gradients so that the system appeared to be controlled by semi-infinite linear diffusion. Analytical applications are possible, particularly in potential regions where a mercury electrode would undergo anodic oxidation. The method has been used to study the effect of various catalysts upon the reduction of oxygen in alkaline solutions. Qualitative information concerning the mechanism and rate of the catalytic activity has been rapidly obtained.

Manuscript received Aug. 25, 1964; revised manuscript received May 18, 1965. Part of this paper was presented at the Boston Meeting, Sept. 16-20, 1962.

Any discussion of this paper will appear in a Discussion Section to be published in the June 1966 JOURNAL.

REFERENCES

1. R. N. Adams, "Treatise on Analytical Chemistry," Part 1, Vol. 4, p. 2381, Interscience Publishers, New York (1963).
2. Y. S. Lyalikov and V. I. Karmazin, *Zarod. Lab.*, **14**, 144 (1948).
3. S N. Flenglas, *J. Chem. Soc.*, **109**, 534 (1956).
4. G. J. Hills, D. Inman, and J. Oxley, "Advances in Polarography," I. Langmuir, Editor, Vol. III, p. 982, Pergamon Press, New York (1960).
5. I. M. Kolthoff and J. J. Lingane, "Polarography," 2nd ed.. p. 494, Interscience Publishers, New York (1952).
6. J. J. Lingane, *J. Electroanal. Chem.*, **2**, 296 (1961)

Errata

In the paper by I. Akasaki and H. Kobayasi "Etching Characteristics and Light Figures of the {111} Surfaces of GaAs" which was published in the July 1965 issue of the *Journal*, [2$\bar{1}\bar{1}$] directions" in line 23 of left column, page 758, should read "<2$\bar{1}\bar{1}$> directions," and Fig. 6 in line 15 of column 1, page 759, should read Fig. 7.

The Effect of Electrode Pretreatment on the Oxygen Reduction on Platinum in Perchloric Acid

Y. L. Sandler and E. A. Pantier

Research Laboratories, Westinghouse Electric Corporation, Pittsburgh, Pennsylvania

ABSTRACT

The effect of pretreatment of a platinum electrode on the electrochemical reduction of oxygen and of hydrogen peroxide in perchloric acid was studied at room temperature. Hydrogen and oxygen pretreatments affect the oxygen reduction in a manner similar to cathodic and anodic pretreatments, respectively. An interpretation of various electrode characteristics is given on the basis of this parallelism. Removal of strongly bound oxygen by hydrogen pretreatment or cathodization accelerates the decomposition of hydrogen peroxide and increases the open-circuit potential and the rate of the oxygen reduction in solutions containing 10^{-5} to $10^{-7}M$ peroxide. Decay rates from a high anodic potential provide a sensitive measure for peroxide concentrations in the electrolyte.

One of the main difficulties in studying the electrochemical oxygen reduction reaction on platinum in acid solution is the lack of reproducibility under varying conditions. This is due to differences in impurity content, the peroxide concentration of the solution, and the physical characteristics of the electrode. This report deals mainly with the influence of the latter on the characteristics of the electrode reaction.

Hydrogen peroxide is either an intermediate (1) or a by-product (2, 3) in the reduction reaction of oxygen. In practice, therefore, it is always present when a cathodic current is drawn, as, for example, in fuel cells.

In clean solutions and at very low peroxide concentrations, open-circuit potentials (OCP) of close to 1.23v *vs.* a hydrogen electrode in the same medium have been obtained in the past by special pretreatments (2-4). The potentials were assumed to be true reversible potentials, corresponding to a four-electron reduction of oxygen to water. The potential cannot be reproduced after a cathodic current is drawn.

At high peroxide concentrations, above 10^{-4} mole per liter, a potential of about 0.84v (5) is set up which is characteristic of the peroxide electrode and is independent of the ambient atmosphere and the peroxide concentration. For the oxygen reduction reaction OCP's usually lie between 0.8 and 1.1v. The oxygen coverage is below one monolayer (6).

In a previous study (7) of the oxygen adsorption on platinum and silver in a dry system, different types of chemisorptions were found varying in binding energy. The activity of the surface for the reaction $O^{16}{}_2 + O^{18}{}_2 \rightarrow 2O^{16}O^{18}$ was found to be affected by the presence of firmly bound oxygen adsorbed at high temperatures and by the presence of hydrogen in the surface.

In the present study the effect of the high-temperature pretreatment of the platinum electrode with oxygen and with hydrogen on the characteristics of the oxygen electrode in perchloric acid solutions was studied. A reproducible effect of gas pretreatment was found and was compared with the effect of electrochemical prehistory. This method of comparison was used to study the influence of the nature of the adsorbed oxygen on the electrochemical characteristics of the electrode.

Experimental

The Cell.—The cell consisted of a flanged 5-in. diameter Pyrex vessel closed by a lid and a Teflon gasket. The electrodes were introduced through the lid via ground joints fitted with Teflon sleeves. The counter-electrode tube and the Luggin capillary tube contained fritted glass disks separating the corresponding electrodes from the main body which contained the test electrode and the oxygen bubbler. A platinized platinum coil served as hydrogen electrode which was frequently checked against a second hydrogen electrode.

Gases.—Commercial electrolytic oxygen was purified by passage through hot copper, Dryerite, Ascarite, and a molecular sieve at dry ice temperature. Hydrogen was also an electrolytically produced commercial product. It was passed over hot palladium asbestos, Dryerite and molecular sieve at liquid nitrogen temperature.

The electrolyte.—Reagent grade perchloric acid was used. It was diluted with water distilled from alkaline permanganate and then double distilled in a quartz still.

The electrodes.—Platinum foils of 99.999% purity were used in form of a square, ½ in. each side. After degreasing in hot 20% KOH, the foils were treated in hot 50% nitric acid and carefully washed in triple distilled water and in condensing steam.

Heat pretreatment.—The foils having platinum lead wires spot welded to them were cleaned, mounted in their quartz electrode holders and fitted into a quartz furnace tube. The foils were treated in a flow of oxygen at increasing temperature with at least 2 hr at 700°C. The tubes were then plugged and transferred to a glove box flushed with pure oxygen. Inside the box the electrode holder and foil were transferred to the cell.

In the case of "hydrogen pretreated foils" the same procedure was adopted except that after the oxygen treatment at 700°C the oxygen was displaced by helium and the foil was treated for 2 hr with hydrogen at 600°C. The foils were then cooled in helium and again exposed to oxygen at a temperature below 100°C for at least ½ hr. Oxygen was bubbled over the electrode, except where stated otherwise.

Instrumentation.—Potentials were read with a Keithley model 660 differential voltmeter. Open-circuit potentials were read at infinite input impedance using the Kelvin-Varley divider on the instrument. A Varian recorder was used only when the lower input impedance of the direct reading device (about 10^7 ohm) was considered not disturbing. Approximately constant currents were obtained by means of mercury batteries giving 28v and a set of fixed and variable resistors in series with the cell. Currents were measured by means of a Keithley electrometer, model 200B, and current shunt.

Results

Reduction of oxygen.—The following experiments are examples of the effect of the electrochemical pretreatment of solution and electrode on the current-voltage characteristics. Measurements shown in Fig. 1 were carried out in 1/10*N* perchloric acid which was pre-electrolyzed for 60 hr at 10 ma with oxygen bubbling through it. Two platinum pre-electrolysis

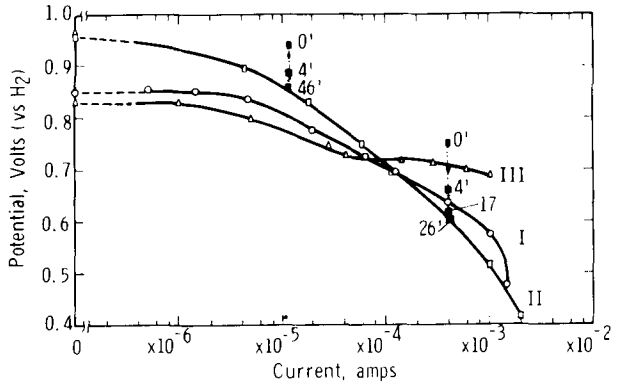

Fig. 1. Cathodic polarization curves of a chemically pretreated electrode; I, first polarization curve; II, after 10^{-4} amp/cm² overnight (■, overshoot on decreasing current); III, after anodization at 1.8v.

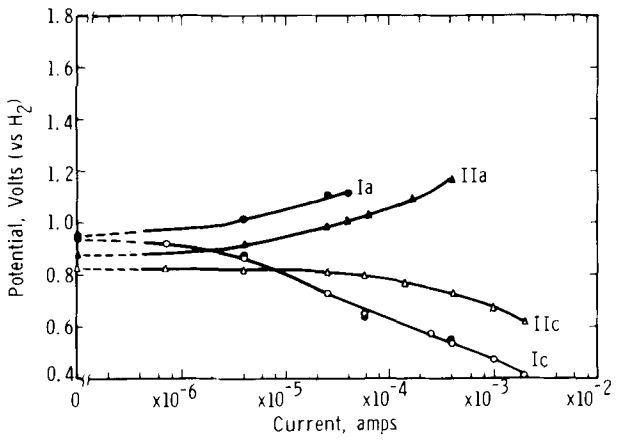

Fig. 2. Polarization curves after thermal gas pretreatments of electrodes: 1, after hydrogen pretreatment; 2, after oxygen pretreatment; c, cathodic, a, anodic.

electrodes of about 1 cm² area were in the main compartment of the cell which was later occupied by the test electrode. This type of pretreatment purifies the solution but generates hydrogen peroxide. The test electrode was dipped for 20 min in hot 50% nitric acid, washed and steamed before use, but was not treated thermally. The open-circuit potential, *vs.* hydrogen in the same medium, varied from 0.80v at a high oxygen bubble rate to 0.88v when the oxygen was shut off. The rise in potential, described in the literature (8), is due to the catalytic destruction of the peroxide at the electrode as is discussed later. The points shown in all figures were taken after 4 min at constant current. Only the open-circuit potentials (OCP) will be given as obtained 30-60 min after immersing the electrode or interrupting the current.

Curve 1 gives the cathodic galvanostatic polarization curve for increasing current settings. An overshoot at first occurred with each new current setting increasing to 25 mv at 10^{-3} amp. The potential then rose and became stationary within the given time. Currents were always cut off when strong fluctuations started indicating approach of the limiting current before drop to low potentials in the hydrogen evolution region. On decreasing the current a stronger overshoot occurred. The overshoot with increasing cathodic polarization is believed to be due to removal, on increasing the current, of strongly bound oxygen which decreases the activity of the electrode, as discussed later. On decreasing the polarization the reverse process occurs.

After leaving the current at 1 x 10^{-4} overnight, the OCP was higher, having risen to 0.962v. Another cathodic sweep then taken is shown in Fig. 1, curve 2. While the polarization was now lower at low currents it was higher at high currents. No good Tafel region was found; the approximate slope was 160 mv between 10^{-5} and 5 x 10^{-4} amp, while it was 115 mv in curve 1. The overshoot on the return curve as a function of time is indicated in Fig. 1 by the points at 4 x 10^{-4} and 1.3 x 10^{-5} amp.

After anodizing the foil several times in the same solution to about 1.8v (to determine the decay rate, as described below) the open-circuit voltage was found to be low, *viz.*, 0.835v. A cathodic curve then taken is shown as curve 3 in Fig. 1. The potential was now relatively low at low currents and high at high currents. The described behavior was qualitatively well reproducible: cathodizing at high current gave a relatively high open-current potential and a steep slope while anodizing gave a low potential at open circuit, but a small decrease in potential with increasing current.

The rate of decay measured after charging the foil anodically to 1.8v was measured oscillographically; it indicated peroxide concentration of the order of 10^{-4} mole/liter (see below).

In Fig. 2 curves obtained after different gas pretreatments of the electrode are presented. Curve 1 was obtained after the hydrogen pretreatment described in the Experimental Section. The initial open-circuit potential was 0.97v. On the following day the OCP was 0.94v. A cathodic sweep for increasing and decreasing current was taken which is shown in Fig. 2, curve Ic. The high open-circuit potential and the steep slope of 160 mv are very similar to what was obtained after cathodizing in Fig. 1. After anodizing, again a low open-circuit potential, 0.83v, and a flat characteristic was obtained (not shown). Curve 2 in the same figure shows the results after thermal oxygen pretreatment of another foil in a new solution. The open-circuit potential was low immediately, 0.85v, and the slope of the cathodic curve was small. This is similar to what was previously obtained after anodizing (Fig. 1).

Several experiments were made with gas pretreated electrodes in which the solution was only anodically pre-electrolyzed (3) for 20 hr at 5 ma. In these experiments the main cell compartment, later used for the test electrode, contained an auxiliary electrode serving as an anode, while the counter electrode was used as the cathode. This resulted in a lower peroxide concentration. Figure 3 shows two sets of curves in which the anodic sweeps were taken first, in 1*N* perchloric acid. Anodic potential values rose steadily and were taken after 4 min. It may be seen that the initial values for the hydrogen pretreated electrode are higher again, 75 mv at open circuit. In the present case this even holds for the cathodic sweeps taken after anodization although this was not always found. The potential

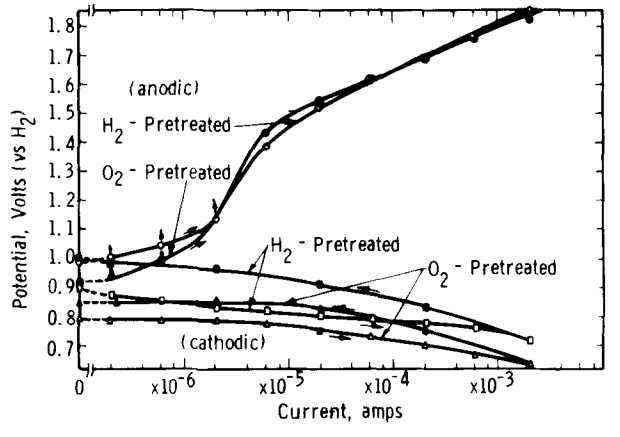

Fig. 3. Polarization curves with oxygen and with hydrogen pretreated foils in anodically pre-electrolyzed 1*N* perchloric acid. Anodic curves taken first. Cathodic curves shown for increasing and decreasing currents.

for an electrode which was not thermally pretreated was intermediate between the values found for oxygen and for hydrogen pretreated electrodes. Similar differences were also obtained when the cathodic sweeps were taken first, giving OCP's of 1.02 and 0.94v, respectively. The peroxide concentration in these experiments was of the order of 10^{-7} mole/liter.

Estimation of the peroxide concentration.—The peroxide concentrations were estimated in two ways, (i) from the anodic limiting current, (ii) from the rate of decay from a given high potential. In Fig. 3 the rate of rise to the oxygen evolution potential (1.45v) became appreciable below 10^{-6} amp/cm^2. The limiting current i_L is related to the diffusion coefficient, D, by the relation

$$i_L = \frac{2FD}{\delta} c$$

Winkelmann's (9) experimental results can be presented by the simple approximate relation

$$i_L(\text{amp/cm}^2) \approx c(\text{mole/liter})$$

Therefore the peroxide concentration in the present case was below 10^{-6} mole/liter.

Figure 4 shows a set of decay curves obtained with different added peroxide concentrations after charging the oxygen electrode to 1.8v. The decay rate may be seen to be a function of the peroxide concentration. A corrosion-like reaction apparently takes place involving the reduction of unstable surface oxygen and the simultaneous oxidation of peroxide. The approximate concentration of 10^{-7} mole/liter was found for the examples given in the previous paragraph by comparing the measured decay curves to the given set of standard curves.

In peroxide-free solutions, the decay (11) of the polarization would give a slope of only about 120 mv. The method, therefore, can be extended to even lower peroxide concentration and by far exceeds the sensitivity limit of chemical tests.

Reduction of peroxide.—The reduction of peroxide in 1*N* perchloric acid in helium-saturated solutions was also studied and compared to the oxygen reduction in the same electrolyte.

In Fig. 5, curves a and b show cathodic polarization curves at a concentration of added peroxide of 10^{-3} mole/liter, as obtained with a hydrogen pretreated electrode in helium and oxygen saturated solutions, respectively. Curves c and d were similarly obtained with a peroxide concentration of 10^{-4} mole/liter. It may be seen that the curves obtained with oxygen and with helium are practically identical up to the sharp potential drop in the helium-saturated solutions when the limiting current for the given peroxide concentration is approached at 10^{-3} and 10^{-4} amp/cm^2, respectively.

Curve e was obtained with an oxygen-pretreated electrode in a 10^{-4}M helium-saturated peroxide solution. In all cases the OCP on immersion was about 0.90v (±25 mv); for all hydrogen pretreated electrodes it decayed to 0.85v within 30 min, while for two oxygen pretreated electrodes the OCP was only 5-10 mv lower. On the other hand, an oxygen pretreated electrode which was exposed to laboratory air for 1 min gave an OCP as low as 0.80v.

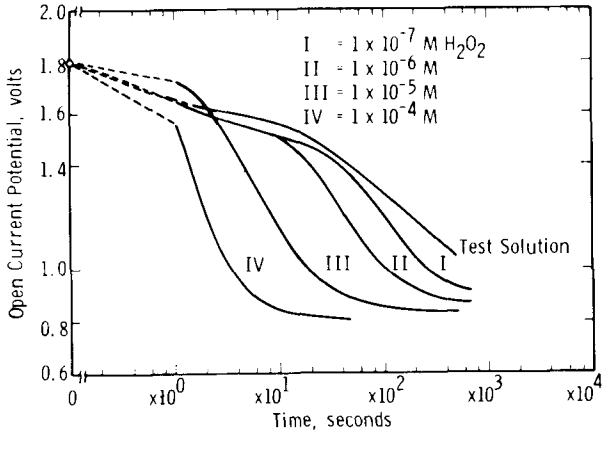

Fig. 4. Decay curves at varying peroxide concentrations

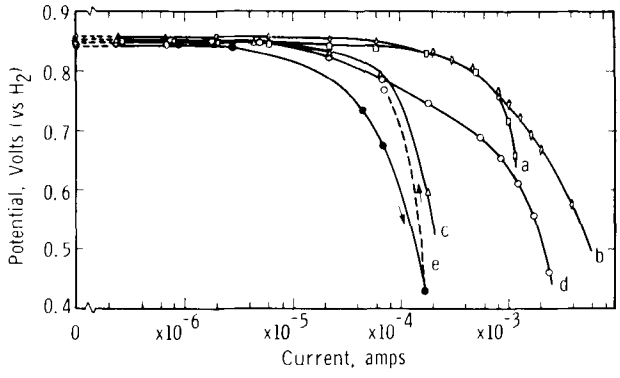

Fig. 5. Cathodic polarization curves at various added concentrations of peroxide: I. Hydrogen pretreated electrode: (a) 10^{-3}M H_2O_2, He-saturated solution; (b) 10^{-3}M, O_2 in solution; (c) 10^{-4}M H_2O_2, He; (d) 10^{-4}M H_2O_2, O_2. II. Oxygen pretreated electrode: (e) 10^{-4}M H_2O_2, He.

In 10^{-5}M peroxide solutions the oxygen reduction curve lies clearly above the peroxide reduction curve, as seen from Fig. 6. Again a hydrogen pretreated foil was used. (The cathodic limiting current was relatively high, about 10^{-4} instead of the 10^{-5} amp/cm^2 expected, presumably due to incomplete oxygen removal from the solution.)

In all cases again a distinct overshoot was found when decreasing the cathodic polarization. It amounted to between 30 and 80 mv on opening the circuit and returned to within 10 mv of the original OCP within about 30 min. Also a small stirring effect on the OCP was found at all peroxide concentrations. The potential in unstirred solutions was about 15 mv higher than at high stirring rates.

Catalytic decomposition of peroxide by platinum.—The higher OCP of the hydrogen pretreated or cathodized platinum electrodes at low peroxide concentrations may be explained by a higher decomposition rate of the peroxide. To test this possibility the catalytic decomposition by differently pretreated electrodes was studied.

Two electrodes which were stored after use in the preceding experiments in triple-distilled water were first used in qualitative tests. An oxygen pretreated electrode stored for one week formed practically no bubbles on the electrode surface when dipped into a 1% aqueous peroxide solution, while a hydrogen-pre-

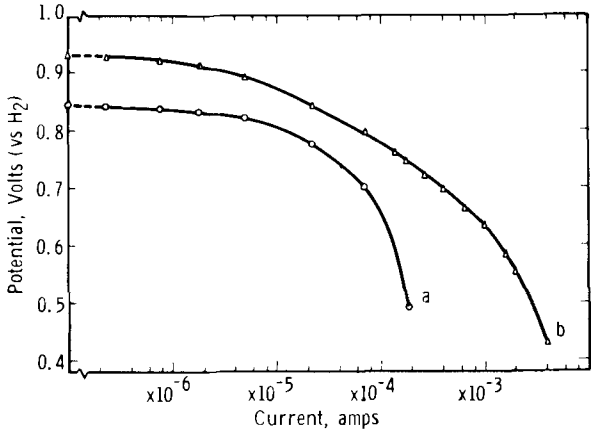

Fig. 6. Cathodic polarization curves at 10^{-5}M H_2O_2: a, He; b, O_2 atmosphere.

treated electrode stored for two weeks rapidly covered itself with oxygen bubbles.

In a more quantitative experiment, a new platinum foil was oxygen pretreated and then dropped into a 1% peroxide solution in perchloric acid. The gas evolved was collected in an inverted buret. A gas evolution rate of 0.01 cc/min of oxygen was measured. The rate gradually decreased to 1/3 in the course of 16 hr.

The experiment was repeated with the same foil after hydrogen pretreatment. After the usual exposure to oxygen at room temperature (see Experimental Section) the oxygen evolution rate in the solution was measured and found to be 0.10 cc/min., *i.e.*, 10 times larger than in the previous experiment.

Discussion

According to Gerischer (10) and Winkelmann (9) the catalytic decomposition of hydrogen peroxide is the result of an over-all anodic process

$$H_2O_2 \rightarrow O_2 + 2H^+ + 2e^- \quad [1]$$

and an over-all cathodic process

$$H_2O_2 + 2H^+ + 2e \rightarrow 2H_2O \quad [2]$$

proceeding at equal rates when no current is flowing. The OCP at, or above, 10^{-4}M peroxide is 0.85v; it is a mixed potential set up by the two given reactions.

Since the gas pretreatment did not change the peroxide potential appreciably, we conclude that the rates of the two reactions, [1] and [2], are about equally affected by the pretreatment. On the other hand, the drop in OCP, found for an electrode poisoned by exposure to the contaminations of laboratory air, is to be explained by a larger decrease in the rate of step [2]. The reduction of peroxide may be expected to be more sensitive to poisoning of the metal surface because, contrary to step [1], step [2] involves the complete dissociation of an oxygen-oxygen bond.

The dependence of the decomposition rate of hydrogen peroxide on the pretreatment suggests a simple explanation for the dependence of the open-circuit potential of the oxygen electrode on pretreatment. At relatively low peroxide concentrations (10^{-5} to 10^{-7} mole/liter), when the peroxide reduction is slower than the oxygen reduction, the O_2/H_2O_2 couple may mainly determine the open-circuit potential, as is often assumed for alkaline solutions (11). (At even higher potentials other equilibria such as oxygen chemisorption may also be of importance or the reduction of oxygen may be balanced by other anodic reactions, such as the oxidation of impurities.) The standard potential of the O_2/H_2O_2 couple is 0.68v (12) and, according to the Nernst equation, the potential rises by 2.30 x $RT/2F$ = 30 mv with each decade of decreasing H_2O_2 concentration. In view of the catalytic activity of the electrode no true equilibrium is established with the bulk of the solution. The rise in OCP after hydrogen pretreatment or cathodization then is a consequence of the increased activity of the electrode which lowers the concentration of peroxide in the diffusion layer. Similarly, the dependence on the gas flow can be explained by a change in convective transport: the concentration of peroxide at the electrode further diminishes as the flow rate decreases. Thus in a stirred solution having a peroxide concentration of roughly 5 x 10^{-8}M (Fig. 3), the peroxide concentration at the oxygen-pretreated electrode (OCP = 0.92v) would be about 10^{-8}M, while at the hydrogen-pretreated electrode (OCP = 0.99v) it would be about 10^{-10}M.

Under current drain, it was also found that in all cases the potential at a given oxygen reduction rate depended on the electrode pretreatment. At low peroxide concentrations, the polarization for hydrogen-pretreated electrodes was smaller than for the oxygen-pretreated electrodes throughout the cathodic range up to the diffusion-limited current (Fig. 3).

The overshoot found on changing the current may also be explained by a change in catalytic activity as the oxygen content of the surface changes. Breiter (13), from a study of periodic sweeps taken at a much faster rate, suggested that adsorbed oxygen hindered the oxygen reduction reaction. The long lasting effects observed in our work show that the change in activity is due to oxygen strongly embedded in the surface (7). The oxygen changes the activity of the surface but does not directly enter into the reaction. The similarity of the effect on the potential of cathodic pretreatment and thermal hydrogen pretreatment seem to confirm this explanation.

In the initial experiments, carried out at higher peroxide concentrations (Fig. 1 and 2), the slope found for the hydrogen or cathodically pretreated electrodes was considerably higher than for the oxygen pretreated electrodes and at higher currents the former showed the larger polarization. No definite conclusions can be drawn on the basis of the present experiments. The electrolyte in the early experiments may not only have contained a higher peroxide concentration but may also have differed in impurity content as a result of the different preelectrolysis procedure used. We are inclined to believe that the greater inhibition of the oxygen reduction for the surface containing the electropositive hydrogen may have been caused by a stronger adsorption of impurity anions (possibly Cl^-). The latter were more thoroughly removed by the anodic preelectrolysis used in the later experiments.

The experiments show the difficulty involved in predicting or analyzing the long-term polarization behavior of the oxygen electrode. The oxygen content of the surface changes with potential and time and thus the activity for the intermediate steps should change in a manner difficult to predict. Similarly, experiments in a dry system (7) have shown that the nature of the adsorbed oxygen tends to change with time; it changes to a more stable form which decreases the catalytic activity. It thus may be expected that a slow deactivation of the platinum electrode would be observed even in absence of impurities.

Acknowledgments

The authors are indebted to Dr. T. Hurlen for stimulating discussions. The work was supported by the Advanced Research Projects Agency through the Office of Naval Research.

Manuscript received March 8, 1965. This paper was presented at the San Francisco Meeting, May 9 to 13, 1965.

Any discussion of this paper will appear in a Discussion Section to be published in the June 1966 JOURNAL.

REFERENCES

1. cf. Klaus Vetter, "Elektrochemische Kinetik," p. 513, Springer (1961).
2. J. O'M. Bockris and A. K. M. Huq, *Proc. Roy. Soc.*, **A237**, 277 (1956).
3. N. Watanabe and M. A. V. Devanathan, *This Journal*, **111**, 615 (1964).
4. J. P. Hoare, *ibid.*, **110**, 1019 (1963).
5. J. O'M. Bockris and L. F. Oldfield, *Trans. Faraday Soc.*, **58**, 249 (1955).
6. Ref. (1), p. 500.
7. Y. L. Sandler and D. D. Durigon, To be published.
8. H. G. Bain, *Trans. Electrochem. Soc.*, **78**, 173 (1940).
9. D. Winkelmann, *Z. Elektrochem.*, **60**, 738 (1956).
10. R. Gerischer and H. Gerischer, *Z. Phys. Chem. N.F.*, **6**, 178 (1956).
11. W. G. Berl, *Trans. Electrochem. Soc.*, **83**, 253 (1943).
12. W. M. Latimer, "Oxidation Potentials," 2nd ed., Prentice-Hall, New York (1953).
13. M. W. Breiter, *Electrochim. Acta*, **9**, 441 (1964).

The Indous Ion: An Intermediate in the Electrochemical Oxidation of Indium Metal

R. E. Visco

Bell Telephone Laboratories, Incorporated, Murray Hill, New Jersey

ABSTRACT

It has been demonstrated that in a stirred acidic noncomplexing medium, the In(I) ion is an important intermediate in the electrochemical oxidation of either indium metal or its amalgam to the In(III) ion. The In(I) ion formed during anodization can be swept away from the electrode surface and can be detected polarographically in the bulk of the solution. The current efficiency in stirred solutions for In(I) production is about 2% in the case of dilute indium amalgams. For indium metal anodes, the current efficiency for In(I) production under the same conditions is at least 75% and is dependent on anodic current density. The effects of mass transport conditions during electrochemical oxidation and of added complexing agents on the quantity of In(I) formed have also been investigated. Based on overpotential decay curves, the polarographic behavior of In(I) and In(III), and coulometric experiments, an electrochemical mechanism is proposed which postulates that the In(I)/In(O) couple is at equilibrium, that the interfacial concentration of In(I) is not vanishingly small, and that an irreversible electrochemical step is associated with the further oxidation of In(I) to In(III).

The aqueous electrochemistry of the higher atomic weight group IIIB elements has been the subject of much scientific interest. For all these elements, the +3 oxidation state is stable in aqueous solution. Vetter (1) has studied both the oxidation and reduction processes for the two-electron Tl(III)/Tl(I) system. Bockris and Enyo (2, 3) have studied the oxidation and reduction processes for the Ga(III)/Ga(O) couple with gallium metal as either a liquid or solid electrode. The In(III)/In(O) couple has been studied using amalgam electrodes by several workers (4-7). In addition to these studies on stationary electrodes, usually made under steady-state conditions, a large body of information, particularly on indium, is available from studies using dropping mercury and dropping amalgam electrodes (8-12).

For the cases of gallium and indium, the over-all electrochemical oxidation is a three-electron process. This multi-electron transfer presents the possibility that during the electrochemical process there may exist detectable quantities of two intermediate oxidation states. Corbett (13) has recently demonstrated that Ga(I) does exist in measurable quantities during the electrochemical oxidation of gallium metal. Hurlen (14, 15) recently reported an extensive study of the oxidation of liquid gallium metal and concluded that lower valent gallium species are formed and can be swept away from the electrode surface.

This paper is a report on a search for In(I) as an intermediate during the electrochemical oxidation of either indium metal or its amalgam. Epelloin (16) has presented coulometric data which suggests that lower valent In(I) species are formed during electropolishing of indium metal in either acetic acid or ethyl alcohol. Losev and co-workers (4-6) have reported on electrochemical and radiochemical studies of the In(III)/In(O) couple using amalgam electrodes. These workers have ascribed a transitory existence to lower valent indium oxidation states and imply that In(III) and In(O) are the only indium oxidation states that can exist during anodization at anything but infinitesimal concentrations. On the other hand there exists a body of information on equilibration of In(O) with solutions of In(III) (17-20) which suggests that at least In(I) can exist at a finite concentration.

Experimental

All chemicals used in this study were reagent grade meeting ACS specification, except those listed below. Indium metal, obtained as shot or rod from American Smelting and Refining Company, South Plainfield, New Jersey, was of 99.999+% purity. The mercury used was triply distilled. Indium amalgams were prepared by determinate weighing of the constituents. Sodium perchlorate was prepared by quantitative neutralization of Na_2CO_3 with $HClO_4$. All solutions were tested for any halide ion by recording the polarographic residual current at potentials anodic of 0v *vs.* saturated calomel electrode (SCE). Residual currents recorded in $NaClO_4$ solutions were identical to those of the $HClO_4$ used, and no wave prior to the oxidation of mercury to Hg^{++} was observed.

The reaction vessel was a thermostatted cell (volume *ca.* 70 ml) similar in design to that sold by Brinkman Instruments. Nitrogen, which was passed through two vanadium (II) wash towers and a water wash, was continuously passed into or above the solution to purge O_2. The amalgam was held in a Riley electrode (Sargent No. S-30438) giving a surface area of 1 cm^2. Indium metal anodes were 0.25 in. in diameter rods. The dropping mercury electrode used was of a conventional design. In addition to the dropping mercury and indium electrodes, a reference and a counterelectrode were also employed; both were saturated calomel electrodes. Each SCE was isolated from the solution by a perchloric acid-silica salt bridge which was similar in composition to the sulfuric acid-silica bridges described by Vinal (21).

The polarograph was a Sargent Model XV modified to have a 1-sec pen response. A Sargent Model IV coulometric current source was employed. Voltage-time curves for the indium electrodes were recorded in several ways. A Keithley Model 610A electrometer and a L&N K-3 potentiometer were used to make steady-state potential measurements. Potential-time transients were recorded using a locally fabricated high-impedance voltage follower (22) and either a Sargent MR Recorder or a Tektronix 565 Oscilloscope with 2A63 preamplifiers. Temperature control was achieved using a thermistor temperature controller so that bath temperature could be controlled to $\pm$ 0.05°C. Micrometer driven syringe burets were used to deliver small quantities of solutions into the glass cell.

Stirring was provided by a Teflon or glass-coated magnetic stirring bar. For a given series of experiments reproducible mass transport conditions in the

cell were maintained by controlling the position and the speed of the stirring bar.

The experimental procedure employed for the analysis of In(III) solutions is described below. To an aliquot of anolyte a quantity of HCl was added to the In(III) solution such that the Cl^- concentration after quantitative dilution became 0.20M. A polarogram was recorded of the In(III) solution and the limiting current at —0.65v *vs.* SCE measured. At this potential and chloride concentration, the polarographic limiting current is diffusion controlled and proportional to the In(III) concentration. Known solutions of In(III) were prepared by determinate weighing of indium metal. The diffusion current constant, *I*, evaluated from the simple Ilkovic equation was found to be 5.20 with a coefficient of variation of 0.6%. The numerical constant used in the Ilkovic equation was 706 since an underdamped current measuring device was employed.

Results

General.—It will be shown that, during anodization of either indium metal or its amalgam, In(I) is an important intermediate in the oxidation. The existence and importance of In(I) can be demonstrated by the detection of In(I) carried by mass transport to the bulk of the solution. The In(I) can be detected at an electrode independent of that used for its generation. To demonstrate the existence and importance of an intermediate in an over-all multi-electron process, the above procedure is preferred to the calculation and subsequent comparison with experiment of a set of current-voltage curves for the case where the interfacial concentration of an intermediate is not vanishingly small.

Polarography of In(I).—Using the dropping mercury electrode as a probe, it is observed that after electrochemical oxidation in stirred solutions of 0.70M $HClO_4$ with anodes of either indium metal or indium amalgam, the anolyte contains a soluble species which can be both oxidized and reduced, Fig. 1 of ref. (20). When corrections are made for the homogeneous decay of the electroactive species (*vide infra*), both the anodic and cathodic process at the dropping electrode are found to be diffusion controlled. For both processes, the limiting current is proportional to the square root of the height of the mercury column and extrapolation to zero column height gives zero current (23). At any given time after termination of the electrolysis, the ratio of the anodic current (—0.20v) to the cathodic current (—0.65v) at the dropping electrode is 2.0, Fig. 2 of ref. (20).

The anodic and cathodic currents decay with time. Plots of log current *vs.* time are linear for at least 4 half-lives. Anodic currents decay completely; after complete decay, the polarogram at potentials more positive than —0.70v *vs.* SCE is identical to the residual current of $HClO_4$. The irreversible reduction of the aquo-indic ion becomes important at potentials more negative than —0.75v. The decrease in polarographic current after anodization results from a homogeneous rather than heterogeneous decay of the electroactive species. This is true since polarograms are recorded in quiet solutions, and because the decay rate is unaffected by periodic stirring. Polarograms recorded with intervening 1-min periods of vigorous stirring show no enhancement in the rate of In(I) disappearance. The intentional addition of In(III) and the build-up of products from repeated anodization experiments do not affect the rate of polarographic current decay.

Based on the above experimentally observed ratios of diffusion-controlled polarographic currents and the potentiometry at indium metal electrodes (*vide infra*), the lower oxidation state of indium present in solution after anodization must be In(I). The electrochemical oxidation process occurring at the dropping electrode therefore is

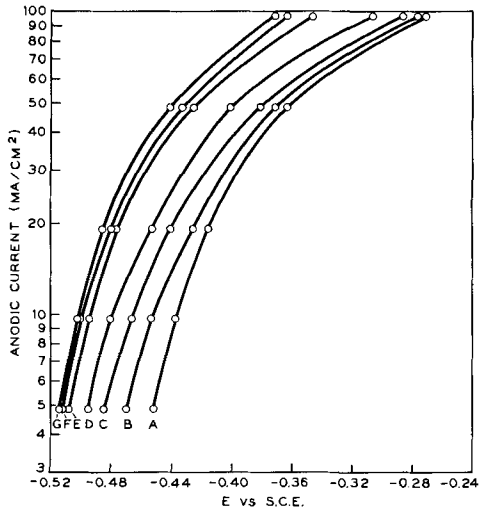

Fig. 1. Current density *vs.* potential for 2 mole % indium amalgam at 20°C as a function of added Cl^- in well stirred 0.70M $HClO_4$ with In(III) of 5 x 10^{-3}M: A, 0; B, 0.016; C, 0.031; D. 0.057; E, 0.091; F, 0.123; G, 0.153.

$$In(I) - 2e^- \rightarrow In(III) \quad [1]$$

while the reduction process is

$$In(I) + 1e^- \rightarrow In(Hg) \quad [2]$$

Homogeneous disappearance of In(I).—The indous ion is observed to decay by a first-order chemical reaction in acidic solution, Fig. 2 of ref. (20). In 0.70M $HClO_4$ solution, the pseudo first-order rate constant at 20°C is 5.28 x 10^{-3} sec^{-1}. This constant decreases linearly with decreasing acidity. A detailed description of the solution chemistry of the indous ion is given elsewhere (20).

Anodization experiments on indium metal and indium amalgam electrodes.—For the stirred solutions and at the high currents used in this study, a plot of log current density *vs.* potential for a 2 mole % amalgam electrode is nonlinear and is shown in Fig. 1, where results for Cl^- containing solutions are also shown. These curves are independent of stirring at the high stirring rates employed. If, during an anodization experiment, stirring is terminated, the electrode potential drifts anodic by about 25 mv. Experiments performed in quiet solutions thus give plots which are similar but displaced with respect to those obtained using stirred solutions. In stirred solutions regardless of the magnitude of the applied current, the potential of the working anode varies by no more than 2 mv during a typical 10-min anodization experiment. The slopes of these Tafel plots at the lowest current densities studied approach 40 mv/decade. Anodization experiments were not carried to current densities below 5 ma/cm^2, and the curvature in Fig. 1 is probably due to amalgam concentration polarization and iR drop. The limiting current density for the 2% amalgam used is somewhat less than 200 ma/cm^2. These data, therefore, place only an upper limit on the Tafel slope. Several workers have already reported on the Tafel experiments at lower current densities, and a value of 27 mv/decade is typical (5-7).

Since in stirred solutions In(I) is observed polarographically in the bulk of solution, it must be either the final product of the anodization or an electrochemical intermediate swept away from the electrode surface. In order to investigate this point further, the efficiency for In(I) formation and escape to the bulk was investigated at both metal and amalgam electrodes. The efficiency for the escape of In(I) from the electrode surface during anodization can be evaluated in two ways. Concentration of In(I) after

anodization and the average valence of indium going into solution are both measures of this efficiency.

During anodization, the steady-state concentration of In(I) is reached in a time equal to 5 half-lives for the decay of In(I), or about 10 min in 0.70M $HClO_4$ at 20°C. The concentration of In(I) as a function of time for the approach to the steady state can be calculated using expressions for the rate of decay of In(I) by the chemical reaction with H^+ (20) and the electrochemical formation rate at the anode. These expressions are given below

$$R_{decay} = k_1[In(I)] \quad [3]$$

$$R_{escape} = k_2(E) \quad [4]$$

and

$$\frac{d[In(I)]}{dt} = k_2(E) - k_1[In(I)] \quad [5]$$

The constant k_1 has been previously defined. The term $k_2(E)$ is a constant describing the rate of formation and escape of In(I) to the bulk; such a constant is surely dependent on the anode potential, E, and the mass transport conditions prevailing in the cell during the experiment.

The solution to Eq. [5] with the initial condition that $[In(I)]_{t=0} = 0$ is

$$In(I) = \frac{k_2(E)}{k_1}(1-e^{-k_1t}) \quad [6]$$

The concentration of In(I) can be evaluated from the polarographic limiting current provided the diffusion coefficient is known. The diffusion coefficient of In(I) is unknown, but it should be very similar to that of Tl(I), 17.9×10^{-6} cm^2 sec^{-1} (24). If only comparisons are of interest, the variation of $k_2(E)$ with anode current and, therefore, anode potential should be independent of the value of the diffusion coefficient for In(I). A comparison of the efficiency for formation and escape of In(I) as a function of potential is therefore meaningful even if the exact value of the diffusion coefficient of In(I) is unknown.

Relevant experimental data for amalgam electrodes are shown in Table I, while the data for solid indium electrodes are given in Tables II and III. Several anode current levels were investigated, and experiments were performed at different times prior to the attainment of the steady-state concentration of In(I). The observed polarographic currents for each type of electrode divided by $(1-e^{-k_1t})$, where t is the length of anodization in seconds, yields a constant value which corresponds to the polarographic diffusion current for the oxidation of In(I) to In(III) when the concentration of In(I) has reached a steady state. The limiting anodic current for the amalgam electrode is less than 200 ma/cm^2, thus, in a potential region where concentration polarization of the amalgam is important, significant quantities of In(I) are observed to escape from the electrode surface to the bulk of the solution.

Since In(I) is observed away from the electrode surface, at least one mass-transport step is required to distribute the product of the anodization throughout the solution. To test the importance of this mass transport step on the quantity of In(I) observed, experiments designed to measure the In(I) concentrations were carried out at several different stirring rates. Data for an amalgam anode are given in Table IV. It is seen that stirring is, indeed, important in determining the quantity of In(I) observed in the bulk. It was observed in other experiments with amalgam electrodes that, at a fixed stirring rate, anodization current and anodization time, the concentration of In(I) reached during that time (< 10 min) was constant. Comparisons within a series of experiments performed in the same solution are, therefore, quantitative, but because of differences in the relative positions of anode, stirrer, and salt bridges, changes in mass transport conditions occur. Thus, comparison of data obtained with different solutions on different days can be only qualitative. These geometry restrictions appear to be less severe for solid anodes. The reproducibility of $\bar{n}$, the average number of electrons transferred per atom of indium dissolved, calculated using Eq. [7], for two different solutions at the same cur-

Table I. In(I) formation in 0.70M $HClO_4$ at 20°C as a function of anode current and time for 2% amalgam electrodes

Anode current, ma/cm^2	Time, sec	i_{DME},* μa	$\frac{i_{DME}}{1-e^{-k_1t}}$	k_2,** $Msec^{-1} \times 10^6$	$\bar{n}$†
96.5	300	0.250	0.309	0.167	
96.5	200	0.207	0.310	0.168	2.93
96.5	100	0.140	0.331	0.179	
48.3	345	0.124	0.146	0.079	
48.3	204	0.116	0.173	0.094	2.93
48.3	140	0.081	0.150	0.081	
19.3	660	0.069	0.071	0.038	2.92
19.3	295	0.066	0.081	0.044	

* i_{DME} corrected for decay of In(I) occurring after termination of anodization.
** The concentration of In(I) at the steady state was evaluated using the simple Ilkovic equation with an assumed D (24), $n = 2$, and the m and τ values appropriate for the capillary employed.
† Solution volume was 50 ml and in this volume an anode current of 96.5 ma/cm^2 corresponds to 20.0×10^{-6} equivalents of charge per liter per second.

Table II. In(I) formation in 0.70M $HClO_4$ at 20°C as a function of anode current and time for metal electrodes*

Anode current, ma/cm^2	Time, sec	$\frac{i_{DME}}{1-e^{-k_1t}}$	k_2, $Msec^{-1} \times 10^6$	$\bar{n}$
24.7	100	20.5	11.7	1.46
24.7	100	21.3	12.2	1.43
12.4	120	13.0	7.4	1.29
12.4	100	12.1	6.9	1.34
4.95	130	5.99	3.42	1.18
4.95	100	5.88	3.35	1.20
2.47	120	3.23	1.84	1.13
2.47	100	3.36	1.92	1.10

* Electrode area was 3.9 cm^2. Volume of the anolyte was 45 ml.

Table III. Effect of chloride on In(I) formation from metal electrodes anodized at 12.4 ma/cm^2 for 100 sec

Cl^- × 10^3	i_{DME}, μa	$\frac{i_{DME}}{1-e^{-k_1t}}$	k_2*	$\bar{n}$
0	5.80	14.1	6.99	1.25
0	5.36	13.0	6.44	1.31
0**	5.86	13.1	6.49	1.30
0.20	4.23	10.3	5.12	1.48
0.80	3.08	7.49	3.71	1.72
2.0	2.05	4.99	2.47	2.05
4.0	1.37	3.33	1.65	2.24
8.0	1.06	2.58	1.28	2.44

* For the 50 ml of solution, the applied current can be expressed as 10×10^{-6} Eq. L^{-1} sec^{-1}.
** Anodization time was 120 sec at 12.4 ma/cm^2.

Table IV. Effect of stirring on the quantity of In(I) from a 2.5 mole % amalgam electrode*

RPM	i_{DME},** μa
0	<0.003
50	0.021
150	0.042
500	0.140

* Anodizations carried out at 50 ma/cm^2 for 150 sec.
** After anodization, the solution was vigorously stirred for about 20 sec, and currents reported were corrected for In(I) decay back to the end of anodization.

Table V. Average valence from electrochemical oxidation of indium in noncomplexing media

Current, ma/cm²	Time, sec	Mole of In dissolved × 10⁶	$\bar{n}$
14.4	100.1	42.6	1.17*
14.4	100.1	41.3	1.21*
14.4	120.2	48.2	1.24*
9.65	480.4	18.1	2.66**
19.30	245.9	18.1	2.73**
48.25	240.4	41.2	2.92**
96.5	124.1	43.6	2.85**

* Anode employed was an indium rod of 3.9 cm².
** Anode employed was a 2.5 mole % indium amalgam of 1 cm² area.

rent density appears satisfactory (Tables II and III).

It is possible to translate the calculated $k_2(E)$ [subject to the assumption of an In(I) diffusion coefficient] into $\bar{n}$ by the equation

$$\bar{n} = \frac{3k}{2k_2(E) + k} \qquad [7]$$

The quantity k in Eq. [7] is the number of equivalents of charge passed per second per liter of anolyte, Tables I, II, and III.

The second method for evaluation of the efficiency of the formation and escape of In(I) during anodic dissolution is the determination of the average number of electrons transferred per atom of indium dissolved, n, by a coulometric technique. Experiments of this type require an analytical method for total dissolved indium. It has been shown (20) that in acidic solutions In(I) is oxidized by H^+ to In(III); therefore, a determination of In(III), provided sufficient time is allowed for In(I) decay, is a satisfactory method of analysis.

Results of the experiment described above for both metal and amalgam anodes are shown in Table V. Experiments of this type should be dependent on mass transport conditions prevailing in the cell during anodization; therefore, quantitative interpretation of the departure from an n value of 3 is difficult. Qualitatively, it can be seen that for amalgam electrodes $\bar{n}$ approaches 3 only at the highest current density employed.

The $\bar{n}$ data for solid electrodes were taken sequentially in the same solution with In(III) samples removed after each anodization. The corresponding polarographic currents for the In(I) ion appear in Table III as the first three entries. The data allow a direct comparison between the two methods of evaluating the importance of In(I).

Agreement between the two methods is quite good. The corresponding values for the same experiment are 1.17 *vs.* 1.25, 1.21 *vs.* 1.31, and 1.24 *vs.* 1.30. These small differences in the two methods of calculating $\bar{n}$ can be rationalized by either (or both) of two explanations. The diffusion coefficient of 17.9×10^{-6} cm² sec^{-1} assumed for In(I) is about 15% high and a value of 15.5×10^{-6} cm² sec^{-1} is correct. The alternate explanation is that since at the anode surface during generation the concentration of In(I) is about tenfold larger than in the bulk, the rate of the reaction with H^+ is also a factor of 10 larger, thus consuming In(I) close to the interface before it can be distributed to the bulk. An approximate tenfold difference in concentration can be shown to exist based on the open-circuit potential curves discussed in the next section.

Open-circuit potentials on indium metal electrodes. —The open-circuit potential of an indium metal electrode was followed as a function of time after anodization. Potential-time curves in stirred and unstirred solutions are shown in Fig. 2 and 3. If the electrolysis carried out in a stirred solution is sufficiently long to build up the In(I) ion concentration to above 10^{-5}M (for example, 150 sec at 14.4 ma/cm²), the decay of

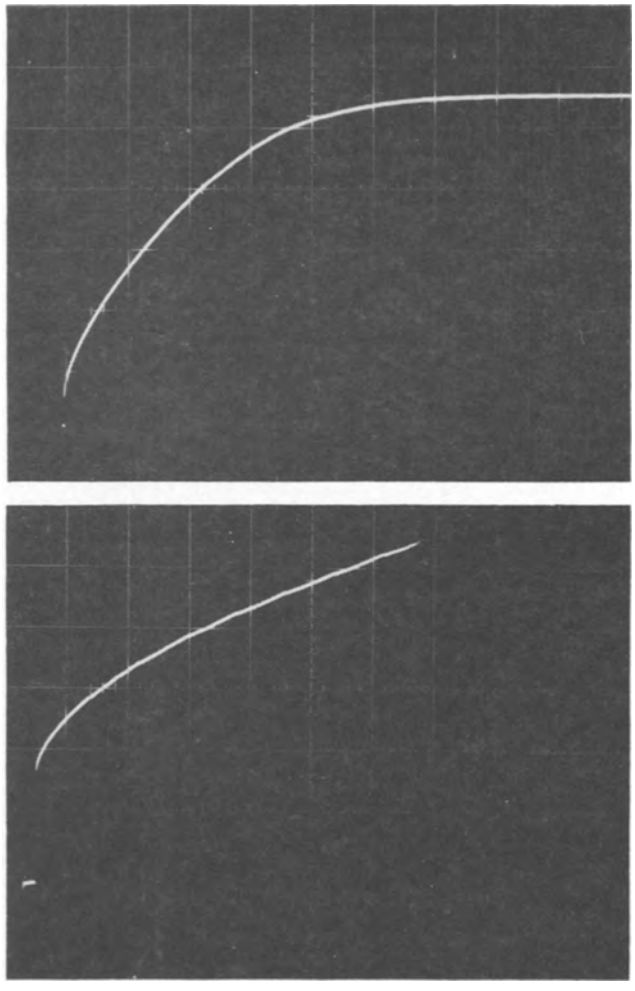

Fig. 2A and 2B. Overpotential decay curves for solid electrodes in stirred solutions of 0.70M $HClO_4$ at 20°C, anodized at 13 ma/cm²; upper curve (Fig. 2A) 20 mv/cm and 0.5 sec/cm; lower curve (Fig. 2B) 5 mv/cm and 20 msec/cm.

open-circuit potential on an indium metal electrode is linear with time for at least 4 min, Fig. 3, curve A. For a short electrolysis (~5 sec at 14.4 ma/cm²) in a stirred solution, the return to the open-circuit rest potential is more rapid, and no linear potential decay is observed, Fig. 3, curve B.

During anodization in a quiet solution, In(I) exists only at or very close to the electrode surface and is not distributed throughout the bulk of solution. When the anodization is terminated, the value of the open-circuit potential for a quiet solution is a few millivolts more positive than that for a stirred solution. It is also observed that the open-circuit potential decays more rapidly for the quiet solution than for a stirred solution. The latter will be true since diffusion of In(I) away from the electrode, as well as oxidation of In(I) by H^+, remove In(I) from the solution volume adjacent to the electrode surface, curves A and C, Fig. 3. For a quiet solution stirred during the measurement of potential decay, Fig. 3, curve D, the potential almost immediately returns (< 10 sec) to the stirred, open-circuit rest potential. The relatively small quantity of In(I) existing close to the electrode surface during anodization in a quiet solution is now distributed by the subsequent stirring through the entire solution. After stirring, the electrode thus sees a solution very little different from that if there had been no anodization at all.

Based on this and the polarographic evidence given earlier, this potential-time behavior of an indium metal electrode depends on the In(I) ion concentration. Two couples involving In(I) are possible

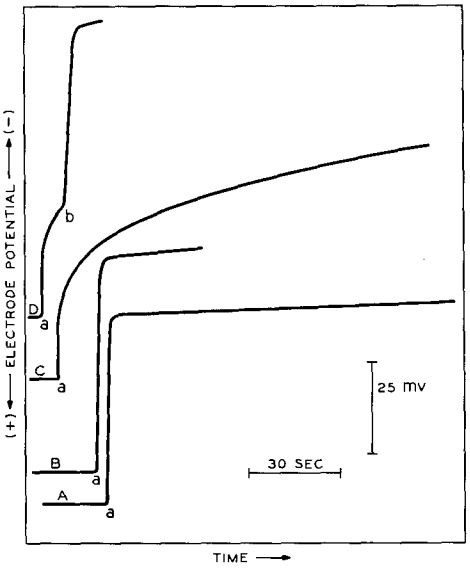

Fig. 3. Open-circuit potential-time curves for an indium metal electrode in 0.70M $HClO_4$ at 20°C with 5 x 10^{-3}M In(III). For each curve the anodization was discontinued at point "a". Curve A, electrode anodized for 150 sec at 14.4 ma/cm^2 in well-stirred solution; curve B, electrode anodized for 5 sec at 14.4 ma/cm^2 in a well stirred solution; curve C, electrode anodized for 150 sec at 14.4 ma in an unstirred solution; curve D, anodization carried out as in C, but during potential decay stirring was commenced at point "b".

$$In(I) + 1e^- \leftrightarrows In(0) \quad [8]$$

and

$$In(III) + 2e^- \leftrightarrows In(I) \quad [9]$$

Because the In(I) ion is unstable with respect to oxidation by H^+, the potential of an electrode responding to In(I) should vary with time. The electrode potential should become more oxidizing if the electrode responds to the In(III)/In(I) couple, but it should become more reducing if it responds to the In(I)/In(0) couple. On open circuit, the potential of the indium metal electrode becomes more reducing; the electrode is, therefore, responding to the In(I)/In(0) couple. The time dependence of the potential can be calculated from the Nernst equation for reaction [8] and the known (20) rate law for the decay of In(I) by the homogeneous reaction with H^+

$$E = E^{0'}_{In(I)/In(0)} + \frac{2.3\,RT}{F}\log[In(I)^0] - \frac{2.3\,RT}{F}k_1 t \quad [10]$$

In Eq. [10], $E^{0'}_{In(I)/In(0)}$ is the formal potential for the In(I)/In(0) couple, $[In(I)^0]$ is the zero time value of the bulk In(I) concentration, and k_1 has already been defined in Eq. [3]. For the initial 4-min linear portion, the observed rate of decay of open-circuit potential is —8.0 mv/min, while the calculated value for the In(I)/In(0) couple, using the k_1 value, at 20°C in 0.70M H^+ is —8.05 mv/min. After the initial 4-min portion, the rate of potential change decreases and, in about 12 min the open-circuit rest potential is reached.

The decay of overpotential recorded on a millisecond time scale is given in Fig. 2B. It can be seen that at 13 ma/cm^2, there is about 8 mv of iR drop. On a slightly longer time scale, Fig. 2A, two distinct segments of overvoltage decay can be seen. The second segment corresponds to that calculated using Eq. [10]. The initial, more rapidly changing portion can be viewed as that brought about by stirring which distributes the high concentration of In(I) in the Nernst diffusion layer throughout the bulk of the solution. The potential difference between the extrapolated zero time value of the potential decay curve changing at 8 mv/min and the initial open-circuit potential (corrected for iR), Fig. 2, is about 60 mv. Such a potential difference for a reversible 1 electron couple corresponds to a concentration difference of a factor of 10 between the electrode interface and the bulk of the solution.

The value of the open-circuit rest potential for indium metal in perchloric acid is dependent on both stirring and the In(III) concentration. For a given In(III) concentration, the rest potential is 10 mv more cathodic in a well-stirred solution than in a quiet solution. If stirring is terminated, the rest potential reaches the value for a quiet solution in less than 2 min, while if a quiet solution is stirred, the potential shifts in less than 10 sec.

The effect of stirring on rest potentials and on open-circuit decay curves is consistent with the metal electrode responding to changes in In(I) ion concentration. The rest potential in a stirred solution is more cathodic than in a quiet solution because In(I) is being swept away from the electrode surface. A finite concentration of In(I) is maintained at the surface in the absence of external current by a cathodic process. The irreversible hydrogen evolution reaction on indium metal (25) is the most likely cathodic process, but the irreversible reduction of In(III) is also possible (4).

Effects of added Cl^- *on the quantity of* In(I) *formed at metal and amalgam electrodes.*—An examination of the quantity of In(I) generated as a function of added Cl^- in experiments performed at the same anodic current for equal times using amalgam electrodes is instructive. Tafel curves for the relevent current densities and Cl^- concentrations are given in Fig. 1. When the solution is made 3.9 × 10^{-3}M in Cl^-, the concentration of indous ion after anodization is half that when no Cl^- is present. It was also observed that the rate of decay of In(I) is unaffected by the addition of Cl^- up to the highest concentration investigated (8.0 × 10^{-3}M). This observation of a decreased efficiency for formation and escape of In(I) is consistent with the change observed in the position and slope of the Tafel plots shown in Fig. 1. The effect of added Cl^- on the quantity of In(I) generated during oxidation of indium metal electrodes is given in Table III. The quantity of In(I) generated at 8 × 10^{-3}M Cl^- is still significant, but is fivefold less than in the absence of added chloride ion.

Discussion

The electrochemical oxidation in noncomplexing media of either indium metal or its amalgam in well-stirred solutions leads to a measurable quantity of In(I) ion in solution. Based on the coulometric and polarographic data from experiments with indium metal electrodes, at least 75% of the current goes to In(I) which escapes to the bulk of solution. For several mole per cent indium amalgams, the polarographic results indicate about 2% of the current goes to In(I) which can be detected at the dropping electrode. Higher but probably less reliable data for In(I) escape are obtained by the coulometric technique for amalgam electrodes.

If only successive one-electron transfers are considered, the slowest electron-transfer step for the oxidation of both the metal and its amalgam must be after the initial formation of In(I). At low current density, a Tafel slope of 27 mv/decade for the oxidation of the amalgam is consistent with the slow step being the oxidation of In(II) to In(III) for which values of between 20 to 30 mv/decade are expected. Further, the polarographic reduction of In(III) in noncomplexing media suggests that the first-electron transfer is the slowest, since the cathodic transfer coefficient is about 0.5.

The early cycling experiments of Heyrovsky (26) at dropping electrodes for In(III) in a $SO_4^=$ media may now be explained by considering the behavior of In(I) produced as an intermediate in the indium amalgam oxidation. Heyrovsky observed no cathodic "kink" or potential arrest, but only an anodic kink on the first

complete voltage cycle. The irreversible reduction of In(III) would produce no obvious kink on the first cycle, but the oxidation of In(0) to In(I) would produce a kink on the first anodic sweep. Heyrovsky also observed that a "warming-up makes the cathodic kinks sharper" on successive cycles. This would be true if the In(I) formed during the previous anodic half-cycle is reduced on the next cathodic half-cycle. The large voltage sweeps of 1-2v employed by Heyrovsky are well suited for such observations.

A mechanism proposed previously (4, 5, 7) for the electrochemical oxidation of indium amalgam is consistent with the data presented here and is given below

$$\mathrm{In(0)} \underset{v_{-1}}{\overset{v_{+1}}{\rightleftarrows}} \mathrm{In(I)} + 1e^-, \quad \text{fast} \qquad [11]$$

$$\mathrm{In(I)} \underset{v_{-2}}{\overset{v_{+2}}{\rightleftarrows}} \mathrm{In(II)} + 1e^-, \quad \text{fast} \qquad [12]$$

and

$$\mathrm{In(II)} \underset{v_{-3}}{\overset{v_{+3}}{\rightleftarrows}} \mathrm{In(III)} + 1e^-, \quad \text{slow} \qquad [13]$$

The previous treatments of this problem have assumed that transport of In(I) and In(II) to the bulk is unimportant; this is equivalent to the assumption that the interfacial concentrations of these intermediates are vanishingly small. Based on the data presented here for both amalgam and metal electrodes, the interfacial concentration of In(I) is not vanishingly small, and, therefore, some account must be taken of its transport to the bulk of solution. Consideration of the rate expressions for reactions [11] to [13] when transport of In(I) is important leads to the following expression for anodic current in the potential region when the cathodic back reaction is no longer important

$$\frac{i}{A} = F\,\mathrm{In(0)} \left\{ 3\,\frac{k_{+3}k_{+2}k_{+1}}{k_{-2}k_{-1}}\, e^{(2+\beta_3)F\Delta\phi/RT} + m\,\frac{k_{+1}}{k_{-1}} e^{F\Delta\phi/RT} \right\} \qquad [14]$$

The several k's are the rate constant for the unit steps in the oxidizing (+) and reducing (—) direction when $\Delta\phi = 0$. The mass transfer coefficient, m, for In(I) can be written D/δ where δ is the Nernst diffusion layer thickness. On examination of Eq. [14], it is clear that as $\Delta\phi$ becomes more positive, the fraction of the current going to In(I) which escapes should decrease, a fact substantiated by the data presented in Tables I, II, IV, and V.

The electrochemical mechanism suggested by Losev (4, 5) is that given above where both the In(I) and In(II) interfacial concentrations are vanishingly small. At the current densities investigated here, several per cent of the current goes to the formation of In(I). Losev suggested that In(I) does exist, but did not consider its interfacial concentration to be important. At the current densities he used, larger fractions of the current should go to In(I) formation than that indicated at the current densities reported here.

It has been reported (27, 28) that metallic indium anodes on electrochemical oxidation disintegrate to give a suspension of finely divided particles of indium metal. Straumanis (27) states that, at current densities greater than 70 ma/cm^2, such particles can be observed. Current densities used with metal anodes in this investigation were at least five times less than the observed lower limit for particulate formation. After oxidation, the electrodes used in this investigation were bright, and some faceting of the polycrystal rods could be seen, but no particles could be observed during or after dissolution.

The system In(0), In(I), and In(III) in acidic solutions where In(I) appears to have a finite chemical lifetime as well as a finite interfacial concentration should be an interesting system to study using one of the newer electrochemical techniques. An impedance method similar to that described by Sluyters-Rehback and Sluyters (29), or the method of faradaic rectification Section to be published in the June 1966 JOURNAL.

Manuscript received Feb. 10, 1965. This paper was presented at the Toronto Meeting, May 3-7, 1964.

Any discussion of this paper will appear in a Discussion Section to be published in the June 1966 JOURNAL.

REFERENCES

1. K. J. Vetter, "Electrochemical Kinetics," p. 376, Springer-Verlag, Berlin (1961).
2. J. O'M. Bockris and M. Enyo, *This Journal*, **109**, 48 (1962).
3. M. Enyo, Ph.D. Thesis, University of Pennsylvania, 1960.
4. V. V. Losev and A. I. Molodov, *Electrochim. Acta*, **6**, 81 (1962); V. V. Losev and A. I. Molodov, *Proc. Acad. Sci. U.S.S.R. Phys. Chem. Sect.* (English Transl.), **135**, 1203 (1960).
5. G. M. Budov and V. V. Losev, *Proc. Acad. Sci. U.S.S.R. Phys. Chem. Sect.* (English Transl.), **129**, 1113 (1959); G. M. Budov and V. V. Losev, *Russ. J. Phys. Chem.* (English Transl.), **37**, 784 (1963).
6. V. V. Losev and A. I. Molodov, *Proc. Acad. Sci. U.S.S.R. Phys. Chem. Sect.* (English Transl.), **130**, 1 (1960).
7. B. Lovreck and V. Markovac, *This Journal*, **109**, 727 (1962).
8. A. I. Busev, "Analytical Chemistry of Indium," Macmillan Co., New York (1962).
9. E. D. Moorhead and W. M. MacNevin, *Anal. Chem.*, **34**, 269 (1962).
10. D. Cozzi and S. Vivarelli, *Z. Elektrochem*, **57**, 408 (1953); D. Cozzi and S. Vivarelli, **58**, 907 (1954).
11. M. Bulnova, *Collection Czechoslav. Chem. Communs.*, **19**, 1123 (1954).
12. K. Z. Brainina, *Proc. Acad. Sci U.S.S.R. Phys. Chem. Sect.* (English Transl.), **130**, 87 (1960).
13. J. D. Corbett, *Inorg. Chem.*, **3**, 634 (1964); J. D. Corbett, *This Journal*, **109**, 1214 (1962).
14. T. Hurlen, T. Valand, and G. Lund, *Electrochim. Acta*, **9**, 1433 (1964).
15. T. Hurlen, *ibid.*, **9**, 1439 (1964).
16. P. Brouillet, I. Epelboin, and M. Fromet, *Compt. rend.*, **239**, 1795 (1954).
17. L. G. Hepler, Z Z. Hugus, Jr., and W. M. Latimer, *J. Am. Chem Soc.*, **75**, 5652 (1953).
18. L. W. Marple, Ph.D Thesis, Massachusetts Institute of Technology, 1960.
19. G. Biedermann and T. Wallin, *Acta Chem. Scand.*, **14**, 594 (1960).
20. R. E. Visco, *J. Phys. Chem.*, **69**, 202 (1965).
21. G. W. Vinal, "Storage Batteries," p. 155, John Wiley & Sons, Inc., New York (1955).
22. H. V. Malmstadt, C. G. Enke, and E. C. Toren, "Electronics for Scientists," p. 355, W. A. Benjamin, Inc., New York (1962).
23. I. M. Kolthoff and J. J. Lingane, "Polarography," Interscience Publishers, New York (1952).
24. I. Shain and K. J. Martin, *J. Phys. Chem.*, **65**, 254 (1961).
25. J. Butler and A. C. Makrides *Trans. Faraday Soc.*, **60**, 1664 (1964).
26. J. Heyrovsky, *Discussions Faraday Soc.*, **1**, 212 (1947).
27. M. Straumanis and R. Martin, *Z. anorg. Chem.*, **334**, 321 (1965).
28. A. Davidson and F. Jirik, *J. Am. Chem. Soc.*, **72**, 1700 (1950).
29. M. Sluyters-Rehback and J. H. Sluyters, *Rec. Trav. Chim.*, **82**, 535 (1963).

The Effect of Cathodic Prepolarization on Capacity Curves of Germanium Electrodes

Christof C. Krischer and Robert A. Osteryoung

North American Aviation Science Center, Thousand Oaks, California

ABSTRACT

Rapid potentiostatic capacity-potential measurements were carried out at Ge electrodes in solutions of pH 1, 7, and 12. Two distinct capacity curves were observed. If cathodic current flow was excluded, capacity-potential curves were measured which are in agreement with results reported in literature. The measuring parameters could be varied within a wide range without affecting the results. These capacity curves occur on an oxidized OH covered surface. Another capacity curve was measured by utilizing a galvanostatic pulse method in order to prepolarize the electrode cathodically prior to the measurement. The capacity curve measured with sufficient prepolarization is shifted 300 to 500 mv cathodic with respect to the curve measured in the absence of prepolarization. These curves correspond to the reduced surface.

The electrochemical behavior of germanium electrodes differs from that of metal electrodes because Ge is a semiconductor. As a consequence of the low electron and (or) hole concentrations there exists a space charge layer on the semiconductor side of the interface. The capacity of this space charge layer is up to three orders of magnitude smaller than the capacity of the Helmholtz double layer in concentrated electrolytes. Both capacitors are considered to be in series (1). The smaller capacitor of the semiconductor determines the measured capacitance of the interface.

The capacity of the space charge layer as a function of potential was calculated by Bohnenkamp and Engell (2) using the Poisson equation and a Boltzmann distribution of the carriers. A semilogarithmic plot of the capacity-potential curves gives V-shaped curves with a rounded minimum which occurs for intrinsic germanium at zero space charge potential difference or "flat band potential" (1). The capacity curves that were measured with a standard a-c bridge technique (2) were in poor agreement with the calculated curves. They were too broad and the minima were at higher capacity values than calculated. With the introduction of a fast pulse technique Brattain and Boddy (3) were able to measure capacity curves in agreement with theory.

It was found experimentally that the potential of the capacity minimum depends on the pH of the solution (2) as well as on the "history" of the electrode (3). Obviously the position of the flat band potential depends on the chemical properties of the surface. Detailed studies of the pH effect (4, 5) yielded the result that the capacity minimum shifts by —58 mv per pH unit at 25°C. This observation and other experimental evidence led to the assumption that the germanium surface is covered with a homopolar bound layer of OH groups (1). The dissociation of the OH groups was made responsible for the observed shift of the curves with pH. Hofmann-Perez and Gerischer (4) called it a "dissociation double layer." The second effect, the dependence of the capacity curves on the "history" of the electrode is reported by Brattain and Boddy in two papers (3, 5). The authors find that the higher the anodic current density prior to the measurement the more anodic was the potential of the minimum. The data (3) show that the potential shift of the capacity minimum is a little over 100 mv per decade of anodic current density, provided the current density does not exceed 50 $\mu a/cm^2$. Later, Boddy and Sundburg (6) published capacity curves which were obtained with a dynamic current sweep method. The minimum measured with a decreasing anodic current density was 180 mv more anodic than the one measured with increasing anodic current density.

The objective of this paper is to show that an electrochemical surface reaction rather than dipole rearrangements are responsible for changes in the capacity curves caused by various pretreatments. A galvanostatic pulse method, which is described elsewhere (7), is used for quantitative prepolarization.

Gerischer and Beck (8) showed that germanium is a corroding electrode. The process can be described by the corrosion theory of Wagner and Traud (9). According to these authors the corrosion process can be separated into two independent partial reactions, one anodic and the other cathodic. In the absence of an external applied potential both reactions proceed at the same rate which is characterized electrochemically in terms of the "corrosion current density." With an external polarizing circuit and a given large overvoltage, one of the reactions prevails and the other can be neglected. Both reactions become comparable in magnitude at external current densities which are close to the corrosion current density (9). It is felt that in the case of Ge electrodes the product of the cathodic partial reaction causes (*a*) the increase in capacity observed with steady-state measurements and (*b*) the cathodic shift and broadening of the capacity curves.

The experimental study of the influence of both partial reactions is possible because the capacity minimum occurs in the potential region of small anodic dissolution currents (6). In the first series of experiments reported here, the capacity potential curves at an anodically polarized electrode are examined with a potentiostatic sweep method (7). The capacity curves are measured dynamically under various conditions. Anodic polarization is, however, maintained throughout these capacity measurements. In a second series of experiments the influence of the cathodic partial reaction on the capacity-potential curves is studied. The electrode is kept at a potential of high anodic dissolution rate. Immediately prior to recording the capacity curve, a constant cathodic current of varying duration is impressed on the electrode. The charge consumption during the capacity measurement, where usually anodic current flows, is kept small by using a fast sweep. Therefore the state of the surface that was created by cathodic charging remains practically unchanged.

Experimental

The measurements were carried out in a cylindrical Pyrex glass cell. The counter electrode consisted of a platinum wire. All potentials are referred to the saturated calomel electrode. Purified argon served as inert gas atmosphere. Solutions were made up of triple distilled water and "reagent" purity chemicals. Na_2SO_4 served as supporting electrolyte, H_3BO_3, H_3PO_4, and

acetic acid, all 0.1M, served as buffer [Prideaux, Ward (10)]. The temperature was at ambient and was close to 25°C.

Germanium rotating disk electrodes were used. Cut from single crystal material in approximately <111> orientation, the Ge was soldered to a rod and imbedded in low melting polyethylene. The electrodes could be rotated from 0 to 3000 rpm.

Results

No Cathodic Prepolarization

Capacity-potential measurements.—In a first series of experiments method (C) of ref. (7) was employed. The germanium electrode is potentiostated at a steady-state potential where the electrode dissolves (E_{dc}). The capacity potential curve is measured by applying a cathodic sweep $E_s = E_{dc} - \nu t$, $\nu = dE/dt$ with superimposed short duration square wave pulses (E_r). In these experiments the transistor (7) was shorted out.

The pulse amplitude E_r was varied from 30 to 100 mv. Positive and negative pulses were used. The measured capacity potential curves were, within the limits of experimental error, the same.

The rate of potential change $\nu = dE/dt$ could be varied from 1 to 300 v/sec without changing the capacity potential curve if E_{dc} was not more than 200 mv anodic to the potential of the capacity minimum. The data are in good agreement with the calculated capacity curve (2), as can be seen in Fig. 1. If E_{dc} was chosen more anodic than the limit specified above, *i.e.*, at high dissolution current densities, best agreement with the calculated curves was obtained if ν was small ($\sim$ 1 v/sec). Higher values of ν yield a vertical shift of the capacity curves toward larger capacity values.

Contrary to the data of Brattain and Boddy (3) results presented here indicate that the potential of the capacity minimum is within wide limits independent of the time required to measure the capacity curve. (Some reservation must be attached to this comparison, however, as the time scales in their work and this work are quite different.) The potential of the minimum in these buffered solutions does not depend on the anodic state of polarization that exists immediately prior to the measurement.

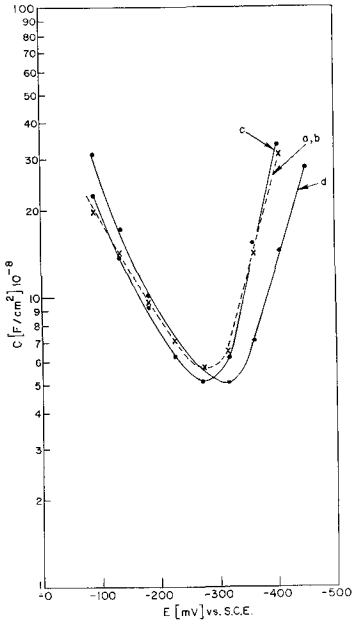

Fig. 1. Dynamically measured capacity potential curves at 10 ohm-cm p-Ge in 0.5 M Na_2SO_4, 0.1M buffer pH 7, unstirred. Curve a (dashed) was measured with —1 v/sec (cathodic going); Curve b which coincides with curve a was measured with a +1 v/sec, anodic going sweep which was started at —500 mv, immediately after the electrode had been potentiostated anodically; curve c was measured like b, but the electrode rested at 0 current for 3.3 sec before sweeping; curve d was measured like b but without the use of the transistor; therefore a short cathodic current spike had prepolarized the electrode. The curves agree favorably with the calculated capacity curve (2). Curve d matches it exactly.

The measurement of the capacity-potential curve with an anodic sweep with approximately the same "history" as the measurements outlined above is described as method A_2 in ref. (7). With the cell potentiostated anodically at E_{dc}, as above, a negative step, $-E_{st}$, makes the potential slightly negative to the potential of the capacity minimum and the capacity potential curve is measured with a positive sweep: $E_s = E_{dc} - E_{st} + \nu t$.

From Fig. 1d it is seen that the capacity curve obtained in this way is shifted 50 mv cathodic with respect to the one obtained employing a cathodic sweep. The corresponding current potential trace, however, showed that there was a short cathodic current spike before the minimum was reached.

To see if exclusion of cathodic charge flow before reaching the minimum could yield the same capacity curve as obtained with the cathodic sweep, method A_1 of ref. (7) was used. A transistor with its reverse bias in the cathodic direction is placed in series with the cell. The cathodic current flow is then, at zero base current, limited to the value of the reverse limiting current which is $\sim$ 1 μa. To make the resistance of the transistor small during the sweep, the gate of the "delayed sweep generator" of the oscilloscope also serves to inject a base current, via E_o. For details see ref. (7). Curve b is obtained in this fashion. As this method excludes major cathodic current flow prior to the sweep we investigated the effect of time that the electrode rests at $\sim$ 0 current prior to the capacity measuring sweep. Curve c is measured after the electrode had been kept for 3.3 sec at $\sim$ 0 current. Coincidence of curves a and b shows that changes of the potential of the minimum during the sweep are negligible. Comparison of curves b and c shows that no significant changes of the surface properties took place when the electrode rested for 3.3 sec at $\sim$ 0 current prior to the sweep.

Cathodic Prepolarization

Charging curves.—In these experiments a transistor was placed in series with the cell. Superposition of a sufficiently high cathodic step $-E_p$ on E_{dc} switched the transistor into its reverse limiting current region [see ref. (7)]. A steady base current was supplied to the transistor via a battery potentiometer. The cathodic limiting current which prepolarizes the electrode during the interval when $-E_p$ is applied could be varied by changing the magnitude of this impressed base current. The consequence of the negative prepolarizing step $-E_p$ is the immediate flow of a constant cathodic current, *i.e.*, a current step. During this galvanostatic period, the potential of the indicator electrode, which is measured differentially between the reference electrode (output of the follower) and the emitter of the transistor, (Fig. 5) of ref. (7), is steadily increasing in the cathodic direction.

In the initial phase of the current step, the increase in cathodic overvoltage is very large. The change in potential at longer times is much less pronounced. Figure 2 gives an example of a charging process measured in alkaline solutions. The individual curves are recorded with various sweep rates of the oscilloscopic trace. As the sweep rate increments are chosen to differ by a factor of 10, intersections of the potential time curves with parallels to the ordinate represent logarithmic time intervals of the charging curve. In Fig. 3, the intersections with parallels to the ordinate at div 1 and 4 are plotted against the corresponding time at which the potential is read. The points of the resulting plot of E *vs.* log t scatter around a straight line with the slope of —100 mv per decade of time.

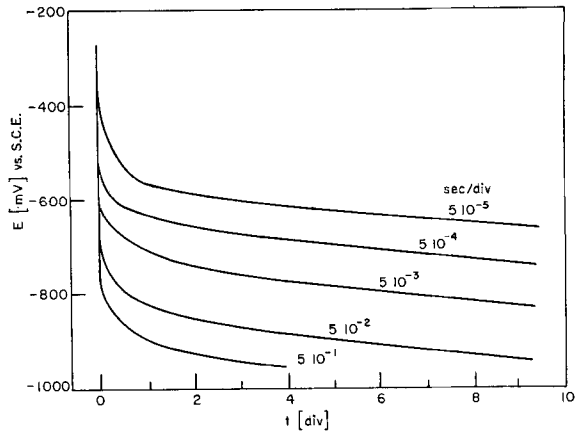

Fig. 2. Buildup of cathodic potential by application of a 0.36 ma/cm² cathodic current step at a 10 ohm-cm n-Ge electrode in 0.5M Na_2SO_4, 0.1M buffer pH 12 solution. Before the step was applied anodic steady-state current of 0.36 ma/cm² was flowing. The corresponding sweep rate of the oscilloscope is marked at each individual curve.

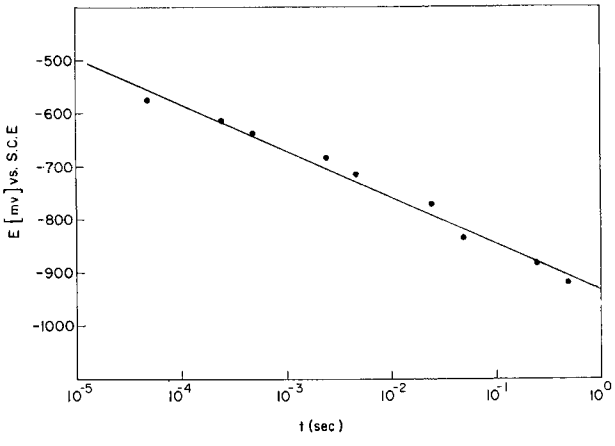

Fig. 3. Potential at div 1 and 4 of Fig. 2 plotted vs. the corresponding time.

Part of the scatter may be caused by the fact that for each individual curve the charging process had to be repeated. This initial E-log t behavior was observed in all charging experiments, both at n- and p-type germanium, in alkaline as well as in neutral and acid solutions. The slope of the E-log t curves (studied in some detail in alkaline solutions at p-Ge) was constant for a given current density. If, however, the current density was varied, the slope also varied. The slope [mv/decade] increased somewhat with increasing current density.

Whereas the potential shift in the beginning of the charging process followed a linear E-log t relationship in solutions of all pH values that were studied, a marked difference in the curves at longer times could be observed at different pH values: in alkaline solutions the curves showed no break (Fig. 2) whereas in acid solutions the curves contained a break, both at n- and at p-Ge. Figure 4, lower curve, gives a typical example. It is seen that the break occurs after the passage of $\sim$ 400 μa sec/cm². To investigate the nature of the break in the cathodic charging curve further, the current density was varied. The time required to reach the break will be called a transition time τ. It was seen that the product of $i\tau$, where i is the current density, was a constant of approximately 400 μa sec/cm². Rotating the electrode with 3000 rpm brought only a slight change in shape of the charging curve which may be attributed to traces of oxygen contamination. These results indicate that the transition time observed in neutral and acid solutions is not caused

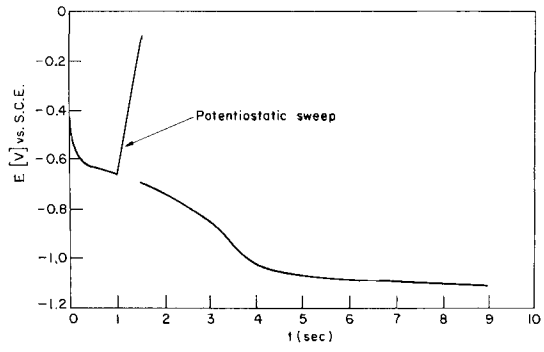

Fig. 4. Potential time behavior for a galvanostatic step (lower curve is the charging curve), interrupted by a potentiostatic sweep (straight line). The electrode was 10 ohm-cm p-Ge in 0.5M Na_2SO_4, 0.1M buffer pH 1. It was rotated at 650 rpm; cathodic current density 0.14 ma/cm²; sweep +1.2 v/sec (anodic going); preceding anodic current density by 0.14 ma/cm².

by exhaustion of a diffusing species. If the latter was the case, the product of $i\tau$ at various values of i should not be a constant [Delahay (11)] and it should be sensitive to stirring. The data presented here are in quantitative agreement with the findings of Turner (12), who attributed the charge required to reach the break to the reduction of the surface hydroxide to a surface hydride.

Capacity-potential measurements.—Capacity measurements with varying cathodic prepolarization were carried out as follows [method PA of ref. (7)]: starting from anodic potentials at which the electrode is rapidly dissolving the cathodic step, $-E_p$, causes a constant cathodic current flow across the electrode interface. At any desired time after the beginning of the pulse, $-E_p$, (which caused a constant current to flow) a positive pulse E_{st} is applied which adjusts the potential to the value that was reached during the charging process. The simultaneous initiation of the anodic sweep $E_s = dE/dt$ (with superimposed short duration pulses) provides a means of measuring the capacity curve in that potential region. Simultaneous injection of a constant base current minimizes the error in the capacity value that is introduced by the transistor (7). Figure 4 represents a typical potential-

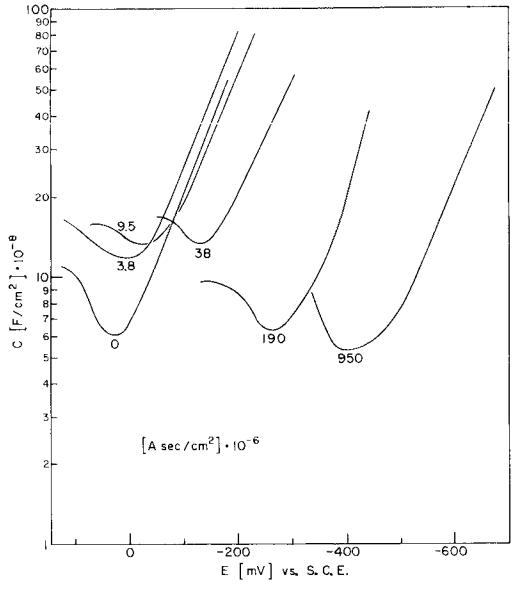

Fig. 5. Dynamically measured capacity potential curves at 40 ohm-cm n-Ge in 0.5M Na_2SO_4, 0.1M buffer pH 1. Electrode was rotated at 900 rpm. Prepolarizing charges are marked at the curves. The sweeps, 100 v/sec, anodic going, were started at the potential of the charging curve.

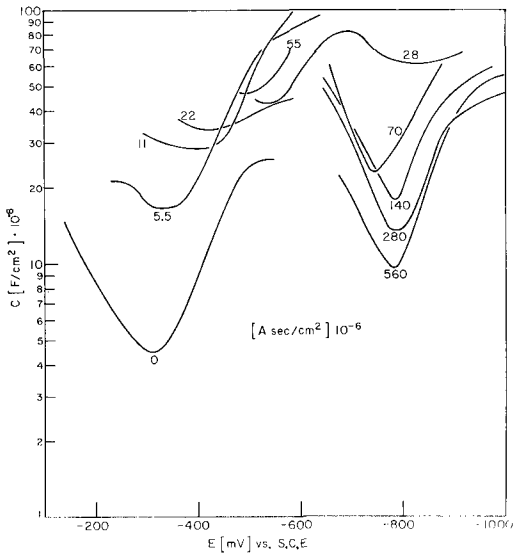

Fig. 6. Dynamically measured capacity potential curves at 10 ohm-cm p-Ge in 0.5M Na_4SO_2, 0.1M buffer pH 7. Electrode was rotated at 900 rpm; sweep, 100 v/sec (anodic going); starting potential coincided with charging curve. Cathodic prepolarization coulombs are marked in figure.

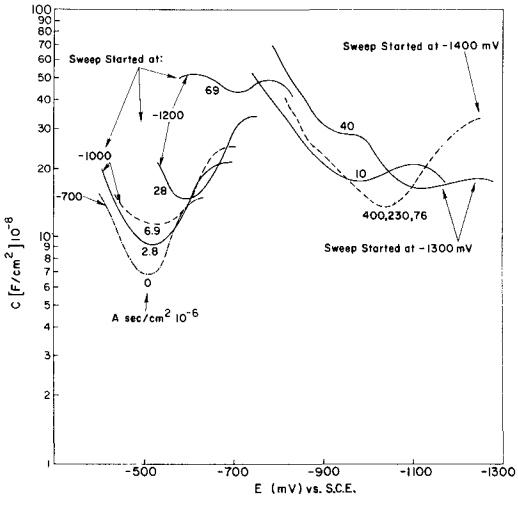

Fig. 7. Dynamically measured capacity potential curves at 10 ohm-cm p-Ge in 0.5M Na_2SO_4 0.1M buffer pH 12, unstirred. Curves to the left +7.2 v/sec (anodic going); dashed curve to the left +2.5 v/sec; solid curves to the right +7 v/sec. Cathodic prepolarization and starting potential are marked in figure.

time trace of these experiments (the short duration pulses cannot be resolved). For the charging curve (lower curve) the electrode is polarized galvanostatically whereas during the sweep the operation is potentiostatic.

Capacity-potential curves obtained in this manner in solutions of pH 1, 7, and 12 are shown in Fig. 5, 6, and 7, respectively. It is seen that at small prepolarization the minimum of capacity increases with increasing prepolarizing charge and the potential of the minimum shifts cathodic. For many of the curves the shift is a little over 100 mv per decade of prepolarizing charge. A maximum increase in capacity is observed at prepolarizations of 70 ± 30 μa sec/cm^2. At sufficiently large prepolarization the minimum decreases again.

Further experiments were carried out in order to examine other parameters. In cases of prepolarizations in the order of 50 μa sec/cm^2 and high enough sweep amplitudes two shallow minima could be observed on one current-potential trace. The corresponding current-potential curves, however, contained characteristic transients indicating that the surface was highly unstable. The current potential curves that correspond to prepolarizations larger than 100 μa sec/cm^2 did not have these transients and were quite reproducible.

The choice of the sweep starting potential E_{st} was of prime importance. If E_{st} is properly chosen, the current level stays approximately constant until the minimum is reached. If E_{st} deviates from this value in the cathodic or anodic direction, a current spike of the same polarity (cathodic or anodic) is observed. This current spike tends to change the capacity curve in the same way as it was described in the experiments with no prepolarization.

Provided E_{st} is properly chosen the sweep rate, $v = dE/dt$, could be varied from 1 to 100 v/sec without a significant change of the capacity curves. Sweep rates larger than 100 v/sec were not employed because the current potential curve showed rapid transients which prevented the evaluation of the capacity curves from the superimposed, short duration current transients that were caused by the pulses (7). Integration of the current as a function of time during such fast sweeps yielded charges in the order of 1 μa sec/cm^2. In most cases this charge represents only a very small fraction of the prepolarizing charge.

The capacity measurement with a cathodic going sweep [method PC of ref. (7)] was studied briefly. This method is less convenient than the one employing an anodic sweep because the exponential nature of the current potential curve in the region of the capacity minimum makes the choice of E_{st} critical. Qualitatively, the same influence of the prepolarization is observed.

Variation of E_{dc} in such a manner that the steady-state anodic dissolution current varied from 700 to 35 μa/cm^2 had no influence on the capacity potential curves.

Discussion

The capacity measurements without cathodic prepolarization showed that when cathodic current flow is excluded and the measurement is carried out rapidly the minimum of capacity lies at one particular potential. The sweep rate and sweep direction may be varied within a wide range without causing a change of the capacity potential curves. In the measurements of Brattain and Boddy (3) the potential of the capacity minimum shifted anodic with increasing steady-state current density prior to the measurement. In the data of ref. (3), Fig. 8, a narrowing of the curves (toward those calculated) takes place coupled with an anodic shift of the capacity minimum. This may be taken as an indication that their method of measurement is quasistationary. The time required to determine an individual experimental point was sufficiently long so

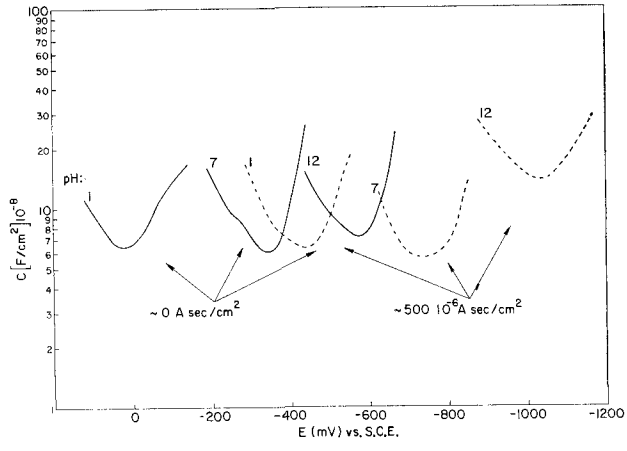

Fig. 8. Collection of dynamically measured capacity potential curves at 10 ohm-cm p-Ge in 0.5M Na_2SO_4, 0.1M buffer, pH marked at curves. Solid curves are measured without cathodic prepolarization, dashed curves after cathodic pretreatment of approximately 500 μcoulomb cm^2.

that at small preceding steady-state current densities the cathodic partial reaction effected the results, as will be discussed below.

Measurements with cathodic pretreatment showed that small amounts of cathodic charge are sufficient to change the potential of the minimum as well as the magnitude of the capacity potential curve. From Fig. 8 it appears that the Ge surface can exist in two different states. The anodic state is well-known and extensively studied (1). The other, the cathodic state of the surface, lies 300 to 500 mv more negative and can be obtained only after considerable cathodic charge has polarized the electrode. The capacity potential curves of the two different surfaces (they may be called oxidized and reduced surfaces) fit, at least in acid solutions and after certain prepolarizations, closely the curves which were calculated on the basis of the Poisson-Boltzmann equation (2).

In the equivalent circuit for a metal (or semiconductor) electrolyte interface a nonohmic resistance, R_p, that corresponds to the faradaic current must be considered to be in parallel with the interface capacitor (11). The applied voltage causes both a faradaic current flow and changes of the space charge capacitor. The occurrence of two different capacity curves at Ge electrodes hence implies that there should also be two d-c current voltage curves. This is indeed what is found experimentally. Figure 9 gives an example of a current voltage curve obtained with a continuous running triangular wave. For comparison, the two capacity curves are also shown in Fig. 9. [Gobrecht and Meinhardt *et al.* reported similar dynamic current voltage curves (13). Their publication, however, does not contain any capacity curves. In another series of papers (14) steady-state capacity curves are published that have more than one minimum of capacity. The authors, however, did not use the result of the dynamically measured current voltage curves to explain the occurrence of more than one capacity minimum in the steady-state measurements.]

The capacity curves that lie in the potential region between the curves measured at the oxidized and reduced surface are characterized by considerably increased capacity minima. An increase in capacity over the calculated value generally is attributed to surface states (1). In the electrical equivalent circuit for the Ge interface the surface states are represented by an additional capacitor in parallel with the space charge capacitor (1). From Fig. 5 to 7 it appears that prepolarization with small amounts of cathodic charge of an OH-covered (oxidized) surface act as surface states. At charges between 70 ± 30 μa sec/cm^2, which corresponds to somewhat less than one unit charge per

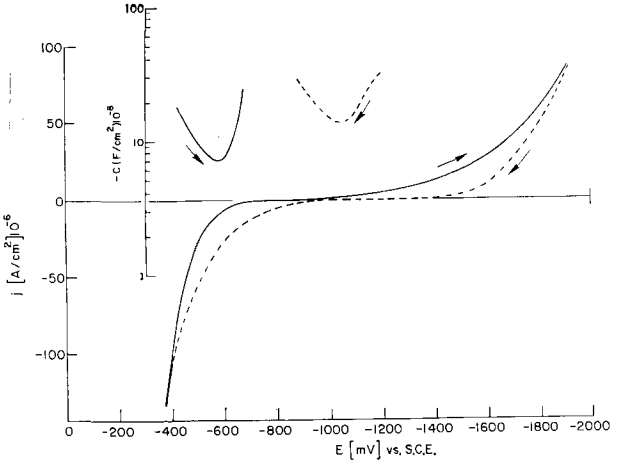

Fig. 9. Dynamically measured current potential curve at 10 ohm-p-Ge in 0.5M Na_2SO_4, 0.1 M buffer pH 12. Free running triangular wave of ±0.73 v/sec; for comparison, the figure contains the simultaneously measured capacity potential curves.

surface atom (12) the additional capacitor has its maximum value. On the other hand, deficiencies from the cathodic charge required to reach the totally reduced surface (hydride surface in acid solutions) also form surface states, as can be seen from the family of cathodic curves in Fig. 6. The experimental results would indicate that at small prepolarizations chemisorbed hydrogen creates surface states on the OH-covered surface whereas at larger prepolarizations empty hydrogen sites act as surface states.

The charging experiments show that in all solutions in the initial phase of the charging process the potential is a linear function of the logarithm of the time. Frumkin (15) also observed logarithmic potential changes with time in connection with his studies of the hydrogen ion discharge at metal electrodes. He showed that this logarithmic relationship is caused by the charging of the double layer or a chemical capacitor (at Pd) via an activation controlled current path. Even though the electrochemical properties of Ge differ considerably from that of typical metal electrodes, the hydrogen overvoltage at Ge is quite similar (1). The experimentally observed slope of the E-log t plot for the charging curve at Ge is 100 mv per decade of time. This is close to the usual values for the slope of an activation controlled current voltage curve (slope of a "Tafel" plot), which holds for both metal and Ge electrodes (1).

The potential shift of the capacity curves with increasing prepolarization indicates that the reaction product of the faradaic reaction is stored at the surface and determines the potential. Without this assumption one could not explain the increase in the value of the capacity at the minimum and the cathodic shift even though the prepolarization has ceased.

The charging curves at longer times, however, give some evidence that the faradaic reactions are different in acid and alkaline solutions. The data in neutral solutions seem to have an intermediate position. In acid solutions Ge hydride is the reaction product (12). The reaction after the break represents hydrogen evolution (12). The capacity curve measured at the hydride surface (Fig. 5) is very close to the calculated curve (compare Fig. 1). In alkaline solutions no break in the charging curve is observed. This can be interpreted in two ways: (*a*) the two possible reactions, surface oxide reduction and water electrolysis occur simultaneously, or (b) the suface hydroxide is not reduced and only water electrolysis takes place. Since the OH groups at the Ge surface are partially dissociated (4, 5) one can attribute some stability to the negative surface in so far as the negative charge of the O^- group may be shared in a mesomeric and tautomeric manner with the germanium and the undissociated OH groups. The arrangement would be analogous to the anion of carboxylic acids. Those anions, too, are in alkaline solutions much more difficult to reduce than in acid solutions. In case (*a*) and (*b*), however, hydrogen ions (or water) are discharged. The increase in the capacity minimum indicates the presence of surface states which may be adsorbed hydrogen. The shift of the capacity curve proves that a potential determining product is stored at the surface.

A recent paper by Hurd and Hackerman (16) involving capacity measurements at the silicon/electrolyte interface has several features in general agreement with the work reported here. There are, however, marked differences in the electrochemical behavior of silicon and germanium. A direct comparison of the two papers is therefore not justified.

The anomalies observed in previously published capacity measurements can now be given an electrochemical explanation.

1. Steady-state measurements yielded capacity curves which were too broad and the minimum of capacity too large. The minimum of capacity lies in a potential region of small current densities, compare Fig. 9. In this region, the two partial reactions of the

corroding Ge electrode are comparable in magnitude. Due to the tendency of Ge to store the charge of the cathodic partial reaction, one therefore observes a cathodic potential shift and an increase of the differential capacity if longer times are required to measure the capacity curves. As the cathodic charging that is responsible for the shift of the curves proceeds during the measurements, the curves appear broader and the minimum larger than calculated (2). Brattain and Boddy (3) were the first authors to publish capacity curves that were in agreement with theory. These authors measured the capacity curves with a pulse method and with an anodic pretreatment of the electrode. The reason for the good agreement of the experimental and calculated curves measured by these authors and in this publication, Fig. 1, is that the dissolution removes the cathodic charge that is generally stored on the electrode if the electrode is allowed to rest a certain length of time at the rest potential. The pulsed capacity measurements are fast enough to exclude storage of cathodic charge.

2. The storage of cathodic charge created by corrosion also explains the shift in the potential of the minimum of the capacity at the dynamically measured capacity curves reported by Boddy and Sundburg (6).

3. In previous investigations of the pH dependence of the potential of the minimum of capacity, it was found that at the extremes of pH the minimum was larger and shifted cathodic with respect to the values that one would expect from the pH dependence observed at intermediate pH values (5) Fig. 4 and (4) Fig. 5. Due to the coupling of anodic and cathodic partial reaction of a corroding electrode (9) both reactions will proceed faster at extremes of pH. In extreme alkaline solutions germanium dissolves readily. The rate of dissolution at a given overvoltage is higher in alkaline than in neutral and acid solutions (17). The anodic partial reaction is the driving force. On the other hand, the hydrogen ion discharge will proceed easily in acid solutions due to the abundance of hydrogen ion. The storage of the reaction product of the cathodic partial reaction causes potential shift and increase of the minimum of the capacity.

Acknowledgment

The authors thank Drs. D. O. Raleigh, K. B. Oldham, and H. W. Wiedersich for many helpful discussions.

Manuscript received March 9, 1965; revised manuscript received June 1, 1965.

Any discussion of this paper will appear in a Discussion Section to be published in the June 1966 JOURNAL.

REFERENCES

1. H. Gerischer in "Advances in Electrochemistry and Electrochemical Engineering," P. Delahay, Editor, Interscience Publishers, New York (1962).
2. K. Bohnenkamp and H. J. Engell, *Z. Elektrochem.*, **61**, 1184 (1957).
3. W. H. Brattain and P. J. Boddy, *This Journal*, **109**, 574 (1962).
4. M. Hofman-Perez and H. Gerischer, *Z. Electrochem.*, **65**, 771 (1961).
5. P. J. Boddy and W. H. Brattain, *This Journal*, **110**, 570 (1963)
6. P. J. Boddy and W. J. Sundburg, *ibid.*, **110**, 1170 (1963).
7. C. C. Krischer and R. A. Osteryoung, *ibid.*, **112**, 735 (1965).
8. H. Gerischer and F. Beck, *Z. Physik. Chem., N. F.*, **23**, 113 (1960).
9 C. Wagner and W. Traud, *Z. Elektrochem.*, **44**, 391 (1938).
10. E. B. R. Prideaux and A. T. Ward, *J. Chem. Soc. (London)*, **125**, 426 (1924).
11. P. Delahay, "New Instrumental Methods in Electrochemistry," Interscience Publishers, New York (1954).
12. D. R. Turner, *This Journal*, **103**, 252 (1956).
13. H. Gobrecht, O. Meinhardt, and M. Lerche. *Ber.*, **67**, 486 (1963).
14. H. Gobrecht, O. Meinhardt, and B. Reinicke, *ibid.*, **67**, 142, 151, 493 (1963).
15. A. Frumkin, *Acta Physicochim. USSR*, **18**, 123 (1943), *ibid.*, **19**, 1 (1944).
16. R. M. Hurd and N. Hackerman, *Electrochim. Acta.* **9**, 1633 (1964).
17. C. C. Krischer, Dissertation, T. H. Stuttgart (1963).

Instrumentation for the Measurement of the Electrical Double Layer Capacitance at Solid Electrodes

Louis Ramaley[1] and C. G. Enke[2]

Frick Laboratory, Princeton University, Princeton, New Jersey

ABSTRACT

Two methods of measurement of double layer capacitance used by the authors are described. One method, involving the application of a rectangular current waveform, is convenient for obtaining qualitative information on the frequency dispersion of the double layer capacitance. The other, involving the application of a small sinusoidally varying potential of constant amplitude, is capable of an accurate and very rapid determination of capacitance over a wide potential range.

The double layer capacitance present at a metal electrode-electrolyte interface is of great interest because of its relation to the chemical and physical properties of the interface. The measurement of this capacitance has presented certain problems due to its nonideality, the effect of solution components and contaminants on it, and the presence of the solution resistance connected with it.

Several different methods of capacitance measurement have been employed. Several authors have used direct current or pulse current charging methods (1-5). Armstrong and Butler (6) proposed the method of current interruption for measurement during a faradaic reaction. Wagner (7) has used a potential step technique. Several authors have applied a controlled sinusoidal potential or current waveform in capacitance studies (8-10). An impedance bridge is often used when high accuracy is desired (11-13).

In general the constant current, current pulse, and potential step methods measure the average capacitance over the region of potential change. Average capacitance may be defined as $C_a = (q_2-q_1)/(E_2-E_1) = \Delta q/\Delta E$. The differential capacitance is obtained from

[1] Present address: Department of Chemistry, University of Arizona, Tucson, Arizona.

[2] Alfred P. Sloan Research Fellow.

the slope of the potential-time curve in the controlled current methods. All the techniques employing sinusoidal waveforms measure the differential capacitance directly if the amplitude of the waveform is kept small.

Capacitance measurements on solid electrodes are complicated by the fact that the electrode surface can become contaminated rapidly with an adsorbed impurity and by the fact that the actual electrode area is not reproducible or exactly measurable. Thus a measurement technique of high accuracy and long measurement time, such as the impedance bridge, probably would not be a good choice. Since the differential capacitance is usually the parameter of interest, a method of direct measurement would be preferred.

The use of a sinusoidal potential of constant amplitude as described below is capable of reasonable accuracy and high measurement speed. In high resistance solutions or for qualitative data on frequency dispersion, the rectangular current pulse technique described below is useful.

Measurements Using a Rectangular Current Waveform

Theory.—In the absence of a faradaic reaction the portion of an electrochemical cell between the reference electrode (or the tip of the Luggin capillary leading to the reference compartment) and the test electrode may be thought of as a resistor in series with a capacitor. The resistor corresponds to the solution resistance and the capacitor to the electrode capacitance. If a current pulse of constant amplitude I is applied through this series network, at time $t = 0$ a discontinuity in the potential across the network will appear corresponding to the IR drop across the resistor. At times greater than $t = 0$ the potential will be a linear function of time according to

$$E = IR_sA + it/C_d \qquad [1]$$

If the current is reversed in sign but held constant in magnitude when the potential reaches E_1, another discontinuity occurs and the slope of the potential reverses. If the current is again reversed at a potential E_2, the same discontinuity appears and the slope of the potential equals the original slope. A triangular shaped waveform as shown in Fig. 1 results. The average capacitance is calculated using

$$C_a = i(t_2 - t_1)/(E_2 - E_1) \qquad [2]$$

where the potential discontinuity due to IR drop is not included in either E_2 or E_1. The differential capacitance is calculated using

$$C_d = idt/dE \qquad [3]$$

The double layer capacitance itself is nonideal, since it is dependent on electrode potential. The change of capacitance with potential is quite gradual in most potential regions in the absence of a strongly adsorbed material. Thus capacitance may be considered independent of electrode potential if small potential increments are used in the measurements.

Finally, nonideality may be caused by a dependence of electrode capacitance on frequency. The curvature imparted to the potential-time waveform by this effect may be explained in the following way: A current pulse may be considered to be a superimposition of sinusoidal currents of different frequencies. The higher frequencies may be looked upon as having the largest effect at the beginning of the pulse and the lower frequencies become more prominent as the pulse lengthens. A change in capacitance with frequency will thus cause a change in the slope of the potential-time waveform during the duration of the pulse.

Elimination of the other causes of nonideality allows a qualitative but extremely rapid determination of the frequency dependence of the double layer capacitance. A study of this dispersion of capacitance may be carried out as a function of potential or time of electrode contact with solution. As a general method of capacitance measurement this technique suffers from inaccuracies in determination of the slope of the potential-time curve. It is reasonably rapid, though not as rapid as the other technique to be described. It does offer the advantage of direct subtraction of the effect of solution resistance in determination of the average capacitance and elimination of this effect on differential capacitance calculation. This can be quite important in high resistance solutions.

Operation.—The block diagram of the apparatus is shown in Fig. 2. Amplifier SF is a stabilized voltage follower and amplifier SX is a stabilized operational amplifier. George A. Philbrick K2-X and K2-P amplifiers were used throughout as the operational units. The voltage follower matches the impedance of the reference electrode to that of the measuring device. Amplifier SX maintains the test electrode at ground potential and adjusts the potential of the counter electrode so that all the current flowing into the summing point of the amplifier flows through the cell.

The reversing current generator RCG supplies the pulses of constant current to the summing point of amplifier SX. The signal that causes reversal of the current is fed into RCG from SF. The wiring diagram for RCG is shown in Fig. 3. The MOD. X amplifier is the same as a G. A. Philbrick K2-X except that a 22K 2W resistor has been placed in the plate circuit of the output cathode follower. This prevents dam-

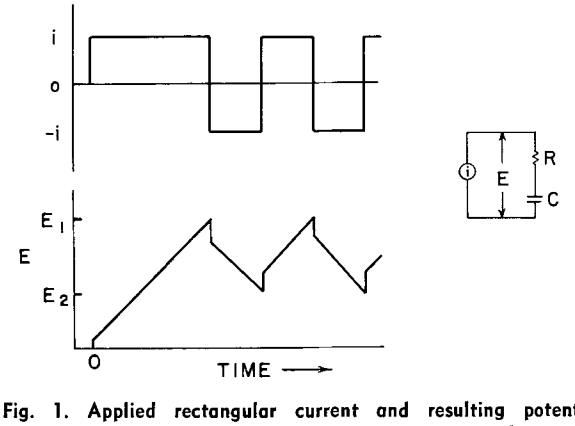

Fig. 1. Applied rectangular current and resulting potential waveform across a series resistance-capacitance network.

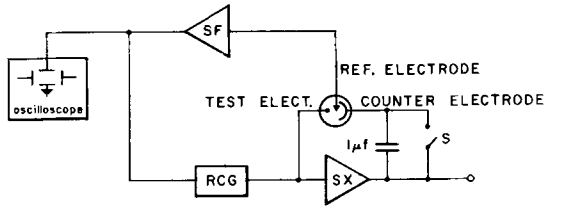

Fig. 2. Block diagram of the apparatus for capacitance measurement with a rectangular current.

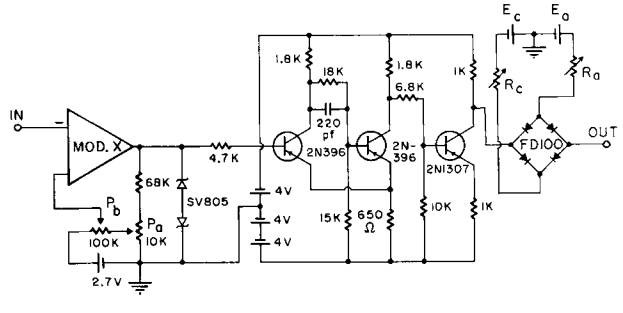

Fig. 3. Wiring diagram of the reversing current generator (RCG).

age to the 6AN8 output tube of the amplifier by preventing an excessive amount of current from flowing through the SV805 zener diodes. A schmidt trigger consisting of the 2N396 transistors squares the output waveform of the MOD. X amplifier. The 2N1307 transistor is an inverter which drives the diode bridge which in turn supplies the current pulses to the cell. The cathodic current is determined by the values of R_c and E_c, the anodic current by R_a and E_a. These values may be varied over a wide range as long as R_c and R_a are much larger than the forward resistance of the diodes, and the current capabilities of amplifier SX and transistor 2N1307 are not exceeded. The current capabilities may be altered by changing the amplifier or the transistor. The potentials, E_1 and E_2, at which the current reverses are determined by the settings of the potentiometers P_a and P_b. The setting of P_a determines the waveform amplitude $(E_1 - E_2)$ and the setting of P_b determines the average potential of the waveform ($E_{avg} = [E_1 + E_2]/2$).

The 1 μf capacitor in the circuit of Fig. 2 detects the presence of a faradaic current flowing in the cell. If no charge crosses the electrode-solution interface, no long term net current will be observed. A faradaic reaction will cause a net direct current. If switch S is open, the direct current must charge the 1 μf capacitor. The presence of such a current is detected by a long term change in the output potential of amplifier SX.

The circuit as described has a current capability of 1 ma and a frequency limit of about 1000 cps (cycles per second). The minimum amplitude $(E_1 - E_2)$ attainable is about 20 mv at 1000 cps and depends to some extent on the cell resistance (or cell geometry) and the frequency of measurement, decreasing somewhat as the frequency decreases. Others have applied square wave currents to capacitance determination (2, 3). The mechanics of the method presented here differs somewhat from the previously reported methods. These methods use a square wave generator to supply symmetrical square current pulses to the test electrode and an auxiliary means to determine the potential of the test electrode. The repetition rate of the wave is determined by the square wave generator and the amplitude of the observed potential-time waveform is determined by the capacitance and resistance of the cell.

The reversing current generator described above supplies the current alternations and also determines the electrode potential. The amplitude of the waveform is determined by the generator, and the repetition rate of the waveform is a function of the cell resistance and capacitance. It is sometimes advantageous to be able to carry out all measurements over the same potential span $(E_1 - E_2)$. The reversing current generator has no low frequency limit, as do ordinary square wave generators, and the current output is genuinely constant and can be made as large as desired by suitable choice of the electronic components. Square wave generators are usually limited to low currents, the lower the current, the more accurate the current control. However, the performance of square wave generators at very high frequencies is superior to that of the generator described above.

Results.—A typical waveform obtained with the reversing current generator is shown in Fig. 4. The results obtained using this method on silver electrodes are published in another article (14).

Use in other areas.—Application of a rectangular current pulse waveform has been discussed with regard to obtaining information on the double layer capacitance. It may be used more widely to obtain information on any process effected by a cyclic reversal of current. For example the circuit in Fig. 2 could be readily used to obtain data on electrochemical

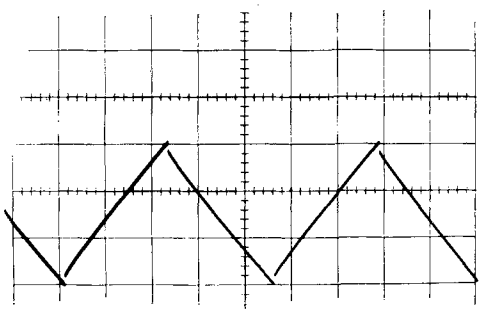

Fig. 4. Potential-time waveform obtained at a silver electrode in molar sodium perchlorate solution. Average potential, minus 340 mv vs. NHE; potential sensitivity, 10 mv/cm; sweep speed 1 ms/cm; current density, 1.7 ma/sq cm.

reactions by cyclic chromopotentiometry (15-17). Herman and Bard (15) describe a circuit for a rectangular current wave generator which employs mechanical switching. The circuit of the generator described above employs electronic switching and is capable of smoother and faster operation.

Measurements Using a Controlled Potential and Constant Frequency

Theory.—If a small sinusoidal potential of constant amplitude is applied across the electrode-solution interface and the sinusoidal current and phase angle are measured, the double layer capacitance can be calculated from

$$C_d = \left(\frac{I_{ac}}{2\pi f A E_{ac}}\right)\sqrt{1/\tan^2\phi + 1} \qquad [4]$$

If the solution resistance is quite small compared to the double layer impedance, $1/\tan^2\phi$ will be small compared to one and Eq. [4] simplifies to

$$C_d = I_{ac}/2\pi f A E_{ac} \qquad [5]$$

The phase angle may be $-76°$ ($-90°$ represents pure capacitive reactance) before a 3% error is made by using the simplified equation.

When Eq. [5] does not apply, the sinusoidal current and phase angle may be measured at one potential and used to calculate the cell resistance R_s. This value of R_s may then be used to calculate the double layer capacitance at all other potentials according to

$$C_d = \frac{1}{2\pi f A}\left[\left(\frac{E_{ac}}{I_{ac}}\right) - R_s^2\right]^{-1/2} \qquad [6]$$

This eliminates the necessity of determining the phase angle at every measurement potential.

An a-c voltmeter or oscilloscope may be used to detect the sinusoidal current directly. The oscilloscope or phase angle meter can be used to determine the phase angle. The sinusoidal current may be rectified and recorded by a servo recorder.

If the sinusoidal potential is superimposed on a linear potential sweep, the capacitance as a function of potential may be obtained. The use of an oscilloscope as the readout device enables sweep speeds of a volt per second or more to be achieved, allowing very rapid determinations of capacitance to be carried out. The linear potential sweep may be cycled between two potential limits, thus providing a recording of capacitance as a function of both potential and time. This technique has been applied by Breiter (10) to double layer measurements on platinum.

This method may be employed in capacitance measurements at an electrode at which a faradaic reaction is proceeding if the measurement frequency is high and the faradaic reaction is kinetically slow.

Operation.—Several types of instrumentation are available for this particular technique. Walker *et al.*

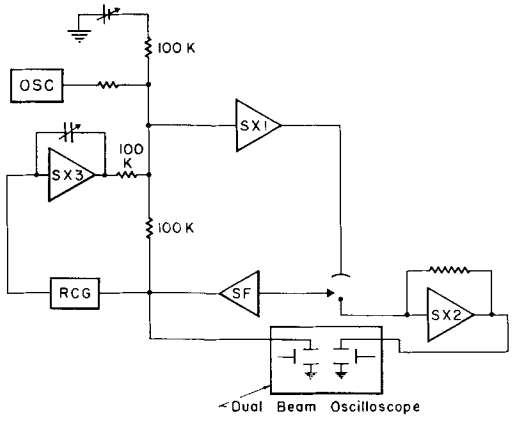

Fig. 5. Block diagram of the apparatus for capacitance measurement with a sinusoidal potential of controlled amplitude and frequency.

(18) used a modified d-c recording polarograph to perform a-c voltammetry at solid electrodes. The sweep speed of this instrument is limited by the polarograph. Breiter (10) replaced the polarograph with an electronic triangular wave generator and oscilloscope, thus greatly increasing the sweep speed.

The circuit used by the authors is shown in Fig. 5. It differs from those previously mentioned in the same way a potentiostatic polarograph differs from an ordinary or two electrode polarograph, thus eliminating or reducing the effect of solution resistance in the same way the potentiostatic polarograph reduces the effect of solution resistance. The circuit is similar to that used by Smith (19) for a-c polarography.

Amplifier SX1 establishes the required potential between the reference electrode and test electrode and amplifier SX2 holds the test electrode at ground potential and provides an output potential proportional to the current through the cell. OSC represents a sine wave generator and RCG and amplifier SX3 combine to provide a triangular sweep generator. The sinusoidal cell current and the potential difference between the test and reference electrodes are displayed simultaneously on a dual beam oscilloscope. A typical display is shown in Fig. 6. The envelope represents the peak-to-peak sinusoidal cell current which is proportional to the capacitance. The other trace represents the potential of the test electrode-reference electrode combination. The phase angle can be determined at a given potential by displaying the sinusoidal potential and current simultaneously on the dual beam oscilloscope and noting the time relationship of one to the other.

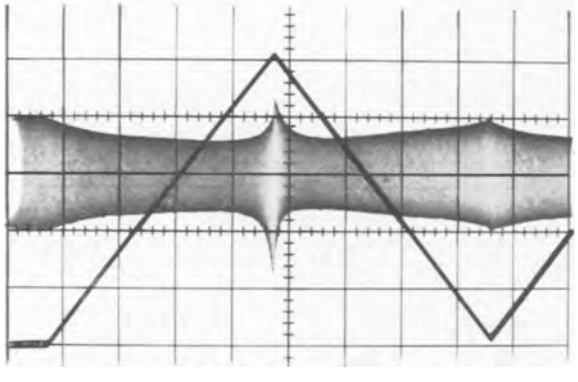

Fig. 6. Potential-time and current-time waveforms obtained at a silver electrode in molar sodium perchlorate solution using a controlled sinusoidal potential. See the text for an explanation. Potential sensitivity, 200 mv/cm; current sensitivity, 0.100 ma/cm; sweep limits, minus 430 mv to plus 570 mv vs. NHE; sweep speed, 200 ms/cm; applied sinusoidal potential, 10 mv peak to peak; electrode area, 0.0401 sq cm.

The frequency limits of the system are determined by the amplifiers. Accuracy begins to fall off rapidly above 2000 cps. The use of higher speed amplifiers could raise this limit. The lower limit of the amplitude of the potential wave form is determined by the signal-to-noise ratio of the instrument. It was found convenient to use a 10 mv peak-to-peak signal, but this could have been made much smaller if tuned amplifiers had been used to suppress the line frequency noise (19). The use of tuned amplifiers would necessitate some sacrifice in measurement speed.

The authors chose to control the sinusoidal potential rather than the sinusoidal current so that a linear potential sweep could be applied, and so that the potential amplitude would not vary with capacitance, causing a change in "resolution" with capacitance. Breiter (9) has used a system that employs a controlled current superimposed on a linear potential sweep which is limited to slower sweep speeds than that described above.

The use of the controlled potential device for the measurement of the double layer capacitance of silver is published in another article (14).

Summary

Speed and ease of measurement, and not extreme accuracy, are important factors in determination of a method of double layer capacitance measurement on solids. Very rapid measurement and good accuracy are obtained with a controlled sinusoidal potential technique. If the cell resistance is small compared with the double layer impedance, the cell capacitance is measured directly by this technique. Kinetically slow reactions do not interfere in the measurements.

With high resistance solutions a constant or pulsed d-c technique has advantages. In the presence of a kinetically rapid reaction a current interruptor method of measurement offers a good solution.

Acknowledgment

This work was in part supported by the Directorate of Chemical Sciences, Air Force Office of Scientific Research under Grant No. AFOSR-151-63.

Manuscript received Feb. 19, 1965; revised manuscript received May 17, 1965.

Any discussion of this paper will appear in a Discussion Section to be published in the June 1966 JOURNAL.

REFERENCES

1. F. P. Bowden and E. K. Rideal, *Proc. Roy. Soc.*, **A120**, 59 (1928) and **A120**, 80 (1928).
2. J. J. McMullen and N. Hackerman, *This Journal*, **106**, 341 (1959).
3. B. D. Cahan and P. Ruetschi, *ibid.*, **106**, 543 (1959).
4. G. M. Schmid and N. Hackerman, *ibid.*, **109**, 243 (1962).
5. H. Angerstein-Kozlowska and B. E. Conway, *J. Electroanal. Chem.*, **7**, 109 (1964).
6. G. Armstrong and J. A. V. Butler, *Trans. Faraday Soc.*, **29**, 1261 (1933).
7. C. Wagner, *This Journal*, **97**, 71 (1950).
8. M. Proskurnin and A. N. Frumkin, *Trans. Faraday Soc.*, **31**, 110 (1935).
9. M. W. Breiter, *J. Electroanal. Chem.*, **7**, 38 (1964).
10. M. W. Breiter, *Electrochim Acta.* **7**, 533 (1962).
11. D. C. Grahame, *J. Am. Chem. Soc.*, **71**, 2978 (1949).
12. D. C Grahame, *Chem. Rev.*, **41**, 441 (1947).
13. D. C. Grahame, *J. Am. Chem. Soc.*, **76**, 4819 (1954).
14. L. Ramaley and C. G. Enke, *This Journal*, **112**, 947 (1965).
15. H. B. Herman and A. J. Bard, *Anal. Chem.*, **35**, 1121 (1963).
16. H. B Herman and A. J. Bard. *ibid.*, **36**, 510 (1964).
17. H. B. Herman and A. J. Bard, *ibid.*, **36**, 971 (1964).
18. D. E. Walker, R. N. Adams, and A. L. Juliard, *ibid.*, **32**, 1526 (1960).
19. D. E. Smith, *ibid.*, **35**, 1811 (1963).

NOMENCLATURE

C	capacitance in farads
q	charge in coulombs
E	potential in volts
I	current in amperes
f	frequency in cycles per second
C_a	average electrode capacitance in farads/cm^2
C_d	differential electrode capacitance in farads/cm^2
A	electrode area in cm^2
i	electrode current in amperes/cm^2
I_{ac}	sinusoidal current in amperes
E_{ac}	sinusoidal potential in volts
ϕ	phase angle between current and voltage in degrees
R_s	solution resistance in ohms

The Double Layer Capacitance of Silver in Perchlorate Solution

Louis Ramaley[1] and C. G. Enke[2]

Frick Laboratory, Princeton University, Princeton, New Jersey

ABSTRACT

The electrical double layer capacitance of silver was studied in 1N sodium perchlorate solutions as a function of pH, method of surface preparation, and electrode potential. The results suggest that the double layer structure on silver and mercury may be very similar. A model explaining the frequency dispersion of the double layer capacitance on solid electrodes is proposed, and qualitative substantiating evidence is given.

Many studies of the electrical double layer capacitance of silver have been carried out in aqueous solution (1-7). The agreement among the values of the capacitance observed in these studies is very poor. This is in part due to the use of different electrolytes over different concentration ranges. However, if the Gouy-Chapman-Stern treatment of the double layer structure is valid for silver, the large differences observed cannot be explained by variations in the type and concentration of electrolyte alone.

Differences in manner of surface preparation and solution purity have probably been the major causes for the discrepancies. Often the surfaces have been mechanically polished or subjected to long and complicated chemical cleansings. The surface state was generally unknown and varied from worker to worker. In the early literature insufficient care was taken to remove adsorbable impurities from solution. These have a dramatic effect on the double layer capacitance.

A frequency dispersion of the double layer capacitance has often been observed (7-15), most notably on solids. Several explanations of this effect have been given (7, 12, 16), but none of these explain all the observed phenomena satisfactorily. Thus it seemed worthwhile to undertake an investigation of the double layer capacitance of silver employing techniques which avoid damaging surface treatments and adsorption of impurities from solution. Information as to the cause of frequency dispersion of the double layer capacitance was also sought.

Experimental

Materials.—Solutions 1M in perchlorate ion were prepared with triply distilled water over a pH range from 0-13 by the mixture of appropriate amounts of Baker and Adamson Reagent Special Grade NaOH and G. F. Smith doubly distilled lead-free 70% $HClO_4$. These solutions were pre-electrolyzed for at least 18 hr using a mercury cathode and platinum anode, and immediately before use were filtered through purified activated charcoal to remove adsorbable impurities. The silver employed was 99.99% pure wire of two sizes, 0.063 and 0.020 cm in diameter. All mercury used was purified by washing with dilute nitric acid followed by vacuum distillation.

Electrode preparation.—Silver electrodes were prepared from wire cleaned in an alcohol solution of KOH, etched in concentrated HNO_3, and suspended in a quartz tube. The tip of the wire was melted and allowed to form a sphere. The size of the sphere was controlled by the amount of wire melted. A stream of pure helium was passed through a liquid nitrogen trap and then through the quartz tube at all times. Hydrogen was not used for this purpose since it has been observed that exposure to hydrogen affects the double layer capacitance of silver (2). The electrodes prepared from the smaller wire were transferred immediately to the electrochemical cell. The electrodes prepared from the larger wire were electropolished in 60% perchloric acid solution for several minutes and then transferred to the cell. The surfaces of both types of electrodes were observed to be bright and specular under the optical microscope.

Hanging mercury drop electrodes were prepared by mercury-coating the tip of a small platinum wire sealed in glass using the method described by Ramaley *et al.* (17). The drops that were hung on this electrode were obtained from a Manostat microburet filled with mercury. These electrodes were used as checks of technique and solution purity.

Electrochemical cell.—A three-electrode system, consisting of the test electrode, a large cylindrical platinum foil counter electrode, and a hydrogen reference electrode, was employed. The counter electrode and test electrode, positioned in a geometrically concentric manner, occupied the main cell compartment. The reference compartment was connected to the main compartment with a Luggin capillary. An atmosphere of nitrogen, passed through a liquid nitrogen trap containing activated charcoal on glass wool and through a presaturator, was maintained in the main cell compartment at all times. Hydrogen, treated in the same manner, was bubbled slowly into the reference compartment. All potentials were measured *vs.* the hydrogen reference electrode in the test solution, and are given here *vs.* the normal hydrogen electrode (NHE).

The cell itself was constructed completely of glass. At no time after the solution had been filtered through activated charcoal did it contact any organic matter, including Teflon. Since silver does not readily seal in glass, the electrodes were suspended from above and allowed to dip into solution.

Methods of measurement.—Double layer capacitance was measured using a small amplitude sinusoidal potential superimposed on a fast linear potential sweep. The electrode was held at a cathodic potential just below hydrogen evolution before the sweep was begun. Experiment demonstrated that adsorbable impurities had less effect at a cathodic potential. The potential was then swept quite rapidly in an anodic direction and then back. Sweep rates of a volt per second were used to minimize completely the effect of

[1] Present address: Department of Chemistry, University of Arizona, Tucson, Arizona.

[2] Alfred P. Sloan Research Fellow.

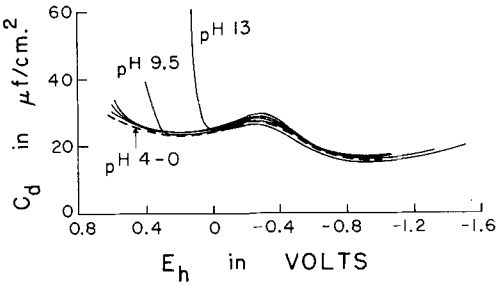

Fig. 1. Variation of the capacitance of mercury in 1M $NaClO_4$-$HClO_4$ solutions with pH and potential. The dotted curve is the data of Grahame (19).

the adsorption of impurities. The frequency of the applied sinusoidal potential was 1000 cps and the amplitude was 10 mv peak to peak.

A rectangular current pulse waveform was employed in capacitance measurements where the object was to determine the extent of frequency dispersion in a qualitative manner. The curvature in the slope of the measured potential-time waveform was taken as a qualitative measure of the extent of frequency dispersion. These measurements were carried out as function of time and potential.

A detailed description of both techniques is given in another article (18).

Results and Discussion

Capacitance-potential data.—The results obtained for mercury using the hanging mercury drop are given in Fig. 1. The effect of pH is as expected and the data agree well with the work of Grahame (19). The wide spread in the curves was caused primarily by background noise on the amplifiers. The signals from the measurements on mercury were small enough so that the signal to noise ratio was unfavorable. In the case of silver, the signal was much greater, and this problem was not encountered. No measurable change in capacitance over periods of 20 min or longer was noted, indicating high solution purity.

The results for silver were much less reproducible than those for mercury. This is in part caused by an uncertainty in the actual area of the electrode. The geometrical area of the silver spheres was calculated from values of their diameters measured with a micrometer. Some error was introduced here due to imperfect sphericity of the electrodes, especially in the case of the electropolished electrodes. The capacitance data are all given in terms of the calculated geometrical area. For a solid, the calculated area will always be smaller than the real area, and from electrode to electrode there is probably no direct proportionality between real area and calculated area. This leads to nonreproducibility in measurements.

Reproducibility was also found to be affected by the manner of electrode preparation. The electropolished electrodes gave the more reproducible values of capacitance which changed very little with time. The electrodes used immediately after cooling of the molten drop (nonelectropolished) gave capacitance-potential curves which contained nonreproducible peaks. The capacitance of these electrodes changed with time over a period of 15 min, becoming higher and approaching the capacitance-potential curves for electropolished electrodes. This behavior is shown in Fig. 2.

In transferring the nonelectropolished electrodes to the electrochemical cell, a brief contact (several seconds) with the atmosphere was necessary. Such a direct contact was not made with the electropolished electrodes. Thus it was assumed that some impurity had adsorbed on electrodes exposed to the atmosphere, and that this impurity slowly desorbed in solution, allowing the behavior of one type of electrode to approach that of the other. A mercury electrode was deliberately exposed to the atmosphere and its capacitance recorded as a function of time. It behaved in exactly the same manner, showing anomalous peaks and an increase in capacitance with time toward the accepted value. Therefore, the capacitance-potential curves of electropolished silver electrodes were taken to be more representative of a clean silver surface.

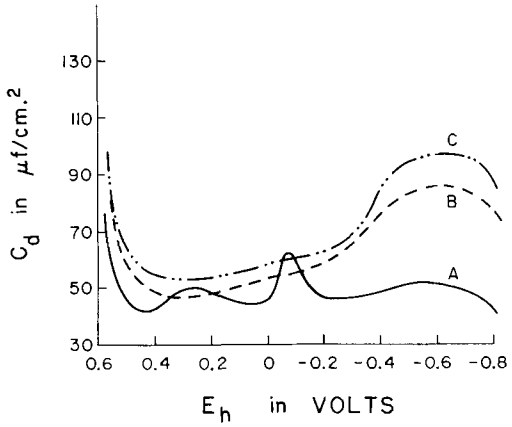

Fig. 2. Capacitance potential behavior of two silver electrodes in 1M $NaClO_4$ at pH 4. Curve A, nonelectropolished silver electrode immediately after immersion in solution; curve B, the same electrode 15 min later; curve C, electropolished silver electrode showing no change in capacitance with time.

Figure 3 describes the results obtained for silver as a function of pH, measurements being made at pH 13, 9.5, 4, 1, and 0. The two large envelopes contain the capacitance-potential curves for thirty-eight electrodes prepared in the two manners previously noted. The values for the nonelectropolished electrodes were taken after their capacitance had increased and the curves had become similar to the electropolished electrodes. The large bandwidth is caused by the nonreproducibility of area mentioned above. The large increase in capacitance at anodic potentials for pH 13 is most probably attributed to the adsorption of hydroxide ion. Similar behavior is observed on mercury in Fig. 1. The values of capacitance for the electrodes run in neutral or acid solution were normalized by assuming that the average value of 65 μf/cm^2 at 0.00v *vs.* NHE is the actual value at this potential. All capacitance values were corrected to 65 μf/cm^2 at 0.00v and the correction factor was used to normalize the capacitance values at all other potentials. All values fell within

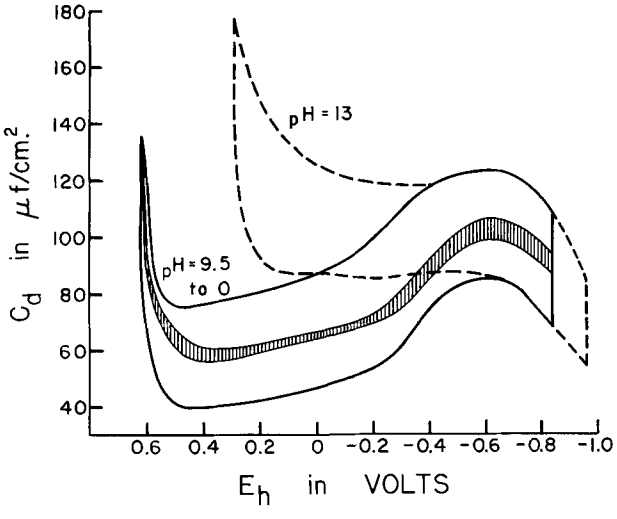

Fig. 3. Variation of the capacitance of silver in 1M perchlorate solutions with pH and potential. Shaded portion normalized at 0v to compensate for varying and unknown surface roughness.

the shaded area in Fig. 3. The width of this band is consistent with about a ±5% measurement error.

The normalization demonstrates the reproducibility of the curve shape. However, it does not give a more accurate measure of the actual double layer capacitance per unit area because the roughness factor is still unknown.

The shape of the curves in Fig. 3 is very interesting in that it resembles the shape of the curves obtained for mercury with the silver curve shifted toward more negative values of potential. For a direct comparison of the curves, the zero point of charge (zpc) of both metals must be known. According to Grahame (19) the zpc for mercury in 1M perchlorate solution occurs within 25 mv of the small capacitance peak shown at 0.30v in Fig. 1. Several values of the zpc have been given for silver, 0.51v (NHE) (20), 0.046v (NHE) (2), and —0.70 ± 0.05v (NHE) (5). If either of the first two values is correct, there is little similarity between the curves for silver and mercury. However, if the zpc for silver is at or near the potential of the capacitance maximum, as would be the case if the third and most recent value is correct, then the double layer structure for the two metals can be assumed to be very similar. A confirmation of the value of —0.70 ± 0.05v should be carried out before any definite statement can be made.

Frequency dispersion.—Several models explaining the variation of capacitance with measurement frequency have been proposed. McMullen and Hackerman (7) have suggested that the change in measured capacitance with frequency is caused not by a frequency dispersion of the double layer, but by a faradaic current due to small amounts of impurities present in solution. Bockris and Conway (12) have proposed that, due to strong adsorptive forces, the water molecules in the inner Helmholtz layer are unable to follow the applied field, resulting in a capacitance dispersion. Frumkin (16) has postulated that for solids, the dispersion is caused by the presence of unevenness and cracks in the electrode surface. This would create paths of differing resistance to different areas of the electrode. These different areas would then have different time constants and a frequency dispersion would result. A shielding of any part of the test electrode surface has the same effect. Grahame (9) has shown that shielding gives rise to dispersion on mercury electrodes.

Any model which attempts to explain the dispersion effect must explain several observed facts: The dispersion is always observed to be much greater on solid electrodes than on liquid electrodes, the measured capacitance always decreases with increasing frequency, the dispersion is potential dependent, the dispersion is observed at low frequencies, and the dispersion increases as the solution conductivity decreases.

The faradaic reaction model fails to explain the increase in dispersion with decreasing electrolyte concentration. It would be expected that the lower the electrolyte concentration, the lower the impurity level, and thus the lower the dispersion.

Experiments were performed in this laboratory by observing both the potential-time waveform and the faradaic current flowing when a rectangular current pulse waveform was applied to the test electrode (18). The curvature of the potential-time waveform (see Fig. 4, curve B) was taken as a qualitative estimate of the frequency dispersion of the double layer capacitance. No relationship between dispersion and faradaic current was observed as long as the faradaic current was a small fraction of the total cell current. The faradaic current, equal to or less than 0.2% of the total current, tended to increase as the potential became more cathodic while the dispersion tended to decrease.

The inner layer relaxation model, as pointed out by Grahame (21), does not explain the dependence of dispersion on solution concentration. It also predicts

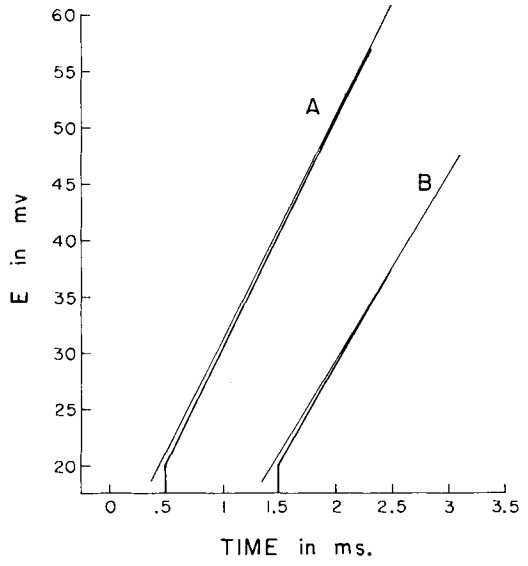

Fig. 4. Curve A, plot of potential vs. time for a constant current according to Eq. [1]; curve B, reproduction of a photograph of an oscillographic potential-time trace for a silver electrode.

that the dispersion of capacitance is noticeable at about 100 megacycles on mercury. If the double layer structures on mercury and solid electrodes are similar, the dispersion on solids should be noted only at high frequencies. Dispersion is easily observable at frequencies of 100 cycles and less on solids.

The cell configuration used in this work was symmetrical and avoided shielding effects, so that all resistance paths to the test electrode should have been equivalent. It was felt that the method of electrode preparation, especially that of electropolishing, avoided the difficulty of uneven and cracked surfaces. Even so dispersion of capacitance with frequency was still observed. No dispersion was noticeable on mercury under the same conditions. If a nonequivalence of resistance paths to different sections of the electrode causes the frequency dispersion, then the potential dependence of the dispersion should be the same as the potential dependence of capacitance. This results because the time constant of the system, which is a function of frequency, changes only as the capacitance changes. A dependence of dispersion on potential was observed, but it was in no way related to the dependence of capacitance on potential. The capacitance is maximum at —0.60v and minimum at +0.45v in neutral or acid solution. The dispersion shows no maximum or minimum, but gradually increases with increasingly anodic potential. Thus the nonequivalent resistance path model does not explain the observed data.

A dispersion of capacitance with frequency will result if various areas of the electrode display different capacitances. The results are the same as for nonequivalent resistance paths to the electrode, but the cause is different. A simple model for this type of behavior can be drawn

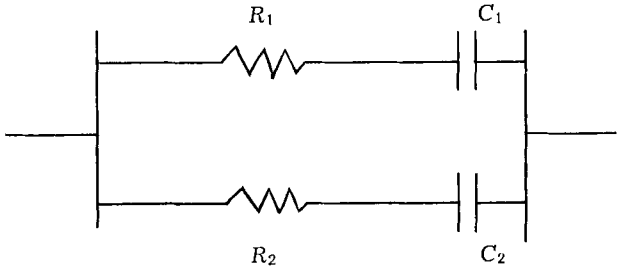

where R_1 and R_2 represent resistant paths to the different parts of the electrode having the different ca-

pacitance values C_1 and C_2. The equation, derived by the method of nodal analysis (22), for the potential across this network as a function of time when a constant current pulse is applied at $t = 0$ is

$$E = \frac{it}{C_1 + C_2} + \frac{iR_1R_2}{R_1 + R_2} + \frac{i(R_1C_1 - R_2C_2)^2}{(R_1 + R_2)(C_1 + C_2)^2}\left[1 - \exp - \frac{(C_1 + C_2)t}{C_1C_2(R_1 + R_2)}\right] \quad [1]$$

Figure 4, curve A shows a plot of this equation assuming an electrode of 1 cm^2 having a capacitance of 60 μf for half its area and a capacitance of 40 μf for the other half. The solution resistance to the electrode is assumed to be 10 ohms and the current is assumed to be 2 ma. Figure 4, curve B shows the actual curve for a silver electrode measured at —0.20v in a solution of pH 13. The current density was 1.8 ma cm^2 and the calculated capacitance was 105 mf cm^2. The curves are quite similar. The majority of electrodes showed less deviation from a linear slope, and thus less dispersion, than did that depicted in Fig. 4, but some showed a greater dispersion.

The network and equation shown above also represent the nonequivalent resistance path model. No choice as to the correct model can be made on the shape of the curves alone. Other information must be obtained before the choice is made. The network shown above is only a very simple approximation of a more complicated system. On a polycrystalline electrode, there must be some variation in the resistance of the solution adjacent to surfaces of various curvature and there are very likely differences in double-layer capacitance among various surfaces of the electrode. The complete network would contain n resistances and capacitances. The point to be made is that in many cases, the variation of C may be much greater than that of R and therefore could be the principal cause of dispersion. Equation [1] is used to show that capacitance variation would result in the observed trends, but it is too simple a model to justify fitting it to the data quantitatively.

The model proposed predicts the decrease of measured capacitance with frequency and the increase in dispersion with increasing solution resistance. (According to the equation as R_1 and R_2 increase, the curvature of the E *vs.* t curve increases, and thus there is an increase in frequency dispersion.) It explains the fact that dispersion is higher on solids than on liquids. Solids present more than one crystal face to the solution, and the crystal faces can have different capacitances (23). Grain boundaries and other imperfections would not show the same capacitance as a more perfect crystal face. There is a probability that an impurity can be preferentially adsorbed on one crystal face, thus drastically changing its capacitance. Finally it can explain the potential dependence of dispersion. The areas of different capacitance may show capacitance-potential behaviors which are not alike, and thus a potential dependent dispersion results. This dispersion need not show any obvious relation to the total measured capacitance-potential behavior of the electrode.

As mentioned above, measurements in this laboratory indicated a potential dependence of dispersion which was not related to the measured capacitance-potential dependence in any obvious way. Another set of measurements was made on a silver electrode in a solution which had not been highly purified. The capacitance of the electrode decreased slowly with time as impurities adsorbed on it. This dispersion was also observed to decrease with time at approximately the same rate. This indicated that as the electrode became contaminated, the adsorbant tended to decrease the nonuniformity of the surface and the dispersion decreased.

Further evidence in support of this model is given by Tsa and Jofa (13). They observed that frequency dispersion decreased when a monocrystalline electrode was used instead of a polycrystalline electrode. This eliminates much of the nonuniformity in the capacitance values of different sections of the electrode.

Summary

Capacitance-potential curves obtained in 1M perchlorate solutions on silver surfaces prepared in two manners without mechanical or extensive chemical treatment indicate the need to avoid any atmospheric contact of the freshly prepared surfaces. After desorption of impurities, the capacitance-potential behavior of the nonelectropolished surfaces approached that of the electropolished surfaces. Since the data on the two types of surfaces agree, the potential dependence of capacitance measured is assumed to be that of a clean silver surface. The data also indicate a similarity between the double layer structure on mercury and silver.

The dispersion of the measured capacitance with frequency is explained on the basis of different portions of the silver electrodes possessing varying capacitance values. This model explains the observed facts concerning the frequency dispersion of the double layer for solids more satisfactorily than those previously proposed.

Acknowledgment

This work was in part supported by the Directorate of Chemical Sciences, Air Force Office of Scientific Research under Grant No. AFOSR-151-63.

Manuscript received Feb. 19, 1965; revised manuscript received May 12, 1965.

Any discussion of this paper will appear in a Discussion Section to be published in the June 1966 JOURNAL.

REFERENCES

1. P. Rüetschi, *This Journal*, **110**, 835 (1963).
2. V. I. Veselavsky, *Acta Physicochim. U.R.S.S.*, **11**, 815 (1939).
3. A. Hickling and D. Taylor, *Discussions Faraday Soc.*, **1**, 227 (1947).
4. C. Wagner, *This Journal*, **97**, 71 (1950).
5. D. I. Leikis, *Doklady Akad. Nauk S.S.S.R.*, **135**, 1429 (1960).
6. F. P. Bowden and E. K. Rideal, *Proc. Roy. Soc.*, **A120**, 59 (1928).
7. J. J. McMullen and N. Hackerman, *This Journal*, **106**, 341 (1959).
8. T. I. Borrisova and M. Proskurnin, *Acta Physicochim. U.R.S.S.*, **12**, 371 (1940).
9. D. C. Grahame, *J. Am. Chem. Soc.*, **68**, 301 (1946).
10. P. Dolin and B. V. Ershler, *Acta Physicochim. U.R.S.S.*, **13**, 747 (1940).
11. T. I. Borrisova and B. V. Ershler, *Zhur. Fiz. Khim.*, **24**, 337 (1950).
12. J. O'M. Bockris and B. E. Conway, *J. Chem. Phys.*, **28**, 707 (1958).
13. Chuan-sin Tsa and S. Jofa, *Doklady Akad. Nauk S.S.S.R.*, **131**, 137 (1960).
14. D. I. Leikis and E. S. Sevast'yanov, *ibid.*, **144**, 1320 (1962).
15. P. Dolin and B. Ershler, *Acta Physicochim. U.R.S.S.*, **13**, 747 (1940).
16. A. N. Frumkin, *This Journal*, **107**, 461 (1960).
17. L. Ramaley, R. L. Brubaker, and C. G. Enke, *Anal. Chem.*, **35**, 1088 (1963).
18. L. Ramaley and C. G. Enke, *This Journal*, **112**, 943 (1965).
19. D. C. Grahame, *Chem. Rev.*, **41**, 441 (1947).
20. M. Proskurnin and A. N. Frumkin, *Z. Physik. Chem., Abt. A*, **155**, 29 (1931).
21. D. C. Grahame in "Soviet Electrochemistry," Vol. 1. p. 31, Consultants Bureau, New York (1961).
22. G. E. Valley, Jr. and H. Wallman, "Vacuum Tube Amplifiers," Chap. 1, 2nd ed., McGraw-Hill Book Co., New York (1958).
23. G. M. Schmid and N. Hackerman, *This Journal*, **109**, 243 (1962).

The Effect of Electrode Separation in Microcells

R. N. O'Brien[1] and K. Kinoshita

College of Chemistry, University of California, Berkeley, California

ABSTRACT

An interferometry cell has been designed with movable electrodes. Interferograms were taken in three cell orientations, shallow vertical, deep vertical, and horizontal cathode-over-anode at various current densities in a 0.1*N* solution of $CuSO_4$, *p*H 4-5. Anomalous maxima and minima were found in concentration gradient change with separation of electrodes and current density in all orientations. Similarly the impressed voltage to maintain a constant current density with increasing electrode separation went through at least one minimum which has been attributed to changes in the convection system in the vertical electrodes and tentatively to migration and field effects in the horizontal orientation. No quantitative interpretation seems possible at this stage.

The thin cell chronopotentiometric work of Anson *et al.* (1) and the recent interest in thin layer ion-exchange electrolytes for fuel cells and electrolytic machining has focussed attention on the effects of having two electrodes very close together.

The authors' interest concerns the very considerable effect of geometry on the transport processes in microcells. It has already been shown (2) that the effect of the orientation of the electrodes is profound varying from pure diffusion (and electromigration) in the cathode-over-anode configuration to almost pure convection in the anode-over-cathode position. All vertical electrodes in cells whose electrolyte depth is greater than 0.2 mm produce natural convection (2), and hence diffusion is limited to some portion of the so-called diffusion layer (3, 4).

It is possible to obtain concentration gradients between working electrodes by the optical means of Schlieren patterns (5) and interferometry (2, 6-8). Interferometry is perhaps the most convenient and is here employed. Since the concentration is directly proportional to the refractive index for all but the most concentrated solutions, the slope of a fringe can be measured to give $\partial c/\partial x$ or the rate of change of concentration with distance from the electrode.

It would be desirable to have a movable probe electrode as well as the ability to move the polarizing electrodes, but since the space limitations are so stringent this was not possible so in all cases the voltages shown are those impressed across the cell, as the distance between the electrodes was varied.

Experimental

The circuit used was a transistorized source, decade resistance boxes of about 100,000 ohms, and the cell of about 200 ohms, whose resistance varies with conditions of electrolysis. The circuit is therefore essentially a constant current circuit.

The interferograms were recorded with an Exacta 35 mm camera using Ilford HPS film.

The cell used was a specially modified one similar to that recently described (9). The Teflon cylinder with coated glass-flat ends had slits for the entry of long slabs of copper which were the movable electrodes. These electrodes were coated with TFE fluorocarbon spray to make them easier to move and so that they would be hydrophobic and thus help prevent leaks around the electrodes. All other parts and manipulations were the same as previously described (4).

The current passing was measured with a multirange microammeter, the impressed voltage with a Simpson Multimeter. The interferograms were taken at 3 min after a desired electrolysis current began to pass. The slope of the fringes were measured as close to the electrode as possible with a straight edge on a light box.

[1] Chemistry Department, University of Alberta; Visiting Scholar, College of Chemistry, University of California, Berkeley, California.

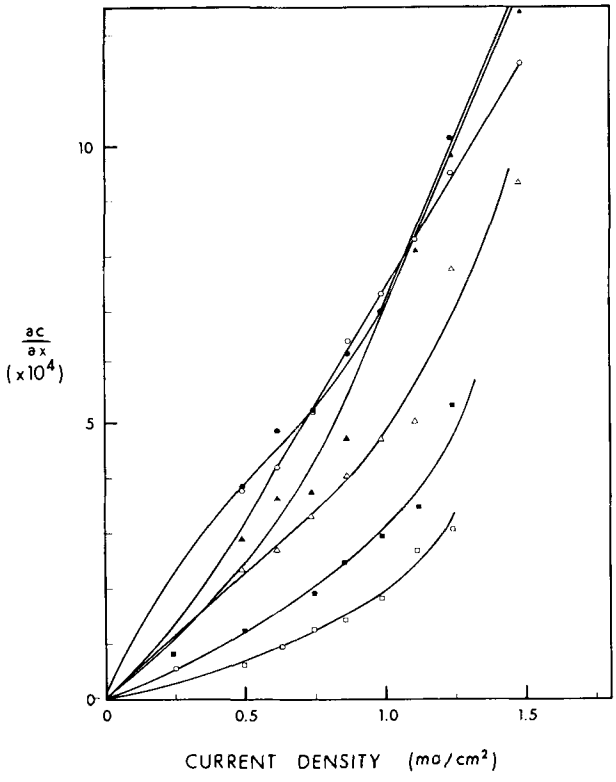

Fig. 1. Concentration gradient *vs.* current density for three different electrode separations, shallow vertical orientation. The separations are: • cathode, ○ anode, 0.0365 cm; ▲ cathode, △ anode, 0.516 cm; ■ cathode, □ anode, 1.115 cm.

Results

Current density, impressed voltage, and interferograms were taken for electrode separations of about 0.4, 0.6, 0.75, 1.0, 2.25, 3.3, 4.2, 5.2, 7.0, 9.5, and 11.0 mm. At each separation 3 orientations of the cell were used and about 10 C.D.'s ranging from about 0.3 ma/cm^2 to about 1.5 ma/cm^2. The range of C.D.'s was dictated by the resolution of the interferometer. At C.D.'s higher than 1.5 ma/cm^2 the fringes lie so close together that they are not measureable with this light-path difference. A thinner cell would of course permit higher current density interferograms. A number of interferograms with similar characteristics to those obtained in this work have been previously published (2, 7-9); therefore none are included here.

Figure 1 is a plot of concentration gradient *vs.* current density at three representative separations in what will be called the shallow vertical position (S/V). This means that the electrodes which were 2 mm by 25.4 mm on the working face were oriented so that

the cell (and hence electrodes and electrolyte as well) was 2 mm deep. The two shortest distances have very steeply increasing gradients with C.D. and the widest separation much less so. Figure 2 shows the same variable plotted for the deep vertical position (D/V) where the electrodes are now 25.4 mm deep and 2 mm wide. A similar relationship obtains.

Since convection is known to occur at all vertical electrodes, the results of Fig. 1 and 2 could be interpreted to mean that convection is a less efficient transport mechanism up to a distance of about 2.3 mm in the S/V and about 7 mm (with one previous change) in D/V and with the possibility of some effect of electromigration and electrode field. But considering Fig. 3 which shows the results for $\partial c/\partial x$ *vs.* C. D. in the cathode-over-anode position (C/A), the fact that the rate of change of $\partial c/\partial x$ with C.D. is constant, although the values of $\partial c/\partial x$ for a given C.D. are different and lower for the two widest separations and have a lower rate of change, suggests that field effects must be important since there is no convection in this position. The change to a constant slope is first noticeable at 2.3 mm separation and a C.D. limitation of about 0.67 ma/cm^2 (impressed voltage 50 mv) and at progressively higher C.D.'s and impressed voltages until, at 4.30 mm separation, there is only slight suggestion of a change (increase) of slope at the highest C.D.'s used.

These effects can be more clearly seen in plots of $\partial c/\partial x$ *vs.* electrode separation at constant current density. Figure 4 is the plot for the S/V orientation. It shows peaks at 1 mm and about 3.5 increasing to just over 4.0 mm at higher C.D.'s and valleys at just under 0.5 mm increasing to 0.6 mm, and at 2.3 mm as well as anomalous variations between the two electrodes at the smallest separations. The first peak is thought to represent the most favorable separation for one convective whorl, the second peak that for two with over and underflow (10) with field effects superimposed.

Figure 5 shows $\partial c/\partial x$ *vs.* electrode separation at constant C.D. for the D/V position. Rapidly dropping values of $\partial c/\partial x$ are evident for low C.D.'s and small separations, but at high C.D.'s there are two peaks at about 0.75 mm and about 4.5 mm. These are also thought to be due mainly to one and two whorl convective flows.

In Figure 6 for the C/A position, $\partial c/\partial x$ values show sharp drops at small separations at all C.D.'s where it was possible to make measurements close to the electrodes. One peak persists from about 1 mm separation

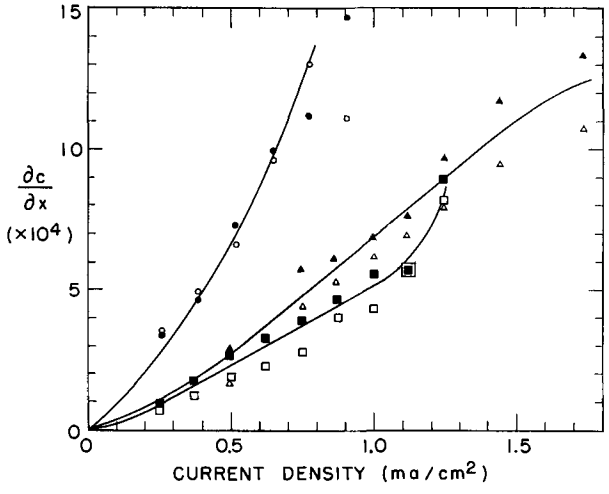

Fig. 2. Concentration gradient *vs.* current density for three different electrode separations, deep vertical orientation. The separations are: • cathode, ○ anode, 0.0245 cm; ▲ cathode, △ anode, 0.532 cm; ■ cathode, □ anode, 1.088 cm.

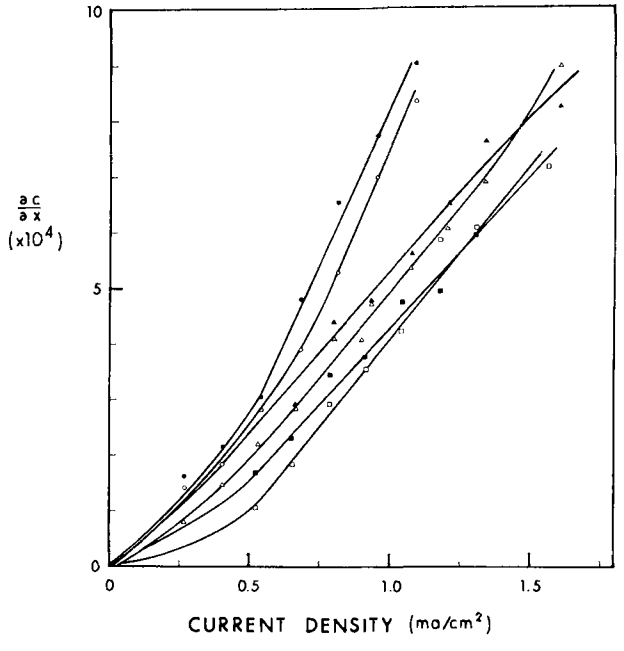

Fig. 3. Concentration gradient *vs.* current density for three different electrode separations, horizontal, cathode-over-anode orientation. The separations are: • cathode, ○ anode, 0.042 cm; ▲ cathode, △ anode, 0.526 cm; ■ cathode, □ anode, 1.112 cm.

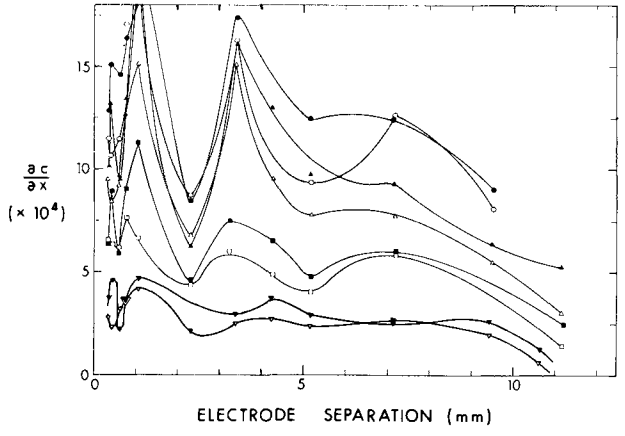

Fig. 4. Concentration gradient *vs.* electrode separation for four different current densities, shallow vertical orientation. The current densities are: • cathode, ○ anode, 1.48 ma/cm^2; ▲ cathode, △ anode, 1.23 ma/cm^2; ■ cathode, □ anode, 0.86 ma/cm^2; ▼ cathode, ▽ anode, 0.49 ma/cm^2.

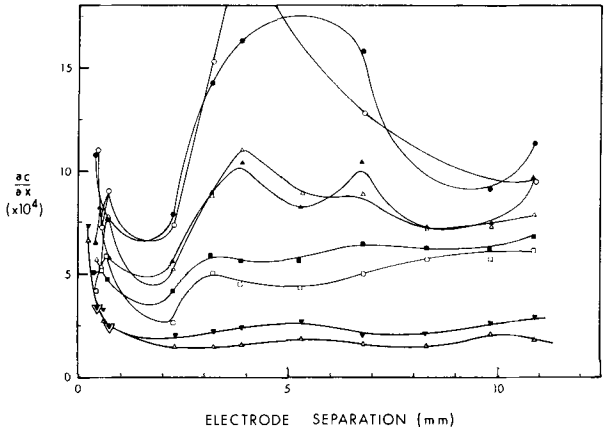

Fig. 5. Concentration gradient *vs.* electrode separation for four different current densities, deep vertical orientation. The current densities are: • cathode, ○ anode, 1.51 ma/cm^2; ▲ cathode, △ anode, 1.26 ma/cm^2; ■ cathode, □ anode, 1.01 ma/cm^2; ▼ cathode, ▽ anode, 0.51 ma/cm^2.

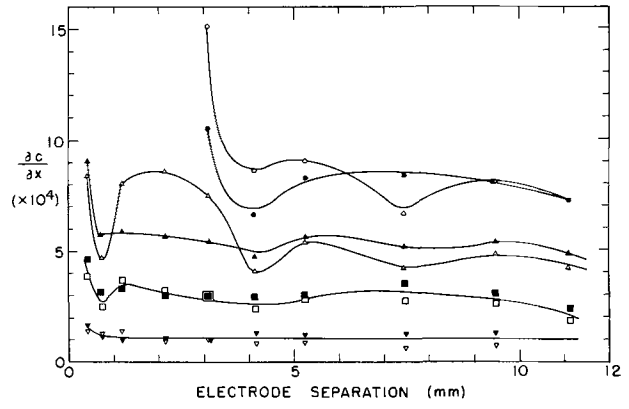

Fig. 6. Concentration gradient *vs.* electrode separation for four different current densities, horizontal, cathode-over-anode orientation. The current densities are: ● cathode, ○ anode, 1.58 ma/cm^2; ▲ cathode, △ anode, 1.07 ma/cm^2; ■ cathode, □ anode, 0.67 ma/cm^2; ▼ cathode, ▽ anode, 0.27 ma/cm^2.

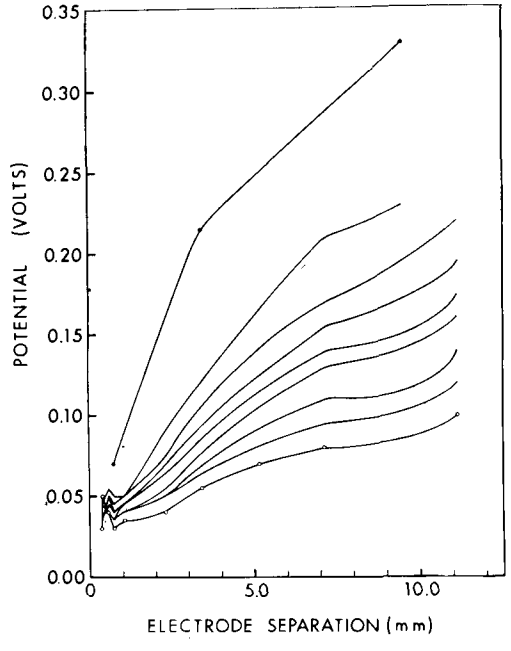

Fig. 7. Impressed voltage to maintain a constant current density at various electrode separations in the S/V orientation. Current densities successively from the top of the plot are: 2.22, 1.48, 1.23, 1.11, 0.99, 0.86, 0.74, 0.62, 0.43 ma/cm^2. Only data points at 2.22 and 0.43 ma/cm^2 are shown to avoid clutter.

up to about 1 ma/cm^2 when the peak begins to broaden. Other minor perturbations to the plot at greater distances persist above 0.5 ma/cm^2.

A plot of the impressed voltage to maintain constant current density should show these anomalous changes in the change in concentration gradient, if they are real. Figure 7 gives the impressed voltage at constant C.D. and various separations for the S/V position. A very sharp drop in required potential has occurred at 0.4 mm electrode separation, the potential then reaches a peak varying from about 0.4 mm to 0.6 mm, increasing with increasing C.D., then again suddenly drops at 0.75 mm to rise again more slowly at greater separations. Up to about 10 mm separation there is no indication that a constant increase in potential with distance will maintain a constant C.D. in this orientation. Figure 8 is the same plot for the D/V position. It again shows a rapidly decreasing potential below 0.4 mm, a peak at about 0.65 mm and a minimum at about 0.80 mm, these distances remaining reasonably constant with C.D. At the greatest current densities and separations the potential is approximately proportional to the separation for constant C.D.

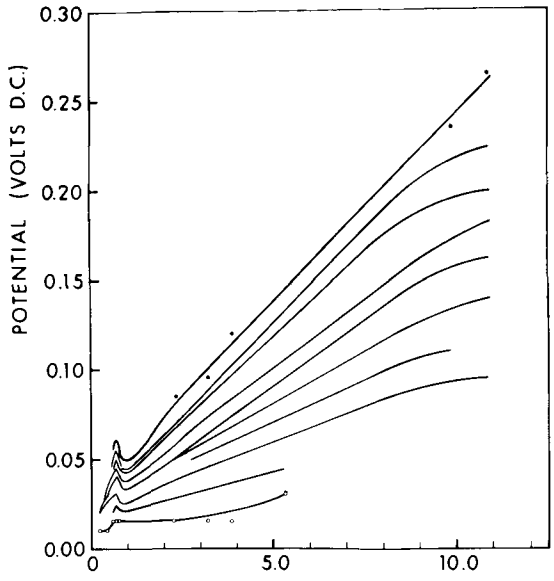

Fig. 8 Impressed voltage to maintain a constant current density at various electrode separations in the D/V orientation. Current densities successively from the top of the plot are: 1.51, 1.26, 1.14, 1.01, 0.88, 0.76, 0.63, 0.51, 0.38, 0.25 ma/cm^2. Only data points at 1.51 and 0.25 ma/cm^2 are shown to avoid clutter.

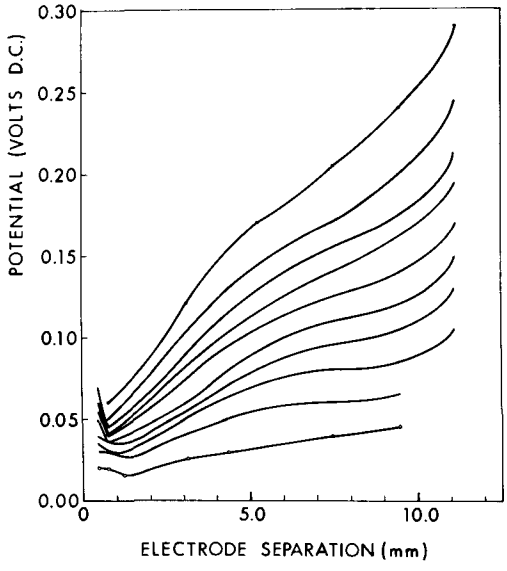

Fig. 9. Impressed voltage to maintain a constant current density at various electrode separations in the C/A orientation. Current densities successively from the top of the plot are: 1.58, 1.33, 1.20, 1.07, 0.94, 0.80, 0.67, 0.53, 0.41, 0.27 ma/cm^2. Only data points at 1.58 and 0.27 ma/cm^2 are shown to avoid clutter.

Figure 9 is the plot for the C/A position. At all C.D.'s the potential to maintain a constant C.D. is increasing with decreasing separation from about 0.75 mm up to about 0.4 mm which is the closest approach that could be measured with this cell. The authors have no doubt that this trend would be reversed at still smaller electrode separation, but they did not find it so. The minima in the family of curves occurred at constantly decreasing separations as the C.D. increased. No further obvious features occurred except that the potential was not proportional to the distance and enough variation at 4.5 mm and 10 mm is present to support the existence of the peaks seen in Fig. 6 at these distances.

Close comparison of Fig. 1, 2, and 3 shows that at the greatest electrode separation ($\sim$ 1.1 cm) and 0.3 ma/cm^2 all three orientations have equal concentration gradients. This is presumably the point at which convection just becomes effective in altering the concentration gradient in this geometry of cell.

Conclusions

The evidence in the presented data for convection when electrodes are oriented vertically is really only reinforcement for already existing evidence. However the anomalies in the plots of $\partial c/\partial x$ *vs.* C.D., $\partial c/\partial x$ *vs.* electrode separation, and impressed voltage *vs.* electrode separation in the C/A orientation clearly indicate the presence of electromigration and field effects. Obviously any quantitative characterization of these effects will require further careful work with a redesigned cell at smaller electrode separation in the C/A position. Preliminary work in the same cell at different concentrations and temperatures shows similar general behavior. This agrees in principle with the findings of Anson who has shown that thin layer chronopotentiometry where his electrolyte layers were 0.01 mm to 0.1 mm thick required less voltage than normal diffusion chronopotentiometry. It should be possible to predict the onset of effective convection in any geometry of cell with further work.

Acknowledgment

The authors gratefully acknowledge the support of the National Research Council of Canada and the Lawrence Radiation Laboratory of the University of California, Berkeley.

Manuscript received June 1, 1965.

Any discussion of this paper will appear in a Discussion Section to be published in the June 1966 JOURNAL.

REFERENCES

1. C. R. Christensen and F. C. Anson, *Anal. Chem.*, **35**, 205 (1963).
2. R. N. O'Brien, W. F. Yakymyshyn, and J. Leja, *This Journal*, **110**, 820 (1963).
3. N. Ibl and R. Muller, *ibid.*, **105**, 346 (1958).
4. R. N. O'Brien, Concentration Gradients at Horizontal Electrodes, To be published.
5. R. S. Cooper, *This Journal*, **105**, 506 (1958).
6. N. Ibl and R. Muller, *Z. Elektrochem.*, **59**, 671 (1955).
7. R. N. O'Brien and C. Rosenfield, *J. Phys. Chem.*, **67**, 643 (1963).
8. R. N. O'Brien, C. A. Rosenfield, K. Kinoshita, W. F. Yakymyshyn and J. Leja, submitted to *Can. J. Chem.*
9. R. N. O'Brien, *Rev. Sci. Inst.*, **35**, 803 (1964).
10. R. N. O'Brien, *Nature*, **201**, 74 (1964).

Technical Notes

Detection of Striae in GaAs by Chemical Etching

T. S. Plaskett and A. H. Parsons

IBM Watson Research Center, Yorktown Heights, New York

Striations in GaAs pulled from the melt in a sealed magnetic puller have been observed by Pilkuhn and Rupprecht (1) by anodic etching of bulk material and by chemical etching of p-n junctions that have been produced by diffusion. Striae have also been observed by Drougard and Gunn (2) by infrared transmission and by LeMay (3) in Te doped GaAs by chemical etching with HNO_3 etch. It has been postulated (4) that the striae in GaAs are associated with segregation of the solute during growth of the crystal, as has been observed in the case of Ge and Si [see review article by Dikhoff (5)] and InSb (6), and result from a variation in the rate of growth (7, 8). In the present investigation a chemical etching technique is described for revealing striations in both the heavily doped, conducting GaAs that is used for the fabrication of injection lasers, and the semi-insulating GaAs that is used for insulating substrate for the epitaxial growth of Ge. The laser material was n-type, selenium or tin doped. The semi-insulating material was obtained by doping with chromium. Striations were clearly evident by infrared examination in the conducting crystals, but could not be detected by this means in the insulating crystal.

The etching solution that was used was $3HNO_3$:1HF:$4H_2O$. Etching was carried out at room temperature for about 2 min on either chemically or mechanically polished surfaces. The striation pattern on a section cut parallel to the growth axis for a 3 x 10^{18} at./cc Sn doped crystal is shown in Fig. 1a. The striation spacing is not constant, but over the distance shown in the photomicrograph it is about 20μ. The spacing calculated from the f/ω relationship where f is the rate of growth of the crystal and ω is the rotation rate is 9μ. As was shown previously (4), agreement with this relationship for a sealed Czochralski system is not good because of an erratic pulling rate characteristic of this type of puller where the pulling mechanism involves magnetic coupling. This etching technique does not detect the finer striation structure reported by Gatos *et al.* (6) to occur between the coarse striae.

A longitudinal section taken from a Se doped crystal (1.5 x 10^{18} at./cc) was given a similar etching treatment as above. Initially, no striae were detected in this material by etching even though the infrared examination indicated that the sample was striated. When, however, the sample was etched under tungsten illumination the striae were clearly visible as shown in Fig. 1b. The etchant only revealed striae on the side of the sample which was closest to a {111} Ga face and was most effective when the surface parallel to the growth axis was a $\{\bar{2}11\}$ (all crystals examined were grown in <111>). For the Sn doped crystal there was no orientation or polarity dependence.

It was found that striae were not detected in the semi-insulating, Cr doped crystal unless the etching was carried out under illumination and on a surface having the same crystal orientation and polarity as required for the Se doped material. The Cr doped crystal showed no striae pattern when examined by infrared transmission but, as shown in Fig. 1c a striation structure is revealed by the chemical etching technique. The Cr level was about 2.8 x 10^{17} as determined by emission spectroscopy; the Se and Sn levels were

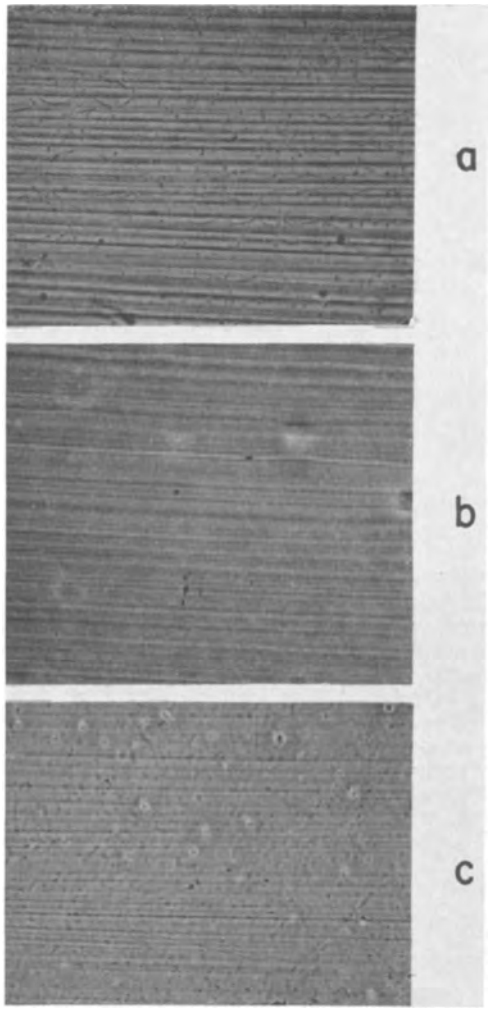

Fig. 1. Striation structures revealed by chemical etching. Sections shown were cut parallel to the growth axis. (a) Sn doped; (b) Se doped; (c) Cr doped. Magnification approximately 45X.

determined by Hall effect measurements. The measured striation spacing for the Se and Cr doped samples was 10 and 15μ, respectively. The calculated spacing from f/ω relationship for the Se was 3μ and for Cr 52μ. The agreement with f/ω relationship is not good and for the same reason as suggested for the Sn doped crystal.

The chemical etching technique with the additional requirement of etching under illumination provides a sensitive means of detecting inhomogeneities in GaAs crystals. The effect of the illumination is to make the etch preferential. The illumination probably injects holes at the surface by some photo process, such as photoconductivity, and makes the surface more reactive. Inhomogeneities in the crystals would affect the amount of the injection of holes and thus give rise to the striated pattern. Semi-insulating GaAs is known to be photoconductive (9), and therefore the striations in this case could be explained by Cr segregation. Similarly the Se doped material had the same etching requirements which would also suggest that the striae represent a chemical segregation pattern. However, for the Sn doped crystal no special etching requirements were needed and thus the striae could represent some other type of crystalline defect such as dislocation loops. The fact that the atomic size mismatch between Sn and Ga or As is much greater than for the other dopants would support a crystalline defect model.

Acknowledgment

The authors wish to thank Dr. S. E. Blum for supplying the crystals.

Manuscript received April 5, 1965; revised manuscript received June 11, 1965. This paper was presented at the Toronto Meeting. May 3-7, 1964.

Any discussion of this paper will appear in a Discussion Section to be published in the June 1966 JOURNAL.

REFERENCES

1. M. H. Pilkuhn and H. Rupprecht, *Trans. AIME*, **230**, 296 (1963).
2. M. E. Drougard and J. B. Gunn, *This Journal*, **111**, 155C (1964).
3. C. Z. LeMay, *J. Appl. Phys*, **34**, 439 (1963).
4. T. S. Plaskett and S. E. Blum, *This Journal*, **111**, 155C (1964).
5. J. A. M. Dikhoff, *Philips Tech. Rev.*, **25**, 195 (1963-64).
6. H. G. Gatos, A. J. Strauss, M. C. Lavine, and T. C. Harmon, *J Appl. Phys*, **32**, 2057 (1961).
7. J. A. Burton, E. D. Kolb, W. P. Slitcher, and J. D. Struthers, *J. Chem. Phys.*, **21**, 1991 (1953).
8. W. A. Tiller, K. A. Jackson, J. M. Rutter, and B. Chalmers, *Acta Met.*, **1**, 428 (1953).
9. C. H. Gooch, C. Hilsum, and B. R. Holeman, *J. Appl. Phys.*, **32**, 2069 (1961).

Chemical Etching of Silicon Carbide with Hydrogen

T. L. Chu and R. B. Campbell

Research Laboratories, Westinghouse Electric Corporation, Pittsburgh, Pennsylvania

Silicon carbide has a large energy gap and is useful for the fabrication of active devices operable at high temperatures. Chemical etching can be used for the preparation of silicon carbide surfaces in the fabrication process; however, the number of etchants is limited due to its chemical inertness. Molten salts, such as sodium peroxide, sodium carbonate, etc., have been used to reveal structural imperfections in silicon carbide (1). Mixtures of chlorine and oxygen have also been used for the etching of silicon carbide at 900°C or above (2). The (0001) and (000$\bar{1}$) faces of hexagonal silicon carbide exhibit different etching behaviors due to the slightly ionic character of the Si-C bond. Using molten sodium peroxide, for example, one face (hereafter face A) remains smooth after etching while the other (face B) becomes "wormy" in appearance with a considerably lower etch rate. However, face B is more readily attacked by mixtures of chlorine and oxygen. No unambiguous conclusions on the nature of these two faces have been reached.

The use of gaseous etchants is more advantageous in certain processes. In the epitaxial growth process, for instance, the substrate surface condition is a very important factor determining the crystal perfection of the grown layer, and the etching of substrates in the reaction tube immediately prior to the growth process is often employed. The chemical reactivity of carbon toward hydrogen at high temperatures suggests that hydrogen could be used as an *in situ* etchant for silicon carbide. We have found that at temperatures above 1600°C, hexagonal silicon carbide crystals are etched at measureable rates yielding smooth surfaces. The results are summarized in this note.

The reaction of carbon with hydrogen proceeds rapidly at high temperatures producing hydrocarbons. At 2000°K, for example, the free energies of forma-

tion of acetylene and methane are 27.97 and 31.19 kcal/mole, respectively (3). The reaction between silicon carbide and hydrogen thus yields a mixture of silicon vapor and hydrocarbons. The use of hydrogen in a flow system shifts the chemical equilibrium toward the formation of gaseous silicon and hydrocarbons, and reasonable etch rates can be obtained. It should be noted that the vapor pressures of the silicon carbide species are very low in the temperature range under consideration. At 2149°K, for example, the principal gaseous species above silicon carbide are Si, SiC_2, and Si_2C, and their partial pressures are 2.1×10^{-5}, 1.9×10^{-6}, and 1.4×10^{-6} atm, respectively (4). Thus, the evaporation of silicon carbide in an inert atmosphere at this temperature or below would not be appreciable.

The etching experiments were carried out in a flow system, using a horizontal, water-cooled quartz tube of 2.5 cm ID with gas inlet and exhaust tubes. Hydrogen was purified by diffusion through a palladium-silver alloy, and its flow rate was measured with a Matheson flowmeter. Hexagonal silicon carbide platelets with main faces of {0001} orientation grown by a sublimation technique (5), were etched in molten sodium peroxide to reveal the polarity of the faces and then mechanically polished. These crystals, usually 3-6 mm across and 0.2 mm thick, were supported on a refractory inert susceptor in the quartz tube (6), and hydrogen was introduced at a constant rate. The susceptor was then heated externally by an rf generator so that the crystals could be maintained at a desired temperature. The temperature of the crystals was measured with a microoptical pyrometer. The measured temperatures should be corrected for the emissivity of the crystals and the reflection loss at the wall of the reaction tube which would be about 100°C under the conditions used here. The etch rate was determined by measuring the thickness of the crystal before and after heating in hydrogen for a measured length of time using both optical microscopy and thickness gauges. In some cases, it was also determined from the surface area of the specimen and its decrease in weight after etching.

The etching of silicon carbide crystals with hydrogen involves such experimental variables as the polarity of the crystal surface, temperature of the crystal, and flow rate of hydrogen. Most experiments were carried out using a hydrogen flow rate of 2.5 l/min which, in our apparatus at room temperature, corresponds to a linear velocity of 8.5 cm/sec or higher. The etch rates of faces A and B of hexagonal silicon carbide in the temperature range 1600°-1750°C (meas.) are summarized in Table I, and the data shown here are believed to be accurate within ±10%. The etch rate was found to decrease with decreasing hydrogen flow rate, as expected. At a hydrogen flow rate of 0.5 l/min, for example, the etch rates at 1700°C were found to be 0.3 and 0.2 μ/min for face A and B, respectively. In all cases, the etch rate of face A by hydrogen is higher than that of face B, contrary to the etching action of chlorine-oxygen mixtures.

Table I. Etch rate of silicon carbide with hydrogen, μ/min (Hydrogen flow rate = 2.5 l/min)

Temperature, °C	Face A	Face B
1600	0.3	0.25
1650	1.5	0.8
1700	2	0.8
1750	4	2

Attempts were made to analyze the products of the silicon carbide-hydrogen reaction using a mass spectrometer, and no hydrocarbons were detected. This is due presumably to the decomposition of the hydrocarbons immediately after reaction (7), depositing carbon at lower temperature regions of the reaction tube.

The hydrogen etch appears to be nonpreferential, and the resulting surface, irrespective of polarity of the surface and growth steps initially present on the crystal, is smooth when examined with an optical microscope. The same results were obtained when the as-grown surfaces of hexagonal silicon carbide were used. A further advantage of this technique is that ultrapure hydrogen can be prepared readily to minimize the contamination of the crystal surface during the etching process. The effectiveness of the H_2 etch technique is indicated by the fact that the structural perfection of epitaxial silicon carbide films has been greatly improved by the *in situ* etching of substrates with hydrogen (6). Furthermore, the use of hydrogen etch also enabled the epitaxial deposition of silicon films of reasonable perfection on silicon carbide substrates (8).

Acknowledgment

This work was supported by the Air Force Avionics Laboratory, Air Force Systems Command, United States Air Force under Contract No. AF33(615)-1440.

Manuscript received June 4, 1965.

Any discussion of this paper will appear in a Discussion Section to be published in the June 1966 JOURNAL.

REFERENCES

1. J. W. Faust, Jr., in "Silicon Carbide," J. R. O'Connor and J. Smiltens, Editors, p. 403, Pergamon Press, New York (1960).
2. R. C. Smith, Electrochem. Soc. Electronics Div. Abstracts, **12** [2] 15 (1963).
3. JANAF Interim Thermochemical Tables, Dow Chemical Co., Midland, Mich., Dec. 31, 1960.
4. J. Drowart, G. DeMaria, and M. G. Inghram, *J. Chem. Phys*, **29**, 1015 (1958).
5. D. R. Hamilton, *This Journal*, **105**, 735 (1958).
6. R. B. Campbell and T. L. Chu, To be published.
7. E. A. Gulbransen, K. F. Andrew, and F. A. Brassart, *This Journal*, **112**, 49 (1965).
8. T. L. Chu, G. A. Gruber, J. J. Oberly, and R. L. Tallman. Paper presented at the Eletrochemical Society Meeting, May 10-14. 1965, San Francisco.

Electrical Conductivity of Fused Potassium Nitrate

C. A. Angell[1]

Department of Metallurgy, University of Melbourne, Parkville, Victoria, Australia

Recently published electrical conductance data for KNO_3 obtained by King and Duke by means of a d-c technique (1) are in agreement, to ±0.1% over the whole temperature range, with a-c measurements made in this laboratory but published only in graphical form (2). Since King and Duke observe that their d-c data show less scatter than previous a-c measurements and as our measurements show less scatter still, it seems appropriate to report the actual conductivity values so that, jointly with those of King and Duke, they may serve as a standard for this salt. The results, together with the "activation energies" [or, preferably, "Arrhenius coefficients" (2)] for the temperature intervals between successive pairs of points are given in Table I. The consistency of activation energies calculated from points only 10°C apart constitutes a severe test of precision of conductance data, *e.g.*, an 0.1°C error in temperature at 385.4°C would be sufficient to

[1] Currently on leave at Argonne National Laboratory, Argonne, Illinois.

Table I.

T, °C	κ	E_κ
410.7	0.8536	3.33
394.6	0.8046	
385.4	0.7559	3.35
371.3	0.7322	3.52
363.1	0.7068	3.50
352.9	0.6749	3.59
336.0	0.6212	3.71

cause the only interruption to the otherwise regular increase of E with T seen in Table I. In view of this, we note that the regular change of activation energy with temperature reported graphically by Cowen and Axon (3) implies a particularly high precision in their measurements, which unfortunately were not tabulated.

In connection with the precision of King and Duke's measurements, it is pertinent to observe that the curvature of their log κ *vs.* $1/T$ plot for the $LiNO_3$-$NaNO_3$-KNO_3 eutectic (4) is of the form to be anticipated for a low-melting eutectic from the free volume interpretation of other molten salt data (2, 5). In fact, the plot runs almost parallel to (but slightly lower than) that for the KNO_3-$NaNO_3$-$NaNO_2$ eutectic shown in Fig. 6 of ref. (2). The curvature represents a systematic increase of E_κ from 3.1 kcal/mole at 370°C to 6.9 kcal/mole at 143°C, which is not sufficient to permit independent calculation of the free volume parameters for this melt. The data are none the less of considerable theoretical value since they cover the temperature range linking the domains of the glass-forming molten nitrate mixtures and the glass-forming aqueous nitrate solutions.

Manuscript received April 2, 1965.

Any discussion of this paper will appear in a Discussion Section to be published in the June 1966 JOURNAL.

REFERENCES

1. L. A. King and F. R. Duke, *This Journal.* **111**, 712 (1964).
2. C. A. Angell, *J. Phys. Chem.*, **68**, 1917 (1964).
3. H. C. Cowen and H. J. Axon *Trans. Faraday Soc.*, **52**, 242 (1956).
4. L. A. King, C. C. Bissell, and F. R. Duke, *This Journal*, **111**, 720 (1964).
5. C. A. Angell, *J. Phys. Chem.*, **69**, 399 (1965).

Brief Communication

Progress toward Single Crystal Silicon Films on Amorphous Substrates

J. D. Filby and S. Nielsen

Royal Radar Establishment, Malvern, England

The preparation of single crystal layers of silicon on insulating substrates has potential advantages in semiconductor technology. Some progress has been made recently toward this with the successful epitaxial deposition of silicon on crystalline quartz (1) and sapphire (2, 3) and with the recrystallization of thin films of silicon on alumina (4,5). We report here encouraging progress toward single crystal layers on fused quartz using a new technique, ultrathin alloy-zone-crystallization, U.T.A.Z.C.

U.T.A.Z.C. involves the use of an extremely thin layer of alloy on the substrate surface and must be differentiated from thin alloy-zone-crystallization, T.A.Z.C., techniques (6, 7) such as the vapor liquid solid technique (8,9). In the T.A.Z.C. technique, material diffuses through a layer of alloy to the substrate surface; in the U.T.A.Z.C. technique the alloy layer is too thin for diffusion to be an important factor and the function of the layer is apparently to alter the energetics of the nucleation and growth processes. The use of the U.T.A.Z.C. technique in the epitaxial deposition of silicon on silicon at low temperatures (10) and on single crystal alumina (11) has been described elsewhere.

When silicon is sublimed, or evaporated, on the surface of fused quartz, polycrystalline layers are obtained. The grain size increases with substrate temperature and may approach 5μ at 1100°C. However, if a very thin layer of gold is evaporated on the fused quartz surface before the silicon is deposited, the grain size is much increased. This is illustrated in Fig. 1, which shows large silicon grains on quartz previously covered with gold on the left, and small silicon grains on quartz with no gold on the right. The grain size can be as large as 300μ, and we believe that with further development even larger grains and possibly single crystal layers may be obtained.

Layers containing grains larger than 50μ, as shown in Fig. 2, were repeatedly obtained by the following procedure. The fused quartz substrate (½ x ¼ in.) was cut from a 3 x 1 in. microscope slide and washed in trichloroethylene, chromic acid, deionized water, and acetone to remove the surface contamination intro-

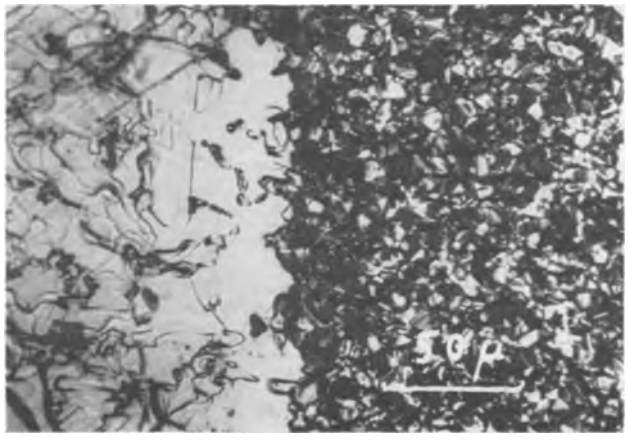

Fig. 1. Surface of evaporated silicon layer deposited on amorphous quartz (right) and on quartz covered by a 1000Å gold film (left).

Fig. 2. Typical area of the surface of a silicon layer sublimed on amorphous quartz using a thin (2000Å) gold film.

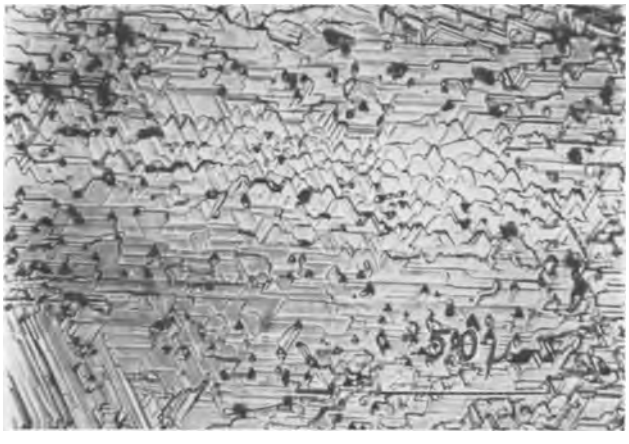

Fig. 3. Growth steps on the surface of a silicon layer deposited on amorphous quartz.

duced during the cutting process. A layer of gold 1000-3000Å thick was evaporated on one surface of the substrate, the substrate being near room temperature. The substrate was then transferred to a sublimation apparatus (7), where silicon was sublimed onto it at a rate of 2 μ/hr, the substrate temperature being in the region 700°-800°C. Layers of silicon up to 20μ in thickness were obtained in this way, but due to differential thermal contraction these were cracked into areas a millimeter or so in diameter. A high proportion of the larger grains had a (111) plane parallel to the surface of the layer, although the grains were randomly orientated with respect to each other. The (111) orientation can be easily seen in Fig. 3, which shows the growth steps on the surface of a large grain, the growth steps being typical of those observed on epitaxial silicon layers grown on (111) surfaces of silicon. Further evidence for the single crystallinity of such large grains was obtained by transmission and reflection electron diffraction, Fig. 4 being a transmission diffraction photograph.

Similar results have also been obtained using evaporation rather than sublimation. In these cases silicon was evaporated as described by Newman (12), and a Varian V120 getter-ion vacuum system used. Although a high proportion of the resultant layer consisted of grains over 50μ across, grains larger than 250μ were less numerous than for sublimed layers. Current results suggest that the grain size is decreased if either the deposition rate or the substrate temperature is too high. Layers containing large numbers of grains

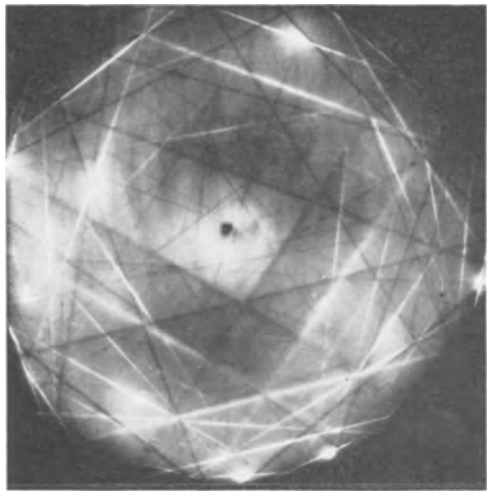

Fig. 4. Transmission electron diffraction photograph of an area of the layer shown in Fig. 2.

50μ or more in diameter were obtained by using 1000Å of gold, an evaporation rate of 50 μ/hr and a substrate temperature of 900°C.

Apart from the thickness of the gold layer, which has been varied between 1000Å and 5μ, with layers below 3000Å giving the best results, no attempt has been made to optimize the experimental conditions. Preliminary experiments using platinum, copper, silver, aluminum, tin, or indium in place of gold, suggest that gold gives the best results. No systematic variation of the experimental parameters, *e.g.*, rate of evaporation, substrate temperature, etc., has been attempted, and no attempt has been made to induce a preferred orientation to the nuclei. The results to date with the U.T.A.Z.C. technique, therefore, seem to offer good prospects of single crystal layers on amorphous substrates.

Acknowledgment

The authors gratefully acknowledge the expert assistance of W. H. Wilgoss and D. G. Coates. British Crown Copyright. Reproduced with the permission of the Controller, Her Britannic Majesty's Stationery Office.

Manuscript received May 7, 1965.

Any discussion of this paper will appear in a Discussion Section to be published in the June 1966 JOURNAL.

REFERENCES

1. B. A. Joyce, R. W. Bicknell, J. M. Charig, and D. J. Stirland, *Solid State Comm.*, **1**. 107, (1963).
2. R. W. Bicknell, J. M. Charig, B. A. Joyce, and D. J. Stirland, *Phil Mag.*, **9**, 965 (1964).
3. H. M. Manasevit and W. I. Simpson, *J. Appl. Phys.*, **35** [4], 1349 (1964).
4. V. Y. Doo, *This Journal*, **111**, 1196 (1964).
5. J. D. Filby and S. Nielsen. *ibid.*, **112**, 534 (1965).
6. D. T. J. Hurle, J. B. Mullin, and E. R. Pike, *Solid State Comm.*, **2**, 197 (1964).
7. J. D. Filby and S. Nielsen, *This Journal*, **112**, 535 (1965).
8. R. S. Wagner and W. C. Ellis. *Appl. Phys. Letters*, **4**, 89 (1964).
9. R. S. Wagner and W. C. Ellis, *Trans. AIME*, **233**, (1965)
10. J. D. Filby and S. Nielsen, *Microelectronics and Reliability*, **4**, (1965).
11. J. D. Filby and S. Nielsen, International Vacuum Congress, Stuttgart, 1965.
12 R. C. Newman, *Microelectronics and Reliability*. **3**, 121 (1964).

The Cathodic Reduction Mechanism of Electrolytic Manganese Dioxide in Alkaline Electrolyte

A. Kozawa and J. F. Yeager

Consumer Products Division, Research Laboratory, Union Carbide Corporation, Cleveland, Ohio

ABSTRACT

Constant-current discharge curves for electrodeposited MnO_2 on graphite showed a two-stage reduction; $MnO_{2.0}$ to $MnO_{1.5}$ and $MnO_{1.5}$ to $MnO_{1.0}$. Potential decreased continuously during the first stage and in some discharges was constant for at least half of the second. The first stage was not influenced by current density, KOH concentration, MnO_2 thickness, or a complexing agent. The constant-potential portion was observed with 9M KOH, low current density; the potential was near the standard redox potential of Mn(II) and Mn(III) species in solution as determined polarographically. The first stage is considered a homogeneous phase reduction, while the second stage involves a heterogeneous system. A new mechanism is suggested for the latter.

The cathodic reduction of electrolytic manganese dioxide (γ-MnO_2) in alkaline electrolyte has been investigated by Cahoon and Korver (1) and also recently by Bell and Huber (2) by taking discharge curves and by chemical and x-ray diffraction analyses.

Cahoon and Korver postulated the following three stages for the reduction process. The electrolytic manganese dioxide is first reduced simultaneously to $Mn(OH)_2$ and Mn_4O_7, then the Mn_4O_7 is reduced to Mn_3O_4 and $Mn(OH)_2$ in the second stage, and the Mn_3O_4 to $Mn(OH)_2$ in the final stage. Their discharge curves, however, did not show steps corresponding to those stages (see Fig. 7).

Bell and Huber postulated the following three stages based on the steps observed in their discharge curves (Fig. 7) (*i*) $MnO_{2.0} \rightarrow MnO_{1.7}$ as a homogeneous phase reduction; (*ii*) $MnO_{1.7} \rightarrow MnO_{1.47}$ as a heterogeneous system, $MnO_{1.7}$ being rhombic groutite (αMnOOH) structure and $MnO_{1.47}$ tetragonal γ-Mn_2O_3 structure; (*iii*) below $MnO_{1.47}$ as a heterogeneous system. In the first stage, the potential decreased continuously as the cathodic reduction proceeded, but in the second and third stages the potential remained practically at the characteristic steady potential values.

Contrary to Cahoon and Korver, Bell and Huber found by x-ray diffraction no $Mn(OH)_2$ as a reduction product at the beginning stage of the discharge. As they (2) pointed out, this discrepancy may be due to the difference in the current density; Cahoon and Korver discharged at about 60 ma/g of MnO_2 and Bell and Huber discharged at 0.5 ma/g of MnO_2.

In the above investigations (1, 2), the discharges of manganese dioxide were performed in the presence of a zinc electrode or even in a KOH solution containing ZnO (2). This may have introduced an additional complication in elucidating the reduction process.

In the present investigation, electrodeposited manganese dioxide on graphite rods was discharged in pure KOH solution under varying conditions of current density, KOH concentration, and thickness of the MnO_2 layer on the graphite. Also the effect of triethanolamine added to the electrolyte was examined in order to see whether $Mn(OH)_2$ is formed on the electrode surface at the beginning stage of the discharge. Triethanolamine forms a stable complex with Mn(II) and Mn(III) ions in alkaline solution; therefore, if $Mn(OH)_2$ is formed on the electrode surface, it will be removed by complexing and an influence will be shown on the discharge curve.

Electrodeposited manganese dioxide on the spectroscopic graphite rod has been extensively used (3-6) in previous studies for the discharge process in neutral or acid solutions and has given satisfactory results, mainly because the rod is porous and provides good adhesion between the manganese dioxide and graphite.

Experimental

Preparation of the MnO_2 *electrode.*—Manganese dioxide was electrodeposited on spectroscopic graphite rods (AGKSP), 7.7 cm long (except for the experiment shown in Fig. 4) and 4.5 mm diameter, from 0.5M $MnSO_4$ + 0.5M H_2SO_4 at 90° ± 1°C at 20.0 ma for 10.0 min. The electrode construction and the electrolysis bath are shown in Fig. 1. The graphite electrodes with electrodeposited manganese dioxide was taken out of the Teflon holder and washed with 0.1*N* H_2SO_4, then washed with water at room temperature for more than 48 hr, and then kept in distilled water until use. Current efficiency of the electrodeposition of manganese dioxide was almost 100% under these conditions. From chemical analysis of the manganese dioxide by the previously reported ferrous sulfate method (7), 10.6 ± 0.4 mg of MnO_2 per electrode and 1.98 ~ 1.99 for the x value in MnO_x were obtained.

Discharge experiments.—The discharge experiments were carried out at room temperature (23° ± 0.5°C) in a cell which was the same as that shown in Fig. 1, except alkaline electrolyte was employed instead of

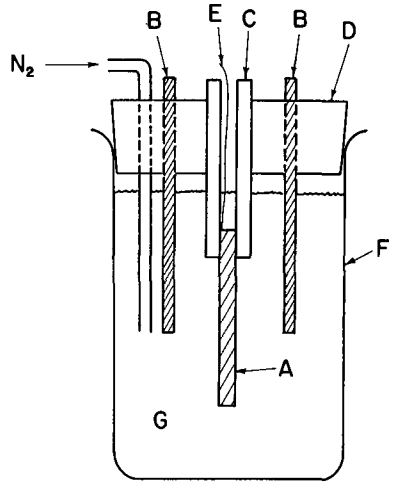

Fig. 1. Electrodeposition bath and discharge cell; N_2 gas was admitted here only when used as a discharge cell. A, Test electrode (MnO_2 deposited on porous graphite); B, counter electrodes of graphite. Showing only 2 of 4; C, Teflon tubing electrode holder; D, Teflon stopper; E, platinum lead wire, epoxy-coated except at the end contact; F, 200 ml beaker; G, electrolyte.

the manganese sulfate solution. Before the discharge, nitrogen was passed through the electrolyte to eliminate dissolved oxygen. Before the discharge, the electrode was immersed in the electrolyte for 12 hr or more unless otherwise noted, and the electrolyte was not stirred during the discharge. During the discharge, the potential was recorded with reference to Hg/HgO electrodes immersed in KOH at the same concentration.

In this experimental arrangement, O_2 may be produced at the counter electrode of graphite. Migration of the O_2 to the manganese dioxide electrode and influence to the current as well as the electrochemical reaction might be considered. This point was examined by calculation as well as experiment. Based on the solubility and diffusion coefficient of oxygen in 9M KOH at 25°C, 3×10^{-5} mole/liter and 5×10^{-6} cm^2 sec^{-1}, respectively (21). The diffusion limiting current was found to be

$$i = \frac{NFDC}{\delta} = \frac{2 \times 10^5 \times 5 \times 10^{-6} \times 3 \times 10^{-8}}{0.05}$$

$$= 0.6 \times 10^{-6} \text{ amp/cm}^2 = 0.6 \ \mu\text{a/cm}^2$$

by assuming $\delta = 0.05$ cm for unstirred aqueous solutions (22). For the graphite rod used in this experiment, therefore the approximate diffusion limiting current is approximately 7μa. This point was also examined by measuring current at the graphite electrode (7.7 cm long) at —0.60v *vs.* Hg/HgO (9M KOH) in 9M KOH saturated with O_2 (1 atm) or N_2. It was found that the current attributable to the dissolved O_2 was less than 3 μa under unstirred conditions. Therefore, the error due to this fact must be very small.

The discharge curves presented in this paper were repeated at least twice, the two curves agreed with each other within 15 mv at any stage of the discharge except at the very end of the discharge curve.

Results

Effect of current density.—Figure 2 shows three discharge curves at three constant current densities; 0.11, 0.33, and 3.0 ma per electrode (apparent area: 10.8 cm^2). The lower abscissa of Fig. 2 shows the amount of electricity in ma-hr and the upper abscissa shows the x value in MnO_x calculated from the electricity drawn. We can see two distinct steps in the discharge curves. In the first step from $MnO_{2.0}$ to $MnO_{1.5}$ the potential decreased continuously and in the second step from $MnO_{1.5}$ to $MnO_{1.0}$ the potential remained practically constant [—0.40v *vs.* Hg/HgO (9M KOH)] for a considerable portion of the discharge period on the 0.11 and 0.33 ma discharges.

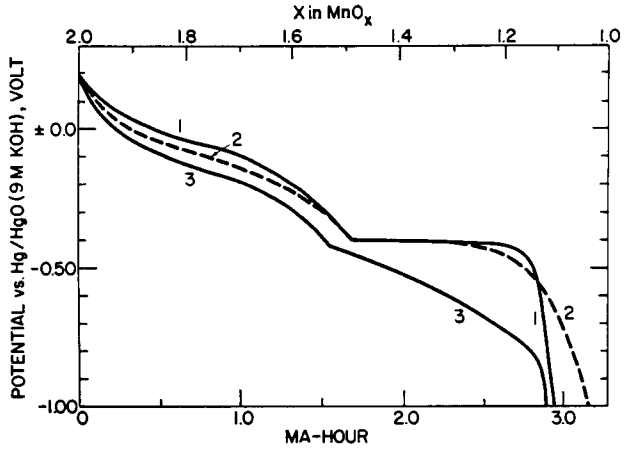

Fig. 2. Discharge curves at constant current in 9M KOH at 23°C. The x value in MnO_2 was calculated from the amount of electricity drawn. Curve 1, at 0.11 ma/electrode; curve 2, at 0.33 ma/electrode; curve 3, at 3.0 ma/electrode.

Table I. Discharge capacities of electrodeposited manganese dioxide in 9M KOH based on the curves shown in Fig. 2. Each graphite rod had 10.6 mg of MnO_2*

Discharge current per electrode, ma	Theoretical discharge time**, hr	Observed discharge time to —1.0v (Fig. 2), hr	Discharge capacity***, %
0.11	30.3	27.0	89.1
0.33	10.1	9.50	94.1
3.0	1.11	0.96	84.4

* Calculated discharge capacity to $Mn(OH)_2$ is 3.33 ma-hr.
** Assuming from MnO_2 to $Mn(OH)_2$.
*** Based on the theoretical discharge time.

Table I shows discharge capacities observed in those discharges (Fig. 2) to —1.0v. The discharge capacity in column 4 of Table I shows values ranging from 84 to 94%. Several additional electrodes prepared and discharged in the same manner as those in curve 2 in Fig. 2 exhibited discharge capacities of 95 ± 3% and the discharge curves were very reproducible.

Effect of KOH concentration.—The effect of KOH concentration was investigated at constant current (3.0 ma) discharge in 0.1, 1.0, and 9M KOH electrolytes. The results are shown in Fig. 3. In these experiments, the potential was measured against Hg/HgO electrodes in 0.1, 1.0, or 9M KOH depending on the electrolyte used in the discharge in order to eliminate the junction potential. We can see in Fig. 3 that the first step ($MnO_{2.0} \rightarrow MnO_{1.5}$) in the discharge is influenced very little by the electrolyte concentration in a range of 0.1-9M, but the second step ($MnO_{1.5} \rightarrow MnO_{1.0}$) is greatly influenced. The second step is essentially absent in 0.1 and 1.0M KOH solutions.

Effect of thickness of MnO_2 layer.—In order to prepare a manganese dioxide electrode which has a thicker MnO_2 layer, a graphite rod 1.5 cm long instead of 7.7 cm long was used for the electrodeposition at the same conditions (20 ma for 10 min at 90°C). The manganese dioxide electrode prepared in this manner had almost the same amount of MnO_2 (10.6 mg) by chemical analysis and therefore should have a MnO_2 layer approximately five times thicker. However, the graphite rod is porous (7) (porosity: 20%) and considerable deposition may have taken place in the pores.

The discharge curves at 3 ma are shown in Fig. 4, which again shows a case where the first step is influenced very little, this time by increasing the MnO_2

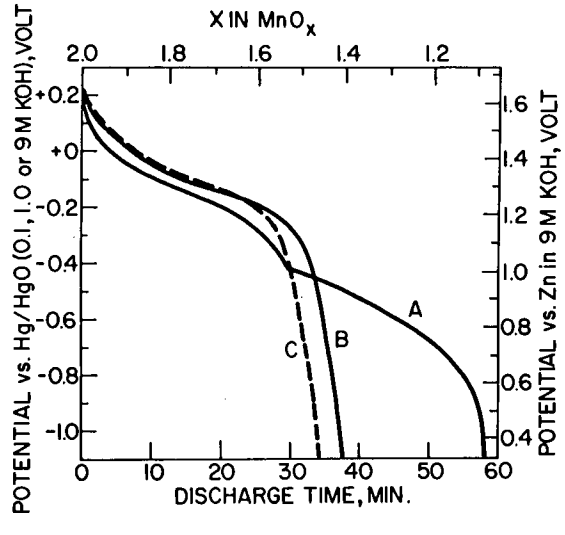

Fig. 3. Effect of KOH concentration on the discharge at a constant current of 3.0 ma. The reference electrodes of Hg/HgO used for discharges in 9, 1 and 0.1M KOH electrolyte were kept in 9 (curve A), 1 (curve B), and 0.1M (curve C), KOH, respectively.

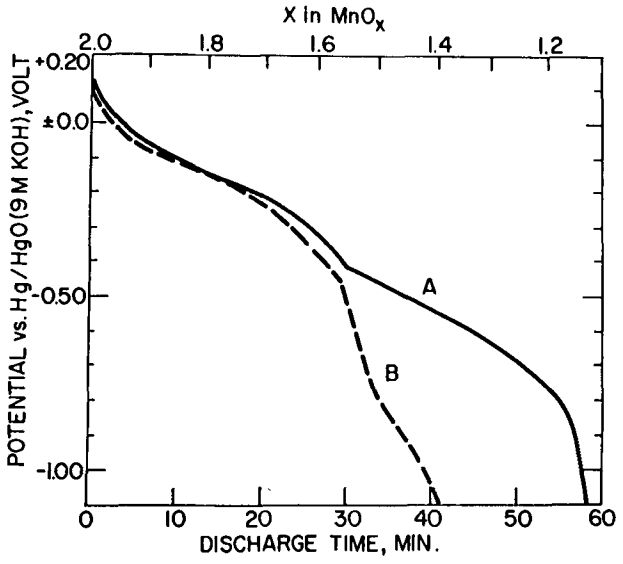

Fig. 4. Effect of thickness of manganese dioxide layer, discharged at a constant current of 3.0 ma in 9M KOH at 23°C. Curve A, MnO_2 on a 7.7 cm graphite rod; curve B, MnO_2 on a 1.5 cm graphite rod.

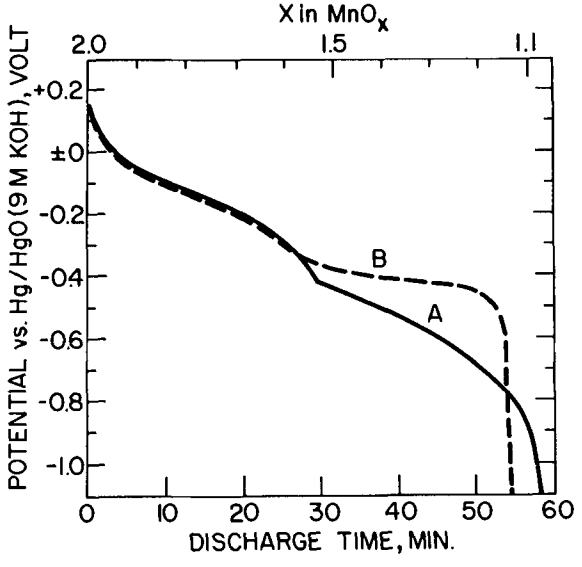

Fig. 5. Effect of triethanolamine (TEA) added to the electrolyte on the discharge at a constant current of 3.0 ma at 23°C. The x in MnO_x was calculated from the amount of electricity drawn. Curve A, 9M KOH; curve B, 9M KOH + 10% (by volume) TEA.

thickness. In the second step, the polarization is much greater with the thicker electrode.

Effect of triethanolamine added to the electrolyte.—Triethanolamine forms stable complexes in alkaline solution with divalent and trivalent metal ions such as Mn^{+++}, Mn^{++}, Fe^{+++}, and Fe^{++} (8, 9). Discharges at a constant current of 3 ma were carried out in 1.0 and 9M KOH solutions containing 10-20% triethanolamine by volume. The results are compared to the discharges in those solutions in which no triethanolamine was added. In these experiments the manganese dioxide electrodes (7.7 cm long) were immersed in the electrolyte for 5 ± 0.5 hr before the discharge. Longer immersion reduced the discharge capacity (20 hr immersion reduced its discharge capacity by about 20%); manganese dioxide was probably slowly reduced by triethanolamine. Figures 5 and 6 show the results. The addition of triethanolamine presents a third instance where the first step of discharge is influenced very little, but the second step

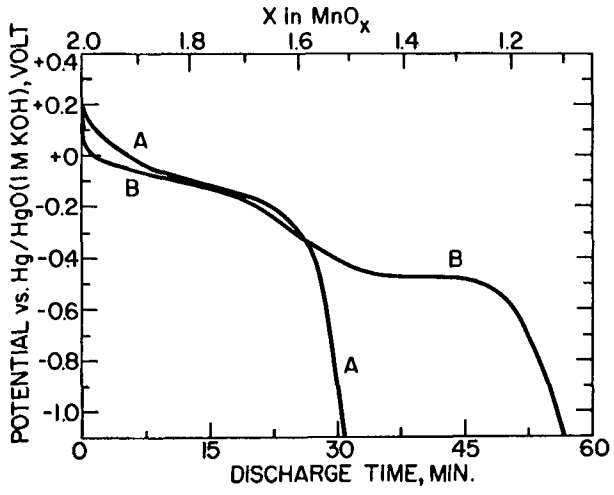

Fig. 6. Effect of triethanolamine (TEA) added to 1M KOH on the discharge at a constant current of 3.0 ma at 23°C. The x in MnO_x was calculated from the amount of electricity drawn. Curve A, 1M KOH; curve B, 1M KOH + 20% (by volume) TEA.

markedly. In the presence of triethanolamine, the second step was kept at a considerably higher and relatively constant potential in 9M KOH as shown in Fig. 5. In 1M KOH containing 10% triethanolamine, the second discharge step can be carried at a relatively high and constant potential, although without triethanolamine the second step did not appear.

Discussion

Discharge curves.—The experimental results obtained above are significantly different from the previously published results by Cahoon and Korver (1) and Bell and Huber (2). This is shown in Fig. 7 in which their results are compared on the same potential scale and also on the basis of x value. The MnO_2 electrodes used in the present investigation could be discharged almost completely to $Mn(OH)_2$ at moderate current densities (11 ~ 33 ma/g of MnO_2), while those used by the other investigators were not. This is probably due to the porous nature of the rod and good contact between the manganese dioxide and graphite, since MnOOH or α-Mn_2O_3 are very poor electronic conductors (10). The three-step reduction curve obtained by Bell and Huber may be due to the extremely slow (low current density) discharge, because under

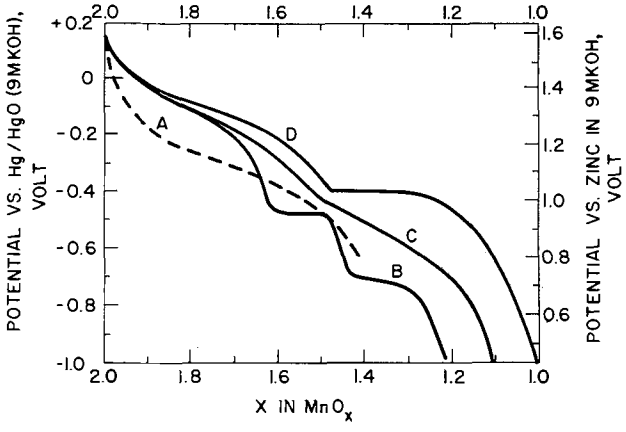

Fig. 7. Comparison of discharge curves of electrolytic manganese dioxide. Curve A, Cahoon and Korver (1), in 7.6M KOH at 30 ohm load continuous discharge (about 60 ma/g of MnO_2); curve B, Bell and Huber (2), in 9.0M KOH at 100 ohm load, 100 hr per week (about 0.5 ma/g of MnO_2); curve C, present work, in 9.0M KOH at 300 ma/g of MnO_2 constant current discharge; curve D, present work, in 9.0M KOH at 11 ~ 33 ma/g of MnO_2 constant current discharge.

such a condition the lower manganese oxide formed in the discharge seems to recrystallize. Bell and Huber cited the fact that the bobbin hardened. Absence of zinc in the present work might be a factor which might make the discharge characteristics different from the others (1, 2).

The present results can be summarized as follows. Generally speaking the discharge curves (the potential-x value in MnO_x relation) consisted of two steps, (*i*) the first step from $MnO_{2.0}$ to $MnO_{1.5}$ where the potential decreased continuously as the x value decreased, and (*ii*) the second step from $MnO_{1.5}$ to $MnO_{1.0}$ where the potential remained almost unchanged at low current densities in KOH electrolytes of high concentration or containing triethanolamine. The first step of the discharge curve was not greatly influenced by the discharge parameters such as current density (11 ~ 300 ma/g of MnO_2), electrolyte concentration (0.1 ~ 9M KOH), and thickness of MnO_2 layer (approximately $2.5 \times 10^{-4} \sim 13 \times 10^{-4}$ cm thick). The second step is greatly dependent on these discharge parameters. The presence of two steps in the reduction and oxidation between MnO_2 and $Mn(OH)_2$ can be substantiated by the charging curves which also clearly show two steps before oxygen evolution on the graphite.

Thermodynamic considerations.—Vetter (11, 12) presented a general thermodynamic theory of the electrode potential of nonstoichiometric conductive metal oxides (or hydroxides). According to this theory, if the system consists of a homogeneous phase, the potential should change in a continuous manner as the oxidation state (x value) changes. Also, according to the theory, if the oxide or hydroxide system consists of two phases (two oxide or hydroxide phases), the potential should remain unchanged as long as the two phases exist in equilibrium. In the first step of the discharge curve from $MnO_{2.0}$ to $MnO_{1.5}$ observed above, the potential decreased continuously. Therefore, this step may be a homogeneous phase discharge. In the second step from $MnO_{1.5}$ to $MnO_{1.0}$ the potential remained constant under certain discharge conditions. Therefore, this process corresponds to a heterogeneous system composed of $MnO_{1.5}$ phase and $MnO_{1.0}$ phase.

Reduction mechanism.—Although thermodynamic considerations provide an interpretation of the two discharge steps as a homogeneous phase reduction followed by a reduction process involving two oxides (or hydroxides), it cannot give or suggest any detailed mechanism. Further discussion of the mechanism for the two steps is necessary.

The first step.—For the first step from $MnO_{2.0}$ to $MnO_{1.5}$ the authors tentatively postulate an electron-proton mechanism; namely, in the discharge, electrons and protons are introduced into the γ-MnO_2 lattice and form α-MnOOH.

$$MnO_2 + H^+ + e^- \rightarrow MnOOH$$

or

$$MnO_2 + H_2O + e^+ \rightarrow MnOOH + OH^-$$

This electron-proton mechanism has been proposed and investigated by Coleman (13), Vosburgh and his co-workers (14, 15), and Scott (16) but not completely proved experimentally. The experimental results presented in this paper substantiate this mechanism. The first step is not greatly influenced by the various discharge parameters investigated such as current density, KOH concentration, MnO_2 thickness, and also addition of triethanolamine to the electrolyte. If formation of lower oxides (or hydroxides) such as $Mn(OH)_2$ at the MnO_2 solution interface in the first step and then subsequent diffusion of such a lower oxide into the MnO_2 were the actual processes, addition of triethanolamine should have an appreciable effect. Any lower oxide formed on MnO_2 surface does not diffuse into the MnO_2 at an appreciable rate (17) and probably accumulates on the surface to some extent. The electron-proton mechanism can be supported by x-ray evidence presented by Brenet (18) and Bell and Huber (2). Bell and Huber found by x-ray that the α-MnOOH structure developed as the discharge proceeded during the first step. The lattice dilation during this discharge step was observed first by Brenet (18) and confirmed by Bell and Huber (2). If the lower oxide is formed on the MnO_2 surface, the x-ray analysis should show the new diffraction lines of the lower oxide rather than the lattice dilation.

The second step.—In order to explain the flat discharge curve of the second step the author proposes here a new mechanism which is based on the appreciable solubility of Mn(II) and Mn(III) in concentrated KOH electrolyte.

The solubilities of Mn(II) and Mn(III) [or $Mn(OH)_2$ and $Mn(OH)_3$] are very small (about 4×10^{-5}M) in neutral or the usual alkaline solutions (*e.g.*, 1M) (19), but the solubility increases rapidly with increasing KOH or NaOH concentration, because of the formation of OH^- coordinated species, $[Mn(OH)_6]^{\equiv}$ and $[Mn(OH)_6]^{\equiv}$ (20). The solubility of Mn(II) and Mn(III) in 9M KOH was found to be about 0.5×10^{-3}M and 4×10^{-3}M, respectively, by a polarographic method.

In the second step in the discharge, two solid phases coexisting in equilibrium must be involved as concluded above from the thermodynamic considerations. Let us assume tentatively that α-MnOOH and $Mn(OH)_2$ are the two phases and also assume that these solid phases are in solubility equilibrium with the dissolved Mn(III) and Mn(II) species, respectively. The potential of such a system can be determined mainly by the dissolved species at an inert electrode such as graphite by the following Nernst equation

$$E = E^0 - \frac{RT}{F} \ln \frac{a_{Mn(II)}}{a_{Mn(III)}} \qquad [1]$$

which corresponds to the electrode reaction, $Mn(III) + e^- \rightleftarrows Mn(II)$. The concentrations of dissolved Mn(II) and Mn(III) are equal to their solubility values as long as the two solid phases exist. Therefore, the ratio $a_{Mn(II)}/a_{Mn(III)}$ in the above equation must be a fixed value, and consequently the potential will remain constant during the discharge at a small current density, because in such a condition the solubility equilibria (Eq. [2] and [4]) are not disturbed appreciably. In other words, we can understand the flat discharge curve if reactions [2] and [4], dissolution of α-MnOOH and precipitation of $Mn(OH)_2$, are fast or at least at a rate comparable to that of the electrochemical reduction, reaction [3].

$$\alpha\text{-MnOOH (solid)} \leftrightarrows Mn(III) \text{ (in solution)} \qquad [2]$$

$$Mn(III) + e^- \rightarrow Mn(II) \text{ (electrochemical reduction)} \qquad [3]$$

$$Mn(II) \text{ (in solution)} \leftrightarrows Mn(OH)_2 \text{ (solid)} \qquad [4]$$

One experimental approach to test the above mechanism is to compare how the potential of the flat discharge portion (Fig. 2) agrees with the potential of the Mn(II)-Mn(III) system in 9M KOH. Polarograms were taken in 9M KOH containing Mn(II) and/or Mn(III) in order to obtain the approximate standard potential of the Mn(II)-Mn(III) system in 9M KOH. Figure 8 shows the results in which we can see that the half-wave potential for the anodic process ($E\frac{1}{2} = -0.290$v) and that of the cathodic process ($E\frac{1}{2} = -0.500$v) are somewhat apart, but the mean values of −0.395v can be taken as the approximate standard potential, because the polarographic reversibility of these processes seems approximately the same from the shape of the polarograms. The potential of the flat discharge portion in Fig. 2 was −0.40v and is in good agreement with this polarographic value −0.395v. In the above comparison, the observed potential in

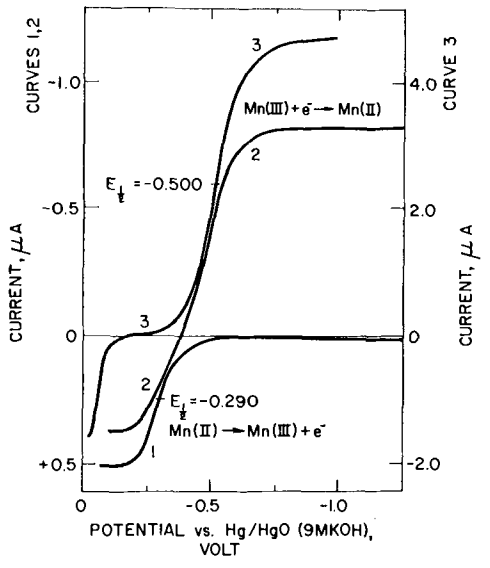

Fig. 8. Polarograms of Mn(II) and Mn(III) in 9M KOH. The curves were corrected for residual current. Polarograms were taken in N_2 saturated 9M KOH at a dropping mercury electrode (m = 1.54 mg/sec, t = 5.4 sec at open circuit in 9M KOH). Curve 1, Approximately 0.5 x 10^{-3}M $MnSO_4$ in 9M KOH, some $Mn(OH)_2$ suspended in solution; curve 2, same as 1, but some of the Mn(II) was oxidized to Mn(III) by passing O_2 gas; curve 3, approximately 2 x 10^{-3}M Mn(III) in 9M KOH. Mn(II) in 9M KOH was completely oxidized to Mn(III) by passing oxygen. Some of the Mn(III) was further oxidized to MnO_2 which was suspended in the solution.

the flat discharge curve was compared directly with the polarographic E° value. This means the logarithmic term, in the Eq. [1] was neglected. This can be justified if we realize that the ratio of the solubility values for Mn(III) and Mn(II) in 9M KOH is about 8 and the second term does not contribute more than 60 mv.

Another test of the above described mechanism is whether the α-MnOOH formed electrochemically by the reduction of γ-MnO_2 can dissolve in 9M KOH or not. During the discharge shown in Fig. 2 a reddish-violet color was observed when the electrode was wrapped with a filter paper. This is evidence that the electrochemically formed trivalent oxide can dissolve in 9M KOH, since manganous ion dissolved in 9M KOH has almost no color.

As mentioned previously the graphite rod on which manganese dioxide was electrodeposited is porous; therefore, a good portion of the manganese dioxide may be deposited on the inner walls of the pores. However, a still larger portion of the bare graphite surface on which no manganese dioxide is deposited must exist, particularly inside the pores. The manganese dioxide may be reduced by the electron-proton addition until the entire phase becomes α-MnOOH. Then further reduction takes place on the bare graphite surface through the dissolved Mn(III), according to the mechanism presented above.

The mechanism described above can explain the discharge behavior in various KOH concentrations and with addition of triethanolamine to the electrolyte, as follows: At low KOH concentrations (0.1 ~ 1M), the solubilities of Mn(II) and Mn(III) are very low; therefore, the concentration of dissolved Mn(III) cannot support the current (Fig. 3). On addition of triethanolamine, the Mn(III) complex forms. This complex is much more soluble and is reversibly reduced to the Mn(II) complex even in 0.5M NaOH (8, 9). Therefore, the discharge can proceed smoothly even in 1M KOH (Fig. 6) and also a much flatter discharge curve can be obtained as shown in Fig. 5.

Acknowledgment

The authors are indebted to Dr. R. A. Powers and Mrs. H. M. Joseph who made various suggestions in the preparation of this paper.

Manuscript received May 17, 1965. This paper was presented at the Buffalo Meeting, Oct. 10-14, 1965.

Any discussion of this paper will appear in a Discussion Section to be published in the June 1966 JOURNAL.

REFERENCES

1. N. C. Cahoon and M. P. Korver, *This Journal*, **106**, 745 (1959).
2. G. S. Bell and R. Huber, *ibid.*, **111**, 1 (1964).
3. A. M. Chreitzberg, D. R. Allenson, and W. C. Vosburgh, *ibid.*, **102**, 557 (1955).
4. W. C. Vosburgh, Mary Jo Pribble, A Kozawa, and A. Sam, *ibid.*, **105**, 1 (1958).
5. A. Kozawa and W. C. Vosburgh, *ibid.*, **105**, 59 (1958).
6. W. C. Vosburgh and Pao-Soong Lou, *ibid.*, **108**, 485 (1961).
7. A. Kozawa, *Memoirs of the Faculty of Engineering, Nagoya University*, **11**, 233 (1959).
8. I. M. Issa, R. M. Issa, I. F. Hewaidy, and E. E. Omar, *Anal. Chim. Acta*, **17**, 434 (1957).
9. I. M. Issa, R. M. Issa, and I. F. Hewaidy, *Chemist-Analyst*, **47**, 88 (1958).
10. C. Drotschman, *Batterien*, **9**, 686 (1964).
11. K. J. Vetter, *This Journal*, **110**, 597 (1963).
12. K. J. Vetter, *Z. Elektrochem.*, **55**, 274 (1951); **66**, 577 (1962).
13. J. J. Coleman, *Trans. Electrochem. Soc.*, **90**, 545 (1946).
14. D. T. Ferrell and W. C. Vosburgh, *This Journal*, **98**, 334 (1951).
15. W. C. Vosburgh, *ibid.*, **106**, 839 (1959).
16. A. B. Scott, *ibid.*, **107**, 941 (1960).
17. A. Kozawa, *ibid.*, **106**, 79 (1959).
18. J. P. Brenet, 8th C.I.T.C.E., Madrid 1956, Butterworth Scientific Publ., p. 394, (1958).
19. R. K. Fox. D. F. Swinehart, and A. B. Garrett, *J. Am. Chem. Soc.*, **63**, 1779 (1941).
20. R. Scholder and A. Kolb, *Z. anorg. Chem.*, **264**, 209 (1951).
21. C. W. Tobias, Private communication. Also M. B. Knaster and L. A. Apelbarm, *Zhur. Fiz. Khim.*, **38**, 223 (1964).
22. G. Kortum and J. O'M. Bockris. "Textbook of Electrochemistry," Vol. II, p. 404, Elsevier Publishing Co. (1951).

Effect of Carbon and Oxygen in Iron on Stress Corrosion Cracking in Nitrate Solution

L. M. Long and H. H. Uhlig

Corrosion Laboratory, Massachusetts Institute of Technology, Cambridge, Massachusetts

ABSTRACT

It was established previously that nitrogen or carbon in iron is necessary for susceptibility to stress corrosion cracking in boiling aqueous 60% $Ca(NO_3)_2$-3% NH_4NO_3. Present measurements show that oxygen in Fe at a concentration as high as 0.07% does not induce similar susceptibility. Pure iron-carbon alloys containing 0.001% N or less are susceptible as quenched from 925°C if they contain more than about 0.002% C. Below this carbon content they are resistant. However, resistant alloys become susceptible when heated subsequently for 3 hr at 550°C, including zone-refined iron containing <0.001% C and <0.0003% N. Only "floating" zone-refined iron of still higher purity is immune as quenched or when heated at 550°C. These results are interpreted in terms of crack-sensitive paths consisting of interstitial atoms associated with imperfections of the grain boundaries. Quenched-in imperfections within grains transport interstitial atoms to grain boundaries which induce susceptibility of an otherwise resistant iron.

Iron or steel stressed in tension and exposed specifically to hot aqueous solutions containing nitrate or hydroxyl ions may crack rapidly along intergranular paths. This type of failure is called stress corrosion cracking (s.c.c.). Uhlig and Sava (1) showed that interstitial carbon or nitrogen in iron is necessary for susceptibility to s.c.c. in boiling nitrate solutions and, presumably, in alkaline solutions as well, in which the mechanism of failure is thought to be similar (2). By reducing both the carbon and nitrogen contents to 0.001% or less, they found iron became essentially immune when either water-quenched from 925°C or cold-rolled to 70-85% reduction in thickness.

For higher C or N contents, the degree of susceptibility was sensitive to heat-treatment. For example, a commercial mild steel (0.06% C, 0.001% N), as quenched, cracked within less than 2 hr. Essential immunity, defined arbitrarily as resistance to cracking for 200 or more hours, was observed for mild steel first quenched from 925°C, then heat-treated at 250°-300°C for ½ hr. The steel became susceptible again if heated at higher temperatures, *e.g.*, 3 hr at 550°C or ½ hr at 700°C, and remained susceptible after long-time heat-treatment, *e.g.*, 3 weeks at 600° or 700°C.

These results were interpreted in terms of crack-sensitive paths formed by interstitial C or N atoms (or transition phase carbides and nitrides) along grain boundaries. Quenching of mild steel from the austenite region produces crack-sensitive paths, but subsequent heat-treatment at 250°-650°C for ½ hr results in resistance to s.c.c. because carbides or nitrides are precipitated which deplete grain boundaries of C or N atoms. Longer heat-treatment, *e.g.*, 3 hr at 550°C, again induces susceptibility because the imperfection structures of grain and grain boundary are altered from arrays characteristic of the material as quenched from 925°C, to arrays characteristic of lower temperatures, *e.g.*, 550°C. In other words, quenched-in imperfections tend at, *e.g.*, 550°C, to migrate from grains to grain boundaries, taking C or N atoms with them. Hence interstitial atoms reverse direction of diffusion at temperatures in the order of 450°-690°C, again entering the grain boundaries from which they originated in concentration sufficient to reinduce susceptibility to cracking. The diffusion of imperfections is slower on the whole than diffusion of interstitial atoms away from or toward grain boundaries, hence, within the intermediate temperature range, immunity precedes ultimate susceptibility.

The observed activation energy is about the same for interstitial atoms diffusing either way, the value for carbon lying within 35-40 kcal. For C atoms migrating toward the grains, the activation energy presumably corresponds to the energy required to dissociate carbon atom-imperfection atmospheres at the grain boundaries of quenched steel. Similarly for diffusion in the reverse direction, the observed value is presumably the energy required to dissociate iron carbides into interstitial carbon and ferrite (or dissociate carbon-imperfection atmospheres at the carbide-ferrite interface). The activation energies for nitrogen steel are somewhat higher, namely, 48 kcal, otherwise the qualitative conditions leading to immunity or susceptibility are similar to those for carbon steels.

It was stated in the earlier paper (1) that the critical minimum concentration of C in iron necessary for s.c.c. appears to be equivalent to the solubility of C in ferrite at 200°-350°C and for nitrogen at 150°-250°C. This was an educated guess based on the information that a quenched mild steel containing 0.06% C becomes immune within about 20 hr on heating at 200°C (¼ hr at 250°C) [Fig. 5, ref. (1)], during which time the carbon associated with grain boundaries is precipitated as carbide particles. By the same token, extrapolation to the time required to reinduce susceptibility to s.c.c. at 200°C [Fig. 7, ref. (1)] is 2900 years (71 years at 250°C). Hence any steel containing less carbon than its solubility in ferrite at 200°C, if immune as quenched, would not be expected to become susceptible if heated for long times at 200°C. It would also not become susceptible at any other temperature of heat-treatment provided crack-sensitive paths depended on a minimum interstitial concentration of carbon established by the solubility of cementite in ferrite at the given temperature. The latter supposition turned out to be not entirely correct, as data presented later show.

Heating a susceptible quenched mild steel (0.06% C) for ½ hr at temperatures up to 690°C, but not above, resulted in immunity presumably because, within the time necessary to reach the upper temperature, rapid precipitation of carbides occurs at intermediate temperatures, depleting grain boundaries of C atoms. Heating for only ½ hr at 690°C does not suffice to alter effectively the imperfection structure of the metal followed by dissociation of precipitated carbides and induced susceptibility; however, heating ½ hr at 700°C succeeds in this respect.

It could also have been assumed, of course, that rate of solution of carbides in ferrite is relatively rapid and that the critical concentration of C in ferrite for susceptibility is close to its solubility at the Ac_1 temperature. Hence heating of quenched mild steel for

½ hr at 690°C would precipitate carbides which lower the carbon content of ferrite below the supposed critical concentration needed for susceptibility. On the other hand, following the same reasoning, when the steel is heated to 700°C, even though carbides may precipitate, enough carbon remains in solution to account for susceptibility. The argument against this process, other than the high solubility of C in ferrite at 690°C (0.02%) (3), is that long time heating at a lower temperature, *e.g.*, 600°C, also produces a susceptible steel which remains susceptible, hence the solubility of C in ferrite at this temperature also suffices to produce crack-sensitive grain boundaries. Any critical concentration of C, therefore, certainly lies below the solubility of carbon in ferrite at 600°C. By the same reasoning it also lies below the value at 550°C at which temperature 3 hr are required to induce susceptibility and, similarly, below 443°C requiring 70 hr. The question remains as to just how far below 443°C the solubility of carbon in ferrite becomes too low for susceptibility to occur within any reasonable time of heat-treatment.

Parkins (4) reported that iron containing less than 0.02% C is immune to s.c.c. in nitrate solution, but Logan (5) reported cracking of iron containing only 0.01% C. Uhlig and Sava (1) reported cracking of a steel containing still less carbon, *i.e.*, 0.001% C, but which steel also contained 0.043% N. It was considered worthwhile checking the minimum concentration of carbon required for susceptibility, taking into account the important factor of heat-treatment and maintaining, at the same time, a low nitrogen content which otherwise also induces susceptibility. Information of this kind is useful to a further understanding of the mechanism of stress corrosion cracking.

Experimental

Pure iron-carbon alloys were produced in the range 0.001-0.03% C. The basis iron was electrolytic grade decarburized to 0.001% C by passing wet H_2 over it for several hours at 760°C. The melt was contained in a crucible of pure dense alumina; carbon additions were made in a vacuum furnace via a 4% carbon master alloy prepared from electrolytic iron and spectroscopically pure graphite. After the iron was melted, helium purified over titanium at 800°C and previously passed through a liquid N_2 trap was allowed to enter the furnace. Castings were then prepared by drawing the melt into 7 mm diameter Vycor tubing followed by water quenching. The castings were encapsulated in evacuated Vycor tubes and homogenized at 1050°C for 15 hr followed by furnace cooling. They were then cold rolled to 0.102 cm (0.040 in.) strip and sheared to specimens measuring 4.45 x 0.48 cm (1-3/4 x 3/16 in.). These were then heated briefly to 925°C in quartz tubes containing an argon atmosphere and water quenched. Some specimens thereafter were heat-treated at lower temperatures in a molten metal bath, the temperature of which was controlled automatically. Specimens were air cooled on removal from the metal bath. Before testing, all specimens were pickled for 4 min in 5 vol. % concentrated commercial HCl at 95°C.

For the s.c.c. tests, specimens were bent beyond the elastic limit to a span of 3.65 cm (1-7/16 in.) and held to this dimension by means of a compression spring. They were totally immersed in boiling 60% calcium nitrate, 3% ammonium nitrate solution employing apparatus described by Uhlig and Sava (1). Failure time was recorded by an electric clock. Variations of the span and corresponding change in flow stress were not found to be critical for specimens essentially immune to stress corrosion cracking. For example, specimens containing 0.0016% C, 0.001% N, bent to a normal span of 3.65 cm (1-7/16 in.) did not fail within 200 hr; they also did not fail within the same test period when bent to a span shorter by 0.65 cm (¼ in.), *i.e.*, to a final span of 3.0 cm (1-3/16 in.).

Table I. Lack of effect of oxygen on stress corrosion cracking of iron

% Oxygen in iron	% C	% N	Cracking time, hr
0.012	0.002	0.002	>200 (2 spec.)
0.066	0.001	0.002	>200 (2 spec.)

Suspected effect of oxygen.—Although it was established that C or N in Fe is necessary for occurrence of stress corrosion cracking, a possible contributing effect of oxygen in Fe also required investigation since oxygen is always present to some extent. It was especially difficult to arrive at a conclusion from analyses of melts already prepared and tested because of the unavoidable experimental variations inherent to all stress corrosion cracking tests, and also because significant amounts of C, N, and O in Fe were at the extreme limits of analytical accuracy. Special melts of iron were prepared, therefore, low in C and N, but relatively high in oxygen. Melts were prepared in vacuum as before; but prior to casting, instead of filling the furnace with the customary purified helium, a mixture of 4 parts He to 1 part O_2 was introduced at a flow rate of 5 liter/min. The He as before was freed of N_2 by passing over hot titanium. In this way, 7 mm diameter castings were obtained which varied in oxygen content, depending on length of contact of melt with the He-O_2 atmosphere, from 0.01 to 0.07% oxygen. These alloys were homogenized, cold rolled to 0.102 cm (0.04 in.), quenched from 925°C, and tested as usual in the boiling nitrate solution. Results summarized in Table I show that oxygen-iron alloys are not susceptible to s.c.c.

Quenched and heat-treated carbon-iron alloys.—Iron specimens as prepared with variable but low C content contained in the order of 0.001% N which marked the limit of usual analytical accuracy for this element. All specimens as quenched from 925°C cracked within 0.6-3 hr except those containing about 0.002% or less carbon. The latter specimens resisted cracking for 70 to 200 or more hours, indicating greater resistance or essential immunity. Data are plotted in Fig. 1.

However, when immune specimens containing 0.002% C or less were heated at 550°C for 3 hr, corresponding to conditions necessary to reinduce sus-

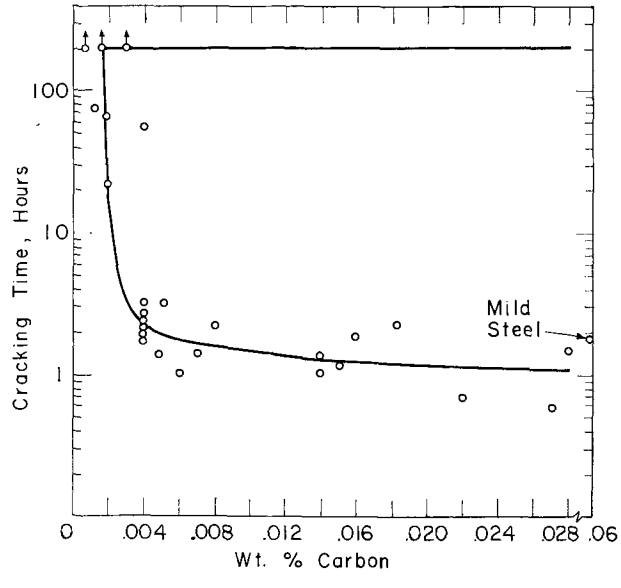

Fig. 1. Effect of carbon in iron quenched from 925°C on susceptibility to stress corrosion cracking.

Table II. Stress corrosion cracking of zone-refined iron

Spec. No.	ppm C	ppm N	ppm O	Cracking time: Quenched from 925°C	Cracking time: Quenched, heated 550°C, 3 hr.	Cracking time: Quenched, heated 550°C, 3 hr Quenched from 925°C
12 C (boat refined)	<10	<3	20	>200 hr (2 spec.)	1.3 ± 0.4 hr (4 spec.)	>200 hr (2 spec.)
72 A (floating refined)	<5 0.8*	0.3 <0.1*	1.4	>200 hr (2 spec.)	>200 hr (2 spec.)	

1 ppm = 0.0001%.

* Determined by internal friction. Upper value for carbon is by combustion-conductometric, and for nitrogen by vacuum fusion. The latter values are higher probably because of interstitial atoms associated with imperfections of grains and grain boundaries which do not contribute to internal friction. (Analysis by W. Rengstorff, Battelle Memorial Institute, 2nd Special Report on Analysis of High Purity Iron to Am. Iron and Steel Inst., July 11, 1963).

ceptibility of quenched mild steel, they all failed within a short time. When, in fact, zone refined iron was examined containing <0.001% C, <0.0003% N which Uhlig and Sava found to be immune as quenched, such specimens also failed on heating at 550°C for 3 hr. Failure time was as short as 1 hr. This result was at first questioned by us on the ground that failure occurred because of possible contamination of the specimens during heat-treatment. For this reason several zone-refined iron specimens were encapsulated in evacuated fused pure quartz tubes so as to minimize contamination that may have resulted from impurities in Vycor both during the quenching and heat-treatment schedules. These specimens, however, also failed by s.c.c. Quenched specimens heated at 550°C for 3 hr, then quenched from 925°C were again immune (Table II) indicating that susceptibility was not caused by contamination through heat-treatment.

The question remained, therefore, whether the very low C and N contents of zone-refined iron were actually high enough to induce the observed cracking. This matter was resolved by obtaining a further sample of pure iron of the so-called "floating" zone-refined quality prepared at Battelle Memorial Institute. This iron was purer than the zone-refined iron first used, as was determined at Battelle by sensitive analytical methods including internal friction measurements. After fabrication and pickling, the purer material was encapsulated in evacuated fused quartz tubes and quenched from 925°C, or heat treated at 550°C for 3 hr. Unlike the first zone-refined iron, specimens of the second material did not crack within 200 hr or more, either as quenched or as heat-treated at 550°C (Table II).

Hence, it can be concluded in accord with earlier conjecture that pure iron is essentially immune to s.c.c. The present results also indicate that the critical carbon content for susceptibility of heat-treated iron lies below 0.001%, which is well under the sensitivity of usual analytical methods for quantitative determinations. For iron quenched from 925°C, the critical carbon content is about 0.002%. The latter value is probably influenced by an unknown small concentration of nitrogen also present.

Discussion

The trace amounts of C in Fe needed for s.c.c. support the suggestion made by Uhlig and Sava that probably only C atoms associated with imperfections of the grain boundary are needed to form crack-sensitive paths, rather than alignment of precipitated carbides along the grain boundaries as had been proposed by other investigators. The present results also suggest that s.c.c. in ammonium nitrate solution of recrystallized iron whiskers after heating above 910°C, reported by Flis *et al.* (6) is caused by impurities in the whiskers instead of by differences, as they suggest, in free energy of iron atoms at grain boundaries and in grains. The partition of C atoms between both interstitial sites and imperfection sites within the grains, and imperfection sites of the grain boundaries corresponding to a 925°C quench, requires an over-all approximate 0.002% C in order to provide crack-sensitive grain boundaries. On the other hand, the over-all required carbon content is much less on heating iron at a lower temperature, *e.g.*, 550°C, presumably because quenched-in imperfections within the grains move at this temperature to grain boundaries accompanied by C or N atoms with which they are associated. The result of such heat-treatment is a final higher concentration of C or N at grain boundaries sufficient to induce susceptibility to s.c.c. Only if the over-all C or N content is extremely low, corresponding to floating zone-refined quality, does iron remain immune after heating in the order of 550°C. The actual lower limit of carbon concentration corresponding to immunity is not readily defined, both because of obvious analytical difficulties and also because the mechanism of sensitization implies that grain size should also be a factor. A large grain size iron with small grain boundary surface would become sensitive at a lower C and N content than would a small grain size iron of larger grain boundary surface. Probably a monolayer or less of C or N atoms along grain boundaries suffices to induce susceptibility. For example, 1 cm^3 of iron containing 1 mm diameter grains would contain about 30 cm^2 of grain boundary surface. Carbon atoms 0.77Å in radius lined up at grain boundaries as close-packed monolayers would account for a carbon content of 0.4 ppm not including C atoms contained within the grains. This value increases appreciably as grain size decreases. Less than a monolayer would perhaps suffice for susceptibility if C and N atoms were available from adjoining regions of the metal by rapid diffusion to the apex of the growing crack, diffusion being aided by plastic deformation accompanying crack growth.

The function of C and N atoms at grain boundaries, as described earlier (1), is supposedly to extend life of emerging surface imperfections of iron during plastic deformation at the tip of the crack sufficient to allow chemisorption of NO_3^- ions (or the reaction product of Fe with NO_3^-) on the imperfection arrays. If the mechanism of crack growth is basically one of surface energy reduction (stress sorption cracking), which has been suggested as a plausible mechanism (7, 8), the reduction is brought about by chemisorption of NO_3^- ions or their reaction products. Chemisorption of this kind substantially reduces affinity of adjoining Fe atoms at the tip of the growing crack, allowing Fe atoms under stress to separate and form a fissure by a mechanism similar to that causing cracking of tensionally stressed metals by specific liquid metals, *e.g.*, brass by mercury. In absence of specific anions which chemisorb, or in absence of surface imperfections of reasonable half-life on which chemisorption can occur, s.c.c. is not observed. Electrochemical action may be required indirectly to form the reaction product which chemisorbs; marked specificity of the anion probably rules out crack growth by direct electrochemical dissolution of disarrayed metal atoms. The marked differences between various anions in causing or not causing cracking are far greater than can be accounted

for on the basis of the parallel, relatively smaller differences they exert on anodic polarization or on film forming characteristics. Similarly, specificity of anion and the fact that pure metals do not fail by stress corrosion cracking make less likely the proposed mechanism of Hoar *et al.* (9) supposedly accounting for rapid electrochemical dissolution of metal at the tip of a crack because the metal undergoing active strain dissolves anodically at appreciably lower overvoltage than does unstrained metal. General incidence of s.c.c. of all metals would probably be much more pronounced were this mechanism to apply. The increase observed by Hoar *et al.* of anodic current at constant potential as a metal is strained may be a function only of the greater surface area produced by numerous cracks, as indeed is not unexpected, since the large increase of current they measured occurs specifically in environments which otherwise induce s.c.c.

The very small amount of C or N in Fe necessary for susceptibility to s.c.c. suggests that a convenient criterion of purity is to subject a stressed specimen of Fe previously heated at about 550°C to boiling nitrate solution. Large grain size Fe would be particularly sensitive to trace amounts of both C and N. Although it was established that oxygen is less effective than C or N in causing susceptibility, it is not known at present to what extent other impurities in iron such as P or S may also contribute.

Acknowledgment

This research was supported by the United States Army Research Office-Durham on Contract DA-31-124-ARO(D)-47 to whom the authors express their appreciation. They also acknowledge helpful contributions of Iwao Matsushima and K. Elaya Perumal to the experimental program, and the contribution of zone-refined iron by the American Iron and Steel Institute.

Manuscript received May 14, 1965. This paper was presented at the Buffalo Meeting, Oct. 10-14, 1965.

Any discussion of this paper will appear in a Discussion Section to be published in the June 1966 JOURNAL.

REFERENCES

1. H. Uhlig and J. Sava, *Trans. Am. Soc. Metals*, **56**, 361 (1963).
2. E. Houdremont, H. Benek, and H. Wentrup, *Stahl u. Eisen*, **60**, 757, 791 (1940).
3. P. Stark, B. Averbach, and M. Cohen, *Acta Met.*, **6**, 149 (1958).
4. R. Parkins, *J. Iron Steel Inst., London*, **172**, 149 (1952).
5. H. Logan in "Physical Metallurgy of Stress Corrosion Fracture," T. Rhodin, Editor, pp. 295-309, Interscience Publishers, New York (1959).
6. J. Flis, J. Mieuluch, and M. Smialowski, Second Int. Congress on Metallic Corrosion, N. Y., National Assn. of Corros. Engrs., Houston, Texas (1963).
7. H. H. Uhlig in "Physical Metalurgy of Stress Corrosion Fracture," T. Rhodin, Editor, pp. 1-17, Interscience Publishers, New York (1959).
8. E. Coleman, D. Weinstein, and W. Rostoker, *Acta Met.*, **9**, 491 (1961).
9. T. Hoar and J. West, *Nature*, **181**, 835 (1958); with J. West, *Proc. Royal Soc.*, **268A**, 304 (1962); with J. Scully, *This Journal*, **111**, 348 (1964). See also D. Van Rooyen, "Proc. First Int. Congress on Metallic Corrosion," p. 309, Butterworths, London (1962).

The Short Time, High Temperature Oxidation of Cobalt

A. R. Reti

Dynatech Corporation, Cambridge, Massachusetts

ABSTRACT

Cobalt was oxidized at 1000°C in 0.5-4.0 atm O_2 over periods of 0.005-100 sec. The reaction rates observed in the 10-100 sec range are of the order of magnitude predicted from long time oxidation studies, checking within 50% with the parabolic constants measured by Carter and Richardson and Bridges *et al.* The reaction rates observed in the initial 0.01-10 sec of oxidation are considerably slower, indicating that cation vacancy diffusion through the CoO layer is no longer the main rate-limiting step. These short-time reaction rates were found to be strongly influenced by the surrounding O_2 partial pressure.

An extensive review of the literature for the oxidation of cobalt metal is presented by Kubaschewski and Hopkins (1). In the oxygen pressure-temperature region where only the cobaltous oxide, CoO, phase is stable, the oxidation mechanism has been explained successfully by considering a model where cation vacancy diffusion through the forming cobaltous oxide layer is the rate-limiting step for the oxidation process (2-4). The experimental oxidation rates measured for all these studies correspond to oxidation times ranging from 1 min to 60 hr, the most recent measurements (3, 4) being performed for oxidation times of 45 min to 31 hr. The corresponding oxide layer thicknesses for such experiments are of the order of 10^{-2} cm. At the initial stages of oxidation, however, the oxide layer is so thin that processes other than cation vacancy diffusion through the oxide scale may control the reaction rate.

Furthermore, for very thin oxide layers, the assumption of a uniform, parallel, and coherent oxide layer may not truly represent the geometry of the system. Because of the total lack of experimental data for the initial oxidation rates of cobalt metal at high temperatures, this investigation was undertaken in order to discover at which point, if any, the parabolic oxidation law breaks down, as well as to understand the nature of any other rate-limiting processes which may exist. The focus of this study was upon the reaction rate over the first 0.005-100 sec of reaction.

Experimental

Apparatus.—The rate of oxidation of cobalt metal was measured by following the oxygen pressure decrease within a closed container of known volume when the metal and oxygen, both at the initial reaction temperature, were suddenly brought into mutual contact. A diagram of the system used is shown in Fig. 1. The reactant cobalt metal was sealed within a Vycor vial under a vacuum of the order of 100μ Hg, and pretreated in any desired fashion. The sealed vial was placed within the pressure container, which was sealed and placed in a furnace where it was brought to the initial reaction temperature. The pressure container was then evacuated and filled with oxygen gas to the desired pressure. After thermal equilibrium was attained, the Vycor vial was broken by means of a rod which slides through a sliding seal, and the reaction rate was followed by recording a signal from a pres-

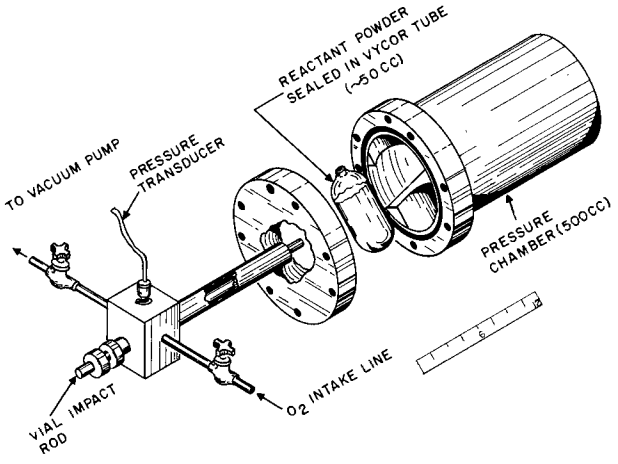

Fig. 1. Experimental apparatus

sure transducer. The entire assembly of the pressure vessel is contained within the furnace except for the end of the extension tube which contains the pressure transducer, the oxygen and vacuum lines, and the end of the vial impact rod. This assembly is maintained at room temperature by use of cooling coils. The pressure transducer used was a Dynisco strain gage transducer with a response time constant of approximately 1 msec, and the electrical signal from the transducer was recorded by a Minneapolis Honeywell Light Beam Oscillograph equipped with a high-frequency response (350 cps) galvanometer or by an Offner Dynograph high-speed recorder (125 cps frequency response). This apparatus provided a means of measuring very rapid pressure changes, and calibration runs involving empty vials indicated that time lags in the apparatus introduced no appreciable error in the reaction rates which were measured.

Oxidation runs were performed at an initial sample temperature of 1000°C under oxygen pressures varying within 0.5 and 4.0 atm.

Materials.—Two types of cobalt metal were used. For the very short time oxidation rate measurements (0.005-0.1 sec), a spectrographic grade cobalt sponge, supplied by the Johnson, Mathey & Company, Limited, was employed. This material had the following certified analysis

Element	Estimated quantity present, %
Silicon	0.0003
Aluminum	0.0001
Copper	0.0001
Iron	0.0001
Calcium, Magnesium, Silver	Each element less than 0.0001

For the longer time (0.1-100 sec) oxidation rate measurements, larger prime particle size material was necessary and had to be used in larger amounts, precluding the use of the spectrographic grade material. Purified cobalt shot, item CB 308, supplied by the Matheson Coleman & Bell Division of the Matheson Company, was employed. A typical analysis of such a material is the following:

Element	Quantity present, %
Co	99.52
Cu	0.009
Ni	0.17
Fe	0.11
S	0.006
P	0.002
C	0.010
Zn and Cd	0.008
Si	0.006
Al	0.034
Mn	0.005
Pb	0.001
H_2	0.00054

Sample preparation.—In order to prevent gas phase diffusion effects from becoming significant, the reactant material configuration must be such that all of its surface is readily accessible to the oxygen gas even at the highest possible reaction rates. Since the finely divided cobalt metal sinters appreciably at 1000°C, if the cobalt sponge were loaded directly into the vial and heated, it would result in a sintered, porous mass of the shape and dimensions of the vial. Oxidation experiments with such a material indicated that only an outside layer, a few millimeters thick, reacted over the initial stages of oxidation. The sample preparation procedure adopted consisted in presintering the cobalt sponge powder for 2.0 hr at 1000°C in an evacuated and sealed Vycor vial, after which the resulting porous sintered body was broken up into porous particles of diameters ranging between 0.5 and 1.0 mm. Such particles were reloaded into a Vycor vial, which was evacuated and sealed. B.E.T. nitrogen adsorption measurements performed on the material prior to heat-treatment, after heating at 1000°C for 2 hr, and after heating at 1000°C for 2 hr and undergoing the heat-up cycle prior to undergoing reaction, indicate that most of the sintering took place during the initial heat-treatment (the surface area decreased from 0.43 to 0.14 m^2/g), with negligible surface area changes occurring during the shorter heat-up period. This later value was used in calculating the cobalt oxidation rate per square centimeter of cobalt surface. Figure 2 shows the appearance of a porous cobalt metal particle cross section after heat-treatment. The average prime particle size, of the order of 10μ, checks well with the measured B.E.T. surface area. The B.E.T. surface measurements, checked against glass spheres (0.24 m^2/g) of known dimensions, were found to be accurate within ±5% in this range. It was found that these particles oxidized uniformly throughout and did not sinter appreciable to each other, leaving sufficiently open path for oxygen to flow into the particle envelope areas and into the internal areas.

For the longer time oxidation experiments, solid cobalt shot, 1-2 mm in diameter was used. The shot was cleaned from surface oxide by surface polishing in an inert atmosphere, after which it was charged into the vial, evacuated, sealed, and annealed at 1000°C for 2 hr. Figure 3 is a photomicrograph of a partially reacted shot, polished and etched in acetic acid, with an oxide layer (darker area) about 15μ thick. The metal grain size, of the order of 10-30μ, can be seen readily. The outside envelope area was used for all reaction rate calculations, as in ref. (3) and (4), neglecting the extent of surface roughness. This procedure is quite valid for oxide layer thicknesses of 1μ or more, where the effects of initial surface roughness will be negligible, but there may be an effect when dealing with smaller oxide thicknesses. The presintering of the pellets at 1000°C should minimize the surface roughness.

Results

Results for the longer time oxidation tests at 1000°C and 0.5-1.0 atm O_2 are summarized in Fig. 4. The oxida-

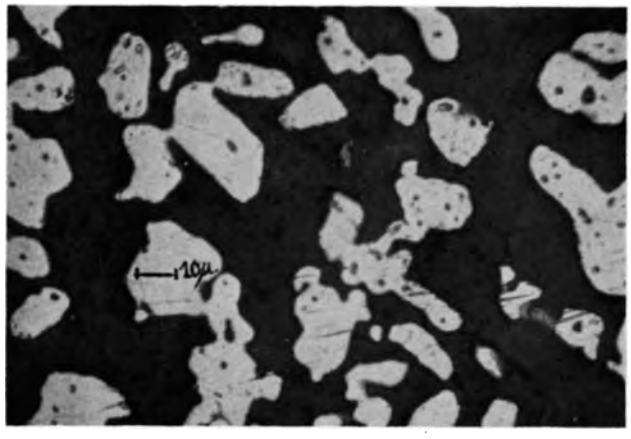

Fig. 2. Photomicrograph of cobalt metal sponge particle

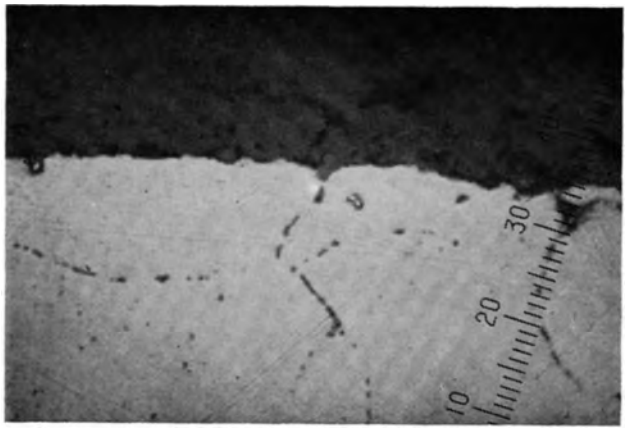

Fig. 3. Photomicrograph of partly oxidized cobalt shot; etched in acetic acid. Magnification, 1.25 μ/division.

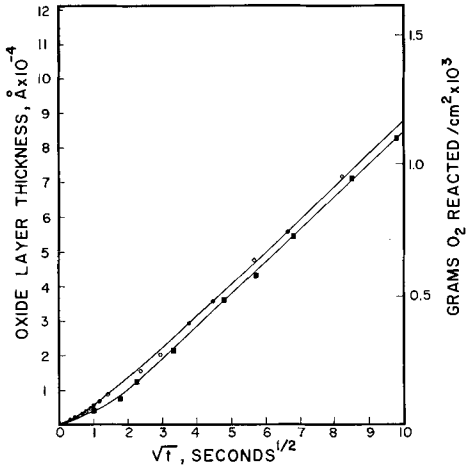

Fig. 4. Oxidation of cobalt shot at 1000°C: ○, PO_2, 1.0 atm; ■, PO_2, 0.5 atm.

tion is essentially parabolic, with a reaction rate constant of 1.46 x 10^{-8} g^2 cm^{-4} sec^{-1}, as compared with the 2.43 x 10^{-8} value obtained by Carter and Richardson (3) and Bridges *et al.* (4). The agreement in the reaction rate constant is quite good considering that the oxidation times studied are 30-3000 times shorter, and remembering that the 0.1% Fe impurity level in the samples used for this series of tests may have an appreciable effect on the vacancy concentration and thus on the reaction rate constant (8). A typical oxide layer formed in these tests is shown in Fig. 3. The oxide-metal interface is by no means completely smooth, and there is definite evidence of preferential attack at the grain boundaries. There is a definite indication that the reaction rates are lower at oxidation times shorter than 4 sec (oxide layer thicknesses smaller than 10,000Å), showing the desirability for even shorter time oxidation data.

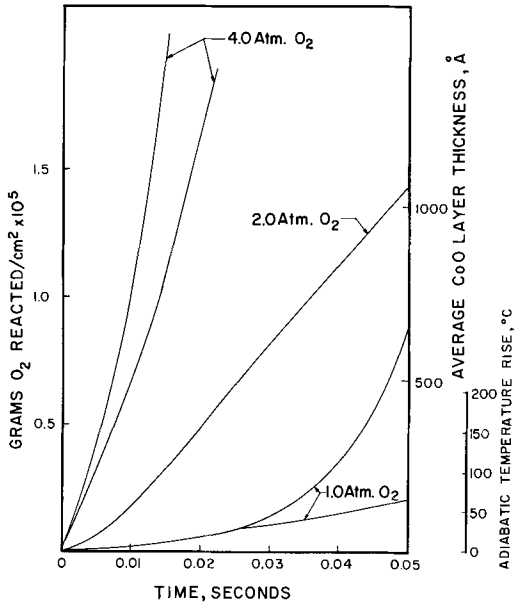

Fig. 5. Oxidation of cobalt sponge at 1000°C; initial sample temperature.

The results of the extremely short time oxidation rate measurements performed on the spectrographic grade cobalt sponge particles are shown in Fig. 5. The initial reaction temperature was 1000°C, and runs were performed at 1.0, 2.0, and 4.0 atm oxygen pressure. These initial reaction rates are highly pressure dependent, and the amount reacted after 25 msec reaction time at 1.0 atm O_2 pressure (1.0 x 10^{-6}g O_2/cm^2) is twenty-five times smaller than the amount that would be predicted from extrapolation of the parabolic reaction rate equation, $\Delta W^2 = K_G t$, obtained from the longer time oxidation studies of Carter and Richardson (3) and Bridges *et al.* (4). A summary of the reaction rate data obtained by other authors and in the present study is presented in Table I.

For the very short time oxidation measurements performed in this study, only the initial stages of the oxidation (up to 2 x 10^{-6}g O_2/cm^2 reacted) have quantitative significance. Such a rapid reaction in the short times considered takes place in an essentially adiabatic system. For this reason, the reactant materials rise rapidly in temperature as they react, since all the heat of oxidation liberated is retained by the reactants as sensible heat. A separate scale in Fig. 5 shows the corresponding adiabatic temperature rise of the reactants for proper reference. This adiabatic temperature raise may account for the autoacceleration effect observed at longer reaction times, rather than the kinetics of reaction. In fact, in runs performed with the fine cobalt sponge and large excess oxygen a decrease in reaction rate was observed as the calculated adiabatic temperature rise of the material indicated that the melting points of Co and CoO had been reached (1490 and 1800°C, respectively), as would be expected from the drastic decrease in surface area that would occur under these conditions. There is no ques-

Table I. Summary of the reaction rate data of several authors

References	Time span	Temperature, °K	K_G, g^2 cm^{-4} sec^{-1}	Predicted oxide layer thickness, Å, after seconds 10	1	0.1	0.025	Activation energy, cal.
Valensi (6)	0.5-10 hr	1293	—	965	306	30.6	8	41,090
Lopez and Suarez (5)	1 min-60 hr	1273	1.875 x 10^{-8}***	28,600	9,050	2,860	1,430	38,900
Phalnikar *et al.* (7)	6 min-30 hr	1273	3.11 x 10^{-8}	41,800	13,200	4,170	2,100	65,500
Carter and Richardson (3)	1-31 hr	1273	2.43 x 10^{-8}	32,600	10,300	3,580	1,790	40,800
Bridges *et al.* (4)	45 min-2 hr	1273	2.44 x 10^{-8}	32,700	10,340	3,600	1,800	58,000
Present study	0.005-100 sec	1273	1.46 x 10^{-8}**	23,500*	5,600*	1,200*	77*	—

* Measured values.
** Constant calculated from 68.5 sec data point.
*** Data obtained in air, Kg multiplied by $(1.0/0.21)^{0.3}$ to compare in 1 atm O_2.

tion, however, that the initial reaction rates, corresponding to average oxide layer thicknesses of less than 200Å, are definitely affected by pressure, increasing by a factor of 30 as the oxygen pressure is increased from 1.0 to 4.0 atm.

Conclusions

The parabolic oxidation law which describes well the oxidation behavior of cobalt metal for high oxide thicknesses breaks down at oxide layer thickness lower than 10,000Å, below which the oxidation rate is significantly slower than that which would be predicted from cation vacancy diffusion rates through a homogeneous CoO layer. The rate-limiting process below this point is strongly affected by the surrounding oxygen pressure, suggesting that either the CoO nucleation rate or the rate of growth of small, freshly formed nuclei control the oxygen uptake.

Acknowledgments

This work was performed under the sponsorship of the Fuels and Lubricants Branch, Technical Support Division, United States Air Force Aero Propulsion Laboratory, Wright-Patterson Air Force Base under contracts AF 33(616)-8295 and AF 33(657)-10797. The authors would like to thank the sponsoring agency for permission to publish this work. Special thanks are due to Mr. M. Dunnam and Mr. C. J. Johnson of the Research and Technology Division of Wright-Patterson Air Force Base for their help and encouragement.

Manuscript received April 19, 1965.

Any discussion of this paper will appear in a Discussion Section to be published in the June 1966 JOURNAL.

REFERENCES

1. O. Kubaschewski and B. E. Hopkins, "Oxidation of Metals and Alloys," pp. 240, 2nd ed., Academic Press, Inc., New York (1962).
2. W. J. Moore and J. K. Lee, *J. Chem. Phys.*, **19**, 225 (1951).
3. R. E. Carter and F. D. Richardson, *J. Metals*, **7**, 336 (1955).
4. D. Bridges, J. Bauer, and W. M. Fassell, *This Journal*, **103**, 614 (1956).
5. J. Lopez and H. Suarez, *Bib. Soc. Chil. Quim.*, **IX**, 38.
6. G. Valensi, *Metaux & Corrosion*, **25**, 283 (1950).
7. C. A. Phalnikar, E. B. Evans, and W. M. Baldwin, *This Journal*, **103**, 429 (1956).
8. H. M. O'Bryan, "Univariant Equilibrium Between the Oxides of Cobalt and Related Reaction Kinetics," Ph.D. Thesis, University of Michigan, 1963.

Oxidation of Manganese in CO_2-CO Mixtures

Kazuo Fueki[1] and J. B. Wagner, Jr.

Materials Research Center and Department of Materials Science, Northwestern University, Evanston, Illinois

ABSTRACT

The kinetics of oxidation of manganese have been studied in CO_2-CO mixtures at temperatures of 800°-1200°C. In most cases the oxidation was parabolic. Activation energies for parabolic oxidation in different gas mixtures were found to range from 40.5 to 45.6 kcal/mole. In a few cases where manganese specimens were oxidized below 1000°C in gas mixtures with a high content of carbon monoxide, weight gains were abnormally large and the parabolic rate law was not obeyed. In these cases carbon deposits were formed on the oxide, and cracks of the scale were observed. Marker studies revealed that manganous oxide grows by the outward migration of manganous ions. From the oxidation data, the self-diffusion coefficient of manganous ions is determined as a function of p_{CO_2}/p_{CO}, and the mechanism of oxidation is discussed.

Only a few kinetic studies have been made of the oxidation of manganese. These have been chiefly in air or in oxygen. Baldwin and his co-workers (1,2) studied oxidation in air and found that parabolic oxidation is obeyed at temperatures between 400° and 1000°C. Their microscopic observations revealed that the scales formed below 825°C consist of layers of Mn_2O_3 plus Mn_3O_4 and MnO. Those formed above 825°C consist of a thin layer of Mn_3O_4 and two layers of MnO, a compact outer one and a porous inner one. They proposed a mechanism whereby the compact layer grows by the outward diffusion of cations and the porous layer grows by the inward diffusion of anions.

Paidassi and Echeverria (3, 4) studied the oxidation of manganese in air at temperatures of 400°-1200°C. They reported that (*a*) the oxidation obeys the parabolic rate law; (*b*) above 900°C the fraction of the oxide layer which was Mn_3O_4 does not exceed several per cent of the total thickness; and (c) the Arrhenius plot of k *vs.* $1/T$ has a break point at about 950°C.

As far as the present authors know, no kinetic study of the oxidation of manganese in CO_2-CO mixtures has been made.

The purpose of the present study is to obtain diffusion data in manganous oxide from the oxidation data and also to elucidate the oxidation mechanism of manganese in CO_2-CO mixtures.

Thermodynamic Consideration

The possible reactions between manganese and CO_2-CO mixtures are discussed with the help of a thermodynamic diagram. Figure 1 shows such a diagram (5, 6) of the Mn-O system superimposed on that of the C-O system. The data were taken from Elliott and Gleisner (7). The ordinate of the diagram represents the chemical potential of oxygen, $\Delta G = RT\ln p_{O_2}$, and the abscissa gives the temperature, T. Lines 1 to 4 represent the equilibrium between two condensed phases of the Mn-O system and divide the $T - \Delta G$ plane into several regions in any one of which a specified condensed phase is most stable. Line 5 gives the equilibrium between carbon and carbon dioxide of 1 atm. A group of lines, denoted by 6, give the equilibrium between carbon and carbon monoxide at specified partial pressures. Similarly, a group of lines, denoted by 7, show the equilibrium between carbon monoxide and carbon dioxide at specified ratios of CO_2 to CO. Lines 5, 6, and 7 divide the $T - \Delta G$ plane into three regions. In a region where the chemical potential of oxygen is high, carbon dioxide is most predominant. In a region where the chemical potential of oxygen is low carbon is the most stable species. At temperatures above the triple point, carbon monoxide

[1] Present address: Department of Industrial Chemistry, University of Tokyo, Tokyo, Japan.

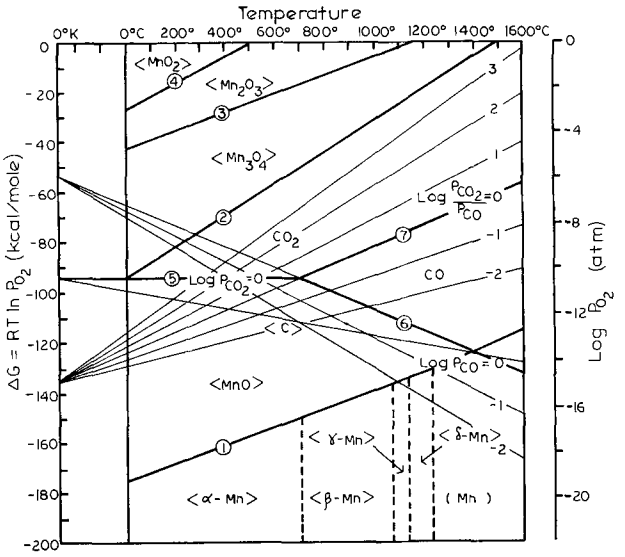

Fig. 1. Superimposed T — ΔG diagrams of the Mn-O system and of the C-O system. The symbol < > denotes a solid phase, ( ) a liquid phase, and the absence of brackets or parenthesis denotes a gas phase.

is the most predominant gas phase. It is seen that manganous oxide is the only oxide formed in CO_2-CO mixtures. When the temperature is above the triple point of the C-O system, which is determined by the partial pressures of CO_2 and CO, the possible reactions between Mn and CO_2 or CO are

$$Mn + CO_2 = MnO + CO \quad [1]$$

$$Mn + CO = MnO + C \quad [2]$$

Since the free energy change of reaction [1] is large and negative, reaction [1] would always occur. The free energy change of reaction [2] is negative only when the content of carbon monoxide is high. It increases as the temperature decreases. Therefore, reaction [2] is likely to occur when the content of carbon monoxide is high and the temperature is low. Carbon monoxide is unstable at temperatures below the triple point. Therefore, under these conditions carbon dioxide would react with manganese to form carbon and manganous oxide by the reaction

$$CO_2 + 2Mn = 2MnO + C \quad [3]$$

Moreover, carbon monoxide might decompose on MnO by the reaction

$$2CO = CO_2 + C \quad [4]$$

When carbon deposition occurs, a carbide such as Mn_7O_3 would be formed by the reaction

$$Mn + C \rightarrow \text{carbide} \quad [5]$$

The present analysis has been made at temperatures above 800°C and at low contents of carbon monoxide so that only reaction [1] could occur.

Experimental and Results

Oxidation rate measurements.—Manganese specimens were prepared from electrolytic manganese chips of 99.9% purity. The main impurities are listed in Table I. The manganese chips were polished with coarse polishing papers on a wheel and finished into coupons of rectangular shape. A typical coupon was 1 cm wide, 1.5 cm long, and 1 mm thick. Two small notches, of about ½ mm radius, were made on both sides of the specimen in order to suspend the specimen by means of a platinum wire. Then the specimens were heated for 6 hr *in vacuo* of 10^{-4} mm Hg at 500°C to remove hydrogen, polished with 2/0 and 4/0 emery

Table I. Spectrographic analysis* of manganese

Impurities	%
Al	0.01
Bi	0.01
Cu	0.01
Fe	0.01
Mo	0.01
Ni	0.01
Si	0.01
Ti	0.01
Pb	0.005
Zn	0.005
Co, Cr, Mg, V, Zr	nil

* Analyzed by Charles C. Kawin Co., Chicago, Ill., before vacuum annealed.

papers and then with Linde "A" alumina abrasive on a wheel, washed with water and then with acetone, and dried. An Ainsworth automatic recording balance and its accessories described by Pettit and Wagner (8) was used for the measurements. Mixtures having ratios of CO_2 to CO of 1:10, 1:3, 1:1, 3:1, 10:1, 30:1, and 100:1 at a total pressure of 1 atm were used. For all runs, a linear flow rate of 0.9 cm/sec was employed.

Figure 2 shows the parabolic plots of oxidation in various atmospheres at 1100°C. With the exception of an initial period, the parabolic law is obeyed. The run denoted by 0.05:0.05 was carried out in a mixture containing CO_2 at 0.05 atm, CO at 0.05 atm, and argon at 0.9 atm. The other runs, denoted by m:n with m and n having integer values, were conducted in CO_2-CO mixtures at a total pressure of 1 atm. Comparison of run 0.05:0.05 with run 1:1 shows that the parabolic rate constants do not depend on the partial pressures of CO_2 and CO but the pressure ratio of CO_2 to CO (mole fractions), and that the linear oxidation is not observed even in low pressures of CO_2 and CO such as run 0.05:0.05. Figure 3 shows the parabolic plots of oxidation at 900°C. The weight gains in a mixture of 1:10 are considerably larger than those in other mixtures and do not follow the parabolic law,

The dependence of parabolic constant on the ratio, p_{CO_2}/p_{CO}, is given in Fig. 4. The plots are not straight but slightly curved.

Arrhenius plots for various gas mixtures are shown in Fig. 5. A break in the Arrhenius plot such as was found by Paidassi and Echeverria for their studies of oxidation in air was not observed in the present study.

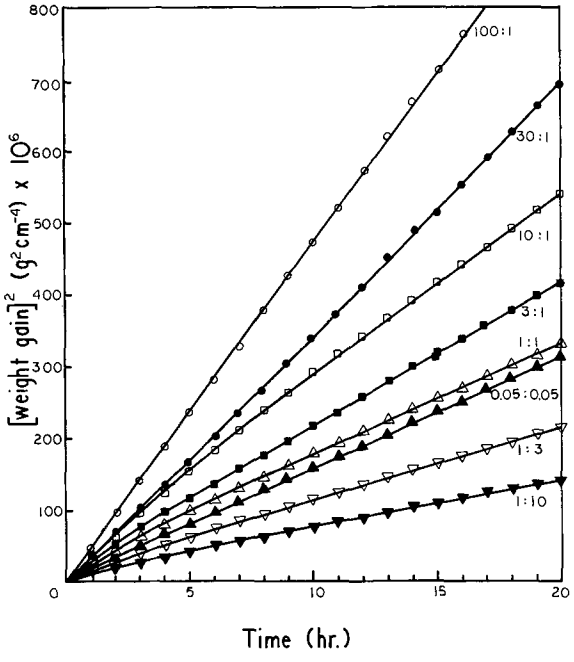

Fig. 2. Parabolic plot of oxidation in CO_2-CO mixtures at 1100°C

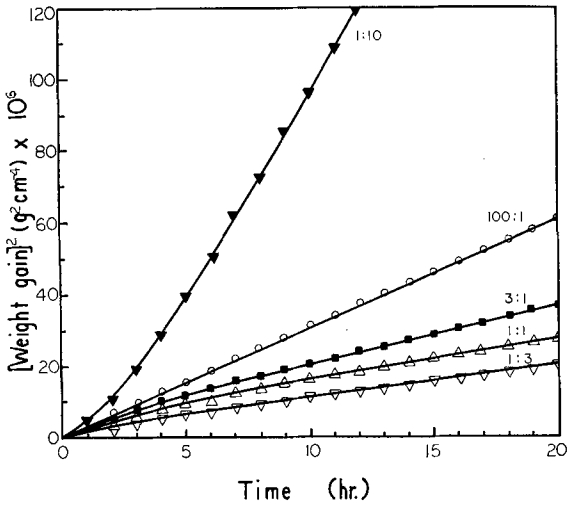

Fig. 3. Parabolic plot of oxidation in CO_2-CO mixtures at 900°C

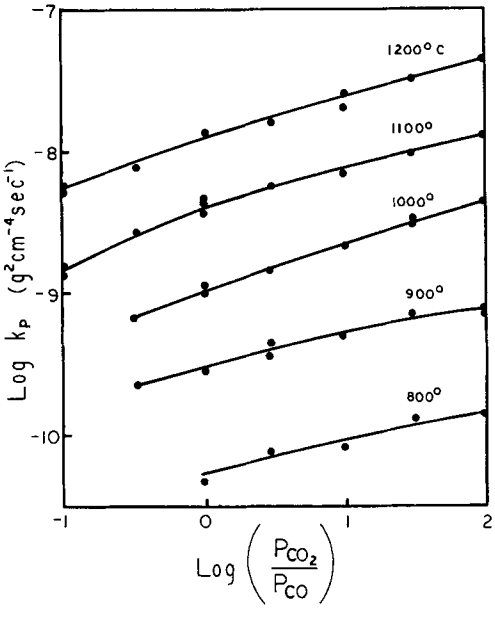

Fig. 4. Pressure dependence of the parabolic rate constant

Activation energies from the present study with errors at a confidence level of 90% are listed in Table II.

Microscopic observations.—The surfaces of oxidized specimens were examined microscopically. Figure 6 shows the surface of specimen oxidized for 24 hr at 1200°C in a CO_2-CO mixture of 5:1. Large oxide grains with growth pyramids are seen. From the fourfold symmetry of growth steps, the habit planes of manganous oxide formed in CO_2-CO mixtures are identified as {100}. This indicates that the surface reactions occur on {100} planes of manganous oxide, as was also observed in the oxidation of iron to wüstite in CO_2-CO mixtures (9).

On the surfaces of specimens which were oxidized at 800° or 900°C in gas mixtures with a high content of carbon monoxide and which exhibited very high oxidation rates, as discussed previously, black carbon deposits were observed on the oxide and cracks in the scales were observed.

The cross section of oxidized specimens that exhibited the normal parabolic behavior were also examined. As shown in Fig. 7, the scales formed in CO_2-CO mixtures were compact, homogeneous, and singly layered. In addition, a few runs were made in 1 atm oxygen, primarily for a marker study described below. The scales formed in oxygen consisted of a

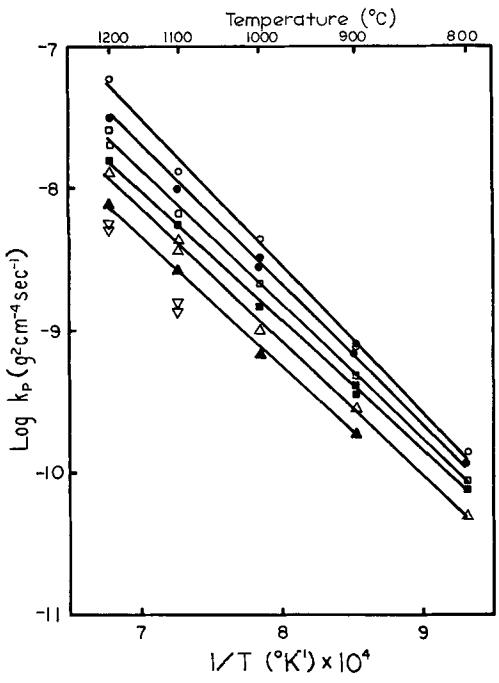

Fig. 5. Plots of log k_p vs. $1/T$: ○, $p_{CO_2}p_{CO}$ = 100:1; ●, 30:1; □, 10:1; ■, 3:1; △, 1:1; ▲, 1:3; ▽, 1:10.

Fig. 6. Growth steps on manganous oxide grains formed at 1200°C (CO_2:CO = 3:1, 24 hr). Magnification approximately 250X.

compact outer layer and a porous inner layer, both of manganous oxide as is shown in Fig. 8. Dispersed precipitates of Mn_3O_4 formed during quenching were also observed in the scales, as was reported by Baldwin and his collaborators and also by Paidassi and Echeverria.

Marker studies.—A thin layer of platinum paste and fine platinum wires, 3 mils in diameter, were placed

Table II. Activation energies of parabolic oxidation

Gas atmospheres, P_{CO_2}:P_{CO}	Activation energies, kcal/mole
100:1	45.6 ± 2.4
30:1	42.8 ± 1.5
10:1	43.5 ± 2.8
3:1	41.7 ± 2.4
1:1	44.0 ± 1.9
1.3	40.5 ± 1.1

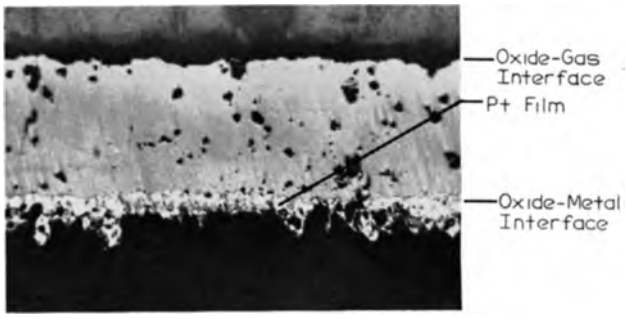

Fig. 7. Cross section of oxide layer with platinum markers (1000°C, p_{CO_2}:p_{CO} = 10:1, 40 hr). Magnification approximately 75X.

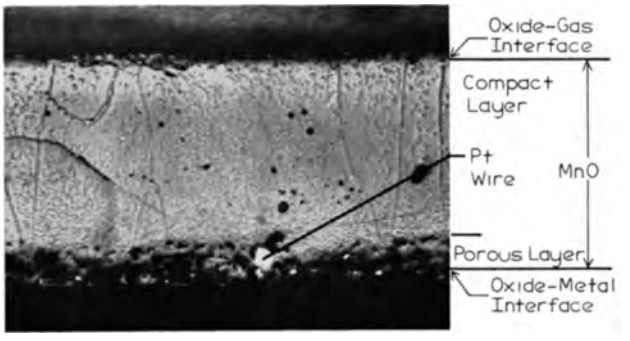

Fig. 8. Cross section of oxide layer with platinum markers (1100°C, 1 atm O_2, 6 hr). Magnification approximately 75X.

on polished specimens. The specimens were heated at 1000°C for 30 min in purified argon to convert the paste into a thin platinum layer and also to fix the platinum wires on the surfaces of the specimens. The specimens were oxidized at 1100°C in a CO_2-CO mixture of 10:1 and cross-sectioned. Manganese metal after oxidation was so brittle that it fell off when the specimens were sectioned and polished. The platinum markers were found at the metal-oxide interface, as is seen in Fig. 7. The location of the markers at the interface between metal and the oxide shows that manganese ions move much faster than oxygen ions in manganous oxide. When manganese was oxidized in 1 atm oxygen, the markers were also found to be located close to the manganese metal-manganous oxide interface as shown in Fig. 8. These findings show that manganese ions play the major role of material transport in manganous oxide under the conditions reported herein.

Discussion

In a previous paper (10), the present authors proposed a method by which the self-diffusion coefficient of the most mobile ions is obtained from the oxidation data as a function of oxygen partial pressure. According to the method, the self-diffusion coefficient of manganous ions in manganous oxide is calculated from the oxidation data, under the assumption that the self-diffusion coefficient of oxygen is negligible, by the equation

$$D_1^* = \frac{1}{2}\left(\frac{M_{MnO}}{M_O \rho_{MnO}}\right)^2 \frac{dk_p}{d \ln (p_{CO_2}/p_{CO})} = 0.1436 \frac{dk_p}{d \log (p_{CO_2}/p_{CO})} \quad [7]$$

where D_1^* is the self-diffusion coefficient of manganous ions, M_{MnO} and ρ_{MnO} are the molecular weight and the density (5.45 g/cc) of manganous oxide, M_O is the atomic weight of oxygen, and k_p is the parabolic rate constant in units of $g^2\ cm^{-4}\ sec^{-1}$. Graphical differentiation of k_p with respect to log (p_{CO_2}/p_{CO}) and multiplication by the factor of 0.1436 yields the value

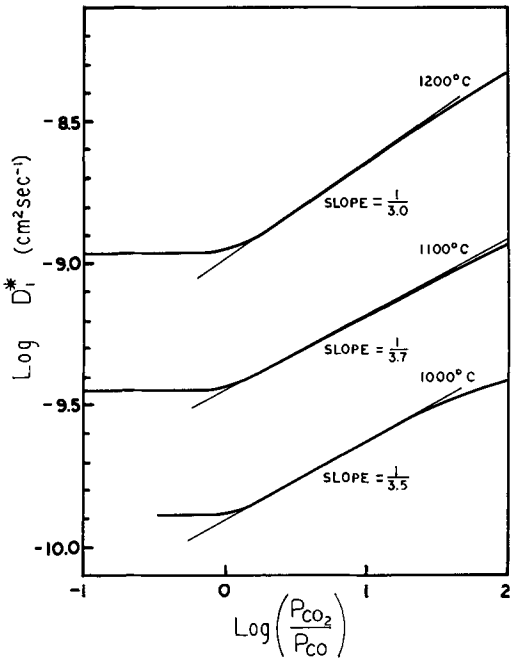

Fig. 9. Plots of log D_1^* vs. log (p_{CO_2}/p_{CO}).

of D_1^* as a function of log (p_{CO_2}/p_{CO}). Figure 8 shows the plots of log D_1^* *vs.* log (p_{CO_2}/p_{CO}) for 1000°, 1100°, and 1200°C. Above the value of log (p_{CO_2}/p_{CO}) = 0, log D_1^* increases almost linearly with the increase in log (p_{CO_2}/p_{CO}). The slope ranges from a value of 1/3.7 to 1/3.0. Cation vacancies would be created in manganous oxide mainly by a mechanism

$$CO_{2(g)} \rightleftarrows CO_{(g)} + Mn_{\square''} + 2\oplus + MnO \quad [8]$$

where $Mn_{\square''}$ is cation vacancy and $\oplus$ is an electron hole. During oxidation manganous ions diffuse via vacancies. Below a value of log (p_{CO_2}/p_{CO}) = 0, log D_1^* is independent of log (p_{CO_2}/p_{CO}).Under those conditions, presumably the intrinsic disorder predominates. Cation defects would be formed mainly by a Frenkel mechanism

$$\text{Null} \leftrightharpoons Mn_{\square''} + Mn_{O''} \quad [9]$$

or by a Schottky mechanism

$$\text{Null} \rightleftarrows Mn_{\square''} + O_{\square''} \quad [10]$$

where the symbols $Mn_{O''}$ and $O_{\square}$ denote an interstitial manganous ion and an oxygen ion vacancy, respectively.

Davies and Richardson (11) have studied the deviations from stoichiometry of manganous oxide at 1500°-1650°C, and they have found that manganous oxide has a composition from $MnO_{1.000}$ to $MnO_{1.045}$. Birchenall (12) has shown that the data of Davies and Richardson are well-explained if cation defects are assumed to be created by mechanism [9] at the stoichiometric composition and by mechanism [8] at large deviations from stoichiometry. The electrical conductivity of manganous oxide has been recently measured by Eror and Wagner (13) in the temperature range of 900°-1150°C in CO_2-CO gas mixtures. The transition of n- to p-type conduction was found to occur near the CO_2-CO ratio of 1:1. These workers (13) also found that above the ratio of 10:1, a $p_{O_2}^{1/6}$ dependence was followed, while a $p_{O_2}^{-1/6}$ dependence was obeyed below the ratio of 1:10. The present results are consistent with those of Birchenall and also with those of Eror and Wagner in the p-type region of manganous oxide.

Paidassi and Echeverria have found in their oxidation studies of manganese in air that the oxide film

formed above 900°C consists chiefly of MnO and that the activation energy above that temperature is 79.8 kcal/mole. The activation energies obtained in the present studies for MnO are much smaller than this value. Additional studies are necessary to clarify the reason for this difference.

Summary

The oxidation of manganese in CO_2-CO mixtures is controlled by the outward diffusion of manganous ions through a single layer of manganous oxide. The self-diffusion coefficient of manganous ions is independent of p_{CO_2}/p_{CO} in a region where the value of log (p_{CO_2}/p_{CO}) is less than 0. The independence is explained by a mechanism whereby intrinsic defects, Frenkel or Schottky, are more prevalent than those formed by the introduction of oxygen into the lattice according to Eq. [8]. In the region where the value of log (p_{CO_2}/p_{CO}) is larger than 0, the dependence of self-diffusion coefficient on p_{CO_2}/p_{CO} is 1/3.7 to 1/3.0. This dependence is explained if the creation of one cation vacancy and two electron holes is assumed.

Manuscript received Jan. 5, 1965; revised manuscript received July 7, 1965. This paper was presented at the Washington Meeting, Oct. 11-15, 1964. This work was supported by a grant from the Advanced Research Projects Agency through the Northwestern University Materials Research Center.

Any discussion of this paper will appear in a Discussion Section to be published in the June 1966 JOURNAL.

REFERENCES

1. B. S. Gurnick and W. M. Baldwin, Jr., *Trans. Am. Soc. Met.*, **42**, 308 (1950).
2. E. B. Evans, C. A. Phalnikar, and M. M. Baldwin, Jr., *This Journal*, **103**, 367 (1956).
3. J. Paidassi and A. Echeverria, *Acta. Met.*, **7**, 293 (1959).
4. J. Paidassi and A. Echeverria, *ibid.*, **11**, 227 (1963).
5. K. Fueki, *J. Electrochem. Soc. Japan*, **26**, E99 (1958).
6. K. Fueki, *ibid.*, **26**, E120 (1958).
7. J. F. Elliott and M. Gleiser, "Thermochemistry for Steelmaking," Vol. 1, Addison-Wesley Publishing Co., Inc., Mass. (1960).
8. F. S. Pettit and J. B. Wagner, Jr., *Acta Met.*, **12**, 41 (1964).
9. F. S. Pettit and J. B. Wagner, Jr., *ibid.*, **12**, 35 (1964).
10. K. Fueki and J. B. Wagner, Jr., *This Journal*, **112**, 384 (1965).
11. M. W. Davies and F. D. Richardson, *Trans. Faraday Soc.*, **55**, 604 (1954).
12. C. E. Birchenall, *Trans. Met. Soc. AIME*, **218**, 1134 (1960).
13. N. G. Eror and J. B. Wagner, Jr., To be published.

The Reaction of Aluminum Electrodes with a Glycol Borate Electrolyte

Robert S. Alwitt and Reginald G. Hills

Engineering Laboratories, Sprague Electric Company, North Adams, Massachusetts

ABSTRACT

Foil electrodes used in aluminum electrolytic capacitors are attacked by glycol borate electrolytes at elevated temperatures. In the work described in this paper it appeared that the dissolution rate was controlled by a reaction step involving OH^- and possibly water, but dissolution proceeded to a significant extent only because the dissolved aluminum was present as a soluble borate complex. The kinetics of electrode attack was studied by means of capacitance and weight change. Cathode foil (not anodized) dissolved at a constant rate and a film of amorphous, nonbarrier oxide was formed. Anodic Al_2O_3 initially dissolved at an approximately constant rate independent of oxide thickness, but at longer times the rate decreased and there was a dependence on thickness. Capacitance and weight loss data correlated as if uniform dissolution were the sole process, despite the fact that electron micrographs showed that the oxide had been penetrated at flaws. The anodizing electrolyte was found to affect the kinetics of dissolution, with and without an applied potential.

Most aluminum electrolytic capacitors contain a glycol borate electrolyte. A typical electrolyte would be ammonium pentaborate dissolved in ethylene glycol, which react to produce glycol borate esters and water. In a previous paper (1) it was shown that some of the common failure modes of low voltage aluminum electrolytic capacitors were the results of slow reactions between the glycol borate electrolyte and the aluminum electrodes. It was found that the primary mode of attack of anode foil was uniform dissolution of anodic oxide, upon which was superposed a more rapid attack at grain boundaries and discrete points within a grain. At these points the substrate metal was pitted and there was a new growth of nonbarrier oxide. Foil that had not been anodized (cathode foil) suffered a weight loss of metal and a gas was evolved that was qualitatively identified as hydrogen. Growth of nonbarrier oxide also occurred on cathode foil.

It was supposed that the slow step for both anode and cathode foil attack was oxide dissolution. When the thin oxide on cathode foil was reduced to its equilibrium barrier layer thickness by this reaction further dissolution was accompanied by a rapid electrochemical reaction to produce new oxide

$$2Al + 3H_2O - 6e \rightarrow Al_2O_3 + 6H^+ \qquad [1]$$

This was accompanied by the cathodic evolution of hydrogen. Oxide dissolution was balanced by formation of oxide at steady state, so the net result was dissolution of metal and production of hydrogen. Quite possibly some dissolved oxygen also was reduced, but this would not affect the qualitative aspects of this description.

Additional data on the kinetics of electrode attack are presented in this paper, as determined by capacitance and weight change both with and without applied potential. Also, the chemistry of oxide dissolution is examined in some more detail. The purpose was to construct a more complete picture of the phenomena and to answer some questions raised by the previous results (1). For example, what fraction of the surface undergoes nonuniform attack, and why was the dis-

solution rate of anodic oxide dependent on oxide thickness? Still no answer has been found to this last question.

Interpretation of anode foil weight change data is complicated by the fact that oxide dissolution is accompanied by some oxide growth, so that observed weight loss is not necessarily a true measure of the loss of anodic oxide. Also, accurate estimation of the weight of oxide deposited during anodization, without resorting to destructive testing, is not an obvious matter. In the discussion that follows on the analysis of weight data, this nomenclature will be used:

Measured quantities:

W_o = initial sample weight..
W_1 = weight after anodization.
W_2 = weight after immersion in electrolyte.
W_3 = weight after oxide stripped in CrO_3-H_3PO_4 solution.
W_4 = weight of metal in solution.
Q_e = equivalents of charge used in anodization.

Calculated quantities:

W_a = weight of anodic oxide dissolved.
W_m = weight of metal dissolved.
W_f = weight of new nonbarrier oxide.
W_{mf} = weight of metal in new nonbarrier oxide.

For cathode foil, the rate of dissolution is derived from data of W_m *vs.* time, where

$$W_m = W_o - W_3 \quad [2]$$

Properties of the corrosion product are given by

$$W_f = W_2 - W_3 \quad [3]$$

$$W_{mf} = W_o - W_3 - W_4 \quad [4]$$

For analysis of anode foil data two assumptions will be introduced. First, that all the charge passed during anodization removes aluminum from the substrate in the +3 state. This is not a stringent assumption since even for anodizations of less than 100% current efficiency it has been found to hold, so long as the anodizing voltage was low enough to prevent oxygen evolution. Under the conditions of the present study this assumption was tested and found to be valid. Second, the anodic film is assumed to be pure Al_2O_3. This is probably not true for any anodic oxide since material from the anodizing solution will be incorporated to an extent dependent on the particular conditions. In this study this was not a serious problem and the method of dealing with it will be presented later.

For anode foil, the weight of substrate metal dissolved is then

$$W_m = W_o - 9Q_e - W_3 \quad [5]$$

and the loss and gain of oxide are, respectively

$$W_a = (102/54)\ [W_4 - (W_m - W_{mf})] \quad [6]$$

$$W_f = (W_2 - W_3) - [(102/48)(W_1 - W_o) - W_a] \quad [7]$$

Unfortunately, Eq. [6] and [7] are a pair of simultaneous equations with three unknowns, W_a, W_f, and W_{mf}. To solve, W_{mf}/W_f could be assumed to be the same as found for cathode foil from Eq. [3] and [4]. If this is done, the resultant expression for W_f has a singularity when $W_{mf}/W_f = 54/102$, *i.e.*, no solution is possible when the new oxide growth is Al_2O_3 and the solution becomes more accurate the more dissimilar is the composition of the new growth from that of the anodic oxide. The best experimental determination of W_{mf}/W_f for cathode foil indicated the ratio was sufficiently close to that of Al_2O_3 to prohibit use of this technique to determine W_a and W_f.

Fortunately, upper and lower limits can be defined for W_a, and the experimental values for these limits were sufficiently close together to provide good estimates of W_a. Thus, the loss of anodic oxide is at least as great as the net observed oxide weight loss, *i.e.*

$$\underline{W_a} = (102/48)(W_1 - W_o - (W_2 - W_3) \quad [8]$$

Similarly, W_a can be no greater than the oxide equivalent to the total amount of metal found in solution, *i.e.*,

$$\overline{W_a} = (102/54)\ W_4 \quad [9]$$

No solution for W_f is possible but its magnitude can be inferred from the range in W_a.

Although aqueous phosphate solutions are the preferred electrolytes for commercial low voltage formations, they were not suitable for this investigation since anodizations in these electrolytes proceed at less than 100% current efficiency and a significant weight of phosphorus is incorporated into the film under some conditions (2). In contrast, Bernard and Cook (3) found that anodization in ethylene glycol containing 30% by weight ammonium pentaborate (E30) at 25°C proceeded at 100% current efficiency and the sole anodic product was Al_2O_3. Bernard and Randall (4) subsequently found that films formed in E30 over the voltage range 40v-150v occluded as much as 0.7% boron (equivalent to about 2% B_2O_3). This electrolyte was used in these present studies.

The first term on the right hand side of Eq. [8] represents the total weight of anodic product and must be modified to account for matter occluded during an anodization at 100% current efficiency. The weight of anodic oxide is simply 102 $Q_e/6$ and the weight gain of oxygen is $8Q_e$. The difference between the observed weight gain and $8Q_e$ represents occluded matter. The modified expression for $\underline{W_a}$ is then

$$\underline{W_a} = (102/6)\ Q_e + [(W_1 - W_o) - 8Q_e] - (W_2 - W_3) \quad [8a]$$

Experimental

Commercially etched 99.97% pure Al foil of 0.003 in. nominal thickness and with a surface roughness factor of about fifteen was used for all capacitance and weight measurements Anodized samples were of 17.6 cm^2 area and samples not anodized (cathode foil) were of 97 cm^2 area. (Areas referred to are projected areas, not true areas.) All samples were given an initial immersion at room temperature in 0.04*N* NaOH for 1 min followed by about 30 sec with gentle agitation in distilled water and then a prolonged soak in acetone. With this treatment the surface oxide was reduced to an amount undetectable by weight change in an oxide-stripping solution. Anodizations were done at constant current in E30 at 25°C. The current was maintained at 25 ma until the desired cell voltage was reached and was then decreased to 2.5 ma where it was held until the particular voltage was again obtained. Anodizations were to either 10v or 40v and the IR drop in the cell was about 0.1v at 2.5 ma.

For the 10v anodizations there were no significant differences between the observed weight gain $(W_1 - W_o)$ and the weight of oxygen calculated from the charge passed $(8Q_e)$. The weight gain in the 40v anodizations was consistently greater than $8Q_e$ by as much as 0.8 $\mu g/cm^2$, or about 2% of the weight of anodic oxide.

After initial capacitance and weight measurements foil samples were immersed in ethylene glycol containing 17% by weight ammonium pentaborate (E17) and kept at 85°C in sealed glass containers. E17 is a typical glycol borate electrolyte and was used in previous studies of electrode attack (1). The ratio of electrolyte volume to foil area was 2.3 ml/cm^2. In a preliminary experiment, only a small increase in the rate of oxide attack in E17 was observed when an anodized Al wire was rotated at several hundred revolutions per minute compared with that obtained with no rotation. In another experiment, no change in the rate of dissolution of cathode foil occurred when the electrolyte viscosity was increased 50% by the addition of a small amount of a thickening agent. These results in-

dicated the absence of significant electrolyte diffusional resistance so no attempt was made to control the natural convective conditions.

After the prescribed immersion time, capacitance and weight were again measured, oxide was stripped and the weight again determined. Between steps the foil was rinsed in distilled water followed by reagent grade acetone.

Oxide stripping was done in an aqueous solution of 2% CrO_3 and 5% H_3PO_4 at 85°C. The rate of attack of the aluminum substrate was only 1.5 $\mu g/cm^2$-min or 0.1 $\mu g/min/cm^2$ of true area, which compared with a rate of 0.2 $\mu g/cm^2$-min reported by Bernard and Randall (5) for electropolished aluminum. The attack of anodic oxide was more than fifty times as fast *e.g.*, a 10v film was completely stripped in 30 sec and a 40v film within 2 min. Samples of 17.6 cm^2 area were stripped for 30 sec, weighed and the cycle repeated until the rate of attack in an interval dropped to that of the base metal. The transition was sharp and unequivocal. The weight preceding the last was taken as the weight of oxide-free metal. The same procedure was used for the 97 cm^2 samples except that a 15 sec stripping interval was used.

Aluminum in solution was determined using a method of Sandell [procedure A in ref. (6)] based on the extraction of aluminum hydroxyquinolate by chloroform and photometry of the resulting yellow extract. For an aluminum concentration of greater than about 2.5 ppm (equivalent to 10 μg Al) the accuracy of the determination was ±5%. At lower concentrations the results were accurate to 5 μg.

All weighings were made on a microbalance accurate to within 10 μg. Capacitance readings were made in an aqueous borate electrolyte at 120 cps using a conventional capacitance bridge with a signal voltage less than 0.3v rms.

Samples for electron microscopy were prepared from 99.99% Al foil, 0.003 in. thick, electropolished in a perchloric acid-acetic anhydride bath. Anodization current densities and other conditions were the same as described for etched foil. Standard methods were used to prepare the micrograph specimens and these have been outlined elsewhere (1). Examination of surfaces was done with carbon negative replicas shadowed 15°.

Results and Discussion

Dissolution chemistry.—Before examining the data on the kinetics of dissolution it may be helpful to consider some results that shed light on the roles of the chemical species involved in the process.

Cathode foil was dissolved in E17 to the extent of 600 ppm Al in solution, with no sign of a precipitate nor decrease in dissolution rate. The solubility product of $Al(OH)_3$ in glycol is not known, but as a comparison, this concentration of Al could be attained in a simple aqueous solution only at a *p*H less than three or greater than ten (7). E17 is an almost neutral electrolyte, so the high solubility of Al appeared likely to be due to formation of complexes, either with glycol or a borate species.

E17 can be considered as a solution of various borates in a mixed solvent of composition 91% glycol + 9% water. Several nonborate solutes were dissolved in this glycol-water solvent, *e.g.*, KCl + HCl, and in each case the *p*H and conductivity were adjusted approximately to that of E17. No significant dissolution of aluminum occurred indicating that the enhanced solubility in E17 is not due to complexing with glycol.

In a saturated aqueous ammonium pentaborate (APB) solution at room temperature (*p*H 7), the concentration of dissolved Al reached 90 ppm. A concentration of less than 1 ppm would have been predicted from solubility data for aluminum hydroxide (7). It is concluded that the enhanced solubility of Al in aqueous and glycol solutions is the result of formation of borate complexes. The structure of the complex is not known, but probably involves a B-O-Al-O-B linkage.

In some simple experiments in aqueous APB solutions it was observed that the rate of weight loss of cathode foil and the rate of dissolution of anodic oxide were independent of the APB concentration, but increased as the *p*H was increased from 7 to 9. The addition of water to E17 increased the rates of attack (1), but it is not known if this was due to direct involvement of water in the rate controlling step or to the effect of water on solvent properties and the several equilibria that exist in this electrolyte. It was proposed (1) that oxide dissolution in E17 proceeded via the over-all reaction

$$Al_2O_3 + 3H_2O + 2OH^- \rightarrow Al(OH)_4^- \quad [11]$$

The results discussed here indicate this is not an accurate description. Although the dissolution rate is apparently controlled by a reaction step involving hydroxyl ion and possibly water, dissolution proceeds to a significant extent only because the dissolved aluminum is present as a soluble borate complex, and not as $Al(OH)_4^-$.

Cathode foil.—Figure 1 shows that etched aluminum foil dissolved in E17 at 85°C at a constant rate of 0.17 $\mu g/cm^2$-hr or, in terms of the equivalent weight of oxide, 0.33 μg Al_2O_3/cm^2-hr. Despite the uniform rate of metal dissolution, the growth of new oxide followed no discernible pattern. The following values of W_f were obtained at the indicated immersion times:

Time (hr)	W_f ($\mu g/cm^2$)
21	3.9, 4.0
67	0.8, 1.0
114	6.7, 6.8
168	0 , 0.3

Apparently, the fraction of dissolved aluminum that entered the oxide phase was determined by factors other than those controlled in these experiments.

No capacitance decrease ever accompanied this film growth so the new oxide was not a barrier film. An attempt was made to learn about the film composition by calculating the per cent Al in the film using the 114 hr data. These were the only data for which both W_f and W_4 were large enough for acceptable accuracy. The data and calculated results are given in Table I. The values of 48% and 52% compare with 53% for Al_2O_3 and 45% for $Al_2O_3 \cdot H_2O$.

A previous examination (1) of electron micrographs of electropolished foil after immersion in E17 showed that the oxide/air surface was similar in appearance to that of anodic oxide and the metal substrate was heavily pitted. The oxide was too thin to permit transmission micrographs. If water is added to a glycol borate electrolyte the reaction with aluminum electrodes is enhanced (1). Some typical results are given in Fig. 1 which show that with 10% water added the reaction rate with cathode foil was increased fourfold. The oxide film on an electropolished specimen immersed in E17 + 10% H_2O for 168 hr at 85°C was sufficiently thick to obtain transmisson electron micrographs. One of these is shown in Fig. 2 along with a selected area electron diffraction (SAD) pattern. The oxide and metal surfaces of this specimen had the same appearance as samples immersed in E17 to which no water had been added (1). The transmission micrograph and SAD pattern indicate that this oxide is amorphous,

Table I. Aluminum content of nonbarrier oxide

Weights in milligrams for 97 cm^2 samples				
W_0-W_3	W_4	W_f	W_{mf}	% Al
1.90	1.56	0.66	0.34	52
1.87	1.56	0.65	0.31	48

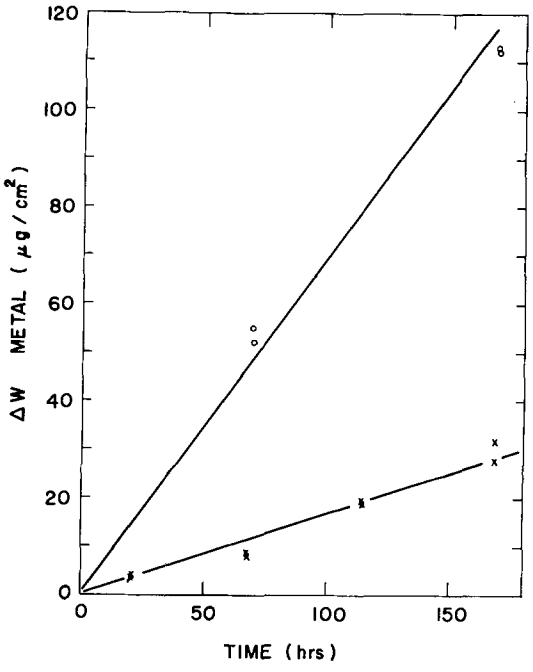

Fig. 1. Cathode foil dissolution in (X) E17 and (○) E(17 + 10% H_2O.

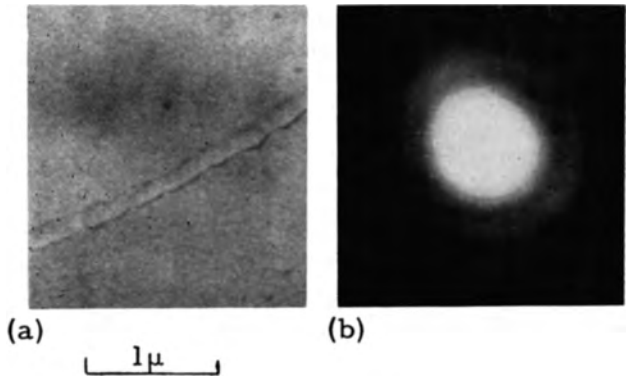

Fig. 2. Oxide film grown in E17 + 10% H_2O; (a) transmission micrograph; (b) electron diffraction pattern.

except for what appears to be a grain boundary in Fig. 2a. Despite the similarity of Al content then, this oxide cannot be $Al_2O_3 \cdot H_2O$ (boehmite), which has a crystalline structure.

Anode foil.—The change of reciprocal capacitance with time of immersion in E17 at 85°C is shown in Fig. 3 for foils anodized to 10 and 40v. Initial values of 1/C were 0.116 ± 6% (10v) and 0.490 ± 2% (40v). For about the first 100 hr Δ1/C was independent of oxide thickness and then the data for each thickness diverged. This behavior at longer times will be discussed in detail later.

The weight loss of anodic oxide during immersion in E17 at 85°C is shown in Fig. 4. Upper and lower limits for the weight loss were calculated from Eq. [9] and [8a] and are indicated in Fig. 4 by tails pointing up and down, respectively. Each point is the average of two samples. Smooth curves drawn through the lowest data points for each thickness are similar in shape to those for reciprocal capacitance in Fig. 3. The linear portion of the 40v curve represents a dissolution rate of 0.20 μg/cm²-hr, which is 2/3 the rate found for cathode foil.

If oxide dissolution proceeded uniformly over the surface, then the fractional loss of oxide calculated from the change in capacitance would equal the corresponding fractional loss in oxide weight. Corresponding points from the curves in Fig. 3 and 4 are plotted

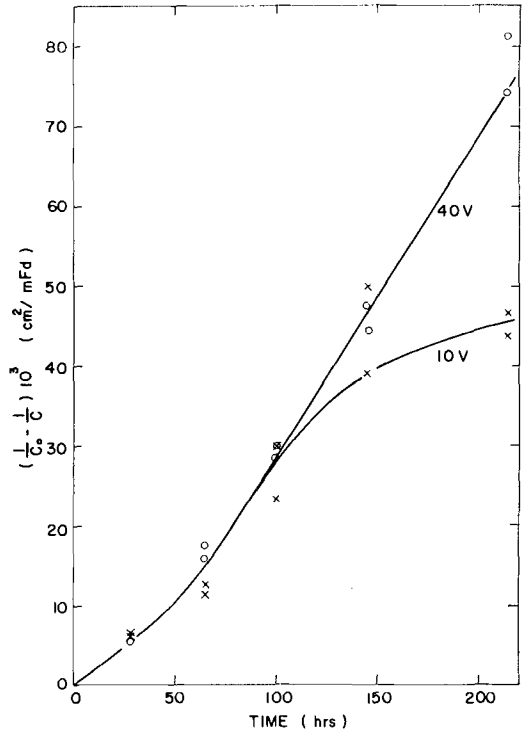

Fig. 3. Reciprocal capacitance change in E17 for two oxide thicknesses.

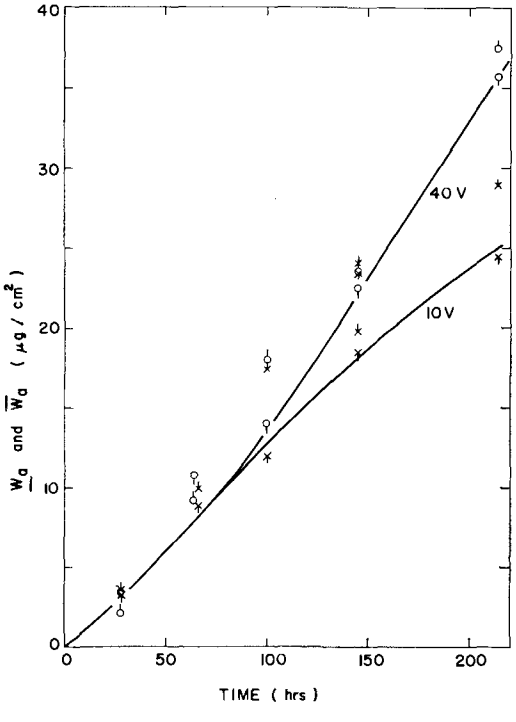

Fig. 4. Dissolution of anodic oxide in E17. (See text for explanation of symbols.)

in this fashion in Fig. 5, where W_{ao} is the initial weight of anodic film. The line is drawn with a slope of one and, except at the highest weight loss with a 10v film, the data are representative of uniform oxide dissolution. This is despite the fact that a significant amount of nonuniform attack took place, as indicated by the electron micrographs to be discussed shortly. This anomaly will be considered further at that time.

If the curves in Fig. 4 were drawn through the upper data points and values of W_a obtained from this curve were used in Fig. 5, all the points would have been below the line of unit slope. This represents a

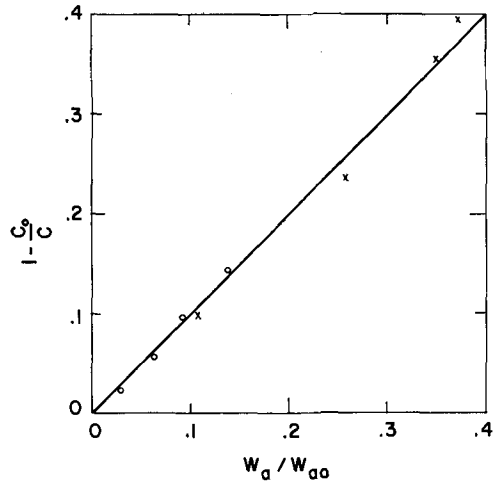

Fig. 5. Equivalence of capacitance increase and oxide weight loss; (X) 10v; (○) 40v.

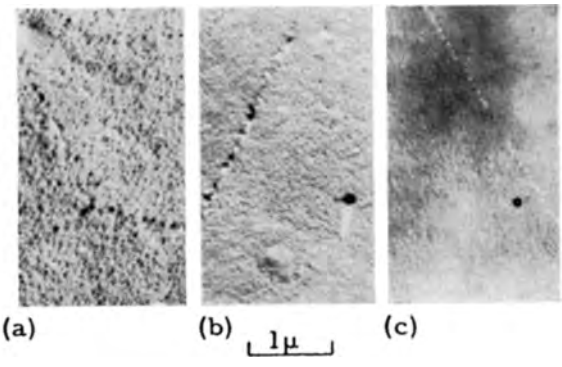

Fig. 6. Electropolished foil anodized to 10v in E30; (a) oxide/air surface; (b) metal surface at metal/oxide interface; (c) oxide film by transmission.

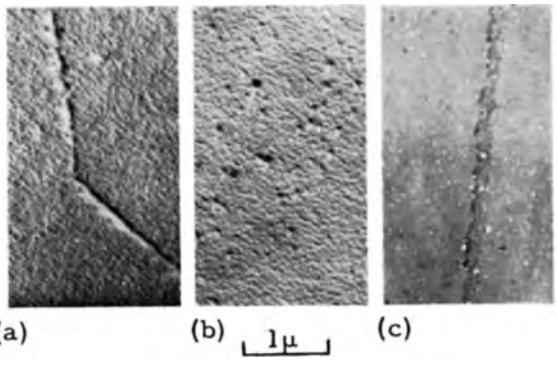

Fig. 7. 10v foil after immersion in E17 for 168 hr at 85°C; (a), (b), (c) same as in Fig. 6.

physically impossible situation since the change of reciprocal capacitance must at least be equivalent to the weight loss of barrier oxide. On this basis, Eq. [8a] probably gives a better estimate of W_a than does Eq. [9]. Since the right hand side of Eq. [8a] equals W_a-W_f, this implies that $W_f << W_a$.

The difference between $\overline{W_a}$ and W_a should be at least equal to the oxide equivalent of the substrate metal dissolved (W_m). In Fig. 4 it can be seen that this difference did not follow a regular pattern but covered a range of values up to the equivalent of 4 μg/cm^2 of dissolved metal, with an average value of 2.5 μg/cm^2. Values for W_m were also calculated from Eq. [5], and for both 10 and 40v films these increased from 2.6 μg/cm^2 at 28 hr to 5.4 μg/cm^2 at 214 hr. Although the ranges of values of W_m calculated by these

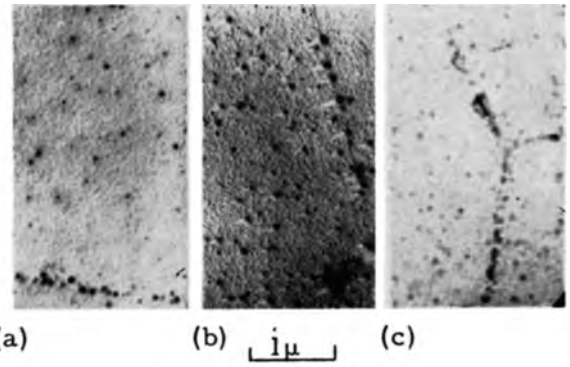

Fig. 8. 10v foil after immersion in E17 for 340 hr at 85°C; (a), (b), (c) same as in Fig. 6.

two methods overlap, those found from the difference between W_a and $\overline{W_a}$ were generally smaller.

Electron micrographs.—The rates of capacitance increase of the electropolished foils examined by electron microscopy were about the same as those of the etched foils. For example, after 168 hr in E17 at 85°C, C_0/C for 10v etched foil was 0.64 compared to 0.62 for polished foil. Examination of electron micrographs showed that significant nonuniform oxide dissolution had taken place. The extent and characteristics of the attack were the same as for polished foils anodized in aqueous phosphate solution that were previously examined (1).

The effect of immersion in E17 on a 10v film formed in E30 is shown in Fig. 6, 7, and 8. After anodization (Fig. 6) the oxide/air surface and metal surface at the metal/oxide interface exhibited uniform texture except for an occasional pit and a noticeable delineation of grain boundaries. The oxide was thinner at grain boundaries and at apparently random sites within a grain. The lower grain in Fig. 6c, in which thin spots are barely discernible, represents the most severe thinning that was observed in an anodized sample. Ten volt films formed in 1 g/liter $NH_4H_2PO_4$ did not exhibit any thin spots (1).

After 168 hr in E17 at 85°C (Fig. 7) there was no change in the oxide/air surface except for enlarged grain boundary grooves. Increased grain boundary attack was also evident at the metal surface and, in addition, numerous pits were present within the grains. The oxide was now thickened at grain boundaries and had a high density of thin spots and holes. After 340 hr in E17, C_0/C was 0.44. In Fig. 8 it is seen that pits were now evident within grains at the oxide/air interface and were more numerous in the metal substrate. Instead of holes, the oxide film now exhibited thickened areas within grains as well as at grain boundaries.

These thickened areas undoubtedly correspond to the points of attack in the substrate and represent a growth of nonbarrier oxide, perhaps similar in properties to that found on cathode foil. Alwitt and Hills (1) have found that this new growth is not too adherent to the surrounding anodic oxide and its presence or absence in a transmission micrograph is dependent on specimen preparation. It is possible that at least some of the holes in Fig. 7c were filled with oxide that was knocked out during specimen handling prior to examination. A general characteristic of the attack is that the metal substrate usually appears more pitted than the oxide/air surface. This may be because the nonbarrier oxide fills the holes in the anodic film so that shadowing of the replica of the oxide/air surface does not reveal their existence.

The pits in Fig. 7b are about 0.03-0.05μ deep and have a diameter of 0.05-0.1μ. After 340 hr immersion these dimensions were not much increased. From the pit depth and the weight loss of metal substrate the

fraction of the total area occupied by pits can be estimated. For a pit depth of 0.04μ and a metal loss of 4 $\mu g/cm^2$, this fraction is 2.5%. This should have resulted in a capacitance increase greater than could be accounted for by the weight loss on the basis of uniform dissolution. For example, assuming a 2v barrier oxide in the pits, it was estimated for a 10v film that when $W_a/W_{ao} \simeq 0.3$, the ordinate in Fig. 5 should be 10% greater and when $W_a/W_{ao} \simeq 0.1$ for a 40v film, $1-C_0/C$ should be 3 times as large. This was clearly not observed. It must be that the electrical resistance of the nonbarrier oxide in the pits was sufficiently high to prevent the capacitance of the underlying dielectric from being measured.

Weight loss and capacitance change are not always found equivalent, *e.g.*, foil anodized to 40v in a phosphate solution and immersed in E17 until $W_a/W_{ao} = 0.23$ had a value for $1-C_0/C$ of 0.32 (1). Perhaps foil anodized in E30 would have shown the same behavior if dissolution had been allowed to proceed to as great an extent.

Decreased dissolution rate at longer times.—The decrease in the rate of attack of thinner films at longer times, shown in Fig. 3 and 4, is a general characteristic of this dissolution process that has been observed previously for films formed in aqueous phosphate solutions (1). It occurred to the same extent whether the foil was left undisturbed in the E17 or removed for periodic capacitance measurements and then replaced. Periodic change of the electrolyte with fresh solution had no effect. The knee in the curve is not always reproducible, as indicated by the 145 hr 10v data in Fig. 3, where only one sample had a decreased rate of dissolution. However, the averaged results from several experiments showed that departure from the parent curve for 10v films occurred usually at about 0.035 cm^2/mfd, and for 20v and 40v films at about 0.050 and 0.085 cm^2/mfd, respectively. These are equivalent to dissolution of 30%, 21%, and 17% of the initial oxide, respectively.

The decrease in the dissolution rate is quite substantial. From the curves in Fig. 4, at 200 hr the 10v oxide was dissolving at only half the rate of the 40v oxide. The capacitance data (Fig. 3) indicates an even larger difference in rates. It is emphasized that even at the longer times when the oxides were dissolving at different rates, the capacitance and weight data behaved as if uniform dissolution was the sole process (Fig. 5). For some reason, the rate of uniform dissolution decreased at longer reaction times as a function of oxide thickness.

Randall *et al.* (8) have found that anodic films formed on tantalum and niobium consist of a layer of stoichiometric pentoxide next to the metal and an outer layer which contains matter characteristic of the anodizing electrolyte. At least in some cases the outer layer was more chemically reactive than the inner portion. At any current density, the relative amounts of the two layers remained constant, independent of the total charge passed. Randall (9) has found that anodic aluminum oxide has a similar structure.

It was thought that the decrease of dissolution rate at longer times in E17 might involve different compositions of inner and outer portions of the oxide. This was tested in the following manner. Four foil tabs were anodized in E30 to 20v, immersed in H_3PO_4-CrO_3 solution for 55 sec at 65°C and then thoroughly rinsed in distilled water. The oxide was now thinned to the thickness of about a 10v film, as determined by capacitance. Two of the tabs were "healed" in E30 at one tenth the anodizing current density until the rapid voltage rise ceased, about 9.5v. Healing produced less than a 3% capacitance decrease which indicated that uniform dissolution had occurred in the stripping solution. These films were now of about the same thickness as normal 10v films but any outer layer was much thinner than normal. If this was an important factor in the dissolution kinetics, these films should undergo a decrease in the rate of dissolution much sooner than normal 10v films. The capacitance increase in E17 of all four samples (two healed, two not healed) was determined in the usual fashion. There were no significant differences among the samples and all data essentially replicated the previous results with normal 10v films.

The agreement between normal and "thinned" 10v oxides means that the observed dependence of dissolution rate on film thickness was not a function of any compositional variations within the oxide. Moreover, lack of any difference between the healed and not healed samples shows that any space charge induced in the oxide by the formation field had no residual effect on the dissolution kinetics. In the absence of any other simple model for the oxide which suggests a thickness-dependent dissolution process, we can offer no explanation for the dissolution kinetics of these oxides.

Sites for oxide penetration.—Rapid penetration of the anodic oxide occurred at points that are probably very similar to the flaws in anodic Ta_2O_5 films discussed in detail by Vermilyea (10). Aside from infrequent gross imperfections, direct evidence of flaws in the as-formed films was found only in the micrographs of 10v E30-formed films (Fig. 6c), and these were at too low a magnification to distinguish any structural features. Inspection of Fig. 6c shows that flaws occurred at grain boundaries and at points within grains, and flaw density varied from grain to grain. These features were intensified by the immersion in E17 as seen in Fig. 7. Most flaws were circular, as inferred from the round pits produced during oxide attack, but larger flaws were sometimes of the types shown in Fig. 9. Though direct evidence is lacking, it is suspected that the annular depressions seen in Fig. 9b were present in the as-formed oxide. The deep slit in the center area was probably developed during immersion in E17. [Vermilyea (10) describes a structure like those in Fig. 9b as being due to a sequence of flaw formation, healing and new flaw formation at the same spot. In the present case, the dimensions of the flaws are too large to have been due to this cause.]

Flaws are presumably the result of surface contamination, either from impurities in the metal or from external sources, and surface roughness. Renshaw (11) has presented evidence that flaws in the oxide formed on chemically etched aluminum tend to be concentrated at the 90° step edges. The internal stresses in the oxide along the step edges would presumably be large enough to cause oxide failure and cracking. In our experiments no micrographs were made of etched foil and the capacitance/weight data were insensitive to the nonuniform dissolution, so no information on the relationship between surface roughness and flaws was obtained. It might have been expected that with foil as heavily etched as that used in these experiments, some difference in the rate of capacitance change between etched and polished foil would have been observed if surface roughness was a factor in flaw generation, but no such difference was seen.

To determine the effect of grain orientation on flaw density, several previously examined samples with

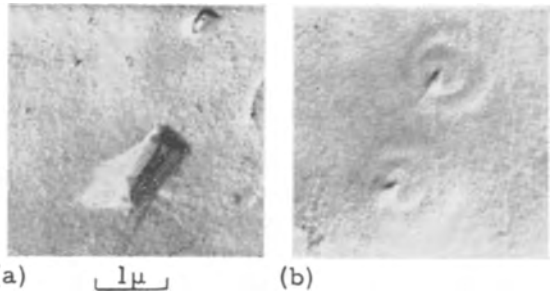

Fig. 9. Flaws in 40v film; oxide/air surface after immersion in E17 for 340 hr at 85°C.

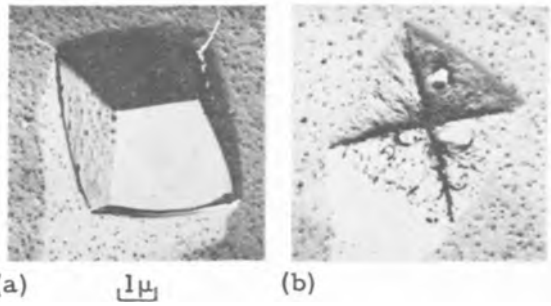

Fig. 10. Characteristic etch figures in (a) grains with high flaw density and (b) grains with low flaw density.

high flaw density were given a metallographic etch in a bath recommended by Lacombe and Beaujard (12). Subsequent examination showed that etch figures such as that in Fig. 10a were in grains with a high flaw density while etch pits such as in Fig. 10b were in grains of low flaw density. This was interpreted to mean that more flaws were present in grains with surfaces parallel to {110} planes than in grains with surfaces parallel to {100} planes. No attempt was made to determine the frequency of the differently oriented grains, nor were any measurements made throughout this study of the relative frequency of grains with high or low flaw densities other than to note that a significant amount of both was always present in a sample.

From electron micrographs, the flaw density within grains (not including grain boundaries) was estimated to be $10^9/cm^2$ for grains exhibiting significant attack, *e.g.*, the grain in Fig. 7b. The same value for flaw density was obtained from the values of pit dimensions and metal weight loss used previously to estimate the area occupied by pits. Neither the anodizing solution nor film thickness had an observable effect on flaw density. Vermilyea (10) estimated 10^7 flaws/cm^2 in oxide films on chemically polished commercial high purity tantalum foil.

Effect of anodizing electrolyte.—Ten volt films were formed at 25°C in the following electrolytes: Aqueous 1 g/l $NH_4H_2PO_4$ (ADP), *p*H 4.74; E30; aqueous 50 g/l H_3BO_3 (NH_4OH added to give *p*H 4.72). For the first two electrolytes the conditions were the same as used previously except that instead of a final current of 2.5 ma, the current was maintained at 25 ma and the anodization continued until the cell voltage was 10v plus the IR drop. The aqueous boric acid electrolyte would not support anodization at this current density so in this case the films were formed at constant voltage to a final current of 25 ma.

The capacitance increase in E17 was followed in the usual manner, with the results shown in Fig. 11. Films formed in the phosphate electrolyte dissolved at a faster rate than did films formed in electrolytes containing borate species. Moreover, the oxide formed in the aqueous borate electrolyte was more resistant to dissolution than that formed in the glycol borate electrolyte. The differences in rates were substantial. For example, the average dissolution rates for the first 24 hr were in the ratio 9:3:2, for the electrolyte order listed above.

It is characteristic of films formed in E30 that their initial dissolution rate is either constant, as in Fig. 11, or there is a period of increasing rate preceding the constant rate, as in Fig. 3. The latter behavior is thought to be due to dissolution initiating at points sufficiently separated so that until the dissolution fronts from these points merge, the attack is occurring over an increasing fraction of the area. On the other hand, films formed in aqueous ADP have never exhibited either of these characteristics, but instead dissolve at a steadily decreasing rate, even at times less than 24 hr.

Although it was shown in a preceding section that compositional differences do not explain the decrease

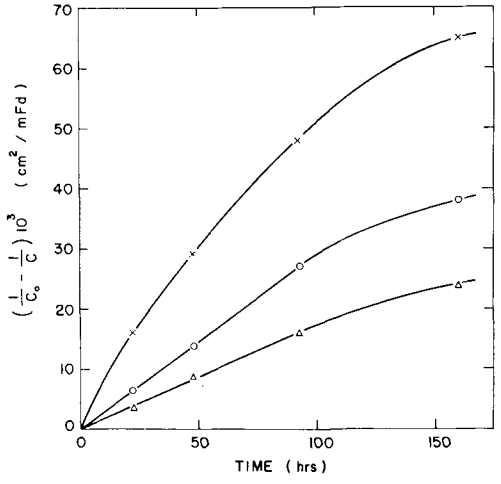

Fig. 11. Effect of anodizing electrolyte on dissolution of 10v films; (X) 1 g/liter ADP: (○) E30; (△) 50 g/liter H_3BO_3.

in dissolution rate for any one oxide, it appears likely that the differences among oxides formed in the three electrolytes are because of the species and concentration of occluded matter in each film.

Effect of applied potential.—Samples of 10v foil were maintained at several positive voltages with respect to a platinized platinum wire cathode, using a storage battery as the constant voltage source. After 96 hr in E17 at 85°C the changes in capacitance and oxide weight were measured. This was done not only with samples anodized in E30 but also with foil anodized in aqueous 1 g/liter $NH_4H_2PO_4$ (ADP). Anodizing conditions with ADP were the same as described in the preceding section. Lastly, tabs of electropolished foil, intended for electron microscopy, were anodized to 10v in E30 and maintained at positive potentials in E17 for 281 hr at 85°C.

The effect of applied potential is illustrated in Fig. 12. The ordinate for weight change is simply the oxide weight after immersion in electrolyte divided by the initial oxide weight. For reasons that will soon

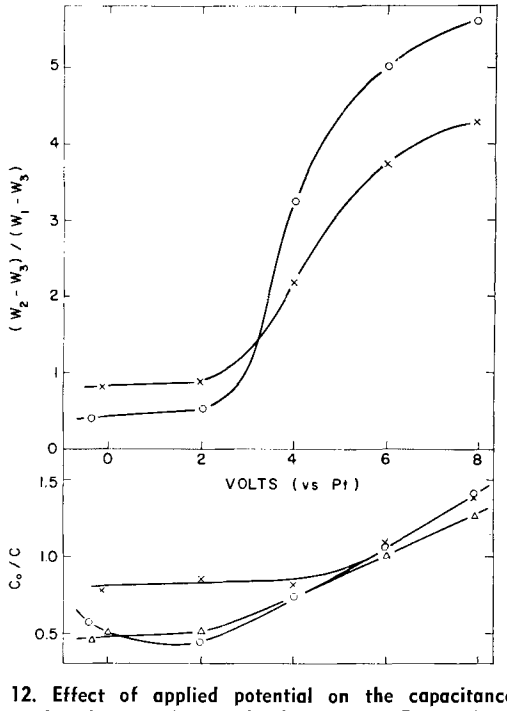

Fig. 12. Effect of applied potential on the capacitance and oxide weight change of several 10v foils in E17. (X) etched, anodized in E30, 96 hr immersion; (○) etched, anodized in 1 g/liter ADP, 96 hr immersion, (△) polished, anodized in E30, 281 hr immersion.

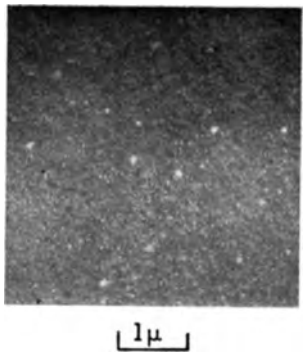

Fig. 13. Transmission micrograph of 10v film after 96 hr in E17 at 85°C with +6v applied potential.

be obvious, C_0/C was a better measure of the fraction of initial barrier oxide remaining than was the change in oxide weight. With foil anodized in E30, small positive potentials had little effect on the dissolution of barrier oxide. This would be expected for a simple chemical dissolution process. Increasing the potential decreased the effect of dissolution until at sufficiently high potentials additional barrier oxide was apparently deposited.

The change in weight of oxide agrees with this description except that the weight gain at higher potentials was far greater than could be accounted for by the capacitance decrease. For example, at 6v there was no change of capacitance but the oxide weight increased almost fourfold. This large a change could only be due to the formation of a porous oxide. To verify this, an electron micrograph was made of the oxide stripped from the electropolished foil kept at 6v. In Fig. 13 it is seen that in addition to the larger holes observed before, a fine network of pores exists throughout the oxide. Formation of porous oxide in electrolytes ordinarily used to produce barrier oxide has been observed previously by Renshaw (11) and by Hunter and Towner (13). The formation of a porous oxide apparently depends only on the relative rates of anodization and oxide dissolution. The observation that porous oxide can be formed in E17 is not of fundamental significance though it could be of importance in interpreting capacitor performance.

Foil anodized in ADP behaved differently from foil anodized in E30. Besides a greater rate of attack on open circuit, small positive potentials accelerated the dissolution, resulting in a minimum barrier thickness at about +2v. The barrier thickness would have been still thinner at higher potentials if the competing process of film formation had not become significant. The same behavior has been observed with foil commercially anodized in ADP (1).

It was thought that the dependence on potential might have been related somehow to the more extensive attack of ADP films at 96 hr compared to E30-formed samples. However, the electropolished tabs were in E17 for sufficient time to produce the same thinning of barrier oxide as the ADP-formed tabs, and yet no increasing attack with increased potential was observed. It is concluded that the different behavior with applied potential is due to a difference in the electrical properties of aluminum oxide formed in a glycol borate electrolyte from that formed in aqueous phosphate solution. In particular, the oxide formed in phosphate solution must contain a higher concentration of mobile charged species. Engell (14) has shown that the dissolution rates of several semiconducting metal oxides are dependent on electrode potential.

It is generally accepted that lattice defects are preferred sites for reaction on a solid surface. The greater dissolution rate of phosphate-formed oxide compared to E30 formed oxide can be explained as the effect of different incorporated material from the electrolyte on defect concentration and type. Phosphorus is found in films formed in aqueous phosphate solutions (2), and in E30-formed films boron, and probably carbon, is occluded (4). The concentration of defects at the surface of oxide formed in 1 g/liter ADP was apparently increased by the application of a potential too low to result in any significant ionic transport, but sufficient for the movement of electrons and/or vacancies. Since we know neither the mechanism of the dissolution reaction nor the state of the incorporated matter in the oxide, it is not possible to be more specific in the interpretation of these results.

Conclusions

1. Dissolution of aluminum and aluminum oxide occurs to a significant extent in glycol borate electrolyte only because of the formation of soluble aluminum-borate complexes.
2. Aluminum oxide is attacked preferentially at flaws that are similar to those found in anodic Ta_2O_5. Despite a significant flaw density in the anodic oxide, the weight of nonbarrier oxide grown at these sites is very small compared to the total weight of anodic oxide dissolved. The resistance of the new oxide growth is sufficiently large so that the capacitance and weight loss correlate as if only uniform dissolution occurred.
3. The dissolution rate of anodic oxide is a function of oxide thickness, but no explanation for this dependency has been found. It is not due to compositional variations within the oxide or to a defect distribution determined by the formation field.
4. Material incorporated from the anodizing electrolyte affects the dissolution kinetics not only on open circuit, but also with an applied potential. This may be a useful tool in learning more about the incorporated species and/or oxide dissolution.

Acknowledgments

The authors wish to thank Miss A. Harvin for the electron micrographs, Mr. R. Vanasse for the aluminum analyses, and Mr. S. Acello for the metallographic etch. Discussions with Drs. J. J. Randall, Jr., S. D. Ross, and D. M. Smyth were most helpful.

Manuscript received May 24, 1965. This paper was presented at the San Francisco Meeting, May 9-13, 1965.

Any discussion of this paper will appear in a Discussion Section to be published in the June 1966 JOURNAL.

REFERENCES

1. R. S. Alwitt and R. G. Hills, Sprague Technical Paper 64-11, presented at 3rd Annual Symposium on Physics of Failure in Electronics, Chicago, September 1964.
2. W. J. Bernard, *This Journal*, **109**, 1082 (1962).
3. W. J. Bernard and J. W. Cook, *ibid.*, **106**, 643 (1959).
4. W. J. Bernard and J. J. Randall, Jr., *ibid.*, **108**, 822 (1961).
5. W. J. Bernard and J. J. Randall, Jr., *ibid.*, **107**, 483 (1960).
6. E. B. Sandell, "Colorimetric Determination of Traces of Metals," 3rd ed., p. 234, Interscience, New York (1959).
7. C. Edeleanu and U. R. Evans, *Trans. Faraday Soc.*, **47**, 1121 (1951).
8. J. J. Randall, Jr., W. J. Bernard, and R. R. Wilkinson, *Electrochim. Acta*, **10**, 183 (1965).
9. J. J. Randall, Jr., Private communication.
10. D. A. Vermilyea, *This Journal*, **110**, 250 (1963).
11. T. A. Renshaw, *ibid.*, **108**, 185 (1961).
12. P. Lacombe and L. Beaujard, *J. Inst. Metals*, **74**, 1 (1947).
13. M. S. Hunter and P. F. Towner, *This Journal*, **108**, 139 (1961).
14. H. J. Engell in "The Surface Chemistry of Metals and Semiconductors," H. C. Gatos, Editor, p. 320, John Wiley & Sons, New York (1959).

The Effect of Phosphor Coating Weight on the Lumen Output of Fluorescent Lamps

R. Gaines Young

Advanced Development Department, Lamp Division, Westinghouse Electric Corporation, Bloomfield, New Jersey

and E. G. F. Arnott

Research Laboratories, Westinghouse Electric Corporation, Pittsburgh, Pennsylvania

ABSTRACT

Brightness measurements have been made in partially coated lamps at both surfaces of 1-cm wide fluorescing Cool White halophosphate stripes for a wide range of coating weights per unit area. The brightness data were used in equations describing the optics of fully coated lamps and the resulting curve was successfully fitted to an experimentally obtained curve of lumens *vs.* coating weight per unit area for such lamps. The values of the differential reflection and absorption coefficients of visible emitted radiation of the coating which gave the best fit were $r = 0.43$ cm²/mg and $a = 0.0012$ cm²/mg, respectively.

It is known that an optimum thickness of phosphor coating is required to produce maximum lumen output from the fluorescent lamp (1). A coating of inadequate thickness does not utilize all the energizing u.v. radiation, whereas an excessively thick coating tends to trap the generated radiation within the lamp and increases absorption losses.

A study was made of the effects on brightness and lumen output resulting from variations in the quantity of coating, *i.e.*, weight per unit area, over a range of thirty-seven to one. These data were sought to increase our understanding of phosphor coating optics and, in particular, the effect of partial trapping of visible light with the phosphor on total output.

Procedure

Twenty-four 48 in. long, 1½ in. diameter, tubular bulbs were coated internally with Cool White halophosphate phosphor, and three more were left bare. Eight different concentrations of phosphor suspended in ethylcellulose lacquer were used on three bulbs each. The lacquer was removed by baking in air. By means of a beam transmittance arrangement, as described by Thayer (1), it was determined that the coating weight at the center of each bulb was within 2½% of the average of its set. A center section was then cut from one bulb in each set, and an analytical balance was used in determining the weight of phosphor per unit area of this section. The coating values varied from zero and 0.36 to 13.4 mg/cm². The other eighteen bulbs were used in the making of 40-w fluorescent lamps.

Other sections of the nine bulbs used in the weight determinations were next used in phosphor brightness studies. All the phosphor except a straight 1-cm wide stripe parallel to the bulb axis was removed from these sections. A G36T5 Sterilamp u.v. source was placed concentrically inside each bulb section, in turn, and the phosphor stripe was irradiated by ultraviolet, Fig. 1. Relative brightness measurements were then made of B_o, the phosphor emission through the outer side of the coating touching the glass, and of B_i, that emitted from the inner side facing the Sterilamp source. A Model UBl-½ Spectra Brightness Spot Meter[1] was used with a red filter (Wratten No. 25) to exclude nearly all of the visible radiation emitted from the mercury discharge of the Sterilamp source. The results shown in Fig. 2 are discussed below.

Total lumen output measurements were made on the eighteen completed lamps. The lumen values include radiation from the discharge, and so the curve in Fig. 3 does not quite drop to zero for zero-coating weight. The measurements were made near zero hours of burning, prior to possible changes in the optical properties of the phosphor caused by interaction with u.v. radiation and the glass bulb. The lamps were operated with a reference ballast and with the rated voltage input, in accordance with ref. (2).

Results and Discussion

The stripe geometry of Fig. 1 was chosen so that practically no radiation would reach it from other phosphor surfaces. In this way the brightnesses aris-

[1] Photo Research Corp., Hollywood, California.

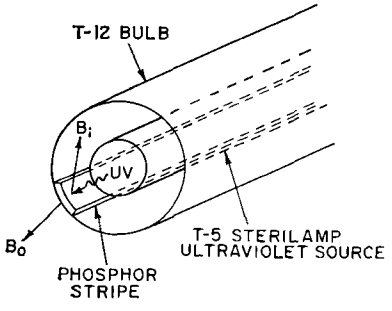

Fig. 1. Schematic view of the phosphor stripe irradiated by a Sterilamp u.v. source.

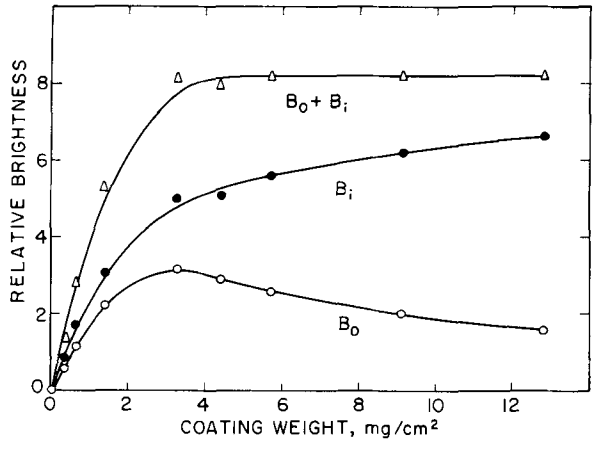

Fig. 2. Relative brightness vs. coating weight per unit area for phosphor stripe shown in Fig. 1.

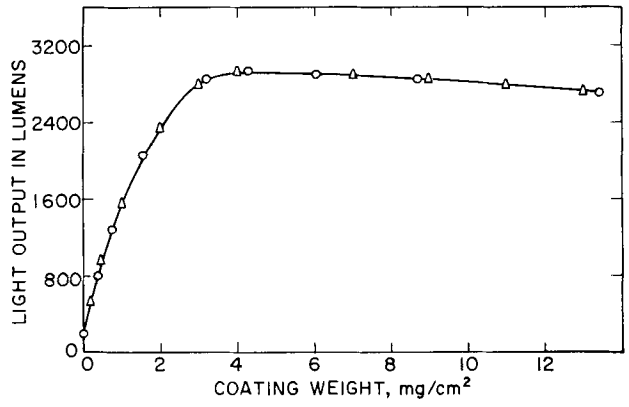

Fig. 3. Lumen output of fully coated fluorescent lamps vs. coating weight per unit area: ○—○, measured values; △—△, calculated values.

ing directly from emission generated in the coating could be studied. Consider first the sum of B_o and B_i, shown in Fig. 2, which is related to the total amount of radiation generated. There is a coating weight per unit area beyond which the amounts of ultraviolet utilized and visible radiation generated are essentially constant. This value is approximately 4 to 5 mg/cm² for the phosphor studied.

It can be seen from Fig. 2 that much of the visible radiation is generated in the layers of the coating nearest the phosphor surface exposed to the gas discharge. Of the portion of the visible radiation which is directed deeper into the phosphor coating, part is transmitted through the phosphor coating and the glass. Another part is reflected internally and passes back through the gas discharge side of the coating. A decreasing proportion of the visible radiation reaches the glass or outer side of the stripe as the coating thickness increases.

The lumen output of a fully coated lamp in Fig. 3 increases with coating weight and reaches a maximum at about the same weight per unit area as does the total brightness of the striped bulb. Because there are interreflections within the lamp and because the phosphor does not have zero optical absorptance for visible radiation, the lumen output decreases for heavier coatings.

It should be possible to use the data in Fig. 2 to predict the lumens *vs.* coating weight per unit area curve for the fully coated lamps, actually measured and given in Fig. 3. In Fig. 4 it is shown how visible light, produced by u.v. radiation striking one portion of the phosphor surface and having brightnesses B_i and B_o eventually escapes the fully coated lamp. The light flux, as it strikes another portion of the phosphor surface, is either transmitted to the outside, absorbed, or reflected to still another internal surface. The process continues until all the light is either transmitted outside or absorbed in the coating.

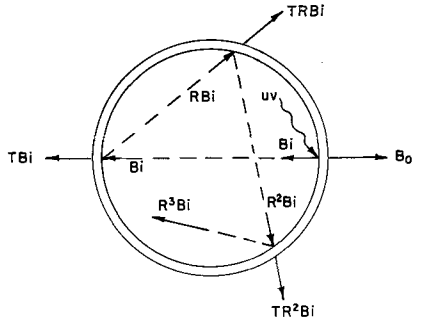

Fig. 4. Schematic cross-section view of fully coated fluorescent lamp, showing the multiple reflections of internal light.

As a result of this, the relative brightness on the outside surface of a fully coated lamp, B, is given by

$$B = B_o + TB_i + TRB_i + TR^2B_i + TR^3B_i + \ldots \quad [1]$$

$$B = B_o + TB_i(1 + R + R^2 + R^3 + \ldots) \quad [2]$$

$$B = B_o + T(1-R)^{-1}B_i \quad [3]$$

where T and R are the transmittance and reflectance of the coating for visible radiation.

The external brightness must be corrected to take into account the visible radiation of the mercury discharge. The latter has a relative brightness of B_{Hg} in an uncoated bulb, and is transmitted and reflected by a coating in the same fashion as is B_i, hence

$$B = B_o + T(1-R)^{-1}(B_i + B_{Hg}) \quad [4]$$

The values of T and R can be found by using equations given by Schuster (3) and applied to powders by others (4-7).

$$T = [\cosh(ps) + (a + r)p^{-1}\sinh(ps)]^{-1} \quad [5]$$

$$R = [\cosh(ps) + (a + r)p^{-1}\sinh(ps)]^{-1}rp^{-1}\sinh(ps) \quad [6]$$

$$T + R + A = 1 \quad [7]$$

where $p^2 = a^2 + 2ar$; s is the coating weight per unit area; a is the differential absorption coefficient of coating for visible radiation; r is the differential reflection (or scattering) coefficient of coating for visible radiation; and A is the absorptance of coating for visible radiation.

Substitution of Eq. [5] and [6] into Eq. [4] gives a final form for the outside surface relative brightness.

$$B = B_o + [\cosh(ps) + ap^{-1}\sinh(ps)]^{-1}(B_i + B_{Hg}) \quad [8]$$

The relative brightness of Eq. [8] must be multiplied by a constant to give total lamp lumens. Evaluation of this constant and of B_{Hg} was made using the measured values of B_i, B_o, and lamp lumens for those thinner coatings for which the term $[\cosh(ps) + ap^{-1}\sinh(ps)]$ of Eq. [8] was known to be nearly unity. The constant equating relative brightness to lumens was found to be 332, and B_{Hg} was 0.64.

Using these figures and the values of B_i and B_o picked for ten different values of coating weight per unit area from the smoothed curves in Fig. 2, it was found that a calculated lumen curve best fits the measured lumen curve of Fig. 3 for values $a = 0.0012$ cm²/mg, $r = 0.43$ cm²/mg, and $p = 0.032$ cm²/mg. This determination was made by the least square method, using a computer. The calculated lumen curve for these optical coefficient values is seen in Fig. 3 to fit the measured data well.

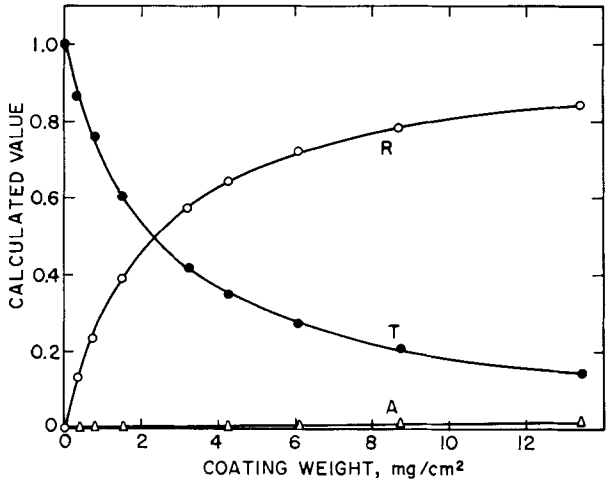

Fig. 5. Reflectance, transmittance, and absorptance calculated for $a = 0.0012$ cm²/mg and $r = 0.43$ cm²/mg vs. coating weight per unit area.

Table I. Calculated values of R and T

Author	Phosphor	R	T	A
Thayer (1)	$ZnBeSiO_3 + MgWO_4$*	~0.60	0.30-0.35	0.07-0.10
Butler and Homer (7)	Halophosphate	0.546	0.439	0.015
Weinstein (9)	Halophosphate	0.55-0.65	0.28-0.40†	0.05-0.07
Young and Arnott	Halophosphate‡	~0.64	~0.35	0.005

* 1.5-2.0 mg/cm².
† Calculated by $T = 1 - R - A$.
‡ 4.0 mg/cm².

Most of the coatings used in this fit of data were sufficiently thick that their u.v. reflectances were maximum for the particular phosphor used. It is thought that the data of the one or two thinnest coatings which had lower reflectance did not affect the fit or evaluation of the coefficients.

No correction has been made for the relatively small loss of radiation at the ends of the lamp.

Calculated values for R, T, and A *vs.* s are shown in Fig. 5. The R and T values are in fairly close agreement with some given in the literature for other phosphor coatings at their normal or optimum thickness (Table I). It appears that the absorptance of visible radiation by commercial phosphors has decreased considerably from the early phosphor reported by Thayer (1).

By letting s approach infinity in Eq. [6], the relationship between the reflectance of an infinitely thick coating and the p, a, and r coefficients is

$$R_\infty = \frac{r}{p + a + r} \qquad [9]$$

Using our evaluation of the coefficients, the value of R_∞ is calculated to be 0.93. This is a very reasonable value; however, no thick-layer measurements were made on this phosphor to check agreement.

Summary

It has been shown that the lumen output of a fully coated fluorescent lamp varies with coating thickness in a manner predictable from the application of Schuster's equations to data of the measured brightness of phosphor stripes. The values obtained for the differential reflection and absorption coefficients of visible emitted radiation of the coating were $r = 0.43$ cm²/mg and $a = 0.0012$ cm²/mg, respectively. The calculated values of reflectance, transmittance, and absorptance of a coating of normal thickness agree well with those given in the recent literature.

Acknowledgment

The authors wish to express appreciation to Dr. J. W. McNall and Mr. R. W. Wollentin for guidance and encouragement, to Mr. G. Hagen for his programming of the computer, and to Mr. J. D. Mongioi for his skillful technical assistance.

Manuscript received June 7, 1964; revised manuscript received July 7, 1965.

Any discussion of this paper will appear in a Discussion Section to be published in the June 1966 JOURNAL.

REFERENCES

1. R. N. Thayer, *Trans. Electrochem. Soc.*, **87**, 413 (1945).
2. "I.E.S. Guide for Photometric Measurement of Fluorescent Lamps," (1957).
3. A. Schuster, *Astrophys. J.*, **21**, 1 (1905).
4. J. W. Coltman, E. G. Ebbighausen, and W. Altar, *J. Appl. Phys.*, **18**, 530 (1947).
5. R. L. Longini, *J. Opt. Soc. Am.*, **39**, 551 (1949).
6. C. H. Haake, *This Journal*, **106**, 866 (1959).
7. K. H. Butler and H. H. Homer, *Ilum. Engrg.*, **55**, 396 (1960).
8. L. R. Koller, "Ultraviolet Radiation," p. 185, John Wiley and Sons, Inc., New York (1952).
9. M. A. Weinstein, *J. Opt. Soc. Am.*, **51**, 723 (1961).

On the Luminescent Properties of Some Rare Earth Ions in Zinc Borate as a Host

L. H. Brixner

Pigments Department, Experimental Station, E. I. du Pont de Nemours & Company, Wilmington, Delaware

ABSTRACT

Zinc borate, ZnB_2O_4, melting at 1000°C, forms a glass of high optical perfection which can be cast readily or pulled into almost any shape. Rare earths can be introduced in the cation sites with compensation by Na^{1+} to give glasses of the generic formula $Ln_xNa_xZn_{1-2x}B_2O_4$. The rare earths Sm^{3+}, Eu^{3+}, Tb^{3+}, Dy^{3+}, and Tm^{3+}, all emitting in the visible, were introduced into zinc borate and emission spectra as well as the optimum of x for fluorescent emission were determined. For a rod of the composition $Nd_{0.02}Na_{0.02}Zn_{0.96}B_2O_4$, stimulated emission was observed at room temperature with a threshold of 1500 joules. Rods containing the optimum concentration of Eu^{3+} and Tb^{3+} did not show laser action.

Although the original solid state laser experiments by Maiman (1) were based on single crystalline ruby and considerable work has been done since with other monocrystalline hosts, such as $CaWO_4$ (2), CaF_2 (3), $CaMoO_4$ (4), $Ca(NbO_3)_2$ (5), and $Ca_3(VO_4)_2$ (6), glasses (7) were soon considered as hosts and found quite useful, particularly in the case of Nd^{3+}. The advantages of glasses over single crystals such as ease of preparation, high optical perfection, low expansion coefficient, homogeneity of the dopant, mechanical strength and greater hardness are quite apparent and are only partially counteracted by some disadvantages such as lower thermal conductivity and higher threshold values. Since the fluorescent transitions occur in the shielded 4f levels of the rare earths, the fluorescent spectra differ not too much in principle between glasses and single crystals although observed halfwidth are considerably narrower in the latter. Never-

theless, glasses definitely do have their established place among the limited list of useful laser hosts.

Most of the glasses studied previously are of the silicate type with SiO_2 as the predominant constituent and at least four or five other components such as Na_2O, CaO, Al_2O_3, and Sb_2O_3. Although in appropriate proportions these constituents do form a homogeneous melt, they still represent a complicated mixture and if nothing else pose a multiple purity problem over less complicated systems. We therefore looked for a simple, well-defined, glass-forming composition with relatively low melting point such as ZnB_2O_4. This compound melts congruently at 1000°C and according to Swanson (8) crystallizes in a cubic structure with $a_o = 7.4726$Å. Rare earth ions can be introduced into the Zn^{2+} site and compensation to achieve electroneutrality can be obtained through the equivalent introduction of Na^{1+} according to $Ln_x^{3+}Na_x^{1+}Zn_{2-2x}^{2+}B_2O_4$, although such compensation may not be necessary in the amorphous glass state. Since the compound melts so low, no problem of volatilization of Na_2O exists. Glass rods can readily be cast in platinum tubes or can be pulled from a melt.

Experimental

The constituent components used in this investigation were of the best commercially available purity, usually 99.9+% pure, and were not given any further purification treatment prior to the reactions. The rare earth oxides were obtained from the Lindsay Chemical Division; ZnO, Na_2CO_3, and H_3BO_3 were Mallinckrodt analytical reagent grade chemicals.

The constituents were weighed to the nearest 0.1 mg according to the desired stoichiometry and were well mixed. In a first step, the mixture was heated to 300°C until all water from H_3BO_3 was removed. The reaction product was homogenized at this point by ball milling under acetone in a mechanical agate ball mill. After drying, 1 in. diameter pellets were pressed under 20,000-40,000 psi. These pellets were given a final heat treatment at 600°-800°C if polycrystalline powders were desired or taken directly to 1000°-1200°C if glass rods were to be cast. Generally ½ or ¾ in. diameter Pt-tubing was used to contain the castings. After a homogeneous melt was obtained, controlled cooling took place at about 1°-2°C/min to room temperature. In each case, the platinum could be readily peeled from the glass rods. Almost invariably, sound, bubble-free rods of good optical perfection were obtained from which stress or strain as indicated under polarized light could be removed by proper annealing at about 650°C, although this proved quite difficult in some cases. Castings up to 12 in. long and ¾ in. diameter were prepared in this fashion. When rods were pulled from a melt, a temperature of 900°C and pulling speeds of ½ to 1 in./sec were found most practical. The hardness of these glasses, as determined with a Reichert microhardness tester is 6.1 mohs (as converted from Knoop). Quartz, used as a standard, gave a 752 Knoop reading, which compares well with the literature (9) value of 750. Although 6.1 mohs for these glasses is considerably softer than ruby (9.0), it is better than the generally low hardness of such single crystals as $CaWO_4$ (4.5), or $CaMoO_4$ (4.3). The surfaces of the glass can readily be polished and were not affected by 100-hr exposure to demineralized water at room temperature.

Although we were primarily interested in the characteristics of the homogeneous glasses, it was of interest to find the limits of solid solubility of the two components, $Ln_{0.5}Na_{0.5}B_2O_4$ and ZnB_2O_4, of the general composition $Ln_xNa_xZn_{1-2x}B_2O_4$. First of all, the structure of $Ln_{0.5}Na_{0.5}B_2O_4$, at least for the cases where Ln = Gd, Dy, or Er, is different from that of the cubic ZnB_2O_4. It is tetragonal with $a_t = 7.304$Å and $c_t = 8.874$Å for $Dy_{0.5}Na_{0.5}B_2O_4$. The compound $Er_{0.5}Na_{0.5}B_2O_4$ with the smaller rare earth ion gave $a_t = 7.273$Å, $c_t = 8.801$Å and $Gd_{0.5}Na_{0.5}B_2O_4$ with the larger Gd^{3+} gave $a_t = 7.375$Å, $c_t = 8.947$Å. This structure could be considered as a tetragonal distortion of the 7.473Å ZnB_2O_4 cube, which is not surprising in view of the fact that the ionic radius of Zn^{2+} (0.74) deviates considerably from the mean value of 0.92 for the Na^{1+}/Dy^{3+} pair. As a result of this discrepancy, very limited solid solubility of the two phases exists in the solid polycrystalline state. The limit of single-phase glass formation was found for all rare earth compounds to be between x = 0.2 and 0.3. Above this rare earth concentration, even at 1300°C, two phases were formed and no homogeneous glasses could be obtained. The Na compensation was retained in the glasses simply to have a precise knowledge of the compositional character, although as was stated in the introduction it may not be necessary.

Fluorescence Studies

Spectra of the polycrystalline powders were obtained in a Beckman DK2 recording spectrometer with a F4T5/BL fluorescent u.v. lamp. Spectra of the glasses were excited with a filtered AH3 mercury discharge lamp (3660Å) and recorded with a Leeds & Northrup 0.5 meter Ebert mount grating spectrometer using a 1P28 photomultiplier detector. The establishment of the optimum for fluorescent emission was based on these data and Fig. 1 gives a typical plot of the concentration dependence for the Sm system. Figure 2 shows the fluorescent emission spectrum of the optimum composition $Sm_{0.05}Na_{0.05}Zn_{0.90}B_2O_4$ at room temperature. It is rather characteristic for all rare earths in this particular host that there was neither a significant shift of emission nor any noticeable narrowing of lines in going from 300° to 77°K. Half-width of the most intense lines was generally between 50-100Å as can be seen in Fig. 3-6 for the corresponding Eu, Tb, Dy, and Tm examples. The latter was a particularly interesting example, since the blue Tm emission, stemming almost exclusively from the 4500Å line, was rather intense compared to Tm in most other

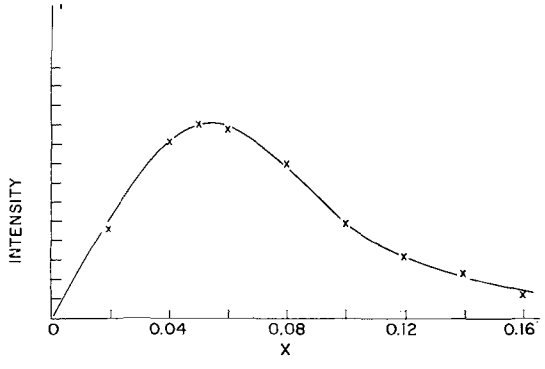

Fig. 1. Intensity of fluorescent emission as a function of x for the $Sm_xNa_xZn_{1-2x}B_2O_4$ system.

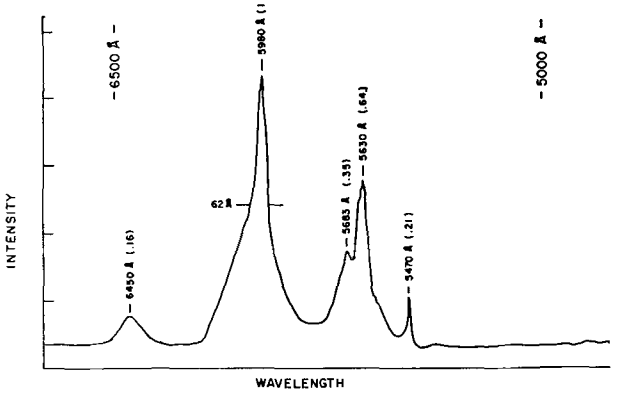

Fig. 2. Fluorescent emission spectrum of $Sm_{0.05}Na_{0.05}Zn_{0.90}B_2O_4$ at 300°K.

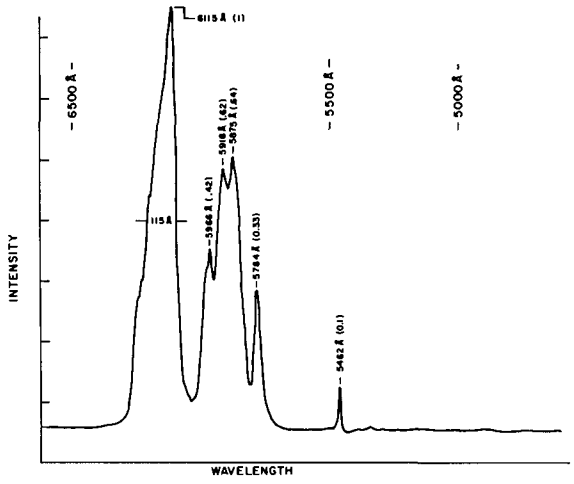

Fig. 3. Fluorescent emission spectrum of $Eu_{0.3}Na_{0.3}Zn_{0.4}B_2O_4$ at 300°K.

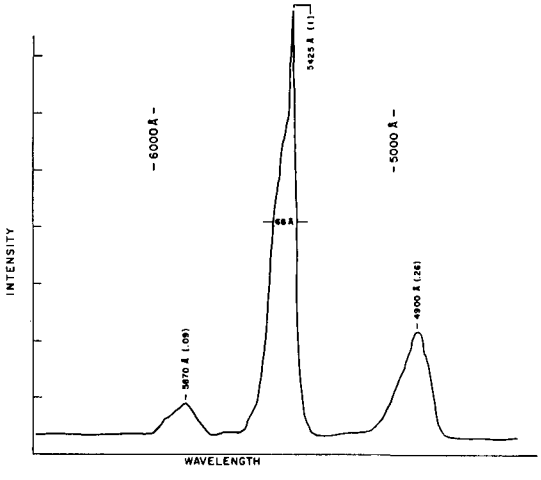

Fig. 4. Fluorescent emission spectrum of $Tb_{0.2}Na_{0.2}Zn_{0.6}B_2O_4$ at 300°K.

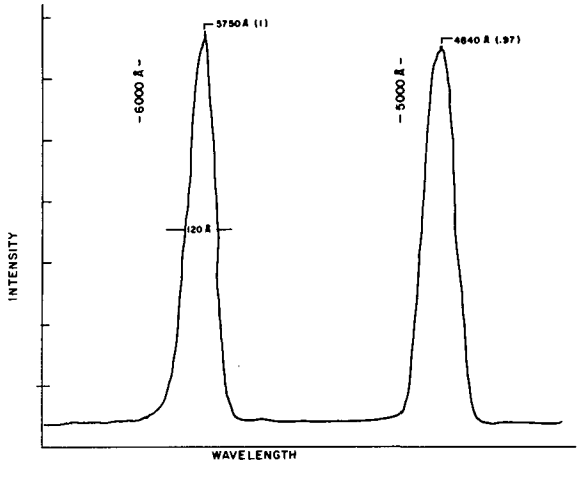

Fig. 5. Fluorescent emission spectrum of $Dy_{0.02}Na_{0.02}Zn_{0.96}B_2O_4$ at 300°K.

hosts. Figure 7 gives the concentration *vs.* emission curve for the Tm example.

For the purpose of a comparison, a summary of the principal emission characteristics of the five rare earths emitting in the visible is given in Table I.

Here again one can see the importance of the host as far as fluorescent emission is concerned. This was pointed out previously specifically for the case of Eu^{3+} in various hosts (6). Whereas for instance, Tb^{3+} just barely emits in a $Ca_3(VO_4)_2$ host, it is by far the most intense emitter in the ZnB_2O_4 host.

Table I. Comparison of fluorescent emission of different rare earths in the $Ln_xNa_xZn_{1-2x}B_2O_4$ system

Rare earth (Ln)	Optimum x	Strongest emission at Å	Intensity at identical slit width (0.2)
Sm	0.05	5980	20 (15)
Eu	0.30	6115	68 (130)
Tb	0.20	5425	1,140 (2,100)
Dy	0.03	5750	95 (135)
Tm	0.02	4540	56 (51)

Table II. Rare earths analysis for some cast rods

Composition	% Ln_2O_3 calc.	% Ln_2O_3 found Top	Bottom	Length of rod, in.
$Ho_{0.01}Na_{0.01}Zn_{0.98}B_2O_4$	1.25	1.27	1.24	3
$Eu_{0.20}Na_{0.20}Zn_{0.60}B_2O_4$	22.02	21.89	21.92	6
$Tb_{0.10}Na_{0.10}Zn_{0.80}B_2O_4$	11.72	11.81	11.75	12
$Nd_{0.02}Na_{0.02}Zn_{0.96}B_2O_4$	2.22	2.24	2.23	2

Since the data in Table I were not corrected for the response of the photomultiplier tube in the different spectral regions, they are merely meant to serve for a qualitative comparison. The numbers in parentheses give the intensities for the corresponding cadmium compounds and it can be seen that at least for the Tb and Eu case the intensity was twice as strong. The emission characteristics of the investigated rare earths in other single phase borates, such as CaB_2O_4, CaB_4O_7 as well as the corresponding Sr and Ba analogues, were very similar to those in ZnB_2O_4.

Analyses by x-ray fluorescence techniques were carried out for a number of cast rods, mainly to demonstrate the homogeneity, which constitutes a significant advantage over practically all single crystalline hosts, where segregation is often a severe problem. Some typical analyses for the rare earth constituents only are summarized in Table II.

Absorption spectra were run for the pure host ZnB_2O_4 as well as the Eu^{3+}, Tb^{3+}, and Nd^{3+} doped glass: ZnB_2O_4 is transparent from 2460Å to 28,500Å. The spectra of the doped materials are given in Fig. 8, 9, and 10. One can see that the Eu sample exhibits much sharper absorption characteristics than Tb^{3+} and the absorption is also considerably more intense in the region of interest for pumping. The Nd absorption spectrum will be considered in the discussion section, but it can already be stated here that the last $4F_{3/2}$ absorption level is not significantly shifted from its location around 0.88μ in most other hosts. An absorption at 0.84μ would, of course, be of interest for injection laser pumping.

Laser Experiments

The three rare earths, Nd^{3+}, Eu^{3+}, and Tb^{3+}, were selected for attempts to observe stimulated emission.

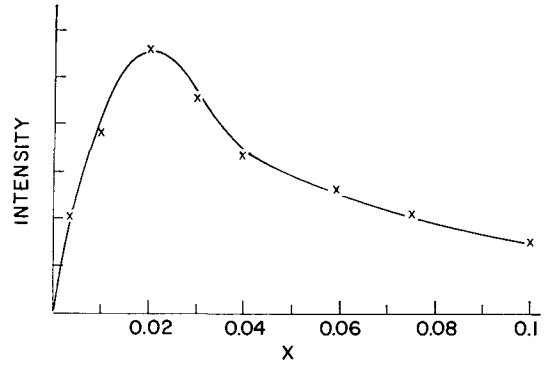

Fig. 6. Intensity of fluorescent emission as a function of x for the $Tm_xNa_xZn_{1-2x}B_2O_4$ system.

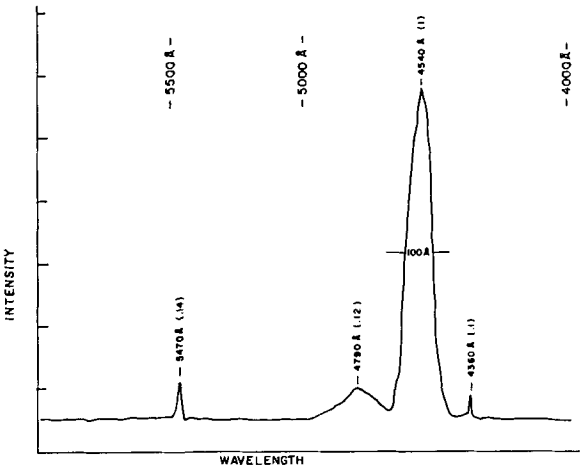

Fig. 7. Fluorescent emission spectrum of $Tm_{0.02}Na_{0.02}Zn_{0.96}B_2O_4$ at 300°K

For the Nd^{3+} case, a ½ in. long, ¼ in. diameter Fabry Perot resonator was machined by grinding and polishing. The ends had dielectric coatings for maximum reflectivity in the 1.06μ region. The composition was $Nd_{0.02}Na_{0.02}Zn_{0.96}B_2O_4$. In a Lear-Siegler LS-3 laser head with a Kemlite FT 100 B helical xenon flash lamp laser action was observed at 300°F with a threshold of 1500 joules. Due to repeated pulsing before reaching threshold, the mirror coatings were severely damaged, so that their effectiveness was probably poor. For the purpose of a comparison with an established laser material, we determined the threshold of a $CaMoO_4$: $NdNbO_4$ (1%) rod of identical size without any coatings at all. It was 500 joules. Such a rod would normally have a room temperature threshold of about 10 joules with appropriate silver or dielectric coatings. For the experiments with the visibly fluorescing composition of Eu^{3+} and Tb^{3+}, 6 in. long x ⅝ in. diameter rods were ground and polished into Fabry Perot cavities. The ends were reflectorized with dielectric coatings to give maximum reflectivity in the region of emission. The rods were placed into a Raytheon LHM-6 system, cooled to near liquid nitrogen temperature and optically pumped with 3 msec light pulses. The output from the rods was monitored at 5400Å (Tb) and 6100Å (Eu), bandwidths 60Å, with a monochrometer-photomultiplier-oscilloscope combination. Maximum storage bank energies were 24,000 joules for the Tb rod and

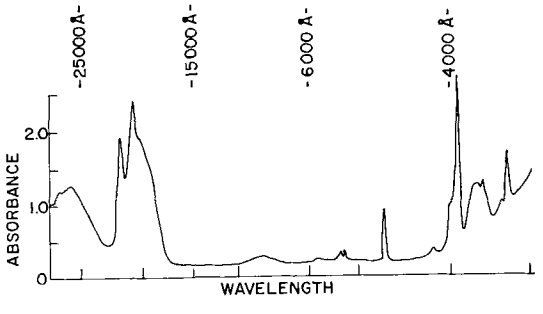

Fig. 8. Absorption spectrum of $Eu_{0.3}Na_{0.3}Zn_{0.4}B_2O_4$ at 300°K

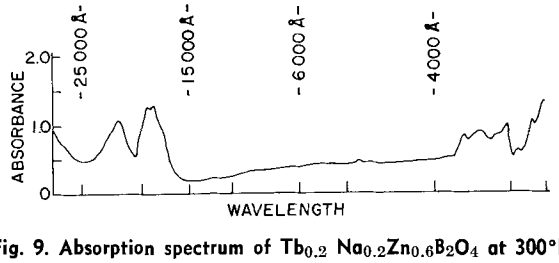

Fig. 9. Absorption spectrum of $Tb_{0.2}$ $Na_{0.2}Zn_{0.6}B_2O_4$ at 300°K

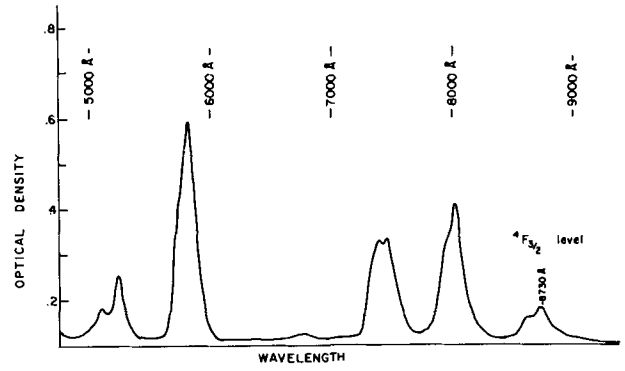

Fig. 10. Absorption spectrum of $Nd_{0.02}Na_{0.02}Zn_{0.96}B_2O_4$ at 300°K

26,100 joules for the Eu rod. In neither case was there evidence for stimulated emission.

The fluorescent signal obtained from the Tb rod was of sufficient intensity to allow an estimate of the fluorescent lifetime, which is approximately 3.3 msec at the temperature of the test.

Discussion

Rare earths in the glass-forming ZnB_2O_4 compound constitute sufficiently interesting compositions to determine as many properties as possible. Due to the isotropic nature of the glass, one can take advantage of the high Verdet constant of several rare earths and make use of the optical Faraday rotation. Since the Verdet constant increases essentially proportional to the rare earth concentration, one is only restricted by the limitation of glass formation and the relatively low density of the host. The magnetic rotation was determined for Dy^{3+} and Tb^{3+} in the compositions $Dy_{0.20}Na_{0.20}Zn_{0.60}B_2O_4$ and $Tb_{0.20}Na_{0.20}Zn_{0.60}B_2O_4$ and the results summarized in Table III. These numbers are in good agreement with those published recently by Rubinstein *et al.* (10), who studied the Faraday rotation of the rare earths in straight rare earth borate glasses. The concentrations achievable in those systems are approximately twice as high as in the ZnB_2O_4 host and therefore the Verdet constants are essentially twice the reported values here.

Thermal conductivity was measured by an absolute technique and found to be 11.5 mwatts/cm-deg which of course for laser work constitutes one of the biggest disadvantages opposite single crystalline hosts such as $CaWO_4$ or $CaMoO_4$, whose conductivities are 3 to 4 times higher. This disadvantage of low thermal conductivity may be compensated for to some degree by the low thermal expansion of about $7 \times 10^{-6}°C^{-1}$ (11). No cracking due to thermal shock was ever experienced on dropping samples directly into liquid nitrogen. The dielectric constant of the pure host was found to be 6.5 at 1 kc/sec and the refractive index, 1.64. These characteristics also compare unfavorably with most single crystalline hosts. The hardness of 6.1, however, is considerably greater than that of $CaWO_4$ (4.5) or $CaMoO_4$ (4.3) and makes polishing of these borates quite easy.

As far as the spectral characteristics of Nd^{3+} in zinc borate are concerned, we made observations similar to those of MacAvoy *et al.* (12); that is, rather intense absorption characteristics as seen in Fig. 10 coupled with quite weak fluorescence. In an attempt to

Table III. Verdet constants of Dy and Tb in ZnB_2O_4 glass

Composition	Intrinsic color of glass	Density g · ml^{-1}	Ions per ml	Verdet constants at 598 mμ min/ gauss/cm
$Dy_{0.20}Na_{0.20}Zn_{0.60}B_2O_4$	Light yellow	3.42	2.54×10^{21}	0.090
$Tb_{0.20}Na_{0.20}Zn_{0.60}B_2O_4$	Colorless	3.40	2.93×10^{21}	0.089
Barium Crown Glass (for comparison				0.022

explain this apparent anomaly, it has been suggested that some quenching process (13) intrinsically associated with the borate network is responsible. In view of the extremely small ionic radius of boron (0.23Å) the nearest Nd-Nd distance will be largely reduced in this host and a shift of the onset of concentration quenching toward lower concentrations seems likely. However, a correct assessment of the structural arrangement of the Nd and other ions in any glass is rather difficult due to the particular amorphous state of the glass, exhibiting rather random distribution of the constituent ions and only a small degree of order around ionic centers such as Nd^{3+}. A coordination number for oxygen of 8 has been suggested for Nd^{3+} in glass (12) and this should create a rather favorable situation for fluorescence. Indeed, Pearson's (14) recently observed laser oscillations in borate glasses closely related to the ones discussed in this paper, and the fact that we obtained stimulated emission in essentially a pure borate host adds another example.

Acknowledgments

The author wishes to thank Drs. P. A. Flournoy and J. C. Caris for carrying out the laser experiments.

Manuscript received May 28, 1965. This paper was presented at the San Francisco Meeting, May 9-13, 1965.

Any discussion of this paper will appear in a Discussion Section to be published in the June 1966 JOURNAL.

REFERENCES

1. T. H. Maiman, *Brit. Commun. Electron.*, **7**, 674 (1960).
2. K. Nassau and A. M. Broyer, *J. Appl. Phys.*, **33**, 3064 (1962).
3. L. F. Johnson, *ibid.*, **33**, 757 (1962).
4. L. H. Brixner, *This Journal*, **111**, 690 (1964).
5. A. A. Ballman, S. P. S. Porto, and A. Yariv, *J. Appl. Phys.*, **34**, 3155 (1962).
6. L. H. Brixner and P. A. Flournoy, *This Journal*, **112**, 303 (1965).
7. E. Snitzer, *Phys. Rev. Letters*, **7**, 44 (1961).
8. H. E. Swanson and E. Tatge, *J. Research Nat. Bur. Standards*, **46**, 321 (1951).
9. M. M. Chrustiov, *Tek. Tid.*, **82**, 37 (1952).
10. C. B. Rubinstein, S. B. Berger, L. G. van Uitert, and W. A. Bonner, *J. Appl. Phys.*, **35**, 2338 (1964).
11. L. Ya. Mazeev, Borate Glasses (Consultants Bureau Enterprises Inc.), New York (1960).
12. T. C. MacAvoy, M. L. Charters, R. D. Maurer, W. H. Dumbaugh, N. F. Borrelli, and P. E. Gordon, Annual Technical Report No. 3833 (00) 52, (1963).
13. Eastman Kodak Co., Semi-Annual Report to ONR Contract 3834(00).
14. A. D. Pearson, S. P. S. Porto, and W. R. Northover, *J. Appl. Phys.*, **35**, 1704 (1964).

Vapor Phase Deposition and Etching of Silicon

W. H. Shepherd

Fairchild Semiconductor, Research and Development Laboratory,

A Division of Fairchild Camera and Instrument Corporation, Palo Alto, California

ABSTRACT

A theory is developed and compared with experiment for the growth and etching of silicon in H_2, $SiCl_4$ and/or HCl mixtures. The horizontal reactor used is operated, as is usual for commercial reactors, under conditions such that the processes are mass-transport controlled. Good agreement between theory and experiment is found if it is assumed that mass transport occurs predominantly by diffusion.

The factors influencing the rate of growth of silicon by hydrogen reduction of $SiCl_4$ in an epitaxial reactor vary with the design of the reactor. In small, single wafer reactors such as described by Theuerer (1) and Tung (2) the rate of growth is found to be highly temperature dependent in the range 900°-1300°C with an apparent activation energy of 37 kcal/mole (1). A similar result has been reported for the hydrogen reduction of $SiHCl_3$, although with a smaller activation energy (3). In larger multiwafer horizontal reactors, such as have been used extensively in commercial operations, the deposition rate, at least above 1150°C, has been found to vary only slowly with temperature (4). Below 1150°C the rate becomes increasingly temperature sensitive. For example, in the reactor described in the present paper an apparent activation energy of 44 kcal/mole has been measured for the hydrogen reduction of $SiCl_4$ between 900° and 1100°C. In multiwafer reactors it appears that the characteristics of the deposition are determined at low temperatures principally by the kinetics of the surface reaction and at higher temperatures by the thermodynamic equilibria involved and by the mass-transfer properties of the gas phase.

The etching of silicon in HCl-H_2 mixtures at elevated temperatures, as shown by the present work (see Fig. 3) and by published work (5), is largely temperature insensitive in the range 1100°-1300°C, and the same conclusions may be drawn concerning the rate-controlling processes.

Theory

At least one worker in the field, Steinmeier (6), has attempted to explain the deposition of silicon from $SiCl_4$-H_2 mixtures on the basis of thermodynamics alone. Certain general characteristics dependent basically on the equilibria in the system can be described by this treatment, for example the fact that with increasing $SiCl_4$ concentrations the growth rate rises to a maximum and then decreases until etching of the silicon actually occurs. However, in order to properly understand the rate of reaction of a component of a fast moving gas stream with a surface it is necessary to take into consideration the rates of transfer of reactants and products to and from the equilibrium region at the surface. This model, *i.e.*, an equilibrium surface layer with the transfer of reactants and products into and out of the layer controlled by gas phase properties is commonly applied to many heterogeneous reactions [see for example Chapter II of ref. (7)].

Thermodynamic data are available for the chemical equilibria of interest and it is now necessary to consider a number of assumptions required to simplify a problem which in a detailed analysis is highly complex.

Under typical operating conditions (see Experimental Section) the Reynolds number for the system used in these experiments is about 20. With such a low value turbulent motions of the gas can be neglected leaving diffusion and convection as possible transport mechanisms. The diffusion coefficients for the species

of interest can be estimated to be in the range 3-10 $cm^2\ sec^{-1}$ at the reaction temperature and it is clear that diffusion must make a strong contribution to the transport process. It is much more difficult to decide if convection also should be considered. However it is assumed that diffusion is the dominant process and convection is neglected.

It is further assumed that diffusive interactions between reactant and product molecules can be ignored so that each component can be treated as if diffusing in hydrogen alone. This is a reasonable assumption for the dilute gas mixtures used. In addition, because of low reactant concentrations, high diffusion coefficients and relatively short diffusion paths, streaming corrections to the mass transport arising from net volume changes in the reactions can be ignored (8).

In the experimental reactor used the gas stream passing directly over the wafers flows through a tube of semicircular section 4 cm in diameter and 15 cm long bounded by the hot, R.F. heated wafer support and the relatively cold wall of the reactor envelope. For such a configuration, because of wall effects for example, it might be expected that across the heated surface considerable variations would exist in gas conditions, including those most responsible for influencing the rate of reaction, *i.e.*, concentrations of reactants and products, gas temperature, and gas velocity. However, it has been experimentally observed that etching and growth rates over individual wafers and over a boat load do not vary more than ±15% from the mean rate and generally only about ±10% from the mean. Still smaller variations are typical of the larger reactors designed for production operation where uniformity is a prime objective. Over-all uniformity is probably due to a delicate balance between rate controlling factors, for example the low transfer coefficients for reactants in the cold gas stream impinging on the front of the boat are balanced by the higher reactant concentrations. However, for the purposes of the treatment to follow it will be assumed that the uniformity in reaction rate implies a uniform gas pattern and reactant distribution. From this an idealized reactor can be pictured which is amenable to a very simple analysis. In such a reactor the heated susceptor and the reactor wall are infinite plane parallel surfaces, thus eliminating edge effects, and the distributions of gas velocity, temperature, and reactant concentrations are assumed to vary so little in the direction of gas flow that they can be treated as invariant. In this way the diffusion of reactants and products in the reactor need be considered only normal to the reacting surface. The simplification is not as extreme as might appear at first glance, as is discussed below.

There is some justification for assuming that the velocity profile and gas temperature in fact do not vary much along the length of the actual reactor. For isothermal flow in a tube a fully developed parabolic profile is established in a distance given by 0.05 R_e times the tube diameter where R_e is Reynold's number (9). Neglecting the non-isothermal nature of the present system and taking $R_e = 20$ suggests that the flow is fully developed in 2-4 cm and hence is stable over the great majority of the boat. As far as temperature uniformity is concerned it is observed that if the flow of hydrogen is increased from 0 to 15 liters/min (normal flow 10 liters/min) only the leading 1/5th (*i.e.*, 3 cm) of the boat is cooled by the gas stream and no effect at all is observed over the last 2/3 of the boat, indicating that the gas is substantially fully heated in the first 3-5 cm.

Derivation of Equations

Concentration gradients of diffusants.—For one-dimensional binary diffusion in the absence of thermal diffusion effects the flux toward the surface, Π, of diffusant in molecules $cm^{-2}\,sec^{-1}$ can be written (10)

$$\Pi = D(y) \cdot N(y) \frac{dx}{dy} \qquad [1]$$

where x is the mole fraction of the diffusant, $D(y)$ is the diffusion coefficient ($cm^2\,sec^{-1}$), and $N(y)$ is the gas density (molecules cm^{-3}). In the system to be considered $D(y)$ and $N(y)$ are functions of y, the distance from the surface because of the temperature gradient along the y-axis, *i.e.*, normal to the surface.

The mole fraction of diffusant, x can be replaced by p/P where p is the partial pressure of the diffusing species and P is the total gas pressure. In the system under discussion, P will be constant and equal to 1 atm so that with p expressed in atmospheres the flux can be written

$$\Pi = D(y) \cdot N(y) \frac{dp}{dy} \qquad [2]$$

Rearranging Eq. [2] and noting that, because of the assumption of one-dimensional diffusion, Π is constant at all points along the concentration gradient gives p as a function of distance from the surface of the form

$$p(y) = \Pi \int_0^y \frac{dy}{D(y) \cdot N(y)} \qquad [3]$$

For an ideal gas the density can be written

$$N(y) = \frac{N_o T_o}{T(y)}$$

where N_o is the gas density at $T_o = 273°K$. The temperature dependence of the gaseous diffusion coefficient (11) results in an expression for $D(y)$ of the form

$$D(y) = D_o \cdot \left(\frac{T(y)}{T_o}\right)^m$$

where D_o is the diffusion constant at $T_o = 273°K$ and where m normally has values between 1.75 and 2.00. The temperature $T(y)$ is that obtaining at a distance y from the surface and, as all temperatures in this paper, is expressed in °K.

Assuming a linear temperature gradient, β, and a temperature T_s at the surface gives for $T(y)$

$$T(y) = T_s + \beta \cdot y$$

where β is negative.

Substituting the above expressions for $D(y)$, $N(y)$, and $T(y)$ into Eq. [3] and carrying out the integration results in the general relationship

$$p(y) = p^* + \Pi \frac{T_o^{m-1}}{D_o N_o} \cdot \frac{(T_s + \beta y)^{2-m} - T_s^{2-m}}{\beta(2-m)} \qquad [4]$$

where p^* is the partial pressure of diffusant at the reacting surface, *i.e.*, at $y = 0$.

Material balance for the reactor.—The general material balance equation for each component is

$$R_1 - R_o = \Pi w l \qquad [5]$$

where w is the width of the susceptor and l the length, R_1 and R_o are the rates at which component molecules are swept into and out of the reactor, respectively. In computing R_1 and R_o only the reactants in the gas stream passing directly over the heated surface are considered. The fraction of the total gas stream passing over the boat is taken as the ratio of the cross-sectional area of the gas path over the boat to the total cross-sectional area of the reactor tube. In the ideal reactor described earlier the area over the boat is simply $w.a$, where a is the separation between the boat and the plane, parallel reactor wall. The value of a is chosen so that $w.a$ is equal to the area determined for the real reactor. Thus R_1 is given by

$$R_1 = F \cdot \frac{w.a.}{A} \cdot N_o \cdot p^o \qquad [6]$$

where F is the total gas flow at 0°C and 1 atm in ml/sec, A is the cross-sectional area of the reactor tube

(cm^2), and N_o is the ideal gas density at 0°C in molecules cm^{-3} atm^{-1}.

The value of R_o is obtained from

$$R_o = w \int_o^a V(y) \cdot N(y) \cdot p(y)\, dy \qquad [7]$$

where $V(y)$ is the gas velocity (cm^2/sec) at distance y cm from the surface and the other symbols are as previously described. For a parabolic gas flow between parallel plates $V(y)$ is given by

$$V(y) = \frac{6 \cdot F_m}{A\, a^2}[y(a-y)] \qquad [8]$$

where F_m is the flow rate in ml/sec at the mean gas temperature, T_m in the reactor, *i.e.*, $F_m = F\,T_m/T_o$.

The integration of Eq. [7] is laborious but straight forward and need not be elaborated on here. Substituting the result for R_o and Eq. [6] for R_1 into Eq. [5] and rearranging leads to the relationship for the flux

$$\Pi = \Psi\,(p^o - p^*) \qquad [9]$$

where the transfer coefficient Ψ is of the form

$$\Psi = N_o D_o \lambda \left[\frac{T_o^{m-1}(\Omega - \lambda\, T_s^{2-m})}{\beta\,(2-m)} + \frac{lAa^2}{6\,FT_m} \cdot D_o\right]^{-1} \qquad [10]$$

All of the symbols above have been described previously except Ω and λ which are given by the following expressions

$$\Omega = \frac{a\beta(4-m)\,(T_s^{3-m} + T_w^{3-m}) + 2(T_s^{4-m} - T_w^{4-m})}{\beta^3(2-m)\,(3-m)\,(4-m)} \qquad [11]$$

and

$$\lambda = \frac{1}{\beta^3} \cdot \left[\alpha\beta\left(T_s(\ln T_s - 1) + T_w(\ln T_w - 1)\right) + \frac{1}{2} \cdot \left(T_s^2(2 \ln T_s - 3) - T_w^2(2 \ln T_w - 3)\right)\right] \qquad [12]$$

In the above expressions T_w is the wall temperature of the reactor, hence $T_w = T_s + \beta a$.

Implicit in the above derivation of Eq. [9] is the assumption that the diffusant does not undergo reactions in the gas phase, or at least that such reactions can be neglected. Such is assumed to be the case for HCl and $SiCl_4$. However, some of the components of the system such as $SiCl_2$ and SiH_2Cl_2, which are stable in the equilibrium layer at the silicon surface, are highly unstable away from the silicon surface where the temperature is considerably lower. Such unstable products can be expected to react rapidly on the walls of the reactor or even in the gas phase. If reaction is complete within the gas phase the concentration of $SiCl_2$ falls to zero at some distance from the surface. For the purposes of the present treatment it will be assumed that the unstable product molecules diffuse away from the surface without reaction for a distance b cm where reaction then occurs so fast that the concentration becomes effectively zero. Because of the very steep temperature gradient and hence rapid decrease in the stability of the product molecules this simplification may be a good approximation to the actual situation.

If the condition that $p(y) = 0$ at $y = b$ is put into Eq. [4] the following result is obtained for the product flux away from the surface

$$\Pi = \frac{D_o N_o}{T_o^{m-1}} \cdot \frac{\beta(2-m)}{(T_s + \beta b)^{2-m} - T_s^{2-m}} \cdot p^* \qquad [13]$$

$$= \mu p^* \qquad [13a]$$

The form of transfer coefficient, μ, has been determined in this case without the need for a material balance but unlike ψ it contains an unknown quantity, b, which can be determined only by experiment.

For the conditions of etching and deposition described in this work, *i.e.*, temperatures above 1100°C and $SiCl_4$ and HCl concentrations below 1.5 mole % and 7 mole %, respectively, the only diffusants of interest are, according to data taken from the JANAF Table (12), $SiCl_4$, HCl, and $SiCl_2$. The diffusion fluxes of $SiCl_4$ and HCl are described by equations of the form of [9] while for $SiCl_2$ an equation similar to [13] has to be used. Using θ, Φ, and χ for the fluxes of $SiCl_4$, HCl, and $SiCl_2$, respectively, leads to the relationships

$$\theta = \psi_1(p_1^o - p_1^*) \qquad [14]$$

$$\Phi = \psi_2(p_2^o - p_2^*) \qquad [14a]$$

$$\chi = \mu p_3^* \qquad [14b]$$

The subscripts 1, 2, and 3 in the above and all subsequent equations refer to properties of $SiCl_4$, HCl, and $SiCl_2$, respectively.

From the condition that thermodynamic equilibrium exists at the silicon surface the surface partial pressure of $SiCl_2$, p_3^* can be written as a function of the surface pressure of HCl, p_2^*

$$p_3^* = K(p_2^*)^2 \qquad [15]$$

where K is the equilibrium constant for the reaction

$$2HCl + Si \gtrless SiCl_2 + H_2 \qquad [16]$$

A relationship exists also between the surface pressures of $SiCl_4$ and HCl, however, for the conditions of temperature and concentration used in this work, p_1^* is so small that it may be neglected entirely.

Chlorine atom balance at the silicon surface.—Here, use is made of the fact that there is no net flux of chlorine atoms at the surface. The flux of chlorine atoms toward the silicon as $SiCl_4$ molecules is 4θ, since each molecule contains four chlorine atoms. Similarly the flux as HCl is Φ and as $SiCl_2$ is -2χ. Hence from Eq. [14] through [15]

$$2\mu K p_2^{*2} - 4\Psi_1 p_1^o - \Psi_2(p_2^o - p_2^*) = 0$$

which is a quadractic in p_2^* solving to give

$$p_2^* = \frac{\Psi_2}{4K\mu}\left[\left(1 + \frac{8K\mu}{\Psi_2}\left[p_2^o + 4\frac{\Psi_1}{\Psi_2} \cdot p_1^o\right]\right)^{1/2} - 1\right] \qquad [17]$$

The total flux of silicon atoms toward the surface is simply $\theta - \chi$ hence the rate of deposition in atoms per square centimeter per second, R_D is

$$R_D = \Psi_1 p_1^o - \frac{\Psi_2^2}{16K\mu}\left[\left(1 + \frac{8K\mu}{\Psi_2}\left[p_2^o + 4\frac{\Psi_1}{\Psi_2} \cdot p_1^o\right]\right)^{1/2} - 1\right]^2 \qquad [18]$$

This equation is a general one for the rate of deposition of silicon from mixtures of both $SiCl_4$ and HCl in hydrogen. For the more normal case of growth in $SiCl_4$-H_2 mixtures, *i.e.*, $p_2^o = 0$, the result becomes

$$R_D = \Psi_1 p_1^o - \frac{\Psi_2^2}{16K\mu}\left[\left(1 + \frac{32K\mu\Psi_1}{\Psi_2^2} \cdot p_1^o\right)^{1/2} - 1\right]^2 \qquad [19]$$

For etching in HCl-H_2 mixtures, *i.e.*, $p_1^o = 0$ the result is

$$R_E = \frac{\Psi_2^2}{16K\mu}\left[\left(1 + \frac{8K\mu}{\Psi_2} \cdot p_2^o\right)^{1/2} - 1\right]^2 \qquad [20]$$

The above deposition and etching rates are in atoms cm^{-2} sec^{-1}. The multiplying factor for conversion to microns/minute is 1.2×10^{-17}.

Evaluation of equations.—To evaluate the above expressions it is necessary to know, (*a*) the equilibrium

Table I. Equilibrium constant for Eq. [16]

Temperature, °K	Equilibrium constant, K
1400	1.44
1500	1.32
1600	1.48

constant K (Eq. [16]), (*b*) the diffusion coefficients for diffusants, and (*c*) the temperature gradient in the gas.

The equilibrium constant K for Eq. [16] has been calculated using thermodynamic data obtained from the JANAF Tables (12). Values are tabulated in Table I for temperatures of interest.

The estimation of diffusion coefficients at reaction temperatures requires evaluation of D_o, the diffusion coefficient at 0°C and the parameter, m, which determines the temperature dependence of the coefficient. Figure 1 shows a plot of diffusion coefficient in hydrogen *vs.* molecular weight for a variety of organic and inorganic molecules (11). A reasonably good correlation seems to exist and this plot was used to obtain values of D_o for $SiCl_4$, HCl, and $SiCl_2$. The parameter m is quoted as having values in the range 1.75 and 2.00 (11) and, although m varies with different molecules, it will be assumed to be the same for all species considered here.

A rough estimate of the temperature gradient in the gas was obtained as follows. With the reactor evacuated the susceptor was raised to a measured temperature of about 1370°C, then, without altering the power setting of the generator, hydrogen was introduced at a typical flow rate of 11 liters/min and the new temperature (about 70°C lower) again measured. The energy radiated at each temperature was then calculated using the Stefan-Boltzmann relationship and the emissivity of molybdenum (13). The difference between the calculated and measured values was the energy conducted away in the hydrogen and using a value of 1×10^{-3} cal sec^{-1} cm^{-2} $°C^{-1}$ for the thermal conductivity of hydrogen at 1250°K (estimated mean gas temperature), the temperature gradient for a susceptor temperature of approximately 1600°K was determined to be 450°C cm^{-1} °C. For the above experiment the water-cooled susceptor support was replaced by a fused quartz holder so that the thermal environment of the susceptor was symmetrical.

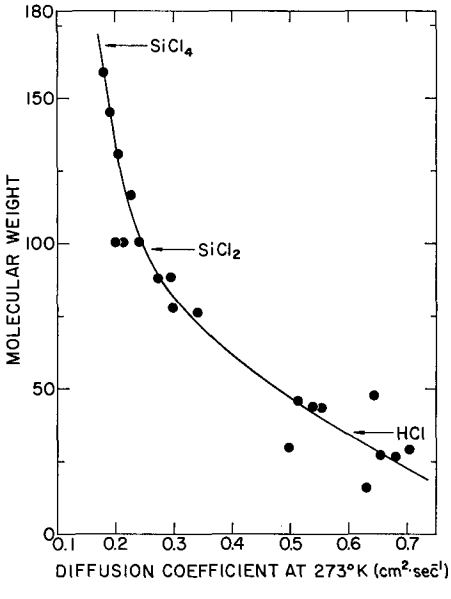

Fig. 1. Diffusion coefficient *vs.* molecular weight for a variety of organic and inorganic molecules in hydrogen at 0°C and 1 atm pressure.

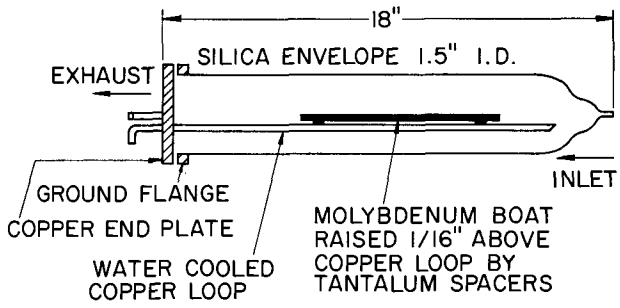

Fig. 2. Epitaxial reactor tube

Apparatus and Experimental Procedures

The reactor was of the horizontal R. F. heated type with a molybdenum susceptor 15 cm long by 3.5 cm wide on which 5-6 wafers could be placed. The essential features of the design are shown in Fig. 2. All flowmeters were calibrated using standard displacement techniques. Silicon tetrachloride was introduced into the reactor by way of a secondary hydrogen stream saturated at 0° ± 0.2°C in a stripping condenser. This arrangement was found to supply $SiCl_4$ at a rate consistent with published vapor pressure data (14) at all flows experimentally used.

For growth studies low resistivity (<0.01 ohm-cm), antimony doped, chemically polished wafers were used and deposit thicknesses were determined from infrared interference measurements. The films were 10-20 microns thick. Etching studies were made on epitaxial n-n+ wafers having 20-40 micron layers. In this way the amount removed could be determined from infrared measurements.

Experimental Results

Etching in HCl-H_2 *mixtures.*—The etching results are presented in Fig. 3 where each point represents a measurement on one wafer. Generally four runs were made at each composition, and more points are not shown because at least two wafers in each run were included for evaluation of etching quality and had no predeposited film, and other wafers gave poor infrared traces which could not be accurately interpreted.

In the temperature range investigated the etching rate is apparently not sensitive to temperature, al-

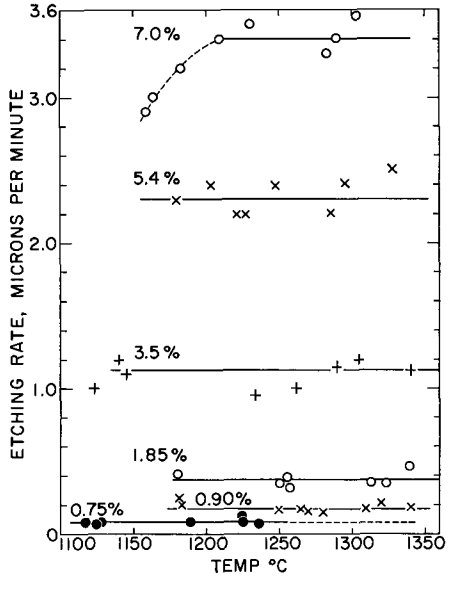

Fig. 3. Rate of etching of silicon in HCl/H_2 as a function of temperature. Numbers refer to HCl concentrations in mole %.

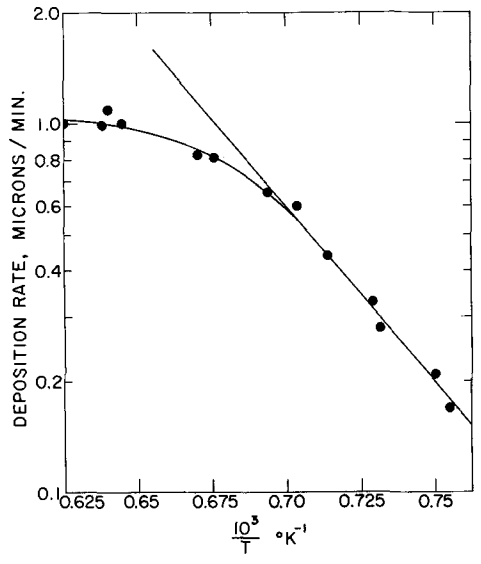

Fig. 4. Arrhenius type plot of temperature dependence of growth rate in $SiCl_4/H_2$. ΔH = 44 kcal/mole; total gas flow, 10 liters/min; $SiCl_4$ concentration, 0.48 mole %.

though the experimental uncertainty is great enough to mask a trend of perhaps 10%. At some temperatures below the lower limit in Fig. 3 a temperature sensitive region is to be expected. However, attempts to investigate this were unsuccessful due to highly preferential etching and even oxide growth which entirely eliminated etching. The oxidation was apparently due to impurities in the HCl since no visible oxide growth occurred when wafers were heated in hydrogen alone at the same temperatures, *i.e.*, 1000°-1100°C.

Growth in $SiCl_4$-H_2 *mixtures.*—Preliminary experiments were carried out to determine the temperature dependence of growth rate for the reactor. The results are shown in Fig. 4, in which the logarithm of the deposition rate is plotted against the inverse of the absolute temperature. Below about 1130°C (*i.e.*, $10^4/T \geqq 0.71$) the plot is linear and the deposition is apparently an activated process with an enthalpy of activation of 44 kcal. The enthalpy quoted by Theuerer (1) for the same reduction is 37 kcal. At higher temperatures, particularly above about 1220°C, (*i.e.*, $10^4/T \leqq 0.67$), the deposition becomes relatively insensitive to temperature. It is within this region that the theory is intended to apply and all growth data have been obtained at 1310° ± 10°C. The results of the growth rate experiments are presented in Fig. 5. Each point is a mean of values obtained on 5-6 wafers.

Growth and etching in $SiCl_4$-HCl-H_2 *mixtures.*—These measurements were made at 1300° ± 10°C. The $SiCl_4$ concentration was maintained constant at 0.40 mole % and the HCl concentration varied from 0-4 mole %. The results are shown in Fig. 6 where each point is a mean of values from 5-6 wafers.

Comparison of Theory and Experiment

For the purposes of calculation the following values are used for quantities appearing in the various equations. The reaction or surface temperature of the silicon, T_s, is taken as 1600°K and the wall temperature, T_w, as 900°K. The separation, a, between the parallel surfaces of the ideal reactor is estimated in the manner previously described as 1.6 cm, so that the temperature gradient, β, is approximately —440°C/cm. The mean gas temperature, T_m, is 1250°K, the cross-sectional area of the reactor, A, is 9 cm^2, and the gas flow at 0°C, F, is 10 liters/min (11 liters/min at 25°C).

The simplest comparison of theory and experiment can be made for growth in $SiCl_4$-H_2 mixtures. As can be seen from the experimental results in Fig. 5, the growth rate is nearly a linear function of concentration in the range investigated. This means that in Eq. [19], which expresses deposition rate as a function of $SiCl_4$ concentration, the second term is relatively insignificant and that the rate may be closely approximated by $\Psi_1 \cdot p_1^o$. Since all of the quantities which determine the magnitude of Ψ_1 are known or can be estimated independently of the experimental data a prediction of the deposition rate can be made. Taking D_o[1], the diffusion coefficient of $SiCl_4$ in hydrogen, as 0.19 cm^2 sec^{-1} (see Fig. 1) and m as 1.9, *i.e.*,

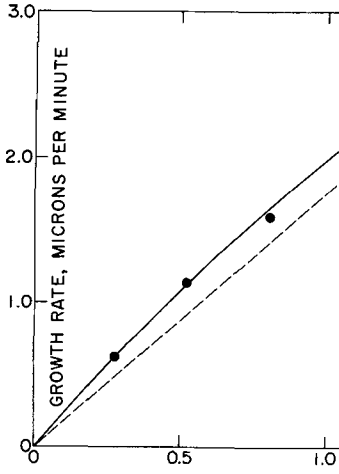

Fig. 5. Growth rate of silicon in $SiCl_4/H_2$ vs. $SiCl_4$ concentration at 1310°C (1583°K): ——, theory; •, experiment; — — —, predicted.

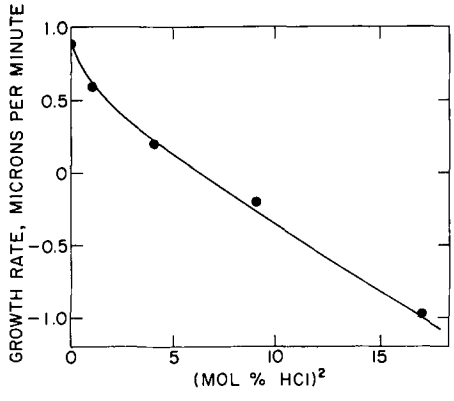

Fig. 6. Growth and etching of silicon in $SiCl_4/HCl/H_2$ at 1300°C: ——, theory; •, experiment.

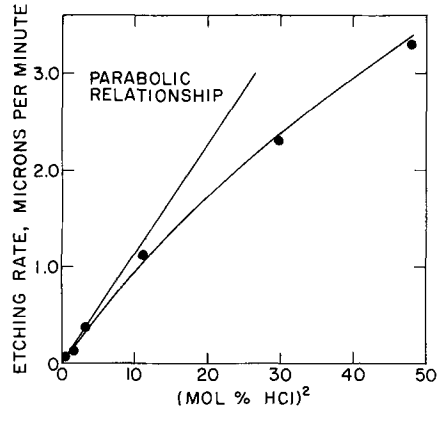

Fig. 7. Etching rate of silicon in HCl/H_2 vs. the square of the HCl concentration: ——, theory; •, experiment.

approximately the mean of the quoted range from 1.75-2.00, gives 176 microns min^{-1} atm^{-1} for Ψ_1. This result is represented by the broken line in Fig. 5, and is remarkably close to the experimental points.

A similar comparison cannot be made for etching since the relevant transfer coefficient, μ, is a function of the distance, b, which can be obtained only by experiment. However the theory can be checked by choosing μ so that a fit is obtained with experiment at one point, and observing the agreement as the etch rate is varied. The variation of etch rate with HCl concentration is sufficiently complex for this to be a good test of the form of the etching equation if not its absolute predictions. A further good test is to use the estimated value of μ to observe agreement between theory and experiment for growth and etching in $SiCl_4$-HCl-H_2 mixtures.

The coefficient μ can be obtained simply from a plot of etching rate against the square of the HCl concentration since, as can be seen from Eq. [20] as $p_2^o \rightarrow 0$, the initial slope of such a plot is $K\mu$. In Fig. 7, R_E is plotted against $(p_2^o)^2$ and the initial slope used to calculate μ is indicated.

The value of Ψ_1 to be used for further comparison of theory and experiment is taken from the initial slope of the experimental plot of growth rate *vs.* $SiCl_4$ concentration shown in Fig. 5. The transfer coefficient for HCl, Ψ_2, like Ψ_1 is described by Eq. [10]. Hence, knowing Ψ_1 it is simple to obtain Ψ_2 by substituting the diffusion coefficient of HCl, D_o^2, for that of $SiCl_4$, D_o^1, and by noting that the length, l, is now the length of etched silicon surface (always maintained at 10 cm) and not the entire heated length of the susceptor as in the case of deposition.

Using 0.60 cm^2 sec for D_o^2 the following values are obtained for the transfer coefficients: $\Psi_1 = 230$ microns min^{-1} atm^{-1}; $\Psi_2 = 507$ microns min^{-1} atm^{-1}; and $\mu = 695$ microns min^{-1} atm^{-1}. With these values, Eq. [18], [19], and [20] have been evaluated and compared with experiment. In Fig. 5 this comparison is shown for deposition in $SiCl_4$-H_2 mixtures. The good agreement observed is not surprising since the plot is only slightly sublinear and the theoretical curve is normalized to the experimental near the origin. However it is obvious that the second term in Eq. [19] is not grossly in error.

Comparison of theory and experiment for etching in HCl-H_2 mixtures is shown in Fig. 7. Again agreement is excellent and in this case more satisfying since the dependence of rate on HCl concentration is a complex one.

Theory and experiment are compared for reactions in $SiCl_4$-HCl-H_2 mixtures in Fig. 6. This, perhaps, is a better test of the equations than either of the above since now the separately determined parameters Ψ_1 and μ are both included in one equation where each has a predominant influence on the curve at different HCl concentrations, Ψ_1 at low HCl concentrations and μ at the higher ones. Again agreement is very good.

Finally now that μ has been measured it is possible to return to Eq. [13] and determine the value of b. Because of the instability of $SiCl_2$ away from the silicon surface and its expected consumption by gas phase reactions, b should be less than a, the susceptor to wall separation. In fact b is calculated to be 3 mm. Equation [13] was evaluated using $m = 2.08$ which is the value of m required to give $\Psi_1 = 230$ microns min^{-1} atm^{-1}, *i.e.*, the experimentally measured value. This is somewhat above the upper limit of 2.0 expected for m but not enough to be of great significance. The values of m for $SiCl_2$ and for HCl probably differ from the value for $SiCl_4$ but, as was pointed out earlier, it has been assumed for the purposes of simplicity that m is the same for all diffusants.

Discussion and Conclusions

It appears that for the reactor geometry and conditions investigated, and these are fundamentally similar to many that have been described, that the rates of reaction in H_2, $SiCl_4$, and/or HCl mixtures can be very satisfactorily described by the theory developed in this paper. The theory takes into account both the thermodynamic and transport aspects of the reaction processes and, since agreement with experiment is good, it is interesting to analyze the equations to determine how these two factors influence the processes.

In Eq. [19] for growth in $SiCl_4$-H_2 compositions the rate is indicated by two terms. The first term on the right hand side of the equation is the rate of transfer of silicon toward the surface as $SiCl_4$ and, apart from being proportional to pressure, is only a function of the transfer properties of the gas stream. The second term, however, contains the thermodynamic equilibrium constant, K, and hence is sensitive to the state of equilibrium at the surface. The second term increases faster than the first as the concentration of $SiCl_4$ is increased and Eq. [19] predicts a maximum in the growth rate curve and eventually a region in which etching takes place. Such behavior is in fact observed (6). However, no attempt has been made to extend Eq. [19] so far since at high reactant and product concentrations many of the assumptions of the theory are no longer valid, *e.g.*, binary diffusion.

The diffusion term for $SiCl_4$ is independent of the surface equilibrium because, under the conditions of temperature and concentration considered, the surface concentration of $SiCl_4$, although varying remains so much smaller than the inlet concentration that it can be totally ignored. At normal epitaxial deposition rates from 0-2 microns/min the second, equilibrium dependent, term in Eq. [19] can be neglected and hence it is true to state that the deposition process is mass-transport controlled since changes in temperature, gas flow rate, or other reactor variables influence the growth rate only through the transfer coefficient.

Etching in HCl-H_2 mixtures is a different situation. As has been pointed out already, Eq. [20] reduces to $R_E = K\mu(p_2^o)^2$ as the HCl concentration approaches zero, which from a practical standpoint is less than 2-3 mole %. Hence at low HCl concentrations the etching rate is proportional to the equilibrium constant, K, as well as the transfer coefficient μ. As a result the etching rate might be expected to be temperature sensitive, but, as can be seen in Table I, K is virtually constant in the temperature range of the present study, *i.e.*, 1100°-1300°C. As the HCl concentration is increased Eq. [20] predicts decreasing influence of the equilibrium constant until finally the rate is simply a function of the transfer coefficient for HCl, Ψ_2. However, as with Eq. [19], the assumptions of the present treatment invalidate predictions for high HCl concentrations.

Manuscript received March 27, 1964; revised manuscript received July 7, 1965.

Any discussion of this paper will appear in a Discussion Section to be published in the June 1966 JOURNAL.

REFERENCES

1. H. C. Theuerer, *This Journal*, **108**, 649 (1961).
2. S. K. Tung, *Metallurgy of Semiconductor Materials*, **15**, 87 (1962).
3. J. M. Charig and B. A. Joyce, *This Journal*, **109**, 957 (1962).
4. E. F. Cave and B. R. Czorny, *R.C.A. Rev.*, **24**, (4), 523 (1963).
5. K. E. Bean and P. S. Gleim, *This Journal*, **110**, 265C (1963).
6. W. Steinmeier, *Philips Research Repts.*, **18**, 75 (1963).
7. D. A. Frank-Kamenetski, "Diffusion and Heat Exchange in Chemical Kinetics," Princeton Univ. Press (1955).
8. H. Schaeffer, *Z. anorg. Chem.*, **286**, 34 (1956).
9. McCabe and Smith, "Unit Operations of Chemical Engineering," 56, McGraw-Hill Book Co., New York (1956).

10. J. O. Hirschfelder, C. F. Curtiss, and R. B. Bird, "Molecular Theory of Gases and Liquids," Equation 8.1-13, John Wiley & Sons, New York (1954).
11. International Critical Tables, 5, 62 (1929).
12. JANAF Thermochemical Data Tables.
13. Metals Handbook, Vol. 1 8th Ed. 1216 (1961).
14. Handbook of Chemistry and Physics, 43rd Ed. (1961-1962).

Semiconduction in Iron Phosphate Glasses

Kent W. Hansen

Research and Development Laboratory, Corning Glass Works, Corning, New York

ABSTRACT

The electrical resistivity. (ρ), and thermoelectric power of iron phosphate glasses were measured over the temperature range 25°-400°C. The resistivity increased as the iron oxide was replaced by magnesium oxide. The resistivity also varied with the Fe^{+3}/Fe_{total} ratio in a glass containing 55% FeO-45% P_2O_5 (on mole basis); ρ passed through minimum at a Fe^{+3}/Fe_{total} ratio approximately equal to 0.5. From thermoelectric data, the glasses were determined to be p-type when the Fe^{+3}/Fe_{total} ratio was less than 0.38 and n-type at higher ratios. The results suggest that the carrier mobility is a thermally activated diffusion process similar to that proposed for crystalline transition metal oxides. The conduction activation energy pertains to mobility rather than to the formation of carriers.

Interest and activity in the field of "electronic" conduction in glassy materials have increased during the past decade. "Electronic" conduction or semiconduction is defined as electrical charge transfer by electrons (or holes) as opposed to ions.

Baynton and co-workers (1) studied the electrical resistivity of glasses in the V_2O_5-P_2O_5 system. They found that the conductivity increased with the V_2O_5 content. This was the first important work reported on semiconducting oxide glasses. The authors suggested that the conduction activation energy is the energy required to excite an electron into the conduction band. Munakata (2) measured the conductivity of vanadium-barium phosphate glasses at various V^{+4}/V_{total} ratios. He found the resistivity was a function of this ratio and that it passed through a minimum at $V^{+4}/V_{total} \approx 0.2$. The conduction mechanism was proposed to be a charge transfer between V^{+4} and V^{+5} ions, similar to the mechanism suggested for transition metal oxides such as Fe_3O_4 (3) and $Li_xNi_{1-x}O$ (4, 5).

Since then, several papers have been published on the electrical properties of semiconducting oxide glasses. Most of these suggest essentially the same mechanism as that proposed by Munakata. MacKenzie (6) has published a review that covers this work.

Very little has been done to correlate Hall effect, Seebeck coefficient, or optical data with resistivity data, to obtain a better understanding of the conduction process. This paper covers work in which a correlation is made between resistivity (ρ) and thermoelectric power (Q) in iron-phosphate glasses. Both ρ and Q were measured as a function of temperature and the ratio Fe^{+3}/Fe_{total}.

Experimental

Glasses containing 55% (FeO + MgO)-45% P_2O_5 (all percentages in this paper are on a mole basis) were melted in fused silica crucibles at 1300°C using reagent grade ferric oxide, magnesium oxide, and phosphoric acid as batch materials. The glasses were annealed between 475° and 500°C. The valence state of the iron in the 55% FeO-45% P_2O_5 glasses was adjusted by adding different amounts of dextrose to the batch. The ferric-ferrous ion concentrations were determined by dissolving glasses in HCl in an inert atmosphere, titrating for ferrous ions, then reducing ferric to ferrous, and titrating for total iron. The percentage of ferric ions, based on total iron, ranged from 4.4 to 87.6%.

X-ray diffraction patterns and transmission electron micrographs of the glasses showed no evidence of crystalline phases. It is difficult to tell from the electron micrographs whether or not a liquid-liquid separation had occurred in the glasses. If separation had occurred, at least one glassy phase is of the order of 30Å or less across.

The d-c electrical resistivity and thermoelectric power were measured as a function of temperature, ρ between 25° and 400°C, and Q between 125° and 400°C. Thermoelectric tests were limited to this temperature range because the resistivity at temperatures below 125°C was too high to obtain meaningful data, and the annealing range of the glasses was about 475°C. The thermal emf's were measured using gold as a reference, and the samples were contained in helium or air atmospheres; no differences were observed between the two ambients. The thermoelectric power was independent of temperature gradients for ΔT's up to at least 20°C.

The d-c resistance was measured across the thickness of glass plates (~2 in. × 2 in. × 3 mm). A guard-ring circuit was used to eliminate surface leakage from the measurements. Both gold and silver were used as electrode materials; essentially the same results were obtained with the two metals. The resistance between electrodes and samples was found to be negligible from data taken using a four-contact technique. Test voltages up to ~300 v/cm indicated the samples are ohmic in this region.

Results and Discussion

The specific resistivities of the glasses obey the general equation

$$\rho = \rho_0 \exp (q/kT) \qquad [1]$$

where q is conduction activation energy and ρ_0 is a constant. As can be seen in Fig. 1 and 3, there is a change in slope between 110° and 150°C. The reason for this break is not completely understood. A few possibilities include: conduction in different phases above and below the break; charge transfer between iron ions in similar positions at low temperatures, and between iron ions in different positions at higher temperatures; and predominately ionic conduction in one temperature range and electronic conduction in the other. The latter possibility is unlikely because no polarization was observed in the samples, *i.e.*, the resistance did not change with time at a constant temperature even though potentials as high as 20v D.C. were applied for 36 hr at 330°C. Under similar conditions the resistivity of a soda-lime-silica glass, Corning Code 0080 glass, increased four orders of magnitude in 64 hr.

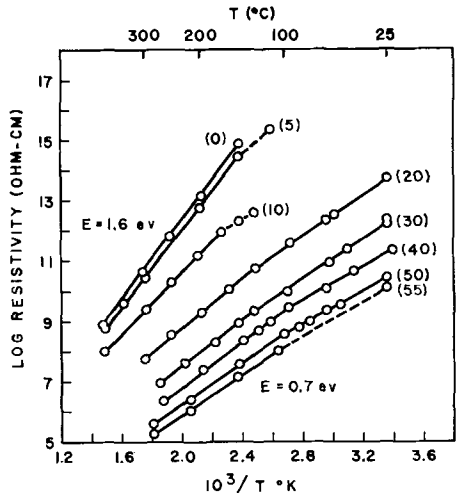

Fig. 1. Logarithm of resistivity vs. $1/T$ for glasses containing 55% (FeO + MgO)-45% P_2O_5. The numbers in parentheses are the percentages of FeO.

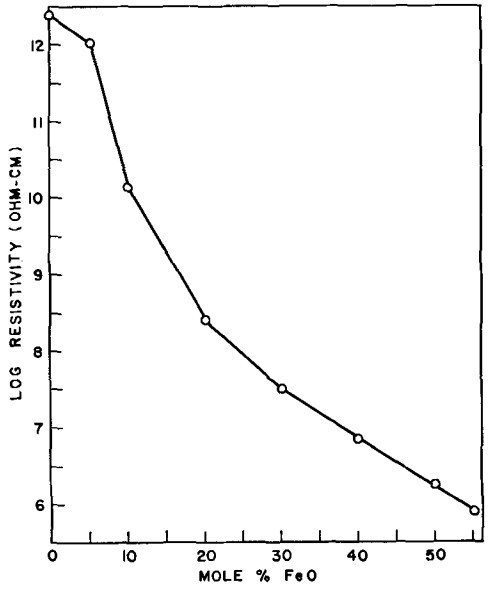

Fig. 2. Logarithm of resistivity at 200°C as function of FeO content

Figures 1 and 2 show the effect of substituting magnesium for iron at a constant P_2O_5 content. As can be seen in Fig. 2, the logarithm of resistivity varies linearly with percentage FeO, down to about 25% FeO. The activation energy is constant in the linear region and increases rapidly as FeO is decreased below 25%. The activation energy of "pure" magnesium-phosphate glass is about twice that of the 55% FeO-45% P_2O_5 glass. These results are similar to those found by Ioffe *et al.* (7) and Kitaigorodskii *et al.* (8) for V_2O_5-P_2O_5 and V_2O_5-BaO-P_2O_5 glasses, and Hansen and Cutler (9) in crystalline $Fe_{1-x}O$-MgO solid solutions. In the latter case, a sharp increase in activation energy was observed when the percentage $Fe_{1-x}O$ decreased below 14%. This was attributed to the fact that, at iron levels below 14%, there is no longer a continuous chain of iron ions by which charge transfer can occur.

The curves in Fig. 3 indicate how the resistivity varies with Fe^{+3}/Fe_{total} at a constant total iron content. This is better illustrated in Fig. 4 where the resistivities at 200°C are plotted *vs.* Fe^{+3}/Fe_{total}. The resistivity passes through a minimum similar to that found in vanadium-phosphate glasses (2). However, the minimum is at Fe^{+3}/Fe_{total} equal to 0.4-0.6 compared with a V^{+4}/V_{total} ratio of 0.2 for the vanadium containing glasses.

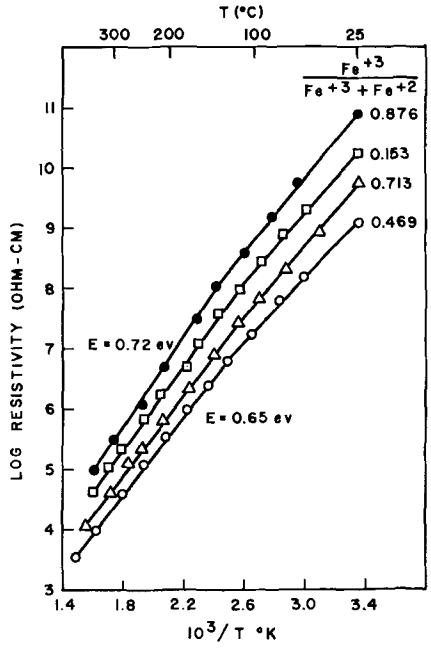

Fig. 3. Logarithm of resistivity vs. $1/T$ for representative glasses containing 55% FeO-45% P_2O_5 with various Fe^{+3}/Fe_{total} ratios.

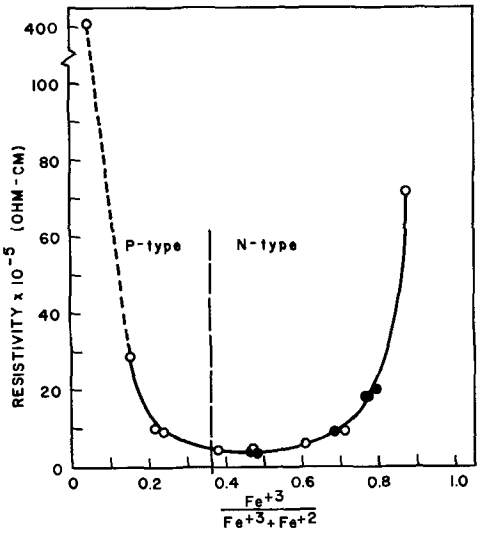

Fig. 4. The effect of Fe^{+3}/Fe_{total} on resistivity at 200°C for glasses containing 55% FeO-45% P_2O_5. • and ○ represent two different series of melts.

Like many crystalline transition metal oxides, the thermoelectric power of the glasses is essentially independent of temperature, as can be seen in Fig. 5. It has been shown in such cases that the carrier concentration (n) is insensitive to temperature (5). Then

$$n \approx N_0 \exp(-|Q|T/kT) \qquad [2]$$

where N_0 is the concentration of total available sites. Figure 6 shows how the glasses changed from n- to p-type as they were reduced, the change in sign occurring at $Fe^{+3}/Fe_{total} \approx 0.38$. Note the agreement obtained between two different sets of melts.

The results reported here and those reported for vanadium-phosphate glasses show a remarkable similarity to those found for transition metal oxides, such as the iron oxides and $Li_xNi_{1-x}O$. A conductance mechanism has been proposed by Heikes and Johnston (4) for these materials. The mechanism involves trapping of charge carriers at cation sites. The conduction mobility in this case is a thermally activated diffusion

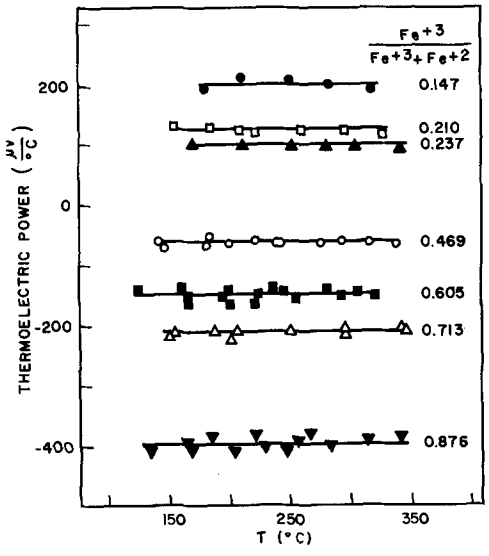

Fig. 5. Thermoelectric power vs. temperature for representative glasses containing 55% FeO-45% P_2O_5 at various Fe^{+3}/Fe_{total} levels.

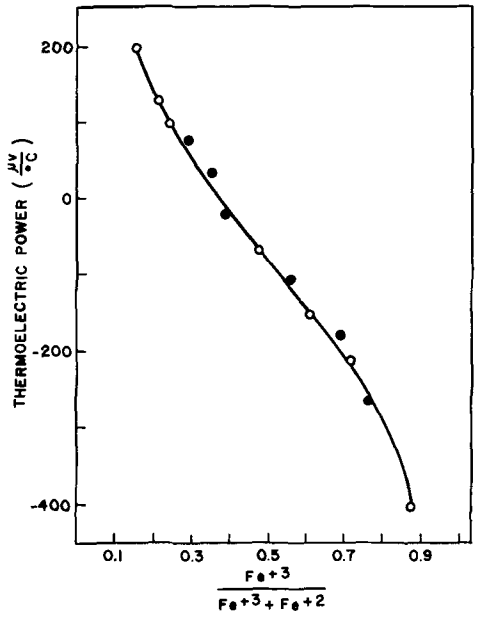

Fig. 6. Thermoelectric power vs. Fe^{+3}/Fe_{total}; 55 FeO-45 P_2O_5 at 200°C. • and ○ represent two different series of melts.

process where the activation energy pertains to the mobility. If such a mechanism occurs in the glasses, the conducting hole (or electron) must reside at a "lattice" site for a time equal to or greater than $1/\nu_0$, where ν_0 is the vibrational frequency ($\sim 10^{13}$ sec^{-1} at 400°K) of the "lattice." The mobility is then given by

$$\mu = \frac{ed^2 \nu_0 e^{-E/kT}}{kT} \quad [3]$$

where d is jump distance, E is activation energy for jump, and e is electronic charge; in this case E is the same as q in Eq. [1]. The mobilities in 55% FeO-45% P_2O_5 glasses containing 87.6 and 14.7% Fe^{+3} were calculated from the following equation

$$\sigma = ne\mu \quad [4]$$

where σ is the conductivity and n is given by Eq. [2]. N_0 was taken as the absolute difference between the ferric and ferrous concentrations. The mobilities ranged from about 10^{-10} $cm^2/v\text{-}sec$ at 400°K to 10^{-7} $cm^2/v\text{-}sec$ at 600°K. Using these mobilities and the activation energies determined from Fig. 3, vibrational frequencies at 400°K were calculated from Eq. [3]. These frequencies were 0.8×10^{13} and 1.7×10^{12} sec^{-1} for the 87.6 and 14.7% Fe^{+3} glasses, respectively. Considering that ν_0 is extremely sensitive to the conduction activation energy, the calculated frequencies are very close to the lattice vibrational frequency.

Collectively, the results are very similar to those for the crystalline transition-metal oxides. Hence, electrical conduction is probably a thermally activated diffusion process in which the electrons (or holes) migrate between Fe^{+2} and Fe^{+3} ions.

In view of the similarity between iron-containing glasses and vanadium-containing glasses, the above conduction model can probably be extended to glasses containing other transition-metal ions when the ions exist in more than one valence state.

Conclusions

1. Conductivity is proportional to the iron content in FeO-MgO-P_2O_5 glasses.
2. Resistivity is a function of the ratio Fe^{+3}/Fe_{total} in iron phosphate glasses, passing through a minimum at 0.4 to 0.6 in a 55% FeO-45% P_2O_5 glass.
3. The thermoelectric power is nearly independent of temperature in the range 125-400°C. This implies that the carrier concentration is insensitive to temperature.
4. Glasses change from n-type to p-type semiconductors as Fe^{+3}/Fe_{total} decreases below 0.38.
5. The mobilities are very low, ranging from about 10^{-10} to 10^{-7} $cm^2/v\text{-}sec$, as temperature varies from 400° to 600°K.
6. The conduction is probably a "hopping" process, *i.e.*, charge transfer between ferrous and ferric ions similar to that proposed in crystalline transition-metal oxides.

Acknowledgments

The author is grateful to Miss M. T. Splann for resistivity measurements, G. B. Carrier for electron micrographs, and Dr. Y. Su for chemical analyses. In addition, the experimental assistance of Mr. F. Voorhees is greatly appreciated.

Manuscript received April 28, 1965.

Any discussion of this paper will appear in a Discussion Section to be published in the June 1966 JOURNAL.

REFERENCES

1. P. L. Baynton, H. Rawson, and J. E. Stanworth, *This Journal*, **104**, 237 (1957).
2. M. Munakata, *Solid-State Electronics*, **3**, 159 (1960).
3. E. J. W. Verwey, *Nature*, **144**, 327 (1939).
4. R. R. Heikes and W. D. Johnston, *J. Chem. Phys.*, **26**, 582 (1957).
5. S. van Houten, *J. Phys. Chem. Solids*, **17**, 7 (1960).
6. J. D. Mackenzie in, "Modern Aspects of the Vitreous State," Vol. III, J. D. Mackenzie, Editor, p. 126, Butterworth, Inc., Washington (1964).
7. V. A. Ioffe, J. B. Patrina, and I. S. Poberovskaya, *Sov. Phys.-Solid State*, **2**, 609 (1960).
8. I. I. Kitaigorodskii and V. G. Karpechenko, *Steklo i. Keramika*, **15**, 8 (1958).
9. K. W. Hansen and I. B. Cutler, To be publshed in *J. Am. Ceram. Soc.*

Oxygen Chemisorption Effects on Photoconductivity in Sintered Layers

Herbert Shear and Edgar A. Hilton

— hp associates —, Palo Alto, California

and Richard H. Bube

Department of Materials Science, Stanford University, Stanford, California

ABSTRACT

Processes involving the adsorption and desorption of oxygen are shown to be of basic importance for the photoconductivity properties of sintered layers of CdS-CdSe and CdSe. Annealing in the light in oxygen decreases photoconductivity and dark conductivity, whereas annealing in the dark in oxygen or in either light or dark in He increases both photoconductivity and dark conductivity. Chemisorbed oxygen decreases the dark conductivity by removing electrons from the conduction band, and decreases the photosensitivity by an effect on the free electron lifetime. The concentration of copper acceptor impurity incorporated in the layer determines the effectiveness of the adsorbed oxygen in establishing a depletion layer, particularly important in the sintered connections between individual particles.

The development of high sensitivity photoconductors of the CdS and CdSe type in single crystal form (1) led directly to the development of high sensitivity photoconductors of these materials in microcrystalline powder and sintered layer forms (2). Although the photosensitive powder differed appreciably in certain basic characteristics from the single crystals (3), the properties of the sintered layers proved to be almost completely similar to those of single crystals. The same type of impurity incorporation led to photosensitive layers, ohmic current-voltage curves could be obtained even down to the microvolt range, photovoltaic effects could be virtually eliminated, and in general the absolute sensitivity and speed of response of the layers were comparable to those of crystals. The chief differences found between sintered layers and single crystals were associated with the relative ease of incorporating high impurity concentrations in the layers; later work with high impurity concentrations in single crystals (4) re-established the close similarity of behavior. Thus in most commercial applications of photoconductors of this type, the sintered layer cell has all but dominated the field.

In spite of the close similarity between the photoelectronic properties of sintered layers and single crystals, there are several effects in the area of reproducibility and stability of the cells made from these layers, which achieve a prominence not ordinarily found in single crystals (5). These stability effects have this importance probably because of two characteristics peculiar to the sintered layers: (i) the microcrystalline or polycrystalline nature of the layers, the actual conductivity links between particles having been formed by the relatively brief sintering process; and (ii) the relatively large ratio of surface to volume as compared with single crystals.

An extensive literature exists on the adsorption of oxygen on n-type semiconductors of many different types: Ge (6-8), PbS (9-11), PbTe (12), BaO (13), ZnO (14-23), ZnS (24), CdS (25-27), and CdSe (28, 29). The significance of photoexcitation in the oxygen sorption phenomena has been investigated particularly for the last four of these compounds. Mark (27) has shown that the free electron lifetime in crystals of insulating CdS is strongly decreased by adsorbed oxygen for strongly adsorbed radiation and has substantiated a previous report (30) that a high density of electron traps can be created in certain CdS crystals by the removal of adsorbed oxygen.

Chemisorption of oxygen in such cases occurs when the oxygen accepts an electron from the crystal and becomes chemically bound in an ionic state. The result of this electronic transfer is the establishment of a depletion layer at the surface, which may reach completely across a thin insulating crystal or layer. When the conductivity path is parallel to the surface, these depletion layer effects may dominate the measured conductivity in the dark.

The results of the present investigation lead to the conclusion that such properties of sintered layer photoconductors as instability, nonreproducibility, variability through low-temperature annealing, and long-time drifts may all be attributed to the effects of adsorption or desorption of oxygen. The long-term stability of sintered layer cells is found to depend significantly on whether the cells are stored in light or dark. The room temperature properties of a sintered layer are also known to depend markedly on the exact environment of a previous low-temperature anneal (50°-250°C), *i.e.*, whether the environment involved light and oxygen or not. It is this effect of environment on the annealing of sintered layers of CdS-CdSe and CdSe that constitutes the major concern of the present investigation. It is believed that the changes that can be brought about rapidly in times of the order of 10 min by annealing at slightly elevated temperatures, are the same as the changes that occur slowly at room temperature and constitute the main source of instability and undesired change with time.

The experiments that are described in this paper demonstrate that oxygen adsorption on sintered layers of this type plays an important role in their over-all photoelectronic behavior. Even more, it is demonstrated that the "normal" sintered layer cell depends on adsorbed oxygen acting as an acceptor to achieve the high dark resistivity typical of these cells. There is at all times a two-way reaction occurring between oxygen being adsorbed on the surface and oxygen being desorbed from the surface. It is the role of the environment to cause this reaction to proceed preferentially in one direction or the other. A nonequilibrium situation at room temperature may be induced by low-temperature annealing. The slow return to the equilibrium state constitutes the observed drift of the photoconductivity with time.

A phenomenological model that considers the formation of depletion layers due to adsorbed oxygen,

particularly at the links between particles, satisfactorily describes a variety of observed phenomena.

Experimental

Apparatus.—The sintered layer to be measured was mounted in a special chamber, the atmosphere in the chamber being variable between air, oxygen, or helium, and the temperature of the layer in the chamber being rapidly variable between 25°and 250°C. The temperature of the layer could be raised from 25° to any desired temperature up to 250°C in a maximum period of about 4 min, held at that temperature for any desired time, and then quenched by water cooling of the chamber substrate to below 75°C in 15 sec.

Optical excitation of the sample was provided by a high-intensity Bausch and Lomb monochromator equipped with a 500w tungsten lamp source. The output of the monochromator was calibrated as a function of wavelength using an Eppley thermopile. The intensity of the excitation was varied over almost seven orders of magnitude, using neutral density filters Set 5A from Optics Technology and stainless steel mesh screens. All measurements were made at 25°C unless otherwise stated.

Materials.—Two types of sintered layers were investigated, one consisting of a solid solution of 45% CdS and 55% CdSe, and the other consisting of CdSe only. A mixture with $CdCl_2$ and $CuCl_2$ was sintered on a ceramic substrate by heating above the melting point of $CdCl_2$ for a short time. Although only layers prepared at hp associates are described in this paper, experience with many other layers produced by a variety of different methods and at different laboratories has established that the effects described are common to all such layers.

Ohmic electrodes of indium were evaporated onto these layers in an interdigital pattern, providing 10 individual cells in parallel, each 0.57 cm long and 0.03 cm wide. The average thickness of the layers was estimated to be about 4μ by weighing the total amount of material on several layers and determining the thickness from the weight per unit area (31).

The peak photoconductivity response for the CdS-CdSe layers at 6550Å and for the CdSe layer at 7250Å is consistent with the known bandgaps of these materials. The wavelength used in all measurement, unless otherwise specified, was 7000Å for the CdS-CdSe and 7400Å for the CdSe layers. These wavelengths were chosen to correspond to approximately homogeneous excitation of the layers, lying as they do at longer wavelengths than the absorption edge.

The layers were highly photosensitive with an electron lifetime of the order of a hundred microseconds. A photoconductivity gain of 150 was typical for 10v applied to the cell. Such data yield an electron mobility between 10 and 100 cm^2/v-sec, consistent with the results of photo-Hall measurements on similar layers (32, 33).

The starting reference for all experiments on the effect of annealing is the cell as it is received from the preparative sintering process. This means that the cell has already passed through an annealing process as it cools in air and room light after firing. By selecting cells for which the photocurrent *vs.* light intensity curve fell within certain narrow limits, however, a reliable reference could be established with which to compare the effects of later annealing. Attempts to choose a more scientifically acceptable reference condition, such as by annealing each cell in the dark at 250°C before any other treatment, proved to be less useful. Although a presumably well-defined and reproducible state of the layer could be achieved in this way, the instability of the resulting cell under normal environmental conditions at room temperature made the use of such a reference impractical.

Results

Although there are some differences in quantitative details, the over-all character of annealing effects is similar for CdS-CdSe and CdSe sintered layers. In discussing the results, therefore, the most complete data available for a given phenomenon will be presented, with comments included to indicate any difference of behavior in details with the other system.

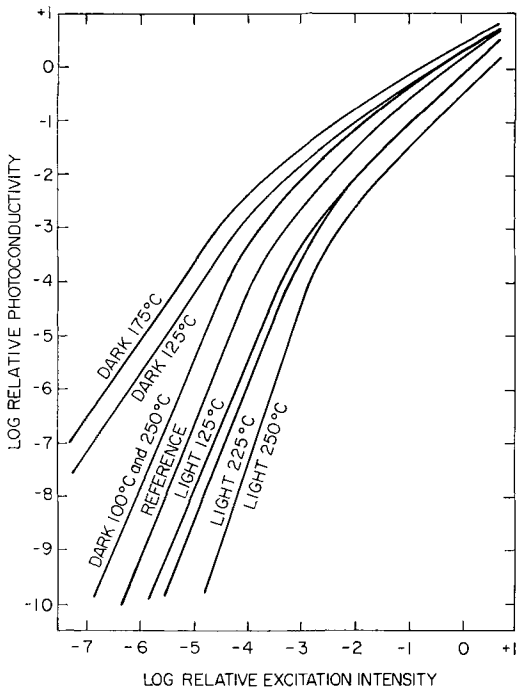

Fig. 1. Room temperature dependence of photoconductivity on light intensity after annealing at elevated temperatures in air. The illumination condition and the temperature are shown on each curve. (The light intensity used for the illumination during annealing corresponds to 0.75 on the log light intensity scale in all cases except where specified. The point 0 on the intensity scale corresponds to 1250 μw/cm^2. The point 0 on the current scale corresponds to 2.45 ma at 1.35v.)

Photoconductivity vs. excitation intensity.—The dependence of photoconductivity on excitation intensity at room temperature was one of the principal types of measurement used to determine the effects of annealing. A summary of such curves after various annealing conditions is given in Fig. 1 for CdS-CdSe layers. All annealing was done for this series of experiments in an atmosphere of air, the only variable being the presence or absence of photoexcitation.

For annealing under photoexcitation, little change occurs in a 10 min anneal until temperatures of 100°C are exceeded. For annealing at higher temperatures, the photoconductivity is reduced. The effect of increasing temperature is small between 125° and 225°C, but becomes larger again at 250°C. For annealing in the dark, quite the opposite effect is found. The photoconductivity increases with increasing annealing temperature, reaching a maximum near 175°C, and then decreases again. The effects obtained with CdSe are quite similar, except that the decrease in photoconductivity after annealing under photoexcitation is not so large.

If either CdS-CdSe or CdSe layers are annealed in He (or another inert atmosphere such as N_2) at 175°C, in either light or dark, the dark conductivity increases by many orders of magnitude and the resulting high-conductivity layer shows little change in conductivity with photoexcitation.

Reversibility of annealing effects.—The effects produced by light or dark annealing in air, as shown in Fig. 1, are completely reversible. Likewise the effects produced by annealing at a given temperature in oxygen or in helium are completely reversible. This latter reversibility is demonstrated by the dynamic curves of Fig. 2, which show the variation of conductivity under various conditions of light or dark, oxygen or

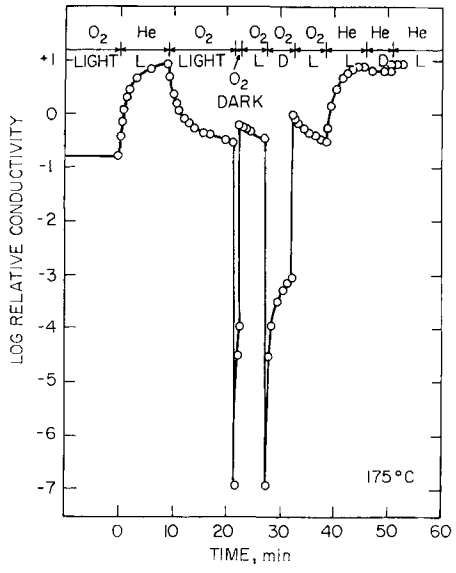

Fig. 2. Dependence of the measured current with variations in illumination and atmosphere at 175°C.

helium atmosphere, at 175°C for a CdS-CdSe layer. Quite comparable results are obtained for a CdSe layer.

The data plotted in Fig. 2 illustrate (*a*) the complete reversibility of oxygen and helium effects on the conductivity, (*b*) the effect of photoexcitation in reducing the dark conductivity of a cell in oxygen, and (*c*) the relative insensitivity of the magnitude of the conductivity in He to the presence or absence of photoexcitation.

Dark conductivity.—Although measurements of dark conductivity as a function of temperature have been made for both the CdS-CdSe and the CdSe layers, it is difficult to draw meaningful conclusions from such curves, since it is virtually impossible to separate true temperature changes of dark conductivity from temperature annealing effects. Representative data are shown in Fig. 3 for a CdS-CdSe layer. Evident from the data are the higher dark conductivity in an oxygen atmosphere produced by annealing in the dark, and also the much higher dark conductivity produced by heating in helium above 140°C. This high dark conductivity produced by a helium anneal persists practically unchanged upon cooling to room temperature in helium; at 260°C, however, the dark conductivity variations between helium and oxygen atmospheres are completely reversible, even as indicated in Fig. 2 for 175°C.

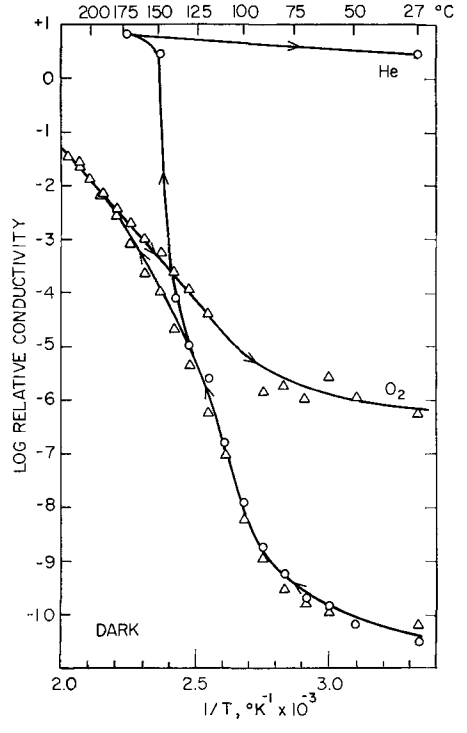

Fig. 3. Temperature dependence of the conductivity in the dark, in an atmosphere of He (○), oxygen (△).

Photoexcitation intensity effects.—The observed dependence of annealing on the intensity of photoexcitation during the annealing is shown for a typical case for a CdS-CdSe layer in Fig. 4. The results are exactly as would be expected from Fig. 1. Since annealing in the dark and in the light produces opposite changes in conductivity, there is some particular light intensity for annealing at a given temperature for which no change in photoconductivity is caused. For light intensities less than this critical intensity, the photoconductivity is increased by annealing. For light intensites greater than this intensity, the photoconductivity is decreased by annealing. For a sufficiently high intensity, the annealing effect appears to saturate.

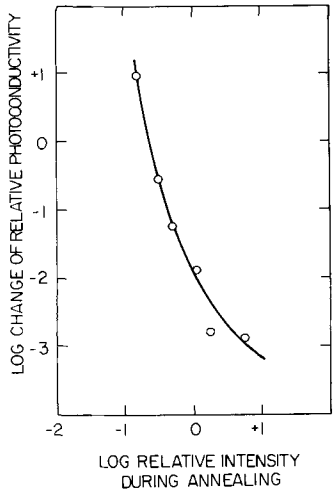

Fig. 4. Change (ratio of current after annealing to before) in the room temperature photoconductivity for a light intensity of —4.1 on the log light intensity scale, after annealing *in air* at 175°C with various intensities of illumination.

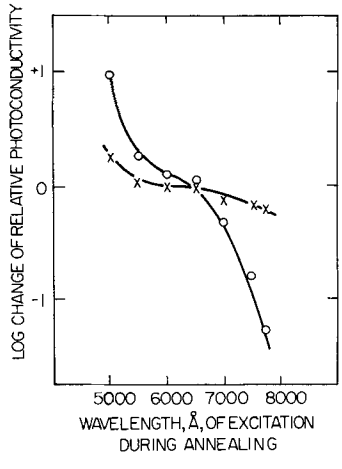

Fig. 5. Change in the room temperature photoconductivity for a light intensity of 0.15 (x) and for a light intensity of —3.6 (○) on the log light intensity scale, after annealing at 175°C in air with various wavelengths of illumination as shown. The intensity of illumination at the elevated temperature was chosen to correspond to equal photocurrent at room temperature for each wavelength.

Photoexcitation wavelength effects.—The dependence of annealing on the wavelength of the photoexcitation is shown for a typical case for a CdS-CdSe layer in Fig. 5. The magnitude of the change in the room temperature photoconductivity at two selected light intensities is plotted as a function of the wavelength used for the photoexcitation during annealing. The intensity of the light at each wavelength was adjusted to give equal photocurrents at room temperature. Wavelengths shorter than the absorption edge are less effective in producing the decrease in photoconductivity than wavelengths longer than the absorption edge. This result may be attributed to the lower efficiency of strongly absorbed light for bringing about oxygen absorption, because of the generation of holes at the surface leading to oxygen desorption as a strongly competing process.

Effects of varying copper concentration.—Additional insight into the processes involved can be obtained by examining the behavior of cells made with both less than and more than the "normal" Cu concentration (0.06 mole %). Cells were prepared of the CdS-CdSe type with 1/3, 3, and 10 times the normal Cu concentration.

Those layers prepared with 1/3 the normal Cu concentration had high dark conductivity. By annealing them in oxygen under photoexcitation, however, the conductivity could be reduced and a cell produced that had a photocurrent *vs.* light intensity curve similar to that of a normal-Cu layer. Typical curves are shown in Fig. 6.

Layers prepared with 3 and 10 times the normal Cu concentration were quite insensitive at room temperature. Their sensitivity and their dark conductivity could be increased, however, by annealing in the dark in air or in helium. Figures 7 and 8 show typical results. If the dark annealing were carried out in air, then a rather normal photocurrent *vs.* light intensity curve was obtained. If the layer were annealed in the dark in He, however, the dark conductivity increased appreciably. If the layer which had been annealed in the dark in He were allowed to stand at room temperature in the air, its properties gradually converted to a much lower conductivity, as is shown in Fig. 7. In other words, the state produced by annealing the layer with

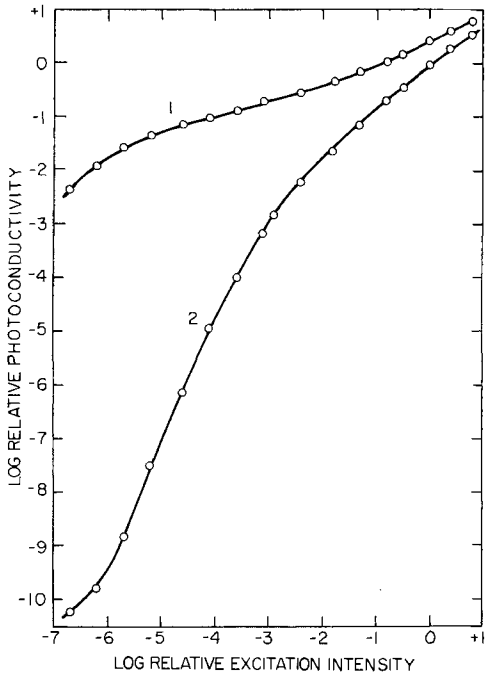

Fig. 6. Dependence of photoconductivity on light intensity at room temperature for a sintered layer of CdS-CdSe with 1/3 the normal Cu concentration, as prepared (curve 1), and after annealing under photoexcitation in air at 260°C for 12 min (curve 2).

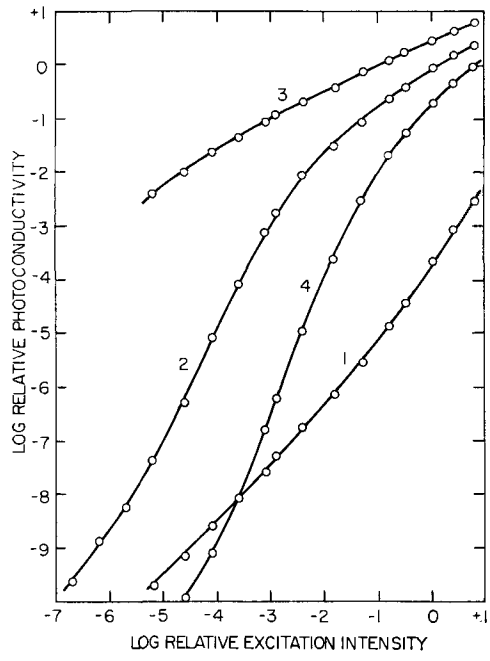

Fig. 7. Dependence of photoconductivity on light intensity at room temperature for two sintered layers of CdS-CdSe with 3 times the normal Cu concentration. The curves for both layers as prepared are given as curve 1. Curve 2 is for one layer after annealing in the dark in air at 175°C. Curve 3 is for the other layer after annealing in the dark in He at 175°C. Curve 4 is again for both layers after the passage of several days during which the cells stood in room light and air at room temperature.

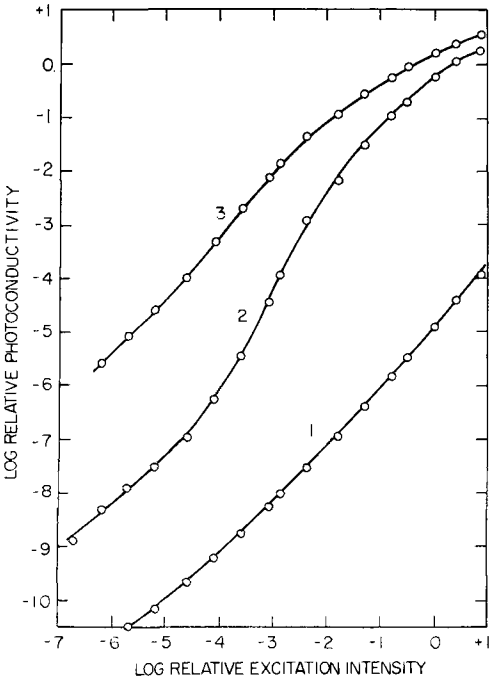

Fig. 8. Dependence of photoconductivity on light intensity at room temperature for two sintered layers of CdS-CdSe with 10 times the normal Cu concentration. Curve 1 is for both layers as prepared. Curve 2 is for one of the layers after annealing in the dark in He at 160°C. Curve 3 is for the other layer after annealing in the dark in He at 180°C.

3 times the normal Cu concentration in the dark in He was extremely unstable at room temperature in air. A curve similar to the one produced by dark annealing in air could be produced by dark annealing in He at a lower temperature than that used to produce the He curve of Fig. 7. The effect of the temperature of the

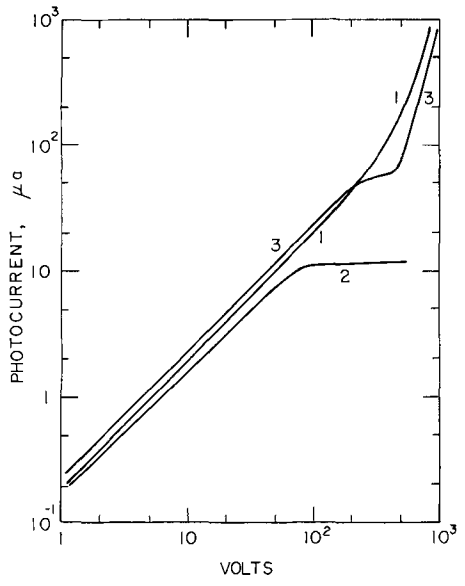

Fig. 9. Photocurrent *vs.* applied voltage for the cell corresponding to curve 2 of Fig. 6 (curve 1), to curve 4 of Fig. 7 (curve 2), and for a standard layer with normal Cu concentration (curve 3). Photoexcitation intensities were chosen to give about the same photocurrent for each cell and correspond respectively to —3.6, —1.8, and —2.9 on the log intensity scale.

dark anneal in He on the layer with 10 times the normal Cu concentration is shown in Fig. 8.

Dependence of photocurrent on applied voltage.—By the previous procedures there were available three quite differently prepared types of cell with similar room temperature dependence of photoconductivity on light intensity. The dependence of the photocurrent in the superlinear range on the applied voltage reveals the difference in these layers. Currents were chosen sufficiently low so that any heating effects in the layers would be eliminated. Results are summarized in Fig. 9, the photoexcitation intensity in each case being adjusted to give about the same photocurrent for each type of cell.

The measured current in the cell with 1/3 the normal Cu concentration, annealed in the light in air to reduce its conductivity (Fig. 5), increases very rapidly with increasing voltage for applied voltages in excess of 100v. In the layer with 3 times the normal Cu concentration, annealed in the dark in He and allowed to stand at room temperature in air (Fig. 7), the current shows a pronounced saturation with voltage for applied voltages in excess of 100v. Finally, in the layer with the normal Cu concentration a region of marked saturation is followed by a rapid increase of current with applied voltage, thus exhibiting both effects seen for the other two types of layers.

Discussion of Results

The significant features of the previous experimental results may be summarized as follows.

1. Annealing in the light in the presence of oxygen causes a decrease in photoconductivity and dark conductivity.

2. Annealing in the dark causes an increase in the photoconductivity and in the dark conductivity, regardless of whether carried out in air or in He, but the effect is more marked if carried out in He.

3. Annealing in the light in He is not substantially different from annealing in the dark in He.

4. All of the above effects are reversible. Annealing in the dark reverses the effect of annealing in light. Annealing in He reverses the effect of annealing in oxygen.

5. Annealing in the light in oxygen has a similar effect to incorporating higher proportions of Cu acceptors in the original layer material.

6. Annealing in the dark has a similar effect to incorporating smaller proportions of Cu acceptors in the original layer material.

7. Although the effects of annealing and varying Cu proportion are superficially interchangeable, the layers exhibit a different dependence of photocurrent on applied voltage depending on the actual proportion of Cu and annealing history.

All of these experimentally demonstrated features can be described by a phenomenological model of the photoconductor layer with the following characteristics. (*A*) Decreases in conductivity are associated with the adsorption of oxygen; increases in conductivity with the desorption of oxygen. (*B*) The effects of adsorbed oxygen are most pronounced at the interparticle links where the development of depletion layers by the adsorption of oxygen can lead to pinch-off of the conductivity.

The process of preparation of the sintered layers makes it a reasonable assumption that the weak links for conductivity are those regions of interparticle contact that had time to sinter in the short time the layer was held above the melting point of $CdCl_2$, the flux for the sintering process. It has been shown that actual interparticle barriers exist in the absence of sintering (3).

The dependence of photoconductivity on light intensity at room temperature shown in Fig. 1 can be described in terms of oxygen sorption effects at the elevated annealing temperature. The rate of oxygen chemisorption on the layer may be attributed to the following mechanisms: (*a*) thermally-activated capture of dark conductivity electrons by oxygen, (*b*) thermally-activated capture of photoexcited electrons by oxygen, and (*c*) thermal release of oxygen from the surface. The possibility of photodesorption of oxygen under suitable circumstances has been mentioned before in connection with Fig. 5, but is probably not a dominant process. A thermal activation step in the capture of free electrons by oxygen must be included to account for the increase in adsorbed oxygen upon annealing at an elevated temperature in light and oxygen. The data indicate that (*b*) is the dominant process below 225°C for annealing in light and oxygen. Above 225°C, process (*b*) is augmented by process (*a*) and the adsorption of oxygen becomes more pronounced. For annealing in the dark and oxygen, (*c*) is the dominant process for temperatures below 175°C, since the dark conductivity is small at lower temperatures. Above 175°C, process (*a*) favoring adsorption reverses the trend established by (*c*) favoring desorption, and the change in photoconductivity with annealing is again negative. Finally, for annealing in helium in either light or dark, process (*c*) is always dominant, and both the photoconductivity and dark conductivity are increased.

Since annealing in the dark in helium for any layer with up to 10 times the normal Cu concentration produces a high-conductivity layer, it may be concluded that the actual proportion of Cu incorporated in the layers is insufficient to give a high-resistivity layer without the contribution of adsorbed oxygen. This is consistent with the observation that the high-conductivity state can be reversibly removed by simply exposing the layer to oxygen, as in Fig. 2. Thus the high-conductivity layer with 1/3 the normal Cu concentration can be transformed to a layer with normal photoconductivity *vs.* light dependence (Fig. 6) by annealing to increase the effect of adsorbed oxygen. Similarly the layer with very low conductivity, prepared with 3 or 10 times the normal Cu concentration, can be transformed to a layer with normal photoconductivity *vs.* light dependence (Fig. 7 and 8) by annealing to decrease the effect of adsorbed oxygen.

The significance of the interparticle conductivity links is brought out in the dependence of photocurrent on applied voltage for the different types of layers. It would be expected that the applied voltage would appear principally across the interparticle links and that

one effect of increasing voltage would be to extract photoexcited holes from these links with a resultant saturation of photocurrent with increasing voltage. This effect is observed both in the layers with normal Cu concentration and in the layers with 3 times the normal concentration (Fig. 9). A second possible effect of increasing applied voltage would be to remove the pinch-off effect of the depletion layer and hence to allow an increased current to flow. This effect is observed both in the layers with 1/3 the normal Cu concentration and in the layers with normal Cu concentration for voltages greater than those involved in the saturation effect.

Acknowledgment

The authors express their appreciation to H. Bratlien who performed some of the measurements.

Manuscript received April 2, 1965.

Any discussion of this paper will appear in a Discussion Section to be published in the June 1966 JOURNAL.

REFERENCES

1. R. H. Bube and S. M. Thomsen, *J. Chem. Phys.*, **23**, 15 (1955).
2. S. M. Thomsen and R. H. Bube, *Rev. Sci. Instr.*, **26**, 664 (1955).
3. R. H. Bube, *J. Appl. Phys.*, **31**, 2239 (1960).
4. R. H. Bube, E. L. Lind, and A. B. Dreeben, *Phys. Rev.*, **128**, 532 (1962).
5. K. W. Böer, R. Boyn, and O. Goede, *Phys. Stat. Sol.*, **3**, 1684 (1963).
6. W. H. Brattain and J. Bardeen, *Bell System Tech. J.*, **32**, 1 (1953).
7. J. Bardeen and S. R. Morrison, *Physica*, **20**, 873 (1954.).
8. E. N. Clarke, *Sylvania Technol.*, **7**, 102 (1954).
9. H. Hintenberger, *Z. Naturforsch.*, **1**, 13 (1946).
10. H. T. Minden, *J. Chem. Phys.*, **23**, 1948 (1955).
11. M. Smollett and R. G. Pratt, *Proc. Phys. Soc. (London)*, **68B**, 390 (1955).
12. D. E. Bode and H. Levinstein, *Phys. Rev.*, **96**, 259 (1954).
13. M. Sakamoto, S. Kobayashi, and S. Ishii, *ibid.*, **98**, 552 (1955).
14. G. Heiland, *Z. Physik*, **138**, 459 (1954); **142**, 415 (1955).
15. S. M. Ryvkin, *Zhur. Tekh. Fiz.*, **22**, 1930 (1952).
16. E. K. Putseiko and A. N. Terenin, *Doklady Akad. Nauk. S.S.S.R.*, **101**, 645 (1955).
17. E. Mollwo, in "Photoconductivity Conference," p. 509, John Wiley & Son, Inc., New York (1956).
18. P. H. Miller, in "Photoconductivity Conference," *loc. cit.*, p. 287.
19. D. A. Melnick, *J. Chem. Phys.*, **26**, 1136 (1957).
20. D. B. Medved, *ibid.*, **28**, 870 (1958); *J. Phys. Chem. Solids*, **20**, 255 (1961).
21. G. Heiland, E. Mollwo, and F. Stöckmann, *Solid State Phys.*, **8**, 268 (1959).
22. B. Hoffman and E. Mollwo, *Z. angew. Phys.*, **14**, 734 (1962).
23. W. Ruppel, H. J. Gerritsen, and A. Rose, *Helv. Phys. Acta*, **30**, 495 (1957).
24. A. Kobayashi and J. Kawaji, *J. Phys. Soc. Japan*, **10**, 270 (1955); **11**, 369 (1956); *J. Chem. Phys.*, **24**, 907 (1956).
25. S. H. Liebson, *J. Chem. Phys.*, **23**, 1732 (1955).
26. R. Williams, *J. Phys. Chem. Solids*, **23**, 1057 (1962).
27. P. Mark, *ibid.*, **25**, 911 (1964); **26**, 959 (1965).
28. R. H. Bube, *J. Chem. Phys.*, **27**, 496 (1957).
29. G. A. Somorjai, *J. Phys. Chem. Solids*, **24**, 175 (1963).
30. R. H. Bube, *J. Appl. Phys.*, **34**, 3309 (1963).
31. Determination carried out by D. Davis.
32. A. B. Fowler, *J. Phys. Chem. Solids*, **22**, 181 (1961).
33. A. L. Robinson and R. H. Bube, *This Journal*, **112**, 1002 (1965).

Photo-Hall Studies of Oxygen Adsorption Effects on Photoconductivity in Sintered Layers

Arthur L. Robinson and Richard H. Bube

Department of Materials Science, Stanford University, Stanford, California

ABSTRACT

The Hall mobility and the free electron density in sintered layers of CdS-CdSe have been measured as a function of photoexcitation intensity, temperature, and ambient atmosphere. Both free carrier density and Hall mobility are reduced by the adsorption of oxygen and increased by the desorption of oxygen. The magnitudes of the effects are such that in all cases the Hall mobility change due to adsorption contributes significantly to the photoconductivity change. Effects associated with photoadsorption of oxygen are reversible by annealing in vacuum. Results can be consistently described in terms of the model for chemisorption of oxygen on sintered layers proposed by Shear, Hilton, and Bube.

The previous paper by Shear, Hilton, and Bube (1) describes the effects of chemisorbed oxygen on the dark conductivity and photoconductivity of sintered layers of CdS-CdSe and CdSe. References to similar phenomena in other materials are also given in the previous paper. Perhaps the most closely related is the investigation of photoinduced chemisorption on insulating CdS single crystals by Mark (2). He found that the free electron lifetime for strongly absorbed light was increased by as much as 35 times by removing the adsorbed oxygen in vacuum.

In order to clarify the mechanism of the processes involved further, photo-Hall measurements were made on sintered layers as a function of photoexcitation intensity, temperature, and ambient atmosphere. By measuring the photo-Hall effect it becomes possible to tell whether a given change in conductivity is due primarily to a change in free carrier density or to a change in free carrier mobility.

Adsorption of oxygen on sintered layers of CdS-CdSe is found to decrease both the free carrier density and the free carrier mobility. Depending on the conditions, the Hall mobility change was comparable to but less than the free carrier change. The observed effects are consistent with a model for the sintered layer in which adsorbed oxygen develops depletion layers because of its acceptor behavior and thereby influences the free carrier density by decreasing the lifetime, and the free carrier mobility by introducing space-charge layer scattering.

Experimental

Apparatus.—Measurements were made in a glass Dewar capable of being evacuated and providing temperature control of a sample between room temperature and 250°C. Atmospheres in the Dewar were either air at atmospheric pressure or a partial vacuum of 10^{-1} Torr obtained with a rotary pump.

A d-c measurement technique for the Hall effect was used, similar to that described by MacDonald and Bube (3). Two Cary vibrating reed electrometers were used, one to measure the potential drop along the sample, and the other to measure the Hall voltage. All normal precautions involving reversal of applied voltage and of magnetic field were taken to insure that the Hall measurements were meaningful. A 6-in. Varian magnet giving a magnetic field of 5000 gauss was used.

Photoexcitation was by an incandescent lamp through a water filter to remove the infrared. Variations in excitation intensity were achieved with calibrated stainless steel, wire-mesh, neutral density filters.

Materials.—Measurements were made on sintered layers of $CdS_{0.45}$-$CdSe_{0.55}$ solid solution with evaporated indium electrodes, prepared by -hp associates-. These layers were prepared on a ceramic substrate with an interelectrode spacing of 6.25 mm, side probe spacing of 1.75 mm, and Hall probe spacing of 1.6 mm. All measurements were made on samples for which ohmic contact behavior had been established. An electric field of 77 v/cm was used for the measurements.

Results

The effects on the free electron density and Hall mobility of successive heating of a sintered layer under photoexcitation in air, and in vacuum, are given in Fig. 1 and 2. Figure 1 shows the variation of free electron density with photoexcitation intensity at room temperature before any annealing experiments, after heating under photoexcitation in air to 250°C, and finally after subsequent heating in vacuum to 250°C. Figure 2 shows the variation of the Hall mobility with photoexcitation intensity at room temperature for the same cycle of experiments. The net effect on the room temperature properties of heating under photoexcitation in air is to decrease the free electron density and the Hall mobility at all photoexcitation intensities. The subsequent vacuum heating restores the Hall mobility to about the same as the initial values, but actually gives a higher free electron density. This higher free electron density under photoexcitation is associated with an appreciably higher free electron density in the dark.

Typical curves showing the variation of free electron density and Hall mobility with temperature for atmospheres of air or vacuum and for extremes of photoexcitation, are given in Fig. 3 and 4. The data are for the same layer as that described in Fig. 1 and 2, the heating in air being followed by the heating in vacuum. The following observations may be

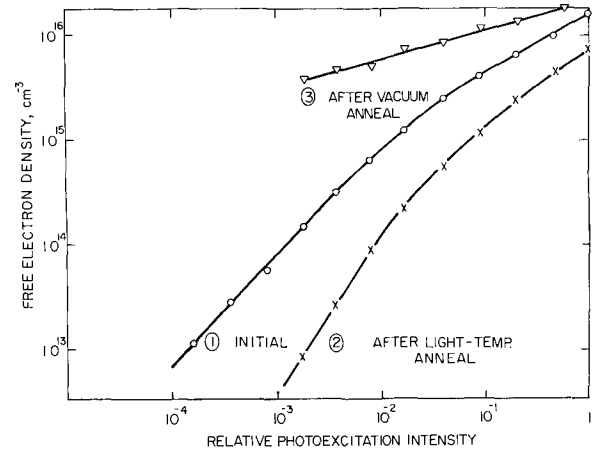

Fig. 1. Free electron density as a function of photoexcitation at room temperature: 1, initial layer; 2, after heating under photoexcitation in air to 250°C; 3, after subsequent heating of same layer in vacuum to 250°C.

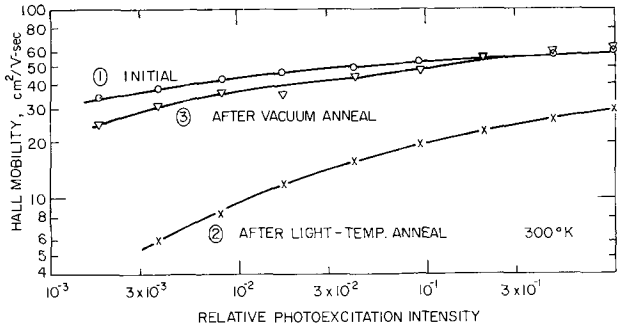

Fig. 2. Hall mobility as a function of photoexcitation intensity at room temperature: 1, initial layer; 2, after heating under photoexcitation in air to 250°C; 3, after subsequent heating of same layer in vacuum to 250°C.

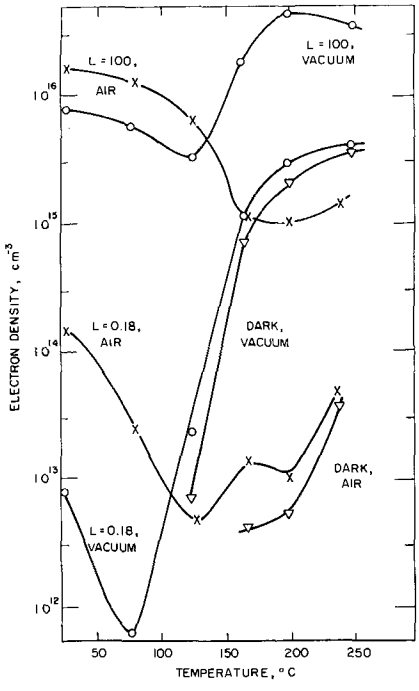

Fig. 3. Free electron density as a function of temperature under excitation conditions corresponding to dark, low intensity (L = 0.18), and high intensity (L = 100), in air and in vacuum. Measurements in vacuum were made on the layer subsequent to the measurements in air.

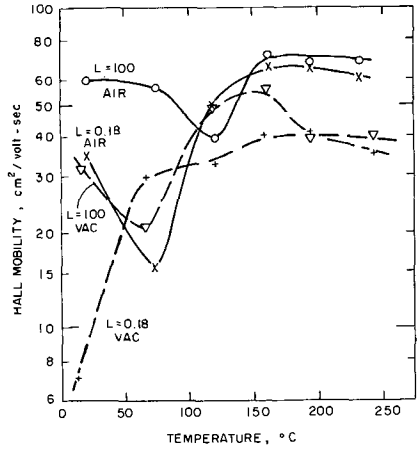

Fig. 4. Hall mobility as a function of temperature under excitation conditions corresponding to low intensity (L = 0.18) and high intensity (L = 100), in air and in vacuum.

Table I. Temperature for beginning of increase of free electron density and Hall mobility

Photoexcitation	Atmosphere	Free electron density, °C	Mobility, °C
Low	Vacuum	75	25
High	Vacuum	125	75
Low	Air	125	75
High	Air	200	125

made from these data, keeping the immediate history of the layer in mind.

1. The free electron density in the dark rises rapidly at a much lower temperature for heating in vacuum than in air.
2. The Hall mobility decreases at first with increasing temperature, but then increases with further temperature increase.
3. The temperature at which the Hall mobility starts to increase is lower the lower the photoexcitation intensity. For heating in air, for example, the Hall mobility for low intensity excitation at 125°C is higher than the Hall mobility for high intensity excitation, quite the reverse of the behavior indicated at room temperature in Fig. 2.
4. The temperature at which the Hall mobility starts to increase is lower for heating in vacuum than in air.

A summary of the temperatures at which increases in free electron density and Hall mobility are found with increasing temperature is given in Table I.

Some of the approximately reversible effects found at constant temperature are illustrated in Fig. 5. A layer held at 195°C experienced varying photoexcitation conditions and atmospheres. Both free electron density and Hall mobility are higher under photoexcitation than in the dark and both are higher in vacuum than in air.

Discussion

The previous paper by Shear, Hilton, and Bube (1) has given evidence for a decrease in photoconductivity upon photoadsorption of oxygen. The results of the photo-Hall studies show that a major part of this decrease in photoconductivity is a decrease in free electron density, through the effect of the adsorbed oxygen on the free electron lifetime as in the work of Mark (2). A significant decrease in free electron mobility also results, however, through the effect of adsorbed oxygen in buiding up a space-charge depletion layer. Space-charge layer scattering is important if the space charge region is of the same thickness as the sample, or is of the same thickness as the excitation absorption depth.

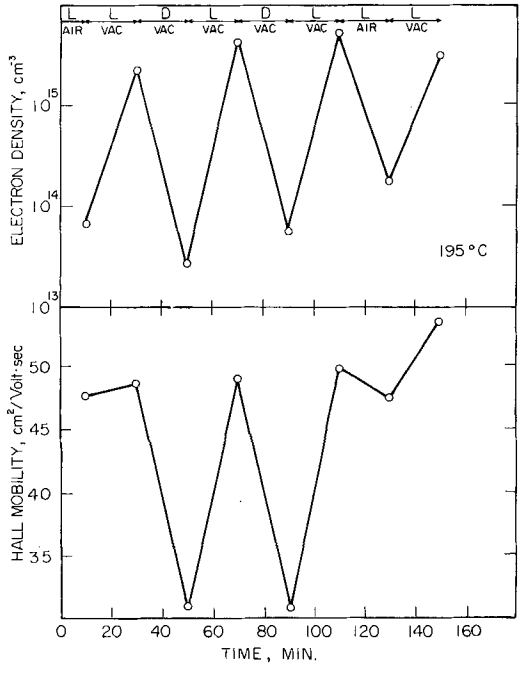

Fig. 5. Variations of free electron density and Hall mobility with photoexcitation and atmosphere changes at 195°C.

The dependence of the free electron density in the dark and under photoexcitation, and of the Hall mobility, on increasing temperature can be understood in terms of the following competing processes. (A) Adsorption of oxygen is increased by increasing temperature in the presence of photoexcitation and air, at least for an intermediate temperature range above room temperature. This effect is consistent with the observation that free electrons thermally excited over the surface barrier could contribute to increased chemisorption. (B) Thermal desorption of oxygen is increased by increasing temperature.

For heating between 25° and 75°C, the free electron density under photoexcitation and the Hall mobility decrease with increasing temperature under all conditions except that for low intensity excitation in vacuum, as shown in Fig. 3 and 4. The exception may not be valid since a very low value of mobility at low intensity excitation exists as the result of the previous heating in air. In this range there is both thermal quenching of photoconductivity in these samples and an increase in photoadsorbed oxygen.

As the temperature is raised still further, a point is reached where the rate of thermal desorption of oxygen exceeds the rate of photoadsorption of oxygen. This temperature is reached first for the measurements in vacuum, next for the measurements with low excitation intensity in air, and last for the measurements with high excitation intensity in air. The Hall mobility in sintered layers at a given temperature normally decreases continuously with decreasing light intensity (4, 5) as indicated in Fig. 2, probably because of photoneutralization of a quasi-continuous distribution of charged scattering centers. At some particular temperature, such as 125°C, for the measurements in air, however, the rate of thermal desorption of oxygen exceeds the rate of photoadsorption of oxygen at low but not at high intensities. The result is the observation of a minimum Hall mobility with decreasing light intensity, followed by an increasing Hall mobility at lower light intensities.

One remaining question is why the mobility starts to increase with increasing temperature consistently about 50° before the free electron density starts to increase. The answer is probably that two factors are decreasing the free electron density with increasing temperature, both thermal quenching of photoconductivity and photoadsorption of oxygen, but only the latter acts to decrease the mobility. As the temperature is reached for which thermal desorption is greater than photoadsorption of oxygen, the Hall mobility increases. However, the effect of thermal desorption of oxygen on the free electron density is only indirectly detectable as a decrease in the rate of thermal quenching. Since thermal quenching of photoconductivity in such materials normally involves a decrease in free electron density by four or more orders of magnitude, it is consistent with the data of Fig. 2 to attribute the much smaller effect of quenching on the compensating effect of oxygen desorption.

The relatively large increase of Hall mobility with photoexcitation in vacuum at 195°C shown in Fig. 5 suggests that photodesorption of oxygen may be a significant process. Photoexcitation in vacuum may be expected to lead to some photodesorption because of the creation of free holes that may be captured by the adsorbed oxygen ions. If this were the case, the observed recovery in the dark must be attributed to readsorption of oxygen in the relatively poor vacuum of 10^{-1} Torr, the dark electron density being high enough at this temperature to provide sufficient free electrons to participate in chemisorption of oxygen.

Acknowledgment

The authors wish to express their appreciation to Dr. P. B. P. Phipps for valuable discussions and assistance during the course of this investigation. This work was sponsored by the Army Research Office (Durham).

Manuscript received April 2, 1965. This investigation constitutes partial fulfillment of the requirements for the degree of M.Sc. in the Department of Materials Science, Stanford University (ALR).

Any discussion of this paper will appear in a Discussion Section to be published in the June 1966 JOURNAL.

REFERENCES

1. H. Shear, E. A. Hilton, and R. H. Bube, *This Journal*, **112**, 997 (1965).
2. P. Mark, *J. Phys. Chem. Solids*, **25**, 911 (1964); **26**, 959 (1965).
3. H. E. MacDonald and R. H. Bube, *Rev. Sci. Instr.*, **33**, 721 (1962).
4. A. B. Fowler, *J. Phys. Chem. Solids*, **22**, 181 (1961).
5. R. H. Bube, H. E. MacDonald, and J. Blanc, *ibid.*, **22**, 173 (1961).

New Glass Compositions Possessing Electronic Conductivities

Donald W. Roe

Electronic Components and Devices, Radio Corporation of America, Lancaster, Pennsylvania

ABSTRACT

This paper describes the use of oxides of the transition elements, V, Mo, W, Fe, Mn, and Ti, in various combinations with oxides of the alkali and alkaline earth metals and oxides of silicon, phosphorus, boron, aluminum, and zinc to produce glass compositions in which conductivity results from movement of electrons rather than ions. Conduction mechanisms in these new glasses are discussed, as well as the principles of glass formation involved in the derivation of the glass compositions.

The program described in this paper had as its goal the preparation of new oxide glasses which would have electronic conductivities ranging from 10^{-11} to 10^{-12} mho/cm. Warburg *et al.* (1) have shown that the resistance of glass films in which ions conduct the current increases rapidly with the passage of direct current. Morey (2) summarized similar results for those glasses containing sodium oxide. Tests on thin films of the new glasses with 10^{12} ohm-cm resistivity or less, however, showed essentially no change in resistance with the passage of direct current. Glasses with greater than 10^{12} ohm-cm were not tested for resistance change with passage of direct current.

Past work on oxide glasses reported in the literature shows that electronic conductivity has been achieved through the use of transition element oxides, usually in combination with modifier oxides of the alkali and alkaline earth metals. The works of interest almost all involve glasses containing V_2O_5, MoO_3, Fe_2O_3, or WO_3. Data from several of these papers will be mentioned briefly.

In 1954 Denton *et al.* (3) reported on glasses containing V_2O_5 as a transition element oxide in combination with a single other oxide that was either P_2O_5, GeO_2, TiO_2, As_2O_3, BaO, or PbO. In some applications V_2O_5 was combined with P_2O_5-BaO and P_2O_5-PbO. Conductivities ranged from 10^{-4} to 10^{-7} $(\text{ohm-cm})^{-1}$.

In 1956 Baynton *et al.* (4) reported on glasses based on Mo, W, and U. The MoO_3 glasses, in 20g batches, contained other oxides in combinations as follows: P_2O_5-Na_2O, P_2O_5-BaO-Na_2O, P_2O_5-K_2O, and Na_2O. Glass formation was also observed in the systems Li_2O-MoO_3, Na_2O-MoO_3, and BaO-MoO_3, all containing high percentages of MoO_3. Because they devitrified readily, these glasses were not made in more than 20 mg lots. The WO_3 glasses K_2O-WO_3 and Na_2O-WO_3 were also limited to this amount because they exhibited the same tendency to devitrify. The WO_3 glasses containing P_2O_5-Na_2O, P_2O_5-K_2O-Na_2O, and P_2O_5 did not crystallize; the conductivities of these glasses and the other 20g batches were of the order of 10^{-8} $(\text{ohm-cm})^{-1}$.

In 1957 Baynton *et al.* (5) reported the formation of glasses containing V_2O_5 in combination with BaO-P_2O_5 and Na_2O-BaO-P_2O_5. Conductivities were of the order of 10^{-5} to 10^{-7} $(\text{ohm-cm})^{-1}$. Also in 1957 Mazurin *et al.* (6) reported that glasses containing SiO_2, B_2O_3, Al_2O_3, CaO, and Fe_2O_3 showed electronic conductivities of the order of 10^{-10} $(\text{ohm-cm})^{-1}$ at 150°C. McMillan (7), at the VI International Conference on Glass, discussed his work in the systems MnO-Al_2O_3-SiO_2, FeO-Al_2O_3-SiO_2, CoO-Al_2O_3-SiO_2, and NiO-Al_2O_3-SiO_2; conductivities were of the order of 10^{-11} to 10^{-13} $(\text{ohm-cm})^{-1}$. MacKenzie (8) at the same conference reported on glasses composed of oxides of Fe, V, and Ti in combination with other nontransition-element oxides. Trap and Stevels (9) at the same conference, reported on the electronic conductivity of glasses that contained (*a*) iron oxides; (*b*) iron oxides, manganous oxide, and cobalt oxides; (*c*) iron oxides and manganous oxide; and (*d*) iron oxides and cobalt oxides in various combinations with oxides of silicon, boron, sodium, aluminum, calcium, and strontium.

Conduction Mechanisms

Verwey (10) mixed the oxides of two or more metals and drove one of the metal ions into different oxidation states. For example, ferric oxide mixed with small amounts of titanium dioxide (up to 1%) and fired at 1200°C in air gives a mixture whose conductivity is 0.1 $(\text{ohm-cm})^{-1}$. The conductivity of pure ferric oxide fired at 1200°C in air is 10^{-9} $(\text{ohm-cm})^{-1}$. The introduction of the titanium dioxide caused the formation of an equivalent amount of ferrous ion to give a semiconductor of the general formula

$$(Ti_x^{IV}\, Fe_x^{II}\, Fe_{1-2x}^{III})_2O_3$$

According to Verwey in inorganic oxides of a more or less polar type, a condition for electronic conductivity is that the lattice contains ions derived from the same element but of different valency in the same crystallographic position. McMillan (7) reported that thin films of MnO-Al_2O_3-SiO_2 glasses exhibited higher conductivities after they were heated in air at 400°-650°C for 4 hr. MacKenzie (8) stated that electronic conduction occurs as a result of transfer of electrons between cations of the same element in different oxidation states. Trap and Stevels (9) reported that electronic conductivity can be effected in a system of inorganic oxides by introduction of elements which are present in different valency states. They found that conductivities were extremely sensitive to melting conditions and thermal treatment during preparation.

In the work described in this paper, transition elements were used to effect electronic conduction. The ratios of the oxidation states of the transition elements were determined, it is believed, by the following factors: (i) the presence of other transition elements;

(ii) the atmospheric composition above the melt; and (iii) the basicity of the glass modifiers and glass formers. A second or third transition element was used in an attempt to drive the transition element into two oxidation states. The atmosphere above the melts during melting and homogenizing operations was provided by a hydrogen-oxygen flame slightly rich in oxygen. After the melting and homogenizing operations, the melts were allowed to cool to blowing temperature and thus approach equilibrium with the room atmosphere before resistivity measurements were made. All these glasses exhibited changes of resistivity of less than 10% after being subjected to repeated 3-4 hr cycles of melting and homogenizing. These results indicated that equilibrium with the atmosphere above the melts was closely approached during melting and homogenizing operations. According to Weyl (11), the equilibria between oxidation states of transition elements oxides are shifted toward the higher states as the basicities of the glasses are increased; thus with greater basicity of the modifier-former medium, lower electronic conduction should be observed if only the higher oxidation state is present in the original constituents of the glass.

Principles of Glass Formation

The glass compositions melted in the work described in this paper were derived from considerations of glass-structure theory. Sun's (12) classification of oxides into glass formers and modifiers was followed in the selection of oxides. Most of the glass compositions used have the Y ratio as defined by Stevels (13), in the proper range for glass formation. The Y ratio is defined as the number of bridging oxygen atoms divided by the number of glass-former atoms. For a Y ratio between 4 and 3 the glass is strong; for Y ratios less than 2, the glass is weak. Between Y ratios of 2 and 3, the cohesion of the glass network decreases rapidly. For calculation of this ratio, coordination numbers for Mo and W were assumed to be 4 as in crystals of $CaWO_4$ (14). Vanadium, titanium, boron, silicon, and phosphorus coordination numbers were taken as 4 as in Sun's article. Because the minor constituents such as Fe and Mn were present in relatively small amounts, they were not considered important contributors to the glass formers and therefore were not used in the calculation of the Y ratio.

Experimental

The melts described were prepared in 100g lots, according to standard procedures, in a 100-cm^3 platinum crucible in a hydrogen-oxygen furnace. The carbonates were used as starting materials for most modifier oxides. Foaming due to CO_2 evolution was a general rule; powders in small amounts produced less foaming than pellets. With experience the proper amounts of powders were added to minimize foaming and loss of material. Melting and homogenizing times averaged 3-4 hr each. Resistivities became constant after this time, or showed less than 10% change after 3 to 4 more hours of melting and homogenizing operations. Weight loss was approximately 2% during melting and homogenizing operations as shown by a weight test on one glass composition.

For volume resistivity measurements, "balloons" of glass were blown from the melts at the proper viscosities for gathering sufficient glass with a 1-in. quartz blowpipe. Suitable "eggshells" were cut from these balloons by use of a small hydrogen-air flame. The volume resistivity apparatus consisted of an RCA microammeter, two 45v dry cells, a mercury well, and a sleeve to contain the mercury on top of the eggshell. A grounded silver-paste ring around the periphery of the eggshell excluded surface resistivity measurements. The number of interferometric fringes for the films was measurable, but because of the color of these glasses no reliable measurements of their indices of refraction could be made. Thicknesses of the films, which were measured with a micrometer, ranged from 0.3 to 0.5 mil. Measurements of the thicknesses of the eggshells at the tips of sharp points of the smallest and flatest pieces kept the error in thickness measurements small. The errors in resistivites were caused by inaccuracies in thickness measurements.

Most glasses were melted in only one batch. When additional batches were prepared, however, resistivities were found to be within 10% of those of the previous batch.

Results and Discussion

The glasses prepared can be divided into the following groups according to transition-element oxides and the predominating glass formers: 1, vanadium - boron; 2, vanadium - iron-boron; 3, vanadium - phosphorus; 4, vanadium - iron-phosphorus; 5, vanadium - molybdenum-phosphorus; 6, vanadium - molybdenum-iron-phosphorus; 7, molybdenum - iron-boron; 8, molybdenum - tungsten-iron-phosphorus; 9, titanium - iron-boron; 10, manganese - iron-phosphorus-boron.

The mole fractions reported for these glasses were calculated from the amounts of starting materials. Properties of the glasses, where measurements were made, are discussed in their respective groups. Where the measurements were made, volume resistivities at room temperature are given, changes in resistivities after a vacuum or nitrogen bake at 400°C and after a direct current of the quantity of 10^{-3} coulomb or more per square centimeter was passed through the thin films are also given.

Electronic conductivities were observed for all the glasses of 10^{12} ohm-cm resistivity or less for the passage of direct current of the quantity of 10^{-3} coulomb/cm^2. Less than 25% changes in conductivities were observed for all the glasses of 10^{12} ohm-cm resistivity or less after the passage of direct current of the quantity of 10^{-3} coulomb/cm^2. In Fig. 1 illustrations of the conductivity changes for a glass with ionic conductivity and for a glass with mainly electronic conductivity but with some ionic conductivity can be seen. This figure shows the current (direct) as a function of time at room temperature for a glass with ionic conductivity (composition as given in Table I) and for glass No. 9, Table III, a glass with mainly electronic conductivity. The conductivity of the glass of composition given in Table I increased rapidly with passage of direct current for 65 hr to give a conductivity 5% as large as in the beginning. Glass No. 9, Table III, after 65 hr of direct current passed, had a conductivity 79% as large as in the beginning, indicating a much smaller amount of ionic conductivity than with the Table I composition. The glass whose composition is given in

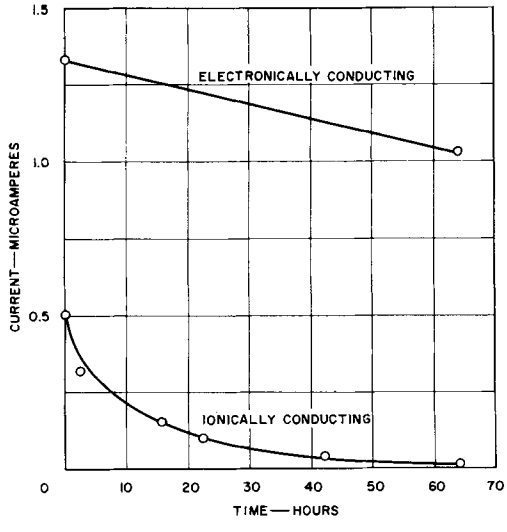

Fig. 1. Comparison of the conductivities of a typical ionically conducting glass (Table I) and an electronically conducting glass (Table III, glass No. 9).

Table I. Composition of a typical ionically conducting glass

Compound	Weight-per cent
Silicon dioxide (SiO_2)	66.59
Iron oxide (Fe_2O_3)	0.045
Aluminum oxide (Al_2O_3)	2.93
Titanium dioxide (TiO_2)	0.017
Calcium oxide (CaO)	7.40
Barium oxide (BaO)	0.08
Magnesium oxide (MgO)	3.83
Sodium oxide (Na_2O)	17.54
Potassium oxide (K_2O)	0.91
Sulfur trioxide (SO_3)	0.04
Arsenic pentoxide (As_2O_5)	0.41
Antimony pentoxide (Sb_2O_5)	0.04
	99.832

Table I has no transition element oxides and has a large mole fraction of Na_2O to give appreciable conductivity by ionic migration of sodium ions. This ionic migration results in a rapid increase of resistance with passage of current.

Conductivities at higher temperatures than room temperature were not measured. Thus activation energies of conduction could not be determined.

No conclusions concerning the effect of a second or a third transition element oxide or the effect of different basicities of the nontransition element oxides could be made from an examination of the tables.

Vanadium-boron glasses.—Twelve melts of vanadium-boron glasses were prepared. Table II shows compositions in mole fractions, melt devitrification results, and resistivities obtained for these glasses.

Devitrification was a problem with five of these glasses. Some relationships between devitrification and the number of constituents of the glasses and the amounts of constituents can be seen from an examination of Table II. Two of the glass compositions that devitrified, No. 9 and 11, had four components, the smallest number in the table. Glass No. 8, another that devitrified, had a small amount of BaO present. A comparison of glass No. 10 with glass No. 5 shows that the latter, which devitrified, had slightly less ZnO. Glass No. 5 and glass No. 4 were similar except that glass No. 5 had no Na_2O and more BaO, ZnO, and CaO than glass No. 4. Glass No. 5 devitrified and glass No. 4 did not.

Resistivities of these glasses can be related to the amount of V_2O_5 present if the compositions are otherwise similar. Glass No. 2, which was very similar in composition to No. 4 except that it had more B_2O_3 and less V_2O_5, had a higher resistivity as expected. The resistivities of glasses No. 7 and 12, a similar pair, are anomalous since glass No. 12 should have a lower resistivity than No. 7, because it had more V_2O_5. Another resistivity anomaly is that glasses No. 7 and No. 12 had a higher resistivities than glass No. 4 even though both glasses No. 7 and No. 12 had more V_2O_5 and less Na_2O than No. 4. The lower Na_2O content in glasses No. 7 and No. 12 should promote more of the lower oxidation state of V_2O_5 in glasses No. 7 and No. 12 than in glass No. 4, and thus give a lower resistivity for No. 7 and for No. 12.

Table II. Compositions and resistivities of vanadium-boron glasses

Glass No.	Mole fractions V_2O_5	B_2O_3	BaO	ZnO	CaO	Na_2O	MgO	SiO_2	Volume resistivity (ohm-cm) × 10^{11}
1	0.213	0.530	0.157	0.074				0.026	7.3
2	0.216	0.556	0.079	0.031	0.070	0.048			10
3	0.227	0.575	0.073	0.040	0.065	0.011	0.009		6
4	0.229	0.547	0.078	0.031	0.069	0.047			2
5	0.232	0.547	0.085	0.051	0.085				*
6	0.234	0.559	0.076	0.041	0.061			0.029	2
7	0.234	0.560	0.080	0.032	0.070	0.024			4
8	0.241	0.567	0.045	0.014	0.133				*
9	0.246	0.525			0.164	0.065			*
10	0.246	0.525	0.082	0.065	0.082				2
11	0.249	0.586		0.073		0.092			*
12	0.250	0.548	0.078	0.031	0.069	0.024			10

* Melt devitrified.

Table III. Compositions and resistivities of vanadium-iron-boron glasses

Glass No.	Mole fractions V_2O_5	Fe_3O_4	B_2O_3	BaO	ZnO	CaO	Na_2O	SiO_2	MgO	Volume resistivity (ohm-cm) × 10^{11}
1	0.168	0.033	0.600			0.136		0.063		100
2	0.195	0.031	0.546			0.127	0.043		0.058	6
3	0.213	0.017	0.562	0.080	0.032	0.071	0.025			40
4	0.215	0.017	0.534	0.075	0.039	0.067	0.044		0.009	4
5	0.217	0.017	0.560	0.080	0.032	0.070	0.024			80
6	0.217	0.035	0.559			0.141	0.048			1000
7	0.220	0.017	0.558	0.079	0.031	0.070	0.025			10
8	0.221	0.017	0.550	0.076	0.041	0.062	0.026		0.009	4
9	0.223	0.017	0.555	0.079	0.031	0.069	0.026			4
10	0.223	0.018	0.548	0.082	0.032	0.072	0.025			3
11	0.225	0.017	0.538	0.077	0.030	0.067	0.046			50
12	0.228	0.036	0.588			0.148				*
13	0.234	0.016	0.531	0.076	0.030	0.067	0.046			20
14	0.235	0.016	0.522	0.075	0.030	0.066	0.056			90
15	0.235	0.016	0.524	0.074	0.029	0.066	0.056			90
16	0.239	0.018	0.520	0.081	0.032	0.072	0.038			3
17	0.240	0.018	0.521	0.112	0.039	0.032	0.038			1

* Melt devitrified.

Devitrification was not a severe problem with these compositions. Only glass No. 12 devitrified. It had the least number of components of any glass in the table.

A test to determine weight loss of a melt was made with these glasses. Glass No. 14 lost only 2% of its total calculated final weight after 72 hr at 800°C.

Several resistivity relationships were observed with these glasses. Glasses No. 3, 5, 7, 8, 9, and 10 had essentially the same mole fractions of modifiers, but differed in amounts of V_2O_5 and B_2O_3. Figure 2 shows that a straight line relationship (except for glass No. 5) exists between the mole fractions ratio B_2O_3/V_2O_5 and the log of the resistivity. This ratio is believed to be significant because B_2O_3 competes with V_2O_5 for the position of glass former. Glasses No. 4, 11, and 13 form a series in which the mole fractions of modifiers are essentially the same and the ratio B_2O_3/V_2O_5 differs. For glasses No. 4, 11, and 13 a plot of the ratio B_2O_3/V_2O_5 (2.48, 2.39, 2.27 for glasses No. 4, 11, and

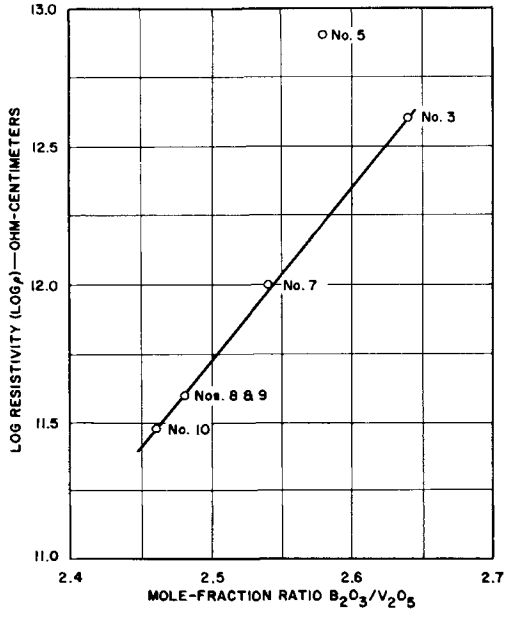

Fig. 2. Resistivity as a function of the mole-fraction ratio B_2O_3/V_2O_5 for the vanadium-iron-boron glasses No. 3, 5, 7, 8, 9, and 10 in Table III.

Table IV. Compositions and resistivities of vanadium-phosphorus glasses

Glass No.	Mole fraction V_2O_5	P_2O_5	CaO	MgO	Volume resistivity (ohm-cm) × 10^{11}
1	0.051	0.618	0.296	0.036	50
2	0.083	0.599	0.301	0.017	5
3	0.110	0.572	0.300	0.018	3
4	0.162	0.518	0.302	0.018	0.06

13, respectively) against log resistivity did not give a straight-line since the resistivity of glass No. 4 was less than that of No. 11 and 13 and not greater as it should have been according to the B_2O_3/V_2O_5 ratio and according to the amount of V_2O_5 present. A comparison of glasses No. 16 and 17 shows that the resistivity decreases slightly with a lower calcium oxide and a higher barium oxide content. The effective higher basicity because of the increased barium oxide should increase the resistivity, however, since more of the higher oxidation state of V_2O_5 is expected.

Vanadium-phosphorus glasses.—Table IV shows the data obtained on 4 vanadium-phosphorus glasses. These glasses were of good quality as thin films and were easy to prepare as melts. Glass No. 4, after being vacuum baked at 400°C for 1 hr, showed a 20% decrease in resistivity. The resistivities of these glasses decrease as the mole fractions of V_2O_5 are increased as shown in Fig. 3. It is remarkable that this straight-line relationship exists for two reasons: (*A*) the compositions differ widely; and (*B*) plot of the mole fraction ratio P_2O_5/V_2O_5 as a function of resistivity is not a straight line.

Vanadium-iron-phosphorus glasses.—Table V presents data on vanadium-iron-phosphorus glasses. Although these glasses were generally of good quality when blown into thin films, they were all on the verge of devitrification in the melt at temperatures at which the viscosity was suitable for blowing bubbles. Without exception the resistivities decreased as the mole fraction of V_2O_5 increased. A plot of mole fraction of V_2O_5 as a function of log resistivity shows essentially a straight-line relationship, as shown in Fig. 4. It is again remarkable that this condition exists, for the same reasons as given for the preceding group of glasses.

Vanadium-molybdenum-phosphorus glasses.—Table VI lists data for two vanadium-molybdenum-phosphorus glasses. These two glasses were of good quality as thin films.

Vanadium-molybdenum-iron-phosphorus glass.—Table VII shows the composition and resistivity of one

Table V. Compositions and resistivities of vanadium-iron-phosphorus glasses

Glass No.	Mole fractions V_2O_5	Fe_3O_4	P_2O_5	SiO_2	Na_2O	CaO	MgO	Al_2O_3	Volume resistivity (ohm-cm) × 10^{18}
1	0.091	0.036	0.584	0.069		0.178	0.042		2
2	0.094	0.029	0.480	0.058		0.283	0.050	0.007	0.6
3	0.100	0.039	0.639	0.057	0.147				0.3
4	0.148	0.033	0.543	0.064		0.165	0.039	0.008	0.003

Table VI. Compositions and resistivities of vanadium-molybdenum-phosphorus glasses

Glass No.	Mole fractions V_2O_5	MoO_3	P_2O_5	CaO	Volume resistivity (ohm-cm) × 10^9
1	0.135	0.043	0.604	0.218	7
2	0.189	0.040	0.566	0.205	1

vanadium-molybdenum-iron-phosphorus glass. This glass was also of good quality as a thin film.

Molybdenum-iron-boron glasses.—Table VIII lists the compositions of two molybdenum-iron-boron glasses. The resistivities of these glasses could not be measured because the melts crystallized on cooling to temperatures at which the viscosities of the glasses would be suitable for bubble blowing.

Molybdenum-tungsten-iron-phosphorus glasses.—Table IX lists the mole fractions and resistivities of five molybdenum-tungsten-iron-phosphorus glasses. The resistivity of glass No. 3 remained the same after 24 hr at 400°C in a nitrogen atmosphere.

No significant resistivity relationships could be determined, primarily because of the presence of three transition elements and also because of wide differences in the compositions of these glasses. The resistivities of glasses No. 1 and 2 were the same even though the compositions differed appreciably; the CaO content was reduced and the MoO_3, Fe_3O_4, and WO_3 contents were doubled for glass No. 2. Glasses No. 3 and 5 had almost the same composition and resistivity. Glass No. 4 had almost the same resistivity as Nos. 3 and 5; however, it had less CaO, WO_3, and Fe_3O_4, no BaO, and much more MgO. Apparently the lower basicity of No. 4, a result of the increase in MgO, compensated for the lower concentration of WO_3 and Fe_3O_4 to provide almost the same resistivity.

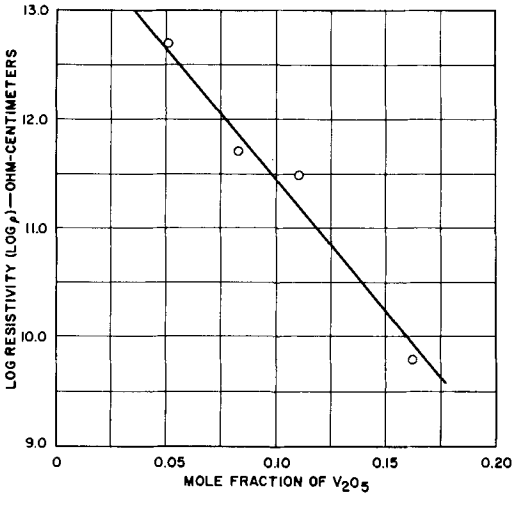

Fig. 3. Resistivity of vanadium-phosphorus glass as a function of the mole fraction of V_2O_5.

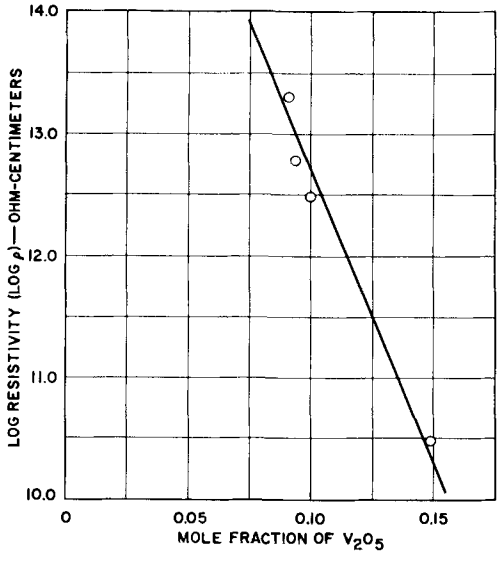

Fig. 4. Resistivity as a function of the mole fraction of V_2O_5 for vanadium-iron-phosphorus glasses.

Table VII. Composition and resistivity of a vanadium-molybdenum-iron-phosphorus glass

Mole fractions						Volume resistivity
V_2O_5	MoO_3	Fe_3O_4	P_2O_5	CaO	BaO	(ohm-cm)
0.195	0.412	0.026	0.167	0.084	0.116	10^{10}

Table VIII. Compositions of molybdenum-boron glasses

Glass No.	Mole fractions						Volume resistivity (ohm-cm)
	MoO_3	Fe_3O_4	B_2O_3	SiO_2	CaO	MgO	
1	0.115	0.036	0.533	0.069	0.206	0.041	Devitrified in melt
2	0.119	0.029	0.533		0.214	0.085	Devitrified in melt

Table IX. Compositions and resistivities of molybdenum-tungsten-iron-phosphorus glasses

Glass No.	Mole fractions							Volume resistivity (ohm-cm) $\times 10^{11}$
	MoO_3	WO_3	Fe_3O_4	P_2O_5	CaO	BaO	MgO	
1	0.060	0.037	0.030	0.612	0.217		0.043	100
2	0.114	0.070	0.053	0.576	0.146		0.041	100
3	0.334	0.124	0.041	0.339	0.068	0.094		10
4	0.339	0.105	0.021	0.343	0.020		0.172	9
5	0.347	0.129	0.043	0.326	0.065	0.090		20

Titanium-iron-boron glasses.—Table X, lists the compositions of two titanium-iron-boron glasses. Because of inhomogeneities, neither of these glasses was satisfactory for bubble formation. A white grainy structure resulted when composition No. 1 was heated in an attempt to dissolve the TiO_2. At this temperature copious evaporation of P_2O_5 also occurred. Neither of these compositions showed glass formation.

Manganese-iron-phosphorus glass.—Table XI shows the composition of the manganese-iron-phosphorus glass. This glass was grain and crystal-free above 1100°C; however, its viscosity was too low for bubble blowing. Below 1100°C crystals formed in the glass melt.

Conclusion

Most of the compositions described in this paper yielded good-quality glasses in the melt. The principles of glass formation discussed appear to be valid for these glass compositions. In those glasses with 10^{12} ohm-cm resistivity or less electronic conductivity was shown to predominate for the quantity of current passed. Ionic migration, although not completely eliminated, did not contribute appreciably to the conduction in the glasses of 10^{12} ohm-cm resistivity or less.

Acknowledgments

The author wishes to express his appreciation to William Kramer for helpful discussions and to Ronald Straley for experimental assistance.

Table X. Compositions of titanium-iron-boron glasses

Glass No.	Mole fraction							Volume resistivity (ohm-cm)
	TiO_2	Fe_3O_4	B_2O_3	SiO_2	P_2O_5	MgO	CaO	
1	0.094	0.008	0.120		0.528	0.042	0.208	Unsuitable for bubble formation
2	0.098	0.008	0.561	0.073		0.043	0.217	

Table XI. Composition of manganese-iron-phosphorus glass

Mole fractions							Volume resistivity (ohm-cm)
MnO_2	MnO	Fe_3O_4	P_2O_5	B_2O_3	CaO	MgO	
0.056	0.033	0.036	0.457	0.174	0.203	0.041	Devitrified in the melt

Manuscript received March 30, 1965; revised manuscript received June 25, 1965.

Any discussion of this paper will appear in a Discussion Section to be published in the June 1966 JOURNAL.

REFERENCES

1. E. Warburg and F. Tegetmeier, *Ann. Physik Chem.*, **35**, 455 (1888).
2. G. W. Morey, "The Properties of Glass," 2nd ed., pp. 465-474, Rheinhold Publishing Co., New York (1954).
3. E. P. Denton, *et al.*, *Nature*, **173**, 1030 (1954).
4. P. L. Baynton, H. Rawson, and J. E. Stanworth, *ibid.*, **178**, 910 (1956).
5. P. L. Baynton, H. Rawson, and J. E. Stanworth, *This Journal*, **104**, 237 (1957).
6. O. V. Mazurin, *et al.*, *Sov. Phys., Tech. Phys. J.*, **2**, 2511 (1957).
7. P. W. McMillan, "The Preparation and Properties of Glasses Containing Major Proportions of Certain Transition Metal Oxides," in "Advances in Glass Technology," VI International Conference of Glass, New York, Plenum Press, 333-47 (1962).
8. J. D. MacKenzie, "Semiconducting Glasses: Principle of Preparation and Typical Examples," in "Advances in Glass Technology," Part 2, VI International Conference on Glass, New York, Plenum Press, 3 (1963).
9. H. J. L. Trap and J. M. Stevels, "New Glasses Showing Electronic Conductivity," in "Advances in Glass Technology," Part 2, VI International Conference on Glass, New York, Plenum Press, 70-78 (1963).
10. E. J. W. Verwey, *et al.*, *Phillips Research Repts.*, **5**, 173 (1950).
11. W. A. Weyl and E. C. Marboe, "The Constitution of Glasses: A Dynamic Interpretation," 306, Interscience Publishers, New York (1962).
12. K. H. Sun, *J. Am. Ceram. Soc.*, **30**, 277 (1947).
13. J. M. Stevels, *Glass Ind.*, **35**, (2), 69 (1954).
14. C. W. Stillwell, "Crystal Chemistry," 1st ed., p. 275, McGraw-Hill Book Co., Inc., New York (1938).

Segregation of Silicon in Gallium Phosphide

M. Rubenstein

Research Laboratories, Westinghouse Electric Corporation, Pittsburgh, Pennsylvania

ABSTRACT

Gallium phosphide was prepared using a horizontal refining technique. The liquid zone was maintained close to the stoichiometric composition. An ingot, doped with silicon, was zone refined. From electrical, optical transmission, and spectrochemical measurements, it is demonstrated that silicon (at concentrations in the range of 10^{18} at./cc) is a donor impurity with an activation energy of 0.06 ev, that silicon substitutes for gallium, and that the segregation coefficient for silicon in GaP is 0.6.

Gallium phosphide (GaP) has been prepared in a number of laboratories from a stoichiometric or nearly stoichiometric melt (1, 2). In this paper such an ingot was prepared using the horizontal zone melting apparatus sketched in Fig. 1. In this apparatus a molten zone is passed through an ingot. If there is an impurity in the GaP, this impurity will tend to concentrate either at the beginning or end of the ingot, depending on whether the segregation coefficient is greater than or less than unity, respectively (3). Since zone refining has produced no great purification in the case of GaP one is led to believe that most impurities which are ordinarily encountered in the preparation of GaP do not have segregation coefficients much less or much greater than unity. In this paper an ingot of GaP, which will be called R-53, was heavily doped with silicon and then the ingot was zone refined. This ingot was then analyzed so that various conclusions could be drawn concerning silicon in GaP.

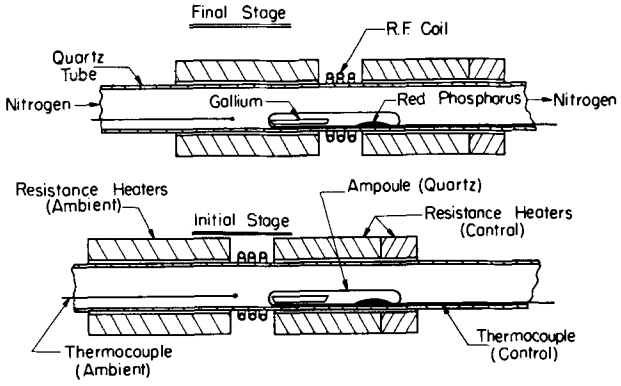

Fig. 1. Schematic view of the furnaces used in the preparation of GaP ingot R-53.

Experimental

Gallium phosphide ingot R-53 was prepared in the following manner. A quartz ampule was sealed at a pressure of 10^{-6}-10^{-5} Torr. Contained in this ampule were weighed amounts of gallium in a boron nitride (BN) boat and phosphorus. The weight of red phosphorus was 10% in excess of the amount necessary to convert all the gallium to GaP plus the amount of phosphorus necessary to maintain the pressure of 16 atm in the ampule.

This ampule was then placed in the furnaces as indicated in Fig. 1 (initial stage). The two resistance heaters determined the phosphorus pressure (the temperature at the right end of the ampule was maintained as the lowest in the ampule). The heating of the gallium and GaP (when it formed) was accomplished with a 10 kw 4 megacycle radio frequency (r-f) generator. The ampule and the boat containing the gallium rested on quartz cradles to prevent the ampule walls from becoming too hot. Nitrogen gas was slowly passed down the outer quartz tube in order to cool the ampule walls. The use of the cradles and the nitrogen was to allow the walls of the ampule to remain cool enough to maintain the pressure of 16 atm while a liquid zone was maintained at about 1500°C.

The phosphorus used in preparing this ingot was purified by aqueous acid treatments, by steam distillations, and by vacuum distillations. The analysis indicating the purity of the phosphorus is shown in Table I.

Table I. Spectrochemical analyses

	Mg	Fe	Al	Cu	Ca	Na	C	B	Si
Phosphorus used in R-53	0.5	ND < 3	ND < 6	ND < 0.5	ND < 0.8	—	98	ND < 14	12
Ga used in R-53									
before degassing	1	ND < 1	ND < 3	ND < 0.3	ND < 2	—	ND < 28	ND < 30	ND < 5
after degassing	2	ND < 1	ND < 3	3	ND < 2	—	ND < 28	ND < 30	ND < 5
GaP section 1	P < 4	P < 9	P < 19(14)	ND < 2	5	—	84	ND < 28	47
section 2	P < 4	P < 9	P < 19(15)	ND < 2	P < 5	ND < 20	76	306	29
section 3	P < 4	ND < 9	ND < 19	ND < 2	P < 5	P < 20	125	52	57
section 4	P < 4	P < 9	P < 19	P < 2	P < 5	P < 20	67	38	129
section 5	P < 4	P < 9	P < 19	2	P < 5	P < 20	285	77	410
section 6	P < 4	P < 9	P < 19	P < 2	P < 5	—	100	92	1,200
section 7	P < 4	P < 5	P < 19	P < 2	6	P < 20	76	120	2,250
section 8*	7	306	ND < 19	46	—	—	—	875	19,200

Detectable limits of other elements checked but not detected:

	Pb	Mn	Sn	Ag	Ba	Se	Na	Li	K	Zn	Cd	Hg	Cr	Sb	Be	Ge
P	1.5	1	1	0.5	2	20	13	9	8	1.5	0.5	15	3	5	—	—
Ga	5	2	1	0.1	1	2	10	20	5	1	0.5	1	1	5	—	—
GaP	5	2	8	2	2	5	20	15	26	5	1	15	10	20	11	15

P indicates that the element was detected but at or just below the limit of detection (beyond the standard curves). Quantities in parentheses are estimations. ND indicates that the element was not detected. All values above are expressed in atomic parts per million.

* Section 8 was a slice taken beyond the slice of section 7. Section 8 was at a distance of 5.7; section 7 was at a distance of 5.2 (see Fig. 6).

Table II. Spectrochemical analysis of boron nitride (expressed in atomic ppm)

	Ca	Si	Al	Fe	Mg
Untreated	6×10^3-6×10^4	2×10^2-2×10^3	60-600	30-300	30-300
Treated	4×10^1-4×10^2	2×10^2-2×10^3	60-600	30-300	3-30

The gallium used was Alcoa 99.9999% material. The analysis for the gallium used is presented in Table I.

In preparing the reactants for this experiment, the gallium was degassed at 800°C for 3 hr at a pumping pressure of about 10^{-5} Torr. The gallium was contained in a quartz boat during this operation. Table I indicates that the silicon concentration in the gallium after degassing was less than 5 ppm (this value was due to improper sampling). The gallium used to prepare the GaP did contain an appreciable amount of silicon (as a two-phase sample). The degassing operation itself incorporated silicon in the gallium by the actual reduction of the quartz (4). However, this silicon was not dispersed throughout the gallium, but was concentrated over a small area on the surface of the gallium. Therefore, using "normal sampling techniques" on the gallium (taking chips from a few sections of the ingot) did not show the large amount of silicon in the gallium ingot. The silicon concentration in the gallium as indicated in Table I is not the real silicon concentration, but the concentration of silicon as indicated using normal sampling techniques.

The boron nitride (BN) boat was machined from a rod and extensively extracted with methanol to remove B_2O_3 and any other impurities which would extract with the methanol treatment. Table II contains an analysis of the BN before and after the treatment with methanol.

Weight losses of 6-7% during the methanol extraction were usual. Almost all of this weight loss was due to the extraction of oxides. B_2O_3 and CaO are both extracted by methanol.

In preparing GaP ingot R-53, a 4 megacycle r-f generator supplied power through a 3 turn work coil. Several mixing zones were passed through the contents of the BN boat at a speed of 1.25 mm/min to react the gallium and phosphorus. Ten refining zones were passed through the GaP at a speed of 0.13 mm/min. The phosphorus pressure during the refining passes was 16 atm. The length of the zone was approximately 2.5 cm. The dimensions of the ingot were $15 \times 1.4 \times 1.2$ cm.

All measurements were made on slices cut perpendicular to the long axis of the ingot. The slices were taken at positions as indicated in Fig. 6.

Spectrochemical analyses.—The impurities in this ingot (see Table I) are primarily silicon, boron, and carbon. One could assume that the iron, magnesium, aluminum, and calcium impurities came from the BN boat (see Table II). The copper impurity could come primarily from the degassed gallium. The sodium impurity could come from any of the sources since sodium determinations were not made on all samples concerned. Since the concentration of silicon is very high in section 8 (see footnote in Table I), it is possible that in this portion of the ingot there are separate silicon and GaP phases. This could account for the unusually high concentrations of magnesium, iron, copper, and boron in slice 8.

Table III. Electrical measurements for R-53

Section	Distance along ingot, x	Temp, °C	Resistivity, ohm-cm	R_H, cm³/coulomb	*Ne*, net electrons/cm³
1	0.8	630	0.383	−8.4	7.45×10^{17}
2	1.2	560	0.524	−14.5	4.3×10^{17}
3	1.8	597	0.292	−5.6	1.1×10^{18}
4	2.6	626	0.084	−2.0	3.1×10^{18}
5	4.0	608	0.030	−0.55	1.1×10^{19}
6	4.8	588	0.035	−0.63	9.9×10^{18}
7	5.2	586	0.037	−0.60	1.04×10^{19}

The carbon contamination certainly has phosphorus as its source, and the boron has the boat as its source. The primary source of the silicon contamination has been discussed above. There is no evidence of segregation caused by zone refining when one considers the concentrations of carbon or boron from section 1 through section 7 (Table I). The concentrations of silicon definitely show a trend of increasing concentration from the beginning to the end of this ingot.

Electrical measurements.—Electrical measurements were made on bridge-cut polycrystalline samples. These measurements were made at temperatures around 600°C because of the nonohmic behavior of polycrystalline GaP at lower temperatures. The samples were approximately 3.5 mm long × 2 mm wide × 0.5 mm thick. Table III contains the compilation of electrical data obtained from the first seven sections of ingot R-53.

A single crystal was cut out of a slice taken from section 3 of ingot R-53. From a bridge-cut sample of this crystal, electrical measurements were made from 700° to −195°C. Figure 2 shows a plot of Hall coefficient as a function of temperature; Fig. 3 contains plots of resistivity and net carrier (electrons) concentrations as functions of temperature. The net carrier concentrations in Table III were calculated $N_e = (e R_H)^{-1}$. As may be seen in Fig. 2, the values of the net electron concentrations given in Table III should be very nearly equal to the exhaustion values. A preliminary analysis of the Hall data indicates that the activation energy of silicon in GaP at these concentrations is about 0.06 ev.

Optical measurements.—Optical transmission measurements were made on polished polycrystalline slices which were about 0.9 mm thick. A Cary Spectrophotometer, model 14 was used to obtain spectra from the band edge of GaP to 2.5μ. Spectra of the first five sections appear in Fig. 4. Sections 6 and 7 did not show any transmission over this wavelength range. The slice from section 2 seems anomalous in that it does not follow the trend set by the series 1, 3, 4, and 5. Although the reason for this is not obvious, the high concentration of boron in this slice (see Table I) may be responsible. The resistivity and Hall coefficient of section 2

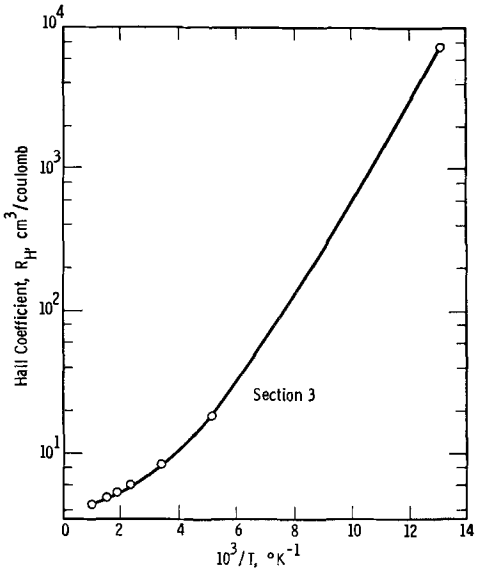

Fig. 2. Hall coefficient plotted as a function of temperature for section 3 of GaP ingot R-53.

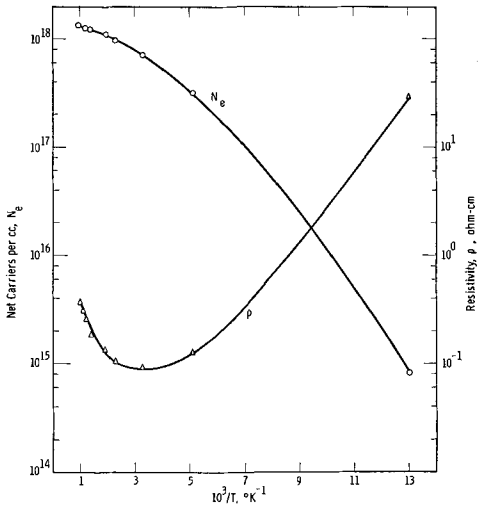

Fig. 3. Net carrier concentration (○) and resistivity (△) plotted as a function of temperature for section 3 of GaP ingot R-53.

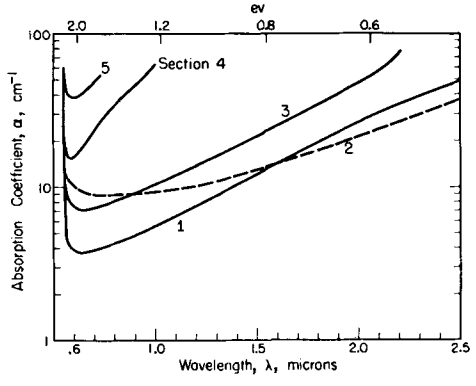

Fig. 4. Optical absorption spectra of polished slices of GaP ingot R-53, sections 1-5 (slice thickness was 0.9 mm).

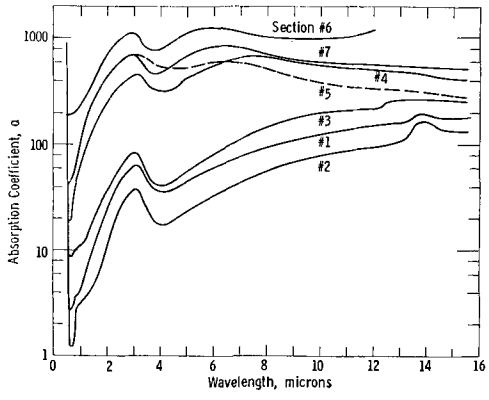

Fig. 5. Optical absorption spectra of polished slices of GaP ingot R-53, sections 1-7 (slice thickness was 0.14 mm).

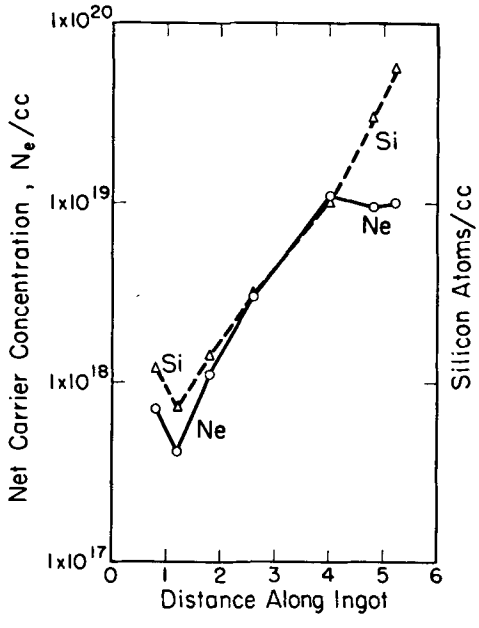

Fig. 6. Net carrier concentration (○) and silicon concentration (△) plotted as a function of distance along GaP ingot R-53.

also does not follow the trend that the other sections do (see Table III).

The slices which were used in Fig. 4 (0.9 mm thick), were lapped and polished to a thickness of about 0.14 mm so that transmission spectra could be obtained for the entire set of 7 sections over a range of wavelengths from the band edge to 15 μ's. A Cary Model 14, and a Perkin-Elmer Model 21 Spectrophotometer were used to obtain the spectra of these slices from the seven sections of this GaP ingot (see Fig. 5). There does not appear to be an inconsistency in section 2. This section has a lower silicon concentration than section 1 according to optical, electrical, and spectrochemical measurements. The spectrum for section 5 seems to be somewhat inconsistent with the other spectra at wavelengths greater than 3μ. This may be due to the nonparallel faces of this slice. On polishing this sample, it was noted that the polished faces were obviously nonparallel.

The absorption band between 1 and 4 μ's was noted by Spitzer *et al.* (5), and the probable interpretation of this band was discussed more recently in ref. (6) and (7). Allen and Hodby suggest that this absorption is due to a transition from a shallow donor impurity to an upper conduction band which has been split off by the lack of a center of symmetry in the crystal (6). The absorption at wavelengths beyond 4 μ's increases with wavelength as λ^n with $n \sim 2$ and is typical of the free carrier absorption found in many semiconductors (6).

Segregation coefficient.—This ingot, which was zone refined with 10 passes, shows the effects of a segregation coefficient less than unity (see Table I, Table III, and Fig. 6). The segregation coefficient can be calculated (3) assuming that the ultimate number of refining passes have been made. In the refining of this ingot, the length of the molten zone is about 2.5 cm, the length of the ingot is 15 cm. Using the equations in ref. (3), one can calculate the segregation coefficient

$$k = \frac{\text{concentration of an impurity in solid GaP}}{\text{concentration of an impurity in molten GaP}} = 0.6$$

Since the ultimate number of zones may not have been passed through this ingot, the true value of k may be somewhat smaller than this value.

Conclusions

Gallium phosphide ingot R-53 has a silicon concentration which varies from about 30 ppm to more than 19,000 ppm from one end to the other end of the ingot. If one were to plot the concentration of silicon as a function of the distance along the ingot and the net carrier concentration as a function of the distance along the ingot, the two curves would seem similar over a range (see Fig. 6). At concentrations greater than 1×10^{19} (400 ppm) the net carrier concentration does not continue to rise as the silicon concentration rises with increasing distance along the ingot. Also the optical absorption curves for sections 5 and 7 are quite similar and the spectrum for section 6, a little greater (see Fig. 5). The trend of increasing optical

absorption for sections 2, 1, 3, 4, and 5 is consistent with the electrical measurements (Table III) and the spectrochemical measurements for silicon (Table I). The beginning of this ingot and also the end of this ingot experienced a different temperature distribution from the main body of the ingot, since the r-f coupling was quite different at these two ends than in the main body. This may be the reason for section 2 having a lower silicon concentration than sections 1 and 3.

The apparent "saturation" of the electrical measurements and to a lesser degree of the optical measurements while the silicon concentration rises (beyond 10^{19} Si at./cc GaP) can be explained if the silicon at these concentrations, as determined by spectrochemical analyses, did not enter the GaP lattice but existed in the slice in grain boundaries or inclusions (as a second phase). The divergence of these two plots (Fig. 6) at silicon concentrations greater than 1×10^{19} could also be explained, if the silicon entered the GaP lattice in gallium and phosphorus sites nonpreferentially. The former explanation seems more reasonable because the absorption for section 6 is greater than the absorption for section 5. The absorption curve for section 7 may be somewhat different than the trend of sections because it is an end section which experiences a different temperature distribution as indicated above. Of course, it is possible that both explanations are partially valid. That is, some of the silicon, at concentrations greater than 10^{19} at./cc, appears as a second phase and some enters the lattice nonpreferentially.

At the lower silicon concentrations, one might expect some difference between the silicon concentrations and the net carrier concentrations because there are other impurities in this material which could be electrically active. If there are about 3×10^{17} acceptors throughout this ingot, a plot of donor (silicon) concentrations measured electrically *vs.* distance along the ingot, and the plot of silicon measured spectrochemically *vs.* distance along the ingot would superimpose for sections 1 through 5.

Since the silicon concentration is the only known parameter that systematically changes in this ingot, since the Hall coefficients indicate that the majority carrier is the electron, and since the silicon concentration changes at the same rate as the net carrier concentration up to 10^{19} carriers per cc, one may conclude that silicon is not only a donor in GaP but that for every silicon atom incorporated into the GaP lattice, one carrier (an electron) is incorporated into the material. Silicon has an activation energy in GaP of 0.06 ev as calculated from the Hall measurements at various temperatures (as plotted in Fig. 2).

Considering only the geometry involved, one might expect the silicon to enter the lattice substitutionally for gallium. The tetrahedral covalent radius of silicon is 7% smaller and 6% larger than that of gallium and phosphorus, respectively. A substitution of silicon for gallium in the GaP lattice, when only considering covalent radii, is consistent with the conclusions derived from the electrical measurements.

Acknowledgment

The author would like to thank Mr. David Dickey who performed the electrical measurements and calculations based on these measurements used in this paper. He would also like to thank Mr. Joseph Rudolph, Mrs. Mary Louise Theodore, and Mr. John Penkrot for the spectrochemical, wet chemical, and carbon analyses, respectively. Discussions with Mr. Dickey and Dr. Hung-Chi Chang were valuable in the writing of this paper.

Manuscript received Nov. 23, 1964; revised manuscript received June 9, 1965. Much of the material in this paper was presented at the Boston Meeting, Sept. 16-20, 1962.

Any discussion of this paper will appear in a Discussion Section to be published in the June 1966 JOURNAL.

REFERENCES

1. O. G. Folberth, *J. Phys. Chem. Solids*, **7**, 295 (1958).
2. C. J. Frosch, M. Gershenzon, and D. F. Gibbs, Paper presented at the Chicago Meeting of the Society May 1-5, 1960, Abstract 97.
3. W. G. Pfann, *J. Metals*, 747, July 1, 1952.
4. C. N. Cochran and L. M. Foster, *This Journal*, **109**, 144 (1962).
5. W. G. Spitzer, M. Gershenzon, C. J. Frosch, and D. F. Gibbs, *J. Phys. Chem. Solids*, **11**, 339 (1959).
6. J. W. Allen and J. W. Hodby, *Proc. Phys. Soc.*, **82**, 315 (1963).
7. R. Zollen and W. Paul, *Phys. Rev.*, **134**, A1628 (1964).

Structural Evaluation of Silicon Oxide Films

W. A. Pliskin and H. S. Lehman

IBM Systems Development Division, Poughkeepsie, New York

ABSTRACT

Techniques for physical and chemical evaluation of silicon oxide films formed by a wide variety of techniques have been developed. It has been established that by the use of infrared absorption spectroscopy, preferential etching procedures, precise optical measurements of thickness, density, and refractive indices, and carefully chosen environmental tests, differences in the oxide films can be determined. Techniques of oxidation studied were: thermal (oxygen and steam), evaporated, pyrolytic, lead catalyzed, sputtered and anodic. In many cases, improvement of oxide film properties can be achieved by simple thermal treatment of the original films.

Silicon dioxide films are presently used for purposes of surface passivation and diffusion masking during fabrication processes of planar silicon devices. In general, these films are obtained by thermal oxidation in oxygen or steam at elevated temperatures. Techniques other than thermal oxidation are of interest in order to (*i*) minimize problems of junction movement and junction degradation (1), (*ii*) avoid thickness limitations, and (*iii*) to obtain high quality insulating films on nonsilicon surfaces.

The general procedure utilized in this study was to compare the physical and chemical properties of the oxide films prepared by low temperature techniques to those of films grown thermally. Films were evaluated for structural differences, stoichiometry, density, porosity, strain, refractive index, and passivation efficiency. Techniques for evaluating the above-mentioned parameters included the use of infrared absorption spectroscopy, preferential etch procedures (2), precise optical measurements of density, refractive index and thickness (3), and passivation efficiency. By the careful application of these techniques to the oxide films studied, small differences in the films can be easily determined.

The low temperature oxidation techniques which have been examined and evaluated include: evaporation, pyrolytic decomposition (4, 5), lead catalyzed growth (6), anodization (7), and reactive sputtering. Valletta, Perri, and Riseman utilized the methods described herein for the detailed evaluation of silicon oxide films prepared by reactive sputtering (8). Consequently, only brief mention will be given to reactively sputtered films.

Experimental Techniques

Infrared spectroscopy.—There are four ways in which infrared spectroscopy is useful for the evaluation of silicon oxides: (*i*) the half-widths and positions of the Si-O stretching bands near 1090 and 805 cm^{-1} are strongly influenced by the bonding character, stoichiometry, density, and porosity of the films; (*ii*) the intensity of the absorption bands near 3650 cm^{-1} (2.74μ) and 3400 cm^{-1} (2.94μ) due to hydrogen bonded hydroxyl groups and adsorbed water are indicative of the quantity of surface hydroxyl groups and porosity of the oxides; (*iii*) impurities other than hydroxyl groups or water can be detected by their characteristic absorption bands; and (*iv*) approximate film thicknesses can be determined by interference fringes in the spectrum.

All infrared spectra were taken on double beam Perkin Elmer Spectrophotometers; Model 221G was used for the earlier work and Model 521 for the later work. Occasionally, quick references were made using a Model 337. In all cases, a bare silicon wafer of the same thickness and from the same crystal as the sample was placed in the reference beam to eliminate lattice absorption bands.

Selective etch techniques.—A selective etch solution consisting of 15 parts hydrofluoric acid (49%), 10 parts nitric acid (70%), and 300 parts water has been developed which is extremely sensitive to differences in density, stoichiometry, bond strain, and impurities in the silicon dioxide films. This etch has been named "P etch" (2). As examples of the sensitivity of this etch to porosity, the etch rate of pyrolytic films formed at 675°C is 13Å/sec; whereas, the etch rate of thermally (1000°C) grown silicon dioxide is only 2Å/sec at 25°C. Films of electron-gun evaporated silicon dioxide, which are less dense than the pyrolytic films and exhibit more bond straining, etched at rates from 20 to 70Å/sec. Densification of the less dense films lowers the etch rate to that of thermally grown oxide. The etch rate is also sensitive to changes in oxygen content of the film, being slower for oxygen deficient films, as in SiO for which the etch rate is negligible.

Optical techniques.—The refractive indices and film thicknesses were measured by use of Vamfo (3), a specially constructed interference microscope. The refractive index of a film is influenced by its density and its stoichiometry. The greater the density, the greater is the refractive index, but the refractive index is also increased by oxygen deficiency. On the other hand, oxygen deficiency will decrease the etch rate of silicon dioxide films and shift the 9.2μ band to longer wavelengths.

Passivation efficiency.—Passivation efficiency was determined by exposing diodes passivated with oxide layers to high temperature steam and monitoring junction degradation due to moisture penetration.

Thus, by a combination of these techniques, the oxide films can be characterized as to density, composition, porosity, and structure.

Results

Densification of pyrolytic oxides.—Pyrolytic films of pure silicon dioxide can be obtained from the thermal decomposition of tetraethoxysilane at deposition temperatures between 625° and 900°C. These somewhat porous films can be densified by short term exposure to temperatures above 800°C. Densification can be achieved at 800°C in steam ambient with a 15 min heat-treatment. Densification of films in dry gas ambients occurs somewhat more slowly and not quite as effectively as with steam. The densified pyrolytic oxide films were compared to thermally grown oxide films in order to determine the extent of densification.

Infrared (Si-O *stretching band*).—The positions of the Si-O vibrational bands in the infrared spectra of thermally grown (steam followed by dry oxygen at 975°C) silicon dioxide films (~1μ thick) are 1093 cm^{-1} (9.15μ) and 805 cm^{-1} (12.42μ); whereas, nondensified pyrolytic oxide films have bands at about 1080-1085 cm^{-1} and at 813 cm^{-1}. The band positions in the spectra of pyrolytic oxide films are a function of porosity and strain. Films with greater porosity and bond strain show even greater shifts than those previously quoted, as shown by their increased reactivity (9). In comparing an oxide film with thermal oxides, comparable thicknesses were used since both the half-widths and band positions of thermal oxides vary slightly with thickness. The bands in the spectra of the thermally grown silicon dioxide films are sharper than those of the nondensified pyrolytic films. The infrared spectra of pyrolytic oxide films become essentially indistinguishable from those of thermally grown oxide films when properly densified. This is shown in Fig. 1 where Spectrum A is that of a tube furnace (T.F.) pyrolytic SiO_2 film formed at 675°C and Spectrum B is the same film after having been densified in steam at 975°C for 15 min. The densified film is indistinguishable from thermally oxidized films of the same thickness. The spectra show the shifts and sharpening of the absorption bands. The 1082 cm^{-1} band with a half-width of 92 cm^{-1} is shifted to 1093 cm^{-1} and the half-width is decreased to 88 cm^{-1} while the film thickness decreased from 1.13 to 1.09μ.

Infrared spectra of various densified pyrolytic oxides show that steam is more effective than dry ambients in densifying pyrolytic oxide films. The band positions of a pyrolytic oxide, after treatment with helium at 850°C for 5 min, shifted from 1081 and 812 cm^{-1} to 1086 and 810 cm^{-1}; whereas, 5 min of steam

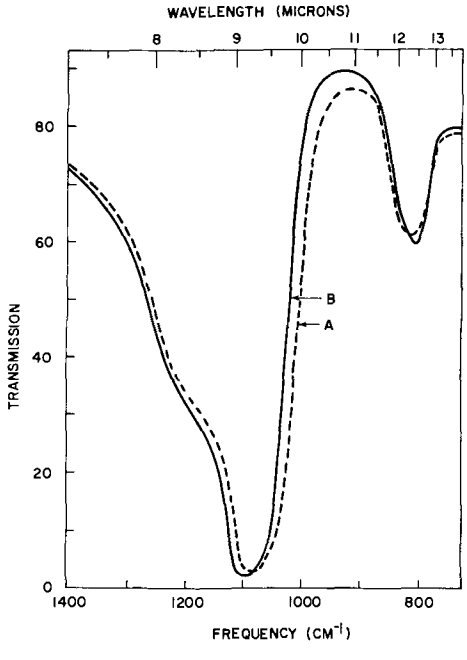

Fig. 1. Steam densification of pyrolytic SiO_2: A, T.F. pyrolytic SiO_2 formed at 675°C, 1.13μ, 1082 cm^{-1}, 92 cm^{-1}; B, densified by exposure to steam for 15 min at 975°C, 1.09μ, 1093 cm^{-1}, 88 cm^{-1}.

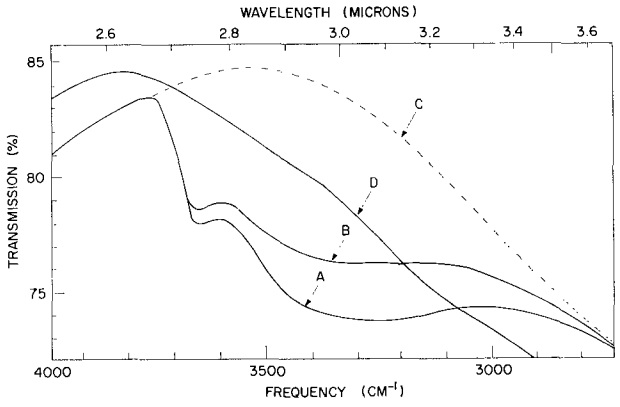

Fig. 2. Spectra showing removal of adsorbed water from a porous pyrolytic oxide: A, spectrum in air (47% R.H.); B, after flushing in N_2 for 20 min; C, estimated background; D, after exposure to argon for 15 min at 800°C (film thickness 1.38μ).

densification at 850°C was sufficient to shift the bands to 1092 and 805 cm^{-1}. In addition, after the steam densification, the vibrational bands were sharper than those after helium densification.

The absorption band at 450-460 cm^{-1} due to the deformation vibration in SiO_2 is not covered in this paper since it behaves in the same manner as the 1080-1090 cm^{-1} band; with increased porosity or strain, the frequency is decreased and the half-width increased.

Infrared (O-H stretching band).—The effect of moisture on the infrared spectrum of a nondensified pyrolytic oxide film is shown in Fig. 2. In Spectrum A, the sample was exposed to air at 47% relative humidity. The amount of water in the sample is indicated by the strength of the broad absorption band in the 3μ region. Some of this water is easily removed as shown by Spectrum B which was obtained by flushing the sample with dry nitrogen in the infrared spectrophotometer for 20 min. By comparison with the background spectrum, it can be seen that this treatment was sufficient to remove about 30% of the adsorbed water. Similar studies on another sample have shown that flushing in dry nitrogen for 4 min removed about 21-22% of the adsorbed water, 10 min flushing removed about 27%, and 160 min removed only 40%. On re-exposure to air, almost all the water was readsorbed within 5 min. After densification by exposure to argon for 15 min at 800°C, Spectrum D was obtained. It shows practically no absorption due to surface hydroxyl groups or adsorbed water. Since similar results were obtained with the other densification procedures, it is concluded that the heat-treatment is sufficient for both removing the surface hydroxyl groups present on the nondensified pyrolytic oxide and densifying the oxide structure such that new moisture is not readsorbed.

Thickness and refractive index.—Figure 2 also shows the effect of shrinkage on the interference pattern of the infrared spectrum by the shift in the maximum from 2.85μ in Spectrum C to 2.61μ in Spectrum D. Considering the variation of refractive index with wavelength and densification, this corresponds to a shrinkage of 9.1%. Before and after densification the thicknesses of many samples were measured with Vamfo, which is a more accurate technique for thickness measurement. The film shrinkage is a measure of the densification. Densifications were also determined based on the refractive index change with the assumption of a linear relationship between density and refractive index. (The relationship is given by $\rho = -4.784 + 4.785\mu$, where ρ is the density in g/cc and μ is the refractive index at 5460Å. It is based on the known densities and refractive indices of various forms of SiO_2.) In some cases where the samples showed appreciable water content, corrections were made for the relative water content. On this basis, good agreement was obtained by the two techniques as shown in Table I from which it is concluded that steam is more effective for densification. This agrees with the infrared results.

Etch rate.—The P-etch rate of nondensified pyrolytic silicon dioxide is much greater than that of thermally grown silicon dioxide or of densified pyrolytic oxides. The etch rate results shown in Table II again show that steam is more effective than dry ambient for densification.

Passivation efficiency.—The passivation characteristics of both densified and nondensified pyrolytic oxide films on silicon devices were determined. Boron

Table I. Densification produced by various treatments

Relative quan. ads. water	Densification treatment			Refrac. index		Density (g/cc)		% Densification	
	Ambient	Temp (°C)	Time (min)	Before dens.	After dens.	Before dens.	After dens.	By R. I.	By film shrinkage
High	Argon	800	15	1.45_0	1.45_5	2.15[b] (1.99)[a]	2.18	1.1[b] (9.2)[a]	9.0
Low	Steam	850	15	1.43_7	1.46_3	2.09	2.22	6.0	6.4
Med.	Nitrogen	975	5	1.44_4	1.45_6	2.12[b] (2.07)[a]	2.18	2.7[b] (5.2)[a]	6.3
Low	Steam	975	15	1.44_4	1.46_5	2.12	2.23	4.7	5.4

[a] Before densification, these samples contained a significant amount of water as shown by their infrared absorption spectra. The relative quantity of adsorbed water was considered in calculating their densities.
[b] The water content was not considered in determining these values.

Table II. Refractive indices and etch rates of various T. F. pyrolytic oxides

Deposition Temp, (°C)	Deposition Time (min)	Densification Ambient	Densification Temp (°C)	Densification Time (min)	Thickness (μ)	Refractive index (5460Å)	P etch Rate, A/sec	P etch Temp (°C)
675	75	—	—	—	0.78	1.44_7	13.2	25.1
675	120	Argon	800	15	1.42	1.45_2	2.9_1	25.1
675	120	Steam	800	15	1.27	1.46_0	2.1_7	25.1
675	120	Steam	975	15	1.09	1.46_5	2.0_3	25.1
835	10	—	—	—	1.56	1.45_3	6.7_5	26.0
~835	10	—	—	—	1.21	1.45_0	10.6_5	26.0
Thermal oxide					0.59	1.46_2	2.07	25.4

Table III. 400°C steam testing

	Passivation	No. of units tested	% Failure after 30 min
5500Å	Thermal SiO_2	96	44
5500Å	Thermal SiO_2 2.3μ pyrolytic SiO_2 no dens.	64	95
5500Å	Thermal SiO_2 2.3μ pyrolytic SiO_2 Densified 15 min. 975° Steam	70	25

Table IV. Relative increase of hydroxyl groups on various types of oxide by exposure to steam at 400°C

Oxide type	Thickness, μ	% Absorption at 2.74μ exposure time 30 Min	120 Min
975°C Steam	1.9	0.1%	0.3%
850°C Pyrolytic Den. 1 hr	2.6	0.1	0.3
850°C Pyrolytic Den. 15 min	2.7	0.1	0.3
850°C Pyrolytic No den.	2.6	0.9	1.5

diffused diodes were used in this experiment. The C_0 of these diodes was 2.5-4.0 x 10^{18} with X_j = 0.11 mils. It had been found that high temperature steam (400°C) exposure at atmospheric pressure causes degradation of the reverse characteristics of thermally oxidized diodes. A 2.3μ, 850°C, high quality, pyrolytic silicon dioxide film was deposited on top of a 0.5μ film of thermally grown silicon dioxide. The wafer was then cut in half with the oxide on one half of the wafer being densified at 975°C for 15 min in steam. Breakdown voltages and reverse currents of the diodes on both halves were measured before and after exposure to steam at 400°C. Results are summarized in Table III. Failures were defined as leakage currents in excess of 1μ amp at 10v reverse bias.

It is readily apparent that there is a great difference between the passivation efficiency of densified and nondensified pyrolytic oxides. Infrared spectroscopy was used to determine the effect of the high temperature (400°C) steam exposure on the oxides. Four oxidized wafers, a thermally grown silicon dioxide, a nondensified pyrolytic oxide, and two steam densified pyrolytic oxides, differing only in densification time, were exposed to steam at 400°C. The pyrolytic oxides were formed at 850°C. The only detectable difference in the oxides on steam exposure was the increase in the absorption of the 2.74μ band due to the formation of hydrogen bonded hydroxyl groups. The results, summarized in Table IV, show that the densified and thermally grown oxide pick up little moisture in comparison with the nondensified oxide. The passivation efficiency of the thermally grown oxide film is reduced by the presence of the nondensified pyrolytic film because it serves as a source of moisture. The moisture is then easily available and diffuses to the junction causing high device leakage currents.

SiO *evaporation.*—Before going into further details of other silicon dioxides, the oxides formed on the evaporation of SiO and SiO_2 will be discussed. The stoichiometry of evaporated silicon oxide films is a strong function of the evaporating parameters and can be followed by observation of the SiO stretching band frequency. The important parameters which determine the type of film formed are the temperature, the rate of evaporation, and the pressure in the evaporating system. Figure 3 shows the spectrum of the film obtained when SiO (Kemet) is evaporated at a fast rate and good vacuum. The rate of evaporation was 375Å/sec and the maximum pressure in the system was less than 1 x 10^{-4} mm of Hg. The transmission spectrum of this film shows one strong absorption band at 10μ

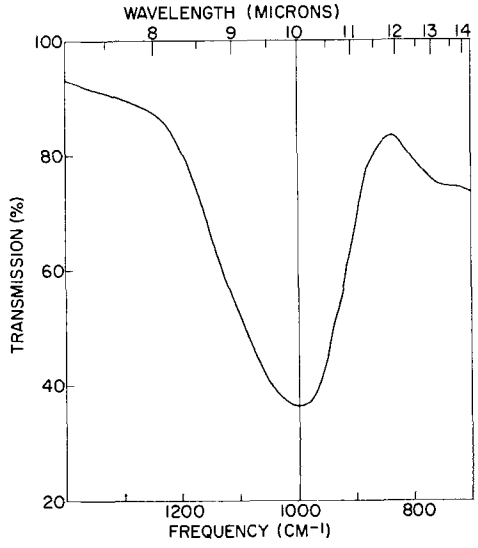

Fig. 3. SiO film formed by evaporation of SiO at a fast rate (375 Å/sec); pressure, <1 x 10^{-4} mm.

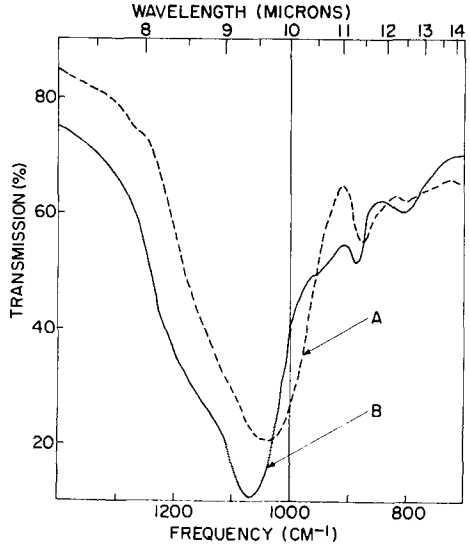

Fig. 4. Films formed by evaporation of SiO at a slow rate (<5 Å/sec) and pressures of: A, <2 x 10^{-4} mm Hg; B, 1 x 10^{-3} mm Hg.

and is the same as the spectrum of the SiO films obtained by Hass and Salzberg (10); whereas, the spectra of SiO_2 show a strong band at 9.2μ, a moderate band at 12.5μ, and a distinct shoulder in the 8-9μ region. At slow evaporating conditions, the spectra shown in Fig. 4 are obtained. With a maximum pressure of 2 x 10^{-4} mm Hg, a film whose spectrum is shown by A in Fig. 4 was obtained. The strongest absorption occurs at an intermediate position between that of SiO and SiO_2. The presence of SiO_2 is indicated by the weak absorption near 12.5μ. In addition, there is a moderate intensity band near 11.5μ which together with part of the strong absorption at 9.6μ is interpreted as being due to Si_2O_3, an oxide intermediate between SiO and SiO_2 (11). Thus, it is felt that this film consists of a mixture of SiO, SiO_2, and Si_2O_3. At slightly higher ambient pressures (1 x 10^{-3} mm Hg of air), a film was produced which is much richer in SiO_2 as shown by Spectrum B. This film consists mainly of SiO_2 with practically no SiO, but some Si_2O_3 is still present as shown by the 11.4μ band. This film was rather porous and in the shorter wavelength region of the infrared some hydrogen bonded Si-OH and adsorbed water was evident. In fact, the weak absorption near 930 cm^{-1} is due to an Si-OH bending vibration.

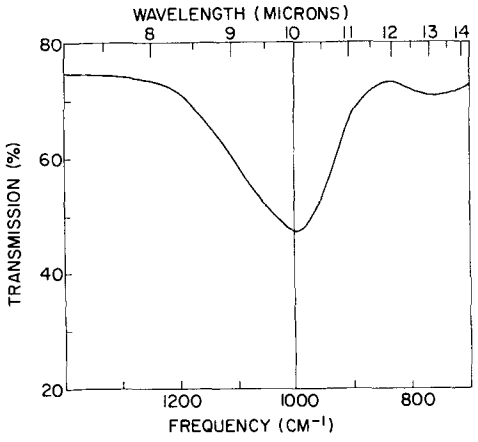

Fig. 5. SiO formed by the evaporation of SiO_2

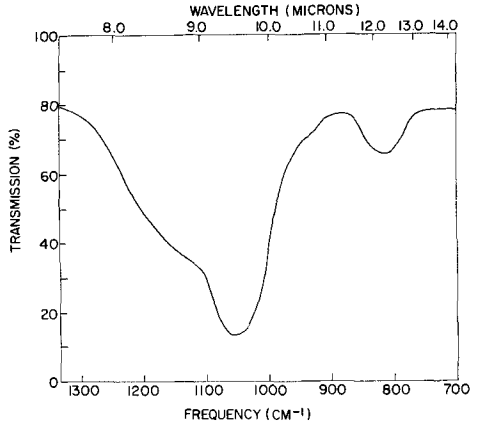

Fig. 6A. Infrared spectrum of electron-gun evaporated SiO_2

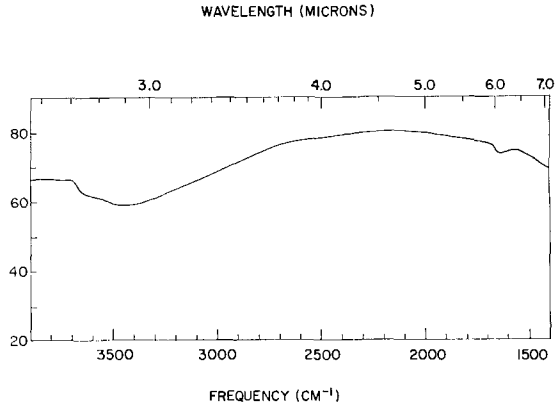

Fig. 6B. Infrared spectrum of electron-gun evaporated SiO_2

All of the previous evaporated films were deposited on unheated substrates. In the case of deposition on heated substrates, decomposition of the SiO to form Si and Si_2O_3 or SiO_2 can occur. The measured refractive index of one such film was found to be 2.02 at 5460Å, but its infrared spectrum indicated the presence of higher forms (intermediate and SiO_2) of oxide. The refractive index of SiO is 1.99_6 and, if the film consisted of pure SiO mixed with higher forms of oxide, the refractive index should be less than 1.99_6. The explanation is that most of the higher oxides in the film were not formed from the oxidation of the SiO with residual O_2 or H_2O in the vacuum system, but were formed by the thermal decomposition of SiO due to the 400°C substrate temperature resulting in a mixture of SiO, Si_2O_3, and Si. With the presence of a significant amount of silicon in the film, the refractive index of the mixed film can be greater than that of pure SiO.

It should be noted that no evidence has been obtained for oxygen deficiency in the pyrolytic SiO_2 films studied. After densification, the refractive indices of the pyrolytic films were comparable to those obtained for thermally grown oxides (1.463 compared to 1.462) and the spectra showed no evidence of Si_2O_3.

Thermal evaporation of SiO_2.—In the straight thermal evaporation of SiO_2 under good vacuum conditions, one obtains films of SiO rather than SiO_2 as shown in Fig. 5. This result is not surprising in view of the fact that the SiO_2-SiO equilibrium highly favors SiO at the elevated temperatures necessary for thermal evaporation of SiO_2 (12).

On the other hand, the films obtained from electron-gun evaporated SiO_2 were more nearly SiO_2 as shown in Fig. 6A. The absorption band position at 9.4μ and the broad half-width are indicative of a porous film. The porosity is also substantiated by the spectrum in the shorter wavelength regions as shown in Fig. 6B where the presence of hydrogen bonded surface silanol groups (Si-OH) is evidenced by the absorption at 3650 cm^{-1} and the presence of water by the absorption at 3400 and 1640 cm^{-1}. The porosity was further substantiated by the very rapid P-etch rate of 30Å/sec.

The shift and half-width of the band at 9μ is not all due to the porosity of the film. A good fraction of it is due to bonding strain in the film. Re-examination of this film after standing for six months at room temperature showed a shift to 1075 cm^{-1} from the initial 1059 cm^{-1} position and significant decrease in half-width. At the same time, the optical density at 3300-3400 cm^{-1} due to adsorbed water increased about 15% showing that there was no significant porosity decrease. But the later spectra showed a moderate intensity band at 930 cm^{-1} due to Si-OH bending which indicated a significant amount of reaction had occurred at room temperature between the oxide and water to form Si-OH. The ease of reaction at room temperature is attributed to the energy stored in the structure due to bond strain. The bond strain and variations in straining can result in broadened spectra. After reaction with the water, the strain is relieved and the bands are shifted to higher frequency and their half-widths decreased. Due to the energy in the strained bonds, strained films would also etch faster than nonstrained films.

The refractive indices (at 5460Å) of electron-gun evaporated SiO_2 samples were higher than that of thermally grown SiO_2 ($\sim$ 1.47 to 1.48 *vs.* 1.462). Normally, a porous SiO_2 film would have a lower refractive index. The explanation is that in addition to being porous and strained, the film is somewhat deficient in oxygen content.

CO_2 *oxidation*.—Another type oxide examined is the CO_2 process silicon dioxide (13). This oxide is generally formed in the epitaxial chamber by the introduction of CO_2 with chlorosilane and hydrogen. Table V shows the etch rates of such samples (14). In columns 1 and 2 are given the deposition times and temperatures. Note that these oxides are formed at much higher temperatures than any of the other type oxides formed other than high temperature thermal oxides. The two films having no post treatment showed etch rates of about 4Å/sec, about twice as fast as that of thermally grown oxides. The refractive index of a thick film of the CO_2 oxide indicated that the oxide was at least as dense as a thermally grown oxide. Its refractive index was 1.465 compared to 1.462 for thermally grown oxide. It was reasoned that this fast etch rate at the surface may be due to the fact that either the oxide near the surface is not as dense as the oxide at greater depths or that the impurity content is greater near the surface. The nonuniformity in the oxide is shown by the results given in Table V. After etching off 1.3μ of oxide from the

Table V. Etch rates of "CO_2 process" silicon dioxide

Deposition Time (min)	Deposition Temp (°C)	Post treatment	Film thickness (μ)	P etch Rate (Å/sec)	P etch Temp (°C)
10	1135	None	0.532	3.90	26.1
36	1135	None	4.33	4.20	26.1
36	1135	Etched off 1.3μ of oxide	2.77	2.42	24.1
4	1125	Additional 5 min at 1125°C	0.784	3.22	22.4
	Thermal oxide		0.581	1.92	24.1
			0.583	2.13	26.1

second sample, the etch rate of the remaining oxide was only 2.4Å/sec. The refractive index was still slightly high but the slower etch rate indicated that the deeper lying portions of the film were either more dense, less strained, or of greater purity. The slightly higher refractive index and faster etch rate can be due to impurities in the oxide such as phosphorus. Part of the slightly faster etch rate may also be due to the high temperature treatment since it has been found that oxides grown in dry oxygen at 1200° or 1000°C thermal oxides which were subsequently treated at 1200°C, etch about 20% faster in P-etch than do 1000°C thermal oxides (15).

A thinner film of the "CO_2 process" oxide was compared with a comparable thickness thermally grown oxide (980°C) using infrared spectroscopy. The results are shown in Fig. 7 and indicate that the oxide is very similar to that of thermally grown oxide. There is only a slight shift of the 9μ band of the "CO_2 process" oxide to longer wavelength. The half-width is also slightly greater than that of the thermally grown oxide.

Reactive sputtering.—Figure 8 shows the infrared spectrum in the 7-14μ region of a reactively sputtered silicon dioxide film. Spectrum A is the spectrum of a reactively sputtered film of 2500Å. Spectrum B is the same film after densification by exposure to nitrogen for 15 min at 980°C. The densified film is nearly the same as that of a thermally grown oxide shown in Spectrum C. The band position of the thermally grown oxide is at slightly higher frequency. From infrared spectra and etch rates, the sputtered oxides when prepared properly, appear to be more dense than T.F. pyrolytic oxides. The etch rate of reactively sputtered

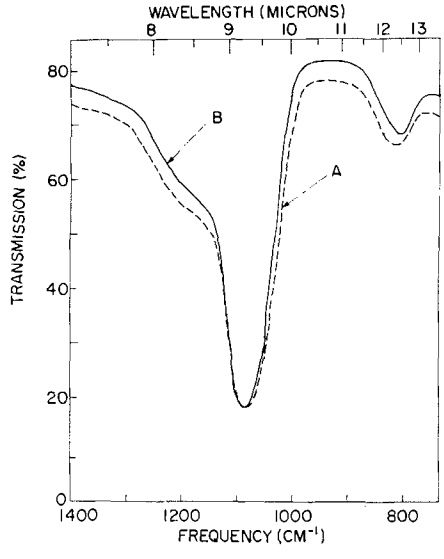

Fig. 7. Band position comparison of: A, "CO_2 process" oxide formed in epitaxial unit; 4600Å, 1083 cm^{-1}, 85 cm^{-1}; B, thermal oxide, 4500Å, 1085 cm^{-1}; 79 cm^{-1}.

	Total Thickness Å	Position cm^{-1}	Half-width cm^{-1}
A	4600	1083	85
B	4500	1085	79

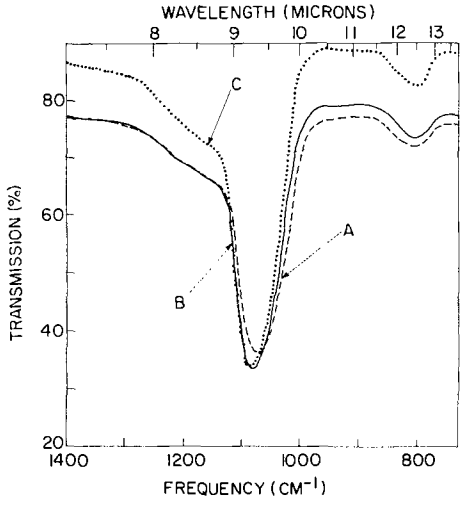

Fig. 8. Nitrogen densification of sputtered SiO_2: A, reactively sputtered SiO_2; B, densified by 15 min N_2 at 980°C; C, thermal oxide for comparison.

	Å	cm^{-1}	cm^{-1}
A	~2500	1070	84
B	~2500	1079	78
C	2820	1081	77

oxides which we had examined varied from about 3.8 to 5.2 Å/sec. The refractive index of these reactively sputtered silicon dioxide films was approximately 1.46.

Anodized SiO_2.—The difference between anodized and thermal oxides is especially noticeable with infrared spectroscopy. In Fig. 9, Spectrum A was obtained for a wafer with 1294Å of anodized oxide on one side and 1207Å of oxide on the back side. (Prepared in a solution of 0.05M KNO_3 in N methyl acetamide with no purposely added water. In preparing some of the films 2½% water was added.) The spectrum of the sample, after densification at 993°C for 15 min in nitrogen, is shown as Spectrum B. The densification was sufficient to decrease the film thickness 3%. For comparison, the spectrum of a wafer with 1155Å thermal oxide (dry oxygen at 975°C) on both sides is shown as Spectrum C. It is readily apparent that the band position (1040 cm^{-1}) of the anodized oxide is at much lower frequencies than the band position (1074 cm^{-1}) for the thermally grown oxide or the densified oxide. Furthermore, the band half-width (96 cm^{-1}) of the anodized oxide is much greater than that (73 cm^{-1}) of

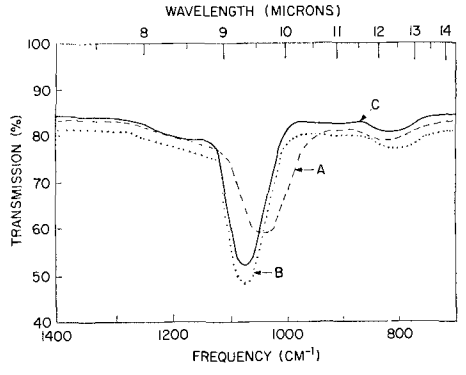

Fig. 9. Spectroscopic comparison: A, anodized with total oxide on both sides of 2501Å (1294 and 1207Å); B, densified by 15 min N_2 at 993°C; C, thermal oxide (dry O_2 at 975°C).

	Total thickness Å	POS cm^{-1}	H.W. cm^{-1}
A	2501	1040	96
B	2426	1074	73
C	2310	1074	73

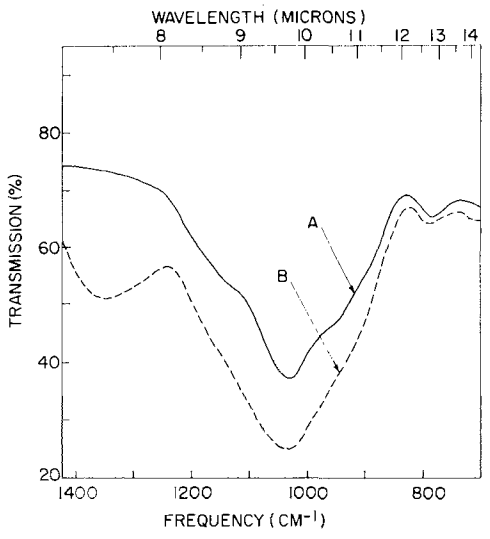

Fig. 10. A, film formed on silicon by 4½ hr in air at 650° above PbO bed; B, 1μ film of a lead borosilicate glass.

the thermally grown or densified oxide. The band position and half-width of this anodized film indicate either a very porous structure or strained bonding or both. The structure is only slightly porous in view of the 3% densification and the relatively small amount of adsorbed water seen in the 3μ region of the infrared spectrum. The refractive index of this anodized film was 1.459 on one side of the wafer and 1.471 on the other (16). Thus, from only the refractive index measurement, one would conclude that the film was similar to thermal SiO_2, but the infrared and the P-etch rate (19Å/sec) show that it is not. Part of the high refractive index and Si-O stretching band shift may be due to a slight oxygen deficiency. A refractive index increase due to oxygen deficiency may be compensated by a refractive index decrease due to the slight porosity such that the over-all refractive index is about the same as thermal SiO_2. It is concluded that the fast etch rate and large band shift were mainly due to bond strain in the oxide. Attempts were made to check for organic impurities by infrared amplification techniques. No organic impurities were visible.

Some of the anodized films which were prepared in glycerin solutions containing more water, were even poorer in quality. They had etch rates as high as 228 Å/sec, low refractive indices (1.30), and showed more water in their spectra, indicating high porosity.

Lead catalyzed oxidation.—We have found that the films formed by catalytic oxidation of silicon using lead oxide (6) are mainly lead silicate as indicated by (*i*) a high refractive index (1.72), (*ii*) extremely fast etch rate in P-etch (600 Å/sec), and (*iii*) by infrared spectroscopy.

A comparison of the infrared spectrum of a lead catalyzed film with that of a lead borosilicate glass film is given in Fig. 10. The latter was formed by fusing a sedimented powder film of known composition (17). Spectrum A is that of an oxide film formed by exposure in air for 4½ hr for 650°C with the wafer just above a lead oxide bed. Except for the B-O stretching vibration near 1360 cm^{-1} in the lead borosilicate glass (Spectrum B), the lead catalyzed film looks more like lead borosilicate than it does SiO_2. It is estimated from the infrared spectra and refractive index that the catalyzed film contains 60 w/o (weight per cent) PbO.

Summary: refractive indices and etch rates.—Table VI summarizes the etch rates of the various silicon dioxides and their refractive indices wherever measured.

Conclusion

On the basis of the described results, the following conclusions can be made:

Table VI. Summary: P etch rates of silicon dioxides

Oxide type and description	Refractive index	P etch rates, Å/sec
T F Pyrolytic	1.44-1.45	6-20
T F Pyrolytic, densified	1.463	2.0
CO_2 process	1.465	2.4-4.2
Reactive sputtering	1.46	3.8-5.2
Anodized	1.30-1.49	18-228
PbO Catalyzed oxidation (lead silicate)	1.72	600
Electron-gun Evaporated SiO_2	1.464-1.487	20-70
Thermal	1.462	2.0

1. Silicon oxide films can be characterized on the basis of refractive index, etch rate, infrared spectra, stoichiometry, passivation efficiency, and thermal densification.
2. Films formed by low temperature techniques have generally inferior properties to those formed by high temperature processes.
3. Porous and strained oxides can be densified to be indistinguishable from thermal oxides.
4. Steam is more effective than a dry atmosphere in causing densification to occur.
5. Surface hydroxyl groups can be removed by densification.
6. For a proper evaluation and differentiation of similar silicon oxide films, all of the described techniques must be accurately utilized.

Acknowledgment

The authors wish to thank Drs. J. A. Perri and J. Riseman for helpful discussions during the course of this work, and W. I. Bitter, R. P. Esch, R. L. Hallen, and R. A. Leonard for help with the experimental work.

Manuscript received April 13, 1965; revised manuscript received June 24, 1965. Portions of this paper were presented at the Toronto Meeting, May 3-7, 1964, and the Washington Meeting, Oct. 11-15, 1964.

Any discussion of this paper will appear in a Discussion Section to be published in the June 1966 JOURNAL.

REFERENCES

1. F. Barson, W. J. Armstrong, and W. E. Mutter, *This Journal*, **111**, 1263 (1964).
2. W. A. Pliskin and R. P. Gnall, *ibid.*, **111**, 872 (1964).
3. W. A Pliskin and E. E. Conrad, *IBM J. Research & Dev.*, **8**, 43 (1964).
4. E. L. Jordan and D. J. Donahue, Paper presented at Chicago Meeting of the Society, May 1960.
5. J. Klerer, *This Journal*, **108**, 1070 (1961).
6. D. A. Kallender, S. S. Flaschen, R. J. Gnaedinger, Jr., and C. M. Duffy, Paper presented at the Indianapolis Meeting of the Society, May 1961.
7. P. F. Schmidt and W. Michel, *This Journal*, **104**, 230 (1957).
8. R. M. Valletta, J. A. Perri, and J. Riseman, Paper presented at the Washington Meeting of the Society, October 1964.
9. W. A. Pliskin, "Reactivity and Bond Strain of Electron Gun Evaporated SiO_2," To be published.
10. G. Hass and C. D. Salzberg, *J. Opt. Soc. Am.*, **44**, 181 (1954).
11. E. Ritter, *Opt. Acta*, **9**, 197 (1962).
12. O. Ruff and P. Schmidt, *Z. anorg. Chem.*, **117**, 172 (1921).
13. W. Steinmaier and J. Bloem, *This Journal*. **111**, 206 (1964).
14. These films were prepared by V. J. Lyons and E. G. Grochowski of IBM Systems Development Division.
15. W. A. Pliskin and R. P. Esch, Unpublished results.
16. With increased Vamfo precision, it is possible to determine the refractive indices of films as thin as 900Å. W. A. Pliskin and R. P. Esch, *J. App. Phys.*, **36**, 2011 (1965).
17. W. A. Pliskin and E. E. Conrad, *J. Electrochem. Tech.*, **2**, 196 (1964).

Epitaxial Growth of Doped and Pure GaAs in an Open Flow System

D. Effer[1]

The Plessey Company Limited, Allen Clark Research Centre, Caswell, Towcester, Northants., England

ABSTRACT

The basic parameters for the transport and epitaxial growth of GaAs in an open flow system have been studied using hydrogen chloride as the transport agent. Selenium- and tin-doped GaAs layers were grown in this system, the maximum doping levels achieved being 3.7 x 10^{18} electrons cm^{-3} and 3.2 x 10^{18} electrons cm^{-3}, respectively. Pure layers of GaAs have been grown by means of the $AsCl_3/Ga/H_2$ reaction. The best layer had a room temperature carrier concentration of 1.75 x 10^{15} electrons cm^{-3} and a mobility of 8800 cm^2/v-sec. At 77°K the mobility value was 38,000 cm^2/v-sec.

Closed tube vapor phase preparations of Group III-V compounds have shown that the basic requirements for their preparation and transport in these systems are: (*a*) a lower valence halide of the Group 3 element, (*b*) arsenic or phosphorus vapor, and (c) a temperature gradient such that the following reversible reaction occurs (1)

$$3MX + 2\,Y \rightleftharpoons MX_3 + 2MY \qquad [1]$$

where M = In or Ga, X = Cl or I, and Y = As or P (of variable atomicity according to the temperature).

In order to extend the applicability of these reactions by using an open tube flow system, the transport of GaAs was studied using H_2/HCl mixtures in an apparatus of the same general form as that illustrated in Fig. 1. Various authors have reported on this method to date (2-7).

Experimental

HCl gas was obtained from a cylinder supplied by B.A.S.F. Germany. The supply lines and needle valve were made of stainless steel. The gas was first dried by means of a trap cooled in solid CO_2/alcohol and then by anhydrous $AlCl_3$. Vessel E, containing concentrated H_2SO_4 served as a constant pressure regulator. During each experiment the gas was slowly bubbled through this vessel and then to waste. The gas was thus passed at constant pressure through the metering capillary, the pressure drop being measured by a gauge containing concentrated H_2SO_4. Oxygen and water vapor were removed from electrolytic purity hydrogen by means of a Deoxo Catalytic Purifier and Linde molecular sieve grade 5A. The flow rate was measured by means of a capillary gauge containing concentrated H_2SO_4.

The GaAs source granules (20-40 mesh) were packed in a demountable quartz tube F which could be weighed.

For most of the work reported here a constant flow rate of 6.9 cc HCl and 45 cc H_2 per minute was used.

Material Balance of the Reaction

In order to study the material balance of the reaction the following quantities have to be known accurately: (*a*) the mass of HCl gas passing through the GaAs source, (*b*) the mass of GaAs reacted, and (c) the mass of either GaAs or $GaCl_3$ formed as products.

To determine the mass of HCl passing per unit time through the metering capillary at a known pressure drop the gas was mixed with hydrogen and absorbed in water. The amount absorbed was determined by titration with standard alkali. The mass of GaAs reacted was determined by weighing the detachable inner source tube F before and after an experiment.

Since it proved difficult to remove the deposited GaAs quantitatively from the walls of the reaction tube, the $GaCl_3$ also formed as a product was dissolved in anhydrous ether and the gallium content determined chemically.

The material balance was studied with the source at various uniform temperatures, the products of the reaction passing down a temperature gradient of approximately 30°/in. In order to account for the reaction occurring during the heating and cooling of the source, for every temperature studied two experiments of different durations were carried out and the net quantities of reactants and products calculated.

The results are shown in Table I.

By the use of the long packed GaAs source and low flow rates of HCl and H_2 the source reaction is assumed to have reached a steady state. At 1000°C the ratio Cl/Ga leaving the source is almost unity. This indicates the formation of GaCl as shown in Eq. [2]. The disproportionation of GaCl in arsenic vapor to form GaAs is shown in Eq. [3]

$$3GaAs + 3HCl \leftrightarrow 3GaCl + 3(As) + 3/2\,H_2 \qquad [2]$$

$$3GaCl + 2(As) \rightarrow 2GaAs + GaCl_3 \qquad [3]$$

Arsenic vapor at these temperatures consists of a mixture of the species As_4, As_2, and As for simplicity (As) is used in equations here and subsequently.

[1] Present address: Ferranti Ltd., Gem Mill, Chadderton, Lancashire, England.

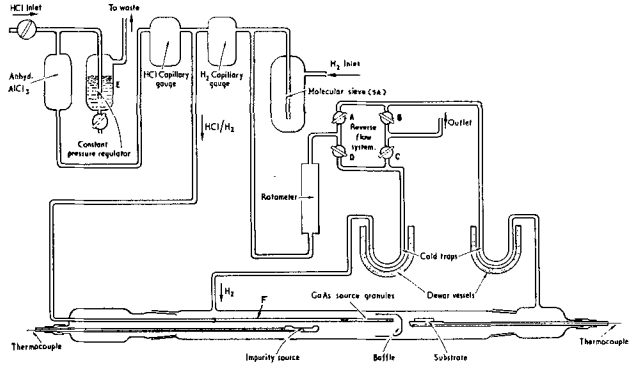

Fig. 1. Apparatus for the growth of doped epitaxial layers of GaAs

Table I. Material balance during transport reaction

Source temp, °C	Source reaction Atoms Cl in / Atoms Ga out	Wt Ga (g) reacted from source in 16 min	Wt Ga (g) found as $GaCl_3$	% Source Ga reformed as GaAs
1000	1.16	0.256	0.051	80.0
900	1.38	0.215	0.050	76.7
800	2.45	0.120	0.070	41.6
750	2.95	0.100	0.066	34.0

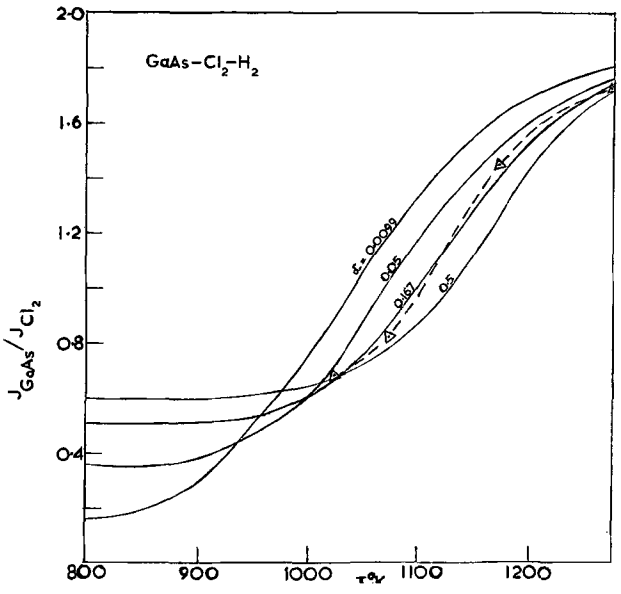

Fig. 2. Theoretical and experimental temperature dependence of GaAs/Cl_2 flux ratios for different chlorine-hydrogen flux ratios.

If the disproportionation reaction were solely responsible for the formation of GaAs the efficiency of conversion would be 66.7%. As an 80% conversion was determined experimentally, Eq. [2] must be reversible to a significant extent. Two reactions are therefore operating at this temperature. From the results it may be calculated that 40% of the GaAs is reformed via the reverse reaction, the balance being formed by the disproportionation reaction. The experimental results shown in Table I may be used to substantiate the theoretical predictions of Fergusson and Gabor (8), on the vapor phase transport of GaAs. In Fig. 2 are plotted the ratio of the flux of Ga to flux of Cl_2 (reciprocal times 2 of source reaction ratio in Table I) against T°K. The conditions of gas flow used in the present system, *viz.*, 6.9 cc/min HCl and 45 cc/min H_2 give a value of

$$\frac{\text{flux } Cl_2}{\text{flux } H_2 + \text{flux } Cl_2} \text{ of } \frac{1}{16}$$

Reasonable agreement is seen between theoretical and practical results.

Effect of Source and Substrate Temperatures on the Rate of Growth

Single crystal substrates of known area cut perpendicular to the {110} direction were chemically polished in a solution of 3 parts H_2SO_4/3 parts 30% H_2O_2/1 part H_2O. They were placed at intervals in a 20 mm diameter reaction tube which was heated by a furnace having a temperature gradient of 30°C/in. The flow rate of gases into the source was 6.9 cc/min HCl and 45 cc/min H_2. The thickness of epitaxial growth was determined by weight measurements. The results are shown in Table II.

The growth rate is reasonably constant at the various source and substrate temperatures except at a source temperature of 750°C when the rate is approximately one half. The results suggest that the reaction leading to the growth of material is limited by the rate of diffusion of reacting species from the vapor phase to the growing layer.

Table II. Rates of growth at various source and substrate temperatures

Source temp, °C	Thickness in microns of layer grown in 20 min at following temperature difference from source					
	25°	50°	75°	100°	125°	150°
1000	4	18	37	20	14	Polycrystalline
900	11	47	47	36	50	Polycrystalline
800	30	47	43	43	Whiskers	
750	16	27	22	Whiskers		
700	Whiskers					

Table III. Rates of deposition on various substrate orientations

Source temp, °C	Substrate temp, °C	Ratios of growing rates (110)	(100)	(111A)	(111B)
750	700	1.44		1	0.85
750	725	1.06		1	0.75
750	725	1.36	1.14	1	
800	750	1.26	1.08	1	
800	750	1.24		1	0.87

Effect of Substrate Orientation on Growth Rate

The rates of growth on various substrate orientations were studied at the two source temperatures 800° and 750°C. In each experiment three chemically polished substrates of different orientations and of known surface area were maintained at a constant temperature 25°-50°C lower than the source. The flow rate into the reaction system was 6.9 cc/min HCl and 45 cc/min H_2. The thickness of the layer was calculated from the change in weight of the substrates. The results are shown in Table III.

It was very noticeable that growths on the (110) slices were smoother than on the other directions. Typical examples of growths are shown in Fig. 3-6.

Growth and Measurement of Se- *and* Sn-*Doped Layers*

Three methods were considered for the study of the controlled doping of a growing epitaxial layer over a range of composition: (*a*) by means of doped source materials, (*b*) by the use of a separate source of solid impurity present as the element or chloride maintained at a controlled temperature, or (c) by doping the gas stream with gaseous impurities. The first method is limited by the fact that a series of sources of known impurity composition would be required and the third requires complicated metering equipment. For initial research the second method presented a relatively simple and controllable system.

Electrical isolation of the grown layers may be achieved by growing layers on substrates of opposite conductivity type such that electrical isolation would be effected by the p-n junction, or by growing on semi-insulating substrates. The former method was preferred as no information was available about the effect of heat treatments on semi-insulating material at the time this work was performed.

The final method adopted involved growing a layer in the shape of a Hall plate as follows.

Substrates doped with zinc to a level 3×10^{17} holes cm^{-3} were cut perpendicular to the {110} direction and chemically polished by a modification of Sullivan's technique (9). For this a metallurgical polishing machine was adapted to take a flat-bottomed Teflon bowl. The slices were waxed to a Teflon block which was moved inside the bowl by the epicyclic motion imposed by the polishing head of the machine. The polish solution comprised 3 volumes concentrated H_2SO_4/1 volume 30% H_2O_2/1 volume H_2O. The slices were washed by circulated deionized water, rinsed in pure water-free alcohol, and dried in warm air. A 6000Å layer of SiO_2 was deposited by the thermal decomposition of tetraethoxysilane and, by means of photoengraving techniques, a Hall shaped window was etched through. This had three contact areas on one side and one on the other. It was therefore possible to check the uniformity of the final grown layer by measuring the voltage drop between the middle and each of the outside contacts. The surface was briefly etched in the polish solution described above, washed thoroughly in circulated water, and rinsed in water-free alcohol. An epitaxial layer approximately 30μ thick was then grown. The average thickness of the layer was measured by means of a microscope using the silica film as a reference. Tin dot contacts were alloyed to the specimen in a hydrogen atmosphere at

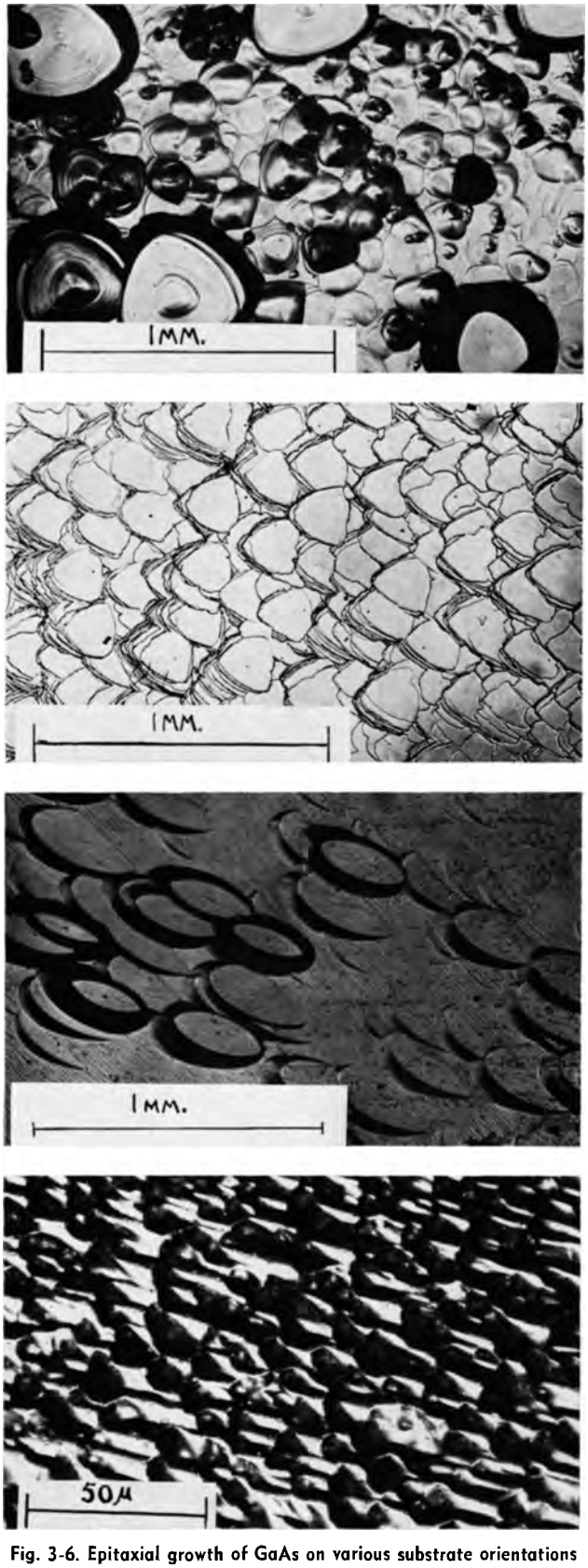

Fig. 3-6. Epitaxial growth of GaAs on various substrate orientations

600°C. The contacts were ohmic to all the layers reported and rectifying to the substrate material. The electrical properties of the layer were then measured at room temperature.

The reproducibility of the electrical properties of epitaxial growths from one identical experiment to another was determined before attempting work on doped layers. Three separate depositions were carried out on to p-type substrates. The results are shown in Table IV. Carrier concentrations were calculated by means of the formula $n = 1/\mathrm{Re}$. These results were taken as a satisfactory basis for future work using this apparatus and technique.

Table IV. Properties of undoped epitaxial layers

Sample	Growth temp, °C	Average thickness of layer after ½ hr growth (μ)	Resistivity (ohm-cm)	Carrier Concentration (cm^{-3})	Mobility $cm^2/v\text{-}sec$
HP12	730	35	0.019	7.6×10^{16}	4330
HP14	730	33	0.020	7.1×10^{16}	4400
HP15	730	31	0.016	9.8×10^{16}	3990
Source material			0.031	4.6×10^{16}	4380

Growth of Selenium-Doped Layers

Several attempts were made to grow selenium-doped layers in an apparatus of a rather simpler design than that shown in Fig. 1. A four zone furnace was used to control the temperature of (*a*) the selenium source, (*b*) an arsenic source if required, (*c*) GaAs source granules, and (*d*) the substrate. The thermal insulation of the furnace winding was kept to a minimum so that long flat uniform temperature zones could be achieved. The temperature of the selenium source and the substrate were monitored by the protected thermocouples as shown. The growth procedure consisted of raising the selenium, GaAs source, and substrate to their operating temperature in a flow of hydrogen and then to commence epitaxial growth by admitting HCl gas to the source. Doped epitaxial layers were successfully grown using relatively low partial pressures of selenium, but at higher pressures a selenium rich layer formed on the substrate which prevented normal growth.

It became obvious that the substrate was reacting with selenium vapor during the heating up cycle and forming GaAs/Ga_2Se_3 compounds. It was necessary therefore to raise the temperature of the selenium and substrate in a reverse flow of hydrogen. The apparatus shown in Fig. 1 has provision for this operation, and selenium doped layers were subsequently grown successfully over a wide range of selenium pressures. Source and substrate temperatures of 800°C and 750°C were used throughout this work. During the warm up period the vapors passed from right to left, the substrate being in a hydrogen atmosphere. When the operating temperature was reached 6.9 cc/min HCl was passed into the GaAs source and sufficient time allowed for steady state conditions to be achieved. The products would again be transported in the opposite direction from the substrate.

Finally the main hydrogen flow was reversed so as to commence epitaxial growth. A hydrogen flow rate of 50 cc/min was passed through both the GaAs source and the side tube. Traps F and G, cooled in solid CO_2/alcohol, served to avoid contamination of the gas metering system. The heating up procedure was tested by placing polished, weighed substrates into the growth position and heating in a reverse flow of hydrogen for 30 min. After this time they were found to have retained their surface polish and had not changed in weight.

A study of the growth of Se-doped epitaxial layers requires a knowledge of the ratio of selenium and gallium atoms present in the gas phase over the growing layer. The number of gallium atoms passing into the vapor phase per unit time may be calculated from the data in Table I. The partial pressure of selenium was determined in the following manner.

A quartz boat was made to fit inside the dopant boat and filled with selenium. At a definite temperature (accurately known by the thermocouple situated under the boat) and in a flow rate of 50 cc/min H_2, the loss in weight of the selenium was noted over a period of 30 min. The weight loss in this time would

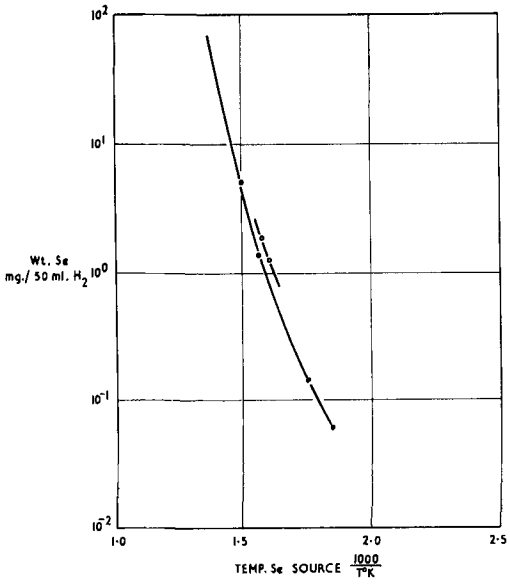

Fig. 7. Partial pressures of selenium vs. temperatures of selenium source.

include that due to the heating up and cooling down of the selenium. A further experiment was conducted at the same temperature over a period of 15 min. The net weight therefore gave the steady weight loss during 15 min at the operating temperature. During this work two different diameter reaction tubes were used. The results are shown in Fig. 7. Several selenium-doped epitaxial layers were grown using the procedure already described. The results are shown in Table V and Fig. 8.

The electrical leakage of the junction between the epitaxial layer and the substrate was determined by etching a channel across the grown Hall plate and through the junction. The two large area diodes so formed were checked for reverse leakage using the tin alloy dot contacts. A typical breakdown voltage of 4-6v was obtained with a reverse leakage of 0.1-0.2 μ-amp.

The behavior of selenium in GaAs has been studied by Vieland and Kudman (10). They find that this element is not fully active electrically in concentrations over 4×10^{17} electrons cm^{-3} and that part enters the lattice as an optically active neutral complex ($VGa Se_3$). The total selenium content in some of their samples was determined chemically and related to the electrically active selenium content. It appeared that the total selenium content of the epitaxial layers could be readily assessed from this data. However, Fuller and Wolfstirn (11) have shown that the electron concentration of selenium is also affected by heat-treatment history of the samples which makes such an assessment untenable.

For one of the Hall shaped layers having a carrier concentration of 3.4×10^{18} electrons cm^{-3} the temperature coefficient of resistivity was determined between room temperature and 280°C. The value —0.08%/°C was obtained.

Table V. Electrical properties of selenium-doped epitaxial layers

Temp Se (°C)	n (cm^{-3})	Mobility (cm^2/v-sec)	Resistivity (ohm-cm)	Diam. reaction tube, mm
285	3.0×10^{17}	2240	9.2×10^{-3}	22
300	9.5×10^{17}	2350	2.8×10^{-3}	22
425	3.5×10^{18}	2550	7.0×10^{-4}	22
455	2.0×10^{18}	2080	1.5×10^{-3}	22
350	3.4×10^{18}	1420	1.3×10^{-3}	28
350	3.1×10^{18}	1190	1.7×10^{-3}	28
345	2.8×10^{18}	1860	1.2×10^{-3}	28
370	3.7×10^{18}	1300	1.3×10^{-3}	28

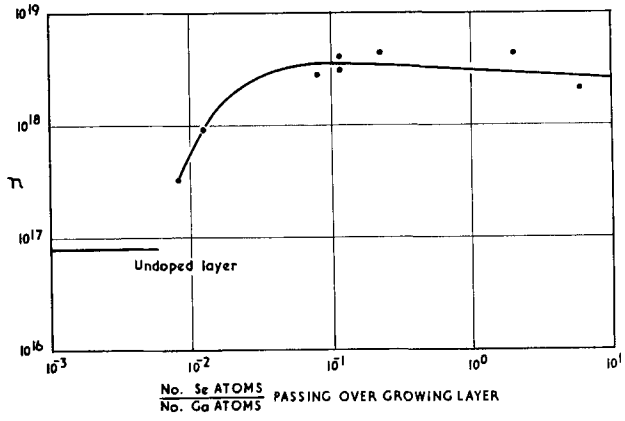

Fig. 8. Electrically active selenium in epitaxial layers vs. Se/Ga atom ratio passing over growing layer.

Growth of Sn-*Doped Layers*

Tin-doped layers were grown by the same procedure as described for selenium-doped layers but using anhydrous $SnCl_2$ as the tin source. Several layers were grown using various partial pressures of $SnCl_2$. The effect also of an increased arsenic pressure was studied by incorporating a separate arsenic source. A complete study of tin-doped layers was however not attempted. The results are shown in Table VI.

The junction characteristics of two of these layers were measured by the method described before. A leakage current of 1 μa was measured in the reverse direction at 2.5v.

It is evident from the low mobility values obtained that a large degree of compensation exists in the tin-doped layers. There appears to be a tendency for layers grown in an excess arsenic atmosphere to have a lower mobility and an increased carrier concentration. The latter would seem to indicate that the additional arsenic atmosphere minimizes the formation of arsenic vacancies in the grown layer and increases the net number of tin atoms on Ga sites.

The Growth of Pure Epitaxial Layers of GaAs

Choice of system.—It has been shown that Group III-V compounds may be prepared and transported by vapor phase reactions in a number of ways (1, 12). In the case of GaAs the following systems are equivalent: (*a*) GaAs, HCl; (*b*) $GaCl_3$, Ga, As, H_2; and (*c*) Ga, $AsCl_3$, H_2.

In order to grow the highest purity layers the choice of system will obviously depend on the initial purity of the reacting species. In this respect system (*a*) has obvious disadvantages unless the GaAs is prepared by vapor phase methods initially. The purification of HCl to semiconductor standards however presents a difficult problem. In the remaining two systems the gallium component is common. It can be obtained commercially 99.9999% pure as confirmed by mass spectrographic and arc spectrographic analysis. $GaCl_3$ may be obtained probably to the same level of purity but arsenic purification has always presented difficulties and many samples are found to contain sulfur (13). System (*c*) was chosen for this work because it has the least number of components and also $AsCl_3$ may be obtained 99.999% pure commercially and may probably be further purified by such simple procedures as fractional distillation and zone refining.

Table VI. Electrical properties of tin-doped epitaxial layers

$SnCl_2$ temp	As temp	n (cm^{-3})	Mobility (cm^2/v-sec)	Resistivity (ohm-cm)
420	—	1×10^{18}	600	1.04×10^{-2}
420	440	1.3×10^{18}	540	8.93×10^{-3}
460	—	1.6×10^{18}	810	4.8×10^{-3}
460	440	3.2×10^{18}	650	3.0×10^{-3}

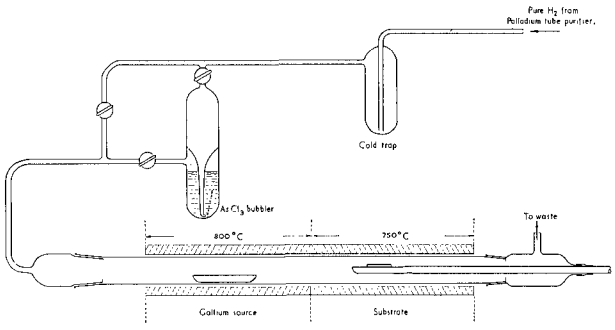

Fig. 9. Apparatus for growth of pure epitaxial layers of GaAS

Reaction mechanism.—An initial study of reaction (c) was carried out in an apparatus similar to that shown in Fig. 9. Initially a furnace was constructed so that the gallium melt, held at 800°C, could be observed. Palladium-diffused hydrogen was bubbled through the $AsCl_3$ at the rate of 50 ml/min. The initial reaction taking place in the furnace was as follows:

$$2AsCl_3 + 3H_2 \rightleftharpoons 6HCl + 2(As) \qquad [4]$$

The arsenic vapor was completely absorbed by the gallium until saturation occurred at a composition 2¼ a/o (atomic per cent) arsenic (14). During this period no free arsenic condensed outside the furnace but gallium was transported as a lower chloride. Disproportionation of this chloride occurred and, outside the furnace, free gallium and $GaCl_3$ condensed. When the melt was saturated with arsenic a skin of GaAs formed over its surface and free arsenic appeared at the furnace outlet.

On cooling the source, GaAs was precipitated from the melt leaving almost pure gallium. The source was again heated to 800°C in a flow of hydrogen. $AsCl_3$ vapors were passed and it was found that an induction period of about 40 min elapsed before free arsenic was seen. Repetitions of this experiment gave the same result. It was initially assumed that the GaAs skin was slowly soluble and that the induction period experienced was the time necessary for the melt to become saturated with arsenic obtained from the GaAs skin. This however was disproved by holding the melt at 800°C for an hour in hydrogen only and then passing $AsCl_3$. An induction period of the same duration was observed. It seems therefore that the GaAs skin is very slowly dissolved by the gallium in this system.

Growth of pure layers.—By the time these experiments were performed semi-insulating GaAs substrate material had been proved to be stable at the temperatures under consideration. All the pure layers were grown on this material, the substrate being cut perpendicular to the {110} direction. The surface preparation techniques used were essentially as described before except that the substrates were given a 10% KCN rinse after the etch polishing operation and before the wash in deionized water. This served to complex any copper ions adsorbed from the acid solution. A final rinse was given in pure, water-free methanol followed by rapid air drying. The substrates were rapidly loaded into the reaction tube through which a rapid stream of pure hydrogen was passed. The furnace was raised to its operating temperature, 800°C for the source and 750°C for the substrate, and the main flow of hydrogen passed through the $AsCl_3$ bubbler at the rate of 50 cc/min. Growth rates of about 1/3 μ/min were observed under these conditions. As the apparatus was extremely simple to operate many successful overnight runs were performed and layers up to 230μ thick were grown. One of these thick layers was checked by x-ray diffraction techniques and the surface shown to be completely epitaxial with the substrate. Normally, layers from 30-60μ were grown and these had a smooth polished appearance with, in many cases, a surface roughness of $\pm 0.2\mu$.

Table VII. Electrical properties of layers grown from the first fraction of $AsCl_3$

Sample	Temperature of measurement	Resistivity (ohm-cm)	n (cm^{-3})	Mobility (cm^2/v-sec)	Duration of growth (hr)
PM127	Room	0.067	3.8×10^{16}	2,460	6½
PM128	Room	0.45	4.0×10^{15}	3,470	5½
	77°K	0.27	2.2×10^{15}	10,500	
PM129	Room	0.43	1.9×10^{16}	7,650	3
	77°K	0.104	1.5×10^{15}	40,100	
	70°K	0.106	1.4×10^{15}	42,100	
	65°K	0.109	1.35×10^{15}	42,500	

The method used for the electrical measurement of the layers consisted of ultrasonically cutting a Hall-shaped sample and alloying tin dot contracts to the relevant positions. The layer thickness was determined on the remainder of the slice by cleaving and then etching the epitaxial junction with 20% cold HNO_3 for 15 min. The first layers measured were found to have a carrier concentration of 1.3×10^{15} to 3×10^{15} donors cm^{-3} with mobilities in the range 5000-6000 cm^2/v-sec.

Two layers grown from the last fraction of $AsCl_3$ were p-type with carrier concentrations of 9×10^{14} cm^{-3} and mobilities of about 500 cm^2/v-sec. The passage of hydrogen through the $AsCl_3$ may be considered as a fractional distillation and it is possible that a higher boiling point p-type impurity chloride is present.

Evidence for the presence of an n-type impurity was obtained by growing layers from a fresh supply of $AsCl_3$. The properties of the first three growths are shown in Table VII.

The following chlorides of n-type impurities have boiling points lower than $AsCl_3$: $SiCl_4$, 58°C; SCl_2, 59°C; $SnCl_4$, 114°C. Se_2Cl_2 boils at the same temperature as $AsCl_3$, 130°C.

These possible impurities may be conveniently minimized therefore by passing hydrogen for several hours into each fresh supply of $AsCl_3$.

Growth on a Vapor Etched Substrate

The effect of cleaning the substrates in situ by vapor etching was studied by reversing the temperature gradient in the reaction tube. The gallium source was kept at a constant temperature of 800°C and the substrates were heated to 900°C. Under the standard flow conditions used an etch rate of approximately 0.5 μ/min was achieved. On cooling the substrates from 900° to 750°C epitaxial deposition took place on to the newly etched surface. The electrical properties of a layer grown in this way are given in Table VIII.

Purification of $AsCl_3$ by Gradient Freezing

A volume of $AsCl_3$ was sealed into an inverted "U" shaped capsule under an atmosphere of argon. The liquid was poured into one of the arms which was then lowered into a freezing mixture at the rate of 1 cm/hr. The last fraction of liquid unfrozen was poured into the empty arm of the capsule. After five such operations the pure liquid was charged into the bubbler and hydrogen passed for several hours. The properties of a layer grown from this material are shown in Table IX.

Growth of Pure Layers in Increased Partial Pressures of Arsenic

An arsenic source was maintained at 425°C in the reaction tube and a layer grown in the normal man-

Table VIII. Electrical properties of layer grown on vapor etched substrate

Temperature of measurement	Resistivity (ohm-cm)	n (cm^{-3})	Mobility (cm^2/v-sec)
Room	0.247	3.3×10^{15}	7,670
77°K	0.083	2.2×10^{15}	34,200

Table IX. Electrical Properties of layer grown from purified $AsCl_3$

Temperature of measurement	Resistivity (ohm-cm)	n (cm^{-3})	Mobility (cm^2/v-sec)
Room	0.550	1.4×10^{15}	8,100
77°K	0.220	1.1×10^{15}	25,800

Table X. Pure layer grown in excess arsenic pressure

Temperature of measurement	Resistivity (ohm-cm)	n (cm^{-3})	Mobility (cm^2/v-sec)
Room	0.407	1.75×10^{15}	8,780
77°K	0.103	1.6×10^{15}	37,900

ner. The arsenic used was of semiconductor purity (99.999%) but the grown layer was found to contain 3×10^{16} electrons cm^{-3}. The introduction of this relatively impure material had obviously invalidated the purpose of the experiment and so a supply of pure arsenic was prepared in the reaction tube by thermal decomposition of the pure $AsCl_3$ in hydrogen. Using this as a source of arsenic the above experiment was repeated. The slice was back-etched prior to growth as described above. The surface polish of all the back-etched slices have been found to be extremely good, a typical surface roughness of $\pm$ 0.25μ being measured on a Talysurf machine. The electrical properties of layers grown by this method are shown in Table X.

The room temperature mobility of this sample is the highest obtained to date. The carrier density however is not unlike previous samples which does not substantiate a report that epitaxial growth of GaAs in increased arsenic pressures reduces the carrier concentration (7).

The purification of the $AsCl_3$ seems to have reduced the concentration of n-type impurity in the grown layer. It is envisaged that a more careful purification of this component may lead to a still further reduction in carrier concentration.

The regular production of high purity GaAs by epitaxial methods has thus made possible the further exploration of GaAs as a high voltage, high temperature rectifier and field effect device material.

Acknowledgments

The author is indebted to G. Whitsey for performing much of the experimental work, to P. R. Evans for the low temperature measurements, and to J. R. Knight, R. W. Ware, and B. Joyce for helpful discussion and review of the manuscript. Thanks are due to the Ministry of Defence and The Plessey Company for permission to publish.

Manuscript received Aug. 17, 1964; revised manuscript received June 29, 1965.

Any discussion of this paper will appear in a Discussion Section to be published in the June 1966 JOURNAL.

REFERENCES

1. G. R. Antell and D. Effer, *This Journal*, **106**, 509 (1959).
2. F. V. Williams and R. A. Ruehrwein Detroit Meeting of the Society, 1961.
3. R. L. Newman and N. Goldsmith, *This Journal*, **108**, 1127 (1961).
4. S. W. Ing and H. T. Minden, *ibid.*, **109**, 995 (1962).
5. R. R. Moest and B. R. Shupp, *ibid.*, **109**, 1061 (1962).
6. N. Goldsmith, *ibid.*, **110**, 588 (1963).
7. N. Goldsmith and W. Oshinsky, *R.C.A. Rev.*, **24**, 546 (1963).
8. R. R. Fergusson and T. Gabor, *This Journal*, **111**, 585 (1964).
9. M. V. Sullivan and L. A. Pompliano, Paper at Spring 1961 meeting of the Society.
10. L. J. Vieland and I. Kudman, *J. Phys. Chem. Solids*, **24**, 437 (1963).
11. C. S. Fuller and K. B. Wolfstirn, *J. Appl. Phys.*, **34**, 8, 2287 (1963).
12. D. Effer and G. R. Antell, *This Journal*, **107**, 252 (1960).
13. D. Effer, *ibid.*, **108**, 357 (1961).
14. R. N. Hall, *ibid.*, **110**, 385 (1963).

The Hydrogen Evolution Kinetics and Hydrogen Entry into α-Iron

J. O'M. Bockris, J. McBreen,[1] and L. Nanis[2]

Electrochemistry Laboratory, University of Pennsylvania, Philadelphia, Pennsylvania

ABSTRACT

An investigation of the permeation rate of electrolytic hydrogen through Armco iron single crystals and polycrystals by an electrochemical technique is described. The variation of the permeation rate with cathodic overpotential has been determined in alkaline (0.1*N* NaOH), alkaline cyanide, acidic (0.1*N* H_2SO_4), acidic iodide, acidic napthalene, and acidic nitrile (valeronitrile, napthonitrile, benzonitrile) solutions. The potential-permeation behavior as a function of temperature has been investigated in acid (0.1*N* H_2SO_4) solutions. The permeation potential behavior in alkaline solutions indicate a coupled discharge recombination mechanism for hydrogen evolution at low overpotentials while at higher overpotentials the mechanism is slow discharge-fast electrochemical. The effects of CN^-, I^-, and napthalene which increase permeation rate has been interpreted in terms of a lowering of the M-H_{ads} bond energy. Nitriles were found to decrease the permeation rate, and their effect on the permeation rate is interpreted in terms of their vertical adsorption on the electrode hindering the discharge process. The results indicate that hydrogen goes through an adsorbed intermediate state on discharge before entering the metal lattice. Grain boundaries play no part in the hydrogen evolution kinetics or in the entry of hydrogen to the metal.

It has been pointed out (1, 2) that an investigation of the permeation-potential relationships on iron can yield diagnostic criteria, from which decisive information on the mechanism of hydrogen evolution on iron can be obtained.

[1] Present address: Yardney Electric Corporation, New York, New York.

[2] Present address: The Institute for Direct Energy Conversion, University of Pennsylvania, Philadelphia, Pennsylvania.

The effect of anions and neutral organic molecules on hydrogen permeation from aqueous electrolytic solutions has been investigated by many workers (3, 4). However, the mechanism by which these anions and poisons effect the permeation remains a topic of dispute (4, 5).

An investigation of the hydrogen permeation rate through α-iron, from acid and alkaline solutions, un-

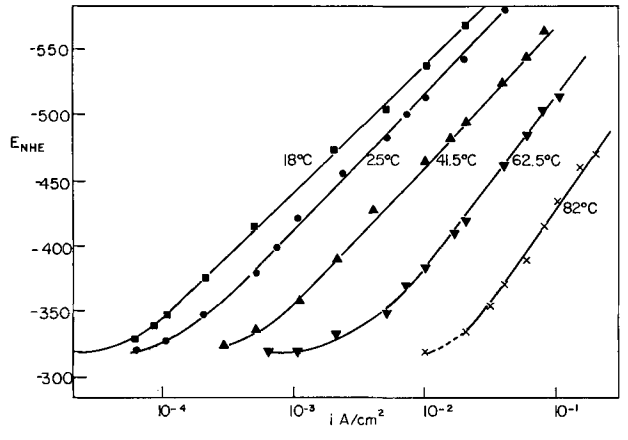

Fig. 1. Current-potential curves for Armco iron in 0.1*N* H_2SO_4 solutions.

der varying conditions of temperature, ambient electrolyte, and cathodic polarization, is presented.

Experimental

Permeation measurements.—Details of the cell and auxiliary apparatus used in this investigation have been described elsewhere (2, 6). Membranes of Armco iron 0.77 mm thick were prepared in a manner described in ref. (7). The Armco iron single crystals used in the investigation were prepared in a similar manner.

Care was taken in acidic solutions to work under conditions of cathodic protection, while doing permeation measurements. In this way, a reproducible electrode surface was always maintained. Temperature control measurements were made in an air thermostat which controlled the temperature to within ±0.5°C. Solutions were prepared from conductivity water and A.R grade reagents. Final purification was made by preelectrolyzing the solutions in an external cell prior to admitting the solution to the cell.

Results

Current-potential behavior in 0.1N H_2SO_4 solutions.—In Fig. 1, current-potential curves for hydrogen evolution on Armco iron in the temperature range 18°-80°C in 0.1*N* H_2SO_4 are given. All curves were obtained galvanostatically. In Table I, the slopes of these curves are tabulated, along with the corresponding transfer coefficient, α. An Arrhenius plot of the current at $V = -0.408$v N.H.E. is given (Fig. 2). This was determined both galvanostatically and potentiostatically. The slopes of the log $i/1/T$ relations obtained by both methods are in agreement and give the heat of activation for hydrogen evolution on iron as 18.1 kcal/mole.

Permeation-potential relationships in acidic solutions.—Permeation-potential plots for Armco iron in 0.1*N* H_2SO_4 solutions, as a function of temperature of 18°-80°C are given in Fig. 3, where J is the steady-state permeation rate; their slopes tabulated in Table I. Because of corrosion on the one hand and

[3] The transmitted hydrogen is measured by the current density as it is anodically oxidized, hence values are reported in microamp/cm².

Table I. Current-potential, permeation-potential parameters and α for Armco iron, 0.1*N* H_2SO_4, at various temperatures

Temperature °C	$(\partial\eta/\partial \log_{10} i)_V$	$(\partial\eta/\partial \log_{10} J_\infty)_V$	α
18	0.097	0.190	0.59
26	0.115	0.240	0.515
41.5	0.125	—	0.498
63	0.135	0.280	0.495
80	0.140	0.280	0.5

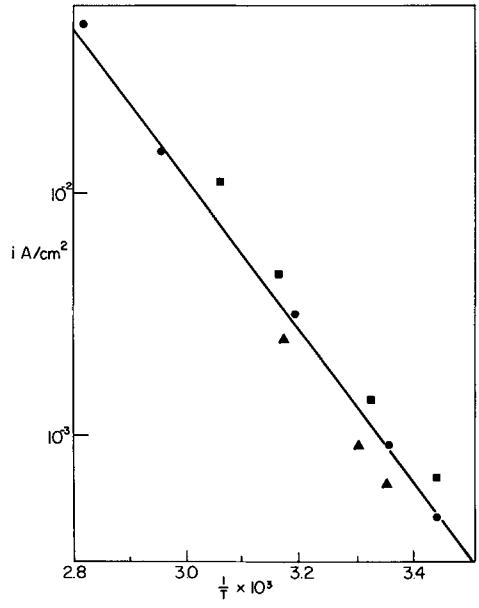

Fig. 2. Arrhenius plot of cathodic current for Armco iron, 0.1*N* H_2SO_4, $E_{NHE} = -0.408$v; ●, galvanostatic measurement; ■, ▲, potentiostatic measurement.

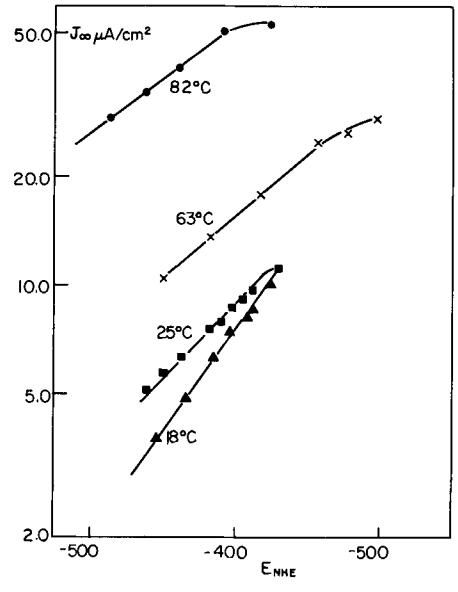

Fig. 3. Permeation-potential curves for Armco iron, L — 0.77 mm, 0.1*N* H_2SO_4.

anomalous permeation effects (which will be described in another publication) on the other, only a limited potential range could be covered.[4] Permeation potential plots are given in Fig. 4 for 0.1*N* H_2SO_4 with additions of potassium iodide. The slope of the curves in each case is —235 mv. Figures 5-7 give permeation potential curves for acidic solutions with additions of valeronitrile, benzonitrile, and naphthonitrile, while Fig. 8 gives the permeation-potential behavior in acidic naphthalene solutions. It may be seen that additions of iodide and naphthalene increase the permeation, while additions of valeronitrile benzonitrile and naphthonitrile decrease it. In all cases these additives increase the hydrogen overpotential, in acid solutions.

Permeation-potential behavior in alkaline solutions.—Permeation potential curves, for pure alkaline (0.1*N* NaOH) and alkaline cyanide (KCN) solutions, are given in Fig. 9. In 0.1*N* NaOH solutions, the Tafel slope

[4] Henceforward, all results are for Armco iron membranes, 0.77 mm thick, at 25°C, unless otherwise stated.

is —122 mv, while the permeation potential curve has a slope of —240 mv below $V = -1.02$v NHE. Above —1.02v NHE the permeation rate increases slowly with potential. Additions of cyanide increase the permeation rate and the hydrogen overvoltage.

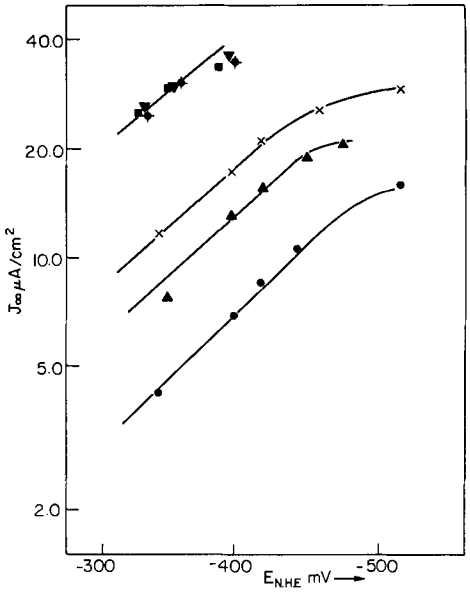

Fig. 4. Permeation-potential curves for acidic iodide solutions, Armco iron, $L = 0.77$ mm, 25°C; 0.1N H_2SO_4 with additions of KI: •, none; ▲, 10^{-4}M; X, 5 x 10^{-4}M; ■, 0.01M; ▼, 5 x 10^{-3}M; solid circle with extended arms, 0.01M.

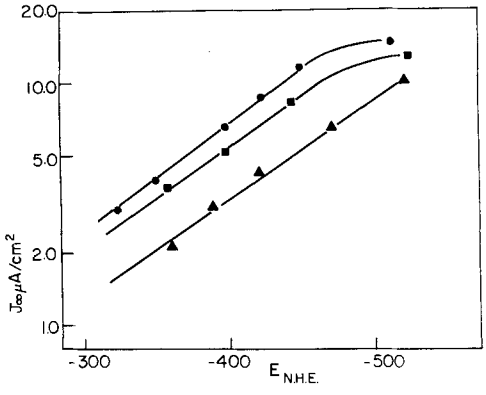

Fig. 5. Permeation-potential plots, Armco iron, $L = 0.77$ mm, 25°C; 0.1N H_2SO_4 with additions of valeronitrile: ○, none; □, 0.01M; △, 0.1M.

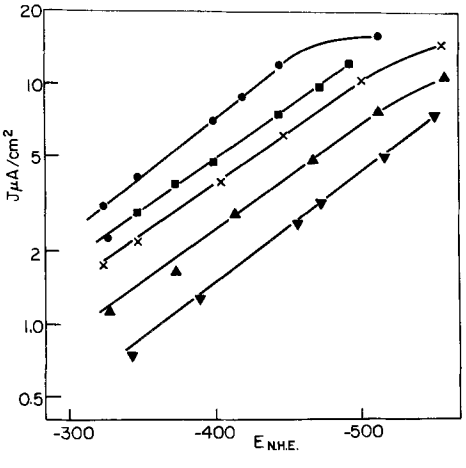

Fig. 6. Permeation potential curves, Armco iron, $L = 0.77$ mm, $T = 25$°C; 0.1N H_2SO_4 with additions of benzonitrile: •, none; ■, 10^{-4}M; X, 5 x 10^{-4}M; ▲, 10^{-3}M; ▼, 10^{-2}M.

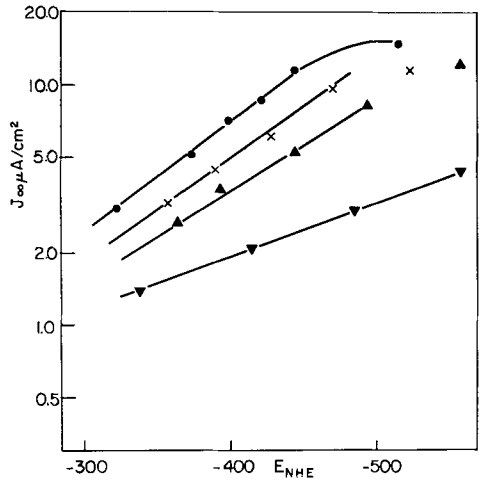

Fig. 7. Permeation-potential curves, Armco iron, $L = 0.77$ mm, $T = 25$°C; 0.1N H_2SO_4 with additions of naphthonitrile: •, none; X, 10^{-6}M; ▲, 10^{-5}M; ▼, 10^{-4}M.

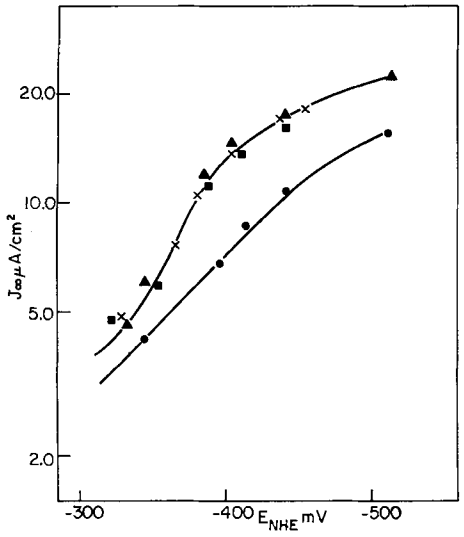

Fig. 8 Permeation-potential curves, Armco iron, $L = 0.77$ mm, $T = 25$°C; 0.1N H_2SO_4 with additions of naphthalene: •, none; ■, 10^{-5}M; ▲, 2 x 10^{-5}M; X, 5 x 10^{-5}M.

Permeation-current relationship.—Figure 10 shows a plot of the permeation rate against the square root of the cathodic current density for acidic (0.1N H_2SO_4) and acidic iodide solutions, while in Fig. 11 a similar curve is shown for 0.1N NaOH. In all cases the curves are linear and the intercept zero.

Single crystals.—The hydrogen concentration directly beneath the cathodic surface of an Armco iron single crystal membrane, at 25°C in 0.1N H_2SO_4, is plotted as a function of potential in Fig. 12, while that for polycrystalline Armco iron is shown for comparison. Both cases yield similar results. The slope of the current potential curve for Armco iron single crystals in acid (0.1N H_2SO_4) solutions is —123 mv while that for the permeation potential curve is —240 mv.

Discussion

Mechanism of the hydrogen evolution reaction in 0.1N H_2SO_4 solutions.—It has been shown elsewhere that, in the case of Armco iron, diffusion through the membrane is rate determining (2). Because of this, the reaction by which hydrogen enters the surface of the metal can be considered to be in equilibrium. If it is assumed that hydrogen, on discharging on the metal, passes through an adsorbed state prior to entering the metal, and that this adsorbed state is the same as that which leads to hydrogen gas evolution, then the permeation rate is directly related to the hydrogen cover-

age on the cathode surface (1, 2). It has been shown elsewhere (8) that

$$\frac{J_\infty}{zF} = \frac{Dc_o}{L} \qquad [1]$$

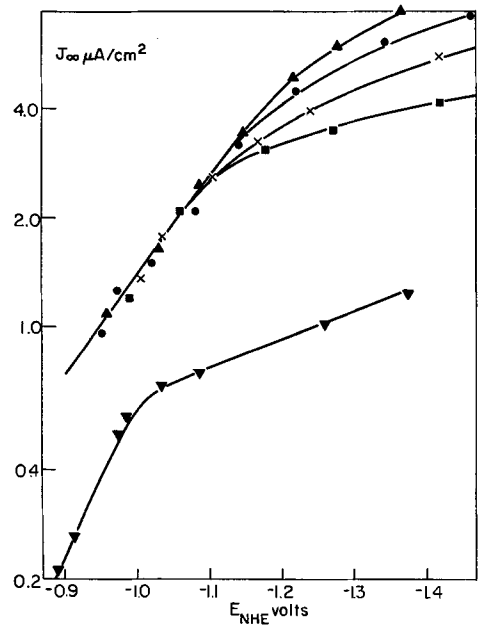

Fig. 9. Permeation-potential curves, Armco iron, L = 0.77 mm, 25°C, 0.1N NaOH, with KCN additions: ▼, none; ■, 1.6 x 10^{-4}M; X, 4 x 10^{-3}M; ●, 0.01M; ▲, 0.1M.

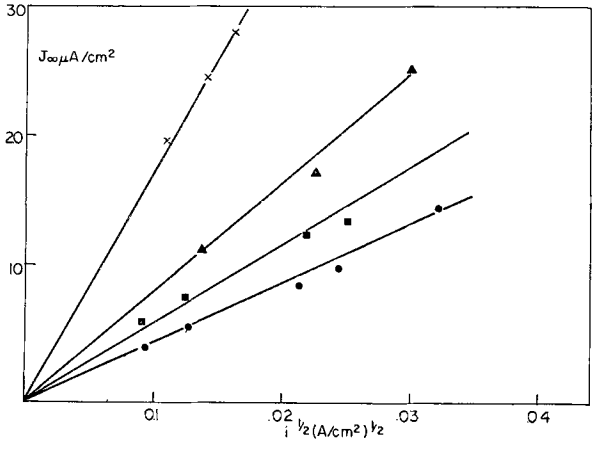

Fig. 10. Permeation-current curves for acidic iodide solutions, Armco iron, L = 0.77 mm, 25°C; 0.1N H_2SO_4 with additions of KI: ●, none; ■, 10^{-4}M; ▲, 5 x 10^{-4}M; X, 5 x 10^{-3}M.

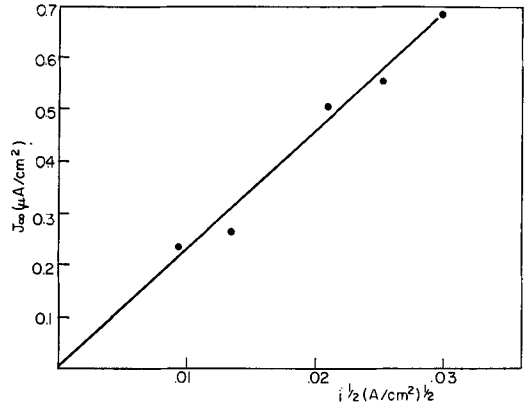

Fig. 11. Permeation-current curves for Armco iron, 0.1N NaOH, L = 0.77 mm, 25°C.

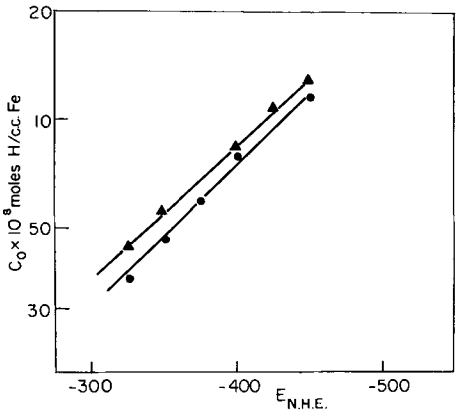

Fig. 12. C_o values for Armco iron polycrystals (▲) and single crystals (●), 0.1N H_2SO_4, 25°C.

where J_∞ is the steady-state permeation rate on amp/cm², D is the diffusion coefficient for hydrogen in the metal, F the Faraday, c_o the hydrogen concentration directly beneath the membrane cathodic surface, and L the membrane thickness. Now for low hydrogen coverages (θ) and dilute solutions of metallic hydrogen (2)

$$k_3\theta = k_{-3}c_o \qquad [2]$$

where k_3 and k_{-3} are the rate constants for the surface to bulk reaction and bulk to surface step respectively. Combining Eq. [1] and [2] gives

$$\frac{J_\infty}{zF} = \frac{D}{L}\left(\frac{k_3}{k_{-3}}\right)\theta \qquad [3]$$

and

$$\frac{\partial\eta}{\partial \ln J_\infty} = \frac{\partial\eta}{\partial \ln\theta} \qquad [4]$$

where η is the hydrogen overpotential. A survey of the data in Table I shows that

$$\frac{\partial\eta}{\partial \ln J_\infty} \simeq -\frac{4RT}{F} \qquad [5]$$

This result is tenable only with a coupled discharge-recombination mechanism for hydrogen evolution at low coverages ($\theta < 0.1$) of hydrogen. The reaction sequence at the cathode surface then is as follows

$$\xrightarrow{+\mathrm{FeH_{ads}}} \quad \xrightarrow{k_2} 2\mathrm{FeH_{ads}} \rightarrow \mathrm{H_2} + 2\mathrm{Fe} \qquad [6]$$

$$\mathrm{H_3O^+} + e + \mathrm{Fe} \xrightarrow[\text{(slow)}]{k_1} \mathrm{FeH_{ads}} \underset{k_{-3}}{\overset{k_3}{\rightleftarrows}} \mathrm{FeH_{abs}} \qquad [7], [8]$$

where FeH_{ads} refers to adsorbed hydrogen on the metal surface, and FeH_{abs} refers to absorbed hydrogen directly beneath the metal surface; k_1, k_2, k_3, and k_{-3} are the rate constants of steps [6], [7], and [8]. The above reaction sequence gives

$$J_\infty = \frac{DzF}{L}\frac{k_3}{k_{-3}}\left(\frac{1}{k_2}\right)^{1/2} i^{1/2} \qquad [9]$$

$$= \frac{DzF}{L} c^{1/2}{}_{H^+}\left(\frac{k_3}{k_{-3}}\right)\left(\frac{k_1}{k_2}\right) e^{-\beta\eta F/RT} \qquad [10]$$

The direct proportionality of the permeation rate to the square root of the current density (*cf.* Fig. 10) is in agreement with Eq. [9], and the slopes of the permeation potential curves in Table I are in agreement with Eq. [10]. From this it may be concluded that in this potential and temperature (18°-80°C) range the mechanism of hydrogen evolution on iron in acidic

(0.1*N* H_2SO_4) solutions is coupled discharge-electrochemical, and that the adsorption of hydrogen on the metal surface is Langmuirean.

Mechanism of hydrogen entry into iron.—Bagotskaya (4) and Frumkin (5) in discussing the effect of poisons in the hydrogen permeation rate have postulated that hydrogen enters the metal in the same elementary act as that in which it is discharged, and that the intermediate state through which hydrogen enters the metal lattice is not identical with the adsorbed intermediate which leads to discharge. They suggest that both reactions (absorption of hydrogen and hydrogen evolution) occur independently. In this case the reaction sequence at the cathode surface is as follows.

$$\begin{array}{ccccc} & & H_{abs} & & \\ & & 4\,\downarrow\uparrow -4 & & \\ & & 1 \quad\quad 2 & & \\ H^+ + e & \rightarrow & H_{ads} & \rightarrow & H_2 \end{array} \qquad [11]$$

Let k_1, k_2, k_4, and k_{-4} be the rate constants for steps 1, 2, 3, 4, and —4, respectively, and β_1 and β_4 the transfer coefficients for steps 1 and 4, respectively. Then the permeation current is as follows

$$J = F\left[k_4 a_{H+} \left(1 - \frac{c_o}{c_s}\right) e^{-\beta_4 \phi F/RT} - k_{-4}\, c_o\, e^{(1-\beta_4)\phi F/RT} \right] \qquad [12]$$

where c_s is the concentration of hydrogen in the lattice at hydrogen saturation, and ϕ is the metal solution potential difference. Substituting for c_o using Eq. [1] gives

$$J = \frac{F k_4 a_{H+}\, e^{-\beta_4 \phi F/RT}}{\left[1 + \frac{L}{D}\left(\frac{k_4 a_{H+}}{c_s} e^{-\beta_4 \phi F/RT} + k_{-4}\, e^{(1-\beta_4)\phi F/RT}\right)\right]} \qquad [13]$$

The only valid limiting case is

$$\frac{L}{D}\left[\frac{k_4 a_{H+}}{c_s} e^{-\beta_4 \phi F/RT} + k_{-4}\, e^{(1-\beta_4)\phi F/RT}\right] >> 1 \qquad [14]$$

since J depends on D and L, *i.e.*,

$$J = \frac{FD}{L\left(\frac{1}{c_s} + \frac{k_{-4}}{k_4 a_{H+}} e^{\phi F/RT}\right)} \qquad [15]$$

Equation [15] in turn yields two limiting solutions

$$J = \frac{FD\, k_4 a_{H+}}{L k_{-4}} e^{-\phi F/RT} \qquad [16]$$

and

$$J = \frac{FDc_s}{L} \qquad [17]$$

the latter (Eq. [17]) being for high negative potentials where the metal approaches hydrogen saturation. Equation [16] gives

$$\frac{\partial \phi}{\partial \ln J} = -\frac{RT}{F} \qquad [18]$$

and

$$J \alpha i^2 \qquad [19]$$

It is thus clear from Eq. [18] and [19] that the model proposed by the Russian workers (4, 5) does not predict the observed result. It may be concluded then that the intermediate through which electrolytic hydrogen passes on entry to the metal substrate is the adsorbed state and is identical to the intermediate which leads to hydrogen evolution. The rate of entry of hydrogen into the metal is determined by the coverage of hydrogen (θ), the energetics of the transfer of hydrogen to the metal bulk, and the energetics of the recombination process which leads to hydrogen evolution.

From the similarity of the experimentally found values of c_o for Armco iron single crystals and Armco iron polycrystals (Fig. 12), it may be concluded that grain boundaries play no part in the hydrogen evolution reaction, or in the absorption of hydrogen on the metal.

Mechanism of hydrogen evolution on iron from 0.1N NaOH solutions.—The Tafel slope, the permeation-potential relationship (Fig. 9), and the permeation-current behavior (Fig. 11) are tenable only with a coupled discharge-recombination mechanism at potentials below —1.02v NHE. Here again, one sees that the hydrogen coverage (θ) is low and that the adsorption of hydrogen is Langmuirean. Since the coverage is low at —1.02v NHE the only explanation for the leveling off of the permeation with potential above —1.02v NHE is a change over to a slow discharge-fast electrochemical mechanism[5] at this potential. These results are in reasonable agreement with Bagotskaya (9) who found, using a qualitative method, that the desorption step changed from recombination to electrochemical at $\eta = -0.34$v in 2*N* NaOH.

In the case of alkaline solutions, it is again clear that hydrogen passes through the intermediate adsorbed state on entry to the metal substrate.

Temperature dependence of the permeation rate and its relationship to the mechanism of hydrogen absorption.—The behavior of the observed slopes of the current potential curve with temperature is in agreement with that predicted from the simple kinetic equations (10), with $\alpha \approx 0.5$ constant with temperature. An analogy may be drawn for the case of nickel (11) where an increase from 9.3 to 16.8 kcal/mole was observed in going from 0.1 to 1*N* HCl. No detailed interpretations of the anomalously high values can be given. However, anion adsorption on Fe and Ni may resemble the adsorption of anions on Pt, which has recently been shown by Balashova to have large regions of potential independence.

Using Eq. [1] and neglecting the membrane thickness change with temperature gives

$$R\left(\frac{\partial \ln J_\infty}{\partial\, 1/T}\right)_L = R\left(\frac{\partial \ln D}{\partial\, 1/T}\right) + R\left(\frac{\partial \ln c_o}{\partial 1/T}\right) \qquad [20]$$

$$= \Delta H_D + R\left(\frac{\partial \ln c_o}{\partial\, 1/T}\right) \qquad [21]$$

where ΔH_D is the heat of activation for diffusion of hydrogen in iron.

From Eq. [9] and [10], one sees that

$$R\left(\frac{\partial \ln c_o}{\partial\, 1/T}\right)_i = R\left(\frac{\partial \ln k_3/k_{-3}}{\partial\, 1/T}\right) - \frac{R}{2}\left(\frac{\partial \ln k_2}{\partial\, 1/T}\right) = \Delta H_{c,i} \qquad [22]$$

and

$$R\left(\frac{\partial \ln c_o}{\partial\, 1/T}\right) = R\left(\frac{\partial \ln c_o}{\partial\, 1/T}\right)_i + \frac{1}{2}\Delta H_\eta = \Delta H_{c,\eta} \qquad [23]$$

where ΔH_η is the heat of activation for the H.E.R. at overpotential η. Calculations on our results give $\Delta H_{c,i} = -1.33$ kcal/mole and $\Delta H_{c,-0.408\text{v NHE}} = 5.0$ kcal/mole, *i.e.*,

$$\Delta H_{c,-0.408\text{v}} - \Delta H_{c,i} = 6.33 \text{ kcal/gram mole} \qquad [24]$$

$$\tfrac{1}{2}\Delta H_{-0.408\text{v}} = 7.2 \text{ kcal/mole} \qquad [25]$$

This internal consistency in the results gives added proof to the fact that hydrogen on entering the metal goes through an adsorbed intermediate which is identical to that which leads to hydrogen evolution. This finding is in disagreement with the hypothesis of Bagotskaya (4), that two parallel paths exists for hydrogen discharge, (one which leads to entry to the

[5] Since θ is small <0.1 up to —1.02v a fast discharge-slow electrochemical reaction above —1.02v would give a Tafel slope of —0.040v.

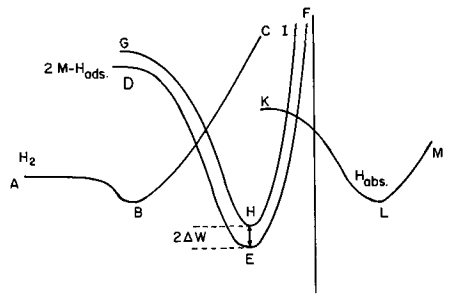

Fig. 13. Schematic representation of the potential energy curves for physical adsorption of molecular hydrogen, chemisorption of atomic hydrogen and absorption of atomic hydrogen.

metal, and the other which leads to hydrogen combination on the surface and evolution of hydrogen gas), each with widely different activation energies.

Mechanism by which anions and poisons increase the permeation rate.—Kabozev and Montblanova (12, 13) on the basis of the assumption that the rate-controlling step in H evolution on iron is recombination, have suggested that the increase in adsorption of anions is due to a lowering of the M-H_{ads} bond. Although the rate-determining step assumed by these workers is no longer an acceptable one for Fe (10), nevertheless, their idea can be incorporated in the mechanism of hydrogen evolution and entry into the metal, deduced in the present work.

In Fig. 13, the potential energy curves for physical adsorption of H_2 (A,B,C), chemisorption of H(DEF), and absorption of H in an octahedral interstitial cavity directly beneath the cathodic surface (KLM) are shown. GHI represents the curve for chemisorption of H when the M-H_{ads} bond strength is lowered by an amount ΔW.

Let J'_i be the permeation rate on lowering the M-H_{ads} bond energy by an amount ΔW. From Eq. [9] it follows that

$$\frac{J'_i}{J_i} = \frac{k'_{-3}k_3}{k_3k_{-3}}\left(\frac{k_2}{k'_2}\right)^{1/2} \qquad [26]$$

where k'_2, k'_3, and k'_{-3} are the rate constants when the potential energy curve for hydrogen adsorption is GHI.

On the basis of the model shown in Fig. 13

$$k'_3 = k_3e^{\alpha\Delta W/RT} \qquad [27]$$

$$k'_2 = k_2e^{2\beta\Delta W/RT} \qquad [28]$$

$$k'_{-3} = k_{-3}e^{(\alpha-1)\Delta W/RT} \qquad [29]$$

where α and β are the slopes of the potential energy curves at the points of intersection. From Eq. [26], [27]-[29] it follows that

$$\frac{J'_i}{J_i} = e^{(1-\beta)\Delta W/RT} \qquad [30]$$

Thus, since $\beta < 1$, it may be seen that a lowering of W by ΔW results in an increase in the hydrogen permeation rate, and on this basis the effect of adsorption of I^- on the permeation rate may be explained.

The question arises as to how adsorption of I^- decreases W. If one supposes, as have Frumkin and Slygin (14) for platinum, that the polarity of the Fe-H_{ads} bond is negative towards the solution, then the lowering of W could be due to electrostatic interaction between I^- and H^-. Interaction between the adsorbed I^- and the d-bond of the metal could lower W, as has been proposed by Bockris and Conway (15). Finally, if adsorption of I^- occurs at sites favorable for hydrogen evolution (*i.e.*, with large W), discharge will then occur at other sites, where W is weaker. The lowering of W may be due to any of the above three effects, or any combination of them, since they can occur simultaneously. Such a model successfully explains the increase in hydrogen permeation and the rise in hydrogen overpotential on absorption of I^-. The increase in the hydrogen permeation rate with concentration of I^- is due to an increased surface coverage with I^-.

The effect of CN^- in alkaline solution can be explained by a mechanism similar to that proposed for I^-. The fact that at low overpotentials the permeation rate is independent of the concentration of cyanide would indicate strong chemisorption of cyanide on the metal surface. This conclusion is in agreement with the findings of Beck *et al.*, who found strong adsorption of CN^- on iron (16). The concentration dependence of the permeation rate in alkaline cyanide solutions at higher overpotentials is due to the fact that here the desorption step is electrochemical instead of combination.

On the basis of the effect of the lowering of W on the permeation rate the increase in permeation on addition of naphthalene to 0.1*N* H_2SO_4 may be explained. Interaction between the π-bonds of naphthalene and the d-band of the metal could lower W and hence increase the permeation rate. This conclusion is in agreement with recent findings of Russian workers (17), who observed a positive shift in the point of zero charge on mercury on adsorption of naphthalene. The similarity in the effects observed in the case of I^- CN^- and naphthalene would suggest that the mechanism of Bockris and Conway is the best explanation for the lowering of the M-H_{ads} bond energy on the adsorption of impurities.

Mechanism of the lowering of permeation rate by organic nitriles.—The effects observed in the case of valeronitrile benzonitrile and naphthonitrile are mutually similar, but give permeation effects in the opposite direction to that observed for naphthalene. The similarity in the effects observed in the case of the aliphatic and aromatic nitrile would indicate that adsorption of the aromatic nitriles occurs vertically. If this were not the case, different effects would be expected in going from the aliphatic to the aromatic nitriles. Adsorption of these compounds in this fashion would thicken the double layer and preclude the interaction of the π-bonds of the aromatic nitriles with the metal. Vertical adsorption of these compounds would hinder the approach of hydrated hydrogen ions from the solution to the metal surface. Since energy would be expended on pushing the hydrogen through the adsorbed organic layer an increase in overvoltage would be expected (5). Thus, the decrease in hydrogen permeation would be due to a decrease in θ_H. At higher surface concentrations of the organic, the effect would be more drastic, and, hence, the concentration dependence of this effect can be explained.

The effects observed by Smialowski *et al.* (18) in the case of dibenzylsulfoxide may be explained by a similar mechanism.

Consistent interpretation of the work of Bagotskaya.—On investigations the permeation from mercury poisoned acid solutions. Bogotskaya (4) had found that the permeation time curve displayed a maximum. Similar results have been observed by us in acid solutions and the mechanism by which this maximum occurs is explained elsewhere (19), as being due to the blistering of the metal and the formation of surface cracks due to supersaturation of the metal with hydrogen. Bagotskaya (4) has found that poisoning the diffusion side with mercury in acidic solutions increases the permeation rate above that observed when only acid (0.1*N* H_2SO_4) was present: the diffusion side in each case was polarized at $i_c = 4 \times 10^{-9}$ amp/cm^2, while the polarization side was polarized at 50 ma/cm^2 in HgO saturated alkaline solutions. In the case of alkaline solutions it was found (4) that, on poisoning with mercury, polarization at $i_c < 4 \times 10^{-4}$ amp/cm^2 decreased the permeation while above $i_c = 4 \times 10^{-4}$ amp/cm^2 the permeation rate was increased, as

compared to that observed in pure alkaline solutions under similar conditions of polarization. Mercury, a strong poison, supersaturates the metal with hydrogen (as is evidenced by the observed maximum in the permeation rate transient). It is suggested, therefore, that, when the diffusion side is poisoned with mercury, fissures form on the surface. Such a damaged surface reduces the entry of hydrogen from the diffusion side. However, hydrogen atoms diffusing from the polarization side can recombine at the bottom of the fissures (out of contact with the electrolyte) and arrive as hydrogen gas at the diffusion side surface. Thus the mercury on the iron diffusion side surface will not affect the permeation. In the case of alkaline solutions it is possible that such damage will not occur until $i_c > 4 \times 10^{-4}$ amp/cm^2 is realized.[6] Below $i_c = 4 \times 10^{-4}$ amp/cm^2, mercury will influence the permeation rate as described here for other poisons, while above 4×10^{-4} amp/cm^2 a situation such as that described for mercury poisoned acid solutions will be operative.

The hypothesis that hydrogen recombines in fissures out of contact with the electrolyte is consistent with the findings of Bagotskaya in an earlier work (20), when it was found that diffusing hydrogen had no effect on the overpotential (η) on polarized mercury poisoned hydrogen electrodes in acid solutions. If the atomic hydrogen cannot reach the sites when hydrogen evolution takes place on the mercury poisoned iron surface, no effect of diffusion hydrogen on η would be expected.

It may be seen that the mechanism described in (19) for the observed maxima in permeation transients offers a rational explanation of the results of Bagotskaya; thus is not necessary to postulate that direct discharge of hydrogen into the metal takes place, in order to explain the observed results (4).

Summary

The investigation of the hydrogen evolution reaction (h.e.r.) on iron has been carried out as a function of ambient and temperature, using permeation rate-potential relationships as a diagnostic criterion for mechanism determination. The evolution on, and entry of hydrogen into single crystal Armco iron, has been studied.

Additions of I^-, CN^-, and naphthalene to the solutions increase, while additions of valeronitrile, benzonitrile and naphthonitrile decrease the permeation rate (J). J through Armco iron single crystals and polycrystals is similar for identical electrode conditions.

From the permeation-potential, permeation-current, and permeation-temperature relationships observed, it has been concluded that hydrogen on entering the metal passes through an adsorbed state on the metal surface which is identical to the intermediate which leads to hydrogen evolution. The similarity of the results obtained for Armco iron, single crystals, and polycrystals indicates that grain boundaries play no part in the hydrogen evolution kinetics or the mechanism of hydrogen entry to the metal.

The current-potential relationships and the dependence of the permeation rate on potential and current density are tenable only with a coupled discharge-recombination mechanism for hydrogen evolution on iron at low overpotentials in acid solutions. This mechanism does not change with temperature. In alkaline solutions the mechanism for hydrogen evolution is coupled-discharge recombination below −1.02v N.H.E. while at more negative potentials, it is slow discharge followed by fast electrochemical desorption.

The effect, of adsorption of I^-, CN^-, and naphthalene, on the permeation rate has been explained by a lowering of the M-H_{ads} bond, while the effect of valeronitrile, naphtonitrile, and benzonitrile is explained by there vertical adsorption hindering the discharge of hydrogen ions and thus lowering θ_H.

It has been shown that the results of Bagotskaya (4) for the effect of mercury poisoning on the permeation rate are not necessarily in disagreement with the hypothesis that hydrogen is adsorbed on the metal surface prior to entry to the metal.

[6] Since at $i_c < 4 \times 10^{-4}$ amp/cm^2 in mercury poisoned alkaline solutions the hydrogen concentration in the lattice will be insufficient to cause any damage of the metal surface.

Acknowledgments

The financial support of the Naval Air Engineering Center, Philadelphia, Pennsylvania, during the course of this work is gratefully acknowledged. The authors wish to express sincere thanks to Dr. H. Wroblowa and Dr. W. Beck for many helpful suggestions and discussions, and to Dr. D. F. Stein, of General Electric Corporation, Schenectady, for supplying the single crystals used in this work. Thanks are also due to Mr. F. S. Williams and Mr. E. Taylor of N.A.E.C. (Philadelphia) for their kind cooperation during the course of the present work. This paper is taken in part from the thesis presented to the University of Pennsylvania by one of the authors (J. McB.) in partial fulfillment of the requirements for the Ph.D. degree.

Manuscript received March 11, 1965; revised manuscript received June 21, 1965.

Any discussion of this paper will appear in a Discussion Section to be published in the June 1966 JOURNAL.

REFERENCES

1. J. O'M. Bockris and R. Thackar, Technical Report No. 3, Office of Naval Research Contract No. NR551(22)NR036-028(1959).
2. M. A. V. Devanathan and Z. Stachurski, *This Journal*, **111**, 619 (1964).
3. A. I. Oshe, *Zhur. Fiz. Khim.*, **32**, 1622 (1958).
4. I. A. Bagotskaya, *ibid.*, **36**, 2667 (1962).
5. A. N. Frumkin, "Advances in Electrochemistry and Electrochemical Engineering," Vol. 3, p. 93, P. Delahay, Editor, Interscience Publishers, Inc., New York (1963).
6. M. A. V. Devanathan and Z. Stachurski, *Proc. Roy. Soc.*, **A270**, 90 (1962).
7. M. A. V. Devanathan, Z. Stachurski, and W. Beck, *This Journal*, **110**, 886 (1964).
8. J. McBreen and L. Nanis, To be published.
9. I. A. Bagotskaya, *Doklady Akad. Nauk S.S.S.R.*, **107**, 843 (1956).
10. J. O'M. Bockris, "Modern Aspects of Electrochemistry," Chap. 4, Butterworths, London (1954).
11. J. O'M. Bockris and E. C. Potter, *J. Chem. Phys.*, **20**, 614 (1952).
12. W. Kobozev and V. Montblanova, *Zhur. Fiz. Khim.*, **6**, 38 (1935).
13. W. Kobozev and V. Montblanova, *Acta. Physiochim. U.R.S.S.*, **1**, 611 (1936).
14. A. N. Frumkin and A. Slygin, *Izvestia, Akad. Nauk. S.S.S.R., Ser. Khim.*, 773 (1936).
15. J. O'M. Bockris and B. E. Conway, *J. Chem. Phys.*, **76**, 532 (1957).
16. W. Beck, A. L. Glass, and E. Taylor, *This Journal*, **112**, 53, (1965).
17. A. N. Frumkin and B. B. Damaskin, "Modern Aspects of Electrochemistry," No. 3, p. 199, J. O'M. Bockris and B. E. Conway, Editors, Butterworths, Washington (1964).
18. M. Smialowski (and others), Electrochemical Conference, Moscow (1956).
19. J. O'M. Bockris, J. McBreen, W. Beck, and L. Nanis, To be published.
20. I. A. Bagotskaya, *Doklady Akad. Nauk. S.S.S.R.*, **110**, 397 (1956).

An All-Metal Cell Technique for the Measurement of the EMF of Molten Metal-Metal Halide Solutions Corrosive to Ceramics

Harry R. Bronstein

Chemistry Division, Oak Ridge National Laboratory, Oak Ridge, Tennessee

ABSTRACT

A new technique is described which permits the measurement of emf using an all-metal cell. The applicability of the method to both aqueous systems and molten metal-metal halide systems is demonstrated. This technique will now permit measurements of the emf of systems such as the molten alkaline earth-alkaline earth halides and the rare earth-rare earth halides which are extremely corrosive to ceramics.

The measurement of equilibrium cell potentials has long been an important means of determining thermodynamic properties of systems. In addition, equilibrium emf measurements can yield information as to the species present and the number of electrons involved in the potential-determining process. The application of this fundamental measurement to a unique group of solutions, namely, the alkaline earth metals, and the rare earth metals dissolved in their respective molten halides (1, 2) has been reported for the lanthanum-lanthanum chloride (3, 4) and the cerium-cerium chloride (5) solutions. However, the results are subject to question because of the corrosiveness of these solutions to ceramic material (6, 7). If dependable emf measurements are to be made on these solutions, a technique must be employed which eliminates the use of ceramic containers and insulators.

This paper describes such a technique which permits the measurement of emf in an all-metal cell.

Discussion of Technique

Aqueous cells such as Hg^{o}, $Hg_2SO_4/H_2SO_4/Ag_2SO_4$, Ag^{o} are contained in glass apparatus. Each electrode compartment is in communication with the sulfuric acid bridging solution by means of a capillary or a sintered glass frit. Electrode leads are platinum wire in contact with the mercury of the $Hg\text{-}Hg_2SO_4$ half-cell and the silver wire of the Ag, Ag_2SO_4 electrode. The open-circuit potential of this cell is measured in the normal manner. The current is comprised of electron transport from the $Hg\text{-}Hg_2SO_4$ electrode, $2Hg \rightarrow Hg_2^{+2} + 2e^-$, via the platinum lead through the potential measuring instrument to the $Ag\text{-}Ag_2SO_4$ electrode, $2Ag^+ + 2e^- \rightarrow 2Ag^{o}$ with the sulfuric acid acting as the transfer medium for the sulfate ion. The over-all cell reaction being $2Hg^{o} + Ag_2SO_4 \rightarrow Hg_2SO_4 + 2Ag^{o}$.

If the same half-cell mixtures Hg^{o}, $Hg_2SO_{4(solid)}$, saturated aqueous solution and Ag^{o}, $Ag_2SO_{4(solid)}$, saturated aqueous solution are placed in separate tantalum tubes, these containers have now the same function as the platinum and silver wires of the glass cells. The tubes are partially immersed in a sulfuric acid solution and communication of the solution in each tube with the bridging liquid is provided by means of a sintered porous tantalum plug welded in the side of each tube. If there were no such communication, a current would not be expected to flow, since the potential difference between the two electrodes is much less than the potential necessary for decomposition of the sulfuric acid (H_2O) and that of the anodic dissolution of tantalum metal. Concomitant with this requirement is the absence in the bridging liquid of any redox process which can occur within the potential developed at the tantalum electrodes. With these requirements met and with the porous metal plug providing an ion path for transport of current, the potential between these all-metal cells should be the same as that measured in the conventional glass insulator apparatus.

The same analysis may be applied to a molten metal-metal halide system. A concentration cell contained in an all-metal system may be schematically illustrated as follows:

$$\underline{\text{Ta}} \quad \begin{matrix}\text{saturated} \\ \text{Cd-CdCl}_2\end{matrix} \quad \begin{matrix}\text{LiCl, KCl} \\ \text{eutectic}\end{matrix} \quad \begin{matrix}\text{unsaturated} \\ \text{Cd-CdCl}_2\end{matrix} \quad \underline{\text{Ta}} \qquad \text{[Cell 1]}$$

The solid line represents the metal tube containing the respective solution, and the dotted line the sintered porous metal frit. The symbol of the metal of construction is placed as shown and the bridging liquid written as normally. The conventional half-cell reaction may be written for each compartment.

The saturated anode

$$Cd \rightarrow Cd^{2+} + 2e^-$$

or [ref. (1), (2)]

$$Cd_2^{2+} \rightarrow 2Cd^{2+} + 2e^-$$

The unsaturated cathode

$$Cd^{2+} + 2e^- \rightarrow Cd^{o}$$

or

$$2Cd^{2+} + 2e^- \rightarrow Cd_2^{2+}$$

For transport of current and measurement of a potential, chloride ions must be able to migrate from the cathode compartment via the bridging liquid to the anode compartment.

As stated previously, if there were no communication of the solutions in the tantalum cells with the bridging liquid and if the decomposition potential of the bridging liquid were greater than the potential developed at the tantalum electrodes, no current could flow. The decomposition potential of the constituents of the molten eutectic mixture (8) is greater than any potential which can be developed in this system (9, 10), but with communication through the porous metal frit, chloride ion migration is possible, and the potential measured should be the same as measured in a conventional ceramic apparatus.

Experimental

For the evaluation of the applicability of this technique to aqueous systems, the following cell was used

$$\underline{\text{Ta}} \quad \begin{matrix}\text{Hg}^{o}, \text{Hg}_2\text{SO}_{4(\text{solid})} \\ \text{saturated solution} \\ \text{in } H_2O\end{matrix} \quad \begin{matrix}1N\ H_2SO_4, \\ H_2O\end{matrix} \quad \begin{matrix}\text{Ag}^{o}, \text{Ag}_2\text{SO}_{4(\text{solid})} \\ \text{saturated solution} \\ \text{in } H_2O\end{matrix} \quad \underline{\text{Ta}} \qquad \text{[Cell 2]}$$

Each mixture was contained in a ⅝ in. diameter tantalum tube 3 in. in height, with a sintered porous tantalum pellet ⅜ in. diameter by ¼ in. thick welded into the wall. The silver wire in contact with both the

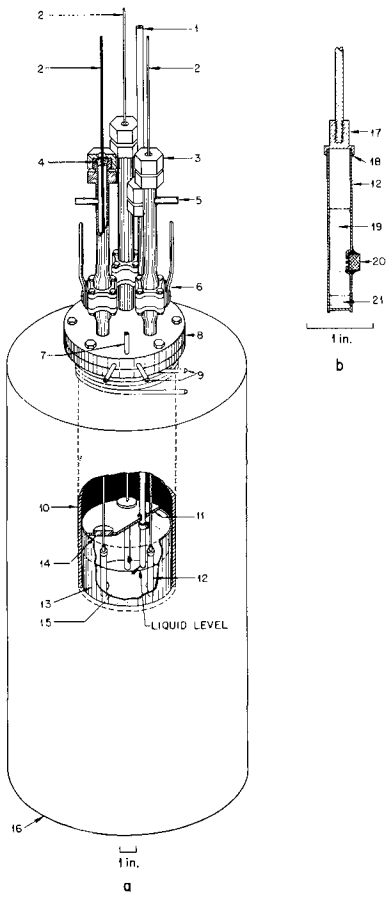

Fig. 1. (a) Apparatus and (b) cell design. 1, Stainless steel thermocouple tube; 2, tantalum electrodes; 3, gasket tightener; 4, Teflon seal; 5, vacuum and pressure line to entry ports; 6, Worchester valve; 7, vacuum and pressure line to tank; 8, Teflon "O" ring seal; 9, water coolant tubes; 10, stainless steel tank; 11, stainless steel spacer plate attached to thermocouple tube; 12, electrode tube (see Fig. 1b); 13, tantalum vessel; 14, Lavite insulators; 15, tantalum jacketed thermocouple tube; 16, Marshall furnace; 17, tantalum threaded cap; 18, weld; 19, solution molten Cd-$CdCl_2$; 20, porous tantalum plug; 21, excess cadmium in reference cell.

solution and solid silver sulfate was clamped to the tantalum cell for good electrical contact. The tubes were suspended in 1*N* H_2SO_4 contained in a tantalum beaker.

For the high-temperature study, the molten Cd-$CdCl_2$ system was used. The inertness of these solutions to Pyrex and quartz has permitted emf measurements to be made in the normal manner. The reproducibility of the data by several investigators (9, 10) has established the reliability of the Cd-$CdCl_2$ system as a standard.

Figure 1a illustrates the apparatus employed for this test. Much of the design of the apparatus was for projected use in the rare earth metal-rare earth halide systems. For the cadmium-cadmium chloride system, three tantalum metal cells (Fig. 1b) were employed, one the saturated Cd(excess)-$CdCl_2$ reference electrode and the other two containing 2 and 10 mole % cadmium dissolved in cadmium chloride, respectively. The 15 mil wall tantalum cells were ⅜ in. ID by 2½ in. in length. One-half inch from the bottom of each electrode capsule, a depression was formed in the wall for placement of a sintered porous pellet of tantalum ⅜ in. diameter by ¼ in. thick. The tantalum pellet was welded to the body of the capsule as illustrated so that only the exposed end of the pellet would be in contact with the bridging liquid. The wall of the capsule in back of the porous tantalum pellet had two holes 0.007 in. in diameter for access of the electrode solution to the porous pellet. The porous pellets were made by the Kawecki Chemical Company from uniform size, 10μ, high capacitance type tantalum powder compressed to 80% of theoretical density. After loading, the cells were capped and welded shut. Loading and welding was performed in a helium dry box. Closure of the cells was necessitated by the volatility of cadmium metal at the temperature to be employed (above 600°C), and escape would be limited by slow diffusion through the porous tantalum plug. By means of threads in the cell caps, 3/16 in. tantalum rods were attached to serve both as electrode leads and as a means of lowering the cells into the melt. The melt, a carefully dehydrated eutectic mixture of LiCl and KCl, was contained in a 3½ in. high tantalum vessel which fitted inside the 5 in. ID by 14 in. high stainless steel tank as illustrated. For this experiment, the tank cover was assembled with the electrode cells and spacer plate positioned such that the cells would be above the eutectic mixture when the tank cover was attached to the tank. The apparatus was evacuated and then pressurized with dry argon by means of a nullmatic valve for maintenance of constant pressure inside the tank. The tank was heated by means of a 6 in. ID by 24 in deep Marshall furnace. Constant temperature of the system was maintained by conventional control devices. At temperature, the cells were lowered into the melt by means of the tantalum rods which extended through Teflon pressure seals in the top of the entry ports, care being taken that the cells did not touch the bottom of the tantalum vessel. Next, the tantalum-jacketed stainless steel thermocouple tube, to which the spacer plate is attached, was lowered into the melt. The temperature was measured with a chromel-alumel thermocouple. The potential of the thermocouple was read on a Brown Electronik recorder, the major part of the voltage being bucked by a Rubicon precision potentiometer. The recorder had a chart span of 3 mv, graduated in 0.01 mv.

Several hours at temperature, 635°C ± 2°, was sufficient for saturation of the reference cell and complete solution in the others as attested by the attainment of a constant potential *vs.* the reference cell. The stability of the system was demonstrated by the constancy of the potential during a period of 16 hr at temperature. Potential measurements were made with a Hewlett-Packard model 425DC microvolt-ammeter.

Results

The potential of the aqueous cell 2 was + 41.5 ± 0.1 mv at 25°C in excellent agreement both with the theoretical value + 42.3 mv and the experimental + 42.0 ± 0.5 mv (11).

Table I compares the values of the emf obtained for the molten system Cd-$CdCl_2$ in cell 1 with those of previous investigations of this system in conventional ceramic cells. The agreement is excellent.

Since pure cadmium chloride was used as the bridging liquid by both Mashovets-Poddymov (10) and Crawford (9) and the eutectic LiCl-KCl in this experiment, the agreement in the experimental data indicates a negligible or nonexistent liquid junction potential in the all-metal cell system.

Summary

It has been experimentally demonstrated, both in an aqueous system and a molten metal-metal halide system, that emf measurements can be made in an all-

Table I. Comparison of emf data for Cd-$CdCl_2$ system at 635°C

Mole % Cd	All-metal cell technique 16 hour period	Conventional quartz cell ref. (10)	Pyrex cell ref. (9)
2	+ 112 ± 2 mv	+ 113 mv*	
10	+ 34 ± 1 mv	+ 35 mv*	36 mv*

* Values obtained from temperature *vs.* emf plots.

metal apparatus by a technique which eliminates the need of ceramic containers and insulators. For the all-metal cell technique to function, the decomposition potential of the bridging liquid, as well as that of any redox process which may be present in that liquid, must be greater than the potential difference between the electrode cells. It will now be possible to measure the emf of systems such as the molten alkaline earth-alkaline earth halides and the rare earth-rare earth halides which are extremely corrosive to ceramics.

Acknowledgment

The author wishes to thank Dr. F. A. Posey of this Laboratory, not only for very helpful and encouraging discussions during the conceptual development of the technique, but also for his continued aid throughout the course of the investigation. The research was sponsored by the United States Atomic Energy Commission under contract with the Union Carbide Corporation.

Manuscript received April 5, 1965; revised manuscript received June 10, 1965. This paper was presented at the San Francisco Meeting, May 9-13, 1965.

Any discussion of this paper will appear in a Discussion Section to be published in the June 1966 JOURNAL.

REFERENCES

1. M. A. Bredig, "Mixtures of Metals with Molten Salts," in "Molten Salt Chemistry," Milton Blander, Editor, Interscience Publishers, Inc., New York (1964).
2. J. D. Corbett, "The Solution of Metals in Their Molten Salts" in "Fused Salts," B. R. Sundheim, Editor, McGraw Hill Book Co., New York (1964).
3. M. V. Smirnov, P. M. Usov, and T. F. Khazemova, *Doklady Akad. Nauk SSSR*, **151**, 591 (1963); English translation, *Doklady Chemistry*, **151**, 583 (1963).
4. M. V. Smirnov and P. M. Usov, *Doklady Akad. Nauk SSSR*, **151**, 862 (1963); English translation, *Doklady Chemistry*, **151**, 606 (1963).
5. S. Senderoff and G. W. Mellors, *This Journal*, **105**, 224 (1958).
6. H. R. Bronstein, A. S. Dworkin, and M. A. Bredig, *J. Phys. Chem.*, **64**, 1344 (1960).
7. A. S. Dworkin, H. R. Bronstein, and M. A. Bredig, *Discussions Faraday Society*, **32**, 188 (1961).
8. W. J. Hamer, M. S. Malmberg, and B. Rubin, *This Journal*, **103**, 8 (1956).
9. G. A. Crawford, Ph.D. Thesis (1960), Imperial College, London.
10. V. P. Mashovets and V. P. Poddymov, *Zhur. Prikl. Khimi*, **37**, 813 (1964).
11. M. H. Lietzke and R. W. Stoughton, *J. Am. Chem. Soc.*, **75**, 5226 (1953).

The Electrochemical Reduction of Oxygen on Platinum Electrodes Partially Immersed in Sulfuric Acid

H. J. R. Maget and R. Roethlein

Fuel Cell Laboratory, Direct Energy Conversion Operation, General Electric Company, Lynn, Massachusetts

ABSTRACT

Reaction rates have been determined for the cathodic reduction of oxygen on submerged and partially immersed smooth and platinized platinum electrodes in 1*N* and 10*N* H_2SO_4. Measurements of local and total electrode currents for various thicknesses of electrodeposited platinum have shown the dependence of current on deposit thickness and surface roughness, observed in 10*N* H_2SO_4. The liquid film theory offers a partial explanation of the observed experimental results. Gas-liquid interfacial geometry relationships have been derived to describe menisci and liquid films obtained on glass, smooth and platinized platinum, and a value of the liquid film thickness immediately above the intrinsic meniscus has been obtained. In all cases, the current is mainly carried by the electrode surface immediately above the conventional "three-zone interface" and decreases rapidly above this level because of appreciable contribution of ohmic polarization to local electrode potentials. Limiting currents were shown to be linearly dependent and square-root dependent on oxygen partial pressure below the meniscus region and above the meniscus, respectively.

It was the general objective of this research program to conduct investigations leading to an understanding and eventual improvement of porous electrodes to be operated as oxidant cathodes in fuel cells. Due to the complexity of practical electrode structures, work was conducted on a simplified model of a single pore, but was expected to yield information regarding the behavior of practical porous electrodes. The simplest study model is a straight cylindrical pore. An early model proposed by Justi (1) suggested a surface diffusion of hydrogen as a rate-controlling step for the electrochemical oxidation of hydrogen, involving the concept of a three-zone interface. However, recent work by Will (2) has shown that the main source of current is confined to a narrow band close to the upper edge of the meniscus. Similar results were observed by Sama *et al.* (3) in the case of oxygen reduction on copper, silver, and nickel electrode sheets. These authors suggest that mass transport of oxygen may be rate limiting. This concept is intriguing since a two-zone thin film region could justify extremely large transport rates. Such a model has raised questions regarding the necessity of basing the diffusion current theory on large exchange currents, larger than usually accepted for gas reactions (4). In addition, meniscus and film stability for practical pore lengths are dependent on pore geometry, the pore material, and potential. Bonnemay (5) has shown for monotubular silver electrodes that applied potentials produce a modified surface state of the pore-wall metal, yielding variations in electrolyte-electrode surface tension, resulting in a dynamic behavior of the liquid in the capillary. As expected, the electrode activity is dependent on the pore diameter, increasing with pore diameters up to 0.3 mm, but abruptly decreasing for diameters greater than 0.3 mm. This result suggests large modifications of meniscus geometry and contact angle. If oxygen diffusion is rate controlling, an increase in contact angle results in a larger diffusion path and smaller gas concentration at the metal-solution interface.

Direct evidence of the existence of these films on metal surfaces has been obtained by Muller (6). A practical contribution to thin film studies was also

reported by Rozenfeld (7) in the case of electrolyte evaporation. Rates of oxygen transport through thin films were observed to increase with rate of evaporation, as a result of spontaneous mixing arising from changes in electrolyte concentration and surface tension. These results indicate that additional complications could be expected in thin film regions if concentration differences, *i.e.*, natural convection, can take place. Detailed and comprehensive calculations on transport processes in pores have been discussed by Wagner (8).

If mass transport of reacting species across the meniscus and film is rate controlling, as it has been shown for some electrochemical processes, it becomes necessary to know the gas-liquid interfacial geometry. Indeed, for extremely small contact angles between the electrolyte and the supporting electrode material, the thickness of the liquid layer near the meniscus-film boundary may become rather small, resulting in appreciable ohmic overvoltage between the electrolyte bulk and the narrow current-carrying region. This would change the local potential and current distribution, which in turn could possibly result in appreciably reduced contribution of the liquid film to the over-all reaction rate. A comprehensive study on such effects has been reported by Guillou (9). This author indicates that potential-concentration relationships are point functions of the current density, and that current-potential relationships have a significance only at discrete points of the electrolyte/electrode.

The following experiments were designed to investigate the effects of thin electrolyte films on the rate of oxygen reduction on platinum electrode surfaces. The results were expected to give a qualitative description of the reaction mechanism and current-potential distribution which occurs in the region immediately above the bulk electrolyte level.

Experimental

Experimental apparatus.—The experiments were carried out in a Pyrex glass cell consisting of five compartments, separate from each other by fine pore fritted glass disks. Two counter electrode compartments were arranged parallel to each other on either side of the central compartment. The counter electrodes have a large surface area composed of platinum-black electrodeposited on platinum mesh. Two other compartments which served as reference cells were joined symmetrically to the remaining sides of the central compartment. Each reference cell had a Luggin capillary extended into the main compartment, allowing the application of potentials near the test electrode. Hydrogen gas was bubbled through the reference compartments, and two platinum black screens served as hydrogen reference electrodes.

The test electrodes, see Fig. 1, were composed of platinum tubing (99.99% pure), 1.0 cm long, 1.5 cm in diameter, and 0.2 cm in wall thickness, sections A and A'. Another electrode, section B, of the same diameter and thickness but only 0.0127 cm (5 mils) in length was inserted between sections A and A'. Electrical connection was made by spot welding Teflon covered platinum wire to the inner wall of the platinum tubing. All three sections were mounted on a Teflon assembly and held rigid by a Teflon coated tantalum rod, which was threaded tightly into a Teflon stopper. This prevented the inner surface from coming in contact with the electrolyte. Insulation was accomplished by inserting 1 mil thick Mylar sheet of the same outside and inside diameter as the platinum tubing between each section.

The test electrode was raised and lowered into solution by means of a specially modified L. S. Starrett Vernier height gauge with an accuracy of $\pm 1.2 \times 10^{-3}$ cm.

Electrode preparation.—The electrode surface was pretreated in several ways: (*a*) finely polished, also electrodeposited with spongy platinum from chloroplatinic acid (with traces of lead acetate) at 10 ma/cm^2 for (*b*) 60 sec, (*c*) 12 sec, (*d*) 4 sec, and (*e*) 240 sec.

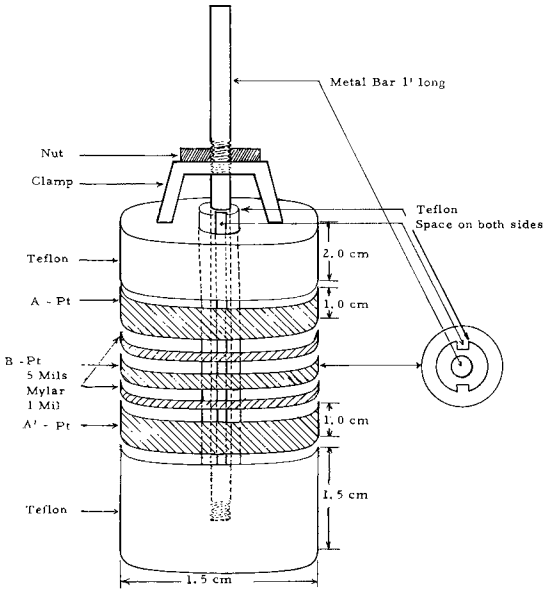

Fig. 1. Experimental cylindrical electrodes for the determination of current densities in meniscus and thin film region.

Measurements of the thickness of the electrodeposited platinum black layers were made by placing the platinum tubing vertically under a microscope and measuring the difference between the platinum substrate and the electrodeposited layers. The magnification was about 200X, with average deviation of $\pm 10\%$ for the thickness of the spongy layer.

Experimental procedure.—Polarization measurements were made by means for two "fast rise" Wenking potentiostats, (Model 61 TR) which have an operating potential source of ± 2v, a current measurement accuracy of 1.5% full scale, and a zero point stability of 5 mv/day.

Surface area measurements for the different electrode roughnesses were made by means of a constant current pulse used in conjunction with the Wenking potentiostat (10). The test electrode was held at a constant potential a few millivolts more positive than the reversible hydrogen potential; then by means of a switching device the potentiostat was disconnected from the circuit and replaced by a constant current anodic pulse. The potential change with time of the test electrode was measured simultaneously with the current variation across a standard resistance by means of a Tektronix type 551 dual-beam oscilloscope. The trace was photographed with a polaroid Tektronix C-12 oscilloscope camera. The number of coulombs required to remove hydrogen from the electrode surface in a N_2 purged, 1N H_2SO_4 solution was then used as a relative measure of the electrodes surface area.

Sulfuric acid of two different normalities (1N and 10N) was made from C. P. Reagent Grade stock solution using doubly distilled water containing less than 0.4 ppm impurities. The gases used in these experiments were of high grade prepurified quality. The temperature was maintained constant at $+23 \pm 1$°C.

The height and shape of meniscus and film formation on various surfaces (glass, smooth platinum, platinized platinum) were examined by optical and electrical methods. The measurements were conducted on cylindrical platinum tubing (99.99% Pt), 1.5 cm in diameter (in absence and presence of electrodeposited platinum black) and on 1.0 cm diameter glass tubing partially immersed in 1 and 10N H_2SO_4.

The meniscus geometry could be determined by projecting the image of the interface on a screen, allowing magnification of about 16X. The liquid film could not be observed clearly by this method.

Electrical resistance measurements were obtained by means of a semicircular platinum foil 1.0 cm in diameter and 1.27 x 10^{-2} cm thick, sealed between two cylindrical glass tubes and finely polished to form a continuous smooth surface. Electrical contact was made by spot-welding a platinum wire to the foil inside of the glass cylinder. The cylinder was raised and lowered into the electrolyte by means of the L. S. Starrett Vernier height gauge. Constant current pulses of less than 3 msec duration were applied between the foil and a counter electrode. The instantaneous potential decay was observed and measured on an oscilloscope and the ohmic resistance calculated therefrom. Similar measurements were also conducted by means of an a-c resistance bridge operating at 1000 cps.

Experimental Results

Interfacial liquid-gas geometry.—The maximum length, h, of the magnified observable meniscus was found to be 0.28 ± 0.01 cm for platinized platinum and glass and 0.27 ± 0.01 cm for polished platinum. The over-all meniscus geometry was similar in all cases. Figure 2 presents the observed geometry for platinized platinum cylinders.

Results obtained from resistance measurements on glass cylinders are reported in Fig. 3, for 1N and 10N H_2SO_4 electrolytes. The ohmic resistance is divided by the electrolyte resistivity, to account for the large variations in electrolyte conductivity. The linear part of the resistance curve is associated with the region of the thin film, allowing the calculation of electrolyte film thickness. Resistance values obtained by a-c measurements and constant current pulses were identical. The point from which a linear relationship between R/ρ and x/h is observed can be used to determine the length of the intrinsic meniscus. These values are in agreement with the measured length obtained from the magnified projected gas-liquid interface, that is 0.28 cm in 1N and 0.265 cm in 10N H_2SO_4.

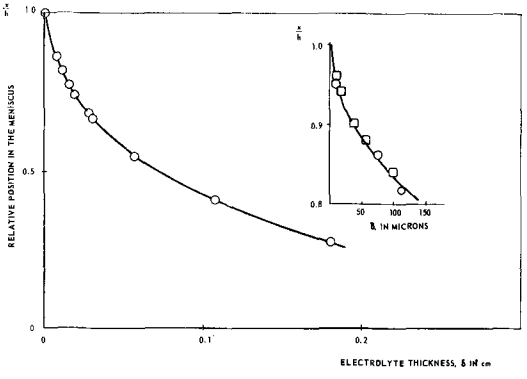

Fig. 2. Gas-liquid interfacial geometry: ○, experimental results; □, calculated values from Eq. [1a].

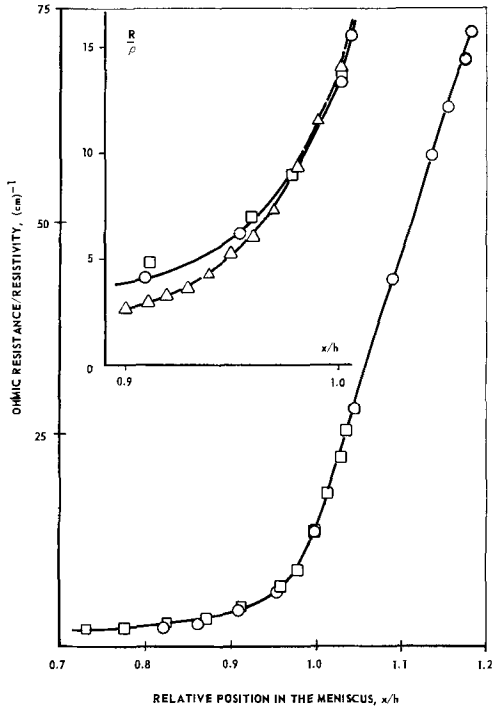

Fig. 3. Resistance in meniscus and thin film, 1N and 10N H_2SO_4. Experimental results: ○, 10N H_2SO_4; □, 1N H_2SO_4; △, calculated values from Eq. [5].

Since the experimental results have shown that relatively thin electrolyte films and relatively large resistance contributions to ionic flow occur for (x/h) values greater than about 0.9, all derivations have been established for (x/h) values near 1. Landau and Lifshitz (11) have derived equations [A1] and [A2] in Appendix A) for the interfacial liquid-gas geometry of menisci on flat surfaces. At the meniscus-film boundary, these equations for the electrolyte thickness, δ in cm, and the relative meniscus height x/h (x is the distance from the liquid level and h the length of intrinsic meniscus), become

$$\delta = \delta_h + A(1 - X)^2 \qquad [1]$$

where $X = x/h$ and A represents the theoretical value

$$A = \frac{1}{2}\frac{5 + 4\sqrt{2}}{4 + 3\sqrt{2}}\left(\frac{2\sigma}{gd}\right)^{1/2} \qquad [2]$$

where σ is the surface tension, g acceleration, d liquid density. For 1N H_2SO_4, $A \simeq 0.25$ cm. However, this value does not check well with the value obtained from the resistance measurements (Appendix B) for the boundary condition $X = 1$, at which the total meniscus resistance R_m should be

$$R_m = \frac{\rho h}{4b(A\,\delta_h)^{1/2}} \qquad [3]$$

where ρ is electrolyte conductivity and, 2b the diameter of the partially immersed cylindical glass tube.

The film thickness, δ_h, can be obtained from experimental results, since

$$\frac{dR_f}{dx} = \frac{\rho}{2\pi b \delta_h} \qquad [4]$$

if high order terms of δ_h are neglected. Indeed, the slope dR_f/dx in the linear region of Fig. 3, allows us to establish that $\delta_h = 2.7 \times 10^{-4}$ cm.

The value of A, thus determined from Eq. [3] and [4], is equal to 0.37 and not too appreciably different for 1 and 10N H_2SO_4. In fact $(A_{1N}/A_{10N})_{\text{theo.}} \simeq 1.14$, whereas the experimental values are $\simeq 1.05$.

Calculated values for the interfacial geometry and ohmic resistance were thus based on

$$\delta = \delta_h + 0.37\,(1 - X)^2 \qquad [1a]$$

and

$$\frac{R(x)}{\rho} = \frac{h}{2b\pi}\frac{1}{(A\delta_h)^{1/2}}\left[\frac{\pi}{2} - \tan^{-1}\left(\frac{A}{\delta_h}\right)^{1/2}(1 - X)\right] \qquad [5]$$

for $X \leq 1$, $A = 0.37$, and $2b = 1$.

Calculated values of δ are plotted against X in the exploded section of Fig. 2 and compared to experimental results obtained for partially immersed platinized platinum surfaces.

Calculated values of $R(x)/\rho$ in 1N H_2SO_4 are plotted against position in the exploded section of Fig. 3 and compared to experimental results obtained for partially immersed glass tubes in 1N and 10N H_2SO_4

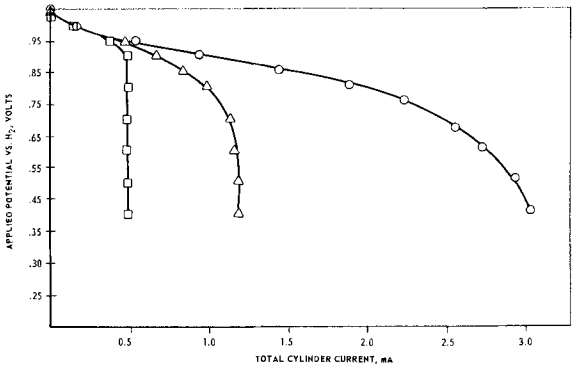

Fig. 4. Current-potential behavior of platinized platinum electrode under various conditions of meniscus and film formation. Electrode position: □, completely submerged; △, partial meniscus formation; ○, full meniscus and film formation (1*N* H_2SO_4).

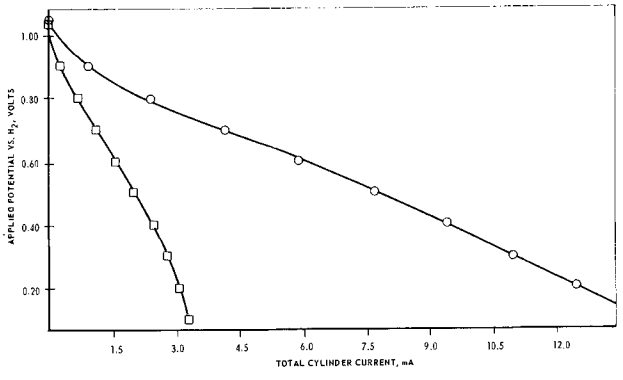

Fig. 5. Polarization behavior of a platinized platinum electrode with full meniscus and film, as a function of concentration. Pt black thickness, 60μ; ○, 10*N* H_2SO_4; □, 1*N* H_2SO_4.

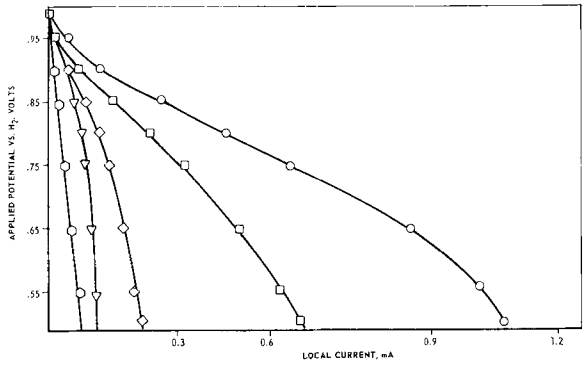

Fig. 6. Local current-potential behavior in various sections of the meniscus and thin film, 1*N* H_2SO_4. Position above electrolyte level, in mils: ○, 0-5; ◇, 90-95; □, 95-100; ○, 106-111; ▽, 125-130.

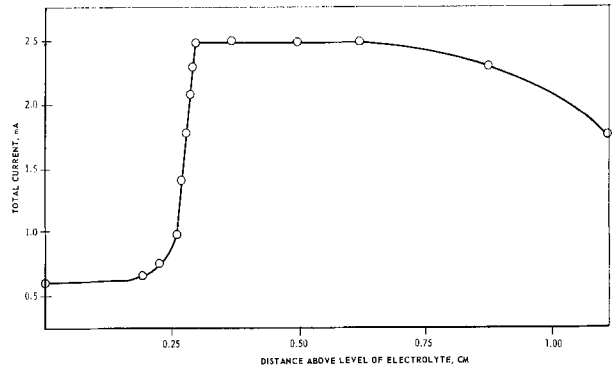

Fig. 7. Current *vs.* height behavior of a platinum electrode at constant potential of +0.400v *vs.* H_2. ○, 1*N* H_2SO_4.

Good agreement is obtained in both cases, with the largest deviations occurring at decreasing values of (x/h), as expected.

Current-voltage characteristics of partially immersed electrodes.—Electrode currents on platinum electrodes are greatly enhanced by raising the electrode partially out of solution as shown in Fig. 4. The data for this plot were taken potentiostatically on a platinized platinum surface of one of the larger sections, A or A′, (total area, 4.7 cm^2; height, 1 cm) of the segmented electrode in 1*N* H_2SO_4. At the limiting current there is, on the average, a fivefold increase in total electrode current from the submerged condition to the one of full meniscus and film formation. In the case of a platinum black electrode surface, drawing the electrode further out of solution does not increase the current past the point of meniscus and film formation. Bright platinum electrodes do show some current increase when partially immersed but large variations are observed with surface pretreatment. Figure 5 shows the effect of acid concentration on polarization behavior for a partially immersed platinum black electrode. This electrode was prepared by deposition of a thick layer of electrodeposited platinum. A fourfold increase in current is observed between 1*N* and 10*N* H_2SO_4. This increase in current for higher acid concentrations is partially explained by the increase in electrolyte conductivity.

Local current-voltage behavior was measured by raising or lowering the thin (5 mil) foil electrode, section B, into meniscus or film zones. Measurements were made with the use of two Wenking potentiostats, one connected to the test electrode and the other to the shorted sections A and A′. By this means the surface of the entire segmented electrode could be kept at relatively the same applied potentials. Figure 6 is representative of the local current-potential variation for the thin segmented electrode, section B, having a platinum black surface. Significant current increases are not realized until the electrode is raised into the highest portion of the meniscus region from 0.28 to 0.30 cm, where the liquid electrolyte layer surrounding the electrode becomes relatively thin. On further withdrawal of the electrode from solution, *i.e.*, displacing the electrode segment upward, the current drops sharply. This is due to the increased resistance to current flow encountered by entering into the thin film region.

Position dependence of the current in the meniscus region. Constant applied potential, —1N H_2SO_4. *Total currents.*—Figure 7 shows a typical behavior for a platinized platinum cylindrical electrode which has been drawn out of solution to various heights above the electrolyte level with an applied potential in the limiting current range. A constant potential of +0.400v *vs.* H_2 was chosen, since this represents a point of maximum oxygen reduction in absence of other reactions such as hydrogen deposition. At higher cathode potentials, the activation polarization represents a large contribution to over-all applied potentials. Thus, the chosen applied potential was representative and reproducible for mass transfer controlled currents for the diffusion of oxygen to the electrode.

The initial portion of the curve represents the currents obtained for a completely immersed electrode and shows very little increase in current until the upper portion of the meniscus is formed. In this region the current rises at an extremely high rate until the meniscus is fully formed. From this point on, the current remains relatively constant dropping slightly near the end of the electrode, since at about 1.0 cm the electrode is nearly completely withdrawn from the electrolyte.

This curve is also representative of the electrode behavior for any thickness of electrodeposited platinum black in 1*N* H_2SO_4 solutions. Three different

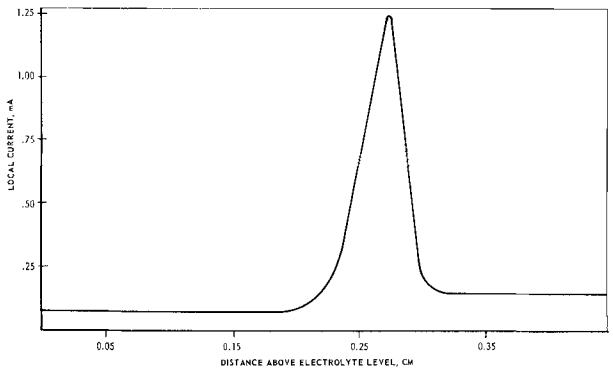

Fig. 8. Local current distribution in the meniscus and thin film at constant potential of +0.400v vs. H_2; 1*N* H_2SO_4.

thicknesses of spongy platinum surfaces were tested, namely 15, 30, and 60μ. The behavior was similar in all cases. Increasing surface roughness had no appreciable effect on electrode performance for this acid concentration. A somewhat different behavior was observed for 10*N* H_2SO_4, as will be described in another section of this paper.

Bright platinum was also tested and showed similar currents for the submerged condition with small increases in current when partially immersed. However, these currents were often transient in behavior and seemed to be largely dependent on surface pretreatment.

Local current.—To determine the local current profile in the meniscus, the height of the thin cylindrical electrode, section B, was varied in the meniscus by means of the Vernier height gauge. A constant potential was applied to the platinized test electrode, while section A and A' were held at the same potential by means of a second potentiostat. A typical curve is shown in Fig. 8. Again the current remains relatively constant until the upper edge of the meniscus zone is reached.

Here the slope rises rapidly until a maximum current is reached, which coincides with the maximum height of the meniscus as determined by optical methods, *i.e.*, approximately 0.28 cm. Further withdrawal of the electrode from the electrolyte displays a rapid current decrease, at approximately the same rate as previously observed for the local current increase. This behavior is due to a sharp increase in electrolyte resistance as the electrode is brought into the thin film region. The current should essentially drop off to zero but there is a small residual current due to stray currents obtained from electrolyte bridging from top to bottom electrode around the Mylar insulating sheet.

The shape of these curves also verifies a previous statement that the polarization potential decreases rapidly to zero in the thin film region.

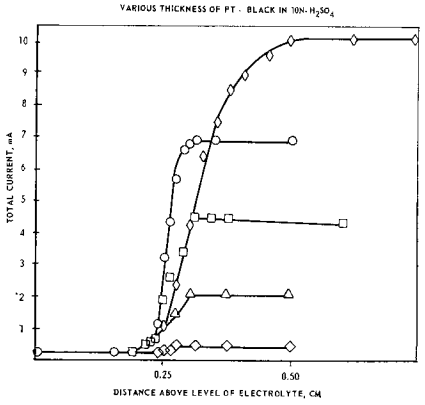

Fig. 9. Current-height behavior at constant potential; +0.400v vs. H_2. Deposition time, in sec: ◇, 240; ○, 60; □, 12; △, 4; ◇, polished.

Table I. Variation of total current with electrode surface treatment

Thickness δ_{sp}, μ	Roughness, millicoulombs/cm^2	Total current, I_T, ma
est. 2.7*	1.3	0.4
15	3.5	2.0
30	7.0	4.5
60	35.0	10.0

* Liquid film.

Position-dependence of the current in the meniscus region. Constant applied potential, 10N H_2SO_4. Total currents.—Using the procedure described above, various thicknesses of electrodeposited platinum and polished platinum were tested in 10*N* H_2SO_4. Figure 9 shows the behavior of polished platinum and four platinized platinum electrodes each one of which was electrodeposited at 10 ma/cm^2 for four different periods of time, i.e., 4, 12, 60, and 240 sec. As shown from the curves there is a distinct increase in current with increasing surface roughness of the electrode. Measurements of the thickness of platinum black layers were made for three different deposition durations by microscopic methods. A relative measure of the surface roughness was also obtained by measuring the number of coulombs required to strip hydrogen from the electrode surface. Table I gives a summary of the data found for surface roughness and platinum black thickness.

Approximate analytical solutions based on two-dimensional oxygen diffusional processes in the spongy platinum layer allow prediction of total electrode currents as a function of electrodeposited platinum layer thickness, δ_{sp}, and a factor (Ψ) describing the state of dispersion of the platinum in the electrodeposited platinum layer. If it is assumed that the roughness, as determined by hydrogen stripping, is representative of this state of dispersion, a qualitative agreement, as presented in Fig. 10, can be obtained between I_T and $(\delta^2_{sp}\,\Psi)^{1/2}$.

Equations developed by Wagner (8) for mass transport controlled processes in an electrolyte-wetted spongy metal surface show that there is a linear relationship between total current, deposit thickness and platinum dispersion

$$I_T = \pi D \left[2 \frac{(\delta^2_{sp}\,\Psi)}{\rho} i_o \frac{RT}{\alpha n F} e^{\frac{\alpha n F}{RT}\eta} \right]^{1/2} \qquad [6]$$

where i_o is exchange current density, D diameter electrode, ρ electrolyte resistivity, ohm-cm, η = polarization, volts, $\frac{\alpha n F}{RT}$ usual electrochemical significance,

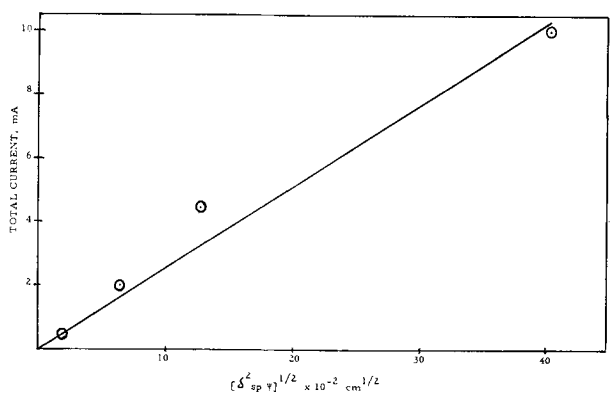

Fig. 10. Total electrode current as a function of platinum deposit thickness, δ_{sp}, and surface roughness Ψ: δ_{sp}, thickness of Pt deposit; Ψ, surface roughness.

and Ψ = (roughness factor/δ_{sp}), cm^{-1}. With appropriate values for the above parameters, calculated values of the current for the various platinum thickness are in close agreement with those obtained from experiment.

Local currents.—In an identical manner to that described for the case of a dilute electrolyte (1*N*), the local current distribution was investigated in 10*N* H_2SO_4.

The currents observed on three platinized electrodes, each one of which was subjected to a different deposition time, increase with increasing surface roughness, which parallels the current variations obtained on the large electrodes.

Effect of oxygen partial pressure.—The partial pressure of oxygen was varied by changing the atmosphere surrounding the electrolyte. The effects of partial pressure on electrode currents were measured potentiostatically. Beside pure oxygen, a mixture of 50% O_2-50% N_2, air, and pure N_2 were tested. In the submerged state there is a linear dependence of current on oxygen partial pressure. For the partially immersed electrode with full meniscus and film formation a square root dependence between current and oxygen partial pressure is observed. This square root relationship exists for both normalities and for all thicknesses of electrodeposited platinum black. Polished platinum tended to show a linear relationship with oxygen partial pressure for total electrode immersion. For partial immersion the results were rather scattered. The problem of getting meaningful results for polished platinum probably lies in the fact that it is so catalytically poor and therefore activation controlled, even at high applied potentials, that true diffusion controlled currents are never realized. When the gaseous atmosphere was changed to N_2 the current essentially dropped to zero. For the submerged electrode this could take more than an hour, however, if the electrode were partially immersed the decay in current occurred within a few minutes. This tends to show again that for the partially immersed condition the diffusion of oxygen across the thin film surface is far more predominant than diffusion from the bulk electrolyte. Table II shows the current variation with partial pressure at a constant applied potential of +0.400v *vs.* H_2 for two different normalities.

Table II. Dependence of electrode current on oxygen partial pressure**

	1*N* H_2SO_4				10*N* H_2SO_4	
	Submerged		Partially immersed		Partially immersed	
Partial pressure of oxygen, P_{O_2}, atm	Total current I_L, ma	I_L/P_{O_2}	Total current I_L, ma	$I_L/(P_{O_2})^{1/2}$	Total current I_L, ma	$I_L/(P_{O_2})^{1/2}$
1.00	0.60	0.60	2.40	2.4	9.75	9.75
0.50	0.30	0.60	1.70	2.4	6.65	9.45
0.21	0.12	0.57	1.15	2.5	4.45	9.75

* Total pressure: 1 atm.
** Platinized platinum electrode. Deposit thickness: 60μ (10 ma/cm² for 240 sec).

Conclusion

For platinized platinum structures the main source of current for the reduction of oxygen at high polarizations (on partially immersed electrodes) is localized to a relatively small region above the meniscus boundary. This fact is shown in a general manner, primarily by the steady increase in current associated with the gradual withdrawal of an electrode from an immersed condition until a full meniscus and liquid film are formed on the extended electrodes' surface. Furthermore, the local current variation in the meniscus exhibits a sharp maximum at a point where the height of the meniscus reaches its maximum length, approximately 0.28 ± 0.01 cm.

Above this region the local current decreases sharply because of large potential gradients, due to ohmic polarization, which are manifested in the thin film region. The sharp increase of resistance in the thin film was also verified by the direct measurement of resistance as a function of height in the meniscus. These measurements also gave a fairly accurate value for the thickness of the thin films, approximately 2.7 x 10^{-4} cm, which are formed above the intrinsic meniscus. Liquid phase continuity at the boundary between the upper edge of the meniscus and the film is obtained, and contact angles identical (or nearly identical) to zero degree can be assumed at the boundary. The height of the intrinsic meniscus decreases, as expected from theory, for decreasing ratios of surface tension/liquid density. However, the theoretical values of the intrinsic meniscus length do not adequately represent the experimental results. Modifications of this length yield quadratic relationships between the liquid electrolyte thickness and the meniscus position, at least near the top of the meniscus. The ohmic resistance, calculated from the interfacial liquid-gas meniscus geometry is linearly dependent on the electrolyte resistivity and can assume rather large values near the meniscus-film boundary.

The relationship obtained for the height-dependence of the meniscus and film can be used to determine if molecular mass transfer can be rate controlling in electrochemical processes. Since transport rates are also dependent on local electrode overpotential, the relationship obtained for the height dependent ohmic resistance, will allow the calculation of ohmic contribution to local potentials, determining to what extent the electrolyte film will contribute to the overall reaction rates.

The liquid film theory, as developed by Will (2), maintains that current depends on electrolyte film thickness. From the measured values of the film thickness, calculations of the current do not check well with those obtained from experiment. Results obtained in 10*N* H_2SO_4 exhibit a distinct electrode current dependence on the electrode surface roughness. The variation in platinum layer thickness, δ_{sp}, does not necessarily affect the thickness of the liquid film, δ_h, which could still form on the spongy metal surface. However since current increase is observed with increasing values of δ_{sp}, it is believed that the longitudinal electrolyte resistance in the spongy platinum layer is decreasing with increasing platinum layer thickness. These changes would vary the potential distribution considerably above the intrinsic meniscus level thereby providing a greater electrode length capable to sustain the electrode current.

If the transport rates are evaluated on the basis of a two-dimensional transport process in the spongy electrolyte-filled platinum layer as developed by Wagner (8), a relationship is obtained between electrode current and the geometric characteristics of the spongy layer, *i.e.*, layer thickness and platinum particle size or layer roughness. Indeed, the currents obtained in 10*N* H_2SO_4 show good agreement with those calculated for the various platinum layer thicknesses by the use of Eq. [6].

Since the values obtained at low acid concentration (1*N* H_2SO_4) show little variation with deposit thickness, it is believed that the lower conductivity value of the 1*N* H_2SO_4 solution does not provide for a long enough active film length above the intrinsic meniscus level to be affected to any great degree by increasing layer thickness. It is therefore concluded that a complete interpretation of the experimental results depends upon an adequate characterization of the electrodeposited platinum layer.

For a partially immersed electrode, which has a full meniscus and film, a square root relationship between oxygen partial pressure and limiting current was obtained. Equation [6] which predicts the diffusion currents for this condition shows that this relationship exists between current and oxygen concentration. The

exchange current, i_o, can be shown to be directly related to oxygen concentration. For fully immersed electrodes there is a linear relationship between current and oxygen partial pressure, which is indicative of a bulk diffusion-controlled process.

Manuscript received Dec. 8, 1964; revised manuscript received June 22, 1965. Part of this paper was presented at the Washington Meeting, Oct. 11-15, 1964.

Any discussion of this paper will appear in a Discussion Section to be published in the June 1966 JOURNAL.

REFERENCES

1. E. Justi, Verlag der Akademie der Wissenschaft und der Literature, Wiesbaden (1959).
2. F. Will, *This Journal*, **110**, 152 (1963).
3. H. C. Weber, H. P. Meissner, and D. A. Sama, Paper presented at the Detroit Meeting of the Society, Oct. 1-5, 1961.
4. E. A. Grens, R. A. Turner, and T. Katan, 145 ACS Meeting, Division of Fuel Chemistry, New York, 1963.
5. M. Bonnemay, *Electrochim, Acta*, **9**, 727 (1964).
6. R. H. Muller, Paper presented at the Washington Meeting of the Society, Oct. 11-15, 1964.
7. I. L. Rozenfeld and K. A. Zhigalova, 4th Soviet Conference on Electrochemistry. Oct. 1-6, 1956, page 24 (English Translation).
8. C. Wagner, Unpublished results.
9. M. Guillou, Thesis, University of Paris, 1963.
10. Butler and Armstrong, *J. Chem. Soc.*, **1934**, 734.
11. L. D. Landau and E. M. Lifshitz, "Fluid Mechanics," p. 235, Pergamon Press, New York (1959).

APPENDIX A

The equation presented by Landau and Lifshitz (11) to describe the liquid-gas interfacial geometry of menisci on flat surfaces

$$\delta = \frac{-a}{\sqrt{2}} \cosh^{-1}\sqrt{2}\frac{a}{x} + a\left[2 - \frac{x^2}{a^2}\right]^{1/2} + \delta' \quad [A1]$$

where

$$a = (2\sigma/gd)^{1/2} \quad [A2]$$

is also equal to h = length of the intrinsic meniscus and σ = surface tension; g = acceleration; d = liquid density, yields the following relationship, if a contact angle $\theta = 0$ is assumed

$$\delta = \frac{a}{\sqrt{2}}\left[\cosh^{-1}\sqrt{2} - \cosh^{-1}\sqrt{2}\frac{a}{x}\right] + a\left[\left(2 - \frac{x^2}{a^2}\right)^{1/2} - 1\right] \quad [A3]$$

The change of variable $X^* = 1 - x/a$ introduced in Eq. [A3] yields

$$\delta = \frac{a}{\sqrt{2}}\left(\cosh^{-1}\sqrt{2} - \cosh^{-1}\sqrt{2}\frac{1}{1 - X^*}\right) + a[(1 + 2X^* - X^{*2})^{1/2} - 1] \quad [A4]$$

or

$$\delta = \frac{a}{\sqrt{2}}\left(\frac{-X^*}{1+\sqrt{2}} + \frac{X^{*2}}{2(1+\sqrt{2})} + \frac{X^{*2}}{2(1+\sqrt{2})^2} - X^* - \frac{X^{*2}}{2}\right) + aX^* - \frac{aX^{*2}}{2} \quad [A5]$$

if Eq. [A4] is simplified for small values of X^*. Ultimately Eq. [A5] will yield a quadratic relationship between δ and X^* for values near the upper limit of the intrinsic meniscus

$$\delta = \frac{aX^{*2}}{2}\frac{5 + 4\sqrt{2}}{4 + 3\sqrt{2}} = A(1 - X)^2 \quad [A6]$$

If a liquid film of constant thickness δ_h is assumed to exist above the intrinsic meniscus, the following general relationship will yield geometry continuity between liquid level and interface geometry

$$\delta = \delta_h + A(1 - X)^2 \quad [A7]$$

where the theoretical value for A should be

$$A = \frac{5 + 4\sqrt{2}}{4 + 3\sqrt{2}}\frac{(2\sigma/gd)^{1/2}}{2} \simeq 0.25 \text{ cm} \quad [A8]$$

APPENDIX B

Since the largest contribution to the resistance to ionic flow is expected near the upper limit of the intrinsic meniscus and in the liquid film, calculations will be restricted to small values of X^*. Resistance variations can be, at least in a simplified manner, expressed by

$$\frac{dR}{dX} = \frac{\rho h}{\pi\delta(2b + \delta)} \quad [B1]$$

where ρ = electrolyte resistivity, $X = x/h$, $2b$ = diameter of the tube supporting the electrolyte, and δ = film thickness.

If $\delta << 1$, which is correct for values of $X > 0.7$, Eq. [B1] can be integrated to yield

$$R(x) = \frac{\rho h}{2b\pi}\frac{1}{(A\delta_h)^{1/2}}\left[\tan^{-1}\left(\frac{A}{\delta_h}\right)^{1/2} - \tan^{-1}\left(\frac{A}{\delta_h}\right)^{1/2}(1 - X)\right] \quad [B2]$$

and since $\delta_h << A$

$$R(x) = \frac{\rho h}{2b\pi}\frac{1}{(A\delta_h)^{1/2}}\left[\frac{\pi}{2} - \tan^{-1}\left(\frac{A}{\delta_h}\right)^{1/2}(1 - X)\right] \quad [B3]$$

where A can be evaluated from the total meniscus resistance, R_m through

$$R_m = \frac{\rho h}{4b(A\delta_h)^{1/2}} \quad [B4]$$

Since Eq. [B3] only applies up to $X = 1$, the total measured resistance will be

$$R(x) = \frac{\rho h}{2b\pi\delta_h}\left[\left(\frac{\delta_h}{A}\right)^{1/2}\left[\frac{\pi}{2} - \tan^{-1}\left(\frac{A}{\delta_h}\right)^{1/2}(1 - X)\right] + X\right] \quad [B5]$$

where the first term of Eq. [B5] applies to $X \leq 1$, and the second term to $X > 1$.

Thermodynamics of Ions: Consistent Standard States for Enthalpies and Free Enthalpies

Philip B. Lorenz

Bartlesville Petroleum Research Center, Bureau of Mines, United States Department of the Interior, Bartlesville, Oklahoma

and Albert Sprague Coolidge

Department of Chemistry, Harvard University, Cambridge, Massachusetts

ABSTRACT

Ions can be treated thermodynamically in the same way as neutral substances if the chemical elements are supplemented by an "element of charge" and if an electrical parameter is added to the variables defining "state." Possible choices for the element of charge are gaseous electrons, electrons in the Schottky state, aqueous hydrogen ion, and metallic electrons. A standard electrical state of zero Volta potential is implied in most discussions, but there are advantages in adopting grounded platinum as a basis for defining standard states.

The application of thermodynamics to electrochemistry would be facilitated if conventions for defining thermodynamic functions of ions were better standardized. Problems have arisen because the hydrogen scale for entropies of aqueous ions contains an internal inconsistency (1), and different standards of reference have been used for ions in gaseous and aqueous states (2). The entropy scale has been discussed critically by several authors (1-5). However, the subject of reference standards seems worthy of further examination.

To an extent greater than may be realized, thermodynamics can be extended to ions in a manner exactly analogous to the treatment used for neutral substances. For each substance C formed from elements A and B, there is a unique formation reaction.

$$aA + bB \rightarrow C \qquad [1]$$

The enthalpy of reaction for [1] when A, B, and C are in their standard states is the standard enthalpy of formation of C; the elements are zero states. If C is a charged species it cannot be synthesized from neutral elements alone, and in order to represent its "formation," there must be inserted into [1] some term playing the role of the element of charge, whose standard state is a zero state for electrically charged species. In the interest of simplicity and in order to conform to basic physical concepts, this term should appear on the left side of [1] and be the same for both cations and anions; therefore, either in one case or in the other, it must have a negative coefficient. It is the purpose of this paper to specify and compare possible choices for the element of charge and its standard state.

Gaseous Electron Standards

The most natural choice for the element of charge would be the electron, with formation reactions of the form

$$aA + bB \mp ze^- \rightarrow C^{z\pm} \qquad [2]$$

where z is the absolute value of the valence of the $C^{z\pm}$ ion. Reactions like this form the basis for tabulations of thermodynamic functions of ions in the gaseous state. However, there is some latitude in what can be taken as the standard state for the electron. The accepted standard enthalpy of formation for gaseous hydrogen ion, given in tabulations (6), is the value of ΔH° for the reaction

$$\tfrac{1}{2}H_2(g) - e^-(g) \rightarrow H^+(g) \qquad [3]$$

where the standard state for electrons and hydrogen ions is the ideal gas at 1 atm. The corresponding free enthalpy of formation is obtained by a straightforward computation using the precise values of entropy for $e^-(g)$ and $H^+(g)$ given by the Sackur equation, in combination with the third-law entropy of $H_2(g)$.

The tabulated value $\Delta H^\circ_f = 367.088$ kcal (6) for reaction [3] is the sum of three terms: the enthalpy of formation of monatomic hydrogen, 52.089 kcal; the ionization energy obtained from the Rydberg constant, 313.518 kcal; and the translational enthalpy 5/2 RT = 1.481 kcal arising from an increase in the number of particles. This latter term can be eliminated by another choice for the standard state of the gaseous electron, conveniently designated (2, 7) by $e^-(0)$. It is defined by

$$\left.\begin{aligned} &\Delta H^\circ = 5/2\,RT \text{ for } e^-(0) \rightarrow e^-(g) \\ \text{and} \quad &S^\circ = 0 \text{ for } e^-(0) \end{aligned}\right\} \qquad [4]$$

For the reaction

$$\tfrac{1}{2}H_2(g) - e^-(0) \rightarrow H^+(g) \qquad [5]$$

the value of ΔH° is then 365.607. In the state $e^-(0)$ the electron has a zero value for entropy and translational enthalpy; this is therefore an example of the "null" state proposed by Schottky (8). The Schottky state has also been described as a state of infinite dispersion with the particles at rest (9). The two descriptions correspond in respect to having zero energy (kinetic and potential), but a state of rest and infinite dispersion is not a unique thermodynamic state, since it can be approached as a limit by endless adiabatic expansion of states having different fixed entropies, the values of each of which will carry over to the limit. It is therefore convenient to specify that $S^\circ = 0$. This is not a definition of a physical state, but a recipe for imagining a reference state; Schottky called it a "harmless fiction."

The state of rest and infinite dispersion is related experimentally to the condition of electrons after gaseous ionization or photoelectric processes at ordinary temperatures. The entropy is unimportant here, as electron work functions for metals are low-temperature approximations which, along with ionization potentials, involve only energies. When the concept of the Schottky state is extended to ions, it becomes fictitious even in respect to the energy, being related to experiment only through neutral combinations formed with the electron. For this purpose it has been necessary to specify that any internal degrees of freedom have the energy that corresponds to statistical equilibrium for the temperature under consideration (9). It seems preferable to avoid a physical description of the fictitious gaseous state (0), but since it is used

in various guises, its numerical characteristics must be clearly recognized.

Aqueous Hydrogen Ion Standard

In aqueous solution, the "element of charge" customarily implied is the ion-molecule couple [$H^+(aq) - \frac{1}{2}H_2(g)$]. Formation reactions take the form

$$aA(\text{std. state}) + bB(\text{std. state}) \pm z[H^+(aq) - \tfrac{1}{2}H_2(g)] \rightarrow C^{z\pm}(aq) \quad [6]$$

Enthalpies and free enthalpies of formation of ions, based on this element of charge, are usually available from standard electrode potentials and their temperature coefficients (6). Naturally, since thermodynamic functions for gaseous ions and aqueous ions are based on different standards, they cannot be compared unless the enthalpy and entropy of hydration for hydrogen ion are known.

Standards Based on Electrons in Platinum

There is another possible standard state for electrons serving as the element of charge, namely the metallic state. It is less closely connected with ordinary conventions, but it has some advantages in helping to correlate gaseous and aqueous states and in clarifying the concepts of standard state in electrochemistry.

Platinum is a convenient choice for the metal because of its involvement in the standard hydrogen electrode (10), which serves as a basis for treatment of all other ions. If $e^-(Pt)$ is the standard (zero) state for the element of charge), it can be connected with the aqueous hydrogen ion standard through the half reaction

$$\tfrac{1}{2}H_2(g) \rightarrow H^+(aq) + e^-(Pt) \quad [7]$$

added $\pm z$-fold to reactions like [6] to give

$$aA(\text{std. state}) + bB(\text{std. state}) \mp ze^-(Pt) \rightarrow C^{z\pm}(aq)$$

Similarly, the connection with the gaseous electron standards is through the reactions

$$e^-(Pt) \rightarrow e^-(g) \quad [8]$$

$$e^-(Pt) \rightarrow e^-(0) \quad [9]$$

added $\mp z$-fold to reactions with the form of [3] and [5].

For reaction [9], the enthalpy change is given by the electron work function for platinum, and the entropy change can be calculated statistically.[1] Although the thermodynamics of reaction [7] has been much investigated, there are some points that have been overlooked. Strictly speaking, this reaction (along with other electrochemical reactions above) is incompletely defined. The parameters necessary to specify the state of electrically charged substances in a conducting medium, besides temperature, pressure, and ordinary composition, must include one that determines electrical condition. For example, a 1-v change in the potential of the platinum, with no other change, would alter the free enthalpy of reaction [7] by 23 kcal.

One way to define electrical condition is by means of the electrostatic (Volta) potential. A zero value of this potential is the standard state that is implied in most discussions. For example, in the calculation of the hydration energy of gaseous ions [*Cf.* (5), (7)] no work term is included for the process of bringing the ion up to the aqueous surface.

However, since it is notoriously difficult to reproduce, the Volta potential is unsatisfactory as a parameter of thermodynamic state. Because of this problem another way is suggested of defining electrical condition, based on electrochemical potentials ($\tilde{\mu}$). For metals, the electron potential, $-\tilde{\mu}_{e^-}/F$, which is a measure of the free enthalpy per mole of transfer of electrons from ground, is a natural parameter to represent electrical state. The standard state of electrons can therefore be taken as grounded platinum,[2] denoted by $e^-(Pt^*)$. An analogous experimental parameter for the electrical state of aqueous hydrogen ion must establish a value for its electrochemical potential $\tilde{\mu}_{H^+}$. For a solution in equilibrium with hydrogen and electrons (*cf.* reaction [7]), it is necessary that

$$\tilde{\mu}_{H^+} = \tfrac{1}{2}\mu_{H_2} - \tilde{\mu}_{e^-} \quad [10]$$

When the hydrogen is in its standard state, this reduces to $\tilde{\mu}_{H^+} = -\tilde{\mu}_{e^-}$. Thus the electrical state of any aqueous solution may be uniquely specified by the electron potential to ground of a standard hydrogen electrode in equilibrium with it. The standard state of the aqueous ion, denoted by $H^+(aq^*)$, may be taken as an acid in its standard state in equilibrium with a reversible standard hydrogen electrode that is grounded. This state is independent of the condition of any of the surfaces involved.[3] It is also independent of the anion associated with the hydrogen ion. In this latter sense it might be more appropriate to speak of $H^+(aq^*)$ as representing a standard electrochemical potential rather than a standard state. Nevertheless, all other thermodynamic functions of the hydrogen ion also have standard values under these conditions, even though only uncertain estimates of their values are available.

Electrical States for Gaseous Ions and Electrons

Electrons emitted from grounded platinum according to reaction [9] are at an electrostatic potential that differs by 0.8v from that of electrons emitted from grounded mercury. Consequently if the enthalpy of reaction [9] is given by the electron work function of platinum, it is not proper to say that the enthalpy of the reaction

$$e^-(Hg) \rightarrow e^-(0)$$

is given by the work function of mercury. An electrical parameter must be added to the conditions that define the state $e^-(0)$. The gaseous states for charged species are obtained by "paper and pencil operations" from experiments involving the removal of single particles from the influence of the opposite charges with which they were associated. Such states cannot be considered appreciably at equilibrium with condensed phases, at least at ordinary temperatures, and therefore the electrostatic potential is the only potential that can be used as an electrical parameter despite its disadvantages. The electrostatic potential of a gas with respect to ground is not an absolute experimental quantity, as it can be measured only relative to the Volta potential of some standard probe that is grounded. Now experimentally platinum is not the best reference material for Volta potentials, but for purposes of uniformity with standards for metallic and aqueous phases it is convenient to define standard gaseous states as having the electrostatic potential of grounded platinum. Symbols such as $H^+(g^*)$ and $e^-(0^*)$ may be used for these states.

Discussion

The word "equilibrium" in the definition of the standard state of $H^+(aq)$ automatically requires that the free enthalpy change for the reaction

$$\tfrac{1}{2}H_2(g) \rightarrow H^+(aq^*) + e^-(Pt^*) \quad [7^*]$$

[1] In platinum at 25°C, with approximately 0.6 free electrons per atom (11), the molar entropy of electrons is about 0.06 e.u.

[2] It is unnecessary to specify the metal that is grounded when only free enthalpy is considered, but entropy and other functions depend on the chemical composition.

[3] Strehlow (12) pointed out that variations in electron work function do not lead to different electrode potentials, but to different values of the Volta potential. At the metal-solution interface variations in the surface condition will be compensated by variations in the amount of adsorption in the electrochemical double layer.

is zero (Eq. [10]). This is not a numerical fiction, but a definition of electrical state.[4] With this definition it follows that $\Delta G^\circ = 0$ for reaction [7]. This statement may come as a surprise in view of the many attempts that have been made at calculation of the standard free enthalpy of reaction [7] (or related calculations) (7, 12-16). Now the most common method of calculation is based on a theoretical hydration energy for the ion and the electron work function of platinum. Consider a standard grounded platinum-hydrogen electrode in contact with a standard acid solution having the equilibrium Volta potential, Ψ°. Reaction [7*] is the sum of the processes

$\frac{1}{2}H_2(g) \rightarrow H(g)$	$\Delta G^\circ = a$
$H(g) \rightarrow H^+(g^*) + e^-(0^*)$	b
$H^+(g^*) \rightarrow H^+(g, \Psi = \Psi^\circ)$	$F\Psi^\circ$
$H^+(g, \Psi = \Psi^\circ) \rightarrow H^+(aq^*)$	$(-c + d)$
$e^-(0^*) \rightarrow e^-(Pt^*)$	$-Fw(Pt)$

The free enthalpies add to zero, and so the contact potential of the metal against the solution is

$$-\Psi^\circ = (a + b - c + d)/F - w(Pt) \qquad [11]$$

The notation is that of de Béthune (13) to show the parallel with his analysis. His value for $-\Psi^\circ$ is -0.459v.[5] The present value of zero for the standard free enthalpy is a consequence of the well-known equation of Lange (19)

$$\tilde{\mu}_i = \alpha_i + z_i F\Psi \qquad [12]$$

according to which the free enthalpy change for zero Volta potential difference is equal to the Volta potential difference for zero free enthalpy change.

The term $(-c + d)/F$ differs from the "real potential," α_{H^+}, by the free enthalpy of the reaction

$$H^+(0) \rightarrow H^+(g) \qquad [13]$$

which, using the Sackur entropy 26.011 kcal for $H^+(g)$, turns out to be -0.272v. Experimental values of the real potentials are limited in accuracy by the uncertainty in work functions and Volta potentials. Reproducible to only one or two significant figures, they are less popular than theoretical estimates of the same thing carried out to four figures. Nevertheless, values of real potentials and their temperature coefficients offer in principle an unexceptionable route for finding ionic entropies, and enthalpies and free enthalpies of formation that are based on a single standard for ions in both gaseous and aqueous states.

[4] It is well to emphasize that we are dealing with total ("electrochemical") free enthalpy change. We do not consider the "purely chemical free enthalpy change" which appears in many electrochemical discussions for the purpose of visualization.

[5] The value back-calculated from the contact potential (17) and standard electrode potential (18) of the standard calomel electrode is -0.447v.

Manuscript received Nov. 12, 1963; revised manuscript received May 15, 1965.

Any discussion of this paper will appear in a Discussion Section to be published in the June 1966 JOURNAL.

REFERENCES

1. P. Van Rysselberghe, *Anales real soc. españ. fis. y quim. (Madrid), Ser. B*, **56**, 515 (1960).
2. R. M. Noyes, *J. Chem. Educ.*, **40**, 116 (1963).
3. F. D. Rossini, "Chemical Thermodynamics," p. 376, John Wiley & Sons, Inc., New York (1950).
4. I. M. Klotz, "Chemical Thermodynamics," p. 353, Prentice-Hall, Inc., New York (1950).
5. B. E. Conway and J. O'M. Bockris in "Modern Aspects of Electrochemistry," J. O'M. Bockris, Editor, Chap. 2, Academic Press, Inc., New York (1954).
6. F. D. Rossini, D. D. Wagman, W. H. Evans, S. Levine, and I. Jaffe, "Selected Values of Chemical Thermodynamic Properties," N. B. S. Circular 500 (1952).
7. R. M. Noyes, *J. Am. Chem. Soc.*, **86**, 971 (1964).
8. W. Schottky, H. Ulich, and C. Wagner, "Thermodynamik," p. 214, J. Springer, Berlin (1929).
9. P. Van Rysselberghe, *Electrochim. Acta*, **5**, 28 (1961).
10. J. B. Ramsey, *This Journal*, **104**, 255 (1957).
11. N. F. Mott and H. Jones, "The Theory of the Properties of Metals and Alloys," Dover Publications, Inc., New York (1958).
12. H. Strehlow, *Z. Elektrochem.*, **56**, 119 (1952).
13. A. J. de Béthune, *J. Chem. Phys.*, **29**, 616 (1958); *ibid.*, **31**, 847 (1959).
14. B. Jakuscewski, *ibid.*, **31**, 846 (1959).
15. M. V. Ionin, *Russ. J. Phys. Chem.* (English Transl.), **37**, 843 (1963).
16. R. H. Stokes, *J. Am. Chem. Soc.*, **86**, 979 (1964).
17. J. E. B. Randles, *Trans. Faraday Soc.*, **52**, 1573 (1956).
18. A. J. de Béthune in "Encyclopedia of Electrochemistry," C. A. Hampel, Editor, p. 414, Reinhold Publishing Corp., New York (1964).
19. E. Lange, "Wien-Harms Handbuch d. Experimentalphysik," XII, Teil II, p. 265, Akad. Verloggesellschaft, Leipzig (1933).

Evaluation of a Pulse Charging Technique for Capacitance Measurements and Double Layer Studies

R. G. Barradas and E. M. L. Valeriote

Department of Chemistry, University of Toronto, Toronto, Ontario, Canada

ABSTRACT

A previously published pulse charging technique for measurements of capacity to derive surface areas of electrodes has been investigated to assess its suitability for studying electrochemical adsorption of inorganic and organic compounds at mercury. Reasonably acceptable results were observed with electrolytic capacitors and for a number of inorganic electrolyte solutions. The method was found to be less suitable for examining the adsorption of organic additives. Unusual dependence of capacitance on potential with varying resistances (R_s) was experienced. Results which conflict with reported data are discussed.

Experimental methods of investigating equilibrium properties of the electrical double layer (1) and electrochemical adsorption of organic compounds at electrodes (2) have recently been reviewed. In the course of our general investigations of electrochemical adsorption (3-9) we were attracted to the pulse-charging technique of measuring capacitance developed by Hackerman and co-workers (10, 11) because of their encouraging results. This method is a modern refinement of an earlier technique due to Bowden and Rideal (12), and differential capacity is determined by analysis of an R-C discharge circuit in which the

electrical double layer provides the capacitative component. The method appeared to be ideally suited to our principal objectives which were to complement the electrocapillary studies of an interesting new class of corrosion inhibitors (furfurylamine, its saturated analogue, and their respective derivatives and ions) on a mercury electrode (9) by capacitance measurements, and to extend the latter to comparison with solid electrodes. There is also the additional advantage of obtaining reliable measurements of electrode areas, which would aid other electrochemical studies, *e.g.*, the kinetics of anodic oxidation of silver (13, 14).

The purpose of this paper is to report on an experimental evaluation of the pulse charging method in terms of specific adsorption of inorganic electrolytes on mercury and also to show some preliminary results concerning its application to adsorption studies of the furfurylamine class of corrosion inhibitors. Certain unexpected behavior and apparently anomalous results were encountered in the course of the investigation and these are discussed below.

Experimental

With the exception of some minor experimental changes, which will be described, the method was essentially similar to that previously reported (10). To ascertain the reliable reproduction of our experimental arrangement and technique, capacity measurements on mercury in a 0.1*N* aqueous solution of Na_2SO_4 were repeated over a wider range of potentials to make better diagnostic comparison with published results (10, 15). The apparent lack of agreement led to further measurements on mercury in aqueous solutions of inorganic electrolytes of varying degrees of specific adsorbability.

A 150 henry choke was used to isolate the square wave from the potentiometer circuits and shielded wire was used for all connections. The cell is shown in Fig. 1 and contains a Ag-AgCl reference electrode which was initially used for potential calibration purposes only. All the reported potential measurements were made with respect to the saturated calomel electrode in order to facilitate comparison with other data (8, 10). A hypodermic syringe, fitted with a ground glass joint and equipped with a Chaney Adaptor (Hamilton Company, Whittier, California), was attached to the cell to supply mercury to the 2.5 cm diameter glass cup. A short platinum wire, sealed in the glass tubing, provided electrical connection between the mercury electrode and the external circuitry. Adjustment of the syringe provided stable and renewable mercury surfaces. The cup was surrounded by a cylindrical 45 x 45 mesh smooth platinum gauze electrode (Johnson, Matthey and Mallory Ltd., Toronto) with an apparent area of approximately 200 cm^2, which served as a counter electrode and as an electrostatic shield for the mercury pool. Although a platinized platinum counter electrode is desirable for reasons stated by McMullen and Hackerman (10), our counter electrode was not platinized in anticipation of the problems associated with its large adsorbent properties in dilute solutions of organic additives. A platinized electrode with a roughness factor of about 500 would increase the area of the counter electrode to such an extent that the bulk concentrations of organic adsorbates would be seriously affected, if not completely depleted, by adsorption on platinum at concentrations of 10^{-3}M or less. Other workers have avoided the use of platinized platinum for similar reasons (16).

Greaseless water-sealed vacuum stopcocks prevented ingress of air and eliminated the possibility of electrode contamination by stopcock lubricants. All solutions were deoxygenated by purified nitrogen gas which was admitted to the cell through sintered glass filters and water-filled presaturator. The solutions were also covered by an inert nitrogen atmosphere during the run by retention of a slight positive pressure of the gas within the cell.

Doubly distilled mercury was further purified by electrolysis in addition to a procedure outlined by Ives and Janz (17). All solutions were made up with "equilibrium water" prepared by redistillation of distilled water in a Barnstead EPR-1/2 still. The conductivity of the final "equilibrium water" was 8 x 10^{-7} mho/cm. The inorganic salts were of high analytical grade and were further purified, where necessary by recrystallization. Furfurylamine (Miles Chemical Company, Elkhart, Indiana) was twice distilled under nitrogen immediately before use. Only solutions of Na_2SO_4 were preelectrolyzed (at 2 ma for 14 hr) before the measurement of capacitances. Comparison between results obtained for solutions which are not preelectrolyzed have been found to show no significant differences within the limits of experimental errors (4, 18).

Results

Using electrolytic capacitors (in place of the cell solution) and a wide range of input wave amplitudes and resistances, R_s [this refers to the series resistance

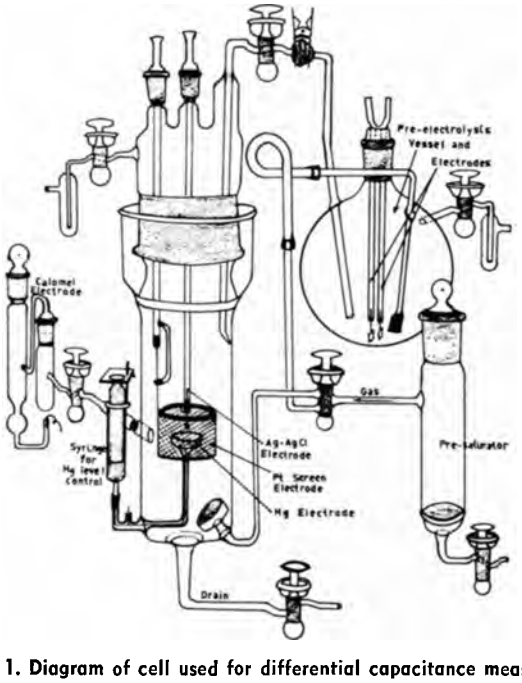

Fig. 1. Diagram of cell used for differential capacitance measurements.

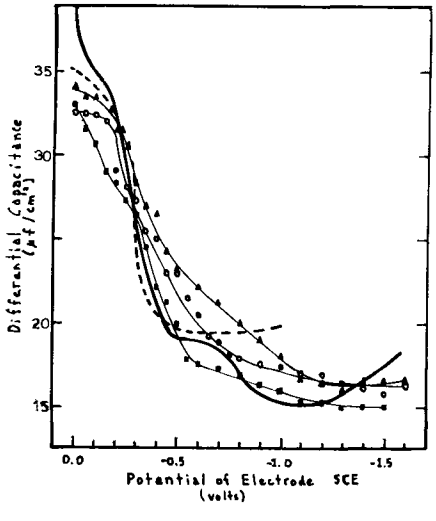

Fig. 2. Dependence of differential capacity on potential and resistance R_s at the mercury-0.1*N* Na_2SO_4 interface. ■, R_s, 16.3K; ○, R_s = 6.5K; ▲, R_s = 2.6K; ——— Grahame (15); - - - - - - McMullen and Hackerman.

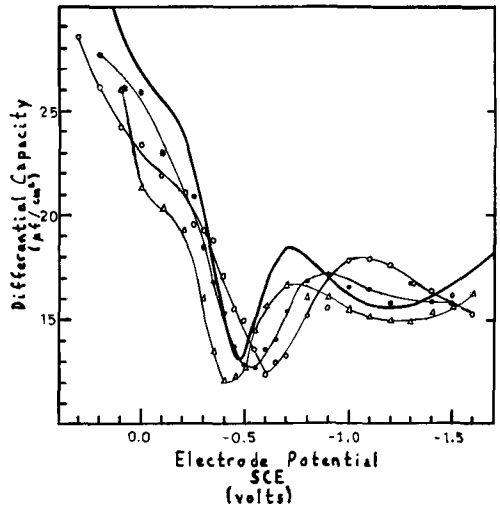

Fig. 3. Dependence of differential capacity on potential and resistance R_S at the mercury-0.01*N* KF interface. △, R_S = 37.9K; •, R_S = 10.8K; ○, R_S = 6.9K; ——— Grahame (19).

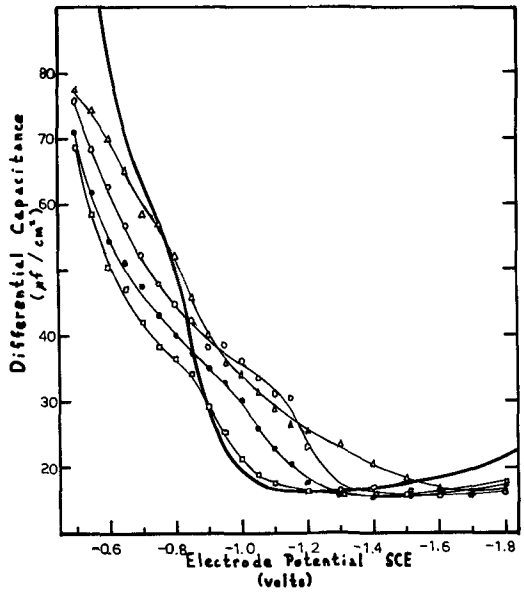

Fig. 4. Dependence of differential capacity on potential and resistance R_S at the mercury-0.1*N* KI interface. □, R_S = 26.7K; •, R_S = 10.8K; ○, R_S = 6.9K; △, R_S = 3.9K; ——— Grahame, Poth, and Cummings (20).

denoted by the same symbol in the circuit diagram reported by McMullen and Hackerman (10)], the capacities of several condensers ranging from 20 to 300 μf were determined at an applied square wave signal of 1000 cps and compared to values obtained using a General Radio Type 1608 A Independence Bridge. The percentage differences between the two sets of determinations had a maximum of 8% and an average of 3% for the eight capacitors tested. This compares favorably with previously reported results (10) of 7-8% differences for 37 and 58 μf electrolytic capacitors.

Differential capacities as a function of potential for various concentrations of aqueous solutions of Na_2SO_4, KF, KCl, and KI were determined by the square wave technique using the lowest amplitude possible so that the potential across the double layer changed by less than 10 mv over a half period of the square wave, and the IR drop in solution was minimized. The value of the series resistance, R_S, and electrode potential, E_{SCE}, was varied systematically, and the results for Na_2SO_4, KF, and KI solutions are displayed in Fig. 2-4. For the sake of clarity, some intermediate values of R_S have been omitted in Fig. 2 to 4 since they are consistent with those shown and do not contribute any further information.

For comparative purposes previously published data (10, 15, 19, 20) are also included on the same figures. Comparison between NaF and KF in Fig. 3 is justifiable because these two substances show similar capacity *vs.* potential behavior (C-E) at equal concentrations [cf. (19) and (20)]. The C-E curves for Na_2SO_4, KF, KI, and KCl (not shown diagramatically because some of the data are reported in Table I) have common characteristics with respect to the effect of varying R_S. Large and small values of R_S shift the curves to more anodic and cathodic potentials, respectively. The shifts of the potential are much more dependent on R_S than are the changes of capacity. This is most easily discernible in Fig. 3 where the C-E curves show clearly defined maxima and minima. It should be noted that the maximum R_S values are 16.3, 37.9, 26.7, and 15.4K for Na_2SO_4, KF, KI, and KCl, respectively, and the C-E curves which correspond to the maximum R_S values are in best agreement with previously published data. In general poorer agreement was observed at anodic potentials with respect to the pzc within a range of 200-300 mv. For Na_2SO_4 (Fig. 2) our C-E curve for R_S = 16.3K conforms more closely to that reported by Grahame than that of McMullen and Hackerman, except for the stated anodic region. The choice of the maximum R_S used was controlled by the magnitude of the highest expected capacitances for the various inorganic electrolytes examined and also by certain instrumental limitations. The variation of C-E curves with changes in R_S reflects the empiricism in assuming an electric analogue of the metal-solution interface.

Owing to the relatively small area of the counter-electrode used, an appropriate correction term was applied to every experimentally observed capacitance according to the following equation

$$1/C_{obs} = 1/C_{Hg} + 1/C_{Pt} \qquad [1]$$

where the terms C_{obs}, C_{Hg}, and C_{Pt} are the experimentally observed capacity and the capacities of the mercury-electrolyte and platinum-electrolyte components, respectively. C_{Pt} was assumed to be 22 μf/cm² on the basis of previously reported constancy of this value for platinum over a potential range from 0.0 to + 0.4v (SCE) in a sodium sulfate solution (10).

In addition a second positive correction of 2% was applied to all C_{obs} to allow for the systematic parallax effects between the photographic images of the oscilloscope graticule and screen. The value of 2% was estimated by comparison of traces on the time axis of the CRO screen, as recorded by the camera, with signals of known frequency (Hewlett-Packard Function Generator 202 A). All experimental values of capacitances reported for the solutions examined have been corrected as described above. To exemplify, the corrections for sodium sulfate (Fig. 2) were approximately 3% and 7% for the respective lowest and highest C_{obs} values. The applicability of Eq. [1], which is based on an assumed C_{Pt} value of 22 μf/cm², to electrolyte systems other than Na_2SO_4 is obviously questionable, but later discussion of this point will show that the correction is not too unreasonable in the absence of organic adsorbates.

Using an R_S value of 15.4K, differential capacities were measured as a function of potential for various concentrations of furfurylamine in aqueous 1.0*N* KCl base electrolyte. Graphical numerical double integration of the C-E curves was carried out to obtain surface tension values (15, 21). The integration constants were obtained from electrocapillary data for identical systems (22). The results of direct measurements of surface tension with those evaluated by double integration of C-E curves are tabulated (Table I). The two sets of surface tensions at various electrode potentials must, of necessity, coincide at the pzc's, but comparison

Table I. Comparison of surface tension from electrocapillary data with that obtained by double integration of capacity data for furfurylamine in 1.0*N* aqueous KCl solutions

E_{pzc} (SCE)	−0.521v		−0.511v		−0.491v		−0.461v		−0.403v		−0.335v	
γ_{pzc}	424.3		422.7		420.6		414.8		406.2		394.8	
C_a	0.000M		0.003M		0.010M		0.030M		0.100M		0.300M	
$-E_{SCE}$, v	$\int\int CdE^2$ γ, dyne/cm		$\int\int CdE^2$ γ, dyne/cm		$\int\int CdE^2$ γ, dyne/cm		$\int\int CdE^2$ γ, dyne/cm		$\int\int CdE^2$ γ, dyne/cm		$\int\int CdE^2$ γ, dyne/cm	
0.10	388.7	387.2	393.1	386.4	391.3	385.6	388.4	384.0	387.0	381.4		
0.15											389.5	383.0
0.20	403.9	402.7	406.9	402.0	404.9	401.5	401.8	395.5	399.3	395.5	392.5	389.0
0.30	415.2	413.8	416.1	413.0	414.5	412.6	410.3	409.4	404.6	403.5	394.7	394.4
0.40	421.5	421.0	420.7	420.2	418.3	418.5	414.3	414.0	406.2	406.2	394.4	394.3
0.50	423.8	424.1	422.5	422.6	420.5	420.5	414.5	414.5	405.1	405.0	393.7	392.3
0.60	423.3	423.2	422.1	421.5	418.9	418.8	412.7	412.5	402.8	402.0	390.1	389.2
0.70			419.8	416.9	415.6	415.0	408.7	408.7	399.7	398.3	386.1	385.5
0.80	411.1	411.7	412.7	410.5	410.6	409.2	403.5	403.6	395.5	393.7	381.5	381.0
0.90			407.7	401.8	401.8	401.3	396.3	397.5	390.8	388.2	377.1	375.6
1.00	390.9	392.1	397.7	391.3	392.6	391.3	388.8	389.0	383.7	381.8	370.6	369.3
1.10	378.8	380.1	390.2	379.2	383.2	379.2	379.6	378.2	375.8	373.5	363.4	362.2
1.20	362.4	365.8	377.1	364.8	369.6	364.8	368.1	363.6	366.8	361.4	355.7	353.6

E_{pzc} and γ_{pzc} are the potentials and surface tensions, respectively, of the electrocapillary maxima. C_a is the concentration of furfurylamine.

at various anodic and cathodic potentials with respect to the pzc gives a good indication of suitability of the pulse-charging method for examining electrochemical adsorption.

Discussion

Reproducibility of results.—The general agreement between capacities of commercial electrolytic capacitors measured on an impedance bridge and that obtained by the square-wave pulse technique are comparable to those previously reported (10), which indicates that there is no significant difference in the electrical circuitry employed in the present work. However, both sets of results show that the pulse-charging method gave less accurate results than that of the impedance bridge. With R_s = 15.4K, the best precision with which we could measure differential capacities in the electrolyte solutions was approximately 4%. In regions of the C-E curves where dC/dE was large the lack of precision was as high as 11% (0.1*N* KI). Smaller values of R_s gave correspondingly poorer precision.

Inorganic electrolytes.—The uniform disparity between our best C-E plots with those of other workers for all inorganic electrolytes examined is obvious from inspection of Fig. 2-4. Hence it will be sufficient to discuss only the Na_2SO_4 case as a typical example. It was suggested by McMullen and Hackerman (10) that the observed discrepancy of results at cathodic potentials in comparison with Grahame's data (15) might be explained by a correction to the mercury surface area of about 1 cm^2 due to meniscus curvature effects. This correction of 20% seems unusually high, and it is not clear why such an effect would not be applicable to both anodic and cathodic branches of the capacity curves. In order to ascertain the magnitude of the area contribution due to meniscus curvature, the profile of our mercury pool electrode was determined using a travelling microscope with a micrometer scale eyepiece. The vertical displacement of the surface was plotted on an exaggerated scale compared to that of the horizontal coordinate. Using a standard analytical expression, the surface area was approximated by successive laminar segments of cones, and the total area found by adding the contributions of each of the laminar elements. A surface area correction of approximately 1% was calculated, which corresponds to an increase of 0.05 cm^2. Our measurements were made for the mercury/glass/air interfaces, but it has been reported (23) that the contact angle for mercury/glass is the same at the air or water interface. Therefore our area correction of about 1% is reasonably valid in the dilute aqueous solutions examined.

In comparison with the results of McMullen and Hackerman (10) for Na_2SO_4 our curves show much closer agreement to Grahame's data at cathodic potentials and greater divergence at anodic potentials.[1] There does not appear to be any simple explanation to resolve these contradictory experimental findings.

Capacitance correction, pzc, and relevant implications.—The correction for C_{Pt} of Eq. [1] is valid for Na_2SO_4 because of the constancy of C_{Pt} = 22 μf/cm^2 over a potential range of 0.0 to + 0.4v (SCE). The same correction for other solutions cannot be strictly applied unless two conditions are satisfied: (i) platinum behaves like mercury at cathodic potentials with respect to their corresponding pzc's; (ii) the pzc for platinum is 0.5 ± 0.2v (SCE). Since the capacity of mercury in most simple inorganic electrolytes is known to be relatively constant and independent of concentration and electrolyte species at extreme cathodic potentials (24) our application of Eq. [1] to electrolytes other than Na_2SO_4 should be justified. However, it is doubtful that the stated conditions are realistic: condition (i) is not supported by conclusive experimental evidence and condition (ii) is apparently erroneous (see Table II).

The value of 0.5 ± 0.2v (SCE) for the pzc of platinum in Table II has been deduced from an inadequately verified hypothesis (25) which relates the electronic work function to the pzc of various metals. It should be pointed out that Robertson (26) showed a capacitance minimum at 0.75v (NCE) for 1.0*N* HCl, but did not define this as the pzc for platinum. Should

[1] Cf. Riney *et al.* (33) using a single pulse method found good agreement with Grahame's data for 1.0*N* Na_2SO_4 (34) at cathodic potentials but poor agreement at anodic potentials.

Table II. Potential of zero charge (pzc) for platinum

Potential, v (Corrected to SCE)	Solution	Literature source
0.5 ± 0.2	1.0*N* Na_2SO_4	McMullen and Hackerman (10)
−0.03 ± 0.01	1.0*N* Na_2SO_4 (acidified)	Gorodetzkaja and Kabanov (30)
0.4	0.2*N* and 0.02*N* Na_2SO_4	Popat and Hackerman (29)
(0.79v)*	1.0*N* HCl	
−0.17 (platinized Pt)	1.0*N* Na_2SO_4 +	Parsons (31)
−0.01 (smooth Pt)	0.1*N* H_2SO_4	
−0.04	1.0*N* acidified Na_2SO_4	Conway (32)
−0.04	0.001*N* KCl 0.01*N* KCl 0.1*N* KCl	Frumkin (25)
−0.05	6.0*N* HCl 1.0*N* HCl 6.0*N* H_2SO_4	Banta and Hackerman (27)

* Attributed by Popat and Hackerman (29) to Robertson (26).

the real pzc for platinum be approximately 0.0v (SCE) as shown in Table II, the use of capacitance techniques to measure surface areas is not invalidated if a calibration procedure is adopted, whereby the area of at least one sample of each metal is determined by BET measurements. The areas of all other samples can then be derived by comparison of capacity values under similar appropriately chosen experimental conditions.

The discussion of pzc's of platinum does not support condition (ii) and the consequent correction factor of Eq. [1]. However, reported capacity values for platinum in various inorganic electrolytes (26-29) indicate that our corrections are in general slightly higher than necessary, but reasonable within experimental limitations.

Adsorption of furfurylamine in 1.0*N* KCl *solution.*—The doubly integrated capacity data in Table I is in moderately good agreement with the direct electrocapillary determinations of surface tension (22) for 1.0*N* KCl. When furfurylamine was present poorer agreement was observed. For 1.0*N* KCl the quantity

$$\Delta \equiv \left(\int\int_{E_{pzc}}^{E} C\,dE^2\right) - \gamma = 1.4 \pm 0.1 \text{ dynes/cm}$$

at the three most positive potentials, and -1.6 ± 0.5 dynes/cm at the three most negative potentials. Positive and negative values of Δ indicate high and low capacitance values, respectively. Hence we note that capacity values are slightly low at anodic potentials (consistent with the other inorganic electrolytes examined) and high at cathodic potentials for the base electrolyte. Although the Δ values are somewhat larger in magnitude than other published comparative differences (21), they are within the estimated experimental error of about 4% which was stated earlier.

In the presence of furfurylamine the average value of Δ is 5.8 ± 1.6 dynes/cm at the extreme potentials (-0.10 and -1.2v). These deviations are positive and greater than the above-mentioned experimental error, and they reflect consistently low capacitance values. The adsorption of some furfurylamine on the platinum counter electrode would reduce C_{Pt} in Eq. [1] to less than 22 μf/cm^2, and this leads to a corrected C_{Hg} which is smaller than its actual value.

Summary

1. A pulse charging technique for capacity and surface area measurements has been evaluated by investigating double layer properties of the mercury/solution interface in a variety of inorganic electrolytes.

2. To make the method suitable for the study of electrochemical adsorption of organic materials, a smooth platinum counter electrode was necessarily introduced. This led to a correction term which gave results only in fair agreement with previously published data for inorganic electrolytes.

3. It was found that the magnitude of the series resistance (R_s) had an appreciable effect on the variation of capacity with electrode potential.

4. Using furfurylamine as a test case the method proved to be less satisfactory in comparison with electrocapillary measurements.

Acknowledgments

The authors are indebted to the National Research Council of Canada and to the University of Toronto for financial support of this work. One of the authors (E. M. L. V.) is the holder of a National Research Council of Canada studentship for 1964-1965.

Manuscript received March 3, 1965; revised manuscript received June 27, 1965.

Any discussion of this paper will appear in a Discussion Section to be published in the June 1966 JOURNAL.

REFERENCES

1. B. B. Damaskin, *Russ. Chem. Rev.*, **30**, 78 (1961).
2. A. N. Frumkin and B. B. Damaskin, "Modern Aspects of Electrochemistry," No. 3, pp. 149 *et seq.*, J. O'M. Bockris and B. E. Conway, Editors, Butterworths, London (1964).
3. B. E. Conway and R. G. Barradas, "Trans. Phil. Symp. on Electrode Processes (1959)," p. 299, E. Yeager, Editor, John Wiley & Sons Inc., New York (1961).
4. B. E. Conway, R. G. Barradas, and T. Zawidzki, *J. Phys. Chem.*, **62**, 676 (1958).
5. R. G. Barradas and B. E. Conway, *J. Electroanal. Chem.*, **6**, 314 (1963).
6. B. E. Conway and R. G. Barradas, *Electrochim. Acta*, **5**, 319 (1961).
7. R. G. Barradas and B. E. Conway, *ibid.*, **5**, 349 (1961).
8. R. G. Barradas and P. G. Hamilton. *Can. J. Chem.*, To be published.
9. R. G. Barradas, P. G. Hamilton, and E. M. L. Valeriote, (a) Paper presented at the Buffalo Meeting of the Society, Oct. 10-14, 1965; (b) *This Journal*, To be published.
10. J. J. McMullen and N. Hackerman, *This Journal*, **106**, 341 (1959).
11. R. J. Brodd and N. Hackerman, *ibid.*, **104**, 704 (1957).
12. F. P. Bowden and E. K. Rideal, *Proc. Roy. Soc. London*, **120A**, 59, 80 (1928).
13. R. G. Barradas and G. H. Fraser, *Can. J. Chem.*, **42**, 2488 (1964).
14. R. G. Barradas and G. H. Fraser, *ibid.*, **43**, 446 (1965).
15. D. C. Grahame, *Chem. Rev.*, **41**, 441 (1947).
16. M. Vorsina and A. Frumkin, *Acta Physicochim.*, **18**, 242 (1943).
17. D. J. G. Ives and G. J. Janz, "Reference Electrodes," pp. 133-135, Academic Press, New York (1961).
18. E. Blomgren, J. O'M. Bockris, and C. Jesch, *J. Phys. Chem.*, **65**, 2000 (1961).
19. D. C. Grahame, U. S. Office of Naval Research, Technical Report No. 14 (1954).
20. D. C. Grahame, M. A. Poth, and J. I. Cummings, *ibid.*, O.N.R. Report No. 7 (1951).
21. M. A. V. Devanathan and P. Peries, *Trans. Faraday Soc.*, **50**, 1236 (1954).
22. P. G. Hamilton, M. A. Thesis, University of Toronto (1964).
23. J. J. Bikerman, "Surface Chemistry-Theory and Applications," pp. 354-356, Academic Press Inc., New York (1958).
24. M. A. V. Devanathan, *Trans. Faraday Soc.*, **50**, 373 (1954).
25. A. N. Frumkin, *This Journal*, **107**, 461 (1960).
26. W. D. Robertson, *ibid.*, **100**, 194 (1953).
27. M. C. Banta and N. Hackerman. *ibid.*, **111**, 114 (1964).
28. J. N. Sarmousakis and M. Prager, *ibid.*, **104**, 455 (1957).
29. P. V. Popat and N. Hackerman, *J. Phys. Chem.*, **62**, 1198 (1958).
30. V. A. Gorodetzkaja and B. Kabanov, *Physik. Z. Sowietunion*, **5**, 418 (1934).
31. Roger Parsons, "Equilibrium Properties at Electrified Interfaces, Modern Aspects of Electrochemistry," No. 1, p. 76, J. O'M. Bockris and B. E. Conway, Editors, Butterworths, London (1954).
32. B. E. Conway, "Electrochemical Data," p. 221, Elsevier Publishing Co., New York (1952).
33. J. S. Riney, G. M. Schmid, and N. Hackerman, *Rev. Sci. Instr.*, **32**, 588 (1961).
34. D. C. Grahame, *J. Am. Chem. Soc.*, **63**, 1207 (1941).

Technical Notes

Beneficial Effect of Lithiated Electrolyte on Iron Battery Electrodes

Stanley Hills

Electric Storage Battery Company, Philadelphia, Pennsylvania

The beneficial effect of lithiated KOH electrolytes in nickel iron and nickel cadmium cells has been recognized for more than a half-century. It was obvious from the time that Edison patented its use (1) that incorporation of lithia in the alkaline electrolyte increased the efficiency of the nickel oxide electrode, since both of the aforementioned cells were and still are designed to be positive limiting. This fact oriented the major portion of the research concerning this phenomenon toward the nickel oxide electrode. Because of this emphasis one finds relatively few references in the literature with regard to the iron electrode (2), and more specifically there is nothing of significance with regard to an additive effect similar to that described previously.

A study of iron active material produced by various techniques, which is still in progress, has shown that the common practice of incorporating lithia in the 20% KOH electrolyte (50g LiOH/liter for formation which is then replaced by 25g LiOH/liter) is of greater benefit to the iron electrode than it is to the nickel oxide electrode. In the attempt to develop a standard procedure with which to evaluate new iron active materials, during the early phases of this investigation, pure 20% KOH was employed as an electrolyte as a result of the mistaken but still widely accepted belief that lithiated electrolytes were of benefit only to the latter electrode (3-5). A great deal of time was lost chasing down blind alleys because of the confusion which arose in the attempt to correlate the mass of seemingly meaningless and irreproducible efficiency data, before it was realized that the presence of lithia in the 20% KOH electrolyte was of greater significance than other variables such as precycling soak time, active material density, fabrication techniques (pressed powder of flat pocket), formation charge and discharge current densities, and extent of overcharge.

Table I. Efficiencies of iron active material stabilized in lithiated and unlithiated 20% KOH

Electrode	Mix weight, g	Weight iron, g	Stabilized Efficiency amp-hr/g Fe	Mean
102	8.11	6.98	0.392 ± 0.009	
103	8.10	6.97	0.392 ± 0.008	
104	8.13	6.99	0.388 ± 0.009	0.392
105	8.13	6.99	0.394 ± 0.010	
106	8.15	7.01	0.295 ± 0.007	
107	8.10	6.97	0.297 ± 0.007	
108	8.16	7.02	0.291 ± 0.007	0.292
109	8.17	7.03	0.288 ± 0.007	

Table I contains efficiency data for eight virtually identical single flat pocket iron electrodes, cycled until stabilization was assured in a pure and in a special lithiated 20% KOH employed solely for such single pocket evaluation (11g LiOH per liter of 20% KOH). These electrodes were fabricated from a batch of active material, prepared by the conventional Edison process described in the literature (6), which had been set aside as a quality control reference standard because of its excellent efficiency. The vast quantity of efficiency data collected with this batch of active material over a span of five years particularly suited it for such a study. Discharge was terminated at the first break in the voltage profile, designated by Salkind, Venuto, and Falk (2) to be the point where the useful capacity derived from the two electron Fe-Fe$(OH)_2$ transition was exhausted.

Theoretical efficiency for this transition is 0.96 amp-hr/g Fe. Individual electrode efficiencies are averages of the values observed over the last eight of the fifteen cycle regime and the excellent reproducibility obtained once stabilization was achieved is readily apparent. The difference in mean values represents a 34% increase in efficiency. Electrodes fabricated with less efficient grades of active material displayed differences of up to 50% when cycled in the same two electrolytes.

Stabilization of iron electrodes in pure 45% KOH yielded efficiencies equivalent to those obtained with lithiated 20% KOH, but use of such a concentrated electrolyte is incompatible with tubular nickel oxide electrodes as presently fabricated, since it results in rupture of the tube from excessive expansion of the active material. It is believed that the increased efficiency obtained with lithiated and more concentrated KOH electrolytes can most logically be explained by a delay in the onset of passivity. The cause of this phenomenon is, as yet, not readily apparent, but probably is related to the maintenance of a desirable crystal morphology.

Manuscript received March 11, 1965; revised manuscript received May 13, 1965.

Any discussion of this paper will appear in a Discussion Section to be published in the June 1966 JOURNAL.

REFERENCES

1. T. A. Edison, U. S. Pat. 876,445 (1907).
2. A. J. Salkind, C. J. Venuto, and S. Uno Falk, *This Journal*, **111**, 493 (1964).
3. L. C. Turnock, *ibid.*, **32**, 405 (1932).

4. J. T. Crennell and F. M. Lea, "Alkaline Accumulators," p. 102, Longmans, Green and Co., New York (1928).
5. K. Hofer, *Batterien*, **12**, 247 (1943).
6. G. W. Vinal, "Storage Batteries," 4th ed., p. 89, John Wiley & Sons, Inc., New York (1955).

Electrode Potentials in Fused Systems

IX. Liquid Junction Potentials in the AgCl-AgBr System

Kurt H. Stern

National Bureau of Standards, Washington, D. C.

Recent transport and liquid junction potential measurements (1) on a variety of molten salt systems indicate that the cationic mobilities in binary molten salt solutions are in general not equal over the entire composition range. Earlier results (2-4) in which zero liquid-junction potentials were obtained now appear as special cases.

Results published so far have included only systems of a single anion, the cation composition being different on the two sides of the junction. In the present paper we report a study of an anion concentration cell, *viz.*

$$\mathrm{Ag|AgCl}(X_1),\mathrm{AgBr}(X_2)\,||\,\mathrm{AgCl}(X_1'),\mathrm{AgBr}(X_2')\,|\mathrm{Ag} \qquad (A)$$

In this cell any nonzero emf is a liquid junction potential and must arise from differences in the anion mobilities and transport numbers.

Following Laity (2), we write for the cell emf

$$-FE/RT = \int_A^B t_1 d\ln a_1 + t_2 d\ln a_2 \qquad [1]$$

where t_1 and t_2 are the chloride and bromide transport numbers, and a_1 and a_2 are the AgCl and AgBr activities, respectively. Introducing the Gibbs-Duhem equation

$$d\ln a_2 = -\frac{X_1}{X_2} d\ln a_1 \qquad [2]$$

into [1] gives

$$-FE/RT = \int_A^B \frac{t_1X_2 - X_1t_2}{X_2} d\ln a_1 = \int_A^B \frac{\phi}{X_2} d\ln a_1 \qquad [3]$$

E can of course be zero only if $\phi = 0$, *i.e.*, $t_1 = X_1$, $t_2 = X_2$, but this is entirely possible even when $t_1 \neq t_2$ since the transport numbers are composition dependent. An explicit solution of Eq. [3] is possible only if some relation between t_1 and t_2 is assumed. This assumption is equivalent to choosing a reference with respect to which the transport numbers are to be measured. By choosing $t_1 + t_2 = 1$ we obtain transport numbers relative to silver ion, *i.e.*, $t_{Ag^+} = 0$. Making this substitution, and remembering that $X_1 + X_2 = 1$, gives

$$\phi = t_1 - X_1 \qquad [4]$$

Substituting [4] into [3] gives

$$-FE/RT = \int_A^B \left(\frac{t_1 - X_1}{X_2}\right) d\ln a_1 \qquad [5]$$

The corresponding expression for bromide ion is obtained by interchanging subscripts, *viz.*

$$-FE/RT = \int_A^B \left(\frac{t_2 - X_2}{X_1}\right) d\ln a_2 \qquad [6]$$

In the present work, using cell (A) the lower limit was fixed at a constant value of $X_1 = X_2 = 0.50$ and the upper limit was varied on both sides of this value.

Experimental

All measurements were carried out at 530°C in a furnace giving temperature control to ±1°. Cells were Pyrex U-tubes, 13 mm OD and 25 cm long, into whose center were sealed fine porosity (5-15μ hole size) quartz disks. These were capable of maintaining a considerable difference in liquid levels for several hours. Resistance measurements served to show that the pores of the frit were indeed wetted by the salt, since the resistance of unwetted glass is of course much higher. Some frits were cut open at the end of the run and examined microscopically to provide direct evidence that the pores were indeed filled with salt.

Twenty grams of each of the appropriate melt compositions were weighed out and melted together in a separate test tube to obtain uniform composition and then poured into the cell. Silver wire electrodes were placed into the cell compartments and the emf measured with a K-2 potentiometer. When a steady value had been reached, a weighed quantity of AgCl or AgBr was added to the variable side and the procedure repeated. Five or six such additions were made. In each run X_1' was both increased and decreased randomly by appropriate additions of AgCl and AgBr; only runs in which the emf varied reproducibly with composition were retained for mathematical analysis.

Results and Discussion

Plots of emf *vs.* the logarithm of AgCl and AgBr activity are shown in Fig. 1. The activities for the experimental compositions were computed from the data in reference (5). The slight curvature in the data suggested that ϕ/X_1 and ϕ/X_2 are not constant over the entire measured concentration range, and they were therefore fitted with a quadratic equation using

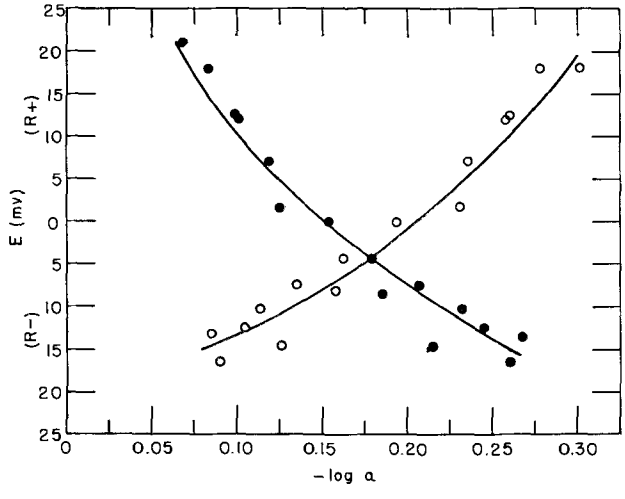

Fig. 1. Liquid junction potential of the cell Ag|AgCl(X_R = 0.5), AgBr| |AgCl(X), AgBr(1 − X)|Ag as a function of the logarithm of the activities of the right-hand compartment. • AgCl, ○ AgBr.

Table I. Relative transport numbers t_{Cl^-} and t_{Br^-} calculated from Eq. [7]. Activity data from (5)

X_{AgCl}	X_{AgBr}	a_{AgCl}	a_{AgBr}	t_{Cl^-}	t_{Br^-}	$(t_{Cl^-} + t_{Br^-})$
0.30	0.70	0.518	0.850	0.30	0.58	0.88
0.40	0.60	0.575	0.782	0.68	0.36	1.04
0.50	0.50	0.660	0.685	1.09	0.039	1.13
0.60	0.40	0.750	0.590	1.22	−0.36	0.86

a least-square procedure. The results of this calculation were used to compute the slopes $dE/d \log a_1$ and $dE/d \log a_2$. Substituting numerical values and solving for t_1 and t_2 gives

$$t_1 = (2.733 + 9.447 \log a_1) X_2 + X_1$$
$$t_2 = (-0.0365 + 5.392 \log a_2) X_1 + X_2 \quad [7]$$

The first term in Eq. [7] gives the deviation from ideality ($t_i = X_i$) which is quite concentration dependent. t_1 and t_2 are of course not independently calculable since (*a*) they are calculated from the same cell, (*b*) the condition $t_1 + t_2 = 1$ was used in deriving [5] and [6], and the activity of AgCl was obtained by a graphical integration of the Gibbs-Duhem equation using the cell Ag|AgBr, AgCl|Br_2 which gives AgBr activities directly (5). The results of the calculation are shown in Table I.

The increasing nonideality of the system with increasing AgCl concentration is quite noticeable. Thus as X_{AgBr} decreases, t_{Br^-} decreases even more rapidly and even becomes negative, suggesting some positive bromide complexes such as Ag_2Br^+. Outside the concentration range of Table I the sum $(t_{Cl^-} + t_{Br^-})$ increasingly drops below unity so that Eq. [7] apparently no longer describes the data adequately.

Although the present results do not yet justify extensive speculations on the nature of anion transport in molten salts, they suggest that the study of this phenomenon, by a variety of techniques, would prove as interesting as the corresponding study of cation transport has been.

Manuscript received Sept. 16, 1964; revised manuscript received April 12, 1965.

Any discussion of this paper will appear in a Discussion Section to be published in the June 1966 JOURNAL.

REFERENCES

1. For references, see A. Berlin, F. Menes, S. Forcheri, C. Manfrini, *J. Phys. Chem.*, **67**, 2505 (1963).
2. R .W. Laity, *J. Am. Chm. Soc.*, **79**, 1849 (1957).
3. K. H. Stern, *J. Phys. Chem.*, **63**, 741 (1959).
4. I. G. Murgulescu and D. I. Marchidan, *Zh. Fiz. Khim.*, **34**, 2534 (1960).
5. I. G. Murgulescu and D. I. Marchidan, *Rev. de Chimie, Acad. Rep. Pop. Roumaine*, **3**, [1] 1 (1958).

The Preparation of Large-Area Silicon Cathodes for Use in Reactive Sputtering

M. Bloom and N. P. Sandler

TRW Space Technology Laboratories, Thompson Ramo Wooldridge Incorporated, Redondo Beach, California

The properties of films of silica (1-3) deposited by reactive sputtering and the conditions under which they are applied (4, 5) are such that these films have great potential value in the fabrication of semiconductor devices. We have had occasion to apply this technique and found ourselves hampered by the lack of suitable large-area silicon cathodes.

The area of the cathode must be larger than the area of the substrate in order to obtain a deposit of uniform thickness (4). Silicon slices are usually used as cathodes, but silicon ingots with diameters larger than 3 in. are difficult to obtain. By slicing an ingot lengthwise, one may obtain a rectangular slab whose length and width are limited by the length and diameter of the ingot. The thickness cannot be reduced below a certain minimum amount because of the necessity of fixing the cathode to its holder. Our attempts to build a large cathode from an assembly of small blocks of silicon have not been successful. The joints, which initially might be quite smooth, are preferentially attacked by the bombarding ions and are soon enlarged to the point where the deposit exhibits nonuniformity.

A similar lack of uniformity is contributed to by the mounting screws. We have used Sinclair and Peter's (5) method of mounting a silicon cathode to its holder with a recessed aluminum screw. In our experience, such a mount causes the deposit to be contaminated with aluminum oxide even at the voltage (1800v) which these authors used. Covering the recessed aluminum screw with an appropriately shaped piece of silicon eliminated the aluminum contamination, but produced a lack of uniformity in the deposit corresponding to the gap between the piece of silicon covering the screw and the remainder of the cathode. Clearly, uniform deposits demand a large cathode having a uniform surface.

It occurred to us that such large-area cathodes might be produced by depositing silicon on a graphite substrate. This has been found to be the case, and it is the purpose of this communication to describe how this was done. The cathode was machined from a piece of graphite so that the front side, the surface from which the silicon was to be sputtered, was flat. The type of graphite was considered to be unimportant since McAleer (6) and co-workers have pointed out that layers of silicon with crystallite sizes ranging from 2 to 200μ across can be deposited by chemical decomposition processes on virtually any type of graphite. The back side of the cathode was machined so that it could be mounted on its holder without interfering with the front side. Figure 1 illustrates a typi-

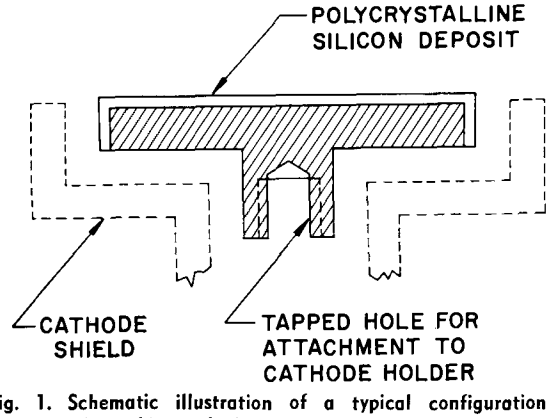

Fig. 1. Schematic illustration of a typical configuration for silicon-coated graphite cathode.

cal configuration. Except at the point of attachment, which was thick enough to allow drilling and tapping, the pieces were 8 mm thick but we know of no reason why the piece could not be thicker. The minimum thickness is determined by the fragility of the graphite.

Silicon was deposited on the cathode by the reduction of trichlorosilane by hydrogen at elevated temperatures in a deposition apparatus similar to that used by Bhola and Mayer (7). The only differences of note are that in our apparatus we used a graphite susceptor and vaporized trichlorosilane by bubbling hydrogen through it. In order to prevent silicon from depositing in the tapped attachment hole, a cathode holder was machined which masked the entire back surface of the cathode during deposition. The entire assembly was heated to 1250°C in the presence of only hydrogen for 30 min to drive off any adsorbed gases and reduce any residue to insure adequate adhesion of the deposited silicon to the cathode surface. This was followed by the deposition of silicon at a very slow rate to optimize complete coverage. The deposition parameters were then adjusted to obtain approximately 4μ of deposited silicon per minute at 1150°C. In this manner, we obtained a uniform layer of polycrystalline silicon whose thickness was approximately 10 mils in 1 hr and whose average grain diameter was approximately 10μ.

The economical use of a sputtering power supply requires that the cathode be shielded to suppress any glow discharge on those portions which do not contribute to the deposition (8). However, such shielding does not prevent oxidation of the exposed graphite during reactive sputtering in oxygen atmospheres when cathodes coated with silicon on only one side are used. During typical runs in 100% oxygen, the loss of graphite from the back side of the cathode, when using a shield, amounted to 0.01 mil/hr. Without a shield the loss was 0.7 mil/hr. For this reason it is better to cover the entire surface of the graphite with silicon. Only a minimal thickness is needed on the back side if a cathode shield is used. This problem might be obviated by depositing the silicon on a piece of polycrystalline alumina (9) which was provided with suitable metal conductors.

The surface of the silicon deposit is rougher and thus has a greater surface area than a lapped slab of silicon of the same diameter. Consequently, one might expect that the former would give a greater rate of deposition than the latter (10). However, after the latter has been used as a cathode for a short time its surface becomes roughened. As a result, the rate of deposition of the two cathodes is essentially the same.

The silica deposits obtained by the use of these silicon-coated graphite cathodes at a current density of about 3 ma/cm^2 appear to be identical to those obtained from cathodes made of slabs of polycrystalline or single crystal silicon.

Manuscript received June 1, 1965.

Any discussion of this paper will appear in a Discussion Section to be published in the June 1966 JOURNAL.

REFERENCES

1. B. H. Claussen and M. Fowler, *This Journal*, **110**, 983 (1963).
2. L. Hesinger and H. Koenig, "Festschrift 100 Jahre Heraeus Platinschlmelz," p. 376, quoted in Holland, p. 491 (Hanau, 1951).
3. C. R. Fuller and S. S. Baird, Paper presented at the Pittsburgh Meeting of the Society, April 1963, Abstract No. 65.
4. L. Holland, "Vacuum Deposition of Thin Films," p. 424, John Wiley & Sons, Inc., New York (1956).
5. W. R. Sinclair and F. G. Peters, *J. Am. Ceram. Soc.*, **46**, 20 (1963).
6. W. J. McAleer, M. A. Kozlowski, and P. I. Pollak, *This Journal*, **111**, 877 (1964).
7. S. R. Bhola and A. Mayer, *RCA Rev.*, **24**, 511 (1963).
8. L. Holland, *loc. cit.*, p. 420.
9. V. Y. Doo, *This Journal*, **111**, 1196 (1964).
10. L. Holland, *loc. cit.*, p. 416.

A Concentration Gradient Profiling Method

Stacy B. Watelski, W. R. Runyan, and R. C. Wackwitz

Texas Instruments Incorporated, Dallas, Texas

Epitaxial depositions are usually such that a thin high resistivity layer is deposited on a low resistivity substrate. If it is desired to make a concentration profile through the interface region, conventional incremental lapping from the front surface is not appropriate because even the removal of thick layers will hardly change the resistance of the remaining sample since most of the carrier contribution comes from the substrate. To circumvent this difficulty, lapping from the back is necessary. Success of the standard incremental lap process hinges on the ability to remove successfully many small parallel sections from the sample. This is difficult to do even when sectioning relatively thin regions and is quite impractical when moving through several hundred microns of material.

These difficulties may be alleviated by beveling from the back at some small, roughly predetermined angle. Sheet resistance readings are made at regular intervals down the slope of the lapped surface using a four-point probe oriented so that the line of probes is perpendicular to their direction of motion (see Fig. 1). Studies of this method thus far have been made using angles as small as 8 min ($\tan \alpha = 0.0023$). The angle is usually determined by sectioning the slice after all electrical measurements are made. Nonuniformity in the angle across and along the face of the bevel is corrected by measuring the sample thickness at several positions along its length.

If the total thickness to be examined is greater than $L \tan \alpha$, where L is the sample length, a sequential process of incremental angle lapping and probing may be employed. When the incremental steps are properly chosen, some overlap of sheet resistance from step to step is possible. A typical sheet resistance profile for a case with three successive laps is shown in Fig. 2. Each sheet resistance curve has a region which decreases with decreasing thickness. This is an edge effect resulting from large probe spacing and was substantially

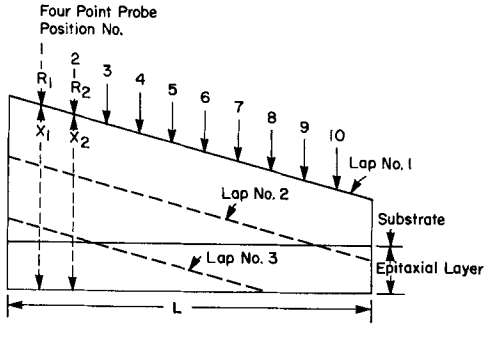

Fig. 1. Diffusion profile determination by incremental angle lapping.

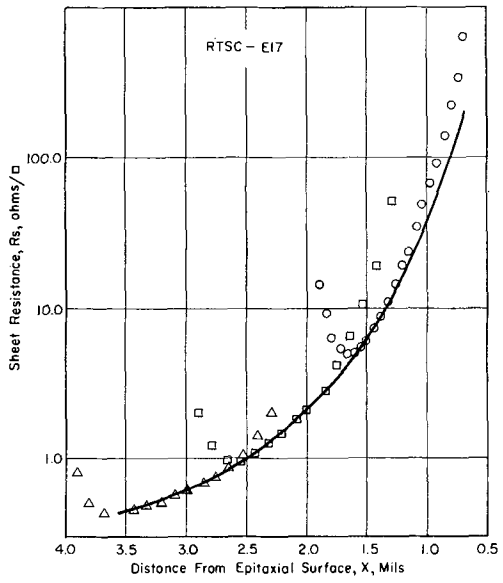

Fig. 2. Measured sheet resistance profile: △, lap No. 1; □, lap, No. 2; ○, lap No. 3.

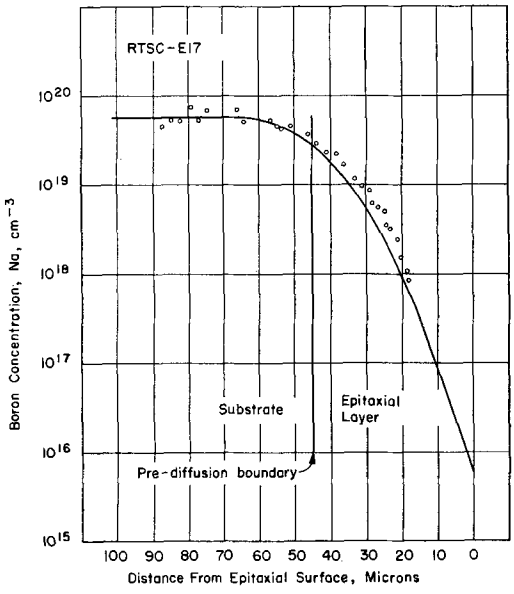

Fig. 3. Comparison of calculated and measured boron concentration profile: ——, calculated; ○ ○ ○, measured.

reduced in later studies by using 250μ probe spacings. An additional edge effect occurs at that portion of each curve corresponding to the thinner end of the blank and causes the apparent sheet resistance to increase at a faster than normal rate. The solid line shown in Fig. 2 compensates for these edge effects and was used for the profile calculations. When the lapped edge intersects the bottom of the slice, *e.g.*, No. 3 of Fig. 1, the readings near the thin edge are very sensitive to damage induced during beveling or by the probes. Probing damage is minimized by securing the sample to a silicon support with a dimensionally stable insulating epoxy layer. This epoxy layer is firm enough to prevent penetration of the probes even at the thin edge extreme. This laminate is also useful when sectioning the sample to correlate probe reading and sample thickness. Induced material damage usually results in readings higher than normal and may be minimized by careful lapping or grinding. Surface roughness comparisons of lapping with 1800 grit *vs.* grinding with an 800 grit diamond wheel show maximum surface excursions of 2.3μ and 0.38μ, respectively. Indeed, a measure of the proficiency of the operation may be obtained by profiling a uniform resistivity slice and observing how thin a section can be measured before the sheet resistance indicates an apparent increase in resistivity. Using 250μ spaced probe, errors $\gtrsim$10% may be realized at distance $\gtrsim$5μ from the surface; however, errors increase rapidly in the 0-5μ region. The technique is valid for substrate to layer resistivity ratios $\lesssim$1.

If R_1 and R_2 are the sheet resistances at x_1 and x_2, respectively, resistivity values in a small interval $(x_1 - x_2) = \Delta x$ may be calculated in the manner of Fuller and Ditzenberger (1) from

$$\rho = \frac{R_1 R_2}{R_2 - R_1} \Delta x \qquad [1]$$

Data reduction may be simplified by computer programing and plotting, in which case it has been found convenient to convert sheet resistance *vs.* thickness to bulk resistivity *vs.* thickness by a method which minimizes the effect of experimental error in the sheet resistance value and does not depend upon the value of Δx used (2). The method consists in relating the logarithm of the sheet conductance values to depth, from which the bulk resistivity ρ for any thickness x can then be found. If $G(x)$ is the sheet conductance for a thickness of material x, then the conductivity $\sigma(x)$ is given by

$$\sigma(x) = \frac{dG}{dx} \qquad [2]$$

The logarithm of sheet conductance has some functional dependence on depth which may be defined as $F(x)$, *i.e.*

$$\ln G(x) \equiv F(x) \qquad [3]$$

Differentiation with respect to x gives

$$(1/G)\,(dG/dx) = dF/dx \qquad [4]$$

so that by combining Eq. [2] and [4]

$$\rho(x) = 1/GF' \qquad [5]$$

The values of $\rho(x)$ thus calculated are converted to concentration values by use of Irvin's curves (3).

A Fortran program has been written for the IBM 7040 computer to calculate $\rho(x)$ *vs.* depth from sheet resistance *vs.* depth measurements using Eq. [5]. A piece-wise smoothing subroutine is first applied to the ln G *vs.* depth values to smooth out random experimental errors in sheet conductance. The smoothing subroutine used reliably follows the physical nature of the curve and does not "over-smooth." A spline subroutine is next applied to the smoothed ln G *vs.* depth values, from which values of $G(x)$ and $F'(x)$ can be calculated for use in Eq. [2] for any depth x desired. The spline subroutine used is based on the spline described by Theilheimer and Starkweather (4), and hence does not require *a priori* values of the first derivative for the first and last data points.

This method has been applied primarily to studies of substrate-epitaxial layer profiles after extended diffusion. For example, a 2.3 ohm-cm, 45μ thick p-type layer was epitaxially deposited on a 0.002 ohm-cm boron-doped substrate blank. The blank was then diffused for 25 hr at 1250°C after which it was beveled and profiled. A comparison of the measured boron concentration profile with one calculated by assuming a boron diffusion coefficient of 8.7 x 10^{-12} cm^2/sec is shown in Fig. 3. The lack of data for $x < 18\mu$ is due to the probe spacing edge effect mentioned earlier.

Acknowledgments

The precision lapping and grinding was done by J. B. Sherer. A portion of this work was supported by the National Aeronautics and Space Administration,

Goddard Space Flight Center, Greenbelt, Maryland under Contract No. NAS 5-3559.

Manuscript received March 29, 1965; revised manuscript received June 21, 1965.

Any discussion of this paper will appear in a Discussion Section to be published in the June 1966 JOURNAL.

REFERENCES

1. Fuller and Ditzenberger, *J. Appl. Phys.*, **27**, 544 (1956).
2. D. L. Kendall, Unpublished work.
3. J. C. Irvin, *Bell Syst. Tech. J.*, **41**, 387 (1962).
4. F. Theilheimer and W. Starkweather, *Math Comp.*, **15**, 338 (1961).

Residual Surface Recombination on Germanium Anodes

P. J. Boddy and W. H. Brattain

Bell Telephone Laboratories, Incorporated, Murray Hill, New Jersey

Capacity measurements on germanium electrodes which had been subjected to anodic dissolution in neutral aqueous electrolytes free from noble metal ion contaminants showed no evidence of charge trapping due to fast surface states (1) (*i.e.*, $N_t < \sim 10^{9.5}$ cm^{-2}). Similarly the value of surface recombination velocity (srv) was reduced to a very low level by the same treatment. In this communication we report measurements of the magnitude of the srv under the conditions which we have adopted as standard (*i.e.*, deoxygenated 10M K_2SO_4, buffered with 15M phosphate to pH 7.4) in several experimental studies of germanium electrodes (2-4). First note that in the Eq. [1] (5)

$$s = (\lambda + \lambda^{-1})(C_nC_p)^{1/2}\{2\cosh(v + \ln\chi) + 2\cosh(Y - \ln\lambda - \ln\chi)\}^{-1} \quad [1]$$

it is the quantity $s(\lambda + \lambda^{-1})^{-1}$, not s, which remains constant for all nondegenerate values of the bulk Fermi level if the other parameters are fixed. Consequently for electrodes which are close to intrinsic, *i.e.*, λ close to unity, the value of s is relatively small. Our previous measurements have been made with near-intrinsic samples to avoid pronounced minority carrier effects, *e.g.*, saturation at small currents. This has reduced the sensitivity of the srv measurements, but not the capacity measurements. A further factor reducing the sensitivity of the srv measurements has been the requirement that the filaments should be sufficiently thick that the ohmic drop between the center and ends of the filament caused by the current flow across the polarized interface is not greater than ~10 mv.

The measurements shown in Fig. 1 were made on a p-type bridge electrode (1) with $\lambda = 19.5$. The srv

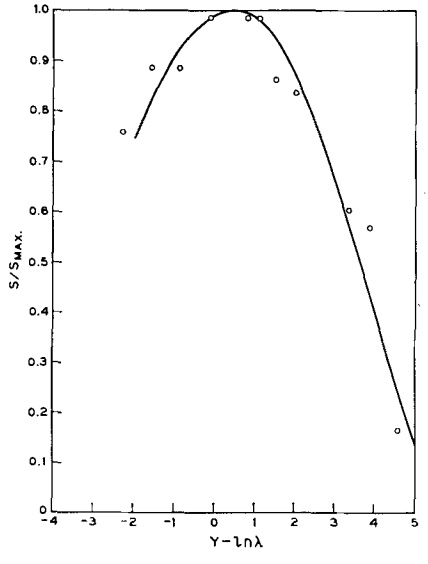

Fig. 1. Measurements made on p-type bridge electrode

was determined from the filament lifetime by the relationship

$$2s = (\tau^{-1}_{fil} - \tau^{-1}_{body})(t^{-1} + w^{-1})^{-1} \quad [2]$$

The surface potential, which was varied by changing the electrode potential, was derived from the interfacial capacity measured by ~1 μsec current pulses (1). The value of s_{max} at 25°C was 39 cm sec^{-1} and hence $s_{max}(\lambda + \lambda^{-1})^{-1}$ was ~2 cm sec^{-1}. As shown in Fig. 1 the data were fitted to a discrete state with parameters: $\ln\chi = 0.4$, $v = +2.6$ or -3.4 kT/e measured positive downward from the intrinsic level. We have no criterion for deciding at which of these two possible levels the state occurs. Within the sensitivity of our measurement we observe no additional capacity (*i.e.*, trapped charge) due to fast surface states. A combination of the uncertainty of about 10% in the surface roughness factor combined with the distortion of the capacity electrode potential curves due to changes in Helmholtz potential difference which occur as a result of polarization (6) precludes the observation of a state with a peak capacity of the same magnitude as the space charge minimum, unless fortuitously it should occur within about 25 mv of the potential of the minimum.

Since $s_{max}(\lambda + \lambda^{-1})^{-1} \approx 2$ cm sec^{-1}, and $(v + \ln\chi) = \pm 3.0$ then from Eq. [1]

$$2 = (C_pC_n)^{1/2}\{2\cosh 3 + 2\}^{-1} \quad [3]$$

since $\cosh(Y - \ln\lambda - \ln\chi) = 1$, when $s = s_{max}$. Hence

$$N_t(\sigma_p\sigma_n v_p v_n)^{1/2} \approx 44 \quad [4]$$

The average cross section $(\sigma_p\sigma_n)^{1/2}$ is taken as approximately equal to atomic dimensions, *i.e.*, 10^{-15} cm^2, on the assumption that an uncharged center has a cross section equal to its physical size while for a charged center the equal and opposite coulombic forces on the holes and electrons will tend to average out. Then taking $(v_pv_n)^{1/2} \approx 7 \times 10^6$ cm sec^{-1}, we have $N_t \approx 6 \times 10^9$ cm^{-2}.

The capacity per unit area due to surface states at a single energy is

$$C = N_t e^2 (kT)^{-1}\{2\cosh \tfrac{1}{2}(Y + v - \ln\lambda)\}^{-2} \quad [5]$$

and, for the N_t derived above, has a peak value of $\sim 1.0 \times 10^{-8}$ farads cm^{-2}. In Fig. 2 is shown the theoretical capacity of the electrode compared with the capacities for surface states of the density and energies we have calculated. The sum of the two is also shown by the dashed lines, and it is clear that, since the experimental curve tends to be broadened by changes in Helmholtz potential difference, the observation of states of these parameters would be quite difficult. For comparison purposes the capacities of surface states produced by contamination of the surface with cupric ion are shown using the energies and densities previously determined (7). In this case it is clear that the additional capacity due to the states is easily measurable. The nature of the residual states in uncontaminated solutions is not known, but the srv data

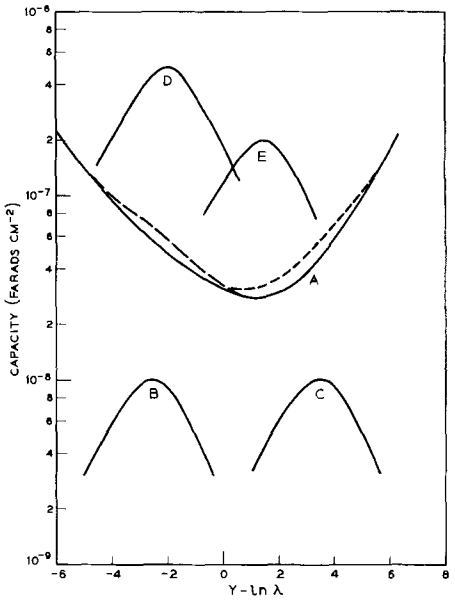

Fig. 2. Theoretical capacity of the electrode

described above have been observed repeatedly and are presumed to be an inherent property of this surface.

Summary

Measurements of srv of an appropriate electrode show that the residual value of $s_{max}(\lambda + \lambda^{-1})^{-1} \approx 2$ cm sec^{-1} on anodically etched surfaces. The parameters of the state are ln $\chi = 0.4$, $\nu = 2.6$ or -3.4 kT/e and $N_t \leq 6 \times 10^9$ cm^{-2} if $(\sigma_p\sigma_n)^{1/2} \leq 10^{-15}$ cm^2.

Manuscript received June 3, 1965.

Any discussion of this paper will appear in a Discussion Section to be published in the June 1966 JOURNAL.

REFERENCES

1. W. H. Brattain and P. J. Boddy, *This Journal*, **109**, 574 (1962).
2. P. J. Boddy and W. H. Brattain, *Ann N. Y. Acad. Sci.*, **101**, 683 (1963).
3. W. H. Brattain and P. J. Boddy, *Proc. Nat. Acad. Sci.*, **48**, 2005 (1962).
4. P. J. Boddy, *This Journal*, **111**, 1136 (1964).
5. D. T. Stevenson and R. J. Keyes, *Physica*, **20**, 1041 (1954).
6. P. J. Boddy and W. H. Brattain. *This Journal*, **110**, 570 (1963).
7. P. J. Boddy and W. H. Brattain, *ibid.*, **109**, 812 (1962).

SYMBOLS

s	surface recombination velocity
p	bulk hole concentration
n_i	intrinsic electron concentration
λ	pn_i^{-1}
N_t	density of recombination centers
$v_{p,n}$	thermal velocity of holes, or electrons
$\sigma_{p,n}$	capture cross sections for holes, or electrons
$C_{p,n}$	$N_t v_p \sigma_p$, or $N_t v_n \sigma_n$
χ	$C_p^{1/2} C_n^{-1/2}$
ν	energy level of a recombination center measured positive downward from the intrinsic level
Y	potential difference across space charge region
τ	minority carrier lifetime
t	thickness of filament
w	width of filament

k, T, and e are the usual constants.

Reaction of Nickel Carbonyl with Carbon Disulfide

S. H. Pitts, Jr.

Chemistry Research and Development Laboratories, The Dow Chemical Company, Golden, Colorado

A program was undertaken to investigate additives which would alter the reaction rate or lower the decomposition temperature of nickel carbonyl. Other investigators have shown that hydrogen sulfide will catalytically lower the decomposition temperature from about 150°C down to 60°-100°C (1). Oxygen or water vapor are rate promoters in the H_2S-$Ni(CO)_4$ reaction (2). Silicon and titanium tetrachlorides are also rate promoters (3). This work revealed that carbon disulfide effects a rapid and unique room temperature reaction.

Figure 1 shows the experimental apparatus. It consists of a one-liter bell jar sealed to a steel base plate with an O-ring. The plate was fitted with the necessary connections to facilitate evacuations and gas chargings. The bell jar served as a precalibrated $Ni(CO)_4$ reservoir. Connected to it was a one-liter round bottom flask reaction vessel. Pressure readings were taken on mercury manometers with a cathetometer. A small reservoir of liquid CS_2 was separated from the flask by a needle valve. A heated decomposition chamber disposed the residual $Ni(CO)_4$ in the waste gases.

The system was designed so that the reaction could be followed through the pressure change. The following 1 to 4 pressure increase occurs in the complete thermal decomposition of $Ni(CO)_4$

$$Ni(CO)_{4(g)} \rightarrow Ni_{(s)} + 4CO_{(g)} \qquad [1]$$

In the CS_2-$Ni(CO)_4$ reaction, the final pressure is usually only 3 times that of the initial pressure. However, the pressure increase does vary by a factor of 2 to 3.5.

A typical run for maximum $Ni(CO)_4$ conversion using the experimental system is made by evacuating the system and charging the reaction flask with 3.5 mm of CS_2. The bell jar is charged with 50 mm of $Ni(CO)_4$. The connecting valve between the two vessels is opened for a minimum time to admit $Ni(CO)_4$ to the reaction flask to an equilibrium pressure of 21.4 mm. Pressure readings are taken after 1 min and as often as necessary thereafter. This procedure is mandatory because of the very fast initial reaction rate. Attempts to meter $Ni(CO)_4$ directly into the reaction flask and get a zero time pressure reading give erratic results. This is due to the simultaneous pressure increase from the CO being formed. After ap-

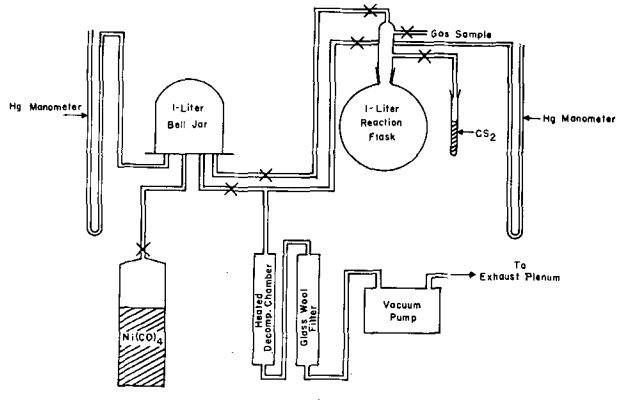

Fig. 1. Experimental system for the $Ni(CO)_4$-CS_2 reaction study

proximately 25 min, no further pressure changes occur.

The reaction can also be made in a modified system which eliminates the reaction flask. This is desirable when using the reaction in practical plating applications where precise measurement is not critical. Both the $Ni(CO)_4$ and the CS_2 can be metered directly into the bell jar. Since the gases react immediately upon contact and the subsequent pressure increase can give erroneous readings, the system in Fig. 1 was used for the experimental work. The CS_2-$Ni(CO)_4$ reaction is apparently not catalytic because of the consumption of CS_2 in the reaction. The maximum conversion is obtained using 13-15% (or higher) volume per cent CS_2. Infrared analyses of residual gases show both the CS_2 and $Ni(CO)_4$ are consumed. Figure 2 shows the effect of CS_2 concentration on the reaction. The $Ni(CO)_4$ conversion increases up to a maximum as the CS_2 concentration is increased to 15%. The rate of reaction and CS_2 concentration could not be correlated.

Sufficient data are not available to postulate a plausible reaction mechanism. It is different than that of thermal decomposition of $Ni(CO)_4$ as implied by the pressure change. Gas analysis shows that 95-100% $Ni(CO)_4$ conversion is obtained even though the pressure increase is only 2 to 3.5 times that of the initial pressure. Carbon monoxide is the major constituent in the residual gas.

Analysis of the nickel deposit is inconclusive because only the following elements were measured: Ni, 81.6%; S, 9.8%; C, 1.8%. It was not determined whether the sulfur exists as a compound or in elemental form, but it does explain the consumption of CS_2. Presumably, the remaining portion of the deposit is oxygen. X-ray diffraction patterns could not be obtained because the deposit is apparently amorphous or very fine grained. Electron microscopy shows the deposit as loosely packed spherical or polyhedral particles of consistent size, approximately 375Å in diameter. Dissolution of the nickel plate in nitric acid leaves an unidentified powdery brown residue. This indicates the deposit to be something other than pure nickel. There was no significant weight change on heating the deposit *in vacuo* to 500°C. After cooling and reheating in an oxygen atmosphere the sample increased in weight 16% and became green-black in color. This is indicative of oxide formation and the deposit is, at least in part, elemental nickel. The deposit imparts a bright, mirror-like finish to smooth surfaces. However, it is quite thin. In a one-liter flask with a 25 mm $Ni(CO)_4$ charge, interferometric measurements show the deposit to be 1700-2100Å thick.

In both the thermal decomposition of $Ni(CO)_4$ and the H_2S-$Ni(CO)_4$ reaction, the accumulation of the CO by-product has a retarding effect. The addition of CO to a CS_2-$Ni(CO)_4$ mixture prior to reacting did not inhibit the reaction. It did produce a 1-2 min induction period.

Both oxygen and water are reported to promote the H_2S-$Ni(CO)_4$ reaction (2). However, neither 6.4% water vapor nor 5.3% air in a CS_2-$Ni(CO)_4$ mixture had any significant effect.

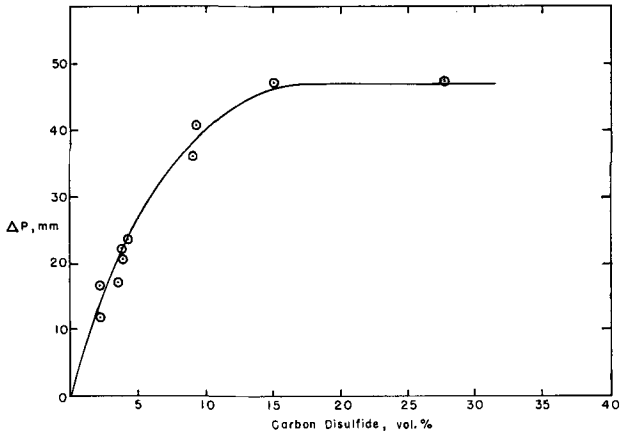

Fig. 2. Effect of CS_2 concentration on reaction with 25mm $Ni(CO)_4$ at 25°C after 25 min.

It is known that $Ni(CO)_4$ will decompose photochemically. However, room light had no apparent effect on the CS_2-$Ni(CO)_4$ reaction. CS_2 and $Ni(CO)_4$ reacted the same in clean glass as they did in a plated flask used 10-12 consecutive times. The metallic coating completely covers the reaction flask after 1-2 passes. The decomposition apparently is initiated and grows from particular surface nucleation sites. This is visually evident from the growth pattern on clean glass. A faster reaction rate was obtained by adding approximately 1-3g of 900 mesh nonactivated alumina. The alumina was loosely adherent to the surface of the reaction flask. Even though complete $Ni(CO)_4$ conversion was obtained, a smaller pressure increase occurs when using alumina. Carbon monoxide adsorption measurements on alumina did not account for this difference. Plating was preferential on the oxide particles. This suggests adsorption of one or both of the reactants on the particle surfaces. The coated particles caused the same effect as uncoated alumina. Powdered nickel oxide also causes a faster reaction rate.

The room temperature reaction of $Ni(CO)_4$ with CS_2 shows some potential for thin films and coating applications. Reaction mechanism studies are being pursued.

Manuscript received Dec. 7, 1964; revised manuscript received May 11, 1965.

Any discussion of this paper will appear in a Discussion Section to be published in the June 1966 JOURNAL.

REFERENCES

1. T. B. Hoover, U. S. Pat. No. 2,881,094, April 7, 1959.
2. T. B. Hoover and T. E. Zava, U. S. Pat. No. 2,886,468, May 12, 1959
3. M. V. Sullivan, U. S. Pat. No. 2,759,848, Aug. 21, 1956.

Brief Communications

PbS Diode Laser

J. F. Butler and A. R. Calawa

Lincoln Laboratory,[1] Massachusetts Institute of Technology, Lexington, Massachusetts

Diode laser action in the Pb salt semiconductors has previously been achieved in PbTe (1) and PbSe (2). Electron beam pumping has recently produced laser action in all three Pb salts (3). The PbS diode laser is described in this note.

Techniques for fabricating diodes of PbS, like those of PbTe and PbSe (4), were based on controlling deviations from stoichiometry. The starting material was a Bridgman grown, n-type single crystal of PbS with a carrier concentration of 3 x 10^{18} cm^{-3}. Wafers with flat planar surfaces were obtained from the boule by cleaving along {100} planes. To diffuse a p-layer into a wafer it was heated in an evacuated, sealed quartz ampoule with a vapor source consisting of a S rich, two phase ingot of PbS (51:49 a/o). A diffusion time of 1 hr at 550°C produced a p-n junction 50μ deep. Dice in the form of rectangular parallelopipeds were obtained from a wafer by further cleaving along {100} planes. Typical dimensions are 500μ between the end faces defining the Fabry-Perot cavity and 200μ in the other two directions. Ohmic contact was made to the p-side with evaporated Au and to the n-side with a Sn-In alloy. The dice were mounted in low inductance packages.

The diode lasers were mounted on the cold finger of a liquid helium dewar. Spectra were measured using a single-pass grating spectrometer and an InSb photovoltaic detector. The detector output was amplified by a lock-in amplifier system.

[1] Operated with support from the United States Air Force.

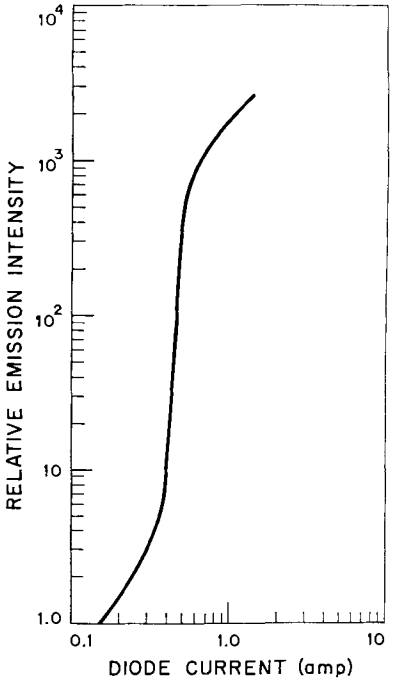

Fig. 1. Infrared emission from an end face of a PbS diode laser at 4.2°K as a function of forward current.

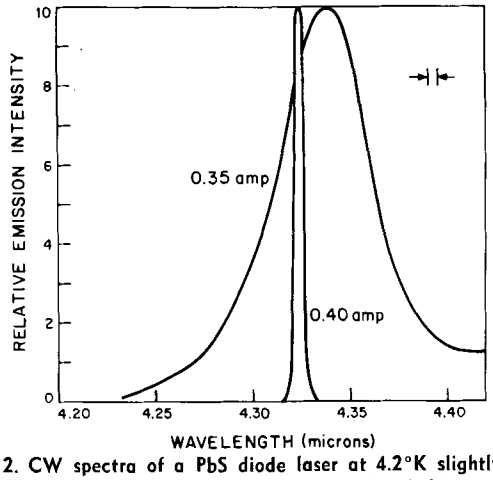

Fig. 2. CW spectra of a PbS diode laser at 4.2°K slightly below (0.35 amp) and slightly above (0.40 amp) threshold.

Figure 1 shows the intensity of the infrared emission from a laser end face as a function of diode forward current. At low currents the intensity is low and increases superlinearly. The sharp rise at about 0.38 amp indicates the onset of laser action and gives a threshold current density of 300 amp cm^{-2}. Since at this temperature the diodes do not overheat for direct current densities of over 1,000 amp cm^{-2}, CW operation at currents greater than three times threshold is possible.

In Fig. 2, CW spectra measured slightly below and slightly above threshold are normalized to the same

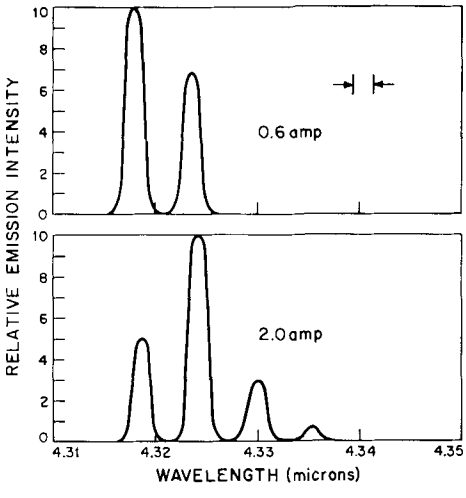

Fig. 3. Multimode emission from a PbS diode laser at 4.2°K forward biased with 0.6 amp direct current and 2.0 amp, 4μsec current pulses.

scale to illustrate the line narrowing associated with laser action. The absolute intensity of the laser peak is much higher than that of the spontaneous emission maximum. The width of the laser line is obviously resolution limited in this figure.

Figure 3 illustrates the multimode emission which occurs at higher currents. The separation between modes of 55Å satisfies the condition that the optical length of the cavity be an integral number of half-wavelengths if $dn/d\lambda = -0.3\ \mu^{-1}$, where n is the refractive index of the material and λ the wavelength of emitted radiation. This result was obtained by using a value of 4.7 for the refractive index of PbS at 4°K, extrapolated from unpublished measurements (5) covering a range down to 77°K. A resolution limited laser linewidth of 15Å has been measured.

Acknowledgment

The authors would like to thank R. Woods for his technical assistance.

Manuscript received June 1, 1965. This paper was presented at the San Francisco Meeting, May 9-13, 1965.

Any discussion of this paper will appear in a Discussion Section to be published in the June 1966 JOURNAL.

REFERENCES

1. J. F. Butler, A. R. Calawa, R. J. Phelan, Jr., T. C. Harman, A. J. Strauss, and R. H. Rediker, IEEE Solid-State Device Research Conference, Boulder, Colo., July 1-3, 1964, abstract in IEEE Trans. on Electron Devices *ED-11,* 536 (November, 1964); *Appl. Phys. Letters,* **5,** 75 (1964).
2. J. F. Butler, A. R. Calawa, R. J. Phelan, Jr., A. J. Strauss, and R. H. Rediker, *Solid State Comm.,* **2,** 303 (1964).
3. C. E. Hurwitz, A. R. Calawa, and R. H. Rediker, *IEEE J. Quantum Electronics,* **1,** (May 1, 1965).
4. J. F. Butler, *This Journal,* **111,** 1150 (1964).
5. J. N. Zemel, J. D Jensen, and R. B. Schoolar, Private communication.

Gallium Arsenide Surface Preparation

Jack Lowen

National Aeronautics and Space Administration, Cambridge, Massachusetts

The preparation of planar devices, for example, field effect transistors, requires polished damage-free surfaces. The following method has consistently yielded flat, polished, and damage-free gallium arsenide.

Material is cut into 0.002 in. thick slices and then into 5/16 in. squares. Heavy coats of wax must be used to avoid breakage. The 5/16 in. squares are removed from their block mounts using heat and then carefully dewaxed and degreased with three successive hot rinses of Solox, tricholorethylene, and methyl alcohol.

The A and B sides are then differentiated using an etch consisting of HF, H_2O_2, and H_2O (1:1:1) for from 1 to 2 min at room temperature. The A side shows up as shiny with rounded orange peel surface. The B or arsenic side has a matte finish and triangular etch pit pattern.

The squares are then mounted on a Teflon block, B side up and chemically polished, with rotation against a flat Teflon surface, in a solution of H_2SO_4, H_2O, H_2O_2, and H_2F_2 (250, 40, 50, and 25), for from 5 to 10 min.

Acknowledgment

The experimental work was carried out at the Sprague Electric Company, Research Center, North Adams, Massachusetts.

Manuscript received May 28, 1965.

Any discussion of this paper will appear in a Discussion Section to be published in the June 1966 JOURNAL.

Addendum

The following additional information is presented for the Technical Note "Notes on the Chemical Polishing of Gallium Arsenide Surfaces" by R. D. Packard which appeared on pp. 871-872 of the August 1965 issue:

"When nitric acid and glycerine are mixed, glyceryl trinitrate (nitroglycerine, a dangerous explosive) may be formed. It is a colorless-to-yellow liquid of specific gravity 1.6 g/cc, and when pure explodes at 260°C.

"The nitric and hydrochloric acids should be mixed first, and then poured into the glycerine slowly, with gentle stirring. The HNO_3-HCl interaction results in the formation of nascent chlorine, which is an oxidant aiding polishing.

"The solution should not be heated nor subjected to violent agitation. Use a constant temperature bath arount the polishing solution. It should be used in a well-ventilated area such as a fume hood, since it is irritating and toxic when breathed.

"The solutions are relatively unstable due to various reactions such as those described; they should be mixed fresh before each etching and discarded by flushing down an acid sink after use. They can be easily and rapidly mixed volumetrically."

Studies of the Molten Carbonate Electrolyte Fuel Cell

A. N. Webb, W. B. Mather, Jr., and R. M. Suggitt

Texaco Research Center, Beacon, New York

ABSTRACT

Fuel cells with $NaLiCO_3$ electrolyte contained in a porous MgO matrix have been operated at 650°C on synthetic, "realistic" fuels containing combinations of H_2, CO, CO_2, H_2O, and N_2. A mixture of air and CO_2 was used as the oxidant. Hydrogen reacted nearly reversibly when a completely oxidized state of the electrode was avoided. No reversible oxidation of CO was observed, and current-time data confirmed that electrode oxidation occurred preferentially. H_2 and CO were oxidized at oxidized electrodes with 0.6v activation polarization. Carbon deposition from the disproportionation of CO occurred even during the oxidation of H_2. The disproportionation can be prevented by addition of H_2O or CO_2.

The molten carbonate fuel cell has been and continues to be under intensive investigation and development (1-11). Rejection of CO_2 by the electrolyte and high operating temperatures of 500°-750°C give promise of practical operation on impure hydrogen and less reactive carbonaceous fuels. Distinct advantages are the reversibility of the silver oxygen electrode and the efficient dissipation of heat at a useful level. Disadvantages are slow starting and the severe testing of materials by the hot, corrosive environment. Considering that these factors are not overruling or can be overcome, there remain problems such as carbon deposition and low anode activity for CO. The objectives of this work were to examine the behavior of realistic fuel gases, especially impure H_2 with CO_2, to develop a working hypothesis of the anode reactions in order to discover and, if possible, remove limitations on cell performance, and to find an electrode catalyst for efficient oxidation of CO. Since CO is present in or formed from all fuel gases (even pure H_2) in the molten carbonate cell, efficient operation will require that CO be consumed at a cell voltage near that of H_2.

Experimental

Experimental cells were disk-type similar to those described by Trachtenberg (11). A binary electrolyte of the composition $LiNaCO_3$ was contained in a porous MgO matrix. Electrodes were of the porous diffusion type formed from silver powders sintered or brazed to silver flame-sprayed areas on either side of the MgO disk. In most cases a dual porosity electrode was prepared by sintering layers of −80 +100 mesh and −20 +40 mesh silver powders at 850°-920°C for 1 hr in a nitrogen atmosphere. The sintered structures were 2 in. diameter and weighed from 10 to 15g.

Anode catalysts were incorporated both by electroplating and as mixed or enclosed powders. Electroplating was performed "internally" by first soaking the porous Ag electrode in the plating solution and then cathodizing it in a similar solution without the reducible metal salt. To overcome limitations on the amount and kind of catalyst which could be introduced by electroplating and the inability to sinter electrode structures containing more than a few per cent of refractory materials, an enclosed powder structure was used. Either a ring of sintered Ag or an Ag gauze basket was filled with a mixture of powdered silver and catalyst, covered with Ag powder, and finally sintered. In some cases the enclosed oxides were "silverized" by coating with $AgNO_3$ and decomposing the nitrate at 500°C using the method of Chambers and Tantram (12). A sintered, uncatalyzed silver cathode was used in all cases.

Cells were heated to 650°C in 4-6 hr with CO_2 flowing through both compartments. The fuel gas then replaced CO_2 in the anode compartment and air at 100 cc STP/min was added to the 40 cc STP/min of CO_2 in the cathode compartment to provide stoichiometric ratio for the reaction

$$\tfrac{1}{2}\ O_2 + CO_2 + 2e^- \rightarrow CO_3^=$$

All operations, unless otherwise noted, were on this cathode mixture of air and CO_2. Electrolytic grade hydrogen, deoxygenated and dried, was used. Carbon monoxide was of C.P. grade; technical grade desulfurized butane and pentane were used. Pentane was picked up in a helium stream and water was injected. Suitable flow meters were used with all gases.

Current-voltage curves were obtained manually by changing the load resistance so that either cell current changed by 50 ma or the cell voltage changed by 50 mv every 2 min. The latter method was preferred since a nearly constant time was required for all cells. Curves were started at open circuit and, if the unloading curve fell appreciably below the initial sweep, retracing was continued until a reproducible path was obtained. Maximum power densities were obtained from the steady-state curve and were based on the area of catalyzed anode.

Measurements of current obtainable at a set voltage as a function of time provided a less tedious approach to steady-state values and a reliable method for distinguishing fuel and electrode oxidations. Anode potential-time curves used in polarization studies were obtained by recording separately current and voltage with time at each of several different cell loads. Voltage and time values for any particular cell current were determined from current-voltage curves (at various times) plotted from the original data. Voltages were not corrected for cathodic or ohmic polarization. Anode and cathode polarizations could not be individually measured since there was no reference electrode in this cell. From other related work, however, both cathode and ohmic polarizations were found to be directly proportional to the current but constant with time at each current density.

Cell Performance

On pure hydrogen.—Performances on H_2 at 650°C of several molten carbonate fuel cells, containing various types of anode structures and various catalysts, are given in Table I. Open-circuit voltages were quite uniform between 1.17 and 1.25v in the absence of anode reaction products. Maximum power densities occurred near 0.6v in all cases and were as high as 45 mw/cm². A more consistent value, however, was 32 mw/cm², and Table I indicates the range of values observed. In most cases 10-20% of the hydrogen entering the anode compartment was oxidized at maximum power.

No one anode type or catalyst was superior to the others although electroplated anodes gave the best performance per gram of catalyst, probably due to better catalyst distribution.

Table I. Fuel cell performance

Cell	Anode type	Catalyst, w/o	Area, cm^2	Max. power density H_2 40 cc/min, mw/cm^2	Max. power density CO-CO_2,[a] mw/cm^2
A	Electroplated	Ni(0.25)	20.2	14.2	—
B	Internally electroplated	Rh(0.35)	20.2	14.2	2.8
C	Internally electroplated	Co(2.2)	20.2	35.6	2.5
D	Internally electroplated	Co,Zn(2.9)	20.2	31.2	2.5
E	Sintered mixed powder	Ni(2.5),ZnO(2.5)	20.2	31.5	—
F	Sintered mixed powder	Ni(5),ZnO(5)	20.2	33.4	—
G	Sintered mixed powder	Ni(5),ZnO(5)	15.5	37.3	—
H	Sintered mixed powder	Ni(5),ZnO(5)	15.5	21.0	—
I	Sintered mixed powder	Ni(10),ZnO(10)	20.2	11.7	—
J	Sintered mixed powder	MnO_2(5),Co_2O_3(5)	20.2	10.0	—
K	Enclosed powder	Rh(5)	11.4	39.7	2.8
L	Enclosed powder	ZnO(Ag),(50)	11.4	42.5	4.2
M	Enclosed powder	ZnO(7.3),Co_2O_3(8.5)	19.7	28.8	6.4
N	Enclosed powder	ZnO(Ag)(30)Co(30)	12.3	45.6	4.3
O	Enclosed powder	ZnO(Ag)(45),MnO_2(10)	14.4	14.2	3.4
P	Enclosed powder	ZnO-Sat % Al(Ag)(50)	13.3	31.2	2.3
Q	Enclosed powder	NiO-Sat % Li(Ag)(50)	15.5	29.0	4.7

[a] CO:CO_2, 1:3 and 1:2, 40 to 120 cc/min.
Porous sintered silver cathodes supplied with air at 100 cc STP/min + CO_2 at 40 cc STP/min.
Cell resistance: 0.15-0.25 ohm.

Cell power could be increased by increasing the flow of hydrogen to the anode compartment probably because fresh fuel replaced reaction products more rapidly. As the H_2 flow was increased from 10 to 100 cc STP/min, open-circuit voltage increased from 1.09 to 1.31v, and cell power at 1.0v increased from 7.4 to 20.2 mw/cm^2. But cell maximum power (at 0.6v) went up by only 50%, from 18.6 to 28.2 mw/cm^2. Moreover, at the higher flow rates there was a considerable decline in per cent H_2 consumed, 5.5% consumed at maximum power at 100 cc STP/min *vs.* 44.0% at 10 cc STP/min. These observations were obtained with cells which had gas chambers of 60-90 cm^3 volume, electrode areas of 11.4-20.2 cm^2, and electrodes 0.2-0.25 cm thick. Since space velocity of the gas feed and the ratio of electrode area to gas volume are undoubtedly important parameters these results cannot be expected to apply directly to cells of different geometry.

On dilute hydrogen.—Pure hydrogen cannot be considered a practical fuel cell fuel. Hydrocarbons and carbon monoxide cannot be used directly in the fuel cell at 650°C because of coke formation (*vide infra*). Hydrogen-carbon dioxide mixtures resulting from steam reforming of hydrocarbons or shifting of carbon monoxide appear to be the most suitable fuel for the molten carbonate fuel cell.

Table II shows the results of using several H_2-CO_2 mixtures as the anode feed. In one case total anode feed rate was kept constant and concentrations of H_2 and CO_2 varied; in the second experiment the H_2 flow was constant and the total flow increased with CO_2. In each case addition of CO_2 lowered open circuit voltage considerably and had a large effect on cell power at 1.0v. Cell power at 0.6v was less affected, decreasing almost linearly with the concentration of H_2 in the gas stream. Increased flow improved cell power at a given concentration by sweeping reaction products from the electrode surface.

Table II. Fuel cell performance on several H_2 + CO_2 anode feeds Cell E

Anode feed H_2(cc STP/min) + CO_2(cc STP/min)		Open-circuit voltage, v	Cell power dens. at 1.0v, ma/cm^2	at 0.6v, ma/cm^2	% H_2 consumed at 1.0v	at 0.6v
Effect of concentration						
40	—	1.22	14.8	27.8	5.3	16.4
30	10	1.08	5.9	23.1	2.8	18.2
20	20	1.02	0.8	20.1	0.5	23.8
10	30	0.97	—	14.2	—	33.6
Effect of flow						
40	—	1.21	13.1	29.6	4.6	17.5
40	10	1.07	5.9	25.6	2.1	15.1
40	20	1.04	2.5	23.4	0.9	13.8
40	40	1.02	1.7	23.0	0.6	13.6

Cathode feed—air (100 cc STP/min) + CO_2 (40 cc STP/min).

These experimental results were anticipated from simple consideration of the Nernst equation as applied to the gas phase compositions of anode reactants and products. At open-circuit CO_2, a product of the anode reaction

$$H_2 + CO_3^{=} \rightarrow H_2O + CO_2 + 2e^-$$

decreased the anode potential. At 0.6v, however, the effect of the CO_2 in the fuel stream was lessened by the formation of H_2O and CO_2 at the anode.

Similar results were obtained for operation on mixtures of H_2 and N_2 except that N_2, an unreactive gas in this system, did not lower cell open-circuit voltage. There was again an almost linear decrease in cell power with decreasing H_2 concentration. These experimental results indicated that it was the concentration (or partial pressure) of H_2 in the anode compartment that determined performance. This fact must be considered when cells are operated on dilute hydrogen fuels and especially when determining the characteristics of battery packs in which feeds are passed serially through the unit. Although it may be possible to oxidize all the hydrogen in a given feed to a battery, the low concentration of H_2 in the fourth, fifth, etc., cells of such a unit may lead to very poor performance of these later cells.

Another problem with such downstream operation is the gradual shifting of residual H_2 in the feed to H_2O and CO by CO_2. To consume most of the H_2 supplied to the unit, CO must be oxidized. Some effort has gone into an attempt to develop an electrode catalyst for the oxidation of CO.

Carbon monoxide oxidation.—The cells with internally plated and enclosed powder catalysts, listed in Table I, were also operated on CO/2CO_2 and CO/3CO_2 mixtures. Maximum power densities were between 2 and 5 mw/cm^2, in most cases less than 10% of the maximum from H_2. At the lowest fuel rate, up to 30% of the fuel was consumed at maximum power. Although fairly high limiting current densities of 35 to 45 ma/cm^2 were attainable from CO, low cell voltage minimized the power. Maximum power was obtained at between 0.13 and 0.26v, in most cells at 0.20v.

The question arose of whether the small amounts of power obtained from CO come from direct oxidation of CO or from H_2 formed by the water gas shift reaction. Kronenberg (7) reported operation of a molten carbonate fuel cell on CO dried to contain less than several ppm H_2O and concluded that a "direct galvanic utilization appears to be the case." It was conceivable that some H_2 could remain for a long time in the cell cycling between H_2O and H_2 by electrode reactions and shifting with CO; however, a seventyfold variation in water input produced no detectable variation in current. Whether the fuel was dried over 4A molecular sieve to contain 0.05 vol % H_2O or was

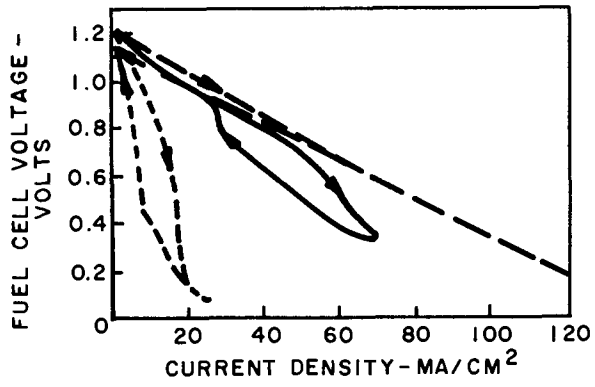

Fig. 1. Typical fuel cell current-voltage curves: —— —— —— cell N; ———— cell C; — — — cell J. Ohmic polarization included was about 0.3v at 107 ma/cm^2. → cell loading; ← cell unloading.

saturated to 3.4 vol % (when shifted to H_2, equivalent to 0.30 amp) the current remained constant with a maximum of slightly over 0.4 amp. This evidence supports Kronenberg's conclusion that CO is directly oxidized, but only at very low cell voltages.

Cell Polarization

Current-voltage curves.—Current-voltage curves have been used to characterize fuel cell performance. Typical current-voltage curves are shown in Fig. 1 for three different fuel cells operated on hydrogen and oxygen. These curves illustrate the range of performance observed in our molten carbonate cells. In each case the cathodes were the same and had a much less important effect on cell polarization than did the anodes. The sigmoid shape of both loading and unloading curves for cells J and C is similar to that of current-voltage curves reported by Broers (1) and Douglas (3) and indicates that at least two different anode reactions are occurring.

For cell N which exhibited no sharp voltage inflection in the hydrogen current-voltage curve, total cell polarization was 1.1v at 100 ma/cm^2. Of this total, ohmic polarization accounted for 0.35v, cathode polarization 0.25v, and anode polarization 0.50v. This same cell when operated on H_2/CO_2 mixtures showed even greater anode polarization. At 50 ma/cm^2 with a $1H_2/4CO_2$ fuel, ohmic polarization was 0.18v, cathode polarization 0.16v, and anode polarization 0.60v.

Table III. Standard potentials for reactions occurring within molten carbonate fuel cell at 650°C

Reactions		Standard potential, v
	Fuel oxidation	
$H_2 + 1/2\ O_2$	$= H_2O$	+1.019
$CO + 1/2\ O_2$	$= CO_2$	+1.047
	Electrode oxidation	
$Co + 1/2\ O_2$	$= CoO$	+0.871
$3Co + 2\ O_2$	$= Co_3O_4$	+0.705
$Mn + 1/2\ O_2$	$= MnO$	+1.664
$3Mn + 2\ O_2$	$= Mn_3O_4$	+1.374
$2Mn + 3/2\ O_2$	$= Mn_2O_3$	+1.246
$Mn + O_2$	$= MnO_2$	+0.914
$Ni + 1/2\ O_2$	$= NiO$	+0.802
$2Rh + 1/2\ O_2$	$= Rh_2O$	+0.287
$Rh + 1/2\ O_2$	$= RhO$	+0.124
$2Rh + 3/2\ O_2$	$= Rh_2O_3$	+0.099
$Ag + 1/2\ O_2$	$= Ag_2O$	−0.144
$Zn + 1/2\ O_2$	$= ZnO$	+1.320

Source: J. P. Coughlin, Bureau of Mines Bulletin 542, 1954, "Contributions to the Data on Theoretical Metallurgy XII. Heats and Free Energies of Formation of Inorganic Oxides."

A sigmoid H_2 current-voltage curve is seen for cell K in Fig. 2. For this cell the current at which the sharp voltage inflection occurred depended linearly on the concentration of H_2 in a mixed H_2-N_2 feed. This relationship between concentration and current is characteristic of a diffusion limited reaction which occurs at cell voltages above 0.8v The increase in current at low cell voltages indicates that a second reaction may be occurring. This cell contained a rhodium catalyst which would be oxidized at a standard potential of 0.287v (see Table III). The cell voltage of 0.2v at 70 ma/cm^2 should be corrected for ohmic polarization totaling 0.15v. The I-R free potential of the low voltage oxidation of 0.35v is not far from the standard potential of $Rh \rightarrow Rh_2O$. The increase in current at low voltages may have been due in part to the oxidation of rhodium and in part to oxidation of H_2 on the rhodium oxide surface. The curve at zero H_2 flow was taken following the others when the rhodium may already have been mostly oxidized.

The cathode reaction contributed less polarization than the anode reaction when stoichiometric feeds were supplied to the fuel cell. When the supply of air was limited, however, the cathode polarization increased. Figure 3 shows the effect of reducing the air content of the cathode feed on the cell current-voltage curve. Limiting currents at very dilute oxygen feeds approached the current equivalent to reduction of all the oxygen (4 electrons/molecule) in the gas feed. This experiment indicates that with the normal air and CO_2 feeds used, the cathode does not limit cell performance.

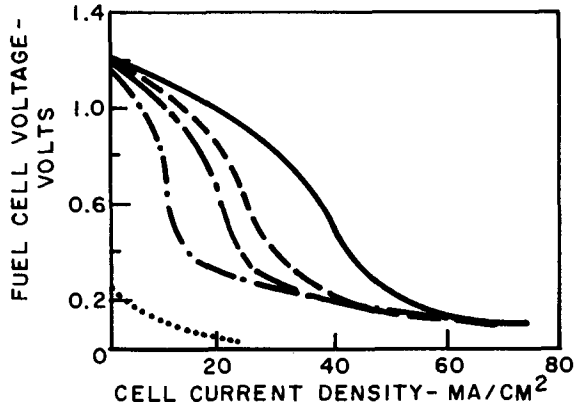

Fig. 2. Fuel cell current-voltage curves, cell K operation on dilute H_2 anode feeds: —— H_2 at 40 cc STP/min; — — — — — H_2 at 30 cc STP/min + N_2 at 10 cc STP/min; —— — —— H_2 at 20 cc STP/min + N_2 at 20 cc STP/min; —— · —— H_2 at 10 cc STP/min + N_2 at 30 cc STP/min; - - - - - N_2 at 40 cc STP/min. Cathode feeds: air at 100 cc STP/min + CO_2 at 40 cc STP/min; complete oxidation of H_2 at 10 cc STP/min would be 126 ma/cm^2. Ohmic polarization totaled 0.15v at 75 ma/cm^2.

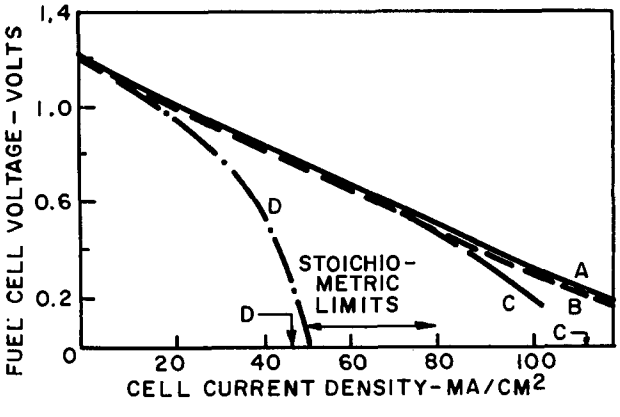

Fig. 3. Fuel cell current-voltage curves, cell N operation on diluted air. Cathode feeds: A —— air at 100 cc STP/min + CO_2 at 40 cc STP/min; B — — — air at 50 cc STP/min + CO_2 at 40 cc STP/min + N_2 at 50 cc STP/min; C — - — air at 25 cc STP/min + CO_2 at 40 cc STP/min + N_2 at 75 cc STP/min; D — · — air at 10 cc STP/min + CO_2 at 40 cc STP/min + N_2 at 90 cc STP/min. Anode feed: H_2 at 40 cc STP/min. Ohmic polarization totaled 0.30v at 107 ma/cm^2.

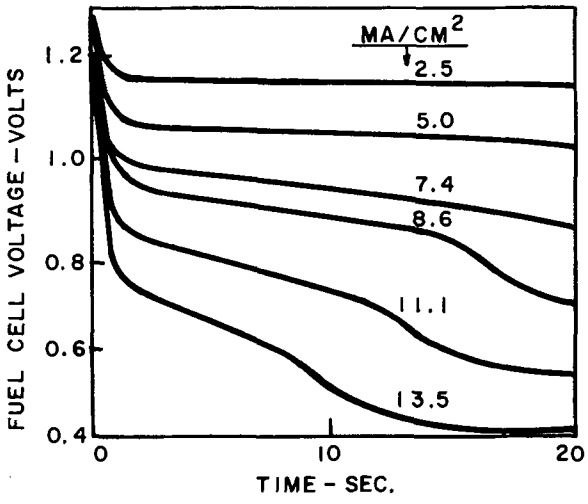

Fig. 4. Voltage-time curves at constant current, Cell A, H_2 at 40 cc STP/min.

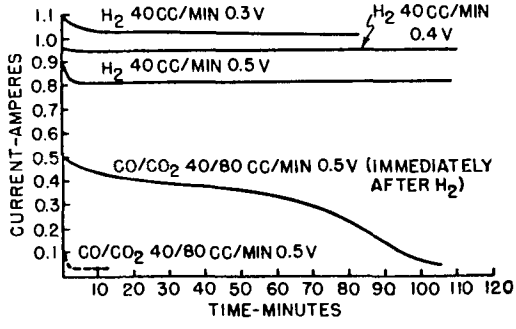

Fig. 5. Current-time curves at constant cell voltage, cell Q

Voltage-time curves.—Voltage-time measurements at constant current have been used to study electrode reactions. From current-voltage studies it was concluded that the anode reactions contributed most to cell polarization. Measurements of cell voltage changes with time reflected reactions occurring at the anode since other experiments indicated cathodic and ohmic polarization, while dependent on current, did not change with time.

A very poor cell was needed to observe any significant voltage time effects within 30 sec. Cell A was constructed with very poor distribution of the fuel gas to the nickel plated anode. Current-voltage curves for H_2, H_2/CO_2 mixtures and a CO/CO_2 mixture were sigmoid shaped. In the voltage-time curves shown in Fig. 4 a voltage inflection for H_2 was observed after 16 sec at 8.6 ma/cm^2 and after shorter times at higher currents. The voltage inflection was followed by a leveling out as a second reaction occurred. The second reaction, occurring about 0.2v lower than the first was probably the oxidation of nickel (standard potential 0.80v, Table III). The first reaction was the oxidation of hydrogen (standard potential 1.02v).

With a mixed H_2-CO_2 feed open-circuit voltage was lower and voltage inflections were observed at lower currents. Again the second reaction occurred about 0.2v lower than the first.

With a mixture of CO and CO_2 no voltage inflection was observed and cell voltage was the same as for the second part of the H_2 anode voltage-time curves. It is probable from this and other experimental evidence that the reaction observed with this feed was just the oxidation of the nickel electrode.

In these three voltage-time studies the only variable was the anode feed. Thus the transition time (dependent on current and H_2 concentration) observed only in the two studies involving hydrogen could not have been due to the cathode reaction or to the electrolyte. It could have been due to a hydrogen species which was dissolved in a thin film of electrolyte at the anode and was in equilibrium with the anode gas.

Current-time curves.—Current-time curves at constant cell voltages for various fuels in cell Q are shown in Fig. 5. With H_2 the stable current values were only slightly below corresponding points on the current-voltage curve indicating that steady-state values were achieved in both observations. With CO-CO_2 the current at 0.5v fell to 0.05 amp after 100 min. The area under this curve corresponds to 19.9 meq or 0.58 g of nickel. Since the electrode contained 2.4g of nickel it is probable that this portion of the nickel had been reduced during the immediately preceding operation on H_2. After the cell had been operated on CO-CO_2 for approximately 2 hr for plotting current-voltage curves the current at 0.5v very quickly fell indicating that very little reduced nickel was present.

Cell L, in which the effect of water on CO oxidation was studied, contained 2.06g of ZnO. Depending on the water content different open-circuit voltages were established: 0.93v for undried and 1.06v for dried fuel. The extent of electrode reduction (the ratio of Zn/ZnO) corresponding to these potentials are calculated by the Nernst equation and found to be in good agreement with the current generated by the cell before the voltage dropped sharply to below 0.3v. Calculated values were 1.6 and 42.6 coulombs compared to 6 and 48 coulombs observed. These experiments indicate that currents observed above 0.3v with CO feed are due to oxidation of the electrode rather than CO.

Discussion of Anode Reactions

Both chemical and electrochemical reactions occur in the anode compartment. Even with pure H_2 fuel there are at least five reactions likely to occur:

$$H_2 + CO_3^{=} \rightarrow H_2O + CO_2 + 2e^-$$

$$\text{Electrolyte} \rightarrow CO_2 \text{ (decomposition and diffusion)}$$

$$H_2 + CO_2 \rightleftharpoons H_2O + CO$$

$$CO + CO_3^{=} \rightarrow 2CO_2 + 2e^-$$

$$2CO \rightleftharpoons C + CO_2$$

These likely reactions, together with possible complications such as the reaction of carbon in the cell with CO_2, H_2, or H_2O in the Boudouard, methanation, and water gas reactions, do not permit detailed material balances to determine the extent of reactions occurring in the anode compartment. Instead current-voltage-time relationships were used to evaluate electrode performance and arrive at a working hypothesis of the electrode reactions. This hypothesis was then used to guide a search for improved electrode catalysts.

The shapes of current-voltage, current-time, and voltage-time curves are interpreted to mean that H_2 reacts nearly reversibly on reduced electrode sites, but, if all accessible sites become oxidized, H_2 reacts electrochemically only with a high activation overvoltage. Carbon monoxide does not react reversibly on either reduced or oxidized sites and most electrode materials are preferentially oxidized. As indicated by Table III only silver would not be oxidized at the potential of the operating anode. Carbon monoxide does appear to react on the oxidized electrode with an activation overvoltage not greatly different from that of H_2.

Stable currents exceeding the electrochemical equivalents of catalyst were obtained from CO only at cell voltages of 0.3v or lower. Activation rather than concentration polarization is invoked to explain the behavior of CO because relatively high current densities are sustained at low voltages.

The situation with regard to H_2, both pure and diluted, is more complex. Some electrodes were particularly susceptible to concentration polarization, and during periods of high current drain almost all the

hydrogen near the reduced electrode sites was consumed. When the cell voltage is reduced to about 0.6v many active electrode sites are oxidized. The cell voltage falls until hydrogen can be oxidized on the irreversible oxide sites. Still higher currents are available from electrode oxidation and, since the limiting current can be sustained indefinitely, from H_2 itself. The electrode recovers to its more active state only if the rate of electrode reduction exceeds that of oxidation. Reduction may be accomplished by increasing the H_2 concentration or by raising the potential above that at which oxidation can occur. The latter requires that the current be reduced to a level considerably below that at which deactivation occurs and results in a large hysteresis loop. The facts argue against operation of a corrosion mechanism which would require the rate of reduction to equal that of electrode oxidation and would preclude the observed hysteresis loop. Much higher power yields are produced by the electrode in the reduced state, but it is metastable, and with temporary overloading the electrode can become trapped in the oxidized state.

The facts that only oxidized electrodes showed appreciable activity for CO and that the high performance of reduced electrodes with H_2 is not stable lead to the conclusion that a reversible oxide anode catalyst would be most desirable. The anodes of cells M and N, which gave the best performance on CO fuel, contained ZnO with Co or Co_2O_3. The presence of a higher valent metal oxide should enhance the n-type conductivity of ZnO. The best impurities for enhancing the n-type conductivity of ZnO are Al_2O_3, Ga_2O_3, and possibly Cr_2O_3, and the firing temperatures should be 1000°C to insure proper doping (13, 14). For comparison purposes both n- and p-types of doped oxides were tried in cells Q and P. Lithia doped nickel oxide and alumina doped zinc oxide each containing 5 a/o of foreign ions were calcined at 1000°C for 3 hr, "silverized," and incorporated in the anodes of these respective cells. The p-type NiO was better at 4.7 mw/cm^2 than the n-type ZnO which yielded only 2.3 from CO, but neither catalyst was distinctly better than undoped materials.

Carbon Formation

Hydrocarbons introduced directly into the molten carbonate cell at 650°C would be expected to crack and form coke; however, pentane was briefly supplied to a cell with a Ag-Ni anode to determine the extent of coking and power production. After 5 hr on 10 cc STP/min of pentane the open-circuit voltage was 0.42v and a current of 0.12 amp was delivered at 0.3v. An exhaust gas sample showed that 87% of the pentane was converted to a distribution of products typical of thermal cracking. The amount of hydrogen in the products including water was within 1% of the input, but the carbon in the exhaust, including some from the electrolyte, was only half the amount entering. On examination of the cell the inlet line was found to be almost plugged, and a soft sooty deposit of carbon nearly filled the anode compartment.

The inlet tube of a cell operated on pure CO at 650°C became plugged in 30 min by carbon from the reaction $2CO \rightleftharpoons C + CO_2$, $K_{650°C} = 2.5$; however, with CO_2 present in the ratio of $2CO_2/1CO$ carbon deposition is prevented, and such fuel mixtures were generally used without difficulty. More serious is the fact that carbon formation can and did occur sufficiently to plug gas lines when H_2-CO, H_2-CO_2, and even pure H_2 fuels were being used. In addition to plugged lines and chemical analyses, evidence of carbon formation has been found in increased cell performance when CO_2 was substituted for a N_2 fuel stream. This effect can be explained by formation of CO by reaction of CO_2 with carbon deposits in the cell.

At 650°C almost any surface catalyzes the water gas shift reaction, $H_2 + CO_2 \rightleftharpoons CO + H_2O$, and CO disproportionation so that conditions thermodynamically favorable for carbon deposition must be avoided. Cairns, Tevebaugh, and Holm (15) have examined these conditions in detail. In general carbon deposition can be prevented by raising the temperature and by increasing the content of H_2O or CO_2 (if a certain minimum is exceeded). Extent of fuel consumption is also a factor. Increased pressure favors carbon deposition.

Addition of H_2O and CO_2, products of the anode reaction, suppresses the open-circuit voltage, but the effect on equilibrium potentials is not large at high levels of fuel consumption. In fact, since the effect of temperature on cell voltage is greater than the effect of the amount of water needed to suppress carbon formation, more power should be obtained from a cell operating at 500°C on a 2:1 H_2:H_2O feed mixture than on pure H_2 at 650°C. In practice the porous diffusion electrodes used in this work limited cell performance when products of the anode reaction were introduced.

Conclusions

It should be emphasized that the results reported in this paper were obtained with porous diffusion electrodes which were quite subject to concentration polarization. The conclusions reached, however, are generally applicable since the problems encountered are common to all molten carbonate fuel cells when the limitations of gas diffusion electrodes are approached.

1. Reduced metals are active and reversible electrodes for the oxidation of H_2 but are not active for CO. Most electrode materials are more easily oxidized than CO.
2. Oxidation of both H_2 and CO can occur on completely oxidized electrodes; however, all those tried (zinc, nickel, cobalt, rhodium, and manganese) showed about 0.6v activation polarization.
3. The reaction of CO on the oxidized electrode is direct and does not involve a water gas shift reaction.
4. Carbon does form in the cell and gas lines when thermodynamically permitted. Favorable conditions for carbon deposition can occur even with pure H_2 as the fuel.

Manuscript received April 6, 1965; revised manuscript received Aug. 11, 1965.

Any discussion of this paper will appear in a Discussion Section to be published in the June 1966 JOURNAL.

REFERENCES

1. G. H. J. Broers and J. A. A. Ketelaar, "Fuel Cells," G. J. Young, Editor, p. 78, Reinhold Publishing Corp., New York (1960).
2. H. H. Chambers and A. D. S. Tantram, ref. (1), p. 94.
3. D. L. Douglas, ref. (1), p. 129.
4. Y. L. Sandler, *This Journal*, **109**, 1115 (1962).
5. G. H. J. Broers and M. Schenke, "Fuel Cells," G. J. Young, Editor, Vol. 2. p. 6, Reinhold Publishing Corp., New York (1963).
6. E. B. Shultz, Jr., K. S. Vorres, L. G. Marianowski, and H. R. Linden, ref. (5), p 24.
7. M. L. Kronenberg, *This Journal*, **109**, 753 (1962).
8. L. G. Marianowski, John Meek, E. B. Shultz, Jr., and B. S. Baker, "New Concepts on High Temperature Hydrocarbon Cells," Proceedings of Seventeenth Annual Power Sources Conference, pp. 72-75.
9. B. S. Baker, L. G. Marionowski, John Meek, and H. R. Linden, "Fuel Cell Systems: Advances in Chemistry Series 47," Robert F. Gould, Editor, p. 247, American Chemical Society, Washington, D. C. (1965).
10. I. Trachtenberg, *This Journal*, **111**, 110 (1964).
11. I. Trachtenberg, ref. (9), p. 196.
12. H. H. Chambers and A. D. S. Tantram, Canadian Pat. 626, 767, Sept. 5, 1961.
13. F. S. Stone in "Chemistry of the Solid State," W. E. Gardner, Editor, p. 367, Butterworths Scientific Publications, London (1955).
14. F. S. Stone in "Advances in Catalysis Vol. 13," D. D. Eley, P. W. Selwood, and P. B. Weisz, Editors, p. 1, Academic Press, New York (1962).
15. E. J. Cairns, A. D. Tevebaugh, and G. J. Holm, *This Journal*, **110**, 1025 (1963).

Analysis of the Charge-Discharge Characteristics of Nickel-Oxide Electrodes by Infrared Spectroscopy

Frederick P. Kober

General Telephone & Electronics Laboratories Incorporated, Bayside, New York

ABSTRACT

Infrared spectroscopy is shown to be a sensitive tool in studies of the structure of electrochemically active materials and in elucidating the mechanism of charge and discharge. The spectrum of the sintered nickel-oxide electrode, impregnated using standard procedures, has been determined in the region between 4000 and 250 cm^{-1}. These spectral data show the discharged state to be $Ni(OH)_2$ having a hexagonal layer structure isomorphic with the space group D_{3d}^3. The hydroxyl groups are parallel to the c-axis of the crystal and are "free" in the sense that hydrogen bonding is absent. Associated with this structure is a relatively small amount of water which is trapped in the crystal lattice through the formation of coordinate-covalent bonds with the nickel ions. The charging process is accompanied by the formation of a hydrogen-bonded structure possessing a higher degree of crystal symmetry than is found in the discharged state. During discharge, these hydrogen bonds are continuously broken, and the structure transforms back to a free hydroxyl configuration.

Many attempts have been made to determine the structure of the active species in nickel-oxide electrodes for rechargeable alkaline batteries. Structure determinations have been based on the analysis of the x-ray diffraction patterns of the active materials (1-5). Because of the amorphous quality of the electrochemically active materials, particularly in sintered electrodes, the x-ray method has been limited to providing information concerning the phases present within the electrode during charge and discharge.

Infrared spectroscopy has been extensively used in the analysis of molecular structure because of the extreme sensitivity of the method to small changes in the vibrational energy states of a molecule. Therefore, infrared analysis of the nickel-oxide electrode should provide valuable information about the structure of the active material and about the changes in chemical bonding which occur during charge and discharge. In this paper the usefulness of this method is demonstrated. The structure of the discharge state of the nickel-oxide electrode is discussed in detail. The infrared data, in addition, provide valuable insight into the changes in chemical bonding which occur during the charging process and provide information about the nature of the charged state.

Experimental Procedure

Pure $Ni(OH)_2$ was prepared from a solution of the nitrate using the method of Glemser and Hartert (6). Electrodes were fabricated from sintered plaques impregnated with $Ni(OH)_2$ by the conventional impregnation technique (7). Samples of the charged and discharged materials were obtained from electrodes which had been cycled at least ten times in 31% KOH at the 3-hr rate. After cycling, the plates were thoroughly washed in hot water and dried at 60°C for 48 hr in an atmosphere of dry nitrogen. The electrodes were then ground to a fine powder (400 mesh).

The near-infrared spectra (2.25-14μ) were obtained using pressed KBr pellets with a Perkin-Elmer model 421 double-beam recording spectrometer. For the far-infrared measurements (14-40μ), samples were dispersed in Nujol, and the spectra obtained with a Beckman IR-7 double-beam instrument equipped with CsBr optics. Although identical results were obtained in the far-infrared using pressed CsBr pellets, Nujol mulls were used because of the ease in preparation.

It was necessary to determine whether the sample preparation technique in any way altered the electrochemical activity of the charged material. Samples of the charged electrode which had been washed, dried, and ground to 400 mesh powder were subsequently discharged in 31% KOH in a pocket-type electrode configuration. These samples yielded normal discharge voltage characteristics and delivered approximately 75% of the capacity obtained from sintered electrodes that were dried but not ground. Consequently, it is concluded that self-discharge of the "higher oxide" is evident to a relatively minor degree during processing of the samples.

Results and Discussion

It is generally assumed that the composition of the discharged state corresponds to $Ni(OH)_2 \cdot xH_2O$, where x has been given many values from zero to ten (1-5). X-ray data indicate that this assumption is essentially correct. However, examination of the literature shows that the structure of the discharge state is, as yet, unresolved.

Pure nickel (II) hydroxide crystallizes with the hexagonal layer structure having the space group D_{3d}^3 (8). Infrared analysis has confirmed this structure (9). In addition, the infrared spectrum shows that the hydroxyl group is "free" in the sense that hydrogen bonding is absent. Because of the absence of

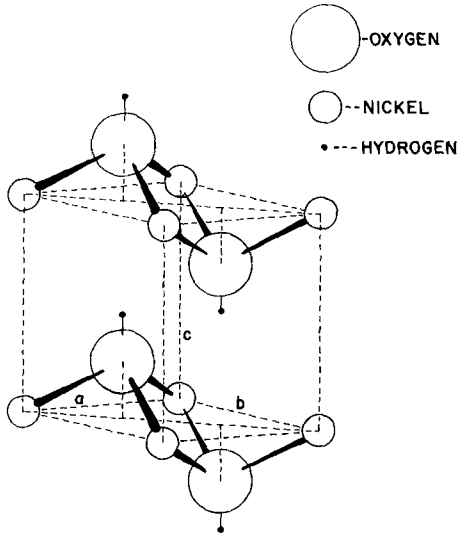

Fig. 1. $Ni(OH)_2$ unit cell showing the hexagonal D_{3d} symmetry. The Ni and O occupy equivalent sites having D_{3d} site symmetry.

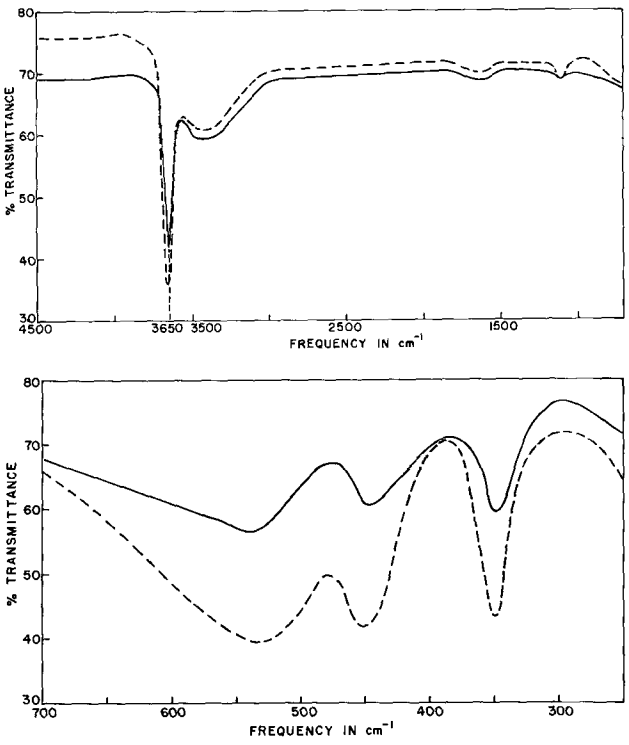

Fig. 2. Spectrum of an impregnated sintered electrode having undergone no cycling compared to that of pure $Ni(OH)_2$: ——, impregnated plate, no cycling; — — —, pure $Ni(OH)_2$.

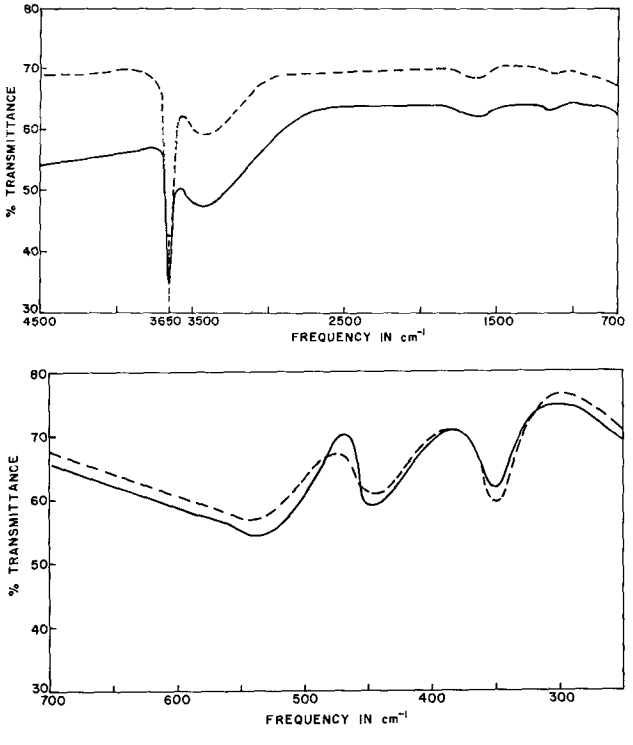

Fig. 3. Spectrum of a sintered electrode in the discharged state: ——, discharged state; — — —, impregnated plate, no cycling.

hydrogen bonding, the vibrational modes of the hydroxyl group do not interact with the lattice modes of the crystal. The hexagonal D_{3d}^3 layer structure of $Ni(OH)_2$ is illustrated in Fig. 1.

In Fig. 2 the spectrum of the pure $Ni(OH)_2$ is compared with that of the freshly impregnated plate which has not undergone any cycling. The spectra are identical, showing that the nickel (II) hydroxide structure is in no way altered during the impregnation procedure. The difference in relative absorption levels in the near infrared is due to dilution of the sample by the nickel matrix. The difference in absorption levels in the far infrared is due to varying sample concentrations in the Nujol mulls. Since the impregnation procedure does not change the structure of $Ni(OH)_2$, the spectrum of the impregnated plate will be used as a reference.

The spectrum of the discharged state is given in Fig. 3. The appearance of the sharp intense band at 3650 cm^{-1} is due to the antisymmetric stretching fundamental of the "free" hydroxyl group (10). With respect to the band centers, the spectrum of the discharged state is identical with that of the pure $Ni(OH)_2$. Therefore, the spectral data show that the discharged state is indeed nickel (II) hydroxide having the same crystal symmetry as the pure compound, *i.e.*, a hexagonal layer structure having the space group D_{3d}^3, and having nonhydrogen bonded hydroxyl groups parallel to the c-axis of the crystal. Although the discharged state may be a highly defect structure and susceptible of considerable disorder (11, 12), the basic hexagonal D_{3d}^3 site symmetry is preserved.

It is not possible to determine the symmetry of the nickel-to-oxygen coordination directly from the infrared spectrum. In lieu of a complete x-ray analysis of the nickel hydroxide molecule, we have estimated the nickel-to-oxygen bond distances from values of the Pauling ionic radii (13) although other data could be used for this estimate (6). From these estimated bond distances, we find that the nickel-to-oxygen coordination is slightly distorted along the c-axis of the crystal from true octahedral symmetry. This slight distortion from true octahedral coordination is consistent with the doubly degenerate nickel-oxygen stretching mode observed at 450 cm^{-1} (Fig. 2b) (9). If the nickel-to-oxygen coordination were truly octahedral, we should then expect to observe the nickel-oxygen stretching mode as a broad intense triply degenerate band in the far infrared (14).

Figure 3 indicates that there is a small amount of lattice water associated with the $Ni(OH)_2$ structure, *i.e.*, water molecules trapped in the crystal lattice by weak coordinate-covalent bonds to the nickel ions. The broad band having a center at 3450 cm^{-1} and the weak absorption at 1620 cm^{-1} can be attributed to the stretching mode and the bending mode of the lattice water, respectively (15). The broad band having a center at approximately 530 cm^{-1} has been attributed to the torsional mode of the lattice water (16). The role and nature of the water associated with electrochemically active $Ni(OH)_2$ will be discussed in detail in a future publication.

The spectrum of the charged state together with that of the discharged state is given in Fig. 4. Several differences are readily observable. The hydroxyl band at 3650 cm^{-1} is no longer present in the spectrum of the charged species. This absorption is replaced by a broad diffuse band having a center at 3450 cm^{-1}. In the far infrared we observe a broadening and shift to a higher frequency of the band at 535 cm^{-1} when going from the discharged to the charged state. These spectral shifts at approximately 3500 and 530 cm^{-1} are definite indications of hydrogen bond formation (17).

In the spectrum of $Ni(OH)_2$ a band at 350 cm^{-1} is observed (Fig. 2). This absorption has been attributed to the interaction of the nickel-oxygen stretching fundamental at 450 cm^{-1} with the librational lattice mode of the free hydroxyl group (< 100 cm^{-1}) (9). By librational mode is meant the torsional motion of the OH group about the Ni-O bond. In the spectrum of the charged material this combination band at 350 cm^{-1} is seen to disappear, accompanied by a broadening of the Ni-O stretching fundamental at 450 cm^{-1}. These spectral data indicate that the charged species is a hydrogen-bonded structure containing no "free" hydroxyl groups. In addition, the broadening of the

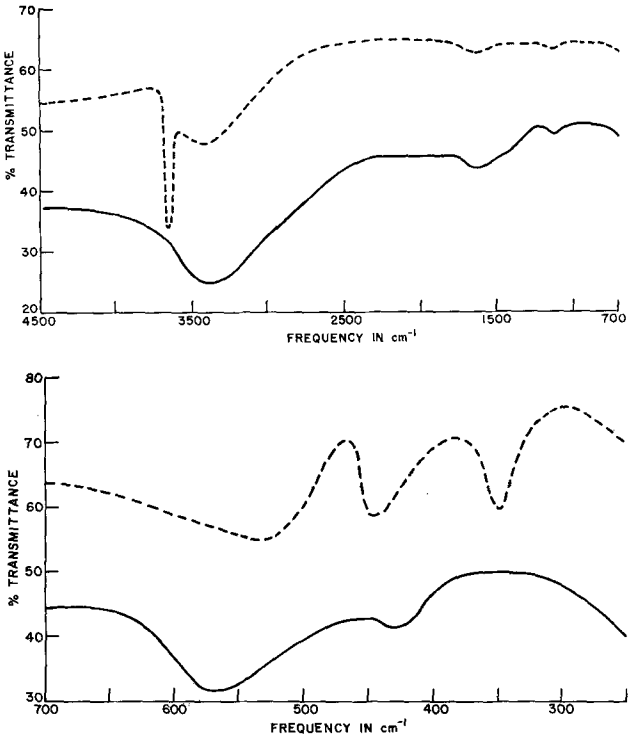

Fig. 4. Spectrum of the charged electrode compared to that of the discharged electrode: ——, charged electrode; — — —, discharged electrode.

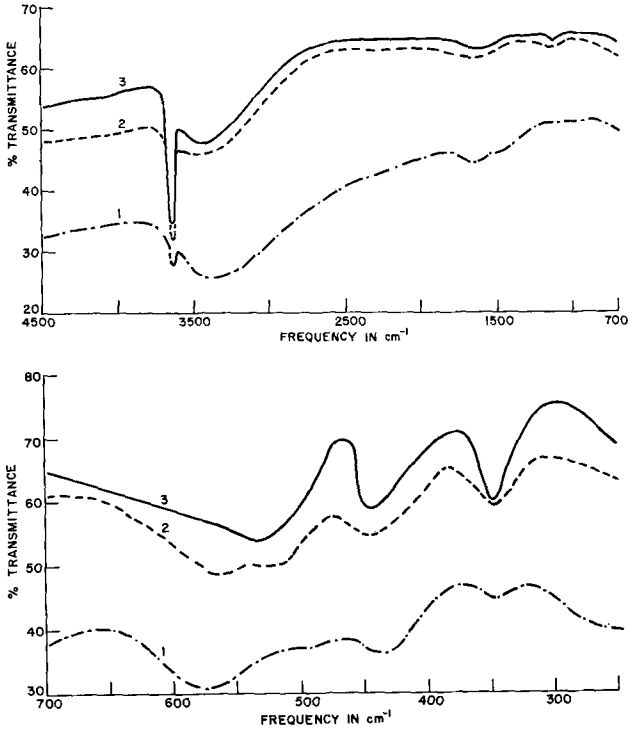

Fig. 5. Spectra of electrodes at various stages of discharge: curve 1, 50% discharge; curve 2, 90% discharge; curve 3, 100% discharge.

band at 450 cm^{-1} indicates that the Ni-O stretch is now triply degenerate (14). This increase in the degeneracy of the Ni-O stretch implies a higher degree of symmetry in the charged state with regard to nickel-oxygen coordination than is found in the discharged state. It is quite probable that the distorted octahedral nickel-oxygen coordination found in the discharge state tends toward regular octahedral coordination as the electrode is charged. This octahedral nickel-oxygen coordination in the charged state has been suggested previously by Tuomi (11). In light of the above evidence, the designation of β-NiOOH for the charged state is, at best, an oversimplification. Similar statements concerning any simple designation for the charged state have been made by others (18, 19).

Okada *et al.* (20), in their x-ray studies of the higher oxides of nickel, suggest that the oxidation of $Ni(OH)_2$ to the higher oxide proceeds through the formation of a series of solid solutions, and discharge of the higher oxide would also proceed through the formation of solid solutions of divalent and trivalent nickel. In Fig. 5 the spectra of the charged nickel positive electrode are shown at various stages of discharge. Curves 1, 2, and 3 differ only in the intensity of the "free" hydroxyl band at 3650 cm^{-1}, showing that $Ni(OH)_2$ is formed continuously during discharge of the higher oxide. Complementing the OH group formation is a continuous disappearance of H bonds as indicated by the changes in the far-infrared spectra. This is evidenced by the continuous shift in the librational water band from 575 to 535 cm^{-1}. If the discharge process involved the formation of solid solutions, the "solute-solvent" interactions should be observed in the spectra. We should expect to observe either a shift or broadening of the hydroxyl band or the appearance of combination bands in the region of 3650 cm^{-1} due to these interactions. Since these interactions are not observed, we conclude that only mixtures (distinct phases) of $Ni(OH)_2$ and the charged species are present. The possibility is not eliminated that the charged state is itself a solid solution of several higher oxides. Tuomi (11) proposes that $Ni(OH)_2$ is transformed into a second phase within which solid solutions of Ni(II) and NI(IV) could be formed. In light of the spectral data, however, this possibility seems unlikely. The formation of mixtures as opposed to solid solutions during charge and discharge has been proposed by Conway and Gileadi (21), Briggs and Wynne-Jones (4), and others (2). Care must be exercised while comparing the results of various investigations since the formation of mixtures as opposed to solid solutions may depend strongly on the method of electrode preparation and the conditions of polarization.

Summary

The sintered positive nickel oxide electrode has been investigated using infrared spectroscopy. The following conclusions can be drawn from the data obtained.

1. The discharged state is $Ni(OH)_2$ having a hexagonal layer structure isomorphic with the space group D_{3d}^3. The hydroxyl groups are parallel to the c-axis of the crystal and are "free" in the sense that hydrogen bonding is absent.

2. A small amount of crystalline lattice water is associated with the $Ni(OH)_2$ structure. The amount of water may be dependent on preparative techniques.

3. The charging process is accompanied by the formation of a hydrogen bonded structure possessing a higher degree of symmetry with respect to nickel-oxygen coordination than is found in the discharged state.

4. The discharge process is accompanied by the continuous formation of "free" hydroxyl groups. In addition, the nickel (II) hydroxide forms mixtures (distinct phases) with the charged species as opposed to solid solutions, *i.e.*, continuous solid solutions from the bivalent state to the higher oxide.

Acknowledgment

The author is indebted to Mr. E. R. Bowerman for his aid in illustrating the symmetry properties of the $Ni(OH)_2$ structure, and to Dr. P. Goldberg for many helpful suggestions during the course of the work. He is also indebted to E. P. Bulan, M. Tomkus, and J. F.

Cosgrove for their assistance in preparing the samples and obtaining the infrared spectra.

Manuscript received June 10, 1965. This paper was presented at the Buffalo Meeting, Oct. 10-14, 1965.

Any discussion of this paper will appear in a Discussion Section to be published in the June 1966 JOURNAL.

REFERENCES

1. O. Glemser and J. Einerhand, *Z. Anorg. Chem.*, **261**, 43 (1950).
2. W. Feitknecht, H. R. Christen, and H. Studer, *Z. anorg. u. allgem. Chem.*, **283**, 88 (1956).
3. E. Jones and W. F. K. Wynne-Jones, *Trans. Faraday Soc.*, **52**, 1260 (1956).
4. G. W. D. Briggs and W. F. K. Wynne-Jones, *ibid.*, **52**, 1272 (1956).
5. S. U. Falk, *This Journal*, **107**, 661 (1960).
6. O. Glemser and E. Hartert, *Z. anorg. u. allgem. Chem.*, **283**, 111 (1956).
7. For a general description of the impregnation procedure see A. Fleischer, *This Journal*, **94**, 289 (1948).
8. R. W. Cairns and E. Ott, *J. Am. Chem. Soc.*, **55**, 527 (1933).
9. F. P. Kober, to be published. This reference contains a complete structural analysis of $Ni(OH)_2$ including a discussion of the local site symmetries of Ni, O, and H within the lattice.
10. K. Nakamoto, "Infrared Spectra of Inorganic and Coordination Compounds," John Wiley & Sons, Inc., New York (1963).
11. D. Tuomi, *This Journal*, **112**, 1 (1965).
12. U. B. Thomas, Private communication.
13. L. Pauling, "The Nature of the Chemical Bond," 3rd ed., Cornell University Press, Ithaca, N. Y. (1960).
14. D. F. Hornig, *J. Chem. Phys.*, **16**, 1063 (1948).
15. P. J. Lucchesi and W. A. Glassen, *J. Am. Chem. Soc.*, **78**, 1347 (1956).
16. J. van der Elskin and D. W. Robinson, *Spectrochim. Acta.*, **17**, 1249 (1961).
17. G. C. Pimentel and A. L. McClellan, "The Hydrogen Bond," Chap. 3, W. H. Freeman and Company, San Francisco (1960).
18. F. Kornfeil, *Proc. 12 Ann. Batt. Res. Div. Conf.*, 18 (1958).
19. B. E. Conway and D L. Bourgault, *Can. J. Chem.*, **37**, 292 (1959).
20. S. Okada, T. Shiraishi, K. Watanabe, and T. Yasuhara, *J. Chem. Soc., Japan, Ind. Chem. Sec.*, **51**, 129 (1948).
21. B. E Conway and E. Gileadi, *Can. J. Chem.*, **40**, 1933 (1962).

Hydrogen Permeation Studies

I. Armco Iron and Iron-Molybdenum Alloys

Robert R. Heinrich, Carl E. Johnson, and Carl E. Crouthamel

Chemical Engineering Division, Argonne National Laboratory, Argonne, Illinois

ABSTRACT

Hydrogen permeation of Armco iron, 5 w/o (weight per cent) molybdenum-iron, and 10 w/o molybdenum-iron alloys was investigated over a temperature range of 350-800°C and at 1 atm hydrogen pressure. Activation energies have been calculated from the experimental data as $E_{(\text{Armco Fe})} = 10{,}260 \pm 29$ cal g-atom^{-1}, $E_{(5\text{ w/o Mo-Fe})} = 9472 \pm 140$ cal g-atom^{-1}, and $E_{(10\text{ w/o Mo-Fe})} = 9592 \pm 191$ cal g-atom^{-1}. Use of iron diaphragm electrodes, in lithium hydride cells under heavy current loads, has resulted in current densities which were 1.5 times greater than those obtainable from data on the permeability of hydrogen through an iron diaphragm at 1 atm hydrogen pressure across the diaphragm. Alpha activation of the hydrogen gas also increases the hydrogen permeation rate of iron. When ionization of the hydrogen gas with alpha particles was used, the activation energy for the process was reduced from -10.3 kcal g-atom^{-1} to -7.9 kcal g-atom^{-1}.

Hydrogen has the unique property of diffusing through certain metals at a rapid rate, and attempts have been made to exploit this property in a thermally regenerative cell system. The use of such a permeable metal diaphragm as an electrode in fused salt systems alleviates some of the problems associated with porous metal gas electrodes, namely, concentration polarization and "flooding" of the electrode with either electrolyte or gas. Materials, on the other hand, which are compatible with a lithium hydride cell environment consisting of liquid lithium, lithium hydride, and a molten alkali halide electrolyte, are somewhat limited. Although iron and some iron alloys have proved to be satisfactory under these conditions, their use as a hydrogen diffusion diaphragm-electrode limits the cell current density and therefore restricts the practical application of such a cell. The purpose of this investigation was to find a metal capable of high rates of hydrogen permeation and therefore capable of high cell current densities when used as a diaphragm-electrode in a lithium hydride cell.

The permeation of a diatomic gas through a metal barrier was considered to be a four step composite rate process; (*i*) the activated adsorption of the gas on the metal surface, (*ii*) the formation of a gas-metal solid solution, (*iii*) the diffusion of atoms through the metal crystal lattice, and (*iv*) the recombination of atoms and the desorption of the gas at the opposite surface. Much experimental evidence has been given to support such a mechanism (1-5). The surface conditions of a metal determine its affinity to adsorb hydrogen, and in the case of aluminum (6), where its oxide film is difficult to remove, this condition was the rate-determining step in the over-all mechanism.

Of great importance to gas permeation is the solubility constant of the gas-metal system. A metal which possesses a high gas solubility, providing optimum surface conditions exist, will in general exhibit a high rate of permeation.

The literature (7) indicates that the solubility of hydrogen in iron-molybdenum alloys reaches a maximum at a composition of about 6 w/o molybdenum. Although this hydrogen solubility differs little from that of pure iron, the iron-molybdenum alloy does occur, along with the silver-palladium alloy, in the same general classification (8) of alloys which exhibit a maximum hydrogen solubility. The silver-palladium alloy, of course, is very permeable to hydrogen, even more permeable than pure palladium. Consequently, it was anticipated that a similar phe-

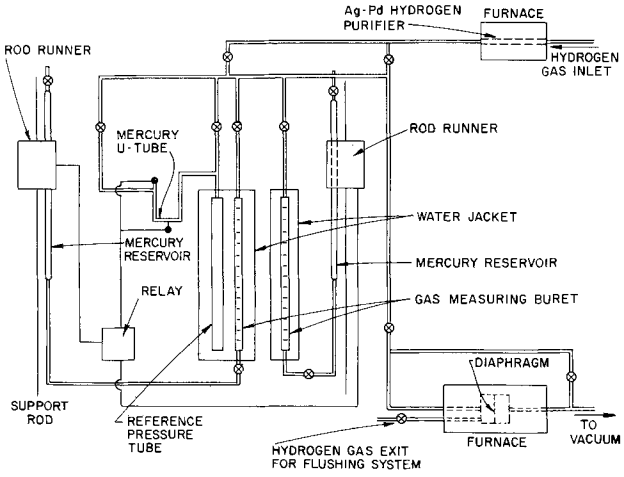

Fig. 1. Gas measuring apparatus

nomena might also exist, but to a lesser degree, for the iron-molybdenum alloy.

Experimental

Apparatus.—Because of greater sensitivity, most investigators have chosen to observe the change in pressure on the vacuum side of the specimen as hydrogen permeates the metal. For this work an apparatus was assembled to measure directly the change in volume of hydrogen permeating the metal. This approach was taken because of anticipated high permeation rates and the simplicity of the volume measuring technique under these experimental conditions. A schematic drawing of this apparatus is given in Fig. 1 and includes the hydrogen gas purifier and diaphragm assembly. The portion of apparatus comprising the gas measuring burets, reference pressure tube, and mercury U-tube and reservoirs was constructed of Pyrex. Stopcocks used in this section were, with one exception, entirely grease free in an effort to keep the introduction of gas impurities into the hydrogen to a minimum. The one exception was not located in the hydrogen flow stream to the diaphragm. This stopcock, isolating the reference pressure tube from the rest of the system, was of the conventional Eck and Krebs precision vacuum type. Other stopcocks were GYCO greaseless high vacuum type. The remaining portion of the apparatus containing the hydrogen purifier and diaphragm assembly was constructed of metal. Connection of these components to the Pyrex system was made by copper to glass seals. Valves used in the metal system were VEECO high vacuum bellows-type.

The hydrogen gas flow into the system was so arranged that the free volume in front of the diaphragm could be flushed with purified hydrogen (from a silver-palladium valve) at the temperature of the measurement. The permeation rates were measured at a constant pressure differential across the diaphragms of 1 atm. This was accomplished by setting the pressure in the reference tube at exactly 1 atm with the aid of a mercury barometer. Any small drop in hydrogen pressure in the system with respect to the reference pressure tube was quickly corrected by the electric motor driven rod runner. The rod runner responds to the closing of an electrical circuit in a U-tube filled with mercury. When the hydrogen pressure in the gas measuring buret dropped below that of the reference pressure tube, the electrical circuit closed by the movement of mercury in the U-tube and the rod runner quickly raised a mercury reservoir until the pressure in the gas measuring buret was exactly equal to that in the reference tube. The permeation rate through the diaphragm was measured directly as the change of gas volume in the measuring buret per unit time.

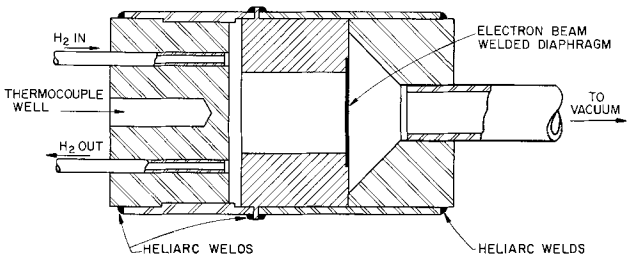

Fig. 2. Diaphragm assembly

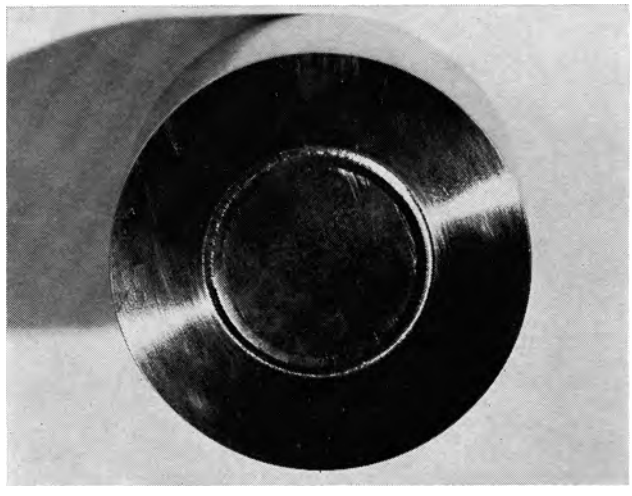

Fig. 3. A typical electron beam welded diaphragm

The design of the gas measuring apparatus does not restrict the presence of mercury vapor on the gas side of the diaphragm. Possible poisoning of the surface of the metal diaphragm could result from the mercury vapor, thereby directly affecting the rate of gas permeation through the diaphragm. A carbon trap was placed in the system to restrict the movement of mercury vapor. However, no differences in rates of permeation were noted either with or without the presence of the carbon trap in the system.

The diaphragm assembly is illustrated in Fig. 2. The diaphragm was first electron beam welded onto a 304 stainless steel support ring. This support ring was in turn heliarc welded into the rest of the assembly. To prevent oxidation of the surface of the metal diaphragm, the heliarc welding operation was carried out under an inert gas blanket. Figure 3 is a photograph of a typical electron beam welded specimen. The uniformity and small width of the electron beam weld enables an accurate measurement of the permeable area of the diaphragm.

To insure that the results were not biased due to hydrogen permeating the diaphragm metal support assembly, the following conditions were met. First, the material of construction of this support was 304 stainless steel which has a permeation rate ten times less than that of Armco iron or the iron-molybdenum alloy. In addition, the wall thickness of the assembly components was kept large compared to the thickness of the diaphragm, the smallest ratio being 10 to 1. Critical dimensions of the diaphragms are given in Table I.

Materials.—Armco iron was used as the pure metal diaphragm and also for the main constituent in the alloy diaphragms. Molybdenum used in the alloys was purchased from Fansteel Metallurgical Corporation, North Chicago, Ill.

Spectrographic analysis of the material is given in Table II.

Method.—Prior to any measurements, the gas measuring system was evacuated to about 10^{-4} mm of mercury and then filled with purified hydrogen gas.[1]

[1] Instrument containing an Ag-Pd valve was purchased from Milton Roy Company, St. Petersburg, Florida.

Table I. Diaphragm dimensions

Diaphragm	Armco Fe	5.04 w/o Mo-Fe	10.0 w/o Mo-Fe
Diameter, mm	24.21	24.00	24.00
Thickness, mm	0.254	0.140	0.140

Table II. Spectrographic analysis

Iron		Molybdenum			
Fe	99.94 (%)	Mo	99.9 (%)	As	0.02 (%)
S	0.025	Si	0.005	Al	0.003
Mn	0.017	Cu	0.002	Co	0.004
C	0.012	Mn	0.01	Pb	0.003
P	0.005	Ni	0.004	Ag	0.0002
		Cr	0.004	Ge	0.002
		B	0.005		

This process was repeated several times before the pressure was set at 1 atm and a measurement taken.

The diaphragm assembly was also evacuated and degassed at 800°C for 16 hr prior to any measurements. Leak rates, on the gas measuring system filled with helium, were undetectable over an 8-hr period. All diaphragm assemblies were leak checked with a helium mass spectrometer prior to connection with the gas measuring portion of the system. In addition, a helium leak check was made at temperature to ensure that the diaphragm or the diaphragm weld did not open on heating. After this testing, pure hydrogen was introduced to the assembly and flushed past the diaphragm for several hours to insure saturation of all the metal system with hydrogen. Reproducibility of successive measurements at temperature was used as an indication that equilibrium had been reached. No decrease in the rate being measured toward the end of a run was observed. A constant rate was taken as indicating that little or no surface contamination of the diaphragm by a reactive impurity occurred during an experiment.

Over-all experimental accuracy was estimated to be ± 2% with the maximum uncertainty occurring in defining the working area of the diaphragm. Accuracy of the burets was considered better than 1% and the reading precision about 0.1%.

Results and Discussion

The general equation for the permeation of a diatomic gas through a metal barrier can be expressed as

$$Q = \frac{KDAt}{d}(p_1^{1/2} - p_2^{1/2}) \exp - \left(\frac{E}{RT}\right)$$

where Q is the amount of gas permeating the diaphragm, cm³ (STP); K is the solubility constant of the gas-metal system; D is the diffusion constant; A is the area of barrier, cm²; d is the thickness of the diaphragm, mm; p_1 is the gas pressure on the upstream side of the diaphragm, atm; p_2 is the gas pressure on the downstream side of the diaphragm, atm; E is the activation energy for the process, cal g-atom^{-1}; R is the gas constant; T is the absolute temperature, degrees Kelvin; and t is the time, hr.

From the equation, it can be seen that the rate of permeation of a diatomic gas through a metal diaphragm varies directly as the area of the diaphragm and as the difference of the square roots of the pressure at each metal face; inversely as the thickness; and exponentially as the reciprocal of the absolute temperature.

In these experiments, the downstream side of the diaphragm was continuously evacuated and the upstream hydrogen pressure held constant at 1 atm which reduces the above equation to the following

$$Q = \frac{KDAt}{d} \exp - \left(\frac{E}{RT}\right)$$

Results of this work are summarized in Table III and are plotted in Fig. 4 as the logarithm of the rate of permeation *vs.* the reciprocal of the absolute temperature. The solid line represents a smoothing of the experimental data by a least squares analysis. Current densities listed in Table III are the equivalent current densities achievable in a cell operating at 100% electrode efficiency.

A comparison has been made in Table IV of the activation energy and permeability derived from this work with that of previous authors for the equivalent hydrogen-metal systems. The reported activation energy for iron was in excellent agreement with literature data (5, 6, 9, 10). No literature data were available for comparison on the 5 w/o Mo-Fe alloy. Rea-

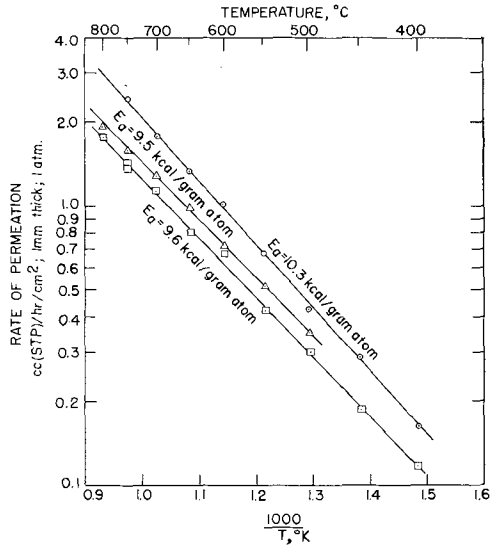

Fig. 4. Hydrogen permeation isobars of Armco iron and iron-molybdenum alloys. Electron beam welded: circle with dot, Armco iron; triangle with dot, 5 w/o Mo-Fe alloy; box with dot, 10 w/o Mo-Fe alloy.

Table III. Hydrogen permeation rates and equivalent current densities cc(STP)/hr/cm², 1 atm, 1 mm thick

Temperature, °C	Armco Fe	Current density,* ma/cm²	5.04 w/o Mo-Fe	Current density,* ma/cm²	10.0 w/o Mo-Fe	Current density,* ma/cm²
350	—	—	6.48×10^{-2}	1.5×10^{-1}	7.56×10^{-2}	1.8×10^{-1}
400	1.63×10^{-1}	3.9×10^{-1}	1.02×10^{-1}	2.4×10^{-1}	1.16×10^{-1}	2.8×10^{-1}
450	2.94×10^{-1}	7.0×10^{-1}	1.96×10^{-1}	4.7×10^{-1}	1.88×10^{-1}	4.5×10^{-1}
500	4.27×10^{-1}	1.0	3.54×10^{-1}	8.5×10^{-1}	3.01×10^{-1}	7.2×10^{-1}
550	6.75×10^{-1}	1.6	5.19×10^{-1}	1.2	4.21×10^{-1}	1.0
600	1.01	2.4	7.28×10^{-1}	1.7	6.81×10^{-1}	1.6
650	1.33	3.2	9.81×10^{-1}	2.3	8.08×10^{-1}	1.9
700	1.78	4.3	1.28	3.1	1.14	2.7
750	2.41	5.8	1.59	3.8	1.41	3.4
800	—	—	1.94	4.6	1.78	4.3

* Current densities for a typical electrode diaphragm 0.127 mm thick would be increased by the factor 7.87.

Table IV. Activation energies and permeabilities for hydrogen metal systems

	E, cal g-atom^{-1}		Q at 500°C, cc(STP) hr^{-1} cm^{-2}, 1 atm, 1 mm thick	
Fe	10,260 ± 29*		0.45*	
	9,600	(5)	0.5	(11)
	9,400	(9)	0.3	(12)
	11,000	(6)		
	9,450	(10)		
5 w/o Mo-Fe	9,470 ± 140*		0.35*	
10 w/o Mo-Fe	9,590 ± 190*		0.30*	
	7,650	(11)	0.4	(11)

* This work.

sonable agreement was observed in the data on the 10 w/o Mo-Fe alloy. There was general agreement when comparing the rates of permeation between this work and previous data (11, 12).

Current densities achievable in a cell which utilizes an iron or iron-molybdenum alloy diffusion electrode are unfortunately low. Actual operation of lithium hydride cells under full load using Armco iron diffusion diaphragms as cathodes produced current densities which were equivalent to 1.5 times the permeation rates obtained with a 1 atm hydrogen pressure differential (1 atm to a vacuum). Apparently, when atomic hydrogen at the iron-fused salt interface was removed as a hydride ion, the over-all permeation rate is increased because of the elimination of the fourth step in the mechanism; namely, the recombination of hydrogen atoms and the desorption of the diatomic gas molecules from the diaphragm surface.

In an attempt to alter the first step of the rate process, *i.e.*, the activated adsorption of the gas on the metal surface, the ionization of the hydrogen gas by a radioactive source was studied. The same type of diaphragm assembly was used but an alpha source (U-233, 5 x 10^8 d/m) was positioned about 10 cm from the iron diaphragm. The same iron diaphragm was used for measurements with and without the alpha source. These results are illustrated in Fig. 5 and indicate that a slight increase in hydrogen permeation of iron was realized when the incoming hydrogen gas was ionized using the radioactive alpha source. At 450°C the increase in rate over that of the same iron diaphragm was 51%; at 550°C the increase 23%; and at 650°C the increase 13%. The activation energy was changed slightly from 10.3 kcal g-atom^{-1} for the plain iron diaphragm to 7.9 kcal g-atom^{-1} for the same diaphragm with the radioactive source.

In view of the above data, indications are that iron or iron-molybdenum alloys probably would not be suitable for use as a diaphragm electrode in a lithium hydride cell where reasonable current densities are required; *i.e.*, 100 ma/cm^2 or greater. In order to fulfill this requirement a material more permeable to hydrogen which is also compatible with the cell environment must be used. The possibility that the Group V-a transition metals may possess these properties will be investigated next.

Acknowledgment

The authors acknowledge the support given this work by the U.S. Atomic Energy Commission. The experimental work was primarily performed by Mrs. G. McCloud.

Manuscript received May 20, 1965; revised manuscript received July 26, 1965.

Any discussion of this paper will appear in a Discussion Section to be published in the June 1966 JOURNAL.

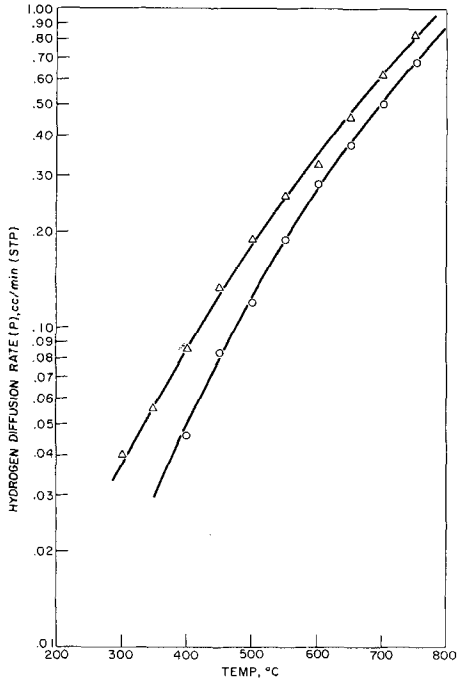

Fig. 5. Hydrogen permeation through an Armco iron diaphragm with alpha activation: △, U^{233} alpha source 5 x 10^8 d/m; ○, no alpha source.

REFERENCES

1. C. J. Smithels, "Gases and Metals," Chapter 2, John Wiley and Sons, Inc., New York (1937).
2. L. D. McGraw, W. E. Ditmars, C. A. Snavely, and C. L. Faust, National Advisory Committee for Aeronautics Report NACA-TN-2696 and NACA-TN-3164 (1954).
3. C. J. Smithels and C. E. Ransley, *Proc. Roy. Soc. (London)*, **A150** (1935).
4. H. M. Ryder, *Elec. J.*, **17**, 161 (1920).
5. W. Baukloh and H. Kayser, *Z Metallik*, **26**, 156 (1934).
6. C. J. Smithels and C. E. Ransley, *Proc. Roy. Soc. (London)*, **A152**, 706 (1935).
7. A. Sieverts and K. Bruning, *Arch. Eisenhutten.*, **7**, 641 (1934).
8. R. M. Barrer, "Diffusion in and Through Solids," p. 159, Cambridge Series on Physical Chemistry, Cambridge University Press (1951).
9. G. Borelius and S. Lindblom, *Annalen. der Physik*, **82**, 201 (1927).
10. H. Bennek and G. Klotzbach, *Technische Mitteilungen Krupp-Forschungberichte*, **4**, 47 (1941).
11. P. L. Chang and W. D. G. Bennett, *J. Iron and Steel Inst. (London)*, **170**, 205 (1952).
12. P. S. Flint, U. S. Atomic Energy Report KAPL-659, December 1951.

Hydrogen Permeation Studies

II. Vanadium as a Hydrogen Electrode in a Lithium Hydride Cell

Robert R. Heinrich, Carl E. Johnson, and Carl E. Crouthamel

Chemical Engineering Division, Argonne National Laboratory, Argonne, Illinois

ABSTRACT

Hydrogen permeation of pure vanadium has been investigated over the temperature range of 450°-550°C and 1 atm hydrogen pressure. An activation energy of 14.2 ± 0.4 kcal g-atom^{-1} has been determined. A lithium hydride cell using a vanadium diaphragm electrode has been operated for a period of 540 hr. Current densities obtained during operation were 180 ma/cm^2 at one-half open-circuit voltage.

The success of a regenerative lithium hydride cell which employs a diaphragm type electrode will depend a great deal on the current density achievable when the cell is operated under load. Current densities in this type of cell are, for the most part, limited by the hydrogen permeation rates of the electrode diaphragm. The permeability of a metal to a diatomic gas has been discussed in a previous investigation (1). The steps in the process can be summarized as: (*i*) the activated adsorption of the gas on the metal surface; (*ii*) the formation of a gas-metal solid solution; (*iii*) the diffusion of the atoms through the crystal metal lattice; and (*iv*) the recombination of the atoms and the desorption of diatomic gas at the opposite surface.

In general, metals which possess high gas solubility, providing optimum surface conditions exist, will exhibit a high permeability to that gas. Transition metals of group V-a possess high hydrogen solubilities and have also been found to be compatible with the lithium hydride cell environment. However, these metals also have the undesirable property of forming very stable oxides and nitrides which are not reduced by hydrogen gas. Thus, pure hydrogen gas and precise control of cell environment must be employed if successful cell operation is to be realized.

In the group V-a transition metals, vanadium is among the highest in hydrogen gas solubility and permeability, is least sensitive to adverse surface effects, maintains good mechanical strength above 400°C in hydrogen atmospheres, and appears to be compatible with all alkali-halide electrolytes and lithium metal.

Experimental

Apparatus.—The diaphragm assembly is illustrated in Fig. 1. The entire apparatus, with the exception of the thin diaphragm, is fabricated from 304 stainless steel. The design of the apparatus is a modification of a basic concept by Brymner and Steckelmacher (2). The seal of the diaphragm is made by tightening the union nut onto the union body which forces the diaphragm to seat in the proper position. The seal itself is achieved by the surface-shearing action between the diaphragm and the male-female components of the assembly. Seals of this type have been shown to withstand several temperature cycles from —188°C to 800°C (2) and still remain gas tight. The technique yields excellent seals; several experiments actually produced cold welding of the diaphragm to the stainless steel.

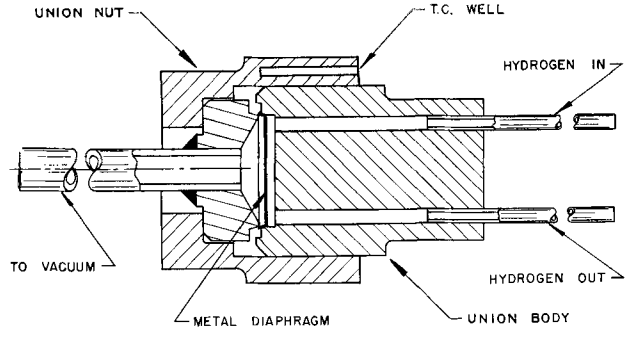

Fig. 1. Swage-type diaphragm holder

The critical diameter of the diaphragm is defined by the diameter of the seat in which the diaphragm fits. This diameter was designed and machined to be 25.40 mm. Diaphragm thickness was 0.254 mm. Wall thickness of the assembly components was kept large in comparison to the diaphragm, the smallest ratio being 10 to 1.

The permeation rates of the diaphragms were measured at 1 atm (absolute) hydrogen pressure by the gas measuring apparatus described previously (1). Pure hydrogen gas was obtainable by passing electrolytic tank hydrogen through a Ag-Pd alloy. The hydrogen gas flow into the system is so arranged that the free volume in front of the diaphragm can be flushed with purified hydrogen at the temperature of measurement.

Materials.—High-purity vanadium metal was purchased from Ames Laboratory, Iowa State University, Ames, Iowa. Our analysis of the material was: V, 99.81%, Fe, 0.019; C, 0.037; N_2, 0.028; H_2, 0.005; and O_2, 0.086.

Method.—Before any measurements were made, the diaphragm and diaphragm assembly were degassed at 850°C for a period of 16 hr. At the end of this time, pure hydrogen was introduced to the assembly and allowed to flush past the diaphragm. With hydrogen flushing past the diaphragm, the temperature was lowered to 450°C. After temperature equilibration had been reached, the first measurement was taken. During the period the diaphragm assembly was being cooled in hydrogen, the gas measuring apparatus was evacuated to 10^{-4} Torr and then filled with purified hydrogen. This process was repeated several times before the pressure in the constant pressure tube was set at 1 atm and connected to the diaphragm assembly.

Leak rates on the gas measuring portion of the system were undetectable over an 8-hr period. The diaphragm assembly was leak checked with a helium mass spectrometer and found to be gas tight. In addition, a helium check was made at temperature to assure that the shear-type seal on the diaphragm was still intact. Accuracy of the gas measuring burets is considered better than 1% and the reading precision about 0.1%.

Results and Discussion

The general equation

$$Q = \frac{KDAt}{d}(p_1^{1/2} - p_2^{1/2}) \exp - \left(\frac{E}{RT}\right)$$

Table I. Hydrogen permeation rates and equivalent current densities

cc(STP)/hr/cm², 1 atm, 1 mm thick		Current density,* ma/cm²	Temperature, °C	
25.0	Average = 26.5 ± 1.0	63.4	447	Range = 450 ± 3
26.8			447	
27.3			447	
24.8			449	
27.3			449	
27.0			452	
27.3			453	
47.2	Average = 51.7 ± 2.8	123.6	496	Range = 500 ± 3
52.1			496	
53.3			496	
47.6			497	
48.0			497	
48.9			497	
52.3			499	
52.3			499	
55.5			499	
56.9			499	
54.1			499	
53.6			499	
51.4			499	
54.0			499	
50.0			503	
50.0			503	
89.8	Average = 86.6 ± 4.3	207.1	549	Range = 550 ± 2
92.2			549	
84.4			549	
90.2			549	
80.6			549	
83.2			549	
82.9			549	
92.1			552	
91.4			552	
83.2			552	
82.6			552	

* Current densities for a typical electrode-diaphragm 0.127 mm thick would be increased by the factor 7.87.

for the permeation of a diatomic gas through a metal diaphragm was discussed previously. With the pressure on the downstream side of the diaphragm essentially a vacuum and the upstream pressure held constant at 1 atm, the equation reduces to

$$Q = \frac{KDAt}{d} \exp - \left(\frac{E}{RT}\right)$$

Results of this investigation are summarized in Table I and are plotted in Fig. 2 as the logarithm of the rate of permeation *vs.* the reciprocal of the absolute temperature. The solid line represents a smoothing of all the experimental data in a least squares sense. Current densities listed in Table I are equivalent current densities achievable in a cell whcih has 100% electrode efficiency and are calculated using the average permeation rate for the particular temperature range listed.

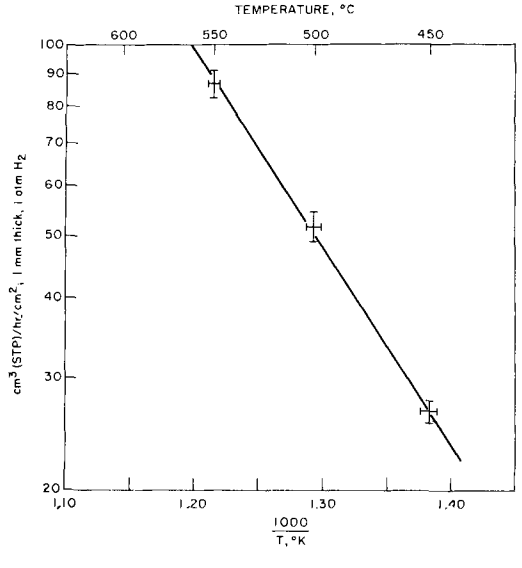

Fig. 2. Hydrogen permeation isobar of pure vanadium. E_a = 14.2 ± 0.4 kcal g—at.$^{-1}$.

Preliminary experiments indicated that, in order for the vanadium to become permeable to hydrogen initially, it was necessary to bake the diaphragm in a vacuum at high temperature (850°C) to eliminate as much surface contamination as possible. Hydrogen was then introduced and the diaphragm thermally activated. It was found that the permeation rate was optimized if the diaphragm was cooled in hydrogen to 450°C before any measurements were taken. Since vanadium absorbs hydrogen with a negative temperature coefficient, this increased permeability is undoubtedly due to the expansion of the vanadium metal lattice. The data of Fig. 2 were collected over a temperature range on four separate days and each time the same activation technique was used. Even so the scatter in the data is attributed to the difficulty in activating the vanadium on four separate occasions.

Difficulty in activating group V-a metals to hydrogen is well-known and for this reason permeation data in the literature are very sparse. Smith (3) has classified these metals as exothermic occluders of hydrogen and has listed a few interesting characteristics of the group. Briefly these are: (*i*) the metal must be raised to an "activation" temperature in order for it to exhibit a high permeability to hydrogen; (*ii*) this permeability may gradually decline due to aging; (*iii*) the metal, if heated and cooled in hydrogen, subsequently shows diminished permeability; (*iv*) reactivation of the metal can only be achieved with difficulty at a temperature higher than the initial activation temperature. These characteristics are interpreted by most investigators as being the result of the expansion and contraction of the metal lattice and possibly surface contamination of the metal. In view of these observations the scatter in our data is not surprising.

Contrary to the findings in the literature (4), vanadium, when used as an electrode material in a lithium hydride cell, was very compatible with the cell environment. A lithium hydride emf cell has been operated in this laboratory for a period of 540 hr using a 0.254 mm thick vanadium diaphragm as an electrode. The electrolyte used was a mixture of lithium chloride-lithium fluoride-lithium hydride. When the cell was operated under a resistive load at 540°C, the average current density obtained was 180 ma/cm² at one-half open-circuit voltage and 1 atm hydrogen pressure. Although this current density was only about one-third of the theoretical, it was achieved without making any attempt to activate the vanadium metal thermally before it was put into the cell. The slope of a plot of cell emf *vs.* the logarithm of hydrogen pressure corresponded to the expected Nernst slope of one, indicating the reversibility of the H_2,H^- couple at a vanadium electrode. Experiments using niobium metal flags as the cathode in a lithium hydride emf cell gave the same equilibrium potential as obtained in cells with pure iron or pure vanadium as the cathode metal flags.

With niobium and vanadium flag electrodes, the rate of achieving the equilibrium potential was very slow. The cell emf was monitored continuously on introduction of each new metal cathode into the cell electrolyte (LiH-LiCl saturated with LiH) operating at 500°C and 1 atm hydrogen pressure. With iron, the initial emf observed was the equilibrium value. However, with vanadium and niobium the equilibrium cell potential was reached only after equilibration in excess of 5 hr. Each of the three metal cathodes (Fe, V, Nb) gave the same equilibrium potential.

The hydrogen electrode in this cell is required to record the potential defined by the over-all equilibrium between molecular hydrogen and hydride ions in the cell electrolyte. But this equilibrium is not freely established in the absence of an active surface, so the electrode must serve in this capacity as well. This makes an additional demand on the electrode because of the reactions that must take place at the electrode surface. The establishment of an equilibrium popula-

tion of atomic hydrogen on the metal surface is achieved only after the bulk metal is saturated with hydrogen. In the case of niobium and vanadium, the hydrogen solubility in the metal is about four to seven thousand times greater than that of iron. At 500°C the slow rate of attaining hydrogen saturation of the bulk metal was reflected in the slow rate of achieving the equilibrium potential.

The following mechanism is consistent with the experimental results and delineates the important features in establishing the equilibrium potential at the hydrogen-hydride electrode.

1. $H_2(g)$	$\rightleftarrows$	2H (surface)	R_1 (moderate)
2. H (surface)	$\rightleftarrows$	H (bulk)	R_2 (slow)
3. H (surface)	$\rightleftarrows$	H^- (solution)	R_3 (very fast)

In this mechanism, rate 1 is the activated adsorption of hydrogen on the metal surface. Rate 2 combines the formation of the gas-metal solid solution and the diffusion of atoms into the metal into a composite rate. The diffusion of hydrogen through the metal lattice is the rate-controlling step. The slow rate at which hydrogen saturates the metal also controls the rate of attaining equilibrium potentials in the cell.

The reaction rate R_3 was assumed to be very fast with respect to rates R_1 and R_2. Atomic hydrogen on the electrode surface was rapidly stripped off as hydride ion by an electron exchange. Voltammetric studies (5) using a microelectrode in a lithium chloride potassium chloride electrolyte have confirmed the rapid rate of this reaction.

The diffusion of atomic hydrogen from the metal surface into the bulk metal lattice was considered the slowest rate. This was consistent with the fact that, when operating a metal diaphragm under a gas pressure differential of 1 atm, the permeation rate was inversely proportional to the diaphragm thickness. The unique feature of vanadium and niobium over that of iron was the extremely high hydrogen solubility in the former two metals. Thus it was not surprising that an equilibrium population of atomic hydrogen could not be maintained on the fresh vanadium or niobium surfaces until the bulk metal was saturated. Once equilibrium had been attained, the reverse was also observed in that the potential of a lithium hydride cell, using a vanadium cathode, dropped only slowly when hydrogen gas was removed from the cell compared to a very rapid drop when iron cathodes were used.

It is realized that more extensive testing of the vanadium diaphragm under severe load conditions must be made before any consideration can be given to its use in a practical cell. However, these hydrogen permeation measurements indicate the use of vanadium as a cathode material is certainly attractive.

Acknowledgment

The authors wish to acknowledge the support given this work by the U. S. Atomic Energy Commission. The experimental work was primarily performed by Mrs. G. McCloud.

Manuscript received May 20, 1965; revised manuscript received July 26, 1965.

Any discussion of this paper will appear in a Discussion Section to be published in the June 1966 JOURNAL.

REFERENCES

1. R. R. Heinrich, C. E. Johnson, and C. E. Crouthamel, *This Journal*, **112**, 1067 (1965).
2. R. Brymner and W. Steckelmacher, *J. Sci. Instruments*, **36**, 278 (1959).
3. D. P. Smith, "Hydrogen in Metals," Chapter 3, University of Chicago Press (1948).
4. TAPCO Report ASD-TDR-62-241, Thompson Ramo Wooldridge Co., 1962.
5. J. P. Elder and J. A. Plambeck, Private communication.

The Voltage Increase of the Cuprous Chloride Electrode by the Addition of Sulfur

R. F. Amlie, H. N. Honer,[1] and P. Ruetschi[2]

The Carl F. Norberg Research Center, The Electric Storage Battery Company, Yardley, Pennsylvania

ABSTRACT

The addition of elemental sulfur to the cuprous chloride active material increases the electrode potential throughout discharge by approximately 0.4v when operated in neutral or acidic media. The greatest benefit is attained by the addition of approximately stoichiometric quantities of sulfur. Cupric sulfide, rather than metallic copper, is the final discharge product. As a result of the increased power density realized by this innovation, the CuCl-Mg water-activated battery constructed for a given power output can be reduced about 15% in weight while the volume is reduced approximately 20%. The effect of sulfur in other similar electrode couples was also investigated.

The cuprous chloride-magnesium water-activated battery is designed to operate under extreme environmental conditions in which most of the conventional dry batteries do not function efficiently. This investigation describes how the addition of elemental sulfur to the cuprous chloride electrode increases the potential during the entire discharge period by approximately 0.4v, which results in a higher energy output per unit weight and volume of the battery.

Since 1949 cuprous chloride-magnesium water-activated batteries have been produced commercially, and their general characteristics have been summarized by Pucher (1). These batteries are characterized by their ability to deliver moderately high current densities with good power output, and they are capable of being discharged at ambient temperatures as low as —50°C, after activation at 0° to 30°C with tap water or salt water. The high energy of hydration of magnesium ions causes internal heating after activation, making these batteries particularly suitable for low-temperature environments.

Cuprous chloride electrodes, either pasted on a supporting grid or pressed to form a flat pellet, are suitable for current densities in the range of 5-70 ma/cm^2 of apparent surface area. The assembled batteries must be stored in dry, sealed containers prior to activation due to the hygroscopic nature of the cuprous chloride. The CuCl-Mg battery has a considerable cost advantage over the silver chloride-magnesium water-acti-

[1] Present address: ESB Company, Ray-O-Vac Division, Special Products, Wonewoc, Wisconsin.

[2] Present address: Leclanché, S. A., Yverdon, Switzerland.

vated system, which has a greater energy output per unit volume because of the higher potential of the Ag/AgCl couple. Cuprous chloride magnesium cells normally produce 1.3-1.4v, while the analogous silver chloride cells give a potential of slightly over 1.5v. Cuprous chloride reserve batteries are used extensively in meteorological balloons and in marine navigation and emergency aids. The life requirements range from periods of about 10 min up to 72 hr for a life-jacket light.

One of the authors (H.N.H.) discovered in 1959 that the addition of sulfur to the cuprous chloride electrode mixture resulted in an operating potential increase of 0.35-0.45 v/cell. Further investigation showed this voltage increase to be completely reproducible even with widely different mix compositions, provided only that the sulfur and cuprous chloride were intimately mixed. It was established that the capacity which could be obtained at the higher voltage level depended on the quantity of sulfur present. The best effect was attained with the addition of about 33% sulfur. With this quantity of sulfur the cell voltage was maintained at a uniform high level during the entire discharge time. The number of cells required for a given battery voltage could thus be decreased with a corresponding reduction in manufacturing costs.

The inclusion of sulfur in the cuprous chloride cathode mix represents a very significant and unique development in the technology of the cuprous chloride-magnesium battery. A patent assigned to The Electric Storage Battery Company is pending.

Elemental sulfur has been employed previously as an additive to the positive electrode active material of the copper oxide-zinc alkaline battery. An early patent by Erwin (2) states that a potential increase of about 0.20v is realized when 1-5% sulfur is mixed with copper oxide for use in an alkaline system. A number of patents were issued to Benner and French (3-6) during the period 1918-1922 and to Armstrong (7) concerning the addition of sulfur to copper oxide electrodes in alkaline electrolytes. Although a sulfur addition as high as 40% is claimed in one patent (4), it was subsequently stated that a concentration in the order of 1% is preferable. More recently, other authors have stated that the potential of the copper oxide electrode can be raised 0.1-0.25v by the addition of a small amount of sulfur (8) or sulfur-containing material (9, 10). Flerov (10) has shown that the steady-state discharge potential of the cupric oxide electrode includes high polarization and the addition of a very small amount of sulfur in the oxide serves to increase the potential as a result of an improvement in the conductivity of the intermediate cuprous oxide layer. His results are discussed further in a later section. Selenium and tellurium are reported to have an effect similar to that of sulfur (9). Elemental sulfur has also been investigated as a cathode active material by itself in neutral electrolytes, but has not gained acceptance due to its low potential (—0.4v *vs.* S.H.E.) and other limitations (11-13).

Experiments with Cuprous Chloride-Sulfur Electrodes in Pile-Type Batteries

The batteries now being manufactured by The Electric Storage Battery Company are of the pile type. A sheet of battery grade magnesium is separated from the cuprous chloride cathode by a porous textile fiber separator material. The cells are stacked in series. Averaged discharge data for a number of CuCl-Mg cells, both with and without the inclusion of sulfur in the cathode, are summarized in Fig. 1. The cell stacks represented in Fig. 1 were discharged through a resistance equivalent to 47.7 ohms/cell after activation with tap water. The average current densities for cells with and without sulfur were 11.4 and 9.0 ma/cm^2, respectively.

Figure 1 shows that a voltage increase of about 0.37 v/cell is achieved by a 30% sulfur addition to the cuprous chloride electrode, and this higher voltage

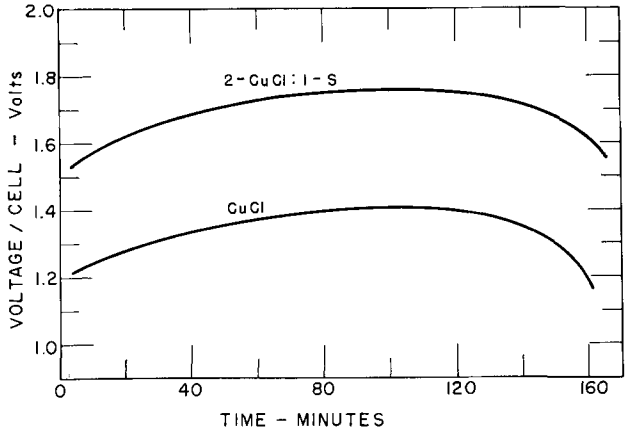

Fig. 1. Effect of sulfur addition to CuCl electrode; discharge through 47.7 ohms/cell; average current density: 11.4 ma/cm^2 w sulfur; 9.0 ma/cm^2 w/o sulfur.

level is maintained throughout the entire discharge. It has been found that, as a result of this innovation, the battery weight and volume for a given power density are reduced approximately 15% and 20%, respectively.

The effect of sulfur content on the discharge capacity is illustrated in Fig. 2, in which the capacity in minutes to the 1.56 v/cell endpoint is plotted against mole per cent of sulfur and cuprous chloride in a S-CuCl mixture. The cell stacks were activated and discharged as described above. It is apparent that the maximum capacity is realized with about 63 mole % sulfur (33% by weight), which approximates a 2:1 mole ratio of sulfur to cuprous chloride.

The effect of the sulfur addition to cuprous chloride is further illustrated in Fig. 3, where the potentials on discharge of single cathodes are measured against a saturated calomel reference electrode. Each cathode was attached to a graphite support and discharged at a constant current of 10 ma/cm^2 in a test cell containing a large excess of 1M magnesium chloride electrolyte. A graphite rod in a separate cell, connected by an electrolyte bridge, served as the counter electrode. The control electrode with no sulfur contained 0.639g of CuCl, equivalent to a theoretical capacity of 0.190 amp-hr, and delivered 74% of this capacity to a cut off of 0.3v below the maximum voltage attained. The electrode with 30% by weight of sulfur maintained a potential about 0.36v above the control throughout the discharge. An efficiency of 87% was realized to a comparable cut-off voltage, based on the weight of the cuprous chloride in the pellet. This single electrode study illustrates that, in addition to the increase in potential, the sulfur also promotes a better electrochemical utilization of the cuprous chloride.

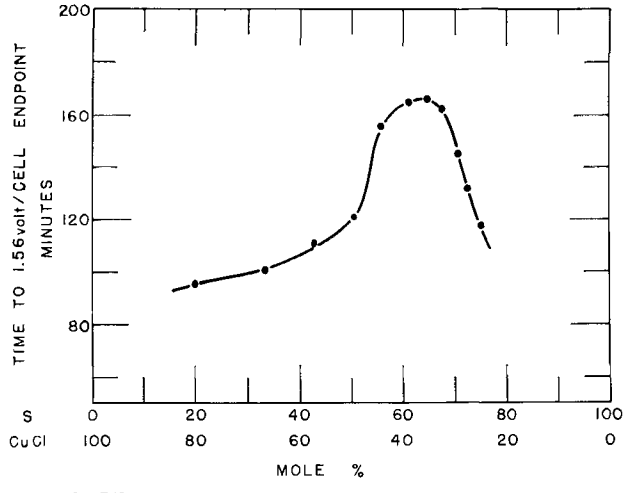

Fig. 2. Effect of S-CuCl ratio on discharge capacity; discharge through 47.7 ohms/cell.

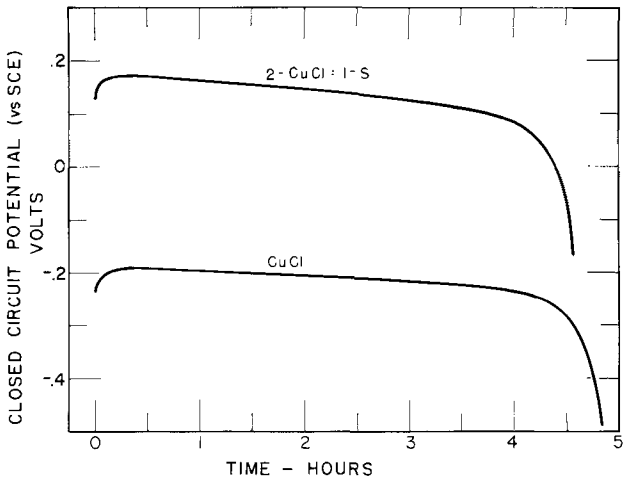

Fig. 3. Single electrode study of S addition to CuCl pellet; 30 ma continuous reduction; 1.0M MgCl electrolyte.

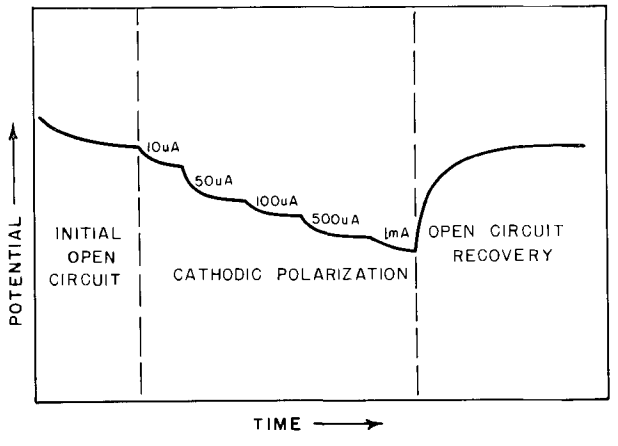

Fig. 4. Illustration of a typical electrochemical sample evaluation

Single Electrode Studies

Experimental.—The addition of sulfur to CuCl and other metal salts which might be employed as positive active materials in electrochemical cells was studied further with small single electrodes in order to achieve a better understanding of the voltage increase mechanism. All of these materials were metal halides or oxides and the measurements were made in a 0.5M $MgCl_2$ or a 30% (7.65M) KOH electrolyte. The experimental technique was discussed and illustrated in detail in the preceding paper (14).

Electrode potentials in 0.5M $MgCl_2$ solution were measured against a saturated calomel reference electrode, while a mercuric oxide reference was employed for the alkaline 7.65M (30%) KOH electrolyte. Initial open-circuit potentials were determined after immersing the sample and allowing the voltage to become constant; the sample pellets were discharged at progressively higher currents, ranging from 10 μa to 5 ma (0.032 to 16 ma/cm^2). A graphic illustration of the test procedure is given in Fig. 4. The ohmic parts of polarization were determined from the recovery of potential after interruption of the current drain and, in most instances, were found to be small enough to be disregarded. Only a small fraction of the total electrode capacity was consumed in making the discharge polarization measurements.

The results of these measurements are summarized in Table I. The difference between the open-circuit value potential and the potential attained at 1.6 ma/cm^2 (500 μa) discharge was selected as a relative measure of polarization for the various samples.

Behavior in neutral or slightly acid chloride electrolytes.—If a mixture of CuCl and sulfur is immersed in water or an aqueous solution, a spontaneous reaction with the formation of CuS occurs (15)

$$2CuCl + S \rightarrow CuS + Cu^{++} + 2Cl^- \quad [1]$$

It can be calculated that this reaction has a free energy change of —2.5 kcal if all the components are in their standard states at unit activity (16). The spontaneous formation of black copper sulfide, accompanied by blue coloration of the solution, can be readily observed. The formation of CuS was confirmed experimentally by x-ray diffraction analysis.

Although an electrode of pure sulfur, without cuprous chloride, attains a steady potential of 0.13v, it is strongly polarized on discharge. Thus, the couple S/H_2S in acidic medium will neither deliver a usable discharge capacity nor influence the potential of other reversible electrode processes.

The electrode mechanism responsible for the potential increase produced by the addition of sulfur was discussed by the authors, in the preceding paper (14). For the present discussion it need only be stated that the presence of solid CuS in the electrode is imperative for the attainment of the higher voltage level and the solid CuS functions as redox catalyst for the $(Cu^{++})/(Cu^+)$ couple which furnishes the discharge current. The theoretical maximum voltage-increase achievable with the addition of sulfur is 0.50v, determined by the free energy of formation of CuS.

As seen from Table I, similar results were also obtained when either cuprous bromide or cuprous iodide were admixed with sulfur.

The potential of the cuprous chloride electrode can also be increased by the addition of certain sulfur-containing compounds such as metal sulfides. Cupric sulfide produced a potential increase of 0.25-0.30v which is significantly less than the increase realized by the addition of sulfur. This increase can be correlated with the formation of cuprous sulfide, Cu_2S, in the electrode during discharge. The reaction responsible for the potential increase is

$$e^- + CuCl + CuS \rightarrow Cu_2S + Cl^- \quad [2]$$

It was found that the maximum electrode capacity at the higher voltage level was realized with a mole ratio of 1:1 between CuCl and CuS.

An experimental potential of —0.26v was observed for a CuO electrode in 0.5M $MgCl_2$. This value was increased by 0.24v with the addition of sulfur. The increase is in close agreement with the theoretical value of 0.25v, calculated from the free energy of formation of CuS. The couple $2e^- + CuO + S + 2H^+ \rightarrow CuS + H_2O$ is however easily polarized in $MgCl_2$ and cannot be utilized in a practical battery device.

When a mixture of silver chloride and sulfur is placed in the magnesium chloride electrolyte no spontaneous reaction can occur since

$$2AgCl + S \rightarrow Ag_2S + Cl_2 \quad [3]$$

has a positive free energy change. Metallic silver, and not Ag_2S, was formed when an electrode of AgCl + S was discharged in 0.5M $MgCl_2$.

The reaction between sulfur and discharged silver according to

$$2e^- + 2AgCl \rightarrow 2Ag + 2Cl^-$$

$$2Ag + S \rightarrow Ag_2S$$

$$2e^- + 2AgCl + S \rightarrow Ag_2S + 2Cl^- \quad [4]$$

appears to be slow. Thus the addition of sulfur will not affect the AgCl/Ag potential.

The addition of sulfur to highly reversible mercurous chloride electrodes has no significant effect on the Hg/Hg_2Cl_2 potential.

Behavior in alkaline electrolyte.—The effect of the sulfur on cupric oxide electrodes in alkaline solution

Table I. Addition of sulfur and sulfides to positive electrode active materials

Electrode composition, w/o, electrolyte	Discharge polarization measurements, v 500 μa (1.6 ma/cm²) (ma-min discharged)	Open-circuit voltage after interruption	Observations during open-circuit recovery
Sulfur			
75% sulfur 25% graphite 0.5*M* $MgCl_2$	−0.60v *vs.* SCE (31 ma-min)	0.13	Increase from −0.1 to +0.13 over 16 hr period (no step)
75% sulfur 25% graphite 30% KOH	−0.36v *vs.* HgO (106 ma-min)	−0.35	Good reversibility, potentials become more negative as sulfur dissolves
Copper compounds			
100% CuCl 0.5*M* $MgCl_2$	−0.22v *vs.* SCE (45 ma-min)	−0.136	Steady after 1 hr
67% CuCl 33% sulfur 0.5*M* $MgCl_2$	0.225 (100 ma-min)	0.230	Increase immediately to +0.230v and is steady for > 4 hr
60% CuCl 30% sulfur 10% graphite 0.5*M* $MgCl_2$	0.220 (30 ma-min)	0.230	Increase to +0.252v after 16 hr
100% CuBr 0.5*M* $MgCl_2$	−0.300 (15 ma-min)	−0.180	Increase to −0.195v after 30 min and −0.180v after 16 hr
75% CuBr 25% sulfur	0.186 (90 ma-min)	0.210	Constant after 1 hr and remains steady > 4 days
90% CuI 10% graphite 0.5*M* $MgCl_2$	−0.43 (59 ma-min)	Approx. −0.24 indeterminate	Slow recovery depending on extent of reduction
67% CuI (1-F.W.)* 23% S (2-F.W.) 10% graphite 0.5*M* $MgCl_2$	0.02 (141 ma-min)	0.21	Rapid rise to 0.15v, slow to final value
90% CuO 10% graphite 0.5*M* $MgCl_2$	−0.4v initial −0.78v after 16 hr	−0.26	−0.29v after 1 hr −0.26v after 5 hr
75% CuO 25% sulfur 0.5*M* $MgCl_2$	−0.55	−0.023	After 1 hr
100% CuO 30% KOH	−0.49v *vs.* HgO (60 ma-min)	−0.22	Steady after 1 hr
95% CuO 5% sulfur 30% KOH	−0.34 (30 ma-min)	−0.075	Steady after 1 hr
71.4% CuO (1-F.W.) 28.6% sulfur (1-F.W.) 30% KOH	−0.22 (186 ma-min)	−0.20	After approx. 1 hr No dissolved S/S⁻⁻
83.2% CuO (2-F.W.) 16.8% sulfur (1-F.W.) 30% KOH	−0.223 (122 ma-min)	−0.177	After 16 hr, sol'n light blue
86.5% CuO (10-F.W.) 3.5% sulfur (1-F.W.) 10.0% graphite 30% KOH	−0.22 (40 ma-min)	−0.170	After 16 hr; sol'n water-clear with sl. blue color
Other heavy metal salts			
90% AgCl 10% graphite 0.5*M* $MgCl_2$	−0.080 (20 ma-min)	−0.025	Increase from −0.50 to −0.025v over 16-hr period
100% AgCl 0.5*M* $MgCl_2$	−0.340 (90 ma-min)	−0.039 (>2 hr)	High resistance, likely due to poor contact
60% AgCl 30% sulfur 10% graphite 0.5*M* $MgCl_2$	−0.079 (50 ma-min)	0.150	−0.031v after 1 hr, increase to 0.150v after 48 hr
30% AgCl 40% Ag_2S 20% sulfur 10% graphite 0.5*M* $MgCl_2$	−0.090 (148 ma-min)	0.150	Remains at approx. −0.042v for 3 hr, increases to 0v at 3½ hr, 6 hr 0.135, 22 hr 0.150
79.5% AgO (1-F.W.) 20.5% sulfur (1-F.W.) 30% KOH	0.21 (538 ma-min)	0.250	Stable potential, finely divided black suspension
87.9% Ag_2O (1-F.W.) 12.1% sulfur (1-F.W.) 30% KOH	0.21 (87 ma-min)	0.300	After 24 hr recovery, OCV increased 50 mv
70.6% Ag_2O (1-F.W.) 9.8% sulfur (1-F.W.) 10.2% Ag_2S 30% KOH	0.215 (110 ma-min)	0.300	Ag_2S addition of no value. Black suspension (Ag_2S) forms
89.1% Ag_2O (2-F.W.) 6.1% sulfur (1-F.W.) 4.8% graphite 30% KOH	0.24 (72 ma-min)	0.315	Rapid final OCV recovery
98.6% Ag_2O (10-F.W.) 1.4% sulfur (1-F.W.) 30% KOH	0.205 (33 ma-min)	0.238	Initial OCV of 0.40v steady for 10 min, then dropped rapidly to 0.27v

Table I. Addition of sulfur and sulfides to positive electrode active materials (con't.)

Electrode composition, w/o, electrolyte	Discharge polarization measurements, v 500 μa (1.6 ma/cm²) (ma-min discharged)	Open-circuit voltage after interruption	Observations during open-circuit recovery
90% Hg_2Cl_2 10% graphite	−0.03 (123 ma-min)	0.00	Immediate recovery to 0v. Stable at 0v for over 16 hr
60% Hg_2Cl_2 30% sulfur 10% graphite 0.5*M* $MgCl_2$	−0.054 (30 ma-min)	0.0	Stable at 0.0v > 16 hr
30% Hg_2Cl_2 40% HgS 20% sulfur 10% graphite 0.5*M* $MgCl_2$	−0.06 (56 ma-min)	0.00	Steady at 0v > 3 days
98.6% HgO (1-F.W.) 1.4% sulfur (1-F.W.) 30% KOH	−0.025v (*vs.* HgO ref) initial OCV. After 4 days open-circuit stand OCV dropped to −0.4v as solution acquired yellow polysulfide color.		

Reference electrode potential *vs.* standard hydrogen electrode
$Hg/HgCl_2$, sat'd KCl + 0.243v
Hg/HgO, 30% KOH + 0.098v
* (F.W.) is formula weight or stoichiometric ratio of active components only.

is different from that in acidic electrolytes. The reaction

$$CuO + S \rightarrow CuS + (1/2)O_2 \qquad \Delta G_o = 18.7 \text{ kcal} \quad [5]$$

has a positive free energy, and consequently the spontaneous formation of CuS cannot occur on open circuit. Stable open-circuit potentials of CuO mixed with increasing amounts of sulfur (weight per cent) are shown in the following tabulation. The electrode potentials were measured in 30% KOH against a mercuric oxide reference electrode.

Electrode composition	Potential, v *vs.* Hg/HgO
CuO + 0% S	−0.22
CuO + 5% S	−0.07
CuO + 16% S	−0.18
CuO + 29% S	−0.23

These results indicate that the increase in electrode potential is greatest with relatively small additions of sulfur. With 30% sulfur the potential is the same as for pure CuO (—0.22v *vs.* Hg). A 40% sulfur addition would be equivalent to a 1:1 stoichiometric ratio. Electrodes of pure sulfur in KOH show a potential of about —0.4v *vs.* HgO, which depends also somewhat on the concentration of dissolved sulfur. The S/S^{--} couple is quite reversible in alkaline electrolytes. The experimental results can therefore be explained by the strong tendency of sulfur to form its own electrode potential in KOH, resulting in a mixed potential with electrodes containing both CuO and S. With very small amounts of sulfur, however, a voltage increase of nearly 0.2v is realized due to the electrode reaction $2e^- + CuO + S + H_2O \rightarrow CuS + 2(OH)^-$. The addition of sulfur to Cu_2O gives a greater voltage increase than that of sulfur to CuO, this in agreement with the free energy of the reaction $2e^- + Cu_2O + 2S + H_2O \rightarrow 2CuS + 2(OH)^-$. During discharge of sulfur-containing copper oxide electrodes at low current densities the duration at the higher voltage level never exceeded the time corresponding to the stoichiometric quantity of sulfur consumed according to the above reactions. However, with large quantities of sulfur present the S/S^{--} couple begins to impose its potential on the electrode, lowering it to —0.4v, which is impractically low.

The effect of the sulfur addition to Ag_2O and HgO positive materials in alkaline solutions was also investigated. Ag_2O is somewhat soluble in alkaline electrolytes and will react with sulfur since the reaction $Ag_2O + S \rightarrow Ag_2S + \frac{1}{2} O_2$ has a free energy of —7.0 kcal.

The electrode potential of Ag/Ag_2O in 30% KOH is 0.25v *vs.* Hg/HgO. The addition of small percentages of sulfur produced potentials as high as 0.35v *vs.* HgO for short periods of time, until the sulfur was substantially consumed at the surface of the electrode. Theoretically, the couple

$$2e^- + S + H_2O + Ag_2O \rightarrow Ag_2S + 2(OH)^- \quad [6]$$

would have a potential of 0.45v *vs.* HgO. With large sulfur additions the open-circuit voltage is about 0.30v *vs.* HgO and steady for several hours, before it decays to the potential of sulfur.

The voltage of the reversible Hg/HgO couple in 30% KOH is not noticeably affected by addition of small amounts of sulfur. With larger amounts of sulfur, the electrode potential is decreased due to the influence of the S/S^{--} couple. The reaction

$$HgO + S \rightarrow HgS + \frac{1}{2} O_2 \qquad \Delta G_o = 3 \text{ kcal} \quad [7]$$

has a positive free energy and does not proceed in the presence of oxygen at atmospheric pressure. The couple, $2e^- + HgO + S + H_2O \rightarrow HgS + 2(OH)$, does not exert a measurable influence.

Discussion

Thermodynamics of the sulfide formation.—An extensive investigation of metal sulfide electrodes in aqueous solutions was carried out by Wrabetz in collaboration with Noddack and Herbst (17-19). These investigators measured the electrode potentials of a large number of metal sulfides in solutions containing the respective cations and found that the sulfides have their own electrochemical potential series which is shifted toward more noble values than that of the respective parent metals. Many of the metal sulfides studied exhibited electrode potentials depending on the activity of the dissolved cation in conformity with the Nernst relationship (17). Wrabetz and co-workers conclude, as Piontelli (20) already had for galena (PbS), that the potential increase ΔE of the metal sulfide electrode over that of the metal is related by

$$\Delta G_o = -z_e F \Delta E \quad [8]$$

to the free energy of formation ΔG_o of the sulfide. According to Wrabetz (17), these sulfide potentials arise as a result of the nonideality, or the nonstoichiometry, of the metal sulfides. The excess of sulfur contained therein reacts according to

$$2e^- + S \text{ (sulfide)} + M^{++} \rightarrow MS \quad [9]$$

Since only a small quantity of excess sulfur or cation vacancies exist in the crystal lattice, very little capacity can be withdrawn in either direction. A comprehensive discussion of the electrode mechanism responsible for the potential of the cupric sulfide elec-

trode is given by Amlie and Ruetschi in the preceding paper (14).

Sulfur addition to the $Cu/CuO/OH^-$ *electrode.*—The electrode mechanism of the cupric oxide electrode during discharge in alkaline solution has been studied recently by Flerov (10). He found that the electrode discharges at two distinct potential levels corresponding to the cupric and cuprous oxide reduction, respectively. He also prepared an "activated" oxide containing about 0.15% sulfur which could be discharged almost entirely at the upper potential level at the 4 ma/cm^2 rate. Flerov suggests that the upper potential level corresponds to the reduction of Cu_2O according to

$$2e^- + Cu_2O + H_2O \rightarrow 2Cu + 2(OH)^- \quad [10]$$

with a potential of —0.35v *vs.* N.H.E. or —0.45v *vs.* Hg/HgO. The cuprous oxide likely exists in a hydrated form and is readily reducible at the Cu/Cu_2O potential. Cuprous oxide is formed by chemical reaction between CuO and Cu, and this formation is shown to be enhanced by intimate mixing, long rest periods, elevated temperature, and preliminary discharge.

Flerov attributes the lower potential level of the two-step discharge curve to the polarized electrochemical reduction of solid-phase CuO

$$2e^- + 2CuO + H_2O \rightarrow Cu_2O + 2(OH)^- \quad [11]$$

He omitted two experiments which would have given greater substantiation to his proposed mechanism. If the CuO electrode had been reduced at sufficiently low discharge rates to allow time for the simultaneous formation of Cu_2O, only the higher potential plateau should have been observed. Also, the discharge of an electrode containing Cu_2O as the only oxide would have provided further confirmation.

Flerov attributes the beneficial effect of the small quantity of sulfur added to an improvement of the conductivity of cuprous oxide. Sulfur is an effective electron acceptor which is said to increase the "hole" conduction of Cu_2O, a p-type semiconductor. Consequently, the reaction between Cu and CuO is accelerated since charge transfer across the intermediate layer of Cu_2O is now facilitated.

It should be emphasized that the higher potential level maintenance mechanism described by Flerov is entirely different from the potential increase phenomena described in the present study. His work explains the improved potential maintenance due to addition of small quantities of sulfur as described in the patent literature (2-7) and elsewhere (8). This mechanism requires that the sulfur be incorporated into the crystal lattice of the cuprous oxide to be effective throughout discharge. In contrast, our findings relate to a new electrode couple in which sulfur is electrochemically consumed, and a potential above that of the Cu_2O/Cu and CuO/Cu_2O electrodes is realized.

Conclusions.—1. The addition of sulfur to the cuprous chloride electrode was found to increase the voltage of the cuprous chloride-magnesium battery by 0.35 to 0.45v and to promote a more efficient utilization of the cuprous chloride active material. This discovery constitutes an important advancement in the technology of this system since a considerably greater power output per cell and is realized by the addition of a very inexpensive substance.

2. Generally, the addition of sulfur to electrochemical couples of the types metal/metal oxide or metal/metal halide may produce a voltage increase which is accounted for by the reaction

$$ne^- + M_xB_y + S \rightarrow M_xS + B_y^{-n} \quad [12]$$

whereby the corresponding metal sulfides are formed. However, this reaction is not always dominant over the component processes

$$ne^- + M_xB_y \rightarrow M_x + B_y^{-n} \quad [13]$$

$$2e^- + S \rightarrow S^{--} \quad [14]$$

Theoretically, the maximum potential increase attainable can be calculated from the free energy of formation of the metallic sulfide, although this increase is not always attainable experimentally.

Traces of free sulfur excess in metal sulfide electrodes in solutions of corresponding cations may produce electrochemical couples analogous to (12), namely

$$ne^- + xM^{n+} + S \text{ (sulfide)} \rightarrow M_xS \quad [15]$$

However, no sustained discharge is possible due to the limited amount of sulfur present.

3. The potential of the copper halide electrodes can also be increased by addition of certain sulfur-containing compounds such as metal sulfides. Cupric sulfide, added to cuprous chloride, produced an increase of 0.25-0.30v which is less than that attained by the addition of sulfur.

4. Sulfur is an electrochemically active material which attempts to establish its own potential when in a solution containing sulfide, polysulfide, or complexed sulfide ions. While the S/S^{--} couple is ineffective in neutral or acid solutions, it is quite reversible in alkaline electrolytes.

If large amounts of sulfur are added to a positive electrode in an alkaline electrolyte, the sulfur will tend to impose its own potential on the system and the electrode potential will approach that of the sulfur/sulfide ion couple, which is impractically low. With small amounts of sulfur present, an increased voltage may be observed over a short transient period on account of the mechanism (12).

5. Sulfur incorporated into the crystal lattice of Cu_2O may greatly decrease the polarization resistance during discharge of copper oxide electrodes, due to increased conductivity.

Manuscript received March 31, 1965; revised manuscript received July 29, 1965.

Any discussion of this paper will appear in a Discussion Section to be published in the June 1966 JOURNAL.

REFERENCES

1. L. E. Pucher, *This Journal*, **99**, 203C (1952).
2. R. W. Erwin, U. S. Pat. 1,282,057, Oct. 22, 1918.
3. R. C. Benner and H. F. French, U. S. Pat. 1,255,283, Feb. 15, 1918.
4. R. C. Benner and H. F. French, U. S. Pat. 1,316,761 Sept. 23, 1919.
5. R. C. Benner and H. F. French, U. S. Pat. 1,375,647 Apr. 19, 1921.
6. R. C. Benner and H. F. French, U. S. Pat. 1,415,860 May 16, 1922.
7. G. W. Armstrong, U. S. Pat. 1,624,460, April 12, 1927.
8. E. A. Schumacher and G. W. Heise, *This Journal*, **99**, 191C (1952).
9. G. W. Vinyl, "Primary Batteries," p. 237, John Wiley & Sons, Inc., New York (1950).
10. V. N. Flerov, *Russ. J. Phys. Chem.*, **37**, 934 (1963).
11. S. F. Walker, U. S. Pat. 361,794, April 26, 1887.
12. C. K. Morehouse and R. Glicksman, *This Journal*, **103**, 94 (1956).
13. C. K. Morehouse and R. Glicksman, *ibid.*, **107**, 651 (1960).
14. R. F. Amlie and P. Ruetschi, *ibid.*, **112**, 665 (1965).
15. G. Vortman and C. Padberg, *Chem. Ber.*, **22**, 2642 (1889).
16. W. M. Latimer, "The Oxidation States of the Elements and Their Potentials in Aqueous Solutions," 2nd ed., Prentice-Hall, Inc., New York (1952).
17. W. Noddack and K. E. Wrabetz, *Z. Elektrochem.*, **59**, 96 (1955).
18. W. Noddack, K. Wrabetz, and W. Herbst, *ibid.*, **59**, 752 (1955).
19. K. E. Wrabetz, *ibid.*, **60**, 722 (1956).
20. R. Piontelli, *Bull. Soc. Chim. France*, Mem (5), **16**, D197 (1949).

Oxidation Studies on Ni and on a 0.37 w/o Cr-Ni Alloy in CO_2 and in CO_2-CO Mixtures

K. Fueki[1] and J. B. Wagner, Jr.

Materials Research Center and Department of Materials Science,

The Technological Institute, Northwestern University, Evanston, Illinois

ABSTRACT

The linear oxidation of pure Ni and a 0.37 w/o (weight per cent) Cr-Ni alloy in reduced pressures of CO_2 was studied between 900° to 1300°C. It was found that the linear rate constants are proportional to the pressure of CO_2 and that the constants of the 0.37 w/o Cr alloy are several times larger than those of pure Ni. The linear oxidation in CO_2-CO mixtures was found not to obey the rate equation, $\overset{o}{n}/A = k' p_{CO_2} - k'' p_{CO}$. Disagreement of the observed results with the above rate equation is interpreted to be due to a nucleation and growth phenomenon whereby the oxide grains are discontinuous over the surface.

The over-all processes of metal oxidation involve the surface reactions at both interfaces and the material transport through the growing oxide layer. When the reaction is governed by the transport process through the compact oxide layer, the oxidation is parabolic, while the linear oxidation is observed when the reaction is controlled by a surface reaction, especially that at the oxide-gas boundary.

Since linear oxidation has been observed only in a few cases, the kinetics of linear oxidation have not been well established. The purpose of this paper is to present kinetic data for the linear oxidation of nickel, undoped and doped with chromium, in CO_2 and in CO_2-CO mixtures.

Linear oxidation in CO_2-CO mixtures has been studied on iron and cobalt. Hauffe and Pfeiffer (1) found the linear rate constant of iron to be proportional to $(p_{CO_2}/p_{CO})^{2/3}$ and have suggested a chemisorption mechanism. Pettit and his co-workers (2, 3) have shown that the linear rate of oxidation of iron obeys a rate equation

$$\overset{o}{n}/A = [k'p_{CO_2} - k''p_{CO}] \qquad [1]$$

where $\overset{o}{n}$ is the number of equivalents of oxide formed per unit time, A is the area, p_{CO_2} and p_{CO} are the partial pressures, and k' and k'' are constants. The second term in brackets of Eq. [1] accounts for the reverse reaction due to the presence of CO in the gas mixture. In general, the constants k' and k'' are functions of the composition of the oxide, in particular, the concentration of excess electrons or electron holes. In the case of the oxidation of iron to wüstite in CO_2-CO mixtures, Pettit and Wagner (3) have inferred that the Fe/O ratio in the wüstite is virtually fixed at that coexisting with metallic iron during the initial kinetics (for thin oxide layers). Accordingly, the concentration of excess electrons and electron holes is fixed and does not appear explicitly in the rate equation, Eq. [1]. Pettit and Wagner (3) have proposed the rate-determining step for the linear oxidation of iron to be the dissociation of carbon dioxide into carbon monoxide and adsorbed oxygen atoms or ions in accordance with a theory of C. Wagner (4).

The linear oxidation of cobalt in CO_2-CO mixtures has been studied by Pettit and Wagner (5). They found that oxidation proceeded by two successive regions of linear kinetics in the initial period of oxidation. It was also found that the rates during the first linear kinetics obeyed Eq. [1] but the second ones did not.

[1] Present address: Department of Industrial Chemistry, University of Tokyo, Tokyo, Japan.

Experimental and Results

Oxidation rate measurements.—Sheets, 0.15 mm thick, of pure nickel and nickel doped with 0.37 w/o chromium were used for the experiments. Their analyses are listed in Tables I and II. Specimens, 8 mm wide and 2 cm long, were cut from the sheets, polished with 1/0, 2/0, 4/0 emery papers and with Linde "A" alumina abrasives, washed with soap and water and then with acetone, and dried. The polished specimens were annealed in purified hydrogen overnight at 550°C to remove strain.

The oxidation rates were measured gravimetrically. The measurements below 1200°C were conducted using an Ainsworth automatic recording balance and its accessories described by Pettit and Wagner (5). The measurements above 1250°C were carried out by means of a quartz spring balance and high-temperature furnace described in a previous paper (6).

The reduced total pressures of the CO_2 and CO were produced by using pure argon as the diluent gas. Linear flow rates of 0.9 and 2.7 cm/sec were employed below 1200° and above 1250°C, respectively.

Table I. Analysis of pure Ni*

Impurities	Amounts, w/o
Fe	0.0005
Si	0.0005
Mg	0.0001
Ca	<0.0001
Cu	<0.0001
Ag	<0.0001

* The nickel sheet and the analysis was furnished by Johnson, Matthey and Co., Ltd., London, England.

Table II. Analysis of the 0.37 w/o Cr alloy

Elements	Amounts, w/o
Cr	0.37
Si	0.01
Fe	0.015
Cu	0.05
Ti	0.05
Al	0.01
Co	0.01
Mg	0.01
Pb	0.005
Zn	0.005
Bi, Mo, Sn, V	Nil

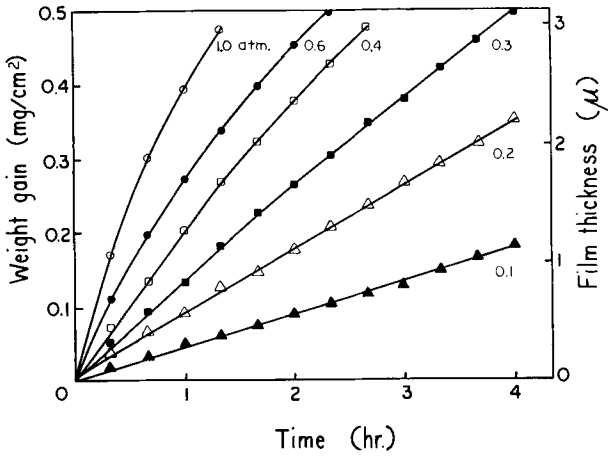

Fig. 1. Oxidation curves of pure Ni oxidized in different pressures of CO_2 at 1100°C.

Figure 1 shows the oxidation curves of pure Ni oxidized in different pressures of CO_2 at 1100°C. The distinct linear portion was observed in the initial period of oxidation, when the pressure of CO_2 was less than about 0.4 atm. The critical film thickness at which the transition from linear to parabolic oxidation rates occurs were found to be 2-5μ depending on the temperature and the pressure of CO_2.

Typical oxidation curves of the 0.37 w/o Cr alloy are shown in Fig. 2. As in the case of pure nickel, linear oxidation is observed for oxidation in reduced pressures of CO_2. The critical film thicknesses for the onset of linear kinetics were found to range from 4 to 36μ.

The linear rate constant, k_L (g-cm^{-2}-sec^{-1}), is determined from the slope of the weight gain *vs.* time plot. The dependence of the linear rate constants of both metals on the pressure of CO_2 is shown in Fig. 3 and 4. The linear rates are proportional to the pressure of CO_2 and are expressed by an equation

$$k_L = k' p_{CO_2} \qquad [2]$$

where k' is a constant and is numerically equal to k_L at 1 atm of CO_2. This result indicates that the rate-determining step of linear oxidation is the surface reaction at the oxide-gas interface.

Figure 5 shows the Arrhenius plots of k'. The plot for pure nickel is straight, while that for the 0.37 w/o Cr alloy has a break point at 1200°C. The rates for the oxidation of the 0.37 w/o Cr alloy are several times larger than those of pure nickel. The activation energies are given in Table III.

Because only a very small content of CO in the gas phase could be tolerated before the oxide would be reduced, the extensive measurements of rate as a function of CO/CO_2 ratio as reported for iron (2, 3) and for cobalt (5) could not be carried out. However, the effect of CO on the oxidation was studied at a pressure of 0.3 atm of CO_2. Typical oxidation curves

Table III. Activation energies of linear and parabolic oxidation

Temperature	Range, °C	Linear, kcal/mole	Parabolic, kcal/mole
Pure Ni	1000-1300	27	37.3
0.37 w/o Cr alloy	900-1200	13	25.1
	1200-1300	38	43.4

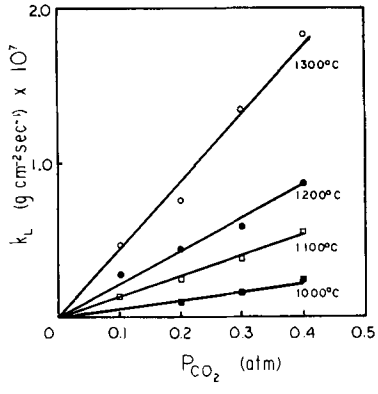

Fig. 3. Dependence of k_L of pure Ni on the pressure of CO_2

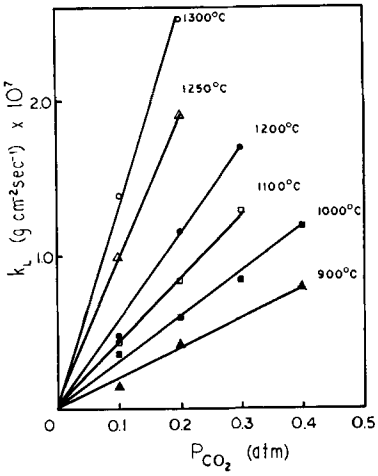

Fig. 4. Dependence of k_L of 0.37 w/o Cr alloy on the pressure of CO_2.

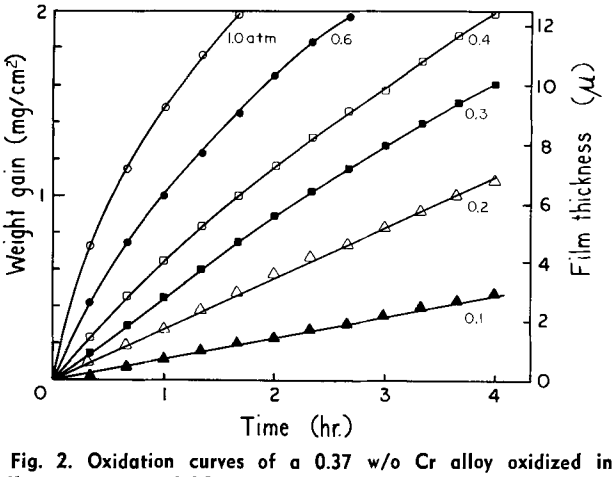

Fig. 2. Oxidation curves of a 0.37 w/o Cr alloy oxidized in different pressures of CO_2 at 1100°C.

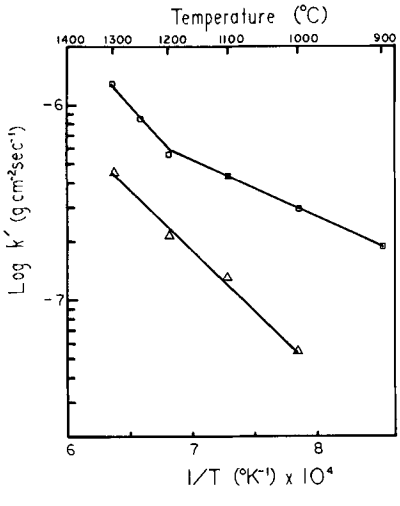

Fig. 5. Temperature dependence of k' of pure Ni and of a 0.37 w/o Cr alloy; △, pure Ni; □, 0.37% Cr alloy.

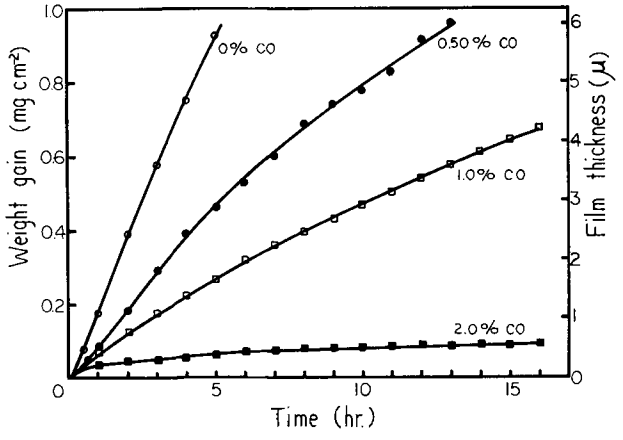

Fig. 6. Effect of CO on oxidation of pure nickel; p_{CO_2} = 0.3 atm, 1200°C.

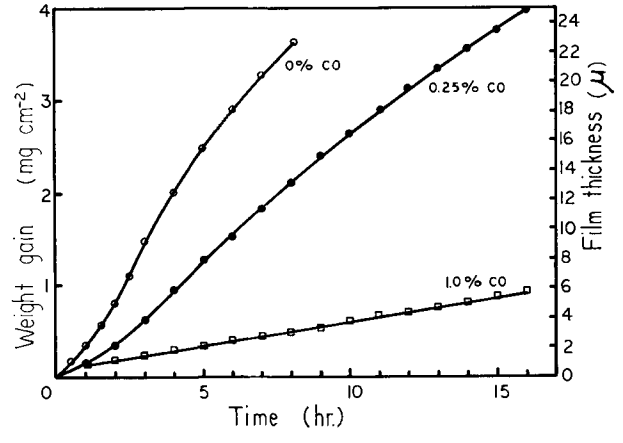

Fig. 7. Effect of CO on oxidation of a 0.37 w/o Cr alloy; p_{CO_2} = 0.3 atm, 1200°C.

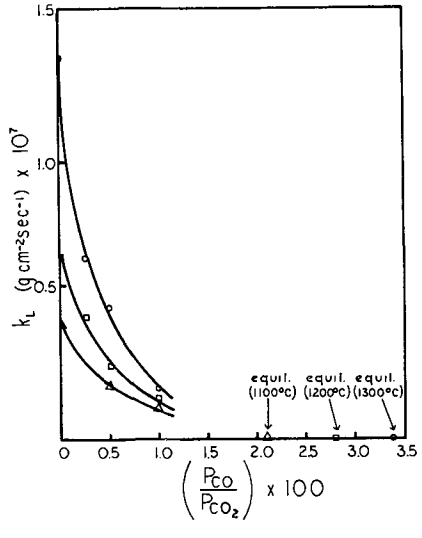

Fig. 8. Effect of CO on k_L of pure Ni; p_{CO_2} = 0.3 atm; ○, 1300°C; □, 1200°C; △, 1100°C.

are shown in Fig. 6 and 7. The percentage of CO given in these figures shows the ratio of p_{CO} to p_{CO_2}. Both the linear rates and the parabolic rates decrease with an increase in the content of CO. Figures 8 and 9 show the plots of k_L *vs.* p_{CO}. In these figures, the notation, equil, denotes the dissociation pressures of nickel oxide in terms of the CO/CO_2 ratio. The linear rate constant, k_L, decreases nonlinearly with the increase

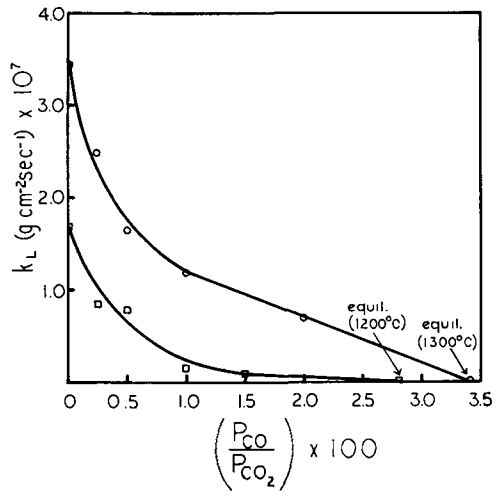

Fig. 9. Effect of CO on k_L of a 0.37 w/o Cr alloy; p_{CO_2} = 0.3 atm; ○, 1300°C; □, 1200°C.

in p_{CO}. These results show that Eq. [1] does not hold since k_L is proportional to n/A (2-4). A nonlinear relation between k_L and p_{CO} was found by Pettit and Wagner for the linear oxidation of cobalt (5) in CO_2-CO mixtures.

It is known that parabolic oxidation kinetics are related to the point defects in the oxide layers formed. In order to obtain information on the defects in nickel oxide doped with chromium oxide, parabolic oxidation was also studied as a function of temperature and oxygen pressure. Figure 10 shows the temperature dependence of parabolic constants at 1 atm of CO_2. In this figure, Ni (II) is the pure nickel used in the present study and Ni (I) is the one employed in the previous work (6). The rate constants of Ni (II) are very close to those of Ni (I). The parabolic rate constants of the 0.37 w/o Cr alloy are about 10 times larger than those of pure Ni. The Arrhenius plot of the data for the 0.37 w/o Cr alloy has a break at 1200°C. The activation energies are given in Table III.

Microscopic observation.—The surface of oxidized specimens was examined microscopically. The surface

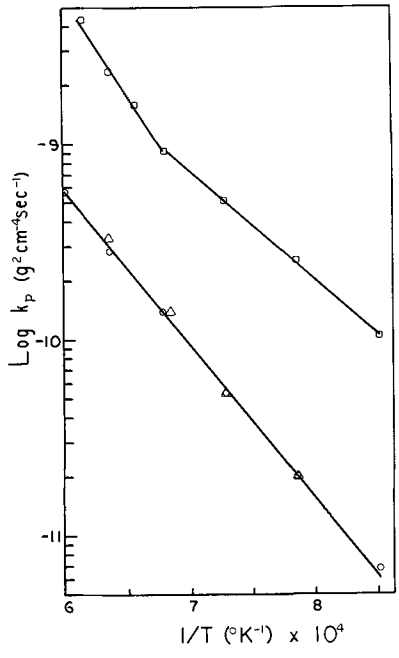

Fig. 10. Temperature dependence of parabolic constants of pure Ni and of a 0.37 w/o Cr alloy; p_{CO_2} = 1 atm; □, 0.37% Cr alloy; △, pure N:(II); ○, pure N:(I) [from ref. (6)].

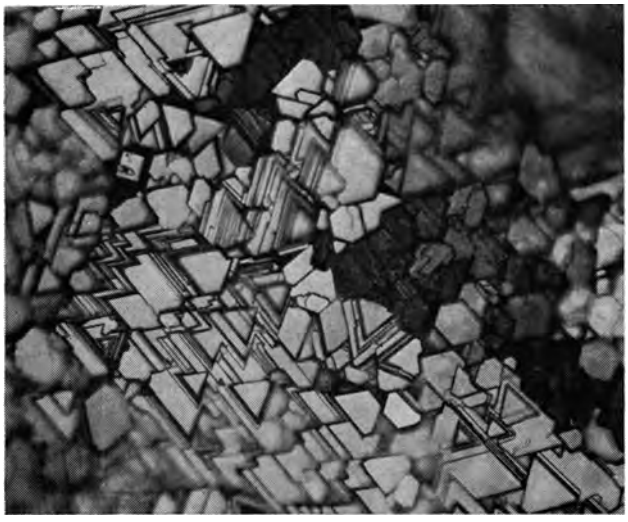

Fig. 11. Surface of pure Ni oxidized at 1300°C in CO_2 of 0.4 atm for 7 hr. Magnification approximately 500X.

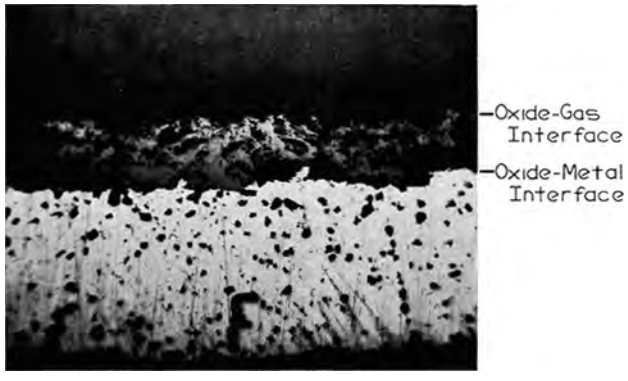

Fig. 12. Cross section of a 0.37 w/o Cr alloy oxidized at 1300°C for 6 hr in 0.3 atm of CO_2. Magnification approximately 400X.

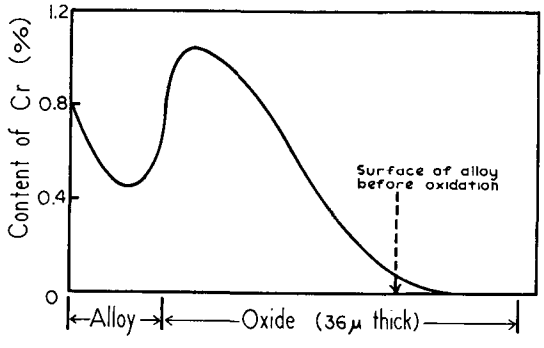

Fig. 13. Distribution of chromium in oxide formed on a 0.37 w/o Cr alloy, 1300°C, 6 hr, 0.3 atm of CO_2.

of nickel oxidized in pure CO_2 was found to be completely covered with well-faceted, coarse oxide grains, as shown in Fig. 11. When pure nickel is oxidized in CO_2-CO gas mixtures, a thin, continuous oxide film consisting of grains of irregular shape was formed. In addition, in some regions there were well-faceted, thick oxide grains. The covering with the well-faceted oxide grains seemed to be high when the content of carbon monoxide was low and the period of oxidation was long. The faceted oxide grains had corners of angles of 60° and 120°, as is seen in Fig. 11. Since nickel oxide is a cubic crystal, the facets are identified as having {111} planes parallel to the substrate.

The cross section of an oxidized alloy is shown in Fig. 12. The scale is thick and distinct oxide layers are not observed. Some apparent voids are present in the oxide. Some second phase (presumably Cr_2O_3) is present in the metal indicating internal oxidation.

Studies by electron microprobe.—In order to investigate the distribution of chromium in oxide film, the cross section of alloy specimens oxidized in 0.3 atm of CO_2 at 1100° and at 1300°C were examined by electron microprobe. A typical distribution of chromium in the oxide is shown in Fig. 13. The concentration of chromium is about three times higher than that in the unoxidized alloy near the metal-oxide interface and is very low at the oxide-gas interface.

The accumulation of chromium near the metal-oxide interface could be a result of the inward movement of particles of chromium oxide as markers. The low concentration at the oxide-gas interface could be due to the low solubility of Cr_2O_3 in NiO and the low diffusivity of chromium ions in NiO, as well as the inward movement of the chromium oxide particles.

Discussion

Nickel oxide is a metal deficit semiconductor exhibiting predominately electronic conductivity *via* electron holes. Excess oxygen may be dissolved in the crystal according to

$$\tfrac{1}{2}\,O_2 = (2-n)\oplus + (Ni_{\square''}\cdot n\oplus) + NiO \qquad [3]$$

where n has values of 0 to 2, and is usually an integer, $Ni_{\square''}$ denotes a cation vacancy and $(Ni_{\square''}\cdot n\oplus)$ denotes a cation vacancy with n trapped electron holes, $\oplus$. Under the usual assumption of dilute solution, the mass action relation is

$$K = [\oplus]^{(2-n)}\left[\left(Ni_{\square''}\cdot n\oplus\right)\right]/p_{O_2}{}^{1/2} \qquad [4]$$

where the brackets denote concentrations. When $n = 0$, the electron holes are completely dissociated from the cation vacancies, and the concentrations of vacancies and holes are proportional to the sixth root of the oxygen partial pressure. Such behavior has been reported at 1300°C for undoped single crystals of NiO by Mitoff (7). At 1000° and 950°C, Wagner and von Baumbach (8) report a pressure dependence of 1/4.5, and between 1200° and 850°C, Eror (9) finds the pressure dependence to be ¼. These data suggest that one electron hole is trapped on each cation vacancy ($n = 1$ in Eq. [4]).

The introduction of Cr_2O_3 in NiO changes the concentration of defects in the crystal. Mass action law consideration (10, 11) shows that the concentration of electron holes is decreased while that of cation vacancies is increased by the addition of Cr_2O_3. Conductivity studies of NiO doped with Cr_2O_3 have been carried out at 800°C by Hauffe and Block (10). Their studies show that the conductivity of doped crystals is 10^3 times smaller than that of the undoped one and therefore the concentration of holes in doped NiO is much smaller. The increase in the concentration of cation vacancies by the introduction of Cr_2O_3 is corroborated by oxidation studies. C. Wagner and Zimens (11) and Zima (12) have found that the parabolic oxidation rate of nickel doped with chromium is greater than undoped nickel. This was also found in the present study. These data show that the cation vacancy concentration in NiO is increased when chromium is added and consequently diffusion of nickel across the reaction product layer is increased during oxidation.

When the oxidation was conducted in pure CO_2, the linear rate constants of pure Ni and of the 0.37 w/o Cr alloy were found to be proportional to p_{CO_2}. It was also found by microscopic observations that the surfaces of specimens are completely covered with coarse grains of oxide during this linear oxidation. These results indicate that the rate-determining step is the surface reaction on the coarse grains of oxide. The surface reaction can be represented by the following elementary steps

$$CO_2 \rightarrow CO + O\ (ads) \qquad [5]$$

$$CO_2 + \ominus \rightarrow CO + O^- \text{ (ads)} \quad [6]$$

$$CO_2 + 2 \ominus \rightarrow CO + O^= \text{ (ads)} \quad [7]$$

If step [5] is predominant, the linear rate should be independent of the activity of electrons in the oxide at the oxide-gas interface, while the linear rate should depend on the activity of electrons, if either step [6] or [7] is predominant.

As discussed above, the concentration of electrons in doped NiO is higher than that in pure NiO. Although the concentration of chromium found at the oxide-gas interface of oxidized alloy is fairly low, a small amount of chromium would be present there. Therefore, the concentration of electrons at the surface of oxide formed on the 0.37 w/o Cr alloy would be higher than that formed on pure Ni. Since the linear rate constants of the 0.37 w/o Cr alloy is much higher than that of pure Ni, a correlation between the linear rate constant and the concentration of electrons is noted. In this case, either one of steps [6] and [7] could be the rate-determining one.

When carbon monoxide was present, the extent of the surface area which was covered with coarse grains of oxide was less than when pure CO_2 was used. Furthermore, the coverage decreased with the increase in CO content. The disagreement of the observed results with Eq. [1] could be due to the incomplete covering with coarse grains, especially since Pettit and Wagner (3) have shown that the linear rate of oxidation is a function of the crystal plane of the oxide that is exposed to the gas.

Summary

The oxidation of nickel and of a 0.37 w/o Cr alloy in reduced pressures of carbon dioxide is linear in the initial oxidation period. The linear rate constants of both metals are proportional to the pressure of CO_2. The rate-determining step is considered to be the surface reaction at the oxide-gas interface. The linear rate constants of the 0.37 w/o Cr alloy are several times larger than those of pure Ni. Thermodynamic consideration of the defects in nickel oxide with or without chromium oxide and the related experiments indicate there is a higher concentration of electrons in doped NiO. Either one of the reaction steps, $CO_2(g) + \ominus \rightarrow O^-$ (ads) + CO(g) or, $CO_2(g) + 2 \ominus \rightarrow CO(g) + O^=$ (ads), is proposed to be rate controlling. Disagreement of the results observed in CO_2-CO mixtures with the equation, $n/A = k' p_{CO_2} - k'' p_{CO}$, is attributed to the fact that the surface was not completely covered with coarse oxide grains which formed during the later stages of linear oxidation.

Acknowledgment

The authors wish to express their sincere thanks to R. Dils of the Advanced Materials and Development Laboratory, Pratt and Whitney Aircraft Company, North Haven, Connecticut, for his electron microprobe studies of the oxide layers. This work was supported by a grant from the Advanced Research Projects Agency through the Materials Research Center of Northwestern University.

Manuscript received April 8, 1965; revised manuscript received Aug. 2, 1965.

Any discussion of this paper will appear in a Discussion Section to be published in the June 1966 JOURNAL.

REFERENCES

1. K. Hauffe and H. Pfeiffer, *Z. Metallk.*, **44**, 27 (1953).
2. F. Pettit, R. Yinger, and J. B. Wagner, Jr., *Acta Met.*, **8**, 617 (1960).
3. F. Pettit and J. B. Wagner, Jr., *ibid.*, **12**, 35 (1964).
4. C. Wagner, Mimeographed notes, Course 3.23, Kinetics in Metallurgy, Massachusetts Institute of Technology (Spring, 1955).
5. F. Pettit and J. B. Wagner, Jr., *Acta Met.*, **12**, 41 (1964).
6. K. Fueki and J. B. Wagner, Jr., *This Journal*, **112**, 384 (1965).
7. S. P. Mitoff, *J. Chem. Phys.*, **35**, 882 (1961).
8. C. Wagner and von Baumbach, *Z. physik Chem.*, **B24**, 59 (1934).
9. N. Eror, Thesis, Northwestern University (1965).
10. K. Hauffe and J. Block, *Z. physik. Chem.*, **196**, 438 (1951).
11. C. Wagner and K. E. Zimens, *Acta Chem Scand.*, **1**, 547 (1947).
12. G. E. Zima, *Trans. Am. Soc. Met.*, **49**, 924 (1957).

The Effect of Nitrogen on the Oxidation of Tantalum at High Temperatures

John Stringer

Metal Science Group, Battelle Memorial Institute, Columbus Laboratories, Columbus, Ohio

ABSTRACT

The effect of nitrogen on the oxidation of tantalum has been studied at 600°, 820°, and 925°C. In all cases, the oxygen partial pressure was close to 360 Torr; nitrogen partial pressures in the range 0 to 250 Torr were investigated. At all three temperatures, nitrogen reduces the rate of oxidation, the effect increasing with temperature. Although the oxidation in pure oxygen follows a linear rate law, with nitrogen present the reaction ceases to be linear. The interpretation of the results in terms of the existing kinetic models is discussed. It is suggested that the pressure drop associated with the flow of the gas through the porous outer scale cannot be neglected.

The oxidation of tantalum at pressures not too remote from atmospheric in the temperature range 500°-950°C has been studied in some detail over the past decade. There is now general agreement on the temperature dependence of the reaction rate, the variation of the reaction rate with oxygen pressure, and the general features of the reaction morphology (the physical distribution of the reaction products in space). In spite of this general agreement, the reaction mechanism remains unclear.

McLintock and Stringer (1) demonstrated that the oxidation of niobium was retarded by the presence of small amounts of nitrogen in the atmosphere, an effect later confirmed by Kolski (2). This effect was somewhat surprising. Mayo *et al.* (3) had oxidized niobium-chromium alloys in mixed atmospheres and found that the presence of nitrogen markedly increased the rate, a result which can easily be rationalized in terms of the Wagner-Hauffe model. It appeared therefore that the effect of nitrogen on the oxidation of

tantalum not only might be interesting in itself, but also might act as an additional experimental variable to assist in the elucidation of the reaction mechanism. This paper describes some results of an investigation of the effect. Before discussing the results of the experiments, it is necessary to describe the reaction of tantalum with oxygen in this temperature range and to outline briefly the kinetic models which have been developed to account for the experimental results.

Reaction of Tantalum with Oxygen

Kinetic Results

All the investigations of the reaction kinetics reported in the literature appear to have been performed on "coupon" specimens, rectangles cut from sheet. For specimens of this shape, the reaction rate over this temperature range is substantially linear

$$w = k_l t + a \qquad [1]$$

where w is the weight of oxygen absorbed at time t, k_l is the linear rate constant, and a is a reaction constant. In some temperature ranges the linear reaction is preceded by a nonlinear step, but this initial reaction is usually short. The empirical rate constant k_l must be regarded with some suspicion, because for coupon specimens the accumulation of oxide on the metal surface is not uniform, thicker layers being formed at the specimen edges and corners. This nonuniformity of oxide accumulation is reflected in the metal removal, which is also greater at the specimen edges and corners, although it has not yet been demonstrated that there is no lateral flow of oxide during the reaction. The nonuniformity is not marked until the temperature exceeds 600°C, and below 950°C the thickness at the corners is only about twice that at the centers of the faces of a specimen. Above this temperature, however, the effect becomes much more marked.

The absolute values of the empirical linear rate constants obtained by different investigations show substantial agreement. Figure 1 shows the rate constants from four investigations, normalized to an oxygen pressure of 760 Torr using the pressure-dependence data of Cowgill (4). Over the range 600°-800°C the temperature dependence of the reaction rate is very small. From 500° to 600°C and from 800° to 950°C, the temperature dependence can be described

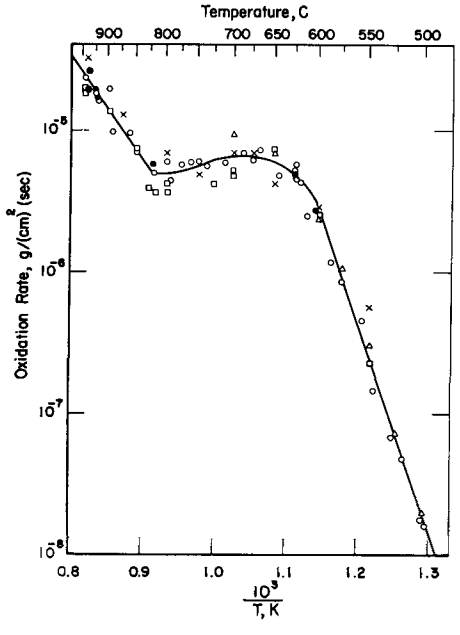

Fig. 1. Arrhenius graph of linear rate constants for the oxidation of tantalum. Rates are normalized to an oxygen pressure of 760 Torr, after Cowgill (4). ○, Cowgill (4); △, Kofstad (5); □, Albrecht (6); x, Peterson (7); •, present investigation.

by Arrhenius relations, although with different activation energies. However, in view of the uncertainty of the absolute significance of the rate constant k_l, this type of analysis is not justified.

The pressure dependence of the rate constant is also well documented. Peterson (7) first studied the pressure dependence over the temperature range 500°-800°C and at pressures from 0.5 through 40 atm. The results could be satisfactorily described in terms of an equation having the form of a Langmuir isotherm

$$k_l = \frac{k_1 k_2 p}{1 + k_2 p} \qquad [2]$$

where p is the oxygen pressure, and k_1 and k_2 are reaction constants. Cowgill and Stringer (8) studied the pressure dependence at lower oxygen pressures and suggested that theirs and Peterson's results would be better described by an equation of the form

$$k_l = k_1 \left(\frac{k_2 p^{1/2}}{1 + k_2 p^{1/2}} \right) \qquad [3]$$

Kofstad (5) has also studied the pressure dependence of the reaction, obtaining results in substantial agreement with Cowgill. More recently, in a study of the oxidation of niobium, McLintock (9) used the empirical equation

$$k_l = k_1 \left(\frac{k_2 p}{1 + k_2 p} \right)^{1/2} \qquad [4]$$

which, although very similar in form to Eq. [3], produced a slightly better fit to his results. Above approximately 750°-800°C, the available experimental results are fitted by the equation

$$k_l = k_3 p^{1/2} \qquad [5]$$

which is in fact the limiting form at high temperatures and low pressures of Eq. [3] and [4].

Morphological Results

The principal reaction product in this range is the low-temperature modification of tantalum pentoxide, Ta_2O_5. In addition, oxygen dissolves in the metal, and specimens cooled and sectioned for metallographic examination after oxidation show light gray, optically active platelets extending into the metal from the metal/oxide interface (5, 10-18). At lower temperatures (below 800°C) these appear to be a metastable tetragonal suboxide, which has been designated TaOz by Kofstad. Above this temperature there is some uncertainty; Kofstad (19) suggests that they may be TaO, with NaCl structure; Vaughan *et al.* (20) have observed similar plates precipitated from supersaturated solid solutions of oxygen in tantalum which were shown to be Ta_2O_5.

The gray suboxide platelets form parallel to prominent crystallographic planes in the tantalum, although there is some disagreement as to which plane they are parallel (10, 14-17).

Although in the very early stages of oxidation more than half the total oxygen absorbed dissolves in the metal, once the linear reaction is well established 95% or more of the oxygen absorbed is present as Ta_2O_5. The pentoxide appears to grow adherently on the metal surface, apparently under considerable compressive stress (21). These stresses eventually cause the oxide to break away from the metal (6), and oxidation starts immediately on the freshly exposed surface. The ruptured oxide forms a detached porous laminated layer. Below 600°C the detached oxide is loose and flaky, falling away from the metal on cooling. However, as the temperature increases, the scale becomes more continuous; at 950°C it has good mechanical strength, although it is still porous.

Figure 2 is a schematic diagram of the cross section of an oxidized tantalum sample after cooling to room temperature.

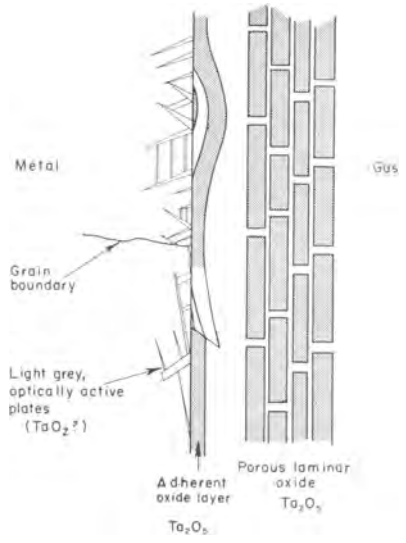

Fig. 2. Schematic drawing of the cross section of an oxidized tantalum specimen after cooling to room temperature.

Effect of Nitrogen

There have been few studies of the tantalum-nitrogen-oxygen system, either kinetic or equilibrium. Schönberg (22) has reported four metallic phases in the pseudobinary TaO-TaN system, and Wasilewski (23) has reported an oxy-nitride having the approximate formula $Ta_2(O_x\ N_{1-x})$. Nitrogen, like oxygen, dissolves interstitially in tantalum. The solubility is approximately 0.5 a/o (atomic per cent) at 950°C, falling to 0.25 a/o at 600°C (24). The oxygen solubility, for comparison, is 2.5 a/o at 950°C and approximately 1.2 a/o at 600°C (10). The diffusion of nitrogen in tantalum is described by the equation

$$D = D_0 \exp(-Q/RT)$$

where $D_0 \cong 0.006$ cm²/sec and $Q = 38.0$ kcal/mole (25) while for oxygen Peterson's (26) analysis of the data leads to $D_0 = 0.02$ cm²/sec, $Q = 27.6$ kcal/mole. At 600°C, this corresponds to a diffusivity of 2.1×10^{-12} for nitrogen and 2.7×10^{-9} for oxygen. At 950°C the figures are 1.1×10^{-9} and 2.5×10^{-7}, respectively. It appears therefore that before the specimen is saturated with oxygen, the amount of nitrogen that will diffuse in will be very small. For example, if oxygen and nitrogen are assumed to be diffusing simultaneously into a tantalum sheet at 950°C in such a manner that the surface concentration is always equal to saturation, then when the sheet has absorbed 90% of all the oxygen it can dissolve, the fractional saturation of nitrogen is 7%. Since the solubility of nitrogen is at least five times smaller than that of oxygen, inward diffusion of nitrogen into the metal is unlikely. Nitrogen apparently does modify the diffusion of oxygen at very low concentrations, but the effect is roughly similar to increasing the oxygen concentration (27).

Albrecht *et al.* (6) have studied the oxidation of tantalum in air but were unable to detect any change in the reaction products. In particular, the lattice spacing of Ta_2O_5 was unaffected, which suggests that any solubility of nitrogen in Ta_2O_5 is small.

Ta_2O_5 has been reported to be an n-type semiconductor containing oxygen vacancies (28), in which case the presence of the higher valent anion N^{3-} should increase the concentration of vacancies. However, Kofstad more recently (29) has reported that the defect structure is more complicated. The oxide is n-type at low oxygen concentrations, but p-type at higher pressures; Kofstad suggests that this implies the presence of reverse Frenkel defects, namely, oxygen interstitials and oxygen vacancies. In this case, the effect of nitrogen cannot be predicted with certainty.

Table I. Manufacturer's analysis of the tantalum sheet

	Ppm
O	70
C	50
N	20
H	5
Cb	300
W	100
Mo	50
Fe	70
Si	<100
Ti	<100
Zr	<100
Al	<50
Mn	<50
Ni	<50
Sn	<50

Tantalum 99.90 min.

It appears therefore that the most likely effect of nitrogen will be to form metallic oxynitrides, presumably at the metal surface. The effect of such new phases on the oxidation reaction again cannot be predicted.

Experimental Materials and Methods

Specimen Preparation

Specimens were cut in the form of rectangles approximately 3 x 0.5 cm from 0.050-in. (0.127 cm) sheet produced by Fansteel. An analysis of the material as supplied by the manufacturer is shown in Table I. Although it appears that the oxidation kinetics are not affected by minor variations in surface preparation, some care was taken to achieve a good surface finish. After hand grinding through 600-grade metallographic polishing papers, the specimens were first chemically polished for 10 min in a 1:2:5 mixture of hydrofluoric, acetic, and sulfuric acids, and then electropolished for 30 sec at a potential of 20v in a sulfuric acid-10% hydrofluoric acid electrolyte at 45°C, using a carbon cathode. After this treatment, the specimen had a bright uniform polish, with a very slight grain-boundary etch. Talysurf measurements indicated that the surface roughness was approximately 2 μin. Immediately prior to the admission of oxygen to the oxidation apparatus, the specimen was vacuum annealed at a pressure of 10^{-6} Torr for 1 hr at reaction temperature. A microhardness traverse of the cross section of a specimen prepared in this way showed that the hardness was quite uniform at 140 DPN, with no tendency for the surface to be harder than the interior. This hardness corresponds closely to that expected on the basis of the manufacturer's analysis.

The specimens had a fine equiaxed grain structure, with a mean grain diameter of approximately 3×10^{-3} cm.

Apparatus

Volumetric methods are preferable to gravimetric for the study of the oxidation of tantalum, because of the loose powdery scale formed at the lower temperatures. Furthermore, volumetric methods are more flexible than gravimetric, although not quite so accurate. Preliminary experiments showed that very little nitrogen was absorbed by the specimen from a mixed atmosphere, so that the problem in a constant-pressure experiment becomes one of replacing the oxygen absorbed from the atmosphere without altering the nitrogen content. This was achieved by bubbling oxygen from the gas buret into the system through a mercury column so that the partial pressures of both gases in the reaction volume remained constant. The total reaction volume is approximately 150 cm³. Details of the design and operation of the apparatus will be published elsewhere.

Metallography and Analysis

In order to prevent the brittle oxide from crumbling during preparation and to prevent "rounding" of the specimen edges, the specimen was mounted between two pieces of glass in epoxy resin and then sectioned, using a diamond cut-off wheel. The cross section was

then prepared mechanically in the conventional manner and lightly etched.

The specimens and scales were analyzed for oxygen and nitrogen, using both vacuum fusion and micro-Kjeldahl methods. In general, the quantity of oxygen was so great that vacuum fusion methods would have been unable to detect quite substantial amounts of nitrogen; for example, in the extreme case of the oxide, 1000 ppm of nitrogen could easily have remained undetected. The micro-Kjeldahl method does not suffer from this disadvantage, but measures the nitrogen directly.

Microhardness traverses on specimen cross sections were performed. Both Knoop and diamond indenters were used, but the diamond indenter gave much more satisfactory results. For most measurements, a 25-g load was used. Because of the fine grain size, it was often difficult to obtain satisfactory microhardness results.

Results

The temperature range 625°-800°C, in which the linear rate constant varies only slightly with temperature, is difficult to interpret and may represent a transition region. Accordingly, for this investigation, temperatures in this range have been avoided. With the dimensions of the present apparatus, the study of very slow reactions is not easy, so low temperatures also have not been studied. These considerations determined three temperatures for detailed study: 925°, 820°, and 600°C. In addition, a small number of oxidations have been performed at 940° and 625°C. The oxygen pressure for most of the experiments was close to 360 Torr; a few experiments were performed with pressures as high as 400 Torr. The nitrogen partial pressure was varied from 10 through 225 Torr.

In addition to these constant-pressure experiments, some "constant volume" experiments of the type described by Stringer and Cowgill (8) were performed at 600° and 625°C.

Effect of Nitrogen at 600°C

The effect of nitrogen on the oxidation rate at 600°C is shown in Fig. 3. The effect is not great; the rate is diminished appreciably by nitrogen, but the appearance of the scale or the suboxide platelets is not appreciably affected. Micro-Kjeldahl analysis shows that neither the scale nor the metal contains any nitrogen. Figure 4 shows a typical cross section of the metal. In addition to the lateral fissures in the scale parallel to the metal surface, the chains of voids through the scale should be noted; these appear in most cases to originate above suboxide plates.

The pressure dependence of the reaction rate in the absence of nitrogen is shown in Fig. 5. As can be seen, the pressure-dependence curve is repeatable and agrees very closely with the constant-pressure results. Furthermore, the curve is reproduced closely from specimen to specimen. The curve drawn through the results is obtained by fitting Eq. [4] through two arbitrary points; the curve shown has

$$k_1 = 3.144 \times 10^{-6}$$

$$k_2 = 3.50 \times 10^{-3}$$

when the rate is given in g/(cm²)(sec). The value of the rate obtained from this equation by setting $p_{O_2} = 760$ Torr is plotted in Fig. 1; it agrees with the results obtained in constant-pressure experiments by other authors.

A number of similar experiments were performed using oxygen-nitrogen atmospheres. In this case, although the curve could be repeated over the same specimen, less satisfactory agreement was obtained with the constant-pressure results. This is scarcely surprising, since as Fig. 3 shows, the rate curves in the mixed atmospheres are not rectilinear. The effect of nitrogen is to increase k_1 and decrease k_2; when $p_{N_2} = 25.6$ Torr, $k_1 = 3.600 \times 10^{-6}$, and $k_2 = 2.00 \times 10^{-3}$; when $p_{N_2} = 112$ Torr, $k_1 = 4.659 \times 10^{-6}$, and $k_2 = 0.873 \times 10^{-3}$.

Effect of Nitrogen at 820°C

As Fig. 6 shows, the effect of nitrogen is much more marked at 820°C. Again, analysis of the scale and the metal showed no detectable amounts of nitrogen. Careful examination of specimen cross sections failed to show any difference in the suboxide morphology as the nitrogen content of the atmosphere increased. Figure 7 shows microhardness traverses performed on three specimens oxidized for the same length of time, but with different amounts of nitrogen present. The hardness profile is the same in each case, indicating that nitrogen does not modify the oxygen solution process.

It seemed possible that the curvature of the rate plots when nitrogen was present might be due to a slow approach to a new linear rate. If this is so, it follows that the slope of the curve, dw/dt, should

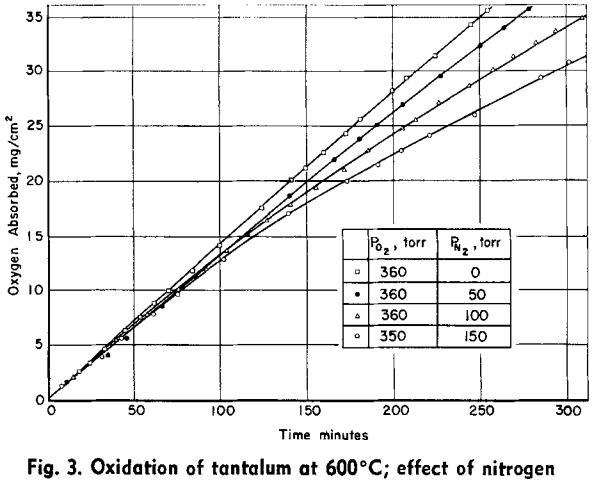

Fig. 3. Oxidation of tantalum at 600°C; effect of nitrogen

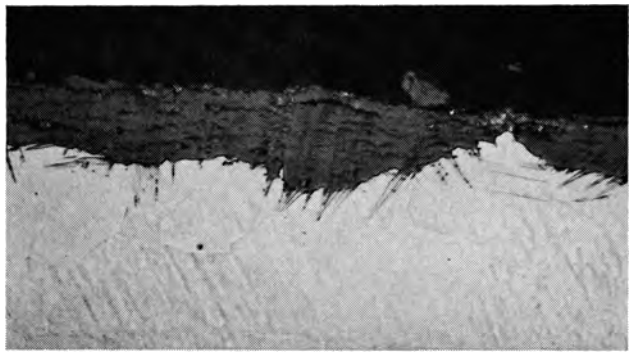

Fig. 4. Cross section of specimen oxidized for 400 min at 600°C; p_{O_2} = 365 Torr; p_{N_2} = 100 Torr.

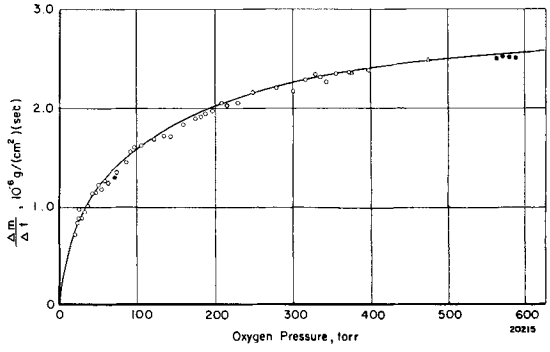

Fig. 5. Oxidation of tantalum at 600°C; effect of oxygen pressure. Full curve drawn according to the equation $\Delta m/\Delta t = 3.144 \times 10^{-6} [(3.50 \times 10^{-3} p)/(1 + 3.50 \times 10^{-3} p)]^{0.5}$ g/cm²-sec. ○, first cycle; ●, second cycle, both constant volume data; △, constant pressure data.

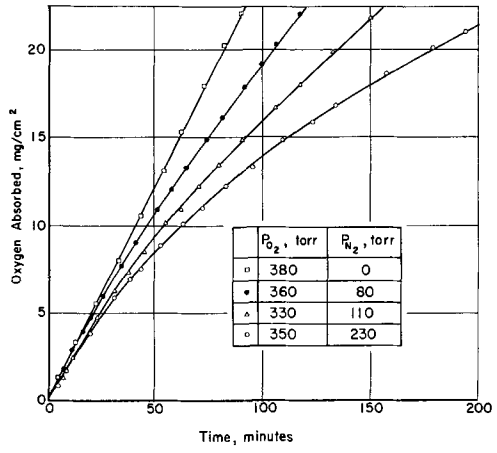

Fig. 6. Oxidation of tantalum at 820°C; effect of nitrogen

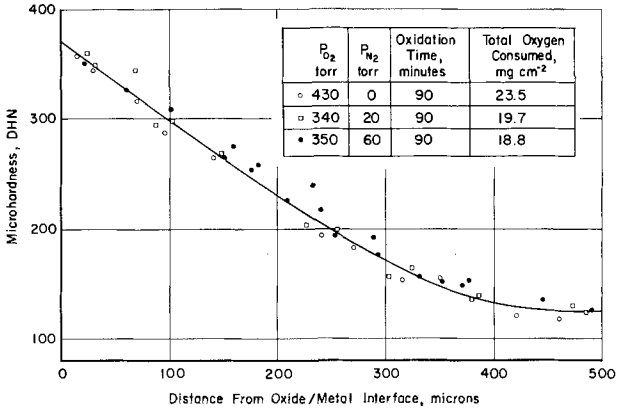

Fig. 7. Oxidation of tantalum at 820°C; microhardness traverses of oxidized specimens.

approach a constant value as t approaches infinity. Such a tendency is difficult to see graphically, but it follows that if dw/dt is plotted against the reciprocal of time, so that $t = \infty$ is the ordinate, a rate curve of any form tending to a straight line at long times should intersect the ordinate horizontally at a positive value. A graph of the rate curves at 820°C plotted in this fashion is shown in Fig. 8. It is clear that for partial pressures of nitrogen in excess of 50 Torr this interpretation is untenable. It cannot be said that the rate curves become linear at any time for nitrogen contents greater than this in the reaction times studied in this investigation.

Cowgill has demonstrated that at this temperature and in this pressure range the rate is proportional to

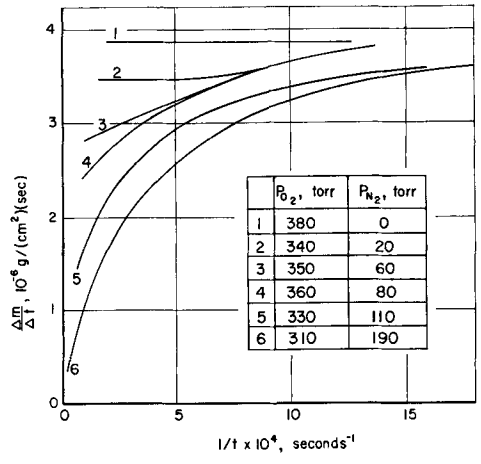

Fig. 8. Oxidation of tantalum at 820°C; effect of nitrogen

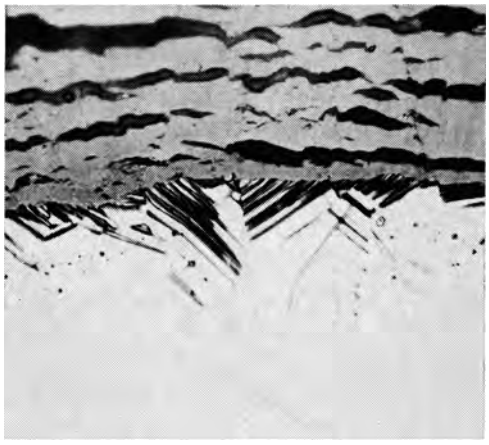

Fig. 9a. Cross section of specimen oxidized for 345 min at 820°C, showing adherent oxide layer; $p_{O_2} = 300$ Torr; $p_{N_2} = 160$ Torr. Normal illumination. Magnification 750X.

Fig. 9b. Same as Fig. 9a except with polarized light

the square root of oxygen pressure; points calculated on this basis from runs performed without nitrogen are included in Fig. 1. Again, the agreement with previous results is very good.

Apart from the change in the oxidation rate, nitrogen produced two effects. The scale appeared to adhere to the metal more strongly as the nitrogen increased, and (for a given weight of scale) the inequality in development of the scale increased, the edge growth becoming more pronounced. It was difficult to determine whether the adherent layer thickness (w_c) increased as the nitrogen content increased, since sufficient scale adhered only to specimens oxidized in atmospheres

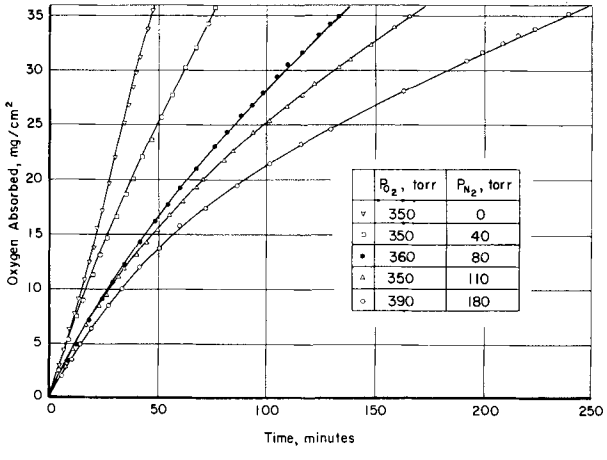

Fig. 10. Oxidation of tantalum at 925°C; effect of nitrogen

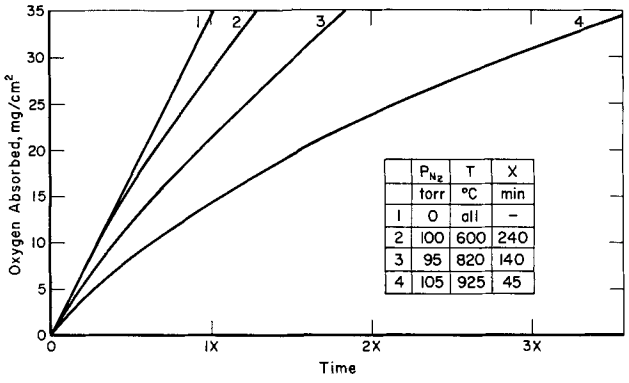

Fig. 11. Relative effect of 100 Torr nitrogen on the oxidation of tantalum at three temperatures; p_{O_2} = 360 Torr. X is chosen so that the curves p_{N_2} = 0 superimpose at all three temperatures.

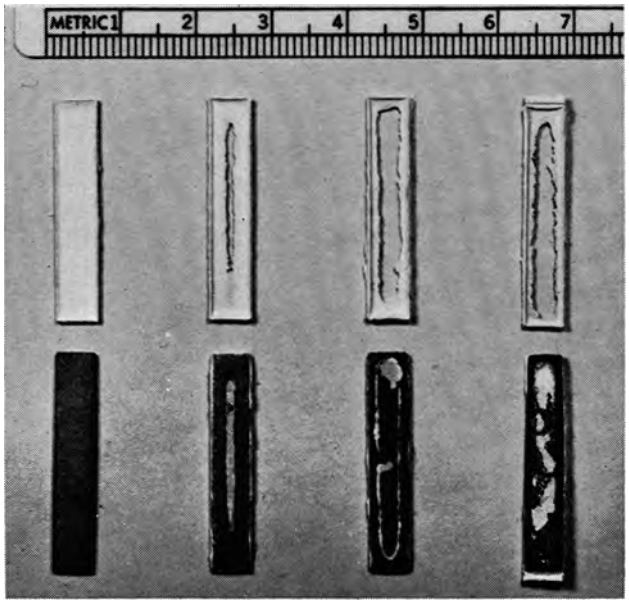

Fig. 12. Oxidation of tantalum at 925°C. The white scales (upper) have separated from the specimens (lower) on cooling. The holes in the separated layers correspond to the still-adhering oxide. All specimens were oxidized in an oxygen partial pressure of approximately 360 Torr to a total weight gain of 45 mg/cm². From left to right, the nitrogen partial pressures and oxidation times, respectively, are: 0 Torr, 54 min; 40 Torr, 100 min; 80 Torr, 180 min; and 180 Torr, 325 min.

containing a significant amount of nitrogen. The adherent layer is shown in Fig. 9a and b for a specimen oxidized in an atmosphere containing 160-Torr nitrogen. Tentatively, it appears likely that the thickness is less on specimens oxidized in atmospheres containing less nitrogen, but this conclusion is based on less than satisfactory metallographic evidence.

Effect of Nitrogen at 925°C

Figure 10 shows the effect at 925°C. Figure 11 shows the effect of 100 Torr of nitrogen on the rate at the three temperatures. The time scale is normalized so that the rate curves for pure oxygen at all three temperatures superimpose. This time the effect of the nitrogen on the oxide morphology and adherence is sufficiently marked to be evident on a photograph; Fig. 12 shows four specimens oxidized to the same total weight gain in atmospheres containing respectively 0-, 40-, 80-, and 180-Torr nitrogen.

Once again, the results in the absence of nitrogen are in excellent agreement with earlier investigations and are included in Fig. 1.

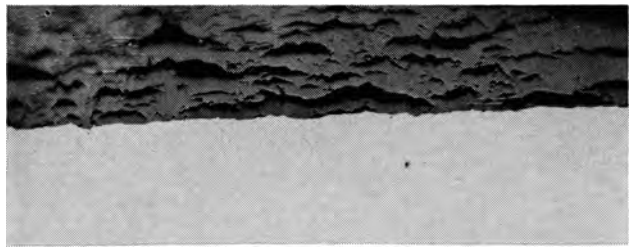

Fig. 13a. Unetched cross section of a specimen oxidized for 106 min at 925°C, showing adherent oxide layer; p_{O_2} = 400 Torr; p_{N_2} = 0. Normal illumination. Magnification 200X.

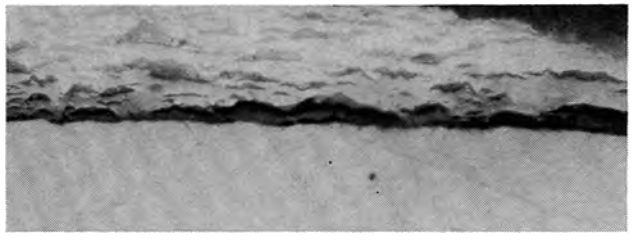

Fig. 13b. Same as Fig. 13a except with sensitive tint illumination

Fig. 14. Cross section of specimen oxidized 185 min at 925°C; p_{O_2} = 355 Torr; p_{N_2} = 110 Torr.

Now, definite differences appear in the scale and platelet morphology. Figures 13a and b show the adherent oxide layer in the absence of nitrogen. Figure 14 shows a specimen oxidized in an atmosphere containing 110-Torr nitrogen. In addition to the dark gray Ta_2O_5 and the light gray optically active platelets, large amounts of a light gray phase can be seen. Although this can only be distinguished with difficulty from the light gray suboxide in this figure, it has little or no optical activity in polarized light. Attempts to identify the phase have failed so far. It is present only in the scale formed on the centers of the large specimen faces, where the scale is adhering; the adherent scale looks dark on the specimen. This specimen contains significant amounts of nitrogen; it is likely therefore that the light gray phase is an oxynitride.

Discussion

A linear oxidation rate may be attained in two ways. The rate-controlling process may be an interface reaction whose rate is independent of the oxide thickness; in this case the rate is truly linear on a microscopic scale. Alternatively, the mechanism may be one of the so-called "paralinear" processes. Suppose that the oxide grows on the metal surface, its rate of growth being determined by the diffusion of one or both of the reactants through the oxide layer. The rate of growth of this adherent layer will in fact be parabolic

$$w^2 = k_p t + a \qquad [6]$$

where k_p is the parabolic rate constant. If the compressive growth stresses in the layer are high enough, the layer will fail, either in shear or by blistering from the metal surface, when the scale reaches a critical thickness ω_c. If the failure process is such that pores or other passage are formed through the separated layer, so that it presents little obstacle to the inward flow of molecular oxygen, a new adherent oxide layer will again grow parabolically on the freshly exposed surface. A thickness, ω_c, is added to the porous outer oxide layer every t_c seconds, where

$$t_c = \frac{\omega_c^2}{k_p}$$

and the over-all rate is therefore linear, with

$$k_l = \frac{\omega_c}{t_c} = \frac{k_p}{\omega_c} \qquad [7]$$

Of course, this description coincides exactly with the observed morphology of the oxidation process. But as Murphy (30) pointed out in 1923, even a coherently forming scale will grow according to a linear rate law if one of the interface processes is slower than the transport process; the scale morphology does not assist, therefore, in determining the reaction mechanism.

However, it is well established that k_l is a function of pressure and, at low enough pressures over this temperature range, varies as the square root of the oxygen pressure. Consequently, if the paralinear mechanism is to account for the reaction rate, either or both of k_p and ω_c must depend on the oxygen pressure. If Ta_2O_5 is an oxygen-vacancy n-type semiconductor, Wagner's mechanism would imply that k_p would be independent of the oxygen pressure provided

$$p_{O_2} >> p_{eq} \qquad [8]$$

where here p_{eq} is the equilibrium pressure for the reaction

$$\frac{4}{5}Ta + O_2 \rightarrow \frac{2}{5}Ta_2O_5$$

At 950°C, p_{eq} is approximately 10^{-25} atm, so that the inequality is satisfied for all attainable pressures. It is difficult to see how ω_c can depend directly on the oxygen pressure, since ω_c should be a function of the growth stresses, the scale adherence, and the scale fracture strength. None of these should depend strongly on the oxygen pressure at low pressures. However, if, as Kofstad suggests, Ta_2O_5 is n-type at low oxygen concentration and p-type at higher, it follows that the adherent scale layer will have an n-p or n-i-p junction within it. The relative position of this boundary, and hence the defect transport rate, will then be pressure dependent. Unless a most unusual ionization is postulated for the mobile species, it is difficult to see how the pressure dependence of k_p can exceed $p^{1/4}$. However, although ω_c is probably not a function of oxygen pressure, it is likely to be a function of the oxidation rate and hence of k_p: if one assumes that, as the rate falls, ω_c increases, then this will magnify the apparent pressure dependence of k_l (32). In fact, there is some evidence that ω_c does increase as the oxidation rate decreases (at constant temperature) in both tantalum (31) and niobium (32). Therefore, it is not impossible that a paralinear process could be compatible with the observed pressure dependence.

A linear reaction rate involving a slow interface process was suggested by Cowgill and Stringer (4, 8). They pointed out that, in order to account for the pressure dependence, the interface must be a solid/gas interface and that, since x-ray evidence suggested that Ta_2O_5 grows coherently on the metal surface, the only available interface was that between the coherent Ta_2O_5 layer and oxygen. In particular, they suggested that the slow step was one of the reactions

$$O_2)_{ads} + 2\,O^{2-}\,\square/Ta_2O_5 + 4e \rightarrow 2\,O^{2-}/Ta_2O_5$$

or

$$O)_{ads} + O^{2-}\,\square/Ta_2O_5 + 2e \rightarrow O^{2-}/Ta_2O_5 \qquad [9]$$

However, it is difficult on the basis of a single process to account for the observed temperature dependence of the reaction rate. In the oxidation of niobium, the change in temperature dependence is apparently associated with the disappearance of suboxide plates, and so it is tempting to locate the rate-controlling reaction at a suboxide/oxygen interface and to postulate that at high temperatures the suboxide either vanishes or changes form. Two models in these terms have been postulated, by Kofstad (19) and by Ong (33). However, no good evidence of the existence of these interfaces has so far been produced; metallography always indicates an adherent Ta_2O_5 layer on the surface of both the metal and the suboxides.

Below 750°C, the results of Peterson (7) and Kofstad (5) are reasonably well fitted by Langmuir adsorption isotherms of the form of Eq. [3] or [4]. However, because of the multiple-specimen technique used by these authors, the fit is less than wholly convincing. For a given pressure range, at high temperatures the Langmuir isotherm becomes

$$\theta \sim k_1 k_2 p^{1/2}$$

where θ is the surface coverage; at low temperatures it becomes

$$\theta \sim k_1$$

so that only in an intermediate temperature range will the results have the form of Eq. [4] and [5]. Most authors are limited to two or three orders of magnitude change in pressure, and for the oxidation of tantalum this restricts the intermediate temperature range to about 100°C. Ong (33) has collected the results of a number of authors over a much wider pressure range, and while the results are compatible with a Langmuir-type behavior, the scatter in the data makes the identification less than certain. Ong's data suggest that for the pressure range attainable in the present apparatus, the optimum temperature for obtaining a Langmuir-type curve should be 600°C; as Fig. 5 shows, the fit to the McLintock Eq. [4] is very good and agrees well with the available results in the literature. On the basis of these results, it seems likely that, at least below 625°C, the oxygen concentration at the reaction interface is determined by an equilibrium adsorption process.

It is important to stress that this adsorption step is compatible with both the linear and paralinear mechanisms; both are demonstrably dependent on the oxygen concentration, and in either case this may be enhanced by adsorption.

Effect of Nitrogen

If nitrogen dissolved in Ta_2O_5, replacing O^{2-} ions on the anion lattice and forming N^{3-} ions, one would expect an increase in the concentration of oxygen vacancies. This should increase the rate of diffusion across the scale for the paralinear model, thus increasing k_p; if the surface reaction in the linear model is a reaction such as [9] the increase in vacancy concentration should also increase this rate.

Both Smith (34) and Kling (35) have remarked that alloy elements which would be expected to increase the oxygen vacancy concentration in Nb_2O_5 nevertheless decrease the linear oxidation rate of niobium. Smith suggests that the increase in vacancies makes plastic deformation of the scale easier, thus increasing ω_c. Kling suggests that the vacancies result in a reduction in the lattice parameter of the oxide, thus improving the scale/metal fit; again, the effect is to increase ω_c. However, Ashbee and Smallman (36) have shown that in the case of TiO_2 increasing the concentration of oxygen vacancies makes the material less, rather than more, ductile; and no change in lattice parameter of the Ta_2O_5 due to the nitrogen has been

detected. In spite of this, nitrogen apparently does improve scale adherence. The effect may be indirect, however; it is known that reducing the rate increases ω_c and hence the scale adherence, so that the improved adherence may be a consequence of the slowing down of the rate, not a cause of it.

Since there is good reason to believe that the oxygen is adsorbed on an interface, nitrogen may affect the surface concentration of oxygen. Nitrogen may be preferentially adsorbed, so that fewer sites are available for oxygen. The effect of this would be to reduce the oxygen concentration and thus the rate. However, in this case the effect should increase as the temperature decreases, as the surface concentration of the adsorbate increases. In fact, the reverse is true. Further, one would expect the establishment of a new linear rate, but in fact the rate becomes nonlinear.

The slow step in the linear model is a surface reaction, and it is therefore possible that a necessary step in the reaction is the formation of a complex of the form $O^{2-}/Ta_2O_5 \cdot O_{ads}$ prior to the actual incorporation. Nitrogen could result in the disruption of this complex by mechanical bombardment with nitrogen molecules and thus, without affecting the adsorption process or the surface oxygen concentration, reduce the rate by reducing the complex lifetime. The chances of this are slight if the surface coverage is noticeably higher than the atmospheric concentration of gas, but they increase relatively as the surface concentration diminishes. The effect would therefore increase with temperature, in agreement with experiment. However, once again, one would expect the establishment of a new linear rate; this model does not lead to a nonlinear process.

The literature survey suggests that the principal effect of nitrogen should be to modify the suboxides; in fact, at 925°C a phase which appears to be an oxynitride is formed. This could affect the oxide fit at the metal surface, and hence modify ω_c. Further, if with Kofstad and Ong one supposes that the reaction interface is that between the atmosphere and a suboxide, a change in rate is not unexpected. The effect of nitrogen on the suboxides is clearly greater at higher temperatures, and although no nitrogen was detected in the specimens oxidized at lower temperatures, the volume fraction of the suboxides is sufficiently small that they still could contain a significant amount of nitrogen. While one would again expect a new linear rate, this is no longer certain; the composition of the suboxynitrides could change as the reaction proceeds. However, as noted above, the metallographic evidence casts some doubt on the existence of oxygen/suboxide interfaces.

Gas-Flow Model

The rate-controlling reaction, irrespective of its nature, occurs in the general vicinity of the metal surface, inside the porous laminated outer scale. It follows that the oxygen pressure p_1 "seen" by the reaction is lower than the external pressure p_o. The difference

$$\Delta p = p_o - p_1$$

is determined by the oxygen flux required by the reaction and the permeability of the outer scale. Since the outer scale is obviously fairly porous, typically containing about 30 v/o (volume per cent) voids, it is customary to assume that Δp is very small and to ignore it. Further, if it were not small, Δp should increase as the porous scale layer thickens, thus leading to a nonlinear reaction rate for constant p_o. However, most of the voids in the scale are the fissures between the scale laminations parallel to the metal surface, and these do not contribute to the permeability through the scale. Further, although the scale is formed in compression on the metal surface, it breaks away to a strain-free position and thereafter is pushed outwards by the newly forming layers. The outer layers of the scale thus fail in tension, with fractures lying normal to the metal surface. The permeability of the porous scale is thus determined by the effectively constant thickness unfailed layer; as a result, the oxidation rate would be linear, and Δp may not be small. Normally, this difference between the external pressure and the reaction pressure will not be evident.

However, if nitrogen is introduced into the atmosphere, the inward-flowing oxygen will transfer momentum to the nitrogen molecules by ordinary collision processes (provided flow through the scale is Poiseuille rather than Knudsen), thus driving it toward the metal surface. The nitrogen pressure between the reaction zone and the porous scale will therefore increase above the external value. This partial pressure difference will produce a dynamic flow of nitrogen outwards, and eventually the system will approach a steady state. Now, however, the transfer of momentum from the oxygen to the nitrogen (and from the outward-flowing nitrogen to the oxygen) will increase the resistance to inward flow of oxygen, thus decreasing the apparent permeability of the scale, increasing Δp, and thus (for a constant external partial pressure of oxygen) decreasing the oxygen pressure at the reaction interface. Again, since this is a steady-state situation, one would expect a new linear rate. However, it appears probable that ω_c increases with decreasing rate; this should lead to a decrease in scale permeability as the rate falls, which again should magnify the effects described above. The rate will therefore become nonlinear. Plainly, the effect also should increase more or less progressively as the nitrogen content increases, in agreement with experiment. Finally, it is clear that the scale permeability decreases as the temperature increases, so that the effect of a given amount of nitrogen also should be greater at higher temperatures. The model is then

1. The reaction process, which may be any process capable of giving a linear or square root pressure dependence, is located in the general vicinity of the metal/suboxide/adherent oxide zone, inside the outer porous oxide.
2. The oxygen concentration "seen" by the reaction is that inside the porous scale and may be enhanced by an adsorption process.
3. The oxygen pressure inside the porous scale is appreciably less than that outside; the difference may not be great, but it is not negligible.
4. Gas flow through the relatively small pores normal to the scale laminations takes place by Poiseuille flow.
5. Nitrogen slows down the rate simply by absorbing momentum, although the effect is enhanced by the rate dependence of the porous scale permeability.

Since the effect of nitrogen is simply to accept momentum, it follows that the model predicts that

1. Argon, since its molecular weight is similar to that of both oxygen and nitrogen, should have roughly the same effect as nitrogen.
2. Helium should also slow the rate down, but because of its smaller weight, the effect should be appreciably less.

These predictions have not been fully checked yet. Although no thermal separation of O_2-N_2 and O_2-Ar atmospheres in the apparatus can be expected, some separation of O_2-He atmospheres will take place, so that the results of these last experiments must be treated with caution. The results of preliminary experiments at 925°C are shown in Fig. 15. As can be seen, the effect of argon is almost the same as that of nitrogen. Varying argon pressures have been used, and in all cases the results lie very close to the results obtained with nitrogen. Relatively few experiments with O_2-He atmospheres have so far been performed, but the results to date are in agreement with the curve shown. A more detailed study of the effect of inert gases will be described in a later paper.

The effect of the inert gases seems to confirm the model. Unfortunately, the model does not help to de-

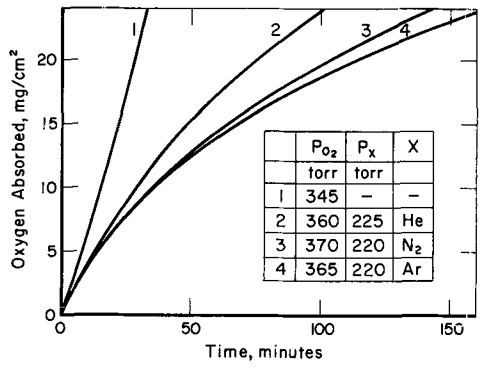

	P_{O_2} torr	P_X torr	X
1	345	–	–
2	360	225	He
3	370	220	N_2
4	365	220	Ar

Fig. 15. Effect of 220 Torr of helium, argon, and nitrogen on the oxidation of tantalum at 925°C; $p_{O_2} \simeq 360$ Torr.

termine the nature of the rate-controlling process. However, since the effect at 925°C can be interpreted entirely in gas-flow terms, although nitrogen clearly modifies the suboxide phases, it does suggest that the Ong mechanism involving suboxides is incorrect.

Clearly, the idea that the rate of oxidation is determined by the pressure the reaction "sees" explains the observed more rapid growth of oxide at the edges and corners of a rectangular specimen, since at these positions fractures penetrate the scale close to the metal. This aspect of the hypothesis is also currently being tested, and results will be published later.

Finally, at 600°C the outer scale is relatively loose and flaky, but at 800°C it is strong and "sintered"; it is possible therefore that since the permeability of the scale clearly falls drastically between these temperatures, the change in temperature dependence may be explainable in this way. This last point has been made in the case of the oxidation of niobium by Aylmore *et al.* (37).

Essentially similar results have been observed in the reduction of hematite by hydrogen by McKewan (38); there, however, the rate remains essentially linear. Helium has slightly less effect on the reduction than nitrogen. These results are well fitted by a modified adsorption equation.

Conclusions

It appears that the pressure drop associated with the flow of gas through the porous outer scale in the oxidation of tantalum in the temperature range 600°-950°C cannot be ignored. Further, the critical scale thickness apparently increases as the rate decreases. These properties account for the observed effect of nitrogen on the oxidation rate and predict that the effect of argon will be much the same. Preliminary experiments confirm this prediction. Although the results do not help much in elucidating the nature of the rate-controlling process, they suggest that models involving suboxide surface reactions are incorrect.

Acknowledgments

Thanks are due to a number of people who have sent me their results and comments on the model described in this paper, most notably Dr. John Sheasby of McMaster University, Hamilton, Ontario, and Dr. William McKewan of the Edgar Bain Laboratories of United States Steel, Monroeville, Pa. Preliminary experiments were performed by Dr. M. G. Cowgill and Dr. C. H. McLintock at the University of Liverpool, England. Mr. R. O. Dodds and Mr. C. R. Rarey assisted with the experimental work, and the metallography was done by Mr. C. H. Brady. The research was supported by Battelle Memorial Institute.

Manuscript received May 17, 1965; revised manuscript received July 30, 1965.

Any discussion of this paper will appear in a Discussion Section to be published in the June 1966 JOURNAL.

REFERENCES

1. C. H. McLintock and J. Stringer, *J. Inst. Metals*, **90**, 190 (1962).
2. T. L. Kolski, *Trans. ASM*, **55**, 1020 (1962).
3. G. T. J. Mayo, W. H. Shepherd, and A. G. Thomas, *J. Less-Common Metals*, **2**, 223 (1960).
4. M. G. Cowgill, Ph.D. Thesis, University of Liverpool, 1963.
5. Per Kofstad, *J. Inst. Metals*, **90**, 253 (1962).
6. W. M. Albrecht, W. D. Klopp, B. G. Koehl, and R. I. Jaffee, *Trans. AIME*, **221**, 110 (1961).
7. H. C. Peterson, W. M. Fassell, and M. E. Wadsworth, *J. Metals*, **6**, 1038 (1954).
8. M. G. Cowgill and J. Stringer, *J. Less-Common Metals*, **2**, 233 (1960).
9. C. H. McLintock and J. Stringer, *ibid.*, **5**, 278 (1963).
10. E. Gebhardt and H. D. Seghezzi, *Z. Metallkunde*, **50**, 521 (1959).
11. N. Norman, *J. Less-Common Metals*, **4**, 52 (1962).
12. N. Norman, P. Kofstad, and O. J. Krudtaa, *ibid.*, **4**, 124 (1962).
13. Per Kofstad, *J. Inst. Metals*, **91**, 209 (1962-1963).
14. R. Bakish, *This Journal*, **105**, 71, 524 (1958).
15. J. V. Cathcart, R. Bakish, and D. R. Norton, *ibid.*, **107**, 956 (1960).
16. R. E. Pawel, J. V. Cathcart, and J. J. Campbell, *ibid.*, **107**, 956 (1960).
17. R. E. Pawel, J. V. Cathcart, and J. J. Campbell, *Acta Met.*, **10**, 149 (1962).
18. G. Brauer, H. Müller, and G. Kühner, *J. Less-Common Metals*, **4**, 533 (1962).
19. P. Kofstad, Tidskrift for Kjemi, Bergvesen og Metallurgi, **6**, 127 (1963).
20. D. A. Vaughan, O. M. Stewart, and C. M. Schwartz, U. S. AEC Rep (1960), BMI-1472, 70 pp.
21. R. E. Pawel, J. V. Cathcart, and J. J. Campbell, *This Journal*, **111**, 551 (1963).
22. N. Schönberg, *Acta Chem. Scand.*, **8**, 620 (1954).
23. R. J. Wasilewski, *Trans. AIME*, **221**, 647 (1961).
24. E. Gebhardt, H. D. Seghezzi, and W. Dürrschnabel, *Z. Metallkunde*, **49**, 577 (1958).
25. R. W. Powers and M. V. Doyle, *J. Appl. Phys.*, **30**, 514 (1959).
26. N. L. Peterson, WADD T-R 60-793 (March 1960).
27. R. W. Powers and M. V. Doyle, *Acta Met.*, **4**, 233 (1956); and *Trans. AIME*, **215**, 655 (1959).
28. W. Hartmann, *Z. Physik*, **102**, 709 (1936).
29. Per Kofstad, *This Journal*, **109**, 776 (1962).
30. Murphy, *J. Inst. Met.*, **29**, 586 (1923), (in discussion of paper by N. B. Pilling and R. E. Bedworth).
31. J. Stringer, Unpublished results.
32. J. Sheasby, Private communication.
33. J. N. Ong, Jr., *Trans. AIME*, **224**, 991 (1962).
34. R. Smith, *J. Less-Common Metals*, **2**, 191 (1960).
35. H. P. Kling, "Technology of Columbium (Niobium)," B. W. Gonser and E. M. Sherwood, Editors, p. 92, John Wiley & Sons, New York (1958).
36. K. H. G. Ashbee and R. E. Smallman, *Proc. Roy. Soc.*, **274A**, 195 (1963).
37. D. Avlmore, S. Gregg, and W. Jepson, *This Journal*, **107**, 495 (1960).
38. W. McKewan, Private communication.

Erratum

In the Extended Abstract book of the Electrothermics & Metallurgy Division for the Buffalo Meeting, Oct. 10-14, 1965, there is an error in Abstract 150, "The Interaction of Iodine with Zircaloy-2" by H. S. Rosenbaum. Delete the last sentence of the first paragraph, the sentence beginning "Since iodine . . ." and ending, ". . . clad with zirconium alloys."

Rotating Disk Study of the Dissolution of Zirconium in $HF-H_2SO_4$

R. E. Meyer and Sandra Massey Zettl[1]

Chemistry Division, Oak Ridge National Laboratory, Oak Ridge, Tennessee

ABSTRACT

The dissolution of crystal bar zirconium in mixtures of hydrofluoric acid and sulfuric acid has been investigated by use of a rotating disk electrode system. The presence of the sulfuric acid in relatively large amounts considerably reduces the rates as compared to solutions of hydrofluoric acid and nitric acid. In addition, the reaction, which is normally first order, changes to second order in the presence of large amounts of sulfuric acid. A kinetic equation which accounts for these results can be derived if it is assumed that both the hydrofluoric acid and the sulfate ion are adsorbed.

Of the common aqueous dissolution media, only solutions of HF significantly attack zirconium metal. Therefore this reaction has been the subject of a number of investigations.

Smith and Hill (1) investigated the dissolution of Zr in various aqueous solutions containing HF by measuring the buildup of ^{95}Zr in a solution that was circulated past a radioactive Zr electrode. They reported that the rate of dissolution is controlled solely by the rate of mass transfer of undissociated HF to the electrode. Their results also showed that the reaction proceeds with a rate of hydrogen evolution exactly equivalent to the rate of dissolution of the metal.

Dissolution rates in mixtures of HNO_3 and HF were determined by Vander Wall and Whitener (2) by use of a tracer method similar to that used by Smith and Hill. According to their results, the reaction is first order with respect to HF and has an activation energy of 6.4 kcal/mole.

Measurements have also been reported by Straumanis, James, and Neiman (3) and by James, Custead, and Straumanis (4). These investigators determined the rate of dissolution by determining the volume of the hydrogen gas evolved. They proposed that the reaction is the result of direct chemical attack of HF molecules on the metal.

The electrochemistry of this reaction was investigated by use of steady state and transient polarization techniques (5) and by use of the rotating disk electrode (6). These investigations show that the reaction is electrochemical in nature and that it proceeds by the continuous formation and dissolution of a film. Rate constants for the surface reaction between HF and the film were determined by the rotating disk study (6).

The electrochemistry of the reaction was investigated by Gilman and Kolotyrkin (7), who also conducted polarization experiments and concluded that the reaction proceeds electrochemically by the formation and dissolution of a film.

In the rotating disk study of the dissolution of zirconium (6), the rate constants of the surface reaction between HF and the zirconium in mixtures of HF and HNO_3 were determined. Interpretation of the results was relatively simple, since the reaction was first order with respect to HF. When the same experiments were done with H_2SO_4 instead of HNO_3, the rates were much lower than the rates in HNO_3, all other factors being equal. Because all factors were identical except that H_2SO_4 was substituted for HNO_3, it appeared that this might be an example of a specific anion effect on a reaction which supposedly was under the influence only of HF. For this reason, a more complete study of the $HF-H_2SO_4$ system was undertaken with the rotating disk electrode. These measurements included the determination of the capacity of the electrodes as a function of rotational velocity.

[1] Oak Ridge Institute of Nuclear Studies Summer Student Trainee (1963) from Texas Wesleyan College, Fort Worth, Texas.

Theory

Derivations of the equations applicable to the rotating disk have been summarized by Levich (8). The current at a rotating disk is given by the expression

$$I = nFSA(C - C_i)\omega^{1/2} \qquad [1]$$

where

$$A = 0.62\, D^{2/3}\gamma^{-1/6}$$

and S is the electrode area, C is the concentration of the reactant in the bulk of the solution, C_i is the concentration of the reactant at the interface, ω is the rotational velocity (rad/sec), D is the diffusion coefficient, and γ is the kinematic viscosity. If the reaction at the surface follows the equation

$$I = nFSk\,C_i^m \qquad [2]$$

then for $m = 1$ (first order)

$$\frac{1}{I} = \frac{1}{nFSk\,C} + \frac{1}{nFSA\omega^{1/2}\,C} \qquad [3]$$

If the reaction is first order, plots of $1/I$ *vs.* $1/\omega^{1/2}$ will be linear, and the rate constant k can be determined by extrapolation of the line to infinite frequency of rotation ($1/\omega^{1/2} \rightarrow 0$).

The treatment for the cases in which the order is not equal to unity is more complicated, and in general, the constant A must first be evaluated in order to determine k. If the reaction is second order ($m = 2$), the current will be given by the following expression

$$I = \frac{A^2\,nFS\omega}{4k}\left[\left(1 + \frac{4kC}{A\omega^{1/2}}\right)^{1/2} - 1\right]^2 \qquad [4]$$

This equation has been plotted for values of C, A, and k which correspond roughly to the values observed in the work here. These plots are illustrated in Fig. 1 and 2. At low values of ω the plots are linear, but they tend to curve at higher values of $\omega^{1/2}$. For the lowest value of C, the term $(4kC/A\omega^{1/2})$ under the square root sign is small compared to unity and a first-order approximation gives $I = nFkSC^2$. The resulting plots do not show a large per cent change in the reciprocal current as the rotational velocity is changed. (Note the greatly expanded scale of the vertical axis on the bottom plot of Fig. 2.)

Experimental

The experimental details are essentially identical to those described in ref. (1) except that solutions were prepared with sulfuric acid instead of nitric acid.

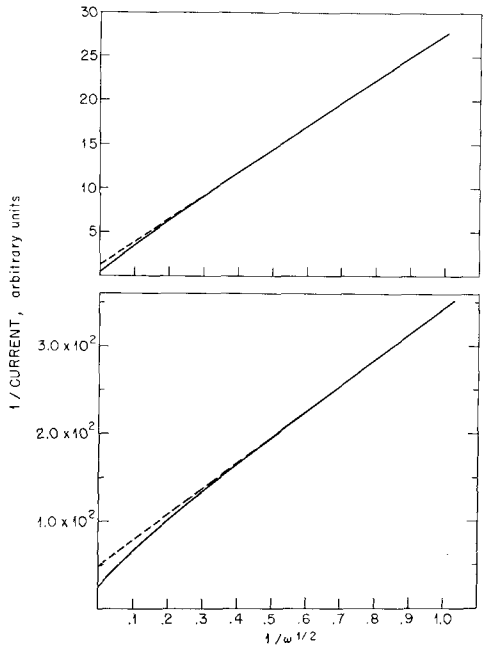

Fig. 1. Calculated $1/I$ vs. $1/\omega^{1/2}$ curves for a second order reaction. Top: C = 10^{-1}, A = 10^{-3}, K = 10^{3}; bottom: C = 10^{-2}; A = 10^{-3}; K = 10^{3}.

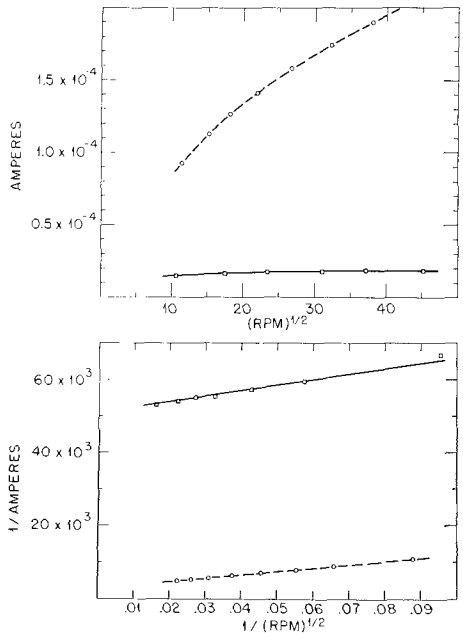

Fig. 3. Comparison of rotating disk plots for zirconium in HF-HNO_3 and HF-H_2SO_4. Electrode area = 0.318 cm^2: ——, 0.0011*N* HF, 1.8*N* H_2SO_4; — —, 0.0011*N* HF, 1.2*M* HNO^3, both —400 mv *vs.* S.C.E.

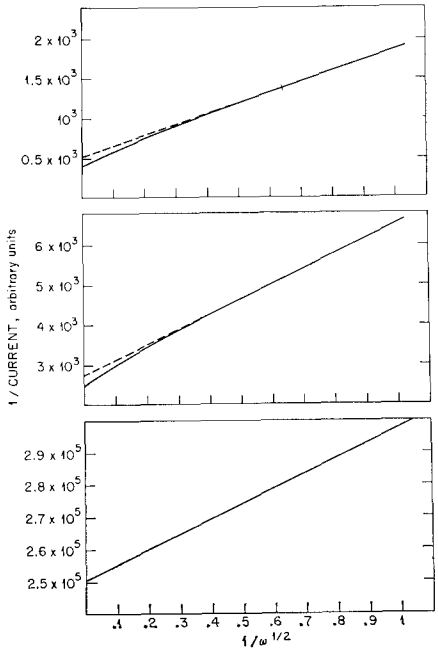

Fig. 2. Calculated $1/I$ vs. $1/\omega^{1/2}$ curves for a second order reaction. Top: C = 2.5 x 10^{-3}; A = 10^{-3}; K = 10^{3}; center: C = 10^{-3}; A = 10^{-3}; K = 10^{3}; bottom: C = 10^{-4}; A = 10^{-3}; K = 10^{3}.

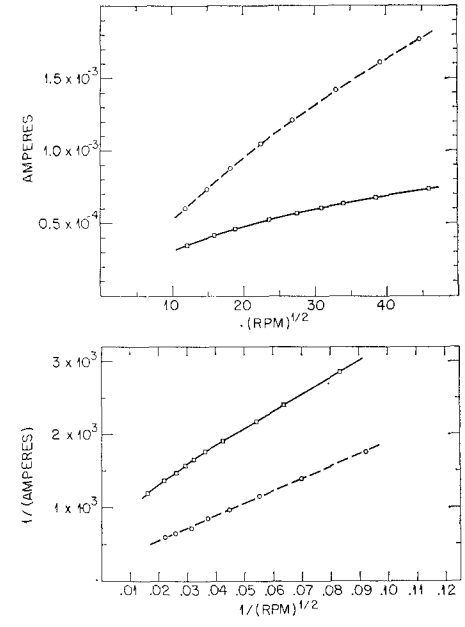

Fig. 4. Comparison of rotating disk plots for zirconium in HF-HNO_3 and HF-H_2SO_4. Electrode area = 0.318 cm^2; — —, 0.00532*N* HF, 1.2*M* HNO_3; ——, 0.0055*N* HF, 1.8*N* H_2SO_4, both —400 mv *vs.* S.C.E.

The capacity was measured by determining the slope of the plot of the electrode potential with time as a constant current pulse was applied. The capacity is then given by the current density divided by this slope, dV/dt. The apparatus used has already been described (5).

Results

The results of these experiments were obtained as a series of determinations of the current as a function of the potential, the rotational velocity, and the composition of the solutions. The potential was varied in steps of 100 mv from —600 to —300 mv *vs.* S.C.E. The concentration of HF was varied from 0.044*N* to about 0.001*N*, and the sulfuric acid concentration was varied from 1.8*N* to 0.0036*N*. The results obtained in HF-HNO_3 (6) are included here for comparison purposes. In Fig. 3-5, comparisons are made between the sulfuric acid and the nitric acid data for three concentrations of HF. Both the current as a function of the square root of the rotational velocity and the reciprocal current as a function of the reciprocal of the square root of the rotational velocity are shown. In each case, the currents for the HNO_3 solutions are greater, this effect being most pronounced for the solutions which contained the lowest concentrations of HF. Examination of the plots also shows that the relative difference increases as the rotational velocity is increased. In the lower sections of Fig. 3-5, com-

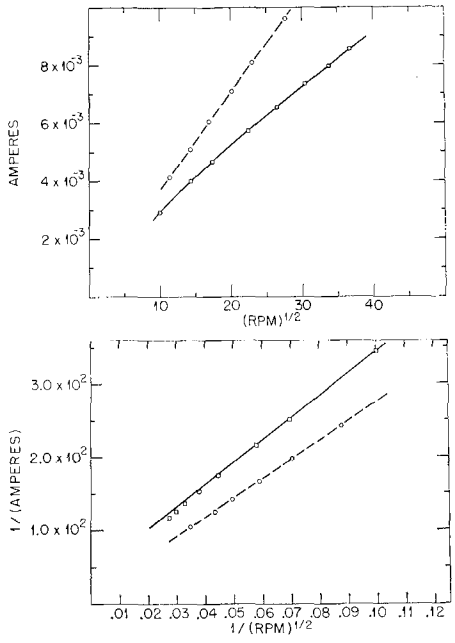

Fig. 5. Comparison of rotating disk plots for zirconium in HF-HNO_3 and HF-H_2SO_4. Electrode area = 0.318 cm^2; ——, 0.0440*N* HF, 1.8*N* H_2SO_4; — —, 0.0426*N* HF, 1.2*M* HNO_3, both —400 mv vs. S.C.E.

parisons are made of the plots of $1/I$ *vs.* $1/rpm^{1/2}$. The plots for the H_2SO_4 experiments are curved, but the plots for HNO_3 are linear.

The effect of potential on the current is illustrated in Fig. 6. At low values of the rotational velocity there is little effect, but at the highest values the current decreases slightly as the potential becomes more anodic, a somewhat unusual result. If a normal Tafel-like logarithmic relation held, a large increase in current as the potential becomes more anodic would be expected.

The effect of change of the concentration of H_2SO_4 is illustrated in Fig. 7. The currents for 0.036*N* and 0.18*N* H_2SO_4 are about the same, but the currents at the higher rotational velocities are markedly smaller for the 1.8*N* H_2SO_4 experiment. Similar patterns were observed in other experiments.

In some experiments, the capacity of the electrodes was also measured as a function of rotational velocity. The results of these experiments are shown in Table I, where it is shown that the capacity is quite small compared to double layer capacities. These results also

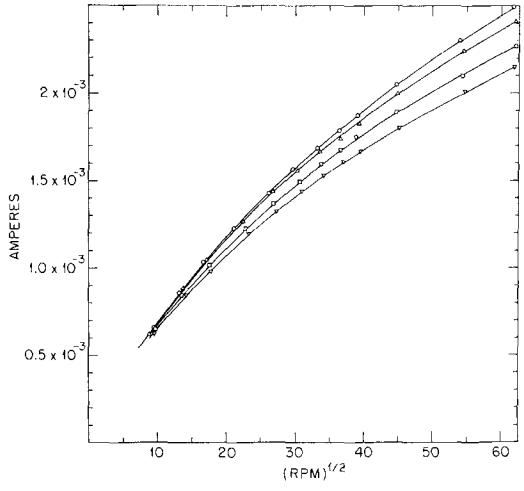

Fig. 6. Effect of potential on *I* *vs.* $(rpm)^{1/2}$ plots for zirconium in 1.8*N* H_2SO_4, 0.011*N* HF. Electrode area = 0.318 cm^2; ○, 600; △, —500; □, —400; ▽, —300 mv vs. S.C.E.

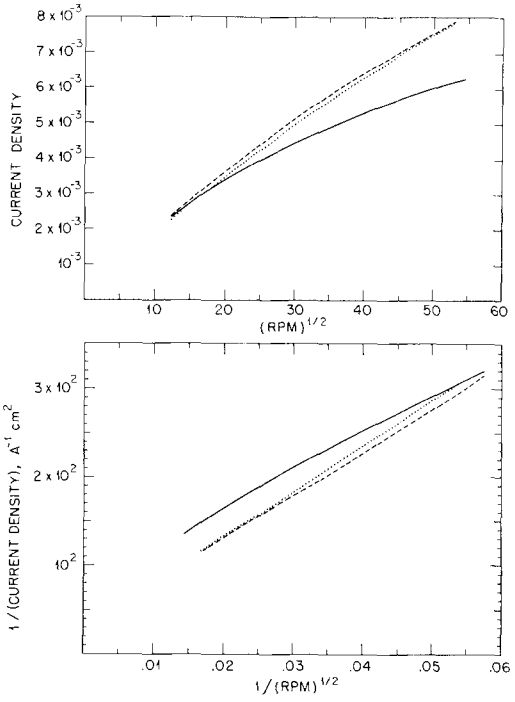

Fig. 7. Comparison of rotating disk plots for zirconium in HF-H_2SO_4. ——, 1.8*N* H_2SO_4; - - -, 0.18*N* H_2SO_4; . . . . ., 0.036*N* H_2SO_4, all 0.01*N* HF, —400 mv vs. S.C.E.

show that the capacity increases significantly as the current and rotational velocities increase.

Discussion

The effect of increasing the rotational velocity is to increase the concentration of the reactant at the interface and therefore to minimize the concentration difference between the interface and the bulk of the solution. If the reaction rate at the surface is fast enough, the reaction will be essentially under complete mass transfer control at the lowest velocities. As the rotational velocity is increased, the concentration at the interface is increased and consequently the rate of the surface reaction rapidly increases. Therefore, if a change in experimental conditions affects only the surface reaction, the effect will be most apparent at the higher rotational velocities. Any effects which change the mass transfer conditions will be present at the lower velocities. Since the effects of 1.8*N* H_2SO_4 were apparent only at the higher rotational velocities, it can be concluded that the sulfuric acid affects the surface reaction and has little or no effect on the mass transfer reaction.

Examination of the plots of $1/I$ *vs.* $1/\omega^{1/2}$ for the data in solutions of H_2SO_4 shows that the plots are not linear but resemble the second order plots shown in Fig. 1-2. In order to determine whether the reaction actually was second order, the logarithm of the concentration at the interface was plotted as a function of the logarithm of the current. The order is numerically equal to the slope of this line. The concentration at the interface was determined by rearranging Eq. [1],

Table I. Capacities of zirconium in 0.0055*N* HF, 1.8*N* H_2SO_4, — 600 mv vs. S.C.E.

Rotation velocity, rpm	Capacity, $\mu F/cm^2$	Current density, amp/cm^2
0	3.34	
186	4.68	1.21×10^{-3}
518	5.08	1.66×10^{-3}
932	5.11	1.95×10^{-3}
1257	5.18	2.10×10^{-3}
2030	5.56	2.37×10^{-3}

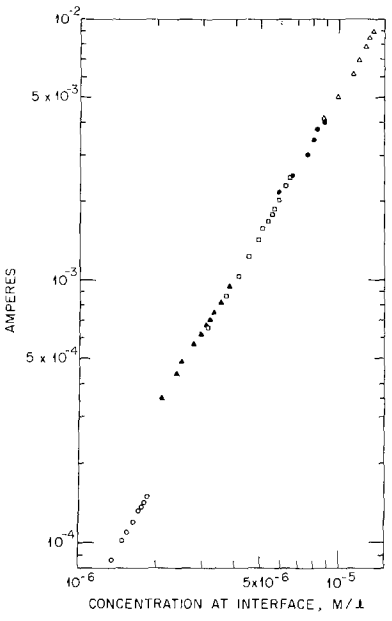

Fig. 8. Relation between concentration of HF at interface and current for zirconium in HF- 1.8*N* H_2SO_4, —600 mv *vs.* S.C.E. Electrode area = 0.319 cm². ○, 0.0011*N* HF; ▲, 0.0055*N* HF; □, 0.011*N* HF; •, 0.022*N* HF; △, 0.044*N* HF.

which is valid generally for reactions of any order, to give

$$C_i = C - \frac{I}{nFSA\omega^{1/2}} \qquad [5]$$

The constant A in Eq. [5] was determined in these experiments from two different experiments at different values of C. Since the current is a function only of C_i, then if the currents are equal in two runs at two different values of C the values of C_i must be identical. Under these conditions, we may write

$$C_1 - I/nFSA\omega_1^{1/2} = C_2 - I/nFSA\omega_2^{1/2} \qquad [6]$$

where the subscripts refer to the two different runs. This equation may be solved to give A (or nFA if n is not known). When this was done, values of nFA between 28 and 29 were found.[2] These values were similar to those found in HF-HNO_3 where values from 28-33 were found.

By use of these techniques, plots of log of C_i *vs.* log I were made for all of the runs at 1.8*N* H_2SO_4 and all of the concentrations of HF. All of the data from 0.0055*N* HF to 0.022*N* HF lay on the same line, which had a slope of about 1.8. The 0.044*N* runs could be made to lie on the line by slight adjustment of the value of nFA. However, the values of the current for the 0.0022*N* and 0.0011*N* HF experiments fell well below the extension of the line. These lines were calculated for all potentials used, and an example of such a plot is shown in Fig. 8. Unfortunately it is difficult to say whether the reaction is exactly second order with experimental error accounting for the discrepancy or whether the order is actually 1.8 because of a complex mechanism or other complicating factors.

The capacity measurements showed that the values were small compared to the values one would expect from a solution double layer. It is difficult to interpret these low values in any other way than as a film capacity. The dissolution reaction, therefore, probably involves the continuous formation and dissolution of a film. As explained in ref. (5), the presence of the film can explain the lack of the dependence of the rate on the potential and also the increase in capacity with increasing current.

In the study of the HF-HNO_3 system, a first order dependence with respect to HF was found. In this study, however, a reaction order slightly less than two was found for high concentrations of H_2SO_4. As the concentration of H_2SO_4 was reduced, the plots of $1/I$ *vs.* $1/(\text{rpm})^{1/2}$ became more linear, indicating that the reaction was approaching first order. Further, the rate constants found by extrapolating these lines at the lower concentrations of H_2SO_4 were about the same as those found for the nitric acid case. The results obtained suggest, therefore, that the sulfate ion, if present in large quantities, is adsorbed on the surface of the film in such a way that the dissolution by HF is inhibited. The affinity of the fluoride and sulfate ions for the zirconium ion is well known and has been discussed extensively (9).

The second order dependence found in the sulfuric acid solutions may also be explained on the basis of adsorption of sulfate. Consider the following equations

$$HF + Zr_l^{+4} \rightarrow Zr(HF)_l^{+4} \qquad [A]$$

$$Zr(HF)_l^{+4} \rightarrow Zr_l^{+4} + HF \qquad [B]$$

$$HF + Zr(HF)_l^{+4} \rightarrow ZrF_2^{+2} + 2H^+ \qquad [C]$$

$$SO_4^{=} + Zr_l^{+4} \rightarrow ZrSO_4^{+2} \qquad [D]$$

$$ZrSO_4^{+2} \rightarrow Zr_l^{+4} + SO_4^{=} \qquad [E]$$

Equations [A] and [B] represent the reversible adsorption of HF; Eq. [D] and [E] represent the reversible adsorption of $SO_4^{=}$. The dissolution reaction is represented by Eq. [C] in which a complex containing two fluoride ions is formed; further complexing may occur in the solution.

The following kinetic expressions may be written

$$R_A = K_A(HF)(1 - \theta_1 - \theta_2) \qquad [7]$$

$$R_B = K_B\theta_1 \qquad [8]$$

$$R_C = K_C\theta_1(HF) \qquad [9]$$

$$R_D = K_D(SO_4^{=})(1 - \theta_1 - \theta_2) \qquad [10]$$

$$R_E = K_E\theta_2 \qquad [11]$$

Here θ_1 and θ_2 represent the fraction of the surface sites occupied by adsorbed HF and adsorbed $SO_4^{=}$, respectively. If steady state coverages in the θ's are assumed, the following expression for the over-all rate may be derived

$$R = \frac{K_AK_CK_E(HF)^2}{K_BK_D(SO_4^{=}) + K_CK_D(HF)(SO_4^{=}) + (K_CK_E + K_AK_E)(HF) + K_BK_E} \qquad [12]$$

If the sulfate ion concentration is very large, then it is possible for the first term in the denominator to dominate, so that

$$R \approx \frac{K_AK_CK_E(HF)^2}{K_BK_D(SO_4^{=})} \qquad [13]$$

Under these conditions, the reaction order with respect to the concentration of HF will be two, and there should be an inverse dependence in $SO_4^{=}$, as observed. If the sulfate ion is reduced, then the other terms containing HF will become significant, and the reaction will tend to approach first order. Again this assumes the appropriate values of the constants.

This explanation is undoubtedly simplified for there are other effects which will affect the rate of the reaction. Among these are possible variations in surface roughness and the influence of the thickness of the film. The zirconium electrodes were very easily passivated by slight anodic pulses in those solutions that contained small amounts of HF, and in extreme cases,

[2] In this computation of nFA, the units of concentration were moles per cubic centimeter and the units of ω were rpm.

this passivation produced visible films. It is quite possible that partial passivation may have occurred, in that only a portion of the surface was actively dissolving. It is also conceivable that the thicker films formed in the more dilute solutions were more resistant than the very thin films formed in solutions containing relatively large amounts of HF. Either of these effects may be the explanation for the very low rates found in the solution containing 0.0011*N* HF.

Manuscript received April 2, 1965; revised manuscript received July 30, 1965. This paper was presented at the San Francisco Meeting, May 9-13, 1965. Research was sponsored by the United States Atomic Energy Commission under contract with the Union Carbide Corporation.

Any discussion of this paper will appear in a Discussion Section to be published in the June 1966 JOURNAL.

REFERENCES

1. T. Smith and G. R. Hill, *This Journal*, **105**, 117 (1958).
2. E. M. Vander Wall and E. M. Whitener, *Ind. Eng. Chem.*, **51**, 51 (1959).
3. M. E. Straumanis, W. J. James, and A. S. Neiman, *Corrosion*, **15**, 286 (1959).
4. W. J. James, W. G. Custead, and M. E. Straumanis, *J. Phys. Chem.*, **64**, 286 (1960).
5. R. E. Meyer, *This Journal*, **111**, 147 (1964).
6. R. E. Meyer, *ibid.*, **112**, 684 (1965).
7. V. A. Gil'man and Ya. M. Kolotyrkin, *Dokl Akad. Nauk SSSR*, **155**, 1155 (1964); Trans. *in Dokl. Phys. Chem.*, **155**, 384 (1964).
8. V. G. Levich, "Physico-Chemical Hydrodynamics," p. 72-78, Prentice-Hall, Englewood Cliffs. N. J. (1962).
9. W. B. Blumenthal, "The Chemical Behavior of Zirconium," D. Van Nostrand, New York (1958).

Devitrification of Tin Oxide Films (Doped and Undoped) Prepared by Reactive Sputtering

W. Robert Sinclair, F. G. Peters, D. W. Stillinger, and S. E. Koonce

Bell Telephone Laboratories, Incorporated, Murray Hill, New Jersey

ABSTRACT

Tin oxide films doped with antimony oxide formed by reactive sputtering of tin-antimony alloy cathodes can be made conductive at room temperature by heating in air at elevated temperatures (*ca.* 710°C) if the atom per cent of antimony in the cathode is between 3.0 and 14%. The kinetics is quite complicated with room temperature resistance of quenched samples showing two minima as a function of time of heating. The kinetics is speeded up if carbon is applied to the sputtered film prior to firing. This treatment introduces oxygen vacancies and allows even indium doped films to be made conductive on firing. For 3500Å thick films of antimony doped tin oxide the highest conductivity obtained is 175 ohms $\square^{-1}$. The temperature coefficient of resistivity ranges from negative to +2000 ppm/°C, depending on composition.

Methods for preparing conductive tin oxide films have been known for some time, and the patent literature is rich on this subject (1). The films are usually prepared by hydrolyzing a volatile tin compound on a hot surface, *e.g.*,

$$SnCl_4 + 2H_2O \xrightarrow{500°\text{-}800°C} SnO_2 + 4HCl$$

In practice the volatile tin compound is dissolved in an organic compound such as ethanol, and the resulting atmosphere is reducing leading to oxygen deficient films.

Aitchison (2) has studied films made by the above reaction as well as films doped with 5% antimony oxide or 5% indium oxide. He found that the conductivity in all cases was electronic and that addition of antimony (presumably +5) ion increased the conductivity whereas addition of indium (presumably +3) ion decreased the conductivity as Verwey had also found (3).

Holland and Siddall (4) have prepared tin oxide films by reactive sputtering. Their technique involved activation of the cathode with oxygen before film deposition, and sputtering was then done in a 95% Ar-5% O_2 atmosphere. The objective was to obtain oxygen deficient conductive films. Heat-treatment of the film to 400°C was necessary, but the results were quite variable and impossible to predict.

We have previously shown (5) that tin oxide films prepared by reactive sputtering with deposition on unheated substrates are amorphous. These films are also electrically insulating. We, therefore, have the opportunity of separating the film deposition step and the crystallization reaction. It was our hope that we could thus obtain insight concerning the properties of conductive SnO_2 films which are far from being understood especially with respect to details involved with the preparation procedure (6).

Experimental Procedures

One of the possibilities for the variability in film resistance obtained by Holland and Siddall was lack of control of the concentration of oxygen vacancies. We decided to sidestep this difficulty as much as possible by completely oxidizing the film by sputtering in pure oxygen and introducing chemical defects by addition of indium or antimony by sputtering from an alloy electrode and/or subsequent reduction with carbon. This approach should allow for better reproducibility from experiment to experiment since precise control of the condition of the cathode or of the oxygen pressure in the system should not be required.

The apparatus used in the sputtering has been previously described (5). Deposition conditions were standardized as much as possible: 2-hr runs, 1500-1600v applied, 30 Mamp and 4 x 10^{-2} Torr of O_2. No attempt has been made yet to maximize the deposition rate which certainly can be increased greatly. Chemical descriptions of the films are in terms of the compositions of the electrodes used. For instance, what is termed a 10% antimony oxide film is prepared from an electrode containing 10 a/o (atom per cent) antimony and 90 a/o tin. The mole per cent of antimony oxide present in the resulting film assuming the products are Sb_2O_5 and SnO_2 is approximately one half of the electrode atom percentage, and in the particular example given is 5.26%.

Films were deposited onto cleaned fused silica rectangular parellelopipeds (1 in. x ca ¼ in. x 1 mm) cut from Amersil fused silica microscope slides and were about 3500Å thick. Film thickness was held approx-

imately constant to avoid effects of film thickness on resistivity noted by Aitchison. In general, six samples were coated on one side in a run. The process of cleaning the silica bars involved the following steps: (*a*) boiling in isopropyl alcohol to remove the wax used in cutting the pieces, (*b*) boiling 30 min in Dreft, (*c*) rinsing in hot tap water, (*d*) boiling in 10% H_2O_2, (*e*) several boilings in deionized water followed by an air dry and storage in a desiccator.

Electrodes (cathodes) were prepared from 99.998 + per cent pure tin (Vulcan Material Company) and Asarco indium (99.999 + per cent pure) and antimony (99.999 + per cent pure). Mixtures of the metals of desired composition were melted in graphite crucibles and poured into a glazed porcelain dish where the alloy solidified. The alloy does not stick to porcelain. During pouring an aluminum screw was suspended above the center of the dish so that the screw head was embedded in the solid alloy, but the threads were still available for attachment to an aluminum piece which served as vacuum seal and electrical conductor and was machined to allow circulating tap water to cool the electrode. The electrode diameter was about 2 in.; the thickness about ¼ in.

After the films had been deposited on the fused silica slides they were removed from the sputtering chamber and fired in air at a desired constant temperature for a given time. No attempt was made to control humidity. After removal from the oven and cooling to room temperature silver electrodes[1] were painted on and fired at 500°C. A separate sample was used for each firing time, *i.e.*, no sample was cooled and then reheated to get another point on the resistance *vs.* firing time curve. Each point in the resistance *vs.* time plots discussed in the next section is an average of about four samples. The room temperature measurements of resistance were made with a Keithley 610A Electrometer. A d-c Wheatstone bridge was employed for temperature coefficient measurements (T.C.R.). To obtain reproducibility in the T.C.R. measurements further heat-treatment was necessary as will be discussed later.

Some samples were coated with carbon previous to firing. The carbon coat was applied by evaporation using a commercial carbon evaporation apparatus (E. F. Fullam, Inc.). The carbon coats were approximately 125Å thick.

Results and Discussion

Structure and composition of films before and after heat-treatment.—The sputtered films as deposited on an unheated substrate are amorphous as indicated both by electron diffraction results on the unsupported film and by x-ray diffraction results on supported films. Upon sufficient heat-treatment these films crystallize to a rutile-like structure with an average crystallite diameter of about 400Å (cf. Fig. 1). If the films are coated with carbon previous to firing and then fired in air, the resulting films are indistinguishable from the uncoated fired film from the point of view of crystallite size, a result different from that of the devitrification of aluminosilicate glass films (7) where the application of carbon was necessary to obtain a very fine grained film of quite uniform crystallite size.

As the ratio of antimony to tin in the film increases the lattice parameters of the crystallized SnO_2 films increase until the 15% Sb-85% Sn film is reached which is nonconducting. The lattice parameters of this film are quite close to those of the pure SnO_2 film. X-ray fluorescence analysis of fired and unfired films shows that within analytical error no antimony or tin is volatilized in air at 710°C in 24 hr. Analysis also indicates that the cation ratio in the film is the same as the atom ratio in the alloy cathode.

These observations can be explained, we believe, by assuming that the true solubility of antimony oxide in tin dioxide films is less than 1 mole % and that such a film is a nonconductor (cf. Fig. 7). This solubility figure is in accord with Loch's measurements (8). The films containing between 1 and 14% Sb then are thermodynamically unstable with respect to exsolution of antimony oxide. We can expect to get supersaturated films easily because the crystallization process probably involves simply bond breaking and reforming with little or no diffusion. Diffusion and consequent exsolution should be slow because our firing temperature is low compared to the melting point of SnO_2. However, since there is no published phase diagram of the SnO_2-Sb_2O_5 system we have been forced here to assume that there is no SnO_2-Sb_2O_5 eutectic at about 1% antimony and at a low temperature of, say, 1000°C. In line with these statements we say that the exsolution of the 15% antimony oxide doped films occurs sufficiently fast at 710°C with the heating schedules employed that the supersaturation is removed and the resulting films are nonconductors.

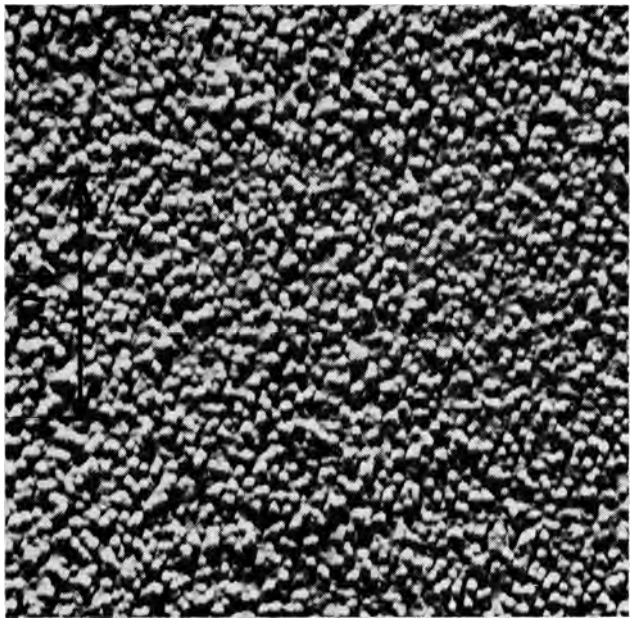

Fig. 1. Electron micrograph (replica) of SnO_2 film on fused silica substrate; fired 3 hr, 710°C in air.

Devitrification kinetics.—Preliminary experiments indicated that the firing temperature should be between 600° and 900°C, and somewhat arbitrarily 710° ± 10°C was selected as the standard firing temperature. The results of firing tin oxide films with various amounts of antimony oxide added are shown in Fig. 2. Obviously the kinetics is complicated and, somewhat surprisingly, the reaction is rather slow. Some light on

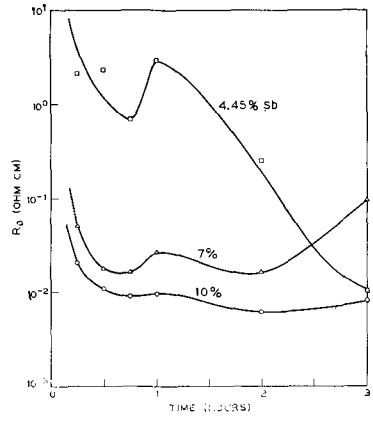

Fig. 2. R_0 in ohm-cm at room temperature of 3500Å thick SnO_2 films doped with indicated amounts of antimony oxide *vs.* firing time at 710°C in air. Films were not carbon treated.

[1] The silver paste consists of finely divided silver and 8 w/o of a lead borosilicate glass suspended in Acryloid A-10, Amylacetate and cellosolve acetate.

the processes involved is shed by the results of devitrification of films which have been carbon coated previous to firing. Before discussing these results, however, we should remark on why this approach was chosen.

In the early stages of this work two difficulties were encountered, poor adhesion of the film after firing and poor reproducibility in resistivity. While these effects existed, considerable effort was applied to understand and overcome them. Although various possibilities such as mismatch of thermal coefficient between film and substrate could be suggested we decided first to investigate the possibility that variable microstructure in the crystallized film was the source of difficulty. It is well known that control of the microstructure is important in control of electrical and other properties of materials (9). As mentioned in the previous section no difference in microstructure with carbon coating could be determined. However, the improvements in reproducibility and elimination of adhesion problems were most dramatic. In addition, the effect of this treatment on the devitrification kinetics was quite noticeable. The results of these studies are indicated in Fig. 3 and 4.

Comparing the results in Fig. 2, 3, and 4 it is apparent that the devitrification reaction is speeded up by the addition of carbon before firing. To explain these results the following tentative reaction scheme is presented.

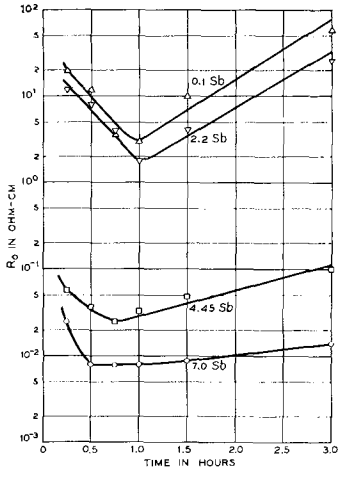

Fig. 3. R_0 in ohm-cm at room temperature of 3500Å thick SnO_2 films doped with indicated amounts of antimony oxide vs. firing time at 710°C in air. Films were coated with *ca.* 125Å carbon film before firing.

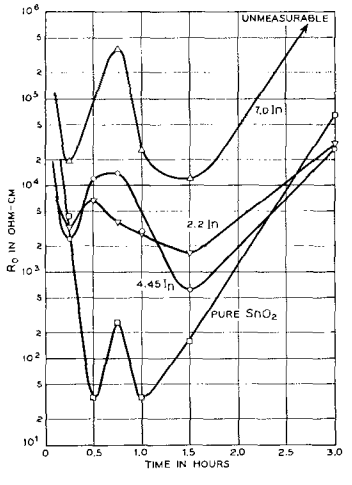

Fig. 4. R_0 in ohm-cm at room temperature of 3500Å thick SnO_2 films doped with indicated amounts of indium oxide vs. firing time at 710°C in air. Films were coated with *ca.* 125Å carbon film before firing.

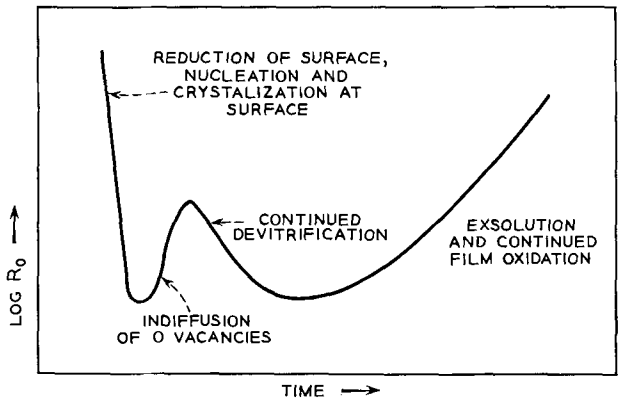

Fig. 5. Postulated reaction steps in heat-treatment of tin oxide films

Presumably the function of the carbon is to reduce the film by abstracting oxygen to form CO or CO_2. We then postulate the nuclei are formed at the surface possibly because the broken Sn-O bonds allow some necessary atomic movements to occur. This should occur more easily with the less stable tin oxide glass. In this picture, then, crystallization of the film starts at the air-film interface and requires breaking of some Sn-O bonds. This occurs more rapidly with a reducing agent like carbon present. In the initial stages of devitrification of the carbon coated stannate glass and to a lessened extent with the uncoated film the crystallized portion should have a high concentration of oxygen vacancies. As time increases there are two competing processes as far as effects on the room temperature resistivity of the film are concerned. Increasing thickness of the crystalline region of the film decreases the resistance whereas decreasing oxygen vacancy concentration due to diffusion into the film, oxidation at the air-film interface (because of the lower dissociation pressure of the crystalline phase), and reduction of Sb^{+5} to Sb^{+3} in the film would act to increase the resistance. Under these conditions one would not expect the resistivity to be a linear function of the vacancy or impurity concentration and, indeed, experimentally does not appear to be so (cf. Fig. 7). Thus as the vacancy concentration gets below a critical value it can be expected that the resistance may sharply increase again despite the continuing increase in the thickness of the crystalline region. Eventually, the resistance drops as the crystallization process continues. The film finally goes to a very high resistivity as the exsolution process becomes dominant. Of course, with the pure tin oxide film exsolution would not occur and reoxidation would be the only mechanism involved in this final upswing in resistance. These processes are summarized in Fig. 5.

In this picture then there is a delicate interplay of several reactions each with its own activation energy and the kinetics could be changed by a variety of influences. The effects of temperature change are indicated in Fig. 6. It is seen that at high temperatures (900°C) the exsolution process becomes dominant. At low temperatures the initial stages of the reaction which are influenced greatly by diffusion of oxygen vacancies are slowed sufficiently that even with carbon coated antimony doped films the first reaction minimum can be seen.

In Fig. 7 the specific resistivity at the second minimum has been plotted as a function of per cent antimony or indium added and the results compared with Aitchison's results. The second minimum was chosen because in our reaction picture the film should be about completely crystallized. In the case of the carbon coated antimony doped films the one minimum obtained was assumed to be the second minimum.

Temperature Coefficient of Resistance

The temperature coefficient of resistance of the nonreduced antimony doped films has been studied in the

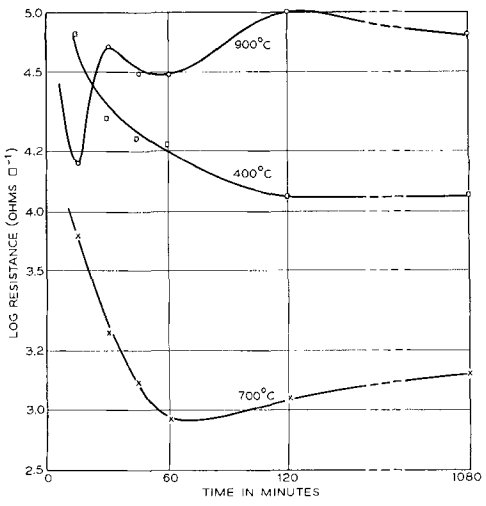

Fig. 6. Devitrification of SnO_2 films containing 4.45% antimony oxide as a function of firing temperature.

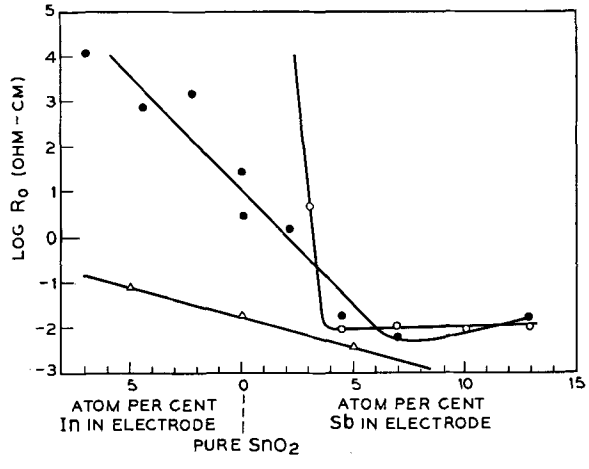

Fig. 7. R_0 (second minimum value) at room temperature of SnO_2 films prepared by reactive sputtering as a function of film composition and carbon treatment. Values quoted from Aitchison (*loc. cit.*) are for sprayed films. △, Aitchison; ○, this work, no carbon treatment; ●, this work, carbon treatment.

range 25°-300°C and the results indicated in Fig. 8. It is seen that the T.C.R. increases monotonically from negative through zero to positive as we progress from insulating films to conducting films. A more detailed discussion of this behavior and of the T.C.R. of the reduced films will be presented in another communication (10).

It is important to note though that the T.C.R. is strongly influenced by the thermal history of the film. This is indicated in Fig. 9 where it is shown that if one cycles the film between 25° and 300°C the T.C.R. can change radically, mostly in the first few cycles. This is possibly due to the fact that initially the film has been quenched from 710° to 25°C and has frozen in a distribution of vacancies, etc., corresponding to a temperature near 710°C. It is known that the resistance of alkali halides is influenced by thermal history at temperatures below a value characteristic of the particular alkali halide and this is attributed to "frozen-in" distributions (11). If one assumes a melting point of 1900°C (12) for tin oxide[2] then one is clearly in a range where mobility of defects should be of importance. It follows also that the processes of quenching and annealing are important in obtaining reproducible resistance values. In general, the values presented in

[2] The melting point of tin oxide is variously reported in different handbooks between 1127° and 1900°C. The 1127°C value we have checked and it is certainly wrong.

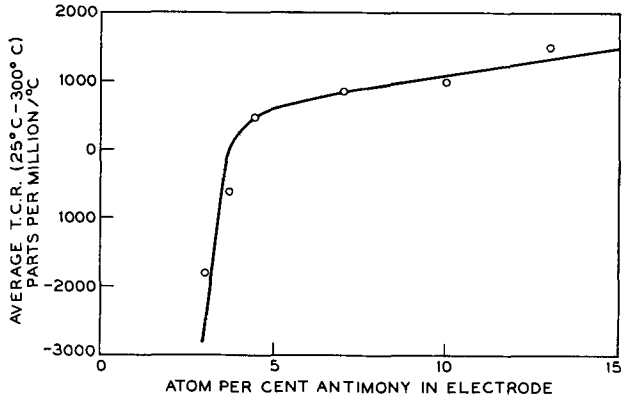

Fig. 8. Average temperature coefficient of resistance (25°-300°C) of tin oxide films at second minimum fired at 710°C in air (3500Å thick) as a function of added antimony oxide. Films were not carbon coated before heat-treatment.

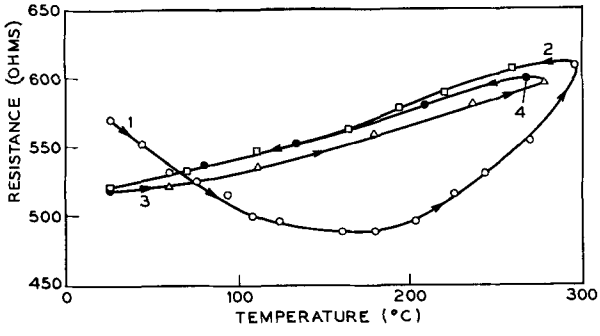

Fig. 9. Resistance of an SnO_2 film doped with 7% antimony oxide as a function of thermal history. Run 1, increasing temperature; run 2, decreasing temperature; run 3, increasing temperature; run 4, decreasing temperature.

Fig. 2 to 4 and 6 are obtained on unannealed samples. Enough corroborative work has been done to assure us that the general shape of these curves is correct. One cannot properly evaluate reproducibility in these systems with only four samples per point, but it appears at the present state of our work as if the resistances of equivalently prepared samples at the second minimum are reproducible to about ±20%, if not carbon treated, and somewhat better, if carbon treated. Preliminary indications are that annealing at 300°C improves the reproducibility.

Summary

We have shown that tin oxide films prepared by reactive sputtering in oxygen of tin or tin-antimony electrodes are crystallized to a rutile-like structure on heating. These films if they contain more than 3.0% Sb and less than 15% Sb are conductive if heated for an appropriate time at a high temperature (*e.g.*, 710°C) in air. The kinetics is complicated. Using the room temperature resistance of a fired film as an index, in general two minima in resistance are noted as a function of time. Films coated with carbon prior to firing devitrify more quickly and display lower conductivity at the second minimum for high antimony concentrations but considerably higher conductivity than the uncoated antimony doped tin oxide film at low antimony concentrations and, in fact, conductivity can be noted even in indium doped films under these circumstances. Long-term heating of these films at high temperatures (*e.g.*, above 900°C) leads to insulating films in all cases. A general picture to explain the kinetic results has been suggested.

The temperature coefficient of resistance of antimony doped tin oxide films which have not been treated with carbon ranges monotonically from negative through zero to +2000 ppm/°C as a function of antimony con-

tent. Annealing of the film at about 300°C is required to stabilize the temperature coefficient of resistivity for the interval 25°-300°C.

Acknowledgments

The interest and constructive criticisms of M. D. Rigterink are appreciated. Mrs. M. H. Read performed a particularly valuable x-ray experiment.

Manuscript received March 23, 1965; revised manuscript received Aug. 2, 1965. This paper was presented at the Pittsburgh Meeting, April 15-18, 1963.

Any discussion of this paper will appear in a Discussion Section to be published in the June 1966 JOURNAL.

REFERENCES

1. J. T. Littleton, U. S. Pat. 2,118,795; H. A. McMaster, U. S. Pat. 2,429,420.
2. R. E. Aitchison, *Austr. J. Appl. Sci.*, **5**, 10 (1954).
3. E. J. W. Verwey, "Semi-Conducting Materials," p. 151, Butterworths (1951).
4. L. Holland and G. Siddall, *Vacuum*, **3**, 375 (1953).
5. W. R. Sinclair and F. G. Peters, *J. Am. Ceram. Soc.*, **46**, 20 (1963).
6. J. A. Marley and T. C. MacAvoy, AFCRL-62-771.
7. J. C. Williams, W. R. Sinclair, and S. E. Koonce, *J. Am. Ceram. Soc.*, **46**, 161 (1963).
8. L. D. Loch, *This Journal*, **110**, 1081 (1963).
9. G. Economos, "Ceramic Fabrication Processes," p. 275, John Wiley & Sons, Inc., New York (1958).
10. W. R. Sinclair and D. W. Stillinger, To be published.
11. F. Seitz, "The Modern Theory of Solids," p. 55, McGraw-Hill Book Co., New York (1940).
12. I. E. Campbell, "High Temperature Technology," p. 31, John Wiley & Sons, Inc., New York (1956).

Impurity Redistribution Processes in Epitaxial Silicon Layers

B. A. Joyce, J. C. Weaver,[1] and D. J. Maule

Allen Clark Research Centre, The Plessey Company Limited, Caswell, Towcester, Northants., England

ABSTRACT

Impurity redistribution processes occurring during the epitaxial growth of silicon layers have been investigated using radiotracer techniques. The final impurity profiles obtained have been measured by the capacitance-voltage technique and the results compared with theoretically computed profiles. It has been shown that the occurrence of the previously postulated etch-back mechanism is unlikely, and that all of the redistributed impurity can be accounted for in terms of solid-state diffusion from the front of the substrate and outdiffusion from the rear. Certain anomalous diffusion rates have been observed in the case of phosphorus doped substrates.

During the growth of epitaxial silicon layers a process occurs whereby impurities initially present in the substrate are redistributed in the growing layer (or in downstream layers in a multislice system) as growth proceeds. This process is usually referred to as autodoping, and the impurity penetration is normally considered to be greater than could be accounted for by solid-state diffusion.

Three possible mechanisms have been suggested for the process, and they are briefly summarized below.

(*A*) The dopant is transferred from the back surface of the slice to the growing layer, the transfer taking place via the gas phase (1).

(B) Transfer occurs from the upper surface of the substrate (or the film after it has begun to grow) into the gas phase, with subsequent reincorporation of the impurities into the growing layer (2, 3). A mathematical treatment is then derived from this countercurrent extraction model by analogy with distillation theory.

(*C*) An extension of (*B*) in which an explicit time dependence for the reaction rate is derived kinetically, and details of the origin of the redistributed substrate impurity are postulated (4). Briefly, a single etch back mechanism is suggested as a natural consequence of the transient behavior involved in initiating a steady-state growth reaction.

The most significant factor in all of this work was the claim that impurity penetration was far greater than could be accounted for by a diffusion mechanism. Recently, however, Grove *et al.* (5) have convincingly demonstrated that normal solid-state diffusion processes are sufficient to account for most of the impurity redistribution observed, particularly with boron and antimony doped substrates, provided that system contamination is eliminated. Further, although they derive a rigorous solution to the diffusion equation based on a moving boundary model, they show that this reduces to a simple complementary error-function-type distribution for all practical growth conditions.

The purpose of this paper is to present results from radiotracer determinations which show that any transfer occurring via the gas phase happens during the substrate pretreatment with hydrogen or via the back of the substrate during growth if this is not adequately sealed. Results of differential capacitance measurements are also presented which confirm that the form of the redistribution profile can be accounted for in terms of solid-state diffusion, coupled with a slight contribution from outdiffusion.

Experimental

It was considered necessary to obtain information on two stages of the autodoping process, namely, the mechanism of any gas phase impurity transfer, and the nature and origin of the redistributed impurity profile. For this reason two experimental techniques have been employed, namely radiotracer methods to investigate gas phase transfer and capacitance voltage measurements on diodes fabricated very close to the epitaxial layer surface in order to determine the impurity profile (6). The details of layer preparation were basically similar for both techniques and are described briefly below.

The films were grown by the hydrogen reduction of trichlorosilane, using a multislice, horizontal, R.F. heated reactor, the susceptor being a block of high-purity graphite encapsulated in fused quartz. Film growth temperatures were in the range 1150°-1250°C, as measured with an optical pyrometer corrected for emissivity and wall transmission losses. The partial pressure of $SiHCl_3$ used was normally 8 mm Hg, and the total flow rate 4 l. min^{-1}.

The substrate slices had an impurity concentration of approximately 10^{19} at. cm^{-3} of either phosphorus, arsenic, or antimony, or approximately 5×10^{17} at. cm^{-3} of gallium and were chemically polished to remove work damage from the surface. Any layer doping was carried out with phosphine.

[1] Present address: Ferranti Ltd., Edinburgh, Scotland.

Table I. Isotope data

Isotope	Half-life	Sensitivity (by β-count) (counts min^{-1} g^{-1})
^{32}P	14.1 days	1.19×10^{10}
^{72}Ga	14.1 hr	1.4×10^{11}
^{76}As	26 hr	4.5×10^{11}
^{122}Sb	2.7 days	3.3×10^{11}

The radiotracer technique employed was to place a labelled slice (containing ^{32}P, ^{76}As, ^{122}Sb, or ^{72}Ga) as number two slice in the reactor, followed by a number of unlabelled substrates. The appropriate growth run or pretreatment was then carried out, and a β-count made on the epitaxial layers grown on the unlabelled substrates (or on the substrates themselves if no deposition was carried out). The isotope data is given in Table I.

Since the actual counts were made on 2.5 cm diameter slices, the calibration from solutions of known specific activity was designed to simulate experimental conditions as nearly as possible. A suitable quantity of solution containing the radio isotope, and of known specific activity, was therefore evaporated on the surface of an inactive silicon slice, the count rate determined using an end window Geiger-Müller counter and the decay rate followed.

In some instances it was ncessary to isolate the radioactive element from a solution, *i.e.*, where it was required to determine impurity concentrations in SiO_2 films formed by oxidation of an active slice. Normally after isotopic exchange had taken place an insoluble compound containing the radioactive element was precipitated, and after chemical, and where necessary radiochemical, purification, the compound was weighed and the count rate determined. Following this a quantity of solution of known specific activity was isolated directly and the count rate determined. The weight of the element in question was then obtained by comparison of count rates and a correction applied for the difference in chemical yields. Such determinations were carried out for ^{32}P, isolated as $(NH_4)_3\ PMo_{12}\ O_{40}$ and weighed as $MgNH_4PO_4 \cdot 6H_2O$ and for ^{72}Ga isolated as $Ga(OH)_3$ and weighed as Ga $(C_9H_6ON)_3$ (gallium oxinate).

Finally impurity profiles were determined by fabricating diodes in the n-type epitaxial layers [using a very shallow (0.3μ) boron diffusion] and measuring the capacitance of the depletion width of the junction as a function of applied reverse bias. The principles of the method have been described by Thomas *et al.* (2) and the technique used here is based on a series R-C network with an applied high-frequency emf. The capacitance in the network is supplied by the depletion region of the diode, whose width is a function of a low-frequency negatively biased emf applied to the junction. As this capacitance varies the change in circuit impedance is measured as a change in potential across the resistor. Since the capacitance is measured at 1 Mc/s, the output signal is modulated at this frequency. After amplification, it is therefore demodulated and applied to the Y plates of an oscilloscope, with the low-frequency bias applied to the X plates. The effective C-V trace thus obtained is calibrated from a single measurement of the capacitance at zero applied bias. Actual capacitance voltage data is then taken from the calibrated trace and processed using an English Electric KDF9 computer to obtain impurity concentration *vs.* distance values.

Gas Phase Transfer Processes, Radiotracer Results, and Discussion

The radiotracer technique was used specifically to study the nature of any gas phase transfer processes occurring under a variety of growth and pretreatment conditions. Basically the conventional epitaxial process may be considered as a pretreatment stage followed by a growth stage, and the back surface of the substrate may be oxidized or left exposed. Initially therefore experiments were devised to obtain information on the stage of the process at which any gas phase transfer occurred and on the effect of sealing the back surface of the substrate with an oxide film. Qualitatively similar results were obtained for all of the labelled impurity elements used in considering the transfer process, but significant differences in the efficiency of an oxide film as a barrier to outdiffusion were observed between group III and group V elements. In an attempt to make the pattern of the results more simple to follow, a brief qualitative picture is presented below of the approach used and the results obtained. The complete quantitative results are subsequently given in detail.

The gas phase transfer experiments were designed to check the possibility of the etch back hypothesis being correct and to find an alternative if this were not so. The only realistic etching mechanism which could be considered was one in which all of the impurities were released initially, since as soon as any low impurity concentration layer growth commenced, substrate impurities could only be released by diffusion through this layer, and under all normal conditions growth rates would be very much faster than diffusion rates. On this basis, therefore, essentially all of the transfer should occur during the very early growth stages and should then virtually cease. As shown in the results below, this did not occur, most transfer occurring during hydrogen pretreatment (to downstream slices) and finally reaching a steady-state level for any layer thickness. Significant differences in the amounts transferred were observed between labelled substrates with the rear surface oxidized and those left unoxidized, so it was apparent that some or all of the transport occurred via this source. Furthermore, some transfer was still observed with a labelled substrate oxidized on all surfaces, so evidently a thermally grown oxide cannot provide a complete barrier. These results in fact seemed to fit best a simple outdiffusion model for gas phase transfer processes, and this was further substantiated by measurement of the amount of impurity transferred via the gas phase from the back of an active substrate into a growing layer in a single slice system, both with the rear surface oxidized and unoxidized. It will in fact be shown that the amount of impurity transferred from the rear surface to the growing layer by outdiffusion closely corresponds to the divergence of the actual impurity profile from the profile derived theoretically, assuming only a solid-state diffusion process to occur.

For gas phase transfer, the results obtained using an arsenic doped substrate may be taken as typical and these will be presented in full. The procedure used was as follows. The substrate containing ^{76}As, doped to a level of 10^{19} at. cm^{-3} and with a 1μ thick oxide layer on the back surface was placed in the horizontal multislice reactor, and the release of impurities was measured by collection on a series of unlabelled substrates placed downstream from this source (slices A, A+1, A+2, A+3).

The various stages of the process which were investigated are shown in Table II. Each of the stages a, b, c, and d was carried out with separate source and collector substrates. The results are illustrated in Fig. 1. The four sets of points show the total amount of active impurity transferred to the four downstream substrates for each separate process stage. From these it may be seen that the bulk of the transport, at least to downstream slices, occurs during

Table II. Stages of the process

Stage	Pretreatment conditions and duration	Growth time and temperature
(a)	Hydrogen, 20 min at 1200°C and 4 $l.min^{-1}$	Nil
(b)	As (a)	1.5 min at 1200°C, (4 $l.min^{-1}$)
(c)	As (a)	2.5 min at 1200°C, (4 $l.min^{-1}$)
(d)	As (a)	6.5 min at 1200°C, (4 $l.min^{-1}$)

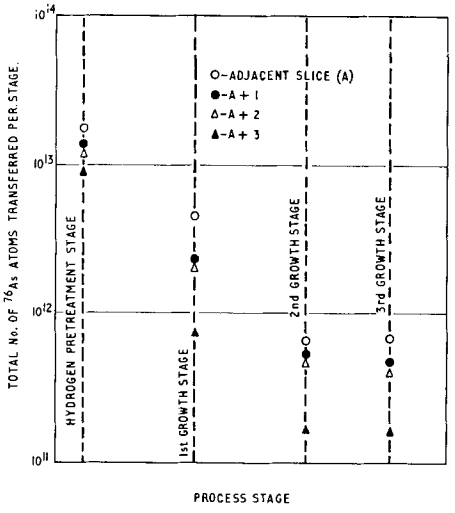

Fig. 1. Impurity transfer occurring during stages of epitaxial growth

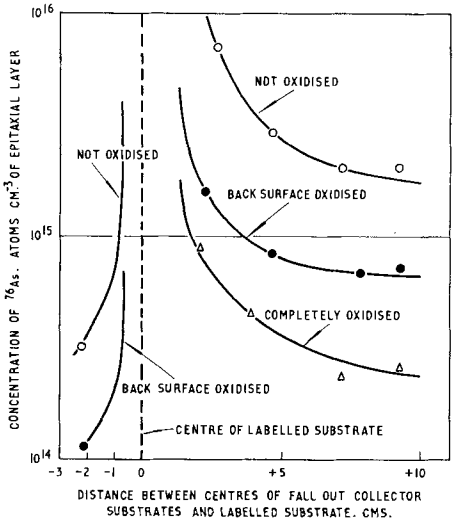

Fig. 2. Effects of oxide barriers on impurity transfer during epitaxial growth.

the hydrogen pretreatment stage. The small amount transferred during growth has been shown to equal, within experimental error, the amount transferred by outdiffusion through the oxide film on the rear surface. The results for this are given later in this section. The observed loss of impurity during hydrogen pretreatment can be correlated with normal outdiffusion processes from silicon, as described by Smits (7).

For comparative purposes the total transfer to the epitaxial layer on an adjacent substrate from substrates containing ^{32}P, ^{76}As, and ^{122}Sb is shown in Table III. The pretreatment and growth conditions were identical in all cases, and correspond to (d) above.

The second aspect of the radiotracer work was designed to study the efficiency of oxide films as barriers to outdiffusion and subsequent gas phase transport. Since significant differences were observed between group III and group V elements the results will be presented in two sections.

Results for Phosphorus, Arsenic, and Antimony

Again the results for the group V elements were qualitatively similar, and only those for arsenic will be presented in detail. The experimental sequence was as follows. Three ^{76}As labelled slices were used in successive runs; for the first the slice was completely unoxidized, for the second the slice had a 1μ oxide film on the back surface only, and for the third a 1μ film on all surfaces. The labelled slice was placed in No. 2 position in a multislice reactor, there being a total of six substrates. They were treated in hydrogen for 20 min at 1200°C, followed by deposition of a 10μ layer at 1μ min^{-1} at 1200°C. The β-activity of the layers on the unlabelled substrates was then measured, and the results are presented in Fig. 2. In this the relative position of the center of each slice is plotted on the distance axis, but the actual count was of course made over the whole of each slice, of 2.5 cm diameter. (The final downstream substrate was semicircular, but of the same diameter.) Thus it may be seen that while an oxide film has a considerable effect as an outdiffusion barrier for arsenic (and similar results were obtained for phosphorus and antimony), some transfer occurs even when the substrate is completely oxidized. This is in accordance with results obtained for the segregation of arsenic between Si and SiO_2 during thermal oxidation, when it was found that ratio of the average concentration of ^{76}As in SiO_2 to the average concentration in the Si was 0.51:1 (for an initial concentration of 1.1×10^{19} at. ^{76}As cm^{-3}, in the silicon, which was oxidized in steam at 1100°C). It should be pointed out that since the growth temperature was 100°C higher than the oxidation temperature some further redistribution of impurities between silicon and silica may occur during the growth of the layers. This compares approximately with the results of Grove *et al.* (8) and indicates that while some accumulation of arsenic in silicon does occur at the silicon-silica interface the extent of this accumulation is quite small. This point is of some importance in considering the surface concentration existing in a substrate which has been oxidized on all surfaces, and then the front surface oxide removed. It will be considered again in the section dealing with solid-state diffusion processes during epitaxial growth. However, the result also indicates that the concentration of arsenic in the silica film is sufficiently high in comparison with the original concentration in the silicon for a considerable amount to be lost by outdiffusion, provided that the diffusion coefficient is large enough, which appears to be the case.

In fact it is possible to make a comparison between the amount of impurity transferred during the actual growth process and the amount transferred by outdiffusion through the oxide film on the rear surface. From Fig. 1, the total number of ^{76}As atoms transferred to the adjacent slice during the growth of a 10μ layer (excluding the hydrogen pretreatment stage) equals 5.6×10^{12}. A labelled substrate with a 1μ oxide film on all surfaces was then used, and a 10-min deposition carried out at a growth rate of 1 μmin^{-1} and a temperature of 1200°C. No hydrogen pretreatment was used. A β-count was made on the adjacent downstream slice and the total number of ^{76}As atoms transferred found to be 5.1×10^{12}. It is considered that the only escape mechanism through an oxide film is outdiffusion, and almost all of this must be via the rear surface, as the front is rapidly covered with a layer of polycrystalline silicon. Thus it appears that transfer during growth can be equated, within experimental error, to transfer by outdiffusion through the oxide on the rear of the slice.

Table III. Pretreatment and growth conditions

Substrate impurity nature and concentration at. cm^{-3}	Substrate rear surface conditions	Adjacent layer contamination at. cm^{-3}
^{32}P, 4×10^{18}	Not oxidized	$<1.5 \times 10^{15}$ (detection
	Oxidized	$<1.5 \times 10^{15}$ limit)
^{76}As, 1×10^{19}	Not oxidized	7.2×10^{15}
	Oxidized	1.6×10^{15}
^{122}Sb, 7.5×10^{18}	Not oxidized	1.1×10^{14}
	Oxidized	4.2×10^{13}

Table IV. Results

Substrate impurity concentration ^{72}Ga at. cm^{-3}	Surface conditions	Concentration of ^{72}Ga in adjacent epitaxial layer, at. cm^{-3}
3.2×10^{17}	No oxide	1.8×10^{15}
3.2×10^{17}	Oxide on rear surface only	8.5×10^{14}
3.2×10^{17}	Oxide on all surfaces	5.6×10^{14}

Results for Gallium

Gallium is the only acceptor to have a suitable isotope, so radiotracer work for group III had to be confined to this element although it is quite possible that other acceptors may behave differently. Further, since the solubility of gallium in silicon is comparatively low the maximum impurity level available was 3.2 x 10^{17} at. cm^{-3}. A series of runs corresponding to those for arsenic doped substrates was carried out, except that in this case only one downstream slice was used to detect transfer because of the much lower impurity concentration in the active substrate. The results are shown in Table IV. (Growth conditions were the same as (d) of Table II.)

Two points are immediately apparent from these results; first, the amount of downstream transfer with respect to the substrate concentration is significantly higher for gallium than for group V impurities, and second, the efficiency of a thermal oxide film as a barrier to outdiffusion is very low in this case. This result is the expected one based on the results of Grove *et al.* (8, 9), who showed that although the segregation coefficient of gallium between silicon and silica favors a larger equilibrium concentration in the silicon, the diffusivity of gallium in silica is so high that it readily escapes into the gaseous ambient, and the over-all effect is a depletion of the impurity from the silicon. As a check, the actual segregation during thermal oxidation was measured radiochemically. It was found that for an oxide film 1μ thick grown at 1100°C in steam the ratio of the concentration of gallium in the silica to the concentration in the silicon was 6.2, for an initial concentration of 3.8 x 10^{17} at. cm^{-3} in the silicon. It appears, therefore, that the value of the segregation coefficient determined radiochemically differs from previously calculated values, and depletion of the silicon might arise from a combination of high diffusivity and higher solubility of gallium in silica. However, the over-all effect is still to allow escape of gallium from the oxide. Thus in a multislice system using gallium doped substrates significant amounts of downstream transfer will always occur, and if a substrate undergoes oxidation followed by partial removal prior to deposition, there will be a considerable depletion of gallium at the substrate surface.

The final transfer problem which was dealt with by radiotracer techniques concerned the transport of material from the rear of the substrate into the epitaxial layer grown on this same substrate. In order to do this a slightly different technique was used. Phosphorus was diffused into a silicon wafer from a phosphine source to give a surface concentration of 5 x 10^{18} at. cm^{-3}, and a junction depth of 7μ (the background concentration was 10^{14} B at. cm^{-3}). This slice was then irradiated and one surface and all sides were removed to a depth of approximately 25μ to yield a rectangle of silicon of area 1.9 cm^2, with phosphorus diffused into one surface. The geometry of this arrangement is shown in Fig. 3. After pretreatment in hydrogen (20 min at 1200°C) a 10μ thick epitaxial layer was deposited on the phosphorus free face (1 μmin^{-1} at 1200°C), and the active phosphorus in this layer, which arose by transport from the back surface, was measured. The experiment was carried out with and without a 1μ thick SiO_2 film over the phosphorus diffused area. The results are shown in Table V.

Table V. Results

Substrate		Epitaxial layer
N_S ^{32}P at. cm^{-3}	Rear surface condition	N ^{32}P at. cm^{-3}
5×10^{18}	Not oxidized	1.8×10^{16}
5×10^{18}	Oxidized	$<6 \times 10^{14}$

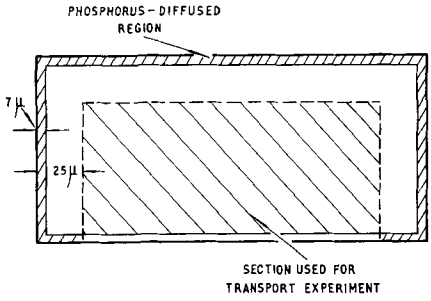

Fig. 3. Slice geometry for rear to front surface transfer experiments

Thus significant transfer from the back surface to the front does occur where no oxide film is present, but a 1μ thick film is sufficient to reduce the phosphorus transfer below the limits of detection of ^{32}P. However the amount of arsenic transferred through a similar film appears to be rather greater, reaching about 8 x 10^{14} at. cm^{-3} under corresponding conditions.

Thus the radiotracer results of gas phase transport effects may be summarized as follows:

(*a*). In a multislice system considerable downstream transfer of impurities is observed, but essentially it all occurs during any pretreatment in hydrogen, by a normal outdiffusion process. There is negligible transfer resulting from any possible etch back mechanism.

(*b*). Oxide films provide much better outdiffusion barriers for group V elements than for gallium, but they are not completely effective for any of the elements studied.

(*c*). A measurable quantity of impurity transfer from the rear surface to the epitaxial layer on the same substrate occurs via the gas phase, as a result of outdiffusion, but again this can be minimized by an oxide film, at least for group V elements.

It is apparent that item (*a*) is by far the most important result obtained from the radiotracer experiments and basically may be taken to mean that "autodoping" as a separate phenomenon based on an etch back mechanism does not occur. All gas phase transfer processes can be accounted for by normal outdiffusion, and in a single slice system where the back of the slice is oxidized, the impurity profile must be accounted for simply by solid-state diffusion, with the exception of a small amount of material which diffuses through the oxide film.

Comparison of Theoretical and Measured Impurity Profiles

Since the radiotracer experiments have shown that there is negligible gas phase transfer occurring from the front of the slice during growth, any redistribution must be accounted for in terms of solid-state diffusion (including outdiffusion through an oxide barrier). "Anomalous diffusion" in epitaxial silicon layers has been reported previously (10) where it was shown that the value of the diffusion coefficient can be as much as nine times greater in the interface region than in bulk material because of poor crystal perfection. However, here the diffusion was carried out after the growth process was complete, so the problem was one of normal diffusion.

It has been suggested by Rice (11) that for the case of concurrent diffusion and growth, *i.e.*, the normal epitaxial process, it is necessary to treat the diffusion as a moving boundary problem in order to obtain an accurate knowledge of the distribution profile. How-

ever, it has been shown by Grove *et al.* (5) that for all normal conditions of epitaxial growth, the solution approximates extremely closely to a simple complementary error-function-type distribution. In addition, it appears that the computations in Rice's paper only give the complementary error function distribution, and do not include the moving boundary effect. Therefore, briefly, the moving boundary solutions are given below, and it is shown, following Grove, how these reduce to the complementary error function distribution for all practical conditions.

The over-all solution is the sum of two component solutions, *i.e.*, (i) final distribution of impurities originally in the substrate and (ii) final distribution of impurities added with the growing layer. The same differential equation governs both cases, although boundary conditions are different.

$$i.e.,\ \partial C/\partial t = D(\partial^2 C/\partial x^2), -\infty < x < x_f, t > 0 \quad [1]$$

where C is the concentration and x the layer thickness at time t. The final thickness is given by $x_f = Vt$, where V is the layer growth rate.

The determination of the final distribution of impurity originally in the substrate is carried out by generating a solution of [1] with the following initial and boundary conditions.

(i) $C(x,O) = M$ (*i.e.*, original impurity concentration in the substrate is constant)
(ii) $\lim_{x\to\infty} C(x,t) = M$ (*i.e.*, concentration far from surface at which deposition occurred not depleted).
(iii) $-D\,(\partial C/\partial x) = (h+V)C$ at $x = x_1$, (*i.e.*, material diffusing to the surface of the layer either escapes or is incorporated into the layer. h is the coefficient of escape of impurities at the surface).

The solution in dimensionless form is then:

$$C(x,t)/M = \tfrac{1}{2}\,\mathrm{erfc}\,[x/2(Dt)^{1/2}] - [(h+V)/2h] \times \exp[(V/D)(Vt-x)] \times \mathrm{erfc}\,[(2Vt-x)/2(Dt)^{1/2}] + [(V+2h)/2h] \times \exp\{[(V+h)/D][(V+h)t-x]\} \times \mathrm{erfc}\,\{[2(V+h)t-x]/2(Dt)^{1/2}\} \quad [2]$$

However, for all normal values of growth rate, *i.e.*, $Vt/(Dt)^{1/2} >> 1$, [2] reduces to

$$C(x,t)/M \simeq \tfrac{1}{2}\,\mathrm{erfc}\,[x/2(Dt)^{1/2}] \quad [3]$$

In order to determine the final distribution of impurity added with the growing layer the following initial and boundary conditions are used

(i) $C_2(x,O) = O,\ x < O$ (*i.e.*, substrate initially contains none of the impurity added with the growing layer)
(ii) $C_2 \to O$ as $x \to -\infty$ (*i.e.*, no impurity added with deposited layer reaches points deep in the substrate)
(iii) $C_2(x_f,t) = K$ (concentration of this impurity is constant at film surface).

The solution is given by

$$C_2(x,t)/K = \tfrac{1}{2}\{1 + \mathrm{erf}[x/2(Dt)^{1/2}] + \exp[(V/D)(Vt-x)] \times \mathrm{erfc}\,[(2Vt-x)/2(Dt)^{1/2}]\} \quad [4]$$

but for $Vt >> (Dt)^{1/2}$, *i.e.*, practical growth conditions, and, in the film, for distances $x > 2(Dt)^{1/2}$ from the interface

$$C_2(x,t) \simeq K \quad [5]$$

Simple complementary error function distributions were therefore used to obtain theoretical impurity profiles.

Thus capacitance-voltage measurements were made on shallow diodes fabricated in n-type epitaxial layers grown on n^+ substrates and impurity profiles determined from these. The only growth variable was temperature, and values in the range 1150°-1250°C were used. The impurity concentration in the substrates was approximately 10^{19} at. cm^{-3}, using both phosphorus and antimony. The growth rate was 1 μmin^{-1}, and 10μ layers were grown. The impurity added with the growing layer was always phosphorus, and the back surface of the substrate was always oxidized in order to minimize transfer from that source.

Impurity profiles were determined from the capacitance voltage data and Fig. 4a to c show the profiles from layers on antimony doped substrates for growth temperatures of 1150°, 1200°, and 1250°C, respectively. The layers were all approximately 10μ thick and were grown at 1 μmin^{-1}. The theoretical profiles are also shown and indicate a reasonable level of agreement. It may be seen that penetration of impurity from the substrate is a function of temperature in the normal way to be expected for a diffusion process. [The theoretical profiles were computed using standard values of diffusion coefficients and activation energies of diffusion (12) and since the over-all agreement between theory and experiment is quite good, it may be assumed that approximately the same values hold in the practical system].

Previous workers (2, 3) have also attributed the comparatively sharp profile close to the substrate-layer interface to a solid-state diffusion process, the so-called diffusion tail, and the results presented here show that the measured profiles do in fact agree closely with those determined theoretically over most of the range.

However, the divergence between measured and computed profiles for impurity concentrations less than about 5 x 10^{14} at. cm^{-3} is probably too great to be accounted for by experimental error. These portions of the curves do in fact correspond closely to those regions which Thomas *et al.* interpreted as arising from an etch back mechanism. Since the radiotracer results have shown that this explanation is not tenable, an alternative must be sought. While no definitive evidence is available it is suggested that this extra impurity is incorporated after outdiffusion through the oxide mask on the back of the slice. It would only require the release of approximately 10^{12} at. of impurity to make up the difference between the observed and calculated values, and the radiotracer experiments have shown that amounts of this order are lost by outdiffusion through the oxide. One further set of results appears to provide evidence in favor of this mechanism. This concerns the radial redistribution of impurities in a slice; it is observed that if capacitance-voltage measurements are made on diodes fabricated across the diameter of an epitaxial layer, the impurity profiles so obtained are not consistent but vary well outside the limits of experimental error. The variation is not random, but is a function of the position of the diode across the slice, and of the temperature of

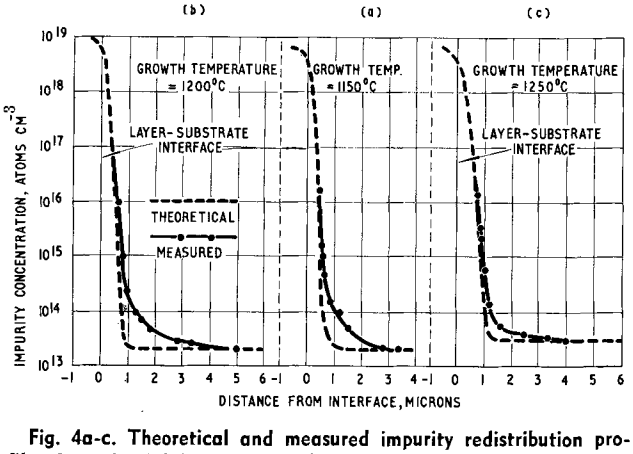

Fig. 4a-c. Theoretical and measured impurity redistribution profiles for epitaxial layers on Sb-doped substrates.

growth. It is found that penetration is greatest on peripheral devices, decreasing to a minimum at the center, and also that the final film doping level follows the same pattern. The effect of temperature is to effect the degree of variability, being very slight at 1150°C, and most pronounced at 1250°C. Some results for 10μ layers on antimony doped substrates (impurity concentration $\sim 10^{19}$ at. cm^{-3}) at three temperatures are presented in Fig. 5a and b. In both cases the ordinate represents the relative position along a radius of the layer, while in Fig. 5a the abcissa represents the penetration depth at which an arbitrarily chosen impurity concentration (5 x 10^{14} at. cm^{-3}) is reached and in Fig. 5b the final film doping level obtained with no deliberately added impurity. Obviously no significance should be attached to the actual shapes of the curves, nor to the absolute values of the ordinate, but the trend is quite apparent. A further point which is brought out by Fig. 5b is that the actual value of the finally achieved impurity concentration is also a function of temperature, irrespective of the position on the slice. Higher growth temperatures in fact lead to higher final doping levels. Qualitatively similar results were obtained for other group V impurities.

It appears that all of these results can be explained on the basis of outdiffusion through the oxidized rear surface. The effect of temperature would be simply to increase the total amount of impurity liberated, in accordance with the observed result, a dynamic equilibrium eventually being achieved for each temperature. The radial distribution would result from the gas flow patterns set up in the reactor, and something of the form illustrated in Fig. 6 seems a reasonable approximation, allowing for the comparatively poor contact which is known to exist between susceptor and slice.

The results so far presented do not show any cases of anomalous diffusion (*i.e.*, abnormally high diffusion rates), but such effects were observed particularly in the case of phosphorus doped substrates. In these circumstances it was necessary to adjust the value of the diffusion coefficient by amounts up to an order of magnitude over the bulk value in order to obtain a reasonable fit between theoretical and calculated profiles. However such values have been determined by Kahng *et al.* (10) and attributed by them to crystal imperfections. Because of the apparently random variations from the normal value of the diffusion coefficient observed during this work, the defect explanation does not seem to be the only plausible one, and system contamination may be responsible, with the possible proviso that phosphorus appears always to penetrate further than the true value of D would allow. A typical profile for a phosphorus doped substrate ($\sim 10^{18}$ at. cm^{-3}) is shown in Fig. 7, for a 10μ layer grown at a temperature of 1200°C.

To obtain the level of agreement shown the value of D was adjusted by a factor of ten, which is about average for phosphorus doped substrates. If the explanation for the anomalous diffusion lies only in terms of crystal defects or system contamination, then it is difficult to account for the behavior of phosphorus. While it is well known that diffusing phosphorus atoms can induce dislocations in silicon (13) the actual impurity concentration for the experiments discussed above is rather lower than the reported concentration necessary to produce a sufficiently high dislocation density to affect diffusion rates significantly. Further, other group V elements should also produce dislocations in the same way, at equivalent, or possibly lower concentrations. However, no evidence to account for this effect in any other way has been produced during this investigation, but it may be worthwhile pointing out one possibility. A good deal of evidence exists to show that the presence of a second impurity can greatly increase the diffusion rate of the first when both impurities are of like charge, and decrease it when they are oppositely charged (14). It has also been shown by one of the authors (J.C.W.), using radiochemical techniques, that epitaxial silicon layers grown from silicon chlorides contain between 10^{16} and 10^{17}

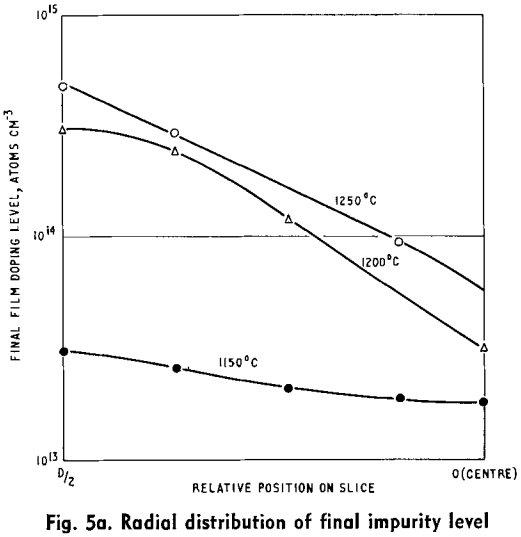

Fig. 5a. Radial distribution of final impurity level

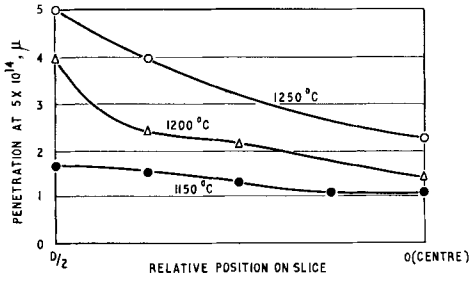

Fig. 5. Radial distribution of impurity penetration

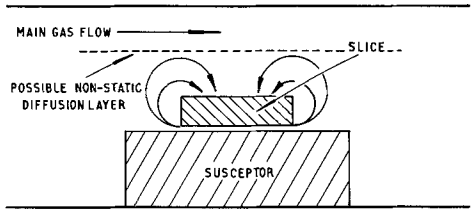

Fig. 6. Possible gas flow patterns in reactor tube

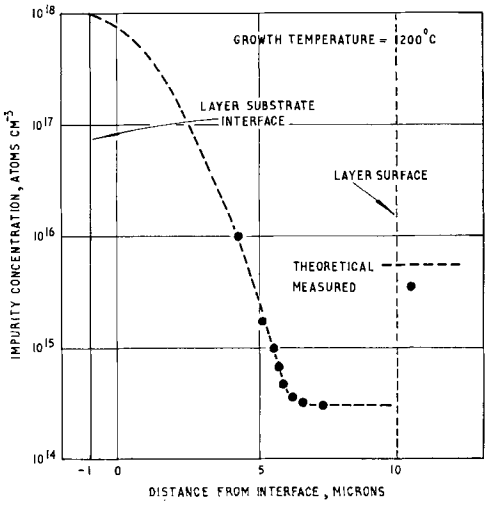

Fig. 7. Theoretical and measured impurity redistribution profiles for a phosphorus doped substrate, showing anomalous diffusion rate.

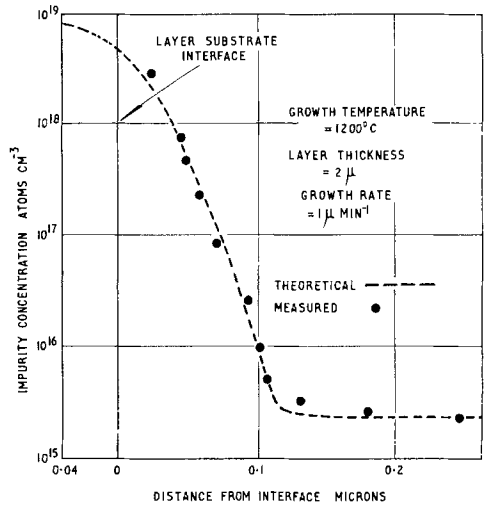

Fig. 8. Theoretical and measured impurity redistribution profiles for a thin (2μ) epitaxial layer.

at. cm^{-3} of chlorine (15) although it is not known in what form the chlorine is present. It is suggested, therefore, that chlorine may increase the diffusion rates of group V impurities, and that the effect is greatest for phosphorus. On this basis, of course, it would be expected to decrease the diffusion rates of group III impurities, but the rate of outdiffusion, at least of gallium, through the oxidized rear surface is so great as to mask any solid-state diffusion effects.

A second way of checking this hypothesis is to consider autodoping effects in silane grown layers, where obviously no chlorine can be present. However, available data are not sufficiently accurate to enable any conclusions to be drawn. The method of profile determination used by Mayer and Shea (16) was rather suspect, and although the capacitance voltage method was used by Bhola and Mayer (17), measurements were not extended sufficiently close to the interface to enable an assessment of the extent of anomalous diffusion to be made. (The diffusion coefficient of arsenic could be increased by a factor of about 60 and still include all of the experimental points shown.) Our own work on silane (18) used a low pressure rather than a hydrogen dilution system and, because of different outdiffusion effects, comparison between this and the chloride systems, is probably not valid.

Finally, in order to check the radiotracer results by means of profile determination, layers of varying thickness were grown and the impurity distribution through them measured. It was thought that, if the single etch back mechanism, in particular, was in any way valid, then the extent of autodoping should be greater in thinner layers, since all of the impurity would be liberated initially, and in thin layers there would be insufficient time for the deliberately added impurity to become the controlling parameter. On the other hand, if the mechanism as determined by radiotracer experiments was correct, and essentially no gas phase transfer occurred via the front of the slice during growth, then autodoping should only be time dependent in accordance with the appropriate diffusion equation. This was in fact found to be the case, and the result for a layer grown for 2 min at 1 μmin^{-1} and a temperature of 1200°C is shown in Fig. 8. The theoretical profile is also shown, and the agreement is extremely good. The substrate was arsenic doped to a level of $\sim 10^{19}$ at. cm^{-3}.

Summary and Conclusions

It has been shown, using radiotracer techniques, that impurity redistribution during the epitaxial growth of silicon does not occur from the front of the slice via the gas phase, but that some outdiffusion from the back does occur, even when this is covered by an oxide film. During any pretreatment in hydrogen at elevated temperatures, the normal outdiffusion processes occur from both surfaces, and impurities are transferred downstream in a multislice system. However, the etch back mechanism proposed in various forms by Thomas *et al.* (2, 3) and by Grossman (4) does not appear to take place.

The form of the final impurity distribution profile can be accounted for almost entirely by normal solid-state diffusion, with two possible exceptions. First, for impurity concentrations less than 5×10^{14} in the growing layer, the outdiffusion of impurities from the back surface, even if this is oxidized, can be the controlling factor. Second, in some cases, and particularly with phosphorus doped substrates, it is necessary to assume values of diffusion coefficients up to an order of magnitude larger than normal to obtain agreement between theoretical and measured profiles. Two possible explanations for this are in terms of enhanced diffusion rates associated with crystal defects or with the presence of a second impurity.

Acknowledgments

The authors are indebted to Mr. J. H. Neave for layer preparation, to Mr. J. Whitworth for some of the radiochemical analyses, and Mr. R. M. Ware for valuable criticism and discussion. Thanks are due to the Plessey Company for permission to submit this paper.

Manuscript received May 17, 1965; revised manuscript received Aug. 3, 1965.

Any discussion of this paper will appear in a Discussion Section to be published in the June 1966 JOURNAL.

REFERENCES

1. H. Basseches, R. C. Manz, C. O. Thomas, and S. K. Tung, A.I.M.E. Semiconductor Metallurgy Conference, Los Angeles, 1961, Interscience Publishers, New York, Vol. 15, p. 69, J. R. Schroeder, Editor.
2. C. O. Thomas, D. Kahng, and R. C. Manz, *This Journal*, **109**, 1055 (1962).
3. D. Kahng, C. O. Thomas, and R. C. Manz, *ibid.*, **110**, 394 (1963).
4. J. J. Grossman, *ibid.*, **110**, 1065 (1963).
5. A. S. Grove, A. Roder, and C. T. Sah, *J. Appl. Phys.*, **36**, 802 (1965).
6. J. Hilibrand and R. D. Gold, *RCA Rev.*, **21**, 245 (1960).
7. F. M. Smits, *Proc. I.R.E.*, **46**, 1049 (1958).
8. A. S. Grove, O. Leistiko, and C. T. Sah, *J. Appl. Phys.*, **35**, 2695 (1964).
9. A. S. Grove, O. Leistiko, and C. T. Sah, *J. Phys. Chem. Solids*, **25**, 985 (1964).
10. D. Kahng, C. O. Thomas, and R. C. Manz, *This Journal*, **109**, 1106 (1962).
11. W. Rice, *Proc. I.E.E.E.*, **52**, 284 (1964).
12. C. S. Fuller and J. A. Ditzenberger, *J. Appl. Phys.*, **27**, 544 (1956).
13. M. L. Joshi and F. Wilhelm, *This Journal*, **112**, 185 (1965).
14. M. F. Millea, *Semiconductor Electronics*, **316**, 3271 (1958).
15. J. C. Weaver, Unpublished work.
16. S. E. Mayer and D. E. Shea, *This Journal*, **111**, 550 (1964).
17. S. R. Bhola and A. Mayer, *R.C.A. Rev.*, **24**, 511 (1963).
18. B. A. Joyce and R. R. Bradley, *This Journal*, **110**, 1235 (1963).

Mechanism of Anodic Germanium Oxide Film Formation

Joseph B. Story[1]

Materials Sciences Laboratory, Lockheed Missiles and Space Company, Palo Alto, California

ABSTRACT

Voltage transient studies were made on the Ge-GeO_2 electrode in a system of acetic anhydride containing small amounts of acetic acid, water, and lithium nitrate. These studies indicate that water diffuses into and through the GeO_2 film, that it reacts electrochemically at or near the Ge-GeO_2 interface, and that the hydrogen ion so produced moves back through the film as the current-carrying species. Increasing the concentration of water in the film increases the conductivity by increasing the jump distance of the hydrogen ion.

Anodic germanium oxide films have been produced by Zwerdling and Sheff (1) who used anhydrous sodium acetate in glacial acetic acid as an electrolyte, and by Wales (2) who used lithium nitrate in acetic anhydride containing small amounts of germanium dioxide, acetic acid, and water. Additional studies of a system similar to that of Wales have shown an unexpected voltage transient effect, an effect which this paper seeks to explain. In the course of the investigation, it was found that the information obtained is relevant to the mechanism of film formation.

Experimental Procedure

Cell.—The cell used for this study (Fig. 1) is almost identical to that used by Wales (2,3). The electrode was mounted outside the cell body, the effective electrode area of 0.50 cm^2 being defined by a circular hole in the cell wall or in the gasket. In voltage decay experiments, the germanium was cemented over the hole in the cell wall with a sodium silicate solution; in all other studies a neoprene gasket was used. The bottom of the cell contained a temperature control "finger" and an argon pump that provided an argon flush and a slow mixing of the electrolyte. A layer of mercury prevented the solution from leaking between the cell wall and cell bottom. For voltage decay work the temperature used was 23°C; for the other experiments, it was 25°C. The cathode was a tantalum sheet.

Flexible salt bridge and Luggin capillary.—The potential was measured between the germanium and the tip of a Luggin capillary placed near the oxide film. By filling a length of No. 22 AWG Teflon tubing with an agar gel of an aqueous potassium chloride solution, a flexible salt bridge and Luggin capillary was created. The aqueous agar gel was satisfactorily stable in contact with the acetic anhydride-based electrolyte. Because this form of flexible salt bridge could be readily manipulated, it was convenient for this application. The end used as the capillary was guided into position by being passed through a glass tube built into the cell, and the opposite end was immersed in a stoppered jar containing an aqueous potassium chloride solution and a commercial calomel electrode.

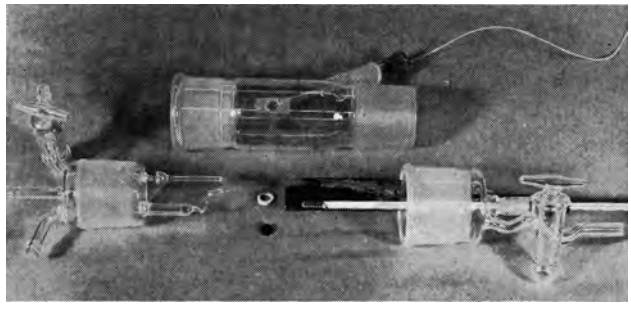

Fig. 1. Photograph of cell

Materials.—The electrolyte employed was acetic anhydride containing 6.0 x 10^{-3} mole/liter lithium nitrate, 0.10 mole/liter acetic acid, and 0.30 mole/liter water. The acetic anhydride, acetic acid, and lithium nitrate were of reagent grade. The germanium used was a single crystal 1-1-1 face p-type with a resistivity of 0.62 to 0.76 ohm-cm. It was etched with CP-4A [3HF (48%), 5HNO_3, and 3HAc, by volume].

Instrumentation.—The potential was measured with a Model 610 Keithley electrometer. Recording of the potential-time curves was made by connecting the electrometer output to an oscilloscope and photographing the trace.

The constant current source was based on the field-effect transistor (8) which contained five individual constant current sources (each variable) that could be connected in parallel in various combinations.

Organization of the study.—Several different kinds of measurement were used in this study. The investigation centers about a particular experimental observation which can be described as follows: (*i*) an anodic GeO_2 film is grown at constant current until the voltage across the film increases to a value V_1; (*ii*) the current is turned off for a few minutes; (*iii*) the constant current is turned on again; (*iv*) the voltage, however, does not immediately rise to V_1, a period of

[1] Present address: University of Arkansas, Graduate Institute of Technology, Little Rock, Arkansas.

Table I. Outline of sequence of experiments

Object	Experiment or plot	Result and conclusion
Determine importance of water in observed effect.	Add small amount of water to solution during film growth.	Major change observed; water assumed to be important in effect.
Determine whether effect occurs within GeO_2 film.	Plot intensity of effect as function of film thickness.	Plot is linear over wide range of film thicknesses; therefore, effect is uniformly distributed within film.
Describe changes occurring in electrical conductivity of GeO_2 film during effect.	At two different stages of effect (a and b) switch current rapidly through series of constant currents (I_1, I_2, etc.); observe voltages Va_1, Va_2, etc., and Vb_1, Vb_2, etc.	Va_1: Va_2: : Vb_1: Vb_2 Va_1: Va_2: : Vb_1: Vb_3, etc. Assuming oxide conduction model is valid, observed effect is result of change in activation distance.
Obtain additional evidence of change in activation distance.	Interrupt current briefly at two different stages; record voltage decay curves.	V *vs.* log t plots of potential decay curves show straight lines of somewhat different slope. Assuming potential decay occurs according to model, difference in slope indicates difference in activation distance.

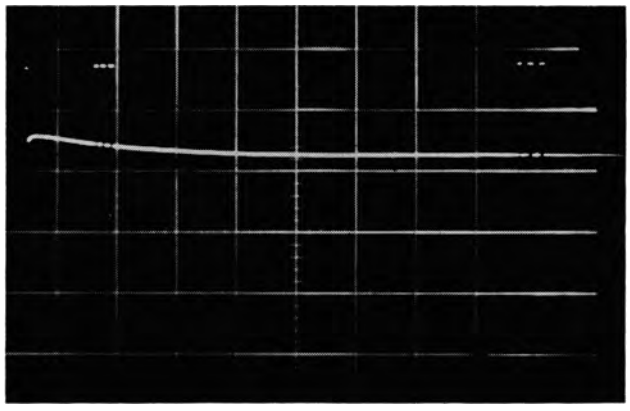

Fig. 2. Voltage transient of Ge-GeO_2 electrode after interruption at low potential. Vertical scale, 20 v/square (read top to bottom, zero potential indicated by dots); horizontal scale, 6.8 sec/square; current density, 120 $\mu a/cm^2$.

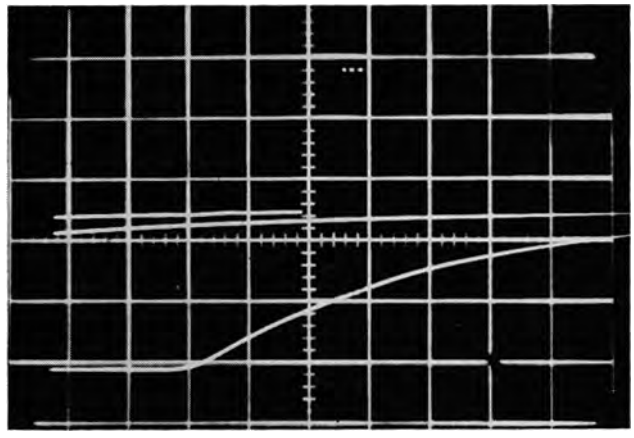

Fig. 3. Hydration of Ge-GeO_2 electrode by addition of 0.5 w/o H_2O to electrolyte. Picture covers 4 min. Vertical scale, 20 v/square; horizontal scale, 6.8 sec/square; current density, 120 $\mu a/cm^2$.

½ to 1 min being required (an oscilloscope trace showing this effect is presented in Fig. 2). Why does this phenomenon occur? Table I lists the sequence of investigational efforts employed to answer this question.

Results

An anodic germanium oxide film was grown in the acetic anhydride-acetic acid-water-lithium nitrate system at constant current. At intervals throughout the growth, the current was turned off for several minutes, then turned on again. Each time this occurred, ½ to 1 min was required for the voltage across the film to rise to its previous value. A typical oscilloscope trace of the voltage change is presented in Fig. 2. Voltage-time curves for interruptions at other voltages can be approximated by multiplying the ordinates of the curve by an appropriate factor, provided that the voltage at interruption is lower than about 60v (at 120 $\mu a/cm^2$). If the voltage is over 60v (at 120 $\mu a/cm^2$), the voltage may continue to rise for several minutes until it exceeds 100v (limit of the Keithley electrometer). If the rise is completed within 1 min, the voltage normally will not exceed the voltage observed before the interruption. If, however, the rise continues for more than 1 min, the voltage can reach values much higher than would be expected if no interruption had occurred.

In Fig. 2, there is an initial "overshoot" in potential. The subsequent decrease in potential appears to be caused by the generation of additional charge carriers as a result of the current. This increase in current carriers has been observed in oxide films on tantalum and several other metals (4). Apparently, a steady-state is reached within a few seconds. The magnitude of the overshoot and the time required for the steady-state to be reached seem to be proportional to the film thickness.

It is convenient to anticipate the results of this study by specifying a name, "dehydration voltage," for the voltage change observed on resumption of the constant current after its interruption. Dehydration voltage will be defined as the difference between the minimum voltage (observed just after the overshoot) and the voltage observed when the steady state is again attained. The dehydration voltage is not defined for cases in which greatly prolonged voltage rise occurs. The oscilloscope trace showing the observed effect will be called the "dehydration trace."

If the small amount of water [0.5 w/o (weight per cent)] present in the acetic anhydride-acetic acid-water-lithium nitrate system is significant in the formation of the germanium oxide film, then the addition of another 0.5 w/o water should have an appreciable effect on the voltage across the film. The effect of such an addition is shown in Fig. 3. The voltage across the film decreased from over 100 to 49v. A dehydration trace made after the addition of this larger amount of water was similar to that for a thinner film, except that the period required for the overshoot to decrease to its steady-state value remained that of the thick film.

In studying the constant current formation of anodic germanium oxide films in a system almost identical with that used in this study, Wales (2) has shown that both the voltage across the film and the film thickness increase linearly with time (after a brief initial period). Thus, the increase in film thickness is proportional to the increase in voltage across the film, and a plot of dehydration voltage *vs.* total voltage across the film at the time of interruption will be linear when the dehydration voltage *vs.* film thickness plot is linear. Such a plot is presented in Fig. 4. Other runs at the same current densities show the same trends, but the values scatter by as much as 20%. Thus, the dehydration voltage varies linearly with film thickness, within the limits of reproducibility of the data.

It was hoped that, by studying and comparing the instantaneous current-voltage properties of the film at two different points along the dehydration trace,

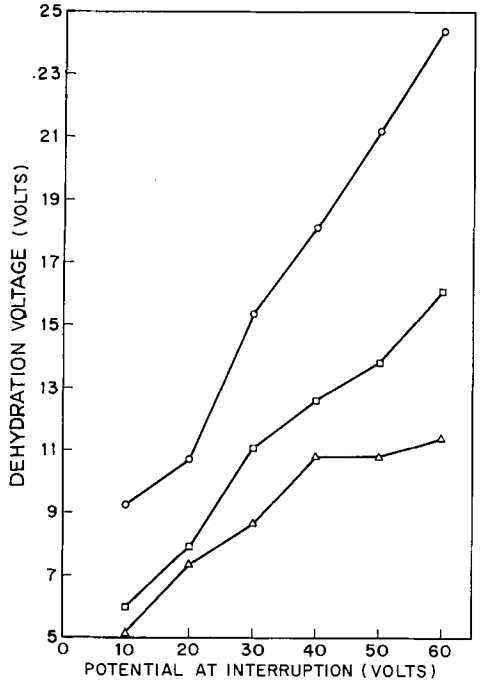

Fig. 4. Dehydration voltage as a function of potential at interruption: circle, 360 $\mu a/cm^2$; box, 120 $\mu a/cm^2$; triangle, 50 $\mu a/cm^2$.

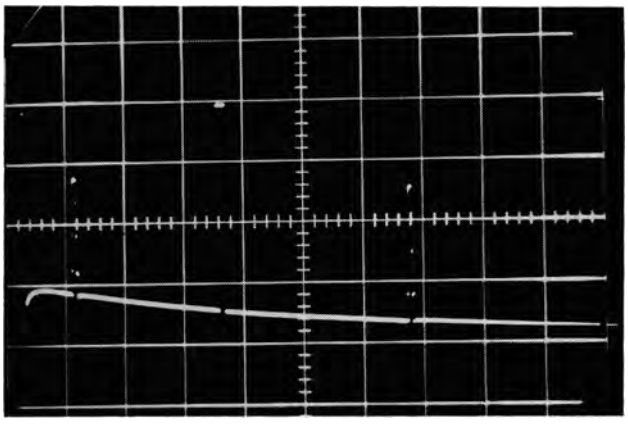

Fig. 5. Dehydration of Ge-GeO_2 electrode after interruption. Vertical scale, 20 v/square; at 7 and 60 sec current decreased in sequence 120, 80, 40, 20, 10 $\mu a/cm^2$, then increased in reverse sequence.

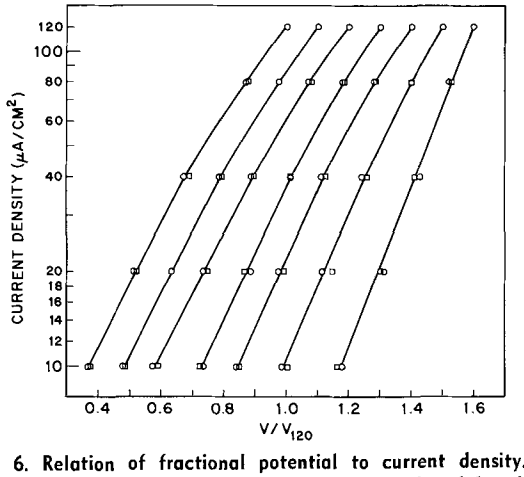

Fig. 6. Relation of fractional potential to current density. Potential at 120 $\mu a/cm^2$ defined as 1.00; curves displaced for clarity. (Dehydration for 7 sec, circle; for 60 sec, box.) From left to right, runs represent interruption 90, 80, 70, 40 30, 20, and 10v, respectively.

some understanding of the nature of the processes occurring within the film could be gained. The comparison was accomplished by switching the current very rapidly through a series of constant currents and observing the corresponding voltages. A trace obtained by this procedure is presented in Fig. 5. In such traces it is significant that there is a constant ratio of voltages for two currents. For example, if the current is switched from 120 $\mu a/cm^2$ to 80 $\mu a/cm^2$ (then quickly back to 120 $\mu a/cm^2$) 7 sec after film growth has been resumed and the voltages Va_1 and Va_2 recorded, then again switched from 120 $\mu a/cm^2$ to 80 $\mu a/cm^2$ 53 sec later and the voltages Vb_1 and Vb_2 recorded, it is observed that $Va_1 : Va_2 : : Vb_1 : Vb_2$. Figure 6 presents such data from a series of dehydration traces. As explained later, this is interpreted to mean that an increase activation distance is associated with the dehydration trace. As a further test of the idea that the activation distance changes during the course of the dehydration trace, voltage decay curves were recorded for the very brief interruption of the dehydration trace at two points. Voltage *vs.* log time plots of these curves are presented in Fig. 7. As discussed below, the difference in slope of the two lines so obtained is interpreted as indicating an increase in activation distance.

Discussion

The decrease in the voltage across the film from over 100 to 49v upon the addition of 0.5 w/o water to the solution suggests that water is important in the formation of the film. This decrease in voltage could not

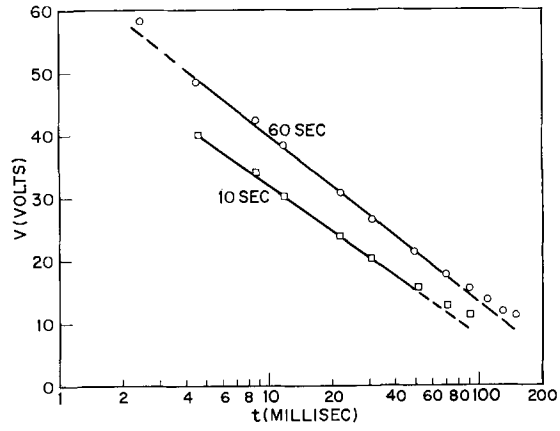

Fig. 7. Open-circuit voltage decay

possibly be the result of half of the film being dissolved because of the following:

1. The process was essentially complete at the end of 4 min. In order for the dissolution of the film to stop at the end of 4 min it would be necessary for the solution to become saturated with germanium oxide within this same period. Common laboratory experience indicates that one cannot saturate 100 ml of a solvent with a slightly soluble substance of limited contact area (0.50 cm^2) within such a short time.
2. It was observed that the addition of another 0.5 w/o water to the solution had a considerably smaller effect on the voltage across the film.
3. The voltage-time curve for the initial period of film growth (almost identical to that given by Wales) does not have the shape that would be expected if an appreciable amount of the germanium oxide being formed were being dissolved to saturate the solution.
4. The period required for the overshoot to decrease to its steady state value did not decrease to the value that would be expected for a thinner film.

The great effect of the small amount of water added can be explained only by assuming that the water penetrated the film and affected its conductivity. The penetration of water into amorphous germanium oxide has been reported (5).

Wales (2,3) has suggested that, because the oxygen in water would be more readily available than that in the acetic anhydride, in the acetic acid, or in the lithium nitrate, water is the source of the oxygen required for film growth and is necessary for such growth. Thus, the stoichiometry of anodic germanium oxide film formation can be represented.

$$Ge + 2H_2O \rightarrow GeO_2 + 4H^+ + 4e$$

It appears that the water within the film and at or near the germanium-germanium oxide interface would react in preference to the more remote water in the bulk of the film or at the germanium oxide-solution interface. If this is true, there will be a decrease in water concentration at the germanium-germanium oxide interface and a transport of water through the film by diffusion. The amount of the concentration decrease will depend on the resistance to mass transport. The major portion of this resistance could occur either in the germanium oxide film or in the stagnant liquid film (diffusion layer) adjacent to the oxide film. If the controlling resistance were in the oxide film, one would not expect the linear voltage-time curve for film growth that was found by Wales (2), since each added increment of film thickness would cause a decrease in the water content and conductivity of the underlying film. This suggests that the controlling resistance to mass transfer is to be found in the liquid phase. The common method used to test for liquid phase diffusional resistance is the stirring of the liquid. Such stirring decreases the thickness of the diffusion layer and thereby decreases the resistance to

mass transport. Such a test was made. It was found that the voltage across the oxide film decreased during stirring and rose to its initial value when stirring was stopped. Thus the controlling resistance to mass transport was in the liquid phase. This is not surprising, if one considers that the diffusion layer is probably more than a thousand times as thick as the film (2,7).

The linear increase in dehydration voltage with film thickness can best be explained by assuming that the dehydration voltage occurs within the film rather than at an interface, and that each element of film thickness (after the initial element) contributes equally to its magnitude. It is unlikely that the dehydration voltage could be an activation overpotential, since the mass transfer and electrode kinetics equations are of such complexity that one would not expect them to interact to produce a linear relation over such a wide range of dehydration voltages. The magnitude of the dehydration voltage is much greater than that usually encountered for activation overpotentials.

A consequence of the existence of a mass transfer resistance in the liquid phase is that the resumption of the current after interruption will not be accompanied by an immediate return of the voltage across the film to its value just prior to interruption. This voltage will be reached only after the mass transfer processes have again attained a steady state condition. Because water addition increases the electrical conductivity of the film, one would expect that the voltage observed shortly after resumption of the current would be lower than at the steady state condition and would then rise to the steady state value. This is what is observed in the dehydration trace. Thus, the reason for the selection of the terms "dehydration voltage" and "dehydration trace" becomes apparent, there is a decrease in water content of the film during the period in which these occur. The concentration of water in the germanium oxide film decreases until the concentration gradient across the diffusion layer is just sufficient to transport water to the film at the rate at which it is being consumed. An approximate calculation shows that the observed ½ to 1 min dehydration time is reasonable for this process.

Figure 6 represents the instantaneous current-voltage relations for a series of dehydration traces. To exhibit the constant ratio between the voltages corresponding to a particular pair of current values, each voltage is divided by the voltage observed at 120 μa/cm^2. The instantaneous current-voltage curves for 7 sec of dehydration are seen to be identical with those for 60 sec of dehydration. It is of interest to interpret these results according to the simple model for oxide film conductivity, although there is no assurance that this model is valid. The current-voltage relation for simple ionic conduction in a film [cf. (4)] can be represented by

$$i = 2eqamv \exp [-(W - eqaV/d)/kT]$$

where i is the current density, e is the electronic charge, q is the charge on the ion, a is the activation distance or half-barrier width, m is the concentration of mobile ions, v is the frequency factor, W is the height of barrier, d is the film thickness, k is Boltzmann constant, and T is the temperature.

Because a given dehydration trace is made at constant current, the voltage change that is observed will reflect a change in one or more of the other variables on the right side of the equation. The only variables that can change and leave the voltage fraction constant are those multiplying the voltage, specifically eqa/d. Because it is not reasonable to expect e, q, or d to change, the change must occur in a. Thus, the activation distance should vary as $1/V$.

It is of interest to plot $1/V$ *vs.* the square root of time ($t^{1/2}$) for: (*i*) the dehydration of the film, (*ii*) the hydration of the film by the addition of water to the solution during film growth, and (*iii*) the hydration of the film by decreasing the current density to a fraction of its initial value. Such plots are shown in Fig. 8, 9, and 10. It is evident that there is a linear relation. In the opinion of the writer, this linearity is a result of both activation distance (proportional to $1/V$) and $t^{1/2}$ being linearly related to the concentration of water at the film-solution interface. The linear relation between interface reactant concentration and $t^{1/2}$ is known from the unsteady state diffusion equation for a constant current process (6). Thus there appears to be a linear relation between the activation distance and the water concentration at the film-solution interface. The writer suspects that there is a linear relation between the water content of the film and the concentration of water at the film-solution interface, and a linear relation between the water content of the film and activation distance.

Additional evidence of a change in the activation distance during dehydration can be found by inter-

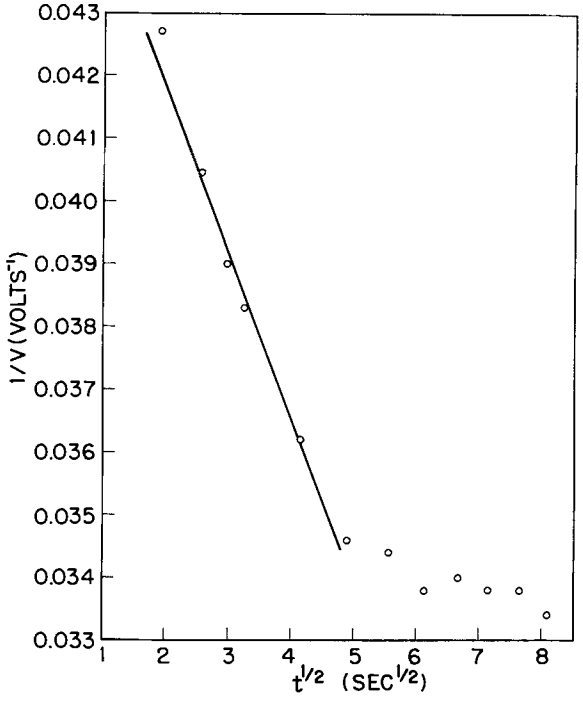

Fig. 8. Dehydration of the Ge-GeO$_2$ electrode (data from Fig. 2)

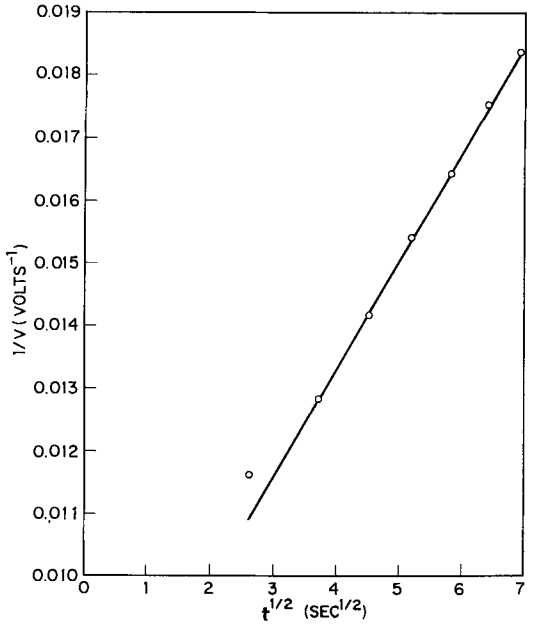

Fig. 9. Hydration of Ge-GeO$_2$ electrode by water addition (data from Fig. 3).

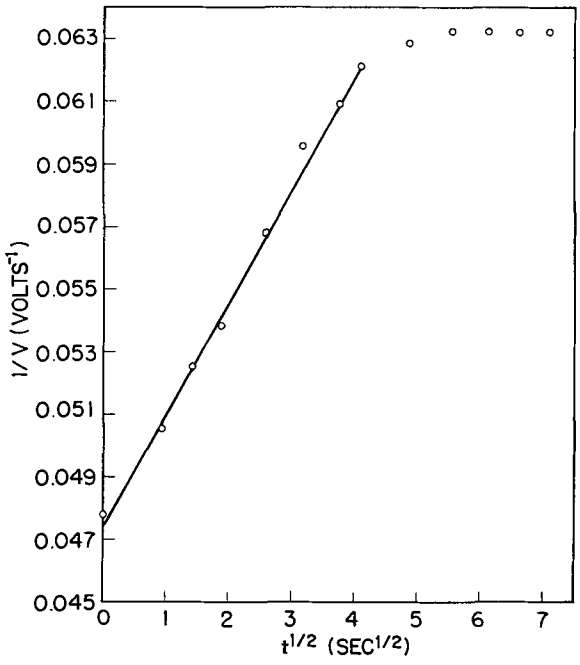

Fig. 10. Hydration of Ge-GeO_2 electrode by decrease in current density from 120 to 10 $\mu a/cm^2$.

preting the voltage decay curves obtained by interrupting the dehydration trace very briefly. If the voltage decay follows a particular simple model it can be represented [cf. (4)] by the equation

$$(1/AB)[\exp(-BV/d) - \exp(-BV_o/d)] = 4\pi \times 9 \times 10^{11}\, t/\epsilon$$

where $A = 2eqam\nu \exp(-W/kT)$; $B = eqa/kT$; and ϵ = dielectric constant.

If A and B are constant during the decay and if V is small compared with V_o, a straight line should be obtained by plotting V *vs.* log t. Such a plot is presented in Fig. 7 for interruptions at 10 sec and at 60 sec. The lines are straight during the major portion of the voltage decay. Measurement shows an increase in slope of about 10% during the dehydration between 10 and 60 sec. This corresponds to a decrease in the value of B. Again, the only apparent explanation is a decrease in activation distance. The displacement of the line toward greater time values is a result of the decrease in film conductivity.

If water moves through the film and reacts to produce germanium oxide at or near the germanium-germanium oxide interface, it is necessary that a mechanism exist whereby the hydrogen of the water can be removed from the film. The only apparent means by which this can happen is for the hydrogen to move through the film as hydrogen ion. The amount of this hydrogen ion would be electrically equivalent to the current producing the reaction

$$Ge + 2H_2O \rightarrow GeO_2 + 4H^+ + 4e$$

Since the germanium oxide is produced with about 80% current efficiency (2), most of the current in the film should be carried by hydrogen ion. Thus the decrease in activation distance on dehydration is a decrease in activation distance for hydrogen ion; that is, the removal of water from the film causes the hydrogen ion to jump between equilibrium positions that are closer together. In the opinion of the writer, this is a result of the water in the film occupying sites that can be used as equilibrium positions by the hydrogen ion when the water is not present.

Conclusions

The oxygen consumed in the formation of an anodic GeO_2 film using an acetic anhydride-acetic acid (0.10M)-water (0.30M)-lithium nitrate (6.0×10^{-3}M) solution, is supplied by the water. This water diffuses through the film and reacts electrochemically at or near the Ge-GeO_2 interface to produce GeO_2 and hydrogen ion. Diffusion of the water results in film growth at the Ge-GeO_2 interface rather than at the GeO_2-solution interface. The hydrogen ion carries the current through the film and jumps between successive available sites. The length of the jumps is increased by the presence of water in the film. It may be that the number of available sites is decreased by the presence of the water. Apparently, the mass transfer of water is controlled by diffusional resistance in the liquid phase, except after interruption of the current through a thick film. In this case, it may be that the diffusional resistance through the thick film dominates, with a severe depletion of water occurring at the Ge-GeO_2 interface.

Manuscript received March 23, 1964; revised manuscript received July 26, 1965. This paper was presented at the Toronto Meeting, May 3-7, 1964.

Any discussion of this paper will appear in a Discussion Section to be published in the June 1966 JOURNAL.

REFERENCES

1. S. Zwerdling and S. Sheff, *This Journal*, **107**, 338 (1960).
2. R. D. Wales, *ibid.*, **110**, 914 (1963).
3. R. D. Wales, Private communication.
4. L. Young, "Anodic Oxide Films," Academic Press, New York (1961).
5. E. R. Shaw, J. F. Corwin, and H. V. Knorr, *J. Phys. Chem.*, **64**, 174 (1960).
6. P. Delahay, "New Instrumental Methods in Electrochemistry," Interscience Publishers, Inc., New York (1954).
7. N. Ibl and R. Muller, *Z. Elektrochem.*, **59**, 671 (1955).
8. J. B. Story and R. D. Wales, *This Journal*, **112**, 536 (1965).

Cross Substitution in InAs

J. C. Woolley, E. W. Williams,[1] and R. Gagnon[2]

Physics Department, University of Ottawa, Ottawa, Ontario, Canada

ABSTRACT

The paper considers cross-substitutional alloys of InAs produced by replacing As by combinations of (Ge,Te), (Sn,Te), or (Ge,Se) so as to keep the ratio of valence electrons to lattice sites equal to four. Limits of solid solution have been determined by x-ray and photomicrograph techniques. All the alloys so produced are degenerate n-type semiconductors of very high carrier concentrations. Values of carrier density and optical energy gap have been determined as a function of composition and the results extrapolated to give data for the conduction band minima of InAs. It is found that at room temperature the <111> minima lie at 0.9 ev above the valence band maximum and that the (000) minimum will accept approximately 4 x 10^{19} electrons/cm^3 before an appreciable number of electrons enter the <111> minima.

It has been shown (1) that new semiconducting compounds can be predicted by using the method of cross substitution. This process, which can be applied to semiconducting elements or compounds, is the replacement in the chemical formula of two or more identical atoms of a given valency by the same number of different atoms, chosen so that the total number of effective valence electrons is unchanged. Thus, for materials of adamantine structure the ratio of valence electrons to lattice sites is kept equal to four. This is the condition of the Grimm-Sommerfeld law (2), and cross substitution is an extension of this law.

In the case of the adamantine structure, the simplest cross-substitutional derivatives are the binary compounds such as GaAs, InSb, etc., which are derived thus from the group IV elements. Further application of the process to such binaries leads to ternary compounds, *e.g.*, $CdSnAs_2$ from InAs. Continued application of the process predicts other ternaries, quaternaries, and more complicated compounds.

One limitation of the production of new materials by this method is the stability of the predicted compound. Thus, for the heavier binary compounds, *e.g.*, InSb, the derived ternaries are unstable and so do not form. However, it is possible to carry out the substitution to a limited extent, *i.e.*, in the case of InSb to replace a limited number of antimony atoms by combination of, say, tin and tellurium atoms. The resulting material may be considered as a solid solution of the derived ternary In_2SnTe in the $A^{III}B^V$ compound (InSb), *i.e.*, a composition in the alloy system InSb-In_2SnTe, even though the derived ternary is unstable. The limits of such solid solution of various ternary derivatives in InSb have been studied recently (3) and the Hall coefficient and optical energy gap measured for samples in the single phase ranges.

All of these InSb alloys are degenerate with high carrier concentrations. These latter occur because the alloys are not completely stoichiometric. For example, in the "anionic" InSb-In_2SnTe system (where anionic indicates substitution for atoms of the element in the $A^{III}B^V$ which has higher electronegativity) some solution of tin atoms in the indium sublattice is to be expected from thermodynamic considerations, leaving excess tellurium on the antimony sites. Both this tin and the resulting excess tellurium will act as donors giving n-type material of high carrier concentration. Very similar results are obtained with InSb-In_2Te_3 and InSb-In_2Se_3 alloys (4, 5).

The variation of Hall coefficient and optical energy gap with composition shows that as donor material is added to InSb, the (000) minimum of the conduction band is filled rapidly and that electrons enter the <111> minima. It is thus possible from the optical data to determine values for the height of the <111> minima above the valence band maximum and, from the Hall data, the approximate number of electrons entering the (000) minimum before appreciable numbers of electrons enter the <111> minima. Hence it is found (3) for InSb itself that at room temperature the <111> minima lie at 0.47 ev above the valence band maximum and that approximately 1 x 10^{19} electrons/cc enter the (000) minimum before the <111> minima are filled appreciably.

Here this work is extended to the cross-substitutional alloys of InAs. The data from these, plus that for the InAs-In_2Te_3 and InAs-In_2Se_3 alloys (6, 5) will give results for the conduction band of InAs similar to those for InSb described above.

Experimental Procedure

Three anionic alloy systems of InAs were investigated, *viz.*, InAs-In_2SnTe, InAs-In_2GeTe, and InAs-In_2GeSe. Standard x-ray powder photograph and photomicrograph methods were used to determine the ranges of solid solution in InAs, and measurements made at room temperature of Hall coefficient R_H and optical energy gap E_g.

The preparation of the alloys and the methods of measurement of R_H and E_g were as described previously (4, 5).

Results

Crystallographic data.—For each of the three systems investigated, samples in the range 0-40 mol. % ternary[3] were investigated. In each case it was found that x-ray photographs of the alloys quenched from the melt at 1050°C and of alloys subsequently annealed for one week at 400°C were practically identical, so that no further annealing was necessary. The variations of the lattice parameter of the zinc blende phase as a function of composition in the three systems are shown in Fig. 1. The curves for the In_2GeTe and In_2SnTe alloys [Fig. 1(a) and 1(b)] are typical of pseudobinary sections and indicate a range of solid solution of 12 mol. % in the case of In_2GeTe and of 3 mol. % for the In_2SnTe alloys. At higher concentrations of ternary, extra lines were observed in the x-ray photographs indicating the presence of other phases, but no attempt was made to investigate these, as the zinc blende type of solid solution was the only phase of interest.

In the case of the In_2GeSe alloys, the graph of lattice parameter against composition [Fig. 1(c)] is not that of a pseudobinary section. For alloys containing more than 5 mol. % In_2GeSe, extra x-ray lines were observed in addition to those of the zinc blende phase,

[1] Present address: Texas Instruments Inc., Dallas, Texas.

[2] Present address: Physics Department, University of Toronto, Toronto, Ontario, Canada.

[3] In calculating molecular per cent in the systems discussed here, InSb has been treated as In_2Sb_2.

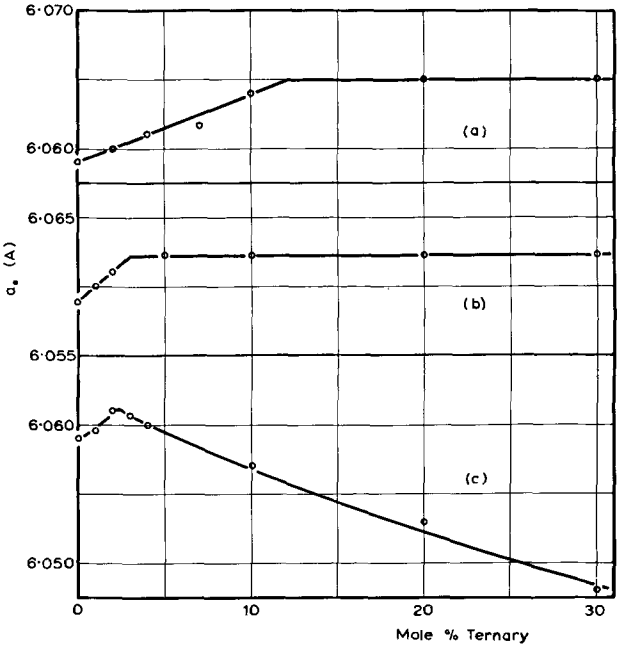

Fig. 1. Variation of lattice parameter a_o of the zinc blende phase as a function of mole percentage "ternary compound" added to InAs: (a) In_2GeTe; (b) In_2SnTe; (c) In_2GeSe.

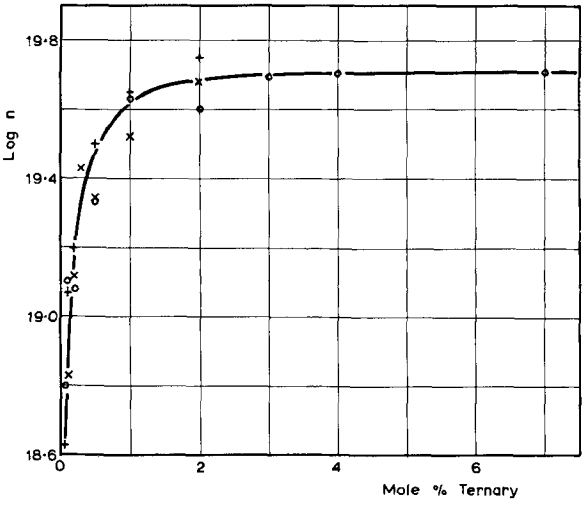

Fig. 2. Variation of log n (where $n = 1/eR_H$) with mole percentage "ternary compound" added to InAs: O, In_2GeTe; x, In_2SnTe; +, In_2GeSe.

indicating the presence of a second phase, but the zinc blende lattice parameter a_o varies in this range. The sharp break in the a_o against composition curve was assumed to represent the limit of single phase behavior, giving a range of solid solution of between 2 and 3 mol. % In_2GeSe. This was confirmed by photomicrograph work.

Semiconductor data.—Measurements of Hall coefficient R_H and optical energy gap E_g were made only on those alloys which were known to be single phase from the data given above. In all cases the specimens were found to be n-type, and the effective carrier concentrations were calculated, assuming that $R_H = 1/ne$. The variation of log n with molecular per cent ternary for the three cases is shown in Fig. 2 while the corresponding variation of E_g is shown in Fig. 3. It is seen that the three sets of data for n and E_g are the same within the limits of experimental error.

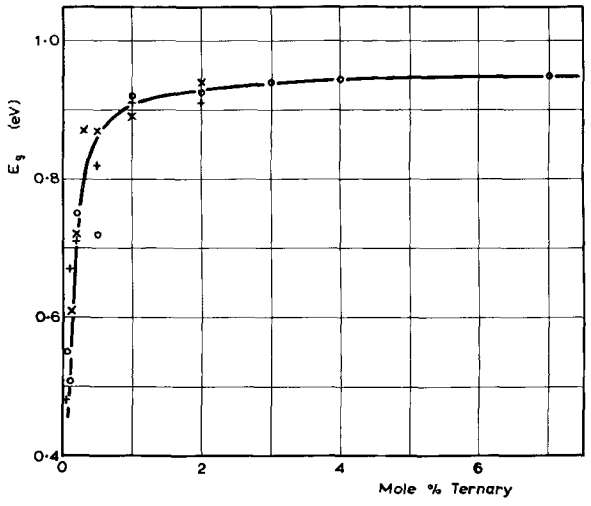

Fig. 3. Variation of room temperature optical energy gap E_g with mole percentage "ternary compound" added to InAs: O, In_2GeTe; x, In_2SnTe; +, In_2GeSe.

Discussion

The curves shown in Fig. 2 and 3 are very similar to the corresponding curves for the InSb cross-substitutional alloys, and they can be explained in the same way. As the ternary In_2 A^{IV} B^{VI} is added to InAs, some A^{IV} atoms enter the indium sites leaving uncompensated B^{VI} atoms on the arsenic sites. Both these A^{IV} and B^{VI} atoms act as donors, resulting in the rapid increase in n seen at low In_2 A^{IV} B^{VI} concentrations. Because of the low density of states in the (000) minimum of the conduction band, the Fermi level moves rapidly up the conduction band, resulting in the observed rapid increase in E_g (Burstein effect). In this region of the curves, the number of A^{IV} atoms occupying indium sites might be expected to vary from one ternary to another. However, the resulting rise in n and E_g is so rapid that it is not possible, within the limit of experimental error, to determine differences among the three cases.

When the Fermi level rises sufficiently in the conduction band, electrons begin to enter the <111> minima. Because of their much higher effective mass, these electrons contribute very little to the Hall coefficient, and to a first order approximation it is possible to assume that $R_H = 1/en_o$ where n_o is the electron density for the (000) minimum alone. Because of the much higher density of states in the <111> minima, the increase in n_o (*i.e.*, $1/eR_H$) with ternary concentration is greatly reduced, *i.e.*, the curve of log $1/eR_H$ against composition flattens out although the total number of electrons in the conduction band continues to increase. Also the Burstein effect in the <111> minima is very small, and so the value of E_g measured in this range is effectively the height of the <111> minima above the valence band maximum.

This behavior is observed in Fig. 2 and 3 at concentrations of ternary larger than about 0.75 mol. %. Here the results for the three cases should coincide unless the band structure of InAs is affected appreciably by the solid solution of small amounts of ternary compound. This coincidence is observed for both n and E_g curves.

Assuming some influence on the band structure due to solid solution, the values for pure InAs can still be obtained by extrapolating this region of the curves back to zero ternary content. On this basis it is found that in InAs at room temperature the <111> minima are 0.9 ev above the valence band maximum and that the number of electrons required to fill the (000) minimum to this level is approximately 4 x 10^{19}/cc. This is in good agreement with the corresponding results for the InAs-In_2Te_3 alloys (6). The values obtained for

the InAs-In_2Se_3 alloys are rather higher than this, but there is some indication that the InAs band structure is appreciably affected by addition of In_2Se_3 (5).

There appears to be no previous experimental data on the energy separation of the <111> conduction band minima and the valence band maximum for InAs. Hilsum (7) has made an empirical estimate of this value, but his figure of 1.5 ev is considerably higher than the value obtained here.

Manuscript received June 21, 1965.

Any discussion of this paper will appear in a Discussion Section to be published in the June 1966 JOURNAL.

REFERENCES

1. C. H. L. Goodman, *J. Phys. Chem. Solids*, **6**, 305 (1958).
2. H. G. Grimm and A. Sommerfeld, *Z. Phys.*, **36**, 36 (1926).
3. J. C. Woolley and E. W. Williams, *This Journal*, **111**, 210 (1964).
4. J. C. Woolley, C. M. Gillett, and J. A. Evans, *J. Phys. Chem. Solids*, **16**, 138 (1960).
5. J. C. Woolley and P. N. Keating, *Proc. Phys. Soc.*, **78**, 504 (1961).
6. J. C. Woolley, B. R. Pamplin, and J. A. Evans, *J. Phys. Chem. Solids*, **19**, 147 (1961).
7. C. Hilsum, Proc. Int. Conf. on Semiconductor Physics, p. 1127, Paris (1964).

The Growth of α-SiC from Various Chromium Alloys by a Travelling Solvent Method

M. A. Wright[1]

Tyco Laboratories, Incorporated, Waltham, Massachusetts

ABSTRACT

Crystal growth of α-SiC from Cr-Si and Cr-Ta alloys has been accomplished using the travelling solvent method. No elaborate surface pretreatments are necessary although kinetic experiments indicate that diffusion is the crystal growth rate-limiting step only when the SiC surfaces are cleaned by electron beam heating or etching in a NaOH + Na_2O_2 salt mixture. At temperatures less than 1760°C the diffusion coefficient for SiC through a liquid chromium—12 w/o (weight per cent) Si alloy can be described by $D = 2.6 \times 10^{-3}\ e^{-1300/RT}$ cm²/sec. It is demonstrated that multiple zone passing results in crystal purification. Large single crytals can also be grown using this method.

The growth of crystals of α-SiC from chromium solution using the travelling solvent method has been reported recently (1). This variant of the temperature gradient zone melting technique (2) consists essentially of maintaining a temperature gradient across an assembly comprising a thin layer of solvent sandwiched between a seed and a source crystal of SiC. At the temperature of crystal growth SiC goes into solution; however, more tends to be dissolved at the hotter than at the cooler crystal-solvent interface. The concentration gradient which is formed provides a driving force to move solute from the hot through the liquid zone to the cooler interface. This latter interface eventually becomes supersaturated, and deposition of SiC occurs. The solvent zone effectively moves through the source crystal until it emerges at some external surface.

The requirements of a solvent are therefore that it should dissolve SiC, that this solubility should increase with increasing temperature, and that the solvent should be insoluble in solid SiC. Elemental chromium meets these requirements; however, it does not wet SiC readily. Cleaning of the SiC surfaces using electron beam heating in ultra-high vacuum, followed by evaporation of chromium *in situ* on the surfaces, produces good wetting and reproducible crystal growth.

Electrical contacting studies (3, 4) indicate that strong ohmic contacts can be produced if metals containing small amounts of Si or Ta are used as contacting material. The small alloying additions effectively react with and remove any contaminating surface film present on the SiC. Chromium alloys were fabricated therefore containing varying proportions of either silicon or tantalum; the following is an account of the growth of single crystal α-SiC from these alloys using the method outlined above.

Experimental Technique

Commercially available "S" type SiC supplied by the Norton Company was used in all the experiments. The specimen dimensions typically 1/4 x 1/4 x 1/20 in. were obtained by cutting and grinding this solid with water-cooled diamond wheels. The chromium alloys were prepared from high-purity materials in an argon arc furnace. The arc was allowed to traverse the specimen several times. Subsequent metallographic observations failed to reveal any segregation. Thin slices of the alloys were cut with a diamond saw, after which the final dimensions were obtained by conventional lapping techniques.

The apparatus used for the growth experiments is shown in Fig. 1. It consisted of an R. F. heated carbon block (A) on which the specimen was placed, contained in a quartz tube. The water-cooled copper end

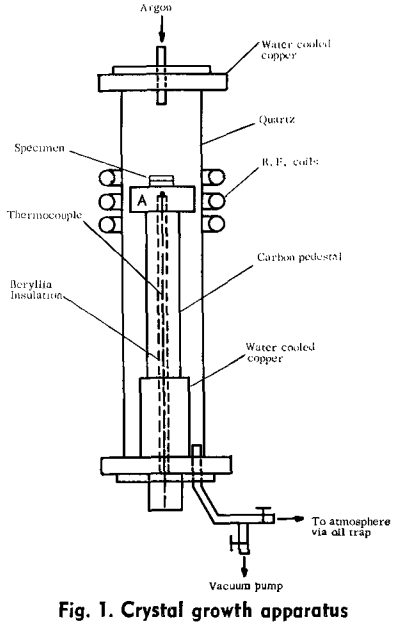

Fig. 1. Crystal growth apparatus

[1] Present address: National Research Corporation, Cambridge, Massachusetts.

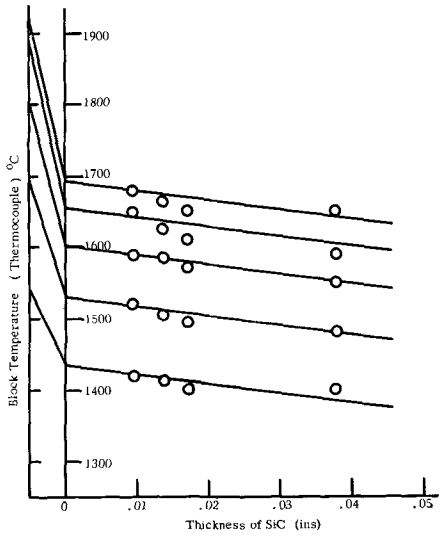

Fig. 2. Effect of block temperature on the temperature gradient through the SiC.

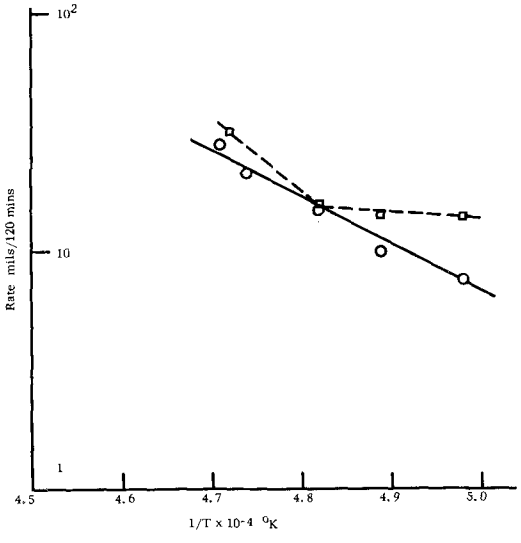

Fig. 3. Effect of temperature on zone movement; □ - - - □, specimens electron beam heated; O—O, specimens degreased only.

caps shown in Fig. 1 were vacuum sealed to the tube with apiezon wax. To prevent oxidation of the chromium at the high-growth temperatures, high-purity argon was passed continuously through the system after first evacuating and back filling three times.

Accurate optical measurement of the temperature of the molten zone proved experimentally difficult due, in part, to unknown emissivity corrections and to the small dimensions (0.005 in.) of the molten zone. The following preliminary experiments were therefore performed:

1. The temperature of the carbon block (A) was measured using both thermoelectric and optical methods.

2. SiC pieces having the same cross section but of different thickness were heated individually to different block temperatures. The surface temperature was measured optically and normalized using the preliminary results discussed above. The effect of specimen thickness is demonstrated in Fig. 2. Assuming that the emissivity of carbon and SiC are approximately equal it was possible with these results and with the continuously recorded temperature of the carbon block to compute the temperature of the molten zone.

Results

Alloys containing 1, 4, 8, and 12 w/o Si in Cr and one alloy containing 5 w/o Ta were used as solvent material. Zone movement was observed in all cases. Figure 3 shows the rate of zone movement *vs.* temperature for the Cr-12 w/o Si alloy.

The polarity observed between opposite (111) faces of zinc blende-type crystals (5) is also shown by the (0001) faces of α-SiC; each face terminates solely in atoms of one kind. The two faces can be identified by etching in a molten NaOH + Na_2O_2 mixture since the rates of dissolution are different. It was thought, therefore, that zone-passing experiments wherein dissolution and recrystallization rates were varied might enable the rate-determining step to be defined. Accordingly, zone-passing experiments were performed using Cr-12 w/o Si as the solvent in which the four possible combinations of face relationships were used. The rate of zone movement was found to be the same, *i.e.*, 5 mils/hr at 1760°C in all cases, suggesting that diffusion of SiC across the solvent zone is the rate-controlling step.

Normal back-reflection x-ray techniques were used to study the effect of growth temperature and zone thickness on the regrown layer. It was found that single crystal growth was achieved easily within wide variations of these parameters. In practice, optimum zone thickness was found to be between 0.006 and 0.015 in. to minimize any tendency of the zone to break up.

The rate of zone movement was studied as a function of zone thickness, but no dependence was observed for the temperature range reported here.

Effect of repeated zone passes.—The principle of multiple zone passing is a well-known technique for preparing ultra pure semiconductor materials. The degree of purification effected by a given number of passes depends only on the relative solubility of the impurity in the liquid and solid phases. Any impurity that exhibits a distribution coefficient much less than or much greater than unity will, therefore, be removed.

A Cr-12 w/o Si alloy zone was made to move through a crystal of SiC. The alloy was removed from the crystal by grinding, and a further zone was made to pass through the crystal in the reverse direction. This process was repeated until a total of six zones, three forward three back, had been passed through the original crystal. The crystal shown in Fig. 4 had then changed from opaque black to translucent green, a definite indication of impurity removal.

Effect of repeated additions of seed crystals.—The passage of a molten-solvent zone through the SiC source crystal results in an increase in size of the seed crystal. The slowest growing direction in the case of hexagonal SiC is the c-direction; thus, thin platelets of relatively pure SiC most commonly produced commercially have maximum dimensions in the c-direction of around 0.050 in.

An experiment was conducted in which one zone was passed through a source crystal, therefore, producing a crystal double the size of the seed crystal. A further source crystal was then added, and the zone was passed through it. This was repeated six times, after which the resultant crystal measured ½ in. in the c-direction (see in Fig. 5).

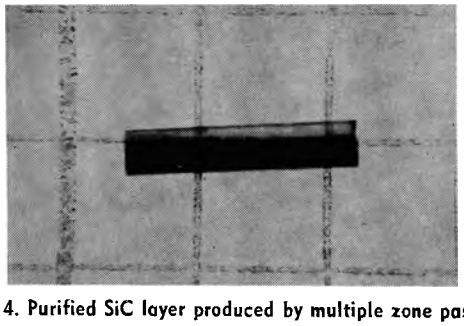

Fig. 4. Purified SiC layer produced by multiple zone passes

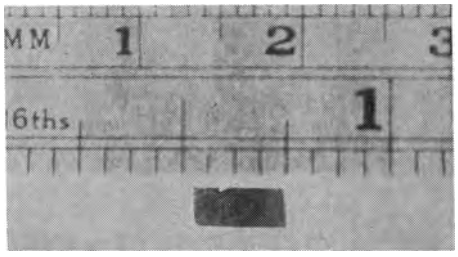

Fig. 5. Large single crystal of SiC produced by successive source crystal additions.

Discussion

SiC can be transported across the solvent zone by two mechanisms, convection and diffusion. The experimental heating geometry would lead one to suppose that convection should be the main transport process, *i.e.*, heat was supplied at the bottom surface of the molten zone; however, no effect of zone thickness could be observed. Since the temperature gradient through the specimen has been shown to be constant, (see Fig. 2), it can be concluded that convection effects are negligible and that diffusion effects predominate. The surface polarity experiments support this conclusion. These experiments also indicate that of the three processes, dissolution, diffusion, and deposition, diffusion is the slowest and is, therefore, rate controlling. The activation energy for the process, using only degreased specimens, computed from Fig. 3 is ~ 90 kcal/mole. This value is not typical of liquid diffusion. Further experiments were performed in which the surface was cleaned by electron bombardment in high vacuum, after which a layer of chromium was immediately evaporated onto the surfaces. Chromium 12 w/o Si was then used as the solvent zone. The effect of temperature on the rate is also shown in Fig. 3.

At temperatures lower than 1807°C the activation energy using these clean samples, is ~ 13 kcal/mole and can be taken as typical for a diffusion-controlled process. If this experiment is taken in conjunction with the surface polarity experiments, then it is apparent that either etching in salt solution or electron beam heating of SiC is sufficient to limit the induction period (presumably by cleaning the surfaces) observed when growth experiments are carried out using only degreased samples.

Above 1807°C a faster transport rate is observed than would be predicted if diffusion effects are still predominant. Since movement of the soluble species by convection has been shown to be negligible, the transport rate can be described by Ficks law, *i.e.*

$$R = -D\frac{dc}{dt}\cdot\frac{dt}{dx}$$

where R is the flux of solute passing through unit area of molten zone, D the diffusion coefficient, dc/dt the variation of concentration with temperature, and dt/dx the temperature gradient.

Figure 2 shows that the temperature gradient through the growing crystal is a constant thus any contribution to the growth rate by this gradient (Soret effect) would also be constant. In addition the variation of the diffusion constant (D) with both temperature and concentration would be expected to be small. It is reasoned, therefore, that the sharp increase in rate is produced by an increase in the value of dc/dt. In physical terms, it would appear that the equilibrium liquidus in the pseudobinary phase diagram (Cr + 12 w/o Si)-SiC begins to turn over quite sharply above 1807°C, however, the experimental data presented here is not sufficient to derive the actual curvature of the liquidus. The equilbrium solubility data for Cr-Si-SiC has not been reported in the literature; however, the pure chromium-SiC equilibrium diagram has recently been determined by Griffiths (6). Using points taken from his curve an accurate plot of dc/dt against $1/T$ for the temperature range reported here was determined. Below 1760°C, dc/dt was constant; above this temperature however, the value began to change quite rapidly until between 1807° and 1857°C an apparent activation energy of 93 kcal/mole was exhibited.

The solute diffusivity was computed by inserting the appropriate values in Ficks equation; thus

$$D = \frac{2.54 \times 13.5 \times 10^{-3} \times 600 \times 10.16 \times 10^{-2}}{120 \times 60 \times 6 \times 50 \times 10^{-2}}\ \text{cm}^2/\text{sec}$$

$$= 9.5 \times 10^{-5}\ \text{cm}^2/\text{sec at } 1700°\text{C}$$

This is a perfectly reasonable value for diffusion through a liquid.

If we insert the values computed above in the expression

$$D = D_o\, e^{-Q/RT}\ \text{cm}^2/\text{sec}$$

where Q is the activation energy for diffusion, R the gas content, and T the absolute temperature, we find that the temperature dependence of the diffusion coefficient below 1760°C can be described by

$$D = 2.6 \times 10^{-3}\, e^{-13000/RT}\ \text{cm}^2/\text{sec}$$

Wernick (7) attempted to measure diffusivities for aluminum-rich and gold-rich zones in silicon and germanium. He obtained reasonable values of D, but found a high activation energy and therefore concluded that true diffusivities were not being measured.

In the case of SiC, it is apparent that, providing rigorous surface cleaning is carried out, acceptable activation energies will be exhibited, and true diffusivities can be computed from zone movement measurements.

Summary

Using and travelling solvent method (A) silicon carbide single crystals can be grown from chromium 5 w/o Ta and various chromium-silicon alloys. In this way the wetting of the SiC surfaces by the solvent is more easily effected such that no elaborate surface cleaning techniques are necessary. (B) Large single crystals of SiC can be produced; (C) Purification of SiC can be achieved; (D) Providing clean surfaces are used, it is possible to measure diffusivities in liquids accurately.

Acknowledgments

The author wishes to thank Mr. T. Fuller for skillful experimental work and Dr. A. I. Mlavsky for his continued interest and encouragement. This work was performed under U. S. Air Force Contract No. AF 19(604)8803.

Manuscript received May 3, 1965; revised manuscript received June 25, 1965. This paper was presented at the New York Meeting, Sept. 29- Oct. 3, 1963.

Any discussion of this paper will appear in a Discussion Section to be published in the June 1966 JOURNAL.

REFERENCES

1. L. B. Griffiths and A. I. Mlavsky, *This Journal*, **111**, 805 (1964).
2. W. G. Pfann, *Trans. AIME*, **203**, 961 (1955).
3. C. A. A. J. Greebe and W. F. Knippenberg, Philips Research Repts, **15**, 120 (1960).
4. R. N. Hall, *J. Appl. Phys.*, **29**, 914 (1958).
5. H. C. Gatos, *Science*, **137**, 311 (1962).
6. L. B. Griffiths, Unpublished information, work performed under Contract No. AF 19(628)4384.
7. J. H. Wernick, *J. Chem. Phys.*, **25**, 47 (1956).

A Study of the Phase Transitions in $PbZrO_3$

Victor J. Tennery

Department of Ceramic Engineering, University of Illinois, Urbana, Illinois

ABSTRACT

An investigation of the linear thermal expansion of high purity specimens of polycrystalline $PbZrO_3$ has revealed that a ferroelectric phase is stable in this compound between 226° and 236°C on heating. The same phase exists between 226° and 212°C on cooling. The data were all obtained at a constant heating and cooling rate of 1°C/min. The thermal expansion of high purity specimens containing about 200 ppm more calcium than those exhibiting the ferroelectric phase did not indicate the existence of such a phase. Hysteresis loop measurements of the low calcium containing materials showed well defined ferroelectric hysteresis loops with $E_c \simeq 2.5$ kv/cm and $P_s \simeq 23\mu$ coulombs/cm^2 at 215°C whereas similar measurements on the more impure material revealed a field induced antiferroelectric → ferroelectric phase transition. The substitution of 0.05 weight per cent of calcium for lead in the purer $PbZrO_3$ resulted in the disappearance of the ferroelectric phase.

The compound $PbZrO_3$ has been the subject of many investigations. Roberts (1) and Smolenskii (2) first reported a dielectric anomaly on the basis of measurements made on polycrystalline specimens. These authors found a peak in the dielectric constant which occurred at about 230°C. Shirane (3) and Smolenskii (4) reported that the sign of the volume anomaly on cooling was negative, in contrast with $BaTiO_3$ in which it is positive. Sawaguchi *et al* (5, 6) established that the phase occurring below 230°C was antiferroelectric, but that in the presence of high electric fields a ferroelectric phase could be induced at temperatures just below the transition temperature of 230°C.

Several systems of solid solutions involving $PbZrO_3$ and various other perovskite-type compounds have been investigated extensively. The system $PbTiO_3$-$PbZrO_3$ has been reported upon by Shirane *et al.* (7-9) and by Sawaguchi (10). These studies indicated that the substitution of even a few atomic per cent of titanium for zirconium in $PbZrO_3$ resulted in the appearance of a rhombohedral ferroelectric phase whose distortion from a cubic perovskite was similar to that observed in the low temperature phase of $BaTiO_3$. Detailed investigations of the piezoelectric properties of poled ceramics in this system have been reported by Jaffe *et al* (11) and by Kulcsar (12). Investigations of the solid solutions $PbZrO_3$-$BaZrO_3$ have revealed that the same rhombohedral phase appears when lead is partially replaced by barium as reported by Roberts (1), Shirane (13), and Shirane and Hoshino (14). On the other hand, investigations of the systems $PbZrO_3$-$SrZrO_3$ and $PbZrO_3$-$CaZrO_3$ reported by Shirane (13) and Krainik (15, 16) revealed that in these systems a ferroelectric phase did not appear when some of the lead ions in the structure were replaced by either strontium or calcium.

In the cases of other divalent ions being substituted for lead in $PbZrO_3$ it appears that the ionic radius of the substituted ion is a critical factor in determining whether or not the ferroelectric rhombohedral phase will appear. If the substituted ion is smaller than the lead ion which it replaced, then the ferroelectric phase does not appear. This is the case for strontium and calcium. In the case of barium, the barium ion is larger than the lead ion and when it is partially substituted for lead the ferroelectric phase is observed.

Experimental

This work consists of a study of the phase transition sequence observed on heating and cooling polycrystalline specimens of high purity $PbZrO_3$. Four different lead zirconates were prepared by using four different zirconium oxides, but the same lead oxide as the raw material from which the compound was synthesized. Two of the zirconias were micronized C. P. zirconium oxide[1] and came from different lots of the oxide. The other two zirconias[2] were somewhat different in that one contained 2% hafnium whereas the other contained only 50 ppm hafnium. The lead oxide used in all cases was an ultra high purity litharge[3] from the same lot and shipment.

The preparation conditions for the lead zirconates were held as constant as experimentally possible. The dried PbO and ZrO_2 were weighed on an analytical balance and the powders were dry mixed for 20 min on a vibratory mixer. Reagent methyl alcohol was then added to the powder and the batch was mixed by hand for 30 min with a mullite mortar and pestle.

After the alcohol was evaporated from the batch, the caked material was broken up to about —100 mesh with the mortar and pestle. This powder was calcined at 800°C for 2 hr in covered platinum crucibles. Measurements of the weights of the calcines prior to and after calcining indicated that negligible lead losses occurred during this stage of preparation. After calcining at 800°C the powders were passed through a 100 mesh screen, a small quantity of distilled water was added to the powder and specimens were pressed from this powder in the form of right cylinders 1.4 cm in diameter by 0.8 cm high. These cylindrical specimens were sintered to high density by placing them on platinum in covered theoretically dense magnesia crucibles and firing them at 1240°C for 1 hr. Weight loss records kept on all of the specimens indicated that about 2 to 3% of the PbO present initially was lost from the specimens when sintering them in this manner. It was apparent from a visual examination of the sintered specimens that most of the PbO loss occurred from a narrow region about the outer surface. After sintering, the specimens were weighed and the lead deficient area of each specimen was included in the weight. The lead deficient area of each specimen was then ground away prior to the thermal expansion measurement. Careful examination of the x-ray patterns of these specimens revealed that only the diffraction lines of $PbZrO_3$ were present. Thus the sintered specimens were not nearly as lead deficient as the weight losses indicated.

The thermal expansion of these specimens was measured by means of an automatic plotting fused quartz dilatometer. The thermal dilation of a specimen was detected by a linear displacement transducer whose output was fed to the Y axis of an X-Y recorder. The junction of a chromel-alumel thermo-

[1] Product of Titanium Zirconium Company, Inc., Flemington, New Jersey.

[2] Product of Titanium Alloy Division, National Lead Company, Niagara Falls, New York.

[3] Product of Hammond Lead Products, Inc., Hammond, Indiana.

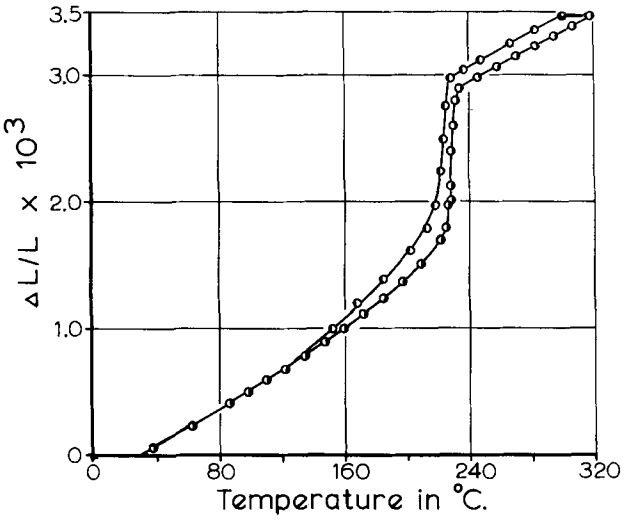

Fig. 1. Linear thermal expansion vs. temperature for $PbZrO_3$-A, half dark circle, right side, heating, half dark circle, left side, cooling.

couple was imbedded in a 1 mm hole in the specimen. The emf output of this couple was fed to the X axis of the recorder. The relative electric permittivity or dielectric constant, loss tangent, and ferroelectric hysteresis loop properties were measured in the conventional manner.

Results and Discussion

The four lead zirconates which were prepared from the four different zirconias as discussed previously will be designated A, B, C, and D throughout the remainder of the text for convenience. The spectrographic analyses obtained for these materials will be given later. The thermal expansion $\Delta L/L$ *vs.* temperature for $PbZrO_3$-A is shown in Fig. 1 for both heating and cooling. The heating and cooling rate in all cases was 1°C/min. The thermal expansion behavior in this case is essentially identical with that reported by Shirane (13). On heating, the specimen underwent a large expansion between 220° and 230°C. This expansion was associated with the transition from the antiferroelectric orthorhombic structure to a paraelectric cubic structure (17). On heating, a discontinuity in the thermal expansion is apparent between 226° and 228°C indicating that a phase transformation takes place. On cooling the paraelectric → antiferroelectric transition occurred at 229°C, whereas the reverse transformation occurred at 234°C on heating.

The thermal expansion of $PbZrO_3$-B is shown in Fig. 2. In this case, on heating, the specimen underwent a sharp contraction between 226° and 227°C. The thermal expansion was then essentially independent of temperature between 229° and 235°C, whereupon it increased essentially linearly with temperature. In this case it appeared that the antiferroelectric phase originally present transformed to some other phase at about 227°C which subsequently transformed to a paraelectric phase at 235°C. On cooling this specimen to 224°C, a very large expansion occurred with $\Delta L/L$ attaining a maximum value of 4.8×10^{-3} at 210°C. At 209°C this intermediate phase transformed to the antiferroelectric phase and a rapid decrease occurred in the thermal expansion.

The thermal expansion of $PbZrO_3$-C was very similar to that of $PbZrO_3$-D shown in Fig. 3. In this case, on heating, the thermal expansion exhibited the usual large increase above 220°C, exhibited a sharp change at 228°C, was temperature independent to 230°C then increased linearly with temperature. On cooling, the thermal expansion exhibited an abrupt increase at 226°C, was temperature independent from 222° to 213°C, and then decreased very rapidly.

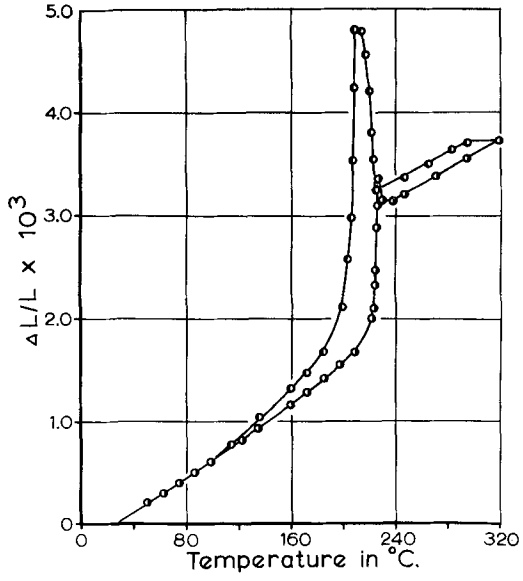

Fig. 2. Linear thermal expansion vs. temperature for $PbZrO_3$-B, half dark circle, right side, heating, half dark circle, left side, cooling.

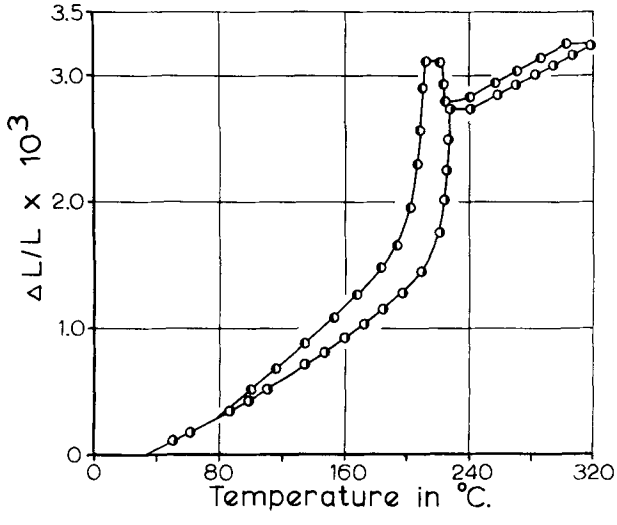

Fig. 3. Linear thermal expansion vs. temperature for $PbZrO_3$-D, half dark circle, right side, heating, half dark circle, left side, cooling.

The thermal expansion of $PbZrO_3$-D is shown in Fig. 3. In this case the thermal expansion on heating was very similar to that observed in $PbZrO_3$-B. There was a slight contraction at 226°C, then a temperature independent region from 226° to 236°C, then the expansion increased linearly with temperature. On cooling there was a large expansion at 226°C, an essentially temperature independent region to 212°C, and then an abrupt contraction at this temperature.

Spectrographic analyses were obtained of all four of the lead zirconates discussed. The analyses agreed reasonably well with those estimated from the analyses obtained from the suppliers of the starting oxides. The analyses of the eleven major impurities present in the four lead zirconates discussed previously are shown in Table I.

It was apparent from the thermal expansion data that there was some critical difference between $PbZrO_3$-A and the others. The spectrographic analyses indicated that $PbZrO_3$-A differed from the others primarily in that it contained higher concentrations of calcium and silicon. However, $PbZrO_3$-D contained nearly as much silicon as did A, but it still exhibited expansion properties very similar to those of B and

Table I. Spectrographic analyses of lead zirconates A, B, C, and D*

	A	B	C	D
Hf	−100	370	1.10%	100
Fe	50	120	30	100
Ca	255	50	25	45
Si	310	58	120	265
Sn	−20	−20	−20	−20
Cr	−20	−20	−20	−20
Al	−20	35	20	65
Na	35	55	40	145
Mg	50	−20	−20	25
K	40	35	50	70
Ti	38	68	45	50

* Concentrations are in ppm except where otherwise noted.

C. Thus, silicon did not appear to be a critical impurity. In order to experimentally evaluate the conclusion that calcium was the critical impurity in $PbZrO_3$, experimental compositions were prepared in which some calcium was intentionally substituted for lead. The following compositions were prepared: $Pb_{0.99965}Ca_{0.00035}ZrO_3$, $Pb_{0.999}Ca_{0.001}ZrO_3$, $Pb_{0.995}Ca_{0.005}ZrO_3$, $Pb_{0.99}Ca_{0.01}ZrO_3$. It was not felt that it would be possible to experimentally provide a homogeneous distribution of the calcium at such small concentrations, but it was thought that some indication of the dependence of the appearance of the intermediate phase on the calcium concentration would be gained. The zirconia used to prepare $PbZrO_3$—D was used for all of these compositions. The thermal expansion of the composition $Pb_{0.99965}Ca_{0.00035}ZrO_3$ differed very little from that shown in Fig. 3. One of these specimens was then crushed, repressed, refired, and measured. The expansion curve of this specimen revealed that the temperature range in which the intermediate phase existed was much narrower than in the previous case where the specimen had been sintered only once. The thermal expansion curves of some of the other compositions noted above are shown in Fig. 4 and 5. It is apparent from these figures that even small concentrations of calcium in $PbZrO_3$ have a profound effect on the phase transition sequence in this compound. In Fig. 5 it is shown that as little as 0.05% by weight of calcium present in the zirconate will completely prevent the intermediate phase from appearing. These data corroborate the results obtained for $PbZrO_3$—A. From Table I it is apparent that $PbZrO_3$—A also contained more magnesium and less hafnium than did B, C, or D. The $PbZrO_3$—A material contained about 25 ppm more magnesium than did $PbZrO_3$—D. It is difficult to access the significance of such a small concentration difference in the presence of other impurities. Because of the small size of the Mg^{+2} ion relative to Pb^{+2}, the amount of magnesium which can substitute for Pb^{+2} in the $PbZrO_3$ structure is probably very limited. Any magnesium ions which do substitute for lead in the structure probably tend to influence the phase transitions of the zirconate in the same way as do calcium ions, since calcium and magnesium are from the same periodic family. The hafnium concentration in $PbZrO_3$—A was slightly less than the lower limit of 100 ppm necessary for reasonably accurate quantitative spectrographic results. $PbZrO_3$—B and D contained somewhat more hafnium than this limit. This difference in hafnium appears to be insignificant as substitutions of hafnium for zirconium in $PbZrO_3$ would be expected to make the appearance of ferroelectricity less likely due to the fact that $PbHfO_3$ is an antiferroelectric crystal at 25°C, and a ferroelectric phase has not been observed in this compound even when it is subjected to intense electric fields at high temperatures.

The electric flux density was examined as a function of electric field and temperature for specimens of $PbZrO_3$—A, B, C, and D to establish if the intermediate

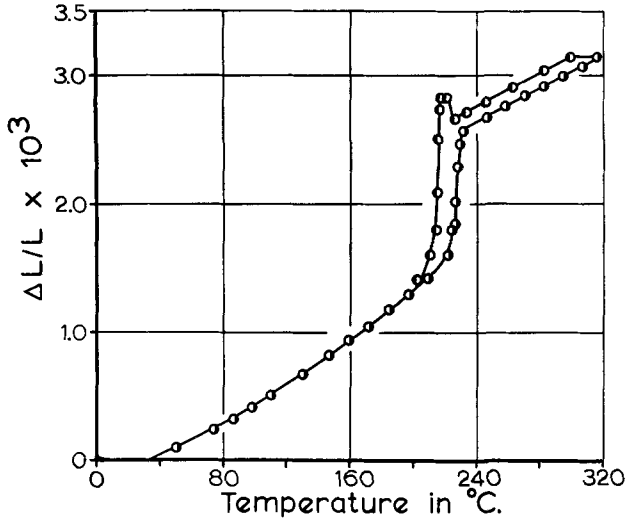

Fig. 4. Linear thermal expansion vs. temperature for $Pb_{0.999}Ca_{0.001}ZrO_3$, half dark circle, right side, heating, half dark circle, left side, cooling.

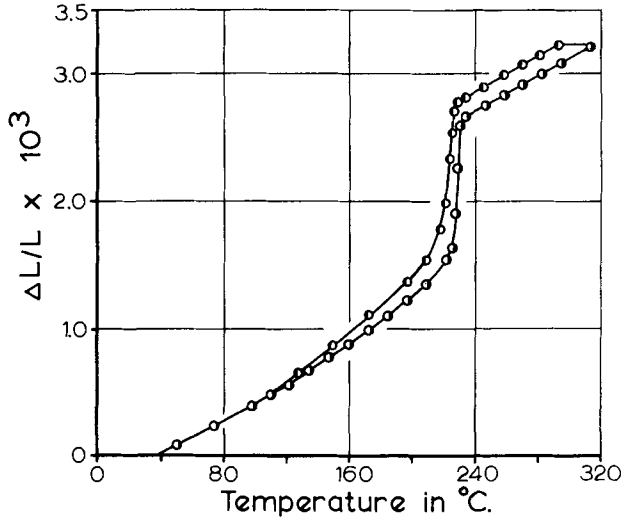

Fig. 5. Linear thermal expansion vs. temperature for $Pb_{0.995}Ca_{0.005}ZrO_3$, half dark circle, right side, heating, half dark circle, left side, cooling.

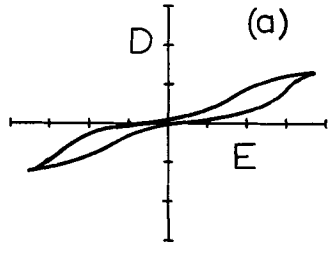

Fig. 6. (a). D-E loop for $PbZrO_3$-A, temperature 220°C, f = 70 cps; E axis, 1 div. = 5 kv/cm., D axis, 1 div. = 10 μcoulombs/cm².

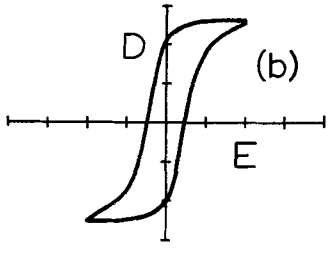

Fig. 6(b). D-E loop for $PbZrO_3$-B, temperature 218°C, other conditions same as Fig. 6(a).

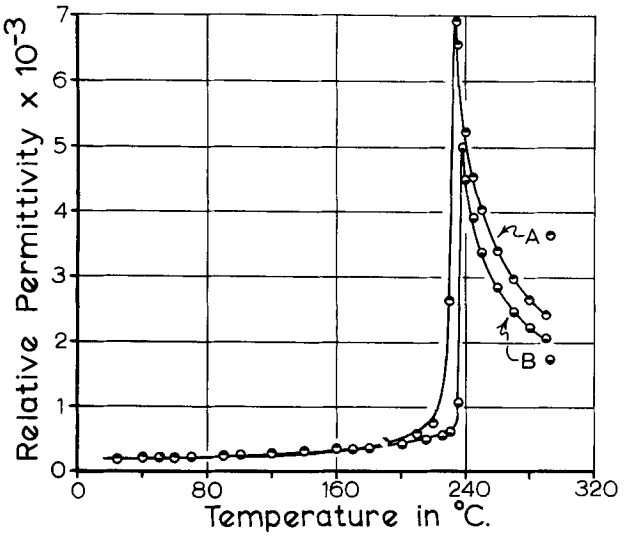

Fig. 7. Dielectric constant *vs.* temperature for $PbZrO_3$-B, curve A, half dark circle, top; and for $Pb_{0.995}Ca_{0.005}ZrO_3$, curve B, half dark circle, bottom.

phase observed in $PbZrO_3$—B, C, and D was ferroelectric. The data obtained for $PbZrO_3$—A are shown in Fig. 6 (a). The trace shown in Fig. 6 (a) is very similar to that reported by Sawaguchi (18) illustrating the transition from an antiferroelectric phase to a ferroelectric phase at some critical field which is temperature dependent. Figure 6 (b) shows that the intermediate phase observed in all of the lead zirconates containing low concentrations of calcium impurities is indeed ferroelectric with a coercive field of about 2.5 kv/cm and a spontaneous polarization of about 23 μcoulombs/cm^2 at 218°C. Just below this temperature the hysteresis loop vanished and was replaced by the linear relationship expected for the antiferroelectric phase.

The relative dielectric constants of specimens of $PbZrO_3$—B and $Pb_{0.995}Ca_{0.005}ZrO_3$ are shown in Fig. 7. The densities of both specimens were approximately 93% of the theoretical for $PbZrO_3$. It is evident that the occurrence of the ferroelectric phase in the material $PbZrO_3$—B was accompanied by a much higher maximum dielectric constant than was the case in $Pb_{0.995}Ca_{0.005}ZrO_3$ where the ferroelectric phase did not appear.

Acknowledgments

The author would like to express his appreciation to Mr. R. M. Brown who helped prepare many of these materials and to Mr. K. Hang and N. Harris for helping with the measurements. This work was supported under contract NONR 1834 (38).

Manuscript received May 14, 1965; revised manuscript received Aug. 2, 1965. This paper was presented at the San Francisco Meeting, May 9-13, 1965.

Any discussion of this paper will appear in a Discussion Section to be published in the June 1966 JOURNAL.

REFERENCES

1. S. Roberts, *J. Am. Ceram. Soc.*, **33**, 63 (1950).
2. G. A. Smolenskii, *Zhur. Tekh. Fiz.*, **20**, 137 (1950).
3. G. Shirane, E. Sawaguchi, and A. Takeda, *Phys. Rev.*, **80**, 485 (1950).
4. G. A. Smolenskii, *Zhur. Tekh. Fiz.*, **21**, 1045 (1951).
5. E. Sawaguchi, G. Shirane, and Y. Takagi, *J. Phys. Soc. Japan*, **6**, 333 (1951).
6. G. Shirane, E. Sawaguchi, and Y. Takagi, *Phys. Rev.*, **84**, 476 (1951).
7. G. Shirane and A. Takeda, *J. Phys. Soc. Japan*, **1**, 5 (1952).
8. G. Shirane, K. Suzuki, and A. Takeda, *ibid.*, **1**, 12 (1952).
9. G. Shirane and K. Suzuki, *ibid.*, **1**, 333 (1952).
10. E. Sawaguchi, *ibid.*, **8**, 615 (1953).
11. B. Jaffe, R. S. Roth, and S. Marzullo, *J. Appl. Phys.*, **25**, 809 (1954); *J. Research Natl. Bur. of Standards*, **55**, 239 (1955).
12. F. Kulcsar, *J. Am. Ceram. Soc.*, **42**, 49, 343 (1959).
13. G. Shirane, *Phys. Rev*, **86**, 219 (1952).
14. G. Shirane and S. Hoshino, *Acta. Cryst.*, **1**, 203 (1954).
15. N. N. Krainik, *Izvest. Akad. Nauk S.S.S.R., Ser. Fiz.*, **21**, 411 (1957).
16. N. N. Krainik, *Zhur. Tekh. Fiz.*, **28**, 525 (1958).
17. E. Sawaguchi, *J. Phys. Soc. Japan*, **1**, 110 (1952).
18. E. Sawaguchi and K. Kittaka, *ibid.*, **7**, 336 (1952).

Diffusion-Controlled Attack of Glass Surfaces by Molten Hydroxides

Roger F. Bartholomew

Research and Development Laboratories, Technical Staffs Division,

Corning Glass Works, Corning, New York

ABSTRACT

The attack of soda-lime-silica, alkali borosilicate, zirconia-silica and alumina-silica glasses by sodium hydroxide and potassium hydroxide melts at temperatures just above their melting points has been studied. Sodium hydroxide attack resulted in a frosty layer bound to the surface; potassium hydroxide left a clear surface. Kinetic measurements were made of the weight loss per unit area as a function of time. Diffusion-controlled mechanisms were indicated in both salts for immersion times equal to or less than 5 min.

The problems associated with the weathering and chemical durability of glass surfaces have been studied extensively (1,2). The rate of attack depends on the nature of the attacking medium. Douglas and Isard (3) studied the attack of a soda-lime and a sodium borosilicate glass in acid and neutral solutions. They showed that the rate was determined by the rate at which the cations diffuse in the glass. A study of the rate of attack of glass surfaces by alkaline solutions made by Schumacher and Schwiete (4) lead to the conclusion that in such systems the weight loss per unit area was proportional to the time of immersion.

The attack of glass surface by molten salts has received little attention in comparison. Many workers in the molten salt field have commented on the attack of glass containers by such media at high temperatures. Lundén (5) has summarized, in a qualitative manner, his experiences of the resistance of glass to various molten salt baths. Elyard and Rawson (6) studied the effect of sodium vapor on the simple Na_2O-SiO_2 system. At 350°C they found that the higher the soda content, the higher the resistance to attack of the glass.

Table I. Major constituents of glasses

	A	B	C	D
SiO_2	73.2	80.0	71.0	62.1
Al_2O_3	0.8	1.9	—	24.1
B_2O_3	—	13.8	—	—
Na_2O	17.0	4.3	11.5	7.6
Li_2O	—	—	1.0	3.4
CaO	5.2	—	—	—
MgO	3.5	—	—	1.5
ZrO_2	—	—	16.5	—

Metal corrosion by molten salts has received more attention because of the use of such systems in nuclear technology. Much of this work has been concerned with equilibrium studies in molten halides (7).

Experimental Procedure

The major components of the glass compositions studied are given in Table I. These compositions will be referred to afterwards as glasses A, B C, or D. Slabs of glasses A, B, and C with approximate dimensions of ½ x ½ x ¼ in. were ground and polished to give a smooth finish. Glass D was similarly treated to give slabs of ½ x ½ x ⅛ in. The chemicals used in this work were Baker Analyzed Reagent grade pellets. The sodium hydroxide was 98.6% pure (0.29% Na_2CO_3), and the potassium hydroxide was 86.0% pure (0.94% K_2CO_3). The major impurity was water. The salts were fused without further purification and left molten for several hours before use, to drive off the water. Nickel crucibles were attacked to a certain extent by fused potassium hydroxide; so all runs were made with the salts fused in zirconium crucibles having a capacity of approximately 50g of salt.

The salts were fused in a tube-type furnace whose temperature could be controlled to within a degree. The sodium hydroxide runs were made at 350°C, the potassium hydroxide at 425°C. The temperature of the furnace was measured by means of a shielded chromel-alumel thermocouple attached to a L&N potentiometer. The slabs were placed in a nichrome wire basket, washed in an ultrasonic cleaner with a detergent, rinsed with distilled water and acetone, and dried in an air oven at 140°C. The samples were then placed in a dessicator, cooled, and weighed. The dimensions of each slab were determined using calipers. The basket plus slabs were preheated in the furnace for at least 2 min, then quickly transferred to the fused salt, and completely immersed. The time of immersion was noted using a stop watch graduated in tenths of a second. The samples were removed from the salt, allowed to cool for 5 min, and then rinsed with tap water. For final cleaning they were placed in an ultrasonic cleaner, and the procedure outlined above was repeated to obtain the loss in weight. The nichrome baskets were attacked to a small extent by the molten salts. Potassium hydroxide melts were observed to be slightly brown in color after several immersions of a basket in the melt. It was assumed that any such impurity would not interfere with the glass attack. These baskets were not exposed to the salt for long times, so while nickel crucibles were badly attacked after several days, the attack of the baskets was very slight. When the brown color was apparent the melt was discarded. The baskets themselves showed no sign of deterioration, beyond a slight blue coloration.

The surface attack was also studied using a Leitz "Ortholux" microscope fitted with an "Aristophot" camera equipped to take 4 x 5 in. Polaroid Land film.

Results and Discussion

There was a major difference in the appearance of a glass sample attacked by sodium hydroxide and one attacked by potassium hydroxide. Sodium hydroxide attack always resulted in a frosty appearance of the surface, making the sample opaque; potassium hydroxide attack left a transparent surface. Photomicrographs were taken of the surfaces after attack. Sodium hydroxide attack is characterized by the topography shown in Fig. 1. This shows the raised character of the frosty layer which causes the samples to be opaque. Close examination of this type of surface shows no crystalline features. This was confirmed by surface x-rays, and by x-ray studies of the surface of glass D which flaked off when dried. In both studies the surface was found to be amorphous. Potassium hydroxide attack, in comparison, gives rise to a featureless surface as shown in Fig. 2. There were slight differences in topographical features between the different compositions treated in the same melts. For instance, the size of the features formed by sodium hydroxide attack on glass A at any one time were much smaller than on glass B.

Fig. 1. Glass B, NaOH, 5 min, 350°C. Magnification approximately 55X.

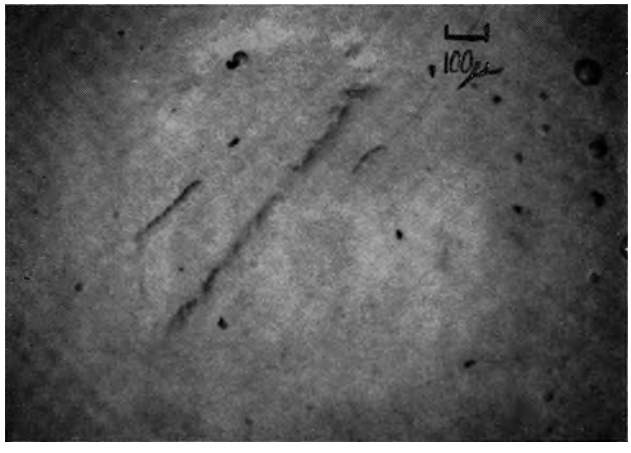

Fig. 2. Glass A, KOH, 1 min, 425°C. Magnification approximately 55X.

Weight Change Studies

The change in weight per unit area was measured as a function of time for all the glass compositions in both molten sodium hydroxide and potassium hydroxide. These runs were made at 350°C in molten sodium hydroxide (mp 322°C) and in molten potassium hydroxide at 425°C (mp 410°C).

The attack of the glasses by molten potassium hydroxide may be considered to proceed by dissolution of the glass. The dissolution of a solid in a liquid may be treated by the method used by Cooper and Kingery (8) in their studies of the dissolution of sapphire in molten calcia-alumina-silica slags. They showed, that in the region where molecular diffusion governs the rate of dissolution, their results could be expressed by the equation

$$Y = 2\alpha\,(Dt)^{1/2} \qquad [1]$$

Y is the change of solute thickness for a semi-infinite slab, D the effective binary diffusion coefficient, and the constant α can be obtained from the expression

$$f(\alpha) = \pi^{1/2}\alpha \exp \alpha^2 \operatorname{erfc} \alpha \cong - \left(\frac{W_1 - W_\infty}{1 - W_1} \right) \quad [2]$$

The function $f(\alpha)$ has been plotted (9), so that α can be obtained once the right-hand side of Eq. [2] has been evaluated. The saturated weight fraction W_1 represents the saturation concentration of the solute in the solvent, and W_∞, the bulk weight fraction, represents the concentration of solute in the solvent before dissolution, and is equal to zero in these systems.

The weight change per unit area, $\Delta W/A$ is related to the change in thickness Y by the expression

$$\frac{\Delta W}{A \cdot \rho} = Y \quad [3]$$

where ρ is the density of the glass. Combining Eq. [3] and Eq. [1] leads to

$$\frac{\Delta W}{A} = 2\alpha \cdot \rho \cdot (Dt)^{1/2} \quad [4]$$

Plots of $\Delta W/A$ against $t^{1/2}$ are shown in Fig. 3. The potassium hydroxide data are represented by the triangles; the sodium hydroxide data by the circles. The bars indicate the spread in the values of the weight change per unit area at a given time. The times of immersion are restricted to 5 min or less, as deviations from linearity were larger for longer immersion times, indicating that diffusion is no longer rate controlling. The data show a certain amount of scatter due to the difficulty in preparing reproducible glass surfaces. A least mean square analysis was applied to all the data. The Student t test, using a 5% confidence level, indicated that in the potassium hydroxide/glass systems there was no significant difference between the calculated intercept and zero, except for the system potassium hydroxide/glass D. The same test applied to the sodium hydroxide/glass systems indicated a significance in the calculated intercept, except for the sodium hydroxide/glass D system, which was not significantly different from zero. It was reported earlier in this discussion that in this system the surface layer flaked off on drying the sample. The points indicate the change in weight per unit area after this layer had been removed. The reason for a significance in the intercept in the potassium hydroxide/glass D system is not too clear. The samples after treatment had the same appearance as the other three compositions treated in potassium hydroxide. A possible explanation is that the diffusion controlled mechanism breaks down before 5 min, in which case the first four points only should be considered. If this is so, then using the statistical treatment outlined earlier, an intercept not significantly different from zero is obtained. The initial slope obtained by this method was used to calculate the effective diffusion coefficient shown in Table II. However, it should be taken as indicating only an approximate value.

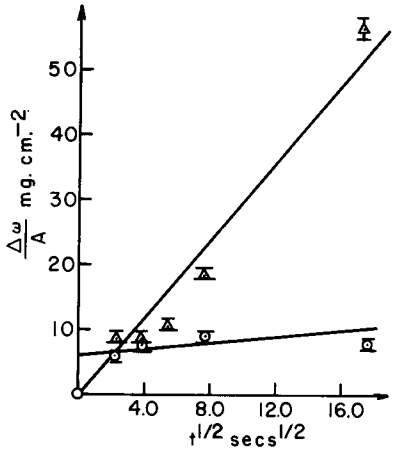

Fig. 3A. Weight loss per unit area as a function of the square root of time. Glass A: ⊙, NaOH, 350°C; △, KOH, 425°C.

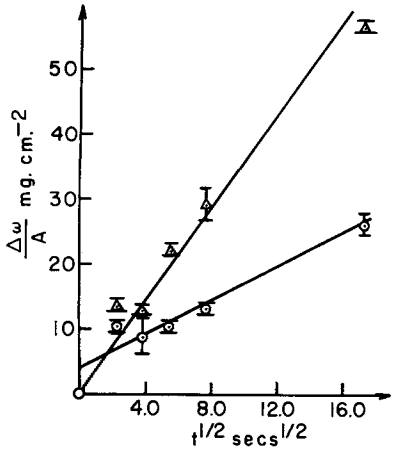

Fig. 3B. Weight loss per unit area as a function of the square root of time. Glass B: △, KOH, 425°C; ⊙, NaOH, 350°C.

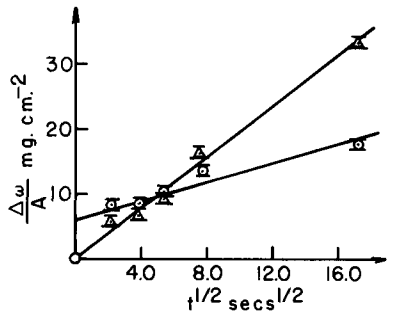

Fig. 3C. Weight loss per unit area as a function of the square root of time. Glass C: △, KOH, 425°C; ⊙, NaOH, 350°C.

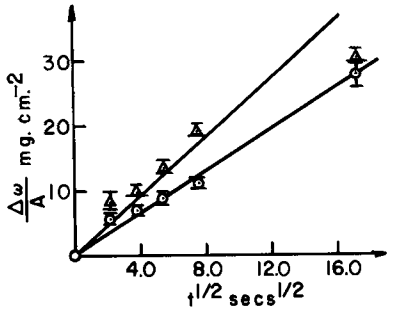

Fig. 3D. Weight loss per unit area as a function of the square root of time. Glass D: △, KOH, 425°C; ⊙, NaOH, 350°C.

The mechanism for surface attack of a glass by sodium hydroxide does not appear to be supported by a simple dissolution process as is found for potassium hydroxide attack. After immersion in sodium hydroxide one, or several, of the reaction products are left strongly bound to the surface, giving rise to the frosted look, and except for glass D are difficult to remove. A diffusion-controlled mechanism is still indicated in these systems by the linear relationship between the weight change per unit area and the square root of the immersion time. The boundary conditions required to apply the treatment of Cooper and Kingery, however,

Table II. Diffusion coefficients in the KOH/glass systems at 425°C

Glass	W_1	ρ, g cm^{-3}	α	D, cm^2 sec^{-1} 10^5
A	0.26	2.47	-0.15_5	1.5
B	0.18_6	2.23	-0.11	5.4
C	0.21_1	2.61	-0.12_5	0.9_2
D	0.22_7	2.44	-0.13	1.3

do not hold. The potassium hydroxide/glass systems, on the other hand, appear to obey these boundary conditions.

A value for the diffusion coefficient in Eq. [4] can be found once W_i, the saturation weight fraction, is known. This latter quantity was obtained by adding known weights of powdered glass slowly to the bath until the melt solidified. The weight of glass in a given weight of salt was then used to obtain W_i. Although this is not an exact measure of W_i, it gives a value which is close enough for calculating diffusion coefficients. The values of D obtained are given in Table II.

All the systems give a value of D of the same order of magnitude, *i.e.*, 10^{-5} cm^2sec^{-1}. This is very similar to values obtained for cation and anion self-diffusion in fused salts at these temperatures (10). However, it should be pointed out that Eq. [4] holds only for molecular diffusion in a binary system. In the dissolution of glass, the system is probably more complicated than a binary system, although one could consider it as a diffusion of potassium hydroxide to the glass surface, followed by the diffusion away from the surface of the reaction products.

Acknowledgments

The author wishes to thank Stanley Lewek for obtaining the weight change data. He also wishes to thank Dr. J. S. Olcott, Dr. R. M. Tichane, Dr. H. M. Garfinkel, and Mr. P. B. Adams for their suggestions and constructive criticism of this paper.

Manuscript received May 25, 1965; revised manuscript received July 22, 1965.

Any discussion of this paper will appear in a Discussion Section to be published in the June 1966 JOURNAL.

REFERENCES

1. L. Holland, "The Properties of Glass Surfaces," pp. 122-192, John Wiley & Sons, Inc., New York (1964).
2. W. Eitel, "Silicate Science," Vol. II, pp. 487-519, Academic Press, New York (1965).
3. R. W. Douglas and J. O. Isard, *J. Soc. Glass Technol.*, **33**, 289 (1949).
4. L. Schumacher and H. E. Schwiete, *Glass Tech. Ber.*, **33**, 1 (1960).
5. A. Lundén, *Corrosion Sci.*, **1**, 62 (1961).
6. C. A. Elyard and H. Rawson, "Advances in Glass Technology," p. 270, Plenum Press, Inc., New York (1962).
7. D. Cubicciotti, "The Encyclopedia of Electrochemistry," C. Hampel, Editor, p. 632, Reinhold Publishing Corp., New York (1964).
8. A. J. Cooper, Jr., and W. D. Kingery, *J. Am. Ceram. Soc.*, **47**, 37 (1964).
9. J. Crank, "Mathematics of Diffusion," pp. 104-105, Clarendon Press, Oxford (1956).
10. B. R. Sundheim, "Fused Salts," pp. 224-231, McGraw-Hill Co., New York (1964).

Vapor Deposition of Metals by Hydrogen Reduction of Metal Chelates

Rudy L. Van Hemert[1]

Lawrence Radiation Laboratory, University of California, Livermore, California

Lyle B. Spendlove[1]

Norton Air Force Base, California

Robert E. Sievers

Aerospace Research Laboratories, ARC, Wright-Patterson Air Force Base, Ohio

ABSTRACT

Thin film deposits of Cu, Ni, and Rh were obtained by hydrogen reduction of $Cu(tfa)_2$, $Cu(hfa)_2 \cdot H_2O$, $Ni(hfa)_2 \cdot 2H_2O$, and $Rh(tfa)_3$ from the gas phase (tfa = trifluoroacetylacetonate anion; hfa = hexafluoroacetylacetonate anion). The chelates are well suited for gas plating purposes by virtue of their high volatility and ease of reduction by hydrogen. The deposition process can be conducted at atmospheric pressure and at temperatures as low as 250°C. The process is potentially cyclic, free chelating agent being regenerated by the reduction reaction.

Chemical vapor deposition processes are the subject of increasing interest for applications in which it is difficult or impossible to use conventional methods for coating objects with metals or metal compounds. Perhaps the greatest obstacle to the widespread use of vapor deposition methods in the past has been the unavailability of suitable volatile metal compounds. Examination of the properties of certain fluorocarbon-β-diketonate metal chelates indicated that these compounds are remarkably well suited for vapor deposition purposes.

This paper discusses a vapor plating technique for the deposition of thin metallic films utilizing hydrogen reduction of volatile metal chelates. Thin films of metallic Cu, Ni, and Rh were obtained by reduction of metal chelates formed from trifluoroacetylacetone and hexafluoroacetylacetone. Although some of these compounds have been known for several years, their potential in chemical vapor deposition has not been previously recognized. The chelates are highly volatile, thermally stable, and readily reduced at atmospheric pressure at temperatures as low as 250°C.

[1] Captain, United States Air Force.

Experimental

Reagents.—1, 1, 1-Trifluoro-2, 4-pentanedione, H(tfa), and 1, 1, 1, 5, 5, 5-hexafluoro-2, 4-pentanedione, H(hfa), were purchased from Peninsular Chemical Research, Inc. The former reagent was used without further purification; the latter was redistilled prior to use. The rhodium nitrate was obtained from Alpha Inorganics, Inc., and was used without further purification.

Sample preparation.—The chelates *bis*(1, 1, 1, 5, 5, 5-hexafluoro-2, 4-pentanedionato) copper (II) hydrate $Cu(hfa)_2 \cdot H_2O$, *bis*(1, 1, 1-trifluoro-2, 4-pentanedionato) copper (II) $Cu(tfa)_2$, and *bis*(1,1,1, 5, 5, 5-hexafluoro-2, 4-pentanedionato) nickel (II) dihydrate

Table I. Analytical and melting point data for the metal chelates

Compound	Exp. mp, °C	Lit mp, °C	Carbon, % Theo.	Carbon, % Exp.	H, % Theo.	H, % Exp.	Metal, % Theo.	Metal, % Exp.
$Cu(tfa)_2$	198-199	200 (2)	24.23	24.50	0.81	0.50	12.82	12.92
$Cu(hfa)_2 \cdot H_2O$	115-126	126-128 (3)	32.49	32.57	2.18	2.14	17.19	17.18
$Ni(hfa)_2 \cdot 2H_2O$	209-210	207-208 (3)	23.60	23.64	1.19	1.22	11.54	11.19
$Rh(tfa)_3$	180-184	*cis* 148.5-149 (1) *trans* 189.5-190 (1)	32.05	31.88	2.15	1.74	18.31	18.15

$Ni(hfa)_2 \cdot 2H_2O$ were prepared by mixing an aqueous solution of the metal chloride with an aqueous solution of H(hfa) or H(tfa) in the proper mole ratios. The ligand solutions were slightly acidic, having been almost neutralized by NaOH prior to addition to the solution of the metal salt. The precipitate resulting from mixing the solutions was isolated by filtration, washed with water, allowed to dry, and then purified by recrystallization from benzene.

The *tris*(1, 1, 1-trifluoro-2, 4-pentanedionato) rhodium (III) $Rh(tfa)_3$ was prepared by the method of Fay and Piper (1).

Elemental analyses were obtained for each of the metal chelates. The analytical results shown in Table I indicate good agreement with the theoretical values. Experimental and literature values of the melting points are also tabulated. Fay and Piper (1) have shown by nuclear magnetic resonance spectroscopy that rhodium (III) trifluoroacetylacetonate exists in two geometrically isomeric forms, the *cis* and *trans* isomers. They were able to separate the isomers by column chromatography and found that the melting points of the pure isomers differ by about 40°. In the present study the isomeric mixture was used without separation, which explains why the melting point does not agree with the values given previously.

Plating equipment.—To test the thermal stability, volatility, and plating characteristics of the metal chelates, a simple apparatus was constructed in which two different temperatures could be maintained simultaneously in two different sections. A schematic of this equipment is shown in Fig. 1.

The function of the "vaporization zone," a Pyrex glass tube 3.2 cm OD and 70 cm long, was to provide a means of volatilizing the metal chelate. This gaseous chelate was then transported by hydrogen, the carrier gas, to the "reduction zone," where it reacted and was reduced to a metal plating on the test specimens. The vaporization zone was maintained between 95° and 150°, depending on the chelate being studied. The temperature of the reduction zone was varied over a broad range to determine the optimum temperature at which reaction occurred.

A thick-wall copper tube 44 cm long wrapped with heating and asbestos tapes was used as a furnace to heat the Pyrex tube. A thermocouple embedded in the copper wall was used to monitor the wall temperature. One end of the Pyrex tube was connected through a Pyrex glass joint to a Predictability Flowmeter, Model FM 1042B, while the other end was used as the exit

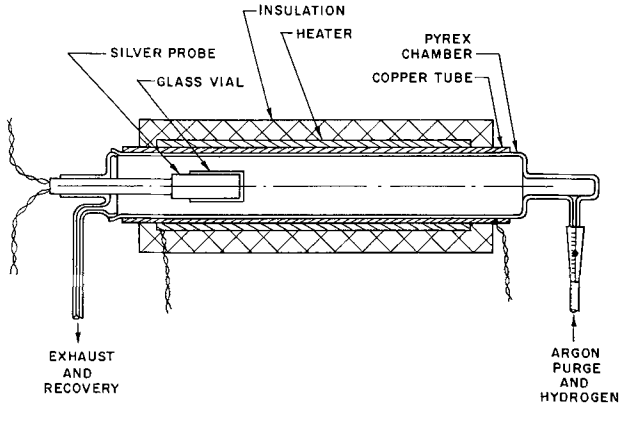

Fig. 1. Schematic of the plating equipment

for the byproducts of the reaction. A 9.5-cm-long, thick-walled, pure silver tube, heated internally by a cartridge heater, was used to heat the test specimens. At steady-state operation there were very small temperature gradients in this silver probe. A thermocouple embedded in this probe measured the reduction zone temperatures. The test specimens were flint glass vials 1.8 cm OD and 7 cm long which securely fitted over the silver probe. These vials were cleaned by dipping them in concentrated nitric acid, rinsing with water and then acetone, and drying in the air.

The heating of both zones was controlled by automatic temperature-regulating equipment capable of maintaining a selected temperature. These vaporization and reduction zone temperatures were continuously monitored and recorded by strip-chart recorders.

Sublimation equipment.—An auxiliary apparatus was used to determine the temperature range which could be used to volatilize the metal chelate at an appreciable rate without causing it to decompose. The lower limit of this range is referred to as the sublimation temperature in Table II. The temperature at which the vaporization zone was actually operated is shown in the second column. Although even higher temperatures can be used, these were judged to be the most satisfactory.

The equipment consisted of a heating bath 22 cm OD and 46 cm high, filled with heating oil. In the oil bath was a coil of glass tubing 4.8 m long. Hydrogen entered one end of the tubing at a carefully controlled flow rate of 16 ml/min and the outlet of the tubing vented to a fume hood. The bottom of the coil contained a glass joint in which the chelates were placed.

The oil bath was agitated vigorously with two stirrers, and the temperature of the bath was continuously recorded. The sublimation temperature recorded in Table II was obtained by very slowly increasing the temperature of the oil bath and observing the value at which crystal growth in the cool part of the glass tubing exposed to the ambient surroundings first became apparent.

Plating experiments.—In each plating experiment the reduction zone was brought to a steady-state temperature, the system was purged with argon and then hydrogen, and the vaporization zone was heated to an appropriate temperature that resulted in reasonably rapid volatilization of the chelate. About 0.01g of the chelate was placed in the vaporization zone of the reaction tube apparatus for each experimental run. The reduction temperature was varied from 200° to 350°C in increments of 10°, while the hydrogen flow rate was varied from 8 to 28 ml/min in increments of 2 ml/min. The best appearing deposits for all four metal complexes were obtained at a reduction temperature of 250° ± 10°C and a hydrogen flow rate of 16 ± 1 ml/min.

Table II. Sublimation, vaporization, and reduction temperatures of the chelates[a]

Compound	Sublimation temp, °C	Vaporization zone, temp, °C	Reduction zone, temp, °C
$Cu(tfa)_2$	85	150	250
$Cu(hfa)_2 \cdot H_2O$	65	90	250
$Ni(hfa)_2 \cdot 2H_2O$	100	135	250
$Rh(tfa)_3$	110	130	250

[a] Hydrogen flow rate of 16 ml/min.

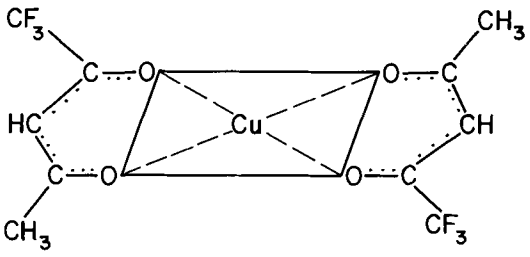

Fig. 2. *Trans* isomer of $Cu(tfa)_2$

Results and Discussion

The reaction of a metal salt with H(hfa) or H(tfa) to form the diketonate complexes may occur by several reactions summarized as follows (1-8)

$$MX_n + n\text{H(tfa) or } n\text{H(hfa)} \rightarrow \text{M(tfa or hfa)}_n + n\text{HX} \quad [1]$$

where X may be Cl^-, NO_3^-, CO_3^{2-}, OH^-, etc. The number n depends on the valence and coordination number of the metal ion. Frequently sodium hydroxide or ammonium hydroxide is used in the synthesis to neutralize the ligand. The structure of a representative complex, the *trans* isomer of $Cu(tfa)_2$, is shown in Fig. 2.

The unusual properties of the metal fluorocarbon-β-diketonates arise from the disposition of the fluorine-containing ligands about the metal ions. The organic ligands with highly electronegative fluorine atoms act as a shroud that surrounds the metal atoms, imparting extraordinary volatility to the complexes (4). The chelates studied all sublime at rates satisfactory for deposition purposes at temperatures much lower than those at which thermal decomposition is appreciable. The compounds are easily prepared and handled and are stable indefinitely to atmospheric hydrolysis, unlike many of the compounds used previously for gas plating purposes. As a matter of fact, the complexes are sufficiently volatile and thermally stable to be subjected to quantitative gas phase chromatography. A recent book (9) summarizes the advances made in this interesting field. The data presented in this paper have direct bearing on problems associated with the gas chromatography of the complexes. Thermal stability, volatility, and ease of reduction are considerations of prime importance. The data in Table II, for example, indicate that unnecessarily high column temperatures and injection port temperatures should be avoided, particularly if hydrogen is used as the gas chromatographic carrier gas, or in conjunction with the flame ionization detector, so that decomposition of the chelates will not occur.

The vaporized chelates were reduced by the hydrogen in the reduction zone according to the following:

$$Cu(tfa)_2 \xrightarrow{H_2} Cu + \text{H(tfa)} \quad [2]$$

$$Cu(hfa)_2 \cdot H_2O \xrightarrow{H_2} Cu + \text{H(hfa)} + \text{HY} \quad [3]$$

$$Ni(hfa)_2 \cdot 2H_2O \xrightarrow{H_2} Ni + \text{H(hfa)} + \text{HY} \quad [4]$$

$$Rh(tfa)_3 \xrightarrow{H_2} Rh + \text{H(tfa)} \quad [5]$$

where HY is 1, 1, 1, 5, 5, 5-hexafluoro-2, 2, 4, 4-tetrahydroxypentane (8, 10).

In a separate experiment a large amount of $Cu(tfa)_2$ was completely vaporized and then reduced by hydrogen. The effluent reaction products were trapped in a U-tube cooled by dry ice and were then analyzed by gas chromatography. The analysis showed that H(tfa), the chelating agent, was regenerated, which suggests that it could be re-used in a cyclic process. HY can be dehydrated to regenerate H(hfa) by treatment with phosphorus pentoxide or concentrated sulfuric acid (8, 10). This step is unnecessary for the regenerative synthesis of the copper chelate, however, because both H(hfa) and HY react with copper (II) salts to form the desired complex.

The thin metallic deposits that were obtained adhered very well to the glass tubes, even though the tubes had not been subjected to any special cleaning or etching treatment other than rinsing with concentrated nitric acid, water, and acetone. Although the experimental plates were very thin, there is, of course, no limit to the thickness that can be obtained since this depends only on the deposition rate and time the reaction is allowed to proceed.

All plates were shiny mirrors on both surfaces and all were electrically conductive. The plates were very ductile and, when scraped from the substrate, could be folded to a sharp crease without breaking. No impurities could be detected by x-ray diffraction measurements on the samples. Lattice constants for the metallic deposits are shown in Table III.

As expected, the thickness of the metal plate was found to be a function of both the surface temperature and the concentration of the metal chelate in the gas contacting the surface. Temperature gradients in the surface caused uneven plating. Also, thinner plates resulted in zones where the chelate concentration in the gas phase was depleted.

Although most of the plating experiments were conducted with flint glass substrates, stainless steel substrates were used in a few cases. As expected, adhesion to the metal was even better than to the glass. Any material, for example, plastics, wood, ceramics, etc., could be plated by this method if the object can be heated to the temperature required for plating. Since the temperature required for the reduction is relatively low, heating could be accomplished with a variety of sources, *e.g.*, resistance, infrared, or induction.

Conclusions

Vapor deposition by hydrogen reduction of metal chelates of fluorocarbon-β-diketones provides a new method of obtaining pure, thin film deposits of various metals. Cu, Ni, and Rh were studied in this investigation, and undoubtedly several other metals can be deposited by reduction of similar chelates possessing the required volatility.

Hydrogen was used both as a carrier gas and as a reducing agent. For complexes of some metals, *e.g.*, copper and rhodium, an inert gas may be used as the carrier, and the chelates will undergo self-reduction to yield the elemental metal via thermal decomposition (11). This method appears to yield a less pure deposit, but like the hydrogen reduction method, it occurs at atmospheric pressure, obviating the problems of operating in a vacuum. Because the reduction occurs at any heated surface, both methods offer significant advantages over line-of-sight plating processes.

Acknowledgment

The authors wish to thank Dr. Eugene Bissell and Douglas B. Fields of the Lawrence Radiation Laboratory for their help in the preparation and testing of the chelates. This work was done under the auspices of the United States Atomic Energy Commission.

Table III. Lattice constants for metallic deposits[a]

Compound	Metal obtained	Lattice constant a, Å	
		Exp	Lit[b]
$Cu(tfa)_2$	Cu	3.615	3.6150
$Cu(hfa)_2 \cdot H_2O$	Cu	3.615	3.6150
$Ni(hfa)_2 \cdot 2H_2O$	Ni	3.523	3.5238
$Rh(tfa)_3$	Rh	3.803	3.8031

[a] Metallic deposits obtained with a hydrogen flow rate of 16 ml/min at experimental conditions shown in Table II.
[b] X-ray Powder Data File, American Society for Testing and Materials, Philadelphia (1962).

Manuscript received March 19, 1965; revised manuscript received July 19, 1965.

Any discussion of this paper will appear in a Discussion Section to be published in the June 1966 JOURNAL.

REFERENCES

1. R. C. Fay and T. S. Piper, *J. Am. Chem. Soc.*, **85**, 500 (1963).
2. E. W. Berg and J. T. Truemper, *J. Phys. Chem.*, **64**, 487 (1960).
3. M. L. Morris, R. W. Moshier, and R. E. Sievers, *Inorg. Chem.*, **2**, 411 (1963).
4. R. E. Sievers, B. W. Ponder, M. L. Morris, and R. W. Moshier, *ibid.*, **2**, 693 (1963).
5. R. A. Staniforth, Doctoral Dissertation, Ohio State University, 1943.
6. R. E. Sievers, R. W. Moshier, and M. L. Morris, *Inorg. Chem.*, **1**, 966 (1962).
7. A. L. Henne, M. S. Newman, L. L. Quill, and R. A. Staniforth, *J. Am. Chem. Soc.*, **69**, 1819 (1947).
8. R. L. Belford, A. E. Martell, and M. Calvin, *J. Inorg. Nucl. Chem.*, **2**, 11 (1956).
9. R. W. Moshier and R. E. Sievers, "Gas Chromatography of Metal Chelates," Pergamon Press, Oxford, 1965, in press, and references cited therein.
10. B. G. Schultz and E. M. Larsen, *J. Am. Chem. Soc.*, **71**, 3250 (1949).
11. R. W. Moshier, R. E. Sievers, and L. B. Spendlove, Patent pending.

A Chronopotentiometric Study of the Silver-Silver Chloride and Silver-Silver Bromide Systems

John D. Van Norman

Brookhaven National Laboratory, Upton, New York

ABSTRACT

The dissolution of silver in its molten chloride and bromide was studied using a chronopotentiometric technique. The solubility of silver in molten AgCl and AgBr was evaluated by adding small amounts of silver to the salts until saturation was reached, as measured *in situ*, by anodic chronopotentiometry. The solubility of silver in its chloride at 520°C was 0.0123 mole % and in its bromide, 0.0118 mole % at 500°C. Analyses of the anodic chronopotentiogram wave shapes indicated that the oxidation of the soluble silver species in the chloride and bromide was a reversible one-electron process. Diffusion coefficients for this species were determined to be 2.0 x 10^{-5} cm^2/sec in AgCl at 520°C and 4.2 x 10^{-5} cm^2/sec in AgBr at 500°C.

The dissolution of metals in their own molten salts is of considerable interest from both the theoretical and practical viewpoints (1,2). Metal-metal halide systems have been examined in detail by using a variety of techniques. In most cases the systems which have been reported are those with appreciable solubility of the metal, *e.g.*, solutions of alkali metals, alkaline earth metals, transition metals, and inner transition metals in their salts. In these cases the solubility of the metal generally exceeds 1 mole % where techniques such as measurement of freezing point depression, vapor pressure, conductivity, and emf, are quite useful. Solubilities have been determined chemically with a fair degree of accuracy, and the phase diagrams in many cases are known.

However, there are certain metal-metal halide systems where the solubility of the metal is small, considerably less than 1 mole %. Examples of such systems are the Pb-$PbCl_2$ (3), Mg-$MgCl_2$ (4), Sb-$SbCl_3$ (5), and the Ag-AgCl (6) systems. In such systems the previously mentioned techniques are not always applicable, while electrochemical techniques have been used with considerable success. Egan (3) utilized a polarographic technique to elucidate the mode of dissolution of lead in its chloride. Van Norman and Egan (4) used a chronopotentiometric technique to study the magnesium-magnesium chloride interaction while Corbett *et al.* (5) employed an emf technique in their study of the Sb-$SbCl_3$ system. In each of these systems the solubility of the metal had been determined chemically. An *in situ* electroanalytical technique may well prove more accurate for determining the metal solubilities while also offering additional information on these systems.

This investigation uses such a technique, anodic chronopotentiometry. The Ag-AgCl and the Ag-AgBr systems were chosen because of their low metal solubility to demonstrate the usefulness of the developed technique. Corbett and von Winbush (6) determined the solubility of silver in its chloride at 490°C by equilibrating the molten salt with excess silver, filtering at temperature through a fine quartz frit, and subsequently analyzing the excess silver content in the AgCl by dissolution of the salt in ammonium hydroxide and weighing the free silver. Since silver recrystallizes in molten silver chloride at these temperatures, finely divided silver not in solution may have passed through the fine quartz frit. For this reason they placed a maximum value of the solubility of 0.03 mole %.

The technique developed in this investigation to determine accurately the solubility of silver in its chloride and bromide is an extension of that used by Van Norman and Egan (4) in their study of the Mg-$MgCl_2$ system. Small amounts of silver were added to the molten silver salts and anodic chronopotentiograms were taken after each addition. From the basic equation of chronopotentiometry

$$i_o\tau^{1/2} = \frac{nF\pi^{1/2}D^{1/2}C}{2} \qquad [1]$$

where i_o is the current density, τ the transition time, D the diffusion coefficient, and C the concentration, it can be seen that the product $i_o\tau^{1/2}$ is directly proportional to concentration. Thus a plot of this product *vs.* the amount of silver added will be a straight line until saturation is reached where $i_o\tau^{1/2}$ becomes constant. The diffusion coefficient D can be calculated from the slope of this plot.

Experimental

Materials.—The silver chloride and the silver bromide used in this investigation were supplied by the Amend Drug and Chemical Company and were of C. P. grade. The AgCl was further treated by passing chlorine gas through the powder while raising the temperature slowly above the melting point, at which point the chlorine was passed through the molten salt for four additional hours. The salt was then cooled, transferred to a filtration apparatus, and filtered in the molten state through a fine quartz frit to remove any insoluble materials. The salt was stored in the

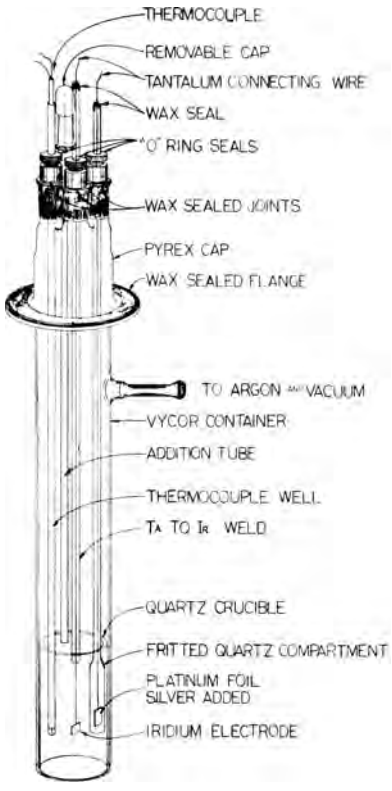

Fig. 1. Experimental cell used for the study of the Ag-AgCl and Ag-AgBr systems.

dark under argon until it was used. The silver bromide was treated in a similar manner with bromine gas. The silver metal used was high-purity foil.

The indicator electrodes used were either tungsten or iridium. It was found that tantalum reacted with molten silver salts to give volatile tantalum salts and silver. Molybdenum oxidized before the soluble silver species was completely oxidized and hence was useless. Tungsten proved satisfactory, but iridium was found to be the best electrode material for both systems.

Apparatus.—The experimental cell shown in Fig. 1 consists of a flanged Vycor jacket sealed with Apiezon wax to a Pyrex cap which has standard tapered joints for insertion of electrodes, a thermocouple well, and an addition tube. The silver salts were contained in an inner quartz crucible. The reference electrode was a platinum foil suspended in a fritted quartz compartment filled with the silver salt and excess silver metal. The indicator electrode was either a tungsten or iridium foil suspended in the main body of silver salt by a fine wire of the same material spot-welded to the foil. Electrical contact was made by a tantalum wire spot-welded to the tungsten or iridium wire. The tantalum wire ran through the quartz tubing which was held by the O-ring seals waxed into the cap. The O-ring seals permitted vertical positioning of the electrodes and thermocouple well. The temperature was measured by a chromel-alumel thermocouple positioned in the well, below the surface of the salt.

The addition tube, sealed through the Pyrex cap, allowed opening of the cell while it was under an argon atmosphere for the addition of small amounts of silver. The cell was contained in a resistance furnace maintained at the proper temperature.

Method.—Pure silver salt was placed in the quartz crucible and the cell assembled and sealed. The cell was then evacuated to a pressure of $<10^{-5}$ mm Hg. Argon was admitted to the cell and the temperature raised to the operating temperature. The fritted quartz compartment, indicator electrode, and thermocouple well were lowered below the surface of the molten salt. Anodic chronopotentiograms were taken of the pure salt by passing a constant current between the reference electrode (which served as the cathode) and the indicator electrode (which served as the anode) while measuring the potential as a function of time. The reference electrode was nonpolarizable as silver was being deposited from a pure silver salt.

The constant current was supplied by an all electronic circuit designed by the Instrumentation Division of Brookhaven National Laboratory and the potential-time curves were recorded on a L&N High Speed Speedomax G recorder which had a pen speed of 0.25 sec, full scale, and a chart speed of 2.0 ips. Transition times for the chronopotentiograms were read directly from the chart recordings with an estimated accuracy of ± 0.025 sec. Transition times were kept between 0.5 and 1.5 sec. Below 0.5 sec the error in reading the transition times became significant, and above 1.5 sec convection due to thermal gradients became important.

A small weighted piece of silver was then added to the pure silver salt and the system equilibrated for at least 20 hr. More anodic chronopotentiograms were taken, and the process was repeated until saturation was achieved. After saturation was established the electrodes and the thermocouple well were withdrawn, and the salt was cooled and weighed.

Results

Anodic chronopotentiograms for the oxidation of the soluble silver species in AgCl at 520°C were obtained at various concentrations; Fig. 2 shows typical examples. Transition times were measured from current onset to the potential break corresponding to the rapid shift of the potential to that of the limiting potential, *i.e.*, the dissolution of the electrode material. In practice, the potential at which this break occurred was determined at each concentration for 4 to 5 waves and subsequent transition times measured to that point.

The product $i_o\tau^{1/2}$ at a given concentration was independent of current density, indicating the validity of this technique for analysis. Final $i_o\tau^{1/2}$ values used in evaluating the solubilities were averages of 8 or more measurements and had an average deviation of $\pm 3\%$. Figure 3 shows a sample plot of $i_o\tau^{1/2}$ *vs.* silver added to silver chloride at 520°C. The diffusion coefficient D for the soluble silver species was calculated from the slope of this plot (see Eq. [1]).

Analysis of the shape of chronopotentiograms can in the ideal case give the number of electrons transferred in an oxidation or reduction process. For the case of the oxidation of silver dissolved in its salts, a plot of potential E *vs.* $-\log(\tau^{1/2}-t^{1/2})$ should be a straight line with a slope of $2.3(RT/nF)$. The quantity t is the time along the chronopotentiogram. A number of such plots gave a straight line with slopes close to that of

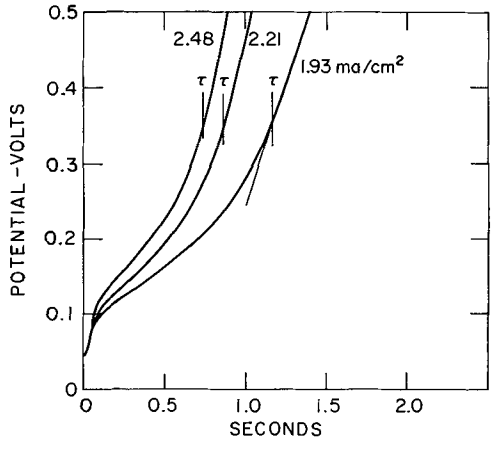

Fig. 2. Typical anodic chronopotentiograms obtained in the Ag-AgCl system using an iridium electrode; temperature, 520°C.

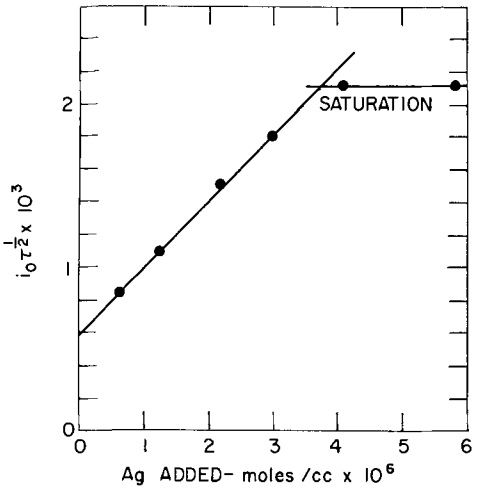

Fig. 3. Plot of $i_0\tau^{1/2}$ vs. silver added to AgCl at 520°C

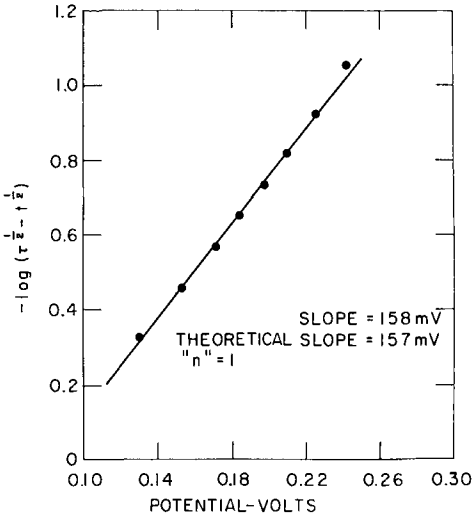

Fig. 4. Plot of E vs. $-\log(\tau^{1/2}-t^{1/2})$ for an anodic wave in the Ag-AgCl system.

a single-electron process at 520°C, namely, 157 mv. Figure 4 shows such a plot.

Table I summarizes the solubility data, the calculated diffusion coefficients, and the slopes of plots of E vs. $-\log(\tau^{1/2}-t^{1/2})$ for the Ag-AgCl system.

The silver-silver bromide system was studied in the same manner. Anodic chronopotentiograms obtained for the oxidation of the silver species in AgBr were quite similar to those obtained in the chloride. The slopes of the solubility plots varied considerably when tungsten was the electrode material, but were constant when iridium was used. Hence diffusion coefficients were calculated from the iridium results. Plots of E vs. $-\log(\tau^{1/2}-t^{1/2})$ were not straight lines when tungsten was the electrode, but were when iridium was used. Table II summarizes the results obtained for the silver-silver bromide system at 500°C.

Table I. Ag-AgCl (520°C)

Electrode material	Solubility, mole %	Diffusion coefficient, cm²/sec	Slope of plot, E vs. $-\log(\tau^{1/2} - t^{1/2})$, mv
Tungsten	0.0121	1.33×10^{-5}	149
Tungsten	0.0131	1.13×10^{-5}	148
Iridium	0.0116	2.01×10^{-5}	158
	Avg 0.0123		157*

* Theoretical slope.

Table II. Ag-AgBr (500°C)

Electrode material	Solubility, mole %	Diffusion coefficient, cm²/sec	Slope of plot, E vs. $-\log(\tau^{1/2} - t^{1/2})$, mv
Tungsten	0.0115		
Tungsten	0.0114		
Tungsten	0.0106		
Iridium	0.0128	4.3×10^{-5}	158
Iridium	0.0126	4.1×10^{-5}	156
	Avg 0.0118	4.2×10^{-5}	154*

* Theoretical slope.

Discussion

The solubility of silver in its chloride at 520°C was found to be 0.0123 mole % as compared with the maximum value set on the solubility at 490°C by Corbett and von Winbush of 0.03 mole %. The observed difference can be accounted for by the inability of the filtration technique to distinguish between dissolved silver and very finely divided silver which may have passed through the quartz frit.

The discrepancy in diffusion coefficients obtained using tungsten as an electrode and that obtained using iridium as an electrode remains a mystery. However, the behavior of the tungsten electrode in the bromide system leads one to suspect these values in the chloride. The probable value of the diffusion coefficient of the soluble silver species in AgCl is 2.0×10^{-5} cm²/sec, quite similar to diffusion coefficients of ions in fused salts.

The plot of E vs. $-\log(\tau^{1/2}-t^{1/2})$ shows a reversible one-electron oxidation process. This can be accounted for by several mechanisms:

$$Ag^0 \text{ (solution)} \rightarrow Ag^+ + e^- \quad [2]$$

$$Ag_2^+ \rightarrow 2Ag^+ + e^- \quad [3]$$

or, in a more general form,

$$Ag_n^{(n-1)+} \rightarrow nAg^+ + e^- \quad [4]$$

where n represents a number of silver ions sharing the excess electron as in an F center. Equation [2] can be rejected as most evidence indicates that metals dissolve in their salts with the formation of an ionic species (1, 2). It is perhaps most meaningful to discuss this system in terms of Eq. [4], where $Ag_n^{(n-1)+}$ represents an F-(color) center with a delocalization of the electron. The number of solute cations, Ag^+, considered bound to the mobile electron is of considerable interest and needs clarification.

The solubility of silver in its bromide at 500°C, approximately the same number of degrees above its melting point as for AgCl, was 0.0118 mole %, which is quite similar to that in AgCl. The diffusion coefficient for the soluble silver species was found to be 4.2×10^{-5} cm²/sec, about twice that found for the chloride system; this is quite reasonable in view of the larger size of the bromide ion. Once again there is a reversible one-electron oxidation process.

The chronopotentiometric technique developed for this study of the Ag-AgCl and the Ag-AgBr systems can easily be extended to other systems where metal solubility is low and difficulties are encountered using other techniques. Valuable information can also be derived concerning diffusion processes in these systems and the nature of the metal-metal salt interaction.

Acknowledgments

The author would like to express his appreciation to Dr. Carl Wagner for suggesting the application of the technique to solubility studies, and to Drs. James Egan and Richard Wiswall, Jr., for many helpful discussions and suggestions. This work was performed under the auspices of the United States Atomic Energy Commission.

Manuscript received July 6, 1965. This paper was presented at the San Francisco Meeting, May 9-13, 1965.

Any discussion of this paper will appear in a Discussion Section to be published in the June 1966 JOURNAL.

REFERENCES

1. J. D. Corbett, "Fused Salts," Chap. 6, B. R. Sundheim, Editor, McGraw-Hill Book Co., New York (1964).
2. M. Bredig, "Molten Salt Chemistry," pp. 367-426, M. Blander, Editor, Interscience, New York (1964).
3. J. J. Egan, *J. Phys. Chem.*, **65**, 2222 (1961).
4. J. D. Van Norman and J. J. Egan, *ibid.*, **67**, 2460 (1963).
5. J. D. Corbett and S. von Winbush, *J. Am. Chem. Soc.*, **77**, 3964 (1955).
6. J. D. Corbett, S. von Winbush, and F. C. Albers, *ibid.*, **79**, 3020 (1957).

Oxygen Overvoltage on Bright Palladium in Acid Solutions

James P. Hoare

Electrochemistry Department, Research Laboratories, General Motors Corporation, Warren, Michigan

ABSTRACT

Oxygen overvoltage measurements were made both galvanostatically and potentiostatically on bright Pd electrodes in O_2-saturated $2N$ H_2SO_4 solutions. The anodic evolution and the cathodic reduction of oxygen were investigated, and, in general, the two measuring techniques gave the same kinetic results. The overvoltage curves exhibited a mixed potential region followed by a Tafel region. In the anodic curves these two regions were separated by a limiting current or passivation region. It was found that Pd is a poorer peroxide-decomposing catalyst than Pt, that a film of adsorbed PdO is a poor electronic conductor, that oxygen is evolved on a Pd anode through an oxide mechanism, the decomposition of PdO_2 to PdO and O_2, and that oxygen is reduced from the adsorbed oxygen molecules on a Pd cathode.

In acid solutions, it appears that the best catalysts for the reduction of oxygen are platinum and palladium. However, in the case of Pd, the metal becomes active in a potential region between 900 and 1100 mv according to Vetter and Berndt (1). Because of this solubility of Pd in H_2SO_4 solutions, the potential-determining mechanism on open circuit does not seem to involve the O_2/H_2O reaction

$$O_2 + 4H^+ + 4e \rightleftharpoons 2H_2O \qquad [1]$$

To explain the observed phenomena that the rest potential is independent of pH but dependent on the partial pressure of oxygen, and that an over-all two-electron process is potential-determining, a mixed potential mechanism composed of the Pd/Pd^{++} and the PdO_2/Pd^{++} half-reactions

$$Pd \rightleftharpoons Pd^{++} + 2e \qquad [2]$$

and

$$O_2 + Pd^{++} + 2e \rightleftharpoons PdO_2 \qquad [3]$$

was proposed (2). The potential is controlled by Eq. [3].

Two oxides are formed by Pd (3), PdO, and PdO_2 but PdO_2 is unstable in acid solutions (3, 4). After a Pd electrode had been anodized above 1500 mv, it was found that, in the absence of peroxide, a steady rest potential of 1470 mv was observed (2) which was assumed to be associated with a Pd/PdO_2 electrode. Since this potential coincides with the point on the charging curves (1, 5, 6), where oxygen is first evolved, it was noted (2) that possibly oxygen is evolved on Pd by a mechanism involving the unstable PdO_2.

In this report an account is given of the oxygen overvoltage measurements obtained on bright Pd both galvanostatically and potentiostatically for the cathodic reduction and the anodic evolution of oxygen in oxygen saturated solutions of $2N$ H_2SO_4.

Experimental

Small beads (0.1 to 0.15 cm in diameter) melted at the end of pure Pd wires (99.97%) in an oxygen torch were cleaned by heating white hot in a hydrogen flame followed by quenching in concentrated HNO_3 in a manner described before (7). As checks, three beads were mounted with Teflon spaghetti over the lead wires (polyethylene was avoided, since it may be attacked by peroxides produced in the polarization procedures) in one side of a dual Teflon cell (7). An α-Pd-H reference electrode (8) was mounted in the other side. All purification techniques and all cell and electrode preparations were the same as before (7).

The galvanostatic measurements were determined by the method already described (9) in which the potential was determined with a General Radio electrometer, Model 1230-A. Potentiostatic measurements were determined with a Model 61R Wenking potentiostat. The value of the current was recorded after the current had remained steady for 60 sec using a Weston microammeter. With an electronic current interrupter, it was found that up to a current density of 1 ma/cm^2 the iR correction to the measured potential was less than a millivolt.

Partial pressure of oxygen, P_{O_2}, experiments were carried out in the same way that was done in the case of Pt (7, 9) using a Beckman Oxygen Analyzer to determine the value of P_{O_2} in the N_2-O_2 gas mixtures. The system was stirred with gas flows of at least 350 cc/min to minimize the effects of mass transfer. In all cases, with this stirring rate mass transfer effects were absent. The overvoltage was determined from 1229 mv, the reversible oxygen potential (10), and all potentials are quoted with respect to the normal hydrogen electrode (NHE) unless otherwise noted. These experiments were carried out at a temperature of 25° ± 1°C.

Finally, it was observed that the Pd bead was still bright after the polarization measurements were taken.

Results

After a Pd/PdO electrode, as prepared in ref. (2), had come to a steady rest potential (~870 mv), the galvanostatic polarization at very low current densities was obtained. A plot of these data is given in Fig. 1. As long as the current density range shown in Fig. 1 was not exceeded, these data could be reproduced within ± 0.5 mv. Each point on the curve is the average value of those obtained from three cycles of increasing and decreasing current through the rest potential.

The cathodic overvoltage for the reduction of oxygen on Pd (galvanostatic) is shown in the bottom curve of Fig. 2. The arrows indicate the direction of polarization. There was some hysteresis observed be-

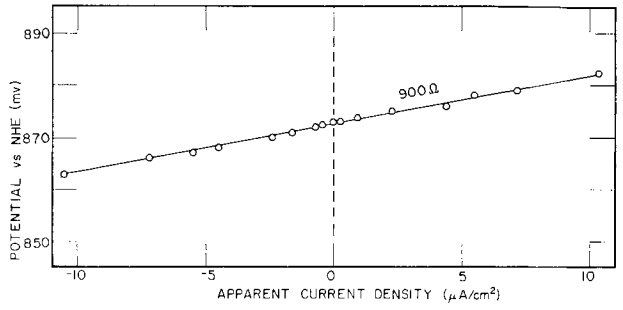

Fig. 1. Plot of potential against apparent current density for a Pd/PdO electrode at very low current densities.

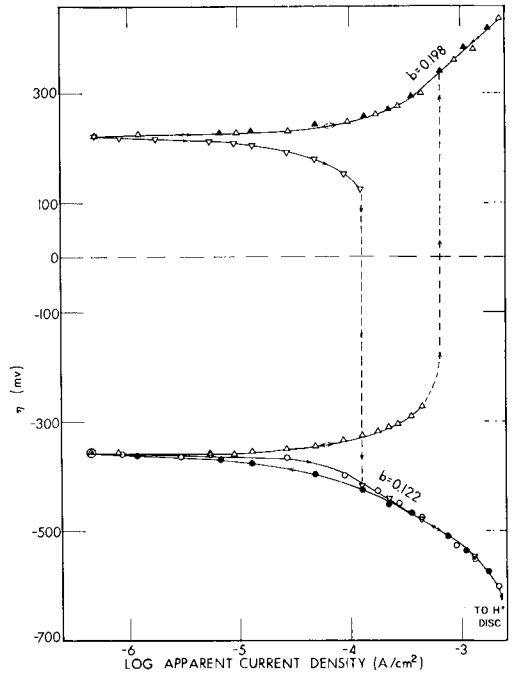

Fig. 2. Oxygen overvoltage curves for the reduction of oxygen (○) and the evolution of oxygen (△) on bright Pd electrodes in O_2-saturated 2*N* H_2SO_4 solution, obtained galvanostatically. The arrows give direction of polarization and, in general, open symbols represent data obtained with increasing current and filled symbols, those with decreasing current. The reduction curve for a Pd/PdO_2 electrode (▽) is also shown.

tween 10^{-4} and 10^{-5} amp/cm². Each point represents the average value of the data obtained from three cycles of increasing and decreasing current, and the deviation from the mean value is within ± 6 mv.

Also in Fig. 2 are presented the anodic overvoltage curves for the evolution of oxygen on Pd. Below a current density value of about 0.7 ma/cm², the curve was highly reproducible (within ± 1 mv) as indicated by the double arrows. Above this point, the potential moved very rapidly (from 960 to 1550 mv within 60 sec) which is depicted by the broken line in Fig. 2 from $\eta = -270$ to $\eta = 320$ mv. Now, a very reproducible curve was obtained in which the points averaged over three cycles of increasing and decreasing polarization deviated within only ± 3 mv from the average value. The steady open-circuit potential value was 1451 mv. When this electrode was cathodized, an irreproducible curve, indicated by the single arrows, was obtained which went into a limiting current above 0.11 ma/cm² (broken line in Fig. 2). Steady state cathodic polarization data after the limiting current was reached gave results identical to the original cathodic overvoltage curve. The complete cycle of events described by the curves in Fig. 2 could be repeated with the same results.

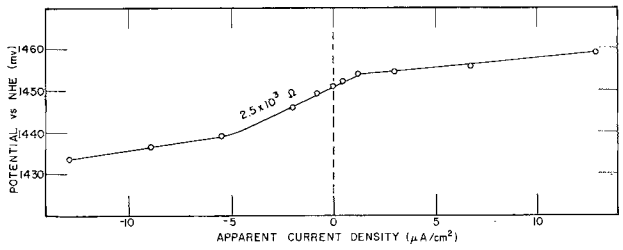

Fig. 3. Plot of the potential against the apparent current density for a Pd/PdO_2 electrode at very low current densities.

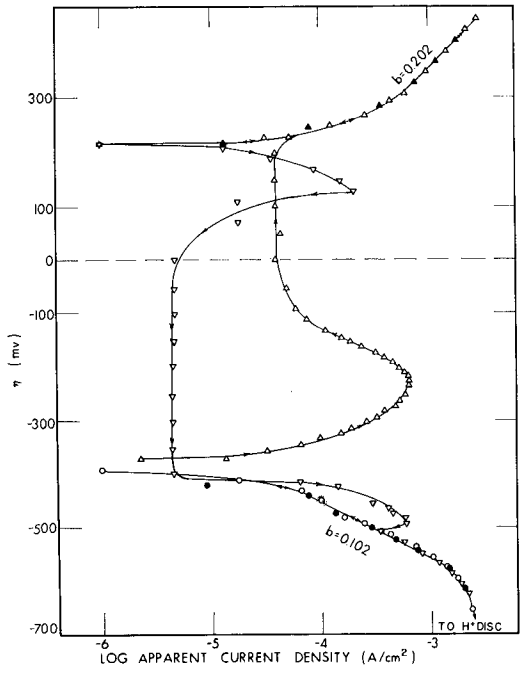

Fig. 4. Oxygen overvoltage curves obtained potentiostatically. The electrode system is the same, and symbols have the same meaning as in Fig. 2.

Polarization data, at very low current densities, obtained on the Pd/PdO_2 electrode are given in Fig. 3. These data are obtained from the anodic polarization curves in Fig. 2 for the electrode with an open-circuit potential of 1451 mv.

The overvoltage curves shown in Fig. 4 were obtained on Pd electrodes potentiostatically. Both the cathodic overvoltage curves below 870 mv ($\eta = -360$ mv) and the anodic overvoltage curves above 1450 mv ($\eta = 220$ mv) are nearly identical to those obtained

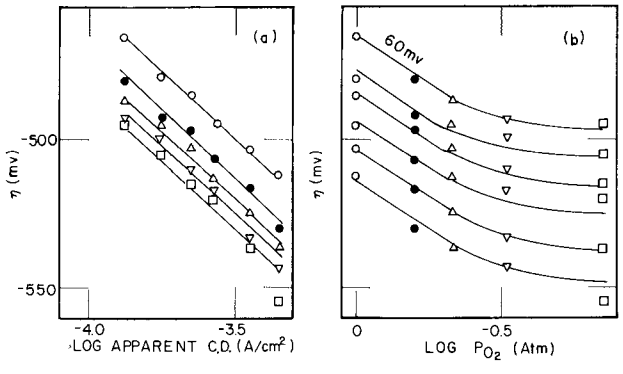

Fig. 5. (a) Oxygen overvoltage curves for the reduction of oxygen on bright Pd obtained galvanostatically with various values of P_{O_2}. P_{O_2} = 1, ○; 0.63, ●; 0.47, △; 0.30, ▽; 0.14, □. (b) Oxygen overvoltage as a function of log P_{O_2}. Lines with a slope of 60 mv were drawn through the first points to show that the data are consistent with a one-electron transfer step.

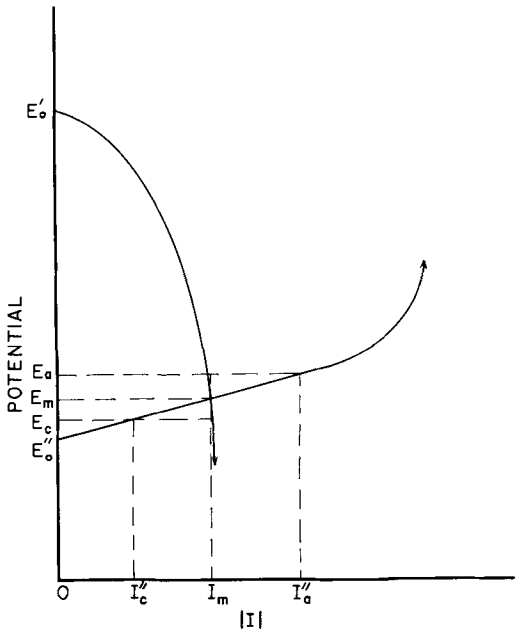

Fig. 6. Sketch of the mixed potential diagram for the Pd-O_2-acid system as a plot of the potential against the absolute value of the local cell current.

galvanostatically. In the potential range between 870 and 1450 mv, where the galvanostatic curves exhibit limiting currents, the potentiostatic curves display typical passivation phenomena. The maximum current density values observed in this potential range correspond well with the limiting current density values observed in the galvanostatic measurements.

Figure 5 contains data showing the variation of the overvoltage with P_{O_2} in the Tafel region for the galvanostatic reduction of oxygen on a Pd cathode. The overvoltage as a function of the current density for various values of P_{O_2} is given in Fig. 5a and as a function of the log P_{O_2} in Fig. 5b. The data in Fig. 5b were obtained from that in Fig. 5a. Similar measurements in the Tafel region for the galvanostatic evolution of oxygen on a Pd anode indicated that the overvoltage is independent of P_{O_2}.

Discussion

Mixed potential region.—As mentioned above, data have been obtained (2) which support the conclusion that the rest potential of a Pd/O_2 electrode is a mixed potential composed of the Pd/Pd^{++} and PdO_2/Pd^{++} half-reactions, with the potential controlled by Eq. [3]. A sketch of a mixed potential diagram that can explain these rest potential observations as well as the polarization data obtained here is given in Fig. 6. E_o' is the equilibrium potential, E_o, for the Pd/Pd^{++} reaction which is 987 mv (10). The E_o for the PdO_2/Pd^{++}, E_o'', is not known, but since the rest potential is 870 mv (2), E_o'' must be less noble than 870 mv, as shown in Fig. 6. To satisfy the requirement that the potential be determined by the PdO_2/Pd^{++} reaction, the Pd/Pd^{++} reaction must be at a limiting current condition at the mixed potential, E_m.

When the system is polarized in the cathodic direction to the potential E_c, the observed external current, I_c, equals the difference between the half-cell currents, I_c' and I_c''. As seen in Fig. 6, I_c' is almost identical to I_m. In like manner, anodic polarization of the system to E_a produces an anodic current $I_a = I_a'' - I_a'$, and again $I_a' \sim I_m$. It may be seen, then, that at very low current densities the system behaves as a reversible PdO_2/Pd^{++} electrode, as shown in Fig. 1. A plot of the reproducible polarization data passes through the open-circuit potential, E_m, without a change of slope. The slope, $di/d\eta$, may be taken as the rate of the electrode process (11) which is 1.1×10^{-3} mho for the PdO_2/Pd^{++} reaction from the data in Fig. 1. It has been shown (9) that the local cell current density, i_m, at open-circuit conditions may be expressed as

$$i_m = \frac{I_m}{A} = (di/d\eta_p)\frac{RT}{F} \qquad [4]$$

where A is the effective electrode area, $\eta_p = E - E_m$, and the other symbols have their usual meaning. From Eq. [4], $i_m = 28.5$ μa/cm^2. Vetter and Berndt (1) found a maximum corrosion current for the dissolution of Pd in N_2-stirred $2N$ H_2SO_4 of about 1 μa/cm^2. It is interesting that in the presence of oxygen a local cell is set up under the driving force of which the dissolution of Pd is increased by an order of magnitude.

Reduction of oxygen region.—With an increase in cathodic polarization, the potential becomes less noble than E_o'', and the mixed potential process can no longer maintain the demanded current density. At this point, the current is obtained from the reduction of oxygen adsorbed on the Pd surface, and a Tafel region is observed (Fig. 2) with a slope of about 0.12. The overvoltage is sensitive to P_{O_2}, and as seen in Fig. 5, a value of 60 mv is obtained as the coefficient of the log P_{O_2} term. As in the Pt/O_2 case, the step favored as the rate-limiting step is

$$O_2(\text{ads}) + e \rightarrow O_2^-(\text{ads})$$

According to an analysis of various mechanisms for the evolution of oxygen (12), it may be shown that a Tafel slope of 0.12 is associated with a mechanism in which the rate-determining step is an electron transfer step.

From Fig. 5b, it is seen that below a P_{O_2} value of about 0.4 the curves deviate from the 60-mv slope by flattening out. Probably this is caused by mass transfer effects. At low values of P_{O_2}, oxygen diffusion becomes rate-determining.

A reproducible hysteresis is observed in the cathodic overvoltage curve in Fig. 2, the values of potential being more noble for increasing than for decreasing current densities. This observation could be explained if the Pd surface were a poor peroxide-decomposing catalyst. The presence of relatively large amounts of peroxide produced at the higher current densities in the neighborhood of the electrode could lower the potential at lower current densities bringing about the hysteresis. By the time a steady open-circuit potential is obtained, this excess peroxide is decomposed, and increasing current densities reproduce the top curve again. This indicates that Pd is a poorer peroxide-decomposing catalyst than Pt, since the overvoltage curves on Pt(9) did not show this hysteresis. The data in Fig. 2 give an $i_o = 5.0 \times 10^{-8}$ amp/cm^2, which is about an order of magnitude larger than that found on Pt (9). Although Pd may be a poorer peroxide-decomposing catalyst than Pt, it may also be a better catalyst for the electron transfer process.

Evolution of oxygen region.—When the system is anodized at progressively higher current densities, a point is reached, as seen in Fig. 6, where the PdO_2/Pd^{++} reaction goes into a limiting current region. At this point, the potential of the system rises rapidly to a more noble value where a new electrode process can supply the demanded current. This behavior is reflected in the anodic overvoltage curve presented in Fig. 2. As long as one remains below a current density of about 0.4 ma/cm^2, steady state reproducible data may be obtained, as shown by the double arrows. Above this point, the system goes into a limiting current region described by the broken line in Fig. 2. Steady state, reproducible, polarization data are obtained again at potentials above 1450 mv ($\eta = 220$ mv).

The overvoltage curve at the top of Fig. 2 has a Tafel region with the very high slope of 0.198. MacDonald and Conway (13) state that anodic electrode mechanisms in which surface oxides play a part are

often accompanied by Tafel slopes of high value. It has been shown (3-6) that PdO_2 is unstable in acid solution. The chemical decomposition of PdO_2 probably proceeds according to the reaction

$$PdO_2 \rightarrow PdO + 1/2O_2 \quad [5]$$

The observed open-circuit potential value of 1451 mv for this anodized electrode is very near the value of 1470 ± 10 mv assumed (2) for the equilibrium potential of the Pd/PdO_2 reaction

$$PdO_2 + 4H^+ + 4e \rightleftharpoons Pd + 2H_2O \quad [6]$$

The small discrepancy between these rest potentials may be due to the presence of peroxides in the electrolyte (2, 7). It was observed that both the rest potential and the overvoltage are independent of P_{O_2}. In Fig. 3, it is seen that the polarization curve for a Pd/PdO_2 electrode, at very low current densities, passes through 1450 mv at zero current density without a change of slope. In view of these experimental observations, it is concluded that the electrode process determining the evolution of oxygen on a Pd/PdO_2 electrode is the chemical decomposition of PdO_2 according to Eq. [5]. The current goes into the conversion of PdO to PdO_2 by the reaction

$$PdO + H_2O \rightleftharpoons PdO_2 + 2H^+ + 2e \quad [7]$$

Over the very low current density range shown in Fig. 3, the electrochemical reaction is the anodic formation and the cathodic reduction of PdO_2 either by Eq. [6] or Eq. [7]. Since it appears that there are two different slopes in the curve of Fig. 3, possibly Eq. [6] predominates in the very low region, ± 2 $\mu a/cm^2$, and Eq. [7] in the higher regions, > ± 2 $\mu a/cm^2$. When the Pd/PdO_2 electrode is cathodized, a polarization curve for the reduction of PdO_2 is obtained until all of the oxide is reduced, after which the system reaches a limiting current as described by the second broken curve in Fig. 2. The system goes rapidly to the reduction of oxygen, and a cathodic polarization curve is found identical to the reduction of oxygen on Pd which was obtained before.

Potentiostatic measurements.—Additional evidence to support the mechanisms described above may be obtained from overvoltage measurements determined potentiostatically on bright Pd electrodes. As seen in Fig. 4, the cathodic overvoltage curve for the reduction of oxygen is almost the same as that found galvanostatically. The Tafel slope seems to be smaller. Possibly this is caused by the influence of peroxide since the hysteresis, observed in the galvanostatic case, was not observed here. With constant current measurements, the rate of the electrode reaction is fixed, and because of the activation energies involved, concentrations of peroxide may build up, producing variations in the potential. The observed effect is the appearance of hysteresis phenomena. With constant potential measurements the rate of the electrode reaction adjusts to the experimental conditions under which the system finds itself, and the effect of the presence of peroxide is added into the over-all electrode kinetics. In this case, the observed effect is the modification of the value of the Tafel slope. Where the build-up of an intermediate is not present, such as in the anodic evolution of oxygen on a Pd/PdO_2 (top curves in Fig. 2 and 4), the constant current and constant potential measurements give identical curves with the same Tafel slope.

The initial part of the anodic potentiostatic curve is almost identical with the corresponding part of the galvanostatic overvoltage curve and may be referred to as the mixed potential region. As the potential is made more anodic, the PdO_2/Pd^{++} reaction enters a limiting current region, as shown in Fig. 6, and a point is reached where a film of PdO begins to form on the Pd surface. The coverage of the surface with PdO is a function of the potential. From the shape of the curve in Fig. 4, it is assumed that this film is a poor electronic conductor, and as the surface becomes covered with PdO with increasing anodic potential, the current decreases. After the surface becomes completely covered with at least a monolayer of PdO, the current falls to a very low value. When the potential has reached values greater than 1450 mv (η = 220 mv), the layer of PdO is converted to one of PdO_2. It is felt that in this region most of the PdO sites have become PdO_2 sites. At higher anodic potentials, the chemically unstable PdO_2 sites decompose to form PdO and O_2, but the newly formed PdO sites are immediately oxidized electrochemically to PdO_2. In this way, oxygen is evolved on a Pd anode by means of an oxide mechanism. There is not enough evidence obtained here to distinguish the nature of the rate-determining step for this mechanism.

When the Pd/PdO_2 electrode is cathodized potentiostatically, a reduction curve similar to that in Fig. 2 is obtained up to the point where all the PdO_2 is removed. Afterward the current falls to a very low value because the surface is covered with the poorly conducting PdO film. Finally, at a low enough potential (about 820 mv, η = —410 mv), a polarization curve for the cathodic reduction of PdO is obtained. When the PdO is used up, the current goes into the reduction of adsorbed oxygen on the Pd surface. This is shown in Fig. 4 by the kink in the curve at about 0.6 ma/cm^2, after which the curve becomes identical with the cathodic overvoltage curve.

Conclusions

From these data, it appears that oxygen may be adsorbed on a bright Pd surface under at least three forms; as adsorbed oxygen atoms, as PdO, and as PdO_2. Oxygen, most likely, is also dissolved in the surface layers of the Pd metal (14,15) but could not be distinguished from the other adsorbed oxygen in this work. Oxygen may be adsorbed as atoms at high negative overvoltages. Reduction of oxygen occurs through the adsorption of molecular oxygen. As in the case of Pt (9), peroxide formed in this process is catalytically decomposed to form oxygen which is adsorbed to complete the cycle. Palladium appears to be a poorer peroxide-decomposing catalyst than platinum.

At low overvoltages, both anodic and cathodic, and at open circuit, the oxygen adsorbed on the surface is in the form of PdO and PdO_2, formed through the mixed potential mechanism. The direction of the local cell is such that the surface should become covered with PdO_2. Since PdO_2 is unstable in this potential region, it decomposes to PdO. However, a complete layer of PdO is also unstable under these conditions, and consequently, bare Pd sites are always available to participate in the local cell reaction. The PdO may be removed from the surface by chemical decomposition, by dissolution in the electrolyte, possibly as a complex ion, or by dissolution in the Pd metal. At open circuit, the over-all result is the corrosion of Pd metal.

In the limiting current region, the Pd surface is completely covered with a monolayer of PdO. The film of PdO is a poor electronic conductor, and the Pd surface is passivated. At high enough potentials (above 1450 mv), the PdO sites may be converted to PdO_2 sites, and in the region above this potential, the surface is considered to be covered mainly by PdO_2. Oxygen is evolved by the chemical decomposition of PdO_2, and the anodic current goes into the formation of PdO_2 from PdO. On open circuit, the Pd/PdO_2 electrode acts like a metal-metal oxide electrode with an electrode reaction corresponding to Eq. [6].

Acknowledgment

The author is grateful to Dr. R. Thacker of General Motors Research Laboratories for many interesting and fruitful discussions.

Manuscript received May 13, 1965; revised manuscript received Aug. 9, 1965.

Any discussion of this paper will appear in a Discussion Section to be published in the June 1966 JOURNAL.

REFERENCES

1. K. J. Vetter and D. Berndt, *Z. Elektrochem.*, **62**, 378 (1958).
2. J. P. Hoare, *This Journal*, **111**, 610 (1964).
3. A. Hickling and G. G. Vrjosek, *Trans. Faraday Soc.*, **57**, 123 (1961).
4. J. A. V. Butler and G. Drever, *ibid.*, **32**, 427 (1936).
5. S. E. S. El Wakkad and A. M. S. El Din, *J. Chem. Soc.*, **1954**, 3094.
6. T. R. Blackburn and J. J. Lingane, *J. Electroanal. Chem.*, **5**, 216 (1963).
7. J. P. Hoare, *This Journal*, **109**, 858 (1962).
8. D. J. Ives and G. J. Janz, "Reference Electrodes," p. 112, Academic Press, Inc., New York (1961); J. P. Hoare, *G. M. Eng. J.*, **9**, No. 1, 14 (1961).
9. J. P. Hoare, *This Journal*, **112**, 602 (1965).
10. W. H. Latimer, "Oxidation Potentials," Prentice-Hall, New York (1952).
11. P. Dolin, B. Ershler, and A. Frumkin, *Acta Physicochim. URSS*, **13**, 782 (1940).
12. J. O'M. Bockris, *J. Chem. Phys.*, **24**, 817 (1956).
13. J. J. MacDonald and B. E. Conway, *Proc. Roy. Soc.*, **269A**, 419 (1962).
14. D. P. Smith, *Z. Physik*, **78**, 815 (1932).
15. J. H. DeBoer and J. D. Fast, *Rec. Trav. Chim Pays-Bas*, **59**, 161 (1940).

Oxygen Reduction at Silver and Silver-Based Alloy Electrodes

S. Z. Beer and Y. L. Sandler

Research Laboratories, Westinghouse Electric Corporation, Pittsburgh, Pennsylvania

ABSTRACT

Current-voltage characteristics for the reduction of oxygen at silver and alloy electrodes formed with silver and elements having oxides of low electron affinity were studied in pre-electrolyzed and in ordinary 15% KOH solution. In impure solutions or at the alloy electrodes straight Tafel lines were obtained, but with pure silver in pure solutions no such behavior was found. This is taken to indicate a dynamic surface of varying catalytic activity. With silver-magnesium oxide surfaces, a potential about 100 mv higher than with pure silver was obtained at open circuit as well as under current drain. The possible mechanistic significance of the results is discussed in terms of the physical properties of the material and the behavior of the constituents in gas-solid reactions.

Much of the effort in current electrochemical research is directed toward the elucidation of the mechanism of the oxygen electrode. Despite the reduction of the oxygen to water, the theoretical emf corresponding to the oxygen-water reaction is rarely observed. The mechanism of the oxygen reduction is not at all simple, and various processes can interfere to yield potentials below the theoretical 1.229v.

In the present work the effect of gases and additions to a silver electrode on the oxygen dissolution reaction was examined. A study of the silver electrode is of special interest because the mode of oxygen adsorption on the dry surface is now better understood (1-3). Chemisorbed oxygen atoms can exist in different binding states. One such state, a molecular weakly bound precursor state, presumably in form of an O_2^- ion, is likely to be involved in the first steps of the oxygen reduction reaction. Pretreating the silver with hydrogen strongly modifies the reversibility of the oxygen adsorption (3). To relate better the electrochemical behavior to knowledge gained in adsorption studies, silver electrodes pretreated in oxidizing and reducing atmospheres were examined with the view of determining the effect of such pretreatments on electrode properties.

The influence of additions on the catalytic oxidation properties of silver has been investigated frequently (1), and their effect has been attributed to a change in the work function of the surface. Changes of this kind thus might be expected to have an influence on the rate of electron transfer in the adsorption of oxygen, or other intermediate steps in the oxygen reduction reaction. Silver alloys containing elements, which themselves or as oxides have superior electron emissive properties (low electron affinity), were examined, and their properties compared with the similarly treated silver electrodes mentioned above. The approach led to the discovery of a new oxygen electrode alloy which operates in basic solutions at much higher potential and considerably lower polarization than silver alone.

Experimental

All the experiments reported here were done in 15% KOH solutions, prepared from chemically pure KOH and degassed, double-distilled deionized water. Some of the effects were examined both in ordinary and pre-electrolyzed KOH solutions.

Two relatively simple cells were used in these investigations. One was of Teflon and the other of thoria. The cells, about 3 in. in diameter, had concentric cylindrical hydrogen reference cells in the center from which emerged the Luggin capillary. The hydrogen electrode was surrounded by an inner porous thoria cup.

Experiments were performed with ordinary KOH and KOH pre-electrolyzed for 20 hr with 2 platinum wire electrodes of about 0.3 cm^2 area at 40 ma. All handling of chemicals, solutions, and electrodes was done in a glove box under a flowing nitrogen atmosphere.

The working electrodes were squares, ½ in. each side and 10 mils thick. They were made at Westinghouse or elsewhere as stated. The electrodes were all lightly etched in dilute nitric acid, washed, and steamed. They were then annealed as described later. The counter electrode was a platinum wire coil of about the same area. The purification train for the gases consisted, for the oxygen and helium, of BTS catalyst (B.A.S.F., Inc., a form of finely divided copper oxide) at 300°C, $CaSO_4$ (Drierite), magnesium perchlorate, and Ascarite CO_2 absorbent, followed by well-baked molecular sieves (Linde 13X) cooled with a CO_2-methanol bath. For hydrogen, a similar train was used except for the substitution of Pd-asbestos at 250°C for the BTS catalyst and the molecular-sieves trap was cooled with liquid nitrogen. The gas lines were of Teflon tubing.

Current measurements were made with a Kiethley Electrometer 200B equipped with a current shunt and the potential with a Kiethley 660 Null Voltmeter. The current source was a set of mercury cells in series with large step and variable resistors.

The oxygen partial pressure in the various rare gas-oxygen mixtures was measured with a Westinghouse oxygen gauge, operating on the principle of a solid electrolyte fuel cell (4).

Cathodic galvanostatic scans were made by manually setting the driving current between values of 10^{-7} to 10^{-3} amp and waiting approximately 2 min to ascertain that a steady state had been attained. An upper limit of current was determined by the onset of fluctuations which always preceded the sudden drop in potential to the hydrogen evolution region.

Results

Pure silver electrodes.—Silver foils (Handy and Harman, 99.99%) were cleaned as described above and annealed at 500°C in an argon-1% oxygen flowing mixture. One foil was quenched and transferred to ordinary KOH solution, and the cathodic galvanostatic sweep was taken. The other foil was heated in an atmosphere of hydrogen at 400°C. This foil was then quenched and transferred to a KOH solution for the same purpose. In this as in the later cases, rapid flow of oxygen was bubbled over the surfaces of the electrodes, agitating the electrolyte vigorously. The resulting curves are shown in Fig. 1; the arrows show the order in which the individual points were measured. Linear portion of each curve extends over one decade or more with Tafel slopes of about —80 mv for the oxygen-treated foil and —70 mv for the hydrogen-treated foil. The potentials of the hydrogen-treated foil are seen to be somewhat lower than those of the oxygen-treated foil.

Another set of experiments was carried out with pre-electrolyzed solutions. The silver electrodes were annealed in oxygen to remove organic impurities and were then either degassed in helium or reduced with hydrogen. In the first experiment a cleaned silver foil was lightly oxidized in a flowing mixture of helium and oxygen (approximately 0.1%) and then degassed for four days at 500°C in pure helium. The foil was inserted into the pre-electrolyzed KOH solution with oxygen bubbling over the electrodes.

The immediate open-circuit potential, o.c.p., was as low as 0.11v, but after 4 hr rose to 0.980v. The cathodic galvanostatic sweep taken at that time is shown as curve 1 in Fig. 2. After anodizing and cathodizing,

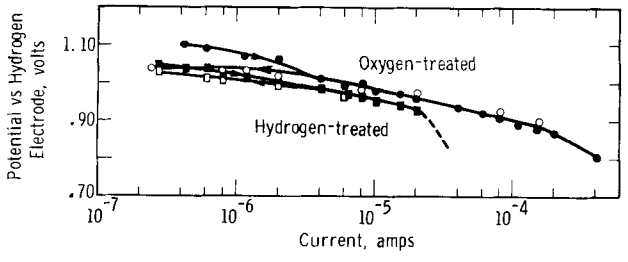

Fig. 1. Cathodic galvanostatic characteristics of silver in ordinary KOH solutions. The arrows indicate the directions in which the points were measured.

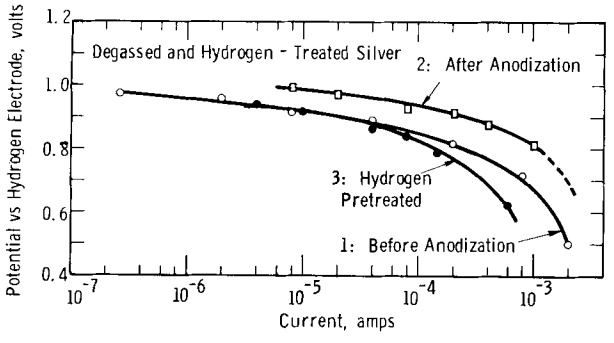

Fig. 2. Effect of pretreatment on cathodic galvanostatic characteristics of silver in pre-electrolyzed KOH solutions.

the o.c.p. rose to 1.034v. The new cathodic galvanostatic sweep taken is shown as curve 2 of the same figure. This galvanostatic characteristic curve corresponds to the highest potentials attained with the silver electrodes regardless of further oxidation and reduction or additional resting in solution. The potentials are now very close to those shown for the oxygen-treated foil as shown in Fig. 1, suggesting that the state of oxygen enrichment of the electrode and the peroxide concentration in solution are about the same for both cases.

The cathodic galvanostatic characteristics of a hydrogen-treated foil can be seen in curve 3, Fig. 2. The foil was treated twice with 20 Torr oxygen in a vacuum system at 500°C, pumped for 16 hr, and then treated with hydrogen at 550°C at 15 Torr pressure before immersion into the pre-electrolyzed solution with oxygen bubbling vigorously over the electrode surface. The o.c.p. was now 0.955v, and the curve is seen to be little different from the degassed electrode (curve 1). Thus, the potentials of electrodes of low oxygen content generally appeared to be somewhat lower than those of the oxygen-pretreated electrodes. A more pronounced effect of this kind was found with platinum in acid solutions (5).

No linear Tafel line portions were obtained in these experiments with pure silver, in contrast to what was found with ordinary KOH solutions. This is seen to be the case even after the potentials have reached the maximum attainable after anodization, where it can be inferred that the peroxide was reduced in concentration comparable to that found in the ordinary KOH solution. It seems possible that some surface property, such as the content in more reversibly adsorbed oxygen, changes continuously with current density. Alternately, this may indicate a change in the dissolution mechanism. This property or mechanism appears to be stabilized by the presence of the impurities which may be present in greater concentration in the ordinary KOH solutions. The possibility of surface stabilization through impurities is seen again later in the results obtained with silver alloys.

Silver-magnesium alloy.—Of the alloys investigated, a silver-1.7 w/o (weight per cent) magnesium alloy yielded the most interesting results. This alloy is used for Dynodes in the construction of phototubes because of its high secondary electron emission (6). In these devices, before the alloy foils are inserted, they are lightly oxidized in an atmosphere containing oxygen in the form of water vapor. The alloy foil, made by Handy and Harman, was annealed in a flow system at 500°C in an argon mixture of low oxygen content for four days. The galvanostatic curve for this foil (Ag-Mg-I) was taken and is shown in Fig. 3. Curve 1 is the curve taken in the direction of increasing currents; curve 2 is the return curve. The open-circuit

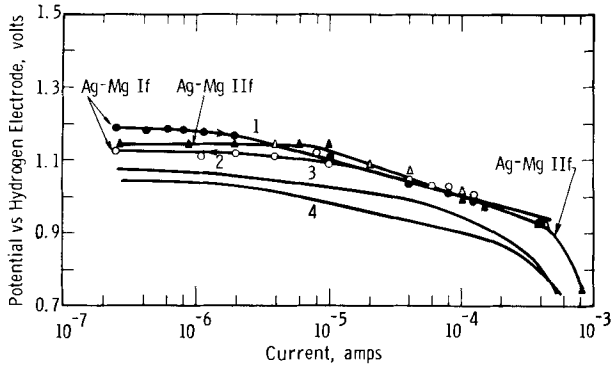

Fig. 3. Cathodic galvanostatic characteristics of silver-1.7 w/o alloy electrodes in ordinary and pre-electrolyzed KOH solutions. The arrows indicate the directions in which the points were measured. Curve 3 of silver in pre-electrolyzed KOH and curve 4 of silver in ordinary KOH are given for reference.

potential stabilized at 1.16v. Straight-line portions are found in these curves over a range of about two decades of current. These yield Tafel slopes of —120 mv.

Another foil of the same composition (Ag-Mg-II) was cleaned and annealed in a helium-0.1% oxygen mixture at 500°-550°C followed by degassing in pure helium. The open-circuit potential in pre-electrolyzed KOH stabilized at 1.14v. Cathodic galvanostatic sweeps were then taken. These results are also shown in Fig. 3 as Ag-Mg-II. Significantly, the potentials are not markedly different from the previous case. Also, contrary to the findings on pure silver in pre-electrolyzed KOH, straight-line portions of the curve are now found. Tafel slopes of —120 mv can be measured.

For comparison purposes, cathodic galvanostatic curves for pure silver are presented in Fig. 3. Curve 3 is that of a silver electrode after anodization in a pre-electrolyzed solution; curve 4 is the same as shown in Fig. 1 for the oxygen-treated silver in ordinary KOH. The over-all potential levels for both Ag-Mg-II and Ag-Mg-I are considerably higher than the highest obtained with pure silver.

To determine whether the open-circuit potentials of 1.16 and 1.14v, found for the electrodes Ag-Mg-I and Ag-Mg-II, respectively, were related in some way to the 1.18v reported for the Ag_2O phase, anodic and cathodic chronopotentiometric measurements were made.

The potentials encountered on anodizing pure silver have been much studied (7). On anodization, the potential rises rapidly, to the first potential plateau of 1.18v, at open circuit, accompanying the formation of Ag_2O. On further oxidation, the potential of the postulated AgO-Ag_2O_3 reaction is encountered at 1.53v, at open circuit. On continued anodization, a third plateau at 1.43v, at open circuit, is attained. This is thought to correspond to the Ag_2O-AgO equilibrium. On cathodization, the voltage falls directly from the 1.43v plateau to the 1.18v level. On anodization, until the 1.53v level is reached it was found by us and others that the current efficiency producing Ag_2O is 100%.

The silver-magnesium alloy electrode Ag-Mg-II was driven anodically to the 1.43v level. On cathodization, more than twice the number of coulombs were driven across the cathode at currents of 10 ma/cm^2. The final open-circuit potential was still 1.135v.

On driving the foil cathodically from the 1.43v level no separate break was found to occur at what might be construed to be a separate 1.18v level. Thus, the 1.14 o.c.p. potential level appears to be some form of stabilized 1.18v level, presumably modified by the presence of MgO in the surface.

Other alloys.—The outstanding behavior of this alloy suggested that other alloying agents having either low work functions or high secondary electron emission characteristics might also be of interest. Thorium, indium, and barium seemed to offer these advantages and so were tried.

A silver 1 w/o thorium alloy was prepared by levitation melting and rolling. Most of the thorium was in the form of the oxide; a photomicrograph showed precipitation at grain boundaries. The foil was cleaned and annealed at 500°C in a helium-oxygen mixture ($P_{O_2} = 0.001$ atm) and was transferred in this state to the pre-electrolyzed KOH. In another set of experiments, a silver 1 w/o indium foil and a silver 1 w/o barium foil, made by William Gold Refining Company, were treated in the same way as the silver-thorium alloy and were then transferred to separate solutions.

The first cathodic sweeps gave rather low potentials. Alternate anodization and cathodic sweeps were performed on each of the alloy electrodes. With each anodization, potential levels of subsequent cathodic polarization curves were higher. The behavior and potentials of these electrodes were much like those of the degassed and hydrogen-treated silver electrodes discussed previously. Thus, no improvement over pure silver was obtained in this last group of alloys. It is, however, of interest to note that linear Tafel regions were found and that these were similar to those found for pure silver in nonpre-electrolyzed solutions, *i.e.*, the slope was about —80 mv.

Discussion

The continuously changing slope found with pure silver in the cleaner solutions may simply indicate that no single step in the reduction reaction is rate determining. The occurrence of distinct Tafel slopes in impure solutions or with alloys, however, indicates that a changing surface may cause this behavior of pure silver. The catalytic properties of the surface may change as a result of a changing oxygen content of the surface, which probably is accompanied by a rearrangement of the surface. Such effects were noted by Germer and his associates in the case of oxygen on nickel (8). Adsorption or incorporation of impurities should reduce the mobility of the surface and may thus cause a more constant activity for the various transfer and chemical steps occurring on the surface.

The fact that the potential of the silver-magnesium oxide surface is higher throughout a relatively broad range of potentials is noteworthy from a practical as well as a mechanistic point of view. The increased activity may be connected with the stabilization of oxygen in the silver lattice by the presence of the magnesium oxide. Alternately, it may be the (silver doped) magnesium oxide that is responsible for acceleration of electron transfer steps. The high activity of this oxide with respect to the recombination of oxygen atoms on surfaces (9) and in the oxygen isotope exchange reaction (10) $O_2^{16} + O_2^{18} \rightarrow 2\,O^{16}O^{18}$ may be related to the superior electron emission properties (6) of the material (low electron affinity) and may explain the higher electrochemical activity.

The outstanding secondary electron emission characteristic of this alloy is well known. The characteristic depends much on the electron mean free path and is somewhat less dependent on surface conditions (11) than is the work function (as a measure of primary emission). The dependence on the latter in the oxygen evolution reaction was studied by Rüetschi and Delahay (12) who concluded that no relationship exists. The same conclusion appears to be warranted on the basis of our results with the Ag-Th, Ag-In, and Ag-Ba alloy electrodes. It must be recognized, however, that the work function is extremely sensitive to surface conditions. The lack of correlation between the work function of the dry solid and related properties of the same solid as an electrode in an electrolyte is not surprising. In the study of this type of dependence, a property such as secondary electron emission might be more useful than the work function. In the light of the unusual behavior of this alloy both in the dry solid-gas state and in an electrolyte, the possibility of an overvoltage dependence on a measurable electron emissive property cannot be dismissed.

The foregoing suggests that other alloys with similar physical properties might show interesting properties as oxygen electrodes. For example, silver-beryllium appears to be promising on the basis of the excellent properties of copper-2 w/o beryllium also much used because of its outstanding emission properties (11). No doubt other alloys of equal promise are possible, however, the paucity of data on these properties makes the selection of other alloys and the comparison with other known systems difficult.

Further work is needed and is at present being carried out to determine the rate-determining step in the reduction reaction on pure silver as well as on the Ag-Mg and other alloys. The analogy with the oxygen isotope exchange reaction indicates that the first adsorption step $O_2 + e^- \rightarrow O_2^-$ might be the slow step in the reaction which is accelerated by the lower electron affinity of the alloy.

Acknowledgment

One of the authors (S. Z. B.) wishes to thank Dr. N. T. Melamed for bringing to the former's attention the availability of the silver-magnesium alloy and Dr. E. J. Sternglass for his stimulating discussions on secondary electron emission.

This work was supported by the Advanced Research Projects Agency through the United States Army Electronics Laboratories and the Office of Naval Research.

Manuscript received April 8, 1965; revised manuscript received July 17, 1965. This paper was presented at the San Francisco Meeting, May 9-13, 1965.

Any discussion of this paper will appear in a Discussion Section to be published in the June 1966 JOURNAL.

REFERENCES

1. L. Ya. Margolis, *Advances in Catalysis*, **14**, 429 (1963).
2. Y. L. Sandler and W. M. Hickham, "Proceedings of the Third International Congress on Catalysis," North Holland Publishing Co., Amsterdam, (1965).
3. Y. L. Sandler and D. D. Durigon, *J. Phys. Chem.*, in press.
4. J. Weissbart and R. J. Ruka, *Rev. Sci. Inst.*, **32**, 593 (1961).
5. Y. L. Sandler and E. A. Pantier, *This Journal*, **112**, 928 (1965).
6. P. Wargo, B. V. Haxby, and W. G. Shepard, *J. Appl. Phys.*, **27**, 1311 (1956).
7. J. A. McMillan, *Chem. Rev.*, **62**, 65 (1962).
8. L. H. Germer, *Ann. N. Y. Acad. Sci.*, **101**, 599 (1963).
9. P. G. Dickens and M. B. Sutcliffe, *Trans. Faraday Soc.*, **60**, 1272 (1964).
10. E. R. S. Winter, *Advances in Catalysis*, **10**, 196 (1958).

11a. E. G. Sternglass, *Phys. Rev.*, **108**, 1 (1957).
11b. M. Kaminsky, "Atomic and Ionic Impact Phenomenon on Metal Surfaces," Academic Press, New York (1965).

12. P. Rüetschi and P. Delahay, *J. Chem. Phys.*, **23**, 556 (1955).

Electrochemistry in Fused Alkali Thiocyanates

Richard E. Panzer and Michael J. Schaer[1]

United States Naval Ordnance Laboratory, Corona, California

ABSTRACT

Detailed polarographic and chronopotentiometric investigations were conducted in molten potassium thiocyanate and the eutectic mixture of 70 mole % KSCN and 30 mole % NaSCN. Between 150° and 325°C, electrochemical oxidation occurred at a potential of +0.25v (vs. Ag/AgCl) to produce thiocyanogen, $(SCN)_2$, which polymerizes to parathiocyanogen, $(SCN)_x$. At the cathode, the SCN^- ion was reduced to sulfide and cyanide ions at a potential of —1.75v. At higher potentials, the half-wave potentials were —2.35v for Na^+ and —2.92v for K^+. In a continuing series of fractional factorial experiments with laboratory prototype pill cells (laminar, 1-3 mm thick, 1 cm in diameter), thiocyanate electrolytes were used with a variety of alkali metal anodes and various cathode materials such as transition metal oxides, silver salts, and organic nitro compounds. At current densities approaching 100 ma/cm², closed-circuit voltages ranged from 1.50 to 2.50v for at least 5 min. At a temperature of 200°C, this performance is approximately equivalent to that of the best previous thermal cells in LiCl-KCl operating at 450°C.

Ionic melt investigations were conducted in both molten potassium thiocyanate and the eutectic mixture of 70 mole % KSCN and 30 mole % NaSCN. Conductivities were measured at various temperatures, polarographic and chronopotentiometric techniques were applied, and a detailed study was made of suitable reference electrode systems.

Only a few investigations have been conducted in molten alkali thiocyanates. Paterno and Mazzuchelli observed the blue coloration of KSCN when it is heated to its decomposition point (1). Kordes, Bergmann, and Vogel were concerned with the manner in which the freezing point was lowered by various transition metal salts in KSCN (2). Greenberg, Sundheim, and Gruen investigated the spectra of sulfur dissolved in molten KSCN (3); Harrington and Sundheim reported the spectra of various transition metal complex ions in that medium (4); and Baddiel and Janz investigated the Raman spectra and structure of molten thiocyanates (5). Frame, Rhodes, and Ubbelohde have summarized the properties of many single molten salts, including alkali thiocyanates (6). Harrington and Tien have written an article on a reference electrode for use in molten salts, including KSCN (7).

Investigations of ionic melts in the range from 80° to 300°C, which have been conducted at NOLC for several years, are continuing in an effort to discover and develop electrolyte systems usable in high energy-density thermal batteries. Approaching the problem from an applied research viewpoint, energy-density requirements are based on a future need for a battery with 100 ma/cm² at 2.00v per cell and 1600 joules per gram of final packaged battery. This objective limits the available materials, since many previously used thermal cell materials do not perform well in this temperature range because their reactivities are drastically reduced at the lower temperatures.

In keeping with the applied research perspective, the method used at NOLC employs a preliminary screening of prospective materials in a beaker-cell environment. Before incorporation into a practical cell, an electrolyte must meet four criteria: (*a*) a melting point within the 80°-300°C range; (*b*) a minimum specific conductivity of 0.1 mho/cm; (*c*) compatibility with anode and cathode materials; and (*d*) absence of surface effects, such as the formation of an insoluble material that might inhibit further reaction. Although other criteria could have been chosen, these four were considered the most important. Failure to meet any one of these, with no discoverable remedy, is considered sufficient reason for halting work on that electrolyte. Several electrolytes have failed to meet the last three criteria in ways unpredictable from any previously existing data.

After an electrolyte has met all four criteria, it is more thoroughly investigated in a laboratory prototype voltaic cell configuration. Statistically designed sets of fractional factorial experiments are used to determine the best operating conditions, anodes, cathodes, electrolyte combinations, absorbents, and resistive loads. Finally, techniques of polarography and chronopotentiometry are used to answer questions of electrochemistry or reaction mechanisms arising during voltaic cell experimentation. Evaluation of responses from

[1] Present address: Department of Chemical Engineering, Montana State University, Bozeman, Montana.

the statistically designed cell experiments is facilitated by a FORTRAN computer program for analysis of variance and by F (level of confidence) tests for significance, using the Laboratory's 7074 IBM digital computer.

Experimental Procedures

Conductivity measurements were made in molten thiocyanates in beaker-cell quantities, using a dipping-electrode system patterned after Crook and Bockris (8) and Van Artsdalen and Yaffe (9). This assembly consists of platinum-bead electrodes 3 mm in diameter that have been somewhat flattened to a wedge shape. Each rests on the top end of a 1 mm ID capillary about 3 cm long. The capillaries are attached to a center Pyrex tube 7 mm ID and 25-35 cm long, which serves as a thermowell and a holder for the electrode assembly. This dip cell was calibrated using 0.1M aqueous KCl solution. Readings were made on a General Radio Model 1650A bridge. Platinized platinum electrodes were used to reduce polarization effects. Conductivities were determined at several frequencies up to 100 kc to determine inductive effects, but the reproducibility of results at 1 kc was satisfactory and it facilitated comparison with data from other investigators.

Conductivities were also determined in a pill-cell environment. The configuration of these cells, the heating apparatus, and the experimental techniques have been described previously (10). The anolyte mixture consists of the electrolyte salt mixed with a sufficient amount of an inert adsorbent, such as kaolin or alumina to immobilize the electrolyte when it is molten. The catholyte mixture consists of the electrolyte salt with at least 65% of the active cathode material, which also serves as the adsorbent to immobilize the molten electrolyte. Carbon was often added to the catholyte mixture for better conduction between the cathector and the active cathode material.

Anolyte or catholyte pills are prepared by pressing 0.10-0.15g of the desired mixture in a steel die under a pressure of 3500 kg/cm^2 to form wafers 1-3 mm thick and 1 cm in diameter. The assembled electrolyte pill stack between strip electrodes is placed between the platens of a heater fixture, which applies approximately 1100g weight to the cell stack.

For conductivity measurements, the electrodes were platinized Pt strips 2 mm wide. Using single pills of anolyte or catholyte composition, the relative conductivity of different compositions could be determined. Temperatures were controlled within ±1°C using a chromel-alumel thermocouple placed in direct contact with the pill-cell stack and regulated by either a Brown Electronik recorder-controller or a Wheelco Amplitrol anticipating controller.

Instrumentation.—The instruments used for polarographic investigations were a Sargent model XXI polarograph, a Keithley model 210 electrometer, and a Moseley model 135 X-Y recorder. The polarograph was used only as a source of slowly varying potential and not as a recorder. The electrometer was used to measure potential because of the reference electrode's high impedance. Current was recorded as the IR drop across a precision resistor. Figure 1 shows the polarographic setup.

Instrumentation for voltammetry at constant current (chronopotentiometry) consisted of a 270v battery pack with several variable resistors in series to provide a constant current of any desired value from 10 μa to 200 ma. Alternatively, an electronic power supply was used, but more spurious transients were observed on the Tektronix type 545A oscilloscope screen with this setup. A Keithley electrometer was used with the high-impedance reference electrode. Voltage-time curves were recorded on the cathode-ray oscilloscope (CRO) with a Dumont type 450 camera, using Polaroid-Land 3000 ASA film. Figure 2 shows the chronopotentiometric circuit.

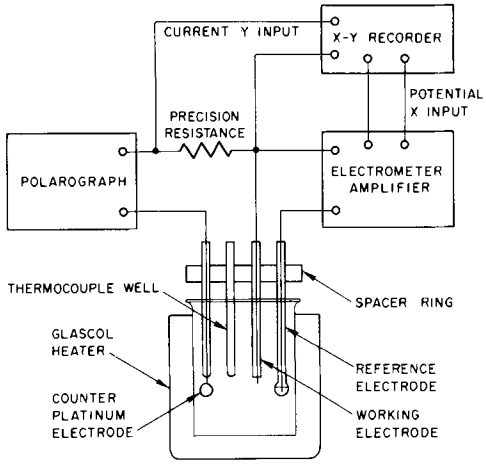

Fig. 1. Polarographic setup

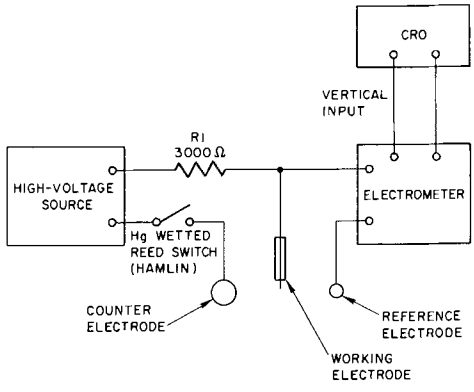

Fig. 2. Chronopotentiometric circuit

All instruments were standardized against a L&N K-3 potentiometer, and all electrode potentials are recorded according to the IUPAC 1953 Stockholm convention.

Reference electrode.—Development of a reproducible, stable, reversible, reference electrode for investigating untried electrochemical systems is almost a research project in itself. The development of a suitable reference electrode for a pill-cell environment has been described previously (11). The electrode mentioned at that time was Mg/MgO, and it was used in LiCl-KCl eutectic at 450°C. However, that electrode was found to be unusable in molten thiocyanates. In this research, the electrodes used and their characteristics were as follows:

Ag-AgCl/$LiNO_3$-KNO_3 *eutectic + sat'd* KCl/*Pyrex glass bulb.*—This electrode consists of a silver wire immersed in a saturated solution of AgCl and KCl in the nitrate eutectic within a thin-walled Pyrex bulb. It is similar to the one described by Inman (12), except for the use of $LiNO_3$ in place of $NaNO_3$. The electrode in this study is stable and reversible within ±2 mv, but an unknown junction potential exists at the external glass interface when the bulb with nitrate on the inside was immersed in the thiocyanate melt. A very large impedance (on the order of 10 meg at 180°C) militates against any fast measurements of polarization and requires the use of an electrometer to avoid loading the electrode during measurements.

5 mole % Na in Hg/soda-glass bulb or capillary.—This electrode, described and discussed by Delimarskii and Markov (13), was found to be stable and reversible when inadvertently loaded. Contact with the sodium amalgam is made with a tungsten wire. Because of the presence of Na^+ ions in the glass, as well as in the melt and amalgam, this electrode behaves as a sodium electrode, reversible to sodium ions. If KSCN is used,

the minute concentration of Na^+ ions required (10^{-5} mole %) may be easily added without changing the melt conditions (14). The bulb-type electrode was used in beaker-cells, and the capillary-type was used in pill-cells 1-2 mm thick. The impedance of the Na-Hg electrodes is quite high, on the order of 1 to 4 meg, depending on the type of glass used. Pyrex glass may also be used with little change in voltage. Against the Ag/AgCl electrode, the amalgam electrode gave 2.11v, measured with an electrometer.

Co/0.1 m $CoCl_2$ in molten KSCN/glass frit or glass bulb.—Harrington and Tien (13) have utilized a similar electrode, but later work by these investigators indicates that the electrode may not be stable enough over reasonably long (24 hr) periods of time (14). The cobalt electrode system contained behind a medium glass frit has a much lower impedance than the glass bulb electrodes, but it is not readily adapted to future use in a pill-cell environment because the small cell precludes use of a fritted separator.

Voltammetric cells.—Beaker-cell investigations were always conducted in the drybox, using three electrodes clamped rigidly in the melt. The chronopotentiometric electrodes were: (*a*) a large platinum counter electrode of about 2 cm^2 area; (*b*) a very small platinum working electrode made of a wire with a cross-sectional area of 8.0×10^{-6} cm^2, fused into a glass tube, and ground flush; and (c) Ag/AgCl chloride reference electrode, previously described.

Polarographic electrodes consisted of the Ag/AgCl reference electrode and the small Pt wire microelectrode only.

When cell investigations outside the drybox were considered desirable, a three-compartment cell with ball joints and medium glass frit separators was loaded in the drybox and then transferred out of the box with the electrodes already in place. The electrodes were essentially the same as for the beaker-cells used in the drybox, but adapted to the smaller column of the tubular compartmented cell.

Voltaic cells.—The configuration of the voltaic cells, called variously pill, wafer, or laminar cells, has been described above.

Fractional factorially designed voltaic-cell experiments were set up in a 2^5 arrangement (five factors were investigated at two levels each). This arrangement has proved convenient for this work and is readily analyzed for variance by the least-squares technique. The independent variables of the statistically designed cells are listed in Table I, but the dependent variables were chosen in order to evaluate the cell performance from various viewpoints. For example, the first set of tests was evaluated on the basis of the change of voltage, ΔE, from peak to final closed-circuit voltage, the cells being activated under load. However, it is possible for a cell starting at a low peak voltage to have a nearly flat discharge and hence a low ΔE. Although a low ΔE would be a desirable criterion, the operation of this cell would not be favorable on an over-all basis because of its generally low voltage. Similar situations arise when considering peak open- or peak closed-circuit voltage, the final closed-circuit voltage level, or some figure based on wattage output.

Table I. Independent variables of statistically designed voltaic-cell experiments

Anodes	
(Lithium metal)	
Li-Ca alloy	80-20 w/o
Li-Zn alloy	80-20 w/o
Li-Mg alloy	75-25 w/o
Li-Mg alloy	50-50 w/o
Li-Pb alloy	Li_4Pb
Cathodes	
$CaCrO_4$	
AgBr	
UO_3 (anhydrous)	
$H_4UO_6(UO_4 \cdot 2H_2O)$	
V_2O_5	
Na,-3,5 dinitrobenzoate	
Electrolytes	
KSCN	
KSCN-LiBr	90-10 w/o
KSCN-NaSCN eutectic	73.7 to 26.3 w/o
KSCN-NaSCN eutectic + 10 w/o NaCl	
Atmosphere	
Laboratory ambient	
Dry argon (drybox)	
Resistive load	
10, 25, 34, 43 ohms	
Temperature	
150°, 175°, 200°, 250°, 300°C	
Electrolyte absorbent	
Kaolin (Edgar, Florida)	
Alumina (Micria AD, Monsanto Chemical Company)	

The error variance was established directly by replicating one of the series of cell tests, rather than by estimating from the effects of factorial combinations or of interactions that were not considered to be significant. By establishing the error variance in this manner, it was learned that the effect of small temperature changes makes close temperature control desirable. Scrutinizing the variances directly also helped in finding how the operational error of uncontrolled (unknown) variables could be reduced. An extremely useful exposition of these statistical methods is given by Davies (16), and the reader is referred to that work for details on the design and analysis of experiments.

The significance of results from the sets of fractional factorially designed experiments is determined by the analysis-of-variance technique. The Laboratory's IBM 7074 computer has been programmed to run this analysis, and the labor involved is thus drastically reduced.

Preparation of materials.—Reagent grade chemicals were used throughout the experimentation and were routinely weighed, transferred, crushed, or melted in a Vac/Atmospheres Company drybox. Potassium and sodium thiocyanates were dried separately in a vacuum oven at 150°C, and the resulting salts poured freely without lumping. No further purification was deemed necessary, since the polarographic residual current on these melts was on the order of 0.5 μa. A definite aging effect on these melts in the drybox was observed as a light yellow color. The polarographic observation of aging will be described in the discussion of polarography. A steel-blue color has been reported by numerous investigators when thiocyanates are heated to temperatures above 300°C, and this color can be obtained readily at any lower temperature in the melt by adding powdered sulfur. The reason for the light yellow color is not known, although the aging effect is reported by Frame *et al.* to cause a large variation in the change of surface tension per degree centigrade (18).

Depleted UO_3 was obtained from Nuclear Materials and Equipment Company, Apollo, Pennsylvania. Hydroxyperuranic acid, H_4UO_6, was prepared from this UO_3 by the method given by Urey (19). The sodium salt of 3,5 dinitrobenzoic acid was prepared by mixing stoichiometric quantities of the acid and sodium hydroxide in water and then evaporating to dryness under vacuum. A portion of the resulting salt was dissolved in water and found to have a *p*H value between 6.5 and 7.0. The salt would not melt, but it decomposed when heated above 500°C.

Lithium alloyed with 20% calcium, with 20% zinc, or with 25% magnesium, respectively, was obtained from Maywood Chemical Works (a Division of Stepan Chemical Company). An alloy of 50-50 w/o (weight per cent) lithium and magnesium was prepared by melting the two metals in an Armco iron crucible. The furnace and crucible were used in the Laboratory's argon-atmosphere drybox, since lithium reacts directly with nitrogen, which was previously used in the drybox.

Kaolin, supplied by the Edgar Kaolin Corporation, Edgar, Florida, was used as an electrolyte immobilizer in pill-cells. Alumina, produced by Monsanto Chemical Company under the trade name Micria AD, was used as an absorbent in some pill-cells.

Analysis of sulfide and cyanide in the presence of excess thiocyanate.—Polarographic techniques were employed to analyze aqueous solutions of sulfide and cyanide in the presence of a large excess of potassium thiocyanate. Because of the difficulties of analyzing for sulfide, cyanide, and thiocyanate in the presence of one another (specially excess thiocyanate), we are presenting in some detail the results of our experience with this method. A Lingane-Laitenen type of H-cell was prepared with the usual dropping mercury-electrode and saturated calomel half-cell separated by a freshly precipitated agar-agar KCl bridge. The supporting electrolyte was a 0.1M solution of NaOH. Prior to the polarographic runs, the solutions were bubbled with nitrogen gas to remove dissolved oxygen.

The method was standardized by taking aliquot portions of prepared solutions of NaCN and Na_2S, determining the half-wave potentials, and then determining the effect of adding various concentrations of KSCN. The latter effect is shown in Fig. 3. It was observed that the KSCN tended to move the limit of analysis (*i.e.*, the decomposition potential of the supporting electrolyte) to more negative values, and this made the analysis of cyanide somewhat more difficult, since the half-wave potential of cyanide occurs very close to the end potential.

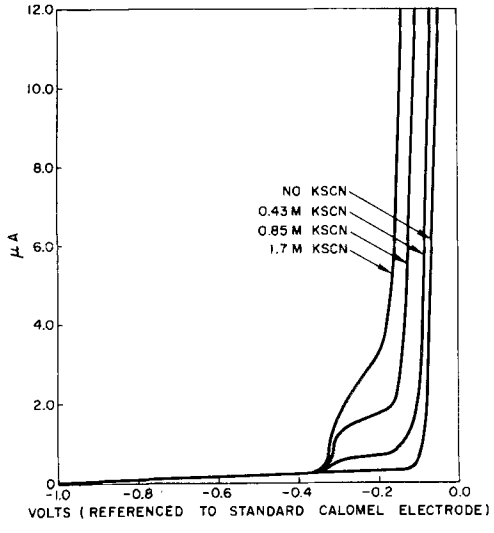

Fig. 3. Polarographic effect of varying the quantity of KSCN in a solution of 0.1M NaOH.

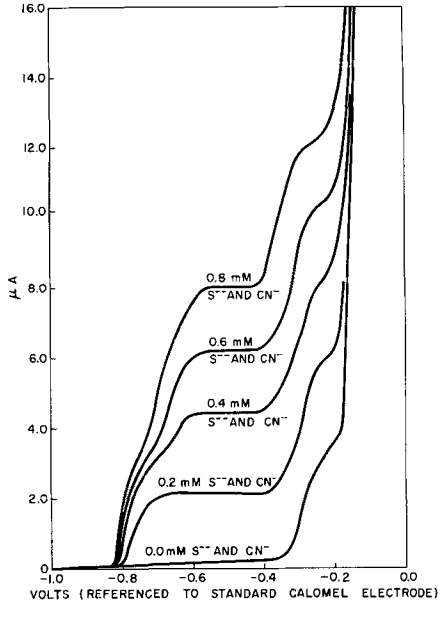

Fig. 4. Polarographic standardization: equal molar concentrations of S^{--} and CN^- in a solution of 1.7M KSCN, 0.1M NaOH.

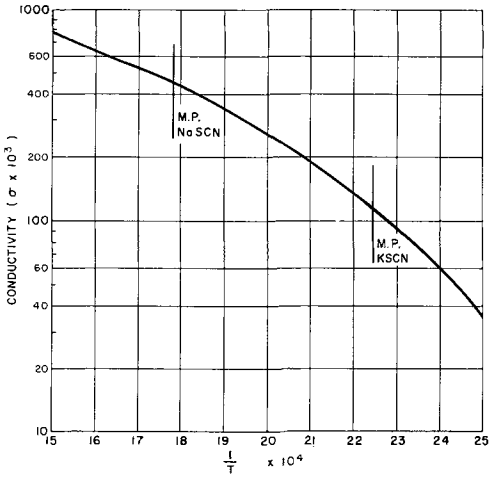

Fig. 5. Specific conductivity as a function of temperature for KSCN-NaSCN eutectic.

When equal molar concentrations of CN^- and S^{--} were used, the curves shown in Fig. 4 resulted. The first wave is caused by the reaction

$$Hg^o \pm S^{--} = HgS + 2e^- \quad [1]$$

The second wave is caused by the reaction

$$Hg^o + 2CN^- = Hg(CN)_2 + 2e^- \quad [2]$$

The final wave is caused by the reaction

$$Hg^o + 2\,OH^- = Hg(OH)_2 + 2e^- \quad [3]$$

which marks the decomposition of the supporting electrolyte. The wave attributable to SCN^- was not observed, because its value is beyond that of the supporting electrolyte.

After this method of analysis had been standardized, it was applied in determining the reaction products that result from the electrolysis of thiocyanate melts, which will be described below in the following section.

Fundamental Results and Discussion

Conductivity.—Conductivities were determined for several electrolytes, namely, KSCN, KSCN-NaSCN eutectic (73 w/o KSCN), KSCN-NH_4SCN (50-50 w/o). Conductivity of the potassium-sodium thiocyanate eutectic, which had not been reported previously, was investigated from 123.5° to 360°C. When the logarithm of the specific conductivity is plotted against the reciprocal of the absolute temperature, the resulting curve is essentially straight until the melting point of NaSCN is reached; with a further temperature drop, the curve is sharper (Fig. 5). This behavior corresponds with that predicted by Delimarskii and Markov for ideal eutectic salt mixtures (20).

It was expected that conductivity of the thiocyanate melts could be increased with additives, so various materials were combined with the melts and the conductivity determined. Additive salts were AgBr, NaI, NaCl, NaBr, KCl, LiCl, and LiSCN. Measured quantities of water were also introduced. Effects of these additives were minimal. There was no great conductivity increase in any case, and in some mixtures there was a decrease.

Addition of water to the eutectic before melting and while molten would be expected to cause some hydrolysis and the formation of such products as H_2S and HCN. While this proved to be true, hydrolysis was minimal because most of the water boiled out during heating. Conductivity was increased only slightly, however, and gassing occurred at the electrodes during polarographic experiments in "wet" melts.

Sodium chloride seemed to cause a slightly increased conductivity. This and the following reasons led to its subsequent addition to the eutectic for cell

electrolytes: (*A*) The Cl^- ion tends to aid anodic depolarization. (*B*) The Na^+ ion has a much smaller charge-to-radius ratio than does the Li^+ ion, and the Na^+ ion does not so readily attract oppositely charged ions, hence its mobility is not reduced.

The conductivity of KSCN-NaSCN-alumina pills (1.4 mm in thickness and 1 cm in diameter) was determined. When subsequent voltaic-cell tests showed that pill cells with kaolin for an absorbent contributed to better performance, further investigation of the anolyte pill conductivity was carried out, using a composition of 65 w/o salt mixture and 35 w/o absorbent at 200°C. Specific conductivities were 0.0606 mho for KSCN-NaSCN-Al_2O_3 and 0.127 mho for KSCN-NaSCN-kaolin. It is believed that the improved cell performance with kaolin results from less ohmic polarization. Possibly the laminar structure of kaolin allows easier passage of the conducting ions than does that of alumina, which has a platelike but irregular structure that grossly lengthens path distance across the cell. In other words, conducting ions may pass through the kaolin particles but must detour around the alumina particles.

Polarography.—Polarographic investigations were conducted in both the pure KSCN and KSCN-NaSCN eutectic melts, electrode reactions were verified by analysis of the melts after prolonged electrolysis, and the effect of aging the melts was determined. All potentials are referenced to the Ag/AgCl reference electrode, unless otherwise stated.

For the pure KSCN, two definite waves occur in the cathodic direction. The first potential increase begins at —1.60v, rising to —1.92v, and the half-wave value ($E_{1/2}$) is —1.75v. The current then decreases to a stable value until the potential reaches a value of —2.93v, whence the current increases without limit. In the anodic direction, the current begins to decrease at a potential of about —2.00v and reaches the residual value at about —1.60v. The current remains at the residual value until the potential reaches a value of approximately +0.20v, whence the current increases for a short span and then returns to the residual value.

The thiocyanate eutectic melt gives essentially the same polarographic waves as the pure KSCN, but with one additional wave, for which $E_{1/2}$ is —2.35v. The current then decreases to an equilibrium value until the potential is approximately —2.93v, where the current rises without limit. Summarized curves of the polarograms for these two melts are plotted in Fig. 6.

These investigations proved that an electrochemical reduction takes place in both these melts at a more positive potential than would be predicted solely on the basis of the reduction of the sodium or potassium ions. The reduction occurring at the half-wave potential of —1.75v is postulated as

$$2\,e^- + SCN^- = S^{--} + CN^- \qquad [4]$$

Experimental proof of this reaction was obtained by analysis of the melt after a prolonged electrolysis,

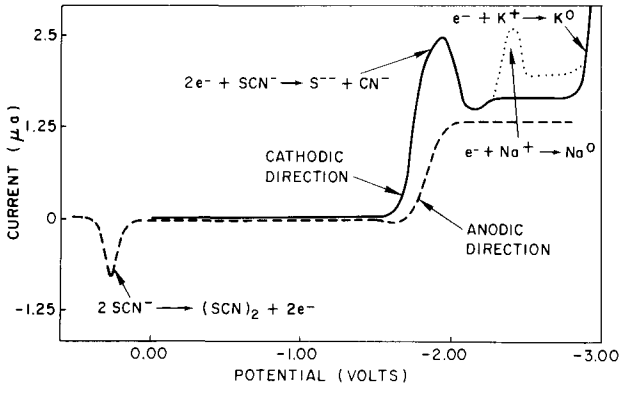

Fig. 6. Characteristic polarographic curves from the KSCN-NaSCN melt.

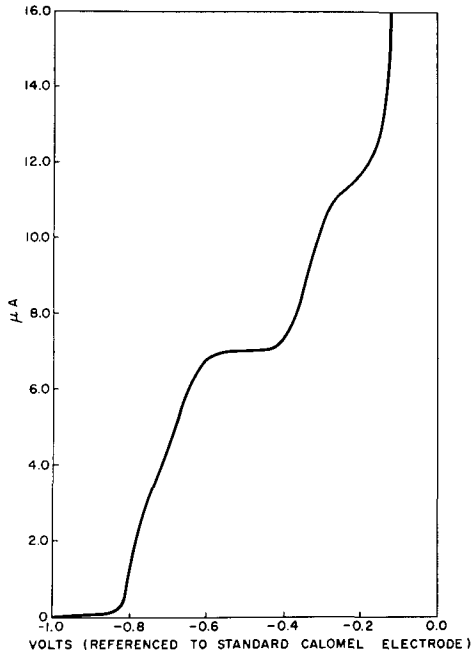

Fig. 7. Polarographic curve of a sample from molten thiocyanate electrolysis in an aqueous solution of 0.1M NaOH.

using the polarographic method in an aqueous 0.1M solution of NaOH, as previously described for the analysis of sulfide and cyanide. The melt electrolysis was carried out between two platinum electrodes, each having an area of 2 cm^2, which were separated by a medium-fritted glass disk. The cathode was enclosed in a known small volume in order to obtain the highest possible concentration of sulfide and cyanide. After electrolyzing the melt with a constant current of 1.6 ma at 1.80v for 20 min, the melt was allowed to cool and was then removed from its container to weighing bottles.

A 1-g sample of the electrolyzed KSCN was dissolved in 12 ml of a 0.1M aqueous solution of NaOH and placed in the H-cell. The resulting polarogram is shown in Fig. 7. These results proved that the total moles of S^{--} and CN^- produced in the electrolysis were faradaically equivalent to the total expected from analysis of the aliquot sample. The results also indicate that these two anions are produced in a one-to-one ratio during electrolysis of the melt. A small error observed in the CN^- determination is probably due to the interference of the KSCN as mentioned previously. Although a strong odor of sulfide is always noted after electrolysis of these melts, the polarographic method was needed to verify its formation.

The second wave observed in the eutectic mixture polarogram is postulated as resulting from the reaction

$$e^- + Na^+ = Na^o \qquad [5]$$

Finally, in the cathodic direction, a third wave in the eutectic-mixture polarogram (it occurs as the second wave in pure KSCN) is apparently due to the reaction

$$e^- + K^+ = K^o \qquad [6]$$

In both depositions of the alkali metals, the metal is not observed in a long-term electrolysis because of the reaction

$$2\ \text{metal} + SCN^- \rightarrow 2\ \text{metal ion}^+ + S^{--} + CN^-$$

The waves resulting from the alkali metal deposition can be observed only because the thiocyanate ion concentration is being lowered by the formation of sulfide and cyanide ions at the cathode-electrolyte interface. At the moment of depletion, current drops to an intermediate value until the potential is reached at which the sodium ion Na^+ is reduced until depleted.

When the Na^+ is depleted, deposition of the potassium begins at its reduction potential.

The anodic polarograms are essentially the same for both types of thiocyanate melts. The increase in anodic current, beginning at a potential of +0.20v, is apparently caused by the reaction

$$2SCN^- = (SCN)_2 + 2e^- \quad [7]$$

The dimeric thiocyanogen, unstable above +2°C, immediately undergoes polymerization to parathiocyanogen $(SCN)_X$. This material is reported by Walden and Audrieth as a yellow-orange solid that is insoluble in most solvents (21). This reported reaction was confirmed in experiments in which much higher currents than those obtaining in polarography were passed across two tungsten electrodes. The anode required a yellow-orange deposit, which formed in bubbles as a gas was given off, and this solid was found to have properties almost identical with those attributed to $(SCN)_X$ by Söderbäck (22). The anode product served as an insulating film on its parent electrode, causing the current to peak at +0.25v before dropping to a very small residual value. On reversing the current (toward the negative direction), the $(SCN)_X$ was not removed at any definite potential, but the film deteriorated with time, probably diffusing away into the melt, in which it has a limited solubility. The vapor that collected over the anode deposited in a cold tube as a light yellow solid that was very inert to solvents and strong mineral acids. No visible signs of reaction were seen on the negative electrode.

Other observations include an effect on the potential caused by aging of the melt. The fresh melts produced a more negative potential at the start of the first wave (*i.e.*, formation of S^{--} and CN^-), but the half-wave potential was essentially the same. Older melts tended to produce varying slopes in the polarographic waves.

Runs made in the ambient laboratory atmosphere produced heavy gassing at the electrodes, even in the low humidity prevailing, while runs in the argon-drybox atmosphere produced comparatively little gas. We analyzed samples of the gas mixture above the electrolysis melt with a mass spectrograph, but this showed only the presence of argon (from the drybox atmosphere), a trace of nitrogen, and very small traces of oxygen and hydrogen.

As the final revision of this manuscript was being prepared, an abstract of a report by Metzger (23) on a similar subject was released. It appears that Mme. Metzger has detected cyanogen above a melt of KSCN. Further investigations may be necessary for a complete determination of the gases evolved in this electrolysis.

Chronopotentiometry.—Chronopotentiometric results in pure KSCN melts verified the polarographic data. All potentials are referenced to the Ag/AgCl electrode. The cathodic current results in two potential plateaus, as shown in Table II. Extrapolation of the first plateau to zero current gives a potential of —1.68v, while extrapolation of the second plateau to zero current gives a potential of —2.90v. The anodic current results in only one plateau, as shown in Table III. Extrapolated to zero current, this potential becomes +0.25v. The time at which the potential remains on the plateau is inversely proportional to the current density.

This method verified the existence of the parathiocyanogen *film*, which appeared to be of constant thickness at the current densities used.

Table II. Cathodic potentials

Current, μa	First plateau, v	Second plateau, v
2.15	−1.72	—
18	−1.99	−2.93
25	−2.08	−2.89
40	−2.12	−3.12

Table III. Anodic potentials

Current, μa	Plateau, v	Time, sec
20.3	+0.27	0.657
100	+0.32	0.301
200	+0.36	0.169

Applied Results and Discussion

Rather extensive preliminary voltaic cell tests, first in beaker cells and then in pill cells, preceded the voltammetric studies in fused alkali thiocyanates. These exploratory cells proved that the thiocyanates would be usable in high energy-density voltaic cells, but did not point conclusively to optimum parameters. However, enough information was gained to proceed with statistically designed sets of fractional factorial tests of voltaic cells at the same time that detailed polarographic and chronopotentiometric investigations were conducted into fundamental characteristics of molten alkali thiocyanates as electrolytes.

Very satisfactory results have been obtained in the search for the optimum operating conditions, anode-cathode-electrolyte combinations, electrolyte absorbents, and resistive loads. Various cell components and operating parameters were used in five series of fractional factorial cell tests. While it manifestly is impossible to list all results obtained from this work, the main results, typical cell configurations, and representative outputs under given conditions can be reported at this time.

As results of each series of factorially designed cell experiments were obtained, developmental work with thiocyanate electrolytes proceeded accordingly. For example, data from the preliminary tests indicated that the mixture of KSCN-LiBr would improve cell performance, *i.e.*, open-circuit performance was good, and closed-circuit performance was acceptable at current densities greater than 50 ma/cm². Because of its melting point at about 175°C, comparison tests were run with this mixture and with the KSCN-NaSCN eutectic. The eutectic proved superior, and the addition of NaCl further improved cell performance, as previously explained in the discussion of conductivity.

The main result that determined the pattern of experimentation and the acceptable limitations of cell components was the optimum operational temperature of 200°C. The effect of temperature was clearly defined. As expected, cells operating at higher temperatures produced higher peak open-circuit (POCV) and peak closed-circuit (PCCV) voltages and higher current densities for longer lifetimes to a given cutoff voltage, but conductivity experiments revealed gassing in beaker melts of alkali thiocyanates above 325°C. Whether this gassing would occur in pill cell configurations is unknown, but some variation in pill-cell performance at high temperatures was observed, and this may have resulted from decomposition of the electrolyte. However, results were found to be consistently good in the temperature range from 200° to 325°C.

Since all of the likely anode materials melted below this temperature, it was necessary to prepare alloys that could be used above 200°C. A mixture of Li 50 w/o Mg melted at about 275°C, and this was used in a factorially designed set of tests for comparison with the Li 25 w/o Mg alloy that had been previously used. While it is thermodynamically predictable that the 50-50 w/o alloy would give a lower potential level, it was actually found that the difference between the potentials of the two was only a few hundredths of a volt. Other results from the 50-50 w/o alloy tests essentially duplicated those from the tests with the 75-25 w/o alloy. In view of these findings, the Li 50 w/o Mg anode material was adopted.

It is in the realm of investigations of cathodic materials that the use of statistically designed cells

Table IV. Configuration and operating parameters of selected thermally activated voltaic cells. All cells were activated under load and discharged between peak and final voltages for a minimum of 300 sec

Cell No.	Configuration[a]	PCCV,[b] v	FCCV,[c] v	Cur. dens., ma/cm²	Temp, °C
1	LiCa/KSCN,Al_2O_3//$CaCrO_4$ + electrolyte/Ni	1.70	1.40	32	200
2	LiZn/KSCN-LiBr,Al_2O_3//UO_3 + electrolyte/Ni	2.20	1.66	37	250
3	Li 25 w/o Mg/KSCN-NaSCN-NaCl,Al_2O_3//H_4UO_6 + electrolyte/Ni	1.95	1.35	45	150
4	Li/KSCN-NaSCN-NaCl,Al_2O_3//Na-dinitrobenzoate + electrolyte/Ni	1.87	1.41	45	150
5	LiPb/KSCN-NaSCN, Kaolin//Na-dinitrobenzoate + electrolyte/Ni	1.57	1.07	39	200
6	Li 25 w/o Mg/KSCN-NaSCN, Kaolin//UO_3 + electrolyte/Ni	2.59	2.01	74	200
7	Li 50 w/o Mg/KSCN-NaSCN-NaCl, Kaolin//V_2O_5 + electrolyte/Ni[d]	2.47	1.75	74	250
8	Li 50 w/o Mg/KSCN-NaSCN-NaCl, Kaolin//UO_3 + electrolyte/Ni	2.35	1.81	73	250

[a] Electrolyte used on the cathode side of cells is the same as that listed on the anolyte side, but with no absorbent except the active cathode material (*i.e.*, UO_3, V_2O_5, etc.).
[b] PCCV is the peak closed-circuit voltage.
[c] FCCV is the final closed-circuit voltage measured 300 sec after the cell output reached the PCCV voltage.
[d] Dry inert atmosphere, all others were operated in ambient atmosphere.

proved most advantageous since there is such a large number of materials that might prove useful.

Preliminary tests showed that AgBr produced potentials on the order of 2.28v (with Li-Mg anodes) at an apparent current density of 45 ma/cm². The first set of statistically designed cells incorporated AgBr, $CaCrO_4$, and UO_3 for the various levels of the cathode factor. Results from this set indicated UO_3 performed significantly better than calcium chromate and slightly better than silver bromide. Since silver bromide has a significant solubility in the electrolyte and could migrate to the anode, it was apparent that UO_3 would be the better cathode material for practical applications.

In later sets of cells, hydroxyperuranic acid, H_4UO_6, and the sodium salt of 3,5 dinitrobenzoic acid (DNBA), were used as cathode materials. Peak open- and closed-circuit voltages were in the range of 1.58 to 1.92v at 200°C. The Na-DNBA gave good performance at all levels of the other factors in the cells (anode, electrolyte, and temperature). However, when the Na-DNBA was then used in a set of cells with UO_3 as the other level of the cathode factor, the latter material again proved its superiority in terms of voltage and current densities achieved.

In work reported previously, V_2O_5 has been used in cells at 450°C, but in the LiCl-KCl eutectic melts (24). The same cathodic material has been used in this research in molten thiocyanates, comparing it with UO_3. Generally, voltage and current levels were about the same as those from UO_3 and in some cases slightly higher. However, V_2O_5 reacts with the electrolyte to an undetermined but obvious extent and is therefore restrictive in cells that must operate for more than a few minutes. Possible reactions of V_2O_5 with the solid salts have not been investigated.

The effect of varying the load resistance was determined so that the cell behavior in a practical battery could be predicted. As the load resistance is lowered for a given electrochemical system, the closed-circuit voltage lowers but the current density rises. In comparing various electrochemical systems, as was done in the statistically designed experiments, the voltage drop for a given time under a high current drain may be much different for one system than it is for another. Thus, the variation under a given load resistance may be used to predict the level of discharge from a given electrochemical system. Although load resistance was used as an independent variable when these series of cell tests were initiated, some other factor of more immediate importance was substituted in later series.

Among the variables that were not significant, it was of interest to note that the atmosphere apparently made little difference; indeed, most cells operated slightly better in ambient atmosphere than in the drybox. This was probably because of a beneficial effect of the slight moisture content of the pill-cell electrolyte.

Summary and Conclusions

Fundamental electrochemistry.—Results of this study indicate that the electrochemical decomposition of thiocyanate melts is bounded on the anodic side by the reaction given in Eq. [7] and on the cathodic side by the reaction given in Eq. [4]. All materials having potentials outside the range of +0.25 to −1.75v (using Ag/AgCl reference electrode) will be thermodynamically unstable in molten thiocyanates and will, ultimately, decompose the SCN^- to either $(SCN)_X$ or sulfide and cyanide ions. Although this study gives a more complete understanding of the basic electrochemistry of fused alkali thiocyanates, we have not investigated the kinetics of such reactions. It is manifestly impossible to predict voltaic-cell performance exclusively from fundamental investigations. For this reason, we have conducted extensive voltaic-cell investigations involving materials that have potentials lying outside the predicted decomposition range of the fused electrolytes. A summary of these results is given in the following section.

Applied electrochemistry.—The configurations and operating parameters of cells selected from the factorially designed sets are given in Table IV. Additionally, discharge curves of representative voltaic cells from the factorial series are shown in Fig. 8. These are cells that have operated presumably at their optimum rate under controlled conditions.

Two things should be kept in mind when evaluating the results of the applied portion of this investigation. In all these tests, more than one factor was changed at a time, and a significant result or difference must be directly attributable to the component under consideration; *i.e.*, there must be no predictable interactions. The other item to remember is the difficulty in extrapolating the results of electrochemical studies made in beaker or laboratory prototype cells into the performance of mass-produced cells or batteries. While screening techniques such as the factorial design of experiments save time and materials, the results cannot be considered final until batteries have been operated and evaluated in the required environment.

Acknowledgment

The authors would like to express their appreciation to their colleagues W. C. Spindler, Dr. W. S. Harris, and Dr. C. P. Haber for many helpful suggestions and consultations during the course of the research. The fine cooperation of L. E. Hanson for initiating the com-

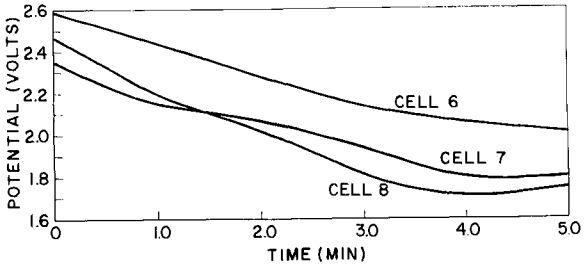

Fig. 8. Discharge curves from representative voltaic cells (see also Table IV).

puter program of the analysis of the statistical cell data should be cited. Dr. Schaer gratefully acknowledges the summer employment offered him by NOLC.

This research was conducted under the Bureau of Naval Weapons Weptask No. R360-FR-104/211-1/R011-01-01 and RRRE-06-017/211-1/F009-06-05.

Manuscript received by ECS March 11, 1964; assigned to JES June 15, 1964; revised manuscript received July 30, 1965. This paper was presented in part at the Toronto Meeting, May 3-7, 1964.

Any discussion of this paper will appear in a Discussion Section to be published in the June 1966 JOURNAL.

REFERENCES

1. E. Paterno and A. Mazzuchelli, *Gazz. Chim. Ital.*, **38**, 137 (1908).
2. E. Kordes, W. Bergmann, and W. Vogel, *Z. Elektrochem.*, **55**, 600-6 (1951).
3. J. Greenberg, B. R. Sundheim, and D. M. Gruen, *J. Chem. Phys.*, **29**, 461 (1958).
4. G. Harrington and B. R. Sundheim, *Ann. N. Y. Acad. Sci.*, **79**, Art. 11, 950 (1960).
5. C. B. Baddiel and G. J. Janz, *Trans. Faraday Soc.*, **60**, 2009 (1964).
6. J. P. Frame, E. Rhodes, and A. R. Ubbelohde, *ibid.*, **55**, Pt. 12, 2039 (1959).
7. G. W. Harrington and H. T. Tien, *J. Phys. Chem.*, **66** [1], 173 (1962).
8. E. H. Crook and J. O'M. Bockris, "The Electrical Conductance and Structure of Simple Molten Electrolytes," Final Technical Report under Contract DA-36-034-ORD-1765, Office of Ordnance Research, U. S. Army. Oct. 1958. Available from DDC, AD 215096.
9. E. R. Van Artsdalen and I. S. Yaffe, *J. Phys. Chem.*, **59**, 118 (1955).
10. R. E. Panzer, *Electrochem. Technology*, **2**, 6 (1964).
11. *Ibid.*
12. D. Inman, *J. Sci. Instrum.*, **39**, 391 (1962).
13. IU. K. Delimarskii and B. F. Markov, "Electrochemistry of Fused Salts," p. 175, Sigma Press, Washington, D. C. (1961). Translated by Adam Peiperl.
14. *Ibid.*, p. 175.
15. Harrington and Tien, *loc. cit.*
16. G. Harrington, "Technical Progress Report," A.E.C. Contract AT(30-1)-2780-Mod. 1, Temple University, Philadelphia, Pa., Jan. 1963.
17. O. L. Davies, Editor, "The Design and Analysis of Industrial Experiments," Hafner Publishing Co., New York (1960).
18. Frame *et al.*, *loc. cit.*
19. H. C. Urey, Columbia University Report, A.E.C. Contract A-743 (1943).
20. Delimarskii and Markov, *op. cit.*, p. 25.
21. P. Walden and L. F. Audrieth, *Chem. Rev.*, **5**, 339 (1928).
22. E. Söderbäck, *Ann.*, **419**, 217 (1919).
23. Giséle Metzger, Report CEA-R-2566 Commissariat à l'Energie Atomique, Centres d'Etudes Nucléaires, Saclay, France [*Nuclear Science Abstracts*, **19**, 1333 (1965)].
24. R. E. Panzer, "Investigations of Chemoelectric Conversion in Fused Salts (II)," Tech Memo 44-10, U. S. Naval Ordnance Lab., Corona, Calif., May, 1961.

Technical Notes

Recrystallization of Anodic Alumina Films

D. J. Barber[1]

National Bureau of Standards, Washington, D. C.

Oxide films on metal surfaces are used increasingly in modern technology. Films formed by anodic or thermal oxidation deviate from stoichiometric composition because of lattice defects and impurities. The electrical, chemical, and mechanical properties of the films depend on stoichiometry, the presence of various phases, grain size, and porosity. This note describes some electron microscope observations on the recrystallization of one type of Al_2O_3 anodic film. Keller *et al.* (1), Franklin and Stirland (2), and Heine and Sperry (3) have already used electron microscopy to study other types of as-grown Al_2O_3 films.

The films were made by the method of Hauser and Kerler (4), as modified by Johnson and Deslattes (5). These samples were conveniently available, but other methods of preparation would have been equally suitable since only small samples were required. The anodizing solution was ammonium citrate and citric acid in distilled water. To avoid charging in the electron beam, the films were backed with a layer of evaporated carbon.

As-grown films are amorphous; grains cannot be resolved and the cellular structure found in some anodic films [for example, those of Keller *et al.* (1)] is absent. Diffraction experiments reveal an intense cloud of scattered electrons about the direct beam but no diffraction rings. The grain size is deduced to be < 30Å. The films are not structureless but show markings related to the rolling direction in the parent aluminum foil. Rolled foil is known to have a fibrous structure (6). The markings in the samples may arise from surface irregularities or rolled-in impurities in the aluminum, or because the apparently amorphous film has a fine crystallinity related to the fibrous structure. Hauser and Kerler (4) showed that their method

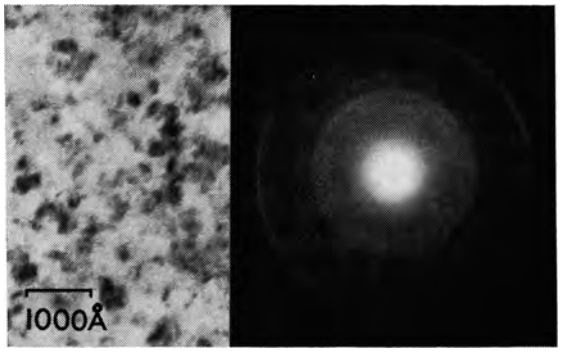

Fig. 1. Aluminum oxide film after type (A) recrystallization, and selected area diffraction pattern.

[1] Present address, Physics Department, the University of Essex, Colchester, England.

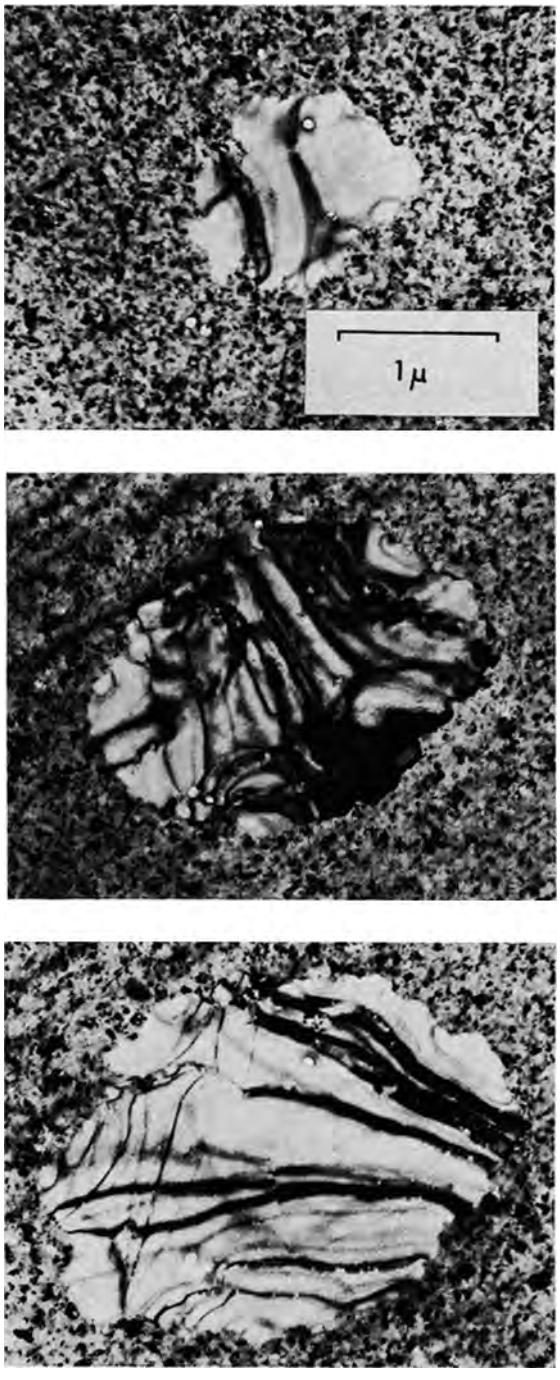

Fig. 2. Successive stages in the development of type (B) recrystallization in the electron beam.

produces films which are gas tight, *i.e.*, free from penetrating pores. Nevertheless, the present samples exhibit many pore-like defects which often nearly penetrate the foil. They apparently result from bubbles which form in the anodizing bath and are incorporated in the growing film. Their occurrence can be substantially reduced by containing the bath in an ultrasonically vibrated vessel. As an added advantage the films are cleaner, showing that there is dross rolled into the aluminum and that some is shaken free during anodization.

Films could be recrystallized by heat treatment at ~ 1250°C in a tube furnace. It was more instructive, however, to cause recrystallization with the electron beam and thus follow its progress. Intense local heating was achieved by using a large condenser aperture and momentarily switching off the second condenser lens.

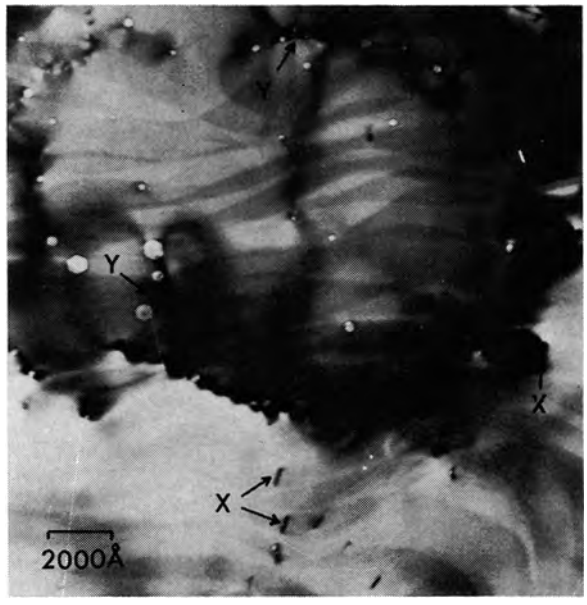

Fig. 3. Completely recrystallized film exhibiting pores, surface terraces (caused by thermal etching in the electron beam), and short dislocations in subgrain boundaries and at pores.

Recrystallization of films in the beam occurs in two stages, which will be referred to as A and B. At an estimated temperature, ~ 1150°C, the film becomes finely polycrystalline (A) with a grain size ~ 250Å. The recrystallization front propagates through the sample like a wave. Further changes (B) occur at ~ 1400°C, and this is shown by the migration of grain boundaries and the rapid growth of large grains. Higher temperatures are needed to cause recrystallization in the beam than in the uniform heat of a furnace. Figure 1 shows a transmission micrograph and selected area diffraction pattern from a sample which had barely undergone (A) recrystallization. The small grains are apparently α-Al_2O_3. Further heating improves the crystallinity and improves the Bragg contrast. Successive views of (B) recrystallization are shown in Fig. 2; these frames were obtained by subjecting the area to short hot pulses from the beam and photographing it between each pulse. The characteristics of stage (B) are typical of normal recrystallization processes.

It is well known that anodic films of Al_2O_3 may contain several phases, including γ-Al_2O_3. In our case the nature of the unrecrystallized films could not be determined by either x-ray or electron diffraction. It is believed, however, that (A) is principally a phase transition to the α-form accompanied by some grain growth; this process leaves the films in a state of high internal strain. Figure 3 demonstrates that dislocations can occur within grains after stage (B) recrystallization. This sample was given prolonged heating in the beam, which explains the surface terraces and equilibrated shape of the pores. Most of the dislocations are nearly perpendicular to the foil (as at X) and thus have minimum energy. Those lying in the plane are usually caught up around pores (as at Y); apparently the pores also impede grain boundary migration. Sub-grain boundaries are somewhat rare and those observed have been of tilt character.

Acknowledgment

The author wishes to thank H. Johnson for supplying the samples.

Manuscript received July 16, 1965.

Any discussion of this paper will appear in a Discussion Section to be published in the June 1966 JOURNAL.

REFERENCES
1. F. Keller, M. S. Hunter, and D. L. Robinson, *This Journal*, **100**, 411 (1953).
2. R. W. Franklin and D. J. Stirland, *ibid.*, **110**, 262 (1963).
3. M. A. Heine and P. R. Sperry, *ibid.*, **112**, 359 (1965).
4. U. Hauser and W. Kerler, *Rev. Sci. Instruments*, **29**, 380 (1958).
5. H. Johnson and R. D. Deslattes, *ibid.*, in press.
6. G. Sachs, "Practische Metallkunde II," Berlin (1934).

Defects in the Structure of Electrodeposited Copper

E. M. Hofer,[1] L. F. Chollet, and H. E. Hintermann

Laboratoire Suisse de Recherches Horlogères, Neuchâtel, Switzerland

The scope of this paper is to describe, compare, and discuss three methods used to obtain characteristic microstructural quantities important for a better understanding of the mechanical properties and the behavior of electrodeposited metals. These techniques are the electron microscopy, the Fourier analysis of the x-ray diffraction line profiles, and the small angle x-ray scattering. In certain cases some of the structural parameters can be measured by two of these methods. Thus the results can be compared.

Electron microscopy permits one by direct counting to determine the dislocation density, the density of inclusions, and the grain size. Its disadvantage is that the results are obtained on a small area which may not be representative of the specimen as a whole.

The x-ray methods do not have this disadvantage. They provide better statistical values for the determination of the crystallite size. However, with these techniques the dislocation density can be calculated only indirectly (1).

The investigated electrodeposits contained inclusions of the additive or a reaction product. The number of inclusions per unit volume can be determined by counting them on an electron micrograph. The inclusion density can also be determined by small angle x-ray scattering provided only that the size of the inclusions is sufficiently small, *i.e.*, smaller than about 100Å. The investigated electrodeposits actually contain inclusions which satisfy this condition (2).

Experimental

Copper deposits, 30μ thick, were produced on laminated and annealed copper sheets, 50μ thick, in an electrolytic cell with a rotating cylindrical cathode (1). The initial composition of the plating bath was 1*N* $CuSO_4$, 1*N* H_2SO_4, prepared and purified as described by Fischer and co-workers (3, 4). Gelatin (mol. wt. $\approx$ 180,000) was used as the additive in concentrations of 80 and 200 mg/l. A fresh solution was used for each deposition. The current density was 20 ma/cm^2 and the temperature was kept constant at 25°C. One portion of each sample was thinned electrolytically perpendicular to the growth direction in a phosphoric acid/ethanol solution, and examined by transmission electron microscopy (Elmiskop I) at electron optical magnifications between 22,000 and 160,000 times using an acceleration voltage of 80 kv. The average grain diameter $\bar{D}$ of these electrodeposits was determined from the formula of Braun (5), which relates the average volume $\bar{V}$ of the grains to its average linear dimensions $\bar{L}$ measured on the electron micrographs, *i.e.*, $V = 2.57\ (\bar{L})^3$. The dislocation density ρ_{el} at the surface of the specimens, the inclusions mean diameter $(\bar{D}^{-3})^{1/3}{}_{el}$ were counted and calculated from 5 or more greatly enlarged electron micrographs (2). The specimen thickness was estimated from extinction fringes at grain boundaries and boundaries of microtwins, to 100-1000Å.

The x-ray diffraction patterns were recorded with a Philips proportional counter diffractometer. Filtered Co Kα radiation (voltage 30 kv, current 10 ma, Fe filter) was used, thus eliminating the copper fluorescent radiation from the sample. The width of the divergence slit was 1°, that of the receiving slit 0.2 mm. The scanning speed was ¼ degree 2θ/min, the chart speed 800 mm/hr.

The background was determined from a sample annealed at 750°C and subtracted from each diffraction pattern of the samples to be analyzed. The electrodeposits were mounted in a stainless steel specimen holder in order to provide reproducible experimental conditions during the recording of the various diffraction patterns. The heat-treatment was performed while the specimen was kept in the holder.

The analytical treatment of x-ray diffraction line profiles has been reviewed by Warren (6). The following quantities can be determined by this method.

The probability α of finding a stacking fault between two (111) layers determined from the relative shift of the 111 and 200 diffraction peaks of the sample as deposited and the same sample annealed for 1 hr at 750°C (7).

$$\Delta(2\theta^0_{200} - 2\theta^0_{111}) = -\frac{45\sqrt{3}\alpha}{\pi^2}\,(\tan\theta_{200} + \tfrac{1}{2}\tan\theta_{111})$$

The probability β of finding a twin fault between two (111) layers determined by the method of Cohen and Wagner (8) from the asymmetry of the diffraction peaks, measured as the relative displacement of the center of gravity (ΔCG) in regard to the peak maximum

$$\Delta CG\,(2\theta^0)_{111} - \Delta CG\,(2\theta^0)_{200} = \beta(11\tan\theta_{111} + 14.6\tan\theta_{200})$$

The Fourier coefficients and the correction of Stokes for the instrumental line broadening are calculated on an electronic computer IBM 1620. From these coefficients the average dimension of the coherently diffracting domains, $\langle D\rangle_{\text{eff hkl}}$, can be obtained.

$$\frac{1}{\langle D\rangle_{\text{eff hkl}}} = -\left[\frac{dA_L{}^S}{dL}\right]_{L\to 0} = \frac{1}{\langle D\rangle} + \frac{(1.5\,\alpha + \beta)}{a_o}\,c_{hkl}$$

The cosine-coefficient A_L can be considered as the product of two coefficients, $A_L{}^S$ and $A_L{}^D$ whereby the former relates to the size (index S) of the crystallites and the latter to the microdeformations, *i.e.*, rms strains (index D). L is a distance perpendicular to the reflecting planes; c_{hkl} has the value of $\sqrt{3}/4$ for the 111 and 222 reflections. The expression $a_o(1.5\,\alpha + \beta)/c_{hkl}$ is defined as $\langle D\rangle_{\text{F hkl}}$, the calculated crystallite dimension due only to the presence of faults. By plotting ln A_L as a function of $h_o{}^2$ where $h_o{}^2 = (h^2 + k^2 + l^2)$ for different values of L, a set of straight lines is obtained whose intersections with the ordinate furnishes the values $A_L{}^S$ and whose slope is proportional to the rms strain $\langle\epsilon^2{}_L\rangle$.

The small angle x-ray scattering diagrams were obtained according to Jan (9). The photometrically measured intensity $I(h)$, where $h = 4\pi\theta/\lambda$, is plotted

[1] Present address: Research Division, American Radiator & Standard Sanitary Corporation, New Brunswick, New Jersey.

as a function of h^2 on a double logarithmic scale, θ being the diffraction angle, λ the wavelength. This experimental curve is superimposed on a network of $I(h)/I(O)$ curves calculated for different values of the parameter $\gamma(\gamma = 1, 2, 3. . .)$ and plotted as a function of $R_o^2h^2$, where R_o is the most probable radius of gyration. From this the $I(O)$, R_o, and γ values can be deducted. It is then possible to calculate the number of scattering centers, N, per unit volume, V_o, according to

$$\frac{N}{V_o} = [I(O)/P_o] \cdot r^2[t\eta\rho^2\kappa^2R_o^6f(\gamma)]^{-1}$$

where P_o is the power of the incident beam, r the distance from the specimen to the film, t the specimen thickness, ρ the electron density of the scattering centers, η a constant equal to 7.94×10^{-26} cm^2, κ a form factor. The function $f(\gamma)$ is calculated using the relation

$$f(\gamma) = \frac{1}{8\gamma^6\sqrt{\pi}}\left[\frac{2\gamma \exp(-\gamma^2)}{1+\Theta(\gamma)}(4\gamma^4 + 28\gamma^2 + 33) + \sqrt{\pi}(8\gamma^6 + 60\gamma^4 + 90\gamma^2 + 15)\right]$$

with $\Theta(\gamma)$ being the Kramp-Laplace error function

$$\Theta(\gamma) = \frac{2}{\sqrt{\pi}}\int_o^\gamma \exp(-x^2)\,dx$$

which can be found tabulated in mathematical tables. The function $f(\gamma)$ takes the values of 23.4, 3.62, and 1.97 for γ equal to 1, 2, and 3, respectively. The radius R of the scattering centers can then be obtained from

$$\overline{R^3} = R_o^3\left[\frac{3+2\gamma^2}{2\gamma^2} + \frac{\exp(-\gamma^2)(1+\gamma^2)}{\gamma^2\pi^{1/2}[1+\Theta(\gamma)]}\right]$$

from which the average diameter $(\overline{D^3})^{1/3}$ of the inclusions can be deducted.

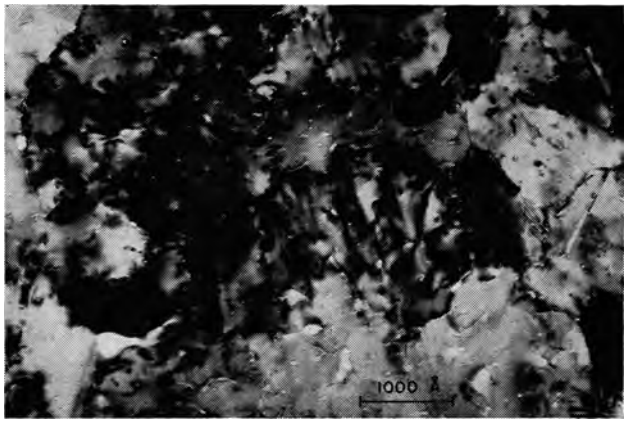

Fig. 1. Electron micrograph of a copper deposit (conditions: 1N H_2SO_4, 1N $CuSO_4$, 20 ma/cm^2, 25°C, 200 mg/l gelatine) showing dislocations and inclusions.

Fig. 2. Electron micrograph of a copper deposit (conditions: 1N H_2SO_4, 1N $CuSO_4$, 20 ma/cm^2, 25°C, 200 mg/l gelatine) showing microtwins, grain boundaries, dislocations, and inclusions.

Results and Discussion

Typical electron micrographs from which the crystallite size and the inclusions and dislocation densities were determined are shown in Fig. 1 and 2. Figure 1 contains more of the randomly distributed inclusions, but only a few microtwins. The dislocations are often seen to interact with the inclusions thereby accounting for the high mechanical strength generally observed in these deposits. The grain boundaries are not always well defined. (Fig. 2).

In general, the crystallite size determined by electron microscopy is larger than that measured by the Fourier analysis. In the first case, an average distance from grain boundary to grain boundary is measured, whereas in the latter case, it is the distance of coherence in the interior of the crystal which may be interrupted by defects such as dislocations and twin faults. Furthermore, with the Bragg-Brentano focalization conditions encountered in the counter diffractograph technique, only the crystallites whose $\{hkl\}$ planes lie parallel to the surface of the sample participate to an hkl reflection. Therefore, the coherence distance is measured perpendicularly to the surface of the sample by the x-ray diffraction technique. Whereas in the electron microscope, the distance corresponds to a cross section of the grains parallel to the surface of the sample, but some electron micrographs taken perpendicularly to the sample surface did not differ essentially from those taken parallel.

The results of the three methods are summarized in Tables I and II. The twin fault density in these electrodeposits is small indeed and a shift of peaks indicating the presence of stacking faults has not been observed. Knowing the values of the rms strains $\langle\epsilon^2_L\rangle_{hkl}^{1/2}$ and assuming a maximal separation and a minimal interaction of the dislocations, it is possible to calculate the dislocation density ρ_{WS} in the sample from the formula proposed by Williamson and Smallman (10)

$$\rho_{WS} = \frac{16\langle\epsilon^2_L\rangle}{b^2}$$

where b is the Burgers vector of the dislocation. This value ρ_{WS} agrees fairly well with the dislocation density ρ_{el} obtained from the electron microscopical study.

The diameters of the inclusions obtained by the small angle x-ray scattering method are in general slightly smaller than those determined with the electron microscope. This is due to the fact that the very smallest inclusions are difficult to observe on the electron micrographs and thus easily escape the counting. As a whole, however, the average sizes of inclusions determined according to the two methods agree reasonably well. The results obtained from the three methods show that each technique is useful in the study of the

Table I. Results of the Fourier analysis of the diffraction line profiles of copper electrodeposited in the presence of gelatin, comparison with the results obtained by electron microscopy

Gelatin conc, mg/l	Annealing temp, (1 hr), °C	$\langle D\rangle_{eff\ 111}$, Å	Crystallite dimension el. micr., Å	$\langle D\rangle_{F\ 111}$, Å	$\langle\epsilon^2_{50}\rangle_{111}^{1/2}$	β
80	20	250	680	4150	0.0031	0.002
80	175	400	720	4150	0.0026	0.002
200	20	360	810	1050	0.0018	0.006

Table II. Dislocation and inclusion density. Comparison between the x-ray results and those from the electron microscope

Gelatin conc., mg/l	Annealing temp, (1 hr), °C	ρ_{WS} x-ray, cm^{-2}	ρ_{el} el. micr., cm^{-2}	N/V_o small angle, cm^{-3}	$(N/V_o)_{el}$ el. micr., cm^{-3}	$\overline{(D^3)}^{1/3}$ small angle, A	$\overline{(D^3)}^{1/3}{}_{el}$ el. micr., A
80	20	2.2×10^{11}	2×10^{11}	13×10^{16}	9×10^{16}	32	40
80	175	—	—	13×10^{16}	9×10^{16}	30	55
200	20	0.8×10^{11}	2×10^{11}	15×10^{16}*	13×10^{16}	49*	55

* According to (10).

structure of galvanic deposits and that a rather complete picture of the faults occurring in the crystalline structure of electrodeposited metals can be obtained.

Acknowledgment

The authors wish to express their thanks to Professor D. Dinichert for his advice and interest in this work and J. P. Jan for his helpful discussions. They are also indebted to I. L. Kalnin who was kind enough to review this manuscript.

Manuscript received April 27, 1965; revised manuscript received July 21, 1965.

Any discussion of this paper will appear in a Discussion Section to be published in the June 1966 JOURNAL.

REFERENCES

1. E. M. Hofer and H. E. Hintermann, *This Journal*, **112**, 167 (1965).
2. S. Steinemann and H. E. Hintermann, *Schweiz. Arch. angew. Wiss. Tech.*, **26**, 202 (1960).
3. H. Binder and H. Fischer, *Z. Metallkde.*, **53**, 161 (1962).
4. H. Seiter and H. Fischer, *Z. Electrochem.*, **63**, 249 (1959).
5. A. Braun, *Rev. Met.*, **52**, 676 (1955).
6. B. E. Warren, *Progr. in Metal Phys.*, **8**, 147 (1959).
7. M. S. Paterson, *J. Appl. Phys.*, **23**, 805 (1952).
8. J. B. Cohen and C. N. J. Wagner, *ibid.*, **33**, 2073 (1962).
9. J. P. Jan, *Z. angew. Math. Phys.*, **14**, 1 (1963).
10. G. K. Williamson and R. E. Smallman, *Phil. Mag.*, **1**, 34 (1956).

Fluorescent Properties of Terbium-Activated Alkaline Earth Alkali Borates

W. L. Wanmaker, A. Bril, and J. W. ter Vrugt

N. V. Philips'Gloeilampenfabrieken, Eindhoven, Netherlands

In recent years several new rare earth activated phosphors have been prepared, especially with europium and terbium as an activator. For instance Van Uitert (1) studied the fluorescence of Tb in many different host materials (scheelites). It was shown in a previous paper (2) that terbium-activated alkaline earth borates are phosphors of medium efficiency, the highest quantum efficiency found being 42%. In this paper we describe the preparation and some fluorescent properties of terbium-activated phosphors which are even more efficient, viz., alkaline earth alkali borates such as, *e.g.*, calcium sodium borate activated with terbium.

The type of host lattice mentioned above was previously used by Tomaschek (3), in the preparation of Eu-activated calcium sodium borate glass. We have not found in the literature any other examples of phosphors with this type of host lattice. In our first paper (2) we presented a short survey of Tb-activated phosphors. Since then, Borchardt (4) has described the preparation of Tb-activated rare earth tungstates and molybdates, and Brixner (5) has prepared phosphors such as $Tb_{0.5}Nb_{0.5}W_{0.5}Ca_{0.5}O_4$ and $Tb_{0.5}Nb_{0.5}Mo_{0.5}Ca_{0.5}O_4$, of which the last was the most efficient one.

The ingredients used in the firing mixtures were luminescent grade $CaCO_3$, $SrCO_3$, $BaCO_3$, $MgCO_3$, and H_3BO_3; Li_2CO_3 ("reinst"), Na_2CO_3, and K_2CO_3 (both A.R.) from the firm Merck (Darmstadt), and the rare earth oxides Tb_4O_7 and Gd_2O_3 which were obtained from the Lindsay Chemical Division of American Potash and Chemical Corporation in purities of 99.9%

In all cases the preparation was carried out in such a way that no glass melts were prepared but polycrystalline powders only. From x-ray analysis it followed that in nearly all cases (except with the compounds $MgLiBO_3$, $MgNaBO_3$, and $BaKBO_3$) well crystallized solids were formed. The powder diagram of calcium sodium borate was in accordance with those found by Lehmann (6). The hitherto unpublished d-spacings of the other compounds will be published elsewhere.

It is important to point out that the phosphors which are discussed in this paper cannot be considered as phosphors comparable to those prepared by us before (2), by merely adding alkali ions for charge compensation. This follows from the fact that, for instance in a compound such as $3CaO \cdot B_2O_3$-Tb, no increase in brightness was observed when adding equimolar amounts of Na and Tb. Only with a high amount of sodium added, accompanied by the appearance of a distinct new phase, a strong increase in brightness could be achieved.

In the case of the preparation of phosphors with varying amounts of activator added, the ratio of the number of cations and anions was kept constant, *e.g.*, $(Ca, Na)_{1-x}Tb_xBO_3$. A small excess of the anions was added, as is common practice in the preparation of most phosphors.

The formula of the phosphors prepared are given as the molar compositions of the firing mixture. One should keep in mind, however, that after the firing, the composition may be different, *e.g.*, due to the volatilization of part of the boric acid added. Moreover an uncertainty of maximum 2% exists in the exact Tb concentration, as we assumed that the Tb-oxide used has the formula Tb_4O_7, and it is known that this compound may have some deviation from this formula.

The excitation, diffuse reflection, and emission spectra, efficiency, and decay times were determined by procedures already described by us (7, 8). All the phosphors investigated show emission lines characteristic of terbium (9), corresponding to transitions from the $^5D_4$ to ^7F_j levels. They resemble those found for the alkaline earth borates, described by us (2) earlier.

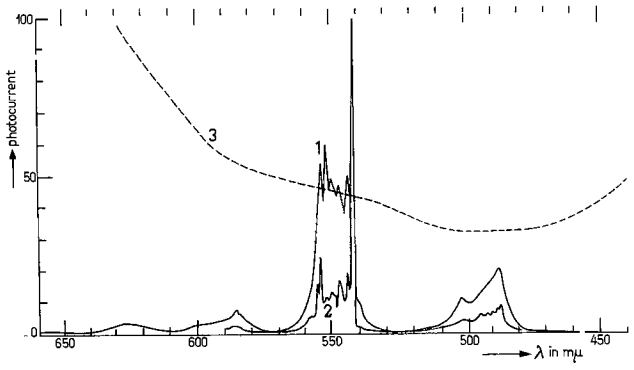

Fig. 1. Spectral energy distribution curves of the emission of $CaNaBO_3$-Tb; molar ratio Tb/B_2O_3 = 0.06. Curve 1, measured at room temperature, 20°C; curve 2, measured at liquid nitrogen temperature, —196°C; curve 3, correction factor with which the ordinates have to be multiplied in order to get relative radiant power.

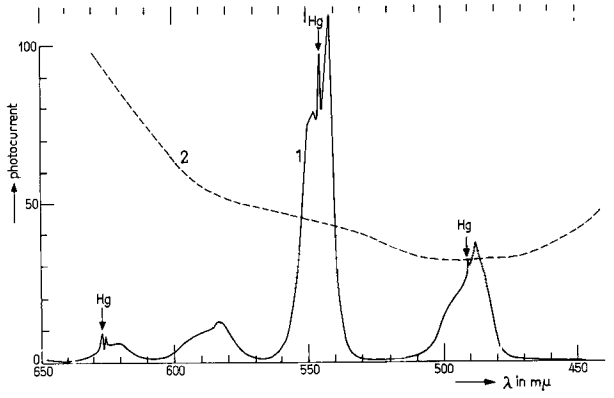

Fig. 2. Spectral energy distribution curves of the emission of $SrLiBO_3$-Tb, molar ratio Tb/B_2O_3 = 0.06 (curve 1). The same correction factor as in Fig. 1 is given in curve 2.

Examples of the emission spectra are given in Fig. 1 and 2, showing uncorrected recorder curves of the photocurrent as a function of wavelength λ. In $CaNaBO_3$-Tb we found that for a low Tb concentration the emission peaks are much sharper than for higher concentrations. The diffuse reflection spectra of the phosphors are similar to those found for the terbium-activated alkaline earth borates, reported before (2). The wavelength dependence of the quantum output (denoted by *L*) of the Tb-fluorescence (excitation spectrum) has been determined for several Tb-activated phosphors. That of calcium sodium borate-Tb is given in Fig. 3. The total intensity of the Tb emission (with $\lambda > 450$ mμ) was continuously monitored as a function of the exciting wavelength in the region from 220 to about 400 mμ Possible changes in the excitation spectra as a function of the fluorescent wavelength were thus not considered. The excitation spectra consist of a continuous part and of a line spectrum. In $CaNaBO_3$-Tb the continuous part of the excitation spectrum becomes somewhat broader with an increasing Tb concentration. This favors the efficiency with 253.7 mμ excitation, as present in a mercury discharge. With the borates containing Sr the peak in the excitation spectrum is located at a shorter wavelength (at about 235 mμ) than in the corresponding Ca-compounds (about 240 mμ). Both in the Ca- and Sr-alkali borates, the continuous bands in the excitation spectra are found to be narrower with the potassium compounds. For many of the latter phosphors the efficiency at 253.7 mμ is already considerably reduced.

Considering the lines found in the excitation spectra, one can distinguish between two groups of lines, *viz.*,

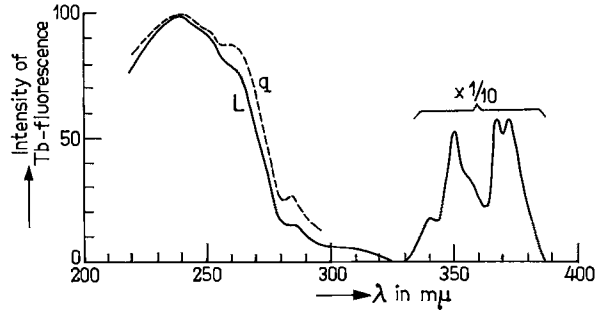

Fig. 3. Relative excitation spectra of the Tb fluorescence of $CaNaBO_3$-Tb (Tb/B_2O_3 = 0.15). Curve denoted with L, quantum output; curve denoted with q, quantum efficiency.

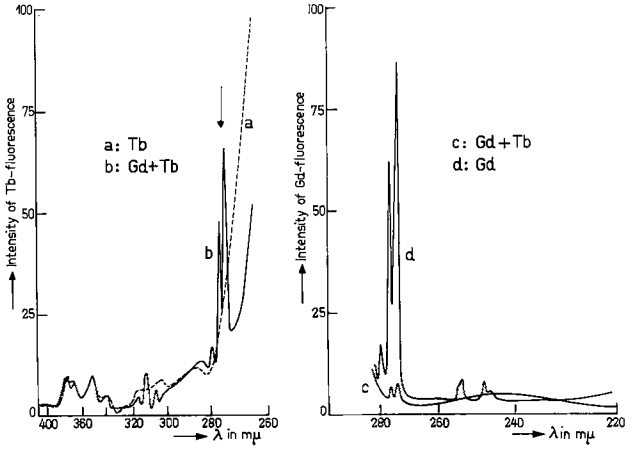

Fig. 4. Relative excitation spectra of the $2CaO \cdot Na_2O \cdot B_2O_3$ phosphors.

Curve	Molar ratio Tb/B_2O_3	Molar ratio Gd/B_2O_3	
a	0.06	0	Tb—fluorescence
b	0.06	0.24	Tb—fluorescence
c	0.06	0.24	Gd—fluorescence
d	0	0.24	Gd—fluorescence

those due to the presence of Tb and Gd, respectively, in the same way as was already discussed by us for the Tb-activated alkaline earth borates (2). When the phosphor contains both Gd and Tb, excitation of the Gd^{3+} ions results in the green Tb fluorescence due to transfer of energy from Gb to Td. (Fig. 4b). The sharp Tb fluorescence peaks indicated by an arrow are due to absorption in the Gd ions. Curves c and d give the excitation spectra of the Gd output (total fluorescent intensity in the 310 mμ region). From d it can be seen that the Gd emission of the phosphor activated with Gd only can indeed be excited in the 275-280 mμ region due to absorption by Gd ions. When incorporating Tb, it is obvious from curve c that the intensity of the Gd fluorescence is very much reduced. An interesting question is whether the observed transfer of energy is due to a quantum-mechanical resonance process or to a radiant process (absorption of the 310 mμ radiation emitted by Gd).

Radiative energy transfer seems rather unlikely, because it follows from the excitation spectra of the Tb emission that the efficiency of this emission is very low for excitation by 310 mμ radiation (see curve C).

Table I presents a survey of the radiant and quantum efficiencies of some terbium-activated borates for excitation in the 250-270 mμ region. These efficiencies are corrected for the reflection of the exciting radiation. In this way the quantum efficiency (the ratio of the number of emitted quanta and the number of absorbed quanta) is obtained. As follows from Fig. 5 the most efficient phosphors are prepared with a molar

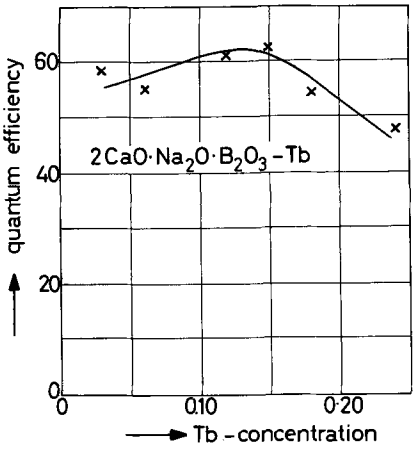

Fig. 5. Quantum efficiency (250-270 mμ excitation) of $2CaO \cdot Na_2O \cdot B_2O_3$-Tb phosphors as a function of the Tb concentration. The Tb concentration is expressed as the mole ratio Tb/B_2O_3.

ratio Tb/B_2O_3 of about 0.12. Concerning the effect of the molar ratio $(Ca + Na + Tb)/B_2O_3$, it was found that the best phosphors are made with a small excess of B_2O_3 added, *viz.*, with about a molar ratio $(Ca + Na + Tb)/B_2O_3$ of 3.75.

As regards the molar ratio Na/Ca of the $CaNaBO_3$-Tb phosphors, it was found that efficient phosphors can also be made with a large excess of sodium, *e.g.*, with a molar ratio Na/Ca = 1.50. From x-ray diffraction analysis it followed, however, that in these cases, apart from the pure $CaNaBO_3$-Tb phosphor, an unknown second phase is present, probably $NaBO_2$. With decreasing values of the molar ratio Na/Ca a gradual decrease in brightness occurs.

In general, the Sr-containing alkaline earth alkali borates are less efficient than the corresponding Ca compounds under excitation with 250-270 mμ radiation. This is in accordance with the shape of the excitation curves of the Ca- and Sr-alkali borates. Since no attempt was made to determine exactly the optimum chemical composition and firing conditions, it may well be possible to make phosphors that are more efficient than those listed in Table I.

Table I. Efficiencies of terbium-activated alkaline earth alkali borates

r = reflection; η = radiant efficiency; q = quantum efficiency; T = relative brightness at 500°C (brightness at room temperature = 100)

Host lattice	Molar ratio Tb/B_2O_3	Molar ratio Gd/B_2O_3	Excitation 250-270 mμ r (%)	η (%)	q (%)	T
$2CaO \cdot Na_2O \cdot B_2O_3$	0.15	0	21	31	65	80
$1.53CaO \cdot 1.15Na_2O \cdot B_2O_3$	0.15	0	43	16	33	—
$1.40CaO \cdot 1.05Na_2O \cdot B_2O_3$	0.15	0.15	30	20	42	—
$2CaO \cdot Li_2O \cdot B_2O_3$	0.06	0	46	4	7	190
$2CaO \cdot Li_2O \cdot B_2O_3$	0.06	0.06	44	11	22	105
$2CaO \cdot K_2O \cdot B_2O_3$	0.06	0	44	10	21	35
$2CaO \cdot K_2O \cdot B_2O_3$	0.06	0.06	44	8	16	45
$2SrO \cdot Li_2O \cdot B_2O_3$	0.06	0	39	8	17	10
$2SrO \cdot Na_2O \cdot B_2O_3$	0.06	0	62	20	43	10
$2SrO \cdot K_2O \cdot B_2O_3$	0.06	0	37	6	13	60
$2MgO \cdot Na_2O \cdot B_2O_3$	0.06	0	37	17	36	—
$2MgO \cdot Na_2O \cdot B_2O_3$	0.12	0	37	25	53	—
$2MgO \cdot Na_2O \cdot B_2O_3$	0.15	0	36	30	63	—
$2MgO \cdot Na_2O \cdot B_2O_3$	0.24	0	36	19	40	—

Table II. Decay times in milliseconds (1/e — values) Excitation: short wavelength ultraviolet.

Host lattice	Molar ratio Tb/B_2O_3	Molar ratio Gd/B_2O_3	Decay time (ms) at 20°C	at −196°C
$2CaO \cdot Na_2O \cdot B_2O_3$	0.03	0	5	5
$2CaO \cdot Na_2O \cdot B_2O_3$	0.15	0	3.5	3.5
$2CaO \cdot Na_2O \cdot B_2O_3$	0.24	0	3	3
$2CaO \cdot Na_2O \cdot B_2O_3$	0.06	0.06	4	4

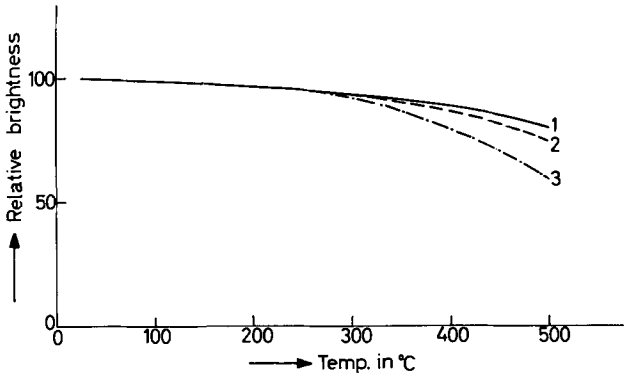

Fig. 6. Variation of brightness with temperature of $2CaO \cdot Na_2O \cdot B_2O_3$-Tb phosphors (with varying Tb concentration). Excitation with germicidal lamp (mainly 254 mμ radiation). The phosphors were twice fired, *viz.*, at 750° and 850°C. Tb/B_2O_3: curve 1, 0.03, 0.12, and 0.15; curve 2, 0.18; curve 3, 0.24.

The radiant efficiency with cathode-ray excitation of some of the phosphors was determined also, in a way described already (10). The highest radiant efficiency, *viz.*, 2.2%, was observed in a sample of $2CaO \cdot Na_2O \cdot B_2O_3$-0.15Tb.

The decay times (*i.e.*, the times in which the intensity of the emission falls to 1/e of the original value) of some of the phosphors prepared are given in Table II. The decay curves were found to be exponential within the accuracy of measurement. At the temperature of liquid nitrogen the decay time is about the same as at room temperature, indicating that the number of radiationless transitions at room temperature is not high.

It may be seen from Fig. 6 and also from the data given in Table I, that the phosphors, like the previously prepared terbium-activated alkaline earth borate phosphors, show a relatively high brightness at elevated temperatures. With a molar ratio $Tb/B_2O_3 = 0.06$, the relative brightness at a certain elevated temperature decreases in the sequence: $CaLiBO_3$-Tb, $CaNaBO_3$-Tb, $CaKBO_3$-Tb. In many cases the phosphors investigated show a stronger absorption of the incident ultraviolet radiation at 500°C than at room temperature. A higher ultraviolet absorption means an increase in brightness, especially for those phosphors having a low ultraviolet absorption at room temperature. This effect may partially explain the increase in brightness at elevated temperatures found for some phosphors.

Acknowledgment

The authors wish to express their thanks to Mr. J. G. Verlijsdonk and Mr. A. A. L. Sleutjes for preparing the phosphors; to Mr. J. A. A. Bertens, Mr. C. D. J. C. de Laat, and Mr. C. J. Loyen for carrying out the measurements of the optical properties of the phosphors investigated, and to Mr. W. Parchen for the x-ray diffraction analysis.

Manuscript received March 15, 1965; revised manuscript received June 22, 1965. This paper was presented at the San Francisco Meeting, May 9-13, 1965.

Any discussion of this paper will appear in a Discussion Section to be published in the June 1966 JOURNAL.

REFERENCES

1. L. G. Van Uitert, *J. Chem. Phys.*, **37**, 981 (1962).
2. W. L. Wanmaker and A. Bril, *Philips Res. Repts.*, **19**, 479 (1964).
3. R. Tomaschek, *Trans. Faraday Soc.*, **35**, 148 (1939).
4. German "Patentamt" "Auslegeschrift" nr. 1.178.965 (1964).

5. L. H. Brixner, *This Journal*, **111**, 690 (1964).
6. H. A. Lehmann and H. Wöckel, *Z. anorg. u allgem. Chem.*, **296**, 199 (1958).
7. A. Bril and W. van Meurs-Hoekstra, *Philips Res. Repts.*, **19**, 296 (1964).
8. A. Bril and W. L. Wanmaker, *This Journal*, **111**, 1363 (1964).
9. M. A. El'Yashevich, "Spectra of the Rare Earths," Vol. 2, p. 528, translated from Russian by United States Atomic Energy Commission, Washington (1961).
10. H. A. Bril in "Luminescence of Organic and Inorganic Materials," p. 479, H. P. Kallman and G. M. Spruch, Editors, John Wiley & Sons, Inc., New York (1962); A. Bril and H. A. Klasens, *Philips Res. Repts.*, **7**, 401 (1952).

Optical Absorption Edges of ZnO and CdS

W. Lehmann

Research Laboratories, Westinghouse Electric Corporation, Pittsburgh, Pennsylvania

The optical absorption edge of n-type InSb has been reported to move to higher quantum energy (*i.e.*, shorter wavelength) with increasing impurity concentration (1). The effect is explained by assumption of an, in k-space, relatively narrow conduction band which fills rapidly with free electrons up to an appreciable height above the bottom of the conduction band. Optical absorption corresponding to an electron transition from the top of the valence band is then possible only into higher, empty conduction band states (2). We observed a qualitatively similar dependence on the impurity concentration of what appeared to be the optical absorption edges of n-type ZnO and n-type CdS.

Measurements so far were restricted to powders. Luminescent or electronic grade ZnO or CdS, respectively, were doped with Al, Ga, or In of various concentrations, prefired in appropriate atmospheres (air for ZnO, H_2S for CdS) to insure well crystallized particles of roughly 10μ mean diameter, and refired in hydrogen gas at relatively low temperatures (700°C for ZnO, 500°C for CdS). The hydrogen reacts slightly with the materials

$$ZnO + H_2 \rightarrow Zn + H_2O$$

$$CdS + H_2 \rightarrow Cd + H_2S$$

so that a slight excess of free Zn or Cd, respectively, remains and the tendency of self-compensation by formation of cation vacancies is reduced. The H_2 firing may also be replaced by firing the powders with a slight excess of the metal in evacuated and sealed quartz tubes with similar results. It is shown by Kröger and co-workers that the n-type conductivity of CdS crystals prepared under such conditions corresponds to approximately one free electron per added impurity atom (3).

Compact but thin (quasi-monoparticle) layers of the powders were stuck with little binder on a piece of aluminum metal and illuminated with the unfiltered light of an incandescent lamp. The light reflected from the samples was passed through a monochromator into a photomultiplier. The readings were normalized on solid $MgCO_3$ (= 100%). Some reflection curves so obtained are shown in Fig. 1 and 2. The reflection remains at a fairly constant, low level at short wavelengths up to a certain point where on it increases rather rapidly. It is estimated from the geometry of the samples that the bulk absorption coefficient of the materials at the "edge" of the absorption curve is in the order of 100 cm^{-1}.

ZnO and CdS crystallize both in the wurtzite structure, and their optical properties are slightly anisotropic. Hence, a determination of the absorption edge on a powder with randomly oriented particles gives only an average between the values corresponding to the directions parallel and perpendicular to the c-axis. This difference is not very large, however. Some values of the optical absorption edge measured by various authors on powders and on single crystals of CdS are collected in Table I.

We observed that the quantum energy corresponding to the optical absorption edge determined as described above increases steadily with increasing impurity concentration up to a certain limit, then on it remains constant. The effect is strong enough in CdS to be noticed on the body color of the sample with the unaided eye. Measured values of the optical absorption edges as functions of the added impurity concentrations are shown in Fig. 3 and 4. They increase up to 2.51 ev at room temperature and to 2.62 ev at 77°K for CdS, and up to 3.33 ev at room temperature and to 3.42 ev at 77°K for ZnO. These values for CdS are higher than any so far reported for CdS (Table

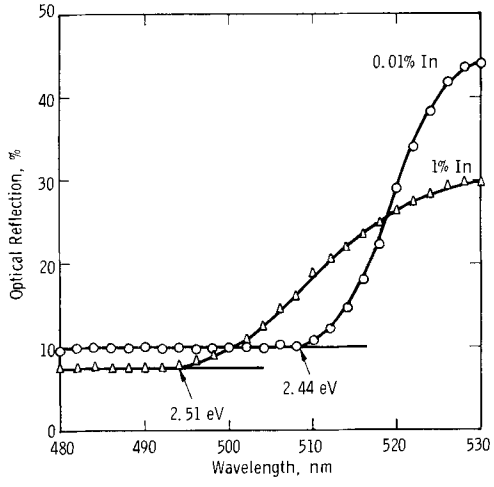

Fig. 1. Spectral reflectance of CdS:In, prefired in H_2S (900°C), refired in H_2 (500°C).

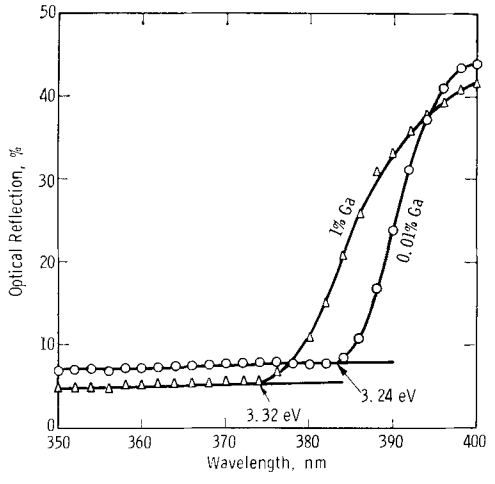

Fig. 2. Spectral reflectance of ZnO:Ga, prefired in air (1200°C), refired in H_2 (700°C).

Table I. Optical absorption edge of hexagonal Cds, in ev

Measured on	at 77°K	at 300°K	Reference
Single crystal	~2.53	~2.40	(4)
Single crystal	~2.53	~2.40	(5)
Single crystal		2.39	(6)
Single crystal*		2.410 + 2.425	(7)
Single crystal*	2.494 + 2.509	2.373 + 2.388	(8)
Powder		2.42	(9)
Powder		2.40	(10)
Powder**	2.54	2.40	

* The two numbers each correspond to the two directions of polarization of the incident light with respect to the crystal orientation.

** Measured in this laboratory on pure CdS fired in H_2S at 1000°C.

I). The situation with ZnO is less clear since considerable controversy exists concerning its optical absorption edge (11). However, most authors agree to a strong onset of absorption of powdered ZnO, at room temperature, in the neighborhood of $\lambda = 385$ nm ($= 3.22$ ev) (12-16).

The variation of the optical absorption edges with the impurity concentrations shown in Fig. 3 and 4 probably can be explained in essentially the same way as proposed by Burstein for InSb (2) with one difference. The density of allowed energy states near the bottom of the conduction band of an ideally perfect crystal clearly is a discontinuous function. However, no crystal is perfect, and any disorder may cause a tailing-off of the density of allowed states below the bottom of the conduction band (17). This tail is probably strong in all conventional II-VI compounds as indicated by the commonly observed exponential (rather than parabolical) dependence of the absorption constant on the quantum energy near the absorption edge (18). Hence, a measured absorption constant in the order of 100 cm^{-1} probably does not correspond to an electron transition into the conduction band but into the tail below the conduction band, and different workers observed different values for the optical absorption "edge" (Table I) because of different degrees of perfectness of their crystals. It appears from Fig. 3 and 4 that increasing n-type conductivity first fills up only the tail below the conduction band, and that the conduction band itself is reached only for high impurity concentrations. Hence, the high energies of the absorption edges, approaching constant values for high impurity concentrations, in Fig. 3 and 4 probably are the true values of the forbidden band gaps of near-perfect ZnO and CdS.

Acknowledgment

The writer wishes to express his thanks to Mr. H. H. Dorman for much good work in preparations and measurements.

Manuscript received July 7, 1965.

Any discussion of this paper will appear in a Discussion Section to be published in the June 1966 JOURNAL.

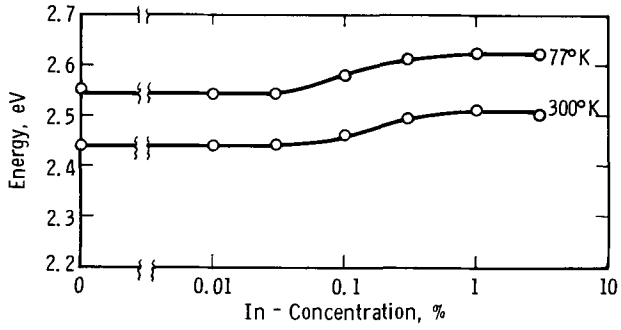

Fig. 3. Variation of the optical absorption edge of CdS:In (H_2, 500°C) as a function of the In concentration.

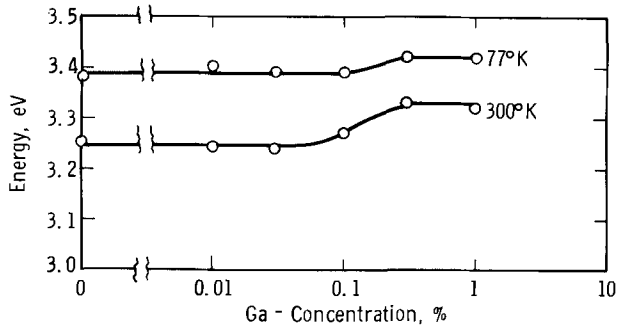

Fig. 4. Variation of the optical absorption edge of ZnO:Ga (H_2, 700°C) as a function of the Ga-concentration.

REFERENCES

1. M. Tanenbaum and H. B. Briggs, *Phys. Rev.*, **91**, 1561 (1953).
2. E. Burstein, *ibid.*, **93**, 632 (1954).
3. F. A. Kröger, H. J. Vink, and J. v. d. Boomgaard, *Z. Phys. Chem.*, **203**, 1 (1954).
4. D. Dutton, *Phys. Rev.*, **112**, 785 (1958).
5. C. Klick, *ibid.*, **89**, 274 (1953).
6. S. J. Czyzak, D. J. Craig, and C. E. McCain, *J. Appl. Phys,*, **23**, 932 (1952).
7. M. Balkanski and R. D. Waldron, *Phys. Rev.*, **112**, 123 (1958).
8. K. W. Böer and H. Gutjahr, *Monatsber. Deutsche Akad. Wissensch.*, **1**, 326 (1959).
9. A. Berton, *Compt. rend.*, **208**, 1898 (1939).
10. F. A. Kröger, *Physica*, **7**, 1 (1940).
11. T. S. Moss, "Optical Properties of Semi-Conductors," p. 203, London (1961).
12. H. Weiss, *Z. Phys.*, **132**, 202 (1952).
13. C. F. Goodeve, *Trans. Faraday Soc.*, **33**, 340 (1937).
14. J. H. Gisolf, *ibid.*, **35**, 170 (1939).
15. M. Luckiesh, *J. Opt. Soc. Am.*, **19**, 1 (1929).
16. E. Mollwo and F. Stöckmann, *Ann. Phys.*, **3**, 223 (1948).
17. R. H. Parmenter, *Phys. Rev.*, **97**, 587 (1955).
18. Ref. (11), p. 38.

Electron Beam Exposure of Photoresists

R. F. M. Thornley and T. Sun

IBM Watson Research Center, Yorktown Heights, New York

The conventional visible or ultraviolet exposure of photoresists is well suited to the parallel exposure of large fields and for resolutions above 3μ. For serial exposures, such as may be required in printed circuit generators, the maximum exposure rates are limited by the sensitivities of presently available resists. For high resolution work, problems of focus adjustment and control of the level of illumination become more critical, making it difficult to carry out routine operations with resist patterns less than 3μ wide. Electron beam exposure can be expected to overcome these problems, at the expense of introducing new ones. The power densities obtainable in electron beams are several orders of magnitude higher than those from conventional optical light sources, permitting exposures to be carried out in well below 1 msec. The diameter

of an electron beam can easily be made less than 0.1μ and the depth of focus for such a beam will be of the order of $\pm 25\mu$. The significant new problems are the need for a high vacuum system and the removal of the resist after etching.

Interaction Mechanism

A negative-working resist is essentially a material which can be caused to polymerize when irradiated with light of a suitable wavelength. The energy of a light quanta is such that it is only able to initiate the polymerization process at certain sensitive points in the resist molecule, and the composition of the resultant polymer is fairly well defined. When an electron, typically with an energy of 20 KeV, enters the resist, the interaction is much less subtle. The electron has so much energy that it opens most of the chemical bonds in its path, permitting a complete reorganization of the molecular structure. Such a process broadens the range of molecular weights in the resist but does not necessarily increase the average molecular weight (1). Experimentally, it is found that the effect of electron exposure is similar to that of light on the negative-working resists. Overexposure with electrons continues the cross linking process and eventually forms a layer which, although a good resist, cannot be stripped after etching in any of the solvents normally used for this operation.

Resist Exposure Characteristics

The resists tested were Kodak Photoresist (KPR), Kodak Metal Etch Resist (KMER), Kodak Ortho Resist (KOR), and Kodak Thin Film Resist (KTFR). The resists were tested on oxidized silicon wafers, coated with an evaporated aluminum layer 1μ thick. Before coating with resist, the wafers were given a 3 min dip in 10% potassium dichromate solution at 65°C to improve the adhesion of the resist to the aluminum surface. The resists were applied, after dilution, by a filter-equipped syringe to the surface of the wafer. KTFR, KOR, and KPR were diluted 1:1 and KMER was diluted 2:1 with the manufacturer's thinner. The wafer was then spun at 7000 rpm for 3 min, producing film thicknesses in the range 1500 to 2500Å. The wafer was then inserted into the vacuum system and pumped down to 10^{-6} Torr, completing the drying process. Prebaking at 45° for 10 min before exposure did not change the sensitivity characteristics.

Exposures were made at 14 and 20 kv using a 1μ diameter beam carrying 1.29 x 10^{-9} amp, which was scanned to cover a 5 x 20 mil area in 50 mS, the line

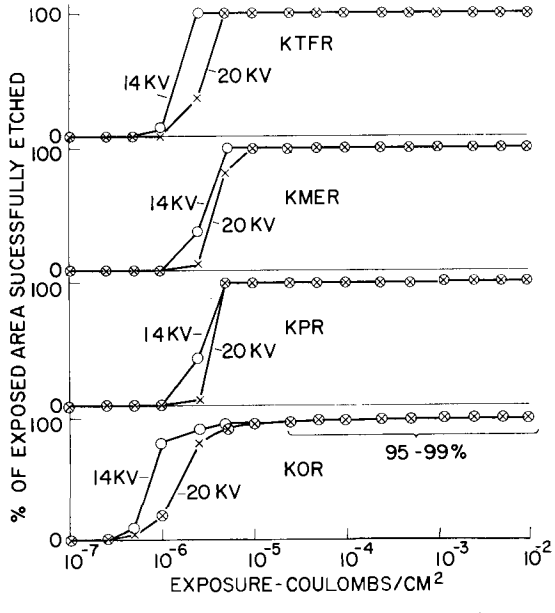

Fig. 1. Exposure characteristics at 14 and 20 kv

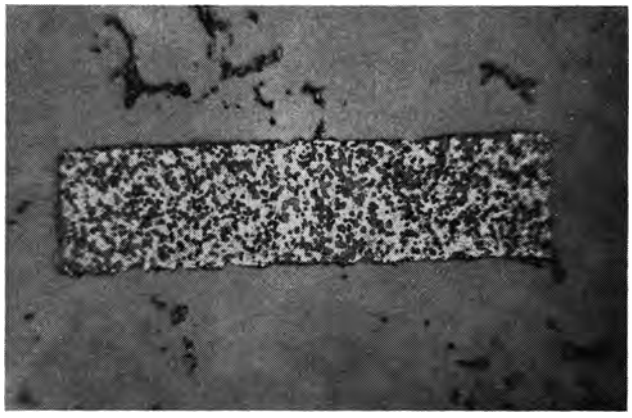

Fig. 2. Pinhole formation in KOR sample exposed with 10^{-5} coulombs/cm^2 at 20 kv.

frequency being adjusted to prevent the scan lines from being resolved. Variations in exposure over a 1000:1 range were achieved by repeated scanning over the same area. A further factor of 100 in range was obtained by increasing the beam current to 1.29 x 10^{-7} amp in a slightly larger beam diameter.

After exposure, the resists were developed, KPR and KOR with the manufacturer's developers, KMER and KTFR with a mixture of three parts toluene, three parts xylene, and one part benzene by volume. The patterns were photographed, baked at 130°C for 30 min, and etched in 20% NaOH at 65°C. No change was found between the areas of the resist patterns of KTFR, KMER, and KPR after development and the areas of the etched aluminum patterns. With KOR, etching revealed the existence of numerous pinholes in the resist image (Fig. 2). The efficiency of resist formation as a function of charge density for 14 and 20 kv electrons is given in Fig. 1. It can be seen that for KTFR, KMER, and KPR, the characteristics are substantially identical, the sensitivities at 20 kv being about 25% less than 14 kv. This is expected since electrons of both energies pass completely through the resist layer and the energy loss/unit length is less for the higher energy beam.

The KOR is about five times more sensitive than the other materials but does not form a satisfactory resist, even with very high exposures. The failure is ten-

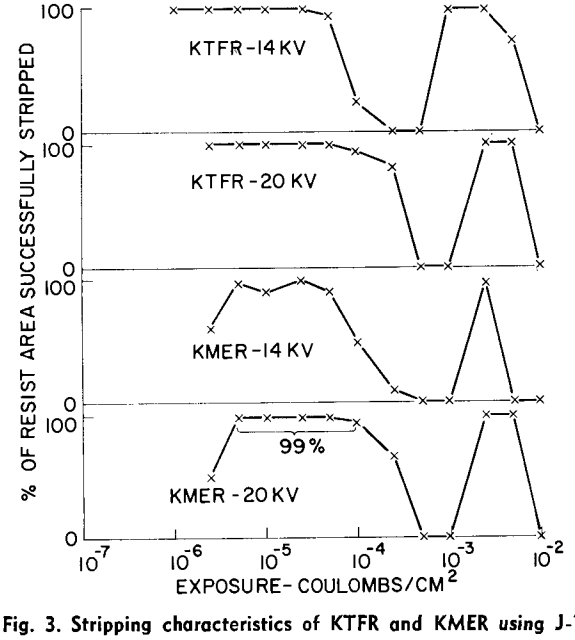

Fig. 3. Stripping characteristics of KTFR and KMER using J-100 at 90° for 4 min.

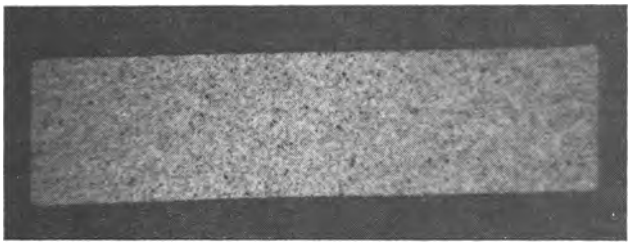

Fig. 4. KTFR exposure, using 10^{-5} coulombs/cm^2 at 20 kv, after etching and stripping.

tatively attributed to the formation of minute bubbles of gas during exposure.

Stripping Characteristics

In most resist operations, the resist must be removed after etching. A very wide variety of solvent mixtures are used for this operation. To restrict the range to be investigated, stripping was attempted for each resist using solvent mixtures that were known to be satisfactory for the same resist exposed with ultraviolet light.

The results for KTFR and KMER, using the commercial stripping solution J-100[1] are shown in Fig. 3. KOR did not strip using a mixture containing 80% trichlorethylene and 20% Stripper 77[2] for 30 min at 70°C. KPR stripped successfully using chromic acid but the aluminum was also attacked, raising doubts as to whether the resist was dissolved off or simply released by the removal of the aluminum. An optimally exposed, etched, and stripped KTFR sample is shown in Fig. 4.

An unexpected feature of the stripping characteristics was the existence of a second area between 10^{-3} and 10^{-2} coulombs/cm^2 for which stripping was possible. The possibility that the effect is due to thermally induced changes during exposure was eliminated by repeating the exposure tests with the beam current reduced by two orders of magnitude. No change was observed.

[1] Litho Aluminum Product Co., Chicago, Illinois.
[2] Shipley Co., Wellesley, Massachusetts.

Exposure Rates

The exposure of any of the resists considered requires the specimen to absorb about 0.1 joules/cm^2. Since this quantity of energy cannot be confined to the irradiated volume without causing an excessive temperature rise, the exposure rate must be low enough to permit most of this energy to diffuse away. For thick (approximating to semi-infinite) substrates, this rate is set by the thermal diffusivity of the substrate and varies from about 10^{-3} for glass or methacrylate plastics up to about 1 cm^2/°C/sec for copper. Experimentally, satisfactory exposures have been made on 0.005 in. thick silicon wafers in 0.25 mS. No upper limit for the exposure rate was reached with the available equipment and silicon wafers.

Conclusions

For applications, requiring high speed, high resolution exposure of resist patterns, electron beams can be usefully employed. There is a range of approximately 10:1 using KTFR for which the resist formation and stripping characteristics are both excellent.

Manuscript received May 10, 1965; revised manuscript received July 7, 1965.

Any discussion of this paper will appear in a Discussion Section to be published in the June 1966 JOURNAL.

REFERENCE

1. R. M. Black and E. H. Reynolds, *Proc. IEE*, **112**, 1226 (1965).

Vapor Phase Equilibria in the Gallium-Chlorine and Gallium Arsenide-Chlorine Systems

M. A. Zuegel

Systems Development Division, International Business Machines Corporation, Boeblingen, Germany

In the vapor growth process, layers are formed by chemical reaction between the substrate and a gas phase which contains compounds of the material deposited on the substrate. The events occurring at the substrate result from the tendency of this reaction toward the establishment of thermodynamic equilibrium. For the process to be practical, the equilibrium conditions must be known.

The importance of III-V compounds, especially of gallium arsenide in the modern technology of semiconductors, was the reason for an experimental investigation of the equilibrium composition in the gallium arsenide-chlorine system. Chlorine, elemental or in form of the compound HCl, is often used as a transporting agent in the vapor growth process of gallium arsenide. To check the stability of the various gallium chlorides at the conditions of the process the gallium-chlorine system was also investigated. The corresponding iodine systems were the object of an earlier study by Lyons and Silvestri (1). A theoretical treatment of the chlorine systems by Fergusson and Gabor (2) makes a comparison of the experimental results with theoretical data possible.

Experimental

The experimental procedure was the same as that used by Lyons and Silvestri (1). The total pressure (P_t) in a sealed quartz ampoule filled with a known amount of chlorine and excess gallium or gallium arsenide, respectively, was measured as a function of temperature.

Figure 1 shows the apparatus used for the experiments. The arrangement of a quartz ampoule prepared for the run is shown in Fig. 2.

The pressure in the reaction vessels was measured with Bodenstein manometers. These manometers (Heraeus Quarzschmelze, Hanau, Germany) are made from a very thin-walled, flat quartz tubing by coiling them into helical spirals. Differences of pressure between the inside of the spirals and the surrounding atmosphere cause a twisting of the spirals from their equilibrium positions. Distortions of the spirals are completely reversible, if they do not become too large and if stresses in the spirals have been removed by annealing at 1000°C. The twisting of the spirals is made visible by a light beam projected on to a scale via a small mirror mounted at the indicator end of the spirals. If a pressure difference causes a distortion of such a spiral, the light mark can be reset to the zero point of the scale by adjusting the pressure surrounding the spiral. This pressure was measured with precision manometers (Wallace & Tiernan, Belleville, New Jersey). With spirals of normal sensitivity, the measuring arrangement permits a clear resolution of pressure differences down to 0.1 mm Hg. To protect the very fragile quartz spirals from glass splinters, a frit was melted into the capillary tubing connecting the reaction vessel and quartz manometer.

In preparing the runs, the reaction vessel was loaded with a quartz hammer and an ampoule which had been sealed in high vacuum after filling it with gallium (99.99%) or gallium arsenide (high resistivity, uncom-

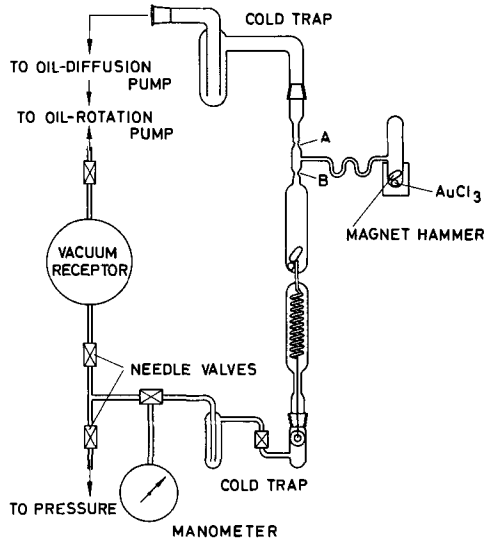

Fig. 1. Apparatus used for the experiments

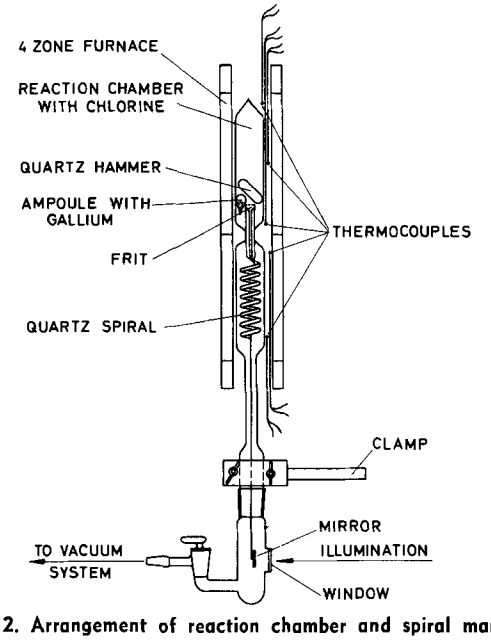

Fig. 2. Arrangement of reaction chamber and spiral manometer in the furnace.

pensated material). The reaction vessel, spiral manometer, and the part of the apparatus in which chlorine was generated were evacuated to 10^{-6} mm Hg, and where possible heated with a torch. The apparatus was sealed at point A, and chlorine was generated by thermal decomposition of gold trichloride ($AuCl_3$) at 250°C. The approximate desired quantity of chlorine was led into the reaction chamber which was then sealed at point B.

For the determination of the initial chlorine concentration, $\frac{n_{Cl}}{V}$, the reaction vessel was placed upside down in a water bath of known temperature, and the pressure in the vessel was determined. The initial chlorine concentration was calculated from the measured pressure and temperature using the ideal gas law.

The small ampoule containing gallium or gallium arsenide was then broken with the quartz hammer by tilting the reaction vessel. Finally, a four-zone furnace was positioned over the reaction vessel and spiral manometer. The voltages of the Pt-Pt/Rh (10%) thermocouples checking the temperatures at the positions shown in Fig. 2 were measured with a L & N millivolt potentiometer.

To prevent a deposition of condensed substances in the spirals, the temperature of the spiral was always

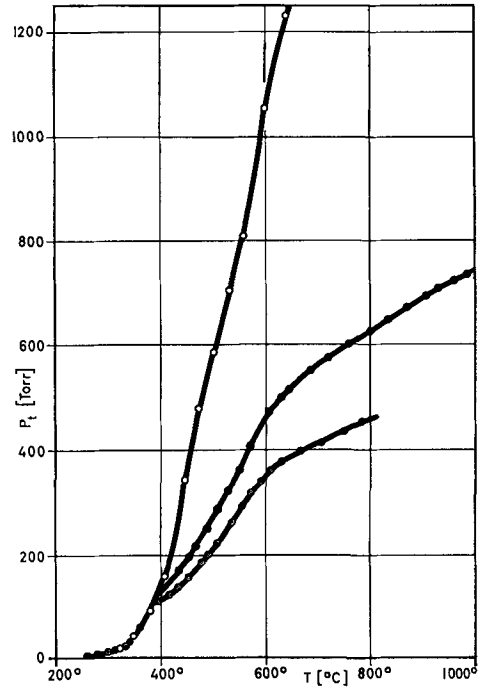

Fig. 3. Gallium-chlorine system: total pressure P_t as a function of temperature for three runs with different initial chlorine concentrations $\frac{n_{Cl}}{V}$

⊙, Run 1, $\frac{n_{Cl}}{V} = 6.92 \times 10^{-3}$ g-at. of Cl/liter

•, Run 2, $\frac{n_{Cl}}{V} = 9.60 \times 10^{-3}$ g-at. of Cl/liter

○, Run 3, $\frac{n_{Cl}}{V} = 2.44 \times 10^{-2}$ g-at. of Cl/liter

kept a few degrees higher than that of the reaction vessel. In most cases, the pressure was measured in the direction of increasing temperature. Since the same pressure values were obtained with decreasing temperatures, this indicates that thermodynamic equilibrium was established during the pressure reading.

Results and Discussion

The gallium-chlorine system.—The reaction between chlorine and gallium occurs at approximately room temperature. A white crystalline material forms with a strong evolution of heat. At 170°C, the crystals melt to a colorless liquid with a high refractive index.

Figure 3 shows the pressure in the reaction chamber as a function of temperature for three runs with different initial chlorine concentrations.

Up to about 400°C the pressure is independent of the chlorine concentration and depends only on temperature. In this range the gallium-chloride system is univariant, and, since it is composed of two components, gallium and chlorine, it consists of three phases, two condensed phases, gallium and a gallium-chlorine compound, and the gas phase. In this temperature range, the pressure in the vessel corresponds to the equilibrium pressure between gallium dichloride and its vapor as measured by Laubengayer and Schirmer (3). Since the physical properties of the compound aforementioned agree with those of gallium dichloride [see ref. (3)], this indicates that chlorine reacts with excess gallium at low temperatures to form gallium dichloride.

At about 400°C, a kink in the pressure curves can be observed. It corresponds to the dew point of gallium dichloride and shifts, as expected, to higher temperatures with increasing initial chlorine concentration. Above the kink the system is divariant and consists of only two phases, a condensed phase of liquid gallium and the gas phase.

From 400° to approximately 600°C, the molar concentration of the gas phase increases with tempera-

ture. An indication of the reaction occurring in this temperature range may be obtained by comparing the molar concentration of the gas phase with the initial chlorine concentration at the kinks of the curves and at high temperatures. At the temperature of the kinks, the molar concentration is only a little higher than one-third of the initial chlorine concentration. Here gallium trichloride ($GaCl_3$) seems to be the predominant vapor species. With increasing temperature, the concentration of the gas phase approaches the initial chlorine concentration indicating the formation of gallium monochloride (GaCl), and it remains constant at temperatures higher than approximately 650°C.

The chlorides, $GaCl_3$ and GaCl, correspond to the iodides, GaI_3 and GaI, as found by Lyons and Silvestri (1) in the gallium-iodine system. In accordance with the gallium-iodine system, the reaction proposed for the gallium-chlorine system is

$$2Ga(l) + GaCl_3(v) \rightleftharpoons 3GaCl(v) \qquad [1]$$

With the pressure data measured above the kinks, the corresponding equilibrium constant

$$K_P(\text{atm}^2) = \frac{p^3_{GaCl}}{p_{GaCl_3}} \qquad [2]$$

was calculated. The partial pressures of GaCl and $GaCl_3$ expressed in terms of total pressure P_t and initial chlorine concentration $\frac{n_{Cl}}{V}$ are

$$p_{GaCl} = \frac{1}{2}\left(3P_t - \frac{n_{Cl}}{V} \cdot RT\right)$$

$$\text{and } p_{GaCl_3} = P_t - p_{GaCl} \qquad [3]$$

The plot $\log K_p$ *vs.* $1/T$ for the three runs of Fig. 3 is shown in Fig. 4. Since the equilibrium constant proves to be independent of the initial chlorine concentration the validity of Eq. [1] is confirmed experimentally.

From the slope of Fig. 4, the enthalpy of reaction was calculated and found to be $\Delta H = 54.2$ kcal/mole.

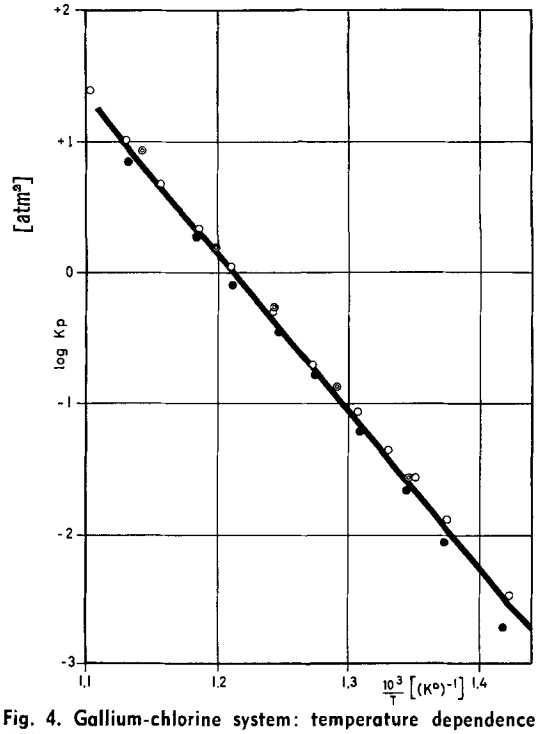

Fig. 4. Gallium-chlorine system: temperature dependence of the equilibrium constant.

○, Run 1, $\frac{n_{Cl}}{V} = 6.92 \times 10^{-3}$ g-at. of Cl/liter

●, Run 2, $\frac{n_{Cl}}{V} = 9.60 \times 10^{-3}$ g-at. of Cl/liter

◉, Run 3, $\frac{n_{Cl}}{V} = 2.44 \times 10^{-2}$ g-at. of Cl/liter

This value is in good agreement with a theoretical value of $\Delta H = 48.9$ kcal/mole (mean value for the temperature range of Fig. 4) calculated with the aid of the heats of formation of GaCl and $GaCl_3$ (2). The temperature dependence of the equilibrium constant for Eq. [1] can be described by the equation

$$\log K_p\ (\text{atm}^2) = -\frac{1.19 \cdot 10^4}{T} + 14.42 \qquad [4]$$

valid between 420° and 630°C.

In the calculation of the partial pressures of the gallium chlorides, the dimerization of $GaCl_3$ was not considered. As can be shown with the data of Fischer and Jubermann (4), Ga_2Cl_6 is almost completely dissociated in the temperature and pressure range of the measurements, and in the most unfavorable case, the Ga_2Cl_6 contents is not higher than a few per cent.

The gallium arsenide-chlorine system.—Chlorine reacts with gallium arsenide already at room temperature. Cooling the top part of the reaction vessel with liquid nitrogen condenses the product of reaction as a colorless liquid which flows down the walls of the vessel and solidifies. Since the substance has a higher vapor pressure than the gallium chlorides, it is presumed to be arsenic trichloride ($AsCl_3$) or more likely a mixture of $AsCl_3$ with gallium di- or trichloride. The pressure curves of four runs with different initial chlorine concentrations are shown in Fig. 5.

At low temperatures, the system is univariant and the pressure is defined by a vaporization equilibrium, probably, of the rather volatile $AsCl_3$. After the complete evaporation of this substance, the slope of the curves decreases suddenly. From the plot dips up to approximately 300°C, the molar concentration of the gas phase increases steadily. At around 300°C, an irreversible reaction takes place indicated by a sudden

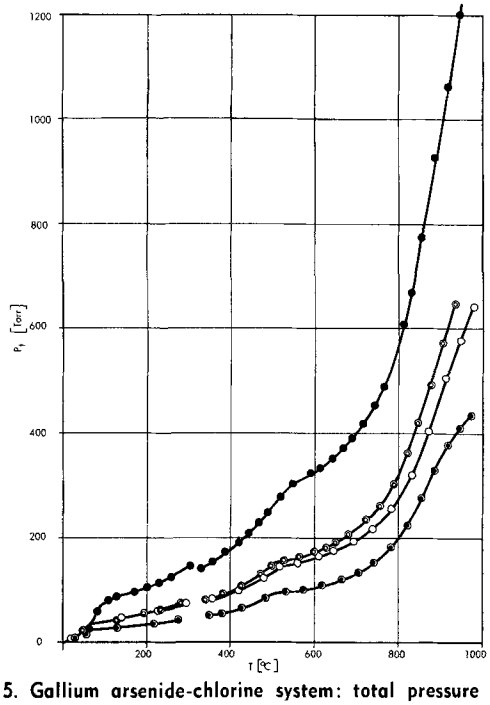

Fig. 5. Gallium arsenide-chlorine system: total pressure P_t as a function of temperature for four runs with different initial chlorine concentrations.

◉, Run 1, $\frac{n_{Cl}}{V} = 4.32 \times 10^{-3}$ g-at. of Cl/liter

◎, Run 2, $\frac{n_{Cl}}{V} = 7.18 \times 10^{-3}$ g-at. of Cl/liter

●, Run 3, $\frac{n_{Cl}}{V} = 1.41 \times 10^{-2}$ g-at. of Cl/liter

○, Run 4, $\frac{n_{Cl}}{V} = 7.03 \times 10^{-3}$ g-at. of Cl/liter

pressure change. Perhaps $AsCl_3$ reacts here with GaAs forming arsenic and gallium trichloride, and the dimerization of $GaCl_3$ causes the observed drop of pressure. The pressure then increases continuously up to the second kinks of the curves at approximately 500°C. The pressure measured here equals that calculated from the ideal gas law, *if* a quantitative formation of completely evaporated $GaCl_3$ and As_4 from the available amount of chlorine is assumed according to the equation

$$2GaAs + 3Cl_2 \rightarrow 2GaCl_3 + \frac{1}{2}As_4 \qquad [5]$$

A further rise of temperature increases the molar concentration of the gas phase more strongly than can be explained by the beginning dissociation of tetrameric arsenic (As_4) into dimeric arsenic (As_2). Therefore, a reaction of the gas phase with unreacted GaAs must be taking place which increases the concentration of the gas phase.

As in the gallium-chlorine system, the pressure at sufficiently high temperatures is the same as would be expected from a quantitative reaction between chlorine and gallium arsenide with formation of only gallium monochloride and arsenic, the latter being partially dissociated. The temperature dependence of the equilibrium constant for the arsenic dissociation is tabulated by Stull and Sinke (5) and obeys the equation

$$\log K_p(\text{Torr}) = \log\left(\frac{p^2_{As_2}}{p_{As_4}}\right) = -\frac{1.31 \cdot 10^4}{T} + 10.99 \qquad [6]$$

From these observations it is likely that the formation of GaCl at temperatures above 500°C is due to a reaction between GaAs and $GaCl_3$ according to the equation

$$2GaAs(s) + GaCl_3(v) \rightleftharpoons 3GaCl(v) + \frac{1}{2}As_4(v) \qquad [7]$$
$$\Updownarrow$$
$$As_2(v)$$

Equation [7] corresponds to the reaction found by Lyons and Silvestri (1) in the gallium arsenide-iodine system.

The partial pressures of the vapor species necessary for the calculation of the equilibrium constant for Eq. [7]

$$K_p = \frac{p^3_{GaCl} \cdot p^{1/2}_{As_4}}{p_{GaCl_3}} \qquad [8]$$

are expressed in terms of total pressure P_t and initial chlorine concentration $\frac{n_{Cl}}{V}$ and dissociation constant for arsenic K_pAs

$$p_{As_4}(\text{Torr}) = 0.2P_t + 0.18K_{pAs} - [(0.2P_t + 0.18K_{pAs})^2 - 0.04P_t^2]^{1/2} \qquad [9a]$$

$$p_{GaCl_3}(\text{Torr}) = \frac{1}{2}\left(\frac{n_{Cl}}{V} \cdot RT - P_{As} - P_t\right), \quad \text{with } P_{As} = p_{As_4} + p_{As_2} \qquad [9b]$$

$$p_{GaCl}(\text{Torr}) = P_t - P_{As} - p_{GaCl_3} \qquad [9c]$$

The partial pressures p_{As_4}, p_{As_2}, p_{GaCl_3}, and p_{GaCl} and the corresponding K_p values were calculated by an IBM 1401 computer using the P_t values measured above the second dips of Fig. 5.

The temperature dependence of the equilibrium constant for the proposed Eq. [7] for four runs with different initial chlorine concentrations is shown in Fig. 6.

Although the temperature dependence of the reaction enthalpy ΔH should be very small in Eq. [7] as calculated from the data of ref. (2) (ΔH 600°C = 104.1 kcal/mole, ΔH 1000°C = 101.4 kcal/mole), the slope of the plot log K_p *vs.* $1/T$ is not even roughly constant for the runs 1-3 of Fig. 6. During these runs dry air or nitrogen was used for the counterpressure. At the high temperatures of the measurements, fused quartz becomes noticeably permeable to the above gases. The permeability of fused quartz for several gases has been measured by Johnson and Burt (6) and Barrer (7).

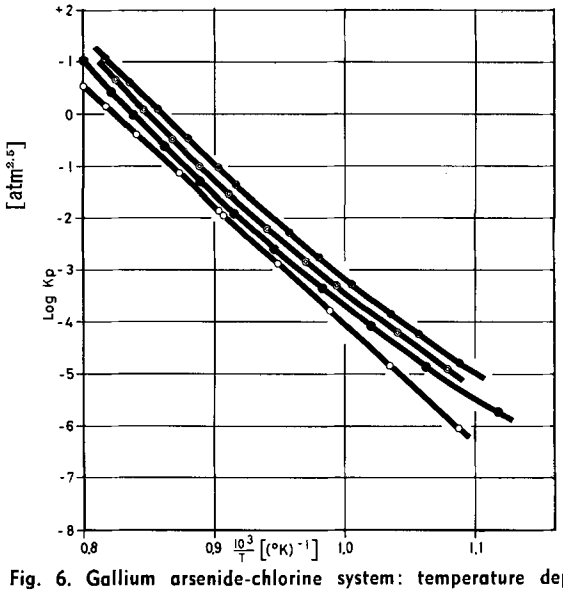

Fig. 6. Gallium arsenide-chlorine system: temperature dependence of the equilibrium constant.

⊙, Run 1, $\frac{n_{Cl}}{V}$ = 4.32 x 10^{-3} g-at. of Cl/liter

⊙, Run 2, $\frac{n_{Cl}}{V}$ = 7.18 x 10^{-3} g-at. of Cl/liter

●, Run 3, $\frac{n_{Cl}}{V}$ = 1.41 x 10^{-2} g-at. of Cl/liter

○, Run 4, $\frac{n_{Cl}}{V}$ = 7.03 x 10^{-3} g-at. of Cl/liter

The value for nitrogen at 900°C, *e.g.*, is about 10^{-10} cm^3/sec of nitrogen gas at normal pressure and temperature related to a sample area of 1 cm^2, a sample thickness of 1 mm, and a pressure difference of 1 Torr across the sample. Thus, with a pressure difference of about 1 atm, with the dimensions of the reaction chamber and the very thin-walled quartz spiral, approximately 0.2 cm^3 of nitrogen would diffuse per hour into the reaction chamber at 900°C. The permeability of quartz glass for air will be approximately the same since its mean molecular weight is similar. The diffused-in gases can react with the contents of the reaction chamber and thereby affect the pressure of the system. In such a case, the pressure will not be due only to the reacting species, $GaCl_3$, GaCl, As_4 and As_2, as has been assumed for the calculation of the equilibrium constant.

During run 4, for which the slope in Fig. 6 is constant in an extended temperature range, argon (99.9%) was used for compensating the deflections of the spiral. The permeability of quartz glass for argon is much smaller, approximately 5 × 10^{-12} cm^3/sec at 900°C. Besides this advantage, argon does not react with the contents of the reaction chamber, so that its effect on the pressure is only an additional partial pressure which can be subtracted from the measured total pressure. The obtained corrected pressure arises then only from the participants of Eq. [7]. As another precaution, the walls of the reaction chamber were made thick for run 4 to keep the penetration of air into the system as small as possible. The amount of diffused-in argon was determined by measuring the pressure in the reaction vessel at a temperature at which the partial pressures of the other constituents are negligibly small. After run 4, the partial pressure of argon was 1.6 Torr at room temperature. Considering the much higher diffusivity of nitrogen or air, it is obvious that no reliable measurements could be made with air or nitrogen as compensating medium.

From the slope of run 4 in Fig. 6, the enthalpy of Eq. [7] was calculated and found to be $\Delta H = 104$ kcal/mole. The temperature dependence of the equilibrium constant for Eq. [7] can be described with the following equation

$$\log K_p\ (\text{atm}^{2.5}) = \frac{-2.28 \cdot 10^4}{T} + 18.79 \qquad [10]$$

which is valid between 640° and 980°C.

Conclusions

The reactions establishing the thermodynamic equilibrium in the gallium-chlorine and gallium arsenide-chlorine systems and the temperature dependence of the corresponding equilibrium constants can be described by the following equations:

Gallium-chlorine system

$$2\text{Ga(l)} + \text{GaCl}_3\text{(v)} \rightleftharpoons 3\text{GaCl(v)} \qquad [1]$$

$$\log K_p\ (\text{atm}^2) = -\frac{1.19 \cdot 10^4}{T} + 14.42 \qquad [5]$$

valid between 420° and 630°C. Gallium arsenide-chlorine system

$$2\text{GaAs(s)} + \text{GaCl}_3\text{(v)} \rightleftharpoons 3\text{GaCl(v)} + \frac{1}{2}\text{As}_4\text{(v)} \qquad [7]$$

$$\Updownarrow$$

$$\text{As}_2\text{(v)}$$

$$\log K_p\ (\text{atm}^{2.5}) = -\frac{2.28 \cdot 10^4}{T} + 18.79 \qquad [10]$$

valid between 640° and 980°C. The mean reaction enthalpy for Eq. [1] or [7] in the above temperature ranges is 54.2 or 104 kcal/mole, respectively.

Acknowledgments

The author wishes to thank Doctors W. Kappallo, M. Michelitsch, and G. Hellbardt for helpful discussions and Miss G. Fritsche for her assistance during the experiments.

Manuscript received Feb. 3, 1964; revised manuscript received July 20, 1965.

Any discussion of this paper will appear in a Discussion Section to be published in the June 1966 JOURNAL.

REFERENCES

1. V. J. Lyons and V. J. Silvestri, *This Journal*, **109**, 963 (1962).
2. R. R. Fergusson and T. Gabor, *ibid.*, **111**, 585 (1964).
3. A. W. Laubengayer and F. B. Schirmer, *J. Am. Chem. Soc.*, **62**, 1578 (1940).
4. W. Fischer and O. Jubermann, *Z. anorg. u. allgem. Chem.*, **227**, 227 (1936).
5. D. R. Stull and G. C. Sinke, "Thermodynamic Properties of the Elements," Advances in Chemistry Series, No. 8, p. 44 (1956).
6. J. B. Johnson and R. C. Burt, *J. Opt. Soc. Amer.*, **6**, 734 (1922).
7. R. M. Barrer, "Diffusion in and through Solids," p. 135, Cambridge (1941).

The Voltage Sweep Method

Electronic Device for Producing Triangle Pulses and Ramps

F. G. Will

Research and Development Center, General Electric Company, Schenectady, New York

Voltage Sweep Method and Its Application

The application of a voltage that changes slowly and linearly with time is well known in polarography (1) and serves to determine the concentration of some oxidizable or reducible species in electrolytes. The linearly varying voltage is usually produced by a motor-operated potentiometer. In oscillographic polarography, periodic sawtooth (2-4) or triangular voltages (5) of much faster rise time are applied to increase the sensitivity of the concentration measurement.

Later, a similar method of applying periodic triangular voltages by means of a potentiostat was introduced (6) to the study of adsorption phenomena and reaction kinetics on solid electrodes. An electronic triangle voltage generator is required to produce the large range of voltage amplitudes and sweep rates that are desired for this purpose. Furthermore, a potentiostat is required to ensure proper control of the potential between the test electrode and an unpolarized reference electrode while the current flows through the test electrode and a counter electrode. In cases where a fixed sweep rate is sufficient and where the currents are small, a conventional polarograph may be used (7,8.)

Originally, the method was applied to measure accurately the amounts of hydrogen and oxygen that are chemisorbed on platinum (9) and other noble metal electrodes (10). Later, the heat of adsorption of hydrogen on polycrystalline platinum (11) and on single crystal platinum (12) was determined by this method. Under the names surface coulometry, cyclic voltammetry, and potentiodynamic method, the voltage sweep method has been used extensively in past years to study the adsorption and oxidation of organic molecules on noble metal electrodes. Examples are investigations on methanol (13-16), formic acid (14-19), and on a number of other organic molecules (15,20). The method has also been used to study the adsorption of carbon monoxide (21) and halide ions (22) on platinum. Recently, an attempt was made (23) to develop a theory that would allow the determination of kinetic parameters with the voltage sweep method.

Application of Periodic Waves vs. Single Pulses

One of the advantages in the study of adsorption phenomena by applying a periodic triangular voltage lies in the periodic removal of impurities ("activation") from the electrode surface (9). This is similar but not equivalent to the periodic renewal of the electrode surface in the case of the dropping mercury electrode. Unfortunately, however, the application of a periodic voltage changes the state of the electrode surface, for example, its roughness (9). In many cases this may not be disturbing as long as the extent of the changing surface roughness is known. In studies of the effect of the surface structure of the electrode on adsorption phenomena, however, the changing surface state is quite undesired. This problem is pointed out in a recent study of hydrogen adsorption on different platinum single crystal faces (12).

In investigations of this kind it is desirable to apply single triangular voltage pulses or ramps that start from controlled d-c voltage levels. In cases where one likes to study the reduction of some adsorbed species immediately following its oxidation, a triangular pulse is applied. In other cases it is preferable either to reduce or oxidize some species and then to wait until a new steady state is obtained. Here, the application of a

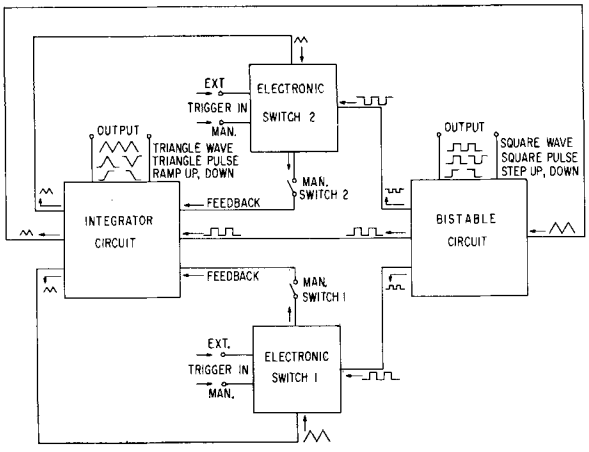

Fig. 1. Block diagram of bistable circuit, integrator circuit, and electronic switches.

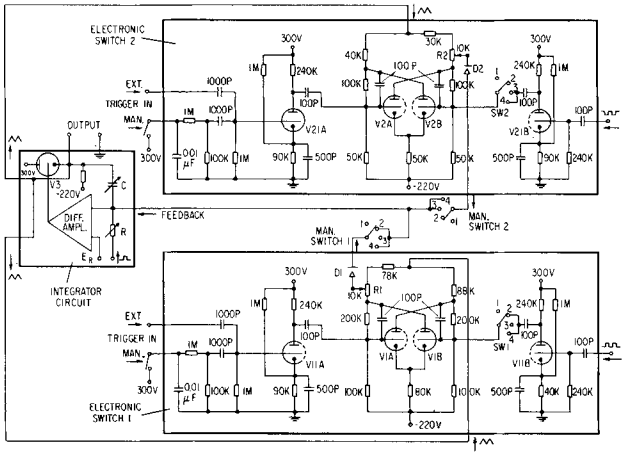

Fig. 2. Circuit diagram of electronic switches in conjunction with integrator circuit. V1, V2, V11, V21 = 12 AX 7; D1, D2 = 1N459.

ramp is required that leads from one controlled d-c voltage level to another. A commercial device[1] is available that produces triangular and sawtooth waves and pulses. However, the d-c level from which these pulses start is not controlled, nor does this instrument produce ramps. In the following, an electronic device is described that is capable of producing triangular pulses, ramps, square pulses, and steps from periodic triangular and square waves. The periodic waves have to be provided by a customary bistable circuit and integrator circuit.

Basic Function of the Electronic Device

Figure 1 shows a block diagram of the new device, consisting of the electronic switches 1 and 2, in conjunction with the bistable circuit and the integrator circuit. The basic operation of the whole instrument is as follows. With both manual switches 1 and 2 open, electronic switches 1 and 2 are also open, and the device produces periodic triangular and square waves in the usual way. The square wave that is produced in the bistable circuit is integrated in the integrator circuit to produce the triangular wave. The triangular wave, in turn, triggers the bistable circuit every time the voltage reaches a predetermined lower and upper voltage reference level. These two voltage levels constitute the positive and the negative turning point of the triangular wave.

With manual switch 1 closed, the electronic switch 1 remains open until the triangle reaches its next negative turning point (lower voltage level). At this point, a negative pulse is produced that closes the electronic switch and stops the triangle. The lower voltage level is controlled by strong negative feedback from the output of the integrator to its input. If a manual or external trigger signal is applied, the electronic switch opens and a single triangular pulse is produced. At the negative turning point, the switch closes again and the voltage is kept at the lower reference level. Concurrently with the triangular pulse, a single square pulse is obtained.

The operation of electronic switch 2 is equivalent to that of switch 1. With manual switch 1 open and 2 closed, the upper voltage level is controlled, and downward triangle and square pulses can be generated by opening electronic switch 2 with a manual or external trigger signal. An internal trigger signal at the positive turning point of the triangle closes electronic switch 2 again and stops the triangle.

With both manual switches closed, electronic switch 1 is always closed when electronic switch 2 is open and conversely. In the former case, the lower voltage level is controlled. When a manual or external trigger signal is applied to electronic switch 1, an upward ramp is generated. During the duration of the ramp, both electronic switches are open until a negative trigger signal is produced at the positive turning point of the triangle that closes electronic switch 2 and causes the upper voltage level to be controlled. In this state, therefore, electronic switch 1 is open and 2 closed. A trigger signal applied to electronic switch 2 opens this switch, too, and a downward ramp is generated. The internal trigger signal that occurs when the ramp voltage reaches the lower reference level closes electronic switch 1 again and results in the control of this voltage level. Concurrently with the upward and downward ramp, at the output of the integrator circuit, an upward and downward step occurs at the output of the bistable circuit.

[1] Exact Electronics function generator.

Description and Operation of the Circuit

Figure 2 shows a circuit diagram of the two electronic switches in conjunction with the integrator circuit. The main part of electronic switch 1 is a bistable circuit V1A/V1B and a diode D1. The manual switches 1 and 2, and SW1 and SW2 are ganged. With these switches in position 1, the bistable circuits are just an additional cathode load to V3 of the integrator circuit, and a periodic triangle wave appears at the output. With the switch in position 2, the bistable circuit 2 continues to be inactive. However, electronic switch 1 becomes closed as soon as the triangle reaches its first negative turning point. At this point, V11B, which is usually nonconducting, becomes momentarily conducting by virtue of the positive flank of the square pulse applied to its grid. The negative pulse that occurs at the plate of V11B makes V1B, which was hitherto conducting, nonconducting. The plate voltage of V1B rises to such a value that the diode D1 becomes conducting, and strong negative feedback is applied from the cathode of V3 to the input of the differential amplifier. In fact, the integrator circuit now operates as a regulated power supply. The magnitude of the controlled d-c voltage that appears at the output depends on the setting of the potentiometer R1 and the magnitude of the reference voltage E_R. If the manual trigger is operated or if a positive trigger signal of at least 30v is applied to the trigger input, V11A becomes momentarily conducting. Hence, V1A becomes nonconducting and V1B conducting. The plate voltage of V1B drops and the diode D1 becomes nonconducting. Consequently, the integrator circuit generates a linearly increasing voltage. The voltage at the plate of V1B has to stay at such a low value that D1 remains nonconducting even at the positive turning point of the triangle pulse. It is only at the negative turning point of the triangle that V11B produces a negative pulse that makes V1B nonconducting and D1 conducting again and, hence, stops the linearly decreasing voltage.

With the switches in position 3, electronic switch 1 becomes inactive and electronic switch 2 functions in an equivalent manner as described for switch 1. The upper voltage level is now being controlled, and a trigger signal produces a downward triangle pulse. The grid of V21B receives the positive flank of the square wave at the positive turning point of the triangle, at which point the triangular sweep is stopped.

With the switches in position 4, both electronic switches are active. A trigger signal applied to electronic switch 2 makes the diode 2 nonconducting. Hence, the voltage at the output decreases from the upper voltage level linearly with time until it reaches the lower voltage level. At this point, the diode 1 becomes conducting and the voltage stops decreasing. A downward voltage ramp has been produced. Accordingly, a trigger signal applied to electronic switch 1 produces an upward ramp.

Conclusions

The electronic device that has been described here broadens the range of applicability for the voltage sweep method and should make this method an even more valuable tool in the study of adsorption phenomena. Further applications are seen in studies of the corrosion (24-27) and electrodeposition of metals. The device also performs as an extremely versatile, fully electronic polarograph. A device of this kind producing ramp amplitudes up to 60v with ramp rise times from 50 μsec to 500 sec (28) has been built and applied to the study of adsorption phenomena.

Acknowledgment

The author is indebted to Mr. J. T. Adamchick for his great efforts in making the device operative.

Manuscript received April 15, 1965.

Any discussion of this paper will appear in a Discussion Section to be published in the June 1966 JOURNAL.

REFERENCES

1. J. Heyrovsky, *Chem. Listy*, **16**, 256 (1922).
2. L. A. Matheson and N. Nichols, *Trans. Electrochem. Soc.*, **73**, 193 (1938).
3. F. C. Snowden and H. T. Page, *Anal. Chem.*, **22**, 969 (1950).
4. K. Cruse and W. Heberle, *Z. Elektrochem.*, **57**, 579 (1953).
5. A. Sevcik, *Collect. Czechoslov. Chem. Communic.*, **13**, 349 (1948).
6. F. G. Will and C. A. Knorr, Internat. Polarographic Colloqu., Bonn 1958; published in *Z. Elektrochem.*, **63**, 1008 (1959); *Z. Analyt. Chem.*, **173**, 87 (1960).
7. T. C. Franklin and S. L. Cooke, Jr., *This Journal*, **107**, 556 (1960).
8. Y. M. Kolotyrkin and A. N. Chemodanov, *Doklady Akad. Nauk*, **134**, 128 (1960).
9. F. G. Will and C. A. Knorr, *Z. Elektrochem.*, **64**, 258 (1960).
10. F. G. Will and C. A. Knorr, *ibid.*, **64**, 270 (1960).
11. W. Boeld and M. Breiter, *ibid*, **64**, 897 (1960).
12. F. G. Will, *This Journal*, **112**, 451 (1965).
13. M. W. Breiter and S. Gilman, *ibid*, **109**, 622, 1099 (1962).
14. R. P. Buck and L. R. Griffith, *ibid.*, **109**, 1005 (1962).
15. W. Vielstich, *Z. Instrumentenkunde*, **71**, 29 (1963).
16. A. L. Juliard and H. Shalit, *This Journal*, **109**, 1002 (1963)
17. M. W. Breiter, *Electrochim. Acta*, **8**, 447 (1963).
18. A. Kutschker and W. Vielstich, *ibid.*, **8**, 985 (1963).
19. D. R. Rhodes and E. F. Steigelmann, *This Journal*, **112**, 16 (1965).
20. R. A. Rightmire, R. L. Rowland, D. L. Boos, and D. L. Beals, *ibid.*, **111**, 242 (1964).
21. S. Gilman, *J. Phys. Chem.*, **66**, 2657 (1962).
22. M. W. Breiter, *Electrochim. Acta*, **8**, 925 (1963).
23. B. E. Conway, E. Gileadi, and H. Angerstein-Kozlowska, *This Journal*, **112**, 341 (1965).
24. M. Prazak, V. Prazak, and Vl. Cihal, *Z. Elektrochem.*, **62**, 739 (1958).
25. M. Prazak, *Corrosion*, **19**, 75t (1963).
26. I. Epelboin, M. Froment, and Ph. Morel, *Electrochim. Acta*, **6**, 51 (1962).
27. N. D. Greene and R. B. Leonard, *ibid.*, **8**, 45 (1964).
28. F. G. Will, To be published

Studies of Hydrocarbon Fuel Cell Anodes by the Multipulse Potentiodynamic Method

I. Behavior of Ethane on Conducting-Porous-Teflon Electrodes

L. W. Niedrach, S. Gilman, and I. Weinstock[1]

Research Laboratory, General Electric Company, Schenectady, New York

ABSTRACT

The adsorption of ethane on semimicro Teflon-bonded, platinum black fuel cell electrodes in the presence of $HClO_4$ electrolyte is both mechanistically and kinetically similar to that on smooth platinum after normalization to "real" (hydrogen adsorption) area. Polarization data obtained under the same conditions as the adsorption experiments allow a comparison of oxidation current with surface coverage over a range of potentials. Additional results obtained with methane and propane are also presented.

The behavior of ethane on smooth platinum microelectrodes in the presence of a perchloric acid electrolyte has been investigated with the multipulse potentiodynamic (MPP) method in this Laboratory (1). This type of study has now been extended to fuel cell anodes of more complex structure. For this purpose a miniature version of a previously described (2) conducting-porous-Teflon fuel cell electrode (containing platinum black as catalyst) has been employed.

Particular attention has been given to the rates of adsorption and the nature of the species that form on the surface of the electrode. Both of these aspects have, in turn, been related to the over-all polarization curve for the fuel electrode. Ethane has been the subject of the most detailed investigation to date in order to obtain maximum correlation with the earlier work with the smooth microelectrodes. However, some work has also been done with several other fuels.

Experimental

The three-compartment, Teflon electrochemical cell is shown schematically in Fig. 1. The anode, a miniature version of a fuel cell electrode, consisted of a 0.20 cm diameter Teflon-bonded platinum black electrode (2). This electrode, which was formed in the center of the thin (approximately 0.012 cm) platinum washer, was mounted horizontally in the cell, with connections for admitting fuel and venting products made from below. The support washer was electrically insulated from the electrolyte by bonding to it a thin, nonporous Teflon film. The electrical connection from the electrode to the external circuitry was made through the bottom of the cell.

A reversible hydrogen reference electrode communicated with the anode through a Luggin capillary. A porous Teflon plug in this leg minimized diffusion of hydrogen to the anode chamber. The counter electrode was also separated from the anode chamber via a porous Teflon plug. Both electrodes were platinized platinum flags. The cell was operated in an air thermostat, enabling control of temperature to ± 0.1°C.

The electronic instrumentation and circuit have been described previously (3).

The 4.3*N* perchloric acid electrolyte solution used for the work was prepared from reagent grade perchloric acid and quartz-distilled water. Electrolytic grade hydrogen was used in the reference electrode chamber, and Phillips research grade hydrocarbons were used as the fuels. Tank argon, deoxygenated by passage over heated copper turnings, was used as the "fuel" for obtaining solvent blanks. Tank argon was also used for de-gassing the solution.

The potential-time sequence applied to the anode for adsorption studies at constant potential is shown in Fig. 2. The significance of the steps is covered below.

A. Pretreatment step (15 sec) to remove oxidizable impurities and to produce a layer of "adsorbed oxygen" which serves to block fuel adsorption. The solution is vigorously stirred and purged with argon to remove molecular oxygen and oxidation products formed.

B. Potential step, during which the oxygen layer formed in *A* is maintained, and the solution is purged for an additional 1 min. The solution is then allowed to become quiescent for 1 min.

C. Reduction step (15 sec), during which the "adsorbed oxygen" layer is reduced. At this low potential

[1] Present address: Battery Product Section, Capacitor Department, General Electric Company, Gainesville, Florida.

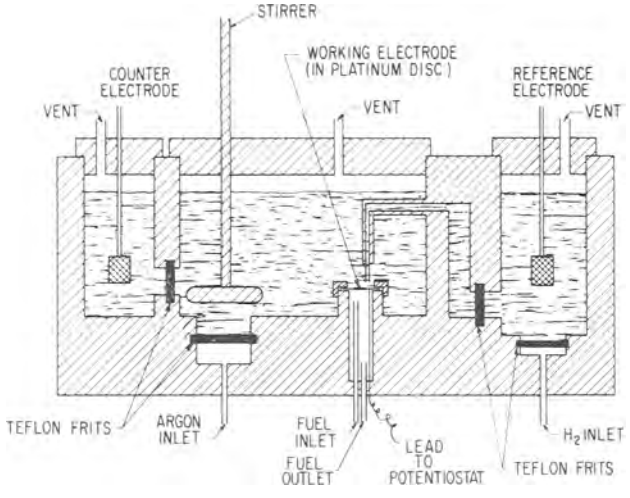

Fig. 1. Schematic diagram of cell

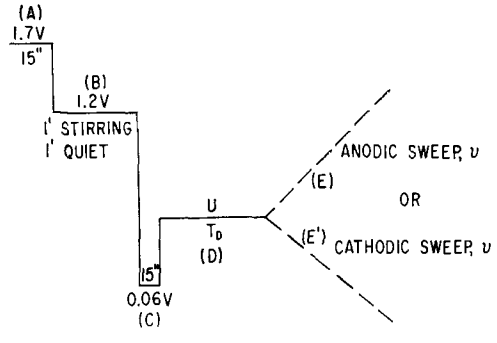

Fig. 2. Potential sequences applied to the test electrode

(0.06v) the adsorption of the hydrocarbons is blocked. This step was included so that the reduction of the surface and the adsorption of the hydrocarbon would not occur simultaneously. However, omission of this step was found to have no detectable effect on the equilibrations.

D. Adsorption step, during which the hydrogen from *C* is rapidly oxidized, exposing a reproducibly clean surface for adsorption. The duration of this step is the adsorption time, T_D.[2]

E. Anodic sweep at 0.1 v/sec. The adsorbed fuel is oxidized and the surface covered with a layer of "adsorbed oxygen." Subtraction of the charge due to surface oxidation from the total charge yields the charge required to oxidize the species derived from the adsorbed fuel.

E'. Alternative to *E*, a cathodic sweep at 0.025 v/sec which is used for determination of the charge $_sQ_H$ corresponding to hydrogen deposition. In this case, argon is substituted for the hydrocarbon fuel.

Steady-state polarization curves such as that in Fig. 12 were obtained in two ways. The first method involved application of steps A-D of Fig. 2 before each measurement of current (after $T_D = 10$ min) at a particular potential *U*. In the second method, steps A-C of Fig. 2 were applied only once, at the lowest value of *U*. The potential was changed in increments and the current recorded for each potential after an apparent constant value was established. The two methods gave essentially identical results.

Results and Discussion

Measurement of $_sQ_H$.—When the sequence of Fig. 2 is terminated in step *E'* (linear cathodic sweep) and applied to a smooth platinum microelectrode, a "hydrogen-deposition" trace may be obtained during step *E'* (3). By drawing the proper construction lines (which make approximate correction for double-layer charging and for hydrogen-evolution) an area $_sQ_H$[3] is defined, which is equivalent to approximately a monolayer of hydrogen, and may be used as a measure of relative surface area. For a smooth platinum microelectrode in an argon saturated solution the charge $_sQ_H$ was found to remain constant (to within a few per cent) for values of the sweep speed up to $v = 800$ v/sec. At much higher values of v, the trace loses "definition" and it is difficult to estimate $_sQ_H$. In the present work, the hydrogen deposition traces obtained with the Teflon-bonded electrodes were similar to those observed previously for smooth microelectrodes, but the traces begin to lose "definition" at much lower values of v. This probably reflects the diffuse structure of the electrode and its resulting inherent internal voltage drops.

Table I records the values of $_sQ_H$ measured on the Teflon-bonded electrode for values of v from 0.01 to 0.25 v/sec. The trace for $v = 0.25$ v/sec was already ill-defined. Over the useful range of $v = 0.01$ to 0.1 v/sec, $_sQ_H$ was found to be reproducible to within 5% according to Table I. A sweep speed of $v = 0.025$ v/sec was subsequently used routinely in making comparative surface area measurements.

If $_sQ_H = 0.21$ mcoul/cm^2 is taken as equivalent to a monolayer of hydrogen on an atomically smooth surface (4), then the value of $_sQ_H$ measured for our electrode corresponds to a roughness factor of approximately 1,800.

Measurement of Q_E.—For these experiments, the sequence of Fig. 2 terminating in step *E* (linear anodic sweep) was employed. When argon is fed to the electrode application of the pulse sequence to the Teflon-bonded electrode results in "oxygen adsorption" traces such as those shown in Fig. 3. The portion between 0.7 and 1.5v on the traces correspond mainly to the oxidation of the platinum surface. At 25°C the trace

[2] The subscript here and for other time intervals refers to the step involved according to Fig. 2.

[3] Previously used symbol was Q_{SH}.

Table I. Effect of sweep rate on charge ($_sQ_H$) corresponding to hydrogen deposition

Sweep speed, v, v/sec	$_sQ_H$, millicoulombs
0.010	12.3
0.015	10.8
0.025	11.9
0.040	11.0
0.060	12.1
0.080	12.4
0.10	10.9
(0.25)	(9.2)
Avg.	11.6 (0.25 v/sec value excluded)

was found to remain essentially invariant for values of T_D upwards of 3 hr without any purification of the solution. This is illustrated by the two superimposed oscilloscope traces in Fig. 3, one made after $T_D = 15$ sec and the other after over 10,000 sec. At 60°C similar reproducibility of the traces was observed.

This behavior contrasts sharply with the approximately 100 sec "clean time" observed for smooth platinum without solution purification (3). The variation of the "oxygen adsorption" trace with time was previously ascribed (3) to the adsorption of impurities from the solution. For the highly "roughened" surface under study here, the rate of flow of impurities to the surface per unit of real area is much diminished. The per cent contamination per unit time is hence also much diminished, and a longer time is required before contamination is noticeable.

The reproducibility of these solvent blanks is important in the determination of the charge associated with the oxidation of adsorbed hydrocarbon species to CO_2 since the latter is derived from the area enclosed by the blank and the corresponding curve for the electrode after equilibration with the hydrocarbon (1). This is illustrated by the data in Fig. 4 where trace A is a solvent blank and traces B through D were obtained when ethane was fed to the electrode and the

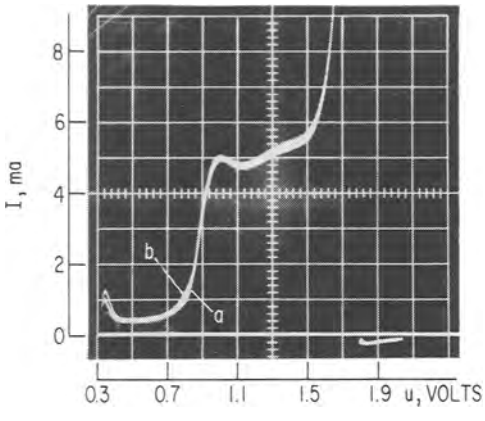

Fig. 3. Comparison of solvent blanks after different equilibration times at 0.3v,; (a) $T_D = 15$ sec; (b) $T_D = 10{,}800$ sec.

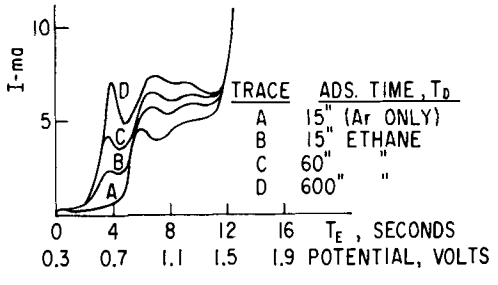

Fig. 4. Current-potential (time) traces for ethane after different adsorption times: 4.3*N* $HClO_4$; 60°C; $\mu = 0.1$ v/sec; U = 0.30v; ME-11.

Table II. Effect of sweep rate on charge to oxidize adsorbed ethane, 4.3*N* $HClO_4$, T = 60°C

Sweep speed, v, v/sec	Q_E', millicoulombs
0.092	21.7
0.18	21.8
0.40	19.8
0.92	15.2

adsorption time, T_D, was varied. The measured charge, Q_E', may include several terms:

$$Q_E' = Q_{E\text{tot}} + Q_E'' + \Delta Q_{\text{cap.}} + \Delta Q_o \qquad [1]$$

where $Q_{E\text{tot}}$ is the charge corresponding to oxidation of the ad-layer formed from ethane during step D; Q_E'' is the charge corresponding to ethane not adsorbed during step D but which oxidizes during step E with or without a preceding adsorption step; $\Delta Q_{\text{cap.}}$ is the difference in capacitive charges included under the "oxygen adsorption" and "ethane" traces due to differences in initial surface states; and ΔQ_o is the difference in charges due to surface oxidation, included under "oxygen adsorption" and "ethane" traces.

It has previously been demonstrated, for smooth platinum (1), that $Q_E' \simeq Q_{E\text{tot}}$ if $v < 20$ v/sec. At higher values of v, $Q_E' < Q_{E\text{tot}}$, at least partially because some of the adsorbed ethane is retained on the surface during sweep E. At the other end of the scale, it is important that the sweep speed not be so slow that appreciable re-adsorption of ethane occur during step E, cause $Q_E'' > 0$. For the present electrode the useful range of v was examined by adsorbing a fixed amount of ethane (corresponding to $T_D = 600$ sec) and measuring Q_E' for a range of sweep speeds. Some results appear in Table II. Below $v = 0.092$ v/sec, a "background" current (corresponding to Q_E'') is distinctly present. Above 0.92 v/sec, the traces tend to lose definition, probably due to the large internal voltage drops in the electrode. A decline in the charge required for the oxidation of the ad-layer is also evident. The range of constancy of Q_E' for the Teflon-bonded electrode extends only from approximately 0.1 to 0.4 v/sec, and in this range we assume $Q_{E\text{tot}} = Q_E'$. Accordingly, a sweep speed of $v = 0.1$ v/sec was used routinely in making the measurements discussed below.

Behavior of ethane.—The general form of the current-voltage trace obtained during the oxidation of adsorbed ethane with a linear potential sweep is shown for a range of equilibration times, potentials, and temperatures in Fig. 4-6. For each experimental condition, trace 2 was obtained in the presence of ethane, while trace 1 was obtained in the presence of argon. Trace 1 serves as the "oxygen adsorption" or "solvent" correction.

From Fig. 4-6, it can be seen that, if ethane is adsorbed at potentials below 0.7v, and a linear anodic

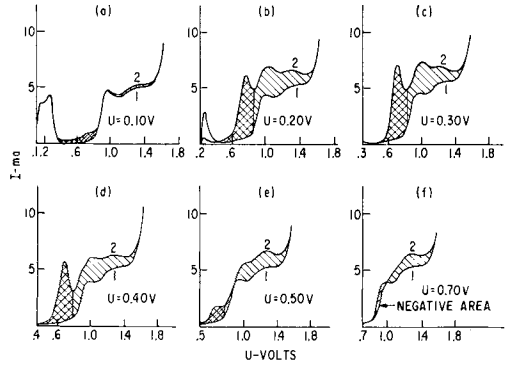

Fig. 5. Current-potential (time) traces for ethane adsorbed at several potentials: 4.3*N* $HClO_4$; 60°C; μ = 0.1 v/sec; T_D = 10 min; 1, Ar blank; 2, ethane; ME-11.

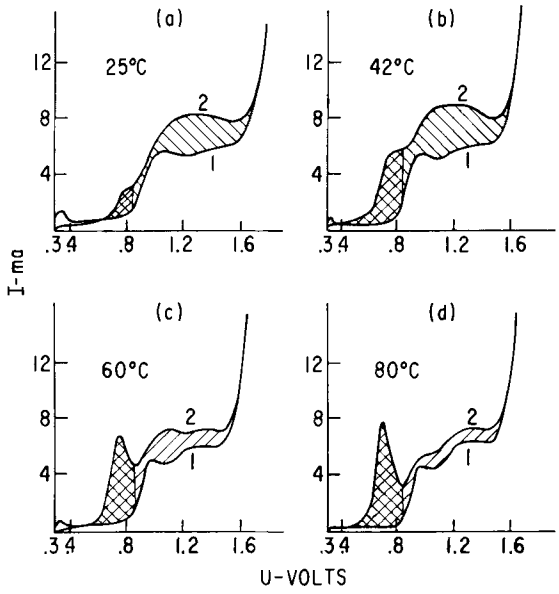

Fig. 6. Current-potential (time) traces for ethane adsorbed at several temperatures: 4.3*N* $HClO_4$; μ = 0.1 v/sec; T_D = 10 min; U = 0.30v; 1, Ar blank; 2, ethane; Me-16.

sweep (l.a.s.) applied to the electrode, the ad-layer is oxidized over a range of potentials part of which is a continuum and part more sharply differentiated as discrete waves. This can be taken as evidence for the existence of a range of reactivities for the individual ad-species which can have their origins in gross differences in chemical composition as well as subtle differences in the activities of individual adsorption sites. Only one sub-division of the ethane ad-layer will be attempted here, since it is suggested by voltammetric and chemical considerations. The various "ethane" traces of Fig. 4-6 reveal that some of the adsorbed ethane is removed at sweep potentials below those (approximately 0.8v) at which the surface itself is normally oxidized. This first wave generally exhibits a well-defined peak. The second wave exhibits a flat maximum which stretches all the way from approximately 0.8v to oxygen evolution potentials. It has already been demonstrated that species associated with wave 2 may be eliminated by cathodic hydrogenation (1, 5) whereas wave 1 is relatively unaffected. Hence waves 1 and 2 represent chemically different species, with the reservation that further sub-divisions are likely also possible.

As previously, Q_E' ($\simeq Q_{E\text{tot}}$ under these conditions) will be used to refer to the entire charge measured

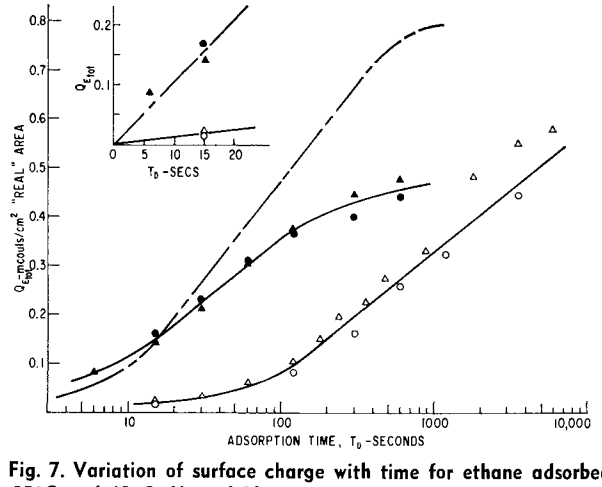

Fig. 7. Variation of surface charge with time for ethane adsorbed at 25°C and 60°C. *U* = 0.30v. —— - ——, Wire electrode, 60°C, 1*N* $HClO_4$ (1). 25°C: ○, ME-11, △ ME-16; 60°C: •, ME-11, ▲, ME-16; 4.3*N* $HClO_4$.

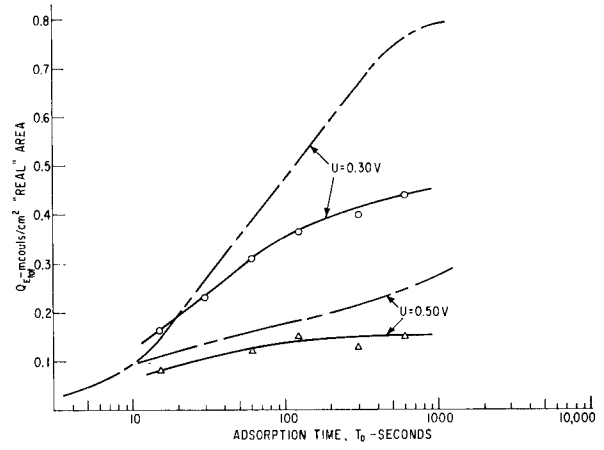

Fig. 8. Variation of surface charge with time for ethane adsorbed at 0.3 and 0.5v. 4.3*N* $HClO_4$; 60°C; ME-11. Broken curves are for wire electrode in 1*N* $HClO_4$ (1).

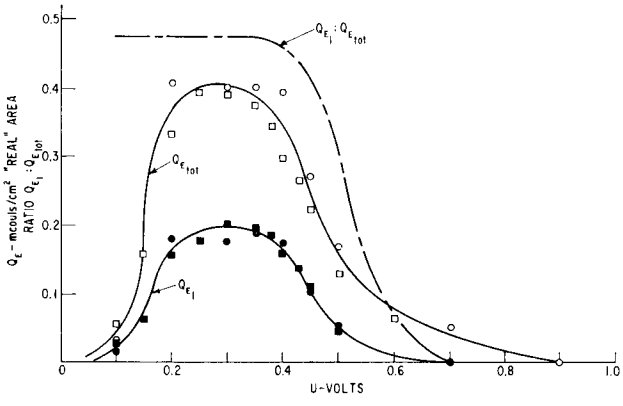

Fig. 9. Surface charge associated with ethane adsorbed at different potentials: 4.3*N* $HClO_4$; 60°C; T_D = 10 min; ○, ●, ME-11; □, ■, ME-16.

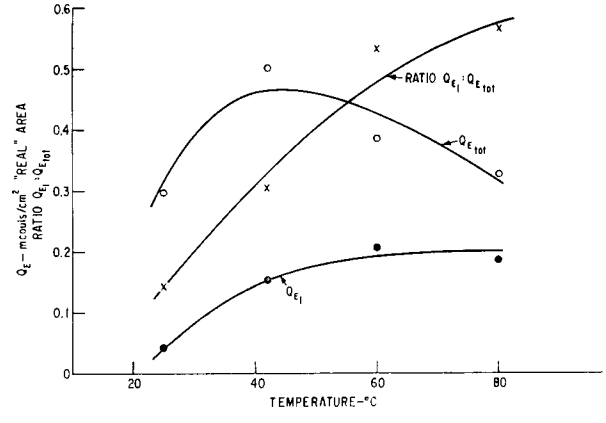

Fig. 10. Surface charge associated with ethane adsorbed at different temperatures: 4.3*N* $HClO_4$; U = 0.3v; T_D = 10 min; ME-16.

on applying a l.a.s. to the ethane-covered surface (entire shaded area of Fig. 5 and 6). The charges Q_{E1} and Q_{E2} will now be taken as the areas of wave 1 and 2 (dark and light-shaded areas of Fig. 5 and 6), respectively. All values of charge reported have been normalized to "real area." For the normalization, the quantity sQ_H was measured for each electrode used, and 0.21 mcoul/cm² was chosen to correspond to 1 cm² of true area (4).

Variation in Q_{Etot} and Q_{E1} with time, temperature, and potential are recorded in Fig. 7 to 10 and in Table III. (The charge Q_{E2} can be readily derived from

Table III. Effect of time and potential on $Q_{E_1}:Q_{E_{tot}}$, T = 60°C

Potential, v	Time, T_D, sec	$Q_{E_1}:Q_{E_{tot}}$
0.3	15	0.36
	30	0.42
	60	0.42
	120	0.41
	300	0.45
	600	0.48
0.35	15	0.50
	60	0.49
	120	0.48
	200	0.47
	600	0.50
0.50	15	0.43
	60	0.38
	120	0.35
	300	0.36
	600	0.33

Q_{Etot} and Q_{E1}.) From Table III and Fig. 9 it is apparent that the ratio of the charge associated with the two ethane "waves" is not a sensitive function of the adsorption time or potential (up to 0.5v). The ratio is sensitive to the adsorption temperature. According to Fig. 10, higher temperatures favor higher relative surface coverages with wave 1 species.

In Fig. 7 and 8, values of Q_{Etot} are plotted against the log of adsorption time for the comparison of results obtained for the Teflon-bonded electrodes with similar results obtained with smooth platinum microelectrodes (1). For both types of electrodes at 60°C, the results are qualitatively similar. The maximum rate of increase of surface coverage occurs in the close vicinity of 0.3v for both systems. At low potentials (<0.3v) adsorption is hindered because the required dissociation of the adsorbing hydrocarbon is repressed by the low potential and/or the presence of atomic hydrogen on the surface. At potentials above 0.3v the surface coverage again declines as the rate of adsorption fails to keep pace with the increasing rate of oxidation of the ad-layer. At 0.3v, the rate of adsorption is initially constant and then falls on a linear semilog plot until quite high surface coverages are achieved. The maximum (initial) adsorption rate is approximately 0.010 mcoul/sec/cm² of "real" area for both the Teflon-bonded and smooth electrodes. Considering the assumptions involved in normalizing the two types of electrode structures to the same real area, the results must be said to represent remarkably good agreement in the adsorptive properties of two platinum surfaces prepared in quite different ways.

With the information presently available, it is not possible to identify firmly the individual species involved on the surface. It is reasonably certain that just as in dry systems (5) the ad-layer does not correspond to undissociated ethane. More than likely, several species are involved. The results of hydrogen codeposition experiments suggest that an average C:H ratio of 1 prevails (1). Additional inferences can be made from the observed temperature effects and other data.

Considering first the data of Fig. 6 and 10 showing the effect of temperature on the oxidation curves for adsorbed ethane, it is noted that wave 1 becomes more prominent as the temperature is raised. An attractive explanation of this phenomenon based on past observations is that this wave is associated with a species derived from the reaction of a primary adsorption species with water. This might be via a direct chemical reaction or via an electrochemical route; the species might itself be either a necessary reaction intermediate along the major route involved in the over-all oxidation of ethane or it could be a by-product that reaches a steady state on the surface.

This new species might thus be the "CO-like" surface species previously suggested by Niedrach (6) or the "reduced CO_2" of Giner (7), both of which appear to refer to identical materials. To obtain additional information bearing on such an interpretation, ex-

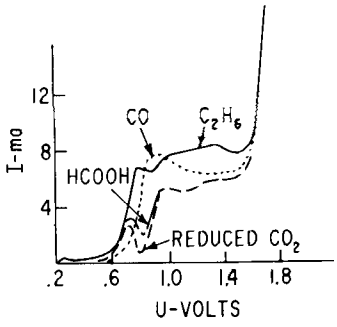

Fig. 11. Current-potential (time) traces for several carbonaceous materials adsorbed on platinum: 4.3*N* $HClO_4$; 60°C; u = 0.1 v/sec; ME-16.

periments were performed at 60°C in which the electrode, after the standard activation procedure, was equilibrated with CO (at 0.3v), CO_2 (at 0.06 and 0.2v), and argon saturated with formic acid vapor at 25°C (at 0.06 and 0.2v) prior to a potential sweep. The results of these experiments are shown in Fig. 11.

The positions of the oxidation waves for the three oxygenated materials relative to that of wave 1 from ethane strongly suggest that a species closely related to them is involved in the oxidation of ethane. This idea is further supported by the observation that wave 1 for ethane is resistant to removal by cathodic hydrogenation of the electrode. As has been previously noted, carbon monoxide behaves in a similar fashion (6), and the waves for reduced CO_2 and formic acid were, of course obtained after equilibrations at hydrogenating potentials, *i.e.*, 0.06v. Additional evidence that wave 1 represents an oxygenated species derives from related galvanostatic and analytical studies of hydrocarbons (8). While the nature of the species associated with wave 1 appears to be narrowed down to a partially oxidized species related to CO and formic acid, additional work will be required to identify it more specifically and to define its role as an active intermediate or by-product. Resolution of the latter point is of particular importance in view of the fact that the "CO-like" species already strongly manifests itself at potentials as low as 0.15v.

As far as the second wave for ethane is concerned, the present work sheds no light in this area. It would appear likely, however, that this wave involves a partially dehydrogenated ethylenic species (1).

In the discussion so far, the effect of temperature on the rate of adsorption has not been considered. The

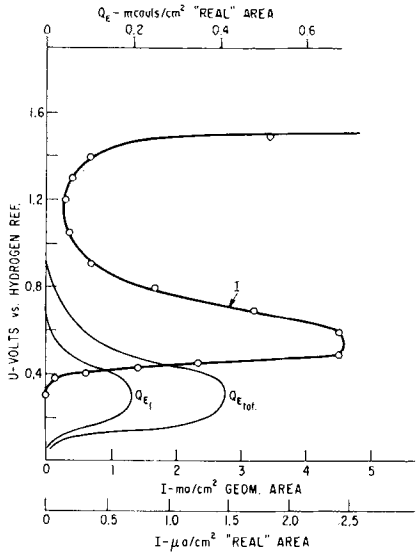

Fig. 12. Polarization and surface charge curves for ethane: 4.3*N* $HClO_4$; T = 60°C; ME-16.

data in Fig. 7 show that the over-all adsorption at 25°C, when expressed in terms of millicoulombs per square centimeter of real electrode area, follows a pattern similar to that observed at 60°C. Similar results were also obtained at 42°C (not shown). Although the equilibrations at the lower temperatures were not continued to "saturation," it is significant that higher total surface charges were realized in both these cases than in the equilibration at 60°C. This appears to reflect the influence of the partially oxidized "CO-like" species on the surface at the higher temperatures.

One additional point for consideration is the relationship between the adsorption data and the polarization curve for the electrode operating on ethane. Such a polarization curve obtained at 60°C is shown in Fig. 12. The abscissa is expressed in terms of the current density per unit of "real" and "geometrical" area of the electrode. Therefore, the data may be related to the adsorption studies as well as performance curves for operating fuel cell devices. Also shown in Fig. 12 are the measured surface coverages, Q_{E_1} and $Q_{E_{tot}}$, from Fig. 9. The form of the polarization curve is typical of those for a variety of fuels when the data are obtained potentiostatically. Even hydrogen shows the minimum in the region from 0.9 to 1.4v on smooth platinum. Over the potential range from 0.3 to 0.45v, the curve has a linear Tafel region with a slope of 0.066 v/decade of current.

It is of interest to compare the value of the maximum current in Fig. 12 with that calculated from the observed adsorption rate on the "clean" surface as measured at 0.3v. In converting the adsorption rate to equivalent current density, it must be recalled that the former is expressed in terms of the change in surface charge with time, $\Delta Q_{E_{tot}}/\Delta t$. Allowance must therefore be made for any oxidation that occurred during the adsorption step itself, *e.g.*, immediate oxidation of dissociated hydrogen. This may be done by multiplying $\Delta Q_{E_{tot}}/\Delta t$ by the ratio of the charge associated with the hydrocarbon fuel molecule to that of the adsorbed species.

While the precise composition of the ad-layer has not been established for ethane, especially after short equilibrations, it is possible to calculate a range of limiting currents from the adsorption data at 0.3v. For ethane it is reasonable to bracket the composition of the ad-layer between one corresponding to C_2H_2 radicals and one corresponding to CO. The observed value of $\Delta Q_{E_{tot}}/\Delta t$ = 0.010 mcoul/sec then corresponds to a range of current densities from 14 to 35 μa/cm². The observed maximum current of 2.5 μa/cm² is much lower than the calculated value. This, as well as the fact that the "maximum" occurs when there is yet an appreciable concentration of adsorbed material on the electrode surface, indicates that the maximum current is established in this case neither by a limiting rate of mass transport nor by a limiting over-all rate of adsorption on a "clean" surface. It could, however, reflect a limiting adsorption rate on a surface partially covered with refractory hydrocarbon residues, oxygen (at 60°C the surface oxide starts to form between 0.6 and 0.7v), and adsorbed ions. Additional work will be required for a definitive understanding of this limiting step.

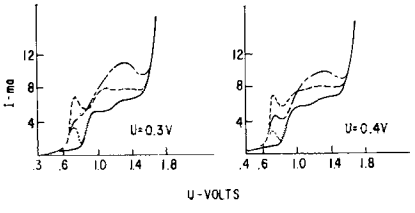

Fig. 13. Current-potential (time) traces for several hydrocarbon fuels after equilibrations at different potentials: 4.3*N* $HClO_4$; 60°C. —— ——, C_2H_6; ----, CH_4; — · —, C_3H_8; ——— Ar blank, ME-16.

Behavior of other fuels.—A limited amount of data have been obtained for fuels other than ethane. Examples of l.a.s. traces obtained after equilibrations with methane and propane at 0.3 and 0.4v are shown in Fig. 13. These data indicate that propane is quite similar to ethane in that the ad-layer on the electrode surface shows two oxidation waves when the l.a.s. is applied. Methane differs markedly, however, in that only wave 1 can be detected during oxidation of the ad-layer. A detailed discussion of the behavior of methane will be the subject of a forthcoming publication (9).

Conclusions

The adsorption and surface behavior of ethane, as a representative hydrocarbon fuel, on semimicro, Teflon-bonded fuel cell electrodes parallels that on wire electrodes. In both cases during adsorption at intermediate potentials a linear law relating measured surface charge and adsorption time is followed at low coverages. At higher coverages the surface charge varies with the logarithm of time. Numerous properties of the first of two waves seen during the oxidation of adsorbed ethane with a linear sweep suggest that one of the surface species is partially oxygenated and related to carbon monoxide and/or formic acid. The behaviors of methane and propane resemble that of ethane, but important differences are seen. In particular adsorbed methane gives only a single wave on oxidation.

Acknowledgment

This work is a part of the program under contracts DA-44-009-AMC-479(T) and DA-44-009-ENG-4909, ARPA Order No. 247 with the United States Army Engineer Research and Development Laboratories, Fort Belvoir, Virginia, to develop a technology which will facilitate the design and fabrication of practical military fuel cell power plants for operation on ambient air and hydrocarbon fuels.

Manuscript received June 21, 1965; revised manuscript received Aug. 27, 1965.

Any discussion of this paper will appear in a Discussion Section to be published in the June 1966 JOURNAL.

REFERENCES

1. S. Gilman, Paper presented at the Washington Meeting of the Society, October 1964, Extended Abstracts, Battery Division, p. 72.
2. L. W. Niedrach and H. R. Alford, *This Journal*, **112**, 117 (1965).
3. S. Gilman, *J. Phys. Chem.*, **67**, 78 (1963).
4. F. G. Will and C. A. Knorr, *Z. Elektrochem.*, **64**, 258 (1960).
5. G. C. Bond, "Catalysis by Metals," p. 183, Academic Press, New York (1963).
6. L. W. Niedrach, *This Journal*, **111**, 1309 (1964).
7. J. Giner, *Electrochem. Acta*, **8**, 857 (1963).
8. W. T. Grubb, To be published.
9. L. W. Niedrach, To be published.

An Experimental Study of the Operation of a Porous Oxygen Cathode

T. Katan and S. Szpak

Materials Sciences Laboratory, Lockheed Missiles & Space Company, Palo Alto, California

and E. A. Grens II

Inorganic Materials Research Division, Lawrence Radiation Laboratory and Department of Chemical Engineering, University of California, Berkeley, California

ABSTRACT

A special oxygen cathode was designed to investigate the film model for operation of porous gas electrodes. This electrode consists of a bed of ~55μ silver spheres behind a thin electroformed mesh facing. The thickness of the bed can be adjusted, and the structure permits holding the electrolyte meniscus out of the electrode body. Measurements in 6.9*N* KOH (23.5°C) confirmed the operation of the film mechanism. The overpotential/current density behavior of the electrode was in agreement with film model analysis with a film thickness of 0.05μ.

It was noted as early as 1839 by Grove that electrodes using a gaseous reactant performed better when only partially immersed in a liquid electrolyte and partially in contact with the gas phase than when totally submerged in the liquid (1). However, the importance of electrolyte films on the surface of those parts of an electrode which are exposed to a gas phase has been clearly recognized only recently (2-7). Now considerable interest has developed in the effect of such films in determining the performance of the porous gas electrodes of fuel cell systems. In this investigation, the behavior of a porous oxygen cathode operating in potassium hydroxide solution was measured and compared with the predictions of a theoretical model based on the film coverage concept. This served to indicate the existence of the films in a porous structure and to confirm the applicability of the model to such systems.

The performance of a porous electrode involving a gas phase reactant supply is determined largely by the location and configuration of charge transfer reaction sites within the pore structure, by the local reaction kinetics, and by the transport of reacting species and electric current to and from the sites. The theoretical models that have been proposed to describe the reaction zone of such electrodes can be broadly classified according to the distribution of reaction relative to the position of the electrolyte meniscus in a pore (usually assumed cylindrical) and the method of gas reactant transport to the points where reaction takes place:

1. Reaction along the pore wall in the liquid filled portion of pore; transport of gaseous reactant by dissolution at the meniscus and diffusion through liquid filled pore to reaction sites (8-9).

2. Reaction along pore wall near the meniscus in the liquid filled portion of pore; transport of gaseous reactant by adsorption on walls of the gas filled section of pore and surface diffusion along pore wall to reaction sites (10-11).

3. Reaction under a liquid film covering pore walls in the gas filled portion of pore; transport of gaseous reactant by dissolution at the surface of the film and

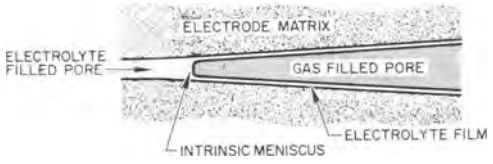

Fig. 1. Idealized pore of gas electrode

diffusion across the thin film to reaction sites along pore wall (2-7).

4. Reaction in liquid filled micropores which intersect walls of the gas filled portion of macropores; gaseous reactant transport by dissolution in electrolyte at mouths of micropores along the macropore walls and diffusion into micropores to reaction sites (12-13).

The first of these models can frequently account for only very low superficial current densities because of the relatively long diffusion paths involved; it cannot explain observed electrode performance in most cases. It can easily be calculated that the contribution of such a mechanism to the operation of the other models listed above is almost always negligible. The last mentioned model may apply to electrodes with a wide range of pore sizes, actually a superimposed coarse and fine pore structure, if the distribution of reaction in the flooded micropores is properly characterized.

For electrodes with a narrow pore size distribution (a single scale of porosity in the bulk of the electrode), or for partially immersed solid electrodes, the "surface diffusion" and "film" models could be considered. However, calculations for the former method indicate that surface diffusion cannot support observed currents for the hydrogen anode (5); similar results can be expected for oxygen cathodes. Thus, the film mechanism remains, perhaps, the most likely explanation for the operation of these gas electrodes. In this model, a thin film of electrolyte covers the walls of the gas filled portion of each pore, extending a very long distance (in relation to pore dimensions) from the intrinsic meniscus (see Fig. 1). Dissolved gas diffuses across this film to reaction sites on the pore wall. Ionic species involved in the reaction move from (or to) the site by diffusion and migration along the film to (or from) the intrinsic meniscus and electrolyte filled part of the pore. The electrons involved are carried by the conducting pore walls. In 1957, Wagner described such a model for the oxygen cathode in molten salt electrolyte (2). He developed overpotential-current density expressions for several limiting cases under the assumption of constant electrolyte conductivity. Will, in conjunction with experimental investigation of a hydrogen electrode, formulated a film model assuming absence of kinetic effects (equilibrium reaction) and uniform conductivity in the film (3). Later, Grens, Turner, and Katan (4), and, independently, Rockett (6), developed film models incorporating electrode kinetic limitations and accounting for variation in electrolyte composition with position along the film. Iczkowski also presented a film model for the hydrogen electrode in sodium hydroxide which included the refinement of considering variation in transport properties with electrolyte concentration (5). One of the significant features of the more refined film models is that they predict active reaction zones extending along the film thousands of film thicknesses from the intrinsic meniscus, particularly when ionic species are formed in the reaction. This phenomenon, among others, is subject to experimental verification.

Measurements by Will using the hydrogen anode in sulfuric acid electrolytes demonstrated the validity of a film mechanism for this system (3). The electrodes employed in that work were exterior surfaces of partially immersed platinum tubes. A later investigation, by Bennion and Tobias, of oxygen reduction at the surface of silver and nickel rods protruding from aqueous potassium hydroxide electrolytes not only established that this reaction occurred under an electrolyte film but also determined the distribution of the reaction along the film above the intrinsic meniscus (7). Further, Muller demonstrated by optical methods the existence and stability of such films on the surface of nickel plates partly immersed in potassium hydroxide solutions and measured film thicknesses on the order of $1 \times 10^{-5} - 5 \times 10^{-5}$ cm (14). Recently, Mazitov found a film mechanism operative for oxygen reduction on silver rod electrodes dipping into KOH solutions (15, 16). However, little in the way of experimental verification of the film model in actual porous structures has been reported.

It was the intent of the present study to examine the operation of a well defined porous gas electrode with a single scale of porosity under conditions where the film model could be expected to apply. By operating in a manner such that electrolyte, except in the form of surface films, was excluded from the body of the electrode, the variation of the performance of the system with electrode thickness could confirm the presence of the film and provide a measure of its active length. Comparison of overpotential-current density relationships for the electrode with those predicted by the film theory would permit verification of the principal assumptions of the model and evaluation of the one parameter not available *a priori*, the effective film thickness on the pore walls.

Experimental

The system selected for study was the oxygen cathode operating in 6.9*N* aqueous potassium hydroxide solution at near ambient temperature. This reaction is important in low temperature fuel cells and has the advantage that it can be conducted, at least for purposes of these experiments, on silver electrode surfaces without use of deposited catalysts. Basic kinetic data for this particular system had been recently determined and were available for use in evaluation of results (17).

Apparatus.—The electrode, shown in Fig. 2, had a superficial area of 1.19 cm^2 and consisted of a thin electroformed silver mesh, which constituted the face in contact with the electrolyte, backed by a bed of 55μ silver spheres. The silver mesh diaphragm was as supplied by the Buckbye Mears Company, ruling number 107, and had regularly spaced 15.8μ square openings with 10.9μ walls between openings and a thickness of 12.0μ. Its porosity was 35%. A single layer of this

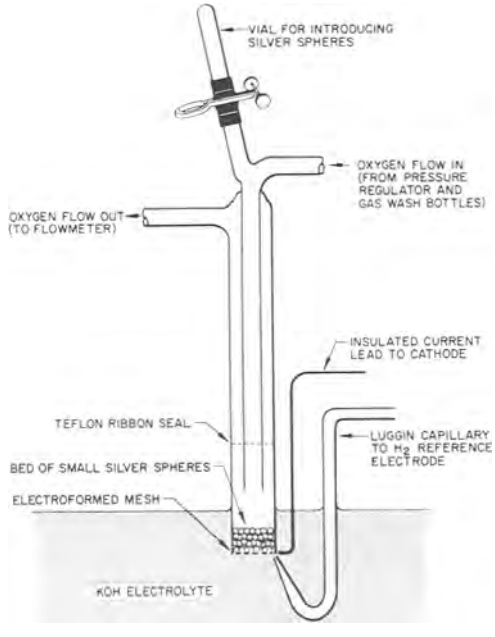

Fig. 2. Experimental oxygen cathode consisting of a bed of silver spheres.

material was cemented across the end of a 15 mm Pyrex tube (cut flat) 45 mm long which served as a carrier for the electrode. Electrical contact existed between the rim of this diaphragm and a gold wire ring which in turn connected to the external circuit through sealed, Teflon insulated leads. Total electrical resistance from the external lead to a silver disk placed on the mesh was 0.14 ohm. The bed of silver spheres, arranged as poured in the carrier tube and nonsintered, comprised the main body of the electrode matrix. The spheres were obtained from the American Platinum Works, and were of 55 $\pm 4\mu$ diameter and visually spherical configuration under 200× magnification. Surface roughness was not measured; however, the surfaces appeared smooth at 3000× magnification. Resistivity of uncompressed beds of these spheres (between silver plates) was measured as 18 ohm-cm.

The Pyrex tube carrying the electrode assembly was fitted flush against a Pyrex gas chamber of similar diameter and sealed with Teflon tape. The gas chamber included an oxygen supply duct extending to within about 2 cm of the electrode bed and a gas outlet leading to a flow control valve and meter. A glass vial could be attached to the gas chamber through a neoprene coupling, equipped with pinchcock, for addition of weighed samples of silver spheres during operation. Oxygen supply to the gas chamber was equilibrated with potassium hydroxide electrolyte at the same concentration and temperature as that in the cell by sparging through this solution. A water column pressure regulator on the supply line allowed control of gas chamber pressure.

The test electrode was mounted in a cell consisting of a glass Dewar flask of 1.4 liters working volume as shown in Fig. 3. Cell contents were held at 23.5°C and continuously sparged with nitrogen to eliminate dissolved oxygen from the bulk electrolyte. The counter electrode consisted of a double layer of 80 mesh platinum screen 7 × 7 cm, and was mounted in the bottom of the cell and connected to the external circuit through an insulated lead. A hydrogen reference electrode, operating in the same electrolyte, with a Luggin capillary leading close to the face of the test electrode furnished voltage reference. The external circuit provided for both galvanostatic (through an Electronic Measurements C612 constant current supply) and potentiostatic (with a Wenking potentiostat) electrode operation. Test electrode potential could be monitored with a Sargent MR potentiometric recorder and cell current measured with a sensitive ammeter (Western Electrical Instrument Corporation 931 or Greibach 500).

The electrolyte solutions used were prepared from reagent grade potassium hydroxide and distilled water.

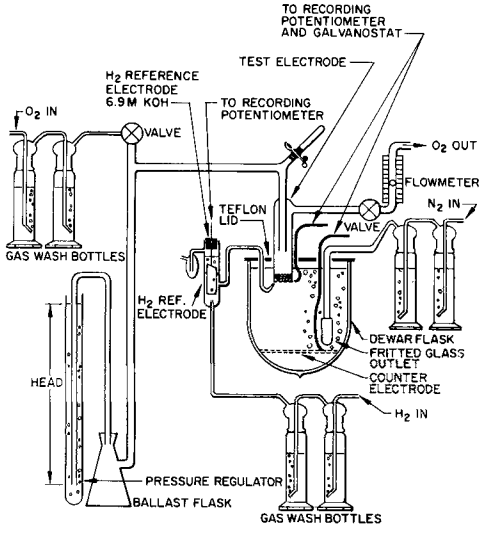

Fig. 3. Arrangement of experimental apparatus

Procedure.—Before each experimental run, the electrode was disassembled, cleaned and dried, and resealed to the gas chamber section. Before immersion, oxygen supply was set to obtain the desired chamber pressure and positive gas flow through the mesh facing; then the electrode was inserted approximately 10 mm into the electrolyte. In this way, the interior of the electrode assembly remained free of liquid. The desired initial quantity of silver spheres was added by means of the attached sample vial and the vial gently tapped to detach adhering particles. During subsequent operation of the electrode, further samples of spheres were introduced in the same way to increase electrode thickness where this effect was under investigation. This procedure yielded sphere beds for which deviations from flatness of the bed surfaces were not visually detectable.

After establishing the initial sphere bed (for some tests, no bed was added initially) the desired current was applied and electrode operation monitored until steady state was reached. Then changes could be made in cell current, oxygen pressure or flow rate, or in sphere bed depth (increases only) as the test series required, and the transient and steady-state effects of these changes observed. Response was recorded as test electrode potential against the hydrogen electrode reference. This value was, in turn, converted to test electrode overpotential by comparison with electrode potential at open circuit.

Characteristics of test electrode.—The test electrode described above was designed to incorporate three principal characteristics:

1. The capability of exclusion of electrolyte, except as surface films, from the body of the porous electrode.
2. A porous electrode thickness which could be easily changed.
3. A porous matrix for the electrode which was sufficiently well described to allow ready determination of specific surface, average wetted perimeter,[1] and other geometric factors.

The pore size of the electroformed mesh was sufficiently smaller than that in the sphere bed that the electrolyte meniscus could be held in the thin mesh face by use of suitable gas pressures in the electrode. The "blow through" pressure of the mesh was measured at 33 ± 1 in. of water while that of the bed was less than 13 in. Thus, the first condition could be satisfied over a wide range of gas chamber pressures.

The ability to establish sphere bed thicknesses as desired has been mentioned earlier. These matrices have properties typical of random packed beds of spheres (18). Measured bed density was 6.6 g/cm² corresponding to a porosity of 0.37, compared to 0.26 for a close-pack arrangement. The specific surface area was calculated, from this observed density, as 690 cm^{-1} and the equivalent wetted perimeter as 390 cm/cm². The average surface tortuosity of the bed,[2] however, could not be directly evaluated.

Results

Effect of sphere bed thickness.—The oxygen cathode overpotential at a current density of 2.1 ma/cm² was measured as a function of sphere bed thickness over a range of bed depths from 0 to ~3 mm. These experiments were conducted under conditions where the electrolyte meniscus was held in the mesh face of the electrode and not allowed to penetrate the bed (23 in. water O_2 pressure). Figure 4 illustrates the effect of bed thickness at steady state. The mesh facing itself was not effective as an electrode. As bed depth was increased, the overpotential decreased markedly up to

[1] Average wetted perimeter is film surface area per unit film length, which here is taken as bed surface area per unit length along sphere surfaces. The actual wetted perimeter will be reduced somewhat below that calculated in this simplified manner by film thickening at points of contact between spheres. As long as film thickness is small compared with sphere radius, this thickening affects the average perimeter by only a few per cent.

[2] Surface tortuosity is average path length along particle surface through a bed of unit depth.

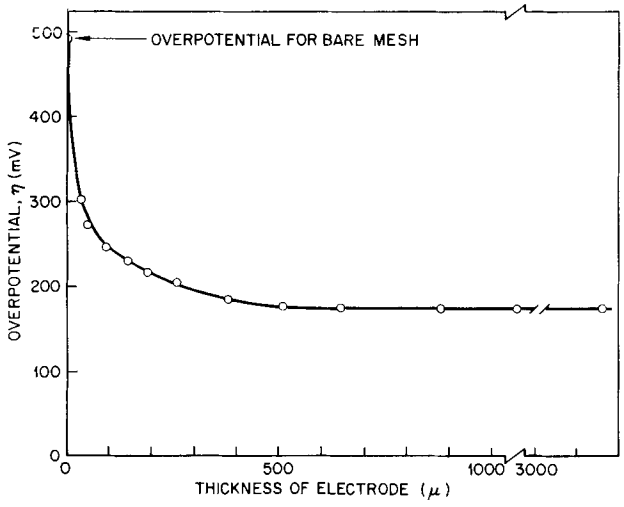

Fig. 4. Effect of increasing electrode thickness on overpotential of oxygen cathode. 6.9*N* KOH, 23.5°C, O_2 at 23 in. H_2O pressure, current density 2.1 ma/cm^2.

a depth of about 0.5 mm. Beyond this, no further improvement in electrode operation was noted. This behavior could be consistently reproduced with electrodes using other electroformed mesh and sphere samples, and corresponding effect of bed depth on current density was observed for potentiostatic operation at an overpotential of 450 mv. Thus, the portion of the bed within 0.5 mm of the electrode face constituted the active part of the electrode. In subsequent experiments investigating effects of other parameters, beds sufficiently deep (3 mm) to exclude effects of bed thickness were used.

When increases in depth were made for beds considerably thinner than the 0.5 mm active depth, the cathode overpotential decreased over a time period of order 1 min to a value perhaps 10% less than its stationary value at the new depth and then increased over a period of order 10 min to its new steady state.

Effect of gas pressure.—The effect of oxygen pressure in the gas chamber on electrode overpotential for a current density of 8.4 ma/cm^2 was determined for a 3-mm thick sphere bed. The performance of the test electrode for gas chamber pressures between 5 and 23 in. of water is shown in Fig. 5. When oxygen pressure was reduced below that necessary to exclude electrolyte (except as films) from the sphere bed (about 13 in.) electrode overpotential increased. For pressures of 7 in. of water or below, capillary action caused complete flooding of the sphere bed and electrode performance became extremely poor.

After a reduction of gas pressure below 13 in., that is after some penetration of bulk electrolyte into the bed

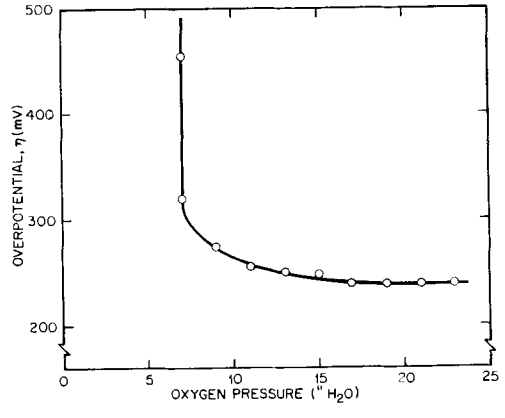

Fig. 5. Effect of oxygen pressure on overpotential of oxygen cathode. 6.9*N* KOH, 23.5°C, 3 mm electrode thickness, current density 8.4 ma/cm^2.

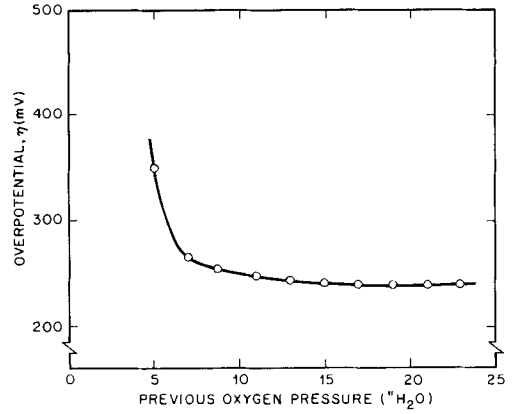

Fig. 6. Effect of previous reduction in oxygen pressure on overpotential of oxygen cathode operating at 23 in. H_2O pressure. 6.9*N* KOH, 23.5°C, 3 mm electrode thickness, current density 8.4 ma/cm^2.

had occurred, later return to original (23 in.) oxygen pressure did not restore electrode performance. This effect is presented in Fig. 6. It is to be expected for such a sphere bed since certain regions, particularly those near points of contact between spheres, cannot be cleared of electrolyte by gas pressure after being flooded.

Variations in oxygen flow rate at 23 in. pressure over the range of 0 to 5 cm^3/min had no measurable effect on electrode behavior.

Effect of current density.—Overpotential-current density relationships were determined for test electrodes under conditions where bulk electrolyte was excluded from the sphere beds (23 in. O_2 pressure) and where these beds were much thicker than their active regions (3-mm thick). These data are shown as the experimental points in Fig. 7. Galvanostatic currents in the range of 0 to 35 ma/cm^2 were applied and overpotential recorded after steady state was reached. The upper limit of currents investigated was set at the point where the resistive potential drop in the sphere bed itself clearly entered as an important effect. This condition would be determined by the linearity of the overpotential-current density curve caused by the resistive loss and was expected above about 20 ma/cm^2 because of the fairly high specific resistivity of the loose packed bed.

Discussion

The observed behavior of the electrode used in this study is in good agreement with the film model for porous gas electrodes (4). With a surface tortuosity factor on the order of 3 to 6 in the sphere bed[3] and a

[3] The tortuosity (path length/bed thickness) of void paths in a random packed sphere bed is about 1.5 and the further tortuosity of the surface, and thus the film, along such a path is $\pi/2$. This gives a minimum film tortuosity of 2.4 which is certainly considerably increased by lack of continuity of pore walls.

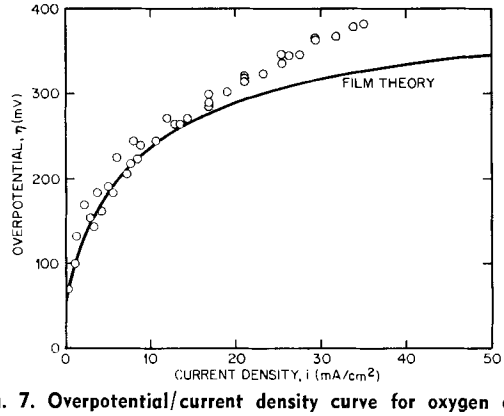

Fig. 7. Overpotential/current density curve for oxygen cathode. 6.9*N* KOH, 23.5°C, O_2 at 23 in. H_2O pressure, electrode 3 mm thick.

Table I. Parameters for silver sphere bed oxygen cathode in 6.9N KOH at 23.5°C

Electrode reaction: $O_2 + 2H_2O + 4e^- \rightarrow 4OH^-$	
Electrons transferred in rate determining step (m)	1
Transfer coefficient (α)*	½
Exchange current density (j_o)*	2×10^{-6} amp/cm²
Diffusion coefficient of OH^- ion (D_-)	2×10^{-5} cm²/s
Diffusion coefficient of dissolved O_2 (D_g)	0.6×10^{-5} cm²/s
Oxygen solubility for 1 atm gas pressure (c_g^o)	7×10^{-5} g-mole/liter

* Using Volmer type kinetic expression [Equation 2, ref. (4)].

film thickness of order of magnitude 10^{-5} cm, the measured active reaction zone extends more than 10^4 film thickness (more than 2 mm) along the surface away from the intrinsic meniscus. This constitutes strong evidence for the film mechanism; active lengths for surface diffusion should be two orders of magnitude less (5). Extreme degradation in electrode performance noted when the meniscus was allowed to enter the sphere bed is also consistent with the film process. The almost negligible residual activity of the flooded electrode indicates the magnitude of the contribution of the mechanism involving reaction under the meniscus itself or in the flooded portions of pores.

For quantitative comparison of measured electrode performance with predictions of the film model, the analog computer implemented computational procedure developed previously by two of the present authors (4) was applied to the electrode system of these experiments. In these calculations, the kinetic parameters for the oxygen reaction were taken from recent measurements for oxygen reduction at silver cathodes in potassium hydroxide solutions (17). Transport properties of the ionic species were derived from transference numbers and conductivities for similar solutions (19-20). The solubility and diffusion coefficient of oxygen in the electrolyte were interpolated from available data for aqueous KOH (21). These values are listed in Table I.

The remaining parameter necessary for film model computations, the film thickness, could not be directly measured. It was determined from the limiting slope of the overpotential-current density relationship for the sphere bed electrode at vanishing currents.[4] The measured limiting slope of 250 mv/ma/cm² yields a film thickness of 0.5×10^{-5} cm. This is of reasonable magnitude; it should be expected that the films on the convex surfaces of spheres of small radii would be thinner than the 1 to 5×10^{-5} cm films observed on flat plates (14).

From the parameters cited above, the overpotential-current density curve and the reaction distributions were calculated for the sphere bed electrode. Figure 7 shows the predicted overpotential compared with experimental values. The model agrees reasonably well with the measured data except for currents large enough for the resistive potential drop in the sphere bed itself to become important. This effect causes an increase in overpotential of about 10 mv at 20 ma/cm² and proportionately higher deviations at higher currents.[5] The resistance of the matrix was not considered in the development of the film model and is negligible where sintered electrodes are involved. The calculations give an active film length of 10^5 film thicknesses or about 0.5 cm for this electrode, a number of the same order as that found experimentally.

For the oxygen cathode under the conditions of these experiments, the reaction distribution and the polarization are determined almost entirely by the electrode reaction kinetics and the transport of ionic species along the film.[6] The transport of dissolved gas across the film does not limit reaction rate nor materially influence electrode performance. This conclusion is supported by the transient behavior observed following increases in bed thickness for beds thinner than the active depth. As the film is very thin when it first forms and increases gradually to its final thickness (14), the overpotential of an electrode whose performance was determined by gas transport across such a film should drop sharply during formation of such new film. Only small temporary decreases in overpotential (<10%), however, were observed. These can be attributed to the elimination of film area by flooding of small regions near the contacts between spheres during film thickening. Exchange current would have to be several orders of magnitude greater than that for oxygen reduction on silver before dissolved gas transport could become a significant factor.

Conclusions

From the experiments with the sphere bed electrode and the comparisons made to film model calculations, several important conclusions can be drawn concerning the operation of porous gas electrodes in KOH electrolytes.

1. The principal mechanism active in gas electrodes with a single scale of porosity is reaction under an electrolyte film on the walls of the gas filled parts of the pores.
2. The electrode reaction is distributed over a length of film extending many thousands of film thicknesses from the intrinsic meniscus.
3. Electrode reactions occurring under the meniscus itself or in the flooded portions of pores do not contribute significantly to the performance of gas electrodes.
4. Those analyses based on the film model which include effects of electrode kinetics and concentration changes in the film (*e.g.*, 4-5-6) provide useful predictions of the performance of gas electrodes of a single scale of porosity.
5. The thickness of aqueous KOH electrolyte films existing on the walls of pores in electrodes composed of spherical or near spherical particles on the 10-100μ size range is on the order of 10^{-6} — 10^{-5} cm at ambient temperatures.

The type of cell used in this work can serve as a tool for investigation of many factors in gas electrode design. Spheres of different materials or of different sizes can be used to examine the influence of matrix material or pore size. The spheres can be uniformly treated with catalyst before being added to the bed for investigation of catalyst activity. In such experiments, the well characterized structure of the electrode and the exclusion of electrolyte menisci from the bed facilitate interpretation of the measurements. Moreover, the applicability of the film model calculation to this electrode permits interpretations in terms of fundamental parameters of the system.

Acknowledgment

The authors wish to acknowledge the financial support of this research by the U. S. Navy, Bureau of Weapons, under research Contract NOw 64-0597-f.

Manuscript received June 10, 1965; revised manuscript received Aug. 6, 1965.

Any discussion of this paper will appear in a Discussion Section to be published in the June 1966 JOURNAL.

REFERENCES

1. W. R. Grove, *Phil. Mag.*, **14**, 127 (1839).
2. C. Wagner, Unpublished work (1957).
3. F. G. Will, *This Journal*, **110**, 145 (1963); **110**, 152 (1963).

[4] Based on the film model analysis (4);
Film thickness = $\delta \simeq \left(\frac{2R^2T^2}{W^2F^3Dc_-{}^oi_o}\right)\left(\frac{1}{\text{Limiting slope of overpotential curve v/a/cm}^2}\right)$
where W is the equivalent wetted perimeter cm/cm², $c_-{}^o$ is KOH concentration g-mole/cm³, F is Faraday's constant, and R is the gas constant.

[5] These resistive potential drops were estimated by adding IR drop in the leads to that generated in the sphere bed assuming the reaction distribution was not significantly altered by bed resistance.

[6] The effects of kinetics and ionic transport predominate over those of dissolved gas transport so long as $\delta i_o/nD_gFc_g{}^o << 1$.
Here this quantity is
$$\frac{(2 \times 10^{-6})(0.5 \times 10^{-5})}{(4)(0.6 \times 10^{-5})(10^5)(7 \times 10^{-8})} = 6 \times 10^{-5}$$

4. E. A. Grens, R. M. Turner, and T. Katan, *Advanced Energy Conversion*, **4**, 109 (1964).
5. R. P. Iczkowski, *This Journal*, **111**, 1078 (1964).
6. J. A. Rockett, "The Performance of Porous Fuel Cell Electrodes," paper presented before the Battery Division of The Electrochemical Society, New York, October 1963.
7. D. N. Bennion and C. W. Tobias, "Current Distribution at a Gas-Electrode-Electrolyte Interface," paper presented before the Battery Division of The Electrochemical Society, Washington, D. C., October 1964.
8. H. B. Urbach, "Theory of Polarization of Porous Gaseous-Diffusion Electrodes," in "Fuel Cells," G. J. Young, Editor, p. 77, Reinhold Publishing Co., New York (1963).
9. L. G. Austin, "Polarization at Diffusion Electrodes," in "Fuel Cells," *ibid.*, p. 95.
10. E. W. Justi, M. Pilkuhn, W. Scheibe, and A. Winsel, "High-Drain Hydrogen Diffusion Electrodes Operating at Ambient Temperature and Low Pressure," *Verlag d. Akademie d. Wissenschaft u.d. Literature* (1959).
11. E. W. Justi and A. W. Winsel, "Kalte Verbrennung," Fran Steiner, Wiesbaden (1962).
12. R. C. Burshtein, A. G. Pshenichnikov, and N. A. Schumilova, *Dokl. Acad. Nauk, SSSR*, **147**, 399 (1962).
13. R. C. Burshtein, V. S. Markin, A. G. Pshenichnikov, V. A. Chismadgev, and Y. G. Chirkov, *Electrochem. Acta*, **9**, 773 (1964).
14. R. H. Muller, Paper presented at the Washington Meeting of the Society, October 1964.
15. Yu. A. Mazitov, *Elektrokhimiia*, **1**, 218 (1965).
16. Yu. A. Mazitov, *ibid.*, **1**, 340 (1965).
17. T. Katan and S. Szpak, Final Report, Bureau of Naval Weapons Contract NOw-64-0597-f, June, 1965.
18. O. K. Rice, *J. Chem. Phys.*, **12**, **1** (1944).
19. S. Lengyel, J. Giber, G. Beke, and A. Vertes, *Acta Chim. Hung. Tomus*, **39**, 356 (1963).
20. M. I. Usanovich and T. I. Sushkenvich, *J. Appl. Chem. USSR*, **24**, 657 (1951).
21. C. W. Tobias *et al.* Final Report, U.S. Army Electronic Lab. Contract and DA36-039 SC-89153 (1965), p. 152 ff.

An Electrochemical Model for the Oxidation of Zirconium

D. H. Bradhurst,[1] J. E. Draley, and C. J. Van Drunen

Metallurgy Division, Argonne National Laboratory, Argonne, Illinois

ABSTRACT

A simple electrochemical model for gaseous oxidation is derived and applied to the oxidation of zirconium at 700°C. It is concluded that the part of reaction involving electron transport is rate-controlling. The factor determining the difficulty of ion transport has not been identified; passage through the oxide film does not seem to be limiting. Half-cell potentials for oxidation and reduction have been calculated to be approximately equal. Some variation in the oxide film defect structure with oxidation time has been deduced. Details are lacking.

The existing theories of oxidation suffer from the disadvantage of limited application. Within the extensively studied class of film-forming metals a number of oxidation theories have been built upon such simplifying assumptions as equilibrium existing at the reacting interfaces, or that the thin film of oxide has properties identical to the corresponding material in bulk. In two of the accepted oxidation theories, those of Cabrera and Mott (1), and Wagner (2), it is implied that a potential gradient exists across the growing oxide such that the metal is positive with respect to the oxide-gas interface. The fact that these assumptions do not always hold limits the applicability of the theories.

In a typical oxidation process it is impossible to measure, using existing methods, the instantaneous values of all the variables which can affect the reaction rate, let alone to predict the values on theoretical grounds. A more reasonable approach in developing a comprehensive theory seemed to be to use a simple model for the reaction in which the number of assumptions is minimal and to measure parameters which are characteristic of a particular reaction. Subsequent analysis of these parameters might be expected to yield useful information from a theoretical viewpoint.

In this paper, evidence is presented in support of a simple electrochemical model for the reaction between zirconium and oxygen at elevated temperatures. However, the model is generally applicable to film-forming oxidation reactions.

Theoretical.—Wagner first applied an electrochemical model to solid-gas reactions involving film formation and published the results in a series of papers in the early thirties. In one of these papers on sulfidation of Ag (2) he derived the familiar expression for the ionic transport number for ions diffusing through a protective layer of silver sulfide, *viz.*

$$\frac{/E/}{E_o} = n_a + n_c \qquad [1]$$

where n_a and n_c are the transport numbers of anion and cation, respectively. E is the potential across the film, and E_o the electrical potential equivalent to the free change for the reaction.

In this treatment the expression derived is independent of the polarity of the potential E developed across the growing layer, while it seems implicit in the derivation that the polarity of E is such that the metal is positive with respect to the outer surface of the growing layer.

In experiments by Misch (3) it was shown that in the oxidation of zirconium, a potential was developed in which the metal was negative with respect to the oxide-gas interface. The following electrochemical model for the oxidation of zirconium was developed in an attempt to allow for the existence of a potential of either polarity.

In the absence of an electric field across an oxide film it can generally be expected that the rates of the ionic and electronic processes will be different. Ionic movement (whether anion or cation moves is for the present purposes immaterial) can be considered to be part of the anodic process since both oxidation of zirconium and ion transport through the oxide produce a negative potential on the metal relative to the exterior of the oxide. The primary anodic driving force is the free energy change in the half-cell reaction which can be written

$$Zr + nZrO_{2-x} \rightleftarrows \left[(n+1)ZrO_{(2-x)} \frac{n}{n+1} \right]^{+4} + 4e^- \qquad [2]$$

[1] Present address: Australian Atomic Energy Commission, Lucas Heights, N.S.W., Australia.

where n is the number of zirconium ions in the oxide film and x is the result of oxygen vacancies. The charge produced in the oxide is distributed in an unspecified manner.

The electrical equivalent of this free energy change is called E_a, and $i_{ionic} = E_a/R_{ionic}$, where R_{ionic} represents the kinetic difficulty of the entire anodic process, including the diffusion of ions. Similarly, $i_{electronic} = E_c/R_{electronic}$, where E_c is for the half-cell reaction which can be written as follows

$$\left(1-\frac{x}{2}\right)O_2 + \left[(n+1)ZrO_{(2-x)}\frac{n}{n+1}\right]^{+4} + 4e^- \rightleftarrows (n+1)ZrO_{(2-x)} \quad [3]$$

So long as the ionic and electronic currents are unequal, a potential will be developed between the metal and the exterior surface of the oxide. For example, ionic flow tends to establish a field which opposes further ionic movement (metal negative). Electronic movement is encouraged by this field and tends to reduce it. A steady potential is established as a result of these processes when their rates are equal. Under these conditions it is expected that for some cases electrons migrate through the oxide against an electric field (but with an electron concentration gradient); for the remaining cases ions migrate against an electric field (but with an ion concentration gradient).

The following equations summarize the situation, where E is defined as the potential of the metal with respect to the exterior oxide surface.

$$E_a + E = iR_i \quad [4]$$

$$E_c - E = iR_e \quad [5]$$

Adding [4] and [5]

$$E_o = E_a + E_c = i(R_i + R_e) \quad [6]$$

which is identical to the equation obtained by Hoar and Price (4).

Also obtainable from Eq. [4] and [5] is the following expression for the potential existing during oxidation

$$E = \frac{\frac{R_i}{R_e}E_c - E_a}{\frac{R_i}{R_e} + 1} \quad [7]$$

The potential is determined by the ratio of the two R's and the values of the half-cell thermodynamic potentials. The possible range of values for E is from $-E_a$ to $+E_c$.

Equation [4] predicts that the reaction rate can be altered by the external application of a potential: if a more positive E is maintained, the oxidation rate will increase, and if a more negative E is applied, the rate will decrease. The rate should decrease to zero when $E = -E_a$.[2]

The unknowns, R_e, R_i, E_a, and E_c can be obtained by experimental means during the course of the reaction, if it is assumed that R_e and R_i act in parallel during a measurement in which a small external current flows. It is also necessary to measure the area effective during the measurement, and the contact resistance. The resistance R is then given by

$$R \cdot \alpha = \frac{R_e \cdot R_i}{R_e + R_i} \quad [8]$$

where α is the fraction of the film area which conducts during the resistance measurement.

Simultaneous solution of Eq. [6] and [8] yields a quadratic equation, providing conjugate expressions for R_e and R_i. It is possible to select which are correct on two bases: (*a*) if applied cathodic current of the same magnitude as the oxidation current causes substantial reduction in oxidation rate (see results), then R_i cannot be much larger than R_e; (*b*) in the case of the present research, calculated values of E_c and E_a seemed reasonable only for one of the two conjugate choices.

Such selection provides the following solution

$$R_e = \frac{E_o}{2i}\left(1 + \sqrt{1 - \frac{4iR\alpha}{E_o}}\right) \quad [9]$$

A knowledge of R_e enables the remaining unknowns to be calculated; values of R_i and R_e indicate the relative importance of the ionic and electronic processes in controlling the reaction rate.

Experimental

Specimen preparation.—Zirconium specimens were prepared in the form of disks approximately 1.3 cm diameter x 0.2 cm thick. "Grade I" Van Arkel crystal bar (iron content 300 ppm) was argon arc melted three times and cold rolled to form sheet from which the disks were machined. The specimens were wet ground to 600 grade SiC paper, rinsed in hot water for 15 min, etched for 2 min in 45:5:50 HNO_3, HF, H_2O mixture, then rinsed in cold water for 30 min, degreased in ethyl alcohol, and swabbed dry.

Weight gain measurements.—The Ainsworth recording balance, together with the furnace and vacuum system are shown in Fig. 1. The balance operates continuously throughout each oxidation experiment and enables weight gain measurements to be made to within ± 10 μg. Samples were brought to temperature under a vacuum of about 10^{-6} mm Hg before the commencement of a run. The reaction was started by admission of oxygen to the furnace, and was stopped after a given period by evacuation of the system. "Blank" experiments were done without a specimen to determine both the buoyancy correction and the small but significant weight gain of the oxide powder used as an electrical contact.

Potential measurements.—The specimen was sometimes immersed in, and at other times rested on the surface of, 100-150 mesh lithium-doped nickel oxide powder (3, 5) contained in a platinum bucket. Comparison of weight change rates and appearances demonstrated that the powder did not seriously limit access of oxygen to the specimen, or otherwise influence reaction rate. This powder approximates an inert electron-conductor in this system.

Electrical contact was effected by means of two platinum wires, one spot-welded to the zirconium specimen (or to a short Zr wire from it) and the other to the platinum bucket. All contacts between dissimi-

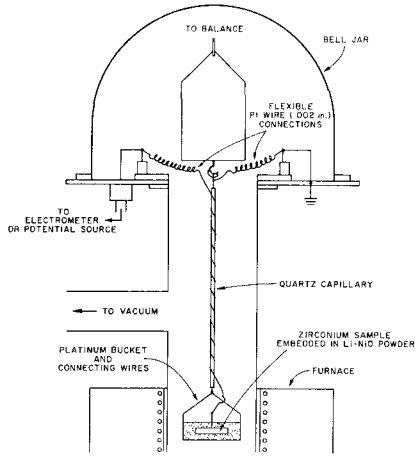

Fig. 1. Apparatus for simultaneous measurement of emf and weight gain.

[2] The value of E_a can be expected to depend on the defect structure of the oxide film (see Eq. [2]), which might be changed by an applied potential; thus the potential just sufficient to stop oxidation might be somewhat different than the E_a applying during unpolarized oxidation. However, oxidation should stop at a negative potential less than E_o.

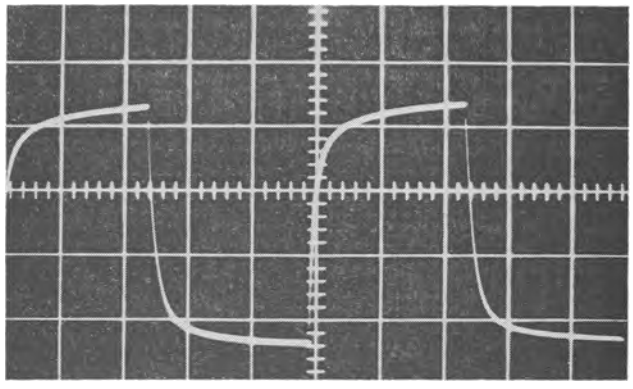

Fig. 2a. Oscilloscope trace of potential across oxide film and contact; 3.33 x 10^{-6} amp square wave; 0.1v (vertical) and 1 msec (horizontal) per large division.

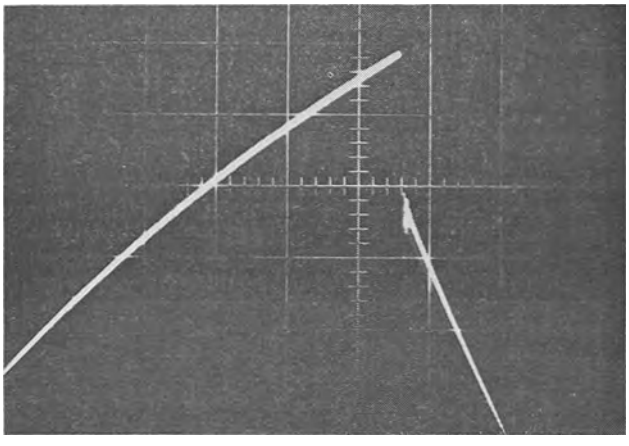

Fig. 2b. 0.01v (vertical) and 0.01 msec (horizontal) per large division.

lar materials were at the same temperature. Two coils of 0.002 in. platinum wire were used to make the connection from the balance to the external circuits for measurement of potential, current, and resistance. The sensitivity of the balance was adjusted prior to each run to compensate for the small damping effect of the coils. Potentials were measured with a Keithley electrometer, Model 610R, having an input impedance of 10^{13} ohms. Typically the output of the electrometer was recorded continuously.

Resistance measurements.—The basic method was to apply small currents, of both polarities, and to determine the slope of the E *vs.* I curve at zero current (polarization resistance). It proved convenient to use a bucking potential and to read only the unbalance produced by the applied current. Currents causing potential changes up to about 20 mv proved suitable for obtaining resistances without giving evidence of long-time disturbance of the oxidizing specimen. Nonlinear response resulted when considerably higher potential changes were used.

Resistances determined in this way required corrections from two causes: (*a*) there was an unknown series resistance consisting of the oxide powder resistance (trivial) and a contact resistance; (*b*) the area of the oxide film which conducted the applied current was unknown.

The series resistance correction was estimated from the oscilloscope trace of an applied square wave alternating current. Such traces for a platinum specimen showed that the potential at the contact points and across the oxide powder decayed rapidly ($<10^{-6}$ sec) and was ohmic. For an oxidizing zirconium specimen there was the iR drop and a more slowly decaying portion, ascribed to the oxide film. Typical traces of this type are shown in Fig. 2. The discontinuity in the

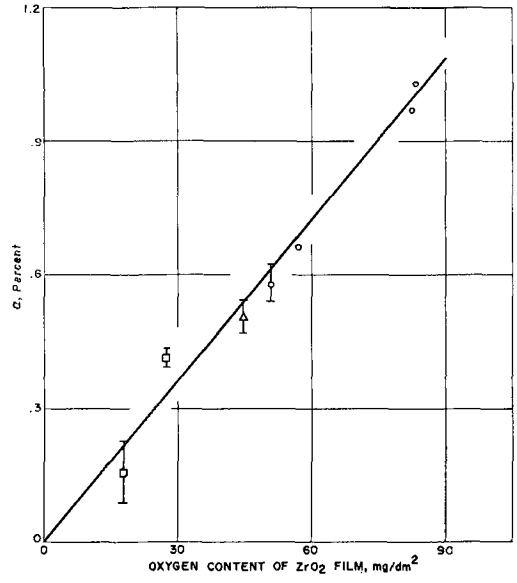

Fig. 3. Calibration curve for alpha: ○, 700°C; △, 650°C; □, 600°C.

decay curve made possible ready measurement of the contact resistance. In practice, a constant current square wave was chosen to give a total potential change in the range 15 to 50 mv. Equivalent results were obtained between 100 and 1000 cps.

The fraction of the film area conducting, α, was determined at the conclusion of the oxidation as the ratio of the resistance (per unit area) immersed in a molten (oxygenated) bath of 28% Li_2CO_3, 33% Na_2CO_3, 39% K_2CO_3 to that obtained in oxygen with the powder contact at the same temperature. In order to obtain the variation in α with film thickness, several tests were terminated at less than typical total exposure. These values were plotted against the film thickness to provide a calibration curve (Fig. 3). To determine film thickness, the amount of oxygen diffused into the metal, as estimated from the data of Pemsler (6), was subtracted from total weight gain.

For small film thicknesses, oxidation rates at 700°C were sufficiently rapid that significant film growth occurred between the last resistance measurement in oxygen and that in the carbonate bath. In order to eliminate this problem, some determinations were made at lower temperatures. Uncertainties were sometimes substantial, but a straight line through the origin is indicated.

Confirmation of the type of calibration curve was obtained with an analogue system. This consisted of a thin layer of 1M $CuSO_4$ solution in a shallow vessel, having a flat copper base. The resistance between a single small-point copper tip just touching the solution surface and the plate is given by: $R = \rho t/A$, where ρ is the measured resistivity of the solution, t its thickness, and A the area effective in conducting the current. The ratio of A to the area of the plate was taken as α for this system.

The thickness to area ratios for these experiments were larger than for the oxidation specimens, the smallest being slightly larger than the largest in Fig. 3. Results approximated a straight line through the origin, providing credence to the calibration curve of Fig. 3.

Results

Preliminary experiments. Potential measurements on zirconium and niobium.—Figure 4 shows a typical measurement of the emf developed during the oxidation of zirconium at 700°C. Before admission of oxygen, when the system is at a pressure of 10^{-6} mm Hg and 700°C, the emf is zero; it rises quickly to a steady value as oxidation proceeds. Finally, when the system is

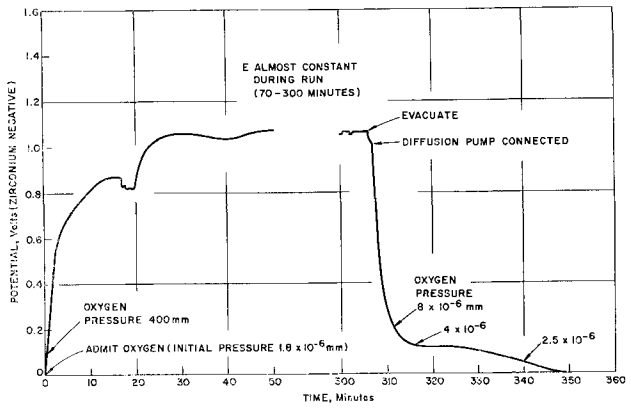

Fig. 4. Behavior of potential developed during oxidation of zirconium at 700°C.

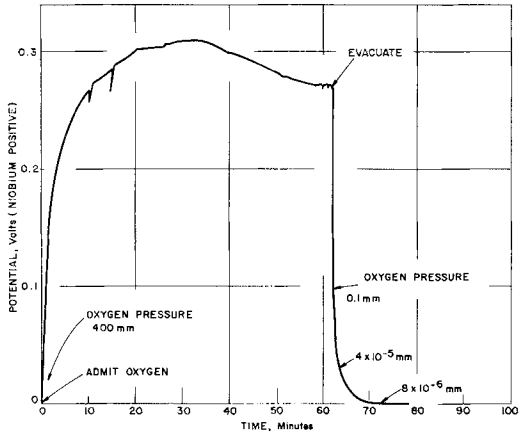

Fig. 5. Behavior of potential developed during oxidation of niobium at 450°C.

evacuated, the emf decays once again to zero. During oxidation of zirconium under these conditions, the emf is slightly greater than 1v with the zirconium negative with respect to the oxide-gas interface.

Figure 5 illustrates that the behavior in emf for niobium at 450°C is similar, except that for this reaction the sign of the emf is reversed.

Forty-six experiments of this type were done for zirconium and all showed the same polarity for the emf. The value of the emf was typically in the region of 1.0 to 1.1v at 700°C, which was in agreement with previous measurements by Misch (3) and Kirkbride and Thomas (7). The emf was steady throughout the experiment in the better runs. There was a small reduction in the value of the emf at longer times of oxidation (from 300 to 5000 min). The majority of measurements were made in the range 0 to 306 min.

Polarization experiments.—A series of specimens were polarized during oxidation in order to determine whether an alteration in rate could be effected as described by Eq. [4]. It was shown that the oxidation rate could be reduced by at least a factor of two by the application of a cathodic potential approximately equal to the reversible emf of the reaction. This is illustrated in Fig. 6 in which the reaction rate (taken as the weight gain during the time interval from 100 to 300 min) is plotted as a function of the applied voltage. The rate decreases as the applied potential becomes more negative, whereas much less change in rate is evident with anodic polarization. The deviation from the prediction from Eq. [4] can be explained from the following. Microscopic examination revealed that the surfaces of the cathodically polarized samples were covered with indentations separated by a distance approximately equal to that between particles of the semiconducting oxide powder used as the contact.

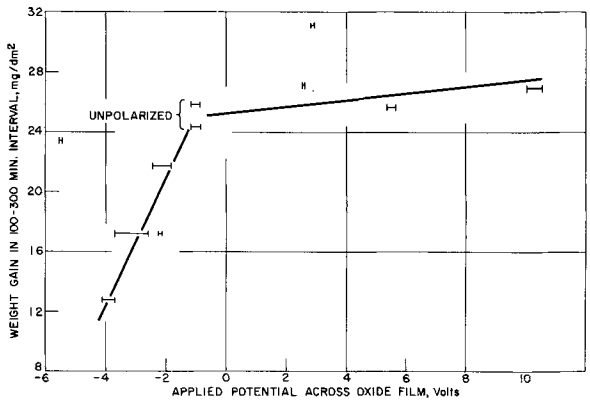

Fig. 6. Variation in oxidation rate with applied voltage: zirconium in oxygen at 700°C.

Unpolarized samples also had some darkened areas corresponding to points of contact, but without depth. The anodically polarized samples had small mounds at points of contact.

These observations suggest that relatively large changes in oxidation rate did occur near the contact points, where the potential was controlled, but that the local changes were not truly represented by the overall weight gain of the specimen. This was more noticeable in the anodic case, since the area of influence was restricted to point contacts as the film grew there, giving rise to a quite small area where the potential was controlled. In the cathodic experiments, the area of contact progressively increased as the oxide thickened around the base of each particle, and the potential was controlled over a significant fraction of the total area.

Experiments using porous metal film contacts.—In an effort to obtain an increased area of contact to the oxide surface, experiments were done in which a layer of gold (approximately 200Å thick) was evaporated onto the surface of the zirconium specimens. A twenty-fold increase in oxidation rate resulted and polarization proved ineffective in changing the oxidation rate. Figure 7 is a photomicrograph of a cross section of an oxidized zirconium specimen, showing the difference between the "normal" oxide thickness (after 300 min) and that achieved beneath the gold layer.

It seems reasonable to expect that an increase in rate might result from contamination of the oxide product by gold, since it is known that zirconium-gold alloys have relatively poor oxidation resistance. The effect was larger than might have been anticipated on this basis. Whether there was a galvanic effect is not known. One face of a single crystal was gold-plated and showed about the same accelerated reaction on that face only. Similar behavior was exhibited during oxidation after evaporating gold on a pre-oxidized specimen.

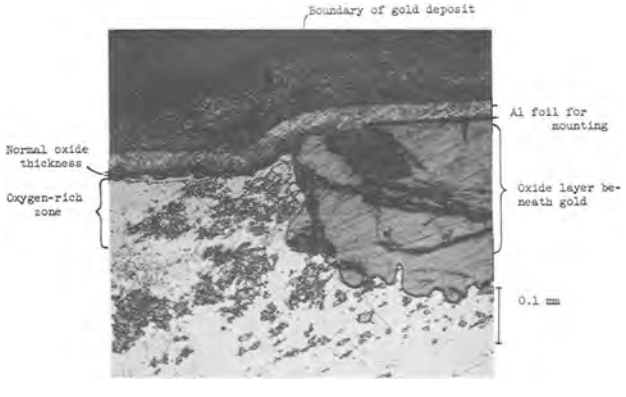

Fig. 7. Cross section of zirconium specimen after 300 min oxidation at 700°C.

In a second series of experiments evaporated films of copper were used in place of the gold. The oxidation rate of unpolarized copper-coated samples was slightly less than that for pure zirconium, after the copper had completely oxidized in about an hour. Variable copper thicknesses apparently caused some irregularity in results, but the oxidation rate changed substantially with applied potentials; positive potentials accelerated oxidation to about the same extent as negative potentials reduced it. The controlled potential at the oxide film surface was apparently more uniform in this case than for the experiments with uncoated zirconium.

Electrochemical Analysis of Oxidation

The reaction rate at 700°C was found to be essentially independent of oxygen pressure in the range 10 to 400 mm Hg, as may be seen from Fig. 8. Kinetics roughly followed the cubic rate expression, although deviation was evident at early and later stages (Fig. 9). The deviation after 100 to 200 min varied from case to case, in some instances being substantial. Detailed examination of the reaction kinetics will be deferred; at this time only the approximate cubic behavior will be used for convenience.

For a number of experiments of about 300 min duration, the potential and weight gain were continuously recorded and the film resistance was determined periodically, using the methods outlined above. Because of some irregularities in the weight gain curves, it was difficult to determine instantaneous slopes (or oxidation "currents") with good precision. It is not clear how much of the irregularity has been due to

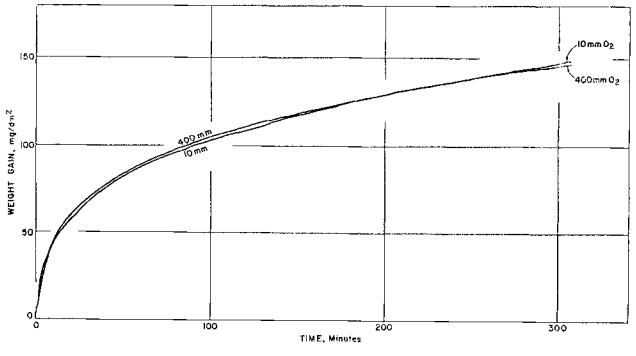

Fig. 8. Weight gain curves for Zr: 700°C and different oxygen pressures.

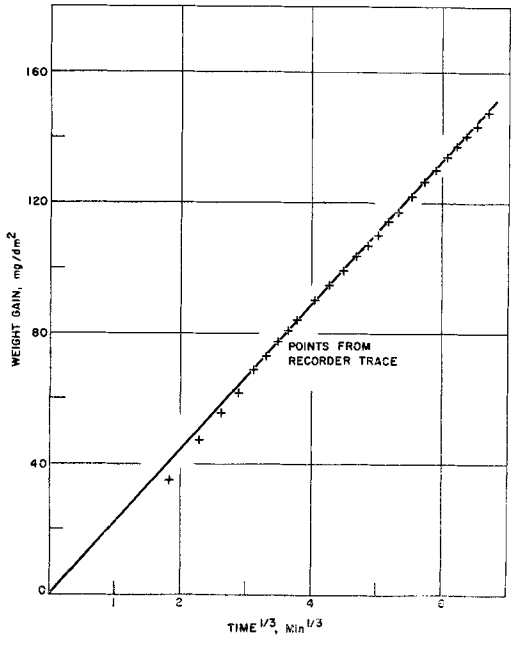

Fig. 9. Cubic plot for oxidation at 700°C

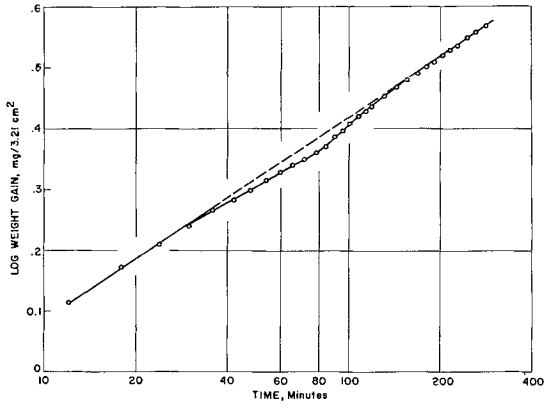

Fig. 10. Weight gain for specimen 69

deficiencies in the apparatus (such as slight balance movement caused by turbulence of the gas in the tube furnace) and how much represents actual irregularity in the oxidation process. Examination of recorder traces has indicated that both of these effects have been significant.

In order to analyze the data effectively, the logarithm of the weight gain was plotted against the logarithm of time. Generally, a straight line was observed; one of the most notable exceptions is shown in Fig. 10. Oxidation currents at times corresponding to resistance measurements were then calculated from slopes of lines such as that in Fig. 10. Values for E_c, E_a, R_e, and R_i were calculated at these times, assuming a constant E_o of 2.344v (at 400 mm O_2 and 700°C) (8).

Results for one specimen are given in Fig. 13; comparison with three other specimens is made in Table I. E_a and E_c were found to be approximately equal. E_a was generally found to have a downward trend with time, and E_c the converse.

R_e and R_i varied smoothly with time, with R_e always considerably the greater. Under these circumstances, and with the knowledge that $\Delta W \approx Kt^{1/3}$, it can be expected (from Eq. [6]) that $i = \dfrac{d(\Delta W)}{dt} \approx \dfrac{K}{3t^{2/3}} \approx \dfrac{E_o}{R_e}$; thus, that $R_e \approx k_e t^{2/3}$.

Figure 11 shows that this is true, with the variation in the middle of the plot peculiar to this specimen (noted in Fig. 12). In spite of this peculiarity, R_i varied smoothly with $t^{1/2}$ for a period, then became erratic. The parabolic rate constants for this increase and the times for which no further regular increase were observed are recorded in Table I. Since R_e and R_i obeyed different rate laws, their ratio changed continuously with time. The ranges of these ratios are also presented in Table I.

Discussion

The rise and fall of the emf across the oxide film with admission and removal of oxygen from the system provide good support for the concept that the potential is produced by the processes occurring. Under

Table I. Calculated electrical constants

	Specimen No. 51	52	69	70*
E_c at 300 min., v	1.25	1.34	1.28	1.48
E_a at 300 min., v	1.09	1.00	1.06	0.86
k_e, ohm-cm^2-min$^{-2/3}$	166	195	181	165
k_i, ohm-cm^2-min$^{-1/2}$	16.5	16.9	32.4	28.5
Last measurement before break in R_i, min	202	244	203	290*
R_e/R_i before break	17-25	13-33	9-14	9-15

* This specimen exhibited an unusually low potential (0.70-0.76, compared to more typical values of 1.0); after an initial period of severe scatter, calculated values of R_i varied with $t^{1/2}$ through the last reading at 290 min.

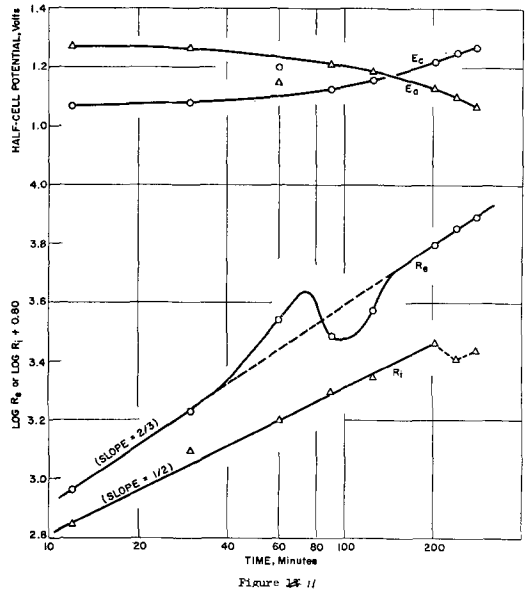

Fig. 11. Calculated constants for specimen 69

these circumstances it is probably wrong to consider the potential as a primary driving force for the reaction.

The appreciable changes in reaction rate which were effected by polarization of zirconium samples during oxidation support the electrochemical model summarized by Eq. [4] and [5]. That this might be a general phenomenon is suggested as well by the work of Jorgensen (9, 10) and of Lacombe *et al.* (11). The fashion in which control of reaction rate by applied potentials was essentially restricted to points of contact demonstrates the need for care in interpreting such results. Reaction rates can be expected to vary with time in a fashion difficult to interpret as the oxide grows into interstices and increases the area of contact, even with constant cathodic polarizing potential (or current).

There are some complications in the application of the theoretical treatment developed here:

1. If there is a potential difference between oxide surface and a zone in the gas phase which is influential in the oxidation process, this will not be included in our measurements and our results for E_a and E_c will be in error. For the present research this error is estimated to be trivial.

2. The R's in Eq. [4] and [5] are integral quantities in that they measure kinetic difficulties in the change from $i = o$ to i. The R_i and R_e in Eq. [8] are differential quantities (for small incremental current values). Assuming that these are the integral R's (in the derivation of Eq. [9]) leads to errors. These have not been evaluated; that the situation is not too bad can at least be hoped from the observations that R (Eq. [8]) remained constant over a fairly wide range of currents, and Eq. [9] was rather insensitive to the value of R.

3. If metal oxidation were not occurring, that portion of an applied current transported through the oxide by electrons would not be involved in an oxidation or reduction reaction. The R_e (and R_i) which would apply for that case would be different from those which are effective during oxidation (and Eq. [1] would hold). However, if applied currents are small compared to an oxidation current, it is believed that such currents can be considered partly to change the ionic current in Eq. [4] and partly to change the electronic current in Eq. [5]. Under these circumstances, the effective R_i and R_e would appear to be nearly those set up by the oxidation reaction. The error due to oversimplified treatment will then be significant only if the kinetic difficulty due to an activation energy in the reduction of oxygen to ions is a significant fraction of R_e.

The results of this investigation suggest (Table I and Fig. 13) that the free energy driving forces for the two half-cell reactions in the oxidation of zirconium at 700°C are approximately equal. Their variation with time is not known, because the variation of E_o with time is not known. Since these quantities can be expected to depend on the defect structure (or nonstoichiometry) of the oxide, it is indicated that there is a variation in this property during oxidation. If knowledge of the free energy of formation and the partial pressure of oxygen in equilibrium with zirconium oxide can be made available as a function of stoichiometry [such as has been reported for the latter by Aronson (12)] it should be possible to determine the stoichiometry of the growing oxide.

The ratio of R_e to R_i ranged from 9 to 33 during this investigation, for times up to 300 min. This indicates the reaction at 700° to be predominantly controlled by an electronic process. Within the meaning of R_e, this process could be any of the following: transport of electrons through the oxygen-rich layer in the metal; entry into the oxide; transport through the oxide; or the surface reaction in which oxygen is reduced. Of these, transport through the oxide seems the most likely, considering both magnitude and variation with time.

The process controlling R_i is apparently not closely related to that controlling R_e, as judged by the different rate law, and the different behavior in experiments showing peculiarities; *e.g.*, the deviation illustrated for R_e, but not R_i, and the irregularity in R_i after some period of exposure (but not in R_e). The process controlling R_i apparently does not reside in an obvious way in the oxide film. Where the weight gain for the specimen illustrated in Fig. 10 was approximately equal to $22.4t^{0.33}$, the estimated oxygen content of the film was $21t^{0.30}$, and R_i was $32.4t^{0.50}$. The diffusion of oxygen into the metal is apparently parabolic (6), and this suggests that this process determines R_i. There appears to be little evidence on this point.

After a period of oxidation, if a sample is evacuated the resistance to the passage of external current is rapidly and sharply reduced (by a factor of a few hundred). Since this resistance is approximately equal to R_i (Eq. [8], where $R_e >> R_i$), it is indicated that this quantity responds quickly in this fashion. The explanation is not clear, but some process at the metal-oxide interface, such as entry of oxygen ions into the metal, is suggested. The failure of R_i to continue to increase (after about 200 min in Fig. 11) might logically be expected on this basis, if the surface layers of the metal became saturated with oxygen at that time.

The calibration curve for α (Fig. 3) indicates that for a film of constant resistivity the measured value of the external resistance should be constant, independent of film thickness. This was observed for the $Cu/CuSO_4$ experiments. During the oxidation of zirconium, however, this resistance increased with time, although sometimes irregularly. This demonstrates that R_i is not a direct measure of some property of a uniform total oxide film.

Under the conditions of the present investigation, the oxide films contain many fine cracks. Interpretation of these results in terms of detailed mechanisms does not seem feasible at this time. It appears desirable to study oxidation under conditions where cracking does not occur before hoping to interpret controlling factors for growing and cracking films.

It is observed (Eq. [9]) that the value of the potential across the growing oxide need not be known in order to calculate R_e and R_i. With measurement of the oxidation rate and the resistance to external current, and knowledge of E_o, it is possible to derive values for the electronic and ionic retardances. These quantities should be quite valuable as an aid in deducing the difficult steps in the oxidation. Their response

to changes in experimental parameters might be quite instructive. Measurement of the potential then makes possible the calculation of E_a and E_c. With these quantities available it might be hoped that interpretation of reaction mechanisms will become possible.

The value of the present treatment appears primarily to be to focus attention on the processes which are most important in determining oxidation behavior. Further analysis of such processes will very possibly involve the use of other techniques. The analogy to electrochemical consideration of corrosion in liquid electrolytes suggests that procedures applicable to such systems might also be applicable to gaseous oxidation.

Acknowledgment

Work on this paper was done under the auspices of the United States Atomic Energy Commission.

Manuscript received April 12, 1965.

Any discussion of this paper will appear in a Discussion Section to be published in the June 1966 JOURNAL.

REFERENCES

1. N. Cabrera and N. F. Mott, *Rept. Prog. Phys.*, **12**, 163 (1948).
2. C. Wagner, *Z. Phys. Chem.*, **21B** 25 (1933).
3. R. D. Misch and G. W. Iseler, USAEC-ANL-6434 (1961).
4. T. P. Hoar and L. E. Price, *Trans. Faraday Soc.*, **34**, 867 (1938).
5. E. J. W. Verwey, P. J. Haaijman, F. C. Romeijn, and G. W. Van Oosterhout, *Philips Research Repts.*, **5**, 173 (1950).
6. J. P. Pemsler, *This Journal*, **105**, 315 (1958).
7. L. D. Kirkbride and D. E. Thomas, Westinghouse Electric Corp., Rept. WAPD-T-308 (1956).
8. JANAF Interim Thermochemical Tables, prepared under the auspices of the Joint Army-Navy-Air Force Thermochemical Panel, Dec. 31, 1960.
9. P. J. Jorgensen, *J. Chem. Phys.*, **37**, 874 (1962).
10. P. J. Jorgensen, *This Journal*, **110**, 461 (1963).
11. Francis Schein, Bernard LeBoucher, and Paul Lacombe, *Compt. rend.*, **252**, 4157 (1961).
12. S. Aronson, *This Journal*, **108**, 312 (1961).

Effect of Impurities in Iron on Corrosion in Acids

Z. A. Foroulis and H. H. Uhlig

Corrosion Laboratory, Massachusetts Institute of Technology, Cambridge, Massachusetts

ABSTRACT

The corrosion rate of annealed pure iron in 0.12*N* deaerated HCl is increased by alloying several hundredths per cent of various nonmetallic elements in the sequence B, N, As, C, S, P. The addition of 0.02% N increases the rate by a factor of only 1.3, whereas for 0.02% S or P the corresponding factors are 23 and 31, respectively. Small amounts of As up to about 0.1% increase the rate; larger amounts, up to at least 0.27%, decrease it. Tin in the amount of 0.1% or more decreases the corrosion rate below that of iron itself; it similarly decreases corrosion of iron in citric or malic acid. Cold work alone has relatively little effect on the corrosion rate except with iron containing carbon, for which the effect is large. Polarization measurements show that hydrogen overvoltage of the added element itself, or as associated with Fe, is the generally important factor controlling corrosion; in some cases change of anodic polarization also enters.

In a previous paper (1), detailed data were presented on the effect of carbon and nitrogen in iron, and of cold work, on the corrosion rate in deaerated 0.12*N* HCl of *p*H 1.01. The present investigation extends these results to iron alloyed with boron, phosphorus, sulfur, arsenic, and tin. The effects on corrosion of some of these elements differ markedly from those induced by nitrogen or carbon. Also cold working of iron containing these elements tends to accelerate corrosion less than in the case of carbon or nitrogen. The reasons for these differences are discussed in relation to the electrochemical mechanism of corrosion.

Experimental Procedure

The procedure was the same as that described previously. Rectangular specimens about 4-6 cm^2 total exposed area were immersed in 1.5 liters of H_2-deaerated 0.12*N* HCl with H_2 continuously bubbling through the acid at a low rate. For the tin alloys, additional runs were made in citric and malic acids. Corrosion rates were determined by periodic colorimetric analyses of the acid for Fe^{++} using the orthophenanthroline method, the rate being taken from the slope of metal dissolution *vs.* time of exposure. Checks were made by weight-loss determinations at the end of each run. Exposure time was usually 4-6 days. The effect of cold work was investigated for all the alloys with the exception of the sulfur alloys which, being brittle, were tested in the as-cast and homogenized condition.

All the alloys were prepared in a vacuum furnace starting with remelted electrolytic iron supplied by courtesy of Westinghouse Electric Corporation (<0.001% Cu, <0.001% Ni). This was further decarburized to 0.002% C by treatment in wet H_2 at 760°C for 48 hr. The alloys were cast in an atmosphere of purified helium (passed over Ti at 850°C) by drawing into ¼ in. Vycor tubing and water quenching. Each specific alloy, encapsulated in evacuated quartz tubes, was homogenized for 48 hr at 1050°C, air cooled, and then cold-rolled to 50% reduction in thickness.

Phosphorus was added in the form of Bureau of Standards ferrophosphorus alloy containing 26.2% P. Other components were added as the purest available form of the element. The alloys were analyzed chemically after the homogenization treatment.

Polarization measurements were conducted in a three compartment glass cell as described earlier (2). Because of slow attainment of steady-state values, anodic polarization values were recorded after constant current flow for 15 min; for cathodic polarization the required time interval was less. Data for tin alloys were especially sensitive to time of previous immersion in the electrolyte.

Results

Iron-boron alloys.—Four alloys prepared for this series contained 0.01-0.099% B with carbon and nitrogen contents of 0.006 and 0.0014%, respectively. An alloy containing 0.15% B was too brittle to cold-roll. Corrosion data are shown in Fig. 1 showing negligible effect of boron on corrosion in 0.12*N* HCl, and with cold-rolled alloys corroding at slightly higher rates

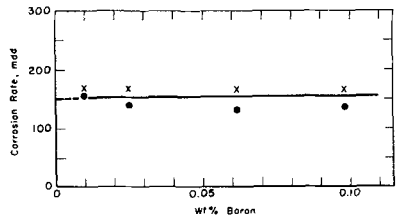

Fig. 1. Effect of alloyed boron on corrosion of iron in deaerated 0.12*N* HCl. • Annealed 2 hr at 950°C; X cold-rolled.

than annealed alloys. The small effect of cold rolling, if any, can probably be ascribed to residual C and N as much as to B.

The cold-rolled B alloys show a maximum in corrosion rate after heat-treating at about 100°C for 2 hr, the maximum rate being almost twice that for the initial cold-rolled material. In view of the fact that a similar effect is found for carbon and nitrogen alloys but not for pure iron (1), the maximum for the present B alloys may also be caused mostly by residual C and N. A similar maximum in corrosion rate of cold-rolled iron alloys containing 0.01-0.105% C and 0.1-1.04% Si was reported by Foroulis (3) after heat-treatment of the alloys at 100°C for 2 hr.

Iron-phosphorus alloys.—Three alloys were prepared containing 0.05-0.15% P, and with C and N contents of 0.002 and 0.005%, respectively. Phosphorus produced the highest corrosion rate in HCl (Fig. 2) compared with any of the other components presently investigated, sulfur also having a marked accelerating effect. Cold rolling produced still higher rates, the effect increasing with phosphorus content. At 0.15% P, for example, 50% reduction in thickness increased the rate by 30%. Heat-treatment of cold-rolled alloys at 100°C decreased the rate instead of increasing it as for C and N alloys.

The marked accelerating effect on corrosion of iron by alloyed P confirms previous results of Endo (4), Edwards *et al.* (5), and of Stern (6).

Iron-arsenic alloys.—Three alloys were prepared containing 0.09-0.29% As and with C and N contents of 0.002% and 0.005%, respectively. The corrosion rate of the 0.09% As alloy is higher than that of alloys containing more, or less, than this amount of As (Fig. 3). Cold working of the alloys has a negligible effect; heat-treatment at 100°C of cold worked alloys neither increases nor decreases the rate.

Iron-sulfur alloys.—Three alloys contained 0.015-0.078% S, with C and N contents of 0.002% and 0.005%, respectively. The corrosion rate of the cast alloys increases linearly with sulfur additions, the increase being appreciable for small amounts (Fig. 4). The effect on corrosion in HCl for a given weight per cent sulfur up to about 0.08% is about 25% less than for the same weight per cent addition of phosphorus. Endo (4) found that the corrosion rate of iron in 5% HCl or 5% H_2SO_4 increased almost linearly with alloyed S up to about 3%. For Fe alloyed with P, on the other

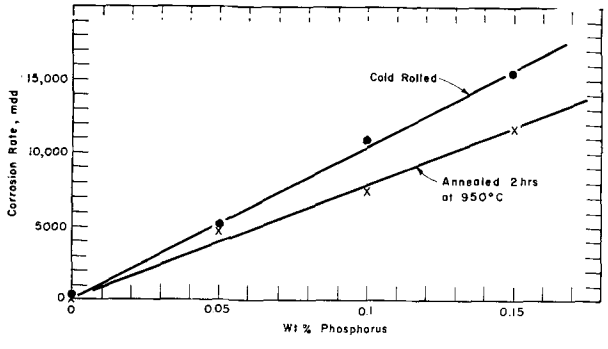

Fig. 2. Effect of alloyed phosphorus on corrosion of iron in deaerated 0.12*N* HCl.

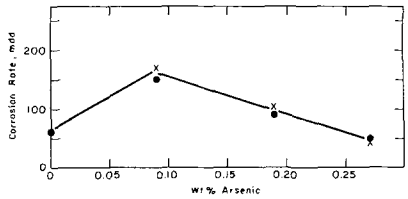

Fig. 3. Effect of alloyed arsenic on corrosion of iron in deaerated 0.12*N* HCl. • Annealed 2 hr at 950°C; X cold-rolled.

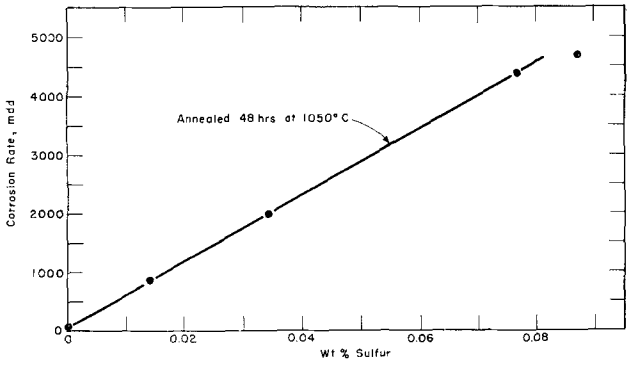

Fig. 4. Effect of alloyed sulfur on corrosion of iron in deaerated 0.12*N* HCl.

hand, he found corrosion to increase up to about 2% P; larger amounts again decreased the rate to appreciably lower values. Edwards *et al.* (5) found alloyed S up to about 0.15% to have little or no effect on corrosion of Fe in 6% H_2SO_4, but their alloys also contained appreciable Cu which counteracts the effect of S. The effect of Cu to reduce the accelerating effect of S on corrosion of iron in nonoxidizing acids was demonstrated by Bardenheuer and Thanheiser (7) and by Stern (6). The latter found Cu to be greatly beneficial in S-Fe alloys exposed to HCl and citric acid, but not to malic acid.

Iron-tin alloys.—Five tin alloys were prepared ranging from 0.039 to 1.38% Sn. Carbon and N contents were 0.002 and 0.005%, respectively. The alloys were cold-rolled except for the 1.38% Sn alloy which was too brittle. Corrosion rates in HCl are given in Fig. 5.

For all alloys in HCl, the initial corrosion rate was higher than the final rate. The cause was either redeposition of tin on the alloyed surface or perhaps build up of a tin-rich surface by preferential dissolution of iron. The decrease of corrosion rate with time is caused by change of alloy surface rather than by change in composition of the acid as shown in Fig. 6. The upper curve represents the weight loss of the 0.039% Sn alloy as a function of time. A steady-state corrosion rate of 25 mdd is reached after 36-40 hr. During this time, a visible black coating forms. If the solution is renewed at the end of six days, the continuing corrosion follows the lower curve of Fig. 6. After an initial period of 3 to 4 hr, the slope is the same as the steady-state upper slope for the initial immersion. Lack of immediate steady-state conditions on

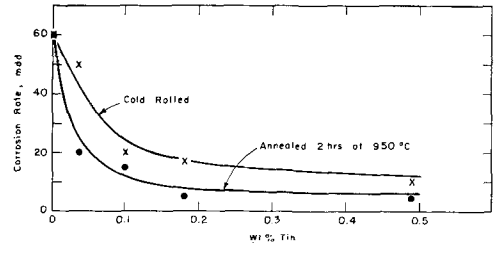

Fig. 5. Effect of alloyed tin on corrosion of iron in deaerated 0.12*N* HCl.

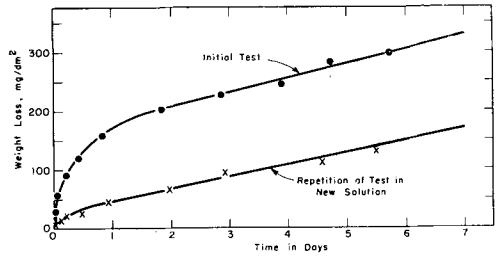

Fig. 6. Weight loss vs. time in deaerated 0.12*N* HCl for cold-rolled 0.039% Sn-Fe. Specimen at the end of corrosion test, upper curve, was introduced into a new solution for repetition of test, lower curve.

transfer of the specimen to the second solution is probably caused by a structural change, or by incipient oxidation of the metal surface during washing, drying, and weighing of the specimen.

It is of interest that the induction time observed in Fig. 6 was reduced in the case of citric and malic acids, with steady-state conditions being achieved within the initial 3-6 hr of the test. Alloyed tin lowered the corrosion rate in the organic acids as well as in HCl.

Rates given in Fig. 5 are steady-state values after exposure to HCl for several days. Tin additions up to 0.1% decrease the rate to about one-sixth the rate for tin-free iron, with little further change for higher Sn additions. The effect of cold-rolling is to increase the rate slightly; subsequent heat-treatment at 100°C had only a small effect either to increase or decrease the rate. Corrosion rates in 0.1*N* citric acid, *p*H 2.05, are similar to those in 0.12*N* HCl, both acids being deaerated (Fig. 7). The rates in deaerated 0.11*N* malic acid, *p*H 2.08, on the other hand, are about one-tenth the rates in either citric acid or HCl (Fig. 8).

Discussion

In our previous paper (1) we showed that zone-refined iron when severely cold-worked corrodes no more rapidly in 0.1*N* HCl than when annealed. In other words, imperfections, such as dislocations, produced by cold work in pure iron have no discernible effect on rate of acid attack. For iron containing carbon, however, cold work markedly accelerates corrosion in the same acid medium, presumably because low hydrogen overvoltage sites form by association of C atoms with imperfections. Nitrogen also markedly increases the rate but more so after heat-treating the alloy at about 100°-200°C at which temperature but not below nitrides readily dissociate allowing N atoms to reach imperfection sites. Carbon or N atoms segregated at imperfections lower hydrogen overvoltage; anodic polarization, on the other hand, is not affected.

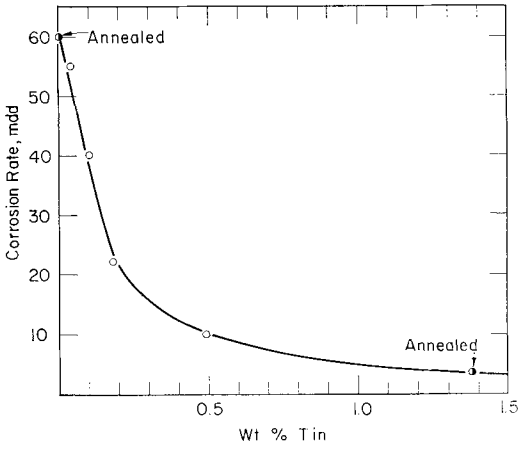

Fig. 7. Corrosion of cold-rolled (or annealed as shown) tin-iron alloys in deaerated 0.1*N* citric acid.

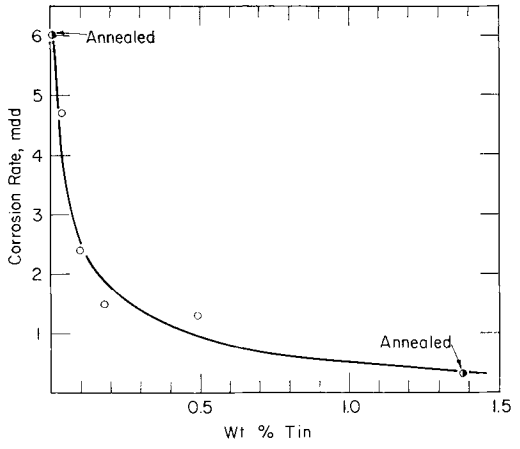

Fig. 8. Corrosion of cold-rolled (or annealed as shown) tin-iron alloys in deaerated 0.11*N* malic acid.

The slight effect of alloyed B up to 0.1% on corrosion of iron indicates that any interstitial impurity substituted for carbon in the iron lattice is not sufficient to reduce hydrogen overvoltage and to accelerate corrosion. Foroulis' results similarly show [Fig. 3, 4, ref. (3)] that alloyed Si up to 0.58% has very little effect on corrosion of cold-worked Fe in 0.1*N* HCl; although in the annealed state Si alters the form of iron carbide to a needle-like precipitate which in turn accelerates corrosion. Hence, chemical properties of the interstitial atoms and their chemical interplay with the surrounding iron atoms are important factors. Cold work apparently accelerates corrosion in nonoxidizing acids like HCl only if the additional imperfections generated by cold work are associated with specific impurity atoms, *e.g.*, C and N atoms, which lower hydrogen overvoltage. In presence of Si and B atoms alone, cold work has little if any effect.

As is noted, phosphorus and sulfur additions accelerate corrosion much more than any of the other elements added to iron. Polarization measurements for phosphorus alloys in Fig. 9 show that increasing P content lowers especially cathodic polarization with simultaneous reduction, although to a lesser extent, of anodic polarization. The corrosion potential moves toward more noble values as the P content of Fe increases in accord with the expected effect of decreased cathodic polarization. The cathodic sites of markedly reduced hydrogen overvoltage may consist of imperfections associated with P atoms but, were this entirely true, the effect on corrosion of cold work, which increases imperfection density, should probably be more pronounced. Instead, the low overvoltage sites probably also consist of iron phosphides.

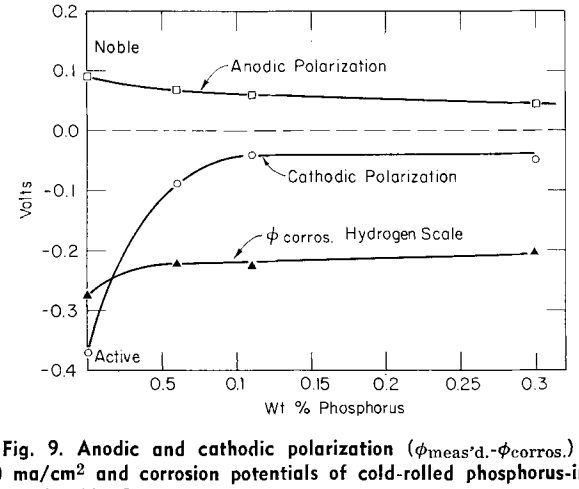

Fig. 9. Anodic and cathodic polarization ($\phi_{meas'd.}$-$\phi_{corros.}$) at 10 ma/cm² and corrosion potentials of cold-rolled phosphorus-iron alloys, 0.12*N* HCl, 25°C.

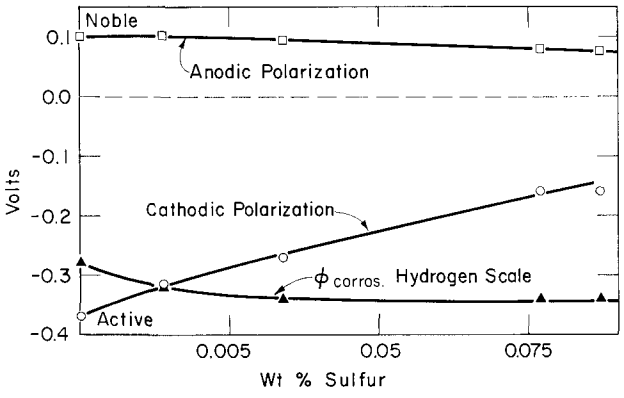

Fig. 10. Anodic and cathodic polarization ($\phi_{meas'd.}$-$\phi_{corros.}$) at 10 ma/cm^2 and corrosion potentials of annealed sulfur-iron alloys, 0.12*N* HCl, 25°C.

Similarly in the case of sulfur additions, the low overvoltage sites very likely consist in large part of iron sulfides. Segregation of S at grain boundaries accounts for the tendency of S-Fe alloys to corrode locally in the form of pits. This effect was previously observed by Stern (6). The corrosion potentials for iron with increasing S content move toward more active values (Fig. 10), opposite to the expected effect accompanying a decrease of cathodic polarization. The reason is not certain, but it is plausibly related to an increasing anode to cathode area ratio as the sulfur content increases (6).

Although the present data show that P increases corrosion of Fe in HCl somewhat more than does an equal weight per cent of S, previous data of Stern showed that the relative effects of S and P depend to some extent on the corrosive medium. In HCl + 4% NaCl at *p*H 1, he found that 0.017% P-Fe alloy (1000 mdd) corroded less rapidly than 0.015% S-Fe alloy (2830 mdd), but the reverse effect applied at *p*H 2, namely the P alloy (480 mdd) corroded at a higher rate than the S alloy (244 mdd). In 0.1*N* citric and malic acids he found that the S alloy corroded much more rapidly, by factors of 4 and 30, respectively, than did the P alloy. It is probably difficult to establish precise relations in this regard because both S and P alloys corrode at increasing rates with time of immersion and never reach true steady-state values. Both gradual change of metal surface composition and structure, and accumulation of P or S corrosion products in solution have an appreciable effect on the rate.

Arsenic added to iron in amounts up to about 0.1% presumably forms a solid solution of As in iron having low hydrogen overvoltage. Above 0.1%, free arsenic of known high hydrogen overvoltage either accumulates on the metal surface or it is redeposited from a solution of reaction products of the Fe-As alloy with HCl.

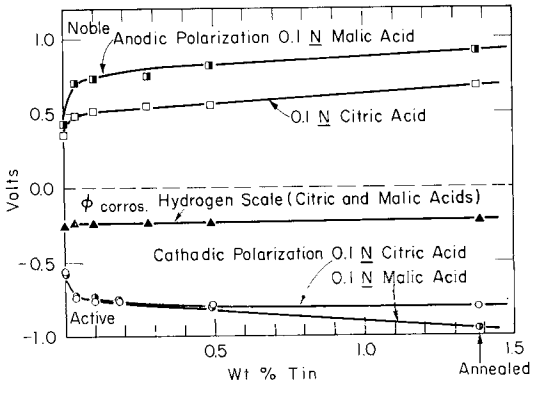

Fig. 11. Anodic and cathodic polarization ($\phi_{meas'd.}$-$\phi_{corros.}$) at 10 ma/cm^2 and corrosion potentials of cold-rolled tin-iron alloys, 25°C.

Tin in solid solution is remarkably effective in reducing the corrosion rate of iron. The steady-state corrosion rate of the 0.1% Sn alloy in 0.1*N* HCl (10 mdd) for example, is below that of zone-refined iron in the same medium (20 mdd) (1). This reduction parallels both an increase of hydrogen overvoltage as well as an increase of anodic polarization with increasing tin content. The lower corrosion rate in 0.1*N* malic acid, compared to 0.1*N* citric acid, is a result largely of increased anodic polarization in malic acid (Fig. 11). Cathodic polarization is about the same in both acids. These facts suggest that malate ions, or their reaction products with iron, adsorb on anodic sites much more, and with stronger bonding, than do citrate ions, thereby more effectively impeding the dissolution of Fe^{++} ions. The effect increases with tin content of iron, parallel to the observed decrease of corrosion.

Recently Greene and Saltzman (8) reported a marked increase in corrosion rate in 1*N* H_2SO_4 or 0.1*N* HCl for zone-refined iron wires torsionally deformed. They ascribed the large effect of cold work which they found to their application of more drastic mechanical deformation in comparison with our 50% cold-reduced material for which no effect was observed. They interpreted their results to indicate, therefore, that plastic deformation increases the number and/or activity of surface dislocations which act as sites for anodic dissolution. Our own work, on the other hand, has not shown an effect of plastic deformation on anodic or cathodic polarization; only in the presence of carbon, for example, is cathodic polarization reduced. Thermodynamic calculations based on residual energy of severely cold-worked iron (approximately 5 cal/g) support the conclusion that change of open-circuit anode potential cannot be more than about 6 mv, a value which is too small to account for a significant increase of corrosion. In agreement with this calculation, Straumanis and Wang (9) found that very severe deformation did not increase the corrosion rate in 1*N* HF of pure aluminum cold reduced 90% in thickness. Similarly Bonnet (10) found no appreciable effect of cold work on the corrosion rate of Ni in deaerated 2*N* HCl of pure Ni sheet cold reduced 70% in thickness. Many lattice imperfections must have been present in both materials. The increase noted by Greene and Saltzman, therefore, may have another explanation which only further experiment can resolve. It is possible in their experiments that torsional straining produced an increase of true surface area with accompanying higher corrosion rates. Their reported increase in rate of corrosion with time suggests that such an effect may have been occurring. Also the discontinuity in the relation between carbon content of their iron and the corrosion rate, instead of a continuous relation (1), suggests that surface contamination may possibly have occurred during the heat-treatment schedules. Our work showed that a few thousandths per cent pick up of carbon easily occurs and can produce large effects. It remains our conclusion, therefore, pending further data, that imperfections, as such, do not have a large effect on corrosion characteristics of relatively soft metals like iron; only when such imperfections are associated with specific impurities, in particular carbon, is the effect marked, and in this case the increase in corrosion results from a lowering of hydrogen overvoltage at such sites.

Acknowledgment

This research was supported by a fellowship grant from the National Steel Corporation to whom the authors express their appreciation.

Manuscript received Feb. 15, 1965, revised manuscript received Aug. 19, 1965. This paper was presented at the Washington Meeting, Oct. 11-15, 1964.

Any discussion of this paper will appear in a Discussion Section to be published in the June 1966 JOURNAL.

REFERENCES

1. Z. A. Foroulis and H. H. Uhlig, *This Journal*, **111**, 522 (1964).
2. R. Covert and H. Uhlig, *ibid.*, **104**, 537 (1957).
3. Z. Foroulis, *Corrosion Science*, **5**, 39 (1965).
4. H. Endo, *Sci. Repts., Tohoku Imp. Univ., Series 1*, **17**, 1245 (1928).
5. C. Edwards, D. Phillips, and D. Thomas, *J. Iron Steel Inst.*, **137**, 223P (1938).
6. M. Stern, *This Journal*, **102**, 663 (1955).
7. P. Bandenheuer and G. Thanheiser, *Mitt. Kaiser Wilhelm Inst. Eisenforsch., Düsseldorf*, **14**, 1 (1932).
8. N. Greene and G. Saltzman, *Corrosion*, **20**, 293t (1964).
9. M. Straumanis and Y. Wang, *ibid.*, **12**, 177t (1956). See also comments in ref. (1).
10. G. Bonnet, M. S. Thesis, Dept. of Metallurgy, M.I.T. (1962).

Logarithmic Oxidation Kinetics of Zinc

Vincent O. Nwoko and H. H. Uhlig

Department of Metallurgy, Massachusetts Institute of Technology, Cambridge, Massachusetts

ABSTRACT

Oxidation rates of cold-rolled zinc are reported at 0.2-0.8 mm O_2 pressure in the temperature range 125°-206°C. Oxide thickness *vs.* time follows a two-stage logarithmic equation similar in behavior to Cu, Ni, and Fe. Activation energies for first- and second-stage oxidation are 0.34 and 0.35 ev, respectively. The data are interpreted in terms of a uniform density space charge oxide, corresponding to first-stage oxidation, underlying a diffuse space charge oxide corresponding to second-stage oxidation, with the rate being controlled in each instance by electron transfer from metal to oxide. The high density of trapped charge in ZnO ($2 \times 10^{17}/cm^3$ at 200°C) explains in part the low initial oxidation rate of Zn compared to Cu and Ni. Second stage logarithmic oxidation kinetics is ascribed to thermal dissociation of trapped charge in the outer regions of oxide when the latter reaches a critical thickness, giving rise to a diffuse space charge.

The oxidation of zinc in accord with parabolic oxidation kinetics has been studied by several investigators (1-4). The initial or low-temperature oxidation rate obeying logarithmic kinetics has also received some attention. Tammann and Köster (5) studied the initial oxidation rate in air in the temperature range 375°-412°C. They were the first to show that the logarithmic equation is obeyed for their particular experimental conditions. An extensive investigation was carried out by Vernon *et al.* (6) who measured the oxidation rate in air between 25°-400°C by weight gain of zinc sheet specimens. They found that the oxidation rate was sensitively affected by method of surface preparation. Abraded or etched surfaces yielded self-consistent but not necessarily the same results. The logarithmic equation was obeyed typically above but only approximately below 225°C, the discrepancy increasing on lowering the temperature or decreasing the time of oxidation.

Previous reports on the initial or thin-film oxidation rate of copper (7-11), Ni (12, 13), and Fe (14) show a two-stage logarithmic behavior. This behavior is also found in data for cobalt by Gulbransen and Andrew (15). Oxides such as NiO and Cu_2O are p-type semiconductors in which cation vacancies characterize the important lattice imperfection sites. It is of interest to learn whether Zn also follows a two-stage logarithmic equation since Zn forms an n-type semiconductor oxide, ZnO, the characteristic lattice imperfections of which are thought to occur as excess interstitial zinc ions. As previously mentioned, Vernon *et al.* (6) found that oxidation of Zn at low temperatures follows a single stage logarithmic equation, but with some discrepancies arising below 225°C. The present measurements on pure Zn cover the thin film oxidation rate at 0.2 to 0.8 mm Hg oxygen pressure in the temperature range 125°-206°C.

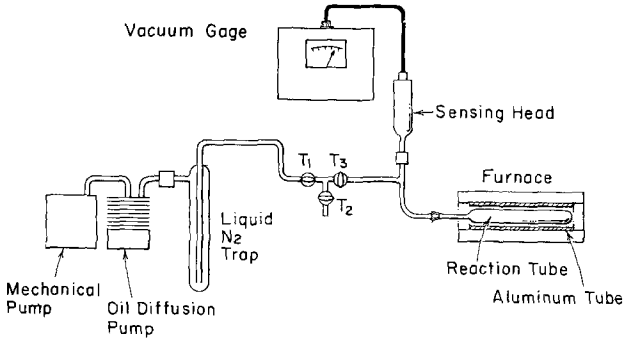

Fig. 1. Apparatus for measuring oxidation rate

Experimental

The oxidation rate was studied using a manometric method. Specimens in the form of thin sheet were contained in a closed glass tube about 60 cm long and 5 cm OD. The glass reaction tube, in turn, was inserted into a heavy wall aluminum tube of slightly larger internal diameter which fitted into an automatically controlled furnace (±1.5°C). The aluminum tube insured a better temperature gradient along the specimen length. The glass tube was connected through a ground glass joint to the vacuum system with details as shown in Fig. 1. The pressure gauge was an "Alphatron" unit which operated by measuring the amplified current in an electrically biased ionization chamber containing the gas and 100 microcuries of radium. The gauge covered seven pressure ranges from 0-100 down to $0\text{-}10^{-4}$ mm Hg; the range used for the present measurements was usually 0-1 mm Hg. The metallic sensing head of the pressure gauge was attached to the vacuum system by means of an O ring connector.

Pure zinc sheet, 0.1 cm thick, was supplied by courtesy of the New Jersey Zinc Company who provided the following analyses: 99.99+% Zn, 0.0009% Pb, 0.0028% Fe, 0.0018% Cd. Specimens 4 x 10 cm were prepared from the original sheet cold rolled to 0.05 cm thickness. These were degreased in benzene and abraded with 2/0 emery paper. A few dimples were then punched in each specimen in order to keep adjoining surfaces separate during oxidation. Specimens were etched in 2*N* HCl at room temperature for 3 min, washed in distilled water, alcohol, and finally benzene. Using clean gloves, the specimens were rolled into spirals having an outer dimension allowing them to be inserted into the glass reaction tube. Twelve and one-half specimens in all were provided for each run

with total apparent area of 1000 cm². The volume (940 ml) of the reaction tube plus specimens, pressure gauge, and connecting glass tubing up to stopcock T_3 was determined by allowing air of known pressure and volume between stopcocks T_3, T_2, and T_1 to expand into the evacuated system and noting the final pressure.

The procedure during a run was to heat quickly the evacuated reaction tube to temperature by inserting the tube into the previously heated furnace. When temperature was established, a specific amount of O_2 dried over $CaCl_2$ was allowed to enter the system. The amount of O_2 reacting with zinc was then determined by pressure decrease. Blank runs were used to establish the extent of slow pressure build-up in the system, particularly from gases adsorbed on the metal sensing head of the pressure gauge which could not be previously degassed by heating. It was found in this way that the pressure increased linearly with time at a rate of about 0.002 mm Hg in 5 hr. This rate of pressure build-up required correction to observed pressures in the latter stages of oxidation for some of the runs. On the basis that ZnO is formed of density 5.47 g/cm³, each 0.01 mm O_2 pressure drop was equivalent to a film of oxide 1.49Å thick, uncorrected for metal roughness factor. Reported values are for oxide thickness overlying a thin air-formed oxide at room temperature.

Results

In view of decreasing pressure during a single run, it was necessary to estimate the effect, if any, of oxygen pressure on the oxidation rate. Two runs were conducted at 157°C, one starting at 0.763 mm O_2 pressure and the other at 0.208 mm. The data, included in Fig. 2 and 3, show that the rates are the same within experimental error despite a threefold change in initial pressure. Hence the normal decrease of pressure during a single run reaching a maximum of 8% of the initial pressure at 125°C and 60% at 206°C did not influence the observed oxidation rates. Oxidation data at various temperatures are plotted in Fig. 2, the initial O_2 pressure being 0.85 mm at 125°C, 0.782 mm at 175°C, and 0.56 mm at 206°C.

Although the data fall on smooth curves in Fig. 2, when plotted semilogarithmically as in Fig. 3, they conform to a two-stage logarithmic equation similar in form to the initial or thin film oxidation behavior of several other metals including Cu and Ni. Earlier data of Vernon *et al.* (6) omitted points for short times of oxidation suggesting that the reported values are for second stage oxidation only. Their observation that deviation from logarithmic behavior increased at temperatures below 225°C and for short oxidation times may have been due to first stage oxidation data lying on a different slope than second stage data for higher temperatures or longer times. They also reported a

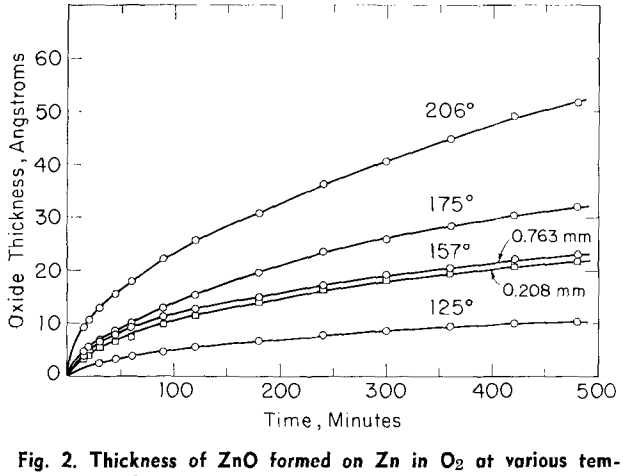

Fig. 2. Thickness of ZnO formed on Zn in O_2 at various temperatures as a function of time.

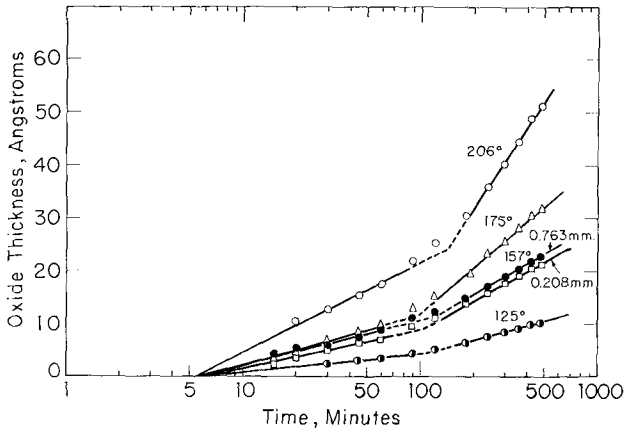

Fig. 3. Thickness of ZnO formed on Zn in O_2 at various temperatures plotted with logarithm of time.

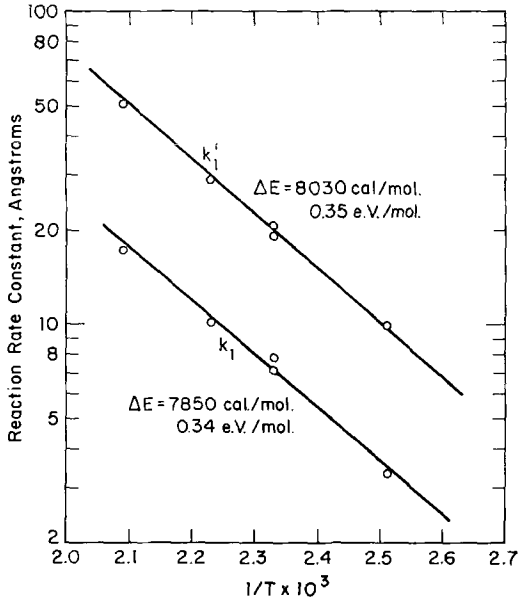

Fig. 4. Logarithm of reaction rate constant of Zn in O_2 as a function of reciprocal absolute temperature. Corresponding activation energies ΔE are inscribed.

maximum in oxidation rate between 25° and 225°C occurring at about 130°C which, however, is not confirmed by the present work. Surface contamination of their specimens, which the authors themselves mention as a cause of irreproducible results, may have been a factor. For the reported data at present, the logarithm of the oxidation rate constant decreases linearly with reciprocal absolute temperature in accord with the Arrhenius equation (Fig. 4). Activation energies ΔE for first and second stage oxidation are found to be nearly the same. Constants based on data of Fig. 3 for the equations:

$$y = k_1 \log\left(\frac{t}{\tau} + 1\right) \qquad \text{(1st stage)}$$

$$y - L = k'_1 \log\left(\frac{t}{\tau'} + 1\right) \qquad \text{(2nd stage)}$$

are listed in Table I where y is the thickness of oxide in Angstrom units, t is time in minutes, τ, τ', k_1, and k'_1 are constants, and L is the thickness of oxide at the beginning of second stage oxidation. Values for τ are obtained by extrapolating to $y = 0$, and for τ' by taking times at which second stage oxidation begins.

Table I. Observed constants for first and second stage logarithmic oxidation kinetics for zinc

Temp, °C	Initial pressure, mm O_2	k_1, A	k'_1, A	τ, min	τ', min	L, A
125	0.85	3.3	9.8	7	110	4.5
157	0.763	7.7	20.6	5.5	120	11
	0.208	7.1	19.0	7	110	9
175	0.782	10.1	29.0	6.5	100	12
206	0.56	17.0	50.5	5.5	140	24

Discussion

The data show clearly that a two-stage logarithmic equation is obeyed by zinc which forms an n-type semiconducting oxide, of the same form as is obeyed by Ni and Cu which form p-type oxides. The basis for a two-stage logarithmic oxidation behavior has been described by Uhlig (10). Two kinds of space charge are presumably formed in thin film oxides in contact with metal, the oxidation rate being controlled by rate of electron transfer from metal to adjoining oxide. The first formed constant density space charge consists of electrons trapped (or electrons lost) at all available imperfection or impurity sites in the oxide, whereas the second stage corresponds to a diffuse space charge with a decreasing fraction of the available sites exhibiting charge as the oxide thickens. Electron transfer is impeded by the increasingly negative (or decreasingly positive) space charge of the oxide which grows, as calculations show, in accord with logarithmic oxidation kinetics. The formation of a diffuse space charge overlying a uniform space charge layer is accompanied by a higher oxidation rate constant because of the lower average charge density per unit oxide thickness acting to slow down electron transfer. For thickness of oxide beyond space charge dimensions, other processes become controlling such as diffusion of ions or ion vacancies through the oxide as described by Wagner (16) to account for parabolic oxidation kinetics.

The theory of logarithmic oxidation kinetics makes it possible to calculate density of imperfections in the oxide at which charge is trapped and relates activation energy for oxidation to metal work function and to electron affinity of oxygen. Information of this kind has been calculated for Cu (10) and Ni (13). The theory furthermore ascribes the observed change in oxidation rate of Ni and of alloys of Ni-Fe and Cr-Fe at the Curie temperature as being caused by changes in metal work function. Similarly the observed change in oxidation rate at the α-γ transformation temperature of iron alloys, and the variation in oxidation rate with crystal face for metals in general are ascribed to changes in work function which affect rate of electron transfer controlling the oxidation process.

The above-described theory was criticized by Fromhold (17) on several grounds, including an implied misinterpretation of Poisson's equation and our alleged ignoring of ionic transport in the oxidation process. However, Poisson's equation can be employed using any set of self-consistent boundary conditions so that our use in the equation of total oxide thickness y to calculate potential at the metal-oxide interface is not considered to be a misinterpretation. In any event, the final equation we obtain appears to be similar to that derived by Fromhold on other assumptions. Furthermore, ionic transport was justifiably ignored in our treatment because it is considered to be the faster process during initial oxidation, with electron transfer being controlling. Perhaps the main difference of Fromhold's treatment from ours is his assumption that the energy of electron transfer from metal to oxide refers only to a tunneling distance equal to the oxide lattice constant, and by further thermal excitation to a distance δ presumably as large as 50Å. In our opinion there is no physical or theoretical reason to believe that an electron entering the oxide at the metal-oxide interface cannot migrate through the conduction band of the oxide to the oxide-oxygen interface in order to ionize adsorbed oxygen, where indeed the electron must eventually go if oxidation is to proceed. In a p-type oxide, a positive hole migrates through the oxide thickness in the opposite direction. We consider that the activation energy for oxidation is equivalent to transfer of an electron from metal to oxide to oxygen adsorbed on oxide, given by $e\ (\phi - v)$ where e is the electronic charge, ϕ is the metal work function ϕ_0 modified by amount χ through contact with the oxide such that $\phi = \phi_0 - \chi$, and v is related to the electron affinity of adsorbed oxygen (approx. 3.6 ev). The total energy of electron transfer is increased by the growing more negative space charge in the oxide accounting for a decreasing oxidation rate as the oxide grows. Fromhold prefers to consider that this energy applies only over thickness δ, beyond which the electron affinity of adsorbed oxygen no longer operates. However, this assumption, besides being unjustified, leads to values of space charge density inconsistent with observed values as is pointed out in his own discussion. Hence the model he describes cannot be considered correct for oxide thickness over which the logarithmic equation applies. His treatment for growth of oxides to thickness values below the tunneling thickness may be valid, but the equations he develops apply largely to growth of air-formed films and not to films forming subsequently at elevated temperatures of the kind represented by practically all available oxidation data.

In accord with the mechanism of logarithmic oxidation kinetics previously described (10), the first stage activation energy ΔE for oxidation of metal is equal to

$$\Delta E = e(\phi_0 - \chi - v)$$

the terms of which have already been defined. For the numerical evaluation of the above expression, the published values of work function for zinc unfortunately show wide scatter. Michaelson (18) considered the average value for polycrystalline zinc to be 3.74v, but for the 0001 face it was reported to be higher, namely 4.26v (19). Since the zinc used in the present experiments was textured by the normal rolling process so that the 0001 face lay in large part parallel to the metal surface, it is probably not unreasonable to accept 4.0v as the value for the Zn sheet used at present. Inserting this number into the above equation and the value of $\Delta E = 0.34$ ev, it is found that $\chi = 0.06$ ev. This value is at best an arbitrary estimate; perhaps the only reasonable conclusion to be made is that χ is small based on values of work function reported at present. As pointed out in an earlier paper (13), the corresponding value of χ for Cu-Cu_2O coincides with the energy necessary to excite an electron from the filled band of Cu_2O to the conduction band. The same coincidence may be noted here for zinc where in this case the small value of χ is apparently the energy required to promote an electron from the donor band of the oxide to the conduction band. Values reported in the literature are 0.02-0.05 ev (20, 21).

The imperfection site density n at which electric charge is trapped in the constant charge density layer of ZnO and the corresponding maximum density n_o in the diffuse space charge layer at which charge may be trapped but not all sites of which exhibit charge, are calculated from the following relations

$$k_o = \frac{\epsilon kT}{4\pi n e^2 l}; \quad v = \frac{4\pi n e l^2}{2\epsilon} = \frac{3.6}{300} \text{ volt}$$

$$k'_o = \frac{\chi_o}{2}\left(\frac{kT}{-C_o e}\right) \text{ where } \chi_o = \left(\frac{\epsilon kT}{2\pi n_o l^2}\right)^{1/2}$$

k is Boltzmann's constant, k_o is $k_1/2.3$, k'_o is $k'_1/2.3$, T is the absolute temperature, ϵ is the dielectric constant of ZnO [approximately 10 (20, 22)], e is the charge on the electron (4.8×10^{-10} e.s.u.), l is the theoretical maximum thickness of the uniform space charge layer, $C_o = -4\pi n e l L/\epsilon - (\phi - v)$ where ϕ, v, and L have

Table II. Calculated values of charge density n in uniform space charge of ZnO, available density of sites n_o in diffuse space charge, and thickness L of ZnO at which 2nd stage oxidation begins

Temp, °C	nl, cm^{-2}	n_o, cm^{-3}	n, cm^{-3}	L, Å
125	1.3×10^{13}	5.0×10^{17}	4.5×10^{18}	13
157	0.64	1.6	1.03	26
175	0.49	0.82	0.60	34
206	0.31	0.33	0.24	53

already been defined, and $-C_o e$ is the activation energy for second stage oxidation.

Values of n and n_o are listed in Table II. It is obvious that n decreases with increase of temperature corresponding to displacement of the following equilibrium to the left

Imperfection site + free electron ⇆ bound electron

A similar apparent shift was also found previously to occur in Cu_2O based on interpretation of thin film oxidation rate data for Cu. The density n_o of available sites for trapped charge in the diffuse layer of ZnO is found to be lower than density n in the constant density layer. Perhaps only higher lying and hence fewer energy levels in ZnO are available for trapped electrons in second stage oxidation. These also decrease with increase of temperature.

The nature of donors and traps in ZnO has been discussed by several investigators at some length (20, 21, 23). The density n of traps here interpolated for the constant density space charge equal to 2×10^{17} at 200°C is certainly larger than the equilibrium concentration of excess zinc atoms in ZnO calculated by Thomas (23) from conductivity measurements (5×10^{13} extrapolated to 200°C). On the other hand, the density of traps estimated by Harrison (20) from low temperature conductivity and Hall effect measurements equal to $3\text{-}8 \times 10^{18}$ is higher, but seemingly still lower than the densities of Table II extrapolated to lower temperatures. Harrison favored oxygen vacancies or paired zinc and oxygen vacancies as contributors to available traps. Impurities, of course, may also be important and would add to other type imperfections, making the total number larger.

It is of interest to know why zinc oxidizes relatively less rapidly at above-room temperatures compared to Ni, Fe, or Cu. For example, the value of k_1 for Ni (13) at 390°C is 350Å, the extrapolated value for Cu (10) is 3650Å, but the extrapolated value for Zn is only 160Å. The oxide thickness formed after 1 hr at 200°C is 70-115Å for iron (24,25) but is only 18Å for Zn. The lower oxidation rate of Zn must be ascribed to a higher density of trapped charge in ZnO (n at 200°C = 2×10^{17}) compared for example to Cu_2O (n at 200°C = 2.5×10^{14}). The value of τ is also higher for Zn than for Cu (approximately 6 *vs.* 0.1 min). Since $\tau = (k_o/A) \exp e(\phi - v)/kT$, the higher value for Zn is related to a higher value for $e(\phi - v)$ which for Zn is 0.34 ev and for Cu is 0.28 ev, and to a lower value of A equal to 8×10^{-7} cm/sec for Zn compared to 6×10^{-4} cm/sec for Cu. The constant A enters the expression for electric current flowing across the metal-oxide interface for a given applied voltage V' as follows:

$$i = (A/\beta) \exp \frac{-e(\phi - V')}{kT}$$

where β is a proportionality constant.

Cause of Two-Stage Oxidation Behavior

Why does a metal oxidizing initially to form a uniform space charge oxide relatively suddenly oxidize at a different rate with formation of a diffuse space charge oxide? The reason apparently resides in a balance within the oxide largely between the electrostatic energy of trapped charge at favorable sites and the thermal energy tending to dissociate trapped charge. The energy of trapped electrons, for example, in the constant space charge layer is a function of the potential exerted by the metal in contact with oxide. The electrostatic energy is largest for electrons trapped in oxide near the metal surface; it becomes less in outer regions of the oxide mostly because of trapped negative charge interposed between outer and inner regions. At a critical thickness of oxide L, the electrostatic energy in the outer oxide approaches the thermal energy kT. Trapped electrons at distance L from the metal surface dissociate increasingly as electrostatic energy decreases in the growing oxide, accounting for the diffuse space charge and a higher oxidation rate constant. As has been shown by others (26), classical statistics apply to this situation.

The approximate oxide thickness L corresponding to balance between kT and the electrostatic energy of an electron in the outer oxide can be calculated from available data as follows: The potential C_o at the metal-oxide interface for an oxide of thickness L corresponding to constant density space charge, is derived in the earlier reference (10).

$$C_o = \frac{-4\pi nelL}{\epsilon} - (\phi - v) \qquad [1]$$

The value of C_o for oxide thickness less than L becomes more negative as the oxide grows. On the other hand, the potential at the oxide-oxygen interface becomes less negative as the oxide grows, and the above expression for thin oxide films becomes

$$C'_o = \frac{4\pi nelL}{\epsilon} - (\phi - v) \qquad [2]$$

Multiplying by electronic charge $-e$ and setting the above expression equal to kT,

$$L = \frac{[e(\phi - v) - kT]\epsilon}{4\pi ne^2 l} \qquad [3]$$

and since $k_o = \dfrac{\epsilon kT}{4\pi ne^2 l}$

$$L = k_o \left[\frac{e(\phi - v)}{kT} - 1 \right] \qquad [4]$$

Equation [4] indicates that the thickness of oxide L at which second stage oxidation begins depends on the initial oxidation rate constant k_o, the activation energy for first stage oxidation $e(\phi - v)$, and temperature. At 125°C, $k_o = 1.43$Å and $e(\phi - v) = 0.34$ ev; hence $L = 13$Å. This value can be compared with the empirical value 4.5Å given in Table I. Corresponding calculated values at other temperatures are listed in Table II, showing that L increases with increase of temperature, as is observed. For Cu, taking data from ref. (10), the observed values of L at 150°, 175°, 225°, and 250°C are 360, 750, 1540, and 1630Å, respectively, compared to calculated values of 600, 990, 1720, and 1510Å, respectively. Considering the approximations that are made in the calculations, and only fair reproducibility of empirical values for L, agreement with experiment is considered reasonable.

Acknowledgment

Support of this research was by the Goodstein Foundation and by the Shell Fellowship Committee to whom the authors express their appreciation.

Manuscript received May 3, 1965; revised manuscript received Aug. 22, 1965. This paper was presented at the Buffalo Meeting, Oct. 10-14, 1965.

Any discussion of this paper will appear in a Discussion Section to be published in the June 1966 JOURNAL.

REFERENCES

1. N. Pilling and R. Bedworth, *J. Inst. Metals*, **29**, 534 (1923).
2. C. Wagner and K. Grünewald, *Z. physik. Chem.*, **40B**, 455 (1938).

3. C. Gensch and K. Hauffe, *ibid.*, **196**, 427 (1950).
4. W. Moore and J. Lee, *Trans. Faraday Soc.*, **47**, 501 (1951).
5. G. Tammann and W. Köster, *Z. anorg. Chem.*, **123**, 216 (1922).
6. W. Vernon, E. Akeroyd, and E. Stroud, *J. Inst. Metals*, **65**, 301 (1939).
7. Ref. (5), p. 196.
8. B. Lustman and R. Mehl, *Trans. AIME*, **143**, 246 (1941).
9. R. Tylecote, *J. Inst. Metals*, **78**, 327 (1950).
10. H. H. Uhlig, *Acta Met.*, **4**, 541 (1956).
11. E. Williams and P. Hayfield, "Vacancies and Other Point Defects in Metals and Alloys," p. 131, Monograph and Report Series No. 23, Institute of Metals, London (1958).
12. W. Campbell and U. Thomas, *Trans. Electrochem. Soc.*, **91**, 623 (1947).
13. H. H. Uhlig, J. Pickett, and J. MacNairn, *Acta Met.*, **7**, 111 (1959).
14. B. Lustman, *Trans. Electrochem. Soc.*, **81**, 359 (1942).
15. E. Gulbransen and K. Andrew, *This Journal*, **98**, 241 (1951).
16. C. Wagner, *Z. physik. Chem.*, **21B**, 25 (1933); **32B**, 447 (1936); **40B**, 455 (1938); *Atom Movements*, pp. 153-73, A.S.M., Cleveland (1951).
17. A. Fromhold, Jr., *Nature*, **200**, 1309 (1963).
18. H. Michaelson, *J. Appl. Phys.*, **21**, 536 (1950).
19. W. Klug and H. Steyskal, *Z. Physik*, **116**, 415 (1940).
20. S. Harrison, *Phys. Rev.*, **93**, 52 (1954).
21. G. Heiland, E. Mollwo, and F. Stockman, "Solid State Physics," Vol. 8, p. 302 (1959).
22. Ref. (21), p. 195.
23. D. Thomas, *J. Phys. Chem. Solids*, **3**, 229 (1957).
24. D. Davies, U. Evans, and J. Agar, *Proc. Royal Soc. (London)*, **225A**, 443 (1954).
25. A. Winterbottom, *J. Iron Steel Inst.*, **165**, 9 (1950).
26. "Crystal Rectifiers," H. Torrey and C. Whitmer, McGraw-Hill, New York (1948).

The Valency of Aluminum Ions and the Anodic Disintegration of the Metal

M. E. Straumanis and K. Poush

Department of Metallurgical Engineering and Graduate Center for Materials Research, University of Missouri at Rolla, Rolla, Missouri

ABSTRACT

It appears from coulometric measurements that Al in Al-amalgam may go into solution in basic electrolytes exclusively as a trivalent ion. Experiments made in aqueous solutions of NaOH, HNO_3, KNO_3, and $K_2Cr_2O_7$ showed that at anodic current densities between 20 and 300 ma/cm^2 dark, nearly black films, which constantly broke down, are formed on the Al electrode. Microscopic examinations revealed the presence of a multitude of metallic particles entangled in the hydrated Al-oxide flakes, causing the dark color of the latter. Depending on the conditions, the diameter of the metallic particles and leaflets varied from almost 10^{-5} to 10^{-2} mm. Such a disintegration of Al was also observed when the partially amalgamated metal merely came in contact with distilled H_2O: dark flakes of hydroxide, containing a multitude of smallest Al particles, were formed. There are indications that the disintegration of Al is caused by the forcible breakdown (*e.g.*, by the current or Hg) of the oxide layers firmly sticking to the surface of the metal. On breaking down of the film the smallest Al particles which remain on the film are torn from the meal. The observed deviation from Faraday's law and the negative difference effect, may be explained in terms of this behavior, without recourse to the hypothesis of lower valency Al ions.

The discoverer of metallic Al, Wöhler, and Buff found in 1857 (1) that, on the anodic dissolution of Al, more metal dissolved than calculated from Faraday's law (that is, from the number of coulombs which passed the anode). Since that time, the search for the reasons for this deviation has continued. Wöhler himself rejected the idea that Al could initially go into solution as an ion of lower valency, *e.g.*, in the form of Al^+

$$Al \rightarrow Al^+ + e \qquad [1]$$

because he could not synthesize Al-lower valency compounds. However, on the assumption that Al^+ is very unstable and immediately reacts outside the anode

$$Al^+ + 2H^+ \rightarrow Al^{3+} + H_2 \qquad [2]$$

the deviation from Faraday's law can well be understood. Therefore, no Al^+ ions are expected to be present in the solution after electrolysis. However, the idea of lower valency ions became less probable when it was found that a dark gray deposit was observed in the electrolyte, especially in the presence of oxidizers (3). It has been assumed for quite a while that the gray color of the deposits is due to metallic Al formed by a disproportionation reaction

$$3Al^+ = 2Al^o + Al^{3+} \qquad [3]$$

Just as in the case of Be (4, 5), reaction [3] appears to be highly improbable; it assumes growth of Al particles in an aqueous solution from nuclei free from an oxide layer. Nevertheless, Al was found later in anodic deposits by Plumb (6). Although he rejected the formation of Al according to reaction [3], he did not mention anodic disintegration, which might well have provided an explanation. Aluminum in anodic deposits and films was also found by McCune (7) and Dmitriev *et al.* (8). Formation of comparatively large, quite regular Al blocks by dropout from an Al piece dissolving in HCl was observed by Roald and Streicher (9).

The reducing power of the anolyte was investigated by many authors (10-16). However, the possibility that the Al particles themselves (rather than Al^+) could act as reducers, was not considered until recently (2).

The intention of the present article is to show that Al during anodic dissolution partially disintegrates into particles and leaflets of irregular shape embedded in an oxide layer, that the particles are much smaller than the blocks previously observed (9), that disintegration of Al also occurs while it is reacting with

H_2O in the presence of Hg, and that Al goes into solution only as Al^{+3} ion.

Anodic Disintegration of Al

Disintegration experiments were made in solutions of NaOH, HNO_3, KNO_3, and $K_2Cr_2O_7$ as electrolytes.

NaOH.—In 1*N* NaOH the Al electrode (99.99% pure) dissolved slowly, evolving H_2 according to the reaction

$$Al + OH^- + H_2O = AlO_2^- + 1.5H_2 \qquad [4]$$

As soon as the switch connecting the Al with the Pt electrode through the battery and resistance was closed, the self-dissolution rate of the Al anode dropped (positive difference effect), and H_2 was evolved on the Pt (17). At anodic current densities between 20 and 300 ma/cm the Al surface became black, and black flakes fell to the bottom of the beaker. The flakes were rinsed in distilled water, then treated with acetone and collected on a slide for microscopic examination. Only at high magnifications, about 1500X, using oil immersion objectives and reflected light, bright shiny metallic particles of various sizes could be seen in a milky looking layer of Al oxide beta trihydrate, as revealed by x-ray powder patterns. The shape of the particles was irregular (Fig. 1). In transmitted light, the same particles were opaque, thus establishing their metallic nature. The black color of the anodic flakes was caused by the presence of the finely divided metal in the oxide layer, in agreement with the theoretical expectations of Ketelaar (18).

HNO_3.—Al does not dissolve in this acid because of formation of a tight oxide layer on the surface of the metal. However, an anodic current of about 300 ma/cm^2 produced in 0.25*N* HNO_3 results similar to those in NaOH. Gray clouds of particles and flakes fell to the bottom of the beaker from the dark anode surface under slight gas evolution at the electrodes. Ultrasonic vibrations of the electrolyte accelerated the breakdown of the flakes. The finest particles dissolved slowly in the HNO_3. Microscopic examination of the flakes revealed groups of fine particles and of objects with plane surfaces having a bright metallic luster, embedded in a milky substance (Fig. 2), which consisted of aluminum oxide. The large plane surfaces exhibited tiny dark spots.

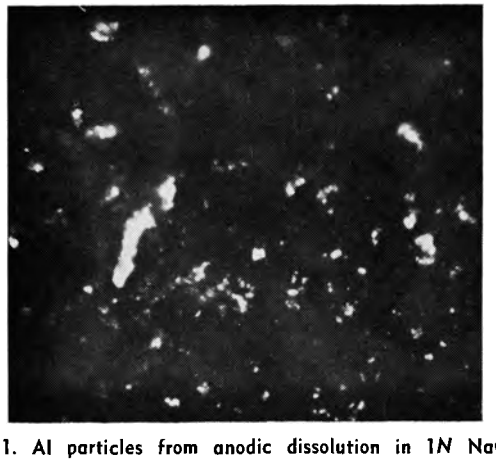

Fig. 1. Al particles from anodic dissolution in 1*N* NaOH or 0.25*N* HNO_3. Magnification 1430X.

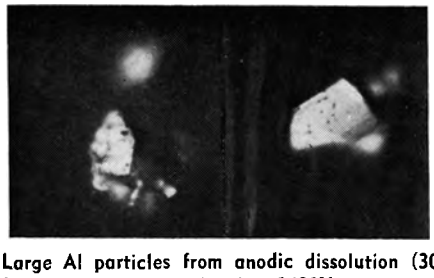

Fig. 2. Large Al particles from anodic dissolution (300 ma/cm) of Al in 0.25*N* HNO_3. Magnification 1430X.

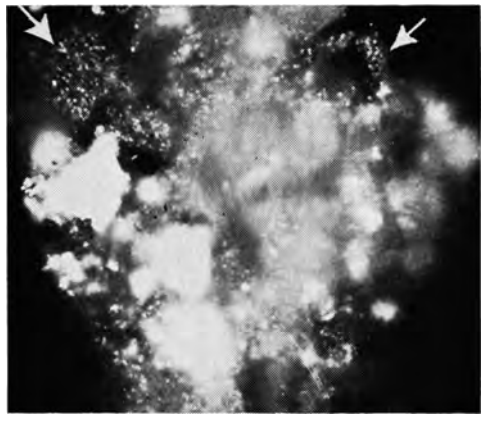

Fig. 3. Bright Al particles, small (arrows) and large ones (with plane surfaces) formed anodically in 3% KNO_3, embedded in Al-oxide. Magnification 1430X.

Fig. 4. Electron micrographs of Al particles formed during anodic dissolution of an Al anode in 3% KNO_3. Round objects are latex spheres. Magnification 2700 to 10000X.

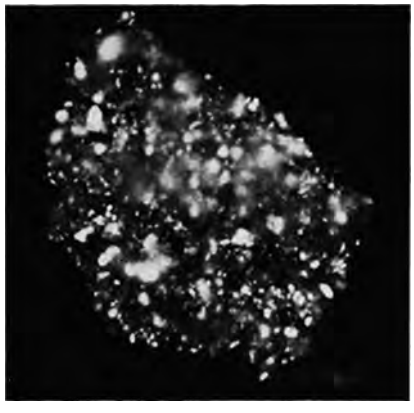

Fig. 5. Al hydroxide flakes containing metallic Al particles formed during anodic dissolution of Al in 3% $K_2Cr_2O_7$. Reflected light. Magnification 1430X.

3% Aqueous **KNO_3.**—Al anodes in this electrolyte behaved very similarly; except that the white oxidic material was more abundant (Fig. 3). To study the shape of the particles, electron microscopic pictures were made. The collected flakes were suspended in ethyl alcohol with an ultrasonic vibrator, and then drops of the suspension were allowed to dry on a small piece of a 200 mesh Cu screen. The magnification was determined from the size of latex spheres which had a diameter of 0.557μ. As can be seen from Fig. 4, the particles look like leaflets torn off the Al surface.

3% **$K_2Cr_2O_7$** *aqueous solution.*—In this solution, the initial current dropped very quickly from 150 to 2 ma, but on adding a few ml of 1*N* NaOH to the solution, a current of 3 ma could be maintained for about 1 hr. Black, finely divided particles accumulated beneath the anode. The microscope revealed aggregates of shiny particles held together by a thin network of Al oxide or hydroxide (Fig. 5). X-ray diffraction patterns

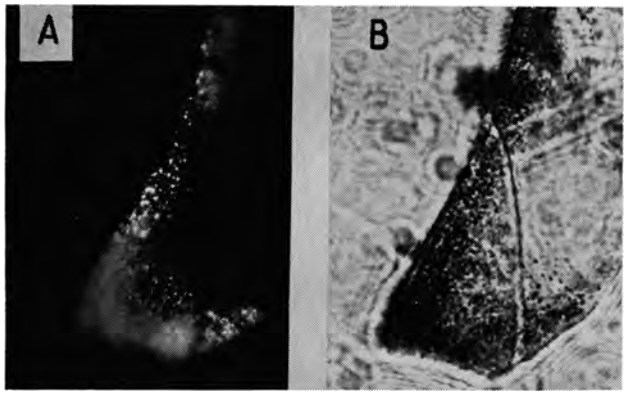

Fig. 6. Al particles embedded in a bayerite flake; particles formed due to disintegration of Al in presence of Hg during reaction [5]. A—in reflected and B—in transmitted light. Magnification 1430X.

showed the presence of faint 200 and 111 lines of metallic Al in addition to the usual oxide pattern.

Disintegration of Al *in* H_2O *in Presence of* Hg

It was observed that on Al pieces (wire or foil) floating on Al-amalgam under distilled H_2O, some dark gray substance was formed around and on the unamalgamated portions in about 0.5 hr. The H_2 (no current was applied) developing according to the reaction

$$Al + 3H_2O = Al(OH)_3 + 1.5H_2 \qquad [5]$$

partially carried the dark gray particles to the water surface. However, particles of gray color did not form after complete amalgamation of the pieces. Large quantities of fluffy, white hydrated Al oxide beta trihydrate (bayerite), as revealed by x-ray diffraction pictures, were also obtained as a consequence of reaction [5]. The nearly black material was carefully removed with a suction tube to avoid mixing with the white oxide and was examined with an optical microscope after drying. Bright spots with metallic luster of the magnitude of about 10^{-5} mm in diameter, embedded in the oxide flakes, appeared in reflected light. The spots became opaque in transmitted light (Fig. 6). Furthermore, as the particles were flat and faded in time, they could only be of metallic Al. These results show that Al can also disintegrate in the presence of Hg.

Trivalency of Al *Ions from Coulometric Measurements*

Clearly, the observed anodic disintegration of Al causes a deviation from Faraday's law. Hence, it may be that Al goes into solution only in form of Al^{3+} ions. In order to test this hypothesis, coulometeric experiments were undertaken by a technique similar to that used with Ga (19): Al amalgam was chosen as an anode. The amount of Al that went anodically into solution was determined by titration with EDTA (20). The apparent valency V of Al ions could then be calculated from Eq. [6] in which a is the number of coulombs

$$V = a/A \text{ (moles)} \times 96490 \qquad [6]$$

However, because H_2 developed in acids on the Pt cathode, as well as in small amounts on the amalgam (self-dissolution), only alkaline solutions (1.0 or 0.1*N* NaOH or KOH) were used, as the self-dissolution rate was much lower there. The anodic dissolution follows the reaction

$$Al + 4\,OH^- = AlO_2^- + 2H_2O + 3e \qquad [7]$$

Aluminates (soluble) are formed at the anode and H_2 is developed at the Pt cathode. Results are given in Table I. The apparent valency fluctuates from measurement to measurement and occasionally approaches 3. The factors which cause the deviation from three are the self-dissolution rate which lowers the apparent valency, and the disintegration of Al. Since the metal floats on the Hg surface (but under the electrolyte) and becomes locally quite "dry" of Hg, disintegration of Al occurs as already mentioned. Experiments with thin amalgamated Al foils which nearly dissolved in Hg gave apparent valencies of 2.93, indicating that there was a minimum of disintegration. Thus, measurements in strong bases are consistent with the assumption that Al goes anodically into solution only as Al^{3+}. The same may also occur in acids, although this is not directly provable.

Table I. Valency of Al ions anodically dissolving from Al amalgam in basic solutions

Electrolyte	Coulombs	Moles Al	*V*, apparent
KOH, 1*N*	27,680	0.1025	2.80
KOH, 1*N*	34,310	0.1241	2.86
KOH, 1*N*	41,855	0.1511	2.87
KOH, 1*N*	30,200	0.1094	2.86
NaOH, 0.1*N*	9,992	0.0352	2.94
NaOH, 0.1*N*	9,705	0.0411	2.45
NaOH, 0.1*N*	24,611	0.0940	2.71
NaOH, 0.1*N*	11,553	0.0450	2.66
NaOH, 0.1*N*	9,992	0.0343	3.02

Discussion and Conclusions

Since the apparent valency lower than 3 may be accounted for by the facts just mentioned, it is unnecessary to assume the formation of lower valency Al ions, either from amalgam or from a pure Al anode.

The presence of metallic Al was also previously found in the anodic flakes (6-8). However, nobody observed the very fine particles (down to about 5 x 10^{-5} mm in diameter) in the deposits, only occasional large chunks and the cubes as found by Streicher *et al.* (9). The mechanism of formation of these entities is, however, quite different from the disintegration described in this paper, because all the particles observed here were embedded in a film consisting of Al oxide (Fig. 3, 5, 6), mainly beta bayerite (21). In NaOH as an electrolyte these oxides dissolve and the particles may appear free (Fig. 1).

The mechanism of formation of such particles is, therefore, as follows. If an active metal (Al) is anodically polarized in aqueous solutions, the oxide film present can thicken. The composition and, therefore, the properties of these films will depend largely on the electrolyte and the applied voltage (22). For one or another reason, these films do not cover the metal anodes uniformly and the anodic current will follow the path of least resistance. At places where the film is thin, or not formed at all (*e.g.*, on inclusions), the current density will be high and anodic dissolution will occur around such high resistance spots, undermining them. After some time, the respective spots, still containing some metal adhering to the protective layer, may drop out. If the protective film is not dissolved by the electrolyte, the metallic particles will appear embedded in the film. Of course, the ions going anodically into solution exert some pressure on the oxide layer and aid the separation. The shape of the metallic particles must, therefore, be irregular and of various sizes as determined by the places of least resistance of the adhering film. This conclusion is confirmed by Fig. 3, 4, and 5. A new oxide film is formed on places where the metal dropped out and the drop-out can occur again after some time. It is clear that with such a mechanism of disintegration, its rate and the particle size and shape will depend on the composition of the electrolyte, temperature (4), and current density (23). In electrolytes which do not further formation of strongly adhering protective films, there may be, with other reasons also excluded, no anodic disintegration at all.

The disintegration of Al, partially amalgamated, proceeds in H_2O in a similar manner: Hg atoms spreading between the oxide film and the metallic surface forcibly loosen the former. The film, on breakdown, takes with it tiny Al particles cracking off the bulk material, as they stick firmly to the film (Fig. 6).

These particles cause the nearly black color of the flakes (18) separating from Al or other metals (4, 5, 23, 24). If the particles are well protected by a film from the action of H_2O, as in case of Al embedded in bayerite, the residue keeps its dark color even in water for a comparatively long time (several days), but where the protection is weak, as with Mg, the dark flakes become white in the presence of moisture much faster (24).

The reducing ability of the anolyte, or of parts of the electrolyte in close vicinity to the anode, is explained simply by the action of the fine metallic dispersion of the active metal coming in contact with an oxidizer, which may be added to the electrolyte, or which may be the solvent itself, *e.g.*, H_2O. In fact, metallic dust (*e.g.*, of Al, Zn, Fe, etc.) is well known as a reducer of organic substances. Whether this reduction proceeds indirectly through the atomic H formed (25) or directly by transfer of the valence electrons from the metal is of lesser importance. The question how this transfer occurs, whether all 3 electrons pass over to the oxidizer molecules simultaneously or in succession, is also insignificant, because at present there is no possibility to check the guess anyway.

Acknowledgment

This investigation was supported by the Office of Naval Research and also partially by the Corrosion Research Council. The authors would like to thank Mr. J. A. Rowland, Director of the U.S. Bureau of Mines at Rolla and Mr. J. W. Jensen for the permission to use the electron microscope of the Bureau.

Manuscript received Jan. 22, 1965; revised manuscript received July 22, 1965.

Any discussion of this paper will appear in a Discussion Section to be published in the June 1966 JOURNAL.

REFERENCES

1. F. Wöhler and H. Buff, *Liebigs Ann.*, **103**, 218 (1957).
2. Literature see paper by M. S. Straumanis, *This Journal* **108**, 1087 (1961).
3. E. Raijola and A. W. Davidson, *J. Am. Chem. Soc.*, **78**, 556 (1956).
4. M. E. Straumanis and D. L. Mathis, *J. Less-Comm. Met.*, **4**, 213 (1962).
5. M. E. Straumanis and D. L. Mathis, *This Journal*, **109**, 434 (1962).
6. R. C. Plumb, *ibid.*, **105**, 498 (1956).
7. H. W. McCune, *ibid.*, **106**, 63 (1959).
8. V. A. Dmitriev, O. I. Avdeeva, and Y. I. Sozin, *Dokl. Akad. Nauk. Ser. Khim.*, **6**, 176 (1961).
9. B. Roald and M. A. Streicher, *This Journal*, **97**, 283 (1950).
10. M. D. Rausch, W. E. McEwen, and J. Kleinberg, *J. Am. Chem. Soc.*, **77**, 2093 (1955).
11. W. E. Bennett, A. W. Davidson, and J. Kleinberg, *ibid.*, **74**, 732 (1952).
12. M. Sborgi and P. Marchetti, *N. Cimento*, **22**, 151 (1921).
13. P. Brouillet, I. Epelboin, and M. Froment, *Compt. rend.*, **239**, 1795 (1954).
14. I. Epelboin and M. Froment, *ibid.*, **238**, 2416 (1954).
15. I. Epelboin, *Z. Elektrochem.*, **59**, 691 (1955).
16. A. W. Davidson in C. A. Hampel's "Encylopedia of Electrochemistry," p. 48, Reinhold Publishing Corp., New York (1964).
17. M. E. Straumanis and Y. N. Wang, *This Journal*, **102**, 304 (1955).
18. J. A. Ketelaar, "Chemical Constitution," p. 292, Elsevier Publishing Co., New York (1953).
19. M. E. Straumanis and K. A. Poush, *This Journal*, **111**, 795 (1964).
20. H. A. Flaschka, "EDTA Titrations," p. 84, Pergamon Press, New York (1959).
21. R. K. Hast, *Trans. Faraday Soc.*, **53**, 1020 (1957).
22. L. Young, "Anodic Oxide Films," Academic Press, New York (1961).
23. W. J. James, M. E. Straumanis, and J. L. Reed, "Anodic Dissolution of Zn in KNO_3," Tech. Rep. No. 10 to ONR, 1964.
24. M. E. Straumanis and B. K. Bhatia, *This Journal*, **110**, 357 (1963).
25. H. H. Uhlig and R. Krutenat, *ibid.*, **111**, 1303 (1964).

Low-Energy Electron Diffraction Studies of Oxygen Adsorption and Oxide Formation on a (001) Iron Surface

A. J. Pignocco and G. E. Pellissier

Applied Research Laboratory, United States Steel Corporation, Monroeville, Pennsylvania

ABSTRACT

The technique of low-energy electron diffraction (LEED) has been used to study oxygen adsorption and oxide formation on a (001) surface of iron. The LEED data indicated that the atomically clean iron (001) surface was an unreconstructed surface. The chemisorbed oxygen layer formed on exposing the clean face of iron to very low oxygen partial pressures consisted of half a monolayer of oxygen atoms arranged in a Fe (001) c(2x2)-O two-dimensional array. With continued oxygen exposure and annealing, a thin layer of FeO was observed to form on the iron crystal with its (001) face oriented parallel to the (001) face of the iron substrate, and with the [110] direction of the FeO parallel to the [100] direction of the iron. These FeO films that were formed and maintained at very low oxygen partial pressures were stable at room temperature.

A thorough understanding of the oxidation behavior of a metal requires a careful study of the manner and rate of growth, the composition, the character, and the structure of the oxide phase from its initiation as a chemisorbed layer to the formation of the thick bulk oxide. Much of the work dealing with the oxidation of metals has been directed toward achieving a better understanding of the formation of thick oxide layers. Vacuum microbalance measurements, transmission and reflection electron microscopy, optical methods, and x-ray and electron diffraction techniques have been utilized successfully in studying this phase of the oxidation process. Despite the great interest in the initial stages of oxidation, studies of the character and mode of growth of the chemisorbed layer, and the subsequently formed very thin oxide layer, have been largely neglected because of the lack of experimental techniques capable of providing such information. Most classical studies of chemisorption have consisted of determinations of adsorption isotherms and isobars, which involve measurements of the quantity of gas taken up or measurements of the changes in various

physical properties of the metal surface that occur as the chemisorption proceeds.

Relatively little has been reported on the arrangement of surface atoms of the metal, or about the conditions and cleanliness of the surfaces under investigation. Although it was well-known since the early Davisson-Germer experiments (1, 2) that low-energy electron diffraction (LEED) is well suited to such studies, only Farnsworth (3-9) and his associates extensively applied the technique to surface and gas sorption studies. Recently Germer (10), Lander (11), and others have perfected a much simpler and more rapid LEED technique. The method, first devised by Ehrenberg (12) in 1934, displays the diffraction pattern of a fluorescent screen. This diffraction pattern can be observed and measured directly, or photographed from the screen for permanent record. In addition to ease of experimentation, this method permits direct observation of many detailed features of a rapidly changing diffraction pattern. Thus, utilizing this improved technique Germer (13-15), MacRae (14, 15), Lander (16-18) and others have generated, in a relatively short time, large amounts of information on the manner in which several kinds of foreign atoms stick and arrange themselves on different faces of many crystalline solids.

This paper describes the results of a LEED study of chemisorption of oxygen on a clean (001) face of a high-purity iron crystal and the subsequent formation, epitaxy, and stability of the thin oxide phase formed under very low oxygen partial pressures.

Material and Experimental Work

Material.—Because the effects of many of the impurity elements found in iron on the oxidation behavior are not well understood, several specimens of the highest purity iron available were used in this investigation. It was possible to achieve an atomically clean surface only on a crystal having a very low carbon content (14 ppm). This was an iron sample obtained from Battelle Memorial Institute in the form of a small polycrystalline section of zone-refined ingot. The analysis of this iron, presented in Table I, indicated that the material had a maximum purity of 99.94%. Other iron specimens, containing carbon in concentrations exceeding 30 ppm, could not be cleaned by conventional techniques. A similar deleterious effect of carbon in the preparation of an atomically clean surface also was encountered by Farnsworth (19) in earlier work on nickel.

Table I. Purity of the iron foil used in the oxidation study (Solids mass-spectrographic analysis)*

Impurity	Parts per million present (1 ppm = 0.0001%)
Arsenic	13
Boron	12
Calcium	2.5
Carbon	14
Chlorine	12
Chromium	19
Cobalt	53
Copper	102
Gallium	50
Germanium	30
Magnesium	5
Manganese	20
Nickel	42
Nitrogen	3
Oxygen	19
Phosphorus	55
Potassium	<20
Silicon	101
Sodium	<20
Sulfur	34
Zinc	2.5
All others**	<0.2-0.7

Maximum purity = 99.941% Fe.
* After all treatments prior to crystal-growing operation.
** Only H, He, Li, Be, F, Al, C, N, and O are not detectable by this method. Of these, C, N, and O were determined by a vacuum-fusion method, while the others are believed to be present in insignificant amounts.

Preparation of the (001) iron crystal surface.—The iron specimen used in these LEED experiments was in the form of a thin platelet (1.0 by 0.5 cm in cross section, and 0.04 cm thick) that consisted of a bicrystal. This bicrystal was prepared from a piece of the polycrystalline Battelle iron by the strain-anneal method. The platelet was oriented and thinned mechanically, ground on a series of successively finer grit emery papers, and then fine-polished with levigated alumina on rotating laps; the polished surface was parallel to the (001) crystal face of one of the grains to within 1 degree. The polished platelet was mounted on two 0.020-in.-diameter clean tungsten support rods, electropolished, washed in absolute methanol, thoroughly dried, and sealed into the LEED tube with the [001] direction of the crystal aligned approximately parallel to the drift tube axis of the electron gun. After the LEED tube was evacuated and "baked out," following conventional ultra-high-vacuum techniques, the residual gas pressure was about 5×10^{-10} Torr.

LEED apparatus.—The LEED apparatus used was of the display type described by Germer *et al.* (10); it had an acceptance angle of approximately 70°, and utilized a planer grid and fluorescent screen assembly. The tube envelope was fabricated of 100-mm OD Pyrex glass tubing, and formed an integral part of an ultra-high vacuum system. Figure 1 is a schematic diagram of the LEED apparatus, showing the fluorescent screen assembly, the iron crystal, and the sputter gear assembly. The energy of the incident electron beam was varied over the range of 50 to 350 ev.

Cleaning of the iron (001) face.—Although a surface prepared by electropolishing has been described as atomically smooth, with relatively little oxide overgrowth, chemisorption studies require that the surface under investigation be atomically clean at the outset. Among the most successful surface cleaning techniques employed by Germer (14), Lander (16, 17), and Farnsworth (19) in their LEED experiments were (*i*) extended high temperature annealing under ultra-high vacuum conditions, (*ii*) alternate oxygen-hydrogen treatments, and (*iii*) low-energy argon ion bombardment. Because high temperature annealing or the oxygen-hydrogen treatments either destroy the single crystal nature of the iron specimen or produce a very unsatisfactory, rough surface, the technique of low-energy argon ion bombardment was used in preparing atomically clean surfaces for these LEED experiments. The (001) iron platelet was subjected to repeated ion bombardment for times ranging from 30 to 60 min. An argon discharge voltage of from 50 to 200v was maintained between the crystal and an anode. The current density at the crystal face was maintained near 50 μamp/cm^2. After bombardment, the LEED tube was evacuated, and the crystal was annealed in high vacuum at 500°C for periods of time ranging from 5 to 15 min. Several such ion bombard-

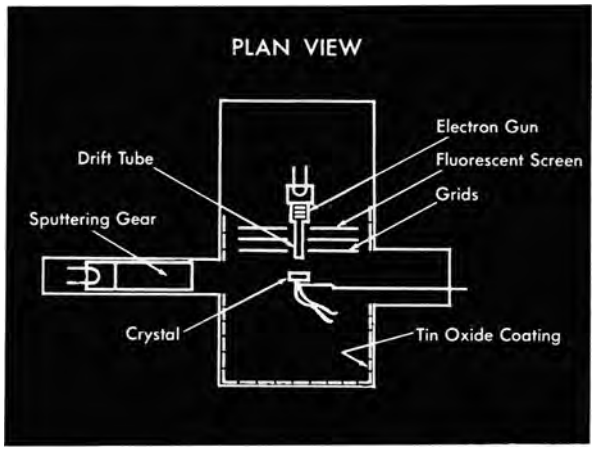

Fig. 1. Schematic diagram of LEED tube

ment-annealing cycles were usually required to prepare a clean (001) crystal face.

LEED nomenclature.—In the energy range of from 50 to 300 ev, the diffraction of electrons from diperiodic surface structures is of paramount importance. Because the arrangement of sorbed atoms on a surface often is related to that of the atoms in a parallel crystal plane of the substrate, a convention of terminology for LEED has been proposed by Wood (20) in which a surface structure is described in terms of a substrate cell; that is, the diperiodic structure of the substrate surface, which initially is known, is taken as the base of reference. In such a diperiodic structure, equivalent points form two-dimensional nets in which the unit areas are unit meshes. A surface structure with the identical mesh of the substrate is then denoted a (1 x 1) mesh; one with its sides equal to twice those of the substrate and with the same orientation as the substrate, a (2 x 2) mesh. A prescript (p) denotes a primitive mesh; and when a mesh contains a centered atom, a (c) precedes the description of the mesh.

For a more complete identification of the structure, Wood further suggests that this term be preceded by the name and orientation of the substrate and followed by the chemical symbol of the sorbed layer. Other notations, such as Miller indices of reflections and indices of a crystallographic direction, generally follow the triperiodic conventions, with the omission of the final index. Such terminology is used to describe the LEED patterns and structures observed in this study.

Observation of Laue diffraction beams.—Under the experimental conditions used in this study, all the sets of diffraction beams obtained from an atomically clean (001) face of iron appear in either the [10] or [11] azimuths. The [10] azimuth beams lie in the planes containing the incident beam and the [100] or the [010] crystal directions; the [11] azimuth beams appear in the planes containing the incident beam and the [110] or [$\bar{1}$10] crystal directions. The first experiments on the clean (001) iron face were made to locate the positions of the LEED beam maxima. The wavelength of the incident beam was varied from 0.6 to 1.6Å, while the azimuths were scanned for beam maxima. When a set of diffraction beams reached maximum intensity, the LEED pattern on the fluorescent screen was photographed, and the electron beam energy was measured to the nearest volt. In addition to these data, a more complete analysis of these beams, revealing the fine structure in the maxima, was desired; for this purpose, a photometer was used to monitor and measure the relative intensity of the 10 diffraction feature as the wavelength of the incident electron beam was varied over the experimental voltage range.

Chemisorption of oxygen on the iron (001) face.—The identification of the two-dimensional lattice structures obtained on exposing the clean (001) crystal face to oxygen for different times and pressures was objective of this series of experiments. The crystal platelet at room temperature was exposed to oxygen at pressures ranging from 1 x 10^{-8} to 5 x 10^{-8} Torr for periods of time ranging from 15 to 60 sec. The exposures (product of time and pressure) were varied from 1.5 x 10^{-7} to 30 x 10^{-7} Torr-sec. After each exposure, the screen was scanned for new diffraction features.

Oxide formation on the iron (001) surface.—According to work reported in the literature (21), the relatively fast chemisorption of oxygen on iron at room temperature is followed by a slow stage that corresponds to the nucleation and growth of crystalline oxide. Nucleation of the oxide has an activation energy that can be overcome by increasing the oxygen pressure. The process of growth of nuclei into a crystalline oxide film also involves an activation energy. This latter activation energy can be overcome by increasing the temperature of the specimen; that is, oxide crystal growth can be facilitated by promoting diffusion of the iron ions to the nucleation sites by annealing the crystal in an ultra-high vacuum after a suitable oxygen exposure. After an oxygen exposure of 55 x 10^{-6} Torr-sec, the LEED features obtained from the (001) surface of an iron crystal were weak and poorly defined. A well developed oxide phase was obtained, however, by subsequently annealing this crystal at 550°C under ultra-high vacuum conditions. The resultant LEED patterns were photographed, and the relative intensity-voltage data were obtained for the 10 beam.

Stability of FeO.—Much of the reported data (22-26) on the wüstite-magnetite transformation ($4FeO \rightleftarrows Fe_3O_4 + Fe$) were obtained under relatively high oxygen partial pressures. The studies generally were performed at the prevailing atmospheric pressures, or under relatively poor vacuum conditions. It was concluded from these data that FeO transformed to Fe_3O_4 at temperatures below 570°C. Gulbransen *et al.* (22) noted some retardation of this transformation with lower oxygen partial pressures; at oxygen pressures near 10^{-6} Torr, the presence of FeO on an iron substrate was observed at temperatures as low as 412°C. An extension of this work to much lower oxygen partial pressures (less than 10^{-10} Torr) was included in this phase of the present LEED study. An iron crystal surface covered with a thin layer of FeO was annealed for 65 hr at each of three temperatures under ultra-high-vacuum conditions, that is, at 480°C [the temperature at which Chaudron and Forestier (26) reported the decomposition rate to be at a maximum], at 100°C, and at room temperature. The LEED patterns and intensity-voltage relationships were determined before and after each experiment.

Results and Discussion

The Clean Iron (001) Crystal Face

Alpha-iron has a body-centered-cubic structure with a lattice constant a_o = 2.86Å. Figure 2 is a solid sphere model of the atomic arrangement in the (001) face of iron. The unit cell of iron is outlined by the square near the top of the figure, and the principal azimuths of the (001) face, that is the [10] and [11] azimuths, are depicted by arrows in the lower part of the figure. The LEED patterns presented in this paper can be brought into register with Fig. 2 by rotating them approximately 5° in a counter-clockwise direction.

The first argon-ion bombardment-annealing cycle sequence did not produce a clean iron surface. A photograph of a LEED pattern taken at 102 ev at this stage of the cleaning process is reproduced in Fig. 3. In addition to the integral-order features in the [10] and [11] azimuths, bright and sharp half-order features {½ ½} were observed. This LEED pattern has been interpreted in terms of a 2-dimensional (2-D), centered two-by-two structure (Fe(001) c(2 x 2)—?).

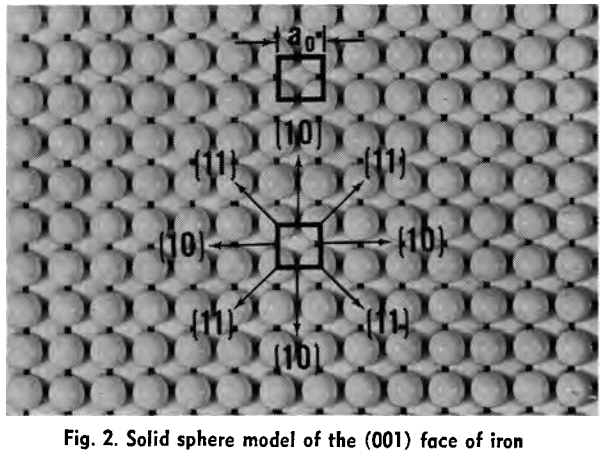

Fig. 2. Solid sphere model of the (001) face of iron

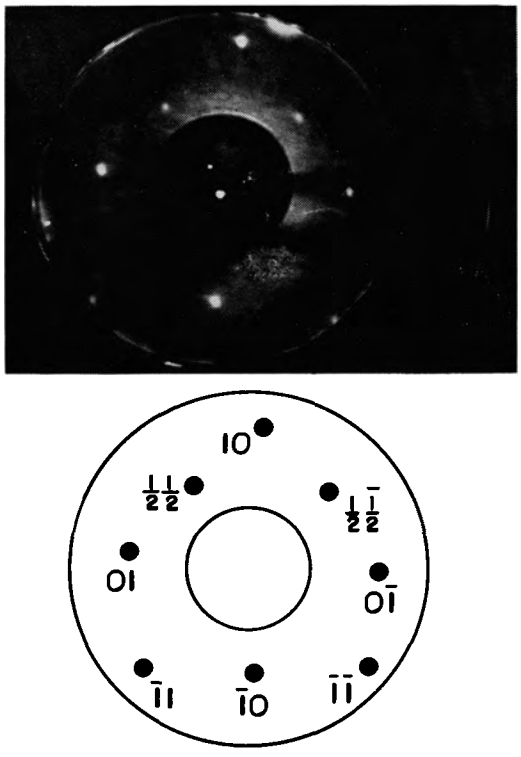

Fig. 3. Photograph of LEED pattern of a contaminated iron surface. The wavelength of the incident electron beam was 1.21Å.

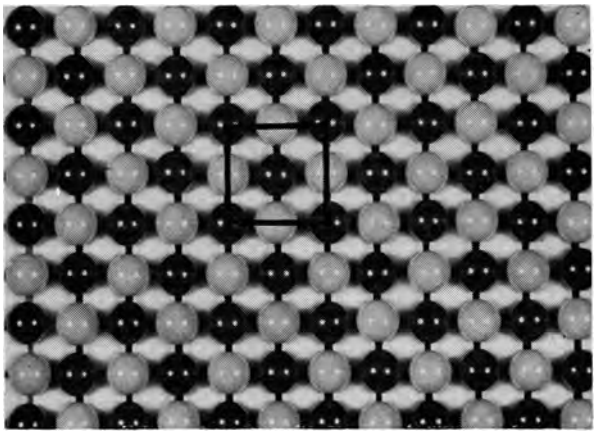

Fig. 4. Suggested solid sphere model of a Fe(001) c(2 x 2)—? structure.

This structure, according to LEED nomenclature, is a superposed net consisting of foreign atoms situated at the corners and at the center of a 2-D mesh. The sides of the mesh are equal to twice the length of the unit mesh of the substrate (iron) with the same orientation as the substrate. The relatively high intensity and sharpness of the half-order beams as compared to that of the integral-order features further suggests that this structure consists of a full monolayer of atoms containing both iron atoms, which occupy the open positions in the c(2 x 2) mesh, and impurity atoms. A suggested model of this structure is illustrated in Fig. 4. The dark spheres represent the impurity atoms and the light spheres the iron atoms. The 2-D unit mesh is outlined in this figure.

Repeated application of low-energy, argon-ion bombardment and annealing removed all fractional order features from the LEED pattern. Figure 5 is a photograph of the LEED maxima in the [10] azimuths obtained at 104 ev from a clean (001) iron surface, where only the integral-order features expected for a clean iron (001) surface, Fe (001) p(1 x 1), are evident.

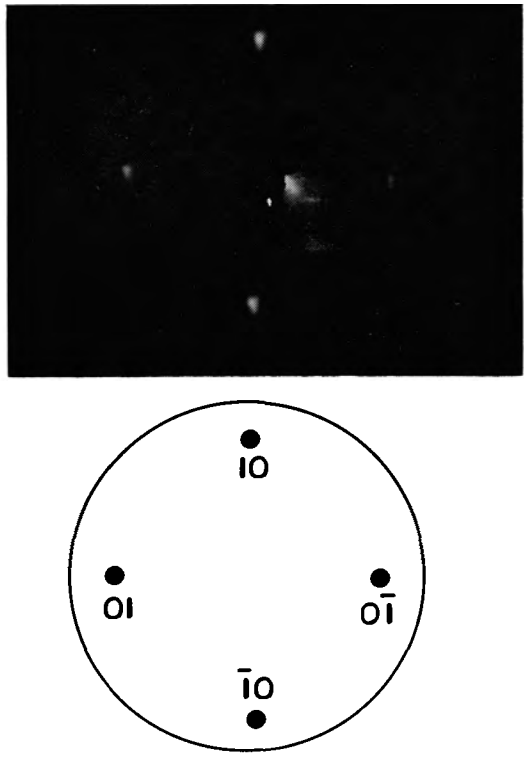

Fig. 5. Photograph of a LEED pattern of a clean iron surface. The wavelength of the incident electron beam was 1.20Å.

All LEED beams back-reflected from a clean iron (001) surface under the conditions of these experiments appear in either the [10] or the [11] azimuths. The surface diffraction grating relationships that apply in these azimuths are

$$\lambda = 2.86 \operatorname{Sin} \phi \text{ (for the 10 reflections)} \quad [1]$$

$$\lambda = 2.03 \operatorname{Sin} \phi \text{ (for the 11 reflections)} \quad [2]$$

These relationships plot as straight lines in Fig. 6, and the calculated positions of the intensity maxima (Laue beams) as deduced from simple kinematic diffraction theory are plotted as circles. The experimental data consisting of the applied electron accelerating voltages and measurements of the resulting LEED patterns (Fig. 5) appear as squares. The relative intensity-voltage data for the 10 beam from a clean iron surface are plotted in Fig. 7. The positions of the Laue beams appear on this plot as inverted arrows. The differences between the experimental and the calculated values of the wavelengths of the beam maxima have been attributed to the interaction of the

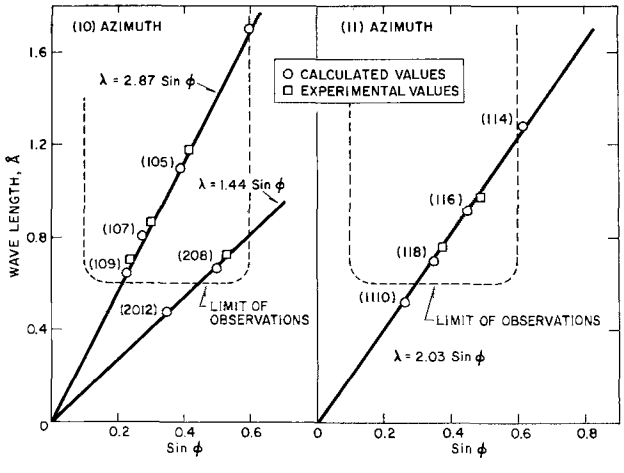

Fig. 6. Laue beams from a clean iron (001) crystal face

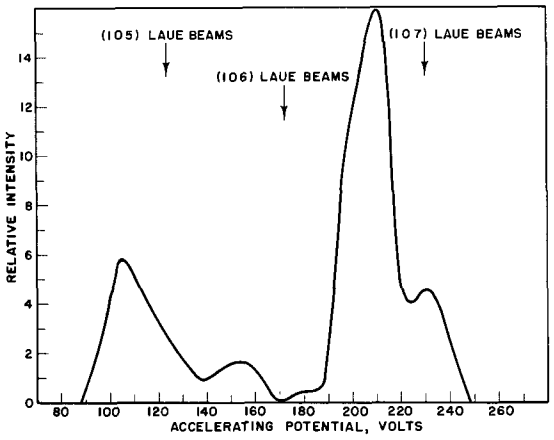

Fig. 7. Relative intensity-voltage data for the 10 reflection from a clean iron (001) crystal face.

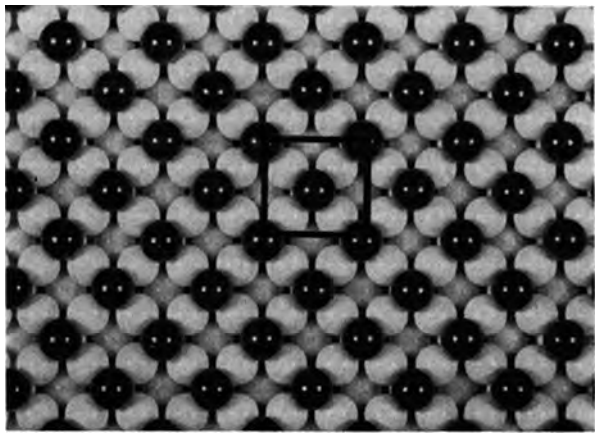

Fig. 9. Suggested solid sphere model of half a monolayer of oxygen on an iron (001) face. The Fe(001) c(2 x 2)—O structure.

electron beams with electrostatic fields existing within the crystal surface, causing refraction of the diffracted beams (the wavelength of the electron beam within the crystal is not the same as that in vacuo outside the crystal), and consequent displacement of the diffraction maxima. These considerations indicate, therefore, that the wavelength characteristic of a diffracted beam is more accurately represented as $[150.4/(V + \psi)]^{1/2}$, where V is the accelerating voltage for the incident electron beam in vacuo and ψ is the inner potential of the surface.

The experimentally observed maxima, appearing at 106 and 210 ev in Fig. 7, are in agreement with the calculated Laue beams (arrows), if an average value of 23v, uncorrected for contact potential, is assumed for the inner potential of this surface. The smaller peaks and/or shoulders appearing at the calculated Laue beam positions, 124 and 230 ev, respectively, generally have been attributed to the interaction of surface beams diffracted from steps on the crystal surface. Because under these conditions the beams do not penetrate into the surface, no inner potential shift is expected. It was concluded from these data, the sharpness of the diffraction features, and the relatively low background, that this surface was clean and that a clean (001) iron surface is an unreconstructed surface; that is, the clean (001) iron surface consists of iron atoms in the positions expected of a mathematical model of atoms arranged in a (001) surface of a body-centered cubic lattice.

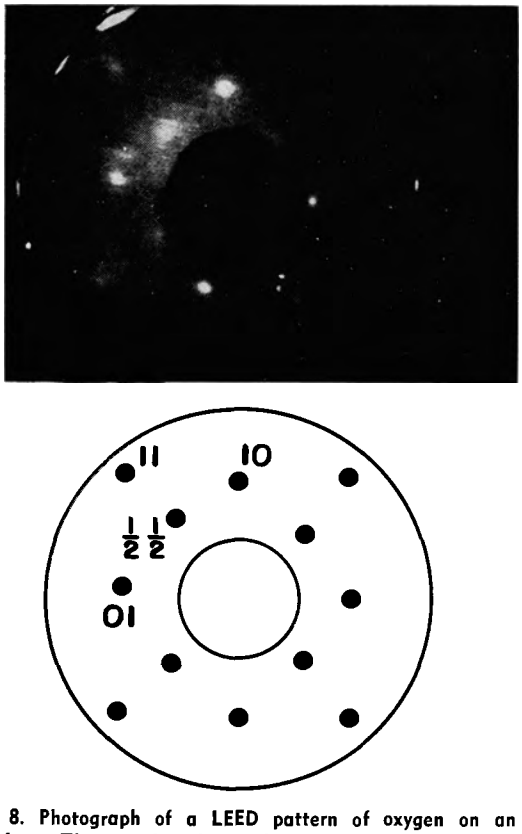

Fig. 8. Photograph of a LEED pattern of oxygen on an iron (001) face. The wavelength of the incident electron beam was 1.03Å.

Chemisorption of oxygen on a clean iron (001) surface.—The first experiments performed on the clean iron surface consisted of the observation and interpretation of LEED patterns obtained on exposure to low pressures of oxygen at room temperature. The initial, relatively slight oxygen exposure (1.5×10^{-7} Torr-sec) served only to weaken somewhat the clean iron surface diffraction features. After a greater exposure of 5×10^{-7} Torr-sec, a weak pattern characteristic of a 2-D, Fe(001) c(2 x 2)-O was observed. This c(2 x 2) pattern reached maximum intensity after an exposure of about 8×10^{-7} Torr-sec. A photograph of the pattern, taken at 140 ev, is presented in Fig. 8; the diffraction features are identified according to their 2-D Miller indices. A photograph of the proposed model of this c(2 x 2) structure, deduced from the LEED pattern, is shown in Fig. 9. The dark spheres represent the chemisorbed oxygen atoms in the top layer; the 2-D unit mesh of the oxygen lattice is outlined in this photograph.

The relatively low intensities of the half-order features, ½ ½, compared to those of the features attributable to the iron substrate 10, suggest that the top surface immediately after an oxygen exposure of 8×10^{-7} Torr-sec probably consists of half a monolayer of chemisorbed oxygen arranged in a c(2 x 2) structure (rather than a full monolayer) containing both iron atoms and oxygen atoms. From these data and the calculated number of oxygen molecules that struck the surface during the exposure, it was evident that essentially every molecule of oxygen that struck the surface dissociated into atoms and was chemisorbed on the surface.

Oxide formation on the iron (001) face.—On further exposure to oxygen at room temperature, the intensities of the beams from the c(2 x 2) structure gradually weakened, with an accompanying increase in background intensity. Also the intensity-voltage relationships for the 10 feature became more complicated with continued exposure. After an exposure of 55×10^{-6} Torr-sec, no diffraction beams were discernible on the screen. However, as a result of a subsequent ultra-high vacuum anneal at 550°C, LEED patterns were obtained that exhibited integral order features only in the [10] and [11] azimuths, and corresponded to the calculated pattern of FeO. The formation of

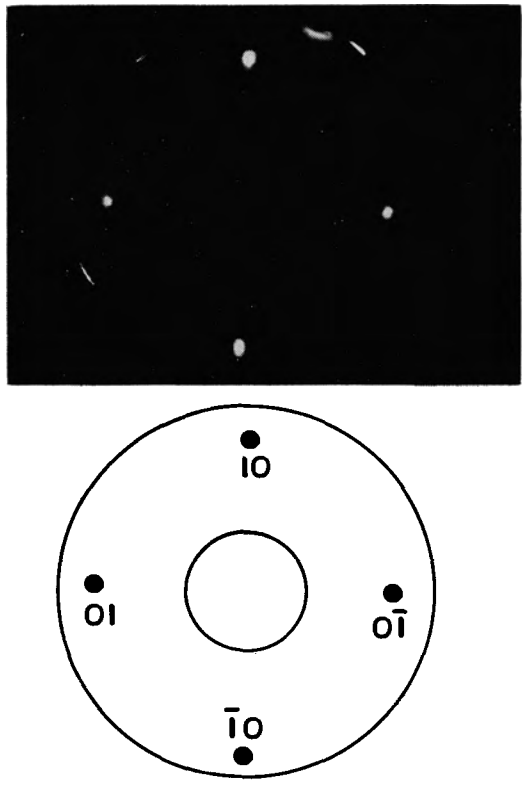

Fig. 10. Photograph of a LEED pattern of iron oxide (FeO) on an iron (001) face. The wavelength of the incident electron beam was 1.33Å.

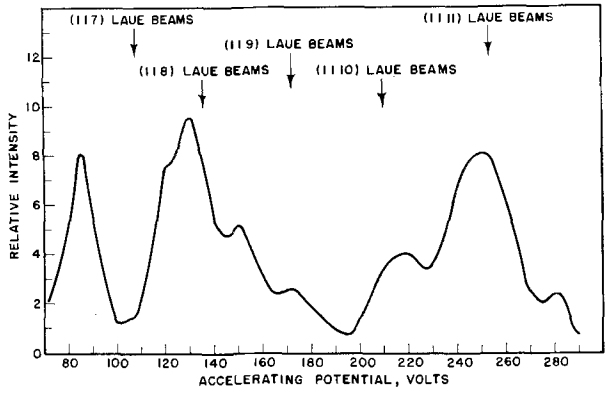

Fig. 11. Relative beam intensity-voltage data for the 10 reflection from a FeO (001) surface.

FeO also was observed to occur at room temperature and very low oxygen partial pressures on a clean (001) face of iron that had been allowed to dwell in an ultra-high vacuum for an extended period of time (~5 days). A photograph of a typical LEED pattern of FeO obtained at 85 ev after an oxygen exposure of 55 x 10^{-6} Torr-sec and subsequent anneal is presented in Fig. 10. The intensity-voltage relationships for the 10 feature are plotted in Fig. 11. The voltages for occurrence of intensity maxima, calculated from a simplified model of FeO (lattice parameter $a_o = 4.32$Å) oriented on the iron substrate with its (001) face parallel to the (001) face of the iron, and with its [110] direction parallel to the [100] direction of iron, are indicated by the arrows.

The maxima appearing at 85 and 150 ev correspond to (117) and (119) Laue beams, respectively, which have been displaced toward lower voltages by approximately 23v, the assumed inner potential of the surface. No correction for the contact potential was employed in these calculations. The large peak appearing at 250 ev is attributed to the (1 1 11) Laue beam, and the smaller peak appearing at 172v, to coherent diffraction from surface steps in the oxide. The intensity maxima observed at 130 and 220 ev, respectively, occur near the voltages calculated for the "forbidden" (118) and (1 1 10) reflections. Because electron scattering phenomena in the low energy range are imperfectly understood, this analysis represents only a first approximation in the calculation of the positions of the occurrence of the intensity maxima. Thus, it is perhaps not surprising that more maxima are observed than can be accounted for by this simple treatment.

Stability of FeO

The thin film of FeO formed on the (001) face of iron was annealed at each of three temperatures (25°, 100°, or 480°C) for 65 hr, at oxygen partial pressures below 10^{-10} Torr. The LEED patterns and the voltage-intensity relationships for the 10 feature, before and after annealing, were identical. Additional features expected for a cubic oxide, such as Fe_3O_4, were not observed under these conditions. Thus, it is concluded that the FeO film, formed and annealed at oxygen partial pressures below 10^{-10} Torr, did not transform to Fe_3O_4, and probably continued to grow as FeO. No evidence of transformation of the FeO to Fe_3O_4 was observed at these low oxygen partial pressures.

There are at least two explanations for this observed stability of FeO. The first assumes that the reaction, 4 FeO $\rightleftarrows$ Fe_3O_4 + Fe, takes place. The equilibrium constant for this reaction calculated from properties of bulk oxide, prepared and investigated at atmospheric pressure, predicts that FeO is unstable at temperatures below 575°C. Gurry and Darken (27), in their investigations of FeO at elevated temperatures, indicated, however, that the free energy of FeO was dependent on oxide composition (that is, on the number of cation vacancies in the oxide) and hence on the manner in which the oxide was prepared. Such variations in the values of the free energies of FeO and/or Fe_3O_4, prepared and maintained at very low pressures, could alter the equilibrium constant and thereby account for the increased stability of FeO at lower temperatures. A second explanation, suggested by Gulbransen (22, 23), is that the nucleation of Fe_3O_4 is rate determining and that the activation energy for the nucleation of Fe_3O_4 is dependent on oxygen pressure, since oxygen concentration should have an influence on the number of vacancies in the FeO lattice, and presumably, therefore, on the number of Fe_3O_4 nucleation sites. This activation energy should become larger at lower oxygen pressures; hence, lower oxygen pressures should inhibit the reaction. Once the activation energy is overcome, the reaction can proceed readily to form the Fe_3O_4 phase. Thus, the very low oxygen pressure utilized in the present experiments may have effectively arrested the reaction through its affect on the nucleation activation energy of Fe_3O_4. Either of these mechanisms satisfactorily account for the observed stability of FeO at room temperature under ultra-high vacuum conditions.

Summary

The LEED technique has been used to investigate the chemisorption of oxygen on an atomically clean (001) iron surface and the subsequent formation and stability of a thin oxide film formed on the iron surface. The surface cleaning treatment consisted of a low-energy argon ion bombardment and a final short period of ultra-high-vacuum annealing at 500°C. It was possible to achieve an atomically clean surface only for crystals obtained from a zone-refined sample having a relatively low carbon content (about 14 ppm or less). The LEED patterns and the intensity-voltage relationships for a clean (001) face of iron indicated that this surface was an unreconstructed surface.

The effects of exposing an atomically clean cube face of iron to low oxygen pressures for different time intervals indicated that after an exposure of 8 x 10^{-7} Torr-sec, formation of the chemisorbed layer was es-

sentially complete. This layer consisted of half a monolayer of oxygen sorbed in a Fe(001) c(2 x 2)-O structure. Germer and Hartman (13) observed a similar structure for the chemisorption of a half of a monolayer of oxygen on the nickel (001) face. A thin layer of FeO was detected on the crystal after an exposure of 55 x 10^{-6} Torr-sec and subsequent annealing at 550°C. FeO also was observed to form at room temperature on a clean (001) face of iron, when the specimen was allowed to dwell under ultra-high-vacuum conditions for an extended period of time. The (001) plane of this film was oriented parallel to the (001) face of the iron substrate, with the [110] direction of the oxide parallel to the [100] direction of the iron which is the usual epitaxy of FeO on iron reported in the literature. Under similar conditions of oxidation Farnsworth (3) and Germer and MacRae (13) also observed the formation of a cubic oxide, NiO, on a nickel crystal. Farnsworth reported that the NiO phase formed at room temperature after a suitable oxygen exposure (10^{-5} Torr) while Germer observed that with lighter oxygen exposures (10^{-6} Torr) heat was generally required to form NiO. In view of these data it appears that it is extremely difficult if indeed not impossible to prepare and maintain for any appreciable time an oxide free surface for such reactive metals as iron and nickel in systems where the oxygen partial pressure is of the order of 10^{-6} Torr or higher.

These LEED studies on iron have also presented data on another phase of the oxidation process; the transformation of FeO to Fe_3O_4. Earlier studies by others had indicated that oxide (FeO) films formed and examined at relatively high oxygen partial pressures, decomposed to form Fe_3O_4 at temperatures below 570°C. The present LEED experiments have demonstrated that FeO films formed and analyzed at very low oxygen partial pressures do not transform to Fe_3O_4 at an appreciable rate at temperatures below 570°C and instead continue to grow as FeO.

Acknowledgments

The authors are indebted to Dr. L. H. Germer for many helpful suggestions and discussions. We also wish to thank Mr. F. J. Malloy and Mr. F. M. Roth for their valuable assistance in the construction of the experimental equipment.

Manuscript received April 22, 1965; revised copy received Aug. 12, 1965. This paper was presented at the Washington Meeting, Oct. 11-15, 1964.

Any discussion of this paper will appear in a Discussion Section to be published in the June 1966 JOURNAL.

REFERENCES

1. C. J. Davisson and L. H. Germer, *Phys. Rev.*, **30**, 705 (1927).
2. C. J. Davisson and L. H. Germer, *Nature*, **119**, 558 (1927).
3. H. E. Farnsworth and J. Tuul, *J. Phys. Chem. Solids*, **9**, 48 (1959).
4. H. E. Farnsworth, *Phys. Rev.*, **34**, 679 (1929).
5. H. E. Farnsworth, *ibid.*, **43**, 900 (1933).
6. H. E. Farnsworth, R. E. Schlier, T. H. George, and R. M. Burger, *J. Appl. Phys.*, **26**, 252 (1955).
7. R. E. Schlier and H. E. Farnsworth, *J. Phys. Chem. Solids*, **6**, 271 (1958).
8. H. E. Farnsworth, R. E. Schlier, and J. A. Dillon, *ibid.*, **8**, 116 (1959).
9. J. A. Dillon, R. E. Schlier, and H. E. Farnsworth, *J. Appl. Phys.*, **30**, 675 (1959).
10. L. H. Germer and C. D. Hartman, *RSI*, **31**, 784 (1960).
11. J. J. Lander, J. Morrison, and F. Unterwald, *ibid.*, **33**, 782 (1962).
12. W. Ehrenberg, *Phil. Mag.*, **18**, 878 (1934).
13. L. H. Germer and C. D. Hartman, *J. Appl. Phys.*, **31**, 2085 (1960).
14. L. H. Germer and A. U. MacRae, *ibid.*, **33**, 2923 (1962).
15. A. U. MacRae and L. H. Germer, *Ann. N. Y. Acad. Sci.*, **101**, 627 (1963).
16. J. J. Lander and J. Morrison, *J. Chem. Phys.*, **37**, 729 (1962).
17. J. J. Lander and J. Morrison, *J. Appl. Phys.*, **34**, 1403 (1963).
18. J. J. Lander and J. Morrison, *ibid.*, **34**, 1411 (1963).
19. H. E. Farnsworth and J. Tuul, *J. Phys. Chem. Solids*, **9**, 48 (1959).
20. E. A. Wood, *J. Appl. Phys.*, **35**, 1306 (1964).
21. M. A. H. Lanyon and B. M. W. Trapnell, *Proc. Roy. Soc.*, **227**, 387 (1955).
22. E. A. Gulbransen and R. Ruka, *Trans. AIME*, **188**, 1500 (1950).
23. E. A. Gulbransen and R. Ruka, *Ind. Engr. Chem.*, **43**, 697 (1951).
24. E. A. Gulbransen, W. R. McMillan, and K. F. Andrews, *Trans. AIME*, **192**, 1027 (1954).
25. G. Chaudron and J. Bénard, *Bull. Soc. Chem. France*, **D88**, 90 (1949).
26. G. Chaudron and C. R. Forestier, *Acad. Sci.*, **178**, 2173 (1924).
27. L. S. Darken and R. W. Gurry, *J. Am. Chem. Soc.*, **68**, 798 (1946).

Epoxy Dielectric Films Produced by Electron Bombardment

A. E. Brennemann and L. V. Gregor[1]

International Business Machines Corporation, Watson Research Center, Yorktown Heights, New York

ABSTRACT

Thin dielectric films have been produced by low energy electron bombardment of a surface which is simultaneously exposed to an evaporating epoxy resin. The rate of film growth is dependent only on the evaporation parameters when the electron flux at the surface is much larger than the molecular flux in the evaporant beam. The polymerized epoxy films are good insulators with d-c dielectric breakdown strengths greater than 10^6 v/cm. The films are stable in normal room atmosphere and may be cycled thermally from room temperature to 77°K many times without damage to their mechanical or electrical properties. A number of multilayer electrical structures consisting of alternating evaporated Pb films and epoxy films have been prepared successfully and tested.

Organic molecules adsorbed on a surface can be converted to solid polymeric films by low energy electron bombardment. Because of the dielectric properties of such films, their use has been suggested as insulation for thin film circuits (1). It has been shown that adsorbed residual pump oil vapor (DC-704) in a vacuum system can be converted by electron bombardment into polymer film with good insulating properties (2). Other investigations have been concerned with the electron bombardment of butadiene (3),

[1] Present address: Systems Development Division, International Business Machines Corporation, Poughkeepsie, New York.

methyl methacrylate, and various conjugated organic monomers (4) with less promising results. The electron bombardment process for producing thin dielectric films is of particular interest for the fabrication and study of cryogenic circuits, since polymer films are not as highly stressed as most evaporated inorganic dielectrics (5) and are more resistant to the additional stresses caused by cooling to very low temperatures. A disadvantage of electron bombardment processes for producing dielectric films is the relatively low rate of film deposition.

In order to be highly compatible with vacuum evaporation techniques for producing multilayer thin film circuits, the material to be used in the electron bombardment process should possess these properties:

1. It should be convertible by bombardment to a solid dielectric.
2. It should have a vapor pressure at room temperature which is negligible compared to the working pressure of the vacuum system, yet which rises to $\sim 10^{-3}$ mm Hg on heating.
3. It should be sufficiently reactive to be polymerized by low energy electron bombardment to the point where essentially no further chemical reactions occur in the film after bombardment. The low molecular weight condensation polymers of epichlorohydrin,

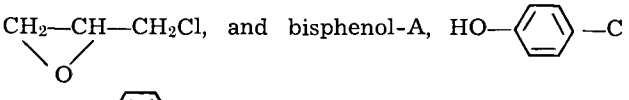

and bisphenol-A,

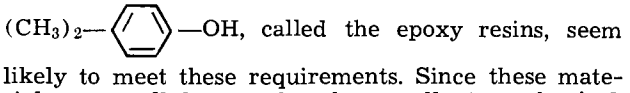

called the epoxy resins, seem likely to meet these requirements. Since these materials are well known for the excellent mechanical, thermal, adhesive, and dielectric properties in bulk, they were chosen for this study.

Experimental Procedures

Evaporation system.—The apparatus for depositing epoxy polymer films was installed in a conventional CVC 18-in. vacuum system operating from 5 x 10^{-5} to 5 x 10^{-6} mm Hg. The schematic diagram (Fig. 1) shows the substrate, electron source or "gun," the epoxy evaporation source, and the magnetic deflection coils for the electron beam. Not shown are the conventional metal evaporation heater and shutter. The epoxy source is mounted 8 in. directly below the substrate, while the electron gun is mounted alongside the epoxy source at an angle to the vertical center line. The deflection coils are positioned between the sources and substrate in such a manner as to allow the evaporating epoxy beam to pass unhindered. The electron beam, aimed at the center of the coils, is deflected on passage through them to become colinear with the molecular beam on arrival at the substrate.

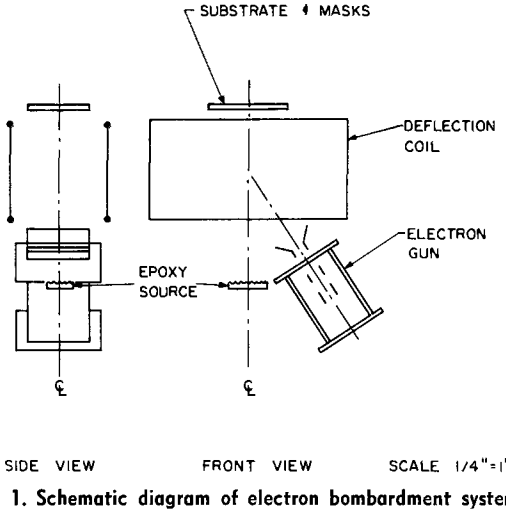

Fig. 1. Schematic diagram of electron bombardment system, side and front views. The electron gun is offset from the center line connecting the epoxy evaporation source and the substrate. Not shown is the vacuum chamber in which the apparatus is situated.

The electron gun is a modification of the Pierce type of electron beam source. The beam can be focused to the shape of a rectangle 4 x ⅜ in. and is capable of static beam current densities up to 5 ma/cm². The focused electron beam is swept across the substrate area, 2 x 2 in., by applying a 60 cycle a-c voltage or other suitable sweep voltages to the deflection electrodes of the gun. The beam current density was maintained at 1.5-2.0 ma/cm² during polymerization, and the accelerating potential was 1200v. The static beam current density was determined by dividing the total target current by the beam area. On sweep deflection, the average dynamic beam density is of course somewhat less than the static value. However, attempts to measure average beam current density during sweep by means of target electrodes or a Faraday gauge at the substrate area did not give consistent results. Thus, the values given for current density can represent only upper limits to the actual current density during polymerization. The rectangular Helmholtz coils used for magnetic deflection of the beam were wound on 5 x 10 in. forms spaced 5 in. apart. A 200-turn coil of No. 32 wire was wound on each frame to produce a 60-amp turn field.

The epoxy resin used in all experiments was Eccomold L-28 manufactured by Emerson and Cummings Inc. It has the molecular structure

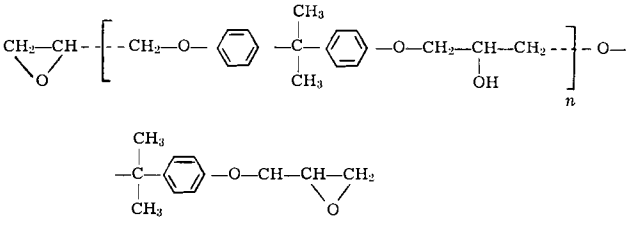

where $n < 10$. The resin is a highly viscous liquid whose vapor pressure is less than 1 x 10^{-6} mm Hg at 25°C. The evaporation source was a shallow trough made of copper sheet or copper tubing, mounted from 6 to 10 in. below the substrate. It was heated by a tungsten or nichrome heater attached to its underside; power input during evaporation was from 5 to 30w for a source temperature from 60° to 130°C, maintained constant to ±1°C. Sources were designed to provide rapid heating, and rapid cooling to room temperature was achieved by means of a copper heat sink.

Evaporation procedure.—The substrate and masks were maintained at room temperature and shielded from the source and electron gun by a movable shutter. At the beginning of a typical run the evaporant source was heated from 25°C to the desired temperature. During the heating period the electron beam was turned on, and the beam current density was adjusted. The beam position and sweep voltages were adjusted by viewing the beam on a phosphor-coated screen on the bottom of the shutter. When the source temperature was stabilized, the shutter was opened to commence film deposition. At the end of deposition, the shutter was closed before either the source or electron gun was turned off. The gun and source were then turned off in no particular sequence. The point to be stressed here is that the substrate should never be exposed to the vapor stream without the presence of the electron beam. Failure to observe this procedure results in unpolymerized epoxy resin on the substrate which is too thick to be polymerized by subsequent scanning with the electron beam.

The temperature of the substrate was monitored during the evaporation. The electron beam power input of 0.5-2.0 w/cm² caused an increase in the substrate temperature from 20° to 40°C after bombardment times of 15-20 min. For longer bombardment times or for larger current densities it was necessary to provide a heat sink and cooling coil for the substrate to

insure that the substrate temperature did not become excessively high.

During the initial experiments, in which a glass bell jar was used, no noticeable polymerization of the epoxy resin in the trough heater was observed. However, subsequent experiments in an all-metal vacuum system resulted in a rapid polymerization of the source epoxy resin and hence a drastic decrease in evaporation rate. The effect may have been due to random bombardment of the source by secondary electrons; in any case, it was prevented by shielding the source with a chimney made of copper.

An undesirable condition is the accidental electrical connection to ground of any metal layer on the substrate. It was observed that if a previous evaporated metal layer became grounded, by shadowing or other means, the subsequent metal layers often became short-circuited to the grounded layer during a subsequent epoxy evaporation. It appears that the short circuit occurs because the ungrounded metal film is charged to some large potential during the electron bombardment. The insulation layer between the grounded and ungrounded layer will then break down due to the large voltage across the film. It is recommended that all metal layers be floating from ground or that all be tied to some fixed potential.

Results

Film growth rates.—Insulating films were produced which were initially reliable (free from short circuits) in a thickness range of 200-10,000Å. Deposition rates were observed from 100 to 900 Å/min on substrates of glass, aluminum, or cast epoxy. Figure 2 shows the rate of film formation as a function of the epoxy evaporation source temperature, with source area as an additional parameter. The substrate temperature was maintained at 25° ± 15°C. The source areas are for shallow open source designs which minimize any collimating or "chimney" effects in the evaporating epoxy resin beam.

The rate of film formation is relatively independent of beam current density between 1.0 and 2.0 ma/cm^2. However, below 1.0 ma/cm^2, the electron beam was difficult to control and the films began to show signs of degradation at current densities above 2.0 ma/cm^2.

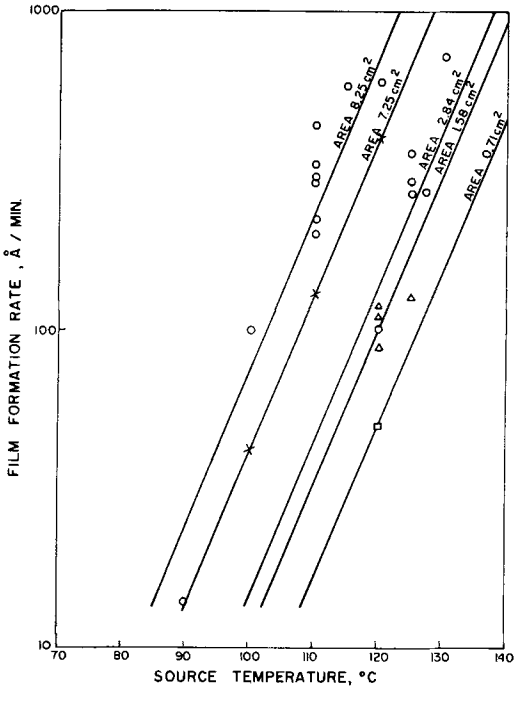

Fig. 2. Polymer film deposition rate (logarithmic scale) vs. temperature of epoxy resin evaporation source for various source areas. Constant accelerating voltage 1200v; constant current density 0.5 ma/cm^2.

Table I. Some dielectric properties of polymerized epoxy resin films at 23°C and 1 kc

Sample No.	Measured thickness, Å	Capacitance, pf	Dielectric constant, k	Dissipation factor, tan δ	Dielectric strength, v/cm
2-44-3	2400	581.8	5.7	0.0063	– (n.m.)
3-47-3	2680	563.4	6.2	0.0070	– (n.m.)
4-50-3	1980	652.2	5.3	0.004	$\geq 1.9 \times 10^6$
2-42-3	1630	1368	5.4	0.0062	$\geq 1.2 \times 10^6$

The degradation consisted of brownish discoloration, increased d-c conductivity, and a much higher incidence of catastrophic failure. Likewise, the rate is relatively independent of the accelerating potential of the gun up to 1200v, but the beam was not controllable for the particular gun design below several hundred volts, setting a lower limit on operating voltage. The upper limit is determined by the voltage at which gas discharge and arcing begin to occur; there appears to be no advantage in operating above 1200v in any case.

Dielectric properties.—The low-frequency dielectric constant k of the polymer film was determined by measuring the capacitance of a structure which embodied the thin film of polymerized epoxy resin as the dielectric medium between two evaporated Pb films approximately 0.5μ thick. The substrate was glass or cast epoxy. The polymer film thickness was measured directly to ±250Å by a Taylor-Hobson Talysurf surface profile instrument. The uniformity of film thickness across a 2 in. substrate deviates less than 2%; the reflection interference color of the film was unchanged across the entire film. Table I summarized the average values for k, tanϑ, and breakdown voltage for films approximately 2000Å thick. The dielectric constant and dissipation factor, tanϑ, were measured from 100 cps to 100 kc, and typical results are shown in Fig. 3. There was no observed variation of either k or tanϑ with a-c signal voltage up to fields of 2 x 10^6 v/cm (rms).

The insulation reliability of epoxy polymer films was examined by fabricating 90 capacitors whose areas ranged from 0.013 to 0.051 cm^2 with the insulating thickness approximately 2000Å. No initial short circuits were found in any of these samples. Thermal cycling between room temperature and 77°K caused no physical damage or short circuits even after hundreds of cycles. Multilayer capacitors with four superimposed metallic films were fabricated with no short

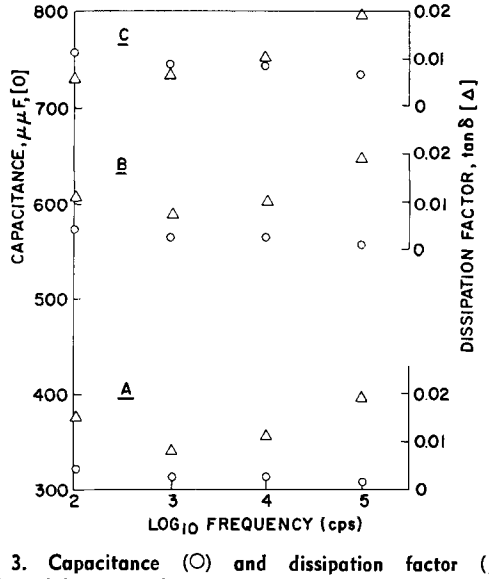

Fig. 3. Capacitance (○) and dissipation factor (△) vs. logarithm of frequency for typical capacitors A (bottom, area 1.37 x 10^{-2} cm^2), B (middle, area 2.76 x 10^{-2} cm^2), and C (top, area 4.03 x 10^{-2} cm^2). Average polymer film thickness 1200-1500Å; measured in air at 23°C.

Table II. D-C breakdown voltage of polymerized epoxy films at 23°C

Film thickness, Å	Breakdown voltage, v
1700	25
1900	40
2100	45

circuits. The dielectric breakdown strength in all samples examined exceeded 1 x 10^6 v/cm (Table II).

Preliminary tests of the epoxy polymer films under conditions of elevated temperature and humidity (85% relative humidity at 85°C) have indicated the occurrence of deleterious effects, such as film buckling and separation from substrate. However, at room temperature and normal humidity (~50%) the capacitors are stable over periods of several months, there being no detectable change in capacitance, dissipation factor, or physical appearance.

The degree of "shadowing," or insulation creepage beyond the edge of the masked areas of the substrate, was found to be comparable to conventional thermally evaporated films. Talysurf measurements of the step width of film approximately 2000Å thick showed the width to be 0.001-0.002 in. The extent of shadowing was determined electrically by varying the width of the insulation mask with respect to the capacitor plate widths until the metallic films were shorted; by this method the extent of electrical shadowing was determined to be $\leq$0.005 in.

Discussion of Results

When used as insulation for capacitors and more complex multilayer thin film structures, the polymerized epoxy films described in this paper have a high degree of initial reliability and are not affected adversely by low-temperature thermal cycling. This implies that the polymer films are homogeneous and adhere well to the surfaces investigated. The structure of the polymer has not been determined, but it is probably a randomly cross-linked network structure; at each end of the molecule the 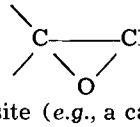 group can be opened to give a reactive site (*e.g.*, a carbonium ion group 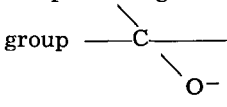), and in the center of the molecule there is the labile —CH_2—CHOH—CH_2— group. In addition to the trifunctional nature of each resin molecule, there is also the possibility of random bond scission and reformation at other points during the bombardment. Many more electrons strike the surface than are required to activate the end or middle reactive groups. For instance, assuming a current density of 1.0 ma/cm^2 and a deposition rate of 150 Å/min, the ratio of electrons to resin molecules reaching the surface is

$$\frac{n_e}{n_m} = \frac{(1.0 \times 10^{-3}\ \text{amp})\,(60\ \text{sec/min})\,(6.2 \times 10^{18}\ e/\text{coul})}{(1\ \text{cm}^2)\,(1.5 \times 10^{-6}\ \text{cm})\,(1.2\ \text{g/cm}^3)\,(6.02 \times 10^{23})\left(\frac{1}{1000\ \text{g/m}}\right)} = \frac{3.7 \times 10^{17}}{1.0 \times 10^{15}} = 370$$

assuming a polymer density of 1.2 g/cm^3 and an average resin molecular weight of 1000 (6). Although the epoxy resins in bulk form are noted for their resistance to electron bombardment after being "cured" (7), the polymer films are apparently adversely affected by prolonged exposure to electron bombardment when the ratio n_e/n_m exceeds ~ 750, corresponding to 2 ma/cm^2 at 1 kv.

The rate of deposition is essentially independent of electron energy and electron flux density within the ranges of these variables which were investigated, since $n_e >> n_m$. The rate of deposition increases exponentially with increasing evaporation source temperature and is proportional to evaporation source area. The film growth rate is essentially determined by the product of the rate of arrival of epoxy resin molecules and the sticking coefficient of the molecules, provided the surface temperature is constant. No accurate epoxy vapor pressure data were available for an attempt to correlate film deposition rate with the rate of epoxy evaporation.

The experimental arrangement allows opportunity for electron-molecule interaction during the time of transit from source to target. In order to estimate the magnitude of this effect, if any, experiments were performed in which the deflection coils were not energized. Under these conditions, the number of electrons striking the surface is greatly reduced; nevertheless an insulating polymer film is formed on the surface at approximately the same rate as during direct bombardment, although the evaluation of the dielectric properties of such indirectly produced polymer films is not complete (8).

The major advantages of epoxy polymer films prepared by electron bombardment appear to be the high degree of insulation reliability, the relatively high rate of film growth, and the compatibility of the process with vacuum evaporation techniques. In addition, the nucleation properties of the surface of the deposited epoxy polymer film can be affected quite strongly by further electron bombardment after deposition. Well-defined patterns have been produced by bombarding selected areas to create nucleation sites, followed by selective growth of metallic films subsequently evaporated onto the polymer surface (9).

Acknowledgment

The authors wish to acknowledge the assistance of H. E. Luhn in performing the experimental work. Several worthwhile discussions and suggestions are due to Dr. H. Seki and E. M. Da Silva. They are grateful for the encouragement of Dr. D. P. Seraphim.

Manuscript received Dec. 17, 1964; revised manuscript received Aug. 6, 1965.

Any discussion of this paper will appear in a Discussion Section to be published in the June 1966 JOURNAL.

REFERENCES

1. D. E. Buck and K. Shoulders, Proc. Eastern Joint Computer Conference, Philadelphia, p. 55 (1958).
2. R. W. Christy, *J. Appl. Phys.*, **31**, 1680 (1960).
3. I. Haller and P. White, *J. Phys. Chem.*, **67**, 1784 (1963).
4. R. A. Fotland and W. J. Burkhard, Paper presented at the Los Angeles Meeting of the Society, May 7, 1962.
5. J. Priest, H. L. Caswell, and Y. Budo, *J. Appl. Phys.*, **34**, 347 (1963).
6. Estimated from data supplied by the manufacturer, Emerson and Cummings, Inc., on "Eccomold L28" epoxy resin.
7. J. V. Pascale, D. B. Hermann, and R. J. Miner, Paper presented at Dielectrics in Space Symposium, Westinghouse Research Center, Pittsburgh, June 25, 1963.
8. E. M. Da Silva, Private communication.
9. H. L. Caswell and Y. Budo, Paper presented at American Vacuum Society Meeting, Chicago, Sept. 29, 1964.

Magnetically Shaped R. F. Discharge for Polymer Film Formation

R. A. Connell[1] and L. V. Gregor[2]

International Business Machines Corporation, Watson Research Center, Yorktown Heights, New York

ABSTRACT

A magnetically contained glow discharge has been developed for production of thin polymer insulating films. The glow discharge is maintained by an electrodeless radio-frequency source external to the system. Film growth rates of 1200Å/min of polystyrene have been achieved with very little substrate heating or shadowing of the polymer films. The controlled glow discharge has been used to make thin film capacitors whose plates are evaporated metal films. Insulating films as thin as 100Å have been produced from several organic monomers.

The formation of thin polymer films on surfaces by means of a gas discharge in an organic vapor has been accomplished by several investigators (1-4). In general, the use of an electrical discharge in a reactive atmosphere is related to the fields of (*a*) chemical plasma reactors for the synthesis of certain compounds (5, 6), and (*b*) electron beam polymerization of absorbed organic or organo-silicon vapors to form insulating films (7-10). The glow discharge source described in this paper attempts to achieve a greater degree of flexibility and control of the discharge and the reaction products evolved than do previous glow discharge polymerization processes.

The analysis of the physical and chemical processes occurring in a discharge involving complex molecules is generally extremely complicated. In such a situation, one wishes to remove as many uncontrolled variables as possible while maintaining maximum control over all other parameters which may influence the results. Accordingly, it was decided to construct a source with the following features: (*a*) rf electrodeless excitation to avoid sputtering and other electrode effects; (*b*) the use of d-c magnetic fields to contain and control the resulting plasma; (*c*) the use of a dynamic flow system to control the relative percentages of constituents of the plasma and the population temperatures within the discharge; and (*d*) the restriction of the target to a passive role in the discharge process.

[1] Present address: Midwest Research Institute, Kansas City, Missouri.

[2] Present address: IBM Corporation, Systems Development Division, Poughkeepsie, New York.

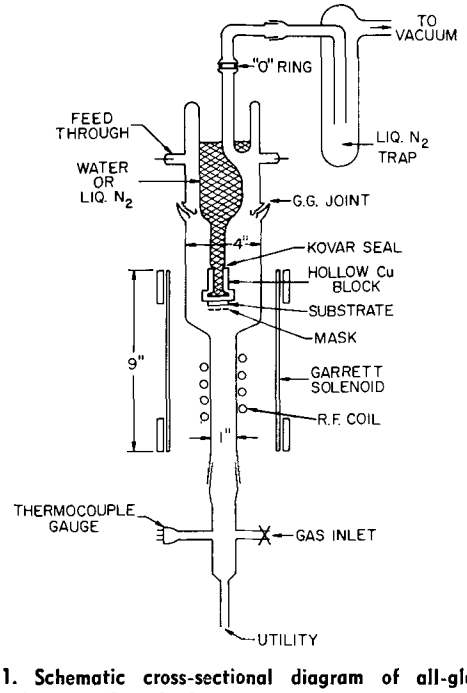

Fig. 1. Schematic cross-sectional diagram of all-glass magnetically focused glow discharge system I.

Apparatus

Cross-sectional diagrams of two versions of the rf discharge apparatus are shown in Fig. 1, a drawing of the original all-glass model for simple experimental work (system I), and Fig. 2, a schematic diagram of the incorporation of such a source into an existing evaporator system (system II). In both models, the monomer vapor is fed into the excitation region through a needle valve and then through a drift zone to the target substrate. In both cases the substrate is attached to a copper block. In system II the block can be alternatively rotated into the discharge stream or faced downward for vacuum evaporation of metal films. A water-cooled rf coil, operating at 0.5 Mc/sec and capable of generating peak fields of the order of 2 oe, was used to excite the gas. The containment coils used in both models provided d-c magnetic fields up to 500 oe. A pinch coil was introduced in the second model as an embellishment to further reduce unnecessary losses by the establishment of a so-called "magnetic mirror" whereby electrons below a certain energy will be reflected by the bunching of magnetic flux. The pinch coil generated a local field intensity of about double the containing field. A separate collimating coil was used for the drift region in system II.

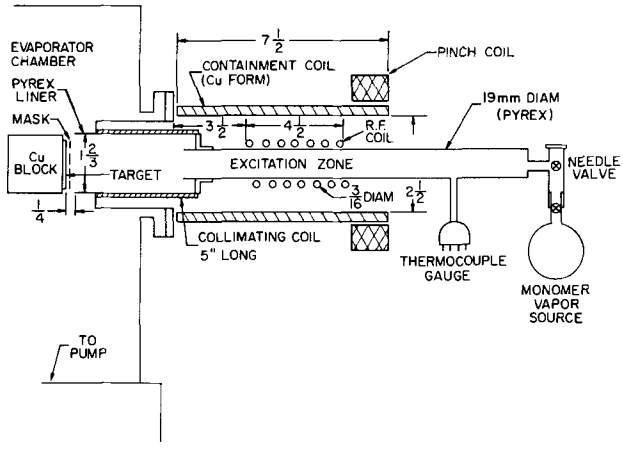

Fig. 2. Schematic cross-sectional diagram of magnetically focused glow discharge system II. Apparatus shown incorporated into the side of a metal bell jar of a vacuum evaporation system.

This coil provided relatively uniform fields up to about 150 oe.

Analysis of the Discharge

An rf electrodeless discharge is essentially diffusion limited (11), and hence the power that must be coupled into the plasma to sustain it in an equilibrium state is determined by the rate at which charged particles are lost from the plasma. Electron drift in a plasma is easily restricted by the application of a modest magnetic field. Under the operating conditions just described, the cyclotron frequency of the electrons, $\omega_e = eB/m$, is of the order of 10^{10} rad/sec with a Larmor radius $\rho_e = mv/He \sim 10^{-2}$ cm. For a typical monomer ion, whose mass number may exceed 100, $\omega_i \sim 10^4$ rad/sec and $\rho_i \sim 5$ cm. The constraint exercised on the heavy ions with the present geometry and fields is therefore indirect, arising from a charge build up on the container walls or a restraining space charge (12).

In a magnetic field, the mean distance and electron moves in a direction perpendicular to the field for an electron-ion collision is l_e (11). For a pressure of 100μ and no applied field, the electronic and ionic mean free paths l_e and l_i are of the order of 1 cm and 1 mm, respectively. The diffusion coefficients of the two species will also be altered accordingly (11, 12). It is obvious that the nature of the discharge will be altered considerably by this field and, in particular, that it may be maintained at pressures and rf field intensities below those which are otherwise possible. Furthermore, it establishes an anisotropy in diffusion losses with a preferred direction parallel to the d-c field.

Magnetic reflection will occur in the pinch field region when the charged particle kinetic energy $W \leq \mu B_m$, where

$$\mu = \tfrac{1}{2}\, mv_c^2/B_0$$

μ is the magnetic moment of the charged particle, B_m is the peak field in the pinch zone (12), and v_c is the velocity component perpendicular to the magnetic field. For an electron energy of 1 ev, the field necessary for electron reflection is of the order of 10^3 gauss.

Two other points should be made before passing on to results of the actual operation of the apparatus. According to Lax *et al.* (11), the mean energy gain of an ion from an rf field between collisions is inversely proportional to the square of the d-c magnetic field. Thus, not only is it possible to sustain a discharge at a low rf power level, but at this level the low-lying excited states and particularly the lowest energy process leading to ionization or excitation should be preferred. This amounts to the exclusion of high energy processes which tend to give rise to a greater variety of reaction products. In this respect, many of the reactions taking place in this discharge should closely resemble those encountered on ultraviolet gas-phase irradiation (14), which can be highly selective. This is in contrast to other discharge sources (1-4), which utilize relatively high energy excitation.

The second point has to do with collimation of the ionized stream impinging on the target surface. The existence of a magnetic field normal to the target surface will severely restrict lateral electronic motion. This applies not only to the primary plasma electrons, but also to any secondary electrons or photoelectrons which might conceivably be ejected from the target or intervening structure, such as a mask. This collimation should reduce shadowing (*i.e.*, unwanted polymer formation) underneath the masked area. In the event that polymerization is achieved via uncharged species such as free radicals (15), the magnetic field would cease to be effective in this respect. However, decreased shadowing would still result from the reduction in the minimum operating pressure and concomitant increase in molecular mean free path, as opposed to the mask-target separation.

Results and Discussion

The observed behavior of the system conforms remarkably well to what might be predicted from the discussion above. Considering system I first, it was found that a pale blue glow could be sustained at a monomer pressure in the range of 20-100μ, as registered on a thermocouple gauge, when $H_{d\text{-}c} \geqq 300$ oe and H_{rf} (peak) ~ 1 oe. A reduction in the d-c field extinguished the glow. For higher rf fields, higher pressures, and decreased d-c field, a bright white, arc-like discharge mode was obtained. (It was observed that it was not possible to strike or sustain a discharge in gases possessing relatively high ionization potentials, such as nitrogen or argon, with this apparatus.) The monomer used most extensively was a mixture of the isomers of divinylbenzene, $CH_2 = CH - C_6H_4 - CH = CH_2$, (DVB), whose vapor pressure at 25°C is approximately 4×10^{-1} mm Hg.

During the blue glow discharge in DVB a tough, coherent, colorless, transparent polymer film was formed on the substrate. The rate of deposition was relatively insensitive to monomer pressure in the glow discharge range. On the other hand, the bright arc-type discharge was characterized by the generation of a great deal of heat, the consumption of comparatively large quantities of monomer (as attested to by a drastic decrease in pressure), and the formation of a thick, brownish deposit on all adjacent surfaces. Some of this is believed to be due to thermal polymerization since it occurred chiefly in the areas heated most strongly, irrespective of magnetic field orientation, and with little or no film formation at the cooler target surface.

The magnetically controlled glow discharge films resembled those formed by ultraviolet polymerization of DVB in many ways (14). There were some differences in physical properties; films prepared by the former process were mechanically much harder with a higher softening temperature, indicative of a higher degree of cross-linking (15). This suggests that the electrons in the discharge may be contributing to cross-linking during polymerization, a conjecture also supported by the absence of almost any shadowing when the target surface was masked off by an aluminum template. For mask-to-substrate spacings as much as 0.020 in, the shadowing, as determined from Talysurf contours, was not more than 0.002 in. This is to be compared to other discharge sources, where the shadowing may extend ten times as far (3).

The average film growth rate, d/t, where d is the

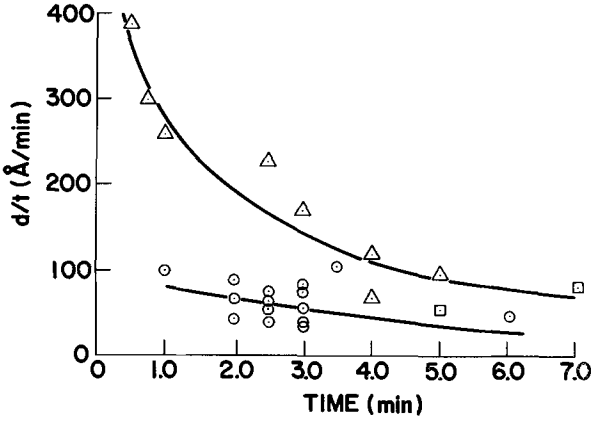

Fig. 3. Rate of deposition of polymer film vs. time for divinylbenzene vapor. Inlet pressure 50μ except for points shown as squares. The decrease in rate is more pronounced for the vertically mounted system in which the thermal contact between substrate and holder is less efficient (system I). Open triangle with dot, vertical mount water-cooled substrate; open circle with dot, horizontal mount; open box with dot, $P_{(DVB)} = 20\mu$.

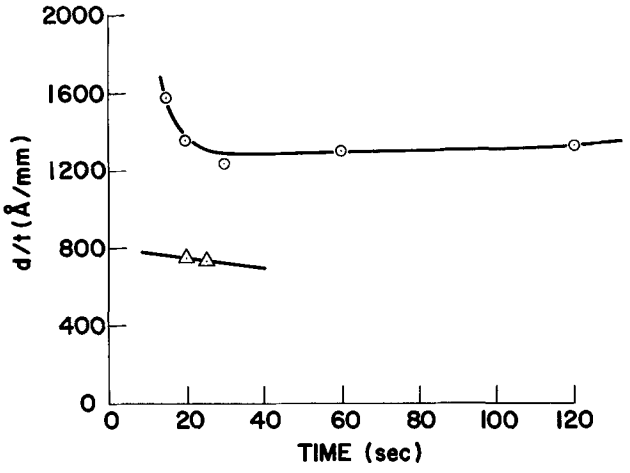

Fig. 4. Rate of deposition of polymer film vs. time for styrene vapor. Inlet pressure 50-75μ, system II; Open circle with dot, Pb film substrate; open triangle with dot, Cu film substrate.

film thickness and t is the deposition time, is plotted as a function of deposition time in Fig. 3 and 4. Thicknesses were ascertained by means of a Talysurf for the thicker films. These readings were then correlated with capacitance measurements of structures comprising films of Pb electrodes above and below the polymer film. For polymer films <1000Å, thicknesses were determined from capacitance measurements alone, assuming the constancy of the polymer dielectric constant (K = 2.8 at 1 kc) as determined from the thicker films. This approach was necessitated by the insensitivity of the Talysurf for thickness values below 1000Å.

Figure 3 shows the deposition rates observed in the all-glass system (I) with DVB as the monomer gas. The triangular points represent values taken with the discharge axis mounted vertically and water cooling of the copper block holding the substrate. The circled points were obtained with the apparatus mounted horizontally with no substrate cooling. Figure 4 shows the rate of deposition as a function of exposure time for films made from styrene, $CH_2 = CH$, in system II. The rate in this case is considerably higher than shown in Fig. 3 and levels off more rapidly. This is probably because the substrate was in better thermal contact with its holder in system II. Included also are two points showing the rate of deposition of polystyrene on an evaporated Cu film in system II.

Although most of this paper concerns itself with divinylbenzene, other monomers such as butadiene, glycidyl methacrylate, and allyl glycidyl ether were also tried, with varying degrees of success. Styrene, deposited via system II, gave the best results to date. With appropriate adjustment in monomer flow rate through the system, deposition rates of the order of 1200 Å/min are readily achievable. Films were deposited on a variety of surfaces, including glass, cast epoxy, evaporated metallic films on glass (Ag, Cu, Pb), polished aluminum and Ni-Fe alloy plated Mylar tape. There did not appear to be any limitation on film thickness up to 10,000Å, the thickest film prepared. Adherence of the polymer film to all substrate materials was excellent. A thick film (7000-9000Å) was deposited on aluminum (25 cm^2 area) and showed no observable deterioration after storage in air at room temperature for nine months.

The capacitor configuration normally used had a rectangular plate area of 7.6 mm^2. The capacitors were fabricated on glass substrates 2.5 x 1.2 cm. The uniformity of polymer film thickness across a circular area 3 cm in diameter is a function of deposition rate, gas flow rate, and thickness. For thick films (> 1μ) deposited at high rates, the decrease in thickness from the center of the circle to the edge was approximately 30%.

In Fig. 3, the apparent drop off in rate with time is believed to be a heating effect at the target surface. The target substrate is only loosely coupled with the cooling block in system I. The cooling block thus serves only to establish an initial surface temperature (approximately 18°C). Under these conditions the most plausible explanation of the observed drop in rate is local heating of the surface. This would be in accordance with rate measurements made as a function of substrate temperature for polymer films formed by both ultraviolet and electron beam irradiation (9, 14), (excluding surfaces so hot as to spontaneously polymerize the vapor).

The use of this type of glow discharge sometimes provides polymer films free of pinholes down to 100Å thickness, although this lower limit will vary somewhat from one monomer to another. Because these films are so thin, electronic conductivity (due to tunneling and Schottky emission) is observed when the electric field across the capacitor is sufficiently high.

Acknowledgment

The authors are grateful to Dr. D. P. Seraphim for his encouragement, and to Messrs. P. Roland, H. J. Martin, and P. L. Ingrassia for assistance in performing much of the experimental work.

Manuscript received Dec. 17, 1964; revised manuscript received Aug. 6, 1965.

Any discussion of this paper will appear in a Discussion Section to be published in the June 1966 JOURNAL.

REFERENCES

1. J. Goodman, *J. Polymer Sci.*, **44**, 551 (1960).
2. A. Bradley and J. P. Hammes, *This Journal*, **110**, 15 (1963).
3. E. M. DaSilva and R. E. Miller, *Electrochem. Tech.*, **2**, 147 (1964).
4. L. L. Alt, S. W. Ing, Jr., and K. W. Laendle, *This Journal*, **110**, 465 (1963).
5. A. G. Massey, *J. Chem. Educ.*, **40**, 311 (1963).
6. E. J. Hellund, "The Plasma State," Reinhold Publishing Co., New York (1961).
7. K. R. Shoulders, Standford Res. Inst. Rep., September 1960.
8. R. W. Christy, *J. Appl. Phys.*, **31**, 1680 (1960).
9. I. Haller and P. White, *J. Phys. Chem.*, **67**, 1784 (1963); P. White, *ibid.*, **67**, 2493 (1963).
10. A. E. Brennemann and L. V. Gregor, *This Journal*, **112**, 1194 (1965).
11. B. Lax, W. P. Allis, and S. C. Brown, *J. Appl. Phys.*, **21**, 1297 (1950).
12. J. G. Linhart, "Plasma Physics," Interscience Publishers Inc., New York (1960).
13. S. Dushman, "Foundations of Vacuum Technique," John Wiley & Sons, Inc., New York (1962).
14. L. V. Gregor and H. L. Mc Gee, Proc. Fifth Elect. Beam Symp., Alloyd Elect. Corp., Cambridge, Mass., p. 211 (1963).
15. P. J. Flory, "Principles of Polymer Chemistry," p. 133, Cornell University Press, New York (1953).

The Effect of Thiourea on Alkaline Electroless Deposition

J. Kivel[1] and J. S. Sallo

Honeywell Research Center, Hopkins, Minnesota

ABSTRACT

C_{14} or S_{35} tagged thiourea were used to follow the uptake of C and S into the electroless nickel deposit and to determine adsorption curves for thiourea on nickel and cobalt. Enhancement of the rate of deposition is observed for cobalt but not for nickel. A Raney nickel type of mechanism and an electron transfer mechanism are proposed to explain the results.

The effect of thiourea and other sulfur-containing compounds on the rate of the electroless deposition process for acid nickel has previously been described (1, 2). Radiochemical studies of this process utilizing sulfur and carbon tagged thiourea have also been reported (3). None of this previous work has dealt with the effect of thiourea on the electroless deposition of nickel or cobalt from alkaline media. The purpose of the present paper is to broaden these studies into the alkaline region for cobalt and nickel and also to report the results of studies utilizing sulfur and carbon tagged thiourea in this type of deposition system.

Experimental

The following systems were studied (i) $NiCl_2 \cdot 6H_2O$, 30 g/l; NH_4Cl, 50 g/l; $NaH_2PO_2 \cdot H_2O$, 20 g/l; Na citrate$\cdot 2H_2O$, 100 g/l. (ii) $CoCl_2 \cdot 6H_2O$, 30 g/l; NH_4Cl, 50 g/l; $NaH_2PO_2 \cdot H_2O$, 20 g/l; Na citrate$\cdot 2H_2O$, 100 g/l. The *p*H of the system was adjusted to the desired levels with NH_4OH.

The temperature of the plating systems was maintained at 85° ± 2°C by means of an electric heating mantle. The substrates used in this investigation were 1 x ½ in. nickel strips. These substrates were sensitized by previously described techniques (4). Deposits were made at 1-hr periods; agitation of the system was accomplished by mechanical stirring. Measurements of *p*H were carried out for all experiments using high temperature glass and calomel electrodes.

In each experiment the desired amount of C^{14} or S^{35} thiourea was added to the system. The activity of the solution during deposition and the activity of deposited samples were determined using previously described techniques (3). All nickel substrates were weighed prior to and following deposition to determine the weight of the deposit. All results are reported as the average of several experimental runs.

Results

The effect of thiourea concentration on the rate of nickel and cobalt deposition from alkaline systems is shown in Fig. 1. Previous work in acid systems has shown a gradual increase in the rate of nickel deposition up to a concentration of about 0.5 mg/liter of thiourea (2). Thiourea concentrations greater than 0.5 mg/liter result in a gradual decrease in the rate until at 1.4 mg/liter, the rate goes to 0. Figure 1 shows that for the electroless deposition of nickel from an alkaline medium, the rate steadily decreases until about 1 mg/liter of thiourea, where there is a very rapid decrease to 0. There is no enhancement of the plating rate due to the addition of thiourea in the alkaline electroless deposition of nickel. The addition of thiourea to an alkaline cobalt electroless system as also seen in Fig. 1 leads to a rate maximum at about 0.2 mg/liter of thiourea. Further increase in the thiourea concentration leads to a rapid falloff in the rate of electroless cobalt plating from alkaline media. This behavior is similar to the behavior previously observed for acid nickel systems; however, the maximum for cobalt occurs at a much lower thiourea concentration. The results of Fig. 1 are obtained at a *p*H of 8. Similar results are obtained at other alkaline *p*H values.

The results of the radioactive uptake of carbon from carbon tagged thiourea are shown in Fig. 2 for both nickel and cobalt deposition from alkaline media. The

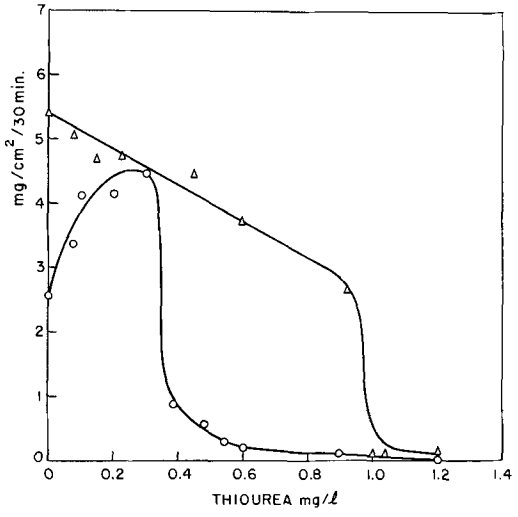

Fig. 1. Rate of electroless deposition *vs.* thiourea concentration at *p*H 8. △, Nickel, ○, cobalt.

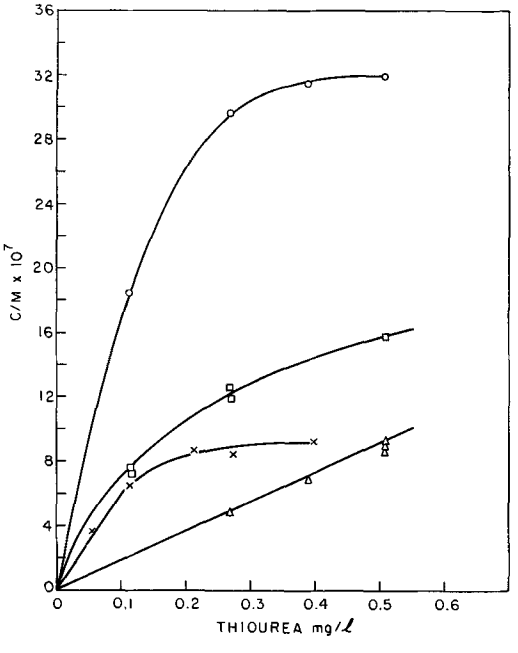

Fig. 2. Carbon-to-metal (Ni or Co) ratio in the deposit *vs.* thiourea concentration. ○, C/Ni at *p*H 7.5; □, C/Ni at *p*H 8.0; △, C/Ni at *p*H 9.5; X, C/Co at *p*H 8.5 to 9.5.

[1] Present address: Atlantic Research Corporation, Alexandria, Virginia.

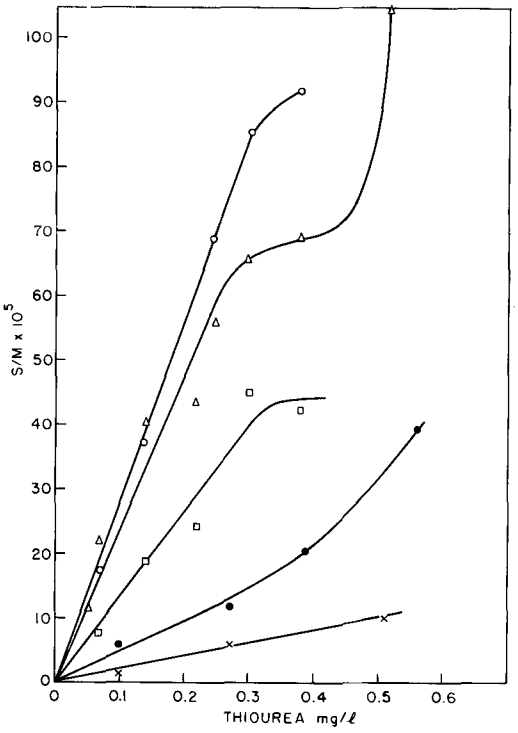

Fig. 3. Sulfur-to-metal (Ni or Co) ratios in the deposit vs. thiourea concentration. ○, S/Co at pH 8.0; △, S/Co at pH 8.5; □, S/Co at pH 9.0; •, S/Ni at pH 7.5; X, S/Ni at pH 9.0.

results are shown as carbon-to-cobalt and carbon-to-nickel ratios. The carbon uptake in the cobalt deposition is virtually independent of pH, whereas in the nickel deposition system the amount of carbon uptake decreases as the pH increases.

The uptake of sulfur in the deposits, shown as sulfur-to-nickel and sulfur-to-cobalt ratios, is seen in Fig. 3. As was previously reported for the acid nickel system (3), there is about a hundred times as much sulfur in the deposit as there is carbon, indicating a high rate of cleavage of the thiourea molecule. It is seen that for both cobalt and nickel more sulfur occurs in the deposit at low pH than at high pH. It is also seen that in the case of cobalt a plateau in the curve occurs which is similar to that which was previously observed in the acid nickel system (3).

Figure 4 shows the results of thiourea uptake on active nickel and cobalt surfaces. The data were taken utilizing a technique which has been previously described (5), in which the nickel surface is slowly withdrawn from a solution of thiourea, dried, and counted. The shapes of these curves are similar to the usual adsorption curve obtained for adsorption from solution, with the plateau representing a monolayer of the adsorbent on the surface. Similar data for adsorption of thiourea on nickel from an alkaline medium fail to show a clear monolayer region. In this case less adsorption is observed than is found from an acid thiourea solution.

Discussion

It is seen from Fig. 1 that cobalt deposition from alkaline media resembles nickel deposition from acid media in that a maximum occurs at a small thiourea concentration followed by a rapid decrease in the rate. This behavior is not followed for nickel in alkaline media where the rate of deposition gradually falls off and no peak or increase in rate is observed at any thiourea concentration. Enhancement in rate is also observed in alkaline cobalt systems.

In the previous work done for nickel in acid media, a plateau in the uptake of sulfur was observed at approximately the same thiourea concentration at which a maximum rate was observed (3). In the case of

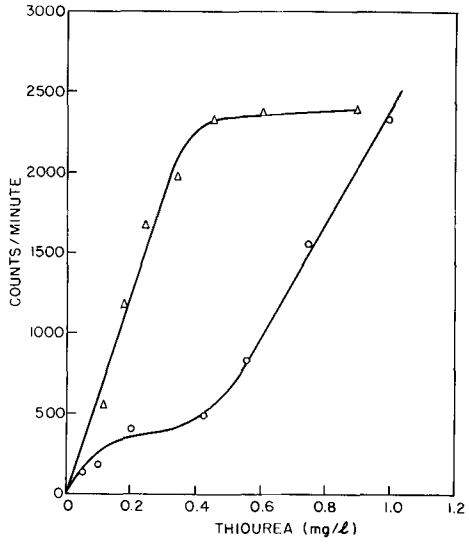

Fig. 4. Adsorption of thiourea. ○, Co surface pH 8; △, Ni surface pH 5.

cobalt deposition a very similar behavior is observed as is seen in Fig. 3. In this case the maximum occurred at 0.3 to 0.4 mg/liter of thiourea. Maxima occurred at higher concentration with thiourea in the acid-nickel system; however, the maximum in the rate also occurred at a higher concentration. In the case of nickel deposition from alkaline media a gradual increase in sulfur uptake into the deposit is observed with no plateau and the curve shapes are entirely different.

The sulfur-to-carbon ratios in the deposit are in the order of 100/1 in all cases. This shows a strong tendency for the thiourea molecule to cleave, leading to the deposition of sulfur, and a very small tendency for carbon to deposit, possibly due to the occlusion of an entire molecule of thiourea. In the acid-nickel system, a volatile sulfur fragment was found (3). When the system was agitated, some of the sulfur counts were lost, presumably in the form of a volatile species. It was speculated that this was hydrogen sulfide which was being lost from the acid system. If this is the case, the alkaline system should show no such loss. A careful investigation has shown that complete sulfur balance is obtained in alkaline systems, and no sulfur is lost during the course of the reaction, even from agitated systems. Furthermore, at the end of the run the system was made acidic and then agitated violently with nitrogen gas and no sulfur loss was observed. It would appear from this result that water soluble sulfide ion forms in the acid system, but not in the alkaline system. This lends support to the suggestion (3) that the sulfide ion in solution results from hydrolysis of nickel sulfide in the deposit. In the alkaline pH region, this nickel sulfide would not hydrolyze, and no sulfide would be found in solution. This finding lends support to the previously suggested Raney mechanism, since one of the previous difficulties was to explain the origin of the sulfides.

In the previous work on this subject, it was suggested that the thiourea acts to enhance the rate of deposition through an electron transfer mechanism. It has been reported (6) that thiourea exists in a redox equilibrium with formamidine disulfide at a potential of —0.42v. It seems quite possible that this reaction between thiourea and its dimer could be the electron transfer mechanism which is used to deposit nickel and cobalt. The reaction suggested is shown below

$$2\,H_2N\text{–}\overset{\overset{S}{\|}}{C}\text{–}NH_2 + Ni^{++} \rightarrow Ni + \left(\overset{\overset{NH}{|}}{C}\text{–}S\text{–}\right)_2 + 2H^+$$
$$\qquad\qquad\qquad\qquad\qquad\qquad\qquad\qquad\qquad\qquad\qquad\qquad\quad \underset{\underset{NH_2}{|}}{}$$

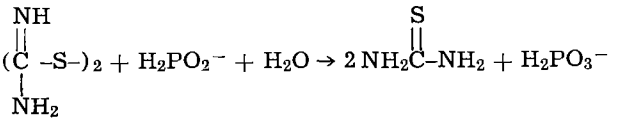

The dimer has been shown in the literature to be unstable with respect to sulfur formation if the *p*H is much above 3 (6). It would seem that the decomposition of this dimer to sulfur and an organic fragment could be one mechanism by which sulfur appears in the deposit. The sulfur uptake data in Fig. 3 show that more sulfur appears in the deposit from the alkaline-cobalt system, where enhancement is occurring, than in the deposit from the alkaline-nickel system where there is no enhancement of the rate. Decomposition of the dimer could explain the excess sulfur formation which is observed when the rate of nickel deposition and cobalt deposition are enhanced.

As a partial check on the possibility that the dimer of thiourea functions as an electron transfer agent, a quantity of the dimer was synthesized (6) and utilized in the reaction as if it were thiourea. In all experiments performed in this way the dimer behaved as if it were thiourea and the normal enhancement of the rate was observed. While this is not proof of the dimer's involvement in the enhancement mechanism, it does lend support to this electron exchange mechanism for the thiourea enhancement of nickel and cobalt deposition.

It would seem that two mechanisms are required to explain the sulfur uptake and the increase in rate in those systems where enhancement of the rate takes place. A Raney mechanism leading to the formation of metal-sulfide and formamidine at the active nickel or cobalt surfaces has previously been suggested (3). The present data lend further support to this notion. The Raney mechanism will not, however, explain the increase in rate which is observed in some of these systems. It is suggested that the large increase in sulfur uptake which is observed after the maximum of the rate of reaction is due to this Raney reaction. This Raney reaction would begin when adsorption beyond the monolayer begins and would explain the large increase in sulfur uptake in the deposit which occurs in these higher thiourea concentrations. In this picture, all of the sulfur uptake in the alkaline-nickel system, where no rate enhancement is observed, is due to the Raney nickel mechanism.

The adsorption data shown in Fig. 4 offer a further insight into the mechanism of the reaction. It is seen that the plateau indicating monolayer formation occurs at about 0.3 mg/liter thiourea for the alkaline cobalt media, and at about 0.5 mg/liter thiourea for the acid nickel media. These points correspond almost exactly to the maximum rate obtainable when thiourea is added to the cobalt or nickel system, respectively. Furthermore, the break upwards in the cobalt curve indicating adsorption beyond the monolayer also corresponds to the thiourea concentrations which begin to inhibit the rate of the reaction. In addition, these adsorption curves are almost identical to the sulfur uptake curves. There is a strong implication from these data that the increase in rate in those systems where enhancement occurs is closely tied to the adsorption of thiourea on the surface.

The reason for the failure of thiourea to enhance the rate of deposition of nickel from alkaline media is not known. Complexation with thiourea appears to occur readily for both nickel and cobalt in alkaline media (7), and there is no reason to believe that the complexes differ in stability. The present work shows that thiourea does not appear to form a monolayer on nickel when adsorption occurs from alkaline media. This monolayer formation seems related to rate enhancement and its absence may explain the failure of thiourea to enhance the rate of alkaline nickel deposition.

Conclusions

Thiourea is shown to increase the rate of cobalt deposition from alkaline media to a maximum at 0.3 mg/liter thiourea. No such enhancement of the rate occurs in the alkaline-nickel deposition systems. It is suggested that the enhancement of the rate which occurs in the alkaline cobalt system and in the acid nickel system is due to an electron transfer mechanism involving the dimer of thiourea and that the excess sulfur which appears in the deposit when enhancement of the rate is taking place is due to the breakdown of this thiourea dimer to give sulfur. It is further suggested that the sulfur appearing in the deposit when excess thiourea is present and during the entire range of thiourea concentration for alkaline nickel systems is due to a Raney mechanism. It is also shown that the region of enhancement of the rate of nickel and cobalt deposition by thiourea is also the region of monolayer formation for thiourea adsorption on nickel and cobalt surfaces. The region where the rate begins to decrease as thiourea concentration is further increased corresponds to adsorption beyond monolayer formation.

Acknowledgments

The authors are indebted for the assistance of Mr. David Prem and Mr. Larry Egan.

Manuscript received June 10, 1965; revised manuscript received Aug. 16, 1965.

Any discussion of this paper will appear in a Discussion Section to be published in the June 1966 JOURNAL.

REFERENCES

1. P. Talmey and G. Gutzeit, U. S. Pat. 2,762, 723.
2. C. H. deMinjer and A. Brenner, *Plating*, **44**, 1297 (1957).
3. J. S. Sallo, J. Kivel, and F. C. Albers, *This Journal*, **110**, 890 (1963).
4. J. S. Sallo, J. I. Swenson, and J. M. Carr, *ibid.*, **109**, 389 (1962).
5. J. Kivel, F. C. Albers, D. A. Olsen, and R. E. Johnson, *J. Phys. Chem.*, **67**, 1235 (1963).
6. P. W. Preisler and L. Berger, *J. Am. Chem. Soc.*, **69**, 323 (1947).
7. J. S. Sallo and R. D. Fisher, *This Journal*, **107**, 277 (1960).

An Evaluation of the Bismuth-Tellurium Phase System

Alfred C. Glatz

Carrier Research and Development Company, Syracuse, New York

ABSTRACT

Phase equilibria studies of the bismuth-tellurium system have been performed by differential thermal analysis (DTA), x-ray diffraction, and metallography. These studies have shown that congruent melting γ-phase (Bi_2Te_3) is stable as a single phase over a very narrow composition range and is separated from a bismuth-rich peritectic β-phase by a narrow two-phase field. DTA studies on annealed samples indicate that there are probably several other peritectic compounds in the region from 30 to 50 mole % tellurium. The departure from equilibrium below the liquidus is considered responsible for some of the previous discrepancies for this system.

The unique electrical properties of bismuth telluride have stimulated many investigations of the physical properties of this compound. However, in spite of these efforts the exact form of the phase diagram below the liquidus appears obscure. In particular, there is considerable disagreement between the reported phase diagrams in the region near the compound Bi_2Te_3 (60 mole % Te) and in the region from 30 to 50 mole % Te. For example, Brown and Lewis (1) and Hansen (2) report a single compound in the system with widely different ranges of compound stability, while Abrikasov and Bankina (3) report a very narrow range of compound stability for Bi_2Te_3 with several other compounds in the system. These apparent discrepancies have indicated that a more detailed investigation of the bismuth-tellurium phase system is required in order to elucidate the true "equilibrium" phase diagram. The study being reported in this paper is concerned primarily with the region near the congruent melting compound with systematic observations in the region from 5 to 50 mole % tellurium and represents a portion of the effort of the thermoelectric materials group of Carrier Research and Development Company to determine the equilibrium phase diagram of the bismuth-tellurium system.

Phase equilibria studies on the bismuth-rich side of Bi_2Te_3 are complicated by the fact that both bismuth and bismuth telluride have the hexagonal C33-type crystal structure with the $R\bar{3}m$ unit cell space group symmetry. This fact limits the use of x-ray diffraction as the only experimental method for interpreting the phase diagram. Consequently, we have employed a combination of x-ray diffraction, differential thermal analysis (DTA), and metallography in these studies.

Although the phase diagram is, by definition, a representation of equilibrium phase boundaries, evidence will be presented to show that in some of the previous studies the samples apparently did not attain thermodynamic equilibrium, which resulted in some erroneous conclusions. For this reason, studies have been made of the effect of "equilibrium" on the phase diagram in the composition ranges mentioned above.

Experimental Procedures

Materials.—Bismuth metal shot (99.9999+%) and elemental tellurium (99.999+%) were obtained from Cominco Products, Inc., and American Smelting and Refining Company, respectively. These elements were used directly in the preparation of the samples.

Preparation of the samples.—For the phase equilibria studies three-gram samples of the appropriate compositions were sealed in evacuated quartz ampoules. The samples were placed in a "Hevi-Duty" tube furnace provided with a rotating mechanism, and the temperature was raised above the liquidus temperature of the alloys for approximately 30 min and then cooled to room temperature. The samples were then placed in a high thermal capacity annealing furnace and initially annealed below the solidus temperature for two weeks. In general, alloys containing greater than 37 mole % tellurium were annealed at 400°C and those containing less than 37 mole % tellurium were annealed at 250°C. After this initial annealing period, the alloys were removed from the ampoules, ground up with a vibrator, and sieved to −50 mesh. Then they were replaced in evacuated, sealed quartz ampoules and annealed at the annealing temperature for approximately two more weeks. In addition, at periodic intervals the powdered samples were removed from the furnace and shaken with the vibrator to ensure homogenization of the composition. To study the effect of "equilibrium" on the phase diagram, alloys having compositions ranging from 5 to 50 mole % tellurium were annealed for varying periods of time up to six months at various annealing temperatures.

The samples prepared in this manner provided annealed powders suitable for x-ray diffraction and DTA measurements. It has been shown by Sato (4) that annealed powders must be used to obtain sharp x-ray diffraction patterns of bismuth telluride.

The compositions of the samples were determined from the constituents. The compositions were verified on representative samples by chemical analysis. In all cases the analyzed compositions indicated that the sample had lost tellurium, but the loss did not exceed 0.05 mole % tellurium.

Phase equilibria examination.—The samples were examined by DTA, x-ray diffraction, and metallographic techniques.

The DTA thermograms were obtained by the conventional technique of plotting the difference in temperature between an aluminum oxide standard and the sample on an X-Y recorder (Honeywell Function Plotter—Model 153X33). The DTA samples were prepared by adding 750 mg of the alloy composition to 250 mg of α-Al_2O_3 (both sieved from −100 to +200 mesh). The aluminum oxide was added to the sample to minimize base-line drift. The standard and the sample were contained in sealed Vycor ampoules with concentric thermocouple wells and placed symmetrically in a high thermal capacity Kanthal furnace. The heating rate of the furnace was controlled at 5°C per min with a cam-type program controller (Honeywell—Model 152).

Alloy compositions in the range from 56 to 62 mole % tellurium were examined by conventional x-ray powder diffraction techniques. The x-ray powder photographs were taken at room temperature with a 14.3 cm Debye-Scherrer camera and nickel filtered $CuK\alpha$ radiation, using the Straumanis method with the samples held in thin-walled silica tubes. The line positions were measured with a Norelco film reader accurate to 1/20 mm. Approximately 25 reflections were indexed for each composition on the basis of

hexagonal lattice employing the data published by Francombe (5). The lattice parameters were determined by extrapolation using Cohen's least squares method (6) with the function, $1/2[(\cos^2\theta/\sin^2\theta) + (\cos^2\theta/\theta)]$, programmed in "Fortran" on a computer. For the calculation of the lattice parameters, 1.54051 and 1.54433Å was assumed for the wavelengths of the $K\alpha_1$ and $K\alpha_2$ radiations, respectively, and 1.54178Å was assumed for the wavelength of the unresolved doublet.

The measured hexagonal lattice parameters of Bi_2Te_3 using the above procedure are $a_{hex} = 4.384 \pm 0.001$Å and $c_{hex} = 30.495 \pm 0.006$Å. The values published by Francombe (5) are in agreement, within the reported precision, with those obtained by this investigation.

Some of the samples were examined by metallography, both at room temperature and as a function of temperature. The metallograph used for these studies was a Bausch and Lomb Research Metallograph, which was equipped with a Unitron HHS-3 Vacuum-Heating Stage. The powdered samples were polished using a Fisher Vibramatic Polisher employing 0.05μ β-Al_2O_3 as a final abrasive. Samples for the hot stage were grown in a Bridgman furnace and polished electrolytically. Vaporization from the surface was reduced during a hot-stage run by introducing approximately 3 atm of argon gas at about 200°C.

Results

Phase equilibria studies by DTA, x-ray diffraction, and metallography, which have been correlated for compositions extending from 56 to 62 mole % tellurium, have established that Bi_2Te_3 exists as a single phase over a very narrow composition range. This congruent melting single-phase field (herein called the γ-phase) is separated from a peritectic phase (herein called the β-phase) by a narrow two-phase field. The phase diagram in this region is shown in Fig. 5, which will be discussed in more detail later.

The range of existence of the single-phase field for the γ-phase and the two-phase field between the β- and γ-phases has been established at room temperature by x-ray diffraction using the parametric method. Shown in Fig. 1 are the hexagonal lattice parameters (a_{hex} and c_{hex}) at room temperature for Bi-Te compositions in the range from 56 to 62 mole % tellurium. It may be observed from the compositional variations of the lattice parameters that at room temperature the γ-phase exists as a single phase from 59.70 ± 0.10 to 60.35 ± 0.15 mole % tellurium and the two-phase

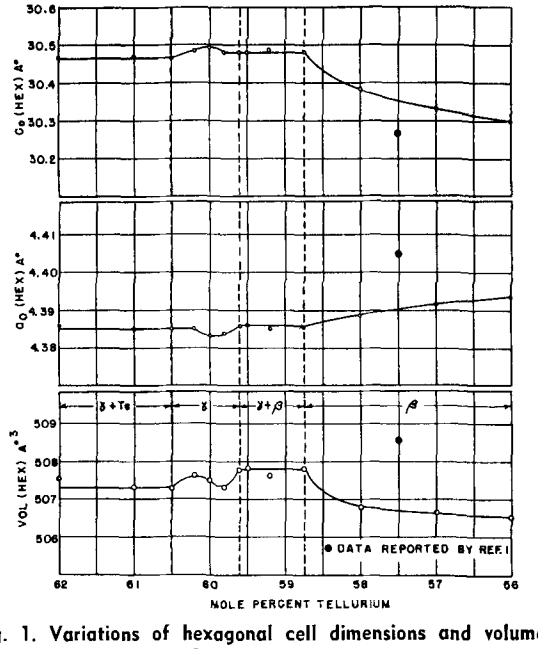

Fig. 1. Variations of hexagonal cell dimensions and volume of Bi-Te compositions at 25°C.

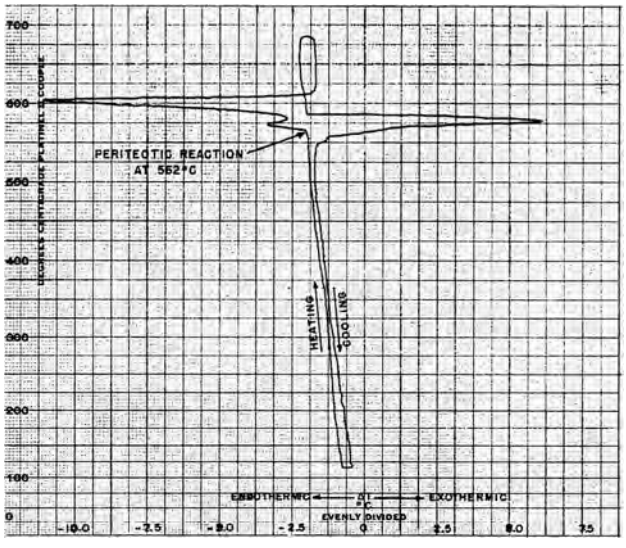

Fig. 2. DTA thermogram for $Bi_{41}Te_{59}$

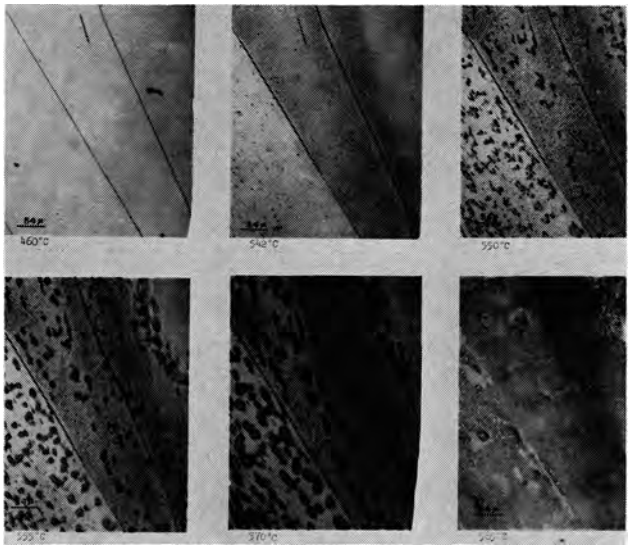

Fig. 3. Photomicrographs at various temperatures for $Bi_{40.4}Te_{59.6}$

field between the β- and γ-phases extends from 58.75 mole % tellurium to the bismuth-rich phase boundary of the γ-phase. The phase boundaries drawn in Fig. 1 represent the maximum ranges for the γ- and β-phases.

The β-phase peritectic with a peritectic reaction temperature of 562° ± 2°C has been observed by both DTA and high-temperature metallography. Shown in Fig. 2 is a DTA thermogram for the composition $Bi_{41}Te_{59}$ and shown in Fig. 3 are photomicrographs of an electrolytically polished section taken at various temperatures for the composition $Bi_{40.4}Te_{59.6}$ (sample 921-B). The existence of the peritectic at 562°C is clearly evident from the DTA thermogram and allowing for the uncertainty in the temperature measurement during a hot stage run, the photomicrographs verify the formation of a liquid phase below the normal melting point of the γ-phase. The peritectic reaction is observed on DTA thermograms extending from the phase boundary of the γ-phase to the liquidus at 50 mole % tellurium. The peritectic reaction was reported by Abrikasov and Bankina (3) at a slightly lower temperature and has apparently been observed by Bolling (7) as the appearance of a liquid below the normal melting point of Bi_2Te_3.

The peritectic point of the β-phase was established at approximately 55 mole % tellurium by metallographic examination of polished sections of alloys quenched from below the peritectic reaction tem-

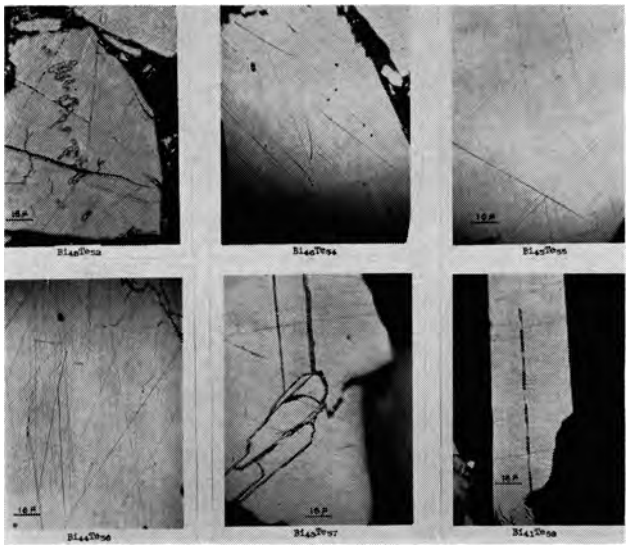

Fig. 4. Photomicrographs of specimens quenched from 553°C

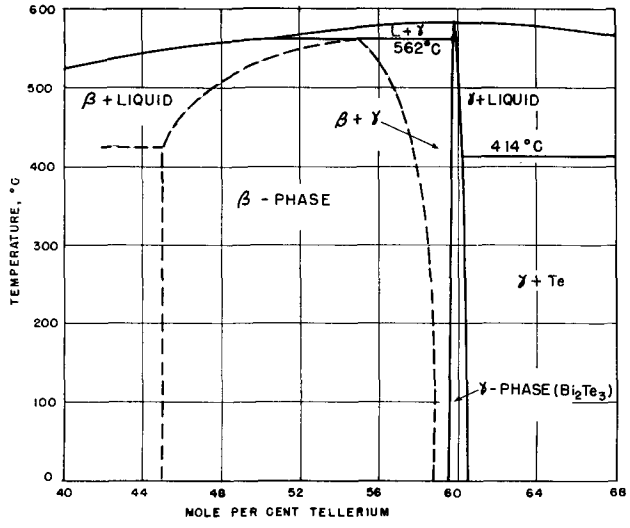

Fig. 5. Phase diagram of the bismuth-tellurium system in the region near the congruent melting compound.

perature. Six powdered alloys having compositions 52, 54-57, and 59 mole % tellurium were maintained at 553° ± 3°C for one week in a "Hevi-Duty" tube furnace mounted in the vertical position and were quenched in ice water. Visual examination of these quenched specimens indicated the appearance of a quenched liquid phase for compositions 52 and 54 mole % tellurium, a sintered mass for compositions 55-57 mole % tellurium, and unaltered powdered sample for 59 mole % tellurium. Employing a mounting technique for powders described by Skinner (8), the peritectic point was established by metallographic observation of polished sections of these alloys. Shown in Fig. 4 are several photomicrographs of these quenched and polished specimens indicating that the peritectic point of the β-phase lies at approximately 55 mole % tellurium. It is of interest to note that the β- and γ-phases are not distinguishable on these photomicrographs in the region between these phases. This is apparently due to the structural similarities between these phases as shown by the x-ray studies. It appears from the photomicrographs that incomplete peritectic reaction or envelopment can be detected in this region.

The β-phase extends over to approximately 45 mole % tellurium as determined by the disappearance of a thermal effect at 430°C. This thermal effect at 430°C will be discussed later.

The range of existence of the γ-phase as a single-phase field at elevated temperatures has been established by DTA studies. On the bismuth-rich side the peritectic reaction at 562°C is observed from the liquidus at 50 mole % tellurium to 59.7 mole % tellurium, and on the tellurium-rich side the eutectic reaction at 414°C is observed from pure tellurium to 60.2 mole % tellurium. The maximum melting composition was determined by the DTA method as the composition having the maximum area under the curve associated with melting. The maximum melting composition determined by this method is $Bi_{40.2}Te_{59.8}$. The existence of the maximum melting point on the bismuth-rich side of the stoichiometric composition is consistent with that reported by other investigators (9, 10).

On the basis of these studies, the equilibrium phase diagram for the Bi-Te system in the region near the congruent melting compound, extending from 45 to 68 mole % tellurium, is shown in Fig. 5.

DTA studies of samples having compositions from 5 to 50 mole % tellurium, that were annealed for periods of time up to six months at various temperatures, indicate that equilibrium is not easily attained for alloys in this composition range. This may be observed on the DTA thermograms shown in Fig. 6.

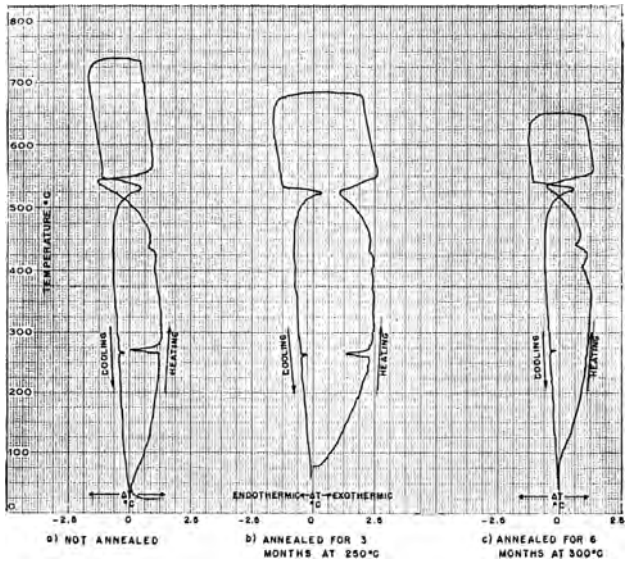

Fig. 6. DTA thermograms of composition, $Bi_{56}Te_{44}$, annealed at various temperatures and periods of time.

This figure illustrates the effect of annealing time and temperature on the observed thermograms for the composition, $Bi_{56}Te_{44}$. It may be observed that the bismuth-eutectic at 266°C can be eliminated by annealing at 300°C for six months; whereas, annealing at 250°C for three months will not eliminate the eutectic reaction, which is also observed on the unannealed sample. DTA studies on unannealed samples indicate that the bismuth eutectic at 266°C is observed on all alloys up to 52 mole % tellurium. For samples annealed at 400°C for one month and at 300°C for six months, the bismuth eutectic is observed on all alloys having compositions less than 40 mole % tellurium. In addition, Fig. 6 shows the appearance of at least two enthalpic effects, occurring at approximately 430° and 375°C. These effects are magnified when the samples are annealed several degrees below these transition temperatures indicating that a closer approach to equilibrium is being achieved. DTA studies of samples annealed at 400°C for one month and 300°C for six months have shown that these enthalpic effects extend over to the liquidus. It is believed that they are probably due to peritectic reactions, but further work is required to validate this point. It may be recalled that Abrikasov and Bankina (3) reported two peritectic compounds in this region of the phase diagram.

Discussion

The results of this phase equilibria study on the Bi-Te system clearly indicate that the congruent melting γ-phase exists as a single phase over a narrow composition range with maximum limits extending from 59.6 to 60.5 mole % tellurium at room temperature. This congruent-melting, single-phase field is separated from a peritectic β-phase by a narrow two-phase field extending from 58.75 to the bismuth-rich phase boundary of the γ-phase at room temperature. The β-phase, which has a peritectic reaction temperature of 562°C, extends from 58.75 to approximately 45 mole % tellurium. Additional studies across the bismuth-rich-phase field from 5 to 50 mole % tellurium have demonstrated the importance of "equilibrium" and have indicated the probable existence of several additional peritectic compounds in this region of the phase diagram.

The samples used in this investigation were annealed below the liquidus for various lengths of time and at various temperatures to investigate the effect of departure from equilibrium upon the phase diagram. These studies have shown that in the region from 30 to 50 mole % tellurium, equilibrium below the liquidus is difficult to attain and requires long annealing time at the proper temperature. This behavior is also observed for some mineral systems (11). It appears that in the region from 55 to 100% tellurium, equilibrium can be easily attained in the laboratory.

Our phase study in the region from 45 to 68 mole % tellurium has demonstrated the importance of using several analytical techniques simultaneously in doing phase studies on this system. For example, Brown and Lewis (1) using only the x-ray method were unable to distinguish between the γ- and β-phases, because these solid solutions have similar symmetries and lattice parameters. Also, their x-ray investigations did not include samples with compositions between the γ- and β-phases so that they erroneously concluded that the β-phase extended up to 60 mole % tellurium. For comparison, the x-ray data reported by Brown and Lewis (1) is shown in Fig. 1. For this reason we have employed both DTA and metallography to corroborate x-ray measurements in this region. It is of interest to note that our phase studies in this region of the phase diagram are consistent with the existence of the mineral phases tellurbismuth and wehrlite as distinct phases (12).

In samples that have not been properly annealed, the bismuth eutectic can be observed on DTA thermograms up to 52 mole % tellurium. This would yield a phase diagram similar to that published by Hansen (2). It is important to note that in systems in which equilibrium is difficult to achieve, thermal methods of analysis must be treated with caution because equilibrium is not attained at each temperature. It is better to corroborate thermal analysis studies with equilibrium studies, *e.g.*, x-ray diffraction at each temperature for establishing phase boundaries. For this reason, our investigations in the region from 5 to 50 mole % tellurium, are presented, only to give an indication of the importance of "equilibrium" in this region of the phase diagram. However, these studies have been performed on carefully annealed samples and probably represent equilibrium at these temperatures. Additional phase equilibria studies on properly annealed samples are required in order to verify the observations mentioned above, and elucidate the equilibrium phase diagram in this region. These studies are in progress and will be reported later.

In conclusion, we have found that the assurance that the sample has reached equilibrium is extremely important in establishing the "true" equilibrium phase diagram for the Bi-Te system. The previously reported phase diagrams for this system appear to be valid representations under the stated conditions. The discrepancies seem to arise due to differences in sample preparation and the limited number of analytical methods that were employed by each investigator.

Acknowledgments

The author wishes to acknowledge the work performed by Mr. Daniel Gaffaney, Mr. Douglas Ingalls, and Dr. Leroy Loewenstern on their observations and helpful discussions. In addition, he wishes to acknowledge the work performed by Mr. James Endress, Jr., of this laboratory for preparing the samples and performing the differential thermal analysis measurements, and Mr. Robert Faxon of Syracuse University for taking the x-ray photographs.

Manuscript received May 21, 1965; revised manuscript received Aug. 16, 1965. This paper was presented at the San Francisco Meeting, May 9-13, 1965.

Any discussion of this paper will appear in a Discussion Section to be published in the June 1966 JOURNAL.

REFERENCES

1. A. Brown and B. Lewis, *J. Phys. Chem. Solids*, **23**, 1597 (1962).
2. M. Hansen. "Constitution of Binary Alloys," 2nd ed., pp. 339-341, McGraw-Hill Book Co., New York (1958).
3. N. Kh. Abrikasov and V. F. Bankina, *Zh. Neorg. Khim.*, **3**, 659 (1958).
4. R. Sato, *J. Phys. Soc. Japan*, **18**, 1344 (1963).
5. M. H. Francombe, *Brit. J. Appl. Phys.*, **9**, 415 (1958).
6. B. D. Cullity, "Elements of X-ray Diffraction," pp. 338-342, Addison-Wesley Publishing Co., Reading, Mass. (1959).
7. C. F. Bolling, *J. Chem. Phys.*, **33**, 305 (1960).
8. B. Skinner, Private communication.
9. G. Offergeld and J. VanCakenberghe, *J. Phy. Chem. Solids*, **11**, 310 (1959).
10. C. Satterthwaite and R. Ure, *Phy. Rev.*, **108**, 1164 (1957).
11. E. H. Roseboom, Jr., *Amer. Mineralogist*, **47**, 1181 (1962).
12. H. V. Warren and M. A. Peacock, *Univ. Toronto Stud. Geol.*, **49**, 55 (1945).

Solubility and Electrical Behavior of Group IV Impurities in Solution Grown Gallium Phosphide

F. A. Trumbore, H. G. White, M. Kowalchik, C. L. Luke and D. L. Nash

Bell Telephone Laboratories, Incorporated, Murray Hill, New Jersey

ABSTRACT

Gallium phosphide crystals doped with silicon, germanium, or tin were grown from solution by using a thermal gradient technique. At low doping levels nearly all of the tin or silicon atoms act as donors, *i.e.*, substitute on gallium sites. At higher doping levels the number of tin and silicon atoms substituting on phosphorus sites increases to about 30% and almost 50%, respectively. In contrast, doping with germanium yields p-type material at the lower doping levels and n-type material at higher doping levels with nearly equal numbers of germanium atoms on both sites at all doping levels.

The purpose of this paper is to present the results of experiments dealing with the concentration dependence of the electrical activities and solid solubilities of silicon, germanium, and tin in GaP crystals grown from gallium solution. This work is an extension of similar studies on zinc, sulfur, selenium, and tellurium in GaP (1), while the behavior of tin in crystals grown from solutions of GaP in pure tin was discussed in an earlier paper (2). Of particular concern here is the amphoteric nature of the Group IV impurities, *i.e.*, the substitution of these impurities on either gallium or phosphorous sites, thus leading to self-compensation.

Experimental

The crystals were grown from doped gallium solutions by using the same sealed tube thermal gradient technique described previously (3) for the growth of germanium or silicon from solution. After crushing and digesting to remove any occluded material, the samples were analyzed using spectrophotometric techniques (4) and, in the case of silicon, emission spectroscopy. Excess donor or acceptor concentrations were determined from surface barrier capacitance measurements involving the evaporation of gold dots on the GaP crystals (5). In order to test for precipitation a few crystals were heated to about 1000°C for several minutes, quenched, and remeasured after etching to eliminate surface effects. Details of the experimental procedures are the same as described previously (1-5).

Results

The results of the chemical analyses and the capacitance measurements are summarized in Table I and plotted in Fig. 1, 2, and 3. The data in Fig. 1 show that for the tin-doped samples the excess donor concentration, $(N_D - N_A)$, is equal to the tin concentration, within experimental error, at the lowest doping level of about 1×10^{17} atoms/cc. At higher tin concentrations the samples remain n-type but the doping efficiency drops until, in the most heavily doped samples grown from a solution of GaP in pure tin, $(N_D - N_A)$ is less than half of the tin concentration. Quenching experiments on crystals grown from pure tin yielded no evidence of precipitation (2). The agreement between duplicate capacitance measurements was especially good for this series of samples.

Although the silicon-doped crystals were grown at a number of different temperatures between 1015° and 1085°C, the scatter in the data masks any temperature dependence of the solid solubility and hence all of the data are plotted in Fig. 2. It is seen that, in the silicon concentration range from about 10^{18} to 7×10^{20} atoms/cc, all the crystals are n-type, although at the higher doping levels the excess donor concentration is only a small fraction of the silicon concentration. No conclusive evidence concerning the presence or absence of precipitation was obtained from quenching experiments, since the capacitance measurements become unreliable at $(N_D - N_A)$ values $\gtrsim 10^{19}$ cm^{-3}. It seems reasonable to assume that there is no significant pre-

Table I. Results of chemical analyses and capacitance measurements on solution grown GaP*

Dopant	C_L, a/o	C_S, atoms/cc Photometric	C_S, atoms/cc Spectroscopic	$\lvert N_D - N_A \rvert$, cm^{-3} Capacitance	Growth temp, °C
Si	18.4	(7.0, 7.4) × 10^{20}	9.0 × 10^{20}	1.0 × 10^{19}	1050
Si	16.3	—	—	(4.6, 7.1) × 10^{18}	1046
Si	9.5	(5.0, 5.3) × 10^{20}	6.6 × 10^{20}	(4.3, 6.6) × 10^{18}	1039
Si	7.7	(2.7, 2.9) × 10^{20}	4.6 × 10^{20}	—	1085
Si	1.95	(7.1, 7.1) × 10^{19}	1.06 × 10^{20}	(5.5, 6.5) × 10^{18}	1015
Si	0.94	(3.4, 3.6) × 10^{19}	6.0 × 10^{19}	(6.5, 7.1) × 10^{18}	1039
Si	0.099	(4.0, 5.1) × 10^{18}	1.06 × 10^{19}	(6.5, 8.3) × 10^{18}	1039
Si	0.0102	—	1.2 × 10^{18}	(4.3, 4.8) × 10^{17}	1039
Si	0.00085	—	< 8 × 10^{17}	(3.2, 6.5) × 10^{16} (p-type)	1039
Ge	88	(1.78, 1.92) × 10^{20}	—	(5.9, 3.4, 2.9) × 10^{18}	950
Ge	80	(1.51, 1.65) × 10^{20}	—	(4.2, 7.2) × 10^{18}	1050
Ge	81	1.47 × 10^{20}	—	(2.4, 4.6) × 10^{18}	1039
Ge	9.3	8.5 × 10^{18}	—	2.2 × 10^{17}	1039
Ge	0.95	4.5 × 10^{17}	—	(1.0, 1.6) × 10^{17} (p-type)	1039
Ge	0.093	—	—	(4.8, 8.3) × 10^{16} (p-type)	1039
Ge	0.0097	—	—	(2.2, 8.5) × 10^{16} (p-type)	1039
Sn	81.3	(1.51, 1.55, 1.69) × 10^{19}	—	(6.05, 6.55) × 10^{19}	1070
Sn	43.4	(4.8, 5.4) × 10^{18}	—	(3.0, 3.2) × 10^{18}	1070
Sn	7.8	(6.3, 10.5) × 10^{17}	—	(7.3, 8.3) × 10^{17}	1070
Sn	0.92	1.26 × 10^{17}	—	(1.49, 1.49) × 10^{17}	1070
Sn	0.01-0.1	—	—	(4.6, 5.1) × 10^{16} (p-type)	1070

* The results of the individual analyses or capacitance measurements are given in order to indicate the reproducibility of these data. All of the $\lvert N_D - N_A \rvert$ values correspond to excess donor concentrations (n-type material) unless noted otherwise. The growth temperatures are uncertain to ±20°C. The value of C_L for the least heavily tin-doped crystal is uncertain but lies between 0.01 and 0.1 a/o as indicated.

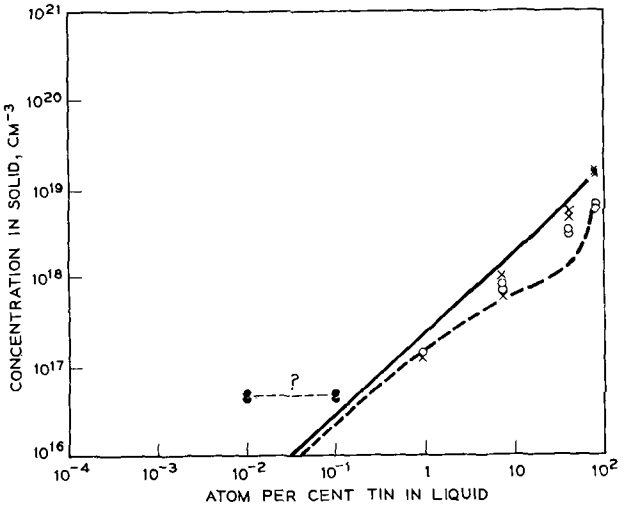

Fig. 1. Tin and excess donor (acceptor) concentrations as a function of the concentration of tin in gallium solution at ~1070°C. The solid and dashed curves are the theoretical curves obtained by fitting the chemical and capacitance data, respectively, for the most heavily doped sample assuming a value of n_i of 3 x 10^{17} cm^{-3}. The p-type behavior at the lowest doping level is believed to be due to a background acceptor. X, Sn concentration, photometric; ○, $(N_D - N_A)$ n-type; ●, $(N_A - N_D)$ p-type.

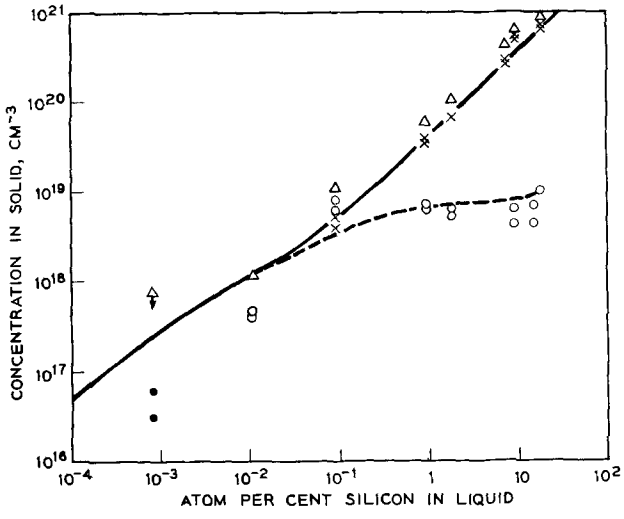

Fig. 2. Silicon and excess donor (acceptor) concentrations as a function of the concentration of silicon in gallium solution at ~1040°C. Actually, points are included for crystals grown at various temperatures between ~1015° and 1085°C (see text). The solid and dashed curves are the theoretical curves obtained by fitting the chemical and capacitance data, respectively, for the most heavily doped sample assuming a value of n_i of 2.5 x 10^{17} cm^{-3}. △, Si concentration, spectroscopic; X, Si concentration, photometric; ○, $(N_D - N_A)$ n-type; ●, $(N_A - N_D)$ p-type.

cipitation in view of the results for tin and germanium (see below). Concerning the chemical analyses, it is seen in Fig. 2 that the spectroscopic results are higher than the photometric values, especially at the lower doping levels. Unfortunately, the scatter in the capacitance data does not help to decide which analyses are more reliable. In general, photometric methods are more accurate and these points are weighted more heavily.

The behavior of germanium (Fig. 3) is quite different from that of tin and silicon. At the higher doping levels of up to about 2 × 10^{20} atoms/cc, the samples are n-type with $(N_D - N_A)$ values between one and two orders of magnitude lower than the germanium concentrations. (No evidence of precipitation was found in quenching experiments.) However, when the

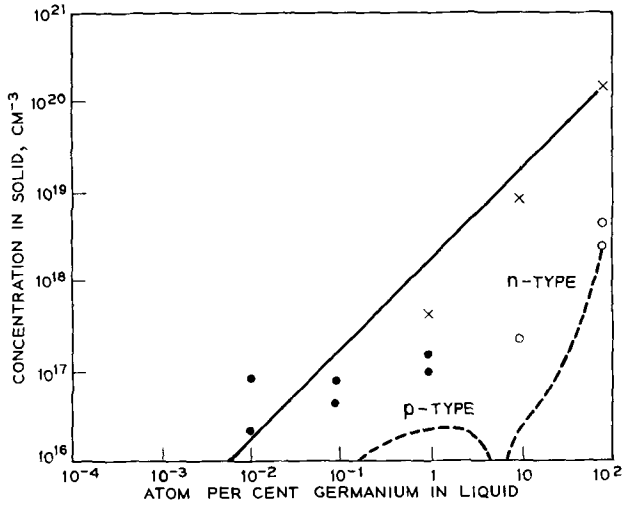

Fig. 3. Germanium and excess donor (acceptor) concentrations as a function of the concentration of germanium in gallium solution at ~1040°C. The solid and dashed curves are the theoretical curves obtained by fitting the chemical and capacitance data, respectively, for the most heavily doped sample assuming a value of $n_i = 2.5 \times 10^{17}$ cm^{-3}. The lowest $(N_D - N_A)$ point is used for fitting to theory. X, Ge concentration, photometric; ○, $(N_D - N_A)$ n-type; ●, $(N_A - N_D)$ p-type.

doping level falls below about 10^{18} atoms/cc p-type material is obtained. The preparation of p-type GaP using Ge as a dopant has also been reported by Weinstein and Mlavsky (6). Data are given in Table I for crystals grown from solutions of GaP in pure Ge at temperatures of ~1040°-1050°C as well as for a crystal grown at ~950°C. There is apparently little temperature dependence of the solid solubility in this temperature range and the distribution coefficient is essentially constant at 4×10^{-3}.

The preceding discussion has included only those samples for which photometric analyses are available. At lower concentrations, where the photometric method is not applicable, capacitance measurements have been made. Crystals grown from the most lightly doped melts are all p-type with $(N_A - N_D)$ values scattering about 5×10^{16} cm^{-3}. This behavior is believed to be due to some unidentified background acceptor impurity or defect. (Crystals grown from undoped gallium solutions were either p- or n-type at the 10^{16}-10^{17} cm^{-3} level.)

Discussion

The incorporation of group IV elements in III-V compounds has been considered by many authors. Kröger (7) gives a detailed discussion and references to most of this work. In considering the incorporation of a group IV element, M, into GaP from a liquid phase we may write the following equations and equilibrium constants involving the gallium and phosphorus vacancies, V_{Ga} and V_P, and the free electrons and holes, e^- and e^+:

$$M(l) + V_{Ga} = M^+ + e^-; \quad K_1 = \frac{(M^+)n}{(M_L)\gamma^{M_L}(V_{Ga})} \qquad [1]$$

$$M(l) + V_P = M^- + e^+; \quad K_2 = \frac{(M^-)p}{(M_L)\gamma^{M_L}(V_P)} \qquad [2]$$

$$O = e^+ + e^-; \quad K_i = np = n_i^2 \qquad [3]$$

$$Ga(l) + V_{Ga} = Ga_{Ga}; \quad K_4 = 1/(V_{Ga})(Ga_L)\gamma^{Ga_L} \qquad [4]$$

$$P(l) + V_P = P_P; \quad K_5 = 1/(V_P)(P_L)\gamma^{P_L} \qquad [5]$$

$$(M^+) + p = (M^-) + n \quad \text{(neutrality condition)} \qquad [6]$$

where the quantities in parentheses denote the concentrations of the respective entities, n and p are the free electron and hole concentrations, n_i is the intrinsic electron or hole concentration, and $\gamma^{M}{}_{L}$, $\gamma^{Ga}{}_{L}$, and $\gamma^{P}{}_{L}$ are the activity coefficients of the respective elements in the liquid phase. Here, we have assumed M to be completely ionized[1] and the solid solutions to be ideal dilute solutions in which all of the entities (M^+, e^-, V_{Ga}, etc.) obey Henry's law. We have also assumed the departures from stoichiometry to be small so that (Ga_{Ga}) and (P_P) are constant. Inherent in this treatment is the assumption that ionized vacancies or other defects or impurities are present in negligible concentrations and the assumption of Schottky type disorder.

The above equations may be solved for (M^+), (M^-), and n to give

$$(M^+) = \frac{K_1 \gamma^{M}{}_{L}(M_L) Q}{n_i} \left\{ \frac{K_i + K_2 \gamma^{M}{}_{L}(M_L) Q^{-1}}{K_i + K_1 \gamma^{M}{}_{L}(M_L) Q} \right\}^{1/2} \quad [7]$$

$$(M^-) = \frac{K_2 \gamma^{M}{}_{L}(M_L)}{n_i Q} \left\{ \frac{K_i + K_1 \gamma^{M}{}_{L}(M_L) Q}{K_i + K_2 \gamma^{M}{}_{L}(M_L) Q^{-1}} \right\}^{1/2} \quad [8]$$

$$n = n_i \left\{ \frac{K_i + K_1 \gamma^{M}{}_{L}(M_L) Q}{K_i + K_2 \gamma^{M}{}_{L}(M_L) Q^{-1}} \right\}^{1/2} \quad [9]$$

where it is convenient to define the quantity Q

$$Q \equiv \left\{ \frac{\gamma^{Ga*}{}_{L}\,(Ga^*{}_{L})}{\gamma^{Ga}{}_{L}\,(Ga_L)} \right\} \quad [10]$$

Here the asterisks denote the values of these quantities in the binary Ga-GaP liquidus alloys. At 1040°C ($Ga^*{}_L$) is about 97 a/o (atom per cent) (8) and $\gamma^{Ga*}{}_{L}$ should be very close to unity (assuming a standard state of pure liquid gallium). In dilute liquid solutions, where (M_L) is low, Q will be approximately unity. It is only in the neighborhood of (M_L) equal to about 10 a/o or more that Q may be expected to depart significantly from unity, at least in the temperature range of interest here ($\leq$ 1070°C). In order to derive values of K_1 and K_2 from the experimental data we may use Eq. [7], [8], and [9] to derive the expressions

$$K_1 = \frac{(M^+)n}{\gamma^{M}{}_{L}(M_L) Q} \quad [11]$$

and

$$K_2 = \frac{(M^+)(M^-)K_i}{K_1 (M_L)^2 (\gamma^{M}{}_{L})^2} \quad [12]$$

Also

$$K_i = n^2 - n\,[(M^+) - (M^-)] \quad [13]$$

The chemical analyses yield $[(M^+) + (M^-)]$ and the capacitance measurements give $[(M^+) - (M^-)]$ so that one can solve for (M^+) and (M^-) assuming, of course, that the concentrations of all other electrically active defects or impurities are negligible. As a first approximation, we may assume both $\gamma^{M}{}_{L}$ and $\gamma^{Ga}{}_{L}$ to be unity, *i.e.*, Raoult's law is obeyed in the liquid phase, and a value for Q can then be calculated.[2] The value of n is assumed to be equal to ($N_D - N_A$), a valid assumption only as long as $n >> n_i$, at the growth temperature. This is a necessary condition since ($N_D - N_A$), measured at room temperature, corresponds to $[(M^+) - (M^-)]$, which in turn only equals n to a good approximation when $[(M^+) - (M^-)] >> n_i$. Therefore, in order to use Eq. [11] to get K_1, it is necessary to use data on a heavily doped sample. This value of K_1 can then be substituted in Eq. [12] to get K_2, if we know K_i. Practically speaking, Eq. [13] is useless in determining K_i since ($N_D - N_A$) or Hall effect data are needed at the growth temperature. In the treatment that follows, values of n_i of 2.5 and 3 $\times$ 10^{17} cm^{-3} were used for the temperatures 1040° and 1070°C, respectively. These values are found to give reasonably good fits to the data and compare with values of between 1 and 3 $\times$ 10^{17} cm^{-3} based on extrapolation of effective mass and band gap data from lower temperatures (9).

The curves in Fig. 1, 2, and 3 are the curves obtained by fitting the photometric and capacitance data on the most heavily doped sample for each system to Eq. [11] and [12] to obtain K_1 and K_2 assuming the above values of n_i. The curves were then calculated from Eq. [7], [8], and [9] assuming the liquid solutions to be ideal, *i.e.*, the activity coefficients were assumed equal to unity.

The agreement between theory and experiment in the case of tin is seen in Fig. 1 to be rather good, especially considering the assumption of Raoult's law for the liquid solutions. The predicted tin solubilities are higher than the measured solubilities, a feature common to germanium and silicon as well. It is interesting that the lower ($N_D - N_A$) values agree well with the predicted values while an intermediate point lies much further off the theoretical curve.

The fit in the case of silicon (Fig. 2) is also good, especially down to a doping level of about 5 $\times$ 10^{18} cm^{-3}, the lowest photometric value. At lower doping levels, if the capacitance measurements at ~5 $\times$ 10^{17} cm^{-3} are taken to be more reliable than the spectroscopic values, the theory predicts a higher solubility than is observed. It is of interest that the predicted concentration of acceptor silicon atoms (on phosphorus sites) is less than 10^{16} atoms/cc at less than about 5 $\times$ 10^{-3} a/o silicon in the liquid phase. Yet, in crystals grown from undoped melts there are strong Si-S (type IA) pair spectra (10). These spectra presumably involve silicon as the acceptor and one concludes that there are less than 10^{16} pairs/cc involved. It would also be expected that Si-Si pair spectra would be observed in these crystals but no such spectra have yet been identified.

In the case of germanium (Fig. 3) the agreement between predicted and observed solubilities is poorer than in the case of tin or silicon. However, the change from n- to p-type is predicted. It should be noted that the magnitude of ($N_D - N_A$) and the concentration at which the crystals change from n- to p-type are extremely sensitive to small changes in the values of ($N_D - N_A$) and n_i used to fit the theory. This is to be expected in view of the very close compensation in these crystals. Liquid phase departures from ideality may be partly responsible for the relatively poor quantitative agreement. Thurmond and Kowalchik (11) showed that the binary Ga-Ge liquidus alloys obeyed Raoult's law closely, at least insofar as the germanium activity is concerned. However, they used a heat of fusion for Ge of 8.1 kcal/g-atom, considerably lower than the recent values of about 8.9 kcal/g-atom obtained by Orr and Sommelet (12) and by Perbix and Tarwater (13). Using the latter values, negative departures from ideality are obtained which are in the direction needed to obtain closer agreement.

Conclusion

The behavior of tin in acting as a relatively strong donor is not unexpected in view of the fact that the tetrahedral radius of tin is 1.40Å while the radii of gallium and phosphorus are 1.25 and 1.10Å, respectively (14). Thus, one would not expect tin to substitute on the phosphorus site nearly as readily as on the gallium site. The behavior of germanium, with a tetrahedral radius of 1.22Å, may be rationalized on

[1] The assumption of complete ionization neglects the possible presence of neutral M atoms due to Fermi level effects; this assumption seems reasonable in view of the close compensation at high doping levels. However, application of this mass action treatment at high doping levels is certainly to be considered only a first approximation.

[2] The values of (Ga_L) and (M_L) were calculated from the binary or pseudobinary Ga-GaP, Sn-GaP, and Ge-GaP liquidus curves (8) assuming the solubilities of GaP in the liquid alloys to vary linearly between the solubility in pure gallium and that in pure tin or germanium. In the case of silicon the solubility of GaP in pure (supercooled) silicon was assumed to be zero and the same linear interpolation was used.

the basis that at low doping levels, due to factors other than size, there is a very slight preference for the phosphorous site, with the increase in gallium vacancy concentration at higher doping levels leading to a preference for the gallium site. From the standpoint of size silicon, with a tetrahedral radius of 1.17Å, would be expected to substitute more predominantly on phosphorous sites than germanium whereas just the opposite is true. This result is also in disagreement with the approximate calculations of Scott and Fredericks (15) who considered the effects of bond and strain energies on the site distribution of group IV elements in III-V compounds. They estimated the free energy of transfer of germanium from a phosphorous to a gallium site to be —10 kcal/mole as opposed to —9 kcal/mole for silicon.

Acknowledgment

The authors are indebted to C. D. Thurmond and R. A. Logan for helpful discussions.

Manuscript received May 19, 1965; revised manuscript received Aug. 25, 1965. This paper was presented at the Buffalo Meeting, Oct. 10-14, 1965.

Any discussion of this paper will appear in a Discussion Section to be published in the June 1966 JOURNAL.

REFERENCES

1. F. A. Trumbore, H. G. White, M. Kowalchik, R. A. Logan, and C. L. Luke, *This Journal*, **112**, 782 (1965).
2. F. A. Trumbore, M. Kowalchik, H. G. White, R. A. Logan, and C. L. Luke, *ibid.*, **111**, 748 (1964).
3. F. A. Trumbore, C. R. Isenberg, and E. M. Porbansky, *J. Phys. Chem. Solids*, **9**, 60 (1959).
4. See, for example, C. L. Luke, *Anal. Chem.*, **36**, 2036 (1964).
5. H. G. White and R. A. Logan, *J. Appl. Phys.*, **34**, 1990 (1963).
6. M. Weinstein and A. I. Mlavsky, *ibid.*, **35**, 1892 (1964).
7. F. A. Kröger, "Chemistry of Imperfect Crystals," Chap. 16, North-Holland Publishing Co., Amsterdam (1964).
8. M. Rubenstein, Electronics Division Abstracts of the Electrochemical Society, **11**, No. 1, p. 129 (1962) (also private communication); A. G. Kalyuzhnaya, I. K. Poluchina, and D. N. Tretyakov, *Zhur. Neorg. Khim.*, **9**, 1497 (1964).
9. M. Gershenzon, Private communication.
10. D. G. Thomas, M. Gershenzon, and F. A. Trumbore, *Phys. Rev.*, **133**, A269 (1964).
11. C. D. Thurmond and M. Kowalchik, *Bell System Tech. J.*, **39**, 169 (1960).
12. R. L. Orr and P. Sommelet, Private communication.
13. G. Perbix and J. P. Tarwater, Private communication.
14. L. Pauling, "The Nature of the Chemical Bond," p. 179. Cornell University Press, Ithaca, New York (1954).
15. A. B. Scott and W. J. Fredericks, *J. Phys. Soc. Japan*, **18**, Supplement II, 136 (1963).

Low-Temperature Epitaxial Growth of Si (Inverted Transport in Close-Spaced Technique)

J. Bloem and J. W. A. Scholte

Semiconductor Development Laboratory, N. V. Philips' Gloeilampenfabrieken, Nijmegen, Netherlands

ABSTRACT

The transport of silicon in a temperature gradient via the vapor phase between two neighboring silicon slices has been analyzed for the chloride system ($SiCl_4$-$SiCl_2$-HCl-H_2). Normal transport of silicon is directed toward the low-temperature side. A reversal of the transport, however, is possible at lower temperatures and at higher $SiCl_4$ partial pressures. Epitaxial layers of good quality can be grown at temperatures as low as 1000°C, an additional advantage is found in the observation that in this case disturbing oxides are transported away from the growing layer. This method offers advantages for the growth of high-resistivity layers on low-resistivity substrates.

The vapor transport of silicon in a temperature gradient between two neighboring silicon surfaces can be realized in a high vacuum (1) or in the presence of silicon halides (2-5) and possibly oxides (6). In most cases the transport of silicon takes place from the higher toward the lower temperature side, as in thermal gradient crystal-growing across a solution (7).

According to Schäfer (2) we may assume that there is equilibrium between the gas phase and the silicon surfaces at both the higher and the lower temperature, giving different vapor pressures of the various reaction partners. By diffusion between the two interface regions in the chloride system a transport of, *e.g.*, $SiCl_2$ from the high to the lower temperature region takes place. At the lower temperature the arriving $SiCl_2$ reacts according to

$$2SiCl_2(g) \rightarrow Si(s) + SiCl_4(g) \qquad [1]$$

$SiCl_4$ again diffuses toward the high-temperature side and the net result is a transport of silicon without a fresh supply of chlorides being necessary.

If the two silicon slices are closely spaced, the rest of the apparatus has little influence, so that high resistivity layers can be grown. A disadvantage of this sandwich system (3), as it is called, is the observation that epitaxial silicon layers with rather high stacking-fault densities are formed. Efficient reduction of surface oxides is difficult in closely spaced structures, and transport of SiO_2 to the lower temperature side interferes with the epitaxial growth of silicon. For the chloride system Steinmaier (8) calculated the resulting equilibrium vapor pressure of HCl, $SiCl_2$, $SiCl_4$, and H_2 in contact with silicon at various temperatures, starting with $SiCl_4$ in H_2 for a system of 1 atm total pressure. For the epitaxial growth of silicon by the sandwich method, use is often made of $SiCl_4$ in H_2 with an open system. Steinmaier's results might be useful in understanding the transport reactions, especially if, as Schäfer suggests, equilibrium vapor pressures can be assumed.[1]

Steinmaier introduced a hypothetical silicon vapor pressure P_{Si}. If the value of P_{Si} is greater than the maximum silicon vapor pressure at that specific tem-

[1] In Schäfer's experiments the distance between the two reaction regions has been so great that diffusion constitutes the rate limiting step. For the close spaced structures this no longer holds, here probably etch and nucleation rates are rate limiting. Near equilibrium in both temperature regions will be postulated nevertheless, as the main interest is in the direction and not in the rate of the transport.

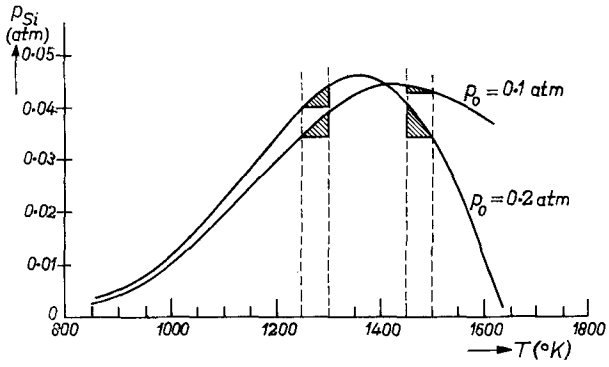

Fig. 1. Variation of p_{Si} with temperature for two initial partial pressures (p_O) of $SiCl_4$ in H_2. The value of p_{Si} refers to a hypothetical silicon vapor pressure, which can be related directly to the growth rate of silicon.

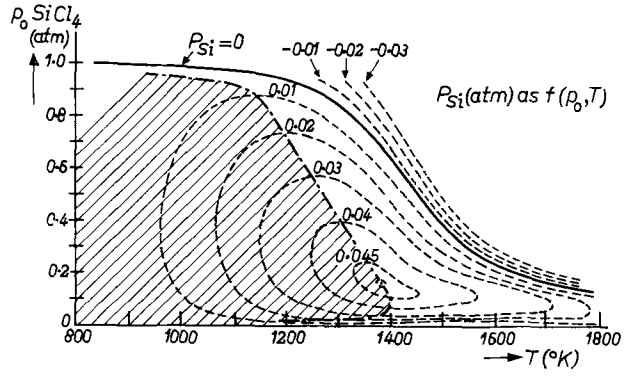

Fig. 2. Variation of p_{Si} (proportional to the growth rate of silicon) with temperature and initial $SiCl_4$ partial pressure (p_O) in the $SiCl_4$-H_2 system. Contours of equal values of p_{Si} are given, together with the line connecting maximum values of p_{Si} vs. temperature. In the shaded area p_{Si} increases with T and reversed sandwich growth is expected.

perature deposition will occur, for a lower value etching will be observed. Figure 1 gives a curve of P_{Si} as a function of temperature for an initial $SiCl_4$ vapor pressure of 10 and 20% in H_2 ($p_O = 0.1$ and 0.2).

In a system with two temperatures of, *e.g.*, 1450° and 1500°K it will be seen that the lower of the two temperatures has the higher value of P_{Si} and thus will give a higher silicon growth rate. In a close-spaced system with the same temperatures it can be expected that the difference in deposition rate between the two interface regions, as deduced from Fig. 1, will constitute the driving force of the transport reaction, the lower temperature side being the receiving part. This being so, then at lower temperatures, *e.g.* 1250°-1300°K in Fig. 1, the transport direction must be reversed, and epitaxial growth of silicon at the high temperature side is to be expected. If some oxide is present a possible transport of SiO_2 toward the low temperature side will not be reversed, but will continue as before. It was, therefore, considered that inverted sandwich growth giving low stacking-fault densities might be

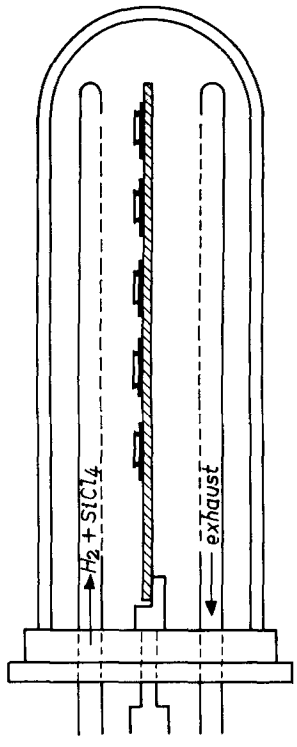

Fig. 3. The horizontal, resistance-heated apparatus used for the sandwich experiments.

possible at relatively low temperatures if the experiments were done in a region where the deposition rate (or rather P_{Si}) increased with temperature. In Fig. 2 values of P_{Si} as given by Steinmaier are depicted as functions of p_O, the initial partial pressure of $SiCl_4$ in H_2, and temperature. The shaded area is the field where transport toward the high temperature side, *i.e.*, the reversed sandwich growth, is expected. Table I gives some numerical results of the calculations of Steinmaier.

Experimental

Apparatus.—The close-spaced sandwich experiments were performed in a horizontal water cooled reactor in which a resistance-heated molybdenum heating element, covered with a quartz glass plate, served as a support for the silicon slices. Gas inlet and outlet tubes were situated as given in Fig. 3. (Figure on side by error.) The silicon sandwich consists of two silicon slices separated by a thin silicon ring or a few silicon chips. The silicon surface temperatures were measured by an optical pyrometer, calibrated by measurement of several melting and alloying temperatures. In the following only the corrected temperatures will be given.

Normal growth.—For normal sandwich growth at higher temperatures (1240°-1300°C) Fig. 4 shows the variation of the growth rate on the low temperature side with the $SiCl_4$ partial pressure of the incoming gas for three different spacer thicknesses (S). The growth rate of silicon not only depends on the spacer thickness and the $SiCl_4$ partial pressure, but also on the total gas flow rate (Fig. 5). For small gas flow rates,

Table I. p_{Si} (atm) as a function of the initial partial pressure of $SiCl_4$ (p_O) and temperature, according to Steinmaier (8)

T (°K) \ p_O (atm) ⟶	0.01	0.05	0.1	0.2	0.3	0.4	0.5	0.6	0.7	0.8	0.9
900	0.0027	0.0043	0.0048	0.0056	0.0058	0.0057	0.0055	0.0045	0.0047	0.0039	0.0030
1000	0.0055	0.0090	0.010	0.0123	0.0128	0.0182	0.0122	0.011	0.010	0.008	0.006
1100	0.0082	0.016	0.0195	0.022	0.023	0.024	0.021	0.0194	0.017	0.0135	0.008
1200	0.0095	0.0245	0.030	0.034	0.034	0.033	0.031	0.027	0.022	0.016	0.0075
1300	0.0097	0.0315	0.0395	0.044	0.043	0.039	0.034	0.027	0.018	0.007	−0.0075
1400	0.0097	0.034	0.044	0.045	0.040	0.030	0.019	0.005	−0.011	−0.0065	−0.025
1500	0.0096	0.034	0.043	0.0345	0.016	−0.0076	−0.032	−0.060	−0.092	−0.03	−0.04
1600	0.0096	0.032	0.038	0.013	−0.028	−0.076	−0.129	−0.186	−0.25	—	—
1700	0.0095	0.029	0.032	−0.029	−0.076	−0.160	−0.256	−0.31	—	—	—

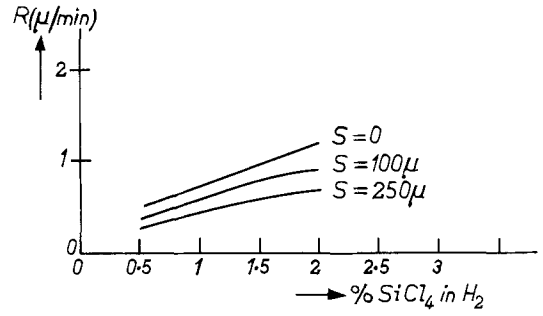

Fig. 4. Growth rate of silicon (R) on the low temperature side of the sandwich vs. initial partial pressure of $SiCl_4$ in H_2. S denotes the thickness of the spacer between seed and source slices. T = 1240°-1300°C.

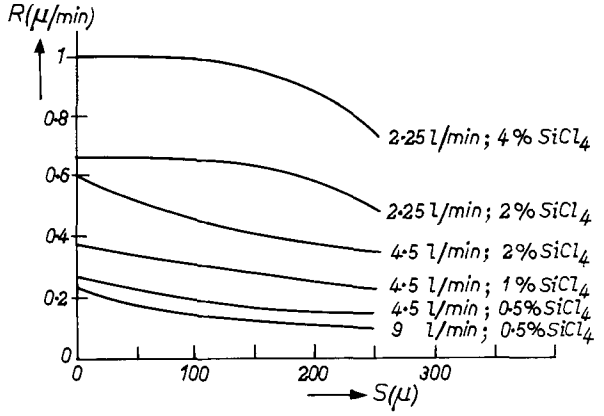

Fig. 5. Influence of the gas flow rate on the sandwich growth rates

however, there is no difference in growth rate for $S = 100\mu$ and $S = 0$ (no spacer).

Reversed growth.—With 1% $SiCl_4$ in H_2, decreasing the heater temperature results in a decreased sandwich growth rate (Fig. 6). In order to obtain reversed sandwich growth lower temperatures and higher $SiCl_4$ partial pressures were studied and results are given in Fig. 7, as can be seen a region indeed exists where reversed growth is observed.

In order to obtain a reasonable temperature gradient at the lower over-all temperatures, the spacing of the slices had to be increased to 200-500μ, otherwise the growth rate was found to be smaller than 0.1 μ/min. With adequate cooling, however, the growth rate at these low temperatures can be increased. The crystallographic quality of the resulting layers is very good, especially if the low growth temperature is considered (9).

It is also possible to start with H_2 + HCl instead of H_2 + $SiCl_4$. In the former case some Si is etched to obtain the necessary $SiCl_4$ and $SiCl_2$ concentration; the same equilibrium concentrations are thus reached from the other side. Reversed epitaxial sandwich growth calls for high HCl concentrations, resulting in a rapid etching of those silicon surfaces that are exposed to the gas phase.

For these experiments, $SiCl_4$ + H_2 was therefore preferred.

Layer quality.—The limited exchange between the close-spaced system and the rest of the apparatus has an advantage in so far as layers with very high resistivity can easily be grown. A disadvantage is the poor reduction possibility prior to growth, giving a high stacking fault density (>3000/cm^2) (3).

In the reversed sandwich growth the growth temperature is lower, but the number of stacking faults is much lower too (<2000/cm^2). This observation gives strong support to the suggestion that transport of SiO_2 toward the low temperature side of the sandwich is one of the major reasons for the growth irregularities.

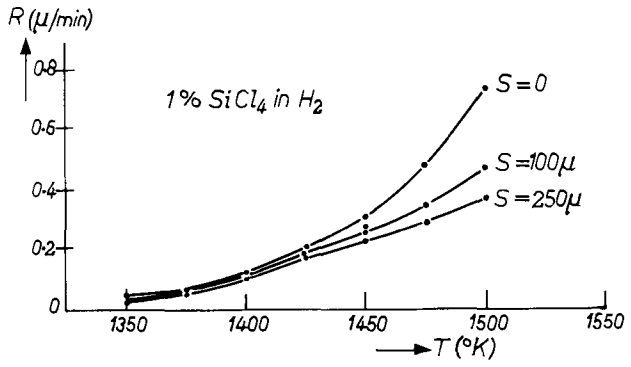

Fig. 6. Influence of the temperature on the sandwich growth rate for 1% $SiCl_4$ in H_2.

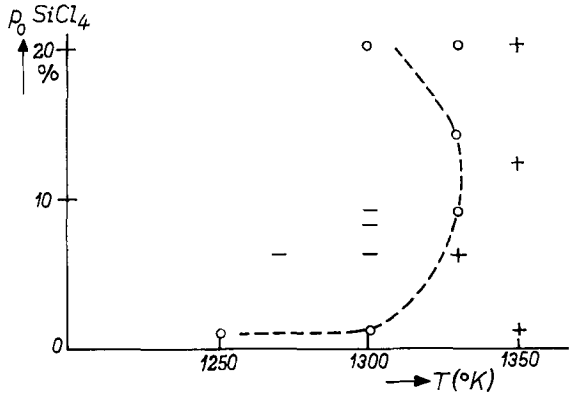

Fig. 7. Regions of normal (+) and inverted epitaxial sandwich growth (—) separated by a neutral zone (O) where no apparent growth on either side of the sandwich structure is observed (compare with Fig. 2). The temperatures given refer to the lower temperature side of the sandwich.

Both in the normal and the reversed sandwich growth the resistivity of the resulting layers mainly depends on the substrate doping level, a refining action being present due to the space between the slices which has to be filled with the gaseous chlorides of the doping elements until ultimately a balance is established between incoming and outgoing dope. The gas phase segregation coefficients for n-type impurities (P, As, Sb) are close to unity. After about 1μ of growth the original resistivity is found again. At greater distances between source and seed crystal the transfer ratio decreases because of a greater loss of dope into the rest of the apparatus. For p-type impurities (B, Al, Ga) the segregation coefficient of B is somewhat smaller than unity. For Al and especially for Ga, the coefficients are very small, *i.e.*, high resistivities result in grown layers of not too great a thickness (see Fig. 8).

Discussion

Equilibrium considerations.—The equilibrium of solid silicon with an atmosphere containing chlorides has been calculated by Steinmaier (8), starting from the following equilibrium reactions

$$SiCl_4(g) + Si(s) \leftrightharpoons 2SiCl_2(g) \qquad [2]$$

giving

$$K_1 = \frac{(p_{SiCl_2})^2}{p_{SiCl_4}}; \quad \log K_1 = 10.081 - 16427/T \qquad (10)$$

and

$$SiCl_4(g) + 2H_2(g) \leftrightharpoons Si(s) + 4HCl(g) \qquad [3]$$

with

$$K_2 = \frac{(p_{HCl})^4}{p_{SiCl_4}(p_{H_2})^2};$$

$$\log K_2 = 13.9 - 13170/T - 1.664 \log T \qquad (11)$$

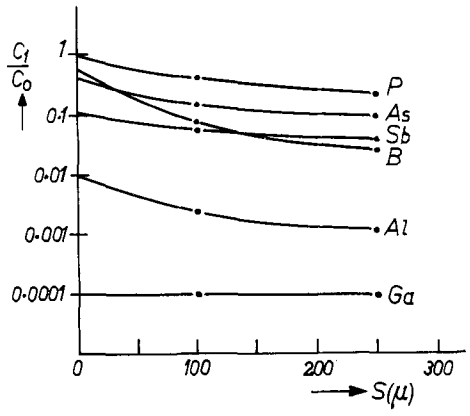

Fig. 8. Some examples of the variation of the segregation coefficient $\frac{C_1}{C_0}$ with distance in sandwich experiments. 1% $SiCl_4$ in H_2, T_1 = 1300°C, T_2 = 1240°C, growth rate 0.8 μ/min, layer thickness 16μ. C_1 = dope concentration in grown layer, C_0 = dope concentration in silicon source.

Further for an open system the sum of all partial pressures is 1 atm

$$p_{SiCl_4} + p_{H_2} + p_{HCl} + p_{SiCl_2} = 1 \quad [4]$$

The total chlorine balance gives

$$p_{SiCl_4} + \tfrac{1}{4}p_{HCl} + \tfrac{1}{2}p_{SiCl_2} = p_0 \quad [5]$$

where p_0 denotes the initial $SiCl_4$ partial pressure.

From [2] and [3] a "silicon partial pressure" p_{Si} is formulated as

$$p_{Si} = \tfrac{1}{4}p_{HCl} - \tfrac{1}{2}p_{SiCl_2} \quad [6]$$

With Eq. [2]-[6] the equilibrium values of the various components can be deduced for any starting concentration of $SiCl_4$ in H_2. Recently Lever (12) has expanded the calculations by introducing also other reaction products of which $SiHCl_3$ proved to be present in greater concentrations, especially at lower temperatures. The arguments used here, fortunately, remain valid, only the maxima in p_{Si} will shift somewhat to lower temperatures.

Direction of transport.—The equilibrium concentrations of the various reaction partners will be different at different temperatures. In a sandwich experiment these different temperature regions are closely spaced and transport occurs because of the existing concentration gradients between the two silicon slices. The transport of n moles of HCl toward any silicon face gives rise to the formation of $\frac{1}{4}n$ mole $SiCl_4$ and the etching of $\frac{1}{4}n$ mole of silicon from the solid (Eq. [3] in reverse direction). On the other hand transport of m moles of $SiCl_2$ toward the same face gives rise to the deposition of $\frac{1}{2}m$ mole of silicon and the formation of $\frac{1}{2}m$ mole $SiCl_4$ on that face (Eq. [2] reverse). The $\frac{1}{4}n + \frac{1}{2}m$ moles of $SiCl_4$ are now present in excess and diffuse back to the other side; here in turn n mole of HCl is formed, $\frac{1}{4}n$ mole of silicon is deposited, also m moles $SiCl_2$ are formed and $\frac{1}{2}m$ mole of silicon is etched away there and the circle is closed.

If the transport of silicon toward the low temperature, T_L, side is called positive and transport toward the high temperature, T_H, negative, then the total transport of silicon is found to be proportional to

$$\tfrac{1}{2}(p_{SiCl_{2H}} - p_{SiCl_{2L}}) - \tfrac{1}{4}(p_{HClH} - p_{HClL}) \quad [7]$$

where the subscripts H and L refer to high and low temperature equilibrium vapor pressure. Equation [7] can also be read as

$$(\tfrac{1}{4}p_{HClL} - \tfrac{1}{2}p_{SiCl_{2L}}) - (\tfrac{1}{4}p_{HClH} - \tfrac{1}{2}p_{SiCl_{2H}}) \quad [8]$$

or, with Eq. [6]

$$p_{SiL} - p_{SiH} \quad [9]$$

It is thus demonstrated that the relative values of p_{Si} can be used anyway to predict the direction of the silicon transport, that side of the sandwich with the highest value of p_{Si} is the receiving side. The magnitude of the growth rate, however, is not strictly proportional to the difference in p_{Si} as for the small diffusion lengths encountered here nucleation rates and perhaps heat transfer difficulties are rate limiting, more than the rate of transport via diffusion as in the experiments of Schäfer.

In the experiments described the total pressure in the open system is kept at about 1 atm, for a closed system the direction of transport is not only temperature dependent as shown here, but also a pressure dependence can be expected analogous to the experiments of Schäfer and Morcher (13).

Under near equilibrium conditions this value of p_{Si} determines the growth rate in normal epitaxial growth and according to Eq. [9] also in sandwich growth; comparison of the experimental Fig. 7 with the calculated Fig. 2 shows that the calculated boundary between the regions of normal and reversed sandwich growth has to be shifted toward the low temperature side by about 100°, dependent also on the actual value of the temperature gradient between the slices. As the presence of $SiHCl_3$ has been neglected in the gas phase in the present calculations, the agreement may be called very satisfactory.

Oxide transport.—The reactions

$$Si(s) + SiCl_4(g) \leftrightharpoons 2SiCl_2(g)$$

and

$$Si(s) + SiO_2(s) \leftrightharpoons 2SiO(g)$$

are comparable to the extent that in both cases transport of silicon toward the low temperature side occurs; for the second system at the high temperature side silicon and SiO_2 react to give SiO, this SiO diffuses toward the low temperature side, the reaction is reversed and solid silicon and solid SiO_2 are deposited again, whereas in the former reaction solid silicon and gaseous $SiCl_4$ are formed. This makes the oxide transport a one way process, the transport stops as soon as the oxide at T_H is used up. As the gas atmosphere is essentially free of oxygen, no new oxide is formed at the high temperature side.

Conclusion

It has been demonstrated that it is possible, using the close-spaced sandwich method, to reverse the growth direction in the epitaxial growth of silicon resulting in a layer of good quality, grown at relatively low temperatures (1000°C). Because of the limited out-diffusion at the low temperatures used, this type of growth has interesting prospects, especially for the growth of high resistivity layers on low resistivity substrates.

Acknowledgment

The authors gratefully acknowledge the very helpful discussions with Dr. J. Tillack of Philips Zentral Laboratorium, Aachen.

Manuscript received June 7, 1965.

Any discussion of this paper will appear in a Discussion Section to be published in the June 1966 JOURNAL.

REFERENCES

1. E. Tannenbaum, Handelman, and E. I. Povilonis, *This Journal*, **111**, 201 (1964).
2. H. Schäfer, "Chemische Transportreaktionen," Verlag Chemie, Weinheim (1962).
3. E. Sirtl, *J. Phys. Chem. Solids*, **24**, 1285 (1963).
4. H. C. Theuerer, U. S. Patent, 3,142,596, July 28, 1964.
5. F. H. Nicoll, *This Journal*, **110**, 1165 (1963).
6. R. F. Lever and F. Jone, *J. Appl. Phys.*, **34**, 3139 (1963).

7. W. G. Pfann, *J. Metals*, **7**, 961 (1955).
8. W. Steinmaier, *Philips Research Repts.*, **18**, 75 (1963).
9. H. C. Theuerer, *This Journal*, **108**, 649 (1961).
10. H. Schäfer and J. Nickl, *Z. Anorg. Chem.*, **274**, 250 (1953).
11. O. Kubaschewski and E. Ll. Evans, "Metallurgical Thermochemistry," Pergamon Press, Oxford (1958).
12. R. F. Lever, *I.B.M. Journal*, **8**, 460 (1964).
13. H. Schäfer and B. Morcher, *Z. Anorg. Chem.*, **290**, 279 (1957).

Electrochemical Behavior of the Quinone-Hydroquinone System in Pyridine

W. Richard Turner[1] and Philip J. Elving

The University of Michigan, Ann Arbor, Michigan

ABSTRACT

The electrochemical behavior of quinone, hydroquinone, and quinhydrone in pyridine solution at the stationary pyrolytic graphite electrode has been studied by conventional and cyclic voltammetry. In the absence of available protons, quinone is somewhat reversibly reduced in a probable 1*e* process to a free radical anion; in the presence of protons, the free radical produced on 1*e* reduction is thought to be oxidized to an N-dihydroxyphenyl pyridinium ion. The latter is also a likely product from the oxidation of hydroquinone. The quinone-hydroquinone system itself is irreversible, *e.g.*, quinhydrone behaves as a mixture of quinone and hydroquinone, the potentials of whose waves are 0.5v apart.

Since the oxidation-reduction behavior of the quinone-hydroquinone system is often used as a test system for electrochemical technics and approaches, its behavior at the pyrolytic graphite electrode was investigated as a part of a systematic investigation of electrochemistry in pyridine as solvent. Previous papers have described the general use of pyridine for polarography with the dropping mercury electrode (1-3), voltammetry with graphite indicating electrodes (4), and an orientative investigation of electrochemical oxidation (5).

Pyridine has a very low proton availability (much lower than the commonly used so-called "aprotic" solvents such as dimethylformamide and acetonitrile), so that reactions carried out in it, *e.g.*, those involving organic compounds, can be compared in the absence of protons and in the presence of known concentrations of available protons present in the form of pyridinium ions.

The results obtained in the present study by both conventional direct-current constant-potential voltammetry and relatively low-frequency cyclic voltammetry indicate the importance of pyridine as a stabilizer of free radicals and carbonium ions, as well as some interesting synthetic possibilities.

Experimental

Reagents.—Analytical reagent grade pyridine (Mallinckrodt) was used without further purification, since it showed the same voltammetric behavior as pyridine, which had been dried over barium oxide and fractionally distilled. Anhydrous lithium perchlorate (G. Frederick Smith) was dried at 200°C. Quinone (Eastman yellow label) was recrystallized from benzene after the benzene solution had been treated with Norit. Hydroquinone and quinhydrone (Eastman white label) were used without further purification. Pyridinium nitrate was prepared by adding cold, concentrated nitric acid to cold pyridine; cooling the resulting solution produced a precipitate, which was filtered and recrystallized from hot acetone, yielding white, nonhygroscopic needles. A colorless, transparent conducting gel, which is excellent for salt bridges, was prepared by heating 5g methyl cellulose (Dow "Methacel," 15 cps viscosity) with 100 ml of 0.5*M* lithium perchlorate in pyridine and cooling.

Apparatus.—The cell, maintained at 25.0° ± 0.1°C, and electrode used have been described (5). The sides of the pyrolytic graphite cylinder (4.0 mm diameter) were insulated by coating with polyethylene; the *ab* plane formed the base of the cylinder. Prior to each run, the electrode was resurfaced by sanding the end with a disk sander using 600A silicon carbide paper.

Procedures.—Conventional voltammograms were obtained with a Sargent Model XV polarograph. The IR drop across the cell was corrected electronically, using an operational amplifier circuit (6). Cyclic voltammograms were obtained by means of a three-electrode polarograph operational amplifier circuit (7), a triangular sweep function supplied by a Hewlett-Packard Model 202A function generator, and an Electro Instruments Model 320 X-Y recorder. All potential measurements are *vs.* the Ag-1.0*M* $AgNO_3$ pyridine reference electrode [$E = +0.09$v *vs.* aqueous S.C.E. including liquid junction potentials (1)].

Behavior of Quinone-Hydroquinone System

The oxidation and reduction of hydroquinone, quinhydrone, and quinone at the stationary pyrolytic graphite electrode were investigated in pyridine solutions, which were 0.5*M* in $LiClO_4$ as background electrolyte.

Cyclic voltammetry.—Typical results of cyclic voltammetry (span: 0.6 to −0.4v; scan rate: 20 mv/sec) are illustrated in Fig. 1.

Oxidation of hydroquinone (4 m*M*) produces a single anodic wave [peak current (i_p) = 83 μa; half-peak potential ($E_{p/2}$) = +0.30v]. On the reverse sweep, only a small wave of 6 μa is observed at a $E_{p/2}$ of −0.12v. The latter wave, which does not appear on the forward sweep and is therefore not a solution impurity, is due to the reduction either of a small amount of the oxidation product of hydroquinone or of a trace amount of quinone, which could be formed by air oxidation of hydroquinone. In either case, the oxidation of hydroquinone is completely irreversible. The product or products of the electrooxidation probably undergo a chemical reaction to form a species which cannot be electroreduced, at least within the potential range involved.

Quinone (4 m*M* solution) is reduced, producing a cathodic wave ($i_p = 45$ μa; $E_{p/2} = -0.18$v). On the reverse sweep, an anodic wave appears in the same region. Since this wave is superimposed on the cathodic process, it is difficult to assess the voltammetric parameters, i_p and $E_{p/2}$, which appear to be very similar to

[1] Present address: Technical Center, Atlas Chemical Industries, Wilmington, Delaware.

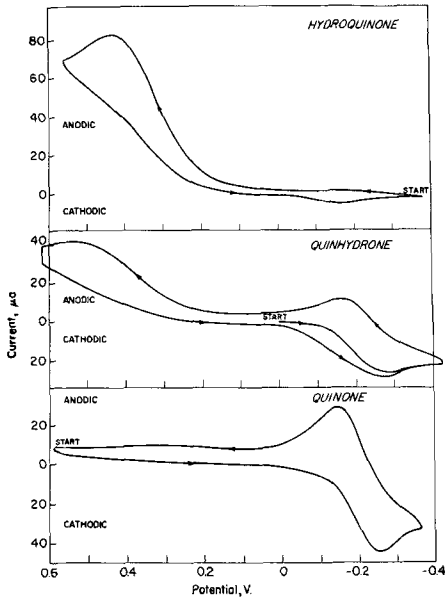

Fig. 1. Cyclic voltammograms at pyrolytic graphite electrode of 4 mM hydroquinone, 2 mM quinhydrone, and 4 mM quinone in 0.5M $LiClO_4$-pyridine solution; scan rate, 20 mv/sec.

those for the cathodic wave. Since a reversible 1e process requires a peak current separation of 57 mv and the present separation is 90-100 mv, the behavior is somewhat irreversible, although in comparison to the hydroquinone oxidation this deviation is minor.

The peak current for the hydroquinone oxidation is almost twice that for the reduction of the same quinone concentration. If the small reduction wave ($i_p = 6$ μa) observed for hydroquinone is due to partial air oxidation of hydroquinone, then i_p for the latter can be corrected to about 89 μa. The ratio of peak currents at a stationary electrode for two reversible processes, one of which is 2e and the other 1e, is 2.8, since the current is proportional to $n^{3/2}$. However, since the oxidation of hydroquinone is quite irreversible so a ratio smaller than 2.8 would be expected. Since the ratio of i_p for the two processes is near 2 and since the ratio of reversible 3e and 4e processes to reversible 1e processes would be 5.2 and 8, respectively, the oxidation of hydroquinone would seem to involve twice as many electrons as the reduction of quinone, and the postulation of a 2e oxidation of hydroquinone and a 1e reduction (and reoxidation) of quinone is quite reasonable.

Similar behavior is observed in the voltammetry of quinhydrone. Although quinhydrone is a 1:1 molecular addition compound of hydroquinone and quinone, cyclic voltammetry clearly shows that the two compounds react independently of each other. The i_p ratio for hydroquinone oxidation and quinone reduction in a quinhydrone solution is 2, *i.e.*, the same as when the two species are independently oxidized and reduced.

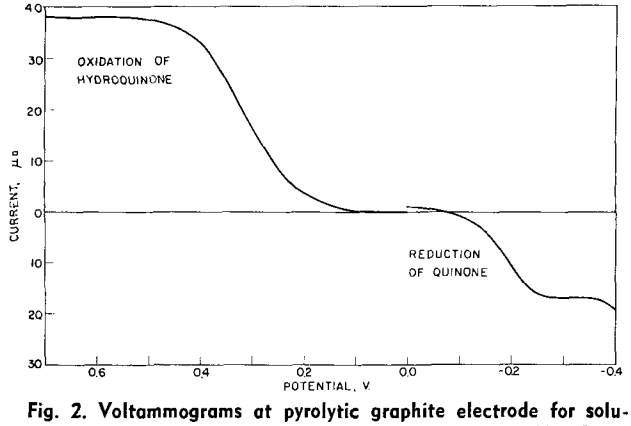

Fig. 2. Voltammograms at pyrolytic graphite electrode for solutions of 4 mM hydroquinone and of 4 mM quinone in 0.5M $LiClO_4$-pyridine solution. Polarization rate, 1.67 mv/sec. The figure is constructed from two voltammograms, one for each compound.

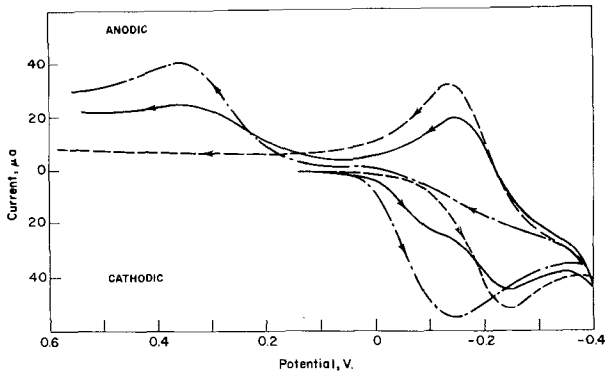

Fig. 3. Cyclic voltammograms at pyrolytic graphite electrode for 4 mM quinone in 0.5M $LiClO_4$-pyridine solution. Dashed line, no pyridinium nitrate added; solid line, 2.0 mM pyridinium nitrate; broken line, 4.0 mM pyridinium nitrate.

Voltammetry.—Typical conventional voltammograms for quinone and hydroquinone are shown in Fig. 2. Hydroquinone produces an anodic wave of 38 μa ($E_{p/2} = 0.31$v); quinone gives a cathodic wave of 17 μa ($E_{p/2} = -0.19$v); these results are in good agreement with the cyclic voltammetry data. The currents, when compared on the basis of current per unit concentration per unit area, correspond to those found for known 2e and 1e electrochemical redox reactions [*cf.* ref. (5).]

Effect of proton addition.—Helpful information in respect to elucidation of the electrode processes involved is obtained on reducing quinone in the presence of available protons or hydrogen ions, *e.g.*, cyclic voltammetry of quinone in the absence of pyridinium ion and in the presence of 0.5 and the same concentrations of pyridinium ion (Fig. 3).

The height of a cathodic wave, which appears at an $E_{p/2}$ of −0.15v, increases with pyridinium ion concentration up to a 1:1M ratio, at which ratio the original quinone wave at −0.18v is no longer visible. In addition, the original anodic reoxidation wave ($E_p = -0.15$v) decreases, and a second anodic wave ($E_{p/2} = +0.25$v) appears, which increases with increasing pyridinium ion concentration up to a ratio of one pyridinium ion per quinone molecule; at this concentration ratio, the anodic wave ($E_p = -0.15$v) has disappeared. Moreover, the ratio of cathodic to anodic peak currents is approximately one and a 1e process is indicated from the magnitude of the peak currents compared with i_p for reduction in the absence of pyridinium ion. Further increase in pyridinium ion has no effect, *e.g.*, a cyclic voltammogram for a solution, in which the molar ratio of pyridinium ion to quinone is 2, is identical to that for a solution, for which the ratio is 1.

Probable Electrode Processes

The voltammetric data can be rationalized on the basis of the following series of electrode reactions, which, as subsequently discussed, involve known reactions of pyridine:

1. Voltammetry of quinone in the absence of pyridinium ion; cathodic wave ($E_{p/2} = -0.18$v; 1e process)

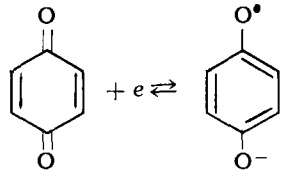

[1]

I

2. Voltammetry of quinone in the presence of pyridinium ion; cathodic wave ($E_{p/2} = -0.05$v; 1e process)

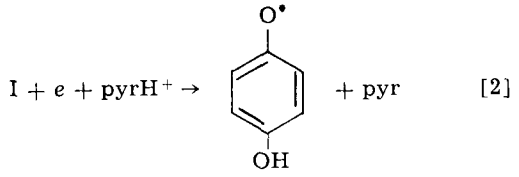

II

For anodic wave ($E_{p/2} = +0.25$v; 1e process)

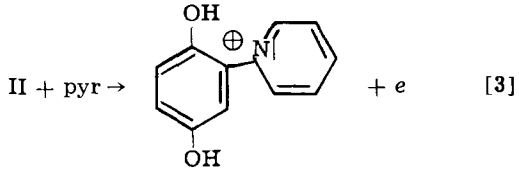

III

3. Voltammetry of hydroquinone; anodic wave ($E_{p/2} = +0.30$v; 2e process)

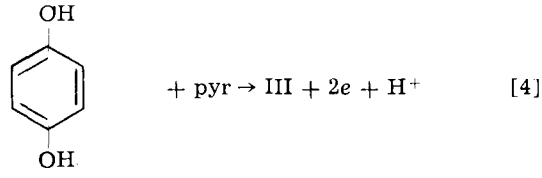

The semiquinone anion radical (I), postulated as the product of the reduction of quinone in the absence of added protons, has also been postulated by Wawzonek *et al.* (8) for the reduction of quinone in anhydrous acetonitrile and dimethylformamide, which are more likely to react with free radicals than pyridine, since they contain hydrogen atoms which are more labile than the hydrogen in pyridine. In addition, one would hardly expect the anodic and cathodic waves to be as close together as shown in the bottom panel of Fig. 1 if there were an intervening chemical reaction such as a dimerization.

Although the N-dihydroxyphenyl pyridinium ion (III) has not been isolated from the reaction, it is a likely product since the following chemical reaction has been observed and the products characterized (9)

The latter reaction proceeds slowly at room temperature and does not compete with the electrochemical reduction. However, when the hydroquinone radical (II) is oxidized, the removal of an electron might produce a protonated quinone in an activated state, which would be readily attacked by pyridine producing (III). In other words, the rate-determining step for the chemical reaction of quinone and pyridinium ion is the protonation of the quinone. The activation energy for this step is decreased, when a protonated quinone is produced during the oxidation of hydroquinone, and the protonated quinone would react rapidly with pyridine.

The reaction of pyridine with positively charged organic oxidation products is by no means unusual, *e.g.*, Lund (10) observed the following reaction in acetonitrile-pyridine mixture:

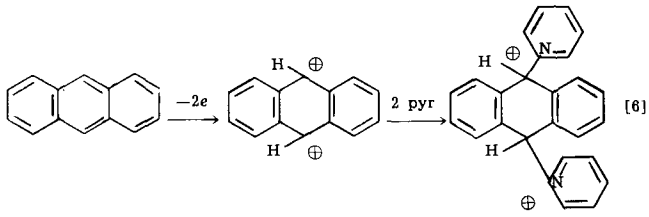

As far as reversibility of the quinone-hydroquinone system in pyridine is concerned, the over-all system is totally irreversible, *e.g.*, Fig. 2 and 3. However, the system involving quinone and the free radical anion resulting from its 1e reduction (Eq. [1]) approaches reversible behavior in the absence of available protons. Wawzonek *et al.* (8) report that 1e reduction of quinone in acetonitrile and dimethylformamide to be reversible.

Discussion

The results of the study of the voltammetric behavior of the quinone-hydroquinone system in pyridine demonstrates the value of the solvent in providing a controlled hydrogen ion environment, where the availability of hydrogen ions for participation in the electrode process is precisely known. The ability of pyridine to react with positively charged organic ions, which may be transient intermediates, is indicated by the oxidation of hydroquinone. This reaction is potentially useful both in trapping reaction intermediates for mechanism elucidation and in synthesis.

Acknowledgment

The authors thank the Petroleum Research Fund of the American Chemical Society, the United States Atomic Energy Commission, and the Horace H. Rackham School of Graduate Studies of The University of Michigan for helping to support the work described. One author (W.R.T.) is indebted to The Institute of Science and Technology of The University of Michigan for a postdoctoral fellowship.

Manuscript received April 6, 1965.

Any discussion of this paper will appear in a Discussion Section to be published in the June 1966 JOURNAL.

REFERENCES

1. A. Cisak and P. J. Elving, *This Journal*, **110**, 160 (1963).
2. A. Cisak and P. J. Elving, *Rev. Polarography*, **11**, 21 (1963).
3. M. Spritzer, J. M. Costa, and P. J. Elving, *Anal. Chem.*, **37**, 211 (1965).
4. P. J. Elving, I. Fried, and W. R. Turner, *Proc. Third International Polarographic Congress*, in press.
5. W. R. Turner and P. J. Elving, *Anal. Chem.*, **37**, 467 (1965).
6. R. Annino and K. J. Hagler, *ibid.*, **35**, 1555 (1963).
7. D. D. DeFord, Division of Analytical Chemistry, 133rd National Meeting, A.C.S., San Francisco, Calif., April, 1958.
8. S. Wawzonek, R. Berkey, E. W. Blaha, and M. E. Runner, *This Journal*, **103**, 456 (1956).
9. E. B. Barnett, J. W. Cook, and E. P. Driscoll, *J. Chem. Soc.*, **123**, 503 (1924).
10. H. Lund, *Acta Chem. Scand.*, **11**, 1323 (1957).

An Electrode Mechanism for the Electrochemical Reduction of M-dinitrobenzene

G. W. Jackson and J. S. Dereska

Consumer Products Division, Research Laboratory, Union Carbide Corporation, Cleveland, Ohio

ABSTRACT

This is an integrated polarographic and potentiostatic study on the mechanism of the cathodic reduction of m-dinitrobenzene for various *p*H values of aqueous electrolytes. The polarographic results confirmed previous results of a two-stage reduction involving four electrons in each step. The supporting coulometric work was performed potentiostatically at a graphite cathode under a nitrogen atmosphere at a controlled potential of —0.48v on a solution of *p*H 6.00. The product of the first step, 3-nitrophenylhydroxylamine, was quantitatively isolated and identified for coulometric equivalencies of 25, 50, 75, and 90% reduction.

There have been a number of theoretical and practical experiments on the electrochemical reduction of m-dinitrobenzene. Some of these reductions have been carried out electrolytically where no attempt was made to control the potential. These reductions have had as their goal the synthesis of a given product such as 2, 4-diaminophenol, m-nitroaniline, 3, 3'dinitroazoxybenzene, and 3-nitrophenylhydroxylamine (1-5). Even though these reductions were carried out in strongly acidic and basic solutions, the *p*H was left doubtful because of the use of large amounts of alcohol.

Pearson (11) polarographically examined a series of dinitro aromatic compounds and concluded that these compounds reduced in two separate stages with each stage equivalent to a four-electron reduction. Such a reaction path has also been postulated by other workers on the basis of polarographic evidence (7-11). Ehlers and Sease (6) used a combination of potentiostatic reduction and polarographic techniques to elucidate the reaction path for the reduction of m-dinitrobenzene and other polynitro aromatic compounds. Their result was the same as above in that a two-step reduction occurred with each step coulometrically equivalent to four electrons. These workers, however, were unsuccessful in obtaining 3-nitrophenylhydroxylamine.

In an effort to more convincingly confirm and describe the representative cathodic process, it appeared advantageous to relate identified isolated products with process-characterizing potentials and the Faradaic amount of electricity required. Polarographic techniques were employed to correlate potentials with reduction processes, while Faradaic equivalence was determined by coulometric measurements at the selected potentials. Finally, confirmation of the reaction path was sought in the isolation and identification of the products. For better interpretive significance in relating potentials to reduction mechanisms, alcohol solvents were avoided and only aqueous solutions of the sparingly soluble m-dinitrobenzene were used in this work. Quantitative isolation and identification of the intermediates were accomplished to confirm the reaction path for the reduction process.

Experimental

Equal importance was placed upon the polarograph, potentiostat, and isolation phases of the experimental work. The specialized polarograph employed in this phase of the nitro compound studies was the one described by Kelly, Jones, and Fisher (12) of the Oak Ridge National Laboratory and made by the Indiana Instrument and Chemical Corporation, Bloomington, Indiana. The polarographic cell was kept at 25°C and used a separate S.C.E. as reference electrode and platinum wire as the anode. The unique feature of this experiment was that no alcohol or other special solvent was used to dissolve the m-dinitrobenzene.

For the potentiostatic work this required that larger volumes of solutions be used; therefore, a special electrolytic cell was designed (Fig. 1). The electrolytic cell for potentiostatic work was a 4000 ml beaker which used three electrodes. The anode compartment consisted of a cylindrical glass tube, 2 in. in diameter, which was separated from the cathode by a cellophane membrane. The anode was silver-silver chloride. The cathode or working electrode was a graphite disk covering the entire bottom of the 4-liter beaker. The reference electrode was a saturated calomel electrode. Adjustment of the reference potential of the graphite electrode with respect to a corresponding S.C.E. was made.

Modification of the electronic circuitry in the standard Wenking model potentiostat was necessary to achieve the higher currents required for this work where substantial amounts of intermediates were isolated and identified. The *p*H meter was a Beckman *p*H meter, Model N.

The m-dinitrobenzene obtained from the Matheson Company, Inc., was first recrystallized from distilled water. The m.p. of the recrystallized material was 89°-89.5°C. All buffer solutions were made from reagent grade materials.

Solutions of m-dinitrobenzene were then prepared by weighing 1g of recrystallized solid into 2 liters of the given buffer. This was heated and vigorously stirred until all of the solid went into solution. The final volume was measured in order to calculate the concentration, since some evaporation took place on

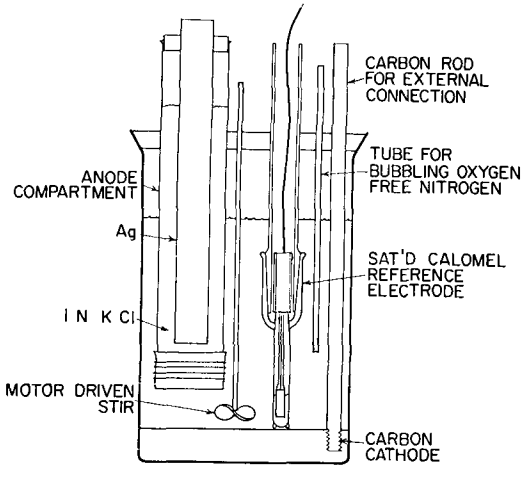

Fig. 1. Drawing of electrolytic cell

heating. The pH of all final solutions was taken on the Beckman pH meter. Solutions of pH 6.00 were used in the potentiostatic experiments.

Dissolved oxygen was removed from the solutions for both polarographic and potentiostatic work by bubbling oxygen-free nitrogen through the solutions for 10 min and 1 hr, respectively. The drop weight was taken at a potential on the limiting current plateau. The values of m and t were 2.53 mgm-sec^{-1} and 3.34 sec. The value of mt was 8.45 mg and $m^{2/3}t^{1/6}$ was 2.27. The diffusion current, I_d, varied slightly for each solution because of the slight differences in the concentration, while the diffusion current, constant, I^*, remained constant.

$$I^* = \frac{I_d}{Cm^{2/3}t^{1/6}} = \frac{I_d}{C \times 2.27} \qquad [1]$$

The potentiostatic reduction was run for a prescribed period of time coulometrically approximated to give 25, 50, 75, and 100% reductions. Siphoning of supernatant ether extracts while under nitrogen was successfully employed to remove products and unreacted meta-dinitrobenzene. After separation and purification of products and any unreacted meta-dinitrobenzene, identification was made by infrared spectra and quantitative chemical analysis. The n values were obtained by coulometric techniques.

Polarographic and Potentiostatic Measurements

Solutions of m-dinitrobenzene were made as described above at all integral values of pH from 1 through 10. These solutions were then diluted by a factor of ten and polarograms were run on the initial and resulting solutions. It will be seen from the polarograms that the half-wave potential, $E_{1/2}$, varies with the pH and in some cases approximately 60 mv per pH unit. A plot of the diffusion current *vs.* the height of the mercury column raised to the one-half power gave a curve that was proportional. A plot of log $I/(I_d - I)$ *vs.* potential gave a straight line whose slope was 0.065. This slope agrees with the experimental findings of Pearson (11). Table I gives the half-wave values and n values as a function of pH. Polarograms are shown in Fig. 2-5. Figure 5 shows a derivative polarogram with peak indicating half-wave values.

The potentiostatic reduction was carried out at preset electronically controlled potentials, and the current was followed on an ammeter. In this case the experiments were run on solutions of pH 6.00, and the potential was set at a potential just below the knee of the first wave as shown on the polarographic curve. This potential was —0.48v *vs.* S.C.E. The amount of current was determined by planimeter integration of the current-time curves and from a copper coulometer. The reduction was carried out under a blanket of nitrogen to insure that no oxygen would become involved in the reaction. This was done because it had been observed in our previous experiments that oxygen could drastically change the products. For example, it was observed that if a reduction was already in progress and oxygen was intentionally added, visible color changes took place and a product was obtained which contained 3, 3'dinitroazoxybenzene. Since the rate of reduction was followed polarographically by determining the amount of m-dinitrobenzene present after a given reduction, a double check was obtained because the rate of reduction of m-dinitrobenzene was also followed coulometrically.

After the reduction, the catholyte was extracted with anhydrous ether while still under the nitrogen atmosphere. To accomplish this, the solution was vigorously

Table I. Half-wave values for the first and second waves equivalent to four and eight electrons

Compound	pH	$E_{1/2}$, v
m-DNB	1.10	0.14
m-DNB	2.10	— 0.14 0.28
m-DNB	3.05	0.27 0.44
m-DNB	4.10	0.33 0.65
m-DNB	5.00	0.34 0.58
m-DNB	6.00	0.40 0.58
m-DNB	7.00	0.44 0.65
m-DNB	7.95	0.50 0.68
m-DNB	9.00	0.62
m-DNB	10.0	0.58 0.75

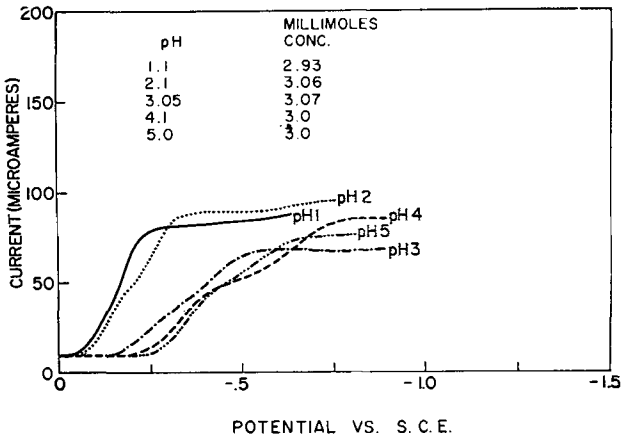

Fig. 2. Polarograms of m-DNB at pH 1 through 5 in the presence of 0.01% gelatin.

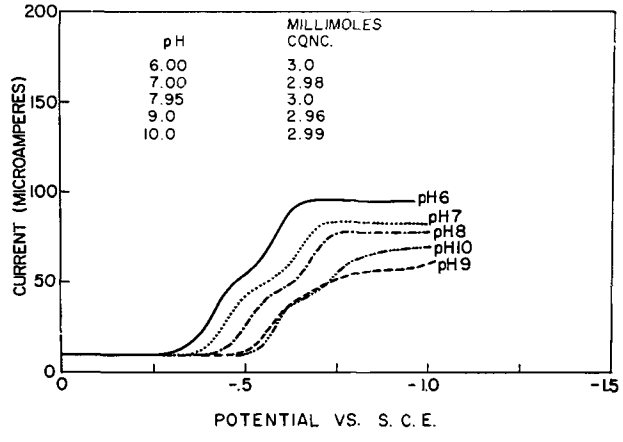

Fig. 3. Polarograms of m-DNB at pH 6 through 10 in the presence of 0.01% gelatin.

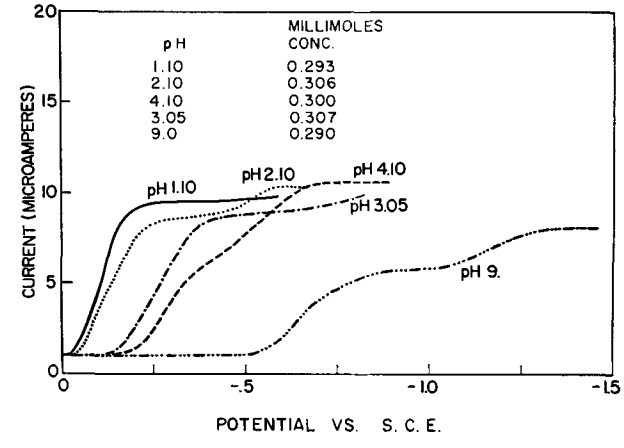

Fig. 4. Polarograms of m-DNB in dilute solutions in the presence of 0.01% gelatin.

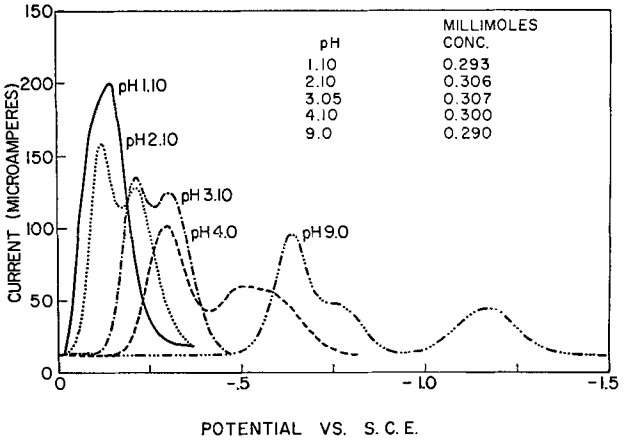

Fig. 5. Derivative polarograms of m-DNB at *p*H 1.10 through 9.0 in dilute solutions.

stirred with a mechanical stirrer and bubbling nitrogen. The ether layers were siphoned off and dried over anhydrous sodium sulfate. The ether was evaporated while still making sure a dry nitrogen atmosphere prevailed. The dried products were weighed and the components separated using a solvent mixture composed of one part chloroform and three parts benzene. This seemed to separate the mixed product into two principal products which were identified as m-dinitrobenzene and 3-nitrophenylhydroxylamine. Table II gives the results of the reduction. Figure 6 shows an infrared curve for the compound formed and identified as 3-nitrophenylhydroxylamine. The medium used for the infrared determination was a KBr disk. Repeated efforts to electrolyze to 100% of the first step in the reduction failed to give all 3-nitrophenylhydroxylamine.

Discussion

From the data listed above and from work of other investigators (1-11), a reaction path for the reduction of m-dinitrobenzene is well established. Above *p*H of 2, the reduction takes place in two steps, polarographically and coulometrically, each wave is of equal height and is equivalent to four electrons. This would mean that the reduction goes as follows

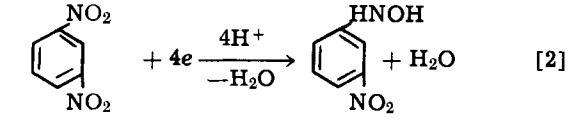

[2]

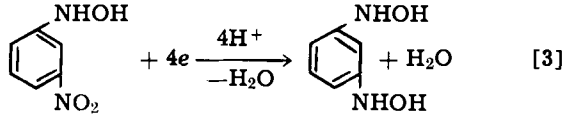

[3]

This reaction path is consistent with experimental results and is inconsistent with the mechanism proposed by Morehouse and Glicksman (13) of a two-step reduction each involving six electrons. Isolation and identification of products in galvanic cells, although somewhat more complex than for the isolated conditions published here, have confirmed at least the initial representative steps and mechanisms described

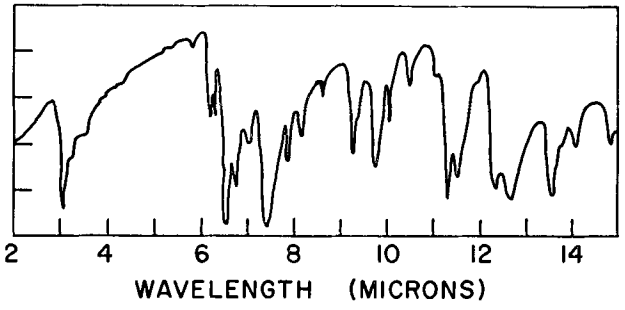

Fig. 6. Infrared spectrum of 3-nitrophenylhydroxylamine on KBr disk.

here. Below *p*H of 2, the reduction goes via 12 electrons as proposed. Even though electron spin resonance evidence (14-19) indicates that the polarographic four electron step is in reality a series of steps involving a free radical, the over-all picture is as shown above.

The results in Table II show no product at 100% reduction. The expected product was all 3-nitrophenylhydroxylamine, but instead of obtaining this compound a mixture was found. This lack of pure product indicates that reduction of the first nitro group does not occur completely before reduction of the second group begins. Several runs gave similar results at 100% reduction.

The product, phenyl dihydroxylamine, which resulted from the complete reduction was not isolated. One reason was the occurrence of a mixture that would not cleanly separate. In alkaline solution, the products were very sensitive to the atmosphere and always contained 3, 3'dinitroazoxybenzene.

Conclusion

1. In a macro sense at least, the initially observable phase of reduction of m-dinitrobenzene above *p*H 3.0 goes in two steps with each step equal to a four electron reduction.

2. The product of a controlled reduction of m-dinitrobenzene equivalent to four electrons is 3-nitrophenylhydroxylamine which is quite reactive and readily undergoes condensation, rearrangement, disproportionation, and oxidation depending on the environmental conditions imposed, *e.g.*, the electrolyte *p*H, temperature, time of its exposure, and competitive side reactions.

3. Alkaline solutions and oxygen tend to increase the probability of the coupling process; *i.e.*, the formation of stable 3, 3'dinitroazoxybenzene, and cause a mixed product; therefore, the presence of this compound and its reduced products, such as the hydrazo, is a result of side reactions and is not to be considered a part of its true reaction path.

Acknowledgment

The authors wish to thank Mr. J. Leonard for his technical assistance also Dr. H. A. Laitinen and Dr. S. Swann, Jr., for helpful suggestions in preparing this manuscript.

Manuscript received May 11, 1965; revised manuscript received July 3, 1965.

Any discussion of this paper will appear in a Discussion Section to be published in the June 1966 JOURNAL.

Table II. Potentiostatic reduction of m-dinitrobenzene

*p*H	% Reduction Coulombic	% Reduction Polarographic	g m-DNB Initially	g of Product	Product g-m-DNB	Product g 3NPHA	3NPHA eq. to m-DNB	Percentages of product m-DNB	Percentages of product 3NPHA	M.P. 3NPHA	Analysis of 3NPHA % Composition C	H	N	O
6.00	26.01	26.5	0.9230	0.8655	0.6274	0.2138	0.2280	73.5	26.5	118°C	46.9	3.90	18.20	31.20
6.00	49.8	49.5	1.0230	1.0089	0.4221	0.3855	0.4100	50.5	49.5	115.5	47.31	4.05	17.44	31.20
6.00	58.5	60.5	0.9795	0.9589	0.3511	0.4633	0.4900	41.5	58.5	115.0	47.94	3.98	17.17	30.91
6.00	72.8	75.1	1.0060	0.7575	0.2093	0.5155	0.5490	27.2	72.8	113.0	46.06	4.00	17.47	31.57
6.00	100.0	100.5	0.9934	Not isolated turned brown	—	—	—	—	—	—	—	—	—	—

REFERENCES

1. H. V. K. Udupa, G. S. Subraminian, and K. S. Udupa, *Research Ind.*, **5**, 309 (1960).
2. S. Kikuchi and T. Utsunomiya, *Kogya Kagaku Zasshi*, **54**, 534 (1951).
3. B. B. Dey and H. V. Udupa, *J. Sci. Ind. Research (India)*, **6B**, 83 (1947).
4. R. H. McKee and C. J. Brockman, *Trans. Electrochemical Soc.*, **62**, 203 (1932).
5. K. Brand, *Ber.*, **38**, 4006 (1905).
6. V. B. Ehlers and J. W. Sease, *Anal. Chem.*, **31**, 16 (1959).
7. M. Shikata and N. Hozaki, *Mem. Coll. Agr. Kyota Imp. Univ.*, **17**, 1 (1931).
8. M. Suzuki, *J. Electrochem. Soc. Japan*, **22**, 112 (1954).
9. L. Holleck and H. Schmidt, *Z. Elektrochem.*, **59**, 56 (1955).
10. S. F. Dennis, A. S. Powell, and M. J. Astle, *J. Am. Chem. Soc.*, **71**, 1484 (1949).
11. J. Pearson, *Trans. Faraday Soc.*, **44**, 683 (1948).
12. M. T. Kelley, H. C. Jones, and D. J. Fisher, *Anal. Chem.*, **31**, 1475 (1959).
13. R. Glicksman and C. K. Morehouse, *This Journal*, **105**, 299 (1958).
14. R. P. Clark, Ph.D. Thesis, University of Illinois (1961).
15. A. C. Testa, Ph.D. Thesis, Columbia University (1961).
16. R. E. Visco, Ph.D. Thesis, University of Illinois (1963).
17. I. Bernal and G. K. Fraenkel, *J. Am. Chem. Soc.*, **86**, 1671 (1964).
18. J. H. Freed and G. K. Fraenkel, *J. Chem. Phys.*, **41**, 699 (1964).
19. H. Freed, P. H. Rieger, and G. K. Fraenkel, *ibid.*, **37**, 1881 (1962).

Electrochemical Studies on Zirconium and Hafnium in Molten LiCl-KCl Eutectic

R. Baboian,[1] D. L. Hill,[2] and R. A. Bailey

Department of Chemistry, Rensselaer Polytechnic Institute, Troy, New York

ABSTRACT

Electrode potential and polarographic studies have been made on solutions of zirconium and hafnium ions in molten LiCl-KCl eutectic at 450°-550°C. Anodic dissolution of Zr at 450°C yielded Zr(IV), but at 550°C, chiefly Zr(II). Only Hf (IV) was observed over this range. Apparent standard electrode potentials were (mole fraction scale, Pt(II)/Pt(0) reference)

Zr(II)/Zr(0); —1.77v at 550°C

Zr(IV)/Zr(0); —1.86v at 450°C

Hf(IV)/Hf(0); —1.88v at 450°C; —1.92v at 550°C

The electrochemical behavior of zirconium and hafnium in molten salt systems has received only slight attention. Yang *et al.* (1, 2), studied the electrode potentials of zirconium and hafnium in fused LiCl-KCl eutectic at 500°-550°C. They found Hf(IV) and Zr(IV) to be the predominant species in equilibrium with the metals, although there was some uncertainty in the latter case (2). More concentrated solutions of $ZrCl_4$ were studied in the same melt by Inman *et al.* (3) at 400°-500°C, but here volatilization of the solute prevented satisfactory potential measurements. It was found that $ZrCl_2$ was the major product of electrolysis at the cathode. Anodization of the metal produced Zr(IV). Work at higher temperatures has been carried out in molten equimolar NaCl-KCl by Grechina and Barchuk (4) and Smirnov *et al.* (5). The former found that at 700°C anodic dissolution of zirconium metal gave Zr(II) as the predominant product, but this disproportionated to Zr(IV) and Zr(0). Chronopotentiometric measurements have been carried out on both the zirconium and hafnium systems at 700° to 800°C in the above melt by Baraboshkin *et al.* (6).

This paper describes potentiometric and polarographic studies of zirconium and hafnium in the LiCl-KCl eutectic at 450°-550°C which yielded values of electrode potentials and information on the oxidation states produced by anodization. Electrode potentials refer to the cell

Metal	Metal Ion, Concentration C, LiCl-KCl Eutectic	Glass Frit	Reference Electrode

[1] Present address: Department of Metallurgical and Material Science, University of Toronto, Toronto, Ontario.

[2] Present address: Department of Chemistry, University of Hong Kong, Hong Kong.

The reference electrode was either the Pt(II)/Pt(0) or the Ag(I)/Ag(0) couple. The apparent standard potential of the metal ion—metal couple, $E^{0\prime}_{M(n)/M(0)}$, is given by the equation

$$-E'_{cell} = E^{0\prime}_{M(n)/M(0)} + \frac{2.303\,RT}{nF}\log C$$

where E'_{cell} is the cell potential with the reference electrode in its standard state of unit mole fraction or molality. $E^{0\prime}_{M(n)/M(0)}$ differs from the true standard potential by the activity coefficient which is included in it, and is constant only if the activity coefficient is constant over the range of concentration studied.

From the free energy of formation of the pure metal chloride, it is possible to calculate the standard potential of the couple, and hence the activity coefficient for the metal ion if that of the reference is known. That of Ag(I) is unity in this melt (7, 8). Other thermodynamic quantities can be found from standard relationships.

Experimental

The purification of the LiCl-KCl eutectic, the electrochemical cell and reference electrodes, and other aspects of the experimental procedure were as described in a previous publication (9). Solutions of zirconium and hafnium were prepared by anodic dissolution of the metal rods using a constant current source (about 10 ma/cm^2). Only low concentration solutions were investigated—generally less than 5 x 10^{-4} mole fraction of zirconium or hafnium.

The zirconium metal used was > 99.9% pure, while the hafnium had a zirconium content of 1-2%, but less than 0.1% of other impurities. The rods were polished with fine emery cloth and slightly etched with HF before use; they were then immediately placed in the

cell where they were maintained under vacuum as the temperature was raised slowly to the desired point. During the electrochemical measurements, the cell was flushed with purified argon which was also used for stirring.

Anodic dissolution of both zirconium and hafnium produced an immediate black precipitate if the melt was inadequately purified, although there was no visible attack of the metal before electrolysis as is the case with titanium under similar conditions. With properly purified melts, this effect was not noticeable. It is evidently due to the formation of oxide and/or oxychloride by reaction of oxide or hydroxide impurities (3). Solubility studies of both metals and their dioxides showed that no detectable amount of material entered solution from them.

Results

The products obtained from anodic dissolution of zirconium depended on temperature. At 450°C, plots of E'_{cell} *vs.* log (zirconium concentration) gave good straight lines with slopes corresponding to a 4-electron process; the average slope of all experiments was 0.037v, while that calculated for a 4-electron transfer at this temperature is 0.0359v. Weight-loss measurements of the rod also indicated that zirconium was dissolved as Zr(IV). At 550°C, a linear plot of the above quantities was also obtained, but with an average slope of 0.073v. This is close to the calculated value for a 2-electron process, 0.0817v, and again weight-loss measurements indicated dissolution as Zr(II). At 500°C, no linear plot could be obtained. At 450° and 550°C, apparent standard potentials were obtained by extrapolating the plots to unit mole fraction; these are given in Table I. The results obtained from different experiments agreed to within 0.01v.

The temperature dependence of the Zr(II)/Zr(0) couple over the range 550°-600°C, given in Table II, was linear and reproducible. This coefficient was used to estimate the potential of the above couple at 450°C which is given in Table I. On the other hand, solutions prepared at 450°C and heated to 550°C and cooled, gave different potentials for increasing and decreasing temperatures. This may have been due in part to loss of Zr(IV) from the melt at higher temperatures, although it is probable that the chief cause was an irreversible reaction such as

$$Zr(IV) + Zr(0) \rightarrow 2Zr(II)$$

Figure 1A shows polarograms recorded at 450°C for different concentrations of Zr(IV) at a platinum microelectrode. No anodic wave was observed, and only a single cathodic wave at about —1.9v appeared. The limiting currents from these polarograms yield an approximate straight line, intersecting the abscissa near zero concentration, when plotted against the concentration of Zr(IV). The slope of this line (the limiting current constant) is about 0.08 amp/mm² per unit mole fraction. In these polarograms, and the others to be discussed, considerable uncertainty is involved in the values of the limiting currents per unit microelectrode area. In part this may be due to the slope of the plateau of the polarogram, but also significant is the fact that measurement of the true microelectrode area is difficult. The limiting current constants quoted, which are the best values from several runs, are reliable to within about 0.01 amp/mm². On reversing the direction of polarization, as in Fig. 1B, the curve is retraced up to the deposition potential, then passes through the zero current axis and changes sign (dotted line). However, the current quickly decreases to nearly zero.

Polarograms in Fig. 2(a), (b), and (c) are for solutions prepared at 450°, 500°, and 550°C, respectively. At 500°C, two cathodic waves occur, at —1.8 and —1.9v. At 550°C, the two waves are at —1.6 and —1.9v. The current of the second wave is quite large with a marked increasing current effect. At 550°C, anodic oxidation waves could be observed; at a fixed potential, the current was more negative with successive additions of Zr(II), but otherwise these polarograms were not reproducible.

Potential measurements in the hafnium system at both 450° and 550°C gave straight lines when E'_{cell} was plotted against log (hafnium concentration). The slopes calculated for a 4-electron process at these temperatures are 0.0359 and 0.0408v, compared with observed values of 0.037 and 0.040v. Weight-loss measurements of the metal rod also agreed with dissolution as Hf(IV). Apparent standard potentials are given in Table I, and the temperature dependence, which was

Table I. Apparent standard electrode potentials

Cell	Temp, °C	Apparent standard potential, volts (based on mole fraction scale)
Zr | Zr(II) || Pt(II) | Pt	450	−1.75[a]
	550	−1.77
Zr | Zr(II) || Ag(I) | Ag	450	−1.12[a]
	550	−1.11
Zr | Zr(IV) || Pt(II)Pt	450	−1.86
Zr | Zr(IV) || Ag(I) | Ag	450	−1.22
Pt | Zr(IV), Zr(II) || Pt(II) | Pt	450	−1.97[b]
Hf | Hf(IV) || Pt(II) | Pt	450	−1.88
	550	−1.92
Hf | Hf(IV) || Ag(I) | Ag	450	−1.24
	550	−1.25
Ag | Ag(I) || Pt(II) | Pt	450	−0.635
	550	−0.667

[a] Extrapolated from data at higher temperatures.
[b] Calculated from experimental data.

Table II. Temperature dependence of apparent standard potentials

Cell	Temperature range, °C	$\Delta E°'/\Delta T$, volts per degree
Zr | Zr(II) || Ag(I) | Ag	550-600	1.2×10^{-4}
Hf | Hf(IV) || Ag(I) | Ag	450-550	1.8×10^{-4}

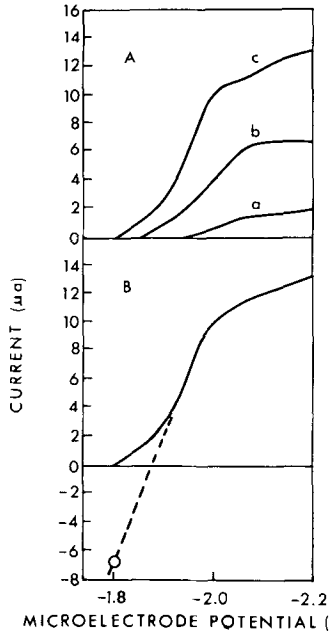

Fig. 1. Polarograms of Zr(IV) reduction in LiCl-KCl eutectic at 450°C.

A. Pt(II)/Pt(O) reference electrode, 2.26 x 10^{-3} mole fraction of Pt(II); 0.85 mm² microelectrode. (a) 0.42 x 10^{-4} mole fraction Zr(IV). (b) 1.25 x 10^{-4} mole fraction Zr(IV). (c) 1.67 x 10^{-4} mole fraction Zr(IV).

B. Reverse of polarogram (c) (dotted line).

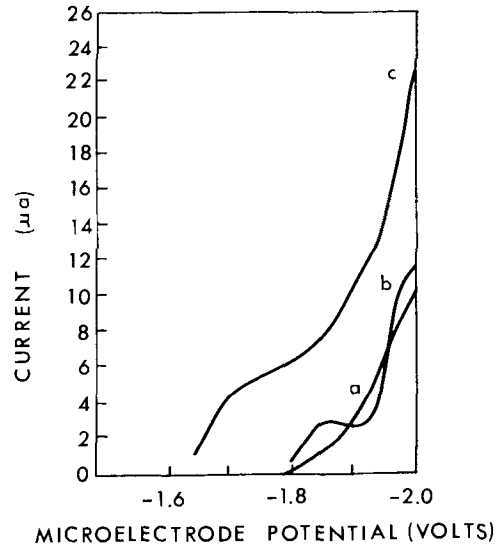

Fig. 2. Polarograms of zirconium solutions prepared by anodic dissolution at different temperatures *vs.* Pt(II)/Pt(O) reference electrode. (a) 450°C, 6.7 x 10^{-4} equivalent fraction of Zr, 2.26 x 10^{-6} mole fraction of Pt(II); 0.85 mm^2 microelectrode. (b) 500°C, 8.2 x 10^{-4} equivalent fraction of Zr, 2.22 x 10^{-3} mole fraction of Pt(II), 0.88 mm^2 microelectrode. (c) 550°C, 3.4 x 10^{-4} equivalent fraction of Zr, 1.34 x 10^{-3} mole fraction of Pt(II), 1.0 mm^2 microelectrode.

linear over this range against a Ag(I)/Ag(0) reference electrode, in Table II.

Polarograms at 450°, 500°, and 550°C showed only a single reduction wave, and no oxidation wave. Figure 3A shows examples at 450°C; those at higher temperatures were similar. Figure 3B shows the curve obtained when the direction of polarization of curve c was reversed (dotted line) but this quickly fell to nearly zero. As in the case of Zr(IV), plots of limiting current *vs.* concentration of Hf(IV) were approximately linear through the origin. The limiting current constants were 0.06, 0.08, and 0.11 amp/mm^2 per unit mole fraction at 450°, 500°, and 550°C, respectively. A plot of log i_d *vs.* $1/T$ (where i_d is the limiting current) was linear also, with a slope corresponding to an activation energy for diffusion of 7 kcal. This may be compared with a value of 10.1 kcal at 800°C in the NaCl-KCl melt reported by Baraboshkin *et al.* (6).

Polarograms at solid microelectrodes may be expected to fit either the Kolthoff-Lingane equation if the reduced metal forms a deposit on the electrode surface, or the Heyrovsky-Ilkovic equation if it alloys with the electrode material. The former predicts a linear relation between the microelectrode potential E_{me} and log $(i_d - i)$, while the latter predicts a linear plot of E_{me} *vs.* log $i/i_d - i$. Here, i is the current on any part of the wave. As shown in Fig. 4, the data for the reduction of Zr(IV) at 450°C, and Hf(IV) at 450°, 500°, and 550°C, fit the Heyrovsky-Ilkovic plot fairly well. The Kolthoff-Lingane plots showed much greater curvature. The slopes observed were: curve (a), 0.040v; curve (b), 0.040v; curve (c) 0.044v; and curve (d), 0.047v. The calculated slopes are 0.036v, 0.036v, 0.038v, and 0.041v. The implication that alloy formation is taking place is supported by the observation that not all the deposited metal could be stripped from the electrode when the current was reversed. The current approached zero before sufficient coulombs had passed to account for the amount of metal deposited originally. However, in the absence of other information, the case is not proved (10).

Discussion

Results of polarographic and potentiometric measurements indicate that Zr(IV) is the stable species in this melt at 450°C. The free energy change and equilibrium constant for the reaction

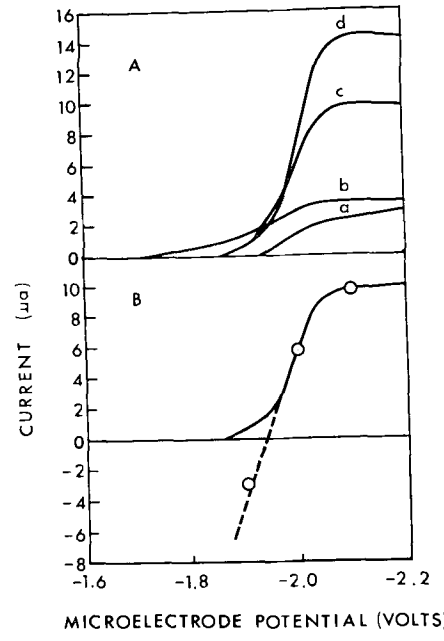

Fig. 3. Polarograms of Hf(IV) reduction in LiCl-KCl eutectic at 450°C.

A. Pt(II)/Pt(O) reference electrode, 0.88 mm^2 microelectrode. (a) 0.44 x 10^{-4} mole fraction of Hf(IV). (b) 0.87 x 10^{-4} mole fraction of Hf(IV). (c) 1.96 x 10^{-4} mole fraction of Hf(IV). (d) 2.61 x 10^{-4} mole fraction of Hf(IV).

B. Reverse of polarogram (c) (dotted line).

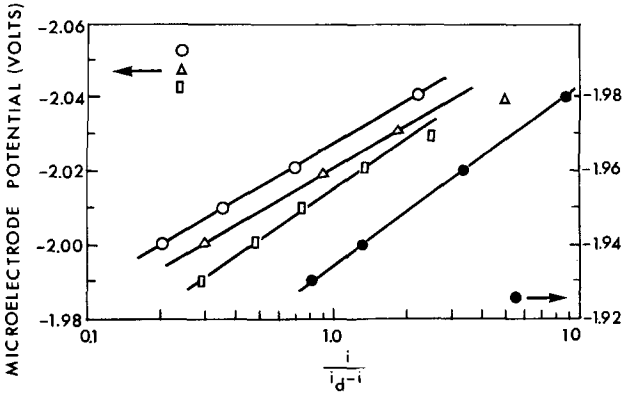

Fig. 4. Plots of log $\frac{i}{i_d - i}$ *vs.* microelectrode potential for Zr(IV) and Hf(IV) reduction in LiCl-KCl eutectic. From left; (b) Hf(IV) at 450°C; (c) Hf(IV) at 500°C; (d) Hf(IV) at 550°C; and (a) Zr(IV) at 450°C.

$$Zr + Zr(IV) \rightleftarrows 2Zr(II) \qquad [1]$$

(in 10^{-5} mole fraction solutions, extrapolated to unit mole fraction) are +9.2 kcal and 1.6 x 10^{-3}, respectively, as calculated from our data. Thus the equilibrium lies to the left at this temperature. The activity coefficient calculated for this solute, utilizing the data of Hamer *et al.* (11), is 9.6 x 10^{-6} (Table III), in agreement with that estimated by Yang *et al.* (1), 10^{-5} to 10^{-6}. This very small value, and the value of the partial molal free energy in Table III, may be interpreted as indicating a high degree of complexing of Zr(IV) in this melt.

At 550°C, Zr(II) is the predominant species produced by anodic dissolution under our conditions. This is indicated by the Nernst plot and the polarographic waves. The first reduction wave at this temperature may be attributed to reduction of the small amount of Zr(IV) in the melt to Zr(II), and the second, larger

Table III. Activity coefficients and partial molal free energies of solutions of metal chlorides in the LiCl-KCl eutectic

Compound	Range of concentration, mole fraction × 10^6	Activity coefficient 450°C	Activity coefficient 550°C	ΔG_s (kcal/mole) 450°C	ΔG_s (kcal/mole) 550°C
$ZrCl_2$	5-50	6.4×10^7	3.1×10^6	+25.7	+24.4
$ZrCl_4$	3-25	9.6×10^{-6}		−16.5	
$HfCl_4$	3-25	24.8	3.1	+4.60	+1.84

wave to reduction of Zr(II) to the metal. These waves were always observed, although their forms were often indistinct. With time, when solutions of higher concentration were used, $ZrCl_4$ could be detected in the argon gas used for stirring, and finely divided zirconium metal appeared in the melt. Evidently Zr(II) disproportionates according to the reverse of reaction [1] above, as it does at higher temperatures in KCl-NaCl (3).

No evidence was found for the existence of a Zr(III) species in this melt. This is in accord with the work of Larson and Leddy (12) on the pure zirconium chlorides, which showed that the equilibrium for the reaction

$$3Zr(III) \rightleftarrows 2Zr(IV) + Zr(0) \qquad [2]$$

lies far to the right at 450°C.

In contrast to the zirconium system, hafnium yielded only Hf(IV) in this melt over the temperature range investigated.

While the activity coefficient for Zr(IV) is very small, the activity coefficients of Zr(II) and Hf(IV) are greater than unity (Table III). Their validity of course depends on the correctness of the free energies of formation of the pure chlorides from which the standard electrode potentials were calculated (11). It does not follow that Zr(II) and Hf(IV) are not complexed in the melt. Flengas and Ingraham (13) have interpreted the activity coefficients of Cr(II) and Sn(II) in KCl-NaCl melts, which were also greater than unity, in terms of a "bond-loosening" effect. If the pure chlorides were composed of more complicated species which break up on dissolution in the melt, an activity coefficient greater than unity could be accounted for in an analogous manner.

Acknowledgment

We wish to thank Mr. Eugene A. Grossi for technical assistance, and the United States Atomic Energy Commission for financial support under Contract No. At(30-1)-2787.

Manuscript received May 28, 1965; revised manuscript received Aug. 31, 1965.

Any discussion of this paper will appear in a Discussion Section to be published in the June 1966 JOURNAL.

REFERENCES

1. L. Yang, R. G. Hudson, and C. Y. Chien, "The Physical Chemistry of Process Metallurgy," vol. 2, p. 925, Interscience Publishers, New York (1961).
2. L. Yang and R. G. Hudson, *Trans. Met. Soc. AIME*, **215**, 589 (1959).
3. D. Inman, G. J. Hills, L. Young, and J. O'M. Bockris, *Ann. N. Y. Acad. Sci.*, **79**, 803 (1960).
4. T. N. Grechina and U. T. Barchuk, *Ukrain. Khem. Zhur.*, **29**, 722 (1963).
5. M. V. Smirnov, V. E. Komarov, and A. N. Baraboshkin, *Fiz. Khim. Rasplavlen. Sobi i Shlakov, Akad. Nauk SSSR, Ural'sk. Filial, Inst. Elektrokhim., Tr. Vses. Soveshch., Sverdlovsk,* **353** (1962); *Chem. Abstr.*, **58**, 5261 (1963).
6. A. N. Baraboshkin, M. V. Smirnov, and N. A. Saltykova, "Proceedings of the All Union Conference on Physical Chemistry of Molten Salts and Slags," Nov. 1960; AEC-Tr-5948, p. 370.
7. S. N. Flengas and T. R. Ingraham, *Can. J. Chem.*, **35**, 1139 (1957).
8. J. B. Raynor, *Z. Elektrochem.*, **67**, 360 (1963).
9. R. Baboian, D. L. Hill, and R. A. Bailey, *Can. J. Chem.*, **43**, 197 (1965).
10. H. A. Laitinen and R. A. Osteryoung, "Fused Salts," B. R. Sundheim, Editor, chap. 4, McGraw-Hill Book Co., Inc., New York (1964).
11. W. H. Hamer, M. S. Malmberg, and R. Rubin, *This Journal*, **103**, 8 (1956).
12. E. M. Larson and J. J. Leddy, *J. Am. Chem. Soc.*, **78**, 5983 (1956).
13. S. N. Flengas and T. R. Ingraham, *This Journal*, **106**, 714 (1959).

A New Class of Molten Salt Mixtures
The Hydrated Dipositive Ion as an Independent Cation Species

C. Austen Angell[1]

Argonne National Laboratory, Argonne, Illinois

ABSTRACT

On the basis of solubility and electrical conductance measurements, a new class of molten salt mixtures involving hydrated multivalent cations as independent cation species is proposed. It is shown that these ions confer essentially the same properties on the solutions as expected theoretically from hard sphere cations of the same charge:radius ratio. The solutions are of considerable potential interest since they have especially low liquidus temperatures for molten salt systems and, as a result, are frequently glass forming. The investigation of ionic liquid behavior at low free volumes (high densities) should, therefore, be possible in a variety of systems. By way of an example, KNO_3 is found to dissolve to the extent of some 70 mol % at 100°C in the "hydrate melt" $Ca(NO_3)_2 \cdot 4H_2O$. The application of free volume transport theory equations to the analysis of electrical conductance data for this system produces striking correlations with electrical conductance behavior in the anhydrous system $Ca(NO_3)_2 + KNO_3$.

Following an account of electrical conductance in the $Mg(NO_3)_2 + H_2O$ system at very high concentrations, it has recently been suggested (1) that aqueous solutions of polyvalent ions in which the water content is insufficient to satisfy more than a first co-ordination sheath for the cation, may most profitably be regarded as molten salts of weak field cations, $M(H_2O)_n^{m+}$. By treating this species as a hard sphere

[1] On leave from Department of Metallurgy, University of Melbourne, Australia.

dipositive ion of radius ($r_{M2+} + 2r_{H_2O}$) it was found that the electrical conductance of these melts could be correlated with that in water-free molten salt systems. The usefulness of this concept was supported by its application in finding tetrahedral $NiCl_4^=$, *i.e.*, 4-coordinated Ni^{++} in aqueous systems for the first time (2).

Extending this idea, it would be expected that "hydrate melts"[2] will dissolve other (unhydrated) salts, in the same way that ordinary molten salts usually dissolve one another. So far we find this to be the case, *e.g.*, KNO_3 whose saturation solubility in water at 100°C corresponds to an 11M (30 mol %) solution, will dissolve in molten $Ca(NO_3)_2 \cdot 4H_2O$, mp 42.7°C, [which is already a 7.2M (20 mol %) solution] to the extent of about 68 mol % at 100°C. Some brief observations on other solutions of this class are noted below.[3] It will be apparent that because of their low liquidus temperatures, these systems may be of considerable value in permitting physicochemical investigations of molten salt behavior in a temperature range otherwise not readily accessible. In this short paper an attempt is made to establish the over-all validity of this view of the aqueous liquids by showing that electrical conductance in the system $Ca(NO_3)_2 \cdot 4H_2O + KNO_3$ is completely analogous to that in other mixed molten salt systems. This particular system is a logical choice for initial study since its anhydrous salt analogue $Ca(NO_3)_2 + KNO_3$ has been studied in some detail (3-5), and the electrical conductance of molten $Ca(NO_3)_2 \cdot 4H_2O$ has recently been measured (1).

We have already reported that electrical transport in molten hydrated Ca^{+2} and Mg^{+2} nitrates is exponentially dependent on $1/(T - T_o)$ in formal accord with the free volume model general equation for conductance (5)

$$\Lambda = AT^{1/2} \exp\left(-\frac{k}{T - T_o}\right) \qquad [1]$$

where Λ is the equivalent conductance, T_o is the theoretical glass transition, or zero free volume, temperature (6), and A and k are constants. The values of k found for the hydrate melts were virtually the same as the value, 690°K, for the molten salt system $Ca(NO_3)_2 + KNO_3$. The same value of k may, therefore, be anticipated for the mixed molten salt-hydrate melt mixtures. Furthermore, since the T_o value for molten KNO_3 (by extrapolation) is greater than the experimental value for $Ca(NO_3)_2 \cdot 4H_2O$ (1), then in the mixed nitrate-hydrate melt T_o should increase with KNO_3 content if the mixed system behaves like a normal molten salt mixture. T_o, which seems to be determined by the electrostatic field strengths of the ions, would thus vary in the opposite manner with KNO_3 content to that in the anhydrous system $Ca(NO_3)_2$-KNO_3. Such a variation of T_o would cause the "activation energy" at a given temperature to increase with KNO_3 content.

[2] For convenience, we will adopt the term "hydrate melts" for a class of molten salts involving independent hydrated cations as constituent species.

[3] *Some General Comments on Hydrate Melts*

1. *Chlorides.*—Molten $MgCl_2 \cdot 6H_2O$ (14.3 mol % $MgCl_2$ or 7.2M at 83.5°C) dissolves considerable amounts of LiCl (saturated solution in H_2O at 100°C = 35 mol % LiCl or ≈ 18M) and somewhat smaller amounts of KCl. As in pure molten $MgCl_2$-$6H_2O$, additions of $NiCl_2$ to this liquid produce blue solutions due to $NiCl_4^=$, *i.e.*, to 4-coordinated Ni^{++}, when hot, changing to yellow on cooling, apparently due to $NiCl_6^=$ or 6-coordinated Ni, through a tetrahedral → octahedral coordination change. Of possible value is the observation that the organic salt, pyridinium chloride, is completely miscible with $MgCl_2 \cdot 4$-$5H_2O$, most compositions being glass forming.

2. *Chloride-nitrates.*—$CaCl_2$ and $MgCl_2$ hydrate melts are completely miscible with the corresponding hydrate nitrates. Where the pure chloride hydrates crystallize on cooling at normal rates, the mixtures with hydrate nitrates generally yield stable viscous liquids at ambient temperatures, and glasses on cooling to lower temperatures, *e.g.*, in liquid nitrogen.

3. *Nitrates.*—The molten hydrate nitrates of Mg and Ca dissolve each and all of the alkali nitrates. In each system there appear to be composition ranges which are glass forming, these presumably corresponding approximately with eutectic regions in the (undetermined) phase diagrams.

Experimental

A. R. grade $Ca(NO_3)_2 \cdot 4H_2O$ was carefully fused without loss of water, and filtered into a Pyrex glass conductance vessel. The latter was seated in the cork of a 1 liter Dewar flask. When filled with water or paraffin at the desired temperature, the Dewar flask restricted the temperature fall rate in the immersed conductance vessel to about 2°C per hour. This rate of change was quite insufficient to affect adversely the accuracy required for the present survey. The temperature of the melt was measured by a precision mercury thermometer and was checked by a fine gauge Cr/Al thermocouple fixed alongside the conductance cell.

The resistances of the melts were measured using a silica dip-type cell (cell constant = 61.85) with platinized electrodes, in conjunction with an Industrial Instruments Inc. Model RC 18 precision conductance bridge. The resistance was measured at 3 kc and 1 kc, but calculations were based on the 3 kc readings since, provided the cell resistance was greater than 1000 ohms, the polarization errors were not sufficient to affect the results plotted in the accompanying graphs, Fig. 1 and 2, detectably.

Composition changes were made by weighed additions of A. R. grade KNO_3, which was used without further purification.

Results

The specific conductances, κ, of the solutions in this system are given in Table I and are shown as a function of composition in the isotherms of Fig. 1 (i). Because of the very low values of conductances recorded in this system at low temperatures a logarithmic scale has been employed in Fig. 1(i) so that the reversal of the composition dependence will be apparent. For a given composition, the "Arrhenius coefficients" (5),

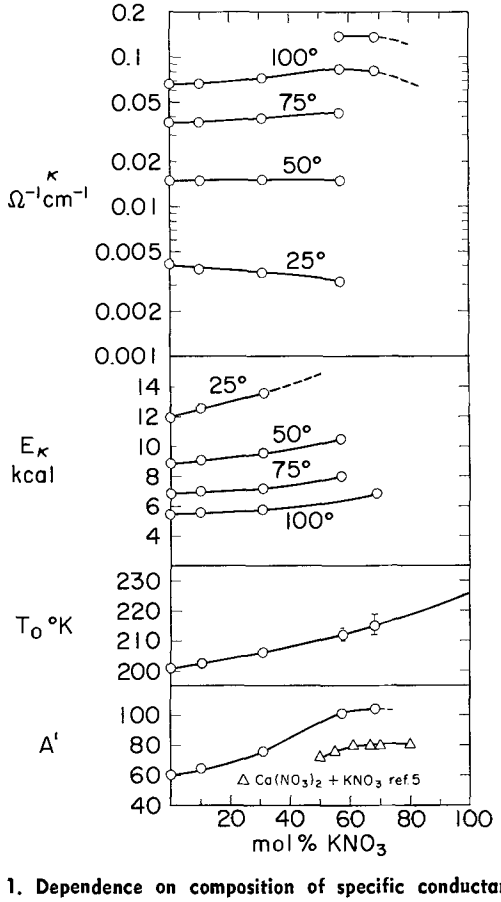

Fig. 1. Dependence on composition of specific conductance, κ, Arrhenius coefficient, E_κ, theoretical glass transition temperature, T_o, and pre-exponential constant, A', in the system $Ca(NO_3)_2 \cdot 4H_2O + KNO_3$.

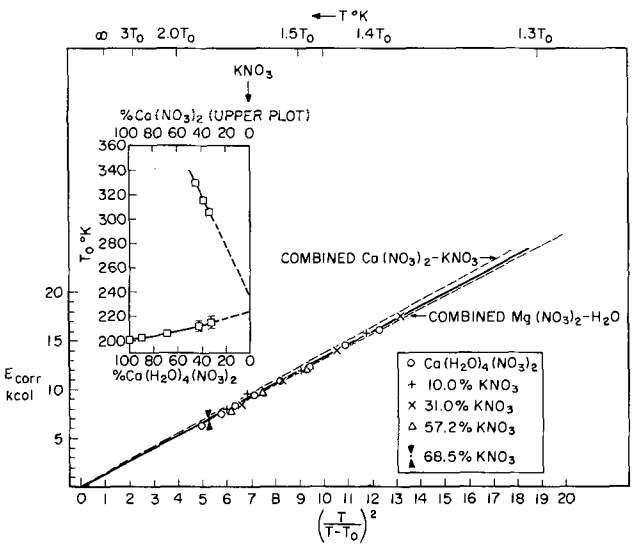

Figure 2. Test of free volume model predictions for the system $Ca(NO_3)_2 \cdot 4H_2O$ + KNO_3, and comparison with other systems. Inset: best fit values of T_o as function of composition for $Ca(NO_3)_2 \cdot 4H_2O$ + KNO_3, and $Ca(NO_3)_2$ + KNO_3 systems.

i.e., "activation energies" E_K, increase rapidly with falling temperature in a manner which has been described in previous publications (5, 1), and which we interpret as due to the probability of ionic movement going to zero at T_o rather than at 0°K as required by the Arrhenius, or other rate process theory, equations. The behavior of the "Arrhenius coefficients" with temperature and composition is summarized in Fig. 1 (ii), where it is seen that at a given temperature the "Arrhenius coefficients" increase with increasing KNO_3 contents as anticipated.

Unfortunately, due to the combination of low temperatures and low conductances in this system, measurements were ceased before E_K reached values as high as were realized in the systems previously studied. As a result, the constants k and T_o of Eq. [1] are in principle more difficult to determine precisely by the graphical method previously employed, since the plot E_{cor} *vs.* $(T/T - T_o)^2$ whose linearity depends on the correct choice of T_o, loses sensitivity to T_o at lower E_{cor} values. This loss of sensitivity was compensated to some extent by an improvement in precision in the measurements, and the value of T_o for $Ca(NO_3)_2 \cdot 4H_2O$ [4] is considered correct to ± 3°K. For the other compositions we have adopted a treatment of results which involved taking the plot for pure $Ca(NO_3)_2 \cdot 4H_2O$ as a reference and making the assumption, based on the similar slopes of these plots for $Mg(NO_3)_2$-H_2O and $Ca(NO_3)_2$-KNO_3 solutions (see Fig. 2), that the other compositions in the present system would have the same value of k. The values of T_o then required to fit the E_{cor} values on the $Ca(NO_3)_2 \cdot 4H_2O$ line were determined for each composition and the validity of the treatment judged by both the degree of fit over the whole T/T_o range, and the behavior of the T_o values with composition. These data are shown in Fig. 2. It seems clear that the assumption of constant k is justified at least up to 31% KNO_3, and, from the continuing regular change of T_o with composition, it is most probably valid at the other compositions. This is consistent with the finding that k for the pure $Ca(NO_3)_2 \cdot 4H_2O$ melt is the same as for the $Mg(NO_3)_2$-H_2O series and about the same as for the anhydrous system KNO_3 + $Ca(NO_3)_2$.

[4] In view of the present finding this composition could be written more informatively as $Ca(H_2O)_4 \cdot (NO_3)_2$ as in the diagrams.

Table I. Specific conductances of solutions

T°C	κ ohm^{-1}cm^{-1}	T°C	κ ohm^{-1}cm^{-1}
$Ca(NO_3)_2 \cdot 4H_2O$		$Ca(NO_3)_2 \cdot 4H_2O$ + 31.0% KNO_3	
96.4	0.0619_0	92.1	0.0612_4
87.4	0.0505_7	75.4	0.0394_4
76.4	0.0382_6	52.4	0.0173_4
66.8	0.0287_1	34.2	0.00666
54.8	0.0187_3	15.0	0.00151_1
41.4	0.0103_8	7.8	0.000698
29.4	0.00535_6		
20.4	0.00289_9	$Ca(NO_3)_2 \cdot 4H_2O$ + 57.2% KNO_3	
10.6	0.00125_6	93.2	0.0716_4
5.8	0.000774	70.2	0.0368_0
$Ca(NO_3)_2 \cdot 4H_2O$ + 10.0% KNO_3		50.5	0.0161_7
		33.7	0.00591
78.7	0.0402_5	$Ca(NO_3)_2 \cdot 4H_2O$ + 68.5% KNO_3	
59.6	0.0216_6		
40.5	0.00937	123.7	0.133_8
17.8	0.00214_0	118.5	0.120_1
10.9	0.00111_7	113.6	0.109_9
		108.0	0.0965
		102.0	0.0837

Discussion

Figures 1 and 2 show that the temperature dependence of conductivity in this system is in complete qualitative accord with the expectations based on the notion that the average cation field strength in the mixtures rises in a regular manner with KNO_3 additions, as K^+ ions ($z_+/r_+ = 0.75$), mix with $Ca(H_2O)_4^{++}$ ions ($z_+/r_+ = 0.53$),[5] *i.e.*, that the hydrated calcium nitrate behaves like a molten salt of a weak field cation. There is a quantitative discrepancy in that the T_o values determined for the present system seem to extrapolate to a value of 225° ± 5°K for pure KNO_3 whereas extrapolation from the data in the anhydrous system $Ca(NO_3)_2$+ KNO_3 indicated T_o = 237° ± 12°K. A comparison of these two sets of data is given in Fig. 2, inset. When the length, and consequent uncertainty, of the latter extrapolation is considered, a discrepancy is not too surprising, and the fact that the same value is approached this closely from opposite directions is enough to give considerable confidence in the general validity of the theoretical approach used in the analysis of these results.

One observes also (Fig. 2) that the application of Eq. [1] has reduced almost to a single straight line plot so-called "activation energies" for conductance varying from 3.5 to 30 kcal in the range 0°-350°C in three different systems whose only common feature is the nitrate anion. This is an impressive correlation.[6a]

While recognizing the danger of circular arguments, the author believes that the general coherence of these observations not only supports the claim that the hydrate melts are no less than molten salts in their important properties,[7] but also indicates the potential usefulness of binary systems with hydrate components, such as the present system, to explore free volume-

[5] The effective radius of the H_2O molecule employed in the estimation of r_- is the generally accepted value of 1.39Å.

[6] Note that the correlation applies only to the slope of the Arrhenius plot, the factor A of Eq. [1] having been eliminated by the logarithmic differentiation. We are thus using two parameters, K and T_o, to describe and unify E_K *vs.* T curves for the form of Fig. 1, ref. 5a, Figure 2 of this paper shows that these curves are all of the family derived from $E_{corr} = K\left(\frac{T}{T - T_o}\right)^2$, which can be written more informatively as $(E_A + \frac{1}{2}RT)^{1/2} = K/(1 - T_o/T)$. Since k seems to have a constant value, this equation indicates that $E_A + RT$ (representing $E_{diffusion}$) depends only on T/T_o, at least for $T/T_o \gtrsim 2$ (5b). The suggestion of a corresponding temperature scale is therefore strong.

[6a] *Note Added in Proof*: A new and attractive theory by Adam and Gibbs (*J. Chem. Phys.*, 43, 139, 1965), which suggests that configurational entropy rather than free volume is transport limiting, provides an alternative explanation of Eq. [1]) ($S_c \to 0$ at $T = T_o$). From the Adam-Gibbs equations it is possible to show that the corresponding temperatures T/T_o (see footnote 6), represent liquid states of equal configurational entropy (suggesting the term "isoentropic states"). To a large extent comments in the present paper on free volume effects can be rephrased in terms of entropy effects without loss of meaning. The quantities concerned should, in fact, be quite closely related.

[7] A discussion of whether or not water at these compositions should be considered completely "bound," is given in a separate publication (1).

determined properties of ionic liquids. We now consider that the high viscosities frequently reported for concentrated aqueous solutions are in general a direct consequence of the reduced free volume in the liquid due to the combination of moderately high charge concentration (and hence T_o) and very low liquidus temperatures.

Because of the long relaxation times for ionic movement, this condition obviously favors glass formation by reducing the probability of nucleation of the crystalline phase during cooling at a given rate. Generally, however, low mobilities due to reduced free volumes will not in themselves be a sufficient condition for glass formation except at extreme quenching rates. A proposal such as that of Urnes (4a) [whose work on the $Ca(NO_3)_2$-KNO_3 system we overlooked in an earlier publication (5)] that the thermal energy at very low temperatures is not sufficient to raise the ions from potential energy minima in the liquid to regroup as crystal nuclei, seems a more acceptable explanation than the chain and network schemes frequently invoked to explain glass formation.[8] Whatever the precise explanation may be, it seems that a large variety of aqueous glasses should exist, some of which may have interesting properties. Mostly, however, the glass transition for these liquids will lie below room temperature.

We have, as yet, no clear idea of why the constant, k, in the exponential of Eq. [1] (*i.e.*, the slope of Fig. 2 x $1/R$) should have almost the same value, 675° ± 15°K, in the three very different systems so far examined in detail (and summarized in Fig. 2). According to Cohen and Turnbull (7) k should be inversely proportional to the expansion coefficient with a proportionality constant of 0.5-1.0 depending on free volume overlap. As seen previously (5), for molten salts k proves to be too small to support the Cohen and Turnbull assumption that the free volume is randomly distributed. Ion-sized holes are apparently much more common than would be expected. If the as-yet-undetermined expansion coefficients of the hydrate melts have about the same value as in the $Ca(NO_3)_2$-KNO_3 melts, then the constant value of k will indicate a rather specific pattern in the distribution of hole sizes in these liquids. On the other hand, if the expansion coefficient increases as the charge concentration decreases, as indicated by a study of the system K, Na, NO_3, NO_2 eutectic + 0-70 mol % H_2O (8), then the constant value of k would indicate that the volume randomness increases proportionately with decrease in binding strength, which would seem reasonable.[8a] The key to this problem may well be in the suggestion of Gruen (9) for the case of the alkali chlorides that the local structure in fused salts is determined by a mobile equilibrium between tetrahedral and octahedral coordination schemes. Such an arrangement could impose considerable uniformity both on the hole size distribution and on the manner in which "diffusion sites" in the liquid or "critical voids" are presented to potential "jumping" ions. The tendency to maintain such electrostatically favored symmetry groups would naturally become less as the coulombic interactions decreased in intensity[9] with, for instance, increasing water content; thus an increasingly random free volume distribution would result.

The behavior of the pre-exponential constant, A, in this system, and particularly the proximity of its value to that found in the anhydrous $Ca(NO_3)_2$-KNO_3 system [Fig. 1(iv)],[10] are not easy to interpret. The slopes of both plots increase when allowance is made for the double charge on the Ca-containing species. The fact that the constants A and k are much the same in the complete absence of the KNO_3 component seems to rule out the possibility (5) that it is a single species (K^+) which determines the conductance behavior in each case.

The reversal of the composition dependence of the isothermal conductance at lower temperatures, Fig. 1 (i), is due to the opposing effects of A and T_o. While the temperature is well above T_o, E_κ changes little with composition, and the increase of A with KNO_3 content leads to a similar dependence of κ. As the temperature falls toward T_o, however, the form of Eq. [1] requires that the exponential term becomes rapidly predominant, so that at low temperature the direction of the T_o change with increasing KNO_3 content imposes a steady decrease on the isothermal conductance.

We conclude that, although there are difficulties in accounting for the values of the constants A and k, the correlations resulting from the use of Eq. [1] in the analysis of conductance data are very significant and indicate that the overlap region between molten salts and polar solvents in general, may prove an interesting field for investigation. In particular it seems that the expansion coefficients of these liquids deserve more systematic study than they have received in the past.

Acknowledgments

Thanks are due to Dr. Dieter M. Gruen of this laboratory for interesting discussions of different aspects of this work. This paper is based on work performed under the auspices of the United States Atomic Energy Commission.

Manuscript received June 10, 1965; revised manuscript received Aug. 16, 1965.

Any discussion of this paper will appear in a Discussion Section to be published in the June 1966 JOURNAL.

REFERENCES

1. C. A. Angell, in press; preliminary report *J. Phys. Chem.*, **69**, 2137 (1965).
2. C. A. Angell and D. M. Gruen, To be published.
3. A. Dietzel and H. J. Poegel, Proceedings of the Third International Glass Congress, Venice, Italy, 1953, p. 219.
4. (*a*) S. Urnes, *Glastechnische Ber.*, **31**, 337 (1958); (*b*) O. Borgen, K. Grjotheim, and S. Urnes, *ibid.*, **33**, 52 (1960); (*c*) S. Urnes, *ibid.*, **34**, 213 (1961).
5. (*a*) C. A. Angell, *J. Phys. Chem.*, **68**, 218 (1964); (*b*) C. A. Angell, *ibid.*, p. 1917.
6. D. Turnbull, *Trans. AIME*, **221**, 422 (1961).
7. M. H. Cohen and D. Turnbull, *J. Chem. Phys.*, **31**, 1164, (1959).
8. C. A. Angell, R. C. Gifkins, and J. A. Corbett, To be published.
9. D. M. Gruen, *J. Chem. Phys.*, **41**, 2569 (1964).
10. C. A. Angell and D. M. Gruen, *J. Chem. Ed.*, In press.

[8] Although it may appear obvious, it is worth re-stating that an explanation of glass formation should focus attention on the failure to crystallize rather than on the resulting amorphous solid. From the present model, rigidity, *i.e.*, glassiness, follows inevitably on the effective disappearance of free volume, which must occur somewhat before the continued contraction of the liquid can produce a close-packed structure [see, e.g., Turnbull, (6)].

[8a] *Note Added in Proof:* Expansion coefficients for liquid $Ca(NO_3)_2 \cdot 4H_2O$ and $Mg(NO_3)_2 \cdot 4H_2O$ by recent measurements are 5.1×10^{-4} and 5.2×10^{-4} at 100°C, respectively [c.f. the smaller value of 3.5×10^{-4} at 100°C for liquid 38% $Ca(NO_3)_2 \cdot 62\%$ KNO_3 (3)].

[9] This is seen, for example, in the two-dimensional magnetic disk ionic liquid model, described by Angell and Gruen (10).

[10] The quantity plotted in Fig. 1 differs from A of Eq. [1] in that it is calculated from specific conductance rather than from equivalent conductance values.

The Theoretical Effect of Electrode Ohmic Losses on the Performance of Diffusion Membrane Electrodes

Ralph Brown

Pratt & Whitney Aircraft, East Hartford, Connecticut

ABSTRACT

Ohmic losses in diffusion membrane electrodes can be significant because current is distributed over the membrane area and must be collected through contacts having considerably smaller area. Explicit mathematical expressions for the ohmic distribution in the electrode, the local current density distribution, and the current-polarization characteristic can be obtained if there is a linear relationship between the local current density and local metal-solution potential difference. A discussion of the kinetics of hydrogen diffusion anodes considers under which conditions the linear approximation is valid. The approximation can apply to each the gas adsorption controlling, diffusion controlling, and electron transfer controlling cases. Three membrane geometries are considered: a hollow tube with external contact at one end, a circular membrane with external contacts around the periphery, and a rectangular membrane with external contacts at the edges. One example shows that ohmic losses in a 10 cm long, 0.005 cm thick tubular membrane will triple the polarization when compared to a membrane with no ohmic losses.

In certain fuel cell electrodes, the ohmic losses in the electrode can be the same order of magnitude as the metal-solution potential. This is particularly true for hydrogen diffusion anodes. In this case the current is distributed over a thin palladium membrane or tube and is collected at the edge of the electrode where the cross-sectional area is relatively small.

There has been some previous work on similar problems in the study of electrolytic cells (1, 2). The problem has also been investigated in reference to a thin wire or tube in contact with an external circuit at one or both ends (3, 4). In the present work, the current distribution and ohmic distribution in both tubes and membranes of various geometries are investigated. Although the analytical solutions consider approximations which are of practical value when applied to the kinetics of hydrogen diffusion anodes, these approximations apply also to a variety of other cases. The effect of electrode ohmic losses are shown by comparing current-polarization characteristics with zero and finite electrode resistivities.

Model.—The model shown in Fig. 1 is for the one-dimensional case of a tubular membrane connected with an external circuit at one end. The external circuit is connected at $x = 0$ to a tube of length L, diameter D, and thickness δ. Consider the current in the tube J, going in the negative x direction. This is related to the local current density on the membrane by taking a balance about an element Δx.

$$\frac{dJ}{dx} = \pi D i \qquad [1]$$

The current in the tube is also related to the ohmic potential, ϕ, in the x direction. This is simply Ohm's law with the conductivity of the metal specified by σ.

$$J = -\pi D \delta \sigma \frac{d\phi}{dx} \qquad [2]$$

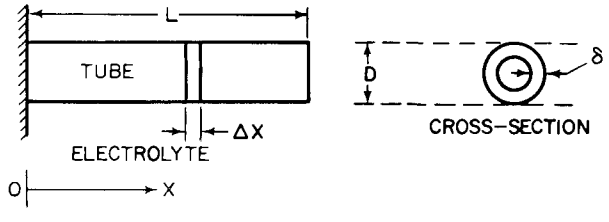

Fig. 1. Model of one dimensional case of tubular membrane

Equation [2] is differentiated with respect to x and substituted into Eq. [1] to obtain a second order differential equation in ϕ.

$$-\delta\sigma \frac{d^2\phi}{dx^2} = i \qquad [3]$$

The electrode is considered to be at a polarization from open circuit of E. If the conductivity of the electrolyte is sufficiently high, the potential in the electrolyte is constant in the x direction. This means that the solution potential can be chosen at zero, and the difference between the metal potential and solution potential at any point is $E - \phi$. The local current density at any point is a function of this local metal-solution potential difference, the specific function being defined by the kinetics of the electrochemical reaction.

$$i = \text{function } [E-\phi] \qquad [4]$$

A boundary condition is given at the connection to the external circuit.

$$x = 0, \quad \phi = 0 \qquad [5]$$

Since there is no current generated beyond the location x_o where ϕ is large enough so that the local current becomes zero, the other boundary condition is

$$x = x_o, \frac{d\phi}{dx} = 0 \qquad [6]$$

The value of x_o will depend on the functional dependence of the local current density on the local metal-solution potential difference, $E-\phi$. If this is a linear dependence, an integration of Eq. [3] will show that x_o is infinite. This means that the value of x_o is given simply by the geometric limitation such as that for the tube, $x_o = L$.

The ohmic distribution, current distribution, and tube current can be found by solution of the differential Eq. [3] if we have knowledge of the kinetics-dependent function in Eq. [4]. Whether or not an analytic solution can be found depends on the specific function. The statement of the problem can be generalized to the two-dimensional membrane.

$$-\delta\sigma\left(\frac{d^2\phi}{dx^2} + \frac{d^2\phi}{dy^2}\right) = \text{function } [E-\phi] \qquad [7]$$

Specific locations for the boundary conditions would depend on the geometry. The boundary conditions

would be $\phi = 0$ at external contacts to the membrane, and

$$\frac{d\phi}{dx} = \frac{d\phi}{dy} = 0$$

at either the ends of the membrane or at the axes of symmetry.

Kinetic Approximations

Mathematically, the solutions to the equations are straight forward when there is a linear local current-potential relationship

$$i = k\,(E - \phi) \qquad [8]$$

These linear current-polarization characteristics are observed experimentally to high current densities when employing membranes at high temperatures (~200°C) and with adequate surface activations (5). This discussion of the reaction kinetics is intended to show these limits on the polarization to which this linear behavior can be expected.

The kinetic relations assume the following sequence of steps: (I) Dissociative adsorption of the hydrogen molecules at the gas-metal surface; (II) desorption of the hydrogen atoms from the gas-metal surface into the metal; (III) diffusion of the hydrogen atoms through the metal to the liquid-metal surface; (IV) adsorption of the hydrogen atoms onto the liquid-metal surface, and finally, (V) transfer of electrons from the hydrogen atoms at the liquid-metal surface.

In alkaline electrolytes, the reaction of the proton with a hydroxyl ion to form water also takes place. This additional step is generally rather fast so is assumed to have no effect on the kinetic relations. Dissociative adsorption and subsequent dissolution of hydrogen in its atomic form is assumed because hydrogen permeability through palladium-silver is proportional to the square root of hydrogen pressure if the surfaces are sufficiently active. A consistent adsorption model must be applied on both sides of the surface in order to maintain the square root dependence in the permeability *vs.* pressure function. Langmuir adsorption kinetics are assumed for the surface both with respect to the fluid and with respect to the bulk metal. The rate equations are as follows:

H_2 adsorption from gas

$$i = K_1P\,(1-\theta)^2 - K_2\theta^2 \qquad [I]$$

H desorption into solid

$$i = \alpha_1\theta - C\alpha_2\,(1-\theta) \qquad [II]$$

H diffusion through solid

$$i = I_D\,(C - C') \qquad [III]$$

H adsorption from solid

$$i = C'\,\beta_2\,(1-\theta') - \beta_1\theta' \qquad [IV]$$

Electron transfer

$$i = k_1\theta' e^{\frac{F(E-\phi)}{2R_oT}} - k_2(1-\theta')\,e^{-\frac{F(E-\phi)}{2R_oT}} \qquad [V]$$

The solid to surface desorption and adsorption reactions are fast so that Eq. [II] and [IV] are assumed to approximate their forms at equilibrium. The hydrogen atom concentrations can then be written in terms of surface coverages and the diffusion equation becomes:

$$i = I_D\frac{\alpha_1}{\alpha_2}\left(\frac{\theta}{1-\theta} - \frac{\beta_1\alpha_2}{\beta_2\alpha_1}\frac{\theta'}{1-\theta'}\right) \qquad [III']$$

At equilibrium, the currents are equal to zero so that θ can be written in terms of K_1P and K_2; and θ' can be written in terms of k_1 and k_2. In order that the equilibrium relationship between θ and θ' given by Eq. [III'] be consistent with the equilibrium values of θ and θ', some simple algebra shows that

$$\frac{\beta_1\alpha_2}{\beta_2\alpha_1} = \frac{k_1}{k_2}\sqrt{\frac{K_1P}{K_2}}$$

The result is substituted into the diffusion equation

$$i = I_D\frac{\alpha_1}{\alpha_2}\left(\frac{\theta}{1-\theta} - \frac{k_1}{k_2}\sqrt{\frac{K_1P}{K_2}}\frac{\theta'}{1-\theta'}\right) \qquad [III'']$$

The kinetic relation for the local current-polarization characteristic is now given in terms of three equations ([I], [III"], [V]) which express the current in terms of θ, θ', and $E - \phi$. The three equations in terms of these three parameters can be rearranged to give one equation for current in terms of $E - \phi$. The algebraic manipulations are not very tractable; for example, a cubic equation is involved when one equates [I] and [III"] in order to solve for θ in terms of θ'. The rate expressions for specific controlling mechanisms can be readily solved, however, by assuming the noncontrolling steps approximate their forms at equilibrium. The results are shown below:

(*A*) *Gas Adsorption Control*

(*i*) High initial coverage $K_1P >> K_2$

$$i = K_2\left[e^{\frac{F(E-\phi)}{R_oT}} - 1\right]$$

$$i \cong K_2\frac{F}{R_oT}(E-\phi) \quad \text{if} \quad E - \phi < \frac{R_oT}{F}$$

(*ii*) Low initial coverage

$$i = K_1P\left[1 - e^{\frac{-F(E-\phi)}{R_oT}}\right]$$

$$i \cong K_1P\frac{F}{R_oT}(E-\phi) \quad \text{if} \quad E - \phi < \frac{R_oT}{F}$$

(*B*) *Diffusion control*

$$i = I_D\sqrt{\frac{K_1P}{K_2}}\left[1 - e^{\frac{-F(E-\phi)}{R_oT}}\right]$$

$$i \cong I_D\sqrt{\frac{K_1P}{K_2}}\frac{F}{R_oT}(E-\phi) \quad \text{if} \quad E - \phi < \frac{R_oT}{F}$$

(*C*) *Activation (Electron Transfer) Control*

$$i = \frac{k_2}{1 + k_2/k_1}\left[e^{\frac{F(E-\phi)}{2R_oT}} - e^{\frac{-F(E-\phi)}{2R_oT}}\right]$$

$$i \cong \frac{k_2}{1 + k_2/k_1}\left[\frac{F}{R_oT}(E-\phi)\right] \quad \text{if} \quad E - \phi < \frac{R_oT}{F}$$

The results show that the linear current-potential expression can be written for the three possible controlling steps in the diffusion membrane. This is subject to satisfying the condition that $E - \phi < R_oT/F$. It has been pointed out that well activated membranes satisfy this condition at typical fuel cell operating current densities.

Hollow Tube with External Contact at One End

The differential equation is given by substituting the linear current-potential characteristic into Eq. [3].

$$\frac{d^2\phi}{dx^2} - \frac{k}{\delta\sigma}\phi = -\frac{k}{\delta\sigma}E \qquad [9]$$

This is a linear, second order equation with constant coefficients for which a solution can be written as a linear combination of hyperbolic sines and cosines. The boundary conditions of Eq. [5] and [6] are applied.

$$\phi = E[1 - \cosh \alpha x - \tanh \alpha L \sinh \alpha x] \quad [10]$$

where: $\alpha = \sqrt{k/\delta\sigma}$. This shows the variation of ohmic potential along the length of the electrode. Substitution of the ohmic relation into Eq. [8] gives the current distribution along the electrode.

$$i = kE(\cosh \alpha x - \tanh \alpha L \sinh \alpha x) \quad [11]$$

The total current from the electrode is given by either integrating the local current over x between 0 and L or by evaluating $\pi D\delta\sigma \frac{d\phi}{dx}$ at x equal to 0.

$$J = kE\left(\frac{\pi D}{\alpha} \tanh \alpha L\right) \quad [12]$$

In order to show the effect of the ohmic losses, the total current can be written as the fraction of the current obtained when there are negligible ohmic losses by dividing by $\pi DLkE$.

$$f = \frac{\tanh \alpha L}{\alpha L} \quad [13]$$

Circular Membrane with External Contacts at the Periphery

The differential equation can be solved most easily if written in cylindrical coordinates

$$\frac{d^2\phi}{dr^2} + \frac{1}{r}\frac{d\phi}{dr} - \frac{k\phi}{\delta\sigma} = -\frac{k}{\delta\sigma}E \quad [14]$$

The boundary conditions are

$$r = 0, \qquad \frac{d\phi}{dr} = 0$$

$$r = R, \qquad \phi = 0 \quad [15]$$

The solution to the equation can be written in terms of Bessel functions

$$\phi = E\left[1 - \frac{I_0(\alpha r)}{I_0(\alpha R)}\right] \quad [16]$$

The current distribution is

$$i = kE\left[\frac{I_0(\alpha r)}{I_0(\alpha R)}\right] \quad [17]$$

The fraction of the current obtained with a zero-resistance membrane is given by

$$f = \frac{2\pi R\delta\sigma}{\pi R^2 kE}\frac{d\phi}{dr}\bigg|_{r=R} \quad [18]$$

and

$$f = \frac{1}{\pi R^2 kE}\int_0^R 2\pi r i dr \quad [19]$$

$$f = \frac{2}{\alpha R}\frac{I_1(\alpha R)}{I_0(\alpha R)} \quad [20]$$

Rectangular Membrane with External Contacts at the Edges

A membrane is considered for which the dimensions are M and L. The differential equation is written in two dimensions

$$-\left(\frac{\partial^2\phi}{\partial x^2} + \frac{\partial^2\phi}{\partial y^2}\right) = \frac{k}{\delta\sigma}(E - \phi) \quad [21]$$

The geometric center of the membrane is chosen as the center of the coordinate axes so that one quadrant of the membrane is considered. The boundary conditions are shown on Fig. 2:

$$\phi(L/2,y) = 0 \quad [22a]$$

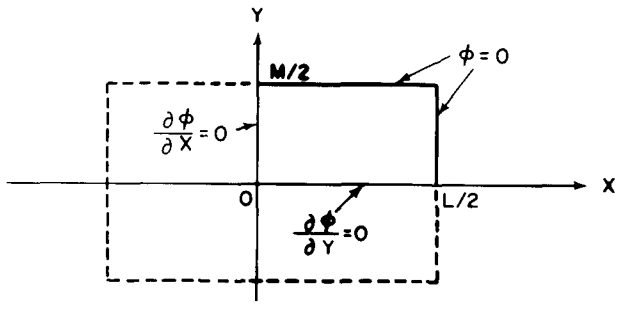

Fig. 2. Boundary conditions of membrane

$$\frac{\partial\phi}{\partial x}(0,y) = 0 \quad [22b]$$

$$\phi(x, M/2) = 0 \quad [23a]$$

$$\frac{\partial\phi}{\partial y}(x,0) = 0 \quad [23b]$$

A solution of the equation is assumed to be in the form

$$\phi(x,y) = \phi_x(x) + \phi_{xy}(x,y) \quad [24]$$

The x-dependent solution is given by solution of the ordinary differential equation in x with $\phi(L/2)$ and $d\phi/dx(0)$ equal to zero.

$$\phi_x = E\left(1 - \frac{\cosh \alpha x}{\cosh \alpha L/2}\right) \quad [25]$$

The result is substituted into the original differential equation to obtain an equation for ϕ_{xy}. The corresponding boundary conditions are also given.

$$\frac{\partial^2\phi_{xy}}{\partial x^2} + \frac{\partial^2\phi_{xy}}{\partial y^2} = \alpha^2\phi_{xy} \quad [26]$$

$$\phi_{xy}\left(\frac{L}{2}, y\right) = 0 \quad [27a]$$

$$\frac{\partial\phi_{xy}}{\partial x}(0,y) = 0 \quad [27b]$$

$$\frac{\partial\phi_{xy}}{\partial y}(x,0) = 0 \quad [27c]$$

By assuming that the solutions take the form of a product of a function of x and a function of y, and applying boundary conditions [27a], [27b], and [27c], the solutions can be written as an infinite series.

$$\phi_{xy} = \sum_{m=0}^{\infty} A_m \cos\left[\frac{2(m + \tfrac{1}{2})\pi x}{L}\right] \cosh\left[\sqrt{\alpha^2 + \frac{4\pi^2(m + \tfrac{1}{2})^2}{L^2}}\, y\right] \quad [28]$$

The complete solution for ϕ is

$$\phi = E\left(1 - \frac{\cosh \alpha x}{\cosh \alpha L/2}\right) + \sum_{m=0}^{\infty} A_m \cos\left[\frac{2(m + \tfrac{1}{2})\pi x}{L}\right] \cosh\left[\sqrt{\alpha^2 + \frac{4\pi^2(m + \tfrac{1}{2})^2}{L^2}}\, y\right] \quad [29]$$

The boundary condition of Eq. [23a] is now employed

$$E\left(\frac{\cosh \alpha x}{\cosh \alpha L/2} - 1\right) = \sum_{m=0}^{\infty} A_m \cosh\left[\sqrt{\alpha^2 + \frac{4\pi^2(m + \tfrac{1}{2})^2}{L^2}}\left(\frac{M}{2}\right)\right]$$

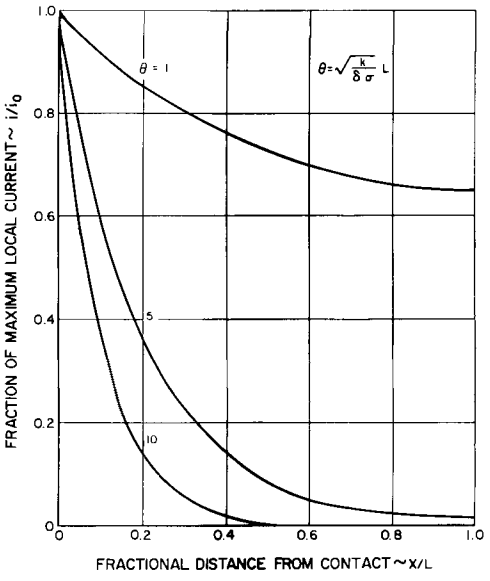

Fig. 3. Local current distribution on tubular membrane

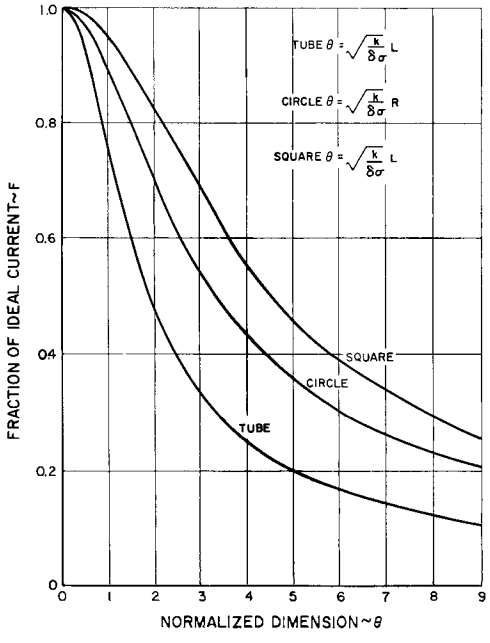

Fig. 4. Effect of ohmic losses on membrane performance

$$\cos\left[\frac{2(m+\tfrac{1}{2})\pi x}{L}\right] \qquad [30]$$

This represents a Fourier cosine series in x. The appropriate coefficients of $\cos[2(m+\tfrac{1}{2})\pi x/L]$ can be evaluated so that the series will converge to the function on the left-hand side. The final solution in x and y is

$$\phi = E\left(1 - \frac{\cosh \alpha x}{\cosh \alpha L/2}\right)$$

$$-\frac{2E}{\pi}\sum_0^\infty (-1)^m \left[\frac{1}{m+\tfrac{1}{2}} - \frac{4(m+\tfrac{1}{2})^2\pi^2}{L^2\alpha^2 + 4(m+\tfrac{1}{2})^2\pi^2}\right]$$

$$\left[\frac{\cosh\sqrt{L^2\alpha^2 + 4(m+\tfrac{1}{2})^2\pi^2}\;(y/L)}{\cosh\sqrt{L^2\alpha^2 + 4(m+\tfrac{1}{2})^2\pi^2}\;(M/2L)}\right]$$

$$\left[\cos\frac{2(m+\tfrac{1}{2})\pi x}{L}\right] \qquad [31]$$

This gives the variation of ϕ, and therefore, of the local current density along the surface of the membrane. The fraction of the total current to that of a zero-resistance membrane is found by integration of i over the quadrant.

$$F = \frac{4}{MLkE}\int_0^{L/2}\int_0^{M/2} i\,dy dx \qquad [32]$$

$$F = \frac{2}{\alpha L}\tanh\frac{\alpha L}{2}$$

$$+\frac{2}{\pi}\sum_0^\infty \left[\frac{1}{m+\tfrac{1}{2}} - \frac{4(m+\tfrac{1}{2})^2\pi^2}{L^2\alpha^2 + 4(m+\tfrac{1}{2})^2\pi^2}\right]$$

$$\left[\frac{\tanh\sqrt{L^2\alpha^2 + 4(m+\tfrac{1}{2})^2\pi^2}\;M/2L}{(m+\tfrac{1}{2})\pi\sqrt{L^2\alpha^2 + 4(m+\tfrac{1}{2})^2\pi^2}\;M/2L}\right] \qquad [33]$$

Discussion

There are certain characteristics of the solutions for the ohmic potential and local current densities that are common to each the linear, circular and rectangular geometries. As governed by the boundary conditions, the ohmic potential has its maximum value at the end or axis of symmetry of the electrode and is zero at the external contacts. This means that the local current is at a minimum near the end or axis of symmetry and at a maximum at the external contacts. The local currents never go to zero leaving part of the electrode inactive, but the local current near the end can be rather small. This is illustrated in Fig. 3 where the fraction of maximum local current density is plotted *vs.* the fractional distance from the external contact. This is plotted for parameters of $\sqrt{k/\delta\sigma}\,L$, this factor being inversely proportional to the square root of membrane thickness and conductivity. Figure 3 illustrates that local currents are reduced in greater proportion as $\sqrt{k/\delta\sigma}\,L$ is larger.

The electrode ohmic losses have a direct influence on the current-polarization characteristic of the electrode. This influence is quantitatively expressed in Eq. [13], [20], and [33] as the ratio of current of the membrane to the current of a zero-resistance or "ideal" membrane. The net current of an actual membrane is then

$$J = f\,A\,k\,E \qquad [34]$$

The reference case of an "ideal" membrane can be approached in practice by employing external circuit contacts along the membrane often called "current-collectors." Small membranes, that is, those with relatively low length or diameter to thickness ratios, also will approach an ideal membrane. The correction factor is independent of the electrode polarization because of the linear current-potential relation. This correction factor is illustrated in Fig. 4 where it is plotted *vs.* a dimensionless parameter defined for each geometry:

$$\text{Tube} \quad \theta = \sqrt{\frac{k}{\delta\sigma}}\,L$$

$$\text{Circle} \quad \theta = \sqrt{\frac{k}{\delta\sigma}}\,R$$

$$\text{Square} \quad \theta = \sqrt{\frac{k}{\delta\sigma}}\,L = \sqrt{\frac{k}{\delta\sigma}}\,M$$

An example of the effect of this ohmic drop is given by considering a tube 10 cm long with a membrane thickness of 0.005 cm. A well activated membrane would show about 20 mv polarization at 0.2 amp/ft^2 when operated at 200°C. The conductivity of a palladium-silver alloy at this temperature and in the presence of hydrogen is about 2 x 10^4 (ohm-cm)$^{-1}$. For this case,

θ is 3.16 and the correction factor from Eq. [13] or Fig. 4 is 0.315. In this example, about three times as much polarization can be expected at a given current density as compared to a tube with current collectors.

Manuscript received by The Electrochemical Society, Feb. 11, 1965, assigned to the JOURNAL, July 28, 1965; revised manuscript received Sept. 9, 1965.

Any discussion of this paper will appear in a Discussion Section to be published in the June 1966 JOURNAL.

REFERENCES

1. Wagner, *This Journal*, **98**, 116 (1951).
2. Tobias and Wijsman, *ibid.*, **100**, 459 (1953).
3. W. W. Harvey, *ibid.*, **109**, 638 (1962).
4. B. E. Conway, E. Gileadi, and H. G. Oswin, *Can. J. Chem.*, **41**, 2447 (1963).
5. H. G. Oswin and S. M. Chodosh, "The Development of a High Efficiency Non-Porous Hydrogen Depolarized Anode for Fuel Cells, presented at 145th National Meeting, ACS, Sept. 8-13, 1963.

Nomenclature

A	Geometric surface area of membrane, cm^2
A_m	Coefficients of Fourier cosine series
C	Concentration of hydrogen atoms in metal at gas side, mole/cm^3
C'	Concentration of hydrogen atoms in metal at electrolyte side, mole/cm^3
D	Outside diameter of tube, cm
E	Polarization from open circuit potential, v
f	Ratio of actual current to the ideal current with no ohmic losses
F	Faraday constant, 96,500 coulomb/equivalent
i	Local current density, amp/cm^2
I_0	Modified zero order Bessel function of the first kind
I_1	Modified first order Bessel function of the first kind
I_D	Diffusion rate constant, amp-cm/mole
J	Current at any location in the tube, amp
k	Proportionality constant between local current and metal-solution potential difference, amp/cm^2-v
k_1	Anodic rate constant for electron transfer, amp/cm^2
k_2	Cathodic rate constant for electron transfer, amp/cm^2
K_1	Hydrogen adsorption rate constant, amp/cm^2-atmosphere
K_2	Hydrogen desorption rate constant, amp/cm^2
L	Length of tube or rectangular membrane, cm
M	Width of rectangular membrane, cm
m	Integer
P	Hydrogen partial pressure, atmosphere
R	Radius of circular membrane
R_0	Gas constant = 8.314 joules/mole-°K
r	Radial distance from center, cm
T	Absolute temperature, °K
x	Linear distance from origin, cm
x_0	Location at which local current equals zero
y	Linear distance from origin, cm
α_1	Hydrogen atom desorption rate constant, amp/cm^2
α_2	Hydrogen atom adsorption rate constant, amp-cm/mole
α	$\sqrt{k/\delta\sigma}$ — cm^{-1}
β_1	Hydrogen atom desorption rate constant, amp/cm^2
β_2	Hydrogen atom adsorption rate constant, amp-cm/mole
Δ	Denotes difference
δ	Membrane thickness, cm
θ	Normalized distance
θ	Fraction coverage of gas-side surface active sites with hydrogen atoms
θ'	Fraction coverage of electrolyte-side surface active sites with hydrogen atoms
ϕ	Ohmic potential, v
ϕ_x	x-dependent solution of ϕ
ϕ_{xy}	x and y dependent, or homogeneous solution of ϕ
σ	Electrical conductivity of membrane, (ohm-cm)$^{-1}$

Electronic Conduction in Anodic Films: The Role of the Forming Solution

D. A. Vermilyea

Research Laboratory, General Electric Company, Schenectady, New York

ABSTRACT

The electronic conductivity of anodic Ta_2O_5 and Nb_2O_5 film depends strongly on the forming solution. Hydrogen peroxide is especially effective; small additions (<1%) may decrease the electronic conductivity by several orders of magnitude. The effect of hydrogen peroxide on conductivity can sometimes be removed by application of large fields in the forward direction. Such major effects of forming bath on conductivity have not been observed with other anodic films or with Ta_2O_5 and Nb_2O_5 films formed on substrates which introduce many flaws into the films.

A previous paper (1) presented current-voltage data for electronic currents in anodic films on several metals. It was found that flaws in the films were very important for all oxides, but that for Nb_2O_5, WO_3, and Ta_2O_5 films electronic currents were passed through films which were nearly flaw free. For those studies only dilute aqueous solutions were used in forming the films, and the results were essentially independent of forming solution. This paper reports studies of the effect of the forming solution on current flow in Ta_2O_5 and Nb_2O_5 films. All films were tested at room temperature using conventional equipment, and the test solution was 0.1M $CeSO_4$ + M H_2SO_4.

It was found that for very thin films (below 100Å) there was little dependence of the electronic current flow on the forming bath or procedure. As the film thickness increased, however, marked differences were observed between films formed in different solutions, and in addition the behavior depended on the rate and temperature of formation. Figure 1 shows some typical data for films formed 2 min at 28v at room temperature on chemically polished zone refined tantalum; the films are essentially flaw free. The data for 1% H_2SO_4 are typical of the behavior of films formed in a variety of dilute aqueous solutions of variable *p*H. The behavior of films formed in 85% H_3PO_4 was not very different, a remarkable fact in view of the report by Randall *et al.* (2) that the films formed on tantalum under similar conditions contain about 0.18 mole of phosphorus per mole of tantalum ions.

Other concentrated forming solutions yield films showing widely different behavior, as shown in Fig. 1. The effect of hydrogen peroxide is especially startling. A film formed in 1% HNO_3 shows a current voltage

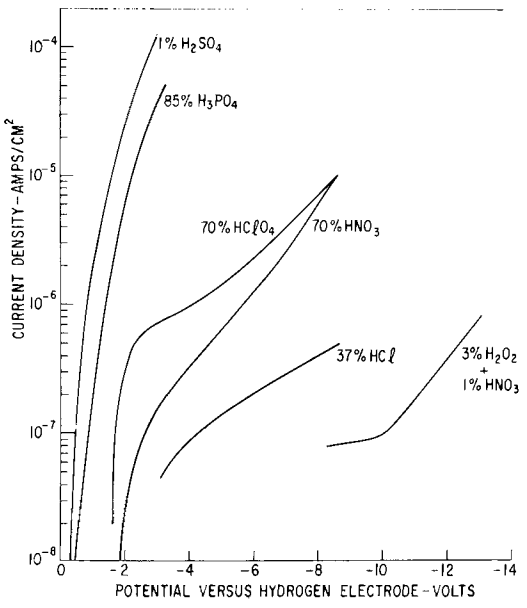

Fig. 1. Films formed at 28v for 2 min at 25°C on chemically polished zone refined tantalum.

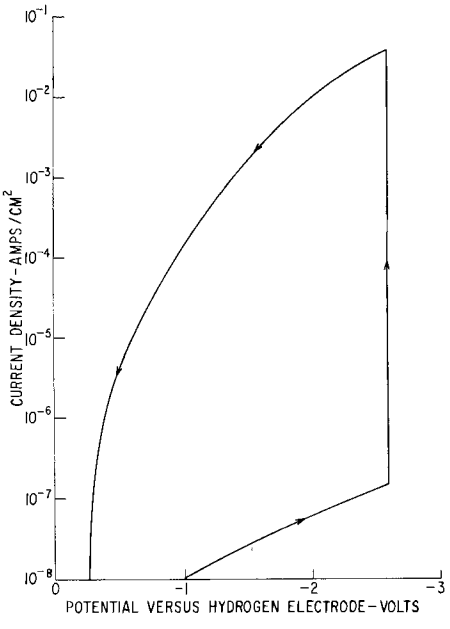

Fig. 2. Film about 200Å thick formed in 1% HNO_3 + 30% H_2O_2 at 25°C.

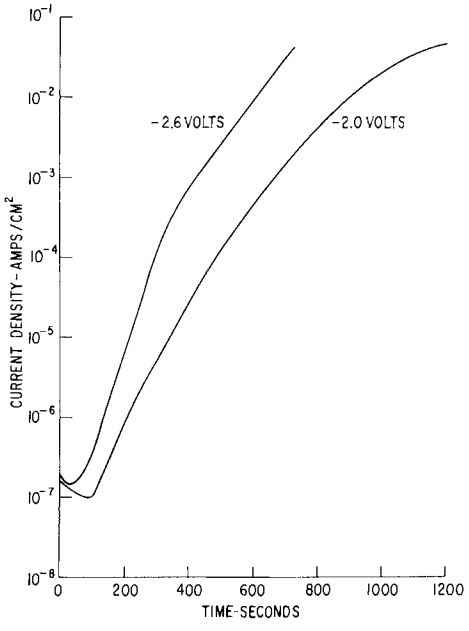

Fig. 3. Films formed as for Fig. 2, held at different negative potentials.

curve like that for 1% H_2SO_4, but the addition of as little as 0.01% H_2O_2 results in a curve similar to that for the 3% H_2O_2, 1% HNO_3 solution. A solution containing 30% H_2O_2, 1% HNO_3 yielded similar films, and the behavior is essentially the same for films formed in 1% H_2O_2 plus a variety of salts in solutions with pH from 1 to 13. It was found that the HF dissolution rates (as measured by changes of interference colors) of the outer portions of films formed in even very dilute H_2O_2 solutions were as much as a factor of two greater than those of the inner portions, a behavior typical of films which contain materials from the forming solution (2, 3). It therefore appears that tantalum oxide has a very strong tendency to occlude hydrogen peroxide or some product of hydrogen peroxide. Niobium oxide is similarly sensitive to H_2O_2, and also, to a lesser extent, to $HClO_4$.

In order to be effective the H_2O_2 must be in the forming bath during film growth. Post formation treatments of any kind do not result in incorporation of H_2O_2 and reduction in current flow. Double formations in which H_2O_2 containing solutions are used for forming part of the film are less effective than when H_2O_2 is present throughout the formation period. It is not possible to remove the H_2O_2 by subsequent long anodization at the same forming potential in a solution which is free of H_2O_2. The H_2O_2 effect is not associated only with the rapidly etching outer layers, for when these are removed with HF the inner portion of the film also has an abnormally low electronic conductivity.

The use of H_2O_2 in forming films is not effective when the metal contains flaw-forming defects (4), films formed with H_2O_2 on such specimens giving nearly unchanged current-voltage curves. On good specimens at sufficiently negative potentials local breakdown occurs and very high currents can be carried at one or a few sites. Attempts to detect uniform conduction in H_2O_2 formed films by gold deposition have not been successful, and it appears that the effect of H_2O_2 is to reduce greatly the conduction in the bulk of the film without changing conduction at flaws.

The high resistivity films produced by H_2O_2 can be altered to low resistivity films by the application of steady negative potentials below those required to cause local breakdown. Figure 2 shows data for a Ta_2O_5 film about 200Å thick formed with H_2O_2 and then held at —4v. The upper portion of the curve is typical for films formed in dilute aqueous solutions, and once the film conductivity has reached that high level it is not possible to regain the initial low conductivity state by any treatment including hour-long formation at the original forming voltage in the original H_2O_2 containing solution. After the conductivity change the outer portion of the film still etches faster than the inner portion, so all the effect of H_2O_2 has not been removed. This "unblocking" is faster at a more negative potential, occurs as readily in mercury as in aqueous solution, and is relatively uniform as shown by gold deposition on the altered specimen. Figure 3 shows data for the current as a function of time for the "unblocking." The curve has a shape very nearly like that for the concentration at one film interface of a substance diffusing across the film from the opposite interface where its concentration is constant.

In summary, it appears that substances from the forming bath which are incorporated into the films may greatly reduce the electronic conduction of the

films. The effects of rate and temperature of film formation may be to change the amounts of such incorporated materials. The effects seem to be primarily associated with bulk conduction and not flaw conduction. The blocking effect is unstable, being removed by long negative polarization, possibly when diffusion adds something to or removes something from the film. Finally, no similar effects of H_2O_2 on conduction in Al_2O_3 and ZrO_2 films was observed; it is believed that conduction in such films occurs mainly at flaws.

Manuscript received June 23, 1965.

Any discussion of this paper will appear in a Discussion Section to be published in the June 1966 JOURNAL.

REFERENCES

1. D. A. Vermilyea, Submitted to *J. Appl. Phys.*
2. J. J. Randall, Jr., W. J. Bernard, and R. R. Wilkinson, *Electrochim. Acta*, **10**, 183 (1965).
3. D. A. Vermilyea, *Acta. Met.*, **2**, 482 (1954).
4. D. A. Vermilyea, *This Journal*, **110**, 250 (1963).

Technical Notes

Direct Observation of the Anodic Oxidation of Aluminum

H. A. Francis

Arthur D. Little, Inc., Cambridge, Massachusetts

Recently, the ionic transport kinetics of the anodic oxidation of aluminum have been investigated using radioactive tracer methods by Davies *et al.* (1). They found that, in the current density range 0.1-10 ma/cm^2, the cation transport fraction (*i.e.*, fraction of total ionic current which is cationic) was 0.6 independent of current density for a nonaqueous electrolyte and increased with current density from 0.4 to 0.7 for an aqueous electrolyte. Transmission electron microscopy has been employed by Doherty and Davis (2) to determine the kinetic mechanisms of the thermal oxidation of aluminum. They found that above 500°C, crystalline oxide forms at the oxide-metal interface by anion transport through the existing amorphous oxide film. Evidence was presented indicating that the thermal amorphous film grows largely by cation transport controlled at the oxide-metal interface. The present investigation utilizes transmission and replica electron microscopy of the oxide in the vicinity of vacancy pits on the metal to investigate the growth mechanisms of anodized amorphous oxide films.

Experimental Technique

Electropolished single crystals of 99.992+% aluminum were grown horizontally from the melt and electropolished in a methanol-perchloric acid solution in the same manner as those used by Doherty and Davis (2). The experiments were performed on (100) and (110) surfaces.

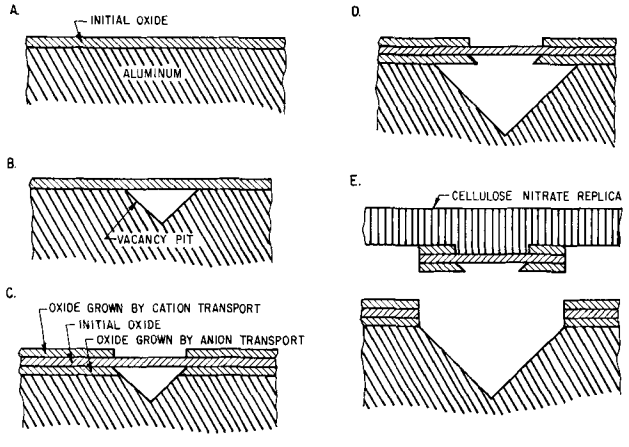

Fig. 1. Schematic representation (not to scale) of experimental technique. (A) Initial surface. (B) After first heating and cooling. (C) After anodizing. (D) After second heating and cooling. (E) Removal of oxide fragment.

The basic experimental technique is illustrated schematically in Fig. 1. The initial oxide film (A) was either the as-electropolished oxide or a thicker film grown either thermally in air or anodically. When the crystal was heated to an elevated temperature (ranging from 400° to 575°C) and cooled (B), micron-sized pits bounded by low-index crystallographic planes nucleated and grew under the oxide in the metal by the condensation of lattice vacancies (3). Oxide was then grown anodically (C) under various controlled voltage conditions to be described later. In all cases the electrolyte was 1% respectively of ammonium citrate and citric acid in distilled water and the cathode was electropolished aluminum of the same purity as the specimens. It is seen that, at the edge of a vacancy pit, a step is produced at the oxide-metal interface whose height is equal to the thickness of oxide grown by anion transport, and a step of height equal to the thickness of oxide grown by cation transport is produced at the oxide-electrolyte interface. Then the crystal was heated a second time, and, on cooling, a fraction of the vacancy pits grew to a larger size (D). An adherent cellulose nitrate replica was used then (E) to remove the oxide over the pits, and these oxide fragments were viewed in normal transmission in the electron microscope. The topography of the oxide-metal interface was observed by shadowing the fragments with platinum after their removal from the crystal. The topography of the oxide-electrolyte interface was observed either by shadowing the surface of the crystal prior to application of the replica or by using conventional techniques to replicate the surface before the second heating without removing any oxide. In all cases, the shadowing angle of incidence was 18°.

The specimens exhibit a slight surface roughness which is observable optically. Hence, it cannot be assumed that the surface in the immediate vicinity of a vacancy pit is precisely parallel to the over-all surface of the specimen or replica which is used as the shadowing angle reference. This and the fact that the oxide over a vacancy pit often bows in either direction prohibit determination of step height from apparent shadow length.

Results

Figure 2 shows a shadowed replica of a (100) surface in the vicinity of a square vacancy pit, the oxide over which was not removed. In this case, the crystal

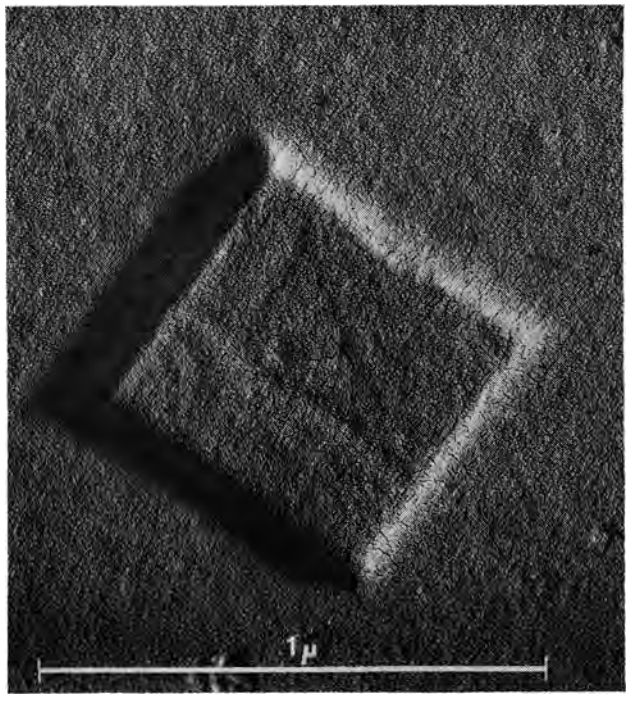

Fig. 2. Shadowed replica of (100) oxide-electrolyte interface showing step along perimeter of vacancy pit.

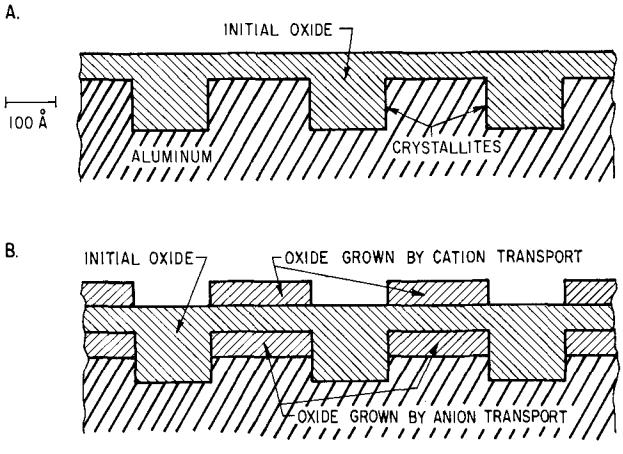

Fig. 3. Schematic representation of surface after nucleation of crystalline oxide. (A) Before anodization. (B) After anodization.

was anodized to 8v, vacancy pitted, and anodized to 27v by instantaneously applying the entire voltage, resulting in a mean current density (averaged over oxide thickness) of 3 ma/cm^2. In addition, (100) surfaces were anodized to voltages ranging from 27 to 42v with the following voltage rates (and mean current densities): 0.24 v/min (0.01 ma/cm^2), 4 v/min (0.3 ma/cm^2), and 15 v/min (1.4 ma/cm^2). The results of replication without oxide removal were identical for the four average current densities. It is seen in Fig. 2 that a step exists along the perimeter of the vacancy pit indicating that cation transport occurred during anodizing.

Doherty and Davis (2) have shown that the high temperature stage of thermal oxide growth consists of the nucleation of oxide crystallites at the oxide metal interface which then grow into the metal. This stage is shown schematically in Fig. 3(A). At room temperature, anodic oxide growth will not occur if the field in the oxide is less than about 1/14 v/Å (4). Thus, if a crystal with this oxide-metal interface topography is anodized by slowly increasing the voltage, growth will not occur at the crystallite sites until the oxide thickness is uniform (Fig. 3B). Growth by cation

Fig. 4. Shadowed replica of (110) surface in vicinity of vacancy pit showing depressions over crystallite sites.

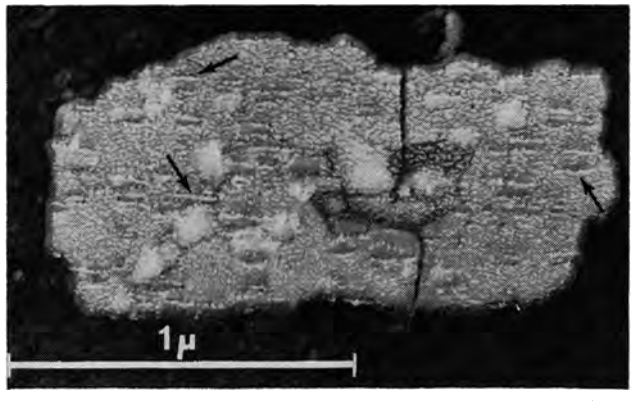

Fig. 5. Fragment of anodized (110) oxide whose oxide-electrolyte interface has been shadowed. Arrows indicate depressions over crystallite sites.

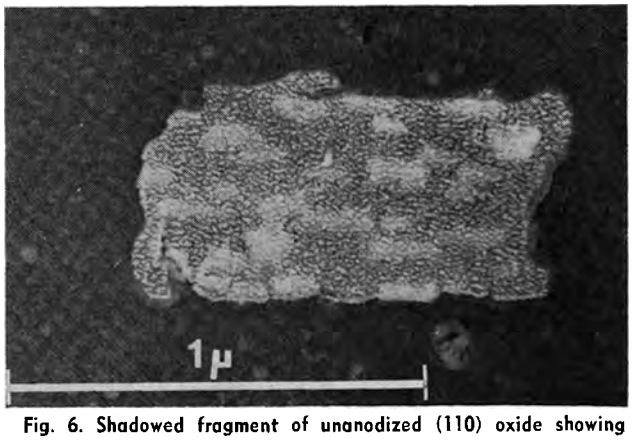

Fig. 6. Shadowed fragment of unanodized (110) oxide showing smooth oxide-electrolyte interface.

transport will result in depressions in the final oxide-electrolyte interface over the crystallite sites. Growth by anion transport will tend to "swallow up" the crystallites.

A crystal was heated to 575°C for 15 min to grow crystallites, cooled to form vacancy pits, and anodized to 20v at about 4 v/min. The mean current density was about 0.3 ma/cm^2. Figure 4 shows a shadowed replica of the (110) surface in the vicinity of a rectangular vacancy pit. The unanodized oxide over the pit has bowed into the pit, and the left half of it has been removed with the replica, directly displaying the crystallites at the oxide-metal interface. The right half

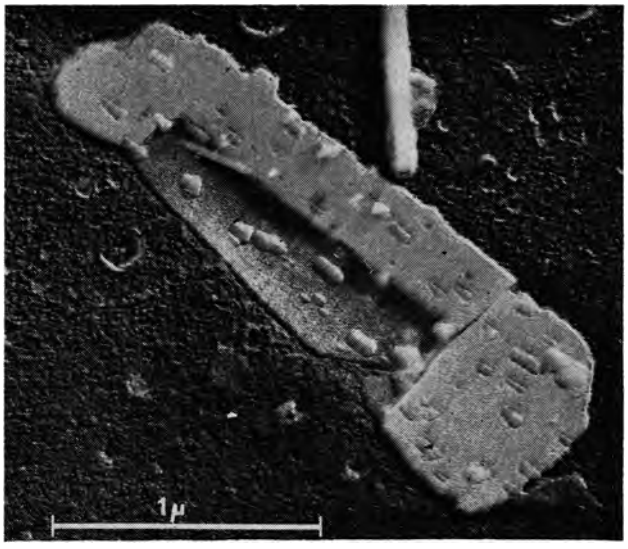

Fig. 7. Fragment of (110) oxide whose oxide-metal interface has been shadowed demonstrating oxide growth by anion transport.

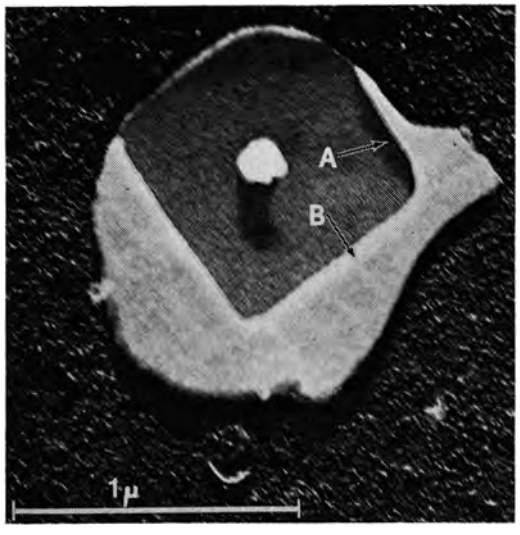

Fig. 8. Fragment of (100) oxide whose oxide-metal interface has been shadowed. Step along original perimeter of vacancy pit is revealed by its cast shadow (A) and platinum build-up on its face (B).

remained in place over the pit, and the replica shows its oxide-electrolyte interface to be smooth. The oxide-electrolyte interface of the anodized oxide surrounding the pit site is seen to contain depressions (rises on the replica) corresponding to the crystallites, indicating growth by cation transport.

Another crystal was treated as described in the preceding paragraph and, after anodizing, heated and cooled a second time to enlarge the existing vacancy pits (see Fig. 1D and 3). Figure 5 shows an oxide fragment removed from the (110) surface, the oxide-electrolyte interface having been shadowed prior to removal. The depressions over the crystallite sites are revealed by the shadowing. For comparison, a fragment of unanodized oxide removed from a pit that did not enlarge is shown in Fig. 6. Its oxide-electrolyte interface is seen to be smooth. The light areas (lower transmitted intensity) correspond to the oxide crystallites. Figure 7 shows an oxide fragment whose oxide-metal interface was shadowed after removal from an enlarged pit. The unanodized region is not in the center of the fragment because either one side of the original pit did not grow or part of the oxide over the pit was not removed. A step can be seen separating the anodized and unanodized regions at the original perimeter of the pit. In addition, the oxide grown by anion transport has surrounded the sides of most of the crystallites, as evidenced by the fact that they do not cast a noticeable shadow. Thus Fig. 5-7 show that for this treatment the anodized oxide grew by both anion and cation transport.

Figure 8 shows an oxide fragment removed from an enlarged pit (see Fig. 1E) on the (100) surface of a crystal which had been anodized to 8v, vacancy pitted, anodized to 27v at 0.24 v/min (0.01 ma/cm^2), and heated and cooled a second time to enlarge the pits. Both a cast shadow and shadowing material (platinum) build-up show that a step exists on the oxide-metal interface along the original perimeter of the pit, hence anion transport occurred. Identical observations were made under experimental conditions differing only in that the 27v was instantaneously applied and the mean current density was 3 ma/cm^2.

Discussion

For the anodizing treatments investigated, which encompass a range of mean current densities from 0.01 to 4 ma/cm^2, we may conclude that both anion and cation transport occur. On one anodized crystal (Fig. 5, 6, 7; 0.3 ma/cm^2) both anion and cation transport were observed. On all others, one or the other was investigated and always observed. There was no observable dependence of the results on surface orientation. The results of the present investigation thus confirm by a new technique previous results which showed that cation and anion transport can occur simultaneously.

For mean current densities of 0.1 ma/cm^2 and 3.0 ma/cm^2 on a (100) surface, 0.3 ma/cm^2 on a (110) surface, and about 30 ma/cm^2 on a (111) surface the oxide grown did not diffract an electron beam. This encompasses the range of current densities for which ionic transport mechanisms were investigated. Thus, while thermal oxide grown at the oxide-metal interface is crystalline (2), apparently anodic oxide grown by anion transport is not. Since anodic oxidation takes place essentially at room temperature, it is reasonable that for kinetic reasons long range order is not produced in the oxide grown at the oxide-metal interface.

One of the most interesting results of the recent work of Davies *et al.* (1) is the apparent dependence of the ionic transport kinetics on the nature of the electrolyte, an effect largely neglected in the literature.

They bombarded unanodized aluminum foils with Xe^{125} and used β-spectroscopy to measure the mean depth of the tracer after anodizing at various constant current densities in the range 0.1-10 ma/cm^2. Independent measurements of the amount of aluminum dissolved in the electrolyte were made for each current density using a neutron activation technique. The final barrier oxide thickness δ was calculated from Bernard and Cook's (5) empirical relationship $i = \alpha \exp(\beta V/\delta)$. The measurements of tracer depth d, dissolved Al a, and δ were converted to equivalent μg/cm^2 of oxide, and the cation fraction t_m (cationic fraction of total ionic current) was calculated from the relationship $t_m = (d + a)/(\delta + a)$. It was found that t_m was 0.6 independent of current density for a sodium tetraborate/ethylene glycol electrolyte and increased with current density for an aqueous 3% ammonium citrate electrolyte.

They inferred that the observed dependence of t_m on current density for the citrate electrolyte may be attributed to pore formation in the oxide. It should be emphasized that the Al in solution may result from either or both of two processes: (*i*) pure cationic leakage (as assumed by Davies *et al.* in their analysis), and (*ii*) dissolution of oxide in the electrolyte to form an electronically conducting porous layer on top of the nonconducting barrier layer (6, 7). Both cases are equivalent with respect to barrier layer growth rate, barrier layer thickness δ, and the field in the barrier layer. For case *ii*, the data must be interpreted in a slightly different fashion. Assuming the density of the porous layer to be homogeneous and independ-

ent of current density, the mass/cm^2 of the porous layer is Ka where K is a constant. The total oxide growth (total ionic current) is thus given by $\delta + a(K + 1)$. The observed Xe^{125} depth d will be less than the actual depth by a "distance" equivalent to the mass/cm^2 of the dissolved oxide. Thus the numerator of t_m will be the same as for case i, and

$$t_m = \frac{d + a}{\delta + a(K + 1)}$$

Although K is not known for this electrolyte, we can predict that the fractional variation in t_m with current density will lie within a certain range. $K = 0$ is case i, for which Davies' values hold. As K becomes very large, the fractional variation in t_m with current density becomes that of the numerator $d + a$. It may be seen from Davies' Table IV that this variation, although less than the variation in t_m for case i, is in the same direction and still well outside of its 10% experimental error. If both cationic leakage and pore formation occur, the fractional variation in t_m will be that for an intermediate value of K. Thus, regardless of the amount of porous oxide formed, the increase of the cation fraction with current density is a real effect for this electrolyte.

It is to be noted that, barring the difficulty of step height measurement, the vacancy pit technique could be used to determine t_m regardless of the amount of pore formation, providing any cationic leakage current is known. The step height at the electrolyte-oxide interface includes both the cationically grown barrier layer and the porous layer.

The nature of the rate-determining steps and the field, temperature, and thickness[1] dependences (*i.e.*, the constants in the appropriate rate equations) of the cation and anion transport rates i_c and i_a remain to be investigated for the various electrolytes. This requires that the total ionic current density $i_t(E, T, \delta)$ be accurately known for the particular electrolyte, even though an approximation is sufficient to determine δ and hence t_m by Davies' method, since δ is probably a relatively insensitive function of the nature of the electrolyte. In addition, if pore formation occurs, the density and growth rate of the porous layer must be known. The fact that $t_m(i_t)$ differs between the two electrolytes investigated by Davies *et al.* strongly suggests that $i_t(E)$ depends on the nature of the electrolyte. For Davies' citrate electrolyte, $i_t(E, T, \delta)$ is not accurately known, so a comparison of $i_c(E, \delta)$ and $i_a(E, \delta)$ between the two electrolytes is not possible.

[1] A thickness dependence is possible according to Dewald's theory for diffusion-limited ionic transport (8).

Assuming Benard and Cook's $i_t(E)$ (5) for an ammonium pentaborate/ethylene glycol electrolyte to hold for Davies' glycol electrolyte, we may conclude from the invariance of t_m that for this electrolyte both $i_c(E)$ and $i_a(E)$ are exponential functions with the same Tafel slope as $i_t(E)$. Since, for the citrate electrolyte, t_m is a function of E, the rate-controlling step of at least one of the two species must be in some way altered between the two electrolytes. Three possible rate-limiting processes for either species are transport across either of the two interfaces of the barrier layer and diffusion within the barrier layer. It is difficult to imagine the structure of the oxide-metal interface to be dependent on the electrolyte. However, it is possible that the nature of the electrolyte could influence the structure of the oxide-electrolyte interface or the structure of the cationically grown oxide, since its growth occurs at the oxide-electrolyte interface (1). If a porous layer exists, anion transport might be limited by oxygen diffusion through the pores to the surface of the barrier layer.

Miles and Smith (9) have anodized aluminum and other metals in an oxygen plasma electrolyte which offers a third, rather different electrolyte for which to investigate the anodic oxidation kinetics. It would be illuminating to know which of the rate equations for i_t, i_c, and i_a differ among the two "wet" electrolytes and the plasma.

Acknowledgments

This research was supported in part by the U.S. Atomic Energy Commission. The author is indebted to Drs. R. S. Davis and P. E. Doherty for much valuable discussion.

Manuscript received April 22, 1964; revised manuscript received Sept. 13, 1965.

Any discussion of this paper will appear in a Discussion Section to be published in the June 1966 JOURNAL.

REFERENCES

1. J. A. Davies *et al.*, *This Journal*, **112**, 675 (1965).
2. P. E. Doherty and R. S. Davis, *J. Appl. Phys.*, **34**, 619 (1962).
3. P. E. Doherty and R. S. Davis, *Acta Met.*, **7**, 118 (1959).
4. M. S. Hunter and P. Fowle, *This Journal*, **103**, 482 (1956).
5. W. J. Bernard and J. W. Cook, *ibid.*, **106**, 643 (1959).
6. M. S. Hunter and P. F. Towner, *ibid.*, **108**, 139 (1961).
7. T. A. Renshaw, *ibid.*, **108**, 185 (1961).
8. J. F. Dewald, *ibid.*, **102**, 1 (1955).
9. J. L. Miles and P. H. Smith, *ibid.*, **110**, 192 (1962).

An Electrically Latched EL-PC Memory Panel

B. Sunners and B. Narken

International Business Machines Corporation, Components Division,

East Fishkill Facility, Hopewell Junction, New York

Electroluminescent memory and display panels have been described by many authors and were reviewed by Henisch (1). They range from a simple EL-PC couple to the very complicated "ELF" (electroluminescent-ferroelectric-photoconductor) display panel. Zim and Krolak recently described an electrically addressed electroluminescent memory panel using hysteretically conducting cadmium selenide as the control element (2).

In its simplest form, a light addressed memory panel is prepared by placing an electroluminescent layer and a photoconductor layer in series and in optical contact, as shown in Fig. 1a. When light strikes the photoconductor, the resistance of the photoconductor falls, and the voltage drop increases across the electroluminescent layer, which then emits light characteristic of the electroluminescent material. Some of this triggering light is fed back to the photoconductor, thus holding it in the "on" position even when the exciting light is removed. The panel remembers the triggering light and can be extinguished only by removing the applied voltage.

In order to display a pattern, the conventional panel (generally in a more complex form) (3) must become one unit in an X-Y matrix (Fig. 1b). The pattern definition is limited by unit size and cross talk between adjacent lines, and the over-all size is limited by the greatly increasing complexity as the number of X and Y drive lines is increased. In addition, this optically latched couple cannot be constructed or used in

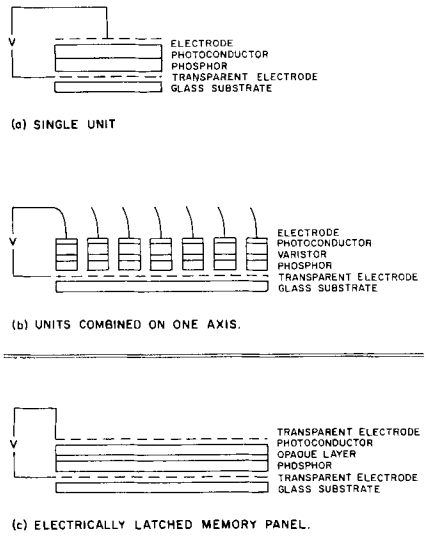

Fig. 1. Schematics of memory panels

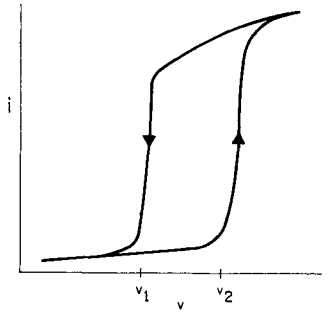

Fig. 2. Current-voltage hysteresis in powder photoconductors (after Nicoll).

a way as to expose the photoconductor to a high ambient light level that would trigger it into the "on" state.

This note describes a panel that does not have the complexity, limited size, and limited resolution of the conventional XY matrix. It is prepared in a continuous sheet (Fig. 1_c), and it has the further advantage of being able to operate in a high ambient light level.

The panel operates on a principle first reported by Nicoll in his work on an image storage device (4). He observed a hysteresis loop in the current/voltage curves of plastic embedded power photoconductors (Fig. 2). Such materials can be triggered into the high conduction state by light when the value of the applied voltage is between V_1 and V_2, and will remain in this state until the voltage drops below V_1. This then forms the basis for a bistable device, switched on by light and switched off by removing (or lowering) the applied voltage.

It is now possible to produce this effect in sintered layer photoconductors. In addition to the usual advantages of sintered layers compared to power photoconductors (*e.g.*, photosensitivity, mechanical strength, ease of fabrication), these sintered photoconductors permit a memory panel that is continuous in structure and does not require the usual complex XY matrix in order to store a pattern. Figure 1c clearly shows the simplicity inherent in this type of construction. As the latching is electrical, not optical, an opaque layer is necessary to prevent feedback from the photoconductor. This construction permits operation of the panel in high ambient light levels, limited only by the desired output contrast level.

The structure is prepared as follows. The semitransparent electrode and the glass electroluminescent and opaque layers are made in the usual ways. The photoconductor is next deposited on top of the opaque layer. In Nicoll's paper, the hysteresis effect was observed in powered materials; these are usually of lower sensitivity than single or polycrystalline materials. The photoconductor discussed here is prepared by sintering CdSe under carefully controlled conditions to yield a material of high sensitivity.

The method of preparation of such a sintered layer is as follows: pure cadmium selenide is thoroughly mixed with glycol, glycerol, an aqueous solution of cupric chloride, and cadmium chloride flux (from 5 to 10% by weight), so as to give a mixture or suspension suitable for depositing by a doctor blading, or similar technique that results in a texture-free layer (thus, screen printing is not entirely satisfactory). The concentration of copper will determine to a large extent many properties (response time, sensitivity, etc.) of the completed photoconductor. As a guide, a suitable concentration of copper under the conditions of our preparations is about 500-1000 ppm by weight. The flux concentration is critical but it is strongly dependent on experimental conditions, such as firing cycle, ambient flow rates, furnace volume, etc.

After depositing the photoconductor in the required grometry, it is slowly dried in air at 200°-300°C and subsequently fired. All samples at present have been fired in a quartz-lined horizontal-tube furnace at 525°-575°C for periods up to 30 min. The ambient is carefully controlled and consists of 98% nitrogen and 2% oxygen by volume, slightly humid, flowing over the sample at a rate of 30 cm/min.

Obviously, these conditions can be varied; sintered layer photoconductors can be prepared under a wide variety of conditions but to obtain a material with the optimum hysteresis properties, a combination of conditions must be chosen so that the sintering action of the cadmium chloride flux is minimal and yet does not lead to typical powder photoconductor properties (e.g., nonlinear current-voltage relationship). The presence of oxygen in the ambient improves adhesion and the mechanical properties of the layer, which otherwise, due to the low flux concentration, would be poor; in addition, it may improve particle-to-particle contact through the formation of a conducting CdO layer (5).

The hysteresis can be greatly enhanced by baking the fired photoconductor at temperatures up to 300°C in an oxygen-containing atmosphere. This process is known to decrease the effective number of donor species in the material (*i.e.*, reduce the number of selenium vacancies). The photoconductor may also be baked in a sulfur or selenium atmosphere, and indeed, some of the better results were obtained with sulfur treatments.

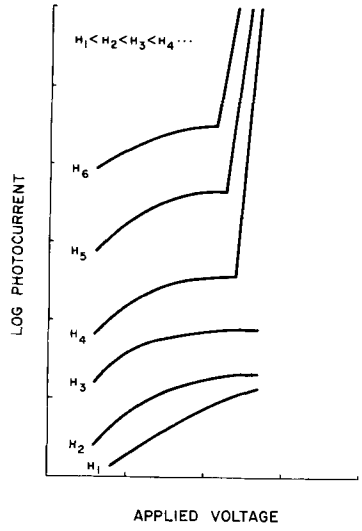

Fig. 3. Photocurrent voltage curves

Preparative techniques that increase hysteresis in general shift the photocurrent-voltage curve to higher voltage levels at a constant light intensity. The voltage breakdown shown has been made to persist in these photoconductors even in the absence of light and thus provide the second stable dark state of the device (Fig. 2).

A layer so prepared has the mechanical properties and sensitivity of the conventional sintered layer and has a linear voltage-current relationship, but, in addition, it shows dark current hysteresis.

Problems have been encountered in applying electrically continuous semitransparent electrodes to the relatively rough surface of this photoconductor, and experiments have been conducted with a view to applying the photoconductor in a glass binder to provide a smooth surface. It is known that photoconductive layers may be prepared in this way and show many advantages over the conventional plastic binder (6), but the required property of hysteresis has not yet been observed in such a structure. Although no panels greater than about 1 in.^{2} have been prepared, no limits to the size are known, nor has any limit to the definition been observed. Ideally, this limit may be the grain or crystallite size of the photoconductor and phosphor; thus the layer should be deposited by doctor blading rather than screen printing to develop optimum resolution. Spreading of the image would, of course, limit the definition and also limit the storage time of the memory. To date, experimental units do not show any spreading or fading of spots about 1 mm in diameter over periods up to 18 hr. The sensitivity of most of the photoconductive layers is such that they are readily triggered by the light from a cathode ray tube, and the intensity of the image is limited only by the performance of existing phosphors.

It is felt that the great advantages of simplicity and consequent ease of manufacture of this type of panel will be of interest to those engaged in fields of display, storage, and opto-electronics.

Manuscript received Jan. 13, 1965; revised manuscript received Sept. 13, 1965.

Any discussion of this paper will appear in a Discussion Section to be published in the June 1966 JOURNAL.

REFERENCES

1. H. K. Henish, *J. Appl. Phys.*, **12**, 660 (1961).
2. Krolak and Zin, *Proc. IEEE.* Conference Electron Devices, 1964.
3. J. O'Connell and B. Narken, *IBM J. Res. Develop.*, **4**, 420 (1960).
4. F. H. Nicoll, *RCA Rev.*, **19**, 77 (1958).
5. B. T. Kolomiets, *Doklady Akad. Nauk S.S.S.R.*, **83**, 561 (1952).
6. B. Sunners and B. Narken, U. S. patent applied for.

Phase Stability Regions of Boron Phosphides in the Ni-B-P System

Robert I. Stearns

Central Research Department, Monsanto Company, St. Louis, Missouri

and Paul E. Greene

—hp associates—, Palo Alto, California

A procedure for the preparation of BP was reported (1) in which mixtures of Ni and B were heated to about 1400°C and then allowed to cool under a phosphorus atmosphere. BP and/or $B_{12}P_2$ (2) was recovered by dissolving away the unwanted material with aqua regia.

In an effort to optimize the preparative procedure, work was undertaken independently by the two laboratories contributing this article. The procedures used were slightly different and are described separately.

The data obtained, although far short of completely defining the system, are sufficient to construct a preliminary phase diagram of the Ni-B-P system, Figure 1.

Experimental

Procedure I.—Mixtures of powdered Ni (A. D. Mackay, carbonyl powder, 99.9%), B (Cooper Metallurgical Associates, Grade AA-325, 99.5%), and red P (American Agricultural Chemical Company, semiconductor grade, ground under distilled water) were made by weighing the individual elements and mixing them thoroughly in a capped bottle. About a half gram of the mixture was sealed under vacuum (about 10μ) in a small quartz ampule and heated to melting and then solidified by quenching. The melting occurred in the same temperature range noted in procedure II below. The weights of the resulting solid masses corresponded to the elements weighed in the small ampules and it was therefore assumed that the vapor pressures at the melting points were small and of the same order given in procedure II. The solidified mass was treated with warm aqua regia until dissolution ceased. The resulting boron phosphides were easily identified by examination. BP is red, transparent, face centered cubic material and $B_{12}P_2$ is black to colorless, rhombohedral material. These identifications were spot checked by x-ray diffraction examination

Procedure II (3).—Weighed samples, 0.2-0.4g of 4.00 w/o B (99.9999% Leytess Metal and Chemical Corporation) in Ni (99.999% Leytess Metal and Chemical Corporation) alloy were taken from a homogenous 20.0g alloy ingot and placed in an alumina crucible in a R. F. heated graphite furnace. These Ni-B samples were then allowed to equilibrate with P_2 at 3.8 Torr partial pressure in H_2 flowing at one 1 l/min. with a total system pressure of 1 atm. Equilibrations were carried out at constant temperatures (± 5°C) ranging from 1085° to 1320°C for 2 hr.

Table I. Tabulation of data

Procedure	At. % Ni	At. % B	At. % P	Phase remaining after acid treatment
I	49.1	8.4	42.5	BP
I	53.4	9.0	37.6	BP
I	54.7	9.1	36.2	BP
I	57.0	28.5	14.5	$B_{12}P_2$
I	57.1	9.5	33.4	$B_{12}P_2$, BP
I	58.9	9.9	31.2	$B_{12}P_2$, BP
I	61.1	10.4	28.4	$B_{12}P_2$
I	62.0	21.4	16.6	$B_{12}P_2$
II	63.7	14.4	21.8	$B_{12}P_2$
II	64.5	11.7	23.7	$B_{12}P_2$
II	64.8	4.8	30.3	$B_{12}P_2$, BP
I	65.0	28.0	7.0	$B_{12}P_2$
II	65.3	2.7	31.9	BP
II	65.7	7.1	27.1	$B_{12}P_2$
II	66.5	8.1	25.3	$B_{12}P_2$
I	67.5	6.5	26.0	$B_{12}P_2$
I	70.6	11.9	17.5	None
I	80.0	13.0	7.0	None

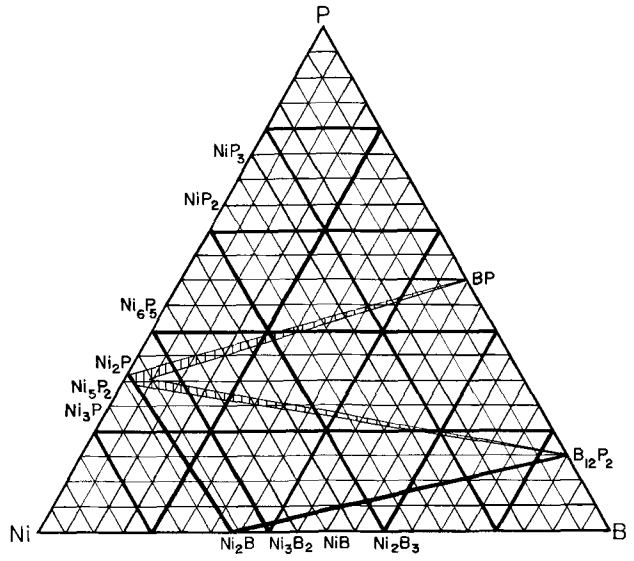

Fig. 1. Phase stability regions of BP and $B_{12}P_2$ in the Ni-B-P system.

The melts were quenched to room temperature, reweighed to within 0.1 mg, and subjected to hot HNO_3 treatment to dissolve the metallic phases and leave the BP and/or $B_{12}P_2$ as residues. The aqueous solutions were analyzed by standard methods (4-6) for Ni, P, and B, while the residues were determined gravimetrically giving a material balance. Identification of the boron phosphides were carried out in the same manner as procedure I.

Discussion

Table I tabulates the data. Figure 1 shows the phase stability regions of BP and $B_{12}P_2$ in the Ni-B-P system. It was constructed (7) by plotting on the binary legs the known binary compounds (1, 2, 8), the data of Table I and then drawing the tie lines from BP and $B_{12}P_2$. The hatched areas represent uncertainty in locating the tie-lines. That a ternary compound in the neighborhood of Ni_2P is indicated corroborates the findings of Rundquist (9) that Ni_2P dissolves B and Ni_3P does not.

The areas outside the area bounded by the four corners Ni_2B, $B_{12}P_2$, BP and the ternary compound cannot be defined by the method employed. Only detailed x-ray work could definitely establish these areas. Nevertheless certain predictions might be made. If no further ternary compounds exist, tie lines from $B_{12}P_2$ to Ni_3B_2, NiB, and Ni_2B_3 are expected, as would be tie lines from the indicated ternary compound to Ni_5P_2, Ni_2P, Ni_6P_5, NiP_2, Ni_3P, and P.

Acknowledgment

The Monsanto portion of this work was performed under a subcontract of MIT Lincoln Laboratory, which is operated with support from the United States Air Force, and the hpa portion under a Wright-Patterson Air Force Base contract (2, 3).

Manuscript received April 30, 1965; revised manuscript received Sept. 2, 1965.

Any discussion of this paper will appear in a Discussion Section to be published in the June 1966 JOURNAL.

REFERENCES

1. B. D. Stone, U. S. Pat. 3,009,780, June 22, 1959.
2. "Investigation of the Boron Phosphide System," Interim Engineering Report No. 4, Air Force Avionics Lab., Wright Patterson AFB, Contract No. AF 33(615)-2001.
3. "Investigation of the Boron Phosphide System," Interim Engineering Report No. 1, Air Force Avionics Lab., Wright Patterson AFB, Contract No. AF 33(615)-2001.
4. Kolthoff and Sandell, "Quantitative Inorganic Analysis," p. 574, The MacMillan Co., New York (1943).
5. N. Furman, "Standard Methods of Chemical Analysis," 6th ed., vol. 1, p. 812, D. Van Nostrand Co., Inc., New York (1962).
6. Kolthoff and Sandell, "Quantitative Inorganic Analysis," p. 223, The MacMillan Co., New York (1943).
7. A. Findlay, "Phase Rule," 9th ed., pp. 314-338, Dover Publications (1951).
8. M. Hansen, "Constitution of Binary Alloys," McGraw-Hill Book Co., Inc., New York (1958).
9. S. Rundquist, *Acta Chem. Scand.*, **16**, 1 (1962).

Preparation and Properties of Lead Hydroxy-Iodide in Single Crystal Form

J. Dennis and H. K. Henisch

Materials Research Laboratory, Pennsylvania State University, University Park, Pennsylvania

and P. Cherin

Fundamental Research Laboratory, Xerox Corporation, Webster, New York

It has been shown (1-3) that a variety of crystals suitable for solid state experimentation can be grown in silica gel. The method is especially useful for substances which, because of their low solubilities or low dissociation temperatures (or both, as in this case), cannot readily be grown in other ways. While preventing turbulence and remaining chemically inert, the gel provides a three-dimensional structure (of silica) which permits reagents to diffuse. It yields mechanically to the growing crystal and, in this way, gross constraining forces which otherwise might arise in a crucible are avoided.

The growth of lead di-iodide in gel media has already been described by Holmes (4) and Hatschek (5). A casual reference to the monoiodide (PbI) has been given by Niewodniezanski (6), but without any kind of detail concerning the circumstances of its formation, its structure, or its properties. Another appears in published tables (7), but without reference to origin and supporting evidence. The crystals here described were indeed the outcome of an attempt to check whether PbI can be obtained. They were grown as follows: Equal volumes of 0.86M sodium metasilicate and 0.68M acetic acid were mixed, and the resulting solution made 0.05M with respect to potassium iodide, giving a pH of 8.0. This was allowed to gel in a heat bath at 40°C. The process takes about 4 min. A raised temperature is necessary to maintain a high degree of hydrolysis and hence the alkaline nature of the gel medium. The top of the gel was covered with a 0.25M solution of lead acetate. Subsequent growth was allowed to take place in darkness. The size and

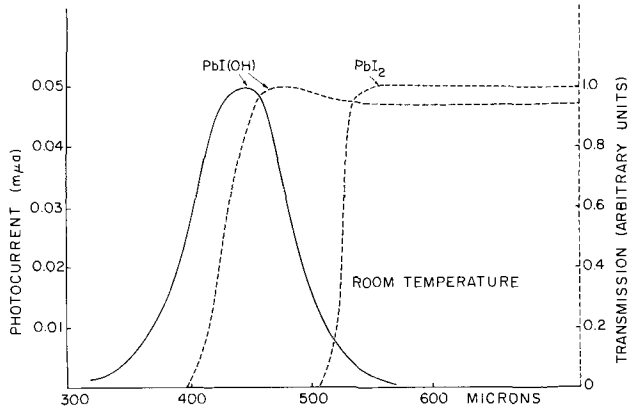

Fig. 1

clearness of the crystals obtained was found to be very sensitive to the *p*H changes of the reagents. Preliminary studies have shown that nucleation is not affected much by light (1) or temperature. However, a decrease in the *p*H causes a decrease in the number of nuclei, until at a *p*H of 7 the crystals which nucleate are PbI_2.

The crystals which result from this procedure are of the order of 1 mm^2 in cross-section, up to 5 mm long, clear, and pale yellow in color. Their appearance is thus entirely different from that of the more familiar PbI_2 which grows in the form of orange-colored hexagonal platelets. X-ray fluorescence, by comparison with PbI_2, showed the ratio Pb:I to be 1:1, within an accuracy of about 1.5%. A result of this kind may have been responsible for the impression that PbI exists. However, PbI(OH) and $PbI_2 \cdot PbO$ satisfy the same criterion while, at the same time, being much more plausible from the valence point of view. Neutron activation studies (by General Dynamics) showed the amount of oxygen to correspond to PbI(OH). The measured lattice parameters of the orthorhombic crystals were $a = 10.43 \pm 0.01$Å [10.41Å], $b = 7.79 \pm 0.004$Å [7.80Å], $c = 4.19 \pm 0.004$Å [4.19Å], the numbers in square parentheses being the parameters for PbI(OH) taken from Wyckoff (8) for the purpose of comparison. The space group is Pbnm, with four molecules per unit cell. The x-ray density is 6.85 g/cc.

As far as is known, PbI(OH) has not previously been prepared in single crystal form. Silicon was known to be present as a contaminant, to the extent of 200 to 500 ppm, no doubt originating from the gel medium. On heating (200°C) in oxygen, the crystals turn to Pb_2O_3.

An exhaustive investigation of properties has not yet taken place, but a few basic results are available. Figure 1 shows that there is an optical absorption edge at about 430μ. It also gives the spectral response of the photoconductivity. The low frequency (10^4 c/s) dielectric constant is about 10.5, and the magnetic susceptibility (averaged over all directions) is -0.256×10^{-6}/g.

The material was shown to be a p-type semiconductor under thermoelectric test. When examined under a scanning electron probe, most of the specimens were found (with a sensitivity of ½%) to be homogeneous as regards Pb:I ratio, and free from gross contaminations by foreign matter. They showed a faint but stable bluish-white cathodoluminescence, in contrast with PbI_2 which luminesces in the green region.

Acknowledgment

Thanks are due to Professor L. Mulay, Mr. S. Lee, and Dr. E. W. White for their help. The present work is supported in part by a grant from the Advanced Research Projects Agency.

Manuscript received Aug. 13, 1965.

Any discussion of this paper will appear in a Discussion Section to be published in the June 1966 JOURNAL.

REFERENCES

1. H. K. Henisch, J. Dennis, and J. I. Hanoka, *J. Phys. Chem. Solids*, **26**, 493 (1965).
2. H. K. Henisch, J. I. Hanoka, and J. Dennis, *This Journal*, **112**, 627 (1965).
3. F. G. Wakim, H. K. Henisch, and H. Atwater, *J. Chem. Phys.*, **42**, 2619 (1965).
4. H. N. Holmes, *J. Franklin Inst.*, **184**, 743 (1917).
5. E. Hatschek, *Z. Chem. Kolloide*, **10**, 77 (1912).
6. H. Niewodniezanski, *Compt. rend.*, **198**, 2159 (1934).
7. "Handbook of Chemistry and Physics," p. 592, Chemical Rubber Publishing Co., Cleveland (1962).
8. R. W. G. Wyckoff, "Crystal Structures," vol. 1, p. 300, Interscience Publishers, Inc., New York (1960).

Cathodic Crossed Hydrocoupling

II. γ-Hydroxy-γ-Methylvaleronitrile and Its Hydrolysis Product from a Mixture of Acetone and Acrylonitrile

Kiichiro Sugino and Tsutomu Nonaka

Department of Applied Electrochemistry, Tokyo Institute of Technology, Ookayama, Meguro-ku, Tokyo, Japan

In a previous paper (1), we mentioned an electrolytic method for the preparation of δ-cyanovaleric acid ester by cathodic crossed hydrocoupling of acrylonitrile with acrylic acid ester.

We have now attempted to extend this to the crossed hydrocoupling of two entirely different types of compounds which can be reduced at the cathode. As a result, we found that a mixture of γ-hydroxy-γ-methylvaleronitrile and its hydrolysis product, γ, γ-dimethylbutyrolactone, could be obtained in a good yield when a mixture of acetone and acrylonitrile was reduced in aqueous sulfuric acid. The yield and the current efficiency were both as high as 70% when calculated on the basis of the amount of acrylonitrile used.

It is interesting to note that the reaction could be obtained even at a potential as low as −1.20v (*vs.* S.C.E.) in a simple electrolyte containing sulfuric acid.[1]

It is well known that acetone is easily reduced in aqueous sulfuric acid at around −1.3v (*vs.* S.C.E.) (2). However, acrylonitrile itself cannot be reduced under the same conditions. It seems to us, therefore, that this crossed hydrocoupling may be the reaction of

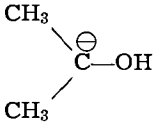

[1] In a neutral electrolyte containing quaternary ammonium salt at −2.3 to −2.4v, the reaction also proceeded smoothly and γ-hydroxy-γ-methylvaleronitrile was obtained without the formation of hydrolysis product. However, the yield was not as good because of the formation of other products.

anion with acrylonitrile. This can be formulated as follows.

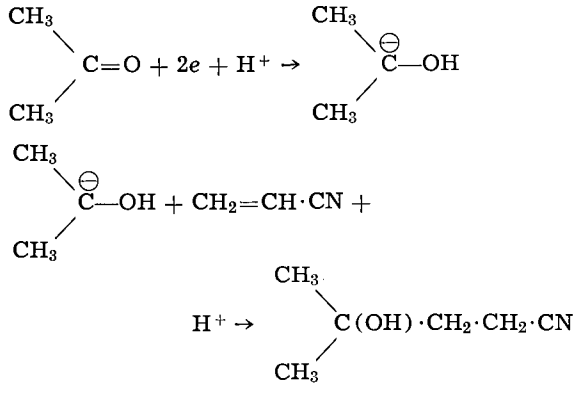

These results have a bearing on the mechanism of pinacol formation by the electrolytic reduction of acetone. This has been considered as the mutual reaction of the radical ($(CH_3)_2\dot{C}OH$) formed at the cathode. However, the result of this research led us to suppose that the usual mechanism might be erroneous and the formation of pinacol from acetone should be the reaction of

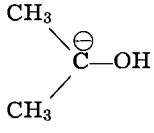

anion with acetone molecule. This gains support from the result of another research (3), which shows that the reduction wave of acetone in tetramethylammonium p-toluenesulfonate has been interpreted as representing a two-electron reduction. The details will be reported in a separate paper.

Experimental

The cell used was the same as described earlier (1): cathode, mercury pool; area, 12.6 cm^2; anode, Pt disk. The electrolysis was carried out by controlling the cathode potential at —1.20v (*vs.* S.C.E.). The electrolysis conditions were: anolyte, 20% sulfuric acid; catholyte, (*a*) 32g acetone and 24g acrylonitrile in 16g 20% sulfuric acid and (*b*) 43g acetone and 3.2g acrylonitrile in 23g 20% sulfuric acid; amperage, (*a*) 0.35-0.24 amp and (*b*) 0.60-0.30 amp; cathodic current density, (*a*) 2.8-1.8 amp/dm^2 and (*b*) 4.8-2.4 amp/dm^2; temperature, (*a*), (*b*) 29°-32°C; amount of current, (*a*) 4.14 amp hr (0.154 Fr) and (*b*) 3.21 amp hr (0.120 Fr, theoretical based on acrylonitrile)

The catholyte turned pale yellow during electrolysis, and a small amount of gas was generated at the cathode.

After the reduction, the catholyte was neutralized with anhydrous potassium carbonate, and the resulting solution was thoroughly extracted with ether. The dried ether extract was analyzed by vapor phase chromatography[2] for isopropyl alcohol[3] and pinacol[4]: (*a*) 0.4g, (*b*) 0.6g of the former and (*a*) a trace, (*b*) 0.2g of the latter were found in it. The extract was then concentrated at diminished pressure, and the resulting concentrate was again analyzed by vapor phase chromatography[2] for γ-hydroxy-γ-methylvaleronitrile[4] (I) and also for its hydrolysis product, γ,γ-dimethylbutyrolactone[4] (II). It consisted of (*a*) 2.5g, (*b*) 1.9g of I and (*a*) 3.7g, (*b*) 2.6g of II. Current efficiency for coupling products was about (*a*) 70% and (*b*) 66%, respectively.

Identity was further confirmed by isolating each compound in nearly pure state by fractional distillation of the concentrate at reduced pressure.

γ-Hydroxy-γ-methylvaleronitrile seemed to be an unknown compound. The fraction corresponding to this compound has the following properties: b.p. 87°-88°C (5 mm Hg), n_D^{24} 1.4351, (molecular refraction 31.05; calculated from the sum of the atomic refractivities, 31.20), d_4^{24} 0.9512; analysis calculated for $C_6H_{11}NO$: C, 63.7; H, 9.8; N, 12.4; found: C. 63.5; H, 10.1; N, 12.3.

Infrared spectrum indicated a very distinct absorption at 2250^{-1} pointing to the presence of nitrile group. It also showed the principal absorption bands at 3400 cm^{-1} (OH), 2950 cm^{-1} (CH_3), and 1468 cm^{-1}($-CH_2-$).

This compound was converted into γ,γ-dimethylbutyrolactone (described below) by hydrolysis with acid.

The γ,γ-dimethylbutyrolactone fraction has the following properties: b.p. 81°C (12 mm Hg) [lit. (4) 208°C], solidify by cooling with ice [lit. (4) mp 10°C], $n_D^{14.5}$ 1.4342 [lit. (5) $n_D^{14.9}$ 1.4349], soluble in water. An infrared spectrum indicated the presence of lactone (C=O) group at 1775 cm^{-1}. It also showed the principal absorption bands at 2960 cm^{-1} (CH_3) and 1460 cm^{-1} ($-CH_2-$). No absorption for CN group was observed in this case. Identity was further confirmed by converting it to γ-hydroxy-γ-methylvaleric acid hydrazide, mp 65-66°C. A mixed melting point with authentic sample[5] showed no depression.

Acknowledgment

This investigation was promoted by a grant for fundamental scientific research from the Ministry of Education of Japan and also a grant from Nippon (Japan) Carbide Industries Inc., for which the authors wish to express their deep appreciation. The authors also wish to acknowledge the collaboration given by other members of this laboratory, especially Dr. K. Shirai, in helping us to carry out this research.

Manuscript received March 16, 1965; revised manuscript received July 27, 1965.

Any discussion of this paper will appear in a Discussion Section to be published in the June 1966 JOURNAL.

REFERENCES

1. K. Sugino, K. Shirai, and T. Nonaka, *Bull. Chem. Soc. Japan*, **37**, 1895 (1964); see also M. M. Baiser, *J. Org. Chem.*, **29**, 1670 (1964).
2. T. Sekine, A. Yamura, and K. Sugino, *This Journal*, **112**, 439 (1965).
3. A. Yamura, T. Sekine, and K. Sugino, Unpublished result.
4. W. A. Noyes, *J. Am. Chem. Soc.*, **23**, 392 (1901).
5. Anderlini, *Gazz. chim. ital.*, **25**, 165 (1895).

[2] 2.5M Stationary phase.

[3] Polyethyleneglycol 4000 at 100°C.

[4] Silicone (DC 550) or Tween 80 at 210°C, carrier gas H_2 (40 cc/min).

[5] The authentic sample was prepared according to the literature (4). The lactone was then converted to γ-hydroxy-γ-methylvaleric acid hydrazide by boiling it with hydrazine for 8 hr in ethanol. mp 65°-66C°.

Czochralski Growth of Iron-59 Doped Calcium Tungstate Crystals and the Determination of Iron Retention by Radiochemical Analysis

V. J. Cobb and J. R. Coleman

Titanium Division, Research Laboratory, National Lead Company, Sayreville, New Jersey

The technique of pulling single crystals from the melt was first used by Czochralski (1) in 1918 to measure the speed of crystallization of different metals. More recently, the technique has been modified for the growth of silicon and germanium single crystals which have found wide use as semiconductors. The first successful application of the Czochralski method to multiple oxide systems was by Nassau and Van Uitert (2, 3). They applied the pulling technique to the growth of both pure and rare earth doped calcium tungstate single crystals. Nassau and co-workers (4, 5) have done extensive research on the growth of calcium tungstate, both pure and with trivalent rare earth substitutions, the latter being useful for laser applications.

The present study has utilized a radioactive tracer to investigate the behavior of iron during the growth of calcium tungstate single crystals by the Czochralski technique. The study was designed to yield information regarding the retention, concentration, and distribution of iron in the finished single crystals.

Initial melts were prepared by dry mixing the calculated amounts of calcium tungstate, radioactive ferrous tungstate containing Fe-59, normal ferrous tungstate, and a 4% excess of tungsten trioxide added as tungstic acid. The mixtures were dry blended until repetitive samples gave equal specific activities (c. min^{-1} g^{-1}) indicative of uniform iron distribution.

The apparatus used for the Czochralski growth of calcium tungstate was similar to that used by Nassau (3). The only significant difference being the use of a Minneapolis-Honeywell "Heat Eye" utilizing a ⅛ in. sapphire rod sighted on the bottom of the iridium crucible, instead of a Pt-PtRh thermocouple immersed in the melt.

A Baird-Atomic Gamma Scintillation Spectrometer, Model 8200, was used to determine the concentration of iron in the initial melts, cold finger samples, and finished single crystals.

All crystals were pulled using a seed crystal oriented in such a way that the a-axis was perpendicular to the melt. The seed was attached to the end of a ⅛ in. diameter rhodium rod by platinum wire. The seed, rotated at a speed of 50 rpm, was lowered into the iron-doped calcium tungstate melt which was held at a temperature of 1625°-1675°C. The seed was allowed to melt slightly, after which the withdrawal mechanism was started and a single crystal pulled from the melt at a rate of 5-15 mm/hr. Samples of the melt were removed at 30-min intervals, during growth of the single crystals, by a cold finger technique and tested for iron content by radioassay. The cold finger sampling involved the immersing of a ⅛ in. rhodium rod in the melt for a few seconds and then withdrawing it. Molten material solidifying on the rod was used as melt samples. Crystals ranging in weight from 8 to 15g were pulled over a period of 2½ to 4¼ hr (~3.3 g/hr).

Table I. Analytical data showing iron retention of calcium tungstate crystals

			Specific activity, c./min/g	Iron content, w/o	Iron distribution coefficient
Run No. 1	Starting material		1046	0.60	
	Cold finger samples	(30 min)	935	0.55	
$K = 5.88 \times 10^{-6}$		(60 min)	918	0.54	
		(90 min)	852	0.50	
		(120 min)	914	0.54	
		(180 min)	904	0.53	
	Average of cold finger samples			0.53	
	Final melt		905	0.53	
	Crystal samples (Top)		28.7	0.017	
			27.0	0.016	
			23.9	0.014	
		(Bottom)	27.3	0.016	
	Average of crystal samples				0.031

Table II. Iron retention of calcium tungstate crystals

Run No.	Melt concentration, w/o	Crystal concentration, w/o	Iron distribution coefficient
1	0.53	0.016	0.031
2	0.55	0.016	0.029
3	0.58	0.016	0.028
4	0.39	0.011	0.028
5	0.41	0.009	0.022
6	0.42	0.014	0.030
7	0.25	0.005	0.020
8	0.25	0.0038	0.015

Calcium tungstate crystals were grown from feeds containing from 0.26 to 0.60 w/o (weight per cent) iron added as iron tungstate. As can be seen from Table I, the concentration of iron in the melt remained essentially constant over the course of the run.

In making material balances for the various runs, both unaccounted weight losses and unaccounted activity losses were found. It was first assumed that the activity loss resulted from loss of iron by volatilization during the melting operation. A careful survey of the operating area gave no indication of radioactivity which might result from condensation of volatilized radioactive iron, however. It was later discovered that the bubble alumina adjacent to the crucible showed the presence of radioactive iron. From the calcium tungstate weight loss and the activity of the contaminated alumina it was estimated qualitatively that the missing iron was present in the alumina asso-

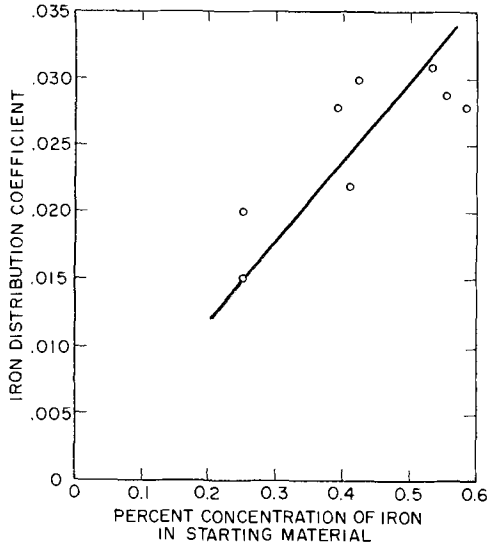

Fig. 1. Effect of change in concentration of iron in the melt on iron retention in the crystal.

ciated with the "lost" calcium tungstate but in a higher concentration than in the starting material.

Careful observation indicated that during growth the calcium tungstate crept up the side and over the lip of the crucible. If iron in molten calcium tungstate is assumed to be a surface active agent, the loss of a disproportionate amount of iron can be explained in this way.

Analytical data for the iron content in the crystals are also shown in Table I and Table II. Samples were taken from the top (first-grown portion) and at intervals of about 3 mm to the bottom (last-grown portion) of the crystal. No significant variation in iron content was observed from place to place, and the iron content was judged to be uniform, as might be expected for this growth technique, over the length of the crystal.

The per cent iron in the crystal increased in a roughly linear fashion with distribution coefficients of iron in the melt as shown in Fig. 1 and ranged from about 0.015 at a melt concentration of about 0.25% Fe (run No. 8) to 0.029 at a melt concentration of 0.55% Fe (run No. 2). Paramagnetic resonance studies by Mergerian (6) disclosed that the majority of the iron was present in the trivalent state. Since these studies were made on a crystal annealed in air at 1200°C for 20 hr, no definitive conclusions can be made with regard to the state of the iron ions at the growth temperature.

Manuscript received May 25, 1965; revised manuscript received Sept. 9, 1965. This paper was presented at the San Francisco Meeting, May 9-13, 1965.

Any discussion of this paper will appear in a Discussion Section to be published in the June 1966 JOURNAL.

REFERENCES

1. J. Czochralski, *Z. Physik Chem.*, **92**, 219 (1918).
2. K. Nassau and L. G. Van Uitert, *J. Appl. Phys.*, **31**, 1508 (1960).
3. K. Nassau and A. M. Broyer, *ibid.*, **33**, 3064 (1962).
4. K. Nassau, Proceedings of the Symposium on Optical Masers, Polytechnic Institute of Brooklyn, April 16-19, 1963.
5. K. Nassau and G. M. Loiacono, *J. Phys. Chem. Solids*, **24**, 1503 (1963).
6. R. Mergerian, Private communication.

On the Use of Galvanostatic Transients for the Study of Fuel Adsorption on Platinum

M. W. Breiter

Research Laboratory, General Electric Company, Schenectady, New York

Galvanostatic or potentiostatic transients have been used in recent years to study the adsorption of formic acid (1-6) and of similar species (7-13) on platinum from aqueous solutions. It is the purpose of this note to compare and evaluate results (1, 4, 5) on the coverage with formic acid as defined subsequently. These results were obtained by two different galvanostatic techniques (1, 4) in N $HClO_4$ with additions of HCOOH. The discussion of the formic acid coverage does not depend on the nature (1, 3-6) of the adsorbed species. Unpublished results of the author on the limitation of the second technique (4) are presented. The conditions for the determination of fuel adsorption from the decrease of hydrogen adsorption are specified for potentials in the hydrogen region.

Anodic charging curves exhibit (1,3) a plateau between about 1.0 and 1.2v in formic acid solutions. The plateau is attributed to the oxidation of adsorbed formic acid. It was found difficult (1) to determine the length of the plateau accurately because of its gradual transition to the subsequent electrochemical process, the formation of the oxygen layer on platinum. Therefore the difference between the anodic charges Q and $Q_{o,an}$, which are required to reach the same potential at the beginning of the O_2 evolution in the presence and absence of formic acid, was suggested (1) as an estimate of the adsorbed amount Q_F of formic acid

$$Q_F = Q - Q_{o,an} \qquad [1]$$

An equivalent procedure was used for potentiostatic transients in other systems (8, 9). It is assumed with Eq. [1] that (*a*) the extent of the formation of the oxygen layer during the fast anodic transient is the same in the presence as in the absence of adsorbable species, (*b*) the double layer charging is the same in each case, (*c*) all the adsorbed species are oxidized, and (*d*) the contribution from species, diffusing to the electrode during the transient, is negligible. The validity of the assumptions (*b*) and (*d*) was demonstrated (1, 3, 4, 8, 9).

The technique was criticized (3, 4) because of the assumptions (*a*) and (c) although experimental findings suggest that they hold approximately. The shape of potential-time curves (U-t curves) or current-time curves (I-t curves) is practically independent of the bulk concentration of the fuel up to 1M in the potential region of O_2 evolution. Oxygen evolution starts on platinum during fast anodic transients after about a monolayer Pt-O has been formed. Another technique which is independent of the assumptions (*a*) and (*c*) was employed (4). The anodic current pulse which is applied during the time τ_a is followed by a cathodic pulse. The charge Q is obtained from the anodic pulse while the charges $Q_{o,cath}$ and Q_H are determined from the cathodic one. Here Q_H designates the charge equivalent of the hydrogen coverage under the given conditions. The charge equivalent of the adsorbed fuel is taken (4) as the difference between Q and $Q_{o,cath}$.

The coverage θ_F is calculated from Q_F and ${}_sQ_F$ where ${}_sQ_F$ represents the saturation value corresponding to the maximum coverage with adsorbed species.

$$\theta_F = Q_F/{}_sQ_F \qquad [2]$$

The hydrogen coverage θ_H

$$\theta_H = Q_H/{}_sQ_H \qquad [3]$$

which coexists in the presence of adsorbed fuel serves as a measure of the part of the surface on which fuel adsorption does not occur.

Comparable results on formic acid adsorption are shown in Fig. 1. The hydrogen coverage is plotted *vs.* the formic acid coverage. Curve a represents the straight line through the data taken from Fig. 5 of ref. (4). The linear extrapolations on both sides are indicated by dashed lines. The ${}_sQ_F$ value of 0.356 mcoul/cm^2 was used in the computation of θ_F. Curve b was constructed from the data in Fig. 5 of ref. (1). These data were obtained by separate anodic and cathodic charging curves at a given formic acid coverage. In general the agreement between the two sets of results may be called fair, taking the reproducibility of about 5% for each of the measurements into account.

Curve b which lies systematically below curve a for $\theta_F \leq 0.85$ consists of a linear portion for $0 < \theta_F < 0.5$

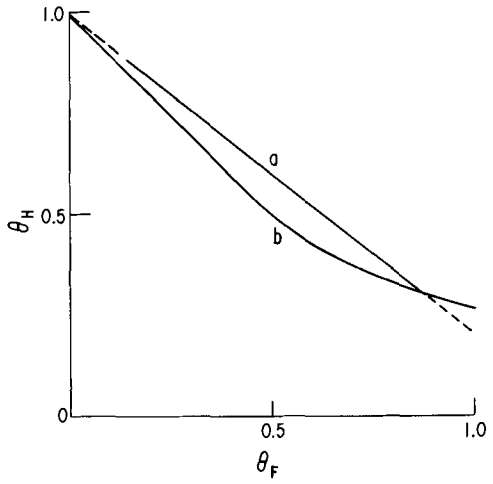

Fig. 1. Hydrogen coverage θ_H as a function of formic acid coverage θ_F on platinum: curve a, ref. (4); curve b, ref. (1).

and a curved portion for $0.5 \leq \theta_F < 1$. It was claimed (4) that a curvature was not found in the case of curve a. However, the experimental points in Fig. 5, and especially in Fig. 6 of ref. (4), indicate the beginning of a curved portion at $\theta_H \approx 0.8$. This suggests that the extrapolated ${}_sQ_F$ values in ref. (4) are too small. Indeed the linear extrapolation of the straight line in Fig. 6 where the curvature is clearly pronounced leads (4) to a ${}_sQ_F$ value of 0.327 mcoul/cm^2 instead of 0.356 mcoul/cm^2.

Larger ${}_sQ_F$ values would lead to a better agreement between the curves a and b of Fig. 1. Thus it is suggested that the two galvanostatic techniques lead to the same results in the case of formic acid adsorption on platinum.

An attempt had been made in 1961 by the author to determine the methanol adsorption on smooth platinum from aqueous solutions by the second technique. However, the technique was abandoned because $Q_{o,an}$ and $Q_{o,cath}$ were not the same in the absence of methanol. The ratio $Q_{o,an}/Q_{o,cath}$ in Table I represents an average of five measurements for each column. The results in Table I demonstrate that $Q_{o,cath}$ is by about 18% smaller than $Q_{o,an}$. A larger effect of this type had been observed (14, 15) previously at smaller values of I_{an} and I_{cath} than here. Although the interpretations (14-16) of the effect are divergent it constitutes a limitation of the second technique. By subtracting $Q_{o,cath}$ from Q an error of unknown magnitude is introduced if $Q_{o,cath}$ and Q are comparable. The error is negligible as in the case (4) of formic acid adsorption if $Q_{o,cath} << Q$.

Table I. Ratio $Q_{o,cath}/Q_{o,an}$ under different conditions in N $HClO_4$

I_{an}, ma/cm^2	160	160	160	140	120
I_{cath}, ma/cm^2	20	60	100	60	60
$Q_{o,cath}/Q_{o,an}$	0.79	0.82	0.84	0.84	0.82

It was suggested (13) to determine the methanol adsorption on platinum solely from the measurements of the hydrogen coverage by cathodic transients. This procedure leads to θ_F values which are too small in the potential region of hydrogen adsorption. The hydrogen coverage which exists at a certain potential in the hydrogen region is not measured by the cathodic transient starting at that potential. The deviations will be the larger the smaller θ_F is. Both an anodic and a cathodic charging curve are required for the determination of fuel adsorption at potentials in the hydrogen region. The discrepancies between the methanol coverage of ref. (8) and (13) in the hydrogen region result from a disregard of the above condition in ref. (13).

Acknowledgment

The author acknowledges helpful suggestions by Dr. S. Gilman, General Electric Research Laboratory.

Manuscript received June 25, 1965.

Any discussion of this paper will appear in a Discussion Section to be published in the June 1966 JOURNAL.

REFERENCES

1. M. W. Breiter, *Electrochim. Acta*, **8**, 447 (1963).
2. C. W. Fleischmann, G. K. Johnson, and A. T. Kuhn, *This Journal*, **111**, 602 (1964).
3. S. B. Brummer and A. C. Makrides, *J. Phys. Chem.*, **68**, 1448 (1964).
4. S. B. Brummer, *ibid.*, **69**, 562 (1965).
5. M. W. Breiter, *Electrochim. Acta*, **10**, 503 (1965).
6. P. R. Johnson and A. T. Kuhn, *This Journal*, **112**, 599 (1965).
7. T. O. Pavela, *Ann. Acad. Sci. Fennicae*, Series A, II. Chemica, 59 (1954).
8. M. W. Breiter and S. Gilman, *This Journal*, **109**, 622 (1962).
9. S. Gilman, *J. Phys. Chem.*, **67**, 78 (1963).
10. A. N. Frumkin and B. I. Podlovchenko, *Doklady Acad. Nauk S.S.S.R.*, **150**, 349 (1963).
11. J. Giner, *Electrochim. Acta*, **9**, 63 (1964).
12. T. B. Warner and S. Schuldiner, *This Journal*, **111**, 992 (1964).
13. O. A. Hasova, Yu. B. Vassiljev, and W. S. Bagotzkii, *Electrochimija, S.S.S.R.*, **1**, 84 (1965).
14. K. Vetter and D. Berndt, *Z. Elektrochem.*, **62**, 378 (1958).
15. S. W. Feldberg, C. G. Enke, and C. E. Bricker, *This Journal*, **110**, 826 (1963).
16. S. Schuldiner and T. B. Warner *ibid.*, **112**, 212 (1965).

Oxidation of Hydrogen on Nickel Electrodes in Sodium Hydroxide Solution

R. N. O'Brien[1] and K. V. N. Rao

Chemistry Department, University of Alberta, Edmonton, Alberta, Canada

The mechanism of the electrochemical oxidation of hydrogen on nickel in alkaline solutions, a reaction of possible fuel cell use, has not been established yet. Several authors observed a limiting anodic current in this system, but different explanations have been offered for the occurrence of the limiting current. Thus Lukowzew, Lewina, and Frumkin (1) suggested that the limiting current is due to the concentration polarization of the hydrogen dissolved in solution and also due to the oxidation of the nickel anode beginning when hydrogen becomes deficient on the surface as a result of concentration polarization. They concluded this on the basis of the observation of the coincidence of the polarization curves obtained on the initial electrodes and on the electrodes subjected to repeated, successive oxidation and reduction, assuming that oxidation-reduction cycling increased the true area of the electrode. However, Weininger and

[1] Visiting Scholar, College of Chemistry, University of California, Berkeley, California.

Breiter (2) reported recently that successive anodic-cathodic sweeps did not increase the surface area of nickel electrodes in KOH by their experimental procedure. Makrides (3), on the other hand, obtained different polarization curves for electrodes of different pretreatment and attributed the limiting current on "initial" electrodes to diffusion control and to activation control of the step $H_2 = H_{ads} + H_{ads}$ on electrodes subjected to anodic-cathodic cycling. However, according to Kandler, Roemer, and Häusler (4), the limiting current obtained potentiostatically on porous electrodes, is due to diffusion control of molecular hydrogen in the solution. Weininger and Breiter (2) concluded that the anodic limiting current cannot be attributed to the Tafel step $H_2 = H_{ads} + H_{ads}$, based on the observation that practically the same current-potential curves resulted for solutions stirred with hydrogen or with argon. Instead, they suggested from the observation of a peak at about —100 mv overvoltage in the differential capacity-potential curve that anodic formation of adsorbed hydroxide due to the reaction $Ni + OH^- = NiOH + e$ might be taking place between —100 and +100 mv overvoltage. It is the purpose of the present study to investigate the cause of the anodic limiting current, which elucidates the mechanism of the electrochemical oxidation of hydrogen.

Experimental

Spectrographically pure nickel rod supplied by Johnson, Matthey, and Company was used for electrodes. A small piece of this rod was tapped, threaded, and attached to a steel rod which served as the electrical lead. The nickel end of this rod was forced into a hole in a small piece of Teflon rod. A thick walled glass tube fitted over the Teflon isolated the steel from the electrolyte. With the aid of a Teflon ring, brass cap, and a nut over the glass tube the electrode was made leakproof (5). A 19/38 ground glass joint was attached to the glass tube to insert the electrode into the cell. The electrode was machined flat so as to expose only the cross section of 0.19 cm^2 area of nickel to the solution. Anodic and cathodic charging curves were obtained with such electrodes. For steady state polarization measurements cylindrical electrodes of large area were used. These electrodes were also constructed in the same manner as described above except that the cylindrical nickel rod was covered with Teflon both at the top and the bottom exposing the middle portion (4.9 cm^2) to the solution.

The electrolytic cell was made of Pyrex glass and consisted of three compartments. Hydrogen or Hg/HgO electrodes placed in one side compartment were used as reference electrodes. Provision was made for bubbling hydrogen or helium in the reference and working electrode compartments. Bright platinum was used as a counter electrode in the other side compartment which was separated from the central compartment by a sintered disk. During the anodic potential-current measurements a cylindrical platinum gauze surrounding the working electrode was used as a counter electrode. Measurements were made in NaOH solutions prepared from Fisher certified electrolytic pellets. Hydrogen purified by passing it through a Serfass hydrogen purifier was bubbled through the solution for at least 3 hr before the start of the experiment. Grade A helium was bubbled through during the pre-electrolysis period of 15-20 hr. The electrodes were abraded with 4/0 emery paper and cleaned with chromic sulfuric acid solution followed by washing with conductivity water. They were made anodic for 5 min at 0.1 ma/cm^2 and then cathodic for at least 10 min at 1 ma/cm^2 in the working cell prior to measurements. Pretreatment of the electrodes at 0.2 ma/cm^2 anodic and 2.0 ma/cm^2 cathodic for 5 min did not produce any difference in results.

Steady state polarization measurements were made using a fast rise Wenking potentiostat. Currents were calculated from the iR drop measured across General Radio Standard resistances with the Keithley Model 660 Differential voltmeter. Charging curves were obtained by employing this potentiostat and a Western Electric 275 B relay. The required potential between the working electrode and the reference electrode was impressed by the potentiostat for 5 min and then the potentiostatic circuit was broken while applying the galvanostatic circuit simultaneously by the relay. The resulting potential-time curve was registered on the Tektronix Type 535 A oscilloscope. A 90v battery was used as a power source for the galvanostatic circuit. All the charging curves were obtained in 1.0*N* NaOH solution at 35° ± 1°C and the data reported refer to apparent surface area.

Results and Discussion

Polarization curves obtained potentiostatically at 35°C in 0.1*N*, 0.5*N*, and 1.0*N* sodium hydroxide solutions stirred vigorously, are shown in Fig. 1. All the potentials reported here refer to the reversible hydrogen electrode in the same solution unless otherwise mentioned. Steady currents were obtained in less than a minute in cathodic measurements (not reported here), whereas time variation of the current was observed in anodic measurements. The current readings taken at the end of 10 min at each potential are reported here. Figure 1 reveals that polarization is higher the smaller the concentration of sodium hydroxide which is likely for the over-all reaction

$$H_2 + 2OH^- = 2H_2O + 2e$$

It can also be seen from Fig. 1 that the current increases first with potential, reaches a limiting or peak value, and then decreases with further increase of potential. This clearly indicates that the oxidation of hydrogen reaction is not limited by either activation control of the step $H_2 = H_{ads} + H_{ads}$ or by diffusion control of hydrogen dissolved in solution because the current is not expected to decrease but level out with increase of potential in both these cases. The anodic limiting current of 14 $\mu a/cm^2$ in 0.1*N* NaOH obtained galvanostatically by Makrides (3) corresponds with the peak current obtained here potentiostatically in 0.1*N* NaOH. If the galvanostatic limiting current can be identified with the potentiostatic peak current, then the peak current, contrary to the results obtained here, should increase with decrease in NaOH concentration according to diffusion as well as activation control mechanisms, because the concentration of dis-

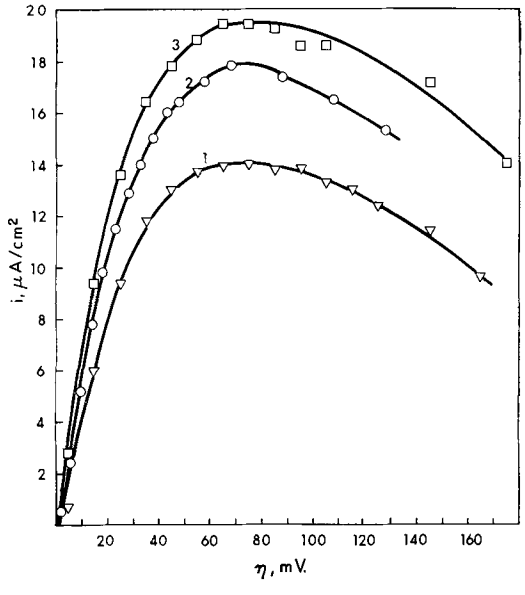

Fig. 1. Anodic polarization curves of the oxidation of hydrogen on nickel in sodium hydroxide solutions: 1, 0.1*N* NaOH; 2, 0.5*N* NaOH; 3, 1.0*N* NaOH.

solved hydrogen increases with decrease in NaOH concentration. As the decrease in current with potential beyond a certain critical value is a phenomenon typical of metal passivity, and since this decrease in current also begins about 35 mv cathodic to the equilibrium potential for the formation of oxide according to the reaction

$$Ni + 2H_2O = Ni(OH)_2 + 2H^+ + 2e$$

at all concentrations of sodium hydroxide investigated, it may be inferred that the decrease in current here is due to oxide film formation on the nickel electrode surface. Frumkin and Aikazyan (6) observed a decrease in current with potential in the studies of oxidation of hydrogen on platinum and suggested that the decrease in hydrogen ionization current is connected with passivation of platinum by adsorbed anions with increasing anodic polarization. Franke, Knorr, and Breiter (7) also observed in the anodic oxidation of hydrogen on platinum that the current decreases as oxidation of the surface occurs.

In order to see whether oxide film forms on the nickel surface, and if so whether the film formation begins from the potential where the anodic current begins to decrease or from lower positive potentials, the surface coverage at different potentials was determined by the method of cathodic charging curves. The galvanostatic reduction curves obtained at 10 ma/cm^2 in 1.0*N* NaOH after potentiostatically oxidizing the electrode at various potentials are shown in Fig. 2 and 3. It can be seen from Fig. 2 and 3 that kinks are present in all the reduction curves. Kinks or

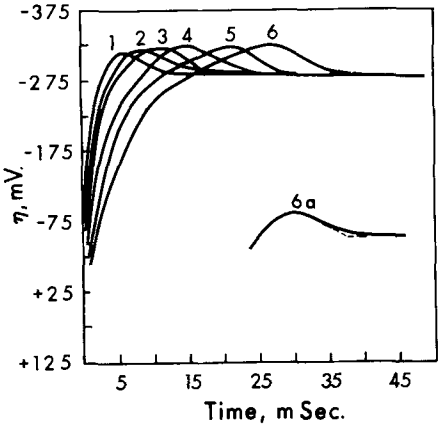

Fig. 2. Galvanostatic cathodic charging curves in 1.0*N* NaOH at 10 ma/cm^2 after anodic oxidation at constant overpotentials of: 1, +25 mv; 2, +45 mv; 3, +65 mv; 4, +85 mv; 5, +105 mv; 6, +125 mv; 6a, +85 mv.

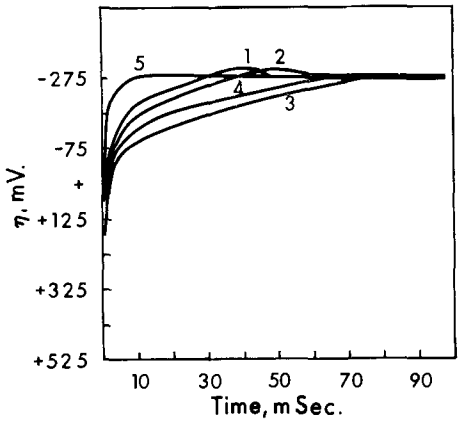

Fig. 3. Galvanostatic cathodic charging curves in 1.0*N* NaOH at 10 ma/cm^2 after anodic oxidation at constant overpotentials of: 1, +145 mv; 2, +165 mv; 3, +225 mv; 4, +325 mv; 5, +525 mv.

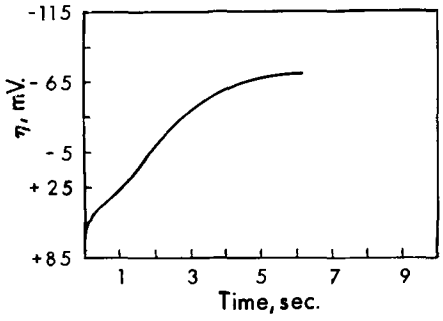

Fig. 4. Galvanostatic cathodic charging curve in 1.0*N* NaOH at 48 μa/cm^2 after anodic oxidation at a constant overpotential of +85 mv.

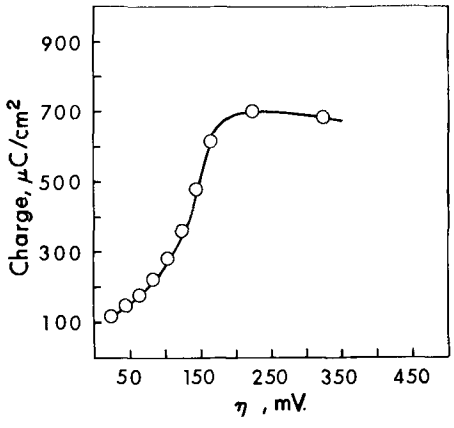

Fig. 5. Variation of charge associated with the step of the reduction curves of Fig. 2 and 3 as a function of overpotential.

overshoots have been frequently noted in the literature, but so far no single view on their nature exists (8). Kinks were not pronounced in the reduction curves obtained at 1 ma/cm^2 and disappeared completely from curves obtained at still lower current densities. Figure 4 is the reduction curve obtained at a current density of 48 μa/cm^2, showing the absence of kink. The appearance of overshoots in the chronopotentiograms makes it difficult to estimate the transition times accurately. Tangents were drawn as shown in Fig. 2, 6A and transition times λ, were measured from origin to the points of intersection of the dashed lines. The cathodic charge ($i\lambda$) which corresponds to surface coverage, was deduced from Fig. 2 and 3 and is shown in Fig. 5 as a function of over-potential. The charge involved as plotted in Fig. 5 may be due to the reduction of the oxide and/or hydroxide formed during potentiostatic oxidation and due to the deposition of hydrogen atoms. As it is not easy to make a distinction between whether oxide or hydroxide is formed on the surface it is assumed here that oxide is formed. Since the shape of the reduction curves, as can be seen from Fig. 2 and 3, starting from various potentials except from +525 mv (graph 5, Fig. 3) is similar and since the charge associated with the reduction step increases with increasing anodic potential, it is likely that most of the charge is involved in the reduction of oxide but not deposition of hydrogen atoms. Hydrogen evolution might be occurring beyond the peak in the chronopotentiograms. The different shape of the chronopotentiogram starting from +525 mv may be attributed to the modification of the surface when potentiostatically oxidized at this potential, the modification being such that it is reduced mostly at the hydrogen evolution potential.

Weininger and Breiter (9) found in the oxidation of nickel in 0.2*N* KOH from potential-current curves that a potential of about +320 mv *vs.* the hydrogen elec-

trode in the same solution is reached on coverage equivalent to about one monolayer of hydroxide. Approximately 600 μc is taken as equivalent to one monolayer. The charge (about 670 μc) at +300 mv obtained here from potential-time curves is in fair agreement with their value. Figure 5 reveals that about 1/6 of a monolayer of surface is covered with oxide even at +25 mv (whereas peak current is at +70 mv) and this increases with increasing potential, reaching a limiting value at about 200 mv. This suggests that the rate of oxidation of hydrogen decreases with increasing potential because of the decrease in area available uncovered with oxide where the rate of electrochemical oxidation of hydrogen is higher, rather than the view that oxidation of the nickel anode begins when hydrogen becomes deficient as a result of concentration polarization.

Although Weininger and Breiter (2), as mentioned earlier, reported that practically the same current-potential curves were obtained for solutions stirred with either hydrogen or argon, it was found that the steady state polarization curves were different for solutions stirred with hydrogen or helium in the region reported here. The currents taken at the end of 10 min were, for instance, 18.2 and 0.5 μa/cm^2 at an overpotential of +85 mv in 1.0N NaOH solutions stirred with hydrogen and helium, respectively. The difference in the results may be attributed to the difference in the techniques employed. Weininger and Breiter (2) obtained the current-potential curves by impressing potentiostatically a linearly increasing potential at a sweep rate of 5 mv/sec. Sato and Okamato (10) reported a difference in the polarization curves of the oxidation of nickel in alkaline solutions at a pH of 11.7, obtained by the transient state method with a 0.33 mv/sec rate of change of potential, and the stationary state method; the currents being about 10.0 and 0.08 μa/cm^2, respectively at —500 mv potential with reference to the standard hydrogen electrode. Hence it may be concluded that polarization is lower in solutions stirred with hydrogen than in solutions stirred with helium due to participation of dissolved hydrogen in the electrode reaction.

Acknowledgment

The authors gratefully acknowledge the support of this work by the Defense Research Board of Canada.

Manuscript received June 23, 1965; revised manuscript received Aug. 23, 1965.

Any discussion of this paper will appear in a Discussion Section to be published in the June 1966 JOURNAL.

REFERENCES

1. P. Lukowzew, S. Lewina, and A. Frumkin, *Acta Physicochim.*, **11**, 21 (1939).
2. J. L. Weininger and M. W. Breiter, *This Journal*, **111**, 707 (1964).
3. A. C. Makrides, *ibid.*, **109**, 977 (1962).
4. L. Kandler, D. Roemer, and E. Hausler, *Electrochim. Acta*, **8**, 233 (1963).
5. M. Stern and A. C. Makrides, *This Journal*, **107**, 782 (1960).
6. A. Frumkin and E. A. Aykazyan, *Doklady Akad. Nauk S.S.S.R.*, **100**, 315 (1955).
7. K. Franke, C. Knorr, and M. W. Breiter, *Z. Elektrochem.*, **63**, 226 (1959).
8. S. Biallozor, *Zhur. Fiz. Khim.*, **38**, 754 (1964).
9. J. L. Weininger and M. W. Breiter, *This Journal*, **110**, 484 (1963).
10. N. Sato and G. Okamato, *ibid.*, **110**, 605 (1963).

Detection and Removal of Traces of Water from Alkali Halides

Irving Warshawsky

Lewis Research Center, National Aeronautics and Space Administration, Cleveland, Ohio

It is well known that analytical reagent grade alkali halides are contaminated with traces of water. The presence of this impurity is a source of difficulty in the following studies:

1. In the preparation of "F" centers in alkali halides, the presence of an impurity such as water or hydroxide may lead to colloid formation (1).
2. When an alkali halide is added to an alkali metal ammonia solution, the water impurity is a source of decomposition of the blue solution (2).
3. In the preparation of solutions of alkali metals in molten salts, the presence of water in the melt not only is a source of decomposition (3), but also leads to corrosion of the container (4).

The purpose of this note is:

1. To present a quantitative method for the detection of traces of water in alkali halides; and
2. To indicate the effectiveness of two methods of removing traces of water from analytical reagent grade alkali halides: (*a*) pumping on the salt at room temperature, and (b) washing with dry liquid ammonia.

Quantitative Method for Detection of Traces of Water

A method for the quantitative detection of traces of water in an alkali halide consists of measuring the amount of hydrogen evolution from the reaction

$$H_2O_{(salt)} + Na_{(NH_3)} \xrightarrow[-78°C]{} NaOH_{(ppt)} + \tfrac{1}{2} H_{2(g)}$$

There is an additional source of hydrogen evolution: the reaction of the blue solution with adsorbed water at the glass-liquid interface (5). At —78°C the homogeneous reaction of sodium with ammonia is negligible.

Experimental

Pumping on the salt at room temperature to remove water impurity.—A small weighed quantity of analytical reagent grade alkali halide was placed in an open vial. The vial was placed into an impule (ID 10 mm) along with a small quantity of sodium. The ampule was then glass-blown to the vacuum line. (The glass-blowing was carried out using a drying tube to minimize the introduction of a new source of moisture.) The salt was dried by pumping on it at room temperature and at pressures less than 10^{-6} mm Hg. For purposes of comparison, one sample of each salt was pumped on for about 20 hr and a second sample of the same salt for about 125 hr. During the final 2 hr of pumping, a liquid nitrogen bath was placed around a trap between the calibrated McLeod gauge and the ampule containing the salt in order to minimize mercury contamination. The latter is believed to catalyze the decomposition of the blue solution (6).

After the drying operation was completed, 3.20 cc of degassed liquid ammonia (previously dried over sodium) were distilled into the ampule which contained the reagent grade salt and sodium at —78°C. This resulted in the formation of a dark blue solution containing an excess of salt. After the saturated solution had been allowed to sit at —78°C for 6 hr, the quantity of hydrogen evolved was determined with a calibrated McLeod gauge, as described previously (5, 7). In one "run" with reagent grade lithium bro-

Table I. Summary of the quantitative data for detection of water in analytical reagent grade alkali halides

Salt	Grams of salt	Hours pumped	*Moles of H_2 evolved $\times 10^7$	*Per cent water by weight
LiCl	0.0382	19	12	0.11
LiCl	0.0618	125	2.9	0.017
LiBr	0.0738	18	240	>1.0
LiBr	0.0624	130	4.1	0.024
NaCl	0.0672	19	11	0.059
NaCl	0.0495	118	3.4	0.025
NaI	0.0814	22	2.9	0.013
NaI	0.0653	118	1.8	0.0099
KCl	0.0340	22	5.8	0.061
KCl	0.0424	118	7.1	0.060
KI	0.0806	22	3.1	0.014
KI	0.100	142	2.9	0.013

* Corrected for the heterogeneous reaction between the blue solution and adsorbed water.

mide (which had been pumped on for 18 hr), the original dark blue solution faded completely in 5 hr. Blank determinations in the absence of the salt were made in order to correct for the quantity of hydrogen evolved from the heterogeneous reaction during the 2 hr. Results are summarized in Table I.

Washing with dry liquid ammonia to remove water impurity.—An ampule containing 0.10g reagent grade sodium iodide with a sidearm holding sodium was glass-blown to the vacuum line. The system was pumped on for 24 hr at room temperature and at a pressure less than 10^{-6} mm Hg. Liquid ammonia, dried over sodium, was distilled into the ampule containing the salt; a saturated solution formed, which was allowed to sit at —78°C for 24 hr. The solvent was then distilled back into a reservoir containing sodium, and the sodium iodide was pumped on for another 24 hr to remove the residual ammonia. This purification procedure was repeated two more times.

In order to test for the presence of water, $\sim 10^{-6}$ moles of sodium was transferred into a saturated solution of the salt in liquid ammonia at —78°C, as previously described (5). This did not result in any additional hydrogen evolution within experimental error (7). Similar results were obtained for the ammonia treatment of lithium chloride (reagent grade) and potassium chloride (reagent grade).

Conclusion

It has been observed quantitatively that extended pumping on analytical reagent grade salts (as described) is not sufficient to remove the last traces of water. However, it is noted that extending the time of pumping on the lithium salts from about 18 hr to about 125 hr does lead to a considerable decrease in the per cent of water impurity present, while for the potassium salts tested, extending the time of pumping (as above) has very little effect on the removal of the water impurity. On the other hand, treatment with liquid ammonia has been shown to be a more effective method for removing traces of water.

Manuscript received Aug. 23, 1965.

Any discussion of this paper will appear in a Discussion Section to be published in the June 1966 JOURNAL.

REFERENCES

1. J. H. Schulman and W. D. Compson, "Color Centers in Solids," p. 267, MacMillan, New York (1962).
2. P. D. Schettler, Jr., and A. Patterson, Jr., *J. Phys. Chem.*, **68**, 2870 (1964).
3. J. Greenberg and I. Warshawsky, *J. Am. Chem. Soc.*, **86**, 3572 (1964).
4. F. R. Duke and L. Bissell, **111**, 717 (1964).
5. I. Warshawsky, *J. Inorg. Nucl. Chem.*, **25**, 601 (1963); *J. Catalysis*, **3**, 291 (1964).
6. J. F. Dewald and G. Lepoutre, *J. Am. Chem. Soc.*, **76**, 3369 (1964).
7. I. Warshawsky, "The Reaction of Adsorbed Water with a Dilute Solution of Sodium in Liquid Ammonia at —78°C," Solutions Metal-Ammoniac: Proprietes Physicochimiques," p. 167, G. Lepoutre and M. J. Sienko, Editors, Catholic University Press, Lille, France, 1963. (Distributed by W. A. Benjamin Inc., New York, N. Y.)

Brief Communications

The $Zn_xCd_{(1-x)}SnAs_2$ Semiconducting Alloy System

B. R. Pamplin, J. S. Shah, and R. A. L. Sullivan

Department of Physics, Bristol College of Science and Technology, Bristol, England

Recent work on semiconducting alloys has shown that a large number of tetrahedrally bonded compounds are isomorphous in pairs. It is found that if two such compounds share a common atom they usually exhibit complete solid solution (1). Ternary compounds $ZnSnAs_2$ and $CdSnAs_2$ which have chalcopyrite structure El 1 (space group $D_{2d}^{12} - I\bar{4}2d$) have been shown to form complete solid solution with InAs (2, 3). The work reported in this note was undertaken to see if the two compounds $ZnSnAs_2$ and $CdSnAs_2$ are also capable of complete solid solution. The compositions chosen for study are those predicted by simple structural arguments to be most likely to show complete or partial ordering (4).

The different compositions used were prepared by reacting the elements of semiconductor grade purity *in vacuo* in quartz ampoules and holding in the molten state for several hours. The ingot so produced was then powdered, annealed at temperatures above 600°C for several weeks, and finally quenched in water. X-ray powder photographs were taken using a Philips 11.46 cm diameter camera and Ni filtered $CuK\alpha$ radiation. The films were interpreted by reference to the end components as being of chalcopyrite structure.

The lattice parameters were determined by the method of least squares. A program was written for the Elliot 803 computer which calculated the lattice parameters with their standard errors. The procedure of Mueller *et al.* (5) was followed in that various correction terms were introduced into the calculation, one at a time. A solution was also calculated using no correction term. However, it was found that the lattice parameters obtained did not differ significantly whichever correction term was used. For consistency Taylor and Sinclair's (6) correction term $\sin^2 2\theta(1/\sin\theta + 1/\theta)$ was used for all results quoted. Since only reflections with a Bragg angle greater than 60° were used weighting each reflection did not significantly affect the results either. Results quoted here were obtained using unweighted reflections.

Table I. Parameters of various alloys

Mole % $CdSnAs_2$	Composition	a, Å	c, Å	c/a	
0	$ZnSnAs_2$	5.852 ± 0.001	11.705 ± 0.002	2.0002 ± 0.0005	Present work
	$ZnSnAs_2$	5.852 ± 0.001	11.705 ± 0.001	2.000 ± 0.0012	Gasson *et al.* (7)
	$ZnSnAs_2$	5.851 ± 0.002	11.710 ± 0.015	—	Masumoto (8)
12.5	$Zn_{7/8}Cd_{1/8}SnAs_2$	5.872 ± 0.004$_4$	11.742 ± 0.010	1.999$_5$ ± 0.0020	Present work
25	$Zn_{3/4}Cd_{1/4}SnAs_2$	5.897 ± 0.002	11.795 ± 0.003	2.0001 ± 0.0007	Present work
37.5	$Zn_{5/8}Cd_{3/8}SnAs_2$	5.907 ± 0.002	11.812 ± 0.005	2.0001 ± 0.0010	Present work
50	$Zn_{1/2}Cd_{1/2}SnAs_2$	5.971 ± 0.003	11.824 ± 0.009	1.9800 ± 0.0020	Present work
62.5	$Zn_{3/8}Cd_{5/8}SnAs_2$	5.986 ± 0.004	11.864 ± 0.009	1.9820 ± 0.0020	Present work
75	$Zn_{1/4}Cd_{3/4}SnAs_2$	5.998 ± 0.001	11.894 ± 0.003	1.9760 ± 0.0010	Present work
87.5	$Zn_{1/8}Cd_{7/8}SnAs_2$	6.047 ± 0.001	11.897 ± 0.002	1.9672 ± 0.0005	Present work
100	$CdSnAs_2$	6.0944 ± 0.0004	11.9182 ± 0.0007	1.9556 ± 0.0002	Present work
	$CdSnAs_2$	6.093 ± 0.001	11.936 ± 0.001	—	Gasson *et al.* (7)
50	$Zn_{1/2}Cd_{1/2}SnAs_2$ (Disordered)	5.949 ± 0.10	—	—	Present work

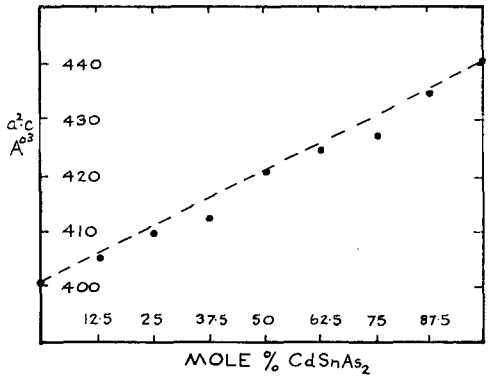

Fig. 1. Variation of unit cell volume (a^2c) *vs.* composition in the system $Zn_xCd_{(1-x)}SnAs_2$.

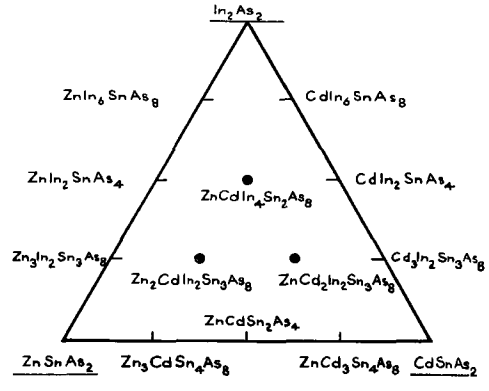

Fig. 2. Pseudoternary system $(Zn_xCd_{(1-x)})_y\ In_{1-2y}Sn_yAs$. Formulas along coordinates and in the diagram indicate compositions rather than ordered phases or compounds.

In the $Zn_xCd_{(1-x)}SnAs_2$ system all the compositions with $x = n/8$ were found to be chalcopyrite. The high angle alpha doublets were clearly resolved in the film of every annealed sample. No convincing evidence for superlattice lines due to further ordering was found. A few weak extra lines found on some photographs were identified as due to As which presumably deposited from the vapor phase on quenching. The "a" and "c" parameters (with their standard errors) of the various alloys in this system are given in Table I. It is worth noting that for all alloys the standard errors in the parameters are larger since the high angle lines in the powder photographs of these were not as sharp as those for pure $CdSnAs_2$ and $ZnSnAs_2$. Figure 1 shows the variation of the unit cell volume (a^2c) as a function of composition. Such departures from Vegard's law as are seen in Fig. 1 are not uncommon in semiconducting alloy systems (1). They are due presumably to the fact that the alloys under study may not quite have achieved their true equilibrium state.

The 50% alloy $ZnCdSn_2As_4$ was found to possess also a disordered sphalerite structure when quenched after anneal above 630°C. It thus seems likely that all zinc rich alloys in the system undergo an order-disorder transition as does $ZnSnAs_2$ itself (7, 8).

It has been shown (9) that the three compositions $ZnCdIn_4Sn_2As_8$, $ZnCd_2In_2Sn_3As_8$, and $Zn_2CdIn_2Sn_3As_8$ in the pseudoternary system $(Zn_xCd_{(1-x)})_y\ In_{1-2y}Sn_yAs$ (Fig. 2) can be obtained single phase with disordered sphalerite structure. Since in the pseudobinary system In_2As_2, $CdSnAs_2$ chalcopyrite structure is found only for the compositions in the vicinity of $CdSnAs_2$ (3), it would be fair to predict that in the phase triangle of the pseudoternary system (Fig. 2) compositions in the vicinity of the base line of the pseudoternary system ($ZnSnAs_2$ — $CdSnAs_2$ line) may possess chalcopyrite structure. All other compositions are likely to have sphalerite structure.

Acknowledgment

The authors wish to thank the Central Electricity Generating Board for the support of this work and to Professor S. H. Ayliffe for the facilities of his department and for his encouragement.

Manuscript received July 26, 1965.

Any discussion of this paper will appear in a Discussion Section to be published in the June 1966 JOURNAL.

REFERENCES

1. J. C. Woolley, "Preparation of III-V compounds," Chap. I, R. K. Willardson and H. L. Goering, Editors, Reinhold Publishing Co., New York (1962).
2. G. Giesecke and H. Pfister, *Acta Cryst.*, **14**, 1289 (1961).
3. N. A. Goryunova and V. D. Prochukhan, *Sov. Phys. Solid State*, **2**, 161 (1960).
4. B. R. Pamplin, *Nature*, **188**, 136 (1960).
5. M. H. Mueller, L. Heaton, and K. T. Miller, *Acta, Cryst.*, **13**, 828 (1960).
6. A. Taylor and H. Sinclair, *Proc. Phys. Soc.*, **57**, 126 (1945).
7. D. B. Gasson, P. J. Holmes, I. C. Jennings, B. R. Marathe, and J. E. Parrott, *J. Phys. Chem. Solids*, **23**, 1291 (1962).
8. K. Masumoto and S. Isomura, *ibid.*, **26**, 163 (1965).
9. B. R. Pamplin and J. S. Shah, *Nature*, **180**, 207 (1965).

Preferential Etching Techniques for Removing Dendrites from Silicon Dendritic Web Material

David W. Ing

Westinghouse Electric Corporation, Research and Development Center, Pittsburgh, Pennsylvania

and Thomas Hunt

Semiconductor Division, Westinghouse Electric Corporation, Youngwood, Pennsylvania

A new, nonmechanical technique for removing dendrites from silicon dendritic web material is described here.

Silicon dendritic web material is produced by growing a silicon sheet between two dendrites. The sheet faces are perpendicular to the [111] direction and possess few dislocations or other surface imperfections. In many applications it is preferable to use only the web portion of the webbed dendrite material. The standard mechanical methods for removing the dendrites often produce undesirable effects. A technique has been developed in which the dendrites are removed by heating dendritic web in KOH or NaOH solutions. Due to the difference in crystal orientations, these solutions preferentially etch the dendrites while leaving the web material relatively unaffected. The etching solution will attack surface imperfections on the web, but this problem is eliminated by oxide masking the sheet prior to etching.

In the new procedure, an oxide film is formed over the entire surface of the webbed dendrite by steam oxidation at 1200°C. Wax is applied to the sheet surface and the oxide coating is removed from the dendrites by an HF etch. Boiling trichloroethylene is used to clean the wax from the web surface. After this preparation, the webbed dendrites are heated in a solution of sodium or potassium hydroxide (10-20% by weight). The solution reacts strongly with the dendrites but the web surface is completely protected by the oxide coating. The web is removed from the solution as soon as the dendrites are completely etched away.

If surface flatness is not a prime requirement, the oxide step may be omitted. The etching solution will react only slightly with the crystallographically perfect sections of the sheet, while it will vigorously etch the dendrites and any surface imperfections on the web. This will result in shallow dimples in the web surface at imperfection sites, but the dendrites will be removed before a significant amount of silicon is etched from the sheet. The resultant web surface is not as flat as that obtained by including the oxide film step but still may be suitable for certain applications.

Manuscript received Aug. 25, 1965.

Any discussion of this paper will appear in a Discussion Section to be published in the June 1966 JOURNAL.

Thin Films Grown on Silicon Surfaces by Excess Nitric Acid Process

William B. Glendinning, Sidney Marshall, and Albert Mark

United States Army Electronics Command, Fort Monmouth, New Jersey

One often observes that following the use of routine laboratory procedures for etching or staining polished silicon wafers the samples are covered with a colored residue or stain film. Several workers have studied this effect and have reported the growth of such films in etchants rich in HF (1-5). Archer concludes that the films are a silicon hydride or another silicon rich form.

This note describes experimental work in which stain films on silicon were produced by both liquid and vapor phase reaction of etchants and silicon wherein the nitric acid concentration of the etchant was exceedingly high.

In the method used in our work a 0.050 in. bead of nitric acid is formed between the tip of a capillary tube and the silicon surface. A polyethylene nozzle directs a mixed stream of HF vapors and oxygen flowing at approximately 7 cc/min at the juncture of the HNO_3 drop and the silicon surface. The silicon substrate is heated to a temperature of 35°-40°C as measured by a Cu-Const thermocouple placed on the upper surface of the sample. When the capillary tube, which can be translated by a micrometer stage, is moved across the surface of a 0.01 ohm-cm p-type sample at a speed of 7 mils/sec a series of ringlike stain film growths occur (Fig. 1). A distilled water rinse was used to quench the etching and film growth reactions.

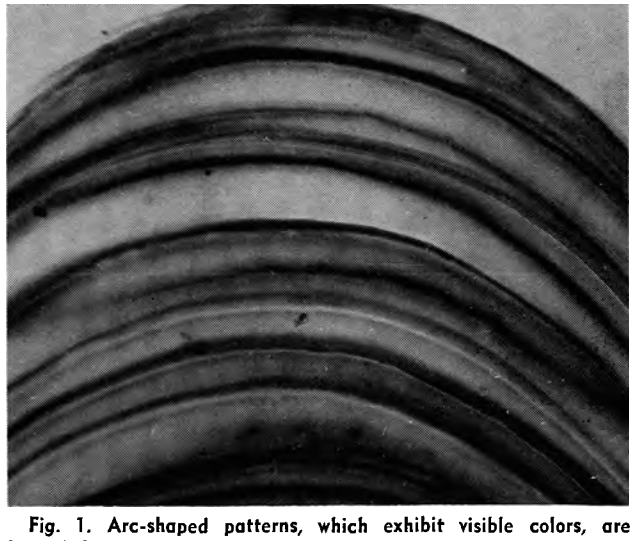

Fig. 1. Arc-shaped patterns, which exhibit visible colors, are formed from liquid HNO_3-vapor HF process.

We observed that the stain films were not noticeably attacked by treatment in a 47% HF solution, but that they could be removed by immersion in a 10% solution of NaOH for 3 min and were also dissolved by concentrated HNO_3.

The surface topology of the silicon samples in the vicinity of the film growth was examined by removing a part of the growth with the 10% NaOH solution, overcoating the sample with aluminum, and studying the fringe pattern obtained with a multiple beam interference technique. Film thickness obtained in this manner ranged from 900 to 1400Å. The surface in the region where the stain film was removed was corrugated and was depressed below the original surface of the silicon sample.

In a variation of the experimental procedure an angle-lapped silicon sample having a nine layer epitaxial structure with two resistivity levels was employed. The HNO_3 bead was formed as before, but this time it remained stationary in the angle-lapped region while the HF vapor stream flowed around it. Film growth was observed here also, but in this case the growth was in the lateral direction outward from the droplet. The extent and rate of growth under these conditions varied with the layer resistivity level and conductivity type. Film growth was most rapid on the 10 ohm-cm n-type, 0.05 ohm-cm p-type, and 10 ohm-cm p-type surfaces. The surface as well as two other 0.05 ohm-cm n-type layers reacted very little during the growth reaction.

Film growths obtained both with the moving HNO_3 bead and with the stationary bead on the angle-lapped surface could be readily scratched, and when this was done small irregularly shaped pieces of the film broke away from the silicon substrate surface.

Further correlation between stain film growth and silicon conductivity type and impurity concentration is being sought. In addition, the potential use of the film growth reaction in a silicon etching process is being evaluated.

Manuscript received July 2, 1965; revised manuscript received Sept. 1, 1965.

Any discussion of this paper will appear in a Discussion Section to be published in the June 1966 JOURNAL.

REFERENCES

1. R. J. Archer, *Phys. Chem. Solids*, **14**, 104 (1960).
2. C. S. Fuller and J. A. Ditzenberger, *J. Appl. Phys.*, **27**, 550 (1957).
3. W. B. Glendinning, USASRDL Technical Report 2211 (June 1961).
4. D. R. Turner, *This Journal*, **105**, 402 (1958).
5. A. Uhlir, *Bell Sys. Tech. J.*, **35**, 333 (1956).

CORRECTION

In the Brief Communication "Gallium Arsenide Surface Preparation" by Jack Lowen which was published in the October 1965 issue of the JOURNAL, the first sentence in the second paragraph should read "Material is cut into 0.020 in. thick slices . . ."

Discussion Section

This Discussion Section includes discussion of papers appearing in the JOURNAL of The Electrochemical Society, Vol. 111, No. 1 and 12 (January and December 1964) and Vol. 112, No. 1, 2, 3, 4, and 5 (January-May 1965). Discussion not available for this issue will appear in the Discussion Section of the June 1966 JOURNAL.

The Crystal Structure and Polarity of Beryllium Oxide

(D. K. Smith, H. W. Newkirk, and J. S. Kahn, pp. 78-87, Vol. 111, No. 1)

Walter C. Allen[1]: In their paper, the linear and angular dimensions of the unit cell of beryllium oxide were given as:

$a_o = 2.6979 \pm 0.0002$Å
$c_o = 4.3772 \pm 0.0002$Å
$c/a = 1.622$
Be-O = 1.659 ± 0.003Å (parallel to C-axis)
Be-O′ = 1.645 ± 0.003Å (to 3 oxygens, O′ in basal plane)
O-Be-O′ = 108° 47′
O′-Be-O′ = 110° 51′

The structure is essentially close-packed hexagonal, but c/a is slightly less than the ratio 1.633 for the ideal HCP structure. Interatomic distances are therefore slightly distorted, and the angles deviate from the true tetrahedral angle of 109° 28′. Each beryllium ion is tetrahedrally coordinated with four oxygens, nesting in the hollow between a triangle of oxygens (O′) in the basal plane with the fourth oxygen straight overhead in a direction parallel to the C-axis.

Preparatory to constructing a model of the beryllia structure, these angles were checked by trigonometry. The angle O-Be-O′ is correct at 108° 47′, but the other angle O′-Be-O′ is incorrect as reported.

From the Law of Cosines,

$$\text{Cos A} = \frac{b^2 + c^2 - a^2}{2bc}$$

$$= \frac{(1.645)^2 + (1.645)^2 - (2.6979)^2}{2(1.645)\ (1.645)}$$

$$= -0.3449$$

$$\text{A} = 110° 10½′$$

The other pair of equal angles in this isosceles triangle was also checked:

$$\text{Cos B} = \frac{(1.645)^2 + (2.6979)^2 - (1.645)^2}{2(1.645)\ (2.6979)}$$

$$= \frac{2.6979}{3.290} = 0.8200$$

$$\text{B} = 34° 55′$$

$$\text{A} = 180\text{-}2\text{B} = 110° 10′$$

The literature value of 110° 51′ can probably be ascribed to an error in reading the trigonometric tables. This revised value of 110° 10′ is herewith presented for the record.

Figure 1 represents a stereoscopic view of the structure model, as made by Mr. Hervey Greenwood and the author. The eyes can be trained to see a three-dimensional image, without a special viewer, by parallel lines of sight instead of focussing convergently.

[1] National Beryllia Corp., Haskell, New Jersey.

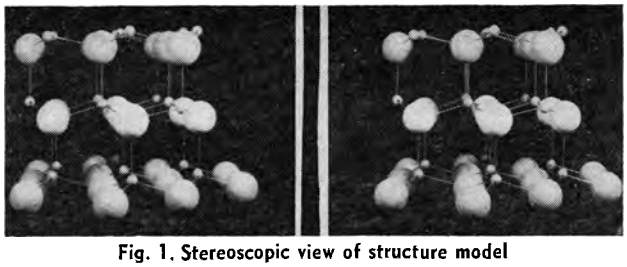

Fig. 1. Stereoscopic view of structure model

Correlation of Limiting Currents; Electrodeposition of Copper in Microelectrolytic Cells

R. N. O'Brien and L. M. Mukherjee[2] (pp. 1358-1362, Vol. 111, No. 12)

Ursula Böhm and **N. Ibl**[3]: The main conclusion of the paper by O'Brien and Mukherjee is that natural convection is still effective in microcells of the type used by one of the authors in his optical experiments. This is in general agreement with the results of a recent investigation of natural convection in narrow spaces open at their upper and lower ends and bounded either by a vertical electrode and a diaphragm or by two vertical electrodes.[4] The latter case corresponds to that studied by O'Brien and Mukherjee. It was found that, depending on the distance d between the electrodes, three regions can be distinguished:

(*A*) For values of d smaller than about 0.5 mm the limiting current reaches a well-defined steady state after some time which varies with d. The steady-state current decreases with increasing d, yielding on a log-log-plot a straight line with a slope of −0.85. The theoretical value of this slope would be −1 for the case that mass transfer from one electrode to the other takes place only by linear steady-state diffusion and migration. The somewhat smaller experimental value of the slope is due to some extent to the nonlinear diffusion toward the ends of the electrodes, and also probably to the fact that there is still some convection. However, the latter is very weak, and, in the region $d < 0.5$ mm, mass transfer occurs almost exclusively by diffusion and migration. The virtual absence of convection is confirmed by the fact that the Nusselt number is here independent of the Grashof number (when both numbers are based on the electrode height).

(*B*) With d lying approximately between 1 and 6 mm [5] the limiting current fluctuates with time, but is almost independent of d. Obviously, in this region, natural convection is already effective and prevents a further decrease of the limiting current with increasing d. The hydrodynamic boundary layers formed at the two electrodes probably interact in a complicated manner, thus causing the unstable character of the mass transfer.

(*C*) For d larger than about 6 mm the usual steady-state limiting current of natural convection was observed.

The thickness of zone (*A*) (virtual absence of convection) was found to increase somewhat with increasing electrode height and decreasing bulk concentration, *i.e.*, with decreasing density differences in

[2] Present address: Chemistry Department, Polytechnic Institute of Brooklyn, Brooklyn, N. Y.

[3] Institute of Industrial and Engineering Chemistry, Swiss Federal Institute of Technology, Zurich, Switzerland.

[4] Unpublished experiments of U. Böhm, Facultad de Ciencias Exactas y Naturales, Buenos Aires, Argentina; see also *Electrochim. Acta*, in press.

[5] For $0.5 < d < 1$ mm the limiting currents are substantially larger than for diffusion alone, but no instability was observed.

the solution. The electrode heights were larger and the density differences smaller than in the investigation of O'Brien and Mukherjee because they worked with $CuSO_4$ solutions whereas in the above-mentioned experiments a redox system was used (reduction of ferricyanide to ferrocyanide at the cathode, oxidation of ferrocyanide at the anode). However, the influence of the height and of the density differences is small. The study of O'Brien and Mukherjee and that reported here are therefore comparable in spite of the differences of electrode heights and of density variations and the two sets of experiments complement each other. Both show that natural convection is quite tenacious when the available space narrows and that it decays substantially only when the distance between the electrodes approaches the thickness of the diffusion layer.

R. N. O'Brien: The comments of Böhm and Ibl and the information given are in good agreement with experiments we have subsequently performed. Their remarks are given systematic consideration below.

(*A*) Confirming Böhm and Ibl's view that convection is present when d is very small we have recently published[6] some data in which three orientations of electrodes have been used, cathode-over-anode, deep vertical and shallow vertical (in all cases including the experiments referred to by Böhm and Ibl, the cell was full, bounded by electrode and glass flats on all sides, allowing no gas-electrolyte interface), and it appears that at small separation the various cell geometries approach each other in electrolytic transport properties suggesting that convection, although tenacious, becomes insignificant finally. An interferogram showing the interelectrode concentration contour at small d has been published.[7] We have also postulated the existence of field effects. In another experiment, the height of the cell and the vertical electrodes were reduced to 0.2 mm.[8] It was impossible to say whether convection was present or not, but when the same cell and electrodes were oriented so that the anode was above the cathode, convection was clearly visible. The effect of laminar and turbulent convection on concentration gradients as seen on an interferogram has been published.[8, 9]

(*B*) As Böhm and Ibl suggest the interaction of convection whorls at 1 mm $< d <$ 6 mm is quite complicated and employing a technique originated in Professor Ibl's laboratory[10] the pattern of convection has been obtained by observing the movement of suspended solids. At a distance of about 0.75 mm in 0.1*N* $CuSO_4$, electrode height 2 mm, there appears to be a transition from one whorl to two whorls with over and underflow between them. The interaction between the whorls seems to be at a maximum for these conditions and geometry at about $d = 2.5$ mm where transport efficiency reaches one of at least three maxima. The more or less circular whorls leave a fairly large volume of solution at the top and bottom of each electrode which is out of the main stream of convection and unpredictable turbulence occurs here. Since this instability affects an appreciable area of the electrode surface, instability would be expected. None of the interferometric data was obtained at greater than 1.5 ma/cm^2 current density, which is far from the limiting current.

(*C*) At c.d.'s much lower than limiting and $d > 6$ mm we also observed no anomalous effects in the interferograms.

N. Ibl: In this interesting investigation it has been found that with cathodes of small height the limiting currents are up to 1.8 times larger than those predicted by the now well established correlation for natural convection at vertical electrodes (Eq. [2]). This is interpreted as being due to an increase in electrode area owing to metal deposition. There is, however, another effect of importance here. The derivation of Eq. [2] from the fundamental differential equations of convective mass transfer implies the usual boundary layer assumptions, *i.e.*, it is assumed that the dimensions of the electrode are very large as compared to the thickness of the diffusion layer and of the hydrodynamic boundary layer. In the present case, with the electrodes of a height of 0.05 mm for instance, this condition is quite far from being fulfilled, the calculated thickness of the diffusion layer being approximately 0.05 mm and that of the hydrodynamic boundary layer of the order of 1 mm. This can lead to substantial departures from Eq. [2] for several reasons, one of which can be easily visualized as follows: near the lower and upper edge the diffusion toward the cathode is no longer perpendicular to the interface and the cross section for diffusion increases with increasing electrode distance, so that the limiting current at small electrodes is larger than that predicted by Eq. [2].

The metal deposition can indeed lead to an increase of electrode area in the region of the limiting current, where very rough or powdery deposits are formed. However, this effect is strongly time dependent and also present (although perhaps to a somewhat smaller degree) with large electrodes. We have studied this phenomenon in some detail with a rotating disk electrode 1 cm in diameter.[11] The increase of electrode area in the limiting current region causes, at constant current, a strong variation of the electrode potential with time. In potentiostatic experiments it leads to an increase of the limiting current. For instance, at a potential of −600 mv (*vs.* a copper reference electrode)[12] the limiting current increased by 20% within 1 min after switching on the current. It increased further to about 4 times its original value during the following 4 min.

R. N. O'Brien and **L. M. Mukherjee**[2]: Professor Ibl's remarks are noteworthy. Indeed, we have not considered any possible explanation on the basis of spherical diffusion in the type of microelectrolytic cells used by us in testing the Tobias equation (Eq. [2]). As suggested by Professor Ibl, it is probably true that as the ratio of the electrode area to the cell wall area decreases the problem approaches one of spherical diffusion. This may completely explain our results, although we believe, from observation of the electrodes following an experiment, that "edge effects" were also important; moreover, the current was practically independent of the position (height) of the electrode along the vertical plane of the cell wall contrary to what would be expected in the case of spherical diffusion. Professor Ibl further points out that the edge effects are strongly time-dependent. We believe that the rate of increase of area of a thin electrode should not be directly proportional to the time of electrolysis, but should decrease rapidly as the electrolysis proceeds. Because of the technique used in our experiments it is unlikely that we would have been able to distinguish this time-dependence, if any, from the normal experimental error.

Extremely Intense Light Sources with Narrow-Band Emission

J. E. Rosenthal and C. F. Eyer (pp. 68-70, Vol. 112, No. 1)

H. F. Ivey[13]: This paper concerns a sodium-seeded flame subjected to a microwave field. It is stated that

[6] R. N. O'Brien and K. Kinoshita, *This Journal*, 112, 951 (1965).

[7] R. N. O'Brien, *Rev. Sci. Inst.*, 35, 803 (1964).

[8] R. N. O'Brien, W. F. Yakymyshyn, and J. Leja, *This Journal*, 110, 820 (1963).

[9] R. N. O'Brien, *This Journal*, 111, 1300 (1964).

[10] N. Ibl and R. Müller, *This Journal*, 105, 346 (1958).

[11] K. Schadegg, Thesis ETH, Zurich, in print.

[12] The solution was 0.7M $CuSO_4$ + 1.5M H_2SO_4, the rotation speed 300 rpm.

[13] Westinghouse Electric Corporation, Research and Development Center, Pittsburgh, Pennsylvania.

in this way "an over-all operating efficiency approaching 50%" is obtained. The value of efficiency calculated in the paper is 140 lpw, but it is claimed that with improved coupling to the microwave field this should be increased to 220 lpw. For purposes of comparison, xenon short-arc lamps with efficiency of 30-40 lpw were selected.

The writer would like to make two points concerning this paper. First, since the C.I.E. visibility function for the wavelength of the sodium D lines (5893Å) has the value 0.765[14], the theoretical maximum luminous efficiency at this wavelength is (0.765) (681) = 521 lpw. The observed (calculated) value of 140 lpw therefore corresponds to an over-all efficiency of 27%, while the predicted value of 220 lpw corresponds to 42.5%. It does not appear that either of these figures "approaches 50%"; the most that can conservatively be said is that the extrapolated value exceeds 40%.

Second, it seems that the efficiencies obtained experimentally in this case should be compared not with xenon lamps but with other sodium sources. With conventional low-pressure sodium-vapor lamps efficiencies of 125-140 lpw have been obtained experimentally, while values of 150-200 lpw have been predicted for improved designs.[15] Efficiencies of 100-145 lpw have also been reported for high-pressure sodium-vapor lamps.[16] It therefore appears that the efficiencies obtained with the apparatus described in this paper do not exceed those obtained with more conventional and simpler sodium sources.

As pointed out by the authors, the intensity and the ability to modulate the type of source described in this paper at high frequencies may be an advantage over conventional sodium lamps in some applications.

J. E. Rosenthal and **C. F. Eyer:** It is obvious that a sodium seeded flame is a very rudimentary light source and that the work described in the article represents only the first stages of development. It is therefore particularly interesting that we have already obtained an efficiency of 140 lpw, which according to Dr. Ivey's references[14,15] is the best that can be obtained with a fully developed sodium lamp operating at one-tenth of our power level. This indicates that the basic principle of our operation is one of high efficiency. Self-absorption is greatly reduced as shown in Fig. 4 of the article so that operation can proceed efficiently at very much higher temperatures and sodium pressures than indicated by van de Weijer[15] for a conventional sodium lamp.

The microwave arrangement used in the original experiments was of the simplest possible type that could be used to demonstrate the existence of the enhancement effect. Replacing it with a properly designed microwave cavity immediately boosts the efficiency of the rudimentary source at least to 220 lpw, or higher with a more efficient magnetron, while still maintaining the same high power output. Using the value of the least mechanical equivalent of light from the 1962-63 edition of the Handbook of Chemistry and Physics which gives 621 lpw at the wavelength of maximum visibility, we obtain 475 lpw as the maximum theoretical luminous efficiency at the wavelength of the sodium D-lines. This gives an efficiency in excess of 46%, which for practical purposes we consider approaching 50%. However, we should like to point out that any improvement in the design of the torch, to say nothing of its eventual replacement by an electrically powered simulated flame, will boost the efficiency.

Following van de Weijer we might try to anticipate the extent of possible improvements. He considers that redesign will boost the efficiency of his lamp from 140 to possibly 200 lpw. We do not anticipate as good an improvement factor. However, the figure of 280 lpw should be a reasonable estimate for the final model. This figure not only approaches but actually exceeds 50% efficiency on the basis of any calculation one may choose. None of these improvements will cause a deterioration either in the power level of the modulability of the source.

[14] A. C. Hardy, "Handbook of Colorimetry," Technology Press, Cambridge, Massachusetts (1963).

[15] M. H. A. van de Weijer, *Philips Tech. Rev.*, 23, 246 (1961/62).

[16] K. Schmidt, *Bull Am. Phys. Soc.*, 8, 58 (1963); *Compt. rend. VI Conf. Intnt. Phen. d'Ion. Gaz, Paris*, 3, 323 (1963).

The Active Iron Electrode, I. Iron Dissolution and Hydrogen Evolution Reactions in Acidic Sulfate Solutions

E. J. Kelly (pp. 124-131, Vol. 112, No. 2)

W. J. Lorenz[17] and **Günter Eichkorn**[17]: Kelly showed by electrochemical investigations with stationary methods the Bockris mechanism of anodic dissolution of iron to be valid. His results agree with data, previously published by Bockris *et al.*[18, 19, 20]

The rate-determining step of transfer reaction if the Bockris mechanism is

$$Fe(OH)_{ads} \rightarrow FeOH^+ + e^- \qquad [1]$$

On the other hand the rate-determining step of transfer reaction given by Heusler,[21, 22, 23] Gerischer,[24] Lorenz *et al.*[25, 26, 27] is

$$Fe(FeOH)_{ads} + OH^- \rightarrow FeOH^+ + (FeOH)_{ads} + 2e^- \qquad [2]$$

Before this transfer reaction of the Heusler mechanism occurs there happens a slow catalytic reaction for the formation of $Fe(FeOH)_{ads}$

$$Fe + Fe(OH)_{ad} \rightleftharpoons Fe(FeOH)_{ad} \qquad [3]$$

In our opinion both mechanism can be found. We explain it in the following way: If there exists a great concentration of active iron sites on the electrode surface, so the equilibrium of Eq. [3] is shifted to the right side. Therefore preferential formation of $Fe(FeOH)_{ad}$ takes place and the following step is the transfer reaction (Eq. [2]), representing the Heusler mechanism. On the other hand, if the concentration of the active places is relatively low, the formation of $Fe(FeOH)_{ads}$ is negligible and the direct transfer reaction of $(FeOH)_{ads}$ happens at once (Eq. [1] of Bockris mechanism).

The proof of this explanation we found by comparing x-ray line width methods and electrochemical anodic dissolution measurements†.

Responsible for the mechanism of anodic dissolution is the substructure, the density of subgrain boundaries, that means the density of dislocations, which act as active places on the surface.

By tempering specimens of Ommet-iron we changed the density of subgrain boundaries in a definite way. On the same material as well the kinetic data of the Heusler mechanism that of the Bockris mechanism could be found. If the density of dislocations is high

[17] Institut für Physikalische Chemie and Electrochemie der Technischen Hochschule, Karlsruhe, Germany.

[18] J. O'M. Bockris, D. Drazic, and A. L. Despic, *Electrochim. Acta*, 4, 325 (1961).

[19] J. O'M. Bockris and H. Kita, *This Journal*, 108, 676 (1961).

[20] J. O'M. Bockris and D. Drazic, *Electrochim. Acta.*, 7, 293 (1962).

[21] K. F. Bonhoeffer and K. E. Heusler, *Z. Phys. Chem. NF*, 8, 390 (1956).

[22] K. F. Bonhoeffer and K. E. Heusler, *Z. Elektrochem.*, 61, 122 (1957).

[23] K. E. Heusler, *ibid.*, 62, 582 (1958).

[24] H. Gerischer, *Electrochim. Acta*, 2, 1 (1960).

[25] H. Fischer and H. Yamaoka, *Chem. Ber.*, 94, 1477 (1961).

[26] W. J. Lorenz, H. Yamaoka, and H. Fischer, *Ber.*, 67, 932 (1963).

[27] W. J. Lorenz, *Corrosion Sci.*, 5, 121 (1965).

† W. J. Lorenz and G. Eichkorn, Ber. Bunsenges. phys. Chem., in press (1965).

(nontempered specimens), the Heusler mechanism is valid. By reducing the number of dislocations that is the density of active places (tempered specimens), we found the kinetic data of the Bockris mechanism. The difference between both mechanism is not due to influences of atomic imperfections, external conditions, or defects of measurements.

E. J. Kelly: In the paper under discussion, it was shown that, subject to appropriate steady-state conditions, the mechanism proposed for the anodic dissolution of iron in acidic sulfate media, Eq. [41]-[45], reduces to a kinetic equivalent of the Bockris mechanism, Eq. [9]-[11]. The objections of Lorenz, Yamaoka, and Fisher[26] to the Bockris mechanism were examined and rejected, and the author is pleased to find that, rather than reiterate these objections, Lorenz and Eichkorn appear to accept the validity of the mechanism. However, they now suggest that both the Heusler mechanism, as modified by Lorenz, Yamaoka, and Fisher {Eq. [53]-[56] of ref. (1), and hereafter referred to as the HLYF mechanism}, and the Bockris mechanism are operative, with the former predominating "if there exists a high concentration of active sites." To be specific, they would add the rate-determining reaction of the Bockris mechanism, Eq. [10], to the system of reactions comprising the HLYF mechanism, while simultaneously invoking the "active site" concept. An examination of the kinetics of the resultant hybrid mechanism reveals that the total steady-state anodic current density corresponding to the iron dissolution process may be represented as a sum of two partial current densities, i_B and i_H, attributable to the Bockris and HLYF mechanisms, respectively, with

$$i_B/i_H \approx \bar{k}_{44}/s \left(\frac{k_{54}}{k_{-54}} \right) \bar{k}_{55} A_{(OH-)},$$

where s represents the concentration of active sites and the other symbols have their customary significance. Therefore, with

$$A_{Fe(FeOH)_{ads}}/A_{(FeOH)_{ads}} \approx s \left(\frac{k_{54}}{k_{-54}} \right),$$

a shift in the equilibrium of Eq. [54] to the right, or an increase in s, would indeed favor the HLYF mechanism. Thus, as an artifice, the hybrid mechanism proposed by Lorenz and Eichkorn is not without merit. However, as a necessary consequence of the nonvalidity of the component HLYF mechanism, a fact already established by a detailed examination, the hybrid must be rejected.

Although Lorenz and Eichkorn refer to ref. (12) for the "proof of this explanation," only the first eleven references were included in the copy of their discussion sent to the author. In the absence of this reference, one is constrained from commenting upon this proof beyond suggesting that, in view of the nonvalidity of the HLYF mechanism, it should prove very interesting.

With regard to the last statement of the discussion of Lorenz and Eichkorn, it has been the experience of the author that in those environments in which the Bockris mechanism has been found to apply, contamination of the electrode surface, as evidenced by the presence of slow polarization hysteresis phenomena, can result in illusory steady-state Tafel behavior, with "apparent" Tafel slopes less than 40 mv/decade and "apparent" hydroxyl ion reaction orders greater than unity, *i.e.*, in data of the type that the HLYF mechanism was devised to explain. When such anomalous behavior was observed in acidic sulfate solutions, the experimental procedure described in this paper was repeated, with the result that the same electrodes then exhibited behavior corresponding to the Bockris mechanism. Hence, there is reason to believe that the Heusler mechanism and its modifications fail because, aside from their faulty constructions, they attempt to explain anomalous electrode behavior without recognizing that this is the case.

Fluorescent Emission Spectra in II-VI Compounds

R. E. Halsted, M. Aven, and H. D. Coghill (pp. 177-181, Vol. 112, No. 2)

W. Lehmann[28]: Emission bands in (Zn, Cd) (S, Se, Te) phosphors do not always shift as monotonously over the spectrum with a variation of the composition of the host lattice, as assumed by Halstead, Aven, and Coghill. Indeed, a steady shift, almost equal to the variation of the band gap, is well established only within the (Zn, Cd) S system. It may occur also with (Zn, Cd) Se and (Zn, Cd) Te, *i.e.*, in all cases where the cation of the host lattice varies from Zn to Cd. However, a strong deviation from such simple behavior does definitely exist within the Zn(S, Se, Te) system, and it may be expected also within the Cd(S, Se, Te) system, *i.e.*, in cases where the anion varies from S to Se to Te. The authors seem to have overlooked the complex influence of an anion variation on the luminescence of II-VI compound phosphors because it may have been not sufficiently stressed in previous reports [29,30,31,32] and because of the apparent restriction of their own work to single crystals of the pure binary compounds.

The situation may be demonstrated for the case of Zn(S, Se, Te) phosphors activated by the incorporation of small amounts of silver and chlorine. Some emission spectra measured at 77°K are shown in Fig. 1, in terms of d (number of quanta)/d (quantum energy) as a function of the quantum energy. This is the physically most senseful presentation because luminescent processes are quantum processes. The spectra are arbitrarily shifted up and down on the logarithmically calibrated ordinate in order to provide a clear picture. Cubic ZnS:Ag,Cl emits primarily in a single emission band in the blue, at about 2.76 ev (somewhat lower than in hexagonal ZnS:Ag, Cl). Replacement of only

[28] Westinghouse Electric Corporation, Research and Development Center, Pittsburgh, Pennsylvania.

[29] H. A. Klasens, *This Journal*, **100**, 72 (1953).

[30] H. W. Leverenz, "An Introduction to the Luminescence of Solids," p. 194, John Wiley & Sons, Inc., New York (1950).

[31] A. A. Bundel, Z. I. Guretskaya, and M. N. Noskova, *Optics and Spectroscopy*, **11**, 352 (1961).

[32] F. F. Morehead, *J. Phys. Chem. Solids*, **24**, 37 (1963).

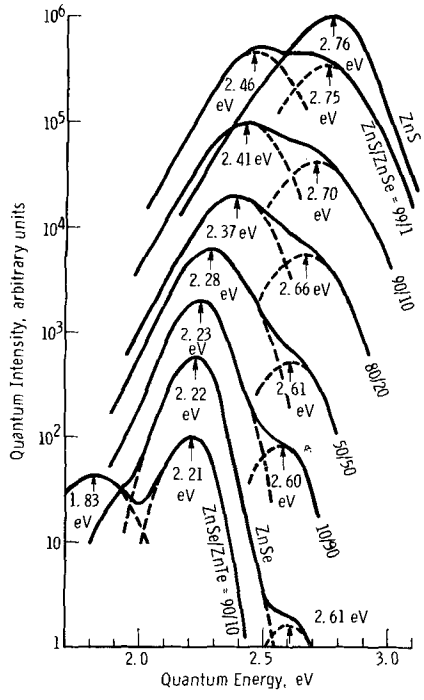

Fig. 1. Some emission spectra of cubic ZnS, Zn (S, Se), ZnSe, and Zn(Se, Te) phosphors made with 0.01 mole % of Ag and 0.1 mole % of Cl, excited to luminescence at 77°K.

(nontempered specimens), the Heusler mechanism is valid. By reducing the number of dislocations that is the density of active places (tempered specimens), we found the kinetic data of the Bockris mechanism. The difference between both mechanism is not due to influences of atomic imperfections, external conditions, or defects of measurements.

E. J. Kelly: In the paper under discussion, it was shown that, subject to appropriate steady-state conditions, the mechanism proposed for the anodic dissolution of iron in acidic sulfate media, Eq. [41]-[45], reduces to a kinetic equivalent of the Bockris mechanism, Eq. [9]-[11]. The objections of Lorenz, Yamaoka, and Fisher[26] to the Bockris mechanism were examined and rejected, and the author is pleased to find that, rather than reiterate these objections, Lorenz and Eichkorn appear to accept the validity of the mechanism. However, they now suggest that both the Heusler mechanism, as modified by Lorenz, Yamaoka, and Fisher {Eq. [53]-[56] of ref. (1), and hereafter referred to as the HLYF mechanism}, and the Bockris mechanism are operative, with the former predominating "if there exists a high concentration of active sites." To be specific, they would add the rate-determining reaction of the Bockris mechanism, Eq. [10], to the system of reactions comprising the HLYF mechanism, while simultaneously invoking the "active site" concept. An examination of the kinetics of the resultant hybrid mechanism reveals that the total steady-state anodic current density corresponding to the iron dissolution process may be represented as a sum of two partial current densities, i_B and i_H, attributable to the Bockris and HLYF mechanisms, respectively, with

$$i_B/i_H \approx \bar{k}_{44}/s \left(\frac{k_{54}}{k_{-54}} \right) \bar{k}_{55} A_{(OH-)},$$

where s represents the concentration of active sites and the other symbols have their customary significance. Therefore, with

$$A_{Fe(FeOH)_{ads}}/A_{(FeOH)_{ads}} \approx s \left(\frac{k_{54}}{k_{-54}} \right),$$

a shift in the equilibrium of Eq. [54] to the right, or an increase in s, would indeed favor the HLYF mechanism. Thus, as an artifice, the hybrid mechanism proposed by Lorenz and Eichkorn is not without merit. However, as a necessary consequence of the nonvalidity of the component HLYF mechanism, a fact already established by a detailed examination, the hybrid must be rejected.

Although Lorenz and Eichkorn refer to ref. (12) for the "proof of this explanation," only the first eleven references were included in the copy of their discussion sent to the author. In the absence of this reference, one is constrained from commenting upon this proof beyond suggesting that, in view of the nonvalidity of the HLYF mechanism, it should prove very interesting.

With regard to the last statement of the discussion of Lorenz and Eichkorn, it has been the experience of the author that in those environments in which the Bockris mechanism has been found to apply, contamination of the electrode surface, as evidenced by the presence of slow polarization hysteresis phenomena, can result in illusory steady-state Tafel behavior, with "apparent" Tafel slopes less than 40 mv/decade and "apparent" hydroxyl ion reaction orders greater than unity, *i.e.*, in data of the type that the HLYF mechanism was devised to explain. When such anomalous behavior was observed in acidic sulfate solutions, the experimental procedure described in this paper was repeated, with the result that the same electrodes then exhibited behavior corresponding to the Bockris mechanism. Hence, there is reason to believe that the Heusler mechanism and its modifications fail because, aside from their faulty constructions, they attempt to explain anomalous electrode behavior without recognizing that this is the case.

Fluorescent Emission Spectra in II-VI Compounds

R. E. Halsted, M. Aven, and H. D. Coghill (pp. 177-181, Vol. 112, No. 2)

W. Lehmann[28]: Emission bands in (Zn, Cd) (S, Se, Te) phosphors do not always shift as monotonously over the spectrum with a variation of the composition of the host lattice, as assumed by Halstead, Aven, and Coghill. Indeed, a steady shift, almost equal to the variation of the band gap, is well established only within the (Zn, Cd) S system. It may occur also with (Zn, Cd) Se and (Zn, Cd) Te, *i.e.*, in all cases where the cation of the host lattice varies from Zn to Cd. However, a strong deviation from such simple behavior does definitely exist within the Zn(S, Se, Te) system, and it may be expected also within the Cd(S, Se, Te) system, *i.e.*, in cases where the anion varies from S to Se to Te. The authors seem to have overlooked the complex influence of an anion variation on the luminescence of II-VI compound phosphors because it may have been not sufficiently stressed in previous reports [29,30,31,32] and because of the apparent restriction of their own work to single crystals of the pure binary compounds.

The situation may be demonstrated for the case of Zn(S, Se, Te) phosphors activated by the incorporation of small amounts of silver and chlorine. Some emission spectra measured at 77°K are shown in Fig. 1, in terms of d (number of quanta)/d (quantum energy) as a function of the quantum energy. This is the physically most senseful presentation because luminescent processes are quantum processes. The spectra are arbitrarily shifted up and down on the logarithmically calibrated ordinate in order to provide a clear picture. Cubic ZnS:Ag,Cl emits primarily in a single emission band in the blue, at about 2.76 ev (somewhat lower than in hexagonal ZnS:Ag, Cl). Replacement of only

[28] Westinghouse Electric Corporation, Research and Development Center, Pittsburgh, Pennsylvania.

[29] H. A. Klasens, *This Journal*, **100**, 72 (1953).

[30] H. W. Leverenz, "An Introduction to the Luminescence of Solids," p. 194, John Wiley & Sons, Inc., New York (1950).

[31] A. A. Bundel, Z. I. Guretskaya, and M. N. Noskova, *Optics and Spectroscopy*, **11**, 352 (1961).

[32] F. F. Morehead, *J. Phys. Chem. Solids*, **24**, 37 (1963).

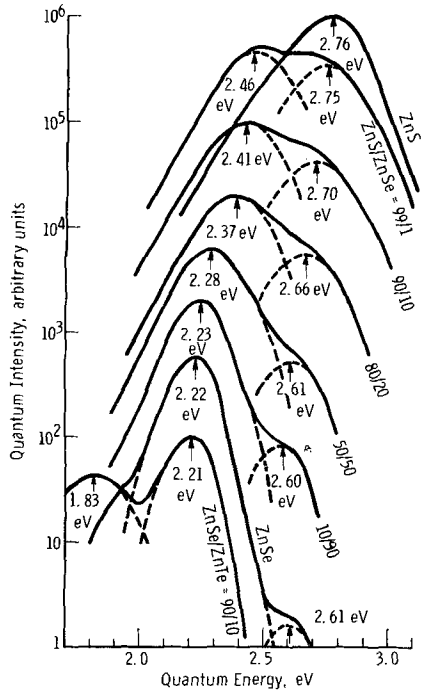

Fig. 1. Some emission spectra of cubic ZnS, Zn (S, Se), ZnSe, and Zn(Se, Te) phosphors made with 0.01 mole % of Ag and 0.1 mole % of Cl, excited to luminescence at 77°K.

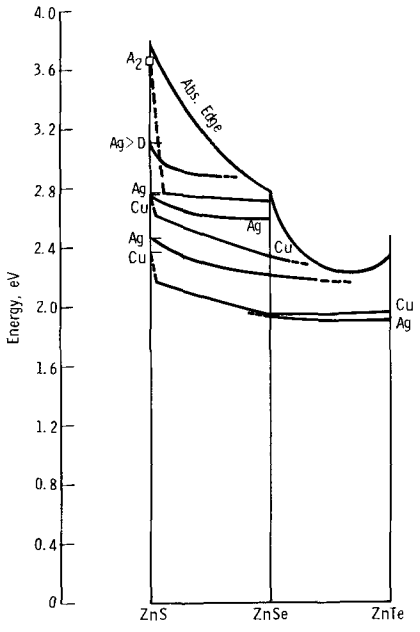

Fig. 2. Fluorescent emission energies in the Zn(S, Se, Te) system (as measured at 77°K).

1% of the ZnS by ZnSe causes a strong green emission band (peak ~ 2.46 ev) besides the blue, and both bands can then be followed through the entire range up to ZnSe.Ag, Cl, Hence, the 2.76 ev band (blue) of ZnS:Ag, Cl corresponds to a band at ~2.61 ev (blue-green) in ZnSe:Ag, Cl, while the 2.22 ev band of ZnSe:Ag, Cl (yellow) corresponds to the (ordinarily almost or completely absent) green emission band of ZnS:Ag, Cl located at ~ 2.46 ev. A similar appearance of a new emission band is to be observed if some of the ZnSe is replaced by ZnTe (also shown in Fig. 1).

This behavior with a variation of the host lattice from ZnS over ZnSe to ZnTe may vary considerably depending on the particular defect or impurity producing the emission. For instance, the complex "A_2-emission" near the optical adsorption edge of ZnSe is no direct continuation of the, also complex, near-edge emission of ZnS, and the two well-known Cu-emission bands in ZnS (blue and green) exhibit a distinct "jump" toward lower quantum energies if only a few per cent of the ZnS are replaced by ZnSe. Except for these irregularities, however, all peak positions vary considerably less than the band gap does over the same variation of the host lattice composition. Hence, if Fig. 4 by Halsted, Aven and Coghill is redrawn in a way as to correspond to experimental evidence in between ZnS and ZnSe, and in between ZnSe and Te, one obtains Fig. 2 here which clearly shows that a simple interpolation can be dangerous.

R. E. Halsted, M. Aven, and H. D. Coghill: W. Lehmann's 77°K results on ZnSSe:Ag provide a worthwhile addition to the literature. They appear to be in accord with the cited 300°K data of Leverenz and of Klasens. The recent analysis of these data by W. H. Fonger[33] is also relevant. The "jumps" apparent in the ZnSSe:Cu data of Lehmann are not evident in the work of Morehead. The jump in his edge emission data is particularly striking, if confirmed. Lehmann's results do indeed suggest that estimates of the positions of spectra derived by simple extrapolation from "analogous" end points may be invalid in ZnSSe:Ag, and perhaps more generally. This would appear to be an important point meriting further study. Our paper was motivated in part by the desire to raise this very question. We clearly distinguish between experimental data and possible implications of the data.

It should be noted, however, that the problem of sample preparation and emission band identification in such investigations is not simple. Trace impurities can exert a profound influence. It is interesting that Bundel's results on self-activated ZnSSe phosphors coincide closely with Morehead's data on the ZnSSe:Cu system. No evidence for the 2.46 ev ZnS:Ag band cited by Lehmann has been found at this laboratory in Cu-free material. We are impressed by Lehmann's conviction that the ZnS edge emission exhibits a 0.8 ev shift with small Se additions. We hope that additional experimental data on the ternary compounds may soon resolve these questions.

[33] W. H. Fonger, *Phys. Rev.*, **137**, A1038 (1965).

Hydrogen Evolution at a Solid Indium Electrode

J. N. Butler and M. Dienst (pp. 226-232, Vol. 112, No. 2)

R. Piontelli and **B. Mazza**[34]: The reference given by the authors to the work done in our Laboratory[35] on the cathode behavior of indium, completely overshadows the main result, which may deserve to be recalled also in view of the study of the hydrogen discharge on indium. This consists in the abrupt increase of the cathode overvoltage (in the order of: 0.4-0.5v), encountered when plating indium from some concentrated baths, and long before attaining the "limit current conditions" (for instance at current densities in the order of 10 amp/m^2).

This phenomenon is typical for: sulfate, sulfamate, perchlorate baths, while in chloride, or by adding adequate chloride amounts to the baths above, the insurgence of this "cathodic passivity" effect is very much displaced toward high values of the current density.

This phenomenon has been successively recognized by Kangro and Weingärtner,[36] who appear to consider it to be correlated with the participation of In^+ to the cathode processes.

In spite of the very extensive work carried out in this laboratory on this matter, some important aspects remain still unexplained, and they will require supplementary effort.

In any case, our results indicate the essential part taken by the hydrogen interference in the electrode processes, and suggest the indium behavior toward hydrogen to be largely different from the mercury one.

Once more the explicit and thorough consideration of the structural properties of the metallic phase and of its surface appears to be an indispensable step to make the kinetic theories some thing more than a formalistic game.

J. N. Butler and **M. Dienst:** Drs. Piontelli and Mazza have pointed out the importance of the hydrogen evolution reaction in the electrodeposition of indium from solution. Although there may be complex interactions between the hydrogen evolution and indium deposition reactions, we hope that studies of each of these processes, under conditions where the other does not occur, will further the understanding of those phenomena observed in practical situations.

Kinetics of the Silicon-Silicontetrachloride Reaction in a Flow System

Ole Alstrup and C. O. Thomas (pp. 319-323, Vol. 112, No. 3)

S. E. Craig, Jr.[37]: The interesting and timely work of Alstrup and Thomas conclusively proves that Mon-

[34] Institute for Electrochemistry, Physical Chemistry and Metallurgy, Milan Polytechnic, Milan, Italy.

[35] R. Piontelli and M. Simonetta, *Gazz. Chim. Ital.*, **79**, 716 (1949); R. Piontelli and G. Poli, Proc. 2nd Meeting C.I.T.C.E., Milan 1950, p. 136, Tamburini, Milan (1951); R. Piontelli, G. Poli, and G. Serravalle, *Rend. 1st Lomb. Sci. Lett.* (A), **93**, 301 (1959); G. Serravalle, *ibid.*, **93**, 653 (1959); G. Serravalle and B. Mazza, *Electrochim. Acta*, **8**, 313 (1963).

[36] W. Kangro and F. Weingärtner, *Z. Elektrochem.*, **58**, 505 (1954).

[37] College of Engineering Science, Arizona State University, Tempe, Arizona.

champ et al.[38] did not measure true kinetic data as they believed but, instead, measured mass transport rates in the gas phase.[39]

Alstrup notes this error in Monchamp's work and then fails to consider mass transport in relation to his own work. Such a failure is always serious in work dealing with a heterogeneous reaction in a laminar flow reactor for such reactors have notoriously slow mass transfer rates.

It is especially unfortunate that Alstrup failed to evaluate the effect of mass transfer on his system since many of his observations are typical of mass transfer controlled reactions. For example, the rate was found to be independent of the surface condition and crystal orientation. The rate was also found to depend on the reactor type, the reactor geometry (above a certain volume), and the velocity of flow. Thomas has adequately explained this last effect as resulting from a difference in composition between the inlet gas and the bulk gas in the reaction mixture caused by the reaction itself. Nevertheless, it is appropriate to examine the gas phase mass transport.

Alstrup's Eq. [5] and [6] are a mass balance on $SiCl_4$ and may be arranged in the following form

$$r = \frac{1}{AM_0}\left(\frac{-dm_0}{dt}\right) = \frac{v_0\rho_0}{A}\left(\frac{y^0_4 - y_4}{1 + y_4}\right) \qquad [1]$$

where r (gram atoms Si removed $-cm^{-2}\text{-}sec^{-1}$) is the rate of reaction, A (cm^2) the active surface area, M_0 the atomic weight of silicon, m_0(g) the mass of the sample, v_0($cm^3\text{-}sec^{-1}$) the volume flow rate, ρ_0 (g moles-cm^{-3}) the molar density at which the volume flow rate is measured and y^0_4 and y_4 are the mole fractions of $SiCl_4$ in the inlet gas and in the reaction chamber, respectively.

A difference in composition will also exist between the bulk gas in the reaction chamber and the gas adjacent to the solid gas interface. This composition gradient is required to transport $SiCl_4$ to the interface and $SiCl_2$ away from the interface. The composition difference is related to the rate of transport by a mass transport coefficient, k'_G (g moles-$cm^{-2}\text{-}sec^{-1}$)

$$r = \frac{k'_G\,(y_4 - y_{4i})}{1 + \dfrac{y_4 + y_{4i}}{2}} \qquad [2]$$

where y_{4i} is the mole fraction of $SiCl_4$ in the gas phase at the solid interface. The numerator of Eq. [2] is derived from the film pressure factor and accounts for the net flow of gas away from the interface.[40] Therefore, k'_G includes only the effects of geometry, flow, and physical properties of the fluid. An equation similar to [2] can be written for the transport of $SiCl_2$. Equations of this form should have been used to calculate the interfacial compositions which could then be used in correlations similar to Alstrup's Eq. [4].

Mass Transfer Controlled Assumption

If the rate of reaction is controlled by the rate of mass transfer in the gas phase, then equilibrium is approached at the solid-gas interface. Since the mass transfer coefficient for $SiCl_4$ will be approximately equal to the mass transfer coefficient for $SiCl_2$, it can be shown that y_{4i} will be equal to the mole fraction of $SiCl_4$ which would remain if the feed gas mixture were brought to equilibrium with the sample at the temperature and pressure of the reactor.

$$y_{4i} = \frac{y^0_4(1 - z)}{1 + zy^0_4} \qquad [3]$$

[38] R. R. Monchamp, W. J. McAleer, and P. I. Pollack, *This Journal*, 111, 877 (1964).

[39] S. E. Craig, *ibid.*, 112, 647 (1965).

[40] O. A. Hougen and K. M. Watson, "Chemical Process Principles," Part III, Chap. 20, John Wiley & Sons, Inc., New York (1949).

where z is the fraction of the $SiCl_4$ in the feed which would be converted at equilibrium.

The general equation for the rate of reaction, assuming mass transfer controlled kinetics, is obtained by combining Eq. [1], [2], and [3].

$$r = \frac{k'_G\left(y^0_4 z - \dfrac{Ar}{v_0\rho_0}\right)}{1 + \dfrac{y^0_4 z}{2} + \dfrac{Ar}{2v_0\rho_0}} \qquad [4]$$

Since for this reaction, $1 >> y^0_4 z/2 + Ar/2v_0\rho_0$ the rate equation may be simplified to

$$\frac{Ar}{v_0\rho_0} = \frac{Ak'_G}{v_0\rho_0}\left[\frac{y^0_4 z}{1 + \dfrac{Ak'_G}{v_0\rho_0}}\right] \qquad [5]$$

Figure 1 is a logarithmic plot of Eq. [4] and is approximately equivalent to Alstrup's Fig. 2. The mass transfer number, $Ak'_G/(v_0\rho_0)$, was taken as 0.3 in order to have the curves fall in the general range of Alstrup's data. The equilibrium conversion, z, was computed from Schafer and Nickl's [41] equation for the equilibrium constant with the assumptions of ideal gas behavior at 1 atm total pressure. Increasing the mass transfer number moves all of the curves upward toward asymptotic values of

$$\frac{Ar}{v_0\rho_0} = y^0_4 z$$

This asymptote is shown for the temperature of 1170°C. Decreasing the mass transfer number merely translates the curves downward as shown for $T = 1170$°C and $Ak'_G/v_0\rho_0 = 0.022$.

An apparent activation energy, E_a, for the reaction can be obtained numerically from Fig. 1 and the definition.

$$\frac{E_a}{R} = \frac{\partial(\ln r)}{\partial(1/T)}$$

The apparent order of the reaction with respect to $SiCl_4$ can be obtained directly from the slope of the curves in Fig. 1.

Two limiting regions can be seen in Fig. 1. The high equilibrium conversion region (high temperature, low y^0_4) and the low equilibrium conversion region (low temperature and high y^0_4). In the high equilibrium conversion region ($z \geq 0.9$) the rate of reaction is controlled by the rate at which $SiCl_4$ gets to the surface. This yields an apparent first order reaction with a very

[41] H. Shafer and J. Nickl, *Z. anorg. u. allgem. chem.*, 274, 250 (1953).

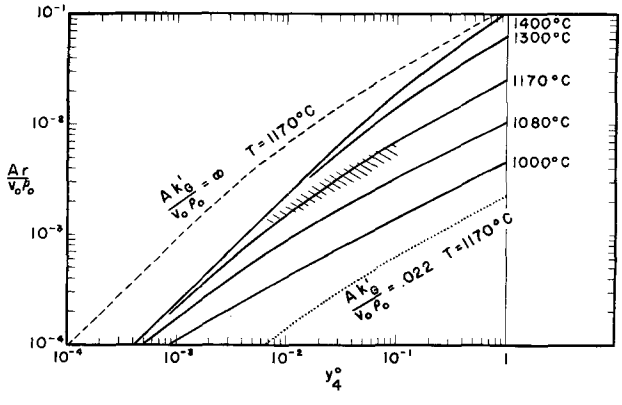

Fig. 1. Reaction rate for the system $SiCl_4$-$SiCl_2$-Si assuming mass transfer controlled kinetics in a well-mixed reactor with no $SiCl_2$ in the feed gas. Solid lines are for $Ak'_G = 0.3$; dashed line is for $Ak'_G/v_0\rho_0 = \infty$ at 1170°C; dotted line is for $Ak'_G/v_0\rho_0 = 0.022$ at 1170°C; shaded area represents the general range of Alstrup's data.

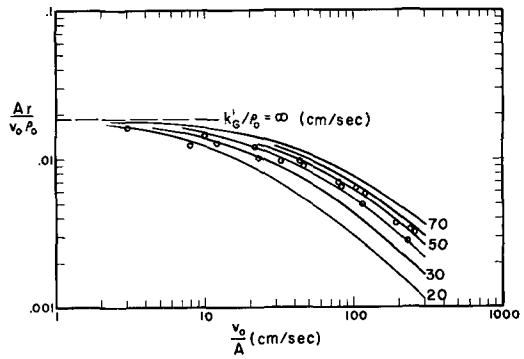

Fig. 2. Effect of velocity on the rate of the $SiCl_4$-$SiCl_2$-Si system assuming mass transfer controlled kinetics. Solid lines are computed from Eq. [4]; data points are from Alstrup's Fig. 5; $y^o_4 = 0.045$.

small apparent activation energy. In the low equilibrium conversion region ($z \leq 0.2$) the reaction kinetics are controlled by the rate at which $SiCl_2$ diffuse into the bulk gas phase. This results in an apparent ½ order reaction with an activation energy equal to ½ the standard free energy of reaction, ΔH^o (in this case about 38 kcal/mole). Both of these regions are fully represented by Eq. [4] and [5]. The apparent order of the reaction and the apparent activation energy are direct results of chemical equilibrium. The mass transfer controlled assumption is therefore able to explain why in a flow reactor, Monchamp[38] and Heinecke[42] obtained results so different from those of Alstrup and Thomas.

The effect of velocity on the mass transfer rate at constant y^o_4 is shown in Fig. 2. The lines are calculated from Eq. [4] while the points are Alstrup data taken from Fig. 5 of his work. From Fig. 2, we see that k'_G is not constant with velocity of flow but increases as the flow rate increases. This is consistent with the mass transfer controlled assumption.

Mass Transfer Coefficient

The mass transfer coefficient used in this discussion is the true local coefficient based on the actual local mole fraction difference driving force. Since the flow is doubtlessly laminar, the mass transfer coefficient can be correlated by the dimensionless equation.[43]

$$\frac{k'_G t}{D\rho} = f\left(\frac{v_o \rho_o}{D\,L\,\rho}\right) \qquad [6]$$

where t is a dimension characteristic of the channel thickness, D is the mass diffusivity (cm²/sec), ρ is the actual molar density of the gas in the reaction chamber (g moles/cm³), and L is the length measured downstream from the start of the reaction zone to the local point on the substrate.

Since Alstrup used a rather unusual reactor geometry, the exact form that the mass transfer correlation should take is unknown for his reactor. Nevertheless, we can infer the form and estimate the values from known solutions for the standard cylindrical tube. For unidirectional flow through a cylinder, $k'_G t/(D\rho)$ is equal to 3.66 if the approach to equilibrium is greater than 90% (very low flow rates or very long lengths). Alstrup's low flow rate region approached this region but did not fully enter it. If the approach to equilibrium is less than 60%, the relationship becomes

$$\frac{k'_G t}{D\rho} = 1.17\left(\frac{v_o \rho_o}{DL\rho}\right)^{1/3} \qquad [7]$$

If k'_G were taken as the mean transfer coefficient based on the average driving force, then the constant in Eq. [7] would be 1.75.[44] Equation [7] is almost

[42] W. J. Heinecke and S. Ing, *J. Appl. Phys.*, 32, 1498 (1961).

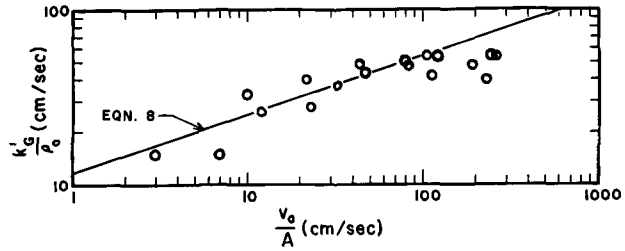

Fig. 3. Comparison of Alstrup's data with the estimated curve for mass transport controlled kinetics; $y^o_4 = 0.045$.

temperature independent. If natural convection is important, an additional temperature dependent term must be added. This additional term increases the mass transfer coefficient and is responsible for a small (0-10 kcal) apparent "activation energy." From the above considerations, we would expect Alstrup's mass transfer relation, neglecting natural convection, to be approximated by Eq. [7]. Additional information on mass transfer coefficients is most easily found in heat transfer texts [43,44] where by rigorous analogy, the group $k'_G t/D\rho$ may be substituted for the Nusselt number and the group $v_o\rho_o/(DL\rho)$, may be substituted for the Graetz number.

Figure 3 is a comparison of Alstrup's data, as interpolated by Eq. [4], with Eq. [7]. In order to plot Eq. [7], estimates had to be made of D, t, L, ρ and ρ_o. The molar densities were calculated from the ideal gas law. D was estimated using the Chapman-Enskog formula.[45] Since the flow in the reactor chamber is bidirectional, t was taken as ½ the tube diameter. One-half the sample length was taken as the average value of L and the width of the sample was assumed to be ½ cm.

The estimated transport relationship becomes

$$\frac{k'_G}{\rho_o} = 1.16\left(\frac{v_o}{A}\right)^{1/3} \qquad [8]$$

Discussion

The fit between Alstrup's data and the estimated transport relationship is surprisingly good in view of the uncertainties in Eq. [8] which may be in error by as much as a factor of 5. Nevertheless, Alstrup's data is definitely in the range where mass transport is important and where it may be controlling.

The mass transfer controlled assumption explains all of the observed phenomena except two; the high activation energy and apparently uniform etching rate. Equation [7] predicts that the upstream edge of the sample will etch faster than the downstream edge. Alstrup does not report whether this occurs or not (it should occur for most kinetic models). In fact, Eq. [7] predicts $k'_G = \infty$ for the extreme upstream edge. This certainly cannot occur. The unreasonably high prediction for $L = 0$ is caused by a simplifying assumption in the derivation of Eq. [7] which makes it invalid for extremely small L's.

As shown earlier, the mass transport assumption yields an apparent activation energy of ½ ΔH^o plus any temperature effects due to natural convection in the reactor. We estimate that the apparent activation energy due to natural convection should not exceed 10 kcal/mole. This would give a total activation energy of 48 kcal/mole which is considerably less than the reported value of 67 kcal/mole. This difference cannot be easily explained. It may be a real difference, indicating mass transport is not fully controlling, or it may be merely an indication of the difficulty in obtaining precise rate data.

[43] W. M. Rohsenow and H. Y. Choi, "Heat Mass and Momentum Transfer," Sections 7.3, 7.7, and 15.7, Prentice-Hall, Inc., New Jersey (1961).

[44] W. H. McAdams, "Heat Transmission," 3rd ed., pp. 229-233, McGraw-Hill Publishing Co., New York (1954).

[45] J. O. Herschfelder, C. F. Curtiss, and R. B. Bird, "Molecular Theory of Gases and Liquids," p. 539, John Wiley & Sons, Inc., New York (1954).

Apparently Alstrup's data represents one of those frustrating cases that can be equally well explained by two widely different kinetic models. These models are not identical and extrapolate to different values. Alstrup's model predicts a rate which is uniform over the whole sample surface and which increases as the total pressure increases (y^{o}_4 held constant). The mass transfer model predicts a rate which will taper the sample and a rate which is essentially independent of the total pressure (y^{o}_4 held constant).

Based on the data presented by Alstrup, it is impossible to choose decisively between the two models. I prefer the mass transport model, however, since with it the correct magnitude for the reaction rate can be predicted a priori.

Ole Alstrup: It is natural to assume that the reaction is limited by diffusion in the gas phase, *e.g.*, because one will not expect a process at the surface to depend on the $SiCl_4$ pressure in a fractional power. A critical analysis of the experiments, however, will show that a diffusion model gives results which deviate so much from the experimental data that one has to reject it.

The diffusion process can take place in two different ways. In the first model we assume laminar flow in the reaction chamber and the mass transport taking place by diffusion across the gas flow. It is apparently this model Craig assumes. If this model is correct, the etch rate should depend on the orientation of the sample in the reaction chamber. Some initial experiments showed that this was not the case. Considering the geometry of the reaction chamber I also find it unlikely to assume laminar flow. We can therefore reject this model.

In our case it is more obvious to assume turbulence in the reaction chamber. The rate-limiting step might then be diffusion through a thin gaseous film at the surface of the sample. From this model one would expect the same etch rate all over the sample surface, in agreement with the experiments. From elementary calculations one obtains an expression for the etch rate which is similar to Craig's Eq. [5]. Both equations can be written

$$\frac{Ar}{v_o\rho_o} \propto \frac{K}{8} \frac{\sqrt{1 + 16\,(P^{o}_4/K)} - 1}{1 + \frac{v_o}{A}\frac{\rho_o}{k'_G}}$$

At 1170°C the equilibrium constant $K = 0.050$ atm, while P^{o}_4 varies from 0.005 to 0.1 atm. From a plot like Craig's Fig. 1 one would expect the etch rate dependency on P^{o}_4 to vary from proportionality to square-root dependency as the $SiCl_4$ pressure increases, and to be independent of the v_o/A value. The experiments however give as shown in our Fig. 2 that the etch rate is proportional to $P^{o}_4{}^{1/2}$ in the whole pressure region, but only for high flow rates ($v_o/A \geqq 3$ cc/sec). This is consistent with our model as we find the etch rate to be proportional to $P_4{}^{1/2}$, and for high flow rates $P_4 = P^{o}_4$ as shown in Eq. [20].

Perhaps more striking is the difference in temperature dependency between the diffusion model and the experiments, a difference which Craig also is aware of. From the above rate expression it is seen that when P^{o}_4 is large the apparent activation energy has its upper limit which is half of the value of that of the equilibrium constant (plus a minor amount from the diffusion constant). The experiments give an activation energy of almost twice that value.

In the diffusion model k'_G depends on v_o since the film thickness decreases with increasing v_o. The reaction rate therefore depends on the absolute value of the flow rate. Craig uses this dependency to explain his Fig. 2. He plots the etch rate *vs.* v_o/A. However this is not the same as plotting the etch rate *vs.* v_o. To verify that, we carried out experiments in which v_o and A were varied, while keeping v_o/A constant. From such experiments we found the same etch rate, whereas from the diffusion model we should get a higher etch rate for the experiments with the higher flow rate.

The conclusion of these considerations is that the diffusion model does not explain any of the parameter dependencies found. So I do not think that for this purpose it is necessary to increase the experimental material. On the other hand we have only been able to give a mathematical treatment that fits the experiments. This analysis makes it evident that the rate-limiting step is located at the surface. To find out what really happens at the surface presumably calls for a considerable expansion of the experimental data.

Studies of the Oxidation of Nickel in the Temperature Range of 900° to 1400°C

Kazuo Fueki and J. B. Wagner, Jr. (pp. 384-388, Vol. 112, No. 4)

Stanislaw Mrowec[46]: Studying kinetics and mechanism of oxidation of nickel at high temperatures, K. Fueki and J. B. Wagner found that dependence of calculated from the kinetic measurement $\sqrt{s}$ values of the self-diffusion coefficients of nickel in nickel oxide on the oxygen pressure can be described by the general equation

$$D_{Ni} = \text{const.}\ p_{O_2}{}^{1/n} \qquad [1]$$

Table I gives the values of the exponent $1/n$ of Eq. [1] computed by these authors for various temperatures.

Table I. Values of exponent $1/n$

Temperature, °C	$1/n$
1000	1/5.6
1100	1/6.0
1200	1/5.1
1300	1/4.0
1400	1/3.5

The data summarized in Table I show that the exponent at first decreases slightly in the temperature range 1000° to 1100°C and then in the temperature range 1100°-1400°C distinctly increases. In order to explain the above given relationship between the calculated values of D_{Ni} and oxygen pressure, Fueki and Wagner considered dependence of the defects concentration in NiO lattice on oxygen pressure on the basis of the mass action law. Results of these considerations did not lead however to the elucidation of the dependence of the $1/n$ exponent on temperature. In the opinion of the author of the present remarks there exists a possibility of interpretation of this dependence.

Let us consider the limiting cases of the ionic and electronic defects of the NiO lattice. On the basis of the studies on self-diffusion of nickel and oxygen in nickel oxide, reported by Moore [47,48] and the marker studies done by Fueki and Wagner one can assume that ionic defects occur practically exclusively in the cation sublattice. As nickel oxide is a metal deficit p-type semiconductor,[49] formation of such defects can be described schematically by the following equations

$$\tfrac{1}{2}\,O_2 \rightleftarrows Ni_{\square''} + 2\oplus + NiO \qquad [2]$$

$$\tfrac{1}{2}\,O_2 \rightleftarrows Ni_{\square'} + \oplus + NiO \qquad [3]$$

$$\tfrac{1}{2}\,O_2 \rightleftarrows Ni_{\square} + NiO \qquad [4]$$

[46] Department of Inorganic Chemistry, School of Mining and Metallurgy, Cravoc, Poland.

[47] M. T. Shi, and W. J. Moore, *J. Chem. Phys.*, 26, 802 (1957).

[48] O'Keeffe and W. J. Moore, To be published.

[49] K. Hauffe, "Reaktionen in und an festen Stoffen," p. 147, Springer, Berlin (1955).

where $Ni_{\square''}$, $Ni_{\square'}$, and $Ni_{\square}$ represent dinegative, uninegative, and neutral cation vacancies respectively, and $\oplus$ is an electron hole. Equation [2] describes the limiting case wherein the dissociation degree in the system electron hole-cation vacancy is equal to 1, whereas Eq. [3] illustrates the case in which the electronic defects are 50% associated with cation vacancies. Finally Eq. [4] represents the other limiting case in which dissociation degree of the ionic and electronic defects is equal to zero, *i.e.*, the defects are entirely associated. As the degree of defects dissociation increases with temperature, one can expect gradual changes of the equilibrium [4] via [3] into [2]. Applying the mass action law to the equilibria given in Eq. [2], [3], and [4], one can obtain the following expressions for the concentrations of cation vacancies as a function of oxygen pressure

$$n_{Ni_{\square''}} = \text{const.}\ p_{O_2}^{1/6} \quad [5]$$

$$n_{Ni_{\square'}} = \text{const.}\ p_{O_2}^{1/4} \quad [6]$$

$$n_{Ni_{\square}} = \text{const.}\ p_{O_2}^{1/2} \quad [7]$$

As the rate of selfdiffusion is directly proportional to the concentration of cation vacancies, one can anticipate in the p-type semiconductors the same dependence of D_{Me} on p_{O_2} as between the concentration of cation vacancies and oxygen partial pressure. The exponent in Eq. [1] should therefore decrease with increasing temperature from 1/2 to 1/6.

As has already been mentioned, dependence of the exponent $1/n$ on temperature indicated, that in the region of lower temperatures, 1000°-1100°C, the dissociation degree of ionic and electronic defects was practically equal to 1, Eq. [5], whereas the degree of dissociation of the defects decreased with increased temperature, reaching at 1400°C a value lower than 0.5. Such dependence of the dissociation on temperature is highly improbable, resulting in Fueki and Wagner abandoning the explanation of this dependence.

Considering the model of the defect structure of semiconductors, one usually neglects the intrinsic defects which involve transfer of electrons from the valence to the conductance bands. Formation of such defects can be illustrated by the equation

$$\text{zero} \rightleftarrows \oplus + \ominus \quad [8]$$

In the region of the moderate temperatures, < 1000°C, participation of the intrinsic electronic defects in the n- and p-type semiconductors is neglected, since it is very small. This is justified particularly when departure from stoichiometric composition is comparatively high. Recent studies, however, showed that nickel oxide exhibits in the high-temperature region very small departures from the stoichiometric composition.[50] Concentration of acceptors in the forbidden energy zone of the oxide is thus small and in the high temperatures one must take into account the increasing participation of the intrinsic defects of NiO lattice with increasing temperature. Formation of the electron holes in the valence band of NiO in these conditions involves superimposing of two processes: (*a*) transfer of electrons from the valence band to the conduction band as a result of reaction [8] and (*b*) transfer of electrons from valence band to acceptor levels according to Eq. [2]. In contrast to reaction [2] formation of the electron holes in valence band in process [8] is independent of oxygen pressure. Therefore one can anticipate that in the very high-temperature region, > 1400°C, total concentration of holes in the valence band of NiO lattice will be practically independent of oxygen pressure, this concentration being determined by reaction [8]. Applying in this case the mass action law to reaction [2] one can get

$$n_{Ni_{\square''}} = \text{const.}\ p_{O_2}^{1/2} \quad [9]$$

as concentration of the electron holes can be taken as being constant. Coming to lower and lower temperatures, participation of reaction [8] in the process of formation of the holes decreases, and at some temperature concentration of these defects in the lattice is determined almost entirely by reaction [2] which consequently gives the dependence of the cation vacancies concentration on oxygen pressure as expressed by Eq. [5].

The discussion given above leads to the following conclusions:
In the region of the not too high temperatures, exponent $1/n$ in Eq. [1] decreases gradually with temperature due to the increase of the dissociation degree of the ionic and electronic defects. In this region, concentration of the electron holes depends almost exclusively on the concentration of acceptor levels resulting from departure from stoichiometry in nickel oxide. In this temperature range one can expect the gradual decrease of the exponent $1/n$ from 1/4 to 1/6 due to the increase with temperature, of dissociation degree of defects. In the high-temperature region the concentration of the electron holes is less and less dependent on the oxygen pressure, as reaction [8] participates more and more in the formation of these defects. In this region of temperatures then, the $1/n$ exponent should increase with increasing temperature from 1/6 to 1/2. Data summarized in Table I indicate that the boundary between those two regions of temperature lies in the vicinity of 1100°C. Below this temperature one can still observe the drop of the value of $1/n$ with rising temperature, whereas above 1100°C the further increase of temperature results in the gradual increase of this exponent.

Kazuo Fueki and **J. B. Wagner, Jr.:** The authors thank Dr. Mrowec for his contribution. We agree with his discussion. We suggested a decreasing amount of association between cation vacancies and electron holes with increasing temperature. Because the value of the exponent, n, in the oxygen partial pressure dependence ($p_{O_2}^{1/n}$) of the diffusion coefficient or the electronic conductivity depends not only on the temperature but on the nickel to oxygen ratio, an additional test of Dr. Mrowec's proposal would be to compare the values of the exponent, n, at different temperatures for constant nickel to oxygen ratios.

Further studies in this laboratory[51] have shown that the isothermal electronic conductivity of single crystalline NiO in oxygen pressures of 10^{-4} to 1 atm and in the temperature range 800°-1200°C is proportional to the 1/4 power of the oxygen pressure. Slight differences in the exponents, $1/n$, of the pressure dependence for the diffusion and for the conductivity studies at the same temperature may be due to differences in the impurity level between the two different materials.

Poisoning and Gettering Effects in Silicon Junctions

E. J. Mets (pp. 420-425, Vol. 112, No. 4)

A. N. Knopp[52] and **R. Stickler**[53]: It is interesting to note that you found significant softening of the blocking characteristics tested on the diffused p-n-p's after exposing them to nitrogen at temperatures above 800°C. We assumed that your nitrogen ambient consisted of approximately 100% nitrogen. In addition, you stated that the resulting silicon nitride formation probably caused the downgrading. We have carried

[50] A. Bielanski, J. Deren, J. Haber, and J. Sloczynski, *Trans. Faraday Soc.*, **58**, 166 (1962).

[51] N. G. Eror, Thesis, Northwestern University, 1965; *Bull. Am. Ceram. Soc.*, **42**, 199 (1963).

[52] Semiconductor Division, Westinghouse Electric Corporation, Youngwood, Pennsylvania.

[53] Westinghouse Electric Corporation, Research and Development Center, Pittsburgh, Pennsylvania.

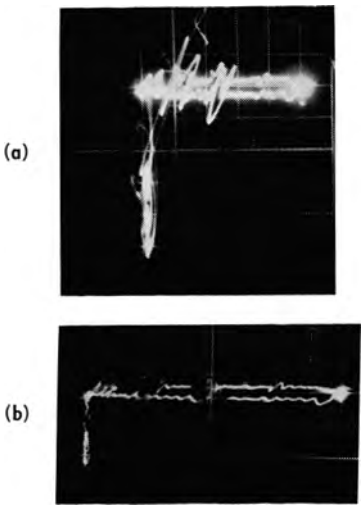

Fig. 1. Electrical characteristics of pnp's. (a) Run A, pnp-diffused, pn = 20-30 ohm-cm, $V_{BD} \approx$ 1250v. Vertical axis 0.5 ma/div., horizontal axis 250 v/div. (b) Run B, pnp-diffused, pN = 12-15 ohm-cm, $V_{BD} \approx$ 920v. Vertical axis 0.5 ma/div, horizontal axis 115 v/div.

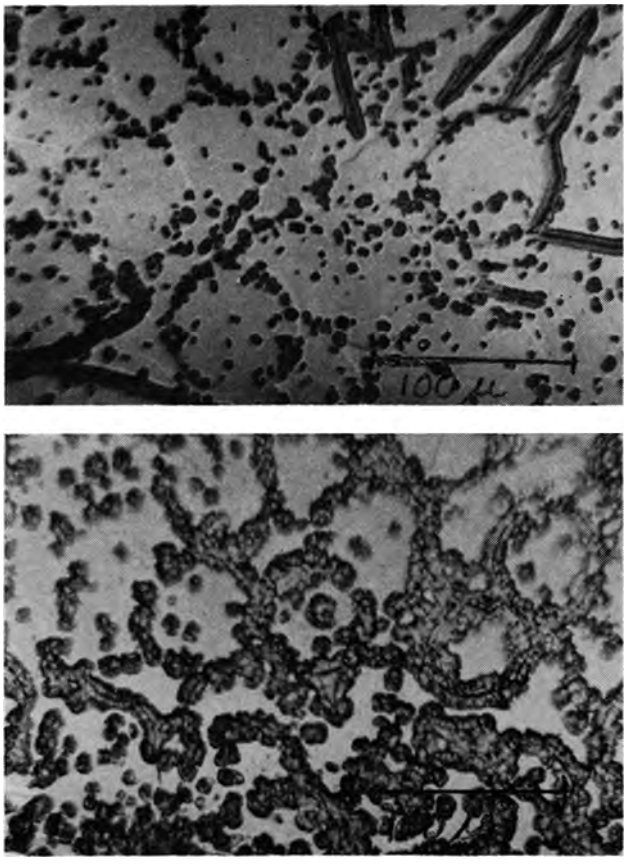

Fig. 2. Silicon nitride on diffused pnp's. (a, top) Silicon nitride on pnp's diffused in run A electrical data See (1a). (b, bottom) Silicon nitride on pnp's diffused in run B electrical data See (1b). Diffusion parameters were the same for run A and run B. Magnification 250X.

out similar studies.[54] In our case, the tested p-n-p structures maintained sharp avalanche breakdown characteristics as shown in Fig. 1a and 1b. Typical surface areas of p-n-p's used for testing are shown in Fig. 2a and 2b which stemmed from two different runs. Si_3N_4 can be clearly distinguished from the silicon substrate.[54] Thus, the silicon nitride formation needs not be responsible for any softening effects.[54]

[54] A. N. Knopp and R. Stickler, *Electrochem. Techn.*, 3, 84 (1965).

On the Equilibrium Properties of Single Crystalline Copper Electrodes

L. H. Jenkins and U. Bertocci (pp. 517-520, Vol. 112, No. 5)

W. W. Harvey[55]: It was gratifying to note that previous work, which indicated a dependence on crystallographic orientation of the equilibrium potential of copper electrodes in copper sulfate solution, has been refuted by the recent experimental results of Jenkins and Bertocci. Certainly their results are in accord with principles of electrochemical thermodynamics. Thus, if the copper-cupric ion equilibrium has been established, then

$$Cu\,(metal) = Cu^{++}\,(in\ CuSO_4\ solution) + 2e^-\,(metal) \quad [1]$$

whence

$$\mu_{Cu} = \mu_{Cu^{++}} + 2e\psi_{electrolyte} + 2\mu_{e^-} - 2e\psi_{electrode} \quad [2]$$

Equation [2] indicates that for massive copper electrodes (*i.e.*, of a size and topography such that the surface free energy is a negligible fraction of the total), and providing there are no extraneous effects such as significant residual strains, the electrode-electrolyte potential difference (p.d.) will be independent of the crystallographic orientation of the surface exposed to the solution.

Arguments in support of seemingly contradictory experimental results, to the effect that observed differences in electrode potential are analogous to the variation of the electronic work function with surface orientation are erroneous. The work function is defined and supposedly measured for the condition of zero net charge on the metal, whereby the metal-vacuum p.d. is made up entirely of the so-called surface potential. By contrast, while the contribution of interfacial dipoles and space charge to the total electrode-electrolyte p.d. may be different for different crystallographic orientations of the electrode surface, the potential due to net charge must adjust itself so as to satisfy Eq. [2] if equilibrium is to be maintained.

R. Piontelli and B. Rivolta[56]: The results and conclusions of the work of Jenkins and Bertocci are in substantial agreement with those of the research carried out in this laboratory[57], concerning the following single-crystal electrodes

$Cu\,[(111), (110)\ (100)]/Cu(ClO_4)_2$
$Ag[(111), (110), (100)]/AgClO_4$
$Pb\,[(111), (110), (100)]/Pb(NH_2SO_3)_2$
$Cd\,[(10\bar{1}0), (11\bar{2}0), (0001)]/Cd(NH_2SO_3)_2$
$Sn\,[(001), (110), (100)]/SnCl_2$

at 25°C, in various conditions, as far as the metal and free acid content of the solutions are concerned.

By a very careful control of the surface conditions of the electrodes and of the purity of the solutions, and with only glass and metal cells, no influence of the crystallographic orientation of the working electrode surface on the equilibrium electrode voltages was encountered (in the accuracy range of the measurements, as a rule less than 1 mV). These equilibrium voltages, in the medium and high metal concentration range, are rather quickly attained and then scarcely influenced by agitation.

The equilibrium electrode voltages thus appear to be strictly independent of the crystallography orientation, in agreement with the requirements of the macroscopic thermodynamics.

On the contrary for the system

$$Zn\,[(11\bar{2}0), (0001)]/Zn(ClO_4)_2$$

[55] Ledgemont Laboratory, Kennecott Copper Corporation, Lexington, Massachusetts 02173.

[56] Institute for Electrochemistry, Physical Chemistry and Metallurgy, Milan Polytechnic, Milan, Italy.

[57] R. Piontelli in "Transactions of the Symposium on Electrode Processes," Ernest Yeager, Editor, p. 67, John Wiley & Sons, Inc., New York (1961); R. Piontelli, B. Rivolta, and M. Rossi, *Atti. Acc. Sci. Torino* (Cl. Sc. Fis.), 99, 199 (1964-65).

which was found very sensitive to agitation [especially for the orientation (0001)] and continuously changing in time, appreciable differences are met with differently oriented electrodes. This last behavior appears to be clearly correlated with the nonequilibrium conditions of the electrode.

L. H. Jenkins and **Ugo Bertocci:** The research was undertaken by the authors because of contradictory reports in the literature. Hopefully, some causes for such conflicts were established and the differences better understood. The authors are aware of the extensive study of Piontelli and co-workers on the electrochemical properties of single crystals and are gratified that our equilibrium data are in agreement with those of this distinguished group.

The authors believe themselves to be in substantial agreement with most of Harvey's conclusions. However, it is not clear to them whether he believes potential differences between orientations must be ruled out as a matter of principle, or only that they are not measurable in the case of large crystals. At any rate, his comments are welcome since they initiate discussion of some matters of interest.

First of all, it seems worthwhile to consider the "massive" electrode. At most, the spacings between atoms in no more than 10 atom layers immediately below a surface would be expected to differ significantly from those of atoms deeper in the interior of the crystal. Even if the electrode were as much as 0.1μ thick, only about 1% of the total atoms present would be contained in these first 10 atom layers. Therefore, since the ultimate concern is the detection of necessarily small differences in the contributions of various surfaces to the total free energy of the system, it is extremely unlikely that potential differences arising from dissimilar surface orientations would be large enough to be observed. Consequently any singularly oriented metal electrode presently capable of experimental realization is either "massive," or an ultra thin specimen of such inherent imperfection, high strain, etc., as to render an unambiguous interpretation of experimental results highly problematical. It appears, then, that failure to observe potential differences between crystal orientations only sets a limit on their possible magnitude, but does not establish definitely the fact they do not exist.

However, the authors feel that the lack of any detectable surface faceting in noncorroding systems, even after extended periods of time, is probably a more sensitive test of potential differences than the measurements themselves. Nevertheless, they do not believe they have established unequivocally that the polar plot of surface energy as a function of orientation of a copper crystal exposed to aqueous copper sulfate is spherical or of such shape that all orientations are stable. It is almost certain that the large surfaces used practically preclude attainment of an equilibrium orientation. So many microscopic transport processes would have to occur to accomplish such a small decrease in free energy that the kinetic process should be immeasurably slow. Even if such is not the case, it is possible that (*A*) although the surface free energies of each of the orientations observed did differ slightly, each was located at a cusp in the Wulff plot. Therefore, any possible decrease in free energy due to spontaneous change from one orientation to another would be more than compensated by the inevitable increase in surface area. Or (*B*) in terms of a Wulff diagram, some or all the orientations studied could have been unstable. In such a case the decrease in free energy due to faceting could be balanced by the increase due to the formation of edges bounding the facets.

Thus the authors agree that failure to measure a potential difference or to observe the formation of facets of preferred orientation in systems at chemical equilibrium is, quoting Piontelli, "in agreement with the requirements of macroscopic thermodynamics." They also agree with Harvey's view that the analogy between electrode potentials and work functions is improper, but would like to point out the following: In vacuum a crystal is in electrical equilibrium regardless of the work functions of the surfaces bounding it (see, for example, Piontelli[58]), but it can be in thermodynamic equilibrium only when it has the Wulff shape. Whereas in an electrochemical system (a metal crystal in contact with a solution of its ions), if the crystal does not have the Wulff shape and is bound by differently oriented surfaces, it is in neither thermodynamic nor electrical equilibrium. Therefore, different orientations should exhibit different potentials, however small the differences might be.

[58] R. Piontelli, Proceedings of 3rd C.I.T.C.E. Meeting, p. 275, Manfredi, Milano (1952).

Cryoscopic Studies of the Melting Point of Silver in High Pressure Oxygen

J. K. Johnstone[1]

Institute for Atomic Research and Department of Ceramic Engineering, Iowa State University, Ames, Iowa

The behavior of gases in metals is becoming increasingly important. Although this subject has received extensive attention for solid metals at pressures up to 1 atm, less emphasis has been placed on liquid metals at pressures above 1 atm.

The purpose of this work is to obtain data on the dissolution and behavior of oxygen in liquid silver at higher pressures. The system was chosen owing to the high solubility of oxygen in the liquid metal. Observations were made on the depression of the freezing point of silver as the oxygen pressure over the silver was increased.

Sieverts and Hagenacker (1) used the silver-oxygen system to show that the solubility of a diatomic gas in a liquid metal is proportional to the square root of the gas pressure, thereby proving that the gas dissolves as atoms rather than molecules (Sieverts' law for dilute solutions). This work was later confirmed by Stacie and Johnson (2) with respect to the solubility of oxygen in solid silver.

The only investigator who has studied the oxygen solubility in liquid silver at pressures substantially greater than 1 atm is Allen (3). The maximum pressure reported by Allen is 13.9 atm. The work also confirmed approximately Sieverts' law up to this pressure. The work reported here extends the pressure range to slightly more than 147 atm.

Since only the freezing point depression was measured, the discussion that follows will be based on the solubility data reviewed in Lumsden (4).

Experimental

The apparatus consisted of a resistance furnace mounted concentrically in a cylindrical, water-cooled pressure-vessel. The apparatus was essentially the same as that used by Baker (5) in a study of calcium carbonate where it is described in detail.

The furnace incorporated a porcelain tube with an inside diameter of 12 mm and a wall thickness of 2 mm. The tube was wound to a length of 9½ in. with 20 gauge 9:1 platinum-rhodium wire.

The pressure-vessel, which has been described previously, was constructed from a section of auto-frettaged gun-barrel with an inside diameter of 5.5 cm and a wall thickness of 2.75 cm. The space between the furnace and the vessel wall was packed with alumina powder.

The pressure and heating (cooling) rate were controlled manually. By this method, the pressures were accurate to ±0.5% and the freezing point temperatures were accurate to ±1°. Three Bourdon test gauges of 10 in. diameter were required to cover the pressure range of 1-147 atm.

Granular silver (— 20 mesh) of 99.9% purity and silver foil 0.004 in. thick and better than 99.9% purity were used for samples. Oxygen gas of 99.5% purity was used. The remaining 0.5% was argon. The available oxygen pressure was the limiting factor in this series of experiments. The oxygen was supplied from standard 2000 psi bottles from which 147 atm was the maximum attainable pressure. All thermocouples were made of Pt-Pt 13% Rh wire.

[1] Mr. Johnstone is the second recipient of the F. M. Becket Memorial Award of the Electrothermics and Metallurgy Division of the Society. See p. 120C of the May 1964 JOURNAL. The research was conducted under the supervision of Dr. E. H. Baker, Nuffield Research Group, Imperial College of Science and Technology.

The general procedure involved placing the sample in a crucible which was then placed in the furnace. The pressure-vessel was sealed in a nearly horizontal position to help eliminate convection currents caused by high-density gases at elevated temperatures and the furnace was heated at a rapid rate—15° to 20°/min —to 600°. At this temperature, the vessel was pressurized to the desired value after several flushings with oxygen at 20 atm pressure. From this point, the procedure was varied according to one of three methods used for the actual freezing point determination.

The first method employed was that of noting the thermal arrest in the cooling curve at the freezing point of the silver. The sample consisted of slightly more than 7g of granular silver placed in a silica crucible. A thermocouple encased in a silica tube was centered in the mass of silver. The sample was raised to a temperature approximately 30° above the expected freezing point of the silver and maintained at this temperature for 40 min. It was then cooled at a rate of 1°/min and the arrest temperature determined.

The method produced satisfactory results up to a pressure of 10 atm. At this pressure, the heat losses, owing to the high gas density, were of such magnitude that the arrest was very indistinct.

The second method involved the use of a D. T. A. technique. A strip of silver foil, 1 mm wide and 5-8 mm long was substituted for the junction of a thermocouple. (The best results were obtained when each end of the silver strip was welded to one of the thermocouple leads.) A standard thermocouple sealed in an alumina sheath was fixed next to the sample to insure an accurate measure of the temperature of the silver strip. The two thermocouples were then placed in a silica crucible and packed with — 10 mesh alumina granules. The alumina particles insured that the silver strip did not come into contact with the crucible as well as helping to eliminate further any convection currents in the gas.

The sample was heated to within 20° of the expected melting point where the heating rate was reduced to approximately 1.5°/min. At the melting point of the silver, the strip broke thus destroying the differential trace; this provided a well defined melting point.

This method provided accurate and consistent results up to a pressure of 50 atm. At this pressure the welds of the differential thermocouple leads to the silver strip oxidized causing an erratic emf.

The third and most reliable method involved the use of an independent electric circuit. The arrangement of the sample and the temperature thermocouple was identical to the D. T. A. method. However, rather than welding the sample to thermocouple leads, it was welded to two pure gold wire leads. The gold leads completed an electric circuit which consisted of a 1.5v dry cell battery, a 5000 ohm series resistance and a milliammeter, thereby providing an independent circuit.

The procedure for heating the sample was described in the previous method. When the silver strip melted, the electric circuit was broken as indicated by the milliammeter.

This method provided an extremely sharp and well defined melting point. Furthermore, at oxygen pressures up to 147 atm, there was no evidence of any oxidation of the welds between the silver strip and

gold wire or of the gold itself. This method was used to check several lower pressure results obtained by the previously described methods and good agreement was found.

At the conclusion of the test series, the thermocouples were checked to see if the surface oxidation of the thermocouple wire reported previously affected the emf which would result in faulty temperature measurement. The thermocouples were tested by determination of the melting point of potassium chloride in an oxygen pressure of 90 atm. Comparison of the observed and known melting point indicated that the thermocouple junctions were not measurably affected by the oxygen gas.

Results and Discussion

The experimental results are presented graphically in Fig. 1, where P is the oxygen pressure and T is absolute temperature. Due to the extremely small solubility of oxygen in solid silver (2), the curve can be regarded as representing the freezing point depression of pure silver.

The inset in Fig. 1 shows the relationship between the freezing point depression (curve A) and the silver oxide dissociation equilibrium (curve B). The equilibrium dissociation pressure of silver oxide was derived experimentally by Lewis (6) and confirmed by Keyes and Hara (7). The curve is defined by the equation

$$\log P = -\frac{2859}{T} + 6.2853$$

and covers a pressure range of from 20.5 atm to 388.3. atm. Brewer (8) has expressed doubt as to the reliability of the work done by Lewis (6) and Keyes and Hara (7) but offers no argument to support his position.

Allen extrapolated his work to intersect the silver oxide dissociation curve to determine a possible eutectic point for the Ag-Ag_2O system. This extrapolation (as well as a summary of past work involving the Ag-O_2-Ag_2O system) has been presented graphically by Vacher (9) and yields a eutectic with a temperature of 507°C and an oxygen pressure of 414 atm (point a,

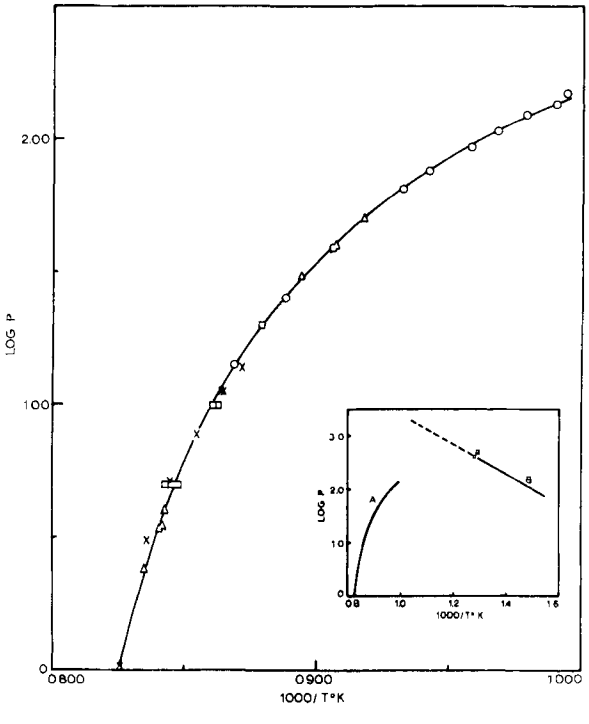

Fig. 1. Pressure-temperature diagram of freezing point depression: □, thermal arrest method; △, D. T. A. method; ○, independent electric circuit method; X, results obtained by Allen (3). Inset: Pressure-temperature diagram of freezing point depression (curve A) in relation to dissociation of Ag_2O (Curve B).

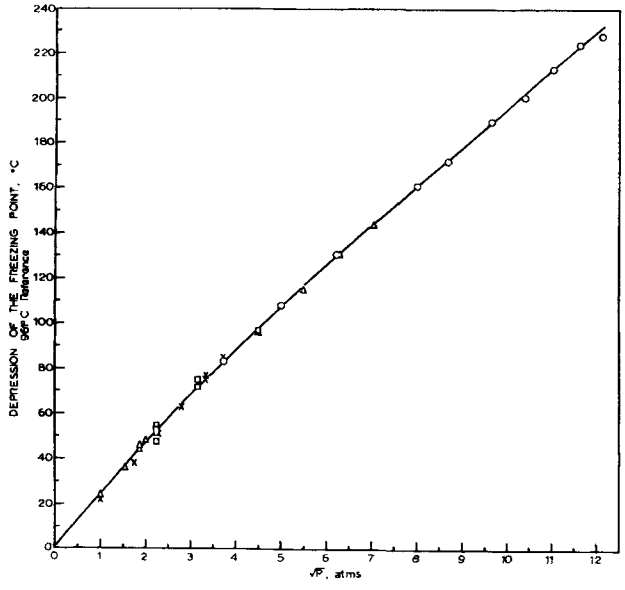

Fig. 2. Freezing point depression — $\sqrt{P}$ diagram

Fig. 1-inset). At the present, this work neither confirms nor disproves the values obtained by Allen. However, the freezing point depression data is tending toward the point suggested.

Allen showed for his range of pressures and temperatures (*i.e.*, to 13.9 atm and 876°C) that the depression of the freezing point was proportional to the $\sqrt{P}$. It is of interest to plot $\sqrt{P}$ against the freezing point depression for the results from the present work (Fig. 2). For pressures up to 4 atm a fair linearity is observed. At higher pressures and correspondingly higher concentrations of oxygen, deviation from the initial slope is apparent. This is to be expected at high concentrations and temperature changes.

The activity of the silver on the freezing point curve can be calculated by the van't Hoff equation in the form of

$$\ln a_{Ag} = \frac{\Delta H_{fus}}{R}\left[\frac{1}{T} - \frac{1}{T_{M.P.}}\right]$$

where $\Delta H_{fus} = 2855$ cal/mole (9) and $T_{M.P.} = 1234$°K. (By application of the Clausius-Clapeyron equation at the maximum pressure observed, it was calculated-assuming that the volume for liquid silver containing dissolved oxygen is not greatly different from the volume of pure liquid silver—that the lowering of the freezing point due to the pressure alone was less than 2°. Therefore, it is valid to consider the lowering of the freezing point of silver to be due solely to the solution of oxygen in the melt.) Using the eutectic temperature given by Allen, the activity of silver is calculated to be 0.508.

If the solution were roughly an ideal solution of oxygen atoms $N_o \cong 0.492$, where N_o is the atom fraction of oxygen in solution. This is greater than the oxygen content of pure liquid Ag_2O ($N_o = 0.333$). It is apparent that the oxygen at higher concentrations is present in some form other than oxygen atoms so that a greater depressive effect could be obtained for a given amount of dissolved oxygen. The possibility of the oxygen combining with silver to form Ag_2O is worth consideration. Such compound formation would certainly explain the observed temperature depression but, unfortunately, said formation can not be confirmed by the present work.

If the oxygen were present solely as oxygen atoms, the eutectic temperature would need to be higher than 642° (obtained through application of the van't Hoff equation for $N_o = 0.333$). It is difficult, however, to assign a reasonable equilibrium pressure at such a eutectic point limit which would fall on the silver-silver oxide line. Consequently, since the true state of

the dissolved oxygen at high concentrations is not known, it is preferable at this stage to regard the system as one involving Ag_2O.

From the above, it can be seen that it is essential to determine the compositions of the melts along the freezing point depression curve and to evaluate the pressure-temperature relation at the true eutectic point. Apparatus is being constructed for the last studies which will be made by Dr. E. H. Baker.

Acknowledgments

The author wishes to thank The Electrochemical Society for the F. M. Beckett award which made his participation in this work possible. Appreciation is also due Dr. E. H. Baker for his patient and invaluable guidance and Professor F. D. Richardson for his cooperation.

References

1. A. Sieverts and J. Hagenacker, *Z. physikal Chem.*, **68**, 115 (1909).
2. E. W. R. Stacie and F. M. G. Johnson, *Proc. Roy. Soc.*, **112A**, 542 (1926).
3. N. P. Allen, *J. Inst. Metals*, **49**, 317 (1932).
4. J. Lumsden, "Thermodynamics of Alloys," pp. 250-253, The Institute of Metals, London (1952).
5. E. H. Baker, *J. Chem. Soc.*, **87**, 464 (1962).
6. G. N. Lewis, *J. Am. Chem. Soc.*, **28**, 139 (1906).
7. F. G. Keyes and H. Hara, *ibid.*, **44**, 479 (1922).
8. L. Brewer, *Chem. Rev.*, **52**, 1 (1952).
9. K. K. Kelley, *U.S. Bur. of Mines Bull.*, No. **584**, 163 (1960).

Manuscripts and Abstracts for Fall 1965 Meeting

Papers are being solocited for the Fall Meeting of the Society, to be held at the Statler-Hilton Hotel in Buffalo, N. Y., October 10, 11, 12, 13, and 14, 1965. Technical sessions probably will be scheduled on: Batteries (including Symposia on Charging Characteristics of Batteries and Characteristics of Electrodes during Charging), Corrosion, Electrodeposition (including Symposium on Thin Film Technology), Electronics-Semiconductors, Electrothermics and Metallurgy (including a Symposium on Zirconium and Its Alloys).

To be considered for this meeting, **triplicate copies of the usual 75-word abstract, as well as of an extended abstract of 500-1000 words** (see notice on page 29C of this issue), must be received at The Electrochemical Society, 30 East 42 St., New York, N. Y., 10017, *not later than May 17, 1965.* (Papers solely sponsored by the Corrosion Division **do not** require an extended abstract.) *Please indicate on 75-word abstract for which Division's symposium the paper is to be scheduled, and underline the name of the author who will present the paper.* No paper will be placed on the program unless one of the authors, or a qualified person designated by the authors, has agreed to present it in person. Clearance for presentation of a paper at the meeting should be obtained before the abstract is submitted. An author who wishes his paper considered for publication in the JOURNAL or ELECTROCHEMICAL TECHNOLOGY should send triplicate copies of the manuscript to the Managing Editor of the appropriate publication 30 East 42 St., New York, N. Y., 10017. Concerning papers to be published in the JOURNAL, see notice on per page charge on page 32C of this issue.

Presentation of a paper at a technical meeting of the Society does not guarantee publication in the JOURNAL or ELECTROCHEMICAL TECHNOLOGY. However, all papers so presented become the property of The Electrochemical Society, and may not be published elsewhere, either in whole or in part, unless permission for release is requested of and granted by the Editor. Papers already published elsewhere, or submitted for publication elsewhere, are not acceptable for oral presentation except on invitation by a Divisional program Chairman.